RESEARCH AND APPLICATIONS IN STRUCTURAL ENGINEERING,
MECHANICS AND COMPUTATION

PROCEEDINGS OF THE FIFTH INTERNATIONAL CONFERENCE ON STRUCTURAL ENGINEERING, MECHANICS AND COMPUTATION, CAPE TOWN, SOUTH AFRICA, 2–4 SEPTEMBER 2013

Research and Applications in Structural Engineering, Mechanics and Computation

Editor

Alphose Zingoni
Department of Civil Engineering, University of Cape Town, Cape Town, South Africa

CRC Press
Taylor & Francis Group
Boca Raton London New York Leiden

CRC Press is an imprint of the
Taylor & Francis Group, an **informa** business

A BALKEMA BOOK

Cover photo: Seto-Ohashi Bridges (courtesy of Honshu-Shikoku Bridge Expressway Co. Ltd, Japan)

CRC Press/Balkema is an imprint of the Taylor & Francis Group, an informa business

© 2013 Taylor & Francis Group, London, UK

Typeset by MPS Limited, Chennai, India
Printed and bound in Great Britain by CPI Group (UK) Ltd, Croydon, CR0 4YY.

All rights reserved. No part of this publication or the information contained herein may be reproduced, stored in a retrieval system, or transmitted in any form or by any means, electronic, mechanical, by photocopying, recording or otherwise, without written prior permission from the publishers.

Although all care is taken to ensure integrity and the quality of this publication and the information herein, no responsibility is assumed by the publishers nor the author for any damage to the property or persons as a result of operation or use of this publication and/or the information contained herein.

Published by: CRC Press/Balkema
P.O. Box 11320, 2301 EH, Leiden, The Netherlands
e-mail: Pub.NL@taylorandfrancis.com
www.crcpress.com – www.taylorandfrancis.com

ISBN: 978-1-138-00061-2 (Hardback + CD-ROM)
ISBN: 978-1-315-85078-8 (eBook)

Research and Applications in Structural Engineering, Mechanics and Computation – Zingoni (Ed.)
© 2013 Taylor & Francis Group, London, ISBN 978-1-138-00061-2

Table of Contents

Preface XXVII
Committees XXIX

1. Keynote lectures

Insights and advances in the analysis of structures 3
K.J. Bathe

Recent studies on long-span bridges: Vibration control, seismic retrofit and monitoring in Japan 9
Y. Fujino & D.M. Siringoringo

Local-distortional interaction in cold-formed steel columns: Non-linear behaviour, ultimate strength and DSM design 17
D. Camotim, P.B. Dinis, B. Young & N. Silvestre

Simulation of multi-physical processes in solar updraft power generation 23
W.B. Krätzig

Mechanics of interfaces and evolving discontinuities 29
R. de Borst, J.J.C. Remmers, C.V. Verhoosel & A. Needleman

Recent controversies and new challenges in structural topology optimization 35
G.I.N. Rozvany

2. Dynamic response, vibration analysis, vibration control

General conditions for instantaneous system inversion in structural dynamics 43
K. Maes, E. Lourens, G. De Roeck & G. Lombaert

Determination of aerodynamic damping of twin cables in wet conditions through passive-dynamic wind tunnel tests 49
M.B. Eriksen, E. Mattiello & C.T. Georgakis

Frequency domain stochastic response of structural systems with uncertain parameters: Closed-form sensitivity 55
G. Muscolino, R. Santoro & A. Sofi

Semi-active control of structural systems with uncertainties using an unscented Kalman filter 61
M.S. Miah, E.N. Chatzi & F. Weber

Guided waves for stress identification 67
A. Pau, G. Ruta & F. Vestroni

Unscented Kalman Filter for the identification of passive control devices 69
R. Ceravolo, A. De Stefano, E. Matta, A. Quattrone & L. Zanotti Fragonara

Vibration elimination analysis of simply-supported bridge under moving loads based on Laplace-Carson integral transform 75
K. Wang, H. Xia & W. Guo

Dynamic identification of Palazzo Marchesale in S. Giuliano di Puglia 81
G. Bongiovanni, G. Buffarini, P. Clemente, D. Rinaldis, F. Saitta, M. Nicoletti, A. De Sortis & G. Rossi

A suspended mass damper for torsional and translational vibration control 87
M. Carlisle & K. Li

Status quo and critical review of PPV safe limits for subsurface construction blasting close to low-rise buildings 93
E.Y. Sayed-Ahmed & K.K. Naji

Dynamic response of rigid pavement under moving traffic load with variable velocity 99
Y. Zhong & M.J. Xu

Assessment of bridge behavior due to the passage of high speed trains 105
A. Graça, L. Guerreiro & F. Virtuoso

Dynamic response of airport building structure due to construction machinery effects 111
J. Benčat & D. Papán

3. Vibration serviceability, human-induced vibrations, human-structure interaction

Data-driven model of random lateral pedestrian excitation 119
V. Racic, J.M.W. Brownjohn & A. Pavic

Simultaneous registration of walking behaviour and structural response 125
K. Van Nimmen, P. Van den Broeck, G. Lombaert & G. De Roeck

Vibrations in a multi-storey lightweight building structure: Influence of connections and nonstructural mass 131
L.V. Andersen & P.H. Kirkegaard

Direct velocity feedback versus a geometric controller design of remotely located vibration control systems 137
D.S. Nyawako, U. Ubaid, P. Reynolds & M.J. Hudson

Sensitivity analysis of coupled crowd-structure system dynamics to walking crowd properties 143
E. Shahabpoor, A. Pavic & V. Racic

Experimental study of the human ability to deliberately excite a flexible floor 149
C. Schwartz, A. Berger, O. Brüls, J.-L. Croisier, B. Forthomme & V. Denoël

4. Non-linear dynamics

Dynamics of structural components subjected to large rotations using a flexible multibody approach (Invited Paper) 157
J. Ambrósio & M.A. Neto

Nonlinear dynamics of a rotating SD oscillator 163
Q. Cao, N. Han & M. Wiercigroch

A hybrid time-frequency procedure for the solution of nonlinear dynamic problems 169
F.N. Correa & B.P. Jacob

Nonplanar vibration and dynamics instability of slender cruciform columns 175
E.C. Carvalho, P.B. Gonçalves, Z.J.G.N. Del Prado & G. Rega

Bifurcation analysis of a Jeffcott rotor with a bearing clearance: Numerics and experiments (Invited Paper) 181
J. Páez Chávez, M. Wiercigroch & S.V. Vaziri Hamaneh

A computational study of the upper Lyapunov exponent and the uniform persistence for monotone skew-product semiflows 183
J.A. Calzada & R. Obaya

Vibrations of cables with bending stiffness by an asymptotic approach 189
T. Canor & V. Denoël

Singularities that induce a breakdown of determinism in mechanics 195
M.R. Jeffrey

On the dynamics of stacks of rigid blocks 201
F. Saitta, P. Clemente & D. Rinaldis

Numerical bifurcation analysis of an impact oscillator with drift 207
J. Páez Chávez, M. Wiercigroch & E.E. Pavlovskaia

5. Seismic response, seismic analysis, earthquake-resistant design

Seismic behaviour and earthquake resistant design of long period structures (Invited Paper) 211
A. Astaneh-Asl

Thinking outside the box: Integrated seismic system evolution in high rises 217
M. Sarkisian, N. Mathias & E. Long

Yokohama-Bay cable-stayed bridge seismic response analysis during the 2011 Great East Japan Earthquake 223
Y. Fujino & D.M. Siringoringo

Large natural draft cooling towers under earthquake excitation 229
M. Andres, R. Woermann & D. Casucci

Future development of the European seismic code, Eurocode 8 235
E.D. Booth

Dynamic shakedown design of structures under repeated seismic loads 241
S. Benfratello, L. Palizzolo & P. Tabbuso

Performance of buildings and other structures during the Tohoku Tsunami 247
I.N. Robertson & G. Chock

Numerical investigation of the cyclic response of CHS braces 253
T. Sheehan, T.M. Chan, J.H. Xing & L. Gardner

Parametric identification of building structures with seismic recordings 259
R. Zhang & L.O. Gargab

Generation of spectrum compatible site-dependent earthquake load histories by evolutionary approach 265
F. Carli & C. Carino

Large-scale dual shake tables testing: An experimental approach to study the non-uniform excitation effects on long span bridges 271
M.M.S. Cheung, C.-Y. Yang, Y. Pan & F. Xiong

Seismic design of the self anchored suspension bridge: San Francisco Oakland Bay Bridge 277
M. Nader & B. Maroney

Seismic performance of an asymmetric base-isolated building in the 2011 Great East Japan Earthquake 283
Y. Fujino & D.M. Siringoringo

Assessment of evaluation methods of dynamic response of multi-span bridge to mining tremor 289
J.M. Dulinska & M. Fabijanska-Kopacz

Characterization of the seismic behaviour of steel pallet racks in cross-aisle direction 295
C. Braham & H. Degée

Passive energy dissipation characteristics of yielding shear panel device produced from steel and stainless steel 301
M. Ashraf & M.R. Hossain

Seismic behaviour of exposed column bases in buckling restrained braced frames 307
Y. Cui, S. Kishiki & S. Yamada

Multi-story steel structures: Seismic energy modal distribution 313
O. Prodan, I. Ladar & N. Chira

Effect of basement rigidity on seismic response of RC buildings 319
A. Koçak, M. Borekci, E.C. Ekinci & A. Kalyoncuoglu

Bidirectional pushover analysis of irregular structures 323
G.P. Cimellaro, D. Lopez-García & T. Giovine

Seismic collapsing response analysis of wooden house retrofitted by ACM braces 329
T. Takatani & H. Nishikawa

Nonlinear behaviour of submerged floating tunnels accounting for seaquake effects 335
C.X. Shi, M. Domaneschi & L. Martinelli

An innovative solution for earthquake resistant hybrid steel-concrete systems with replaceable dissipative steel links 341
A. Zona, G. Leoni, A. Dall'Asta, T. Bogdan, C. Braham & H. Degée

Effectiveness of seismic protection by added damping: An energy approach 347
I. Ladar, O. Prodan & N. Chira

Seismic Safety Screening Method (SSSM) for slum clearance 353
P.O. Caglayan

Experimental study on the performance of hollow reinforced concrete bridge piers subjected to lateral seismic loads 357
O. Lopez-Batiz, R. Gomez-Martinez, J.A. Escobar-Sanchez, F. De la Serna-Hernandez & G. Aguilar-Ramos

Evaluating the seismic performance of RCC dams, subjected to near-field and far-field earthquakes via FEA approach 363
M.R.A. Ala, H.R. Vosoughifar, N. Hasani & S.K.S. Shokouhi

6. Material modelling, composite materials, functionally-graded materials

Some advances in functionally graded materials (Invited Paper) 369
L. Nunziante

Numerical implementation of the Hoek-Brown material model with strain hardening 375
E.S. Sørensen, J. Clausen & L. Damkilde

Simulation of the mechanical behaviour of W/Cu composites containing FGM related interpenetrating microstructures under consideration of phase dependent damage limits 381
S. Schmauder & U. Weber

Determination of effective elastic constants of two phase composites 387
O. Bulut, N. Kadioglu, S. Ataoglu, M. Yuksek & E. Sancak

Strain induced product properties of magneto-electric composites 393
J. Schröder, M.-A. Keip, M. Labusch & D.C. Lupascu

Microstructural image-based modelling of weld failure 399
O. Barrera, A.C.F. Cocks & E. Tarleton

Flame straightening application on structural steels: Effects on mechanical and fracture properties 405
R. Lacalle, J.A. Álvarez, D. Ferreño, J. Portilla, E. Ruiz, B. Arroyo & F. Gutiérrez-Solana

Statistically similar RVE construction based on 3D dual-phase steel microstructures 411
L. Scheunemann, D. Balzani, D. Brands, J. Schröder & D. Raabe

A study of local mechanical properties of 304L SS welded joints subjected to cyclic straining using depth-sensing instrumented indentation 417
D. Ye, F. Mi & X. Yin

Biological tissue mechanics with fibres modelled as one-dimensional Cosserat continua: Applications to cardiac tissue in healthy and diseased states 423
K. Sack, S. Skatulla & C. Sansour

Buckling analysis of thin composite plates reinforced by carbon nanotubes (CNTs) using finite strip methods (F.S.M) 429
M. Pazoki, M. Azhari & A. Heidarpour

Identification of nonlinear hyperelastic material parameters for healthy myocardial tissue via an inverse method based on modelling the passive filling stage of the cardiac cycle 435
M. Essack & S. Skatulla

Numerical properties of second order integration algorithms for plasticity models 443
M. Jahanshahi

7. Numerical modelling, FEM modelling

A layered shell element for the thermal analysis of plates exposed to non-uniform heating 451
A.E. Jeffers

Co-rotational FEM for fast geometrically nonlinear static and dynamic algorithms 457
D. Marinkovic & M.W. Zehn

Finite element modelling of shear tab connections including damage simulation 463
A. Mirzaei, C.A. Rogers & R. Tremblay

Nonlinear static and dynamic analysis of an electrically-actuated microbeam modelled by means of the strain gradient elasticity theory 469
P. Belardinelli & S. Lenci

Peak shear stress distribution in finite element models of concrete slabs 475
E.O.L. Lantsoght, C. van der Veen, J.C. Walraven & A. de Boer

Elimination of slip-locking in composite beam analysis by using a meshfree method 481
R.E. Erkmen

Nonlinear analysis of semi-rigid steel frames subjected to blast or fire 487
A. Heidarpour

Coupling different FE-models for the calculation of the thermo-mechanical behavior of ultra high performance concrete components under high temperature load 493
M. Siemon, D. Hosser & J. Zehfuß

FE modelling of semi-rigid flush end plate joints with concrete-filled steel tubular columns 499
A. Ataei & M.A. Bradford

Development and testing of a technique for the simulation of the rock cutting process 505
M.J. Mikl, R. Tichy, W. Ecker, T. Antretter & G. Pittino

Material influence on the strength of aluminium column web in tension 511
G. Sarracco, G. Brando & G. De Matteis

8. Impact, blast, damage mechanics, damage modelling

Interaction forces between huge cargo vessels and quay walls 519
M. Bahr & V. Sigrist

Response of a building envelope system to near field blast events 525
H.D. Hidallana-Gamage, D.P. Thambiratnam & N.J. Perera

Impact velocity and initial length influence on the crushing behaviour of TWCF open section members under axial impact 531
M. Kotełko, R.J. Mania & M. Jankowski

Computational modelling of reinforced concrete wall subjected to transformer tank rupture 537
M.A. Seman, M.A. Nasly, Y.T. Feng & Z.M. Jaini

Blast test and numerical simulation of point-supported laminated glass curtain wall 541
S. Chen, C.G. Zhu, G.Q. Li & Y. Lu

Thermodynamics-based constitutive modeling of coupled dissipative phenomena in engineering materials 547
H. Egner, W. Egner & M. Ryś

Heterogeneous structures studied by an interphase elasto-plastic damage model 553
G. Giambanco, G. Fileccia Scimemi & A. Spada

A coupled local-nonlocal framework for modeling hydraulic fracturing in the Karoo 559
D.Z. Turner

Tensile and compressive buckling of shear deformable damaged beams 565
S. Caddemi, I. Caliò & F. Cannizzaro

9. Fracture, fatigue

The use of the theory of critical distances in fracture and structural integrity assessments 573
S. Cicero, V. Madrazo, I. Carrascal & T. García

Fracture mechanics as an improvement of fatigue life assessment in orthotropic bridge decks 579
W. Nagy, H. De Backer & Ph. Van Bogaert

Analogies in the fracture mechanisms of concrete and ice 585
B. Chiaia, A.P. Fantilli & B. Frigo

An investigation of the double torsion geometry using peridynamics 591
T.H. Becker & D.Z. Turner

Propagation of non-planar pressurized cracks from a borehole 597
J.A.L. Napier & E. Detournay

Hydraulic fracture simulation: Comparison with exact solutions 603
C. Detournay, P.A. Cundall & B. Damjanac

Optimisation of the Double Torsion geometry 609
S.P. Goqo, S. Skatulla & T.H. Becker

An experimental validation of residual stresses in weld clad pipelines 613
G. Schnier, J. Wood & A. Galloway

Assessment of fracture toughness in strain hardening cement-based composite (SHCC) made from fine and coarse sand 619
S.C. Paul & G.P.A.G. van Zijl

Polymeric facades: Fatigue performance of pultruded panel connections 625
P.T. Gates, T.J. Ibell, A.P. Darby & M. Evernden

Experimental evaluation of the fretting fatigue behaviour of high-strength steel monostrands 631
J. Winkler, C.T. Georgakis & G. Fischer

10. Wind loading, robustness, progressive collapse, tall buildings

Revised wind loading for linear and non-linear design of cooling towers (Invited Paper) 639
H.-J. Niemann & W. Hubert

Wind-tunnel investigations of pressure distribution over high-rise buildings 645
M. Cwik, M.A. Gizejowski & A.M. Goliger

Probabilistic models for design of structures against wind loads 651
J.V. Retief, C. Barnardo-Viljoen & M. Holicky

Computational fluid dynamics simulations and validation of results 657
M.A. Sitek, M. Cwik, M.A. Gizejowski & A.M. Goliger

Equivalent static wind loads for structures with non-proportional damping 663
N. Blaise, V. Denoël & T. Canor

Robustness of structures: State of art 669
Seema, N. Baldassino & R. Zandonini

Performance-based plastic design of earthquake resistant tall building frames 675
W.-C. Liao, M.R. Bayat & S.C. Goel

Parametric study of pyramid-like tubular structure 681
G.S. Liou & H.-C. Kuo

More optimal seismic design of highrise structures using nonlinear analysis techniques 687
S.A. Ashrafi

Progressive collapse prevention of drive-in steel storage racks 693
S. Yadwad & L.H. Teh

Assessment of column removal time for progressive collapse evaluation of high rise structures 699
O.D. Stephen, D. Lam & V.V. Toropov

Rotational capacity of concrete slabs and its influence on tensile membrane action in the framework of robustness analysis 705
D. Gouverneur, R. Caspeele & L. Taerwe

The impact of fire scenario to the collapse of a tall structure 711
S. Selamet

Behaviour of tall buildings under blast loading with direct simulation method 717
F. Fu

A modal property analysis of linked tall buildings using a matrix model 721
K.T. Tse & J. Song

11. Bridge engineering, bridge girders

Composite steel-concrete cable-stayed bridges: Developments and future trends 729
J.J. Oliveira Pedro & A.J. Reis

Analysis of steel and steel-concrete bridge girders through a higher order beam model (Invited Paper) 735
R.F. Vieira, F.B. Virtuoso & E.B.R. Pereira

Full-scale testing of concrete deck slabs under fatigue-causing axle loads 741
G. Borkowski, K. Thoma & P. Roos

Cable stressing sequence of an asymmetrical cable stayed bridge 747
J.R.B. Anderson

Design curves for stiffened flanges used in steel box girder bridges 751
P.S. Ferreira & F. Virtuoso

Fatigue life assessment of existing motorway bridge 757
L. D'Angelo, A. Nussbaumer, M.A. Fenart & A.-G. Dumont

Comparing two types of fatigue and tsunami resisting medium span bridges 763
Ph. Van Bogaert

Are short span reinforced concrete bridge girders cost effective? 769
T.N. Haas & D. Smith

Effect of constraint in-plane displacement conditions for the unloaded edges of stiffened flanges used in steel box girder bridges 775
P.S. Ferreira & F. Virtuoso

Buckling resistance with combined shear of steel curved bridge girder webs 781
Ph. Van Bogaert

The weathering steel bridges maintenance practice in Poland 787
M. Łagoda & T. Wierzbicki

Study on high speed railway prestressed continuous rigid frame bridges 793
J.Q. Lei & K. Zhang

Experimental study on hybrid FRP-concrete bridge superstructure 799
Y.L. Wang, J.H. Ran, Y.Y. Li & M.M. Cao

12. Lightweight structures, roof systems, membranes, cables, bars, rods, struts

Design of tension components according to Eurocode 3 Part 1-11 (Invited Paper) 807
K. Kathage

Extraordinary possibilities using fabric to form concrete structures (Invited Paper) 813
J.J. Orr, T.J. Ibell, A.P. Darby & M. Evernden

The Porsche Pavilion in the Autostadt Wolfsburg, Germany (Invited Paper) 819
H. Pasternak & T. Krausche

Computational model for simulation of rigid foldable origami structures 823
J.D. van der Woerd, R. Chudoba & J. Hegger

Performance analysis of a membrane roof project 829
E.F. Nunes, J.B.M. de Sousa Jr, B. Baier & A.M.S. de Freitas

Collapse behaviour of double-layer grid structures in steel 835
J.M. Adams & A. Zingoni

Behaviour of composite bar structures: Theory and examples (Invited Paper) 841
J.B. Obrębski

A method for reconstructing the shape of highly flexible, slender objects from distributed strain measurements 847
M.D. Todd, C.J. Stull & M. Dickerson

Rod-in-tube buckling – Comparative analysis of numerical and test results 853
V.S. Tikhonov & O.S. Bukashkina

On load drop phenomenon in axially compressed elasto-plastic columns 859
L. Kwasniewski

Eulerian formulation for an extensible elastic rod 865
A. Huynen, E. Detournay & V. Denoël

Some results of experimental investigations of thin-walled bars 871
J.B. Obrębski

13. Plates, shells, laminated composite structures, sandwich structures

Bending and buckling of circular sandwich orthotropic plates with corrugated cores (Invited Paper) 879
K. Magnucki, M. Walachowski & E. Magnucka-Blandzi

Modeling and simulation of large amplitude vibrations of layered composite and smart structures 885
R. Schmidt, M.N. Rao & T.D. Vu

Simplified modelling of stiffened panels for simultaneous static and dynamic optimisation 891
L. Weiß, H. Köke & C. Hühne

Finite element vibration analysis of pole structures made of advanced composite materials 897
G.-D. Kim & S.-Y. Lee

Experiments on fatigue behaviour of sandwich panels 901
H. Nelke & J. Lange

Modelling and nonlinear FE analysis of composite shells at finite rotations (Invited Paper) 907
R. Schmidt, M.N. Rao & T.D. Vu

Using the polynomial annihilation edge detection for locating delamination in laminated composite plates 911
C. Surace, H. Darwich & M. Gherlone

On the design of plates and stiffeners of rectangular industrial ducts 917
T. Thanga, K.S. Sivakumaran & B. Halabieh

Structural behaviour of flexible straws 923
B. Zhang & Z. You

A strain gradient Reissner-Mindlin micro-plate model obtained through an asymptotic analysis 929
M. Serpilli

Inelastic buckling of annular plates in shear 933
J. Becque

A novel analytical solution of orthotropic rectangular thick plate 939
B. Pan & H. Liu

14. Renewable energy structures

Wind loading on solar chimneys: From wind tunnel experiments to CFD simulation 947
F. Lupi, C. Borri & H.-J. Niemann

Stability and nonlinear behaviour of RC solar updraft towers 953
R. Harte

An analysis of an optimised solar thermal chimney for desert deployment 959
P. Cottam, P. Duffour & P. Fromme

Solar energy systems under impact of aeolian sand and dust 965
C. Kalender-Wevers, U. Winkelmann & R. Höffer

Constructability-aspects for reinforced concrete solar updraft power plants chimneys: From construction technology and logistics to schedules and costs – data-requirements for economical evaluation 971
L. Laußat, N. Warkus & M. Helmus

SHM strategies, application and measurements on tripod offshore wind energy converters within the German offshore park Alpha Ventus 977
W. Rücker, S. Thöns, S. Said & W. Schmid

A comparative study about the effects of linear, weakly and fully nonlinear wave models on the dynamic response of offshore wind turbines 983
E. Marino, G. Stabile, C. Borri & C. Lugni

Structural health monitoring for life-cyle estimation of on-shore wind energy converters 989
R. Höffer, D. Hartmann, S. Lachmann, X. Liu & K.R. Leimbach

15. Cold-formed steel structures, thin-walled sections

Analysis and design of perforated cold-formed steel members in compression (Invited Paper) 997
Z. Yao & K.J.R. Rasmussen

A semi-discretized thin-walled beam element including distortion 1003
M.J. Andreassen & J. Jönsson

Generalised Beam Theory (GBT) for stiffened sections 1009
G. Taig, G. Ranzi, G. Piccardo & A. Luongo

Cold-formed steel design and research assisted by testing (Invited Paper) 1015
D. Dubina

On the response of cold-formed steel sections under compression 1023
N. Baldassino, G. Torresani, R. Zandonini, G. Manzini & F. Scavazza

Local and global vibration analysis of thin-walled steel frames using Generalised Beam Theory (GBT) 1029
C. Basaglia, D. Camotim & H.B. Coda

Moment redistribution in cold-formed steel continuous beams 1035
C. Hui, L. Gardner & D.A. Nethercot

Shear strengths of lipped channel beams with stiffened web openings using numerical studies 1041
P. Keerthan & M. Mahendran

Coupled instability behaviour of members with thin-walled welded box sections loaded in bending and compression 1047
A. Taras, H. Unterweger & S. Hafner

Performance of reinforced web openings of cold-formed steel joists 1053
K.S. Sivakumaran

A linear one-dimensional model for the flexural-torsional vibrations of tapered thin-walled bars with open cross-sections 1059
A. Andrade, P. Providência & D. Camotim

Design models for the bolted joints of cold-formed steel pitched roof portal frames 1065
D. Dubina, V. Ungureanu & P. Perneş

Tests of cold-formed steel lipped channel columns undergoing local-distortional-global interaction 1071
B. Young, D. Camotim & P.B. Dinis

Shear design of cold-formed steel beams using direct strength method 1077
P. Keerthan & M. Mahendran

Influence of cross-section geometry on the distortional post-buckling strength of cold-formed steel columns 1083
A. Landesmann, D. Camotim & C. Basaglia

Cold-formed steel beams of corrugated web 1089
D. Dubina, V. Ungureanu & L. Gîlia

Post-buckling behaviour and strength of cold-formed steel lipped channel columns: When is local-distortional interaction relevant? 1095
P.B. Dinis, D. Camotim & A.D. Martins

Design of Z-section purlins under combined axial compression and bending 1101
J. Becque & K.J.R. Rasmussen

Buckling of cold-formed lipped-channel stub columns 1107
M. Dundu & J. Lim

Continuous beam tests on aluminium alloy SHS and RHS with internal stiffeners 1113
M. Su, B. Young & L. Gardner

Rational DSM design of thin-walled cruciform and angle columns 1119
P.B. Dinis & D. Camotim

Flexural-torsional analysis of shear-deformable monosymmetric thin-walled open members – I. Closed-form solution 1125
M.A. Hjaji & M. Mohareb

Flexural-torsional analysis of shear-deformable monosymmetric thin-walled open members – II. Finite element formulation 1131
M.A. Hjaji & M. Mohareb

Flexural strength of single channels restrained by angle cleats 1137
G.M. Bukasa & M. Dundu

Single shear screwed connection tests of thin sheet steel at elevated temperatures 1143
S. Yan & B. Young

Finite element simulation of perforated rack section columns 1149
A.M. Sarmanho Freitas, M.S.R. Freitas & F.T. Souza

16. Steel structures: Stability, strength, design

Inelastic post-buckling GBT analysis of tubular thin-walled metal members 1157
M. Abambres, D. Camotim & N. Silvestre

Direct stability analysis of steel beam-column with an elastic restraints 1165
I. Misiunaite & A. Juozapaitis

Stabilization of members with I-sections against flexural torsional buckling 1171
R. Stroetmann

Lateral-distortional buckling formulae for hollow tubular flange plate girders with slender unstiffened webs 1177
M.F. Hassanein & N. Silvestre

Modeling of force deformation characteristic of angle bracing members (Invited Paper) 1183
M.A. Gizejowski & A.M. Barszcz

Experimental and numerical research on longitudinally stiffened tapered steel plate girders subjected to shear 1189
A. Bedynek, E. Mirambell & E. Real

A new design methodology for steel hollow sections: The Overall Interaction Concept 1195
J. Nseir, E. Saloumi & N. Boissonnade

Use of the Overall Interaction Concept for the practical design of steel sections and members 1201
N. Boissonnade, J. Nseir & E. Saloumi

Influence of imperfections and geometrical discontinuities on the behavior of the steel towers 1207
A.I. Dogariu & D. Dubina

Nonlinear finite element modelling of castellated steel beams lateral torsional bucking 1213
F.O.M. da Gama, L.R.O. Lima, J.G.S. Silva, P.C.G.S. Vellasco & M.M.B.R. Vellasco

Buckling mode decomposition of thin-walled members with holes 1219
M. Nedelcu, N. Chira, H.L. Cucu & A.G. Popa

Resistance assessment of the sinusoidal openings in cellular beams 1225
S. Durif & A. Bouchaïr

GBT buckling analysis of I-section steel girders under concentrated loads 1231
P. Natário, N. Silvestre & D. Camotim

Design by inelastic analysis – 2010 AISC specification 1237
R.D. Ziemian

Three-dimensional joist member design using equivalent beam theory 1243
S.J. Kilber & A.E. Surovek

Behaviour of I-section columns experiencing local–global mode interaction: Analytical and finite element modelling 1249
M.A. Wadee, L. Bai, D. Camotim & C. Basaglia

Influence of the cross section slenderness on the buckling behaviour of steel welded tapered beam-column 1255
I.M. Cristutiu & D.L. Nunes

Analyzing portal frames using rotational springs 1261
T.N. Haas, H.L. Albertyn & P.E. Dunaiski

Behaviour of pitched-roof portal frames with tapered web and flange members considering lateral restraints 1267
I.M. Cristutiu & D.L. Nunes

Compressive resistance of circular hollow sections with squashed ends 1273
M. Dundu & J. Tumkou

The influence of pallets on the behaviour and design of drive-in steel storage racks – Part I: Behaviour 1279
B.P. Gilbert, L.H. Teh, R.X. Badet & K.J.R. Rasmussen

The influence of pallets on the behaviour and design of drive-in steel storage racks – Part II: Design 1285
B.P. Gilbert, L.H. Teh, R.X. Badet & K.J.R. Rasmussen

Extension of the DSM to welded H profile cross-sections 1291
B. Rossi & Y. Li

On the strength of T-section columns 1297
F. Sena Cardoso & K.J.R. Rasmussen

Stability, failure and design of I-section steel beams subjected to tension 1303
J. Tomás, J. Nseir, D. Camotim & N. Boissonnade

17. Steel joints, steel connections

Lateral-torsional buckling behaviour of members in steel structures with hanging-profile connections 1311
D. Liu & J. Lange

Design bearing stresses for injection bolts with short and long duration high loads 1317
A.M. Gresnigt & D. Beg

On evaluation of a unified moment-rotation characteristic of steel and steel-concrete composite joints 1323
M.A. Gizejowski, W. Barcewicz, J. Uziak & A.A.K. Saleh

The influence of the bolt grade on its behaviour under combined tension and shear 1329
A. Renner & J. Lange

Finite element modeling of CHS T-joints strengthened using through bolts 1335
M.A. Mohamed, A.A. Shaat & E.Y. Sayed-Ahmed

In-plane shear flexibility evaluation of fastened steel flat plate by numerical simulation considering the interaction between connectors and thin plate 1341
F. Bakhti, R. Tremblay & C.A. Rogers

New experimental method for determining the stiffness and strength of steel storage rack floor connections 1347
F. Roure, M.M. Pastor, M.R. Somalo & M. Casafont

Seismic behaviour of welded and bolted I-beam to box column connections 1353
Q.Y. Song, A. Heidarpour & X.L. Zhao

Analytical approach for the determination of the strength and stiffness of the T-stub with four rows of bolts 1359
N. Mehidi, F.Z. Mimoune, M. Mimoune & A. Bouchaïr

Axial capacity of transverse branch plate-to-CHS T-joints 1365
A.A. Shaat

18. Steel-concrete composite construction

Sustainable composite beams with deconstructable bolted shear connectors 1373
S.S.M. Lee & M.A. Bradford

Numerical simulations of concrete-composite-slabs with perforated metal sheets 1379
S. Pirringer & J. Kollegger

A computer method for design and M-N-Φ analysis of composite steel-concrete cross-sections 1385
C.G. Chiorean, A. Chira & M. Buru

Load-carrying capacity of steel and high-strength concrete composite columns 1391
M. Karmazínová & J.J. Melcher

Behaviour of multi-span composite steel-concrete beams subjected to combined flexure and torsion 1397
E.L. Tan, B. Uy & G. Hummam

Considerations on the long-term behaviour of composite steel-concrete bridges 1403
G. Ranzi, G. Leoni, L. Dezi & R. Zandonini

Nonlinear inelastic analysis of 3D composite steel-concrete frameworks 1409
C.G. Chiorean, M. Buru, A. Chira & I. Marchis

Square concrete filled steel hollow columns 1415
M. Dundu

Study on the loading transferring efficiency of large dimension CFT column in joint zone with internal stiff ring 1421
Y. Chen, X.Z. Zhao, N.N. Yan & S.Y. Wu

Connections by adherence – A numerical analysis of preliminary push-out tests 1427
H.J.F. Diógenes, A.L.H.C. El Debs & M.K. El Debs

19. Stainless steel structures

Constitutive equations for stainless steels: Experimental tests and new proposal 1435
I. Arrayago, E. Real & E. Mirambell

Direct strength method and continuous strength method for cold-formed lean duplex stainless steel columns 1441
Y. Huang & B. Young

Numerical study of lean duplex stainless steel plate girders with stocky flanges and slender unstiffened webs under bending 1447
M.F. Hassanein & N. Silvestre

Structural response of stainless steel cross-sections under combined compression and biaxial bending 1453
M. Theofanous, L. Gardner & E. Koltsakis

Investigating the role of gradual yielding in stainless steel columns and beams by virtual testing 1459
P. Hradil & A. Talja

Experiments on ferritic stainless steel columns in fire 1465
B. Rossi, J.M. Franssen & N. Tondini

Buckling response of ferritic stainless steel columns at elevated temperatures 1471
S. Afshan, L. Gardner & N.R. Baddoo

Interaction effects of constituent plate elements on cold-formed high strength stainless steel cross-section behaviour in compression 1477
F. Zhou, Y. Chen & B. Young

Mechanical properties of austenitic stainless steel after exposure to fire 1483
X.Q. Wang, Z. Tao, T.Y. Song & L.H. Han

Study on ferritic stainless steel and its application on architecture structure 1489
M. Li & W. Dong

20. Concrete structures, concrete design

Assessing the reliability of existing concrete bridges in terms of shear strength 1497
D. Busse, L. Eckfeldt & M. Empelmann

Dismantleable joints of load-bearing reinforced concrete units of prefabricated concrete building system with controlled stiffness (Invited Paper) 1503
J. Witzany, T. Čejka & R. Zigler

Numerical investigations on the shear capacity of reinforced concrete slabs under concentrated loads 1507
K. Reissen & J. Hegger

Analysis of the structural behaviour of shear-critical prestressed and reinforced concrete beams using digital image correlation 1513
K. De Wilder, G. De Roeck, L. Vandewalle, P. Lava, D. Debruyne & Y. Wang

The effect of steel fibres on the compressive ductility in lightweight aggregate concrete structures 1519
J.A. Øverli & T.M. Jensen

Full-range behavior of FRP-to-concrete bonded joints with trilinear bond-slip law 1525
H. Yuan & L. Wu

A comparison of the variable strut inclination and alternative stirrup design methods 1531
K.K. Mensah, C. Barnardo-Viljoen & J.V. Retief

Shear strength of reinforced concrete plastic hinges subjected to seismic action 1537
R.V. Mehrabani & V. Sigrist

Experimental and numerical investigations on punching behaviour of thick footings with and without shear reinforcement 1543
D. Kueres, C. Siburg, K. Reissen & J. Hegger

Reliability of EN1992 crack model applied to South African water retaining structures 1549
C.H. McLeod, J.V. Retief & J.A. Wium

New design approach for crack width calculation in reinforced concrete structures 1555
H.A. Elgohary & M.M. Assas

21. Fibre-reinforced concrete, polymer-reinforced concrete, cement composites

Multi-functional fiber reinforced concrete for sustainable structures (Invited Paper) 1561
N. Banthia

Comparison of strain measurement techniques for the characterization of brittle, cementitious matrix composites 1567
D. Arboleda, S. Yuan, J. Giancaspro & A. Nanni

Strut and tie models for disturbed regions: Steel fibre reinforced concrete dapped end beams 1573
J.M. Hisdal, G. Zirgulis, E.V. Sarmiento & T. Kanstad

Study of the properties of hybrid fibre reinforced concretes 1579
T. Zych

A review of the shear behaviour of reinforced steel fibre concrete 1587
S. Zeranka & G.P.A.G. van Zijl

Time-dependent behaviour of pre-cracked polypropylene fibre reinforced concrete (PFRC) under sustained loading 1593
A.J. Babafemi & W.P. Boshoff

Effect of temperature on the behaviour of polymer reinforced concrete façade 1599
J.O. Akinyele

Flexural behaviour of normal and high strength concrete beams reinforced with GFRP rods 1603
N.F.O. Evbuomwan

Flexural behaviour of GFRP prismatic beams in composite action with concrete 1611
N.F.O. Evbuomwan

22. High strength concrete, high performance concrete

UHPC – a challenging material for innovative structures (Invited Paper) 1619
E. Fehling

Modular constructions made of UHPC 1625
N.V. Tue & M. Reichel

Development of ultra-high performance concrete and applications to bridges in Korea 1631
C. Joh, S.Y. Park, K.T. Koh, S.W. Kim, Y.J. Kim & B.S. Kim

Behaviour of hybrid PVA-steel fibre reinforced ultra high performance concrete at high temperature 1637
S. Sanchayan & S.J. Foster

Sustainable building with ultra-high performance concrete (UHPC) – coordinated research program in Germany 1643
M. Schmidt

Composite structures of steel and filigree UHPC-elements – experimental and numerical investigations 1649
T. Lechner, O. Fischer & G. Seidl

Optimization process for thin-walled high performance concrete sandwich panels 1655
K. Hodicky, T. Hulin, J.W. Schmidt & H. Stang

Quality control of UHPC by using non-destructive ultrasonic testing methods 1661
B. Middendorf & A. Glaubitt

Statistical model for compressive strength prediction of high-performance concrete 1667
A. Kapelko, M. Kapelko & R. Kapelko

Experimental tests and analytical modeling of UHPC beams subjected to torsion 1673
E. Fehling, M. Ismail & T. Leutbecher

Compressive strength of high-performance concrete with absorption capacity of Super-Absorbing-Polymers (SAP) 1679
B.J. Olawuyi & W.P. Boshoff

A model for spalling of HPC thin plates exposed to fire 1685
T. Hulin, K. Hodicky, J.W. Schmidt, J.H. Nielsen & H. Stang

Micro structural optimization of high strength performance air hardened foam concrete 1691
B. Middendorf & A. Just

The anchorage of rebars in UHPC 1697
P. Lorenz & E. Fehling

Next generation nano-based carbon concrete 1703
P.S. Nagaraja, F.A. Khan, K.N.N. Gowda, S.A.K. Zai & H.R. Srinivas

Evaluation of behaviour and ductility of polymer modified steel fiber reinforced high performance concrete beams 1709
S.A.K. Zai, N. Munirudrappa, K. Muthumani, R. Naveen & H.R. Srinivas

Structural behaviour of high performance fibre-reinforced flowable concrete beams and plates 1715
S.G. Ladkany & A.T. Berhe

Influence of fiber orientation on the properties of strain hardening Ultra-High Performance Fiber Reinforced Concrete (UHPFRC) under direct tensile loading 1721
C. Hollmann & K. Wille

23. Durability, creep, shrinkage, transport processes in concrete

The origin of plastic settlement cracking and the effect of re-vibration 1729
R. Combrinck & W.P. Boshoff

Composite material under influence of moisture 1735
J. Skramlik, M. Novotny & K. Suhajda

Chimney cracked reinforced concrete walls as a problem of durability exploitation 1739
M. Kaminski, M. Maj & A. Ubysz

Water transport in surface layer of fair-face concrete 1745
P. Reiterman, F. Vogel, O. Holčapek, K. Kolář, P. Konvalinka, M. Keppert, M. Čáchová & E. Vejmelková

Creep influence on concrete slabs, pre-stressed in both directions 1749
G. Sossou

Frost resistance property of concrete doped with scrap rubber powder 1755
B.M. Wang, Y. Han & S. Liu

24. Construction materials, construction technology, building performance

Determination of the relation between the content of used reclaimed asphalt material and deformation characteristics of asphalt concretes 1763
K. Miláčková, P. Mondschein & J. Valentin

Feasibility of lightweight aggregate concrete for structural and non-structural works in Tanzania 1769
A.L. Mrema & H.A. Mboya

Mechanical properties of aluminous cement paste at high temperature 1775
O. Holčapek, P. Reiterman, F. Vogel, P. Konvalinka & E. Vejmelková

The influence of percentage replacement from coarse recycled concrete aggregate 1779
D.W. Immelman & W. de Villiers

Full-scale model of road structure 1785
M. Varaus, P. Hyzl & D. Stehlik

Monitoring of experimental sections with recycled waste materials 1789
D. Stehlik, M. Varaus & P. Hyzl

Experience with experimental designs and performance assessment of cold asphalt mixtures – New type of pavement structure in the Czech Republic 1795
J. Suda, J. Valentin, J. Žák, J. Šedina & K. Miláčková

Knowledge sharing and constructability in structural design 1801
V. Kuo & J. Wium

Processes of ID-based linking of structural relevant construction phase data to planning phase data using auto-ID techniques 1807
L. Laußat, A. Kelm, A. Meins-Becker & M. Helmus

Verification of MZELWE module in ESP-r programme with experimental confrontation 1813
A.M. Čekon, M. Kalousek & B.J. Hraška

Thermal comfort of the rooms in the designing of commercial buildings 1819
K. Nowak, K. Nowak-Dzieszko & M. Rojewska-Warchał

25. Timber structures

Behaviour of steel to timber connections in fire and normal conditions (Invited Paper) 1827
A. Bouchaïr, P. Racher & D. Dhima

Shaking table tests on a large scale moment resistant timber frame with post-tensioning and energy dissipating system 1833
F.C. Ponzo, A. Di Cesare, M. Simonetti, D. Nigro, T. Smith & S. Pampanin

Fracture process under moisture content variation in timber structures 1839
R. Moutou Pitti, F. Dubois, E. Fournely & B. Mbangagoye

The resilience of timber buildings 1845
G. Faller

Numerical modeling of a post-tensioned timber frame building with hysteretic energy dissipation 1851
A. Di Cesare, F.C. Ponzo, M. Simonetti, T. Smith & S. Pampanin

26. Masonry structures

In situ full-scale tests for old masonry elements: The out-of-plane response 1859
A. Borri, M. Candela & R. Fonti

Seismic behaviour of masonry walls with soft-layer wall bearings 1865
N. Mojsilović, B. Stojadinović, A. Barandun & C. Vögeli

Application of sequentially linear analysis to the seismic assessment of slender masonry towers 1871
V. Mariani, A.T. Slobbe, M.A.N. Hendriks & J.G. Rots

Experimental evaluation of the response of ferrocement strengthened lightweight masonry walls to impact loads 1877
M.A.N. Abdel-Mooty

Externally applied retrofit system for existing masonry buildings subject to progressive collapse 1883
A. Kousgaard & E. Erdogmus

Non-linear static analysis of masonry-infilled RC frames 1889
A. Koçak, B. Doran, A. Kalyoncuoglu & B. Zengin

Sisal reinforced cement-based masonry units 1895
G. Coetzee, W.P. Boshoff & R.D. Toledo Filho

Structural design for earth buildings 1901
A.C. Heath & P.J. Walker

Affordable, sustainable and resilient tornado shelter design using compressed stabilized earth block construction 1907
B. Wagner, E. Erdogmus & A. Schwer

27. Performance of structures in fire, design for fire resistance

Global structural behaviour in fire and consolidated testing of steel structures (Invited Paper) 1915
M. Fontana, M. Knobloch & A. Frangi

Structures in fire or fires in structures? Assessing the true performance of structures in fire (Invited Paper) 1919
J.L. Torero

Numerical simulation of thin RC structures exposed to fire (Invited Paper) 1925
R. Harte

Shear capacity of steel plate girders with slender webs in fire 1931
T. Ohtsuka, M. Knobloch & M. Fontana

Modeling and assessment of the response of super-light elements to fire 1937
K.D. Hertz, B.M. Campeanu, M. Giraudo & L. Giuliani

Composite floors with steel fibre reinforced concrete slabs exposed to fire 1943
J. Bednář, F. Wald, J. Vodička & A. Kohoutková

Engineering solutions for structures in fire: Should concrete care? 1947
L.A. Bisby

The application of fire engineering methods for the design of open steel car parks 1953
G. Woźniak & R. Obiała

Numerical study on structural behaviour of cold-formed steel columns under fire conditions 1959
S.J.C. Almeida, J.M. Neto & J.P.C. Rodrigues

An analytical method for determining the loading on connections in heating and cooling during a fire 1965
D. Lange & J. Albrektsson

Fire protection of multi-storey straw bale buildings 1971
J. Wachtling, D. Hosser & J. Zehfuß

Structural analysis at the fire limit state: Practical applications 1977
A. Jowsey & P. Scott

Fire design of wooden box floors 1981
D. Dhima & R. Blondeau-Patissier

No-sway collapse of steel frames under fire conditions: A parametric investigation 1987
A. Monti, T. Pariciani, F. Gentili & F. Petrini

Numerical studies of load bearing LSF walls under realistic design fire conditions 1993
P. Keerthan, A. Ariyanayagam & M. Mahendran

Numerical study of travelling fire in full-scale experimental building 1999
K. Horová & F. Wald

Numerical and experimental investigation of the toxicity and light extinction of fire smoke using experimental data from fire tests of polymers 2003
A. Löhnert, N. Monreal, C. Knaust & U. Krause

Development of a simplified design method to predict the fire rating of LSF walls 2009
S. Gunalan & M. Mahendran

Fire resistance assessment of steel structure exposed to fire for differentiated safety requirements 2015
M. Maślak

Numerical experimental design approach to evaluate the fire resistance of timber connections 2021
M. Audebert, D. Dhima & A. Bouchaïr

Performance of reinforced concrete structures in post-earthquake fire 2027
B. Behnam, H. Ronagh & M. Ashraf

Behaviour of structural steel subjected to post-earthquake fire 2033
S. Sinaie, A. Heidarpour & X.L. Zhao

28. Structural safety, structural reliability, risk assessment

Target reliability for engineering structures (Invited Paper) 2041
M. Holický

Reliability evaluation and design of steel frames with BRBs under severe earthquakes 2047
Y.S. Liu, G.Q. Li & X.K. Guo

Reliability analysis of corroding pipelines by enhanced Monte Carlo simulation 2053
B.J. Leira, A. Naess & O.E. Brandrud Næss

Some practical aspects of statistics methods of estimation reliability computed for existing silo constructions 2059
M. Kaminski & M. Maj

Model uncertainties in reliability analysis of reinforced concrete structures 2065
M. Holický, M. Sykora, C. Barnardo-Viljoen, K.K. Mensah & J.V. Retief

Safety in design for industrial and mining structures 2071
T. Langbecker & S. Loganathan

Risk-based design in mining structures 2077
M. Mmusi & A. Masarira

Simulated virtual portfolio for masonry buildings 2081
A. Mühlhausen, U.E. Dorka, F. Obón Santacana, A. Smolka & M. Stupazzini

29. Structural optimisation, manufacturing processes

Effective lightweight design of a rocket interstage ring through mixed-integer optimization 2089
H. Köke, L. Weiß & C. Hühne

Topology optimization with local stress contraints in a simultaneous analysis and design setting 2095
D.P. Munro & A.A. Groenwold

Reliability-based robust optimization using variance based methods 2101
G. Karaki

Designing adaptive structures for whole life energy savings 2105
G. Senatore, P. Duffour, S. Hanna, P. Winslow & C. Wise

Softening some effects of the no free lunch (NFL) theorems in optimization via parallel computing 2111
S.S. van Huyssteen & A.A. Groenwold

Exploring the domain of application of adaptive structures 2117
G. Senatore, P. Duffour, P. Winslow, S. Hanna & C. Wise

Effect of serviceability limits on optimal design of steel portal frames 2123
T.D. Phan, J.H. Lim, J.B.P. Lim, W. Sha, T.T. Tanyimboh & M. Dundu

Optimization of the injection molding processes using the Moldflow simulation program on the example of electrical connectors 2129
M. Szostak & R. Staniek

Comparison of simulation results of injection molding process obtained by Moldflow and Moldex3D programs 2133
M. Szostak & R. Staniek

The use of modified three axes forging to strengthen Nb for superconducting radio frequency cavities 2137
P.N. Kalu, N. Bembridge & I. Dagwa

Biomass in materials processing: Using cassava leaves to case-harden mild steel 2143
R. Gordon, K.J. Akinluwade, A.R. Adetunji, P.N. Kalu & O.O. Adewoye

30. Structural health monitoring, damage detection, non-destructive evaluation

Non-destructive evaluation (NDE) practice for concrete bridges in USA (Invited Paper) 2151
A. Ghorbanpoor & S. Boone

Rapid and economical condition assessment of concrete bridge decks through automation of NDE data collection, analysis and interpretation 2157
N. Gucunski, A. Maher, H. Ghasemi & F.S. Ibrahim

Making sense of bridge monitoring: Vision for the future (Invited Paper) 2163
A. Pavic & J.M.W. Brownjohn

Structural model updating using combined global mode and local primary frequency 2169
J.L. Hou, J.P. Ou & Ł. Jankowski

On the application of artificial boundary condition frequencies in structural identification (Invited Paper) 2175
Y. Lu, L. Mao & Z.G. Tu

A novel two-step method for localization and assessment of cracks in beams 2181
G.R. Gillich & Z.I. Praisach

Model updating of strategic building structures under real earthquake loading 2187
R. Ceravolo, A. De Stefano, E. Matta, A. Quattrone & L. Zanotti Fragonara

A frequency analysis applied to force identification 2193
M. Thiene, U. Galvanetto, M. Ghajari & M.H. Aliabadi

Influence of multiple cracks upon the dynamic behaviour of beams 2199
Z.I. Praisach & G.R. Gillich

Structural health monitoring of continuously welded underground pipelines based on quasi-distributed wireless inclinometers 2205
S. Li, M. Zhao & N. Gao

Cable break detection in pre-stressed bridges, parking decks and girders 2211
B. Hillemeier & S. Knapp

Detection of damage due to salt crystallization through the Scaling Subtraction Method 2217
P. Antonaci, P.G. Bocca, A.S. Gliozzi & M. Scalerandi

A damage evaluation method for bridge substructures using longitudinal impact dynamic responses 2223
J.W. Zhan, H. Xia & N. Zhang

Structural damage identification in small scale models of bridge decks 2229
R. Carrazedo & T.M. Juliani

An application of the local flexibility method to hyper-static beams using non-local virtual forces 2235
T.Y. Hsu, S.Y. Shiao, W.I. Liao & C.H. Loh

Effect of load redistribution of a steel truss bridge due to fracture of a truss member on vibration-based fault detection 2239
C.W. Kim, S. Kitauchi, K. Hashimoto, K. Sugiura & M. Kawatani

A system model for lifecycle monitoring of bridges 2247
M. Wild, O. Fischer, G. Dori & A. Borrmann

The opportunities of blind source separation techniques in the automation of modal identification for vibration based SHM 2253
C. Rainieri & G. Fabbrocino

Transducers frequency influence on ultrasonic velocity measurements in concrete specimens 2259
G. Concu, B. De Nicolo, N. Trulli & M. Valdés

Application of SHM system based on modal filtration to the truss structure 2263
K. Mendrok, T. Uhl & W. Maj

System identification of masonry buildings in Vienna 2269
F. Kopf, D. Schäfer, M. Pietsch & H. Wenzel

Shear wave travel times in multi-story buildings for system identification and damage detection 2275
E. Şafak, E. Çaktı & E. Zengin

Application and developments of the infrared thermography in the building construction sector 2281
S. Knapp & B. Hillemeier

Automated devices for inspection and maintenance 2285
E. Kuhn & C. Zimmermann

Structural health monitoring of the Basilica S. Maria di Collemaggio 2291
V. Gattulli, F. Graziosi, F. Federici, F. Potenza, A. Colarieti & M. Lepidi

Experimental study on bridge damage identification based on wavelet packet energy curvature difference method 2297
Z. Yu, H. Xia & J. Zhan

Damage detection on reinforced concrete framed structures using a band-variable filter 2303
F.C. Ponzo, R. Ditommaso, G. Auletta & A. De Muro

Damage identification in the mistuned bladed system utilizing the outlier analysis 2309
A.U. Rehman, F.H. Shah, K. Worden & J.A. Rongong

Modal characteristics-based damage identification in repeating structures 2315
A.U. Rehman, F.H. Shah, S. Nazar, C.E. Lord & A. Javed

Research on corrosion monitoring for steel-reinforced concrete structures using fiber optic sensing technique 2321
X.F. Zhao, L. Wang, Q. Liu, S.J. Shan, H. Dong, Y.F. Zhu, Y.H. Jiang & Y. Yu

Steel reinforced concrete structures dynamic damage monitoring using guided wave testing technique 2327
D.S. Li, J.H. Yuan, W. Yang & W.Y. Zhang

Structural condition assessment based on modal flexibility from operational modal analysis and model updating 2333
L.-M. Zhang, T. Wang & X.-K. Lin

31. Structural assessment, damage assessment, failure analysis, forensic engineering, disaster management

The art of the forensic engineer 2341
D. Charrett

Lessons for structural engineers: The Hillsborough disaster (Invited Paper) 2347
R.A. Smith

Causal models for the forensic investigation of structural failures 2353
S. Arangio, C. Crosti & F. Bontempi

Capacity assessment of damaged school buildings after 2011 Van earthquake 2359
R.A. Oyguc

Structural failures and monitoring of structural health with use of WiSeNe^{MONIT} system 2365
S. Wierzbicki, M.A. Gizejowski & Z. Stachura

Approaches to quantify the safety gain for existing concrete bridges due to surveillance 2371
C. Siegert, L. Eckfeldt & M. Empelmann

An investigation on the collapse sequence of an RC frame during L'Aquila 2009 earthquake 2377
M.G. Mulas, L. Martinelli & F. Perotti

Structural assessment during the demolition of an arch bridge by advanced modal techniques 2383
K. Islami & R. Betti

EQvis: A consequence based risk management software tool 2389
D. Schäfer, M. Pietsch & H. Wenzel

Measuring degree of interdependencies at the infrastructure level during emergencies 2395
D. Solari, G.P. Cimellaro & A.M. Reinhorn

Back-analysis of the collapse of a metal truss structure 2401
C. Crosti & F. Bontempi

FE models for evaluating damages in churches hit by L'Aquila earthquake 2407
G. Brando, E. Criber & G. De Matteis

32. Repair, strengthening, retrofitting, sustainable construction

The strengthening and widening of the Okavango River Bridge in Northern Namibia 2415
W. Martin

CFRP strengthening of steel I-beam against local web buckling: A numerical analysis 2421
M.A. Ghareeb, M.A. Khedr & E.Y. Sayed-Ahmed

Timber beams with external strengthening based on CFRP and GFRP composites 2427
M. Karmazínová

Bond characterization between historical concrete substrate and SRG/SRP strengthening systems 2433
E. Stievanin, F. da Porto, M. Panizza, E. Garbin & C. Modena

Methods of silo strengthening walls in practice 2439
M. Kaminski & M. Maj

Study on mechanical behaviour of circular concrete columns confined by HFRP under axial compressive load 2445
L.J. Li, S.D. Xu, L. Zeng & Y.-C. Guo

Research on concrete repair materials 2451
G. Lagoda & T. Gajda

Energy harvesting for the sustainability of structures and infrastructures 2457
K. Gkoumas, F. Petrini, S. Arangio & C. Crosti

Sustainability considerations for tunnel projects 2463
J. Sauer & O. Fischer

Challenges in rehabilitation techniques in strengthening cracked concrete beams 2467
M.K. Murthy, N. Munirudrappa, S.A.K. Zai, J. Guruswamy & S. Krishnan

33. Soil-structure interaction, foundations, geotechnical engineering

The second order solution of Boussinesq's problem 2473
E. Ferretti

Upper and lower bound calculations of the bearing capacity of strip footings near slopes in cohesionless soil 2479
S. Krabbenhoft, L. Damkilde & K. Krabbenhoft

Stress state of massive foundation slabs – Measurements and simulation 2485
K. Stopp

Soil-structure-interaction: Analysis through measurements 2491
F. Kopf, D. Schäfer & J. Pistrol

Numerical calculation of damping for monopile foundations under cyclic load during steady-state vibration 2497
M. Bayat, L.V. Andersen, S.M. Andersen & L.B. Ibsen

Improved subgrade reaction model in designing embedded piles exposed to static lateral head loads 2503
M. Pulsfort & T. Welskopf

Field test of soil-steel arch with ribs and calculation of internal forces on the basis of measured strains 2509
B. Kunecki & L. Korusiewicz

Alternative shape of suction caisson to reduce risk of buckling under high pressure 2515
S. Madsen, L.V. Andersen & L.B. Ibsen

Qualitative and quantitative assessment of liquefaction in a saturated road embankment 2521
A. Borowiec & K. Maciejewski

A study of frictional interface properties between typical South African sands and construction materials 2525
Z. Bhengu, D. Kalumba & F.C. Chebet

Dynamic soil-structure interaction behaviour of building frames with raft foundation 2531
G. Narayana, H. Sharada Bai & M.P. Jyothi

Using the shear strength reduction method to assess the stability of retaining structures adjacent to excavations for the University of Cape Town's New Engineering Building 2537
C.J. Warren-Codrington & D. Kalumba

34. Structural engineering education

Efforts to reduce the drop-out rate in civil and structural engineering programs (Invited Paper) 2545
U. Quapp & K. Holschemacher

Teaching and learning of fundamentals of structural engineering in undergraduate level 2549
M.R. Karim

Structural stability and the complement to the differential equation 2555
R.D. Ziemian

International master program in structural engineering at Leipzig University of Applied Sciences (HTWK Leipzig) 2561
K. Holschemacher & U. Quapp

Author index 2565

Research and Applications in Structural Engineering, Mechanics and Computation – Zingoni (Ed.)
© 2013 Taylor & Francis Group, London, ISBN 978-1-138-00061-2

Preface

The International Conference on Structural Engineering, Mechanics and Computation (SEMC) was inaugurated in 2001 with the aim of "bringing together from around the world academics, researchers and practitioners in the broad fields of structural mechanics, associated computation and structural engineering, to review recent achievements in the advancement of knowledge and understanding in these areas, share the latest developments, and address the challenges that the present and the future pose". Held every 3 years since then, SEMC has attracted an ever-increasing level of participation from all over the world. The fifth conference in the series, SEMC 2013, was held in Cape Town (South Africa) from 2 to 4 September 2013. Well over 400 participants from 60 countries worldwide attended the conference.

These Proceedings contain over 420 papers that were presented at the Fifth International Conference on Structural Engineering, Mechanics and Computation. The Proceedings are divided into 34 sections for ease of reading. The six keynote lectures delivered at the Conference have been collected together into Section 1, while the rest of the papers have been classified under the most appropriate topics, and appear in Sections 2 to 34 of the Proceedings. As expected, many papers have subject matter that spans more than one topic, and could equally have been placed in any one of two or more sections of the Proceedings. In trying to access papers on a particular subject, readers should therefore be mindful of the overlapping nature of the topics, and make sure they look through all relevant sections of the Proceedings.

Every contribution that was submitted for the Conference was prepared as a full paper of length 6 pages, and a shortened version of the paper of length 2 pages. The Proceedings have been published in the form of a printed book containing the short papers, and a CD-ROM containing the full papers. All papers were reviewed by members of the International Scientific Advisory Board and other identified experts acting independently, and only those papers that were accepted have been included in the Proceedings. The editor would like to thank all reviewers for their input in enhancing the quality of the Proceedings.

The SEMC 2013 International Conference was wide in scope, and on opening the Proceedings, one immediately sees this in the diversity of the subject matter treated by the six keynote papers, from analytical and computational considerations to practical issues of design and monitoring. The first section is followed by a cluster of sections covering the topics of vibration, dynamics, vibration control and seismic design. Immediately after these appear papers on the mechanics of materials and modelling in general, and these specifically cover material modelling, composite materials, numerical modelling, finite-element modelling, damage mechanics, fracture, fatigue and other problems. The more design-oriented considerations of robustness, progressive collapse, tall buildings and bridge engineering are dealt with next, followed by a series of papers on lightweight structures, roofing solutions, plates, shells, laminated and sandwich construction, and the growing area of renewable energy structures (solar chimneys, wind-turbine structures, and the like).

Not unexpectedly, the Proceedings feature several sections devoted to various aspects of steel structures (thin-walled sections, cold-formed steel construction, stainless-steel structures, steel joints and connections, steel-concrete composite construction) as well as concrete structures (reinforced-concrete design, prestressed concrete, fibre-reinforced concrete, high-strength concrete, high-performance concrete, properties of concrete, creep, shrinkage and durability). There is also a significant number of contributions on masonry and timber structures. Performance of structures in fire, and design for fire resistance, are topics which are attracting the attention of many researchers worldwide, and this is reflected in the large number of papers making up the section on fire. There is also a healthy number of papers dealing with more general issues of structural safety and reliability, as well as the important topic of optimization in structural design.

Towards the end of the Proceedings, one finds papers related to the integrity and long-term performance of structures. The large section on structural health monitoring, damage detection and non-destructive evaluation reflects the intensity of global research activity in these areas. This is followed by sections on the related topics of structural assessment, damage assessment, failure analysis, forensic engineering, repair, strengthening and retrofitting of structures. Papers on soil-structure interaction and foundation design have been collected together in the second-last section of the Proceedings. The last section features papers on structural-engineering education.

The editor is most grateful to all the many authors who contributed to these Proceedings. It is hoped that this rich collection of research and technical papers will serve as an enduring resource for all researchers and practitioners working in various fields, and also provide direction for future activity in these areas.

The financial support of the following organisations, who were the offical sponsors of the SEMC 2013 International Conference, is gratefully acknowledged:

- The National Research Foundation of South Africa
- The South African National Roads Agency Limited
- Anglo American Corporation
- ADINA (USA)

In his capacity as Conference chair, the editor is also grateful to colleagues and postgraduate students who assisted with various aspects of the organisation of the Conference, and to all session chairs for managing the oral presentations so competently. Last but not least, the editor wishes to acknowledge the support of his wife Lydia and children Ratidzo, Tafadzwa and Simbarashe, for their patience and understanding in giving him the space required to accomplish this work.

A. Zingoni
Editor

Research and Applications in Structural Engineering, Mechanics and Computation – Zingoni (Ed.)
© 2013 Taylor & Francis Group, London, ISBN 978-1-138-00061-2

Committees

LOCAL ORGANISING COMMITTEE

A. Zingoni, *University of Cape Town (Chairman)*
A. Masarira, *Anglo American Corporation*
M. Latimer, *Joint Struct. Div. of SAICE & IStructE*
S. Skatulla, *University of Cape Town*
D. Kalumba, *University of Cape Town*
L. Zingoni, *University of Cape Town*

INTERNATIONAL SCIENTIFIC ADVISORY BOARD

Professor S. Adali
University of KwaZulu-Natal, South Africa

Professor H. Adeli
Ohio State University, USA

Professor M.G. Alexander
University of Cape Town, South Africa

Professor C.J. Anumba
Pennsylvania State University, USA

Professor B. Baier
University of Duisburg-Essen, Germany

Professor C. Bailey
University of Manchester, UK

Professor T. Balendra
National University of Singapore, Singapore

Professor Y. Ballim
University of the Witwatersrand, South Africa

Professor J.R. Banerjee
City University, UK

Professor N. Banthia
University of British Columbia, Canada

Professor K.J. Bathe
Massachusetts Institute of Technology, USA

Professor Z.P. Bazant
Northwestern University, USA

Professor D. Beskos
University of Patras, Greece

Professor F.S.K. Bijlaard
Delft University of Technology, The Netherlands

Professor Z. Bittnar
Czech Technical University in Prague, Czech Republic

Professor F. Bontempi
University of Rome La Sapienza, Italy

Profesor G. Borino
University of Palermo, Italy

Professor H. Bouchaïr
Blaise Pascal University, France

Professor M. Bradford
University of New South Wales, Australia

Professor O. Buyukozturk
Massachusetts Institute of Technology, USA

Professor S. Caddemi
University of Catania, Italy

Professor D. Camotim
Technical University of Lisbon, Portugal

Professor W. Cantwell
University of Liverpool, UK

Professor R. Cerny
Czech Technical University in Prague, Czech Republic

Professor C.K. Choi
Korea Advanced Institute of Science & Technology, Korea

Professor A.K. Chopra
University of California at Berkeley, USA

Professor K.F. Chung
Hong Kong Polytechnic University, China

Professor J.G.A. Croll
University College London, UK

Professor R. de Borst
University of Glasgow, UK

Professor G. De Matteis
University G. d'Annunzio of Chieti-Pescara, Italy

Professor G. De Roeck
Catholic University of Leuven, Belgium

Professor G. Domokos
Budapest University of Technology & Economics, Hungary

Professor A. Elnashai
University of Illinois at Urbana-Champaign, USA

Professor M. Fontana
Swiss Federal Institute of Technology, Switzerland

Professor D.M. Frangopol
Lehigh University, USA

Professor E. Fehling
University of Kassel, Germany

Professor J. Feix
University of Innsbruck, Austria

Professor F.C. Filippou
University of California at Berkeley, USA

Professor Y. Fujino
University of Tokyo, Japan

Professor A. Ghobarah
McMaster University, Canada

Dr. L. Giuliani
Technical University of Denmark, Denmark

Professor M. Gizejowski
Warsaw University of Technology, Poland

Professor P.L. Gould
Washington University, USA

Professor A.A. Groenwold
University of Stellenbosch, South Africa

Dr. S. Guest
University of Cambridge, UK

Professor W. Guggenberger
Technical University of Graz, Austria

Professor G. Hancock
University of Sydney, Australia

Professor R. Harte
Bergische University Wuppertal, Germany

Professor N.M. Hawkins
University of Illinois at Urbana-Champaign, USA

Professor S. Heyns
University of Pretoria, South Africa

Professor M. Holicky
Czech Technical University in Prague, Czech Republic

Professor K. Holschemacher
Leipzig University of Applied Sciences, Germany

Professor T. Ibell
University of Bath, UK

Professor K. Jarmai
University of Miskolc, Hungary

Professor J. Katsikadelis
National Technical University of Athens, Greece

Professor A. Kaveh
Iran University of Science and Technology, Iran

Professor K. Kayvani
Aurecon Group, Australia

Professor S. Kitipornchai
City University of Hong Kong, China

Professor J.M. Ko
Hong Kong Polytechnic University, China

Professor J.G. Korvink
University of Freiburg, Germany

Professor W.B. Kratzig
Ruhr University Bochum, Germany

Professor T. Laursen
Khalifa University, United Arab Emirates

Professor R.W. Lewis
University of Wales at Swansea, UK

Professor H.N. Li
Dalian University of Technology, China

Professor A. Long
Queen's University of Belfast, UK

Professor J. Loughlan
Loughborough University, UK

Professor Y. Lu
University of Edinburgh, UK

Professor H.A. Mang
Vienna University of Technology, Austria

Professor H. Matsunaga
Setsunan University, Japan

Professor F.M. Mazzolani
University of Naples Federico II, Italy

Professor J. Melcher
Brno University of Technology, Czech Republic

Professor C. Mota Soares
Technical University of Lisbon, Portugal

Professor A. Mufti
University of Manitoba, Canada

Professor R.S. Narayanan
Clark Smith Partnership, UK

Professor D.A. Nethercot
Imperial College London, UK

Professor H.J. Niemann
Ruhr University Bochum, Germany

Professor A. Nowak
University of Michigan, USA

Professor G.N. Nurick
University of Cape Town, South Africa

Professor J.B. Obrebski
Warsaw University of Technology, Poland

Professor R. Ohayon
Conservatoire National des Arts et Metiers, France

Professor J.P. Ou
Harbin Institute of Technology, China

Professor D.R.J. Owen
University of Wales at Swansea, UK

Professor M. Papadrakakis
National Technical University of Athens, Greece

Professor A. Pavic
University of Exeter, UK

Professor F. Perotti
Politecnico di Milano, Italy

Professor E. Ramm
University of Stuttgart, Germany

Professor K. Rasmussen
University of Sydney, Australia

Professor B.D. Reddy
University of Cape Town, South Africa

Professor J.V. Retief
University of Stellenbosch, South Africa

Professor J.M. Rotter
University of Edinburgh, UK

Professor U. Schneider
Technical University of Vienna, Austria

Professor S.A. Sheikh
University of Toronto, Canada

Professor S. Shrivastava
McGill University, Canada

Professor R.A. Smith
Imperial College London, UK

Professor H.H. Snijder
Eindhoven University of Technology, The Netherlands

Professor U. Starossek
Technical University of Hamburg, Germany

Professor C. Szymczak
Technical University of Gdansk, Poland

Professor T. Tarnai
Budapest University of Technology & Economics, Hungary

Professor J.G. Teng
Hong Kong Polytechnic University, China

Professor D. Thambiratnam
Queensland University of Technology, Australia

Professor S. Timashev
Russian Academy of Sciences, Russia

Professor V. Tvergaard
Technical University of Denmark, Denmark

Professor H.C. Uzoegbo
University of the Witwatersrand, South Africa

Professor B.W.J. van Rensburg
University of Pretoria, South Africa

Professor G.P.A.G. van Zijl
University of Stellenbosch, South Africa

Professor R. Vaziri
University of British Columbia, Canada

Professor O. Vilnay
Technion Israel Institute of Technology, Israel

Professor T. Vogel
Swiss Federal Institute of Technology, Switzerland

Professor F. Wald
Czech Technical University in Prague, Czech Republic

Professor J.C. Walraven
Delft University of Technology, The Netherlands

Professor A.C. Wijeyewickrema
Tokyo Institute of Technology, Japan

Professor W. Wunderlich
Technical University of Munich, Germany

Professor Y.B. Yang
National Taiwan University, China

Professor D. Yankelevsky
Technion Israel Institute of Technology, Israel

Professor R. Zandonini
University of Trento, Italy

Professor A. Zingoni
University of Cape Town, South Africa

1. Keynote lectures

Research and Applications in Structural Engineering, Mechanics and Computation – Zingoni (Ed.)
© 2013 Taylor & Francis Group, London, ISBN 978-1-138-00061-2

Insights and advances in the analysis of structures

Klaus-Jürgen Bathe
Massachusetts Institute of Technology, Cambridge, Massachusetts, USA

ABSTRACT: The objective in this presentation is to survey our recent research accomplishments to advance the state of computational simulations in engineering and the sciences. We present our novel insights and recent advances in the analysis of transient and wave propagation problems, the simulation of large strain conditions of shells, the prediction of more accurate solutions using low-order elements, and the coupling of structures to general fluid flows and electromagnetic effects. At the conference, applications are given in the analysis of traditional structures and in the modeling of nano-structures, specifically, proteins and DNA assemblies. Also, major challenges are outlined for further advances in the field.

1 INTRODUCTION

Although the analysis of solids and structures has been much researched during the recent decades, and finite element methods are nowadays used abundantly, there are many analysis areas where further advances are still much needed. These areas primarily pertain to the solution of dynamic, nonlinear, and multiphysics problems. The objective in this paper is to briefly present some advances that we have recently accomplished. Due to space limitations, we mention only our books and papers, and refer the reader to the many references given therein.

When considering research achievements in the field, it is important to realize the philosophy that a research group adheres to in its research on computational methods. Our philosophy – as pursued for about 40 years now – is to focus on the development of methods that are general, reliable and efficient, and advance the current state of the art as practiced in industry and the sciences (Bathe 1996, Bathe 2009, Bathe 2012a).

The ultimate test as to whether a computational scheme is of value is, indeed, whether the scheme, once published, is used widely in industry and scientific investigations. Since there is a keen interest in engineering and the sciences to solve ever more complex and difficult physical problems, significant new, reliable and effective analysis procedures are quickly adopted.

Our research focus is on the conception of novel and general methods, their mathematical analyses and their testing to establish the generality, reliability and efficiency.

A finite element method is *general* if it is applicable to many varied problems in a certain problem area; for example, a general shell element can be used for all shell problems described by a general mathematical model like the 'basic shell model' identified in references (Chapelle & Bathe 2000, 2011).

A finite element method is *reliable* and *efficient* if identified as such; for example, a finite element discretization is reliable and efficient if the ellipticity and inf-sup conditions are satisfied without the use of any artificial factors, and the scheme shows optimal convergence at a low computational cost (Bathe 1996, Chapelle & Bathe 2011).

In the next sections, we present our recent developments, according to the above research aims, regarding the analysis of wave propagations, large strains in shells, prediction of more accurate solutions when using low-order elements, and the simulation of fluid-structure interactions including electro-magnetic effects. These schemes are widely applicable in traditional areas of analysis and also in novel areas, like the analysis of proteins and DNA structures.

2 INSIGHTS AND ADVANCES

We briefly focus in the following sections on some of the research we have pursued.

2.1 *Wave propagation problems*

The accurate analysis of transient wave propagations and the accurate solution of time harmonic problems at high frequencies have remained a significant challenge. The essential difficulties are that the waves need to be captured accurately by the mesh and the time integration scheme used. If high frequency waves are to be simulated, very fine meshes of conventional finite elements may be needed. However, even with such very fine meshes, to calculate a transient response accurately, the numerical dispersion and dissipation of waves due to the spatial and temporal discretizations must be small. To address these solution difficulties, spectral methods, spectral element methods, and spectral finite element methods have been proposed, for the solution of specific problems.

We have developed a finite element method 'enriched for wave propagation problems' (Ham & Bathe 2012). In this method the standard low-order Lagrangian finite element interpolations are simply enriched with harmonic functions, governed, as usual, by nodal degrees of freedom. An important point is that the usual fundamental theory of finite element methods is applicable.

For two-dimensional solutions, the basic displacement interpolations for a typical solution variable $u(r,s)$ are

$$
\begin{aligned}
&u(r,s)= \\
&\sum_{\alpha} h_\alpha(r,s) \\
&\left[U_{(\alpha,0,0)} + \sum_{k_x=1}^{n} \left\{ \cos\left(\frac{2\pi k_x x}{\Lambda_x}\right) U^{C}_{(\alpha,k_x,0)} + \sin\left(\frac{2\pi k_x x}{\Lambda_x}\right) U^{S}_{(\alpha,k_x,0)} \right\} \right. \\
&+ \sum_{k_y=1}^{m} \left\{ \cos\left(\frac{2\pi k_y y}{\Lambda_y}\right) U^{C}_{(\alpha,0,k_y)} + \sin\left(\frac{2\pi k_y y}{\Lambda_y}\right) U^{S}_{(\alpha,0,k_y)} \right\} \\
&+ \sum_{k_x=1}^{n}\sum_{k_y=1}^{m} \left\{ \cos\left(\frac{2\pi k_x x}{\Lambda_x}+\frac{2\pi k_y y}{\Lambda_y}\right) U^{C+}_{(\alpha,k_x,k_y)} + \sin\left(\frac{2\pi k_x x}{\Lambda_x}+\frac{2\pi k_y y}{\Lambda_y}\right) U^{S+}_{(\alpha,k_x,k_y)} \right. \\
&\left. \left. + \cos\left(\frac{2\pi k_x x}{\Lambda_x}-\frac{2\pi k_y y}{\Lambda_y}\right) U^{C-}_{(\alpha,k_x,k_y)} + \sin\left(\frac{2\pi k_x x}{\Lambda_x}-\frac{2\pi k_y y}{\Lambda_y}\right) U^{S-}_{(\alpha,k_x,k_y)} \right\} \right]
\end{aligned}
$$

where the $U_{(\alpha,k_x,k_y)}$ with superscripts are the nodal degrees of freedom, α is the local element node, with h_α the conventional finite element interpolation function, and the S, C, and $+$ and $-$ are used in the superscripts to correspond to the harmonic expressions. The interpolations for one- and three-dimensional analyses directly follow from the above equation. Here, the two fundamental wavelengths Λ_x and Λ_y, typically equal to twice the element lengths, and the wave cut-off numbers n and m with $1 \le k_x \le n$, $1 \le k_y \le m$, typically $n, m \le 3$, need to be chosen by the analyst.

These functions can directly be used to solve time harmonic and transient problems. Figure 1 shows the finite element solution of the Helmholtz equation corresponding to a 2D planar pressure wave

$$
\begin{aligned}
&\nabla^2 P + k^2 P = 0 && \text{in } V \\
&\frac{\partial P}{\partial n} = g(x,y) && \text{on } S_f \\
&\lim_{r\to\infty} \sqrt{r}\left(\frac{\partial P}{\partial r} - ikP\right) = 0
\end{aligned}
$$

Here good accuracy is seen, although a very coarse mesh is used (Ham & Bathe 2012).

For transient analysis also an effective time integration scheme needs to be employed. Considering implicit schemes, we use the Bathe method (available in ADINA) which shows good cut-off characteristics of waves that can spatially not be resolved (Bathe 2007, Bathe & Noh 2012, Noh, Ham & Bathe, In Press).

Figure 2 gives the relative wave speed errors when traditional 2-node elements are used to solve a 1D wave propagation problem, here the CFL number is defined as $\mathrm{CFL} = c_0 \Delta t / \Delta x$. The key point to note is that for

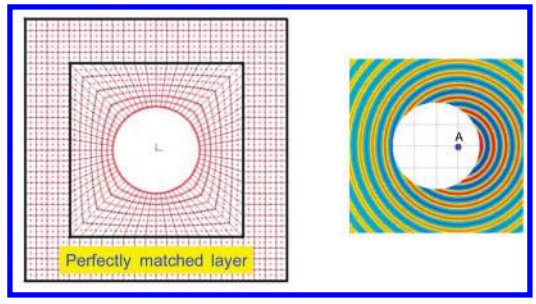


Figure 1. Solution of Helmholtz problem; 9-node elements and $\mathrm{n} = m = 2$; S_f = surface of the cylinder; point A is the pole.

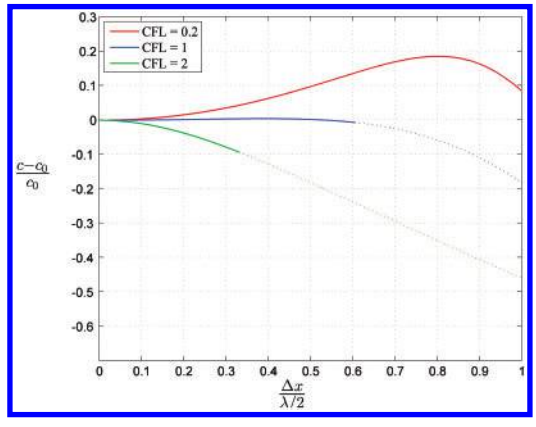


Figure 2. Relative wave speed errors of the Bathe method for various CFL numbers; results for discarded wave modes are given by dotted lines.

CFL = 1.0, the wave speed error is very small for reasonable spatial discretizations – hence the dispersion error is small for those waves that can be represented spatially – and waves of lengths less than 3 elements are 'cut-out' of the response.

The corresponding behavior of the widely-used trapezoidal rule of the Newmark method is given in Figure 3, here the property of cutting out the high-frequency modes is not present.

Figure 4 describes an illustrative 1D problem solved using standard 2-node elements. The response is given in Figure 5 using the Bathe method with CFL = 1.0 and the trapezoidal rule with CFL = 0.65, these being the optimal numbers to use. Less oscillations are seen when using the Bathe method. This better response prediction is due to cutting out those waves that cannot be accurately captured.

For further solutions, see Ham & Bathe 2012, Bathe & Noh 2012, Noh, Ham & Bathe, In Press, and Kazancı & Bathe 2012. Also, using the Bathe method, an added benefit is that the load at the half-step can be selected for optimal accuracy, like for rapidly varying loads, the mean value of the loads at times t and $t + \Delta t$ is best used. An explicit time integration scheme with

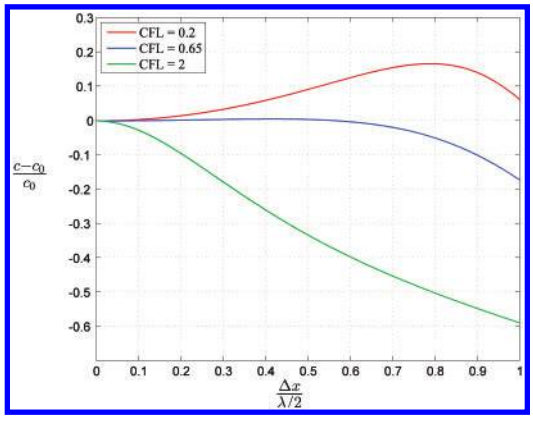


Figure 3. Relative wave speed errors of the trapezoidal rule for various CFL numbers.

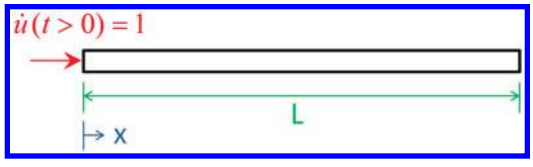


Figure 4. 1D bar impact problem, initial velocity = 0.

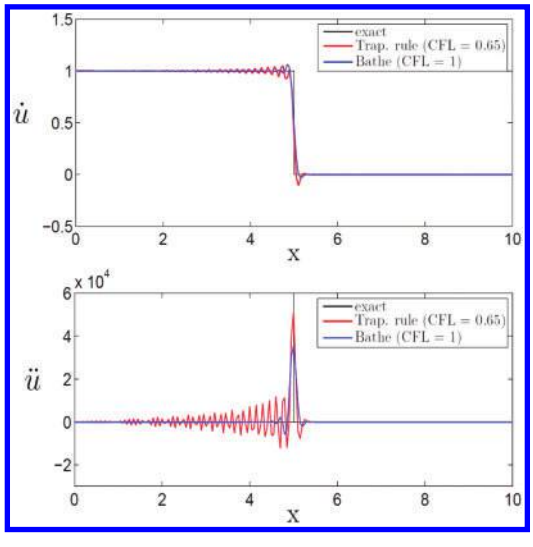


Figure 5. 1D bar impact problem, 200 2-node elements.

the property of 'cutting out' undesirable frequencies, as in the Bathe method, is given in Noh & Bathe 201x.

2.2 *3D-shell elements for large strain analysis*

Significant research efforts over many decades have focused on the analysis of shells, but there are still many outstanding challenges in the field (Chapelle & Bathe 2011); one such is the analysis of large strain behaviors. The 3- and 4-node MITC 3D-shell elements build upon the classical MITC shell elements but include important three-dimensional effects (Kim & Bathe 2008, Sussman & Bathe, In Press). The elements (available in ADINA) can be used to model very large deformations with large elastic or plastic strains. They are employed like the conventional MITC shell elements with 5 or 6 degrees of freedom at each mid-surface node and additional nodal degrees of freedom to represent through-the-thickness straining and warping of the transverse fibers. In the formulations, MITC interpolations are used on the transverse fiber motions to preserve the volume and prevent shear locking, and in incompressible analysis the u/p formulation is employed (Chapelle & Bathe 2011, Sussman & Bathe, In Press).

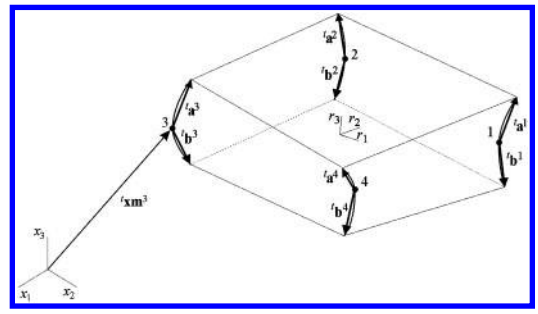


Figure 6. Nodes and control vectors of the 4-node 3D-shell element.

Figure 6 shows schematically a 4-node element. The important point is that at each node two control vectors are used to describe the deformations. To eliminate shear locking, the motions of the transverse fibers are described by a tying rule that represents an extension of the rule used for the classical MITC shell elements (Chapelle & Bathe 2011), namely we employ

$$\begin{bmatrix} \frac{\partial {}^t x_1}{\partial r_1} & \frac{\partial {}^t x_2}{\partial r_1} & \frac{\partial {}^t x_3}{\partial r_1} \\ \frac{\partial {}^t x_1}{\partial r_2} & \frac{\partial {}^t x_2}{\partial r_2} & \frac{\partial {}^t x_3}{\partial r_2} \\ \left(\frac{\partial {}^t \mathbf{x}}{\partial r_1}\times\frac{\partial {}^t \mathbf{x}}{\partial r_2}\right)_1 & \left(\frac{\partial {}^t \mathbf{x}}{\partial r_1}\times\frac{\partial {}^t \mathbf{x}}{\partial r_2}\right)_2 & \left(\frac{\partial {}^t \mathbf{x}}{\partial r_1}\times\frac{\partial {}^t \mathbf{x}}{\partial r_2}\right)_3 \end{bmatrix} \begin{bmatrix} \left(\frac{\partial {}^t x_1}{\partial r_3}\right)^{AS} \\ \left(\frac{\partial {}^t x_2}{\partial r_3}\right)^{AS} \\ \left(\frac{\partial {}^t x_3}{\partial r_3}\right)^{AS} \end{bmatrix} = \begin{bmatrix} {}^t_r C_{13}^{AS} \\ {}^t_r C_{23}^{AS} \\ \det {}^t_r \mathbf{X}^{DI} \end{bmatrix}$$

where ${}^t x_i, i = 1, 2, 3$ are the components of ${}^t\mathbf{x}$, $\partial {}^t\mathbf{x}/\partial r_i$ are the covariant base vectors, ${}^t_r C_{ij}$ are the components of the Cauchy-Green deformation tensor referred to the isoparametric description, $\det {}^t_r \mathbf{X}^{DI}$ is the determinant of the deformation gradient directly calculated, the superscript t denotes at time t, and the superscript AS denotes "assumed".

Figure 7 shows a large strain solution obtained with the MITC4 3D-shell element. Here the large strains in the structure result into a significant downward shifting of the midsurface nodes during the response.

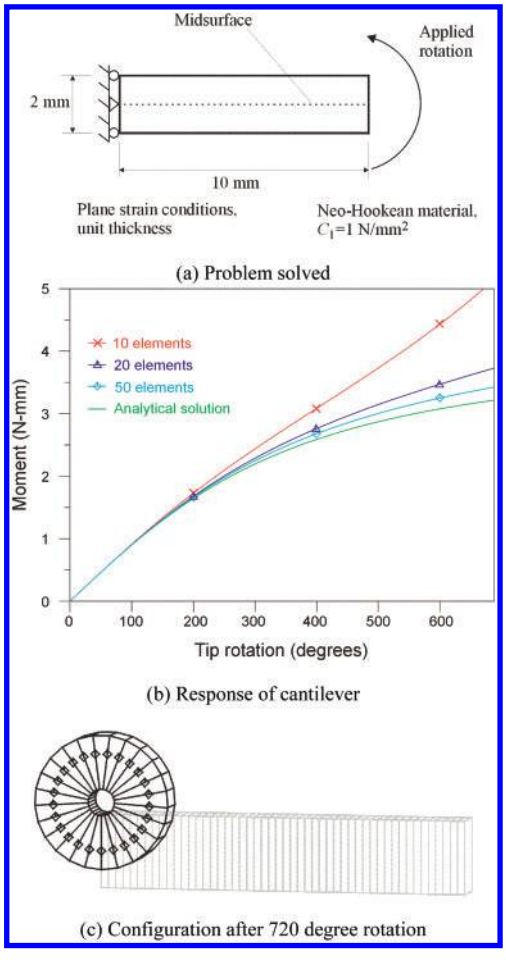


Figure 7. Large strain analysis of thick plane strain cantilever.

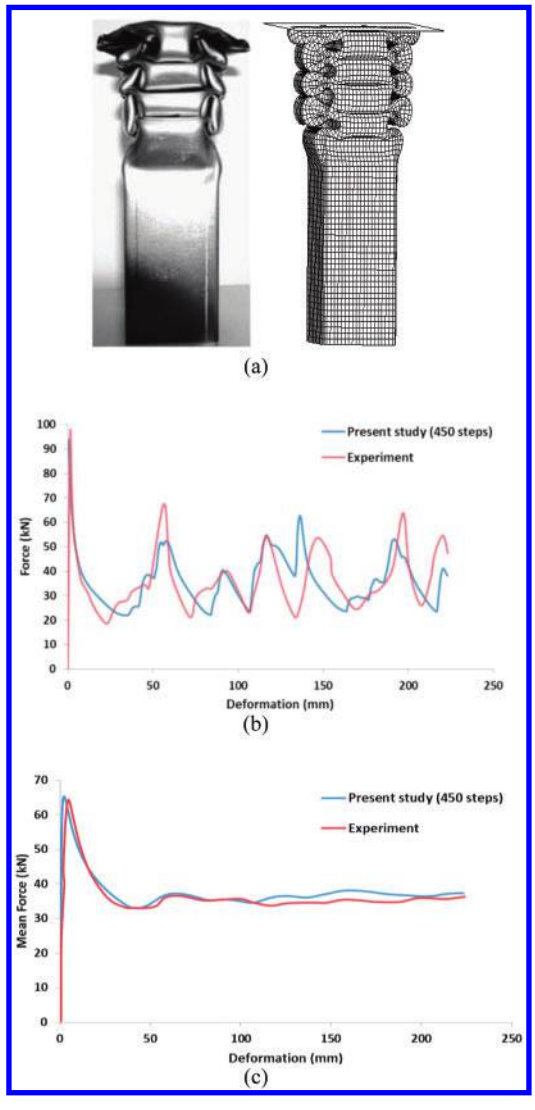


Figure 8. Quasi-static crushing of a square-section tube, length of tube is 310 mm; (a) experimental and computed results in final configuration; (b) force–displacement curves; (c) mean crushing force–displacement curves.

Figure 8 shows some analysis results obtained in a slow crush analysis of a square tube using the MITC4 3D-shell element and the Bathe time integration scheme; for details and also crash solution results see Kazancı & Bathe 2012.

2.3 *Procedures for solution improvements*

As well known, the 3-node triangular and 4-node quadrilateral elements in 2D solutions and 4-node tetrahedral and 8-node brick elements in 3D solutions lead to well-conditioned small bandwidth assembled matrices, they are robust but are not effective in predicting stresses accurately. Very fine meshes are needed in practice. Hence, it is of much interest to increase the order of stress convergence of these elements.

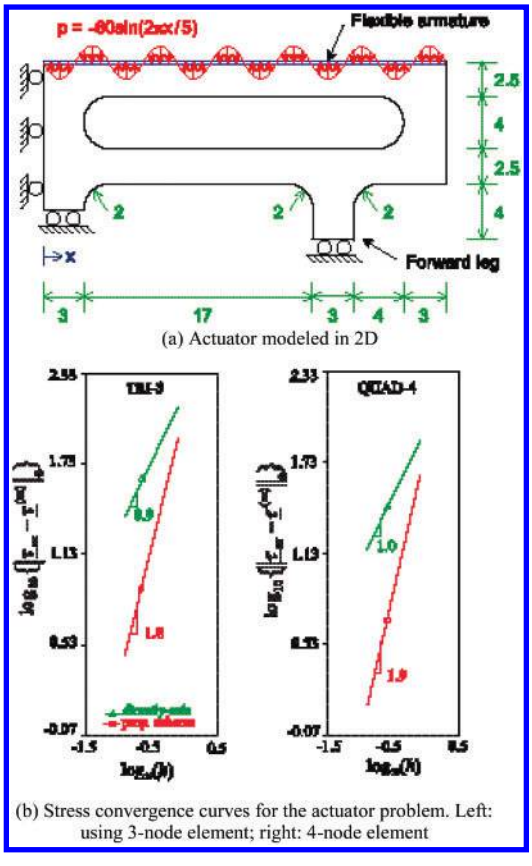
We have developed schemes to improve the predictions of stresses (Payen & Bathe 2012) and, both, displacements and stresses (Kim & Bathe 2013). To establish more accurate stresses from calculated displacements, we use two projection equations over the patch of elements that contains the element, for which improved stresses are sought, and those surrounding it (Payen & Bathe 2012)

$$\sum_{m=1}^{N_P}\left(\int_{V^{(m)}}\delta\underline{\bar{\tau}}^{(m)T}\left\{\underline{\tau}^{(m)}-\underline{\tau}_h^{(m)}\right\}dV\right)=0\quad\forall\,\underline{\bar{\tau}}^{(m)}\in\bar{\mathbf{V}}^{\tau}$$

$$\sum_{m=1}^{N_P}\left(\int_{V^{(m)}}\delta\underline{\zeta}^{(m)T}\left\{div\left[\underline{\tau}^{(m)}\right]+\underline{f}^{B}\right\}dV\right)=0$$

$$\forall\;\underline{\zeta}^{(m)}\in P_1$$

where P_k denotes the kth order polynomial, $\underline{\tau}^{(m)}$ represents the enhanced stresses to be calculated in P_2, $\underline{\tau}_h^{(m)}$ are the directly-calculated stresses, $\underline{\bar{\tau}}^{(m)}$ is an element in $\bar{\mathbf{V}}^{\tau}$, the subspace of P_2 in which all stress



(a) Actuator modeled in 2D

(b) Stress convergence curves for the actuator problem. Left: using 3-node element; right: 4-node element

Figure 9. Analysis of actuator subjected to Lorentz force.

functions satisfy the equilibrium equations $div\,[\,\underline{\bar{\tau}}^{(m)}] = \underline{0}$, and N_P is the number of finite elements in the patch considered.

The scheme is effective, needs to only be applied in certain critical stress areas, and can be used in linear and nonlinear, static and dynamic analyses.

Figure 9 shows an actuator analyzed and the results obtained. It is seen that with the scheme used the stresses converge with almost second order, i.e. with the same order as the displacements.

This scheme only improves the stresses. We have also researched another approach in order to improve all solution variables when using 3-node 2D triangular and 4-node 3D tetrahedral elements through 'enriching the finite element method by interpolation covers' (Kim & Bathe 2013). These covers are also applied only in those regions where higher accuracy is sought in the solution.

Considering a patch of 2D 3-node elements, the essence of the enrichment scheme is to interpolate the solution variable using

$$u_h = \sum_{i=1}^{3} h_i u_i + \sum_{i=1}^{3} \underline{\tilde{H}}_i\, \underline{\tilde{a}}_i \qquad \text{in the } \textit{element}$$

where u_i is the usual nodal degree of freedom and $\tilde{a}_i$ lists additional degrees of freedom with

$$\underline{\tilde{H}}_i = h_i \left[\bar{x}_i \quad \bar{y}_i \quad \bar{x}_i^2 \quad \bar{x}_i\bar{y}_i \quad \bar{y}_i^2 \quad \cdots \quad \bar{y}_i^p \right]$$

Here, the $(\bar{x}_i, \bar{y}_i)$ are coordinates measured from the node i,and p is the cover order used.Important considerations pertain to choosing computationally effective covers and having a well-conditioned coefficient matrix (Kim & Bathe 2013).

2.4 *Coupling of structures to fluid flows and electromagnetic effects*

Separate solutions of solids, structures, fluid flows, and electromagnetics have been obtained for decades. However, the solution of multiphysics problems involving fully coupled fluid-structure interactions with temperature and electromagnetic effects has hardly been tackled and presents special difficulties. Such fully coupled problems need to be solved, for example, in biomedical engineering, metal processing, and plasma physics.

We have developed a novel finite element scheme for the solution of the general Maxwell's equations to simulate fluid flows, solids, and structures coupled with electromagnetic effects (Bathe 2012a, Bathe, Zhang & Yan 201x). The finite elements used are similar to those we proposed for the solution of the Navier-Stokes equations (Bathe & Zhang 2009).

The basic equations we solve are, considering Faraday's law and Ampere's law with the Maxwell term, in the E-H form

$$\nabla\Box\left(\left(p + \rho_0/\varepsilon^*\right)\mathbf{I} - \nabla\mathbf{E} + \mathbf{I}\times\mathbf{K}\right) = \mathbf{0} \quad in\ \Omega_e$$

and

$$\nabla\Box\left(q\mathbf{I} - \nabla\mathbf{H} - \mathbf{I}\times\mathbf{J}\right) = \mathbf{0} \quad in\ \Omega_m$$

where Ω_e and Ω_m denote the domains of electric and magnetic fields, resp., $\mathbf{K}$ and $\mathbf{J}$ are source terms for the electric and magnetic field intensities, ρ_0 is the charge density, ε^* is the effective permittivity (for static and harmonic solutions), $\mathbf{I}$ is the identity tensor, and we introduced

$$p = \nabla\Box\mathbf{E} - \rho_0/\varepsilon^*$$

$$q = \nabla\Box\mathbf{H}$$

Of course, these equations specialize to specific cases by omitting certain terms, and the equations must be used with appropriate boundary and interface conditions.

However, for certain problems, a potential formulation can be more effective, in which the electric and magnetic potentials, ϕ and $\mathbf{A}$, are used

$$\mathbf{E} = -\nabla\phi - \frac{\partial\mathbf{A}}{\partial t}; \qquad \mathbf{B} = \nabla\times\mathbf{A}$$

with $\nabla\cdot\mathbf{A} = g_A$ and g_A a gauge condition. Solutions using these formulations in ADINA are shown at www.adina.com.

3 CONCLUDING REMARKS

In this paper we briefly summarized some of the research we have pursued during the recent years, with our research philosophy adhered to in these developments.

Significant advances in many areas are still to be accomplished – in particular when the actual *practice* of simulations in engineering and the sciences is focused upon. Here the reliability and efficiency of procedures is very important. Major challenges exist in solving multiphysics problems, at small and large scales, and in multiscale conditions.

In all applications, the endeavor is, in essence, to 'understand nature and try to predict the future through analysis'. This endeavor will be of increasing interest and value throughout the sciences and engineering, and the hierarchical process of analysis will be of particular value, see references (Bathe 1996, Bucalem & Bathe 2011). However, while novel areas of simulations will attract exciting attention, it is also important to continuously increase the efficiency of methods in traditional areas of analysis, like for the analysis of shells and for the solution of large finite element systems (Chapelle & Bathe 2011, Bathe 2012b).

ACKNOWLEDGEMENTS

I would like to acknowledge my most valuable collaboration with my students and colleagues, referred to in the references.

REFERENCES

Due to space limitations, we only refer to some of our publications; please refer to the many references given therein.

Bathe, K.J. 1996. *Finite Element Procedures*. Englewood Cliffs: Prentice Hall, republished by K.J. Bathe 2006.

Bathe, K.J. 2007. Conserving energy and momentum in nonlinear dynamics: A simple implicit time integration scheme. *Computers & Structures*, 85:437–445.

Bathe, K.J. 2009. The Finite Element Method, in *Encyclopedia of Computer Science and Engineering*, (B. Wah, ed.), Wiley and Sons, Inc.

Bathe, K.J. 2012a. Advances in the Multiphysics Analysis of Structures, in *Computational Methods for Engineering Science*, (B.H.V. Topping, ed.), Saxe-Coburg Publications, Stirlingshire, Scotland.

Bathe, K.J. 2012b. The subspace iteration method – revisited. *Computers & Structures*, 10.1016/j.compstruct.2012.06.002.

Bathe, K.J. & Noh, G. 2012. Insight into an implicit time integration scheme for structural dynamics. *Computers & Structures*, 98–99: 1–6.

Bathe, K.J. & Zhang, H. 2009. A mesh adaptivity procedure for CFD and fluid-structure interactions. *Computers & Structures*, 87:604–617.

Bathe, K.J., Zhang, H. & Yan, Y. 201x. The solution of Maxwell's equations in multiphysics. In prep.

Bucalem, M.L. & Bathe, K.J. 2011. *The Mechanics of Solids and Structures – Hierarchical Modeling and the Finite Element Solution*. Springer.

Chapelle, D. & Bathe, K.J. 2000. The mathematical shell model underlying general shell elements. *International Journal for Numerical Methods in Engineering*, 48: 289–313.

Chapelle, D. & Bathe, K.J. 2011. *The Finite Element Analysis of Shells – Fundamentals*. 2nd edition, Springer.

Ham, S. & Bathe, K.J. 2012. A finite element method enriched for wave propagation problems. *Computers & Structures*, 94–95: 1–12.

Kazancı, Z. & Bathe, K.J. 2012. Crushing and crashing of tubes with implicit time integration. *International Journal of Impact Engineering*, 42:80–88.

Kim, D.N. & Bathe, K.J. 2008. A 4-node 3D-shell element to model shell surface tractions and incompressible behavior. *Computers & Structures*, 86: 2027–2041.

Kim, J.H. & Bathe, K.J. 2013. The finite element method enriched by interpolation covers. *Computers & Structures*, 116: 35–49.

Noh, G. & Bathe, K.J. 201x. An explicit time integration scheme for the analysis of wave propagations. In prep.

Noh, G., Ham, S. & Bathe, K.J. In Press. Performance of an implicit time integration scheme in the analysis of wave propagations. *Computers & Structures*.

Payen, D.J. & Bathe, K.J. 2012. A stress improvement procedure. *Computers & Structures*, 112–113: 311–326.

Sussman, T. & Bathe, K.J. In Press. 3D-shell elements for structures in large strains. *Computers & Structures.*

Research and Applications in Structural Engineering, Mechanics and Computation – Zingoni (Ed.)
© 2013 Taylor & Francis Group, London, ISBN 978-1-138-00061-2

Recent studies on long-span bridges: Vibration control, seismic retrofit and monitoring in Japan

Y. Fujino & D.M. Siringoringo
Bridge & Structure Lab., Department of Civil Engineering University of Tokyo, Japan

ABSTRACT: The paper describes three important issues on the long-span bridges, namely, vibration problem and control, seismic retrofit and vibration-based structural health monitoring. Specific studies on these topics are discussed based on recent experiences and practices in Japan.

1 INTRODUCTION

Dynamic performance is an important consideration in bridge designs especially the long-span ones. Various types of vibration from various sources of excitation such as wind, earthquake, vehicle movement, and human motion could occur during a lifetime of a long-span bridge. They can have several levels of consequence, from a potentially hazardous effect such as causing immediate structural failure; to a more subtle but have more extended effect such as structural fatigues. Vibration can also affect users' safety and comfort and limit bridge serviceability. Extensive research and development has been carried out to understand bridge vibration mechanisms. Some vibration mechanisms are now well understood and results of the research have been adopted in bridge design codes and put into practices by specifying methodologies and guidelines for countermeasures, or by introducing new structural elements or devices as vibration control.

Vibration problems are not only considered when designing new bridges but also when improving safety, durability and long-term performance of existing bridges. Seismic retrofit, for example is an important effort to improve seismic safety of existing bridges against foreseeable earthquakes in the future. Durability and long-term performance of existing bridges are also important issues nowadays and more efforts are now being devoted to enhance the implementation of technologies and methodologies for structural health monitoring (SHM) of bridges.

In this paper, we describe recent studies and developments on bridge vibration and control, seismic retrofit and vibration-based monitoring in Japan. We discuss specific cases involving the author and some important lessons from structural engineering viewpoints. New development, implementation of passive, and control of stay cable of the cable-stayed bridges in Japan are described. The paper also discusses case-studies on seismic retrofit of large bridges and vibration monitoring of long-span bridges under wind and seismic excitation.

2 VIBRATION AND CONTROL OF LONG-SPAN BRIDGES

2.1 *Wind-induced vibration and control of bridge structure*

Wind-induced vibration is the most critical among various types of dynamic excitation for long-span bridges. Type and level of vibration depend on bridge structural properties (i.e. mass, stiffness and damping), wind force condition and interaction between wind and bridge. The wind-induced vibration mechanisms on a bridge can be classified based on force excitation into four mechanisms: forced vibration, self-excited vibration, combination of forced and self-excited vibration and random vibration.

The bluff body of bridge components such as deck, pylon and cable immersed in a wind flow can move and create a motion that in turn affects the wind flow around the body. Vibration created by this interaction is known as the *self-excited* vibration and the resulted aerodynamic force is known as *motion-dependent* force. A phenomenon wherein structural motion and aerodynamic force interact significantly is called aeroelastic phenomenon. The aeroelastic phenomena commonly observed on long-span bridges are the galloping, torsional flutter, coupled flutter and vortex-induced vibration.

Long-span bridge girders are susceptible to torsional flutter. It is generally recognized now that the dramatic collapse of the Tacoma Narrows Bridge was due to torsional flutter. The weak torsional rigidity and aerodynamically unstable cross-section of the girder are two main factors responsible for the collapse. Since the Tacoma Narrows Bridge incident, flutter instability had become the most important issue in the design of long-span bridges. To avoid this instability

two different design approaches have been proposed; one is by streamlining the girder using box section that was promoted in UK such as Severn Bridge and Humber Bridge; and another one is using the truss-stiffened girder, which was promoted in the US, such as New Tacoma Narrows Bridge, Mackinac Bridge and Verrazano Narrows. Pressure difference between the girder upper and lower surface is considered as the main mechanism that induces flutter instability. To reduce such pressure difference, part of the deck floor can be made open using grating, or in case of box girder, by applying the central slot concept. For truss girder bridge, the use of vertical stabilizer and center barrier are effective to reduce the possibility of flutter instabilities. Such countermeasures are adopted in the Akashi-Kaikyo Bridge.

Vortex-induced vibration (VIV) is one of major issues in long-span bridge vibration. Although the vibration is self-limited and does not create divergent type of motion; maximum amplitude, fatigue problem and serviceability of the bridge associated with VIV are the main concern. VIV mainly occurs on bridge girder and pylon. VIV on cables of cable-supported bridge is also common; but the amplitude is usually small and can be suppressed completely by adding a small amount of damping. VIV on bridge deck is more serious and usually affects the girder vertical or torsional mode. Modern long-span bridges usually use box girder deck in the trapezoid form. This form has superior aerodynamic instability performance that is higher critical wind speed for flutter, but may suffer from VIV at low wind speed. Amplitude of VIV depends on wind turbulence, where larger turbulence intensity creates smaller vibration amplitude, shape of girder and structural damping.

A notable example of VIV problem in the girder of long-span bridge in Japan is the one that occurred on the Trans-Tokyo Bay Bridge (Fujino and Yoshida 2002). The Trans-Tokyo Bay Highway Crossing is a combination of tunnel and multiple bridge sea-crossing highways, completed in 1997, with total length of 11 km. The bridge section includes a ten-span continuous steel box-girder bridge with a total length of 1630 m. The two longest spans of this bridge are of 240 m. Significant vibration due to vortex shedding occurred under prevailing winds almost transverse to the bridge axis during construction stage. The vortex-induced first-mode vibration peaked at a wind velocity around 16–17 m/s, with maximum amplitude exceeding 50 cm (Figure 1).

Extensive wind tunnel testing using sectional models as well as three dimensional models had been conducted in the design stage and the VIV was indeed observed in the experiments. As countermeasures, 16 units of TMD were installed inside the box girder and aerodynamic flaps were added on deck side before opening the bridge to traffic. These countermeasures significantly reduced the vibration.

The VIV is also commonly observed on the long-span bridge pylons, especially during construction. During the free-standing construction period, the

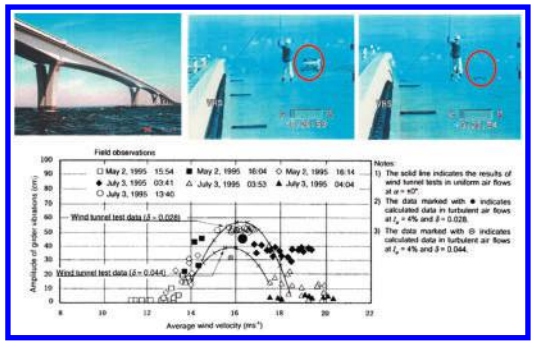
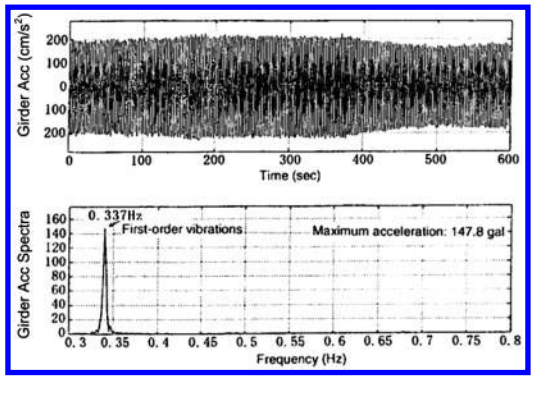


Figure 1. Observed 1st Mode Vortex-Induced Vibration at the Trans-Tokyo Bay Bridge. Note the disappearance of a car in the circle (After Fujino & Yoshida 2002).

pylons have low natural frequency and their bluff body would normally cause the out-of-plane VIV. Vibration could be excessive and obstruct the construction process, especially for pylons made of low-damped steel. Such vibration was observed during construction of Akashi-Kaikyo Bridge (Hata & Katsumi 1998), the Kurushima-Kaikyo Bridges (Suzuki et al. 1996). The excessive level of vibration obstructed construction process so that vibration control is required. Recently a unique in-line vortex combined with interference type of vibration has been observed on tower of Hakucho suspension bridge in Hokkaido Japan. Wind under certain velocity range and direction created vortices behind the windward tower leg and induced an in-line vibration on the leeward tower leg (Figure 2).

Two countermeasure strategies commonly employed are aerodynamic and mechanical counter measures. Aerodynamic countermeasures include cutting off the corners or making slits, and attaching the aerodynamic appendages such as deflectors or side-plates. Cutting the corner of bridge pylon reduces drag force and crosswind vibration at low wind speed. This approach was implemented in Higashi Kobe Bridge and Akashi-Kaikyo Bridge pylon. Mechanical countermeasures such as tuned mass damper (TMD), tuned liquid damper (TLD), tuned sloshing damper (TSD) and tuned liquid column damper (TLCD) (Fujino et al. 1992) are also commonly used in recent bridges in Japan. The first application of TMD scan be found



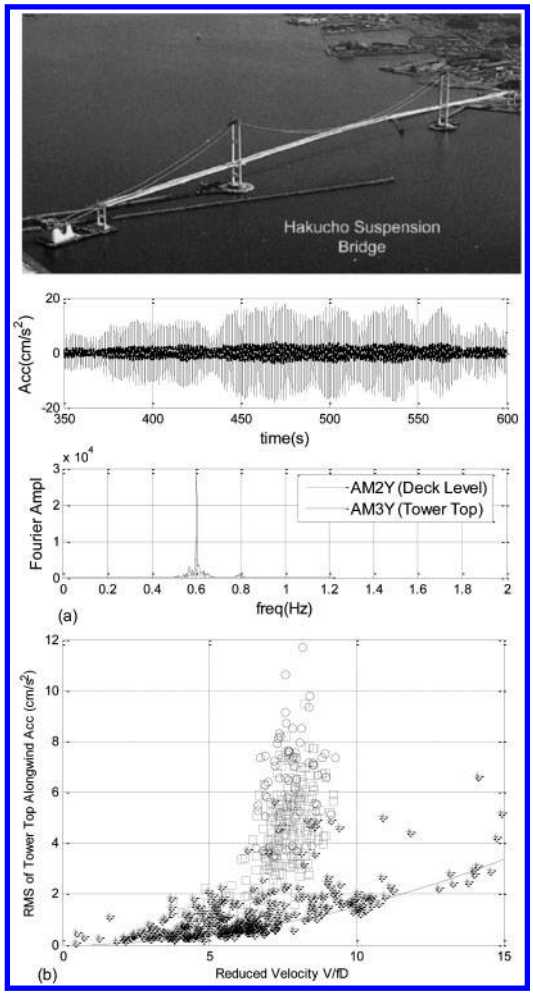


Figure 2. Hakucho Suspension Bridge and observed in-line VIV of the tower (After Siringoringo & Fujino 2012).

in the Meiko Bridge. TLD is used in Higashi Kobe Bridge and Toda Bridge. It should be noted that during construction, changes in pylon height lead to the changes in natural frequency, so that tuning frequency should be adjusted accordingly. This means several mass dampers of different natural frequencies should be prepared. To overcome this inefficiency, actively controlled mass dampers have been developed and this technology has been applied. One example of such application is the Hybrid-Mass Damper (HMD) used during construction of the Akashi-Kaikyo Bridge pylons (Fujino et al. 2012).

2.2 *Cable vibration and control*

Cables are essential component of long-span bridges and they are prone to vibrate because of their large flexibility, small mass and low mechanical damping. Main cable of suspension bridge, stay cables of cable-stayed bridge and hangers are generally very flexible

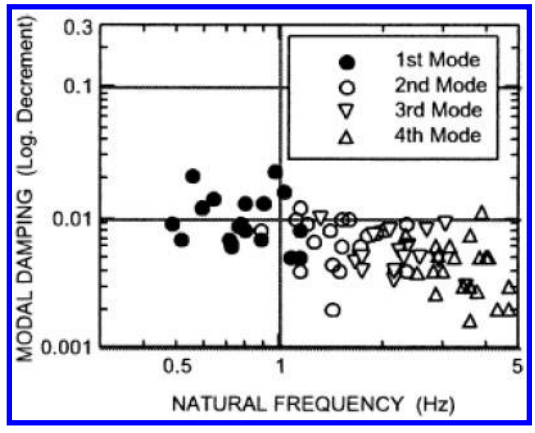


Figure 3. Relationship between modal damping and natural frequency of stay cable (After Yamaguchi & Fujino 1998).

compared to other bridge components, and therefore prone to vibrate. In long-span cable-stayed bridges, stay cable can be as long as 500 m, resulting in low natural frequencies of about 0.2–0.3 Hz in the lowest mode. A survey on inherent damping of stayed cables of cable-stayed bridges in Japan show that structural damping could reach as low as 0.1% critical damping ratio (Yamaguchi & Fujino 1998, Figure 3). Occurrences of large cable oscillation may cause damage to the anchorage and fatigue of the cable.

Vibration of objects caused by interference due to certain arrangements and proximities are very complex in nature. In the case of long-span cable-supported bridges, wake interference has been observed on the stay cables of cable-stayed bridge. It is observed in the range of $-2 < y/d < 2$ and $1 < x/d < 4$, where x and y denote the longitudinal and lateral spacing between cables, respectively and d is cable diameter (Matsumoto et al. 1989). The oscillation starts at the critical reduced velocity of around 40, which typically corresponds to the wind speed of 5–20 m/s, and generally produces an elliptical trajectory with the maximum amplitude of less than $3d$. The motion is known to be sensitive to the Scruton number (Sc), and becomes hardly recognizable at $Sc > 50$. Stay cables of Yobuko Bridge in Japan (Yoshimura 1992) and the parallel suspender cables of Akashi-Kaikyo Bridge (Furuya & Miyazaki 1998) were reported to have experienced the wake-flutter.

Rain-and-wind-induced (RWIV) cable vibration is probably the most well-known vibration problem of stay cable. It was firstly observed by Hikami on the stay-cables of the Meiko-Nishi Bridge in Japan (Hikami & Shiraishi 1998). The vibration occurs under certain wind velocity range but only during the raining condition. It occurs only on the inclined cables and the vibration amplitude on vertical plane is visible and can reach up to ten times cable diameter. The occurrence of RWIV was observed in many cable-stayed bridges around the world; such as Tempozan and Aratsu Bridge in Japan

Vibration with instability characteristics similar to RWIV has been reported on inclined stay-cables in tunnel tests during in dry (without rain) condition. It was shown that if the wind is in an oblique direction against the cable plane, the cable could have similar response characteristics as galloping instability. The instability phenomenon has been observed on several wind tunnel investigations and it appears to share the characteristics, namely, occurring on dry inclined cable at specific Reynolds number range and on the few specific geometrical cable positions. Dry galloping vibration would pose a very serious problem if it takes place as predicted in wind tunnel tests. However, unlike the RWIV, incident related to this type of cable motion has been rarely observed in real bridges. Perhaps a clear indication of dry galloping on stay cable was reported only recently in Japan (Matsumoto et al. 2005), where a 187 m length stay cable showed intense vibration with amplitude up to 1.5 m at the wind speed of 18 m/s.

In case of long-span cable-stayed bridge, natural frequency of the stay cables in local horizontal vibration (f_y) can be almost equal to the natural frequency of the girder global horizontal vibration (f_h), a condition that leads to the linear interaction known as parametric vibration. Since the cable is much lighter compared to girder and pylons, its vibration can develop easily in large amplitude so that the geometrical non-linearity of the cable cannot be ignored. This creates the *nonlinear interaction*. The linear internal resonance occurs when the natural frequency ratio of the local cable motion to the girder- or pylon-dominant global mode is 1:1. In the forced excitation experiment of cable-stayed bridges, cable local vibration is often excited and this is mostly due to the linear internal resonance. Mechanisms and estimation of the maximum amplitude of vibration interaction between pylon, girder and cables in the parametric and auto-parametric excitations are explained in the studies by Fujino et al. (1993).

Cable vibration can be controlled by aerodynamic, structural and mechanical countermeasures. For RWIV, the aerodynamic countermeasures aim at breaking up formation of the upper water rivulet on cable surface. This can be achieved by whirling helical wire on the cable surface, adding dimples to cable surface, or using axially protuberated surface (Figure 4). To suppress wake interference vibration, structural countermeasures by installing spacer and cable crossties between cables are commonly applied in an attempt to increase cable stiffness. This, however, may not be effective for very long cables.

Currently, mechanical countermeasure is the most widely used method. Main purpose of this approach is to increase cable damping by installing various types of dampers near the anchorage points or between cables. The relative motion between the cables and between cable and girder generate damping force. This method, however, has a limited performance and adequate damping force cannot be provided for extremely long stay cables. The damper has customarily been designed by neglecting several influencing factors; one

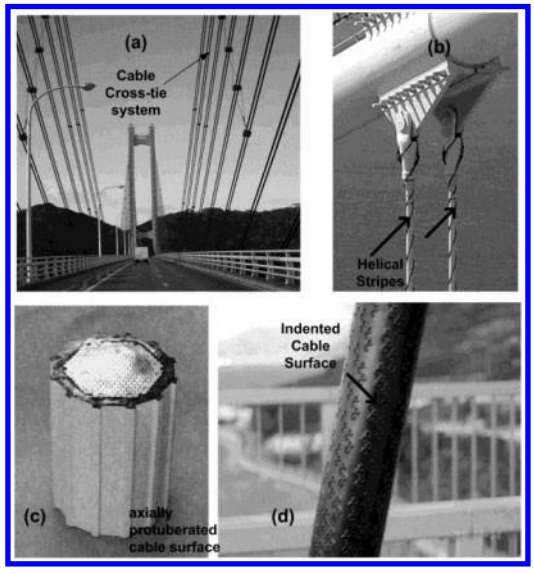


Figure 4. Aerodynamic countermeasures for cable vibration control at (a) Yobuko Bridge (Cross-tie), (b) Akashi-Kaikyo Bridge (Helical stripes), (c) Higashi-Kobe Bridge (axially protuberated surface) and (d) Tatara Bridge (indented surface).

of which is the cable flexural rigidity. It can be anticipated that the small flexural rigidity possessed by real cable systems affects performance of the damper since it is usually installed near the anchorage. As a result, additional damping given to the cable may not be as high as designed. Recent studies by author (Fujino & Hoang 2007, 2008) on the theoretical aspects have provided deeper understanding on the effects of sag, bending stiffness of cable and the flexibility of damper supports on the optimal performance of the dampers.

3 SEISMIC RETROFIT OF LARGE BRIDGES

Vibration problems are not only considered in the designing of new bridges but also when improving safety, durability and long-term performance of existing bridges. Seismic retrofit, for example, is an important effort to improve safety of existing bridges against foreseeable earthquakes in the future. In Japan, many bridges including the long-spanones were designed and constructed before the 1995 Hyogo-ken Nanbu (Kobe) Earthquake. Experience and lessons learned from the earthquake are very valuable and incorporated in the new seismic design code in 1997. According to the new code bridges must be designed for two levels of ground motions; one is a moderate ground motion with a return period of several tens year and the other is one for the maximum credible earthquakes with a return period of 500 to 2000 years. For the level 1 ground motion, the bridge is expected to receive no damage or very mild damage after the earthquake. For the level 2 ground motion, damage to

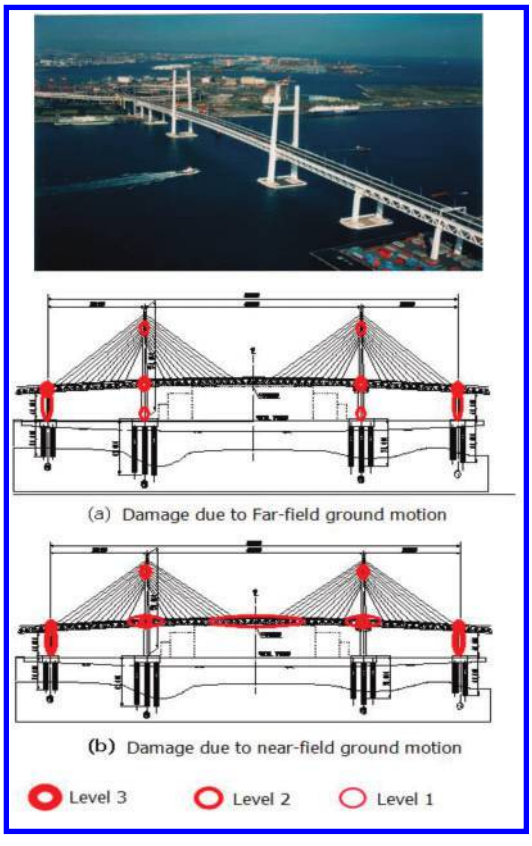


Figure 5. Yokohama-Bay Bridge. Several damage locations and levels due to simulated ground motions in retrofit program.

bridge after the earthquake is explicitly permitted, but functionality should be maintained after very severe ground motion.

Seismic performances for two levels of ground motions prescribed in new code must be evaluated and necessary retrofit strategies must be taken for existing bridges. Two case-studies on seismic retrofit of long-span bridges namely the Yokohama-Bay Bridge and Minato Truss Bridge are described in this section.

3.1 *Seismic retrofit of Yokohama-Bay Bridge*

Yokohama Bay Bridge (Figure 5), completed in 1988 is a double deck cable-stayed steel truss-box bridge with a central span of 460 m and two side spans of 200 m in length. It is located at the mouth of the Yokohama harbor. In 2005 a seismic retrofit program for safety assurance of level-2 earthquake according to Japan's bridge seismic code was conducted. The retrofit program considered two types of maximum credible earthquakes: magnitude 8 far-field or moderately far-field large earthquakes taking place in subduction zone of the Pacific plate with and near-field inland earthquake occurring beneath the site or close to the site.

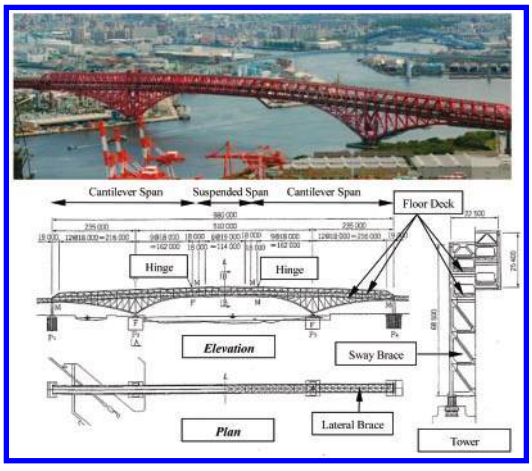


Figure 6. Minato Truss Bridge and its structural characteristics.

Based on seismological model, the ground motions were simulated assuming seven scenarios with fault geometry that resembles the 1923 Kanto Great earthquake (Fujino et al. 2008). Simulations identified potential damages for both types of ground motion and concluded that significant damage would occur on the towers and bearings under such excitations (Figure 5 (a),(b)). Furthermore, the far-field ground motion would create more damage and induce 1.5 m longitudinal displacement of the girder. Accordingly, a fail-safe design concept was introduced and the following strategies for major structural elements were implemented:

1) Providing adequate seating on the approach span to avoid unseating during a large earthquake.
2) Constructing additional cables connecting girder and end-piers in case that large transverse excitation damages the two link-bearing connections (LBC) at the end-piers.
3) Adding stiffeners inside the towers and piers to increase the ultimate strength and ductility in case a large longitudinal excitation damages the edge of steel frame.
4) Installing cable inside the lateral upper-beam near the top of tower to prevent the beam from falling in case of large deformation.
5) Providing additional seats on the lateral beam under the girder to prevent impact force from girder in case a large transverse excitation damages the tower links and stay cables near the towers.

3.2 *Seismic retrofit of Minato Truss Bridge*

The Minato Truss Bridge, completed in 1974 is located in Osaka, Japan. It is a 980 m-long cantilever-truss bridge and currently the third longest truss bridge in the world (Figure 6). Application of conventional retrofitting methods by strengthening the existing members is considered ineffective for this bridge for the concerns of low ductility, additional weight, large

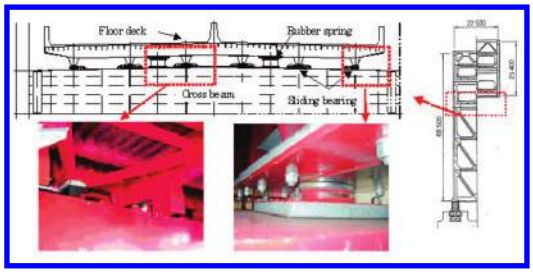


Figure 7. Floor deck seismic isolation system using sliding bearings (After).

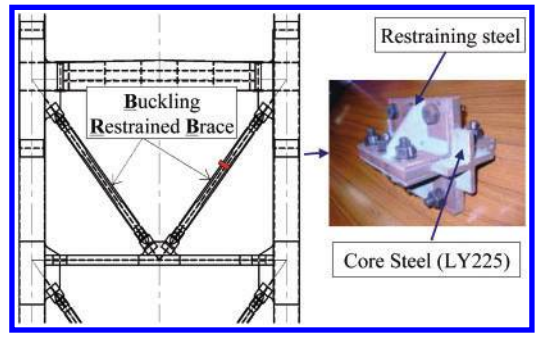


Figure 8. Buckling restrained brace (BRB) to give adequate damping to the entire bridge and also to avoid buckling. In transverse direction.

response force, working difficulties, and huge cost. Therefore it was decided to perform seismic retrofit by modifying and controlling seismic response (Kanaji et al. 2008).

Response spectrum analysis as well as time history analysis using the site-specific earthquake motions is carried out. Response spectrum analysis revealed that acceleration for the first mode in the longitudinal direction is larger than that of the original design acceleration, which implies that the 1st natural period should be shifted so that retrofit would be effective. On the other hand, the natural period of the 1st mode in the transverse direction is adequate, while for the 2nd mode the retrofit by increasing the damping would be effective.

Evaluation of *Demand/Capacity* ratio of each structural member under the site-specific prescribed ground motion is conducted. The results show that response in the longitudinal direction causes yielding ($R < -1.0$) or buckling ($R > 1.0$) in chord members located near the edges of side-spans, and around hinges between the cantilever span and the suspended span. On the other hand, the response in the transverse direction causes inelastic behavior in chord members located near the edges of the bridge, as well as, in lower chord members, diagonal or vertical members of the side-spans near the towers, and also in towers' diagonal members.

The retrofitting strategy applied herein considers the damage control concept in which damage is allowed only in sub members supporting lateral forces. These sub-members are expected to behave elasto-plastically and to generate adequate hysteretic damping. On the other hand, the main members supporting vertical forces such as dead load and live load should remain almost elastic.

To realize the retrofit concept, several strategies were examined using dynamic analysis. Among them, it was confirmed that floor deck isolation for the longitudinal direction (Figure 7) and buckling restrained braces (BRB) for the transverse direction (Figure 8) is the most effective way considering their cost. Parametric study for the floor isolation properties gives the relationship between the bearing displacement and the response ratio of chord member force and shows that the optimal combination of the vibration period, 3.0 secs and the friction coefficient, 0.05. BRBs of lower lateral braces and sway braces of towers are extremely effective to provide large damping. The test of the frame incorporating BRBs shows the stable hysteretic curve with the equivalent damping coefficients is 32%.

4 BASED STRUCTURAL HEALTH MONITORING OF LONG-SPAN BRIDGES

A large number of long-span bridges were constructed in Japan in the past decades. These bridges, especially the cable-supported ones, are expensive to inspect and maintain. They have long service periods of over 100 years, during which they inevitably suffer from environmental long-term loads effects such as fatigue, material deterioration and other extreme load effects. To this end, structural health monitoring (SHM) becomes important, and more concerted efforts are now being devoted to enhance our understanding in implementation of both monitoring technologies and methodologies.

Structural health monitoring using vibration data is recommended for global assessment of bridges. The system consists of bridge instrumentation, signal processing, data transmission and storage, and the most important part is data analysis and interpretation. Many large bridges such as long-span cable-supported bridges are now instrumented in Japan. Some of them are continually monitored using vibration response recorded from normal traffic, wind, typhoon and seismic responses (see examples of continuously monitored bridges in Tokyo metropolitan area Figure 9). The objectives of vibration-based SHM can be broadly categorized in two: environment and disaster prevention, and stock management.

Monitoring for seismic response has been widely employed especially for structures with special features such as long span bridges (Siringoringo & Fujino 2008a, 2008b), and bridges with new technology such as base-isolated bridges (Chaudhary et al. 2000). One example is dense monitoring system installed on the Yokohama-Bay Bridge (Figure 9a) (Siringoringo & Fujino 2006, 2008a). The study shows that by employing a system identification technique, dynamic characteristics of the bridge can be evaluated and global

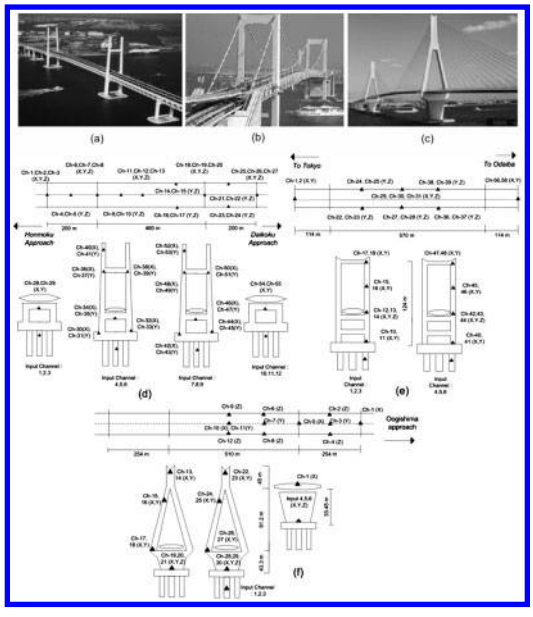


Figure 9. Three permanently instrumented long-span cable-supported bridges in Japan (a&d) Yokohama-Bay Bridge, (b&e) Rainbow Bridge, (c&f) Tsurumi-Tsubasa Bridge.

structural behavior under various levels of earthquake can be investigated. In addition to global behavior such as amplitude dependency of damping ratios, variations of local components were also observed. This variation was a result of non-linear response of link-bearing connection – a seismic isolation device between girder and tower.

Another popular method of monitoring of long-span bridges is ambient vibration measurement. Ambient vibration measurement uses loading from wind, waves, vehicular or pedestrian traffic or any combination of service loading. This offers economical advantage since it eliminates the need for loading testing devices and also does not re-quire the suspension of structure services during measurement. One of such analysis in conducted in Hakucho Suspension Bridge (Siringoringo & Fujino 2008). During ambient tests the bridge response was monitored by densely distributed vibration measurement system.

To estimate dynamic characteristics of the bridge system identification using random response is implemented. In this approach, dynamic signatures that have the characteristics of free vibration responses were extracted from random response. Using these dynamic signatures, effect of randomness and transient can be eliminated to obtain the dynamic characteristics such as natural frequencies, damping ratios and mode shape vectors. Important results of wind-induced monitoring are evaluation of influence of aerodynamic damping, bearing rotational stiffness on the girder vibration characteristics. It was found that the contribution of aerodynamic force was smaller than the effect of friction force from the bearing. These results are consistent with the expected increase in equivalent stiffness and decrease in damping when the amplitude level is small enough to suppress any relative movement at the bearing or extension devices (Nagayama et al. 2005).

5 CONCLUSIONS AND FUTURE CHALLENGES

Vibration mechanisms and control are critical factors in the design and construction of long-span bridges. In this paper, we present several studies on vibration mechanisms commonly observed for long-span bridges in Japan, especially cable-supported ones. Countermeasures against vibration problems have been developed based on the present understanding of vibration mechanisms. Performance improvement for these engineering countermeasures is still a subject for further study, especially for bridge with longer spans and taller pylons. One particular aspect of the countermeasures is the use of control technology for long-span bridge vibration problems. While passive control strategies have been widely applied, active control strategies have yet to reach a mature state to be directly applied to solve long-span bridge vibration problems, which provides both challenges and opportunities for bridge researchers and engineers in the future.

The recent advancement on computer technology has provided us with strong simulation tool to investigate vibration problems. Computational fluid dynamics (CFD) technique, for example, has been developed and used extensively as a supplement in recent years. Rapid development of CFD is expected to become a strong tool, although it may take some time to become a complete replacement for wind tunnel testing because of the high complexity of the geometry of the bridge section and the three-dimensional nature of the bridge.

For seismic-induced vibration analysis, the use of computer simulation and site-specific ground motions have improved our understanding on the behavior of bridge components under specific earthquakes, which is essential in the performance-based design and seismic retrofit of existing bridge.

We note also recent advancement in sensing and monitoring technologies applied in long-span bridges. Such monitoring systems have provided data that is useful for improving our understanding of bridge vibration problems. Furthermore, monitoring data will be essential for validation of structural model and providing feedback on the performance of current vibration countermeasures. Newly observed vibration phenomenon in authors' experience are the results of continuous monitoring of long-span bridges. One direction in bridge structural health monitoring is toward realizing a low-cost, smart, continuous and reliable monitoring system using wireless sensor network. The objective is to combine bridge engineering knowledge with developments in sensor technology and network/information management in order to provide a solution that is a robust and significantly lower-cost as an alternative to traditional wired monitoring systems.

REFERENCES

Chaudhary MTA, Abe M, Fujino Y, Yoshida J, (2000), System Identification of Two Base-Isolated Bridges Using Seismic Records, *J. of Struct. Eng. ASCE* , 126 (10), 1181–1194.

Fujino Y, Sun L, Pacheco BM and Chaiseri P, (1992), Tuned Liquid Damper (TLD) for suppressing horizontal motion of structures, *J Eng. Mechs ASCE*, 118(10), 2017–2030.

Fujino Y, (1990), Countermeasures of vibration of civil engineering structures (in Japanese). *J Wind Eng JAWE*, 44, 53–69.

Fujino Y, Pennung W, Pacheco B, (1993), An experimental and analytical study of autoparametric resonance in a 3DOF model of a cable-stayed-beam, *Nonlinear Dynamics*, 4, 111–138.

Fujino Y and Yoshida Y, (2002), Wind-induced vibration and control of Trans-Tokyo Bay Crossing Bridge, *J. Struct. Eng. ASCE.*, 128, 1012–1025.

Fujino Y, Kikkawa H, Namikawa K, Mizoguchi T, (2008), Seismic Retrofit Design of Long-Span Bridges on Metropolitan Expressways in Tokyo, Transportation Research Record: *Journal of the Transportation Research Board*, 335–342.

Fujino Y, Kimura K, Tanaka H, (2012). Wind Resistant Design of Bridges in Japan: Developments and Practices, 2012, Springer.

Fujino Y. and Hoang N. (2008), Design Formulas for Damping of a Stay Cable with a Damper, *J. Struc. Eng, ASCE*, 2008,134, 2: 269–278.

Furuya M, Miyazaki M. (1998), Wind induced vibration of parallel hangers in Akashi Kaikyo Bridge and its aerodynamic remedy. *Proc. 2nd Cable Dynamics Seminar*, Norway.

Hata K and Tatsumi M, (1998), Vibration control of the main towers of the Akashi Kaikyo Bridge. *Proc. IABSE symposium Kobe*, 57–62.

Hikami Y and Shiraishi N, (1998), Rain-and wind-induced vibration. *J. Wind Eng. and Ind. Aerodyn* 1988, 29, 409–418.

Hoang N and Fujino Y. (2007), Analytical Study on Bending Ef-fects in a Stay Cable with a Damper *J. Engrg. Mech ASCE.* 133(11), 1241–1246.

Kanaji H. Fujino Y. Watanabe E. (2008), Performance-Based Seismic Retrofit Design of a Long-Span Truss Bridge—Minato Bridge—Using New Control Technologies, Structural Engineering International Vol. 18(3), pp. 271–277.

Matsumoto M. Yokoyama K, Miyata T, Fujino Y and Yamaguchi H, (1989), Wind-induced Cable Vibration of Cable-Stayed Bridges in Japan, *Proc. Canada-Japan Workshop on Bridge Aerodynamics*, Ottawa, Canada.

Matsumoto M, Yagi T, Liu Q, Oishi T, Adachi Y, (2005), Effects of axial flow and Karman vortex interference on dry-state galloping of inclined stay-cables, *Proc. 6th Intl Symp Cable Dynamics*, 2005, 247–254.

Nagayama T, Abe M, Fujino Y, Ikeda K, (2005), Structural Identification of a Nonproportionally Damped System and Its Application to a Full-Scale Suspension Bridge, *Journal of Structural Engineering*, Vol. 131, No. 10: 1536–1545.

Siringoringo D.M and Fujino Y, (2006), Observed dynamic performance of the Yokohama-Bay Bridge from system identification using seismic records, *Journal of Structural Control and Health Monitoring*, Vol. 13(1), 226–244.

Siringoringo D.M and Fujino Y, (2008), System identification applied to instrumented long-span cable-supported bridges using seismic records, *Earthquake Engineering & Structural Dynamics,* Vol. 37, 361–386.

Siringoringo D.M and Fujino Y, (2008), System identification of suspension bridge form ambient response measurement, *Engineering Structures*, 30 (2), 462–477.

Siringoringo DM and Fujino Y, (2012), Observed Along-Wind Vibration of a Long-Span Suspension Bridge Tower, *J. Wind Eng Ind Aerodyn*., 103, 107–121.

Suzuki S, Sasaki M, Yamaguchi K, (1996), Countermeasures to suppress vibration of the towers in the Kurushima Kaikyo Bridge in the erection stage (in Japanese). *Honshi Technical Report BOEA* 1996, 20(80): 27–39.

Yamaguchi H and Fujino Y, (1998), Stayed cable dynamics and its vibration control. *In: Esdahl S (ed) Larsen A. Balkema, Bridge aerodynamics*, 1998, 235–253.

Yoshimura T, (1992), Aerodynamic Stability of Four Medium Span Bridges in Kyushu District, *J. Wind Eng Ind Aerodyn*. 41–42, 1203–1214.

Research and Applications in Structural Engineering, Mechanics and Computation – Zingoni (Ed.)
© 2013 Taylor & Francis Group, London, ISBN 978-1-138-00061-2

Local-distortional interaction in cold-formed steel columns: Non-linear behaviour, ultimate strength and DSM design

D. Camotim & P.B. Dinis
Civil Engineering Department, ICIST, Instituto Superior Técnico, Technical University of Lisbon, Portugal

B. Young
Department of Civil Engineering, The University of Hong Kong, Pokfulam Road, Hong Kong, China

N. Silvestre
Civil Engineering Department, ICIST, Instituto Superior Técnico, Technical University of Lisbon, Portugal

ABSTRACT: This paper provides an overview of the most recent research activity concerning the (i) non-linear behaviour (elastic and elastic-plastic), (ii) ultimate strength and (iii) Direct Strength Method (DSM) design of cold-formed steel columns experiencing local-distortional (L-D) interaction. After briefly introducing and illustrating this mode coupling phenomenon, both numerical (ABAQUS 4-node shell finite element analysis) and experimental results are presented, compared and discussed. The numerical investigation make it possible to characterise the L-D interactive behaviour and failure of columns with different cross-section shapes (lipped channels, hats, zeds and racks) and includes fairly extensive parametric studies, carried out in order to (i) assess how the relevance of the L-D interaction effects varies with the ratios between the competing (local and distortional) critical buckling stresses and the steel yield stress, and (ii) gather a substantial ultimate strength data bank. Then, the experimental tests, dealing with lipped-channel and rack-section columns, provides experimental (i) evidence of the occurrence of clear L-D interaction and (ii) failure loads and collapse mechanisms. Next, after showing the inadequacy of the current DSM local and distortional column strength curves to predict L-D interactive failures, the paper presents and assesses the merits of recently developed DSM-based design procedures against such interactive column failures. Finally, the paper closes with some concluding remarks and a few comments on developments planned for the near-to-intermediate future.

1 INTRODUCTION

Most cold-formed steel members display very slender thin-walled open cross-sections, making them highly susceptible to instability phenomena involving cross-section in-plane deformations: local (L) and distortional (D) buckling. Moreover, since commonly used members exhibit cross-section geometries (shape and dimensions) that may be associated with close local and distortional critical buckling stresses, their post-buckling behaviour (elastic or elastic-plastic), ultimate strength and failure mode are bound to be heavily affected by the coupling between these two buckling modes.

A fair amount of research has been recently devoted to L-D interaction, involving mostly lipped channel columns and consisting of numerical simulations, experimental investigations and design proposals (e.g., Yang & Hancock 2004, Yap & Hancock 2011, Kwon *et al* 2009). The aim of this paper is to present a unified overview of the authors' recent research on the (i) non-linear behaviour (elastic and elastic-plastic), (ii) ultimate strength and (iii) Direct Strength Method (DSM – Schafer 2008) design of cold-formed steel columns affected by L-D interaction – this is part of an ongoing investigation on coupled instabilities involving distortional buckling (e.g., Camotim & Dinis 2011). Both numerical and experimental research was carried out, concerning pin-ended and fixed-ended columns with various geometries ensuring close L and D critical buckling stresses. The numerical simulations, carried out at the Technical University of Lisbon, employed ABAQUS shell finite element analyses (SFEA) and dealt with the elastic and elastic-plastic non-linear behaviour and strength of lipped channel (C), hat (H), zed (Z) and rack-section (R) columns. They involved the identification of key mechanical features concerning the member response, such as the most detrimental initial imperfection shapes and elastic-plastic failure modes (Dinis *et al* 2007, 2013a). These findings were then included in extensive parametric studies aimed at determining failure loads of imperfect columns with various geometries, support conditions and yield stresses (covering wide slenderness ranges). The experimental investigation, performed at The University of Hong Kong, clear evidenced the occurrence of L-D interaction in C (Young *et al* 2013) and R (Dinis *et al* 2012a) fixed-ended columns and provided the failure loads of the tested specimens. The numerical and experimental ultimate strength "data bank" gathered was the starting point to develop and validate DSM-based approaches to predict failure loads of columns influenced by L-D interaction (Silvestre *et al* 2009, 2012, Dinis *et al*

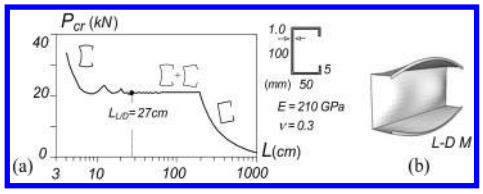


Figure 1. (a) Column critical buckling curve and (b) "combined" L-D buckling mode shape – $L_{L\text{-}D} = 27$ cm column.

2013a, Young *et al* 2013). This paper aims at providing an overview of the above research effort, namely the numerical simulations, experimental studies and quest for an efficient DSM design against L-D interactive failures.

2 NUMERICAL SIMULATIONS

Following a brief presentation of the most relevant issues concerning the buckling, post-buckling and strength behaviour of columns with $P_{crL}/P_{crD} = 1.0$, the performance of parametric studies, intended to gather a extensive failure load data bank involving mostly fixed-ended columns under strong L-D interaction and covering a wide slenderness range, is addressed. The numerical simulations were carried out by means of ABAQUS SFEA, using an existing model: (i) columns discretised into fine 4-node isoparametric element meshes (length-to-width ratio ≈1.0), (ii) fixed-ended conditions modelled by attaching rigid plates to the column end sections and (iii) steel material behaviour described by Prandtl-Reuss's elastic-perfectly model – details to be found in Dinis *et al*. (2007, 2013a).

2.1 *Buckling behaviour*

The column geometry (cross-section dimensions, length) selection, ensuring different levels of L-D interaction, was made by trial-and-error buckling analysis sequences. Figure 1 illustrates this procedure for a simply supported C column: while Figure 1(a) provides the P_{cr} vs. L (logarithmic scale) curve, Figure 1(b) shows the "combined" L-D buckling mode shape of the selected $L_{L\text{-}D}$ column ($P_{cr.L\text{-}D} = 21.1$ kN): 3 local and 1 distortional half-waves.

2.2 *Initial geometrical imperfections*

The initial geometrical imperfection shape plays a crucial role in mode interaction investigations, as its choice may alter considerably the column post-buckling behaviour and strength. Therefore, it is necessary to study the post-buckling behaviour of members with various critical-mode initial shapes, combining arbitrarily the competing L and D buckling modes and sharing the same amplitude (Dinis *et al* 2007) – the outcome of this study is the most detrimental imperfection shape (lowest column strength). Figure 2 illustrates the methodology adopted, for the $L_{L\text{-}D}$ column in section 2.1. The initial shapes are linear combinations of 3 half-wave local and 1 half-wave distortional buckling modes, normalised to exhibit amplitudes equal to 10% of the wall thickness t (0.1 mm). The coefficients $C_{L.0}$ and $C_{D.0}$ satisfy $(C_{L.0})^2 + (C_{D.0})^2 = 1$

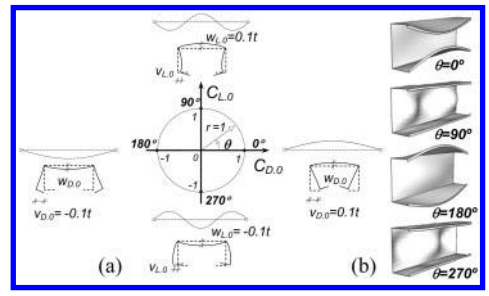


Figure 2. (a) Initial imperfection representation in the $C_{L.0}-C_{D.0}$ plane and (b) $\theta = 0°$, 90°, 180° and 270° column initial imperfection shapes.

and the initial imperfection is defined by an angle θ, such that $C_{L.0} = \sin\theta$ and $D_{D.0} = \cos\theta$ in Figure 2(a). Figure 2(b) shows the pure L ($\theta = 90°$ or 270° – inward-outward mid-span web bending) and D ($\theta = 0°$ or 180° – inward-outward mid-span flange-stiffener motion) initial imperfections.

2.3 *Post-buckling behaviour*

The influence of L-D interaction on the column elastic and elastic-plastic post-buckling behaviour is shown through the previous C $L_{L\text{-}D}$ column, with (i) 8 initial imperfection shapes ($\theta = 0°$, 45°, 90°, 135°, 180°, 225°, 270°, 315°) and (ii) 4 yield-to-critical stress ratios ($f_y/f_{cr} \approx 1.2$, 2.0, 3.5, $\infty - f_y = 120$, 200, 355 MPa and elastic behaviour). Figure 3(a) shows, for $P/P_{cr} > 0.6$, the P/P_{cr} *vs.* v/t elastic equilibrium paths (v: mid-span flange-lip corner vertical displacement) of the $\theta = 0°$, 180° and $\theta = 90°$, 270° columns (pure distortional and local imperfections). Figure 3(b) shows the evolution, along the equilibrium paths, of the mode coupling ratio C_L/C_D (for all columns). The following conclusions can be drawn from these results:

(i) All equilibrium paths merge into 2 common curves, associated with inward or outward flange-lip motions – the initial imperfection shape determines which curve is joined by a given equilibrium path.

(ii) The two straight lines in Figure 3(b), with slightly different slopes ($C_L \approx -0.34C_D$ and $C_L \approx -0.25C_D$, for outward and inward flange-lip motions), define the coupled buckling modes, combining distortional and local deformations (opposite mid-span web flexure).

(iii) The pure distortional outward imperfections ($\theta = 180°$) are the most *detrimental*, as they lead to the lowest strength. Similar studies involving H and R columns showed that the $\theta = 0°$ imperfections (inward mid-span flange-lip motions) are the most detrimental (Dinis *et al* 2013a) – in Z columns, both the $\theta = 0°$ and $\theta = 180°$ imperfections are equally detrimental (the associated post-buckling behaviours are identical).

In order to illustrate the elastic-plastic post-buckling behaviour and strength of columns experiencing strong L-D interaction, Figure 4(a) shows the upper portions ($P/P_{cr} > 0.6$) of the P/P_{cr} *vs.* v/t paths concerning the previous C $L_{L\text{-}D}$ columns with (i) $\theta = 180°$ imperfections and (ii) three yield-to-critical

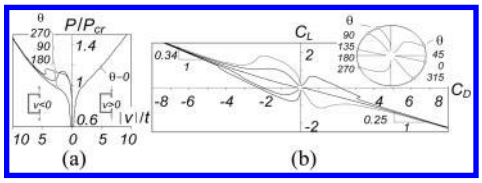


Figure 3. (a) Column critical buckling curve and (b) "combined" L-D buckling mode shape – $L_{L\text{-}D} = 27$ cm column.

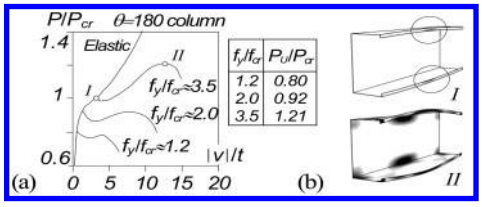


Figure 4. (a) Elastic-plastic P/P_{cr} *vs.* v/t paths ($\theta = 180° + f_y/f_{cr} \approx 1.2; 2.0; 3.5; \infty$) and (b) configurations and plastic strains ($\theta = 180° + f_y/f_{cr} \approx 3.5$).

stress ratios: $f_y/f_{cr} \approx 1.2; 2.0; 3.5$. Figure 4(b) concerns the $f_y/f_{cr} \approx 3.5$ column and displays the plastic strain diagrams at the equilibrium states shown on the equilibrium path (including the failure mode). This investigation led to the following conclusions:

(i) The nature and characteristics of the column elastic-plastic post-buckling behaviours and failure mode clearly depend on the f_y/f_{cr} value.

(ii) For f_y/f_{cr} close to 1.0 (e.g., $f_y/f_{cr} \approx 1.2$), yielding starts when the normal stresses are still fairly uniform and, therefore, precipitates a rather abrupt collapse.

(iii) For higher f_y/f_{cr} values (e.g., $f_y/f_{cr} = 3.5$), yielding starts when the normal stresses are already heavily non-uniform and, thus, collapse is not immediate (it only occurs after a mild snap-through phenomenon, followed by a further strength increase up to a limit point). The elastic-plastic strength reserve increases with f_y/f_{cr}, but the erosion due to L-D interaction is considerable (e.g., for $f_y/f_{cr} \approx 1.2; 2.0; 3.5$, the column ultimate load ratios are $P_U/P_{cr} = 0.80; 0.92; 1.21$).

(iv) Plasticity appears first at the mid-span section lip free ends and failure occurs after the full yielding of the column central zones located around the web-flange corners (see Fig. 5(b)).

2.4 *Parametric studies – failure load data*

ABAQUS SFEA parametric studies were performed to obtain numerical failure loads of imperfect C, H, Z and R columns with geometries leading to strong L-D interaction (Silvestre *et al* 2009, 2012, Dinis *et al* 2013a). These data were then used to (i) assess the merits of the current DSM design curves in predicting L-D interactive failures and (ii) to guide/validate the search for DSM-based design approaches able to capture this interaction.

The column cross-section geometries were selected to control the closeness between the critical buckling loads P_{crL} and P_{crD}. This was achieved by slightly altering a dimension of previously identified "base cross-sections" with identical P_{crL} and P_{crD} (see Fig. 2). This procedure led to several columns with close (but not coincident) P_{crL} and P_{crD} – the changes ensured $0.9 \leq P_{crL}/P_{crD} \leq 1.1$. Furthermore, to cover a wide distortional slenderness $\lambda = (f_y/f_{crD})^{0.5}$ range, various yield stresses were considered for each column. Failure loads of (i) 111 pin-ended C columns, (ii) 210 fixed-ended C, H and Z column triplets, and (iii) 234 fixed-ended R columns were obtained.

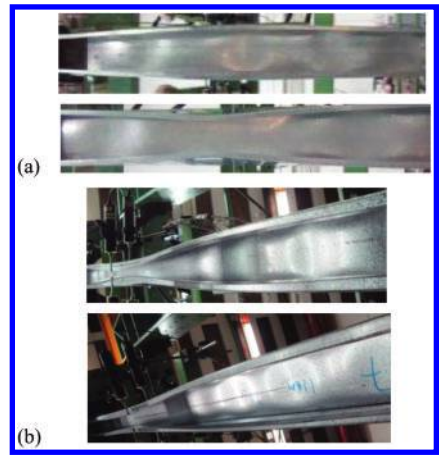


Figure 5. Experimental evidence of the occurrence of L-D interaction in the UHK (a) lipped channel and (b) rack-section column tests.

3 EXPERIMENTAL INVESTIGATIONS

Concerning C, H, Z and R columns, the occurrence of L-D interaction and ensuing ultimate strength erosion had only been experimentally observed by Kwon *et al* (2009) at Yeungnam University (YU – 6 C column tests) – note however, that these authors, and also Yang & Hancock (2004) and Yap & Hancock (2011) from the University of Sydney, reported experimental evidence on L-D interaction in web and/or flange-stiffened lipped channel columns (outside the scope of this study). Thus, it was decided to perform an experimental investigation at The University of Hong Kong (UHK), involving (i) 16 fixed-ended C (Young *et al* 2013) and (ii) 10 fixed-ended R (Dinis *et al* 2012a) columns with geometries selected to ensure strong L-D interaction. Although the specimens tested at YU and UHK showed sheer evidence of L-D interaction (see Fig. 5(a)–(b)), it was subsequently found that their P_{crL} and P_{crD} values were not that close (clearly not in the $0.9 \leq P_{crD}/f_{crL} \leq 1.1$ interval). Indeed, numerical calculations, based on the actual/measured specimen geometries (different from the requested ones) showed that local buckling always preceded distortional buckling – the P_{crD}/P_{crL} ratio varied from 1.34 to 3.23 (YU Cs), 1.73 to 2.71 (UHK Cs) and 1.31 to 1.46 (UHK Rs).

In order to explain this somewhat surprising feature, Figures 6(a)–(b) display the elastic equilibrium paths and four cross-section buckled configurations of C columns with P_{crD}/P_{crL} equal to 1.05 (Fig. 6(a)) and 1.4 (Fig. 6(b)): while the former concerns a "true interaction" (L-D coupling starts at the early loading stages),

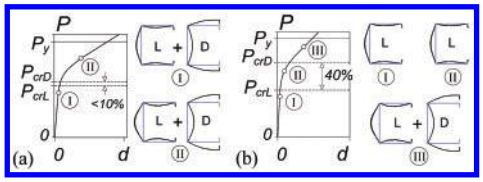


Figure 6. *P vs. d* equilibrium paths and cross-section buckled shapes for lipped channel columns with P_{crD}/P_{crL} equal to (a) 1.05 and (b) 1.4.

Table 1. UHK test programme: specimen dimensions, yield stresses, critical and yield-to-critical load ratios, and failure loads.

Sp.	b_w (mm)	b_f (mm)	b_s (mm)	b_l (mm)	L (mm)	t* (mm)	f_y (MPa)	$\frac{P_{crD}}{P_{crL}}$	$\frac{P_y}{P_{crD}}$	P_U (kN)
C1	104.9	81.6	15.2	–	2498	0.962	523	1.80	3.52	39.9
C2	101.8	82.1	15.5	–	2499	0.984	536	1.73	3.44	42.1
C3	94.9	80.9	16.9	–	2499	0.978	536	1.80	2.97	42.0
C4	152.5	131.2	14.7	–	1425	1.227	588	1.73	5.58	68.1
C5	152.4	131.0	15.8	–	1426	1.227	588	1.92	5.03	71.0
C6	154.5	141.0	15.0	–	1426	1.206	588	1.76	6.10	67.7
C7	110.5	82.2	16.1	–	1148	1.459	494	1.84	1.53	109.0
C8	118.5	82.0	15.7	–	1149	1.453	494	1.97	1.63	102.8
C9	118.6	81.9	15.9	–	1148	1.469	494	1.98	1.59	103.6
C10	203.7	192.7	19.0	–	1852	1.478	494	1.83	5.99	92.9
C11	204.7	191.9	20.6	–	1849	1.459	494	2.14	5.22	94.7
C12	182.1	113.1	19.2	–	1030	1.934	336	2.46	1.20	145.2
C13	181.1	112.5	20.2	–	1026	1.915	336	2.71	1.09	146.1
C14	182.5	122.5	19.4	–	1027	1.974	336	2.34	1.23	142.5
C15	238.9	162.7	21.1	–	1946	1.966	336	2.00	2.53	129.7
C16	238.2	162.3	23.1	–	1947	1.947	336	2.24	2.28	131.6
R1	73.0	37.1	17.3	21.3	1300	1.002	550	1.37	1.91	58.2
R2	78.4	47.4	17.2	21.0	1800	0.998	550	1.35	2.30	54.4
R3	83.6	52.3	17.1	20.4	2100	0.982	550	1.46	2.49	54.3
R4	88.6	57.2	17.2	21.3	2499	0.999	550	1.40	2.83	51.4
R5	88.6	57.2	17.5	21.4	2500	0.981	550	1.45	2.85	51.0
R6	83.5	52.5	17.3	21.6	1397	1.193	500	1.31	1.81	81.6
R7	88.5	57.9	17.7	21.0	1599	1.186	500	1.38	1.95	79.8
R8	93.7	67.3	17.4	20.8	1902	1.227	500	1.31	2.20	79.8
R9	98.7	72.2	17.0	21.0	2501	1.201	500	1.32	2.54	75.5
R10	98.8	72.2	17.2	20.8	2501	1.175	500	1.36	2.57	74.3

the latter deals with a "secondary bifurcation" – L-D interaction only starts close to the distortional buckling load level and it will cause ultimate strength erosion provided that the squash load P_y is "high enough" ($P_y > P_{crD}$) to allow for it – all the YU and UHK tests fell into this category.

3.1 *The University of Hong Kong test programme*

The UHK test programme is briefly addressed in this sub-section – more details in Young *et al* (2013) and Dinis *et al* (2012a). It comprised 16 C and 10 R fixed-ended cold-formed steel specimens brake-pressed from high strength and mild steel zinc-coated structural steel sheets – the zinc coating was removed by acid etching. Table 1 provides the various specimen geometries, yield stresses, P_{crD}/P_{crL} and P_y/P_{crD} ratios, and failure loads P_U. The specimens were cut to specified lengths, ranging from (i) 1026 to 2500 mm (Cs) and (ii) 1300 to 2500 mm (Rs), and their ends were milled flat electronically and welded to 25 mm thick steel plates, ensuring full contact with the test machine end bearings and contributing to achieve fully fixed end supports.

The specimen material properties were obtained by means of tensile coupon tests. Moreover, initial geometrical imperfection measurements were made at the column mid-height cross-section prior to testing, providing information on the local and distortional imperfections ("combined" with torsional rotation and minor-axis flexural information, in the case of the R column tests).

A servo-controlled hydraulic testing machine was used to apply the compressive axial force to the column specimen (with steel plates welded to their ends), whose top end plate was bolted to its bearing plate, which was restrained against warping, twist and major and/or minor axis flexural rotations – this setting may be said to correspond to a fully fixed-ended support condition. A data acquisition system recorded the readings of the applied load cell and displacement transducers (located at the top and mid-span cross-sections) at regular intervals during the tests.

All the C and R specimens failed in local-distortional interactive modes – Figures 5(a)–(b) show the deformed configurations near collapse of two C (Fig. 5(a)) and two R (Fig. 5(b)) specimens, exhibiting a very clear combination of local and distortional deformations. As mentioned earlier, these L-D interaction effects do not stem from the closeness of P_{crL} and P_{crD} – instead, the interaction takes place because $P_{cr.L} < P_{cr.D}$ and P_y is sufficiently larger than $P_{crD.}$: the $P_y/P_{cr.D}$ ratio varies from (i) 1.09 to 6.01 (Cs) and (ii) 1.83 to 2.88 (Rs).

4 DIRECT STRENGTH METHOD (DSM) DESIGN

The current DSM column strength curves are defined by "Winter-type" expressions that (i) were calibrated against fairly large numbers of experimental and/or numerical failure loads and (ii) predict efficiently the ultimate loads of columns failing in local (f_{NL}), distortional (f_{ND}), global (f_{NE}) and local-global (f_{NLE}) interactive modes, on the sole basis of yield and elastic buckling stresses – the expressions providing the above DSM nominal strengths can be found in Schafer (2008).

4.1 *L-D interaction – $P_{crL} \approx P_{crD}$*

Two distinct (but similar) DSM strategies to estimate the failure loads of columns experiencing L-D interaction were originally proposed by Schafer (2002): replace f_y either (i) by f_{ND} in the f_{NL} equations (NLD approach – f_{NLD}) or (ii) by f_{NL} in the f_{ND} equations (NDL approach – f_{NDL}). Then, the nominal strength against L-D interactive failure can be estimated by the equations

$$f_{NLD} = \begin{cases} f_{ND} & \text{if} \quad \lambda_{LD} \le 0.776 \\ f_{ND}\left(\frac{f_{crL}}{f_{ND}}\right)^{0.4}\left[1-0.15\left(\frac{f_{crD}}{f_{ND}}\right)^{0.4}\right] & \text{if} \quad \lambda_{LD} > 0.776 \end{cases}, \tag{1}$$

$$f_{NDL} = \begin{cases} f_{NL} & \text{if} \quad \lambda_{DL} \le 0.561 \\ f_{NL}\left(\frac{f_{crD}}{f_{NL}}\right)^{0.6}\left[1-0.25\left(\frac{f_{crD}}{f_{NL}}\right)^{0.6}\right] & \text{if} \quad \lambda_{DL} > 0.561 \end{cases}, \tag{2}$$

where $\lambda_{LD} = (f_{ND}/f_{crL})^{0.5}$ and $\lambda_{DL} = (f_{NL}/f_{crD})^{0.5}$ – local-distortional and distortional-local slenderness.

Later, Silvestre *et al.* (2009) used numerical failure load data to assess the performance of these two approaches for C columns and concluded that they provide similar predictions, even if the quality of the f_{NDL} estimates was marginally higher. Moreover, these authors showed that (i) regardless of the column end support conditions, the f_{ND} values predict the ultimate strength quite accurately in the low-to-moderate distortional slenderness range ($\lambda_D < 1.5$), but perform much worse for the more slender columns ($\lambda_D \geq 1.5$), and (ii) the f_{NDL} values only provide reasonably accurate failure load predictions for simply supported columns with moderate-to-high distortional slenderness ($1.4 \leq \lambda_D \leq 2.6$). Then, Silvestre *et al* (2012) went a step further and, on the basis of a larger numerical failure data bank, proposed a novel DSM approach for fixed-ended C columns: the NL-D approach – $f_{NL\text{-}D}$. It adopts the current DSM distortional strength curve for $\lambda_D < 1.5$ (i.e., $f_{NL\text{-}D} = f_{ND}$ – no relevant L-D interaction) and, for $\lambda_D \geq 1.5$, proposes a modified local strength f_{NL}^*, which (i) depends on the critical half-wave length ratio L_{crD}/L_{crL} (obtained from simply supported column signature curves), and (ii) provides ultimate strength estimates by replacing f_{NL} with f_{NL}^* in the NDL equations (2) – the f_{NL}^* values are given by the expressions

$$f_{NL}^* = \begin{cases} f_y & \text{if} \quad \frac{L_{crD}}{L_{crL}} \leq 4 \\ f_y + \left(1 - 0.25\frac{L_{crD}}{L_{crL}}\right)\left(f_y - f_{NL}\right) & \text{if} \quad 4 < \frac{L_{crD}}{L_{crL}} < 8 \\ f_{NL} & \text{if} \quad \frac{L_{crD}}{L_{crL}} \geq 8 \end{cases} . \qquad (3)$$

Note that these equations lead to the f_{ND} and f_{NDL} values for $L_{crD}/L_{crL} \leq 4$ and $L_{crD}/L_{crL} \geq 8$, respectively.

The above findings were very recently extended to columns with other cross-section shapes, in order to assess their generality and pave the way for the codification of a DSM-based design approach for columns undergoing L-D interaction. The authors (Dinis *et al.* 2013a) performed numerical simulations on (i) H and Z columns with cross-section dimensions equal to those exhibited by the C columns analysed previously (which implies the same local and distortional critical buckling loads), and (ii) R columns. It was found that (i) the C, H and Z column triplets behave quite similarly, and (ii) the L-D interactive failure loads of the four column sets exhibit similar f_U/f_y distributions/"clouds" – see Figures 7(a)–(d), which also show the DSM strength curves providing the f_{NL}/f_y, f_{ND}/f_y and f_{NDL}/f_y values (assuming $f_{crL} = f_{crD}$).

It may then be concluded that the $f_{NL\text{-}D}$ DSM design approach developed by Silvestre *et al.* (2012), in the context of C columns, predicts the L-D interactive failure loads of C, H, Z and R columns with equal efficiency. Its merits can be assessed in Figures 8(a)–(b), providing the variation of f_U/f_{NDL} (Fig. 8(a)) and $f_U/f_{NL\text{-}D}$ (Fig. 8(b)) with λ_D for the four column sets. It is clearly shown that the novel $f_{NL\text{-}D}$ failure load predictions exhibit higher quality than the f_{NDL} ones – the associated ultimate-to-predicted load ratios have an average closer to 1.0 (1.05 *vs.* 1.25), a smaller standard deviation (0.07 *vs.* 0.16) and a lower maximum value (1.26 *vs.* 1.81), with an expected "trade-off": higher underestimations (minimum 0.84 *vs.* 0.96).

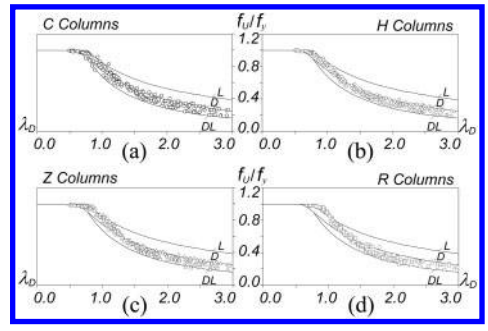


Figure 7. f_U/f_y *vs.* λ_D for the (a) C, (b) H, (c) Z and (d) R columns.

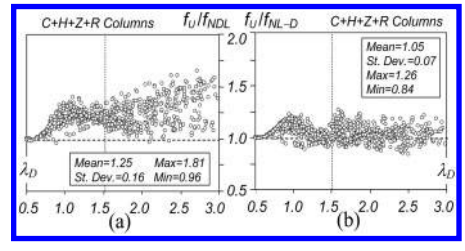


Figure 8. Variation of (a) f_U/f_{NDL} and (b) $f_U/f_{NL\text{-}D}$ with λ_D for the C, H, Z and R columns.

4.2 *L-D interaction* – $P_{crL} < P_{crD}$

As mentioned in section 3, it was found that all the available C, H, Z and R column experimental failure load data (Kwon et *al* 2009, Young *et al* 2013 and Dinis *et al* 2012a) concerns specimen geometries for which (i) P_{crL} always precedes P_{crD} by a substantial amount and (ii) P_y is almost always considerably larger than P_{crD} – the exceptions are a few test with $P_y/P_{cr.D}$ values close to 1.10. Since no numerical failure loads were obtained for columns exhibiting these mechanical characteristics, unveiled by the experimental investigations, it is not possible to assess adequately the merits of the novel DSM approach presented in the previous sub-section – this will be done in the near future, after concluding an ongoing investigation on the relevance of L-D interaction with respect to the P_{crD}/P_{crL} ratio (Dinis *et al* 2013b). Therefore, the available experimental failure loads are compared with their estimates provided by the DSM design approach proposed by Young *et al* (2013) on the basis of the YU and UHK fixed-ended lipped channel column tests – they suggested that, regardless of the closeness between P_{crD} and P_{crL}, the fixed-ended column ultimate strength can be fairly well predicted by the f_{NLD} estimates obtained from Eq. (1) and that had already been used by Yang & Hancock (2004), Kwon *et al* (2009) and Yap & Hancock (2011) to predict failure loads of lipped channel columns with web and/or flange intermediate stiffeners.

Figure 9(a) shows that (i) the C and R column sets exhibit similar f_U/f_y value distributions/"clouds", particularly for $\lambda_D > 1.0$, and (ii) all the experimental failure loads test ultimate loads are clearly below the DSM distortional strength curve, thus confirming

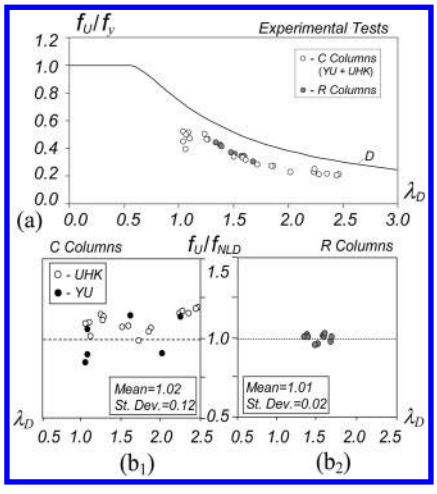


Figure 9. Variation with λ_D of the experimental (a) f_U/f_y values (C and R columns), and (b) f_U/f_{NLD} values for the (b_1) C and (b_2) R columns.

the ultimate strength erosion due to L-D interaction. The merits of the proposed DSM approach, which provides lower estimates that the $f_{NL\text{-}D}$ values defined in sub-section 4.1, can be assessed by looking at Figures 9(b), showing the variation of f_U/f_{NLD} with λ_D for the C (Fig. 9(b_1)) and R columns (Fig. 9(b_2)) – also given are the associated averages and standard deviations. These results make it possible to conclude that f_{NLD} provides mostly safe and accurate failure load estimates (higher overestimations for 3 YU tests): f_U/f_{NLD} averages and standard deviations of 1.01–0.02 (Rs) and 1.02–0.12 (Cs: 1.10–0.06 and 0.94–0.11 for the UHK and YU tests, respectively).

5 CONCLUDING REMARKS

The paper provided an overview of the most recent research activity on the non-linear behaviour, ultimate strength and DSM design of cold-formed steel columns with four cross-section shapes and experiencing L-D interaction. After illustrating this coupling phenomenon and providing its mechanical characterisation, numerical and experimental results were presented, compared and discussed – in particular, two types of L-D interaction were identified, corresponding to P_{crD}/P_{crL} values close to and clearly above 1.0, respectively. Next, after showing the inadequacy of the current DSM local and distortional strength curves to predict column L-D interactive failures, the paper presented and assessed the merits of recently developed DSM-based design procedures against such failures. The first one, more accurate and intended for columns with P_{crD}/P_{crL} close to 1.0, was compared against extensive numerical failure load data. The merits of the second one, less accurate (more conservative) and intended for columns with P_{crD}/P_{crL} above 1.0.

Research planned for the near future includes (i) continuing the work of Dinis *et al* (2013b), by further assessing how the relevance of L-D interaction varies with the P_{crD}/P_{crL} ratio, as well as its impact on the DSM design, and (ii) investigating L-D interaction in lipped channel columns with web and/or flange intermediate stiffeners, particularly when local buckling is triggered by the flanges, following the very recent numerical and experimental studies carried out by Dinis *et al* (2012b) and taking advantage of the available test results, which have been reported by Yang & Hancock (2004), Kwon *et al* (2009) and Yap & Hancock (2011).

REFERENCES

Camotim D & Dinis PB 2011. Coupled instabilities with distortional buckling in cold-formed steel lipped channel columns. *Thin-Walled Structures*, 49(5): 562–575.

Dinis PB & Camotim D 2013a. Cold-formed steel columns undergoing local-distortional coupling: behaviour and direct strength prediction against interactive failure. *Submitted for publication*.

Dinis PB, Camotim D & Silvestre N 2007. FEM-based analysis of the local-plate/distortional mode interaction in cold-formed steel lipped channel columns. *Computers & Structures*, 85(19–20): 1461–1474.

Dinis PB, Young B & Camotim D 2012a. Local-distortional interaction in cold-formed steel rack-section columns. In J. Loughlan, D. Nash, J. Rhodes (eds.), *Coupled Instabilities in Metal Structures* (CIMS 2012). *Proc. 6th intern. conf.*: 523–530.

Dinis PB, Young B & Camotim D 2012b. Strength, failure and design of web-stiffened lipped channel columns exhibiting distortional buckling. In J. Loughlan, D. Nash, J. Rhodes (eds.), *Cououpled Instabilities in Metal Structures* (CIMS 2012). *Proc. 6th intern. conf.*: 531–538.

Dinis PB, Camotim D, Martins AD 2013b. Post-buckling behaviour and strength of cold-Formed steel lipped channel columns: when is local-distortional interaction relevant? In A. Zingoni (ed.), *Structural Engineering, Mechanics and Computation* (SEMC 2013). *Proc. 5th intern. conf.*: in press.

Kwon YB, Kim BS & Hancock GJ 2009. Compression tests of high strength cold-formed steel channels with buckling interaction. *Journal of Constructional Steel Research*, 65(2): 278–89.

Schafer BW 2002. Local, distortional and Euler buckling in thin-walled columns, *Journal of Structural Engineering* (ASCE), 128(3): 289–299.

Schafer BW 2008. Review: the Direct Strength Method of cold-formed steel member design. *Journal of Constructional Steel Research*, 64(7–8): 766–78.

Silvestre N, Camotim D & Dinis PB 2009. Direct strength prediction of lipped channel columns experiencing local-plate/distortional interaction. *Advanced Steel Construction*, 5(1): 49–67.

Silvestre N, Camotim D & Dinis PB 2012. Post-buckling behaviour and direct strength design of lipped channel columns experiencing local-distortional interaction. *Journal of Constructional Steel Research*, 73(June): 12–30.

Yang D & Hancock GJ 2004. Compression tests of high strength steel channel columns with interaction between local and distortional buckling. *Journal of Structural Engineering* (ASCE), 130(12): 1954–1963.

Yap DCY & Hancock GJ 2011. Experimental study of high strength cold-formed stiffened web steel sections. *Journal of Structural Engineering* (ASCE), 137(2): 162–72.

Young B, Silvestre N & Camotim D 2013. Cold-Formed Steel Lipped Channel Columns Influenced by Local-Distortional Interaction: Strength and DSM Design. *Journal of Structural Engineering* (ASCE), in press.

Research and Applications in Structural Engineering, Mechanics and Computation – Zingoni (Ed.)
© 2013 Taylor & Francis Group, London, ISBN 978-1-138-00061-2

Simulation of multi-physical processes in solar updraft power generation

W.B. Krätzig
Department of Civil and Environmental Engineering, Ruhr-University Bochum, Germany
Krätzig & Partner Civil Engineering Consultants, Bochum, Germany

ABSTRACT: After elucidating Schlaich's classical evaluation of the generated electricity of solar updraft power plants, the paper derives and discusses the numerical simulation concept for the thermo-fluid-mechanical processes of the airflow therein. This then will be supplemented by the description of the capture of solar irradiation through the collector glazing in the absorber soil and further the internal air, leading to a highly nonlinear simulation. A special fast solution concept is explained, and illustrated by few typical properties of physical variables of the plant. Finally, simulated results for the generated electricity are presented.

1 INTRODUCTION INTO SUPPS

Solar updraft power plants (SUPPs) form a rather modern and highly efficient concept of generating electricity from solar irradiation. SUPPs consist of large glass-covered collector areas (CA), huge central solar chimneys (SC), and turbo-generators as power conversion units (PCUs), see Figure 1.

The solar irradiation penetrates through the CA glass cover, heats the absorber soil which then warms up the internal collector air. This air expands and moves towards the elevated CA centre, where it is released into the ambience via the SC. This high stack acts as the engine of a SUPP, since the buoyancy of the heated air leads to a continuous airflow through the SUPP, drawing permanently fresh cold air into the CA from its rim. Parts of the kinetic energy of this airflow are extracted by the turbines and transformed into electricity by the coupled generators of the PCUs (Schlaich 1995).

Such power generation concept had been proposed first in 1903 by the Spanish Army Officer I. Cabanyes. In the years 1979 to 1982 J. Schlaich constructed the first pilot SUPP in Manzana-res/Spain which he and his team operated very successfully for more than 7 years. All data which are presently used for SUPP-designs stem from this prototype (Krätzig et al. 2009; Schlaich et al. 2005).

2 GLOBAL SUPP MODELS

2.1 *Schlaich's classical SUPP model*

In (Schlaich 1995) the author derived a clear, simple and evident concept for the determination of the maximum electric power of a SUPP. This concept, re-organized in Equation 1, catches all essential parameters correctly. It has been derived to determine

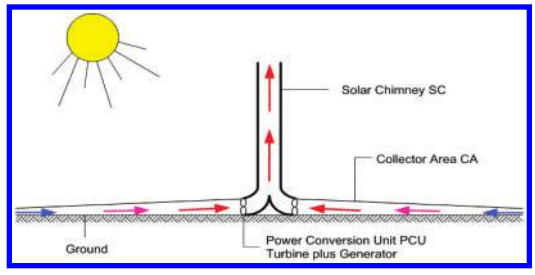


Figure 1. Working scheme of a solar updraft power plant.

the actual power P_{el}, G represents the actual solar irradiation in kW/m^2. But it serves also for estimates of the annually harvested electric energy E_{el}, in this case G stands for the annually irradiated energy:

$$P_{el} = 2/3\ \eta_{turb}\ \frac{g \times h_c}{c_p \times T_0}\ \eta_c\ \eta_{coll}\ A_{coll}\ G. \qquad (1)$$

In formula (1) we used the following abbreviations:

η_{turb} Degree of efficiency of the turbo-generators,
$g = 9.81$ m/s^2 Acceleration due to gravity,
h_c Effective height of the chimney in m,
$c_p = 1005$ J/kg K Specific heat capacity of the air,
T_0 Ambient temperature in K,
η_c Influence of mean chimney diameter d_c on P_{el},
η_{coll} Degree of efficiency of the collector in P_{el},
A_{coll} Effective ground area of the collector m^2,
G Solar irradiation in W/m^2 (or kWh/m^2 a).

At the time of the Manzanares pilot plant the designers had only single glazing of the collector in mind. Thus for this case of collector efficiency η_{coll} (Schlaich 1995) proposed the following expression:

$$\eta_{coll} = \alpha - \beta \times \Delta T/G. \qquad (2)$$

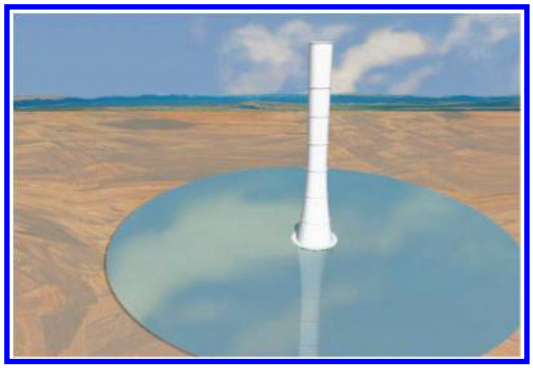


Figure 2. Computer vision of a solar updraft power plant.

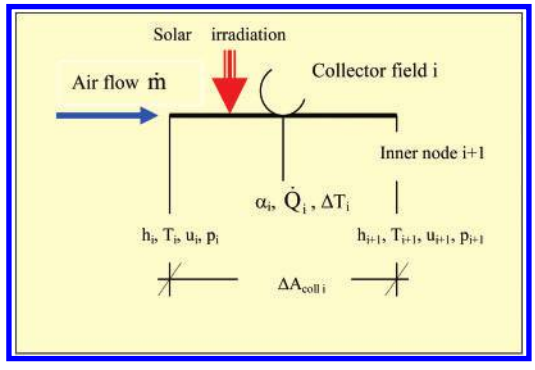


Figure 3. ith collector volume element.

Herein $\alpha = 0.75 \div 0.80$ denotes the heat absorption coefficient, and $\beta = 5 \div 6\,\mathrm{W/m^2K}$ a heat-loss coefficient for consideration of the collector size.

2.2 *Improvement of the model*

The expressions η_{coll} and η_c, the latter in SCHLAICH's concept equals 1, can be improved by use of computer simulated results. In P_{el} the collector efficiency η_{coll} follows the interpolation relation:

$$\eta_{coll} = 0.680\ (\ 1 - 0.229\ \sqrt{d_{coll} - 2.000}\ ), \qquad (3)$$

in which the diameter of the collector is measured in [km]. The influence of the mean chimney diameter d_c on P_{el} has been evaluated to:

$$\eta_c = 1 + 0.420\ f_c\ \frac{d_c - 200.0}{200.0} - 0.400\ f_c \left(\frac{d_c - 200.0}{200.0}\right)^2,$$
$$\text{with} \qquad f_c = 1 + 0.250\sqrt{d_{coll} - 2.000}\,. \qquad (4)$$

In f_c the effective diameter d_{coll} of the collector is again measured in [km]. These expressions fit well with examples taken from (Pretorius 2007).

This improvement changes the classical model to a rather comfortable instrument for pre-designs of SUPPs. However, desired modifications of the collector roof or of the absorber require mathematically much more rigor models which shall be treated now.

3 THERMO-FLUIDMECHANICAL MODEL OF THE ENTIRE SUPP

3.1 *Pre-requisites*

Overlooking Chapter 2 we observe a SUPP-model which has hidden all thermo-physical and fluid-mechanical knowledge in the efficiency parameters η_{coll}, η_c, and η_{turb}. For extensions of MANZANARES SUPP designs this might be sufficient. But for advanced designs a deeper insight into the thermo-fluid-radiation-mechanics is advantageous, as now based on the following pre-requisites:

- The collector bottom is horizontal with equal ambient air pressure everywhere.
- The thermo-fluiddynamics is modeled within one-dimensional flow-tube theory.
- Air is assumed as an ideal gas.
- The entire model is approximated as stationary.

3.2 *Collector model*

The collector is discretized into a number of i ring-shaped finite volumes:

- $\Delta A_{colli} = \pi(r_{i+1}^2 - r_i^2)$ denote ground/top surfaces,
- h_i, h_{i+1} are the respective collector heights,
- r_i, r_{i+1} stand for radial distances from the centre,
- $A_i = 2\pi r_i h_i$ are circular boundaries at i's inflow,
- $A_{i+1} = 2\pi r_{i+1} h_{i+1}$ boundaries at i's outflow.

The following conditions describe the thermo-fluidmechanical processes in the collector:

Conservation of mass: $\dot{m} = \text{const.}$, (5)

Conservation of momentum:

$$\dot{m}u_i - \dot{m}u_{i+1} + p_i A_{colli} - p_{i+1} A_{coll.i+1} = 0\,, \qquad (6)$$

Conservation of energy: $\Delta\dot{Q}_i = \dot{m}\, c_p\, \Delta T_i\,.$ (7)

Herein $\dot{m}$ abbreviates the rate of air mass flow (kg/s) in the plant, u the air velocity (m/s), p the air pressure (N/m^2), ΔQ_i the specific heat flux increase (W), and ΔT_i the temperature increase of the airflow (K). Again c_p stands for the specific heat capacity (J/kg K). The solar irradiance G (W/m^2) is coupled with the collector heat power by the relations:

$$\Delta\dot{Q}_i = \alpha_i\, G\, \Delta A_{coll.i} \ldots \Rightarrow \ldots \dot{Q}_i = \Sigma_i \Delta\dot{Q}_i\,, \qquad (8)$$

in which α_i denotes the efficiencies of the collector ring surface $\Delta A_{coll.i}$ in transforming G into heat increase ΔQ of the collector airflow, see Figure 3.

The initial conditions: $p = p_0$, $u = 0$ along the rim outside the CA are coupled to those corresponding values on the inflow border of the 1st finite volume by BERNOULLI's equation

$$p_0 = p_{i+1} + 0.5\rho_{i+1} u_{i+1}^2\,. \qquad (9)$$

Assuming further air as an ideal gas, the gas law

$$\rho_i = p_i / R\, T_i, \tag{10}$$

with R as general gas constant (J/kg K) and T_i as absolute temperature, couples the fluid-mechanic Equations (5, 6, 9) with the thermodynamic ones (7, 8, 10). All these equations formulate an initial value problem, nonlinear because of Equation 10. Its final values: u_{turb}, p_{turb} have to be coupled at the turbines' exits with the corresponding values of the chimney.

3.3 *Solar chimney model*

On the turbines' exits, the chimney's start, the heated air inside has smaller mass density ρ_{i0} as ρ_{o0} the colder air outside. So in the chimney there exists an updraft, which serves as the engine of the SUPP:

$$\Delta p = g \int_0^H \{\rho_o(h) - \rho_i(h)\}\, dh. \tag{11}$$

From this equation we receive with standard approximations expressions for the maximum pressure

$$\Delta p_{max} = g\, \rho_0\, H\ \ \Delta T / (T_0 + \Delta T) \tag{12}$$

of the airflow or for its maximum velocity:

$$u_{max} = \sqrt{2 g\, H\ \ \Delta T / (T_0 + \Delta T)}. \tag{13}$$

Because of the square-root in Equation (11), the above mentioned coupling to the collector airflow increase the initial nonlinearity.

Both density profiles $\rho_i(h)$, $\rho_o(h)$ in Equation (11) influence the buoyancy of the solar chimney. At least the outside profile $\rho_o(h)$ as meteorological variable is unknown at the design state. Thus intensive studies have been carried out proving that Equations (12, 13) give excellent approximations, if $\rho_o(h)$ describe a standard (polytrophic, $\kappa = 1.235$, $\Delta T = 6.5$ K/km) atmosphere, and $\rho_i(h)$ a special polytrophic one, with the following parameters ($\kappa = 1.100$, $\Delta T = 3.0$ K/km).

3.4 *Turbine model*

The turbines are pressure-staged, so they withdraw parts of the pressure out of the airflow, and transform them into electric power. With the pressure withdrawal factor κ of the turbine, and the maximum airflow velocity u_{max} from Equation (13) we receive:

$$\Delta p_{turb} = \kappa\, \Delta p_{tot} : u_{turb} = \sqrt{1-\kappa}\ \ u_{max}. \tag{14}$$

Δp_{turb} and u_{turb} stand for the average pressure jump and air velocity in the turbines, respectively. From the kinetic power of the airflow, $P_{tot} = m u_{max}^2/2$, the harvested effective power P_{eleff} is gained, introducing η_{turb} for the turbines' degrees of efficiency:

$$P_{el\,eff} = \eta_{turb}\, \Delta p_{turb}\ \dot{m}/\rho = \eta_{turb}\, \kappa\ \dot{m}\, u_{max}^2/2. \tag{15}$$

For more details see (Gannon & Backström 2003).

3.5 *Flow losses and initial value problem*

For simplicity, all equations (5) until (13) have been derived without any consideration of flow losses of the airflux, which reduce the flow pressures, and so the efficiency of the SUPP. Their integration is straight forward and will not be detailed here.

From all given fluid-thermodynamic conditions a (moderately) nonlinear initial value problem in the air mass flow $\dot{m}$ can be formulated. Its numerical solution by incremental-iterative techniques delivers all design parameters of the SUPP, provided, the collector efficiencies α_i introduced in Equation (8) are known. This is not the case, so their rigor determination shall now be elaborated.

4 SOLAR RADIATION INPUT

4.1 *Collector: Thermodynamics of radiation*

This determination of the collector efficiencies α_i requires the modeling of the complicated physical transformation process of solar irradiation G into heat increase ΔQ of the airflow $\dot{m}$. If further SUPPs shall be optimized, the collector turns out to be the most important component for its economy, because the convective/radiation heat power transfers determine largely the plant efficiency. At this point many specific properties of the collector design come into play which were not considered up to now, e.g. double glazing. Interactions of the heat power transfers and the flow velocity of the air will be neglected.

All essentials of this thermodynamics of radiation can be found in the monograph (Duffie & Beckman 2006) Bases of our modeling of the solar heat input are first the convective heat transfers (qc)

$$qc_i = hc_i\ \ T_i \tag{16}$$

with the convective heat power transfer coefficients hc_i, qc depending on absolute temperature T_i. Second, there are the radiation heat power transfers (qr) due to Boltzmann's radiation law. This reads for the radiation between two parallel plates

$$qr_1 = qr_2 = \frac{Q_r}{A} = \frac{\sigma(T_2^4 - T_1^4)}{1/\varepsilon_1 + 1/\varepsilon_2 - 1}, \tag{17}$$

or for the radiation between one plate and the sky

$$qr_1 = \varepsilon\sigma(T_1^4 - T_{sky}^4). \tag{18}$$

In these conditions, the ε-values abbreviate optical emittances of opaque bodies, T always absolute temperatures, and σ the Stefan-Boltzmann constant equal to 5.6697×10^{-8} (W/m^2 K^4). Necessary emittances ε can be found in (Duffie & Beckman 2006), convective heat power transfer coefficient hc in the standard literature.

4.2 *Heat transfers*

In each collector volume element the convective/ radiation heat power transfers now shall be modeled. To

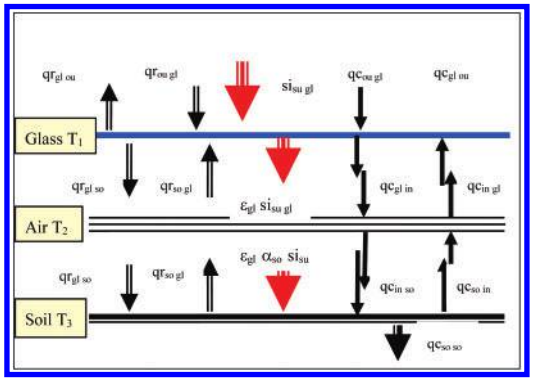


Figure 4. Heat transfers for glass/air/soil collector construction.

introduce our reader into this and to prepare the later formulation of the heat power balance equations of the collector, we select due to Figure 4 the simplest collector construction consisting of one panel of glass (temperature T_1), the heated airflow (T_2) and the soil-absorber (T_3). We consider a unit cell of the collector and distinguish therein the following thermal transfers qr due to radiation and qc due to heat convection. As emphasized in connection with Equations (16) to (18), they all are assumed to depend on their respective absolute temperatures T_i:

- $qr_{ou\,gl}$ thermal transfer by radiation (qr) from outer air (ou) into glass sheet (gl),
- $qr_{gl\,ou}$ thermal transfer by radiation (qr) from glass sheet (gl) into outer air (ou),
- $qr_{gl\,so}$ thermal transfer by radiation from glass sheet into soil, and analog for further transfers (qr),
- $qc_{ou\,gl}$ thermal transfer by convection (qc) from outer air (ou) into glass sheet (gl),
- $qc_{gl\,ou}$ thermal transfer by convection (qc) from glass sheet (gl) into outer air (ou),
- $qc_{gl\,in}$ thermal transfer by convection from glass sheet into inner air, and analog for further (qc),
- $si_{su\,gl}$ solar irradiance from the sun into glass sheet.

The solar irradiation penetrates through the glazing and then into the absorber soil. All this and further details can be seen from Figure 4.

4.3 *Heat balance conditions*

The stationarity condition of the solar radiation input process requires, that the vector sum of all heat transfers each into/from the glass, the inner air flow, and the soil absorber have to vanish. This leads to three coupled heat balance conditions, nonlinear equations in the temperatures T_1, T_2, T_3:

$$\begin{aligned}
\text{glass:}\quad & qr_{ou\,gl} - qr_{gl\,ou} - qr_{gl\,so} + qr_{so\,gl} + qc_{ou\,gl} \\
& - qc_{gl\,ou} - qc_{gl\,in} + qc_{in\,gl} + (1-\varepsilon_{gl})\, si_{su\,gl} = 0, \\
\text{air:}\quad & qc_{gl\,in} - qc_{in\,gl} + qc_{so\,in} + qc_{in\,so} = \alpha_i\, si_{su\,gl}, \\
\text{soil:}\quad & qr_{gl\,so} - qr_{so\,gl} + qc_{in\,so} - qc_{so\,in} - qc_{so\,so} \\
& + \varepsilon_{gl}\, \alpha_{so}\, si_{su\,gl} = 0. \qquad (19)
\end{aligned}$$

In these heat power balance equations, α_{so} denotes the broadband absorptance of the absorbing soil. Obviously, for this simplest collector construction with the first and last Equations (19) two coupled algebraic conditions have been received, depending on forth (qr) and first (qc) power of temperatures T_1, T_2 and T_3. The centered Equation (19), also algebraic and coupled to the other two, is written in such a way, that the heat flux increase

$$\Delta\dot{Q}_i = \alpha_i\, si_{su\,gl} \qquad (20)$$

in the i-th collector element stands on the right, and determines directly the desired efficiency parameter α_i, related to the solar irradiance input $si_{sugl} = G$. Nonlinear algebraic conditions like (19) have to be formulated for each collector ring element $\Delta A_{coll.i}$. For more complicated collector constructions (double glazing, water heat reservoirs, double air compartments), these conditions increase in number.

4.4 *Simulation concept for the entire SUPP*

In Chapter 3 we have established the initial value problem describing the thermo-fluiddynamics of the entire SUPP. This problem is now supplemented by one heat balance condition for each collector cell. These heat balance conditions are highly nonlinear.

If we just add them to the original initial value problem, e.g. in the form of so-called thermal networks (Bernardes 2004), and use an arbitrary nonlinear solver algorithm, we would run into endless automatic iterations.

It seems to be much more suitable to solve each heat balance condition i separately by a fast nonlinear solver for the corresponding α_i, and correct the initial value problem iteratively.

So the repeatedly mentioned nonlinear initial value problem from Chapter 3 is solved for a first guess of the efficiencies $\alpha_{i\,(1)}$ in all collector ring elements. This leads to a first approximation $\dot{m}_1$ for the airflow, and vice versa for the harvested electrical power $P_{eleff(1)}$. For each of the i collector elements we further find a 1^{st} approximation of the air temperatures $T_{int.air(1)}$, which then are inserted into the respective power balance conditions. Solution of all of these (highly nonlinear) conditions leads to a new set of collector efficiencies $\alpha_{i\,(2)}$, with which the computing process of the initial value problem has to be repeated. Introducing all new air temperatures $T_{int.air\,(2)}$ into the heat balance conditions with solutions lead to a new improved set of $\alpha_{i\,(3)}$. This iteration process is continued until the desired exactness for P_{eleff} has been achieved, see (Krätzig 2012b).

This analysis process is fast and extremely stable. It leads to unique solutions in rather short computing times, as has been proven in intensive theoretical studies and in many program runs.

5 ENERGY OUTPUT OF SUPPS

Up to now we have in great detail elucidated our simulation concept for day hours with solar irradiation.

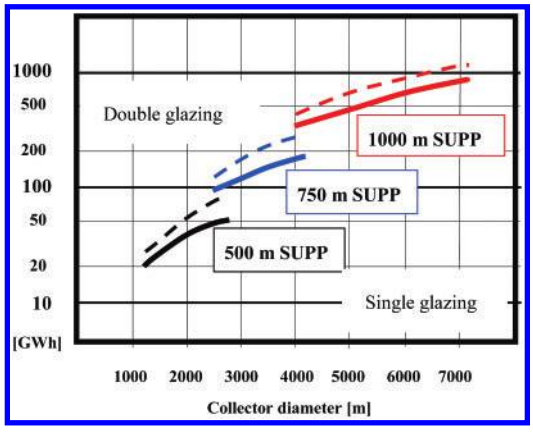


Figure 5. Annually harvested solar energy for different SUPPs.

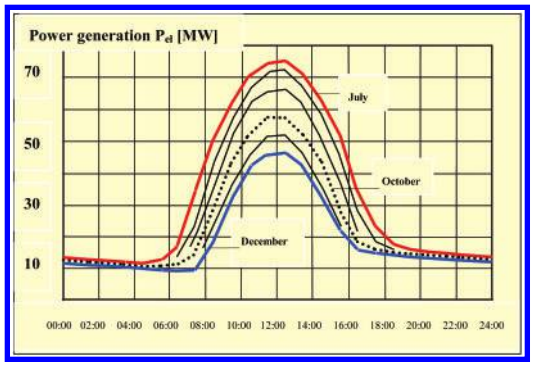


Figure 6. Power generation of 750/3500 SUPP over solar day.

Table 1. Results of an optimization study for 2 SUPP families.

	500/2000	750/3500
SUPP DIMENSIONS		
Chimney height [m]:	500.00	750.00
Throat diameter of chimney [m]:	45.00	67.50
Top diameter of chimney [m]:	50.00	75.00
Outer collector diameter [m]:	2 000.00	3 500.00
SERVICE PARAMETERS		
Total annual energy harvest [GWh/a]:	54.9	219.7
Max.electric power $P_{el\,max}$ at $G = 1088$ W/m^2 [MW]:	18.5	74.3
Values for max. solar irradiance of 1088 W/m^2:		
Maximum air mass flow [kg/s]:	37 501	106 705
Air temperature increase Δ_{turb} for $T_0 = 24°C$ [K]:	57.80	61.16
Medium air velocity u_{turb} [m/s]:	37.04	43.97
INVESTMENTS		
Chimney [M€]:	23.9	60.5
Double glazed collector (22.25 €/m^2) [M€]:	69.5	213.3
Turbo-generators (0.65 M€/MW of $P_{el\,max}$) [M€]:	12.2	48.8
Additionals + Engineering + Tests [M€]:	5.4	15.0
Total investments [M€]:	111.0	337.6
FINANCIAL AND SERVICE RESULTS		
Annuity including annual insurance [M€]:	7.4	22.8
Levelled electricity costs LECs (33 years) [€/kWh]:	0.131	0.099

This procedure has to be supplemented by a similar concept for night times, in which no solar irradiation can feed the SUPP with energy. Then the required heat has to be taken from the absorber soil, in which it had been stored automatically from the solar irradiance for night uses.

If we so have a simulation tool at hand applicable for 24 hours of a solar day, we can evaluate with hourly values of the solar irradiation and the actual temperatures the daily harvested energy, from which we compute the entire annually produced energy of a certain SUPP. Figure 5 shows such simulation results for SUPPs with suitably coated double glazing, an artificially blackened soil absorber, and for a location with annual solar energy irradiation of 2.20 MW/m^{2}a (logarithmic scale in the vertical).

Basis of such an annual energy evaluation of a SUPP are the courses of generated power over a typical solar day. Such a plot is shown in Figure 6 for different months of the last two seasons of a year. One clearly recognizes the strong influence of the sun shine during day hours, but also over different months. Very interesting is the fact, that the SUPP technology – in contrast to concentrating solar techniques CSP and PVT – the solar updraft concept possesses a natural storage component due to the heat storage property of the absorber soil.

Starting with such a simulation tool we are able to carry out optimization studies for SUPP families, to systematically find those plant alternatives with minimum levelled electricity cost LECs. Some results of such studies are presented in Table 1. The reader may observe the enormously low LECs, namely 0.131 €/kWh for MINI-SUPPs with 500 m SC, and 0.099 €/kWh for those ones with 750 m SC. Independent from this, (Bergermann & Weinrebe 2010) came to rather identical LECs for SUPPs with 1000 m SC.

Comparing these values e.g. with LECs for parabolic trough plants, central receiver works or photovoltaic installations, we observe the high economic efficiency of the solar updraft technology. In addition, this technology requires only water for glass cleaning, neither for steam formation nor for re-condensation, a great advantage in deserts with high solar irradiance (Backström et al. 2008).

Finally, Figure 7 shows the computer vision of a SUPP arrangement with solar chimneys of 1000 m of elevation and 6000 m of collector diameter. The maximum power is of the order of 300 MW, and the annual electric energy close to 900 GWh.

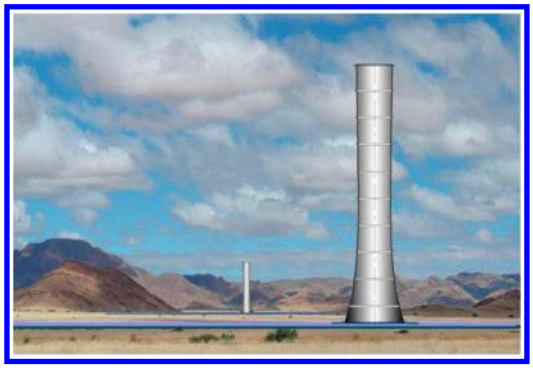


Figure 7. Computervision of 1000 m/6000 m SUPPs.

6 CONCLUSIONS

SUPPs are at the very beginning of their technical existence as an extremely sustainable electricity generation concept for countries with high solar irradiation. Many improvements are in discussion, as can be observed from the proceedings of the last two international conferences on this matter, see (Bottenbruch et al. 2010) and (Zhou 2012). Clearly one has to solve the problem of praiseworthy storing the solar energy at least for several hours after sundown when power is demanded. Many improvements in this direction are under discussion, e.g. storage of low-concentrated heat in water-filled basins under the CA (Schlaich 1995) or the storage of the generated electricity in modern devices. But all this is beyond the scope of this manuscript, and thus it is left for more deeply interested readers (Krätzig 2012a).

ACKNOWLEDGEMENT

Long time assistance of Drs. M. Andres, U. Montag and R. Wörmann from Krätzig & Partners Civil Engineering Consultants is gratefully acknowledged.

REFERENCES

Backström, T.W. von, Harte R., Höffer R., Krätzig W.B., Kröger D.G., Niemann H.-J., Zijl G.P. van, 2008. State and Recent Advances of Solar Chimney Power Plant Technology. PowerTech, 88(7), 64–71.

Bergermann, R., Weinrebe, G., 2010. Realization and costs of solar updraft towers. In: *Proc. of the SCPT 2010 – Intern. Conf. Solar Chimney Power Technology*. Bochum, Germany: Ruhr-University, 63–68.

Bernardes, M.A. dos S., 2004. *Technische, ökonomische und ökologische Analyse von Aufwindkraftwerken*. Dr.-Ing.-Thesis, Institut für Energiewirtschaft und Rationelle Energieanwendung, U Stuttgart.

Bottenbruch, H., Harte, R., Höffer, R., Krätzig, W.B., Mark, P., Niemann, H.-J. (eds.), 2010. *Proc. SCPT 2010, 2nd Int. Conf. on Solar Chimney Power Technology*. Bochum, Germany: Ruhr-University.

Duffie, J.A., Beckman, W.A., 2006. *Solar Engineering of Thermal Processes*, 3rd Edition. Hoboken, New Jersey: John Wiley & Sons Inc.

Gannon, A.J., Backström, T.W. von, 2003. Solar chimney turbine performance. *ASME Journ. Solar Energy Eng.* 125: 101–106.

Krätzig, W.B., Harte, R., Montag, U., Woermann, R., 2009. From large natural draft cooling tower shells to chimneys of solar upwind power plants. In: *A. Domingo, C. Lazaro (eds.), IASS Symposium on Evolutions and Trends in Design, Analysis and Construction of Shells*. CD-publication: Univ. of Valencia.

Krätzig, W.B., 2012a. Solar updraft power technology – State and advances of low-concentrated thermal solar power generation. *VGB PowerTech* 92(11), 34–39.

Krätzig, W.B., 2012b. Physics, Computer Simulation and Optimization of Thermo-fluidmechanical Processes of Solar Updraft Power Plants. In: Zhou, X.P. (Ed.) *Proc. SUTPT 2012, 1–12*. Wuhan, China: Huazhong University of Science and Technology.

Pretorius, J.P., 2007. *Optimization and Control of a Large-Scale Solar Chimney Power Plant*. PhD-thesis, University of Stellenbosch.

Schlaich, J., Bergermann, R., Schiel, W., Weinrebe, G. 2005. Design of Com. Solar Updraft Tower Systems. *ASME J. Solar Energy Engineering,* 127, 117–124.

Schlaich, J. 1995. *The Solar Chimney, Electricity from the Sun*. Edition A. Menges, Stuttgart.

Zhou, X.P. (ed.), 2012. *Proceedings SUTPT 2012, 3rd Int. Conf. on Solar Updraft Tower Power Technology*. Wuhan, China: Huazhong University of Science and Technology.

Research and Applications in Structural Engineering, Mechanics and Computation – Zingoni (Ed.)
© 2013 Taylor & Francis Group, London, ISBN 978-1-138-00061-2

Mechanics of interfaces and evolving discontinuities

René de Borst
School of Engineering, University of Glasgow, Glasgow, UK

Joris J.C. Remmers & Clemens V. Verhoosel
Department of Mechanical Engineering, Eindhoven University of Technology, Eindhoven, The Netherlands

Alan Needleman
Department of Materials Science and Engineering, University of North Texas, Denton, TX, USA

ABSTRACT: The two main approaches to the modelling of discontinuities are reviewed concisely, followed by a discussion of cohesive models for fracture. Emphasis is put on a novel approach to incorporate triaxiality into cohesive-zone models, and on the representation of cohesive crack models by phase-field models.

1 INTRODUCTION

The modelling of discontinuities, including interfaces, is of a growing importance in the mechanics of materials. Basically, two methods exist to capture discontinuities: one can either distribute them over a finite width, or handle them as true discontinuities, i.e. in a discrete sense.

When a discontinuity has a stationary character, such as in grain boundaries, it is fairly straightforward to describe it in a discrete manner, since it is then possible to make the discretisation such that the discontinuity, either in displacements or in displacement gradients, is modelled explicitly. An evolving or moving discontinuity, however, is more difficult to describe. A possibility is to adapt the mesh upon every change in the topology, as was done by Ingraffea and co-workers in the context of linear elastic fracture mechanics (Ingraffea & Saouma 1985), and later for cohesive fracture (Camacho & Ortiz 1996).

Another approach is to model fracture within the framework of continuum mechanics. A fundamental problem then emerges, namely that standard continuum models do not furnish a *length scale* which is indispensible for describing fracture. More pre- cisely, they result in a zero length scale. Since the energy dissipated in the failure process is given per unit area of material that has completely degraded, and since a zero internal length scale implies that the volume in which failure occurs goes to zero, the energy dissipated in the failure process also tends to zero. Two approaches have been followed to avoid this physically unrealistic situation, namely via discretisation and via regularisation of the continuum.

Along the first line, researchers have let the spacing of the discretisation take over the role of the missing internal length scale. The idea is then to choose the discretisation such that the spacing of the discretisation coincides with the internal length scale that derives from the physics of the process. Evidently, a good knowledge of the problem is required and solutions, including the proper choice for the discretisation, are dependent on the problem and the numerical method. Nevertheless, this approach has been used successfully to obtain insight in various issues in materials science (Ruggieri et al. 1996).

Yet, this approach cannot be called a proper solution in the sense that the mathematical setting of the initial value problem remains unchanged. Indeed, the introduction of degradation of the material properties in a standard, rate-independent continuum model – and therefore, the introduction of a stress-strain curve with a descending slope – can locally cause the governing differential equations to change character. Without special provisions such as the application of special interface conditions between both domains at which different types of differential equations hold, the initial value problem becomes ill-posed. Numerically, this has the consequence that the solution becomes fully dependent upon the discretisation (Bažant 1976).

As a more rigorous solution, various regularisation methods have been proposed, including non-local averaging, the addition of viscosity or rate dependency, or the inclusion of couple stresses or higher-order strain gradients (de Borst et al. 1993). The effect of these strategies is that the discontinuity is transformed into a continuous displacement distribution. The internal length scale is now set by the constitutive model, and for a sufficiently fine discretisation, the numerically calculated results only change in a sense that is normally expected upon mesh refinement.

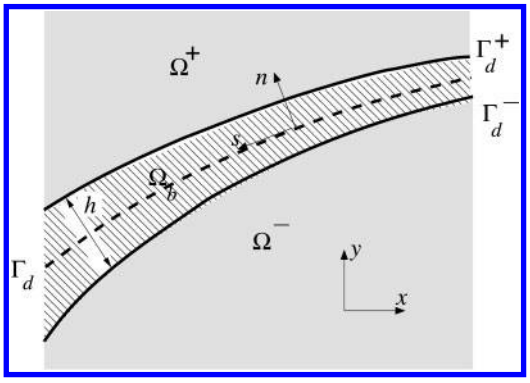


Figure 1. Cohesive surfaces at an internal discontinuity Γ_d.

2 COHESIVE SURFACE MODELS

Most engineering materials are not perfectly brittle in the Griffith sense, but display some ductility after reaching the strength limit. In fact, there exists a zone ahead of the crack tip, in which small-scale yielding, micro-cracking and void initiation, growth and coalescence take place. If this fracture process zone is sufficiently small compared to the structural dimensions, linear-elastic fracture mechanics concepts can apply. However, if this is not the case, the cohesive forces that exist in this fracture process zone must be taken into account. The most powerful and natural way is to use cohesive surface models, which were introduced by Dugdale (1960) and by Barenblatt (1962).

2.1 *General formulation*

We consider a volume Ω with an internal discontinuity boundary Γ_d as shown in Figure 1. As a starting point we consider the potential energy for the case of a discrete description of brittle fracture (Francfort & Marigo 1998):

$$\Psi_{\text{pot}} = \int_{\Omega} \psi^e(\boldsymbol{\varepsilon})\,\mathrm{d}V + \int_{\Gamma_d} \mathcal{G}_c\,\mathrm{d}A \tag{1}$$

with the elastic energy density ψ^e a function of the infinitesimal strain tensor ε. The elastic energy density is expressed by Hooke's law for an isotropic linear elastic material as $\psi^e(\varepsilon) = \frac{1}{2}\lambda\varepsilon_{ii}\varepsilon_{jj} + \mu\varepsilon_{ij}\varepsilon_{ij}$ with λ and μ the Lam'e constants. In Equation (1) the fracture energy, i.e. the amount of energy dissipated upon the creation of a unit of fracture surface) is denoted by $\mathcal{G}_c$. The potential energy Ψ_{pot} governs the balance between elastic energy in the bulk material and the fracture energy.

An essential difference between brittle and cohesive fracture models is the dependence of the fracture energy on the crack opening in the latter case, as the fracture energy is released only gradually, and energy dissipation is governed by a *fracture energy function*:

$$\mathcal{G} = \mathcal{G}(\llbracket \boldsymbol{u} \rrbracket, \kappa) \tag{2}$$

which depends on the jump of the displacement field $[\![u]\!]$ across the discontinuity Γ_d and on a history parameter κ, which obeys the Kuhn-Tucker loading/unloading conditions. The potential energy now takes the form:

$$\Psi_{\text{pot}} = \int_{\Omega} \psi^e(\boldsymbol{\varepsilon})\mathrm{d}V + \int_{\Gamma_d} \mathcal{G}(\llbracket \mathbf{u} \rrbracket, \kappa)\mathrm{d}A \tag{3}$$

and the cohesive tractions are obtained through differentiation of the fracture energy function with respect to the crack opening:

$$\boldsymbol{t} = \frac{\partial \mathcal{G}}{\partial \llbracket \boldsymbol{u} \rrbracket} \quad \rightarrow \quad \boldsymbol{t} = \boldsymbol{t}(\llbracket \boldsymbol{u} \rrbracket, \kappa) \tag{4}$$

2.2 *An extension: the cohesive-band model*

The cohesive surface model as outlined in the preceding section is a two-dimensional model embedded in a three-dimensional continuum, and only the crack opening and the crack sliding modes are available. The normal strain parallel to the cohesive surfaces is absent, and so is the normal stress in this direction. This hampers the accurate computation of failure modes in metals where stress triaxiality plays a role, but also prevents the prediction of splitting cracks in concrete or masonry structures where a large compressive stress induces cracks that are aligned with the normal stress (Rots 1991). To circumvent this deficiency of the cohesive surface model it has been proposed to take the normal stress from a neighbouring integration point in the continuum and to insert this stress component in the failure criterion for the cohesive surface model (Keller et al. 1999, Tijssens et al. 2000).

A more rigorous solution is to define a small band with a thickness h_0, which can be conceived as the value of the crack opening, h, in a reference state (Remmers et al. 2013), see Figure 1. In this cohesive band we define a strain tensor expressed in the n, s, t local frame of reference:

$$\bar{\boldsymbol{\mathcal{E}}} = \begin{bmatrix} \mathcal{E}_{nn} & \mathcal{E}_{ns} & \mathcal{E}_{nt} \\ \mathcal{E}_{sn} & \mathcal{E}_{ss} & \mathcal{E}_{st} \\ \mathcal{E}_{tn} & \mathcal{E}_{ts} & \mathcal{E}_{tt} \end{bmatrix} \qquad \forall\ \mathbf{x} \in \Omega_b \tag{5}$$

Under the assumption that the normal strain component ε_{nn}, and the shear strain components ε_{ns} and ε_{nt} are completely determined by the crack opening v_n, and the crack sliding components v_s and v_t, respectively, we can define:

$$\mathcal{E}_{nn} = \frac{v_n}{h_0} \tag{6}$$

and

$$\mathcal{E}_{ns} = \frac{v_s}{2h_0} \quad \text{and} \quad \mathcal{E}_{nt} = \frac{v_t}{2h_0} \tag{7}$$

The in-plane terms of the strain tensor in the band, ε_{ss}, ε_{tt} and $\varepsilon_{st} = \varepsilon_{ts}$ are independent of the magnitude

of the displacement jump. They represent the normal strain components in the s- and t-directions, respectively, and the in-plane shear strain. In view of the assumption that the strains in the band are piecewise constant at either side of the discontinuity Γ_d in the n-direction, and enforcing continuity for the in-plane strain components across Γ_d^- and Γ_d^+ these strain components are defined as:

$$\begin{aligned}\mathcal{E}_{ss} &= \frac{1}{2}\left(\mathcal{E}_{ss}|_{\Gamma_d^-} + \mathcal{E}_{ss}|_{\Gamma_d^+}\right)\\ \mathcal{E}_{tt} &= \frac{1}{2}\left(\mathcal{E}_{tt}|_{\Gamma_d^-} + \mathcal{E}_{tt}|_{\Gamma_d^+}\right)\\ \mathcal{E}_{st} &= \frac{1}{2}\left(\mathcal{E}_{st}|_{\Gamma_d^-} + \mathcal{E}_{st}|_{\Gamma_d^+}\right)\end{aligned} \tag{8}$$

Allowing for a wide range of cohesive relations, we postulate a tangential relation between the stress rate in the band $\dot{\boldsymbol{\mathcal{S}}}^{\mathrm{T}} = (\dot{\mathcal{S}}_{nn}, \dot{\mathcal{S}}_{ss}, \dot{\mathcal{S}}_{tt}, \dot{\mathcal{S}}_{ns}, \dot{\mathcal{S}}_{yt}, \dot{\mathcal{S}}_{st})$ and the strain rate in the band, $\boldsymbol{\varepsilon}$:

$$\dot{\boldsymbol{\mathcal{S}}} = \mathbf{D}_b \dot{\boldsymbol{\mathcal{E}}} \tag{9}$$

We assume that the tangential stiffness matrix $\mathbf{D}_b$ in the band has a transversely isotropic structure, and is obtained by differentiating the cohesive relation $\boldsymbol{\mathcal{S}} = \boldsymbol{\mathcal{S}}(\boldsymbol{\varepsilon}, \kappa, E_b, \nu_b)$, with κ an array of one or more internal variables, and E_b and ν_b the Young's modulus and the Poisson's ratio in the band, respectively. For the general three-dimensional case, a closed-form expression for $\mathbf{D}_b$ can be rather complicated. For this reason, a compliance format is sometimes preferred:

$$\mathbf{D}_b^{-1} = \begin{bmatrix} \frac{1}{k_n} & -\frac{\nu_b}{E_b} & -\frac{\nu_b}{E_b} & 0 & 0 & 0 \\ -\frac{\nu_b}{E_b} & \frac{1}{E_b} & -\frac{\nu_b}{E_b} & 0 & 0 & 0 \\ -\frac{\nu_b}{E_b} & -\frac{\nu_b}{E_b} & \frac{1}{E_b} & 0 & 0 & 0 \\ 0 & 0 & 0 & \frac{1}{k_s} & 0 & 0 \\ 0 & 0 & 0 & 0 & \frac{1}{k_t} & 0 \\ 0 & 0 & 0 & 0 & 0 & \frac{2(1+\nu_b)}{E_b} \end{bmatrix} \tag{10}$$

with

$$k_n = \frac{\partial \mathcal{S}_{nn}}{\partial \mathcal{E}_{nn}}$$

the stiffness that derives from the cohesive relation for mode-I behaviour, and with

$$k_s = \frac{\partial \mathcal{S}_{ns}}{\partial \mathcal{E}_{ns}} \quad \text{and} \quad k_t = \frac{\partial \mathcal{S}_{nt}}{\partial \mathcal{E}_{nt}}$$

the tangential shear stiffnesses in the s- and t-directions, respectively.

We observe that the standard cohesive stiffnesses between the tractions and the relative displacements are incorporated, but that the matrix also includes the in-plane stiffness and the coupling between the normal relative displacement and the stretching of the fracture plane via the Poisson ratio ν_b in the band. The assumed transversely isotropic structure of equation (10) has limitations, in particular when ductile fracture processes are considered which involve metals, ductile polymers, or adhesives. An appropriate band constitutive relation could then involve a significant shear-normal stress/strain coupling and the response cannot be characterised by an isotropic constitutive relation.

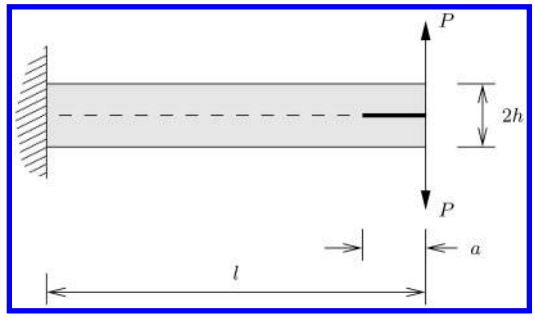


Figure 2. Geometry and boundary conditions of a double cantilever peel test.

2.3 *Double cantilever peel test*

We next consider the double cantilever test shown in Figure 2. The structure with length $l = 10$ mm consists of two layers with the same thickness $h = 0.5$ mm and with the same (isotropic) material properties: a Young's modulus $E = 100$ MPa and a Poisson ratio $\nu = 0.3$. The two layers are connected through an adhesive with a tensile strength $t_{\max} = 1$ MPa and an interfacial fracture toughness $\mathcal{G}_c = 0.1$ N/mm. The initial delamination extends over $\alpha = 1$ mm. An external load P is applied at the tip of both layers.

The specimen has been analysed with four-noded quadrilateral elements: 100 elements in the horizontal direction and 11 elements in the vertical direction. The elements in the centre of the specimen, i.e. the elements that are crossed by the discontinuity, are square with dimensions $l_e \times l_e = 0.1 \times 0.1$ mm. The solutions have been obtained using the energy dissipation arc-length method (de Borst et al. 2012).

The constitutive behaviour of the cohesive band is governed by an isotropic, plane-strain continuum damage relation:

$$\boldsymbol{\mathcal{S}} = (1 - \omega)\mathbf{D}_b^e \boldsymbol{\mathcal{E}} \tag{11}$$

where $\mathbf{D}_b^e$ is the plane-strain elastic stiffness matrix, that is constructed using the Young's modulus E_b and the Poisson's ratio ν_b in the band. The damage parameter ω is function of the history parameter κ, such that prior to reaching the tensile strength there is no accumulation of damage, while the residual strength decreases linearly thereafter. The relation between the classical, interfacial fracture toughness $\mathcal{G}_c$ and the volumetric fracture toughness is:

$$g_c = \frac{\mathcal{G}_c}{h_0} \tag{12}$$

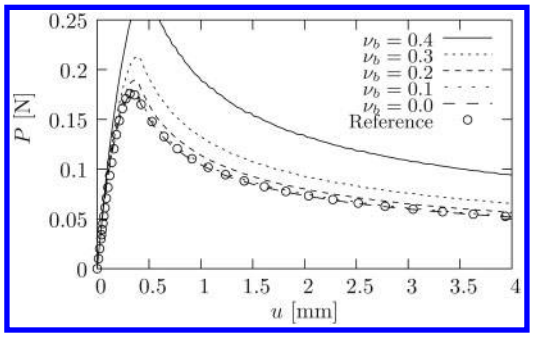


Figure 3. Effect of the Poisson ratio in the band, ν_b, on the strength and the ductility of a double-cantilever beam.

The results of the simulations for different values of the Poisson's ratio in the band, ν_b, are compared with a standard cohesive surface model in Figure 3. We clearly observe the effect of the in-plane strains, which are generated through the coupling to the crack opening displacement through ν_b, the Poisson ratio in the band. The additional strains and ensuing stresses give rise to an additional term in the internal virtual work, thus resulting in a higher peak load and a more ductile behaviour. Evidently, the effect diminishes for smaller values of the Poisson's ratio, and disappears for $\nu_b = 0$, when the results of the standard cohesive surface model are retrieved.

3 CONTINUUM REPRESENTATIONS OF THE COHESIVE MODEL

The cohesive-zone model is essentially a discrete concept. However, it can be transformed into a continuum formulation by distributing the fracture energy $\mathcal{G}_c$ over the thickness w of the volume in which the crack localises (Bažant & Oh 1983). The disadvantages of the formulation are that a pseudosoftening modulus is introduced which is inversely proportional to the number of elements, and, more importantly, that the boundary-value problem becomes ill-posed, implying a dependence on the discretisation. As discussed before, this anomaly is inherent in all smeared formulations without proper regularisation. A smeared formulation that is properly regularised, and therefore exhibits no mesh dependence, can be obtained using the phase-field concept, and will be outlined below.

3.1 *Cohesive fracture and phase fields*

As the starting point of the derivation of the phase field approximation to cohesive fracture we take the potential energy, equation (3) and we define $x_n = (\mathbf{x} - \mathbf{x}_c) \cdot \mathbf{n}(\mathbf{x}_c)$, with $\mathbf{n}(\mathbf{x})$ the unit vector normal to the fracture surface and $\mathbf{x}_c$ the position vector of a point on the fracture surface. The Dirac function δ can then be used to relate the infinitesimal surface area $\mathrm{d}A$ to the infinitesimal volume $\mathrm{d}V$ of the surrounding body:

$$\mathrm{d}A(\mathbf{x}_c) = \int_{-\infty}^{\infty} \delta\,(x_n)\ \mathrm{d}V \tag{13}$$

Equation (13) allows for smeared descriptions of the fracture surface by an approximation of the Dirac function. As in (Miehe, Welschinger, & Welschinger 2010, Miehe, Hofacker, & Welschinger 2010) we consider the approximated Dirac function

$$\delta_\epsilon(x_n) = \frac{1}{2\epsilon}\exp\left(-\frac{|x_n|}{\epsilon}\right) \tag{14}$$

with $\varepsilon > 0$ a length scale parameter. Evidently

$$\int_{-\infty}^{\infty} \delta_\epsilon(x_n)\mathrm{d}x_n = 1 \tag{15}$$

for arbitrary ϵ. Clearly, the fracture surface is distributed over a larger volume for higher values of ϵ. The corresponding infinitesimal fracture surface area then follows from

$$\mathrm{d}A_\epsilon(\mathbf{x}_c) = \int_{-\infty}^{\infty} \delta_\epsilon\,(x_n)\ \mathrm{d}V \tag{16}$$

Using the approximation to the Dirac function expressed in equation (14), the internal energy, equation (3), is approximated by

$$\Phi_{\mathrm{pot},\epsilon} = \int_\Omega \left(\psi^e(\boldsymbol{\varepsilon}^e) + \mathcal{G}(\mathbf{v},\kappa)\delta_\epsilon\right)\mathrm{d}V \tag{17}$$

Note that, compared to equation (3), we have replaced the infinitesimal strain tensor ε by the "elastic" infinitesimal strain tensor ε^e, and the jump in the displacement field $[\![\mathbf{u}]\!](\mathbf{x}_c)$ by an auxiliary field $\mathbf{v}(\mathbf{x})$. This is necessary since in the phase-field formulation, the crack only exists in a smeared sense. Hence, the clear distinction between the bulk and interface kinematics, i.e. between the strain tensor ε^e and the crack opening $[\![\mathbf{u}]\!]$, is lost.

In the phase-field formulation for cohesive fracture it is crucial to derive kinematic relations that are consistent with the discrete problem, in the sense that as the length scale parameter o approaches zero, the kinematics of the discrete problem are recovered. In order to arrive at such relations, we first introduce the distributed internal discontinuity

$$\Gamma_\epsilon = \{\mathbf{x} \in \Omega | d(\mathbf{x}) > \mathrm{tol}\} \tag{18}$$

with $\mathrm{tol} \ll 1$ being a small tolerance that truncates the support of the smeared crack, which provides the support for the auxiliary field $\mathbf{v}(\mathbf{x})$. Hence, the auxiliary

field is only present at the smeared crack, and the kinematics away from the crack are governed by the displacement field $\mathbf{u}(\mathbf{x})$. Next, we define the normal to the smeared crack based on the point closest to the discrete boundary Γ_d, denoted by $\mathbf{x}_c$, as

$$\mathbf{n}_c(\mathbf{x}) = \mathbf{n}(\mathbf{x}_c) \quad , \quad \mathbf{x}_c(\mathbf{x}) = \underset{\mathbf{y}\in\Gamma_d}{\operatorname{argmin}} \left(\|\mathbf{y}-\mathbf{x}\|\right) \tag{19}$$

In the discrete formulation, the displacement jump is strictly defined at the internal discontinuity Γ_d. In the phase-field approach the crack exists in smeared sense, and so does the crack opening. Therefore, we approximate the discrete displacement jump at $\mathbf{x}_c$ in terms of the auxiliary jump field $\mathbf{v}(\mathbf{x})$ as

$$[\![\mathbf{u}]\!](\mathbf{x}_c) \approx \int_{-\infty}^{\infty} \mathbf{v}(\mathbf{x})\delta_\epsilon \mathrm{d}x_n \tag{20}$$

Under the condition that the auxiliary field is constant in the direction normal to the fracture, i.e. $\frac{\partial v}{\partial x_n} = 0$, we have

$$\mathbf{v}(\mathbf{x}) = \mathbf{v}(\mathbf{x}_c + \zeta\mathbf{n}) = \mathbf{v}(\mathbf{x}_c) \tag{21}$$

with $\mathbf{n}$ the vector normal to the crack, and ζ the coordinate along $\mathbf{n}$. Back-substitution into equation (20) shows that $\mathbf{v}(\mathbf{x})$ reflects the crack opening at the closest point x_c on the discrete internal boundary. Consequently, in equation (17) the crack opening $[\![\mathrm{u}]\!]$ that appears as an argument of the fracture energy is directly replaced by the auxiliary field $\mathbf{b}(\mathbf{x})$. In the limiting case that the length scale parameter ϵ goes to zero, the smeared crack Γ_ϵ coincides with the discrete crack Γ_d and the auxiliary displacement field consides with the discrete displacement jump. The requirement that the auxiliary jump field is constant in the direction normal to the crack is now enforced weakly through an additional term in the internal energy functional:

$$\Phi_{\mathrm{pot},\epsilon} = \int_\Omega \left(\psi^e(\varepsilon^e) + \mathcal{G}(\mathbf{v},\kappa)\delta_\epsilon + \frac{1}{2}\alpha \left\| \frac{\partial \mathbf{v}}{\partial x_n} \right\|^2 \right) \mathrm{d}V \tag{22}$$

with α a positive constant parameter.

With the discontinuity kinematics determined through the auxiliary jump field, the elastic strain tensor ε^e can be derived by requiring the auxiliary field not to exert any external power on the problem, such that the balance of power is given by

$$\int_\Omega \left(\sigma^e_{ij}\dot{\varepsilon}^e_{ij} + t_i(\boldsymbol{v},\kappa)\delta_\epsilon \dot{v}_i \right) \mathrm{d}V = \int_{\partial\Omega} t_i \dot{u}_i \mathrm{d}A \tag{23}$$

Application of Gauss' theorem to the right-hand side of this equation, and requiring the traction to be in equilibrium with the elastic stress, $\sigma^e_{ij}n_j = t_i$, yields

$$\int_\Omega \sigma^e_{ij} \left(\dot{\varepsilon}^e_{ij} + \delta_\epsilon \,\mathrm{sym}\left(\dot{v}_i n_j\right) \right) \mathrm{d}V = \int_\Omega \sigma^e_{ij} \dot{u}_{(i,j)} \mathrm{d}V \tag{24}$$

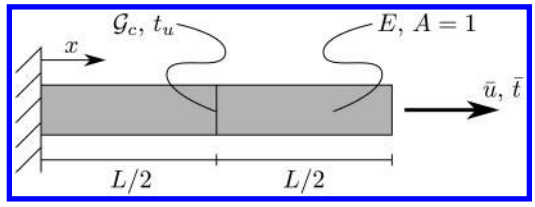


Figure 4. Schematic representation of a uniaxial rod with a cohesive interface.

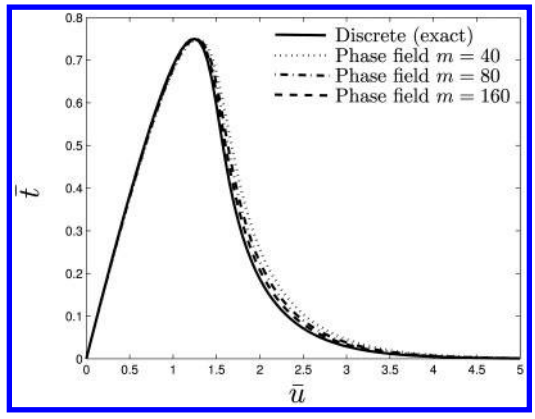


Figure 5. Force-displacement curve for the one-dimensional cohesive zone problem.

From the balance of power it is directly observed that the elastic infinitesimal strain tensor is related to the displacement field $\boldsymbol{u}(\boldsymbol{x})$ and auxiliary field $\boldsymbol{v}(\boldsymbol{x})$ as

$$\varepsilon^e_{ij} = u_{(i,j)} - \mathrm{sym}\left(v_i n_j\right)\delta_\epsilon \tag{25}$$

In this expression the first part is the symmetric part of the gradient of the displacement field. The second part can be interpreted as the strain caused by the displacement jump. Hence the elastic strain is defined as the symmetric gradient of the displacment field, minus the strain caused by the crack opening. We note from equation (25) that away from the crack, i.e. for $\boldsymbol{x} \notin \Gamma_\epsilon$, the continuum expression is recovered. In the limiting case that ϵ goes to zero, the elastic equivalent strain is equal to the symmetric gradient of the displacement field at every point in the interior of the domain. The unbounded strain term at the discontinuity is caused by the jump of the displacement field over this internal boundary.

3.2 *Cohesive fracture of a rod*

As an example we consider the one-dimensional bar loaded in tension as shown in Figure 4. The bar has a unit length and also the modulus of elasticity equals unity. The fracture toughness and fracture strength are taken as $\mathcal{G}_c = 1$ and $f_t = 0.75$, respectively. Figure 5 shows the response obtained using various mesh sizes for the phase-field model and compares it with the

exact solution to the discrete problem. It is observed that upon mesh refinement the phase-field model converges to the discrete solution.

4 CONCLUSIONS

The cohesive approach to fracture is simple, flexible, yet very powerful, and capable of capturing a wide range of fracture phenomena. A shortcoming of existing cohesive surface models is that the inplane strains, and therefore the in-plane stresses, are absent in the formulation, which makes it difficult, if not impossible to capture fracture phenomena like splitting cracks in reinforced concrete, or crazing in polymers. A simple and elegant extension of the classical cohesive surface methodology has been proposed Remmers et al. (2013), which can be incorporated straightforwardly in numerical methods, such as interface elements, partition-of-unity finite methods, and isogeometric analysis.

Another issue is the implementation of cohesive surface models in finite element methods. Since a cohesive surface represents an evolving, two-dimensional body in a three-dimensional continuum, this necessarily involves remeshing, or the use of another discretisation method that involves the addition of degrees of freedom during the computation, e.g. the finite element methods that exploit the partition-of-unity property of finite element shape functions. Smeared (or continuum) approaches avoid this, but tend to result in ill-posed boundary value problems when the damage exceeds a certain threshold. Herein, we have suggested that a phase-field approach to cohesive fracture can be a possible solution, since it operates on a fixed grid, but does not result in an ill-posed boundary value problem.

REFERENCES

Barenblatt, G. I. (1962). The mathematical theory of equilibrium cracks in brittle fracture. *Advances in Applied Mechanics 7*, 55–129.

Bažant, Z. P. (1976). Instability, ductility, and size effect in strain-softening concrete. *ASCE Journal of the Engineering Mechanics Division 102*, 331–344.

Bažant, Z. P. & B. Oh (1983). Crack band theory for fracture of concrete. *RILEM Materials and Structures 16*, 155–177.

Camacho, G. T. & M. Ortiz (1996). Computational modeling of impact damage in brittle materials. *International Journal of Solids and Structures 33*, 2899–2938.

de Borst, R., M. A. Crisfield, J. J. C. Remmers, & C. V. Verhoosel (2012). *Non-linear Finite Element Analysis of Solids and Structures* (second ed.). Chichester: John Wiley & Sons.

de Borst, R., H. B. Mühlhaus, J. Pamin, & L. J. Sluys (1993). Fundamental issues in finite element analyses of localization of deformation. *Engineering Computations 10*, 99–121.

Dugdale, D. S. (1960). Yielding of steel sheets containing slits. *Journal of the Mechanics and Physics of Solids 8*, 100–108.

Francfort, G. A. & J. J. Marigo (1998). Revisiting brittle fracture as an energy minimization problem. *Journal of the Mechanics and Physics of Solids 46*, 1319–1342.

Ingraffea, A. R. & V. Saouma (1985). Numerical modelling of discrete crack propagation in reinforced and plain concrete. In *Fracture Mechanics of Concrete*, pp. 171–225. Dordrecht: Martinus Nijhoff Publishers.

Keller, K., S. Weihe, T. Siegmund, & B. Kröplin (1999). Generalized cohesive zone model: incorporating triaxiality dependent failure mechanisms. *Computational Materials Science 16*, 267–274.

Miehe, C., M. Hofacker, & F. Welschinger (2010). A phase field model for rate-independent crack propagation: Robust algorithmic implementation based on operator splits. *Computer Methods in Applied Mechanics and Engineering 199*, 2765–2778.

Miehe, C., F. Welschinger, & F. Welschinger (2010). Thermodynamically consistent phase-field models of fracture: Variational principles and multi-field fe implementations. *International Journal for Numerical Methods in Engineering 83*, 1273–1311.

Remmers, J. J. C., R. de Borst, C. V. Verhoosel, & A. Needleman (2013). The cohesive band model: a cohesive surface formulation with stress triaxiality. *International Journal of Fracture.*

Rots, J. G. (1991). Smeared and discrete representations of localized fracture. *International Journal of Fracture 51*, 45–59.

Ruggieri, C., T. L. Panontin, & R. H. Dodds (1996). Numerical modeling of ductile crack growth in 3-D using computational cell elements. *International Journal of Fracture 82*, 67–95.

Tijssens,M. G. A., E. van der Giessen E, & L. J. S. LJ (2000). Modeling of crazing using a cohesive surface methodology. *Mechanics of Materials 32*, 19–35.

Research and Applications in Structural Engineering, Mechanics and Computation – Zingoni (Ed.)
© 2013 Taylor & Francis Group, London, ISBN 978-1-138-00061-2

Recent controversies and new challenges in structural topology optimization

G.I.N. Rozvany
Department of Structural Mechanics, Budapest University of Technology and Economics, Budapest, Hungary

ABSTRACT: This keynote lecture deals with structural topology optimization, a relatively new but rapidly expanding field of structural mechanics. After discussing its fundamental features and defining its subfields (layout optimization and generalized shape optimization), we review the early history of both exact and discretized topology optimization and show extensive applications in the car, machine and aerospace industries, as well as in architecture and medicine. . Then a brief summary of both theoretical developments and numerical methods is given, and computational difficulties and quality control in topology optimization discussed. This includes a detailed review of basic features of optimal structural topologies, including some recent controversies in basic theory and numerical techniques. Finally, some new challenges and future perspectives are outlined.

1 INTRODUCTION

Structural topology optimization is becoming an extremely popular field of structural mechanics, because it results in substantial savings in industrial applications and has interesting theoretical implications in mathematics, mechanics, multi-physics and computer science.

Various theoretical aspects, as well as a great variety of numerical methods and applications are discussed extensively in the literature. At the ISSMO world congress in Seoul, over 160 papers dealt with topology optimization (out of some 400 papers). In this keynote lecture, we review basic features, history, applications, current status, recent controversies and future perspectives of structural topology optimization.

2 FUNDAMENTAL FEATURES OF STRUCTURAL TOPOLOGY OPTIMIZATION

As explained earlier (e.g. Rozvany et al. 1995), structural topology optimization consists of two main subfields.

Layout optimization deals with grid-like (low volume fraction) structures (trusses, grillages, shell-grids, and dense systems of intersecting shells), optimizing simultaneously the topology (connectivity of the members), geometry (location of the joints) and sizing (cross-sectional dimensions).

Generalized shape optimization finds the best topology of the internal boundaries and the optimal shape of both internal and external boundaries of perforated or composite continua.

In **layout optimization (LO)**, we start off with a 'ground structure', which contains all potential members ('ground elements'). During the optimization procedure, we remove non-optimal ground elements and determine the optimal sizes of the optimal ones.

In discretized LO, the number of ground elements is finite. In exact LO, it is infinite. A ground structure with an infinite number of elements is sometimes called 'structural universe' (Rozvany et al. 1995). Alternatively, a structural universe may be replaced by a 'design domain', at all points of which members may run in any direction.

The simplest form of structural topology optimization concerns so-called **ISE topologies** (with **I**sotropic **S**olid or **E**mpty elements).

In **generalized shape optimization** (GSO) the structural domain is divided into a finite number of ground elements. For ISE topologies, the thickness or density of each ground element may only take on a zero value ('white element') or a pre-assigned other value ('black element'). In a normalized formulation, the pre-assigned value is unity, and then we have a 0–1 problem.

In discretized GSO, we have a finite number of ground elements. In exact GSO, we have an infinite number of ground elements, which shrink to points. In other words, exact GSO consists of assigning optimally either 'material' or 'no material' to each point of the design domain.

GSO can be generalized into **multi-material optimization**, in which for each ground element (or at each point of the design domain) we may chose one out of several given materials or no material.

Structural topology optimization may consist of minimizing an objective function (typically the total structural volume, weight or cost) within **constraints** on the structural response (e.g. stresses, displacements, buckling load, natural frequency, etc.). Alternatively, we may maximize or minimize some structural responses or their combination for given volume, weight or cost.

In the following two sections, we review briefly the history of exact and numerical branches of structural topology optimization.

3 BRIEF HISTORY OF EXACT (ANALYTICAL) STRUCTURAL TOPOLOGY OPTIMIZATION

The first paper on exact structural topology optimization was published more than a century ago by the ingenious Australian inventor A. G. M. ('George') Michell (1904). It dealt with the **least-volume topology of trusses** with a single load condition and a stress constraint. This pioneering effort was completely ignored for over a half a century, when it was re-discovered by Cox (1958), who applied Michell's criteria to new load conditions. Later Hemp worked on Michell structures most of his professional life. His and his coworkers' results were summarized in his book (Hemp 1973).

The theory of the **optimal topology of grillages** (beam systems) actually preceded the development of the optimal layout theory (Prager and Rozvany 1977a). The grillage theory (e.g. Rozvany 1972a and b) was developed by the author's research group, but it has some elements of Morley's (1966) theory for optimal reinforcement in concrete slabs. Reviews of the grillage theory may be found in several texts (e.g. Rozvany and Hill 1976, Prager and Rozvany 1977b, Rozvany 1989 and Rozvany, Bendsoe and Kirsch 1995).

Exact optimal grillage topologies should actually be used more often as benchmarks, because they have the following advantages.

(i) The optimal grillage theory has advanced much further than the truss theory, because exact optimal grillage topologies are available for almost all possible support and load conditions, and these analytical solutions can even be generated by computer (see e.g. Fig. 38, Rozvany et al. 1995).
(ii) Michell trusses ignore buckling, which plays a much more important role for trusses than for grillages.
(iii) Grillages may have three types of boundary conditions (clamped and simply supported boundaries, and free edges), whilst trusses may only have two (support or no support).
(iv) A large number of extensions of the grillage theory exist (see Rozvany 1992, pp. 125–127)
(v) Whilst most Michell trusses are mechanisms, most optimal grillages are stable structures.

3.1 *The Prager-Rozvany (1977a) optimal layout theory*

The **first general theory of exact topology optimization** was introduced in effect in the author's first book (Rozvany 1976) for flexural systems (e.g. grillages, shells), and formulated in a more concise form later (Prager and Rozvany 1977a). It is based on the Prager-Shield (1967) optimality condition for plastic design and its extensions (Charrett and Rozvany 1972). However, the new element in the layout theory is, that it also gives optimality conditions for 'vanishing' members (of zero cross-sectional area) in terms of 'adjoint' strains along these members. In other words, optimal layout theory starts off with a ground structure or structural universe of all potential members, and selects the optimal members (of non-zero cross-sectional area) out of those.

In the Prager-Rozvany (1977a) layout theory, it is necessary to find a

(i) kinematically admissible 'adjoint' displacement/strain fields (satisfying kinematic continuity and boundary conditions),
(ii) statically admissible stress fields (satisfying equilibrium and statical boundary conditions),
(iii) such that certain ('static-kinematic') optimality criteria are also fulfilled.

In these optimality criteria, the adjoint strains are given by the subgradient of the 'specific cost function' with respect to stresses or stress resultants (e.g. member forces F or beam moments M).

The subgradient of a function is the usual gradient, but at discontinuities of the gradient any convex combination of the adjacent gradients can be taken.

For sign-independent stress-based design of trusses and grillages of given depth, for example, the 'specific cost functions' (representing in this text cross sectional areas A) are, respectively

$$A = k|F| \text{ and } A = k|M|, \tag{1}$$

where k is a constant, F is the member force and M is the beam bending moment. Then, e.g. for trusses, the optimality conditions reduce to those of Michell (1904)

$$\bar{\varepsilon} = k \operatorname{sgn} F \text{ (for } F \neq 0), \; |\bar{\varepsilon}| \leq k \text{ (for } F = 0), \tag{2}$$

where $\bar{\varepsilon}$ is the adjoint strain (see Fig. 1a). For a prescribed minimum cross section with equal and unequal permissible stresses in tension and compression the optimality criteria are shown in Figs. 1b and c, respectively.

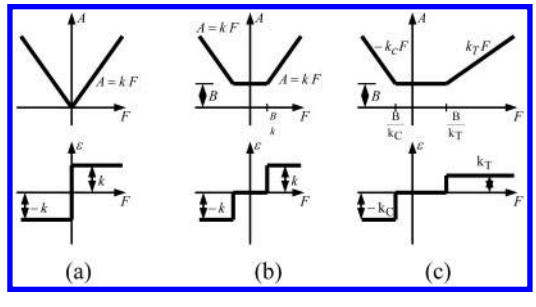


Figure 1. Optimality criteria for various types of trusses.

3.2 *Optimal regions in Michell trusses and grillages*

It follows from (2) that in Michell trusses, the members are in the direction of the adjoint principal strains of a constant magnitude (k), and the absolute value of adjoint strains may nowhere exceed this value. The optimal topology usually consists of several 'regions'. Denoting the principal adjoint strains by $(\bar{\varepsilon}_1, \bar{\varepsilon}_2)$, at any point of a 2D truss, *for equal permissible stresses in tension and compression* we may have the following **optimal regions**.

T-region with a tensile and a compression member at right angles, $\bar{\varepsilon}_1 = \bar{\varepsilon}_2 = k$,

S-region with members having forces of the same sign in any direction, $\bar{\varepsilon}_1 = \bar{\varepsilon}_2, |\bar{\varepsilon}_i| = k (i = 1, 2)$,

R-regions with only one member at any point, $|\bar{\varepsilon}_1| = k, |\bar{\varepsilon}_2| \le k$, or

O-region with no members $|\bar{\varepsilon}_1|, \le k, |\bar{\varepsilon}_2| \le k$ with $k = 1/\sigma^{(p)}$, where $\sigma^{(p)}$ is the permissible stress in both tension and compression.

Within O-regions we may have Z-regions with $\bar{\varepsilon}_1 = \bar{\varepsilon}_2 = 0$ and V-regions with $|\bar{\varepsilon}_1| \le k, \bar{\varepsilon}_2 = 0$

Most of the Michell literature deals with T-regions, because of the link with slip-lines (Hencky-Prandtl nets).

The symbols for optimal regions are shown in Fig. 2a. We have similar optimal regions for grillages of given depth.

3.3 *Example of determining an optimal truss topology*

In Fig. 2b we show some optimal topologies and in Fig. 2c the corresponding optimal adjoint displacement fields. The boundary conditions consist of two line supports at right angles. We use a normalized formulation with $k = 1$.

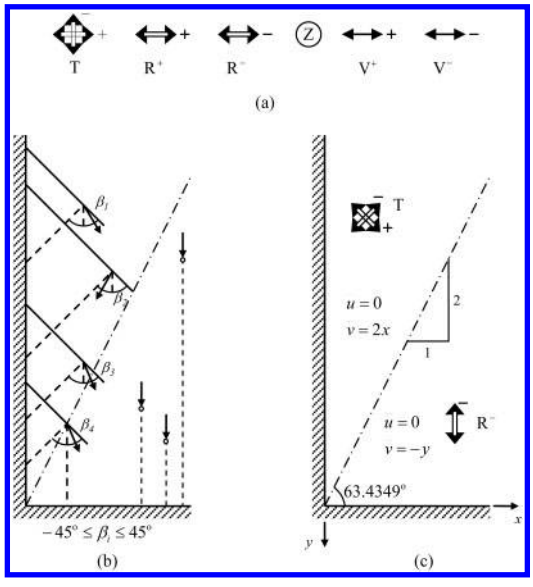


Figure 2. (a) optimal regions for Michell trusses and (b,c) example of determining an optimal truss topology.

Elementary calculations show that in the upper region we have the principal adjoint strains

$$\bar{\varepsilon}_1 = -\bar{\varepsilon}_2 = 1 \tag{3}$$

at ±45° to the horizontal. This corresponds to a T-region, denoted by an arrow cross in Fig. 2c. In the lower region we have

$$\bar{\varepsilon}_1 = 0, \ \bar{\varepsilon}_2 = -1, \tag{4}$$

which signifies an R^- region denoted by a double arrow. Both (3) and (4) *satisfy the optimality conditions* in (2).

It can be readily seen that along the line supports with $x = 0$ and $y = 0$ we have $u = v = 0$, satisfying the *kinematic boundary conditions*. Moreover, along the region boundary with $y = -2x$ both adjoint displacement fields in Fig. 2c give

$$\bar{u} = 0, \ \bar{v} = -2x \tag{5}$$

satisfying *kinematic continuity*.

3.4 *Shortcomings of Michell's truss theory*

One of the controversies discussed in this lecture concerns the limited range of validity of Michell's optimality criteria.

After re-examining Michell's proof, the author concluded (Rozvany 1996) that Michell's original optimality criteria are valid only if one or both of the following two conditions are satisfied:

(a) the structural domain is subject to prescribed external forces only, or equivalently, to 'statically determinate supports' (supports in which the reactions can be uniquely determined from equilibrium), or

(b) the permissible stresses in tension and compression are the same.

3.5 *Extension of Michell's theory to unequal permissible stresses and statically indeterminate support conditions*

If neither of the conditions (a) or (b) under Section 3.4 are satisfied, then Michell's optimality conditions are not valid, and must be modified.

For different permissible stresses σ_T, σ_C in tension and compression, and statically indeterminate support conditions, one must use the following optimality criteria (for proofs see Rozvany 1996).

$$\begin{aligned} &\bar{\varepsilon} = -1/\sigma_C \ (\text{for } F < 0), \ \bar{\varepsilon} = 1/\sigma_T \ (\text{for } F > 0), \\ &-1/\sigma_C \le \bar{\varepsilon} \le 1/\sigma_T \ (\text{for } F = 0), \end{aligned} \tag{6}$$

in which $\bar{\boldsymbol{\varepsilon}}$ represents a fictitious strain-field termed 'adjoint' strain field. We sometimes use the shorter notation

$$1/\sigma_C = k_C, \ 1/\sigma_T = k_T. \tag{7}$$

For $\sigma_T = \sigma_C = \sigma^{(p)}$ we have

$$k_T = k_C = k = 1/\sigma^{(p)}, \tag{8}$$

and then (6) reduces to (2). Relations (2) or (6) are necessary and sufficient conditions of optimality for the relevant class of problems if a feasible solution exists, the adjoint strains $\bar{\varepsilon}$ are kinematically admissible, and the member forces F statically admissible (i.e. satisfying equilibrium).

3.6 *More recent developments in Michell's truss theory*

New classes of solutions using the classical theory (relation (2)) were derived in papers by Rozvany and Gollub (1990) Lewinski et al (1994a and b), Rozvany et al. (1997), Lewinski and Rozvany (2007, 2008a and b), Sokol and Lewinski (2010, 2011), Sokol and Rorvany (2012).

Using the extended theory (relation (6)), a number of new solutions were derived by Graczykowski and Lewinski (2006a and b, 2007a and b), Rozvany and Sokol (2012), Sokol and Rozvany (2013), and Pichugin et al. (2012).

4 NUMERICAL METHODS IN STRUCTURAL TOPOLOGY OPTIMIZATION

4.1 *The origins of the SIMP algorithm*

The idea of FE-based topology optimization is due to Rossow and Taylor (1973), who used an unpenalized density-stiffness relation (continuous line in Fig. 3) and therefore obtained solutions with intermediate thicknesses In a pioneering publication, Bendsoe and Kikuchi (1988) suggested homogenization based on square or rectangular holes, which also produced some degree of penalization (dotted line in Fig. 3).

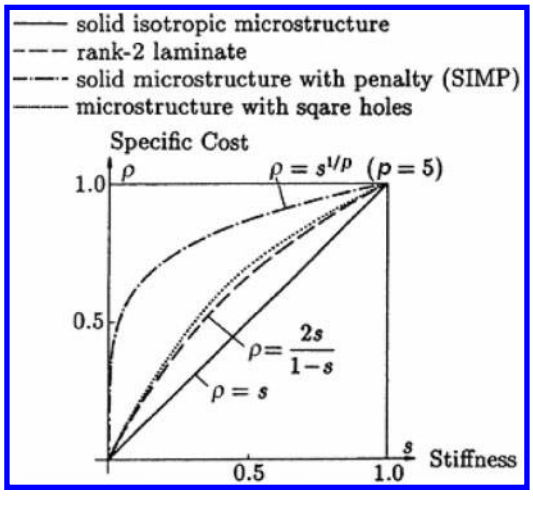


Figure 3. Normalized stiffness (s) – specific cost or density (ρ) relations in topology optimization methods (after Fig. 81 in Rozvany et al. 1995).

A year later Bendsoe (1989), in another milestone paper, considered a SIMP-like method based on the power-law relation

$$\rho = s^{1/p} \tag{9}$$

(see Fig. 2), but expressed as yet preference for homogenization with square holes. This he justified by referring to mesh dependence and fictitiousness of material properties in (9), which was quite reasonable from his viewpoint. Mlejnek (e.g. 1992) proposed later an independently conceived SIMP-like procedure.

The author and Zhou based the relation (9) on combined cost of material and manufacturing, assuming that only one plate thickness is available originally, and other thicknesses must be obtained by a machining process. Zhou developed the computational details of the SIMP method, with suitable re-design formulae for thicknesses (densities) and Lagrange multipliers. At a Karlsruhe conference in 1990, Zhou and the author presented already advanced solutions (Zhou and Rozvany 1991). The term 'SIMP' was coined by Rozvany et al. (1992).

Zhou and the author initially applied the DCOC optimality criteria method (Zhou and Rozvany 1992/1993) to solve the optimization problem under SIMP formulation. While DCOC offers unique capability in the handling of stress constraints, general optimization codes such as CONLIN and MMA (Fleury 1989, Svanberg 1987) based on dual method of convex programming offer robust black-box solutions to multiply constrained optimization problems.

SIMP was gradually accepted by other topology groups as well, particularly after Sigmund, who started working in the author's research group in Essen on topology optimization, moved back to Denmark and contributed much to explaining SIMP to the optimization community. Sigmund's (2001) educational article with a 99-line SIMP-code played an important role in SIMP's general acceptance. Moreover, Bendsoe and Sigmund (1999) generated microstructures corresponding to the power law in (9) above. The complete acceptance of SIMP can be seen also from the fact that the second edition of Bendsoe's trendsetting book (Bendsoe and Sigmund 2003) uses almost exclusively SIMP for its main part (on what we call here ISE topologies), whilst its earlier edition (Bendsoe 1995) mentioned the "penalized variable thickness approach" only in one sentence under "Bibliographical notes" (p. 230) .

4.2 *Application of SIMP in commercial software*

The author's former co-worker Ming Zhou moved from Essen University to the Altair software company in California, where he is currently the Vice President for research and development. He has incorporated the SIMP algorithm into the OptiStruct software, which is now used most extensively by the aerospace, car and machine industries, but also for very tall buildings in architecture. In the lecture, several examples of these

industrial applications will be shown. But other commercial software is also using exclusively the SIMP method for structural topology optimization.

4.3 *Other numerical methods of structural toplogy optimization*

Earlier the **homogenization method** was also used, in which in each element the dimensions and orientation of square or rectangular holes were optimized, and such elements were homogenized for the subsequent FE analysis in each iteration. Other investigators used earlier **optimal microstructures** in each element, and subsequently penalized intermediate densities. However, currently SIMP is used in preference to the latter two methods.

Moreover, Fleury and Beckers used **discrete dual programming** successfully for topology optimization (e.g. Beckers 1999).

More recent methods are the **topological derivative and level set methods**, which have very much promise, but have not reached as yet the stage of industrial applications.

Rather controversial are the completely heuristic '**sudden death**' or '**hard kill**' methods, in which in each iteration elements with some low response function values are taken out. The most publicized of these methods is the '**ESO**' (**E**volutionary **S**tructural **O**ptimization) method, which is not used currently in commercial software. A comprehensive review of established methods in structural topology optimization was published by the author four years ago (Rozvany 2009).

4.4 *Computational difficulties in structural topology optimization*

Some of these difficulties are the checkerboard (discretization) error, singular optima, local optima and special difficulties with local and global buckling constraints. These will be discussed in greater detail in the lecture, together with a review of the most recent research, particularly by Sigmund's research school in multi-physics applications.

5 CONCLUDING REMARKS

In the lecture we will also examine such controversial issues as the relative importance of gradient (e.g. SIMP) and non-gradient (e.g. nature-inspired) methods in topology optimization. It has been suggested recently in a paper by Sigmund (2011), that publication of the latter should be severely restricted in topology optimization, because the efficiency and resolving power of the former is several orders of magnitude higher. Moreover, it is not correct that we call non-gradient methods in general 'global methods', because there exists no proof of convergence to a global optimum for most of them. In fact in many examples in the literature they produce a highly non-optimal solution. It is true that gradient methods find the nearest local optimum only, but they are just as likely to locate the global optimum if we use several starting points in the design space.

Another issue to be discussed is the importance of exact analytical solutions in topology optimization, pointing out that they can be used (a) as benchmarks for checking on numerical methods, (b) for establishing fundamental properties of optimal topologies, and (c) for deriving non-heuristic numerical algorithms by discretization. On the other hand, new numerical methods (e.g. Sokol 2011a and b, Pichugin et al. 2012) can optimize problems with billions of variables for checking accurately on analytically derived optimal topologies.

REFERENCES

Beckers M (1999) Topology optimization using a dual method with discrete variables. Struct Optim 17:14–24

Bendsoe MP (1995) Optimization of structural topology, shape and material. Springer, Berlin, 1995

Bendsoe MP, Sigmund O (1999) Material interpolation schemes in topology optimization. Arch Appl Mech 69: 635–654

Bendsoe MP, Sigmund O (2003) Topology optimization, theory, methods and applications. Springer, Berlin

Charrett DE, Rozvany GIN (1972) Extensions of the Prager-Shield theory of optimal plastic design. Int J Non-Lin Mech 7:51–64

Cox HL (1958) The theory of design. Rep Aeronaut Res Council No 2037

Fleury C (1989) CONLIN: An efficient dual optimizer based on convex approximation concepts. Struct. Opt. 1:81–89

Graczykowski C, Lewinski T (2006a and b, 2007a and b) Michell cantilevers constructed within trapeziodal domains – Parts I-4: Struct Multidisc Opt 32:347–368, 463–471, 33:1–19, 113–129

Hemp WS (1973) Optimum structures. Clarendon, Oxford

Lewinski T, Rozvany GIN (2007) Exact analytical solutions for some popular benchmark problems in topology optimization II: three-sided polygonal supports. Struct. Multidisc. Optim. 33, 337–350

Lewinski, T, Rozvany, GIN (2008a) Exact analytical solutions for some popular benchmark problems in topology optimization III: L-shaped domains. Struct. Multidisc. Optim., 35: 165–174

Lewinski T, Rozvany GIN (2008b) Analytical benchmarks for topology optimization IV: square-shaped line support. Struct Multidisc Optim 36:143–158

Lewinski T, Zhou M, Rozvany GIN (1994a) Extended exact solutions for least-weight truss layouts. Part I: cantilevers with a horizontal axis of symmetry. Int J Mech Sci 36: 375–398

Lewinski T, Zhou M, Rozvany GIN (1994b) Extended exact solutions for least-weight truss layouts. Part II: unsymmetric cantilevers. Int J Mech Sci 36:399–419

Michell AGM (1904) The limits of economy of material in frame structures. Phil Mag 8, 589–597

Mlejnek HP, Schirrmacher R (1993) An engineering approach to optimal material distribution and shape finding. Comp Meth Appl Mech Engrg 106: 1–26

Morley CT (1966) The minimum reinforcement of concrete slabs. Int J Mech Sci 8:305–319

Pichugin AV, Tyas A, Gilbert M (2012) On the optimality of emp's arch with vertical hangers. Struct Multidisc Optim 46:17–25

Prager W, Rozvany GIN (1977a) Optimization of the structural geometry. In: Bednarek, A. R.; Cesari, L. (eds.) Dynamical Systems (proc. Int. Conf. Gainsville, Florida). pp. 265–293. Academic Press, New York

Prager W, Rozvany GIN (1977b) Optimal layout of grillages. J Struct Mech 5: 1–18

Prager W, Shield RT (1967) A general theory of optimal plastic design. J Appl Mech 34:184–186

Rossow MP, Taylor JE (1973) A finite element method for the optimal design of variable thickness sheets. AIAA J 11: 1566–1569

Rozvany GIN (1972a) Grillages of maximum strength and maximum stiffness. Int. J. Mech. Sci. 14, 1217–1222

Rozvany GIN (1972b) Optimal load transmission by flexure. Comp. Meth. Appl. Mech. Engrg. 1, 253–263

Rozvany GIN (1976) Optimal design of flexural systems. Pergamos Press, Oxford

Rozvany GIN (1989) Structural design via optimality criteria. Kluwer, Dordrecht

Rozvany GIN (1992) Shape and layout optimization of structural systems and optimality criteria methods. CISM Courses and Lectures No. 325, Springer-Verlag, Vienna-New York

Rozvany GIN (2009) A critical review of established methods in structural topology optimization. Struct Multidisc Optim 37:217–237

Rozvany GIN (1996) Some shortcomings of Michell's truss theory Struct Optim 12:244–250

Rozvany GIN, Bendsoe MP, Kirsch U (1995) Layout optimization of structures Appl Mech Rev ASME 48:41–119

Rozvany GIN, Gollub W (1990) Michell layouts for various combinations of line supports – I. Int J Mech Sci 32: 1021–1043

Rozvany GIN, Gollub W, Zhou M (1997) Exact Michell layouts for various combinations of line supports – Part II. Struct Optim 14:138–149

Rozvany GIN, Hill RH (1976) General theory of optimal load transmission by flexure. Advances in Appl Mech 16: 184–308

Rozvany GIN, Sokół T (2012) Exact truss topology optimization: allowance for support costs and different permissible stresses in tension and compression – extensions of a classical solution by Michell. Struct Multidisc Optim 45:367–376

Rozvany GIN, Zhou M, Birker T (1992) Generalized shape optimization without homogenization. Struct Optim. 4, 250–254

Sigmund O (2001) A 99 line topology optimization code written in matlab. Struct. Multidisc. Optim. 21:120–127

Sigmund O (2011) On the usefulness of non-gradient approaches in topology optimization. Struct Multidisc Optim 43:589–596

Sokół T (2011a) A 99 line code for discretized Michell truss optimization written in Mathematica, Struct Multidisc Optim 43:181–190

Sokół T (2011b) Topology optimization of large-scale trusses using ground structure approach with selective subsets of active bars. In: Borkowski A, Lewiński T, Dzierżanowski G (eds) 19th int conf on 'computer methods in mechanics', CMM 2011, 09–12 May, Warsaw, Book of Abstract, pp 457–458

Sokół T, Lewiński T (2010) On the solution of the three forces problem and its application in optimal designing of a class of symmetric plane frameworks of least weight, Struct Multidisc Optim 42:835–853

Sokół T, Lewiński T (2011) Optimal design of a class of symmetric plane frameworks of least weight. Struct Multidisc Optim 44:729–734

Sokół T, Rozvany GIN (2012) New analytical benchmarks for topology optimization and their implications. Part I: bi-symmetric trusses with two point loads between supports. Struct Multidisc Optim 46:477–486

Sokół T, Rozvany GIN (2013) Exact least-volume trusses for two symmetric point loads and unequal permissible stresses in tension and compression. Struct Multidisc Optim 47:151–155

Svanberg, K (1987) The method of moving asymptotes – a new method for structural optimization. Int. J. Numer. Methods Eng. 24: 359–373

Zhou M, Rozvany GIN (1991) The COC algorithm, Part II: topological, geometrical and generalized shape optimization. Comp Meth Appl Mech Engrg 89:309–336

Zhou M, Rozvany GIN 1992/1993: DCOC: An optimality criterion method for large systems. Part I: Theory. Part II: algorithm. Struct. Optim. 5: 12–25, 6:250–262

2. Dynamic response, vibration analysis, vibration control

Research and Applications in Structural Engineering, Mechanics and Computation – Zingoni (Ed.)
© 2013 Taylor & Francis Group, London, ISBN 978-1-138-00061-2

General conditions for instantaneous system inversion in structural dynamics

K. Maes, E. Lourens, G. De Roeck & G. Lombaert
KU Leuven, Department of Civil Engineering, Leuven, Belgium

ABSTRACT: In structural dynamics, the forces acting on a structure are in many cases not well known. System inversion techniques may then be used to estimate these forces from the measured response of the structure. This paper presents conditions for the invertibility of linear system models, that apply generally to any instantaneous input estimation algorithm. The conditions ensure the identifiability of the dynamic forces, the stability of the system inversion and the uniqueness of the identified quantities. For the specific case of modally reduced order models, which can be obtained either from first principle models or from experimental data using system identification techniques, the conditions can be directly expressed in terms of the modal properties of the structure. This physical insight can then be used to design vibration experiments that aim for system inversion. Each of the conditions is derived and illustrated by a conceptual example.

1 INTRODUCTION

The dynamic forces acting on a structure are of great importance to many engineering applications. Often, however, the dynamic forces cannot be obtained by direct measurements, e.g. for wind loads, and have to be determined indirectly from dynamic measurements of the system response.

Force identification problems were initially solved off-line in a deterministic setting. Many methods were proposed, most of them based on the frequency response function (Guillaume et al. 2002, Liu and Shepard 2005, Parloo et al. 2003) or making use of a time domain approach (Klinkov and Fritzen 2007, Nordström and Nordberg 2002, Jacquelin et al. 2003, Adams and Doyle 2002). A recursive deterministic method was presented by Klinkov and Fritzen (2006), estimating both the input and system states from a set of output measurements. Currently, the attention is shifted to the development of recursive combined deterministic-stochastic approaches (Hwang et al. 2009, Ma et al. 2003). These methods do not only account for measurement errors, but also for modelling errors and additional unknown vibration sources. An algorithm was proposed by Gillijns and De Moor (2007), where the input estimation is performed separately from the state estimation step. The algorithm was applied in structural dynamics by Lourens et al. (2012). A similar approach was proposed by Niu et al. (2011). Alternatively, the dynamic forces and system states can be jointly estimated using a classical Kalman filter, hereby including the unknown forces in an augmented state vector (Lourens et al. 2012).

This paper focuses on instantaneous system inversion, i.e. inversion without any time delay, covering the majority of inversion algorithms applied in structural dynamics. The invertibility of a system in general requires three conditions. Firstly, the dynamic forces must be identifiable from the given set of response measurements. Secondly, the system inversion must be stable, such that small perturbations on the measurement data do not give rise to unbounded errors on the identified quantities. Thirdly, if the dynamic forces can be identified in a stable way, the estimates obtained must be uniquely defined by the measurement data. In the literature, the main requirements on the system description for instantaneous invertibility are extensively documented for the general case of linear systems (Antsaklis 1978, Massey and Sain 1968, Moylan 1977). For the specific case of linear modally reduced order models, as often used in structural dynamics, the general conditions can be directly translated into a number of requirements on the output vector, i.e. sensor types, sensor locations, and number of sensors. These requirements are important for the design of vibration experiments that aim for input estimation.

Starting from the general conditions on system invertibility, as given in the literature, the requirements on the output vector are derived. A conceptual example is used to illustrate the theoretical derivation.

2 PROBLEM FORMULATION

In structural dynamics, first principle models, e.g. finite element (FE) models, are widely used. In many cases, modally reduced order models are applied, constructed from a limited number of structural modes. When proportional damping is assumed, the

continuous-time decoupled equations of motion for modally reduced order models are given by:

$$\ddot{\mathbf{z}}(t) + \mathbf{\Gamma}\dot{\mathbf{z}}(t) + \mathbf{\Omega}^2\mathbf{z}(t) = \mathbf{\Phi}^{\mathrm{T}}\mathbf{S}_{\mathrm{p}}(t)\mathbf{p}(t) \tag{1}$$

where $\mathbf{z}(t) \in \mathbb{R}^{n_{\mathrm{m}}}$ is the vector of modal coordinates, with n_{m} the number of modes taken into account in the model. The excitation force is written as the product of a selection matrix $\mathbf{S}_{\mathrm{p}}(t) \in \mathbb{R}^{n_{\mathrm{dof}} \times n_{\mathrm{p}}}$, specifying the force locations, and a time history vector $\mathbf{p}(t) \in \mathbb{R}^{n_{\mathrm{p}}}$, with n_{p} the number of forces. For the remainder of this paper, the selection matrix $\mathbf{S}_{\mathrm{p}}(t)$ is assumed to be time-invariant. The results, however, can be readily extended to the case where $\mathbf{S}_{\mathrm{p}}(t)$ is varying over time. The number of degrees of freedom is indicated by n_{dof}. $\mathbf{\Gamma} \in \mathbb{R}^{n_{\mathrm{m}} \times n_{\mathrm{m}}}$ is a diagonal matrix containing the terms $2\xi_j\omega_j$ on its diagonal, where ω_j and ξ_j are the natural frequency and modal damping ratio corresponding to mode j, respectively. $\mathbf{\Omega} \in \mathbb{R}^{n_{\mathrm{m}} \times n_{\mathrm{m}}}$ is a diagonal matrix as well, containing the natural frequencies ω_j on its diagonal, and $\mathbf{\Phi} \in \mathbb{R}^{n_{\mathrm{dof}} \times n_{\mathrm{m}}}$ is a matrix containing the eigenvectors $\boldsymbol{\phi}_j$ as columns.

The decoupled governing equations can be written into state-space form, which after time discretization yields:

$$\mathbf{x}_{[k+1]} = \mathbf{A}\mathbf{x}_{[k]} + \mathbf{B}\mathbf{p}_{[k]} \tag{2}$$

The state vector $\mathbf{x}_{[k]} \in \mathbb{R}^{n_{\mathrm{s}}}$ consists of the modal displacements and velocities:

$$\mathbf{x}_{[k]} = \begin{bmatrix} \mathbf{z}_{[k]} \\ \dot{\mathbf{z}}_{[k]} \end{bmatrix} \tag{3}$$

The specific form of $\mathbf{A}$ and $\mathbf{B}$ depends on the time discretization scheme and will not be further considered. The reader is referred to Franklin et al. (1998) for a detailed overview of common time discretization schemes. As an alternative to models based on first principles, models can be directly identified from experimental data using system identification techniques, e.g. Reynders and De Roeck (2008).

The output vector is generally written as

$$\mathbf{d}(t) = \mathbf{S}_{\mathrm{d,a}}\mathbf{\Phi}\ddot{\mathbf{z}}(t) + \mathbf{S}_{\mathrm{d,v}}\mathbf{\Phi}\dot{\mathbf{z}}(t) + \mathbf{S}_{\mathrm{d,d}}\mathbf{\Phi}\mathbf{z}(t) \tag{4}$$

where $\mathbf{S}_{\mathrm{d,a}}$, $\mathbf{S}_{\mathrm{d,v}}$, and $\mathbf{S}_{\mathrm{d,d}} \in \mathbb{R}^{n_{\mathrm{d}} \times n_{\mathrm{dof}}}$ are selection matrices indicating the degrees of freedom corresponding to the acceleration, velocity and displacement measurements, respectively. The output vector is composed of $n_{\mathrm{d,d}}$ displacement or strain measurements, $n_{\mathrm{d,v}}$ velocity measurements and $n_{\mathrm{d,a}}$ acceleration measurements, where n_{d} is the sum of $n_{\mathrm{d,d}}$, $n_{\mathrm{d,v}}$, and $n_{\mathrm{d,a}}$.

Eq. (4) is transformed into its state-space form, using Eq. (1):

$$\mathbf{d}_{[k]} = \mathbf{G}\mathbf{x}_{[k]} + \mathbf{J}\mathbf{p}_{[k]} \tag{5}$$

The expression for the state-output matrix $\mathbf{G}$ and the direct transmission matrix $\mathbf{J}$, in general, does not depend on the discretization scheme and is given by Eq. (6) and Eq. (7), respectively.

$$\mathbf{G} = \begin{bmatrix} \mathbf{S}_{\mathrm{d,d}}\mathbf{\Phi} - \mathbf{S}_{\mathrm{d,a}}\mathbf{\Phi}\mathbf{\Omega}^2 & \mathbf{S}_{\mathrm{d,v}}\mathbf{\Phi} - \mathbf{S}_{\mathrm{d,a}}\mathbf{\Phi}\mathbf{\Gamma} \end{bmatrix} \tag{6}$$

$$\mathbf{J} = \begin{bmatrix} \mathbf{S}_{\mathrm{d,a}}\mathbf{\Phi}\mathbf{\Phi}^{\mathrm{T}}\mathbf{S}_{\mathrm{p}} \end{bmatrix} \tag{7}$$

When process noise and measurement noise are added to Eq. (2) and Eq. (5), respectively, the following discrete-time combined deterministic-stochastic state space description of the system is obtained:

$$\mathbf{x}_{[k+1]} = \mathbf{A}\mathbf{x}_{[k]} + \mathbf{B}\mathbf{p}_{[k]} + \mathbf{w}_{[k]} \tag{8}$$

$$\mathbf{d}_{[k]} = \mathbf{G}\mathbf{x}_{[k]} + \mathbf{J}\mathbf{p}_{[k]} + \mathbf{v}_{[k]} \tag{9}$$

where $\mathbf{x}_{[k]} \in \mathbb{R}^{n_{\mathrm{s}}}$ is the state vector, $\mathbf{d}_{[k]} \in \mathbb{R}^{n_{\mathrm{d}}}$ is the output vector, assumed to be measured, and $\mathbf{p}_{[k]} \in \mathbb{R}^{n_{\mathrm{p}}}$ is the unknown input vector. The deterministic system behaviour is described by the system matrices $\mathbf{A}$, $\mathbf{B}$, $\mathbf{G}$ and $\mathbf{J}$. The process noise $\mathbf{w}_{[k]} \in \mathbb{R}^{n_{\mathrm{s}}}$ and measurement noise $\mathbf{v}_{[k]} \in \mathbb{R}^{n_{\mathrm{d}}}$ are of no importance for the invertibility of the system, and will not be considered in the following theoretical derivation. When the optimal sensor configuration is to be determined, i.e. the configuration of sensors giving rise to the smallest error on the identified forces, the noise statistics will, however, be important.

In structural dynamics, the problem of input estimation consists of estimating the excitation forces $\mathbf{p}_{[k]}$, acting on a structure at known locations, from a set of response measurements.

3 IDENTIFIABILITY CONDITIONS

System identifiability requires that the measured output contains information on the estimated system input. This condition can be subdivided in two separate requirements, the observability requirement and the direct invertibility requirement.

3.1 *Observability*

System observability requires that all states are represented in the system output. The following definition holds (Kalman 1960).

Definition 3.1. *A system described by Eq. (8) and Eq. (9) is called observable if, in the absence of noise, the knowledge of the input* $\mathbf{p}_{[k]}$ *and the output* $\mathbf{d}_{[k]}$ *over a finite interval* $(k = 0, \ldots, n)$ *is sufficient to determine the state vector* $\mathbf{x}_{[0]}$.

In general, system observability is tested by means of the rank of the observability matrix $\mathcal{O}$:

$$\mathcal{O} \equiv \begin{bmatrix} \mathbf{G} \\ \mathbf{GA} \\ \vdots \\ \mathbf{GA}^{n_{\mathrm{s}}-1} \end{bmatrix} \tag{10}$$

Theorem 3.1. *The system described by Eq. (8) and Eq. (9) is observable if and only if* $\text{rank}(\mathcal{O}) = n_s$*, with* n_s *the number of system states.*

When a modally reduced order model is used, system observability requires that all structural modes contribute to the measured output. From the definition of the observability matrix in Eq. (10), and the definition of the output vector in Eq. (4), the observability test can be formulated in a more straightforward and comprehensible way.

Theorem 3.2. *The modally reduced order system described by Eq. (8) and Eq. (9) is observable if and only if the matrix*

$$\begin{bmatrix} \mathbf{S}_d\boldsymbol{\Phi} \end{bmatrix} = \begin{bmatrix} \mathbf{S}_{d,d}\boldsymbol{\Phi} \\ \mathbf{S}_{d,v}\boldsymbol{\Phi} \\ \mathbf{S}_{d,a}\boldsymbol{\Phi} \end{bmatrix} \tag{11}$$

does not contain any zero columns.

Proof. Theorem 3.2 directly follows from the expression of the matrix **G** and the structure of the matrix **A** for the case of modally reduced order models. The full proof is omitted here for the sake of brevity. □

The observability requirements in Theorem 3.1 and Theorem 3.2 hold for continuous-time systems and discrete-time systems. The observability of a discrete-time system in addition depends on the sampling frequency. On the one hand, the sampling frequency has to be chosen, in accordance to the Nyquist theorem (Franklin, Powell, & Workman 1998), taking into account the largest natural frequency of the model. When the sampling frequency becomes too large, on the other hand, the observability matrix becomes numerically rank-deficient. The influence of the sampling frequency is, however, not further considered in this paper.

When only force identification is aimed at and the system states as such are not of interest, the observability requirement can be relaxed, as not all n_m modes have to be observable. For the identifiability of the forces, it suffices that at least n_p modes, which are excited by these forces, contribute to the given set of output measurements. This requirement is referred to as relaxed observability hereafter. Relaxed observability can be ascertained, based on the system description.

Theorem 3.3. *Relaxed observability holds for the reduced order system described by Eq. (8) and Eq. (9) if and only if the matrices*

$$\begin{bmatrix} \mathbf{S}_d\boldsymbol{\Phi} \end{bmatrix} \text{and} \begin{bmatrix} \mathbf{S}_p^T\boldsymbol{\Phi} \end{bmatrix}$$

have at least n_p *non-zero columns in common.*

The concept of relaxed observability is illustrated by means of a conceptual example.

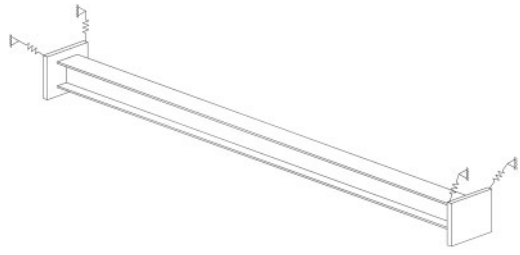


Figure 1. Structure as considered for the illustration of the theoretical derivation, three dimensional view.



Figure 2. Force and sensor locations as considered for Example 3.1, (a) side view and (b) top view.

Example 3.1. The structure under consideration is a steel beam with I-shaped cross section. The structure, as constructed at the laboratory, is shown in figure 1. The beam has steel plates welded to its ends and is connected to the environment by springs. In this way, free-free boundary conditions are obtained. Details on the structure and its modal characteristics, though not required for the remainder of this paper, can be found in Lourens et al. (2012).

Assume a modally reduced order model constructed from two modes of the beam, one torsional mode (mode T1) and one vertical bending mode (mode B1). A single vertical force, indicated as p_1, is acting eccentrically on the beam (figure 2). The response of the structure is measured using one accelerometer, a_1, placed on the beam axis. The force and sensor locations are shown in figure 2.

The force p_1 excites both the vertical bending mode and the torsional mode. The matrix $\mathbf{S}_p^T\boldsymbol{\Phi}$ becomes

$$\begin{bmatrix} \mathbf{S}_p^T\boldsymbol{\Phi} \end{bmatrix} = \begin{bmatrix} \overset{\text{T1}}{*} & \overset{\text{B1}}{*} \end{bmatrix} \tag{12}$$

where $*$ indicates a generally non-zero number. Since only bending of the beam contributes to the measured acceleration response, it is clear that in general

$$\begin{bmatrix} \mathbf{S}_{d,d}\boldsymbol{\Phi} \\ \mathbf{S}_{d,v}\boldsymbol{\Phi} \\ \mathbf{S}_{d,a}\boldsymbol{\Phi} \end{bmatrix} = \begin{bmatrix} \overset{\text{T1}}{0} & \overset{\text{B1}}{0} \\ 0 & 0 \\ 0 & * \end{bmatrix} \tag{13}$$

Since mode T1 is not observed by the sensor, the system is not observable and, consequently, the observation matrix $\mathcal{O}$ will not have rank n_s $(= 2n_m = 4)$. Relaxed observability holds, however, as there is only one force to be identified.

3.2 *Direct invertibility*

Direct invertibility requires that the system input can be estimated from the output without a time delay, which is called instantaneous inversion. The necessary and sufficient condition for direct invertibility is extensively documented in the literature (Massey and Sain 1968, Moylan 1977), and is given by the following theorem.

Theorem 3.4. *The system described by Eq. (8) and Eq. (9) is instantaneously invertible if and only if* $\text{rank}(\mathbf{J}) = n_\text{p}$.

For modally reduced order models, this condition results in two important requirements which have to be taken into account when performing instantaneous system inversion.

1. The number of forces n_p cannot become larger than the number of modes excited by these forces, which not necessarily equals the total number of modes. This has to hold for each subset of forces. The underlying physical explanation directly follows from the assumption of an uncoupled reduced order model. The forces must be able to control at least n_p modes independently, in order to be distinguishable. This requirement is referred to as relaxed controllability hereafter.

If requirement 1. holds, the matrix $\mathbf{\Phi}^\text{T}\mathbf{S}_\text{p}$ will be of rank n_p. An illustration is found in Example 3.2.

2. The contribution from at least n_p modes excited by the forces must be distinguishable from the measured acceleration signals. This has to hold for each subset of forces. This conclusion ensures a direct coupling between the measured acceleration responses and the estimated forces through at least n_p modes composing the model.

If requirements 1. and 2. hold, the matrix $\mathbf{J}$ will be of rank n_p and the system will be instantaneously invertible. The required number of independent acceleration measurements depends on the particular force and sensor locations, but can never become smaller than the number of forces n_p. An illustration is found in Example 3.3. From the direct coupling between the acceleration responses and the forces, it is clear that direct invertibility of the system also implies relaxed observability (see Theorem 3.3).

Example 3.2. Assume a modally reduced order model constructed from three modes of the beam, two torsional modes (modes T1 and T2) and one vertical bending mode (mode B1). Three vertical forces are acting on the beam, one of them eccentrically, two others centrically, indicated as p_1, p_2, and p_3, respectively. The force locations are shown in figure 3.

Force p_1 excites the torsional modes and the bending mode, whereas forces p_2 and p_3 only excite the bending mode. The matrix $\mathbf{S}_\text{p}^\text{T}\mathbf{\Phi}$ becomes

$$\left[\ \mathbf{S}_\text{p}^\text{T}\mathbf{\Phi}\ \right] = \begin{matrix}\text{T1} & \text{T2} & \text{B1}\end{matrix}\begin{bmatrix} * & * & * \\ 0 & 0 & * \\ 0 & 0 & * \end{bmatrix}\begin{matrix}p_1\\ p_2\\ p_3\end{matrix}$$

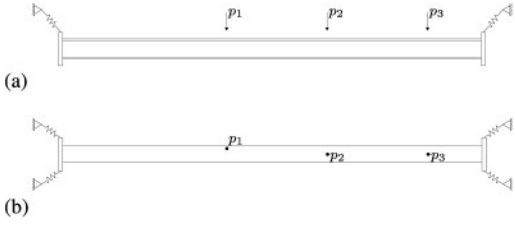


Figure 3. Force locations as considered for Example 3.2, (a) side view and (b) top view.

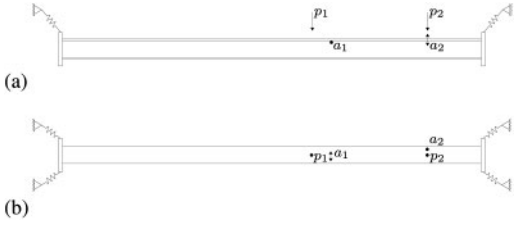


Figure 4. Force and sensor locations as considered for Example 3.3, (a) side view and (b) top view.

All modes are excited by the forces and, in general, the three forces are independent. However, $\mathbf{S}_\text{p}^\text{T}\mathbf{\Phi}$ is not of rank n_p, since the two torsional modes cannot be controlled independently by the forces assumed.

Example 3.3. Assume a modally reduced order model constructed from three modes of the beam, one torsional mode (modes T1) and two vertical bending modes (modes B1 and B2). Two vertical forces are acting centrically on the beam, indicated as p_1 and p_2. The response of the structure is measured using two accelerometers. The first accelerometer, a_1, measuring the horizontal accelerations, is placed at the web plate, right below the upper beam flange. The second accelerometer, a_2, measuring the vertical accelerations, is placed eccentrically. The force and sensor locations are shown in figure 4.

Forces p_1 and p_2 excite the bending modes of the beam. The torsional mode is not excited. The matrix $\mathbf{S}_\text{p}^\text{T}\mathbf{\Phi}$ becomes

$$\left[\ \mathbf{S}_\text{p}^\text{T}\mathbf{\Phi}\ \right] = \begin{matrix}\text{T1} & \text{B1} & \text{B2}\end{matrix}\begin{bmatrix} 0 & * & * \\ 0 & * & * \end{bmatrix}\begin{matrix}p_1\\ p_2\end{matrix}$$

Acceleration a_1 only contains a contribution from the torsional mode, whereas acceleration a_2 contains a contribution from all modes. The matrix $\mathbf{S}_{\text{d,a}}\mathbf{\Phi}$ becomes

$$\left[\ \mathbf{S}_{\text{d,a}}\mathbf{\Phi}\ \right] = \begin{matrix}\text{T1} & \text{B1} & \text{B2}\end{matrix}\begin{bmatrix} * & 0 & 0 \\ * & * & * \end{bmatrix}\begin{matrix}a_1\\ a_2\end{matrix}$$

The two forces excite the two bending modes independently. The system will, however, not be instantaneously invertible, since there is not a direct coupling between acceleration a_1 and the excitation forces. Consequently, matrix $\mathbf{J}$ ($= \mathbf{S}_{\mathrm{d,a}} \boldsymbol{\Phi} \boldsymbol{\Phi}^{\mathrm{T}} \mathbf{S}_{\mathrm{p}}$) will not be of rank n_{p}.

4 STABILITY CONDITIONS

Stability of system inversion is mainly an issue for recursive inversion algorithms, and is defined by the following definition:

Definition 4.1. *The inversion of a system is stable if, starting from an arbitrary initial state estimate* $\hat{\mathbf{x}}_{[0]}$*, the force estimates* $\hat{\mathbf{p}}_{[k]}$ *and/or state estimates* $\hat{\mathbf{x}}_{[k]}$ *converge to the true input and system state values,* $\mathbf{p}_{[k]}$ *and* $\mathbf{x}_{[k]}$*, respectively (in the absence of modelling errors and noise processes).*

The stability of the system inversion depends on the conditions under which the poles of the inverse system can be assigned. These conditions are directly related to the transmission zeros λ_j of the original system (Moylan 1977).

Theorem 4.1. *If all transmission zeros of the system described by Eq. (8) and Eq. (9) are located at the center of the unit circle* ($\lambda_j = 0$, $j = 1, \ldots, n_{\mathrm{s}}$)*, there exists a system inverse for which the poles can be arbitrarily assigned. If the system has no unstable transmission zeros* ($|\lambda_j| < 1$, $j = 1, \ldots, n_{\mathrm{s}}$)*, the poles of the system inverse can be chosen such that the system inversion is stable.*

Theorem 4.1 holds for instantaneous system inversion, as well as for time delayed inversion (e.g. Hsieh (2009)). If the system contains any unstable zeros ($|\lambda_j| \geq 1$), there does not exist a stable instantaneous inverse. By applying a time delay in the inversion process, the inverse system can stabilized. The issue of time delayed inversion is not further considered in this paper, however.

The transmission zeros of a system depend on all four system matrices $\mathbf{A}$, $\mathbf{B}$, $\mathbf{G}$ and $\mathbf{J}$ and are found by solving a generalized eigenvalue problem (Emami-Naeini and Van Dooren 1982). When a modally reduced order model is used, not only the mode shapes ϕ_j but also the natural frequencies ω_j and the modal damping ratios ξ_j determine the location of the system transmission zeros. In addition, the system zeros depend on the type and number of sensors used to measure the response (i.e. on the selection matrices $\mathbf{S}_{\mathrm{d,d}}$, $\mathbf{S}_{\mathrm{d,v}}$, and $\mathbf{S}_{\mathrm{d,a}}$), on whether these measurements are collocated with the forces (i.e. the relation between $\mathbf{S}_{\mathrm{d,d}}$, $\mathbf{S}_{\mathrm{d,v}}$, $\mathbf{S}_{\mathrm{d,a}}$ and $\mathbf{S}_{\mathrm{p}}$), on the time discretization scheme used, etc. For these reasons, a direct relation between the output vector and the occurrence of systems zeros cannot be derived and the system transmission zeros have to be checked systematically for each experiment design. Based on the physical background of system transmission zeros, however, a few rules of thumb can be drawn. Firstly, for collocated response measurements, i.e. when for each force a coinciding response measurement is available, the system will not have any unstable transmission zeros. Secondly, if only acceleration or velocity measurements are used, which are insensitive to static excitation, there will always be at least one transmission zero $\lambda_j = 1$, located at the unit circle. This transmission zero corresponds to excitation at a frequency of 0 Hz. If none of the other system zeros is unstable, the instantaneous inversion will be marginally stable. In structural dynamics, however, acceleration measurements are used extensively, as they can be obtained in a reliable way and at an acceptable cost. The problem of marginal stability of the system inversion can be resolved by including displacement and/or strain measurements, in accordance to the following theorem.

Theorem 4.2. *Transmission zeros of the system described by Eq. (8) and Eq. (9), corresponding to a frequency of* 0 Hz*, can be resolved by including displacement and/or strain measurements, such that* rank $(\mathbf{S}_{\mathrm{d,d}} \boldsymbol{\Phi} \boldsymbol{\Phi}^{\mathrm{T}} \mathbf{S}_{\mathrm{p}}) = n_{\mathrm{p}}$.

If the system is instantaneously invertible (see Theorem 3.4), the matrix $\mathbf{S}_{\mathrm{p}}^{\mathrm{T}} \boldsymbol{\Phi}$ is of rank n_{p}, and one additional requirement needs to be drawn, in order to ensure that the rank criterion, as stated in Theorem 4.2, holds:

1. The contribution from at least n_{p} modes excited by the forces must be distinguishable from the measured displacement and/or strain signals. This has to hold for each subset of forces. This conclusion ensures a direct coupling between the measured displacement and/or strain responses and the estimated forces through at least n_{p} modes composing the model.

If requirement 1. holds, $\mathbf{S}_{\mathrm{d,d}} \boldsymbol{\Phi} \boldsymbol{\Phi}^{\mathrm{T}} \mathbf{S}_{\mathrm{p}}$ will be of rank n_{p} and all transmission zeros corresponding to a frequency of 0 Hz are resolved. The required number of independent displacement and strain measurements depends on the particular force and sensor locations, but can never become smaller than the number of forces n_{p}. The choice of displacement or strain measurements (number of measurements, measurement locations and directions) is based on the same principles as the choice of acceleration measurements, needed for system invertibility (section 3.2). The reader is referred to Example 3.3 for an illustration of the concept.

5 UNIQUENESS CONDITIONS

The uniqueness of the identified forces depends on the system transmission zeros, as stated in the following theorem:

Theorem 5.1. *The input of a system with at least one transmission zero cannot be uniquely reconstructed.*

This follows directly from the definition of a system transmission zero: there exists an input and an initial state for which the system output is zero. As a consequence, the input cannot be uniquely reconstructed from the measured output.

Example 5.1. When the system output only consists of acceleration measurements, the static component of both the identified forces and system states cannot be retrieved from the measurements. By adding displacement and/or strain measurements, in accordance to Theorem 4.2, the static component is retained from the identification procedure as well.

6 CONCLUSIONS

In this paper, general conditions on the invertibility of linear system models have been presented. The conditions apply generally to any instantaneous input estimation algorithm. The main focus is on the identifiability of the dynamic forces, as well as the stability and the uniqueness of the identified quantities. It is shown that, for the specific case of modally reduced order models, the general invertibility conditions can be ascertained based on the knowledge of the modal characteristics of the structure. The resulting set of simplified requirements can then be used to design a measurement setup in a very straightforward and comprehensible way.

ACKNOWLEDGMENTS

The research presented in this paper has been performed within the framework of the project G.0738.11 "Inverse identification of wind loads on structures", funded by the Research Foundation Flanders (FWO), Belgium. Their financial support is gratefully acknowledged. The authors are all members of the KU Leuven – BOF PFV/10/002 OPTEC – Optimization in Engineering Center.

REFERENCES

Adams, R. & J. Doyle (2002). Multiple force identification for complex structures. *Experimental Mechanics 42*(1), 25–36.

Antsaklis, P. (1978). Stable proper nth-order inverses. *IEEE Transactions on Automatic Control 23*(6), 1104–1106.

Emami-Naeini, A. & P. Van Dooren (1982). Computation of zeros of linear multivariable systems. *Automatica 18*(4), 415–430.

Franklin, G., J. Powell, & M. Workman (1998). *Digital control of dynamic systems* (third ed.). Menlo Park, CA: Addison-Wesley.

Gillijns, S. & B. De Moor (2007). Unbiased minimum-variance input and state estimation for linear discrete-time systems with direct feedthrough. *Automatica 43*(5), 934–937.

Guillaume, P., E. Parloo, & G. De Sitter (2002). Source identification from noisy response measurements using an iterative weighted pseudo-inverse approach. In *Proceedings of ISMA2002 International Conference on Noise and Vibration Engineering*, Leuven, Belgium, pp. 1817–1824.

Hsieh, C. (2009). Optimal time-delayed joint input and state estimation for systems with unknown inputs. In *Proceedings of the 48th IEEE Conference on Decision and Control*, Shanghai.

Hwang, J., A. Kareem, & W. Kim (2009). Estimation of modal loads using structural response. *Journal of Sound and Vibration 326*, 522–539.

Jacquelin, E., A. Bennani, & P. Hamelin (2003). Force reconstruction: analysis and regularization of a deconvolution problem. *Journal of Sound and Vibration 265*, 81–107.

Kalman, R. E. (1960). On the general theory of control systems. In *Proceedings of the First International Congress of IFAC*, Moscow.

Klinkov, M. & C.-P. Fritzen (2006, September). Online estimation of external loads from dynamic measurements. In P. Sas and M. D. Munck (Eds.), *Proceedings ISMA2006*, Leuven, Belgium, pp. 3957–3968.

Klinkov, M. & C. Fritzen (2007). An updated comparison of the force reconstruction methods. *Key Engineering Materials 347*, 461–466.

Liu, Y. & W. Shepard (2005). Dynamic force identification based on enhanced least squares and total least squares schemes in the frequency domain. *Journal of Sound and Vibration 282*, 37–60.

Lourens, E., C. Papadimitriou, S. Gillijns, E. Reynders, G. De Roeck, & G. Lombaert (2012). Joint input-response estimation for structural systems based on reduced-order models and vibration data from a limited number of sensors. *Mechanical Systems and Signal Processing 29*, 310–327.

Lourens, E., E. Reynders, G. De Roeck, G. Degrande, & G. Lombaert (2012). An augmented Kalman filter for force identification in structural dynamics. *Mechanical Systems and Signal Processing 27*, 446–460.

Massey, J. & M. Sain (1968). Inverses of linear sequential circuits. *IEEE Transactions on Automatic Control 17*(4), 330–337.

Ma, C., J. Chang, & D. Lin (2003). Input forces estimation of beam structures by an inverse method. *Journal of Sound and Vibration 259*(2), 387–407.

Moylan, P. (1977). Stable inversion of linear systems. *IEEE Transactions on Automatic Control 22*(1), 74–78.

Niu, Y., M. Klinkov, & C.-P. Fritzen (2011). Online force reconstruction using an unknown-input Kalman filter approach. In *Proceedings of the 8th International Conference on Structural Dynamics, EURODYN 2011*, Leuven, Belgium, pp. 2569–2576.

Nordström, L. & T. Nordberg (2002). A critical comparison of time domain load identification methods. In *Proceedings of the 6th International Conference on Motion and Vibration Control*, Saitama, Japan, pp. 1151–1156.

Parloo, E., P. Verboven, P. Guillaume, & M. Van Overmeire (2003). Force identification by means of in-operational modal models. *Journal of Sound and Vibration 262*(1), 161–173.

Reynders, E. & G. De Roeck (2008). Reference-based combined deterministic-stochastic subspace identification for experimental and operational modal analysis. *Mechanical Systems and Signal Processing 22*(3), 617–637.

Research and Applications in Structural Engineering, Mechanics and Computation – Zingoni (Ed.)
© 2013 Taylor & Francis Group, London, ISBN 978-1-138-00061-2

Determination of aerodynamic damping of twin cables in wet conditions through passive-dynamic wind tunnel tests

M.B. Eriksen & E. Mattiello
FORCE Technology, Hydro- and Aerodynamics, Kgs. Lyngby, Denmark

C.T. Georgakis
Department of Civil Engineering, Technical University of Denmark, Kgs. Lyngby, Denmark

ABSTRACT: Moderate amplitude cable vibrations continue to be reported on the cable-stayed Øresund Bridge, despite the presence of helical fillets and dampers. The vibrations are particularly notable in wet conditions, which would suggest a form of rain-wind induced vibrations (RWIV). A statistical operational modal analysis of the monitored vibrations revealed, in certain conditions and for specific wind velocities, the presence of negative aerodynamic damping. To investigate the observed aerodynamic damping of the twin cable arrangement further, a series of 1:2.3 scale passive-dynamic wind tunnel tests was performed at the DTU/FORCE Technology Climatic Wind Tunnel facility in Kgs. Lyngby, Denmark. Tests were performed for both dry and wet conditions, with and without helical fillets. The specific relative cable-wind angle tested was identified as critical from the aforementioned full-scale monitoring of the bridge cables. For the wet tests, the twin cable surfaces were treated in order to obtain uniform upper and lower water rivulets. The interaction between water rivulets, surface properties and the flow was found to govern the activation of the RWIV mechanism. The resulting aerodynamic damping from wet passive-dynamic wind tunnel tests showed the effect of the helical fillets in preventing the occurrence of negative aerodynamic damping, contrary to the plain cables.

1 INTRODUCTION

Bridge cable vibrations remain a problem for bridge designers and operators notwithstanding the wide research efforts spent in the last couple of decades. Two approaches have generally been followed so far to minimize these vibrations and their effects: application of fillets or dimples onto the cable surface to improve the aeroelastic behaviour, and addition of mechanical dampers to increase energy dissipation. The cable-stayed Øresund Bridge, linking Denmark and Sweden, was one of the first bridges to incorporate this dual approach. Nevertheless, vibrations of the cables have been observed since before its opening in 2000.

More recently, Acampora & Georgakis (2011) reported moderate vibration incidences in both dry and wet conditions and for a narrow range of cable-wind angles. Various mechanisms may be responsible for the reported vibrations, including dry inclined galloping and forms of rain-wind-cable interaction. In the wet case, water rivulets form on the cable surface interacting with the flow. An equilibrium between rain intensity, droplet size, wettability, aerodynamic and gravitational forces is required for the water rivulets to form and be sustained (de Sá Caetano 2007, Lemaitre et al. 2010). The subsequent non-symmetric cross-section of a cable with rivulets, does not completely describe the RWIV mechanism (Matsumoto et al. 1995). In fact, RWIV occur in a restricted range of wind velocities, as the water rivulets oscillate on the cable surface (Hikami & Shiraishi 1998). A possible explanation for the restricted velocity range is the resonance between the natural frequencies of the rivulets and of the cable, as proposed by Hikami & Shiraishi (1998). Furthermore, for a cable declining in the wind, the rivulets interact with the axial flow, and with three-dimensional vortex shedding (Matsumoto et al. 2001). Cosentino et al. (2003) reported that the thin water layer acts as an added roughness close to the separation line. It obstructs the separation-reattachment mechanism allowing for changes in the flow regime, and an enhanced vortex shedding may be observed (Matteoni & Georgakis 2012). These changes depend on the relative cable-wind angle and the wind angle of attack. In specific cases, the unfavourable changes of aerodynamic forces may lead to the formation of positive velocity-proportional forces corresponding to negative aerodynamic damping.

The specific twin-cable arrangement of the Øresund Bridge cables may further influence the aerodynamic and/or aeroelastic behaviour of the stays. The cable spacing to diameter ratio of the Øresund Bride cables, $S/D = 2.68$, generates a flow pattern with two wakes equal in size, leading to synchronised vortex shedding (Zdravkovich 2003). The Øresund Bridge cable arrangement was originally studied by Larose & Smitt

(1999), and its aerodynamic damping was recently estimated from full-scale measurements using an Operational Modal Analysis (OMA) technique (Georgakis & Acampora 2011) as well as an Eigenvalue Realisation Algorithm (ERA), as reported by Acampora et al. (2012). Negative aerodynamic damping was found from the monitoring of specific stays of the Øresund Bridge in wet condition for specific cable wind-angle orientations (Georgakis & Acampora 2011).

To further investigate the aerodynamics of the Øresund Bridge twin cables, a series of passive-dynamic wind tunnel tests has been undertaken in both dry and simulated rain conditions on a scaled model of the twin stays. The present paper details the investigations in wet conditions.

2 EXPERIMENTAL WORK

2.1 *Test facility*

The experimental work was carried out in the closed-circuit DTU/FORCE Technology Climatic Wind Tunnel (Georgakis et al. 2009). The tests were performed in the $2\,m \times 2\,m \times 5\,m$ test section with turbulence intensity $I_u \approx 1\%$ in the flow direction in the test section with local increases up to 3% at the wall panel openings, as described in section 2.3.

2.2 *Cable model preparation*

A 1:2.3 scale section model was produced using PVC piping of diameter $D = 110\,mm$, and thickness $t = 6\,mm$. Two 3 m long pipes were rigidly connected to each other at the ends to form the twin cable arrangement as shown in Figure 2.1. The pipes were sanded to reproduce the surface roughness and a scaled double helical fillet was added.

The surface properties of a prototype cable change over time due to the effects of various agents including ageing, sun, sea water and pollutants (Larose & Smitt 1999). In particular the wettability, described as the contact angle between a water droplet and the surface, increases (contact angle decreases). Therefore a polyvinyl coating was applied to the surface of the PVC pipes with a soft brush to achieve similar surface properties as the prototype cable. The applied solution consisted of 5% weight Gohsenol KP-08R dissolved in water at 70–75°C.

2.3 *Test set-up*

The cable configuration with inclination $\theta = 30°$ and horizontal yaw angle $\beta = 70°$ (see Figure 2.2) was identified as critical from full-scale monitoring of the bridge cables and thus chosen for the tests. The axial component of the model weight was carried by a steel wire.

A 1-DoF dynamic rig was designed to restrict the motion of the cable model to the in-plane degree of freedom, i.e. direction of motion in the plane containing the two cable axes. Two linear elastic springs per



Figure 2.1. Wind tunnel twin cable set-up.

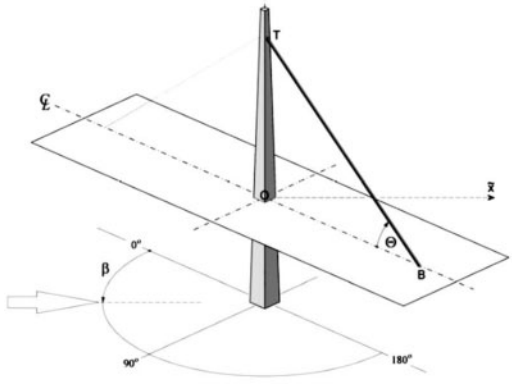


Figure 2.2. Cable-wind angle convention.

end were mounted perpendicular to the axes of the PVC pipes. The springs were chosen and adjusted to match the 1st in-plane natural frequency $f = 1.1\,Hz$ (model scale) of the bridge cables, identified as problematic from full-scale monitoring. The dynamic rig was designed to minimize the structural damping, which was measured to be $\zeta_s = 0.2\%$. In order to improve the likelihood for RVIW to occur, the Scruton number, was set to $Sc = m\zeta_s/(\rho D^2) = 1.35$, (FHWA 2007).

The blockage coefficient estimated as the ratio between the model frontal area inside the test section and the tunnel cross section was $S/A = 12.7\%$. No blockage corrections were made on aerodynamic damping or lift force coefficients though.

To allow attachment to the rig and movement of the model, the test section was partially open ($0.3\,m \times 0.9\,m$) at the cable ends. The influence of panel openings on flow velocity and turbulence intensity was investigated through flow profile measurements conducted along the model axis position and along the wall openings, respectively.

2.4 *Rain simulation system*

A rain simulation system was built inside the test section to provide the cable model with enough water to

form both upper and lower water rivulets. The water flow was optimized to obtain the biggest rivulets. The flow rate was measured to be 4.2 l/m for the filleted cable tests and 3.2 l/min for the plain cable tests (without fillets). More water was sprayed in the first case because the presence of the fillets redirected some of the water off the cables. The system was not designed to reproduce natural rain, but to form the rivulets on the cables.

Ten nozzles were fixed on two piano wires perpendicular to the flow and inclined as the model. The wires were positioned 0.8 m and 1.35 m upstream the upper and lower end of the model respectively. The wires were spaced from each other in order for the nozzles to direct the spray onto the cables. Five tubes channelling the water were led along the floor and vertically up to the wire where each of them was split in two to feed all the nozzles.

A balanced wettability was found to be necessary for the water rivulets to form, sustain and eventually cause vibrations. The model was subjected to a pre-wash prior to test in order to remove the excessive polyvinyl coating from the PVC surface. A water film was then formed on the windward side of the treated cables and upper and lower rivulets built up and oscillated near the separation lines.

2.5 *Test programme*

The wet tests were conducted on the twin cable model in two states: filleted and plain i.e. without helical fillets.

The model was manually excited to approximately 1D in amplitude and the free decay monitored by laser displacement transducers at both the upper and lower end. The model was also left steady to be excited only by the wind in the velocity range where the previous tests showed slow or zero decay. The free growth was logged with the same measuring technique. Five repetitions were made for every velocity tested from approximately 2 m/s to 30 m/s in steps of 1 m/s.

3 RESULTS AND DISCUSSION

The objective of the tests was to investigate the aerodynamic damping for the specific cable configuration described above. The negative aerodynamic damping reported from full-scale monitoring by (Georgakis & Acampora 2011) was of particular interest and the attempt to reproduce a situation leading to negative aerodynamic damping was emphasised.

The results were described as a function of Reynolds number, $\mathrm{Re} = \mathrm{UD}/\nu$, where U is the flow velocity, D is the single cable diameter and ν is the kinematic viscosity of the air.

3.1 *Formation of water rivulets*

The upper water rivulets started to form at velocities corresponding to $\mathrm{Re} \approx 0.2\text{–}0.25 \cdot 10^5$ and both



Figure 3.1. Filleted twin cable with lower water rivulet.

upper and lower rivulets were fully formed at velocities with $\mathrm{Re} \approx 0.5 \cdot 10^5$, see Figure 3.2. For flow velocities $\mathrm{Re} > 1.5 \cdot 10^5$, the rivulets were no longer continuous, but were partly blown off the cable surface.

3.2 *Aerodynamic damping*

The aerodynamic damping ratio of the cable model ζ_a was determined by subtracting the damping of the rig measured at zero wind velocity ζ_s from the total measured damping ζ and scaled to represent full-scale values. Following Macdonald & Larose (2006). aerodynamic damping can be described with the form:

$$\zeta_a = \frac{\mu Re}{4m\omega} f(Re, C_D, C_L, \alpha, \phi) \tag{1}$$

For cylinders with similar aerodynamic properties, such as a full-scale bridge cable and a scaled cable model, only mass m and natural frequency ω vary. This requires that flow characteristics and fluid dynamic behaviour are the same, i.e. Reynolds number and dynamic viscosity of air have to remain unchanged. Hence, the resulting scaling factor depends on the mass-frequency ratio between the full-scale cable and the scaled model, such that:

$$\lambda_{\zeta a} = \frac{\zeta_{a,model}}{\zeta_{a,full}} = \frac{m_{full}\omega_{full}}{m_{model}\omega_{model}} \tag{2}$$

The main results in terms of aerodynamic damping for in-plane motion are presented in Figure 3.2 as the mean value (solid lines) plus/minus the standard deviation (dashed lines). The aerodynamic damping ratio is given as a function of Re.

The figure shows the aerodynamic damping for the tests with and without helical fillets (plain). The black curve (◁) representing the filleted cables shows that the aerodynamic damping increased following an approximately linear trend until it reached the maximum value of $\zeta_a = 0.37\%$ for $\mathrm{Re} = 1.65 \cdot 10^5$.

The aerodynamic damping for the plain cables is represented by the dark grey curve (○). At low

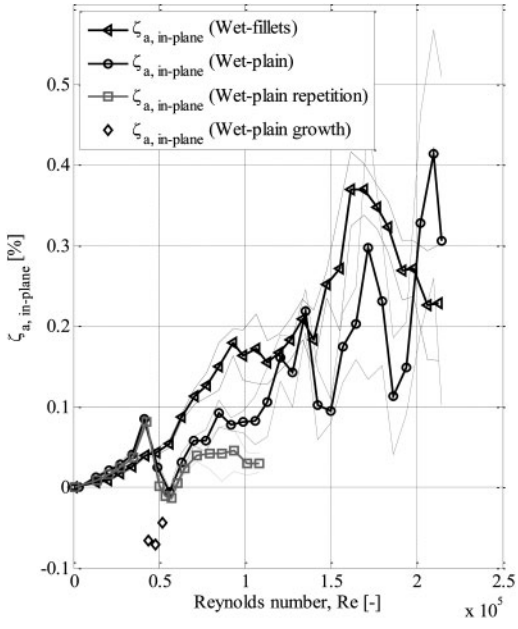


Figure 3.2. Aerodynamic damping ratios for in-plane motion.

flow velocities up to $\mathrm{Re} = 0.35 \cdot 10^5$ it followed a trend similar to the filleted cables, but after a rapid and short increase, a drop to negative values for $\mathrm{Re} \approx 0.5\text{–}0.6 \cdot 10^5$ was observed. The minimum value $\zeta_a \approx -0.01\%$ was observed for $\mathrm{Re} = 0.56 \cdot 10^5$. Hereafter the damping increased and remained positive in the tested flow velocity range. In general the aerodynamic damping for the filleted cables was found to be larger than for the plain cables.

The drop in aerodynamic damping to negative values for the plain cables was further investigated in two steps: first the free decay test was repeated and then a growth test was performed.

The repeated decay test represented in Figure 3.2 by the light gray curve (□) was performed as before, but with steps in velocity of 0.5 m/s in the range of interest until 15 m/s. This resulted in values similar to the first test.

Representative displacement time histories are illustrated in Figure 3.3 and Figure 3.4 for flow velocities of 8 m/s ($\mathrm{Re} = 0.56 \cdot 10^5$) and 11 m/s ($\mathrm{Re} = 0.77 \cdot 10^5$), respectively. The lines at the curve envelope represent the logarithmic fittings for the damping estimation. It is seen that the damping was lower at 8 m/s ($\mathrm{Re} = 0.56 \cdot 10^5$). Note that negative aerodynamic damping may still be achieved despite a total positive damping, when the structural damping is subtracted.

For the plain cables limited amplitude vibrations were observed in a narrow velocity range $\mathrm{Re} = 0.44\text{–}0.52 \cdot 10^5$ without any manual excitation of the model. This agrees with the incidences of RWIV documented in literature (Matsumoto et al. 1995; Cosentino et al. 2003). The damping determined from the growth tests is represented by the ◇-shaped points in Figure 3.2. Figure 3.5 shows a displacement time history for the growth at $\mathrm{Re} = 0.52 \cdot 10^5$. Again, the logarithmic fitting was used to determine the damping.

The aerodynamic damping determined from the increasing response was significantly larger in absolute value compared to the values determined from the free decay tests at the same flow velocities. The minimum value $\zeta_a \approx -0.07\%$ was observed for $\mathrm{Re} = 0.48 \cdot 10^5$.

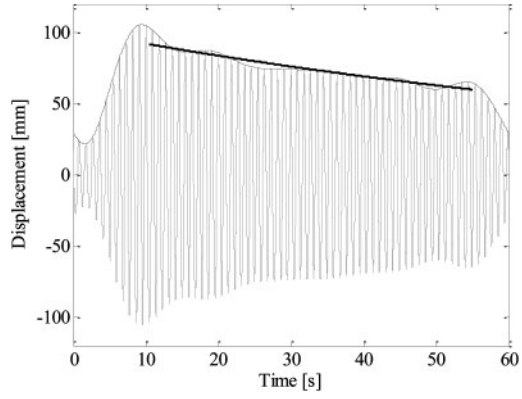


Figure 3.3. Time history, $\mathrm{Re} = 0.56 \cdot 10^5$ – decay test.

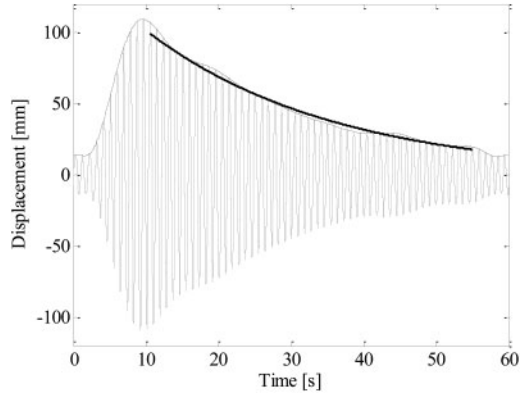


Figure 3.4. Time history, $\mathrm{Re} = 0.77 \cdot 10^5$ – decay test.

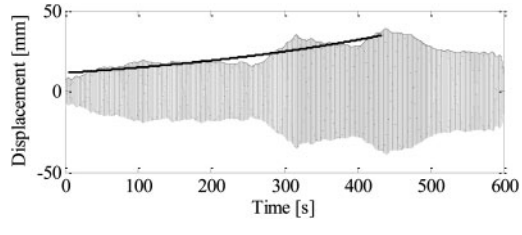


Figure 3.5. Time history, $\mathrm{Re} = 0.52 \cdot 10^5$ – growth test.

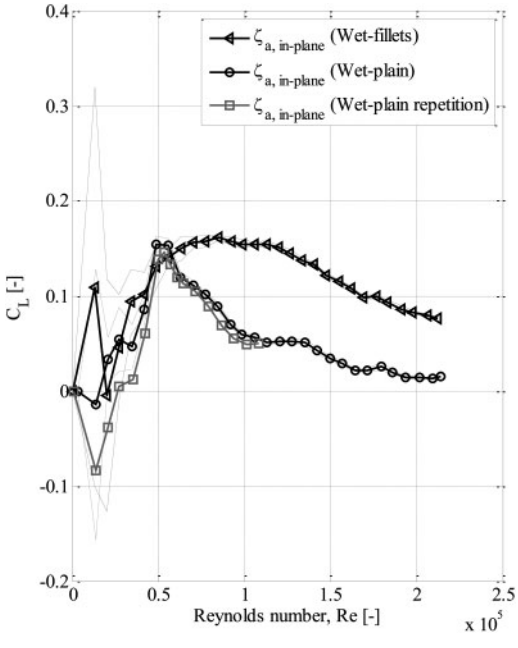


Figure 3.6. Lift force coefficients.

The excitation mechanism may have been triggered differently, generating diverse extreme values of negative aerodynamic damping for the two different tests. From Figure 3.5 it is seen that the growth continued to build up over a period of 450 s. The decay tests were carried out with sample time of 60 s. The excitation mechanism may require some interaction between flow and cable motion, which could be hardly obtained when the model was excited manually. Furthermore the amplitude levels (1D for the free decay test and 1/3D for growth test) were different.

Nevertheless, negative aerodynamic damping was observed for the plain cables, which may lead to undesired moderate amplitude vibrations. It was noticed that the drop in aerodynamic damping for the plain cable coincided with the complete formation of the rivulets, though at higher velocities the aerodynamic damping reached positive values in the presence of rivulets. The filleted cables did not suffer from instability and negative aerodynamic damping contrary to what had been monitored and observed for the Øresund Bridge cables.

3.3 *Lift force coefficients*

The mean lift forces were derived from the mean displacement and the stiffness of the system in the in-plane direction. Lift coefficients C_L for the wet tests are shown in Figure 3.6 as a function of Re.

It should be noted that the curve gradient for the plain cable (○) changes sign in the same range where the negative aerodynamic damping was found i.e. $Re = 0.5 \cdot 10^5$. At flow velocities $Re < 0.5 \cdot 10^5$ the standard deviations (dashed lines) in lift are significantly larger then for the higher flow velocities. This may be linked to the non-fully formed water rivulets at lower velocities. For flow velocities $Re > 0.6 \cdot 10^5$ the lift was observed to be higher for the filleted (◇) than for the plain cables (○).

4 CONCLUSIONS

A series of passive-dynamic wind tunnel tests was conducted on a scaled model of the twin stayed cables of the Øresund Bridge, to investigate the aerodynamics of this particular cable arrangement, for the critical conditions, i.e. weather precipitation and cable-wind angle, as shown by monitoring. Aerodynamic damping results showed no evidence of instability for the filleted cables in wet conditions. In the case of the plain cables, a region of instability zone with negative aerodynamic damping ratio was found between $Re \approx 0.4–0.6 \cdot 10^5$. This critical range could also be observed from the lift curve in correspondence to its abrupt change in gradient. This suggested the activation of a RWIV mechanism in the reported Re range. The results of the test campaign were consistent with the observation of RWIV incidences on the full-scale bridge cables.

REFERENCES

Acampora, A., Macdonald, J.H.G., Georgakis, C.T., & Nikitas, N. 2012. Identification of aeroelastic forces on twin bridge cables from full-scale measurements in skewed winds. *10th UK Conference on Wind Engineering, Southampton, UK.*

Acampora, A. & Georgakis, C.T. 2011. Recent monitoring of the Øresund Bridge: Observations of rain-wind induced cable vibrations, *13th International Conference on Wind Engineering, Amsterdam, NL.*

Caetano, de Sà. E. (1st ed.) 2007. *Cable Vibrations in Cable-Stayed Bridges* Zürich: IABSE-AIPC-IVBH.

Cosentino, N., Flamand, O. & Ceccoli, C. 2003. Rain-Wind Induced Vibration of Stay Cables. Part I: Experimental Investigation and Physical Explanation. *Wind and Structures* 6(6): 471–484.

FHWA. *Wind-Induced Vibration of Stay Cables*. Federal Highway Administration, Research, Development and Technology Turner-Fairbank Highway Research Center, 6300 Georgetown Pike, McLean, VA 22101–2296.

Georgakis, C.T. & Acampora, A. 2011. Determination of the aerodynamic damping of dry and wet bridge cables from full-scale monitoring, *9th International Symposium on Cable Dynamics (ISCD), Shanghai, CN.*

Georgakis, C.T., Koss, H.H. & Ricciardelli, F. 2009. Design specification for a novel climatic wind tunnel for testing of structural cables. *8th International Symposium on Cable Dynamics, Paris, FR.*

Hikami, Y. & Shiraishi, N. 1988. Rain-wind induced vibrations of cables in cable stayed bridges. *Journal of Wind Engineering and Industrial Aerodynamics* 29: 409–418.

Larose, G.L. & Smitt, L.W. 1999. Rain/wind induced vibrations of the stays of the Øresund High Bridge. *IABSE Conference, Malmö, SW.*

Lemaitre, C., de Langre, E. & Hémon, P. 2010. Rainwater rivulets running on a stay cable subject to wind. *European Journal of Mechanics B/Fluids* 29: 251–258.

Macdonald, J.H.G & Larose, G.L. 2006. A unified approach to aerodynamic damping and drag/lift instabilities, and its application to dry inclined cable galloping. *Journal of Fluids and Structures*, 22: 229–252.

Matsumoto, M., Saitoh, T., Kitazawa, M., Shirato, H. & Nishizaki, T. 1995. Response characteristics of rain-wind induced vibration of stay-cables of cable-stayed bridges. *Journal of Wind Engineering and Industrial Aerodynamics* 57: 323–333.

Matteoni, G. & Georgakis, C.T. 2012. Aerodynamic force coefficients of plain bride cables in wet conditions, *7th International Colloquium on Bluff Body Aerodynamics and Applications, Shanghai, CN.*

Zdravkovich, M.M. (1st ed.) 2003. *Flow around circular cylinders. Volume 2: Applications.* New York: Oxford University Press.

Research and Applications in Structural Engineering, Mechanics and Computation – Zingoni (Ed.)
© 2013 Taylor & Francis Group, London, ISBN 978-1-138-00061-2

Frequency domain stochastic response of structural systems with uncertain parameters: closed-form sensitivity

G. Muscolino & R. Santoro
Department of Civil, Information, Building, Environmental Engineering and Applied Mathematics, Messina, Italy

A. Sofi
Department of Civil, Energy, Environmental and Materials Engineering, Reggio Calabria, Italy

ABSTRACT: This study deals with the sensitivity analysis of the response of linear discretized structures with uncertain stiffness parameters subjected to stationary multi-correlated Gaussian random excitation. The proposed procedure relies on the use of the so-called *rational series expansion* (*RSE*), recently proposed by the authors as an alternative explicit form of the Neumann series expansion of the inverse of an invertible matrix with a modification of rank r. The *RSE* allows to derive approximate explicit expressions of the sensitivities of the probabilistic characteristics of the stationary stochastic response in the frequency domain by direct differentiation. The accuracy of the proposed procedure and computational issues related to sensitivity analysis are scrutinized through numerical results.

1 INTRODUCTION

Sensitivity plays an important role to evaluate the performance of structures subject to changes of model parameters.

From a mathematical point of view, sensitivity analysis involves computation of derivatives of the structural response quantities with respect to desired design variables (see e.g. Elishakoff & Ohsaki 2010). Within the context of structural applications, sensitivity derivatives are useful for performing optimization, structural health monitoring, identification, reliability etc.

There has been a great interest in developing methods for computing structural response sensitivities (Haftka & Adelman 1989). The approaches proposed for evaluating the partial derivatives of a performance measure can be classified in numerical, analytical and semi-analytical (Jensen 1995).

The availability of the exact or approximate explicit dependence of the response on the structural parameters allows an efficient sensitivity analysis.

The evaluation of the sensitivities of response statistics to variations of the design variables is of great interest for design purposes (Bhattacharyya & Chakraborty 2002, Chaudhuri & Chakraborty 2004) when the random nature of the main excitation sources, such as earthquake, wind etc., is taken into account besides the inevitable occurrence of uncertainty due to variation of design variables.

The present paper concerns the stochastic sensitivity analysis of linear discretized structures with uncertain structural parameters subjected to stationary multi-correlated Gaussian random excitation. The formulation is provided in the frequency domain. The proposed approach relies on approximate closed-form expressions of the mean-value and power spectral density (*PSD*) function of the stationary response obtained by applying the so-called *rational series expansion* (*RSE*) (Muscolino & Sofi 2012a, Muscolino & Sofi 2012b, Muscolino et al. 2012). Direct differentiation of these expressions allows to determine the sensitivities of response statistics in closed-form. Sensitivity information may be exploited to improve the computational efficiency of the *RSE* by eliminating the series terms associated to the design parameters whose variation has negligible influence on the response.

For validation purposes, the proposed procedure has been applied to a seismic-excited portal frame subject to variations of the Young's moduli.

2 PROBLEM FORMULATION

2.1 *Equations of motion*

The present study deals with the analysis of a quiescent n – DOF linear structural system with uncertain stiffness properties subjected to a stationary multi-correlated Gaussian stochastic process $\mathbf{f}(t)$. The equations of motion can be cast in the form:

$$\mathbf{M}\ddot{\mathbf{u}}(\boldsymbol{\alpha},t)+\mathbf{C}\dot{\mathbf{u}}(\boldsymbol{\alpha},t)+\mathbf{K}(\boldsymbol{\alpha})\mathbf{u}(\boldsymbol{\alpha},t)=\mathbf{f}(t) \tag{1}$$

where $\mathbf{M}$ and $\mathbf{C}$ are the $n\times n$ mass and damping matrices of the structure; $\mathbf{K}(\boldsymbol{\alpha})$ is the $n\times n$ stiffness

matrix depending on the vector $\boldsymbol{\alpha} = [\alpha_1, \alpha_2, \ldots, \alpha_r]^{\mathrm{T}}$ which collects the r dimensionless fluctuations of the uncertain parameters, α_i, around their nominal values; $u(\alpha, t)$ is the stationary Gaussian vector process of displacements; a dot over a variable denotes differentiation with respect to time r.

In structural engineering problems, the uncertainties affecting the geometrical and mechanical properties are usually small, so that it can be reasonably assumed that $|\alpha_i| \ll 1$, where the symbol $|\bullet|$ means absolute value. Under this assumption, the classical modal analysis can be applied by introducing the following coordinate transformation:

$$\mathbf{u}(\boldsymbol{\alpha}, t) = \boldsymbol{\Phi}_0 \, \mathbf{q}(\boldsymbol{\alpha}, t) \tag{2}$$

where $q(\alpha, t)$ is the vector gathering the first m modal coordinates $q_j(\alpha, t)$ $(j = 1, 2, \ldots, m \leq n)$; Φ_0 is the nominal modal matrix of order $n \times m$, solution of the following eigenproblem:

$$\mathbf{K}_0 \boldsymbol{\Phi}_0 = \mathbf{M} \boldsymbol{\Phi}_0 \boldsymbol{\Omega}_0^2; \quad \boldsymbol{\Phi}_0^{\mathrm{T}} \mathbf{M} \boldsymbol{\Phi}_0 = \mathbf{I}_m \tag{3a,b}$$

where $\mathbf{I}_m$ denotes the identity matrix of order m; $\mathbf{K}_0 = \mathbf{K}(\boldsymbol{\alpha}_0)$ is the stiffness matrix pertaining to the nominal configuration where the uncertain parameters are set equal to their nominal values, i.e. $\boldsymbol{\alpha} = \boldsymbol{\alpha}_0$; $\boldsymbol{\Omega}_0^2 = \boldsymbol{\Phi}_0^{\mathrm{T}} \mathbf{K}_0 \boldsymbol{\Phi}_0$ is the spectral matrix of the nominal structural system, say a diagonal matrix listing the squares of the natural circular frequencies of the structure, $\omega_{0,i}$, for $\boldsymbol{\alpha} = \boldsymbol{\alpha}_0$. According to Eq. (2), the modal matrix of the structural system with uncertain parameters is approximated by the nominal one, i.e. $\boldsymbol{\Phi}(\boldsymbol{\alpha}) \approx \boldsymbol{\Phi}_0$, being $|\alpha_i| \ll 1$.

By applying the coordinate transformation (2), the equations of motion in the modal subspace are obtained:

$$\ddot{\mathbf{q}}(\boldsymbol{\alpha}, t) + \boldsymbol{\Xi} \, \dot{\mathbf{q}}(\boldsymbol{\alpha}, t) + \boldsymbol{\Omega}^2(\boldsymbol{\alpha}) \, \mathbf{q}(\boldsymbol{\alpha}, t) = \mathbf{p}(t) \tag{4}$$

where $\boldsymbol{\Omega}_2(\boldsymbol{\alpha}) = \boldsymbol{\Phi}_0^{\mathrm{T}} \mathbf{K}(\boldsymbol{\alpha}) \boldsymbol{\Phi}_0$; $\boldsymbol{\Xi} = \boldsymbol{\Phi}_0^{\mathrm{T}} \mathbf{C} \boldsymbol{\Phi}_0$ is assumed to be a diagonal matrix; $\mathbf{p}(t) = \boldsymbol{\Phi}_0^{\mathrm{T}} \mathbf{f}(t)$ is the modal forcing vector. It is worth mentioning that, due to the assumption $\boldsymbol{\Phi}(\boldsymbol{\alpha}) \approx \boldsymbol{\Phi}_0$, the spectral matrix $\boldsymbol{\Omega}^2(\boldsymbol{\alpha})$ is not diagonal and the modal equations of motion in Eq. (4) are always coupled.

The external load vector $\mathbf{f}(t)$ in Eq. (1) is modelled as a stationary multi-correlated Gaussian random process fully characterized from a probabilistic point of view by the mean-value vector, $\boldsymbol{\mu}_{\mathbf{f}}$, and the correlation function matrix, $\mathbf{R}_{\mathbf{ff}}(t_1, t_2) \equiv \mathbf{R}_{\mathbf{ff}}(t_2 - t_1)$, given, respectively, by:

$$\begin{aligned} &\boldsymbol{\mu}_{\mathbf{f}} = \mathrm{E}\left\langle \mathbf{f}(t) \right\rangle; \\ &\mathbf{R}_{\mathbf{ff}}(t_2 - t_1) = \mathbf{R}_{\mathbf{ff}}(\tau) = \mathrm{E}\left\langle \mathbf{f}(t_1) \mathbf{f}^T(t_2) \right\rangle - \boldsymbol{\mu}_{\mathbf{f}} \, \boldsymbol{\mu}_{\mathbf{f}}^T \end{aligned} \tag{5a,b}$$

where t_1 and t_2 are two generic time instants and $E\langle \cdot \rangle$ denotes the stochastic average operator.

The input process $\mathbf{f}(t)$ can be conveniently split as sum of two terms, i.e.:

$$\mathbf{f}(t) = \boldsymbol{\mu}_{\mathbf{f}} + \tilde{\mathbf{X}}_{\mathbf{f}}(t) \tag{6}$$

where $\boldsymbol{\mu}_{\mathbf{f}} = \mathrm{E}\langle \mathbf{f}(t) \rangle$ is a deterministic vector denoting the mean-value of the excitation, whereas $\tilde{\mathbf{X}}_{\mathbf{f}}(t)$ is a zero-mean stationary multi-correlated Gaussian random process. Since the addition of a deterministic function has no influence on the autocorrelation function of a stochastic process, the following relationship holds:

$$\mathbf{R}_{\tilde{\mathbf{X}}_{\mathbf{f}} \tilde{\mathbf{X}}_{\mathbf{f}}}(\tau) = \mathrm{E}\left\langle \tilde{\mathbf{X}}_{\mathbf{f}}(t_1) \tilde{\mathbf{X}}_{\mathbf{f}}^T(t_2) \right\rangle \equiv \mathbf{R}_{\mathbf{ff}}(\tau). \tag{7}$$

The zero-mean stationary multi-correlated Gaussian random process $\tilde{\mathbf{X}}_{\mathbf{f}}(t)$ is completely characterized by the correlation function matrix $R_{\tilde{\mathbf{X}}_{\mathbf{f}} \tilde{\mathbf{X}}_f}(\tau)$ or, alternatively, by the power spectral density (*PSD*) function matrix:

$$\mathbf{S}_{\tilde{\mathbf{X}}_{\mathbf{f}} \tilde{\mathbf{X}}_{\mathbf{f}}}(\omega) = \frac{1}{2\pi} \int_{-\infty}^{\infty} \exp(-\mathrm{i}\omega\tau) \, \mathbf{R}_{\tilde{\mathbf{X}}_{\mathbf{f}} \tilde{\mathbf{X}}_{\mathbf{f}}}(\tau) \, \mathrm{d}\tau \tag{8}$$

where $i = (-1)^{1/2}$ denotes the imaginary unit.

2.2 *Stationary stochastic response in the frequency domain*

In view of the linearity of the structural system, the stochastic response to the stationary multi-correlated Gaussian random process $\mathbf{f}(t)$ is Gaussian too (Lutes & Sarkani 1997).

Based on the decomposition (6) of the input vector process $\mathbf{f}(t)$, the stochastic response can be split as follows:

$$\mathbf{u}(\boldsymbol{\alpha}, t) = \boldsymbol{\mu}_{\mathbf{u}}(\boldsymbol{\alpha}) + \tilde{\mathbf{U}}_{\mathbf{u}}(\boldsymbol{\alpha}, t) \tag{9}$$

where $\boldsymbol{\mu}_{\mathbf{u}}(\boldsymbol{\alpha}) = E\langle \mathbf{u}(\boldsymbol{\alpha}, t) \rangle$ denotes the mean-value vector; $\tilde{\mathbf{U}}_{\mathbf{u}}(\boldsymbol{\alpha}, t)$ is the zero-mean stationary Gaussian stochastic response vector process due to the random excitation $\tilde{\mathbf{X}}_{\mathbf{f}}(t)$.

The mean-value of the stationary response process is given by:

$$\boldsymbol{\mu}_{\mathbf{u}}(\boldsymbol{\alpha}) = \mathbf{K}^{-1}(\boldsymbol{\alpha}) \boldsymbol{\mu}_{\mathbf{f}} \tag{10}$$

where $\boldsymbol{\mu}_{\mathbf{f}}$ is the mean-value of the input process.

The correlation and *PSD* function matrices of the vector $\tilde{\mathbf{U}}_{\mathbf{u}}(\boldsymbol{\alpha}, t)$ coincide with those pertaining to the response vector process $\mathbf{u}(\boldsymbol{\alpha}, t)$. Furthermore, it is well-known that, after performing the projection into the modal subspace through Eq. (2), the *PSD* function matrix of the response, is related to the *PSD* function matrix of the zero-mean stationary Gaussian stochastic input, $\mathbf{S}_{\tilde{\mathbf{X}}_{\mathbf{f}} \tilde{\mathbf{X}}_{\mathbf{f}}}(\omega)$, by means of the following relationship (Lutes & Sarkani 1997):

$$\mathbf{S}_{\mathbf{uu}}(\boldsymbol{\alpha}, \omega) = \boldsymbol{\Phi}_0 \, \mathbf{H}^*(\boldsymbol{\alpha}, \omega) \mathbf{S}_{\tilde{\mathbf{X}}_{\mathbf{p}} \tilde{\mathbf{X}}_{\mathbf{p}}}(\omega) \mathbf{H}^T(\boldsymbol{\alpha}, \omega) \boldsymbol{\Phi}_0^T \tag{11}$$

where the asterisk means complex conjugate; $\mathbf{\Phi}_0$ is the modal matrix of the nominal structural system obtained by solving the eigenproblem (3); $S_{\tilde{\mathbf{X}}_p\tilde{\mathbf{X}}_p}(\omega)=\mathbf{\Phi}_0^{\mathrm{T}}\,S_{\tilde{\mathbf{X}}_\mathbf{f}\tilde{\mathbf{X}}_\mathbf{f}}(\omega)\,\mathbf{\Phi}_0$ is the *PSD* function matrix of the modal input vector process $\mathbf{p}(t)=\mathbf{\Phi}_0^{\mathrm{T}}\mathbf{f}(t)$ and $H(\alpha,\omega)$ is the modal *frequency response function* (*FRF*) matrix also referred to as *transfer function*, defined as:

$$\mathbf{H}(\boldsymbol{\alpha},\omega)=\left[-\omega^2\,\mathbf{I}_m+\mathrm{i}\omega\mathbf{\Xi}+\mathbf{\Omega}^2(\boldsymbol{\alpha})\right]^{-1}. \tag{12}$$

Once, the *PSD* function matrix, $\mathbf{S_{uu}}(\boldsymbol{\alpha},\boldsymbol{\omega})$, is known (see Eq. (11)), the covariance matrix of the random response can be evaluated as:

$$\mathbf{\Sigma_{uu}}(\boldsymbol{\alpha})=\int_{-\infty}^{\infty}\mathbf{S_{uu}}(\boldsymbol{\alpha},\omega)\,\mathrm{d}\omega. \tag{13}$$

In conclusion, the probabilistic characterization of the stationary Gaussian random response process in the frequency domain involves the inverse of the parametric stiffness matrix (see Eq. (10)) and the modal *FRF* matrix (see Eq. (12)) which in turn requires the inversion of a parametric frequency-dependent matrix.

3 RATIONAL SERIES EXPANSION

3.1 *Approximate inverse of the stiffness matrix*

It is assumed that the stiffness matrix $\mathbf{K}(\boldsymbol{\alpha})$ of a linearly-elastic structure can be expressed as a linear function of the uncertain parameters:

$$\mathbf{K}(\boldsymbol{\alpha})=\mathbf{K}_0+\Delta\mathbf{K}(\boldsymbol{\alpha})=\mathbf{K}_0+\sum_{i=1}^{r}\mathbf{K}_i\,\alpha_i \tag{14}$$

where $\mathbf{K}_0=\mathbf{K}(\boldsymbol{\alpha}_0)$ is a positive definite symmetric matrix representing the stiffness matrix of the nominal system introduced in the previous section; $\mathbf{K}_i=\partial\mathbf{K}(\boldsymbol{\alpha})/\partial\alpha_i|_{\boldsymbol{\alpha}=\boldsymbol{\alpha}_0}$ denotes a $n\times n$ semi-positive symmetric matrix of rank p_i. According to Eq. (14), the stiffness matrix $\mathbf{K}(\boldsymbol{\alpha})$ results from a rank-r modification $\Delta\mathbf{K}(\boldsymbol{\alpha})$ of the nominal matrix $\mathbf{K}_0$.

The computation of the inverse of modified matrices is a crucial step in the solution of various engineering problems involving changes in the design parameters. By properly modifying the Neumann series expansion, recently the authors derived a novel series expansion, called *rational series expansion* (*RSE*), which provides an approximate explicit expression of the inverse of an invertible matrix with a rank-r modification. The starting point to derive the *RSE* is the decomposition of the $n\times n$ matrix $\mathbf{K}_i$ in Eq. (14) as sum of n rank-one matrices, i.e.:

$$\mathbf{K}_i=\sum_{\ell=1}^{n}\mathbf{k}_i^{(\ell)}\mathbf{i}^{(\ell)\mathrm{T}},\quad(i=1,2\cdots r) \tag{15}$$

where $\mathbf{k}_i^{(\ell)}$ is the ℓ-th column of $\mathbf{K}_i$ and $\mathbf{i}^{(\ell)}$ is a vector of order n containing zeros except the ℓ-th entry which is equal to 1. Then, the stiffness matrix of the structural system with r uncertain parameters (Eq. (14)) can be recast as:

$$\mathbf{K}(\boldsymbol{\alpha})=\mathbf{K}_0+\sum_{i=1}^{r}\alpha_i\left[\sum_{\ell=1}^{n}\mathbf{k}_i^{(\ell)}\mathbf{i}^{(\ell)\mathrm{T}}\right]. \tag{16}$$

Based on Eq. (16) and modifying the Neumann series expansion, the authors derived the *RSE* which yields the following approximate explicit expression of the inverse of the stiffness matrix (Muscolino & Sofi 2012a, Muscolino & Sofi 2012b, Muscolino et al. 2012):

$$\begin{aligned}\mathbf{K}^{-1}(\boldsymbol{\alpha})&=\left[\mathbf{K}_0+\sum_{i=1}^{r}\sum_{\ell=1}^{n}\alpha_i\,\mathbf{k}_i^{(\ell)}\mathbf{i}^{(\ell)T}\right]^{-1}\\&\approx\mathbf{K}_0^{-1}-\sum_{i=1}^{r}\sum_{\ell=1}^{n}\frac{\alpha_i}{1+\alpha_i\,d_{i\ell}}\mathbf{D}_{i\ell}\end{aligned} \tag{17}$$

where only first-order terms are retained being $|\alpha_i|\ll 1$. In Eq. (17), the following quantities appear:

$$d_{i\ell}=\mathbf{i}^{(\ell)T}\mathbf{K}_0^{-1}\mathbf{k}_i^{(\ell)};\quad\mathbf{D}_{i\ell}=\mathbf{K}_0^{-1}\mathbf{k}_i^{(\ell)}\mathbf{i}^{(\ell)T}\mathbf{K}_0^{-1}. \tag{18a,b}$$

Notice that Eq. (17) holds if and only if the following conditions are satisfied $|\alpha_i d_{i\ell}|<1$.

3.2 *Modal frequency response function matrix*

Upon substitution of the decomposition of the stiffness matrix given by Eq. (16), the spectral matrix of the structural system with uncertain parameters takes the following form:

$$\mathbf{\Omega}^2(\boldsymbol{\alpha})=\mathbf{\Omega}_0^2+\sum_{i=1}^{r}\alpha_i\left[\sum_{\ell=1}^{n}\mathbf{w}_i^{(\ell)}\,\mathbf{v}^{(\ell)\mathrm{T}}\right] \tag{19}$$

where

$$\mathbf{w}_i^{(\ell)}=\mathbf{\Phi}_0^{\mathrm{T}}\mathbf{k}_i^{(\ell)};\quad\mathbf{v}^{(\ell)\mathrm{T}}=\mathbf{i}^{(\ell)\mathrm{T}}\mathbf{\Phi}_0. \tag{20a,b}$$

Introducing Eq. (19) into Eq. (12), the *FRF* matrix can be recast as:

$$\mathbf{H}(\boldsymbol{\alpha},\omega)=\left[\mathbf{H}_0^{-1}(\omega)+\sum_{i=1}^{r}\sum_{\ell=1}^{n}\alpha_i\,\mathbf{w}_i^{(\ell)}\mathbf{v}^{(\ell)T}\right]^{-1} \tag{21}$$

where $\mathbf{H}_0(\omega)$ is the *FRF* matrix of the nominal structural system, given by:

$$\mathbf{H}_0(\omega)=\left[-\omega^2\,\mathbf{I}_m+\mathrm{i}\,\omega\mathbf{\Xi}+\mathbf{\Omega}_0^2\right]^{-1}. \tag{22}$$

For the nominal systems here studied the matrix $\mathbf{H}_0(\omega)$ is diagonal. Conversely, the *FRF* matrix $\mathbf{H}(\boldsymbol{\alpha},\omega)$ in Eq. (21) (or Eq. (12)) is not diagonal since, as already mentioned, the spectral matrix $\mathbf{\Omega}^2(\boldsymbol{\alpha})$ in Eq. (19) is a full matrix. This implies that in

order to determine the matrix $\mathbf{H}(\boldsymbol{\alpha},\omega)$, the inverse of a frequency-dependent parametric matrix has to be performed.

In this regard, it is useful to observe that the decomposition (16) of the stiffness matrix allows to express the deviation of the *FRF* matrix with respect to the nominal value as sum of $r \times n$ modifications of rank one, as shown in Eq.(21). Thus, by applying the *RSE* (Muscolino & Sofi 2012a, Muscolino & Sofi 2012b, Muscolino et al. 2012), the following approximate explicit expression of the *FRF* matrix is obtained:

$$\mathbf{H}(\boldsymbol{\alpha},\omega) = \mathbf{H}_0(\omega) - \sum_{i=1}^{r}\sum_{\ell=1}^{n} \frac{\alpha_i}{1+\alpha_i\, b_{i\ell}(\omega)}\, \mathbf{B}_{i\ell}(\omega) \tag{23}$$

where the following complex quantities have been introduced:

$$\begin{aligned} b_{i\ell}(\omega) &= \mathbf{v}^{(\ell)T}\mathbf{H}_0(\omega)\,\mathbf{w}_i^{(\ell)}; \\ \mathbf{B}_{i\ell}(\omega) &= \mathbf{H}_0(\omega)\,\mathbf{w}_i^{(\ell)}\mathbf{v}^{(\ell)T}\mathbf{H}_0(\omega). \end{aligned} \tag{24a,b}$$

Equation (23) holds if and only if the following conditions are satisfied:

$$\left\| \alpha_i\, b_{i\ell}(\omega) \right\| < 1 \tag{25}$$

where the symbol $||\bullet||$ means modulus of $\bullet$.

4 SENSITIVITY ANALYSIS OF THE STATIONARY STOCHASTIC RESPONSE

The main aim of the present study is to perform a sensitivity analysis of the probabilistic characteristics of the random response of structures with uncertain stiffness properties under stationary Gaussian random excitation in the frequency domain.

The sensitivity of the generic scalar response quantity $R(\boldsymbol{\alpha})$ to the i-th structural parameter α_i is expressed, by definition, as the partial derivative of $R(\boldsymbol{\alpha})$ with respect to α_i evaluated at $\boldsymbol{\alpha} = \boldsymbol{\alpha}_0$, i.e. $\partial R(\boldsymbol{\alpha})/\partial \alpha_i | = \boldsymbol{\alpha}_0$.

In this section, the sensitivities of both the mean-value and *PSD* of the random response to the uncertain parameters α_i are derived in closed-form by direct differentiation of the explicit expressions of $\boldsymbol{\mu}_{\mathbf{u}}(\boldsymbol{\alpha})$ and $\mathbf{S}_{\mathbf{uu}}(\boldsymbol{\alpha},\omega)$ obtained by applying the *RSE*.

The closed-form approximate inverse of the stiffness matrix $\mathbf{K}(\alpha)$ and *FRF* matrix $\mathbf{H}(\boldsymbol{\alpha},\omega)$ obtained in the previous sections by applying the *RSE* allow to derive explicit expressions of the mean–value, $\boldsymbol{\mu}_{\mathbf{u}}(\boldsymbol{\alpha})$, and *PSD* matrix, $\mathbf{S}_{\mathbf{uu}}(\boldsymbol{\alpha},\omega)$, of the stationary random response (see Eqs. (10) and (11)). Indeed, substituting Eq. (17) into Eq. (10), the following explicit approximate expression of the mean value vector is obtained

$$\boldsymbol{\mu}_{\mathbf{u}}(\boldsymbol{\alpha}) = \mathbf{K}^{-1}(\boldsymbol{\alpha})\,\boldsymbol{\mu}_{\mathbf{f}} \approx \boldsymbol{\mu}_{\mathbf{u},\mathbf{0}} - \sum_{i=1}^{r}\sum_{\ell=1}^{n} \frac{\alpha_i}{1+\alpha_i\, d_{i\ell}}\, \mathbf{D}_{i\ell}\,\boldsymbol{\mu}_{\mathbf{f}} \tag{26}$$

where $\boldsymbol{\mu}_{\mathbf{u},\mathbf{0}} = \boldsymbol{\mu}_{\mathbf{u}}(\boldsymbol{\alpha})|_{\boldsymbol{\alpha}=\boldsymbol{\alpha}_0} = \mathbf{K}_0^{-1}\boldsymbol{\mu}_{\mathbf{f}}$ is the nominal mean-value vector.

The influence of the i-th uncertain parameter α_i on the mean-value of the response can be investigated by evaluating the sensitivity of $\boldsymbol{\mu}_{\mathbf{u}}(\boldsymbol{\alpha})$ to α_i $(i = 1,2,\ldots,r)$ through direct differentiation of Eq. (26) which yields the following explicit expression:

$$\left.\frac{\partial \boldsymbol{\mu}_{\mathbf{u}}(\boldsymbol{\alpha})}{\partial \alpha_i}\right|_{\boldsymbol{\alpha}=\boldsymbol{\alpha}_0} = -\sum_{\ell=1}^{n}\left[\frac{1}{\left(1+\alpha_i d_{i\ell}\right)^2}\right]_{\boldsymbol{\alpha}=\boldsymbol{\alpha}_0} \mathbf{D}_{i\ell}\,\boldsymbol{\mu}_{\mathbf{f}}. \tag{27}$$

Similarly, substituting Equation (23) into Eq. (11) the *PSD* matrix of the random response process $\mathbf{S}_{\mathbf{uu}}(\boldsymbol{\alpha},\omega)$ is obtained in closed-form and the explicit expression of the sensitivity to the i-th uncertain parameter α_i $(i = 1,2,\ldots,r)$ can be derived analytically by direct differentiation, i.e.:

$$\begin{aligned} &\left.\frac{\partial \mathbf{S}_{\mathbf{uu}}(\boldsymbol{\alpha},\omega)}{\partial \alpha_i}\right|_{\boldsymbol{\alpha}=\boldsymbol{\alpha}_0} = \\ &= \boldsymbol{\Phi}_0 \left.\frac{\partial \mathbf{H}^*(\boldsymbol{\alpha},\omega)}{\partial \alpha_i}\right|_{\boldsymbol{\alpha}=\boldsymbol{\alpha}_0} \mathbf{S}_{\hat{\mathbf{X}}_p\hat{\mathbf{X}}_p}(\omega)\,\mathbf{H}^T(\boldsymbol{\alpha},\omega)\boldsymbol{\Phi}_0^T \\ &+\boldsymbol{\Phi}_0\mathbf{H}^*(\boldsymbol{\alpha},\omega)\mathbf{S}_{\hat{\mathbf{X}}_p\hat{\mathbf{X}}_p}(\omega) \left.\frac{\partial \mathbf{H}^T(\boldsymbol{\alpha},\omega)}{\partial \alpha_i}\right|_{\boldsymbol{\alpha}=\boldsymbol{\alpha}_0} \boldsymbol{\Phi}_0^T \end{aligned} \tag{28}$$

where $\mathbf{H}(\boldsymbol{\alpha},\omega)$ is given by Eq. (23) and

$$\left.\frac{\partial \mathbf{H}(\boldsymbol{\alpha},\omega)}{\partial \alpha_i}\right|_{\boldsymbol{\alpha}=\boldsymbol{\alpha}_0} = -\sum_{\ell=1}^{n}\left[\frac{1}{\left(1+\alpha_i b_{i\ell}(\omega)\right)^2}\right]_{\boldsymbol{\alpha}=\boldsymbol{\alpha}_0} \mathbf{B}_{i\ell}(\omega). \tag{29}$$

Finally, the sensitivities of the covariance matrix of the random response, $\boldsymbol{\Sigma}_{\mathbf{uu}}(\boldsymbol{\alpha})$, to the uncertain parameters can be determined straightforwardly from Eq. (28) as:

$$\left.\frac{\partial \boldsymbol{\Sigma}_{\mathbf{uu}}(\boldsymbol{\alpha})}{\partial \alpha_i}\right|_{\boldsymbol{\alpha}=\boldsymbol{\alpha}_0} = \int_{-\infty}^{\infty} \left.\frac{\partial \mathbf{S}_{\mathbf{uu}}(\boldsymbol{\alpha},\omega)}{\partial \alpha_i}\right|_{\boldsymbol{\alpha}=\boldsymbol{\alpha}_0} \mathrm{d}\omega. \tag{30}$$

The above explicit expressions of the sensitivities enable designers to gain a deeper insight into the effects and relative importance of each stiffness parameter on structure's performance. Specifically, we may determine how the statistics of the random response change due to a given change in the stiffness parameters.

5 NUMERICAL APPLICATION

A very simple reasoning, based on the knowledge of sensitivities to the various uncertain parameters, allows to reduce the number of series terms in the *RSE* (23). Specifically, if for a given degree-of-freedom, sensitivity analysis shows that the variability of some

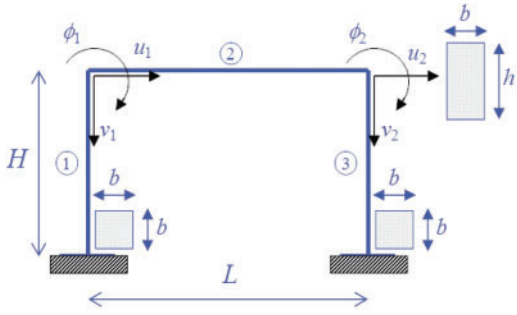


Figure 1. Portal frame with uncertain Young's moduli.

Table 1. Sensitivities of the variances of the nodal horizontal displacements with respect to α_i $(i = 1, 2, 3)$.

$\|\|\partial\sigma^2_{u_s}/\partial\sigma_i\|_{\alpha=\alpha_0}\|\|$	μ_1	μ_2
α_1	3.06809×10^{-7}	3.06809×10^{-7}
α_2	5.30716×10^{-8}	5.30716×10^{-8}
α_2	3.06809×10^{-7}	3.06809×10^{-7}

stiffness parameters does not affect the response, then the corresponding terms can be dropped from the *RSE*. This provides substantial computational savings especially when a large number of uncertain parameters is involved.

As an application, a portal frame with uncertain Young's moduli is considered (see Fig. 1). It is assumed that the elastic moduli of the beam and columns exhibit fluctuations $|\alpha_i| < 1$ around the nominal value $E_0 = 2.85 \times 10^7$ kN/m^2, i.e. $E_i = E_0(1 + \alpha_i)(i = 1, 2, 3)$. The geometrical properties of the portal frame are indicated in Figure 1, where $b = 0.30$ m, $h = 0.60$ m, $L = 3$ m and $H = 2$ m. Furthermore, each node possesses a lumped mass $M = 500$ kg. The modal damping ratio is set equal to $\xi = 0.05$.

The ground acceleration is modelled as a Tajimi Kanai process with *PSD* given by:

$$S(\omega) = S_W \frac{4\zeta_g^2\omega_g^2\omega^2 + \omega_g^4}{\left(\omega_g^2 - \omega^2\right) + 4\zeta_g^2\omega_g^2\omega^2} \tag{31}$$

where $S_W = 0.05$ m^2/s^3, $\zeta_g = 0.6$ and $\omega_g = 4\pi$ rad/s.

The sensitivity analysis provides information on response variability due to changes of Young's moduli in the beam and columns. The analysis is performed here by evaluating the sensitivities of the covariance matrix given by Eq. (30). In Table 1, the values of the sensitivities of the variances, $\sigma^2_{u_s}(\boldsymbol{\alpha})$, of the horizontal displacements, u_1 and u_2, with respect to the parameters α_1, α_2 and α_3 are reported.

Any response variable depending on the uncertain parameters can be expanded in the Taylor series about its nominal value. For small uncertainties, the first-order term of this expansion turns out to be the most significant contribution to the deviation of the response from the nominal value due to the variability of the model parameters. Such term is given by the summation of the first-order partial derivatives of the response with respect to the uncertain parameters multiplied by the uncertainties. Then, a percentage measure of the influence of a generic design variable on the response can be defined by introducing the so-called *coefficient of sensitivity* that measures the global variability of the response with respect to its nominal value. In particular, for the variance of the s-th DOF the *coefficient of sensitivity* with respect to the i-th uncertain parameter can be defined as:

$$\varepsilon_{i,\sigma^2_{u_s}}\% = \frac{1}{\sigma^2_{u_s}(\boldsymbol{\alpha}_0)}\left(\frac{\partial\sigma^2_{u_s}(\boldsymbol{\alpha})}{\partial\alpha_i}\right)\Bigg|_{\boldsymbol{\alpha}=\boldsymbol{\alpha}_0} \Delta\alpha_i \times 100. \tag{31}$$

Table 2. Coefficients of sensitivity of the variances of the horizontal displacements with respect to α_i $(i = 1, 2, 3)$.

$\varepsilon_{i,\sigma^2_{u_s}}$ %	u_1	u_2
α_1	4.6%	4.6%
α_2	0.8%	0.8%
α_3	4.6%	4.6%

In Table 2, the coefficients of sensitivity for the variances of the horizontal displacements u_1 and u_2 with respect to the uncertain parameters α_i $(i = 1, 2, 3)$ are reported.

As expected, the variances of the horizontal displacements are sensitive to variations of the parameters α_1 and α_3, while they are almost unaffected by the variation of the parameter α_2.

The results provided by sensitivity analysis allow an efficient evaluation of the approximate *PSD* of the response by the *RSE* (see Eq. (11) and Eq. (23)). To assess the validity of sensitivity analysis outcomes, comparisons in terms of *PSD* function of the nodal horizontal displacement u_1, $S_{u_1}(\omega)$, are reported in Figures 2a–c.

In Figure 2a, the proposed estimate of the *PSD*, obtained by retaining all terms in the *RSE*, is contrasted with the exact one for $\alpha_i = \alpha = 0.05$ $(i = 1, 2, 3)$. For completeness, in the same plot the nominal *PSD* is also depicted.

Figure 2b shows a similar comparison where the proposed *PSD* is estimated by retaining in the *RSE* (see Eq. (23)) only the terms associated to the parameters resulting as the most influential for the selected response quantity from the preliminary sensitivity analysis (see Table 1), namely the parameters α_1 and α_3. By inspection of Figure 2b, it can be seen how the accuracy of the estimated *PSD* is not affected by neglecting the term associated to the parameter α_2. Further validation of the sensitivity analysis is provided considering another comparison among the *PSD* functions as reported in Figure 2c.

The proposed *PSD* of the horizontal displacement u_1 plotted in Figure 2c is evaluated by neglecting the

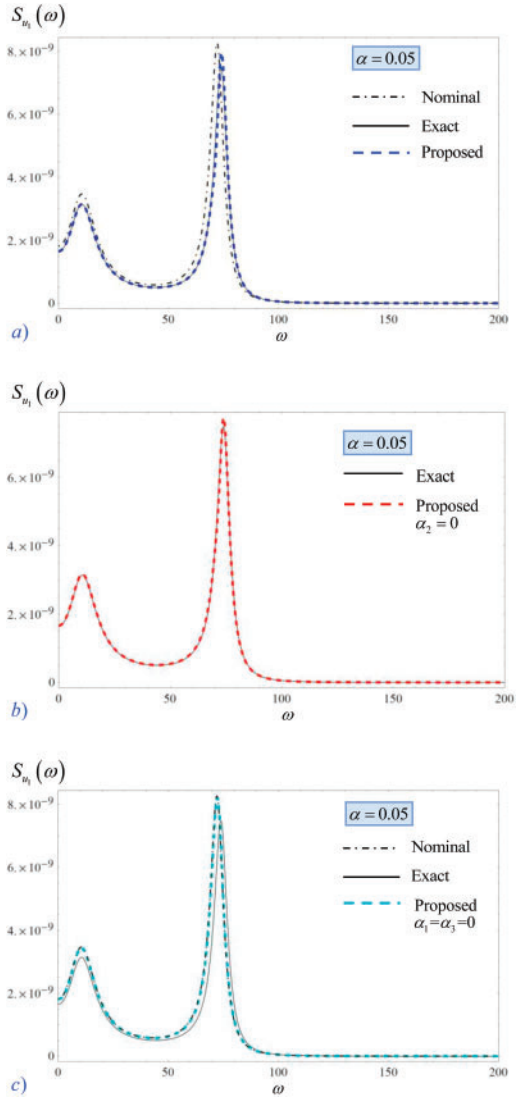


Figure 2. Comparison between the proposed estimate of the *PSD* function of u_1 and the exact one: a) retaining all terms in the *RSE* (see Eq. (23)); b) neglecting the term associated to α_2; c) neglecting the terms associated to α_1 and α_3.

terms associated to the parameters α_1 and α_3. Notice that the estimated *PSD* matches the nominal one, thus confirming the negligible influence of the parameter α_2 on the *PSD*, detected via sensitivity analysis.

6 CONCLUSIONS

Sensitivities give information about the variability of the response due to a change in a given design parameter and play an important role also in structural identification, optimization and anti-optimization problems.

In the paper, a novel procedure for deriving approximate explicit expressions of the sensitivities of the mean-value and covariance matrix of the stationary response of randomly excited structures subject to variations of the stiffness parameters has been presented. The proposed approach relies on the use of the so-called *RSE*, recently proposed by the authors for evaluating in approximate closed-form the inverse of an invertible matrix with a modification of rank r.

The present study has also focused on the usefulness of sensitivity analysis to improve the computational efficiency of the *RSE* which involves a summation over the fluctuating properties.

The accuracy and efficiency of the proposed procedure for sensitivity analysis of randomly excited structures has been demonstrated through numerical results concerning a frame structure with variability of the Young's moduli.

REFERENCES

Bhattacharyya B. Chakraborty S. 2002. Stochastic dynamic sensitivity of uncertain struc-tures subjected to random earthquake loading, *J. Sound Vib.* 249, 543–556.

Chaudhuri A. Chakraborty S. 2004. Sensitivity evaluation in seismic reliability analysis of structures, *Comput. Methods Appl. Mech. Engrg.* 193, 59–68.

Elishakoff I. Ohsaki M. 2010. *Optimization and Anti-Optimization of Structures under Uncertainties*, Imperial College Press, London.

Haftka R.T. Adelman H.M. 1989. Recent developments in structural sensitivity analysis", *Struct. Optim.* 1, 137–151.

Jensen H.A 1995. Global sensitivity analysis in structural mechanics, *Comput. Struct.* 56, 903–915.

Lutes L.D. & Sarkani S. 1997. *Stochastic Analysis of Structural and Mechanical Vibrations*, Prentice-Hall, Upper Sudale River.

Muscolino G. & Sofi A. 2012a. Explicit solutions for the static and dynamic analysis of discretized structures with uncertain parameters. In: B.H.V. Topping (Ed.), *Computational Methods for Engineering Science*, Volume 30, Chapter 3: 47–73. Stirlingshire, Scotland: Saxe-Coburg Publications.

Muscolino G. & Sofi A. 2012b. "Bounds for the stationary stochastic response of truss structures with uncertain-but-bounded parameters", Mech. Syst. Signal Process., http://dx.doi.org/10.1016/j.ymssp.2012.06.016 (2012).

Muscolino G. Santoro R. & Sofi A. 2012. Frequency response functions of discretized structural systems with uncertain parameters, *Proc. 5th International Conference on Reliable Engineering Computing (REC 2012)*, June 13-15, Brno, Czech Republic, 407–425.

Research and Applications in Structural Engineering, Mechanics and Computation – Zingoni (Ed.)
© 2013 Taylor & Francis Group, London, ISBN 978-1-138-00061-2

Semi-active control of structural systems with uncertainties using an unscented Kalman filter

M.S. Miah & E.N. Chatzi
Institute of Structural Engineering, ETH Zurich, Zurich, Switzerland

F. Weber
Empa, Structural Engineering Research Laboratory, Duebendorf, Switzerland

ABSTRACT: This work presents a novel semi-active control approach for the mitigation of vibrational response of structures. As is often the case for structural systems, the underlying mathematical/simulation model is not entirely deterministic due to uncertainties related to both the system properties as well as the noise content of the measured information. Therefore, in order to successfully monitor the system, it is essential to develop suitable algorithms that can incorporate dynamic feedback into the computation. In order to meet the aforementioned challenges, in the approach introduced herein a nonlinear joint state and parameter estimation algorithm is employed. The combination of an LQR controller with a linear Kalman Filter is already well established and is commonly known as Linear-Quadratic-Gaussian (LQG) control. In what follows the combination of a nonlinear filter equivalent, namely the Unscented Kalman Filter (UKF) with a Linear Quadratic Regulator (LQR) semi-active controller is numerically investigated. The proposed methodology is validated through two numerical applications, a first one assuming uncertain structural parameters, and a second one employing online tuning of the design parameter R.

1 INTRODUCTION

Over the past few decades smart materials, intelligent structures and emerging associated technologies have led to increasingly complex structural systems. As a result, the efficient design and precise monitoring of such systems are non-trivial tasks. Several techniques have in fact been developed involving the use of control strategies for the mitigation of vibrations (Weber & Boston 2011, Weber & Maslanka 2012, Preumont 2004). One of the inherent difficulties in the field of structural control is that in most cases the anticipated extreme event forces are not entirely known. Therefore, even though a controller might be optimally designed for some predefined type of input forces, in effect it may not be capable of handling a wider range of uncertain inputs. In order to eliminate such a drawback, this study investigates the applicability of an online system identification technique for the real-time updating of the control scheme. As shown later on, this leads to a nonlinear identification problem of joint state and parameter estimation (Chatzi et al. 2009). A novel structural control approach is proposed, combining the Unscented Kalman Filter (UKF) with an LQR controller. The UKF surfaced through the work of Julier & Uhlmann (1997) who introduced the Unscented Transform. Later on Merwe & Wan (2004) introduced the sigma-point Kalman filters (SPKF), a special class of which is the UKF, as an upgraded version of the Extended Kalman Filter (EKF). The performance of the UKF algorithm in real-time nonlinear identification problems has been verified by several studies (Chatzi & Smyth 2010, Xie & Feng 2011, Wu & Smyth 2007, Mariani & Ghisi 2007) noting its robustness against available alternatives.

In a previous study, Araki & Okada (2005) firstly perform parameter identification of an Acrobot system using the UKF, and an energy based control approach is proposed in a second, separate step. Bisgaard et al. (2010) have also employed a UKF filter for estimating the slung load states of a helicopter system. Marafioti (2010) explores the efficacy of the UKF and EKF within the context of Model Predictive Control (MPC) where simulation-based results prove the advantages of using the UKF as an alternative to the EKF. Rigatos (2011) demonstrates the use of Particle Filter and other nonlinear state estimation algorithms for industrial control applications using a reduced number of sensors. Aiming to achieve optimal control Wang (2011) combines nonlinear estimators with fuzzy control of nonlinear systems with general performance criteria.

Concerning the control approach utilized herein, the LQR controller is employed as one of the most commonly used and robust algorithms for mitigating structural vibration (Johnson & Erkus 2002, Rajamohan et al. 2011). However, the LQR controller is associated with two significant drawbacks. One concerns the full observation of the state vector. When this is

not possible, as is frequently the case due to a limited number of sensors, the LQR is combined with a Kalman Filter state estimator yielding the LQG control (Athans 1971). This is commonly performed for the case of linear systems, however not much work has dealt with combining the LQR with nonlinear filters (Jimenez et al. 2011, Gawronski 2008). An additional drawback is the selection of optimal weight matrices $\boldsymbol{Q}$ and $\boldsymbol{R}$. Conventionally, this is performed based on designer experience or the trial and error method. Several studies have tried to overcome this limitation and proposed an automated design usually based on evolutionary processes (Mobaieen et al. 2012, Coelingh et al. 1997). Li et al. (2008) propose a multi-objective evolutionary algorithm for selecting the optimal weight matrices. More interestingly Oral et al. (2010) propose an approach that is based on a mathematical formulation relying on the knowledge of the characteristics of the particular system. In the work presented herein, the online identification problem is appropriately formulated in order to regulate the optimal weight matrices in an online regime.

2 THE SHEAR FRAME SETUP

In order devise the envisioned control scheme, an online approach is devised based on feedback from measurements of structural response. A 5-storey shear frame is considered as the case study, relying on an actual experimental setup assembled on the uniaxial shaking table of the Structural Engineering laboratory in EMPA. The experimental setup (without controller) is shown in Figure 1. Each floor is assumed to have a mass of 5.95 kg. A non parametric simulation has been performed yielding the natural frequencies ($f_1 = 1.33$ Hz, $f_2 = 3.94$ Hz, $f_3 = 6.23$ Hz, $f_4 = 8.04$ Hz, $f_5 = 9.28$ Hz) and modal shapes of this test structure as well as the estimated damping. By synthesizing the results, an analytical model is additionally put together (physical model of the system). In formulating the simple model of only five degrees of freedom (dof), symmetry is taken into account. Additionally no rotation is considered for horizontal sections at the floor levels, i.e., the simplified model corresponds to a shear-type frame. The physical model is essentially the representation of the dynamic equation of motion of this 5 dof system.

$$\boldsymbol{M}_{sf}\ddot{x}(t)+\boldsymbol{C}_{sf}\dot{x}(t)+\boldsymbol{K}_{sf}x(t)=F(t) \tag{2.1}$$

where $\boldsymbol{M}_{sf}$ (5×5) is the mass matrix and $\boldsymbol{K}_{sf}$,$\boldsymbol{C}_{sf}$ are the associated stiffness and damping matrices. Due to the nature of the considered system, the mass matrix is assumed to be diagonal and the stiffness and damping matrices contain non-diagonal terms only in the case of consecutive storey dofs. It is clear that due to the number of simplifying assumptions the system matrices are not idealized. Nonetheless, the numerical simulation of the system using the identified matrices agrees well with the experimentally measured response.

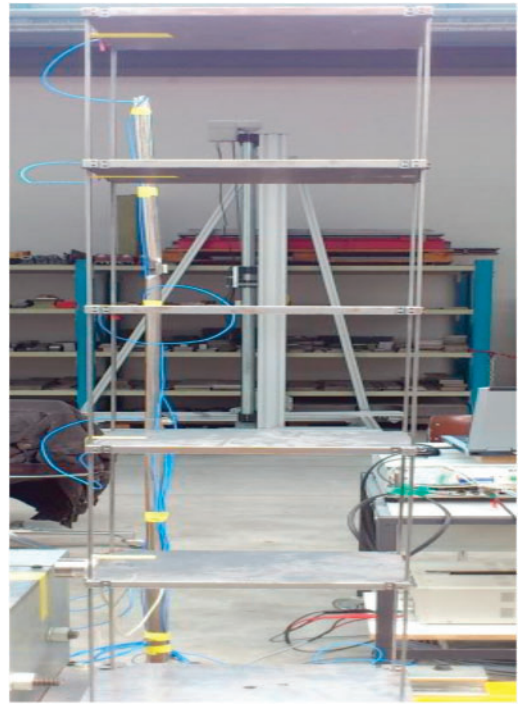


Figure 1. Experimental setup of 5-storey shear frame at EMPA.

In order to apply the framework proposed herein the system is brought into a state-space formulation. Equations 2.2 are known as the process (or system) and measurement (or observation) equations of the continuous system and can be easily derived from Equation 2.1.

$$\dot{x}(t)=A_c x(t)+B_c u(t) \;\;\&\;\; y(t)=C_c x(t)+D_c u(t) \tag{2.2}$$

where in the general case: $A_c[.]$ = system matrix $(n \times n)$, $B_c[.]$ = input matrix $(n \times p)$, $C_c[.]$ = output matrix $(m \times n)$, $D_c[.]$ = feed-forward matrix $(m \times p)$, $x(.)$ = state vector (R^n), $y(.)$ = output vector (R^m), $u(.)$ = input vector (R^p). The input vector $u(.)$ holds the exogenous input (ground excitation) and the actuator control force as appears in Equation 2.3.

$$u(t)=\begin{bmatrix} f_{cont}(t) \\ a_g(t) \end{bmatrix} \tag{2.3}$$

where $f_{cont}(t)$ = control force, $a_g(t)$ = exogenous input. In this study a_g is a harmonic excitation with a frequency chosen exactly equal to the first resonant frequency of the shear frame, $f_1 = 1.33$ Hz. The control force is provided by means of an actuator assumed to act horizontally on the first floor level. In order to calculate the control force, the full-state vector (displacement & velocity) needs to be fed to the controller. Using an appropriate integration algorithm,

the continuous system can be brought to its discrete equivalent:

$$x_{k+1} = Ax_k + Bu_k \quad \& \quad y_k = Cx_k + Du_k \tag{2.4}$$

3 THE LQR CONTROL STRATEGY

Complex structures such as bridges or high-rise buildings often incorporate systems for their monitoring and control. However, most real world structures come with inherent uncertainties related to their structural properties or even to the lack of knowledge concerning the loading involved. This renders the control task non trivial.

In this study, a semi-active control strategy based on the LQR is deployed for the shear frame presented earlier. A detailed concept of semi-active control, employing clipping of the active force, and its applications are studied by Weber & Boston (2011) and Lazar et al. (2012). Active control comes with several drawbacks. The most significant one is associated with the possibility of electrical power loss during an emergency event (i.e. earthquake, significant wind, etc.) in which case the control scheme is non-operational. In order to tackle this limitation, semi-active control strategies can be implemented.

The LQR is a well-known full-state feedback control algorithm, frequently met in the fields of structural dynamics and mechanical control. For reasons of completeness we provide here the basic form of the discrete-time quadratic strategy for a discrete LTI system of the form of Equation (2.4). This control strategy minimizes the cost-to-go function J defined in Equation 3.2.

$$J = \sum_{k=0}^{\infty} (x_k^T Q x_k + u_k^T R u_k) \tag{3.2}$$

The first part of this equation corresponds to the state response contribution whereas the second part reflects the contribution of the control force.

$$u_k = -K_{opt} x_k \tag{2.3}$$

where K_{opt} is the optimal closed-loop gain of the control law, which minimizes the performance index J by feeding in the state response. The minimization strictly depends on the optimal set of weight matrices $\boldsymbol{Q}$ & $\boldsymbol{R}$. The selected weight matrices must satisfy the following conditions; $\boldsymbol{Q}$ must be positive semi-definitive, $x_k^T Q x_k \geq 0$; $\boldsymbol{R}$ must be positive definitive, $u_k^T R u_k > 0$; and both must be symmetric. As already mentioned in section 1, the choice of optimal weight matrices $\boldsymbol{Q}$ & $\boldsymbol{R}$ is conventionally performed by trial and error or relying on the designer's experience. In this study a novel online approach is demonstrated for optimal tuning of the weight matrices based on the measured structural response. For further information on the LQR, the interested reader is referred to Anderson & Moore (1989).

4 THE UKF FOR NONLINEAR SYSTEM ESTIMATION

As aforementioned, the UKF algorithm was introduced in an effort to eliminate the computational drawbacks of the EKF, associated with linearizations and the calculation of Jacobians. The UKF models the state as a Gaussian random variable whose distribution can be approximated by a carefully chosen set of deterministic points (sigma points). These points capture the prior mean and covariance of the state and when propagated through the nonlinear function, provide the estimation of the posterior/transformed state. This process is known as the Unscented Transformation (UT) (Julier & Uhlmann 1997).The assumed process and observation functions are shown in Equations 4.1 and 4.2 where functions f, h can be nonlinear.

$$x_k = f(x_{k-1}, u_{k-1}) + w_{k-1} \tag{4.1}$$

$$y_k = h(x_k) + v_k \tag{4.2}$$

where w_{k-1} = process noise, v_{k-1} = measurement noise, assumed white, Gaussian.

The sigma points are calculated as follows:

$$x_k^a = \left[\hat{x}_{k-1}^a \quad \hat{x}_{k-1}^a + \sqrt{(L+\lambda)P_{k-1}^a} \quad \hat{x}_{k-1}^a - \sqrt{(L+\lambda)P_{k-1}^a} \right] \tag{4.3}$$

where L = state dimension, x_k^a = sigma point vector, augmented to account for the process noise dimension, λ = scaling parameter indicating the spread of the sigma points, P_{k-1}^a = covariance of the state. The sigma points are propagated through the process/system equation in a prediction step and, subsequently, the weighted estimate is updated in a correction step. The estimation of the posterior is performed by minimizing the error between the estimated and actually measured quantities. At this point, it is important to note for what follows, that the observations do not need to correspond to the full system state. In other words a limited number of sensors can be employed. For a deeper insight into the UKF, the interested reader is referred to Wan & Merwe (2001); Julier & Uhlmann (1997).

5 APPLICATIONS

5.1 *Calibration of "**Q**" and "**R**"*

The initial task of this work is to design an optimal LQR controller. As a preliminary step, and in order to obtain a better understanding of the problem at hand, the optimal selection of the weight matrices Q & R is numerically performed, by employing a number of different nonlinear optimization techniques in place of trial and error. These include (i) the Genetic Algorithm (GA) and (ii) Particle Swarm Optimization (PSO) (Kennedy & Eberhart 1995) which constitute evolutionary methods, and (iii) a gradient/algebraic

Table 1. Summary of the optimization techniques.

Algorithm	GA	PSO	CNO
Q/R	1082	1042	1097
Fitness Value	39.15	38.57	38.03
Time (sec)	2414.25	5822.24	29.64

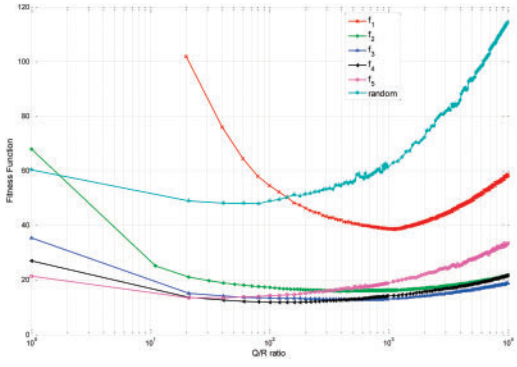


Figure 2. Fitness Function plot for a range of Q/R ratios.

approach for Constrained Nonlinear Optimization (CNO).

The test structure and the assumed loading is already described in Section 2. The fitness function f to be optimized aims at the minimization of the amplitude of response quantities for all five stories:

$$f = \sum_{i=1}^{5} \left\{ w_1 |x_i|_{\max} + w_2 |\dot{x}_i|_{\max} + w_3 |\ddot{x}_i|_{\max} \right\} \tag{5.1}$$

where w_1, w_2, w_3, are appropriate scaling factors. A summary of the results of the different optimization techniques and the corresponding calculation times are presented in Table 1. As noted in the figure, and is well established in the literature, the optimal pair depends only on the ratio Q/R since scaling the LQR cost function does not change the optimal control law. Additionally, it is obvious that the gradient based method requires considerably less computational effort than the GA and PSO schemes.

In Figure 2 the fitness function value is plotted for a range of plausible Q/R ratios given harmonic excitations of frequency equal to the structure's natural frequencies, as well as one random input. As is evident, the optimum lies in a valley-like space which clearly explains the faster convergence of the gradient based method against evolutionary ones.

It is obvious that as the nature of the simulated ground motion varies, the optimal point can be shifted, yielding different optimal Q & R configurations. This, in combination with the fact that the actual extreme event loading is generally unknown a-priori, confirms the need for the weight parameters to be tuned online. In Section 5.2 predefined values of the Q & R parameters are utilized for the controller, assuming an uncertain system, whereas in Section 5.3 the structure is assumed known and the Q & R are tuned online. In both cases limited sensor information is assumed. The required algorithms are programmed in MATLAB®/Simulink and the sampling frequency for the simulations is set to 200 Hz.

5.2 *Joint states and parameter estimation*

In this application the system's stiffness characteristics are assumed to be unknown. The goal is therefore the joint state & parameter estimation of the system based on limited sensor measurements, i.e. the state vector is only partially observed. Therefore in order to conduct the LQR control, a state estimator is required. When introducing the stiffnesses as unknowns, the problem becomes nonlinear. We therefore utilize the UKF as the state observer. The state vector is augmented to include all floor stiffnesses $k_1 \ldots k_5$, and the dimension of the state vector size is now 15:

$$x = \begin{bmatrix} x_1 & \ldots & x_5 & \dot{x} & \ldots & \dot{x}_5 & k_1 & \ldots & k_5 \end{bmatrix}^T \tag{5.2}$$

where, x = state vector, $x_1 \ldots x_5$ = 1st–5th floor displacement, $\dot{x}_1 \ldots \dot{x}_5$ = 1st–5th floor velocity, and $k_1 \ldots k_5$ = 1st–5th floor stiffness.

$$A = \begin{bmatrix} 0_{5\times5} & \mathrm{I}_{5\times5} & 0_{5\times5} \\ -M_{sf}^{-1}K_{ident} & -M_{sf}^{-1}C_{sf} & 0_{5\times5} \\ 0_{5\times5} & 0_{5\times5} & 0_{5\times5} \end{bmatrix} \tag{5.3}$$

where $0_{5\times5}$ = null matrix, $\mathrm{I}_{5\times5}$ = unit matrix.

$$B = \begin{bmatrix} 0_{1\times5} & m_1^{-1} & 0 & 0 & 0 & 0 & 0_{1\times5} \\ 0_{1\times5} & -1 & -1 & -1 & -1 & -1 & 0_{1\times5} \end{bmatrix}^T \tag{5.4}$$

where $0_{1\times5}$ = null matrix (1×5).

The need for an online update of the stiffness matrix stems not only from a possible incomplete knowledge of the properties, but also from changes that might occur during the life of a structure owing to deterioration, damage, loosening of bearings, etc. The analysis is performed for a duration of 10sec for a harmonic input of 1.33 Hz (1st natural frequency). In this example, the weight matrices Q & R are considered preselected and set equal to Q = 5e-8, R = 7.5e-10. We assume that only acceleration signals from floors 1, 3 and 5 are observed, and the UKF is able to reconstruct the full state estimate. A process noise of 0.5% RMS noise to signal ratio is set, indicating confidence in the physical state-space model and a measurement noise of 7% RMS is added to the simulated, "clean" response signal which is generated using an accurate 4th order Runge-Kutta scheme. The discrete state space formulation is carried out using a 2nd order Taylor expansion approximation

Table 2. Summary of the identified stiffness.

Parameters	Original	Identified	Error (%)
k_1	481.30	491.10	2.00
k_2	545.50	514.90	5.93
k_3	554.10	558.40	0.77
k_4	544.70	571.90	4.76
k_5	553.00	541.60	2.10

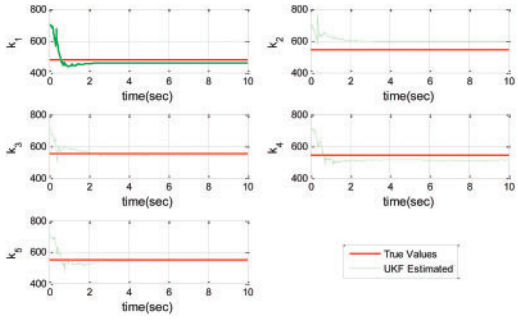


Figure 3. Identified/estimated stiffness vs. the true values.

for the matrix exponential formula applied on $A_c dt$, where dt is the sampling time & $A_c\,dt$ is convergent. This simplified assumption keeps the process online.

The summary of the converged identified stiffness values is presented in Table 2. Also a graphical representation over time is provided in Figure 3. The method seems to effectively estimate the unknown parameters despite an initial guess of 700 units, which is about 30% off the actual values. It is worth noting that even as the order of the system increases (for more dofs), the sigma point evaluation can be carried out in parallel computations and it is hence possible to maintain the computational time to a low.

It should be stated, that convergence is affected by the assumed levels of measurement noise and by the initial choice of covariance for the state. As the problem is nonlinear, the choice of initial covariance for the constant parameters has to lie within a reasonable range or the algorithm might be disoriented early on in the estimation process.

Additionally, Figure 4 displays the results for the first floor displacement. The blue line is the real response from the online control (stiffness unknown a-priori), the red line is the UKF estimate (quite close), and the green line is what the controlled response would be if the stiffness was known a-priori (fixed k value).

The nature of observations is an important factor. For instance in this example additional displacement info would improve the estimation by mitigating integration issues stemming from the analog to digital system conversion. These issues will be the topic of more extended research.

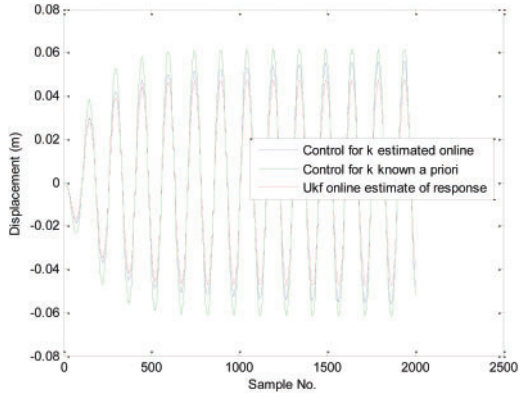


Figure 4. The top floor online response i) as would actually occur for online control, ii) as would occur is k was known a-priori and iii) as is estimated from the UKF in an online manner.

5.3 *Online Estimation of weight factor "**R**" assuming known properties*

As a next step, it is now assumed that the structural characteristics are this time known a-priori, while the optimal control force weight factor R is unknown. As already mentioned Q & R are linearly dependent and therefore only one of the two needs to be defined as a parameter, otherwise the system would become unobservable. The aim is to tune the control force in an online manner. For this purpose, the state vector is augmented to a dimension of 11, so as to include the weight factor.

$$x = \left[x_1 \quad . \quad . \quad . \quad x_5 \quad \dot{x}_1 \quad . \quad . \quad . \quad \dot{x}_5 \quad R\right]^T$$

The system matrices are again appropriately formulated. The estimation of R is achieved by defining an additional set of observations, other than the floor accelerations. These are "*artificial, zero observations*" of the five first states, requiring that the corresponding floor displacements are minimized, i.e., $x_i(t) = 0, i = 1 \ldots 5$. For these artificial observations a relatively sizeable measurement noise is assumed; namely 30% RMS noise to signal ratio. The remaining noise levels are the same as before, as is the input ground excitation. Since R is now a design variable, the control loop has to be checked for stability in every update of its value. Therefore, the computational time now increases and, unless this process is carried out in parallel, the control scheme is not online. It could however become near-online by enforcing the update of R at intervals scarcer than the time step. Further research will investigate this.

As shown in Figure 5, the proposed approach indeed yields a reduced vibration response as compared to the empirically calibrated equivalent.

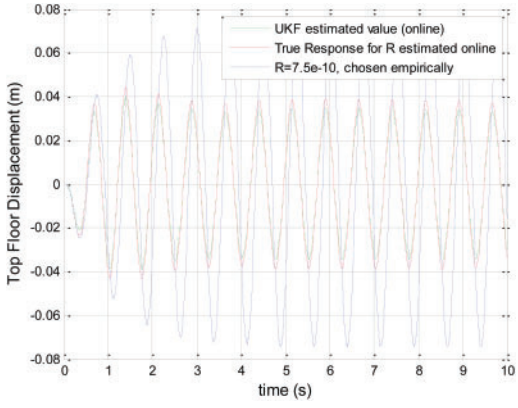


Figure 5. The top floor online response as would actually occur for online control (red), as would occur is R was empirically chosen a-priori (blue) and as is estimated from the UKF in an online manner (green).

6 CONCLUSION

This paper proposes a framework for the online tuning of an LQR controller by employing a nonlinear filter, namely the UKF, as the state estimation algorithm. Three main applications are presented; firstly the weight matrices *Q & R* are calibrated in an offline mode; then joint state and parameter estimation is achieved, corresponding to a system with uncertainties; and finally the control parameter *R* is tuned in an online manner. The overall results of the simulated performance of the shear frame confirm that the proposed approach provides a promising adaptive control scheme. In future work, the sensitivity of system to noise and the coupling of joint state & parameter estimation with the tuning of the control parameter *R* will be explored.

REFERENCES

Anderson, B. & Moore, J. 1989. Optimal control LQ method. *Prentice-Hall International, Inc*.

Araki, N., & Okada, M. 2005. Parameter identification and swing-up control of an Acrobot system. *IEEE International Conference on Industrial Technology* 14–17 Dec. 2005.

Athans M. 1971. The role and use of the stochastic Linear-Quadratic-Gaussian problem in control system design. *IEEE Transaction on Automatic Control AC-*16 (6): 529–552.

Bisgaard, M. La C. A. & Bendtsen, D. J. 2010. Adaptive control system for autonomous helicopter slung load operations. *Control Engineering Practice* 18(7): 800–811.

Chatzi, E. N. & Smyth, A. W. 2009. The unscented Kalman filter and particle filter methods for nonlinear structural system identification with non-collocated heterogeneous sensing. *Structural Control and Health Monitoring* 16: 99–123.

Chatzi, E. N., Smyth, A. W. & Masri, S. F. 2010. Experimental application of on-line parametric identification for nonlinear hysteretic systems with model uncertainty. *Structural Safety* 32(5): 326–337.

Coelingh, H. J., de Vries, T. J. A, van Lochem. P. B. T. & Amerongen, J. 1997. Automated optimal controller design in mechatronics. *7th IFAC Symposium on Computer Aided Control Systems Design*, Gent, Belgium.

Gawronski, W. 2008. Modeling and Control of Antennas and Telescopes, *Mechanical Engineering Series*, Part 3: 95–134.

Jiménez, A., Al-Hadithi, B. M. & Matía, F. 2011. Extended Kalman Filter for the Estimation and Fuzzy Optimal Control of Takagi-Sugeno Model. *Fuzzy Controllers, Theory and Applications*, book edited by Lucian Grigorie, ISBN 978-953-307-543-3

Johnson, E.A. & Erkus, B. (2002). Structural Vibration Mitigation using Dissipative Smart Damping Devices. 15th ASCE Engineering Mechanics Conference (EMI2002), *Columbia University, New York, New York*, June 2–5, 2002. CD-ROM Proceedings (A. Smyth, ed.), paper 442, 8 pages

Kennedy, J. & Eberhart, R. (1995). Particle swarm optimization. *Proceedings of ICNN'95-International Conference on Neural Networks*, (4): 1942–1948.

Julier, S. J. & Uhlmann, J. K.1997. A New Extension of the Kalman Filter to Nonlinear Systems. Int. Symp. *Aerospace/Defense Sensing, Simul. and Controls* 3: 1–12.

Leyffer, S. & Mahajan, A. 2010. *Nonlinear constrained optimization: methods and software*. Argonee National Laboratory, Argonne, Argonne, Illinois.

Li, Y., Liu, J., & Wang, Y. (2008). Design approach of weight matrices for LQR based on multi-objective evolution algorithm. *International Conference on Information and Automation* (2): 1188–1192.

Marafioti, G. 2010. *Enhanced Model Predictive Control: Dual Control Approach and State Estimation Issues*. Norwegian University of Science and Technology. Norway.

Mariani, S. & Ghisi, A. (2007). Unscented Kalman filtering for nonlinear structural dynamics, *Nonlinear Dynamics* 49(1):131–150.

Merwe, R. van der& Wan, E. 2004. Sigma-point Kalman filters for integrated navigation. *In 60th Annual Meeting of The Institute of Navigation*.

Mobaieen, S., Mohamady, B., Ghorbani, H., & Rabii, A. 2012. Optimal Control Design Using Evolutionary Algorithms with Application to an Aircraft Landing System. Journal of Basic and Applied Scientific Research 2(2): 1876–1882.

Oral, E., Çetin, L., & Uyar, E. 2010. A novel method on selection of Q and R matrices in the theory of optimal control. *Journal of Systems Control* 1: 84–92.

Preumont, A. (2nd ed.) 2004. *Vibration control of active structures: an introduction*. Kluwer Academic Publishers.

Rigatos, G. 2011. Filtering and Estimation Methods for Industrial Systems. *Modelling and Control for Intelligent Industrial Systems*, (ii): 119–140.

Wang, X. 2011. *Nonlinear Control and Estimation with General Performance Criteria*, Marquette University, Milwaukee, Wisconsin.

Weber, F. & Boston, C. 2011. Clipped viscous damping with negative stiffness for semi-active cable damping. *Smart Materials and Structures* 20(4), 045007 (13pp).

Weber, F. & Maślanka, M. 2012. Frequency and damping adaptation of a TMD with controlled MR damper. *Smart Materials and Structures* 21(5), 055011 (17pp).

Wu, M. & Smyth, A. W. 2007. Application of the unscented Kalman filter for real-time nonlinear structural system identification. *Structural Control and Health Monitoring*, 14: 971–990.

Xie, Z. & Feng, J. 2011. Real-time nonlinear structural system identification via iterated unscented Kalman filter. *Mechanical Systems and Signal Processing* 28:309–322.

Research and Applications in Structural Engineering, Mechanics and Computation – Zingoni (Ed.)
© 2013 Taylor & Francis Group, London, ISBN 978-1-138-00061-2

Guided waves for stress identification

A. Pau, G. Ruta & F. Vestroni
Department of Structural and Geotechnical Engineering, "Sapienza" University, Rome, Italy

ABSTRACT: The measurement of stress in structural components would be of great value in engineering. Here, a numerical model is set up to expound experimental tests on a prestressed plate in the light of acoustoelasticity and in view of the formulation of an inverse problem, in which response is measured and stress is identified. The theory of acoustoelasticity is used to describe wave propagation in a prestressed guided wave, accounting for selected sources of nonlinearities. In particular, finite strains are used, and energy is written as a third-order function of the strains. The experiments are performed on a rectangular plate held by a machine, inducing prestress in the plate and applying in-plane impulsive loadings by an instrumented hammer. The time histories of both loading and dynamic response are recorded and the variation of the relevant dynamic response quantities are investigated. The aim of the experimental tests is to observe the transmission of waves in the plate, relating the prestress to the variation of the propagation speed of waves.

1 INTRODUCTION

This study aims at developing techniques of stress evaluation in structural elements. The starting point for a numerical and experimental analysis is that the speed of wave propagation varies as a function of the stress in the material. Acoustoelasticity (Murnaghan 1951, Cantrell 2004) is the basic theory relating the change of wave speed to the initial stress in the medium. The early studies on this phenomenon assume that the body is hyperelastic, and finite strain acting on the natural (unstressed and unstrained) state causes prestress. Waves of small amplitude are then superimposed on the strained initial state (Hughes & Kelly 1953, Egle & Bray 1976, Pao & Gamer 1985). The velocity of waves changes as a function of both the state of stress and the kind of propagating wave, e.g. plane, shear, Rayleigh, Lamb waves (Chen & Wilcox 2007, Gokhale 2007). Here, acoustoelasticity is applied to investigate the phenomenon in the case of a plane strip of solid (Figure 1) acting as a waveguide for waves propagating in longitudinal direction. The same problem is examined also with experimental tests.

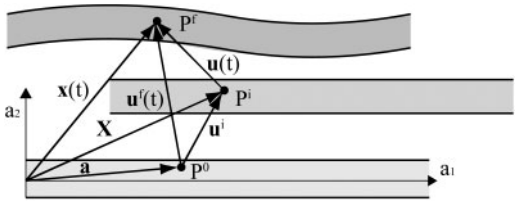


Figure 1. Natural (0), initial (i) and final (f) configurations.

2 ANALYTICAL MODEL

A longitudinally unbounded strip with two free surfaces reaches its initial state by stretching the solid parallel to its length. Three different configurations are considered (Figure 1). In the natural configuration, free of stress and strain, the material point P is retrieved by the vector **a**, with components a_1 and a_2. Physical quantities in this configuration are referred to by the superscript "0". The initial configuration is stressed and strained, and the vector **X**, with components X_1 and X_2, defines the position of P as follows:

$$\mathbf{X} = \mathbf{a} + \mathbf{u}^i \tag{1}$$

In (1) $\mathbf{u}^i$ is the displacement vector from the natural to the initial state. The physical quantities of the latter are referred to by the superscript "*i*". We assume that this initial state is attained by a static homogeneous transformation $\mathbf{u}^i = \mathbf{A}\mathbf{a}$. The final configuration is due to a dynamic disturbance superimposed on the initial state. The vector **x**, with components x_1 and x_2, defines the position of P as follows:

$$\mathbf{x}(t) = \mathbf{a} + \mathbf{u}^i + \mathbf{u}(t) = \mathbf{X} + \mathbf{u}(t) \tag{2}$$

In (2) $\mathbf{u}(t)$ represents the displacement from the initial to the final state, the physical quantities of which are referred to by the superscript "*f*". We may write:

$$\mathbf{u}(t) = \mathbf{u}^f(t) - \mathbf{u}^i \tag{3}$$

The tensor of finite strains is:

$$\mathbf{E}^f = \frac{1}{2}\left(\nabla_a \mathbf{u}^{f\,T} + \nabla_a \mathbf{u}^f + \nabla_a \mathbf{u}^{f\,T} \nabla_a \mathbf{u}^f\right) \tag{4}$$

In (4) the derivatives are calculated with respect to the position **a** in the natural configuration.

Let us denote by **S** the first Piola-Kirchhoff stress tensor. In the initial frame of reference, and in the absence of body forces, the equations of motion are:

$$\mathrm{div}_{\mathbf{a}}\mathbf{S} = \rho^{i}\ddot{\mathbf{u}} \tag{6}$$

since $\mathbf{u}^i$ is a static displacement. The strain energy Φ of a hyperelastic and isotropic material can be written as a power series of the invariants I_1, I_2 and I_3 of the strain tensor $\mathbf{E}^f$. Neglecting infinitesimals of order higher than three in Φ, it is:

$$\Phi = \frac{1}{2}(\lambda + 2\mu)I_1^2 + 2\mu I_2^2 + \frac{l+2m}{3}I_1^3 + 2mI_1I_2 + nI_3 \tag{7}$$

where λ and μ are the Lamé constants and l, m, n are the Murnaghan constants. Since in a plane state of strain $I_3 = 0$, the constitutive relation expressing the first Piola-Kirchhoff stress tensor as a derivative of the strain energy (7) is:

$$\mathbf{S} = \mathbf{F}\frac{\partial\Phi}{\partial\mathbf{E}^f} = \mathbf{F}\{[\lambda I_1 + lI_1^2 + (2m\text{-}n)I_2]\mathbf{I} + \\ + [2\mu + (2m-n)I_1]\mathbf{E}^f + n\ co(\mathbf{E}^f)\} \tag{8}$$

where *co* stands for the cofactor of the indicated matrix and $\mathbf{F} = \nabla_{\mathbf{a}}\mathbf{x}$. To obtain a displacement formulation of the equations of motion in the initial frame of reference, equation (8) is substituted into (6). The speed of wave propagation is then obtained by substituting a given harmonic wave for $\mathbf{u}(t)$ in the equation of motion (6), which gives an expression depending on the initial state of prestress and on Lamé and Murnaghan constitutive constants.

3 EXPERIMENTAL TESTS

The experimental tests have been performed on a steel plate 1 m in length, 10 cm in height and 1 cm in thickness. As a first step, the constitutive relationship for the material was determined by performing a static stress-strain test on a specimen cut from the plate. The elastic range was defined on the basis of the amplitude of the unloading branch (about up to 500 N/mm^2). A curve fitting of the experimental stress-strain relationship to straight lines in four strain ranges enables to evaluate the percent variations of the elastic modulus in the related elastic range (2, 5, 15, 43%). Two kinds of dynamic tests were performed on the plate, according to the sketches of Figure 2. The time-history of the

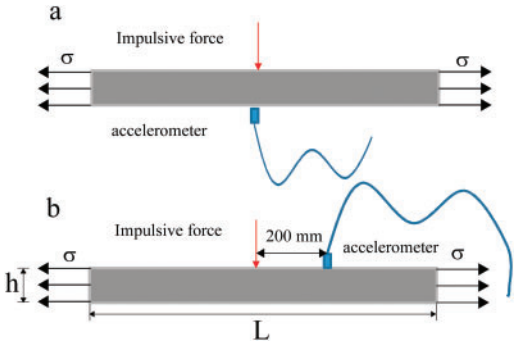


Figure 2. Sketch of the dynamic tests.

dynamic response to an impulsive force was measured on the opposite side of the plate with respect to the excitation (test a) and on the same side of the plate (test b). The impulsive force was applied by means of an instrumented hammer, the time-history of which was also measured, revealing a frequency range extending up to 15 kHz. Both tests were repeated in three different states of prestress, corresponding to tensile stresses of 200, 300 and 400 N/mm^2, respectively, and the related wave speed was observed. These tests showed that, while it is difficult to observe the variation of *p* wave speed within this range of prestress and frequency band (tests a), the transverse waves measured in tests b are more sensitive to a variation in the state of stress. These results are in agreement with the results of the developed analytical model (Gokhale, 2007) and provide a basis for the development of techniques for the measurement of stress in structural elements.

REFERENCES

Cantrell J.H. 2004. Fundamentals and applications of nonlinear ultrasonic ND evaluation. in *Ultrasonic ND Eval. Eng. and Biol. Material Charact.*, Kundu T. Ed., CRC Press.

Chen F., Wilcox P.D. 2007. The effect of load in guided wave propagation. Ultrasonics 47: 111–122.

Egle D.M., Bray D.E. 1976. Measurement of acoustoelastic and third-order elastic constants for rail steel, *Journal of the Acousical Society of America*, 60(3): 741–744.

Gokhale S. 2007. Determination of applied stress in rails using the acoustoelastic effect of ultrasonic waves, Master of Science Thesis, Texas A&M University.

Hughes D.S., Kelly J.L. 1953. Second-order elastic deformations of solids, *Physical Review A*, 92: 1145–1149.

Murnaghan F.D. 1951. *Finite Deformation of an Elastic Solid*, John Wiley and Sons.

Pao Y.H., Gamer U. 1985. Acoustoelastic waves in orthotropic media. *Journal of the Acoustical Society of America*, 77 (3): 806–812.

Research and Applications in Structural Engineering, Mechanics and Computation – Zingoni (Ed.)
© 2013 Taylor & Francis Group, London, ISBN 978-1-138-00061-2

Unscented Kalman Filter for the identification of passive control devices

R. Ceravolo, A. De Stefano, E. Matta, A. Quattrone & L. Zanotti Fragonara
Department of Structural, Geotechnical and Building Engineering, Politecnico di Torino, Torino, Italy

ABSTRACT: The Unscented Kalman Filter (UKF) is a technique which allows dealing with nonlinear systems and it is able to handle any type of non-linearity. In detail, differently from Extended Kalman Filter (EKF), UKF does not require the computation of the Jacobian of the non-linear function. Estimation of parameters through the UKF approach is an indirect procedure, consisting of transforming the parameter estimation problem into a state estimation problem. This is done by augmenting the system state vector by artificially defining the unknown parameters as additional state variables. In the present study the UKF is proposed to the purpose of the nonlinear identification of rolling-pendulum tuned vibration absorbers.

1 INTRODUCTION

In the field of nonlinear system identification several methods have been proposed in the past (Kerschen et al. 2006; Bursi et al. 2012). In the field of on-line methods the most promising are probably those belonging to the family of Kalman Filter algorithms. Though the Kalman Filter (1960) has been originally proposed for linear applications, different extensions of the method to the nonlinear field have been proposed.

The first group descends from the Extended Kalman Filter (EKF) (Jazwinski, 1966). The EKF allows applying the Kalman Filter to nonlinear optimal filtering. It forms a Gaussian approximation to the joint distribution of state and measurements by resorting to a Taylor series based transformation. When working with nonlinear processes the optimality of the estimation is lost and, even worst, the estimate may diverge (Stengel 1994). The EKF has some flaws: (i) it is not an optimal estimator; (ii) it may diverge due to its linearization approach if the initial estimate of the state vector is wrong or the process is modelled incorrectly; (iii) its estimated covariance matrix tends to underestimate the true covariance matrix so that it risks becoming inconsistent in the statistical sense without the addition of a "stabilising noise".

State-Dependent Riccati Equation Filter (SDRE) overcomes the EKF flaws, since it does not involve the Jacobian evaluations, but it entails direct parameterization (Beikzadeh & Taghirad 2009). Briefly, it fully captures the nonlinearities of the system and brings the nonlinear system into a nonunique linear structure having state-dependent coefficients (SDCs). This nonuniqueness of the SDC form provides design flexibility which can be exploited to overcome serious difficulties such as singularities and loss of observability in traditional filtering methods.

Among the family of Particle Filters the most widely used and applied is the Unscented Kalman Filter (UKF). This technique has been recently proposed by Julier and Uhlman (2000) having the advantage, with respect to the canonical filters, of being able to treat any type of nonlinearity. In detail, UKF does not require the computation of the Jacobian of the nonlinear function; in fact it does not approximate the measurement equation of the system but it approximates the posterior probability density by a Gaussian density, by using a set of deterministic points (the so-called Sigma points). This allows dealing with also non differentiable nonlinear systems. When the Sigma points are propagated through the nonlinear transform, they capture the true mean and covariance of the Gaussian random variables, and the posterior mean and covariance accurately to the 3rd order Taylor series expansion for any nonlinearity.

In the last few years, the UKF has been successfully applied for the identification of nonlinear mechanical systems in several numerical case studies, e.g. (Wu & Smyth, 2008; Ceravolo et al. 2012). Due to the uncertainty in the dissipation laws of real dynamic systems (nonlinear damping, hysteresis, friction, etc.), very few experimental applications to real case studies are known. As a consequence, any experimental applications should be previously validated through extensive numerical simulations.

The capability of UKF to deal with the nonlinear identification of system parameters has been tested on a numerical model aimed to describe the dynamic behaviour of a new prototype of vibro-protective control device recently proposed by Matta et al. (2009). The device consists of an innovative type of rolling-pendulum tuned vibration absorber which, relying on an optimal three-dimensional guiding receptacle, can simultaneously control the response of the supporting structure along two orthogonal horizontal directions.

Through preliminary numerical simulations, the effectiveness of the UKF in identifying the structural parameters of the new device is investigated for different alternative descriptions of the nonlinear dissipation model introduced to simulate rolling friction at the interface between the ball bearing and the rolling surface.

2 THE NEW BIDIRECTIONAL PENDULUM VIBRATION ABSORBER

In recent years, many vibration control strategies have been developed for enhancing serviceability and safety of Civil Engineering structures against natural and manmade hazards. Among them, tuned vibration absorbers have been extensively studied and widely applied because of their simplicity, efficiency and low maintenance cost.

In its basic configuration, a tuned vibration absorber merely consists of a viscously damped single-degree-of-freedom (SDOF) auxiliary system attached to the main structure. By properly tuning its natural frequency to that of the selected target mode of the main structure, part of the vibratory energy of that mode is transferred to the auxiliary system and dissipated through its damping (Warburton & Ayorinde, 1982).

Tuned absorbers have found through the years a variety of technological implementations (Matta & De Stefano, 2009). Among them, the rocking pendulum, the ball pendulum and the rolling pendulum share the same idea of using curved rolling surfaces to derive the necessary restoring force, which makes them more compact and durable than hanging pendulums as well as more suitable to tuning to low-period structures for seismic applications. Several variants of rolling pendulum vibration absorbers are described in the literature (Legeza, 2005; Pirner, 2002), however arranged either in a planar configuration (constrained to move in a vertical plane) or in an axial-symmetrical configuration (constrained on a spherical cavity).

In order to simultaneously achieve bidirectional tuning to two distinct in-plan orthogonal structural modes, a new bidirectional pendulum vibration absorber was proposed by the first author in (Matta et al. 2009), based on an innovative non-axial-symmetrical rolling guide. An analytical non-linear dynamic model was first derived using Appell's nonholonomic mechanics, and then a laboratory scaled prototype was tested which eventually demonstrated the bidirectional tuning capability and validated the mathematical model. Yet, the nonlinear dissipation law governing the rolling problem was outside the scope of the analytical model and therefore was only roughly identified from the experiments.

Aiming at more accurately characterizing the dissipative term, the same prototype absorber is here reconsidered. This consists of two identical plexiglass plates having dimensions $400 \times 300 \times 25\ mm^3$, each carved with five identical toroidal concavities (Fig. 1).

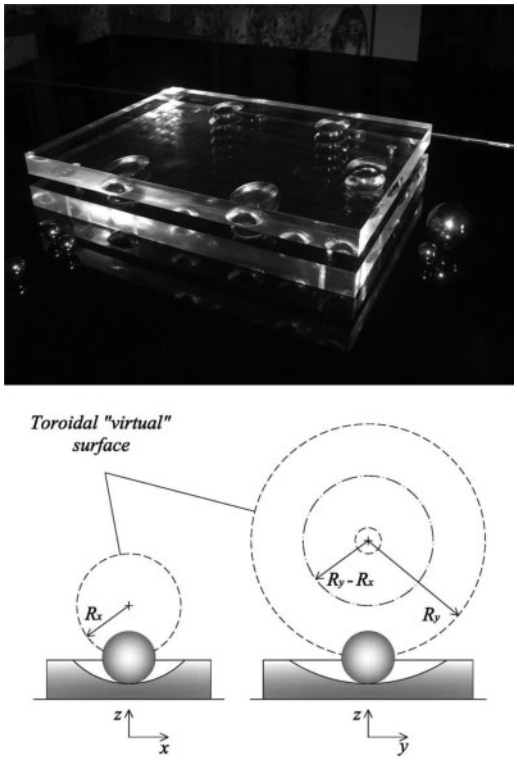


Figure 1. The prototype: (left) the test assembly; (right) a scheme of the toroidal concavities.

The plates are deployed with their concavities symmetrically facing each other, with three out of the five pairs of concavities sandwiching a stainless steel ball of radius $R = 10$ mm. The mass of each plate is $m = 3.42$ kg. The "physical" concavities have radii of curvature $R_{xp} = 29.9$ mm and $R_{yp} = 54.7$ mm, and are 9 mm deep. Correspondingly, being $R = 10$ mm, the "virtual" radii are $R_x = 19.9$ mm and $R_y = 44.7$ mm.

In (Matta et al. 2009), with four accelerometers attached to each plate along the lateral faces (two in the x direction and two in the y direction), two kinds of experimental tests were conducted: fixed-base free motion tests, through imparting an initial non-zero relative displacement of the upper plate; and base shaking tests, through imparting a (non-stationary) random bidirectional translational motion to the lower plate. In the present paper, as an intermediate step towards using the UKF for the experimental identification of the dissipative rolling mechanism from those tests, the latter are preliminary replaced with numerical simulations, for simplicity circumscribed to unidirectional motions in the yz vertical plane only.

3 THE NONLINEAR MODEL

The thorough nonlinear model describing the three-dimensional rolling-without-slipping motion of each ball with respect to both the lower and the upper plates,

and therefore of the upper plate with respect to the lower plate, is given in (Matta et al. 2009). As long as ball bearings' inertia is neglected and motion is restrained to the yz plane, that model reduces to the following nonlinear SDOF one (Matta & De Stefano, 2009):

$$\ddot{\theta} + c_1 \left|\dot{\theta}\right|^{c_2} \operatorname{sgn}(\dot{\theta}) + \frac{g}{R}\sin\theta = -\frac{1}{R}\ddot{x}_g \cos\theta \qquad (1)$$

where θ is the pendulum angular deflection, is the absolute acceleration of the lower plate, $R = 2R_y$ is the effective pendulum radius, g is the gravity constant, c_1 and c_2 are the two parameters governing the dissipation mechanism, here assumed to be velocity-dependent and someway intermediate between dry friction ($c_2 = 0$) and linear viscous damping ($c_2 = 1$), as suggested by experiments (Matta et al. 2009). Notice that, for the assigned value of R_y, the undamped linearized natural period, defined as $T = 2\pi/\omega = 2\pi\sqrt{(R/g)}$, happens to be exactly equal to 0.60 s.

4 UKF WITH BOUNDARIES

The equations of a general dynamic system in discrete form can be defined by resorting to the state-space equation and its measurement equation as follows:

$$\begin{aligned} \mathbf{X}_k &= f\left(\mathbf{X}_{k-1}, u_{k-1}\right) + \mathbf{q}_k \\ \mathbf{Y}_k &= h\left(\mathbf{X}_k\right) + \mathbf{r}_k \end{aligned} \qquad (2)$$

where $\mathbf{X}$ is the state vector in its augmented form, $\mathbf{Y}$ is the output vector, u is the input whilst $\mathbf{q}$ and $\mathbf{r}$ are the process and measurement noises, respectively.

In this paper the UKF algorithm (see Table 1 or, for further information, (Julier et al. 2000)) is applied to the system described in Equation 1 using a modified version which allows for interval constraints on the state vector:

$$\mathbf{X}_L \le \mathbf{X}_k \le \mathbf{X}_U \qquad (3)$$

In (Kolas et al. 2009) several steps were identified in the original UKF algorithm where constrains can be introduced: on the sigma points (step 1 and 2), on the state vector prediction (step 3), on the output Sigma points (step 5), on the output (step 6) or on the updated state vector (step 10).

The bounds used in this paper have been applied according to the methods proposed in (Teixera et al. 2010) and in (Vachani et al. 2006). It has been chosen to deal with this problem by using both constraints on the unscented transform, on the predicted and updated state vector. In order to generate Sigma points satisfying Equation 3 one can use the following equations:

$$\mathcal{X}_k^- = \mathbf{X}_k + \begin{bmatrix} \mathbf{0}_{nx1} & \theta_{1,k}\,\mathrm{col}_1\left[\left(\mathbf{P}_{XX_k}\right)^{1/2}\right] & \dots \\ \dots & \theta_{n,k}\,\mathrm{col}_n\left[\left(\mathbf{P}_{XX_k}\right)^{1/2}\right] & \dots \\ \dots & -\theta_{n+1,k}\,\mathrm{col}_{n+1}\left[\left(\mathbf{P}_{XX_k}\right)^{1/2}\right] & \dots \\ \dots & -\theta_{2n,k}\,\mathrm{col}_{2n}\left[\left(\mathbf{P}_{XX_k}\right)^{1/2}\right] & \end{bmatrix} \qquad (4)$$

where n is the length of the state vector and θ is defined as follows:

$$\theta_{j,k} = \min\left(\mathrm{col}_j\left(\Theta\right)\right) \qquad (5)$$

Table 1. The UKF algorithm as proposed by Julier and Ulhmann (Julier et al. 2000).

1. Unscented transform and computation of sigma points

$$\mathcal{X}_{k-1}^- = \left[\hat{\mathbf{X}}_{k-1} \quad \hat{\mathbf{X}}_{k-1} + \sqrt{(n+\lambda)\mathbf{P}_{XX_{k-1}}} \quad \dots \quad \dots \hat{\mathbf{X}}_{k-1} - \sqrt{(n+\lambda)\mathbf{P}_{XX_{k-1}}}\right]$$

2. Nonlinear propagation of sigma points

$$\mathcal{X}_{k,i}^{-\mathcal{X}} = f\left(\mathcal{X}_{k-1}^-, u_{k-1}\right)$$

3. State vector prediction

$$\hat{\mathbf{X}}_k^- = \sum_{i=0}^{2n} W_i^{(m)} \cdot \mathcal{X}_{k,i}^{-\mathcal{X}}$$

4. State covariance matrix prediction

$$\mathbf{P}_{XX_k}^- = \sum_{i=0}^{2n} W_i^{(c)} \left[\mathcal{X}_{k,i}^{-\mathcal{X}} - \hat{\mathbf{X}}_k^-\right]\left[\mathcal{X}_{k,i}^{-\mathcal{X}} - \hat{\mathbf{X}}_k^-\right]^T + \mathbf{Q}_k$$

5. Propagation of sigma points through measure equation

$$\mathcal{Y}_{k,i} = h\left(\mathcal{X}_{k,i}^{-\mathcal{X}}\right)$$

6. Measurement prediction

$$\hat{\mathbf{Y}}_k^- = \sum_{i=0}^{2n} W_i^{(m)} \cdot \mathcal{Y}_{k,i}$$

7. Measurement covariance matrix prediction

$$\mathbf{P}_{YY_k}^- = \sum_{i=0}^{2n} W_i^{(c)} \left[\mathcal{Y}_{k,i} - \hat{\mathbf{Y}}_k^-\right]\left[\mathcal{Y}_{k,i} - \hat{\mathbf{Y}}_k^-\right]^T + \mathbf{R}_k$$

8. Cross covariance matrix prediction

$$\mathbf{P}_{XY_k}^- = \sum_{i=0}^{2n} W_i^{(c)} \left[\mathcal{X}_{k,i}^{-\mathcal{X}} - \hat{\mathbf{X}}_k^-\right]\left[\mathcal{Y}_{k,i} - \hat{\mathbf{Y}}_k^-\right]^T$$

9. Kalman gain

$$\mathbf{K}_k = \mathbf{P}_{xy}^- \left(\mathbf{P}_{yy}^-\right)^{-1}$$

10. State vector update

$$\hat{\mathbf{X}}_k = \hat{\mathbf{X}}_k^- + \mathbf{K}_k\left(\mathbf{Y}_k - \hat{\mathbf{Y}}_k^-\right)$$

11. State covariance matrix update

$$\mathbf{P}_{XX_k} = \mathbf{P}_{XX_k}^- - \mathbf{K}_k \mathbf{P}_{YY_k} \mathbf{K}_k^t$$

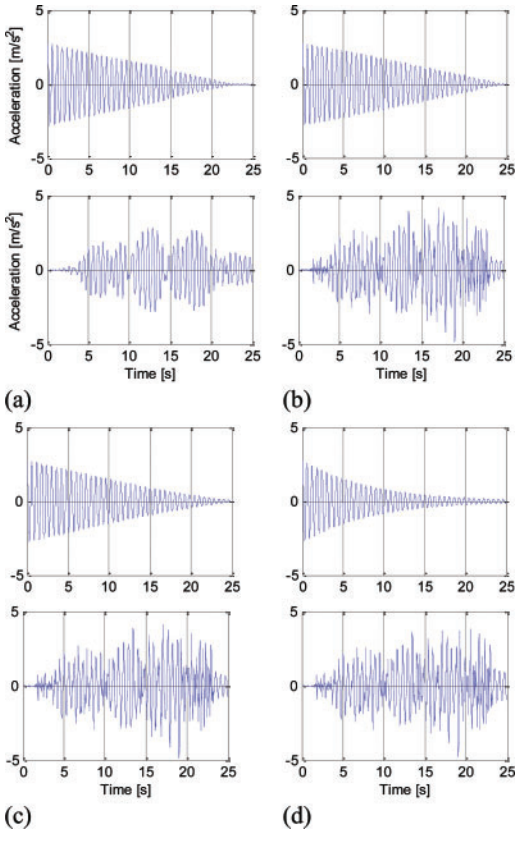


Figure 2. The free decay (above) and random shaking (bottom) responses of: (a) the real test device; (b) the model with $c_1 = 0.2$ and $c_2 = 0.0$; (c) the model with $c_1 = 0.2$ and $c_2 = 0.3$; (d) the model with $c_1 = 0.25$ and $c_2 = 1.0$.

$$\Theta_{(i,j)} = \begin{cases} \sqrt{n+\lambda} & \text{if } \mathbf{S}_{(i,j)} = 0 \\ \min\left(\sqrt{n+\lambda}, \dfrac{\mathbf{X}_{U,i} - \hat{\mathbf{X}}_k}{\mathbf{S}_{(i,j)}}\right) & \text{if } \mathbf{S}_{(i,j)} > 0 \\ \min\left(\sqrt{n+\lambda}, \dfrac{\mathbf{X}_{L,i} - \hat{\mathbf{X}}_k}{\mathbf{S}_{(i,j)}}\right) & \text{if } \mathbf{S}_{(i,j)} < 0 \end{cases} \quad (6)$$

$$\mathbf{S} = \left[\left(\mathbf{P}_{XX_k}\right)^{1/2} \quad -\left(\mathbf{P}_{XX_k}\right)^{1/2} \right] \quad (7)$$

Weights applied to the Sigma points are given by $W_i = [W_{0,k} W_{1,k} \ldots W_{2n,k}]$ satisfying $\sum_{j=0}^{2n} W_{1,k} = 1$ where:

$$W_{0,k} = b_k, \quad W_{j,k} = a_k \cdot \theta_{j,k} + b_k \quad (8)$$

with a_k and b_k determined using the equation proposed by Teixera (2010). Furthermore, in order to apply the constraints on step 3 and 10, a simple clipping procedure on the vector $\mathbf{X}_k$ is performed. It is worth noticing that the clipping procedure, even if it is rough, is the optimal solution in most of the usual problems (see (Vachani et al. 2006)) and without doubt the most computationally efficient.

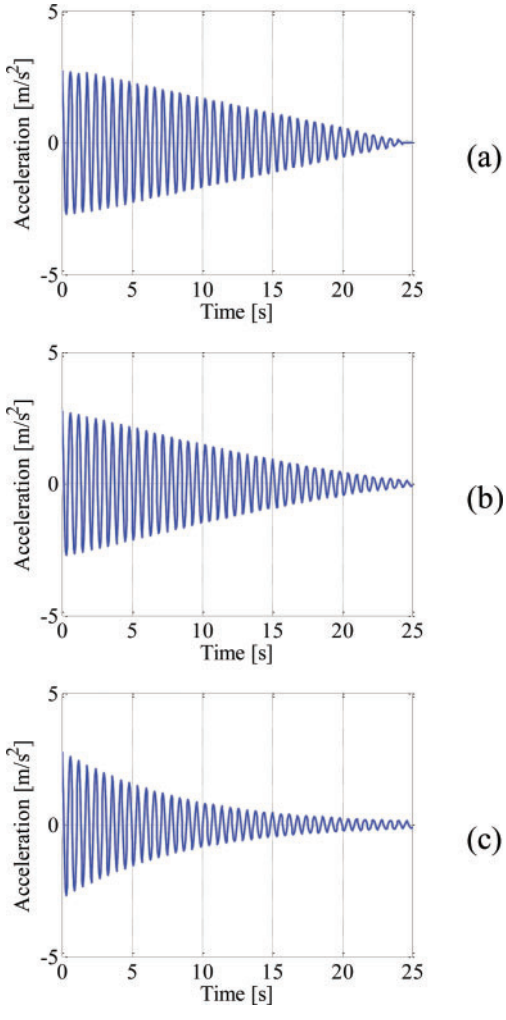


Figure 3. UKF matching of the free decay response for: (a) $c_1 = 0.2$ and $c_2 = 0.0$; (b) $c_1 = 0.2$ and $c_2 = 0.3$; (c) $c_1 = 0.25$ and $c_2 = 1.0$ – Simulated model (thick grey line) vs. estimated model (thin blue line).

5 NUMERICAL EXAMPLES

The UKF is here applied to estimate the two states and the two dissipation coefficients c_1 and c_2 of the nonlinear model defined by Equation 1, i.e. to identify the following joint state vector:

$$\mathbf{X} = [x_1, x_2, x_3, x_4] = [x, \dot{x}, c_1, c_2] \quad (9)$$

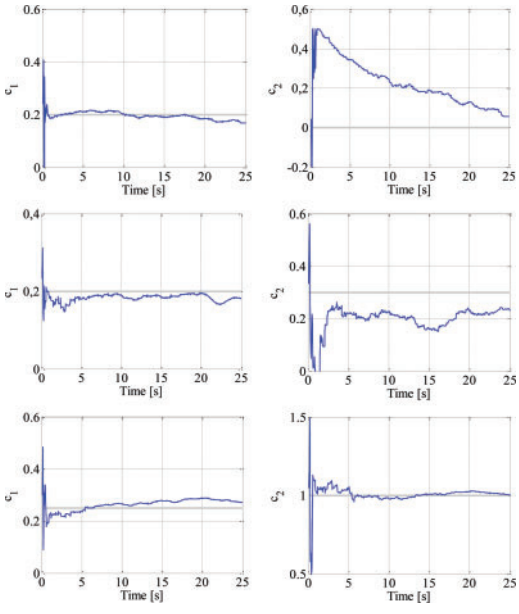


Figure 4. UKF esteems from the free decay response for: (above) $c_1 = 0.2$ and $c_2 = 0.0$; (middle) $c_1 = 0.2$ and $c_2 = 0.3$; (bottom) $c_1 = 0.25$ and $c_2 = 1.0$ – Simulated model (thick grey line) vs. estimated model (thin blue line).

while the two remaining parameters, g and R, are assumed to be exactly known. For the sake of validation, the identification is repeated for a number of simulated scenarios, chosen to roughly reproduce the two experimental test cases, i.e. the free decay oscillation and the random base shaking. Namely, three distinct models are simulated, each described by a different pair $[c_1, c_2]$ of the model parameters, and each responding to the experimental inputs in nearly the same way as the real device, as can be appreciated from Figure 2. For each model, the UKF identification is then repeatedly run for different additive measurement noise levels and different initial estimation errors.

Some of the results obtained for the free decay input scenario are exemplified in Figure 3.

One example of the results obtained for the random shaking input scenario is reported in Figure 4.

For both the free decay and the random shaking scenarios, a satisfactory performance of the UKF estimation can be generally appreciated. The simulated response can be tracked with good accuracy and the estimated parameters tend to rapidly converge to the assumed numerical values in nearly all cases. This is a promising result in view of the application to the real experimental data, which is left for future work.

6 CONCLUSIONS

In the present work, a preliminary numerical investigation is reported in order to assess the viability of UKF for the nonlinear identification of a new prototype of vibro-protective control device. The device

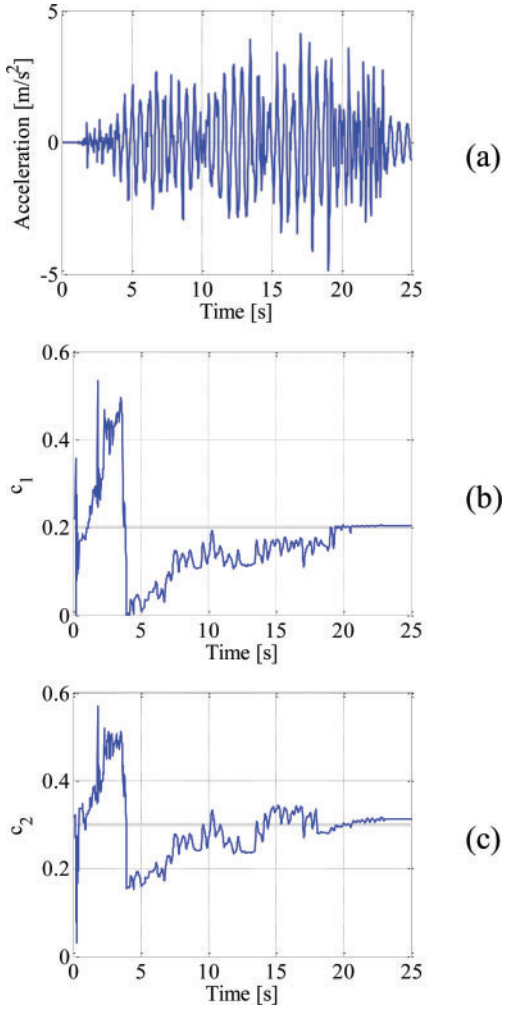


Figure 5. UKF applied to the random shaking response for $c_1 = 0.2$ and $c_2 = 0.3$ – Simulated model (thick grey line) vs. estimated model (thin blue line).

consists of an innovative type of rolling-pendulum tuned vibration absorber which, relying on an optimal three-dimensional guiding receptacle, can simultaneously control the response of the supporting structure along two orthogonal horizontal directions.

Through preliminary numerical simulations, the effectiveness of the UKF in identifying the structural parameters of the new device is investigated for different alternative descriptions of the nonlinear dissipation model introduced to simulate rolling friction at the interface between the ball bearing and the rolling surface. The experimental characterization of the real test prototype is left for future work.

REFERENCES

Beikzadeh, H. and Taghirad, H.D. 2009. Robust H8 Filtering for Nonlinear Uncertain Systems using State-Dependent

Riccati Equation Technique. *Joint 48th IEEE Conference on Decision and Control and 28th Chinese Control Conference*.

Bursi, O.S., Ceravolo, R., Erlicher, S. and Zanotti Fragonara, L. 2012. Identification of the hysteretic behaviour of a partial-strength steel-concrete moment-resisting frame structure subject to pseudodynamic tests. *Earthquake Engineering & Structural Dynamics* 41(14): 1883–1903.

Ceravolo, R., Matta, E., Quattrone, A., Surace, C. and Zanotti Fragonara, L. 2012. On-line identification of time-varying systems equipped with adaptive control. *Journal of Physics: Conference Series* 382.

Jazwinski, A.H. 1966. Filtering for nonlinear dynamical systems. *IEEE Transactions on Automatic Control* 11(4): 765–766.

Julier, S.J., Uhlmann, J.K. and Durrant-Whyte, H.F. 2000. A new method for the nonlinear transformation of means and covariances in filters and estimators. *IEEE Trans. Automat. Control* 45(3): 477–482.

Kalman, R.E. 1960. A New Approach to Linear Filtering and Prediction Problems. *ASME Journal of Basic Engineering* 82: 35–45.

Kerschen, G., Worden, K., Vakakis, A.F. and Golinval, J.C. 2006. Past, present and future of nonlinear system identification in structural dynamics. *Mechanical Systems and Signal Processing* 20: 505–592.

Kolas, S., Foss, B.A. and Schei, T.S. 2009. Constrained nonlinear state estimation based on the UKF approach. *Computers and Chemical Engineering* 33: 1386–1401.

Legeza, V.P. 2005. Analytic determination of the amplitude-frequency characteristic of a nonlinear vibroprotective system with roller damper. *Strength of Materials* 37(2): 214–224.

Matta, E. and De Stefano, A. 2009. Seismic performance of pendulum and transaltional roof-garden TMDs. *Mechanical Systems and Signal Processing* 23: 908–921.

Matta, E., De Stefano, A. and Spencer, B.F.J. 2009. A new passive rolling-pendulum vibration absorber using a non-axial-symmetrical guide to achieve bidirectional tuning. *Earthquake Engineering & Structural Dynamics* 38: 1729–1750.

Pirner, M. 2002. Actual behaviour of a ball vibration absorber. *Journal of Wind Engineering and Industrial Aerodynamics* 90: 987–1005.

Stengel, R.F. 1994. *Optimal Control and Estimation*. Dover.

Teixera, B.O.S., Torres, L.A.B., Aguirre, L.A. and Bernstein, D.S. 2010. On unscented Kalman filtering with state interval constraint. *Journal of Process Control* 20: 45–57.

Vachani, P., Narasimhan, S. and Rengaswamy, R. 2006. Robust and reliable estimation via Unscented Recursive Nonlinear Dynamic Data Reconciliation. *Journal of Process Control* 16: 1075–1086.

Warburton, G.B. and Ayorinde, E.O. 1982. Optimum absorber parameters for various combination of response and excitation parameters. *Earthquake Engineering & Structural Dynamics* 10: 381–401.

Wu, M. and Smyth, A.W. 2008. Real-time parameter estimation for degrading and pinching hysteretic models. *International Journal of Non-Linear Mechanics* 43: 822–833.

Research and Applications in Structural Engineering, Mechanics and Computation – Zingoni (Ed.)
© 2013 Taylor & Francis Group, London, ISBN 978-1-138-00061-2

Vibration elimination analysis of simply-supported bridge under moving loads based on Laplace-Carson integral transform

Kunpeng Wang, He Xia & Weiwei Guo
School of Civil Engineering, Beijing Jiaotong University, Beijing, China

ABSTRACT: The displacement solution for dynamic equation of simply-supported bridge under moving loads is derived using the method of Laplace-Carson integral transform. By introducing two non-dimensional parameters to describe the influence of load speed and damping of bridge respectively, the moving load induced vibration elimination phenomenon is studied. The result shows that the phenomenon of vibration elimination will appear, i.e. the displacement and velocity of bridges become zero when the load leaves the bridge at a certain speed. The elimination speed and resonance speed obtained in case of no damping also are applicable to case of light damping.

1 INTRODUCTION

With the raise of trains speed, the vehicle has a higher demand on the quality of railway lines. To increase the quality of the line, more bridges are built in high-speed railways in China, which has accounted for a large part of the line. Take Beijing-Shanghai High-speed Railway as example, the rate of bridge length is 86.5%. Therefore, it is necessary to study the problem of train going through the bridges. In studying the resonance and elimination of train-bridge system, the vehicle load is usually simplified as moving load series (Xia et al. 2011).

The problem of moving load going through simply supported bridge is a basic problem, which has been studied in many references, where the dynamic equation of the bridge is solved by numerical integration methods (Cao et al. 1987, Gao et al. 2005 & Garinei et al. 2008), such as the Duhamel integral method. Numerical integration method is applicable. However, it only gives us an integral expression, but not shows the influence of load speed nor bridge damping. In this paper, the displacement solution for dynamic equation of the simply supported bridge under moving loads is derived using the method of Laplace-Carson integral transform, and the vibration elimination of the bridge is analyzed.

2 ANALYSIS MODEL AND SOLUTION

2.1 *Problem*

Assumed the simply supported beam has a constant section (EI is a constant), a uniform the mass ($\bar{m}$ is a constant), the moving load $P(t)$ goes through the beam from left to right at a constant speed V, and zero initial deflection and velocity are assumed for the beam vibration. The model is shown in Fig. 1.

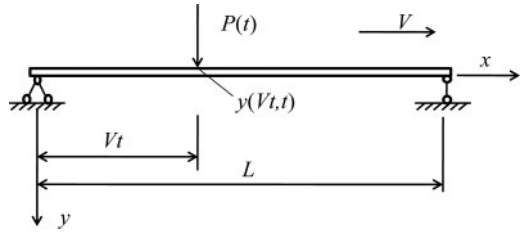


Figure 1. Moving load passing the simply supported beam.

Assume the beam remains small deformation and has a viscous damping coefficient c, the forced vibration equation of the beam can be expressed as

$$EI\frac{\partial^4 y(x,t)}{\partial x^4}+\bar{m}\frac{\partial^2 y(x,t)}{\partial t^2}+c\frac{\partial y(x,t)}{\partial t}=\delta(x-Vt)P(t) \quad (1)$$

and the initial condition is

$$y(x,0)=0;\quad \left.\frac{\partial y(x,0)}{\partial t}\right|_{t=0}=0 \quad (2)$$

where $y(x,t)$ is the vertical displacement of the beam; and δ is Dirac function.

2.2 *Solution*

Equation (1) can be solved by the modal superposition method. Thus, the displacement of the beam can be expressed as

$$y(x,t)=\sum_{i=1}^{\infty}\phi_i(x)\cdot q_i(t) \quad (3)$$

where $\phi_i(x)$ is the i-th vibration mode of the beam; $q_i(t)$ is the generalized coordinate of the i-th mode. For an ideal simply supported beam, $\phi_i(x)=\sin(i\pi x/L)$ (Clough, et al. 2003).

Substitute Eq. (3) into (1), multiply $\phi_n(x)$ on both sides of the equation, and then integrate both sides of the equation along the beam. Basing the orthogonality of mode shapes, the motion equation of the generalized coordinate of the n-th vibration mode can be obtained as

$$\ddot{q}_n(t)+2\omega_b\dot{q}_n(t)+\omega_n^2 q_n(t)=\frac{2}{\bar{m}L}P(t)\sin n\omega t \tag{4}$$

where ω_n is the n-th circular frequency of the beam; $\xi_n=c/2\bar{m}\omega_n$ is the damping ratio of the n-th mode of the beam; $\omega_b=\xi_n\omega_n$ is the critical circular frequency of the beam with damping; and $\omega=\pi V/L$ is the circular frequency expressing the load motion.

Equation (4) is usually solved by Duhamel integral method, but in this paper, it is solved by the Laplace-Carson integral transform method. The basic relations of this transform are as follows:

$$\begin{cases} F(s)=s\int_0^\infty f(t)\mathrm{e}^{-st}\mathrm{d}t \\ f(t)=\dfrac{1}{2\pi\mathrm{i}}\int_{a_0-\mathrm{i}\infty}^{a_0+\mathrm{i}\infty}\mathrm{e}^{st}\dfrac{F(s)}{s}\mathrm{d}s \end{cases} \tag{5}$$

where s is a complex variable.

In view of the initial condition Eq. (2), we only solve the displacement of the beam induced by the moving load. After transform using Eq. (5), Eq. (4) becomes

$$\begin{aligned} &s^2Q_n(s)+2\omega_b sQ_n(s)+\omega_n^2Q_n(s) \\ &=\frac{2}{\bar{m}L}\frac{s}{2\mathrm{i}}\left[\frac{P^*(s-\mathrm{i}n\omega)}{s-\mathrm{i}n\omega}-\frac{P^*(s+\mathrm{i}n\omega)}{s+\mathrm{i}n\omega}\right] \end{aligned} \tag{6}$$

$$\begin{cases} Q_n(s)=s\int_0^\infty q_n(t)\mathrm{e}^{-st}\mathrm{d}t \\ P^*(s)=s\int_0^\infty P(t)\mathrm{e}^{-st}\mathrm{d}t \end{cases} \tag{7}$$

Using Eq. (6), it is not difficult to computer the transformed solution as

$$\begin{aligned} Q_n(s)=&\frac{2}{\bar{m}L}\frac{1}{(s+\omega_b)^2+\omega_D^{n2}} \\ &\times\frac{s}{2\mathrm{i}}\left[\frac{P^*(s-\mathrm{i}n\omega)}{s-\mathrm{i}n\omega}-\frac{P^*(s+\mathrm{i}n\omega)}{s+\mathrm{i}n\omega}\right] \end{aligned} \tag{8}$$

where $\omega_D^{n2}=\omega_n^2-\omega_b^2$ is the circular frequency of a beam with light damping.

The integral transform can be realized by means of the tables (Frýba 1999). Using the table, the inverse Fourier transform $q_n(t)$ of the original $Q_n(s)$ shown in Eq. (8) can be easily obtained as

$$q_n(t)=\frac{2\int_0^t P(\tau)\sin n\omega\tau\mathrm{e}^{-\omega_b(t-\tau)}\sin\omega_D^n(t-\tau)\mathrm{d}\tau}{\bar{m}L\omega_D^n} \tag{9}$$

where $\omega_D^n=\omega_n(1-\xi_n^2)^{0.5}$ is the n-th circular frequency of the beam with damping.

Using the generalized coordinate $q_n(t)$ obtained in Eq. (9) and the modal superposition method, the displacement of the beam induced by the moving load can be obtained as

$$\begin{aligned} y(x,t)=&\frac{2}{\bar{m}L}\sum_{n=1}^\infty\frac{1}{\omega_D^n}\sin\frac{n\pi x}{L} \\ &\times\int_0^t P(\tau)\sin n\omega\tau\mathrm{e}^{-\omega_b(t-\tau)}\sin\omega_D^n(t-\tau)\mathrm{d}\tau \end{aligned} \tag{10}$$

In Eq. (10), the load $P(t)$ can be in various forms. When the vehicle is simplified as moving load series for simplified analysis, two special condition are studied, i.e. $P(t)=P$ and $P\sin\bar{\omega}t$.

To discuss more easily the effect of different factors on the dynamic responses of the beam, two dimensionless parameters α and β are herein introduced, to represent the effect of load speed and beam damping, respectively.

$$\begin{cases} \alpha=\dfrac{\omega}{\omega_1}=\dfrac{VL}{\pi}\left(\dfrac{\bar{m}}{EI}\right)^{1/2}=\dfrac{V}{V_{cr}} \\ \beta=\dfrac{\omega_b}{\omega_1}=\dfrac{\omega_b L^2}{\pi}\left(\dfrac{\bar{m}}{EI}\right)^{1/2}=n^2\xi_n \end{cases} \tag{11}$$

where $V_{cr}=2f_nL/n^2=\pi(EI/\bar{m})^{1/2}(n=1,2,3,\dots)$ is the critical speed of beam under the moving load.

3 SOLUTION AND DISCUSSION OF SPECIAL CASES

3.1 *Case of* $p(t)=p$

If moving load $P(t)$ equals to P, the Laplace-Carson integral transform of $P(t)$ is shown below

$$P^*(s)=s\int_0^\infty P\mathrm{e}^{-st}\mathrm{d}t=P \tag{12}$$

Accordingly, Eq. (8) can be transformed into

$$Q_n(s)=\frac{2Pn\omega}{\bar{m}L}\frac{s}{s^2+n^2\omega^2}\frac{1}{(s+\omega_b)^2+\omega_D^{n2}} \tag{13}$$

Ditto, the inverse Fourier transform $q_n(t)$ of original $Q_n(s)$ in Eq. (13) can be obtained. The displacement of the beam induced by the moving load P can be obtained as

$$\begin{aligned} y(x,t)=v_0\sum_{n=1}^\infty&\frac{1}{n^2\left[n^2(n^2-\alpha^2)^2+4\alpha^2\beta^2\right]} \\ &\times\Big\{n^2(n^2-\alpha^2)\sin n\omega t \\ &-\frac{n\alpha\left[n^2(n^2-\alpha^2)-2\beta^2\right]}{(n^4-\beta^2)^{1/2}}\mathrm{e}^{-\omega_b t}\sin\omega_D^n t \\ &-2n\alpha\beta(\cos n\omega t-\mathrm{e}^{-\omega_b t}\cos\omega_D^n t)\Big\}\sin\frac{n\pi v}{L} \end{aligned} \tag{14}$$

where $v_0=PL^3/48EI\approx 2PL^3/\pi^4EI=2P/\bar{m}L\omega_1^2$ is the deflection at mid-span of a simply supported

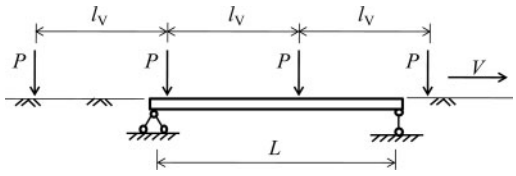


Figure 2. Moving train load passing through beam.

beam loaded with static force P at point $x = L/2$; $\omega_b = \beta\omega_1 = \beta\omega/\alpha$; $\omega_D^n = \sqrt{n^4 - \beta^2}\omega/\alpha$. The zero time in Eq. (14) is the instant of force arrival, and the range of time t is $0 \le t \le L/V$.

Equation (14) is the displacement of the beam induced by one moving load P. Usually, the vehicle is simplified as moving load series with equal load spacing l_v, which is equal to the length of the vehicle, as shown in Fig. 2. Based on the small deformation theory, the displacement of the beam under moving load series is the superposition of all displacement components induced by each single load P, which can be expressed as

$$y(x,t) = \sum_{i=0}^{N-1} y_i\left[x, (t - \frac{i \cdot l_V}{V})\right] \tag{15}$$

where $y_i(x,t)$ is the displacement component of beam induced by the i-th moving load P. When the i-th moving load P is on the beam, $y_i(x,t)$ is calculated by Eq. (14), while after the i-th moving load P leaves the beam, $y_i(x,t)$ is the free vibration induced by the i-th moving load P, which is calculated by Eq. (21).

In this paper, based on Eq. (14), three special cases are discussed detailed.

3.1.1 *Static case ($\alpha = 0$)*

If the load is static, i.e. $\alpha = 0$, Eq. (14) can be converted to

$$y(x,t) = v_0 \sum_{n=1}^{\infty} \frac{1}{n^4} \sin\frac{n\pi x}{L} \sin\frac{n\pi Vt}{L} \tag{16}$$

In this case, Eq. (16) is the static deflection of the beam at point x, if the beam loaded with force P at point Vt. Herein, Vt is considered as a combined variable to express the location of load P.

When it is divided by v_0, Eq. (16) can be considered as the influence line of the beam deflection at point x expanded in the Fourier series, which can also be considered as the deflection of the beam induced by force P at point Vt, expanded in the Fourier series.

3.1.2 *Case with no damping ($\beta = 0$) — analysis of elimination and resonance*

3.1.2.1 α is not an integer, $\beta = 0$

In this case, Eq. (17) can be obtained from Eq. (14)

$$y(x,t) = v_0 \sum_{n=1}^{\infty} \sin\frac{n\pi x}{L} \frac{1}{n^2(n^2 - \alpha^2)} \left(\sin n\omega t - \frac{\alpha}{n} \sin\omega_n t\right) \tag{17}$$

From Eq. (17), it can be seen that the first vibration mode has the largest contribution to the displacement of the beam. Shen et al. (1996) and Yang et al. (2004) indicated that using the first vibration mode of the beam to calculate the dynamic response of the beam could achieve high solution precision. In this case, Eq. (17) can be simplified as

$$y(x,t) = \frac{v_0}{1-\alpha^2} \sin\frac{\pi x}{L} \left(\sin\omega t - \alpha \sin\omega_1 t\right) \tag{18}$$

Assumed the part in the parentheses of Eq. (18) equal to zero at the instant of moving load P leaves the beam (i.e. $t = L/V$), will give us

$$\begin{aligned} \left(\sin\omega t - \alpha \sin\omega_1 t\right)\Big|_{t=\frac{L}{V}} &= \sin\pi - \alpha \sin\frac{\pi}{\alpha} = 0 \\ \Rightarrow \alpha &= \frac{1}{k};\ (k = 2, 3, \cdots) \end{aligned} \tag{19}$$

From Eq. (19), it can be seen that when $\alpha = 1/k$, the displacement component of the beam contributed by the first vibration mode of the beam will be zero at the instant of moving load P leave the beam. In this condition, the displacement of the beam will approaches zero, for the first vibration mode has the largest contribution to the displacement of the beam. In this paper, the speed $V_D = 2f_1 L/k$ expressed in Eq. (19) is named elimination speed (f_1 is the first natural frequency of the beam).

At the instant of moving load P leaves the beam, the velocity of beam is expressed as

$$\dot{y}(x,t)\Big|_{t=\frac{L}{V}} = \frac{v_0\omega}{1-\alpha^2} \sin\frac{\pi x}{L} \left(\cos\pi - \cos\frac{\pi}{\alpha}\right) \tag{20}$$

After the moving load P leaves the beam (i.e. $t > L/V$), the free vibration of beam can be expressed as

$$y(x,t) = \frac{\dot{y}_0}{\omega_1} \sin\omega_1 t + y_0 \cos\omega_1 t \tag{21}$$

If the moving load P pass through the beam at speed V_D, at the instant of moving load P leaves the beam, the velocity of the beam is expressed as

$$\dot{y}(x,t)\Big|_{t=\frac{L}{V}} = \frac{v_0\omega}{1-\alpha^2} \sin\frac{\pi x}{L} \left(\cos\pi - \cos k\pi\right) \tag{22}$$

where y_0 and is the displacement and velocity of the beam, at the instant of moving load P leaves the beam, respectively.

In order to keep the beam still after the moving load P leaves the beam, according to Eq. (21), the displacement and velocity of the beam should be zero at the instant of moving load P leaves the beam. From Eq. (22), it can be seen that the velocity of the beam may not be zero at the instant of the moving load P leaves the beam at speed V_D.

When k is an odd, Eq. (22) is equal to zero, i.e. both displacement and velocity of the beam are zero at the instant of the moving load P leaves the beam. According to Eq. (21), the beam will keep still after the moving load P leaves the beam. In this paper the speed $V_{D1} = 2f_1 L/2i - -1)$ (i is an integer) is named true elimination speed.

When k is an even, Eq. (22) is not equal to zero, only displacement of the beam is zero at the instant of the moving load P leaves the beam. In this case, the beam will continue vibrate after the moving load P leaves the beam. In this paper the speed $V_{D2} = 2f_1 L/(2i)$ is named false elimination speed.

When moving load series pass through the beam at true elimination speed V_{D1}, the displacement component of the beam induced by one of the moving load series will be zero at the instant of this load leaves the beam. The beam will keep still at this condition, for the displacement of the beam under moving load series is the superposition of displacement components induced by single load P, which is useful for determining the operation speed of the vehicle on the bridge. True elimination speed V_{D1} is also applicable to moving load series with unequal load spacing and load values.

3.1.2.2 α is an integer, $\beta = 0$

If α is equal to one of the number $i = 1, 2, 3, \ldots$, say to number k, in this case $\alpha = \omega/\omega_1 = k$, $\omega_k^2 = k^4\omega_1^2 = k^2\omega^2$. The Laplace-Carson integral transform of generalized coordinate $q_k(t)$ of k-th vibration mode will be Eq. (23) rather than Eq. (13), whereas for the remaining ones, $i = 1, 2, \ldots, k--1, k+1, \ldots$ there hold the preceding solution of Eq. (13) as

$$Q_k(s) = \frac{2Pk\omega}{\bar{m}L}\frac{s}{(s^2 + k^2\omega^2)^2} \tag{23}$$

Similarly, using Eq. (13) and Eq. (23), the displacement of the beam can be obtained, which consists of two parts as

$$\begin{aligned} y(x,t) &= v_0 \frac{1}{2k^4}(\sin k\omega t - k\omega t \cos k\omega t)\sin\frac{k\pi x}{L} \\ &+ v_0 \sum_{n=1,n\neq k}^{\infty} \sin\frac{n\pi x}{L}\frac{1}{n^2(n^2-\alpha^2)}\left(\sin n\omega t - \frac{\alpha}{n}\sin\omega_n t\right) \end{aligned} \tag{24}$$

The first part in Eq. (24) can be considered as the limit values of the k-th term in Eq. (17) for $\alpha \to k$. It can be seen from Eq. (24) that the displacement of the beam is increased with the time t, the maximum of which is appeared at the instant of moving load P leaves the beam. This can be considered the resonance of the beam induced by a single moving load P. The resonance of the beam can also be induced by moving load series at a special speed for the cyclic loading (Gao et al. 2005 & Xia et al. 2006).

When the circular frequency expressing the load motion ω is k times of the first circular frequency of the beam, in this case $\sin(k\pi Vt/L) = \sin k^2\omega_1 t$, the resonance of the k-th vibration mode of the beam will be induced by the moving load. In this paper, the speed $V_R = 2kf_1 L$ is named resonance speed. If k is equal to 1, the resonance of the beam is strongest. Take $L = 32$ m, $f_1 = 4.5$Hz, $k = 1$ as example, in this case the critical speed of beam V_R equal to 1036.8 (km/h), which is far more than the actual train speed, so resonance speed resonance speed V_R only has meaning in mathematics.

3.1.3 *Case with light damping ($\beta << 1$)*

3.1.3.1 α is not an integer, $\beta << 1$

When the beam damping is very light, terms contain β or β^2 can be neglected in Eq. (14), approximately, the expression of the displacement of the beam can be given as

$$\begin{aligned} y(x,t) \approx v_0 \sum_{n=1}^{\infty} \sin\frac{n\pi x}{L}\frac{1}{n^2(n^2-\alpha^2)} \\ \cdot\left(\sin n\omega t - \frac{\alpha}{n}\mathrm{e}^{-\omega_b t}\sin\omega_n t\right) \end{aligned} \tag{25}$$

For $\alpha \to k$, the calculation error of Eq. (25) will be too large to be applicable. Because the actual operation speed of the vehicle cannot reach the critical speed V_R and the damping of actual bridge is very light, so Eq. (25) is very practicable in engineering practice. If the speed of the vehicle is very low, i.e. $\alpha << 1$, and using the first vibration mode of the beam to express the displacement of the beam, Eq. (25) can be simplified as

$$y(x,t) \approx v_0 \sin\frac{\pi x}{L}\sin\omega t \tag{26}$$

3.1.3.2 α is an integer, $\beta << 1$

This case is similar to the case in Section 3.1.2.2, the expression of the displacement of the beam is given directly as

$$\begin{aligned} y(x,t) \approx \frac{v_0}{2k^4}\left[\mathrm{e}^{-\omega_b t}\sin k\omega t - \frac{k^2}{\beta}\cos k\omega t(1-\mathrm{e}^{-\omega_b t})\right] \\ \cdot\sin\frac{k\pi x}{L} + v_0\sum_{n=1,n\neq k}^{\infty}\sin\frac{n\pi x}{L}\frac{1}{n^2(n^2-\alpha^2)} \\ \cdot\left(\sin n\omega t - \frac{\alpha}{n}\mathrm{e}^{-\omega_b t}\sin\omega_n t\right) \end{aligned} \tag{27}$$

The cases of light damping ($\beta << 1$)and no damping ($\beta = 0$) are very similar, the elimination speed V_D and resonance speed V_R obtained in case of no damping also are applicable to the case of light damping, the error induced by the damping of the beam within the acceptable range.

3.2 *Case of $p(t) = P\sin\bar{\omega}t$*

One dimensionless parameter γ is herein introduced, to represent the effect of circular frequency of moving load $P\sin\bar{\omega}t$.

$$\gamma = \frac{\bar{\omega}}{\omega_1} \tag{28}$$

If moving load $P(t)$ equals $P\sin\bar{\omega}t$, the Laplace-Carson integral transform of $P(t)$ is shown as

$$P^*(s) = s\int_0^{\infty} P\sin\bar{\omega}t\mathrm{e}^{-st}\mathrm{d}t = \frac{P\bar{\omega}s}{s^2+\bar{\omega}^2} \tag{29}$$

Accordingly, Eq. (8) can be transformed into

$$Q_n(s) = \frac{P}{\bar{m}L}\left(\frac{1}{s^2+r_2^2} - \frac{1}{s^2+r_1^2}\right)\frac{s^2}{(s+\omega_b)^2+\omega_D^{n2}} \tag{30}$$

where $r_1 = \bar{\omega} + n\omega$; $r_2 = \bar{\omega} - n\omega$

Ditto, the inverse Fourier transform $q_n(t)$ of original $Q_n(s)$ in Eq. (30) can be obtained. In this case, the displacement of the beam induced by the moving load $P\sin\bar{\omega}t$ can be obtained as

$$y(x,t)=\frac{v_0}{2}\sum_{n=1}^{\infty}\left\{\frac{\omega_1^2}{(\omega_n^2-r_2^2)^2+4\omega_b^2r_2^2}\left[(\omega_n^2-r_2^2)\right.\right.$$
$$\cdot\left(\cos r_2t-\mathrm{e}^{-\omega_bt}\cos\omega_D^nt\right)+2\omega_br_2\sin r_2t$$
$$\left.-\frac{\omega_b}{\omega_D^n}(\omega_n^2+r_2^2)\mathrm{e}^{-\omega_bt}\sin\omega_D^nt\right]-\frac{\omega_1^2}{(\omega_n^2-r_1^2)^2+4\omega_b^2r_1^2}\quad(31)$$
$$\cdot\left[(\omega_n^2-r_1^2)\left(\cos r_1t-\mathrm{e}^{-\omega_bt}\cos\omega_D^nt\right)+2\omega_br_1\sin r_1t\right.$$
$$\left.\left.-\frac{\omega_b}{\omega_D^n}(\omega_n^2+r_1^2)\mathrm{e}^{-\omega_bt}\sin\omega_D^nt\right]\right\}\sin\frac{n\pi x}{L}$$

If $\alpha<<1$, $\beta<<1$ and using the first vibration mode of the beam to calculate the dynamic response of the beam, in this case, Eq. (31) can be simplified as (Frýba 1999)

$$y(x,t)=v_0\frac{1}{\gamma^2}\frac{1}{\left(\frac{1}{\gamma^2}-1\right)^2+4\left(\frac{\alpha^2}{\gamma^2}+\frac{\beta^2}{\gamma^2}\right)}$$
$$\cdot\left\{\left[\left(\frac{1}{\gamma^2}-1\right)^2+4\frac{\beta^2}{\gamma^2}\right]^{1/2}\sin\left(\frac{\gamma\omega t}{\alpha}+\varphi\right)\sin\omega t\right.\quad(32)$$
$$\left.+2\frac{\alpha}{\gamma}\left(\cos\frac{\gamma\omega t}{\alpha}\cos\omega t-\mathrm{e}^{-\omega_bt}\cos\frac{\omega t}{\alpha}\right)\right\}\sin\frac{\pi x}{L}$$

where $\tan\varphi=-\dfrac{2\omega_b/\bar{\omega}}{\omega_1^2/\bar{\omega}^2-1}=-\dfrac{2\beta\gamma}{1-\gamma^2}$

When the circular frequency $\bar{\omega}$ of moving load is closed to the first circular frequency ω_1 of the beam, the displacement of the beam is very large. In this case, Eq. (32) can be simplified as

$$y(x,t)=\frac{v_0}{2}\frac{\cos\omega_1t}{\alpha^2+\beta^2}\sin\frac{\pi x}{L}\quad(33)$$
$$\cdot\left[\alpha(\cos\omega t-\mathrm{e}^{-\omega_bt})-\beta\sin\omega t\right]$$

4 NUMERICAL RESULTS

4.1 *Model parameters*

According to the theory above, the displacement of the beam induced by moving load P or $P\sin\bar{\omega}t$ is calculated and analyzed.

Model parameters of the beam: the span of the beam $L=32$ m. The first natural frequency of the beam $f_1=4.5$ Hz, which is a composite reflection of section stiffness EI and mass $\bar{m}$ of the beam. The damping ratio of the first vibration mode $\xi_1=0.0$ or 0.1, i.e. the damping factor $\beta=0.0$ or 0.1. In engineering practice, the damping ratio of concrete bridge and steel bridge

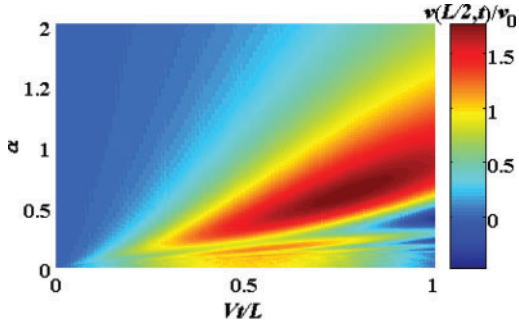


Figure 3. Mid-span displacements *vs* time and load speed ($\beta=0$).

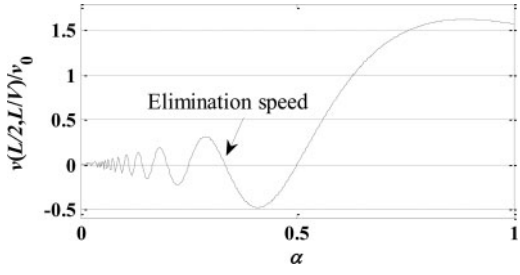


Figure 4. Mid-span displacement *vs* load speed as load leaves the beam ($\beta=0$).

are taken as 0.05 and 0.03, respectively, which is much lesser than 0.1. In this case, the critical speed of beam $V_R=1036.8$ (km/h), while the actual operation speed of the vehicle is 0∼300 km/h, i.e. $\alpha=0.0$∼0.3.

4.2 *Displacement of the beam induced by moving load*

Figure 3 is the displacement of the beam, induced by moving load P at different velocities, in no damping case. From Fig. 3, it can be seen that the maximum mid-span displacement will appear when moving load located near the mid-span of the beam when load speed is low. With the load speed increased, the maximum mid-span displacement will appear when moving load located near the right support of the beam. The phenomenon shown in Fig. 3 is applicable to the beam with different section stiffness EI.

Figure 4 is the mid-span displacement of the beam at the instant of moving load leaves the beam, i.e. $t=L/V$, induced by moving load P at different velocities. As the preceding discussion, the displacement of the beam becomes zero when the load leaves the beam at an elimination speed V_D, i.e. $\alpha=1/k$.

Figure 5 is the relationship between displacement of the beam and speed factor α, and the range of α is 0.0∼0.3 in no damping case. From Fig. 5, it can be seen that the maximum mid-span displacement increases in sinusoidal way with gradually increasing amplitude, instead of in monotonous way, which is also indicated by Wang et al. (2010), by studying the sprung mass through the simply supported bridge. The damping of

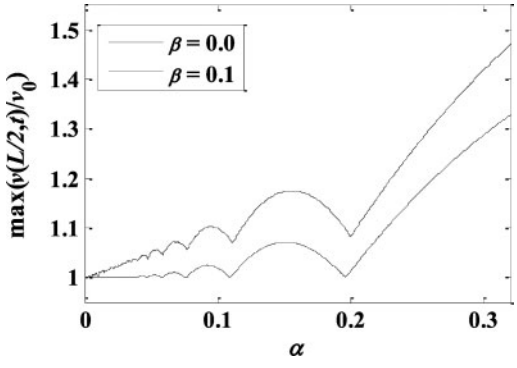


Figure 5. Maximum mid-span displacement *vs* load speed.

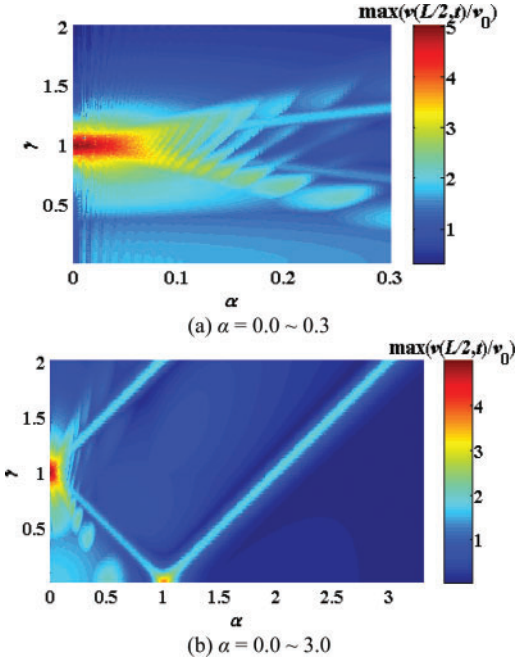


Figure 6. Dynamic amplification factor vs load frequency and speed ($\beta = 0.1$).

the beam can reduce the maximum mid-span displacement of the beam and the elimination speed V_D, but the difference of elimination speed V_D is within the acceptable range. If the damping factor β equals to 0.05, the difference can be smaller, which indicates the elimination speed V_D obtained in case of no damping also are applicable to case of light damping.

From Figs. 4 and 5, it is seen that when the speed factor α equals to 0.2, i.e. $k = 5$, the maximum mid-span displacement of the beam is small, and the beam keeps still after the moving load P leaves the beam. Therefore, in the design, the section stiffness EI, mass $\bar{m}$ and span L of the bridge should be carefully selected.

Figure 6 is the displacement of the beam, induced by the moving load $P \sin \bar{\omega} t$ at different speeds and circular frequencies, in case of low damping. The displacement of the beam is affected by circular frequencies $\bar{\omega}$ and ω. When speed factor α is low, the displacement of the beam is the largest on condition of γ equal to 1. With the increase of speed factor α, the displacement of the beam becomes smaller on condition of γ equal to 1, and the maximum displacement of the beam appears on condition of γ equal to other value. From Fig. 6, an interesting phenomenon is found that if consider coordinate planes as mirror surfaces, the form of maximum displacement of the beam looks like the incidence light at angle of 45° reflected by mirror surfaces, which is named generic-light reflection effect phenomenon in this paper.

5 CONCLUSIONS

The following conclusions can be summarized up from this paper:

(1) There are special speeds $V_{D1} = 2f_1 L/(2i-1)$ (i is an integer), when moving load P through the beam at speeds V_D, the beam will keep stationary after the moving load P leaves the beam.
(2) The maximum mid-span displacement increases with load speed in sinusoidal way with gradually increasing amplitude, instead of in monotonous way.
(3) The elimination speed V_D and resonance speed V_R obtained in case of no damping also are applicable to case of light damping, the error induced by the damping of the beam within the acceptable range.

REFERENCES

Cao, X.Q. & Liu, B.S. 1987. *Dynamic Analysis of Bridge Structure*. Beijing: China Railway Publishing House.

Clough, R. & Penzien, J. 2003. *Dynamics of Structures*. Berkeley: Computers & Structures, Inc.

Frýba, L. 1999. *Vibration of solids and structures under moving loads*. London: Thomas Telford,.

Gao, C.W., Tang, Y.R. & Yu, H. 2005. China Railway Science. *Study on the vibration of rail transit bridge based on moving load passing bridge* 26(2): 73–76.

Garinei, A. & Risitano, G. 2008. Engineering Structures. *Vibrations of railway bridges for high-speed trains under moving loads varying in time* 30(3): 724–732.

Shen, R.L. 1996. China Railway Science. *Research of Vertical Vibration Response of Simple Supported Beam Bridge on High Speed Railways* 17(3): 24–34.

Wang, S.Q., Xia, H. & Guo, W.W. 2010. Journal of Vibration and Shock. *Dynamic response and resonance analysis of simply bridge under speed- varying Loads* (2): 26–30.

Xia, H., Zhang, N. & Guo, W.W. 2006. Journal of Sound and Vibration. *Analysis of resonance mechanism and conditions of train-bridge system* 297: 810–822.

Xia, H, Roeck, G. Re. & Goicolea, J.M. 2011. *Bridge Vibration and Controls*, New York: Nova Science Publishers.

Yang, Y.B., Yau, J.D. & Wu, Y.S. 2004. *Vehicle-bridge interaction dynamics*. Singapore: World Scientific Publisher.

Research and Applications in Structural Engineering, Mechanics and Computation – Zingoni (Ed.)
© 2013 Taylor & Francis Group, London, ISBN 978-1-138-00061-2

Dynamic identification of Palazzo Marchesale in S. Giuliano di Puglia

G. Bongiovanni, G. Buffarini, P. Clemente, D. Rinaldis & F. Saitta
ENEA, Centro Ricerche Casaccia, Roma, Italy

M. Nicoletti & A. De Sortis
Italian Civil Protection Dept., Roma, Italy

G. Rossi
Office for the reconstruction of San Giuliano di Puglia, Italy

ABSTRACT: Palazzo Marchesale in San Giuliano di Puglia (Italy) is an old masonry structure hosting the new City Hall. It is quite complex and is characterized by several parts with different height and foundation levels, and includes an internal court. After the earthquake of October 31st ($M_L = 5.4$) and November 1st, 2002, ($M_L = 5.3$), the building was retrofitted and seismic joints were realized between the different buildings, in order to regularize the dynamic behaviour. The structure has been considered for seismic monitoring in the framework of a research project funded by the Office for the reconstruction of San Giuliano di Puglia. Therefore a permanent accelerometric array has been designed and installed. It was tested by deploying also a temporary array in different configurations and recording ambient vibrations and weak motion effects. The experimental results were compared with those obtained by means of a finite element model. Thus, linear and nonlinear analysis allowed to evaluate the seismic safety of the structure. Modal identification and model updating are shown in the paper.

1 INTRODUCTION

Identification of dynamic characteristics of historical buildings is an important step that is necessary for two basic reasons: to assess possible dynamic behaviour of such complex structures during strong events and to gain experience on the dynamic behavior of historical buildings such that the experience and data base can be used in future design and analyses.

Past efforts in determination of dynamic behaviour of historical buildings allowed the development of data bases, which in turn have been used in design codes. Actually, data on dynamic behaviour of complex structures such as historical buildings are scarce.

The data bases are in general obtained from dynamic testing of structures (forced vibration, ambient vibration, etc.), and from analyses of data from instrumented structures. With this purpose, ENEA, the Italian Civil Protection and the Municipality of San Giuliano di Puglia organized a research project for seismic monitoring of relevant structures in the framework of the reconstruction of San Giuliano di Puglia, Italy. A permanent accelerometric array was designed and installed as part of the Seismic Observatory of Structures (OSS) of the Italian Civil Protection. The OSS (Spina et al., 2011) is the Italian State permanent network that monitors the seismic response of public structures, including 133 buildings (schools, city halls, hospitals, etc.), 7 bridges and 1 dam. The array was designed after a detailed study of the expected dynamic behavior of the structure and then installed and tested by recording ambient vibrations and weak motion effects also using a temporary array. The experimental results were compared with those obtained by means of a finite element model. Thus, linear and nonlinear analysis allowed to evaluate the seismic safety of the structure. All the steps of the modal identification, the model updating and the seismic analysis are summarized in the paper.

2 THE BUILDING

The Palace, located in the historical center of San Giuliano di Puglia, is composed of a series of masonry buildings, arranged around a central courtyard. They spreads over several levels, two completely above the ground emerging from the courtyard (level 0 and level 1), two below (level -1 and level -2) and then partially buried by the presence of a slope, which affects the site. In more detail four buildings can be distinguished, which are structurally separated (Fig. 1). For the seismic monitoring the following buildings have been considered:

- building A, developed from level -1 to level 1; a little room on level -2 is present in the left corner in Fig. 1;
- building B, which includes levels 0 and 1 but also levels -1 and -2 in some parts;
- the tower T, which starts from level 0 and presents levels 1, 2 and 3.

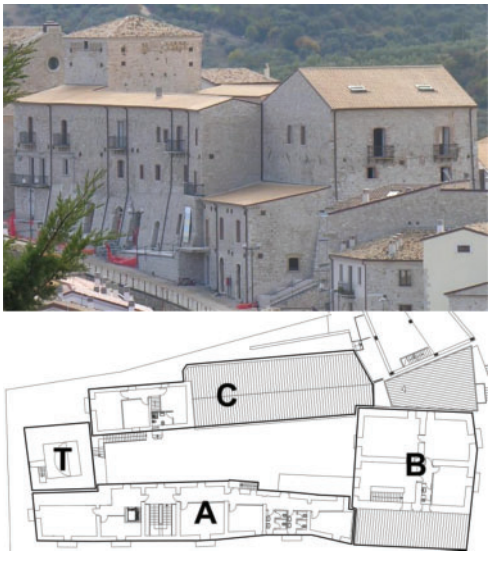


Figure 1. View and plan of Palazzo Marchesale.

Seismic improving interventions have recently been done. These consisted in mortar injections in masonry, substitution of some floors with new ones having laminated wood structure, and retrofit of vaulted roofs by means of FRP. Furthermore, the Palace was divided into buildings of regular shape (T, A, B and C), with seismic joints between them. Therefore, the tower, at the entrance of the courtyard is separated structurally and so are the buildings A and B, where the municipal offices are placed. In these buildings, which belong to the local municipality, an accelerometric network has been installed.

3 ACCELEROMETRIC NETWORK

The accelerometric network was designed on the basis of previous dynamic tests carried out on Palazzo Marchesale (Fig. 2). It is composed by 26 sensors, 4 of them are triaxial, 8 are biaxial sensors and 14 are uniaxial accelerometers. The total number of channel is 48. In more details, in building A three sensor (A1) were deployed on the floor and two sensor (A4) under the ceiling at level −1. Three other sensor (A9) were put on level 0 as well as two sensor respectively on the floor (A6) and under the ceiling (A7). On level 1, five accelerometers are on the floor and six under the ceiling. This deployment should be able to record both longitudinal and transversal movements of building A, in which one size is much higher than the other.

In building B three accelerometers (A2) were put on level −1, three (A10) on level 0 and three (A16 and A17) on level 1. The latest should be able to analyze both the translational and torsional modes of building B. The tower was instrumented by means of four accelerometers (A21, A22, A23 and A24) on level 2, four on the floor of level 3 (A8 and A19) and four under the ceiling of level 3 (A24, A25, A26 and A27).

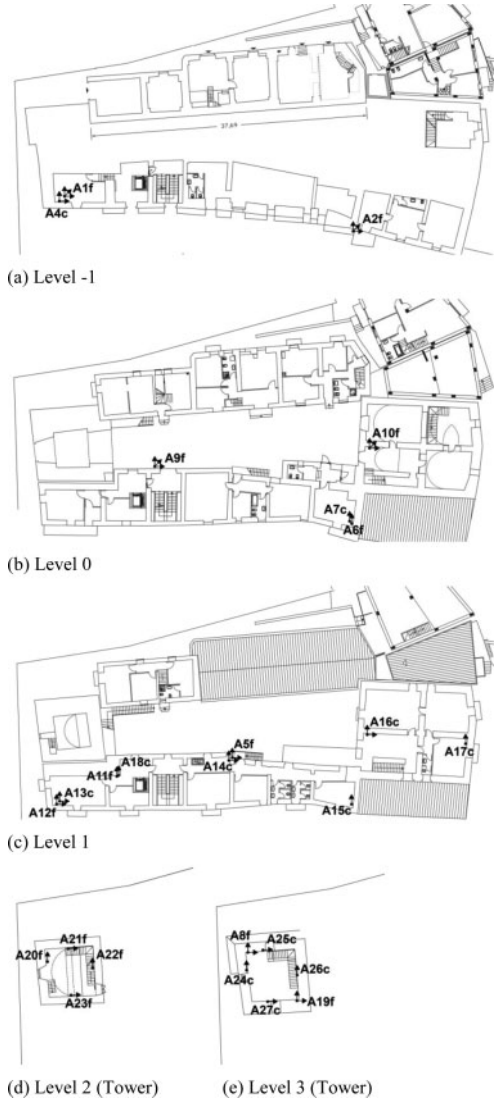


Figure 2. Accelerometric network (f = floor, c = ceiling).

Another triaxial accelerometer is in the courtyard, about 10 m below the ground level. This should record the seismic input to the building.

4 AMBIENT VIBRATION ANALYSIS

The ambient vibration analysis were carried out by using a Granite acquisition system and seismometers SS-1. Sensors were deployed in 2 configurations. In the first one 15 seismometers were deployed in the tower T (Fig. 3), in the second 17 seismometers were positioned in buildings A and B (Fig. 4). In both cases sensors positions were very close to the accelerometers of the fixed network. In the case of accelerometers placed at the top of the level, seismometers were positioned on the above floor. In Tab. 1 each seismometer in

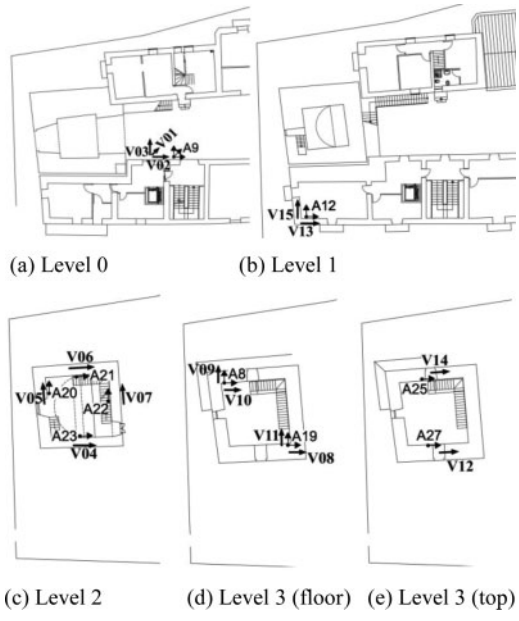


Figure 3. Configuration 1 – Tower.

the two configuratons is associated to the corresponding accelerometer in the tower T and in buildings A and B. Also the direction is associated to each sensor, x being the longitudinal, y the transversal and z the vertical one.

Several test for each configurations were carried out, each lasting 5 minutes, with the sampling rate of 250 samples/sec ($\Delta t = 0.004$ sec) in analogy to the sampling rate of the fixed accelerometric network (Clemente et al., 2012).

For all recordings the analysis was performed in the time and frequency domains. The velocimetric data were first derived in order to obtain accelerations. Then the corresponding auto- and the cross-spectral densities were compared with those of the accelerometric recordings. All recordings gave similar results. So only one test for each configuration was reported here in detail.

4.1 *Ambient vibration of the tower*

The resonance frequencies and the dynamic behavior of the tower, which is taller than the other portion, are apparent from the first configuration.

The main peak in the X direction is at 6.59 Hz, while in the Y direction the main peak is at 5.73 Hz. A resonance frequency is also at 10.10 Hz, apparent in all sensors, which is associated to a torsional mode, as demonstrated by the phase factors.

To assess the degree of connection of the tower T with building A, sensors V13x and V15y were placed just beyond the joint. The transversal sensor V15y followed the behavior of the sensors in the tower, while the longitudinal sensor V13x recorded the presence of the tower but also other peaks typical of building A, which will be analyzed later. For low levels

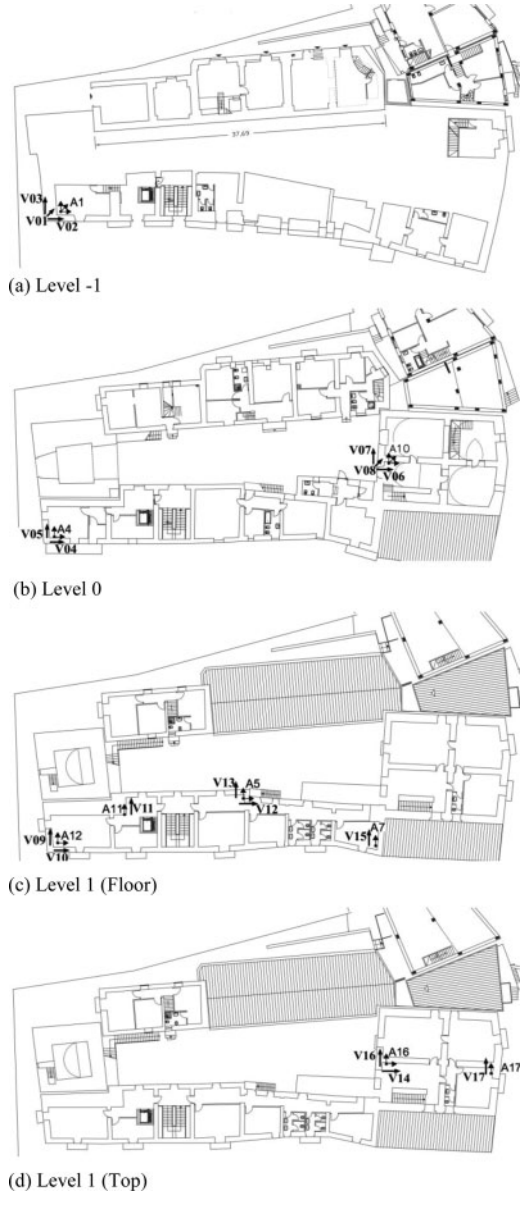


Figure 4. Configuration 2 – Buildings A and B.

of excitation the links with non-structural elements across the joint form a continuous link in the direction perpendicular to the joint (V15y).

Other resonance frequencies apparent in the spectra can be attributed to the local modes present in such complex structure. These make difficult the interpretation of the global behavior but have less importance in the interpretation of the general dynamics of this part of the building. The frequencies recorded by seismometers in the tower are shown in Table 2, while the first and second modal shapes obtained with accelerometric recordings are in Figs. 5a and 5b with the associated frequencies.

Table 1. Correspondence between seismometers and accelerometers in the tower and in buildings A and B (configuration 1 and 2, respectively).

Seismometers	Accelerometers in Tower	Accelerometers in buildings A and B
V01z	A9z	A1z
V02x	A9x	A1x
V03y	A9y	A1y
V04x	A23x	A4x
V05y	A20y	A4y
V06x	A21x	A10x
V07y	A22y	A10y
V08x	A19x	A10z
V09y	A8y	A12y
V10x	A8x	A12x
V11y	A19y	A11y
V12x	A27x	A5x
V13x	A12x	A5y
V14x	A25x	A16x
V15y	A12y	A7y
V16y	–	A16y
V17y	–	A17y

Table 2. Experimental frequencies of the tower.

Freq. (Hz)	Modal shape
5.73	Transversal Traslation Y
6.59	Longitudinal Translation X
10.10	Torsional

4.2 *Comparison with the accelerometric recordings*

To perform the comparison the operation of derivation of the velocity recordings was performed, in order to make the data consistent to accelerations recorded from the fixed network. For these comparisons the frequency range was expanded up to 30 Hz. Then the comparison was performed in the frequency domain, through the auto-spectra and cross-spectra and the difference between the auto-spectra of the corresponding sensors.

The analysis of the diagrams showed significant values of the coherence function in the studied frequency range, while the phase factor assumes almost everywhere values around $\pi/2$, consistent with the derivation operation performed in the frequency domain.

Particularly significant is also the difference between the auto-spectra of the two measuring systems. Actually, the spectral shapes of the velocimeter recordings are always in agreement with the accelerometer ones while the amplitudes of velocimeters at the foundation level are not very similar to the corresponding accelerometric recordings (A9x, A9y, A9z). Proceeding to the positions at the upper levels of the structure a good compliance between the amplitudes is apparent. The presence of a low frequency component in the recording of A20y is apparent, which does not influence the spectrum but could affect the peak in the time domain.

Table 3. Experimental frequencies of buildings A and B.

Freq. (Hz)	Building	Modal shape
8.17	A	Transversal Y
9.88	A	Longitudinal X
6.22	B	Transversal Y
8.54	B	Longitudinal X

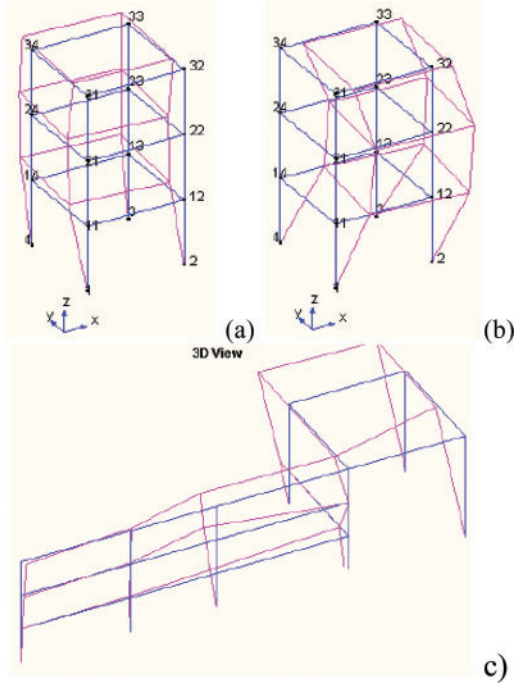


Figure 5. Experimental modal shapes with accelerometric data: (a) f = 5.6 Hz (Translational Y Tower), (b) $f = 6.7$ Hz (Translational X Tower), (c) $f = 6.2$ Hz (Translational Y building B).

4.3 *Ambient vibration of buildings A and B*

In the second configuration seismometers were deployed in buildings A and B. The complexity of the structures made the interpretation of the dynamic behaviour very hard. In the records of sensors in the transversal direction in the central portion of building A (V13y) the prevalent resonance frequency is at 8.17 Hz. This is associated to a bending modal shape with maximum amplitude in the central portion. In the records of sensors close to the tower (V05, V09) the same resonance of the tower, 5.73 Hz, was found. In the longitudinal direction (V04, V10 and V12) the main resonance is at 9.88 Hz.

With reference to building B, records of sensors in transversal direction (V16 and V17) showed an apparent peak at 6.22 Hz. Only V16 presents peaks at higher frequencies, between 10 and 11 Hz. In the longitudinal direction the record of sensor V14 has the main peak at 8.54 Hz. Both 6.22 Hz in the transversal direction and 8.54 Hz in the longitudinal one, can

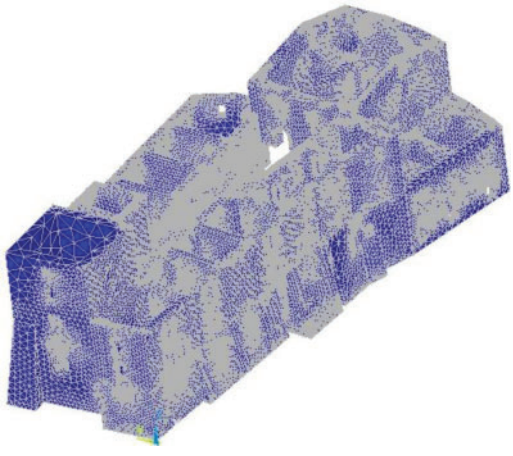


Figure 6. Mesh with solid elements.

be assumed as structural resonances. In Tab. 3 the structural resonances and the corresponding modal shapes are listed. The modal shape obtained with accelerometric recordings is in Fig. 5c.

4.4 *Comparison with the accelerometric recordings*

The low level of excitation and the stiffness of the structure determine a higher influence of the noise in both accelerometric and velocimetric recordings. The analysis showed significant values of the coherence function, while the phase factor is always equal to about $\pi/2$, due to the derivation in the frequency domain. The power spectral densities have very similar shape but some differences in the amplitudes are apparent. These could be related to the distance between accelerometers, which are often just below the floor or at the vault springing, and the velocimeters, which are above the corresponding floor.

5 FINITE ELEMENT MODEL

A finite element model was set up by using the code ANSYS. The elastic modulus was equal to 2120 N/mm^2 and was obtained by matching the first frequency with the experimental value. The model has 189236 nodes, and a total of 567 708 degrees of freedom. Finite element SOLID45 of prismatic or tetrahedral shape were used.

The mesh with solid elements is shown in Fig. 6. In the first step, here reported, the building was considered as a whole, without seismic joints. This hypothesis could be useful to analyze the behaviour under very low vibrations, such as the ambient vibrations. Then the mesh was generated obtaining. The frequencies of vibrations and the corresponding modal shapes were extracted by mean of the *subspace iteration method*. The first eleven modes were found, whose frequencies are listed in Tab. 4.

The first and second modal shapes are associated to a transversal and to a longitudinal movement of

Table 4. Numerical frequencies.

Mode	Freq. (Hz)	Building
1	5.73	T
2	6.50	T
3	6.74	B
4	6.96	C
5	7.43	A
6	7.87	A
7	8.20	All
8	8.36	All
9	8.43	All
10	8.62	All
11	9.08	All

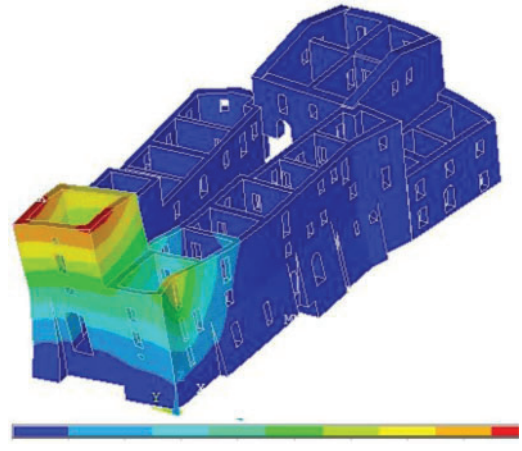


Figure 7. Mode 1 ($f = 5.73$ Hz).

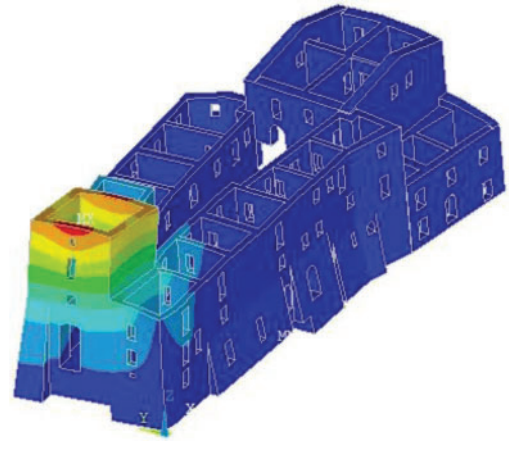


Figure 8. Mode 2 ($f = 6.50$ Hz).

the tower, respectively (Figs. 7 and 8). The portion around the tower is also involved in the modes. The third modal shape consists in the transversal movement (Y direction) of building B (Fig. 9), while the fourth mode interests building C, not considered in

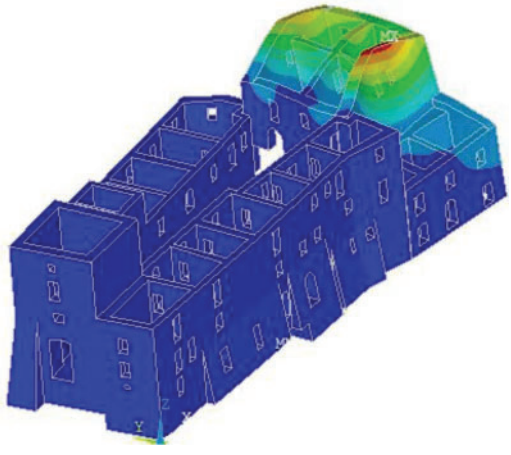


Figure 9. Mode 3 ($f = 6.74$ Hz).

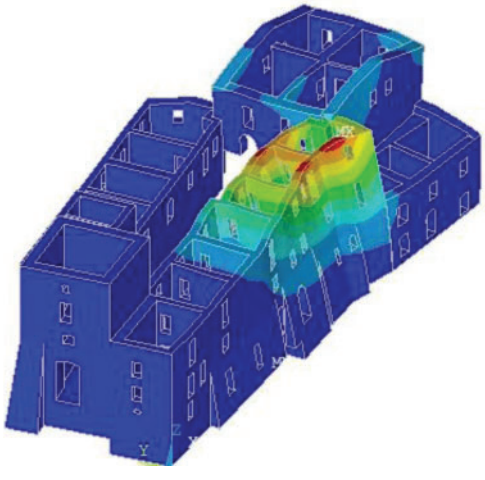


Figure 10. Mode 5 ($f = 7.43$ Hz).

the seismic monitoring. Modes 5 and 6 are relative to the longitudinal building A (Figs. 10 and 11).

The model was updated in order to obtain the coincidence between the first experimental and numerical frequencies. The comparison with the other frequencies gave quite good results (Tab. 5) and the same conclusion can be gathered in terms of modal shapes (Fig. 5 with Figs. 7–10). The comparison between the higher frequencies and the corresponding modal shapes is quite hard, especially for building *A*. Further recordings, including seismic events, could be useful.

6 CONCLUSIONS

The experimental campaign on Palazzo Marchesale by using both a temporary array, composed by velocimeter sensors, and a permanent array, composed by accelerometer sensors, gave the following results:

- the first three resonance frequencies of the tower were found; due to its slenderness its vibrations were detected using ambient noise only, which was quite hard for the other portions;
- the resonance frequencies of building B were also found but the modal shapes are not very clear;
- the longitudinal building A requires more data and a more detailed analysis;
- the comparison between accelerometric and velocimetric recordings gave good results.

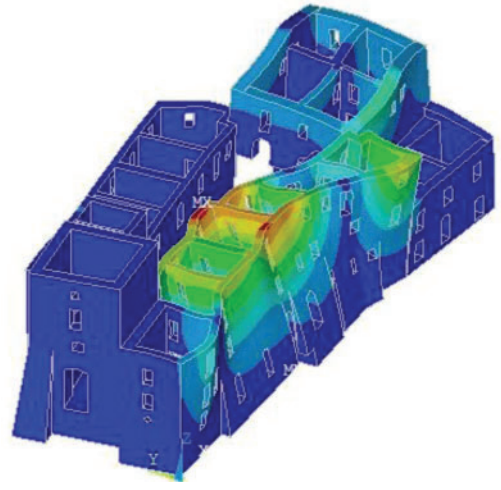


Figure 11. Mode 6 ($f = 7.78$ Hz).

Table 5. Comparison between experimental and numerical frequencies.

Num. Freq. (Hz)	Exp. Freq. (Hz)	Modal shape	Building
5.73	5.73	Translational Y	T
6.50	6.59	Translational X	T
6.74	6.22	Translational Y	B

The numerical model seams to interpret very good the experimental results. Anyway, further analyses will be very useful, especially in case of seismic recordings.

ACKNOWLEDGEMENTS

The activities here described are part of a research project funded by the Office for the reconstruction of San Giuliano di Puglia.

REFERENCES

Clemente, P. et al. 2012. *Palazzo Marchesale. Dynamic test and modeling*. Report to Office for the reconstruction of San Giuliano di Puglia. ENEA

Spina, D., Lamonaca, B.G., Nicoletti, M., Dolce, M. 2011. Structural monitoring by the Italian Department of Civil Protection and the case of 2009 Abruzzo seismic sequence, *Bulletin of Earthquake Engineering*, Vol. 9, No.1.

Research and Applications in Structural Engineering, Mechanics and Computation – Zingoni (Ed.)
© 2013 Taylor & Francis Group, London, ISBN 978-1-138-00061-2

A suspended mass damper for torsional and translational vibration control

M. Carlisle & K. Li
The University of the Witwatersrand, Johannesburg, South Africa

ABSTRACT: A Suspended Mass Damper (SMD) is a passive vibration control device consisting of a mass which is suspended in the top region of a structure and is forced into motion, due to inertia, when the structure is excited. A test structure is used to carry out this experimental investigation. The damper mass is connected to the structure to be controlled by a group of inelastic ropes. It moves relative to the structure, utilising and dissipating energy as it swings, and in this way, the vibrational energy of the structure is absorbed and the vibrations are controlled. Free vibration tests are carried out on the test model to determine the damping effects of the SMD. The results reveal that a SMD, without tuning or specific adjustment, can provide significant control on translational, torsional and coupled vibration of the structure, making it versatile, uncomplicated and therefore ideal for engineering applications.

1 INTRODUCTION

The control of the dynamic response of structures to certain loads is an important focus of study in Civil Engineering. It aims to eliminate unwanted vibrations and to maintain a safe and comfortable environment for the inhabitants of a structure. Vibrations can occur in floor systems of tall, flexible buildings due, most commonly, to excitation from human activity, wind, and seismic activity. The dynamic nature of these loads causes vibrations which are not usually a safety concern but rather a serviceability issue, causing discomfort to the occupants. In relatively recent years, the research of vibration control on Civil Engineering structures has increased with the development of active and passive control devices. Passive control devices are those which are activated by the excitation of the structure and possess no feedback capability. They seem to be favoured due to the fact that they do not require power for their use as well as their mechanical simplicity and efficiency. A common passive control device which is frequently featured in the literature is the Tuned Mass Damper (TMD). A TMD is, in its basic configuration, a SDOF auxiliary mechanism consisting of a mass, spring and a dashpot which is connected to the main structure. The TMD's natural frequency is tuned to the natural frequency of the fundamental mode of the structure and therefore, under excitation, the damper will resonate out of phase with the structure's motion due to inertia. In this way, a portion of the structure's vibratory energy is transferred to the TMD and is dissipated. The World Trade Center Towers (1973) in New York and the John Hancock Tower (1976) in Boston were among the first practical applications of this type of control device.

It is obvious from observing the results of TMD applications that this system of vibration control for the protection of Civil Engineering structures has been widely successful and accepted. Although TMDs have achieved a great amount of success, the main shortfall of their use is their need to be tuned to a particular modal frequency of the structure and the fact that their efficiency depends strictly on this frequency. Unfortunately, a structure's fundamental frequency can change with time due to changes in building use or occupancy and changes to non-structural elements. These modifications may adjust the building's mass or stiffness and therefore alter its modal frequencies. Research has been conducted into other types of dampers, including multiple tuned mass dampers (Xu & Igusa 1992), active mass dampers (Scheller & Starossek 2011) and semi-active tuned mass dampers (Nagarajaiah & Sonmez 2007), with the aim of increasing the robustness of the TMD to mistuning. Attempts have also been made to produce a damper which can control the vibration in more than one direction, such as the rolling pendulum vibration absorber proposed by Matta *et al.* (2009) and the bidirectional and homogenous tuned mass damper proposed by Almazan *et al.* (2007). However, these devices need to be tuned and are therefore also subject to mistuning.

Although the research and application of the control of translational vibrations in structures has become more common, the control of torsional vibrations is significantly more challenging. A small amount of research has been done into reducing the torsionally coupled response of irregular structures (Lynch 1998, Lin *et al*. 1999, Yoshida & Dyke 2005). The control devices which have been studied for torsional control are mainly semi-active or active, and often multiple dampers are required in order for them to be effective.

The purpose of this investigation is to attempt to come up with an effective yet simplistic way of controlling torsional vibrations on buildings, as well as

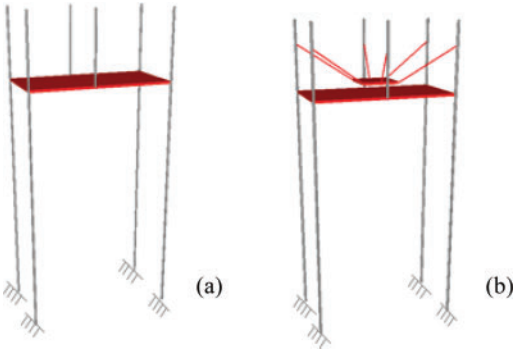


Figure 1. (a) The primary test model (b) The test model containing the SMD.

bidirectional translational vibrations, using only one control device, whilst also eliminating the problem of mistuning. The proposed SMD is completely passive and does not require any tuning to be effective. The inelastic ropes tighten and loosen as the damper moves during excitation, and in this way, the stiffness of the system can vary passively from zero to infinity as required. The proposed system effectively controls torsional and coupled vibrations of the structure. Furthermore, the translational vibrations of the structure, in two orthogonal directions, can be controlled. This paper uses experimental results to demonstrate the performance of an SMD.

2 EXPERIMENTS

2.1 *Experimental structure and setup*

Experimental tests were carried out on a tall, flexible test model. The primary, undamped model is illustrated in Figure 1a, whilst the model containing the SMD is shown in Figure 1b. The primary model consists of four 1.3 m high, 12 mm threaded rods and a 300 mm × 600 mm × 10 mm thick steel plate. The plate is secured at a height of 1m using nuts. The columns are bolted rigidly to the base such that the ends are rotationally fixed, and the base is fixed to a unidirectional shaking table. Prokon was used to simulate the behavior of the primary model, and to determine its first three natural frequencies and associated mode shapes. It was ensured that the values obtained during the Prokon simulation closely matched those which would be expected for a real-life tall, flexible structure. A number of model dimensions were entered and simulated until suitable frequency values were obtained, and therefore the suitable model dimensions were decided. The simulated model's first three natural frequencies, corresponding to the first three mode shapes are $f_{n1} = 2.66$ Hz, $f_{n2} = 2.69$ Hz and $f_{n3} = 4.24$ Hz.

The suspended mass damper, shown attached to the primary model in Figure 1b, is a 15 cm square metal plate with a thickness of 10 mm. It has a mass of 0.75 kg which is about 5% of the primary model's mass of 14.13 kg. It is tied, with inelastic ropes, to the threaded rod at a height of 20 cm above the plate. The damper mass sits 5 cm above the plate.

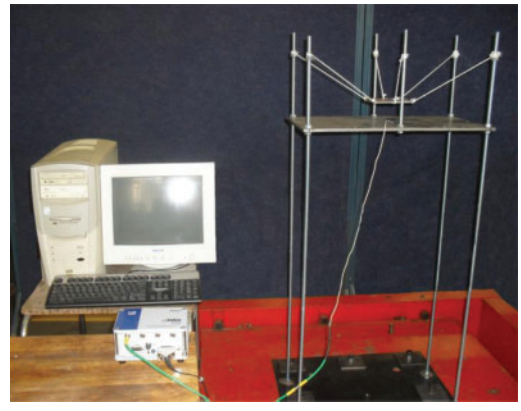


Figure 2. The experimental setup showing the test model, accelerometer, data logger and computer.

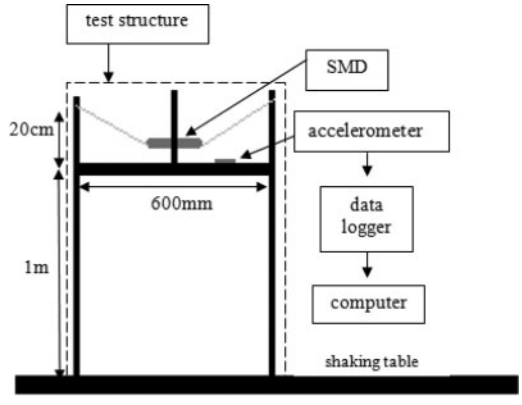


Figure 3. A schematic diagram of the experimental setup.

The test setup is shown in a photograph in Figure 2 and in a schematic diagram in Figure 3. An accelerometer is attached to the primary model in order to measure the accelerations after excitation. The accelerometer is connected to a data logger which records the acceleration readings over time. The data logger is connected to a computer so that the data acquired during the test can be viewed, analysed and processed using the programs TCE Build and Matlab.

2.2 *Experimental procedure*

2.2.1 *Free vibration tests*

Free vibration tests were carried out on the primary test model. The model was excited by giving it an initial displacement, which was measured using a dial gauge, and then releasing it. The tests were done for five different excitations of the test structure – it was excited in two translational directions; torsion; and lastly it was given two coupled excitations. The two translational directions were the orthogonal x and y-directions,

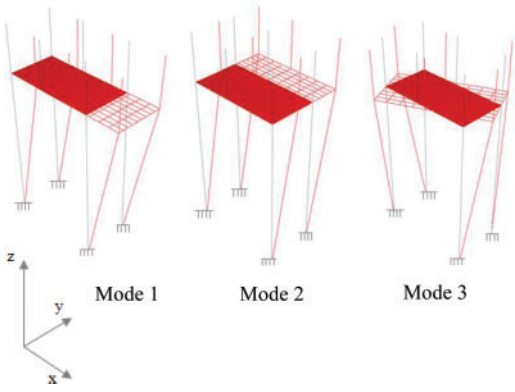


Figure 4. The model's first three mode shapes.

depicted by mode shapes 1 and 2 respectively in Figure 4 below. It was excited torsionally, as shown by mode 3 in Figure 4, by applying an initial twist to the model and then releasing it. Lastly, the model was subjected to two coupled excitations which were achieved by giving it initial torsional as well as translational displacements simultaneously.

The SMD was then added to the primary structure and the tests described above were repeated. The sampling frequency chosen for these experiments was 250 Hz, meaning that 250 acceleration readings were collected by the data logger per second.

3 RESULTS AND COMPARISON

3.1 *Translational vibration in the x-direction*

In the first test, an initial displacement of 30 mm was given to the undamped and damped models in the x-direction before releasing them. Figure 5 below shows a high peak at 2.36 Hz which is the model's first natural frequency, with a smaller peak at half of this value, 1.18 Hz. It is observed that the natural frequencies obtained by simulation (2.66 Hz) and by experimentation (2.36 Hz) do not match up exactly, however they are close in value. This is to be expected as the simulation results represent the results of an 'ideal' test and were merely obtained in order to get a basic idea of what could be expected during experimentation. Figure 5 shows that the SMD provides a high level of attenuation at both of the peaks, with the peaks of the damped model being reduced almost to zero. The time history of acceleration response for the first 25 seconds of the test can be seen in Figure 6. Near the beginning of the test, as the SMD starts moving, the acceleration peaks generated in the damped model are very high, exceeding those generated in the undamped model. These high accelerations subside and the accelerations rapidly become less than those found in the undamped model; however these initial high accelerations are undesirable. It was discovered by doing some further testing, that by making the inelastic ropes tighter i.e. reducing the height at which they are tied

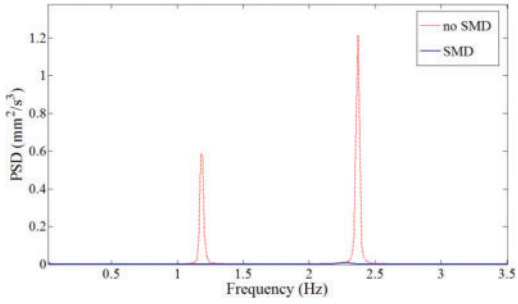


Figure 5. Power spectral density (PSD) of the acceleration response in the x-direction.

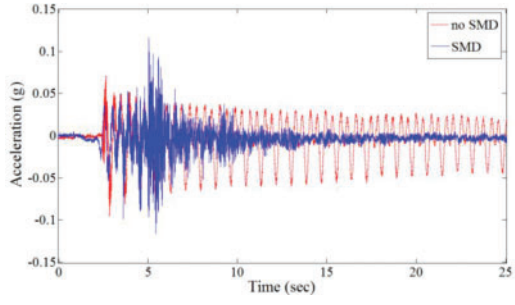


Figure 6. Time-history of acceleration response in the x-direction.

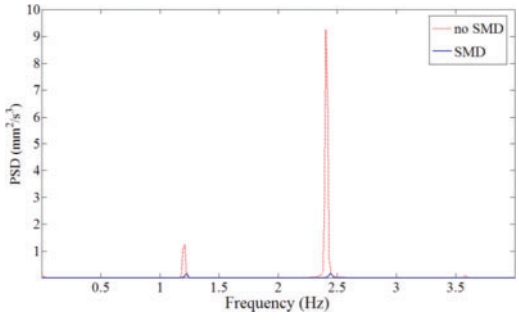


Figure 7. Power spectral density (PSD) of the acceleration response in the y-direction.

onto the threaded columns from 20 cm to 15 cm, the high accelerations decrease in value, becoming equal to or less than the undamped peaks. However, regardless of this small modification, the positive damping effects of the SMD evident in Figures 5 and 6 are still significant.

3.2 *Translational vibration in the y-direction*

Next, the damped and undamped models were given an initial displacement of 30 mm in the y-direction before being released. The PSD graph shows a high peak at 2.4 Hz, which is the model's natural frequency in that direction. Again, this is slightly different to the simulated result of 2.69 Hz, which is to be expected.

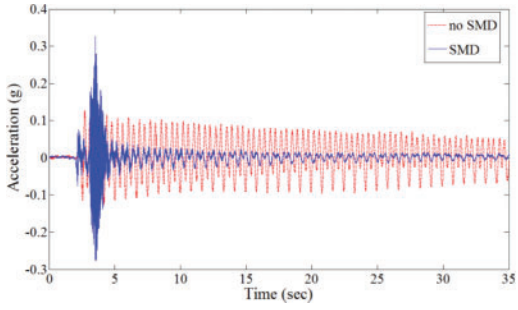


Figure 8. Time-history of acceleration response in the y-direction.

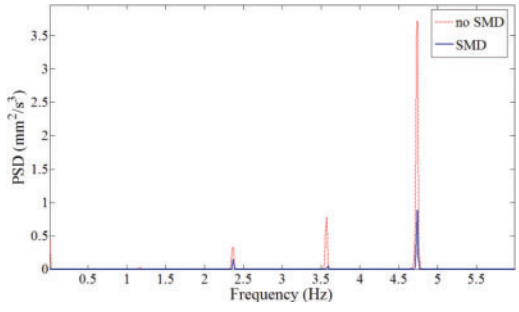


Figure 9. Power spectral density (PSD) of the acceleration response for torsional vibration.

A smaller peak can be seen at half of this value, 1.2 Hz. Again, the peaks are reduced as the structure is controlled by the addition of the SMD. The time history of acceleration response, shown in Figure 8, also contains high acceleration peaks for the damped model as the SMD starts moving, with these peaks rapidly decreasing to well below those of the undamped model as time progresses. Again, these initial high accelerations can be controlled by the slight tightening of the inelastic ropes of the SMD, which does not affect the positive damping results.

3.3 *Torsional vibration*

The damped and undamped models were then given a torsional displacement of 30 mm which was measured using dial gauges. The PSD graph below shows a high peak at 4.75 Hz, the torsional frequency of the model, as well as smaller peaks at 1.2 Hz, 2.4 Hz and 3.6 Hz. The torsional frequency obtained during simulation was 4.24 Hz, which is relatively close to the experimental value. The fact that there is a peak at 2.4 Hz means that although the model was excited in torsion, it had some movement in the y-direction as well. Once again, all of the peaks are reduced by the addition of the SMD. The time history of acceleration response for the damped model shows a more gradual decrease in accelerations as opposed to the translational time history graphs. However, the effect of the SMD is still obvious as time passes.

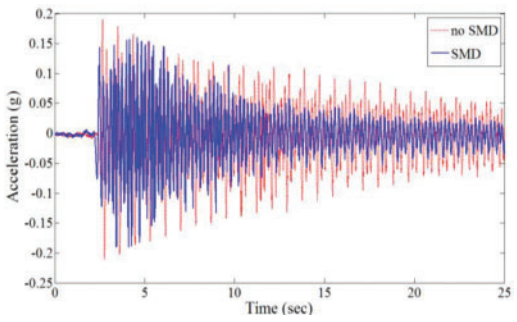


Figure 10. Time-history of acceleration response for torsional vibration.

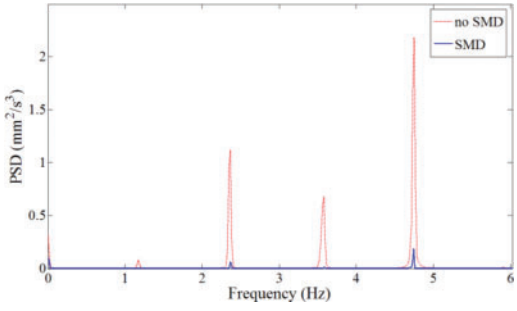


Figure 11. Power spectral density (PSD) of the acceleration response for coupled vibration (x-direction and torsion).

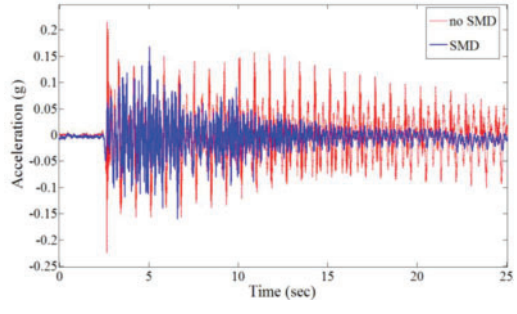


Figure 12. Time-history of acceleration response for coupled excitation (x-direction and torsion).

3.4 *Coupled vibration (translation in x-direction and torsion)*

Next, the model was subjected to a coupled excitation. It was given initial translational and torsional displacements simultaneously and then released. In Figures 11 and 12, the model was displaced in the x-direction as well as twisted. As can be seen, there are peaks at the torsional natural frequency, 4.75 Hz and at the natural frequency of translation in the x-direction, 2.35 Hz as well as smaller peaks at 1.2 Hz and 3.6 Hz. All of these peaks are decreased substantially by the addition of a SMD, indicating its control effect. This control is also obvious in the time history of acceleration response where the acceleration peaks generated in the damped

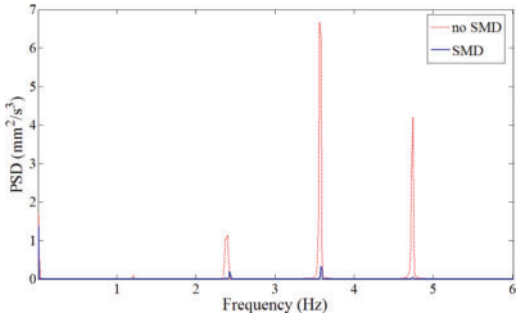


Figure 13. Power spectral density (PSD) of the acceleration response for coupled excitation (y-direction and torsion).

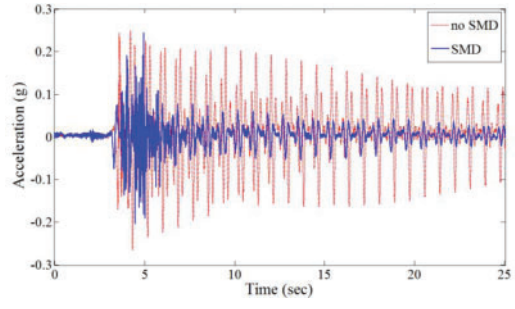


Figure 14. Time-history of acceleration response for coupled excitation (y-direction and torsion).

test decrease much more rapidly than those generated in the undamped test.

3.5 *Coupled vibration (translation in y-direction and torsion)*

Lastly, the model was subjected to a second coupled excitation. It was given a translational displacement in the y-direction and a torsional displacement simultaneously. The PSD shows peaks at the natural frequency for torsion, 4.75 Hz and the natural frequency for translation in the y-direction, 2.4 Hz, as well as a peak at 3.6 Hz. The control effect of the SMD is obvious for all peaks in the PSD graph and in the time history of acceleration response.

4 CONCLUSIONS

The proposed control device is effective, yet also simple and versatile. The free vibration tests which have been carried out, demonstrate the proposed SMD's capability of providing considerable vibration control to structures such as the tall, flexible test structure. The SMD did not need to be tuned during the tests and no specific adjustment took place. This is a significant advantage over traditional TMDs which are often the subject of mistuning due to changes in the structure's mass or stiffness and therefore changes in its natural frequency, which can render the TMD ineffective. The SMD's stiffness varies, as needed, during excitation by virtue of inelastic ropes, making it an uncomplicated yet efficient passive control device.

A further advantage of the proposed SMD is its ability to significantly control torsional and coupled vibrations, which has previously proven to be considerably more difficult than the control of translational vibrations. Moreover, the translational vibrations in the two principle, orthogonal directions, direction x and direction y were controlled effectively in the free vibration tests. High acceleration peaks were seen to occur in the damped model soon after the SMD was excited; however these were reduced by the slight tightening of the inelastic ropes connecting the damper to the structure. This modification does not reduce the positive damping effects which are obvious in all of the tests.

REFERENCES

Almazan, J.L., De la Llera, J.C., Inaudi, J.A., Lopez-Garcıa, D. & Izquierdo, L.E. 2007. A bidirectional and homogeneous tuned mass damper: A new device for passive control of vibrations, *Eng. Struct.*, 29, 1548–1560.

Lin, C.C., Ueng, J.M. and Haung, T.C. (1999), "Sesimic Response Reduction of Irregular Buildings Using Passive Tuned Mass Dampers", *Eng. Struct,* **22,**512–524.

Lynch, J. P. 1998. Active Structural Control Research at Kajima Corporation. *The National Science Foundation's Summer Institute in Japan Program*. Stanford University, U.S.A.

Matta, E., De Stefano, A. & Spencer, B.F. 2009. A new passive rolling-pendulum vibration absorber using a non-axial-symmetrical guide to achieve bidirectional tuning. *Earthquake Engng Struct. Dyn*., 38, 1729–1750.

Nagarajaiah, S. & Sonmez, E. 2007.Structures with semiactive variable stiffness single/multiple tuned mass dampers, *J. Struct. Eng.*, 133(1), 67–77.

Scheller, J. & Starossek, U. 2011. A versatile active mass damper for structural vibration control, *Proceedings of the 8th International Conference on Structural Dynamics EURODYN 2011*, Leuven, Belgium, July.

Xu, K. & Igusa, T. 1992. Dynamic characteristics of multiple substructures with closely spaced frequencies, *Earthquake Engng. Struct. Dyn*., 21, 1059–1070.

Yoshida, O. and Dyke, S. (2005), "Response control of full-scale irregular buildings using magnetorheological dampers." *J. Struct. Eng.*, 131(5), 734–742.

Research and Applications in Structural Engineering, Mechanics and Computation – Zingoni (Ed.)
© 2013 Taylor & Francis Group, London, ISBN 978-1-138-00061-2

Status quo and critical review of PPV safe limits for subsurface construction blasting close to low-rise buildings

E.Y. Sayed-Ahmed
The American University in Cairo and Professor (on leave), Ain Shams University, Egypt

K.K. Naji
Facilities and IT, Qatar University, Qatar

ABSTRACT: Subsurface construction blasting may result sever man-made ground vibrations. Waves generated due to detonating a charge in a solid medium like rock generate particle movement and travel at different wave velocities. As such, ground-borne vibrations have effects on nearby buildings that range from disturbing the occupants to causing severe threshold "cosmetic" or structural damage. The said ground vibrations are usually monitored to assess their impact on nearby structures. Currently, codes of practice adopt safe limit criteria which are mainly based on field observations where the structural damage is correlated to the soil Peak Particle Velocity (PPV) produced on the ground surface close to the structure. For example, the criteria limit the PPV of the ground vibration to 51 mm/s at the nearest "non-owned" structure to the blasting site. On the contrary, it is not the soil PPV that matter but it is the structural response to the ground vibration which causes the damage: all the blast-vibration complaints are actually due to the structure vibration not the ground vibration. In this paper, some of the currently adopted safe limit criteria of ground vibration generated by subsurface construction blasting are reviewed. Two real case studies have been performed on low rise buildings (houses) located nearby an excavation performed by blasting in rock. The PPV and the vibration frequency due to excavation by blasting measured close to these low-rise buildings satisfied the existing safe limit criteria for subsurface blasting ground vibration. Despite this fact, both buildings suffered threshold cracks and one of them even had structural cracks. Thus, it is argued that the current safe limit criteria ignore a very important factor which is the structural response to the ground vibration. It is also argued that ground vibrations with low level frequencies affected the structural response of the two houses may have caused resonance and wall rattling. These, in turn, caused threshold, and even structural, cracks beside the severe disturbance to the residents. So, as an urgent modification, it is recommended that the PPV for low level frequency vibrations (4–30 Hz) should be multiplied by a magnification factor before comparing them to the current safe limits of the codes of practice. This would simulate the resonance or wall rattling which may occur to low rise buildings subjected to ground-born vibrations with low level frequencies.

1 INTRODUCTION

Rock excavation is commonly adopted by blasting which generates a family of waves that travel at different wave velocities. Approximately 15% of the total blast energy is utilized for actual breakage and mass displacement with the reminder spent on undesirable activities Niclson (2005). Among these are the ground-borne vibrations which may have an effect on residential buildings ranging from disturbing the occupants to causing severe threshold "cosmetic" or structural damage. Problems may occur as a result of large amplitude (low frequency) vibrations, repeated occurrence of smaller amplitude vibrations, or from differential settlement induced by soil particles rearrangement. Classifying ground vibrations types, monitoring their effects and establishing their severity were investigated (Dowding1985; Franfield 1996; Dowding 1996; Massarsch 1993; Wiss 1981; Skip 1984). The level of ground vibration resulting from subsurface blasting and the structural response depends on the explosive type and weight, delay time, blasting technology, soil properties, distance between the structure and the blasting centre, susceptibility ratings of the adjacent and remote structures, and the age and type of the structure. A simple equation estimating the PPV in terms of distance from the blasting location (D in m) and the charge weight per delay (W in kg) is:

$$PPV = 1725 \cdot \left(D/\sqrt{W}\right)^{-1.6} \quad (1)$$

Many attempts have been made to relate the vibration parameters (displacement, velocity, acceleration and frequency) with the observed human annoying, disturbance of sensitive devices and structural damage (Medearis 1976; Siskind et al. 1980; Wiss 1981; Svinkin 1993; Dowding 1996). Currently, codes of

practice adopt safe limit criteria which are mainly based on field observation (Svinkin 2004; ISEE 1998). Most of these criteria correlate the structural damage to the soil Peak Particle Velocity (PPV) produced on the ground surface and limit the PPV to 51 mm/s at the nearest "non-owned" structure to the blasting site. Three factors of ground vibration affect the structural response: ground vibration amplitude defined via the PPV, ground vibration duration (which is not the same as the blast duration), and ground vibration frequency. Usually seismographs report the PPV and the frequency and often ignore the duration. Reducing ground vibration duration would reduce the structure response but increase the perception of the occupants to the ground vibration.

This paper shows that it is not the soil PPV that matter but it is the structural response to the ground vibration: all the blast-vibration complaints are actually due to the structure vibration not the ground vibration. Thus, the currently adopted criteria cannot define reliable and acceptable safe limits for subsurface construction blasting. Two case studies have been performed and discussed for two residential houses (one- and two-storeys) located adjacent to an excavation where blasting was to be used for excavating the rock. Data recorded during blasting are compared to currently adopted ground vibration safe limit criteria: PPV and the vibration frequency due to excavation by blasting measured close to these houses satisfied the existing safe limits criteria. Despite this fact, both houses suffered threshold cracks and one of them had some structural cracks. Thus, a new approach that is based on relating the PPV and the ground vibration frequency to the structural response is proposed and a safe limit criterion for sub-surface construction blasting is developed.

2 CURRENT SAFE LIMIT CRITERIA

The International Standards ISO 4866-1990 lists some major regulations of ground vibrations for different types of buildings. Further, it was continuously argued that damage could be related to the PPV of the ground vibration (Duvall and Fogelgon 1962; Wiss 1968; ISEE 1998).

A 10-year research programme of the United States Bureau of Mines (USBM) led to the widely adopted criterion for the safe-limit vibration against structural and threshold damage of buildings resulting from ground vibrations generated by blasting (Nichollas et al. 1971). The safe limit for the resulting PPV was set at 51 mm/s in the frequency range of 3–100 Hz. This limit could not prevent the frequent residents' complaints from construction blasting. To take into account the effect of the dominant vibration frequency to assess the ground vibration effect on structures, an alternative USBM frequency-based safe limit was proposed (Siskind et al. 1980). This criterion is known as USMB-RI 8507 (Figure 1) for providing safety against ground vibrations resulting from blasting.

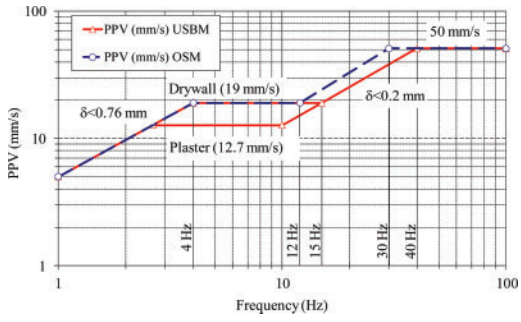


Figure 1. USBM and OSM safe limit criteria against ground-born vibrations due to subsurface blasting.

Table 1. PPV and Scaled Distance (US-OSM).

Distance m	PPV mm	Scaled Distance m
0∼91	31.8	22.6
92∼1524	25.4	24.9
>1524	19.1	29.4

The USMB-RI 8507 criterion was modified by US Office of Surface Mining (OSM). It is shown graphically in Figure 1 and compared to the previously mentioned USMB-RI 8707 criterion.

The OSM adopted two other methods. In the first method, the PPV is limited to the values shown in Table 1 without the need for monitoring the vibration frequency. In the second method, the amount of explosive is designed based on a scaled distance (SD) using the following Equation:

$$W = (D / SD)^2 \quad (2)$$

where W is the allowable charge per delay (kg), D is the distance (m) and SD is the scaled distance given in Table 1 (m). The scaled distance method is very conservative and there is no need to fit seismograph to measure the PPV or the vibration frequency during the blasting operation.

The British Standard BS 7385 criterion for safe limit against ground vibrations due to blasting is plotted in Figure 2 and compared to the OSM criterion. It is very close to both USBM-RI 8507 and OSM criteria. The BS 7385 adopts two lines for the safe limit depending on the building type: line 1 (independent of the vibrations' frequency) is used for commercial large buildings and line 2 (frequency based) is used for residential or small buildings.

The DIN 4150 and the Swiss Standards criteria for safe limits against ground vibrations resulting from blasting are also plotted in Figure 2. It is evident that these two criteria are significantly conservative. It is argued that the DIN 4150 criterion is not damage-based; it is intended to minimize the perceptions and complaints of housing residents who live adjacent to blasting sites.

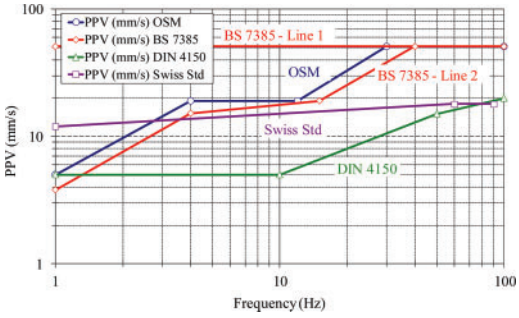


Figure 2. OSM versus other safe limit criteria against construction vibrations.

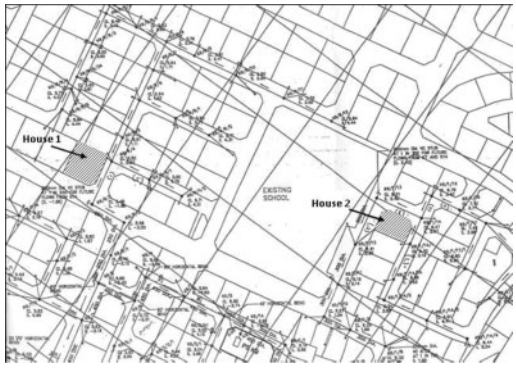


Figure 3. The two houses outlined on the layout of the sewerage system project (Blast locations are along the solid lines representing the sanitary sewer of the city).

3 PROPOSED DAMAGE CRITERIA

The current safe limit criteria make no distinction for the type, age or stress history of the structure; all of which considerably affect the safe limits. The y are all based on the PPV and frequency of the ground vibrations and thus, they fail in many situations (ISEE 1998; Quesne 2001). A major drawback is in the concept of the safe limit criteria itself: they only correlate the structural damage to the intensity of the ground vibration. However, a safe limit criterion against ground-born vibrations due to blasting should be based on the structure vibration/response not the ground vibration. In other words, the 51 mm/s safe-level criterion should be applied to the PPV of the structural vibration due to blasting not to the soil vibration.

The intensity of the vibration depends on the soil-structure interaction that determines the structure responses to the ground excitation. A ground vibration frequency which is 40% (or more) greater than the fundamental frequency of the structure introduces a structure PPV that is less than the PPV of the ground vibration. On the other hand, a ground vibration with a frequency below the fundamental frequency of the structure causes the structure to vibrate at least as much as the ground. If the ground vibration frequency is close to the structural natural frequency, a state of resonance may be generated and the PPV of the structure will increase considerably beyond the PPV of the ground vibration. This phenomenon is totally disregarded in all the currently adopted safe limit criteria against ground-born vibrations due to subsurface blasting.

Low-rise buildings have a natural frequency in the order of 4～12 Hz (Medearis 1977; Siskind 1980; ISEE 1998). The structures and their parts (e.g. floor, walls, etc.) respond differently to ground vibration as they have different natural frequencies. For example, the natural frequencies are 12～20 Hz for interior walls' horizontal vibrations and 8～30 Hz for floors vertical vibrations. Mid-walls' vibrations cause residential buildings to "rattle" making vibration more noticeable and aggravate human response to annoyance from ground vibration. It is difficult, if not impossible, to follow a uniform vibration standard to reduce the human perception of vibration due to subsurface blasting (Baliktsis 2001).

For the currently adopted safe limit criteria which are based on threshold/structure damage prevention, it is proposed to apply an amplification factor ranging between 2 and 4.5 to the soil PPV in the frequencies range of 4 Hz to 30 Hz as a modification to these criteria in order to consider the structure's resonance effect (Svinkin 2004).

4 PROPOSED CRITERIA VERFICATION

A project for sewerage system was executed in rock soil; part of the project layout plan is shown in Figure 3. The excavation was performed using subsurface blasting. The blasting events were officially supervised and the resulting soil PPVs and vibration frequencies were recorded using seismograph.

All the safe limits criteria for ground vibration resulting from the subsurface blasting, particularly those of the USBM and OSM, were accurately followed. The readings recorded by the seismographs for all the blasting events were well below the 51 mm/s limit. However, complaints were reported from many residents who blamed the blasting operation for causing threshold cracks to their houses. The readings of the seismographs recorded nearby two houses are compared to the currently adopted safe limit ground vibration criteria. The proposed safe limit criterion is also applied to these two houses to investigate the effect of the ground vibration resulting from the excavation by blasting on the two houses.

4.1 *House 1*

The first investigated house is a two-storey residential building which was newly built. When excavation by blasting started the house was almost one year old. It is a common reinforced concrete skeletal structure (solid slabs, beams and columns). The foundation of the house is composed of isolated footings constructed

Table 2. PPVs recorded for some blasting events – House 1.

Event No.	281	282	280	283	177	185	288
PPV mm/s	14.7	22.7	23.2	20.8	14.9	27.5	20.1
Event No.	294	287	219	218	220	284	285
PPV mm/s	15.7	19.8	25.5	28.8	20.5	19.3	12.4
Event No.	279	147	163				
PPV mm/s	14.2	24.8	23.3				

1.20 m below the lowest ground level and tied together with strong ground beams. The mid-wall partitions of the house consist of concrete block masonry walls. The house contains one stair case joining its two storeys.

After the excavation by blasting, many cracks appeared inside and outside the house (Figure 4). Most of the thresholds cracks started from the window frames, propagated vertically for a short distance then continue to propagate diagonally at an angle ranging between 30° and 60°. One structural crack was visible in the beam carrying the reinforced concrete slab of the second storey over the stair case.

Samples of ground PPV measured during the excavation by the blasting process around the house are listed in Table 2. The date of the event and its position with respect to the house were eliminated from the table. The seismographs also recorded the blasting event frequency in the vertical, radial and circumferential directions. These frequencies are plotted against the PPV for every blasting event in Figure 5 and compared to some of the currently available safe limit ground vibration criteria. The PPV of the low frequency vibrations (between 10–20 Hz) are magnified, as recommended by the proposed safe limit criterion, and also plotted in Figure 5: these events are enclosed by the dotted line in the figure to highlight their sever effects.

4.2 *House 2*

The second investigated case study is a one-storey residential house which was about twenty years old when the excavation by blasting started. The house had been renovated about two years before the start of the excavation work. It is an ordinary reinforced concrete structure with solid slabs carried by reinforced concrete beams which are supported over columns. The foundation of the house consists of isolated footings. The partitions of the house consist of concrete block masonry walls. Some of the cracks which appeared in this house after excavation are shown in Figure 6. Samples of ground PPV measured during the excavation by blasting process are list in Table 3. The vertical, radial and circumferential frequencies recorded by the seismographs are plotted against the PPV for every blasting event in Figure 7 and compared to some of the currently available safe limit ground vibration criteria. Ground PPV which have low frequency vibrations are magnified and plotted in Figure 7.

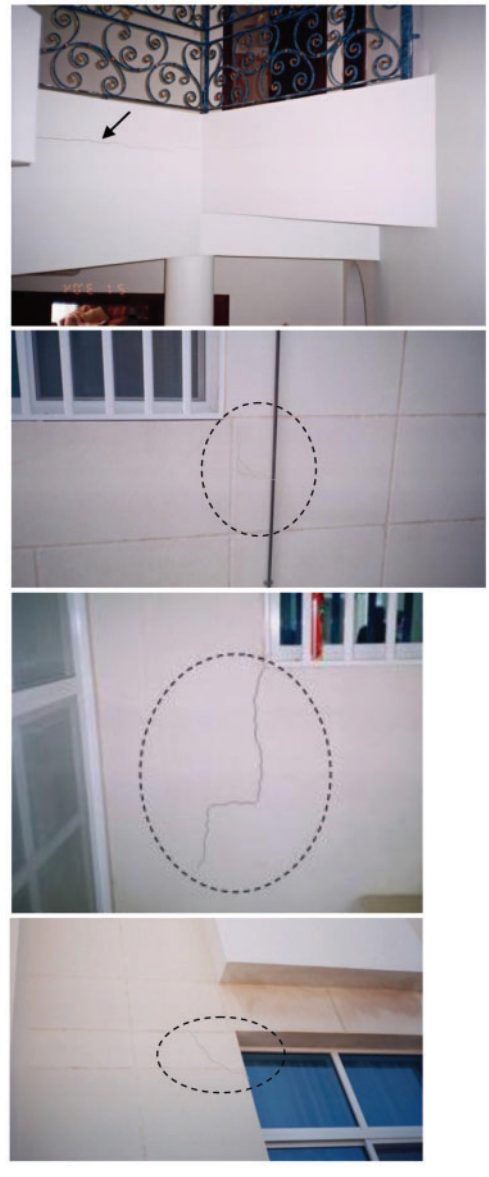


Figure 4. Examples of cracks appeared on House 1 after excavation by blasting (Cracks circled by dotted lines have been enhanced by plotting grey lines on top of them).

4.3 *Discussion*

Data recorded for the two case studies of houses located nearby subsurface blasting were examined. It is evident form the readings of the seismographs (samples of them are summarized in Tables 2 and 3) that the PPVs recorded for all blasting events were well below 51 mm/s; the limit defined in most of the available safe limit criteria. Furthermore, plotting the relations between the PPVs and the frequencies of the ground vibrations for these events (Figures 5 and 7) reveals that the ground vibrations satisfy the safe limit criteria set by the USBM, the OSM and the BS 7385. Some

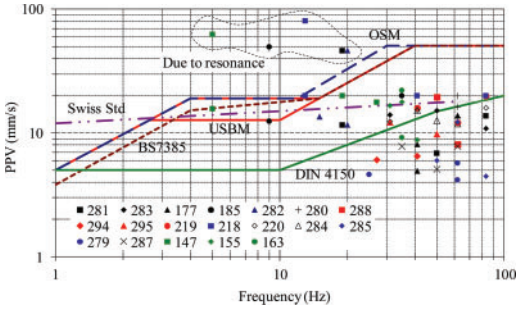


Figure 5. Ground PPVs and vibration frequencies of the blasting events recorded for House 1.



Figure 6. Examples of cracks appeared on House 2 after excavation by blasting (Cracks circled by dotted lines have been enhanced by plotting grey lines on top of them).

the events do not satisfy the Swiss Standards and most of them are unsafe compared to the DIN 4150 specifications. However, these two standards are human annoyance driven as opposed to structural damage driven criteria.

Table 3. PPVs recorded for some blasting events – House 2.

Event No.	269	270	175	176	266	267	182
PPV mm/s	18.8	22.3	23.0	12.7	21.9	15.7	22.4
Event No.	183						
PPV mm/s	16.9						

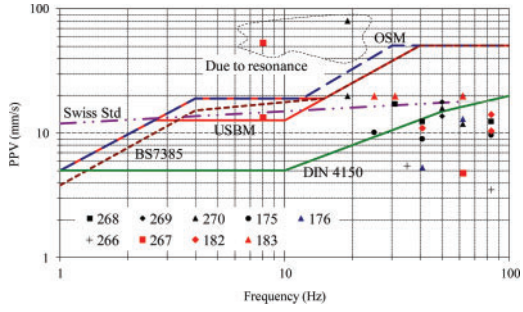


Figure 7. Ground PPVs and vibration frequencies of the blasting events recorded for House 2.

Despite satisfying all these criteria, threshold cracks, and even structural cracks, appeared in these houses after the excavation by blasting. Furthermore, the residents complained that the blasting effects were significantly pronounced.

It is evident that the currently adopted safe limit criteria ignore a very important factor which is the structural response to the ground vibration. It is argued that ground vibrations with low level frequencies affected the structural response of these two houses causing resonance and wall rattling. These, in turn, caused threshold, and even structural, cracks beside the severe disturbance to the residents.

So, as a modification, the PPVs of the low level frequency vibrations (4–30 Hz) should be magnified by a certain factor (estimated as 4.0 in the current investigation) before comparing them to the currently adopted safe limit criteria. This would simulate the resonance or wall rattling which may occur to the houses subjected to ground-born vibrations with low level frequencies. With this modification, Figures 5 and 7 reveal that some of the ground vibrations are significantly outside the safe limit defined by the safe limit criteria and would cause damage to the structures.

Gad *et al*. (2005) presented an investigation which agrees with the reached conclusion of this paper. They investigated the effects of blast vibrations on a single storey brick veneer house, which was monitored for over 1 year and was subjected to 43 blasts with ground PPV ranging from 1.5 to 222 mm/s. They recommended an amplification factor ranging between 2.0 and 4.0 for the ground PPV depending on the PPV value where:

$$\begin{aligned} \lambda &= 4.0 \quad for\ PPV \le 5\ mm/s \\ \lambda &= 2.0 \quad for\ 5\ mm/s < PPV \le 100\ mm/s \end{aligned} \tag{3}$$

No evidence was clear for this stepped function and further research is required to investigate if a smoother function for the magnification factor.

The amplification factor was adopted in calculating the wall shear strain γ resulting from ground vibration (Gad *et al*. 2005) where:

$$\gamma = \frac{PPV_{hl}}{2\pi f}\frac{\lambda}{H} \quad (4)$$

where PPV_{hl} is the horizontal ground peak component velocity, H is the floor height and f is the natural frequency of the structure. It is evident from equation 4 that the shear strain (causing structural/threshold damage) is dependent on both the PPV and the dynamic properties of the building.

Other data collected by Niclson (2005) for residential houses located nearby subsurface blasting had PPVs ranged between 0.06 mm/s and 11.5 mm/s which were well below the 51 mm/s defined by common safe limit criteria. Despite this fact, many complaints of structural/threshold damages were reported which also confirm the conclusions reached in this work.

5 CONCLUSIONS

The currently adopted safe limit criteria for ground-born vibrations resulting from subsurface blasting were discussed. All these criteria do not focus on resonance or wall rattling which may occur to a residential building if it is subjected to low-level frequency ground vibrations.

Data recorded for two houses located nearby subsurface blasting were examined. The two houses suffered cracking despite satisfying the current safe limit criteria required for subsurface blasting. It is argued that ground vibrations with low level frequencies affected the structural response of these two houses causing resonance and wall rattling. These, in turn, caused threshold, and even structural cracks in addition to causing severe disturbance to the residents.

Thus, it is recommended that the PPV for low level frequencies (4–30 Hz) be multiplied by a certain magnification factor before comparing them to the current safe limits. The magnification factor adopted in the current investigation was 4.0; however, the value of this factor should be refined to include the ratio between the ground vibration frequency and the natural frequency of the nearby structure. Furthermore, this proposed concept still needs to be explicitly verified using more data.

REFERENCES

Baliktsis E.K. 2001. Blasting vibration limits to prevent human annoyance remarks from some case studies. *Mineral Resources Engineering* 10(1): 71–81.

Dowding, C.H. 1985. Blasting vibrations monitoring and control. Prentice Hall, New Jersey, USA.

Dowding C.H. 1996. Construction Vibrations, Prentice Hall, New Jersey, USA.

Duvall W.I., and Fogelgon 1962. Review of criteria for estimating damage to residences from blasting vibrations. US Bureau of Mines, RI 5868.

Franfield, R.A. 1996. Do you think you are monitoring peak particle velocity. *12th Annual Symposium on Explosives and Blasting Research, Orlando, Florida, USA*, pp. 13–20.

Gad E.F., Wilson J.L. Moore A.J., 2005. Richards A.B. Effects of mine blasting on residential structures. *Journal of Performance of Constructed Facilities, ASCE*. 19(3): 222–228.

ISEE 1998. Blaster's handbook. 17th edition. International Society of Explosive Engineering, Cleveland, Ohio, USA.

ISO 4866-1990. International Standards, Mechanical vibrations and shock – vibrations of buildings – guidelines for the measurement of vibrations and evaluation of their effects on buildings.

Medearis K. 1976. The development of rational damage criteria for low-rise structures subjected to blasting vibrations. Report to the National Crushed Stone Association, Washington, D.C. USA.

Nichollas H.R., Johnson C.F., and Duvall W.I. 1971. Blasting vibrations and their effect on structures. US Department of Interior, Bureau of Mines Bulletin 656.

Niclson R. F. 2005. Determination of blast vibration using peak particle velocity at Bengal Quarry. MSc thesis, Lulea University of Technology. 72p.

Quesne J.D. 2001. Blasting vibration from limestone quarries and their effect on concrete block and Stucco homes, Vibration Problem. Geo-Discussion Forum, www.geofrum.com

Siskind D.E., Stagg M.S., Kopp J.W. and Dowding C.H. 1980. Structure response and damage produced by ground vibrations from subsurface blasting. RI 8507, US Bureau of Mines, Washington DC, USA.

Skipp. B.O. 1984. Dynamic ground movements – man-made vibrations. *In Ground movement and their effects on structures, Attewell, P.B. and Taylor R.K. (Eds)*, Chapman and Hall, New York, pp. 121–130.

Svinkin M.R. 2004. Drawbacks of blast vibration regulations, http://www.vulcanhammer.org.

Svinkin M.R.1993. Analyzing man-made vibrations, diagnostics and monitoring. *3rd International Conference on Case Historic in Geotechnical Engineering, Rolla, Missouri, USA*, Vol. 1, pp. 663–670.

Wiss J.F. 1968. Effect of blasting vibration on buildings and people, *Civil Engineering. ASCE*, July 1968, pp. 46–48.

Wiss J.F. 1981. Construction vibrations: State-of-the-art. Journal of *Geotechnical Engineering Division, ASCE* 107(2):167–181.

Research and Applications in Structural Engineering, Mechanics and Computation – Zingoni (Ed.)
© 2013 Taylor & Francis Group, London, ISBN 978-1-138-00061-2

Dynamic response of rigid pavement under moving traffic load with variable velocity

Yang Zhong & Mei-Jie Xu
School of Civil and Hydraulic Engineering, Dalian University of Technology, Dalian, Liaoning, China

ABSTRACT: In this paper, the dynamic response of an infinity plate resting on an elastic foundation subjected to moving traffic load with variable velocity (accelerating or decelerating) is investigated by using a triple Fourier transform in time and space. The effects of the load moving velocity, acceleration and deceleration are discussed respectively. The numerical results indicate that the main affecting parameters are initial velocity, acceleration or deceleration. Numerical examples are presented to compare the results of static analysis and those of dynamic analysis with a constant moving velocity. The results show that the dynamic response of rigid pavement under a moving traffic load with variable velocity is not only different from that caused by static load, but also different from that generated by load with a constant moving speed. Displacement of the plate is reduced with increasing of moving velocity and acceleration. But, stresses of the plate increase with the moving velocity at given acceleration. Both the velocity and acceleration of a moving vehicle shall be considered in the analysis of rigid pavement.

1 INTRODUCTION

In the analysis of pavements of highway and airport, a rigid pavement structure is usually regarded as a plate resting on an elastic foundation, which is often modeled as a Winkle foundation. In general, the loads exerted on the plate are moving traffic load such as wheel loads from moving vehicles and from air planes. When a vehicle accelerates or decelerates or a plane takes off or lands, the loads applied to the plate structure are moving loads with acceleration or deceleration. Therefore, the investigation of dynamic response of the plate resting on an elastic foundation subjected moving traffic loads is interesting and important, as the results can be applied to understand the dynamic behaviors of pavements of highway and airport.

Many research works have appeared in the literature on the dynamic response of a beam resting on the foundation subjected to moving loads and free vibration of plate. In comparison, plates on an elastic foundation subjected to moving loads have only attracted the attentions of few researchers. Sun el at studied the effects of initial stress on the dynamic response of infinity long and simply supported composite plate under cylindrical bending by means of model superposition approach. Wu et al. used the finite element method to study the dynamic response under moving loads. Lin and Gbadeyan discussed the dynamic behavior of a beam and a rectangular plate under moving loads, paying more attention to moving mass. Takabataka investigated the dynamic response of rectangular plate with stepped thickness subjected to moving loads, including moving mass. Existing research on dynamic analysis of plates on elastic foundation pertains to analytical models with simple and regular boundary conditions. Gbadeyan and Oni gave a closed-form solution by using double Fourier sine integral transformation to analyze a simply supported rectangular plate resting on elastic Pasternak foundation traversed by an arbitrary number of moving concentrated masses. Kim and Roesset investigated an infinite plate resting on an elastic Winkler foundation subjected to moving loads with transformed field domain analyses using Fourier transform. The response to moving loads with acceleration (or deceleration) has not been well studied before. Existing research on response to accelerated moving loads can only be found for plate and beam structures without an elastic foundation. Suzuki investigated the influence of the acceleration of the traveling load on the response of a finite beam. Wu et al. used the finite element method to investigate the response of flat plate structures and studied the effects of eccentricity, span length, acceleration and initial velocity of moving load. Lin and Trethway used the finite element method to analyze response of elastic beams to a moving load, which could be specified as a general excitation force. This paper studies the dynamic response of an infinity plate resting on an elastic foundation. The effects of acceleration, initial moving velocity and initial position are investigated and discussed. In order to prove the correctness of formulations derived in the paper, the numerical results are presented and compared with results for the same problem with a constant velocity. The dynamic response of a plate resting on an

elastic foundation subjected moving traffic loads is interesting and important. The results can be applied to understand the dynamic behaviors of pavements of highway and airport.

2 GOVERNING EQUATIONS AND SOLUTION ANALYSIS

The governing differential equation for the dynamic vertical displacements $w(x,y,t)$ in a Cartesian coordinate system $\{x,y\}$, based on the Kirchhoff small deflection plate theory, can be written as

$$D\left[\frac{\partial^4 w}{\partial x^4}+\frac{\partial^4 w}{\partial x^2\partial y^2}+\frac{\partial^4 w}{\partial y^4}\right]+Kw +C\frac{\partial w}{\partial t}+\rho h\frac{\partial^2 w}{\partial t^2}=F \tag{1}$$

where D is the flexural rigidity of the plate defined by $D=Eh^3/12(1-\mu^2)$, the parameters ρ, h, E, μ and C are the unit density, thickness, modulus, damping coefficient and Poisson's ratio of the plate respectively. K is the reaction modulus of the foundation. F is external dynamic load acting on the surface plate. The plate is assumed to extend to infinity in the horizontal plane. The load pressure within the contact area is assumed to uniformly distribute in a rectangular area.

When the loads moving along the x direction are considered and the loads, for this case, can be expressed as:

$$F(x,y,t)=F_0\{U[x+a-X(t)]U[y+b] -U[x-a-X(t)]U[y-b]\} \tag{2}$$

where U is the unit step function and X(x) denotes a function describing the motion of the force at time t defined

$$X(t)=x_0+Vt+\frac{1}{2}at^2 \tag{3}$$

where F_0 is the amplitude function of the load. x_0 is the load positions, V is the initial speed, and a, is the constant acceleration. The uniform velocity type of motion, of course, is given by

$$X(t)=x_0+Vt \tag{3'}$$

Equations (1), (2) and (3) are total formulations for the analytical model of the plate on elastic foundation, subjected to moving concentrated loads.

In order to solve the problem described above double dimensions Fourier transform is adopted as defined by following:

$$\bar{f}(\varsigma,\eta,t)=\int_{-\infty}^{\infty}\int_{-\infty}^{\infty} f(x,y,t)e^{-i(\varsigma x+\gamma\eta)}dxdy \tag{4}$$

The inverse Fourier transform is

$$f(x,y,t)=\frac{1}{4\pi^2}\int_{-\infty}^{\infty}\int_{-\infty}^{\infty} f(\varsigma,\eta,t)e^{i(\varsigma x+y\eta)}d\varsigma d\eta \tag{5}$$

Using the Fourier transform defined as Eq. (4), the Eq. (1) can be presented as

$$\frac{d^2\bar{w}}{dt^2}+\frac{C}{\rho h}\frac{d\bar{w}}{dt}+\frac{1}{\rho h}\left[D(\xi^2+\eta^2)^2+K\right]\bar{w}=\frac{\bar{F}}{\rho h} \tag{6}$$

Fourier transforming equation (3) gives

$$\bar{F}=F_0\frac{4\sin\xi b}{\xi}\frac{\sin\eta c}{\eta}e^{i\xi[x_0+t(V+\frac{1}{2}at)]} \tag{7}$$

Substituting Eq. (7) into Eq. (6) and using Duhamel Integration and the inverse Fourier transform, the solution for Eq. (1) in temporal domain can be obtained as

$$w=\frac{F_0}{\rho h\pi^2}\int_{-\infty}^{\infty}\int_{-\infty}^{\infty}\int_0^t\frac{\sin\xi b\sin\eta c}{\xi\eta}e^{i\xi[x_0+\tau(V+\frac{1}{2}a\tau)]-B(t-\tau)} \frac{\sin A(t-\tau)}{A}e^{i(\varsigma x+\eta y)}d\xi d\eta d\tau \tag{8}$$

where $B=\frac{\rho hC}{2}$; $A=\sqrt{D(\xi^2+\eta^2)^2/\rho h-B^2}$.

Using Mathematica and integrating for τ in Eg. (8), gives

$$w=\frac{(-1)^{1/4}F_0}{\rho h\pi^2\sqrt{2a\pi}}\int_{-\infty}^{\infty}\int_{-\infty}^{\infty}\frac{e^{i\{\xi(x+x_0)+\eta y+\frac{(A+iB-\xi B)^2}{2a\xi}\}-pt}}{A} \frac{\sin\xi b\sin\eta c}{\xi\eta}\left\{e^{A(\frac{2B}{a\xi}-it)}\left[erf(Z_1)-erf(Z_2)\right]\right. \left.e^{iA(\frac{2V+at}{a})}\left[erf(Z_3)-erf(Z_4)\right]\right\}d\xi d\eta \tag{9}$$

where $erf(x)=\frac{2}{\sqrt{\pi}}\int_0^x e^{-t^2}dt$ is the error function

$$Z_2=\frac{(1+i)(\xi V-A+iB)}{2\sqrt{a\xi}};\quad Z_1=\frac{(1+i)[\xi(V+at)-A+iB]}{2\sqrt{a\xi}}$$

$$Z_3=\frac{(1+i)(\xi V+A+iB)}{2\sqrt{a\xi}};\quad Z_4=\frac{(1+i)[\xi(V+at)+A+iB]}{2\sqrt{a\xi}}$$

The transverse stresses are the longitudinal stresses at the bottom of the plate can be obtained respectively.

$$\sigma_x=\frac{Eh}{(1-\mu^2)}\left(\frac{\partial^2 w}{\partial x^2}+\mu\frac{\partial^2 w}{\partial y^2}\right) \tag{10}$$

$$\sigma_y=\frac{-Eh}{(1-\mu^2)}\left(\frac{\partial^2 w}{\partial y^2}+\mu\frac{\partial^2 w}{\partial x^2}\right) \tag{11}$$

The stresses considered in this study are tensile stresses in the longitudinal direction at the bottom of the plate because the transverse stresses are smaller than the longitudinal stresses.

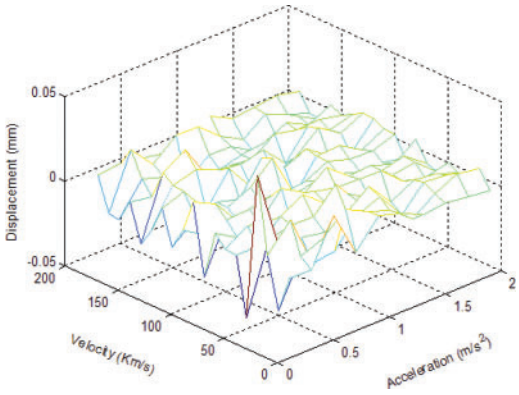


Figure 1. Displacements of the plate with different accelerations and velocities.

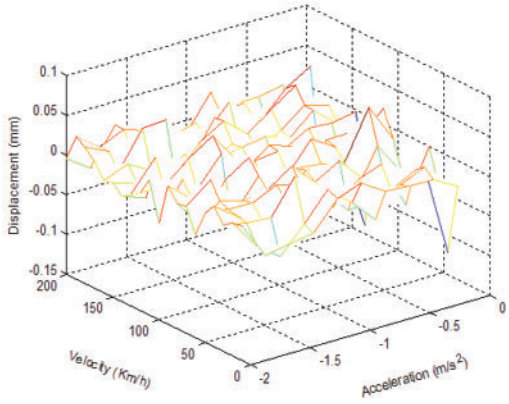


Figure 2. Displacements of the plate with different decelerations and velocities.

3 DYNAMIC RESPONSE TO MOVING ACCELERATED OR DECELERATION LOAD

An infinity plate resting on the elastic Winker foundation subjected to moving traffic load with variable velocity (accelerating or decelerating) is considered in this and the following sections. The data for the plate and load amplitude used in the all the numerical examples are

$E = 3.45 \times 10^4$MPa, $\mu = 0.15$, $K = 1.36$ MN/m^3, $C = 2.0 \times 10^5$Ns/m^3, $b = 0.35$ m, $F_0 = 1.0 \times 10^5$N; $h = 0.30$ m, c $= 0.25$ m, $t = 1.0$ s, $x_0 = 0.0$.

A range of acceleration and velocity values are considered in the numerical examples treated in order to study the effect of acceleration and velocity on the dynamic response of the plate.

Fig. 1 and Fig. 2 show the deflected shapes of the plate with different acceleration, deceleration and velocity at time of 1s and at load positions of 0.5 m respectively. Fig. 3 shows stresses of the plate with different acceleration and velocity at time of 1 second and at load positions of 0.5 m. It can be seen that the deflected shapes and the stresses of the plate and the

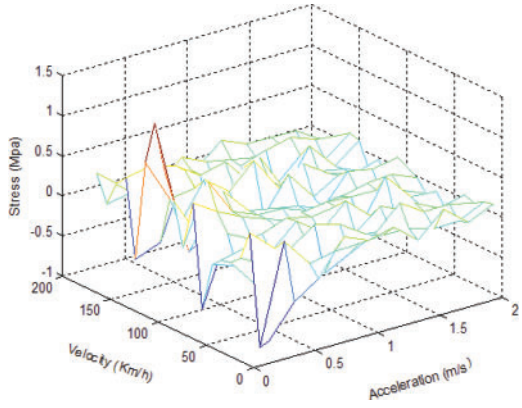


Figure 3. Stress of the plate with different accelerations and velocities.

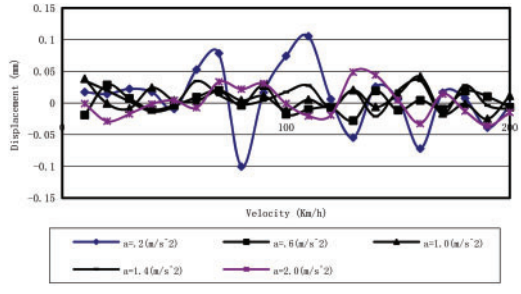


Figure 4. Displacement of the plate with different velocities and given acceleration.

change with the load moving acceleration, deceleration and velocity and occur different maximum values. This feature can also be seen from Fig. 4 to Fig. 9 which illustrates the dynamic deflections and stresses of the plate under the different moving load acceleration, deceleration and velocity when one of them is given.

From Fig. 4, it can be seen that when the load acceleration is given, the deflection of the plate increases with the load moving velocity and appear peak values. At the acceleration of 0.2 m/s^2 and velocity of 100 km/h the displacement occurs maximum value. When acceleration is given 2 m/s^2 the displacement will have a peak value at the velocity of 130 km/h.

Fig. 5 shows the results of displacement with different velocities when the deceleration is given. It can be seen that there are same results as shown in Fig. 4, the deflection of the plate increases with the load moving velocity addition and appear peak values. But the increasing speed is larger than that when the load moves with acceleration. Also, at the deceleration of -0.2 m/s^2 and velocity of 100 km/h the displacement occurs maximum value. But when deceleration is given -2 m/s^2 the displacement has a peak value at the velocity of 190 km/h. Fig. 6 and Fig. 7 illustrates the results of displacement with different acceleration and deceleration when the load moving velocity is given. It can be seen that the displacement reduces with the

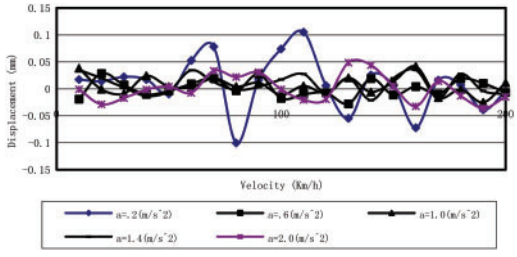


Figure 5. Displacement of the plate with different velocities and given deceleration.

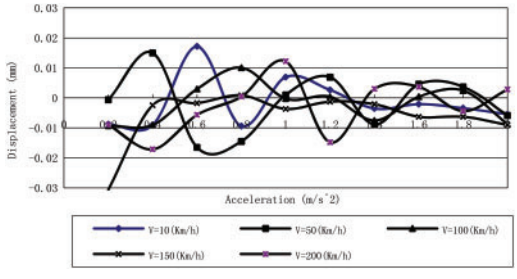


Figure 6. Displacement of the plate with different accelerations and given velocity.

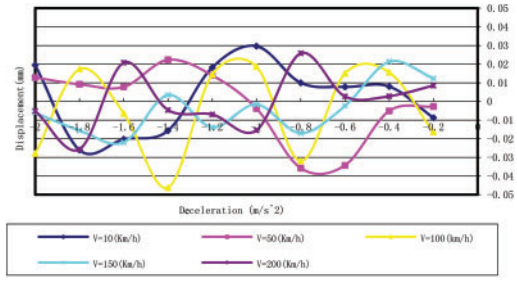


Figure 7. Displacement of the plate with different decelerations and given velocity.

acceleration and deceleration increasing when the load moving velocity is given.

Fig. 8 presents the results of the stresses of the plate with different acceleration when the load moving velocity is given. It can be seen that the stresses of the plate reduces with the acceleration and deceleration increasing when the load moving velocity is given. At small values of velocity (less than 50 km/h) the reducing is slowly. At large values of velocity the reducing is rapidly.

Fig. 9 is the results of the stresses of the plate with different velocity when the load moving acceleration is given. It can be seen that the stresses of the plate increase with the acceleration increasing when the load moving velocity is given. At the acceleration of 0.2 m/s^2 and velocity of 140 km/h the stresses of the plate reaches the maximum value. When aceleration is given 2 m/s^2 the plate stresses appear a peak value at the velocity of 170 km/h.

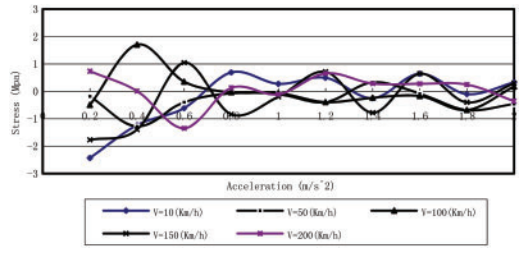


Figure 8. Stresses of the plate with different accelerations and given velocity.

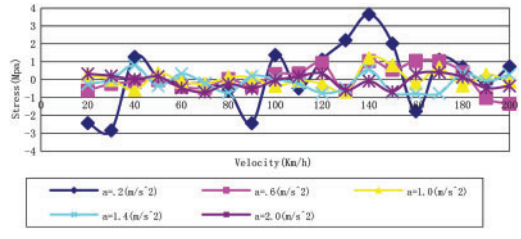


Figure 9. Stresses of the plate with different velocities and given acceleration.

4 CONCLUSION

In this paper, the dynamic response of an infinity plate resting on an elastic foundation subjected to moving traffic load with variable velocity (acelerating or decelerating) is investigated by using a triple Fourier transform. The effects of the load moving velocity, acceleration and deceleration are discussed respectively. The numerical results illustrate that the deflected shapes and the stresses of the plate change with the load moving acceleration, deceleration and velocity. Both the deflection and the stresses reach different maximum values. The dynamic displacements and stresses of the plate increase with the load moving velocity and decrease with the load moving acceleration and deceleration. This phenomenon indicts that the design of the rigid pavement shall consider the effect of the dynamic load caused by variable moving vehicles.

REFERENCES

Fryba L. Vibration of Solids and Structures under Moving Loads [M]. Noorhoff International Publishing, 1971.

Gbadeyan JA, Oni ST. Dynamic response to moving concentrated masses of elastic plates on a non-Winkler elastic foundation. Journal of Sound and Vibration 1992;154(2):343–58.

Huang, M-H., Thambiratnam, D.P. Free vibration of rectangular plates on elastic intermediate supports. Journal of Sound and Vibration 2001;354(6): 643–58.

Huang MH, Thambiratnam D P. Dynamic response of plates on elastic foundation to moving loads [J]. Journal of Engineering Mechanics 2002, 128(9):1017–1022.

Kim SM, Roesset JM. Moving loads on a plate on elastic foundation. Journal of Engineering Mechanics 1998;124(9):1010–7.

Lu Sun Analytical dynamic displacement response of rigid pavements to moving concentrated and line loads [J] International Journal of Solids and Structures 2005, 317(12):1830–1844.

Matsunage H. Vibration and stability of thick plates on elastic foundations [J]. J. Eng. Mech., 2000, 126(1):27–34.

Saha KN. Dynamic stability of a rectangular plate on non-homogeneous Winkler foundation [J]. Comput. Struct., 1997, 63(6):1213–1222.

Thambiratnam D P, Zhuge Y. Dynamic analysis of beams on an elastic foundation subject to moving loads [J]. J. Sound and Vibration 1996, 198(2):149–169.

Vallabhan C V G, Straughan W T, Das Y C. Refined model for analysis of plates on elastic foundations [J]. J. Eng. Mech., 1991, 117(12):2830–2844.

Research and Applications in Structural Engineering, Mechanics and Computation – Zingoni (Ed.)
© 2013 Taylor & Francis Group, London, ISBN 978-1-138-00061-2

Assessment of bridge behavior due to the passage of high speed trains

A. Graça
Grid S.A.,Lisboa, Portugal

L. Guerreiro & F. Virtuoso
Instituto Superior Técnico, Lisboa, Portugal

ABSTRACT: The railway bridges, due to the passage of high speed trains, can suffer high resonance phenomena that cause, for example, ballast instability, endangering the railway line. Therefore, the main goal of this paper was to develop a simplified but efficient MATLAB model able to reproduce and analyze the dynamic response of bridges to the passage of high speed trains, in order to obtain static (bending moments, shear forces and reactions) and cinematic (accelerations, displacements and rotations) envelopes along the bridge. The implementation of this methodology took place using a continuous beam model subjected to moving point loads, which was based on the determination of the free vibration modes, generated semi-analytically, considering simple supports model, or by finite elements, using spring supports model. Extensive parametric studies were performed, which contributed to raise the sensibility to results, particularly for continuous bridges, the less studied type.

1 INTRODUCTION

In modern societies, transports play a crucial role in economic growth and globalization. Among the other transports, High speed trains can be more competitive for distances about 100/200 km and 400/600 km, comparing with terrestrial and aero transportation, respectively (Ureña, 2010). With the increase of high speed trains usage, some resonance problems were identified (e.g. ballast liquefaction due to high accelerations produced by the passage of the trains (Gustafsson, 2008)), being essential to evaluate the bridge response due to their passage. Bridge's safety studies should be performed through dynamic analyses.

Full dynamic analyses gives more accurate results, which are important if the designer intends to compare model with experimental results, evaluate the passenger comfort or have a more sophisticated analysis of an important bridge. The dynamic analysis are complex and time consuming because of the large amount of information required to define the input and the difficulty in solving the equilibrium equations, which lead to slow computational models (Wilberg, 2009) (Azevedo et al., 2007).

The goal of this work was to study the bridge response with simple models, by using the moving load beam model. This model, implemented in MATLAB, although less accurate than the more complex models (Barbero, 2001), is able to quick reproduce a large amount of different structural solutions. As the objective of this work was to perform extensive parametric studies, it was important to have a reliable and simplified model with capacity to reproduce any train and several dynamic parameters of the bridge. All the studies were done for the set of HSLM-A trains, presented in EN1991-2. Velocities between 40 and 120 m/s were considered.

2 THEORETICAL BACKGROUND – BRIEF REVIEW

As shown in Fig. 1, the bridge superstructure is modeled as a continuous beam with a total length L, constant flexural stiffness EI, constant mass per unit length m and viscous proportional damping C. The beam is assumed to be a Bernoulli-Euler beam, in which the effects of shear deformation and rotary inertia are not taken into account.

Considering the group of forces p_j moving from left to right at a constant speed, the equation of motion is given as

$$m\,\frac{\partial^2 u(x,t)}{\partial t^2} + C\,\frac{\partial u(x,t)}{\partial t} + EI\,\frac{\partial^4 u(x,t)}{dx^4} = p(x,t) \quad (1)$$

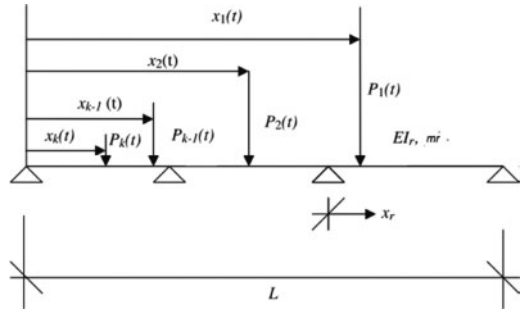


Figure 1. Bridge model.

Based on modal superposition, the solution of Eq. (1) can then be expressed as

$$u(x,t) = \sum_{n=1}^{\infty} \emptyset_n(x) q_n(t) \quad (2)$$

where $q_n(t)$ is the nth modal amplitude and $\Phi_n(x)$ is the nth mode shape function of the beam. Substituting Eq. (2) into (1), the result leads to an equation in terms of modal amplitude (Yang & Lin, 2004)

$$\frac{d^2 q_n(t)}{dt^2} + 2\xi_n \omega_n \frac{d\, q_n(t)}{dt} + \omega_n^2 q_n(t) = \\ = \frac{1}{M_n} \sum_{j=1}^{N_l} f_j(x,t)\, \varepsilon_j(t) \quad (3)$$

where ω_n, ξ_n are modal frequency and damping ratio of the nth mode, respectively, and

$$M_n = \int_0^L m\, \emptyset_n^2(x) dx \quad (4)$$

$$\varepsilon_j(t) = H\left(t - t_j^{in}\right) - H\left(t - t_j^{out}\right) \quad (5)$$

$$f_j(x,t) = \emptyset_n\left(x_j(t)\right) p_j \quad (6)$$

where M_n, H(t), $\Phi_n(x)$ and $t_j^{in/out}$ are the modal mass, Heaviside function, nth mode shape and the time instant when the jth force enter and leave the bridge.

To solve the problem it is only necessary to calculate the mode shapes, since they are responsible to define the modal participation. Therefore, after the computation of mode shape $\Phi_n(x)$ a numerical integration of Eq. (3) should be done. It was used the Newmark-β method (Newmark, 1959) to perform this integration. The analysis was not restrained to the first vibration mode. A mode superposition model using the resonant modes resented a good fit on the studied cases.

In this paper, a semi-analytical method to obtain frequencies and modal amplitudes were used. For the rth span of the general case, shown in Fig. 1, the analytical solution of the problem is given by

$$\emptyset_{nr}(x) = A_{nr} \cos(\lambda_n x) + B \cos h(\lambda_n x) + \\ C_{nr} \sinh(\lambda_n x) + D_{nr} \sin(\lambda_n x) \quad (7)$$

where $\Phi_{nr}(x)$ is the nth modal shape function of the rth span and the constants A_{nr}, B_{nr}, C_{nr}, D_{nr} and λ_n are the problem unknowns of the span r and nth eigenvalue.

The constants (Eq. (7)) are determined from the boundary and initial conditions. The calculation of eigenfunctions is just a matter of substituting the appropriate boundary conditions in Eq. (7). The complete development of the equations and solution of the problem are presented in (Graça, 2011).

3 COMPUTATIONAL IMPLEMENTATION

In order to apply the theoretical background, a MATLAB program and three routines were implemented.

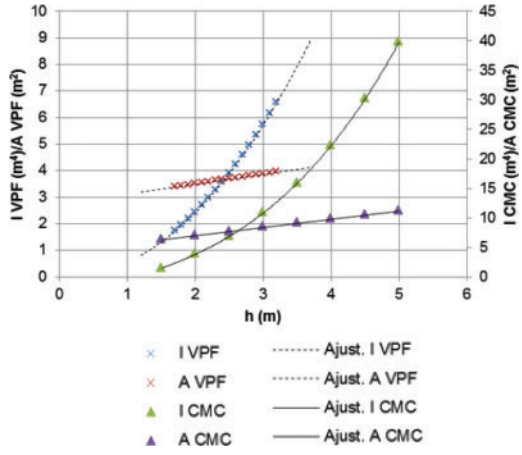


Figure 2. Moment of inertia and area versus section height (VPF – prefabricated box girder, CMC – one cell box girder).

The main program computes, for a defined velocity and train, the accelerations and displacements time response. In addition, the routines perform: (i) computation of general envelopes, for a defined interval of passage velocities, (ii) parametric studies, function of transversal section slenderness ($\lambda = h/L$), and (iii) analysis of foundation flexibility on the final response, in terms of acceleration and vertical reaction.

Fig. 2 shows the moment of inertia and area, functions of section height. It defines the domain of validity of the parametric studies carried out.

4 SUITABILITY OF EN1991-2 ACCELERATION PEAK CRITERION

A set of rules and limitations are prescribed in EN 1991-2 and EN1990-A2. One of them is the limitation of peak acceleration to 3.5 m/s^2 (ballasted bridges) and 5 m/s^2 (non-ballasted bridges). Some authors (Zacher & Baessler, 2005) consider that the implementation of a different criterion leads to a more economical design, without compromise the bridge safety. They state that the peak criterion should be replaced by a 5 peak criterion. So, the new proposed criterion is:

1) Ballasted bridges – 5 successive peaks are allowed (with the same signal) surpassing 3.5 m/s^2 with a maximum peak of 5.5 m/s^2;
2) Non-ballasted bridges – 5 successive peaks are allowed (with the same signal) surpassing the 5.0 m/s^2 with a maximum peak of 5.5 m/s^2.

The present section intends to analyze the dynamic response characteristics, particularly the difference between criterions, of a vast group of structural solutions – simple supported and continuous bridges. Consequently, conclusions about the suitability of the new criteria can be drawn, with the premise that, the smaller the difference between criterions, the more adjusted the code limits are.

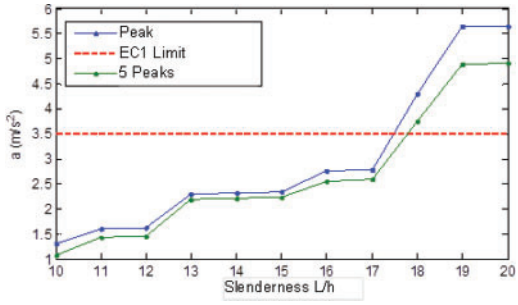


Figure 3. Evolution of the two peak criterion with the slenderness of the bridge.

4.1 *Case studied*

In order to illustrate the differences between criterions, only one geometrical example was used (a continuous bridge with 5 spans – 35 m long inner-spans and 28 m long end-spans) with different cross section slenderness (λ = span/height), varying from 10 to 20. Additional death load of 100 kN/m, a modulus of elasticity of 34 GPa and 1% damping were considered. Fig. 3 the differences for the set of HLSM-A trains are presented.

The analysis of the results presented on Fig. 3 prompts the following remarks:

1) Both acceleration values grow with the increase of slenderness. The evolution is made by steps. Each step is caused only by one determined critical train (Graça, 2011).
2) Differences between criterions are very small, smaller than 0.5 m/s^2, for slenderness's inferior to 17, and increases (not much) for $\lambda > 17$ (very high slenderness).
3) Differences similar to 2 m/s^2 (difference between 3.5 and 5.5 m/s^2) were never registered.

4.2 *Simple supported bridges*

The existence of any appreciative differences in simple supported bridges was also evaluated. In terms of geometric examples, Fig. 4 and 5 show the results for bridges with lengths varying from L = 20 m to 40 m, and slenderness's between 8 and 14.

After analyzing both figures, the following comments, for simple supported bridges, are appropriate:

1) Fig. 4 shows that all the differences between criteria are lower than 2 m/s^2. A higher difference only exists for more slender specimens and spans length equal or lower than 30 m. Spans of 35 m and 40 m do not suffer much difference with slenderness increasing;
2) To confirm the acceleration scale factor argument, which leads to higher differences, Fig. 5 illustrates the absolute accelerations registered for peak criterion. It is clearly visible that upper differences are related with large accelerations, much higher than the limits;

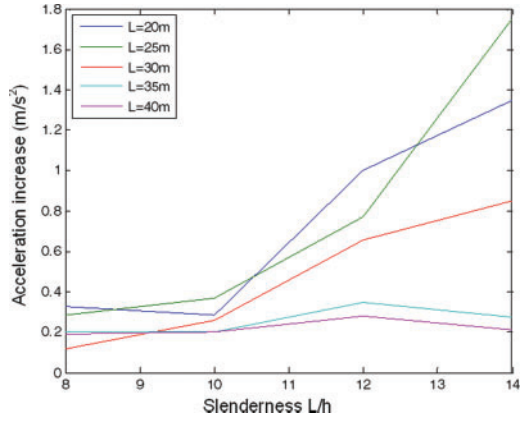


Figure 4. Evolution of the two peak criterion differences $\Delta a = (a_{peak} - a_{5\,peak})$ with the slenderness of the bridge.

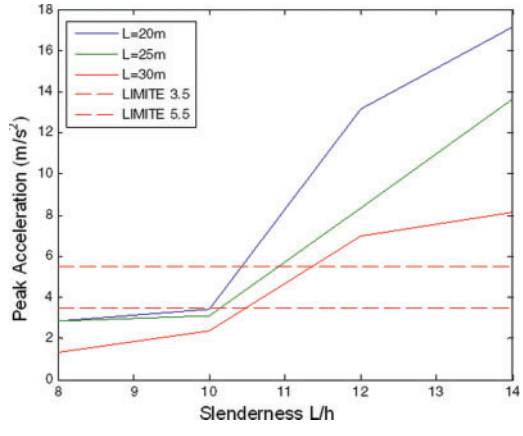


Figure 5. Evolution of the two accelerations with the slenderness of the bridge.

Table 1. Key parameters for the continuous bridge analysis.

Parameter	Variation Domain
Slenderness	10, 12, 14 and 16
Number of inner spans	1, 2 and 3
Length of inner span (m)	30, 35 and 40

3) Results show that if a solution does not verify the peak criterion, will also not check the 5 peak one.

4.3 *Continuous bridges*

Additionally, the continuous bridge analysis was made with a vaster group of geometrical examples. It was used cross sections bridges with end/inner span relationship of 0.75. While Table 1 shows the varying key parameters, Table 2 presents the results for differences in peak criterion for all the different tested parameters.

Table 2. Difference between peak criteria ($\Delta a = a_{peak} - a_{5\,peak}$) for continuous bridges.

Span	Slenderness	Δa (m/s^2) Number of inner spans 1	2	3
30 m	10	0.25	0.25	0.20
	12	0.41	0.35	0.29
	14	0.55	0.61	0.30
	16	1.63	0.53	0.35
35 m	10	0.35	0.16	0.08
	12	0.74	0.49	0.25
	14	0.75	0.45	0.40
	16	0.35	0.54	0.30
40 m	10	0.45	0.21	0.21
	12	0.70	0.15	0.37
	14	0.35	0.15	0.20
	16	0.28	0.35	0.14

The conclusions that can be drawn from the analysis of Table 2 are:

1) The maximum registered difference was 1.63 m/s^2 for the solution with slenderness of 16, inner span length of 30 m and one inner span only. This solution presents an acceleration of 6.39 m/s^2 with peak criterion and 4.77 m/s^2 with 5 peak criterion, both values higher than the limits;
2) Differences tend to diminish with the increasing of the number of inner spans (except for $\lambda = 16/L = 35$ m and $\lambda = 12/L = 45$ m);
3) Once again, results show that if a solution does not verify the peak criterion, will also not check the 5 peak one.

5 PARAMETRIC STUDIES

In this section the results concerning the parametric studies for vertical acceleration behavior of bridges are presented and discussed.

5.1 *Influence of inner span number – N*

To analyze the influence of inner spans number N, models with slenderness from 10 to 17, span lengths of 30 m, 35 m and 40 m, additional death load of 100 kN/m, and end/inner span length relationship $\beta = 0.75$ were used. Fig. 6 depicts the acceleration evolution with N. To explain some of the results, Fig. 7 presents the curve decomposition in critical trains, for L = 30 m and $\lambda = 0.14$, which leaded to envelope one.

From the observation of Fig. 6, the following remarks can be drawn:

1) Higher slenderness produces always larger accelerations than lower slenderness;
2) N = 1 gives the response maximum;
3) On average, acceleration decrease with N. However, it is clearly visible local maxima and minima. Acceleration fluctuates around a straight line between points N = 1 and N = 8. It can be explain

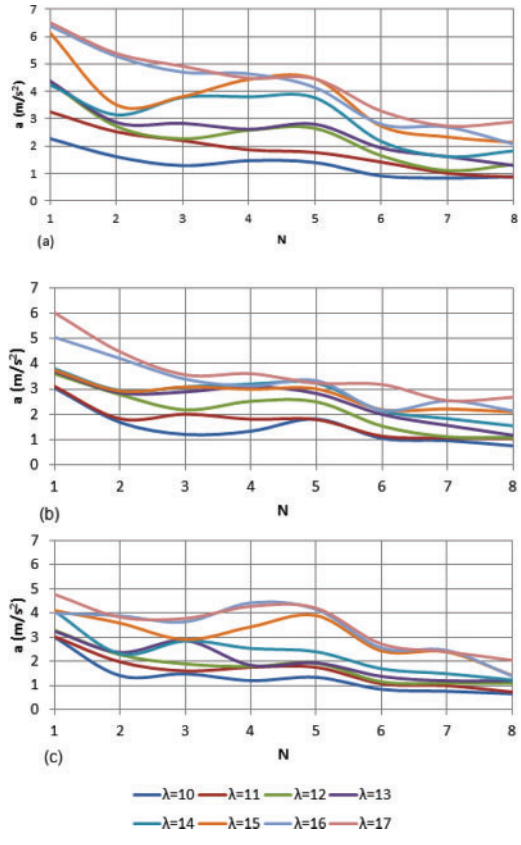


Figure 6. Evolution of bridge acceleration with the number of inner spans N for (a) L = 30 m, (b) L = 35 m and (c) L = 40 m.

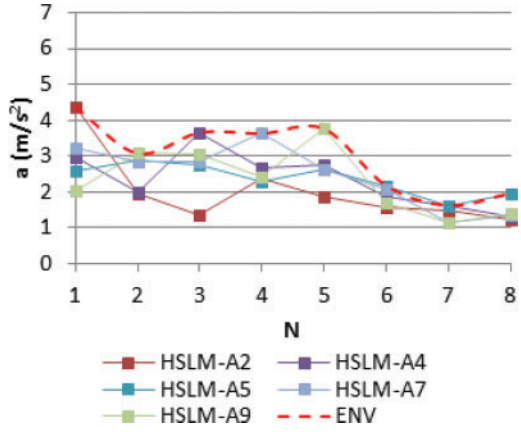


Figure 7. Decomposition in critical trains for L = 30 and $\lambda = 14$.

by the observation of Fig. 7, where is shown that local maximums come from resonances of a particular HSLM-A train. Local minimums appear when there is no train with a clear resonance;
4) For this reason, it does not seem to exist a simple mathematical explanation to the results. In truth,

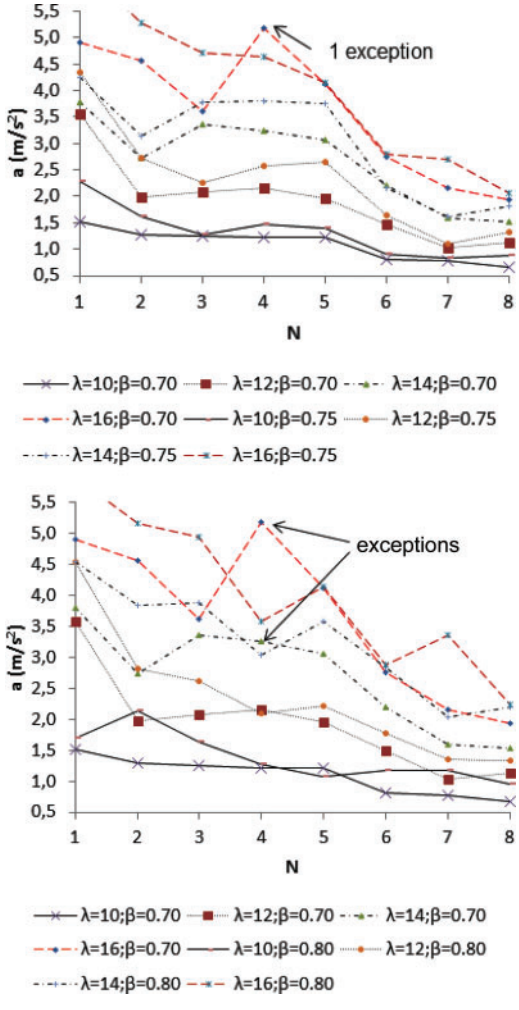


Figure 8. Comparison between $\beta = 0.70/\beta = 0.75$ (top) and $\beta = 0.70/\beta = 0.80$ (bottom) for L = 30 m.

there are 10 times 7 (critical trains times used frequencies) possibilities to create resonance;

5) The usage of L = 35 m gives smoother curves. The same can be said for $\lambda \leq 13$. Those slenderness's have much better performance, both in terms of it regularity as in acceleration greatness;
6) Finally, for $N \geq 5$ the acceleration is always lower than the one registered for $N < 5$. From $N \geq 6$, it can be considered as constant.

5.2 *Influence of end/inner span length relationship*

In order to evaluate the influence of end/inner span length relationship the presented in Fig. 8 were obtained. It was only compared relations of 0.70, 0.75 and 0.80, typical in design situation.

Analysis of Fig. 8 results prompts the following observations:

1) For inner span length of 30 m, over 90% of analyzed situations show that the usage of $\beta = 0.70$ produces lower accelerations than the usage of $\beta = 0.75$ and $\beta = 0.80$;
2) On the other hand, for spans of L = 35 and 40 m, using the same relationship, guarantee 70% of the cases (lower value);
3) Thus, one can consider that in design situation preference should be given for $\beta = 0.70$.

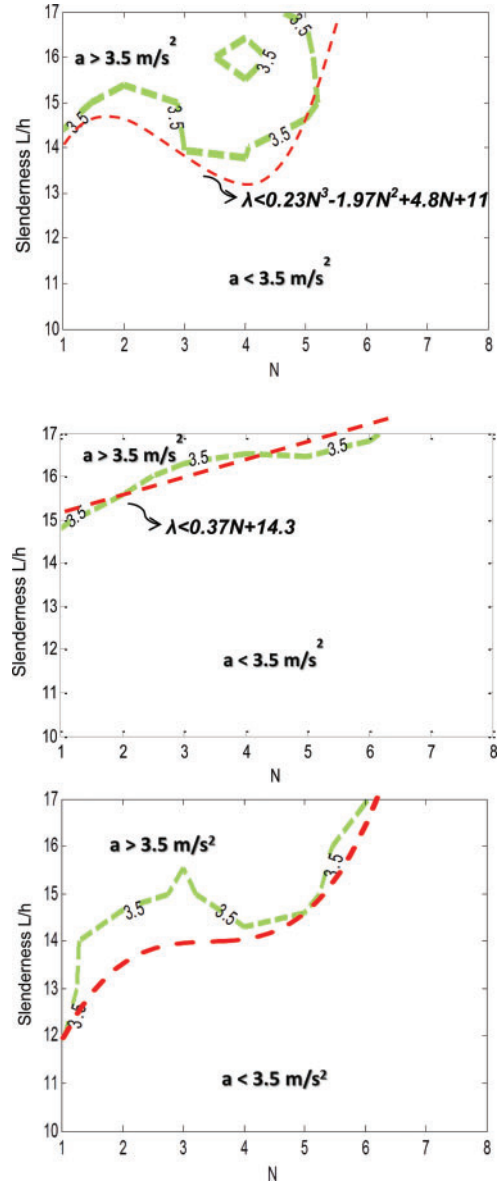


Figure 9. Peak criterion verification curves for L = 30 m (top), L = 35 m (middle), L = 40 m (bottom).

5.3 *Criterion verification curves for* $\beta = 0.70$

Taking into account the conclusions made in de last section, a relation N versus λ curves were produced, which guarantee the peak criterion verification. Fig. 9

displays the results and includes criterion verification formulas. Some conclusion from their analysis:

1) For $L = 30$ m, acceleration is only restrictive with $N = 1$, where the curve indicates $\lambda = 12$. For higher N values, slenderness raises to 14, which is considered current and for $N > 6$ it's completely non-restrictive;
2) Bridges with $L = 35$ m only have problems with $N = 4$;
3) In longer span bridges ($L = 40$ m) acceleration restrictions don't put much limitations to design, because designer can use slenderness's equal or higher than 15.

6 CONCLUSION

This paper dealt with the use of a simplified but efficient computational implementation, in order to assess the effect of high speed trains on bridges. Hence, several studies were made.

Focusing on the results about the suitability of code acceleration peak criterion, one showed that, apparently, there is no reason to change the existing rules. It should be noted that, conclusion is based only on the present paper structural analysis model.

Relatively to parametric studies, one can prompt the following general conclusions:

1) About influence of N parameter, analysis showed a tendency to acceleration decrease with several local minima and maxima. The usage of less slender cross sections leads to a smoother decrement and lower accelerations. For $N \geq 6$, acceleration can be considered constant and with inferior values;
2) Usually, the most convenient end/inner span length relationship, which cover over 70% of the cases, is $\beta = 0.70$.

REFERENCES

Azevedo, A., Neves S., Calçada, R. 2007, Dynamic Analysis of the Vehicle-Structure Interaction: a Direct and Efficient Computer Implementation, CMNE/CILAMCE.

Barbero, J.D. 2001. Dinámica de puentes de ferrocarril para alta velocidad: métodos de cálculo y estudio de la ressonancia. Tesis Doctoral, Escuela Tècnica Superior de Ingenieros de Caminos, Caneles y Puertos, UPM.

Gustafsson, A. 2008, Reduced models for dynamic analysis of high-speed railway bridges, Lund University.

Graça, A. 2011, Modelação da Resposta em Pontes Devido à Passagem de Comboios de Alta Velocidade, Master Thesis (in portuguese), IST, Lisbon.

Newmark, N. M. 1959, A Method of Computation for Structural Dynamics, ASCE, Journal of the Engineering Mechanics Division, Vol. 85 No. EM3.

Ureña, J.M. 2010. New metropolitan processes encouraged by High-Speed Rail: the cases of London and Madrid, 12th WCTR, Madrid, July 2010.

Wiberg, J. 2009, Railway bridge response to passing trains, Doctoral Thesis, KTH, Stockholm.

Yang, Y. & Lin, C. 2004, Vehicle bridge interaction dynamics with applications to high speed railways, World Scientific.

Zacher, M. & Baessler, M. 2005, Dynamic behaviour of ballast on railway bridges. In: Proceedings of the advanced course on dynamics of high-speed railway bridges, Portugal.

Research and Applications in Structural Engineering, Mechanics and Computation – Zingoni (Ed.)
© 2013 Taylor & Francis Group, London, ISBN 978-1-138-00061-2

Dynamic response of airport building structure due to construction machinery effects

J. Benčat & D. Papán
University of Žilina, Žilina, Slovakia

ABSTRACT: In spite of the wide use of driven piles and sheet piles and the increasing awareness of the public and authorities for environmental problems, little progress has been made in the understanding of ground vibrations caused by vibration pile driving. The construction vibrations can be reduced by planned and controlled use of construction machinery. We studied the effect of the construction vibration on the Bratislava Airport buildings caused by sheet piledriving during the construction works near present operating Airport buildings.

1 INTRODUCTION

Construction activity such as driving piles, vibrating compaction of earth materials, and driving heavy construction machinery, can result in varying degrees of ground vibration, depending on the equipment and methods employed. Operation of construction equipment causes ground vibrations which spread through the ground and diminish in strength with distance. Vibration which usually also has a negative impact on security and stability of the structures, facilities performance and peoples should be controlled by experimental analysis and results compared with relevant standards prescription values and criteria (Eurocodes, national codes, etc.). Sometimes it is necessary to predict or monitor vibration level of projected or constructed structures and buildings.

In the case study the results of the theoretical and experimental investigation of the M. R. Stefanik Bratislava Airport building structures vibrations caused by piling operations were analyzed mainly from the aspects of the safety of the building structures (Bencat et al. 2011). Also the influence of these vibrations on production process conditions and people being in production halls were analysis, too.

2 CONSTRUCTION VIBRATIONS

2.1 *Sources of vibrations*

Vibratory hammers for driving non-displacement piles usually have low to moderate force amplitudes and operating frequencies above 20 Hz. Displacement piles are driven by vibratory hammers with frequencies of around 10–40 Hz and commonly along with much higher force amplitudes (Warrington, 1992). The soil resistance to pile penetration and the seismic effect of vibratory driven piles depend substantially on soil conditions, pile type and vibratory hammer model. A coincidence of the operating frequency with the soil layer frequency may generate large ground vibrations of the soil surrounding the pile. The use of vibratory hammers with variable frequency and force amplitude may minimize damage due to accidental ground vibration amplification.

Ground vibrations. The main characteristic waves that are generated when a vibrating load is placed on the surface of a soil are the compression wave (P-wave), the shear wave (S-wave), and the surface wave (Rayleigh-wave). Each of these waves has a characteristic velocity calculated from the following equations:

$$CW \rightarrow C_P = (\lambda + 2\mu/\rho)^{1/2}, SW \rightarrow C_S = (\mu/\rho)^{1/2} \text{ and } RW \rightarrow C_R = (0.87 + 1.12\nu/1 + \nu)C_S,$$

where λ and μ are Lame coefficients of elastic medium, ν – Poisson ratio and ρ is soil density. The correspondence principle (Rizzo & Shippy 1971) can be applied to model material damping in the elastic medium by the use of a complex Lame coefficients $(\lambda + 2\mu)(1 + \mathrm{i}\delta)$, where $\delta \approx \delta_E \approx \delta_G$ represents the hysteretic material damping ratio for the compression and shear waves respectively. Natural ground conditions permits the ground to be modelled as a damped, viscoelastic half space. The viscoelastic model of soil simulation *using the complex modulus conception* $\mathrm{E}^* = E(1 + i\delta_E)$ and $G^* = G(1 + i\delta_G)$ respectively, offers a very good approach to the actual soil behavior (E, G and $\delta_E \approx \delta_G$ *are real and imaginary components of complex modulus*). The basic equations used to describe the viscoelastic half space analysis of wave propagation through ground with modulus in complex form cannot be fully described here, see Bencat (1992), Martinček (1975).

Sources of construction vibrations generate body and surface waves in soil medium. Body waves propagate through the soil deposits and rock. Compression

and shear waves are the main types of body waves that should be taken into consideration at relatively small distances from the construction sources. Surface waves, of which Rayleigh waves are the primary type, propagate along the upper ground surface. Rayleigh waves have the largest practical interest for structural engineers because building foundations are generally placed near the ground surface. In addition, surface waves contain more than 2/3 of the total vibration energy and their peak particle velocity are dominant on velocity records.

The proximity of the frequency of horizontal soil vibrations to one of the building's natural frequencies may generate the conditions of resonance in that building. Moreover, vertical ground vibrations can cause dangerous structural settlements. To prevent the unacceptable effect of construction vibrations, it is important to accurately predict expected ground and structure vibrations and also it is useful to perform the monitoring of the structure response due to construction vibrations. The construction vibration monitoring enables the vibratory pile drivers operating mode regulation to avoid undesirable vibrations level of the structures and also undesirable effects on facilities performance and peoples.

2.2 *Structure vibrations due to construction activities*

Harmful vibration effects of construction activities occur frequently. Vibrations may produce direct damage to structures when excitation frequencies of ground vibrations do not match natural frequencies of structures. Such damage usually occurs in nearby structures at distances about one pile length from driven piles. Intensity of structure vibrations depends on soil-structure interaction which determines structure response to the ground excitation. Building vibrations having low and high frequencies are usually generated by Rayleigh and compression waves, respectively. There are two frequency ranges of structure responses: 2–30 Hz and 30–450 Hz. Perhaps structure vibration damage obtained without the effect of resonant structure response can be considered mainly to be due to particle velocities (PPV) of ground vibrations higher than about 50 mm/s for frequencies of 2–30 Hz and all PPV obtained in the frequency range of 30–450 Hz (Svinkin 1999).

Resonant structure response. The proximity of the frequency ground vibrations to one of the building's natural frequencies may generate the condition of resonance. The PPV of structure vibrations can increases from two to seven times as high as vibrations measured at the ground. Under the condition of resonance, the maximum dynamic amplification even may be much higher (Quesne 2001). Dynamic settlements – ground and foundation settlements as a result of relatively small ground vibrations in loose soils may occur at various distances from the source. Densification and liquefaction of soils can occur under the vibration effects of construction activities. Additional causes of damage – soil excavation associated with pile driving and made in close proximity to existing building can produce structural damage, Dowding (1996) observed that permanent excavation deformations induced in adjacent structure generally exceeded those from pile driving equipment and suggested taking into account the accumulated effect of repeated dynamic loads, from production pile driving. This approach is especially important for historic and old buildings and also for building in those great number people are allocated (theatres, airports, schools, hospitals, etc.).

3 PREDICTION AND MONITORING OF THE BUILDING VIBRATION

3.1 *Assessment of building vibration due to construction activities*

Assessment of building vibration due toconstruction activities caused by pile driving is a problem that can be solved through the application of research. This research consists mainly of defining the relationship between intensity fluctuations in the soil, the pile driving energy quantity and the distance from the vibration source. Through intensity fluctuations can appear in different physical quantities, such as the *oscillation velocity, acceleration, frequency, ground motion intensity, displacement and energy*. There are accessible several standards in the field of measurement of vibration in the construction industry in the European Union and USA.

In Slovakia in the field of measuring and assessing of building vibrations due to ground motion the most commonly used standard is Slovak Standard STN EN 1998 – 1/NA/Z1 (2010) based on EC8.

The usual concern related to construction vibration is building damage. A considerable amount of research has been done to define acceptable levels of construction-induced vibration to limit damage to neighboring buildings. Pre- and post-construction inspections and real-time monitoring systems are used to avoid damage claims associated with the construction process. For sensitive equipment or historic and old building also in the case of buildings with allocation of many people, however, the vibration levels of concern are two to three orders of magnitude lower than those associated with even minor cosmetic damage. In such cases, more sophisticated monitoring systems are needed to measure and assess the potential adverse effects of construction-related vibration. This article describes also the evolution of remote monitoring systems being used for the special case related to vibration in sensitive facilities of airport near construction sites.

3.2 *The analytic – experimental prediction models*

The analytic – experimental approach suggests the test and the theory data combination to calculate the prediction level of ground vibration. In this process

as an input signal can be used accelerations (velocities) spectrum $\overline{S}_{\ddot{w}\ddot{w}}(\omega)$ measured at the nearest ground point to the different kind of piles and hammers and generate experimental spectra data bank for authorized driving equipment and the same procedure to use for individual case study. On the surface of a linear viscous–elastic half space, the displacement response spectrum $S_{ww}(\omega)$ can be expressed in terms (Bendat & Piersol 1993). to the input spectrum of ground vibration accelerations $\overline{S}_{\ddot{w}\ddot{w}}(\omega)$, by

$$S_{\ddot{w}\ddot{w}}(\omega) = |H(\omega)|^2 \overline{S}_{\ddot{w}\ddot{w}}(\omega), \quad (1)$$

where $|H(\omega)|$ is the frequency response function magnitude for the half space medium and $\ddot{w}(t)$ is vibration accelerations of the surface measured at a distance l from the measured point near the driving pile. In this approach it can be used as the input spectra $\overline{S}_{\ddot{w}\ddot{w}}(\omega)$ measured at nearest ground point to the pile. The frequency response function (transfer function) of the ground can be derived via experimental impulse seismic method (ISM) or cross–hole test data, from which elastic and attenuation parameters of the ground can be obtained, too. The measuring output response acceleration spectrum at the distance $S_{\ddot{w}\ddot{w}}(\omega)$ due to input accelerations spectrum $\overline{S}_{\ddot{w}\ddot{w}}(\omega)$ the FRF – $H(\omega)$ is possible derived by (1), too.

4 MEASUREMENTS ON SITE

4.1 *The building site description*

The new part of the M. R. Štefánik Bratislava Airport building development involved the relocation of the old technological collector under area of the operated airport buildings into the part of reinforced concrete collector along the new terminal and the terminal under reconstruction. Reinforced concrete tube collector cross section has internal dimensions of 2.5 m wide and 3.3 m high. The thickness of the walls, ceiling and base plate are consistently 300 mm tube is structurally designed as a reinforced concrete structure using a U-shaped, covered with prefabricated ceiling. Foundation of the collector and its technical chambers and it is about one meter below the ground water level and therefore it was necessary to make earth works using steel sheet pile (profiles Larsen 3n, length 10 m), which enabled to encircle the collector site very shortly after water pumps installation and the performing water pressure insulation. Sheet piles driving were performed by vibration ramming machines (MS 16HFV and 206H40). Trench shoring was insured by Larsen 3n steel sections for an average pit bottom depth of 5.3 m (Figure 1).

4.2 *The experimental tests at nearby construction site and airport building*

The ground vibrations and airport building response due to pile driving were measured by accelerometers



Figure 1. Vibratory pile driving in collector site. Location L2 Airport Bratislava.

BK – 8306 (Brüel–Kjaer). The output signals from the accelerometers were preamplified and recorded on portable PC equipped with A/D converters software packages *NI* and *DISYS*. The experimental analysis has been carried out in the Laboratory of the Department of Structural Mechanics, University of Žilina (Bencat et al. 2011). The ground and structure vibrations frequencies were obtained using spectral analysis of the recorded ground response dynamic components, which are considered as ergodic and stationary. Spectral analysis (spectra, PSD) was performed via National Instrument software package NI LabVIEW. The wave velocities have been investigated by means of the correlation and spectral analysis (Bendat & Piersol 1993) in order to obtain cross correlation functions $R_{xy}(t)$ and coherence function $\gamma^2_{xy}(f)$.

(i) Ground dynamic parameters.To calculate the predicted vibration level and projected dynamic response for a new airport terminal T2 building and adjacent operating T1 terminal building, it was needed to know the soil dynamic parameters and FRF for the building site. In situ impact tests in the T2 terminal building site (location L1 – 35.0 m distance from T1) were performed (Bencat et al. 2011), see also Figs. 2.3. The objective of experimental measurements of transient signal was to find:

- the Raleigh's and share wave velocities by using standard equipment of ISM,
- the same dynamic characteristics as mentioned in stationary signals investigation (at nearby pile region) via the spectral and correlation procedures. The impulse test results are as follows: $C_R = 155.10\,\mathrm{ms}^{-1}$; $\delta_G = 0.117$; $E_o = 149.20$ MPa; $G_0 = 55.95$ MPa,

The calculation includes data: $\lambda_R = 9.2$ m, $\rho = 1950\,\mathrm{kgm}^{-3}$, $\alpha = 0,0398(\mathrm{m}^{-1})$, $l = 16$ m, (B2–B3, ISM points distance) $F_{RE} = 1.061457$ and $\nu = 0.33$.

The attenuation coefficient α (m^{-1}), was obtained by Golicyn's formula via standard deviations $\sigma(0)$, $\sigma(y)$ of displacement amplitude

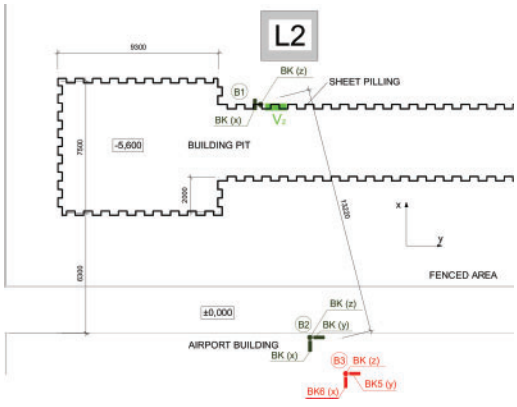


Figure 2. Measured points in L2 location (Position S2).

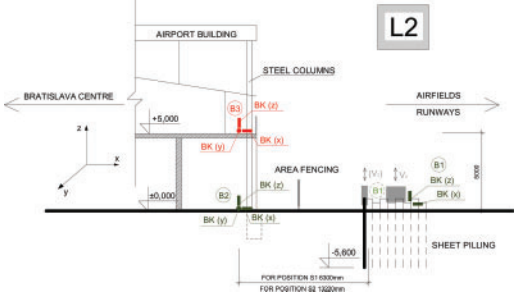


Figure 3. Measured points position in L2 location.

vibration at the distances l_0, l_y from source of excitation using the *displacement* PSD $G_{ii}^{(0)}$ and $G_{kk}^{(y)}$ (Bencat & Papan 2011).

(ii) Buildings structure dynamic response (BSDR). The main purpose of the pile driving tests at the site was to determine the distance where ground vibrations could be expected to be lower than the limiting value recommended e.g. by STN EN 1998-1/NA/Z1 (2010) or vibratory pile drivers (VPD) op-erating mode regulation. From Swedish Standard (1999) the maximum allowable calculated vibration velocity (vertical component) is $v_{\max} = 7.8$ mm/s. Before starting of tests and monitoring BSDR series, the operation mode rating of all pile drivers was set up to avoid unfavorable level of vibration on airport terminal structure (calibration). However, some concern was expressed with regard to environmental considerations (occupants). It was reason to carry out 9 measurements and 10 days continual monitoring of the dynamic response of the airport terminal buiding structure at selected representative points, (Figs. 2.3). Information about the measured objects, type of measurement and the distances to the source of vibration caused by the VPD are given in Table 1. The Airport Bratislava building site layout and accelerometers and DLP positions during the experimental tests are shown in Figures 2–3.

Figure 5 shows a schematic overview of used monitoring system. The sensors are connected to an analyzer that also provides power to the sensors. The analyzer is connected to a laptop computer that can either be an integral part of the analyzer (the analyzer software runs on the laptop) or it can serve only as a communication device to pull data off the analyzer (Newmark et al. 2011). The laptop is connected to the internet, which allows remote control, remote data download and a conduit for alarm notifications.

Results of experimental tests and monitoring via extreme values of all measurements are summarized in the accompanying Figure 6. As an example of the of the VPD induced vibrations velocities spectral analysis result (PSD) in the structure at point BK2 and the ground and structure velocities time depended functions $v(t)$ at points BK1 and BK2 at are plotted on Figure 4.

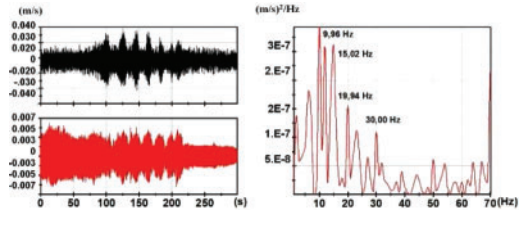


Figure 4. Vibration velocities and PSD at Location L2 Airport Bratislava **BK1(z)** and BK2(z). Test Nr. 6.

Table 1. Essential measurements data.

Measured location (L2)	Measured point	Test type (T)	Vibration horizontal distance [m]	Pick up position
Pile	B1 (x,z)	T1-T4	6.30	S1
		T5-T9	13.22	S2
Foundament	B2 (x,y,z)	T1-T4	6.30 (E0.0)	S1
		T5-T9	13.22 (E0.0)	S2
1st. floor	B3 (x,y,z)	T1-T4	6.30 (+5.0)	S1
		T1-T9	13.22 (+5.0)	S2
		Monitoring	Variable	Variable
1st. floor (ceiling)	B3 (z)	T5-T9	21.40 (+5.0)	S2
		Monitoring	Variable	Variable

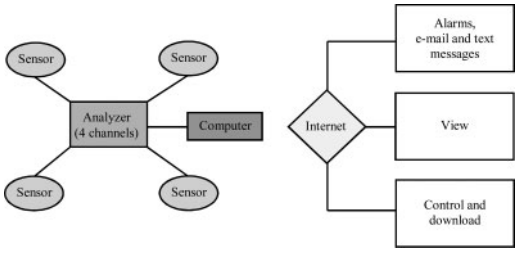


Figure 5. Monitoring system scheme.

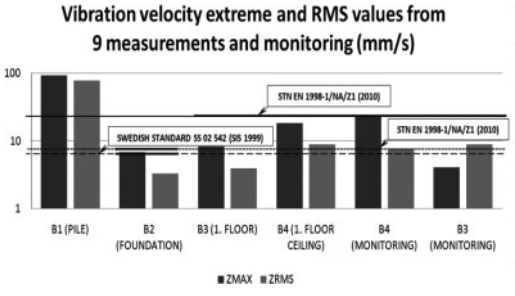


Figure 6. Results of experimental tests and monitoring.

5 CONCLUSIONS

This paper presents an overview of some prediction model for the ground-borne vibrations and the buildings structure dynamic response due to pile driving process. The numerical an numeric-experimental based on spectral analysis approach for ground response at the distance and dynamic response of building structures calculation procedure were introduced and also in the experimental process was carried out using this approach.

The relevant calculated data values following from experimental spectral and amplitude analysis of the Airport Bratislava building dynamic response (spectral picks limit, vibration levels, etc.) were compared with relevant standards prescription values and criteria (Figure 6). From these comparisons it follows that the standards prescription values and criteria regarding building structure during vibratory driving of sheet piles in the adjanced construction site were fulfilled.

ACKNOWLEDGEMENTS

We kindly acknowledge the research project VEGA, Nr.G1/0169/12 granted by Scientific Grant Agency of the Slovak Republic Ministry of Education. We should also like to thank the Civil Engineering Faculty – University of Žilina for additional feed in this field research activity.

REFERENCES

Bencat, J. 1992. Microtremor due to Traffic. *Research report A–4–92/b*, (In Slovak) UTC, Zilina.

Bencat, J. at al. 2011. Construction Machinery Effect on Bratislava Aiport Building Structure. *Research report A – 3 11/b*, (In Slovak) UTC, Zilina.

Bencat, J. & Papan, D.2011. Building Structure due to Railway Traffic Prediction Model in *Proceedings of the Eighteenth International Congress on Sound and Vibration*, *Rio de Janeiro, 10–14 July, 2011*, Intern. Inst. of Acoustics and Vibration Publishing, paper No. R39.

Bendat, J. S. & Piersol, A.G.1993. *Engineering Applications of Correlation and Spectral Analysis*, New York: Wiley & Sons.

Dowding, C. H. 1996. *Construction vibrations,* New York: Prentice-Hall, Upper Saddle River.

Martinček, G. (1975). Some Problems of the Viscoelastic Bodies Dynamics. *Research Report III–6–8/18*, USTARCH–SAV, Bratislava.

Newmark, M. S. et al. 2011. Monitoring Construction Vibrations at Sensitive Facilities. *Acentech Incorporated*, Cambridge, Massachusetts.

Quesne, J. D. 2001. Blasting vibration from limestone quarries and their effect on concrete block and stucco homes. *Vibration problems. Geo Discussion Forum,* May 6, 2002.

Rizzo, F.J. & Shippy, D.J. 1971. An application of the correspondence principle of linear viscoelasticity theory. SIAM *Journal on Applied Mathematics*, 21(2):321–330.

Slovak National Annex 2010. to Eurocode 8: Design of structures for earthquake resistance. Part 1: General rules, seismic actions and rules for buildings, (In Slovak). STN EN 1998-1/NA/Z1. Slovak Institute of Standards, SUTN, Bratislava.

Svinkin, M. R. 1999. Prediction and calculation of construction vibrations. *DFI 24th Annual Members' Conf, Decades of Technology-Advancing into the Future,* Deep Foundation Institute, Englewood Cliffs, N.J., 53–69.

Swedish Standard 1999. Vibration and shock – Guidancelevels and measuring of vibrations in buildings originating from piling, sheet piling, excavating and packing to estimate permitted vibration levels, (In Swedish). SS 02 5211. Swedish Institute of Standards, SIS. Stockholm.

Warrington. D. C. 1992. Vibratory and impact-vibration pile driving equipment. *Pile Buck. Inc.* Second October Issue: 2A–28A.

3. Vibration serviceability, human-induced vibrations, human-structure interaction

Research and Applications in Structural Engineering, Mechanics and Computation – Zingoni (Ed.)
© 2013 Taylor & Francis Group, London, ISBN 978-1-138-00061-2

Data-driven model of random lateral pedestrian excitation

V. Racic, J.M.W. Brownjohn & A. Pavic
The University of Sheffield, UK

ABSTRACT: Randomness and narrow band nature are the two essential features of lateral walking loading not addressed adequately in the existing design guidelines for footbridges. One of the reasons for this is the lack of a comprehensive database of lateral walking forces in the form of continuously recorded time series that can be used for development of statistically reliable characterisation of these forces for application in the civil engineering context. This paper has addressed the issue by establishing a large database of measured lateral walking time series recorded by a state-of-the-art instrumented treadmill at the University of Sheffield. Another reason is the lack of an adequate modelling strategy which can simulate reliably the actual forcing records. Motivated by the existing models of wind and earthquake loading, speech recognition techniques and a method of replicating electrocardiogram (ECG) signals, a data-driven mathematical model has been developed to generate synthetic force signals with realistic temporal and spectral features. This multi-disciplinary modelling strategy offers a radical departure from traditional Fourier-based representations of lateral walking loads towards more reliable and more realistic vibration serviceability assessment of footbridges.

1 INTRODUCTION

More than a decade after the London Millennium Bridge debacle (Fitzpatrick et al. 2001), structural designers still have to manage significant uncertainties in lateral dynamic loads induced by pedestrian occupants due to crude guidance based on insufficient and fragmented science (Zivanovic et al. 2005, Ingólfsson et al. 2011). The present study takes a step forward by bringing together a comprehensive database of continuously measured lateral walking loads and their mathematical model which can simulate accurately the measurements. Since the measured loads were generated on a ground-mounted instrumented treadmill (Figure 1), the model simulates the forces induced by individuals walking on stiff surfaces, i.e. without the lateral bridge motion and hence discounting effects of human-structure dynamic interaction. Such a model is an essential prerequisite for future quality models of group and crowd lateral pedestrian loading under a wider range of conditions. From the structural engineer's point of view, guidance is still lacking on the proportion of pedestrians in a given situation who coordinate their body motion and the scale and character of the resulting net dynamic loads on the structure, with or without influence of the motion of the structure itself. In fact, motion of the structure is just one type of cue or stimulus among several others affecting group/crowd pedestrian loads (Racic et al. 2009), such as proximity of individuals and different audio, visual and tactile stimuli.

2 EXPERIMENTAL DATA ACQUISITION

All walking tests were carried out in the Light Structures Laboratory in the University of Sheffield (Figure 1). The acquisition of walking forces started at a speed of 2 km/h and continued in increments of 0.5 km/h up to the maximum walking speed, i.e. an ultimate self-selected speed at which jogging, rather than walking, is more comfortable for a test subject. Pacing rate was not prompted by any stimuli such as a metronome, and it was determined only from sub-sequent analysis of the generated force signals.

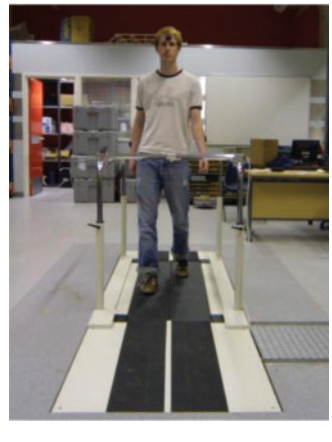


Figure 1. Experimental setup.

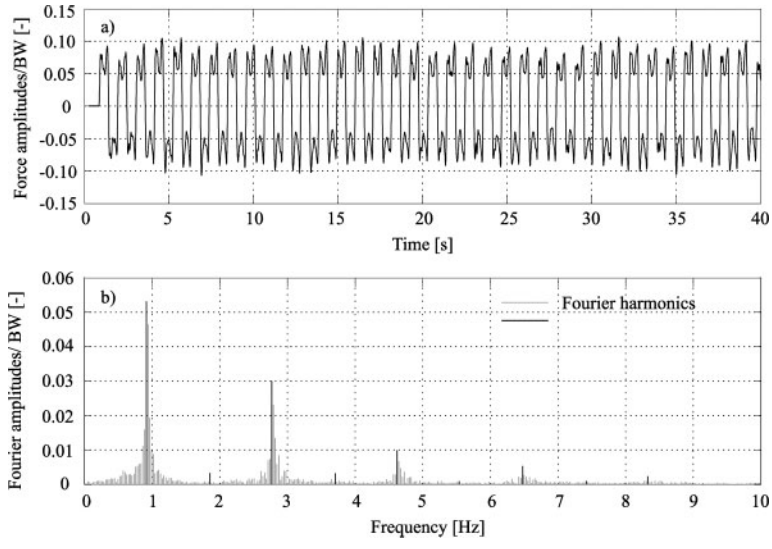


Figure 2. An example of measured (a) force-time history and the corresponding (b) Fourier amplitude spectrum. Dominant harmonics at integer multiples of lateral walking frequency $f_w = 0.92$ Hz are bold.

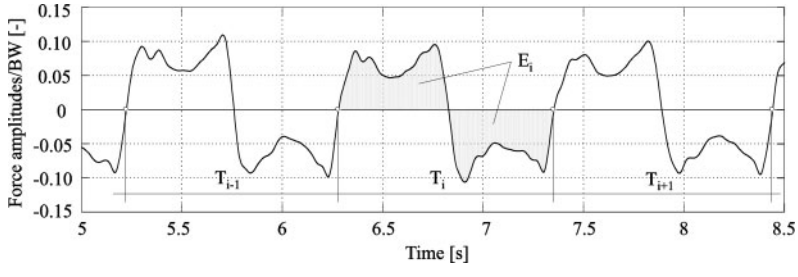


Figure 3. A portion of a force-time history after applying a fourth-order low-pass Butterworth digital filter with cut-off frequency 15 Hz. The force is recorded at fixed treadmill speed of 4.5 km/h, while the estimated average lateral frequency is 0.92 Hz.

Each test was completed when at least 64 successive footfalls were recorded. A typical measured force-time history and the corresponding Fourier amplitude spectrum is shown in Figure 2.

In total, 85 volunteers (57 males and 28 females, body mass 75.8 ± 15.2 kg, height 174.4 ± 8.2 cm, age 29.8 ± 9.1 years) were drawn from students, academics and technical staff of the University of Sheffield. All together they generated 850 lateral walking force time series of kind illustrated in Figure 2a. Each walking time series was sampled at 200 Hz.

The next section describes the concept of modelling individual lateral force records as a narrow band process. In Section 4 this model is fitted to all 850 force records, yielding a numerical generator of random walking time series.

3 MODELLING OF IMPERFECT REAL WALKING

As humans are not perfect robots, force measures fluctuate invariably with time from one walking cycle to the next (Figure 2). A walking cycle can be defined between any two nominally identical events of the total force-time history. In this study, the point of intersection between the force trace and time axis at which the first derivative of the force is positive was selected as starting (and completing) event (Figure 3).

From the 40 s long force signal given in Figure 2a and yielding about 40 cycles, a window comprising 34 successive cycles was extracted from the middle of the signal. Three cycles at the beginning and end of the force record were cast aside as their natural variability might be affected by the measuring process. In the next section, the selected 34 cycles will be used to curve fit morphology of the force, a so called "template cycle", which can be scaled (stretched and compressed) along the synthetic time and amplitude axes to reflect inter-cycle variability present in the actual force-time history. This modelling strategy is motivated by an existing numerical generator of electrocardiogram (ECG) signals (McSharry et al. 2003) which have similar near-periodic features as walking time series. Modelling variability of the cycle intervals and force amplitudes is presented respectively in

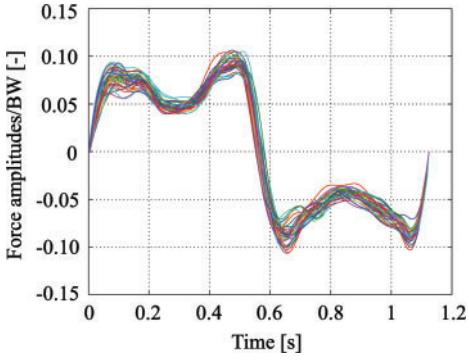


Figure 4. Resampled weight-normalised cycles.

Sections 3.2 and 3.3, while generation of synthetic force signals is outlined in Section 3.4.

3.1 *Template cycle*

The 34 weight-normalised walking cycles have been temporarily displaced and resampled to the length of the longest cycle, as shown in Figure 4.

Visual inspection does suggest that there is a common waveform of the force which distorts along time and amplitude axes on a cycle-by-cycle basis. Their average is considered an inadequate representative of the force morphology due to misalignments of the common events, such as positions of the local extreme values. To line up the force cycles, a technique called dynamic time warping (DTW) had been applied before their average was computed. More details can be found in Racic & Brownjohn (2012).

The underlying shape of the template cycle can be modelled mathematically as a sum of 29 equidistant Gaussian functions (Racic & Brownjohn (2012)):

$$Z(t)=\sum_{j=1}^{29} A_j e^{-\frac{(t-t_j)^2}{2\delta^2}} \tag{1}$$

where $Z(t)$ is the curve fit, the parameter A_j is the height (also called weight) of the j-th Gaussian peak, t_j is the position of the centre of the peak, and the common parameter δ controls the width of the Gaussian bell functions. Aiming for the minimum number of Gaussians in the sum necessary to describe accurately the template cycle, values of parameters δ, t_j, and A_j were optimised using non-linear least-square curve fit (Bates & Watts 1998). As a result, the positions of Gaussian centres are optimally located in every eight sample (29 of them), the optimal common width is $14/f_s$, while the optimal heights are illustrated in Figure 8a.

3.2 *Variability of cycle intervals*

Variations of cycle intervals T_i $(i=1,\ldots,34)$ can be represented by a dimensionless set of numbers τ_i:

$$\tau_i=\frac{T_i-\mu_T}{\mu_T} \tag{2}$$
$$\mu_T=mean(T_i)$$

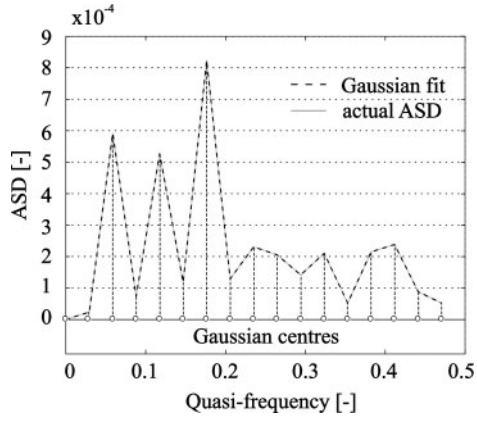


Figure 5. ASD of τ_i and its fit.

Taking τ_i as a series having zero mean value, variance of τ_i can be obtained as the integral of its auto spectral density (ASD) (Newland 1993). Assuming that the variation of τ_i does not change for the given test subject, pacing rate and duration of walking (e.g. due to fatigue and physical discomfort), the aim here is to use the ASD of the actual τ_i data to generate synthetic series τ'_k $(k=1,\ldots,N)$ of arbitrary length (e.g. $N \gg 34$) with the same statistical properties, such as standard deviation and "pattern" of variation between successive τ_i values.

The ASD of τ_i can be calculated as (Newland 1993):

$$S_\tau(f_m)=\frac{A_\tau^2(f_m)}{2\Delta f},\quad f_m=\frac{m}{34},\quad m=0,\ldots,16 \tag{3}$$

where $A_\tau(f_m)$ is a single-sided discrete Fourier amplitude spectra and $\Delta f=1/34$ is the spectral line spacing (Figure 5).

Similarly to the template cycle (Section 3.1), the ASD $S_\tau(f_m)$ can be analytically described by a sum of Gaussian functions (Figure 5):

$$S'_\tau(f)=\sum_{j=1}^{17} W_j e^{-\frac{(f-c_j)^2}{2b^2}} \tag{4}$$

Here, parameter W_j is the height of the j-th Gaussian peak, c_j is the position of the centre of the peak, and b is the common width of the Gaussian function. The Gaussian centres c_j, are placed in each sample on the quasi-frequency axis to fit exactly the actual ASD (Figure 5). For such fixed positions of c_j and predefined widths $b=\Delta f$, Gaussian heights W_j can be computed using the non-linear least-square method (Bates & Watts 1998).

Generation of synthetic series τ'_k $(k=0,\ldots,N)$ starts by calculating $S'_\tau(f_n)$ values using Equation (5) at discretely spaced frequency points $f_n=n\Delta f'$, where $n=0,\ldots,N/2-1$ and $\Delta f'=1/N$. The synthetic ASD amplitudes are then used in conjunction with Equation (4) to generate a set of Fourier amplitudes $A'_\tau(f_n)=\sqrt{2\Delta f' S'_\tau(f_n)}$. Finally, assuming random

distribution of phase angles in the range $[-\pi, \pi]$, $A'_\tau(f_n)$ are used in inverse FFT algorithm to generate a set of N synthetic variations τ'_k. Different realisations of the random phases may be specified by varying the seed of the random number generator, hence many different series τ'_k can be generated with the same spectral properties.

According to Equation (2), scaling τ'_k by μ_T and adding the offset value μ_T, results in a series of synthetic intervals T'_k. Moreover, assuming that the test subject does not vary significantly their gait in a narrow range of (lateral) walking rates, μ_T value can be slightly changed in the scaling process to generate cycle intervals at rates close to $1/\mu_T$. Empirical evidence for this is presented in Section 4.

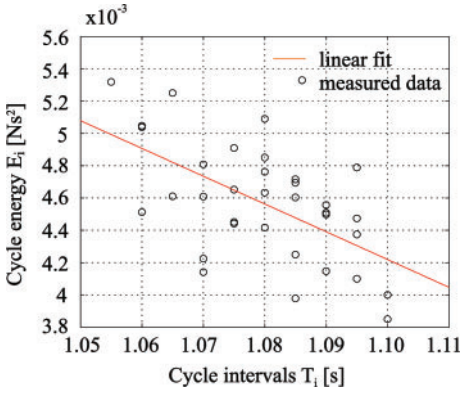


Figure 6. Cycle energy vs. cycle intervals.

3.3 *Variability of force amplitudes*

Energy of weight-normalised walking cycles E_i can be defined as the integral of squared weight-normalised force amplitudes over the corresponding cycle intervals T_i (Figure 3). The linear trend between these two parameters (Figure 6) makes it possible to describe energy transfer between successive cycles using the following linear regression model (Bishop 2006):

$$E_i = \rho_1 T_i + \rho_0 + \Delta E_i \tag{5}$$

Here, $\rho_1 = -0.017$ and $\rho_0 = 0.023$ are regression coefficients and ΔE_i is the subsequent error (also known as a disturbance term), which is a random variable and is usually modelled as a random Gaussian noise (Bishop 2006).

Given a set of synthetic cycle intervals T'_k $(k = 1, \ldots, N)$ generated as explained in Section 4.2, the corresponding synthetic series E'_k can be calculated using Equation (6). These energies can be assigned to template cycles by scaling their amplitudes by factors α_k:

$$\alpha_k = \sqrt{\frac{E'_k}{E_{tc}}} \tag{6}$$

where E_{tc} is the energy of the template cycle. Arranged in a sequence along the time axis, the scaled template cycles reflect the smooth variations of the force amplitudes on a cycle-by-cycle basis, as presented in the next section.

3.4 *Generation of synthetic forces*

Visual comparison of Figure 7a to 1a and Figure 7b to 1b shows apparent similarity between a measured

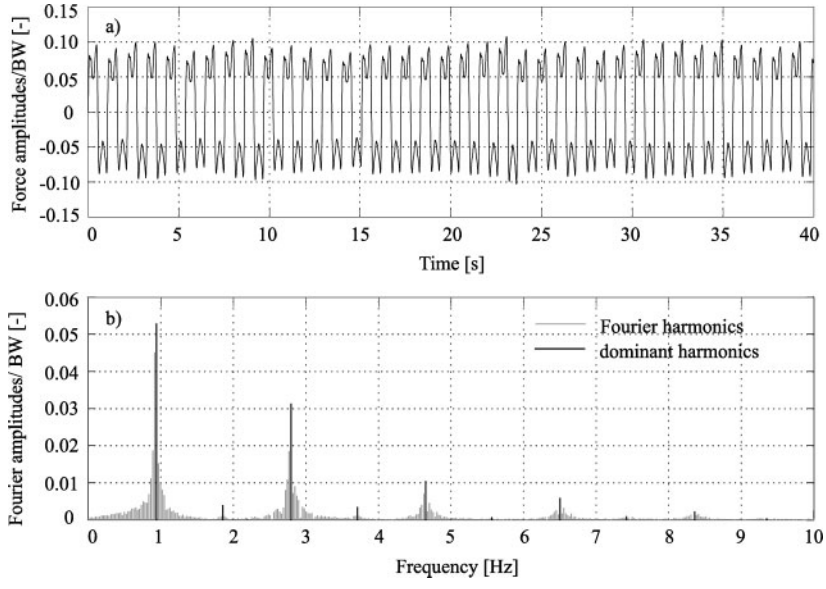


Figure 7. (a) An example of synthetic time series and (b) the corresponding discrete Fourier amplitude spectrum.

signal and an example artificial force signal in both time and frequency domain.

4 DEVELOPMENT OF RANDOM NUMERICAL GENERATOR OF FORCE SIGNALS

Each of the 850 force records in the database (Section 2) was processed using the concept described in Section 3. Multiple sets of information, such as parameters of the template cycle $Z_k(t)$, the ASD $S'_\tau(f)$, disturbance term $\Delta E_i(t)$ and the regression coefficients ρ_1 and ρ_0, were extracted and stored in MATLAB structure files (MathWorks 2011). These are called "mat files" in the remaining part of the paper.

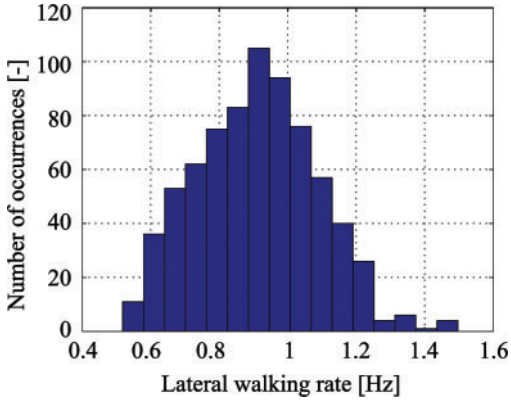


Figure 8. Histogram of lateral walking frequencies f_w.

The mat files were classified into 16 categories (clusters) with respect to the lateral walking frequency, as shown by the histogram in Figure 8. As each bar in the histogram is only 0.06 Hz wide, it can be assumed that any mat file in a cluster can be used to generate synthetic walking time series at any frequency within the cluster's narrow frequency range. As already mentioned in Section 3.2, this means that the modelling parameters extracted from real walking at a certain rate can be used to synthesise walking forces at close rates in the same cluster. The flow chart in Figure 9 outlines the algorithm of creating synthetic force signals.

For the same set of input parameters – lateral walking rate 1 Hz and walking period 40 s, Figure 10 illustrates examples of force signals generated after the model was run twice in succession. A visual comparison of the time series provides convincing evidence that the model does account for the inter-subject variability. On the other hand, the ability to generate different degrees of the intra-subject variability is more obvious from comparison between the corresponding

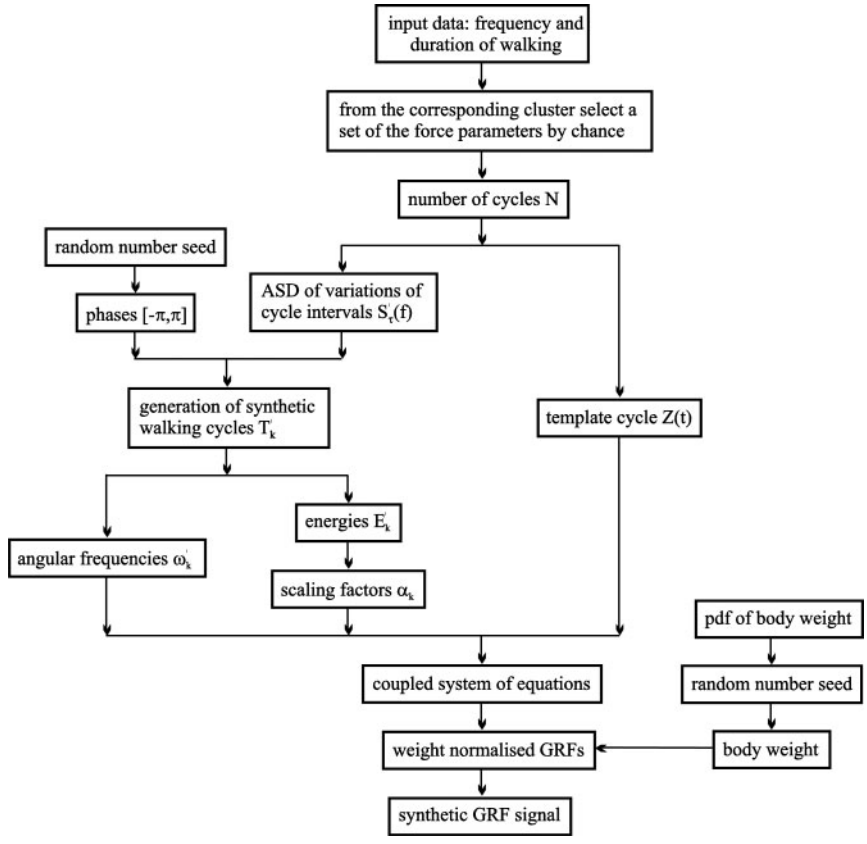


Figure 9. Flow chart.

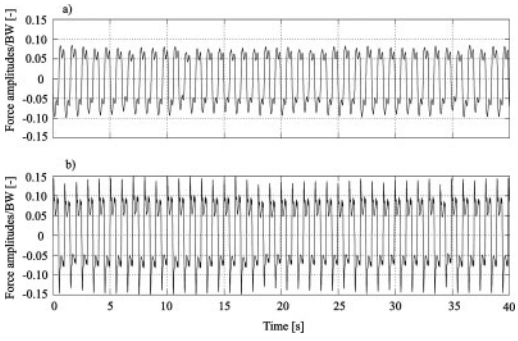


Figure 10. Examples of walking time series for specified $f_w = 1$ Hz and duration 40 s.

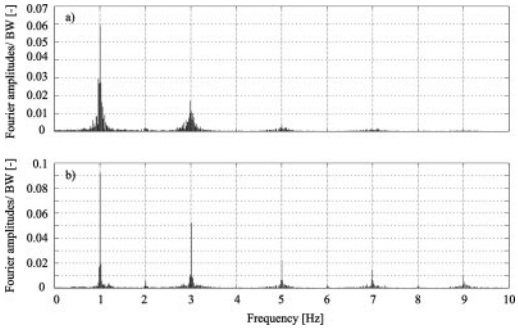


Figure 11. Fourier amplitude spectra of the signals given in Figure 10.

frequency spectra (Figure 11). The broader spread of energy around dominant harmonics in Figure 11a relative to 11b indicates that walking of the first "virtual" pedestrian is characterised by greater intra-cycle variability.

ACKNOWLEDGEMENTS

The authors would like to acknowledge the financial support provided by the UK Engineering and Physical Sciences Research Council (EPSRC) for grant reference EP/E018734/1 ("Human Walking and Running Forces: Novel Experimental Characterisation and Application in Civil Engineering Dynamics") and to thank all test subjects for participating in the data collection.

REFERENCES

Bates, D.M. & Watts, D.G. 1998. *Nonlinear regression and its applications*. New York: Wiley.

Bishop, C.M. 2006. *Pattern recognition and machine learning*. New York: Springer.

Fitzpatrick, T., Dallard, P., Le Bourva, S., Low, A., Ridsdill-Smith, R. & Willford, M. 2001. *Linking London: the Millennium Bridge*, Report No. L12.32. London, UK: The Royal Academy of Engineering.

Ingólfsson, E.T., Georgakis, C.T., Ricciardelli, F. & Jönsson, J. 2011. Experimental identification of pedestrian-induced lateral forces on footbridges. *Journal of Sound and Vibration* 330 (6) 1265–1284.

MathWorks 2010 Matlab user guides www.mathworks.com

McSharry, P.E., Clifford, G.D., Tarassenko, L. & Smith, L.A. 2003. A dynamical model for generating synthetic electrocardiogram signals. *IEEE Transactions of Biomedical Engineering* 50, 289–294.

Newland, D.E. 1993. *An introduction to random vibrations, spectral and wavelet analysis*, 3rd edn, Harlow: Pearson Education Limited.

Racic, V. & Brownjohn, J.M.W. 2012. Mathematical modelling of random narrow band lateral excitation of footbridges due to pedestrians walking. *Computers & Structures* 90–91, 116–130.

Racic, V., Pavic, A. & Brownjohn, J.M.W. 2009. Experimental identification and analytical modelling of human walking forces: Literature review. *Journal of Sound and Vibration* 326, 1–49.

Zivanovic S., Pavic A. & Reynolds P. 2005. Vibration serviceability of footbridges under human-induced excitation: a literature review. *Journal of Sound and Vibration* 279, 1–74.

Research and Applications in Structural Engineering, Mechanics and Computation – Zingoni (Ed.)
© 2013 Taylor & Francis Group, London, ISBN 978-1-138-00061-2

Simultaneous registration of walking behaviour and structural response

K. Van Nimmen
KU Leuven, Department of Civil Engineering, Leuven, Belgium
KAHO Sint-Lieven, Department of Industrial Engineering, Ghent, Belgium

P. Van den Broeck
KAHO Sint-Lieven, Department of Industrial Engineering, Ghent, Belgium

G. Lombaert & G. De Roeck
KU Leuven, Department of Civil Engineering, Leuven, Belgium

ABSTRACT: The present contribution demonstrates the possibilities of a 3D motion tracking technique, originating from the movement science and entertainment industry, for the in situ analysis of the walking behaviour of pedestrians. Based on the registered movement, stride-to-stride variations are identified which enable to simulate the imperfect real walking forces. The technique is used in a unique experiment to simultaneously register the behaviour of (groups of) pedestrians and the structural response of a lightweight steel footbridge. The calibrated numerical model of the structure and the information gathered using the motion tracking system enable detailed step-by-step simulations. Accounting for the in situ identified imperfect walking behaviour of the test-subjects increases the agreement between the measured and the simulated response significantly. The remaining difference in magnitude between measurements and simulations, may be explained by an increase in damping due to the increase in amplitude of the structural response or the presence of pedestrians.

1 INTRODUCTION

Due to the trend towards greater slenderness, footbridges are very often lively structures, prone to human-induced vibrations (Brownjohn et al. 2004, Van den Broeck et al. 2011). Predicting the dynamic response of these structures due to crowd-induced loading has therefore become a critical aspect of the vibration serviceability design (Caetano et al. 2010, Živanović et al. 2005).

The human-induced forces and walking behaviour have been studied thoroughly in laboratory conditions (Racic et al. 2009). A remaining challenge is the analysis of the walking behaviour of pedestrians and crowds *in situ*. In view of this challenge, the authors see great potential in a 3D motion tracking technique originating from the movement science and entertainment industry.

A full-scale experiment is performed in which the structural response of a lively footbridge and the walking behaviour of the pedestrians are registered simultaneously. Numerical simulations are performed based on the calibrated numerical model of the structure and information gathered using the motion tracking system.

The outline of this paper is as follows. First, the 3D motion tracking technique is presented. Second, it is shown that the registered movement of the test-subject allows to identify the imperfect walking behaviour. In the final section, the in situ experiments are presented and the results of the numerical simulations are discussed.

2 3D MOTION TRACKING

The Xsens MTw Development Kit measurement system consists of multiple wireless inertial units (figure 1), incorporating 3D accelerometers, gyroscopes, magnetometers and a barometer. The accompanied Awinda radio protocol ensures time synchronisation between the MTw's across the wireless network. The sensors are securely fixed onto the test-subject with specially designed click-in full body straps.

3 APPLICATION IN LABORATORY CONDITIONS

The preliminary research by Van Nimmen et al. (2013) considered experiments in laboratory conditions and studied the relation between the accelerations of the body segments and the measured ground reaction forces. It is shown that the same main step frequency of the test-subject is identified from the frequency analysis of the measured ground reaction forces and the lower back accelerations. This step frequency along with the static weight of the test-subject, determine the vertical single foot force as defined by Li et al. (2010).

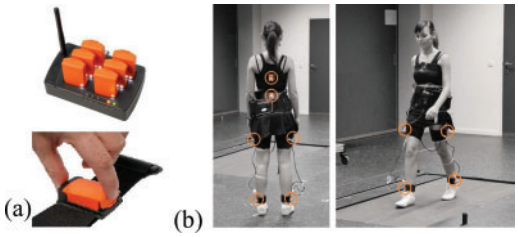


Figure 1. © Xsens – MTw Development Kit consisting of multiple wireless inertial units (MTw's) and specially designed click-in full body straps (a). Configuration setup of the wireless inertial units (MTw's) in laboratory conditions (b).

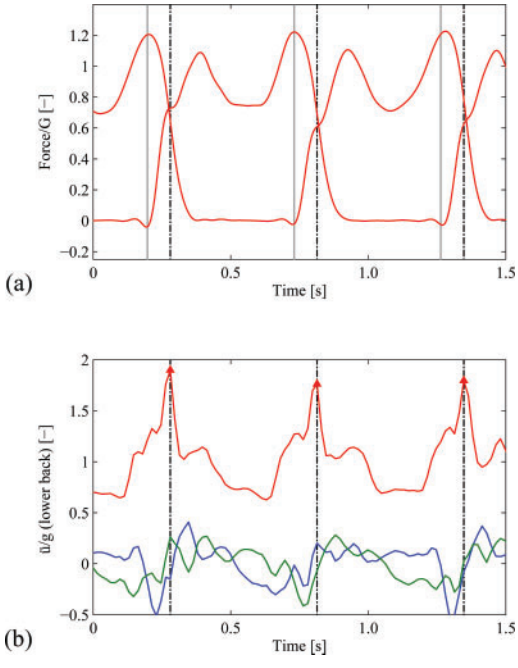


Figure 2. For a normal walking of speed of 5 km/h: (a) normalised ground reaction forces registered by the instrumented split-belt treadmill and (b) normalised measured accelerations at the lower back for the longitudinal (blue), lateral (green) and vertical (red) component.

Secondly, it is shown that both the acceleration levels measured at the lower back and at the ankles, enable to identify the time period in between two successive steps, and therefore, the pacing rate of the test-subject (figure 2). Figure 3 shows that the simulation of ground reaction forces based on a generalised single foot force model and the in situ identified pacing rate, allows for a good approximation of the imperfect real walking forces.

4 APPLICATION IN SITU

In this section, the 3D motion tracking technique is applied in a unique experiment to simultaneously

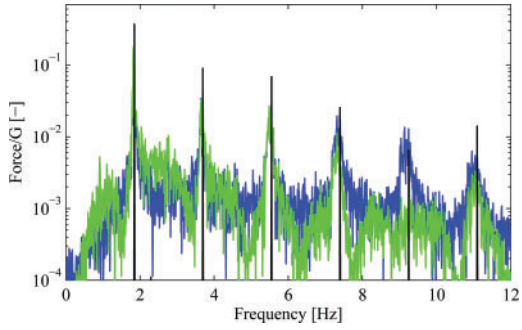


Figure 3. The Fourier series coefficients of the measured vertical ground reaction forces for a normal walking speed of 5 km/h (blue) and the corresponding simulated vertical walking forces according to Li *et al.* with main step frequency f_s and pacing rated identified based on the tracked motion of the body segments of the test-subject (green) and the perfectly periodic forces with the identified average step frequency and the time in between two successive steps equal to $1/f_s$ (black).



Figure 4. Eeklo footbridge.

register the behaviour of pedestrians and the structural response of a lightweight steel footbridge. The in situ identified modal characteristics of the structure are applied to calibrate its numerical model. Numerical simulations are performed applying step-by-step force models and the impact of the in situ identified imperfect walking behaviour of the test-subjects is assessed. This section consists of four parts: (1) the description of the footbridge and (2) the different experimental setups, (3) the analysis of the walking behaviour *in situ*, and (4) the numerical simulations and discussion of the results.

4.1 *Eeklo footbridge*

The footbridge considered in these experiments is located in Eeklo, at Aalstgod, and forms a safe passage across the N49 for pedestrians and cyclists. The bridge (2002) has three spans, a main middle span of 42 meters (across the N49) and two side spans of 27 meters (figure 4). The bridge is simply supported with land abutment at the sides and two pillars at the midspan. Both the abutments and the pillars are equipped with neoprene supports.

An extensive measurement campaign was carried out to obtain the operational modal characteristics of the footbridge. Output-only system identification is

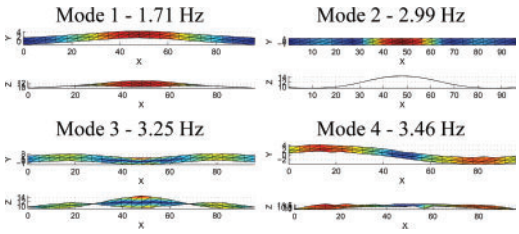


Figure 5. The first four identified modes of the Eeklo footbridge: respectively the top and side view.

performed based on ambient vibrations, mainly due to wind and nearby highway traffic (Peeters and De Roeck 1999, Reynders and De Roeck 2008). In total, 14 modes were identified with a frequency up to 12 Hz (table 1). Some of the lower operational eigenmodes and eigenfrequencies identified by this analysis, are presented in figure 5 which clearly illustrates that combined lateral-torsional modes alternate with vertical bending modes.

The FE model was constructed in great detail according to the as-built plans and is calibrated using the results of the operational modal analysis: model parameters are adopted such that an optimal correspondence is found between measured and calculated modal characteristics. This will result in a better representation of the dynamic behaviour of the structure and, therefore, increase the accuracy of the numerical predictions of the response to pedestrian loading. For the presently considered footbridge, the updating variables are limited to the stiffnesses of the neoprene supports, modelled with three translational springs (one in vertical, lateral and longitudinal direction) at each support.

Table 1 summarizes the results of the updating procedure. It lists the values of the measured natural frequencies $\tilde{f}$, calculated natural frequencies f, the relative error ε_j, and MAC values between measured and calculated mode shapes. This table shows that an excellent agreement is found between the numerical model and the measurements. The relative errors on the frequencies of all modes are limited to 1.76% and the MAC values are high.

4.2 *Experimental setups*

In this experimental study, different types of setups were considered including free walking and synchronised walking. In case of synchronised walking, the step frequency (or its second harmonic) of the test-subjects was chosen so as to match one of the natural frequencies of the structure. These resonant conditions were realized for both the first ($f_s = \tilde{f}_1 = 1.71$ Hz) and the second mode ($f_s = \tilde{f}_2/2 = 1.49$ Hz) of the structure. The step frequencies of the pedestrians were synchronised using a metronome signal, a process which was practiced by the test-subjects in laboratory conditions beforehand.

Different group sizes, ranging from one pedestrian up to six, are considered in various formations: two by two or all lined up one by one, and symmetrically (figure 6b) or asymmetrically (figure 6a) distributed with respect to the longitudinal axis of the structure. The response of the structure is registered with five triaxial sensors, for which the location was determined using an optimal sensor location algorithm (Papadimitriou and Lombaert 2011). The walking behaviour of the pedestrians is registered with the 3D motion tracking technique. Due to the limited number of MTw's, only one sensor is fastened to each test-subject (figure 6). For reasons of visibility and connectivity, the location of the sensor was set at the front of the torso instead of the back. Although good results were obtained using this sensor configuration, in future experiments preference will again be given to the lower back position because this limits the influence of skin motion artifacts resulting into an even clearer picture of the registered pedestrian motion.

Table 1. Identified modal characteristics (mode number $\tilde{N}$, natural frequencies $\tilde{f}$, damping ratios $\tilde{\xi}$) for all modes with a natural frequency blow 13 Hz and corresponding predicted natural frequencies of the calibrated numerical model (f), the calculated Modal Assurance Criterion (MAC) and the relative frequency deviation (ε).

$\tilde{N}$	$\tilde{f}$ [Hz]	$\tilde{\xi}$ [%]	N	f [Hz]	ε [%]	MAC [−]
1	1.71	1.94	2	1.71	0.26	0.99
2	2.99	0.19	3	3.02	0.90	1.00
3	3.25	1.45	4	3.30	1.76	0.98
4	3.46	2.97	5	3.43	−0.67	0.98
5	5.77	0.23	6	5.75	−0.31	0.99
6	5.82	0.16	7	5.80	−0.46	0.97
7	6.04	2.08	8	6.10	0.89	0.97
8	6.47	0.60	9	6.47	0.00	1.00
9	6.98	3.38	10	6.94	−0.48	0.96
10	7.44	4.77	11	7.36	−1.09	0.97
11	9.64	0.87	15	9.80	1.67	1.00
12	9.89	2.50	14	9.71	−1.76	0.96
13	10.48	1.43	16	10.65	1.62	0.97
14	12.01	3.49	17	12.16	1.30	0.93

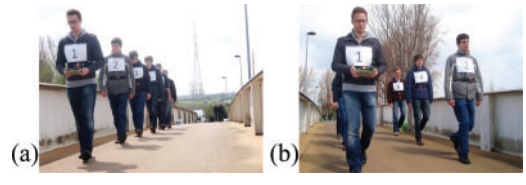


Figure 6. Synchronized walking of (a) 6 persons in a row and (b) two by two.

4.3 *Analysis of the walking behaviour in situ*

The identification of the pacing rate *in situ* is illustrated for a setup where the second harmonic of the walking load is set to match the frequency of the second mode of the structure ($f_s = \tilde{f}_2/2 = 1.49$ Hz). For this setup, it takes about 90 seconds to cross the

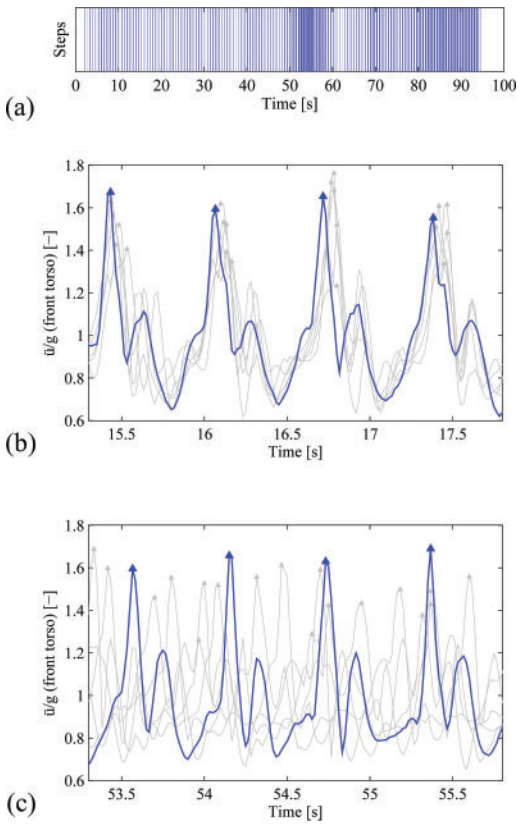


Figure 7. Identified pacing rate for a setup considering synchronised walking ($f_{metronome} = \tilde{f}_2/2 = 1.49$ Hz): visualisation of each step in time (a) and corresponding accelerations measured at the front of the torso for the 6 test-subjects (b–c) for times characterised by a high (b) and a low (c) synchronisation rate.

footbridge. Figures 7b and 7c present the accelerations measured at the front of the torso for the 6 test-subjects. For reasons of clarity, the signal of the first pedestrian is emphasized. These signals are clearly similar to the results obtained in laboratory conditions, as presented in figure 2b. Based on this registered movement, the beginning of each step and thus the pacing rate can be identified for each test-subject. As a result of the time synchronisation among the MTw's, the identified in situ walking behaviour also allows to study the synchronisation rate of the different test-subjects.

In figure 7a, all steps of all test-subjects are visualised in time with a single vertical line. If these lines coincide, it means that the different test-subjects are taking their steps at more or less the same time. A high rate of synchronisation has therefore been obtained. Times characterised by a high sychronisation rate, can be identified in figure 7a as equally spaced lines. The lack of white spacing will therefore indicate a lower synchronisation rate. As discussed in section 3, the induced forces can be simulated based on the in situ identified pacing rate and the generalised single foot force model that accounts for the identified mean step frequency and the weight of every test-subject. For this setup, the rate of synchronisation is relatively high during the first 40 seconds. The synchronisation is lost between 50 and 60 seconds and gets partially restored towards the end (figure 7c).

4.4 *Numerical simulations*

The essential features of the simulation model are the dynamic footfall load, the dynamic behaviour of the footbridge and the response calculation.

The vertical component of the walking force, as discussed in section 3, is modelled as a series of moving single footsteps for which the time history of the vertical component is described by Li et al. (2010). The lateral component is described by a rectangular force with an alternating sign for left and right foot and with a contact time equal to the vertical force. A dynamic loading factor of 0.04 is adopted as recommended by Butz et al. (2007).

The dynamic behaviour of the footbridge is characterized by the modal parameters (natural frequencies, mode shapes and damping factors). The natural frequencies and mode shapes of the calibrated finite element model of the structure (section 4.1) are applied together with the in situ identified modal damping factors. The response calculation is based on the time integration of the state-space equations formulated in terms of the modal coordinates. For the presented simulations, all modes with a natural frequency below 20 Hz are taken into account.

Figure 8 presents the measured and simulated acceleration response at midspan for the setup where the subjects were walking on one side of the bridge, with a pacing rate targeted at $\tilde{f}_1$. This figure presents the lateral response which is in accordance with the dominant component of the first mode. In total, 4 different responses are presented: the simulated acceleration response due to (1) the perfectly periodic forces based on the step frequency as set by the metronome signal, (2) perfectly periodic forces based on the identified mean step frequency of the test-subjects, (3) the imperfect walking forces as a result of the identified pacing rate and (4) the measured response. This figure illustrates that the response of the structure is clearly overestimated by the perfectly periodic forces. Although accounting for imperfect walking behaviour by applying the identified pacing rate still seems to overestimate the response, a good qualitative agreement is found with the measured response i.e. the two signals are almost equal up to a scaling factor. For both this simulated and measured response, a decrease in acceleration level can be observed after about 40 seconds, which is due to a reduced synchronisation of the test-subjects. A comparison of the responses in the frequency domain shows that again the simulation model that accounts for imperfect walking behaviour, gives the best approximation of the measured response. The underestimation at low frequencies is mainly due to ambient excitation of the bridge due to wind and nearby traffic, which is unaccounted for in this analysis. The errors on the predicted response for higher

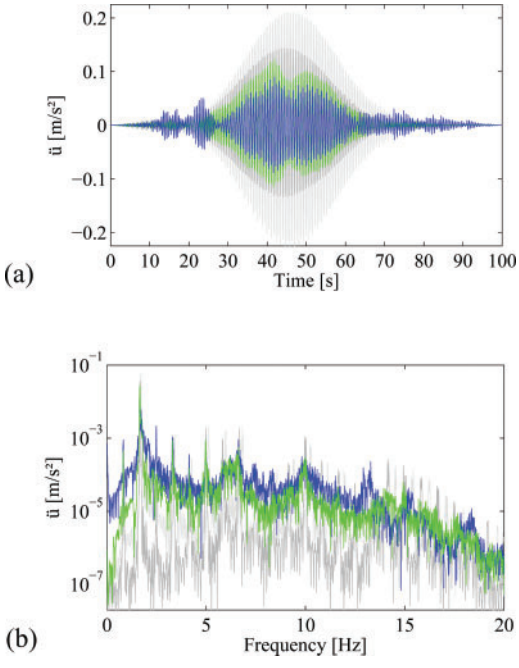


Figure 8. (a) Time series of the lateral acceleration levels in the center span of the bridge and (b) corresponding Fourier series coefficients: (blue) measured (green) simulated accounting for the identified pacing rate of each pedestrian (gray) simulated only applying the main step frequency.

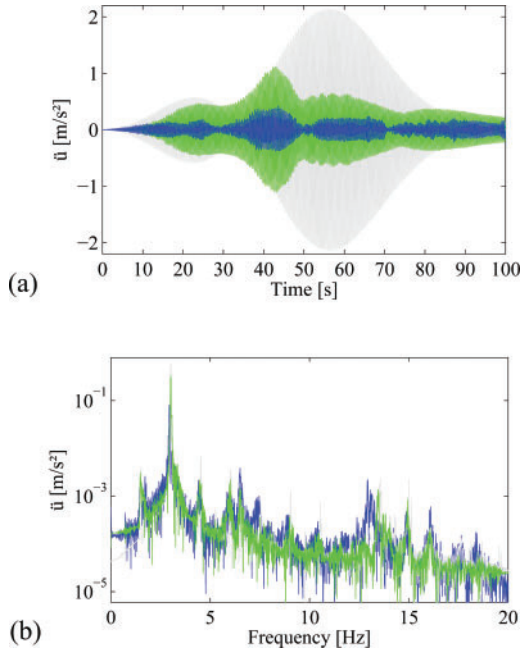


Figure 9. (a) Time series of the vertical acceleration levels in the center span of the bridge and (b) corresponding Fourier series coefficients: (blue) measured (green) simulated accounting for the identified pacing rate of each pedestrian (gray) simulated applying the average step frequency as set by the metronome signal.

frequencies, are for the greatest part attributed to modelling errors still present in the calibrated finite element model. The good qualitative agreement between the two responses but the difference in amplitude, may be explained by an increase in damping. This increase can be due to the presence of the pedestrians (Brownjohn et al. 2004) but structural damping has also been found to increase with amplitude (Kijewski-Correa and Pirnia 2007, Hudson and Reynolds 2012). Moreover, it has to be acknowledged that the in situ identified damping ratios are also subject to a significant degree of uncertainty (Reynders et al. 2008).

Figure 9 presents the measured and simulated vertical acceleration response at midspan for the setup where the subjects were walking two by two, with a targeted pacing rate equal to $1/2\tilde{f}_2$. Since the mean step frequency of all the test-subjects was equal to the rhythm guided by the metronome signal for this setup, this figure presents only three responses: the simulated acceleration response (1) due to the perfectly periodic forces based on the step frequency as set by the metronome signal, (2) due to the imperfect walking forces accounting for the identified pacing rate and (3) the measured response. This figure again illustrates that the response of the structure is clearly overestimated by the perfectly periodic forces. Accounting for imperfect walking behaviour by applying the identified pacing rate predicts in this case a response almost three times larger then the measured response but again, but again a good qualitative agreement is found between the two signals. The comparison of the responses in the frequency domain, shows again that the simulation model that accounts for imperfect walking behaviour leads to the best approximation of the measured response. The comparison in frequency domain shows that both simulated and measured responses are clearly dominated by the contribution of the second mode ($\tilde{f}_2$).

The results of the numerical simulations should be analysed critically. Although the modelling errors of the calibrated model of the structure are limited to the higher frequencies, all identified damping ratios are subject to a significant degree of uncertainty. The identification of the main step frequency and pacing rate from the registered walking behaviour of each test-subject, enables a good approximation of the imperfect real walking forces with small differences due to the application of the generalised force model. The difference in amplitude between the predicted and measured response presented in figure 9, is striking and cannot simply result from these remaining uncertainties. The difference may be explained by an increase in damping as a result of the larger vibration amplitudes or the presence of the pedestrians. Due to the fact that the dominant mode has a very small modal damping ratio ($\tilde{\xi}_2 = 0.19\%$) and a low modal mass (2217 kg), it can be expected that even six persons (together 477 kg) have a non-negligible impact on the dynamic behaviour of the structure.

The present analysis shows that the considered lightweight steel footbridge is highly sensitive to human induced vibrations and can be an interesting case to study human-structure interaction. In view of this objective, additional experiments will be performed including motion tracking for multiple test-subjects.

5 CONCLUSIONS

A 3D motion tracking technique is presented for the in situ analysis of the walking behaviour of pedestrians. The technique enables to identify the main step frequency and pacing rate of the test-subject. Applying a generalised model for the ground reaction forces available in literature, based on the weight of the test-subject and the identified pacing rate, provides a good approximation of the imperfect real walking forces.

The technique is applied in a unique experiment where simultaneously the behaviour of (groups of) pedestrians and the structural response of a lightweight steel footbridge is registered. From the registered motion of the pedestrians, the pacing rate and the rate of synchronisation among the pedestrians can be identified. Numerical simulations are performed applying series of moving single footsteps and a calibrated numerical model of the structure. The results show that the traditionally assumed perfectly periodic forces clearly overestimate the structural response. A good qualitative agreement is found between the simulations that account for imperfect real walking behaviour and the measured response. The remaining difference in amplitude of the predicted and measured response may be explained by an increased damping as the result of the increase in amplitude of the structural response and human-structure interaction.

ACKNOWLEDGMENTS

We thank Prof. I. Jonkers and Prof. B. Vanwanseele for the cooperation and the support in the framework of the interdepartmental research laboratory (MALL) at Faber at KU Leuven.

This research is funded by the Agency for Innovation by Science and Technology in Flanders (IWT). Their financial support is gratefully acknowledged.

REFERENCES

Brownjohn, J., P. Fok, M. Roche, & P. Moyo (2004). Long span steel pedestrian bridge at Singapore Changi Airport-part 1: Prediction of vibration serviceability problems. *The Structural Engineer 82*(16), 21–27.

Brownjohn, J., P. Fok, M. Roche, & P. Omenzetter (2004). Long span steel pedestrian bridge at Singapore Changi Airport part 2: Crowd loading tests and vibration mitigation measures. *The Structural Engineer 82*(16), 28–34.

Butz, C., M. Feldmann, C. Heinemeyer, & G. Sedlacek (2007). SYNPEX: Advanced load models for synchronous pedestrian excitation and optimised design guidelines for steel footbridges. Report, Research Fund for Coal and Steel.

Caetano, E., A. Cunha, F. Magalhães, & C. Moutinho (2010). Studies for controlling human-induced vibration of the Pedro e Inês footbridge, Portugal. Part 1: Assessment of dynamic behaviour. *Engineering Structures 32*, 1069–1081.

Hudson, M. & P. Reynolds (2012). Implementation considerations for active vibration control in the design of floor structures. *Engineering Structures 44*, 334–358.

Kijewski-Correa, T. & J. Pirnia (2007). Dynamic behaviour of tall buildings under wind: insights from full-scale monitoring. *The Structural Design of Tall and Special Buildings* (16), 471–486.

Li, Q., J. Fan, J. Nie, Q. Li, & Y. Chen (2010). Crowd-induced random vibration of footbridge and vibration control using multiple tuned mass dampers. *Journal of Sound and Vibration* (329), 4068–4092.

Papadimitriou, C. & G. Lombaert (2011). The effect of prediction error correlation on optimal sensor placement in structural dynamics. *Mechanical Systems and Signal Processing*.

Peeters, P. & G. De Roeck (1999). Reference-based stochastic subspace identification for output-only modal analysis. 13(6), 855–878.

Racic, V., A. Pavic, & P. Reynolds (2009). Experimental identification and analytical modelling of walking forces: a literature review. *Journal of Sound and Vibration 326*, 1–49.

Reynders, E. & G. De Roeck (2008). Reference-based combined deterministic-stochastic subspace identification for experimental and operational modal analysis. *Mechanical Systems and Signal Processing 22*(3), 617–637.

Reynders, E., R. Pintelon, & G. De Roeck (2008). Uncertainty bounds on modal parameters obtained from Stochastic Subspace Identification. 22(4), 948–969.

Van den Broeck, P., K. Van Nimmen, B. Gezels, E. Reynders, & G. De Roeck (2011, July). Measurement and simulation of the human-induced vibrations of a footbridgee. In G. De Roeck, G. Degrande, G. Lombaert, and G. Müller (Eds.), *Proceedings of the 8th International Conference on Structural Dynamics EURODYN 2011*, Leuven, Belgium, pp. 941–948. CD-ROM.

Van Nimmen, K., P. Van den Broeck, G. Lombaert, & G. De Roeck (2013, June). Identification of near-periodic walking behaviour from inertial motion tracking. In *Proceedings of the 4th International Conference on Computational Methods in Structural Dynamics and Earthquake Engineering*, Kos, Greece.

Živanović, S., A. Pavic, & P. Reynolds (2005). Vibration serviceability of footbridges under human-induced excitation: a literature review. *Journal of Sound and Vibration 279*(1–2), 1–74.

Research and Applications in Structural Engineering, Mechanics and Computation – Zingoni (Ed.)
© 2013 Taylor & Francis Group, London, ISBN 978-1-138-00061-2

Vibrations in a multi-storey lightweight building structure: Influence of connections and nonstructural mass

L.V. Andersen & P.H. Kirkegaard
Department of Civil Engineering, Aalborg University, Aalborg, Denmark

ABSTRACT: This paper provides a quantification of the changes in vibration level that can be expected in a lightweight multi-storey wooden building due to reduced connection stiffness or added nonstructural mass. Firstly, the impact of changes in the floor-to-wall connections is examined. Secondly, a study is performed regarding variations of the vibration level due to different placements of nonstructural mass inside the building. The analyses are carried out by means of a modular three-dimensional finite-element model. Each floor and wall panel is modelled in high detail, including door and window openings. By a substructure approach, the panels are assembled to construct a global building model that allows analysis within a reasonable computation time.

1 INTRODUCTION

Timber is an environmentally friendly building material and with the recent progress in construction methods and structural engineering it has become possible to construct large multi-storey wooden buildings. However, transmission of noise and vibrations between residential units in such lightweight structures is a potential risk. Assessment of the dynamic performance in the design stage is therefore necessary. In this context, a correct modelling of the connections between wall and floor panels and the main structure may be important. Further, since the building itself has limited mass, furniture and other nonstructural elements can have significant impact on the dynamic properties of the structure.

In the low and mid-frequency range, statistical energy analysis (Craik 1996) and the European standard EN12354-1 (European Committee for Standardization 2000) provide unreliable results for lightweight structures (Mahn 2007). Instead, analysis can be performed by utilization of a finite-element (FE) model as proposed by, for example, Brunskog and Davidsson (2004), Løvholt et al. (2011), Maluski and Gibbs (2000), or Fiala et al. (2007). However, a solid FE model including structural details such as individual joist and studs will contain millions of degrees of freedom if several wall and floor panels are to be included in a model of a multi-storey building.

Andersen et al. (2012) proposed the use of a modular FE model in which the walls and floors are treated as substructures, leading to a significant reduction of the number of degrees of freedom. This approach is employed in the present paper for dynamic analysis of a four-storey building. The analyses have been made in the frequency domain within the range 0–250 Hz.

In order to study the influence of nonstructural mass in terms of furniture or persons present in the rooms of the building, the model is constructed such that discrete masses can be added at a number of points on each floor. Ohayon and Soize (1998) suggested the application of fuzzy structures for these unknown secondary systems. However, for simplicity a mass of 100 kg is utilized to represent a nonstructural element in the present analyses. The impact of placing additional mass on a dynamically excited floor, or by placing the mass on other floors, has been examined. Further, the influence of having hinged, semihinged or rigidly coupled connections between walls and floors has been examined.

2 FINITE-ELEMENT BUILDING MODEL

A finite-element (FE) model of the building has been created in the commercial software code Abaqus 6.12-2 (Dassault Systèmes Simulia Corp. 2012), utilizing Python scripting and a substructure approach. Firstly, based on rigorous FE models and system reduction, substructures are extracted for each wall and floor panel. These substructures are then assembled to form a building model that is two rooms in length, four storeys high, and one room wide. The module sizes in the length (x), height (y) and width (z) directions are $L = 6.0$ m, $H = 3.0$ m, and $W = 4.2$ m, respectively. Figure 1 provides an illustration of the global FE model. In the following subsections, more details will be given about the panel substructure models as well as the assembly of the global model.

2.1 *Panel substructures*

Three different lightweight panels are modelled and analysed, i.e. wall panels to be used as vertical divisions in the global x and z-directions, and floor panels to form the horizontal divisions in the global

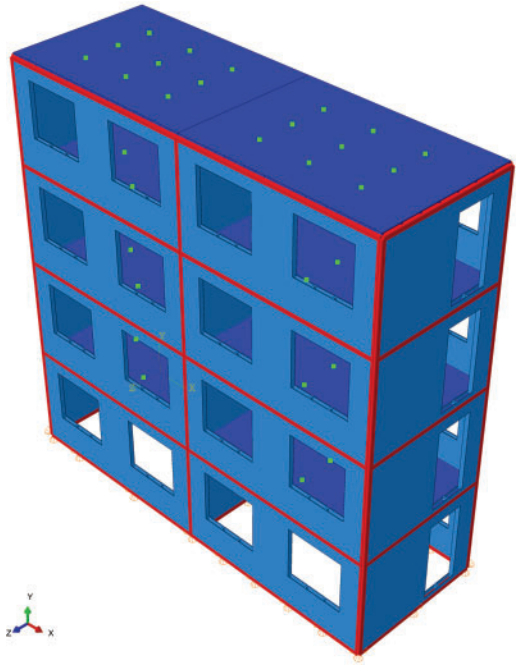


Figure 1. Building model. The green dots indicate positions at which loads or discrete nonstructural masses may be applied.

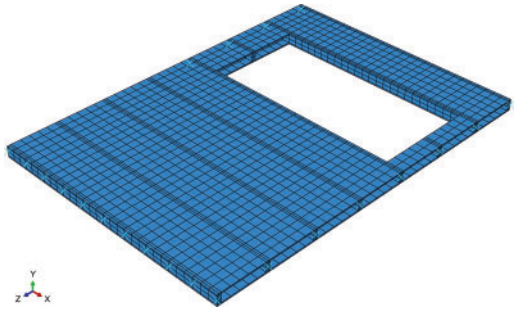


Figure 2. FE model of $4.2 \times 3.0\,\mathrm{m}^2$ (width × height) wall panel for vertical divisions in the global x-direction.

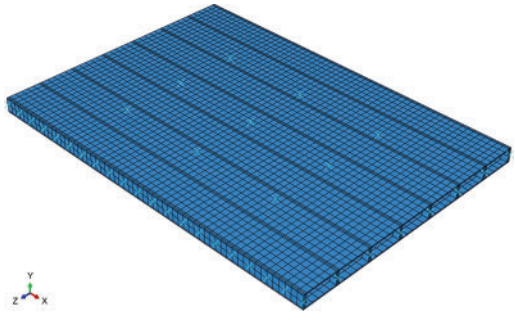


Figure 3. FE model of $6.0 \times 4.2\,\mathrm{m}^2$ (length × width) floor panel for horizontal divisions in the global y-direction.

y-direction. All panels are made of wood, simplified as an isotropic linear viscoelastic material with Young's modulus 9.5 GPa, Poisson's ratio 0.35, and mass density $455\,\mathrm{kg/m}^3$. Structural damping with a loss factor of 1% has been employed in all parts of the model.

The walls parallel to the (y,z)-plane have the overall dimensions $(W \times H) = 4.2 \times 3.0\,\mathrm{m}^2$ and a thickness of 130 mm. They are made as double-leaf panels with two 15 mm thick plates connected to a set of vertical studs. The studs have a cross-sectional area of $100 \times 50\,\mathrm{mm}^2$, and the centre-to-centre distance is 600 mm, leading to a total of eight studs in each panel including the two members placed along the sides of the panel. Glued connections are assumed between the plates and the studs, i.e. the structural members are fully tied on the interfaces, and a door opening has been cut in each wall panel as illustrated in Figure 2. The opening is 2.40 m high, 1.15 m wide, and it is placed 0.20 m from the bottom of the panel. The model is discretized into 20-node brick finite elements with quadratic spatial interpolation of the displacement field and full integration of the mass and stiffness. A maximum mesh size of 100 mm is allowed in the structured hexahedral mesh. The cross sections of the studs are subdivided into four elements, two in each of the width and thickness directions.

Similarly, the floors of the building are made as lightweight timber panels with the dimensions $(L \times W) = 6.0 \times 4.2\,\mathrm{m}^2$. They consist of two plates connected to joists placed along the length direction. The plates have a thickness of 20 mm, whereas the joists are 50 mm wide and 200 mm high, providing a total panel height of 240 mm. The distance between the joists, centre-to-centre, is 600 mm. An illustration is given in Figure 3. Again 20-node brick elements have been employed, using the same meshing rules as for the wall panel providing the horizontal divisions in the x-direction.

Finally, the walls parallel to the (x,y)-plane have the dimensions $(L \times H) = 4.2 \times 3.0\,\mathrm{m}^2$ and a thickness of 130 mm. The model contains two window openings as illustrated in Figure 4. Each window has a height of 1.6 m and it is placed 1.0 m from the bottom of panel. As in the case of the other two panel models, a discretization into 20-node brick elements with a maximum mesh size of 100 mm is carried out.

For each of the three panels, a system reduction is carried out in order to provide a substructure macro finite element. As proposed by Craig and Bambton (1968) and further explained by Craig (1981), the system matrices achieved by Guyan reduction (Guyan 1965) of the system matrices has been enriched by a set of internal modes of a model fixed at the retained degrees of freedom.

In the present analyses, original nodes have been retained on along the edges of the panels with a distance of 300 mm. Only the nodes at the middle plane of the panels are retained. For example, 11 nodes are retained along the sides of the wall panels, one per

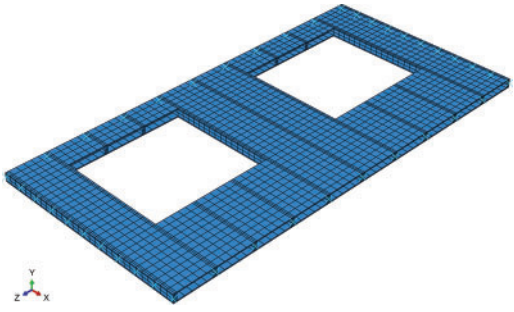


Figure 4. FE model of $6.0 \times 3.0\,m^2$ (length × height) wall panel for vertical divisions in the global z-direction.

three elements over the height direction, and one node is retained at the centre of the end cross sections of the studs. For the wall panel shown in Figure 2 this provides a total of 34 retained nodes. Additional retained nodes are included in the floor panel substructure to allow the application of loads as well as discrete nonstructural masses. The nodes are placed on the top of the floor in the one-half and one-quarter points, leading to a total of nine additional retained nodes per floor panel. The retained nodes are marked by crosses in Figures 2–4.

In the original panel FE models, nodes are only associated with translational degrees of freedom. To allow coupling of rotations between adjacent panels, artificial shell elements have been introduced in the cross sections of the beams at the positions of the retained nodes along the panel edges. These shells have a thickness of 10 mm, a mass density of $0.01\,kg/m^3$ and a Poisson's ratio of 0. The elements are only intended to provide rotational stiffness. In the reference model, Young's modulus is 10^7 GPa, ensuring full rotational rigidity. Two alternative models of each panel are analysed: A model with semi-hinged connections in which Young's modulus of the shells is 10^4 GPa, and a model with hinged connections, obtained by defining Young's modulus of the shells as 10 GPa.

2.2 *Global assembly and analysis*

The substructures created from the FE models of the wall and floor panels are assembled to form the building illustrated in Figure 1. Following the approach proposed by Andersen et al. (2012) and Kiel et al. (2012), the individual substructures are attached to an artificial skeleton made of beam elements with nearly no mass. The stiffness of the skeleton is made high enough to avoid spurious modes of vibrations and low enough to prevent significant impact on the overall static and dynamic properties of the building. In the present case, 3-node Timoshenko beam elements with a node distance of 300 mm and a cross-sectional area of $10 \times 10\,mm^2$ are adopted. A mass density of $1\,kg/m^3$ and a Young's modulus of 1 GPa are applied. The total mass of the building is 11,294 kg, and the global model has 35,000 degrees of freedom.

Two types of analysis are carried out. Firstly, the undamped eigenfrequencies are determined in the frequency range 0–250 Hz. Secondly, the steady state response of the building to time-harmonic excitation is determined at 2001 uniformly distributed discrete frequencies in the interval 0–250 Hz. The load is applied as a concentrated force with unit amplitude and acts vertically in the middle of the Floor 1-2-1 which is the floor belonging to room 1 in the x-direction, room 2 in the y-direction, and room 1 in the z direction. With reference to Figure 1, this is the leftmost room of the second storey. Likewise, Floor 1-3-1 is the floor right above Floor 1-2-1, and Floor 2-4-1 belongs to the rightmost room of the top storey. The eigenvalue problem is solved in 104 s on an Intel i7 CPU 860@ 2.80 GHz, using a single core. Computation time for the steady state analysis is about 3.0 s per frequency. The analyses are performed for buildings with different connection stiffness and added nonstructural mass. The following models are considered:

- A reference building model with rotationally rigid joints and no added mass,
- a model with 100 kg of nonstructural mass placed at each of the nine points on every floor in the left side of the building, i.e. the side where the force is applied,
- a model with 100 kg of nonstructural mass added to the similar points in the right side of the building, i.e. the unloaded side,
- a model with 100 kg of nonstructural mass added to all points in all rooms,
- a model with semi-hinged connections obtained by reducing the stiffness of the shell elements used for coupling of the rotational degrees of freedom,
- a model with hinged connections obtained by a further reduction of of the shell stiffness.

3 RESULTS AND DISCUSSION

3.1 *Eigenfrequencies*

Figure 5 shows a mode count for different floor panels. The first natural frequency of the reference floor, fixed at the retained edge nodes, is 42.5 Hz, while the corresponding values for the semi-hinged and hinged floors are 35.3 Hz and 30.1 Hz, respectively. For a pinned floor, all models provide a first natural frequency of 30.1 Hz. Hence, the hinged connections and the reference building model provide two limits. In the first case, the building will act as if only the translational degrees of freedom are tied at the connections between adjacent panels, whereas all degrees of freedom (including rotational degrees of freedom) are effectively tied in the reference building model.

Further, in Figure 5 it is observed that the modal density is not significantly influenced by the boundary conditions, i.e. the overall mode count is the same for all models. However, a pronounced increase of the modal density occurs beyond 300 Hz.

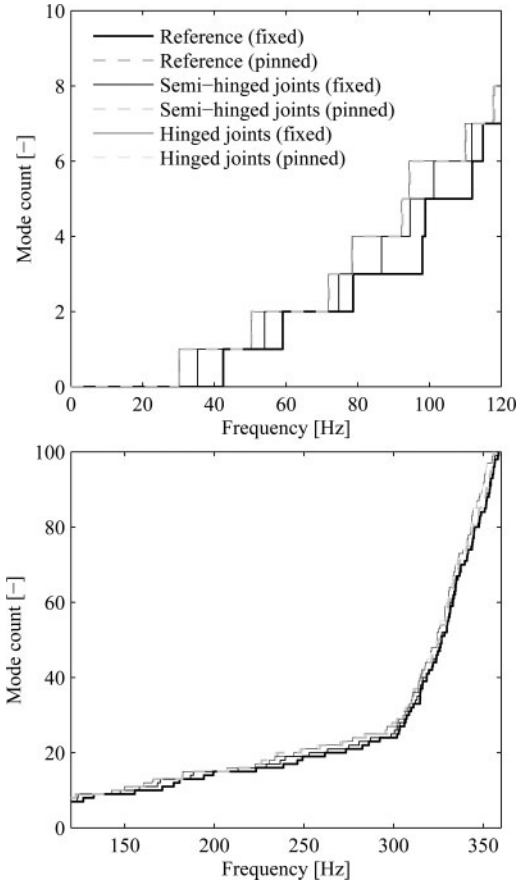


Figure 5. Mode count for floor panels with different connection stiffness and pinned or fixed along the edge. Top: Frequency range 0–120 Hz. Bottom: Frequency range 120–360 Hz.

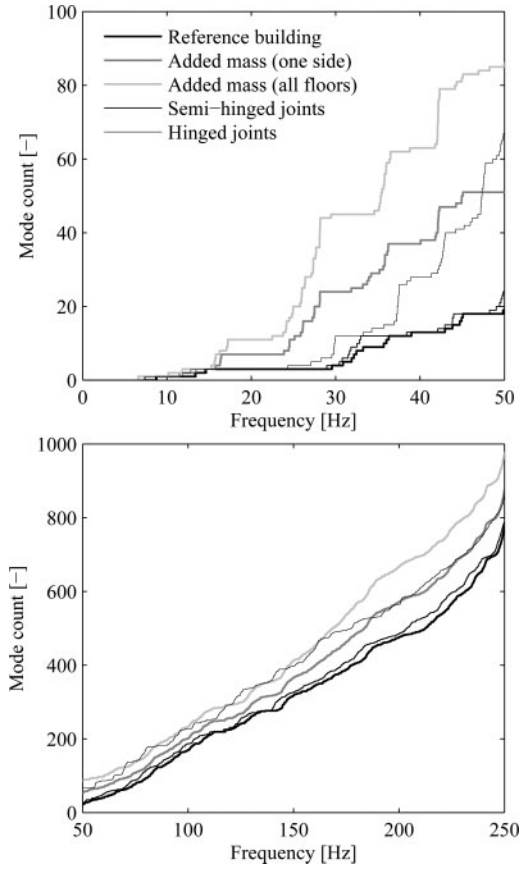


Figure 6. Mode count for global building models with different added mass and connection stiffness properties. Top: Frequency range 0–50 Hz. Bottom: Frequency range 50–250 Hz.

Mode counts for the building models listed above are provided in Figure 6. As expected, added nonstructural mass leads to a higher modal density in the low-frequency range. Especially, the first natural frequencies related to resonance of the floors with added mass are 15.6–17.2 Hz, and several additional floor vibration modes occur in the range 24.0–28.2 Hz. For the reference building with no added mass, the first floor vibration modes occur around 30 Hz, and the next modes occur near 50 Hz.

In the low-frequency range, only small differences are observed in the mode counts for the reference building and the model with semi-hinged connections—especially within the low-frequency range. As expected, the reduced stiffness leads to a small reduction of the natural frequencies related to floor vibrations, but it has only got a marginal impact on the global modes of the building. However, compared to the reference building model, the model with hinged connections has significantly more modes in the frequency range 25–50 Hz. At frequencies near 80 Hz and from 120–145 Hz, the mode count for the model with hinges is even higher than the model with nonstructural mass added to every floor.

3.2 *Steady state response to harmonic excitation*

For each floor panel in the building, the steady state response has been extracted at the nine nodes which are retained on the top of the floor. The complex amplitudes of velocity are considered, and a root-meansquare (RMS) value is obtained for each floor as:

$$\langle V \rangle_{\mathrm{RMS}} = \sqrt{\frac{1}{9} \sum_{n=1}^{9} \mathbf{V}_n^H \mathbf{V}_n}, \tag{1}$$

where $\mathbf{V}^n$ is the complex velocity amplitude vector at node n, and $\mathbf{V}_n^H$ denotes its conjugate transpose. Figures 7 to 12 show the RMS velocity response measured in decibel according to the definition

$$\langle V \rangle_{\mathrm{RMS}}^{\mathrm{dB}} = 20 \log_{10} \left(\frac{\langle V \rangle_{\mathrm{RMS}}}{V_0} \right), \quad V_0 = 1 \text{ nm/s}. \tag{2}$$

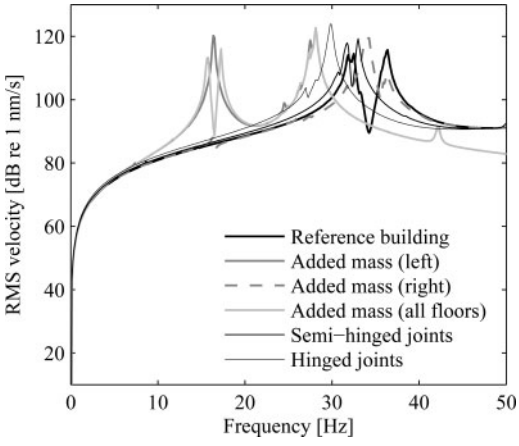


Figure 7. Steady state response to harmonic point force excitation in the middle of Floor 1-2-1; RMS velocities of Floor 1-2-1 in the low-frequency range 0–50 Hz.

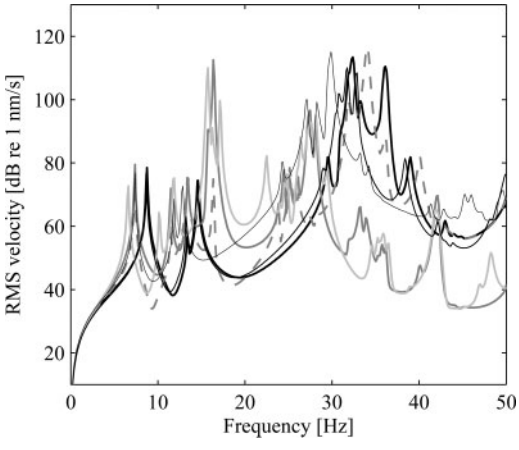


Figure 8. Steady state response to harmonic point force excitation in the middle of Floor 1-2-1; RMS velocities of Floor 1-3-1 in the low-frequency range 0–50 Hz.

In Figures 7 and 10 it is observed that the maximum response occurs near the natural frequencies of the loaded floor, i.e. Floor 1-2-1. When nonstructural mass has been added on the floor, the velocity response is overall decreasing with an increase of the frequency, whereas the trend is the opposite for a floor with no added mass. No influence of added mass in the other (right) side of the building is visible.

Figures 8 and 11 show results for Floor 1-3-1 which is placed in the room right above the room with the loaded floor. As expected, added nonstructural mass has led to a reduction of the frequencies related to the first global modes of resonance of the building. At higher frequencies, the response is again lower (about 40 dB lower) for the two cases with added mass on the loaded floor, but no significant impact of added mass in the other side of the building can be observed. Further, the hinged connections lead to a response

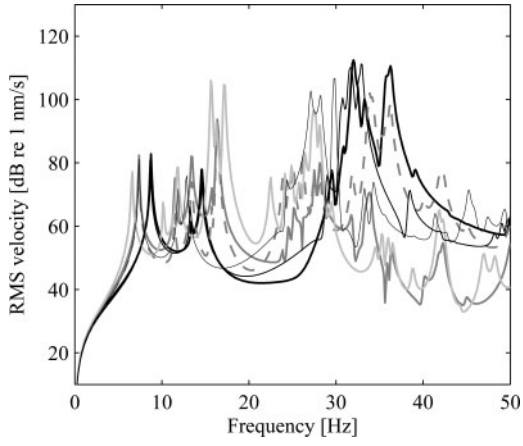


Figure 9. Steady state response to harmonic point force excitation in the middle of Floor 1-2-1; RMS velocities of Floor 2-4-1 in the low-frequency range 0–50 Hz.

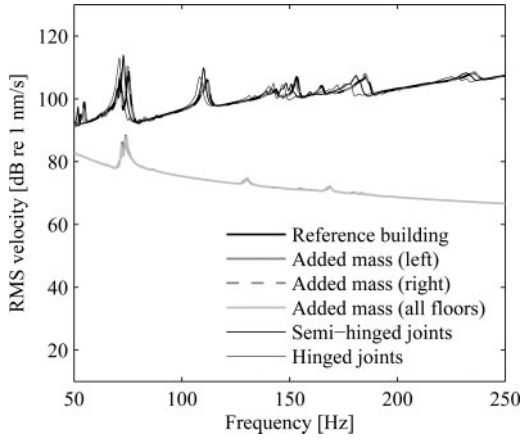


Figure 10. Steady state response to harmonic point force excitation in the middle of Floor 1-2-1; RMS velocities of Floor 1-2-1 in the mid-frequency range 50–250 Hz.

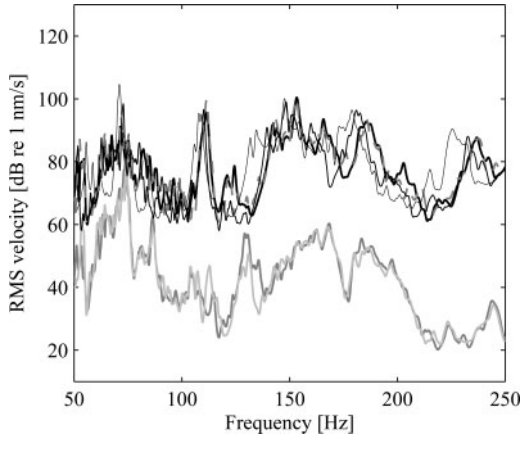


Figure 11. Steady state response to harmonic point force excitation in the middle of Floor 1-2-1; RMS velocities of Floor 1-3-1 in the mid-frequency range 50–250 Hz.

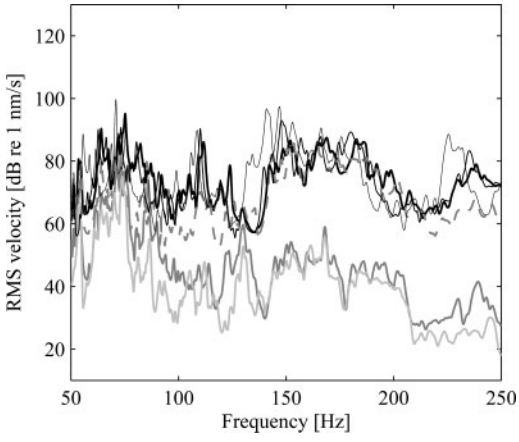


Figure 12. Steady state response to harmonic point force excitation in the middle of Floor 1-2-1; RMS velocities of Floor 2-4-1 in the mid-frequency range 50–250 Hz.

which is in some frequency intervals 10–20 dB higher or lower than the response in the reference case.

Finally, Figures 9 and 12 illustrate the response of Floor 2-4-1 in the room that is farthest away from the loaded floor. Interestingly, there is only a small influence of adding nonstructural mass on the floor itself, i.e. in the right side of the building. Again, the main influencing factor is nonstructural mass placed in the left side of the building, i.e. where the load is applied.

4 CONCLUSIONS

The influence of added nonstructural mass and reduced wall–floor connection stiffness in a lightweight multi-storey wooden building has been examined regarding the dynamic structural response.

It has been found that a significant change in the stiffness of the connections between walls and floors can occur without any substantial influence on the global dynamic response. In the considered case of a concentrated vertical harmonic force, vibrating in the middle of a single floor, differences less than about 10 dB are generally obtained in the RMS velocities related to floor vibration. Hence, variations of the connection stiffness due to, for example, craftsmanship are not likely to have an impact on the overall dynamic response of a building dramatically. However, the stiffness of the individual floors, and therefore the local modes of resonance, may be influenced.

When nonstructural mass is added to the loaded floor, the response of the entire building is generally change significantly. Differences of about 40 dB have been observed in the RMS floor vibration velocities. On the other hand, placing nonstructural mass on the floors in the other side of the building has minor impact on the response—even in rooms in the other side of the building far away from the load. This is an important result regarding performance and analysis of vibration measurements in real lightweight buildings.

ACKNOWLEDGEMENT

The present research is part of the Interreg project "Silent Spaces", funded by the European Union. The authors highly appreciate the financial support.

REFERENCES

Andersen, L., P. Kirkegaard, K. Persson, & B. Niu (2012). A modular finite element model for analysis of vibration transmission in multi-storey lightweight buildings (Paper 189). In B. Topping (Ed.), *Proceedings of the Eleventh International Conference on Computational Structures Technology*, Volume 99 of *Civil-Comp Proceedings*, Stirlingshire, Scotland. Civil-Comp Press.

Brunskog, J. & P. Davidsson (2004). Sound transmission of structures. A finite element approach with simplified room description. *Acta Acustica united with Acustica 90*, 847–857.

Craig, R. (1981). *Structural dynamics: An introduction to computer methods*. New York: John Wiley & Sons Inc.

Craig, R. & M. Bambton (1968). Coupling of substructures for dynamic analysis. *AIAA Journal 6(7)*, 1313–1319.

Craik, R. (1996). *Sound Transmission Through Buildings: Using Statistical Energy Analysis*. Aldershot: Gower.

Dassault Systèmes Simulia Corp. (2012). *Abaqus 6.12 Analysis User's Manual*. Providence, RI, USA: Dassault Systèmes Simulia Corp.

European Committee for Standardization (2000). *EN 12354-1:2000 Building Acoustics. Estimation of Acoustic Performance in Buildings from the Performance of Elements. Airborne Sound Insulation between Rooms* (3rd ed.). European Committee for Standardization.

Fiala, P., G. Degrande, & F. Augusztinovicz (2007). Numerical modelling of ground-borne noise and vibration in buildings due to surface rail traffic. *Journal of Sound and Vibration 301*, 718–738.

Guyan, R. (1965). Reduction of stiffness and mass matrices. *AIAA Journal 3(2)*, 380.

Kiel, N., L. Andersen, N. Niu, & K. Persson (2012). Different modelling approaches to coupling wall and floor panels within a dynamic finite element model of a lightweight building (Paper 190). In B. Topping (Ed.), *Proceedings of the Eleventh International Conference on Computational Structures Technology, Volume 99 of Civil-Comp Proceedings*, Stirlingshire, Scotland. Civil-Comp Press.

Løvholt, F., C. Madshus, & K. Norén-Cosgriff (2011). Analysis of low frequency sound and sound induced vibration in a Norwegian wooden building. *Noise Control Engineering Journal 59(4)*, 383–396.

Mahn, J. (2007). Prediction of flanking noise transmission in lightweight building constructions: A theoretical and experimental evaluation of the application of en12354-1. Technical report, University of Canterbury, Acoustics Research Group.

Maluski, S. & B. Gibbs (2000). Application of a finite-element model to low-frequency sound insulation in dwellings. *Journal of the Acoustical Society of America 108(4)*, 1741–1751.

Ohayon, R. & C. Soize (1998). *Structural Acoustics and Vibration*. San Diego: Academic Press.

Research and Applications in Structural Engineering, Mechanics and Computation – Zingoni (Ed.)
© 2013 Taylor & Francis Group, London, ISBN 978-1-138-00061-2

Direct velocity feedback versus a geometric controller design of remotely located vibration control systems

D.S. Nyawako, U. Ubaid, P. Reynolds & M.J. Hudson
Departments of Civil and Structural Engineering and Automatic Control and Systems of Engineering, The University of Sheffield, Sheffield, UK

ABSTRACT: The mitigation of human induced vibrations in floors continues to be a key area of research particularly as a result of advancement in material and design technologies enabling the design of light, slender and more open plan structures. These floors are typically characterised by low and close natural frequencies as well as low modal damping ratios, and these combinations of factors contribute to their increased susceptibility to human induced vibrations. Amongst the remedial measures pursued to enhance their vibration serviceability performance, active vibration control (AVC) technologies are emerging as a viable technology and predominantly direct output feedback approaches have been pursued in past analytical studies and field trials.

It has often been assumed that actuators and sensors can be located where vibration attenuation is desired and this may not always be feasible. The research work presented in this paper compares the vibration mitigation performances of the direct velocity feedback scheme that has been extensively used in past floor vibration control researches against a geometric controller design approach that has been developed to provide a design freedom for reducing vibration in both local and remote locations. The geometric controller design approach assumes the inability to locate the actuators and sensors at the remote location but acknowledges that this measurement can be obtained during the commissioning stage and used during the design phase to enhance both local and remote locations. All the analytical and experimental studies are based on a laboratory structure. The work demonstrates comparable vibration mitigation performances of the dominant mode of vibration of the laboratory structure for both approaches but also demonstrates potential for additional enhancement to the second vibration mode of the laboratory structure with the geometric controller design approach. Approximately 20–25 dB attenuation in the first and second vibration modes of the laboratory structure were achieved.

Keywords: active control, human-induced vibrations, geometric controller design

1 INTRODUCTION

Vibration serviceability is now the dominant design criterion for many floor structures, mainly in the commercial sector due to two key factors. Firstly, modern floors are more slender and lightweight than in the past as a result of improved design methods, structural materials and constructiontechnologies. The drivers for improved construction technology include reduced economic cost, increased flexibility of usage, and lower carbon footprints due to reduced material usage. Secondly, there is a trend towards more open plan floor layouts that have fewer full height partition walls than in the past. This reduces the amount of inherent damping present in finished floor structures and hence increased levels of response to human induced excitation. These floors are also characterised by low and close natural frequencies which fall within the range of frequencies produced by human activities as well as their harmonics.

Amongst the remedial measures pursued to enhance the vibration serviceability performance of office floors, AVC technologies are emerging as a promising and viable technology. This has been seen in some past field trials. In those investigations, combinations of direct output feedback (DOFB) and model-based AVC control schemes were successfully used to augment damping for selected vibration modes in each of the floors studied and in the process suppress human-induced vibrations[1,2,3,4,5,6]. Predominantly single-input-single-output (SISO) and multi-SISO collocated sensor and actuator pairs were utilized in both the DOFB, for example, direct velocity feedback (DVF) and model-based controller schemes. In most of these past implementations of AVC in office floors, it was possible to site actuator and sensor pairs at required locations. There was one case in which it was not possible to site the actuators and sensor pairs at a desired location.

Recently, a geometric controller design approach for harmonic or broadband control of remotely located vibration has been developed for trials in the marine and aerospace sectors for large scale structures or those exposed to harsh environments[7,8,9]. The concept behind this controller design approach is that for large scale structures or where the system environment is harsh, it may not be feasible to locate sensors or even actuators where vibration attenuation is desired or this may be prohibitively expensive. The optimal control of local vibration may in turn result in an enhancement at remote locations. These researches therefore define a design freedom for reducing vibration both at local and remote points, and can be applied for either discrete frequency and/or broadband control and often involves an inversion of the local path plant dynamics. The geometric controller design approach assumes the inability to locate the actuators and sensors at the remote location but acknowledges that this measurement can be obtained during the commissioning stage and used during the design phase to enhance both local and remote locations. This approach may in turn be beneficial for floor vibration control in which, as the authors have found out, the presence of services or other facilities may often hinder the siting of actuators and sensors at desired locations.

The research work presented here compares vibration mitigation performances between the DVF control scheme and the geometric controller design approach. An overview of the design methodologies for each of the controller schemes and appropriate compensators designed to achieve desired closed-loop specifications with the plant model known are presented. Some stability studies are shown as well as a brief insight into the use of the geometric controller approach for controlling both local and remote vibration. The work in this paper is organized as follows: section 2 introduces the plant and actuator dynamics as well as an overview of the design methodologies with DVF and the geometric controller design approach. Also shown are results of stability studies for both controller design approaches. In section 3, the results of uncontrolled and controller frequency response functions (FRFs) in both the analytical studies and experimental implementation are presented and some conclusions are included in section 4.

2 PLANT MODEL AND CONTROLLER SCHEMES

The laboratory structure used for the AVC studies is a simply-supported in-situ cast post-tensioned slab strip with a span of 10.8 m, width of 2.0 m and depth of 275 mm. The dynamic properties for the AVC studies are evaluated from a point accelerance FRF test in figure 1c using a collocated sensor and actuator pair (S1, A1) as shown in figures 1a and 1b. Figure 1c also shows the transfer function between actuator A1 and remote sensor S2 which is an additional measurement used for the geometric controller design. An analytical

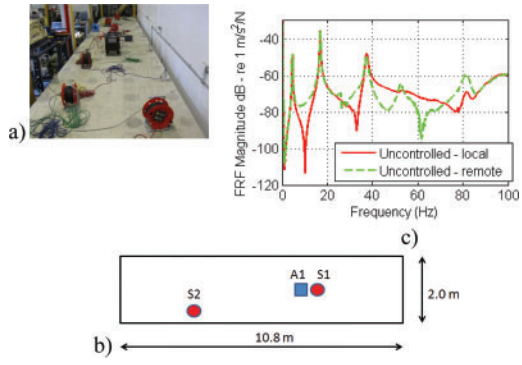


Figure 1. Plan view of laboratory structure showing test location for AVC studies and measured point mobility FRF for AVC design (A1 – actuator 1, S1 – local sensor 1, S2 – remote sensor 2).

Table 1. Estimated modal properties of laboratory structure.

Mode	f_i (Hz)	ζ_i (%)
1	4.45	1.0
2	16.80	0.4
3	37.30	1.0

model of the point accelerance FRF is obtained in the Laplace domain using the modal expansion approach as shown in Eq. 1. s is a complex variable, $\mu_i \geq 0$, ζ_i and ω_i are the inverse of the modal mass, damping ratio and natural frequency associated with the ith mode of vibration. A summary of the modal properties of the first three bending modes of vibration estimated from the EMA test are shown in Table 1.

$$G_s(s) = \sum_{i=1}^{3} \frac{\mu_i s^2}{s^2 + 2\zeta_i \omega_i s + \omega_i^2} \tag{1}$$

The actuators are APS Dynamics model 400 electrodynamic shakers. Their dynamic characteristics, expressed by the transfer function between the force applied to the structure, $f(t)$, and the input voltage command, $v(t)$, can be described by the linear second order system in Eq. 2 when they are driven in the current drive mode, which is the mode of operation used here. $K_c = 300$, $\zeta_{act} = 0.07$ and $\omega_{act} = 8.168$ rads/s are the force-voltage constant, damping ratio and natural frequency, respectively.

$$G_{act}(s) = \frac{K_c s^2}{s^2 + 2\zeta_{act}\omega_{act} s + \omega_{act}^2} \tag{2}$$

DVF with an inner loop compensation for the actuator is shown in figure 2. $C_0(s)$ is a lossy integrator that includes a feedback gain component, γ_{dc}, as shown in Eq. 3. This is designed to impart significant damping in the structure. The designed inner loop actuator

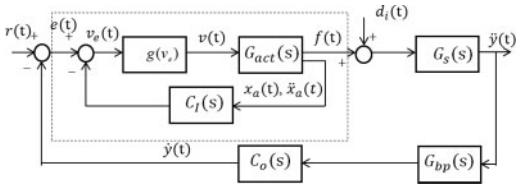


Figure 2. Direct velocity feedback with inner loop actuator compensation.

compensator, $C_I(s)$, is shown in Eq. 4. This achieves a closed-loop transfer function of the actuator inner loop with a frequency of 1.30 Hz and a damping ratio of 0.60. As noted before, DVF is implemented in a SISO set-up with the collocated actuator and sensor pairs A1, S1 shown in figure 1b. $\gamma_{dc} = 300$ and the DVF scheme is designed to achieve damping ratios of 0.16 and 0.075 in modes 1 and 2, and ensures a gain margin (GM) of 9.5 dB and phase margin (PM) greater than 30°. A second-order Butterworth filter with cut-off frequency 1.0–100 Hz is also implemented in both analytical and experimental studies. Stability studies are evaluated using both the root locus plot $G_s(s)G_{act}(s)G_{acomp}(s)C_o(s)$ as shown in figure 3.

$$C_0(s) = \frac{\gamma_{dc}}{s+\beta},\ C_I(s) = \frac{s^2+1.14s+66.72}{s^2+9.80s+66.72} \tag{3,4}$$

where:
$G_s(s)$ Floor model
$G_{act}(s)$ Actuator model
$G_{bp}(s)$ Band pass filter
$f(t)$ Actuator force
$d_i(t)$ Input disturbance
$e(t)$ Error signal
$r(t)$ Reference signal
$g(v_e)$ Saturation nonlinearity
$\ddot{y}(t)$ Structural acceleration response
$\dot{y}(t)$ Structural velocity response
$C_0(s)$ Transfer function of outer loop
$v(t)$ Final control voltage signal
$C_I(s)$ Transfer function of inner loop
$v_e(t)$ Initial control voltage signal
$x_a(t)$ Displacement of actuator moving mass
$\ddot{x}_a(t)$ Acceleration of actuator moving mass

The formulation of the geometric controller design approach is derived from the works of[8,9,10] assuming a two input two output system with the transfer function matrix relating the disturbance and control inputs to the remote (S2 in figure 1c) and local (S1 in figure 1c) vibration outputs as shown in Eq. 5. $y(s)$ and $z(s)$ are the locally measured and remote vibration whilst $u(s)$ and $d(s)$ are the local control force and remote disturbance force, respectively. Eq. 6 shows the control input as a function of the locally measured vibration. These past works have also been extended to deal with stable controller designs for non-minimum phase dynamics. Through the definition of a design variable, $\alpha(s)$ in Eq. 7, the location vibration output, $y(s)$ and remote vibration output, $z(s)$, in the presence of the feedback

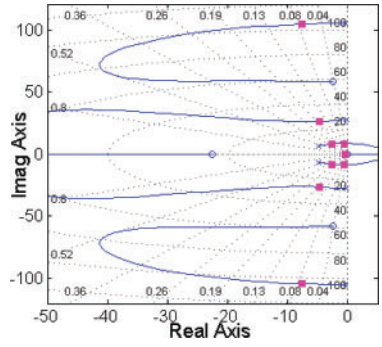


Figure 3. Root locus plot for DVF control scheme.

control signal in Eq. 6 can be expressed as shown in Eqs. 8 and 9. Various design objectives can be outlined through the selection of the design variable, $\alpha(s)$, for example, attenuation of remote vibration without increment in local vibration, or attenuation in vibration of both the remote and local vibration. Further details of specifying the design objectives for either harmonic or global controller can be seen in[8,9,10].

$$\begin{bmatrix} y(s) \\ z(s) \end{bmatrix} = \begin{bmatrix} g_{11}(s) & g_{12}(s) \\ g_{21}(s) & g_{22}(s) \end{bmatrix} \begin{bmatrix} u(s) \\ d(s) \end{bmatrix} \tag{5}$$

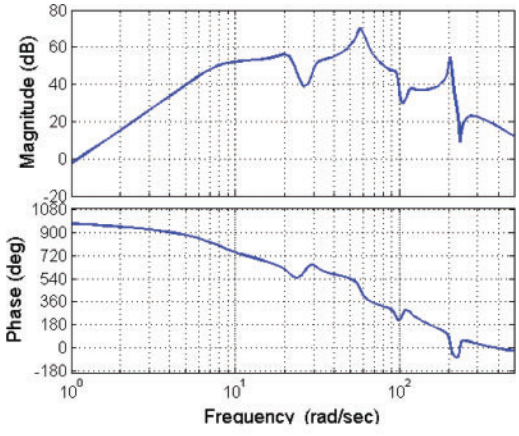
$$u(s) = -k(s)y(s) \tag{6}$$

$$\alpha(s) = -\frac{g_{11}(s)k(s)}{1+g_{11}(s)k(s)} \tag{7}$$

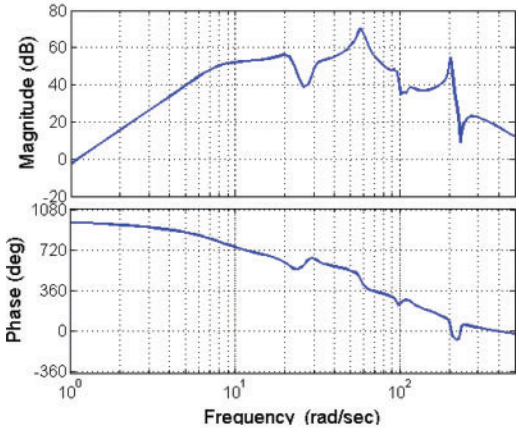
$$y(s) = [1+\alpha(s)]g_{12}(s)d(s) \tag{8}$$

$$z(s) = \left[1+\alpha(s)\frac{g_{12}(s)g_{21}(s)}{g_{11}(s)g_{22}(s)}\right]g_{22}(s)d(s) \tag{9}$$

In the work presented here, $k(s)$ is selected using a parametric design of $\alpha(s)$ to attenuate vibration at both the local point (S1) and remote point (S2) shown in figure 1b. The derived compensators for two different designs: geometric controllers 1 and 2 with this procedure are shown in figures 4a and 4b and figures 5a and 5b show the Nyquist contours for the stability studies. Controller 1 is tuned to offer similar vibration mitigation performance as DVF in both the first and second vibration modes of the laboratory structure whilst with controller 2, it is demonstrated that there is potential to achieve further attenuation in the second mode of vibration i.e. flexibility to isolate and enhance target modes of vibration. From figures 6a and 6b, since the centres of both design 'mobius' circles derived for both local and remote locations from Eqs. 5 to 9 almost overlap[7,8,9], this gives the design freedom to enhance damping at both locations simultaneously. The geometric controller design here includes a 3rd order band pass filter with cut-off frequency 1.75–26.5 Hz.



a) $k_1(s)$



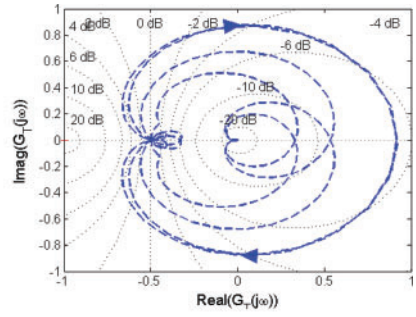
b) $k_2(s)$

Figure 4. Bode plots of compensators $k_1(s)$ and $k_2(s)$ for geometric controller schemes 1 and 2.

3 UNCONTROLLED AND CONTROLLED FREQUENCY RESPONSE FUNCTIONS

The results of uncontrolled and controlled frequency response functions (FRFs) predicted analytically and measured experimentally for both the local and remote locations are shown in figures 7 and 8 for DVF, and geometric controller schemes 1 and 2. They reflect approximately 20–25 dB attenuations of the first and second modes of vibration of the laboratory structure. With the geometric controller (GC) design scheme, since the compensator design incorporates approximate inversion in the plant dynamics, feedback gains have to be curtailed so that the influence of the anti-resonances in the open loop FRF do not degrade the vibration mitigation performances as seen in figures 7 and 8 or in the worst case become sources of instability.

a)



b)

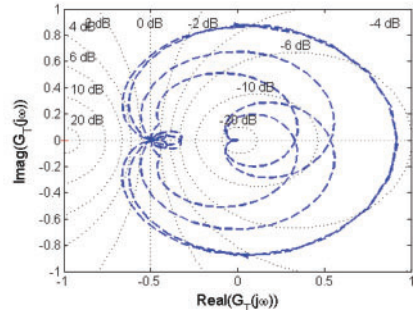
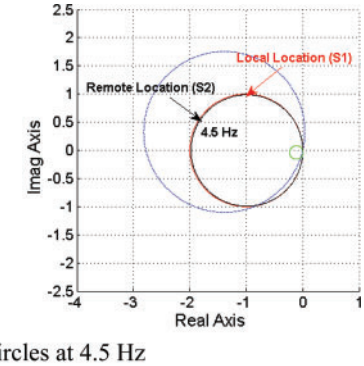
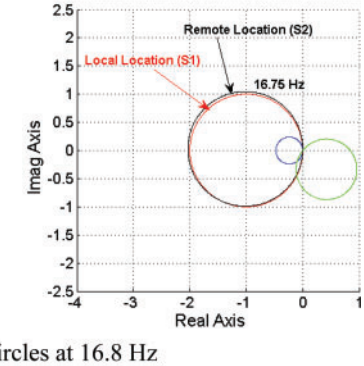


Figure 5. Nyquist contour plots of $G_T(s) = G_s(s)\, G_{act}(s) G_{acomp}(s) k(s)$ for geometric controller schemes 1 and 2.



a) Circles at 4.5 Hz



b) Circles at 16.8 Hz

Figure 6. Design 'mobius' transformation circles showing the lowest bending modes of vibration of the laboratory structure can be enhanced at both at the local (S1) and remote (S2) points with actuator at local location.

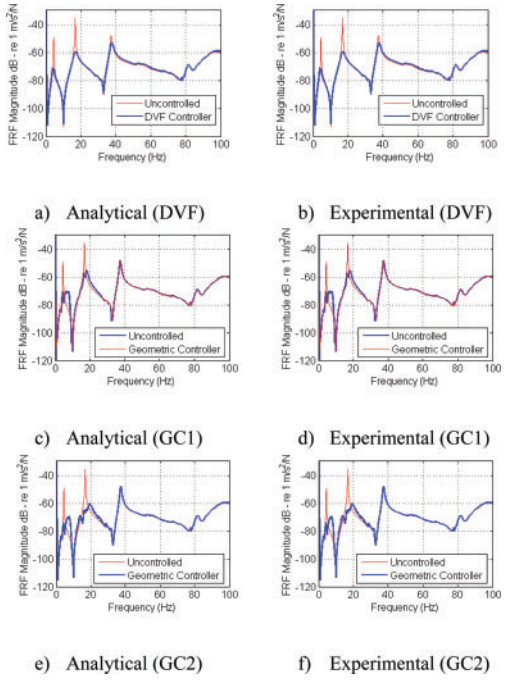


Figure 7. Uncontrolled and controlled FRFs with DVF and Geometric controllers 1 and 2 – FRFs at local location S1 (Local).

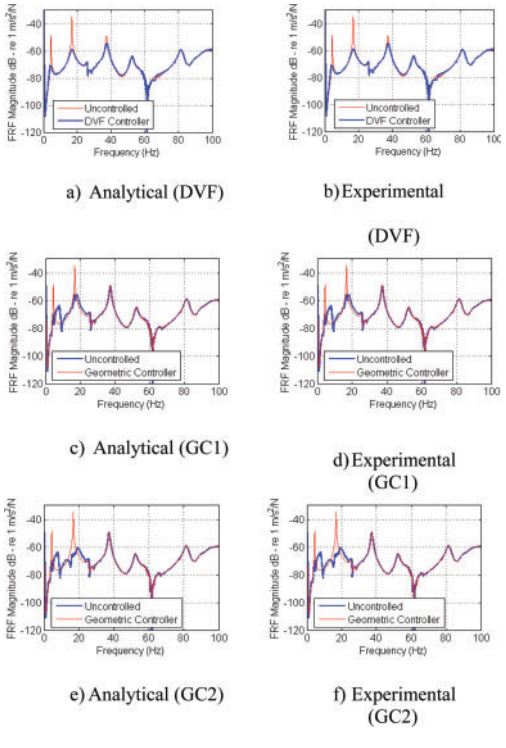


Figure 8. Uncontrolled and controlled FRFs with DVF and Geometric controllers 1 and 2 – FRFs at remote location S2 (Remote).

4 CONCLUSIONS

The geometric controller scheme offers a new design freedom for controlling vibration at both a local and remote location by using design mobius circles. This can be tuned to guarantee that a controller designed does not degrade the vibration serviceability performance at both the local and remote location as outlined in the works of[7,8,9]. This approach to design can be beneficial to AVC of human induced office floor vibrations where the presence of services and other facilities would mean that there are restrictions on the potential locations of sensors and actuators. As a result of the approach making use of an inversion in plant dynamics, additional compensation or gain regulation can be used to ensure the anti-resonances of the open loop system do not degrade the vibration mitigation performance objective. In this work, vibration mitigation performances of DVF and the geometric controller schemes have been found to be quite comparable and there is potential for further attenuation of the second mode of vibration with the geometric controller formulation.

ACKNOWLEDGEMENTS

The authors would like to acknowledge the financial assistance provided by the UK Engineering and Physical Sciences Research Council (EPSRC) through a responsive mode grant entitled “Active Control of Human-Induced Vibration” (Ref: EP/H009825/1), Leadership Fellowship grant entitled “Advanced Technologies for Mitigation of Human-Induced Vibration” (Ref: EP/J004081/1) and Platform Grant entitled “Dynamic Performance of Large Civil Engineering Structures: An Integrated Approach to Management, Design and Assessment” (Ref: EP/G061130/1).

REFERENCES

[1] Reynolds, P., Diaz, I.M., and Nyawako, D.S., Vibration testing and active control of an office floor, In Proceedings of the 27th International Modal Analysis Conference, Orlando, Florida, USA (2009).

[2] Diaz, I.M., and Reynolds, P., Acceleration feedback control of human-induced floor vibrations, Engineering Structures 32, 163–173, (2010).

[3] Diaz, I.M., and Reynolds, P., Robust saturated control of human-induced floor Vibrations via a Proof-Mass Actuator, Smart Materials and Structures 18, 1–10, (2009).

[4] Nyawako, D.S., Reynolds, P., and Hudson, M.J., Findings with AVC design for mitigation of human induced vibrations in office floors, In Proceedings of the 31st International Modal Analysis Conference, Orange County, California, USA (2013).

[5] Diaz, I.M., Pereira E., and Reynolds P., Casado, C.M., Human-induced vibration cancellation using an active mass damper modified by an inner loop, Proceedings of the 8th International Conference on Structural

Dynamics, EURODYN 2011, Leuven, Belgium, 4–6 July, (2011).
[6] Nyawako, D., Diaz, I.M., Reynolds P., and Hudson, M., Enhancing velocity feedback with inner loop compensators for the actuators, SMART Conference 2011, Germany, 629–639, (2011).
[7] Daley, S., Wang, J., A geometric approach to the design of remotely located vibration control systems, Journal of Sound and Vibration, 318, 702–714, (2008).
[8] Wang, J., Daley, S., Broad band controller design for remote vibration using a geometric approach, Journal of Sound and Vibration, 329, 3888–3897, (2010).
[9] Ubaid, U., Daley, S., Pope, S., Broadband design of remotely located vibration control systems: a stable solution for non-minimum phase dynamics, Inter-Noise 2011, Osaka, Japan, September 2011.

Research and Applications in Structural Engineering, Mechanics and Computation – Zingoni (Ed.)
© 2013 Taylor & Francis Group, London, ISBN 978-1-138-00061-2

Sensitivity analysis of coupled crowd-structure system dynamics to walking crowd properties

E. Shahabpoor
Department of Civil & Structural Engineering, University of Sheffield, UK

A. Pavic
College of Engineering, Mathematics and Physical Sciences, University of Exeter, UK

V. Racic
Department of Civil & Structural Engineering, University of Sheffield, UK

ABSTRACT: Increasing vibration serviceability problems of modern structures have drawn researchers' attention to the walking-induced vibration modelling and assessment of floors and footbridges. Changes of dynamic properties of structure due to presence of stationary people have been studied extensively in the literature. However, little is known about the similar effects of walking people, mainly due to the lack of experimental evidence and credible models capable of simulating human-structure dynamic interaction (HSI) in the vertical direction. This paper uses a single degree of freedom mass-spring-damper (MSD) model to simulate dynamics of walking crowd on structure and investigates the sensitivity of the coupled crowd-structure system frequency and damping to properties of crowd model. Results of this study show that when the natural frequency of the crowd model is less than the natural frequency of the structure, both natural frequency and damping ratio of occupied structure are more sensitive to crowd's model stiffness. Similarly, when the natural frequency of the crowd model is greater than the natural frequency of the structure, both natural frequency and damping ratio of occupied structure are more sensitive to crowd's model mass. It also can be seen that natural frequency of theoccupied structure has no sensitivity to damping of the crowd model while its damping ratio shows a limited sensitivity to the crowd's model damping with the maximum where both natural frequencies are equal.

1 INTRODUCTION

Recent increase in vibration serviceability problems of flexible structures under human dynamic loading have led to concerns about both safety and comfort of pedestrians using such structures. Hence, there is demand for more accurate and inclusive design methods (Shahabpoor & Pavic 2012, Zivanovic et al. 2010, Kasperski 1996, Reid et al. 1997, SCOSS 2001). As to the walking-induced dynamic loading, current design approaches, such as those in BS 5400 (2006) and Eurocode 5 (2004), use deterministic walking force models and simply ignore human-structure interaction effects and inherent stochasticity of the walking force (Shahabpoor & Pavic 2012, Zivanovic et al. 2010, Dougill 2006). Research (Shahabpoor & Pavic 2012, Zivanovic et al. 2010, Ellis & Ji 1997,Willford 2002, Brownjohn et al. 2004, Pavic 2011), mostly based on full-scale measurements, have indicated that interaction of the human body, as a bio-mechanical system, with the structure have significant effects on dynamic properties of the joint human-structure system and should be considered. It often leads to a considerable reduction in response and some change in the natural frequency of the structure (Shahabpoor & Pavic 2012, Zivanovic et al. 2010, Dougill 2006, Pavic 2011).

To address HSI, different types of mechanical or biomechanically-inspired models, such as single/ multiple degrees of freedom mass-spring dampers MSDs (Archbold 2004, 2008, 2011, Caprani et al. 2011) and single/bipedal inverted pendulum (Bocian 2011), are used to simulate kinematics of human motion for both vertical and horizontal directions and different postures and types of activities (Macdonald 2009, Matsumoto & Griffin 2003, Wei & Griffin 1998). This paper uses a classic single degree of freedom mass-spring-damper (S-MSD) model to simulate crowd-structure interaction during walking by using human body MSD properties. Although this S-MSD model may not be the best option for modeling human, the simplicity of its dynamics allows easy investigation of highly relevant coupled human-structure system dynamics under different loading conditions. The principal aim of this study is to improve understanding of the sensitivity of the occupied structure dynamic

[1] In this paper, 'crowd' is called to any group of people with more than a single person.

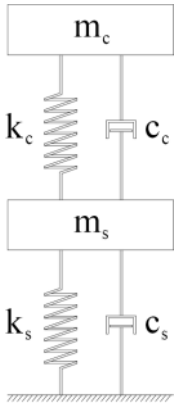


Figure 1. Conceptual 2DOF model of coupled crowd-structure system (stationary walking people).

properties to each of the currently uncertain *crowd* parameters. This is done for a range of common structures and crowd occupation scenarios and should help dealing with large uncertainty when modeling crowds on structures during design process.

Section 1 of the paper presents a very short introduction into the subject and rationale of this research. Section 2 describes the proposed coupled S-MSD model and its formulation for the considered crowd occupation scenarios. Section 3 presents the analysis specifications and Section 4 illustrates the parameters used in the models. Section 5 presents the results of the parametric study and sensitivity analysis and finally Section 6 closes the paper by highlighting the important findings and making conclusions.

2 S-MSD MODEL DESCRIPTION

To simulate the problem, only the first mode of structural vibration is considered and is conceptualized using a SDOF oscillator with the corresponding modal properties (m_s, k_s and c_s). Considering only one structural mode does not affect the generality of the results as mode superposition principle applies to linear structures which is an acceptable assumption for this kind of problem.

In all simulations, a S-MSD model (m_c, k_c and c_c) is used to simulate the effects of the crowd's MSD properties on the structure. This model represents 'stationary' walking pedestrian an imaginary case in which people are 'walking' on the 'anti-node' of the first mode of vibration but their location on the structure does not change[2]. Being stationary, such coupled crowd-structure system can be represented as a simple conventional two degrees of freedom system as illustrated in Figure 1, the behavior of which can be studied using closed form solutions of 2DOF equations of motion.

[2] e.g. assume walking on a series of treadmills distributed over the length of a beam-like structure

More detailed discussion about the selected 2DOFs crowd-structure model and its equations of motion are presented by Shahabpoor et al. (2013).

3 ANALYSIS SPECIFICATIONS

The natural frequency f_{os} and damping ratio ζ_{os} of the occupied structure are chosen to represent dynamics of the occupied structure. In the first step, crowd's properties (m_c, k_c and c_c) are changed one at a time and the effect of this single parameter on natural frequency f_{os} and damping ratio ζ_{os} of the occupied structure are calculated.

In the next step, the *rates of change* of f_{os} and ζ_{os} of the occupied structure with respect to change of crowd's model properties m_c, k_c and c_c is considered as the sensitivity criteria. The chosen rate of change provides a measure of '*how fast'* the occupied structure properties f_{os} and ζ_{os} change as uncertain crowd's parameters m_c, k_c and c_c change.

To allow for comparison, as units of MSD parameters are different, a typical set of initial values for structure and crowd's parameters (m_{ci}, c_{ci}, $k_{ci,}$ f_{si} and ζ_{si}), are selected and unit-less ratios m_c/m_{ci}, c_c/c_{ci}, $k_c/k_{ci,}$ f_{os}/f_{si} and ζ_{os}/ζ_{si} are used for presentation. To ensure generality of results, the same analysis is repeated for several initial values and results are compared. The effects on f_{os} and ζ_{os} are considered for the changes of m_c (Case 1), k_c (Case 2), and c_c (Case 3).

In all three cases, the selected crowd parameter is varying over a certain range and other two parameters of the crowd model are kept constant and equal to the initial set of values.

4 MODEL PARAMETERS

The exact parameters used in the crowd – structure 2DOF model are described in this section. These parameters are selected to be realistic and to cover a range of possible values (in the case of the varying parameter).

4.1 *Dynamic parameters of structure model*

The dynamic parameters of the crowd and structure models that are used in simulations are presented in for different analysis cases. An imaginary simply supported beam is selected as the structure and its first mode properties m_{si}, k_{si} and c_{si} are selected in a way to be both realistic and corresponding to a light weight structure. The latter is needed to highlight the crowd-structure interaction effects better. Three different natural frequencies (and therefore stiffnesses for the same mass m_{si} of 6500 kg) are selected for the structure to cover the scenarios in which the natural frequency of the structure is lower, close to and higher than the assumed natural frequency of the crowd model.

Table 1. Dynamic parameters of human and structure models used in different analysis cases.

Analysis case	Initial values	Case 1	Case 2	Case 3	Unit
Structure model parameters					
Mass			6500		kg
Damping ratio			0.005		–
Natural frequency			2–4		Hz
Crowd model parameters					
Mass	168	8.4–462	168	168	kg
Stiffness	61698	61698	3085–169669	61698	N/m
Damping	1803	1803	1803	90–4958	N · s/m
Damping ratio	0.28	1.25–0.169	0.984–0.133	0.014–0.770	–
Natural frequency	3.05	13.64–1.84	0.68–5.06	3.05	Hz

4.2 *Dynamic properties of crowd model*

The initial parameters of the crowd model m_{ci}, c_{ci} and k_{ci} are adopted from the results of studies done by the author to simulate crowd's dynamics on a real-life test structure. An extensive set of experiments were carried out on the Sheffield laboratory test structure (2 meters wide and 11 meters long pre-stressed concrete beam) with the groups of 2-15 pedestrians walking on it. An S-MSD crowd model was then fitted to each test scenario and the corresponding crowd's parameters were found. Properties corresponding to a group of 6 walking people are selected as the initial values for the crowd model. A six-people group represents a normal spatially-unconstrained crowd on the assumed test structure and is a very good starting point to study the effects of varying crowd parameters.

The ranges of possible crowd parameters m_c, c_c, k_c, are adopted from the values reported by researchers for individuals and groups of people (Archbold et al. 2011, Zhang et al. 2000, Rapoport et al. 2003, Bertos et al. 2005, Lee & Farley 1998, Geyer et al. 1998) and are presented in Table 1.

5 ANALYSIS RESULTS

Distinction should be made between the results that are presented in Sections 5.1 and 5.2. The former provide a measure of '*how effective*' crowd parameters m_c, k_c and c_c are on occupied structure dynamics (represented by f_{os} and ζ_{os}) while the latter gives a measure of the sensitivity of f_{os} and ζ_{os} to crowd's uncertain parameters.

5.1 *Parametric analysis*

Figure 2 and Figure 3 present a typical set of results for $f_{si} = 4$ Hz. Results of analysis Cases 1, 2 and 3

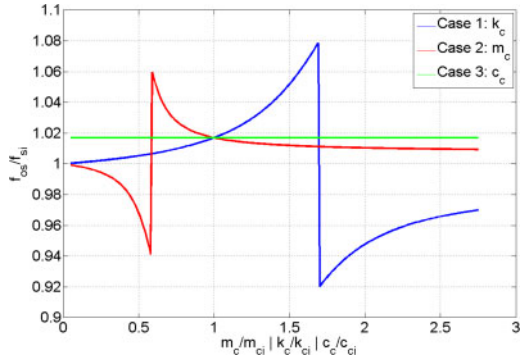


Figure 2. Effects of the m_c, k_c and c_c on f_{os} ($f_{si} = 4$ Hz).

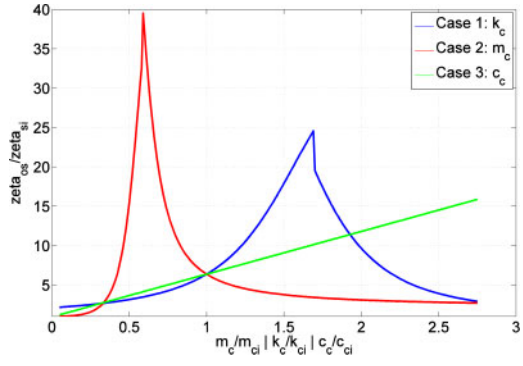


Figure 3. Effects of the m_c, k_c and c_c on ζ_{os} ($f_{si} = 4$ Hz).

corresponding to changing crowd's m_c, k_c and c_c are plotted on the same graph to be able to compare them. The horizontal axis presents the ratio of the crowd parameters to their initial values 'X', while the vertical axis presents the ratio of the changes in the occupied structure parameters 'Y'. These parameters are presented in equations 1 and 2, respectively.

$$X = {}^{x_c}/_{x_{ci}} \;\therefore\; (x_c = m_c, c_c, k_c) \tag{1}$$

$$Y = {}^{y_{os}}/_{y_{si}} \;\therefore\; (y_{os} = f_{os},\ \zeta_{os}) \tag{2}$$

As the natural frequency of a SDOF is proportional to k/m, increase of stiffness or decrease of mass leads to the increase of the natural frequency. Keeping this in mind and knowing that $f_{ci} = 3.05$ Hz and $f_{si} = 4$ Hz in Figure 2 and Figure 3, increasing stiffness of the crowd model k_c (blue trace) or

decreasing its mass m_c (red trace) leads into an increase of the crowd's natural frequency f_c and makes it closer to the structure's initial frequency f_{si}.

A closer look at Figure 2 and Figure 3 shows that the extreme values of m_c and k_c graphs (red and blue traces) represent the cases where natural frequencies of the crowd and initial structure model are equal ($f_{si} = f_c$). This means that m_c and k_c have maximum effects on f_{os} and ζ_{os} when $f_{si} = f_c$. It also can be

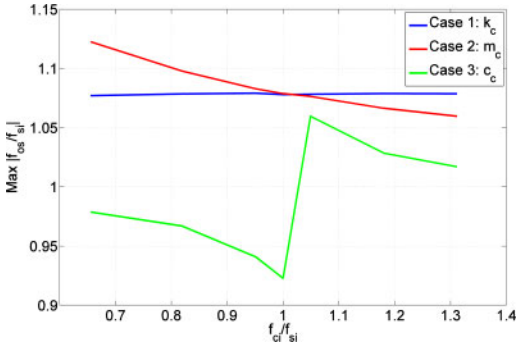


Figure 4. Maximum effects of the m_c, k_c and c_c on f_{os} for $f_{ci} = 3.05$ Hz and f_{si} varying from 2–4 Hz.

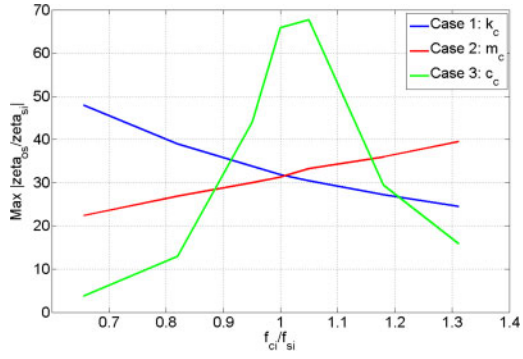


Figure 5. Maximum effects of the m_c, k_c and c_c on ζ_{os} for $f_{ci} = 3.05$ Hz and f_{si} varying from 2–4 Hz.

seen that increasing ζ_c has no significant effects[3] on f_{os} but increases ζ_{os}. An extensive discussion of the observed trends in Figure 2 and Figure 3 is presented by Shahabpoor et al. (2013).

To compare the effects of the crowd's parameters m_c, c_c, k_c, on the occupied structure's dynamics, a family of initial values is considered in which initial natural frequency of crowd model f_{ci} is 3.05 Hz and structure initial natural frequency f_{si} varies from 2 to 4 Hz. For each (f_{ci}, f_{si}) pairs, a set of XvsY curves similar to the ones presented in Figure 2 and Figure 3, are plotted. Maximum absolute value of each of XvsY graphs are then plotted against their corresponding f_{ci}/f_{si} (which is equal to $3.05/f_{si}$) and are presented for f_{os}/f_{si} and ζ_{os}/ζ_{si} in Figure 4 and Figure 5 accordingly.

As it can be seen in Figure 4 and Figure 5, as $3.05/f_{si}$ increases, maximum effects of m_c on f_{os} decrease and its effects on ζ_{os} increase. k_c has the opposite effects and as $3.05/f_{si}$ increases, its maximum effects on f_{os} increase and on ζ_{os} decrease. Maximum effects of crowd's damping c_c on both f_{os} and ζ_{os} is highest when $f_{ci} = f_{si}$.

5.2 *Sensitivity analysis*

Sensitivity here is defined as the rate of change of f_{os} and ζ_{os} to the changes in m_c, k_c and c_c. The sensitivity here is an indicator of '*how fast*' the effects of the crowd parameters on the occupied structure parameters change. Results of this section are presented in Figure 6, Figure 7, Figure 8 and Figure 9. In these figures, the horizontal axis presents the ratio of the crowd parameters X as is given in equation 1 and the vertical axis presents derivative of Y (given in equation 2) with regards to X.

Figure 6 displays the sensitivity of ζ_{os} and Figure 7 displays the sensitivity of f_{os} for two typical initial

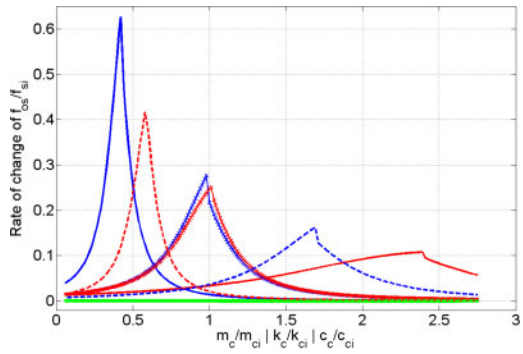


Figure 6. Sensitivity of f_{os} to m_c (red trace), k_c (blue trace) and c_c (green trace): Continues traces: $f_{si} = 2$ Hz; Crossed traces: $f_{si} = 3$ Hz; Dashed line: $f_{si} = 4$ Hz.

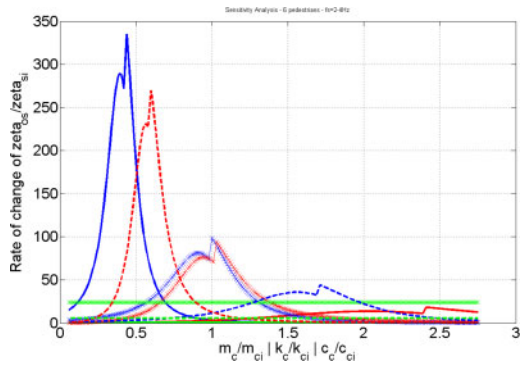


Figure 7. Sensitivity of ζ_{os} to m_c (red trace), k_c (blue trace) and c_c (green trace): Continues traces: $f_{si} = 2$ Hz; Crossed traces: $f_{si} = 3$ Hz; Dashed line: $f_{si} = 4$ Hz.

structural frequencies $f_{si} = 2$ and 4 Hz. Similar to the findings in Section 5.1, sensitivity of ζ_{os} and f_{os} to m_c and k_c increase significantly when frequency of the crowd and structure models are close in value.

For the case $f_{ci} < f_{si}$ (when $f_{si} = 4$ Hz), as both Figure 6 and Figure 7 show, when k_c (dashed blue trace) increase from k_{ci} and mass m_c (dashed red

[3] The case presented in Figure 2. Effects of the m^c, k^c and cc on fos ($fsi = 4$ Hz and Figure 3 is corresponding to the system with proportional damping matrix. In systems with non-proportional damping distribution, natural frequency is dependent on damping but its effects is not significant. Further discussion about details of this issue is beyond the scope of this paper.

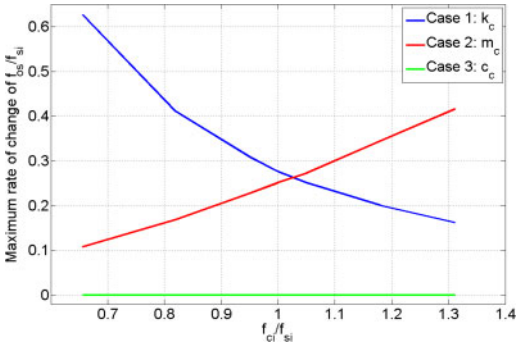


Figure 8. Maximum sensitivity of the f_{os} to m_c, k_c and c_c for $f_{ci} = 3.05$ Hz and f_{si} varying from 2–4 Hz.

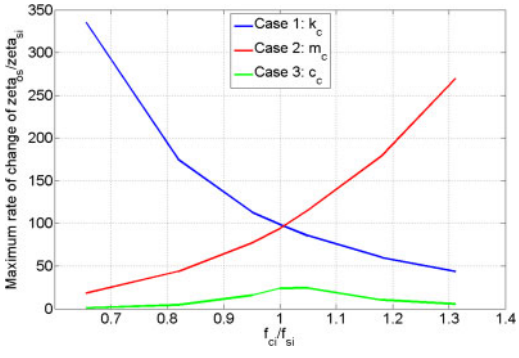


Figure 9. Maximum sensitivity of the ζ_{os} to m_c, k_c and c_c for $f_{ci} = 3.05$ Hz and f_{si} varying from 2–4 Hz.

trace) decrease from m_{ci}, their corresponding sensitivity curves show a peak. These peaks can be shown to correspond to $f_{si} = f_c$. The same applies when $f_{ci} > f_{si}$ (when $f_{si} = 2$ Hz) and the sensitivity curves show maximum when k_c (blue trace) decrease and m_c (red trace) increase. Also, as Figure 6 illustrates, rate of change of f_{os} is not sensitive to c_c while sensitivity of ζ_{os} is maximum when $f_{si} = f_{ci}$ (crossed green line in Figure 7).

To compare the sensitivity of f_{os} and ζ_{os} to m_c, k_c, and c_c, the same family of initial values that is described in the previous section is considered in which $f_{ci} = 3.05$ Hz and f_{si} varies from 2 to 4 Hz. For each (f_{ci}, f_{si}) pairs, then, a set of X vs Y′ curves similar to the ones presented in Figure 6 and Figure 7 are plotted. Maximum values of X vs Y′ graphs are then plotted against teir corresponding f_{ci}/f_{si} and are presented for f_{os} and ζ_{os} in Figure 8 and accordingly.

It can be seen in Figure 8 and Figure 9 that by increasing the f_{si}, maximum sensitivity of the f_{os} and ζ_{os} to k_c decrease (blue traces) and its maximum sensitivity to m_c increase (red traces). This means that when $f_{ci} < f_{si}$, both f_{os} and ζ_{os} are more sensitive to k_c, while when $f_{ci} > f_{si}$, both f_{os} and ζ_{os} are more sensitive to m_c. It also can be seen that f_{os} has no sensitivity to c_c while ζ_{os} shows a limited sensitivity to c_c with the maximum at $f_{ci} = f_{si}$.

6 CONCLUSION

Modelling crowd dynamics on structures have always been a challenge due to uncertainty of human parameters. This paper combines results of the parametric study and sensitivity analysis that are done on a 2DOF mass-spring-damper human-structure model to describe effects and sensitivity of the occupied structure to the crowd model parameters m_c, k_c and c_c. Results of this analysis provide valuable insight for engineers to choose more realistic crowd properties during design process and researchers to understand better the human-structure interaction mechanisms.

REFERENCES

Archbold, P., Novel interactive load models for pedestrian footbridges, *PhD thesis, University College Dublin*, 2004.

Archbold, P. 2008. Evaluation of novel interactive load models of crowd loading on footbridges, *Proceedings of 4th Symposium on Bridge and Infrastructure Research in Ireland*, National University of Ireland, Galway, 35–44.

Archbold, P., Keogh, J. & Caprani, C. 2011. A Parametric Study of Pedestrian Vertical Force Models for Dynamic Analysis of Footbridges, *Proceedings of EVACES 2011*.

Bertos, G., Childress, D. & Gard, S. 2005. The vertical mechanical impedance of the locomotor system during human walking with applications in rehabilitation, *Proceeding of the 2005 IEEE Ninth International Conference on Rehabilitation Robotics*.

Bocian, M., Macdonald, J. & Burn, J. 2011. Modelling of self-excited vertical forces on structures due to walking pedestrians, *Proceedings of the 8th International Conference on Structural Dynamics*, *EURODYN 2011*.

Brownjohn, J. M. W., Fok, P., Roche, M. & Omenzetter, P. 2004. Long span steel pedestrian bridge at Singapore Changi Airport – part 1 and 2.

BSI. 2006. Steel, Concrete and Composite Bridges, Part 2: Specification for Loads; Appendix B: Vibration Serviceability Requirements for a Foot and Cycle Track Bridges.BS5400, British Standards Institution.

Caprani, C.C., Keogh, J., Archbold, P. & Fanning, P. 2011. Characteristic vertical response of a footbridge due to crowd loading, *Proceedings of the 8th International Conference on Structural Dynamics, EURODYN 2011*.

Dougill, J. W., Wright, J. R., Parkhouse, J. G. & Harrison, R. E. 2006. Human structure interaction during rhythmic bobbing, *The Structural Engineer*, 84(22).

Ellis, B. R. & Ji, T. 1997. Human-structure interaction in vertical vibrations, Structures of Buildings, *the Proceedings of Civil Engineers*, 122(1), 1–9.

EN. 2004. Eurocode 5: Design of timber structures – Part 2: Bridges, EN 1995-2:2004, *European Committee of Standardization*.

Geyer, H., Seyfarth, A. and Blickhan, R. 1998. Compliant leg behavior explains basic dynamics of walking and running, *Proc. of the Royal Society B: Biological Sciences*, 273(1603), pp. 2861–2867.

Kasperski, M. 1996. Actual problems with stand structures due to spectator-induced vibration, *Proceedings of Structural Dynamics-EURODYN '96*, p. 455–461.

Lee, C. & Farley, C. 1998.Determinants of the center of mass trajectory in human walking and running, *The Journal of Experimental Biology*, 201, 2935–2944.

Macdonald, J. H. G. 2009. Lateral excitation of bridges by balancing pedestrians, *Proc. Royal Society* A, 465(2104), pp. 1055–1073.

Matsumoto, Y. & Griffin, M. 2003. Mathematical models for the apparent masses of standing subjects exposed to vertical whole-body, *Journal of Sound and Vibration*, 260(3), 431–451.

Pavic, A. 2011. Vertical crowd dynamic action on footbridges: review of design guidelines and their application, *Proceedings of Footbridge Conference* 2011.

Rapoport, S., Mizrahi, J., Kimmel, E., Verbitsky, O. & Isakov, E. 2003. Constant and variable stiffness and damping of the leg joints in human hopping, *Journal of Biomechanical Engineering, ASME*, 125, 507–514.

Reid, W. M., Dickie, J. F. & Wright, J. R. 1997. Stadium structures: are they excited. *The Structural Engineer*, (75), pp. 383–388.

SCOSS. 2001. Structural Safety 2000-01, *13th Report of the Standing Committee on Structural Safety*, pp. 23–24.

Shahabpoor, E. & Pavić P. A. 2012. Comparative evaluation of current pedestrian traffic models on structures, *Conference Proceedings of the Society for Experimental Mechanics Series.* V 26, pp. 41–52.

Shahabpoor, E., Pavić, A.& Racic, V. 2013. Using MSD Model to Simulate Human-Structure Interaction during Walking, *Conference Proceedings of the Society for Experimental Mechanics Series*.

Wei, L. & Griffin, M. J. 1998. Mathematical models for the apparent mass of the seated human body exposed to vertical vibration, *Journal of Sound and Vibration*, 212(5), 855–75.

Willford, M. 2002. Dynamic actions and reactions of pedestrians, *the proceedings of Footbridges conference*.

Zhang, L., Xu, D., Makhsous, M. & Lin, F. 2000. Stiffness and viscous damping of the human leg, *Proceedings of the 24th Annual Meeting of the American Society of Biomechanics*.

Živanović, S., Díaz, I. M. & Pavić, A. 2009. Influence of walking and standing crowds on structural dynamic properties, *Proceedings of the IMAC-XXVII*.

Živanović, S., Pavić, A. & Ingólfsson, E. T. 2010. Modelling spatially unrestricted pedestrian traffic on footbridges, *ASCE Journal of Structural Engineering*, 136(10), pp. 1296–1308.

Research and Applications in Structural Engineering, Mechanics and Computation – Zingoni (Ed.)
© 2013 Taylor & Francis Group, London, ISBN 978-1-138-00061-2

Experimental study of the human ability to deliberately excite a flexible floor

C. Schwartz
LAMH, Laboratoire d'Analyse du Mouvement Humain, University of Liege, Belgium

A. Berger
Structural Engineering Division, University of Liege, Belgium

O. Brüls
LAMH, Laboratoire d'Analyse du Mouvement Humain, University of Liege, Belgium
Department of Aerospace and Mechanical Engineering, University of Liege, Belgium

J.-L. Croisier & B. Forthomme
LAMH, Laboratoire d'Analyse du Mouvement Humain, University of Liege, Belgium
Department of Motivity Sciences, University of Liege, Belgium

V. Denoël
LAMH, Laboratoire d'Analyse du Mouvement Humain, University of Liege, Belgium
Structural Engineering Division, University of Liege, Belgium

ABSTRACT: Human-structure interactions are not completely understood yet. This paper presents an experimental study focusing on the interaction between a human and a flexible support, with a major aim to better understand how the behavior of a human subject, bouncing on a flexible structure, adapts to the support motion. Exploratory experiments are undertaken with a 7 m-span timber footbridge tested in the Human Motion Analysis Laboratory of the University of Liege. The movements of the coupled system composed of the subject and the footbridge are recorded by Motion Capture technology; the subject's 3-D body motion is defined by three important angles: ankle, knee and hip. The interaction between the subject and the footbridge is also quantified by means of force platform measurements. The experiments indicate an influence of the support amplitude and natural frequency on the phase shift between the oscillatory floor motion and the three angles characterizing the motion.

1 INTRODUCTION

Vandalism is coined as a specific kind of footbridge loading characterized by the intentional and wellcoordinated action of one or several persons, moving their own body with the sole aim to increase the structural vibration level to a maximum value. The term *vandalism* actually covers several kinds of action (Zivanovic S. 2005), among which only bouncing—sometimes also referred to as bobbing or yogging—is considered in this paper. It consists in a near harmonic knee-extension motion at a frequency equal to, or as close as possible to, a structural natural frequency, which brings the structure into resonance. Of major importance is the reaction force under the vandal's feet, i.e. the basic information required for the structural design of the footbridge since it may be seen as an external loading from the designer's point of view. A proper estimation of this force and of the resulting structural response allows estimation of occurrence of possible harmful vibrations which could, for instance, result in negative vertical reaction forces at the abutments. Several models of reaction forces resulting from bouncing do exist, but are essentially limited to motionless rigid supports (Duarte E. 2009). Recently, Harrison et al. (Harrison R. E & Dougill 2006, Harrison R. E. 2008) have studied this humanstructure interaction on flexible supports as a function of a number of parameters including the structural mass and damping. A mass- and damping-dependent reduction of the reaction force was observed, while approaching resonance. In contrast with existing literature which mainly relies on the body motion description as a single degree-of-freedom system, experimental results reported in this paper include the measurement of three representative body motion angles as well as the floor reaction force and the structural response. The paper is divided into a short description of the experimental setup, a presentation of the main results, followed by the proposition of a simple loading model.

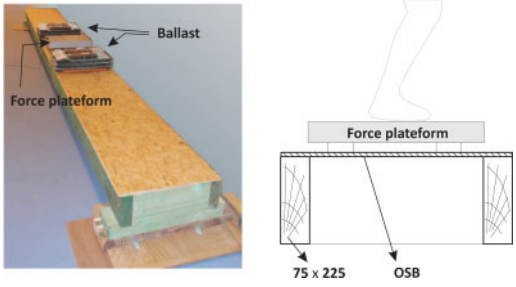


Figure 1. Picture of the toy footbridge, with a force platform at mid-span. Laboratoire d'Analyse du Mouvement Humain (LAMH).

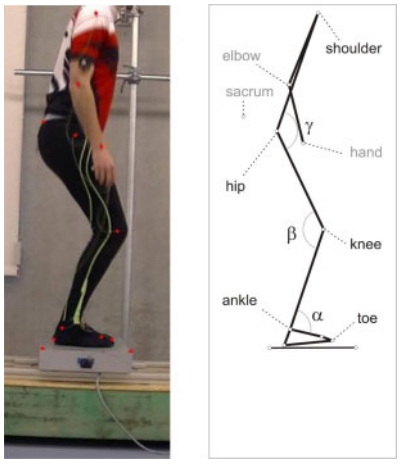


Figure 2. Markers location and reconstructed model with rigid body segments. (Red dots in the picture indicate the full set of measured anatomical references – only four of them are used to define the kinematic angles).

2 DESCRIPTION OF THE EXPERIMENTAL SETUP

2.1 *The footbridge*

A toy footbridge composed of two timber beams with a cross-section of 75 × 225 mm is designed to behave as a simply supported span of 6.7 m. The two main beams are covered by oriented strand board (OSB) screwed on top of them. This bare structure is ballasted with steel load in order to tune the natural frequency in the range [2.4; 4.2] Hz, see Fig. 1. These additional dead loads are securely fastened to the structure in order to hinder any relative vertical motion. During the experiment, the vandal stands at midspan, where a force platform is installed in order to record the reaction forces. The structure responds in its fundamental vibration mode.

2.2 *Instrumentation of the human-structure system*

The instrumentation is performed with a Motion Capture system composed of cameras, markers and the *CODAmotion* software. The system localizes in space the diodes (markers) placed in various strategical points of the investigated system. Figure 2 shows a snapshot of the planar model constructed with rigid body segments connecting the measured joints, as well as a picture of the vandal in a similar position. Essentially instrumentation of two corners of the force plate allow estimation of the structural motion at mid-span while five anatomical references, namely the great toe, the ankle, the knee, the hip and the shoulder, provide information about the posture during the excitation. Because the body motion is studied in a vertical plane, these four anatomical references define three *kinematic angles* α, β and γ, that describe the motion precisely enough.

The reaction force is acquired with a force platform *Kistler, 9281 EA* which is firmly fastened to the footbridge in order not to disturb the subject's motion. The recorded data are logged and properly synchronized between the markers and the force platform with the software *CODAmotion, V6.79.2*. The force platform data is sampled at 1000 Hz and immediately downsampled to match the 200 Hz sampling frequency of the markers for further postprocessing.

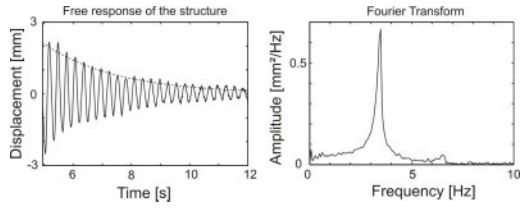


Figure 3. Free-response of the footbridge in the 3.4 Hz configuration: time series and Fourier transform. Estimated damping ratio is 2%.

Table 1. Modal masses m, natural frequencies f of the ballasted structure and natural frequencies f_{eff} of the human-structure system.

Configuration	1	2	3	4	5	
m	1154	811	615	412	275	kg
f	2,4	2,8	3,4	3,9	4,6	Hz
f_{eff}	2,3	2,8	3,2	3,7	4,2	Hz

2.3 *Considered configurations*

Five configurations are considered. Each of them corresponds to a different ballast and thus to a different natural frequency. The effective natural frequency involving the coupled human-structure system is slightly less than the natural frequency of the ballasted structure itself, see Tab. 1. Figure 3 represents the free response of the beam in configuration 3, with the corresponding frequency spectrum. Such free decay responses are used to identify a damping ratio of 2% in each configuration.

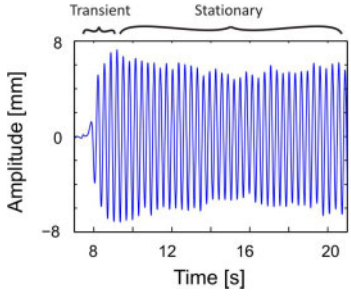


Figure 4. Vertical displacement of the flexible floor, measured with respect to the static deflection of the footbridge under the own weight of the experimenter.

2.4 *Test instructions and measurement protocol*

The results presented next are obtained with a unique subject weighting 87 kg, male, aged 23. The sole test instruction is to bring the structure into resonance as fast as possible, while keeping heels in contact with the support, and to hold a constant excitation level during at least 15 seconds. A typical response signal thus features two distinct parts: a short transient regime followed by a stationary response with a somewhat constant amplitude.

Tests are reproduced 20 times targeting various levels of amplitude in this stationary regime (slight, weak, medium, large, very large), which is feasible because the sole experimenter was trained and could judge how much energy should be imparted in the test, before it starts.

These two regimes are illustrated in Figure 4, with an example of the displacement of the flexible support, measured with the opto-electronic system, and expressed with respect to the static deflection under the own weight of the test subject.

3 RESULTS

3.1 *Overview of a typical result*

Figure 5 represents the displacement, velocity and acceleration of the footbridge in configuration 3. The transient phase is apparently as short as 1 second. This is by no means much shorter than the transient phase associated with a linear time-invariant system of natural frequency 3.2 Hz and damping ratio 2% ($t_r \simeq 1/(3.2 \cdot 0.02) = 15$ s), which evidences the existence of a strong human-structure interaction, *reductio ad absurdum*.

The corresponding time evolution of the reaction force is represented in Figure 6, together with the phase shift between the force and the structural displacement. The typical profile of the force further illustrates the shortness of the transient phase. It systematically starts with a decreasing magnitude, down to half of the body weight (BW), as the subject pumps down, lowering his center of mass—this corresponds to a decrease of the three angles α, β and γ—. The structural motion

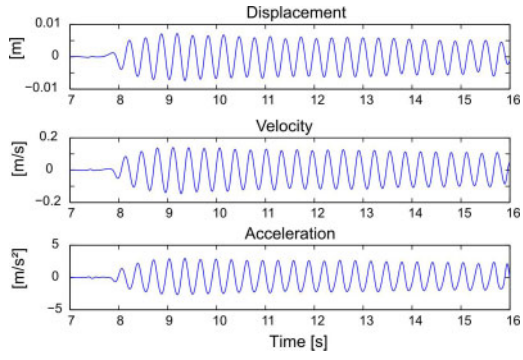


Figure 5. Typical response of the footbridge in configuration 3.

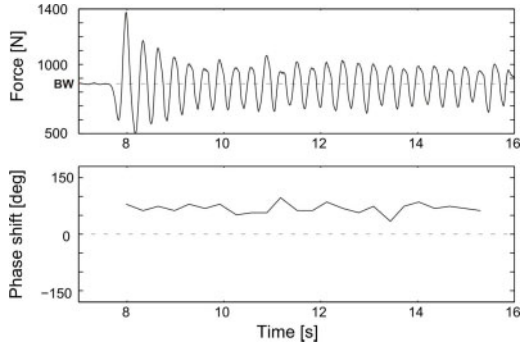


Figure 6. Force reaction and phase shift between force reaction and structural displacement.

is thus initiated upward. Then the subject sets forth, with a knee-bending motion, which results in a significantly increased reaction force, up to 1.6 times the body weight and triggers the structure oscillations. A couple of such pumping cycles is sufficient to reach the steady regime.

A key event in this human-structure interaction is the sensibility of the test subject to adequately identify the right instant when to set forth (around 7.85 s in this example). In this particular test setup, the pump-down phase results in a perceptible motion ($v \simeq 1$ mm/s) because the potential energy stored in the footbridge under the full body weight transforms into a significant kinetic energy as the reaction force drops to half of the body weight.

Once the stationary regime is achieved, the phase shift between the reaction force and the structural displacement oscillates with slight amplitudes around approximately 70°.

Figure 7 shows the time evolution of the kinematic angles α, β and γ, as well as their phase shift with respect to the structural displacement. Starting from a more or less vertical rest position, the subject bends his knees, identifies the structural natural frequency from the weak initial motion and performs a quasiperiodic motion. A couple of cycles only is enough for the subject to adapt his excitation frequency, amplitude and

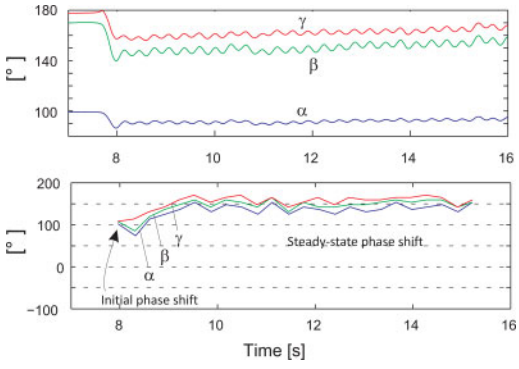


Figure 7. Kinematic angles and phase shift between them and the structural displacement.

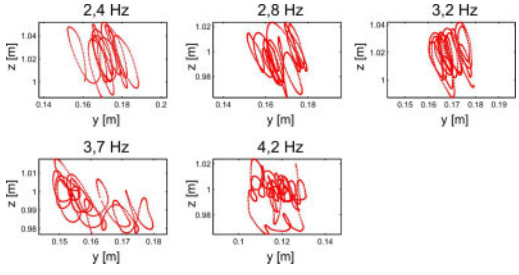


Figure 8. Trajectories of the centre of mass of the subject,for various natural frequencies of the support. While an quasiperiodic motion is observable for 2.4 Hz, 2.8 Hz and 3.2 Hz, the response for 3:7Hz and 4:2Hz is rather chaotic.

delay in order to maximize the structural response. The slight long-term drift in the kinematic angles indicates a slow change of the posture, which may be attributed to the weariness of the subject. Average phase shifts in the steady regime $\bar{\alpha} = 138°$, $\bar{\beta} = 150°$ and $\bar{\gamma} = 157°$ show that these angles are all a phase ahead of the structural displacement. Furthermore, the small advance of the chest-leg angle γ indicates that the human motion seems to be initiated from the chest to the knees, and then feet.

Actually, trajectories of the center of mass of the subject (estimated with a sensor located on the sacrum) indicate a kind of quasi-periodic elliptical motion, at least in cases where resonance is achieved 2.4 Hz, 2.8 Hz and 3.2 Hz, see Figure 8, while the motion is rather chaotic for larger natural frequencies.

Interestingly, the phase shifts between kinematic angles and the structural motion seem to witness a longer transient regime, as it takes from 8 s to 9 s before the phase shifts between kinematic angles and the structural displacement stabilize. For this reasons, results of the parametric study are analyzed next in the light of two different shifts, the *initial phase shift* which is measured as the force starts increasing and the *steady-state phase shift* which corresponds to the long term phase shift, see Figure 7.

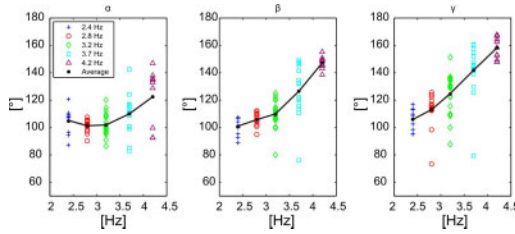


Figure 9. Initial phase shifts for various natural frequencies of the footbridge.

3.2 *Parametric study*

Figure 9 shows the initial phase shift for each measurement and for each angle. The black line connects average results. Despite a significant scatter in the data, this diagram shows a clear trend: initial phase shift of angles β and γ roughly exhibit an augmentation rate of about 30°/Hz, with a larger initial phase shift for γ. The ensemble average for angle α is approximately equal to 100° for frequencies equal to 2.4 Hz, 2.8 Hz and 3.2 Hz and increases up to 120° for higher natural frequencies. Also, the initial phase shift associated with α is smaller than the phase shifts associated with β and γ, which suggests that the motion is well initiated from top to bottom, which generalizes what was observed for configuration 3.

Steady-state phase shifts are reported in Figure 10 as a function of the maximum displacement of the footbridge on the left, and as a function of the natural frequency on the right. Again, despite a significant scatter in the data, there is a clear trend indicating that the higher the natural frequency, the larger the phase shift. More precisely the rates of increase of angles α, β and γ are approximately equal to 8°/Hz, 16°/Hz and 10°Hz, respectively.

Figure 11 represents the phase shift between the reaction force and the footbridge displacement, as a function of the maximum structural displacement (left) and of the natural frequency (right). While the optimum phase shift between a harmonic force and the response of a single-degree-of-freedom that maximizes the energy pumping into the system is, from a mechanical viewpoint, equal to 90°, the human brain-body controller is not able to adjust to this optimality of control. Figure 11 indicates that this optimum delay is only materialized when vibration amplitudes of the footbridge are small. Even for moderate structural displacements and accelerations, this optimum phase shift is hardly hold by the subject. Indeed, the time delay required for communication between the brain and the sensorimotor activities, the treatment of information generated by sensory organs, the identification of a natural frequency and finally the muscle activation make it impossible for a human being to adjust to this mechanical optimum.

For natural frequencies of 2.4 Hz, 2.8 Hz and 3.2 Hz, the phase shift seems to stabilize around 110° for displacements in the range 1.5–4.5 cm. For smaller amplitudes, large scatterness indicates that the subject

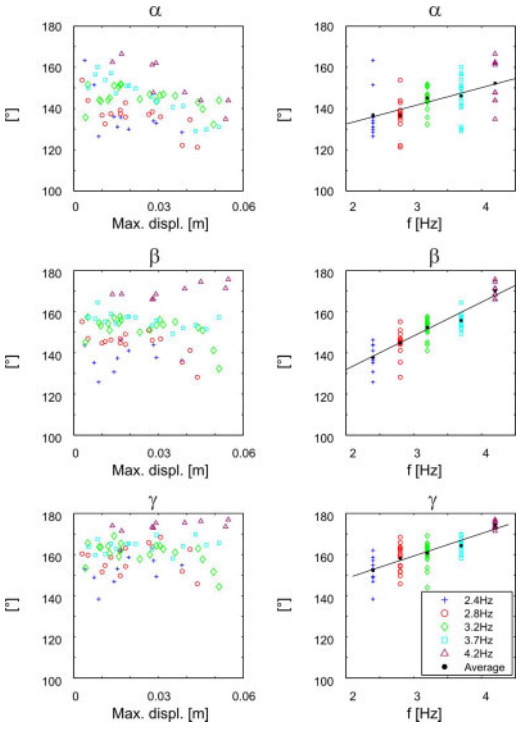


Figure 10. Steady-state phase shift between the kinematic angles and the structural displacement represented as a function of the maximum displacement (left) and of the structural natural frequency (right).

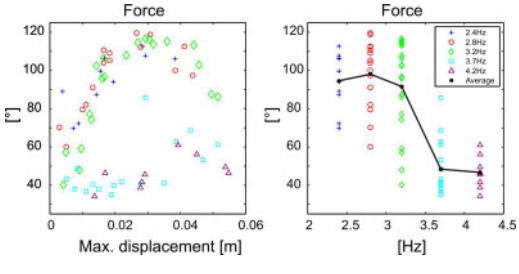


Figure 11. Steady-state phase shift between the force and the structural displacements represented as a function of the maximum displacement (left) and of the structural natural frequency (right).

has difficulties in feeling a sufficient level of vibration, and in adapting its motion to that frequency; he thus provides the impulse with a smaller delay (80°).

A similar explanation may justify the short delay (40°–60°) for frequencies of motion equal to 3.7 Hz and 4.2 Hz. In this case, the frequency of the motion is too high and the subject is not able to move that fast. The existence of this discontinuity in the response, when considered as a function of the natural frequency of the footbridge, is however not observable in the body posture, i.e. in angles α, β and γ, see Figure 10. This indicates that, despite an apparently similar body behaviour, the subject is not able to impose an optimum phase shift in the force.

4 CONCLUSIONS

This experimental study of the human-structure interaction in a bouncing motion has objectivized a series of facts. First, the human body motion—parametrized in this study with three kinematic angles, which is a major innovation of this experiment—seems to be initiated from chest to feet. Second, there are basically two conditions in which the subject is not able to tune his excitation frequency on the structural motion. On the one hand, for small amplitudes of vibration, the subject is not capable of identifying the natural frequency and the phase of the structural loading, which makes it impossible for him to properly synchronize. On the other hand, for large frequencies of support oscillations, the subject has not the physical reactivity to excite the footbridge fast enough, which finally translates into a chaotic uneffective motion. This is presumably due to the communication with the brain feedback, and the delay in the muscle activation. In both cases, this results in a reaction force, i.e. the force transmitted from the vandal to the structure, that is not optimally synchronized with the support motion, and consequently turns into small amplitudes of vibration. Actually in these cases, the phase shift between the support motion and the reaction force may even drop down to 40°–60° in the latter case.

The results obtained with a single subject indicate the existence of a critical natural frequency (in the range [3.2; 3.7] Hz for this particular subject) beyond which synchronization of the force and structural displacement is not achieved. As perplexing as it may appear, this discontinuity in the reaction force does not replicate in the steady-state phase shift between the kinematic angles and the support motion. Additional experimental work, involving EMG in order to survey muscle activity, will be carried out in a near future in order to clarify this point.

ACKNOWLEDGMENT

The authors would like to acknowledge the Federation Wallonie-Bruxelles for their support in the development of the laboratory (http://www.lamh.ulg.ac.be).

REFERENCES

Duarte E., J. T. (2009). Action of individual bouncing on structures. *Journal of Structural Engineering*, 818–827.

Harrison R. E, Wright, J. R. & J. W. Dougill (2006). Video monitoring of human-structure interaction for bouncing on a flexible structure. In *Proc., 24th Int. Modal Analysis Conf. (IMACXXIV), Society for Experimental Mechanics SEM*, Bethel, Conn.

Harrison R. E., Yao S., W. J. R. P. A. R. P. (2008). Human jumping and bobbing forces on flexible structures: Effect of structural properties. *Journal of Engineering Mechanics*, 663–675.

Zivanovic S., Pavic A., R. P. (2005). Vibration serviceability of footbridges under human-induced excitation: a literature review. *Journal of Sound and Vibration 1–74*, 279–.

4. Non-linear dynamics

Research and Applications in Structural Engineering, Mechanics and Computation – Zingoni (Ed.)
© 2013 Taylor & Francis Group, London, ISBN 978-1-138-00061-2

Dynamics of structural components subjected to large rotations using a flexible multibody approach

J. Ambrósio
IDMEC, Instituto Superior Técnico, Lisbon Technical University, Lisbon, Portugal

M. Augusta Neto
Mechanical Engineering Department, Faculty of Science and Technology, University of Coimbra, Coimbra, Portugal

ABSTRACT: Different finite element formulations handle the dynamics of deployable structures, being the co-rotational approaches popular. Flexible multibody dynamics formulations of complex structural and mechanical systems, including rigid and elastic components, use the finite element method to represent the flexibility of the components while describing the large rigid body motion using the fundaments of rigid body dynamics. Here, bodies of a multibody system deform while undergoing large rigid-body motions. A set of reference conditions is imposed to define a unique displacement field that includes the large rigid body motion and the system elastodynamics. The efficiency in the computer implementation is achieved by using a component synthesis approach involving vibration and static correction modes. The approach is demonstrated byanalyzing the deployment of a space satellite antenna in which the elastodynamic coupling with the large rotations plays a major role.

1 INTRODUCTION

Earlier work dealing with the elastodynamics of mechanical systems the deformations of the system components, assumed elastic and small, is superimposed to their large rigid body motion. Erdman and Sandor (1972) and Thompson and Sung (1986) discuss the inertial coupling between the small deformation of the elastic linkages of the system and their gross motion with some contradictory views.

Using reference frames fixed to planar flexible bodies, Song and Haug (1980) suggest a finite element based methodology, which yields coupled gross rigid body motion and small elastic deformations. Shabana and Wehage (1986) further developed and generalized the approach by using substructuring and the mode component synthesis to reduce the number of generalized coordinates required to represent the flexible components. Yoo and Haug (1986) account for the contribution of the truncated modes by introducing static correction modes. The selection of the modes to use, in order to improve accuracy and efficiency, has been addressed by Koutsovasilis (2013) while Heckmann (2010) discusses the suitability of boundary conditions for modes of vibration. Other type of system reductions are proposed by Fehr and Eberhard (2011).

The structure of the equations of motion for flexible multibody systems include the mass and stiffness matrices, commonly used for finite element models, the mass and inertia matrices and the gyroscopic and centrifugal force vectors, always present in multibody formulations, and the inertia coupling terms, which are only encountered in these formulations. The coupling terms involve matrices involving the finite element shape functions that are not available in the common finite elements. Using a lumped mass formulation for the inertia terms Ambrósio and Gonçalves (2001) showed not only that all the terms required in the flexible body equations of motion are readily available from any commercial finite element code but also that any type of linear finite element can be used in the model. The recovery of the stresses that develop in the flexible bodies of the system, generally necessary during design, can be achieved using procedures such as that proposed by Tobias and Eberhard (2011).

The space dynamics community was naturally involved with the dynamics of flexible bodies undergoing large rigid body motion. Kane, Ryan and Banerjee (1987) showed that though most of the flexible multibody methods, at the time, could capture the inertia coupling between the elastodynamics of the system components and their large motion but they would still produce incorrect results because they neglected the dynamic stiffening effects.

Geradin and Cardona (1991) show that the floating reference frame methods used in flexible multibody dynamics have the ability to lower the geometric nonlinearities of the flexible bodies, but not to eliminate them because the moderate rotation assumption about the floating reference frame is still required. The work of researchers in the finite element community, such as that by Belytschko and Hsieh (1973) or Simo and Vu-Quoc (1988), among others, addressed similar problems from different points of view.

Defining it as an absolute nodal coordinate formulation, Shabana (1997) used finite rotations nodal coordinates enabling the capture of the geometric nonlinear deformations. Further work on this approach is developed by Maqueda and Shabana (2007) to include nonlinear material constitutive models. Another approach taken by Ambrósio and Nikravesh (1992) to model geometrically nonlinear flexible bodies is to relax the need for the structures to exhibit small moderate rotations about the floating frame using an incremental finite element approach within the flexible body description. Approaches to flexible multibody modeling using meshless methods are proposed by Ibanez and Orden (2011).

The work presented here assumes linear deformations when measures in the body fixed coordinate frame of the moving bodies of the system. Methods dealing with nonlinear or material deformations are not discussed here.

2 FLEXIBLE MULTIBODY SYSTEMS: A FINITE ELEMENT APPROACH

Let the principle of the virtual works be used to express the equilibrium of the flexible body in the current configuration $t + \Delta t$ and an updated Lagrangean formulation be used to obtain the equations of motion of the flexible body (Ambrosio, 1996). Let the finite element method be used to represent the equations of motion of the flexible body. Referring to Fig. 1, the assembly of all finite elements used in the discretization of a single flexible body results in its equations of motion written as

$$\begin{bmatrix} \mathbf{M}_{rr} & \mathbf{M}_{r\phi} & \mathbf{M}_{rf} \\ \mathbf{M}_{\phi r} & \mathbf{M}_{\phi\phi} & \mathbf{M}_{\phi f} \\ \mathbf{M}_{fr} & \mathbf{M}_{f\phi} & \mathbf{M}_{ff} \end{bmatrix} \begin{bmatrix} \ddot{\mathbf{r}} \\ \dot{\boldsymbol{\omega}}' \\ \ddot{\mathbf{u}}' \end{bmatrix} = \begin{bmatrix} \mathbf{g}_r \\ \mathbf{g}'_\phi \\ \mathbf{g}'_f \end{bmatrix} + \begin{bmatrix} \mathbf{s}_r \\ \mathbf{s}'_\phi \\ \mathbf{s}'_f \end{bmatrix} - \begin{bmatrix} \mathbf{0} \\ \mathbf{0} \\ \mathbf{f} \end{bmatrix} - \begin{bmatrix} \mathbf{0} & \mathbf{0} & \mathbf{0} \\ \mathbf{0} & \mathbf{0} & \mathbf{0} \\ \mathbf{0} & \mathbf{0} & \mathbf{K}_L + \mathbf{K}_{NL} \end{bmatrix} \begin{bmatrix} \mathbf{0} \\ \mathbf{0} \\ \mathbf{u}' \end{bmatrix} \tag{1}$$

where $\ddot{\mathbf{r}}$ and $\dot{\boldsymbol{\omega}}'$ are the translational and angular accelerations of the body fixed reference frame, respectively, and $\ddot{\mathbf{u}}'$ denotes the nodal accelerations measured in body fixed coordinates. The local coordinate frame $\xi\eta\zeta$, attached to the flexible body, is used to represent the gross motion of the body and its deformation.

In Eq. (1) it is not assumed any type of reference conditions that relate the displacement of the finite elements to the body local frame. Eq. (1) describes thoroughly the motion of the flexible body. Even if only small elastic deformations occur, this equation is highly nonlinear due to a variant mass matrix, nonlinear external applied forces, gyroscopic and centrifugal forces and non-constant stiffness matrices. The variant mass matrix for the flexible body results from the assembly of the individual contributions of each finite element. Submatrices $\mathbf{M}_{rr}$ and $\mathbf{M}_{ff}$ are constant and

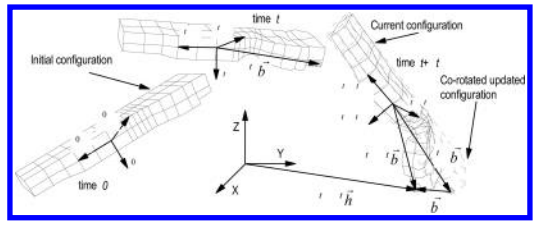


Figure 1. General motion of a flexible body.

represent respectively the mass of the entire body and the standard finite element mass matrix. $\mathbf{M}_{rf}$ and $\mathbf{M}_{\phi f}$ are the time variant matrices responsible for the inertia coupling between the gross motion of the body and its deformations.

The major differences between the equilibrium equations expressed by Eq. (1) and the standard nonlinear finite element equations consists in the fact that Eq. (1) is expressed with respect to a body fixed coordinate system $\xi\eta\zeta$ while in standard nonlinear finite elements only the global referential exists and, consequently, all quantities are measured directly in the *XYZ* coordinate system.

2.1 *Linear deformations in a flexible body*

If the deformations of the flexible body are linear elastic the nonlinear term $\mathbf{K}_{NL}\Delta\mathbf{u}'$ on Eq. (1) disappears, the nodal displacement increments $\Delta\mathbf{u}'$ are replaced by the nodal displacements $\mathbf{u}'$ and the equivalent nodal force vector $\mathbf{f}$ vanishes. The equations of motion for the linear elastic flexible body are finally given as

$$\begin{bmatrix} \mathbf{M}_{rr} & \mathbf{M}_{r\phi} & \mathbf{M}_{rf} \\ \mathbf{M}_{\phi r} & \mathbf{M}_{\phi\phi} & \mathbf{M}_{\phi f} \\ \mathbf{M}_{fr} & \mathbf{M}_{f\phi} & \mathbf{M}_{ff} \end{bmatrix} \begin{bmatrix} \ddot{\mathbf{r}} \\ \dot{\boldsymbol{\omega}}' \\ \ddot{\mathbf{u}}' \end{bmatrix} = \begin{bmatrix} \mathbf{g}_r + \mathbf{s}_r \\ \mathbf{g}'_\phi + \mathbf{s}'_\phi \\ \mathbf{g}'_f + \mathbf{s}'_f - \mathbf{K}_L\mathbf{u}' \end{bmatrix} \tag{2}$$

For a finite element model that involves elements with three nodal translations and three nodal rotations the nodal coordinates vector is

$$\mathbf{u}' = \left[\boldsymbol{\delta}_1'^T \; \boldsymbol{\theta}_1'^T \; \boldsymbol{\delta}_2'^T \; \boldsymbol{\theta}_2'^T \cdots \boldsymbol{\delta}_n'^T \; \boldsymbol{\theta}_n'^T \right]^T \tag{3}$$

Eqs. (1) and (2), cannot be solved without the reference conditions, which ensure that the displacement field of the flexible body is unique. Different types of reference conditions are discussed next.

2.1.1 *Body-fixed frames*

A straightforward type of reference conditions corresponds to that of the fixed body frame in which a given number of nodal degrees of freedom (dof), never less than 6, are constrained. The body-fixed reference conditions are written as:

$$\boldsymbol{\Phi}^{(bf)} \equiv \begin{Bmatrix} \boldsymbol{\delta}'_k \\ \boldsymbol{\theta}'_k \end{Bmatrix} = \mathbf{0} \qquad (k = 1,..,n_c) \tag{4}$$

where k refers to the fixed nodes that are not successively numbered in the finite element mesh and the

superscript *(bf)* denotes that the constraints are related to the body fixed conditions. Although Eq. (4) seems to imply that all dof of the fixed nodes are constrained, such is not necessary, provided that among all nodes at least 6 dof are constrained.

The constraints described by Eq. (4) are added to the equilibrium equations of the flexible body, given by Eq. (2), using Lagrange multipliers, as

$$\begin{bmatrix} \mathbf{M}_{rr} & \mathbf{M}_{r\phi} & \mathbf{M}_{rf} & \mathbf{0} \\ \mathbf{M}_{\phi r} & \mathbf{M}_{\phi\phi} & \mathbf{M}_{\phi f} & \mathbf{0} \\ \mathbf{M}_{fr} & \mathbf{M}_{f\phi} & \mathbf{M}_{ff} & \left(\Phi_{\mathbf{u}'}^{(bf)}\right)^T \\ \mathbf{0} & \mathbf{0} & \Phi_{\mathbf{u}'}^{(bf)} & \mathbf{0} \end{bmatrix} \begin{bmatrix} \ddot{\mathbf{r}} \\ \dot{\boldsymbol{\omega}}' \\ \ddot{\mathbf{u}}' \\ \boldsymbol{\lambda}^{(bf)} \end{bmatrix} = \begin{bmatrix} \mathbf{g}_r + \mathbf{s}_r \\ \mathbf{g}'_\phi + \mathbf{s}'_\phi \\ \mathbf{g}'_f + \mathbf{s}'_f - \mathbf{K}_L \mathbf{u}' \\ \boldsymbol{\gamma}^{(bf)} \end{bmatrix} \quad (5)$$

in which the constraint Jacobian matrix $\boldsymbol{\Phi}_{u'}^{(bf)}$ is made of unit and null entries and the right-hand-side of the acceleration $\boldsymbol{\gamma}^{(bf)}$ is null.

Usually the body fixed reference conditions are implicitly included by removing the nodal coordinates in Eq. (4) and the corresponding lines and columns of the stiffness and mass matrices.

2.1.2 *Mean axis conditions*

These conditions are defined by 6 constraints that enforce the kinetic energy associated with the deformation, measured with respect to an observer stationed on the flexible body,to be minimum (Cavin and Dusto, 1977). Setting the partial derivatives of the kinetic energy with respect to the translational and rotational velocity vectors to zero leads to

$$\dot{\boldsymbol{\Phi}}^{(ma)} \equiv \begin{Bmatrix} \sum_{k=1}^{n} m_k \dot{\boldsymbol{\delta}}'_k \\ \sum_{k=1}^{n} m_k \tilde{\mathbf{b}}'_k \dot{\boldsymbol{\delta}}'_k + \sum_{k=1}^{n} \boldsymbol{\mu}_k \dot{\boldsymbol{\theta}}'_k \end{Bmatrix} = \mathbf{0} \quad (6)$$

Eq. (6) represents in the 6 equations that form the mean axis conditions. They imply that the linear and the angular momentum due to the elastic deformation are null.

To add Eq. (6) as a constraint to the equation of motion of the flexible body, described by Eq. (2), let

$$\dot{\boldsymbol{\Phi}}^{(ma)} \equiv \boldsymbol{\Phi}_{\mathbf{u}'}^{(ma)} \dot{\mathbf{u}}' = \mathbf{0} \quad (7)$$

in which the Jacobian matrix $\Phi_{u'}^{(ma)}$ is given by

$$\boldsymbol{\Phi}_{\mathbf{u}'}^{(ma)} = \begin{bmatrix} m_1\mathbf{I} & \mathbf{0} & \cdots & m_k\mathbf{I} & \mathbf{0} & \cdots & m_n\mathbf{I} & \mathbf{0} \\ m_1\tilde{\mathbf{b}}'_k & \boldsymbol{\mu}_1\mathbf{I} & \cdots & m_k\tilde{\mathbf{b}}'_k & \boldsymbol{\mu}_k\mathbf{I} & \cdots & m_n\tilde{\mathbf{b}}'_n & \boldsymbol{\mu}_n\mathbf{I} \end{bmatrix} \quad (8)$$

The time derivative of Eq. (7) yields the constraint acceleration equation

$$\ddot{\boldsymbol{\Phi}}^{(ma)} \equiv \boldsymbol{\Phi}_{\mathbf{u}'}^{(ma)} \ddot{\mathbf{u}}' = \mathbf{g}^{(ma)} \quad (9)$$

The Jacobian matrix given by Eq. (8) and vector $\boldsymbol{\gamma}^{(ma)}$ in Eq. (9) are now used in Eq. (5) instead of the equivalent quantities that refer to the body fixed conditions.

2.1.3 *Principal axis conditions*

The reference conditions that associate the origin of the reference frame to the instantaneous center of the referential and its directions to the principal inerta directions are designated by principal axis conditions (Nikravesh and Lin, 2003)

$$\boldsymbol{\Phi}^{(pa)} \equiv \sum_{k=1}^{n} \begin{Bmatrix} m_k \boldsymbol{\delta}'_k \\ \left(m\, b_\xi b_\eta + \mu_\eta \theta_\zeta\right)_k \\ \left(m\, b_\eta b_\zeta + \mu_\zeta \theta_\xi\right)_k \\ \left(m\, b_\xi b_\zeta + \mu_\xi \theta_\eta\right)_k \end{Bmatrix} = \mathbf{0} \quad (10)$$

in which the vector that locates node k with respect to the body reference frame is $\mathbf{b}'_k = \begin{bmatrix} b_\xi & b_\eta & b_\xi \end{bmatrix}^T$. The second time derivative of Eq. (10) and the corresponding Jacobian matrix $\boldsymbol{\Phi}_{\mathbf{u}'}^{(pa)}$ and the right-hand side vector $\boldsymbol{\gamma}^{(pa)}$ are now used in Eq. (5) instead of the quantities that refer to the body fixed conditions.

2.2 *Generalized elastic coordinates reduction*

The equations of motion for the linear flexible body, in the form described by Eq. (5), is computationally inefficient due to the large number of coordinates necessary to describe complex models. This problem is overcome using component mode synthesis technique, static condensation approaches or a combination of both, reducing considerably the size of the problem. For the sake of conciseness only the mode synthesis technique is explored here.

The modes used may be the natural modes of vibration, static correction modes or other deformation modes (Yoo and Haug, 1986). Let the nodal displacements of the flexible part of the body be described by a weighted sum of deformation modes

$$\mathbf{u}' = \mathbf{X}\,\mathbf{w} \quad (11)$$

where the vector of modal coordinate $\mathbf{w}$ represents the contributions of the vibration modes towards the nodal displacements and $\mathbf{X}$ is the modal matrix.

Let the set of modes used in the mode synthesis, in Eq. (11), include a set of modes of vibration $\mathbf{X}_v$ and a set of static condensation modes $\mathbf{X}_s$ as

$$\mathbf{X} = \begin{bmatrix} \mathbf{X}_v & \mathbf{X}_s \end{bmatrix} \quad (12)$$

The evaluation and selection of the modes to be used in mode component synthesis is of fundamental importance for numerical accuracy and efficiency.

2.2.1 *Modes of vibration*

The modal matrix includes a selected number of modes of vibration $\mathbf{x}_i$ that are obtained by solving the eigenproblem associated to the finite element description of the flexible body

$$\mathbf{K}_L \mathbf{x}_i = \varpi_i \mathbf{M}_{ff} \mathbf{x}_i \quad (13)$$

The modes of vibration obtained, defined as free modes, correspond to those of a structure that is free in space. The modes of vibration $\mathbf{x}_0$ associated to the 6 lowest frequencies ϖ_i of the eigenproblem, generally null, represent the rigid motion with respect to the body reference frame, and are included in the modal matrix $\mathbf{X}_v$.

2.2.2 *Static correction modes*

The use of a small number of modes of vibration is unable to represent local deformations of the flexible body. Even if no external loads are applied on the flexible body, the points at which the kinematic joints are attached have to transmit the joint reaction loads and, consequently, their neighbourhood experiences local deformations. The use of the static condensation modes $\mathbf{X}_s = \left[\, \boldsymbol{\varphi}_1 \cdots \boldsymbol{\varphi}_s \cdots \boldsymbol{\varphi}_S \,\right]$ describes local deformations (Yoo and Haug, 1986; Geradin and Cardona, 1991).

To calculate each static correction mode let a nodal load vector $\mathbf{f}_a$ be defined with all its entries are null, except for the degree of freedom of the node in which an unit concentrated force or moment is applied. The force cannot be applied to the flexible body because no reference conditions are implied when the vibration analysis is performed. Instead, a pseudo-static equilibrium force $\mathbf{f}_e$, in which the unit force $\mathbf{f}_a$ is balanced by the rigid body inertial forces, is used. The pseudo-static equilibrium force is

$$\mathbf{f}_e = \left(\mathbf{I} - \mathbf{M}_{ff}\mathbf{X}_0\mathbf{X}_0^T\right)\mathbf{f}_a \tag{14}$$

The deformation mode $\hat{\boldsymbol{\varphi}}_s$ associated to the pseudo-static equilibrium force is obtained by solving the static equilibrium equation for the flexible body

$$\mathbf{K}_{ff}\hat{\boldsymbol{\varphi}}_s = \mathbf{f}_e \tag{15}$$

Before the deformation mode can be used it has to be orthogonalized and normalized with respect to the vibration modes and to the other static condensation. Let vectors $\boldsymbol{\alpha}_0$ and $\boldsymbol{\alpha}_v$ be defined as

$$\begin{aligned} \boldsymbol{\alpha}_0 &= \mathbf{X}_0^T\mathbf{M}_{ff}\hat{\boldsymbol{\varphi}}_s \\ \boldsymbol{\alpha}_v &= \mathbf{X}_v^T\mathbf{M}_{ff}\hat{\boldsymbol{\varphi}}_s \end{aligned} \tag{16}$$

Then, the new deformation modes orthogonal to the rigid body and kept vibration modes are obtained as

$$\breve{\boldsymbol{\varphi}}_s = \hat{\boldsymbol{\varphi}}_s - \mathbf{X}_0\boldsymbol{\alpha}_0 - \mathbf{X}_v\boldsymbol{\alpha}_v \tag{17}$$

The new deformation modes have to be orthogonal to each other also. The procedure is implemented by using successively Eqs. (16) and (17) with the vibration modes substituted by the other deformation modes. The result is that all modes are orthogonal to each other. The final step in obtaining the static deformation modes is the normalization. For the purpose let the β_s be defined as

$$\beta_s = \breve{\boldsymbol{\varphi}}_s^T\mathbf{M}_{ff}\breve{\boldsymbol{\varphi}}_s \tag{18}$$

in which the deformation modes $\breve{\boldsymbol{\varphi}}_s$ are assumed to be orthogonal to each other. Then, each one of the static correction modes is finally obtained as

$$\boldsymbol{\varphi}_s = \frac{1}{\sqrt{\beta_s}}\breve{\boldsymbol{\varphi}}_s \tag{19}$$

The pseudo-natural frequencies associated to each of the static correction mode are evaluated as

$$\varpi_s^2 = \boldsymbol{\varphi}_s^T\mathbf{K}_L\boldsymbol{\varphi}_s \tag{20}$$

The balance between the number of vibration modes and static correction modes used in each flexible body model is problem dependent. It is not necessary that a static correction mode is associated to every degree of freedom to which a joint reaction or external force is applied. However, static correction modes must be associated to dof where the most significant forces are applied.

2.2.3 *Mode synthesis*

Due to the assumption of linear elastic deformations the modal matrix is invariant. A simpler system of equations is obtained by using the orthonormality of the modes with respect to the mass matrix, which implies that $\mathbf{X}^T\mathbf{M}_{ff}\mathbf{X} = \mathbf{I}$ and $\mathbf{X}^T\mathbf{K}_{ff}\mathbf{X} = \Lambda$, where Λ is a diagonal matrix containing the squares of the flexible body natural and pseudo-natural frequencies. This leads to

$$\begin{bmatrix} \mathbf{M}_{rr} & \mathbf{M}_{r\phi} & \mathbf{M}_{rf}\mathbf{X} & \mathbf{0} \\ \mathbf{M}_{\phi r} & \mathbf{M}_{\phi\phi} & \mathbf{M}_{\phi f}\mathbf{X} & \mathbf{0} \\ \mathbf{X}^T\mathbf{M}_{fr} & \mathbf{X}^T\mathbf{M}_{f\phi} & \mathbf{I} & \left(\boldsymbol{\Phi}_{\mathbf{u}}^{(bf)}\mathbf{X}\right)^T \\ \mathbf{0} & \mathbf{0} & \boldsymbol{\Phi}_{\mathbf{u}}^{(bf)}\mathbf{X} & \mathbf{0} \end{bmatrix} \begin{bmatrix} \ddot{\mathbf{r}} \\ \dot{\boldsymbol{\omega}}' \\ \ddot{\mathbf{w}} \\ \boldsymbol{\lambda}^{(bf)} \end{bmatrix} = \begin{bmatrix} \mathbf{g}_r + \mathbf{s}_r \\ \mathbf{g}'_\phi + \mathbf{s}'_\phi \\ \mathbf{X}^T\left(\mathbf{g}'_f + \mathbf{s}'_f\right) - \Lambda\mathbf{w} \\ \boldsymbol{\gamma}^{(bf)} \end{bmatrix} \tag{21}$$

where any reference condition previously described can be used instead of the body fixed condition implied by the superscript (bf).

Although Eq. (22) represents the dynamic equilibrium of a flexible body with the reference conditions included it is seldom found in the literature. When the body fixed condition is used, the nodal degrees of freedom of the flexible body to which the coordinate frame is attached are null. In this case, such degrees of freedom are removed from the nodal displacement vector $\mathbf{u}'$ and the corresponding lines and columns of $\mathbf{K}_L$ and $\mathbf{M}_{ff}$ are eliminated before the eigenproblem is solved. These are referred as fixed modes and are not discussed here.

3 APPLICATION TO THE DEPLOYMENT OF A SATELLITE

The antenna consists in two identical subsystems, each with three coupled planar 4-bar links that unfold two panels on each side. The central panel is attached to the main body of the satellite. Each system has 2 dof, driven individually by actuators. During launching the antenna and the solar array are folded, as shown in Fig. 2a. Upon unfolding the satellite achieves the configuration in Fig. 2b.

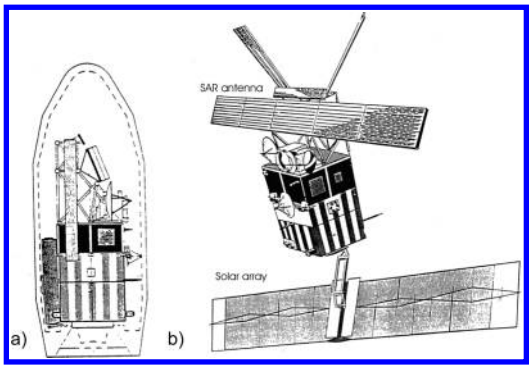


Figure 2. Satellite with the antenna a) folded and b) unfolded.

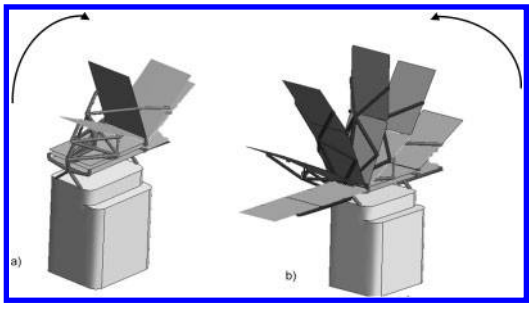


Figure 3. Unfolding process: a) 1st phase b) 2nd phase.

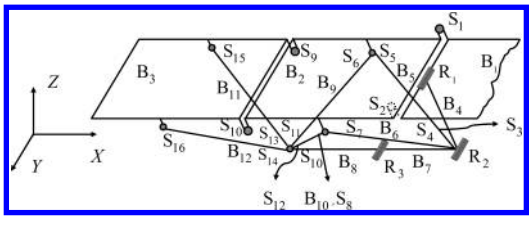


Figure 4. Multibody model of the antenna.

The unfolding process consists in two phases, schematically represented in Fig. 3. Functional requirements for the final configuration impose that the alignment between panels is obtained within a tolerance smaller than 0.5°.

The model used for one half of the folding antenna, schematically depicted Fig. 4, is composed by 12 bodies (B_1,…, B_{12}), 16 spherical joints (S_1,…, S_{16}) and 3 revolute joints (R_1, R_2, R_3). The geometry of each panel is $1.994 \times 1.300 \times 0.002$ m. All truss members have a circular cross-section (Anatharaman and Hiller, 1991). The material used in the model is a carbon reinforced plastic IM6/SC1081 with a matrix of Epoxy SC1081 and fibers in Carbon IM6. Note that the material model is not necessarily that of the real satellite antenna, as the characteristics of such material are not publicly available. Referring to Fig. 5, the properties of the composite material, for a single layer with an orientation of 0° relatively to the X axis are: $E_1 = 177$ GPa; $E_2 = 10.8$ GPa; $G_{12} = G_{13} = 7.6$ GPa; $G_{23} = 8.504$ GPa; $\nu_{12} = 0.27$; with a specific mass of 1600 kg/m^3.

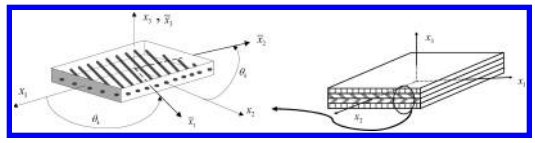


Figure 5. Coordinate system and layer numbering used for a typical laminated plate and orthotropic layer.

Table 1. Layer orientations of the satellite panels before and after optimization.

Panels	Design variable	Lower bound	Initial value	Optimal value	Upper bound
2 = 3	ϕ_1/ϕ_2	−90°/−90°	55°/−55°	+1°/−47°	+90°/+90°

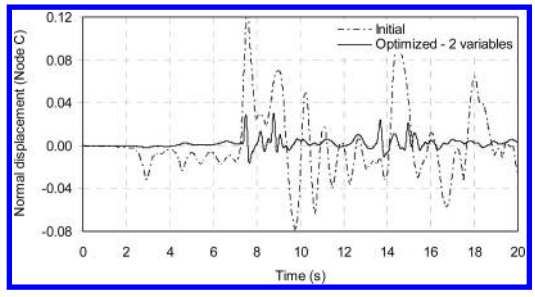


Figure 6. Normal displacements of node coincident with S_9 (see Fig. 4) for the initial and optimal laminates.

The actuator, applied in revolute joint R_3, is modeled as a nonlinear spring and damper actuator. The spring-damper-actuator has piecewise-linear characteristics with damping. The actuation law presented here is different from that reported by Anantharaman and Hiller (1991), which was used to model the antenna with panels made of isotropic material.

The flexibility of the multibody systems components made of composite materials is very sensitive to the layer orientation of the lay-ups that form the laminate. In order to get a stiffer antenna, an optimization problem is formulated as the minimization of the deformation energy of the panels (Ambrósio et al., 2007). In order to avoid that at a given instant the deformation of the panel exceeds predefined limits, the maximum value of the deformation energy, in each panel, is constrained to be below a given threshold. All material models considered for the optimal problem were symmetric laminates. The layer orientations of the panel material for the original and optimal configurations are depicted in Table 1.

The normal displacements of the panels, with respect to the body fixed frame, are greatly reduced in the optimized model with respect to the original one, as shown in Figs. 6 and 7. It is also observed that in the initial design the panel deformations involve mostly the bending mode while the optimal panel oscillations are mostly torsion deformation.

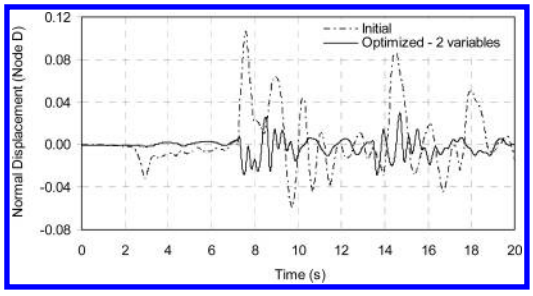


Figure 7. Normal displacements of node coincident with S_{10} (see Fig. 4) for the initial and optimal laminates.

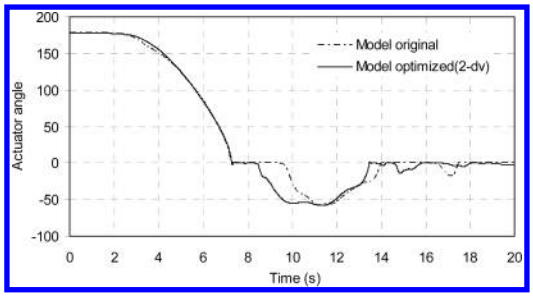


Figure 8. Actuator angle for the initial and optimal laminates during the first phase.

In Fig. 8, the actuator angle history during the first phase of the unfolding antenna is presented for the original and the optimum designs. It is clear that both designs lead to similar end alignments of the panels without any qualitative difference between the angle histories.

4 CONCLUSIONS

A computationally efficient methodology to handle the large displacements and rotations of flexible multibody systems involving linear elastic deformations is presented here. By using reference conditions as algebraic constraints it is possible to apply free-free vibration and static modes in a component mode synthesis approach to reduce the size of the problem. The application of the methodology to the deployment of a satellite demonstrates its virtues and exemplifies the modelling possibilities of structural mechanisms made of composite materials.

REFERENCES

Ambrósio, J. & Nikravesh, P. 1992. Elastic-plastic deformations in multibody dynamics. *Nonlinear Dynamics*, 3: 85–104.

Ambrósio, J. 1996. Dynamics of structures undergoing gross motion and nonlinear deformations: a multibody approach, *Comp. & Structures* 59(6): 1001–1012.

Ambrósio, J. & Gonçalves, J. 2001. Complex flexible multibody systems with application to vehicle dynamics. *Multibody Systems Dynamics* 6(2): 163–182.

Ambrósio, J., Neto, M.A. & Leal, R. 2007. Optimization of a complex flexible multibody systems with composite materials. *Multibody Systems Dynamics* 18(2): 117–144.

Anantharaman, M. & Hiller, M. 1991. Numerical simulation of mechanical systems using methods for differential-algebraic equations. *Int J Nume Methods in Engng*, 32: 1531–1542.

Belytschko, T. & Hsieh, B.J. 1973. Nonlinear transient finite element analysis with convected coordinates. *Int. J. Nume. Methods in Engng.* 7: 255–271.

Cavin, R.K. & Dusto, A.R. 1977. Hamilton's principle: finite element method and flexible body dynamics, *AIAA Journal*, 15(12): 1684–1690.

Erdman, A. & Sandor, G. 1972. Kineto-elastodynamics – a review of the state of the art and trends. *Mechanisms and Machines Theory* 7: 19–33.

Fehr, J. & Eberhard, P. 2011. Simulation process of flexible multibody systems with non-modal model order reduction techniques. *Multibody System Dynamics* 25(3): 313–334.

Geradin, M. & Cardona, A. 1991. A modelling of superelements in mechanism analysis, *Int. J. Nume Methods in Engng.* 32: 1565–1594.

Gestmayer, J. & Ambrósio, J. 2008. Component mode synthesis with constant mass and stiffness matrices applied to flexible multibody systems. *Int. J. of Num. Methods in Engineering* 73: 1518–1546.

Heckmann, A. 2010. On the choice of boundary conditions for mode shapes in flexible multibody systems. *Multibody System Dynamics* 23(2): 141–163.

Ibáñez, D.I. & Orden J.C. 2011. Galerkinmeshfree methods applied to the nonlinear dynamics of flexible multibody systems. *Multibody System Dynamics* 25(2): 203–224.

Kane, T., Ryan, R. & Banerjee, A. 1987. Dynamics of a cantilever beam attached to a moving base. *AIAA J of Guidance, Control and Dynamics* 10: 139–151.

Koutsovasilis, P. 2013. Improved component mode synthesis and variants. *Multibody System Dynamics* 29(4): 343–359.

Maqueda, L. & Shabana, A. 2007. Poisson modes and general nonlinear constitutive models in the large displacement analysis of beams. *Multibody System Dynamics* 18: 375–396.

Neto, M.A., Ambrósio, J. & Leal, R. 2006. Composite materials in flexible computational multibody dynamics, *Comp. Meths in Appl. Mech. Enging* 195: 6860–6873.

Nikravesh, P. & Lin, Y.-S. 2003. Body reference frames in deformable multibody systems, *Int. J. for Multiscale Computational Engineering* 1: 1615–1683.

Shabana, A. & Wehage, R. 1989. A coordinate reduction technique for transient amalysisos spatial structures with large angular rotations. *J. of Structural Mechanics* 11: 401–431.

Shabana, A. 1997. Definition of the slopes and the finite element absolute nodal coordinate formulation. *Multibody System Dynamics* 1: 339–348.

Simo, J.C. & Vu-Quoc, L. 1988. On the dynamics in space of rods undergoing large motions – a geometrically exact approach, *Comp. Methods Appl. Mech. Eng.* 66: 125–161.

Song, J. & Haug, E.J. 1980. Dynamic analysis of planar flexible mechanisms. *Computer Methods in Applied Mechanics and Engineering* 24: 359–381.

Thompson, B. & Sung, G. 1986. Survey of finite element techniques for mechanism design, *Mechanisms and. Machines Theory* 21: 351–359.

Tobias, C. & Eberhard, P. 2011. Stress recovery with Krylov-subspaces in reduced elastic multibody systems. *Multibody System Dynamics* 25(4): 377–393.

Yoo, W.S. & Haug, E.J. 1986. Dynamics of flexible mechanical systems using vibration and static correction modes, *ASME J. of Mechanisms, Transmissions and Automation in Design* 108: 315–322.

Research and Applications in Structural Engineering, Mechanics and Computation – Zingoni (Ed.)
© 2013 Taylor & Francis Group, London, ISBN 978-1-138-00061-2

Nonlinear dynamics of a rotating SD oscillator

Qingjie Cao & Ning Han
Centre for Nonlinear Dynamics Research, School of Astronautics, Harbin Institute of Technology, Harbin, China

Marian Wiercigroch
Centre for Applied Dynamics Research, School of Engineering, University of Aberdeen, King's College, Aberdeen, Scotland, UK

ABSTRACT: In this paper, we present a novel model which comprises a conventional pendulum and the presently proposed SD oscillator being of an oblique spring pinned to its rigid support. This model provides a cylindrical dynamical system with both smooth and discontinuous regimes depending on the value of a system parameter and also the dynamics transient relying on the coupling strength between the pendulum and the SD oscillator. The unperturbed system behaves both standard (smooth) and nonstandard (discontinuous) nonlinear dynamics of equilibrium bifurcations, periodic patterns and their separatrices of homoclinic and heteroclinic orbits of the first type, second-type and double heteroclinic orbits. Chaotic attractors are presented when the system is excited under the perturbation of viscous damping and external harmonic forcing within smooth regime. The results presented herein this paper show the dependency of the demonstrate attractors depending the coupling strength of the the pendulum and the SD oscillator exhibiting pendulum-type, SD-type and their mixture.

1 INTRODUCTION

Complex nonlinear phenomena always exhibited in a simple model, such as pendulum and SD oscillator. We will start from a smooth and discontinuous (SD) oscillator (Cao et al. 2006, Cao et al. 2008, Cao et al. 2008) and a mathematical pendulum (Nelson & Olsson 1986, Formalskii 2006) to introduce an archetype nonlinear model which is coupled with an SD oscillator and a pendulum to form the so called rotating SD oscillator. Both the SD oscillator and the pendulum are the reliable nonlinear system to reflect the nature behaviours of the nonlinear system without any truncation. The motivation of this paper is to present an archetype oscillator by combining the classical pendulum with the recently proposed SD oscillator to explorer the complex dynamics behaviour resulted by the coupling strength of the oscillators.

2 RELIABLE NONLINEAR OSCILLATORS

In this section we will give briefly introduction to the SD oscillator and the conventional pendulum, by using which an archetype rotating SD oscillator is proposed with both smooth and discontinuous dynamics.

2.1 *SD oscillator*

The SD oscillator was firstly proposed and investigated by Cao, Wiercigroch, Pavlovskaia, Grebogi, & T. Thompson (2006) which is an archetype nonlinear dynamical system with both smooth and discontinuous

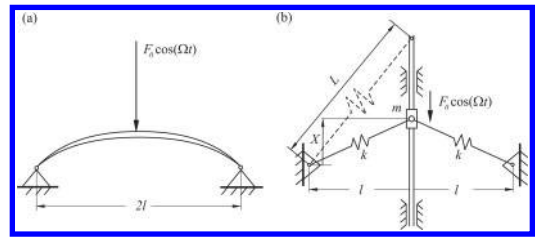


Figure 1. A shallow elastic arch and the simplified oscillator; (a) an elastic arch consisting of a beam and the rigid supports at each end; (b) vertically governed oscillator with a pair of springs pinned to rigid supports.

nonlinear dynamics due to the geometry configuration, see also Cao et al. (2008) and Cao et al. (2008) for details. This model is based upon a simple elastic beam, seen Thompson & Hunt (1973), as shown in Fig. 1a. This oscillator is similar to a snap through truss system composing of a mass m linked by a pair of inclined elastic springs which are capable of resisting both tension and compression. Each of the springs is of stiffness k pinned to a rigid support, as shown in Fig. 1b or Fig. 4a. Although the springs themselves provide linear restoring resistance, the resulting vertical response on the mass is a strong nonlinear force because of the geometric configuration.

The dimensionless equation of motion can be written in the following form by letting $w_0^2 = \frac{2k}{m}$, $x = \frac{X}{L}$ and $\alpha = \frac{l}{L} \geq 0$,

$$\ddot{x} + \omega_0^2 x(1 - \frac{1}{\sqrt{x^2 + \alpha^2}}) = 0, \qquad (1)$$

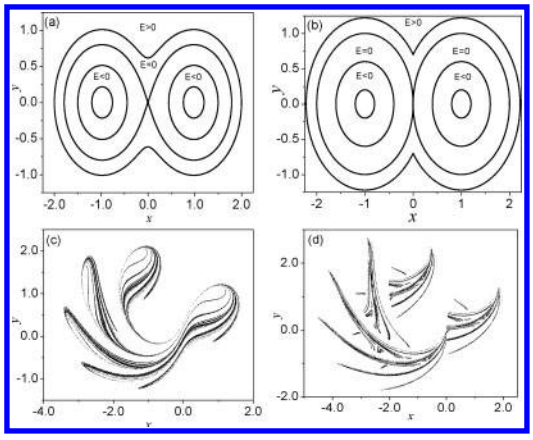


Figure 2. Phase portraits: (a) and (b) for $\alpha = 0.5$ and $\alpha = 0$, respectively, and the SD attractors: (c) and (d) for for $\alpha = 0.25$ and $\alpha = 0$, respectively, for $f_0 = 0.8$, $\xi = 0.015$ and $\omega = 1.015$ with the largest Lyapunov exponents 0.09432, 0.0473 and the Lyapunov dimension 1.5432, 1.4025.

in which, the smoothness parameter α defines the ge ometry of the oscillator (as shown in Fig. 1b) governing the property of the system. For $\alpha > 1$ the system epresents a pre-tensional discrete elastic string, while if $\alpha = 0$, the model corresponds to an oscillating mass supported by two parallel vertical springs.

When $\alpha = 0$ system (1) can be written in the following form,

$$\ddot{x} + \omega_0^2(x - \mathbf{Sign}(x)) = 0. \tag{2}$$

It is worth reiterating here that the discontinuous system (Filippov 1960, Filippov and Arscott 1992, Leine et al. 1998, Leine et al. 2000, Leine and Van Campen 2002) is obtained by decreasing of the smoothness parameter α to 0. Both system (1) and system (2) are call the SD oscillator.

Again the perturbed dimensionless system of (1) can also be obtained by letting $\tau = \omega_0 t$, $f_0 = \frac{F_0}{2kL}$, $\xi = \frac{\delta}{2mw_0}$ and $\omega = \frac{\Omega}{\omega_0}$,

$$x'' + 2\xi x' + x(1 - \frac{1}{\sqrt{x^2 + \alpha^2}}) = f_0 \cos\omega\tau, \tag{3}$$

where "′" denotes differentiation with respect to τ.

Attentions have been paid to the investigation of the nonlinear behaviours of the system in the past years. Tian, Cao, & Li (2010) and Lai & Xiang (2010) generalised the conventional averaging technique and the multiple scale method the this system to get the Hopf bifurcations and the semi-analytical solutions. Tian, Cao, & Yang (2010) investigate the detailed analysis about the co-dimension two bifurcation behaviour near the equilibrium bifurcation point at $\alpha = 1$. Cao, Wiercigroch, Pavlovskaia, Grebogi, & Thompson (2008) and Cao, Xiong, & Wiercigroch (2011) studied the limit case dynamics when parameter $\alpha = 0$ showing the complicated resonant behaviour and also the discontinuous chaotic sea with detailed formulation of the resonances which is no longer satisfying the law of $n\omega_0 = m\omega_1$, n, m are the relative prime integers. This formulation provides a better understanding of the complex resonant behaviours and a further application to describe chaos symbolically. Wang, Zhang, & Hong (2011) investigated the interior crisis of the SD Oscillator by using mapping cell method.

As for the irrational properties of the SD oscillator with both smooth and discontinuous phases, there occurs barrier for the conventional methodologies. An open problem was proposed by Cao, Wiercigroch, Pavlovskaia, Michael, Thompson, & Grebogi (2008) for the construction of the analytical solutions for the SD oscillator. Tian, Yang, Cao, & Wu (2012) tried a transformation to covert this irrational system to a new parametric space to get the further step to the problem. Cao, Wang, Chen, & Wiercigroch (2012) provides a series of irrational elliptic function to present the analytical solutions for the SD Oscillator, by using which the chaotic threshold can be derived by expanding the Melnikov method.

Applications and the experimental investigations are also made about the original SD oscillator. Leger, Pratt, & Cao (2012) considered the fully nonlinear dynamics with impact and friction by introducing Coulomb cone presented all the possible equilibrium bifurcations of the SD oscillator with impact and friction. Han, Cao, Chen, & Marian (2012) presented a rig-coupled SD oscillator showing the bifurcations of the multiple stability, dynamic bucklings and also the conditions of the bifurcations. Tian, Yang, Cao, & Han (2012) modelled the bridge-vehicle intersection to explorer the dynamic behaviour by using a variable stiffness SD oscillator, the results show the excellent agreement withe the experiment data. Chen, Cao, Feng, & Tian (2012) set up a experimental rig to investigate the nonlinear behaviour approaching the real system and the numerical studies.

2.2 *Pendulum*

None can ignore the influence of pendulum on the history of science, which is a frequent topics in a modern universities. Even the first application of pendulum can be dated back to AD 132, when it is used in Seismograph, see (Bielenstein 1980) for instance, until 1582, Galileo found the law of isochronism (Galileo 1592) through classical experiments, which marked the beginning of scientific research of pendulum. In 1674, Huygens discovered the periodicity of large swings (Michael, Matthews, & Gauld) which deviates from the law of isochronism. This is one of the earliest records of nonlinear phenomenon.

In modern times, several kinds of pendulum systems have been proposed and investigated, such as mathematical pendulum (Liang & Brian 2006) , double pendulum (Dullin 1994), spring pendulum (Lee & Park 1997) and spherical pendulum (Miles 1984) as well. Recent years, nonlinear behaviour of pendulum still attracts the study, such as Lobas, Kovalćhuk, & Bambura (2007) investigated the nonlinear behaviour

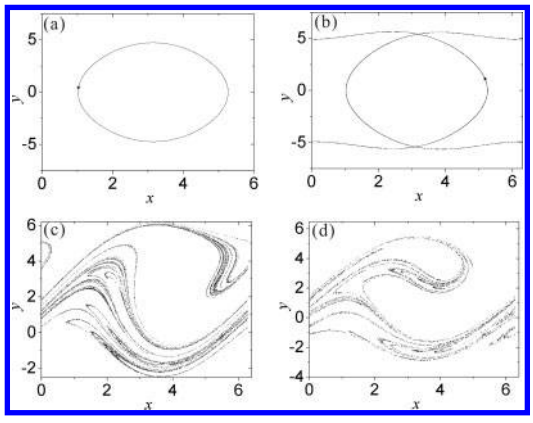


Figure 3. Pendulum trajectories for $\xi = 0.125$, $f_0 = 5.0$: (a) and (b) for the type I and type II periodic solution when $\omega = 1.05$ and $\omega = 2.1$, respectively; (c) and (d) are the classical pendulum ($h = 0$) for $f_0 = 5.0$, $\xi = 0.25$ with the largest Lyapunov exponents 0.3248 and 0.3342, the corresponding Lyapunov dimension 1.5651, 1.5717, respectively, for $\omega = 1.05$ and 1.7.

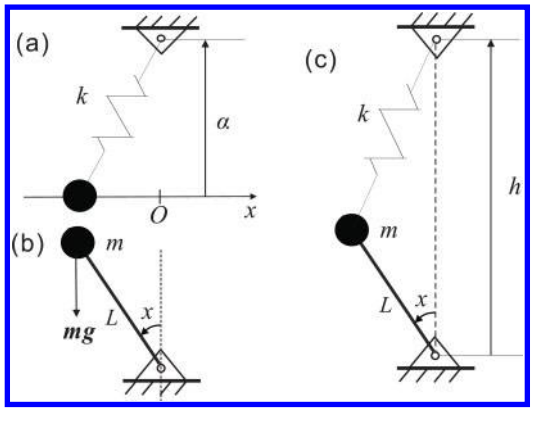


Figure 4. (a) SD Oscillator, (b) inverted pendulum and (c) the rotating SD oscillator comprising an SD oscillator and an inverted pendulum.

of the inverted pendulum systems subjected to a linear spring providing a follower force, and others demonstrated a rich behaviour for pendulum systems, see Nelson & Olsson (1986) and Formalskii (2006) for example.

Here we present some primary attractors for the classical inverted pendulum, as shown in Fig. 4b. The dimensionless equation of motion with damping and external excitation of frequency ω and amplitude f_0 can be obtained as the following by re-scalling transformations (omitted).

$$\ddot{x} + 2\xi\dot{x} - \omega_0^2 \sin x = f_0 \cos \omega t. \tag{4}$$

Fig. 3 shows the phase portraits for the periodic solutions (Fig. 3a and 3b) and the chaotic attractors in Fig. 3c and 3d, the detail explanation can be seen in the corresponding captions.

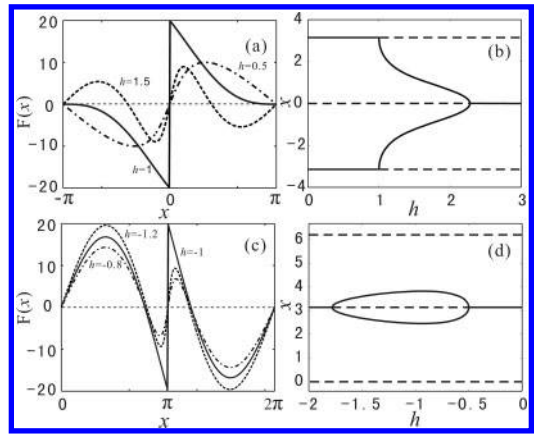


Figure 5. Restoring forces and the equilibrium bifurcations for $\omega_0 = \sqrt{20}$: (a) and (c) nonlinear restoring force $F(x)$ for $h > 0$ and $h < 0$ respectively, (b) and (d) bifurcation diagrams for x versus h, for $h \geq 0$ and $h \leq 0$, respectively.

3 ROTATING SD OSCILLATOR

3.1 *Equation of motion*

Let us consider a so called rotating SD oscillator, shown in Fig. 4a, which comprises the original SD oscillator, with a spring of stiffness k and relax length l linked by a mathematical pendulum of length L and a lump mass m. The governing equation of the dimensionless form can be written as the following by letting $L = 1$, $l = 1$, and $\omega_0^2 = \frac{k}{m}$.

$$\ddot{x} - F(x) = 0, \tag{5}$$

where $F(x) = g \sin x - \omega_0^2 h \sin x - \frac{\omega_0^2 h \sin x}{1+h^2-2h\cos x}$, and the graphs are plotted in Figs. 5a and 5c, respectively, for $\omega_0 = \sqrt{20}$ for the different values of parameter h.

It can be seen that this system is smooth for $|h| \neq 1$ and discontinuous at $x = 0$ for $h = 1$ and $x = \pi$ for $h = -1$. The equilibria of system (5) can be obtained, by letting $F(x) = 0$, written as

$$\begin{aligned} &x_1 = 0, x_{2,3} = \pm\pi, \\ &x_{4,5} = \pm \arccos\left(\tfrac{1+h^2}{2h} - \tfrac{\omega_0^4 h}{2(g-\omega_0^2 h)^2}\right), \end{aligned} \tag{6}$$

which exist only for $\left|\frac{1+h^2}{2h} - \frac{w_0^4 h}{2(g-\omega_0^2 h)^2}\right| < 1$.

Figs. 5b and 5d plot the branches of the equilibria for $\omega_0 = \sqrt{20}$ and show the pitchfork bifurcations of the equilibria, the solid curves denote the stable branches and the dashed indicate the unstable ones.

In the same way the perturbed equation of the dimensionless system can also be obtained by letting $f_0 = \frac{F_0}{mL}$ and $\xi = \frac{\delta}{2m}$.

$$\ddot{x} + 2\xi\dot{x} - F(x) = f_0 \cos \omega t. \tag{7}$$

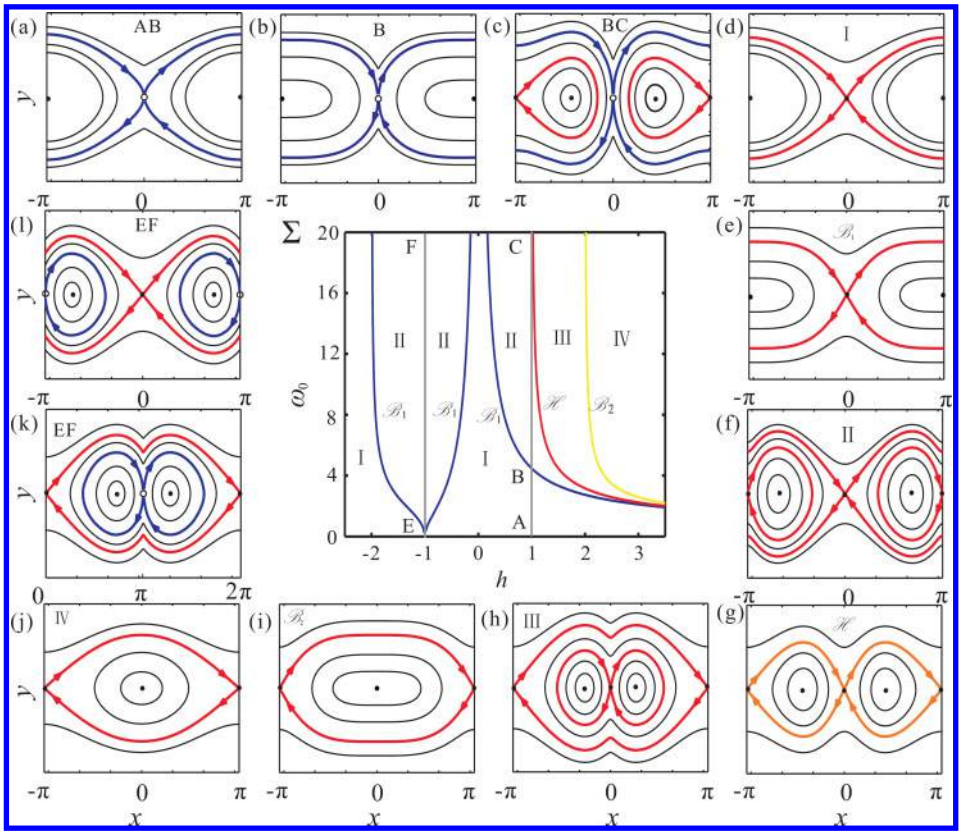


Figure 6. $\sum$. Bifurcation diagram, and (a)–(l) the corresponding phase portraits, the details seen in the context.

3.2 *Unperturbed dynamics*

Letting $\dot{x}x = y, \dot{y} = F(x)$ in system (5) yields the Hamiltonian of system as the following.

$$H(x,y) = \frac{y^2}{2} + (g - \omega_0^2 h)\cos x - \omega_0^2\sqrt{1+h^2-2h\cos x} - (g-\omega_0^2 h) + \omega_0^2|1-h|, \tag{8}$$

with the help of which, the trajectories of system (5) can be classified and analyzed. To do so, we calculate the transient sets on the surface of $F(x)$ in the parameter space (h, ω_0) plane as the following (Golubitsky, Stewart, & Schaeffer 1988).

$$\sum = \mathscr{B} \cup \mathscr{H} \cup \mathscr{D} = \mathscr{B}_1 \cup \mathscr{B}_2 \cup \mathscr{H}, \tag{9}$$

where $\mathscr{B}$ and $\mathscr{H}$ correspond to bifurcation set and hysteresis set, respectively, while $\mathscr{D}$ refers to the double limit set.

$$\begin{cases} \mathscr{B}_1 = \{\omega_0^2 h(1 - \frac{1}{|1+h|}) - g = 0\}, \\ \mathscr{B}_2 = \{g - \omega_0^2 h(1 - \frac{1}{|h-1|}) = 0\}, \\ \mathscr{H} = \{\omega_0^2(h-1) - g = 0\}, \\ \mathscr{D} = \emptyset. \end{cases} \tag{10}$$

which divides parameter space (h, ω_0) into four persistence regions, marked I, II, III and IV, as shown in Fig. 6$\sum$, $\mathscr{B}_1$, $\mathscr{B}_2$ and $\mathscr{H}$ are plotted with solid blue, yellow and red respectively, while the solid lines, marked grey, correspond to the discontinuous regimes for $|h| = 1$. All possible phase portraits of system (5) in parameter space, $(h, \omega_0 0)$, as shown in Fig. 6$\sum$, are plotted in Figs. 6a–6l, marked with the same symbols as in the corresponding parameter space in Fig. 6$\sum$.

The bold dots denote the centre and saddle points of the smooth equilibria connecting the corresponding heteroclinic, see Fig. 6g for example, homoclinic orbits, marked red, of the first, and the second kind in Fig. 6, respectively. While small cycles indicate nonstandard or saddle-like (Cao et al. 2006, Cao et al. 2008) for details, equilibria connecting the corresponding homoclinic-like orbits, marked blue, as shown in Figs. 6a–6c, 6k and 6l, respectively. Those dynamics present the global bifurcations for both smooth and discontinuous phenomena (Lamba and Budd 1994, Bressloff 1990) of pitchforks for equilibria and transitions for homoclinic and heteroclinic orbits. For example, smooth dynamics for $|h| \neq 1$ are displayed in Figs. 6d–6j, demonstrating two types of pitchfork bifurcations, seen Fig. 6, from Figs. 6d, 6e to Fig. 6f. Bifurcations of discontinuous for $|h| = 1$ are also given, for example Figs. 6a–6c, 6k and Fig. 6l,

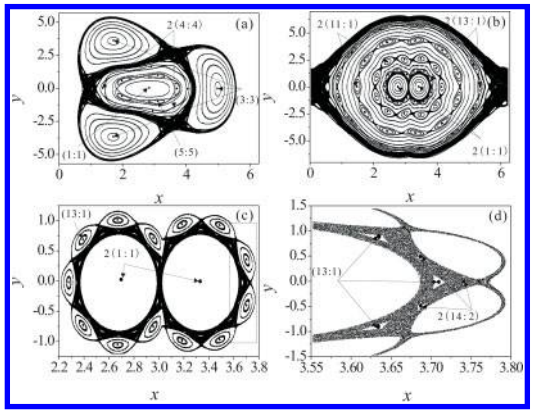


Figure 7. Chaotic sea and the quasi-periodic trajectories (islands) for $\xi = 0$: (a) Poincaré section for $f_0 = 10$, $\omega = 5.5$, $h = 1$, $\omega_0 = \sqrt{19.5}$, (b) Poincaré section for $f_0 = 20$, $\omega = 30$, $h = -1$, $\omega_0 = \sqrt{5}$, (c) the amplified area for the center part in (b), (d) locally amplified for the boxed area in (c).

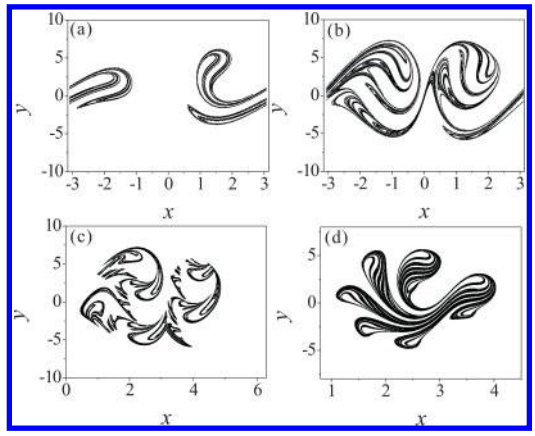


Figure 8. Rotating attractors:(a) and (b) for $h = 0.8$, 1.22 with the largest Lyapunov exponents 0.536155, 0.464603 and the corresponding Lyapunov dimension 1.52763, 1.49214, respectively, for $f_0 = 10$, $\xi = 0.24$, $\omega = 4.75$ and $\omega_0 = \sqrt{50}$; (c)–(d) for $h = -1$, -1.47 with the largest Lyapunov exponent 0.545585, 0.400991 and the Lyapunov dimension 1.73175, 1.67245, respectively, for $f_0 = 10$, $\xi = 0.1$, $\omega = 5.5$ and $\omega_0 = \sqrt{28}$.

which reveal a pitchfork bifurcation of the saddle-like equilibrium (0, 0) as well.

3.3 *Perturbed dynamics*

The time-dependent Hamiltonian can also be derived for the undamped system (7) for $\xi = 0$, written in the following form.

$$H(x,y,t) = \frac{y^2}{2} + (g - \omega_0^2 h)\cos x - (g - \omega_0^2 h) - \omega_0^2\sqrt{1 + h^2 - 2h\cos x} + \omega_0^2|1 - h| - f_0 x\cos\omega t, \quad (11)$$

in which time "t" is regarded the parameter, while system (7) acts as an one and half degree of freedom system with natural frequency ω_0 and the excitation frequency ω. The motions of this system are restricted within an torus with both action and angular variables (Chernikov, Sagdeev, Usikov, Zakbarov, & Zaslavsky 1987) for instance. The most interesting situation is the resonant behaviour (Lichtenberg & Lieberman 1992) occurred for $m\omega_0 - n\omega = 0$, m and n the related prime integers, which implies that the resonant motion can return to the starting point after m cycles of longitude and $n$cycles of latitude along the torus. Even the winding number of the resonance is defined $\alpha = \frac{n}{m}$, the period of the motion might be the integer times of the winding number (Guckenheimer & Holmes 1999). As examples, we show the Poincaré section, or a resonance web, for $f_0 = 10, \omega = 5.5, h = 1$, $\omega_0 = \sqrt{19.5}$ in Fig.7a with resonant solutions of (1:1), (3:3), (5:5), and a pair of (4:4). Fig.7b shows the Poincaré section for $f_0 = 20, \omega = 30, h = -1, \omega_0 = \sqrt{5}$ with resonant solutions of a pair of (1:1), a pair of (11:1), a pair of (13:1), a pair of (14:2) and (15:3) respectively.

In the following, numerical analysis are carried out to detect the complex behaviour for system (7) in the presence of both viscous-damping and external excitation of amplitude f_0 and frequency ω.

As the attractors we have presented for SD type in Fig. 5c and Fig. 5d and the conventional pendulum type in Fig. 3c and Fig. 3d when $h = 0$, Figs. 8a and 8b are the attractors for $h = 0.8$ and $h = 1.22$, respectively, and Figs. 8c and 8d are the attractors for $h = -1$ and $h = -1.47$, respectively, for the mixture of the SD and pendulum type. The attractors presented here show the chaotic transition among the pendulum and the SD oscillator and also the transition between the smooth and discontinuous ($h = -1$). It is interesting that the attractors of the system vary from the classical pendulum to the SD type depending on the strength of coupling.

4 CONCLUSIONS

In this paper, we have proposed and investigated an archetype oscillator exhibiting both smooth and discontinuous regimes. This system couples the conventional pendulum and the recently proposed SD oscillator. All the possible trajectory patterns of the unperturbed system have been demonstrated for the choosing of parameters h and ω_0 with various kinds homoclinic and heteroclinic orbits of the first and second type on the cylinder and the bifurcation transition. The system exhibits similar behaviour with the conventional pendulum and inverted pendulum and a bistable behaviour as parameter varying. For the perturbed system, numerical investigations show different type of attractors which are similar with that of pendulum or SD type or their mixture depending on the degree of coupling of the nonlinearities.

ACKNOWLEDGEMENTS

The authors would like to acknowledge the financial support from the Natural Science Foundation of China (Grant No. 11072065).

REFERENCES

Bielenstein, H. (1980). *The Bureaucracy of Han Times*. Cambridge: Cambridge University Press.

Bressloff, P.C. and Stark, J. (1990). Neuronal dynamics based on discontinuous circle maps. *Physics Letters A 150*(34), 187–195.

Cao, Q., D.Wang, Y. Chen, & M. Wiercigroch (2012). Irrational elliptic functions and the analytical solutions of SD oscillator. *Journal of Theoretical and Applied Mechanics 50*(3), 701–715.

Cao, Q., M. Wiercigroch, E. E. Pavlovskaia, C. Grebogi, & J. M. T. Thompson (2006). Archetypal oscillator for smooth and discontinuous dynamics. *Phys. Rev. E 74*, 046218:1–5.

Cao, Q., M. Wiercigroch, E. E. Pavlovskaia, C. Grebogi, & J. M. T. Thompson (2008). The limit case response of the archetypal oscillator for smooth and discontinuous dynamics. *International Journal Of Non-Linear Mechanics 43*(6), 462–473.

Cao, Q., M. Wiercigroch, E. E. Pavlovskaia, J. Michael, T. Thompson, & C. Grebogi (2008). Piecewise linear approach to an archetypal oscillator for smooth and discontinuous dynamics. *Phi. Tran. Roy. Soc. A 366*(1865), 635–652.

Cao, Q., Y. Xiong, & M. Wiercigroch (2011). Resonances of the sd oscillator due to the discontinuous phase. *Journal of Applied Analysis and Computation 1*, 183–191.

Chen, E., Q. Cao, M. Feng, & R. Tian (2012). The preliminary investigation on design and experimental research of nonlinear characteristics of SD oscillator. *Chinese Journal of Theorctical and Applied Mechanics 44*(3), 1–7.

Chernikov, A. A., R. Z. Sagdeev, D. A. Usikov, M. Zakbarov, & G. M. Zaslavsky (1987). Minimal chaos and stochastic webs. *Nature 326*, 559–563.

Dullin, H. R. (1994). Melnikov's method applied to the double pendulum. *Z. Physik B – Condensed Matter 93*, 521–528.

Filippov, A. & F. Arscott (1992). *Differential Equations with Discontinuous Righthand Sides: Control Systems*. New York: Springer.

Filippov, A. F. (1960). Differential equations with discontinuous right-hand side. *Mat. Sb. (N.S.)*, 99–128.

Formalskii, M. (2006). An inverted pendulum on a fixed and a moving base. *Journal of Applied Mathematics and Mechanics* 70(1), 56–64.

Galileo, G. (1592). *De Motu (On Motion), Chapter 8*.

Golubitsky, M., I. Stewart, & D. G. Schaeffer (1988). *Singularities and Groups in Bifurcation Theory, II*. New York: Springer.

Guckenheimer, J. & P. Holmes (1999). *Nonlinear Oscillations, Dynamical System, and Bifurcation of Vector Fields*. New York: Springer.

Han, Y., Q. Cao, Y. Chen, & W. Marian (2012). A novel smooth and discontinuous oscillator with strong irrational nonlinearities. *Science China-Physics Mechanics & Astronomy* 55(10), 1832–1843.

Lai, S. & Y. Xiang (2010). Application of a generalized senatorbapat perturbation technique to nonlinear dynamical systems with an irrational restoring force. *Computers and Mathematics with Applications 60*(7), 2078–2086.

Lamba, H. & C. J. Budd (1994, Jul). Scaling of lyapunov exponents at nonsmooth bifurcations. *Phys. Rev. E 50*, 84–90.

Lee, W. & H. Park (1997). Chaotic dynamics of a harmonically excited spring-pendulum system with internal resonance. *Nonlinear Dynamics 14*, 211–229.

Leger, A., E. Pratt, & Q. Cao (2012). A fully nonlinear oscillator with contact and friction. *Nonlinear Dynamics 70*(1), 511–522.

Leine, R. I. & D. H. Van Campen (2002, August). Discontinuous bifurcations of periodic solutions. *Math. Comput. Model. 36*(3), 259–273.

Leine, R. I., D. H. Van Campen, A. DE Kranker, & v. d. L. Steen (1998). Stick-slip vibrations induced by alternate friction models. *Nonlinear Dynamics 16*.

Leine, R. I., D. H. Van Campen, & B. L. Van De Vrande (2000). Bifurcations in nonlinear discontinuous systems. *Nonlinear Dynamics 23*(Section 2), 105–164.

Liang, Y. & F. F. Brian (2006). Parametric identification of a base-excited single pendulum. *Z. Phys. B 93*, 17–29.

Lichtenberg, A. J. & M. A. Lieberman (1992). *Regular and Chaotic Dynamics*. New York: Springer.

Lobas, L. G., V. V. Koval'chuk, & O. V. Bambura (2007). Influence of material and geometrical nonlinearities on the bifurcations of equilibrium states of a two-link pendulum. *Physica D: Nonlinear Phenomena 43*, 924–934.

Michael, R., C. F. Matthews, & A. S. Gauld. *The Pendulum: Scientific, Historical, Philosophical and Educational Perspectives*.

Miles, J. (1984). Resonant motion of a spherical pendulum. *Physica D: Nonlinear Phenomena 11*, 309–323.

Nelson, R. A. & M. G. Olsson (1986). The pendulum-rich physics from a simple system. *American Journal of Physics 54*, 112–121.

Thompson, J. & G. Hunt (1973). *A general theory of elastic stability*. London: John Wiley & Sons.

Tian, R., Q. Cao, & Z. Li (2010). Hopf Bifurcations for the recently proposed smooth and discontinuous oscillator. *Chinese Physics Letters 27*(7), 074701:1–5.

Tian, R., Q. Cao, & S. Yang (2010). The codimension-two bifurcation for the recent proposed SD oscillator. *Nonlinear Dynamics* 59(1–2), 19–27.

Tian, R., X. Yang, Q. Cao, & Q. Wu (2012). Bifurcations and chaotic threshold for a nonlinear system with an irrational restoring force. *Chinese Physics B 21*(2), 020503:1–12.

Tian, R. L., X. W. Yang, Q. J. Cao, & Y. W. Han (2012). The Study on the midspan deflection of a beam bridge under moving Loads based on SD oscillator. *International Journal of Bifurcation and Chaos 22*(5), 1250108:1–15.

Wang, J., X. Zhang, & L. Hong (2011). Study of the interior crisis in SD oscillator. *Journal of Dynamics and Control (in Chinese) 9*(4), 331–336.

Research and Applications in Structural Engineering, Mechanics and Computation – Zingoni (Ed.)
© 2013 Taylor & Francis Group, London, ISBN 978-1-138-00061-2

A hybrid time-frequency procedure for the solution of nonlinear dynamic problems

F.N. Correa & B.P. Jacob
LAMCSO – Laboratory of Computer Methods and Offshore Systems/COPPE/UFRJ – PostGraduate Institute of the Federal University of Rio de Janeiro, Civil Engineering Department, Rio de Janeiro, Brazil

ABSTRACT: This work presents extensions on the formulation of a Hybrid Time-Frequency domain Green Approach method (HTF-GA) for the solution of structural dynamic problems. The HTF-GA method is based on a step-by-step time domain solution procedure associated to the convolution between the Green functions of the problem and the vector of external loads. The hybrid approach is characterized by the fact that the Green functions are implicitly calculated in the frequency domain. Here the method is modified to uncouple the Green Function and represent complex problems with strongly non-linear behavior.

1 INTRODUCTION

The challenge of exploiting deep water offshore oil has been motivating studies on new alternatives for structural systems to support deepwater platforms, leading to the development of fixed compliant structures [1] and of moored floating platforms [2]. The behavior of such systems is characterized by large displacements leading to severe nonlinear dynamic effects, and also may have frequency-dependent mass, damping and stiffness properties.

This characteristic is associated not only to the intrinsic structural behavior of the system, but also to hydrodynamic effects due mainly to the fluid-structure interaction at the platform hull and sloshing effects that must be considered in the calculation of hull motions. In this context, this paper presents enhancements on the formulation of the hybrid time-frequency domain Green approach method (HTF-GA) for the solution of dynamic problems (see [3, 4] and the references thereof), modified here to solve strongly non-linear problems comprising an explicit method.

Classical numerical time-domain integration methods for the solution of equilibrium equations in dynamic analysis are based on the use of finite difference operators (or arbitrarily defined functions), that define the variation of the unknown values of displacements, velocities and accelerations within each time interval [5]. Solution procedures that combine time and frequency domain methods have been proposed to combine computational efficiency and the ability of dealing with frequency-dependent properties and time-dependent nonlinear effects [6, 7, 8, 9]. The HTF-GA method is based on the evaluation of the Green's function of the problem by Discrete Fourier Transform, adding advanced mathematical techniques to overcome numerical problems due to discontinuous functions and periodic effects.

The extension of the hybrid HTF-GA method presented in this work may be particularly suited for complex nonlinear applications, since it solves the equations of motion implicitly in the frequency domain, without explicitly calculating response spectra. The solution is presented directly in the time domain, without the need of transforming the domain of the external loadings acting on the structure. This way, to represent nonlinear effects without recalculating the Green Function and avoiding high CPU costs, the HTF-GA method is modified to solve the dynamic equation with the elastic forces placed at the right hand side. This means that the elastic forces are evaluated by the convolution integral of the method.

The resulting method may be classified as an explicit method, which will be particularly useful for instance on transient applications with severe nonlinear behavior. In comparison to current standard frequency-domain solution procedures, the main advantages of the hybrid method will be its ability to deal with highly nonlinear problems without compromising computational efficiency, and preserving all the advantages of a time-frequency method.

2 FORMULATION

It is well known [5, 10] that the spatial discretization via the Finite Element Method yields a set of second-order "semi-discrete" ODE – Ordinary Differential Equations, which in turn can be discretized and solved in time by an appropriate integration algorithm. For linear problems, this ODE corresponds to the equations of motion:

$$\mathbf{M}\,\ddot{\mathbf{u}}(t) + \mathbf{C}\,\dot{\mathbf{u}}(t) + \mathbf{K}\mathbf{u}(t) = \mathbf{F}(t) \tag{1}$$

where $\ddot{\mathbf{u}}(t)$, $\dot{\mathbf{u}}(t)$ and $\mathbf{u}(t)$ are vectors containing the unknown nodal values of, respectively, accelerations,

velocities and displacements; F(t) is the vector of external loads; **M, K** and **C** are the mass, stiffness and damping matrices.

2.1 *Green function*

The Green functions $\mathbf{G}(t)$ represent the transient response of a structural system due to the application of an impulsive load $\mathbf{F}_j(t) = I_j\delta(t-\tau)$ applied at the degree of freedom j at a given time $t = \tau$ (where δ is the Dirac delta function, and $\mathbf{I}_j$ is a vector with a unit non-zero entry only at dof j).

The Fourier transform of the Dirac delta function δ is simply $1/T$, one has the following expressions for the Green function matrices expressed in terms of harmonic components:

$$\mathbf{G}(t) = \frac{1}{T}\sum_{n=0}^{N-1}\mathbf{H}_n\, e^{jn\bar{\omega}t} \tag{2}$$

$$\dot{\mathbf{G}}(t) = \frac{1}{T}\sum_{n=0}^{N-1} jn\bar{\omega}\,\mathbf{H}_n\, e^{jn\bar{\omega}t} \tag{3}$$

where the transfer function matrix $\mathbf{H}_n$ is:

$$\mathbf{H}_n = (\mathbf{K}_n + \mathbf{C}_n.j.n.\varpi - \mathbf{M}_n.n^2.\varpi^2)^{-1} \tag{4}$$

Equations (2) and (3) include consequently periodicity effects associated to a Discrete Fourier Transform. This means that to solve transient responses without periodicity effects and without the need of extending the period of the Fourier transform the HTF-GA uses an advanced mathematical formulation [3] to express the matrix of Green functions $\mathbf{G}(t)$ and its time-derivative $\dot{\mathbf{G}}(t)$ as the sum of steady-state periodic components and "corrective" components, intended to represent the effects of unsatisfied initial conditions in the discrete Fourier transform procedure.

More details of the procedure to evaluate the Green Functions without periodicity effects may be found in [3].

2.2 *Basic formulation of the HTF-GA method*

Generalizing for MDOF systems such as those governed by Eq. (1), subjected to a general loading **F**(t) and with initial conditions $\mathbf{u}(0)$ and $\dot{\mathbf{u}}(0)$, an analytical solution for the displacement vector $\mathbf{u}(t)$ can then be expressed using Green Functions, as follows:

$$\mathbf{u}(t) = \left[\dot{\mathbf{G}}(t)\mathbf{M} + \mathbf{G}(t)\mathbf{C}\right]\mathbf{u}(0) + \mathbf{G}(t)\mathbf{M}\dot{\mathbf{u}}(0) + \int_0^t \mathbf{G}(t-\tau)\,\mathbf{F}(\tau)\,d\tau \tag{5}$$

A similar expression for the velocity response $\dot{\mathbf{u}}(t)$ can be derived:

$$\dot{\mathbf{u}}(t) = \left[\ddot{\mathbf{G}}(t)\mathbf{M} + \dot{\mathbf{G}}(t)\mathbf{C}\right]\mathbf{u}(0) + \dot{\mathbf{G}}(t)\mathbf{M}\dot{\mathbf{u}}(0) - \int_0^t \dot{\mathbf{G}}(t-\tau)\,\mathbf{F}(\tau)\,d\tau \tag{6}$$

Considering the equilibrium equation for $t \neq 0$ with $\mathbf{G}(t)$ as unknown, $\mathbf{M}\ddot{\mathbf{G}}(t) + \mathbf{C}\dot{\mathbf{G}}(t) + \mathbf{K}\mathbf{G}(t) = 0$, this last equation can be written in the following alternative form:

$$\dot{\mathbf{u}}(t) = -\mathbf{G}(t)\mathbf{K}\,\mathbf{u}(0) + \dot{\mathbf{G}}(t)\mathbf{M}\dot{\mathbf{u}}(0) + \int_0^t \dot{\mathbf{G}}(t-\tau)\,\mathbf{F}(\tau)\,d\tau \tag{7}$$

In establishing a recursive time-domain step-by-step solution, equations (5) and (7) are written taking $t = \Delta t$. Thus the response for the time step in the future is provided in terms of the convolution integral between the Green functions and the external force in this interval, added to terms that depend on the previous initial conditions $\mathbf{u}(t - \Delta t)$ and $\dot{\mathbf{u}}(t - t)$.

2.3 *Extension for mild non-linear problems*

Those last equations are oriented for linear transient analysis, but the HTF-GA method can be adapted for systems with nonlinear behavior.

For linear problems, the Green function matrices can be calculated only once. This will also be the case for problems where the degree of nonlinearity is such that allows the use of a pseudo-force technique, where the nonlinear component of the internal forces $\mathbf{R}(t)$ are included in the right-hand side of the equations.

The incorporation of the pseudo-force approach in the algorithm is simple. One needs only to add the nonlinear internal forces $\mathbf{R}(t)$ to the external loadings $\mathbf{F}(t)$ in the expressions that determine the numerical convolution integrals.

3 EXTENSION TO STRONGLY NON-LINEAR PROBLEMS

Up to this point, the HTF-GA method has been formulated to deal with linear and mildly nonlinear problems, with physical properties that may be frequency-dependent, focusing on inertial or structural dynamic problems. It is well known that implicit algorithms are in general more suited for the solution of inertial problems, since they allow the use of time steps larger than those required by explicit algorithms.

On the other hand, many dynamic problems are governed by intermediate or high-frequency components, such as in the case of slender offshore structures in transient and/or accidental situations. This is the case, for instance, of moored floating platforms during the rupture of one of its mooring lines; also, of the behavior of flexible jumpers (to convey fluids between floating plafforms) with bending restrictors presenting a multi-linear behavior. These cases are characterized by transient responses with severe nonlinear behavior, exciting higher components of the response. For these problems, conventional time-integration procedures would require the use of explicit algorithms with very small time steps. The advantage of explicit

schemes lies on the fact that the dynamic equations are reduced to a system of algebraic equations where the matrix of coefficient is diagonal, therefore not requiring expensive solvers for coupled systems. However, such schemes depend on using time steps smaller than a given critical value.

Following this line of reasoning, here the HTF-GA method is modified to uncouple the matrices of the Green functions and its derivative, and incorporate the elastic response on the vector of external loads. The goal is to solve, without high computational costs, such strongly nonlinear problems.

Recalling the equations of motion expressed by Eq. (1), this goal can be achieved by adding, on both sides of the equation, the fictitious elastic term $\eta\mathbf{I}\mathbf{u}(t)$, and transferring the actual elastic term to the right-hand side:

$$\mathbf{M}\ddot{\mathbf{u}}(t)+\mathbf{C}\dot{\mathbf{u}}(t)+\eta\mathbf{I}\mathbf{u}(t)=F(t)+\eta\mathbf{I}\mathbf{u}(t)-\mathbf{K}\mathbf{u}(t) \quad (8)$$

The fictitious elastic term is comprised by the identity matrix $\mathbf{I}$ affected by a real constant η, both multiplying the vector of unknown displacements $\mathbf{u}(t)$. The purpose of this elastic term is to stabilize the transfer function of the modified system, recalling that the transfer function becomes unstable if only mass and damping terms are incorporated.

In summary, the new transfer function can be assembled from Eq (8) following a procedure similar to the presented previously, now considering the fictitious elastic term along with the mass and damping matrices. This way, the new transfer function $\mathbf{H}_n^*$, the Green matrices and its derivative ($\mathbf{G}(t)^*$, $\dot{\mathbf{G}}(t)^*$) will be diagonal, thus uncoupling the system of equations:

$$\mathbf{H}_n^* = (\eta\mathbf{I}+\mathbf{C}i.n.\varpi-\mathbf{M}(n.\varpi)^2)^{-1} \quad (9)$$

$$\mathbf{G}(t)^* = \frac{1}{T}\sum_{n=0}^{N-1}\mathbf{H}_n^*.e^{i.n.\bar{\omega}.t} \quad (10)$$

$$\dot{\mathbf{G}}(t)^* = \frac{1}{T}\sum_{n=0}^{N-1}i.n.\bar{\omega}\,\mathbf{H}_n^*.e^{i.n.\bar{\omega}.t} \quad (11)$$

The displacements and velocities will then be expressed by the following equations:

$$\mathbf{u}(t) = \left[\dot{\mathbf{G}}(t)^*\mathbf{M}+\mathbf{G}(t)^*\mathbf{C}\right]\mathbf{u}(0) + \mathbf{G}(t)^*\mathbf{M}\dot{\mathbf{u}}(0) + \int_0^t \mathbf{G}(\tau)^*\left(\mathbf{F}(t-\tau)-\mathbf{F}_u(t-\tau)+\eta\mathbf{I}\mathbf{u}(t-\tau)\right)d\tau \quad (12)$$

$$\dot{\mathbf{u}}(t) = -\mathbf{G}(t)^*\eta\mathbf{I}\mathbf{u}(0) + \dot{\mathbf{G}}(t)^*\mathbf{M}\dot{\mathbf{u}}(0) + \int_0^t \dot{\mathbf{G}}(\tau)^*\left(\mathbf{F}(t-\tau)-\mathbf{R}(t-\tau)+\eta\mathbf{I}\mathbf{u}(t-\tau)\right)d\tau \quad (13)$$

As a consequence, both the actual and fictitious elastic terms ($\mathbf{F}_u(t)=\mathbf{K}\mathbf{u}(t)$) and $\eta\mathbf{I}\,\mathbf{u}(t)$ respectively, will be incorporated on the convolution integrals for the external forces.

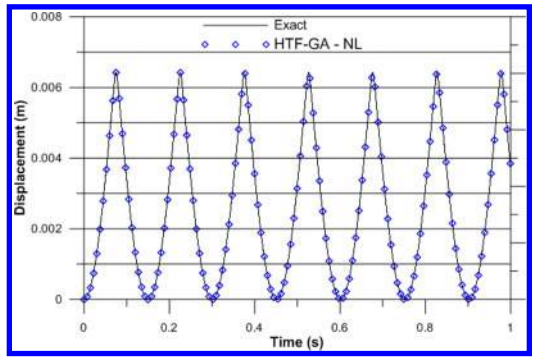


Figure 1. N-L SDOF Displacements.

It can be observed that, since $\mathbf{G}(0)^*=0$, the displacements $\mathbf{u}(t)$ are determined without the need of previously calculating the external loads, elastic forces and velocities on time t. Once $\mathbf{u}(t)$ is obtained, the elastic forces can be calculated, and then the velocity vector $\dot{\mathbf{u}}(t)$.

In general a value for the constant η can be attributed so as to make the natural periods of the modified system (with the added elastic term $\eta\mathbf{I}\mathbf{u}(t)$) greater than the natural periods of the original system.

4 CASE STUDY: SDOF SYSTEM

This section presents results for a SDOF spring-mass system, applying the new nonlinear formulation. This case represents a contact/impact condition restricting the motion of the spring. Consequently, the spring presents a nonlinear behavior, with stiffness varying with displacement, assuming an elastic bilinear spring, but with the second segment (for displacements larger than 0.006 m) presenting a much higher stiffness value, equal to 200 times the original value. The time step value is taken as $\Delta t = 0.0015$ s.

Figure 1 compares the displacements between the analytical (exact) and numerical responses. No visible difference can be observed. In the same figure, one can notice the small penetration of the system beyond the elastic contact condition, characterized by the higher stiffness value for displacements larger than 0.006 m.

5 CASE STUDY: OFFSHORE SYSTEM

This section presents results of the application of the proposed N-L HTF-GA method to solve the dynamic equations of an actual offshore engineering problem – a flexible riser that connects a floating platform to a subsea equipment to convey fluids that result from the oil exploitation procedures.

The riser, with nominal outer diameter equal to 581 mm, has a total length of 2000 m and connected to a platform installed at a water depth of 1000 m as illustrated on Figure 2. It is installed in a free-hanging catenary configuration, characterized by an angle of 7° at the top connection, between the axis of the riser and

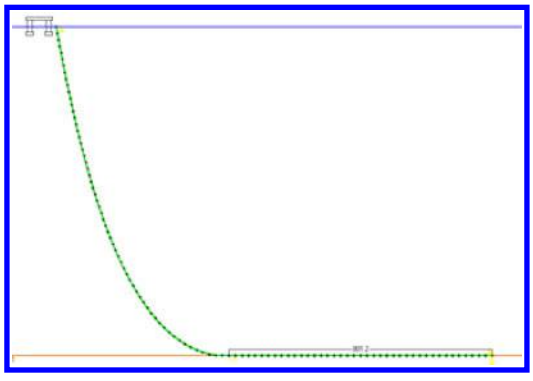


Figure 2. Flexible Catenary Riser.

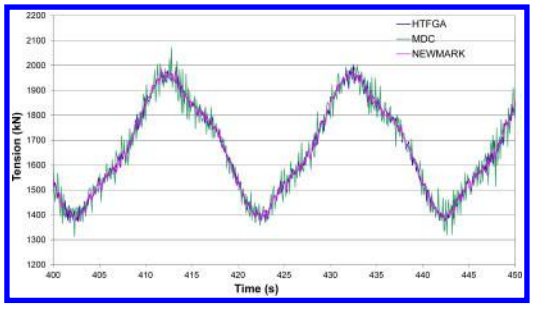


Figure 3. Riser Top Tension.

Table 1. Computational Performance (CPU times, s).

α-Newmark	Central Difference	HTF-GA
654.2	158.8	124.7

the vertical direction. The numerical model comprises a FE mesh of 500 frame elements with variable length (more refined at the top and touch-down regions).

The riser is submitted to its dead weight, marine currents, and a horizontal harmonic motion prescribed at its top. The results are expressed in terms of tensions at the top of the riser. Three algorithms are compared: the N-L HTF-GA method presented here, along with the classical Central Difference method [5], and a non-linear implementation of an implicit alpha-Newmark method with numerical damping [11, 12]. The total simulation time is 1000s, and all methods employ the time step value of 0.01 s.

Figure 3 compare the results obtained by all three methods, for a short time window of the complete response. It can be observed that the green curve, corresponding to the Central Difference method, presents considerable numerical noise, while the other two methods (alpha-Newmark and HTF-GA) presents smoother responses.

Table 1 presents the CPU times, in seconds, required for the execution of each method. It can be observed that the HTF-GA is about five times faster than the implicit alpha-Newmark method, and even faster than the explicit Central Difference method, with the additional advantage of presenting more accurate responses without spurious noise.

6 FINAL REMARKS

In this work, the HTF-GA method (originally presented in [3]) is enhanced to solve non-linear problems with the characteristics of an explicit algorithm. The main advantage of this new method is its ability to remove the stiffness matrix from the Green function, while keeping the transfer functions stable. The elastic behavior is solved by the convolution integrals of the method. Because the Green functions do not incorporate the non-linear stiffness matrix, this matrix may be calculated only once for the entire analysis, assuming the mass and damping matrix are constant; the explicit characteristic is retained (that is, the Green functions are completely decoupled) when diagonal, "lumped" mass matrices are considered.

The Green function matrices (which are characterized in the time-domain) are still implicitly determined in the frequency domain in terms of its steady-state harmonic components defined by a Fourier transform, therefore the method keeps its ability to deal with frequency-dependent mass and damping matrices.

The aspects related to causality and convergence of the Fourier series were presented in [3], where it was observed that the calculation of the Green function matrices $\mathbf{G}(\Delta t)$ and $\dot{\mathbf{G}}(\Delta t)$ also influences the accuracy of the method, depending not only on the selection of the time step Δt, but also on the adequate selection of the value N that define the number of terms in the truncated series. While the analysis of the properties of the original method was presented in [3], a detailed analysis of its new explicit form presented here will be presented in subsequent works.

The two case studies presented here were intended to illustrate the use of the N-L explicit formulation of the HTF-GA method for two different classes of dynamic problems: respectively impact and inertial (structural dynamic) problems. The results indicated that the method is able to deal with both classes of problem with good results. The method will be most suited to deal with transient problems associated to large F.E. models and strong non-linear behavior, which could not be evaluated efficiently by the standard form presented in [3].

Further studies on this line of research are being performed, and include other enhancements on the method such as adaptive time-step selection to assure the stability of the explicit N-L HTF-GA method.

REFERENCES

[1] Benjamim AC, Mourelle MM, Jacob BP and Ebecken NFF, Coupled and Uncoupled Solutions for the Nonlinear Dynamic Behavior of Guyed Deepwater Platforms, *Adv. Engng Software*, 1988, **10**, 2–7.

[2] Rodrigues MV, Correa FN, Jacob BP. Implicit Domain Decomposition Methods for Coupled Analysis of Offshore Platforms, *Communications in Numerical Methods in Engineering*, 2007, **23**, 599–621, DOI: 10.1002/cnm.945.

[3] Correa, FN; Jacob, BP; Mansur, WJ. *Formulation of an efficient hybrid time frequency domain solution procedure for linear structural dynamic problems*. Computers & Structures, v. 88, pp. 331–346, 2010.

[4] Correa, FN; Jacob, BP;. *An Efficient Time-Frequency Domain Solution Procedure for the analysis of Offshore System*. Procs. of the ASME 2011 30th International Conference on Ocean, Offshore and Arctic Engineering OMAE, v. 30. pp. 1–10, 2011

[5] Bathe KJ, *Finite Element Procedures*, Prentice-Hall, NJ, USA, 1996.

[6] Matthees W. A strategy for the solution of soil dynamic problems involving plasticity by transform. Int. J. Numer. Methods Eng. 18, 1601–1611, 1982.

[7] Wolf JP. Dynamic Soil–Structure Interaction. Prentice-Hall, Englewood Cliffs, NJ, 1985.

[8] Kawamoto JD. Solution of nonlinear dynamic structural systems by a hybrid frequency–time domain approach. In: MIT Research Report R83-5, Department of Civil Engineering, 1983.

[9] Aprile A, Benedetti A, Trombetti T. On non-linear dynamic analysis in the frequency domain. Earthquake Eng. Struct. Dyn. 3, 363–388, 1994.

[10] Belytschko T. An Overview of Semidiscretization and Time Integration Procedures, in *Computational Methods for Transient Analysis*, eds. Belytschko T, Hughes TJR, 1-65, 1983, Amsterdam: Elsevier Science Publishers.

[11] Wood WL, Bossak M, Zienkiewicz OC, 1980. "An Alpha Modification of Newmark's Method", *International Journal for Numerical Methods in Engineering*; 15, 1562–1566.

[12] Jacob BP, Ebecken NFF. An Optimized Implementation of the Newmark/Newton-Raphson Algorithm for the Time Integration of Nonlinear Problems, *Communications in Numerical Methods in Engineering*, 1994, **10**, 983–992.

Research and Applications in Structural Engineering, Mechanics and Computation – Zingoni (Ed.)
© 2013 Taylor & Francis Group, London, ISBN 978-1-138-00061-2

Nonplanar vibration and dynamics instability of slender cruciform columns

E.C. Carvalho & P.B. Gonçalves
Pontifical Catholic University, Rio de Janeiro, RJ, Brazil

Z.J.G.N. Del Prado
Federal University of Goiás, Goiânia, GO, Brazil

G. Rega
University of Rome, Rome, Italy

ABSTRACT: The three-dimensional motions and instabilities of a clamped-free, inextensible cruciform column under axial loads are investigated in this paper. Special attention is given to the nonlinear oscillations of columns with low torsional stiffness and its influence on the bifurcations and instabilities of the structure, a problem not tackled in the previous literature on this subject. For this, the nonlinear integro-differential equations describing the flexural-flexural-torsional couplings of the column are used, together with the Galerkin method, to obtain a set of discretized equations of motion, which are in turn solved by numerical integration using the Runge-Kutta method. Both inertial and geometric nonlinearities are considered in the present analysis. Using several tools of nonlinear dynamics, a complex dynamic behavior of the column is observed near to the region where a 1:1:1 internal resonance occurs. In this region several bifurcations leading to multiple coexisting solutions, including planar and nonplanar motions are obtained. Finally, the paper shows how the tools of nonlinear dynamics can help in the understanding of the global safety and integrity of the model, thus leading to a safe structural design.

1 INTRODUCTION

The stability of slender cruciform columns under static loading has been a frequent research topic due to its low torsional stiffness and the dangerous flexural-torsional coupling in the post-buckling regime. One of the first studies on this topic was conducted by Hutchinson and Budiansky (1976). Later, Dabrowski (1988), Cimetire *et al*. (2004) and Schurig and Bertram (2011) also studied the torsional stability of cruciform columns under compressive loads and their design was discussed by Kim and Hirohata (2005) and Trahair (2012), among others. However, little is known on the nonlinear vibrations and dynamic stability of cruciform columns.These columns can, when excited, exhibit large displacements, as well as nonplanar motions, leading to various types of bifurcations, coexistence of different solutions and dynamic jumps, causing sudden changes in the stress and strain states of the structure.

When the first torsional frequency is well above the minimum flexural frequencies, a simplified two-degree-of-freedom model is used in the nonlinear nonplanar vibration analysis of slender columns (Crespo da Silva and Glynn, 1979; Nayfeh and Pai, 1989; Pai and Nayfeh, 1990; Arafat, Nayfeh and Chin, 1998). However, for a slender cruciform column the lowest torsional frequency may be of the same order as the flexural frequencies and a strong flexural-flexural-torsional coupling may occurs. In particular, for certain geometries,such as the cruciform one, a 1:1:1 internal resonance can be observed leading to a complex nonlinear dynamic behavior. Many others cross section geometries exhibit low torsional stiffness, such as cold formed steel sections (Davies, 2000), leading to similar phenomena.

To correctly describe the dynamic characteristics of slender columns with low torsional stiffness, it is necessary to consider in the equations of motion both geometric and inertial nonlinearities. Crespo da Silva and Glynn (1978a; 1978b) derived the equations of motion for a three-dimensional inextensible beam, including both types of nonlinearity. Due to its high accuracy, their formulation was the basis for several investigations (Lee *et al*, 2008; Aghababei *et al*, 2009), including the present work.

So, our aim here is, using the tools of nonlinear dynamics, to study three-dimensional motions and instabilities of a clamped-free, inextensible cruciform column under axial loads with emphasis on the influence of a static preload on the linear frequency spectrum, nonlinear frequency-amplitude relation, stability boundaries in the force control space, dynamic bifurcations and basins of attraction, thus giving a detailed description of this problem.

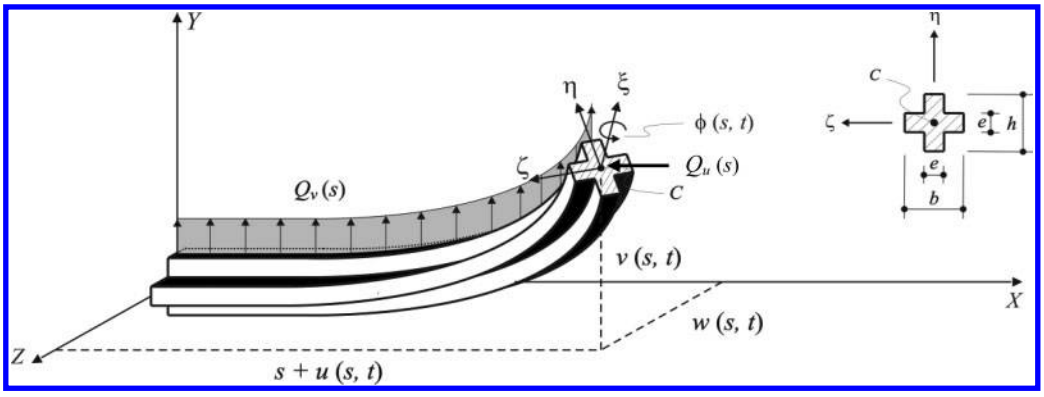


Figure 1. Coordinate systems, displacements, loads and column cross section.

2 DYNAMIC SYSTEM

A uniform, homogeneous, inextensible and initially straight column of isotropic linear elastic material, length L and mass m per unit length is considered in this analysis. A deformed column segment of length s is shown in Figure 1, where the axes X, Y and Z define the inertial rectangular coordinate system, while ξ, η and ζ denote a local orthogonal curvilinear coordinate system of the column at arc length s in the deformed configuration, which coincides with the principal axes of the column cross section.

The column has a cruciform cross section with height h, width b and wall thickness e, as shown in the Figure 1. The system is subjected to an axial load applied at the free end and given by $Q_u(t) = P_s + q_u\cos(\Omega_u t)$, where P_s is the static load and $q_u\cos(\Omega_u t)$ is a harmonic excitation with frequency Ω_u, magnitude q_u and t is the time. Additionally, in the Y direction a uniformly distributed lateral harmonic excitation defined by $Q_v(t) = q_v\cos(\Omega_v t)$ is also considered, where q_v is the excitation magnitude and Ω_v the excitation frequency.

3 EQUATIONS OF MOTION

Using only one mode approximation in the Galerkin procedure, the following third-order dimensionless PDEs equations of motion are obtained:

$$\left[\int_0^1 F_\gamma^2 ds\right]\ddot{\gamma} + \left[c_\gamma \int_0^1 F_\gamma^2 ds\right]\dot{\gamma} - \left[\beta_\gamma \int_0^1 F_\gamma'' F_\gamma \, ds\right]\gamma = \alpha_{\gamma 1}\,\gamma\, v^2 + \alpha_{\gamma 2}\,\gamma\, w^2 + \alpha_{\gamma 3}\, v\, w + \left[\alpha_{\gamma 4}\,(v\,w)^{\bullet} + \alpha_{\gamma 5}\, v\,\dot{w}\right]^{\bullet} + \alpha_{\gamma 6}\,\gamma\,\dot{v} + \alpha_{\gamma 7}\,\gamma\,\dot{w} + \alpha_{\gamma 8}\,\dot{v}\,\dot{w}\,, \tag{1}$$

$$\left[\int_0^1 F_v^2 ds - J_\zeta \int_0^1 F_v'' F_v ds\right]\ddot{v} + \left[c_v \int_0^1 F_v^2 ds\right]\dot{v} + \left[\beta_y \int_0^1 F_v^{IV} F_v \, ds + \int_0^1 [P_s + q_u \cos(\Omega_u t)]F_v F_v'' \, ds\right] v = \alpha_{v1}\,\gamma\, w + \alpha_{v2}\, v\,\gamma^2 + \alpha_{v3}\, v\, w^2 + \alpha_{v4}\, v^3 + \alpha_{v5}\left(v^2\right)^{\bullet\bullet} v + \alpha_{v6}\left(w^2\right)^{\bullet\bullet} v + \alpha_{v7}\, v^2\,\ddot{v} + \alpha_{v8}\, v\, w\,\ddot{w} + \alpha_{v9}\,\dot{w}\,\dot{\gamma} + \alpha_{v10}\, w\,\dot{v}\,\dot{w} + \alpha_{v11}\, v\left(\dot{w}\right)^2 + \alpha_{v12}\left(\dot{v}\,\gamma^2\right)^{\bullet} + \alpha_{v13}\,\gamma\,\ddot{w} + \alpha_{v14}\, v\left(\dot{v}\right)^2 + \alpha_{v15}\, w\,\dot{\gamma} + \int_0^1 F_v\, q_v \cos(\Omega_v t) ds\,, \tag{2}$$

$$\left[\int_0^1 F_w^2 ds - J_\eta \int_0^1 F_w'' F_w ds\right]\ddot{w} + \left[c_w \int_0^1 F_w^2 ds\right]\dot{w} + \left[\beta_y \int_0^1 F_w^{IV} F_w \, ds + \int_0^1 [P_s + q_u \cos(\Omega_u t)]F_w F_w'' \, ds\right] w = \alpha_{w1}\,\gamma\, v + \alpha_{w2}\, w\,\gamma^2 + \alpha_{w3}\, w\, v^2 + \alpha_{w4}\, w^3 + \alpha_{w5}\left(w^2\right)^{\bullet\bullet} w + \alpha_{w6}\left(v^2\right)^{\bullet\bullet} w + \alpha_{w7}\, w^2\,\ddot{w} + \alpha_{w8}\, w\, v\,\ddot{v} + \alpha_{w9}\,\dot{v}\,\dot{\gamma} + \alpha_{w10}\, v\,\dot{w}\,\dot{v} + \alpha_{w11}\, w\left(\dot{v}\right)^2 + \alpha_{w12}\left(\dot{w}\,\gamma^2\right)^{\bullet} + \alpha_{w13}\,\gamma\,\ddot{v} + \alpha_{w14}\, w\left(\dot{w}\right)^2\,. \tag{3}$$

Details of this formulation, not considering the axial loads, can be found in Crespo da Silva (1991), where $v = v(t)$ and $w = w(t)$ are the deflections of the column in the Y and Z directions, respectively, and $\gamma = \gamma(t)$ is the angle of torsion. The nondimensional parameters of stiffness β_y and β_γ are used and c_v, c_w and c_γ, are the linear viscous damping coefficients. The superscript ($'$) denotes partial differentiation with respect to s and the superscript ($''$) means differentiation with respect to time t. Finally, the eigenfunctions $F_v(s)$, $F_w(s)$ and $F_\gamma(s)$ are of the following form:

$$F_{v,w} = C_{v,w}\{\cosh(r_{1,3}\,s) - \cos(r_{2,4}\,s) - K_{v,w}[\sinh(r_{1,3}\,s) - (r_{1,3}/r_{2,4})\sin(r_{2,4}\,s)]\}, \quad (4)$$

$$F_\gamma = C_\gamma \sin[(\pi/2)s]. \quad (5)$$

The quantities r_1 to r_4 are obtained from the solution of the characteristic equation:

$$r_{1,3}^4 + r_{2,4}^4 + 2\,r_{1,3}^2\,r_{2,4}^2\cosh(r_{1,3})\cos(r_{2,4}) + r_{1,3}\,r_{2,4}(r_{2,4}^2 - r_{1,3}^2)\sinh(r_{1,3})\sin(r_{2,4}) = 0\,. \quad (6)$$

In the above equations α_{vi}, α_{wi} e $\alpha_{\gamma i}$ (for $i = 1, 2, 3, \ldots$) are the Galerkin coefficients (Carvalho, 2013).

4 NUMERICAL RESULTS

4.1 *Influence of the axial load on the frequency-amplitude relation*

For the numerical analysis, a column with $h/b = 1.0$, $e = 0.06b$ (see Figure 1), $L = 25b$, distributed moments of inertia $J_\eta = J_\xi = 6.8978 \cdot 10^{-5}$ and $J_\xi = 1.3796 \cdot 10^{-4}$, stiffness parameters $\beta_y = 1.0$ and $\beta_\gamma = 6.9123 \cdot 10^{-4}$, and normalized modal amplitudes $C_v = C_w = 1.0$ and $C_\gamma = 1.4142$, is adopted.

The lowest natural flexural frequencies of the unloaded column are $\omega_{0v} = \omega_{0w} = \omega_{0\gamma} = 3.5161$. Figure 2a shows that as the axial load increases the square natural frequency decreases linearly, becoming zero when the static axial load reaches its critical value, $P_{cr} = (\pi^2 EI/4L^2)$.

In addition, Figure 2b illustrates the influence of the static axial load on the nonlinear frequency-amplitude relation. The unloaded column exhibits a small degree of geometric nonlinearity with hardening behavior. As the axial load increases, the degree of geometric nonlinearity decreases, but the importance of inertial nonlinearities in the equations of motion increases. At a certain load level, the curve starts to bend to left. For high load levels, it exhibits a strong softening behavior.

The described behavior is typical of bar structures, where geometric nonlinearities lead to increasing effective stiffness, while inertial nonlinearities lead to a loss of stiffness.

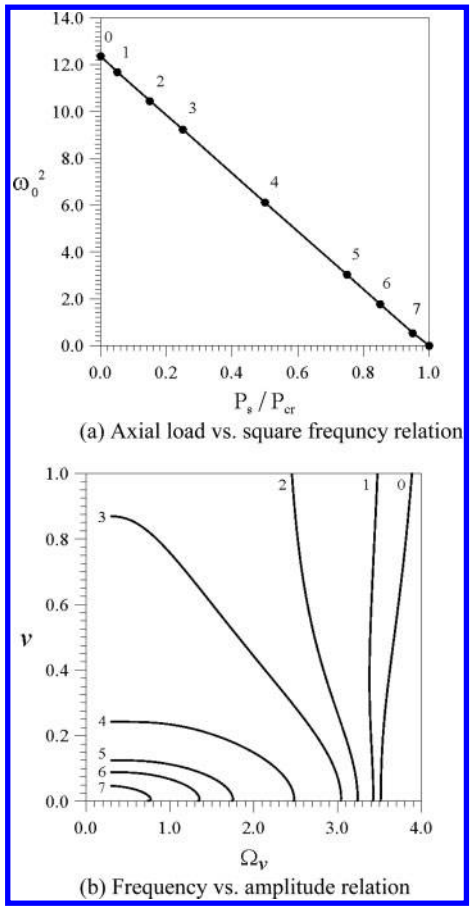


Figure 2. Influence of axial load on the lowest natural frequency and on the nonlinear frequency vs. amplitude relation.

4.2 *Parametric instability at principal and fundamental resonance regions*

Now, the nonlinear dynamic behavior of the clamped-free column subjected only to a harmonic axial load is studied.Here and in the following sections the linear viscous damping coefficients are $c_v = c_w = c_\gamma = 0.6\%$. Figure 3 shows the parametric instability boundary of the column in the excitation frequency Ω_u – excitation magnitude q_u control space.The first important parametric instability region is associated with the fundamental resonance, which occurs when the excitation frequency is equal to the lowest natural frequency ($\omega_0 = 3.5161$). The second V-shape region, on the right side, is associated with the principal parametric instability region, occurring when the excitation frequency is two times the lowest natural frequency of the column ($2\omega_0 = 7.0322$).

To understand the loss of stability and the bifurcations associated with the instability boundary, a study of the three-dimensional motions of the column in these two parametric instability regions ($\Omega_u = 2\omega_0$ and $\Omega_u = \omega_0$) is carried out.

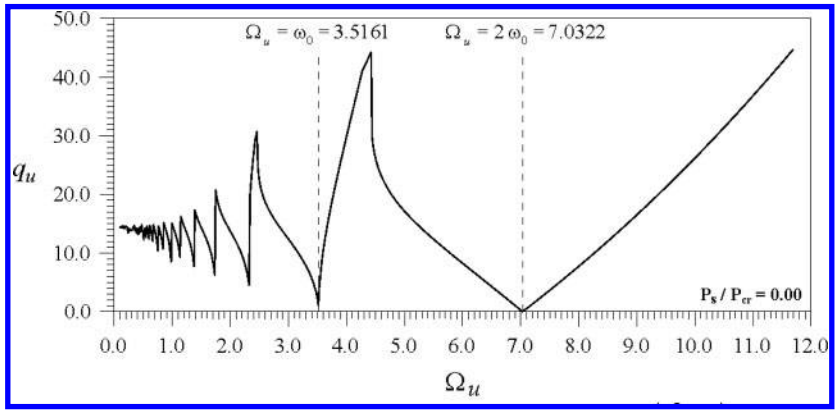


Figure 3. Parametric instability boundary in the force control space. Axial load: $q_u\cos(\Omega_u t)$.

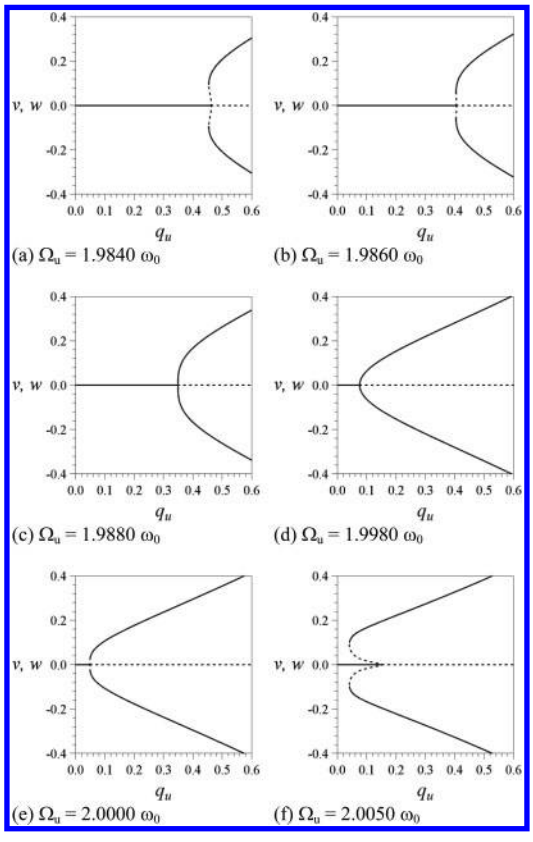


Figure 4. Bifurcation diagrams in the vicinity of the principal parametric instability region ($\Omega_u = 2\omega_0$).

As a starting point, Figure 4 displays the bifurcation diagrams for $\Omega_u \approx = 2\omega_0$. This bifurcation diagram is obtained by using the continuation algorithm and by taking the excitation magnitude q_u as control parameter.

In all cases the trivial solution (T) becomes unstable leading to a nontrivial solution (NT) with a period equal to twice of the forcing period. However, for $1.986_1\omega_0 < \Omega_u < 2.000_1\omega_0$ the trivial solution losses stability through a supercritical bifurcation, being subcritical out of this range. In addition, Figure 5 shows, at $\Omega_u = 2\omega_0$, the bifurcation diagram obtained by the use of the force brute algorithm. So, unstable solution branches are not identified in Figure 5. The transversal displacements v and w are analogous, as shown in Figure 5a. So, the angle of torsion is zero, as shown in Figure 5b.

A time history associated with the non-trivial solution (NT) is shown in Figure 6, considering $q_u = 0.70$. The period two of the non-trivial solution is confirmed by the existence of two fixed points of the Poincaré map (NT1 and NT2) shown in Figure 6b, which illustrates the three-dimensional motion of the column. Figure 7 show the bifurcation diagram for $\Omega_u = \omega_0$, which corresponds to the lowest critical load in the fundamental resonance region (see Figure 3).The trivial solution (T) becomes unstable at $q_u \approx 1.378$ where the column suffer a subcritical pitchfork bifurcation, leading to two non-trivial solutions with period equal to that of the forcing, denoted by NTA and NTBin Figure 8. Thus, between $q_u \approx 1.113$, where a saddle-node bifurcation along the nontrivial path occurs, and $q_u \approx 1.378$, threecoexistingperiodic solutions are observed (Figure 8) and the response of the structure is a function of the initialconditions.In this region the displacements v and w are no analogous due to the symmetry breaking effect of the pitchfork bifurcation. So, the angle of torsion, although small, is not zero (Figure 7b), leading to a flexural-torsional coupled motion of the structure.

4.3 *Influence of the static preload on the parametric instability boundary*

To illustrate the effect of the static preload (P_s) on the parametric instability of the system, Figure 9 shows four bifurcation diagrams for increasing values of the static preload, where, in each case, ω_0 is the lowest natural frequency of the loaded column, as shown in Figure 2a.

So, this corresponds to the lowest parametric instability load in the principal parametric resonance

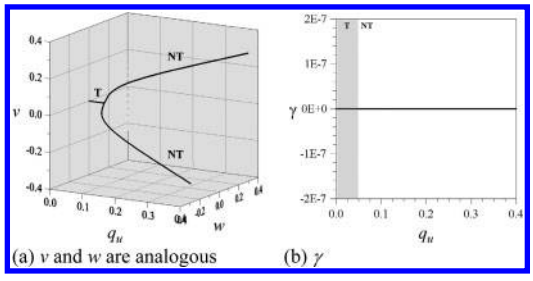


Figure 5. Bifurcation diagrams for $\Omega_u = 2\omega_0$ obtained by the force brute method.

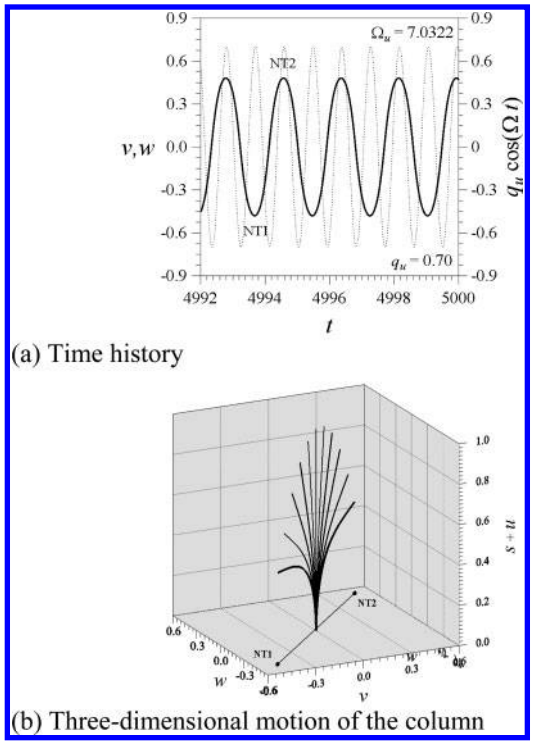


Figure 6. Time history v vs. t (analogous w vs. t) and nontrivial solution of the column (NT), considering $q_u = 0.70$ and $\Omega = 2\omega_0$.

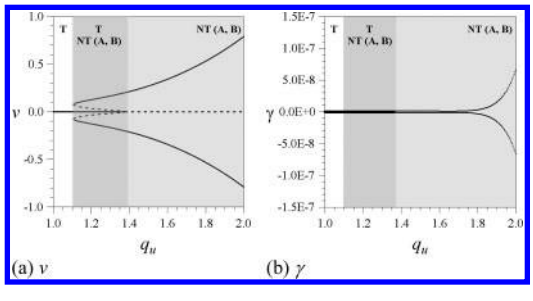


Figure 7. Bifurcation diagrams for $\Omega_u = \omega_0$.

region. These diagrams are obtained by increasing the axial load (q_u) and considering $\Omega_u = 2\omega_0$. Comparing the diagrams in Figure 9, one observes that, as P_s increases, the parametric critical load increases

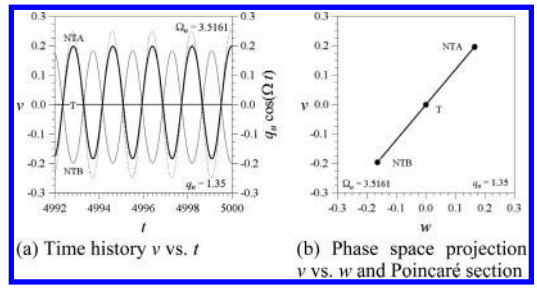


Figure 8. Stable solutions at $q_u = 1.35$ and $\Omega_u = \omega_0$.

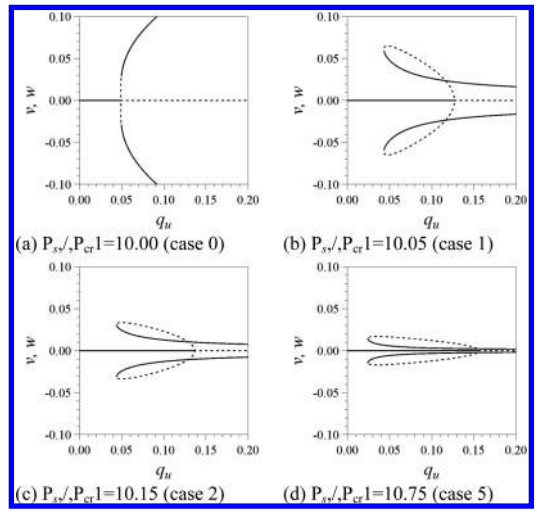


Figure 9. Bifurcation diagrams for the column under increasing static preload at $\Omega = 2\omega_0$. In each case, ω_0 is the lowest natural frequency of the loaded column.

while the load associated with the saddle-node bifurcation along the nontrivial path decreases, increasing the range of q_u where coexisting solutions can be observed.

4.4 *Influence of the static preload on the nonlinear response of the column under lateral excitation*

Next, we investigate the influence of static axial load on the dynamic nonlinear behavior of the beam under a distributed lateral harmonic excitation given by $Q_v(s) = q_v \cos(\Omega_v t) = 0.025 \cos(\Omega_v t)$ at the primary resonance region $\Omega_v = \omega_0$, applied in the Y direction (see Figure 1). Figure 10 showstwo projections of the resonance curves considering $P_s/P_{cr} = 0.00$ and $P_s/P_{cr} = 0.15$. The continuation *software* AUTO (Doedel*et al.*, 1998) is used in Figure 10a and brute force algorithm in Figure 10b.

As the static load increases, the natural frequency of the structure decreases (Figure 2) and the resonance region moves to the left, approaching zero, and most stable solution branches observed in the Figure 10a become unstable, as shown in Figure 10b for $P_s/P_{cr} = 0.15$. For this load level, a region without stable periodic solution appears. Figure 11 shows the time

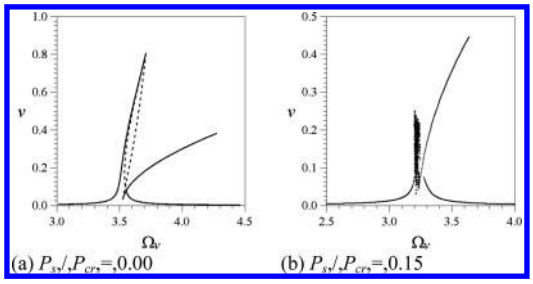


Figure 10. Influence of static preload on the resonance curvesof the column under lateral harmonic excitation ($q_v = 0.025$).

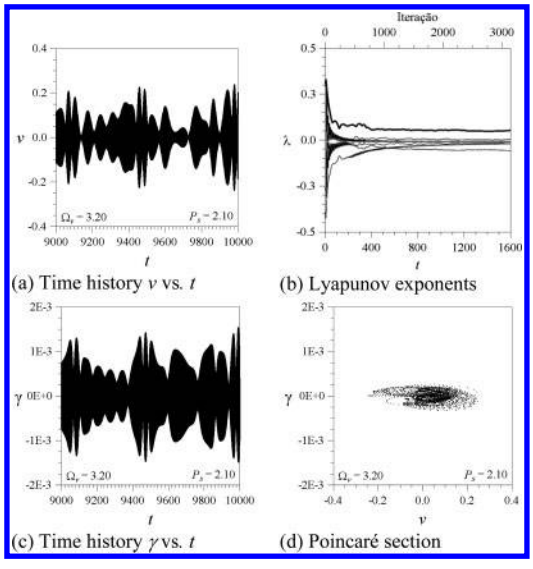


Figure 11. Characteristic chaotic response of the preloaded column. $P_s/P_{cr} = 0.15$, $q_v = 0.025$ and $\Omega_v = 3.20$.

history and the evolution of Lyapunov exponents (λ_i, for $i = 1, \ldots, , 6$) at $\Omega_v = 3.20$. At least one of the exponent is positive ($\lambda_i > 0$), characterizing the motion as chaotic.

5 CONCLUSIONS

The flexural-flexural-torsional response of a cruciform column with low torsional stiffness was investigated by taking into account geometric and inertial nonlinearities. The column geometry is such that all three lowest natural frequencies are of the same order. The column was subjected to a static preload plus a harmonic axial excitation. A bifurcation analysis shows that the static pre-load has a profound influence on the frequency-amplitude relation and on the resonance curves, which become more complex when the lateral harmonic excitation is considered. Multiplicity of solutions is observed as well as, regions without any stable periodic solution, where chaotic motions are detected.

ACKNOWLEDGMENTS

The authors gratefully acknowledge the support of FAPERJ, CAPES and CNPq.

REFERENCES

Aghababei, O., Nahvi, H., and Ziaei-Rad, S. 2009. Non-linear non-planar vibrations of geometrically imperfect inextensional beams, Part I: Equations of motion and experimental validation. *International Journal of Non-Linear Mechanics* 44: 147–160

Arafat, H., Nayfeh, A. H., and Chin, C. 1998. Nonlinear nonplanar dynamics of parametrically excited cantilever beams. *Nonlinear Dynamics* 15: 31–61.

Carvalho, E.C., 2013, Nonlinear and Non-planar Vibrations and Dynamic Instability of Slender Bars *D.Sc. Thesis*, PUC-Rio, Rio de Janeiro, Brazil.

Cimetire, A., Lger, A., and Potier-Ferry, M., 2004. Sur le flambage plastique de l'éprouvette cruciforme. *C. R. Mec* 332 (1): 67–72.

Crespo da Silva, M. R. M. 1991. Equations for nonlinear analysis of 3D motions of Beams. *Applied Mechanics Reviews* 44: 51–59.

Crespo da Silva, M. R. M., and Glynn, C. C. 1978a. Nonlinear flexural-flexural-torsional dynamics of inextensional beams. I. Equation of motion. *Journal of Structural Mechanics* 6(4): 437–448.

Crespo da Silva, M. R. M., and Glynn, C. C. 1978b. Nonlinear flexural-flexural-torsional dynamics of inextensional beams. II. Forced motions. *Journal of Structural Mechanics* 6(4): 449–461.

Crespo da Silva, M. R. M., and Glynn, C. C. 1979. Nonlinear nonplanar resonant oscillations in fixed-free beams with support asymmetry. *International Journal of Solids and Structures* 15: 209–219.

Dabrowski R. 1988. On torsional stability of cruciform columns, *J. Constr. Steel Res*. 9: 51–59.

Davies, J. M. 2000. Recent research advances in cold-formed steel structures. *Journal of Constructional Steel Research* 55: 267–288.

Doedel, E. J., Champneys, A. R., Fairgrieve, T. F., Kuznetsov, Y. A., Sandstede B. and Wang X. 1998.*AUTO 97*. Concordia University, Montreal, Canada.

Hutchinson, J., and Budiansky, B. 1976.Analytical and numerical study of the effects of initial imperfections on the inelastic buckling of a cruciform column. In: Budiansky, B. (Ed.), *Proc. of IUTAM Symp. on Buckling of Structures*. Springer: 98–105.

Kim, Y., and Hirohata, M. 2005. Ultimate strength of cruciform column corrected by heating.*Steel Structures* 5: 167–171.

Lee, W. K., Lee, K. S., and Pak, C. H. 2008.Stability analysis for nonplanar free vibrations of a cantilever beam by using nonlinear normal modes.*Nonlinear Dynamics* 52: 217–225.

Nayfeh, A. H., and Pai, P. F. 1989. Nonlinear nonplanar parametric responses of an inextensional beam. *International Journal of Non-Linear Mechanics* 24: 139–158.

Pai, P. F., and Nayfeh, A. H. 1990. Nonlinear nonplanar oscillations of a cantilever beam under lateral base excitations. *International Journal of Non-Linear Mechanics* 25: 455–474.

Schurig, M., and Bertram, A. 2011. The torsional buckling of a cruciform column under compressive load with a vertex plasticity model. *International Journal of Solids and Structures* 48: 1–11.

Trahair, N. S. 2012. Strength design of cruciform steel columns. *Engineering Structures* 35: 307–313.

Research and Applications in Structural Engineering, Mechanics and Computation – Zingoni (Ed.)
© 2013 Taylor & Francis Group, London, ISBN 978-1-138-00061-2

Bifurcation analysis of a Jeffcott rotor with a bearing clearance: Numerics and experiments

J. Páez Chávez
Centre for Applied Dynamics Research (CADR), School of Engineering, University of Aberdeen, Aberdeen, UK
Facultad de Ciencias Naturales y Matemáticas, Escuela Superior Politécnica del Litoral, Guayaquil, Ecuador

M. Wiercigroch & S.V. Vaziri Hamaneh
Centre for Applied Dynamics Research (CADR), School of Engineering, University of Aberdeen, Aberdeen, UK

ABSTRACT: We introduce a two-degrees-of-freedom, non-smooth model of a Jeffcott rotor with a bearing clearance. During operation, the rotor makes intermittent contact with a snubber ring with viscoelastic support. This configuration gives rise to a rich and complex dynamical behaviour, which is explored both theoretically and experimentally. This work extends the previous investigations undertaken by the CADR within University of Aberdeen to gain a deeper insight into the system response (Gonsalves et al. 1995, Karpenko et al. 2002, Karpenko et al. 2002). To this end, careful numerical simulations are carried out and then compared with experimental data obtained from a rig (see Fig. 2) previously constructed and designed at the CADR.

1 PHYSICAL AND MATHEMATICAL MODELLING

Consider a two-degrees-of-freedom rotor with a bearing clearance excited by an out-of-balance rotating mass as shown in Fig. 2. This physical setting allows the rotor to make intermittent contact with the outer snubber ring during operation. The mathematical description of the system is made under the following assumptions: the snubber ring is massless and with viscoelastic support; there is no dry friction between the rotor and the snubber ring; there are no gyroscopic forces acting on the system; and the gravity force is neglected. To derive the equations of motion, we choose the coordinate system shown in Fig. 3, centered at the static position of the snubber ring O_{s_0}. We denote by $(\varepsilon_x, \varepsilon_y)$ the eccentricity between the center of the equilibrium position of the rotor O_{r_0} and O_{s_0}. Due to the physical configuration of the system, we must have $D \leq \gamma$, where γ denotes the radial clearance between the rotor and the snubber ring. According to the physical and geometrical setting shown in Figs. 1 and 3, the equations of motion are

$$M\ddot{x}_r + c_r\dot{x}_r + k_r(x_r - \varepsilon_x) + N_{sx} = m\rho\omega^2\cos(\omega t + \theta_0), \quad (1)$$

$$M\ddot{y}_r + c_r\dot{y}_r + k_r(y_r - \varepsilon_y) + N_{sy} = m\rho\omega^2\sin(\omega t + \theta_0), \quad (2)$$

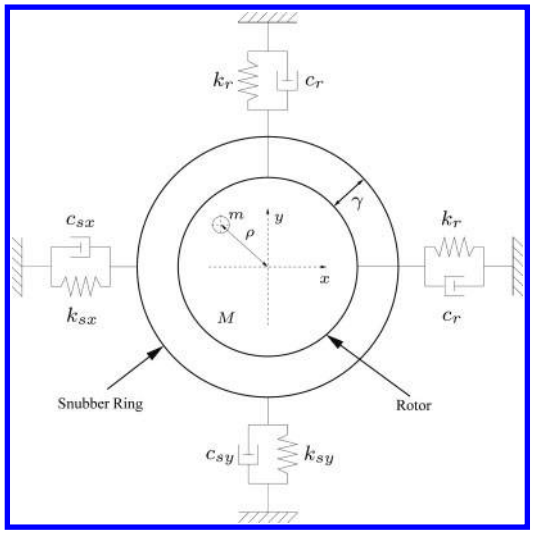


Figure 1. Physical model of a Jeffcott rotor with a snubber ring. The rotor of mass M is excited by an out-of-balance rotating mass producing a centrifugal force of magnitude $m\rho\omega^2$.

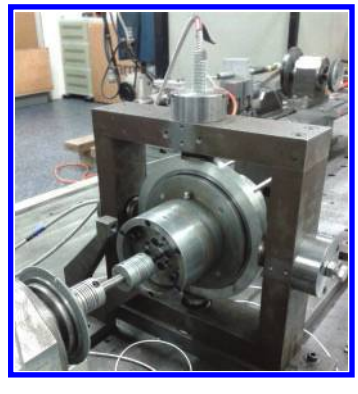


Figure 2. Photograph of the experimental setup.

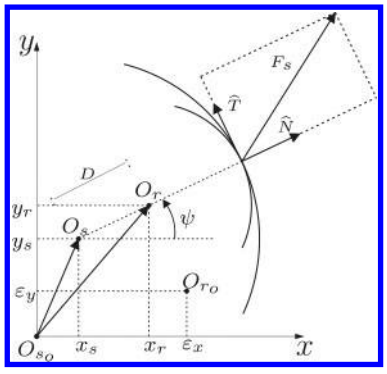


Figure 3. Geometrical representation of the force produced by the snubber ring when an impact occurs. $\widehat{T}$ and $\widehat{N}$ represent tangential and normal unit vectors, respectively, at the contact surface.

$$\dot{x}_s = \chi_t(x_r, y_r, \dot{x}_r, \dot{y}_r, x_s, y_s, k_{sx}, k_{sy}), \tag{3}$$

$$\dot{y}_s = \Upsilon_t(x_r, y_r, \dot{x}_r, \dot{y}_r, x_s, y_s, k_{sx}, k_{sy}). \tag{4}$$

Here, $(N_{sx}, N_{sy})^T = N_s$ stands for the normal force produced when the rotor hits the snubber ring. It is computed as the normal component of the snubber ring force F_s (see Fig. 3), which is given by

$$\begin{pmatrix} N_{sx} \\ N_{sy} \end{pmatrix} = \begin{cases} \begin{pmatrix} \langle F_s, \widehat{N} \rangle \cos(\psi) \\ \langle F_s, \widehat{N} \rangle \sin(\psi) \end{pmatrix}, & D \geq \gamma, \\ 0, & D < \gamma. \end{cases}$$

When there is no contact ($D < \gamma$), the equations 3 and 4 reduce to

$$k_{sx}x_s + c_{sx}\dot{x}_s = 0, \quad k_{sy}y_s + c_{sy}\dot{y}_s = 0$$

and when the snubber ring and the rotor are in contact ($D \geq \gamma$), the motion of the snubber ring is assumed to obey the Principle of Minimum Total Potential Energy and thereby χ_t and Υ_t are computed.

The mathematical model of the rotor given by the equations 1–4 defines a piecewise-smooth dynamical system, which is linear for $D < \gamma$ (i.e. no contact with the snubber ring) and nonlinear otherwise. Thus, an intermittent contact of the rotor with the snubber ring produces a complex dynamical behaviour which will be numerically and experimentally explored.

2 MAIN RESULTS

In order to validate the mathematical model experimentally, the parameters of the rig were carefully identified as follows: rotor mass $M = 10.2$ kg, vertical and horizontal eccentricities $(\varepsilon_x,\ \varepsilon_y) = (0.04,\ 0.32)$ mm, mass imbalance $m = 0.06$ kg, $\rho = 3.5$ mm, radial clearance $\gamma = 1$ mm, stiffness of the rotor $k_r = 79$ kN/m, damping of the rotor $c_r = 1.75$ kg/sec, vertical and horizontal stiffness of the Snubber ring $(k_{sx},\ k_{sy}) = (2.8,$ 4) kN/mm, vertical and horizontal damping of the snubber ring $(c_{sx},\ c_{sy}) = (55.79,\ 350.42)$ kg/sec.

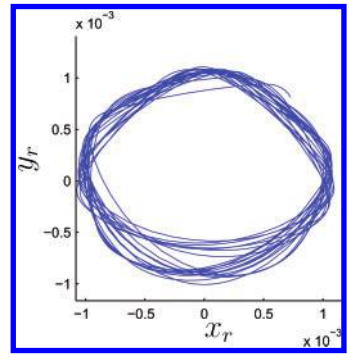


Figure 4. Numerical result: motion of the rotor center o_r showing quasi-periodic response, for the rotational frequency 16.23 Hz.

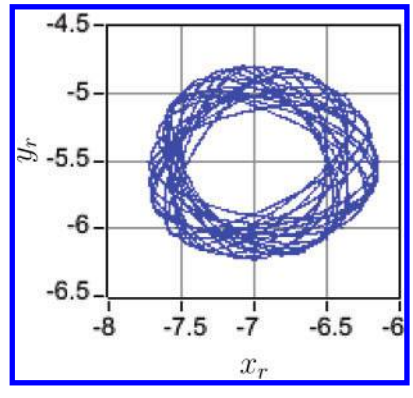


Figure 5. Experimental result: motion of the rotor center o_r (in Volts), for the rotational frequency 16 Hz.

Using the identified physical parameters, the mathematical model (1)–(4) was integrated and the phase response is shown in Fig. 4. In this picture, we can identify a quasi-periodic motion. Moreover Fig. 5 depicts the corresponding experimental results measured from the rig shown in Fig. 2, where a good agreement with the numerical simulation can be observed.

REFERENCES

Gonsalves, D. H., R. D. Neilson, & A. D. S. Barr (1995). A study of response of a discontinuously nonlinear rotor system. *Nonlinear Dynamics* 7, 451–470.

Karpenko, E. V., M. Wiercigroch, & M. P. Cartmell (2002). Regular and chaotic dynamics of a discontinuously nonlinear rotor system. *Chaos, Solitons and Fractals 13*, 1231–1242.

Karpenko, E. V., M. Wiercigroch, E. E. Pavlovskaia, & M. P. Cartmell (2002). Piecewise approximate analytical solutions for a Jefcott rotor with a snubber ring. *Internat. J. of Mech. Sci. 44*, 475–488.

Research and Applications in Structural Engineering, Mechanics and Computation – Zingoni (Ed.)
© 2013 Taylor & Francis Group, London, ISBN 978-1-138-00061-2

A computational study of the upper Lyapunov exponent and the uniform persistence for monotone skew-product semiflows

J.A. Calzada & R. Obaya
Departmento Matemática Aplicada, E. Ingenierías Industriales, Universidad de Valladolid, Valladolid, Spain

ABSTRACT: In this paper the authors study almost-periodic neural networks of Hopfield type given by variable delayed differential equations. They main result of the work states the stabilization role for the fast or instantaneous inhibitory self-connections. We describe a computational method based on the numerical calculus of a continuous separation that provides the upper Lyapunov exponent of the system. As an example we develope a numerical simulation of a neural network with variable delayed interconexions.

1 INTRODUCTION

The study of artificial neural networks, and in particular of its dynamics, is of great interest due to the application to different scientific and technical problems such as biological modeling, pattern recognition, cognitive simulation and engineering applications (Chua & Yang 1988a, Chua & Yang 1988b, Grossberg 1988, Wu 2001). One of the more outstanding models in artificial neural network was introduce by Hopfield (Hopfield 1982, Hopfield 1984) in terms of a system of ordinary differential equations (ODE), which describes the voltage on the input of each neuron.

A single constant delay $\tau > 0$ was introduced for the first time by Marcus and Westervelt (Marcus & Westervelt 2009) and Gopalsamy and He (Gopalsamy & He 1994) introduced the existence of several constant delays in the distinct communication channels between neurons. In the works of van den Driessche *et. al.* (van den Driessche & Zou 1998, van den Driessche, Wu, & Zou 2001) and Arratia *et al.* (Arratia, Obaya, & Sansaturio 2012) it is shown, for the case of several delays, how the specific values of τ_{ij} can change to a significant extent the dynamic of the system.

A new dynamical theory for deterministic monotone non-autonomous differential equations has recently been developed (Shen & Yi 1998, Novo, Obaya, & Sanz 2007, Novo, Obaya, & Villarragut 2009). Such equations are described using the skew-product formalism in the terms given by Sell (Sell 1967a, Sell 1967b) and Johnson *et. al* (Johnson & Moser 1982).

The objective of this work is to introduce computational methods based on the calculus of the upper Lyapunov exponent to study neural networks with variable delay.

2 PRELIMINARIES

Let us consider a non-autonomous system of delayed functional differential equations (FDE)

$$y_i' = -a_i(t)\, y_i(t) + \sum_{j=1}^{n} b_{ij}(t)\, f_j(y_j(t-\tau_{ij}(t))) + c_i(t), \quad (1)$$

which modelize a network of n neurons with decaying coefficients $a_i(t)$, delayed transmission signal coupled by a interconnection matrix $B(t) = [b_{ij}(t)]$ and external input $c_i(t)$. The matrix of delays $[\tau_{ij}(t)]$ is variable with $\tau_{ij}(t) \geq 0, i, j = 1, \cdots, n$. The coefficients $a_i(t) > \alpha > 0, \forall t$, $b_{ij}(t)$, $c_i(t)$ and delays $\tau_{ij}(t) > 0$ are almost-periodic.

We are going to apply methods of the dynamical theory of non-autonomous monotone differential equations to study the long time behaviour of the solutions of (1).

We assume the following conditions over the activation functions $f_i, i = 1, \cdots, n$

(A1) $f_i \in C^1(\mathbb{R}), f_i(0) = 0$.

(A2) $\lim_{s\to\infty} f_i(s)/s = 0$.

(A3) $0 < f_i'(s) \leq 1 = \sup_{t\in\mathbb{R}} f_i'(t)$.

We take $\tau = \max_{1\leq i,j\leq n}\{\tau_{ij}(t),\ t \in \mathbb{R}\}$ and introduce the state space $X = C([-\tau, 0], \mathbb{R}^n)$ endowed with the norm $\|x\|_\infty = \sup_{s\in[-\tau,0]} \|x(s)\|$ for every $x \in X$, which converts it into a Banach space. For each $k > 0$, $B_k = \{x \in X |\ \|x\|_\infty \leq k\}$ will represent the closed ball of center 0 and radius k. We denote by r he maximal size of external input which is physically admissible.

The standard theory of FDE (Hale 1977, Hartung & Turi 1997) provides, for every $t \in \mathbb{R}$, $t \geq 0$ and $x \in X$ a vectorial solution $y(t, x)$ of (1) with $y(s, x) = x(s)$ for all $s \in [-\tau, 0]$. From the vectorial solution we can

define the functional solution, which stores the vectorial solution during the last period of lenght τ, that is $u(t,x)(s)=y(t+s,x)$ for every $s\in[-\tau,0]$, $t\in\mathbb{R}$, $t\geq 0$. Obviously $u(0,x)=x$ for every $x\in X$.

We apply methods of the dynamical theory of monotone non-autonomous FDE (Novo, Obaya, & Villarragut 2009, Novo & Obaya 2013, Arratia, Obaya, & Sansaturio 2012) to deduce conditions which imply, for every external input, the existence of a unique almost-periodic solution which is globally exponentially stable.

For each almost-periodic function $d(t)$ we denote

$$d^+(t)=\max(d(t),0),\quad d^-(t)=\max(-d(t),0)\,.$$

and represent by $|d|_\infty=\sup\{\|d(s)\|,\ s\in\mathbb{R}\}$. We consider supplementary conditions for the FDE (1)

(A4) The diagonal delay corresponding to a non-positive coefficient b_{ii} vanish on $\mathbb{R}$; i.e. $\tau_{ii}(t)\equiv 0,\forall t\in\mathbb{R}$.

(A5) The diagonal delay corresponding to a non-positive coefficient b_{ii} is small enough, satisfying

$$0\leq\tau_{ii}(t)\leq\frac{1}{|a_i+e\,b_{ii}^-|_\infty},\quad i=1,\cdots,n$$

Let us consider the map $M:\mathbb{R}\to\mathcal{M}_{n\times 2(n+1)}$ with $M(s)=[a(s),b_{ij}(s),\tau_{ij}(s),c_i(s)]$. For every $t\in\mathbb{R}$ we take $M_t(s)=M(t+s)$. The hull of M is the set $\Omega(M)=\text{closure}\{M_t,\ t\in\mathbb{R}\}$ for the compact open topology. This is a compact set where is defined a continuous flow $\sigma:\mathbb{R}\times\Omega\to\Omega$, $\omega\mapsto\omega\cdot t$ by time translation (see Novo & Obaya 2013, Arratia, Obaya, & Sansaturio 2012).

We consider the family of FDE on the hull

$$y_i'=-a_i(\omega\cdot t)\,y_i(t)+\sum_{j=1}^{n}b_{ij}(\omega\cdot t)\,f_j(y_j(t-\tau_{ij}(\omega\cdot t)))+c_i(\omega\cdot t)\,, \tag{2}$$

Following the arguments of van den Driessche, Wu, & Zou 2001 and Arratia, Obaya, & Sansaturio 2012 we introduce a set of new variables given by $y_{n+i}=-y_i$, $i=1,\ldots,n$, and taking the new activation functions $g_i(x)=-f_i(-x)$, for every $x\in\mathbb{R}$, $i=1,\ldots,n$, we obtain the extended family of FDE ($i=1,\ldots,n$)

$$\begin{aligned}y_i'=&-a_i(\omega\cdot t)\,y_i(t)+b_{ii}(\omega\cdot t)\,f_i(y_i(t-\tau_{ii}(t)))\\&+\sum_{\substack{j=1\\j\neq i}}^{n}b_{ij}^+(\omega\cdot t)\,f_j(y_j(t-\tau_{ij}(t)))\\&+\sum_{\substack{j=1\\j\neq i}}b_{ij}^-(\omega\cdot t)\,g_j(y_{n+j}(t-\tau_{ij}(t)))+c_i(\omega\cdot t)\end{aligned}$$

$$\begin{aligned}y_{n+i}'=&-a_i(\omega\cdot t)\,y_{n+i}(t)+b_{ii}(\omega\cdot t)\,g_i(y_{n+i}(t-\tau_{ii}(t)))\\&+\sum_{\substack{j=1\\j\neq i}}^{n}b_{ij}^+(\omega\cdot t)\,g_j(y_{n+j}(t-\tau_{ij}(t)))\\&+\sum_{\substack{j=1\\j\neq i}}b_{ij}^-(\omega\cdot t)\,f_j(y_j(t-\tau_{ij}(t)))-c_i(\omega\cdot t)\,,\end{aligned}$$

which satisfies all the conditions (A1)–(A5) stated before. If we set $\tilde{y}_1=(y_1,\ldots,y_n)\in\mathbb{R}^n$, $\tilde{y}_2=(y_{n+1},\ldots,y_{2n})\in\mathbb{R}^n$ and $\tilde{y}=(\tilde{y}_1,\tilde{y}_2)\in\mathbb{R}^{2n}$, we can represent the family of FDE in short form by

$$\begin{cases}\tilde{y}_1'=\tilde{F}_1(\omega\cdot t,\tilde{y}_t)+C(\omega\cdot t)\\ \tilde{y}_2'=\tilde{F}_2(\omega\cdot t,\tilde{y}_t)-C(\omega\cdot t)\end{cases} \tag{3}$$

Let us introduce the extended phase space $\tilde{X}=C([-\tau,0],\mathbb{R}^{2n})=X\times X$. For each $\omega\in\Omega$ and $\tilde{x}\in X$, $\tilde{y}(t,\omega,\tilde{x})$ will denote the vectorial solution of (3) for $t\geq 0$ with $\tilde{y}(s,\omega,\tilde{x})=\tilde{x}(s)$ for all $s\in[-\tau,0]$. Likewise $\tilde{u}(t,\omega,\tilde{x})$ will represent the functional solution defined by $\tilde{u}(t,\omega,\tilde{x})(s)=y(t+s,\omega,\tilde{x})$, $s\in[-\tau,0]$.

If the FDF (1) satisfies (A1)–(A3) and (A4) then the solutions of (3) satisfies monotony properties for the standard ordering: that is if $\tilde{x}_1,\tilde{x}_2\in\tilde{X},\tilde{x}_1\leq\tilde{x}_2$ for the standard order then $\tilde{u}(t,\omega,\tilde{x}_1)\leq\tilde{u}(t,\omega,\tilde{x}_2)$ for every $t\geq 0$, $\omega\in\Omega$.

Next we describe a different order which is technically more complex but it is important in applications. Let $D=(d_{ij})$ a real matrix with $d_{ij}\geq 0$ for every $1\leq i,j\leq n$. We introduce the definition of the D-exponential ordering on X. If $x_1,x_2\in X$ $x_1\leq_D x_2\Leftrightarrow x_1\leq x_2$ and it is verified for $-\tau\leq s\leq t\leq 0$.

$$(x_2(t)-x_1(t))\geq e^{D(t-s)}(x_2(s)-x_1(s)),$$

If the FDE (1) satisfies (A1)–(A3) and (A5) then the solution of (3) satisfies monotony properties for the exponential ordering, that is if $\tilde{x}_1\leq_D\tilde{x}_2$ then $\tilde{u}(t,\omega,\tilde{x}_1)\leq_D\tilde{u}(t,\omega,\tilde{x}_2)$ for $t\geq 0$, $\omega\in\Omega$.

It is clear that $x(t)$ is an almost-periodic solution of (2) through $\omega\in\Omega$ if and only if $\tilde{x}(t)=(x(t),x(t))$ is an almost-periodic solution of (3) through $\omega\in\Omega$.

For each $k\in\mathbb{R}$ we denote by $\bar{k}_m=(k,\ldots,k)\in\mathbb{R}^m$ and by $\hat{k}_m\in C([-\tau,0],\mathbb{R}^m)$ the constant function $\hat{k}_m(s)=\bar{k}_m$ for every $s\in[-\tau,0]$.

We define $\rho(r)$ as the inferior of all the real positive numbers k_1 such that for every $k\geq k_1$

$$\begin{aligned}&\tilde{F}_1(\omega,\hat{k}_{2n})<<-\bar{r}_n,\qquad \tilde{F}_2(\omega,\hat{k}_{2n})<<-\bar{r}_n,\\&\bar{r}_n<<\tilde{F}_1(\omega,-\hat{k}_{2n}),\qquad \bar{r}_n<<\tilde{F}_2(\omega,-\hat{k}_{2n})\,,\end{aligned} \tag{4}$$

where $<<$ means that the strong inequality verifies for all the components of the vector.

Let us consider $r\geq 0$. We define for $i=1,\cdots,n$

$$\delta_i(r)=\inf\{f_i'(s)|\ |s|\leq\rho(r)\}>0\,. \tag{5}$$

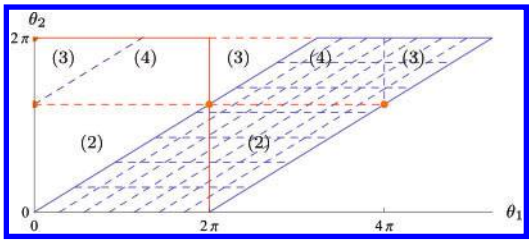


Figure 1. Equivalence of $\mathbb{T}^2$ and $\mathcal{R}$ as base space for flux construction.

It is proved (Arratia, Obaya, & Sansaturio 2012) that if $x(t)$ is an almost-periodic solution of (1) then $\|x\|_\infty \leq \rho(r)$.

We introduce the linear FDE (LFDE) that will be used to control the size of the solutions of the linearized equations of the FDE (1)

$$\begin{aligned} z_i' = & -a_i(\omega\cdot t)\, z_i(t) \\ & + [b_{ii}(\omega\cdot t) - \delta_i(r) b_{ii}(\omega\cdot t)]\, z_i(t-\tau_{ii}(\omega\cdot t)) \\ & + \sum_{j=1}^{n} |b_{ij}(\omega\cdot t)| z_j(t-\tau_{ij}(\omega\cdot t))\,. \end{aligned} \tag{6}$$

For each $\omega\in\Omega$ and $x\in X$, $z(t,\omega,x)$ will denote the vectorial solution of (6) with $z(s,\omega,x) = x(s)$, for all $s\in[-\tau,0]$ and $v(t,\omega,x)$, with $v(t,\omega,x)(s) = z(t+s,\omega,x)$, for all $s\in[-\tau,0]$ and $t\geq 0$, will represent the corresponding functional solution.

The solution of (6) satisfies the same conditions of monotony mentioned for (3).

We now state the main result of this section that is a version, for a neural network with variable delays, of theorem 5.1 of Arratia, Obaya, & Sansaturio 2012.

Theorem 1.
Let us assume that the FDE (1) verifies (A1)–(A3) and one of the conditions of (A4) or (A5). If the LFDE (6) is uniformly exponentially stable then for every arbitrary input $C(t) = (c_1(t),\ldots,c_n(t))$ with $\|C\|_\infty \leq r$ there is an unique almost-periodic solution of (1) $e:\mathbb{R}\to\mathbb{R}^n$ such that for all $k>0$ there are constants $\kappa,\alpha>0$ fulfilling

$$\| u(t,x) - e(t) \| \leq \kappa\, e^{-\alpha t} \| x \|, \tag{7}$$

for every $x\in B_k$, $t\in\mathbb{R}$ with $t\geq 0$.

This results confirms the stabilization role for the fast or instantaneous inhibitory self-connetions. The objetive of this work is to describe computational methods based on the numerical calculus of a continuous separation, that provides the upper Lyapunov exponent of (3). In particular if this exponent is negative (3) is uniformly exponentially stable and the conclusions of the previous statement applies.

3 NUMERICAL SIMULATION

In order to illustrate the results of the work we consider the non-autonomous system of FDE with variable delay given by

$$\begin{aligned} y_1'(t) = & [-1+0.3\cos(\alpha t)]\, y_1(t) \\ & + [-1.5+\sin(t)]\, \tanh(y_1(t)) \\ & + [1.4-\sin(t)]\, \tanh[y_2(t-(2-\cos(t)))] + c_1(t) \end{aligned} \tag{8}$$

$$\begin{aligned} y_2'(t) = & [-1+0.3\sin(\alpha t)]\, y_2(t) \\ & + [-1.3+0.3\cos(t)]\, \tanh[y_1(t-(2-\cos(t)))] \\ & + [-1+0.3\cos(t)]\, \tanh[y_2(t)] + c_2(t)\,, \end{aligned}$$

where $\alpha = (\sqrt{5}-1)/2$ and $c_i(t)$, $i=1,2$ are the external inputs with $c_i(t) = d_i + d_i^\star \sin(\alpha t)$, $i=1,2$ and $\|c_1\|_\infty$, $\|c_2\|_\infty \leq 0.3$. This equations verify conditions (A1)–(A3).

If we consider the map $M:\mathbb{R}\to\mathcal{M}_{2\times 4}(\mathbb{R})$

$$M(s) = \begin{pmatrix} a_1(s) & b_{11}(s) & b_{12}(s) & \tau(s) & c_1(s) \\ a_2(s) & b_{21}(s) & b_{22}(s) & \tau(s) & c_2(s) \end{pmatrix}$$

being a_i, b_{ij} and c_i the elements of formula (1) and $\tau(t)$ the variable delay present in the system. The hull of M is homeomorphic to the 2-torus $\mathbb{T}^2$ and a flow can be obtained by time translation (Cornfeld, Fomin, & Sinay 1982, Arratia, Obaya, & Sansaturio 2012)

$$\begin{aligned} \sigma : \mathbb{R}\times\mathbb{T}^2 &\longrightarrow \mathbb{T}^2 \\ (t,\theta_1,\theta_2) &\mapsto (\theta_1,\theta_2)\cdot t = (\theta_1+\alpha t, \theta_2+t)\,. \end{aligned}$$

Under this flux the orbits in $\mathbb{T}^2$ are dense and $(\mathbb{T}^2,\sigma)$ is uniquely ergodic: that is admits a unique invariant meausure. Let us consider, as a more suitable base space for the flux, the rhomboid

$$\mathcal{R} = \{(\theta_1,\theta_2) = (x_0+\alpha t, t), \quad x_0, t\in[0, 2\pi]\},$$

defined by translation of $\mathbb{T}^2$ and which is constituted by trajectories of the system. This change can be done by the 2π-periodicity of the system as can be seen in figure 1.

Finally the flux $(\mathcal{R},\sigma)$ and the flux $(\mathbb{T}^2,\sigma)$ are homeomorphic.

Let us consider the following family of FDE defined over the hull, $y' = F((\theta_1,\theta_2)\cdot t, y_t)$, given by

$$\begin{aligned} y_1'(t) = & [-1+0.3\cos(\theta_1+\alpha t)]\, y_1(t) \\ & + [-1.5+\sin(\theta_2+t)]\, \tanh(y_1(t)) \\ & + [1.4-\sin(\theta_2+t)]\, \tanh[y_2(t-(2-\cos(\theta_2+t)))] \\ & + c_1((\theta_1,\theta_2)\cdot t) \end{aligned} \tag{9}$$

$$\begin{aligned} y_2'(t) = & [-1+0.3\sin(\theta_1+\alpha t)]\, y_2(t) \\ & + [-1.3+0.3\cos(\theta_2+t)]\, \tanh[y_1(t-(2-\cos(\theta_2+t)))] \\ & + [-1+0.3\cos(\theta_2+t)]\, \tanh[y_2(t)] + c_2((\theta_1,\theta_2)\cdot t) \end{aligned}$$

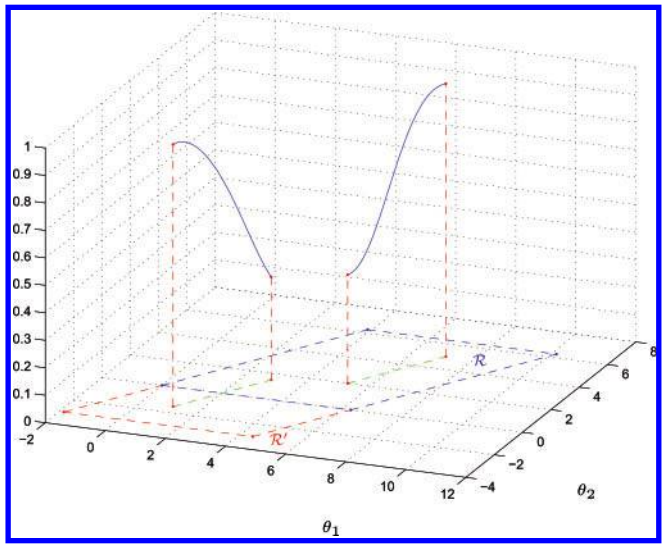


Figure 2. Vectorial solutions defined over the extended rhomboid $\mathcal{R}'$ (dashed blue and red line) and the corresponding functional solutions defined over the rhomboid $\mathcal{R}$ (dashed blue line).

whose solutions induce the skew-product semiflow

$$\varphi : \mathbb{R}_+ \times \mathcal{R} \times X \longrightarrow \mathcal{R} \times X$$
$$(t, \theta, x) \mapsto (\theta_1 + \alpha t, \theta_2 + t, u(t, \theta, x))$$

where $X = C([-\tau, 0], \mathbb{R}^2)$. Let $\tilde{y}(t, \omega, \tilde{x})$ denote the vectorial solution of (9). The functional solution $\tilde{u}(t, \omega, \tilde{x})$ is obtained by means of the vectorial solution $y(t, \theta, x)$ in the point ω and τ units of time backwards across the trayectory (see figure 2)

$$u(t, \theta, x)(s) = y(t + s, \theta, x), \quad s \in [-\tau, 0], t \geq 0.$$

In order to represent this solution we have introduced the extended rhomboid (full graph in the plane θ_1–θ_2 of figure 2)

$$\mathcal{R}' = \{(x_0 + \alpha t, t), \quad x_0 \in [0, 2\pi], t \in [-\tau, 2\pi]\}.$$

The system (8) is the element of this family corresponding to $(\theta_1, \theta_2) = (0, 0)$. We embed this family into a four dimensional group of FDE fullfiling conditions (A1)–(A5) defining new variables $y_3 = -y_1$ and $y_4 = -y_2$ and taking new activation functions $g_i(x) = -f_i(-x)$, $i = 1, 2$

$$\begin{aligned}
&g_i(x) = -f_i(-x),\ i = 1, 2\\
&y_1'(t) = [-1 + 0.3\cos(\theta_1 + \alpha t)]\, y_1(t)\\
&\quad + [-1.5 + \sin(\theta_2 + t)]\tanh(y_1(t))\\
&\quad + [1.4 - \sin(\theta_2 + t)]\tanh[y_2(t - (2 - \cos(\theta_2 + t)))]\\
&\quad + c_1((\theta_1, \theta_2) \cdot t)
\end{aligned}$$

$$\begin{aligned}
y_2'(t) &= [-1 + 0.3\sin(\theta_1 + \alpha t)]\, y_2(t)\\
&\quad + [1.3 - 0.3\cos(\theta_2 + t)]\tanh[y_3(t - (2 - \cos(\theta_2 + t)))]\\
&\quad + [-1 + 0.3\cos(\theta_2 + t)]\tanh[y_2(t)] + c_2((\theta_1, \theta_2) \cdot t)\\
y_3'(t) &= [-1 + 0.3\cos(\theta_1 + \alpha t)]\, y_3(t)\\
&\quad + [-1.5 + \sin(\theta_2 + t)]\tanh(y_3(t))\\
&\quad + [1.4 - \sin(\theta_2 + t)]\tanh[y_4(t - (2 - \cos(\theta_2 + t)))]\\
&\quad + c_1((\theta_1, \theta_2) \cdot t)\\
y_4'(t) &= [-1 + 0.3\sin(\theta_1 + \alpha t)]\, y_4(t)\\
&\quad + [-1 + 0.3\cos(\theta_2 + t)]\tanh[y_4(t - (2 - \cos(\theta_2 + t)))]\\
&\quad + [1.3 - 0.3\cos(\theta_2 + t)]\tanh[y_1(t)] + c_2((\theta_1, \theta_2) \cdot t)
\end{aligned} \tag{10}$$

which in a short form can be written as

$$\begin{cases} \tilde{y}_1' = \tilde{F}_1(\theta \cdot t, \tilde{y}_t) + C(\theta \cdot t) \\ \tilde{y}_2' = \tilde{F}_2(\theta \cdot t, \tilde{y}_t) - C(\theta \cdot t) \end{cases}$$

where $\tilde{y}_1 = (y_1, y_2)$ and $\tilde{y}_2 = (y_3, y_4)$ and $\tilde{F}_i : \mathbb{R} \times X \to \mathbb{R}$, $i = 1, \ldots, 4$ are the components of the field. The system (10) is monotone for the usual ordering.

We are going to determine the variation region for the almost-periodic solution. Let us consider $r = 0.3$. In order to find the value of $\rho(0.3)$ given by (4) we must find the inferior of $k > 0$ verifying simultaneously the following inequalities

$$\begin{cases} -0.7k - 0.1\tanh k \leq -0.3 \\ -0.7k + 0.3\tanh k \leq -0.3, \end{cases}$$

A direct calculus let us obtain $\rho(0.3) = 0.6828810924$. Taking in to account the definiton of δ_i, $i = 1, 2$ in (5) and the fact that, in this case, the values of $\delta_1 = \delta_2$, we get

$$\delta(0.3) = 1 - \tanh^2[\rho(0.3)] = 0.6478892387.$$

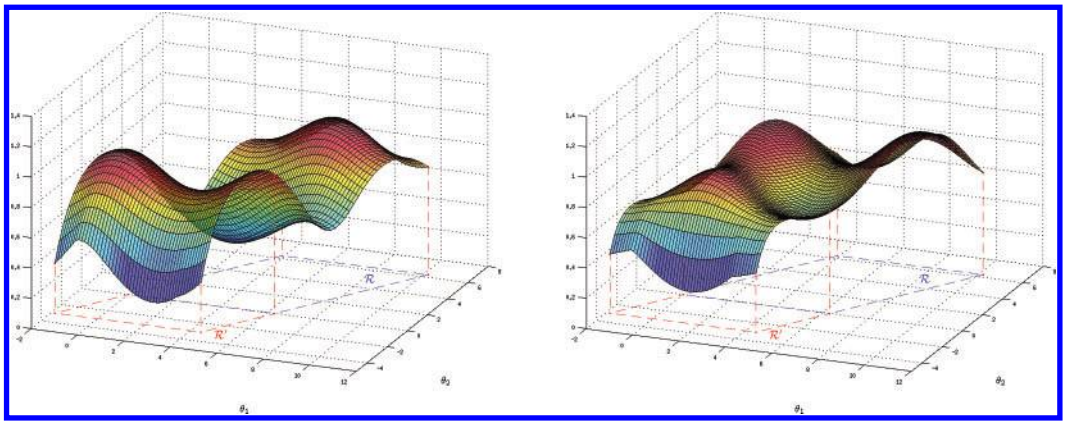


Figure 3. Vectorial and functional solutions for the first (right image) and second (left image) component of system (11). In both figures we represent the rhomboid $\mathcal{R}$ (dashed blue line) and the extended rhomboid $\mathcal{R}'$ (dashed blue and red line).

The family of LFDE given by (9) is

$$\begin{aligned} z_1' &= -[1-0.3\cos(\theta_1+\alpha t)+\delta(0.3)\,(1.5-\sin(\theta_2+t))]\,z_1(t) \\ &\quad +[1.4-\sin(\theta_2+t)]\,z_2[t-(2-\cos(\theta_2+t))] \qquad (11) \\ z_2' &= -[1-0.3\sin(\theta_1+\alpha t)+\delta(0.3)\,(1-.3\cos(\theta_2+t))]\,z_2(t) \\ &\quad +[1.3-0.3\cos(\theta_2+t)]\,z_1[t-(2-\cos(\theta_2+t))]\,. \end{aligned}$$

The solutions of the LFDE (11) define a linear skew-product semiflow $\eta{:}\mathbb{R}_+ \times \mathcal{R} \times X \to \mathcal{R} \times X$ that is monotone for the standard ordering and admits a continuous separation of type II in terms given by Novo *et al.* (Novo, Obaya, & Sanz 2013b). We remark that this concept introduce a slight modification of the classical concept given by Poláčik *et al.* (Poláčik & Tereščák 1993) that does not require the strong monotony of the semiflow and finds specific application in the case of finite delay FDE. This means that the existence of subspaces $\{X_1(\theta_1,\theta_2)\}_{(\theta_1,\theta_2)\in\mathcal{R}}$, $\{X_2(\theta_1,\theta_2)\}_{(\theta_1,\theta_2)\in\mathcal{R}}$ satisfies the following properties

(S1) $X_1 = X_1(\theta_1,\theta_2) \oplus X_2(\theta_1,\theta_2)$ and $X_1(\theta_1,\theta_2)$, $X_2(\theta_1,\theta_2)$ vary continously in K

(S2) $X_1(\theta_1,\theta_2) = \mathrm{span}\{x(\theta_1,\theta_2)\}$ with $x(\theta_1,\theta_2) \gg 0$ and $\|x(\theta_1,\theta_2)\| = 1$ for any $(\theta_1,\theta_2) \in K$.

(S3) there exits a $t_0 > 0$ such that if for some $(\theta_1,\theta_2) \in \mathcal{R}$ there is a $z \in X_2(\theta_1,\theta_2)$ with $z > 0$ then $v(t,\theta_1,\theta_2,z) = 0$ for any $t \geq t_0$

(S4) for any $t > 0$, $(\theta_1,\theta_2) \in \mathcal{R}$
$$v(t,\theta_1,\theta_2)\,X_1(\theta_1,\theta_2) = X_1(\eta(t,\theta_1,\theta_2))$$
$$v(t,\theta_1,\theta_2)\,X_2(\theta_2,\theta_2) \subset X_2(\eta(t,\theta_1,\theta_2))$$

(S5) there are $M > 0$, $\delta > 0$ such that for any $(\theta_1,\theta_2) \in \mathcal{R}$, $z \in X_2(\theta_1,\theta_2)$ with $\|z\| = 1$ and $t > 0$,
$$\| v(t,\theta_1,\theta_2,z) \| \leq M e^{-\delta t} \| v(t,\theta_1,\theta_2,x(\theta_1,\theta_2)) \|\,.$$

We are interested in the calculus of the upper Lyapunov exponent for this system. For this purpose first we calculate the main direction $X_1(\theta_1,\theta_2)$. The vectorial solution, $z((\theta_1,\theta_2)\cdot t)$ for all $(\theta_1,\theta_2) \in \mathcal{R}'$ and t in an adequate interval, is given by the integration of (11). For this numerical integration we use the Matlab *ddesd* solver for delay differential equations with general delays (Shampine 2005). This routine belongs to a family of Runge-Kutta based methods endowed with a interpolating scheme so not only the solution in final integration point is achive but also a continous extension along the integration interval. This methods estimate and bound not the local error on each integration step but the defect of the continuous extension (Enright 1989). In this way the achived accuracy is independent of the method itself.

Calculating this integration for the points of $\mathcal{R}'$ we obtain the surfaces of figure 3 (for the two components of the solution). The second type of solution is the functional one $v(\theta_1,\theta_2)(s) = z((\theta_1,\theta_2)\cdot s)$ for all $s \in [-\tau, 0]$. This solution is obtained integrating over the rhomboid $\mathcal{R}$.

Using general theoretical results of uniform persistence related to a minimal set of a monotone skew-product semiflow (Novo, Obaya, & Sanz 2013b, Novo, Obaya, & Sanz 2013a) and the numerical method of Calzada *et al.* (Calzada, Obaya, & Sanz 2013) we are going to calculate numericaly the upper Lyapunov exponent for this system.

The exponent is calculated by means of a double integration along the rhomboid $\mathcal{R}$. The first integration develops for lines crossing the rhomboid's base at a point $x_0 \in [0, 2\pi]$. For one of this lines we start the integration and let pass a enough quantity of time to assure we are in $X_1(\theta_1,\theta_2)$ when we arrive at the rhomboid's base point $(x_0, 0)$, $x_0 \in [0, 2\pi]$. Then we integrate along the 2π length time interval to reach the top of the rhomboid. The second integration is made in x_0 variable and gives us the final estimation of the Lyapunov exponent (Calzada, Obaya, & Sanz 2013).

For the external inputs $c_1 = 0.3$ and $c_2 = -0.3$ we have obtained a value for the upper Lyapunov exponent of $\lambda = -0.00437662$. So for every arbitrary input $c(\omega)$ such that $\|c(\omega)\| \leq 0.3$ there is a continuous invariant function $e{:}\Omega \to X$ such that for every $(\omega, x) \in \Omega \times X$ (see theorem 5.1 in Arratia, Obaya, & Sansaturio 2012)

$$\lim_{t\to\infty} \| u(t,\omega,x) - e(\omega\cdot t) \| = 0\,,$$

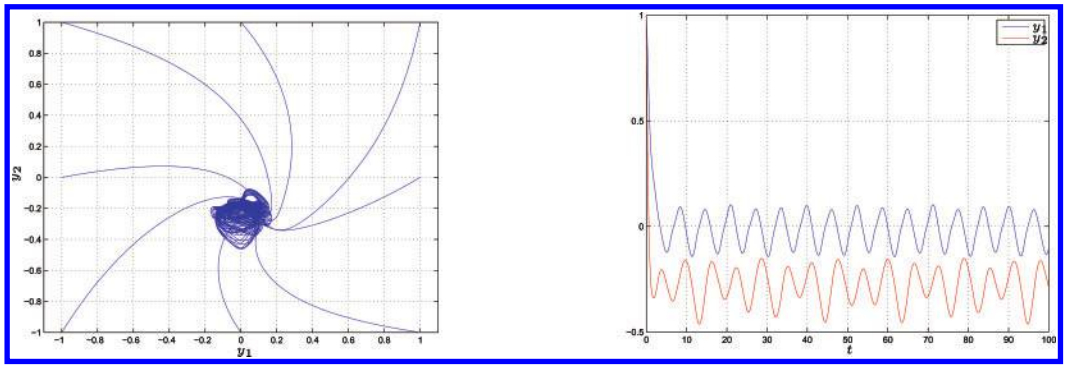


Figure 4. Numerical simulation for solutions of FDE (9). We show the trajectories proyected over the (y_1, y_2) plane (left image) for $0 \leq t \leq 100$ and on the plane (y_1, t) (right image).

The family of FDE (9) has only one minimal set of the phase space and the solutions of (1) are asymptotically almost-periodic. The exponential convergence in theorem 1 depends on the value of constant $-\alpha$ (which is equal to the Lyapunov exponent) given by (7). In our example the near to zero value for the exponent justifies the slow exponential convergence in the short term (see fig. 4).

ACKNOWLEDGEMENTS

This work has been partially supported by Junta de Castilla y León and Ministerio de Economía y Competitividad under projects VA118A12-1 and MTM2012-30860.

REFERENCES

Arratia, O., R. Obaya, & M. E. Sansaturio (2012). Applications of the exponential ordering in the study of almost-periodic delayed hopfield neural networks. *Physica D. 241*, 1551–1566.

Calzada, J. A., R. Obaya, & A. Sanz (2013). Continuous separation for monotone skew-product semiflows: from theoretical to numerical results (preprint).

Chua, L. O. & L. Yang (1988a). Cellular neural networks: theory. *IEEE Trans. Circuits. Syst. 35*, 1257–1272.

Chua, L. O. & L. Yang (1988b). Cellular neural networks: applications. *IEEE Trans. Circuits. Syst. 35*, 1273–1290.

Cornfeld, I. P., S. V. Fomin, & Y. G. Sinay (1982). *Ergodic Theory.* Berlin, Heidelberg, New York: Springer-Verlag.

Enright, W. H. (1989). A new error-control for initial value solvers. *Appl. Math. Comput. 31*, 588–599.

Gopalsamy, K. & X. Z. He (1994). Stability in asymmetric hopfield nets with transmission delays. *Physica D 76*, 344–358.

Grossberg, S. (1988). Nonlinear networks: principles, mechanisms and architectures. *Neural Netw. 1*, 17–61.

Hale, J. K. (1977). *Theory of Functional Differential Equations, in: Applied Mathematical Sciences, vol* 3. Berlin, Heidelberg, New York: Springer-Verlag.

Hartung, F. & J. Turi (1997). On differentiability of solutions with respect to parameters in state–dependent delay equations. *J. Differential Equations 135*, 192–237.

Hopfield, J. J. (1982). Neural networks and physical systems with emergent collective computational abilities. In *Proc. Nat. Acad. Sci. 79*, USA, pp. 2554–2558.

Hopfield, J. J. (1984). Neurons with graded response have collective computational properties like those of two-state neurons. In *Proc. Nat. Acad. Sci. 81*, USA, pp. 3088–3092.

Johnson, R. & J. Moser (1982). The rotation number for almost periodic potentials. *Comm. Math. Phys. 84*, 403–438.

Marcus, C. M. & R. M. Westervelt (2009). Stability of analog neural networks with delay. *Phys. Rev. A 39*, 347–359.

Novo, S. & R. Obaya (2013). Non-autonomous functional differential equations and applications. Stability and bifurcation for non-autonomous differential equations. *Lecture Notes in Math. 2065*, 185–264.

Novo, S., R. Obaya,& A. Sanz (2007). Stability and extensibility results for abstract skew-product semiflows. *J. Differential Equations 235 (2)*, 623–646.

Novo, S., R. Obaya, & A. Sanz (2013a). Topological dynamics for monotone skew-product semiflows with applications (preprint).

Novo, S., R. Obaya, & A. Sanz (2013b). Uniform persistence and upper lyapunov exponents for monotone skew-product semiflows (preprint).

Novo, S., R. Obaya, & V. Villarragut (2009). Exponential ordering for nonautonomous neutral functional differential equations. *SIAM J. Math. Anal. 41 (3)*, 1025–1053.

Poláčik, P. & I. Tereščák (1993). Exponential separation and invariant bundles for maps in ordered banach spaces with applications to parabolic equations. *J. Dynamics Differential Equations.* **5**(2), 279–303.

Sell, G. R. (1967a). Non-autonomous differential equations and topological dynamics i, the basic theory. *Trans. Amer. Math. Soc. 127*, 241–262.

Sell, G. R. (1967b). Non-autonomous differential equations and topological dynamics ii, limiting equations. *Trans. Amer. Math. Soc. 127*, 263–283.

Shampine, L. F. (2005). Solving odes and ddeswith residual control. *Appl. Numer. Math. 52*, 113–127.

Shen, W. & Y. Yi (1998). *Almost automorphic and almost periodic dynamics in Skew-Product Semiflows*. Providence: Mem. Amer. Math. Soc., vol 647, Amer. Math. Soc.

van den Driessche, P., J. Wu, & X. Zou (2001). Stabilization role of inhibitory self-connections in a delayed neural network. *Physica D. 150*, 84–90.

van den Driessche, P. & X. Zou (1998). Global attractivity in delayed hopfield neural networks models. *SIAM J. Appl. Math. 58 (6)*, 1878–1890.

Wu, J. (2001). *Introduction to Neural Dynamics and Signal Transmission Delay.* Berlin: Walter de Gruyter.

Research and Applications in Structural Engineering, Mechanics and Computation – Zingoni (Ed.)
© 2013 Taylor & Francis Group, London, ISBN 978-1-138-00061-2

Vibrations of cables with bending stiffness by an asymptotic approach

T. Canor
F.R.S.-FNRS, National Fund for Scientific Research of Belgium, ArGEnCo Department, University of Liege, Belgium

V. Denoël
ArGEnCo Department, Structural Engineering Division, University of Liege, Belgium

ABSTRACT: Vibrations of cables with a small bending stiffness concerns many engineering applications such as the fatigue assessment of stay cables. With the Finite Element (FE) method, the analysis can be performed with nonlinear truss elements, but bending effects are not taken into account. Otherwise, beam elements can be used, but the smallness of the bending stiffness may lead to numerical instability and mediocre results in boundary regions.

In this context, the paper presents an alternative method to calculate the time evolution of the profile of bending moments in boundary layers of cables, avoiding heavy FE analysis. The developments combine the theory of vibrations of extensible rods with asymptotic methods. The equations are decoupled between the slow dynamics of the boundary regions and the fast dynamics of the span. Then, a composite solution is constructed by means of a matched asymptotic procedure.

1 INTRODUCTION

The vibration analysis of cables with a small bending stiffness is a problem encountered in many engineering applications such as the fatigue assessment of stay cables (cable stayed bridges or prestressed concrete beams), the modeling of pipeline laying operation or the determination of bending stresses in drillpipe assemblies. The elastic theory of rods models the static and dynamic deflections of general elastic beams and cables (Antman 2005, Coleman et al. 1993). However, the smallness of the bending stiffness leads to consider a singularly perturbed equations and the existence of boundary layers near the anchors (Hinch 1991). In these small regions, the curvature and the bending moment change sharply compared with the rest of the cable especially. This phenomenon is magnified for clamped beams. Standard numerical techniques fail to solve these problems efficiently.

Static deflection of cables with a small bending stiffness is a widely covered topic. A matched asymptotic expansion has been used (Stump & van der Heijden 2000) to study the spatial deflection of a bent and twisted inextensible cable. Denoël & Detournay (2010) propose an application of multiple scales methods to study a beam with a small bending stiffness, offering a better accuracy for a larger range of bending stiffness than the matched asymptotic method. From another viewpoint, Denoël & Canor (2013) have developed a patching method allowing to quantify the size of the boundary layer of the cable using an Eulerian description of a catenary in the span and a nonlinear beam model in the boundary layers.

Concerning nonlinear vibration of cables, the finite element method widely used in structural dynamics presents some weaknesses. The use of nonlinear truss elements (Impollonia et al. 2011) neglects completely the bending effects, while nonlinear beam elements may lead to instability because of the smallness of the bending stiffness. Mediocre results can be obtained for indirect excitations in boundary layers. These zones in which the bending moment increases sharply, require an expensive mesh refinement with small elements which leads to increase the computational burden or to have ill-conditioned systems. In the range of analytical or semi-analytical methods, Stump & Fraser (2000) have used matched asymptotic expansion to study the boundary layer behaviour of moving strips in a steady state deflection (no inertial forces). Pellicano et al. (1998) study the dynamical behaviour of an axially moving beam with hinged extremities: a linear modal analysis associated with matched asymptotic expansion allows to decouple quite efficiently the equation of the beam, eventhough the potential nonlinear bending behaviour is not considered. The modal analysis for cable with small bending stiffness is also presented in the works of Ricciardi et al. (2008) and Lacarbonara et al. (2008). The modal approach may seem attractive, nevertheless the complex analytical shape of modes is a drawback just to take into account small

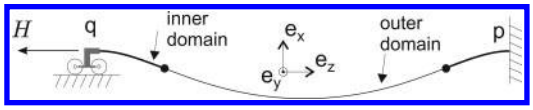


Figure 1. Sketch of problem.

perturbations in the boundary regions. Furthermore, modal analysis of slack cables is usually based on rough approximations.

As an alternative to numerical methods and modal analysis, provided the complexity of the analytical developments does not preclude their application, these problems may be tackled with appealing analytical procedures such as matched asymptotic or multiple scales methods (Hinch 1991). This work proposes to start with classical theory of rod vibration and to use the potentiality of asymptotic methods to derive an efficient and smart formulation to analyse the vibration of taut and clamped cable with bending stiffness as sketched in Figure 1.

2 FORMULATION OF THE PROBLEM

2.1 *Theory of extensible rods*

The classical theory of rods (Antman 2005) models the motion of elastic structures submitted to external forces in large displacements and large rotations. The rod deflection is described with a configuration vector $\mathbf{r}(s,t)$ which defines a curve $C(t)$. The variable s identifies the position of a material point of the rod in the stress-free reference configuration $\mathbf{r}^0(s)$, while t denotes the time. The function $\mathbf{r}(s,t) : [0, l] \times \mathbb{R}^+ \to \mathbb{R}^3$ is a continuous function with l the length of the rod in $\mathbf{r}_0(s)$. The tangent vector to $C(t)$, noted $\partial s\mathbf{r}$, is defined as the strain vector $\mathbf{v}$ such that $\partial s\mathbf{r} = \mathbf{v}$. The norm of $\mathbf{v}$ is usually called the *stretch*.

A local basis, different from the Frenet basis related to the curve $C(t)$ at a point s, is usually introduced. The cross section is determined by the orientation of two orthogonal vectors $\tilde{\mathbf{d}}_1(s,t)$ and $\tilde{\mathbf{d}}_2(s,t)$. The local basis is completed by the definition of a third vector $\tilde{\mathbf{d}}_3(s,t) = \tilde{\mathbf{d}}_1 \times \tilde{\mathbf{d}}_2$ which is normal to the surface of the cross section of the rod. If the rod in unshearable but extensible, the strain vector in the local basis has a single component defined such that $\mathbf{v} = [0, 0, 1 + v_3]^T$ with $v_3 \in [-1, +\infty]$ the strain in the axial direction of the rod.

The dynamics of rods is modelled by a set of partial differential equations in space and time. The conservation of linear and angular momenta yields

$$\partial_s \mathbf{N} + \mathbf{F} = \rho A \partial_t^2 \mathbf{r} \tag{1}$$

$$\partial_s \mathbf{M} + \partial_s \mathbf{r} \times \mathbf{N} = \rho I \left(\tilde{\mathbf{d}}_1 \times \partial_t^2 \tilde{\mathbf{d}}_1 + \tilde{\mathbf{d}}_2 \times \partial_t^2 \tilde{\mathbf{d}}_2 \right) \tag{2}$$

where $\mathbf{M}(s,t)$ and $\mathbf{N}(s,t)$ are the vectors of internal moments and forces for a material point s at a time t, respectively. Furthermore, ρ, A and I are the mass density of the beam material, the cross section area and the second moment of area per unit of reference length. The parameters of the cable are independent of t and s. The section is supposed to be circular, so the second moment of area is independent of $\tilde{\mathbf{d}}_1$ and $\tilde{\mathbf{d}}_2$ as principal axes.

The conservation of planar cross section, or the Euler-Bernoulli hypothesis (Bernoulli 1694), is commonly assumed in rods and cables when the shear forces do not induce significant strain energy. The constitutive equation for internal moments with this assumption yields

$$\mathbf{M} = EI \left(\kappa_1 \tilde{\mathbf{d}}_1 + \kappa_2 \tilde{\mathbf{d}}_2 \right) + GJ\kappa_3 \tilde{\mathbf{d}}_3 \tag{3}$$

with E the Young modulus, G the shear modulus, GJ torsional stiffness, $\kappa_{1,2}$ the curvature in the direction $\tilde{\mathbf{d}}_{1,2}$ and κ_3 the twist density. The constitutive equation for internal forces takes into account the extensibility and the unshearability of the rods, such that

$$N_3 = EAv_3. \tag{4}$$

At this stage, because of the assumption of unshearability, the complete set of 9 equations involves 9 unknowns, which leads to a well-posed problem.

2.2 *Euler angles*

Euler angles (Antman 2005, Coleman et al. 1993) can be interpreted as a generalization of the spherical coordinates. In the theory of elastic rods, they are often used because they provide an efficient description of the orientation of a cross section compared with a reference system, in spite of some drawbacks, as discontinuities. The method consists in mapping the fixed basis $\{\mathbf{e}_x, \mathbf{e}_y, \mathbf{e}_z\}$ with the local basis of the cross section by a set of three successive rotations of angles $\psi(s,t)$ (precession), $\theta(s,t)$ (nutation) and $\varphi(s,t)$ (spin). In the reference configuration $\mathbf{r}^0(s)$, the axis of the rod lies on the $\mathbf{e}_z$-axis and the two principal axes of the cross section are parallel to $\mathbf{e}_x$- and $\mathbf{e}_y$-axes.

The first two rotations match the vector $\mathbf{e}_z$ with the unit vector $\tilde{\mathbf{d}}_3(s,t)$ normal to the cross section of the rod. In spherical coordinates, this normal vector reads

$$\tilde{\mathbf{d}}_3 = \cos\psi \sin\theta \mathbf{e}_x + \sin\psi \sin\theta \mathbf{e}_y + \cos\theta \mathbf{e}_z. \tag{5}$$

The two unit vectors $\tilde{\mathbf{d}}_1(s,t)$ and $\tilde{\mathbf{d}}_2(s,t)$ at abscissa s are contained in a plane perpendicular to $\tilde{\mathbf{d}}_3(s,t)$. The transformation between the fixed basis and the local basis is completed by a last rotation $\phi(s,t)$ around $\tilde{\mathbf{d}}_3(s,t)$ such that $\tilde{\mathbf{d}}_1(s,t)$ and $\tilde{\mathbf{d}}_2(s,t)$ are expressed in terms of $\psi(s,t)$, $\theta(s,t)$ and $\phi(s,t)$ (see (Antman 2005)). At this stage, the nine components of the local basis depend on three angles only. The curvature vector in terms of Euler angles reads

$$\begin{aligned} \boldsymbol{\kappa} = {} & (\sin\phi\partial_s\theta - \cos\phi\sin\theta\partial_s\psi)\tilde{\mathbf{d}}_1 + (\cos\phi\partial_s\theta \\ & + \sin\phi\sin\theta\partial_s\psi)\tilde{\mathbf{d}}_2 + (\cos\theta\partial_s\psi + \partial_s\phi)\tilde{\mathbf{d}}_3. \end{aligned} \tag{6}$$

However, because the cable is reasonably assumed to have a circular cross section, the orientation of $\tilde{\mathbf{d}}_1(s,t)$ and $\tilde{\mathbf{d}}_2(s,t)$ is independent of the rotation $\phi(s,t)$, because every couple of orthogonal unit vectors normal to $\tilde{\mathbf{d}}_3(s,t)$ are principal axes (Coleman et al. 1993). A new local basis may be defined by imposing a clockwise rotation $\phi(s,t)$ around $\tilde{\mathbf{d}}_3(s,t)$ to the couple $\tilde{\mathbf{d}}_1(s,t)$ and $\tilde{\mathbf{d}}_2(s,t)$, such that

$$\mathbf{d}_1 = \cos\psi\cos\theta\mathbf{e}_x + \sin\psi\cos\theta\mathbf{e}_y - \sin\theta\mathbf{e}_z \quad (7)$$

$$\mathbf{d}_2 = -\sin\psi\mathbf{e}_x + \cos\psi\mathbf{e}_y \quad (8)$$

and $\mathbf{d}_3 = \tilde{\mathbf{d}}_3$. The same clockwise rotation imposed to the curvature vector yields

$$\boldsymbol{\kappa} = (\cos\theta\partial_s\psi + \partial_s\phi)\mathbf{d}_3 + \partial_s\theta\mathbf{d}_2 - \sin\theta\partial_s\psi\mathbf{d}_1. \quad (9)$$

2.3 *Dimensionless formulation*

A dimensionless formulation is introduced. Dimensionless vectors, variables and parameters are mentioned with Greek letters and bar symbols. The material coordinate s is scaled with respect to the stressfree rod length l, such as $\xi = s/l$ with $\xi \in [0, 1]$. The internal and external forces $\mathbf{N}$ and $\mathbf{F}$ are scaled by the total weight of the rod wl and the bending moment $\mathbf{M}$ is scaled by wl^2; w is the weight per unit of length. This choice is motivated by the time-invariance of w and l. The dimensionless time τ is obtained by scaling the time t with a reference period $T_1 = \sqrt{l/g}$ with g the gravitational acceleration. The dimensionless bending stiffness is given by $\varepsilon^2 = EI/wl^3$ and the position vector $\mathbf{r}$ is scaled by l. A parameter $\varepsilon_b = wl/EA$ is introduced in the constitutive equation of extensibility and a parameter γ is defined as the ratio between the torsional stiffness GJ and the bending stiffness EI.

The kinematic condition of unshearability but extensibility implies $\partial_\xi\bar{\mathbf{r}} = (1+v_3)\mathbf{d}_3$ and the curvature vector becomes

$$\bar{\boldsymbol{\kappa}} = (\cos\theta\partial_\xi\psi + \partial_\xi\phi)\mathbf{d}_3 + \partial_\xi\theta\mathbf{d}_2 - \sin\theta\partial_\xi\psi\mathbf{d}_1 \quad (10)$$

with $\bar{\kappa} = l\kappa$. Then, the equations of motion become

$$\partial_\xi\bar{\mathbf{N}} + \bar{\mathbf{F}} = \partial_\tau^2\bar{\mathbf{r}} \quad (11)$$

$$\partial_\xi\bar{\mathbf{M}} + \partial_\xi\bar{\mathbf{r}}\times\bar{\mathbf{N}} = \varepsilon^2\varepsilon_b\left(\mathbf{d}_1\times\partial_\tau^2\mathbf{d}_1 + \mathbf{d}_2\times\partial_\tau^2\mathbf{d}_2\right) \quad (12)$$

and the constitutive equations read

$$v_3 = \varepsilon_b\bar{N}_3 \quad (13)$$

$$\bar{\mathbf{M}} = \varepsilon^2\left(\bar{\kappa}_1\mathbf{d}_1 + \bar{\kappa}_2\mathbf{d}_2\right) + \varepsilon^2\gamma\bar{\kappa}_3\mathbf{d}_3 \quad (14)$$

Dimensionless variables offer the opportunity to compare efficiently the parameters of the problem. A cable is a structural element between a rod and a string. A string is supposed to be perfectly flexible and extensible ($\varepsilon = 0$), contrarily to a rod, a more complex element which is flexible, shearable and extensible. A cable is supposed to be an extensible rod with a small bending stiffness, i.e. ε is a small parameter. For classical cable structures made up of steel cables, the Young modulus of the material is so high that the ratio ε_b between the axial stiffness and the weight of the cable is also a small parameter.

For the sake of simplicity, the bar over all the dimensionless variables is deliberately omitted in the following developments.

3 ASYMPTOTIC APPROACH

3.1 *Outer solution*

The equation of motion in the outer domain is obtained by supposing that the bending effects are small in this region. In this domain, a regular asymptotic expansion in terms of ε for all variables of the problem reads

$$\mathbf{w} = \mathbf{w}_c + \varepsilon\mathbf{w}_{c,1} + \varepsilon^2\mathbf{w}_{c,2} + \ldots \quad (15)$$

with $\mathbf{w}(\xi, \tau)$ a generic vector representing the vectors $\mathbf{N}$, $\mathbf{F}$, $\mathbf{r}$ or the Euler angles.

After injecting Eq. (15) into Eq. (11) and Eq. (12), the leading order equation reads

$$\partial_\xi(\mathbf{N}_c) + \mathbf{F}_c = \partial_\tau^2\mathbf{r}_c \quad (16)$$

with the subscript c referring to the leading order in the outer domain. Equation (16) is the classical form of the equation of motion of extensible strings. The unshearability assumption in the angular momentum equation leads to $N_{c,1} = N_{c,2} = 0$. Euler angles in the outer domain are $\theta_c(\xi,\tau)$ and $\psi_c(\xi,\tau)$. The methods to solve this equation are numerous, as finite element method (Impollonia et al. 2011) or modal analysis (Warnitchai et al. 1995). The modal approach is probably less accurate, because it usually neglects the axial displacements and is limited to nonlinear vibrations of taut cables. The modal analysis assumes also synchronous vibration of material points.

3.2 *Inner solution*

The assumption of clamped-clamped beams (Fig. 1) explains the existence of two boundary layers at both anchors. To analyse the behaviour of the cable in these two boundary layers, a stretched coordinate ζ is introduced $\xi = \varepsilon\zeta$, modelling the fast variation of the curvature close to the anchors. This stretched variable $\zeta \in [0, \varepsilon^{-1}]$ is introduced in the equations of motion.

For the equilibrium equation in rotation, the rotational inertial forces are three orders of magnitude less than the variation of the bending moment in the boundary layer and they are thus neglected. Equation (12) becomes

$$\varepsilon^{-1}\partial_\zeta\mathbf{M} + (1+v_3)\mathbf{d}_3\times\mathbf{N} = \mathbf{0} \quad (17)$$

because of the kinematic equation. The stretched variable ζ is also introduced in the constitutive equation of $\mathbf{M}$ through the curvature vector κ, Eq. (10) becomes

$$\varepsilon\boldsymbol{\kappa} = (\cos\theta\partial_\zeta\psi + \partial_\zeta\phi)\mathbf{d}_3 + \partial_\zeta\theta\mathbf{d}_2 - \sin\theta\partial_\zeta\psi\mathbf{d}_1. \quad (18)$$

With Eq. (18) and Eq. (14), Eq. (17) becomes

$$\begin{cases} \partial_\zeta(\sin\theta\partial_\zeta\psi) + (1+v_3)N_2 & = 0 \\ \partial_\zeta^2\theta + (1+v_3)N_1 & = 0 \end{cases} \quad (19)$$

and $\partial_\zeta\kappa_3 = 0$, this latter one meaning that the twist moment is constant along the cable in the boundary layer, $\kappa_3 = \kappa_3^\star$. Actually, the twist moment is constant all along the rod, because of the hypothesis of unshearability.

Introducing the stretched variable in Eq.(11) yields

$$\partial_\zeta\mathbf{N} = \varepsilon\left(\partial_\tau^2\mathbf{r} - \mathbf{F}\right). \quad (20)$$

The right-hand side must be analysed more precisely to evaluate the real order of the inertial forces and the external forces. If no concentrated load acts in the boundary layer and if the external forces are at most of the same order of magnitude as wl, the term $\varepsilon\overline{\mathbf{F}}$ is at least of order ε.

The magnitude of the inertial forces requires more attention. The use of the stretched variable leads actually to consider two different problems in the outer and in the inner domains. The matched asymptotic approach is just a method to compose a solution. Therefore, the equation of motion can be considered separately in the boundary layer and in the span. The characteristic time scale in the boundary layer is not the same as in the span. Indeed, the boundary layer may be considered as a cantilever beam with a dimensionless length of ε (Denoël & Canor 2013), a unit dead load per unit length and a bending stiffness of ε^2. The ratio of the characteristic time in the inner domain τ_b and the one in the outer domain is thus of order ε (Clough & Penzien 1993). Because of the smallness of ε, the period τ_b corresponds to the period of a very rigid structure. Using a multiple scales approach in time, the time τ can be split into two contributions $\tau_1 = \tau$ related to the span and τ_2 related to the boundary layer with $\tau_2 = \varepsilon\tau$. The inertial forces read now

$$\partial_\tau^2\mathbf{r} = \partial_{\tau_1}^2\mathbf{r} + 2\varepsilon\partial_{\tau_1\tau_2}^2\mathbf{r} + \varepsilon^2\partial_{\tau_2}^2\mathbf{r} \quad (21)$$

and the conservation of linear momentum becomes

$$\partial_\zeta\mathbf{N} = \varepsilon\partial_{\tau_1}^2\mathbf{r} + 2\varepsilon^2\partial_{\tau_1\tau_2}^2\mathbf{r} - \varepsilon\mathbf{F} + \mathcal{O}(\varepsilon^3). \quad (22)$$

with $\mathbf{N}$ now a function of τ_1, τ_2 and ζ.

A regular asymptotic expansions in term of ε for all variables of the problem reads

$$\mathbf{u} = \mathbf{u}_0 + \varepsilon\mathbf{u}_1 + \varepsilon^2\mathbf{u}_2 + \ldots \quad (23)$$

with $\mathbf{u}(\zeta, \tau)$ a generic vector representing the vectors $\mathbf{N}$, $\mathbf{F}$, $\mathbf{r}$ or the Euler angles. With Eq. (23) into Eq. (20), the leading order of $\mathbf{N}$ is given by

$$\partial_\zeta\mathbf{N}_0 = \mathbf{0} \quad (24)$$

which is equivalent to disregard the external forces and the inertial forces in the boundary layer at a lower order of magnitude. This result must be understood with regard to the presumed small dimension of the boundary layer and that the forces are distributed along the cable in a quite regular manner, as the dead load and the inertial forces. The smallness of τ_b compared with τ_1 means also a quasi-static response of the boundary layer to an excitation at period close to τ_1. This short comment aims to explain intuitively that the boundary layer responds in a quasi-static manner with regard to the fast dynamics of the outer domain.

The leading order of the internal forces $\mathbf{N}_0$ can be projected in the leading order basis $\{\mathbf{d}_{1,0}, \mathbf{d}_{2,0}, \mathbf{d}_{3,0}\}$, and especially

$$N_2 = \mathbf{N}_0 \cdot \mathbf{d}_{2,0} = -\sin\psi_0 N_x + \cos\psi_0 N_y \quad (25)$$

with N_x, N_y and N_z the projections of $\mathbf{N}_0$ in a fixed basis $\{\mathbf{e}_x, \mathbf{e}_y, \mathbf{e}_z\}$. These components are constant in this basis because of Eq. (24). Therefore, $\partial_\zeta N_2 = 0$ is only satisfied if ψ_0 is also constant in the boundary layer. The curvature vector is $\varepsilon\kappa = \partial_\zeta\theta_0\mathbf{d}_{2,0} + \partial_\zeta\varphi_0\mathbf{d}_{3,0}$ and the angular momentum equation reads

$$\partial_\zeta^2\theta_0 + (1+v_3)N_1 = 0 \quad (26)$$

and $N_2 = 0$. So, the constant $\psi_0 \in [0, 2\pi]$ is determined as $N_y = N_x \tan\psi_0$. The use of reciprocal function leads to discontinuity in the calculation of ψ_0. From a computational viewpoint, it is more convenient to calculate $\psi_0 = \arctan\left(\frac{N_y}{N_x}\right)$ and to adapt ψ_0 according to the signs of N_x and N_y.

Therefore, the equilibrium equation for the bending moment and the extensibility constitutive equation become

$$\partial_\zeta^2\theta_0 + (1+v_3)(V\cos\theta_0 - H\sin\theta_0) = 0 \quad (27)$$

$$v_3 = \varepsilon_b(V\sin\theta_0 + H\cos\theta_0) \quad (28)$$

with $V = (\cos\psi_0 N_x + \sin\psi_0 N_y)$ and $H = N_z$. These developments highlight two interesting results which make our approach very elegant: (i) the quasi-static response of the boundary layer avoid the computation of spatial beam dynamics, (ii) the low frequency oscillations in the boundary layer are contained in a plane characterized by the angle ψ_0, (iii) the torsion is decoupled from the bending dynamics.

By multiplying Eq. (27) by $\partial_\zeta\theta_0$, a first integral is found, such as

$$\begin{aligned} A(\tau) &= \frac{1}{2}(\partial_\zeta\theta_0)^2 + (H\cos\theta_0 + V\sin\theta_0) \quad (29) \\ &+ \frac{\varepsilon_b}{2}\left(\frac{(H^2 - V^2)}{2}\cos 2\theta_0 + VH\sin 2\theta_0\right) \end{aligned}$$

with $A(\tau)$ a first integration constant, which is determined by using the van Dyke's rule (Hinch 1991). The matching condition is usually formulated as the inner limit of a given variable equals the outer limit of this variable, such that

$$\left(\lim_{\varepsilon\to 0} y_{in}(\tau,\zeta)\right)_{\xi \text{ fixed}} = \left(\lim_{\xi\to 0} y_{out}(\tau,\xi)\right)_{\varepsilon \text{ fixed}} \quad (30)$$

with y a variable of the system. This equality leads to identify the internal forces $\mathbf{N}_0$ in the boundary layer to the reactions at the anchors calculated with the string dynamics and the angle ψ_0 to the rotation angle of the string at the anchor, such as

$$\lim_{\varepsilon\to 0,\xi \text{ fixed}} \mathbf{N}_0(\zeta,\tau) = \lim_{\xi\to 0,\varepsilon \text{ fixed}} \mathbf{N}_c(\xi,\tau) = \mathbf{N}_{c,p}(\tau) \quad (31)$$

$$\lim_{\varepsilon\to 0,\xi \text{ fixed}} \psi_0(\zeta,\tau) = \lim_{\xi\to 0,\varepsilon \text{ fixed}} \Psi(\xi,\tau) = \Psi_p(\tau) \quad (32)$$

with the subscript p denoting the anchor at $\xi = 0$. Concerning the rotation angle θ_0 in the plane orthogonal to $\mathbf{d}_2$, we have

$$\lim_{\varepsilon\to 0,\xi \text{ fixed}} \theta_0(\zeta,\tau) = \lim_{\xi\to 0,\varepsilon \text{ fixed}} \vartheta(\xi,\tau) = \vartheta_p(\tau) \quad (33)$$

$$\lim_{\varepsilon\to 0,\xi \text{ fixed}} \partial_\zeta\theta_0(\zeta,\tau) = \lim_{\xi\to 0,\varepsilon \text{ fixed}} \partial_\zeta\vartheta(\xi,\tau) = 0. \quad (34)$$

The constant $A(\tau)$ is calculated with these two matching conditions. Furthermore, if we note that $V = H\tan\vartheta_p$ which comes from Euler angles in the string dynamics, the equation in θ_0 becomes

$$\frac{1}{2}\left(\partial_\zeta\theta_0\right)^2 = 2f_p\sin^2\left(\frac{\Delta\theta_0}{2}\right) + \varepsilon_b\frac{f_p^2}{2}\sin^2\left(\Delta\theta_0\right) \quad (35)$$

or, in a differential formalism,

$$\frac{d\theta_0}{\sin\left(\frac{\Delta\theta_0}{2}\right)\sqrt{1+\varepsilon_b f_p\cos^2\left(\frac{\Delta\theta_0}{2}\right)}} = \pm 2\sqrt{f_p}d\zeta \quad (36)$$

with $\Delta\theta_0 = \theta_0 - \vartheta_p$ and $f_p(\tau) = \frac{H}{\cos\vartheta_p}$. A direct integration leads to

$$-\frac{1}{\sqrt{1+\varepsilon_b f_p}}\operatorname{arctanh}\left(\frac{\sqrt{2(1+\varepsilon_b f_p)}\cos\left(\frac{\Delta\theta_0}{2}\right)}{\sqrt{2+\varepsilon_b f_p+\varepsilon_b f_p\cos\left(\Delta\theta_0\right)}}\right) = \pm\sqrt{f_p}\zeta + B(\tau) \quad (37)$$

with $B(\tau)$ a second integration constant. For usual cable, the term $\varepsilon_b f_p$ which expresses the ratio between the tension in the cable and the axial stiffness, is small. According to some classical hyperbolic function properties, an explicit expression for θ_0 can be approximated by

$$\theta_0(\zeta,\tau) = \vartheta_p(\tau) + 4\arctan\left(B(\tau)\exp\left(\pm\sqrt{f_p\left(1+\varepsilon_b f_p\right)}\zeta\right)\right) \quad (38)$$

Only the minus sign is kept for stability reasons. The constant $B(\tau)$ can be calculated by imposing the rotation angle at the anchor p, such that

$$B(\tau) = \tan\left(\frac{\theta_p - \vartheta_p(\tau)}{4}\right) \quad (39)$$

with $\theta_p = \theta_0(0,\tau)$ the imposed boundary condition.

A composed solution can be expressed all along the beam in term of the initial space variable ξ, such that

$$\theta_0(\xi,\tau) = \vartheta(\xi,\tau) + 4\arctan\left(B(\tau)\exp\left(-\frac{\xi}{\varepsilon}\sqrt{f_p\left(1+\varepsilon_b f_p\right)}\right)\right) + 4\arctan\left(B(\tau)\exp\left(-\frac{1-\xi}{\varepsilon}\sqrt{f_q\left(1+\varepsilon_b f_q\right)}\right)\right) \quad (40)$$

with the subscript q denoting the anchor at $\xi = 1$.

4 APPLICATIONS

4.1 *In-plane vibration*

The first application aims at validating the previous developments by studying the response of a horizontal cable submitted to harmonic horizontal displacement of the anchor q (see Figure 1). In this example, the vibrations are contained in the vertical plane to simplify the comparison at this first stage.

The dimensionless properties of the system are $\varepsilon = 0.02$ and $\varepsilon_b = 5.6\cdot 10^{-5}$. The static deflection is characterized by a sag-to-span ratio equal to 5‰. The excitation is the function $2\cdot 10^{-4}\sin(2\omega_1\tau)$ with ω_1 the dimensionless natural circular frequency of the cable equal to 3.3. In this example, a classic analysis with beam finite elements is compared to the proposed approach in which the string dynamic is computed with truss finite elements. The bending moment at the anchors is calculated according to Eq. (40) and $M(\xi) = \varepsilon^2\partial_\xi\theta_0$. In this application, 70 elements are considered for the beam model against 30 for the truss model. Nonlinear corrotational finite elements are used in the numerical simulations. For the beam model, the mesh is adapted to be denser in the boundary regions. Because the number of nodes and the number of DOF per node are reduced, the computational time is drastically reduced between the truss and the beam models.

Furthermore, the instabilities susceptible to appear in the boundary layers are avoided.

Figure 2 highlights the good correspondence between the two methods. The values of the bending moment are identical in both applications, in spite of a short shift between the two time series, explained by the important sensitivity of the transient phase to the natural frequency and the damping model.

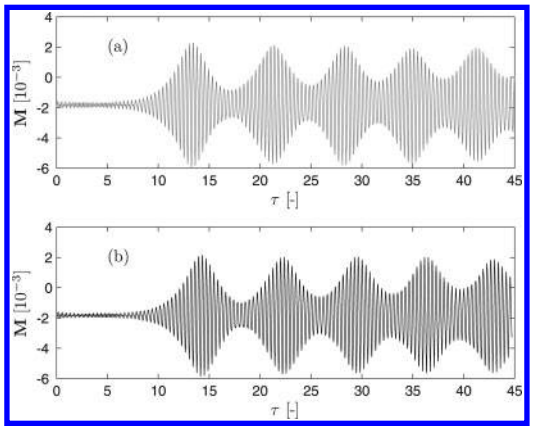


Figure 2. Bending moment $\mathbf{M}$ $[10^{-3}]$ at the fixed anchor p calculated with the proposed method (a) and a beam finite element model (b).

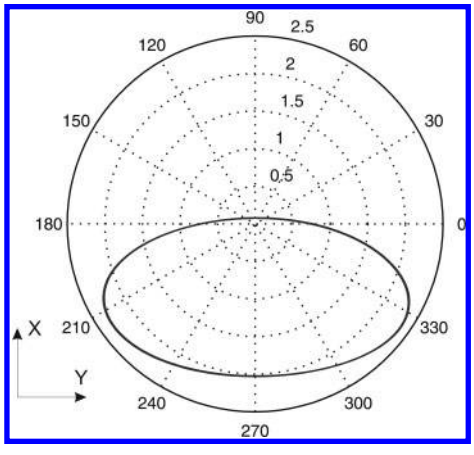


Figure 3. Polar plot of bending moment $\mathbf{M}[10^{-3}]$ in steady-state vibration at the fixed anchor p for different orientations ψ_0.

4.2 *Spatial vibration*

The second application illustrates the proposed developments for spatial vibrations. The characteristics of the cable are $\varepsilon = 0.01$, $\varepsilon_b = 10^{-4}$, the sag-to-span ratio is about 5‰. The cable is excited by an elliptic displacement of the anchor q, such as $x_q(\tau) = e_{0,x}\sin(\omega_2\tau)$ and $y_q(\tau) = e_{0,y}\sin(\omega 2\tau)$, with $e_{0,x} = 10^{-3}$ and $e_{0,y} = e_{0,x}/2$, with ω_2 the first in-plane natural frequency. The outer solution is calculated with only 20 truss finite elements.

In spatial steady-state vibration, the diagram of the bending moment is adequately shown in a polar graph with the value of the bending moment in the orientation $\psi_0(\tau)$ as in Figure 3. For spatial vibrations, the proposed method offers a real efficiency, because the mesh in the boundary layer must not be refined, the instability due to the twist and the smallness of the bending stiffness are discarded and the number of DOF is reduced (substantial in larger models).

5 CONCLUSION

In this paper, an analytical approach using matched asymptotic expansion has been developed. This method allows to calculate the bending moment in the boundary layers by decoupling the equation of motion between the span and the boundary layer. Because these regions respond in a *quasi*-static way, the proposed formula allows to build the curvature and the bending moment in the boundary layers only by the knowledge of the span vibration.

ACKNOWLEDGEMENT

The authors acknowledge the National Fund of Scientific Research of Belgium for its support.

REFERENCES

Antman, S. (2005). *Nonlinear Problems of Elasticity* (2nd ed.). Applied Mathematical Sciences. Springer-Verlag.

Bernoulli, J. (1694). Curvatura laminae elasticae. *Acta Eruditorum 13*, 262–275.

Clough, R.W. & J. Penzien (1993). *Dynamics of structures* (2nd ed.). New-York: McGraw-Hill.

Coleman, B. D., E. H. Dill, M. Lembo, Z. Lu, & I. Tobias (1993). On the dynamics of rods in the theory of kirchhoff and clebsch. *Archive Rational Mechanics Analysis 121*, 339–359.

Denoël, V. & T. Canor (2013). Patching asymptotics solution of a cable with a small bending stiffness. *Journal of Structural Engineering – ASCE 139*, 180–187.

Denoël, V. & E. Detournay (2010). Multiple scales solution for a beam with a small bending stiffness. *Journal of Engineering Mechanics 136*(1), 69–77.

Hinch, E. (1991). *Perturbation Methods*, Volume 1. Cambridge: Cambridge University Press.

Impollonia, N., G. Ricciardi, & F. Saitta (2011). Vibrations of inclined cables under skew wind. *International Journal of Non-Linear Mechanics 46*(7), 907–918.

Lacarbonara, W. & A. Pacitti (2008). Nonlinear modeling of cables with flexural stiffness. *Mathematical Problems in Engineering* 2008.

Pellicano, F. & F. Zirilli (1998). Boundary layers and nonlinear vibrations in an axially moving beam. *International Journal of Non-Linear Mechanics 33*(4), 691–711.

Ricciardi, G. & F. Saitta (2008). A continuous vibration analysis model for cables with sag and bending stiffness. *Engineering Structures 30*(5), 1459–1472.

Stump, D. M. & W. B. Fraser (2000). Bending boundary layers in a moving strip. *Nonlinear Dynamics 21*(1), 55–70.

Stump, D. M. & G. H. M. van der Heijden (2000). Matched asymptotic expansions for bent and twisted rods: applications for cable and pipeline laying. *Journal of Engineering Mathematics 38*(1), 13–31.

Warnitchai, P., Y. Fujino, & T. Susumpow (1995). A nonlinear dynamic model for cables and its application to a cablestructure system. *Journal of Sound and Vibration 187*, 695–712.

Research and Applications in Structural Engineering, Mechanics and Computation – Zingoni (Ed.)
© 2013 Taylor & Francis Group, London, ISBN 978-1-138-00061-2

Singularities that induce a breakdown of determinism in mechanics

Mike R. Jeffrey
Department of Engineering Mathematics, University of Bristol, Bristol, UK

ABSTRACT: We will show that determinism can break down at certain singularities that arise in the mechanics of semi-rigid bodies. An example system consists of a wheel slipping and rolling along a surface, such that dry friction applies a torque to the wheel via a standard nonlinear tyre-like interaction. In a certain configuration the force on the wheel and its ensuing motion acquire many possible values. The subsequent motion is therefore infinitely sensitive to perturbation, constituting a point of non-determinism in an otherwise deterministic system. Moreover the device returns to the singularity repeatedly, so that it suffers repeated bursts of unpredictability, constituting an extreme non-deterministic form of chaos. A non-deterministic chaotic attractor was found for a range of parameters and tyre/friction models in (2013). Here, we explore the building blocks of this dynamics by stripping the model down to its key elements. We investigate the non-deterministic phenomenon when subjected to relaxations of the model that allow for smoothing, noise, and hysteresis. This is part of a wider theory currently emerging in the study of dynamical systems that undergo sharp switches in behaviour, whereby singularities can violate traditional rules of smooth dynamical systems.

1 INTRODUCTION

In dynamical systems modeling, discontinuities are widely used to model abrupt switches such as electronic relays, mechanical impact, and stick-slip motion; see e.g. (1999, 2008). Their application is increasingly reaching beyond traditional problems to include extreme nonlinearity and slow-fast timescale separation in electronics, mechanics, and the life sciences; e.g. (2011, 2010, 2003). Previous studies have progressed largely by extending established concepts from dynamical systems theory for smooth models, into a theory of *piecewise-smooth dynamics*. In recent years, however, certain discontinuity-induced phenomena have come to light that have no counterpart in smooth systems. They represent novel topological sources of unpredictable behaviour, and offer insight into the idealizations that are made in deriving empirical models of switching behaviour.

In (2010, 2011, 2013), certain physical models were shown to exhibit singularities at which determinism breaks down, meaning that, when the system is in one particular configuration, solutions of its differential equations become multi-valued.

The singularity occurs due to switching associated with stick-slip mechanics in (2013), and with a superconductivity threshold in (2011). A general classification of such singularities appears in (2011). Perhaps the most provocative outcome of these studies is an unconventional form of chaotic dynamics, driven by a loss of determinism at the so-called *Teixeira singularity* (2011). The singularity can occur in MIMO (multiple-input multiple-output) circuit models (2010), and was shown to create *non-deterministic chaos* in a mechanical friction model (2013).

The simplicity of the phenomenon itself is somewhat obscured in these preliminary studies, due to irrelevant nonlinearities in the practical models, and due to the rigours of normal form analysis in the general theory. Is the loss of determinism an artefact of modelling fundamentally smooth underlying physics using discontinuities, or does it provide insight into behaviour that is encountered daily, but dismissed as unmodelled error? To begin addressing these questions we focus here on the simple mechanism behind non-deterministic chaos, and the complex behaviour it creates; both appear for the first time in this paper.

In the mathematical sense, the configurations of interest are described by so-called two-fold singularities. They are *generic* in systems with at least two dimensions with one switch (2009), or two dimensions with more than one switch (2013). In the relatively young field of piecewise-smooth systems, however, it remains unclear whether 'genericity' implies a prevalence of such configurations in real systems. It also remains unclear exactly how one should recognize such behaviour in experimental data. Here we will present simulations of the typical dynamics in a stripped down model, which we then subject to smoothing, hysteresis, and noise.

We introduce the phenomenon of non-deterministic chaos by deriving a caricature encapsulating only the essential features of previous mechanical and electronic models. Our starting point is a mechanical system involving friction between a tyre and a dry revolving surface. In this conceptual model introduced

in (2013), a rolling wheel experiences a torque due to standard tyre-like contact forces, and this creates highly unpredictable rattling due to a singularity. The wheel system is introduced in sec. 2, and in sec. 3 the concept of non-deterministic chaos is introduced. A caricature model is derived in sec. 4, generalized to consider smoothing, noise, and hysteresis, and then these systems are simulated in sec. 5.

2 A MECHANICAL EXAMPLE

The mechanical device depicted in fig. 1 consists of a disc rotating with constant angular speed ω_0, on top of which sits a wheel, which is free to roll along a line placed a distance d from the disc axis. The wheel is fixed at an angle γ to this line. A tyre model for the contact force between the wheel and the disc then translates the frictional contact force into a torque on the wheel. The specifics of the tyre model (discussed in (2013)) are not vital to the dynamics observed.

The constraint by which the wheel moves along a line is also not crucial here, but is achieved by mounting it on a slider, embedded in a housing which is essentially another disc mounted coaxially above the lower disc; constants c_d, c_w, and k_w, give damping and spring coefficients between the housing and lower disc (subscript h) or wheel (subscript w).

For the time-varying displacement r and velocity v of the wheel, and the angular speed of the housing, ω, one obtains dynamical equations of the form

$$\begin{aligned} \dot{r} &= v \\ \dot{v} &= a_1(r,v,\omega) - b_1(r,v,\omega)\mathbf{sign}(h) \\ \dot{\omega} &= a_2(r,v,\omega) - b_2(r,v,\omega)\mathbf{sign}(h) \end{aligned} \qquad (1)$$

where a_i and b_i are nonlinear functions. The a_i capture the system geometry, while the b_i contain the contact model (for details we refer the reader to (2013)). More crucial is the function sign(h), which expresses the relative direction of the wheel's motion with respect to the disc, measured in the plane of the wheel. The function h is

$$h = (v - d(\omega - \omega_0))\sin\gamma + r(\omega - \omega_0)\cos\gamma\,. \qquad (2)$$

When this quantity vanishes for a period of time it means the wheel and the disc are in sticking contact. The equations governing sticking motion can be derived using Filippov's method (1988, 2003), which we describe briefly in the next section, and the resulting equations can be solved to simulate the device's dynamics (see (2013)). An alternative to Filippov's method, particularly suited to numerical simulation, is to smooth out the discontinuity in the sign function at $h=0$, so that it transitions smoothly between ± 1 in a small region $|h| < \varepsilon$ for small ε. The system is simulated by this method in fig. 2.

Although a smoothed-out model of the system is solvable using standard numerical tools, the system is then more stiff, as controlled by the parameter ε.

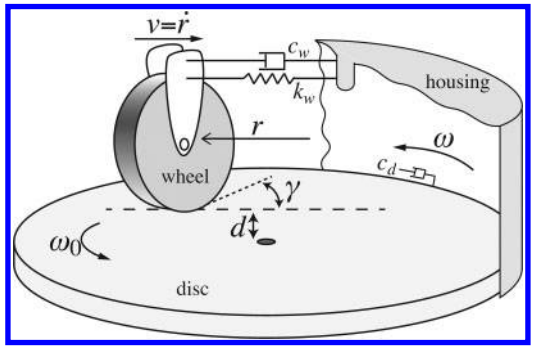


Figure 1. Sketch of the wheel assembly. Friction between the revolving disc, and a tyre on the wheel rim, apply linear and angular forces on the wheel as it rolls along the dashed line. The wheel-disc contact can stick or slip at different times.

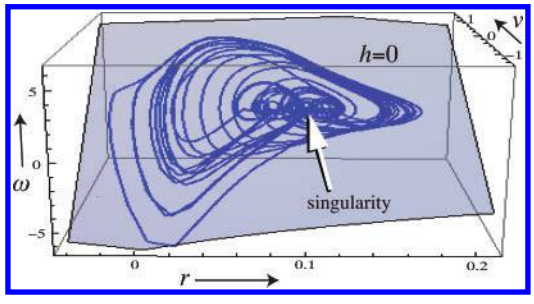


Figure 2. Simulation of the dynamics of the wheel assembly in fig. 1, indicating the sticking surface $h=0$, and the singularity. A solution of (1) is found by replacing the function sign(h) by tanh (h/ε), with stiffness parameter $\varepsilon = 10^{-3}$; [all simulations made in Mathematica™ using NDSolve].

Besides affecting computation time, smaller ε introduces instability to the simulation in ways that are poorly understood. As we describe below, the dynamics in fig. 2 involves the funnelling of solutions into and out of a singularity. In the discontinuous system this means that all trajectories at some time pass through the same point. That point represents a configuration of the physical device which can be reached from any initial conditions, and from which many different configurations of the system are possible at some later time. If the discontinuity is smoothed out, the system becomes extremely sensitive to initial conditions near the singularity. These problems are general properties, not specific to one system, but attributable to a specific class of singularities. Let us therefore isolate the features of the model that create these conditions.

3 A SCHEMATIC DEFINITION

At the heart of the mechanical system in fig. 2 lies a Teixeira singularity, a generic feature of discontinuous systems first studied in (1988, 1990). The discontinuity surface can be divided into regions where trajectories cross through it, are attracted to it, or

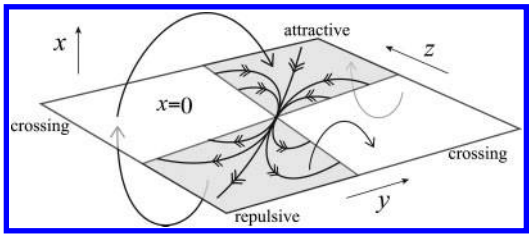


Figure 3. The Teixeira singularity – an isolated point in three dimensions, or an $n-3$ dimensional set in n dimensions. At a discontinuity surface ($x=0$) trajectories can cross (unshaded regions) or stick (double arrows, shaded regions). The sticking regions attract or repel the surrounding trajectories. The boundaries of the different regions intersect at the singularity.

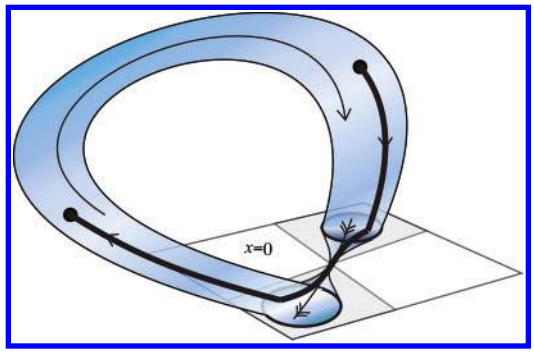


Figure 4. The mechanism of non-deterministic chaos: a Teixeira singularity on $x=0$, and a re-injection, that forces all trajectories to repeatedly visit the singularity. Any two points can be connected by a trajectory passing through the singularity, so which of these connections will persist under perturbation?

are repelled from it. All three types of behaviour are brought together at the singularity, as shown in fig. 3.

Consider a system

$$(\dot{x},\dot{y},\dot{z}) = \begin{cases} \mathbf{f}^+(x,y,z) & \text{if} \quad x>0 \\ \mathbf{f}^-(x,y,z) & \text{if} \quad x<0 \end{cases} \tag{3}$$

(we can increase the dimensionality, but three is the minimum required to understand the singularity), where $\mathbf{f}^{\pm}$ are smooth vector fields. The system switches between $\mathbf{f}^+$ and $\mathbf{f}^-$ at the discontinuity surface $x=0$ (which was $h=0$ in sec. 2). The standard way to define dynamics at $x=0$ (1988) is to take a linear combination of the two vector fields, say $\mathbf{g}^\lambda = \lambda\mathbf{f}^+ + (1-\lambda)\mathbf{f}^-$, and if there exists $\lambda\in[0,1]$ for which $\mathbf{g}^\lambda$ lies tangent to the surface, then $\mathbf{g}^\lambda$ defines a *sliding vector field* on $x=0$. This 'sliding' dynamics prescribes 'sticking' motion (double arrows in fig. 3), and the requirement $\lambda\in[0,1]$ (meaning $\mathbf{g}^\lambda$ lies somewhere between $\mathbf{f}^+$ and $\mathbf{f}^-$), confines sticking to the shaded regions in fig. 3, where $\mathbf{f}^+$ and $\mathbf{f}^-$ have opposing directions with respect to $x=0$. Elsewhere, the fields $\mathbf{f}^{\pm}$ cause trajectories to cross $x=0$ transversally. The boundaries between sticking and crossing are where $\mathbf{f}^+$ or $\mathbf{f}^-$ lie in the plane $x=0$, and a singularity forms where *both* $\mathbf{f}^+$ and $\mathbf{f}^-$ lie in the plane.

Various forms for this singularity are possible. Here we are interested in the case shown in fig. 3, when all sticking trajectories traverse the singularity, but moreover, they do so in the counterintuitive direction *from* the attractive region *to* the repulsive region. A local normal form for this scenario is known (1988, 1990, 2009), given by (3) with

$$\mathbf{f}_0^+(y) = (-y,1,v)\,, \qquad \mathbf{f}_0^-(z) = (z,w,1) \tag{4}$$

in terms of constants $v,w<0$ satisfying $vw>1$; from these equations one can easily sketch fig. 3. The point $(x,y,z)=(0,0,0)$ is the Teixeira singularity. Observe that a whole volume of trajectories will fall into the attractive sticking region, and then enter the singularity. Conversely, a whole volume of trajectories can be traced backwards in time to the repulsive sticking region, and thence to the singularity.

It is easy to show that passage through the singularity takes a finite amount of time (2009). This implies that when a trajectory traverses the singularity, its possible histories and possible futures are momentarily multi-valued — an instant of non-determinism.

The dynamics becomes more striking if we introduce a feedback to the system, as exists in the mechanical problem of sec. 2, so that every trajectory, once ejected from the repulsive side of the singularity, is eventually re-injected via the attractive side (see fig. 4). Although the system's immediate future becomes unpredictable when it arrives at the singularity, whichever exit path it follows will lead eventually back to the singularity, giving rise to repeating yet unpredictable dynamics, describable as *chaotic* (2009).

Without specifying the method of re-injection, we can understand very powerfully what this *non-deterministic chaos* represents. Taking *any* two points in the chaotic set, we can find a finite-time trajectory that connects them (see fig. 4). This means any configuration of the system can evolve into any other configuration (within the chaotic set). In a *deterministic* system, chaos arises when all trajectories pass exponentially close to one other given sufficient time. In a *discontinuous* system this is taken to an extreme, so that all trajectories intersect given sufficient time, when they pass through the singularity.

If we approximate the system by something deterministic, which of the possible trajectories through the singularity will persist? In the spirit of deterministic chaos, we expect the singularity to lead to an infinite sensitivity to initial conditions. To investigate its effect on the dynamics let us now give a specific form for the re-injection described above. To the local normal form (3), we must add a nonlinear term that dominates far from the singularity, steering trajectories from the repulsive sticking region, back towards the attractive region.

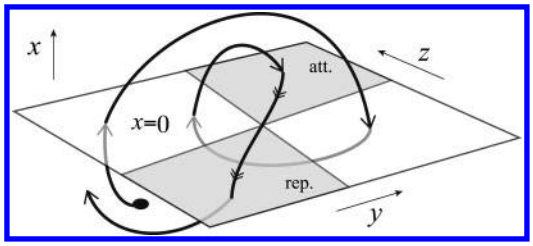


Figure 5. A typical trajectory of (5).

4 ANALYSIS OF A SIMPLIFIED MODEL

The required effect is easily achieved by adding a drift term in the $(0,1,1)$ direction, of strength α, and an attraction term $(0,-y,-z)$ of strength β, for some constants $\alpha,\beta>0$. Multiplying these by $|\mathbf{x}|^2=x^2+y^2+z^2$ ensures they only become significant far from the singularity, and we obtain a model

$$\begin{aligned}\mathbf{f}^+(x,y,z)&=(-y,1,v)+(0,\alpha-\beta y,\alpha-\beta z)|\mathbf{x}|^2\,,\\ \mathbf{f}^-(x,y,z)&=(\ z,w,1)+(0,\alpha-\beta y,\alpha-\beta z)|\mathbf{x}|^2\,.\end{aligned}\quad(5)$$

Any initial condition in a neighbourhood of the origin leads to a trajectory of the form shown in fig. 5.

By simulating this system, respecting crossing and sticking dynamics as described in the previous section, one finds that there exists a region around the origin where all trajectories intersect the origin in forward and backward time.

At the origin, the singularity dictates that no single path can be chosen uniquely from the continuum of possible trajectories. Nor is there any unique way to resolve this ambiguity. The discontinuous model is representative of a range of systems that become extremely sensitive to initial conditions near the singularity. To gain some insight we will smooth out the discontinuity, which restores determinism, and then add noise and hysteresis to the model. We define these models in the rest of this section, then we simulate each of them in sec. 5.

As a preparatory step, we relax the definition of (3) so that the switch takes place over a region $|x|<\varepsilon$, which collapses to a discontinuity at $x=0$ as ε tends to zero. We replace the system (3) with

$$(\dot{x},\dot{y},\dot{z})=\mathbf{f}^{\varepsilon}(x,y,z)\,,\quad(6)$$

for some small $\varepsilon\geq 0$, such that

$$\lim_{\varepsilon\to 0}\mathbf{f}^{\varepsilon}(x,y,z)=\begin{cases}\mathbf{f}^+(y) & \text{if}\quad x>0\,,\\ \mathbf{f}^-(z) & \text{if}\quad x<0\,.\end{cases}\quad(7)$$

This can be achieved by letting $\mathbf{f}^{\varepsilon}$ be a linear combination of $\mathbf{f}^{\pm}$, and considering

$$(\dot{x},\dot{y},\dot{z})=\mathbf{f}^{\varepsilon}=\mathbf{f}^-+(\mathbf{f}^+-\mathbf{f}^-)\phi\quad(8)$$

where (7) places a requirement on ϕ that

$$\phi=\{1\ \text{ for }\ x>+\varepsilon\ \ \&\ \ 0\ \text{ for }\ x<-\varepsilon\}+\mathsf{O}(\varepsilon)\ .\quad(9)$$

4.1 *Smoothing*

A smooth system is now found by letting ϕ be a smooth function $\phi=\phi(x/\varepsilon)$ (e.g. for the simulations to follow, we will mainly consider $\phi=\frac{1}{2}[1+\tanh(x/\varepsilon)]$). Substituting $x=\varepsilon u$ gives

$$(\varepsilon\dot{u},\dot{y},\dot{z})=\mathbf{f}^-(\varepsilon u,y,z)+[\mathbf{f}^+(\varepsilon u,y,z)-\mathbf{f}^-(\varepsilon u,y,z)]\phi(u)\,.$$

The result is a system where u varies on a fast timescale t/ε, while y and z vary on the slow timescale t. For such slow-fast systems, much is known about the correspondence between, for example, Fenichel's slow manifolds (1979), which occupy a region of space where the u component of $\mathbf{f}^-+(\mathbf{f}^+-\mathbf{f}^-)\phi$ vanishes, and the sticking regions which form as $\varepsilon\to 0$ (2007); these are recent but well established developments, so we do not explore them more deeply here.

4.2 *Noise*

A thorough study of how noise distributions propagate in the system is beyond the scope of the present paper. For brevity, we simulate noise in the system (8) by adding a random perturbation of size ε to the state $(x(t),y(t),z(t))$, after each time interval $\Delta t=0.3$. We let $\phi=\frac{1}{2}[1+\tanh(x/\varepsilon)]$.

4.3 *Hysteresis*

To introduce hysteresis to (1), let ϕ be a variable (which adds a dimension to the system), by adding to (8) the equation

$$\varepsilon'\dot{\phi}=\psi([x+\varepsilon(2\phi-1)]/\varepsilon')-\phi\quad(10)$$

where ψ is another function that satisfies

$$\psi=\{1\ \text{ for }\ w>+\varepsilon'\ \ \&\ \ 0\ \text{ for }\ w<-\varepsilon'\}+\mathsf{O}(\varepsilon)'$$

for some small ε'. Then ϕ is attracted (on the fast timescale t/ε') towards $+1$ if $x+\varepsilon(2\phi-1)>\varepsilon'$ and towards 0 if $x+\varepsilon(2\phi-1)<-\varepsilon'$. For the simulations to follow we let $\psi=\frac{1}{2}[1+\tanh(w/\varepsilon')]$ and $\varepsilon'=10\varepsilon$.

One further generalization that will not be considered here (due to space restrictions, and because the effect is in some ways similar to hysteresis), is to consider a delay in the switching function ϕ, for example $\mathbf{f}^{\varepsilon}=\mathbf{f}^-+(\mathbf{f}^+-\mathbf{f}^-)\phi(x(t-\delta)/\varepsilon)$ for some $\delta>0$.

5 SIMULATIONS

The purpose of the simulations below is to demonstrate the sensitivity of the model (5). For a standardized method we solve the ordinary differential equations using the default NDSolve function in Mathematica™. All simulations start from an initial point $(x,y,z)=(0.2,0,-1)$, with $\mathbf{f}^{\pm}$ fixed by parameters $v^+=-1.2$, $v^-=-1.4$, $\alpha=10^{-3}$, $\beta=10^{-5}$, and with stiffness parameter $\varepsilon=10^{-3}$.

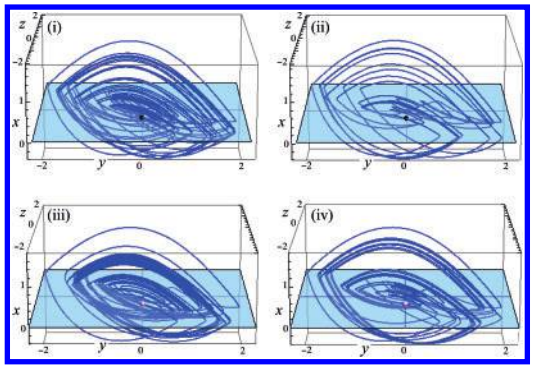


Figure 6. Simulation of: (i) the system in sec. 4.1 for $\phi = \frac{1}{2}[1 + \tanh(x/\varepsilon)]$; (ii) the hysteretic system (10), (iii–iv) the noisy system described in sec. 4.2, showing two separate simulations from the same initial conditions.

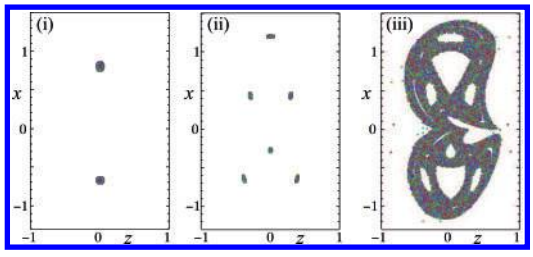


Figure 7. Poincaré sections for the system in sec. 4.1 with $\phi = \frac{1}{2}[1 + \tanh(x/\varepsilon)]$, for different iteration schemes: dividing the trajectory into time intervals (i) 20, (ii) 40, (iii) 100.

Each image in fig. 6 shows a single trajectory, winding around and revisiting the singularity repeatedly over a time $t = 150$. Despite some overall similarity, the detailed shape of the orbits differs markedly, exhibiting less organisation in the basic smoothed model (i) than when hysteresis is applied in (ii), and revealing changes in structure sensitive to random noise in (iii)–(iv).

Given the complexity of the phase space trajectories, more insight is gained by taking a Poincaré section, recording only coordinates where a trajectory passes through the plane $y = 0$. All of the sections below are simulated over a time $t = 2 \times 10^5$, but plotting only the latter half of the trajectory to omit transients.

We first highlight the sensitivity of the system to the method of simulation itself. One could use different numerical iteration schemes with different levels of precision to solve the dynamical system. We show one simple variant in fig. 7, dividing the total trajectory time into fixed intervals that force the adaptive NDSolve function to restart periodically. With this seemingly redundant change, the numerical simulation settles to different attractors (for the same time and initial conditions); we present examples of a periodic orbit, a period three orbit, and the seeming appearance of deterministic chaos.

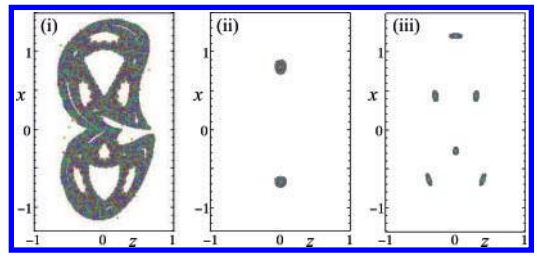


Figure 8. Poincaré sections for the system in sec. 4.1 with $\phi = \frac{1}{2}[1 + \tanh(x/\varepsilon)] + \sigma\sqrt{\varepsilon}e^{-x^2}$ and: (i) $\sigma = 0.01$, (ii) $\sigma = 0.1$, (iii) $\sigma = 0.13$.

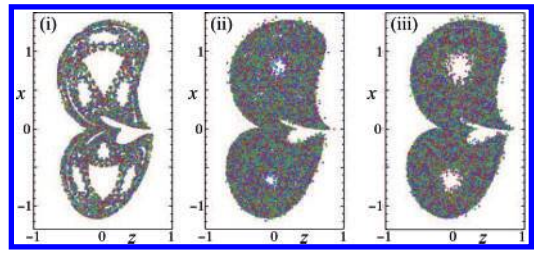


Figure 9. Poincaré sections for the system in sec. 4.1 with $\phi = \frac{1}{2}[1 + \tanh(x/\varepsilon)]$: (i) with hysteresis as described in sec.4.3; (ii) with noise as described in sec. 4.2 for two different runs.

One assumes that a more sophisticated simulation will reveal which result from fig. 7 is correct, but the ambiguity is compounded by other sensitivities in the system, such as the choice of how to smooth out the discontinuity. In fig. 8 we repeat the simulation in fig. 7(iii) using a perturbed smoothing function ϕ, which still tends to sign(x) as $\varepsilon \to 0$; this is no less valid, therefore, as an approximation of the discontinuous system (5). Small changes in the size of this perturbation give different attractors, as before.

Finally, in fig. 9, more physically realistic scenarios are simulated by repeating fig. 7(iii) with hysteresis added in (i) or noise added in (ii–iii).

These various simulations show for the first time the sensitive behaviour associated with non-deterministic chaos. We observe that many different deterministic systems lie close to the discontinuous system. The ambiguity of selecting between outcomes can be attributed to the existence of a non-deterministic singularity in the discontinuous limit, which amplifies even tiny changes in parameters. For some parameters the deterministic system exhibits stable periodic orbits (figs. 7(i–ii) and 8(ii–iii)), while for others the dynamics appears chaotic over some intricate attractor (figs. 7(iii), 8(i), 9(iii)), only some of which is washed out by noise (figs. 9(i–ii)). The important point is that all of these systems differ by only small changes in the defining model. Under these small changes the system jumps between regimes of periodicity or (deterministic) chaos.

6 CLOSING REMARKS

Renewed interest in recent years in a general theory of switching systems relevant to engineering applications, has inspired closer inspection of certain singularities where switching causes extreme sensitivity in a model, modeled dynamically by a breakdown of determinism. In this paper we described a mechanical model that exhibits such behaviour, constructed a toy model to study the phenomenon itself, and simulated its dynamics under relaxations of the model that take account of smoothing, hysteresis, and noise. This revealed unpredictability, partially organised by underlying structure, that survives from such a singularity when the idealization of discontinuity is relaxed.

REFERENCES

Bachar, G., E. Segev, O. Shtempluck, E. Buks, & S. W. Shaw (2010). Noise induced intermittency in a superconducting microwave resonator. *EPL 89*(1), 17003.

Brogliato, B. (1999). *Nonsmooth mechanics – models, dynamics and control*. Springer-Verlag (New York).

Colombo, A., M. di Bernardo, E. Fossas, & M. R. Jeffrey (2010). Teixeira singularities in 3D switched feedback control systems. *Syst.&Contr.Letters 59*(10), 615–622.

Colombo, A. & M. R. Jeffrey (2011). Non-deterministic chaos, and the two-fold singularity in piecewise smooth flows. *SIAM J. App. Dyn. Sys. 10*, 423–451.

Desroches, M. & M. R. Jeffrey (2011). Canards and curvature: nonsmooth approximation by pinching. *Nonlinearity 24*, 1655–1682.

di Bernardo, M., C. J. Budd, A. R. Champneys, & P. Kowalczyk (2008). *Piecewise-Smooth Dynamical Systems: Theory and Applications*. Springer.

Fenichel, N. (1979). Geometric singular perturbation theory. *J. Differ. Equ. 31*, 53–98.

Filippov, A. F. (1988). *Differential Equations with Discontinuous Righthand Sides*. Kluwer Academic Publ.

Jeffrey, M. R. (2011). Non-determinism in the limit of nonsmooth dynamics. *PRL 106*(254103), 1–4.

Jeffrey, M. R. (2013). On the problem of uniqueness in multiple switching dynamics: hierarchy & isonomy. *In draft*.

Jeffrey, M. R., A. R. Champneys, M. di Bernardo, & S. W. Shaw (2010). Catastrophic sliding bifurcations and onset of oscillations in a superconducting resonator. *Phys. Rev. E 81*(1), 016213–22.

Jeffrey, M. R. & A. Colombo (2009). The two-fold singularity of discontinuous vector fields. *SIAM Journal on Applied Dynamical Systems 8*(2), 624–640.

Jeffrey, M. R. & S. J. Hogan (2011). The geometry of generic sliding bifurcations. *SIREV 53*(3), 505–525.

Jeffrey, M. R. & R. Szalai (2013). Non-deterministic dynamics of a mechanical systems. *In draft*.

Kuznetsov, Y. A., S. Rinaldi, & A. Gragnani (2003). One-parameter bifurcations in planar Filippov systems. *Int.J.Bif.Chaos 13*, 2157–2188.

Teixeira, M. A. (1990). Stability conditions for discontinuous vector fields. *J. Differ. Equ. 88*, 15–29.

Teixeira, M. A., J. Llibre, & P. R. da Silva (2007). Regularization of discontinuous vector fields on R3 via singular perturbation. *J.Dyn.Diff.Equat. 19*(2), 309–331.

Research and Applications in Structural Engineering, Mechanics and Computation – Zingoni (Ed.)
© 2013 Taylor & Francis Group, London, ISBN 978-1-138-00061-2

On the dynamics of stacks of rigid blocks

F. Saitta, P. Clemente & D. Rinaldis
ENEA, Rome, Italy

ABSTRACT: The rocking motion of real bodies under external excitation can be often modeled by means of the theory of rigid body dynamics, neglecting the elastic deformations. Several studies paid attention to the dynamics of one block, under deterministic or stochastic excitation, whereas only few works focused on the case of two stacked blocks. In this paper the general problem of stacks with more than two rigid blocks is analyzed, typical of monumental ancient columns made of multiple stone blocks and also of stacks of drums filled with various material. Differing from previous papers, a vector based approach is adopted to write the equations of motion in a straightforward manner. Assuming non sliding rocking, the rotation angles are the Lagrangian parameters appearing in the equations of motion. Taking advantage of the Lagrange equations, the vector equation of motion is derived in a smart way. The impact has been accounted for by means of the conservation of angular momentum. Finally, the model is applied to the evaluation of seismic safety of the stack.

1 INTRODUCTION

Rocking motion of rigid blocks has been the subject of many research works. Indeed, many real structures under various kind of loads can be modeled in such way.

A first study on the subject was due to Housner (1963), which was inspired by the survival of some structure to the Chilean earthquake of May 1960. The work gave attention on the dynamics of the single rigid block and showed how the period of the structure varied with motion amplitude. The analysis of a tall slender block showed a major stability of such structures to earthquakes than expected. The equations of motion were obtained in direct way assuming the tilt angle as Lagrangian coordinate. The block could rotate with a rotation axis located at one base corner. Therefore, the inertia moment relative to that axis was considered in the equations.

A probabilistic approach to the study of the dynamics of a single block was proposed by Facchini et al. (1994). The tilt angle was the only Lagrangian coordinate and the friction coefficient was assumed sufficiently high to prevent the sliding of the block. The distribution of extreme values of the tilt angle of the block was used to investigate the stability of some monuments in Rome.

Zhang & Makris (2001) gave conditions for block overturning under cycloidal pulses, motivated by the similarities of such loads with fault-parallel and fault-normal component of motions recorded near the source of strong earthquakes. Makris & Konstantinidis (2003) gave a detailed comparison between the response of a single degree of freedom oscillator and the rocking response of a rigid block, introducing the concept of rocking spectrum.

Lenci and Rega (2006) introduced the recent developments in nonlinear dynamics to evaluate overturning conditions and charts, characterizing the response in the parameter space. The equations of motion were the same given by Housner. The excitation was periodic and, differing from previous works, the influence of the excitation phase in the block overturning was pointed out.

The slide-rocking behavior of a non-symmetric block was examined by Di Egidio and Contento (2009), with the aim of analyzing the dynamics of statues under seismic and impulsive ground motions. The exact nonlinear equations of motion were written in direct way for the different phases of motion and the rocking block was supposed isolated or not at the base.

A recent attempt to overcome the single block problem was proposed by Spanos et al. (2001), considering a system composed of two stacked blocks. Assuming the hypothesis of non-slide rocking response, the paper established the governing equations of motion for all the involved patterns, so as the impact and transition from a pattern to another. The model was applied for free vibrations or seismic induced motion. Another study on a two-block system was proposed by Kounadis et al. (2012), which discussed conditions for overturning under ground motion with different frequencies. They found that in some case the two-block system is more stable than the single one.

Other works focused their attention on the three-dimensional dynamics of the single block (Chatzis & Smyth 2012; Zulli et al. 2012).

In this paper the study of the dynamics of more than two stacked rigid blocks is shown. The motivation was given by the practice needs of evaluating the seismic stability of overpacks composed by several blocks. In addition, the extension of the analysis of two blocks to the case of several blocks is a complicate task due to the enormous number of patterns involved, which makes difficult the solution of the problem. Thus, a different vector way is chosen to write the equations of motion and the tilt angle with respect to the lower block was chosen as Lagrangian parameter. Assuming non sliding rocking, the angles are the only parameters in the equations of motion. The coordinates of the center of gravity of each block depend only on these tilt angles. Therefore, taking advantage of the Lagrange equations, the vector-form equation of motion is derived in a smart way.

2 ROCKING KINEMATIC OF STACKED RIGID BLOCKS

Consider first a single block as in Fig. 1 and suppose that the block can only rotate around the lower corners. The rotation angle θ is assumed to be positive for counterclockwise rotation. The following vector and matrices are introduced:

$$\boldsymbol{\Omega}_G(\theta)=\begin{bmatrix}\xi_G\\ \eta_G\end{bmatrix};\ \boldsymbol{\Gamma}(\theta)=\begin{bmatrix}sgn(\theta) & 0\\ 0 & 1\end{bmatrix};\ \boldsymbol{v}=-\begin{bmatrix}b\\ 0\end{bmatrix}$$

$$\mathbf{R}(\theta)=\begin{bmatrix}\cos(\theta) & -\sin|\theta|\\ \sin|\theta| & \cos(\theta)\end{bmatrix};\qquad (1a\text{-}g)$$

$$\boldsymbol{w}_G=\begin{bmatrix}b\\ h\end{bmatrix};\ \boldsymbol{w}_T=\begin{bmatrix}b\\ 2h\end{bmatrix};\ \boldsymbol{u}=\begin{bmatrix}0\\ h\end{bmatrix}$$

where $sgn(\bullet)$ is the sign function, $|\cdot|$ is the absolute value, b is the half base of the block, h the half height.

The coordinates in a planar reference system $O\xi\eta$ of the center of gravity are given by the following equation:

$$\boldsymbol{\Omega}_G(\theta)=\boldsymbol{\Gamma}(\theta)\left[\boldsymbol{v}+\mathbf{R}(\theta)\boldsymbol{w}_G\right] \qquad (2)$$

The coordinates of the middle point of the top base, are obtained as follows:

$$\boldsymbol{\Omega}_T(\theta)=\boldsymbol{\Gamma}(\theta)\left[\boldsymbol{v}+\mathbf{R}(\theta)\boldsymbol{w}_T\right] \qquad (3)$$

With some manipulation:

$$\boldsymbol{\Omega}_T(\theta)=\boldsymbol{\Gamma}(\theta)\left[\boldsymbol{v}+\mathbf{R}(\theta)(\boldsymbol{w}_G+\boldsymbol{u})\right]=\boldsymbol{\Omega}_G(\theta)+\mathbf{P}(\theta) \qquad (4)$$

where:

$$\mathbf{P}(\theta)=\boldsymbol{\Gamma}(\theta)\mathbf{R}(\theta)\boldsymbol{u} \qquad (5)$$

In the case of more than one block, Eq. (1) can be applied recursively to derive the coordinates of the centers of gravity of each block. As an example for two blocks (Fig. 2), the coordinates of the centre of gravity of the upper block, with reference to the $T_1\xi\eta$ system, are given by $\boldsymbol{\Omega}_G(\theta_2)$. In the global reference system Oxy, the coordinates are obtained adding the coordinates of T_1 (referred to O) with $\boldsymbol{\Omega}_G(\theta_2)$ multiplied by a rotation matrix $\boldsymbol{\Lambda}(\theta_1)$:

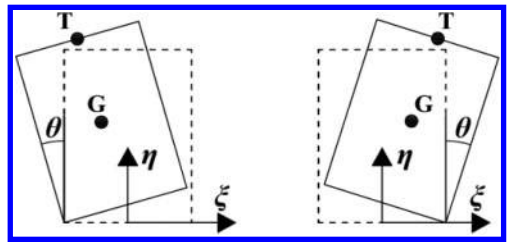


Figure 1. Rocking motion of a single block.

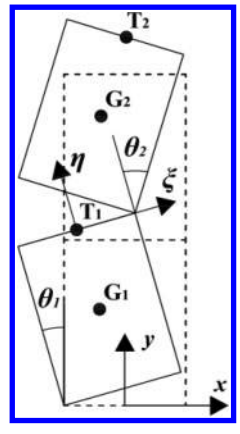


Figure 2. Rocking motion of two blocks.

$$\mathbf{x}_{G_1}(\theta_1)=\boldsymbol{\Omega}_G(\theta_1) \qquad (6)$$

$$\mathbf{x}_{G_2}(\theta_1,\theta_2)=\boldsymbol{\Omega}_T(\theta_1)+\boldsymbol{\Lambda}(\theta_1)\boldsymbol{\Omega}_G(\theta_2) \qquad (7)$$

Taking into account Eq. (4), the latter can be rewritten as follows:

$$\mathbf{x}_{G_2}(\theta_1,\theta_2)=\boldsymbol{\Omega}_G(\theta_1)+\mathbf{P}(\theta_1)+\boldsymbol{\Lambda}(\theta_1)\boldsymbol{\Omega}_G(\theta_2) \qquad (8)$$

In the general case of several blocks, the coordinates of the centre of gravity of the k-th block are given by:

$$\begin{aligned}&\mathbf{x}_{G_k}(\theta_1,\theta_2,..,\theta_k)=\\ &=\mathbf{x}_{T_{k-1}}(\theta_1,\theta_2,..,\theta_{i-1})+\boldsymbol{\Lambda}(\theta_1)..\boldsymbol{\Lambda}(\theta_{k-1})\boldsymbol{\Omega}_G(\theta_k)=\\ &=\sum_{i=1}^{k-1}\left\{\left[\prod_{j=0}^{i-1}\boldsymbol{\Lambda}(\theta_j)\right]\left[\boldsymbol{\Omega}_G(\theta_i)+\mathbf{P}(\theta_i)\right]\right\}+\\ &+\prod_{j=0}^{k}\boldsymbol{\Lambda}(\theta_j)\boldsymbol{\Omega}_G(\theta_k)\end{aligned} \qquad (9)$$

whereas the coordinates of the middle points of the top bases of each block are given by:

$$\mathbf{x}_{\mathrm{T}_k}(\theta_1,\theta_2,..,\theta_k)=\sum_{i=1}^{k}\left\{\left[\prod_{j=0}^{i-1}\mathbf{\Lambda}(\theta_j)\right]\left[\mathbf{\Omega}_{\mathbf{G}}(\theta_i)+\mathbf{P}(\theta_i)\right]\right\} \quad (10)$$

where the assumption $\theta_0 = 0$ has been done.

3 EQUATIONS OF MOTION

In order to derive the equations of motion, the following derivatives with respect to θ are useful:

$$\mathbf{\Omega}_{\mathbf{G}}'(\theta)=\mathbf{\Phi}(\theta)\boldsymbol{w}_G;\quad \mathbf{\Omega}_{\mathbf{T}}'(\theta)=\mathbf{\Phi}(\theta)(\boldsymbol{w}_G+\boldsymbol{u}) \quad (11)$$

$$\mathbf{\Omega}_{\mathbf{G}}''(\theta)=\mathbf{\Psi}(\theta)\boldsymbol{w}_G;\quad \mathbf{\Omega}_{\mathbf{T}}''(\theta)=\mathbf{\Psi}(\theta)(\boldsymbol{w}_G+\boldsymbol{u}) \quad (12)$$

where the following matrices have been introduced:

$$\mathbf{\Phi}(\theta)=\begin{bmatrix}-sgn(\theta)\sin(\theta) & -\cos(\theta)\\ sgn(\theta)\cos(\theta) & -\sin(\theta)\end{bmatrix} \quad (13)$$

$$\mathbf{\Psi}(\theta)=\begin{bmatrix}-sgn(\theta)\cos(\theta) & \sin(\theta)\\ -sgn(\theta)\sin(\theta) & -\cos(\theta)\end{bmatrix} \quad (14)$$

The coordinates of the N blocks can be put into a vector $\mathbf{x}_{\mathbf{G}}$:

$$\mathbf{x}_{\mathbf{G}}=\begin{bmatrix}\mathbf{x}_{\mathbf{G}_1} & \mathbf{x}_{\mathbf{G}_2} & \cdots & \mathbf{x}_{\mathbf{G}_N}\end{bmatrix}^{\mathrm{T}} \quad (15)$$

In order to evaluate the equations of motion the following derivative is necessary:

$$\frac{\partial\mathbf{x}_{\mathbf{G}}}{\partial\boldsymbol{\theta}}=\nabla_{\boldsymbol{\theta}}^{\mathrm{T}}\otimes\mathbf{x}_{\mathbf{G}}=\begin{bmatrix}\frac{\partial\mathbf{x}_{\mathbf{G}_1}}{\partial\theta_1} & \cdots & \frac{\partial\mathbf{x}_{\mathbf{G}_1}}{\partial\theta_N}\\ \vdots & \ddots & \vdots\\ \frac{\partial\mathbf{x}_{\mathbf{G}_N}}{\partial\theta_1} & \cdots & \frac{\partial\mathbf{x}_{\mathbf{G}_N}}{\partial\theta_N}\end{bmatrix} \quad (16)$$

In the previous equation:

$$\nabla_{\boldsymbol{\theta}}^{\mathrm{T}}=\begin{bmatrix}\frac{\partial}{\partial\theta_1} & \cdots & \frac{\partial}{\partial\theta_N}\end{bmatrix} \quad (17)$$

and $\otimes$ is the Kronecker product. The matrix in Eq. (16) is lower triangular, of order $2N \times N$, and can be rewritten as follows:

$$\begin{bmatrix}\mathbf{\Omega}_{\mathbf{G}}'(\theta_1) & 0 & \cdots & 0\\ \mathbf{\Omega}_{\mathbf{G}}'(\theta_1)+\mathbf{P}'(\theta_1)+\mathbf{\Lambda}'(\theta_1)\mathbf{\Omega}_{\mathbf{G}}(\theta_2) & \mathbf{\Lambda}(\theta_1)\mathbf{\Omega}_{\mathbf{G}}'(\theta_2) & & \vdots\\ \vdots & & \ddots & \vdots\\ \mathbf{\Lambda}(\theta_{N-1})\mathbf{\Omega}_{\mathbf{G}}'(\theta_N) & \mathbf{\Lambda}(\theta_1)\left[\mathbf{\Omega}_{\mathbf{G}}'(\theta_2)+\mathbf{P}'(\theta_2)\right] & \cdots & \mathbf{\Lambda}(\theta_{N-1})\mathbf{\Omega}_{\mathbf{G}}'(\theta_N)\end{bmatrix} \quad (18)$$

The second derivative is:

$$\frac{\partial^2\mathbf{x}_{\mathbf{G}}}{\partial\boldsymbol{\theta}^2}=\nabla_{\boldsymbol{\theta}}^{\mathrm{T}}\otimes\left(\nabla_{\boldsymbol{\theta}}^{\mathrm{T}}\otimes\mathbf{x}_{\mathbf{G}}\right)=\nabla_{\boldsymbol{\theta}}^{\mathrm{T}[2]}\otimes\mathbf{x}_{\mathbf{G}}=$$
$$=\begin{bmatrix}\frac{\partial^2}{\partial\theta_1^2} & \cdots & \frac{\partial^2}{\partial\theta_1\partial\theta_N} & \cdots & \frac{\partial^2}{\partial\theta_N\partial\theta_1} & \cdots & \frac{\partial^2}{\partial\theta_N^2}\end{bmatrix}\otimes\mathbf{x}_{\mathbf{G}} \quad (19)$$

In the previous matrix, the first row contains nil values except for the term $\partial^2\mathbf{x}_{\mathbf{G}_i}/\partial\theta_1^2=\Omega_{\mathbf{G}}''(\theta_1)$. The second row contains non nil values for derivatives involving the variables θ_1 and θ_2:

$$\frac{\partial^2\mathbf{x}_{\mathbf{G}_2}}{\partial\theta_1^2}=\mathbf{\Omega}_{\mathbf{G}}''(\theta_1)+\mathbf{P}''(\theta_1)+\mathbf{\Lambda}''(\theta_1)\mathbf{\Omega}_{\mathbf{G}}(\theta_2) \quad (20)$$

$$\frac{\partial^2\mathbf{x}_{\mathbf{G}_2}}{\partial\theta_2^2}=\mathbf{\Lambda}(\theta_1)\mathbf{\Omega}_{\mathbf{G}}''(\theta_2) \quad (21)$$

$$\frac{\partial^2\mathbf{x}_{\mathbf{G}_2}}{\partial\theta_1\partial\theta_2}=\mathbf{\Lambda}'(\theta_1)\mathbf{\Omega}_{\mathbf{G}}'(\theta_2) \quad (22)$$

Other rows can be constructed in the same way. Therefore, most of the elements are nil. The matrix is of order $2N \times N^2$.

The equation of motion can be easily derived applying the Lagrange equations, using the rotations θ_i $(i=1,..,N)$ as coordinates. Therefore, the i-th equations is:

$$\frac{d}{dt}\left(\frac{\partial T}{\partial\dot{\theta}_i}\right)-\frac{\partial T}{\partial\theta_i}+\frac{\partial V}{\partial\theta_i}=0 \quad (23)$$

or in vector form:

$$\frac{d}{dt}\left(\frac{\partial T}{\partial\dot{\boldsymbol{\theta}}}\right)-\frac{\partial T}{\partial\boldsymbol{\theta}}+\frac{\partial V}{\partial\boldsymbol{\theta}}=0 \quad (24)$$

where the kinetic and potential energy are given by:

$$T=\frac{1}{2}\left[\dot{\mathbf{x}}_{\mathbf{G}}^{\mathrm{T}}(\boldsymbol{\theta})\mathbf{M}\dot{\mathbf{x}}_{\mathbf{G}}(\boldsymbol{\theta})+\dot{\boldsymbol{\theta}}^{\mathrm{T}}\mathbf{I}_{\mathbf{G}}\dot{\boldsymbol{\theta}}\right] \quad (25)$$

$$V=g\boldsymbol{\delta}^{T}\mathbf{M}\mathbf{x}_{\mathbf{G}}(\boldsymbol{\theta}) \quad (26)$$

where $\boldsymbol{\delta}$ is a vector composed by N couples $[0,1]^T$.

The derivatives in Eq. (24) are expanded as follows:

$$\frac{\partial T}{\partial\dot{\boldsymbol{\theta}}}=\frac{\partial\dot{\mathbf{x}}_{\mathbf{G}}}{\partial\dot{\boldsymbol{\theta}}}^{\mathrm{T}}\mathbf{M}\dot{\mathbf{x}}_{\mathbf{G}}+\mathbf{I}_{\mathbf{G}}\dot{\boldsymbol{\theta}} \quad (27)$$

$$\frac{\partial V}{\partial\boldsymbol{\theta}}=\mathrm{g}\frac{\partial\mathbf{x}_{\mathbf{G}}}{\partial\boldsymbol{\theta}}^{\mathrm{T}}\mathbf{M}\boldsymbol{\delta} \quad (28)$$

$$\frac{\partial T}{\partial \boldsymbol{\theta}} = \frac{\partial T}{\partial \dot{\mathbf{x}}_G}\frac{\partial \dot{\mathbf{x}}_G}{\partial \boldsymbol{\theta}} = \frac{\partial \dot{\mathbf{x}}_G}{\partial \boldsymbol{\theta}}^{\mathrm{T}} \mathbf{M}\dot{\mathbf{x}}_G \tag{29}$$

By substituting Eqs. (27)–(29) into Eq. (24), and taking into account the chain rule of derivation:

$$\dot{\mathbf{x}}_G = \frac{\partial \mathbf{x}_G}{\partial \boldsymbol{\theta}}\dot{\boldsymbol{\theta}} \tag{30}$$

with some manipulation the equation of motion in vector form is obtained:

$$\begin{aligned}\left(\mathbf{I}\otimes\dot{\boldsymbol{\theta}}\right)^{\mathrm{T}}\left(\nabla_{\boldsymbol{\theta}}^{\mathrm{T}[2]}\otimes\mathbf{x}_G\right)^{\mathrm{T}}\mathbf{M}\frac{\partial \mathbf{x}_G}{\partial \boldsymbol{\theta}}\dot{\boldsymbol{\theta}} + \frac{\partial \mathbf{x}_G}{\partial \boldsymbol{\theta}}^{\mathrm{T}}\mathbf{M}\frac{\partial \mathbf{x}_G}{\partial \boldsymbol{\theta}}\ddot{\boldsymbol{\theta}} + \\ + \mathbf{I}_G\ddot{\boldsymbol{\theta}} + \mathrm{g}\frac{\partial \mathbf{x}_G}{\partial \boldsymbol{\theta}}^{\mathrm{T}}\mathbf{M}\boldsymbol{\delta} = 0\end{aligned} \tag{31}$$

where the following equality has been considered:

$$\nabla_{\boldsymbol{\theta}}^{\mathrm{T}}\otimes\left(\frac{\partial \mathbf{x}_G}{\partial \boldsymbol{\theta}}\dot{\boldsymbol{\theta}}\right) = \left(\nabla_{\boldsymbol{\theta}}^{\mathrm{T}[2]}\otimes\mathbf{x}_G\right)\left(\mathbf{I}\otimes\dot{\boldsymbol{\theta}}\right) \tag{32}$$

and $\mathbf{I}$ is the identity matrix of order N

The following $N \times N$ matrices are introduced:

$$\boldsymbol{\mu}(\boldsymbol{\theta}) = \frac{\partial \mathbf{x}_G}{\partial \boldsymbol{\theta}}^{\mathrm{T}}\mathbf{M}\frac{\partial \mathbf{x}_G}{\partial \boldsymbol{\theta}} + \mathbf{I}_G \tag{33}$$

$$\boldsymbol{\gamma}(\boldsymbol{\theta},\dot{\boldsymbol{\theta}}) = \left(\mathbf{I}\otimes\dot{\boldsymbol{\theta}}\right)^{\mathrm{T}}\left(\nabla_{\boldsymbol{\theta}}^{\mathrm{T}[2]}\otimes\mathbf{x}_G\right)^{\mathrm{T}}\mathbf{M}\frac{\partial \mathbf{x}_G}{\partial \boldsymbol{\theta}}\dot{\boldsymbol{\theta}} \tag{34}$$

The moment due to the weight of the blocks gives the following vector:

$$\boldsymbol{\rho}(\boldsymbol{\theta}) = \mathrm{g}\frac{\partial \mathbf{x}_G}{\partial \boldsymbol{\theta}}^{\mathrm{T}}\mathbf{M}\boldsymbol{\delta} \tag{35}$$

Finally, the equation of motion is rewritten in a more concise form:

$$\boldsymbol{\mu}(\boldsymbol{\theta})\ddot{\boldsymbol{\theta}} + \boldsymbol{\gamma}(\boldsymbol{\theta},\dot{\boldsymbol{\theta}}) + \boldsymbol{\rho}(\boldsymbol{\theta}) = \mathbf{0} \tag{36}$$

In first order form:

$$\dot{\boldsymbol{\Theta}} = \mathbf{A}(\boldsymbol{\Theta}) + \mathbf{v}(\boldsymbol{\Theta}) \tag{37}$$

where the following quantities are introduced:

$$\boldsymbol{\Theta} = \begin{bmatrix}\boldsymbol{\theta}\\ \dot{\boldsymbol{\theta}}\end{bmatrix};\ \mathbf{A}(\boldsymbol{\Theta}) = \begin{bmatrix}\dot{\boldsymbol{\theta}}\\ -\boldsymbol{\mu}^{-1}(\boldsymbol{\theta})\boldsymbol{\gamma}(\boldsymbol{\theta},\dot{\boldsymbol{\theta}})\end{bmatrix} \tag{38}$$

$$\mathbf{v}(\boldsymbol{\Theta}) = \begin{bmatrix}\mathbf{0}\\ -\boldsymbol{\mu}^{-1}(\boldsymbol{\theta})\boldsymbol{\rho}(\boldsymbol{\theta})\end{bmatrix} \tag{39}$$

This equation is solved numerically by means of the Runge-Kutta method, accounting for the conservation of the angular momentum during impact between blocks as will be shown in section 5.

4 GENERALIZED FORCES

In the framework of the Lagrange method, forces acting on the system allow to derive generalized forces β_h related with Lagrangian coordinates θ_h:

$$\beta_h = \sum_{i=1}^{N}\mathbf{F}_i^T\frac{\partial \mathbf{x}_{G_i}}{\partial \theta_h} \tag{40}$$

Assuming that the only forces are inertial due to ground motion, with some manipulation, the vector of N generalized forces can be written as follows:

$$\boldsymbol{\beta}(\boldsymbol{\theta},t) = -\left(\frac{\partial \mathbf{x}_G}{\partial \boldsymbol{\theta}}\right)^T\mathbf{M}\boldsymbol{\tau}\ddot{u}_g(t) \tag{41}$$

where $\boldsymbol{\tau}$ is a vector composed by N couples $[1, 0]^{\mathrm{T}}$.

In first order form, the vector to be added to the second member of Eq. (37) to derive the forced equation of motion is:

$$\mathbf{Q}(\boldsymbol{\Theta},t) = \begin{bmatrix}\mathbf{0}\\ \boldsymbol{\mu}^{-1}(\boldsymbol{\theta})\boldsymbol{\beta}(\boldsymbol{\theta},t)\end{bmatrix} \tag{42}$$

5 IMPACT BETWEEN BLOCKS

The variation of angular velocity of each block is accounted for by the conservation of the angular momentum, which can be written as the sum of two contributes, one due to the motion of the center of mass and a second contribute due to the instantaneous rotation with respect to the center of mass.

Given n blocks, the involved patterns are $3^n - 1$. Therefore, at each time step, the vector $sign(\boldsymbol{\theta})$ establishes the current pattern. When an impact occurs the system can switch to another pattern, characterized by a vector $\boldsymbol{\theta}$ with: *i*) a sign variation at the component related with the impact point; *ii)* the same sign as before impact; *iii)* the blocks remain in contact after impact.

The total angular momentum of the system with respect to a generic pole O is written as follows:

$$K_O = \sum_{i=1}^{N}\mathrm{K}_O^{(i)} = \sum_{i=1}^{N}I_{Gi}\dot{\psi}_i + \left[OG_i\times m_i\dot{\mathbf{X}}_{G_i}\right]_3 \tag{43}$$

In the previous equation $\mathbf{X}_{G_i} = [\mathbf{x}_{G_i}, 0]^T$ is the three-component vector of the coordinates of the center of mass, the pedix 3 indicates the third component, ψ_i is the tilt angle of the i-th block with respect to the vertical, related with θ_i as follows:

$$\psi_1 = \theta_1;\quad \psi_2 = \theta_1 + \theta_2;\quad \psi_3 = \theta_1 + \theta_2 + \theta_3\ \ldots\ldots \tag{44}$$

Obviously, N equations are necessary to obtain the N velocities. They can be derived by the imposition of the conservation of the angular momentum, before and after the impact, for the whole system with respect

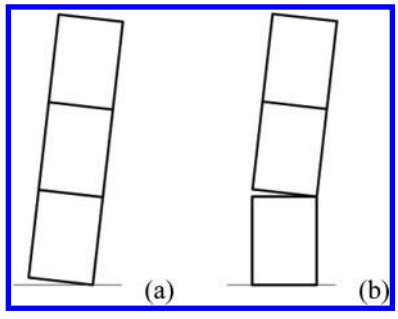


Figure 3. Initial conditions for the free rocking examples.

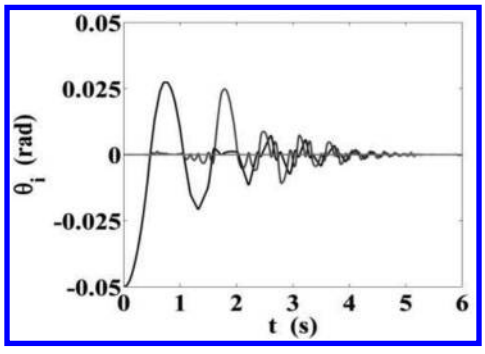


Figure 4. Tilt angle versus time for the three blocks: (Gray-level: Block 1 = Black; Block 2 = Dark gray; Block 3 = Light gray).

to the base vertex which is the center of rotation of the base block, if the block is rocking. Another equation can be written for the $N-1$ top blocks with respect to the vertex of the base of second block, if the block is rocking, and so on. At the level of impact, the pole of the momentum could switch to the other vertex or eventually the two blocks could remain in contact and behave as a single block. In this latter case the equations necessary become $N-1$ The assumed hypotheses are equivalent to those given in Spanos et al. (2001).

6 APPLICATIONS

A three-block pile is considered in the first application. The blocks have the following characteristics: $b_i = 0.440$ m and $h_i = 0.545$ m ($i = 1, \ldots, 3$). The mass of each block is $m_i = 1000$ kg and the inertia moment is $I_{Gi} = 292.61$ kgm^2.

The free oscillations with the initial conditions $\theta_{1,0} = -0.05$ rad (Fig. 3a), all the other rotations and velocities being zero, have been studied, using a time step of 0.001 sec in the numerical integration. In Fig. 4 the response is plotted, using decaying gray levels from the lower to top block. Fig. 5 reports the response in the phase plane. Shifts in velocity after impacts ($\theta = 0$) can be observed. In this case, after the first impact, the two top blocks start rocking approximately together.

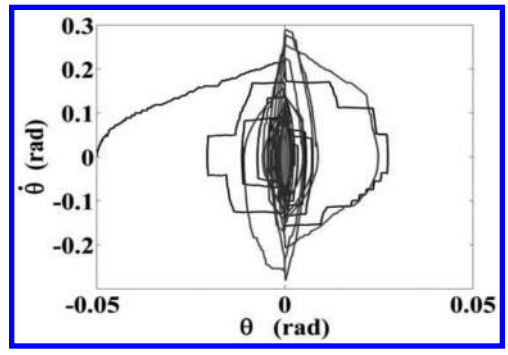


Figure 5. Response in the phase plane for free rocking with $\theta_{1,0} = -0.05$ rad.

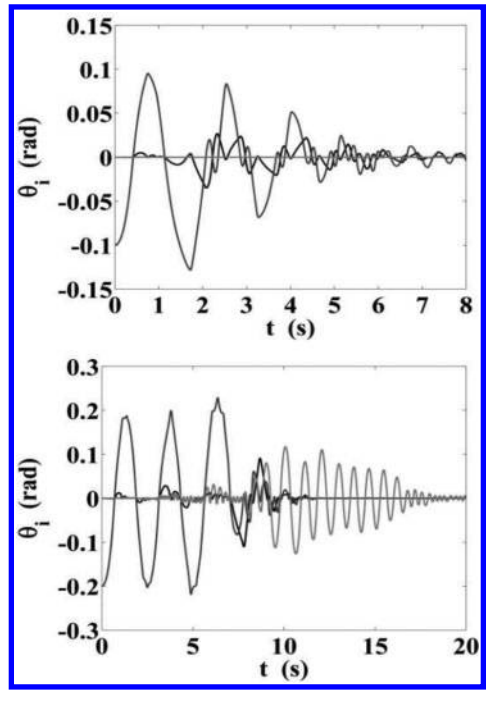


Figure 6. Tilt angle versus time for the three blocks: a) $\theta_{2,0} = -0.1$ rad; b) $\theta_{2,0} = -0.2$ rad.

In another example (Fig. 3b) the two cases of initial conditions $\theta_{2,0} = -0.1$ rad or $\theta_{2,0} = -0.2$ rad all the other rotations and velocities being zero, have been considered. The results are plotted in Figs. 6a and 7a and in Figs. 6b and 7b, respectively.

In this second example, jumps in velocity during impacts are more evident. Fig. 6a shows clearly changes in velocity of the top blocks due to impacts of the lower block with ground.

Finally, the analysis of a five-blocks system under seismic action has been considered. The base excitation, horizontally directed, is given by the N-S component of the 1940 El Centro earthquake (Fig. 8). The geometrical and mechanical characteristics of the blocks are the same used in the previous examples.

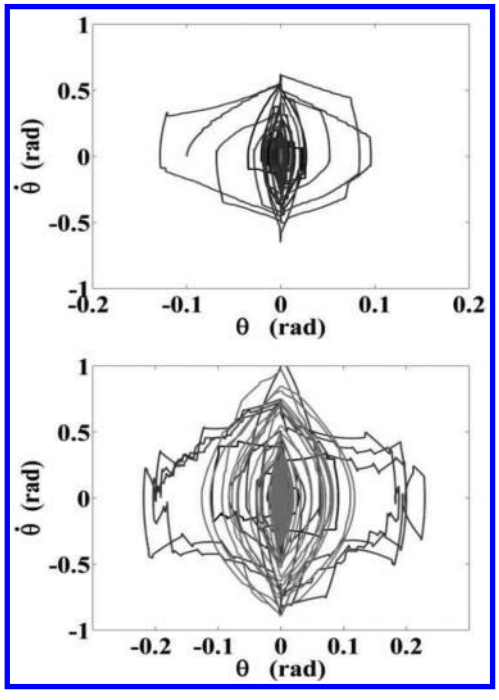


Figure 7. Response in the phase plane: a) $\theta_{2,0} = -0.1$ rad; b) $\theta_{2,0} = -0.2$ rad.

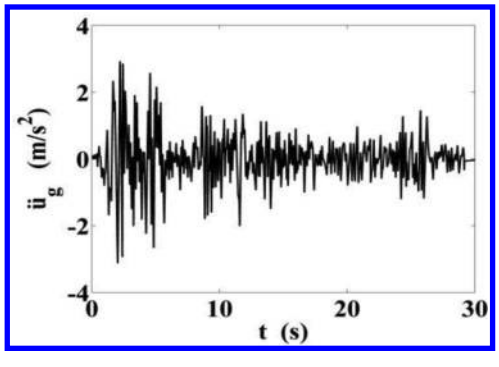


Figure 8. N-S component of El Centro earthquake.

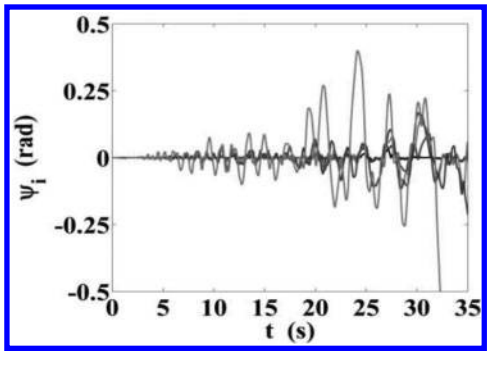


Figure 9. Time histories of tilt angles, with respect to the vertical, for the five blocks under seismic excitation.

Fig. 9 shows the time history of the tilt angles ψ_i. The system rocks with increasing amplitude for the whole event. Only at about 32 s, when the forcing action stops, the top block overturns.

7 CONCLUSIONS

A vector method for the rocking analysis of multiple block systems has been proposed in the paper. The method allows writing the equations of motion easily. Indeed, methods present in the literature, dealing with one or two blocks, becomes burdensome in these cases from a computational point of view. In order to show the suitability of the method in solving practical problems, some applications have been presented, with reference to free rocking response under imposed initial rotation or under seismic-induced motion. The first results are promising. Further verification would be necessary in order to check the accuracy and reliability of the procedure in practical applications. Besides, based on real materials behavior, more dissipative models for impact could be implemented and verified on the basis of experimental analysis. Furthermore, the method can be extended to three-dimensional cases.

REFERENCES

Chatzis, M.N. & Smyth A.W. 2012. Modeling of the 3D rocking problem. *International Journal of Non-Linear Mechanics* 47(4): 85–98.

Di Egidio, A. & Contento A. 2009. Base isolation of slide-rocking non-symmetric rigid blocks under impulsive and seismic excitations. *Engineering Structures* 31(11): 2723–2734.

Facchini L., Gusella V. & Spinelli P. 1994. Block random rocking and seismic vulnerability estimation. *Engineering Structures* 16(6): 412–424.

Housner, G.W. 1963. The behavior of inverted pendulum structures during earthquakes. *Bulletin of the Seismological Society of America* 53(2): 403–417.

Kounadis, A.N., Papadopoulos G.J. & Cotsovos, D.M. 2012. Overturning instability of a two-rigid block system under ground excitation. *ZAMM – Journal of Applied Mathematics and Mechanics* 92(7): 536–557.

Lenci, S. & Rega, G. 2006. A dynamical systems approach to the overturning of rocking blocks. *Chaos, Solitons and Fractals* 28(2): 527–542.

Makris, N. & Konstantinidis, D. 2003. The rocking spectrum and the limitations of practical design methodologies. *Earthquake Engineering and Structural Dynamics* 32(2): 265–289.

Spanos, P.D., Roussis, P. C. & Politis N.P.A. 2001. Dynamic analysis of stacked rigid blocks. *Soil Dynamics and Earthquake Engineering* 21(7): 559–578.

Zhang, J. & Makris, N. 2001. Rocking Response of Free-Standing Blocks Under Cycloidal Pulses. *Journal of Engineering Mechanics* 127(5): 473–483.

Zulli, D., Contento, A. & Di Egidio, A. 2012. 3D model of rigid block with a rectangular base subject to pulse-type excitation. *International Journal of Non-Linear Mechanics* 47(6): 679–687.

Research and Applications in Structural Engineering, Mechanics and Computation – Zingoni (Ed.)
© 2013 Taylor & Francis Group, London, ISBN 978-1-138-00061-2

Numerical bifurcation analysis of an impact oscillator with drift

J. Páez Chávez
Centre for Applied Dynamics Research (CADR), School of Engineering, University of Aberdeen, Aberdeen, UK
Facultad de Ciencias Naturales y Matemáticas, Escuela Superior Politécnica del Litoral, Guayaquil, Ecuador

M. Wiercigroch & E.E. Pavlovskaia
Centre for Applied Dynamics Research (CADR), School of Engineering, University of Aberdeen, Aberdeen, UK

ABSTRACT: Mechanical systems with impacting components have received considerable attention in the past due to their wide engineering applications. In this work, we study numerically a physical model that accounts for viscoelastic impacts and is able to reproduce the effect of the vertical progression (drift) observed e.g. in drilling applications (Pavlovskaia et al. 2001). The model is comprised of a harmonically excited mass simulating the penetrating part of the system and a viscoelastic slider, which represents the soil resistance. During operation, the system can move downwards in stick-slip phases, resulting in complex dynamical behaviour, which includes fold, period-doubling and grazing bifurcation of periodic orbits, as well as chaotic motion. The present work extends the previous investigations undertaken by the CADR within Aberdeen University (Pavlovskaia et al. 2001, Pavlovskaia and Wiercigroch 2007) to gain an insight into the bifurcation structure of the underlying system. Specifically, the system is analyzed numerically by means of the software TC-HAT, a toolbox of AUTO 97 allowing numerical continuation and bifurcation detection of periodic orbits in non-smooth dynamical systems.

1 PHYSICAL MODEL

In Fig. 1, we present a physical model describing the interaction between a harmonically forced impactor of mass m which collides with a medium modelled as a viscoelastic slider (Pavlovskaia et al. 2001).

Systems of this type are often described by piecewise smooth ODEs, due to the presence of non-smooth or discontinuous phenomena in the physical model. This results in fascinating and complex dynamical behaviour, ranging from various periodic responses to chaotic motion (Pavlovskaia et al. 2001). The equations of motion of the system can be given in compact form as follows (cf. (Pavlovskaia and Wiercigroch 2007)):

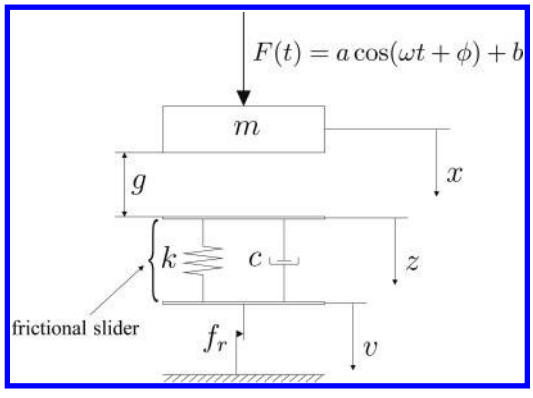


Figure 1. Physical model of a viscoelastic impact oscillator, with the dimensionless parameters $m = 1$, $c = 2\xi$, $k = 1$ and $f_r = 1$.

$$p' = y - P_1 P_3 \left(y + \frac{1}{2\xi}(q-1) \right), \tag{1}$$

$$\begin{aligned}
y' &= a\cos(s+\phi) + b - P_1 P_2 (1-P_3)(2\xi y + q) - P_1 P_3, \\
q' &= -\frac{1}{2\xi} q + P_1 P_2 (1-P_3) \left(y + \frac{1}{2\xi} q \right) + \frac{P_1 P_3}{2\xi}, \\
v' &= \left(y + \frac{1}{2\xi}(q-1) \right) P_1 P_3, \\
s' &= \omega,
\end{aligned}$$

with $P_1 := H(p-q-g)$, $P_2 := H(2\xi y + q)$ and $P_3 := H(2\xi y + q - 1)$, where $H(\cdot)$ stands for the Heaviside step function. In (1), the linear transformation $p = x - v$, $q = z - v$ has been introduced in order to decouple the periodic component of the system response captured by the variables (p, y, q) from the vertical progression v.

In our numerical study, we will consider a periodic solution $(p(t), y(t), q(t))$ of (1) of period $T > 0$ and we introduce the average rate of vertical progression (ROP) as solution measure, which is defined as

$$\text{ROP} := \frac{1}{T} \int_0^T \left(y(t) + \frac{1}{2\xi}(q(t)-1) \right) P_1 P_3 \, dt.$$

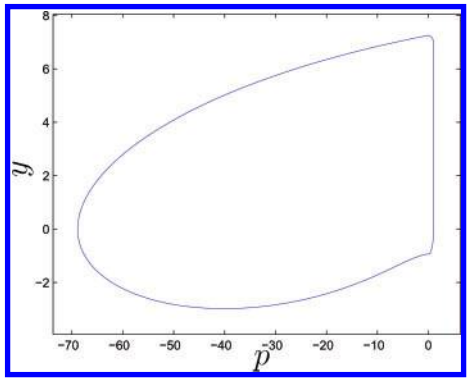


Figure 2. Initial periodic orbit of (1) for the parameter values $a = 0.3$, $\omega = 0.1$, $\xi = 0.05$, $b = 0.15$, $g = 0.02$ and $\phi = 0$.

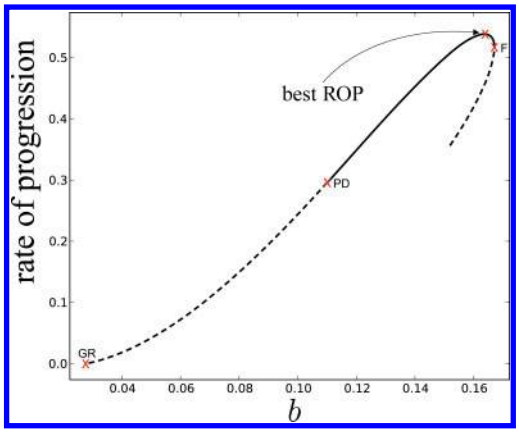


Figure 3. Numerical continuation of the periodic orbit shown in Fig. 2 with respect to the static force b. Dashed and solid segments denote unstable and stable periodic solutions, respectively.

This measure will allow us to monitor the efficiency of the periodic solution under the change of the external loading parameters, i.e. dynamic amplitude a, static force b and excitation frequency ω.

2 MAIN RESULTS

The previous analysis (Pavlovskaia et al. 2001) has shown that the best ROP is obtained when the system response is periodic and the frequency of the response is the same as the frequency of external excitation. Therefore we will concentrate on studying numerically this type of periodic response and its typical trajectory is depicted in Fig. 2. The results presented in this section are obtained by performing the numerical continuation of the period-1 orbit via TC-HAT (Thota & Dankowicz 2008), taking the ROP as solution measure and a, b and ω as the main bifurcation parameters.

In Figs. 3, 4 and 5, we can observe the dependance of the ROP on the control parameters b, a and ω, respectively. Here, the main role played by the parameters in the system can be identified, i.e., stability control of

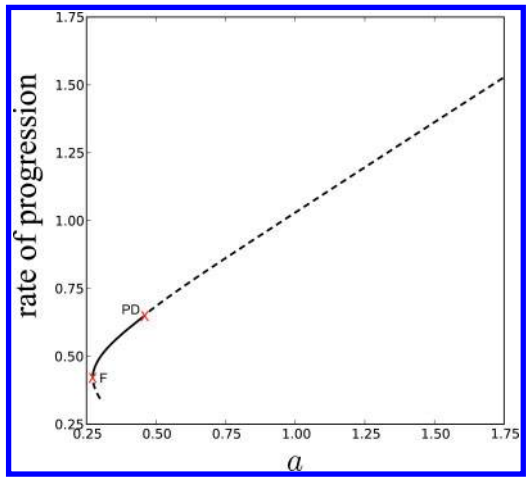


Figure 4. Continuation of the period-1 motion shown in Fig. 2 with respect to a.

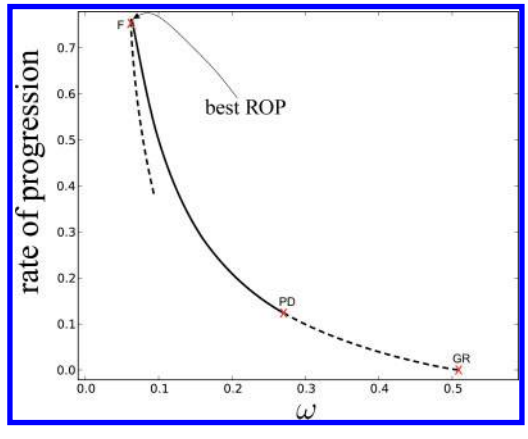


Figure 5. 1-parameter continuation of the periodic orbit shown in Fig. 2 with respect to the frequency of external excitation ω.

the period-1 motion and ROP adjustment. The stability windows are limited by fold and period-doubling bifurcations, while the ROP becomes zero at a grazing bifurcation. The present study thus provides accurate calculations for determining the stability windows as well as choosing the optimal penetration rates. This analysis may provide fundamental insight for designing and tuning control systems in various engineering applications.

REFERENCES

Pavlovskaia, E. E., M. Wiercigroch, & C. Grebogi (2001). Modeling of an impact system with a drift. *Physical Review E 64*(5).

Pavlovskaia, E. E. & M. Wiercigroch (2007). Low-dimensional maps for piecewise smooth oscillators. *Journal of Sound and Vibration 305*(4), 750–771.

Thota, P. & H. Dankowicz (2008). TC-HAT: A Novel Toolbox for the Continuation of Periodic Trajectories in Hybrid Dynamical Systems. *SIAM J. Appl. Dyn. Sys. 7*(4), 1283–1322.

5. Seismic response, seismic analysis, earthquake-resistant design

Research and Applications in Structural Engineering, Mechanics and Computation – Zingoni (Ed.)
© 2013 Taylor & Francis Group, London, ISBN 978-1-138-00061-2

Seismic behaviour and earthquake resistant design of long period structures

A. Astaneh-Asl
University of California, Berkeley, California, USA

ABSTRACT: The studies summarized in this paper focus on the effects of *far-field* ground motions on the response of long period structures such as long span bridges and tall buildings. In the studies two long span suspension bridges and two tall office buildings, with their fundamental period ranging from 5.9 to 17.5 seconds were subjected to a strong near field and a relatively weak far field ground motions and their response were studied. All structures were steel structures. The research indicated that the force and displacement response of these long period structures to far field, but weak ground motion were far greater than the response of the same structures to much stronger ground motion recorded close to the epicenter. The main parameter affecting the response was the long dominant period of vibration for far field motions being close to or longer than the fundamental period of vibration of the structures.

1 INTRODUCTION

Long period structures, such as long span bridges and tall buildings, are sensitive to long period content of the ground motion. Two characteristics of ground motion affect the response of long period structures the most. These are: (1) the *near field* velocity pulse, and (2) the long period component of *far-field* strong motions.

The first phenomenon, the *near field* velocity pulse, results in permanent displacement at the site of structures located near the ruptured fault. Ground motions with such permanent displacements cause larger force and displacement response in the structure than the ground motions that are base corrected and have a zero permanent displacement after the motion stops (McCallen et al, 2009).

The subject of the remainder of this paper is the second phenomenon, the *far-field* long period ground motions, arriving at the site of a long period bridge or building.

Long span bridges and tall buildings have relatively long fundamental period of vibration in the range of 3–20 seconds and sensitivity to ground motions with dominant long periods. The objective of this study was to investigate dynamic response of actual tall buildings and long span bridges with relatively long fundamental period of vibration to ground motions with dominant long period.

In the main study, a total of 12 steel buildings and bridge structures with their fundamental period ranging from three to 17.5 were subjected to two different ground motions, one a strong ground motion recorded relatively close to epicenter and the other a relatively weak motion recorded at a far-field distance from the epicenter. Later, Section 4 provides more details on the ground motions.

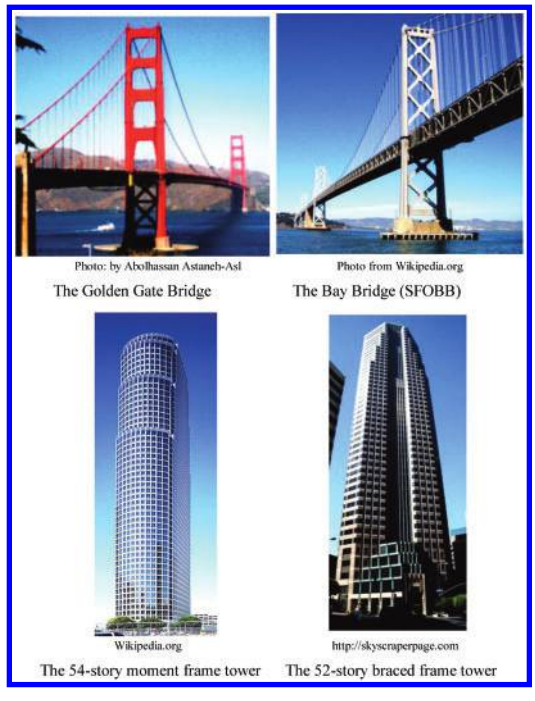


Figure 1. The four structures studied.

Figure 1 shows four of the 12 study structures summarized in this paper. They are the Golden Gate Bridge and the San Francisco Oakland Bay Bridge in the San Francisco Bay, and the 54-story moment frame and the 52-story braced frame towers in Los Angeles. For full report of studies of these four structures see Over,

Astaneh-Asl and Dreger (2010), Naeem and Astaneh-Asl (2012), Fan and Astaneh-Asl (2013), Zajac and Astaneh-Asl (2013), Leung and Astaneh-Asl, (2013) and Chen and Astaneh-Asl (2013.)

2 OBSERVATIONS DURING ACTUAL EARTHQUAKES

Far field long period ground motions and their effects on the structures have been recognized and studied since the 1960's. According to Koketsu and Miyake (2008), the far field long period, ground motions were first found in the seismograms of the 1968 Tokachi-oki and the 1966 Parkfield earthquakes.

Adnani, Marto and Hendriyawan, (2004) studied seismological effects of the far field ground motions obtained from the 2002 Sumatra, Mw = 7.4, earthquake on the peninsular Malaysia. According to the results, acceleration at the bedrock had been amplified about 2 to 7 times at the surface of Penang and Kuala Lumpur.

Observations on actual seismic performance of long span bridges and tall buildings located relatively far from the epicenter also points to the effects of far field long period ground motions. As an example, on August 23, 2011 a magnitude $M_w = 5.8$ earthquake with a focal depth of 6 km occurred in the US State of Virginia (USGS, 2013) and (Horton Jr. 2012). Although not very large quake, it resulted in damage to the Washington Monument, which is a 170 m tall structure located about 130 km from the epicenter. The reported damage was primarily in the form of cracks in the stones near the top of the monument. The monument has been closed since the quake, expected to open after three years of repair and retrofit efforts.

3 FAR FIELD GROUND MOTIONS

When a fault ruptures, the shock waves emanating from the ruptured fault particularly the surface waves while travelling through the ground loose their short period components and become a long period motion. During the travel, while the period of vibration is elongating the maximum peak ground accelerations decrease and the duration increase.

When long period surface waves arrive at the site of a structure, with fundamental period of vibration close to the dominant period of vibration of the ground motion, there will be resonance and the response of the structure to such ground motions can be quite significant even when the maximum peak ground acceleration can be quite small.

4 GROUND MOTIONS USED IN THE STUDY

Two ground motions recorded during past earthquakes were used in the studies. One ground motion representing the strong near field and relatively short period

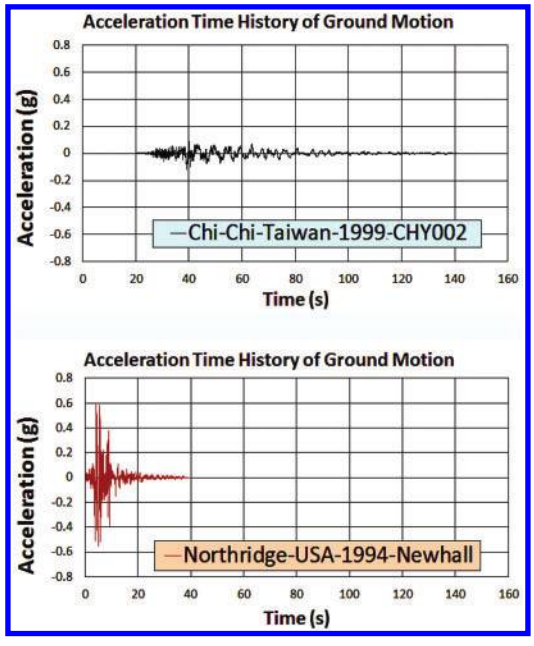


Figure 2. Time history of acceleration for N-S component of the ground motions used in the study.

motions, was the Newhall record obtained during the 1994 Northridge, California earthquake. The other was the CHY002 record of the 1999 Chi-Chi Taiwan earthquake representing relatively weak (small MPGA), far field and long period earthquakes. Figure 2 shows time history of acceleration for the N-S component of these two earthquakes. The other two components had similar features (Taing and Astaneh-Asl, 2013).

These two ground motions have profound differences. The Chi-Chi CHY002 ground motion (Figure 2, top) has relatively long duration of about 140 seconds while the Northridge Newhall ground motion has only 40 seconds durations. The maximum peak ground acceleration for the Northridge Newhall ground motion is about 0.60 g, while for the Chi-Chi CHY002 motions it is very small and only 0.08 g. The dominant period for the Northridge Newhall ground motion is about 2.5 seconds and for the Chi-Chi CHY002 ground motions it is about 6 seconds.

5 ANALYTICAL MODELS

In these studies the structural analysis software SAP2000 (CSI, 2013) was used to subject a 3-D elastic model of each long span bridge or tall building to three components of ground motions of the 1994 Northridge-Newhall and the 1999 Chi-Chi-CHY002 earthquakes. In the previous section, we discussed the ground motions. Since in all structures the response remained elastic, there was no need to introduce nonlinear member or connection elements in the models.

The main objective was to investigate the response of two existing long span bridges and two tall buildings

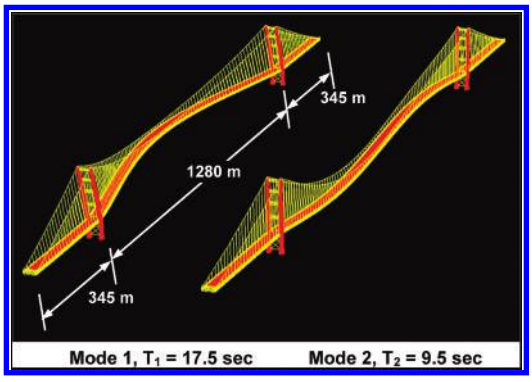


Figure 3. Two higher modes of the Golden Gate Bridge.

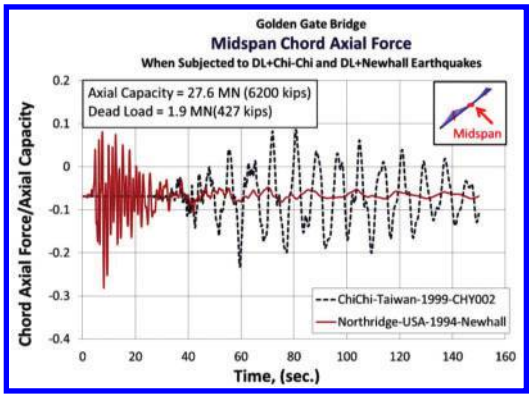


Figure 4. Time history of axial load in the midspan truss chords (Leung and Astaneh-Asl, 2013).

designed according to the governing design codes, to two different earthquake ground motions, one strong and near field and the other relatively weak but emanating from far field sources.

6 THE RESULTS

6.1 *The Golden Gate Bridge results*

The Golden Gate Bridge opened to traffic in 1937. Figure 3 shows the span lengths along with two highest mode shapes and periods of vibration. The seismic design of original bridge was based on 10%g horizontal acceleration acting on the mass. Since the 1989 Loma Prieta earthquake during which this bridge had only minor damage to its expansion joints, the entire bridge has been undergoing major seismic retrofit.

The Chi-Chi CHY002 ground motions with maximum peak acceleration of 0.08 g created almost the same axial forces in the stiffening truss chords for almost the same number of cycles that the Northridge Newhall ground motions with MPGA of 0.60 g produced, Figure 4.

Figure 5 shows midspan transverse displacements. For the strong near field Northridge Newhall motions, transverse displacements were relatively small and

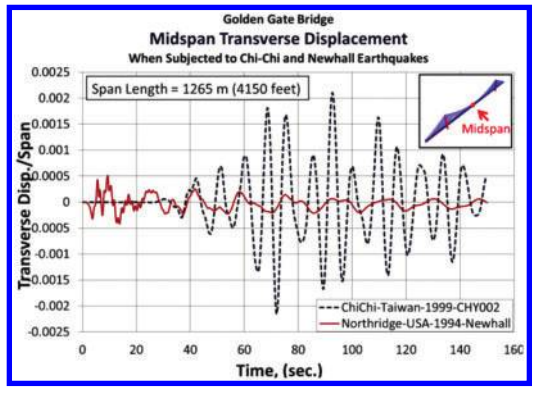


Figure 5. Time history of transverse displacement of the deck.

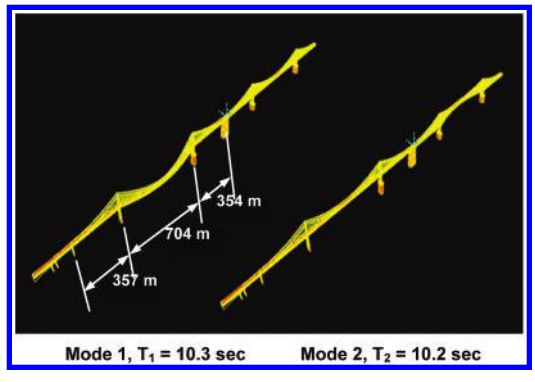


Figure 6. Two higher modes of the San Francisco Oakland Bay Bridge.

only for four cycles, Figure 5. For Chi-Chi CHY002 ground motions, transverse displacements were more than five times larger than the ones for Newhall ground motions and the number of cycles was quite large for Chi-Chi CHY002 motion.

6.2 *The San Francisco-Oakland Bay Bridge results*

The San Francisco-Oakland Bay Bridge opened to traffic in 1936. It was designed for a horizontal seismic force of 10% of its weight. Figure 6 shows the structural model used in the studies and higher modes of vibrations for the bridge as well as span length. The bridge is a double deck structure.

The longitudinal displacement response to the Northridge Newhall ground motion generated a maximum peak displacement of 0.0075 times the span length, while the maximum displacement for Chi-Chi CHY002 ground motion was 0.0063 times the span length, Figure 7. However, the number of large cycles generated by the Northridge Newhall case was only 3 while the Chi-Chi ground motion generated more than 20 displacement cycles. The large number of cycles in longitudinal direction is significant since the dampers placed between the stiffening trusses and the towers to control longitudinal motions are more effective for

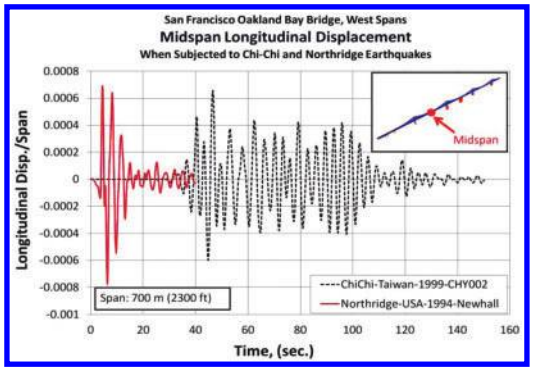


Figure 7. Time history of longitudinal displacement of the deck of the San Francisco Oakland Bay Bridge at midspan.

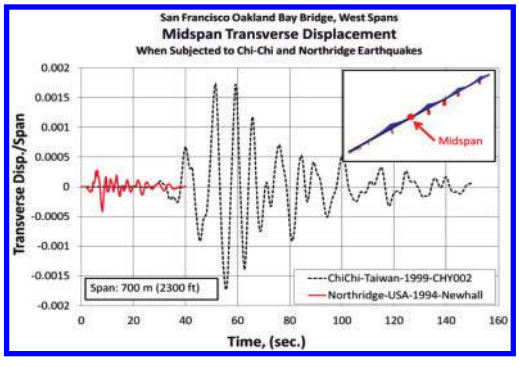


Figure 8. Time history of transverse displacement of the of the San Francisco Oakland Bay Bridge at midspan.

Chi-Chi ground motion with large number of displacement reversal cycles than for the Northridge motion with relatively small number of load reversal.

Figures 8 shows transverse displacement of the deck at midspan of the west main span. The transverse response to the much weaker ground motion of Chi-Chi was considerably greater than the response to much stronger ground motion of the Northridge earthquake.

More importantly, the maximum transverse displacement at midspan for Chi-Chi earthquake being 0.0017 times the span length, would most likely cause damage in the expansion joint while the almost negligible transverse displacements due to the Northridge ground motions would not cause any consequential damage.

6.3 *The 54-story steel moment frame tower results*

The 54-story moment frame structure is in Los Angeles built in 1990 as an office building. The tower height is about 214 m. The lateral force resisting system consists of perimeter tubular Special Moment Frames. Figure 9 shows a view of the tower and mode shapes one and three.

The building is instrumented by the California Strong Motion Instrumentation Program (SMIP, 2013). Using the data collected by the instrumentation during the 1994 Northridge earthquake, we verified the elastic 3-D model (Over, Astaneh-Asl, Dreger, 2010).

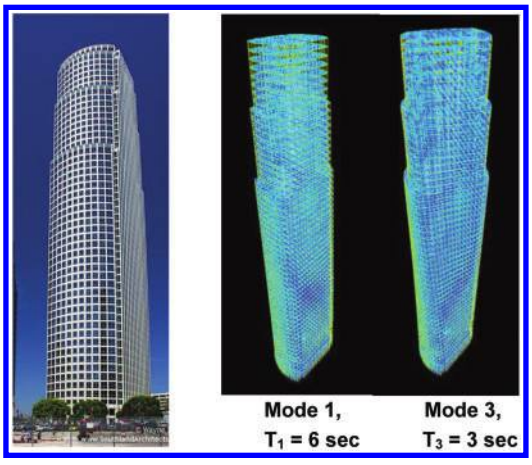


Figure 9. Modes 1 and 3 of the 54-story moment frame tower.

Table 1. Inter-story Drift Values and Non-structural Damage.

Type of Non-Structural Element	No Visible Damage	Visible but easily repairable damage	Severe Damage
Pre-cast concrete claddings	0.004	0.008	0.015
Glass windows, aluminum sash, hardened mastic	0.002	0.003	0.004
Glass windows, wood sash, soft (new) mastic	0.010	0.020	0.030
In-fill partitions	0.0025	0.004	0.008

Table 1 shows the relationship between drift and level of damage to non-structural elements of steel structures (Astaneh-Asl, 2003). The orbit roof drift response shown in Figure 10 indicates that the maximum roof drift for the Northridge ground motion is about 0.005, causing minor non-structural damage according to limits given in Table 1.

The maximum roof drift for Chi-Chi ground motion was 0.01, Figure 10, which could cause serious non-structural damage and some structural damage.

6.4 *The 52-story concentrically braced frame tower*

The 52-story concentrically braced frame structure was built in 1990, with a height of 219 m. The main lateral force resisting system in this office building is Special Concentrically Braced Frames within moment frames (Dual System). The braced bays have Chevron and V braces in both directions located around the

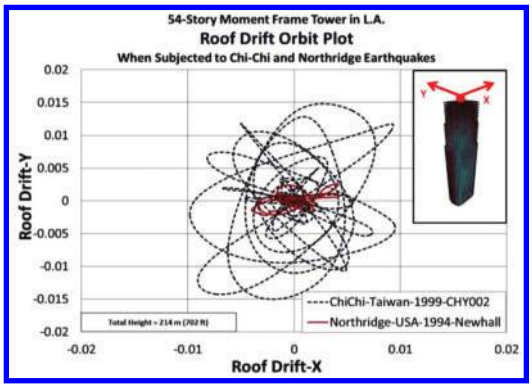


Figure 10. Orbit plot of roof drift for 54-story moment-frame tower.

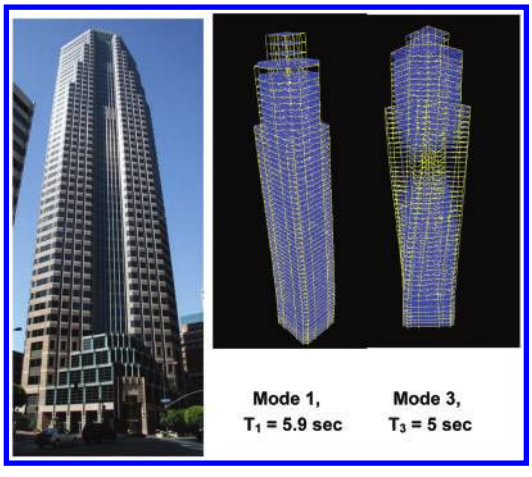


Figure 11. Modes 1 and 2 of the 52-story braced frame tower.

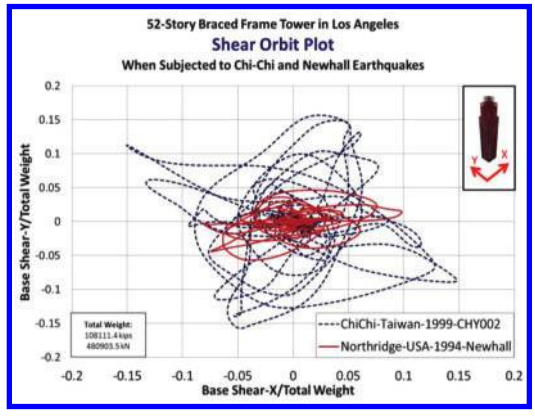


Figure 12. Orbit plot of base shear for 52story tower.

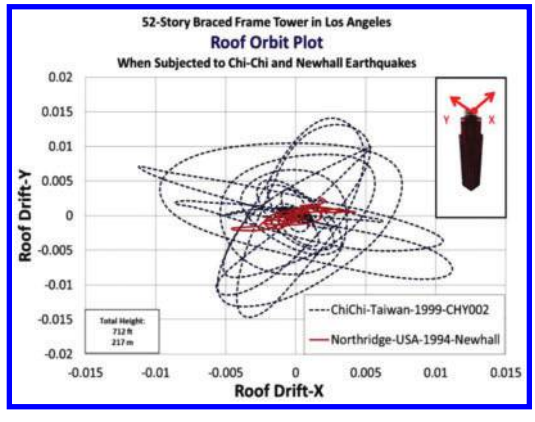


Figure 13. Orbit plot of time history of roof drift for 52-story concentrically braced frame.

core. The building is instrumented by the California Strong Motion Program (SMIP, 2013). Using the data collected by the instrumentation during the 1994 Northridge earthquake, we verified the elastic 3-D model (Naeem and Astaneh-Asl, 2012).

Figure 11 shows first two modes of the structure as well as its primary dimensions. Maximum base shear for the 52-story braced tower along the principle axes was 0.15 W (along x-x axis, Figure 12). Maximum drift along principle axes was 0.015 along the y-y axis, Figure 13, strong enough to cause serious non-structural and some structural damage such as buckling of the bracing members.

7 CONCLUSIONS AND RECOMMENDATIONS

In the studies summarized here, we subjected elastic 3-D models of the Golden Gate Bridge, the San Francisco Oakland Bay Bridge, a 54-story moment frame tower and a 52-story braced frame tower to ground motions recorded during the 1994 Northridge and the 1999 Chi-Chi, Taiwan earthquakes. The elastic time history analysis was done using SAP2000 structural analysis software.

The 1994 Northridge Newhall ground motion represents a *near field* motion with relatively short period (2.5 seconds), large maximum peak acceleration (0.6 g) and short duration (40 sec). The 1999 Chi-Chi CHY002 was selected to represent a *far field*, distant earthquake that has relatively low peak ground acceleration (0.08 g), relatively long dominant period (6 seconds) and long duration (140 sec). These two different ground motions allowed us to examine how the long span bridges and tall buildings, which have relatively long fundamental period of 6 seconds or longer, respond to near field and far field ground motions.

Based on the studies summarized herein we concluded that:

1. The study structures, which had a fundamental period of 5.9 to 17.5 seconds, had quite large response, in some cases sustaining serious non-structural damage and in a few case some structural damage to long period and weak, far field Chi-Chi CHY002 ground motion.

2. The same structures had equal or much smaller response to the much stronger near field Northridge Newhall ground motions.
3. The main parameter affecting the response was the dominant period of ground motion being close or greater than the period of vibration of the higher modes of the structure.
4. The maximum peak ground acceleration did not appear, at least in these four cases, to result in large responses.
5. The conclusions reached here were limited to the case study steel structures and should not be generalized for all long span bridges and tall buildings. More studies of long period structures subjected to far field long period, long durations, but low amplitude ground motions, are needed to develop generalized recommendations on how the effects of far field earthquakes should be considered in actual seismic design of long period structures.

REFERENCES

Adnani, A., Marto, A. and Hendriyawan, "Lessons Learned from the Effects of Recent Far Field Sumatra Earthquake to Peninsular Malaysia", *Proceedings*, 13th World Conf. in Earthq. Engrg, Vancouver, B.C., Canada, Aug, 2004.

Astaneh-Asl, A. "Performance of Buildings Subjected to Ground Shaking," *Report to Sponsor,* Lawrence Livermore National Laboratory, May 2003.

Chen, J. and Astaneh-Asl, A. "Response of the Bay Bridge to a Far Field and a Near Field Earthquake Records," *Report No. UCB/CEE-STEEL-2013/2*, Dept. of Civil and Env. Engrg, Univ. of Calif., Berkeley, May 2003.

CSI, 2013. "SAP2000 Software" Computers and Structures Inc. www.csiberkeley.com/

Gong, F., and Astaneh-Asl, A. "Response of a 54-story Steel Moment Frame Building to a Far Field and a Near Field Earthquake Records," *Report No. UCB/CEE-STEEL-2013/4*, Dept. of Civil and Env. Engrg, Univ. of Calif., Berkeley, May 2003.

Graizer, V., and Kalkan, E., "Ground Motion Attenuation Model for Peak Horizontal Acceleration from Shallow Crustal Earthquakes," *Earthquake Spectra,* Earthq. Engrg Res. Institute, Volume 23, No. 3, August 2007, pp. 585–613.

Horton Jr., J. W. , (2012) "The 2011 Virginia Earthquake: What Are Scientists Learning?", *EOS Transactions,* American Geophysical Union, Vol. 93, No. 33, 14 August 2012, pp. 317–324.

Koketsu K. and Miyake, H. "A Seismological Overview of Long-Period Ground Motion," *J Seismol* (2008) 12:133–143.

Leung, M. and Astaneh-Asl, A. "Response of the Golden Gate Bridge to a Far Field and a Near Field Earthquake Records," *Report No. UCB/CEE-STEEL-2013/5*, Dept. of Civil and Env. Engrg, Univ. of Calif., Berkeley, May 2013.

McCallen, D. B., Astaneh-Asl, A., Larsen, S. C., and Hutchings, L. J. "The Response of Long-Span Bridges to Low Frequency, Near-Fault Earthquake Ground Motions", *Proceedings*, Technical Council on Lifeline Earthquake Engineering Conference (TCLEE) 2009, Oakland, California, June 28–July 1, 2009.

Naeem, M. and Astaneh –Asl, A. "Seismic Studies of 52 Story Instrumented Structure in Los Angeles," *REP. No. UCB/CEE-STEEL-2012/1*, Dept. of Civil and Env. Engrg, Univ. of Calif., Berkeley, December 2012.

Over, M., Astaneh-Asl, A., and Dreger, D. "The Elastic Time History analysis of a Long Period Structure undergoing Long Distance, Low Amplitude and Long Duration Earthquake Excitations", *Report No. UCB/CEE-STEEL-201/1*, Dept. of Civil and Env. Engrg, Univ. of Calif., Berkeley, May 2010.

SMIP, 2013. "California Strong Motion Instrumentation Program", "http://www.conservation.ca.gov/

Taing, J. and Astaneh-Asl, A. "Response of a Proposed Steel Single Tower Curved Bridge to a Far Field and a Near Field Earthquake Records," *Report No. UCB/CEE-STEEL-2013/9*, Dept. of Civil and Env. Engrg, Univ. of Calif., Berkeley, May 2003.

Zajac, M., and Astaneh-Asl, A. "Response of a 52-Story Steel Braced Frame Building to a Far Field and a Near Field Earthquake Records," *Report No. UCB/CEE-STEEL-2013/1*, Dept. of Civil and Env. Engrg, Univ. of Calif., Berkeley, May 2003.

Research and Applications in Structural Engineering, Mechanics and Computation – Zingoni (Ed.)
© 2013 Taylor & Francis Group, London, ISBN 978-1-138-00061-2

Thinking outside the box: Integrated seismic system evolution in high rises

M. Sarkisian, N. Mathias & E. Long
Skidmore, Owings & Merrill LLP, San Francisco, CA, USA

ABSTRACT: International building codes typically tend to offer limited prescriptive design options for the seismic load resisting systems of high-rise structures. This, inevitably and unfortunately, has tended to restrict the creativity of designers, leading to a preponderance of "boxy" tall buildings, particularly in seismic regions. Codes do, however, offer opportunities for designers to use more strenuous but rewarding non-prescriptive design methodologies to develop and substantiate unique lateral system solutions. These methodologies, typically involving performance based design, rely on engineering first principles, non-linear analysis, and sometimes testing to accomplish desired ends.This paper will illustrate, using examples in regions of moderate and high seismicity, the integrated evolution of unique non-prescriptive high-rise structural systems and innovations in response to the specific architectural program, environmental control system, and aesthetic challenges in each case.

1 INTRODUCTION

When designing high-rise building structures, in regions of high seismicity, engineers find they have to contend with stringent prescriptive requirements that typically limit them to the use of only a few lateral systems: moment frames, shear walls, and various types of braced frames; alone or in combination. Codes furthermore impose strict requirements on building regularity. The result is that if strictly followed, prescriptive code requirements leave structural engineers with little room for innovation limiting the opportunities for architects and building services engineers to in turn be creative. Today's cities are replete with such buildings; relatively anonymous rectangular boxes with conventional structural systems.

It is possible, fortunately, to overcome this limitation by using non-prescriptive design methodologies permitted by most building codes. These typically involve the use of advanced analytical techniques and sometimes testing to validate designs and provide at least the same level of robustness as prescriptive designs. While the engineering effort is usually significantly greater than that involved in prescriptive design, the rewards in terms of being able to participate in innovative design coming up with creative solutions make it more than worthwhile.

In the following pages, examples of design solutions that were born of the interaction between programmatic, aesthetic and building system needs are presented. Examples are selected from recent work in areas of moderate and high seismicity in China, where the codes and review procedures for non-prescriptive design are well developed.Given their uniqueness, all the project examples presented were reviewed by panels of seismic experts in accordance with Chinese regulations.

2 CASE STUDIES

2.1 *Gemdale Plaza, Beijing*

The Gemdale Plaza project in Beijing consists of two high-rise reinforced concrete office towers, one 100 m tall and the other 150 m tall, and a retail podium along Chang-an boulevard, Beijing's principal thoroughfare (Fig. 1).

The architectural design envisioned the use of sun screens for shading purposes on the south and west facades of the towers. The sun screen expression was inspired by traditional oriental screens. Initially, the



Figure 1. Gemdale Plaza, Beijing.

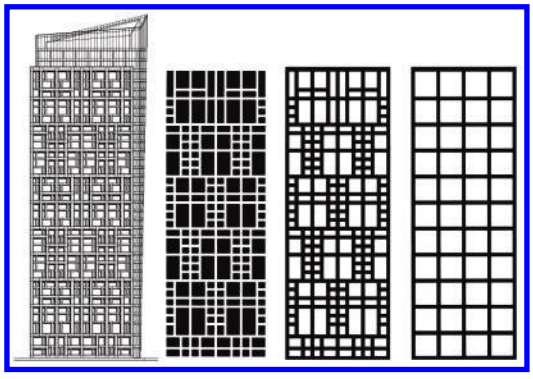


Figure 2. Screen Frame Mega Frame and Infill.

structural lateral system of the towers was conceived of as a core-perimeter moment frame system, with columns spaced at 6 m on center and girders at every floor. The sun screens, however, yielded an interesting possibility; to serve dual functions as the architectural aesthetic and shading devices as well as structure; thereby eliminating redundancy and adding rentable space to the plans. The concept of "screen frames" was thus born.

2.1.1 *Challenges and solutions*

The first challenge was to rationalize seemingly random screen members into a pattern that could serve as moment frames. Figure 2 shows an example of how this can be achieved; by creating a regular, multi-story mega-frame of primary members that carry the gravity loads of the tower as well as provide lateral resistance, and then using secondary "infill" members within the mega-grid to provide lateral stiffness only. For the Gemdale Plaza project, this resulted in screen frame mega columns at 9 m on center and mega girders every three stories. Gravity loads from the floor framing were directed only to the mega columns of the screen frames, allowing the frames to be pulled away from the edge of the floors creating a vertical gap between themselves and the exterior glazing (Fig. 3). The frames on the north and east facades, subject to less direct sunlight, had conventional moment frames with columns at 6 m on center and girders at every floor (Fig. 4).

Once the screen frames were rationalized, the next step was to "tune" their lateral stiffneses to match those of the conventional frames on the opposite faces each tower to minimize torsional irregularity. In order to keep gravity loads from straying into the secondary lateral stiffening infill members of the screen frames, delayed pour techniques were employed, where the infill member connections to the mega-frame members were only finalized after the towers were topped out and dead loads were in the primary mega-frame members. Extensive study of diaphragm demands where the floor framing connected to the screen frames across the gaps was needed to assure adequate capacity even in rare earthquakes and appropriate steel reinforced concrete details developed.

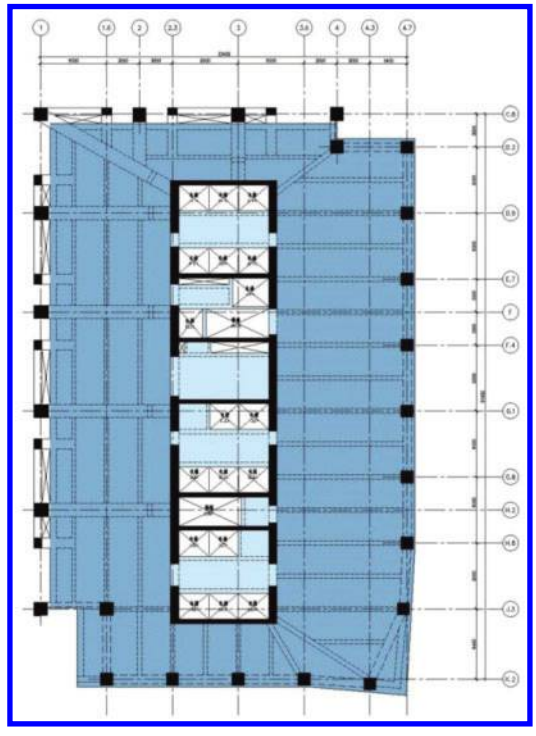


Figure 3. Typical Framing Plan.



Figure 4. Screen Frames and Conventional Frames.

2.2 *Poly International Plaza, Guangzhou*

Located along the Pearl River in Guangzhou, the design of Poly International Plaza's two mixed-use



Figure 5. Poly International Plaza, Guangzhou.

towers blended familiar structural systems with architectural form to shape an innovative slender high-rise design solution with an aspect ratio of 8:1, framing riverfront views in a hot climate. Although Poly International Plaza used conventional seismic systems, such as a dual system composed of moment frames, braced frames, and outrigger trusses, the elements and materials of these systems were creatively integrated to define a distinctive solution that addressed the issues related to the slender proportions of the building (Fig. 5).

2.2.1 *Challenges and solutions*

To create the slender plan of each tower, a combination of reinforced concrete and steel elements were used in its lateral system (Figs 6, 7). Consequently, composite columns (in the north) were tied to reinforced concrete piers (south) with three-story high interior outrigger truss frames located in the mid-height and top sections of the building, and end frames composed of steel braced frames (east and west). Adjacent to this structure, the conventional reinforced concrete framed core was placed to the south, outside the moment resisting and braced frame perimeter, and tied back to the structure through slab diaphragms. The offset location of the core moved the bulk of service facilities and elevators out of the building to open the interior space to natural light and enhance the slender appearance of the towers.

The overall effect from the compilation of these lateral force resisting elements was a premium of open views in the north, sun-shading in the south, and a column-free interior office space. Moment frames maximized the amount of desirable natural indirect light in the building, while the core and braced frames

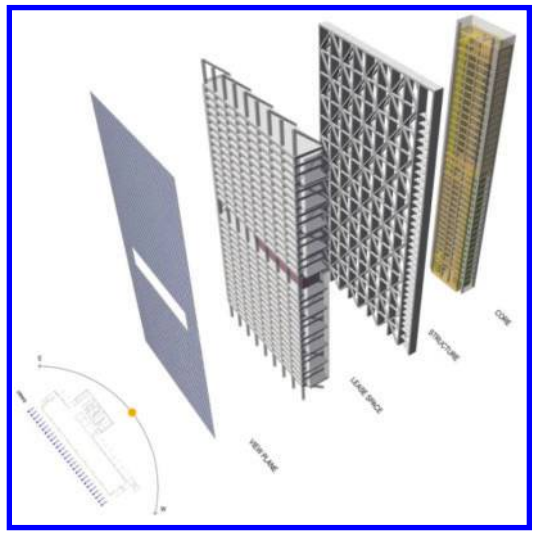


Figure 6. Structural System Components.

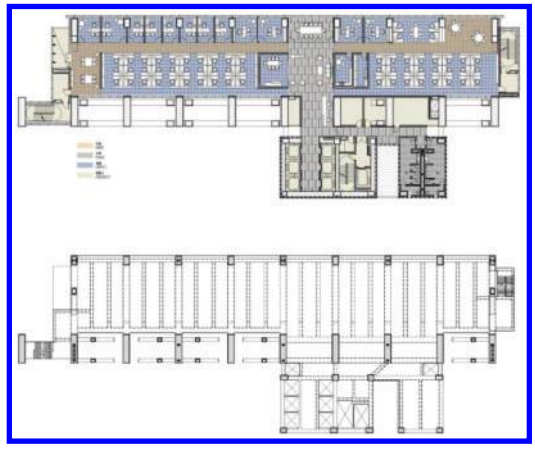


Figure 7. Typical Floor Plans, Architectural and Structural.

blocked direct light from overheating the building in the south, minimizing the demands on the HVAC system. Further, the double line of diagonal elements in the braced frames filtered light into dynamic patterns in the interior space.

In addition to its sun shading effects, the structural system yielded an unusually efficient design. The spine comprising the reinforced concrete piers and the double line of braced frames was very stiff, and served to resist in-plane seismic forces through brace action as well as out-of plane seismic forces acting as a stressed skin flange. This effectively achieved the strict drift requirements of the building codes in China. Three-story high openings penetrating both towers at the location of the mid-height outrigger truss frames also served dual roles by reducing wind loads and becoming social spaces that could double as refuge floors during an emergency.

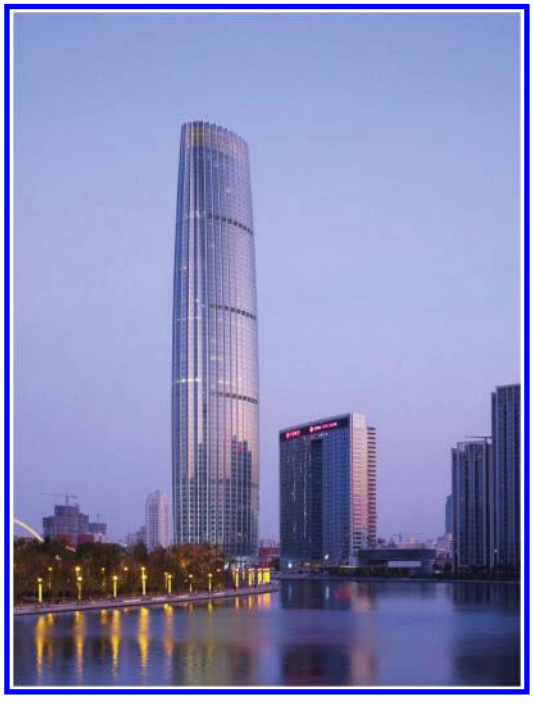


Figure 8. Jinta Tower, Tianjin.



Figure 9. Chinese Paper Art Inspiration.

2.3 *Tianjin Global Financial Tower, Tianjin*

At less than one kilometer from the main railroad station in the heart of downtown Tianjin, the Tianjin Global Financial Tower site is bounded on three sides by prominent urban thoroughfares and on the fourth by the Haihe River (Fig. 8).

Clad in a pleated glass exterior wall that recalls the structure and lightness of Chinese paper arts (Fig. 9), the 336.9 m tall office tower's uniquely folded surface catches light and maximizes views for occupants; its architectural expression combining the strength of a minimal form with an elegance of material and detail.

2.3.1 *Challenges and solutions*

Because of the tower's slender form—it has an overall aspect ratio close to 1:8—a key design challenge was to develop an efficient lateral system capable of resisting significant wind and seismic lateral loads while simultaneously keeping wind-induced lateral drifts and oscillations under acceptable limits.

Several structural system options were considered in the concept and early schematic design phases including an all concrete dual system with perimeter moment resisting frames and core shear walls;

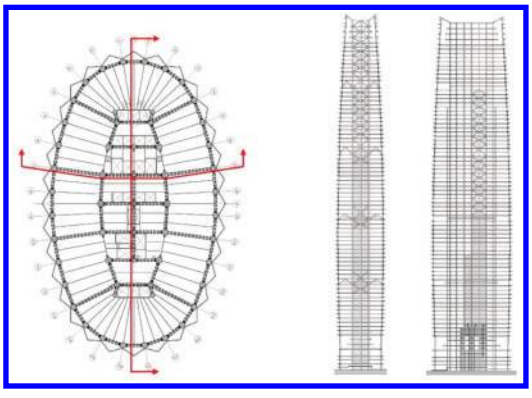


Figure 10. Typical Framing Plan and Sections.

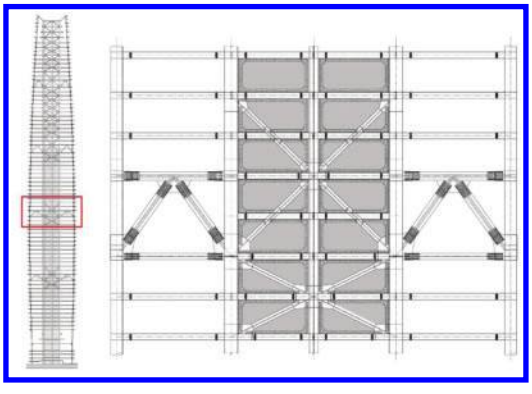


Figure 11. Outrigger Truss Elevation.

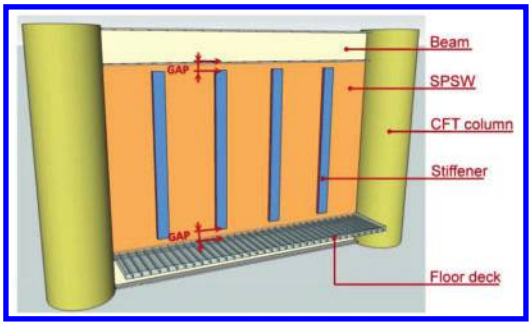


Figure 12. Steel Plate Shear Wall System Components.

composite systems with perimeter steel moment resisting frames, steel floor framing and composite metal deck slabs, and composite concrete and steel plate shear walls; and all steel systems with perimeter moment resisting frames and braced or steel plate shear wall (SPSW) cores; all in combination with outriggers in the slender direction. After relative evaluation of technical and financial merits, an all steel dual system utilizing slender stiffened SPSWs and core and perimeter frames was selected (Figs 11, 12, 13). The core and perimeter structures were connected to each other in the slender direction using steel outriggers. Columns were composite concrete filled tubes



Figure 13. Steel Plate Shear Wall.



Figure 14. Jinao Tower, Nanjing.

(CFT) to reduce dimensions and increase ductility.The minimal dimensional needs of SPSWs, the availability of substantial code provisions and design guides, research and testing data that highlighted the superior ductility of SPSWs, excellent predicted structural performance and a highly developed local steel industry, all contributed to a decision to use SPSWs in the tower core and an all steel structure.

2.4 *The Jinao Tower, Nanjing*

The 232 m tall Jinao Tower's (Fig. 14) structural system arose out of the demands of its mixed use program and unique environmental control system. The program consisted of office space in approximately the lower two thirds of its height and a hotel in the upper one third.

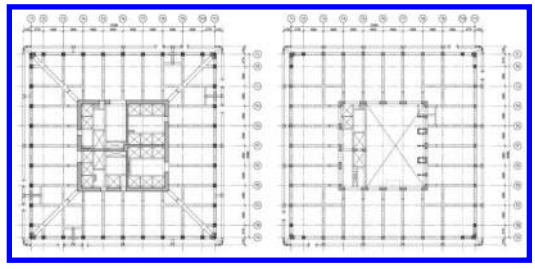


Figure 15. Typical Office and Hotel Framing Plans.

2.4.1 *Challenges and solutions*

In order to satisfy the stringent requirements of the Chinese codes, a concrete dual system consisting of a core and perimeter frame was selected. The hotel program, however, required a central atrium in the core necessitating that the core walls be extensively perforated to act as a central light well (Fig. 15). This resulted in a softening of the lateral system. Although strength requirements could be met, it was not possible to satisfy drift requirements without additional measures.

A unique solution was hit upon, noting that the project was shaped like a Chinese lantern with external folds in its double skin façade. The double skin facade system, which included slots in the outer facade to allow the entry of air, was part of the projects environmental control system, creating a temperature buffer between the inner and outer exterior wall systems. A tertiary structural system—an exterior steel mega-braced frame that only served to stiffened the building laterally to meet drift requirements without participating in gravity load support—was introduced, aligning itself with the folds of the double façade (Figs 16, 17, 18).

The steel braces, only 500 mm in diameter with a typical wall thickness of 25 mm, are designed to resist only lateral loads and superimposed live loads by stipulating a delayed construction sequence and appropriate joint details in order to keep proportions slender. The brace connections were finalized approximately a year after topping out the structure, allowing creep and shrinkage vertical building shortening to take place without impacting the braces.

The braces efficiently direct lateral wind and seismic loads from the superstructure to the foundation. Loads are managed, optimally shared between the core, perimeter moment frame and external steel braces through the "tuned" stiffness of the individual systems.Introducing the wrapping diagonal steel brace system on each side of the concrete tubular structure resulted in additional stiffening, a 40% design reduction in concrete and rebar in the lateral load resisting system, and a 20% design reduction in concrete and rebar for the overall building structure.

Several special studies were conducted to explicitly ensure the redundancy, ductility, and overstrength of the structural system. First, 3D non-linear pushover and time-history analyses were conducted to verify "life-safety" performance during rare earthquake

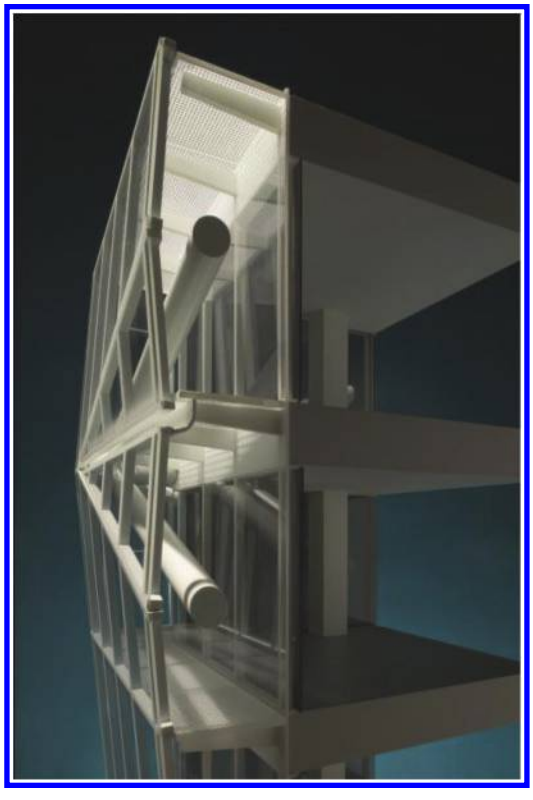


Figure 16. Perimeter System Model.

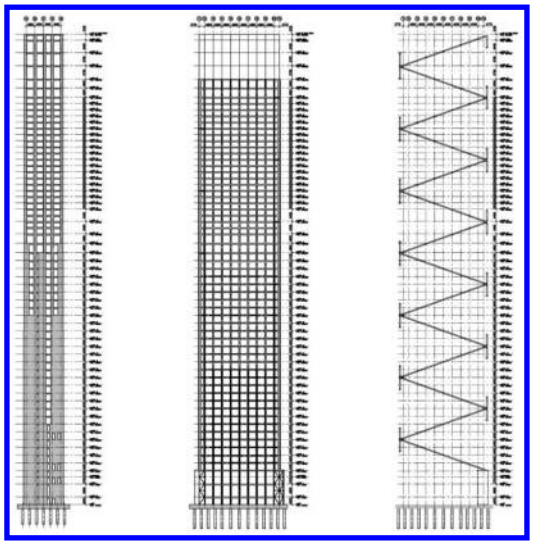


Figure 17. Inner Shear Wall Core, Perimeter Moment Frame, and Exterior Steel Brace Elevations.

demands (2000 year return) exceeding "collapse prevention" goals typically associated with such events. Second, key members and components including the steel pipe braces were designed to enhanced criteria to

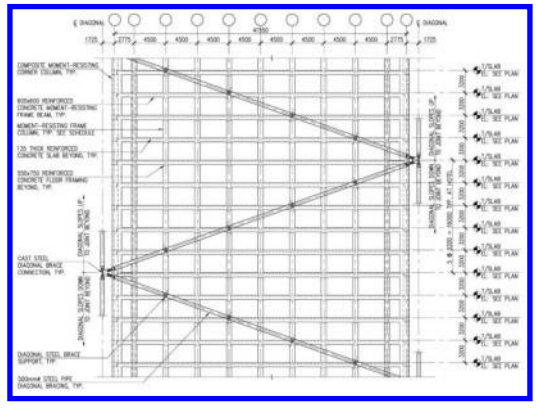


Figure 18. Enlarged Composite Elevation.



Figure 19. Full Scale Joint Testing.

ensure that they would remain elastic well beyond the baseline frequent earthquake (50 year return). Third, the force levels in the perimeter steel pipe braces were rechecked after the removal of any one brace to verify the redundancy of the structural system. Lastly, reduced scale shake table testing of the entire building and full scale testing of the typical exterior brace corner connection (Fig. 19) were conducted to validate expected performance.

3 CONCLUSIONS

It is hoped that the provided examples of structures in seismic regions will serve to show that the constraints and challenges of a real project, whether they be aesthetic, programmatic, related to site or any other reason can serve as design opportunities for structural engineers; giving them opportunities to arrive at appropriate and innovative structural solutions. With innovation, however, comes the responsibility for due diligence, and engineers who choose this course should be prepared to go the extra distance in terms of additional analysis and computation as well as peer reviews to ensure safety and efficiency of their designs.

Research and Applications in Structural Engineering, Mechanics and Computation – Zingoni (Ed.)
© 2013 Taylor & Francis Group, London, ISBN 978-1-138-00061-2

Yokohama-Bay cable-stayed bridge seismic response analysis during the 2011 Great East Japan Earthquake

Y. Fujino & D.M. Siringoringo
Bridge & Structure Lab., Department of Civil Engineering, University of Tokyo, Japan

ABSTRACT: Yokohama Bay Bridge with the total span length of 860 m is the second longest span cable-stayed bridge in east of Japan and one of the most densely instrumented bridges in Japan. On March 11, 2011, northeastern Japan was shaken by the Great East Japan earthquake and at the bridge location JMA seismic intensity 5. This paper describes response analysis of the bridge, system identification, observation of the changes in dynamic characteristics, performance evaluation of link-bearing connection and post-earthquake field observation.

1 INTRODUCTION

1.1 *Bridge description*

Yokohama-Bay Bridge is a part of the Tokyo-Yokohama Bay Shore expressway link that connects Tokyo and Yokohama harbor area. The bridge is a continuous three-span double-deck cable-stayed with the total span length of 860 m (200 m–460 m–200 m). Bridge towers are of H-shaped, welded as monolithic section with the height of 172 m and width of 29.25 m. The girder is suspended from towers and piers by means of link bearings in such a way that the inertia force of superstructure on substructure is reduced during an earthquake by maintaining a longitudinal fundamental period about 7.7 seconds. By lengthening natural period, the structure is expected to have lower acceleration but larger displacement during an earthquake. Short links with the length of 2 m in a shape of inverted pendulum were utilized to connect the girder to the towers.

The bridge has eighty-five sensors measuring acceleration and displacement installed at 36 locations. Along the girder, sensors are installed at 12 locations with spacing of 115 m (Figure 1). At 14:46 on March 11, 2011, northeastern Japan was struck by the Great East Japan earthquake (moment magnitude of 9.0), the largest ever recorded in Japan. Epicenter of the earthquake was about 398 km away from the bridge, with the focal depth of 24 Yokohama-Bay Bridge dimension and sensor layout km. Even though the epicenter is very far away from the bridge, the fault rupture consists of about 500 km long from north to south and 220 km wide area of northeast Japan, which means that the closest distance from the bridge to the rupture fault area is about 180 km. JMA seismic intensity 5+ (equivalent to scale VII in MMI), out of the maximum scale of 7 was recorded on the bridge location.

This paper describes response analysis of Yokohama Bay Bridge under 2011 Great East Japan earthquake. The paper focuses on the response of superstructure, system identification, observation of the changes in dynamic characteristics, performance evaluation of link-bearing connection and post-earthquake field observation.

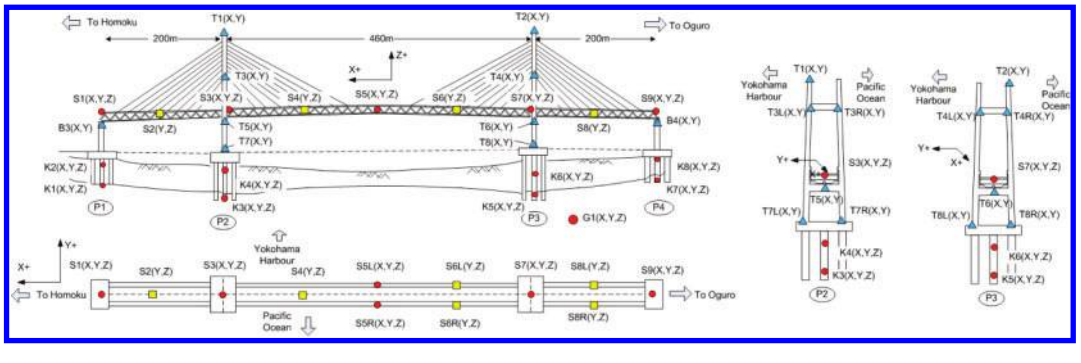


Figure 1. Yokohama-Bay Bridge dimension and sensor layout.

Table 1. Recorded accelerations and displacements during the main shock (March 11, 2011 14:47).

Sensor Code	Max Acceleration [direction] (cm/s^2)	Max Displacement (cm)
S5R	51.14 [L], 299.17 [T], 194.25 [V]	19.60 [L], 61.80 [T], 19.50[V]
S4	250.78 [T], 163.58 [V]	47.15 [T], 11.32 [V]
S2	335.77 [T], 165.80 [V]	20.50 [T], 6.94 [V]
T1	252.99 [O], 635.94 [I]	25.00 [O], 54.60 [I]
T2	418.67 [O], 656.87 [I]	24.28 [O], 48.36 [I]
T3	124.37 [L], 344.41 [T]	23.40 [L], 43.40 [T]
T4	138.80 [L], 411.73 [T]	22.50 [L], 42.70 [T]
T8	71.38 [L], 67.27 [T]	17.50 [L] , 18.00 [T]

Note: L = Longitudinal, T = Transverse, V = Vertical, O = out-of-plane, I = in-plane

2 CHARACTERISTICS OF SEISMIC RESPONSE

2.1 *Characteristics of girder responses*

The girder responses were characterized by large transverse vibration as can be seen in Table 1. For girder, the maximum acceleration was in transverse direction, with the maximum girder displacement of more than 62 cm recorded in the middle of center-span. The girder large vibration is mainly due to one mode that is the first girder transverse mode at 0.28–0.32 Hz. Meanwhile, the girder vertical vibration is dominated by the first five vertical bending modes between 0.32 Hz and 1.2 Hz. The maximum girder vertical displacement is about 20 cm measured at the middle of the center span.

The frequency characteristics during main shock indicate that the predominant girder frequencies are closely-spaced around 0.32 Hz in both vertical and transverse direction. The results are different from previous investigation using seismic records of several smaller earthquakes (Siringoringo and Fujino 2006), where the first vertical and transverse mode was identified at 0.34 Hz and 0.28 Hz, respectively. Time-frequency wavelet analysis of girder transverse acceleration shows frequency peak at the initial response appears at 0.29 Hz. The frequency increases and reaches up to 0.32 Hz during the largest excitation (i.e.100–200 sec) before later decreases to 0.27 Hz near the end of response. On contrary for the vertical acceleration, the frequency peak at the initial response appears at 0.34 Hz. The frequency decreases slightly to 0.32 Hz during the largest excitation before increases to 0.34 Hz near the end of the response. The similar result was also observed during aftershock 1 (March 11, 2011 15:16). Changes in transverse and vertical frequency indicate non-linearity of the response.

2.2 *Characteristics of tower responses*

Maximum acceleration larger than 600 cm/s^2 was recorded on the top of both towers, which result in the maximum tower in-plane displacement of more than 50 cm. The large tower transverse vibrations were mainly dominated by the modes that correspond to the tower local frequency at 0.42 Hz. In out-of-plane direction the maximum accelerations were 252 cm/s^2 and 418 cm/s^2 for P2 and P3, respectively. The tower out-of-plane vibrations were mainly due to the bridge global modes associated with girder vertical modes such as the first vertical bending (0.32 Hz–0.34 Hz) and the first torsional mode (0.83 Hz), with the largest component is due to the second vertical bending modes at 0.48 Hz–0.52 Hz.

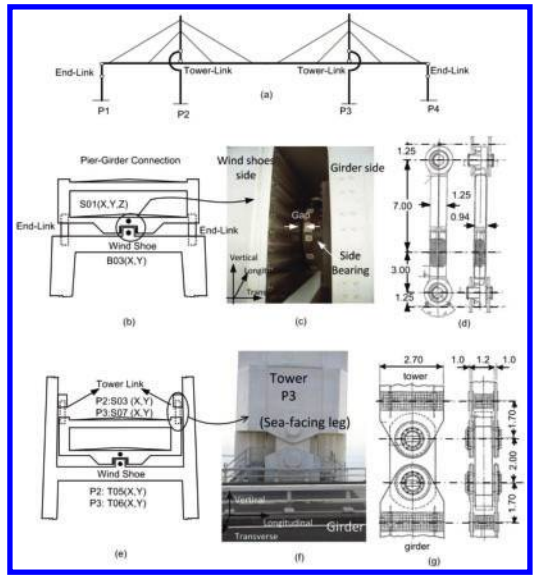


Figure 2. (a) Characteristics of pier-to-girder and tower-to-girder connections, (b) Schematic figure of tower-to-girder connection (c) snapshot photo of wind shoe transverse gap between tower/pier and girder, (d) detail figure of end-link, (e) Schematic figure of pier-to-girder connection, (f) photo of tower link, and (g) detail figure of tower-link.

2.3 *Characteristics of vibration on pier-girder and tower-girder connections*

Girder motion in longitudinal direction is accommodated by link-bearing connections (LBC) namely end-link at the end of girder (P1 and P4) and tower-link at the towers (P2 and P3) (Figure 2). In transverse direction the girder movement is restricted by wind shoes at all piers and towers. Note that there is small transverse gap between wind shoes and girder to accommodate tower-girder relative motion. The surface of wind shoes are made of stainless steel, while the girder's connection that faces the wind shoes have the form of side bearing with concave surface made of Teflon PTEE. The side bearing at end-piers and towers were designed to resist transverse load of 2,820 ton and 4,930 ton, respectively.

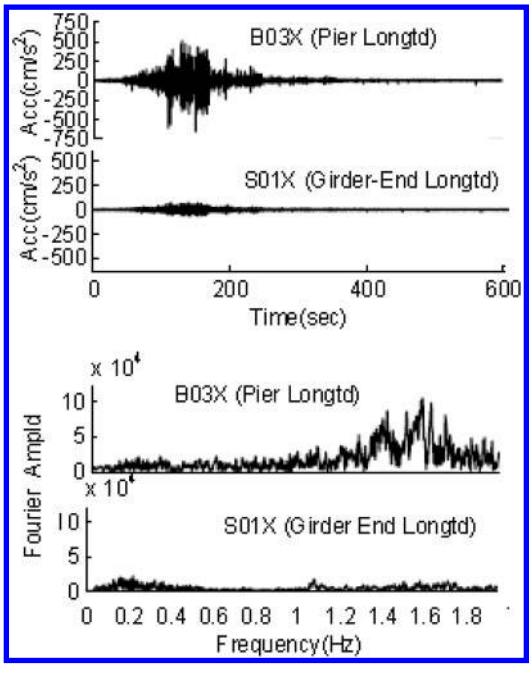


Figure 3. Longitudinal acceleration recorded on pier P1 (B3X) and on the girder above P1 pier (S1X), along with their Fourier spectra.

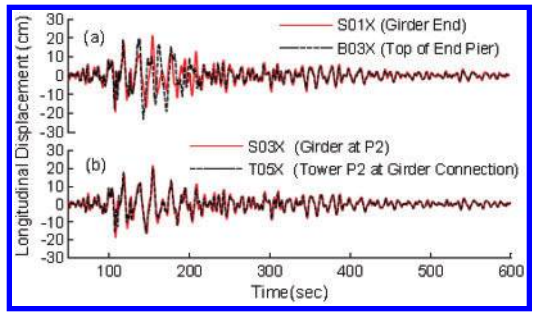


Figure 4. Comparison of longitudinal displacement (a) at end-pier P1 (B3X-S1X), (b) at tower P2 (S3X-T5X).

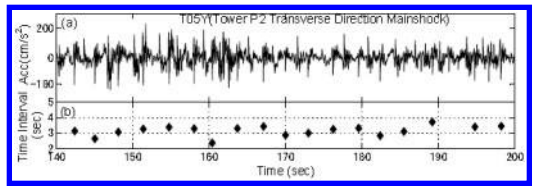


Figure 5. Accelerations of tower at deck level showing spike indicating impulses.

In design, the link bearing that connects pier and girder in longitudinal direction is expected to form a high type of connection so that large vibration energy from the pier or tower would not be transferred to the girder (Maeda et al. 1991). In such condition, relative displacement between pier and girder; and between tower and girder will be large and the high frequency components of pier and tower vibration will not be transferred to girder.

Figure 3 shows that pier longitudinal acceleration (B3X) was characterized by frequency peaks around 1.5 Hz and 2 Hz, while the girder longitudinal acceleration (S1X) located on the top of B3X, and was dominated by frequency peaks around 0.13 Hz. The maximum acceleration on the pier is about 500 cm/s^2 while the maximum acceleration at the girder is only about 50 cm/s^2. Moreover spectra plots of accelerations at the end of girder show that vibration energy is significantly smaller compared to that of the pier. The facts that girder longitudinal acceleration is dominated by low frequency component, significant reduction in amplitude of high frequency components of girder longitudinal acceleration and the large difference of vibration amplitude between pier and girder suggest that vibration energy from the pier was not transferred to the end-girder. Similar results were also observed on longitudinal responses of tower at the deck level (T5X and T6X).

Girder longitudinal displacement is one of the main concerns since excessive longitudinal displacement during a large earthquake may cause pounding to the approach spans and result in damage to the pier-to-girder connections. The results show, however, that the girder maximum longitudinal displacement (processed from acceleration) was relatively small in the order of 20 cm, which is still far below the maximum displacement 1.5 m as expected in the seismic retrofit program.

Relative displacement between girder and tower or between girder and piers at connections can be used as indicators of pier-to-girder and tower-to-girder performance during earthquakes. The results show that relative displacement between pier and girder in longitudinal direction are relative large (in order of 5–10 cm) (Figure 4). In fact at P1, pier-cap displacement (B3X) was lagged behind the girder (S1X) displacement during the largest excitation (time: 150–200sec) suggesting that girder movement was completely decoupled from pier movement for that short period of time. Meanwhile relative longitudinal displacements between girder and tower at connection are smaller than that of pier (1–5 cm).

In transverse direction, wind shoes limit girder transverse movement over the pier and tower. Small gap exists between girder and pier at wind shoes to allow for small relative displacement. This gap, however, most likely be exceeded during large excitation. Tower transverse accelerations are characterized by many periodic spikes similar to a periodic impulse response especially during the largest excitation between 100 s and 300 s. Figure 5 shows a close-up look of the acceleration response where periodic impulse exists between tower and girder indicating the occurrence of transverse pounding. In addition to the main shock, only the aftershock 1 (March 11,15:16) shows the same periodic impulse in the transverse

response of tower-to-girder connection. By observing time intervals between successive impulses during the largest excitation, we can estimate structural mode that triggers the pounding. The average time interval between consecutive impulses is about 3.2 second, which is equivalent to periodic motion at frequency range of 0.31–0.32 Hz. This result indicates that the transverse impulse at the tower-to-girder during the largest excitation period of the main shock was mainly caused by the girder first transverse mode.

3 SYSTEM IDENTIFICATION

Multiple-input multiple output (MIMO) system identification was employed to identify modal parameters of the bridge under seismic excitation. The methodology used in this study utilizes correlations between input-output data for realization of a state-space model and estimation of modal parameters. Detail information on the system identification algorithm and its application to Yokohama-Bay Bridge is given in reference (Siringoringo and Fujino 2008). In order to effectively implement the system identification, a set of input-output data was selected. As inputs, responses from triaxial accelerometers located at the bottom of the towers (P2 and P3) and the end-pier (P1) were selected (see sensor location in Figure 1). These responses were utilized, instead of the free-field responses as to minimize the effect of soil-structure interaction. As outputs 41 channels of acceleration from super structures were selected. These channels consist of accelerations from girder (23 channels), pier P1 (2 channels), tower P2 (8 channels) and tower P3 (8 channels). Since the input and output data are derived from multiaxial accelerations, the identified mode shapes have three-dimensional shape.

The system identification is based on assumption that modal parameters remain constant during a specific time-window in which the input-output data was analyzed. However, since the input excitation is large and the bridge may enter non-linear region during large excitation this assumption may not always be satisfied for the whole responses. Therefore, the analysis was conducted using a moving window scheme of a shorter time frame, during which the modal parameters were assumed to remain constant. For this reason, the total time history responses were divided into several shifted time windows consisting of 50 seconds of input and output data. Each time window generates a set of modal parameters, from which the change of parameters with respect to time can be evaluated.

3.1 *Results of system identification*

System identification generated fourteen modes between 0.1 Hz and 2.5 Hz where the girder modal displacement dominates the mode shapes. Their identified natural frequencies were in good agreement with the results from the previous earthquakes and the finite element model. In the following sections we shall focus discussion on the characteristics of three most dominant modes in respective motion direction that is the girder first longitudinal, first transverse and first vertical mode. The three modes dominate the girder vibration in three respective directions and they are most sensitive to the input amplitude.

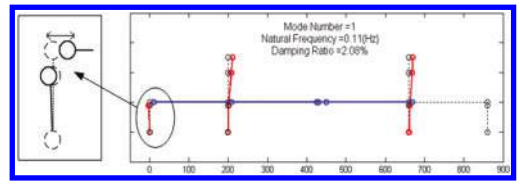


Figure 6. Longitudinal Mode shape with slip characteristic at the end-pier and girder connection.

The first mode identified by SI is the longitudinal sway mode. The mode is characterized by dominant girder longitudinal modal displacement with minimum coupling in vertical and lateral direction. Mode shape and natural frequency characteristic of this mode depend on the behavior of link-bearing connection (LBC) during the vibration. In design, the LBC is expected to function – thus modeled in FEM, as a longitudinal hinge connection. This means that relative modal displacement between girder and end piers are expected to be significantly large. Longitudinal mode shape with such condition is denoted as *slip mode*. Previous observations from seismic response reveal that this is not necessary true for all cases. For small earthquakes, system identification gives small relative modal displacements between end-piers and girder and higher frequency of longitudinal mode. Longitudinal mode shape with such condition is denoted as *stick mode*. The *stick mode* suggests that LBCs have not functioned as full-hinged connections and as a result force distribution on the end-piers and tower may be different than intended in design. A significant amount of additional force will be distributed to pier and tower if the LBCs remain stuck during large earthquake. Therefore it is important to investigate performance of LBC during large earthquake.

Figure 6 shows the mode shape of longitudinal mode identified from main shock, frame 4 (during the largest excitation) and the mode was identified at 0.13 Hz. Results of identification for the entire main shock response show that the mode was identified at around 0.12 Hz–0.13 Hz with large relative modal displacement between pier and girder indicating the *slip mode*. This is in agreement with the result of displacement of girder and pier at the pier-to-girder connection that shows a large relative displacement. It is also supported by the frequency characteristics of girder and pier accelerations at the pier-to-girder connection.

The second and the third identified global mode were the first transverse bending and first vertical bending, respectively. The two modes have distinct characteristics in that their natural frequencies and modal displacements depend on the amplitude of input excitation. During a large excitation, such as the 100–200 seconds of the main shock, frequency of the first transverse mode increases from 0.27 Hz to

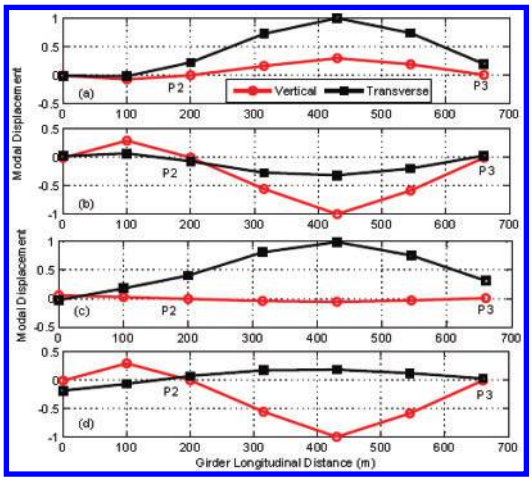


Figure 7. Characteristics of mode shapes with strong transverse-vertical coupling during the largest excitation of main shock 14:47 (Frame 4, t = 150–200 s): (a) girder first transverse mode and (b) girder first vertical mode. Characteristics of mode shapes with weak transverse-vertical coupling during the end of main shock 14:47 (Frame 11, t = 500–550 s): (c) girder first transverse mode and (d) girder first vertical mode.

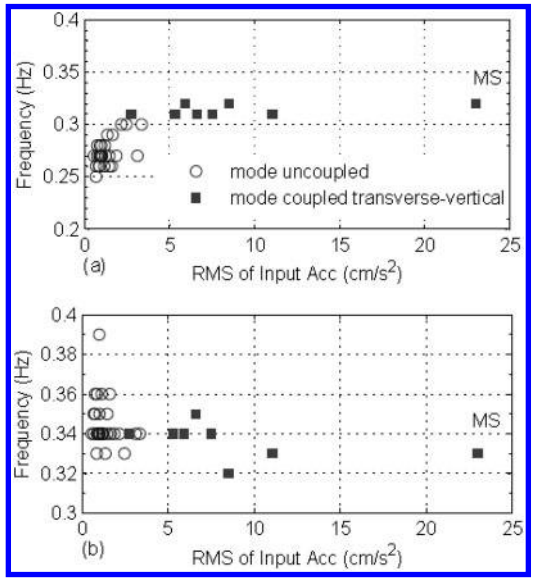


Figure 8. Variation of natural frequencies with respect to input acceleration for all analyzed seismic records: (a) 1st Transverse bending mode and (b) 1st Vertical bending mode (MS:main shock).

0.32 Hz, while frequency of the first vertical mode decreases from 0.35 Hz to 0.33 Hz.

The change in frequency is followed by the change in mode shape characteristics especially the girder transverse-vertical coupling pattern. During large excitation, strong transverse-vertical coupling of girder modal displacement was observed in both transverse and vertical modes. In this condition, the vertical mode has significant modal displacement in transverse direction and the transverse mode has significant modal displacement in vertical direction (Figure 7). At smaller excitation, as in the beginning and near the end of response, the transverse-vertical coupling becomes weaker, in that the vertical mode has very small transverse modal displacement and vice versa (Figure 7). Variations of natural frequency and coupling behavior of the first lateral and first vertical bending modes with respect to input amplitude for all records analyzed are shown in Figure 8.

The change in natural frequencies and transverse-vertical coupling behavior with respect to input amplitude indicate that the bridge response has entered the non-linear region during the main shock. Non linearity in cable-stayed bridge seismic response is known to be caused by several factors such as material nonlinearity, geometric nonlinearity due to large displacement in cable and behavior of pier-to-girder and tower-to-girder connections. However, considering the displacement resulted from seismic response is not so large as to cause significant geometric or material nonlinear, behavior of tower-girder and pier-girder connections are thought as a possible source of nonlinearity.

4 POST-EARTHQUAKE VISUAL INSPECTION

The main objective of inspection was to investigate condition of pier-girder and tower- girder connections after the earthquake. The bridge did not show any signs of serious damage and was in full operation following the earthquake. Visual inspection findings are as follows.

1. Circular marks left on the surface of wind shoes on the pier P1 and tower P2 suggesting that the girder had experience large relative longitudinal movement. The marks show that relative displacement between girder and tower (and pier) in the order of 8–10 cm had occurred (Figure 9(b)). For this relative displacement to occur, the link-bearing connection between girder and tower (and pier) must have slipped. Therefore the scratch mark on the surface of wind shoes supports the results of response analysis and the type of longitudinal mode generated by system identification.
2. In transverse direction, several marks of scraped paint were observed on the link head of tower P2. Nuts of several bolts on the upper disc of the lower head of P2 tower link were crushed and signs of scraped paint were clearly seen on the surface of the disc (Figure 9(c) and (d)). The scraped paint and broken nuts could be caused by transverse pounding between tower and girder at tower link and by combination of transverse and excessive vertical motion of girder at tower-to-girder connection.

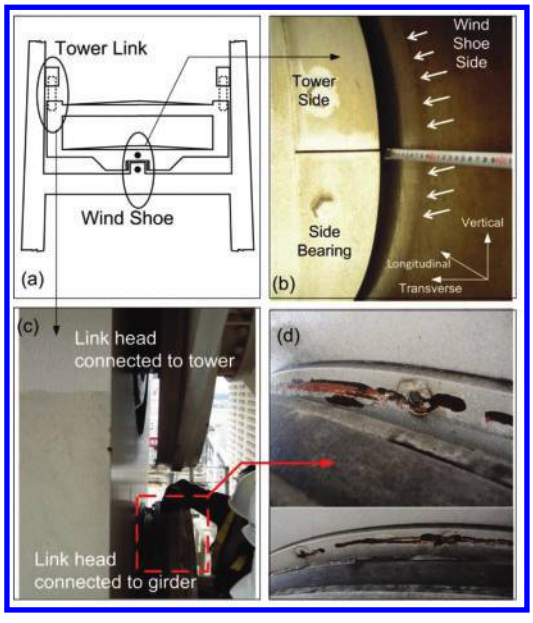


Figure 9. (a) Schematic figure of wind shoe and tower link. (b) Circular scratch marks on the surface of wind shoe as a result of side bearing movement indicate girder longitudinal movement. Distance between the marks and side bearing stationary is about 8 cm. (c) Location of head of tower link (P2) bottom head is connected to girder, top head is connected to tower. (d) Scratch marks on the surface of the bottom link head caused by combination of vertical and transverse movement of the girder. The arrows point to locations of three broken bolts caused by the movement.

5 CONCLUSIONS

Response analysis of Yokohama Bay Bridge under the 2011 Great East Japan earthquake has been discussed in this paper. During the main shock the bridge experienced intense shaking for about 10 minutes, but no structural damage was reported. Based on response analysis and system identification, the following conclusions can be drawn. (1) The input excitations recorded on the bridge foundation are still below the design and seismic-retrofit ground motions. The bridge experienced intense shaking for about 10 minutes, but no structural damage reported. (2) The bridge response during main shock was dominated by transverse movement of girder and tower. (3) During the main shock and aftershock March 15:16, girder accelerations show indication of response nonlinearity as denoted by the time variation of natural frequencies and the change in transverse-vertical coupling of the first transverse and vertical mode shapes. (4) Relative displacement response, characteristics of acceleration spectra and type of longitudinal mode at the pier-to-girder and tower-to-girder connections suggest that the link bearing have slipped as intended in design. (5) Recorded accelerations, results of system identification and visual inspection indicate that transverse pounding between girder and tower have occurred. Despite its occurrence, transverse pounding does not cause any structural damage at the present earthquake. In the future, however, effect of transverse pounding between girder and tower on bridge should be investigated in more detail and countermeasure if necessary must be taken, especially in anticipation for larger earthquake excitation.

REFERENCES

Fujino, Y. Kikkawa, H. Namikawa, K. and Mizoguchi, T. (2005). Seismic Retrofit Design of Long-Span Bridges on Metropolitan Expressways in Tokyo, Proc. the 6th International Bridge Engineering Conference, Transportation Research Board, Boston Mass, USA, CD-ROM.

Siringoringo, D.M. and Fujino, Y. (2006), Observed dynamic performance of the Yokohama-Bay Bridge from system identification using seismic records. Structural Control and Health Monitoring; 13, 226–244.

Maeda, K. Otsuka, A. Takano, H. (1991), The design and construction of Yokohama Bay Bridge, Cable-Stayed Bridges Recent Developments and their Futures, M. Ito et al. (Editors). Elsevier Science Publisher B.V. 377–395.

Siringoringo, D.M. and Fujino, Y. (2008), System identification applied to long-span cable-supported bridges using seismic records. Earthquake Engineering & Structural Dynamics, 37, 361–386.

The Yokohama Bay Bridge (1991), Published by Metropolitan Expressway Public Corporation, Tokyo Japan, (in Japanese), 164–172.

Research and Applications in Structural Engineering, Mechanics and Computation – Zingoni (Ed.)
© 2013 Taylor & Francis Group, London, ISBN 978-1-138-00061-2

Large natural draft cooling towers under earthquake excitation

M. Andres & R. Woermann
Krätzig & Partner Engineering Consultants, Bochum, Germany

D. Casucci
Institute of concrete structures and structural engineering, University of Kaiserslautern, Kaiserslautern, Germany

ABSTRACT: The paper deals with the behavior of large hyperbolic cooling towers under dynamic excitation of earthquakes. The column support is that component of a cooling tower which leads the entire loading from the shell into the foundation. Therefore a comparison between the traditional "V"- and "A"-columns and the most recent radial support was carried out. A parametric calculation has been performed, under consideration of three different sites and three different soil classes. Moreover, some analyses are performed to considerate the influence of wind in combination with earthquake loading as required by the previous version of the German VGB-guideline. Finally, the pushover approach of EN 1998-1 (2004) has been applied in order to perform a simplified non-linear verification in terms of displacements.

1 INTRODUCTION

Up to now the most common column support systems for a cooling tower are diagonal frameworks with different inclination and a circular or square cross section of the columns. Their efficiency is well known and proved by use in many cooling towers all over the world.

Since 20 years also radial support columns are increasingly used for different reasons, especially in countries like Germany and France. However, a few doubts remain about their applicability in areas prone to earthquakes. Due to higher internal forces and resulting higher ratios of reinforcement they are more expansive in terms of material. One advantage of this kind of support system is the simplification of construction. The installation does not require complex spatial scaffolding, which can be highly cost intensive. Another positive aspect is the larger air inlet area, due to smaller number of columns and bigger spacing between them. Furthermore, when flue gas is directly discharged into the centre of cooling towers, there is the need to transport huge gas tubes into the cooling tower. This may become difficult with inclined columns. It can be solved by skipping one column at construction phase and replacing it after pipe transportation. Another advantage of radial columns is the wide access opening to the tower for maintenance.

The behavior under earthquake loading of these different support systems are investigated in the following to evaluate the structural advantages of these different systems.

2 CASE STUDY

2.1 *Cooling tower for case study*

As case study the cooling tower of the E.ON hard coal power plant in Datteln has been chosen. This hard coal power plant is situated close to the city of Dortmund in Germany. Its net power capacity is 1055 MW, which is one of the most powerful single block plants of Europe. The cooling tower shell has a hyperbolic shape and rests on 36 radial supports, which are situated on a ring foundation (Fig. 1).

The tower has a height of 178.10 m with a diameter of 114.40 m at the base and 71.20 m at the throat. The thickness of the shell decreases from 1.00 m at the lower edge down to 0.20 m for the main part of the shell area. The cross section of the 36 radial columns varies

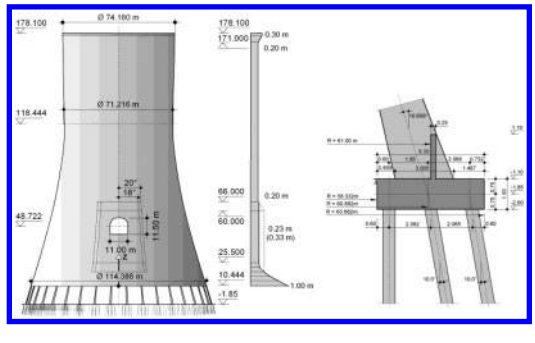
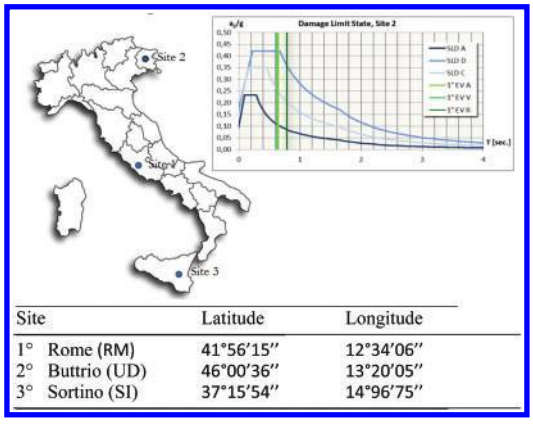


Figure 1. Dimensions of Natural Draft Cooling Tower Datteln.



Site	Latitude	Longitude
1° Rome (RM)	41°56′15″	12°34′06″
2° Buttrio (UD)	46°00′36″	13°20′05″
3° Sortino (SI)	37°15′54″	14°96′75″

Figure 2. Sites of study in Italy and seismic design spectra.

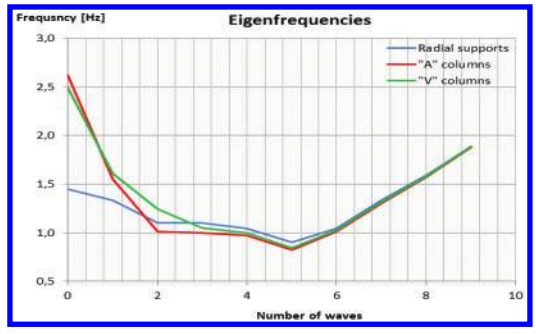


Figure 3. Eigenfreq. and wave no. of different column systems.

from 3.00 × 1.10 m at the bottom to 1.00 × 1.10 m at the top. The ring foundation has a thickness of 1.50 m and a width of 5.35 m (Andres & Woermann 2007). At Datteln power plant the cleaned flue gases, after having passed the electrostatic precipitator, are exposed directly through the cooling tower. For this reason a hole in the cooling tower shell as well as a thickening of the surrounding area for supporting the pipe is required. The main loadings which are decisive for the design of this cooling tower are wind and temperature, which both are defined by the German VGB-guideline (VGB 2010).

2.2 *Performed analyses*

In addition to the original radial support system, two alternative column arrangements are taken into account, the so-called "A"- and "V"-columns. These notations refer to the spacing between the columns heads at the lower shell edge. "V" denotes a diagonal arrangement that divides the lintel in equal divisions to reduce the bending stress at the shell base. "A" refers to the arrangement forming a true triangulated support framework at the shell base. For both of these two alternatives the diameters of the columns are chosen to 0.80 m with a pedestal at the foot of the columns.

To achieve a higher seismic load the tower is hypothetically located in three different regions in Italy (Fig. 2). To investigate the behavior of the different columns under earthquakes, three sites with different characteristics have been taken into account. The first location with low to medium base accelerations, the second with medium to high acceleration and the third with very high accelerations. Furthermore, to extend the carried out research, three subsoil classes of Eurocode A, C and D are considered.

The flue gas hole and the thickening are not considered in this parametric analysis. At first the seismic analysis is carried out with dynamic modal analysis for all 27 alternatives. Because the time-domaining non-linear analysis is computationally too burdensome in engineering practice, a non-linear static pushover analysis, as described in EN 1998-1 (2004), will be performed.

The significant construction costs and the immense consequences of a shutdown time due to possible structural failure prefer normally the elastic design, because reserves for the material ductility enhance the overall safety of the structure. EN 1998-4 (2006) clause 2.4 indeed prescribes a behavior factor 1.0 for the damage limitation state, and not greater than 1.5 in ultimate limit state verification. The seismic action is evaluated in dependence on a reference period of service life. For cooling towers normally a lifetime V_n of 100 years and an importance class of IV should be chosen for the seismic design.

All following analyses are performed with the finite elements program SOFiSTiK (2012).

3 LINEAR ANALYSIS

3.1 *Mode shapes*

All investigated cooling towers with the alternative support systems fulfill the requirements of the VGB (2010) regarding buckling safety, which impose a factor of buckling safety of 5.0 for wind and dead load.

Figure 3 shows the natural vibration eigenfrequencies correlated with the wave number of hyperbolic shell. The eigenfrequency is strictly related to the stiffness of the structure. The tower on radial supports is always stiffer for vibration wave numbers greater than 3 and generally more flexible for lowest wave numbers 0 and 1. It means that they are much less rigid for torsional motion of the shell, and quite less for translational motions. Moreover, it can be noticed that for higher wave numbers the difference between the alternative column support systems becomes smaller because of the decreasing amplitudes.

As Figure 4 shows, the larger deformations are located at column head level, while the shell is subject to a rotational/translational movement close to a rigid body. This behavior is more evident for those supports which are more flexible at lower wave number vibrations, such as radial ones and "V"-columns.

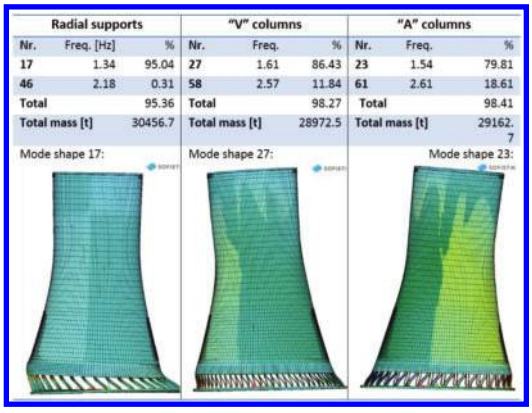


Figure 4. Mode shapes of different column systems.

It is worth to notice that the tower with radial supports has about 20% lower frequencies compared to the other solutions. This means that it has higher vibration periods, which lead to lower accelerations for most seismic design spectra.

Without taking earthquakes into account, results of the linear analysis show that towers on diagonal columns have a better behavior, especially with respect to the shells. Radial supports lead to higher thermal stresses and bending moments at the lower lintel of the shell.

3.2 *Serviceability limit state*

The VGB (2010) does not impose restriction on the serviceability limit state and therefore verification is formally not necessary. On the other hand in areas of high seismic risk, it seems to be appropriate to investigate this aspect also. Hence, in this section, it is shown how to impose a limitation for such structures.

For importance classes I and II it has to be verified that seismically action does not produce damage to construction elements without structural function, in order not to render the structure temporarily unusable. For example the limitation for a common frame building of these classes is the difference of the displacement between each floor level. The limit depends on the kind of structure and especially on the non-load-bearing walls.

The natural draft of a cooling tower will function until the structure hypothetically collapses. Normally a gap between the shell and the internal fill structures exists, so an uncoupled system can be assumed.

Since these proofs are not required in detail in EN 1998-1 (2004), the Italian design code is additionally observed (NTC 2008). For structures of importance class III and IV two verifications are necessary. The first one, regarding the Operational Limit State (O.L.S.), requires the avoidance of cracking under weak earthquake. To impose a limitation on the displacements, a couple of columns has been analyzed: Also under the strongest earthquake the calculated displacements are far below the limitation of the serviceability limit state.

The second requirement is concerned with the Immediate occupancy Limit State (I.L.S.), verifying the resistance as indicated below. At the I.L.S., in order to limit the suffered damage, the code requires a resistance verification for exceptional situations. In this case the ordinates of the spectra can be reduced by a factor $\eta = 2/3$. Furthermore, since it is an exceptional situation, all partial safety factor of the material can be set to 1.0. Because of the fact that in the Ultimate Limit States with behavior factor 1.0 all partial safety factors are the same this verification can be neglected.

3.3 *Capacity design on a cooling tower*

Capacity design is based on the fact that energy released by an earthquake is absorbed by the structure through damage of structural and nonstructural components. Seismic damages should occur in a controlled way and at precise points to avoid collapse of the whole structure. This behavior is normally achieved through cracking of reinforced concrete members or yielding of diagonal steel braces. The structure has to sustain significant deformation without failure. To achieve the desired failure mechanism, the members not participating in the failure are provided by additional strength or overcapacity. This method has a considerable advantage: with minimum increase of cost it is able to satisfy the requirements in terms of earthquake resistance. However, it must be considered that this method has been developed for frame structures, for which the behavior described above is relatively easy to obtain. The capacity design would necessarily have to provide overcapacity to the columns, as the weakest link of the structural integrity of the system. However in diagonal arrangement, one finds slender columns under high compression, hence there is no chance of a plastic hinge. Instead, it seems possible that this method may be successfully applied, although with modest benefit, on cooling towers with radial supports.

3.4 *Effects on the shell*

The effects of earthquakes on cooling tower shells are small in comparison with those ones of wind and temperature. Indeed wind bends the shell acting with different pressure coefficient over height and circumference. Earthquakes instead give horizontal impulses nearly constant along the ring foundation which firstly affect the columns. Radial support columns, which bend the lower shell edge at area with minor stiffness, lead to high internal forces at the first two shell meters. In this area the shell thickness and the reinforcement ratio are high. So forces can be distributed to adjacent areas without additional strengthening. The situation improves for diagonal arrangements, where the largest part of the seismic action is carried by the columns which are located under the stiff area of the shell with respect to the direction of the seismic action.

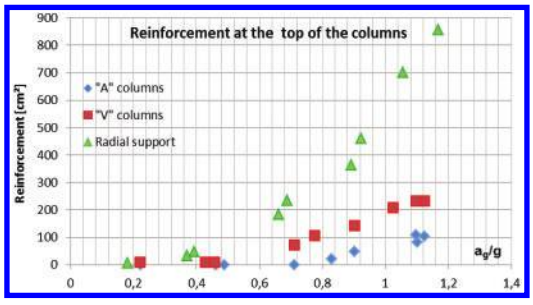


Figure 5. Reinforcement at columns head acc. to acceleration.

Above this edge-near shell area, effects of earthquake are negligible because of the rigid behavior of the shell.

3.5 *Effects on the columns*

Linear analysis shows that diagonal column arrangements resist well to horizontal acceleration. The columns are almost only affected by axial forces. That holds especially true for "A"-columns which lead horizontal forces effectively to the foundation. For "V"-columns instead bending moments become more important and axial forces are higher, because of minor inclination between the two columns. Thus the study shows that "A"-columns can resist to all investigated earthquakes without additional reinforcement with respect to the basic design for wind load, but "V"-columns require some additional longitudinal reinforcement for middle to strong earthquakes, as shown in Figure 5.

This situation gets significantly more worse for radial supports, which resist to horizontal acceleration only by bending. The behavior is less efficient than for the other cases and the reinforcement which results from the basic design is sufficient only for weak and medium earthquakes. Usually the dimensions of the columns have upper limits, because this affects the flow of incoming air. Also the reinforcement ratio is limited by the regulations of the design codes. Because of both limits, radial support columns should not be chosen in case of high earthquake excitation.

3.6 *Effect of wind on earthquake combination*

Regarding seismic actions, VGB-guideline requires to refer to the design code of the respective country where the tower will be built. In modern design codes often wind loading must not to be taken into account in combination with earthquakes. This is because the very low probability that both actions occur simultaneously. However, for tall structures such as cooling towers or shafts of wind turbines, it is far more probable that wind action is present than not. For this reason, the VGB-guideline, up to the previous edition, required to include a percentage of wind on the earthquake combination. In this case, the exceptional design situation for earthquake was assumed.

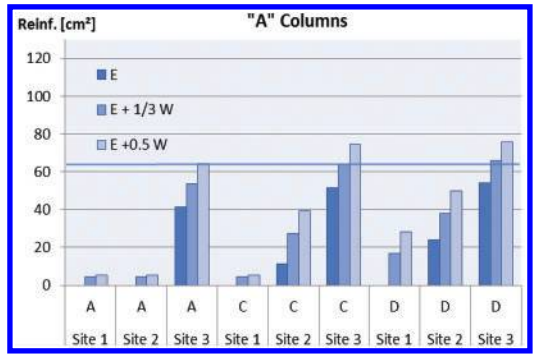


Figure 6. Reinforcement for wind-earthquake combination.

The effects of this combination on the columns are now evaluated. The following combinations will be considered in order to get certain information about the influence of the wind:

$$\sum G_{k,i} + A_R + 0.333W + \sum \psi_{2,i} \cdot Q_{k,i}$$

$$\sum G_{k,i} + A_R + 0.5W + \sum \psi_{2,i} \cdot Q_{k,i}$$

The main effects, if wind is involved, are bending and traction in the shell and additional compressive or tensile strengths in the columns. Since the shell continues to have no considerable problems with such low wind actions, we check again the effects on the columns, starting with the stiffer ones.

By observing the computed results the following remarks can be made:

1) "V"-columns require more reinforcement by rise of the base acceleration,
2) on "A"-columns the effect of wind load is more incisive, but generally they require less reinforcement than all the other cases,
3) in combination with wind load, the earthquake may become decisive also for "A"-columns (Fig. 6).

Furthermore also the influence of the wind direction with respect to earthquake excitations has been investigated. It can be shown that the influence is not very high, always less than 5%.

4 PUSHOVER ANALYSIS

In recent years this method has asserted itself increasingly, for the following reasons. Elastic analysis is not capable of providing reasonable estimates of inelastic deformation or damage. On the other hand nonlinear dynamic time history analysis is capable of providing this information, but is very time-consuming for larger structures.

The pushover analysis of a structure is a static nonlinear analysis under permanent vertical loads and gradually increasing lateral loading. The equivalent

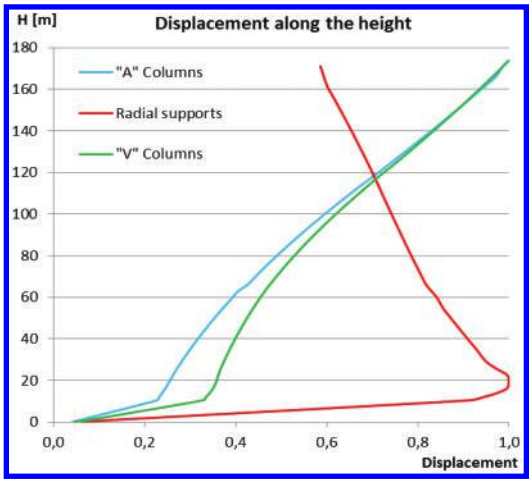


Figure 7. Normalized displacement of first mode shape.

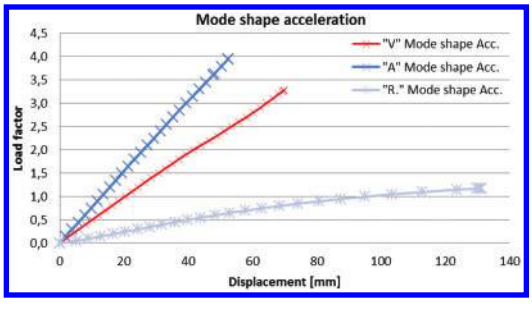


Figure 8. Pushover analysis with mode shape acceleration.

static lateral loading approximately represents earthquake induced forces. The analysis is carried out up to failure, thus it enables determination of collapse load and ductility capacity. For the pushover analysis two load distributions are generally applied. One distribution is constant over height, and the second is proportional to the first mode shape which activates the highest possible percentage of mass.

The second distribution varies over height. The average displacement of the nodes of each parallel circle has been calculated, generating a curve along the whole height. This curve was normalized to the maximum displacement and used to scale the acceleration. In Figure 7 the normalized displacement of the first mode shape is shown.

Figure 8 shows for example one of the results of this analysis. It can be seen that the radial column support is the only one which shows a ductile behavior. In this case the system is able to distribute the forces after reaching yield stresses into the neighbored areas.

The N2-method of EN 1998-1 (2004) is a nonlinear method for performance-based seismic design where the displacement demand must be compared with the displacement capacity of the structure. Such analysis methods are typically recommended for the performance assessment of existing structures. We use this method to evaluate the impact of earthquakes on the

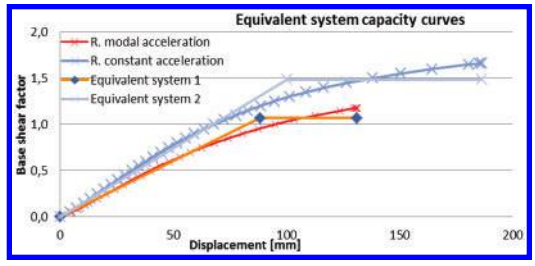


Figure 9. Equivalent capacity curve for radial support system.

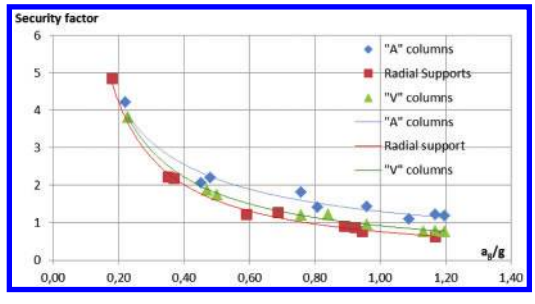


Figure 10. Security factors depending on the base acceleration.

cooling towers previously designed. Once the capacity curve of the whole structure is calculated, an equivalent system with only one degree of freedom is defined with a bilinear equivalent capacity curve (Fig. 9).

The theory of this method is simple and can be directly taken from EN 1998-1 (2004). In the case of a cooling tower, things are simplified because the shell can be considered as a rigid body.

Figure 10 shows the security factor, which is the quotient between the maximum displacement of the capacity curve and the demand for the specific acceleration. It can be seen that the results are nearly the same as from a linear analysis. “A”-columns still resist all investigated earthquakes, whereas radial and “V”-columns loose their capacity for stronger earthquakes.

5 COOLING TOWER AT KORADI POW. PLANT

This actual project comprises the design of three similar cooling towers with a height of 185.00 m in the state of Maharashtra, India for the TPS Expansion Project 3 × 660 MW, unit 8, 9 & 10 at Koradi near the city of Nagpur in central India. These cooling towers, being under construction now, are situated on extremely weak ground. Further information can be taken from Andres et al. (2012).

The above described studies concerning earthquake and the low soil bearing capacity lead to the stiff deep foundation system which is shown in Figure 11.

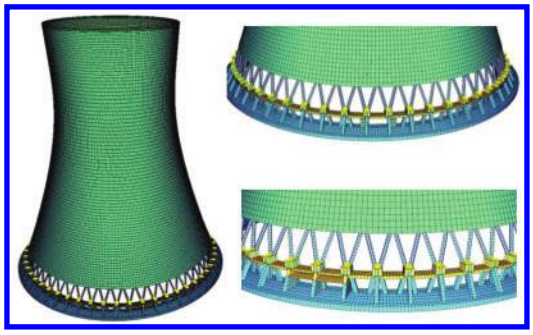


Figure 11. FE-Model of Koradi Tower.

6 CONCLUSIONS

Finally we affirm that radial columns are the less statically efficient ones, because of the temperature loads and the higher spacing at the lower lintel, which confer higher stresses to the shell. Since the cross section can not be enhanced, in order not to obstruct the air entrance surface, the reinforcement ratio rises quickly with the horizontal load exceeding the maximum allowable limit.

For "A"- and "V"-column systems the need of additional reinforcements for seismic actions results for higher horizontal loadings. However they are able to resist at most of the sites and soil conditions which were investigated. Furthermore they are the best choice for the shell because the lower lintel is divided in equal spaced pieces allowing to reduce internal forces and required materials.

Summarizing the results, radial columns, although more expensive and not extremely efficient, became recently most popular for many different not properly structural reasons. "V"-columns appear to be the best compromise until the seismic action does not reach too high values. Indeed, "V"-columns seem to be suitable for almost all sites where steam power stations will be built (Casucci 2012).

REFERENCES

Andres, M., Eckstein, U., Peters, J. & Suryanarayanan, NK. 2012. Cooling tower practice in different countries with and without consideration of VGB guidelines, In Harte, R. & Meiswinkel, R. (eds.) *Proc. of 6th International Symposium on Cooling Towers, Cologne, Germany, June 20–23, 2012:* 217–222.

Andres, M. & Woermann, R. 2007. Anwendung der neuen Normen im Kraftwerksbau am Beispiel flach- und pfahlgegründeter Kühltürme (in German), In *Tagung 2007, Bauen auf gutem Grund, 30. November 2007, Dortmund, Germany,* 127–152.

Casucci, D. 2012. Stress analysis and structural design of a cooling tower under seismic loads, Master thesis, University of Fiorenze, Italy.

EN 1998-1: 2004. Eurocode 8: Design of structures for earthquake resistance – Part 1: General rules, seismic actions and rules for buildings, CEN, Brussels, Belgium.

EN 1998-4: 2006. Eurocode 8: Design of structures for earthquake resistance – Part 4 Part 4: Silos, tanks and pipelines, CEN, Brussels, Belgium.

NTC 2008. Nuove norme tecniche per le costruzioni, (in Italian), Decreto Ministeriale 14 gennaio 2008, Italy.

SOFISTIK 2012. Manuals for Finite Element System, SOFISTIK AG, Oberschleissheim, Germany.

VGB 2010. VGB-PowerTech: Structural Design of Cooling Towers, VGB Guideline on the Structural Design, Calculation, Engineering and Construction of Cooling Towers, VGB-R 610e, VGB Powertech e.V., Essen, Germany.

Research and Applications in Structural Engineering, Mechanics and Computation – Zingoni (Ed.)
© 2013 Taylor & Francis Group, London, ISBN 978-1-138-00061-2

Future development of the European seismic code, Eurocode 8

E.D. Booth
Edmund Booth Consulting Engineer, Tring, UK

ABSTRACT: Publication of the ten structural Eurocodes during the first decade of the 21st century represented one of the most ambitious projects of European collaboration in structural engineering. Eurocode 8 – design of structures for earthquake resistance – was published in 2004, and its six parts gave it a scope which exceeded any other seismic code anywhere in the world; thus, it covered not just buildings, but also bridges and a range of other civil and industrial structures. Moreover, it applied to a very wide range of seismic hazard conditions, from the low seismicity of Northern Europe to the highly active regions of the South. Many of the provisions of the code were among the most advanced available at the time of publication, and represented a distinctly different tradition and approach from that found in US seismic codes such as ASCE 7 and ACI 318. However, earthquake engineering is a rapidly advancing discipline, and since the code was originally drafted there have been many important developments, including those in seismic hazard assessment, foundation and structural design, seismic performance specification and seismic analysis. Moreover, societal expectations for structural and non-structural performance in an earthquake are becoming much more demanding. Work on revising all the Eurocodes, including Eurocode 8 (EC8), is due to start in 2014, with the intention of publishing revised standards for use in around 2020. The paper reports on the current proposals for upgrading EC8. In the opinion of the author, who has been involved in EC8's development for over twenty years, a broad ranging review of objectives for EC8 should also be undertaken, to set out a framework for its development after the current revision process is complete.

1 INTRODUCTION

1.1 *Evolution of the structural Eurocodes*

The ten structural Eurocodes were published as finally approved standards during the period 2002 to 2005, and since 2010 they have superseded the national codes of many of the 33 European countries which are members of the European Committee for Standardisation (Comité Européen de Normalisation or CEN). This major change in practice represented a great challenge to European engineers; therefore, CEN decided that a period of stability was needed after the initial introduction of the Eurocodes. No changes to the Eurocodes were to be allowed for at least ten years after first publication, apart from essential corrections and clarifications. However, that period of stability is now complete and a formal review of all the Eurocodes will start in 2014. It is hoped that the revised standards emerging from the review will be approved for use from around 2020.

At the time of writing (March 2013), CEN/TC250, which is the Technical Committee of CEN overseeing all the Eurocodes, was about to submit a proposal to the European Commission identifying the work needed to update all the Eurocodes, including the seismic standard Eurocode 8 (EC8). This proposal requests funding from the European Commission for certain parts of the work, with the remainder intended to be carried out by voluntary activity. The Commission's response is due at the end of 2013. Funding from the Commission is expected to be very limited.

One primary aspiration for the next generation of Eurocodes will be to bring national practices more into line, by reducing the number of parameters and procedures for which national choice is permitted, as expressed in each nation's National Application Document. Another major aspiration is to simplify the codes. While those aspirations may be sufficient for many of the Eurocodes, the recent rapid and radical developments in earthquake engineering demand suggest more extensive changes will be needed to EC8.

1.2 *Eurocode 8 (EC8) – design of structures for earthquake resistance*

Creating a comprehensive and coordinated set of design rules to cover a very wide range of seismic engineering situations was a major task. The scope of the six parts of EC8 (see Table 1) exceeded that of any of the pre-existing European seismic codes, or indeed that of any seismic code anywhere in the world. It had to cover the very wide range of seismic hazard and construction types that exists over the various parts of Europe, and it also covered not only building structures but also bridges and a wide range of industrial and civil structures. Some innovative features made aspects of

Table 1. The six parts of EN1998 (EC8): Design of structures for earthquake resistance.

Number	Title
EN 1998-1	General rules, seismic actions and rules for buildings Section 1: General Section 2: Performance requirements and acceptance criteria Section 3: Ground conditions and seismic action Section 4: Design of buildings Sections 5–9: Specific rules for buildings in concrete, steel, composite steel-concrete, timber and masonry Section 10: Base isolation
EN 1998-2	Bridges
EN 1998-3	Assessment and retrofitting of buildings
EN 1998-4	Tanks, silos and pipelines
EN 1998-5	Foundations, retaining structures and geotechnical aspects
EN 1998-6	Towers, masts and chimneys

EC8 more advanced than any other code available in 2004; for example, the treatment of geotechnical issues was particularly ambitious. Therefore, the successful publication of EC8 nine years ago was a considerable achievement, and it has subsequently been used as a model for codes in countries outside Europe, such as Egypt and Vietnam.

However, earthquake engineering is a rapidly developing field, perhaps changing more rapidly than applies to the topic of any other Eurocode. The long period of drafting, which took over 15 years, means that many of the procedures and approaches in the code are considerably older than nine years. The feedback from users during the next revision process will of course provide much useful information on what needs changing and simplifying, and the process of harmonizing national choices will also be useful. However, more wide ranging changes are also needed.

2 THE EVOLUTION OF EC8

2.1 *Areas identified for redrafting by CEN*

As explained above, CEN Technical Committee TC250, which is responsible for the Eurocodes, is submitting proposals to the European Commission for the work required to revise and update the Eurocodes. The proposals relating to EC8 were prepared by the CEN sub-committee on EC8; the work items identified were as follows.

2.1.1 *European seismic zonation*

At present, EC8 specifies the seismic ground motions to be used in design in terms of a response spectrum. This is defined by means of the peak ground acceleration (PGA) on rock, which is used to scale standard spectral shapes depending on both the ground conditions at a particular site, and the magnitude of the earthquake controlling the seismic hazard. The return period of the PGA to be used for design is recommended as 475 years, although this is a 'nationally determined parameter (NDP)' which countries may vary. Similarly, spectral shapes are recommended but are also subject to national choice. However, EC8 gives no guidance on the seismic zonation itself – i.e. the values of design PGA to be used at a particular location. That is left for the national standard authority in the country concerned to define in its 'National Annex' (NA) to EC8 Part 1.

Each country has used somewhat different models and methods to define its seismic zonation and this has led to a lack of harmonization between CEN member countries. For example, the seismic hazard defined in the NA of one country on one side of a national border may be very different from that on the other side, as defined in the adjacent country's NA.

To address this, a major European collaborative project now nearing completion called SHARE (www.share-eu.org/), funded by the European Commission, has attempted to define a standard approach and common models to produce a harmonized European approach to seismic zonation, and has also proposed changes to EC8 procedures. In particular, the use of a single parameterfor defining hazard has been questioned. Currently EC8 specifies PGA at 475 year return period as the single defining parameter, but SHARE recommends use of multiple parameters based on spectral response at different periods. Allowing for the dependence of site amplification on the intensity of motion, not currently included in EC8, is also recommended. Both these changes were adopted some time ago in US seismic codes.

The results and recommendations of SHARE will be a major source for the proposed task of harmonizing European seismic zoning and more generally of improving the specification of design ground motions in EC8.

2.1.2 *Displacement based design*

Currently, the standard analysis method for buildingsin most seismic codes, including EC8, is based on an equivalent static or response spectrum method, with reduction factors (q in EC8 and R in the US seismic codes) modifying response to allow for the availableductility. These essentially linear elastic methods give no information on the distribution of plastic strains in the building, and the reduction factors are a crude measure of the ductile response available. In the last 20 years, efforts have been made to develop analysis methods which give a better indication of seismic performance without resulting in an unacceptable increase in complexity. These 'displacement based' methods involve idealizing the structure as an elasto-plastic single degree of freedom (SDOF) system, and setting the maximum displacement demand, rather than force demand as in more traditional methods, as the principle parameter determining design. The

distribution of displacements throughout the building structure, and the corresponding distribution of plastic strains, is then found by imposing the maximum displacement found from the SDOF model onto a non-linear model of the building structure in a process known as 'static pushover' or 'equivalent static' analysis.

It is claimed that these procedures result in more efficient and reliable structures, and facilitate better control of performance under serviceability as well as ultimate limit states. They form the basis of 'performance based design'.

Displacement based analysis methods in fact already appear in EC8, particularly for bridges in Part 2, and also for buildings in Part 1, although the latter are not fully described. During the current redrafting of EC8, the intention is to ensure that they are fully usable in practical terms, particularly for the design and retrofit of buildings. This would be relatively easy to do by building on the current procedures given in Annex B of EC8 Part 1, which are based on the N2 method of Fajfar (2000).

Revisions to the standard after 2020 might consider more radical departures. One possibility is that the direct displacement based design method of Priestley et al. (2007) could be adopted by EC8 as one of a number of options available to the designer. Sullivan et al. (2012) have described the procedure in code format suitable for inclusion in EC8.

2.1.3 *Steel, timber, masonry and aluminium building structures*

The current provisions in EC8 Part 1 for steel, timber and masonry building are recognized as needing significant updating. For steel buildings, the European Convention for Constructional Steel Works (ECCS) has prepared proposals for clarifying a number of issues in EC8. The ECCS proposals need to be reviewed and refined as necessary, taking into account recent research into the seismic design of steel structures. In particular, EC8 needs to reflect the results of work in the USA intended to address the issues which caused numerous failures of welded steel buildings in the Northridge, California and Kobe, Japan earthquakes of 1994 and 1995 respectively (AISC, 2010).

There have been many recent innovations in factory prefabricated timber panels for house construction, and these have included the development of new timber systems with earthquake resistance. Draft revisions to EC8 Part 1 reflecting these innovations have been prepared by Follesa et al. (2011) and these need to be reviewed and refined as necessary.

Masonry buildings form a large proportion of the domestic housing stock in Europe, but the current rules in EC8 Part 1 have been found to be onerous to apply in the low seismicity regions of Northern Europe. Moreover, the simple rules for masonry buildings given in EC8 are in need of overhaul, and are probably excessively conservative. These rules enable low rise masonry buildings to be designed without recourse to a seismic analysis by specifying minimum values of parameters such as the ratio of the total cross sectional area of walls to floor plan area. Updating is also needed to the rules for preventing walls failing out of their plane (as distinct from in-plane shear failures).

Eurocode 9 presents rules for the (non-seismic) design of aluminium structures, but none are given in EC8 and it is intended to redress this during its current revision.

2.1.4 *Infill frames and cladding*

Steel, and more especially concrete, frames infilled with brick masonry to form the external building envelope represent a common form of construction in Southern Europe. There is a complex interaction during an earthquake between the masonry infill and the frame which encloses it; in well-designed cases, the interaction can be favourable, but often it is highly deleterious. The rules in EC8 Part 1 are considered adequate to prevent the unfavourable interactions but need updating to allow designers to take more benefit from the favourable ones. There is also a need to improve the rules on providing restraint to prevent out-of-plane failures of the infill.

More generally, cladding has suffered damage in recent European earthquakes, particularly in portal-frame industrial buildings where the structure itself has performed well but the cladding has failed, giving rise to costly consequences. Improved design guidance is needed.

2.1.5 *Retrofit of buildings and bridges*

Part 3 of EC8 provides rules for the seismic assessment and retrofitting of existing buildings. Since most deaths and much of the loss due to earthquake shaking are caused by the collapse of inadequately designed existing buildings, this part is clearly of great importance, but in the author's view is the least satisfactory part of EC8. The procedures presented are rather general and theoretical, and more practical methods of assessing buildings are found in US documents, particularly ASCE 41 (ASCE, 2013).

It is hoped that the revisions to Part 3 will be able to improve this situation. It also intended to extend Part 3 to cover the retrofitting of not only buildings, but also bridges.

2.1.6 *Flat slab systems*

Flat slabs (floors which are supported by columns without an intermediate framework of beams) are currently not permitted by EC8 as a primary seismic resisting system, although they are permitted as a secondary system supporting gravity loads if the seismic loads can be taken by another system, such as a perimeter frame or series of shear walls. As a secondary system, it must be demonstrated that the flat slabs and their supporting columns can continue to carry the imposed gravity loads without yield occurring, under the deflections experienced during the design earthquake. However, some engineers in Northern Europe have found the EC8 rules for flat slabs difficult to

implement in practice, and improvements will be prepared. The rules for secondary systems more generally need review.

2.1.7 *Design of deep and shallow foundations*

It is considered that Part 5 of EC8 needs updating to include specific seismic design provisions for modelling, analysis, dimensioning and detailing of piles and shallow foundations, and some issues relating to the design of retaining walls and assessing slope stability also need review. One particular concern is to identify levels of seismicity below which particular issues, such as liquefaction or soil-pile interaction, can be safely neglected.

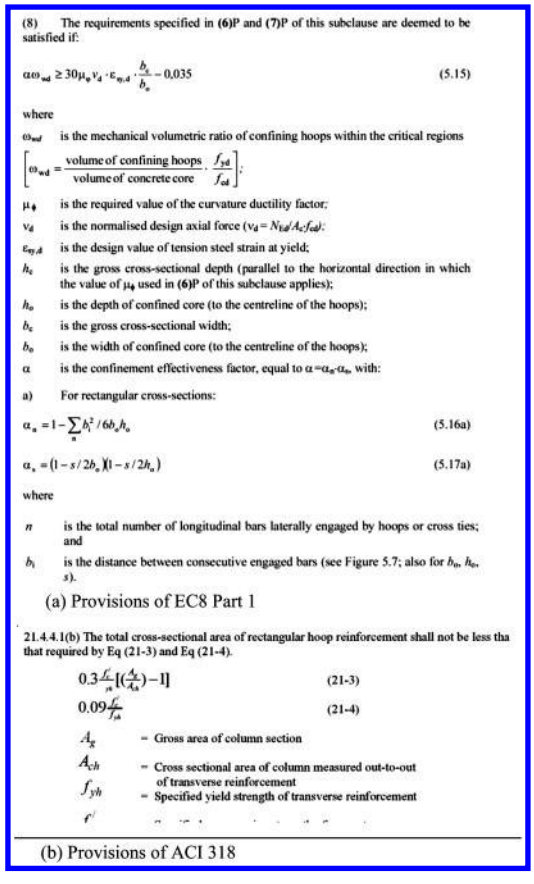
2.1.8 *Ductility classes*

EC8 specifies three ductility classes for buildings, called Ductility Class Low, Medium and High (DCL, DCM and DCH). DCL has no additional design and detailing requirements to those in the non-seismic Eurocodes, and is only recommended for areas of low seismicity. However, for medium or high seismicity areas, DCM or DCH must be chosen; DCM has higher lateral strength requirements than DCH but the design and detailing requirements are less complex. The distinction between DCM and DCH is particularly significant for reinforced concrete buildings, with relatively minor differences for steel and steel-concrete composite buildings and no practical distinctions for timber and masonry.

Similar distinctions between levels of ductility are found in US codes, and they serve an essential purpose in balancing the complexity of design and detailing requirements against the anticipated extreme seismic demand. In low seismicity areas, DCL structures can be detailed to non-seismic standards, with sufficient lateral strength for seismic resistance being provided in just the same way as for wind; this simplifies design while providing adequate safety. However, where seismic loading is the dominant consideration, more complex measures become necessary; these are currently provided by EC8 in ductility classes DCM and DCH.

The original intention was that the simpler rules for DCM would mean that safe but perhaps conservative designs could be achieved by small design offices, while larger more sophisticated practices could use the DCH rules to achieve more economy, and/or more complex structures.

In practice, this laudable aim has not in the author's opinion been achieved. As noted above, the DCH/DCM distinction is almost irrelevant to masonry and timber buildings, and there are few advantages in adopting DCH over DCM for steel or composite structures. The main differences are in the provisions for concrete, where the much more complex rules for DCH have been found in some cases to be impossible to apply. However, although the DCM rules are less extensive, in some cases they are still excessively complex whereas in other cases they are insufficiently rigorous.



(8) The requirements specified in **(6)P** and **(7)P** of this subclause are deemed to be satisfied if:

$$\alpha\omega_{wd} \geq 30\mu_\phi \nu_d \cdot \varepsilon_{sy,d} \cdot \frac{b_c}{b_o} - 0{,}035 \qquad (5.15)$$

where

ω_{wd} is the mechanical volumetric ratio of confining hoops within the critical regions $\left[\omega_{wd} = \frac{\text{volume of confining hoops}}{\text{volume of concrete core}} \cdot \frac{f_{yd}}{f_{cd}}\right]$;

μ_ϕ is the required value of the curvature ductility factor;

ν_d is the normalised design axial force ($\nu_d = N_{Ed}/A_c f_{cd}$);

$\varepsilon_{sy,d}$ is the design value of tension steel strain at yield;

h_c is the gross cross-sectional depth (parallel to the horizontal direction in which the value of μ_ϕ used in **(6)P** of this subclause applies);

h_o is the depth of confined core (to the centreline of the hoops);

b_c is the gross cross-sectional width;

b_o is the width of confined core (to the centreline of the hoops);

α is the confinement effectiveness factor, equal to $\alpha = \alpha_n \cdot \alpha_s$, with:

a) For rectangular cross-sections:

$$\alpha_n = 1 - \sum_n b_i^2 / 6 b_o h_o \qquad (5.16a)$$

$$\alpha_s = (1 - s/2b_o)(1 - s/2h_o) \qquad (5.17a)$$

where

n is the total number of longitudinal bars laterally engaged by hoops or cross ties; and

b_i is the distance between consecutive engaged bars (see Figure 5.7; also for b_o, h_o, s).

(a) Provisions of EC8 Part 1

21.4.4.1(b) The total cross-sectional area of rectangular hoop reinforcement shall not be less tha that required by Eq (21-3) and Eq (21-4).

$$0.3\frac{f'_c}{f_{yt}}\left[\left(\frac{A_g}{A_{ch}}\right) - 1\right] \qquad (21\text{-}3)$$

$$0.09\frac{f'_c}{f_{yt}} \qquad (21\text{-}4)$$

A_g = Gross area of column section

A_{ch} = Cross sectional area of column measured out-to-out of transverse reinforcement

f_{yh} = Specified yield strength of transverse reinforcement

f'

(b) Provisions of ACI 318

Figure 1. Comparison between EC8 and ACI 318 requirements for transverse steel at the ends of columns.

For example, the rules for confinement steel in the columns of moment resisting frames are based on a complex theoretical formula which is not easy to apply in practice (Figure 1(a)). They require a detailed calculation of the effectiveness of the confinement steel and are based on the 'mechanical volumetric ratio' of the steel, not a concept with which most structural engineers are familiar. The equivalent rules in the US standard ACI 318 are not only much simpler (Figure 1(b)), but also relate to a much simpler measure than volumetric ratio of steel, namely the ratio between the hoop steel's area and the concrete. There is no doubt that the EC8 formula is theoretically sounder. However, for DCM it only needs to be applied at the base of the columns, with steel at other locations governed by much simpler and less onerous rules, which in the author's opinion are likely to be insufficient in some cases.

By contrast, the rules for checking columns which are not part of the lateral load resisting structure (called 'secondary' elements by EC8) are less rigorous than their equivalents in ACI 318 and recent experience from earthquakes in New Zealand (Canterbury Earthquakes Royal Commission, 2012) and elsewhere suggest they are inadequate.

Simple rules to allow small practices to achieve safe designs are certainly very valuable, but the mean of achieving this in concrete buildings needs a radical overhaul, and also needs careful review for steel, timber and masonry buildings.

2.1.9 *New technologies for earthquake resistance*

Great advances have been made in developing a range of systems which result in better seismic performance than conventional structures. One such system, base isolation, is covered in section 10 of EC8 Part 1, but these rules do not provide the comprehensive guidance now found in US standards. Other technologies have been developed which are become widely used, such as provision of supplemental damping. These are not currently covered in EC8, though they are in US codes, and EC8 will have to be extended to provide rules for these new technologies if it is to maintain its position as a leading international standard.

2.1.10 *Part 4 (Silos, tanks and pipelines) and Part 6 (Towers, masts and chimneys)*

A review will be carried out of these parts, which will be updated as necessary.

3 LONGER TERM OBJECTIVES FOR EC8

The areas of EC8 identified as needing revision in CEN's proposals to the European Commission were described in Section 2. All the topics that they address need attention, and they will significantly improve the code. They will be supplemented by a clause by clause 'systematic review' of the standard, to identify further issues of detail that need revision.

Both this systematic review and the more fundamental review described in Section 2 will be constrained by a general desire to limit changes as far as possible to those intended to improve ease of use and to reduce the topics for which national choice is allowed. The intention is to maintain a large measure of stability in the form of the standard, so that design engineers using it do not have to face yet another taxing new learning period.

However, in the opinion of the author, over a longer period more radical changes are essential. To provide a framework for these changes, an overview of the future direction in which EC8 should be carried out. The Americans have produced overviews of this sort very successfully in the past, for example in SEAOC's vision 2000 report (SEAOC 1995).

Some suggestions of the form such a roadmap could take are provided by Booth and Lubkowski (2012), who propose the following ten characteristics of the ideal EC8.

1) Incorporates state-of-the-art technology, yet remains user friendly.
2) Allows state-of-the-art buildings to be designed without undue restrictions on creativity, yet provides clear and practical guidance for standard buildings implementable without unnecessary or impracticable demands on designers' expertise and time.
3) Provides the appropriate level of earthquake performance for a variety of limit states without excessive conservatism, allowing designers and their clients to define and control with confidence structural response to an earthquake.
4) Provides guidance on the use of emerging technologies, at least to some extent, and where such technologies are not explicitly referred to, does not prevent their use.
5) Applicable across a wide range of seismic hazard conditions, from very low to very high.
6) Provides procedures for specifying design ground motions adequate for standard cases, but also provides comprehensive guidance on more sophisticated procedures for non-standard cases.
7) Provides straightforward analysis methods for superstructure and foundations which are adequate for standard cases, but also provides comprehensive guidance on more sophisticated methods.
8) Applicable across the entire range of structural types covered by the Eurocode suite, including different construction materials (steel, concrete, masonry, timber etc.), and different end uses (commercial, residential, industrial, infrastructure, etc.).
9) Within its coverage of building design, applicable to a wide range of types, from high rise, high tech to simple low rise unreinforced masonry.
10) Gives guidance on the seismic assessment and retrofit of existing structures, as well as on design of new buildings.

Booth and Lubkowski (2012) discuss these ten objectives in more detail. They recognise that some of them may be hard to reconcile with each other – for example, the goal of providing user friendly provisions with that of keeping pace with state-of-the-art technology. Nevertheless, many of the objectives are already achieved, at least to some extent, in the Eurocode as it stands, and these include a number of objectives which US and other international codes do not address to nearly the same extent. Moreover, some others are addressed in CEN's current proposals, outlined in section 2. However, the author believes that defining a clear set of overall objectives would greatly enhance the rather piecemeal approach represented by the proposals described in Section 2 of this paper.

Defining overall objectives and setting a roadmap for EC8 is unlikely to influence the objectives of the current revision process, which have already been fixed. Moreover, radical changes to EC8 are not being encouraged at this stage, because of the desire to maintain stability in the standard. However, in the longer term, EC8 will have to develop in ways which are likely to be quite fundamental, given the rapid change in analysis techniques, technical solutions and societal requirements that are likely to continue to affect the discipline of earthquake engineering. An overarching review of the type proposed would help

ensure EC8's future position as a leading and distinct international seismic code, when its next major evolution is undertaken in the 2020's.

4 CONCLUSIONS

- The seismic Eurocode, EC8, is currently undergoing a major review, as part of a process expected to lead to publication of revised versions of all the Eurocodes for use in about 2020.
- Proposals by CEN (the body responsible for European Standards) for the topics to be included in this review are being submitted for approval to the European Commission. The proposals will greatly strengthen EC8, helping it to maintain its position as a leading and distinct international seismic standard.
- Major objectives for the current review are to simplify the Eurocodes, and to reduce the possibility for variation among CEN member nations in the ways they are implemented.
- The current revision process is constrained to some extent by the desire to limit the number of major changes to the Eurocodes, in order to maintain their stability.Moreover, CEN's proposals for the evolution of EC8 are somewhat piecemeal and lack a guiding vision.
- In the longer term, more radical changes to EC8 are needed, to reflect the rapid improvements in analytical techniques and technical solutions available to seismic engineers, as well as the changing demands of society for structural and non-structural performance in an earthquake.
- In order to guide changes to EC8 after the current review is complete, it is recommended that a 'road map' should be prepared. This would define the objectives that EC8 should aim for in future, and provide an overall framework for how to achieve those objectives, which may be less constrained by the need to limit radical changes.

ACKNOWLEDGEMENTS

The help by Professor Peter Fajfar (University of Ljubljana) and Zygmunt Lubkowksi (Ove Arup Partnership) in preparing this paper is gratefully acknowledged.

REFERENCES

AISC 2010.ANSI/AISC 358-10. Prequalified Connections for Special and Intermediate Steel Moment Frames for Seismic Applications. Chicago: American Institute of Steel Construction.

ASCE 2013. ASCE/SEI 41-13: Seismic evaluation and rehabilitation of existing buildings. Reston, VA: American Society of Civil Engineers.

Booth E. and Lubkowski Z.A. 2012. Creating a vision for the future of Eurocode 8. Paper 3501, 15th World Conference on Earthquake Engineering, Lisbon, September 2012.

Canterbury Earthquakes Royal Commission 2012. Final Report Volume 2: The performance of Christchurch CBD buildings. http://canterbury.royalcommission.govt.nz/

Fajfar P. 2000. A nonlinear analysis method for performance-based seismic design. Earthq Spectra 16(3):573–592.

Follesa, M., Fragiacomo, M. and Lauriola, M.P. 2011. A proposal for revision of the current timber part (Section 8) of EC8 Part 1. Working Commission W18-Timber Structures, CIB, International Council for Research and Innovation, Alghero (Italy), paper No. CIB-W18/44-15-1, 13 pp.

Priestly, M.J.N, Calvi, G.M. and Kowalsky, M.J. 2007. Displacement-based seismic design of structures. Pavia, Italy: IUSS Press.

SEAOC 1995. Vision 2000 Report: Performance-Based Seismic Engineering of Buildings. Structural Engineers Association of California, Sacramento, CA, USA.

Sullivan T.J., Priestley M.J.N., and Calvi G.M. editors 2012. DBD12: A model code for the displacement-based design of structures. Pavia, Italy: IUSS Press.

Research and Applications in Structural Engineering, Mechanics and Computation – Zingoni (Ed.)
© 2013 Taylor & Francis Group, London, ISBN 978-1-138-00061-2

Dynamic shakedown design of structures under repeated seismic loads

S. Benfratello, L. Palizzolo & P. Tabbuso
Department of Civil, Environmental, Aerospace, Materials Engineering, University of Palermo, Italy

ABSTRACT: The paper is devoted to the formulation of an optimal design (minimum volume) problem of elastic perfectly plastic structures subjected to suitable combinations of static (fixed) and dynamic (seismic) loads. The structure is constrained to simultaneously respect two different safety criteria; actually, it must exhibit an elastic shakedown behaviour for the combination of loads characterizing the serviceability conditions and it must prevent the instantaneous collapse for the highest expected load condition (combination of loads characterized by the presence of fixed loads and maximum expected intensity of seismic action). The shakedown limit behaviour for the optimal structure will be imposed according with the unrestricted dynamic shakedown approach. The numerical application is devoted to the optimal design of a simple six floor plane steel frame and the solution is reached by utilizing a suitable harmony search algorithm.

1 INTRODUCTION

As it is well known, in the last decades several researchers devoted their studies to the optimal design problem of structures subjected to quasi-static loads and the main results are reported in several interesting books (see, e.g., Rozvany 1976, Save et al. 1985, Rozvany 1989, Haftka et al. 1990). These works contain original formulations characterized by different chosen objective functions, different special admissibility conditions as well as different computational approaches.

Other formulations have been proposed for the elastic optimal design (see, e.g., Cinquini et al. 1980), for the shakedown optimal design (see, e.g., Cohn et al. 1973, König 1975, Giambanco et al 1994a,b) and for the standard limit design (see, e.g., Maier et al. 1972).

Unfortunately, imposing just one of the cited criteria it is possible to make safe the structure just with reference to the selected corresponding structural limit state; on the contrary, the observance of suitable safety factors for the other limit states is disregarded. In order to extend the study to a more general case, some new formulations, in which suitably chosen different admissibility criteria (constraints) are simultaneously considered, have been proposed (see, e.g., Palizzolo 2004a).

Furthermore, for load conditions above the elastic shakedown limit, an alternating plasticity behaviour (plastic shakedown) is certainly preferable with respect to an incremental collapse one. A first formulation of the so-called plastic shakedown (no ratchet) optimal design of structures subjected to a combination of fixed and cyclic loads has been proposed, (see, e.g., Giambanco et al. 2002); in this formulation the restrictive hypothesis that the cyclic part of the load be a perfect one has been adopted, namely for each cyclic basic load condition an opposite one exists in the load space. Improved formulations and further applications (see, e.g., Giambanco et al. 2004, Palizzolo 2004b) have been also proposed.

Recently, further design formulations have been proposed for elastic plastic structures subjected to appropriate combinations of fixed and seismic loadings simultaneously preventing the overcoming of the elastic shakedown for serviceability conditions and the instantaneous collapse for full seismic conditions (see, e.g., Benfratello et al. 2009, Giambanco et al. 2011). In the referenced formulations the dynamic elastic response, to be utilized both for the shakedown limit and for the instantaneous collapse one, is evaluated by making recourse to a classical modal technique appropriately combining the single frequency responses; in other words, the response takes into account the dynamic features of the structures, and of the seismic action, but the shakedown yield condition is satisfied as in the case of quasi static cyclic loads.

Therefore, the present paper is devoted to the formulation of a special optimal design problem of elastic perfectly plastic frame structures subjected to different combinations of static (fixed) and dynamic (seismic) loads. In particular, the structure must be designed so as to be able to behave elastically when subjected to the action of the solely fixed load, to remain in the elastic shakedown domain in presence of serviceability conditions and to prevent the instantaneous collapse for suitably chosen combinations of fixed and high seismic loading. In the previous statement the serviceability conditions are conventionally defined as the superposition of suitably amplified fixed loads and seismic loads of appropriate low intensity.

In the present context the elastodynamic structural response is obtained by using a standard step-by-step method based on the mode superposition. Moreover, according to the unrestricted dynamic shakedown theory (see e.g., Borino et al. 1995), suitable domains are deduced by the cited responses, utilized in the elastic shakedown analysis as well as in the instantaneous collapse one.

Anyway, whatever the special formulation is utilized, substantially depending on the special limiting criterion imposed on the structure behaviour, it is very useful to know if the optimal structure, at the prescribed limit state, fulfils special limits on its functionality . In the present context these dangerous limit conditions will be disregarded, namely it is accepted the simplifying hypothesis that no secondary collapse modes can occur.

As known, the optimal design problem is a strongly non linear one, so in the scientific literature several different efforts have been devoted to the proposition of suitable computational approaches aimed to solve the relevant optimal design problem. In the present paper, the numerical application is devoted to the search for the minimum volume design of a flexural elastic perfectly plastic plane steel frame constituted by six floor. A suitable harmony search technique (see, e.g., Lee et al. 2005, Degertekin 2012) has been utilized.

The behavioural features of the obtained optimal structure for different load conditions are emphasized through the determination and interpretation of the related Bree diagram.

2 FUNDAMENTALS

In order to appropriately describe the proposed optimal design formulation, some fundamentals must be introduced mainly regarding the definition of some appropriate model both for the frame structure and for the acting loads.

2.1 *The structural model*

As known, the classical formulation of the static linear elastic analysis problem for plane frames constituted by n_b beam type elements, described by the Navier kinematical model, and n_N standard nodes (each characterized by three degrees of freedom) is given as follows:

$$\boldsymbol{d} = \boldsymbol{C}\boldsymbol{u} \tag{1a}$$
$$\boldsymbol{Q} = \boldsymbol{D}\boldsymbol{d} + \boldsymbol{Q}^* \tag{1b}$$
$$\tilde{\boldsymbol{C}}\boldsymbol{Q} = \boldsymbol{F} \tag{1c}$$

where $\boldsymbol{d}$ is the element nodal displacement vector of dimension $6 \cdot n_b$, $\boldsymbol{C}$ is the compatibility matrix with order $6 \cdot n_b \times 3 \cdot n_N$, $\boldsymbol{u}$ is the frame nodal displacement vector of dimension $3 \cdot n_N$, $\boldsymbol{Q}$ is the generalized stress vector evaluated at the extremes of the elements with order $6 \cdot n_b$, $\boldsymbol{D}$ is the frame internal (square block diagonal) stiffness matrix with order $6 \cdot n_b \times 6 \cdot n_b$, $\boldsymbol{Q}^*$ is the perfectly clamped element generalized stress vector with the same dimension of $\boldsymbol{Q}$, and $\boldsymbol{F}$ is the frame nodal force vector with the same dimension of $\boldsymbol{u}$. The solution to problem (1) is given by:

$$\boldsymbol{u} = \boldsymbol{K}^{-1}\boldsymbol{F}^* \tag{2a}$$
$$\boldsymbol{Q} = \boldsymbol{D}\boldsymbol{C}\boldsymbol{u} + \boldsymbol{Q}^* = \boldsymbol{D}\boldsymbol{C}\boldsymbol{K}^{-1}\boldsymbol{F}^* + \boldsymbol{Q}^* \tag{2b}$$

in terms of displacements and generalized stresses, respectively, with $\boldsymbol{K} = \tilde{\boldsymbol{C}}\boldsymbol{D}\boldsymbol{C}$ frame external square stiffness matrix of order $3 \cdot n_N \times 3 \cdot n_N$, and $\boldsymbol{F}^* = \boldsymbol{F} - \tilde{\boldsymbol{C}}\boldsymbol{Q}^*$ is the equivalent (in terms of structure node displacements) nodal force vector, where the over tilde means the transpose of the relevant quantity. Making reference to the seismic actions, let us consider the relevant frame as a flexural plane frame just subjected to an horizontal ground acceleration $a_g(t)$, where the masses are concentrated at each node, modeled as a Multi-Degree-Of-Freedom (MDOF) structure in which the dynamic equilibrium equations can be written in the following form:

$$\boldsymbol{M}\,\ddot{\boldsymbol{u}}(t) + \boldsymbol{B}\,\dot{\boldsymbol{u}}(t) + \boldsymbol{K}\,\boldsymbol{u}(t) = \boldsymbol{f}(t) \tag{3}$$

being $\mathbf{f}(t) = -\boldsymbol{M}\tau a_g(t)$, where $\boldsymbol{M}$ and $\boldsymbol{B}$ are the mass and damping matrices and τ is the influence vector. As known only the node horizontal displacements are dynamically significant and then the following static condensation procedure can be adopted. Let us operate a suitable partition and reordering of the above described matrices and vectors in such a way that in the case of free vibrations the equations of motion can be written:

$$\begin{pmatrix} \boldsymbol{M}_{tt} & \boldsymbol{0} \\ \boldsymbol{0} & \boldsymbol{0} \end{pmatrix} \begin{pmatrix} \ddot{\boldsymbol{u}}_t(t) \\ \ddot{\boldsymbol{u}}_r(t) \end{pmatrix} + \begin{pmatrix} \boldsymbol{K}_{tt} & \boldsymbol{K}_{tr} \\ \boldsymbol{K}_{rt} & \boldsymbol{K}_{rr} \end{pmatrix} \begin{pmatrix} \boldsymbol{u}_t(t) \\ \boldsymbol{u}_r(t) \end{pmatrix} = \begin{pmatrix} \boldsymbol{f}(t) \\ \boldsymbol{0} \end{pmatrix} \tag{3a}$$

where $\mathbf{u}_t$ is the vector that collects the structure node horizontal displacements while $\mathbf{u}_r$ collects the vertical displacements and the rotations of the nodes. Equation (3a) can be usefully rewritten in the following form:

$$\boldsymbol{M}_{tt}\,\ddot{\boldsymbol{u}}_t(t) + \boldsymbol{K}_{tt}\,\boldsymbol{u}_t(t) + \boldsymbol{K}_{tr}\,\boldsymbol{u}_r(t) = \boldsymbol{f}(t) \tag{3b}$$
$$\boldsymbol{K}_{rt}\,\boldsymbol{u}_t(t) + \boldsymbol{K}_{rr}\,\boldsymbol{u}_r(t) = \boldsymbol{0} \tag{3c}$$

the first of which represents a system of differential equations while the second one is a system of algebraic equations. The solution of the equation (3c) assumes the form:

$$\boldsymbol{u}_r(t) = -\boldsymbol{K}_{rr}^{-1}\boldsymbol{K}_{rt}\,\boldsymbol{u}_t(t) \tag{3d}$$

Substituting equation (3d) into equation (3b) one obtains:

$$\boldsymbol{M}_{tt}\,\ddot{\boldsymbol{u}}_t(t) + \boldsymbol{K}_c\,\boldsymbol{u}_t(t) = \boldsymbol{f}(t) \tag{3e}$$

that represents the condensed equation of motion for free vibration and where $\boldsymbol{K}_c = \boldsymbol{K}_{tt} - \boldsymbol{K}_{tr}\boldsymbol{K}_{rr}^{-1}\boldsymbol{K}_{rt}$ is the

condensed stiffness matrix. By performing analogous steps it is possible to define a matrix $\boldsymbol{C}_d$ obtained by condensation of matrix $\boldsymbol{B}$.

As usual the equation (3e) can be solved with a classical modal technique according to the initial conditions that hereinafter are assumed to be $\boldsymbol{u}_t(0)=\boldsymbol{0}$, $\dot{\boldsymbol{u}}_t(0)=\boldsymbol{0}$. The dynamic characteristics of the structural behaviour are identified in terms of natural frequencies as well as damping coefficients. In this framework, as usual, the following coordinate transformation is adopted:

$$\boldsymbol{u}_t(t)=\boldsymbol{\Phi}\boldsymbol{z}(t) \tag{4}$$

being $\boldsymbol{z}(t)$ the modal displacement vector and $\boldsymbol{\Phi}$ the so-called modal matrix, normalized with respect to the mass matrix and whose columns are the eigenvectors of the undamped structure, given by the solution to the following eigenproblem:

$$\boldsymbol{K}_c^{-1}\boldsymbol{M}_{tt}\,\boldsymbol{\Phi}=\boldsymbol{\Phi}\,\boldsymbol{\Omega}^{-2} \tag{5a}$$

$$\tilde{\boldsymbol{\Phi}}\,\boldsymbol{M}_{tt}\,\boldsymbol{\Phi}=\boldsymbol{I} \tag{5b}$$

$$\tilde{\boldsymbol{\Phi}}\,\boldsymbol{K}_c\,\boldsymbol{\Phi}=\boldsymbol{\Omega}^2 \tag{5c}$$

In equations (5a,c), besides the already known symbols, $\boldsymbol{I}$ represents the identity matrix while $\boldsymbol{\Omega}^2$ is a diagonal matrix listing the square of the natural frequencies of the structure.

Once the modal matrix $\boldsymbol{\Phi}$ has been determined, the structure can be defined as a classically-damped one if $\tilde{\Phi}\,\boldsymbol{C}_d\,\boldsymbol{\Phi}=\boldsymbol{\Xi}$ is a diagonal matrix whose typical non zero element Ξ_{jj} is equal to $2\,\zeta_j\,\omega_j$, being ω_j and ζ_j the jth natural frequency and the jth damping coefficient, respectively. The equation of motion in the modal space can be written as:

$$\ddot{\boldsymbol{z}}(t)+\boldsymbol{\Xi}\,\dot{\boldsymbol{z}}(t)+\boldsymbol{\Omega}^2\boldsymbol{z}(t)=\boldsymbol{g}(t) \tag{5d}$$

where $\boldsymbol{g}(t)=\tilde{\Phi}M_{tt}\boldsymbol{f}(t)$.

The solution of the decoupled system of equations (5d) together with the corresponding initial conditions provides the complete structural response in terms of horizontal displacements. Once the horizontal displacements are known the remaining ones can be determined by means of equation (3d).

2.2 *The seismic loading model*

In order to formulate the relevant design problem a suitable loading model must be defined. For the purposes of the present paper reference will be made to civil and/or industrial constructions usually subjected to combinations of fixed (gravitational) loads and dynamically variable actions (earthquake). Furthermore, the cited load combinations must be able to describe the real significant state that the structure can suffer during its lifetime. So, three different load combinations will be considered: the first is constituted by the action of the solely fixed loads (basic condition); the second one is defined by the contemporary action of a suitably amplified fixed load and a low intensity seismic action (serviceability condition); the third one takes into account the simultaneous presence of amplified fixed loads and high seismic loads (ultimate load condition). It is clear that different behaviours will characterize the structure response for the different load combinations: purely elastic behaviour for the basic loads, shakedown for serviceability conditions, preventing of the instantaneous collapse for ultimate load conditions.

For the purposes of the present paper it is necessary to conveniently model the dynamic (seismic) action on the structure, especially with reference to the shakedown condition. Actually, as known, the real load history is unknown and, as a consequence, reference must be made to a suitably defined admissible load domain. The definition of such a domain is quite easy in the case of static and/or quasi-static load, while in the case of dynamic (seismic) actions reference will be made to the unrestricted dynamic shakedown theory (Borino et al. 1995). Following this theory the seismic acceleration $\ddot{u}_g(\tau)$ is expressed as the superposition of a discrete set of single-frequency wave components $\overline{\Psi}_{ij}(\tau)$, that is

$$\ddot{u}_g(\tau)=\sum_{i=1}^{n}\sum_{j=1}^{4}\xi_{ij}\,\overline{\psi}_{ij}(\tau)\quad 0\le\tau\le T \tag{6}$$

being T the duration of the seismic action and ξ_{ij} some coefficients required to satisfy the following admissibility conditions:

$$\xi_{ij}\ge 0\quad \sum_{i=1}^{n}\sum_{j=1}^{4}\xi_{ij}=1 \tag{7}$$

in order to fulfill the convex hull theorem (De Martino et al. 2000).

In equation (6) the intensity of the ith single-frequency wave component is related to the power spectral density of the considered earthquake corresponding to ith structural natural mode (Borino et al. 1995). The latter is here modeled by the well-known Kanai-Tajimi filter model as follows:

$$S_g(\omega_i)=\frac{\left[1+4\zeta_g^2\left(\omega_i/\omega_g\right)^2\right]S_0}{\left[1-\left(\omega_i/\omega_g\right)^2\right]^2+4\zeta_g^2\left(\omega_i/\omega_g\right)^2} \tag{8}$$

where ω_g, ζ_g are ground parameters and S_0 is the seismic intensity.

3 OPTIMAL DESIGN FORMULATION

The optimal design problem formulation for a given structure strongly depends on two elements: the selected objective function and the imposed limit states characterizing the optimal structural limit behavior.

It is important to emphasize that usually the optimal structure is regarded as the lowest weight one, the latter often being also the lowest cost one.

Therefore, let us consider an elastic perfectly plastic frame structure as above described and, according to the assumed loading model, let it be subjected to fixed mechanical loads and dynamic (seismic) loads. The minimum volume design problem formulation, where suitable constraints are imposed on the purely elastic behavior, on the elastic shakedown behavior, and on the instantaneous collapse, can be written as follows:

$$\min_{(\boldsymbol{t},\boldsymbol{u}_0,\boldsymbol{u}_d,\boldsymbol{\rho}_0,\boldsymbol{\rho}_1,\boldsymbol{\rho}_2)} V \tag{9a}$$

$$\boldsymbol{t}_{min} \le \boldsymbol{t} \le \boldsymbol{t}_{max} \tag{9b}$$

$$\boldsymbol{H}\boldsymbol{t} - \bar{\boldsymbol{h}} \ge \boldsymbol{0} \tag{9c}$$

$$\boldsymbol{K}\boldsymbol{u}_0 = \boldsymbol{F}_0^* \tag{9d}$$

$$\boldsymbol{Q}_0 = \boldsymbol{D}\boldsymbol{C}\boldsymbol{u}_0 + \boldsymbol{Q}_0^* \tag{9e}$$

$$\boldsymbol{M}_{tt}\,\ddot{\boldsymbol{u}}_t^S(t) + \boldsymbol{C}_d\dot{\boldsymbol{u}}_t^S(t) + \boldsymbol{K}_c\,\boldsymbol{u}_t^S(t) = -\boldsymbol{M}_{tt}\boldsymbol{\tau}\ddot{u}_g^S(t) \tag{9f}$$

$$\boldsymbol{u}_r{}^S(t) = -\boldsymbol{K}_{rr}{}^{-1}\boldsymbol{K}_{rt}\,\boldsymbol{u}_t{}^S(t) \tag{9g}$$

$$\boldsymbol{Q}^S(t) = \boldsymbol{D}\boldsymbol{C}\boldsymbol{E}\begin{pmatrix}\boldsymbol{u}_t{}^S(t)\\ \boldsymbol{u}_r{}^S(t)\end{pmatrix} \tag{9h}$$

$$\boldsymbol{Q}_+^S = \max_{0\le\tau\le t}\boldsymbol{Q}^S(t) \tag{9i}$$

$$\boldsymbol{Q}_-^S = \min_{0\le\tau\le t}\boldsymbol{Q}^S(t) \tag{9j}$$

$$\boldsymbol{M}_{tt}\,\ddot{\boldsymbol{u}}_t{}^I(t) + \boldsymbol{C}_d\dot{\boldsymbol{u}}_t{}^I(t) + \boldsymbol{K}_c\,\boldsymbol{u}_t{}^I(t) = -\boldsymbol{M}_{tt}\boldsymbol{\tau}\ddot{u}_g{}^I(t) \tag{9k}$$

$$\boldsymbol{u}_r{}^I(t) = -\boldsymbol{K}_{rr}{}^{-1}\boldsymbol{K}_{rt}\,\boldsymbol{u}_t{}^I(t) \tag{9l}$$

$$\boldsymbol{Q}^I(t) = \boldsymbol{D}\boldsymbol{C}\boldsymbol{E}\begin{pmatrix}\boldsymbol{u}_t{}^I(t)\\ \boldsymbol{u}_r{}^I(t)\end{pmatrix} \tag{9m}$$

$$\boldsymbol{Q}_+^I = \max_{0\le\tau\le t}\boldsymbol{Q}^I(t) \tag{9n}$$

$$\boldsymbol{Q}_-^I = \min_{0\le\tau\le t}\boldsymbol{Q}^I(t) \tag{9o}$$

$$\boldsymbol{\varphi}_+^E = \xi_0\tilde{\boldsymbol{G}}_p\boldsymbol{Q}_0 - \boldsymbol{R} \le \boldsymbol{0} \tag{9p}$$

$$\boldsymbol{\varphi}_-^E = -\xi_0\tilde{\boldsymbol{G}}_p\boldsymbol{Q}_0 - \boldsymbol{R} \le \boldsymbol{0} \tag{9q}$$

$$\boldsymbol{\varphi}_+^S = \xi_0^S\tilde{\boldsymbol{G}}_p\boldsymbol{Q}_0 + \xi^S\tilde{\boldsymbol{G}}_p\boldsymbol{Q}_+^S + \boldsymbol{\rho}_0 - \boldsymbol{R} \le \boldsymbol{0} \tag{9r}$$

$$\boldsymbol{\varphi}_-^S = -\xi_0^S\tilde{\boldsymbol{G}}_p\boldsymbol{Q}_0 - \xi^S\tilde{\boldsymbol{G}}_p\boldsymbol{Q}_-^S - \boldsymbol{\rho}_0 - \boldsymbol{R} \le \boldsymbol{0} \tag{9s}$$

$$\boldsymbol{\varphi}_+^{I1} = \xi_0^I\tilde{\boldsymbol{G}}_p\boldsymbol{Q}_0 + \xi^I\tilde{\boldsymbol{G}}_p\boldsymbol{Q}_+^I + \boldsymbol{\rho}_1 - \boldsymbol{R} \le \boldsymbol{0} \tag{9t}$$

$$\boldsymbol{\varphi}_-^{I1} = -\xi_0^I\tilde{\boldsymbol{G}}_p\boldsymbol{Q}_0 - \xi^I\tilde{\boldsymbol{G}}_p\boldsymbol{Q}_-^I - \boldsymbol{\rho}_1 - \boldsymbol{R} \le \boldsymbol{0} \tag{9u}$$

$$\boldsymbol{\varphi}_+^{I2} = \xi_0^I\tilde{\boldsymbol{G}}_p\boldsymbol{Q}_0 + \xi^I\tilde{\boldsymbol{G}}_p\boldsymbol{Q}_+^I + \boldsymbol{\rho}_2 - \boldsymbol{R} \le \boldsymbol{0} \tag{9v}$$

$$\boldsymbol{\varphi}_-^{I2} = -\xi_0^I\tilde{\boldsymbol{G}}_p\boldsymbol{Q}_0 - \xi^I\tilde{\boldsymbol{G}}_p\boldsymbol{Q}_-^I - \boldsymbol{\rho}_2 - \boldsymbol{R} \le \boldsymbol{0} \tag{9w}$$

$$\tilde{\boldsymbol{A}}\boldsymbol{\rho}_0 = \boldsymbol{0} \quad \tilde{\boldsymbol{A}}\boldsymbol{\rho}_1 = \boldsymbol{0} \quad \tilde{\boldsymbol{A}}\boldsymbol{\rho}_2 = \boldsymbol{0} \tag{9x}$$

In equation (9b,c) $\boldsymbol{t}$ is the design variable vector, $\boldsymbol{H}$ is the technological constraint matrix, $\bar{\boldsymbol{h}}$ represents a suitably chosen technological vector. In equations (9c-o): $\boldsymbol{u}_0$ and $\boldsymbol{Q}_0$ are the purely elastic response to the assigned full fixed loads; $\boldsymbol{u}_t^S$, $\boldsymbol{u}_r^S$, $\boldsymbol{Q}_+^S$, $\boldsymbol{Q}_-^S$ are the elastic response to low seismic actions; $\mathbf{u}_t^I$, $\boldsymbol{u}_r^I$, $\boldsymbol{Q}_+^I$, $\boldsymbol{Q}_-^I$ are the elastic response to high seismic actions; $\mathbf{E}$ is a matrix necessary to reordering the structural displacements. In equations (9p-w): $\boldsymbol{\phi}_+^E$, $\boldsymbol{\phi}_-^E$, $\boldsymbol{\phi}_+^S$, $\boldsymbol{\phi}_-^S$, $\boldsymbol{\phi}_+^{I1}$, $\boldsymbol{\phi}_-^{I1}$, $\boldsymbol{\phi}_+^{I2}$, $\boldsymbol{\phi}_-^{I2}$ are the plastic potential vectors related to the purely elastic limit (apex E), to the elastic shakedown limit (apex S) and to the instantaneous collapse limit (apex I), respectively; $\boldsymbol{\rho}_0$, $\boldsymbol{\rho}_1$, $\boldsymbol{\rho}_2$ are the self-equilibrated stress vectors satisfying the equilibrium conditions expressed by equation (9x). In addition: $\tilde{\boldsymbol{G}}_p$ is an appropriate equilibrium matrix which applied to element nodal generalized stresses provides the generalized stresses acting upon the plastic nodes of the elements; A is a compatibility matrix which applied to element node displacements provides the plastic strains evaluated at the strain points; $\boldsymbol{R}$ is the relevant plastic resistance vector. Finally, ξ_0, ξ_0^S, ξ^S, ξ_0^I, ξ^I are scalar load multipliers suitable to define the load combinations.

4 APPLICATION

The optimal design of a steel frame has been obtained referring to the previously proposed formulation. The minimum volume design problem (9) has been solved, utilizing a suitable harmony search algorithm (Degertekin 2012), for the frame plotted in Fig. 1. The frame is constituted by square box cross section elements (Fig. 2) with $\ell = 250$ mm. The constant thickness t has been assumed as design variable.

Furthermore, the following geometrical and material characteristics have been assumed: $L_1 = 7.00$ m, $L_2 = 5.00$ m, $H = 4.00$ m, Young modulus $E = 210$ GPa, yield stress $\sigma_y = 235$ MPa. Two rigid perfectly plastic hinges are located at the extremes of all elements, considered to be purely elastic (Fig. 3); an additional hinge is located in the middle point of the longer beams.

The structure is subjected to a fixed uniformly distributed vertical load on the beams, $q_0 = 60$ kN/m and to seismic actions. Seismic masses are equal at each floor: $m_1 = 21.40$ kNs^2/m, $m_2 = 36.69$ kNs^2/m, $m_3 = 15.29$ kNs^2/m, and located at each structural nodes.

In the case of serviceability conditions the ground acceleration $\ddot{u}_g^S$ has been characterized by the following Kanai-Tajimi parameters: $\zeta_g = 0.65$, $\omega_g = 18$ rad/s and $S_0 = 0.0012$. In the case of ultimate limit load conditions, the ground acceleration $\ddot{u}_g^I$ has been characterized by the same parameters except for $S_0 = 0.0032$. The adopted load combinations are defined by the following load multipliers $\xi_0 = 1$, $\xi_0^S = 1.25$, $\xi^S = 1$, $\xi_0^I = 1.25$, $\xi^I = 1$. The results in terms of optimal volume and optimal thicknesses are reported in Table 1.

The obtained design features have been investigated through the determination of the relevant Bree diagrams related to the combinations of suitably amplified fixed loads and seismic actions. In Fig. 4 the cited diagrams are plotted where ξ_0 represents the fixed load multiplier and ξ_c the dynamic load one. It is easy to

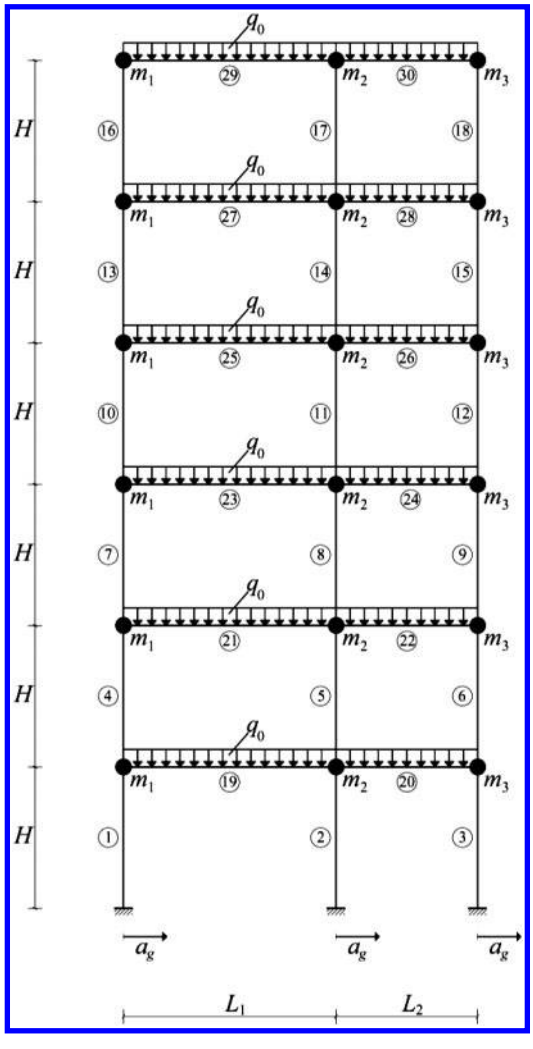


Figure 1. Six floor steel frame: geometry and load conditions.

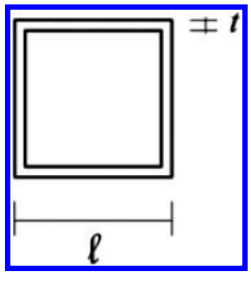


Figure 2. Typical square box cross section.

observe that, as expected, all the imposed behavioural constraints are satisfied. In particular, the structure shows to especially suffer the load combination involving high seismic loads: actually, it exhibits a certain safety margin in serviceability seismic conditions with to the shakedown limit, and it finds itself in a condition of impending collapse for fixed and high seismic loads.

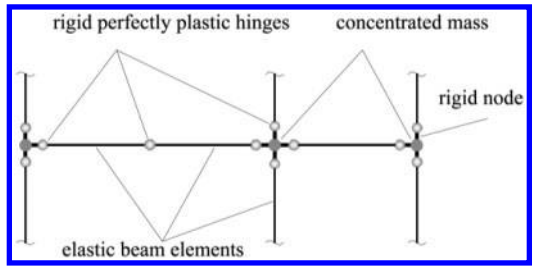


Figure 3. Structural scheme.

Table 1. Optimal volume (m^3) and optimal thicknesses (mm).

Volume: 1.478					
El.	**1**	**2**	**3**	**4**	**5**
t	9.96	10.19	10.17	10.63	9.31
El.	**6**	**7**	**8**	**9**	**10**
t	9.28	9.48	11.86	8.10	19.75
El.	**11**	**12**	**13**	**14**	**15**
t	21.20	20.47	21.50	19.84	19.32
El.	**16**	**17**	**18**	**19**	**20**
t	8.85	8.34	8.03	8.00	8.70
El.	**21**	**22**	**23**	**24**	**25**
t	9.14	8.99	8.23	8.18	8.09
El.	**26**	**27**	**28**	**29**	**30**
t	8.17	8.58	8.35	9.20	8.09

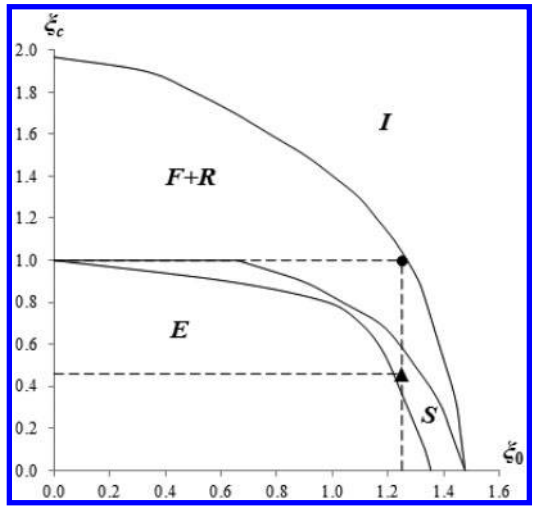


Figure 4. Bree diagrams related to the combinations of amplified fixed loads and seismic actions (▲ imposed serviceability condition, ● imposed instantaneous collapse condition).

5 CONCLUSIONS

The present paper has been devoted to the optimal design of elastic perfectly plastic frames subjected to fixed and dynamic actions. The optimal design problem has been formulated as the search for the minimum

volume structure and three different resistance limits have been simultaneously considered: the purely elastic limit, the elastic shakedown limit and the instantaneous collapse limit. In the proposed formulation, in order to take into account the seismic load, reference has been made to the unrestricted dynamic shakedown theory. In particular, a basic load condition has been defined as constituted by the solely assigned fixed loads; the serviceability conditions have been defined as the combination of amplified fixed loads and low seismic actions; the ultimate limit conditions have been defined as the combination of amplified fixed loads and high seismic actions. A computational application has been developed related to a six floor plane. The features of the obtained optimal structure have been deduced by the interpretation of the related Bree diagrams. It has been found that the structure obtained by the solution of the proposed optimal design problem guarantees a safe behaviour with respect to all the imposed limit states. The obtained results are encouraging and further numerical applications applied to practical engineering problems are expected as well as more restrictive descriptions of the basic loads utilized for the dynamic shakedown formulation.

REFERENCES

Benfratello, S. & Giambanco, F. & Palizzolo, L. 2009. Optimal design of structures under dynamic loading, *XIX Congresso Nazionale AIMETA*, Ancona (Italy), September 14–17.

Borino, G.& Polizzotto, C. 1995. Dynamic shakedown of structures under repeated seismic loads. *J. Eng. Mech. ASCE* 121(12), 1306–1314.

Cinquini, C. & Guerlement, G. & Lamblin, D. 1980. Finite element iterative methods for optimal elastic design of circular plates. *Comp. and Struct*. 12(1), 85–92.

Cohn, M.Z. & Parimi, S.R. 1973. Optimal design of plastic structures for fixed and shakedown loadings. *J. Appl. Mech.* 595–599.

De Martino, A & Di Paola, M. 2000. Dynamic shakedown analysis under stochastic loads. In *Euromech 413 Colloquium on "Stochastic Dynamics of Nonlinear Mechanical Systems",* June 12–14, Palermo, Italy.

Degertekin, S.O. 2012. Improved harmony search algorithms for sizing optimalization of truss structures. *Comp. and Struct*., 92–93, 229–241.

Giambanco, F. & Palizzolo, L. & Polizzotto, C. 1994a. Optimal shakedown design of beam structures. *Structural Optimization* 8, 156–167.

Giambanco, F. & Palizzolo, L. & Polizzotto, C. 1994b. Optimal shakedown design of circular plates. *J. of Eng. Mech.* 120(12), 2535–2555.

Giambanco, F. & Palizzolo, L. & Caffarelli, A. 2002. An optimal plastic shakedown design, *The Sixth International Conference on Computational Structures Technology*, Prague, Czech Republic, September 4–6.

Giambanco, F. & Palizzolo, L. & Caffarelli, A. 2005. Optimum design of structures with limited ductility, IX Int. Conf. on Computer Aided Optimum Design in Eng., WIT Press (Henrnandez & Brebbia Eds.) Skiathos, Grecia, May 23–25.

Giambanco, F. & Benfratello, S. & Palizzolo, L. & Tabbuso, P. 2011. Multicriterion design of frames with constraints on buckling, *XX Congresso Nazionale AIMETA*, Bologna, September 12–15.

Haftka, R.T. & Gürdal, Z. & Kamat, M.P. 1990. *Elements of structural optimization*. The Nederlands, Dordrecht: Kluwer Academic Publishers.

König, J. A. 1975. On optimum shakedown design. In: Sawczuk, A.; Mroz, Z.: *Optimization in structure design*, 405–414, Berlin: Springer-Verlag.

Lee, K.S & Geem, Z.W. 2005. A new meta-heuristic algorithm for continuous engineering optimalization: harmony search theory and practice. *Comp. Methods Appl. Mech. Engrg*., 194, 3902–3933.

Maier, G. & Zavelani Rossi, A. & Benedetti, D. 1972. A finite element approach to optimal design of plastic structures in plane stress. *Int. J. Num. Meth. Eng.* 4, 455–473.

Rozvany, G.I.N. 1976. *Optimal design of flexural systems*. Oxford: Pergamon Press.

Rozvany, G.I.N. 1989. *Structural design via optimality criteria*. The Nederlands, Dordrecht: Kluwer Academic Publishers.

Save, M.A. & Prager, W. 1985. *Structural optimization*. New York: Plenum Press.

Palizzolo, L. 2004a. Optimization of continuous elastic perfectly plastic beams. *Comp. & Struct.*, 82, 4–5, 397–411.

Palizzolo, L. 2004b. Optimal design of trusses according to a plastic shakedown criterion. *J. of Appl. Mech.*, 71, 2, 240–246.

Research and Applications in Structural Engineering, Mechanics and Computation – Zingoni (Ed.)
© 2013 Taylor & Francis Group, London, ISBN 978-1-138-00061-2

Performance of buildings and other structures during the Tohoku Tsunami

I.N. Robertson
University of Hawaii at Manoa, Honolulu, Hawaii, USA

G. Chock
Martin & Chock, Inc., Honolulu, Hawaii, USA

ABSTRACT: In April, 2011, the American Society of Civil Engineers, ASCE, sponsored a team of engineers to survey tsunami effects on structures along the Tohoku coastline of Japan. The team was lead by Gary Chock, S.E., and consisted of 7 members of the recently formed ASCE 7 subcommittee on Tsunami Loads and Effects. The survey objectives were to investigate structural successes, failures and near failures in order to evaluate design provisions being considered for a new chapter on Tsunami Loads and Effects in the ASCE 7 design load standard for the USA. The survey results are extensively documented in a 350 page ASCE report (ASCE, 2013).

This paper gives an overview of the tsunami survey, and introduces the analysis methodology used to evaluate tsunami design provisions using full-scale field tsunami damage observations. Examples of building failure analysis will be used to demonstrate the potential for field validation of actual loading conditions most significant to structural response. The authors discuss how these findings influence the direction of the forthcoming ASCE 7 chapter on Tsunami Loads and Effects.

1 INTRODUCTION

On March 11, 2011 2:46 pm, the Great East Japan Earthquake of Moment Magnitude 9.0 generated a tsunami of unprecedented height and spatial extent along the northeast coast of the main island of Honshu. The ASCE SEI Tohoku Tsunami Reconnaissance Team conducted an investigation into the performance of buildings and other structures along the Tohoku coast region of Japan. In the course of two weeks the team was able to examine nearly all the towns and cities with significant damage due to the tsunami. The Japanese government estimated that over 250,000 buildings either collapsed or partially collapsed predominately from the tsunami. Topics covered in the scope of this investigation included: tsunami warning and evacuations, tsunami flow velocities, debris loading, building structural performance, bridge performance, seawalls and tsunami barriers, breakwaters, piers, quays, and wharves, scour effects, other structures, failure mode analyses, and economic impacts and initial recovery efforts. Detailed results of the survey are available in a 350 page report (ASCE, 2013).

2 TSUNAMI DETAILS

The primary affected coastline was on the main island of Honshu along the Tohoku region Figure 1. This area can be geographically subdivided further into the Sanriku coast of the three prefectures of Miyagi (north portion), Iwate, and Aomori, which has a 600 km saw-tooth coastline with numerous estuaries and coastal valleys, and the middle coastline from the city of Sendai in southern Miyagi leading southward towards Fukushima prefecture, where the coastline has broader low-lying plains. Along the Sanriku coast, in most instances the tsunami occurred as a long period high amplitude surge. Along the coastal plain south of Sendai southward to Natori City and Soma City, the offshore bathymetry caused the tsunami to break into a series of bores, which were seen on worldwide television networks as videos taken from Japanese news helicopters.

Approximately 20,000 people lost their lives as a consequence of the tsunami. The vast majority of these were located in the numerous coastal communities along the Tohoku coastline.

3 TSUNAMI WARNING AND EVACUATION

Japan's tsunami response plan did not rely on physical countermeasures alone. Japan, having a history of damaging historical tsunamis, has a variety of tsunami awareness signage established throughout the coastal regions by local government. There are signs clearly entreating evacuation immediately after an earthquake in the expected tsunami inundation zones.

In addition, in areas were high ground is too far removed from the coastline, selected buildings have been designated as vertical refuges from tsunamis.

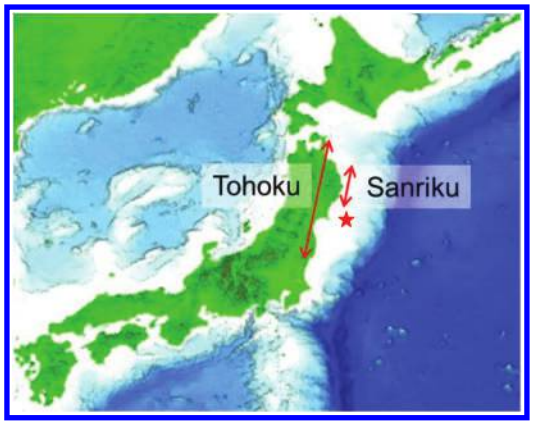


Figure 1. Earthquake epicenter and impacted coastline (ASCE).



Figure 2. Minamisanriku apartment building designed as vertical evacuation building (Robertson/ASCE).



Figure 3. Vertical refuge on roof of Minamisanriku coastal apartment building (Google Earth and ASCE).

Most of these are existing buildings that were evaluated for their suitability as vertical evacuation structures, while some are recently built specifically to serve a vertical evacuation function. Figure 2 shows an apartment building built on the coastline in Minamisanriku with the roof specifically designated as a vertical refuge from tsunamis (Figure 3).



Figure 4. Rikuzentakata City Hall Community Center and Gym designated as official tsunami evacuation center.

Access to the evacuation area was provided by external elevator and staircase accessible without entering the rest of the building. The roof level evacuation area measured a total of 660 square meters and was surrounded by a well braced 2 meter high guard fence. Even though this building was overtopped by 0.7 meters, the 44 people who sought refuge on the roof survived the tsunami.

Unfortunately, due to underestimation of the potential tsunami height, many of the designated vertical evacuation centers were not high enough to provide safe refuge during the tsunami (Figure 4) Japanese guidelines for selection, evaluation and design of vertical evacuation structures have been revised subsequent to the Tohoku Tsunami.

4 TSUNAMI FLOW CHARACTERISTICS

In order to evaluate tsunami loading on structures, it is important to obtain estimates for the flow depth and velocity at the site of interest. The Tohoku tsunami provided an unprecedented opportunity to analyze tsunami flow conditions based on video and field evidence. Much of this analysis can be performed remotely using only the captured videos and satellite imagery tools such as Google Earth. However, field verification of dimensions provides valuable confirmation of the assumptions made during video analysis. Field investigation is also necessary to determine flow depth which may be difficult to estimate from the video evidence alone.

Because this tsunami took place during daylight hours it was captured on video by numerous sources. After the Mw 9.0 earthquake, a number of news media helicopters and light planes were in the air to survey earthquake damage and fires initiated by the shaking. They were still in the air when the tsunami came onshore, so captured numerous videos of the incoming flow and its destructive path. In addition, numerous citizens witnessing the tsunami inundation and drawdown videoed the event. Many of these videos are now available online for analysis of the flow characteristics.

Figure 5 shows a typical analysis of aerial video footage of the tsunami surge passing over farmland

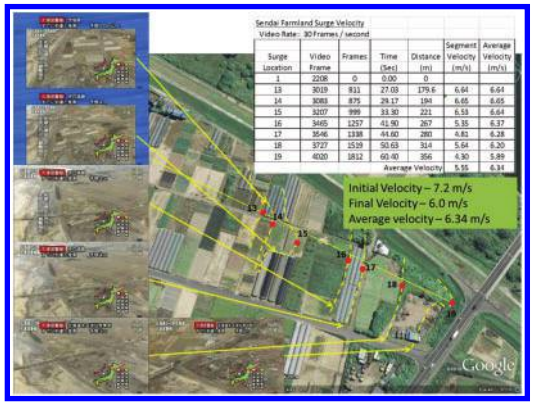


Figure 5. Aerial video analysis to determine flow velocity (Robertson/ASCE).



Figure 6. Light standard adjacent to coastal Takada Matsubara building in Rikuzentakata (Robertson/ASCE).

in the Sendai coastal plane. Maximum flow velocities captured by video analysis range from 5 to 8.5 m/s (18 to 30 kph).

Video evidence of tsunami flow characteristics is only available at certain locations depending on where helicopters or observers were located at the time of the inundation. Because of the variability in tsunami flow characteristics from location to location due to changes in bathymetry, topography and physical obstructions it is not always possible to base flow characteristics at one location on those determined for another location. If video evidence is not available at a location of interest, it is possible to estimate the flow characteristics by reverse analysis of a "flow surrogate".

Figure 6 shows a light standard that served as "flow surrogate" for analysis of a major shearwall blow-out inside the adjacent Takada Matsubara building. Based on structural analysis, the pushover of the light standards during the 10 meter deep inflow had the following sequence: under flexural bending, initial buckling of the thin walls occurred above the stiffeners of the base plate, resulting in rotation of the pipe until the initially dry light fixture frame at the top of the pole was lowered into the flow and captured debris. This debris load at the top of the pole greatly increased the moment at the base and initiated much more rotation until it generated tensile rupture of the anchor bolts (Figure 6). A depth-averaged flow velocity of at least 7.25 m/s was determined from structural analysis of the pole in order to create the initial buckling.

Similar analysis of other "flow surrogates" generated maximum flow velocities are various locations along the Tohoku coastline ranging from 4 to 10 m/s (14 to 36 kph).

5 DEBRIS IMPACT DAMAGE

As a tsunami flows over land it accumulates an enormous amount of debris consisting of vegetation, building materials, automobiles, boats and ships, and in some cases entire buildings. The resulting debris flow will impact structures in the path of the tsunami, often leading to localized damage due to debris impact strikes or overloading of structural elements or of the entire structure through the effects of debris damming.



Figure 7. Ship impact damage to steel framed building in Kamaishi harbor (Robertson/ASCE).

A particularly dramatic impact occurred when a large cargo ship in Kamaishi harbor broke free from its moorings and rammed into a steel framed warehouse building supported on concrete piled foundations (Figure 7). Analysis of a survivor video from a nearby building shows that the ship was traveling at 7.13 m/s (25.6 kph) immediately prior to impact. The impact destroyed two of the concrete piled foundations and collapsed half of one side of the steel warehouse framing. The ship subsequently grounded on an adjacent pier (Figure 7).

Accumulation of debris against structures leads to increased hydrodynamic loading due to damming effects. Even though a structure is designed with relatively open structural framing at the lower levels, accumulation of debris from collapsed surrounding buildings can result in dramatically increased drag loading on the "open" structure (Figure 8).



Figure 8. Debris accumulation on surviving building (Robertson/ASCE).



Figure 9. Surviving and damaged reinforced concrete buildings in Minamisanriku (Robertson/ASCE).

6 BUILDING STRUCTURAL PERFORMANCE

Along the Tohoku coast, tsunami inundation height was in the range of 5 to 30+ meters. In general, light-frame residential construction subject to about a story height or more of inundation will collapse. Therefore, complete collapse of residential light-frame construction occurred in nearly 100% of all affected areas extending to the edge of the inundation limit. In commercial and industrial areas, low-rise building collapses occurred in the approximate range of 75% towards 95%, with the higher collapse rate occurring as tsunami height reached the upper range (Figure 9). In these inundated coastal zones, buildings taller than 5 stories were uncommon. Despite this devastation, there were a number of these multi-story buildings that survived the tsunami without loss of structural integrity of their vertical load carrying system or foundation. In fact, a significant proportion of the surviving buildings did not appear to have significant structural damage. This provides some encouragement regarding the potential resilience of larger buildings having robust seismic designs and scour and uplift-resistant foundations.



Figure 10. Overturned structural steel building on mat foundation in Onagawa (Robertson/ASCE).



Figure 11. Buoyancy of the sealed cold storage room on the ground floor of this reinforced concrete building in Onagawa was sufficient to lift the building off its compression piles (Chock/ASCE).

In the town of Onagawa, a number of multi-story structural steel and reinforced concrete buildings overturned due to the combination of buoyancy and lateral hydrodynamic loading (Figure 10). A common feature of these buildings was the lack of a deep foundation system designed for uplift. Buildings on mat foundations or compression-only piles may not have sufficient resistance to overturning, sliding or buoyancy during inundation. Based on field measurements the two-story cold storage fishery building in Figure 11 was estimated to have a deadweight of 9000 kN. The refrigerated space on the ground floor was effectively sealed, leading to a neutrally buoyant condition as soon as the water inundation depth reached 7 meters. Video evidence confirms field measurements that the flow exceeded 10 meters at this location, resulting in this building floating off its foundations and flipping over.

7 BRIDGE STRUCTURAL PERFORMANCE

Numerous road and railway bridges in the inundation zone suffered severe damage or even total failure.



Figure 12. Road bridge failure in Rikuzentakata (Robertson/ASCE).



Figure 13. Surviving road bridge in Minamisanriku (Robertson/ASCE).

A relatively new three span road bridge in Rikuzentakata suffered collapse of all three deck spans and severe scour behind the abutments (Figure 12). The failure is attributed to a combination of buoyancy, enhanced by air pockets trapped between the bridge girders, and lateral hydrodynamic loading. Measurements of the bridge deck sections showed that when fully submerged, the deck had only 11% residual dead load to resist uplift. A number of road bridges survived even though they were fully submerged and subjected to flow velocities exceeding 7 m/s. In the case of a road bridge in Minamisanriku, survival is attributed to steel brackets which appear to have been installed as a seismic retrofit of the concrete bridge (Figure 13).

A coastal railway line along the Tohoku coastline suffered numerous bridge failures (Figure 14). In some cases the bridge girders were washed off the support piers, but in other cases the piers themselves failed in bending due to the lateral hydrodynamic loads. Road bridges can be replaced with temporary structures, however railway bridges are much more difficult to replace, hampering cargo and passenger transport for many months and even years.



Figure 14. Damage to railway bridge in Otsuchi (Robertson/ASCE).

8 FAILURE MODE ANALYSIS

A number of partial or near-collapse structures were surveyed in detail to serve as full-scale candidates for hydrodynamic loading evaluation. Failure analysis of these structures has provided valuable confirmation of loading expressions derived based on small scale laboratory experiments.

The Takada Matsubara Road Station in Rikuzentakata (Figure 6) endured a 10.5 meter tsunami inundation depth with flow of about 7–1/2 m/s, but suffered a failure of its principal transverse shear wall due to unbalanced hydrostatic and hydrodynamic forces of the incoming tsunami (Figure 15). Reinforcing steel was sampled and tested at 510 MPa average yield strength, consistent with JIS G3112 SD 490. A nonlinear finite element analysis of the wall identified the following sequence leading to the observed damage state:

1. Flexural yielding of the base of the wall as soon as the flow level reached 1.6 meters above grade.
2. Bottom half of side edge supports of the wall and the two ends of the mid-height horizontal beam yield when the flow level reached 2.2 meters.
3. The top and upper portions of the side supports of the wall yield and concrete shear cracks occur at the bottom when the flow reaches 2.7 meters.
4. Side supports and horizontal beam supports reach concrete shear failure cracking when the flow reaches 7.2 meters.
5. The top and upper portions of the side supports reach concrete shear failure cracking when the flow reaches 9.5 meters.
6. At 10.5 meters, the upper portion of the concrete wall hanging in tension drops down and relieves further loading increase; the unbalanced hydrostatic forces are relieved.

9 TSUNAMI DESIGN CODE DEVELOPMENT

Similar failure analyses were performed on numerous reinforced concrete and structural steel buildings,



Figure 15. Partial collapse of shear wall due to combined hydrostatic and hydrodynamic loading (Takagi/ASCE).

helping to verify loading expressions for use in a new chapter of ASCE 7, Minimum Design Loads for Buildings and other Structures (Chock *et al*, 2011). ASCE 7 is the basis for all loading conditions used in the International Building Code, the building code used in all 50 States in the USA. It does not currently provide guidance on tsunami design. An ASCE sub-committee was established in January 2011 to develop a chapter on Tsunami Loads and Effects. The sub-committee is currently working on a draft of the code provisions, with the hope that this chapter will be added to the 2016 edition of ASCE 7.

Lessons from the Tohoku Tsunami have also been incorporated into the second edition of FEMA P-646, Guidelines for Design of Structures for Vertical Evacuation from Tsunamis (FEMA, 2012). This document provides non-mandatory guidance to coastal communities considering construction of a tsunami refuge, either as a multi-story structure or a mound simulating high ground. Because it was developed specifically for vertical evacuation refuges, P-646 has greater conservatism than would be economically justified for non-refuge buildings. The Tsunami Loads and Effects chapter in ASCE 7 will provide more economical design requirements for all buildings exceeding 20 m in height.

10 CONCLUSIONS

The Tohoku Tsunami was a truly devastating natural disaster that caused considerable loss of life and tremendous economic hardship for the affected coastline of Japan. Recovery and reconstruction following this event will be expensive and protracted. In order to avoid similar consequences in other tsunami-prone communities, it is essential that greater resilience be incorporated during community development. Part of this resilience can be provided by designing mid- to high-rise coastal buildings for the anticipated tsunami loading. Lessons from the Tohoku Tsunami, and failure analyses performed on full-scale building failures, have provided valuable validation for tsunami loading expressions derived from laboratory experiments. These findings are being incorporated in a new chapter on Tsunami Loads and Effects being developed for ASCE 7. When adopted by coastal communities these code requirements will enhance the structural performance of multi-story steel and concrete buildings during future tsunamis.

REFERENCES

ASCE (2010). ASCE 7 Minimum Design Loads for Buildings and other Structures, American Society of Civil Engineers, Reston, Virginia.

ASCE (2013). Tohoku Japan Tsunami of March 11, 2011 – Performance of Structures, American Society of Civil Engineers, Reston, Virginia.

Chock, G., Robertson, I.N., Riggs, H. R., (2011), Tsunami Structural Design Provisions for a New Update of Building Codes and Performance-Based Engineering, Solutions to Coastal Disasters 2011, ASCE Coasts, Oceans, Ports and Rivers Institute, June, 2011, Anchorage, Alaska.

FEMA P646 2nd Ed. (2012). Guidelines for Design of Structures for Vertical Evacuation from Tsunamis, Federal Emergency Management Agency, Washington, D.C., USA.

Research and Applications in Structural Engineering, Mechanics and Computation – Zingoni (Ed.)
© 2013 Taylor & Francis Group, London, ISBN 978-1-138-00061-2

Numerical investigation of the cyclic response of CHS braces

T. Sheehan & T. M. Chan
School of Engineering, University of Warwick, UK

J.H. Xing & L. Gardner
Department of Civil and Environmental Engineering, Imperial College London, UK

ABSTRACT: The behaviour of seismic-resistant buildings relies heavily upon the inclusion of energy dissipating elements. For concentrically-braced frames, the function of energy dissipation is accomplished by diagonal bracing members, whose performance depends upon both cross-sectional properties and global slenderness. Rectangular hollow sections are traditionally preferred in such applications. However these sections are susceptible to local buckling and, particularly in the case of cold formed tubes, have high residual stresses and reduced corner ductility. Hence as an alternative, this paper focuses on the hysteresis response of hollow circular tubes under cyclic axial loading. The uniformity of the circular cross-section may provide improved performance under cyclic loading over rectangular sections. In this paper, finite element analysis and a damage assessment method are first validated against experimental data on both hot-rolled and cold formed hollow CHS members. A series of parametric investigations is then carried out to access the influence of the local slenderness, global slenderness and steel material type on the hysteresis behaviour. Predictive expressions for displacement ductility and energy dissipation, incorporating both local and global slenderness, are proposed.

1 INTRODUCTION

The inclusion of dissipative devices is crucial in earthquake-resisting structures in order to absorb the energy from seismic loading, reduce element forces and moments around the frame and prevent catastrophic failure. This function is achieved by diagonal bracing members in concentrically-braced frames, but the performance is often compromised by buckling of the slender braces under compression, leading to an asymmetric response of the system between tension and compression. Tubular sections are becoming increasingly popular for this application owing to their inherent buckling resistance in compression, together with their visual appeal, ductility and torsional resistance. A considerable degree of attention has been paid to rectangular tubular sections owing to the ease of connection design, with experiments conducted by Nip et al. (2010a) comparing the response of hot-rolled carbon steel, cold formed carbon steel and cold formed stainless steel RHS braces. In recent years, research has also been conducted on curved tubular sections, which offer several advantages both aesthetically and structurally, owing to superior geometrical continuity around the section perimeter. Tests have been performed on circular hollow sections under monotonic loading, e.g. Packer et al. (2010), and elliptical hollow sections by Chan & Gardner (2008). Research has also been carried out on braces under cyclic axial loading, e.g. Elchalakani et al. (2003) tested twenty cold formed CHS braces to failure. However, there is scope to conduct further research to enhance current design recommendations in BS EN 1998-1 (2004) and to predict the ability of members to meet the displacement demands under seismic actions.

Numerical modelling is becoming increasingly popular since it requires less time and expense than that associated with laboratory experiments. Takeuchi & Matsui (2011) and Nip et al. (2010a) developed numerical models of tubular steel braces in ABAQUS, using the inbuilt nonlinear isotropic/kinematic hardening model to capture the material behaviour. Modelling has also been conducted on concrete-filled tubular columns in ABAQUS, such as by Goto et al. (2010), with a user subroutine to define the steel material behaviour. Following the success of these, ABAQUS was utilized in this study to examine the response of hollow hot-finished and cold formed circular braces. Results from recent experiments on CHS braces (Sheehan & Chan (2013)) were used to validate the simulation technique, enabling further parametric studies to be conducted, covering a wider range of cross-section and global slenderness values. Full 3-dimensional models, including geometric imperfections were created in order to capture both the overall load-displacement hysteresis response and the local behaviour. A strain-based fatigue model and suitable counting techniques were implemented to predict the number of cycles to fracture. The main results of interest were the total number of cycles endured and the

Table 1. Summary of test specimens for model calibration.

Specimen ID	$\bar{\lambda}$	Section type	Core
CF-H-1500	0.90	Cold formed	Hollow
CF-H-3000	1.98	Cold formed	Hollow
HF-H-1500	0.78	Hot-finished	Hollow
HF-H-3000	1.72	Hot-finished	Hollow

energy dissipation capability, as well as the influence of specimen dimensions on these parameters.

2 MODELLING OF HOLLOW STEEL BRACES

2.1 *Specimens*

Initially, models were generated to simulate the results from a series of experiments involving CHS braces under cyclic axial loading (Sheehan & Chan (2013)). A summary of the test specimens is provided in Table 1.

The tested sections were manufactured in two ways – hot-finished and cold formed – both with a nominal yield stress of 355 N/mm^2. All sections had the same nominal diameter of 48.3 mm and two wall thicknesses were utilised: 3.0 mm for the cold formed tubes and 3.2 mm for the hot-finished sections.The type of steel section is indicated by the first part of the specimen ID in Table 1, with 'CF' denoting cold formed steel and 'HF' signifying hot-finished specimens. The middle part of the specimen name refers to the fact that the member is hollow, since concrete-filled braces were also tested by Sheehan & Chan (2013) and numerical simulations of these are planned at a later stage. The brace length is also included in the specimen identification by the last four digits. Two lengths were employed: 1500 mm and 3000 mm. $\bar{\lambda}$ is evaluated in accordance with BS EN 1993-1-1 (2005).

2.2 *Element type and mesh size*

The steel tube was modelled using S4R general purpose shell elements. These are three-dimensional, double-curved elements consisting of 4 nodes with 6 degrees of freedom per node. A more refined mesh was employed at the end and mid-lengths over a distance equal to 3.0 times the section radius, since large local deformations were expected in these locations.

2.3 *Boundary conditions and loading*

Fixed-ended conditions were employed at the end of the tested brace and this was achieved in the models by constraining the ends of the tubes to a rigid plate. The models were subjected to the ECCS axial cyclic loading protocol (ECCS, 1986), as used for the experiments, and this was implemented by applying an axial displacement to one end of the tube. This loading protocol entailed symmetric cycles of compression and tension and was defined by means of axial displacements. The displacement amplitudes comprised one cycle at each of the first four values and three cycles at each of the higher displacements, following the sequence: $0.25\delta_y$, $0.5\delta_y$, $0.75\delta_y$, $1.0\delta_y$, $2.0\delta_y$, $2.0\delta_y$, $2.0\delta_y$, $4.0\delta_y$, $4.0\delta_y$, $4.0\delta_y$, $6.0\delta_y$, $6.0\delta_y$, $6.0\delta_y$, etc. up to failure. The yield displacement parameter δ_y, which was used to define the loading protocol was determined using the material yield stress, f_y, and the specimen length, L.

2.4 *Material modelling*

In order to accurately simulate the behaviour of steel under cyclic loading, a material model was required that would take into account phenomena such as the expansion of the yield surface during repeated cycles and the Bauschinger effect. The nonlinear isotropic/kinematic hardening model in ABAQUS was adopted for this study, which is based on the two-surface plasticity model of Chaboche (1986). This model consists of two surfaces in 3D stress-space, a yielding surface, within which the behaviour is elastic and the bounding surface, which defines the maximum stress. The main disadvantage of the ABAQUS inbuilt model is that the material parameters cannot be updated as the analysis progresses but the ease of implementation renders it favourable – only five input variables are required. The success of using this model has been previously demonstrated by Nip et al. (2010a) and Takeuchi & Matsui (2011). In the absence of experimental data, the ABAQUS material input parameters were adopted from the material tests of Nip et al. (2010b) and scaled suitably according to the yield stress.

2.5 *Fracture prediction*

A strain-based fracture model was employed for predicting fracture of the tube, using a relationship proposed by Coffin (1954) and Manson (1954) to calculate the number of cycles to failure for a specimen under repeated cycles of the same strain. This was given as

$$\frac{\Delta\varepsilon_p}{2} = \varepsilon'_f \left(2N_f\right)^c \tag{1}$$

where $\Delta\varepsilon_p/2$ is the plastic strain amplitude, $2N_f$ is the number of reversals to failure, ε'_f is the fatigue ductility coefficient and c is the fatigue ductility exponent. In the adopted approach, values of ε'_f and c were taken from material tests, previously conducted by Nip et al. (2010b) and using these, N_f was computed for each plastic strain amplitude, $\Delta\varepsilon_p/2$. Since the strain range varied significantly throughout the tests, the total accumulated damage was determined using Miner's rule (Miner (1945)). This consisted of a damage index, D, given by:

$$D = \sum_{i=1}^{n} \frac{n_i}{N_{fi}} \tag{2}$$

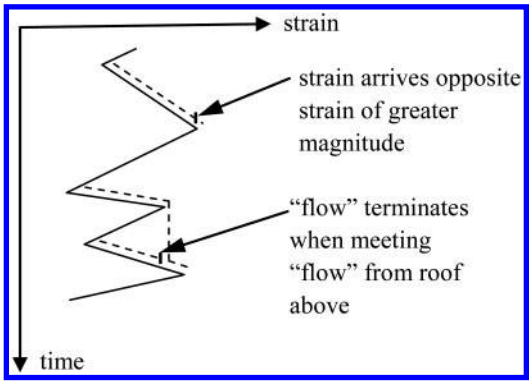


Figure 1. Illustration of 'rainflow' counting technique.

where N_{fi} is the number of cycles to failure for a particular strain amplitude and n is the number of cycles undergone by the test specimen at that strain. According to this damage model, failure occurred when D reached a value of 1. Two approaches were considered for evaluating the strain amplitudes in each cycle. The first was a "rainflow" counting algorithm proposed by Matsuishi & Endo (1968) to define strain amplitudes for a specimen undergoing irregular loading patterns. In this approach, the strain in successive cycles was envisaged as water flowing between levels of a pagoda roof, as depicted in Figure 1.

Strain was counted in half cycles, and under cycles of increasing amplitude, the 'flow' continued from one cycle to the next and the increase in strain amplitude was added onto the previous cycle. The half cycle terminated when interrupted by 'flow' from a previous cycle or when it arrived opposite a peak/trough of greater magnitude than that from which it originated. Compression and tension half cycles were initially counted separately. Half cycles of the same amplitude and opposite sense were then added together to form complete cycles. The second approach involved counting the differences between individual peaks and troughs in the strain progression as they occurred, accumulating the damage continuously.

The buckled shape at the mid-length is shown in Figure 2. This comprised a relatively flat portion in the centre of the compression face, with a region of higher curvature towards the edges. The most favourable predictions were attained by computing the average strain across the entire compression face, including both of these regions, and using the strains on the outside face.

Both the 'rainflow' counting technique and counting the individual ramps in the strain sequence provided reasonable estimations of the number of cycles to failure, with the 'rainflow' technique tending to slightly overestimate the number of cycles and counting the individual half cycles generally underestimating the performance. Hence these provided suitable upper and lower bounds to the anticipated number of cycles to fracture.

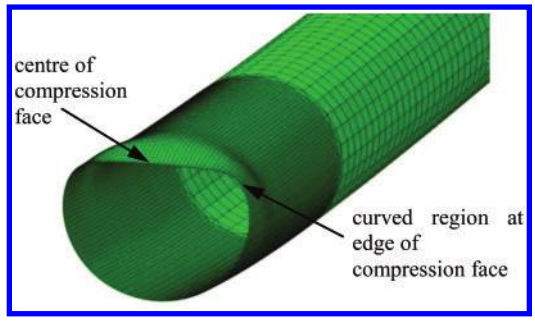


Figure 2. Deformed shape at brace mid-length.

Table 2. Number of cycles to failure for hollow steel brace models.

	No. of cycles to					
	global buckling		local buckling		fracture	
Specimen	FE	test	FE	test	FE	test
CF-H-1500	5	5	8	8	11	14
HF-H-1500	6	5	11	15	11	17
CF-H-3000	3	3	8	9	11	17
HF-H-3000	3	4	9	8	17	24

2.6 *Geometric imperfections*

Global imperfection amplitudes were determined following a sensitivity study. The most satisfactory results were found using imperfection amplitudes equal to $L/1000$ and $L/750$ for the 1500 mm and 3000 mm specimens respectively. The global imperfection was implemented in the model by applying a lateral load at the mid-length. A study was also conducted to establish the most suitable local imperfection amplitude. The best agreement between test and FE results was achieved by using an imperfection of $t/100$, where t was the tube wall thickness, with models being less sensitive to changes in local imperfection at amplitudes lower than this. This was incorporated into the model by directly altering the nodal positions prior to commencing the analysis. The shape of the local imperfection was a sinusoidal wave along the length.

2.7 *Verification of FE model*

The accuracy of the models was assessed by comparing the numbers of cycles to local buckling, global buckling and fracture with the laboratory test results of Sheehan & Chan (2013). Results for the hollow steel tubes are presented in Tables 2 and 3 in addition to the maximum tensile and compressive forces. The numbers of cycles to local and global buckling showed close agreement in most cases except for the local buckling of specimen HF-H-1500. The number of cycles to fracture was underestimated by the numerical model in all cases. In spite of this, the models

Table 3. Maximum tensile and compressive forces for hollow steel brace models.

	Max tension force (kN)		Max compression force (kN)	
Specimen	FE	Tests	FE	tests
CF-H-1500	234	209	147	151
HF-H-1500	229	180	130	155
CF-H-3000	250	209	69	71
HF-H-3000	227	187	86	81

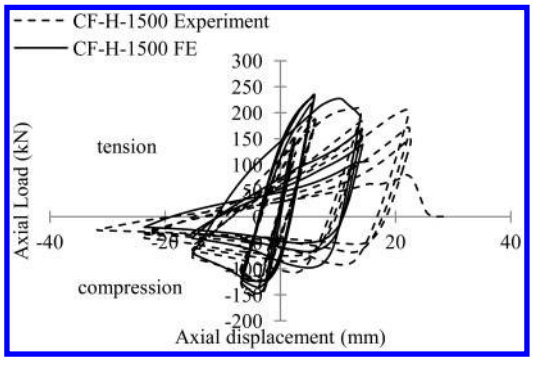


Figure 3. Load-displacement hysteresis curves for CF-H-1500.

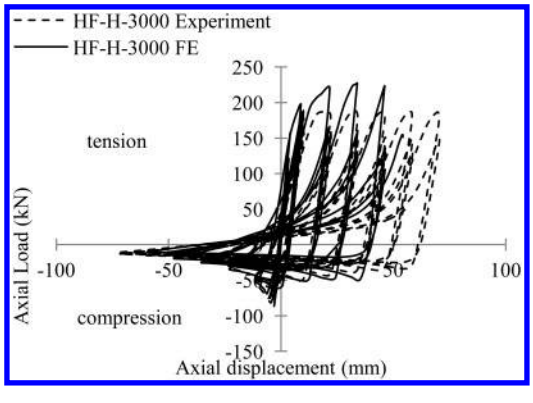


Figure 4. Load-displacement hysteresis curves for HF-H-3000.

provided a reliable prediction of the maximum tensile and compressive resistances.

Figures 3 and 4 compare the load-displacement hysteresis curves for two typical specimens.

Despite undergoing an earlier failure than their experimental counterparts, the numerical models produced similarly-shaped hysteresis curves, indicating an accurate simulation of the energy dissipation capability and general specimen behaviour.

2.8 *Parametric studies*

Once a suitable approach to numerical modelling was established, parametric studies were conducted for both the cold-formed and hot-finished sections. The specimens are summarised in Table 4.

Table 4. Specimens for parametric studies.

Specimen ID.		$D/t\varepsilon^2$			
Cold formed	Hot-finished	Cold formed	Hot-finished	Class	$\bar{\lambda}$
CF1	HF1	36.11	26.7	1	0.5
CF2	HF2	36.1	26.7	1	1.0
CF3	HF3	36.1	26.7	1	1.5
CF4	HF4	36.1	26.7	1	2.0
CF5	HF5	60.3	60.9	2	0.5
CF6	HF6	60.3	60.9	2	1.0
CF7	HF7	60.3	60.9	2	1.5
CF8	HF8	60.3	60.9	2	2.0
CF9	HF9	78.9	77.5	3	0.5
CF10	HF10	78.9	77.5	3	1.0
CF11	HF11	78.9	77.5	3	1.5
CF12	HF12	78.9	77.5	3	2.0
CF13	HF13	102.6	100.3	4	0.5
CF14	HF14	102.6	100.3	4	1.0
CF15	HF15	102.6	100.3	4	1.5
CF16	HF16	102.6	100.3	4	2.0

where:
D = cross-section outer diameter
t = tube thickness
A = cross-section area
L = specimen length
$\varepsilon = \sqrt{235/f_y}$, where f_y is the material yield stress
$\bar{\lambda}$ = global slenderness calculated in accordance with BS EN 1993-1-1 (2005).

Four specimen lengths were utilised for each section type to give values of $\bar{\lambda} = 0.5$, 1.0, 1.5 and 2.0 in accordance with BS EN 1993-1-1 (2005). Therefore all braces were within the recommended limit of $\bar{\lambda} \leq 2.0$ given in BS EN 1998-1 (2004). The tube diameter was kept constant and four different wall thicknesses were employed to provide a cross-section in each of the classifications 1, 2, 3, and 4 defined in BS EN 1993-1-1 (2005). The same material properties were used as those for simulating the experiments. It is evident from the experimental and numerical results that the number of cycles to failure and maximum displacement amplitude are influenced by both the local and global slenderness values. Figure 5 shows the variation in number of cycles to failure with global slenderness for each cross-section class and Figure 6 presents the relationship between the number of cycles to failure and cross-section slenderness for members of each global slenderness value. Similar trends were observed for each section type and hence the results are only displayed for cold formed sections in Figure 5 and for hot-finished sections in Figure 6.

For both hot-finished and cold formed tubes, the number of cycles to failure generally increased with global slenderness. Conversely, the total number of cycles generally decreased with increasing cross-sectional slenderness, $D/t\varepsilon^2$. However, these observations only reflect the predominant trends across the results and did not occur in all cases. Hence, relating

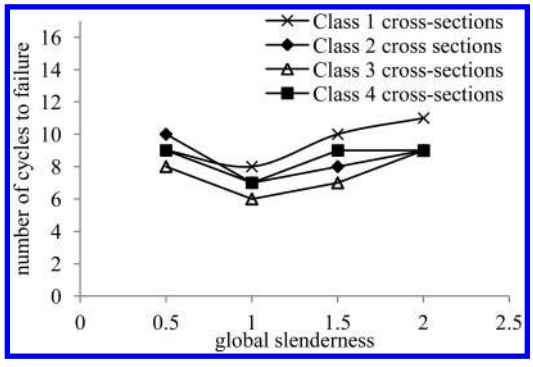


Figure 5. Relationship between number of cycles to failure and global slenderness for cold formed specimens.

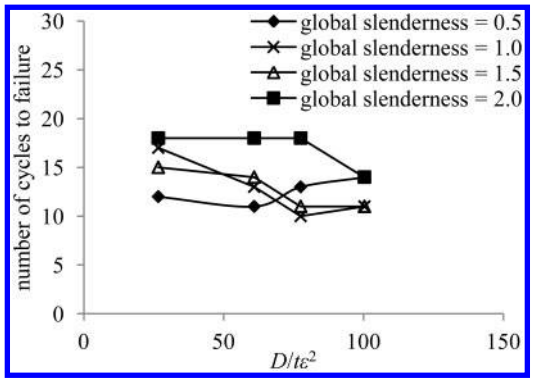


Figure 6. Relationship between number of cycles to failure and cross-section slenderness for hot-finished specimens.

the number of cycles to failure to a single slenderness parameter did not appear to be sufficient.

Relationships have been proposed previously to predict the maximum displacement amplitude as a multiple of the yield displacement of RHS braces, μ_Δ, by relating it to the local and global slenderness parameters separately, such as Goggins et al. (2006) but a combination of the two has also been proposed by Nip et al. (2010a). Using the parametric results, the following expressions were developed to predict the number of cycles to fracture for CHS braces.

For hot-finished specimens:

$$\mu_\Delta = 6.17 + 3.36\,\bar{\lambda} - 0.052 D/t\varepsilon^2 + 0.00045(D/t\varepsilon^2)^2 - 0.022\,\bar{\lambda}\, D/t\varepsilon^2 \quad (3)$$

For cold-formed specimens

$$\mu_\Delta = 6.08 + 1.39\,\bar{\lambda} - 0.1 D/t\varepsilon^2 + 0.00073(D/t\varepsilon^2)^2 - 0.013\,\bar{\lambda}\, D/t\varepsilon^2 \quad (4)$$

These were formulated based on the parametric results that employed counting of the individual strain half-cycles as they occurred, since this provided a more conservative estimation than the 'rainflow' counting algorithm, and also showed a closer agreement with the failure observed from the load-displacement hysteresis relationship and deformed shape. Figure 7 compares the predicted displacement ductility μ_Δ, from Equations (3) and (4) with the results from the parametric studies. The numerical simulations show a reasonable correlation to the predictions.

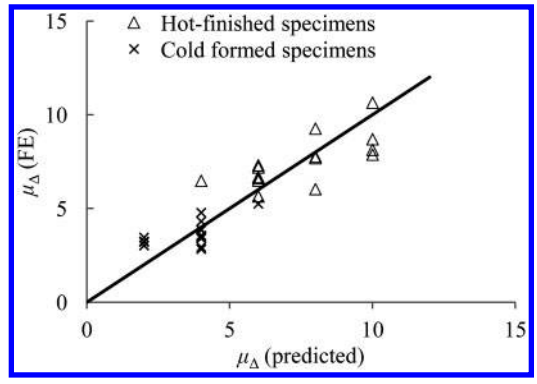


Figure 7. Load-displacement hysteresis for CF-H-3000.

Since a key function of the diagonal braces is to absorb the energy of seismic forces acting on the structure, expressions were also proposed for the anticipated energy dissipation of the brace. Two equations were proposed for each section type: one to predict the energy dissipated in the 8th loading cycle and the second to compute the total energy dissipation. The 8th cycle was selected following Goggins et al. (2006), who examined the energy dissipation at this particular displacement amplitude. The relationships are given by Equations (5) to (8).

For hot-finished specimens:

$$W_8 = 9.2 - 0.036\, D/t\varepsilon^2 - 4.46\bar{\lambda} + 0.016\bar{\lambda}\, D/t\varepsilon^2 + 0.77\bar{\lambda}^2 \quad (5)$$

$$W_T = 66.39 - 5.86\, D/t\varepsilon^2 - 345.3\bar{\lambda} + 0.092\left(D/t\varepsilon^2\right)^2 + 0.65\bar{\lambda}\, D/t\varepsilon^2 - 278.2\bar{\lambda}^2 - 0.0004\left(D/t\varepsilon^2\right)^3 - 0.0076\bar{\lambda}\left(D/t\varepsilon^2\right)^2 + 0.68\bar{\lambda}^2\left(D/t\varepsilon^2\right) + 58.62\bar{\lambda}^3 \quad (6)$$

For cold formed specimens:

$$W_8 = 7.98 - 0.029\, D/t\varepsilon^2 - 2.38\bar{\lambda} + 0.011\bar{\lambda}\, D/t\varepsilon^2 + 0.075\bar{\lambda}^2 \quad (7)$$

$$W_T = 155.5 - 2.75\, D/t\varepsilon^2 - 91.6\bar{\lambda} + 0.0057\left(D/t\varepsilon^2\right)^2 + 2.26\bar{\lambda}\, D/t\varepsilon^2 + 0.00011\left(D/t\varepsilon^2\right)^3 - 0.015\bar{\lambda}\left(D/t\varepsilon^2\right)^2 \quad (8)$$

where W_8 refers to the energy dissipated in the 8th loading cycle and W_T is the total energy dissipated. In both cases the energy is normalized with respect to $Af_y\delta_y$, where A is the cross-sectional area, f_y is the steel yield stress and δ_y is the yield displacement.

3 CONCLUSIONS

The behaviour of cold formed and hot-finished CHS braces under cyclic axial loading has been successfully

simulated using finite element modelling. Satisfactory analysis of the fatigue behaviour has been achieved by employing a strain-based approach in conjunction with Miner's rule (Miner (1945)) and the Coffin-Manson relationship (Coffin (1954), Manson (1954)). Expressions have been developed to predict the displacement ductility and energy dissipation capability in terms of both local and global slenderness parameters. The following conclusions can be drawn:

The nonlinear isotropic/kinematic hardening material model in ABAQUS provides a reliable prediction of the maximum compressive and tensile forces in the member and of the load-displacement hysteresis response.

The number of cycles to failure were generally underestimated by the ABAQUS models.

For estimating the number of cycles to failure, counting individual successive half cycles provides a suitable lower bound, whereas the rainflow algorithm gives an upper bound.

The displacement ductility, μ_{Δ}, was found to increase with increasing global slenderness, $\bar{\lambda}$, and decrease with increasing cross-sectional slenderness, $D/t\varepsilon^2$.

ACKNOWLEDGEMENT

The authors wish to thank Dr. Alan K. H. Nip from the Hong Kong Polytechnic University and Dr. Jihui Xing from Beijing Jiaotong University for their advice in conducting the analysis.

REFERENCES

BS EN 1998-1. 2004. Design of structures for earthquake resistance. Part 1: General rules, seismic actions and rules for buildings. CEN.

BS EN 1993-1-1. 2005. Design of steel structures. Part 1-1: General rules and rules for buildings. CEN.

Chaboche, J.L. 1986. Time independent constitutive theories for cyclic plasticity. *International Journal of Plasticity*, 2(2): 149–188.

Chan, T.M. & Gardner, L. 2008. Compressive resistance of hot-rolled elliptical hollow sections. *Engineering Structures* 30(2): 522–532.

Coffin, Jr. L.F. 1954. A study of the effects of cyclic thermal stresses on a ductile metal. *Transactions of ASME*. 76(6): 931–950.

ECCS (European Convention for Constructional Steelwork). 1986. Recommended Testing Procedure for Assessing the Behaviour of Structural Steel Elements under Cyclic Loads. ECCS, Brussels, Belgium.

Elchalakani, M., Zhao, X.L. & Grzebieta, R. 2003. Tests of cold-formed circular tubular braces under cyclic axial loading. *ASCE Journal of Structural Engineering* 129(4) 507–514.

Goggins, J.M., Broderick, B.M., Elghazouli, A.Y. & Lucas, A.S. 2006. Behaviour of tubular steel members under cyclic axial loading. *Journal of Constructional Steel Research*. 62(1–2): 121–131.

Goto, Y., Kumar, G., and Kawanishi, N. 2010. Nonlinear finite-element analysis for hysteretic behaviour of thin-walled circular steel columns with in-filled concrete. *ASCE Journal of Structural Engineering* 136 (11): 1413–1422.

Manson, S.S. 1954. Behaviour of materials under conditions of thermal stress. National Advisory Commission on Aeronautics: Report 1170. Lewis Flight Propulsion Laboratory, Cleveland, USA.

Matsuishi, M. & Endo, T. 1968. "Fatigue of metals subjected to varying stress", paper presented to Japanese Society of Mechanical Engineers (Jukuoka, Japan).

Miner, M.A. 1945. Cumulative damage in fatigue. *Journal of Applied Mechanics*. 12(3): A159-A164.

Nip, K.H., Gardner, L. & Elghazouli, A.Y. 2010a. Cyclic testing and numerical modelling of carbon steel and stainless steel tubular bracing members. *Engineering Structures* 32(2): 424–441.

Nip, K.H., Gardner, L., Davies, C.M. & Elghazouli, A.Y. 2010b. Extremely low cycle fatigue tests on structural carbon steel and stainless steel, *Journal of Constructional Steel Research* 66(1): 96–110.

Packer J. A., Chiew, S.P., Tremblay, R. & Martinez-Saucedo, G. 2010. Effect of material properties on hollow section performance. *Proceedings of the ICE – Structures and Buildings* 163(6): 375–390.

Sheehan, T. & Chan, T.M. 2013. Cyclic response of hollow and concrete-filled CHS braces. *Proceedings of the ICE – Structures and Buildings* (In press).

Takeuchi, T. & Matsui, R. 2011. Cumulative cyclic deformation capacity of circular tubular braces under local buckling. *ASCE Journal of Structural Engineering*. 137(11): 1311–1318.

Research and Applications in Structural Engineering, Mechanics and Computation – Zingoni (Ed.)
© 2013 Taylor & Francis Group, London, ISBN 978-1-138-00061-2

Parametric identification of building structures with seismic recordings

Ruichong Zhang
Colorado School of Mines, Golden, Colorado, USA

Lotfi O. Gargab
Tripoli, Libya

ABSTRACT: This study presents system identification of ten-story Millikan Library in Pasadena, California with a pair of the Yorba Linda earthquake of September 3, 2002. The proposed identification approach is based on wave features of generalized impulse and frequency response function (GIRF or GFRF), i.e., wave response at one structural response location to an impulsive motion at another reference location in time and frequency domains respectively. With a pair of seismic recordings at the two locations, GIRF/GFRF is obtainable. With a continuous-discrete model for the structure, a closed-form solution of GFRF, and subsequent GIRF with Fourier transformation of GFRF, can also be found in terms of structural physical properties above the impulse location. Matching the two sets of GIRF/GFRF from recordings and the model helps identify system parameters such as wave velocity or shear modulus.

1 INTRODUCTION

For seismic design, vibration control, and damage diagnosis of multi-story buildings, such as ten-story Millikan Library building located in Pasadena California, response characterization and system identification are fundamental and typically carried out with a discrete, multi-degree-of-freedom (MDOF) model. As far as one-dimensional (1D) horizontal motion is concerned, the Millikan Library building as shown in Fig. 1a can be modeled as a 10-DOF system with each floor mass and inter-story stiffness (i.e., physical parameters) calculable based on design configuration and materials. These physical parameters can also be calibrated in terms of identified vibratory features (i.e., modal frequencies, damping, and shapes—a function of physical parameters), through Fourier spectral analysis of 11-set acceleration recordings of the Yorba Linda earthquake of September 3, 2002.

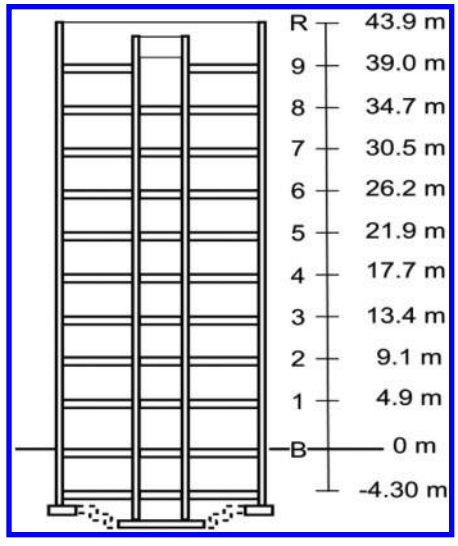


Figure 1a. Vertical cross-section of 10-story Millikan Library, Pasadena, California.

While the aforementioned discrete modeling is overwhelmingly used in structural engineering (e.g. Chopra, 1995), it has limitation in characterizing comprehensive seismic motion in structures with a finite number DOF modeling in general, and distorting time-space or wave features of seismic motion in buildings in particular. Misrepresenting the seismic responses in structures would falsely predict, likely underestimate, the maximum inter-story drift, a key index of seismic demand for structural design. This is due to the fact that time-delay peak waves at two neighboring floors would have the drift calculated as difference between one peak amplitude and one non-peak value, which is typically larger than the difference between two peak values without time-delay effect. This time-delay feature would also affect the efficacy of vibration control, if actuators installed in different floors are operated with a central feedback-control device.

More importantly, understanding and utilization of the wave features could create an alternative wave-based approach for system identification of multi-story buildings, which can be used to improve greatly

the efficiency of post-earthquake structural condition assessment. As well known, effectiveness of discrete-modeling-based system identification in general, and recognition of local physical parameters in particular, relies on a large number of recordings exemplified as 11-set recordings for the Millikan Library, which is neither common nor practical for most structures currently or in the near future. In contrast, a wave-based approach requires only a few of recordings. For example, the peak-to-peak wave traveling time between two different heights is measurable and directly related to wave velocity of the building segment. Similarly, the corresponding peak-amplitude reduction is associated with the segment damping. Both identified velocity and damping can then be related to local physical parameters such as shear modulus and hysteretic damping ratio if the building segment is modeled as a uniform shear-beam.

In fact, seismic responses are the result of wave propagation in large-scale structures such as high-rise buildings, pipelines, and towers, in which some wave-propagation features, such as time delay of traveling waves from one location to the other, play an important role in in-depth understanding of seismic recordings and effective identification of local structural features. Recent studies indeed show advantages of continuous-modeling over traditional discrete-modeling in some seismic response analyses and damage diagnosis of building structures. For example, Iwan (1996) proposed to use 1D uniform shear-beam model for buildings and obtained seismic drift spectrum for design. Safak (1999) introduced 1D continuous/discrete modeling for structure-soil system with impulsive seismic excitation in bedrock. Todorovska et al. (2001) modeled 2D anisotropic wave propagation for a real seven-story building. Snieder and Safak. (2006) employed seismic interferometry (SI) to extract structural responses from seismic recordings. Kohler et al. (2007) studied seismic propagating waves in a 3D steel moment-frame building and verified with ETABS finite-element modeling, among others. Building upon the aforementioned advances and others in relevant literature, this study uses recently-proposed 1D continuous-discrete modeling for wave propagation in building structures and examines response characterization and system identification.

2 MODELING OF WAVE PROPAGATION

In this study, a multi-story building is modeled as a series of continuous shear-beam layers for inter-story columns/walls and discrete lumped-masses for floors, as shown in Fig. 1b. Each inter-story is characterized with shear wave speed $v = \sqrt{G/\rho}$ where G and ρ are respectively equivalent shear modulus and mass density, hysteretic damping ratio γ_c, story height h, and cross-sectional area A, while each floor with lumped mass m_f, which excludes the mass overlapped with

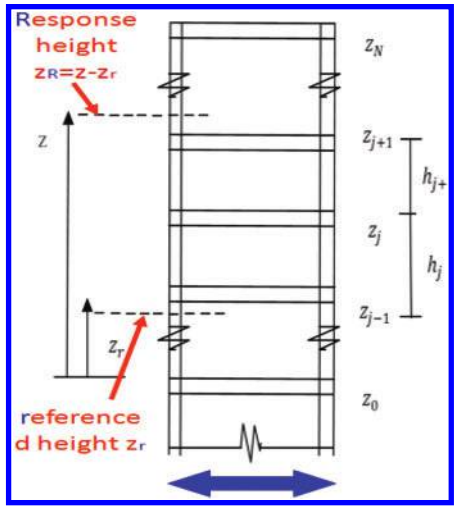


Figure 1b. A model for an N-story building subjected to seismic excitation.

columns and walls, and damping γ_f ($=c_f/m_f$) where c_f is the hysteretic damping coefficient.

The displacements $u(z,t)$ and $u(z_r,t)$ at two locations, referred to as response location z (or $z_R = z - z_r$) and referenced location z_r, can be found

$$u(z,t) = \int_{-\infty}^{\infty} D_{Rr}(\omega) U_{z_r}(\omega) e^{i\omega t} d\omega = \int_{-\infty}^{\infty} d_{Rr}(t-\tau) u(z_r,\tau) d\tau \qquad (1)$$

where D_{Rr} and d_{Rr} are respectively displacement responses at z (z_R) to displacement impulse at z_r in frequency and time domains, and U_{Z_r} is the frequency counterpart of $u(z_r,t)$. Equation (1) can also be interpreted as displacement response at z to a displacement input at z_r, which has the same mathematical form as traditional, vibration representation of displacement response to an external force (e.g., convolution integral), except the difference between force and motion inputs. Because of that, D_{Rr} and d_{Rr} are referred here to as wave-based or generalized frequency response function (GFRF) and generalized impulse response function (GIRF) respectively.

By definition, GFRF is the ratio of frequency displacements at the two locations, obtainable from FFT of the two recordings. With the continuous-discrete model (Zhang et al., 2011)], a closed-form solution of GFRF, and subsequent GIRF with Fourier transformation of GFRF, can be found as

$$D_{Rr}(\omega) = \frac{U_{z_R}}{U_{z_r}} = \frac{(1+R_{NR})T_{Rr}}{(1-R_{rR}R_{NR})(1+R_{Nr})}, \qquad d_{Rr}(t) = \int_{-\infty}^{\infty} D_{Rr} e^{i\omega t} d\omega \qquad (2a,b)$$

where wave transmission coefficient T_{Rr} is the up-going wave at z (z_R) which is propagated upward from an impulsive up-going wave input at z_r (i.e., $\delta(t)$ in time domain and unit in frequency domain), reflection

coefficient R_{Nr} (similar to other Rs) is down-going wave at z_r resulted from an impulsive up-going wave input at z_r which travels upward first, reflects at the free-top Nth story, and then propagates downward to z_r. Expressions of Ts and Rs can be found as function of building physical parameters above z_r. In particular, for the jth inter-story bounded with (z_{j-1}, z_j^-),

$$T_{j^-(j-1)} = T_{z_j^- z_{j-1}} = e^{-\gamma_{ij}|\omega|h_j/v_j} e^{-i\omega h_j/v_j} = T_{(j-1)j^-}$$
$$R_{j^-(j-1)} = R_{(j-1)j^-} = 0 \tag{3}$$

For the jth floor bounded with (z_j^-, z_j)

$$T_{jj^-} = \frac{2}{1 + r_{I_j} - r_{D_j} + ir_{M_j}} = B_{f_j} e^{-i\omega h_{ej}/v_j}$$
$$R_{jj^-} = T_{jj^-} - 1 \quad , \quad T_{j^-j} = T_{jj^-} r_{I_j} \quad , \quad R_{j^-j} = T_{j^-j} - 1 \tag{4}$$

where coefficients r_{Ij}, r_{Dj} and r_{Mj}, amplitude B_{fj} and equivalent floor-height h_{ej} can be found in terms of inter-story impedance (ρv) ratio, cross-sectional area (A) ratio, mass ratio (r_m), wave travelling time through inter-story length (h/v), i.e.,

$$r_{I_j} = \frac{\rho_{j+1} v_{j+1}}{\rho_j v_j} \frac{A_{j+1}}{A_j}, \quad r_{D_j} = \gamma_{f_j} r_{M_j}$$
$$r_{M_j} = r_{m_j} \frac{h_j}{v_j} \omega, \quad r_{m_j} = \frac{m_{f_j}}{m_j}$$
$$B_{f_j} = \frac{2}{\sqrt{(1 + r_{I_j} - r_{D_j})^2 + r_{M_j}^2}} \tag{5}$$
$$h_{ej} = \frac{v_j}{\omega} \tan^{-1} \frac{r_{M_j}}{1 + r_{I_j} - r_{D_j}}$$

For a composite building segment bounded with (z_l, z_n), or simply (l, n), with intermediate location z_m ($z_l < z_m < z_n$ or $z_l > z_m > z_n$) such as (z_{j-1}, z_j) with z_j^-, T and R in (l, n) can be found in terms of those in two sub-segments in (l, m) and (m, n) as

$$T_{ln} = \frac{T_{lm} T_{mn}}{1 - R_{mn} R_{lm}}, \qquad R_{ln} = R_{mn} + \frac{T_{mn} R_{lm} T_{mn}}{1 - R_{mn} R_{lm}} \tag{6}$$

3 SYSTEM IDENTIFICATION

With the aforementioned model for wave propagation at hand, this section shows system identification of the Millikan Library with the use of the general and degenerated models with a limited number of seismic recordings after the Yorba Linda earthquake of September 3, 2002.

In general, with a pair of seismic recordings at two locations, GFRF is obtainable as Fourier spectral ratio of the two recordings. One can first calculate the recording-based GFRF as

$$\tilde{D}_{j0} = \frac{\tilde{U}_j \tilde{U}_0^*}{|\tilde{U}_0|^2 + \varepsilon} \xrightarrow{\varepsilon \to 0} \frac{\tilde{U}_j}{\tilde{U}_0} \tag{7}$$

where $\tilde{U}$ is the seismic recordings in the frequency domain, superscript asterisk indicates the complex conjugate, and ε is a positive small number, implying the added white noise. The white noise is used primarily to avoid unstable calculation of GFRF at some frequencies near the notches in the spectrum $|\tilde{U}_0|^2$. As ε approaches zero, $\tilde{D}_{j0}(\omega) \Rightarrow \tilde{U}_j / \tilde{U}_0$, which is the Fourier spectral ratio or the definition of GFRF in Eq. 2a. Note that the tilde over quantities D and U is used to distinguish the recording-based quantities from those based on modeling or Eq. 2a.

With the continuous-discrete model for the structure, model-based GFRF can also be found in terms of wave transmission and reflection coefficients, which are related to structural physical properties above the impulse location. Matching the two sets of GFRF from recordings and the model helps identify structural parameters such as wave velocity or shear modulus.

3.1 *One-layer model*

One can examine a special case of the general model, i.e., uniform shear-beam or one-layer model without lumped floor mass. The GFRF of Eq. 2a becomes

$$D_{Rr} = \frac{\left(1 + e^{-i\omega(2H_r - 2z_R)/v_c} e^{-\gamma_c|\omega|(2H_r - 2z_R)/v_c}\right) e^{-i\omega z_R/v_c} e^{-\gamma_c|\omega|z_R/v_c}}{1 + e^{-i\omega 2H_r/v_c} e^{-\gamma_c|\omega|2H_r/v_c}} \tag{8}$$

where $H_r = z_N - z_r$ denotes the height of the building portion bounded by (z_r, z_N). The GIRF can then be found by substituting GFRF of Eq. 8 into Eq. 2b, where the integration can be evaluated with the method of residues. In particular, the integrand for d_{Rr}, a function of the real variable ω, is treated as a function of variable y, which has an infinite number of poles y_j ($j = 1,2,\ldots,\infty$) in the upper half complex plane, namely

$$\omega_j = (2j-1)\omega_0 \ , \ \omega_0 = \frac{\pi v_c}{2H_r}, \quad j = 1,2\ldots,\infty \tag{9a,b}$$

The integration of Eq. 2b can then be found as

$$d_{Rr} = 8\omega_0 \sum_{j=1}^{\infty} (-1)^{j+1} e^{-\gamma_c \omega_j t} \cos\left(\frac{\omega_j (H_r - z_R)}{v_c}\right) \sin(\omega_j t) \tag{10}$$

Equation 10 indicates that GIRF consists of an infinite number of motion modes, each of which has exponentially decaying damping factor, modal shape with cosine factor, and sinusoidal motion with modal frequency ω_j. This is essentially the traditional vibration perspective for seismic motion in buildings, in which the 1st modal frequency ω_1 (similar to higher-order modal frequencies) is interpreted as fundamental vibration feature of building's periodic, horizontal motion. Since ω_1 corresponds to $T_1 = 4H_r/v_c$ obtainable from Eqs. 9a,b, the fundamental period can also be viewed as four times of wave traveling time through the building height, i.e., wave interpretation.

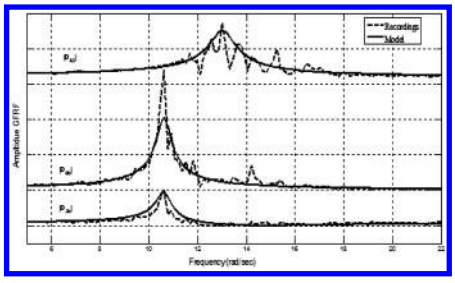


Figure 2. GFRFs at the 3rd and 8th floors with respect to basement and 3rd floors' motion.

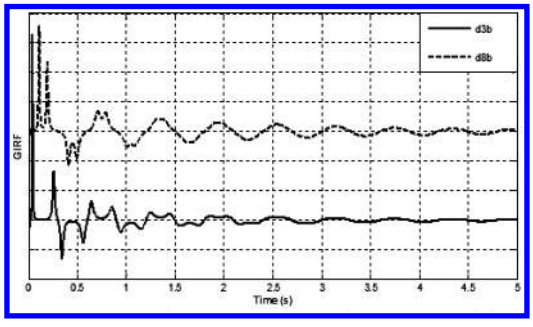


Figure 3. GIRFs at the 3rd and 8th floors with uniform shearbeam model ($v_c = 322$ m/s, $H_r = 48.2$ m, and $\gamma = 0.044$).

Figure 2 shows the match of recording- and uniform-model-based GFRFs of acceleration at the 3rd and 8th floors with respect to referenced motion at the basement and 3rd floors, in which ε is selected as 5% of total power spectrum of basement motion. The identified shear wave speeds for the whole building and the 3rd-floor-up building portion are 326 and 289 m/s, respectively; indicating that shear modulus (G) of the 3rd-floor-up building portion is less than that of the whole building if mass density (ρ) is assumed the same. Alternatively, the lower portion of the building (i.e., from the basement to the 3rd floor) is more rigid in shear resistance than the upper portion (from the 3rd floor to the top). The corresponding damping ratios are 0.028 and 0.040 respectively for the whole and the 3rd-floor-up building portion. The identified parameters indicating that the uniform shear-beam model is good enough to characterize the fundamentals of wave and vibration motion in multi-story buildings.

To validate the wave response features of the uniform shear-beam model, this study examines GIRF at the 3rd and 8th floors with respect to the basement motion shown in Fig. 3 where $v_c = 322$ m/s and $\gamma = 0.044$ are used based on Snider and Safak (2006). In particular, the first peak at the 3rd floor is rooted from the impulse propagation from the basement, which propagates further to the first peak at the 8th floor with damping-related reduced amplitude. That first peak at the 8th floor is then propagated to the top and then reflected to travel downward to the 8th and 3rd floors to generate the second peaks with sequential reduced amplitudes. The second peak at the 3rd floor continues propagating downward to the basement. Since the motion will disappear at the basement due to the fixed boundary, a negative, same-amplitude peak, balancing the positive one at the basement, is generated and propagated upward. That negative peak propagates to the 3rd and 8th floors with further reduced amplitudes, and continues following previous wave propagation cycle. As time goes on, the vibration features at those floors are then dominated by the character of the resonance of the whole building, while high-order motion modes are also involved. All these fundamental features are literally consistent with wave-propagation theory as well as pertinent others (e.g., Snieder, 2006).

3.2 *Two-layer model*

While the uniform shear-beam model captures fundamental features of a multi-story building, piecewise shear beams would be natural in characterizing the changing-properties of the structure along the height. For simplicity, one can examine a two-layer model without floor masses, which leads Eq. 2a to

$$D_{R0} = \frac{\left(1+\alpha\left(e^{-2i\omega(\tau_1-\tau_z)}+e^{-2i\omega\tau_2}\right)e^{-2i\omega(\tau-\tau_z)}\right)e^{-i\omega\tau_z}}{1+\alpha\left(e^{-2i\omega\tau_1}+e^{-2i\omega\tau_2}\right)+e^{-2i\omega\tau}} \quad (11a)$$

$$0 \le z \le h_1, \quad \tau_z = \frac{z}{v_1}$$

$$D_{R0} = \frac{2\left(1+e^{-2i\omega(\tau-\tau_z)}\right)e^{-i\omega\tau_z}/\left(1+r_{I_1}\right)}{1+\alpha\left(e^{-2i\omega\tau_1}+e^{-2i\omega\tau_2}\right)+e^{-2i\omega\tau}} \quad (11b)$$

$$h_1 \le z \le h_1+h_2, \ \tau_z = \frac{h_1}{v_1}+\frac{z-h_1}{v_2}$$

where τ_z is the flight time for waves traveling from referenced level z_0 to response location z_R, and

$$\alpha = \frac{1-r_{I_1}}{1+r_{I_1}}, \ \tau_1 = \frac{h_1}{v_1}, \ \tau_2 = \frac{h_2}{v_2}, \ \tau = \tau_1+\tau_2 \quad (12a,b,c,d)$$

The GIRF can be found by substituting GFRF of Eqs. 11a,b into Eq. 2b, where the integration can be obtained in a closed form with the method of residue for some special cases and numerically for general cases. Below are presented some special cases, which could help understand the characteristics of wave propagation in piecewise-uniform buildings and subsequently aid in system identification.

For $\gamma_1 = \gamma_2$ and $\tau_1 = \tau_2$, one can find

$$\omega_{2j-1} = \frac{(2j-1)\pi-\beta}{\tau}, \ \omega_{2j} = \frac{(2j-1)\pi+\beta}{\tau} \quad (13)$$

$$\gamma_{eq} = \gamma_1 = \gamma_2, \ \alpha = \pm\cos\beta$$

The closed-form solution of GIRF with Eq. 2b for $r_{I_1} = 1$, which could be, but not necessarily, the uniform or one-layer model, can be found with the same

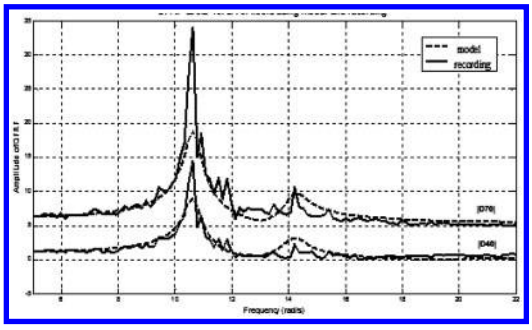


Figure 4. Comparison of GFRF amplitudes at the 4th and 7th floors with respect to impulsive basement acceleration obtained from seismic recordings and model.

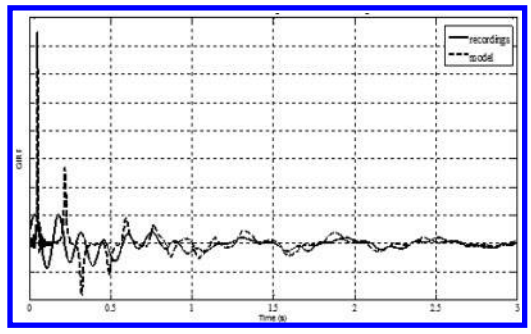


Figure 5. Comparison of GIRF at the 4th floor with respect to basement acceleration motion obtained from seismic recordings and model.

as Eq. 10. Accordingly, wave-propagation features of the two-layer model will be similar to those observed in the uniform shear-beam model.

For a pair of recordings available at the basement and floor 4 or floor 7, for example, the GFRF of $\tilde{D}_{40}$ or $\tilde{D}_{70}$, with $\varepsilon = 5\%$ of the total power spectrum of basement motion can be found in Fig. 4. In principal, all the frequencies corresponding to the spectral peaks in Fig. 4 can be regarded as modal frequencies and then used for system identification. For simplicity in practice and also for illustration with the use of a two-layer model without floor masses, parametric identification is carried out here based on two modal frequencies identified from Fig. 4 as $\omega_1 = 10.62$ rad/s and $\omega_2 = 14.21$ rad/s.

With the use of Eqs. 12a$\sim$d, the following are found: $\tau = 2\pi/(\omega_1 + \omega_2)$, $\beta = \pi(\omega_1 + \omega_2)/(\omega_1 + \omega_2)$, which yields $\tau = 0.253$ s and $\beta = 0.454$ rad, and subsequently $r_{I1} = 0.053$, $v_1 = 361.85$ m/s, $v_2 = 19.18$ m/s, $h_1 = 45.77$ m, $h_2 = 2.43$ m with Eqs. 13a$\sim$d & 14a$\sim$d. The identified slower velocity in the very-thinner layer 2 than those in layer one below makes sense, for the real building has one portion that consists of large floor masses and rigid columns and walls, which is below the very thin roof top, the other portion. It should be noted that the aforementioned identification is under special condition of $\gamma_1 = \gamma_2$ and $\tau_1 = \tau_2$. In general, parameters r_{I1}, v_1, v_2, h_1 and h_2, together with γ_1 and γ_2, can be found by minimizing the mean-square error of the model-based GFRF from recording-based GFRF in certain frequency range (say 5$\sim$22 rad/s), among many other identification algorithms.

While it is doable, this study instead presents the comparison of model-based GFRFs with the aforementioned, pre-selected parameters with recording-based ones, aiming to show the influences of some parameters in GFRF and GIRF. Figures 4 and 5 show, respectively, the comparison of recording-based GFRF at the 4th and 7th floors and GIRF at 4th floor with respect to band-limited ($\varepsilon = 5\%$) impulsive motion at the basement against model-based counterparts with respect to pure ($\varepsilon = 0\,\%$) impulsive motion at basement. These two figures indicate that the two-layer model is able to capture the fundamental wave and vibration features shown in the recordings, exemplified as the first and second modal frequencies in Fig. 4, and proximity of first couples of wave arrival times and well-matched resonant vibration features in Fig. 5. The major difference in spectral amplitudes at the first modal frequency in Fig. 4 and in wave amplitude and arrival time in the 0$\sim$0.5 s time window in Fig. 5 can be minimized with appropriate system-identification algorithm.

3.3 *General continuous-discrete model*

In general, the more the number of DOF used for the building system, the more robust the system identification is. This sub-section shows some results of the system identification using the continuous-discrete model with seismic recordings provided at the basement and 8th floor. The identification algorithm is carried out by numerically minimizing the mean squared difference of recording- and model-based GFRF with match at two pairs of identified modal frequencies, i.e., (10.62, 11.67) rad/s for one case and (10.62, 14.21) rad/s for the other.

Figures 6a,b shows the match between recording- and model-based GFRF with modal frequencies (10.62, 11.67) and (10.62,14.21) rad/s respectively. These results show that continuous-discrete model could flexibly capture dominant dynamic features of the system, exemplified as any two (or more in principle) modal frequencies identified from seismic recordings. They also indicate that the floor-to-column mass ratio, one of model parameters, plays a major role in determining the other parameters.

Figure 7 shows the GIRFs at selected locations with the building modeled as 11 continuous layers for inter-stories and 10 discrete masses for floors. In general, the wave features shown in Fig. 7 bear the similarity with those with uniform shear-beam model in Fig. 3. Besides the aforementioned fundamental wave features, multiple higher-frequency waves are also observed at those presented floors after the first motion peaks in Fig. 7. That is primarily caused by wave scattering at each and every of 10 floor-to-column boundaries, characterized with transmission

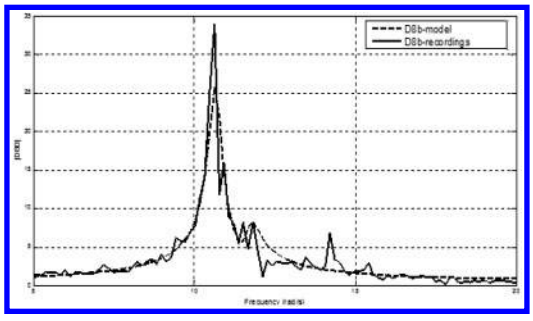


Figure 6a. System identification using seismic recordings at the basement and 8th floors with continuous-discrete model matching two modal frequencies (10.62,11.67) rad/s.

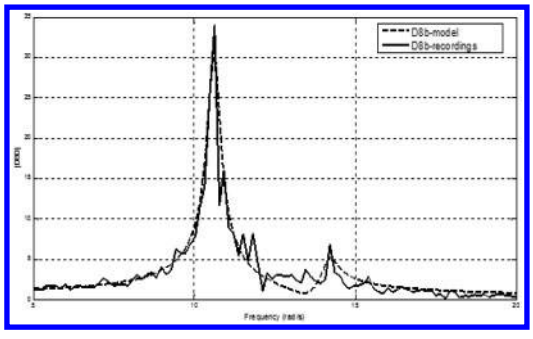


Figure 6b. System identification using seismic recordings at the basement and 8th floors with continuous-discrete model matching two modal frequencies (10.62,14.21) rad/s.

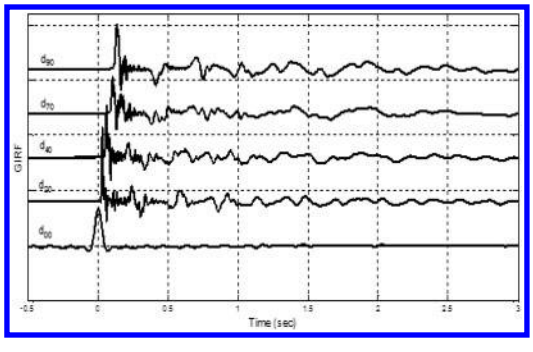


Figure 7. GIRFs at selected floors with continuous-discrete model.

and reflection coefficients in Eqs. 4 and 5. In other words, besides the dominant motion peaks at one floor (say the 1st and 2nd dominant peaks at around 0.1 and 0.25s for the GIRF at the 4th floor), other multiple peaks after the 1st peak are attributed to the arrival waves reflected and transmitted from other floors. All these make the wave responses complicated after initial arrival of impulse waves.

4 CONCLUSIONS

This study first presents continuous-discrete modeling of seismic wave propagation in multi-story building structures. It then derives the generalized impulse and frequency response functions (GIRF and GFRF) which are fundamentally important in constructing response to the motion input to a system, not the traditional force input. The features of GIRF and GFRF as well as seismic responses are also examined in detail, revealing not only well-observed vibration features of building structures, but also some perspective of seismic wave behaviors of structures which traditional vibration-based approach does not show clearly. The model is then used for system identification of Millikan Library building with recordings of Yorba Linda earthquake of September 3, 2002. Results show the proposed approach is efficient. While this study shows some applications of the modeling in system identification, it can be easily extended for damage diagnosis in post-earthquake conditional assessment for a pair of available recordings of an earthquake, which is the subject of future study.

REFERENCES

Chopra, A., 1995. *Dynamics* of *Structures- Theory and Applications to Earthquake Engineering*, Prentice-Hall, Inc.

Iwan, W.D. 1996. Drift Spectrum: Measure of Demand for Earthquake Ground Motions, *Journal of Engineering Mechanics-ASCE,* 123(4): 397–404.

Safak, E. 1999. Wave Propagation Formulation of Seismic Response of Multistory Building, *Journal of Structural Engineering ASCE*, 125(4): 426–437.

Todorovska, M.I., Ivannovic, S.S. and Trifunac, M.D. 2001. Wave Propagation in A Seven-Story Reinforced Concrete Building I: Theoritical Models, *Soil Dynamics and Earthquake Engineering*, 21(3): 211–223.

Snider, R. and Safak, E. 2006. Extracting The Building Response using Siesmic Interferometery: Theory and Application to The Millikan Library In Pasadena, California, *Bulletin of the Seismological Society of America,* 96(2):. 586–598.

Kohler, M.D., Heaton, T. and Bradford, S.C. 2007. Propagating Waves in The Steel Moment-Frame Factor Building Recorded During Earthquakes, *Bulletin of the Seismological Society of America,* 97(4): 1334–1345.

Zhang, R., Snider, R. Gargab, L. and Seibi, A. 2011. Modeling of Seismic Wave Motion in High-Rise Buildings, *Probabilistic Engineering Mechanics,* 26(4), 520–527.

Research and Applications in Structural Engineering, Mechanics and Computation – Zingoni (Ed.)
© 2013 Taylor & Francis Group, London, ISBN 978-1-138-00061-2

Generation of spectrum compatible site-dependent earthquake load histories by evolutionary approach

F. Carli & C. Carino
Dipartmento di Ingegneria Civile e Architettura, Univ. di Pavia, Pavia, Italy

ABSTRACT: In this work a generation procedure for sets of simulated accelerograms is formulated on the basis of an assigned target design spectrum. The proposed approach accounts for both energy release and frequency content variability in time. The discussed evolutionary model is based on the assumption of decoupling the distribution in time of the energy release from the changing of the frequency content that is obtained by means of an amplitude modulation function and a frequency modulating function. The decoupling of the two main sources of the non-stationary behavior of natural time-histories allows the recognition of strict relations between recorded accelerograms at a site and the underlying evolutionary model here proposed. The numerical example is based on a specific record at a reference Italian seismic site and on the corresponding design spectrum from the national design code.

1 INTRODUCTION

In modern performance based design codes the specification of design forces for earthquake resistant design is often obtained via design spectra consistent at the specific site with the performance requirements. In many cases this underlying equivalent linear static/dynamic approach by modal combination rules can't be considered sufficient especially when studying the dynamics of large nonlinear systems. In that case the seismic load must be represented by a suitable set of earthquake time histories. Records of natural seismic events rarely comply with the design code requirement to be 'response spectrum compatible' at the specific site. This lack produces the need of suitable methods for the digital generation of synthetic accelerograms from the knowledge of a target response spectrum given by the code. Different methods are present in literature at this purpose (Cacciola & Zentner 2012): models bases on filtering and windowing Gaussian noise, others based on filtering white-noise of Kanai-Tajimi type, auto regressive approaches, autoregressive with moving average and recently also wavelet based models (Giaralis & Spanos 2009). More recently significant efforts were made to include both the amplitude variation and the changing in time of the frequency content (Sgobba et al. 2011). The present work is concerned with the formulation of a generation procedure for sets of simulated accelerograms on the basis of an assigned target design spectrum. The proposed approach is able to take into account for both the energy release in time and the contemporary variability of the frequency content on the basis of a possible decoupling of the two main sources of non-stationarity (Carli 1997). In particular the evolutionary approach is obtained by means of an amplitude modulation function and a frequency modulation function in time. That allows the recognition of strict relations between recorded accelerograms at a site and the underlying evolutionary model here proposed for the generation of spectrum compatible time histories. The work is completed by a numerical example in which a specific recorded sample at a reference site and the corresponding site dependent design spectrum prescribed by the Italian design code (Ministero delle Infrastrutture 2008) give all the information used for the complete definition of the simulation procedure.

2 FUNDAMENTAL RELATIONS

A complete and detailed description of a generic natural time signal $r(t)$ can be obtained by means of a suitable one-to-one mapping of $r(t)$ in the time t and frequency f domain by means of its complex spectral representation $R(f,t)$ (Newland 1993). Moreover in presence of a quasi-stationary stochastic process $r(t)$ of limited duration, an estimate of its power spectral density function $G_r(f,t)$ can be obtained as:

$$G_r(f,t) = R(f,t)^2 / d_0 \tag{1}$$

where $R(f,t)$ is defined as a smooth version of the amplitude spectrum of the underlying stochastic process $r(t)$, while d_0 represents the equivalent stationary duration of the signal. Previous works (Carli 1997) show the possibility and effectiveness of the separation

of the amplitude variability in time from the changing of the frequency content by the following basic relation:

$$R(f,t) = i(t)\, A_s(f,t) \tag{2}$$

with $i(t)$ the intensity function of the process $r(t)$ and $A_s(f,t)$ the amplitude stationary and frequency non-stationary amplitude spectrum. Therefore $A_s(f,t)$ represents a function with constant release in time of the power while allowing the variation of the frequency content, that is:

$$\int G_s(f,t_i)df = \text{constant}, \qquad \forall t_i \tag{3}$$

with $G_s(f,t) = A_s(f,t)^2/d_0$.

In this approach the intensity function $i(t)$ is therefore the only responsible of the power release of the process. That can be considered a suitable approximate description of the signal behavior only when smooth fluctuation in time of the energy release are involved.

In that context for the analytical formulation of $A_s(f,t)$ different approaches can be followed like seismological models based on multi-filtering techniques from source to site including attenuation law, or more empirical relations with less hints from the physical description of the natural event, till pure analytical models using suitable approximating functions. The main objective of this work is the formulation of a model suitable for the generation of load histories having spectral compatibility with a target response spectrum at the site prescribed by a building design code. Moreover the existence of a strict relation between the amplitude spectrum of an accelerogram and its zero damping pseudo-velocity response spectrum is also considered. The previous considerations suggested to test a formulation based on the following description of the $A_s(f,t)$ spectrum:

$$A_s(f,t) = A_s(f, f_0(t)) \tag{4}$$

whose analytical shape at time t changes on the basis of a single frequency parameter $f_0(t)$ that can change in time accordingly to a suitable function. In this model the $f_0(t)$ function is the only responsible of the changing of the spectral shape in time, assuming from that the term of frequency modulation function. In particular the following relation is here tested:

$$f_0(t) = \begin{cases} f_0(t_r), & 0 \le t \le t_r \\ e^{c_0 + c_1 t + c_2 t^2}, & t_r \le t \le t_{end} \end{cases} \tag{5}$$

Few time parameters are highlighting: t_{end} total duration of the accelerogram and t_r rise-time or ramp up time, that can be related to the starting point of the decay portion t_d simply by $d_0 = t_d - t_r$ that is the strong-ground-motion part of the load history, also known in literature as equivalent stationary duration. The proposed piece-wise function derives from the observation of the natural behavior of seismic records in which the frequency content is changing in time with regularity from high frequency content during the initial ramp up, to lower frequency content in time with important changing during the strong motion part and then slowly decreasing along the last part of the signal. From this model comes out the importance of the time characterization of the energy release in time to be expected at the considered site.

To play the role of single-parameter characterization of the variation in the frequency content $f_0(t)$ is here assumed to be the central frequency of the spectral representation in time. By this approach the decoupling of the two main sources responsible for the non-stationary behavior of strong ground motions is almost complete. The only connection between time and frequency formulations remains the frequency modulating function with the job of driving the variation of the frequency content in time.

3 TIME PARAMETERS

In the estimation process of the time parameters needed for the characterization of the accelerograms an important role is played by the intensity function $i(t)$ and the derived estimate of the equivalent stationary duration d_0 with its time location t_r and t_d. In particular $i(t)$ gives the distribution in time of the energy while d_0 gives the basis for the estimate of the frequency modulating function.

In literature different methods were proposed for the estimate of the equivalent stationary duration of a recorded time history but all the proposals show pro and cons. Here is used a method introduced by (Carli, 1997) where the equivalent stationary duration is estimated on the basis of the intensity function of the record as:

$$d_0 = \int_0^{t_{end}} i(t)dt \tag{6}$$

where $i(t)$ comes from the convolution of the strong ground motion by a suitable 'bell-shaped' window function $w(t)$ accordingly the followings:

$$e(t) = w(t) * r(t) \quad \text{with: } i(t) = e(t)/\max[e(t)] \tag{7}$$

The placement of d_0 in time is then obtained looking for the maximum energy release step of the record during a d_0 time portion. In particular, defining the cumulate function of $r(t)$ as:

$$C_r(t) = \int_0^t r^2(\tau)d\tau \tag{8}$$

d_0 can be easily located by the following maximizing condition (Carli 1997) solved for t:

$$\max\left[C_r(t+d_0) - C_r(t)\right], \quad 0 \le t \le (t_{end} + d_0) \tag{9}$$

t_r is therefore obtained leading to $t_d = t_r + d_0$.

It can be observed that the presented procedure for the evaluation of the envelope function $i(t)$ and

the time parameters allowing the definition of the strong motion part of a seismic record are somehow dependent on the selection of the smooth convolution window $w(t)$. Favorably the level of subjectivity of any reasonable choice is limited to the window function only and moreover it can be shown that the time characterization remains stable to that.

4 FREQUENCY SHAPES

As previously stated the observation of the evolution of the frequency content in time of natural seismic records suggested the adoption of the piece-wise function $f_0(t)$ in Eq. (5) with constants c_0 , c_1 and c_2 obtained by least squares fitting. To define the analytical form for $A_s(f,t)$, the amplitude stationary and frequency non-stationary amplitude spectrum to be used for the simulation of the spectrum compatible accelerograms, some hints can be obtained by the following general observations. It is known that the zero damping elastic (absolute) velocity response spectrum $S_{av}(f)$ of a generic seismic record $r(t)$ can be considered a reasonable approximation of its Fourier amplitude spectrum $R(f)$. It can be also taken into account that the spectral response $S_{av}(f)$ can be superposed with the elastic pseudo-velocity response spectrum $S_v(f)$ of $r(t)$ in a wide range of significant frequencies. Therefore a commonly used piecewise function, normalized to unit, $A_{su}(f)$ is here adopted for the analytical description of the spectral representation of a stationary simulated accelerogram $s(t)$:

$$A_{su}(f)=\begin{cases}\left(f/f_1\right)^2 & , \quad 0\le f\le f_1\\ 1 & , \quad f_1\le f\le f_2\\ \exp\left[\dfrac{(f_2-f)}{f_1}\right] & , \quad f_2\le f\end{cases} \tag{10}$$

with f_1 and f_2 the characteristic corner frequency of the spectral representation. The shape of the $A_{su}(f)$ resembles the one of the elastic design spectrum given by the Italian design code for seismic structure. For given values f_1 and f_2 a central frequency value f_0 of $A_{su}(f)$ can be easily calculated. Therefore assuming $f_0(t|f_1,f_2)$ to be the suitable modulating function $f_0(t)$ as previously defined in Eq. (5), the following time-frequency spectral representation $A_s(f,t)$ of a random process $a_s(t)$, stationary in time but non-stationary in frequency, can be obtained:

$$A_s(f,t) = c_s(t)\ A_{su}(f\,|\,f_1(t),f_2(t)) \tag{11}$$

being $f_1(t)$ and $f_2(t)$ in one-to-one relation with $f_0(t|f_1(t),f_2(t))$ estimated at time t, and $c_s(t)$ a normalizing factor to guarantee a constant energy release in time.

5 SPECTRUM COMPATIBILITY PROCEDURE

On the basis of the previously defined relations, the logical scheme used in the present work for the generation of evolutionary and spectrum compatible site-dependent earthquake load histories $a(t)$ can be summarized in the following steps.

5.1 *Time characterization*

a) selection from a public database of recorded seismic signal of a suitable record $r(t)$ to be used as a reference descriptor of the local seismicity
b) evaluation of the intensity function $i(t)$, equivalent stationary duration d_0, rise-time t_r, decay time t_d and signal duration t_{end} employing the approach described in Eqs. (7–9)
c) estimation of the continuous function $f_0(t)$ by approximation of the time varying values of the central frequency $f_0(t_i|\Delta t)$, with Δt a suitable moving time interval, using Eq. (5). A usual selection for seismic signals is $\Delta t = 1$ sec. The values $f_0(t_i|\Delta t)$ can be easily obtained by common methods usually employed for the estimation of the time-frequency amplitude spectra $R(f,t_i)$ of a non-stationary natural record $r(t)$ by time-segmented approach (Geckinli & Yavuz 1983).

5.2 *Frequency characterization*

d) definition of the two corner frequency functions $f_1(t)$ and $f_2(t)$ on the basis of the just estimated central frequency $f_0(t)$, e.g. assuming $f_2(t) = f_1(t) + 1$
e) construction of one sided real valued amplitude spectrum $A_s(f,t)$ from Eq. (6) having constant power per unit time, that is:

$$\int A_s^2(f,t)df\,dt = \left(\int r^2(t)dt\right)_{end} / d_0 \tag{12}$$

5.3 *Simulation procedure*

f) generation of the an initial amplitude stationary simulated accelerogram $a_s(t)$ by the classic approach:

$$a_s(t) = \sum_i A_s(f_i,t)\cos(2\pi f_i\, t+\varphi_i) \tag{13}$$

g) amplitude modulation of $a_s(t)$ to obtain the initial simulated accelerogram $a(t)$:

$$a(t) = i(t)\ a_s(t) \tag{14}$$

h) evaluation of the pseudo-velocity elastic response spectrum $S_v(f)$ of $a(t)$
i) estimation of the unit difference factor $\Delta S_v(f)$ calculated as:

$$\Delta S_v(f) = \left[S_{vd}(f)-S_v(f)\right]/S_{vd}(f) \tag{15}$$

with $S_{vd}(f)$ the elastic design response spectrum given by the building code at the considered site

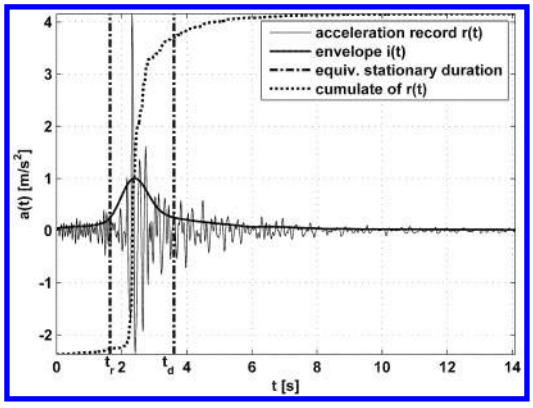


Figure 1. The reference record $r(t)$, its cumulate $C_r(t)$. The calculated envelope function $i(t)$ and the position of the equivalent stationary duration $d_0 = 1.96$s, $t_r = 1.65$s, $t_d = 3.61$s.

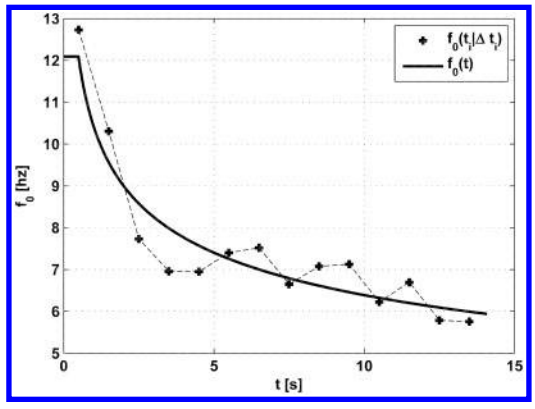


Figure 2. The data points corresponding to the central frequency values of the segmented record at time intervals Δt_i, and the corresponding approximation function $f_0(t)$.

j) correction of $A_s(f,t)$ by the $\Delta S_v(f)$ factor
k) iterate steps from f) to j) till some convergence criterion is fulfilled

6 NUMERICAL EXAMPLE

The main objective of the numerical application here reported is to show the behavior and effectiveness of the proposed procedure for the generation of synthetic time histories. In particular the level of compatibility with the target elastic spectrum prescribed at the selected site by a building design code is verified while employing as site dependent input data a single significant seismic record used as the reference indicator for the time characterization of the simulation procedure. In particular the site here selected is Ancona (Italy). It was selected considering the following features: it is located in a seismic active zone of medium level (classified as seismic Zone 2 with peak ground acceleration $0.15g < a_g < 0.25g$), public seismic records are available (Ambraseys et al. 2002), the records from the main 1972 seismic event show a significant variation of the frequency content in time.

The recorded signal $r(t)$ here used as reference for the time-frequency characterization of the proposed model is the NS component of the acceleration recorded at Ancona-Palombina station in date 21.06.1972, h.15.06.44 starting time, sampling period: 0.01 s, record length: 14.080 s. The record is here characterized in time and frequency following the approach described in Eqs. (6–9). At first the intensity function $i(t)$ is estimated by the convolution with a window function $w(t)$ of Gaussian type with standard deviation set equal to 1 s. The equivalent stationary duration is estimated, $d_0 = 1.96$ s, and then located in time, $t_r = 1.65$ s and $t_d = 3.61$ s, with the aid of $C_r(t)$ the cumulate of $r^2(t)$.

The original record $r(t)$ and the obtained results are summarized in Figure 1.

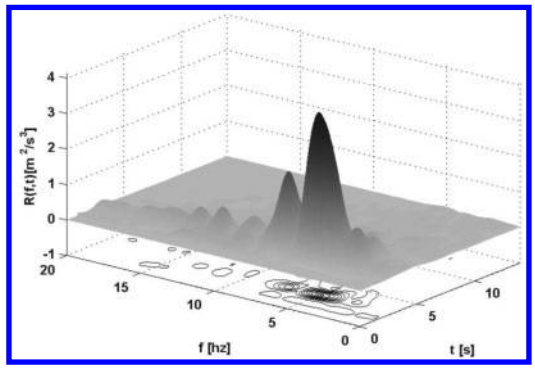


Figure 3. One sided time-frequency spectral representation $R(f,t)$ of the reference record $r(t)$.

A short time spectral representation of the frequency content of the record is then performed adopting for the segmentation of the signal a time-tapering window function of Tukey type and time-width $\Delta t = 1$ s (Geckinli & Yavuz 1983).

Naming $R_i(f)$ the one-sided amplitude spectrum of the corresponding time segment $r_i(t)$ the central frequency $f_0(t_i|\Delta t)$ of $R_i(f)$ can be promptly calculated allowing the evaluation of the approximating function $f_0(t)$ given in Eq. (5). The estimated values $f_0(t_i|\Delta t)$ for the selected record and the corresponding central frequency function obtained by least-square fitting procedure are shown in Figure 2 while Figure 3 gives a smoothed version of the one-sided spectral representation of the reference accelerogram in time and frequency $R(f,t)$ (Eq. 1). The obtained central frequency function allow the numerical evaluation of both $f_1(t)$ and $f_2(t)$ in Eq. (10) with the assumption of a constant width of the flat part: $f_2(t) - f_1(t) = 1$. From that the stationary one-sided spectrum $A_s(f,t)$ is evaluated (Fig. 4).

The iteration procedure is then performed using as global convergence criterion that the norm of the unit difference factor have to be less than 20% of the

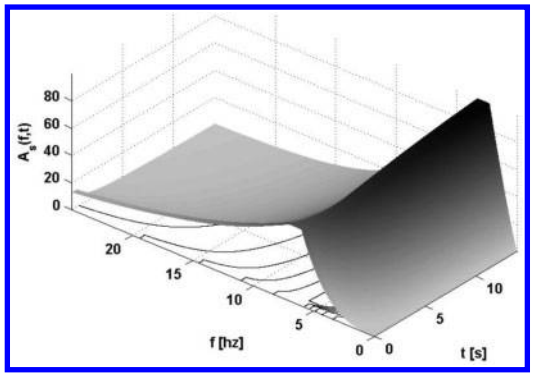


Figure 4. The normalized frequency evolutionary spectrum $A_s(f,t)$ with constant energy release in time of the proposed model.

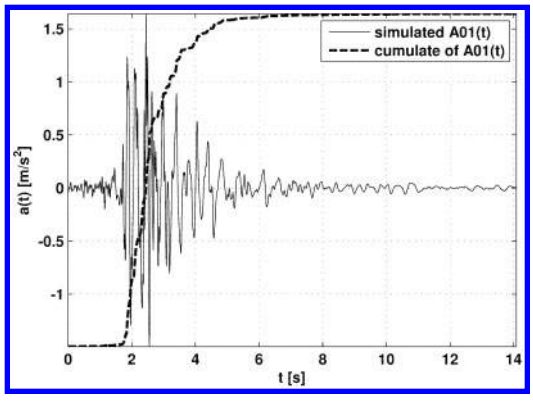


Figure 5. The simulated accelerogram $A01(t)$ obtained at the first step of the iteration procedure towards a target design spectrum signal and it's cumulate function.

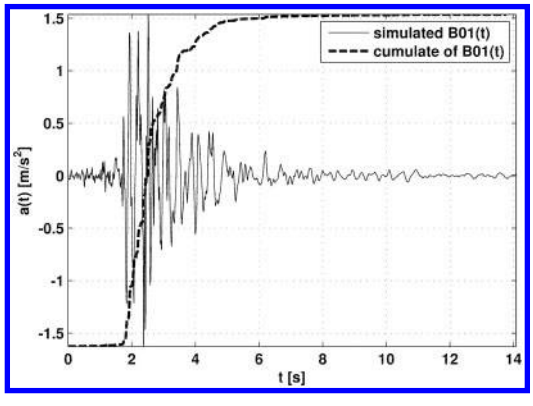


Figure 6. The simulated accelerogram $B01(t)$ obtained at the first step of the iteration procedure towards a target design spectrum signal and it's cumulate function.

target zero damping velocity design spectrum estimated at the site. The target spectrum is obtained in agreement with the Italian Design Code (Ministero delle Infrastrutture 2008) using the suitable parameters given for the selected site. In Figures 5, 6 two

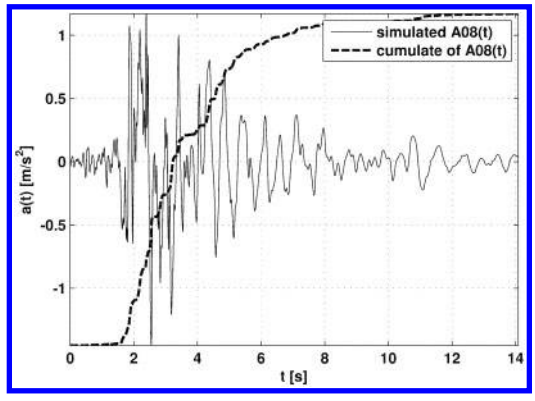


Figure 7. The simulated accelerogram $A08(t)$ obtained at convergence of the iteration procedure towards a target design spectrum signal and it's cumulate function.

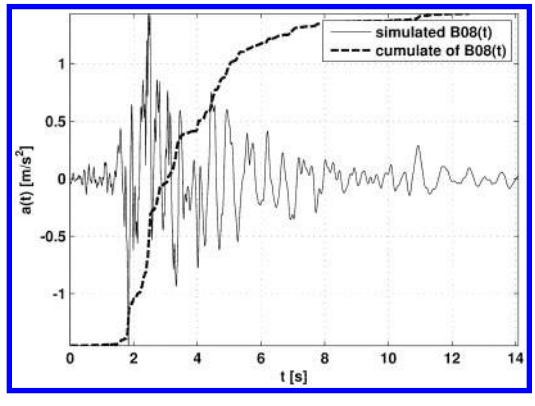


Figure 8. The simulated accelerogram $B08(t)$ obtained at convergence of the iteration procedure towards a target design spectrum signal and it's cumulate function.

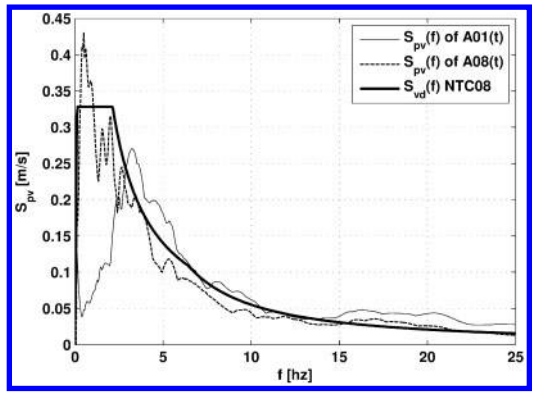


Figure 9. The pseudo-velocity response spectra, 5% damping, of $A01(t)$ and of $A08(t)$ plotted vs. the target design response spectrum prescribed by the Italian design code *NTC08*.

simulated accelerograms $A01(t)$ and $B01(t)$ obtained at the first iteration are presented, while in Figures 7, 8 are reported the same two simulated accelerograms as obtained at the last iteration, n. 8, used in

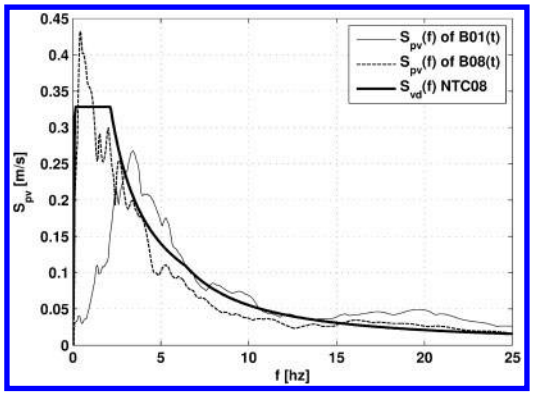


Figure 10. The pseudo-velocity response spectra, 5% damping, of $B01(t)$ and of $B08(t)$ plotted vs. the target design response spectrum prescribed by the Italian design code *NTC08*.

this example $A08(t)$ and $B08(t)$. The pseudo-velocity response spectra calculated for $A01(t)$ and $B01(t)$ are plotted vs. the reference design spectrum at the site in Figure 9. The same comparison is presented in Figure 10 for the signals $A08(t)$ and $B08(t)$ at convergence.

7 CONCLUSIONS

In this paper a first proposal for the generation of synthetic acceleration time histories is presented. The main distinctive feature of the proposed approach is the generation of evolutionary signals in which both amplitude and frequency content change during the time resembling the natural behavior of recorded seismic signals. The complete non-stationary behavior is obtained in simplified way introducing a decoupled description of the frequency content from the amplitude non-stationarity. The numerical example is set up to show the step by step characterization of the model. It can be recognized the need of a small amount of data for its site localization. The obtained accelerograms show a natural appearance and the corresponding spectra significantly approach the target design spectrum. Nevertheless more work is needed to obtain a more strict convergence to the desired target.

REFERENCES

Ambraseys, N. & Smit, P. & Sigbjornsson, R. & Suhadolc, P. & Margaris, B. 2002. *Internet-Site for European Strong-Motion Data*, European Commission, Research – Directorate General, Environment and Climate Programme.

Bozorgnia, Y. & Campbell, K.W. 2004. Engineering Characterization of Ground Motion. In Bozorgnia, Y. & Bertero, V.V.(ed.), *Earthquake engineering: from engineering seismology to performance-based engineering.* CRC Press 2004.

Cacciola, P. & Zentner, I. 2012. Generation of response-spectrum-compatible artificial earthquake accelerograms with random joint time-frequency distributions, *Probabilistic Engineering Mechanics* 28(12):52–58.

Carli, F. 1997. Generazione di accelerogrammi spettrocompatibili. *Proc. Convegno Nazionale ANIDIS "L'Ingegneria Sismica in Italia", Taormina, 21–24 Settembre 1997*.

Geckinli, N.C. & Yavuz, D. 1983. *Discrete Fourier Transformation and Its Application to Power Spectra Estimation*. Amsterdam: Elsevier.

Newland, D.E. 1993. *An Introduction to random vibration, spectral and wavelet analysis. 3rd Ed*. NewYork: Longman Scientific & Technical.

Giaralis, A. & Spanos, P.D. 2009. Wavelet-based response spectrum compatible synthesis of accelerograms – Eurocode application (EC8). *Soil Dynamics and Earthquake Engineering* 29(09):219–235.

Ministero delle Infrastrutture. 2008. Norme tecniche per le costruzioni. *Suppl. Ord. G.U. 4.2.2008, n.29*.

Sgobba, S. & Stafford, P.J. & Marano, G.C. & Guaragnella, C. 2011. An evolutionary stochastic ground-motion model defined by a seismological scenario and local site conditions. *Soil Dynamics and Earthquake Engineering* 31(11):1465–1479.

Research and Applications in Structural Engineering, Mechanics and Computation – Zingoni (Ed.)
© 2013 Taylor & Francis Group, London, ISBN 978-1-138-00061-2

Large-scale dual shake tables testing: An experimental approach to study the non-uniform excitation effects on long span bridges

Moe M.S. Cheung
Western China Earthquake and Hazards Mitigation Research Centre, Sichuan University, Chengdu, China

Cheng-Yu Yang
State Key Laboratory of Disaster Reduction in Civil Engineering, Tongji University, Shanghai, China

Yuxin Pan & Feng Xiong
Western China Earthquake and Hazards Mitigation Research Centre, Sichuan University, Chengdu, China

ABSTRACT: The traditional approach for seismic analysis is based on a uniform excitation assumption, which works well for normal buildings, but is not quite accurate for long span structures, such as bridges, dams, and pipe network systems. For long span bridges, different supports might be subjected to significantly different seismic excitations, foundation types, soil conditions, seismic inputs, with different incidence angles. In general, four main factors may contribute to the spatial variation of earthquake excitations: a) incoherence effect, b) attenuation effect, c) site effect and d) propagation effect. During the last 30 years, many researchers have been working on the numerical analysis of seismic behavior of long span bridges under uniform or non-uniform ground motion; however, few experimental studies of large scale bridge models subjected to earthquake loading have been carried out. Although there are many shake tables in universities and research institutes all over the world, few have a multiple shake table system which can provide non-uniform excitations to different parts of the structural model. A dual shake table testing system has been developed at the Hong Kong University of Science and Technology and a 1:120 reduced scale model of a cable-stayed bridge with a main span of 430 m is designed and constructed for the purpose of this study. This paper describes the factors involved in the scale factor selection and the detailed design processes of different components of the model, including towers, girders, stayed-cables as well as artificial masses. The earthquake records from the SMART-1, as well as the PEER Strong Motion Database, are used in the shake table test. The results of the modal tests, the identical-input excitation tests and the varying-input excitation tests are presented, for the purpose of a) evaluating the design of the reduced scale model and the experimental method, b) studying the dynamic performance of long span bridges, and c) improving understanding of the response of long span bridges subjected to spatially varying earthquake ground motion.

1 INTRODUCTION

The traditional approach for seismic analysis is based on a uniform excitation assumption, which postulates that earthquake excitations at all the points along the base are identical. The assumption works well for normal buildings but is not quite accurate for long span structures, such as bridges, dams, and pipe network systems, etc. For long span bridges, which are long with respect to the wavelengths of the input earthquake ground motions, different supports might be subjected to significantly different seismic excitations (Nazmy & Abdel-Ghaffar 1992). This complicated correlation phenomenon is attributed to the fact that different piers may have different foundation types, soil conditions, seismic inputs, with different incidence angles as well as different travel paths due to reflections/refractions. In general, four main factors may contribute to the spatial variation of earthquake excitations (Kiureghian et al. 1992, Kramer 1996, Mylonakis et al. 2001, Lupoi et al. 2005): a) Incoherence effect. The seismic source is not a single point but a finite-sized region and the ground material is not homogeneous, but consists of different types of materials. Reflection and refraction of waves in the strata cause losses of coherency of the seismic wave. b) Attenuation effect. The energy of the wave may also decrease along with propagation, and this causes a reduction in excitation amplitude. c) Site effect. Different site conditions may lead to different influences on the seismic excitation. Different soils have different wave characteristics. When a wave travels through various strata, some strata may amplify the response, however some may do just the opposite. d) Propagation

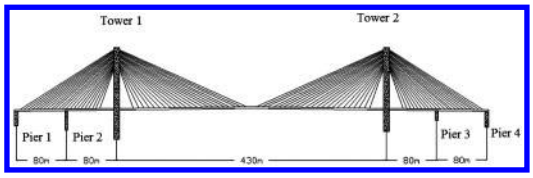


Figure 1. Elevation of the cable-stayed bridge.

effect. The wave travel speed isn't infinite, which will result in different arrival times of the ground motion at the piers.

During the last 30 years, many researchers have been working on the numerical analysis of seismic behavior of long span bridges under uniform or non-uniform ground motion; however, few experimental studies of full bridge models subjected to earthquake loading have been carried out in the past few decades. Three reasons can be given as follows: a) Full scale field testing is almost impossible for this research area. b) It is a very difficult and complex task to perform reduced scale model testing for earthquake loading. c) One prerequisite for dynamic model testing of non-uniform excitation is the multiple shake table system. Although there are many shake tables in universities and research institutes all over the world, few have a multiple shake table system which can provide non-uniform excitations to different parts of the structural model.

Based on the above reviews and considerations, a dual shake table testing system is developed and a 1:120 reduced scale model of a cable-stayed bridge with a main span of 430 m is designed and constructed for the purpose of this study. This paper describes the factors involved in the scale factor selection and the detailed design processes of different components of the model, including towers, girders, stayed-cables as well as artificial masses. The earthquake records from the SMART-1, as well as the PEER Strong Motion Database, are used in the shake table test. The results of the modal tests, the identical-input excitation tests and the varying-input excitation tests are presented, for the purpose of a) evaluating the design of the reduced scale model and the experimental method, b) studying the dynamic performance of long span bridges, and c) improving understanding of the response of long span bridges subjected to spatially varying earthquake ground motion.

2 MODEL DESIGN

2.1 *Characteristics of the prototype*

The prototype is a double-deck cable-stayed bridge with a main span of 430 m and side spans of 160 m on either side, as shown in Figure 1. Most of the main span, 387 m, is of steel/concrete composite construction, consisting of steel frames, steel webs and concrete slabs. The rest of the main span and both side spans are constructed using prestressed concrete box girders. The bridge girder is vertically supported by 4 piers and 2 towers. The two H-shape concrete towers are founded on bedrock, with a height of 150 m above the water level. Each tower consists of 2 shafts and 3 cross beams. The bridge consists of 176 stay cables, arranged in two vertical planes.

Table 1. Summary of scale factors used in physical model.

Quantity	Scale factor	Quantity	Scale factor
Length	1:120	Stress	1:11.812
Disp.	1:120	Strain	1:1
Velocity	1:10.954	Mass density	N/A
Accel.	1	Force	1:161022
Time	1:10.954	G-accel.	1:1
Frequency	1:0.0913	Model weight	1:161022
Modulus		1:11.182	

2.2 *Design of the reduced scale model*

In model testing, it is the "similitude requirements" that relates the reduced scale model to the prototype structure. The similitude requirements are based on the theory of modeling, and can be derived from dimensional analysis (Harris 1979; Liam Finn & Gohl 1987, Blaney & Mallow 1987). The Pi theorem was proposed by Buckingham in 1914. The theorem states that "*any dimensionally homogeneous equation involving certain physical quantities can be reduced to an equivalent equation involving a complete set of dimensionless products*".

In order to derive the scale factors for all the quantities, two parameters should be determined: the geometric scale S_L and the scale factor for Young's Modulus S_E. The geometric scale S_L is determined by the dimensions of the dual shake table and the length of the prototype. An innovative dual shake table testing system has been designed and constructed for the purpose of this study (Yang 2007). Each table is 1.5 m * 1.5 m, with a maximum payload of 2 ton and an operation frequency of 0–50 Hz. Another parameter which should be determined in advance is S_E, which relates to the selection of material for the model construction. Based on the results of material testing and comparison, acrylic is finally selected for the fabrication of the reduced scale model. After determining S_L and S_E, all the scale factors for different quantities can be derived accordingly. A summary of scale factors adopted in the proposed physical model can be found in Table 1.

Considering that the AMS (Artificial Mass Simulation) model can adequately simulate the dynamic behavior of the prototype and provide a practical modeling method for shake table testing, a reduced scale model of the prototype bridge is designed based on the scaling law of AMS model in this study. Figure 2 shows the finished 3-D spatial model.

3 SHAKE TABLE TESTING

An instrumentation scheme, including 10 channels of accelerometers, 8 channels of displacement



Figure 2. Finished model of the cable-stayed bridge.

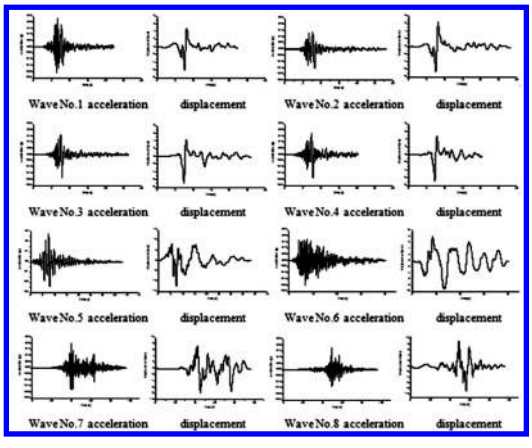


Figure 3. Acceleration and corresponding displacement inputs used in this study.

transducers and 15 channels of strain gauges, is designed for the shake table testing. The data are recorded at a rate of 256 Hz. These channels are fixed on either the dual shake table or bridge model, to measure the response of the overall bridge.

3.1 *Input ground motion and test protocol*

The ground acceleration records from the SMART-1 as well as the PEER Strong Motion Database are adopted in this test. The SMART-1 are used as the non-uniform ground motion input, while the PEER records is used to study the wave propagation effects on long span bridges under different soil conditions.

The numerical processing scheme suggested by the USGS (United States Geological Survey) is adopted here to transform the collected acceleration records to the displacement records, since it is very important that an appropriate data processing scheme should be adopted to minimize the effects of noise, as well as produce reliable and reasonable signals. The acceleration time-histories and the corresponding displacement time-histories of all the inputs in this study are shown in Figure 3.

The test protocol for the shake table testing is divided into three stages. Firstly, in test stage I, a modal test is performed by using 0.1 g white noise input excitation. Secondly, in test stage II, two groups of

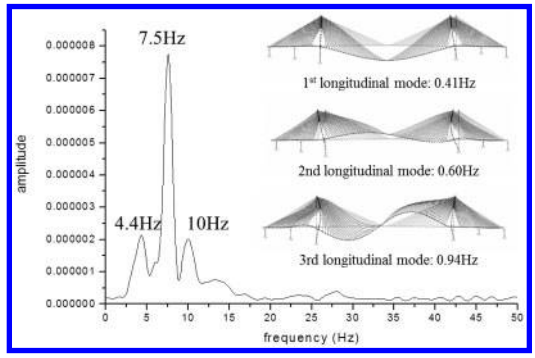


Figure 4. Comparison of modal test results with numerical modal analysis results.

earthquake records from SMART-1 (waves No. 1 & No. 2; waves No. 3 & No. 4) are used for performing the uniform and non-uniform excitation tests. In the "identical input" test, both tables have the same input wave; while in the "varying input" test, different input waves are applied to different tables. The wave propagation effect is studied by changing the wave passage velocity, including five cases, 400 m/s, 600 m/s, 1000 m/s, 2000 m/s and infinite. The distance between the two main towers (430 m) is used to calculate the difference of the arrival time for the two tables. Finally, in test stage III, four input waves (waves No. 5–No. 8), representing different site classifications, are used for the test, and the effect of wave propagation is taken into consideration.

3.2 *Test results and discussions*

3.2.1 *Test stage I: Modal testing*

The modal test is carried out before the earthquake ground motion excitation tests. The vibration of the reduced scale model is induced by 0.1 g white noise input excitation. A refined finite element model of the prototype bridge is developed in this study and the modal test result is compared with the result from the FEM analysis for evaluating the design of the reduced scale model. As shown in Figure 4, from the spectral response of the signals recorded by the strain gauge near the bottom of Tower 2, the frequencies of the first three longitudinal vibration modes of the physical model can be easily identified, i.e., 4.4 Hz, 7.5 Hz and 10 Hz. Since the scale factor for the frequency is 0.0913 (see Table 1), the natural frequencies of the corresponding prototype bridge can be calculated accordingly, i.e., 0.40 Hz, 0.68 Hz and 0.91 Hz. Compared with the results from the finite element analysis, which are 0.41 Hz, 0.60 Hz and 0.94 Hz, the reduced scale model represents the dynamic nature of the prototype quite well, which thereby verifies the design of the reduced scale model.

3.2.2 *Test stage II: Identical input & varying input excitation test*

Typical results of test stage II-Group A (Input waves No. 1 & No. 2) are presented in Figs.9–11. From

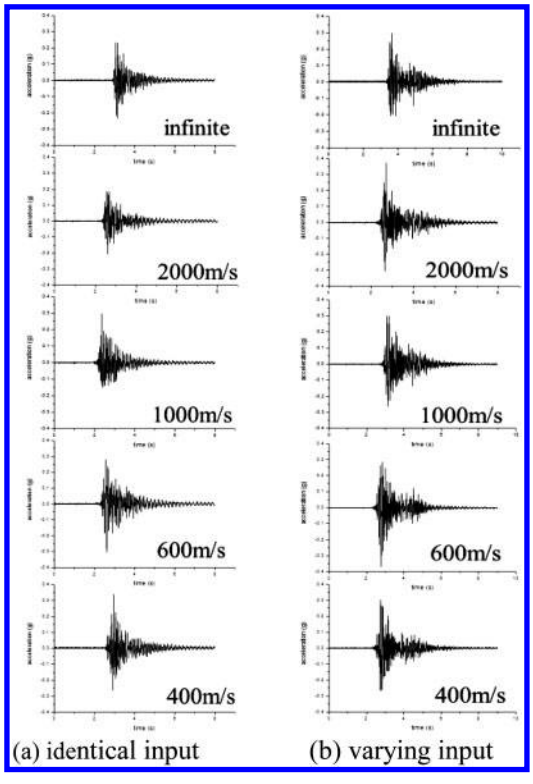


Figure 5. Vertical acceleration time-histories at quarter location of the girder under test stage II-Group A.

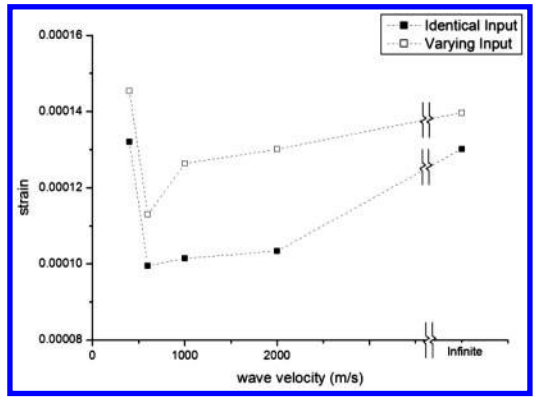


Figure 6. Strain gauge records near the top of Tower 2 under test stage II-Group A.

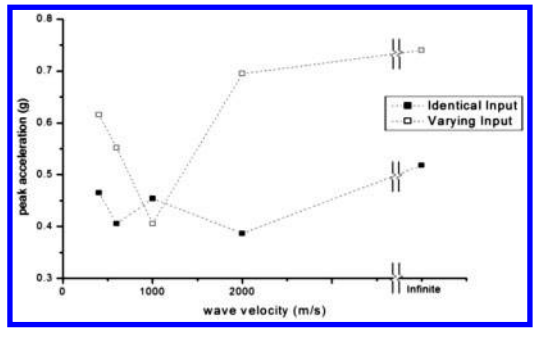


Figure 7. Peak longitudinal accelerations at the top of Tower 1 under test stage II-Group B.

these figures, one can find that non-uniform excitation strongly influences the dynamic response of the bridge model. Comparing the results at the same wave velocity, in most cases, the "varying input" excitation results in a much larger response than the "identical input", and an amplification of the response to an extent of 20–50% can be observed. The wave propagation effect also has a significant influence on the results. As shown in Figure 5, in most cases, the wave propagation effect observably increases the vertical acceleration at the quarter location of the girder (except in the case where the wave velocity is equal to 2000 m/s, in Figure 5a). Compared with the recorded time-history under uniform excitation (infinite wave velocity), an amplification of about 50% can be observed in some cases. However, from Figure 6, it can be seen that except for the case of a wave velocity equal to 400 m/s, the wave propagation effect slightly reduces the strain at the top of the tower. Since the strain gauges attached along the tower shaft are installed for measuring the longitudinal bending response of the tower, the above results imply that, in general, the wave propagation effect may increase the vertical response while slightly reducing the longitudinal response of the cable-stayed bridge. The exceptions found in above results also indicate that the value of the wave propagation velocity may play an important role in studying the bridge response subjected to non-uniform excitation.

Typical results of test stage II-Group B (Input waves No. 3 & No. 4) show that the spatial variation effect of the input ground motion has significant influences on the dynamic response of the bridge model. In most cases, the responses under the "varying input" mode are larger than the ones under the "identical input" mode. The response amplification from the effect of "varying input" excitation can be easily observed from these figures. The wave propagation effect also affects the results. When comparing the vertical acceleration time-histories at the quarter location of the girder under the "identical input" condition, with different wave velocities, one finds that the wave propagation effect increases the vertical response of the girder by a maximum extent of 50% (in the case of a wave velocity of 1000 m/s). Figure 7 presents the non-uniform excitation effect on the longitudinal response of the bridge. It can be seen that the wave propagation effect may slightly weaken the longitudinal response of the model. A maximum reduction of 40% can be observed in terms of the longitudinal peak acceleration.

3.2.3 *Test stage III: Identical input excitation test (Different site classifications)*

Typical results of test stage III-Input wave No.5 are presented in Figure 8. It can be seen that the wave propagation effect has a high visible influence on the

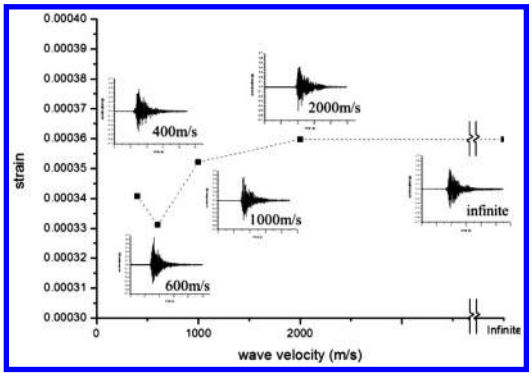


Figure 8. Vertical acceleration time-histories at the quarter location of the girder and strain gauge records near the bottom of Tower 2 under test stage III-Wave No. 5.

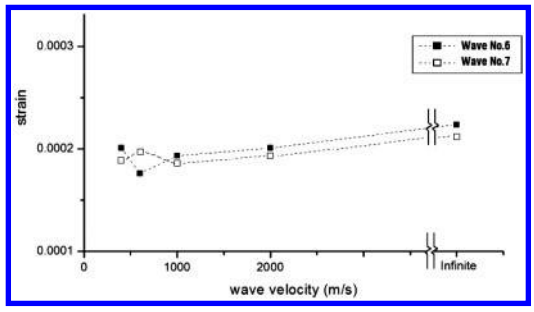


Figure 9. Strain gauge records near the bottom of Tower 2 under test stage III-Wave No. 6 & No. 7.

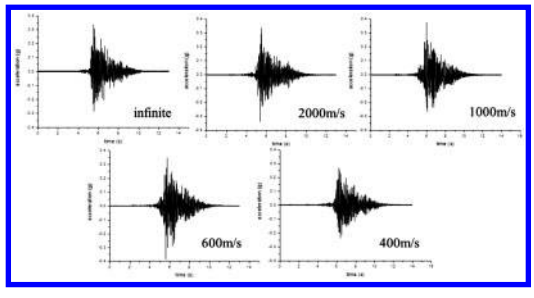


Figure 10. Vertical acceleration time-histories at the quarter location of the girder under test stage III-Wave No. 8.

bridge response when subjected to earthquake excitation in the site of soft soil. Comparing the case of uniform excitation with the cases of wave velocities of 1000 m/s or 600 m/s, the peak vertical acceleration at the quarter location of the girder increases more than 30%. However, when studying the longitudinal vibration of the tower, a reduction of approximately 10% and 25% can be observed in the recorded strain near the bottom of Tower 2. Therefore, the conclusion that can be drawn from the test results of stage III-Input wave No. 5 is that, in general, under the site classification of soft soil, the vertical response of the girder is amplified while the longitudinal response of the tower is reduced, when considering the wave propagation effect. This conclusion tallies with the previous findings of test stage II.

Similar results are observed from test stage III-Input wave No. 6 and No. 7 that the wave propagation effect significantly increases the vertical response of the bridge significantly. A maximum increase of 40% can be observed from the two tests when comparing the peak acceleration value of the uniform excitation with the one for the case of wave velocity set equal to 1000 m/s. Figure 9 shows the strain gauge records near the bottom of Tower 2 under test stage III-Wave No. 6 and No. 7. In test No. 6, it can be seen that the longitudinal response of the bridge is slightly reduced when considering the effect of the wave passage. However, in test No. 7, comparing the results from non-uniform excitation cases with those from the uniform input, the longitudinal vibration response of Tower 2 decreases.

Figure 10 shows the time-histories of the vertical acceleration at the quarter location of the girder under test stage III-Input wave No. 8 at different wave velocities. It can be seen that no significant changes, in terms of peak value and wave form, can be observed, when comparing the results from uniform excitation with the ones considering wave propagation effects. Investigating the results from Input wave No. 8 with the ones from Input wave No. 5–7, one can see that the wave propagation effect has the least influence on the dynamic response of the bridge model under Input wave No. 8, which is a recorded earthquake ground motion from a site classified as rock.

4 CONCLUSIONS

To study the dynamic response of long span bridges subjected to non-uniform excitation, 1:120 reduced scale model of a cable-stayed bridge with main span of 430 m is designed and tested on a dual shake table system. Based on this experimental test, the general comments can be made.

A reduced scale model of a cable-stayed bridge is designed and constructed in this research, based on the scaling law for an AMS (Artificial Mass Simulation) model. By choosing a "more flexible" material for model construction (with a smaller Young's Modulus compared with the prototype material), the self-weight of the reduced scale model can be significantly decreased. The design of the artificial mass is a key point in developing an AMS model, which has a significant influence on whether or not the reduced scale model can represent the structural nature of the prototype.

Seismic records from SMART-1 array and PEER Strong Motion Database are used in this study. The records from digital arrays of strong-motion seismographs can represent the nature of the spatial vibration, and are more applicable and reliable than artificial earthquake records in the study of non-uniform excitation. During the transformation of the acceleration

time history to a displacement time history, the numerical processing scheme suggested by USGS provides a comparatively effective and dependable solution and can produce rational and stable results.

In Test Stage I, the modal test is performed by using 0.1 g white noise input excitation. The modal test results tally with the numerical modal analysis results of the prototype bridge fairly well, and thereby verifies the design of the reduced scale model. In Test Stage II, two groups of earthquake records from SMART-1 are used for performing varying input and identical input excitation tests. The results of varying-input excitation show that non-uniform excitation strongly influences the dynamic response of the bridge model. In most cases, the "varying input" excitation results in a much larger response than the "identical input". The value of the wave propagation velocity plays an important role in studying the bridge response subjected to non-uniform excitation. The wave propagation effect increases the vertical responses of the bridge, while reducing the longitudinal responses. In Test Stage III, four input waves, representing different soil conditions, are used to study the effect of wave propagation for different site classifications. For the site classified as having soft and medium soil, the effect of wave propagation tallies with the previous findings from test stage II. However, for harder sites like rock, less obvious changes can be noticed and less consistent rules are obtained, implying that the wave propagation effect has less influence on the dynamic response of the bridge model for a site classified as having harder soil.

REFERENCES

Blaney, G.W. and Mallow, W.A. 1987. Synthetic clay soil for dynamic model pile tests. *Dynamic response of pile foundations–experiment, analysis, and observation: proceedings of a session of the Geotechnical Engineering Division of the American Society of Civil Engineers in conjunction with the ASCE Convention in Atlantic City, New Jersey*, 27 April, 1987. pp. 127–148.

Harris, H.G. 1979. Use of structural models as an alternative to full-scale testing. *Full-scale load testing of structures: a symposium / jointly sponsored by ASTM Committee E06 on Performance of Building Constructions and the American Society of Civil Engineers Committee on the Professional Practice for Full-Scale Structural Testing, American Society for Testing and Materials, Philadelphia, Pa.* 2 April, 1979. pp. 25–44.

Kiureghian, A.D. and Neuenhofer, A. 1992. Response spectrum method for multi-support seismic excitations. *Earthquake Engineering and Structural Dynamics*, 21, pp. 713–740.

Kramer, S.L. 1996. *Geotechnical Earthquake Engineering*, Prentice-Hall International Series in Civil Engineering and Engineering Mechanics.

Liam Finn, W.D. and Gohl, W.B. 1987. Centrifuge model studies of piles under simulated earthquake lateral loading. *Dynamic response of pile foundations–experiment, analysis, and observation: proceedings of a session of the Geotechnical Engineering Division of the American Society of Civil Engineers in conjunction with the ASCE Convention in Atlantic City, New Jersey*, 27 April 1987. pp. 21–37.

Lupoi, A., Franchin, P., Pinto, P.E. and Monti, G. 2005. Seismic design of bridges accounting for spatial variability of ground motion. *Earthquake Engineering and Structural Dynamics*, 34, pp. 327–348.

Mylonakis, G., Papastamatiou, D., Psycharis, J. and Mahmoud, K. 2001. Simplified modeling of bridge response on soft soil to nonuniform seismic excitation. *ASCE Journal of Bridge Engineering*, 6(6), pp. 587–597.

Nazmy, A.S. and Abdel-Ghaffar, A.M. 1992. Effects of ground motion spatial variability on the response of cable-stayed bridges. *Earthquake Engineering and Structural Dynamics*, 21, pp. 1–20.

Yang, C.Y. 2007. *Seismic Analysis of Long Span Bridges Including the Effects of Spatial Variation of Seismic Waves on Bridges*. PhD Thesis, Department of Civil Engineering, The Hong Kong University of Science and Technology.

Research and Applications in Structural Engineering, Mechanics and Computation – Zingoni (Ed.)
© 2013 Taylor & Francis Group, London, ISBN 978-1-138-00061-2

Seismic design of the self anchored suspension bridge: San Francisco Oakland Bay Bridge

M. Nader
T.Y. Lin International

B. Maroney
Caltrans

ABSTRACT: The seismically vulnerable East Span of the San Francisco-Oakland Bay Bridge is being replaced with a dual east bound and west bound 3.6 km long parallel structure. The iconic single tower asymmetric self-anchored suspension bridge was selected by an international panel of experts from a total of four design alternatives that were developed for the signature main span. Analytically, geometrically, and in the design of practical details for fabrication and durability, the Self Anchored Suspension Bridge is a unique structure requiring innovative solutions and departures from conventional design. Whether a similar bridge of this scale will ever again be proposed is unknown. However, the set of methods and technologies developed to meet these challenges offer an illustrative study of designing a world class structure, an architectural icon, and a seismic innovation all at one time in one of the most seismically challenging areas in the world. The bridge will be open to traffic by the summer of 2013.

1 INTRODUCTION

The seismically vulnerable East Span of the San Francisco-Oakland Bay Bridge is being replaced with a dual east bound and west bound 3.6 km long parallel structure. The Bay Bridge lies between the Hayward and the San Andreas faults which can generate magnitude 7.5 M and 8.1 M earthquakes, respectively. Performance criteria require that the bridge must be operational immediately following a 1500-year return period earthquake from either of these two faults.

Four distinct structures will make up the new bridge crossing: a low-rise post-tensioned concrete box girder near the Oakland shore; a 2.4 km long segmental concrete box girder; a self-anchored suspension signature span; and a post-tensioned concrete box girder that connects to the east portal of the Yerba Buena Island tunnel (Figure 1).

Comparable to the levels specified in the 1930 Uniform Building Code for buildings, the Bay Bridge was designed for only 10 percent gravity (0.1g) earthquake accelerations. In 1989, the Loma Prieta earthquake measuring 7.1 on the Ritcher scale with an epicenter 70 miles to the south of San Francisco caused a 15 m section of the upper deck of the East Span of the San Francisco-Oakland Bay Bridge to collapse. A more severe earthquake is expected to occur in the next 30 years and will cause significant damage and possibly the collapse of the existing East Span's truss structures. Retrofitting the structure was not only determined to be expensive and unreliable but also very difficult to implement while the bridge is under heavy use.

2 GEOTECHNICAL CONDITIONS

The site geology varies dramatically along the length of the bridge. Figure 2 is a geological profile at the bridge alignment. At the western end of the bridge (YBI), the piers are founded on rock. As the bridge alignment progresses east towards Oakland, the bedrock Franciscan Formation drops abruptly and the remaining piers overlie deep Bay muds, followed by the inter-layered clays and sands of the Alameda Formation. The main span tower structure is sited on relatively shallow, sloping bedrock. The remainder of the skyway is founded on a significant thickness of sediment.

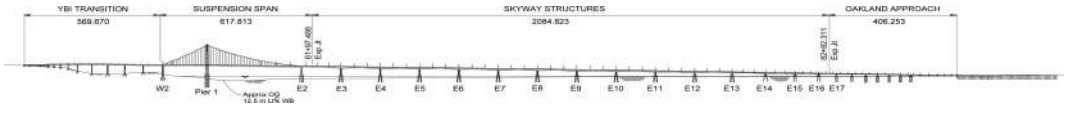


Figure 1. The New San Francisco Oakland Bay Bridge.

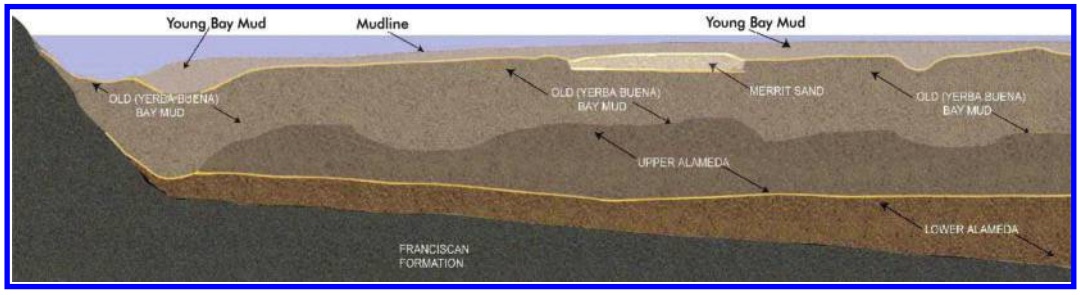


Figure 2. Soil Profile.

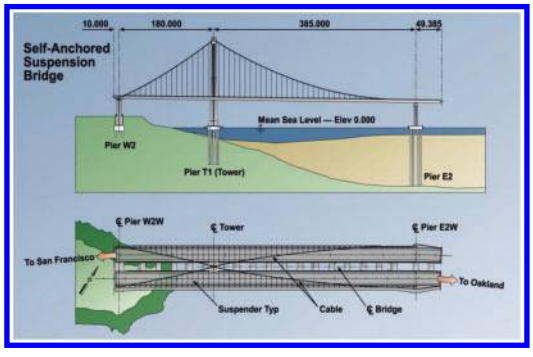


Figure 3. Elevation of the Self Anchored Suspension Bridge.

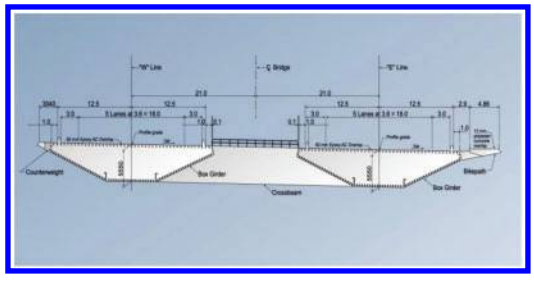


Figure 4. Typical Cross Sections of Bridge – Dual Box Girders.

3 SEISMIC PERFORMANCE CRITERIA

The bridge is designed to provide a high level of seismic performance. It is designed to resist two levels of earthquake, a functional evaluation earthquake (FEE) and a safety evaluation earthquake (SEE). After a functional evaluation earthquake, the bridge will provide full service almost immediately and there will be minimal damage to the structure. Minimal damage implies essentially elastic performance and is characterized by minor inelastic response, narrow cracking in concrete, no apparent permanent deformations, and damage to expansion joints. After a safety evaluation earthquake, the bridge will provide full service within days and will sustain repairable damage to the structure. Repairable damage is damage that can be repaired with minimum risk of losing functionality; it is characterized by yielding of reinforcement, spalling of concrete cover and limited yielding of structural steel.

4 SELF ANCHORED SUSPENSION BRIDGE

The Self-Anchored Suspension (SAS) portion of the new East Span of the San Francisco-Oakland Bay Bridge consists of dual box girders suspended from cables which are supported on the 160 m tower located off of the eastern shore of the Yerba Buena Island. The SAS spans 565 m between the piers E2 and W2, with a 385 m main span, over the navigational channel, and a 180 m back span (Figure 3).

The asymmetry of the bridge subjects pier W2 to a vertical uplift while the bridge is lightly supported on pier E2. The main tower therefore carries most of the bridge dead load. The uplift at pier W2 is fully counterbalanced by the pre-stressed concrete cap beam at pier W2. This ensures that the bridge is always balanced without relying on the pier to carry any tension. In order to balance the moments in the box girder caused by the 49 m cantilever at the east anchorage, suspenders do not support a 35 m segment of eastern end of the main span.

The box girders are not supported by the tower and are therefore "floating" at the tower with the suspenders providing the only connection between the box girders and the tower. This implies that while the tower carries most of the bridge dead load, the tower is not the primary element that carries the bridge seismic loads. The tower seismic response is mainly governed by its own mass and stiffness (the tower acts as a propped cantilever with a spring support at the tower saddle). The gap between the tower and the deck is designed to be large enough to prevent any impact during a Safety Evaluation Earthquake. Piers E2 and W2 are designed to provide the main lateral seismic support of the bridge.

The 0.78 m diameter cable is anchored to the east anchorage and is looped around the west bent through deviation saddles. The suspenders are splayed to the exterior sides of the box girders and are spaced at 10 m.

The superstructure consists of dual hollow orthotropic steel box girders (Figure 4). These girders are in longitudinal compression (reacting against the cable tension force) and are a part of the gravity load system. Transverse diaphragms spaced at 5 m

support the orthotropic deck and distribute the suspender loads to the entire box. The box girders are connected together by 10 m wide by 5.5 m deep cross-beams spaced at 30 m on center. These cross beams carry the transverse loads between the suspenders (span of 72 m) and ensure that the dual boxes act compositely during wind and seismic loads (Vierendeel truss action).

The bridge carries a pedestrian path on the south side of the eastbound deck. The pedestrian path eccentric load is balanced by a counter-weight on the north side. At the west bent, the steel box girders frame into the prestressed cap beam. The connection between the orthotropic steel box girders and concrete cap beam is subjected to the compressive reaction forces to the cables. Additional prestress is added through post-tension strands connected at each steel orthotropic rib.

The 160 m main tower is composed of four shafts interconnected with shear links along its height. The tower shafts are stiffened pentagonal steel box sections which taper along the height. The tower shafts are provided with diaphragms spaced at 4 m. The tower shafts are rigidly connected at the top and bottom by tower saddle grillage and tower base grillage, respectively (Figure 5).

The tower is fixed to a 6.5 m deep pile cap with anchor rods and dowels. The pile cap consists of a steel moment resisting frame encased with concrete and is supported on thirteen (13) 70 m long 2.5 m diameter steel shell pipe piles filled with concrete and embedded into rock. The rock slope is benched to give the piles equal lateral stiffness and to reduce torsional response (approximate clear length is 20 m).

The hinges in the transition spans between the SAS and Skyway as well as the SAS and YBI structures are designed to allow the structures to move relative to each other in the longitudinal direction and to rotate about the longitudinal axis of the bridge. The hinges are comprised of compact steel beam pipe section capable of transferring live loads and seismic loads. These hinge pipes are designed to fuse before any other bridge components in case of an overload (Figure 6).

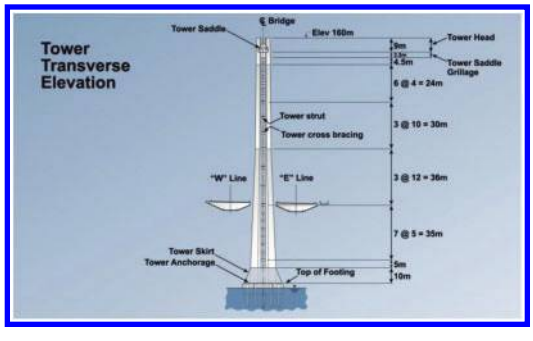


Figure 5. Single Tower with Four Shafts Interconnected with Shear Links.

5 SINGLE TOWER DESIGN

The tower shear links play a significant role in resisting the seismic loads as well as to supply the tower with the proper stiffness during service load conditions. The tower shear links are designed to satisfy the following criteria:

- Supply the tower with the required stiffness for service load conditions.
- Remain almost elastic during a functional evaluation earthquake (FEE)
- Plastify during a safety evaluation earthquake (SEE); thus dissipating energy
- Limiting the damage in the tower shafts (shafts are designed to remain almost elastic).
- To be replaceable after an SEE, if necessary

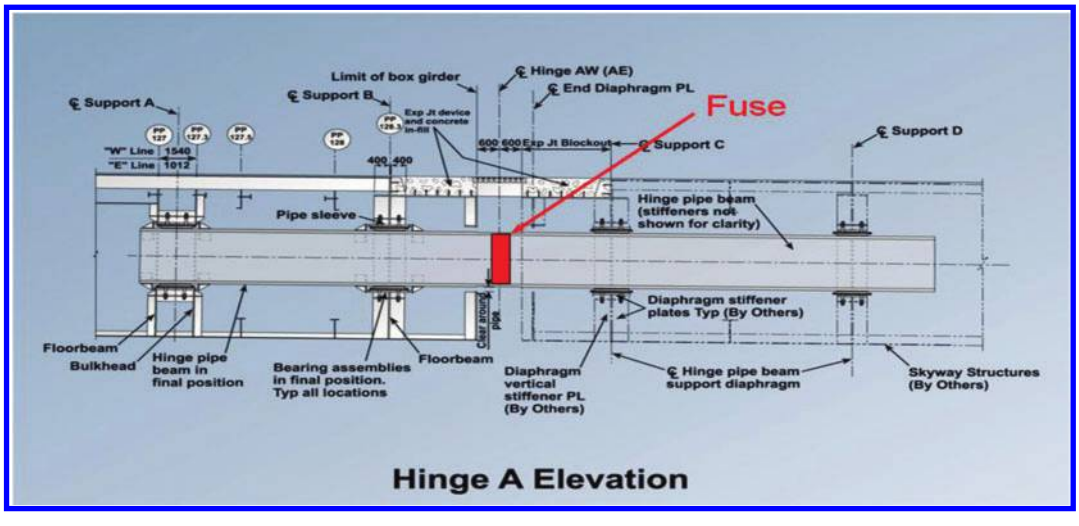


Figure 6. SAS to Skyway Hinge.

In order to satisfy the above requirements, various configurations of the tower were evaluated where the strength and stiffness of the shear links as well as their location along the height of the tower were varied. These studies were primarily done in the form of static pushovers to determine the response of the tower during service loads, wind loads, FEE and SEE loads. An optimal layout of these links was then established as well as the stiffness and yield strength of the shear links.

Although the tower shafts are designed to remain elastic during SEE, the shafts were designed as stiffened box section per ATC-32. This insured that the shafts could undergo large inelastic compressive strains without locally buckling.

A pushover analysis of tower is shown in Figure 7. This analysis was performed to evaluate the base shear versus top of tower displacement relationship; to optimize the design of the tower shear link and shaft; to evaluate the lateral ductility of the tower before collapse; and to evaluate the ductility demands on the shear links and tower shafts at various levels of displacement demand. Figure 14 shows the effects of using shear links on the lateral behavior of the tower. As noted the tower has stable behavior for displacements much larger than the SEE displacement demands (1 m). Figure 8 shows a full-scale test specimen tested at the University of California at San Diego at a rotation of 0.07 radians.

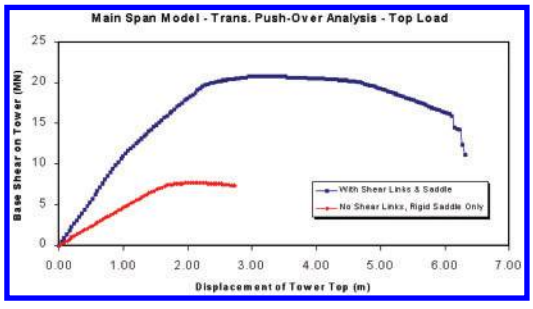


Figure 7. Pushover Analysis of the Single Tower.

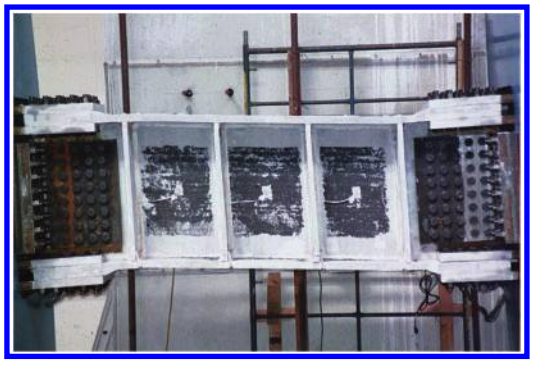


Figure 8. Full Scale Test of Shear Link Type 1 at UCSD.

6 SEISMIC PERFORMANCE

Seismic analysis was performed using the ADINA general-purpose finite element program. Three forms of analysis were employed: time history analysis (global model), pushover analysis and local detailed analysis. Time history analysis was used as the primary means of analysis for several reasons. Foremost among these is that the bridge foundations are subjected to different excitations. The tower and west pier of the bridge are founded on rock while the east pier is supported in deep soil. The ground motions at these supports are completely different in character and intensity. This was reflected in the analysis by applying different time histories of ground displacement at the supports.

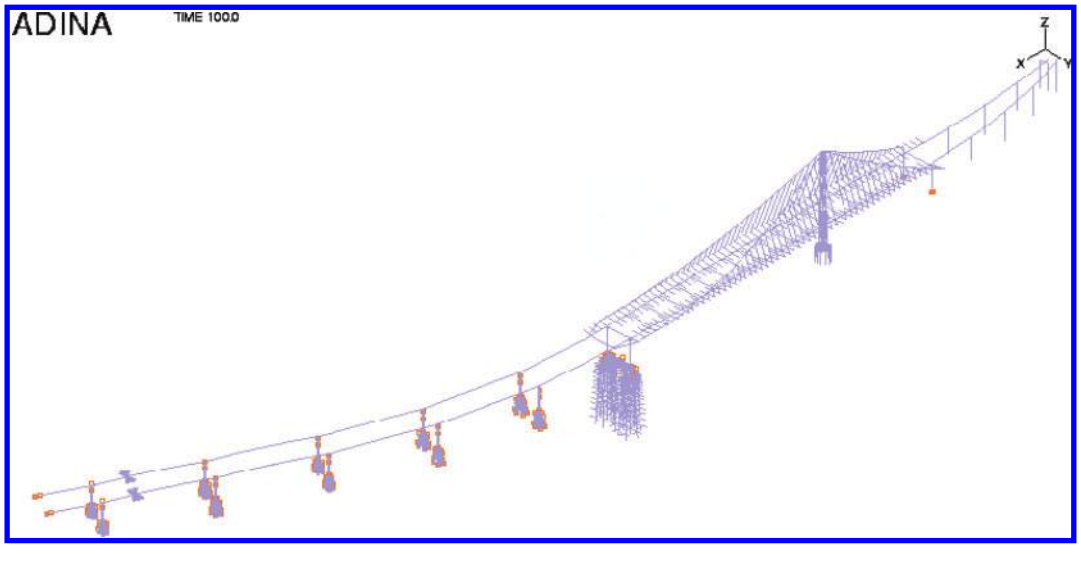


Figure 9. Adina Model of the Suspension Bridge.

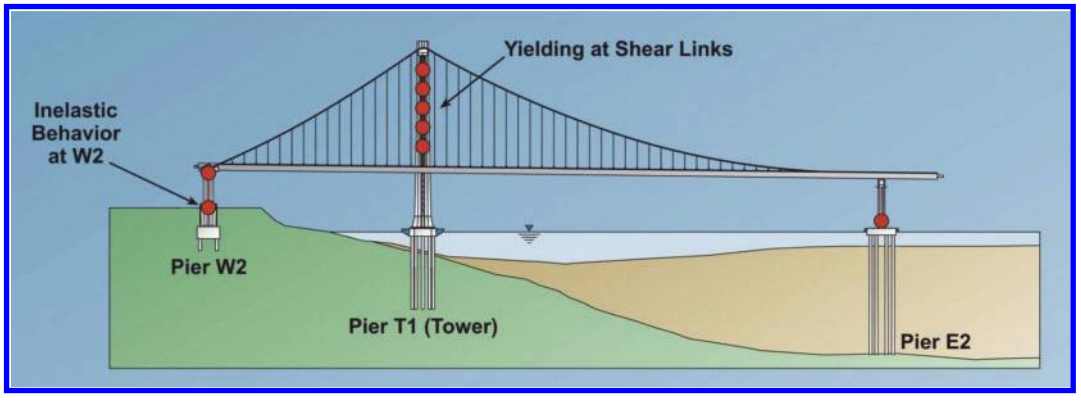


Figure 10. Seismic Response of the Bridge.

A large-displacement analysis and the use of non-linear material where necessary to allow the designers to capture the true behavior of the bridge (geometric stiffness of bridge, P-delta effects, slacking of suspenders, plastic hinging of piers, tower shear links, etc.). The model was "built" in a single step, in the dead load state. Initial strains in the deck, cables and suspenders were applied in this single step rather than simulating the construction sequence of the bridge. Time history analyses were done as restart analyses from the dead load state. Push Over analysis was primarily used to evaluate ductility of critical elements and to establish failure mode sequence. Local detailed analysis was used to establish local strain/stress demands and to evaluate the modeling used for the global model. The ADINA global model of the Self-Anchored Suspension Bridge is shown in Figure 9.

As discussed earlier the bridge is designed based on a limited ductility design in which plastic deformations are clearly defined and predetermined. Figure 10 summarizes the seismic response of the bridge. As noted the bridge is designed to remain largely elastic with the exception of the east and west piers which are designed to form plastic hinges. The plastic strain in these piers is limited to 2/3 the ultimate strains based on Manders equation for confined concrete columns. The shear links between the tower shafts are also designed to yield in shear during the SEE earthquake. The maximum rotation demand on these links is 0.04 radians compared with an ultimate rotation of 0.09 radians. The piles were designed to sustain minimal damage (strains less than 0.01 for concrete and 0.02 for steel) when subjected to the SEE displacement demands. The tie down at the west pier was designed with a factor of safety of two.

Research and Applications in Structural Engineering, Mechanics and Computation – Zingoni (Ed.)
© 2013 Taylor & Francis Group, London, ISBN 978-1-138-00061-2

Seismic performance of an asymmetric base-isolated building in the 2011 Great East Japan Earthquake

Y. Fujino & D.M. Siringoringo
Bridge & Structure Lab., Department of Civil Engineering, University of Tokyo, Japan

ABSTRACT: Analysis of strong motion recordings during the March 11, 2011 Great East-Japan Earthquake of an asymmetric base-isolated building located in Tokyo-Bay area is reported in this paper. The building, whose structural configuration is of braced steel frames, consists of two parts: seven-story and fourteen-story building with vertical void. Seismic responses were recorded including the strongest shaking (PGA 0.80–1.40 m/s^2) experienced during the Great East-Japan Earthquake. The building survived the earthquake without structural damage. Response analysis shows that despite the considerable shift in effective frequency of the building due to the increase in flexibility of isolation system during the main shock, large acceleration was recorded on the superstructure with the peak floor accelerations of nearly 3 m/s^2. Contrary to common symmetric base-isolated buildings where vibration is dominated by translational mode, the seismic responses of superstructure were dominated by torsional modes that caused large peak floor acceleration.

1 INTRODUCTION

Base isolation as a seismic mitigation technique for buildings and bridges has gained popularity in Japan especially after the 1995 Hyogo-ken Earthquake. The favorable responses during an earthquake, ability to limit structural damage to a low and repairable level and ability to maintain functionality of structure even after a large earthquake are some advantages that have increased the acceptance of base isolation technology among engineers and building owners.

There are two main concerns regarding the torsional response of asymmetric base-isolated buildings: the asymmetricity of isolation system and the asymmetricity of superstructure system. In both cases the asymmetricity could be caused by the eccentricity either in superstructure or in isolation system. When eccentricity exists in superstructure system, the coupled lateral-torsional motions occur as they do in the non-isolated buildings. Effect of torsional motion can be significant when the building has large eccentricity. The outer isolators will experience larger force than the inner isolators when torsional motion is dominant. Large rotation of the building contributes significantly to the corner deformation in that the outer columns of the structure will experience larger shear force as a result of combined shear and moment from floor eccentricity.

This paper describes a study from strong motion recordings of an instrumented building. The study described in the paper includes: 1) seismic response evaluation of instrumented asymmetric base-isolated building during main shock of March 11, 2011 Great East Japan earthquake using system identification, 2) investigation on the seismic response characteristics considering the building asymmetricity and 3) evaluation of the long-term seismic response characteristics of the building for over a year that includes the foreshock, main shock and aftershocks and various amplitude earthquakes in 2011-2012. The high-quality seismic responses recorded on the building is significant considering the earthquake magnitude and seismic intensity recorded on site and the number of vibration sensors used in the building is larger than those usually used in other buildings.

1.1 *Description of building and monitoring system*

The monitored structure is the SIT Building located in Tokyo Bay area. The building consists of two parts: building B seven stories tall and building C fourteen stories tall (Figure 1). Building B is 81 m long, 21.6 m wide and 31.2 m high with 16 bays in longitudinal direction and 3 bays in transverse direction. Building C is 97.2 m long, 43.2 m wide and 67.5 m high with 19 bays in longitudinal direction and 6 bays in transverse direction. Both buildings are of braced steel frames and connected at the corner by elevator shaft to form an L-shaped asymmetric structure. The fourteen-story research building has vertical opening in the middle starting from the second to the seventh floor, which divides the building into the northwest section and northeast section, named hereafter as Section C-NW and Section C-NE, respectively. Meanwhile, the seven-story classroom building has some voids on its floors to provide access for escalator. Both buildings are connected by concrete slab on the basement level, on top of which the isolation systems are located.

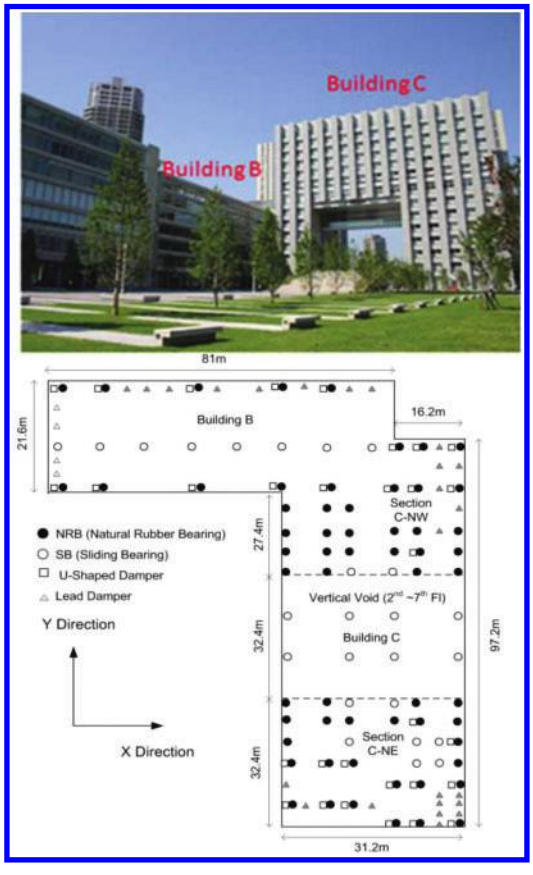


Figure 1. SIT Building and isolation layout.

The isolation system consists of 37 natural rubber bearing (NRB) and 34 sliding bearing (SB). In order to limit the horizontal motion, dampers are added to the isolation system. Two type of dampers are used namely the lead damper (28 units) and of U-shaped steel dampers (33 units). Layout of isolators and dampers is given in Figure 2. Owing to its L-shaped and vertical void, eccentricity ratios of some floors are larger than 10%, indicating significant asymmetricity of the building.

2 CHARACTERISTICS OF SEISMIC RESPONSE

2.1 *Characteristics of ground motions*

Figure 3. shows time histories of ground acceleration obtained from free-field Acc-112 during the main shock. The excitation lasted for about 10minutes, in which the significant duration (i.e. 95% energy of the excitation) remained for about 6 minutes since the arrival of the primary wave. The maximum ground acceleration in X, Y and vertical direction were 0.16 g, 0.17 g and 0.08 g, respectively. The ground accelerations have dominant frequency content between 0.7 Hz and 1.2 Hz in both X and Y directions.

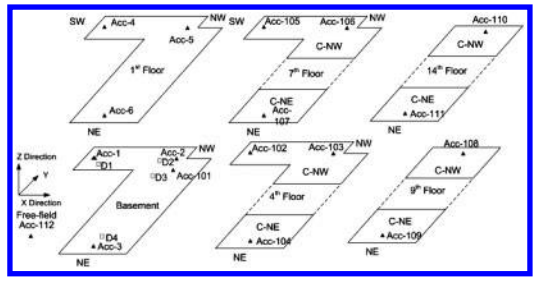


Figure 2. Layout of seismic monitoring system.

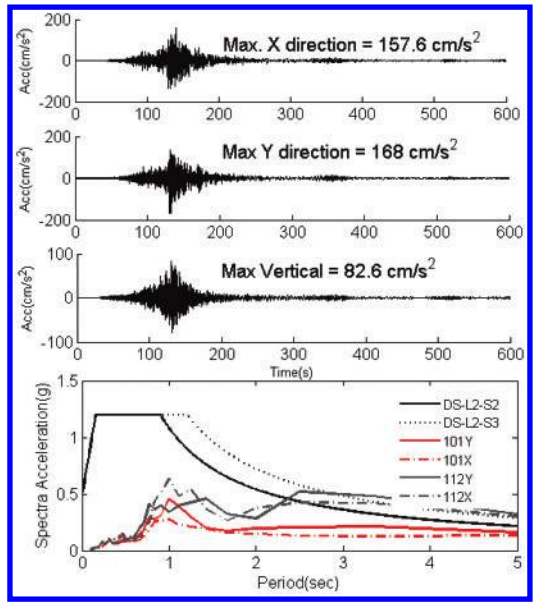


Figure 3. Ground motions accelerations and their response spectra.

In Figure 3, response spectra of two ground accelerations, namely Acc-101 (basement level) and Acc-112 (free-field sensor) are plotted together with the design response spectra for Level-2 earthquake with soil condition class 2 and 3, as specified in the Japan's Building Code. As can be seen, spectra of the main shock are still smaller than the original design spectra, especially for the period range below 3 sec, which is the range of the building's natural periods. Considering this fact, ground motions of the present earthquake are not potentially damaging to the bridge. Moreover, spectra of the main shock have large amplitude in the period range of 0.8–1.2 s (0.83 Hz–1.25 Hz), which will be shown later is the range for certain natural frequencies of the building.

2.2 *Characteristics of building response*

The building responses are characterized by large horizontal vibration of the superstructure. In the building B, the largest horizontal vibration is recorded in Y direction, with the peak acceleration on the 7th floor

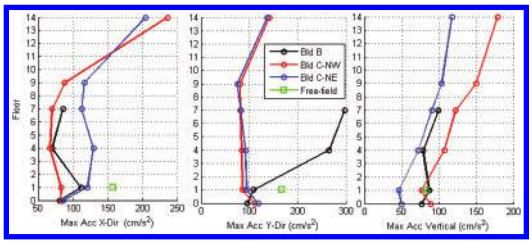


Figure 4. Recorded maximum acceleration amplitude for each floor in each direction (Note: 0 = basement level, free-field sensor: Acc-112).

nearly 300 cm/s^2 (Figure 4), or about three times of the basement acceleration. Large acceleration on the southeast section of building B was also recorded on the 5th floor, with peak acceleration of 265 cm/s^2. This large acceleration can be considered exceptional considering that the peak acceleration on the basement level of southeast section of building B is only 96 cm/s^2. Response amplification of the superstructure was also observed on building C in X direction. Peak accelerations on the 14th floor of the NE and NW sections were about 204 cm/s^2 and 236 cm/s^2, respectively, or about 2.5 times of the ground acceleration (Figure 4).

The transfer functions of accelerations on top floors of Building B and C in Y and X directions respectively are shown in Figure 5. We can see that the response of Building B is dominated by frequency peak at 0.86 Hz, while for the Building C is mainly due to frequency component at 0.58 Hz. The significant acceleration amplification of superstructure is rather unexpected in a base-isolated building. One of assumptions in design of seismically isolated structure is that lateral deformation is concentrated on the isolator level and the superstructure behaves rigidly without significant dynamic amplification. In Japan, the common design practice is to limit the horizontal floor acceleration to the maximum 300 cm/s^2 in design for Level 2 ground motion (Peng et al. 2005). Limiting large floor acceleration is necessary to protect nonstructural components, highly sensitive equipments, and computer facilities that can be found in the building. In the following sections we shall discuss the reason behind significant dynamic amplification of the superstructure.

3 SYSTEM IDENTIFICATION

Seismic behavior of the building is examined thoroughly by evaluating the vibration modes pertinent to the seismic responses using system identification procedures. A multiple-input multiple output (MIMO) system identification is utilized in this study. The methodology is based on the System Realization using Information Matrix (SRIM) (Juang 1997), which utilizes correlations between input-output data for realization of a state-space model and estimation of modal parameters. Detail information on the algorithm and

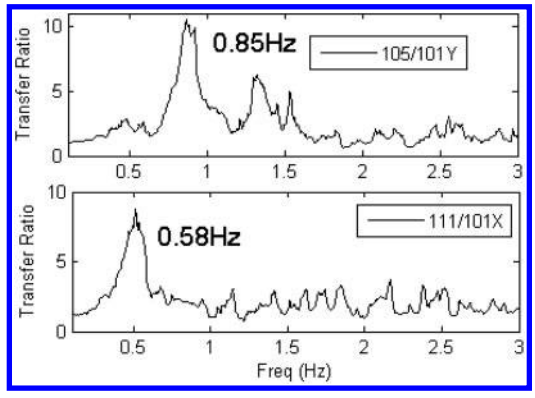


Figure 5. Transfer Functions of recorded accelerations on top floors of Building B and C in Y and X direction, respectively.

its application seismic-induced excitation is given in reference (Siringoringo and Fujino 2008).

To effectively implement the system identification, a set of input-output data was selected. Responses from triaxial accelerometers located at the basement, the same level as the isolators (i.e. Acc-1, Acc-2, Acc-3 and Acc-101), were selected as inputs. Meanwhile accelerations from the superstructure (i.e. Acc-4, Acc-102 until Acc-111) were selected as outputs. Note that the input and output data are derived from multiaxial accelerations, so that the identified mode shapes have three-dimensional shape.

It should be mentioned that in the time-invariant assumption, modal parameters remain constant during a specific time-window in which the input-output data was analyzed. However, considering that the response of base-isolated building may enter nonlinear region during large excitation this assumption may not be satisfied throughout the whole responses. Therefore, a piece-wise linear analysis was conducted using moving time window. Shorter time window was selected for analysis, during which the modal parameters were assumed to remain constant. For this reason, the total time history responses were divided into several shifted time windows consisting of 50 seconds of input and output data. Each time window generates a set of modal parameters, from which the change of parameters with respect to time can be evaluated. By applying this procedure, the 600 s main shock response was divided into twelve time windows of input-output data.

3.1 *Results of system identification*

The multi-input multi-output time-invariant SRIM system identification results in three dominant modes: the first translation mode identified at 0.44 Hz–0.55 Hz, the first torsional modes identified at 0.58 Hz–0.68 Hz and the second torsional mode at 0.85 Hz–0.95 Hz. As illustrated in Figure 6, the first mode has characteristic of large modal displacement at the isolator layer and small modal displacement of

the upper-stories resembling the rigid body motion of the superstructure, which is typical characteristics of the fundamental base-isolation mode. The second is the torsional mode with large modal displacement concentrated on the corner of Building C. On the hand, the third mode is the torsional mode with large modal displacement concentrated on the corner of Building B and small modal displacements on the superstructure of Building C.

In design, two scenarios of isolator behaviors and the effect to modal parameters were considered, one is the case for small and medium earthquake in which the initial stiffness of isolators were considered, the other one is during exceptionally large earthquake, where the isolators enter the secondary stiffness. In the first scenario, isolators are expected to enter the initial stiffness and the estimates of building's natural frequencies are 0.5 Hz, 0.64 Hz and 1.05 Hz for the first, second and third modes, respectively. For the second scenario, large deformation of isolation 40 cm is assumed and as the result the building's motion will be dominated by the first translation mode. In such condition, the first natural frequency of the building could reach as low as 0.16 Hz and the superstructure moves as rigid body. When large deformation occurs on the isolators during significantly large earthquake, it is expected in design that the torsional modes of superstructure become insignificant and the translation mode due to the flexibility of isolation will govern vibration of the building. Comparing the identified natural frequencies with the estimates from two scenarios, one can see that the identified frequencies are closer to the estimates for small and moderate earthquake. The identified frequencies of the first the modes, however, are lower the analytical estimation.

3.2 *Variation of modal parameters during main shock*

The general trend (Figure 7) shows that the strong shaking causes significant reduction in effective frequency. The natural frequency of the first mode decreases from about 0.6 Hz in the beginning of the response to about 0.44 Hz during the largest excitation (t = 150−−250 sec). The similar reduction in natural frequencies was also evident from the second and the third modes. Reduction of natural frequencies identified during the largest excitation. The second and the third mode also show the reduction from 0.68 Hz and 0.95 Hz in the beginning of the response to 0.58 Hz and 0.85 Hz, respectively, during the largest excitation. The frequencies increase slightly near the end of excitation when excitation amplitude become smaller but do not recover to their conditions before the arrival of seismic.

Damping ratios of the all modes increase from about 3–4% in the beginning of the response to nearly 15% during the largest excitation. At the end of the responses, the damping ratios are generally decreasing nearly to their original values. The increase in damping is related to the performance of isolators and dampers that become fully engaged during largest excitation, as shown by the largest isolator deformation occurring during t = 130–170 second. Large damping in the present earthquake is in agreement with common practice in Japan that is to design number of dampers so that the equivalent damping is about 15 to 20% (Peng et al. 2005).

4 RELATIONSHIP BETWEEN MODE SHAPES, ISOLATION DEFORMATION AND INTENSITY OF GROUND MOTION

The influences of excitation intensity on the isolator's relative displacement for the first three dominant modes are described in Figure 8. In this figure, abscissa represents the ground motion amplitude in term of response spectra of acceleration Acc-101 for 5% damping. The response spectra of horizontal ground acceleration were calculated at the frequencies that correspond to the first three modes (i.e. 0.44 Hz for the first mode, 0.58 Hz for the second mode and 0.85 Hz for the third). In such a way, we can quantify the frequency components of the ground motion that are relevant to the natural frequencies of the structure.

To quantify the influence of excitation intensity on isolator displacement, an index called Relative Isolator Modal Displacement (RID) index is used for the ordinate. For each mode shape, the RID measures relative modal displacement at isolator level with respect to the modal displacement at the roof level, which is normalized to unity. When isolator displacement is large, the RID value will become closer to unity, and for

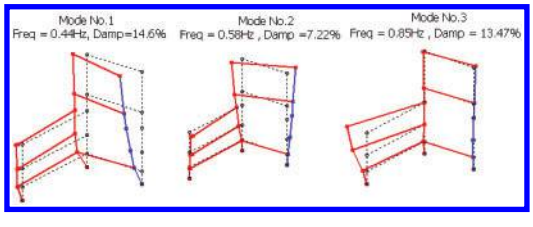


Figure 6. Mode shapes of the Building identified during the largest excitation of the main shock.

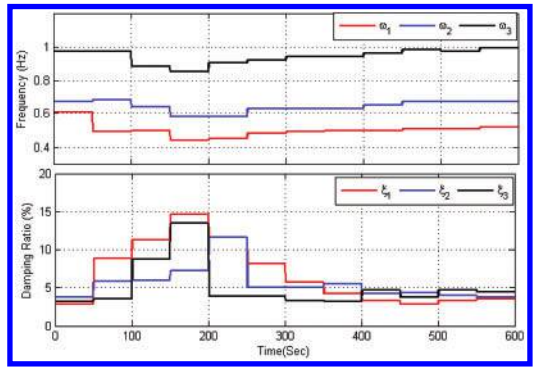


Figure 7. Time variation of identified frequencies and damping ratios during the main shock.

an ideal rigid superstructure; the RID value is equal to one. The RID index also describes the influence of isolator displacement on the global modal displacement for each mode. As can be seen on the figure, only the first mode shows a strong relationship between the RID and spectra acceleration, in that the RID values increase significantly as the spectra acceleration increases.

The foregoing results provide an explanation on the large amplification experienced by the superstructure during the main shock. As mentioned previously, responses of the top floors are dominated by vibration modes that correspond to the torsional modes. These torsional modes lie within the dominant frequency range of excitation as demonstrated by the response spectra of Acc-101, indicating the occurrence of resonance between input excitation and structural torsional modes. Furthermore, from the RID plot we know that isolator displacements do not have significant influence on the torsional modes as illustrated by Figure 8. This suggests that even though the base-isolation system had worked during the main shock, its function was inadequate to prevent torsional effect on the superstructure response due to characteristics of the building. It should be mentioned, however, that this condition depends upon the excitation intensity and the amplitude of isolator displacement.

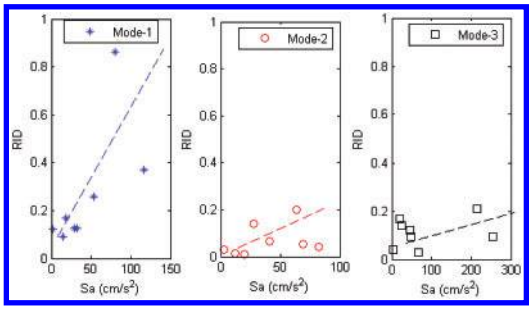


Figure 8. Influence of the excitation intensity on isolator's relative displacement.

In the design process, it is described that when larger excitation occurs (i.e. level 2 earthquake in Japan's seismic design code), isolator displacement will be significantly larger and natural frequency of the building will drop to 0.16 Hz, in which case the effect of torsional motion on the total response of the building will be minimized. Nevertheless, significant response amplification in the moderate excitation (i.e. earthquakes smaller than level 2) is still possible, and this

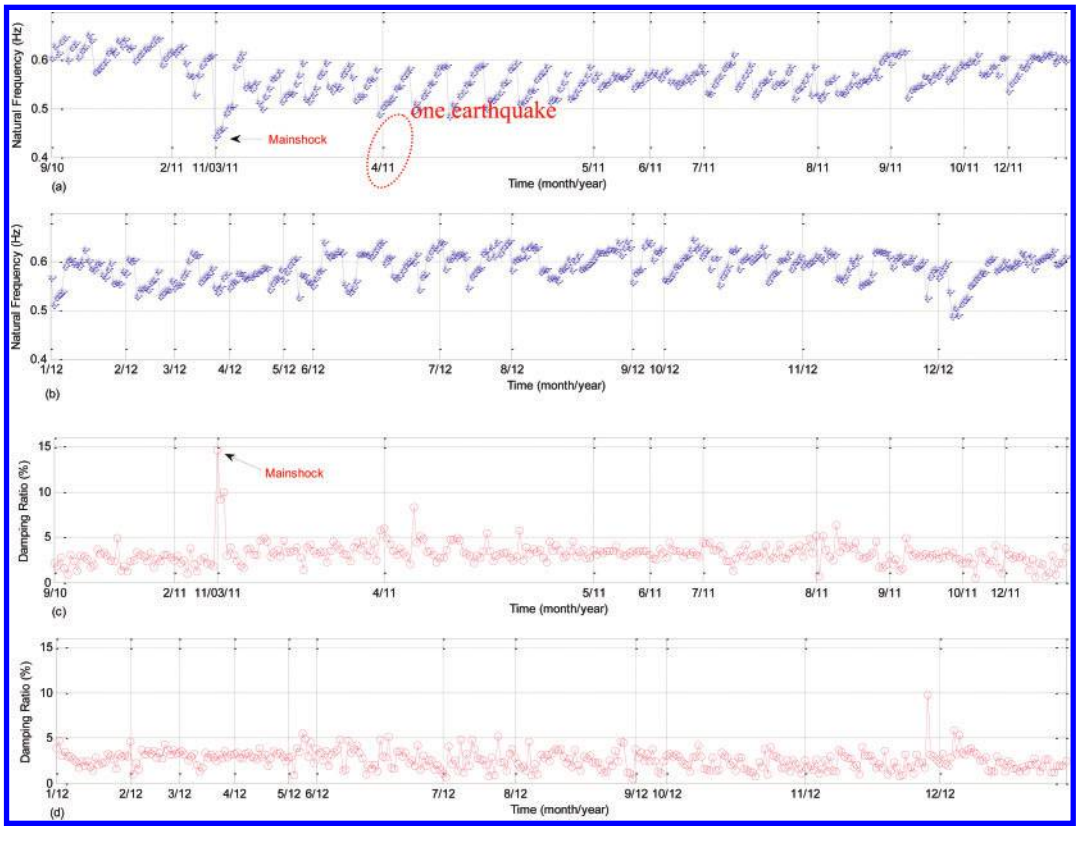


Figure 9. Long-term time sequential variation of the first mode: (a) Natural frequency Sept 2010–Dec 2011, (b) Natural frequency Jan 2012–Dec 2012, (c) Damping ratio Sept 2010–Dec 2011 and (d) Damping ratio Jan 2012–Dec 2012. Note the circle in (a) showing the variation of frequency in one earthquake event.

could be critical to nonstructural elements or sensitive equipments in the building.

5 LONGTERM VARIATION OF NATURAL FREQUENCY AND DAMPING RATIO

Since installed in September 2010, about 140 seismic events have been recorded by the monitoring system until December 2012. Most of the earthquakes were of small and moderate scale (JMA seismic intensity 3 or less) and only ten events including the March 11,2011 main shock have seismic intensity larger than 4. With relatively large earthquake database, we can investigate behavior of the building and observe the trend in modal parameters with respect to the level of seismic excitation and their long-term variations.

Figure 9 shows the sequential long-term variation of the first mode. Note that we focus discussion on the first mode, since it is the mode that is significantly affected by isolator behavior. As shown on the figure, for one seismic event, the natural frequency reaches the minimum value in the beginning of the record that is during the largest excitation and increases gradually towards the end of the record. Similar behavior is repeated in the next earthquake event. These repetitions result in the sharp turns in alternating directions as time progresses. The minimum frequency of the first mode for the entire monitoring records is 0.44 Hz observed during the main shock of the March 11, 2011 earthquake. Prior to that event, the lowest observed frequency was slightly higher 0.55 Hz, recorded during the foreshock event on February 9, 2011. Note that natural frequency of the first mode was higher before the foreshock event with an average of 0.6 Hz. The main shock of the March 11, 2011 earthquake was followed by several aftershocks with moderate level of excitations, and in the course of two months the building experienced frequent earthquakes with JMA seismic intensity 3–4. One can note from the figure that it takes about two months (May 2011) for the natural frequency to return to its pre-main shock value.

The prolonged effect of reduction in natural frequency is thought to be caused by the stiffness reduction of isolator system as results of the property known as the Mullins' effect (Clark et al. 1997), which is a temporary and recoverable reduction in modulus due to cyclic straining history on a rubber. The reduction in effective modulus with cycling of elastomeric isolator system depends on the material properties of elastomer and the strain history. Large excitation, long duration experienced during the main shock, and the occurrences of many moderate level aftershocks that follow immediately within a short period of time are thought to contribute significantly to the prolonged effect on the strain history of isolator system and delay the recovery of isolator's effective modulus.

6 CONCLUSIONS

Based on response analysis and system identification during the 2011 Great East-Japan Earthquake, the following conclusions are drawn:

1. The building experienced frequency reduction and increase of damping during the main shock. Frequency reduction indicates the increase in flexibility due to base-isolation system, as demonstrated by reduction of the first mode from about 0.6 Hz in the beginning of the response to about 0.44 Hz during the largest excitation. Meanwhile, the increase in damping is a consequence of shear deformation in isolation system and functioning of the damper system during the large excitation.
2. Despite the functioning of base-isolation system, strong response amplifications on the upper-stories were during the main shock. Unlike typical base-isolated building where the first sliding mode dominates the response, the torsional modes dominate the horizontal accelerations of the superstructure, and amplification of superstructure is caused by the torsional modes. Torsional modes were not significantly influenced by performance of the isolation system. Moreover, natural frequencies of the torsional modes coincided with the frequencies of ground motions that have the largest energy. These combined factors are thought to be the reason behind strong amplification of the superstructure.
3. Large excitation, long duration experienced during the main shock, and the occurrence of many moderate level aftershocks that follow immediately within a short period of time contribute significantly to the prolonged effect on the strain history of isolator system and delay the recovery of isolator effective modulus.

REFERENCES

Clark, P. W., Aiken, I. D., and Kelly, J. M. (1997). Experimental studies of the ultimate behavior of seismically-isolated structures (Vol. 97, No. 18). Earthquake Engineering Research Center, University of California.

Juang J.N., (1997). "System Realization Using Information Matrix." *J. Guidance, Control, and Dynamics*, **20**(3), 492–500.

Peng, P.A.N., Zamfirescu, D., Nakashima, M., Nakayasu, N., & Kashiwa, H. (2005). "Base-isolation design practice in Japan: introduction to the post-Kobe approach". *Journal of Earthquake Engineering*, 9(01), 147–171.

Siringoringo, D.M. and Fujino, Y. (2008), System identification applied to long-span cable-supported bridges using seismic records. Earthquake Engineering & Structural Dynamics, 37, 361–386.

Research and Applications in Structural Engineering, Mechanics and Computation – Zingoni (Ed.)
© 2013 Taylor & Francis Group, London, ISBN 978-1-138-00061-2

Assessment of evaluation methods of dynamic response of multi-span bridge to mining tremor

J.M. Dulinska & M. Fabijanska-Kopacz
Institute of Structural Mechanics, Cracow University of Technology, Krakow, Poland

ABSTRACT: In this paper assessment of evaluation methods of dynamic response of a 4-span bridge to a mining tremor in Legnica-Glogow Copperfield, Poland (LGC) was presented. The time history analysis including spatial variability of ground motion was performed. It occurred that non-uniform excitation may cause the increase of stresses in comparison with uniform excitation. The time history analysis with simplifying assumption of uniform excitation does not always lead to conservative assessment of dynamic response. The response spectrum method was also performed. The elastic spectrum recommended in Eurocode-8 and the local spectrum established for the LGC were used. The results indicated that the Eurocode 8 spectrum strongly overestimated the dynamic response of the long bridge with low natural frequencies. Better results were obtained for the local spectrum. For comparison dynamic response of a shorter bridge with higher natural frequencies was evaluated. For that bridge the results obtained for both spectra were almost identical.

1 INTRODUCTION

Numerous studies involve research on analyzing and designing of engineering structures located in seismic areas. In Poland natural seismic incidents occur very rarely, but there are mining activity regions where mining tremors frequently happen. The evaluation of dynamic responses of engineering structures subjected to mining tremors became a task of intensive studies in recent years. However, the vast majority of these studies focuses on the influence of mining tremors on residential buildings (Kuzinar 2005; Tatara 2002; Tatara, 2006). The recognition of effects of mining shocks on other structures, like bridges are still insufficient (Dulinska 2011; Dulinska & Fabijanska-Kopacz 2012).

Since energy and amplitudes of vibrations caused by highly energetic mining tremors are comparable with those resulting from small earthquakes, methods used for evaluation of dynamic responses of structures to mining tremors are identical with methods applied in seismic engineering. Two main evaluation methods of dynamic response of a structure to kinematic excitation are commonly used: the time history analysis (*THA*) based on numerical integration of equation of motion, and the response spectrum analysis (*RSA*) based on spectral curves provided for a variety of soils by Eurocode 8 (2004).

In this paper both methods were introduced in the dynamic analysis of a 4-span bridge subjected to a mining tremor registered in the LGC (Legnica-Glogow Copperfield), which is the major mining activity region in Poland.

The *THA* method was implemented considering non-uniformity of kinematic excitation resulting from spatial variability of ground motion. This effect is typical for long structures, such as bridges, pipelines and dams (Crewe & Norman 2006; Dulinska 2006; Dulinska 2011; Sextos & Kappos 2009; Zerva 2009). For comparison uniform excitation was also introduced. The results of the dynamic response of the bridge obtained with the *THA* method for both uniform and non-uniform kinematic excitation were assessed. The *RSA* method was also used to evaluate the dynamic response of the bridge to the mining tremor. Two response spectra were applied in the analysis: the horizontal elastic response spectrum recommended in Eurocode 8 and the local elastic response spectrum established for LGC (Tatara 2002). The assessment of applications of both spectra in case of mining tremor was conducted according to the accuracy of the obtained of results.

2 THE MAIN DATA OF THE BRIDGE

The evaluation of the dynamic response to a strong mining shock was conducted for the existing 4-span cable concrete bridge with elastomeric bearings located in Poland (Fig. 1). The bridge is 157.5 m long. The length of the longest span is 56 m. The height of the piers varies from 7 to 21 m. The abutments are situated 32 and 34 m away from the extreme piers. The height of the cross section of the concrete deck changes along the length of the bridge form 1.9 m at the abutments to 3.3 m at the central pier.

The geometry of the superstructure cross section and the view of the central pier are presented along with the main dimensions in Figure 2. The bridge



Figure 1. View of the existing 4-span bridge (157,5 m long).

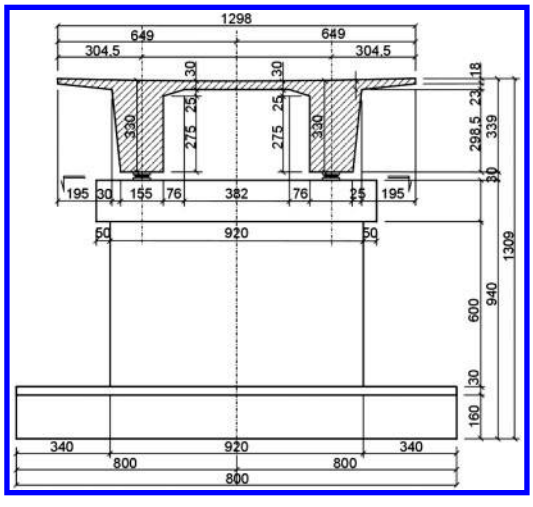


Figure 2. Main dimensions of the cross-section of the superstructure and the view of the central pier.

is equipped with elastomeric bearings as linking elements between the superstructure and the piers. The elasticity modules are taken as 4.4 and 3.8 GPa for the superstructure and the piers, respectively. The fixed boundary conditions reflected the high rigidity of the foundation rock.

Numerical analyses of the bridge were performed with the Abaqus software – a general-purpose system for static and dynamic calculations in engineering (Abaqus 2010). A mesh of 8-node linear brick and 10-node quadratic tetrahedron finite elements was used. The numerical model of the bridge with cross sections selected for the dynamic analyses is shown in Figure 3.

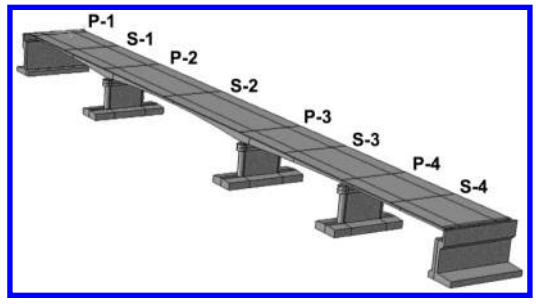


Figure 3. Numerical model of the bridge with cross sections selected for dynamic analyses.

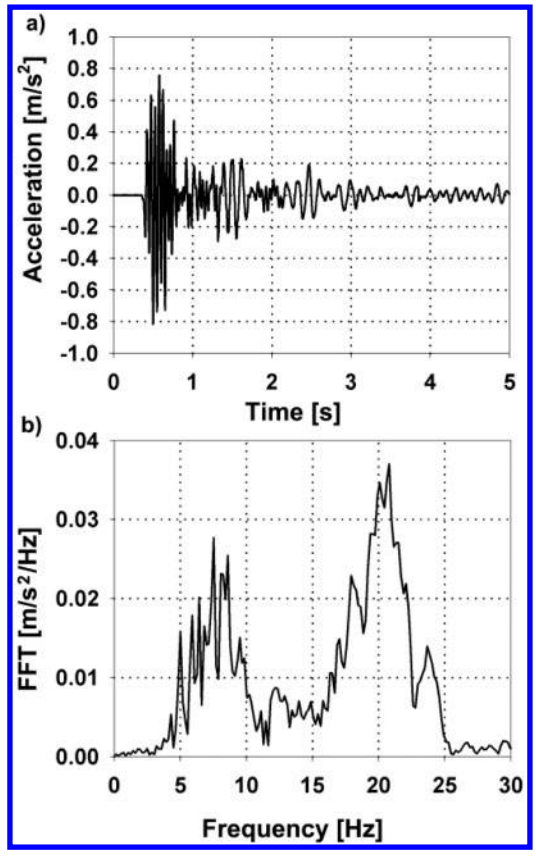


Figure 4. Ground vibration resulting from mining tremor in horizontal NS direction: (a) time history of accelerations, (b) amplitude-frequency spectrum of the signal.

3 MINING TREMOR DATA

For the analysis of the dynamic response of the bridge a real mining tremor registered in the Legnica-Glogow Copperfield was selected (Tatara 2002). The time history of accelerations in horizontal direction NS, parallel to the longitudinal axis of the bridge, as well as the frequency spectrum of the signal are shown in Figure 4.

The maximum acceleration of 0.8 m/s^2 occurred during the shock in horizontal direction NE (see Fig. 4a). The frequency-amplitude spectrum of this high-frequency shock shows maxima at the dominant frequencies of about 7 and 20 Hz (see Fig. 4b). The maximum acceleration of 0.38 and 0.45 m/s^2 occurred in horizontal direction WE and in vertical direction Z, respectively. A similar range of dominant frequencies in these directions was be observed.

4 ASSESSMENT OF DYNAMIC RESPONSE UNDER UNIFORM AND NON-UNIFORM KINEMATIC EXCITATION (*THA* METHOD)

The objective of this study was to assess the effect of non-uniformity of kinematic excitation on the dynamic response of the long bridge which is commonly neglected in the time history analysis. A model of non-uniform kinematic excitation, which takes into consideration the wave passage effect only, was applied for the dynamic analysis (Dulinska 2006; Dulinska 2011). In this model it is assumed that subsequent points of the ground in the direction of wave propagation undergo the same motions with a certain time delay dependent on the wave passage velocity. Neither loss of coherence of the signal nor possible changes of the vibration amplitudes with regard to different local ground conditions are taken into consideration (Zerva 2009).

The time history analysis was carried out with the Hilber-Hughes-Taylor time integration algorithm provided in the ABAQUS software for a direct step-by-step solution. In order to evaluate the relation between the dynamic response of the bridge and the wave passage velocity, the investigation of the response to non-uniform excitation propagating with velocities ranging from 500 to 4000 m/s was performed. For the purpose of comparison the dynamic response to uniform kinematic excitation was also evaluated (this corresponds to the infinite wave passage velocity).

Figure 5 presents the time histories of maximal principal stresses at cross-section F1 (see Fig. 3) computed for uniform and non-uniform kinematic excitation (with wave passage velocities 1500 and 500 m/s). It could be observed in Figure 5 that the maximal principal stresses obtained with the assumption of uniform kinematic excitation were larger then maximal principal stresses obtained for the non-uniform kinematic excitation with the wave passage velocity of 1500 m/s. At the wave passage velocity of 500 m/s maximal principal stresses increased again.

The relation between the maximal principal stresses and the wave passage velocity for selected cross sections is presented in Figure 6. Generally, the plots show the reduction of maximal principal stresses to a certain wave velocity. The initial decrease results from the reduction of the average values of excitation amplitudes.

Further reduction of the wave velocity causes the increase in maximal principal stresses. At low velocities the wave passage produces significant quasi-static effects which can be attributed to the changes of the subsoil geometry during the passage of the wave. It happened that the stresses obtained for non-uniform kinematic excitation with low wave passage velocity occurred greater than stresses obtained for uniform excitation (see Fig. 6, cross section P2).

The *THA* method, based on direct integration of equations of motion, in case of the investigated long bridge correctly evaluates the dynamic response only when non-uniformity of kinematic excitation is considered. The presented analysis highlights that the simplifying assumption of uniform kinematic excitation is not recommended for long structures. No doubts, including the correct wave passage velocity in the model is also essential for the accurate assessment of the dynamic response of the bridge to non-uniform kinematic excitation.

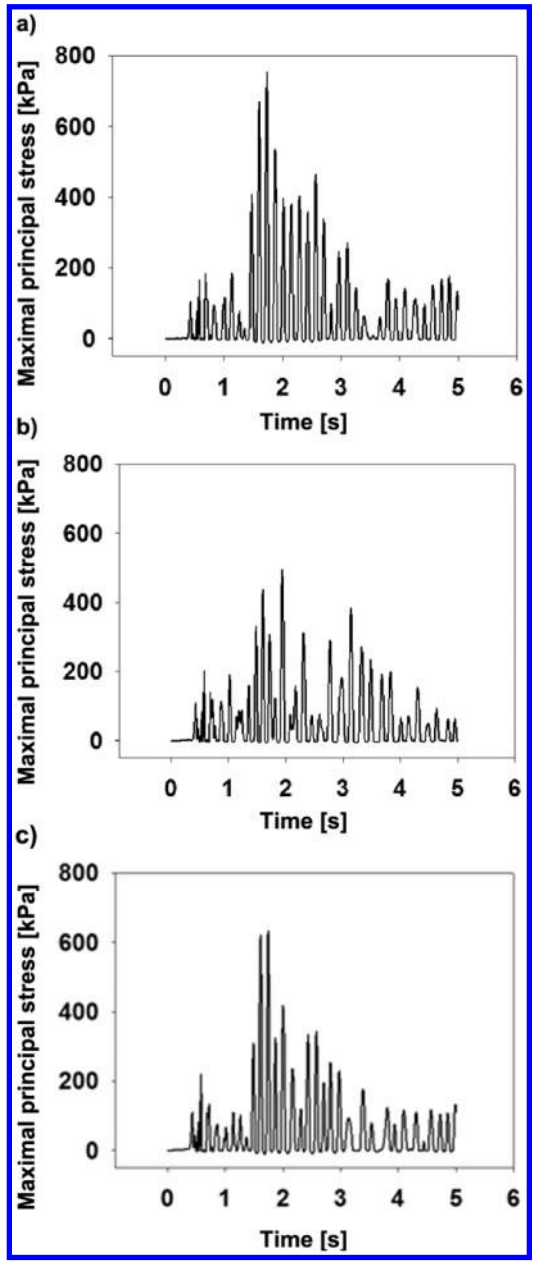


Figure 5. Time histories of maximal principal stresses at cross-section P1: (a) uniform kinematic excitation, (b) non-uniform kinematic excitation, v = 1500 m/s, (c) non-uniform kinematic excitation, v = 500 m/s.

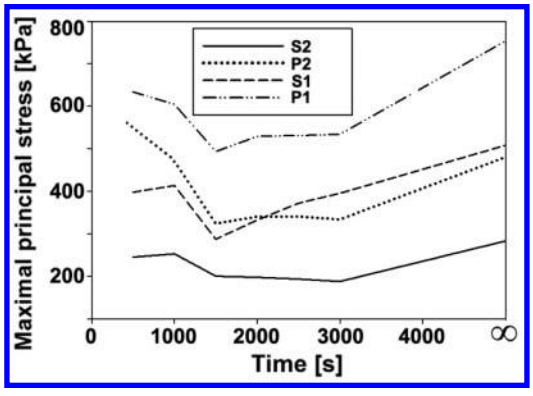


Figure 6. Relation of maximal principal stresses and wave passage velocity for selected cross-sections of the bridge.

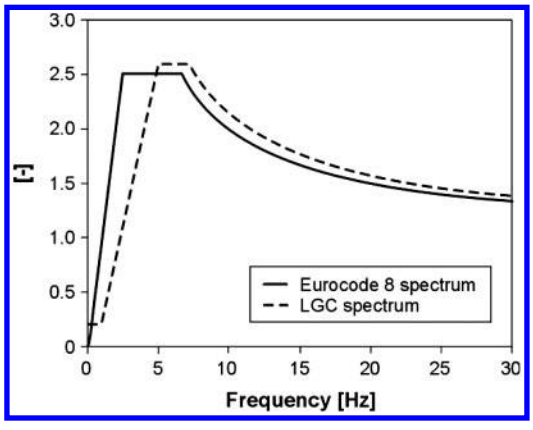


Figure 7. The shapes of the horizontal response spectrum recommended in Eurocode 8 and established for LGC region.

5 ASSESSMENT OF DYNAMIC RESPONSE OBTAINED WITH DIFFERENT ELASTIC RESPONSE SPECTRA (*RSA* METHOD)

The evaluation of the dynamic response of the bridge with the *RSA* method was also carried out. The method is only approximate, but it estimates the peak response of a structure to a particular base motion. Two spectra were applied in the analysis, using the *SRSS* method for modal summation (Abaqus 2010). Firstly, the elastic response spectrum recommended by Eurocode 8 (ground type A, damping 5%) was implemented. Then, the elastic response spectrum established for the LGC region was used. The proposed local spectrum is based on studies of a selected set of ground motion data resulting from mining tremors in the LGC region (Tatara 2002).

In Figure 7 the horizontal elastic response spectrum from Eurocode 8 is compared with the local spectrum established for the LGC region.

The presented horizontal elastic response spectra were applied in both horizontal directions with the maximum ground acceleration of 0.8 and 0.38 m/s^2 in the direction parallel and perpendicular to the bridge longitudinal axis, respectively. Since three direction of the ground motion during the mining tremor were taken into account in *THA* method, the vertical response spectra were also taken into consideration with the maximum ground acceleration of 0.45 m/s^2.

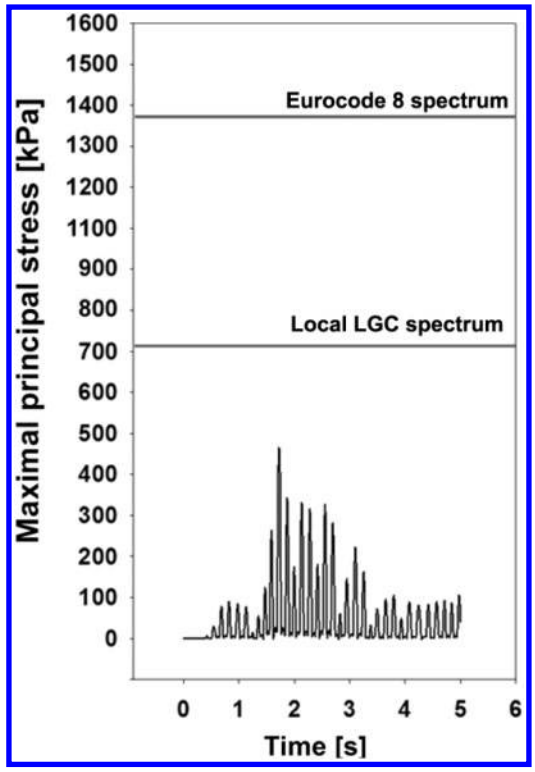


Figure 8. Relation between maximal principal stresses at cross section S3 obtained from *THA* and *RSA* method with the Eurocode 8 and the local LGC elastic response spectrum.

The relation between maximal principal stresses at cross section S3 (see Fig. 3) obtained from the time history analysis and from the response spectrum analysis with both abovementioned elastic response spectra is presented in Figure 8. Similar relation for cross section P3 is shown in Figure 9.

In Table 1 the differences between maximal principal stresses obtained from *THA* and *RSA* method with the elastic response spectrum recommended in Eurocode 8 are presented for all selected cross sections (see Fig. 3). The differences between stresses obtained from *THA* and *RSA* method with the local elastic response spectrum established for the LGC region are summarized in Table 2.

On the basis of the results presented in Figures 8 and 9 as well as in Table 1 it could be noticed that the differences between maximal principal stresses obtained from the exact *THA* and the approximate *RSA* methods reached up to 270%. The results obtained from both methods differed less significantly when the local LGC elastic response spectrum was used in the analysis. They reached up to 80% (see Table 2).

In summary, the dynamic response of the bridge to the mining tremor was significantly overestimated

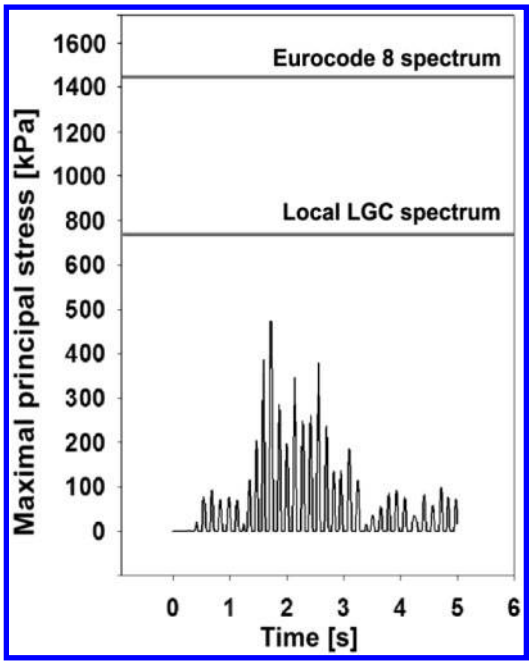


Figure 9. Relation between maximal principal stresses at cross section P3 obtained from *THA* and *RSA* method with the Eurocode 8 and the local LGC spectrum.

Table 1. Differences between maximal principal stresses at all selected cross sections (see Fig. 3) obtained from *THA* and *RSA* method with the elastic response spectrum recommended in Eurocode 8.

Cross section	Maximal principal stress [kPa]		Difference [%]
	THA	*RSA* (EC8 spectrum)	
P1	459	1587	245
S1	472	1261	167
P2	491	1753	257
S2	417	1283	208
P3	403	1480	267
S3	439	1377	213
P4	352	705	101
S4	322	725	125

if the elastic response spectrum recommended by Eurocode 8 was introduced. More accurate results were obtained if the local elastic response spectrum established for the Legnica-Glogow Copperfield region was applied.

For the purpose of comparison exactly the same dynamic analysis was performed for a bridge with different dimensions. This bridge was four times shorter than the previous one, its total length was 40 m (Dulinska & Szczerba 2013). The main dimensions and points selected for the dynamic analysis are presented in Figure 10.

The relation between maximal principal stresses at point BS1 (see Fig. 10) obtained from the time history

Table 2. Differences between maximal principal stresses at all selected cross sections (see Fig. 3) obtained from *THA* and *RSA* method with the local elastic response spectrum established for LGC region.

Cross section	Maximal principal stress [kPa]		Difference [%]
	THA	*RSA* (LGC spectrum)	
P1	459	770	67
S1	472	662	40
P2	491	893	81
S2	417	673	61
P3	403	719	78
S3	439	708	62
P4	352	412	17
S4	322	437	35

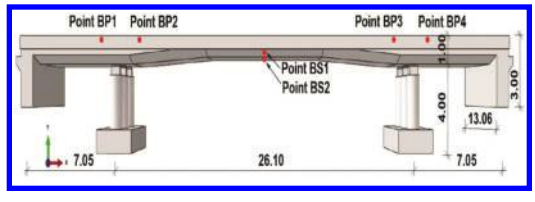


Figure 10. Numerical model of the short bridge (40 m) with points selected for dynamic analyses.

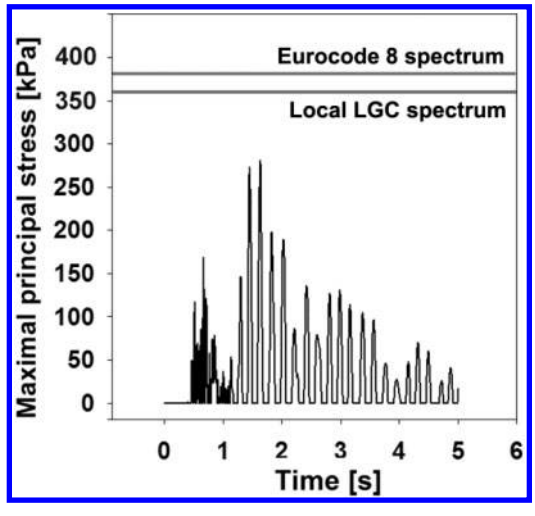


Figure 11. Relation between maximal principal stresses at point BS1 of the short bridge (see Fig. 10) obtained from *THA* and *RSA* method with the Eurocode 8 and the local LGC spectrum.

analysis and from the response spectrum analysis with both the Eurocode 8 and the local LGC elastic response spectra is presented in Figure 11.

It may be observed from Figure 11 that for the shorter bridge the results obtained for both response spectra were almost identical.

The main reason of the dissimilarity of results obtained for the investigated bridges lies in the differences in the length and stiffness of the structures.

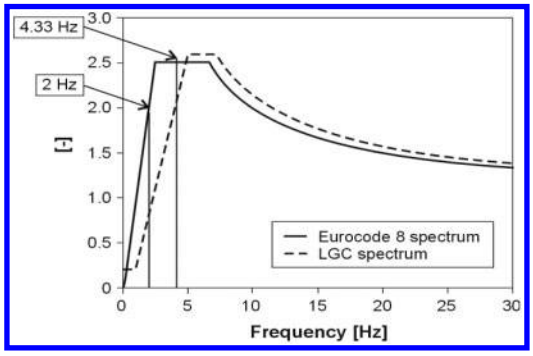


Figure 12. Location of first natural frequencies of the bridges on the investigated spectral curves.

These differences resulted in different values of natural frequencies of the bridges.

The first natural frequency of the longer bridge was 2 Hz, whereas the first natural frequency of the shorter bridge was 4.33 Hz. These frequencies were associated with vibrations in transverse direction.

The second natural frequencies which correspond to the vertical mode of vibrations of both bridges also differed distinctly. The value of 2.40 Hz was evaluated for the longer bridge, whereas the value of 7.09 Hz was obtained for the shorter bridge.

Figure 12 localizes the first natural frequencies of both bridges on the investigated spectral curves.

The local spectrum established for the LGC region is shifted towards higher frequencies. The maximum values of accelerations in the spectrum recommended in Eurocode 8 start from 2.5 Hz, whereas in the local spectrum – from 5.0 Hz. Therefore, for the longer bridge with the first natural frequency of 2.0 Hz, the value of the spectrum recommended in Eurocode 8 is 2.5 times greater than the value of the local LGC spectrum. Such a discrepancy does not occur for the shorter bridge with the first natural frequency of 4.33 Hz. The value of the spectrum recommended in Eurocode 8 is only 20% greater than the value of the local LGC spectrum.

6 CONCLUSIONS

In this paper the dynamic response of the 4-span prestressed bridge to the mining tremor was studied. The performed dynamic analysis allowed to assess the *THA* and the *RSA* methods of evaluation of the dynamic response of bridges to mining tremors.

The following conclusions as well as some general remarks for engineering practice may be drawn from the three-dimensional FE dynamic analysis:

In the case of the long bridge the *THA* method correctly evaluated the dynamic response only when the non-uniform kinematic excitation was taken into account. It occurs that the simplifying assumption of uniform excitation does not always lead to conservative assessment of the dynamic response of bridges to mining tremors. Proper recognition of the wave passage velocity is necessary for accurate assessment of the dynamic response of bridges to non-uniform kinematic excitation.

The approximate *RSA* method estimated the peak response of the long bridge to the mining tremor with accepted accuracy, provided that local elastic response spectrum established for the LGC region was introduced. The proposed response spectrum was based on the local ground motion data resulting from mining tremors in this particular mining activity area. The application of the elastic response spectrum recommended in Eurocode 8 (ground type A, damping 5%) significantly overestimated the dynamic response of the long bridge (with relatively low natural frequencies) subjected to the mining tremor.

The problem pertain only to long bridges with low natural frequencies. The analysis of the dynamic response of the shorter bridge with higher natural frequencies showed that the results obtained for both elastic response spectra were almost identical.

REFERENCES

ABAQUS. 2010. *Users Manual V. 6.10-1*. Dassault Systemes Simulia Corp., Providence, RI.

Crewe, A.J. & Norman, J.A. 2006. Experimental modelling of multiple support excitation of long span bridges. In *4th International Conference on Earthquake Engineering, Taipei, Taiwan, 12–13 October 2006, paper no. 127.*

Dulinska, J. 2006. In situ investigations of dynamic response of earth dam to non-uniform kinematic excitation. *Archives of Civil Engineering* 52(1): 37–58.

Dulinska, J.M. 2011. Influence of wave velocity in the ground on dynamic response of large dimensional structures. *International Journal of Earth Sciences and Engineering,* 4(6 SPL): 538–541.

Dulinska, J.M. & Fabijanska-Kopacz, M. 2012. Evaluation methods of dynamic response of RC bridge to spatially varying mining shock. *International Journal of Engineering and Technology* 4(5): 638–641.

Dulinska, J.M. & Szczerba, R. 2013. Simulation of dynamic behaviour of RC bridge with steel-laminated elastomeric bearings under high-energy mining tremors. *Key Engineering Materials* 531–532: 662–668.

EN 1998-1:2004 Eurocode 8 – Design of structures for earthquake resistance. Part 1: General rules, seismic actions and rules for buildings, ENV 1998-1, CEN, Brussels.

Kuzniar, K. 2005. Neural network prediction of response spectra from mining tremors with the problem decomposition. Archives of Civil Engineering 51(3): 311–321.

Sextos, A.G. & Kappos, A.J. 2009. Evaluation of seismic response of bridges under asynchronous excitation and comparisons with Eurocode 8-2 provisions, *Bulletin of Earthquake Engineering* 7 (2): 519–545.

Tatara, T. 2002. *An Influence of Mining-Induced Seismicity on Low-Rise Buildings*. Scientific Notebooks of Cracow University of Technology, no. 74, Krakow.

Tatara, T. 2006. Influence of rigid lintels for dynamic response of low masonry buildings due to mining-related surface vibrations. *Technical Transactions, Civil Engineering, Cracow University of Technology* 103(13): 143–157.

Zerva, A. 2009. *Spatial variation of seismic ground motion. Modeling and engineering applications*. CRC Press, Taylor & Francis Group, Boca Raton, FL.

Research and Applications in Structural Engineering, Mechanics and Computation – Zingoni (Ed.)
© 2013 Taylor & Francis Group, London, ISBN 978-1-138-00061-2

Characterization of the seismic behavior of steel pallet racks in cross-aisle direction

C. Braham & H. Degée
Structural Engineering Division, University of Liege, Belgium

ABSTRACT: Stability of steel storage racks in the cross-aisle direction is typically ensured by cold-formed steel bolted upright frames with diagonal bracing. Accurately determining the shear behaviour of these frames is essential for a proper seismic design and stability of the rack. In this paper, an experimental study of cross-frame designed to resist earthquake action is summarized. Structures are tested under transverse loading representative of the earthquake action, in static and cyclic conditions, with the objective of assessing the actual shear stiffness, shear resistance and deformation capacity of a set of earthquake-resistant cross-frames with different bracing configurations. The work is part of a larger research project called Seisracks2 (Storage Racks in Seismic Areas) carried out at European level.

1 INTRODUCTION

Racking systems are not regular buildings but a very particular form of steel construction. They differ from buildings in terms of their use, the loads that are supported, the geometrical dimensions and the components used in their construction. These components are normally thin-gauge cold-formed profiles and, in the case of uprights, are typically continuously perforated. This gives the required functionality, adaptability and flexibility needed to cope with the great variation in the different types of goods that are stored.

Prediction of the structural behavior of pallet racks is difficult because affected by the particular geometry of their structural components, i.e. members made by high slenderness thin-walled elements hence prone to global, local and, for the uprights, distortional buckling problems. Moreover specific modeling and design rules are required for these non-traditional steel structures, especially for the beam-to-upright and base-plate joints in the down-aisle direction (Fig. 1) that exhibit a strongly non linear behavior. In the cross-aisle direction, stability is ensured by frames consisting of two uprights connected by bracing members as shown in Fig. 1.

Rack design is even more complicated for storage racks installed in seismic zones, where they must be able to withstand horizontal and vertical dynamic forces and where, besides the usual global and local collapse mechanisms, additional limit states such as for instance the fall of the pallets with subsequent damage to goods, people and to the structure itself must be considered.

Whilst the basic technical description of an earthquake is obviously the same for all types of structures, it is of great importance to define whether or not it is possible to apply the "general design rules" (applicable to ordinary steel structures) to a rack. Furthermore it is necessary to consider how to modify correctly the general principles and technical requirements, in order to take into account the peculiarities of racking and to achieve the requested safety level. For instance, many specific physical phenomena strongly affect the structural behaviour of a racking system during an earthquake, such as the energy dissipated in the deformation of stored goods or when pallets slide on their supports.

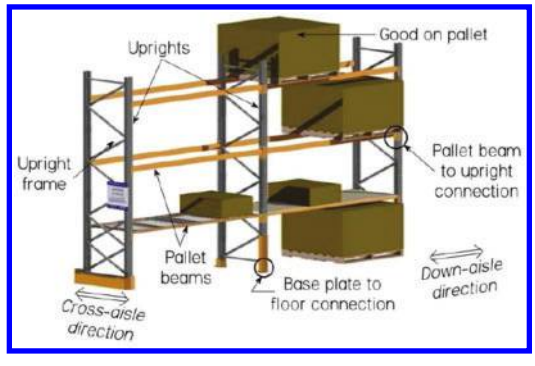


Figure 1. Typical storage rack configuration.

To this purpose, a working group had been initiated by the European Racking Federation. The main outcome of this working group is a new Code of Practice issued in September 2010 [8] and relying on a number of pre-existing standards. It includes also outcomes of the most recent researches carried out in Europe and the USA (see Ref. [9] for a comprehensive state of art and critical comment on FEM 10.2.08). In January 2011, the ERF working group has been converted into

a CEN working group (within TC 344) with the aim of transposing the Code of Practice into a European standard EN. Alternatively, reference can be made to the Rack Manufacturers Institute (R.M.I.) specifications which include few pages proposing a way to account for seismic actions.

However, only a limited number of experimental results are available to cover these issues, which questions the reliability of the rules implemented in the various reference design procedures.

Results presented in this paper are part of a wide research project "Seisracks2 – Storage Racks in Seismic Areas" (which is an extension of Seisracks1 project) funded by the European Union (RFCS research program). This research program aims at constituting a scientific background document for the conversion of the Code of practice FEM 10.2.08 to a European Standard and is intended to cover various items such as:

- The out-of-plane behavior of the beams and of the beam-to-upright connections;
- The actual structural behavior in cross-aisle direction depending on the geometrical configuration and on the type of connections of bracings between the uprights;
- The actual behavior in the down-aisle direction in presence of eccentric vertical bracings;
- The influence of the rate occupancy and of the location of the palletized goods;
- The reactions transferred to the concrete slab.

Within this project, these issues are planned to be investigated by means of component testing, full scale (push-over) testing and in-situ testing of racking systems in operating warehouses, all of these testing complements by numerical simulations.

More specifically, the present paper intends to summarize the current situation of one of the main aspects of this research, namely the investigations carried out on the cross-aisle behavior, with the objective of covering a wide range of configurations (D/Z/X type of cross bracing including different types of connection) and to investigate their consequences on the transverse stiffness, resistance and deformation capacity of the frame.

It must be emphasized however that, at the time of concluding the present paper, experimental activities are still under way and that the paper must then be considered as a milestone and not as definitively conclusive.

2 TEST SETUP AND TEST SPECIMENS

The European Standard EN 15512 [1] requires testing to evaluate the transverse stiffness per unit length of an upright frame. In the recommended test setup, shown in Fig. 2, an upright frame composed of at least two bracing panels is restrained in the transverse direction at two corners. One upright is pinned in the longitudinal direction at one end and a longitudinal load F is applied at the opposite end of the other upright through its centroidal axis. The exploitation of the experimental measurements consists then in determining the upright frame longitudinal shear stiffness and deriving then the transverse shear stiffness using Timoshenko and Gere's [2] shear formulae. It is generally considered that, upright frames braced with diagonal bracing members only, considering the full cross-section of the diagonals may lead to an overstimation of the shear stiffness by a factor up to 20. The purpose of the test is thus to estimate the reduction of the diagonal cross-section to be used in further analysis. Finite element models developed in some studies available in the literature [3,4,5] were also not really able to accurately reproduce the experimental test results and produced stiffness values that are 2 to 5 times greater than the observed results. The authors attribute the difference between FE results and experimental test results to the joint flexibility and the distortion of the upright, caused by the eccentricity between the uprights and the bracing members at the joints, which was not considered in the FE analysis.

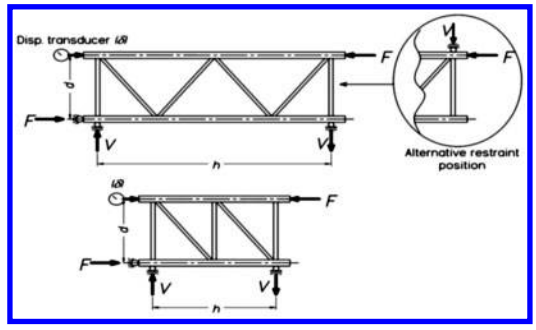


Figure 2. Upright frame shear stiffness setup in EN 15512 [1].

The EN 15512 test is however characterizing the behavior under pure shear, while the reality of the earthquake situation implies the combination of a shear loading varying over the height of the frame and combined with a significant overall bending contribution.

The purpose of the alternative test setup proposed in the present study is thus to aim at a more realistic loading procedure with the perspective of assessing the transverse stiffness, resistance and deformation capacity of cross-frames under seismic conditions; the cross-frame tests are carried out on specimens similar to those classically used for the characterization of the pure shear behavior (although longer) but with an adapted loading. Tests are carried out statically ("pushed over") and cyclically under transverse loading representative of the earthquake action.

Eurocode 8 [10] recommends that, when the fundamental mode shape is dominant, it can reasonably be approximated by horizontal modal displacements increasing linearly along the height. The associated horizontal forces F_i should be taken as being given by:

$$F_i = F_b \frac{z_i m_i}{\Sigma z_j m_j} \quad (1)$$

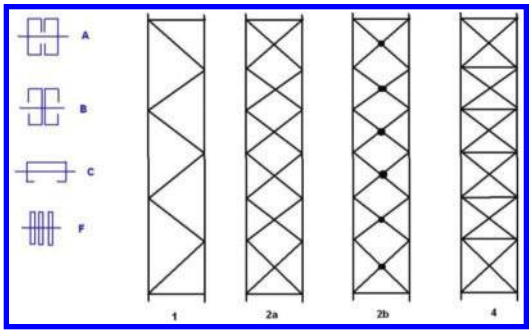


Figure 3. Typologies of upright frames.

where:

- z_i, z_j are the heights of the masses m_i, m_j above the level of application of the seismic action (foundation or top of a rigid basement);
- F_i is the horizontal force acting on storey i;
- F_b is the seismic base shear in accordance with expression (4.5) of Eurocode 8;
- m_i, m_j are the storey masses computed in accordance with 3.2.4(2) of Eurocode 8.

Industrial partners involved in the project (4 European companies) were invited to provide at least one configuration out of the types suggested in Fig. 3 with the objective of getting a wide range of situations (design for high/moderate seismicity, D/Z/X type of cross bracing). For confidentiality reasons the names of the Industrial partners are not given here nor the details of the profile sections, diagonal-to-upright connection or upright to base-plate connection. 4 basic typologies have been selected regarding the geometrical pattern of the diagonals, as well as 4 types of diagonal-to-upright connections, shown in Figure 3.

In the standard shear test, a frame assembly with a minimum number of two bracing panels shall be connected to a rigid vertical column by pin-connecting the upright ends and tested horizontally for the ease of the execution, as reminded in Fig. 2. In the present study, a more realistic configuration has been chosen (although complicating the setup) consisting in 8 meter high frames tested transversally with 4 load levels equally distributed over the height of the frame with a constant spacing of 2 m. These load levels correspond to the beam levels of the case-studies configurations, i.e. to levels where the masses are actually present. Vertical side guides are placed at each of these levels to prevent out-of-plane instabilities. The objective is clearly to test the frame in a real loading configuration in terms of shear and overall bending moment distribution.

In practice, the loads are indirectly applied on the structure by mean of one single jack F acting on a distribution beam that is acting then on two other beams, in such a way that the support reactions of this two-levels loading system satisfy Eq. (1). Loads acting directly on the upper side, transfer hoops are foreseen to distribute the load between the two uprights. No

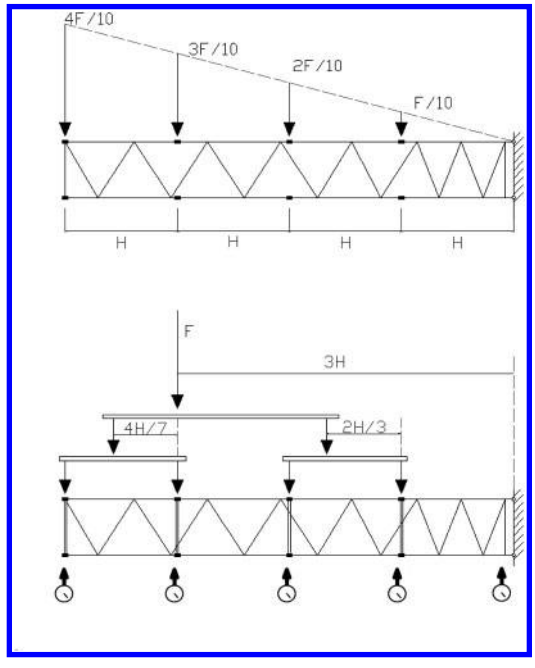


Figure 4. Test setup.

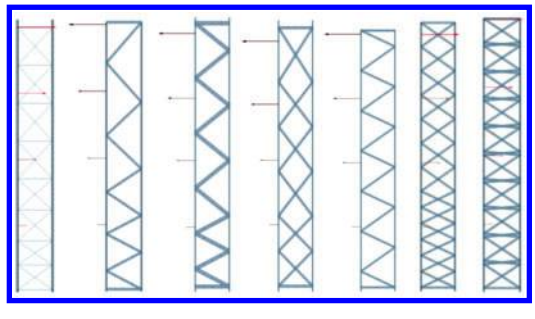


Figure 5. Tested configurations.

direct axial force is applied on the uprights, implying the base connection to be design, and if necessary reinforced appropriately, to resist the tension induced by the overall bending of the system, in order to focus on a collapse in the main part of the frame and not in its connections to the floor. Displacement transducers are located next to the bottom horizontal bracing member and at each beam level. Two extra transducers measure the relative displacement between uprights at the first two beam levels.

Figure 5 depicts the 7 different configurations of cross-frames to be tested. For confidentiality reasons no dimensions are revealed, nor of the bracing panels neither of the element cross-sections. For symmetric configurations (configs. 1, 4, 6 and 7), 1 pushover and 1 cyclic test are planned, whereas for asymmetric configurations, (configs. 2, 3 and 5), 2 pushover (one in each direction) and 1 cyclic test will be carried out.



Figure 6. Artificial hinge.



Figure 7. Original connection.

3 PRELIMINARY OBSERVATIONS

At the time of issuing the paper, experimental tests have been realized on one configuration so far (config. 1 of Fig. 5, with X bracings and horizontal members, designed with account taken for both the compression and tension diagonals as part of the resisting system), considering different ways of executing the base connection. The behavior of the upright-to-base-plate connection is intended to be covered by the research project Seisracks2 but with tests that are not discussed here. The aim of the study presented in this paper is specifically to emphasize on structural failure modes of the cross-frame either in the upright or in the bracing members but not in the upright-to-base-plate connection which is tested separately.

According to the traditional design assumptions, the upright-to-base-plate as well as the base-plat-to-floor connections are supposed to be simple pinned connections. Therefore, in order to stick as close as possible to his assumption, a first approach was to add an artificial hinge under the base-plate as seen in Figure 6. The rotation is thus supposed to occur in this artificial hinge instead of in the base-plate, resulting in an offset of the point of zero moment and to a slight change of the distribution of internal forces in the very bottom part of the structural system.

As a matter of comparison, a second configuration consisted in reproducing the same test but with connecting the frame to the vertical support according to the real way of doing. This connection is represented in Figure 7 where the base-plate is fixed with its original bolts.

3.1 *Cross-frame partially loaded – Test 1*

These first two tests were realized by applying only the two bottom loads (corresponding to F/10 and 2F/10 on Fig. 4). In this case, the loading is mainly in shear

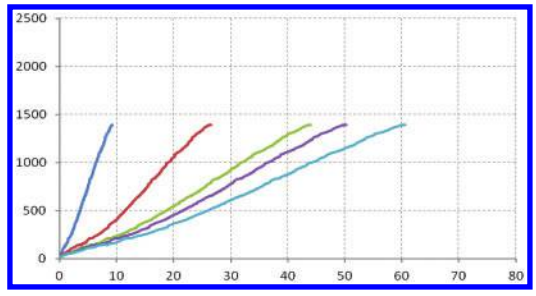


Figure 8. Total force F_b [daN] vs. displacement of the different beam-levels [mm] for the hinged connection (2 levels loaded).

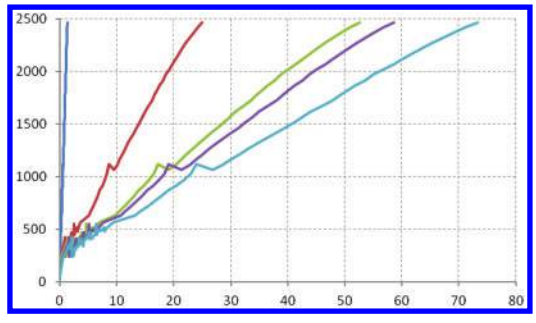


Figure 9. Total force F_b [daN] vs. displacement of different beam-levels [mm] for the original connection (2 levels loaded).

with a limited contribution of the overall bending. Displacements measured during the tests are represented in Figure 8 for the hinged connection and in Figure 9 for the normal connection:

The hinged configuration results in large displacements of the bottom horizontal diagonal situated at around 70 mm from the base-plate because of the rotation induced at the hinge level. The displacement reached 10 mm at failure for a total load of 1390 daN where the system fails by buckling of the lower compressive diagonal, followed by a load transfer to the tension diagonal finally resulting in the shearing of the bolts of the lower diagonal in tension of the bottom panel.

The original configuration collapses for a much larger applied load (up to 2400 daN) with the same failure mode: buckling of diagonals in compression followed by shearing of bolts of diagonals in tension. But the transverse displacement of the bottom horizontal member close to the base-plate is much lower than in previous case, only 1 mm.

The additional hinge induces actually a significant drift of the frame since its lower part behaves like a quasi-articulated parallelogram delimited by the additional real hinge on one side and the upright-to-base-plate connection behaving quasi like an hinge (as assumed in design) on the other hand.

This first case with additional hinges is thus finally found as not really representative of what is observed

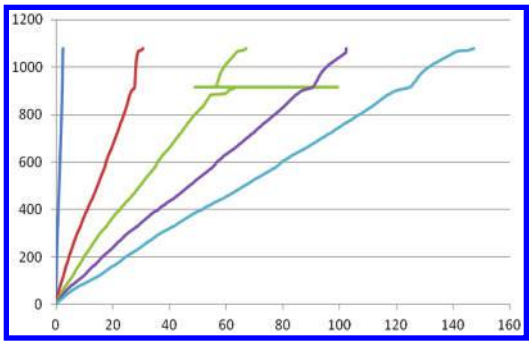


Figure 10. Total force F_b [daN] vs. displacement of different beam-levels [mm] with 4 load levels – rigid connection.

in reality and is therefore abandoned. All following tests will be realized without the additional hinges.

3.2 *Cross-frame fully loaded – Test 2*

An additional test has been realized on the same frame without the additional hinge and with the loads applied as illustrated in Figure 4. The total applied force vs. displacements of the different beam-levels is shown in Figure 10.

Failure of the cross-frame occurs now for a much lower total transverse load (1000 daN) compared to the previous test with 2 load application points and with the same base conditions. The failure mode is completely different as well, i.e. failure in shear of all bolts connecting the upright to the base-plate of the upright on the tension side due to the higher overall bending. However, in normal conditions, the uprights of the cross-frames are not subjected to such high tension forces: pallets stored on the rack provide a pre-compression of these uprights, and thus of their base connections, and overturning due to the earthquake would only decompress these connections. The case of uprights in tension should not be met in practice and base connections are therefore not meant to withstand uplift forces. New tests will thus be carried out on a system with over-designed base connection in order to focus on failure modes of interest for the present study.

4 FINITE ELEMENT ANALYSIS

The frames have been modelled with the non linear finite element software FinelG developed in University of Liège. They consist of 8 meter long uprights pinned at their bottom and linked up with diagonals which are simply hinged at their ends.

4.1 *Cross-frame partially loaded – Test 1*

A numerical analysis has been realized on the cross-frame partially loaded with F_b equal to 2066 daN (cf §3.1), applying 1/3rd on the first beam-level and 2/3rd on the second, leading to the results shown in the last line of Table 1, where the reduced area of the diagonals A_{red} calibrated to match the measured displacements is equal to $A_{real}/10$. These results have to be compared with those obtained with the test with the standard base-plates.

Table 1. Displacements of beam-levels.

	$\delta_{H\sim70\,mm}$ mm	$\delta_{H=2\,m}$ mm	$\delta_{H=4\,m}$ mm	$\delta_{H=6\,m}$ mm	$\delta_{H=8\,m}$ mm
Test	1.1	17.6	33.2	46.5	58.5
FinelG	1.1	20.1	36.4	41.3	44.4

Table 2. Displacements of beam-levels.

	$\delta_{H\sim70\,mm}$ mm	$\delta_{H=2\,m}$ mm	$\delta_{H=4\,m}$ mm	$\delta_{H=6\,m}$ mm	$\delta_{H=8\,m}$ mm
Test	2.4	27.9	58.1	95.9	132
A/28	1.2	28.4	56.1	81	98.1
A/40	1.6	39.9	78	111.5	134.1

Displacements resulting from the numerical analysis match relatively well as far as the bottom beam-levels are concerned. Beam-levels 3 and 4 reveal lower displacements with the numerical analysis which might result of the fact that this part of the cross-frame is unloaded.

4.2 *Cross-frame fully loaded – Test 2*

The same numerical model has been used applying the load at failure resulting from the test described in §3.2 (F_b equal to 1000 daN) and distributed as illustrated on Fig. 4. The area of the diagonals has now to be reduced by dividing the gross area by 28 in order to fit the bottom measured displacements and by 40 to fit the top measured displacements; these displacements are shown in Table 2.

It appears actually quite difficult to make the experimental and numerical displacement match at the same time for the two lower and the two upper levels. Different reduced areas have to be chosen. This may be due to the variation of the diagonal's inclination from bottom to top of the frame. Additional investigations are in progress to investigate this issue.

4.3 *Fully loaded additional cross-frames*

All cross-frames to be tested during this project have been modeled in FinelG using a reduced area for the diagonals. This reduced area is the one obtained with the standard shear test in accordance with the European Standard EN 15512 [1]. These shear tests have been realized on portions of cross-frames with the same profiles; the portions are generally composed of two bracing panels. Test results on 8 meter long cross-frames tested transversally will probably

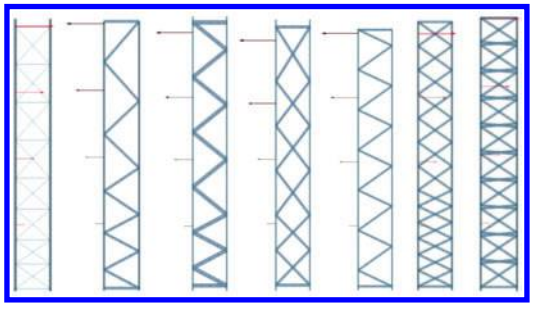


Figure 11. Cross-frames to be tested during this project.

Table 3. Maximum expected base shear F_b [kN] and corresponding displacement [cm] with a linear elastic analysis for the frames of figure 11.

18	21	8.5	21	6	28	24
7.5	5.3	22	12.4	3.8	8	6.8

require to adapt these reduced areas in order to calibrate the results which may be different than the ones obtained by calibrating results comming from longitudinal shear tests, in accordance with the preliminary observations and conclusions of section 4.2.

However the values obtained numerically can be considered as a preliminary assessment, in terms of maximum displacements of the top of each cross-frame ans of the corresponding total shear force are represented in Figure 11.

The first line in table 3 gives the maximum expected total base shear F_b in kN applied on the frame in an elastic linear analysis until failure of either the diagonals or the upright. The second line gives the corresponding top displacement in cm.

5 CONCLUSIONS

This paper has presented the general context of a study currently in progress to investigate the behavior of cross frames of pallet racks under earthquake loading. More specifically, the paper presents the motivations of the study, the set of planned test specimens, the test set-up and some preliminary results on one of the configuration.

Although the results are still very partial, some tentative conclusions can already be drawn:

- The common assumption of a purely pinned behavior of the base connections in the plane of the cross-frame seems adequate. This implies that no additional hinge need to be used in the test set-up to avoid the development of local mechanisms;
- The design of cross-frames considering compression and tension diagonals as part of the resisting system results in a brittle behavior with no plastic deformation capacity;
- The reduction of the cross-sectional area of the diagonals calibrated on standard shear tests should be modulated according to the paneling of the structural system.

These conclusions are of course to be confirmed and quantified (specifically regarding the cross-section reduction) for the remaining test configurations.

REFERENCES

[1] EN 15512. Steel static storage systems – adjustable pallet racking systems – principles for structural design.
Brussels, Belgium: European Committee for Standardization (CEN); 2009.

[2] Timoshenko SP, Gere JM. Theory of elastic stability. 2nd edition. New York, USA: McGraw-Hill Book Company, Inc; 1961.

[3] Sajja SR, Beale RG, Godley MHR. Factors affecting the shear stiffness of pallet rack uprights. In: Camotim D, et al, editor. Stability and ductility of steel structures, Lisbon, Portugal; 2006. P. 365–72.

[4] Sajja SR, Beale RG, Godley MHR. Shear stiffness of pallet rack upright frames. J Constr Steel Res 2008; 64:867–74.

[5] Godley MHR, Beale RG. Investigation of the effects of looseness of bracing components in the cross-aisle direction on the ultimate load-carrying capacity of pallet rack frames. Thin-Walled Struct; 2008;46:848–54.

[6] Gilbert B.P., Rasmussen K.J.R., Baldassino N, Cudini T, Rovere L. Determining the transverse shear stiffness of steel storage rack upright frames. Journal of Constructional Steel Research; 78(2012): 107–116.

[7] Degée H, Denoël V. Numerical modeling of storage racks subjected to earthquake. ECCOMAS Thematic Conference on Computational Methods in Structural Dynamics and Earthquake Engineering, Rethymno, Crete, Greece; 2007.

[8] FEM 10.2.08 – "Recommendations for the design of static steel racks in seismic conditions", version 1.00, European Racking Federation, September 2010.

[9] Degée H. New European recommendations for the design of static steel pallet racks in seismic conditions – the FEM 10.2.08 Code of Practice. Proc. of the ICTWS 2011 Conference, Timisoara (2011).

[10] EN 1998 – Eurocode 8 – "Design of structures for earthquake resistance", CEN, 2005.

Research and Applications in Structural Engineering, Mechanics and Computation – Zingoni (Ed.)
© 2013 Taylor & Francis Group, London, ISBN 978-1-138-00061-2

Passive energy dissipation characteristics of yielding shear panel device produced from steel and stainless steel

M. Ashraf
School of Engineering and IT, The University of New South Wales, Canberra, Australia

M.R. Hossain
School of Civil Engineering, The University of Queensland, Australia

ABSTRACT: Yielding Shear Panel Device (YSPD) is a newly developed passive energy dissipation device that exploits the stable hysteretic shear energy dissipation characteristics of a metal plate. YSPD is a simple device, which is composed of a thin metal diaphragm plate welded within a small segment of a square hollow section (SHS). The device is designed to be fitted on to a structure in such a way that it automatically gets activated to absorb excessive energy during the horizontal excitation as a result of any seismic activity. Performance of YSPDs produced from ordinary carbon steel has recently been evaluated both experimentally and numerically. Stainless steel offers significantly higher ductility, which makes stainless steel favourable for use in energy absorption. The current research exploits already validated numerical models for steel YSPDs to examine the characteristics of YSPDs produced from stainless steel. Two stainless steel alloys austenitic 1.4301 and lean duplex 1.4162 grades are used in the developed finite element models using ANSYS. Obtained results show that stainless steel could be considered as a viable option for manufacturing passive energy dissipation devices to mitigate damages due to seismic excitations.

1 INTRODUCTION

Recent catastrophic earthquakes demonstrate the possible severity of seismic activity that could cause significant damages to structures resulting in complete demolition of buildings. Damaged structures need to go through complex and expensive retrofitting techniques to be used for the purpose. Minimization of structural damages due to earthquake is a major area of research which contributed to the development of a number of active, semi-active and passive control mechanisms during the last few decades. Added damping and stiffness ADAS (Whittaker et al. 1991), Triangular added damping and stiffness TADAS (Tsai & Hong 1992) and steel plate shear wall SPSW (Timler and Kulak 1992) are commonly used metal yielding devices in design. ADAS and TADAS use out-of-plane bending deformation of steel plates to dissipate energy, whilst SPSW exploit the in-plane shear deformation of metal plates. Yielding shear panel device (YSPD) is a newly proposed passive energy dissipation device that is designed to utilise the diagonal tension field that develops in the post-buckling regime of a thin steel plate under shear. Williams and Albermani (2003) initially proposed the concept and performed experimental investigation followed by further experimental, theoretical and numerical evaluation of YSPD by Chan et al. (2009), Hossain et al (2011) and Hossain and Ashraf (2012).

The current research investigates the relative performance of different constituent metals i.e. three grades of ordinary steel and two stainless steel alloys, when used to produce YSPD. Hossain et al. (2011) developed finite element models for steel YSPD using ANSYS and verified their performance against available monotonic and cyclic test results. These models will be used in the current paper to investigate changes in energy dissipation characteristics of YSPD as a result of using different constituent material.

2 YIELDING SHEAR PANEL DEVICE (YSPD)

YSPD is a simple passive energy dissipation device, which relies on the in-plane shear deformation of a thin metal diaphragm plate welded inside a square hollow section (SHS). YSPD is designed to be placed beneath a structural beam using a V-brace so that it automatically comes into play in the event of any horizontal excitation. Figure 1 shows the basic geometry and the proposed assembly for installing YSPD within a building frame.

Chan et al. (2009) conducted a series of monotonic and cyclic tests using various plate thickness and device configurations for YSPD. The tested specimens were fabricated using a short segment of a square hollow section (SHS) with a steel diaphragm plate welded inside the SHS. Four bolt holes were drilled on each

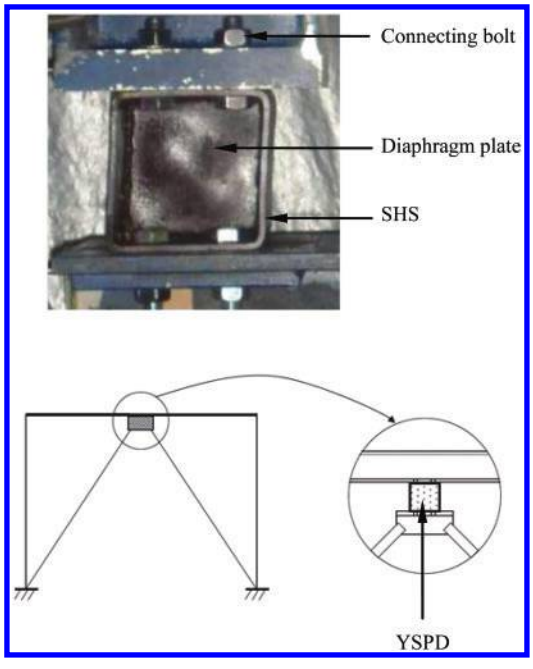


Figure 1. Basic geometry and the proposed assembly for YSPD.

of the two opposite SHS flanges for connecting the device to the test setup; this connection is analogous to the practical assembly where YSPDs are proposed to be connected using bolts to ensure easy installation and replacement. The SHS provides a boundary to the diaphragm plate so that shear forces can be applied to the plate, in addition to providing necessary detail for connections to the parent structural frame. Most importantly, the SHS serves as a boundary element allowing the tensile strips to be formed and the tension field to be developed following the post-buckling of the thin diaphragm plate. As a result of sufficiently large displacements occurring in the diaphragm plate, the input energy originating from an earthquake could be dissipated through plastic deformation.

3 ANALYTICAL FORMULATION OF YSPD

Chan et al. (2009) classified YSPDs into two different categories based on the slenderness ratio of the diaphragm plate for theoretical evaluation. Material stress-strain response was considered elastic, perfectly-plastic with a von Mises yield criterion. Diaphragm plates were assumed to be simply supported by the SHS and were classified as either compact or slender depending on whether or not the critical shear buckling stress τ_{cr} exceeds the material yielding stress. The critical shear stress for a simply supported plate is given by Equation 1 (Timoshenko 1961),

$$\tau_{cr} = k_e \frac{\pi^2 E}{12(1-\nu^2)} \left(\frac{t}{d}\right)^2 \quad (1)$$

where k_e is a coefficient which depends on the aspect ratio and end restraints of the plate e.g. k_e is equal to 9.34 for square pates, whilst E and ν are Young's modulus and Poisson's ratio respectively. Assuming an insignificant contribution from the SHS, Chan et al. (2009) proposed Equation (2) to estimate the theoretical elastic in-plane lateral stiffness of YSPD

$$k_{YSPD} = Gt \quad (2)$$

where G is the shear modulus of steel and t is the thickness of the diaphragm plate. The proposed Equation 2 is too simplistic and does not consider effects of boundary conditions in predicting initial stiffness. Hossain et al. (2011) carried out further investigation and proposed Equation 3 to obtain an appropriate expression for k_{YSPD} including the contribution from both diaphragm and SHS in addition to incorporating the effects of support rotation using a reduction factor ϕ.

$$\frac{1}{k_{YSPD}} = \frac{1}{k_{diaphragm}} + \frac{1}{\emptyset k_{SHS}} \quad (3)$$

All necessary details on theoretical formulation for YSPD are available elsewhere (Hossain & Ashraf 2012).

4 FINITE ELEMENT MODELLING OF YSPD

Finite element (FE) models for steel YSPDs were developed using ANSYS and the obtained results were verified using available test results. The basic assumptions and formulations adopted in the FE modelling process are briefly discussed herein, whilst the detailed description is available in Hossain et al. (2011).

Bilinear kinematic hardening model available in ANSYS was used as the constitutive model for both the diaphragm plate and the SHS. General purpose shell element 'SHELL181' was used for its suitability in large rotation, and/or large strain nonlinear applications. SHELL181 is a four-noded full integration quadrilateral shell element with six degrees of freedom at each node. An appropriate mesh size was achieved through convergence analysis. Developed FE models were analysed elastically to obtain suitable Eigenmodes to model initial geometric imperfections for use in the subsequent nonlinear analysis. Obtained results, however, showed insignificant effect of initial geometric imperfections on the force-displacement response of YSPD. Diagonal tension in the diaphragm plate makes the incorporated initial imperfections less effective when compared to its significance in other types of loading e.g. members subjected to longitudinal compression. The 1st Eigenmode was, therefore, used to define the distribution of initial imperfections as this normally represents the lowest buckling capacity. Amplitude of 0.2t, where t is the thickness of the diaphragm plate, was used to obtain a reasonable imperfection distribution.

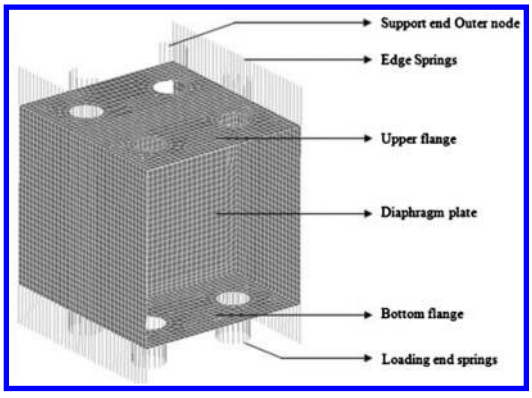


Figure 2. FE model in ANSYS for a typical YSPD.

Modelling appropriate support conditions for YSPD was one of the challenging tasks in FE modelling as it showed significant effects on the overall load-deformation response. Deformations and movements observed in the bolts and the edges of YSPD were modelled using a combination of hinge and spring supports as shown in Figure 2. All nodes along four edge lines are supported by 'COMBIN39' spring elements, which act as a tension-compression element. Stiffness of the spring elements in tension and compression are defined separately to allow the elements exhibit appropriate force-displacement response in tension as well as in compression.

It is worth noting that residual stresses were also incorporated within the FE models and a marginal reduction on the initial slope of the load-deformation behaviour was observed; the overall effect of assumed typical residual stresses on YSPD was negligible.

5 LOAD-DEFORMATION CHARACTERISTICS OF STAINLESS STEEL YSPD

The effect of material properties on the energy dissipation characteristics of YSPD is examined by using stainless steel as the constituent material. Stainless steel shows significantly higher ductility than mild steel. Austenitic stainless steel EN 1.4301 and lean duplex stainless steel EN 1.4162 have been used as constituent materials for YSPD in developed FE models. Chaboche Model (Chaboche 1989, Chaboche 1991) is used to accurately simulate the nonlinear stress strain behaviour exhibited by stainless steel alloys. Material properties and model parameters for the considered stainless steel alloys are summarized in the Table 1. Figure 3 compares the Chaboche model prediction for the austenitic stainless steel stress-strain response against those obtained from test results.

Three YSPDs with size $100 \times 4 \times 2$, $110 \times 5 \times 3$ and $120 \times 6 \times 4$ are considered to evaluate the performance of stainless steel in energy dissipation. Three grades of ordinary steel HA250, HA300 and HA350 as specified in AS/NZS 1594:2002 with nominal yield strength of 250, 300 and 350 MPa respectively are also

Table 1. Chaboche model parameters for the considered stainless steel alloys.

Stainless Steel Grade	Material properties		Model parameters					
	E GPa	$\sigma_{0.2}$ MPa	α_1	γ_1	α_2	γ_2	α_3	γ_3
1.4301	187	398	28246	758	2441	8.66	50	0
1.4162	198	635	28260	310	2631	29.62	10	0

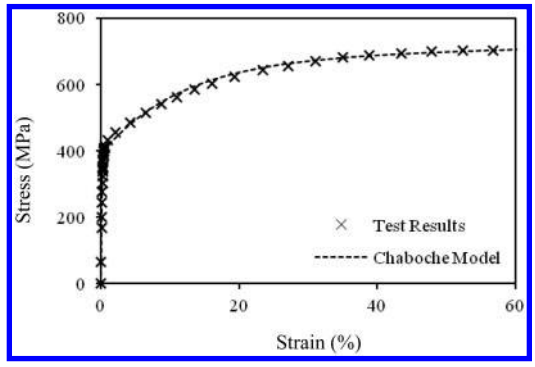


Figure 3. Chaboche model prediction for austenitic Grade 1.4301.

considered for comparison. Figure 4 shows the monotonic force displacement response of YSPDs for the considered constituent materials. Austenitic and lean duplex stainless steel shows similar initial stiffness and yielding deformation but demonstrates potential for higher energy absorption.

Three considered YSPDs were subjected to cyclic loading – a four cycle loading history of amplitudes 1, 5, 10 and 20 mm was applied for the cyclic loading as shown in Figure 5. Figure 6 shows the load-deformation response of YSPDs when subjected to the cyclic loading. Austenitic and lean duplex stainless steel showed considerably larger force-deformation loops when compared against those obtained for the considered steel grades. Higher yield strengths of the considered stainless steel grades obviously contributed to larger loops. Additional displacement would have been useful to investigate the effects of significant strain hardening observed in stainless steel. Further analysis is currently underway to examine the energy absorption of stainless steel YSPDs subjected to rather extreme loading conditions.

The amount of energy dissipated in one cycle is measured by calculating the area bounded by the cyclic response. Total amount of dissipated energy for the developed finite element models were calculated and the comparison for energy dissipation with the cumulative number of cycles are plotted in Figure 7. Lean duplex YSPDs absorbed energy at a higher rate and eventually dissipated approximately 1.8 times more energy than that of a similar 250 MPa steel

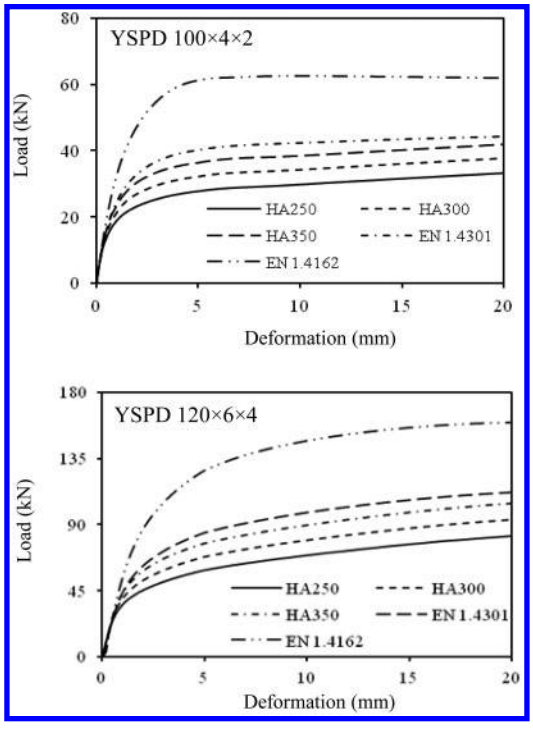


Figure 4. Force displacement response of steel and stainless steel YSPDs under monotonic loading.

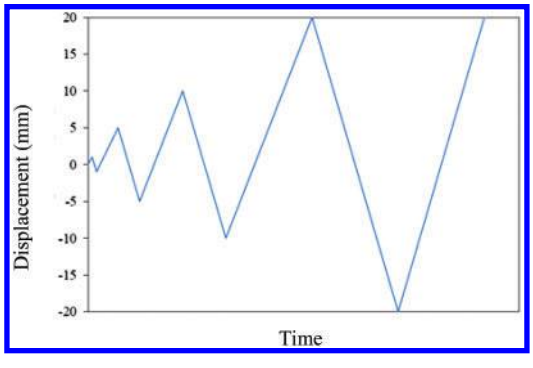


Figure 5. Displacement history applied for cyclic loading.

YSPD. Austenitic stainless steel, however, demonstrated slightly improved performance when compared against HA350 grade steel.

The performed study provides some understanding of the behavior of stainless steel YSPD and presents a preliminary comparison against its steel counterpart. The main barrier in promoting stainless steel in construction is its high material cost. In the case of small devices like YSPD, the material cost is insignificant. The higher strength of lean duplex grade should provide means for absorbing more energy in the event of seismic excitation. In the event of a prolonged or a severe earthquake, significantly high ductility offered by stainless steel alloys should allow the YSPDs to act as "structural fuse" and should be able to

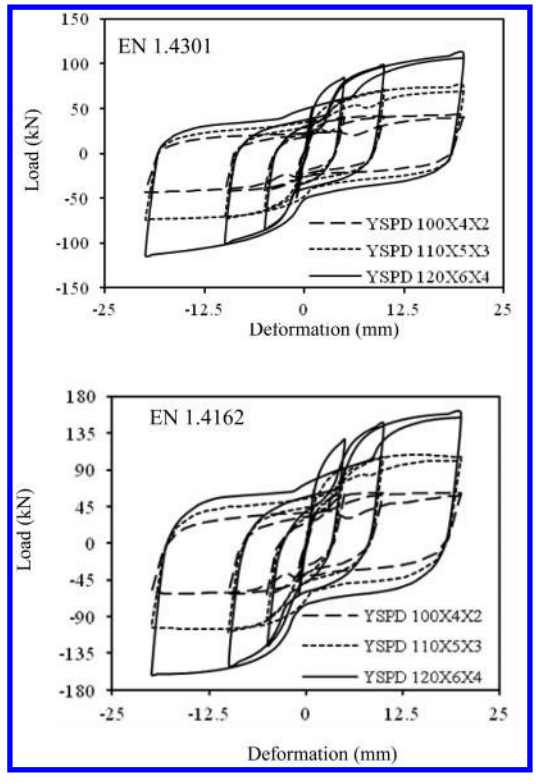


Figure 6. Response of stainless steel YSPDs subjected to cyclic loading.

absorb significant amount of excessive energy exerted on to the structures; this could play significant role in maintaining the integrity of the main structural components.

6 CONCLUSION

The structural performance of a newly developed passive energy dissipation device YSPD has been evaluated using finite element modelling techniques. FE models developed for steel YSPDs were verified using available test results and are used in the current paper to investigate the characteristics of YSPD produced from stainless steel. Two grades of stainless steel – austenitic 1.4301 and lean duplex 1.4162 are used in the current study in addition to three AS/NZS steel grades –HA250, HA300 and HA350. Results obtained both for monotonic and cyclic loading using the developed FE models show that stainless steel YSPDs could absorb more energy than their steel counterparts, with lean duplex exhibiting significantly better performance. Higher 0.2% proof strength and significant strain hardening of lean duplex 1.4162 allowed more energy absorption. Higher ductility of stainless steel should facilitate YSPDs to dissipate more energy in extreme loading conditions and hence could provide better resistance to main structural components.

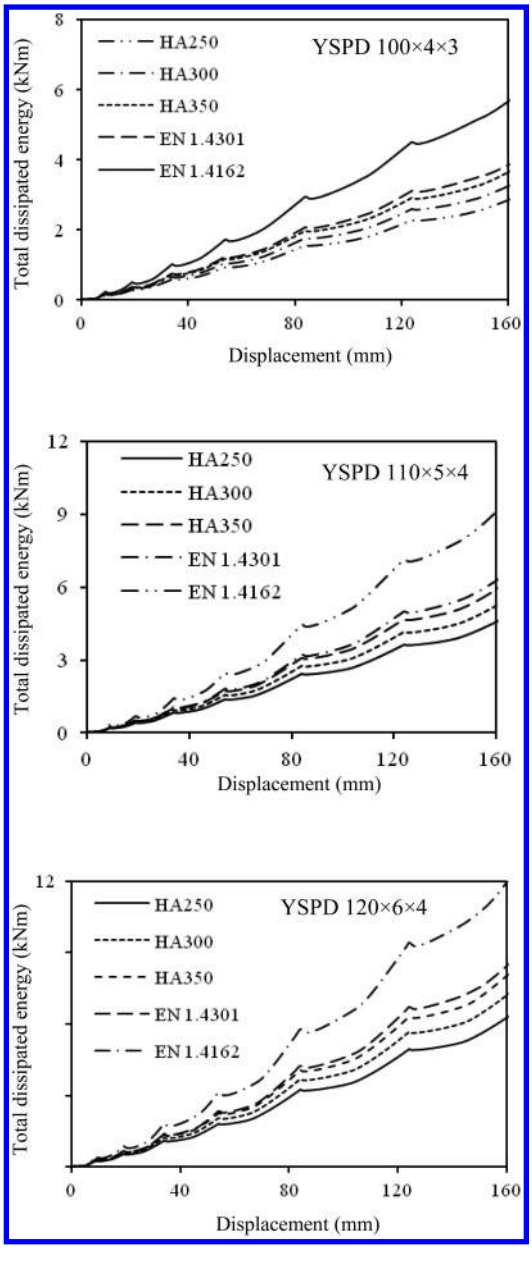


Figure 7. Cumulative energy absorption of stainless steel YSPDs subjected to cyclic loading.

The current research paves the way for further investigation in this area to explore the full potential of using stainless steel in passive energy dissipation devices.

REFERENCES

ANSYS 2007. Release 11.0 Documentation for ANSYS. *ANSYS Inc.*, Southpointe, 275 Technology Drive, Canonsburg, PA 15317.

Chaboche, J. L. 1989. Constitutive-Equations for Cyclic Plasticity and Cyclic Viscoplasticity. *International Journal of Plasticity*. 5: 247–302.

Chaboche, J. L. 1991. On some modifications of kinematic hardening to improve the description of ratchetting effects. *International Journal of Plasticity*, 7:661–678.

Chan, R. W. K., Albermani. F., Williams, M. S. 2009. Evaluation of yielding shear panel device for passive energy dissipation. *Journal of Constructional Steel Research*. 65(2):260–268.

Hossain, M. R. and Ashraf, M. 2012, Mathematical modelling of yielding shear panel device. *Thin-Walled Structures*. 59:153–161.

Hossain, M. R., Ashraf, M. and Albermani, F. 2011. Numerical modelling of yielding shear panel device for passive energy dissipation, *Thin-Walled Structures*. 49(8): 1032–1044.

Timler, P. and Kulak, G.L. 1983. Experimental Study of Steel Plate Shear Walls. *Structural Engineering Report No. 114*. Department of Civil Engineering. University of Alberta.

Timoshenko S. 1961. *Theory of elastic stability*. New York: McGraw-Hill.

Tsai, K. C. and Hong, C. P. 1992. *Constructional steel design: world developments.* Elsevier Applied Science.

Whittaker, A. S., Bertero, V. V., Thompson, C. L. and Alonso, L. J. 1991. Seismic testing of steel plate energy dissipation devices. *Earthquake Spectra*. 7(4):563–604.

Williams, M. and Albermani, F. 2003. Monotonic and Cyclic Tests on Shear Diaphragm Dissipators for Steel Frames. *Civil Engineering Bulletin No. 23*. Department of Civil Engineering, University of Queensland, Australia.

Research and Applications in Structural Engineering, Mechanics and Computation – Zingoni (Ed.)
© 2013 Taylor & Francis Group, London, ISBN 978-1-138-00061-2

Seismic behavior of exposed column bases in buckling restrained braced frames

Yao Cui
Dalian University of Technology, Dalian, China

Shoichi Kishiki
Osaka Institute of Technology, Osaka, Japan

Satoshi Yamada
Tokyo Institute of Technology, Tokyo, Japan

ABSTRACT: In Buckling Restrained Braced (BRB) frames, the axial and shear force on the column base is more critical compared with conventional moment resisting frames. Quasi-static tests of exposed column bases with BRB were conducted. It was found that the column base was uplifted when the BRB force increased to maximum tension strength. The friction force between base plate and mortar lay will be absent and then slip of base plate will occur. In this paper, a numerical study was conducted to investigate the effect of the slip of base plate on the BRB behavior. The effects of the number and size of anchor rods on the slip were briefly discussed.

1 INTRODUCTION

Buckling restrained braces (BRBs) are commonly used as primary energy dissipation elements in new construction and seismic retrofit project. It was commonly used in high-rise building and showed good ability in energy dissipation. However, there are around 80% buildings were low-to-rise structures. However, the use of BRB in low-to-medium rise building is rare. Considering the benefit of BRB, it is necessary to promote the use of BRB in low-to-medium rise building.

Exposed column base are commonly used in low-to-medium rise Moment Resisting Frames (MRFs) because of easy construction and promising seismic behavior. In Japan, it is recommended to design the column base failed at the anchor bolts rather than at the column bottom. Previous experimental studies on the seismic behavior of exposed column base in conventional braced frames (Hatanaka et al. 2002, Fukuhara et al. 2010) indicated that the anchor rods of exposed column base would experience severe shear deformation. The study on the exposed column base with BRB is not extensively studied. In this study, both experimental and numerical studies were conducted to investigate the effect of BRB on the exposed column base.

2 EXPERIMENTAL STUDY

2.1 *Test program*

The details of the test could be found in Cui et al. (2012). The test program is briefly introduced here.

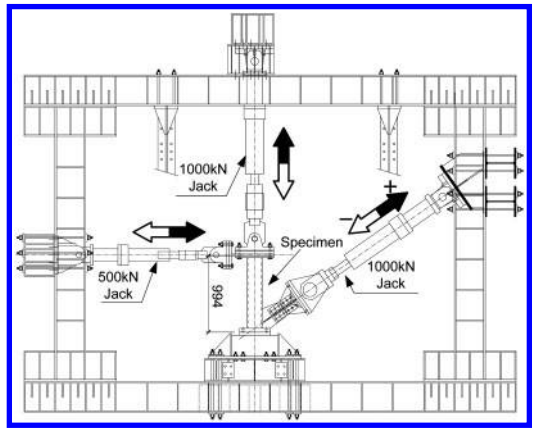


Figure 1. Test setup (unit:mm).

Three specimens were fabricated at approximately 2/3 scale. Each of specimens comprised a cold-formed square-tube cross sections column having the width of 200 mm and the thickness of 12 mm, a shop-welded hot-rolled square base plate (300 and 50 mm in the width and thickness, respectively), four or six machined anchor rods with the nominal diameter of 30 mm and a concrete foundation beam confined in a steel box.

The test specimen was placed in the loading frame shown in Figure 1. The foundation steel box was clamped to the reaction floor. The column top was clamped to two hydraulic jacks, one is the horizontal direction and the other is the vertical direction. The

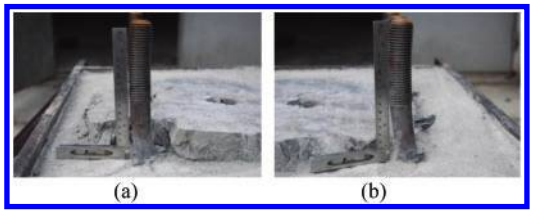


Figure 2. Deformed anchor rod: (a) in gusset plate side; (b) in the opposite side of gusset plate side.

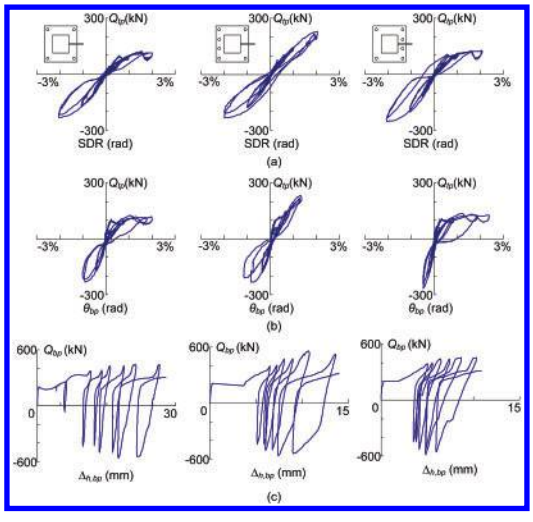


Figure 3. Test results: (a) Q_{tp}–SDR relationship; (b) Q_{tp}–θ_{bp} relationship; (c) Q_{bp}–Δ_{slip} relationship.

gusset plate was clamped to one hydraulic jack, which was used to reproduce the BRB behavior. The positive loading was defined when the BRB was in tension. The positive loading directions of each jack are illustrated in Figure 1.

2.2 *Test results*

No damage was observed in the concrete foundation during the test. All the anchor rods experienced sever lateral deformation as shown in Fig. 2. It is notable that the anchor rods in the opposite side of gusset plate (Fig. 2(b)) deformed more serious than that in the gusset plate side (Fig. 2(a)). Anchor rods in the opposite side of gusset plate is elongated and shear.

The test results till the story drift of 2% are shown in Figure 3. Figure 3(a) shows the relationship of the shear force on the top of column (Q_{tp}) and the relative story drift angle. Figure 3(b) shows the relationship of the shear force on the top of column (Q_{tp}) and the rotation of base plate (θ_{bp}). Compared these two figures, it is notable that the base plate rotation contribute mostly to the story drift angle in the positive loading (when BRB in tension). On the contrary, the column deformed mainly in the negative loading (when BRB in tension) due to the increased compressive axial force from BRB vertical component. Therefore, the anchor

Table 1. Test results.

(a) Moment resistance, M_{bp}(kNm)

	Positive loading		Negative loading	
Spec.	Measured	Calculated	Measured	Calculated
BRCB1	132	138	246	260
BRCB2	248	270	246	260
BRCB3	138	138	278	341

(b) Shear resistance in positive loading, Q_{bp}^{+} (kN)

Spec.	Measured	Calculated	
		Q_f	Q_{ab}
BRCB1	455.5	191	318
BRCB2	573.6	419	318
BRCB3	462.2	191	636

rods in the opposite side of gusset plate showed severe deformation compared with the other side as observed in Figure 2.

The measured moment and designed moment is compared in Table 1. The moment resistance was evaluated as suggested by AIJ (2006). It should be noted that the moment could be evaluated well at the peak loading with the current design guide. As shown in Table 1(b), the calculated friction forces between base pate and mortar are smaller than the measured shear resistance in positive loading, Q_{bp}^{+}. It indicated the slip of base plate could be noted in the design. Different from the moment resisting frame, the shear resistance should not be considered by the minimum of the friction force and the anchor rods resistance in design.

2.2.1 *Shear behavior*

The friction capacity depends on the normal force (compression) between the base plate and the mortar and the friction coefficient. The slip of base plate was suddenly increased when the shear force at the base plate is around 200 kN for all specimens. It is primary because the friction force lost as the vertical force on the base plate was reduced by the vertical component of BRB tensile force. The amount of BRB force when the friction force is absent could be calculated using Equation 1:

$$F_{\mathrm{br}} \cdot \cos 35^\circ + M_{bp}/L = \mu \cdot (N_0 - 2.5F_{br} \cdot \sin 35^\circ) \quad (1)$$

where F_{br} = brace axial force; M_{bp} = moment at base plate; L = specimen height; N_0 = axial force contributed by moment-resisting frame (500 kN); and μ = friction coefficient between base plate and mortar layer (0.5).

Since M_{bp} is relatively small when the friction force is broken, it is omitted in the calculation. According the equation 1, friction force is broken when the

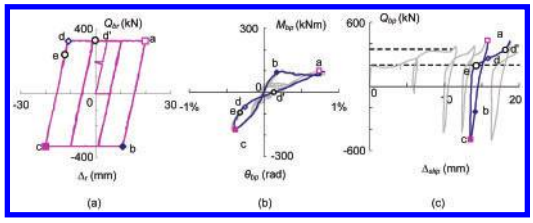


Figure 4. (a) Braced behavior; (b) column base slip behavior; (c) column base rotation behavior.

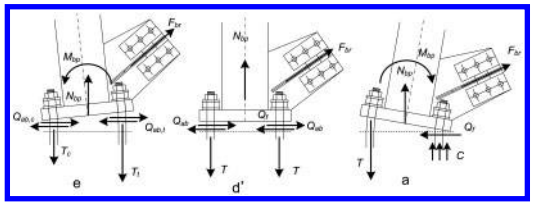


Figure 5. Resisting mechanism of column base with BRB.

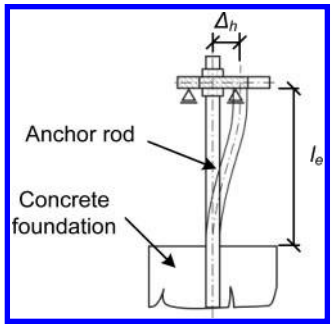


Figure 6. Horizontal deformation of anchor rods.

brace force is 163 kN, which is coincident with the experimental results.

As discussed in Cui et al. (2012), the slip of base plate occurred when the friction force between base plate and mortar layer is broken, point e in Fig. 4, and recovered when the base plate touched with the mortar ($\theta_{bp} > 0$), point d′ in Fig. 4. In this region, the resisting mechanism of column base is described in Fig. 5.

At increasing horizontal displacement the shear force increases till it reaches the friction capacity. Before the friction force was recovered, the column base experienced the direction change of the moment resistance. Because the mortar does not have sufficient strength to resist the bearing stresses between the anchor rods and the mortar, considerable bending of the anchor rods may occur, as shown in Figure 2. Tension, shear and bending will occur in the anchor rods due to the horizontal displacement. The deformation of anchor rods could be described as shown in Figure 6. Such horizontal deformation was cumulated, since such deformation developed in one loading direction (load from negative loading to positive loading). Equation 2 was used to evaluate the horizontal displacement in the very beginning.

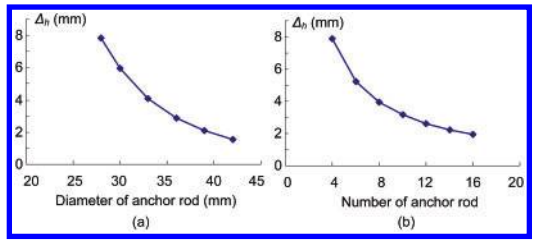


Figure 7. Effect of parameters on the horizontal displacement of anchor rod: (a) diameter of anchor rod; (b) number of anchor rod.

$$\Delta_h = \frac{F_{br,y}/n \cdot \cos 35° \cdot l^3}{12EI} \tag{2}$$

$$I = \frac{\pi d^4}{64} \tag{3}$$

where, n = the number of anchor rods; $F_{br,y}$ = the yield strength of BRB force, 400 kN; E = the young modulus of anchor rod; d = the diameter of anchor rod; l = the effective length of anchor rod (the sum of base plate thickness and the mortar layer thickness). Should be noted that the lateral load on the top of column was ignored, since it is far less than the lateral components of BRB yield force.

Using Equation 2, it is calculated that the horizontal displacement of the three specimens are 8 mm and 5 mm, which are close to the measured slip at the 1st loading cycle. However, Equation 2 is a simple way to roughly evaluate the slip at the very beginning. The effect of anchor rods arrangement is not able to be traced. But it still could give the designers the general image of the horizontal deformation of anchor rods.

Figure 7 shows the effect of diameter and number of anchor rods on the horizontal displacement. The horizontal displacement is reduced as the diameter or number of anchor rod increased. But it is notable that the horizontal displacement could not be completely overcome by simply increase the size or number of anchor rods.

3 NUMERICAL STUDY

3.1 *Numerical model*

The general-purpose finite element program ABAQUS version 6.9 (2010) was used to the effect of column base slip on the BRB frames behavior. The prototype frame of the experiment discussed above was modeled as shown in Figure 8 (a). Half of the specimen was modeled.

Beam elements (B31) were used for the column in the frame part. Truss elements (T3D2) were used for the BRB. The column base part was modeled in details, as shown in Figure 8 (b). A four-node linear reduced integration with an hourglass control shell

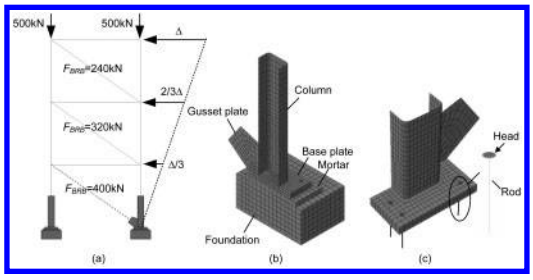


Figure 8. Numerical model: (a) loading condition; (b) modeling of column base model; (c) modeling of anchor rod.

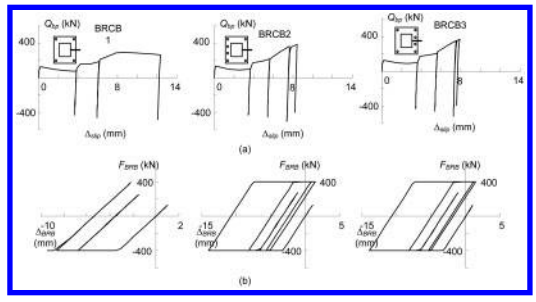


Figure 9. Analysis results: (a) Q_{bp}-Δ_{slip} relationship; (b) BRB behavior.

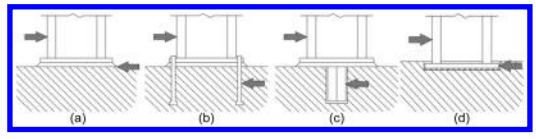


Figure 10. Shear transfer mechanisms: (a) surface friction; (b) anchor rod bearing; (c) shear key; (d) foundation bearing.

element (S4R) was used for the column. Two layers of eight-node hexahedral incompatible mode elements (C3D8I) were adopted to model the base plate to accurately trace the bending behavior. The foundation beam and mortar were considered as an elastic component to reduce the calculation time. Interaction between the bottom of base plate and the upper surface of the mortar was modeled to allow for contact behavior with friction. As shown in Figure 8 (c), the bolts were modeled as beam elements, having a diameter equal to the nominal bolt diameter of 28 mm and restrained at the lower node. The heads of the bolts were modeled as shell disks, S4R, having a constant thickness equal to the average thickness of the actual bolt head. The sections were modeled as rigid by giving them a linear elastic material response.

The multilinear kinematic hardening option was adopted to simulate the material behavior of steel, with the parameter value provided by the associated material tests. For the column and base plate, the stress-strain curve was assumed to be bilinear with a strain hardening ratio of E_s/100, where E_s is Young's modulus of steel. For the anchor bolts, a fracture strain was assigned to consider the rupture of anchor bolts. Bilinear hysteresis curve of BRB is applied to the truss element.

Lateral displacement on the 3rd story was controlled. Story drift angle of 1/300 rad, 1/150 rad, and 1/100 rad of each two cycles were controlled. However, due to the serious lateral deformation of anchor rods, the analysis was stopped in the very early loading age.

3.2 *Numerical results*

The analysis results are shown in Fig. 9 (a) and (b). It is noted that the slip was reduced nearly half by using extra two anchor rods, which is similar as observed in the experimental study. Because of the slip of the base plate, the axial deformation of BRB was reduced. As shown in Fig. 9(b), the BRB behaved different from the expected one, which is shown in Fig. 4(a). Although the frame with 'BRB3' showed the smallest slip, the BRB behavior is nearly the same as the one with 'BRB2'.

Based on the analytical results, it concludes that the BRB contribution was significant reduced due to the slip of base plate. It would limit the develop of the BRB application in low-to-medium rise building. As discussed above (Fig. 7), the slip of base plate could not be completely overcome by using larger or more anchor rods. Other method should be developed to avoid the slip and to ensure the BRB behavior in the low-to-medium rise building.

4 FURTHER DISCUSSION

There are four mechanisms for shear forces to be transferred from the column base into the supporting concrete foundation. They are friction between the base plate and mortar layer (Fig. 10 (a)), shear and bending of the anchor rods (Fig. 10 (b)), shear key bearing on the foundation (Fig. 10(c)) and bearing of the column embedded in a slab or foundation beam (Fig. 10 (d)).

It was observed that the first two mechanisms were not promising and sufficient for heave shear loads. The other two mechanisms, shear key and embedded column, showed great shear resistance in other studies. Further study should be continued to investigate the effect of these two mechanisms in the column base of BRB frames.

5 CONCLUSIONS

In moment frames, the shear is often transferred through friction developed in the bearing potion of the base plate. However, when such a bearing zone is not present (e.g., in braced frames or in moment frames where the columns have tensile axial loads), shear transfer mechanisms must be carefully considered and designed. The main findings of this paper are summarized as follows:

1) The exposed column base in BRB frames showed unsymmetrical hysteresis behavior in positive and negative loading.

2) The shear behavior is critical for the exposed column base in BRB frames. The friction force between the base plate and foundation beam was broken when the BRB force was in tension. Significant slip occurred then.
3) The slip of base plate was cumulated in cyclic loadings. And such slip would reduce the effect of BRB behavior.
4) The slip was reduced by increasing the number of anchor rods. However, the arrangement of the anchor rods had slightly contribution to increase the seismic behavior of exposed column base.
5) Other methods to reduce the slip of base plate should be studied, such as stopper in front of base plate or shear key under base plate.
6) In the design, not only the shear resistance should be checked, but also the deformations at serviceability.

ACKNOWLEDGEMENTS

The authors acknowledge the support from the Japan Iron and Steel Federation and KAKENHI (21686051).

REFERENCES

ABAQUS/Standard user's manual, version 6.9. 2010. Hibbitt, Karlson and Sorensen, Inc.

Architectural Institute of Japan (AIJ). 2006. Recommendations for design of connections in steel structures. Tokyo.

Cui, Y., Kishiki, S., and Yamada, S. 2012. Hysteretic behavior of exposed column bases in buckling restrained braced frame. *Proceedings of 15th world conference on earthquake engineering, Lisbon, 24–28 September 2012.*

Fukuhara, A., Yamanishi, T., et al. 2010. Anchor-bolt-yield-type exposed column-base subjected to tensile and shearing forces: Part 2 cyclic loading test. *Summaries of technical papers of annual meeting AIJ* C-1(III):843–844.

Japanese Society of Steel Construction (JSSC). 2009. Recommendation and commentary for construction of exposed column bases with structural anchor bolts. Tokyo.

Tanaka, T., and Masui, A. 2002. Study on seismic retrofit for exposed column bases of steel frames with braces. *Summaries of technical papers of annual meeting Kinki Branch AIJ* 42: 221–224.

Research and Applications in Structural Engineering, Mechanics and Computation – Zingoni (Ed.)
© 2013 Taylor & Francis Group, London, ISBN 978-1-138-00061-2

Multi-storey steel structures: Seismic energy modal distribution

O. Prodan, I. Ladar & N. Chira
Technical University of Cluj-Napoca, Romania

ABSTRACT: The Present contribution reviews the already classical transformations of seismic input energy into multi-storey structures and emphasizes the less developed distribution of this energy to the natural modes of vibration. The computation is conducted on two scaled down steel multi-storey frames dynamically modeled as mdof systems. The main objective of the intended contribution is to introduce a modal approach to energy based analysis and design. While the structural engineer enjoys a good command of transformation of seismic input energy into kinetic, strain, damping (inherent viscous and hysteretic) energy components, the modal distribution of seismic input energy is less exhibited and practiced. A short theoretical part dealing with modal energy based analysis is developed. It is followed by several numerical results carried out on steel multi-storey structures seismically acted on via a laboratory shaking table. Associated relevant results in terms of input energy and its structural modal components are presented. Inferred conclusions and an avaricious bibliography are presented.

1 INTRODUCTION

Why is the energy approach to seismic analysis and design of structures a new and, eventually, a more general technique to the analysis and design of structures located in seismic areas? First, the answer to the question may start with the direct evidence that what the earthquake introduces, primarily, into a structure is energy. Not stresses and not displacements/ deformations. They come later as the result of energy input. Then, the energy is a synthetic parameter comprising both, vector quantities (stresses, displacements, velocities, accelerations) and scalar quantities (masses, damping associated parameters, elastic and plastic properties of the structures). It has to be emphasized that a synthetic quantity, as the seismic induced energy, will allow a synthetic approach to structural analysis and, most important, design. Energy approach [1], [2], [3] will not lead to (numerical) values of stresses and displacements that may be compared to some allowable limits. Energy approach, as it is formulated [4], [5], [6] will not lead to any mechanical (static and kinematic) state of a seismically acted upon structure that is specified in seismic design codes. If this is a shortcoming, it is not a shortcoming of the energy approach. The shortcoming could be of the analysis and design techniques. This shortcoming is not going to last, the energy based analysis and design are, already, firmly formulated [7], [8], and are rapidly and successfully catching up [9], [10]. The mass distribution and, mainly, the proposed modal distribution of seismic input energy into multi-story structures may constitute useful tools in the hands of structural engineer to an optimal structural conceiving. It may be helpful in assigning an optimal location of dampers into the design structure aiming at fulfilling the fundamental requirement of energy based design criterion:

Energy dissipating capacity ≥ Energy demand

where, energy demand is the input energy of the design (code provided) earthquake.

The study refers to the energy formulations of seismic analysis of multi-story structures in its relative form. A short emphasize on the relevance of the two forms is added and commented. Mass and proposed modal decompositions of seismic input energy are developed and followed by numerical analysis results obtained from energy based analysis of steel multi-story structures seismically acted upon.

2 MASS AND MODAL APPROACH TO THE SEISMIC INPUT ENERGY

Following (nxn) matrices and (nx1) vectors are associated to a classical dynamic n dof viscously damped model (Fig. 1) seismically acted in elastic domain: inertia matrix $\mathbf{M}$, stiffness matrix $\mathbf{K}$, classical [11] viscous damping matrix $\mathbf{C}$, modal matrix $\mathbf{\Phi}$, kinematic relative vectors $\mathbf{u}$ (displacements), $\dot{\mathbf{u}}$ (velocities) and $\ddot{\mathbf{u}}$ (accelerations), unit vector $\mathbf{1}$, inertia vector $\mathbf{m} = \mathbf{M} \cdot \mathbf{1}$ and recorded ground acceleration vector $\ddot{\mathbf{u}}_g$. The modal orthogonal eigen vectors $\mathbf{\Phi}_j$ and eigen values ω_j $(j = 1 \div n)$ associated to natural mode of vibration j are, also, considered. An elastic elementary displacement set $d\mathbf{u}$ compatible with structural constraints is considered. The elementary work equation – associated to linear elastic behavior – reads:

$$\ddot{\mathbf{u}}^T \cdot \mathbf{M} \cdot d\mathbf{u} + \dot{\mathbf{u}}^T \cdot \mathbf{C} \cdot d\mathbf{u} + \mathbf{u}^T \cdot \mathbf{K} \cdot d\mathbf{u} = - \mathbf{m}^T \cdot \ddot{u}_g \cdot d\mathbf{u} \quad (1)$$

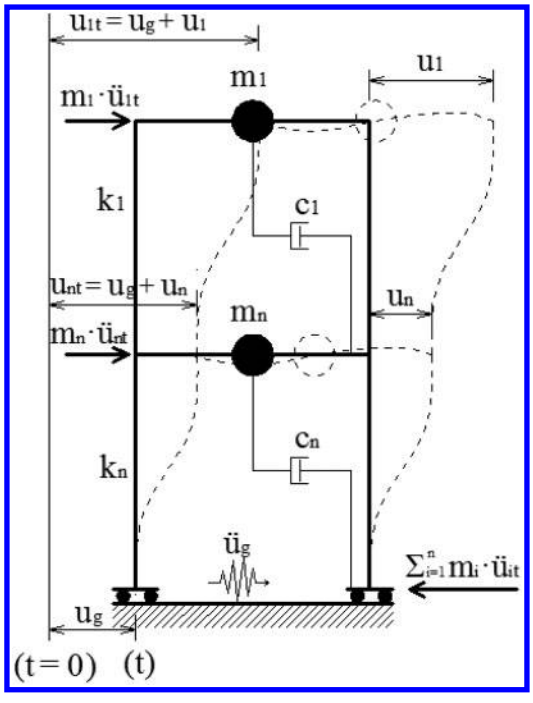


Figure 1a. Seismically induced displacements to mdof structure.

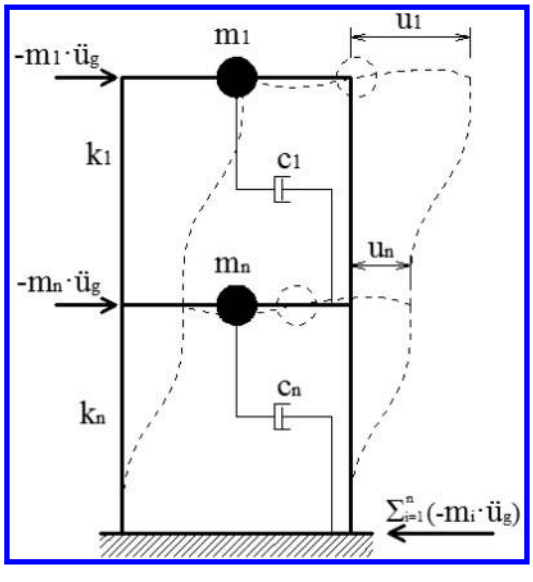


Figure 1b. Relative displacements **u**.

where^T denotes matrix transposition and δ is the virtual differential operator. Modal coordinates **u** are transformed into a new set **x** of coordinates through:

$$\mathbf{u} = \mathbf{\Phi}\cdot\mathbf{x} \qquad (2a)$$

The elastic elementary displacement in **x** reads:

$$d\mathbf{u} = \mathbf{\Phi}\cdot d\mathbf{x} \qquad (2b)$$

Substituting coordinates **u** by the new modal set **x** leads to the work equation:

$$\ddot{\mathbf{x}}^T\cdot\mathbf{\Phi}^T\cdot\mathbf{M}\cdot\mathbf{\Phi}\cdot d\mathbf{x}+\dot{\mathbf{x}}^T\cdot\mathbf{\Phi}^T\cdot\mathbf{C}\cdot\mathbf{\Phi}\cdot d\mathbf{x}+\mathbf{x}^T\cdot\mathbf{\Phi}^T\cdot\mathbf{K}\cdot\mathbf{\Phi}\cdot d\mathbf{x}=-\mathbf{m}\cdot\ddot{u}_g\cdot\mathbf{\Phi}\cdot d\mathbf{x} \quad (3)$$

Taking into account the orthogonality property of **M**, **C** and **K** matrices, a simple mathematical processing of virtual work equation (3) leads to the differential equation in x_j:

$$\mathcal{M}_j\cdot\ddot{x}_j + \mathcal{C}_j\cdot\dot{x}_j + k_j\cdot x_j = -(\mathbf{\Phi}_j)^T\cdot\mathbf{M}\cdot\mathbf{1}\cdot\ddot{u}_g(t) \qquad (4)$$

Subscript j denotes the natural mode of vibration and scalar L_j is given by:

$$L_j = (\mathbf{\Phi}_j)^T\cdot\mathbf{M}\cdot\mathbf{1} = (\mathbf{\Phi}_j)^T\cdot\mathbf{m} \qquad (5)$$

Integration of differential equation (4) leads to the classical solution $x_j(t)$ $(j = 1 \div n)$ of the traditional convolution integral associated to natural mode of vibration j in the form:

$$x_j(t) = -(\Gamma_j/\omega_j)\cdot\int_0^\tau \ddot{u}_g(\tau)\cdot e^{-\zeta_j\omega_j(t-\tau)}\cdot\sin[\omega_j(t-\tau)]\cdot d\tau \qquad (6)$$

where time variable $\tau \in [0, t_c]$, ω_j is j^{th} mode circular frequency and ζ_j is the modal critical viscous damping ratio. Modal participation factor $\Gamma_j = L_j/\mathcal{M}_j$ is, also, traditional. If the nxn diagonal matrices $\mathcal{M} = \mathbf{\Phi}^T\cdot\mathbf{M}\cdot\mathbf{\Phi}, \mathcal{C} = \mathbf{\Phi}^T\cdot\mathbf{C}\cdot\mathbf{\Phi}$ and $\mathcal{K} = \mathbf{\Phi}^T\cdot\mathbf{K}\cdot\mathbf{\Phi}$ are introduced in (3), the set of n simultaneously uncoupled differential equations reads:

$$\ddot{\mathbf{x}}^T\cdot\mathcal{M}\cdot d\mathbf{x} + \dot{\mathbf{x}}^T\cdot\mathcal{C}\cdot d\mathbf{x} + \mathbf{x}^T\cdot\mathcal{K}\cdot d\mathbf{x} = -\mathbf{m}^T\cdot\mathbf{\Phi}\cdot\ddot{u}_g\cdot d\mathbf{x} \qquad (7)$$

where the non-zero entries $\mathcal{M}_j$, $\mathcal{C}_j$ and $\mathcal{K}_j$ of diagonal matrices $\mathcal{M}, \mathcal{C}$ and $\mathcal{K}$ are given by:

$$\mathcal{M}_j = (\mathbf{\Phi}_j)^T\cdot\mathbf{M}\cdot\mathbf{\Phi}_j,\ \mathcal{C}_j = (\mathbf{\Phi}_j)^T\cdot\mathbf{C}\cdot\mathbf{\Phi}_j \text{ and } \mathcal{K}_j = (\mathbf{\Phi}_j)^T\cdot\mathbf{K}\cdot\mathbf{\Phi}_j \quad (8)$$

By substituting (8) into equation (7), the work equation takes the scalar form:

$$\sum_{j=1}^n \mathcal{M}_j\ddot{x}_j dx_j dt + \sum_{j=1}^n \mathcal{C}_j\dot{x}_j dx_j dt + \sum_{j=1}^n \mathcal{K}_j x_j dx_j dt = -\mathbf{m}^T\cdot\mathbf{\Phi}\cdot\ddot{\mathbf{x}}\cdot d\mathbf{x}\cdot dt \quad (9)$$

where $d\mathbf{x}$ is the usual differential: $d\mathbf{x} = \dot{\mathbf{x}}\cdot dt$.

Integration of (9) from $t = 0$ to $t = t_c$ (earthquake duration) leads to the (relative) modal energy balance equation:

$$E_{kj} + E_{dj} + E_{sj} = E_{ij} \qquad (10)$$

where energy modal j^{th} components read:

$$\text{Relative kinetic energy } E_{kj} = \int_0^t \mathcal{M}_j\cdot\ddot{x}_j\cdot\dot{x}_j dt \qquad (11a)$$

Dissipated energy by (inherent) viscous damping

$$E_{dj} = \int_0^t \mathcal{C}_j\cdot\dot{x}_j\cdot\dot{x}_j dt \qquad (11b)$$

Elastic strain energy $E_{sj} = \int_0^t K_j \cdot x_j \cdot \dot{x}_j dt$ (11c)

Seismic relative energy input $E_{ij} = -\int_0^t \mathbf{m}^T \cdot \mathbf{\Phi}_j \cdot \dot{x}_j \cdot \ddot{u}_g dt$ (12)

Similar mathematical incursion associated to total displacement $\mathbf{u}_t = \mathbf{u} + \mathbf{1} \cdot u_g$ (Fig. 1) leads to the absolute modal kinetic and absolute modal seismic input energy formulation (not dealt with here). The dissipated energy by viscous damping and strain energy preserve their form in both (relative and absolute) formulations [5]. All above integrating computation corresponds to [0, t_c] time interval. Energy balance at every instant $t \in [0,t_c]$ requires the emphasize of instant values of energy components. Energy balance at $t = t_c$ would "eliminate" stored (kinetic + strain) energy components as they vanish at the end of earthquake action.

3 NUMERICAL RESULTS

A set of two steel multistory scaled frames (Fig. 2) have been numerically analyzed. The frames have been experimentally tested aiming at a comparative study of added damping effect on energy input and distribution (not included here). Traditional n dof ($n = 2$ and $n = 3$) dynamic model is adopted. Applied seismic inputs are several scaled down accelerograms associated to the shaking table. Presented results have been selected form applying Kobe 1995 recorded and scaled down accelerogram (Fig. 3). The results are part of an entire set of laboratory results and are focused at energy decomposition into its modal components. No reference is made here to the laboratory calibration, selection of appropriate structures, lumped masses and digital recordings.

Experimentally analyzed structures (Figs 2a–2b) exhibit an accentuated flexibility (mainly lateral) that allows (by the large values of modal vibration periods T_j) a relevant emphasize of modal contributions to total seismic response. Processing relations 8) with computed modal analysis associated parameters (T_j, ω_j, $\mathbf{\Phi}_j$, ζ_j) the following numerical results (Table 1 and Table 2, respectively) have been obtained in the case of a critical damping ratio $\zeta_j = 2\%$ for all natural vibration modes:

Induced kinematic parameters $\mathbf{u}$ (displacements), $\dot{\mathbf{u}}$ (velocities) and $\ddot{\mathbf{u}}$ (accelerations) have been digitally recorded for each floor (lumped masses) via installed digital transducers. Numerical integrations of relations (6), (11) and (12) have been carried out numerically, following a recurrence numerical integration procedure [11] for a constant time interval step $\Delta t = 0.001$ sec.

Eloquent images of the obtained numerical results (modal energy components) are presented (Figs 4–5).

The classical mechanical energy (the stored energy) is presented as the sum of its kinetic and strain energy components. Also, it is computed in its cumulated form during the earthquake duration t_c. The surface by the mechanical energy curve (Fig. 4a) is the energy that

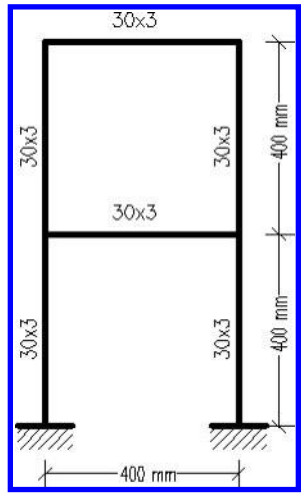


Figure 2a. Two dof structure.

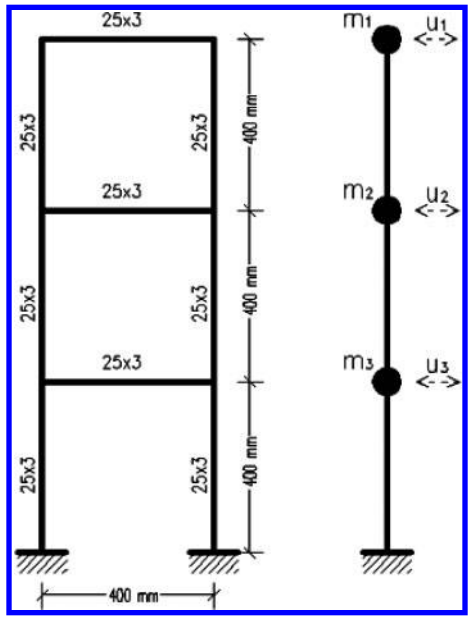


Figure 2b. Three dof structure and dynamic model.

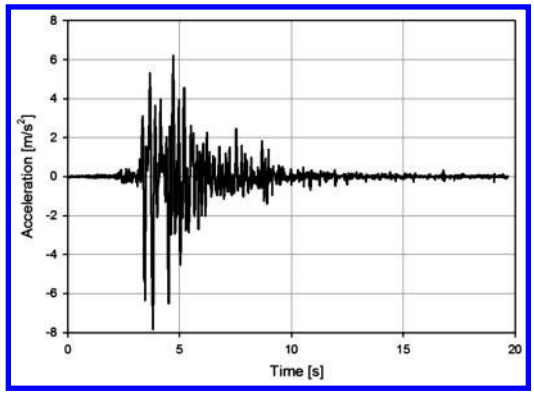


Figure 3. Kobe 1995 scaled down accelerogram.

Table 1. Modal parameters for n = 2 dof structure.

j	ω_j [s^{-1}]	T_j [s]	$\mathcal{M}_j$ $\left[\frac{Ns^2}{mm}\right]$	$\mathcal{C}_j$ $\left[\frac{Ns}{mm}\right]$	k_j $\left[\frac{N}{mm}\right]$	Γ_j
1	11.693	0.5379	$8.824 * 10^{-3}$	0.01	1.239	1.201
2	37.772	0.1663	0.036	0.139	53.184	−0.201

Table 2. Modal parameters for n = 3 dof structure.

j	ω_j [s^{-1}]	T_j [s]	$\mathcal{M}_j$ $\left[\frac{Ns^2}{mm}\right]$	$\mathcal{C}_j$ $\left[\frac{Ns}{mm}\right]$	k_j $\left[\frac{N}{mm}\right]$	Γ_j
1	8.539	0.73546	$8.261 * 10^{-3}$	$7.209 * 10^{-3}$	0.622	1.25
2	27.677	0.2269	0.015	0.043	12.131	−0.328
3	48.39	0.12978	0.07	0.492	164.041	0.079

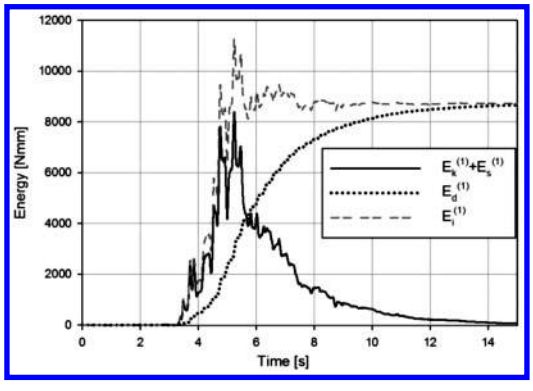


Figure 4a. Modal energy components $E^{(1)}$ n = 2 dof structure.

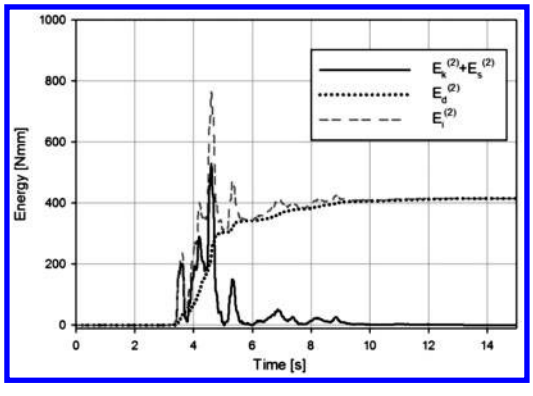


Figure 4b. Modal energy components $E^{(2)}$ n = 2 dof structure.

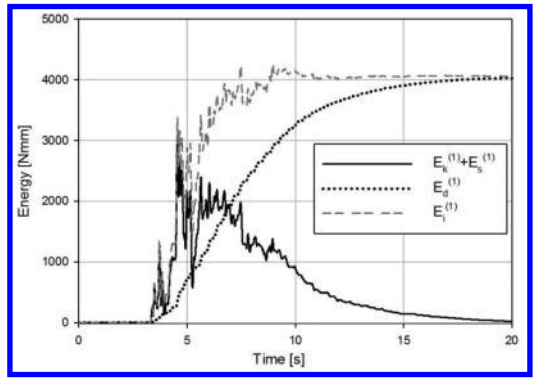


Figure 5a. Modal energy components $E^{(1)}$ n = 3 dof structure.

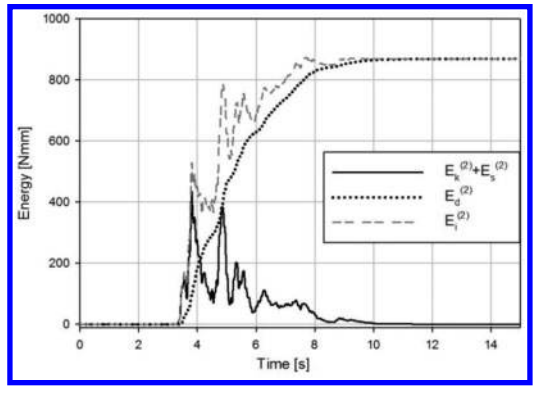


Figure 5b. Modal energy components $E^{(2)}$ n = 3 dof structure.

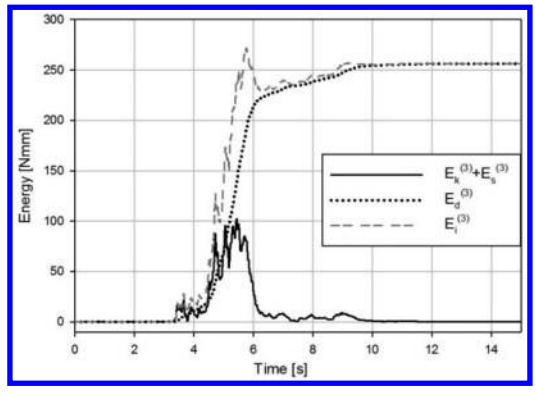


Figure 5c. Modal energy components $E^{(3)}$ n = 3 dof structure.

has to be "taken care" by the structural engineer by appropriate added damping equipment.

A clear difference (of about 1 to 10) between the 1st and 2nd modal values (of input energy and dissipated energy (by viscous damping) components may by ascertained (Figs 4–5) in in the case of both (n = 2 dof and n = 3 dof) structures. The ratio of modal value of energy component and the value of input energy may constitute a modal participation factor in terms of energy.

Indeed, in the case of n = 2 dof structure the assessment of modal energy participation would lead to a 95% participation of the first mode and of about 5% participation of the 2nd mode (Figs 4a, 4b and 6a). In the case of n = 3 dof structure, the energy share of the 1st mode would be about 83% (Fig.6b).

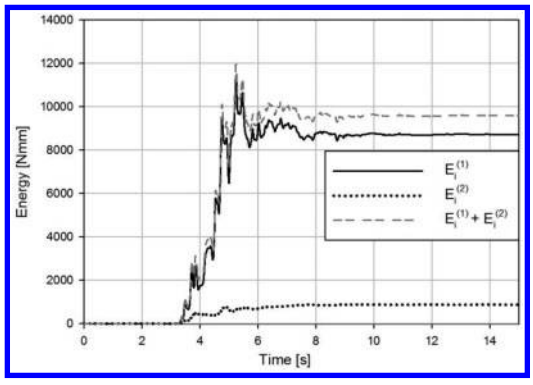


Figure 6a. Total energy $\sum E_i$ n = 2 dof structure.

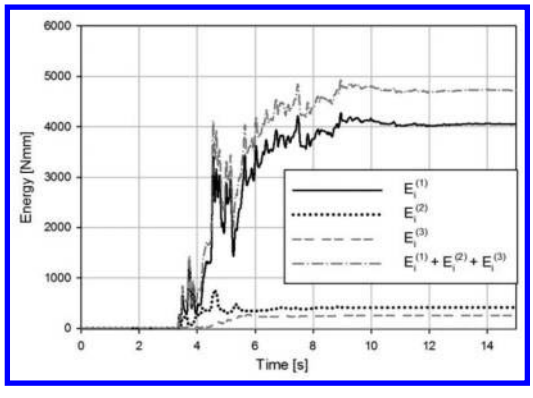


Figure 6b. Total energy $\sum E_i$ n = 3 dof structure.

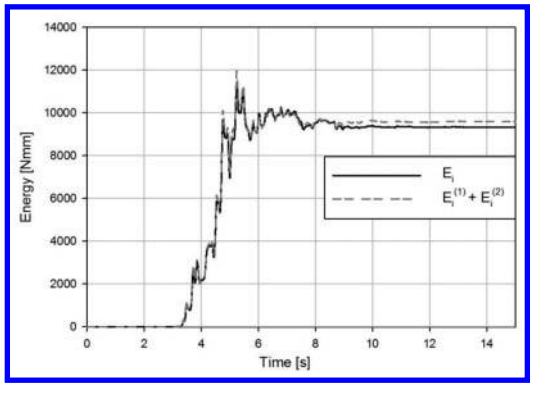


Figure 7a. Total input energy $\sum E_i$ n = 2 dof.

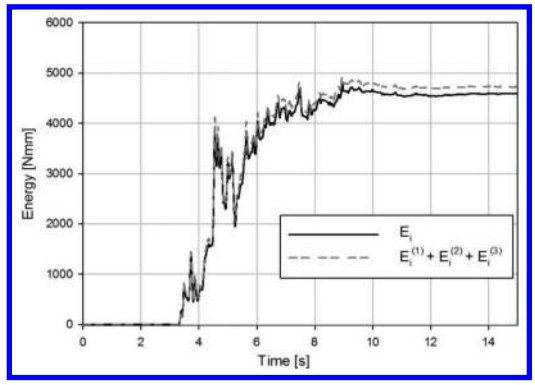


Figure 7b. Total input energy E_i n = 3 dof.

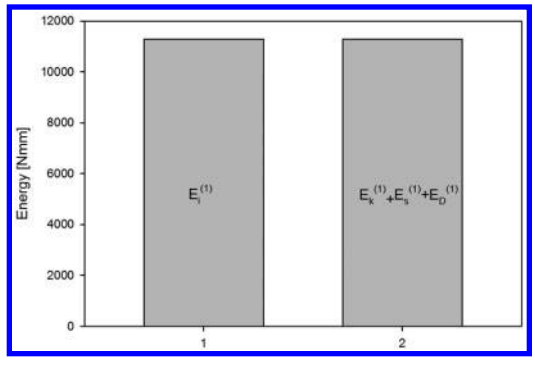


Figure 8a. Modal (j = 1) energy balance at t = 5.253 sec. n = 2 dof structure.

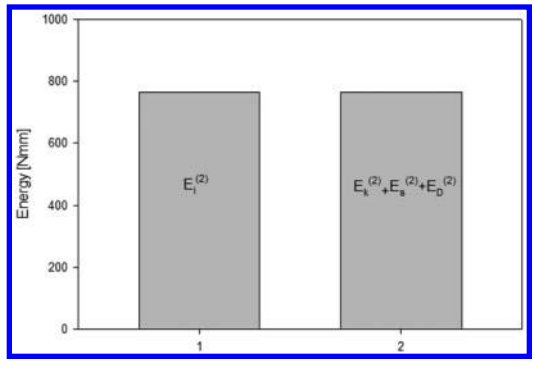


Figure 8b. Modal (j = 2) energy balance at t = 4.607 sec. n = 3 dof structure.

An energy balance may be ascertained at "modal level" associated to every instant t (Figs 8a, 8b) as well as the global (structural) level. Such an instant balance may express the required dissipation capacity (design provided) according to the (code) earthquake type (shock, long duration, etc.).

Computed modal coordinates x_j allow for the computation of (total) seismic response by applying the coordinate transformation (2a). Developing (2a) for the case of total (seismically induced) displacement u_i of mass m_i it takes the classical form of modal summing up:

$$u_i = \Sigma_j \Phi_{ij} \cdot x_j \tag{13}$$

Total seismic response in energy terms (Fig. 6) is, simply, the summing up of corresponding energy modal responses:

$$E = \Sigma_j E_j \tag{14}$$

Table 3. Energy modal participation – input energy.

	nmv	Classical modal participation factor Γ_j	Energy modal participation factor
n = 2 dof	j = 1	1.201	0.952
	j = 2	−0.201	0.048
n = 3 dof	j = 1	1.249	0.776
	j = 2	−0.328	0.17
	j = 3	0.079	0.054

Table 4. Modal participation – dissipated and stored energy.

	nmv	Dissipated energy modal participation E_d/E_i	Stored energy $(E_k + E_s)/E_i$
n = 2 dof	j = 1	0.4	0.6
	j = 2	0.39	0.61
n = 3 dof	j = 1	0.575	0.425
	j = 2	0.69	0.31
	j = 3	0.59	0.41

It is customarily to compare obtained numerical results to homologous values computed via a traditional approach. Consequently, a set of results computed in SAP2000 computer program versus the results computed by proposed technique are, also, provided (Fig. 7).

4 CONCLUSIONS

A modal approach to seismic response in energy terms and energy based elastic analysis of seismically acted upon multi-story steel structures is presented. Energy components are associated to the relative motion only. The values of left-hand-side of equation (10) is very close to the value of right-hand-side of this equation as it may be ascertained in Fig. 6. Also, an acceptable accuracy may be seen (Fig. 7) in the values of both sides of equation (14), exhibiting – numerically – the validity of proposed modal decomposition.

Closeness inside cca. 3% difference may be noted between the results of proposed modal approach and those computed via SAP2000 computer program (Fig. 8).

Modal contribution to the total seismic response may be more profoundly exhibited and assessed. It may be extended over post-elastic behavior and over seismically protected structures via added damping and added mass.

Regarding the proposed modal energy decomposition, one may note the easiness of expressing modal participation in terms of energy. It is customarily [11] to express modal participation in terms of displacements (mainly lateral), base shear, stress resultants. Similar participation may be straightforward express in energy quantities. It may be expressed in total input energy and, also, in its (kinematic, strain, dissipated) components. The modal participation to (total) input energy is presented in Table 3. Such modal participation assessment may open the possibility of expressing the effectiveness of added damping to seismic mitigation.

Modal participation of dissipated energy may be the most useful tool in the hands of structural engineer. For the analyzed cases, such results are presented in Table 4 at t = 5.5 sec.

An energy expressed modal participation avoids the negative values of modal participation factors. Also, energy approach to modal participation allows for a time variation of modal participation that, in its turn, expresses instant state in modal participation at important instants of seismic action.

REFERENCES

[1] Housner, G.W., 1956. Limit design of structures to resist earthquake. Proceedings of the 1st WCEE, EERI, Berkeley, California.

[2] Berg, G. V. and Thomaides, S. S., 1960. Energy consumption by structures in strong-motion earthquakes. Proceedings of the 2nd World Conference. on Earthquake Engineering, Tokyo, Japan, Vol. 2, pp. 681–696.

[3] Tembulkar, J. M. and Nau, J. M., 1987. Inelastic modeling and seismic energy dissipation. Journal of Structual Engineering, ASCE, Vol. 113, pp. 1373–1377.

[4] Fajfar, P., Vidic T. and Fischinger M., 1989. Seismic demand in medium and long period structures. Earthquake Engineering Structural Dynamics, 18: 1133–1144.

[5] Uang, C.M. and Bertero V.V., 1990. Evaluation of seismic energy in structures. Earthquake Engineering Structural Dynamics, 19: 77–90.

[6] Bertero V. V. and Teran – Gilmore A., 1993.Use of energy concepts in earthquake – resistant analysis and design: Issues and future directions. Memorias del VIII Seminario Latinoamericano de Ingenieria Sismoresistente y Primeras Jornadas de Ingenieria Estructural, 5–8 Julio de 1993, Merida, Venezuela.

[7] Surahman A., Merati W., 1992. Input energy based seismic design code. Earthquake Engineering, Tenth World Conference, Balkena, Rotterdam.

[8] Akbas B., Shen J. and Hao H., 2001. Energy approach in peformance-based seismic design of steel moment resisting frames for basic safety objective. The Structural Design of Tall Buildings Vol. 10 Issue 3 pages 193–217, September 2001.

[9] Takewaki, I., 2004. Bound of earthquake input energy, Journal of. Structural Engineering, ASCE, Vol. 130, pp. 1289–1297.

[10] Lieping Ye, Guangyu Cheng and Zhe Qu, 2009, Study on energy-based seismic design method and the application for steel braced frame structures, Sixth International Conference on Urban Earthquake Engineering March 3–4 2009 Tokyo Institute of Technology, Tokyo, Japan, pp. 417–428

[11] Chopra A. , K., 1995. Dynamics of Structures: Theory and Applications to Earthquake Engineering, Prentice Hall.

Research and Applications in Structural Engineering, Mechanics and Computation – Zingoni (Ed.)
© 2013 Taylor & Francis Group, London, ISBN 978-1-138-00061-2

Effect of basement rigidity on seismic response of RC buildings

A. Koçak, M. Borekci & E.C. Ekinci
Yildiz Technical University, Istanbul, Turkey

A. Kalyoncuoglu
Istanbul Gelişim University, Istanbul, Turkey

ABSTRACT: A building which has rigid basement and has dominant first mode, is separated into two parts as rigid basement and upper stories in determining of seismic loads. It is clear that separating the building which has rigid basement into two parts is reasonable. However, separating the building into two parts does not hold true if the building has semi-rigid basement. In this study, we used RC frame buildings which have different rigidity level in basement to investigate the effect of the basement rigidity on seismic response of RC buildings. The level of the ratio of the column width and total frame span length which makes the floor as rigid was investigated. Also we investigated the difference between equivalent seismic load method and mode superposition method which are used to determine seismic base shear for sample buildings while shear walls ratio increases.

1 INTRODUCTION

Many buildings have basement and most of them are surrounded by continuous perimeter walls. The basement stories with RC peripheral walls and rigid diaphragms is called as *rigid basement.* In buildings with RC peripheral walls in their basement and basement floor behaving as rigid diaphragm in their horizontal direction, seismic loads are determined based on the mass of upper stories from the top of basement floor according to Turkish Seismic Code 2007 (TSC 2007) and Eurocode 8 (EC 8). There are two common analysis techniques for seismic design such as linear and nonlinear analysis. Both techniques have two procedure as static and dynamic. In this study, linear static analysis was performed for the seismic analysis of buildings. If participation of first mode is dominant on response than higher modes, most of codes allow us to assume the building as single degree of freedom (SDOF) system. If participation of first mode is higher than 70% it is assumed that first mode is dominant according to TEC 2007. First mode of building can be considered in determining the seismic load and it is called as *equivalent seismic load method.* Taking into account the higher modes of the building additional to first mode in seismic analysis is named as *mode superposition method.* Both methods are linear static seismic analysis. A building which has rigid basement and has dominant first mode, is separated into two parts as rigid basement and upper stories in determining of seismic loads. It is clear that separating the building which has rigid basement into two parts is reasonable. However, does that hold true for the buildings which has *semi-rigid* basement?

In this study, rigidity of the first floor of frames was increased gradual. Effect of shear wall ratio on response of vibration modes and the ratio of base shear of equivalent seismic load and base shear of mode superposition method were investigated. Also, the limit of shear walls are ratio that makes the basement rigid was investigated. Sample frames were modeled by using SAP2000 as 2D frame.

2 SAMPLE FRAMES

5-storey, 3 bays 2D RC frame building have been considered within the scope of this study. 11 sample buildings were generated based on the ratio of column width and total frame span length. Sample buildings were named based on rigidity ratio. Columns width were increased gradually to achieve the rigidity ratio and rigidity ratio was increased with the interval of 10% from 0% to 100%. First frame was named as 0% and dimension of outer columns is 40 × 30 cm × cm, dimension of inner columns is 60 × 30 cm × cm. First floor represents basement in the buildings. Column and beam dimensions are same for all sample buildings except first floor. Schematic view of frames were given in Figure 1. In Figure 1b horizontal dimensions of columns of first floor were increased to determine the 70% rigidity ratio. In Figure 1c, the frame has continuous shear wall.

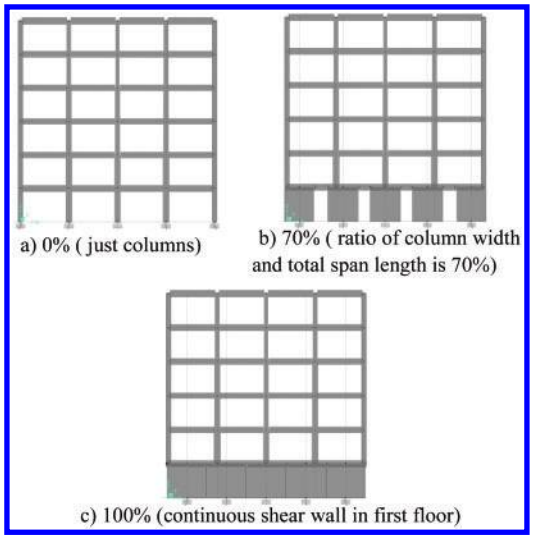


Figure 1. 2D frame used in the study.

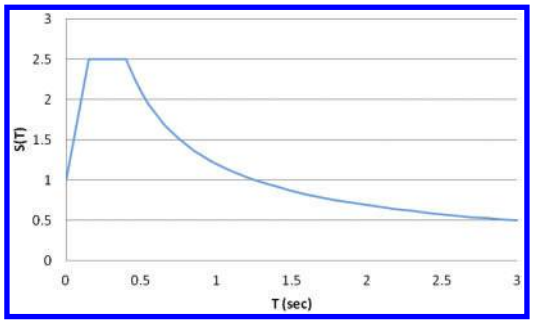


Figure 2. Standard acceleration spectrum (TSC 2007).

3 LINEAR STATIC SEISMIC ANALYSIS METHODS

3.1 *Equivalent seismic load method*

If the response of a structure is controlled by fundamental mode, the structure can be assumed as SDOF and seismic base shear is determined based on fundamental mode T_1.

$$V_t = \frac{W \times S(T) \times A_0 \times I}{R} \quad (1)$$

W is weight of building, A_0 effective ground acceleration coefficient, I is building importance factor, S(T) spectrum coefficient and R strength reduction factor. An example of standard acceleration spectrum was given in Figure 2.

Additional equivalent seismic load (ΔF_N), acting at the top storey of the building is determined by Equation 2.

$$\Delta F_N = 0.0075\ N\ V_t \quad (2)$$

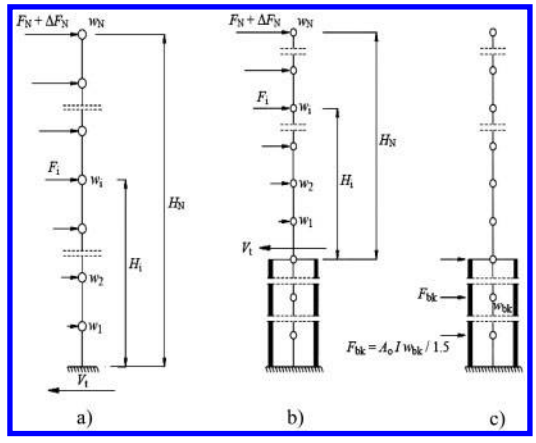


Figure 3. Seismic load distribution to stories of the building (TSC 2007).

Total equivalent seismic load (V_t) is distributed to stories of the building in accordance with Equation 3. This distribution is applied excluding the ΔF_N.

$$F_i = (V_t - \Delta F_N)\frac{w_i h_i}{\sum_{j=1}^{N} w_j h_j} \quad (3)$$

Total equivalent seismic load distribution was given in Figure 3a. w_i is weight of i'th storey of building, F_i is design seismic load acting at i'th storey of building, F_{bk} is equivalent seismic load acting at rigid basement and H_i is the height of i'th storey of building measured from the top foundation level. In buildings with rigid peripheral basement walls, height of i'th storey is measured from the top of ground floor level.

In buildings with RC peripheral walls at their basements being very rigid relative to upper stories and basement floors behaving as rigid diaphragms in horizontal planes, equivalent seismic loads acting on the basement stories and on the upper stories are calculated independently. Calculation and distribution of total equivalent seismic load for upper stories and rigid basement stories were given in Figure 3b and Figure 3c, respectively.

In calculating equivalent seismic loads acting on rigid basement stories, seismic weights of basements only are taken into account and Spectrum Coefficient is taken as S(T) = 1. In determining equivalent seismic loads acting on basement storey, R is equal to 1.5.

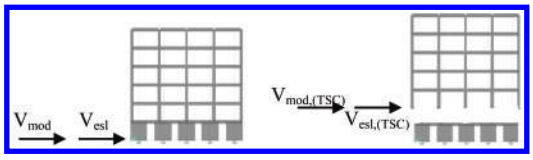
3.2 *Mode superposition method*

In this method, base shear is determined by the statistical combination of maximum contributions obtained from each of the sufficient number of vibration modes considered. The criterion of sufficient number of vibration mode to be considered in determining the seismic load is sum of effective participating masses calculated for each mode shall in no case be less than 90% of the total building mass (Chopra 2001, TSC 2007).

Table 1. Periods of the sample structures.

	Sample Buildings (Rigidity Ratio)										
Mode No	0%	10%	20%	30%	40%	50%	60%	70%	80%	90%	100%
1	1.419	1.319	1.253	1.243	1.238	1.234	1.232	1.231	1.230	1.230	1.230
2	0.521	0.481	0.457	0.454	0.452	0.451	0.450	0.450	0.450	0.449	0.449
3	0.307	0.284	0.271	0.269	0.268	0.268	0.267	0.267	0.267	0.267	0.267
4	0.232	0.219	0.209	0.208	0.207	0.206	0.206	0.206	0.205	0.205	0.205
5	0.176	0.163	0.153	0.151	0.150	0.149	0.149	0.149	0.148	0.148	0.148
6	0.128	0.100	0.097	0.096	0.095	0.094	0.094	0.093	0.093	0.093	0.092
7	0.105	0.099	0.094	0.093	0.092	0.092	0.092	0.091	0.091	0.091	0.091
8	0.102	0.098	0.091	0.090	0.089	0.088	0.088	0.088	0.088	0.088	0.088
9	0.098	0.094	0.088	0.087	0.087	0.086	0.086	0.086	0.086	0.086	0.086
10	0.095	0.090	0.086	0.085	0.085	0.085	0.084	0.085	0.085	0.085	0.084
11	0.093	0.089	0.067	0.053	0.044	0.037	0.035	0.034	0.034	0.034	0.034
12	0.039	0.037	0.036	0.035	0.035	0.035	0.034	0.034	0.034	0.034	0.034

Table 2. Base shears and base shear ratios based on equivalent seismic load and mode superposition method



Sample Buildings	V_{mod} (kN)	V_{esl} (kN)	V_{mod}/V_{esl}	$V_{mod,(TSC)}$ (kN)	$V_{esl,(TSC)}$ (kN)
0%	243.34	249.97	0.97	224.50	230.77
10%	242.62	267.36	0.91	224.50	230.77
20%	241.10	279.72	0.86	224.50	230.77
30%	239.95	283.40	0.85	224.50	230.77
40%	238.65	286.45	0.83	224.50	230.77
50%	235.28	289.12	0.81	224.50	230.77
60%	225.75	291.50	0.77	224.50	230.77
70%	225.19	293.76	0.77	224.50	230.77
80%	224.96	295.98	0.76	224.50	230.77
90%	224.81	298.11	0.75	224.50	230.77
100%	224.69	300.27	0.75	224.50	230.77

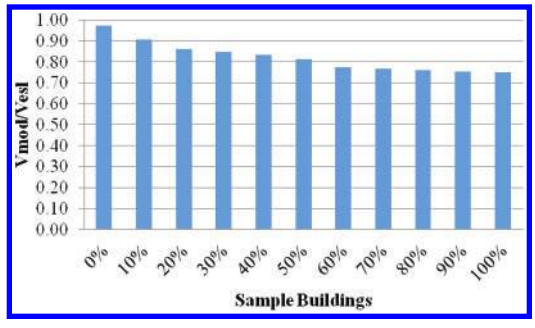


Figure 4. Base shear coefficients of sample frames.

4 RESULTS

Periods of sample buildings were given in Table 1. Seismic base shears of sample buildings based on equivalent seismic load method and mode superposition method and their ratio were given in Table 2. Effect of basement rigidity on base shear ratios (the ratio of the base shear which was determined according to mode superposition method and the base shear which was determined according to equivalent seismic loading method) was given in Figure 4.

In Table 2, V_{mod} is the base shear which was determined according to mode superposition method, V_{els} is the base shear which was determined according to equivalent seismic loading method and $V_{esl,(TSC)}$ is the base shear which was determined according to equivalent seismic loading method with separating rigid first floor and upper stories. According to Table 1, it can be seen that periods nearly constant after 50% rigidity. Thus, seismic base shear is determined separating rigid basement and upper stories (TSC 2007; EC 8) for the buildings which have a rigidity ratio higher than 50%.

It can be seen from Table 2, the ratio between V_{mod} and V_{esl} changes according to rigidity ratio. V_{mod}/V_{esl} is 0.97 for 0% value of rigidity ratio and 0.83 for 40% value of rigidity ratio while it is 0.75 for 100% value of rigidity ratio. According to the results, ratio of V_{mod}/V_{esl} decreases while rigidity of basement increases. If the building does not have shear walls in its basement, there is no important difference between the methods of determining of base shear. However, it is important that which method is used for determining base shear while shear walls ratio increases. If the building has rigid basement V_{mod} and $V_{mod,(TSC)}$ are nearly same.

Modal amplitudes of three modes were given in Figure 5. Changing of top storey amplitude was given in Figure 6. It is clear from the figures of amplitude, amplitudes are nearly same for all the sample buildings after 30% rigidity ratio. However, the amplitude is constant after 50% rigidity ratio.

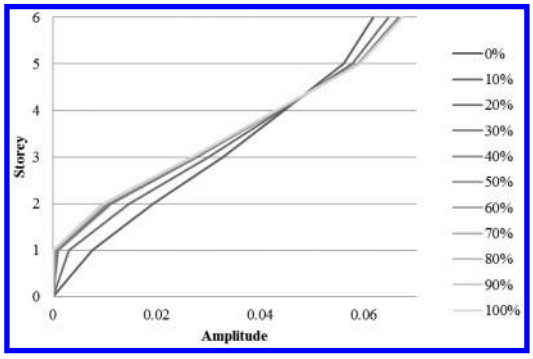


Figure 5. First mode amplitude of sample buildings.

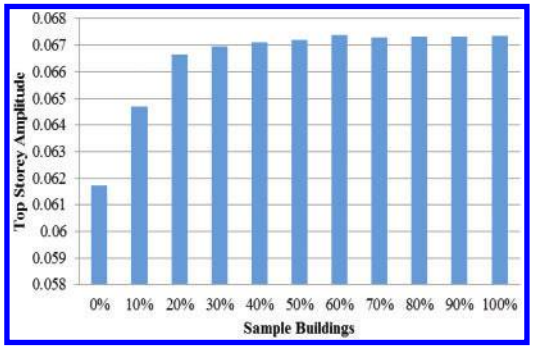


Figure 6. Top storey amplitude of sample buildings.

5 CONCLUSIONS

Following conclusions can be drawn from the results of the current study:

- Periods of the sample buildings are nearly constant after level of the 50% basement rigidity ratio. That means, modal behavior are nearly same after 50% ratio level. Basement behaviors as semi-rigid less than that rigidity ratio.
- According to the results, difference between base shear determining methods increases. In fact, codes allow us to neglect basement if it is rigid. However, there is no information about neglecting semi-rigid basement. If a building has semi-rigid basement, nearly 20% difference between base shears of equivalent seismic load and mode superposition methods.
- If a building does not have rigid basement, the base shears of mode superposition method and equivalent seismic loading method are nearly same. If the building have rigid basement equivalent seismic loads acting on the basement stories and on the upper stories are calculated independently. Thus, there will be no difference between the methods of determining base shear. However, it is important that which method is used to determine the base shear if the building has semi-rigid basement.
- Further studies are needed to determine the rigidity ratio level which provides rigid basement behavior.

REFERENCES

Chopra, A. K., 2001. *Dynamics of Structures*, Prentice-Hall, New Jersey.

Eurocode 8: Design of Structures for Earthquake Resistance, 2004. European Committee for Standardization

Turkish Seismic Code 2007. Ministry of Public works and Settlement, Turkey

Research and Applications in Structural Engineering, Mechanics and Computation – Zingoni (Ed.)
© 2013 Taylor & Francis Group, London, ISBN 978-1-138-00061-2

Bidirectional pushover analysis of irregular structures

G.P. Cimellaro
Department of Structural, Building and Geotechnical Engineering (DISEG), Politecnico di Torino, Turin, Italy

D. Lopez-García
Departamento de Ingeniería Estructural y Geotécnica, Pontificia Universidad Catolica de Chile

T. Giovine
Department of Structural, Building and Geotechnical Engineering (DISEG), Politecnico di Torino, Italy

ABSTRACT: The Nonlinear Static Pushover analysis is extensively used for the seismic assessment of structures for every type of building. The paper proposes the Bidirectional Pushover Analysis (BPA) to overcome the torsional problems in plan and elevation of asymmetric buildings, when bidirectional ground motion is considered. Different reinforced concrete frame structures are selected and modeled in 3D. The N2 method is then applied bidirectional to estimate the actual non linear response. Results in term of floor interstory drifts and floor rotations from the bidirectional pushover analysis, are compared with the nonlinear dynamic time history analysis. A suite of twenty European bidirectional seismic ground motions were selected. It was found that BPA matches with the bidirectional non linear time history analysis when the ratio Y/X is around 0.6, which is different from the ratio of 0.3 provided by the European seismic code when bidirectional linear analysis is performed.

1 INTRODUCTION

Among the nonlinear static methods (Pushover) implemented in codes, one relatively simple that incorporates performance-based engineering concepts is the *N2 method* formulated by Fajfar and Gaspersic (1996) as a variant of the *capacity spectrum method* (CSM) (Fajfar, 1999).

The *N2 method* combines the pushover analysis of a multi-degree-of-freedom (MDOF) system model with the response spectrum analysis of an equivalent single-degree-of-freedom (SDOF) system. The applicability of the method is restricted to 2D planar analysis, and it is based on three main assumptions: (i) the structure vibrates predominantly in the first mode; (ii) the deformation shape is time independent; (iii) the inelastic response spectra used in the analysis is obtained by applying a reduction factor R_μ to the elastic response spectra. The limitation of the *N2 method* is that it is not suitable in the case of high-rise buildings and/or torsionally flexible plan-asymmetric buildings (Kilar and Fajfar, 1997). In the first case for example, higher mode effects are important, and some demand quantities determined by the *N2 method* may be underestimated (De Stefano and Pintucchi, 2008, 2010).

Nowadays the research efforts are directed toward extending the applicability of pushover methods considering: (i) the contribution of highest modes of vibration (Gupta and Kunnath, 2000; Chopra et al., 2004a–b, Kalcan and Kunnath, 2006; Kim and Kurama, 2008), (ii) the effect of stiffness degradation (Kim and Kurama, 2008)), (iii) the changes in dynamic properties after the formation of first plastic mechanism as a function of the level of inelasticity and the torsional effects of irregular buildings (Fajfar et al., 2005) and (iv) and the effect of bi-directional seismic ground motion (Lin and Tsai, 2008). Chopra and Goel (2002, 2004a–b) proposed an appropriate modal combination rule assuming several displacement shapes, representing the predominant vibrating modes determined by one pushover analysis.

The main goal of this paper is to verify the accuracy of the extended N2 pushover method on 3D vertically irregular structural models under bidirectional seismic ground motions. A bidirectional use of the N2 method for asymmetric structures that allows the assessment of the maximum floors displacements and rotations on both X and Y directions at the same time, is proposed. The procedure consists on imposing different ratios of lateral load patterns applied simultaneously on orthogonal directions to an irregular structure and evaluate the maximum displacements through the N2 method (Fajfar, 1999). Finally the results of a parametric study are presented in term of displacements and storey drifts, obtained by the bidirectional pushover analysis and compared with the results of a more accurate approach (NRHA).

2 BIDIRECTIONAL PUSHOVER ANALYSIS

Standard practice consists in determining separately the two peak responses of the structure due to each ground motion component (NS and EW) and combine these peak responses according to one of the multi-component combination rules: the simplified square root of sum of squares (SRSS) rule (Lopez, 2001), the CQC3 rule (Menun, 1998) etc.

The SRSS rule have been adopted to combine the simultaneous effect of bidirectional ground motions used during the analysis. The maximal floor displacements and maximal floor rotations of *bidirectional pushover analysis* (BPA) along the X and Y directions have been compared with the median results of the *non linear response history analysis* (NRHA). The procedure can be summarized in the following steps:

Step 1: The Seismic demand is obtained by using the inelastic acceleration displacement response spectra (ADRS) format (Fajfar, 1999). The acceleration spectrum can be determined by applying a reduction factor R_μ such that $S_a = S_{ae}/R_\mu$; where R_μ is the reduction factor which is defined as follows:

$$R_\mu = \begin{cases} (\mu - 1)\dfrac{T}{T_C} + 1 & T < T_c \\ R_\mu = \mu & T \geq T_C \end{cases} \quad (1)$$

Step 2: the first vibration mode is evaluated by eigenvalues analysis and normalized to the roof top displacement.

Step 3: The modal participation factor Γ is evaluated as follow

$$\Gamma = \frac{\Phi^T M 1}{\Phi^T M \Phi} = \frac{\sum m_i \Phi_i}{\sum m_i \Phi_i^2} = \frac{m^*}{\sum m_i \Phi^2_i} \quad (2)$$

where is $m_i^* = \Sigma m_i \cdot \Phi_i$. is the modal mass.

Step 4: first mode shape lateral load profile is applied both in X and Y direction in order to perform pushover analysis. Lateral load is maintained constant in the X direction, while it is amplified in the Y direction as shown in Table 1 for example and with the direction represented in Figure 1. It assumed that the ratio g of the lateral load pattern for bidirectional simultaneous pushover analysis is given by:

$$\gamma = Y/X \quad (3)$$

where $X = m_i \Phi_i$ and $Y = \gamma m_i \Phi_i$.

Table 1. Bidirectional pushover lateral load ratios.

20%: R = X + 0.2Y	30%: R = X + 0.3Y	40%: R = X + 0.4Y
50%: R = X + 0.5Y	60%: R = X + 0.6Y	70%: R = X + 0.7Y
80%: R = X + 0.8Y	90%: R = X + 0.9Y	100%: R = X + Y

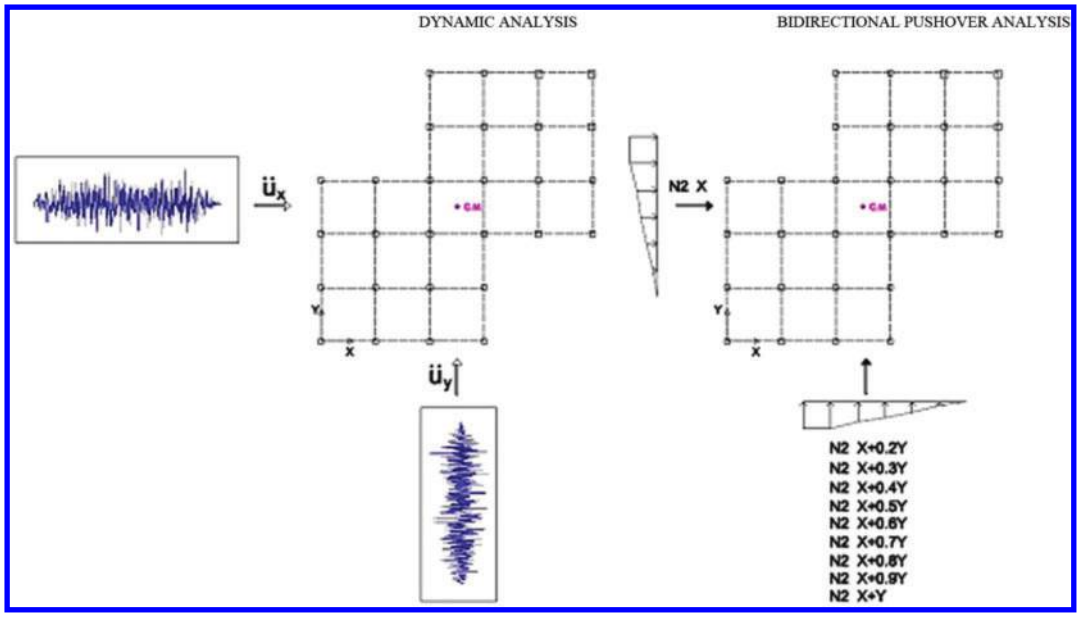


Figure 1. Bidirectional excitation adopted for dynamic non linear analysis and bidirectional pushover analysis.

Step 5: Transform the MDOF system capacity curve into an equivalent SDOF system using the following formulas

$$D^* = D_t/\Gamma ; F^* = V/\Gamma \quad (4)$$

where D_t is the target displacement of the MDOF system in the x direction, usually at the top of the building.

- Evaluate the displacement seismic demand of the SDOF system using the graphical procedure proposed in the N2 method;
- Transform SDOF displacement demand to maximum top displacement D_t of the MDOF system (target displacement);
- Determination of the associated displacement in the transversal direction Y.
- The torsional effects are evaluated numerically as ratio between corners and mass centre displacements (u_c/u_{cm}) on each floor (Fajfar *et al*., 2005). In other words, the floor rotations are evaluated numerically to calculate the torsional correction factors.

3 DESCRIPTION OF THE SIX STOREY BUILDINGS USED IN THE ANALYSIS

The proposed BPA is applied to an ensemble of six irregular six-story RC frames structures (Figure 2) that have been designed according to the requirements of EC8 (CEN, 1994). All the buildings are plan asymmetric in both X and Y directions, and irregular in elevation. The frames are equally spaced at a distance of 4 m with a storey high of 3.5 m. Each model is designed using a tapered square shape columns system. The reinforced concrete floors slabs are 20 cm thick.

3.1 *Numerical modeling*

The buildings are designed and selected using a parametric approach considering two parameters γ and α which quantify the torsional effects. The parameter α is defined as the ratio between the lower rotational frequency and the lower translational frequency. The parameter γ is defined as ratio between the moment of inertia evaluated around the global center of stiffness ($M_l \cdot d_l^2$) and the polar moment of inertia evaluated around the center of mass I_q. Analytically they are defined as follow:

$$\alpha = \min_{n \le N}\left(\frac{\omega_{\theta,n}}{\min\left(\omega_{x,n};\omega_{y,n}\right)}\right); \quad \gamma = \frac{M_l \cdot d_l^2}{I_{\theta,l}}; \text{ with: } l = n \quad (5)$$

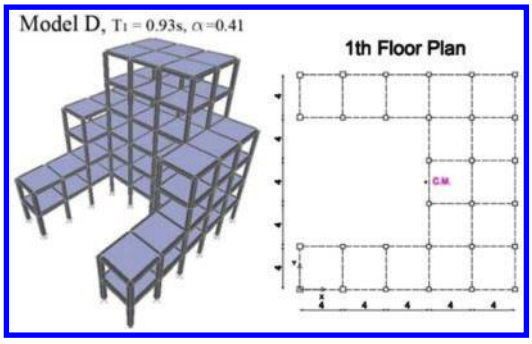


Figure 2. One of the six 3D reinforced concrete structural models adopted in the analysis.

The 3D building structures have been modelled in SAP2000 (CSI, 2011) using the rigid diaphragm constrains in the horizontal plane. The column-beam end connections were modelled with rigid offsets. The number of degree of freedom is three times the number of stories ($N = 6$). Five percent damping is used in all the analyses. The P-Δ effect is not taken in account in the analysis. The first mode is translational in the X-direction, the second is translational in the Y-direction, whereas the third mode is mainly torsional in all the structural models considered. The inelastic member model used is the beam element with concentrated plasticity at both end parts of each element. A bilinear is usually used. A simplified elasto-plastic (Isotropic) model for RC material has been adopted.

3.2 *Ground motion selection*

Two ensembles of 20 earthquake bi-directional records are selected from the Italian earthquake ITACA database (Working Group ITACA, 2010) website. All the selected records have local Magnitude M_L between 4.0 and 7.0, and source distance R between 2 and 50 km, with peak ground acceleration (pga) bigger than 0.15 g at least in one horizontal component. Each of the recorded accelerograms is amplitude-scaled in such a way that the median spectrum of both *unidirectional* and *bidirectional* set match to the target elastic spectrum, which is the EC8 spectrum for soil type C shown in Figure 3.

The scaling procedure used for the *bidirectional ensemble* is the same of the one used for the *unidirectional ensemble*, but in this case both North-South and East-West components have been considered for the scaling procedure. The response spectrum at 5% damping calculated from the North-South and East-West components of each earthquake are combined with the *SRSS* rule.

4 COMPARATIVE EVALUATION OF THE NON LINEAR STATIC ANALYSIS

Lateral forces with a modal load pattern are applied to all models first in one direction and then in both directions. In the first case, the classical pushover analysis is performed, while in the second case bidirectional pushover analysis (BPA) is performed.

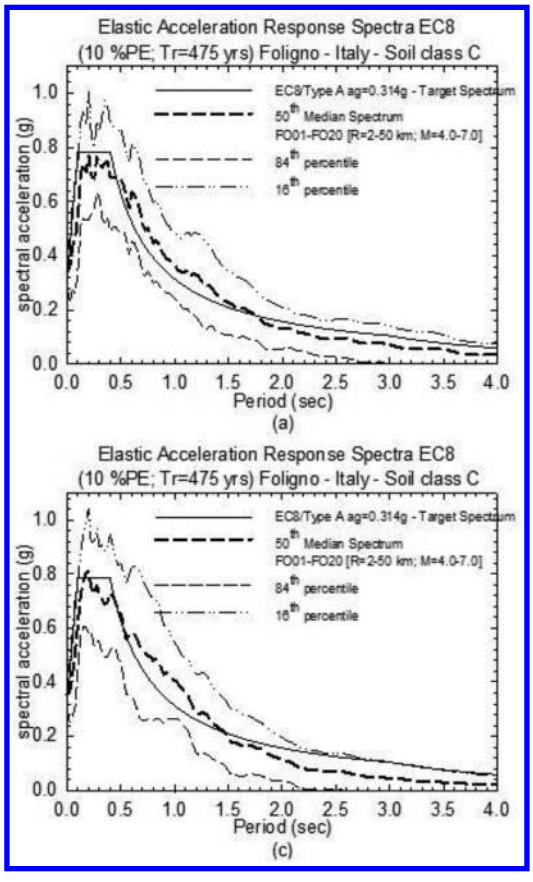


Figure 3. (a) Acceleration response spectrum of the 20 earthquake records used in the unidirectional analysis. (c) Acceleration and displacement response spectrum of the 20 earthquake records used in the bidirectional analysis.

4.1 *Comparison of pushover analysis vs. non linear response history analysis*

Pushover analyses are performed in the two horizontal directions with lateral loads based on the fundamental mode shapes in the relevant direction, i.e. x-components of the first mode shape is used in the X-direction, and Y-component of the second mode shape is used in the Y-direction.

Pushover analysis is performed in both North-South and East-West direction separately using the modified N2 method (Fajfar, 2005, Kreslin and Fajfar, 2011). The displacements of the center of mass of each floor of the buildings analyzed are evaluated using N2 pushover method and the results are compared with the median values of the displacements obtained by the time history analysis using the 20 earthquake records selected in previous section. The time history median results are identified in each plot with NRHA.

Numerical results at a given location are amplified by a correction factor calculated for each location. All models (six) have been analyzed. The accuracy of the proposed procedure is illustrated for example in

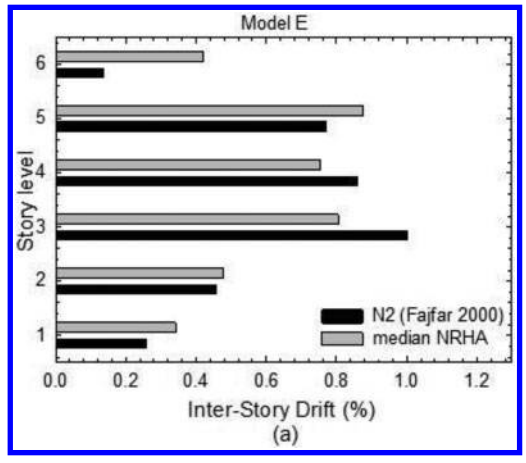


Figure 4. Pushover curves in the X direction of the analyzed models.

Figure 4 by comparing the maximum building interstory drifts of the traditional pushover analysis (N2) with the interstory drifts of the nonlinear response history analysis (NRHA). The floor relative rotation is evaluated comparing the ratio between the displacement measured at predefined corner points of the building and the displacement measured at the center of mass of the respective floor. The estimation of the floor relative rotations with the traditional N2 method is compared with the median time history response (NRHA) obtained from the 20 selected scaled records corresponding to the *unidirectional set*. In particular for the *E model* ($\alpha = 0.03$), which is symmetric with respect to a direction oriented at 45° with respect to the orthogonal axis X and Y, the floor displacement errors with respect to the time history analysis (NRHA) are respectively 11% at 6th floor, 3% at 5th floor, 2% at 4th floor 12% at 3rd floor and finally 16% and 9% at 2nd and 1st floor. The comparison shows a good approximation of the floor rotations in the upper stories, while differences are evident in the lower stories (Cimellaro et al., 2013).

4.2 *Assessment of the new bidirectional pushover analysis procedure vs. time history analysis*

In order to obtain accurate estimation of X and Y displacements when considering bi-directional simultaneous pushover analysis the ratio $\gamma = Y/X$ in the pushover lateral loads is considered.

In Figure 6 is shown the comparison of the top story (6th level) displacement for one of the six analyzed models. The top story total displacement and rotation obtained by the BPA is compared with the results of the nonlinear response history analysis (NRHA). In particular, the selection of the optimal lateral load distribution ratio γ that optimizes the X and Y displacement is obtained by minimizing the index $F(\gamma)$ which represents the sum of the differences of translational and rotational displacements at each floor between

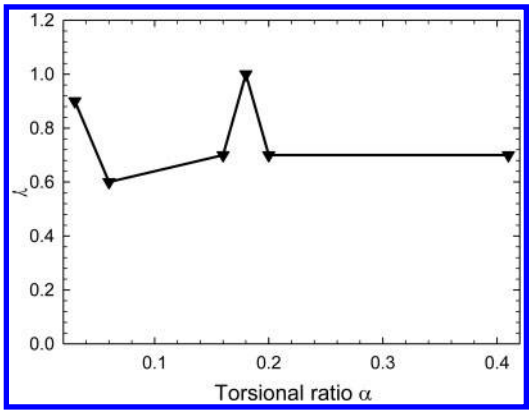


Figure 5. Optimal bidirectional ratio g = Y/X for different structural models.

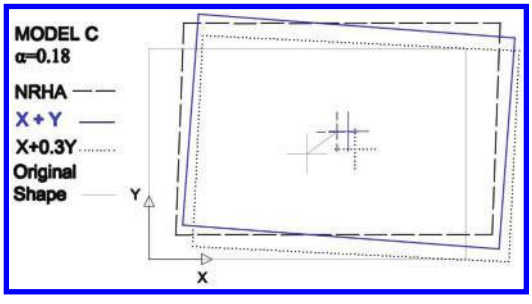


Figure 6. Comparison of time history analysis with different ratio of bidirectional pushover Analysis at 6th floor.

bidirectional pushover analysis (BPA) and nonlinear response history analysis (NRHA).

$$F(\gamma)=\sum_{1}^{6}\left[\left(X_{i\,TH}-X_{i\,PA}\right)^2+\left(Y_{i\,TH}-Y_{i\,PA}\right)^2+\left(\vartheta_{i\,TH}-\theta_{PA}\right)^2\right] \quad (6)$$

where X, Y = translational story displacement measured at the center of mass; $\theta_{R,i} = X_i/X_{cm,i}$ rotational story displacement where X_i is the maximum corner floor displacement in the X direction normalized with respect to $X_{cm,i}$ which is the floor center of mass displacement.

The optimal γ ratio obtained by minimizing the index F(γ) given in Equation (6) is plotted in Figure 5 for the different structural models considered in the analysis, while the optimal top story displacements obtained with the BPA are shown in Figure 6 and compared with the displacements obtained with the BPA using a γ ratio of 0.3 ($X + 0.3Y$) as suggested for linear dynamic analysis in the European seismic standard (CEN, 1994). Regardless the torsional ratio α, the γ ratio ranges between 0.6 and 1. This ratio is therefore different from the value provided in the European seismic provision which uses a value to combine earthquake records of 0.3. The relative rotation $\theta_{R,i}$ can be plotted for different torsional ratio α related to six different structural models considered. The floor relative rotation $\theta_{R,i}$ are evaluated for all bidirectional pushover lateral load ratios γ and compared with median relative rotations obtained at each floor by the bidirectional time history analysis for each model. Bidirectional pushover analysis ($X + 0.6Y$) shows better results with respect to the classical pushover analysis (N2) especially at the lower stories, while similar results in agreement with time history analysis and N2 method can be obtained at the upper stories.

5 CONCLUDING REMARKS

Nonlinear static procedures are less time-consuming than nonlinear response history analysis, therefore nowadays are extensively used by practicing engineers for virtually every type of building. However, since the majority of real structures are irregular, pushover methods need to be improved to take into account the torsional effects of buildings and the directivity of the seismic ground motion, before being implemented in design codes. In this paper an extension of the N2 method to overcome the torsional problem in plan and elevation of asymmetric buildings is proposed. The proposed bidirectional pushover analysis (BPA) method, applicable when bidirectional ground motion is considered, led to better results than the traditional N2 method when compared with nonlinear response history analysis (NRHA). In particular, the BPA method estimates accurately the response of the CM when the torsional effects are not relevant (Model E with $\alpha = 0.03$), while the response is overestimated when the torsional effects are relevant (Model F with $\alpha = 0.16$). Based on the numerical results provided from the analysis, it was found that the ratio $\gamma = Y/X$ equal to 0.3, which is provided by the European seismic code when bidirectional ground motion wants to be considered in the analysis, is not adequate when nonlinear static analysis is performed. Instead, the ratio $\gamma = Y/X$ equal to 0.6 for the bidirectional pushover analysis (BPA) is proposed. Using this ratio, floor mass center displacements have been estimated relatively accurately, while fair results have been obtained in the estimation of floor relative rotations. The reason of this discrepancy is probably due to the fact that the factor is obtained from the statistical analysis of linear dynamic simulations.

ACKNOWLEDGEMENTS

The research leading to these results has also received funding from the European Community's Seventh Framework Programme – Marie Curie International Reintegration Actions – FP7/2007-2013 under the Grant Agreement n° PIRG06-GA-2009-256316 of the project ICRED – Integrated European Disaster Community Resilience.

REFERENCES

ATC-40. (1996). "Seismic Evaluation and Retrofit of Concrete Buildings Volume 1." *Report No. SSC 96-01, November 1996, APPLIED TECHNOLOGY COUNCIL, 555 Twin Dolphin Drive, Suite 550*, Redwood City, California 94065.

Bhatt, C. & Bento, R. (2011). "Extension of the CSM-FEMA440 to plan-asymmetric real building structures." *Earthquake Engineering & Structural Dynamics, 40(11), 1263–1282.*

CEN. (1994, 1995). "Eurocode 8: Design provisions for earthquake resistance of structures (ENV 1998-1-Parts 1, 2, 3)." *ENV 1998-1-Parts 1, 2, 3, European Committee for Standardization.*

Chopra, A. K. & Goel, R. K. (2002). "A modal pushover analysis procedure for estimating seismic demands for buildings." *Earthquake Engineering & Structural Dynamics, 31(3), 561–582.*

Chopra, A. K. & Goel, R. K. (2004a). "A modal pushover analysis procedure to estimate seismic demands for asymmetric-plan buildings." *Earthquake Engineering & Structural Dynamics, 33(8), 903–927.*

Cimellaro, G. P., Reinhorn, A. M., D'Ambrisi, A., and De_Stefano, M. (2011). "Fragility Analysis and Seismic Record Selection." *ASCE Journal of Structural Engineering, 137(3), 379–390.*

Cimellaro, G. P. (2013). "Correlation in spectral accelerations for earthquakes in Europe." *Earthquake Engineering & Structural Dynamics, 42(4), 623–633.*

Cimellaro, G. P., Giovine, T., and Lopez-Garcia, D. (2013). "Bidirectional Pushover analysis of irregular structures." *Journal of Structural Engineering, ASCE*, in review.

CSI. (2011). "SAP2000-Linear and Nonlinear Static and Dynamic Analysis and Design of Three-Dimensional Structures." *Computers and Structures, Inc., Berkeley, California, USA.*

De Stefano, M. & Pintucchi, B. (2008). "A review of research on seismic behaviour of irregular building structures since 2002." *Bulletin of Earthquake Engineering, 6(2), 285–308.*

De Stefano, M. & Pintucchi, B. (2010). "Predicting torsion-induced lateral displacements for pushover analysis: Influence of torsional system characteristics." *Earthquake Engineering & Structural Dynamics, 39(12), 1369–1394.*

Dolsek, M. & Fajfar, P. (2005). "Simplified non-linear seismic analysis of infilled reinforced concrete frames." *Earthquake Engineering & Structural Dynamics, 34(1), 49–66.*

Dolsek, M. & Fajfar, P. (2007). "Simplified probabilistic seismic performance assessment of plan-asymmetric buildings." *Earthquake Engineering & Structural Dynamics, 36(13), 2021–2041.*

Fajfar, P. (1999). "Capacity spectrum method based on inelastic demand spectra." *Earthquake Engineering & Structural Dynamics, 28(9), 979–993.*

Fajfar, P. & Gaspersic, P. (1996). "The N2 method for the seismic damage analysis of RC buildings." *Earthquake Engineering & Structural Dynamics, 25(1), 31–46.*

Fajfar, P., Marusic, D. & Perus, I. (2005). "Torsional effects in the pushover-based seismic analysis of buildings." *Journal of Earthquake Engineering, 9(6), 831–854.*

Gupta, B., Kunnath, SK. (2000). "Adaptive spectra-based pushover procedure for seismic evaluation of structures." *Earthquake spectra, 16(2): 367–392.*

Kalkan, E. & Kunnath, S. K. (2006). "Adaptive modal combination procedure for nonlinear static analysis of building structures." *Journal of Structural Engineering-Asce, 132(11), 1721–1731.*

Kilar, V. & Fajfar, P. (1997). "Simple push-over analysis of asymmetric buildings." *Earthquake Engineering & Structural Dynamics, 26(2), 233–249.*

Kim, S.-P. & Kurama, Y. C. (2008). "An alternative pushover analysis Procedure to estimate seismic displacement demands." *Engineering Structures, 30(12), 3793–3807.*

Lin, J.-L. & Tsai, K.-C. (2008). "Seismic analysis of two-way asymmetric building systems under bi-directional seismic ground motions." *Earthquake Engineering & Structural Dynamics, 37(2), 305–328.*

Menun, C. & Der Kiureghian, A. (1998). "A Replacement for the 30%, 40%, and SRSS Rules for Multicomponent Seismic Analysis." *Earthquake Spectra, 14(1), 153–163.*

Working Group ITACA (2010) – Data Base of the Italian strong motion records: http://itaca.mi.ingv.it

Research and Applications in Structural Engineering, Mechanics and Computation – Zingoni (Ed.)
© 2013 Taylor & Francis Group, London, ISBN 978-1-138-00061-2

Seismic collapsing response analysis of wooden house retrofitted by ACM braces

T. Takatani
Department of Civil Engineering & Architecture, Maizuru National College of Technology

H. Nishikawa
Education and Research Supporting Centre, Maizuru National College of Technology

ABSTRACT: 3-D non-linear collapsing process analysis of two-story wooden house was conducted against several strong earthquake ground motions with the seismic intensity of 6+ to 7 level in order to investigate the seismic behaviour of the wooden house retrofitted by ACM braces. A non-linear behaviour of timber elements in wooden house during earthquake motion can be simulated by this collapsing analysis. As a result, seismic response of the wooden house depends on the seismic intensity of input earthquake ground motion in the collapsing analysis. Also, there seems to be a possibility that the wooden house with the upper structural seismic index value of less than 1.0 may be collapsed by a strong earthquake motion with 7 level.

1 INTRODUCTION

In recent years, major earthquakes in Japan caused serious damage to a great number of existing wooden houses built by some old seismic design codes before 1981. One of the authors has already developed an advanced seismic retrofitting method for existing wooden house using ACM bracing method which consists of Carbon Fiber Reinforced Plastic (CFRP) plate and steel plates (Takatani 2012). It is very important for a structural engineer to take account of a seismic response of wooden house in the design process of seismic retrofit and also to make an accurate evaluation of the seismic collapsing behaviour of the retrofitted wooden house during a strong earthquake ground motion. In this paper, 3-D seismic collapsing process analysis of wooden house based on the theory of the Distinct Element Method (Cundall et al. 1979) is conducted in order to accurately evaluate the seismic behaviour of wooden house with or without ACM bracing seismic retrofit. The effect of the seismic retrofit using ACM bracing method on the collapsing behaviour is numerically investigated. Five earthquake ground motions with the Japan Meteorological Agency (JMA) seismic intensity, $I_{\mathrm{JMA}} = 6+ \sim 7$, are used in this 3-D collapsing process analysis of a typical traditional two-story wooden house in Japan.

2 COLLAPSING ANALYSIS OF WOODEN HOUSE

Target of the collapsing process analysis in this paper is a Japanese traditional two-story wooden house built in 1961. The upper structural seismic index of this wooden house is 0.45 in the span direction. ACM bracing seismic retrofit can be designed so as to satisfy the upper structural seismic index of 1.0. Figure 1 shows the wooden house floor plans before and after seismic retrofit. This wooden house was retrofitted by outside, inside and corner ACM bracing techniques. Some red lines of X sign in Figure 1(b) mean ACM brace locations. Some types of ACM bracing seismic retrofit for wooden house have already developed by Takatani (2012).

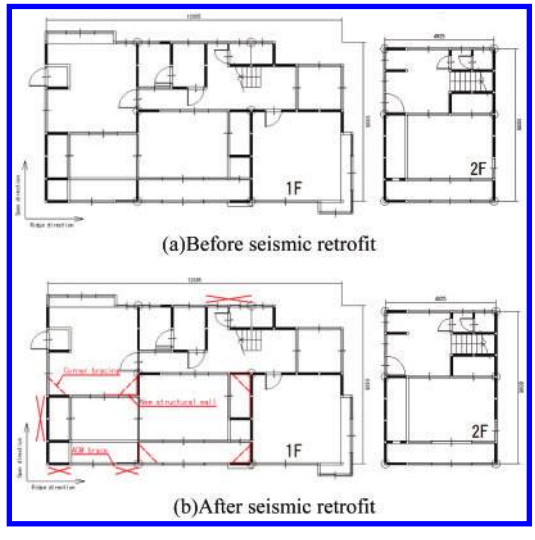


Figure 1. Floor plan of wooden house.

A collapsing process analysis software of "Wallstat" is conducted in order to investigate the seismic response behaviour and the collapsing process of wooden house during a strong earthquake ground

motion. This software has an original analysis technique (Nakagawa et al. 2010) using the basic theory of the Distinct Element Method.

Figure 2 illustrates a typical framing plan of Japanese two-story wooden house built by a traditional wooden-based building method. In the collapsing process analytical calculation, a wooden house can be modelled by a lot of timber elements such as beam and column connected with non-linear spring as shown in Figure 2, and also can be modelled by lumped mass and the weight of each floor in wooden house model can be obtained from each structural element as illustrated in Figure 3.

2.1 *Modelling of frame*

Timber frame is modelled by two elasto-plastic rotational springs (plastic hinge) and an elastic beam component as shown in the left-hand side of Figure 4. The spring can be defined by a relationship between the bending moment M and the angle of rotation θ with the skeleton curve indicated in the right-hand side of Figure 4. The bending moment starts to fall once if it is over the maximum bending moment, and the rotating spring changes to a pinned joint state at the point if the bending moment reaches 0, and then the beam component can be judged to have been broken.

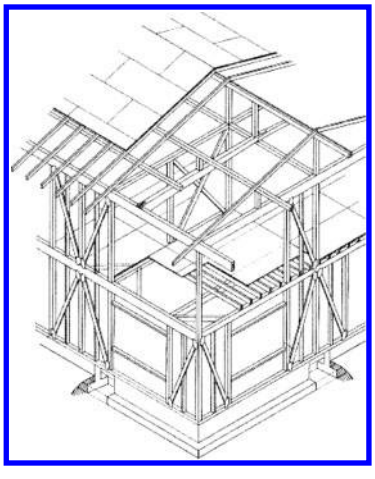


Figure 2. Framing plan of wooden house.

2.2 *Modelling of joint spring*

Joint spring can be modelled by both an elasto-plastic spring and a rotational spring as shown in Figure 5(a). Timber characteristic of the compression and tensile elasto-plastic spring consist of an elastic part and slip-type part indicated in Figure 5(b), and also timber characteristics of the rotational spring is assumed to be a slip-type relationship between ending moment M and angle of rotation θ shown in Figure 5 (c). When the elasto-plastic spring or the rotational spring of the joint exceeds the maximum structural strength or moment and their strength values becomes 0, the joint will be adjudged to have been broken and then the spring will be annihilated.

2.3 *Modelling of shear wall and bracing*

Vertical shear wall indicated in Figure 6 can be modelled by the replacement of truss component with a load-displacement non-linear relationship shown in Figure 8. Also, bracing shear wall illustrated in Figure 7 can be modelled by the replacement of compression and tensile truss components defined by a set of bi-linear and slip skeleton curve shown in Figure 8, too.

2.4 *Parameters of structural element*

In this paper, Young's modulus and the maximum bending moment of timber component are assumed to be 2,000 MN/m^2 and 10 kNm, respectively. External and internal walls in wooden house can be assumed to be lath mortal wall and clay wall, respectively. For seismic retrofit work, plywood is used as internal wall. Parameters of hysteretic characteristics of their walls are shown in Table 1. Parameters of stub tenon jointed at the interface between beam, column

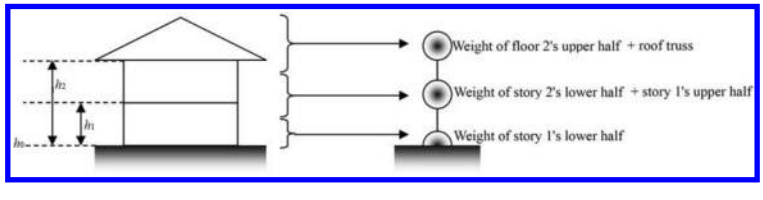


Figure 3. Weight of floor in the analytical model of wooden house (Nakagawa 2010).

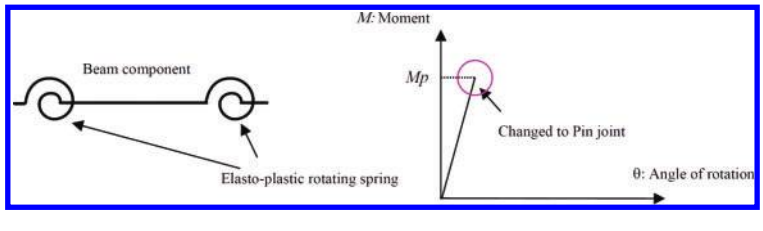


Figure 4. Schematic diagram and skeleton curve of frame spring (Nakagawa 2010).

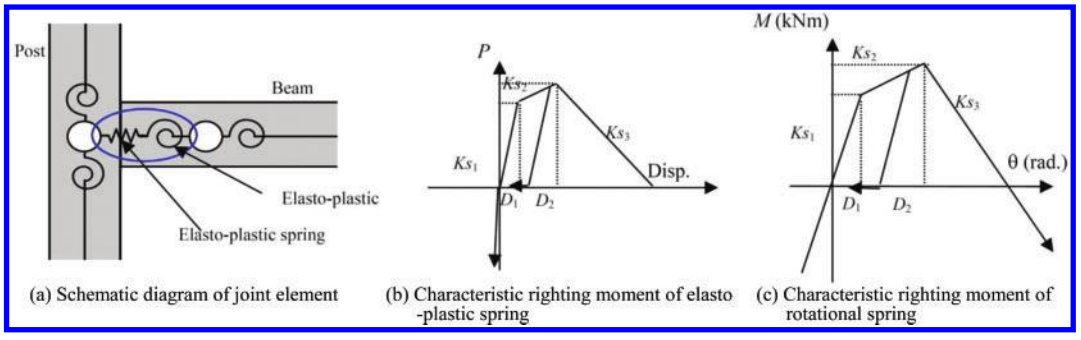


Figure 5. Outline of joint modelling (Nakagawa 2010).

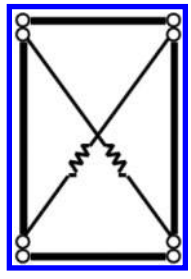


Figure 6. Shear wall spring.

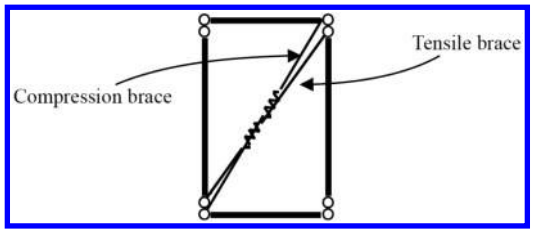


Figure 7. Outline of bracing shear wall.

and corner bracing used for seismic retrofit work are described in Table 2. Table 3 shows the parameters of hysteretic characteristics of timber brace and ACM brace element. This software has an original analysis technique (Nakagawa et al. 2010) using the basic theory of the Distinct Element Method, and can be taken into consideration the extremely non-linear properties of timber members breaking or being disperse. Nishikawa et al. (2012) conducted collapsing analysis of a two-story wooden house with and without ACM bracing seismic retrofit against some earthquake motions to investigate the effect of seismic retrofit of the wooden house.

3 EVALUATION OF COLLAPSING PROCESS OF WOODEN HOUSE

3.1 *Input earthquake motion*

Table 4 shows five earthquake records in K-NET and KiK-net systems used in this paper, which were obtained in the earth's crust between 2000 and 2008 in Japan and were the moment magnitude $M_W = 6.6 \sim 6.9$ with the seismic intensity of $I_{JMA} = 5 + \sim 7$. Three earthquake acceleration waves in Table 4 and their Fourier spectra are indicated in Figures 9 and 10, respectively. Three seismic intensities I_{JMA} are 6.3∼ 6.7 and their predominant frequencies are about 1 Hz.

3.2 *Collapsing process and seismic response*

Figure 11 illustrates collapsing behaviours before and after seismic retrofit of a wooden house against K-NET Ojiya in the Mid Niigata prefecture Earthquake in 2004. Wall elements in wooden house during earthquake are indicated in yellow, orange and red colours with the increase of damage degree of wooden house. In addition, as can be seen from the upper structural seismic index values in Table 5, the difference between the upper structure seismic index values before and after seismic retrofit have a significant effect on the seismic response against a strong earthquake motion, because the upper structural seismic index of the first floor in the ridge direction increases more than 0.2 by a seismic retrofit. Upper structure seismic index of wooden house means a ratio of the holding strength to the necessary one of wooden house, and also indicates the resistant strength against a strong earthquake motion with $I_{JMA} = 6 +$ level. Therefore, if the upper structural seismic index value is over 1.0, the retrofitted wooden house has an enough seismic resistant strength against a strong earthquake with the seismic intensity of $I_{JMA} = 6 +$ level. It is found from Table 5 that the wooden house after seismic retrofit doesn't have an enough seismic resistant strength. As can be found from the collapsing behaviour during K-NET Ojiya in Figure 11, the first floor of wooden house before seismic retrofit begins to destroy after 8 seconds and then collapses after 12 seconds. On the other hand, the damage degree of wooden house after seismic retrofit is slightly smaller than before seismic retrofit and then collapses after 12 seconds, too. This is because the displacement wave of K-NET Ojiya in Figure 9(a) was measured under a strong earthquake motion with the seismic intensity of $I_{JMA} = 7$ level and the amplitude of displacement was over 0.3 m.

Figure 12 illustrates collapsing behaviours before and after seismic retrofit of wooden house during K-NET Anamizu in the Noto Peninsula Earthquake in 2007. Although wooden house before seismic retrofit collapses after 16 seconds, wooden house after seismic

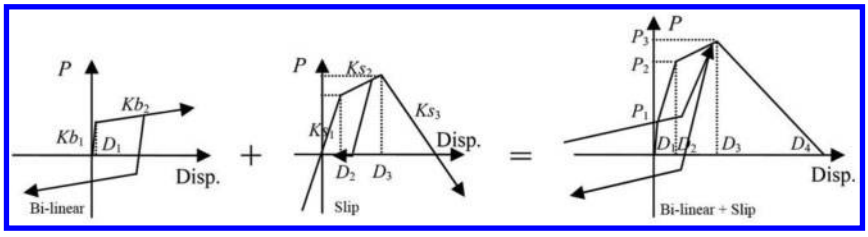


Figure 8. Hysteretic characteristics of shear wall and bracing (Nakagawa 2010).

Table 1. Parameters for hysteretic characteristics of vertical shear wall (Nakagawa 2010).

	P_1	P_2	P_3	P_4	D_1	D_2	D_3	D_4	h
Wall	(kN)			(m)			(%)		
Clay Wall	0.5	1.75	2.0	0.0	0.010	0.05	0.10	0.5	2
Lath Mortal Wall	1.0	3.50	4.3	0.0	0.002	0.01	0.05	0.2	2
Structural Plywood	3.0	9.50	10.5	0.0	0.010	0.06	0.12	0.3	2

h: viscous damping factor

Table 2. Parameters for hysteretic characteristics of elasto-plastic spring (Tajima et al. 2000, Nakagawa 2010).

	Ks_1	Ks_2	Ks_3	D_1	D_2
	(kN/m)			(m)	
Stub Tenon	900	−18.919	−33.333	0.0015	0.02
Corner Bracing	5,128	651	−154	0.0027	0.015

Table 3. Parameters for hysteretic characteristics of bracing spring.

Brace	P_1	P_2	P_3	P_4	D_1	D_2	D_3	D_4	h
	(kN)			(m)			(%)		
Timber Brace	0.500	2.500	2.800	0.000	0.001	0.015	0.050	0.250	2
ACM Brace (e-plate)	3.193	6.387	9.580	0.000	0.010	0.021	0.031	0.043	2

Table 4. Earthquake ground motion records.

	Number of Records	
Earthquake	K-NET	KiK-net
The Western Tottori prefecture Earthquake in 2000	5	3
The Mid Niigata prefecture Earthquake in 2004	5	2
The Noto Peninsula Earthquake in 2007	4	0
The Niigataken Chuetsu-oki Earthquake in 2007	2	0
The Iwate-Miyagi Nairiku Earthquake in 2008	2	4

retrofit has no large damage after 50 seconds. This implies that the seismic retrofit has a significant effective effect on the collapsing behaviour against an earthquake with the seismic intensity of $I_{JMA} = 6 +$ level.

Figure 13 indicates collapsing behaviours before and after seismic retrofit of wooden house during KiK-NET Hino in the Western Tottori prefecture Earthquake in 2000. The first floor of wooden house before seismic retrofit in Figure 13(a) begins to destroy after 8 seconds and then collapses after 12 seconds. On the other hands, the damage degree of wooden house after seismic retrofit in Figure 13(b) is almost the same collapsing behaviour of wooden house before

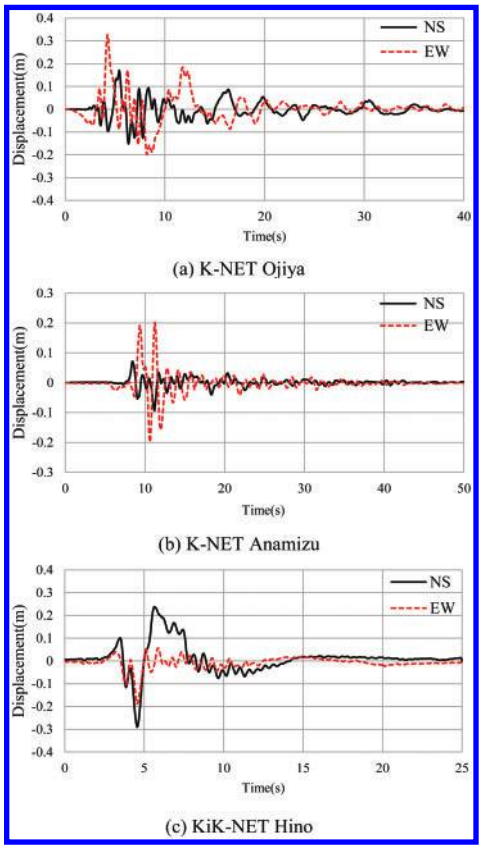


Figure 9. Displacement waves of input motion.

Table 5. Upper structural seismic index value.

		No Seismic Retrofit	Seismic Retrofit
2F	Ridge Direction	0.51	0.51
	Span Direction	1.02	1.02
1F	Ridge Direction	0.47	0.71
	Span Direction	0.45	0.57

seismic retrofit. This is because the displacement wave of KiK-NET Hino in Figure 9(c) was measured under a strong earthquake motion with the seismic intensity of $I_{JMA} = 7$ level.

In this collapsing analysis, there are three wooden houses collapsed before seismic retrofit and two wooden houses collapsed after seismic retrofit against earthquake motions in Table 5. Because two earthquake motions, which was collapsed the wooden house after seismic retrofit, have seismic intensity of $I_{\mathrm{JMA}} = 7$, any other effective seismic retrofit countermeasure seems to be needed for a strong earthquake motion with the seismic intensity of $I_{JMA} = 7$. Consequently, the upper structural seismic index value of wooden house must be over 1.0.

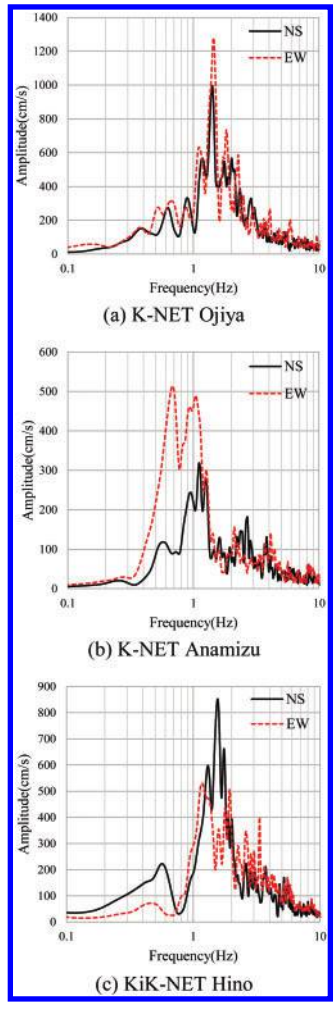


Figure 10. Fourier spectra of acceleration.

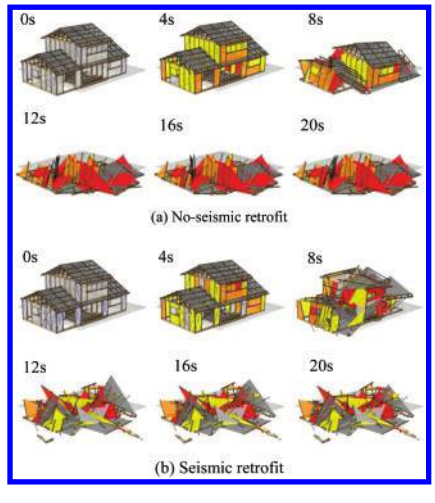


Figure 11. Collapsing process behaviour of wooden house under K-NET Ojiya ($I_{JMA} = 6.7$).

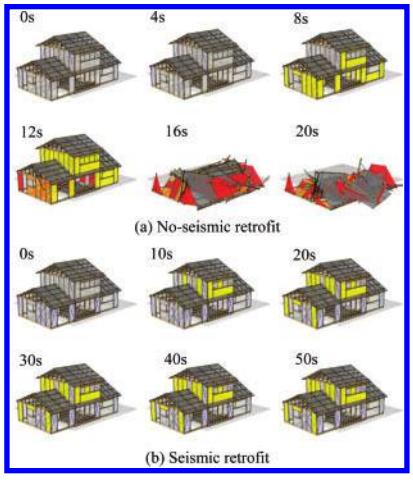


Figure 12. Collapsing process behaviour of wooden house under K-NET Anamizu ($I_{JMA} = 6.3$).

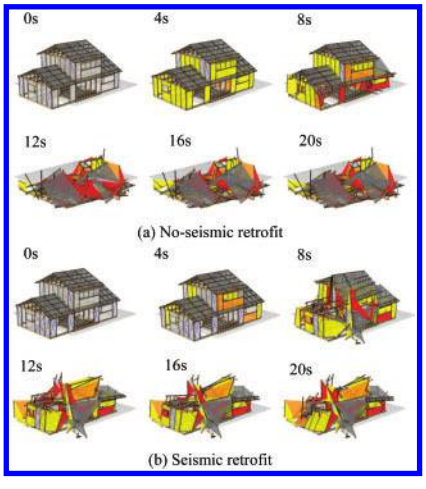


Figure 13. Collapsing process behaviour of wooden house under KiK-NET Hino ($I_{JMA} = 6.6$).

4 CONCLUSIONS

In this paper, a structural analysis based on the Distinct Element Method was conducted in order to investigate the collapsing behaviour of wooden house during a strong earthquake ground motion and the seismic performance effect of ACM bracing method using e-plate. A traditional two-story wooden house was modelled before and after ACM bracing seismic retrofit, and the collapsing behaviour of the wooden house against some earthquake motions with the seismic intensity of $I_{\mathrm{JMA}} = 6 + \sim 7$ were investigated by 3-D seismic collapsing process analysis.

In summary, the following conclusions can be made based on the results presented in this paper.

(1) Seismic performance of an old wooden house retrofitted by ACM bracing method can be numerically confirmed by a collapsing process analysis. Seismic response of the wooden house greatly depends on the seismic intensity of input earthquake ground motion used in the collapsing analysis.
(2) There seems to be a possibility that the wooden house with the upper structural seismic index value of less than 1.0 is easily collapsed by a strong earthquake motion with the seismic intensity of $I_{JMA} = 7$ level even if the wooden house is retrofitted by ACM bracing method.
(3) As the wooden house retrofitted by ACM bracing method does not suffer severe damage against any earthquake ground motion with the seismic intensity of $I_{\mathrm{JMA}} = 6 +$ level, ACM bracing method for old wooden house may be one of the effective seismic retrofitting countermeasures.

Although the effect of earthquake ground motion spectrum on the seismic response of wooden house is not presented in detail in this paper, it is necessary for an intensive study on the effect of earthquake ground motion spectrum on the seismic response of the retrofitted wooden house during some earthquake ground motion wave data, which have the same level intensity with a different peak frequency in Fourier spectra. In addition, further investigation may be needed to simulate the seismic collapsing process phenomenon of an existing wooden house with or without seismic retrofit and make some concrete conclusions.

ACKNOWLEDGMENTS

The authors would like to thank the Japan Meteorological Agency and the National Research Institute for Earth Science and Disaster Prevention in Japan for their earthquake ground motion wave data in K-NET and KiK-net system.

REFERENCES

Cundall, P. A. and Strack, O. D. L. 1979. A discrete numerical model for granular assemblies, *Géotechnique*, Vol.29, No.1, 47–65.

Nakagawa, T., Ohta, M. 2010. Collapsing process simulations of timber structures under dynamic loading III: Numerical simulations of the real size wooden houses, *Journal of Wood Science*, Vol.56, No.4, 284–292.

Nishikawa, H., Takatani, T. 2012. Collapsing simulation of wooden house retrofitted by ACM braces during seismic ground motion, *Proceedings of the 2102 World Congress on Advances in Civil, Environmental and Materials Research* (ACEM-2), Seoul, South Korea, 2048–2060.

Tajima, M., Murakami, M., Gotou, M., Inayama., M and Fukuda, M 2000. Development of structural design method on conventional post and beam structures: Part 35 Result of Shearthed Diaphram with Angle Brace Test, *Summaries of Technical Papers of Annual Meeting*, Architectural Institute of Japan, 25–26 (in Japanese).

Takatani, T. 2012. Load-displacement relationship of ACM wooden-house retrofitting brace, *Proceedings of World Conference on Timber Engineering* (WCTE 2012), Auckland, New Zealand.

Research and Applications in Structural Engineering, Mechanics and Computation – Zingoni (Ed.)
© 2013 Taylor & Francis Group, London, ISBN 978-1-138-00061-2

Nonlinear behavior of submerged floating tunnels accounting for seaquake effects

Chunxia Shi, Marco Domaneschi & Luca Martinelli
Department of Civil and Environmental Engineering, Politecnico di Milano, Italy

ABSTRACT: Submerged Floating Tunnels, also known as Archimedes Bridges, are a new structural conceptual way for strait and waterways crossing, which are catching more and more worldwide attention. In this paper, a 3D finite element model is developed in a commercial finite element code, accounting for material and geometrical nonlinearities, soil-structure interaction and multiple-support seismic excitation, to give a broad angle view on the structural behavior under seismic motion. Elastic-plastic springs at tunnel shores, simulating passive control devices, are applied to reduce relative displacements between the tunnel and shores. Beside the traditional earthquake loading on the structure foundations' connections, the motion transmission from the seabed through the water (called *seaquake*) is newly introduced as an additional hydrodynamic pressure working on the floating tunnel. The velocity field due to seaquake is derived from its velocity potential which is deduced from the wave equation considering the boundary conditions. The force on the moving tunnel body in the oscillatory flow, simulating the seaquake, is modeled by using Morison's equations. A comparison between transient dynamic response in case of 'earthquake' and 'earthquake plus seaquake' is also given, which shows how seaquake loading affects the responses of anchor bars, shore connections and tunnel sections in terms of stresses, strains and displacements. The outcome indicates a larger displacement capacity is required to the control system in the mitigation of dangerous structural responses, as well as the significant role played by the seaquake loading source, and highlights the need of further investigations on seaquake effects.

1 INTRODUCTION

Submerged Floating Tunnels (SFTs), also named Archimedes Bridges, are a promising alternative to cross sea-straits, lakes and waterways. Entirely immersed at specific depth, they serve different types of traffic efficiently connecting the shores. A circular cross section is commonly adopted in SFTs' design and the tunnel, subject to positive buoyancy, is anchored at the seabed by suitable structural elements. The first proposal about SFTs was formulated by S. Preault in 1860. The concept caught the attention of several bridges and links specialists from Italy, Norway, China, Japan, USA and other countries, and is the object of a working group for SFTs established in 1989 (Ingerslev 2010).

Owing to the special siting of the SFT, several research fields have to be covered to give a thorough view of the dynamic loading and the resulting structural behavior, such as:

- seismic engineering analysis, studying both support-transmitted and fluid-transmitted loads,
- fluid-structure interaction, leading to the definition of forces due to sea waves and vortex shedding,
- vehicle-structure interaction, resulting in forces due to traffic loading,
- phenomena related to impact and explosions, for both internal and external events.

The study on the dynamic response of SFTs subjected to strong seismic motion made significant progress in the last decades (Di Pilato et al. 2008a, b, Martinelli et al. 2010, Martinelli et al. 2011, Shi et al. 2012a, b). The response due to hydrodynamic loads has been treated in detail in (Di Pilato et al. 2008b). In (Hong & Ge 2010), the SFT response to the accidental load due to the impact of a sinking boat is discussed. Fewer works have been found in the field of vehicle-structure interaction.

In seismic analysis, both the earthquake loads due to direct ground motion transmission to the structural supports and the so-called "seaquake" loading, due to the water transmission of compressive waves originated at the seabed, are worth more attention. Especially for seaquake, research work on SFTs has only been recently started (Shi & Martinelli 2013). However, a number of other different cases called for attention to the effects of propagating seismic waves in water due to seaquakes, and to the potential damaging effects that such waves may cause on offshore structures and floating systems (Hove et al. 1982). As a new type of external loading, this load works as a hydrodynamic pressure due to compression waves, since water cannot transmit a shear wave, traveling through the water and excited by the motion of the seabed during an earthquake.

Such complex loading conditions can induce dangerous responses in SFTs, about safety and reliability

performances. Structural control solutions can help to meet the required high standards of safety, mitigating the tunnels responses and protecting their structural elements. Moreover, several fruitful applications of passive and semi-active control systems to long span structures, such as cable-stayed and suspension bridges under seismic loading (Domaneschi 2010, 2012, Domaneschi & Martinelli 2012, Ismail et al. 2013), seem promising also when SFTs are considered.

In this paper, the first part is devoted to introduce the earthquake and seaquake motions. Then, a SFT model, simulated in the commercial finite element (FE) framework ANSYS, has been accounted for as a case study: it has been equipped with suitable passive control devices in the way of elastic-plastic axial springs which restrain the tunnel at the shores, and inelastic anchoring bars mooring the tunnel to the seabed. Finally, some conclusions are given about comparison between the cases of 'earthquake' and 'earthquake plus seaquake'.

2 SEISMIC MOTIONS

2.1 *Multiple-support earthquake loading*

The seismic excitation is applied at each ground connection points (shores and anchoring foundations) in the form of a multiple-support one. The stochastic modeling of the space-time variation of the seismic excitation is based on the Kanai-Tajimi power spectral density (PSD) modified by Clough and Penzien, which has been adopted to describe the seismic motion at a point. In addition, the coherency model of Luco and Wong was introduced representing the spatial variation of the ground motion.

The coherency function is defined in terms of the cross-power spectral density of ground acceleration $S_{i,j}(\xi_d, \omega)$ between two stations i and j at a separation distance ξ_d.

$$\gamma(\xi_d, \omega) = \frac{S_{i,j}(\xi_d, \omega)}{\left[S_{i,i}(\omega) \cdot S_{j,j}(\omega)\right]^{1/2}} \tag{1}$$

where ω is the circular frequency; $S_{i,i}(\omega)$, $S_{j,j}(\omega)$ the direct PSDs at the station sites.

Luco and Wong 1986 model was here adopted in the form:

$$\gamma(\xi_d, \omega) = \exp\left[-\left(\frac{\alpha_c \omega \xi_d}{v_s}\right)^2\right] \exp\left[i \frac{\omega \xi_d^L}{v_{app}}\right] \tag{2}$$

where ξ_d is the horizontal separation distance between two stations i and j, v_s the shear wave velocity, α_c a parameter controlling coherence decay, ξ_d^L the projected horizontal distance along the wave propagation direction, v_{app} the surface apparent velocity of "dominant" waves.

The adopted PSD function is the well-known modified Kanai-Tajimi spectrum of ground accelerations (Clough and Penzien 1975), expressed as (Monti et al. 1996)

$$S(\omega) = S_0 S_{CP}(\omega) = S_0 \frac{\omega_g^4 + 4\zeta_g^2 \omega_g^2 \omega^2}{(\omega_g^2 - \omega^2)^2 + 4\zeta_g^2 \omega_g^2 \omega^2} \frac{\omega^4}{(\omega_f^2 - \omega^2)^2 + 4\zeta_f^2 \omega_f^2 \omega^2} \tag{3}$$

where S_0 is the intensity of the ideal white noise process as bedrock acceleration, $S_{CP}(\omega)$ the normalized Clough-Penzien spectrum, ω_g and ζ_g the characteristic ground frequency and damping, ω_f and ζ_f parameters of an additional filter introduced to guarantee finite power for displacements.

The parameters in Equation 3, defining the modified Kanai-Tajimi power spectral density, have been selected according to the procedure presented in Martinelli et al. 2010 and Martinelli et al. 2011, to achieve acceleration time histories satisfying a code compatible response spectrum.

2.2 *Seaquake loading*

When seaquake effects are introduced, the hydrodynamic pressure is assumed associated with the water-transmitted seismic vibration from the seabed to the SFT. The velocity field due to seaquake is derived from its velocity potential. The velocity potential is deduced from the wave equation considering the boundary conditions (Hamamoto 1995). The force on the moving body in the oscillatory flow is modeled by using Morison equation (Chakrabarti 1987), which is adopted for simulating the seaquake loading on the tunnel.

3 SFT MODEL

3.1 *General outline and the control system*

In this paper, a prize-winning proposal for a SFT between Calabria and Sicily across the Messina strait in Italy is selected as case study. The model accounts for soil-structure interaction, geometrical and material non-linearities as well as for 3D multiple-support seismic excitation and seaquake.

The length of the proposed SFT project across the Messina Strait is 4680 m, the maximum depth is 325 m, and the location of the floating tunnel is set 40 m under the water level. Figure 1 shows the SFT's front and section views. The tunnel has a circular

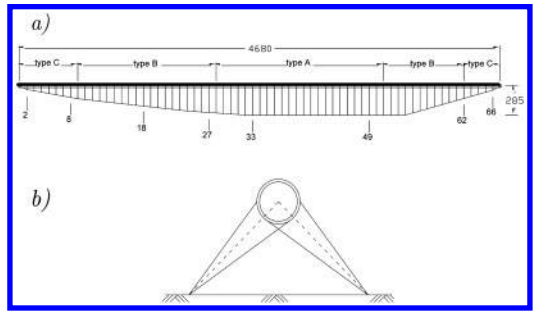


Figure 1. SFT, front view (a), section view (b).

composite steel-concrete section having a 15.95 m outside diameter. It is connected to the seabed by means of slender steel beams having hollow circular section and pile foundations.

For the supporting system, there are three kinds of bar sections along the whole length of the tunnel. The composite section is treated as an equivalent homogeneous one, having elastic modulus equal to 2.943×10^7 kN/m^2. The steel elastic modulus for the anchoring system is assumed equal to 2.06×10^8 kN/m^2, while the yielding stress and the hardening ratio are assumed respectively 210×10^6 N/m^2 and 0.02.

In light of the requirements of energy dissipation under severe seismic excitation, passive hysteretic control devices are suggested to be applied, acting in longitudinal direction at the tunnel's ends. These devices are implemented in the FE model as nonlinear elastic-plastic springs. Their design stiffness is derived from the yielding displacement and yielding force fixed respectively to 10 cm and 5% of tunnel weight. Additionally, the mooring system can have elastic-plastic behavior as well.

The role played by the passive control systems at the shores is twofold: first, to dissipate part of the seismic energy imparted to the SFT by the earthquake motion. This results attempts also to concentrate the inelastic deformation at specific and selected positions on the whole structure. The second aim of the control system is to decouple the structural motion from those of the shore, shifting the structural response to lower frequencies and, consequently, far from the higher frequencies characterizing the earthquake excitation. The expected consequence is to allow internal forces and stresses reductions at cost of larger structural displacements.

3.2 *The ANSYS implementation*

The ANSYS FE code is used to simulate the seismic response of the SFT by implementing a 3D model. In Figure 2, an illustration of the first natural vibration shape in transversal direction is depicted.

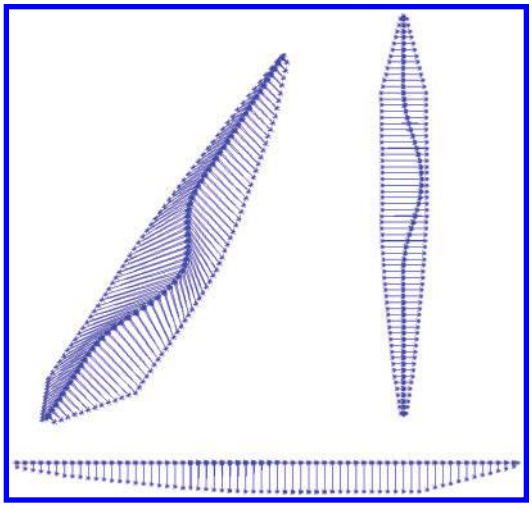


Figure 2. Mode shape of tunnel first transversal mode.

4 TRANSIENT ANALYSES

Two different loading conditions have been implemented for the dynamic analyses: the first accounts for the earthquake excitation, identified in the remaining of this section with the 'Eq' acronym, the second is the combination of both earthquake and seaquake excitations (identified with the 'Sq+Eq' notation). The transient dynamic responses of passive control devices, tunnels and anchor bars under such loading conditions are presented in the following sub-sections.

In the following figure legends (Figures 3–7), solid lines represent the responses under the combination of seaquake and earthquake excitations while dashed lines stand for the responses under earthquake alone.

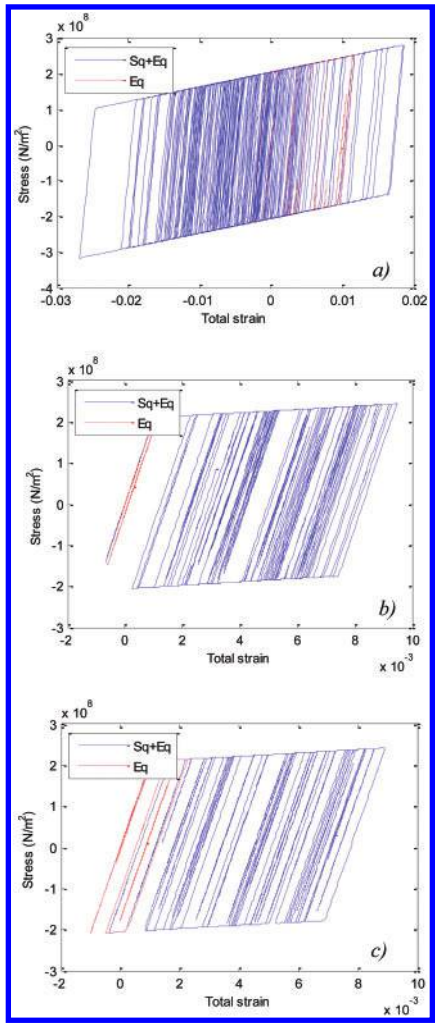


Figure 3. Strain-stress relationships of anchoring bars: the mid-section of bar close to the shore (a), at the quarter-span of tunnel (b), at the mid-span of tunnel (c).

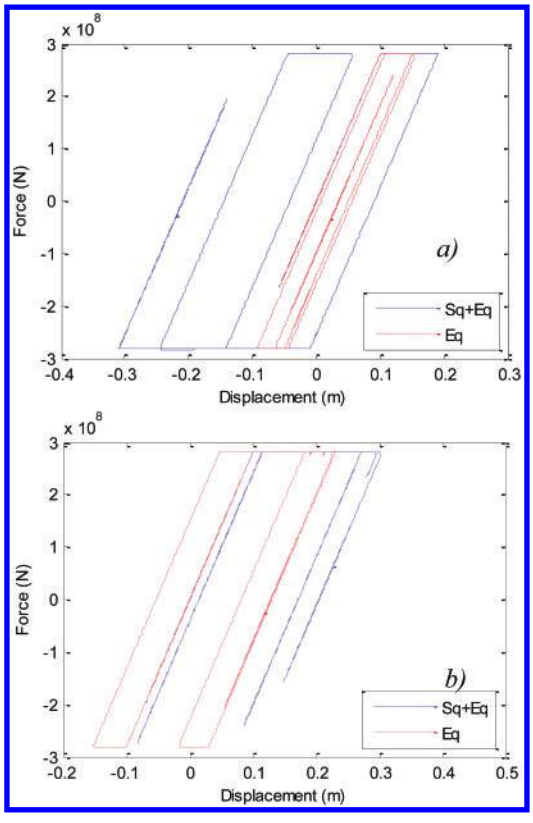


Figure 4. Elastic-plastic springs' nonlinear behaviors.

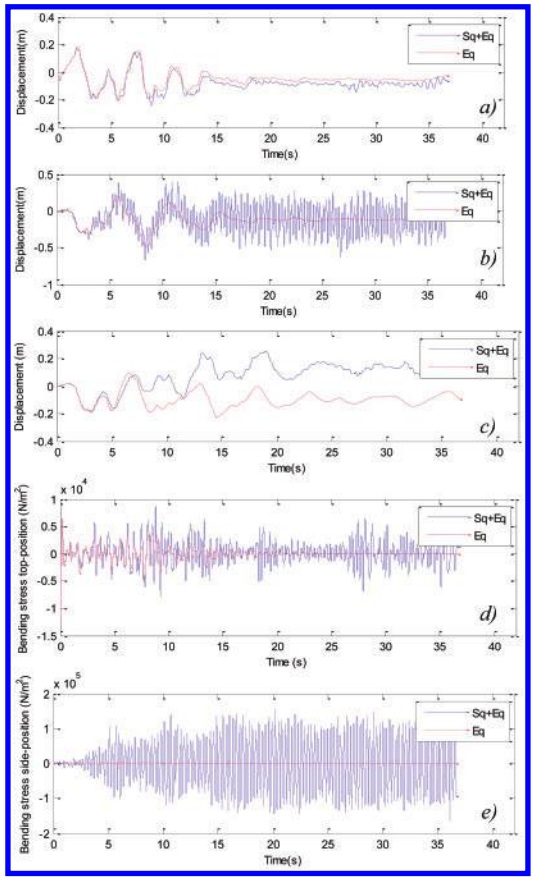


Figure 5. Tunnel section 1 (close to the shore). Transversal displacement (a), vertical displacement (b), longitudinal displacement (c), bending stress at top-position (d), bending stress at side-position (e).

4.1 *Response of anchoring bars*

In Figure 3, the inelastic behavior of the anchor bars is depicted. Figure 3a shows the strain-stress relationship at the mid-section of the bar close to the shore; Figure 3b gives the mid-section of the bar at the quarter-span of tunnel; meanwhile Figure 3c the mid-section of the bar at the mid-span of tunnel.

From the general overview of Figures 3a-c it arises that the bars close to the shore show ten times larger plastic deformations if compared with those at quarter-span and mid-span. The seaquake effect influences the behavior of the anchoring system, especially causing a significant strain increment in the bars at the middle span. Larger hysteretic cycles are induced by the 'Sq+Eq' loading.

4.2 *Passive control devices' response*

Figure 4 reports the longitudinal displacement-force paths for the devices at both tunnel ends.

From Figures 4a-b, the passive control devices, both in cases of 'Sq+Eq' and 'Eq', dissipate satisfactorily the seismic energy through hysteresis cycles. Larger displacements in 'Sq+Eq' than that in 'Eq' case can also be recognized, highlighting the more severe condition represented for the SFT by the coupled earthquake and seaquake excitation.

4.3 *Tunnel response*

Tunnel responses in terms of vertical (y axis), longitudinal (z) and transversal (x) absolute displacements, together with bending stresses (at top-position and side-position in the tunnel cross-section) are discussed in this subsection. Three locations along the longitudinal tunnel axis have been considered: close to the shore, at the quarter-span, and at the mid-span. The outcomes are depicted respectively in Figures 5–7.

The transversal displacements of tunnel sections near the shore, at the quarter-span of tunnel and at the mid-span of tunnel for the 'Sq+Eq' loading condition show similar time variation as those in the 'Eq' one, meaning that the vertical seaquake loading has small influence in the transversal direction for the inelastic model (Figure 5a, Figure 6a and Figure 7a).

The longitudinal displacements show a drift of the tunnel sections. Particularly, the tunnel section near the shore shows the largest drift, caused by the high yielding deformation in the anchoring bars at this position and the proximity to the dissipative control devices, see Figure 5(c), Figure 6(c) and Figure 7(c).

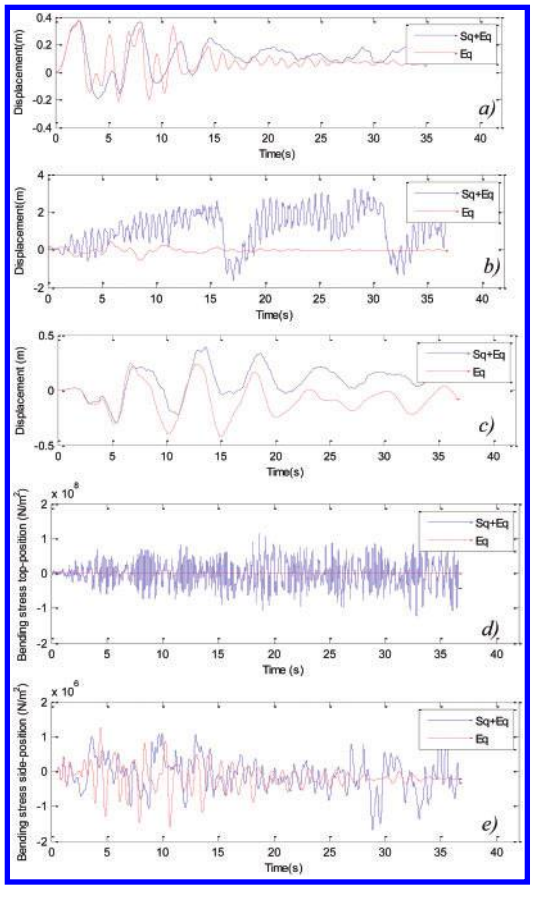


Figure 6. Tunnel section 18 (quarter-span). Transversal displacement (a), vertical displacement (b), longitudinal displacement (c), bending stress at top-position (d), bending stress at side-position (e).

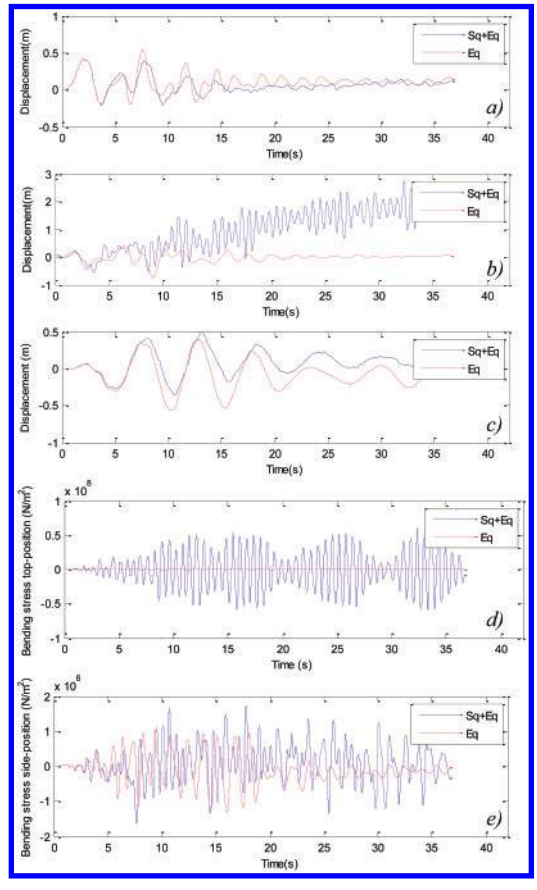


Figure 7. Tunnel section 33 (mid-span). Transversal displacement (a), vertical displacement (b), longitudinal displacement (c), bending stress at top-position (d), bending stress at side-position (e).

From Figures 5b-7b, the vertical displacements for the 'Sq+Eq' loading are larger than those in 'Eq' conditions, particularly at the quarter and the mid-span. Especially, the 'Sq+Eq' loading leads to larger values of the bending stress in the tunnel top-position (see Figures 5d–7d). Furthermore, taking a comparison between bending stress at the tunnel top-position in Figure 6d and Figure 7d, the seaquake effects enlarge the bending stress to a large degree, compared with only earthquake excitation.

Finally, comparing the bending stress in tunnel side-position at quarter-span and mid-span, see Figure 6e and 7e, the amplitudes in the 'Sq+Eq' case are close to those of the 'Eq' case, showing how the seaquake has little influence on the bending stress on the section side-position due to being these positions close to the neutral axis for bending when the bending moment acts in the vertical plane.

5 CONCLUSIONS

In this paper a SFT case study in a finite element software has been developed under different earthquake excitations, namely the multiple-support and the seaquake one. Dissipation devices have been implemented and, from the results so far obtained which relate to a single earthquake realization, they perform efficiently especially when both multiple-support and seaquake loading are considered together. As it concerns the other source of energy dissipation herein considered, that is to say energy dissipated by exploiting the inelastic behavior of the mooring system material, the anchoring bars largely exceed the yielding stress not only near the shore, where is can be expected due to the shorter length of the bars, but also at the quarter-span and mid-span along the tunnel.

The seaquake effect mainly induced a response in the vertical plane. Related to this aspect, it mainly affects the vertical displacement and the bending moment in the horizontal plane, and also this influences more the tunnel bending stress at the cross-section top position.

It can be thus inferred that seaquake effects will increase the probability of damage, both for the higher stress in the tunnel and for the higher deformation in the mooring bars. It follows that to this source of

excitation it should be paid a larger attention in the future designs.

ACKNOWLEDGEMENTS

The first author's work is partially supported by CSC (China Scholarship Council).

The remaining author are partially supported by MIUR (Italian Ministry of University and Research) under the project 'Dynamic response of linear and non-linear structures: modeling, testing and identification' (PRIN 2009).

Prof. F. Perotti (Department of Civil and Environmental Engineering – Politecnico di Milano) is also gratefully acknowledged for his scientific contributions and stimulating guidance.

REFERENCES

Ansys Rel. 14 2012. Ansys Inc, USA.

Chakrabarti, S.K. 1987. Hydrodynamics of Offshore Structures. *Computational Mechanics Publications*.

Clough, R.W. & Penzien, J. 1975. *Dynamics of structures*. Mc Graw Hill, New York N.Y.

Di Pilato, M., Feriani A., Perotti, F. 2008a. Numerical models for the dynamic response of submerged floating tunnels under seismic loading. *Earthquake Engineering and Structural Dynamics* 27(9): 1203–1222.

Di Pilato, M., Perotti, F., Fogazzi, P. 2008b. 3D dynamic response of submerged floating tunnels under seismic and hydrodynamic excitation. *Engineering Structures* 30: 268–281.

Ismail, M., Rodellar, J., Carusone, G., Domaneschi, M., Martinelli, L. 2013. Characterization, modeling and assessment of Roll-N-Cage isolator using the cable-stayed bridge benchmark, *Acta Mechanica* 224: 525–547.

Domaneschi M. 2010. Feasible control solutions of the ASCE benchmark cable-stayed bridge. *Structural Control and Health Monitoring* 17(6): 675–693.

Domaneschi, M. 2012. Simulation of Controlled Hysteresis by the Semi-active Bouc-Wen Model. *Computers and Structures* 106–107: 245–257.

Domaneschi, M., Martinelli, L. 2012. Performance Comparison of Passive Control Schemes for the Numerically Improved ASCE Cable-Stayed Bridge Model. *Earthquakes and Structures* 3(2): 181–201.

Hamamoto, T. 1995. Stochastic Fluid-Structure Interaction of Large Circular Floating Islands during Wind Waves and Seaquakes. *Probabilistic Engineering Mechanics* 10: 209–224.

Hong, Y. & Ge, F. 2010. Dynamic response and structural integrity of submerged floating tunnel due to hydrodynamic load and accidental load. *Procedia Engineering*, 4: 35–50.

Hove, K., Selnes, P.B., Bungum, H. 1982. Seaquakes, A potential threat to offshore structures, *Behaviour of Offshore Structures*; *Proceedings of the Third International Conference, Cambridge, USA, 1982*, 561–571.

Ingerslev, C. 2010. Immersed and Floating Tunnels. *Procedia Engineering* 4: 51–59.

Martinelli, L., Barbella, G., Feriani, A. 2010. Modeling of Qiandao Lake submerged floating tunnel subject to multi-support seismic input, *Procedia Engineering* 4: 311–318.

Martinelli, L., Barbella, G., Feriani, A. 2011. A numerical procedure for simulating the multi-support seismic response of submerged floating tunnels anchored by cables. *Engineering Structures* 33: 2850–2860.

Monti, G., Nuti, C., Pinto, P.E. 1996. Nonlinear response of bridges under multisupport excitation. *Journal of structural engineering*, 10: 1147–1159.

Shi, Chunxia, Domaneschi, M., Perotti, F. 2012a. Submerged Floating Tunnels under seismic motion: vibration mitigation issures. *5th European Conference on Structural Control (EACS2012), Genoa, Italy, June 18–20, 2012*.

Shi, Chunxia, Domaneschi, M., Martinelli, L. 2012b. Nonlinear Behaviors of Submerged Floating Tunnels under Seismic Excitation. *Applied Mechanics and Materials* 226–228: 1124–1127.

Shi, Chunxia, Martinelli, L. 2013. On the generation of seaquake velocity fields for Submerged Floating Tunnel structures. 4th International Conference on Manufacturing Science and Engineering (*ICMSE2013*), *Dalian, China.*

Research and Applications in Structural Engineering, Mechanics and Computation – Zingoni (Ed.)
© 2013 Taylor & Francis Group, London, ISBN 978-1-138-00061-2

An innovative solution for earthquake resistant hybrid steel-concrete systems with replaceable dissipative steel links

A. Zona, G. Leoni & A. Dall'Asta
Univesity of Camerino, Italy

T. Bogdan, C. Braham & H. Degée
University of Liège, Belgium

ABSTRACT: In this work innovative Hybrid Coupled Shear Walls (HCSW) are considered, their design is discussed, their efficiency and limitations evaluated by means of nonlinear static (pushover) analysis. Different numbers of storeys, wall geometries and design assumptions are studied in order to give an overview of situations of interest in European seismic prone areas. The design of an experimental test regarding the performance of the connection of a seismic link embedded in a concrete shear wall is presented. This study is part of a larger research project named INNO-HYCO (INNOvative HYbrid and COmposite steel-concrete structural solutions for building in seismic area) funded by the European Commission.

1 INTRODUCTION

Steel-concrete hybrid structures are of current limited application for construction in seismic areas, compared to classical steel-concrete composite structures. However, their use seems promising provided that suitable structural schemes and proper design methods are identified and developed. While the deformation demands for the steel and concrete components in traditional composite structures are in the same range (since concrete and steel are part of a same structural member), hybrid structures allow a more efficient design of both the reinforced concrete and the steel structural elements. In this context, the present paper proposes an innovative hybrid solution coupling concrete shear walls by steel link elements tailored to act as dissipative replaceable fuses. The concrete wall is designed to control the stiffness while the links are controlling the resistance and optimized for an efficient dissipation of the seismic energy. Preliminary design is discussed and efficiency and limitations of the system are evaluated by means of nonlinear static and dynamic analyses. Different numbers of storeys and different global geometries of the structural system are examined in order to give an overview of situations of interest in European seismic prone areas.

Objective of the research project INNO-HYCO (INNOvative HYbrid and COmposite steel-concrete structural solutions for building in seismic area), funded by the European Commission, is the study of steel-concrete hybrid systems obtained by coupling reinforced concrete elements (e.g., walls and shear panels) with steel elements (e.g., beams and columns). Such systems should permit to exploit both the stiffness of reinforced concrete elements, necessary to limit building damage under low-intensity earthquakes, and the ductility of steel elements, necessary to dissipate energy under medium- and high-intensity earthquakes. Such hybrid systems might represent a cost- and time-effective type of construction since: (i) simple beam-to-column connections could be used for the steel frame constituting the gravity-resisting part, (ii) traditional and well-known building techniques are required for the reinforced concrete and steel components.

2 COUPLED SHEAR WALL SYSTEMS

2.1 *Conventional systems*

Coupled shear wall systems obtained by connecting reinforced concrete shear walls by means of beams placed at the floor levels constitute efficient seismic resistant systems characterized by good lateral stiffness and dissipation capacity. Structural steel coupling beams (Figure 1) or steel-concrete composite coupling beams provide a viable alternative (e.g. El-Tawil et al. 2010), particularly for cases with restrictions on floor height. The coupling beam-wall connections depend on whether the wall boundary elements include structural steel columns or are exclusively made of reinforced concrete elements. In the former case, the connection is similar to beam-column connections in steel structures. In the past decade, various experimental programs (El-Tawil et al. 2010) were undertaken to address the lack of information on the interaction between steel coupling beams and reinforced concrete shear walls. Coupled shear wall systems suffer from being difficult to be repaired after strong earthquakes.

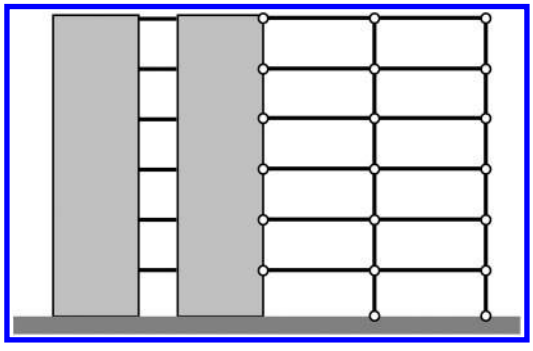


Figure 1. Example of conventional hybrid coupled shear wall system connected to a gravity-resisting steel frame with pinned beam-to-column joints.

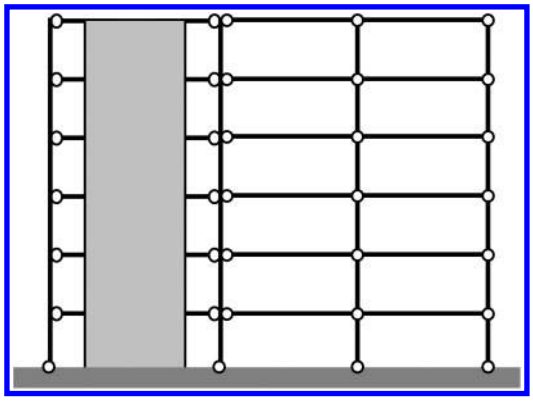


Figure 2. Example of innovative hybrid coupled shear wall system connected to a gravity-resisting steel frame with pinned beam-to-column joints.

2.2 *Innovative systems*

An example of innovative hybrid system is the reinforced concrete shear wall with steel links depicted in Figure 2. The connections between steel beams (links) and the side steel columns are simple: a pinned connection ensures the transmission of shear force only while the side columns are subject to compression/traction with reduced bending moments.

The structure is simple to repair if the damage is actually limited to the link steel elements. To this end, it would be important to develop a suitable connection between the steel links and the concrete wall that would ensure the easy replacement of the damaged links and, at same time, the preservation of the wall. Clearly, the proposed hybrid system is effective as seismic resistant component if the yielding of a large number of links is obtained.

3 DESIGN OF HCSW SYSTEMS

3.1 *Case study*

Two case studies are considered: 4-storey and 8-storey steel frames with the same floor geometry as shown in Figure 3. For each floor the vertical loads are $G_k = 6.5\,\text{kN/m}^2$ and $Q_k = 3.0\,\text{kN/m}^2$, while the floor total seismic mass is $1200\,\text{kNs}^2/\text{m}$. Interstorey height is $h = 3.40\,\text{m}$. The gravity-resisting frame has continuous columns (Table 1) pinned at the base. Beams (IPE500) are pinned at their ends. Steel S355 is used for columns, beams, and links. Selected materials for the reinforced concrete walls are concrete C25/30 and steel reinforcements S500.

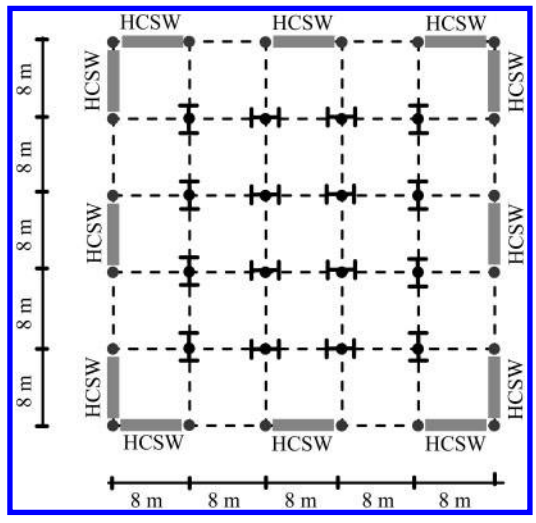


Figure 3. Floor geometry of the benchmark structures with positions of the HCSWs.

Table 1. Wide-flange cross sections of the columns of the vertical-resisting structure.

Storey #	4-storey case	8-storey case
8	–	HE 220 B
7	–	HE 220 B
6	–	HE 300 B
5	–	HE 300 B
4	HE 220 B	HE 450 B
3	HE 220 B	HE 450 B
2	HE 300 B	HE 450 M
1	HE 300 B	HE 450 M

The assumed seismic action is represented by the Eurocode 8 type 1 spectrum with $a_g = 0.25\,\text{g}$ and ground type C. Both verifications of the ultimate limit state (ULS) and of the damage limit state (DLS) are required.

3.2 *Preliminary design*

Preliminary designs based on the conventional force approach were made in order to identify possible optimal geometries. Two conditions were required in the design: (i) strength verification at ULS under the lateral forces derived from the design spectrum following the prescriptions in Eurocode 8.

A large number of HCSWs with different dimensions of the reinforced concrete shear walls and link lengths were evaluated and the seismic behaviour of the most promising designs was assessed through nonlinear static (pushover) analysis and multi-record incremental nonlinear dynamic analysis.

In the 4-storey case it is observed that reinforcements in the concrete wall yield together with yielding in bending of the steel links in the first three storeys. Afterwards, further plastic dissipation is fostered by the successive yielding in bending of the links at the last storey. Then the peak strength of the reinforced concrete wall is achieved leading to the maximum sustained base shear before leading the bracing system to failure due to failure of the reinforced concrete wall. A different seismic performance is observed in the 8-storey design, where the steel links at all storeys yield in bending before any damage in the reinforced concrete wall. Afterwards reinforcements yields and shortly afterwards all links yield in shear. The concrete peak strain is attained but the bracing system is still able to exhibit global hardening. Collapse is reached when the link at the fifth storey fails in combined banding and shear. Despite these differences, pushover verifications are satisfied (capacity displacement larger than target displacement) in both case studies. In addition, it is observed that the HCSW systems designed are not prone to soft storey formation, even when the yielding of the steel links is not simultaneous, thanks to the contribution of the reinforced concrete wall.

3.3 *Design based on rules inherited from other systems*

The results obtained in this first design stage directed the research towards the definition of a design approach that inherits recommendation for capacity design from other structural systems involving similar dissipative mechanisms in the links, i.e. eccentric braces in steel frames, as well as indication to reduce damages in the reinforced concrete wall. The design procedure attempted in this second stage of this research is subdivided in the following steps:

- Step 1: assign dimensions of the reinforced concrete wall by selecting height-to-length ratio and thickness;
- Step 2: design of the steel links based on bending and shear obtained from linear analysis (e.g. spectrum analysis) with assigned uniform overstrength; design of the steel side columns using the summation of the yield shear forces of the links (amplified with $1.1\gamma_{ov}$) as design axial force;
- Step 3: design of the wall longitudinal reinforcements to provide an assigned over-strength compared to the bending moment obtained from linear analysis; design of the transverse reinforcements to avoid shear collapse of the wall considering the maximum shear at the base derived from the limit condition of yielded steel links and yielded wall in bending; reinforcement detailing according to Eurocode 8 DCM rules.

The application of the above design rules and the necessity to limit the shear force at the base of the wall brought to the adoption of six HCSW systems for each direction (Figure 3). In order to investigate the main geometric and design parameters, 18 cases were designed, comprising three height-to-length ratios of the wall taken with constant thickness and relevant links (length 600 mm for the 4-storey case and 660 mm for the 8-storey case) designed with over-strength equal to one, longitudinal reinforcements in order to obtain three values of wall over-strength (1.00 in cases labelled as R10, 1.25 in cases labelled as R12, 1.50 in cases labelled as R15), as detailed in preliminary report “” produced by ULg. Reinforcement bars were concentrated in the lateral confined parts of the wall as for Eurocode 8 DCM rules. Significant quantities of longitudinal bars were required, especially for R15, in some cases exceeding Eurocode upper limits.

4 DESIGN OF DOWN SCALED CONNECTION

4.1 *General assumptions*

The tests aim to characterize the performance of the connection of a seismic link embedded in a concrete shear wall and the efficiency of the capacity design of such a system, with the objective of developing a plastic hinge in the replaceable part of the link, acting as a fuse, with all other components of the connection remain undamaged. For the materials, design values are used concrete C 25/30, steel grades (S275 for the link, S355 for the embedded part and S500 for reinforcements). The links are defined as being intermediate and the link stiffeners number is determined using a linear interpolation and the link rotation angle value θ_p. Face bearing plates are placed at the face of the concrete wall, in order to keep the integrity of the concrete part and for the yielding to take place in the profile section or rebars. The concrete wall dimensions are consistent with the experimental stand dimensions and the embedment length of the steel profile into the concrete part.

Two topologies are considered for what regards the embedment of the profile in the concrete shear wall and the connection of the replaceable part of the link to the embedded part.

– *Configuration No. 1 (Figure 4)* – The bending moment transferred by the link to the wall is resisted by shear studs, while the beam splice connection is placed at a distance of 100 mm from the top face of the concrete wall in order to allow an easy bolting of the removable part.

The design assumptions consists in forcing the creation of a plastic hinge in the replaceable part of the link and to capacity-design the part of the fixed part of the link embedded in the shear wall, the link-to-shear-wall connection and the bolted beam splice connection between the fixed and replaceable parts of the link.

The required number of shear studs is influenced by the value of the fore V, as shown in Figure 4. The

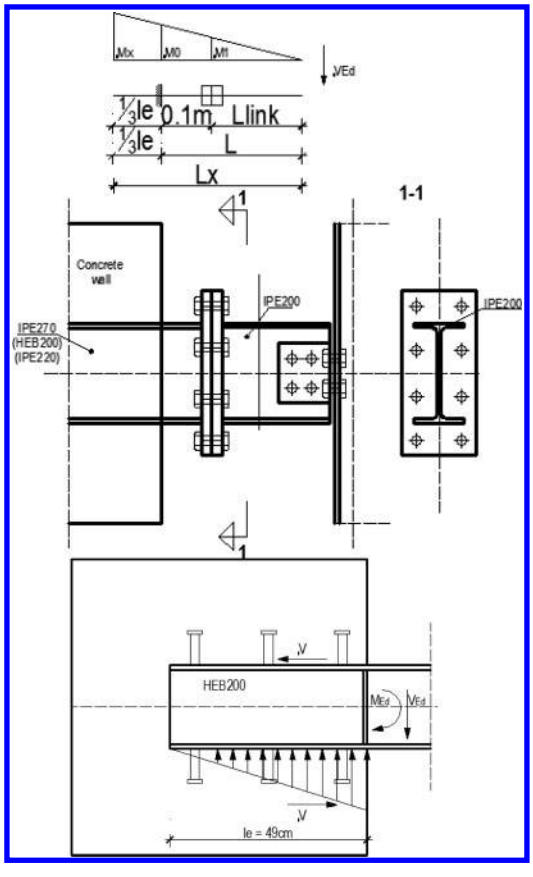


Figure 4. Configuration No. 1 – mechanical model.

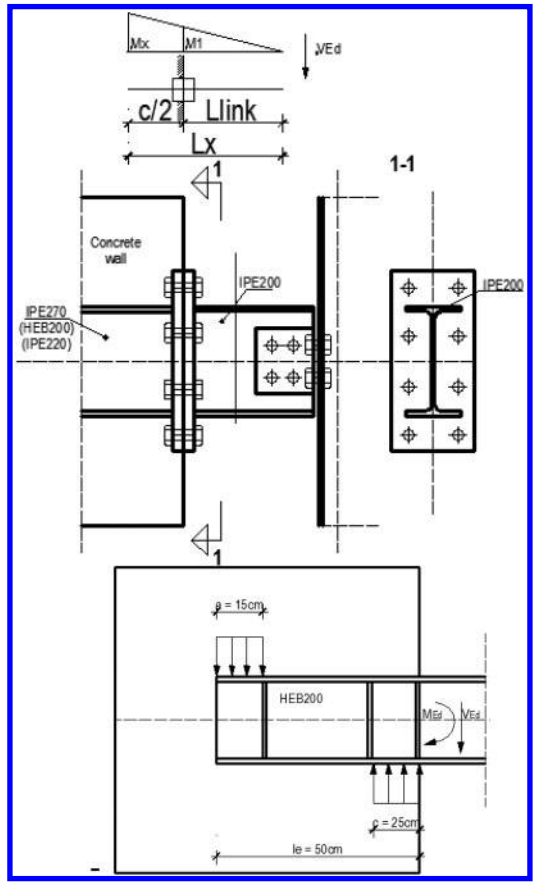


Figure 5. Configuration No.2 – mechanical model.

embedment length is determined using equilibrium equations of the mechanical model.

– *Configuration No. 2 (Figure 5)* – The bending moment transferred by the link to the wall is balanced by a couple of vertical forces. The connection link – embedded steel profile is placed at the top of the wall using threaded bushings.

The main differences with configuration 1 are:

- The positioning of the beam-splice connection of the fuse with the embedded part of the link. The end-plate is positioned right at the face of the shear wall, acting thus also as face bearing plate. Moreover, the connection is assumed to be realized in practice with threaded bushes instead of regular bolts;
- The assumed load transfer mechanism between the embedded part of the link and the concrete shear wall. In this case, no shear studs are used and a longer embedded part is considered in order to develop a static scheme where the applied bending moment is resisted by a couple of vertical load, activating the compression resistance of the contact profile-concrete.

According to the transfer mechanism, the embedded part of the profile is designed assuming conservatively that the bending moment increased linearly until the location of the first reaction force applied by the concrete on the profile.

The design of the beam splice connection has been realized with CoP, software developed by Universities of Aachen and Liege, based on the component method. The aimed and governing failure of the connection is failure of the steel bolts, before yielding of the beam flange of the profile.

5 SEISMIC BEHAVIOUR OF HCSW SYSTEMS

5.1 *Modelling assumptions and selected results*

The seismic behaviour of the designed HCSW systems was assessed through displacement-controlled nonlinear static analysis under applied lateral loads (pushover analysis), using the software FinelG. For the sake of simplicity, the evaluation of the seismic performances is based on a plane model of a single HCSW connected to two continuous columns equivalent to the relevant parts of the gravity-resisting steel frame, as shown In Figure 6 (4-storey case).

The reinforced concrete shear wall is represented by frame elements using a fibre description for the behaviour of the concrete in the longitudinal direction, allowing an accurate estimation of the behaviour

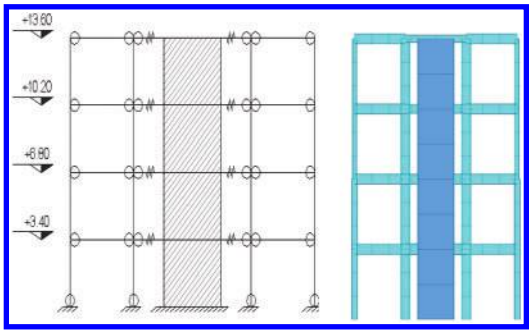


Figure 6. Numerical model.

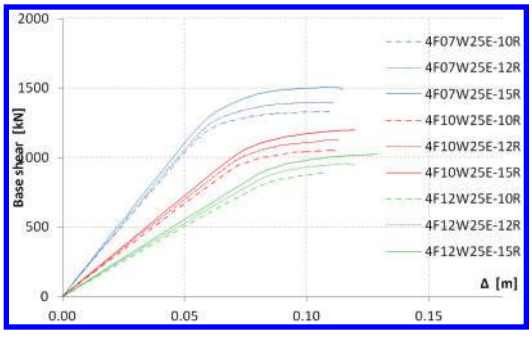


Figure 7. Pushover curve – global comparison.

in bending and thus of the possible plastic hinge at the bottom of the wall. Reinforcement of the shear wall is assumed to be sufficient to avoid a shear failure of the wall. The steel shear links are modelled using non linear frame elements for the bending contribution as well as non linear shear springs introduced at mid span of each steel link to account for the shear deformability of the link and for the possible yielding in shear of the links. This additional shear spring is required for a correct modelling of the system since most links are classified as intermediate according to EC8 definition and are thus more or less equally prone to shear or bending failure. Interaction between flexural and shear plastic deformations is considered in the post-processing of the results.

For all materials, the design values of the resistance are used ($f_{cd} = 20$ MPa, $f_{y,s} = 435$ MPa, $f_{y,p} = 355$ MPa). Steel behaviour is modelled by a bilinear elastic-perfectly-plastic law without strain hardening. Concrete is by a parabola-rectangle in compression and a linear behaviour in tension with tension stiffening. Particular values of the strain are $\varepsilon_{c2} = 0.002$ (end of the parabolic behaviour) and $\varepsilon_{cu2} = 0.0035$ (end of the rectangular behaviour). No confinement is considered for the concrete in compression.

Pushover curves (total base shear versus top displacement) for the 4-storey cases are shown in Figure 7, while for the 8-storey case is shown in Figure 8.

It is observed that increasing the wall over-strength has positive effects as the yielding of reinforcements and failure of the wall (attainment of the ultimate strain

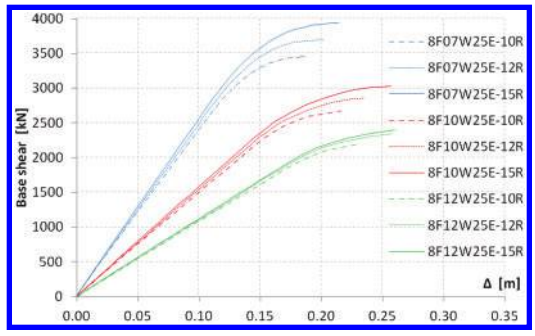


Figure 8. Pushover curves – global comparison.

in the concrete) are delayed, resulting in an increment of the lateral load capacity as well as in an increment of the global ductility of the HCSW systems. However, these benefits are obtained at the expenses of an often excessive congestion of reinforcements. It is also observed that a reduction of the wall aspect ratio allows a higher lateral load capacity as well as a higher ductility. Given that a reduction of the aspect ratio means smaller steel links and longer walls that allow more space for reinforcements, the design should be based in practice on a limitation of the wall aspect ratio, possibly limited to suggested values $H/l_w \leq 10$.

5.2 *ULS and DLS verifications*

Outcomes in terms of pushover curves presented in section 5.1 can be analyzed with respect to different ULS and DLS criteria. This allows in particular the calculation of specific performance points associated the activation with different limit states and hence, based on the N2 method proposed in Annex B of Eurocode 8, the calculation of the acceleration level corresponding to these performance points. In the present contribution, only preliminary assessments are given. The outcomes will be more deeply investigated in the next publications on the INNO-HYCO project. Three different limit states are taken into consideration:

- *ULS1: Maximum compressive strain reached in the concrete shear wall*. No confinement is conservatively taken into account. Accounting for the confining effect by imposing rules similar to those prescribed by EC8 for reinforced concrete walls could certainly improve the global behaviour of the system.
- *ULS2: Maximum rotation of the steel links*. In this preliminary assessment, indicative conservative values of the maximum possible rotation capacity are estimated according to the criteria proposed by FEMA 356 for seismic links in eccentrically braced structures. The values must be adjusted in a next stage on the base of experimental test results to be carried out in the context of the INNO-HYCO project.
- *DLS: Maximum allowable inter-storey drift.* Associated values of the acceleration should be referred to acceleration level for DLS, smaller than the reference design value of 0.25 g.

Table 2. Maximum sustainable accelerations from pushover curves and ULS/DLS criteria [in g].

ID step1	ULS1	ULS2	DLS
4F07W25E – 10R	0.22	0.19	0.11
4F07W25E – 12R	0.23	0.18	0.11
4F07W25E – 15R	0.26	0.14	0.07
4F10W25E – 10R	0.18	0.18	0.11
4F10W25E – 12R	0.18	0.18	0.09
4F10W25E – 15R	0.15	0.14	0.06
4F12W25E – 10R	0.14	>0.14	0.08
4F12W25E – 12R	0.14	>0.14	0.08
4F12W25E – 15R	0.13	>0.13	0.06
8F07W25E – 10R	0.27	0.24	0.14
8F07W25E – 12R	0.3	0.25	0.15
8F07W25E – 15R	0.35	0.29	0.18
8F10W25E – 10R	0.24	0.24	0.11
8F10W25E – 12R	0.26	0.25	0.12
8F10W25E – 15R	0.29	0.26	0.12
8F12W25E – 10R	0.21	>0.24	0.10
8F12W25E – 12R	0.24	0.24	0.10
8F12W25E – 15R	0.25	0.25	0.10

Table 3. Behaviour factors at $a_g = 0.25$ g.

ID step1	10R	12R	15R
4F07W25E	2.77	2.59	2.30
4F10W25E	2.81	2.94	2.55
4F12W25E	1.86	2.15	1.97
8F07W25E	1.30	1.28	1.41
8F10W25E	1.22	1.23	1.24
8F12W25E	1.17	1.21	1.19

Results are provided in Table 2 in terms of maximum acceleration for the 4-storey and 8-storey cases. Additionally, Table 3 gives the values of the behaviour factor estimated from an equivalent bilinear curve on the base of the ductility.

6 CONCLUDING REMARKS

A selection of results involving an innovative steel-concrete hybrid coupled shear wall systems developed under the European research project INNO-HYCO was briefly illustrated. The analysis of the case studies designed according to the adoption of existing rules in the Eurocodes has highlighted the potentialities of the proposed innovative HCSW systems, namely: it is actually possible to develop a ductile behaviour where plastic deformation are attained in the steel links and limited damage occurs in the reinforced concrete wall; the interstorey drifts up to collapse are quite regular regardless of the non-simultaneous activation of the plastic hinges in the steel links and/or in the reinforced concrete wall; the adopted design approach based on well-known concepts and procedures already available in the Eurocodes give a promising starting design solution, although it appears that using the behaviour factor proposed by Eurocode 8 for composite walls overestimates the deformation capacity of the HCSW, in particular for short walls. On the other hand, the following issues have been encountered: the designed solutions require additional studies to clarify the relationships between wall and links in order to provide additional design recommendations as integration of the Eurocodes; the slenderness of the HCSW systems needs to be better controlled in order to limit the negative effects of geometric nonlinear effects and improve the behaviour at the damage limit states. However, the sensitivity of the response to rotation capacity of the links and to confinement of the concrete needs also to be deeper studied, including in the context on time-history analysis. The upcoming developments of this research work involve the definition of a design procedure compatible with the current Eurocode 8 recommendations and in-depth experimental studies on the connections between reinforced concrete wall and replaceable dissipative steel links.

ACKNOWLEDGMENT

Support for this research from the European Commission, Research Fund for Coal and Steel, Steel Technical Group TGS 8 “Steel products and applications for building, construction and industry”, is gratefully acknowledged. H. Degée also acknowledges the support received from F.R.S.-FNRS.

REFERENCES

ASCE, 2009. *Recommendations for seismic design of hybrid coupled walls*, ASCE Composite Construction Committee.

Dall’Asta, A., Leoni, G., Zona, A., 2011. INNO-HYCO INNOvative HYbrid and COmposite steel-concrete structural solutions for building in seismic area, First Annual Report.

Dall’Asta, A., Leoni, G., Zona, A., 2012. INNO-HYCO INNOvative HYbrid and COmposite steel-concrete structural solutions for building in seismic area, Mid-term Report.

T. Bogdan, H. Degée, 2013. INNO-HYCO INNOvative HYbrid and COmposite steel-concrete structural solutions for building in seismic area: pushover analysis protocol, Preliminary report.

El-Tawil, S., et al., 2010. Seismic design of hybrid coupled wall systems: state of the art, *Journal of Structural Engineering*, **136**(7), 755–769.

FEMA356: Guideline for seismic rehabilitation of buildings, Federal Emergency Management Agency, 2002.

Paulay, T., Priestley, M.J.N., 1992. *Seismic design of reinforced concrete and masonry Buildings*, Wiley.

Zona, A., Braham, C., Degée, H., Leoni, G., Dall’Asta, A., 2011. Innovative hybrid coupled shear walls for steel buildings in seismic areas. *XXIII Italian Steel Structure Conference (CTA)*. 9–12 October, Ischia, Italy.

Zona A., Leoni, G. Dall’Asta, A., Braham, C., Bogdan, T., Degée, H., 2012. Behaviour and design of innovative hybrid coupled shear walls for steel buildings in seismic areas. 15th World Conference on Earthquake Engineering, 24–28 September, Lisbon, Portugal.

Research and Applications in Structural Engineering, Mechanics and Computation – Zingoni (Ed.)
© 2013 Taylor & Francis Group, London, ISBN 978-1-138-00061-2

Effectivenss of seismic protection by added damping: An energy approach

I. Ladar, O. Prodan & N. Chira
Technical University of Cluj-Napoca, Romania

ABSTRACT: The contribution proposes an analytical tool to assess the energy demand to be used in energy based structural design. An important step in energy based structural design is the assessment of energy demand that is going to take the unprepared structure into post-elastic incursions. While added damping may reduce this amount of energy, the designer is, still, uncertain of its efficacy. Proposed technique allows for an immediate and simple check of this efficacy. Several numerical studies have been performed on full scale steel multistory structures aiming at computation of energy components developed during seismic action. Also, a set of laboratory seismic tests have been conducted to the same objective on scaled down steel structures. Processed results have been synthetized into the proposed ratio for assessing the efficacy of added damping. Its values and time-variation emphasize allow for immediate conclusions and, possible, changes regarding the amount of added damping during the design activity.

1 INTRODUCTION

The objective of the present contribution is to introduce an energy approach to the assessment of effectiveness of passive protection of steel multistory structures equipped with passive seismic protection via added viscous damping. Numerical and experimental studies have been carried out to back up the assessment technique of the added viscous damping. Current techniques are, mainly, based on checking the values of several static and kinematical parameters against their code prescribed maximum values. This is the standard and correct way in the case of structure design. A rather popular approach is to compare the reduction in lateral displacements induced by seismic excitation. Indeed, the reduction – via seismic protection – in lateral displacements of shear multistory structures seismically induced is an easy, immediate and visible effect of any system of seismic protection. Nevertheless, the seismic response of structures is a broader concept that includes, beside classical components (such as stresses and deformations), synthetic and stronger components such energy quantities. Since Housner's pioneering work on energy approach to seismic input [1], several outstanding works and results have paved the way to present day energy based seismic design. Among the first objectives of the new field of research has been the assessment of seismic input energy [2], [3], [4], [5]. Next clear cut objective consists in exploiting the new analysis tool to assess the future damages that a prescribed earthquake will in inflict into a given structure [6], [7]. Based on possible seismic induced damages, the computation of structure capacity to dissipate the seismic input energy – the already popular – seismic energy demand became a new performance objective [8], [9]. As expected, the structures had to be equipped with industrial devices that increase their energy dissipating capacity. Almost entire scene has been set for the structural design based on energy approach while the results appeared continuously [10], [11], [12]. This is the most advanced stage in the new domain of energy based structural computation. The up to day level of energy approach to structural computation did not prevent a continuous research over the whole issue of the field. Present contribution belongs to the narrow topics of assessing the effectiveness of added viscous damping by using energy concepts and quantities. The supplementary damping is provided in the form of linear viscous damping by viscous dampers inserted into steel multistory structures. The assessment of effectiveness of seismic protection is not just a tool to check the quality of the final product (seismic protection). It is necessary in the more elaborated activity of structural design, mainly, in designing the (hysteretic) energy demand of future structure. Providing for energy demand (hysteretic dissipating capacity of designed structure) is a must of today structural engineering. The relevance of an adequate tool to measure the effectiveness of seismic protection system is generated by the importance of providing for energy demand in structural design activity. Since the seismic protection via energy dissipating equipment has been implemented, several "instruments" for assessing effectiveness of seismic protection have been proposed [13], [14]. Energy approach to structural computation requires an energy based technique to such an assessment. The contribution introduces such a scalar parameter that focuses on expressing the capacity of a structure to absorb seismic energy. If E_i is the seismic input energy and E_d is the total dissipated energy (by inherent and added damping), the quantity (E_i–E_d) expresses the energy that has to be "faced" by the

equipped structure through deformations. Since the structure has been provided with added damping, the deformations are allowed in the elastic domain only, usually limited by design codes to small values. The smaller the quantity (E_i–E_d) the smaller seismically induced elastic deformations. Consequently, the ratio $E_i/(E_i–E_d)$ is directly proportional to the capacity of designed structure to avoid plastic deformations and to keep elastic deformations inside the code provided limits. The contribution proposes the above ratio as a measure of the effectiveness of seismic protection by added damping. The proposed ratio is capable to express the effectiveness of added damping at every instant of seismic action. Usually, at the end of seismic action, the energy balance may be "reduced" to its simplest form (1)

$$E_d = E_i \tag{1}$$

since the kinetic energy E_k and elastic strain energy E_s do no longer contribute (due to their tendency to vanish towards to the end of seismic action) to the energy balance

$$E_k + E_s + E_d = E_i \tag{2}$$

valid at an instant t of seismic action. By expressing the effectiveness of added damping at every instant, an adequate seismic behavior of designed structure could be achieved over the entire duration of earthquake.

The contribution is structured into four parts: a general view of energy balance of multi degree of freedom steel structures, a theoretical study of a set of multistory steel structures via energy approach, a presentation of numerical results specific to energy approach associated to a set of laboratory tested structures seismically acted and finally, an emphasize on proposed technique of assessing the effectiveness of added damping together relevant concluding remarks.

2 ENERGY FORMULATION OF MDOF STRUCTURES UNDER SEISMIC ACTION

Classical technique regarding the dynamic model, energy components, energy balance equation of seismically acted shear multistory steel structures is adopted: the n – dimension vector of degrees of freedom u(t) together the associated velocities $\dot{u}(t)$ and accelerations ü(t), ground seismically induced acceleration $\ddot{u}_g(t)$, the nxn inertia matrix **M**, nxn damping matrix **C** (inherent Rayleigh type and added damping), the nxn stiffness matrix **K**, unit n vector dimension 1.

Modal analysis of damped free vibrations lead to the well-known modal results: eigen periods T_j, eigen circular frequencies ω_j, eigen n vectors Φ_j, modal nxn matrix Φ.

In what regards damping, the Rayleigh type damping matrix is processed from its proportional form (3)

$$\mathbf{C} = \alpha\cdot\mathbf{M} + \beta\cdot\mathbf{K} \tag{3}$$

to its diagonal form (4) following [15].

$$\mathbf{c} = \mathbf{\Phi}^T\cdot\mathbf{C}\cdot\mathbf{\Phi} \tag{4}$$

The relative energy components associated to seismic behavior over the entire duration t_c of the earthquake read:

Seismic input energy

$$E_i = -\int(\dot{\mathbf{u}})^T\cdot\mathbf{M}\cdot\mathbf{1}\cdot\ddot{u}_g(t)\cdot dt \tag{5}$$

Kinetic energy

$$E_k = \int(\ddot{\mathbf{u}})^T(t)\cdot\mathbf{M}\cdot\dot{\mathbf{u}}\cdot dt \tag{6}$$

Elastic strain energy

$$E_s = \int(\mathbf{u})^T(t)\cdot\mathbf{K}\cdot\dot{\mathbf{u}}(t)\cdot dt \tag{7}$$

Energy dissipated (inherent linear viscous and added viscous damping)

$$E_d = \int(\dot{\mathbf{u}})^T(t)\cdot\mathbf{c}\cdot\dot{\mathbf{u}}(t)\cdot dt \tag{8}$$

The relative energy balance equation takes the form:

$$E_k + E_s + E_d = E_i \tag{9}$$

Relative forms (5–8) of energy components and energy balance equation (9) have been adopted as the results of laboratory tests proved to be more accurate in the case of the values of relative story displacements/velocities/accelerations in what regards their measured and computed values. The computation of integral quantities has been performed following a linear integration procedure associated to a time interval $\Delta t = 0.02$ sec.

3 THEORETICAL STUDIES

Theoretical studies have been carried out on three structures six story one bay steel frames of the same general geometry (Fig. 1), while the lateral stiffness is gradually increased through higher stiffness values of

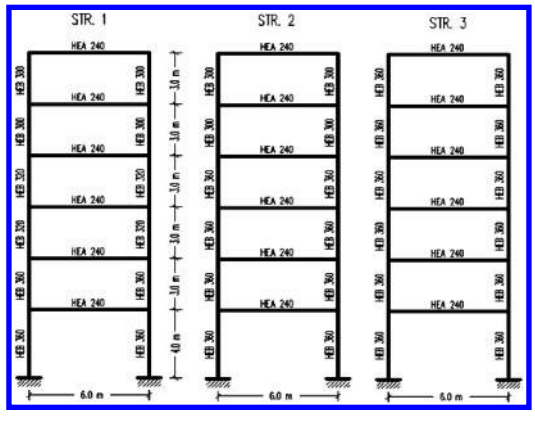


Figure 1. Steel frames STR1, STR2 and STR3.

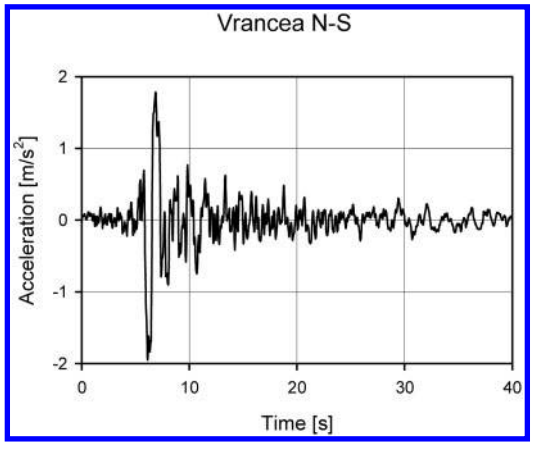


Figure 2a. Vrancea 1977 earthquake.

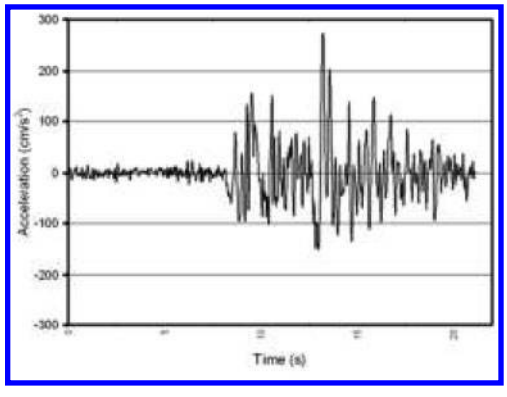


Figure 2b. Focsani 1986 earthquake.

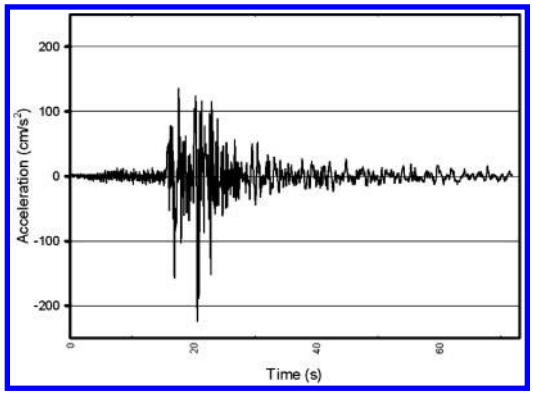


Figure 2c. Focsani 1990 earthquake.

the columns cross sections. The three structures have been designed for a peak seismic acceleration value of $a_g = 0.3\,g$ according to Romanian seismic code applied simultaneously with a gravitational loading of 60.0 kN/m on current beams and 40.0 kN/m on top beam. Several levels of damping have been considered: a reference level of 1.0% and two increased damping levels (ratio of critical damping ζ) of 5.0% and 9.0%, respectively. Story lateral displacements u_i ($i = 1 \div 3$)

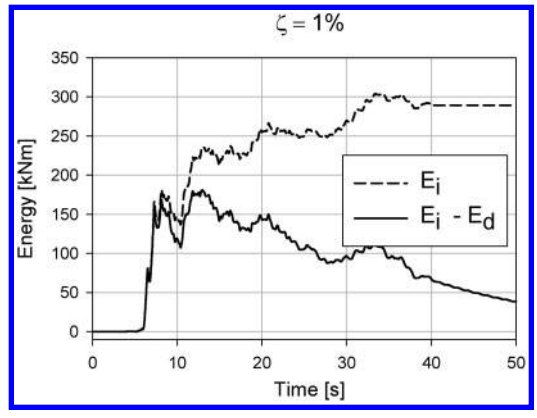


Figure 3. Energy quantities for $\zeta = 1\%$.

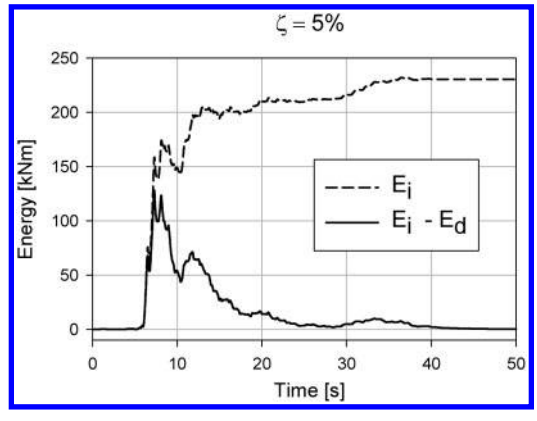


Figure 4. Energy quantities for $\zeta = 5\%$.

collected in the three degrees of freedom vector **u** ad to the general picture of dynamic MDFO model. Seismic actions are applied in the form of three recorded (in Romania) earthquakes: Vrancea 1977 (Figs 2), Focsani 1986 and Focsani 1990 – reference earthquakes in this country.

Modal and time history analyses of each frame under each earthquake have been performed and kinematical parameters (displacements, velocities and accelerations) associated to seismic behavior have been computed. The most relevant primary results (kinematical parameters) and processed parameters (energy quantities) results for the structure STR1 are presented (Figs 3–5). The area defined by E_i–E_d is the amount of energy the structure has to "face".

4 LABORATORY RESULTS

A set of three scaled down steel frames have been tested using a small seismic platform. A high flexibility has been provided to the tested frames to ensure large lateral deformations exclusively inside the elastic behavior of the tested structure. Dynamic model of the three story tested frame includes the lumped masses located in the frame joints (Fig. 6). The tests have been conducted in two cases: on the reference frames (no added

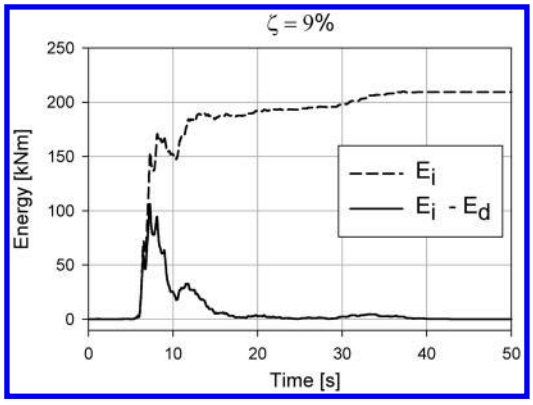


Figure 5. Energy quantities for $\zeta = 9\%$.

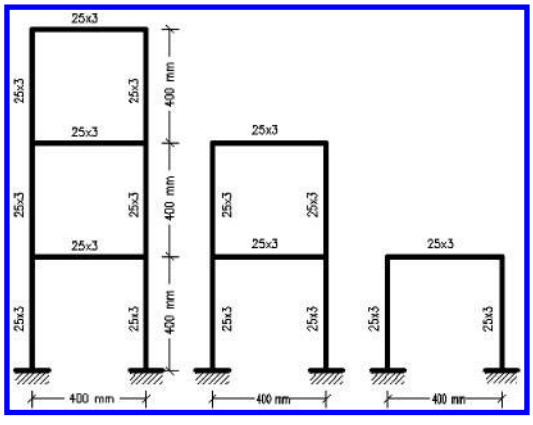


Figure 6. Laboratory tested frame. Geometry.

damping) and on the frame equipped with linear fluid viscous dampers (Fig. 7). Seismic load has been applied in the form of three recorded and processed accelerograms (Northridge 1994, Kobe 1995, Chi–Chi 1999) provided together with the shaking table.

Using digital transducers, the lateral displacements and accelerations have been recorded. In accordance to their values, the energy components are computed from equations (5–8). Variations of energy components E_i and $(E_i–E_d)$ for Kobe 1995 and Northridge 1994 emphasize their expected shape (Figs 8–9).

Proposed ratio (10) of effectiveness assessment and its variation in time have been graphically emphasized for Kobe-1995 earthquake (Fig. 10). The pseudoconstant amount of energy demand between $t = 2$ seconds and $t = 6$ seconds (Fig. 10) closely follows the shape of Kobe 1995 recorded and scaled earthquake

$$\varepsilon = (E_i - E_d)/E_i \qquad (10)$$

Variation (in time) of proposed ε for the reference structure (Fig. 10) expresses an almost constantly decreasing need of energy dissipating capacity (area under each of the two curves). Again, this shape is in accordance with the shape of accelerograms associated to the two earthquakes (a strong initial shock in the case

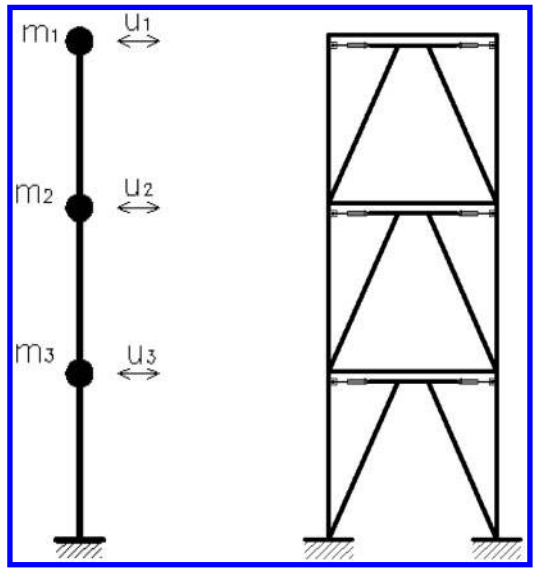


Figure 7. Dynamic model and the frame equipped with viscous dampers.

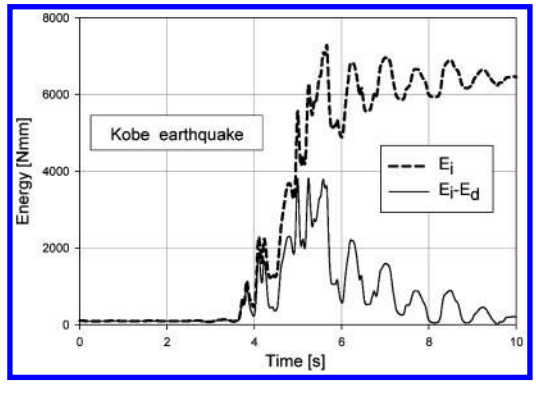


Figure 8. Reference 3 story structure.

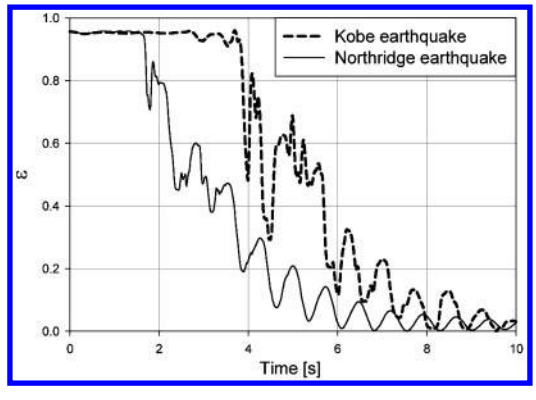


Figure 9. Reference 3 story structure.

of Northridge earthquake). Once this initial energy "hunger" is satisfied, the structure may carry on the remaining induced vibration motion. It may transmit a clear message to the structural engineer in what regards

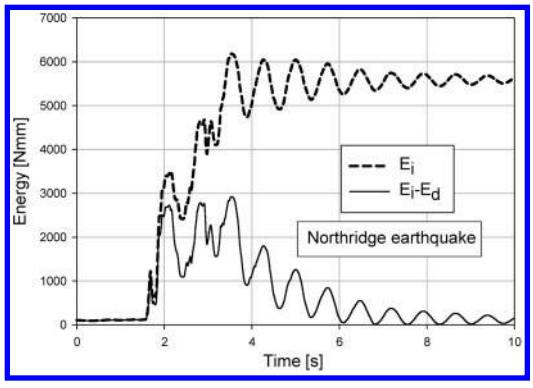


Figure 10. Effectiveness ε ratio. Reference structure.

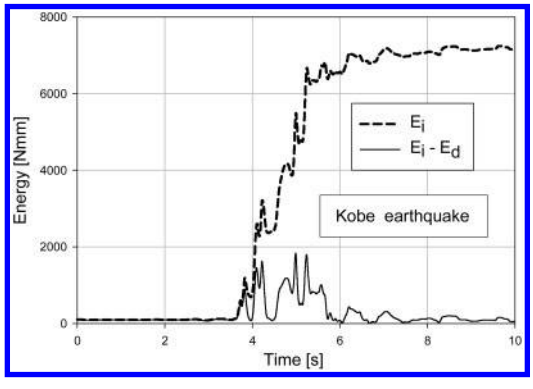


Figure 11. Structure with dampers.

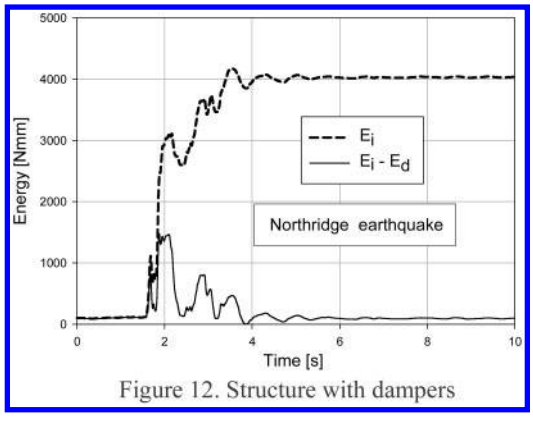


Figure 12. Structure with dampers.

the seismic protection in terms of required amount of added damping or energy absorbing devices.

Similar variations of energy quantities E_i and (E_i–E_d) for the case of structure equipped with fluid viscous dampers are, further presented (Figs 11–12). It can be noticed the small amount of energy absorbing capacity "uncovered". Indeed, the installed dampers (Fig. 7) are performing their "job" of providing energy absorbing capacity.

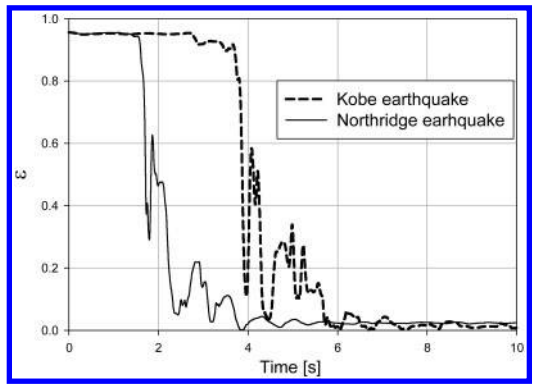


Figure 13. Equipped structure. Effectiveness ratio ε.

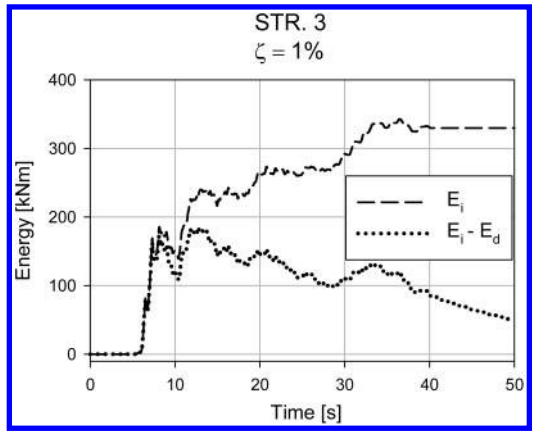


Figure 14. Energy quantities for $\zeta = 1\%$.

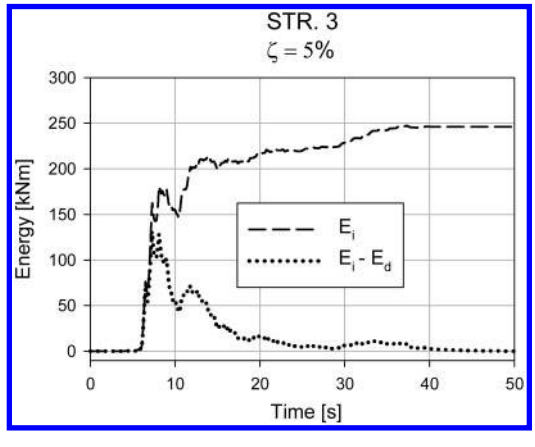


Figure 15. STR3 with $\zeta = 5\%$ damping.

A corresponding variation of proposed ratio ε for the case of structure equipped with fluid viscous dampers is presented in Figure 13.

Several other results obtained in terms of seismic input energy E_i, energy demand (E_i–E_d) in the case of structure STR3 are presented for critical damping ratio $\zeta = 1\%$ (Fig. 14), $\zeta = 5\%$ (Fig. 15) and $\zeta = 9\%$

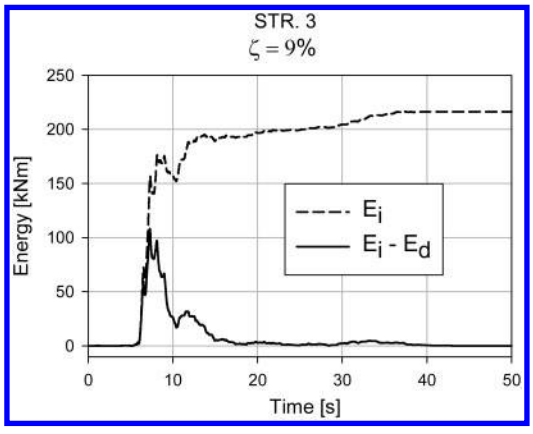


Figure 16. STR3 with $\zeta = 9\%$ damping.

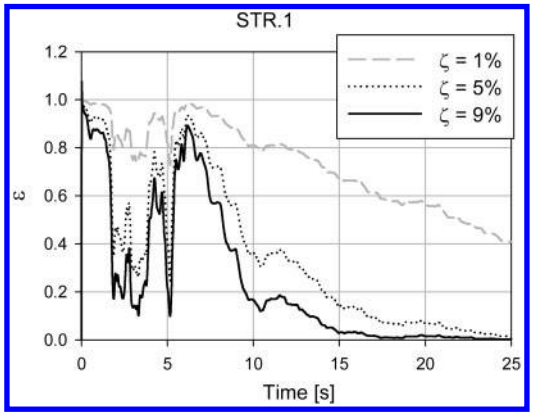


Figure 17. STR1. Effectiveness ratio ε.

(Fig. 16) are presented. The relevance of proposed effectiveness ratio ? in the case of structure STR1 for all three levels of damping, also, presented (Fig. 17).

5 CONCLUSIONS

A simple technique to assess the effectiveness of seismic protection via added damping has been proposed – in the form of energy ratio – and presented in several cases of full scale steel structures and scaled down models. Both, the values of proposed ratios and, mainly, their variation in time are capable of expressing the degree of reduction in the amount of dissipated energy by (inherent and added) viscous damping and the amount of energy that is still stored in the structure – the energy demand. The energy demand is a decisive criterion in the ingoing modern tendency of the energy based structural design. The time variation form of proposed ? ratio provides a direct, immediate, versatile and visual tool to assessing the structural weaknesses at every instant of seismic action. The possibility of assessing the contribution of added damping to seismic protection during the design process opens, in its turn, the opportunity of corroborating the added damping with an adequate (lateral, mainly) stiffness. Structural optimization regarding seismic response in terms of rigidity is an important aspect of modern design activity [16], [17], while the designer's option concerning stiffness is a decisive economical step in structural design process.

REFERENCES

[1] Housner, G.W., 1956. Limit design of structures to resist earthquake. Proc. 1st WCEE., 5: 1–5.
[2] Akiyama, M., 1985. Earthquake Resistant Limit-State Design for Buildings. 1st Edn., University of Tokyo Press, Tokyo.
[3] Uang, C.M. & V.V. Bertero, 1990. Evaluation of seismic energy in structures. Earthquake Eng. Struct. Dyn., 19: 77–90.
[4] Khashaee, P., 2003. Distribution of earthquake input energy in structures. National Institute of Standards and Technology Interagency Report 6905. United States Department of Commerce Technology Administration National Institute of Standards and Technology.
[5] Kuwamura, H. and T.V. Galambos, 1989. Earthquake load for structural reliability. J. Struct. Eng., 115: 1446–1462.
[6] Riddell R and Garcia J E. Hysteretic energy spectrum and damage control [J]. Earthquake Engineering & Structural Dynamics, 2001:vol.30, 1791∼1816.
[7] Sutat Leelataviwat et al. Application of Energy Balance Concept in Seismic Evaluation of Structures Volume 135, Issue 2 (February 2009).
[8] Manfredi G. Evaluation of seismic energy demand [J]. Earthquake Engineering & Structural Dynamics, 1995:vol.24, 1195∼1213.
[9] B. Akbas, J. Shen and H. Hao Energy approach in peformance-based seismic design of steel moment resisting frames for basic safety objective The Structural Design of Tall Buildings Vol 10 Issue 3 pages 193–217, September 2001.
[10] Fajfar, P., T. Vidic and M. Fischinger, 1989. Seismic design in medium and long period structures. Earthquake Eng. Struct. Dyn., 18: 1133–1144.
[11] Chai, Y.H., Fajfar, P., Procedure for estimating input energy spectra for seismic design, Journal of Earthquake Engineering, 2000, 4(4):539–561.
[12] Jinkoo Kim and Hyunhoon Choi Energy-Based Seismic Design of Buckling-Restrained Braces 13th World Conference on Earthquake Engineering Vancouver, B.C., Canada August 1–6, 2004 Paper No. 2113.
[13] Prodan, O., I. Ladar, and P. Alexa. "Effectiveness of passive seismic control of steel structures." Risk Analysis VII & Brownfields V 43 (2010): 283.
[14] Prodan, O., N. Chira I. Ladar, and P. Alexa. "Spatial steel structures with passive seismic protection." Behaviour of Steel Structures in Seismic Areas, STESSA 2012: 797.
[15] Chopra Anil K. – Dynamics of structures, Prentice Hall International, Inc. 1995.
[16] Karkauskas, R. 2007. Optimization of geometrically non-linear elastic-plastic structures in the state prior to plastic collapse, Journal of civil engineering and management: international research and achievements 13(3): 183–192.
[17] Yanglin Gong Optimal Stiffness Distribution of Steel Moment Frames under Extreme Earthquake Loading – Advances in Structural Engineering Volume – Volume 8 Issue – 6 pp.573–584.

Research and Applications in Structural Engineering, Mechanics and Computation – Zingoni (Ed.)
© 2013 Taylor & Francis Group, London, ISBN 978-1-138-00061-2

Seismic Safety Screening Method (SSSM) for slum clearance

P. Ozdemir Caglayan
Istanbul Technical University, Turkey

ABSTRACT: After October 23rd, 2011 M7.2 Tabanli-Van earthquake which caused damage in a widespread area across the Van province, government of Turkey announce that "revolutionary measures will be taken in the area of housing and public works with respect to the life safety in structures, and urban regeneration will be started soon". When the existing stock of RC buildings in Turkey with a large variety of design and construction defects is considered it is vital importance to use not only simplified but also reliable techniques, which can predict the seismic safety of the existing buildings in relatively shorter time. Seismic Safety Screening Method (SSSM), is an adaptation of the Japan Seismic Index Method considering "Specification for Buildings to be Built in Seismic Zones (2007)", some technical/non-technical properties of existing building stock in Turkey. The outcome of SSSM is the determination of buildings which are not safe enough to keep the life alive inside, or another words to decide the "Slum Clearance" by spending minimum time with reliable results.

1 INTRODUCTION

In the past, big earthquakes in Turkey have caused huge numbers of casualties and damage to structures. The Marmara earthquake in 1999 reportedly killed 17.480 persons; injured 23.781 persons and damaged 328,113 buildings in Marmara region. Though being a seismic country, earthquake-resistant standard has not been effectively applied to new constructions because of adequate control and being be unaware of earthquakes always occur suddenly without prior notice. There is a higher possibility of large number of buildings will not perform life safety level during a large seismic event. Recent earthquakes in Van province in 2011 were proved that above statement, unfortunately. Then, the government of Turkey announce that "Revolutionary measures will be taken in the area of housing and public works with respect to the life safety in structures" after October 23rd, 2011 M7.2 Tabanli – Van earthquake which caused damage in a widespread area across the Van province. They also declared that "regeneration of urban areas and slum clearance will be started soon". Turkey is an earthquake prone country where 92 % of total areas of 783,562 km^2 are located at seismic zone.

A high priority task of urban regeneration or of the slum clearance is to decide weak structures in terms of safety during the earthquakes. Determining the location of seismically vulnerable buildings structures in the current building stock is therefore a high priority task within the concept of urban renovation issues.

When the existing stock of buildings in Turkey with a large variety of design and construction defects is considered it is clear that it is practically impossible to carry out detailed structural analysis for all of the buildings. Therefore, it is vital importance to use not only simplified but also reliable techniques, which can predict the seismic safety of the existing buildings in relatively shorter time.

Seismic Safety Screening Method (SSSM), is an adaptation of the Japan Seismic Index Method, considering Turkish Earthquake Resistant Design Code and some technical or non-technical properties of existing building stock in Turkey such as older design standards, or non-engineered design, etc . The outcome of SSSM is the determination of buildings which are not safe enough to keep the life alive inside, or another words to decide the "Slum Clearance" by spending minimum time with reliable results.

The procedure presented in this paper is the secondary screening phase of a two-phase procedure for identifying potentially hazardous buildings. The first phase is much easier and used as a quick safety check to generate list of building stock and sort the inventory for the second stage.

Since reinforced concrete frame, shear wall or dual frame-shear wall structural systems are nationwide, the SSSM procedure is intended to be applicable for RC building types having number of stories free to vibrate (excluding basements) is 6 or less. Steel structures, precast structures, and other non-building structure types, however, are not covered by the procedure. SSSM is designed to calculate the capacity of a building in terms of seismic index of a building (I_S). Seismic index, I_S, will be compared with the demand of the seismicity in terms of required seismic index of a building (I_D).

Buildings identified by this procedure must be interiorly inspected. The detailed description of building characteristics based on the five basic parameters;

building location based on seismicity region and soil condition, number of floors, building plans (particularly a plan of the most critical floor), the floor height and occupancy type. The structural characteristics of the building are necessary for calculating the seismic capacity of buildings.

A large number of the buildings in Turkey have not received proper civil engineering service and they do not have any civil engineering drawings of the structural system. The data and information gathered after recent earthquakes indicated that average concrete compressive strength is as low as 10 MPa and the amount of longitudinal reinforcement bar is 1% of gross cross sectional area of columns with the tensile strength of 220 MPa on the large number of buildings. Both longitudinal and transverse bars are generally plain bars with large spacing between stirrups like 20~30 cm. Due to these facts some assumptions were made to simplify the quick assessment procedure. However, if blue prints and the construction material information are available actual values also could be used in this method.

The original method JSIM have been applied to a number of buildings damaged during 1992 Erzincan, 1998 Adana-Ceyhan and 1999 Marmara and Duzce Earthquakes. These results have been used for adaptation of the JSIM to SSSM depending on initially adopted seismic design code requirements. The calibrations of several coefficients in this method have been done after examining certain buildings in Zeytinburnu, and nine school building in Istanbul. Reliability of the method has been tested by analyzing buildings respect to requirement of "Specification for Buildings to be Built in Seismic Zones (2007)".

2 SEISMIC SAFETY SCREENING METHOD (SSSM)

Basic concept of SSSM and the original JSIM is the equal energy concept. In case of structures with relatively short natural period, dissipation energy is almost equal to maximum potential energy of the elastic system. Seismic index of a building, I_S value, is calculated by using Equation 1 below.

$$I_S = P \times D \times K \quad (1)$$

where P = seismic capacity index; D = structural irregularity index; and K = time dependent deterioration index.

Seismic index I_S is calculated with penalties if there is a irregularity or/and a deterioration on a building. I_S should be calculated separately for both earthquake directions for all critical stories of a building and the most unfavorable result should be compared with the required seismic index I_D. The required seismic index, I_D should be calculated by Equation 2.

$$I_D = P_0 \times B \times Z \times U \quad (2)$$

where P_0 = index for basic seismic demand; B = index for regional seismicity; Z = index for local soil conditions; and U = index for usage. Index B should be taken as 1.0 for high seismicity and never lower than 0.5 in any case. Index Z varies for soil conditions from 0.80 (for rock or stiff soil) to 1.00 (soft soil). Usage index, U is 1.0 for residential buildings, 1.5 for buildings to be utilized immediately after the earthquake.

Based on comparison of indices, the seismic safety of the building can be estimated. If for any of the comparison cases is $I_S < I_D$, then it is concluded that the performance of the building is not enough for life safety, and preventive measures should be taken.

Table 1. Classification of Vertical Members.

Elements	Definition	Ductility Index R
Columns	$h_0/D > 2.0$	$Rc = 1.0$
Short Columns	$h_0/D < 2.0$	$Rsc = 0.8$
Walls	shear wall	$R_w = 1.0$

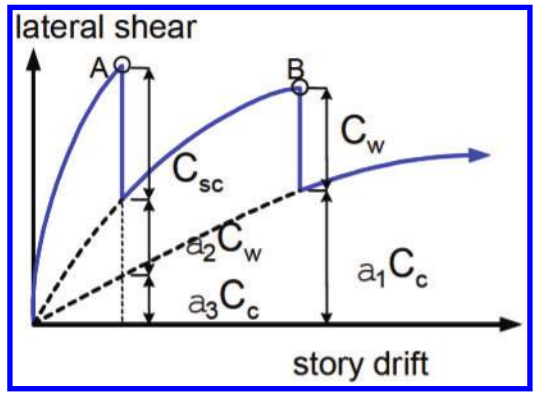


Figure 1. Displacement compatibility of vertical members.

2.1 *Seismic capacity index, P*

Seismic capacity index, P, is a function of strength index, C and ductility index, R. The C is computed with the lateral strength of vertical members based on the assumption that beams are strong enough and the expected structural damage on beams cannot be as important as vertical elements' damages. Vertical structural members are classified into three groups as columns, short columns and shear walls since ductile behavior of elements are different. The definitions of these groups are given in Table 1.

The calculation of P index differs at each floor of the building in accordance with Equation 3.

$$P_i = \frac{(n+1)}{(n+i)} \sum (a \times C) \times R \quad (3)$$

where n = number of stories of a building; i = number of the story where the calculation is done (for a ground floor i = 1); C = strength index of a vertical member, and R = ductility index, a = strength reduction factors due to displacement compatibility as shown Figure 1.

On the figure above C_c = strength index of a column; C_w = strength index of a shear wall; C_{sc} = strength index of a short column, and a1 = 0.7; a2 = 0.7; a3 = 0.5.

$$P = (n+1/n+i) * (C_{sc} + a_2 C_w + a_3 C_c) * R_{sc}$$
$$P = (n+1/n+i) * (C_w + a_1 C_c) * R_w \quad (4)$$
$$P = (n+1/n+i) * (C_c) * R_c$$

2.2 *Structural irregularity index, D*

Structural irregularity index is related with the irregularities in plan and irregularities in elevation of a building. In the "Specification for Buildings to be Built in Seismic Zones (2007)" six types of irregularities are described. Three of these are in plan and three in elevation. Since the seismic index, I_S is a production of three sub-indices (Eqn. 1) structural irregularity index, D, negatively affects the result. If building is an irregular structure, the seismic index, I_S could be reduced 40% by the structural irregularity index, D. The details of structural irregularity index, D will not be given in this study.

2.3 *Time dependent deterioration index, K*

Influence of structural defects such as deflection, cracking, and corrosion is taking into account with time dependent deterioration index, K on the seismic index, I_S. Site inspection is necessary for the estimation of the time dependent deterioration index, K. The seismic index, I_S could be reduced 30% by the time dependent deterioration index, K.

3 BASIC SEISMIC DEMAND INDEX, P_0

Seismic index of a building, I_S should be greater than the required seismic index, I_D. The basic seismic demand index, P_0 is the most critical parameter for the method. In TERDC-2007, Total Equivalent Seismic Load (base shear), V_t acting on the entire building in the earthquake direction considered will be determined by Equation 5 below:

$$V_t = \frac{W x A_0 x I x S(T)}{R_a(T)} \geq 0.10 x A_0 x I x W \quad (5)$$

where W = total weight of the building ($\Sigma G + nQ$); A_0 = effective ground acceleration coefficient; I = building importance factor; $S(T)$ = spectrum coefficient, $R_a(T)$ = seismic load reduction factor; and T = natural period of the building.

The lateral load carrying capacity of the ground floor, Q_g can be expressed by Equation 6 in the SSSM, and it should be greater than the base shear, V_t.

$$Q_g = P_g x W \;\; ; \;\; Q_g \geq V_t \;\; ; \;\; P_g \geq \frac{A_0 x I x S(T)}{R_a(T)} \quad (6)$$

where P_g = seismic capacity index of ground floor; and W = total weight of the building.

When a non-ductile ($R_a(T) = R = 4.0$), residential building ($I = 1.0$) is considered, whose natural period is relatively short and nearly matching with soil's natural period ($S(T) = 2.5$) and located on seismic zone 1 ($A_0 = 0.40$), its seismic capacity index of ground floor (P_g) should be equal to or greater than 0.25.

$$P_g \geq \left(\frac{0.40 x 1.00 x 2.5}{4} = 0.25 \right) \quad (7)$$

If we calculate the seismic index, I_s for the same case with assuming structural irregularity index, D and time dependent deterioration index, K equal to 1.0 we can say that I_s should be equal to or greater than 0.25. Then; the required seismic index, I_D value should be equal to 0.25 at least because the seismic index, I_s value will be judged against to the required seismic index, I_D value. If we repeat the same conditions ($B = 1$; $Z = 1$; $U = 1$) in Equation 2 to calculate I_D, the result implies that P_0 should be equal to 0.25 as the first approach.

$$I_s \geq I_D$$
$$\left(I_s = 0.25 x 1.0 x 1.0 x 1.0\right) \geq \left(I_D = P_0 x 1.0 x . 1.0 x 1.0 x 1.0\right) \quad (8)$$

The value of 0.25 is very conservative as a basic seismic demand index P_0 in case of buildings with high ductility. For calibration of this index, a pilot study was carried out in Zeytinburnu, Istanbul to the residential buildings and nine school buildings at different locations of Istanbul, but has a same hazard zone level 1. Calibration and validation of the seismic demand index P_0 and the whole procedure will be continuously done as more data becomes available, there for some school builds are under consideration from data of Van.

4 CALIBRATION

The value of the seismic capacity index, P has a fundamentally important effect on the decisions about the basic seismic demand index, P_0.

For the calibration of the SSSM, the results of nonlinear static analysis carried out for 12 of 2401 buildings are utilized for seismic safety during Istanbul Earthquake Master Plan Project.

In this study, nine reinforced concrete school buildings that can represent typical school buildings in Turkey are examined by SSSM. The analyses have been done by the seismic loads given in the Turkish Earthquake Resistant Design Code. The result was none of them were satisfying the code expectation. After retrofit designs of these buildings are done considering the seismic loads given by the Turkish Earthquake Resistant Design Code, SSSM is utilized once more for each of these retrofitted buildings. Then detailed structural analysis is carried out both for the existing and retrofitted states of these buildings. Finally a comparison of the results obtained by the quick seismic safety

Table 2. P values obtained for existing and retrofitted school buildings by SSSM.

	Existing			Retrofitted		
Code	P_x	$P_{y\ \min}$	$(V/W)_{x,y}$	P'_x	$P'_{y,\min}$	$(V/W)_{x,y}$
ANT	0,15	0,14	0,14	0,24	0,40	0,18
HAY	0,06	0,07	0,06	0,15	0,22	0,13
MHV	0,03	0,04	0,03	0,12	0,32	0,14
MSF	0,14	0,15	0,14	0,28	0,51	0,21
SB	0,17	0,25	0,17	0,32	0,58	0,22
UEML	0,18	0,25	0,18	0,35	0,77	0,23
RD	0,18	0,14	0,14	0,48	0,39	0,20
MEV	0,18	0,25	0,18	0,51	0,50	0,20
TIOK	0,10	0,12	0,10	0,35	0,38	0,17

evaluation method before and after retrofitted is presented. Since this comparison is separately carried out for each principal direction, an important amount of data is obtained in terms of the relation between results of the detailed structural analysis and quick evaluation method. Then the ratios of base shear force capacity to structural weight were calculated. The ratios for x and y directions (Vx/W, Vy/W) and the structural seismic capacity indices (Px, Py), which are the ratios of strength indices to the structural weight determined by SSSM are presented in Table 2.

5 CONCLUSIONS

Based on the proposed study in the paper the Seismic Safety Screening Method, SSSM, which is adopted and modified from Japanese Seismic Index Method, can be used to rank buildings according to their building performance indices. Estimation of the existing seismic safety levels for medium/low rise RC buildings due to the structural analysis. are in good agreement with the results obtained by the SSSM. Calibration and validation of the scores and the whole procedure will be continuously done as more data becomes available in different seismic regions.

REFERENCES

Standard for Seismic Evaluation of Existing Reinforced Concrete Buildings, Japan Building

Specification for Buildings to be Built in Seismic Zones, 2007, Ministry of Public Works and Settlement Government of Republic of Turkey

The Study on a Disaster Prevention/Mitigation Basic Plan in Istanbul, Japan International Cooperation, Istanbul Metropolitan Municipality, 2002, Istanbul

Earthquake Master Plan for Istanbul, Istanbul Metropolitan Municipality Construction Directorate Geotechnical and Earthquake Investigations Department, 2003, Istanbul

İlki, A., Ozdemir, P., Boduroglu, M.H. et al. Comparison Of The Results Obtained By Seismic Index Method And Structural Analysis For Existing And Retrofitted Buildings, Fifth National Conference on Earthquake Engineering, 26–30 May 2003, Istanbul, Turkey

Ozdemir, P., Boduroglu, M.H. and Ilki, A., "Seismic Safety Screening Method", Proceeding for SPEAR International Workshop, Joint Research Centre, 2005, Ispra Italy

Ozdemir, P., Taskin, B., Seismic Safety Screening Method For İstanbul Metropolitan City, The Tenth East Asia-Pacific Conference on Structural Engineering and Construction (EASEC-10), 3–5 August 2006, Bangkok, Thailand

Boduroglu, M.H., Ozdemir, P., A Screening Method For The Evaluation Of Existing Buıldıngs Sixth National Conference on Earthquake Engineering, 16–20 October 2007, Istanbul, Turkey

Çopur, S., Deprem Güvenliği Tarama Yöntemi ve İtme analizi Sonuçlarinin Karşilaştirilmasi, Master Thesis, 2010, Institute of Science and Technology, Istanbul Technical University, Istanbul, Turkey

Research and Applications in Structural Engineering, Mechanics and Computation – Zingoni (Ed.)
© 2013 Taylor & Francis Group, London, ISBN 978-1-138-00061-2

Experimental study on the performance of hollow reinforced concrete bridge piers subjected to lateral seismic loads

O. Lopez-Batiz
National Center for Disaster Prevention (CENAPRED), Mexico

R. Gomez-Martinez, J.A. Escobar-Sanchez, F. De la Serna-Hernandez & G. Aguilar-Ramos
Institute of Engineering, UNAM, Mexico

ABSTRACT: This paper presents the results of a comparative evaluation of the seismic performance of two RC bridge columns, one of a full cross section and the other of a hollow cross section. The full section specimen has a cross section of 120 × 80 cm and a height of 500 cm, whereas the hollow column has an interior section of 96 × 56 cm, and 12 cm for thickness. The specimens were subjected to a cyclic reversal loading pattern. Experimental tests were carried out in order to evaluate the performance of the specimens at the limit and ultimate stage; flexural and shear strengths, and ductility capacity were observed as well. Tests were performed at the laboratory of great structures of CENAPRED.

1 INTRODUCTION

Up to date, the results of a large amount of experimental works related to bridge piers under lateral loads indicate that the most brittle way of failure is produced by shear, where cracks with inclination produce the crushing and spalling of the concrete cover and the breaking and/or separation of the stirrups. Another form of failure is the loss of confinement at the plastic hinge zones, where flexure cracks, crushing and spalling of the concrete cover produce the buckling of the longitudinal reinforcement or a compression failure due to the deterioration at the plastic hinges. Also, it has been observed that pier element specimens fail because of the sliding of the longitudinal reinforcement splices; the degradation of the flexure capacity can quickly happen in zones where there are small joints and confinement is restricted (Priestley et al, 1996).

In Mexico, historically, failures of bridge structures due to earthquakes are unusual. Earthquake effects observed to date only show minor damage or partial failures of elements. More scarce are the studies on the structural evolution of bridges and their components, in spite of the policy implemented in the late 90's for the construction of high standards highways.

This work is intended to start a research line related to the laboratory experimental response of RC pier models for highway bridges. In a first stage the experimental response of two piers specimens under lateral loads that simulate the actions of an earthquake is studied. The work is aimed to compare the performance of highway bridge prototype pier models: one with a solid cross section of reinforced concrete, and another with a hollow cross section of the same material. These models are representative of columns used in the construction of bridges piers in Mexico. Results of the solid cross section model will be used to establish comparative parameters and differences in behavior with respect to the hollow cross section model. The influence of the void in the pier, the displacement capacity of the tested element as well as its pattern of damage and failure will be observed. In a second stage a reliable mathematical model will be developed and calibrated in order to reproduce the hysteretic behavior of laboratory models.

In the first part of this paper a brief description of the studied models is presented, as well as the experimental procedure used. Location of sensors for instrumentation, both external and embedded in the specimens, the device and load history, and the general test procedure are also described. This is followed by an analysis of some basic design and experimental parameters: strength, displacement, stiffness, degradation of stiffness and energy dissipation capacity; all of them from the perspective of the influence of the gap in the section of the pier column on the characteristics of response under lateral loads of the seismic type. Finally, the results of greater importance are presented.

The experimental work described herein was carried out at the Laboratory of Large Structures of the National Center for Disaster Prevention (LEG-CENAPRED).

2 DESCRIPTION OF THE MODELS

In order to achieve the objectives of the study, laboratory tests were carried out in two RC specimens

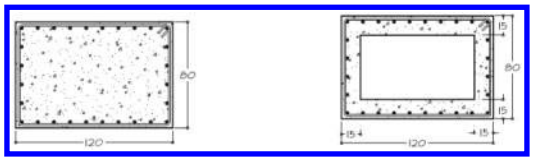


Figure 1. Cross section of the models studied. Dimensions and reinforcement.

of columns, one with a solid cross section and another with a hollow cross section; both specimens aimed to represent piers used in the construction of highway bridge substructures. Cross sections of the models are shown in Figure 1, whereas the nominal properties of the materials were: concrete for footing, $fc' = 350\,\text{kg/cm}^2$; concrete for pier $fc' = 300\,\text{kg/cm}^2$; and longitudinal and transverse steel, $fy = 4200\,\text{kg/cm}^2$; which are similar to those used in the construction of bridges.

The first model studied in the laboratory was the solid cross section model and herein will be referred as the "standard" or "pattern" model. This model has a longitudinal reinforcement ratio of 0.0148 and a ratio of volume of transverse reinforcement of 0.0040.

The second model studied, called herein "ch-01", had the same external dimensions than the "pattern" model, but with a hollow cross section and a wall thickness of 15 cm; it has a longitudinal reinforcement ratio of 0.0278, a ratio of volume of transverse reinforcement of 0.0081.

Both models were built using the regular procedures employed in this type of civil works. Steel bars of 25 mm were used for the longitudinal reinforcement being distributed uniformly in the cross section. For the transverse reinforcement, 13 mm bars were used. In both models a concrete cover of 5.0 cm was implemented.

In order to carry out a preliminary calibration of the models, using the values for confined concrete (Kent and Park, 1971), and the program BIAX (Wallace, 1989), moment-curvature relationships of the cross sections were obtained. Confined and unconfined regions considered in the analysis; moment curvature and interaction diagram obtained for the solid and hollow cross sections were obtained.

In the interaction diagram, it was easily observed that in order to consider the axial load in the experiments, its magnitude has to be very large to influence the results; also, from the moment-curvature graph, for a ultimate moment of 320 t-m corresponds a lateral load of 66.7 t and an ultimate displacement of 35 cm.

On the other hand, a 64 cm length for the plastic hinge was obtained using the expression provided by Priestley et al (1996). Also, a ductility factor of 8 was derived.

For the hollow section, the ultimate moments is 340.3 t-m for a lateral load of 70.9 t; the ductility factor is 11, and the plastic hinge length is the same as in the solid section.

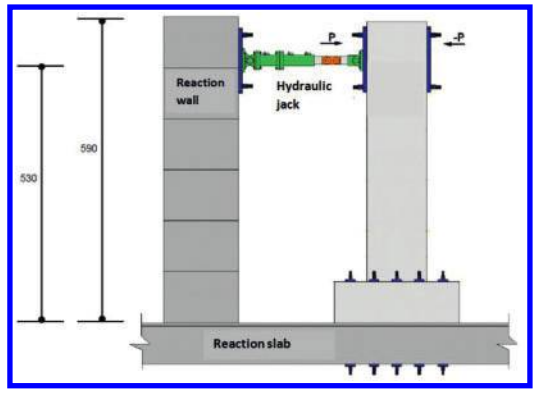


Figure 2. General array of the loading device (dim: cm).

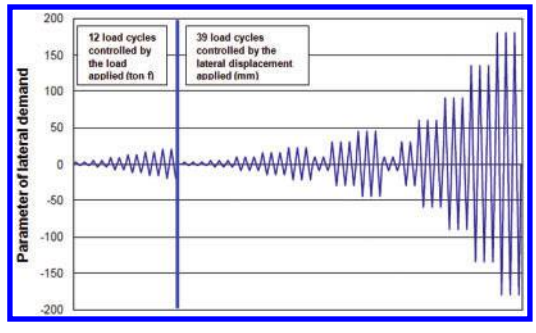


Figure 3. Load history.

3 LOAD HISTORY

Specimens were subjected to one-way reversible cyclic loading with a configuration of a cantilever load type, as shown in Figure 2.

Load history was designed to allow the observation of elastic and inelastic behaviors, as well as the "low cyclic fatigue" phenomena. Loading was initially defined considering 12 load controlled cycles, up to the theoretical cracking stress produced by flexural bending at the critical section of the pier (at the base). Once the lateral load corresponding to cracking was attained, the test was then controlled using the displacement of the point where the load was applied, and applying 39 additional load cycles with re-runs of three cycles for each range of amplitude. The graphical representation of the load history is shown in Figure 3.

During testing the magnitude of strains occurring in the longitudinal and transversal steel were recorded, allowing the identification of plastic hinges.

4 INSTRUMENTATION AND RECORDING SETUP

Instrumentation of the models comprised 126 strain gauges placed in the longitudinal and transverse reinforcing bars. The strain gauges were basically placed

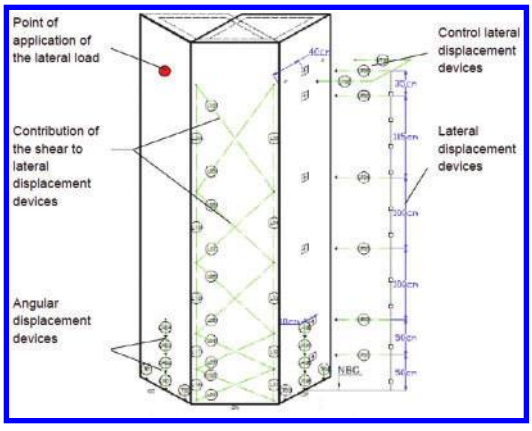


Figure 4. Graphic representation of the external instrumentation.

within the influence length of the plastic hinge, defined for this study as a section with a size equivalent to greater dimension of the cross section measured from the critical section. In a first instance, these recorded strains were aimed to identify the level of demand in the reinforcement, and therefore, their possible incursion in the yielding area.

Additionally, external instrumentation was used and it was conformed with LVDT's. The objective of this instrumentation is, in addition to control the test parameter or the displacement at the point of application of load, to identify characteristics of displacement, rotation, and contributions of the mechanisms of flexural bending and shear to the total displacement, among other issues.

The distribution of sensors is presented in Figure 4, whereas Figure 5 shows a general view of the load set-up during the test.

4.1 *General behavior of the models*

Load – displacement relationships

As a result of the application of the reversible cyclic lateral loading, load-displacement histories of the response of both models were obtained as shown in Figure 6. Two graphs are presented, one for the response of the two models in the range of elastic behavior (defined until the yielding of the longitudinal reinforcement), and the other one for the complete test, also for the two models, including the incursion on the inelastic range.

Analysis of the load – displacement graph in the range of elastic behavior (Figure 6) shows a difference in the initial stiffness between the two models. This fact produces a variation in the values of the lateral force associated with flexural cracking, as well as in the displacement magnitudes observed for these conditions. On the other hand, Figure 6.b shows a similar trend of behavior between the two models after incursioning in the inelastic range. Regarding the capacity of deformation and degradation of resistance for the same



Figure 5. General view of the model and testing set-up at LEG – CENAPRED.

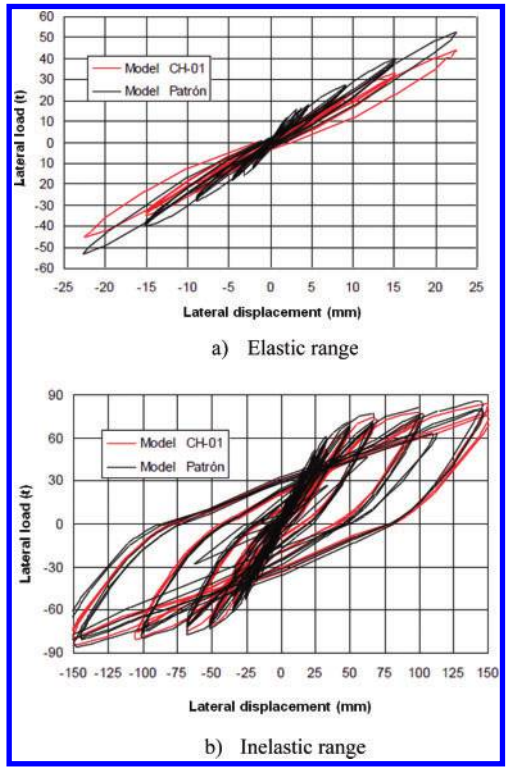


Figure 6. Lateral load-displacement behavior of the two models.

Table 1. Theoretical and experimental strengths of the models.

MODEL	MODEL	Solid model	Hollow model
Cracking	Experimental resistance (V_{crEXP}, t)	14.92	9.95
	Theoretical resistance (V_{crTEO}, t)	16.48	12.92
	V_{crEXP}/V_{crTEO}	0.92	0.77
	Experimental displacement (δ_{crEXP}, mm)	3.14	2.81
	Theoretical displacement (δ_{crTEO}, mm)	1.60	1.60
	$\delta_{crEXP}/\delta_{crTEO}$	1.96	1.48
Yielding	Experiemental resistance (V_{yEXP}, t)	44.17	44.06
	Theoretical resistance (V_{yTEO}, t)	40.64	40.44
	V_{yEXP} V_{yTEO}	1.09	1.09
	Experimental displacement (δ_{yEXP}, mm)	18.10	25.03
	Theoretical displacement (δ_{yTEO}, M-φ, mm)	26.90	26.00
	Theoretical displacement (δ_{yTEO}, Sugano, mm)	15.50	19.70
	$\delta_{yEXP}/\delta_{yTEO}$ (M-φ)	0.67	0.96
	$\delta_{yEXP}/\delta_{yTEO}$ (Sugano)	1.17	1.27

consecutive demands of displacement, no significant differences between the performance parameters of the two models were observed. Information on parameters such as degradation of instant stiffness, peak to peak degradation of stiffness, energy dissipation, coefficient of equivalent damping, among other important parameters of structural performance has not yet been processed, as well as other concepts that will be introduced in a future work.

Based on the analysis of similar graphs, together with the review of information recorded during the test and a review of the level of unit deformation required in the longitudinal steel reinforcement of the models, values of load and displacement associated with the first cracking of tension due to flexural bending, were identified, as well as the load magnitude associated with the manifestation of yielding of the longitudinal reinforcement. These values are presented in Table 1 for the two models.

On the other hand, based on moment-curvature (M-φ) relationships, theoretical values of the lateral forces associated with the first cracking and the first yielding, V_{cr}TEO and V_yTEO, respectively, were identified. Also, based on the theoretical relationship between flexural moment, curvature, rotation and deflection, theoretical deflections at cracking and yielding were derived and identified as δ_{cr}TEO and δ_yTEO, respectively. Additional displacement magnitudes at yielding were obtained using the empirical expressions of Sugano (AIJ, 1987). This one defined in Table 1 as δ_yTEO, Sugano.

Analysis of resistances shows that the dispersion between the experimental and theoretical values are slightly higher for the CH-01 model, mainly for the resistance at cracking with a difference of 23% between the experimental and the theoretical for the CH-01 model, and 9% for the standard model. Regarding the yielding resistance, the difference between the theoretical, and experimental value, for both models, is 9%; this is an expected behavior since after yielding the prevailing structural performance parameter is the amount of longitudinal steel reinforcement.

On the other hand, from the analysis of displacements, it is observed that the experimental state for cracking, nominally equal to the limit values of linear elastic behavior, was considerably higher than the theoretical: 96% for the pattern model and 48% for model CH-01. In this regard it is important to mention that the difference of initial stiffness, defined as the relationship between load and displacement at cracking due to tension by bending, is 34% higher than that of the pattern model; a difference of 28% was expected.

Analyzing the yielding condition or limit state of service, and calculating for the two models the experimental stiffness up to the yielding point, the ratio between the stiffness at the yield point (K_y) and the initial stiffness (K_{cr}) is equal to 0.51 and 0.50 for the pattern and CH-01 models, respectively; therefore, there is no difference in the parameter of degradation of stiffness between the two models considering only the limit points in the service range (cracking and yielding by bending).

4.2 *Cracking patterns*

Cracking patterns of the two models showed similar trends in the distribution and orientation of the cracks; no gross differential effect was identified due to the presence of the void in the model CH-01. Figure 7 shows the cracking pattern of the standard model at the final stage of the testing which was reached when the crushing of the fiber of maximum compression was observed.

The final mechanism of failure of both models was observed during the failure of the third stirrup at the critical section. This failure was observed at its bend of 135 degrees around the longitudinal corner bars. It is worth to mention that the manufacture of stirrups used in the two models was made using a mechanical bending device and complying with the radii of curvature specifications. Even so, damage in the area of the bend of the crossbar that shapes the stirrup was observed. This damage was observed previous to the lateral loading demand applied on the model.

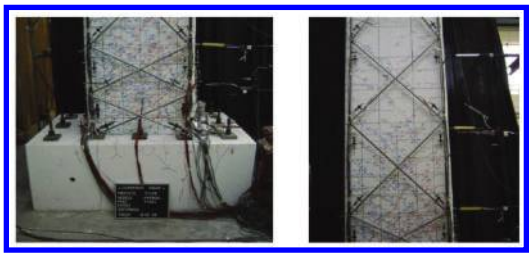


Figure 7a. Final cracking patterns on both models.



Figure 7b. Failure mode at the base of the standard model.

4.3 *Analysis of lateral displacements*

As indicated in Figure 8, regarding specifically the devices used to measure the configuration of lateral displacements of the models, experimental normalized deformed configurations for the two models were identified for the first ten cycles, corresponding to the applied load history controlled by the magnitude of the applied lateral force, in the interval of behavior previous to cracking due to tension by flexural bending. Using concepts of the theory of elasticity and strength of materials, expressions to calculate the deformed configuration of the models were derived. For each load cycle, Figures 12 presents a comparison of the deformed configurations of the models including the theoretical one.

Studying the distributions of displacements along the height of the models, and comparing with a theoretical configuration, it can be asserted that for the pattern model (solid cross section), its displacements are quite different from the theoretical values in a length of 100 cm near the base of the pier. The rest of the configuration shows a configuration similar to the theoretical.

On the other hand, although for a small number of cycles, the trend is the same for the CH-01 model as described for the standard model. For most of the cycles, the behavior observed/measured reasonably matches the theoretical behavior expected along the 100 cm near the base of the pier.

The difference between the observed behavior at the bottom of the pier can be assumed as a consequence of the greater geometric inertia and mass of the pattern model, which could generate a local rotation at

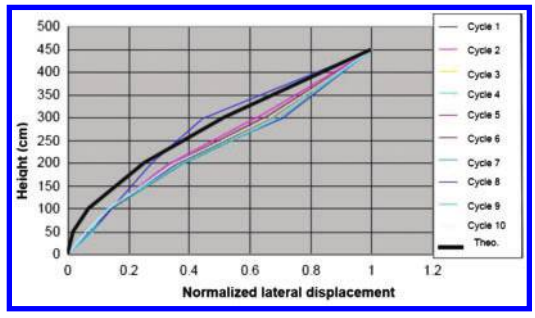


Figure 8a. Configuration of normalized lateral displacements for the pattern model, interval previous to cracking by flexure.

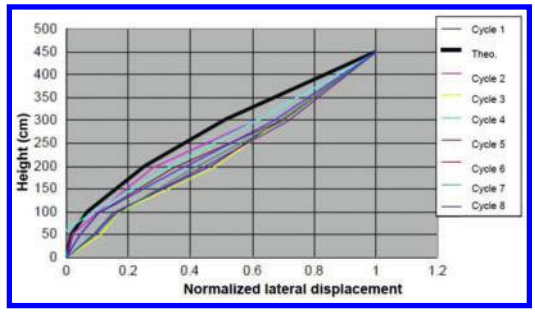


Figure 8b. Configuration of normalized lateral displacements for the CH-01 model, interval previous to cracking by flexure.

the base of the pier starting at load levels lower than those associated to flexural cracking, aspect that was not observed in the pier of the hollow section model. This aspect will have to be revised and, if necessary, confirmed with the analysis of external and internal information in the vicinity of the bases of the two models.

5 CONCLUSIONS

As a result of this experimental study, and taking into account only part of the information recorded with the external instrumentation, the most important conclusions can be summarized as follows:

(1) Regarding the mechanism of failure, the presence of the void in the section of the pier does not significantly modify the overall performance of the model. This is inferred from the direct comparison of the results of the solid section model with those of the hollow section;
(2) There are differences in performance characteristics between the models in the elastic range, between cracking and the first yielding due to flexural bending; more specifically, differences were observed in the cracking resistance and the values of initial stiffness and yielding, resulting

higher than those expected for the pattern model (solid section); and,

(3) From the analysis of the deformed configuration of the two models in the elastic range, a possible rotation of the base of the pattern model was observed, feature which was not fully observed in the CH-01 model, probably due to the large difference in inertia and mass between the models.

ACKNOWLEDGMENTS

The authors are grateful to technicians Pablo and Carlos Olmos-Ibarra, at LEG-CENAPRED, for their participation in the experimental testing. Also, enthusiastically, Jaime Lorenzo-Camargo provided assistance at the laboratory during his social service stage. Assistance of Salvador Barrios, Ivan I. León, Ronald Gomez, Joel Aragon, Raúl Sánchez and Oscar Rosales is appreciated as well.

Financial support for the manufacturing of the models was provided from remnants funds of a project sponsored by the Secretariat of Communications and Transport of Mexico to the Institute of Engineering at the National University of Mexico.

REFERENCES

Architectural Institute of Japan (1987), "Data for Ultimate Strength Design of Reinforced Concrete Structures". Tokyo, Japan, September.

Kent, D C and R Park (1971), "Flexural members with confined concrete", Proceedings ASCE, Vol. 97, ST 7, July, pp. 1969-1990.

Priestley, M., Seible, F. and Calvi, G. M. (1996). "Seismic Design and Retrofit of Bridges", John Wiley.

Wallace, J. (1989), "BIAX user manual", A Computer Program for the Analysis of Reinforced Concrete Sections, University of California.

Research and Applications in Structural Engineering, Mechanics and Computation – Zingoni (Ed.)
© 2013 Taylor & Francis Group, London, ISBN 978-1-138-00061-2

Evaluating the seismic performance of RCC dams, subjected to near-field and far-field earthquakes via FEA approach

Mohammad Reza Abedini Ala & Hamid Reza Vosoughifar
Department of Civil Engineering, Islamic Azad University, South Tehran Branch, Tehran, Iran

Nemat Hasani
Department of Civil Engineering, Power and Water University of Technology, Tehran, Iran

Seyed Kazem Sadat Shokouhi
Department of Civil Engineering, Islamic Azad University, South Tehran Branch, Tehran, Iran

ABSTRACT: The safety and stability of Roller Compacted Concrete (RCC) dam under strong earthquake shaking has long been an issue of practical importance, and has attracted and continues to attract considerable research interest. In this paper the evaluation of seismic performance of RCC dam subjected to near-field and far-field earthquakes was undertaken. In this attempt, an RCC dam was modeled using the Finite Element (FE) software considering dam-reservoir interaction. Then dynamic analysis procedure has been performed via non-linear time history analysis. Verification of FE model was done with experimental data by a statistical test which the obtained results indicated a good conformity.The obtained seismic strain, stress and lateral displacement demonstrated that RCC dam include different seismic behavior subjected to near and far field earthquakes which the near-field earthquakes have more greater effects on the RCC dams in comparison with far-field earthquakes.

Keywords: Seismic performance, Finite Element Analysis (FEA), Roller Compacted Concrete (RCC) dam, Near-field and far-field earthquakes

1 INTRODUCTION

Roller compacted concrete (RCC) technology has revolutionized the dam construction industry during the past decades. The advantages of more economical and rapid construction brought these dams into the engineers' attention; hence seismic analysis of suchlike structures to assess its resistance during earthquake and some phenomena such as cracking has become important. It is recommended to perform nonlinear analysis based on fracture mechanics theory to assess performance of a new or an existing concrete dam with regard to dam safety [1,2].

The design of gravity dams constructed by RCC is similar to the design of concrete gravity dams constructed by conventional methods. The largest differences are in the used construction methods and in the composition of the concrete used to allow roller compaction [3]. Ground motion effect on RCC dams in the earthquake zone should be taken into account for the most critical conditions.

This paper aims to present the evaluation of RCC seismic performance against near-field and far-filed earthquakes.

2 FINITE ELEMENT MODEL AND ANALYTICAL DYNAMIC CHARACTERISTIC OF ZIRDAN DAM

Zirdan dam was taken place in Kajoo River in north of Chabahar city in Iran. Zirdan, is one of the gravity dams which was constructed by RCC method in 2011. (fig 1)

Using about 545,000 m^3 concrete which is contained two material (CVC and RCC). FE model of the dam that is shown in Figure 1 is 64.5 m high, with a sharp slope change on the upstream face at the level of 20 m and 35 m (fig 2,4).

In the finite element modeling of the RCC dam that is shown in Fig 2, openings are not considered in the modeling. In the finite element model of Zirdan Dam, the dam body is created firstly by the FEM software. In the dam body, areas are used. Each areas has 8 node and each node has three degree of freedoms: translations in the nodal x, y, and z directions. The finite element model of Zirdan Dam is developed considering reservoir. Reservoir affects the dynamic response of gravity dams considerably. So they must be well represented to obtain realistic result. In the model, the

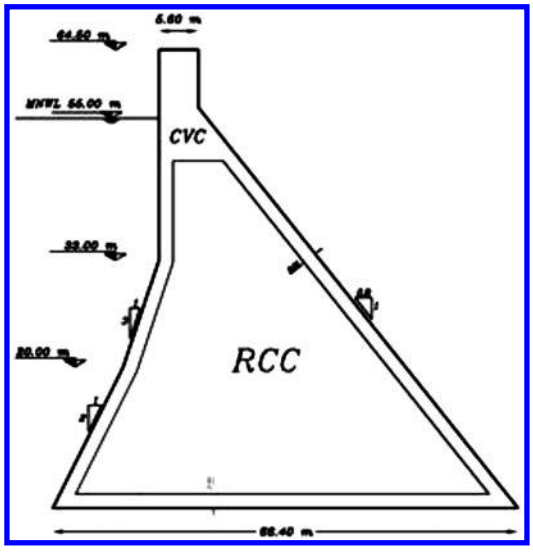


Figure 1. Zirdan Dam.



Figure 2. Zirdan Dam.

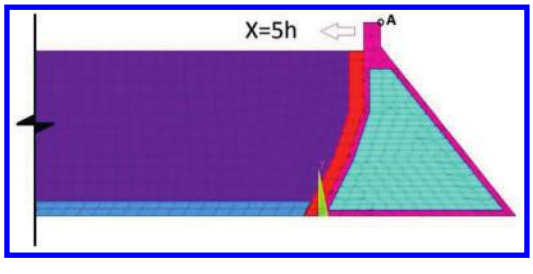


Figure 3. Zirdan Dam Finite Element model.

length of the reservoir is taken as much as fifth times of dam high to represent the impounded water [4]

In this Study, material properties assumed in the analyses are listed in Table 1.

3 AMBIENT VIBRATION AND GEOTECHNICAL TEST OF ZIRDAN DAM

Several vibration tests were conducted to Zirdan. Site classification and wave velocity of the dam foundation

Table 1. Material properties of Zirdan Dam.

Material Properties			
Element Type	Elasticity Modulus (GPa)	Poisson Ratio	Mass Density (KN/m^3)
RCC	16.7	0.18	23,0
CVC	22.5	0.18	24,0



Figure 4. Zirdan Dam.

were carried out during the tests. We classified the soil characteristics by USGS method and we assume the foundation soil type is Type A, and also we found out the design base earthquake (DBE) and Maximum credible earthquake (MCE).

4 VERIFICATION OF NUMERICAL MODEL

To Confirm the Validity of the numerical model we studied Koyna Dam researches [5].

Koyna Dam is a gravity dam in India that was damaged by during the earthquake in 1967, the Koyna Dam is considered a classic problem for experimental studies and validation of numerical procedure for predicting the seismic response of concrete gravity dams [6] for this purpose we made the FE model of Koyna dam (fig 5) to control the modal properties of Koyna dam and verify the FE Software , so for theses control we used the results of V. Valamanesh et al [7,8].

We analyzed the model of Koyna Dam and Compared the results in Table 2.

For this comparison we used SPSS Program by Mann-Whitney U method.

Mann-Whitney test is a statistics method for one of two samples of independence number and it is one of the most well-known non-parametric significance tests [9].

Mann-Whitney U test showed that asymp sig is 0.873 so it is clarified that Analytical mode shape of Koyna dam is convergence and we can trust on our outputs.

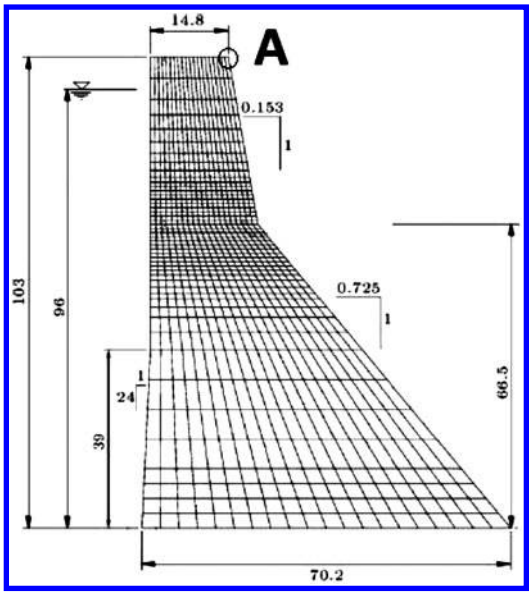


Figure 5. Koyna Dam.

Table 2. Modal properties of Koyna Dam

Mode	Analytical Frequency	Analytical Period	Reference Period
1	2.88	0.346	0.387
2	7.72	0.129	0.149
3	10.13	0.098	0.093
4	15.00	0.067	0.078
5	22.73	0.044	0.053
6	22.94	0.043	0.042

5 MODEL ANALYSIS

First of all we must select the accurate records for time history method for near field and far field earthquakes, for this purpose we accumulated the seismic records data which are conformed to local soil characteristics. We must modify the accelerators to gain the best interaction between the foundation, dam and reservoir because the record doesn't match with Zirdan Dam location, to reach the target we studied faults and histories of the earthquakes then we recognized that we should amend the accelerators by MCE records.

On this inquiry we selected Northridge, Koceali and Whittier Narrows seismic records on FE Software and discussed on the lateral displacements on dam.

Near-filed earthquake means that the faults are very close to dam structure and it can be about 10 km or less,

In Figures 6 and 7 are showed that the lateral displacements of Point A on Zirdan Dam Via Near and far-field Northridge earthquake records.

It is denoted that the time the displacement of the near-field earthquake is greater than far field earthquake.

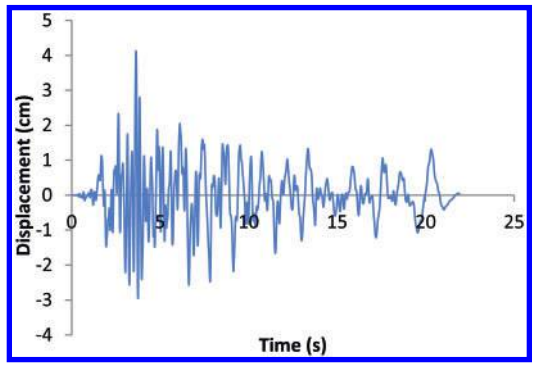


Figure 6. Lateral Displacement – Near-Field Northridge records.

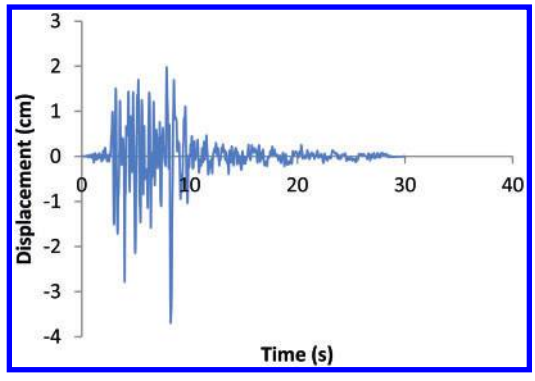


Figure 7. Lateral Displacement – Far-Field Northridge records.

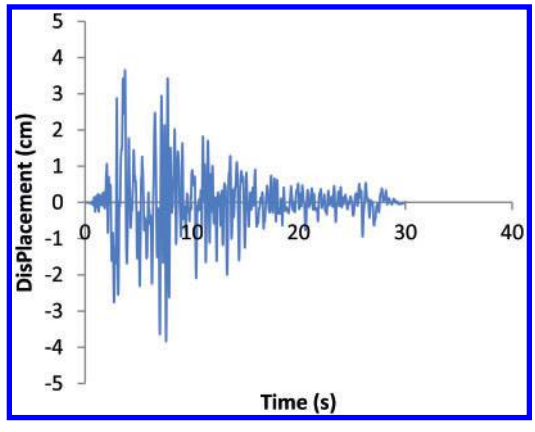


Figure 8. Lateral Displacement – Near-Field Koceali records.

In Figures 8 and 9 are showed that the lateral displacements of Point A on Zirdan Dam Via Near and far-field Koceali earthquake records.

It is showed that the maximum displacement of point A is happened in far filed earthquake that is denoted the point A moved towards the reservoir of dam.

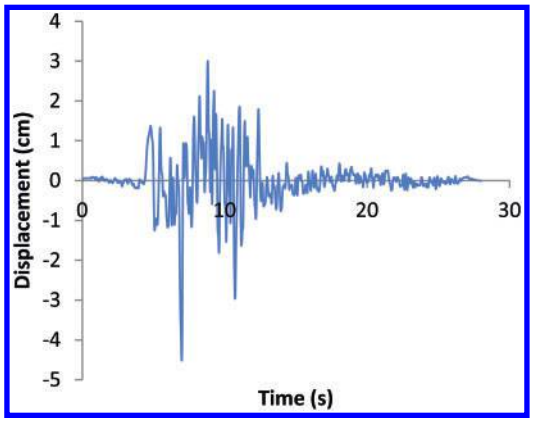


Figure 9. Lateral Displacement – Far-Field Koceali records.

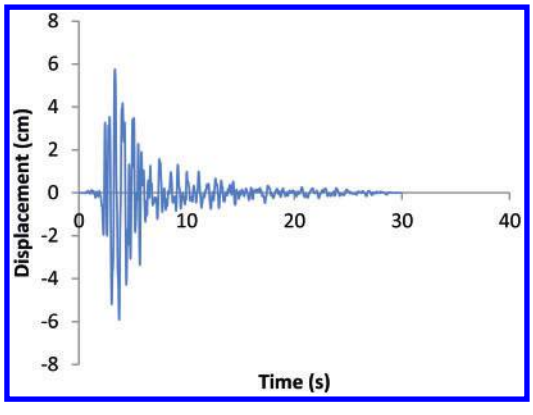


Figure 10. Lateral Displacement – Near-Field Whittier Narrows records.

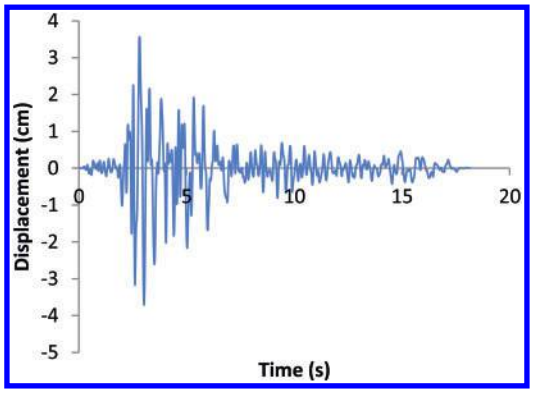


Figure 11. Lateral Displacement – Far-Field Whittier Narrows records.

In Figures 10 and 11 are showed that the lateral displacements of Point A on Zirdan Dam Via Near and far field Whittier Narrows earthquake records.

It is denoted that the time the displacement of the near field earthquake is greater than far field earthquake.

The obtained results were compared between near and far filed earthquakes that were modified.

6 CONCLUSIONS

This paper compares nonlinear seismic responses of RCC Dam – reservoir systems obtained for near field and far-field earthquakes by FE models on MCE records.

- The displacement of three near field and far-field seismic records were showed that near-filed earthquakes are much stronger than far field one indeed , although there are some lateral displacements that are excessive than near filed but the average of displacement is not.
- The direction of the displacement of far filed earthquake is showed that the maximum of movements are towards the reservoir so it can be very dangerous for dam stability.

ACKNOWLEDGEMENTS

The authors gratefully acknowledged the Pazhoohab company especially Mr Mansoor Karimi and Islamic Azad university of south Tehran Branch department.

Appreciation is also expressed to Dr. Arash Razmkhah, Dr Iman shoar, and Mrs Toosi.

REFERENCES

US Army Corps of Engineers (USACE). (1995) Seismic design provision for roller compacted concrete dams, EP 1110-2-12, Department of The Army, USA

A. Mazloumi, M. Ghaemian, A. Norrzad (2012), Nonlinear Seismic Analysis of RCC Dam Considering Orthotropic Behavior of Layers, International symposium on dams for a changing world, Kyoto, Japan.

G. Monterio and R.C. Barros (2008), Seismic analysis of a roller compacted concrete gravity dam in Portugal, The 14th Word Conference on Earthquake engineering, Beijing, China.

USACE, Time-history dynamic analysis of concrete hydraulic structures Engineering and Design, USA. (2003).

Z. Heirany and M. Ghaemian (2012) The effect of foundation's modulus of elasticity on concrete gravity dam's behavior, Indian Journal of Science and Technology.

US Army Corps of Engineers (USACE) (2001), Seismic Testing of a 1/20 scale Model of Koyna Dam, ERDC TR-01-17, Construction engineering Research laboratory.

Chopra, A.K. and Chakabarti, P. (1972) 'The earthquake experience at Koyna dam and stresses in concrete gravity dam", Earthq. Eng. Struct. Dyn.

V. Valamanesh, H.E. Estekanchi, A.Vafai, M. Ghaemian, (2011), Application of the endurance time method in seismic analysis of concrete gravity dams, Scientia Iranica.

Lehmann, Erich L. (1975); Non parametrics: Stati stical Methods Based on Ranks.

6. Material modelling, composite materials, functionally-graded materials

Research and Applications in Structural Engineering, Mechanics and Computation – Zingoni (Ed.)
© 2013 Taylor & Francis Group, London, ISBN 978-1-138-00061-2

Some advances in functionally graded materials

Luciano Nunziante
University of Napoli Federico II. Napoli. Italy

ABSTRACT: Some new solutions for mechanical response of composite circular cylinders are shown, by means of a mathematical treatment of Navier-Cauchy elasticity equations, based on suitable choice of Boussinesq-Somigliana Galerkin potentials. The set of Euler differential equations is transformed in to an algebraic one, by means of compatibility and equilibrium boundary conditions. All load cases de Saint-Venant like are solved. An homogenization technique is used to obtain particular stiffness features, by coupling of materials with Poisson modulus of opposite sign. Finally, the solution of technical problems is shown: design of optimum assembling aimed to maximize stiffness in cases of bending and shear, design of optical fibre sensors for distributed strain measurements, prediction of collapse load of concrete columns confined by Fiber Rinforced Polymers.

1 INTRODUCTION

1.1 *Composites and functionally graded materials*

Composites are highly inhomogeneous media made up of a matrix and of a reinforcement, designed to enhance overall mechanical properties and destined to optimize elastic stiffness or to gain resistance of the designed objects to face up mechanical actions or limiting damage effects, in cases of dynamic impact, wear, thermal loads, fatigue and fracture. Sometime the composite is made up by an assembling of several composite lamina, each of them constituted by a mono or two-phase component. Among Composites, Functionally Graded Materials (FGMs) are formed of two or more constituent phases with a continuously variable composition, where volume fraction of particles varies in one or several directions. FGMs possess a number of advantages that make them attractive in several applications, since they eliminate stress discontinuities of composites, avoiding delaminating effects, also mitigating thermal stress concentrations [1,2,3]. When the cylinder is strained symmetrically it was already shown by the Author [7] that all mechanical quantities can be obtained in closed form starting from the Navier-Cauchy elastic equilibrium equation of the single phase for vanishing body forces:

$$\nabla^2\mathbf{u}+1/(1-2\nu)\,grad\,div\mathbf{u}=-\mathbf{b}/\mu=0 \qquad (1)$$

where **u** is the displacement field, **b** are body forces, ∇^2 is the Laplacian operator; μ and ν are the first Lamè constant and the Poisson modulus of the material phase, respectively.

It is well known that for the problem at hand for the displacement **u** there exists a vector ***F*** (Boussinesq-Somigliana Galerkin potential) such that following equations hold true:

$$\mathbf{u}=\nabla^2\boldsymbol{F}-2(1-\nu)\,grad\,div\boldsymbol{F} \quad , \quad \boldsymbol{F}\in\mathcal{C}^{(4)} \, , \, \nabla^4\boldsymbol{F}=0. \qquad (2)$$



Figure 1. Structures in composites materials.

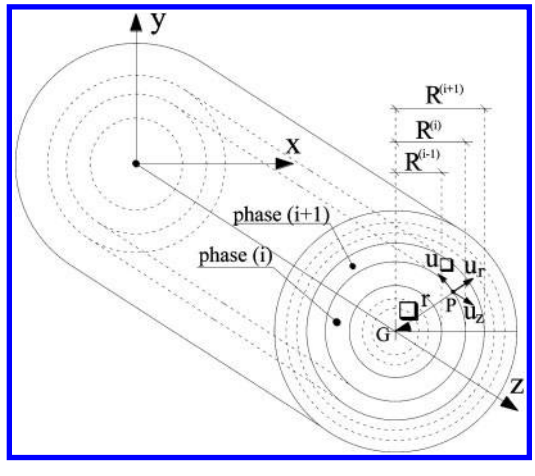


Figure 2. Composite Cylinder.

The problem of the whole composite cylinder was solved in analytical form [4,7,9] for a variety of load cases, by choosing suitable form for the potential of displacement of single material phase. From displacement, strains are obtained by differentiation and stresses by application of Hooke's law of linear elasticity. Finally on displacements and on stresses are applied constraints of continuity on the boundary surfaces between couples of material phases, expressing compatibility and equilibrium. These conditions follow the assumption of perfect bonding among constituting phases.

2 NEW SOLUTIONS FOR COMPOSITE CYLINDER UNDER SAINT-VENANT LOADS

For the already defined composed cylinder, were obtained new analytical elastic solutions, in presence of pure bending, and of bending and shear [7,9]. Also the well known literature's solutions for cases of axial force and of torque, were obtained, thanks to a unitary mathematical procedure starting from following assumptions:

a) Existence of a Love's function, [3] defining an irrotational potential giving displacement field for the case of axial force

$$\begin{aligned} u_r &= -(1/2)\left(\chi_{,rz}/\mu\right),\ \ u_\vartheta = 0, \\ u_z &= (1/2)\left[\left(\nabla^2\chi\right)/(\mu+\lambda)+\left(\chi_{,rr}+r^{-1}\chi_{,r}\right)/\mu\right] \end{aligned} \tag{3}$$

where χ is a bi-harmonic function satisfying equation $\nabla^4\chi = 0$

b) Existence of a solenoidal potential of displacement field for torque, bending moment and shear. As matter of fact, symmetry and skew-symmetry conditions on displacement in to the section allow to split in each phase displacement components in two parts: the first ones u_r, u_z symmetric, and the second one u_θ as skew-symmetric, so that the divergence takes in to account the relevant terms: $\nabla\cdot\mathbf{u} = g_1 + g_2$, where $g_1 = u_{r,r} + r^{-1}u_r + u_{z,z}$, is symmetric and $g_2 = r^{-1}u_{\theta,\theta}$, is skew-symmetric. Above Figure shows displacement's symmetry and skew-symmetry features respect to axes x and y for bending moment M_x. It was shown [7] that the integral of the divergence of displacement field over any cross section is equal to zero:

$$\int_\omega \nabla\cdot\mathbf{u}\, d\omega \tag{4}$$

The above integral condition (weak condition) corresponds to a vanishing volumetric change of cross-section and of whole solid. It was shown that

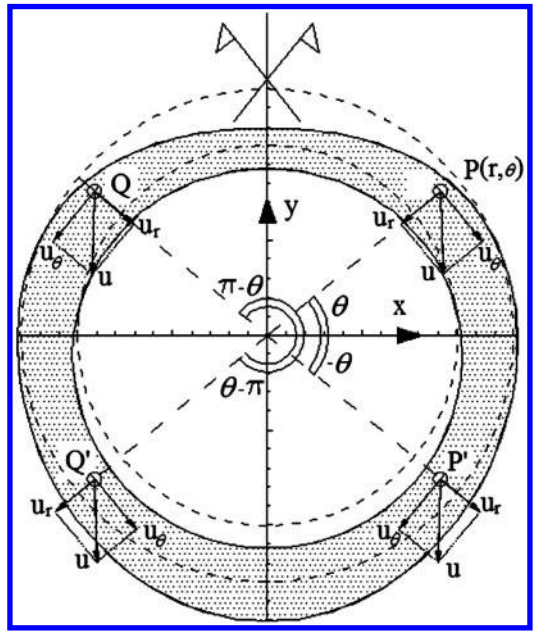


Figure 3. Symmetry and skew-symmetry features of displacement field in cross section of bending composite cylinder.

divergence of displacement can assume the unified expression:

$$\nabla\cdot\mathbf{u} = 1/4\ k\,\alpha^2\ \ 7-3\alpha\ \ z^{\alpha-1}y\ = \\ = \left\{\begin{array}{l} = 0, \alpha = 0, torque; = k\,y, \alpha = 1, bending; \\ = k\,y\,z, \alpha = 2, shear + bending \end{array}\right\} \tag{5}$$

By substituting above condition in to the Navier-Cauchy equations, resulting displacement field is obtained as the sum of the two following displacements

$$\mathbf{u} = \mathbf{u}^h + \mathbf{u}^p \tag{6}$$

where:

$$\begin{aligned} &u_r^h = r^{-1}G_{,\theta z},\ \ u_\theta^h = \left[\ 1/2\ r\nabla^2 G - G_{,r}\right]_{,z},\ \ u_z^h = -\ 1/2\ \left[\nabla^2 G\right]_{,\theta} \\ &u_r^p = \left[\alpha\ 3\mu+\lambda\ \ 7-3\alpha\ \ k\,z^{\alpha+1}\sin\theta\right]/\left[4\ 1+\alpha\ \ \mu\right] \\ &u_\theta^p = \left\{\frac{\alpha\,k\,z^{\alpha-1}\ \ 3\alpha-7}{\left[4\ 1+\alpha\ \ \mu\right]}\left[\alpha\ 1+\alpha\ \ 2\mu+\lambda\ r^2 - 3\mu+\lambda\ z^2\right]\cos\theta\right\} \\ &u_z^p = \left[\ \mu+\lambda\ \ 3\alpha-7\ \ \alpha\,k\,r\,z^\alpha\sin\theta\right]/\ 4\mu \end{aligned} \tag{7}$$

The first one $\mathbf{u}^h$ is characterized by divergence equal to zero (pure torsion), and corresponds to the solution of the homogeneous differential equation system, and is denoted by the symbol "h". This solution will not more treated in what follows.

The second one $\mathbf{u}^p$ is characterized by divergence equal to function reported in (5) with $\alpha \neq 0$, is a particular integral and will be denoted by the symbol "p" (bending and shear);

By substituting the components of displacement $\mathbf{u}^p$ corresponding to the "particular" solution in to the stress-strain relationships, were obtained for each phase the stress components related to this part of displacement with volumetric strain not locally vanishing:

$$\begin{aligned}
&\sigma_{rr}^p = -\Gamma\lambda\sin\theta,\ \sigma_{\theta\theta}^p = -\Gamma\ 4\mu+3\lambda\ \sin\theta,\\
&\sigma_{zz}^p = \Gamma\ 2\mu+\lambda\ \sin\theta,\ \tau_{r\theta}^p = \Gamma\ 2\mu+\lambda\ \cos\theta,\\
&\tau_{rz}^p = -\Gamma\ 2\mu z\sin\theta\ /\ \alpha r\ ,\\
&\tau_{\theta z}^p = \Gamma\left[-2\mu z^2+\alpha\ 2\mu+\lambda\ \ \alpha-1\ r^2\right]\cos\theta\ /\ \alpha\ r z\ ,\\
&\text{where } \Gamma = k\alpha^2\ 3\alpha-7\ r z^{\alpha-1}\ /4\ .
\end{aligned} \tag{8}$$

2.1 *Combined bending and shear force*

For the problem of bending and shear, functions $G^{(i)}$ are assumed as bi-harmonic in each phase. Also in this case the integral of divergence of solving displacement vanishes on every cross section. In presence of constant shear on the solid, shear stresses $\tau_{\theta z}^{(i)}, \tau_{rz}^{(i)}$ must be independent on z. Since the bending moment is linear along z direction, the remaining stresses depend linearly upon z direction. By applying the above hypotheses, we obtain [7,9] for each material phase function $G^{(i)}$ as:

$$\begin{aligned}
&G^{(i)} = \left(G_0^{(i)} + G_1^{(i)} z^2 + G_2^{(i)} z^4\right)\cos\theta,\\
&k^{(i)} = 2\left[2V_3^{(i)} - 9V_2^{(i)}\right]\Big/\Omega^{(i)}
\end{aligned} \tag{9}$$

the solving displacement field is finally obtained for each phase satisfying equilibrium and compatibility equations inside each generic *i-th* phase of multilayered cylinder subjected to shear and bending moment:

$$\begin{aligned}
u_r^{(i)} &= \left\{V_5^{(i)} + V_2^{(i)} z^2 + (1/2)V_4^{(i)} r^{-2} + \left(r^2/2\Omega^{(i)}\right)\left[V_3^{(i)}\left(\mu^{(i)} - \lambda^{(i)}\right) + 6V_2^{(i)}\lambda^{(i)}\right]\right\} z\sin\theta\\
u_\theta^{(i)} &= \left\{V_5^{(i)} + V_2^{(i)} z^2 - (1/2)V_4^{(i)} r^{-2} + \left(r^2/2\Omega^{(i)}\right)\left[6V_2^{(i)}\lambda^{(i)} - V_3^{(i)}\left(3\lambda^{(i)} + 5\mu^{(i)}\right)\right]\right\} z\cos\theta\\
u_z^{(i)} &= \left\{\begin{array}{l} V_6^{(i)} + -3V_2^{(i)} z^2 + V_7^{(i)} r^{-2}\left(1-\delta_{0i}\right) + \\ +\left(r^2/2\Omega^{(i)}\right)\left[3\left(2\lambda^{(i)} + 3\mu^{(i)}\right)V_2^{(i)} - \left(\lambda^{(i)} + \mu^{(i)}\right)V_3^{(i)}\right] \end{array}\right\} r\sin\theta
\end{aligned} \tag{10}$$

Above displacements produce by differentiation and by means of Hooke equations suitable expressions for strain and stress components. Under assumption of perfect contact at the cylindrical interfacial boundaries (no de-lamination or friction phenomena), equilibrium and compatibility equations at the interfaces between two generic adjacent phases allow to determine constants V_i. The followed mathematical approach reduces the Euler partial differential equation's system governing the elastic problem and relevant boundary conditions in to a simpler linear algebraic problem, where a prescribed number of coefficients have to be determined. The found analytical solutions allows to controlling the evolution of the local stress field inside each object's layer and at the material interfaces when volume fractions and elastic modulus of the constituents are prescribed.

2.2 *Homogenization of multilayered cylinder*

The derived analytical solutions lend themselves to define a homogenized one-dimensional beam-like model, representing the overall behavior of multilayered cylinder under the action of the DSV load conditions, by explicitly constructing the corresponding stiffness governing the elastic law among generalized beam stresses and strains. In case of bending, for the infinitesimal beam element under moment M_x the external virtual work becomes $dL_E = M_x\, d\phi(z)$ where $d\phi(z)$ is the flexural rotation increment. The inner virtual work is

$$dL_I = dz\sum_{i=0}^{n}\int_{\omega^{(i)}} \boldsymbol{\sigma}^{(i)} : \boldsymbol{\varepsilon}^{(i)} ds = \tag{11}$$

where

$$\begin{aligned}
&\Psi_\chi = \sum_{i=0}^{n}\int_{\omega^{(i)}} \boldsymbol{\sigma}^{(i)} : \boldsymbol{\varepsilon}^{(i)} ds = \sum_{i=0}^{n}\frac{4E^{(i)}I^{(i)}}{\left(1+\nu^{(i)}\right)}\\
&\cdot\left[\frac{U_4^{(i)2}\left(1-\delta_{0i}\right)}{R^{(i)4}R^{(i-1)4}} + \frac{4U_3^{(i)2} + \chi_0^2\left(3-\nu^{(i)}\right) - 8\chi_0 U_3^{(i)}\nu^{(i)}}{4\left(3-4\nu^{(i)}\right)}\right];
\end{aligned} \tag{12}$$

The curvature χ ,which is constant on the whole cross section in agreement with Bernulli's theory of beam, can be defined on each material phase as follows:

$$\begin{aligned}
&\chi = \varphi_{x,z} = \left[u_z^{(i)}/\left(r\sin\theta\right)\right]_{,z} = \chi_0 = const\\
&M_x = k_\chi\,\chi = k_\chi\,\varphi_{x,z} \ \Rightarrow\ d\varphi_x(z) = M_x\, k_\chi^{-1} dz
\end{aligned} \tag{13}$$

By means of Virtual Work Equation we obtain the overall bending stiffness k_χ of multilayered cylinder: $k_\chi = M_x^2\,\Psi_\chi^{-1}$ and the overall bending stiffness is $k_\chi = \Psi_\chi^{-1} = \sum_{i=0}^{n} E^{(i)}I^{(i)}\psi_\chi^{(i)}$ where $\psi_\chi^{(i)}$ is a correction term that depends on geometrical and mechanical parameters:

$$\psi_\chi^{(i)} = \eta_\chi^{(i)} \Big/ \left[\sum_{i=0}^{n} E^{(i)}I^{(i)}\eta_\chi^{(i)}\right]^2 = \left(dL_I^{(i)} / dL_I^2\right) / E^{(i)}I^{(i)} \tag{14}$$

where coefficient $\eta_\chi^{(i)}$ is given by following expression:

$$\begin{aligned}
&\eta_\chi^{(i)} = 1/E^{(i)}I^{(i)}\int_{\omega^{(i)}} \boldsymbol{\sigma}^{(i)} : \boldsymbol{\varepsilon}^{(i)} ds\ = 4/\left(1+\nu^{(i)}\right).\\
&\left[\frac{U_4^{(i)2}\left(1-\delta_{0i}\right)}{R^{(i)4}R^{(i-1)4}} + \frac{4U_3^{(i)2} + \chi_0^2\left(3-\nu^{(i)}\right) - 8\chi_0 U_3^{(i)}\nu^{(i)}}{4\left(3-4\nu^{(i)}\right)}\right]
\end{aligned}$$

where, without loss of generality, $U_3^{(i)}, U_4^{(i)}, \chi_0$ are coefficients to determine by setting $M_x = 1$. It is hence evident that, in the expression found for bending stiffness, an important role is covered by the value of Poisson modulus of each material phase. Following a similar procedure [4,7,9], the shear stiffness of homogenized composed cylinder was obtained as: $k_\gamma = \sum_{i=0}^{n} \mu^{(i)}\omega^{(i)}\psi_\gamma^{(i)}$ where $\omega^{(i)}$ is the area of i-th

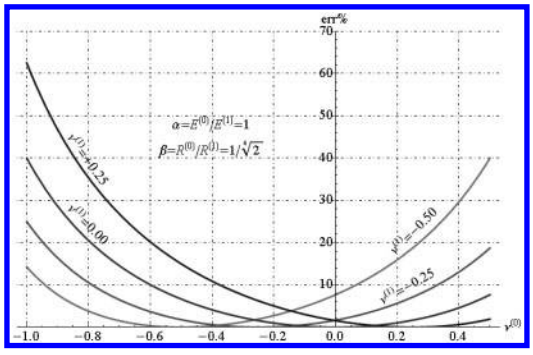


Figure 4. Error percentage of bending stiffness as function of different Poisson modulus values of materials.

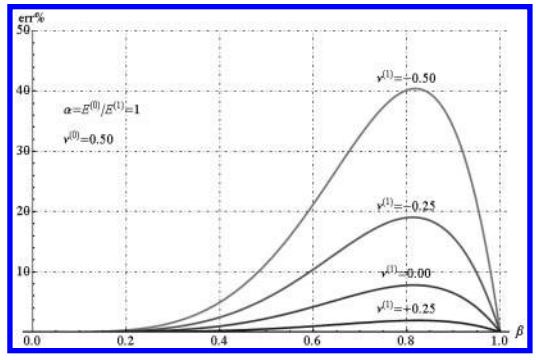


Figure 5. Error percentage of bending stiffness for different Poisson modulus values of materials, as function of radii ratio.

phase and $\psi_\gamma^{(i)}$ is a coefficient depending on geometrical and mechanical parameters of the i-th phase. Also for the shear stiffness a crucial role is covered by the elastic modulus (Lamè constants, and Poisson modulus) of each component phase. The numerical values of the found stiffness's expressions were tested on a two phase multilayered cylinder (a central core perfectly bonded to a sole surrounding hollow cylinder), for which relevant bending stiffness is $k_\chi = \Psi_\chi^{-1} = \sum_{i=0}^{n} E^{(i)} I^{(i)} \psi_\chi^{(i)}$ that was compared with the approximate bending stiffness of current literature $\bar{k}_\chi = \sum_{i=0}^{1} E^{(i)} I^{(i)}$, evaluated as the sum of the single phase's stiffness, ($I^{(i)}$ are the inertia, and $E^{(i)}$ the Young modulus of single phase, respectively). In order to stress the influence of Poisson's moduli, the error percentage between and $\bar{k}_\varepsilon$ was carried out by applying the formula $err\% = 100(k_\chi - \bar{k}_\chi)/\bar{k}_\chi$, that for pure bending gives:

$$err\% = \frac{400\,\alpha\,\beta^4\left(1+\beta^4\right)\left(\nu^{(0)}-\nu^{(1)}\right)^2}{\left[\beta^4(\alpha-1)+1\right]} \cdot \frac{1}{\left\{\left(\beta^4-1\right)\left(3-\nu^{(0)}-4\nu^{(0)2}\right)+\alpha\left(1+\nu^{(1)}\right)\left[\beta^4\left(4\nu^{(1)}-3\right)-1\right]\right\}} \tag{14}$$

where α, β are parameters expressing ratios between Young modulus and of radii of two phases, respectively.

By assuming same area and same Young's modulus for two phases: $\alpha = 1$, $\beta = 1/\sqrt[4]{2}$, the defined percentage error becomes following function of Poisson's modulus of two phases:

$$err\%\left(\alpha=1,\beta=\frac{1}{\sqrt[4]{2}}\right) = \frac{200\left(\nu^{(1)}-\nu^{(0)}\right)^2}{8+\nu^{(1)}\left(1-4\nu^{(1)}\right)-\nu^{(0)}\left(1+4\nu^{(0)}\right)} \tag{15}$$

Figure 4 shows that by coupling an external tube shoving negative values of Poisson modulus ν with a core cylinder with positive values of ν, the homogenized stiffness of composite can assume values greater than 40% respect the approximate averaging

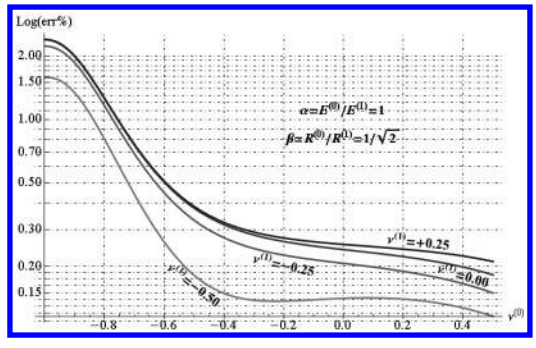


Figure 6. Error percentage of shear stiffness as function of different Poisson modulus values of materials.

value ($\alpha = E^{(0)}/E^{(1)} = 1$, $\beta = R^{(0)}R^{(1)} = 1/\sqrt[4]{2}$). Figure 5 shows same effect when it is assumed variable the ratio β between radii of phases, for negative values of Poisson modulus of external material ($\alpha = E^{(0)}/E^{(1)} = 1, = 0.5$). By means of the same homogenization procedure also the shear stiffness was obtained, which is given by:

$$\bar{k}_\gamma = 6\pi R^{(1)}\mu^{(1)}\left[\frac{\beta^2\mu^{(0)}\left(1+\nu^{(0)}\right)}{7+2\nu^{(0)}\left(7+4\nu^{(0)}\right)} + \frac{\left(1-\beta^2\right)\left(1+\beta^2\right)^2\left(1+\nu^{(1)}\right)}{\left[7+2\nu^{(1)}\left(7+4\nu^{(1)}\right)\right]\left(1+\beta^4\right)+\left[34+4\nu^{(1)}\left(17+8\nu^{(1)}\right)\right]\beta^2}\right] \tag{16}$$

and the relevant error percentage is given by formula

$$err\% = 100\left(k_\gamma - \bar{k}_\gamma\right)/\bar{k}_\gamma. \tag{17}$$

Following Figures 6 and 7 show the considerable growing of shear stiffness for particular chooses of mechanical and geometrical parameters, namely for Poisson modulus of components of opposite sign.

Above solutions were successfully applied to a few of technical problems aimed to maximize stiffness in cases of bending and shear, design of optical fibre sensors for distributed strain measurements, prediction of collapse load of concrete columns confined by Fiber Rinforced Polymers.

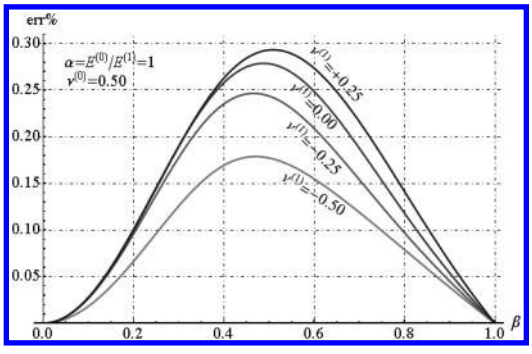


Figure 7. Error percentage of shear stiffness for different Poisson modulus values of materials, as function of radii ratio.

3 TECHNICAL APPLICATIONS

In the following, some applications of above theory are presented, that show interesting new results obtained by the Author, in a few of new fields of modern structural engineering.

3.1 *Optical fibre sensors for distributed strain readings*

New sensors for distributed readings, composed by a three phase Functionally Graded Cylinder [Figure 8] were studied by means of the above presented theory [5,6,8]. The optical fibre (Figure 8), a composed cylinder whose axis is x_3, is composed by an internal glass core, covered by a glass cladding and by a polymeric jacket. The external diameter can reach a few of hundreds of micrometers. For many engineering works of strategic significance like bridges, pipes, high rise buildings, dams and tunnels, safety should be continuously assessed over their complete lifetimes. Because optical fibre length reaches tens of kilometres, they can be used for the monitoring and safety assessment of these large structures.

When optical fibre is strictly bonded to the structure, its deformation follows that of the supporting object, and thanks to the strain, changes in to the density of the glass core occur. This effect con be read by means of distributed optical fibre sensors based on *stimulated Brillouin scattering* (SBS) that rely on the interaction between two light waves and an acoustic wave in the optical fibre. The measurement principle is based on the fact that the Brillouin frequency of the optical fibre is shifted when strain changes occur.

A necessary condition for a good reading of strain, is that the strain present in the object in the direction of axis x_3 on the external boundary of optical fibre, may be transmitted without decaying until the central core of sensor. This condition becomes the so-called mechanical condition of *no-decaying* of ε_{33} strain component in the radial direction [4], passing through the three material phases of sensor. The mechanics of the three-phase composed cylinder constituting the sensor was analysed, by imposing the inner constraint

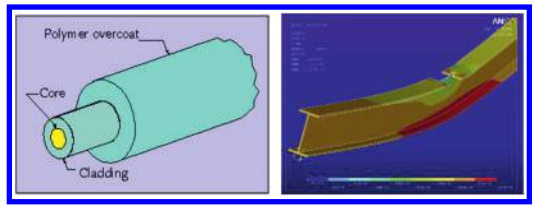


Figure 8. Optical Fibre. FEM analysis of bent defected beam.



Figure 9. Laboratory Tests on large beams.

of no-decaying of the ε_{33} strain component in radial direction. It was shown that under this internal constraint on deformation, only the following conditions of loads are allowed: a) radial pressures with linear variation in x_3 direction applied on the cylindrical external surface of sensor; b) axial force applied on two bases; c) uniform shear tractions applied on the cylindrical external surface of sensor in x_3 direction accompanied by equilibrating normal forces on bases of cylinder.

By means of this new mechanical solutions, and of an experimental optical-electronic apparatus, some laboratory tests on large steel beams and rods, were carried out to measure the strain profile all over the length of structure (Figure 9). This technique was then successfully utilised to predict the damage present in a bending beam, showing optimal accuracy and agreement between the read strains and the calculated ones. FEM numerical results were also utilised for assessment of experimental results (Figure 8).

3.2 *Load carrying capacity of reinforced concrete columns confined with fiber reinforced polymers*

By means of the above presented theory of composite cylinders [4,5], the elastic and ultra-elastic response of concrete columns confined by Carbon Fiber Reinforced Polymers (CFRP) was analyzed. The concrete column was modeled as a composed circular cylinder constituted by a concrete's central core with a surrounding tube of concrete in which are present axial steel reinforcements, surrounded by a CFRP thin bandage.

Under the hypotheses of axis-symmetrical boundary conditions, elasticity and perfect bond between the phases, analytical solutions for self-equilibrated axial forces applied at the extremities of the object were derived (Figure 10).

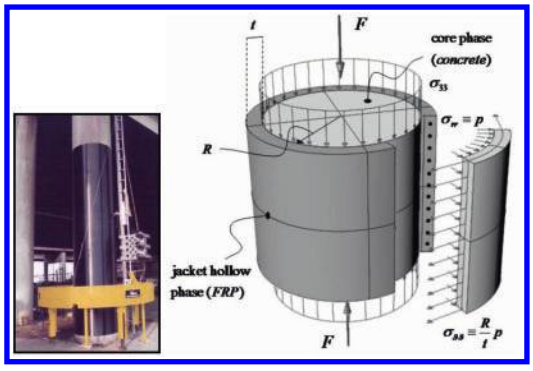


Figure 10. RC Column reinforced with FRP. Mechanical model.

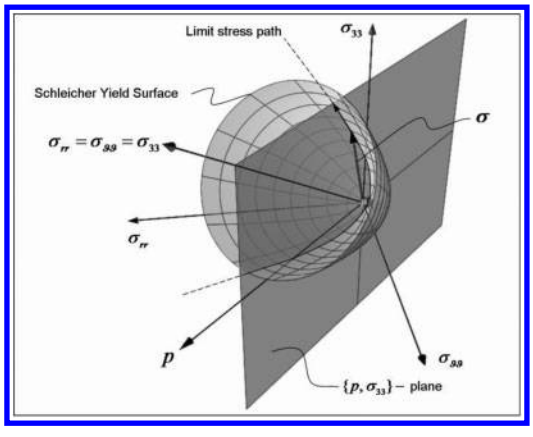


Figure 11. Limit stress path on Schleicher Yield surface.

The initial elastic analysis was based here on the hypotheses of isotropic response of concrete and on cylindrically anisotropy of FRP bandage. Also in this case, the differential Boundary Value Problem (BVP) of the three phase composite cylinder was reduced to the equivalent linear algebraic one, by means of a special matrix-like arrangement of the governing equations and invoking the Complex Potential Theory for anisotropic materials.

When axial load increases, the response of cylinder "moves" toward the post-elastic range in which the stress field in the core follows the Intrinsic Curve or Schleicher-like elastic-plastic behavior whit associate flow rule.

The cylindrically orthotropic hollow phase modeling FRP sheets surrounding reinforced concrete column obeys to an elastic-brittle Tsai-Hill anisotropic yield criterion. By means of this strategy, predictive formulae for estimating the overall collapse mechanism, the concrete ultimate compressive strength and the confining pressure effect were derived.

The obtained results were compared with several experimental literature data, highlighting good agreement with each other [5,6].

Also a formula for design thickness of confining FRP sheet was obtained, as well as an assessment formula for the whole reinforced column [5].

REFERENCES

[1] Lekhnitskii, S. G., (1981), Theory of Elasticity of an Anisotropic Body, Mir, Moscow.

[2] Ting, T. C. T., (1999), Pressuring, shearing, torsion., Proc. Roy. Soc. Lond. A452, 2397–2421. [3] Love, A. E. H., (1944), A treatise on the mathematical Theory of Elasticity, Dover Publications, Inc, New York.

[4] Nunziante, L., Fraldi, M., Carannante, F. (2007) "Axis – Symmetrical Solutions for n-plies Functionally Graded Material Cylinders under Strain no-decaying conditions". *Mechanics of Advanced Materials and Structures* – Taylor & Francis. **vol. 14**, No 3.

[5] M. Fraldi, L. Nunziante & Al. (2008). On the Prediction of the collapse load of circular concrete columns confined by FRP. J. Engin. Struct., Vol. 30, 11.

[6] Fraldi, M., Nunziante, et al. (2009), Mechanics of distributed fibre optic sensors for strain measurements on rods. J. Struct. Engin., 35, No 5.

[7] M. Fraldi, L. Nunziante at al. (2012), Analytical solutions for n-phase Functionally Graded Material Cylinders under de Saint Venant load conditions: Homogenization and effects of Poisson ratios on the overall stiffness. Composites Part B: Vol.45, No 1.

[8] Bernini, R., Nunziante, L. et al. (2006). Identification of. Smart Mat. and Struct. Vol. n. 15.

[9] F. Carannante. (2013). Some new thermo-elastic solutions for cylindrical and spherical composites. PhD Thesis, Construction Engineering, Dept of Structures for Engineering and Architecture, University of Napoli Federico II. Napoli. Italy.

Research and Applications in Structural Engineering, Mechanics and Computation – Zingoni (Ed.)
© 2013 Taylor & Francis Group, London, ISBN 978-1-138-00061-2

Numerical implementation of the Hoek-Brown material model with strain hardening

E.S. Sørensen, J. Clausen & L. Damkilde
Department of Civil Engineering, Aalborg University, Aalborg, Denmark

ABSTRACT: A numerical implementation of the Hoek-Brown criterion is presented, which is capable of modeling important aspects of the different post-failure behaviors observed in jointed rock mass. This is done by varying the material parameters based on the accumulated plastic strains. The implementation is for use in finite element calculations, and is based on the return mapping framework. The updated stress state is found in principal stress space based on the principles of boundary planes and a consistent constitutive matrix is found for better convergence of the global equilibrium iterations. The constitutive model is demonstrated on a simulation of a tunnel excavation and the results are compared with an analytical solution for a tunnel excavation in elastic-brittle rock material.

1 INTRODUCTION

Rock masses are often encountered within the fields of civil and mining engineering. Examples include tunnel excavations, foundations and slope stability problems. According to Hoek & Brown (1997), the post-failure behavior of rock masses falls into three categories. A very good quality hard rock mass tends to show an elastic-brittle behavior, where the strength drops rapidly once yielding occurs. Average quality rock mass is believed to show a strain-softening behavior, where the strength decrease with an increase in plastic strains. Rock mass of poor quality behaves in an elastic-perfectly-plastic fashion. The analytical solutions of a tunnel excavation provided by Sharan (2008) demonstrate the impact of an elastic-brittle behavior compared to a perfectly plastic behavior.

To model the strength of rock masses, the Hoek-Brown yield criterion is often applied (Hoek et al. 2002). This paper seeks to implement a Hoek-Brown material model able to incorporate all three post-failure behaviors for use in finite element calculations.

2 THE HOEK-BROWN CRITERION

The Hoek-Brown criterion has evolved from the original Hoek-Brown criterion used for hard rock masses into the more versatile generalized Hoek-Brown criterion, which states that plastic deformations develop once

$$\sigma_1' = \sigma_3' + \sigma_{ci}\left(m_b\frac{\sigma_3'}{\sigma_{ci}} + s\right)^a \tag{1}$$

where σ_1' is the largest effective principal stress, σ_3' is the smallest effective principal stress, σ_{ci} is the uniaxial compressive strength of the intact rock material and m_b, s and a are material parameters. Compression is taken as positive. Throughout the rest of this paper, effective stresses are implied and the primes will thus be left out for simplicity. The material parameters m_b, s and a and the Youngs modulus, E can be found based on the Geological Strength Index, GSI, the disturbance factor, D, and the intact rock parameter, m_i (Hoek et al. 2002), (Hoek & Diederichs 2006).

3 PLASTICITY FUNDAMENTALS

The basic theory behind plasticity relies on one or more yield functions, $f_1, \ldots, f_n$, which are scalar functions of the stress state, $\boldsymbol{\sigma}$, and some hardening parameters, $\boldsymbol{K}$. Plastic strains start to develop once the material reaches its yielding limit, which is defined by the yield criteria

$$f_i(\boldsymbol{\sigma}, \boldsymbol{K}) = 0, \quad i = 1, \ldots, n \tag{2}$$

Any combination of $\boldsymbol{\sigma}$ and $\boldsymbol{K}$ fulfilling one or more of the criteria leads to additional plastic straining. Any combination of $\boldsymbol{\sigma}$ and $\boldsymbol{K}$ resulting in negative values of all yield criteria does not result in additional plastic straining and any combination resulting in a positive value of any of the functions is inadmissible. The manner in which the plastic strains develop is governed by the plastic potential functions, $g_1, \ldots, g_n$, which are also functions of $\boldsymbol{\sigma}$ and $\boldsymbol{K}$, and the non-negative plastic multipliers $\lambda_1, \ldots, \lambda_n$, such that

$$d\boldsymbol{\varepsilon}^p = \sum_{i=1}^{n} \alpha_i \, d\lambda_i \frac{\partial g_i}{\partial \boldsymbol{\sigma}} \tag{3}$$

where α_i is 1 if yield criterion i is active, and 0 otherwise. The hardening parameters, $\boldsymbol{K}$, are functions of

the state variables, $\boldsymbol{\kappa}$, that define the internal state of the material

$$\boldsymbol{K} = \boldsymbol{K}(\boldsymbol{\kappa}) \tag{4}$$

The evolution of the state variables is defined by the evolution law

$$d\boldsymbol{\kappa} = \sum_{i=1}^{n} \alpha_i \, d\lambda_i \boldsymbol{k}_i(\boldsymbol{\sigma}, \boldsymbol{K}) \tag{5}$$

where $\boldsymbol{k}_1, \ldots, \boldsymbol{k}_n$ are some functions, that must be appropriately chosen.

Further details of the FE-method and plasticity can be found in Ottosen & Ristinmaa (2005), de Souza Neto, Perić, & O wen (2008) and Clausen (2007).

4 RETURN MAPPING

The numerical implementation relies on return mapping, which initially assumes that the strain increment, $\Delta\boldsymbol{\varepsilon}$, from the global equilibrium iterations, is entirely elastic, resulting in an elastic predictor stress increment

$$\Delta\boldsymbol{\sigma}^e = \boldsymbol{D}\Delta\boldsymbol{\varepsilon} \tag{6}$$

which combined with the initial stress state, $\boldsymbol{\sigma}^A$, results in a predicted elastic stress state

$$\boldsymbol{\sigma}^B = \boldsymbol{\sigma}^A + \Delta\boldsymbol{\sigma}^e \tag{7}$$

If the evaluation of one or more of the yield criteria with this stress state and the initial hardening parameters, $\boldsymbol{K}^A$, results in a positive value, the stress state is inadmissible, cf. figure 1.

To find the updated stress state, a plastic corrector, $\Delta\boldsymbol{\sigma}^p$, is introduced

$$\begin{aligned} \Delta\boldsymbol{\sigma}^p &= \boldsymbol{D}\Delta\boldsymbol{\varepsilon}^p = \boldsymbol{D}\sum_{i=1}^{n} \alpha_i \int_{\lambda_i^A}^{\lambda_i^C} \frac{\partial g_i}{\partial \boldsymbol{\sigma}} d\lambda_i \\ &\approx \sum_{i=1}^{n} \alpha_i \Delta\lambda_i \boldsymbol{D} \left.\frac{\partial g_i}{\partial \boldsymbol{\sigma}}\right|_C = \sum_{i=1}^{n} \alpha_i \Delta\lambda_i \boldsymbol{s}_i \end{aligned} \tag{8}$$

where (3) has been used. Thus, the plastic corrector is some linear combination of the directions

$$\boldsymbol{s}_i = \boldsymbol{D} \left.\frac{\partial g_i}{\partial \boldsymbol{\sigma}}\right|_C \tag{9}$$

given by each active yield surface. The updated stress state becomes

$$\boldsymbol{\sigma}^C = \boldsymbol{\sigma}^B - \Delta\boldsymbol{\sigma}^p = \boldsymbol{\sigma}^B - \sum_{i=1}^{n} \alpha_i \Delta\lambda_i \boldsymbol{s}_i \tag{10}$$

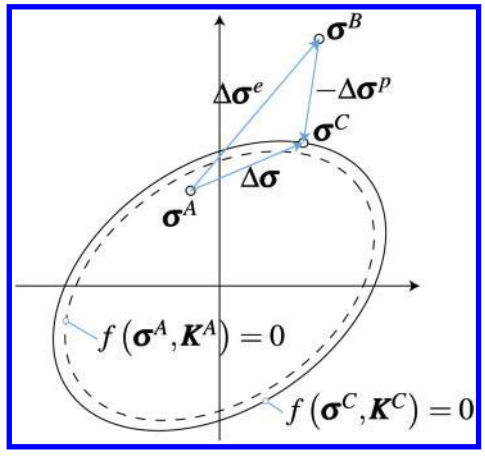


Figure 1. Sketch of the updating scheme.

In this regard, α_i is 1 for the yield criteria, which are satisfied for the updated stress state and zero otherwise. The updated stress state must fulfill

$$\alpha_i f_i\left(\boldsymbol{\sigma}^C, \boldsymbol{K}^C\right) = 0 \tag{11}$$

where $\boldsymbol{K}^C$ has been found from $\boldsymbol{\kappa}^C$, which in turn has been found using (5) such that

$$\boldsymbol{\kappa}^C = \boldsymbol{\kappa}^A + \sum_{i=1}^{n} \alpha_i \int_{\lambda_i^A}^{\lambda_i^C} \boldsymbol{k}_i d\lambda_i \approx \boldsymbol{\kappa}^A + \sum_{i=1}^{n} \alpha_i \Delta\lambda_i \, \boldsymbol{k}_i|_C \tag{12}$$

5 STRAIN HARDENING HOEK-BROWN MODEL

5.1 *Basic premises*

In order to implement the strain hardening Hoek-Brown model, the above mentioned aspects must be accounted for. With tension taken as positive, the Hoek-Brown criterion of (1) can be rewritten

$$f = \sigma_{\max} - \sigma_{\min} - \sigma_{ci}\left(s - m_b \frac{\sigma_{\max}}{\sigma_{ci}}\right)^a = 0 \tag{13}$$

where $\sigma_{\max}$ is the largest principal stress and $\sigma_{\min}$ is the smallest principal stress. Equation (13) forms a six-sided pyramid with curved sides in principal stress space along the hydrostatic axis, which bounds the allowable stress states, as seen on figure 2.

The plastic potential function is assumed to take the form of the Hoek-Brown criterion as well, however, the parameters are different from those of f, thus

$$g = \sigma_{\max} - \sigma_{\min} - \sigma_{ci_g}\left(s_g - m_{b_g} \frac{\sigma_{\max}}{\sigma_{ci}}\right)^{a_g} \tag{14}$$

The hardening parameters are comprised of

$$\boldsymbol{K} = \{\sigma_{ci}, m_b, s, a, \sigma_{sci_g}, m_{b_g}, s_g, a_g\} \tag{15}$$

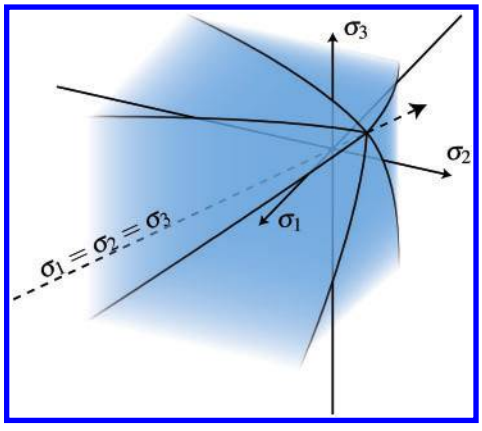


Figure 2. Sketch of Hoek-Brown criterion in principal stress space.

The state parameters, $\boldsymbol{\kappa}$, are assumed to be expressed by a single scalar value, $\bar{\varepsilon}^p$, called the accumulated plastic strain, which is assumed to evolve according to

$$d\bar{\varepsilon}^p = \sum_{i=1}^{n} \alpha_i \, d\lambda_i \tag{16}$$

i.e. $\boldsymbol{k}_i(\boldsymbol{\sigma}, \boldsymbol{K})$ is assumed to be 1, cf. (5). Thus, the change in accumulated plastic strain is the sum of the plastic multipliers involved. The state of the hardening parameters, $\boldsymbol{K}$, are found based on an arbitrary user defined set of points

$$\left(\bar{\varepsilon}_1^p, \boldsymbol{K}_1\right), \ldots, \left(\bar{\varepsilon}_k^p, \boldsymbol{K}_k\right) \tag{17}$$

Thus, the hardening parameters are found by linear interpolation between these points. If $\bar{\varepsilon}^p$ exceeds $\bar{\varepsilon}_k^p$, the hardening parameters are set according to the last point, and perfect plasticity is assumed during further plastic straining. Using this method, the model is able to simulate different kinds of behaviour, including elastic-brittle, strain hardening, strain softening and elastic-perfectly-plastic behaviour.

The return mapping scheme is carried out in principal stress space. This reduces the unknowns of $\boldsymbol{\sigma}^C$ from six to only three components, which can be visualized in a 3D space, and thus geometrical arguments can be applied. The predicted stress state, $\boldsymbol{\sigma}^B$, is thus transformed to principal stress space, denoted $\bar{\boldsymbol{\sigma}}^B$, and the corresponding updated stress state in principal stress space, $\bar{\boldsymbol{\sigma}}^C$, is found, which is then converted back to the original coordinate system, giving the updated stress state, $\boldsymbol{\sigma}^C$, that is of interest in the FE-model.

5.2 *Yield criterion regions*

Figure (3) shows the Hoek-Brown criterion seen from the hydrostatic axis.

If by definition we state that $\sigma_1 \geq \sigma_2 \geq \sigma_3$, when we transform $\boldsymbol{\sigma}^B$ to $\bar{\boldsymbol{\sigma}}^B$, then only surface f_1, f_2 and f_6 are of interest. There are four possible locations of

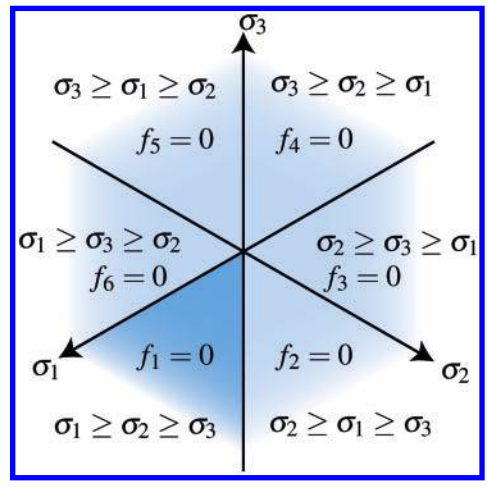


Figure 3. Sketch of Hoek-Brown criterion in principal stress space seen from the hydrostatic axis.

the updated stress state. Either the stress state lies on surface f_1, the intersection between f_1 and f_2, the intersection between f_1 and f_6 or the intersection of f_1, f_2 and f_6, known as the apex. Even though the apex point is comprised of all six yield criteria, only three of them are needed to form a basis for the plastic strains. Thus, we are dealing with three yield functions

$$f_1 = \sigma_1 - \sigma_3 - \sigma_{ci}\left(s - m_b\frac{\sigma_1}{\sigma_{ci}}\right)^a = 0 \tag{18}$$

$$f_2 = \sigma_2 - \sigma_3 - \sigma_{ci}\left(s - m_b\frac{\sigma_2}{\sigma_{ci}}\right)^a = 0 \tag{19}$$

$$f_6 = \sigma_1 - \sigma_2 - \sigma_{ci}\left(s - m_b\frac{\sigma_1}{\sigma_{ci}}\right)^a = 0 \tag{20}$$

with the appertaining plastic potentials g_1, g_2 and g_6. Because the updated stress state can be situated at four different locations, four different return algorithms are required. However, before they can be put to use, it must first be clarified, which one to use for a given predictor stress state.

This is handled in a similar fashion to Clausen & Damkilde (2008), with the use of boundary planes. By evaluating (9) along the boundaries of each yield criterion, the principal stress space is divided into regions. The updated stress state of a given predictor stress state belongs to the yield criteria f_i, where $\boldsymbol{s}_i$ define the region, in which the predictor stress state is located.

For the Hoek-Brown model, $\boldsymbol{s}_1$ is given by

$$\boldsymbol{s}_1 = \frac{E}{(1+\nu)(1-2\nu)}\begin{Bmatrix}(1-\nu)k_g - \nu \\ \nu k_g - \nu \\ \nu k_g - 1 + \nu\end{Bmatrix} \tag{21}$$

where

$$k_g = \frac{\partial g_1}{\partial \sigma_1} = 1 + a_g m_{b_g}\left(s_g - m_{b_g}\frac{\sigma_1}{\sigma_{ci_g}}\right)^{a_g - 1} \tag{22}$$

similarly $\boldsymbol{s}_2$ and $\boldsymbol{s}_3$ is given by

$$\boldsymbol{s}_2 = \left\{s_{1,2},\ s_{1,1},\ s_{1,3}\right\}^T,\ \boldsymbol{s}_3 = \left\{s_{1,1},\ s_{1,3},\ s_{1,2}\right\}^T \quad (23)$$

where $s_{1,k}$ is the k'th component of $\boldsymbol{s}_1$. From (21) and (22), it is seen, that $\boldsymbol{s}_i$ only depend on σ_1.

If perfect plasticity is assumed, the boundaries given by $\boldsymbol{s}_i$ does not change during plastic flow. However, if hardening plasticity is applied, the boundaries of each criteria as well as $\boldsymbol{s}_i$ change as the hardening parameters change. Since the hardening parameters of the updated stress state, $\boldsymbol{K}^C$, is unknown, these boundaries are also unknown. Nonetheless, by evaluating $\boldsymbol{s}_i$ with the initial hardening parameters, $\boldsymbol{K}^A$, the correct return algorithm can be estimated and applied. The resulting updated stress state and hardening parameters can then be used to check, whether the correct return algorithm has been employed. This is done if any of the return algorithms fail to converge. The new boundaries are calculated using the hardening parameters of the last iteration, $\boldsymbol{K}_l^C$, and if the predictor stress state has fallen into a new region, that return algorithm is applied. If that is not the case, then it is suggested to decrease the load step of the global finite element calculations and try again.

5.3 *Return to f_1*

If the predictor stress state is believed to return to $f_1 = 0$, then only one plastic multiplier is in play and only $\alpha_1 = 1$. This leads to four unknowns, namely the three principal stresses $\overline{\boldsymbol{\sigma}}^C$ and $\Delta\lambda_1$, which is sufficient to compute the accumulated plastic strain, $\overline{\varepsilon}^p$, and the updated hardening parameters. The solution is required to obey

$$\sigma_1^C = \sigma_1^B - \Delta\lambda_1 s_{1,1} \quad (24)$$

$$\sigma_2^C = \sigma_2^B - \Delta\lambda_1 s_{1,2} \quad (25)$$

$$\sigma_3^C = \sigma_3^B - \Delta\lambda_1 s_{1,3} \quad (26)$$

$$f_1\left(\overline{\boldsymbol{\sigma}}^C, \boldsymbol{K}^C\right) = 0 \quad (27)$$

cf. (10) and (11). However, since $\boldsymbol{s}_1$ only depends upon σ_1^C, the unknowns σ_2^C and σ_3^C are known once σ_1^C is known cf. (25) and (26). Thus we only need two equations, and with a little rewriting of (24), we obtain

$$\sigma_1^C - \sigma_1^B + \Delta\lambda_1 s_{1,1} = 0 \quad (28)$$

$$f_1\left(\overline{\boldsymbol{\sigma}}^C, \boldsymbol{K}^C\right) = 0 \quad (29)$$

This system of equations is solved using a Newton-Raphson iteration scheme, where

$$\boldsymbol{R}_l = \begin{Bmatrix} \sigma_{1,l}^C - \sigma_1^B + \Delta\lambda_{1,l} s_{1,1} \\ f_1\left(\overline{\boldsymbol{\sigma}}_l^C, \boldsymbol{K}_l^C\right) \end{Bmatrix} \quad (30)$$

until $|\mathrm{norm}(\boldsymbol{R}_l)| < \mathrm{TOL}$, where TOL is the required tolerance. $\boldsymbol{K}_l^C$ is interpolated from the points of (17) based on $\overline{\varepsilon}_l^{p,C}$ given by

$$\overline{\varepsilon}_l^{p,C} = \overline{\varepsilon}^{p,A} + \Delta\lambda_{1,l} \quad (31)$$

To start the iterations, an initial guess is needed. $\sigma_{1,0}^C$ is based on the σ_1 value that would fulfill (18) if $\sigma_3 = \sigma_3^B$ and $\Delta\lambda_{1,0}$ is assumed equal to 0. If $\sigma_{1,l+1}^C$ exceeds the current apex of the yield criteria, a fail safe is adapted in which

$$\sigma_{1,l+1}^C = \rho\sigma_{a,l+1}^C + (1-\rho)\sigma_{1,l}^C \quad (32)$$

where $\sigma_{a,l+1}^C$ is the current apex of the Hoek Brown criterion based on $\boldsymbol{K}_{l+1}^C$, and $\rho = 0.99$.

The solution of (28) and (29) does not ensure that $\sigma_1^C \geq \sigma_2^C \geq \sigma_3^C$. The solution is thus checked to ensure this. If it turns out that $\sigma_2^C > \sigma_1^C$, the return to f_1 & f_2 is applied. If $\sigma_3^C > \sigma_2^C$, the return to f_1 & f_6 is applied.

5.4 *Return to f_1 & f_2*

If the updated stress state resides on the intersection between f_1 and f_2, where $\sigma_1 = \sigma_2$, then two yield criteria are active, $\alpha_1 = \alpha_2 = 1$, and two multipliers, $\Delta\lambda_1$ and $\Delta\lambda_2$, are needed. Based on a similar procedure as the f_1 return, it ends up in three equations, with three unknowns

$$\sigma_1^C - \sigma_1^B + \Delta\lambda_1 s_{1,1} + \Delta\lambda_2 s_{2,1} = 0 \quad (33)$$

$$\sigma_1^C - \sigma_2^B + \Delta\lambda_1 s_{1,2} + \Delta\lambda_2 s_{2,2} = 0 \quad (34)$$

$$f_1\left(\overline{\boldsymbol{\sigma}}^C, \boldsymbol{K}^C\right) = 0 \quad (35)$$

Note that (34) corresponds to $\sigma_1^C = \sigma_2^C$, which ensures that $f_2(\overline{\boldsymbol{\sigma}}^C, \boldsymbol{K}^C) = 0$. This system is solved in a similar manner to the system of the f_1 return.

5.5 *Return to f_1 & f_6*

If the updated stress state resides on the intersection between f_1 and f_6, where $\sigma_2 = \sigma_3$, then two yield criteria are active, $\alpha_1 = \alpha_6 = 1$, and two multipliers, $\Delta\lambda_1$ and $\Delta\lambda_6$, are needed. Based on a similar procedure as above, it ends up in three equations, with three unknowns

$$\sigma_1^C - \sigma_1^B + \Delta\lambda_1 s_{1,1} + \Delta\lambda_6 s_{6,1} = 0 \quad (36)$$

$$\sigma_3^C - \sigma_2^B + \Delta\lambda_1 s_{1,2} + \Delta\lambda_6 s_{6,2} = 0 \quad (37)$$

$$f_1\left(\overline{\boldsymbol{\sigma}}^C, \boldsymbol{K}^C\right) = 0 \quad (38)$$

Again (37) corresponds to $\sigma_2^C = \sigma_3^C$, which ensures that $f_6(\overline{\boldsymbol{\sigma}}^C, \boldsymbol{K}^C) = 0$.

5.6 *Return to f_1, f_2 & f_6*

The return algorithm where the updated stress state resides on the apex, is comprised of three active yield criteria, f_1, f_2 and f_6, $\alpha_1 = \alpha_2 = \alpha_6 = 1$, and thus three plastic multipliers are also needed, $\Delta\lambda_1$, $\Delta\lambda_2$ and $\Delta\lambda_6$. However, the return algorithm is a little different than the other algorithms, because the location of $\overline{\boldsymbol{\sigma}}^C$ is known to coincide with the intersection of the three active yield criteria, where $\sigma_1^C = \sigma_2^C = \sigma_3^C = \sigma_a^C$. The apex, σ_a^C, is known once $\boldsymbol{K}^C$ is known. Thus only the three equations of (10) are needed to solve the problem, i.e.

$$\sigma_a^C - \sigma_1^B + \Delta\lambda_1 s_{1,1} + \Delta\lambda_2 s_{2,1} + \Delta\lambda_3 s_{3,1} = 0 \tag{39}$$

$$\sigma_a^C - \sigma_1^B + \Delta\lambda_1 s_{1,2} + \Delta\lambda_2 s_{2,2} + \Delta\lambda_3 s_{3,2} = 0 \tag{40}$$

$$\sigma_a^C - \sigma_1^B + \Delta\lambda_1 s_{1,3} + \Delta\lambda_2 s_{2,3} + \Delta\lambda_3 s_{3,3} = 0 \tag{41}$$

If associated flow is assumed, the apex of the yield criteria and the plastic potentials coincide. Since the gradient of the plastic potential tends toward infinity on the apex, cf. (22), the plastic multipliers must approach zero in order to give finite strains. For this reason, perfect plasticity is assumed in the associated case with a return to the apex.

5.7 *Consistent constitutive matrices*

It can be shown, that the consistent constitutive matrix is given by

$$\boldsymbol{D}^{epc} = \boldsymbol{D}^c - \boldsymbol{D}^c \sum_{i=1}^{n}\sum_{k=1}^{n} \alpha_i \alpha_k \left(\boldsymbol{A}^{-1}\right)_{ik} \frac{\partial g_i}{\partial \boldsymbol{\sigma}} \left(\frac{\partial f_k}{\partial \boldsymbol{\sigma}}\right)^T \boldsymbol{D}^c \tag{42}$$

where $\boldsymbol{A}$ is the $n \times n$ matrix given by

$$A_{ik} = \alpha_i \alpha_k \left(\left(\frac{\partial f_i}{\partial \boldsymbol{\sigma}}\right)^T \boldsymbol{D}^c \frac{\partial g_k}{\partial \boldsymbol{\sigma}} + \left(\frac{\partial f_i}{\partial \boldsymbol{K}}\right)^T \frac{\partial \boldsymbol{K}}{\partial \overline{\boldsymbol{\varepsilon}}^p} \right) + (\alpha_i - 1)(\alpha_k - 1)\,\delta_{ik} \tag{43}$$

where $\boldsymbol{D}^c$ is the modified elastic stiffness matrix and δ_{ik} is the Kronecker delta. For further details see Clausen (2007) and Ottosen & Ristinmaa (2005). Once perfect plasticity is reached, the modified consistent constitutive matrices mentioned in Clausen (2007) is used in the calculations.

6 EXAMPLE: TUNNEL EXCAVATION

The numerical implementation is tested on a simulation of a tunnel excavation. The simulation models 1 m of a tunnel with a radius, r_T, of 10 m along the tunnel axis, z, using axissymmetry, cf. figure 4. The extend of the model reach out to $r_{BC} = 300$ m from the tunnel axis. The excavation is simulated by reducing the pressure, p, on the tunnel wall from the in-situ

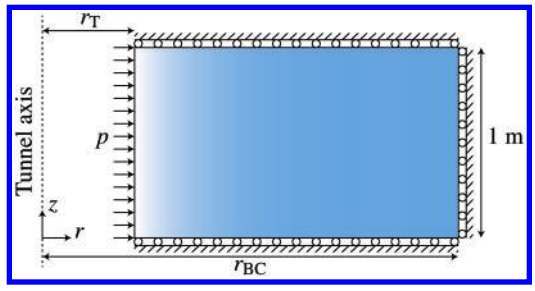


Figure 4. Sketch of the tunnel model.

Table 1. Hoek Brown parameters of tunnel rock mass material.

σ_{ci}	a	m_b	s	E	ν
80 MPa	0.51	2.01	0.0039	9 GPa	0.25
80 MPa	0.53	0.34	0	9 GPa	0.25

Table 2. Plastic potential parameters of tunnel rock mass material.

σ_{ci_g}	a_g	m_{b_g}	s_g
80 MPa	1.00	1.15	0
80 MPa	1.00	1.15	0

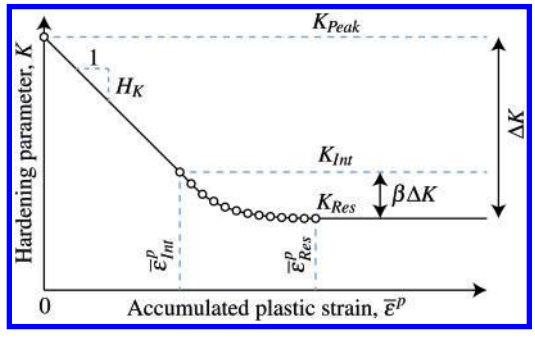


Figure 5. Evolution of the hardening parameters based on the accumulated plastic strain, $\overline{\varepsilon}^p$.

pressure, p_∞, to 0. The self weight of the rock material is neglected.

The parameters of the Hoek-Brown material are taken from example B of Sharan (2008). The parameters consists of peak parameters and residual parameters, cf. table 2. Notice however, that the numerical implementation is incapable of implementing the drop in Young's modulus described in Sharan (2008). Because of this, the peak modulus is assumed throughout the simulation, and the solution method in Sharan (2008) is utilized to get an analytical solution for an elastic-brittle rock material.

The plastic potential parameters are listed in table 2. These parameters result in non-associated flow and gives a constant dilation parameter, K_d, of 1.15, which makes comparing with the solution of Sharan (2008) possible.

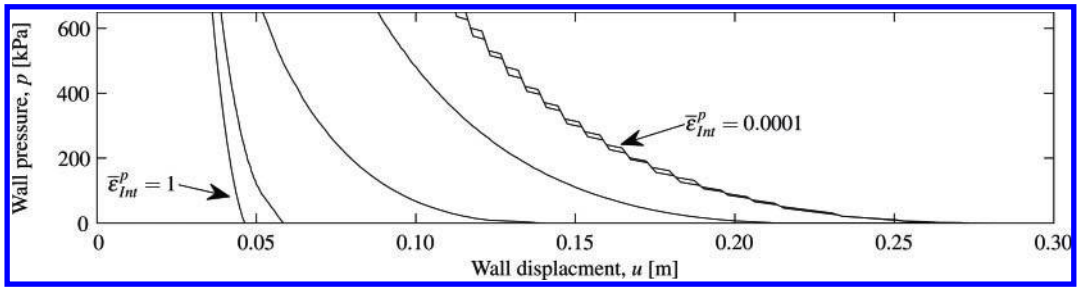


Figure 6. Tunnel wall movement, u, as a function of wall pressure, p. Notice that the curve for $\bar{\varepsilon}^p_{Int} = 0.0010$ and $\bar{\varepsilon}^p_{Int} = 0.0001$ almost overlap.

In the simulations, it is chosen, that during plastic straining, the hardening parameters drop from the peak parameters to the residual parameters according to figure 5.

As can be seen, the hardening parameters drop linearly from the peak value at zero plastic strain, to some intermediate value, K_{Int}, at some intermediate accumulated plastic strain, $\bar{\varepsilon}^p_{Int}$, followed by a non-linear evolution leading to perfect plasticity at $\bar{\varepsilon}^p_{Res}$. The intermediate value of the hardening parameter, K_{int}, is based on the parameter β, cf figure 5, which is set to 0.1. By setting the residual parameters equal to the peak parameters, perfect plasticity is achieved. The intermediate and residual accumulated plastic strains, $\bar{\varepsilon}^p_{Int}$ and $\bar{\varepsilon}^p_{Res}$, can be used to control the rate of softening. By letting these tend towards zero, an elastic-brittle behavior is achieved. $\bar{\varepsilon}^p_{Res}$ is chosen as $2\bar{\varepsilon}^p_{Int}$, and the simulation is performed for $\bar{\varepsilon}^p_{Int} = \{1; 0.1; 0.01; 0.005; 0.0025; 0.0010; 0.0001\}$, which spans an almost perfectly-plastic behavior, through strain softening to almost elastic-brittle behavior. Based on this, 300 points are calculated and used in the simulations, cf. (17). The model is meshed using 1600 linear-strain triangular elements with a gauss order of 13 and solved using a standard Newton-Raphson solution method with a maximum step length of $\Delta t = 5 \cdot 10^{-4}$, in order to get a detailed view of the equilibrium path, which can be seen on figure 6.

The analytical solution predicts a wall displacement of 0.0454 m in the elastic-perfectly-plastic case, and a wall displacement of 0.2789 m in the elastic-brittle case. The results from the finite element model results in a wall displacement between 0.0456 m and 0.2826 m respectively for $\bar{\varepsilon}^p_{Int} = 1$ and $\bar{\varepsilon}^p_{Int} = 0.0001$. A difference of 0.4% and 1.3% respectively. Further, the results of the simulations in between the elastic-perfectly-plastic and the elastic-brittle behaviour shows results between these two values, which is what would be expected.

The FE-simulations showed some mesh dependency, and the jagged nature of the more brittle rock simulations is believed to stem from a too coarse mesh. If the elastic predictor stress state falls just outside the yield surface, the yield surface shrinks very rapidly, and thus a large plastic multiplier is needed, which leads to large plastic strains. If the mesh is coarse, each gauss point represents a large portion of the model, and thus large displacements are also expected. If a finer mesh is employed, each gauss point represents smaller portions of the model, and thus smaller and more continuous displacements are expected. However, if a finer mesh is employed, the global equilibrium iterations become troublesome. This could perhaps be due to the stability issues surrounding numerical non-associated plasticity.

7 CONCLUSION

A strain hardening Hoek-Brown material model has been developed, which is capable of modeling many aspects of the observed behavior of jointed rock masses. A total of eight parameters are allowed to evolve based on the accumulated plastic strains. The model has been deployed on a FE-simulation of a tunnel excavation utilizing non-associated plasticity and the results obtained are in good agreement with the analytical solutions, however, some mesh dependency was observed.

REFERENCES

Clausen, J. (2007). *Efficient Non-Linear Finite Element Implementation of Elasto-Plasticity for Geotechnical Problems*. Ph. D. thesis, Computational Mechanics, Esbjerg Institute of Technology, Aalborg University Esbjerg. http://vbn.aau.dk/files/14058639/JCthesis.pdf.

Clausen, J. & L. Damkilde (2008). An exact implementation of the Hoek-Brown criterion for elasto-plastic finite element calculations. *International Journal of Rock Mechanics & Mining Sciences 45*, 831–847.

de Souza Neto, E., D. Perić, & D. Owen (2008). *Computational Methods for Plasticity*. London: Wiley.

Hoek, E. & E. T. Brown (1997). Practical estimates of rock mass strength. *Internation Journal of Rock Mechanics & Mining Sciences 34*, 1165–1186.

Hoek, E., C. Carranza-Torres, & B. Corkum (2002). Hoek-Brown failure criterion – 2002 edition. *Proc. NARMS-TAC Conference, Toronto 1*, 267–273.

Hoek, E. & M. S. Diederichs (2006). Empirical estimation of rock mass modulus. *Internation Journal of Rock Mechanics & Mining Sciences 43*, 203–215.

Ottosen, N. S. & M. Ristinmaa (2005). *The Mechanics of Constitutive Modeling*. London: Elsevier.

Sharan, S. (2008). Analytical solutions for stress and displacements around a circular opening in a generalized Hoek-Brown rock. *International Journal of Rock Mechanics & Mining Sciences 45*, 78–85.

Research and Applications in Structural Engineering, Mechanics and Computation – Zingoni (Ed.)
© 2013 Taylor & Francis Group, London, ISBN 978-1-138-00061-2

Simulation of the mechanical behavior of W/Cu composites containing FGM related interpenetrating microstructures under consideration of phase dependent damage limits

S. Schmauder & U. Weber
Institute for Materials Testing, Materials Science and Strength of Materials (IMWF), University of Stuttgart, Stuttgart, Germany

ABSTRACT: Coarse isotropic interpenetrating microstructures are often found in powder metallurgically fabricated composites in the regime of 25%–75% volume fraction, or result from the infiltration of a porous material with a molten metal of a lower melting point. The phases in most of these technical composites are usually randomly arranged. Besides the volume fraction such an interpenetrating microstructure requires at least one further parameter called matricity to describe the material more precisely. The "matricity" describes the mutual circumvention of both phases and can be measured from a representative micrograph of a microstructure via an image analyzing system. In order to characterize the elastic and elastic-plastic properties of composites with interpenetrating microstructures a self-consistent unit cell model is applied. This so called matricity model is a combination of two self-consistent unit cells, which consider the enclosure of the phases of a two-phase microstructure. Thereby, in every cell, depending on the volume fraction, every phase is once considered as the matrix and as inclusion. The matricity model is applied on several ranges of volume fractions for a W/Cu composite. In addition a damage criterion based on critical normal stresses and on the von Mises stress is applied to predict load limits for the composite.

1 INTRODUCTION

1.1 *General*

Composites consisting of phases with strongly different properties have the potential to be used in new application fields as they comprise otherwise incompatible properties. While the deformation behaviour of inclusion-type microstructures has been successfully modeled in the past for brittle fiber or particulate reinforced metal matrix composites (Zahl & Schmauder & McMeeking, 1994, Dong & Schmauder, 1996a, Schmauder & Mishnaevsky, 2009) this was not achieved until recently in the case of interpenetrating microstructures where both phases are connected throughout the material. Such microstructures are typically observed in the composition range of 30–70% while inclusion type of microstructures are typical for dilute systems with phase volume fractions between 0–30%. Specifically, functionally graded materials can depict the full composition range in material transitions. As processing techniques are nowadays available to design material transitions, experience in modeling of the full composition range is still lacking. This paper is intended to bridge the gap in the case of W/Cu composites where the full compositional range is experimentally available from a powder-metallurgical route (Jedamzik & Neubrand & Rödel, 1997).

1.2 *Model*

The matricity model is used for the simulation of the elastic-plastic material properties of the W/Cu composite with phases α and β in this paper. In the case of an inclusion type of microstructure the self-consistent embedded cell model is applied which is described in (Dong & Schmauder, 1996a, b, c, Sautter, 1995, Zahl & Schmauder & McMeeking, 1994). The embedded cell model has been introduced to simulate the mechanical behaviour of composites with randomly distributed inclusions. The volume fraction of the inclusions is the main parameter in the model. To take the matricity M as a second microstructural parameter into account, the self-consistent embedded cell model has been extended by a second self-consistent embedded cell model (Figure 1). In this "matricity model" the parameter M can be defined in the same manner as the matricity is defined for a real microstructure: First the single phases are reduced to skeleton lines. The lengths of the skeleton lines of the inclusions (Figure 1; left: β, right: α) are zero as the inclusions are spherical and are, therefore, reduced to a point in the process of obtaining the matricity of the phase.

The lengths of the skeleton lines S_α and S_β in the matrices are given as the circumference of a circle with a diameter which is obtained from the arithmetic average of the diameter of the embedded cell and the

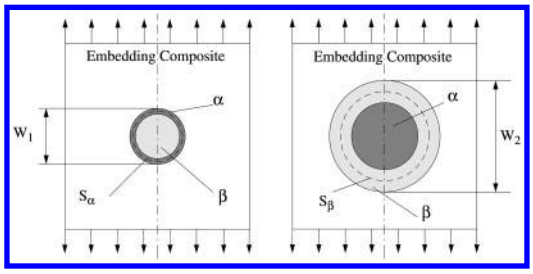


Figure 1. Matricity model (schematic) with skeleton lines (dashed) to adjust for the measured parameter "Matricity" in the model via the factors W_1 and W_2.

diameter of the inclusion phase (Figure 1; left: S_α, right: S_β). The diameters of the embedded cells are denominated as W_1 and W_2. The diameters of the inclusion part of the embedded cells depend on the volume fraction of the inclusions and the corresponding factors W_1 or W_2. The matricity M can be calculated as a function of the sizes of the embedded cells and the volume fraction of one of the two phases, as the volume fraction of the phases is held constant in both parts of the matricity model.

$$W_1 = W_2\left(\sqrt[3]{1-f_\beta}\right)\cdot\frac{1-M_\beta}{M_\beta\left(\sqrt[3]{f_\beta}+1\right)},\ W_2 = 1 \text{ for } M_\beta \geq 0.5$$
$$W_2 = W_1\left(\sqrt[3]{1-f_\alpha}\right)\cdot\frac{1-M_\alpha}{M_\alpha\left(\sqrt[3]{f_\alpha}+1\right)},\ W_1 = 1 \text{ for } M_\alpha \geq 0.5 \quad (1)$$

As can be seen in Figure 1, the volume fractions of the phases as well as the diameters W_1 and W_2 of the embedded cells are adjustable. To achieve a matricity M_i ($i = \alpha, \beta$) in the model, the measured volume fraction of the phases in the model is realized and the diameters W_1 and W_2 are calculated according to equation 1 (Leßle & Dong & Soppa & Schmauder, 1998). If the geometrical boundary conditions are modeled at a distance of about 5 times the radius of the embedded cell, they are of almost no influence on the model's mechanical behaviour. If the boundary conditions are kept remote, the embedded cell can be modeled with the surrounding composite in different manners. As the remote boundary conditions have almost no influence on the mechanical behaviour of the embedded cell it is assumed that the continuum mechanical stress-strain state in the embedded cell is hardly influenced as well. Taking this into account, a unit cell for a specific volume fraction can be used in each part of the matricity model. Moreover, due to the virtual independency from remote boundaries, it is not necessary to model the matricity as an absolute parameter of the FE-mesh. It is rather possible to introduce the matricity by adjusting weighting factors W_1 and W_2 only in the evaluation of the results from the inclusion type geometries. As the results have to be determined by an iterative procedure in about 3 to 5 iterations, the adjusting weighting factors W_1 and W_2 must be introduced in the evaluation of each iteration step.

The stress-strain curves of the two-phase composite are determined from the matricity model in the same iterative manner as it is done for the simple self-consistent embedded cell model: In each increment the components for stress and strain are determined. This is done by a weighted averaging of the stress and strain values over all integration points of both embedded cells in loading direction.

2 RESULTS AND DISCUSSION

2.1 *Microstructures and matricity*

W/Cu compositions in different ranges till 75% Cu were produced by a sintering and infiltration method (Jedamzik & Neubrand & Rödel, 1997).

The corresponding microstructures are presented in Figure 2. Besides the volume fraction, the second parameter, the so-called matricity parameter M which represents the degree of mutual interpenetration and circumvention of the phases and which was introduced by (Poech & Ruhr, 1993) is also given in the Figure. In the following, composites of two phases α and β are considered. Matricity is then defined as the ratio of the length of the skeleton lines of one phase, S_α, and the length of the skeleton lines of the participating phases:

$$M_\alpha = \frac{S_\alpha}{S_\alpha + S_\beta} \quad (2)$$

By definition, the sum of the matricities of all phases equals to one:

$$M_\alpha + M_\beta = 1 \quad (3)$$

To obtain the skeleton lines of a certain phase, this phase is selected within an image analysing system and the detected structure is reduced to a typically non-connecting line maintaining the topology. In Figure 2 the matricities have been determined for a graded W/Cu composite. The structure parameters, volume fraction f, and matricity M, have been determined to be: $M_{Cu} = 0.26$, 0.45, 0.59 and 0.72 for $f_{Cu} = 21\%$, 40%, 50% and 75%, respectively.

2.2 *Material properties*

To predict the stress-strain curves of the W/Cu composite with the corresponding volume fraction and matricities of the real microstructure using the matricity model, the elastic-plastic behaviour of the bulk materials W and Cu are needed. Because W can be assumed as a brittle metal, a pure elastic behaviour is assumed for this phase. The elastic-plastic properties of the Cu-phase are given in Table 1.

The tensile strength and the yield stress of the W- and Cu-phase, respectively, are used later on as critical damage stresses.

Figure 3 shows the calculated stress strain behaviour of the W/Cu composite for the given volume fractions and matricities of Cu (see Figure 2). As indicated

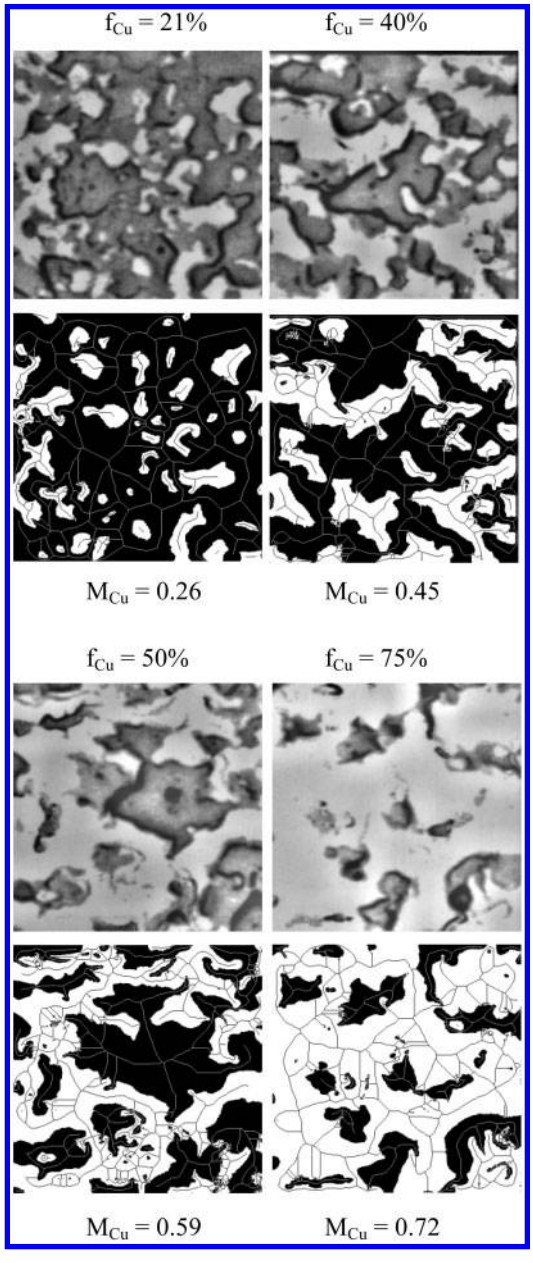


Figure 2. Microstructures and matricities (Cu-phase) of different W/Cu composites at different volume fractions of Cu.

in Figure 3, there is especially a strong variation in the mechanical behaviour of the W/Cu composite for $f_{Cu} = 40\%–50\%$. In order to derive later on limit curve at additional interpolation points, additional volume fractions of Cu have to be considered.

The unknown matricities for these additional volume fractions are determined by interpolation. In Figure 4 it can be seen, that there exists a nearly linear relationship between the two parameters f (volume fraction) and M (matricity).

Table 1. Material Properties of the Bulk Phases W and Cu: μ = Poisson's Ratio, E = Young's Modulus, σ_y = yield stress, R_m = tensile strenth, ε_{ue} = uniform elongation

Setting	μ	E (GPa)	σ_y (MPa)	R_m (MPa)	ε_{ue}
W	0.17	411	–	800	–
Cu	0.35	130	95	230	0.22

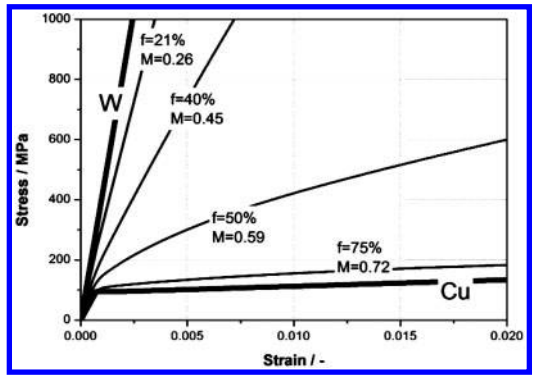


Figure 3. Calculated stress-strain curves of the W/Cu composite for selected compositions and according matricities (see Figure 2) (f = volume fraction of Cu, M = Matricity of Cu).

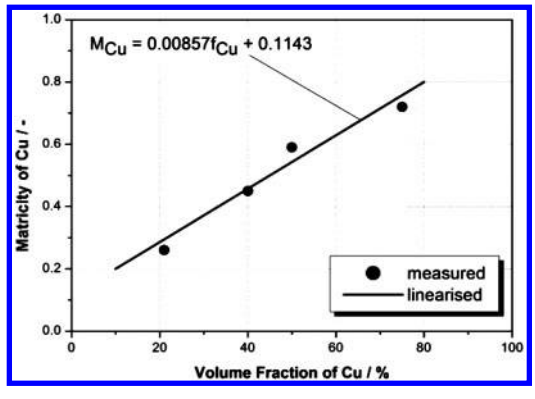


Figure 4. Correlation between volume fraction of Cu (f_{Cu}) and matricity of copper (M_{Cu}) for different W/Cu microstructures.

To close the gap of unknown stress-strain curves between 40% and 50% and between 50% and 75% volume fractions of Cu (see Figure 3), respectively, additional simulations are performed at $f_{Cu} = 46\%$ ($M_{Cu} = 0.51$) and $f_{Cu} = 60\%$ ($M_{Cu} = 0.63$). More model details and further results are given in Schmauder & Weber & Hofinger & Neubrand.

2.3 *Damage*

W/Cu composites are mostly applied as electrodes to erode, electrical contacts and welding electrodes.

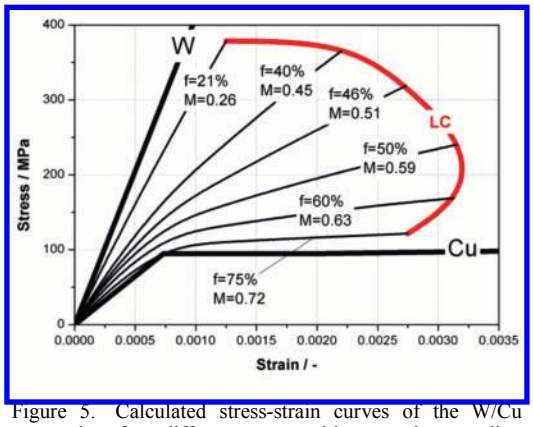


Figure 5. Calculated stress-strain curves of the W/Cu composite for different compositions and according matricities (f = volume fraction of Cu, M = matricity of Cu). LC = limit curve at which the averaged von Mises stress in the Cu-phase reaches 95 MPa.

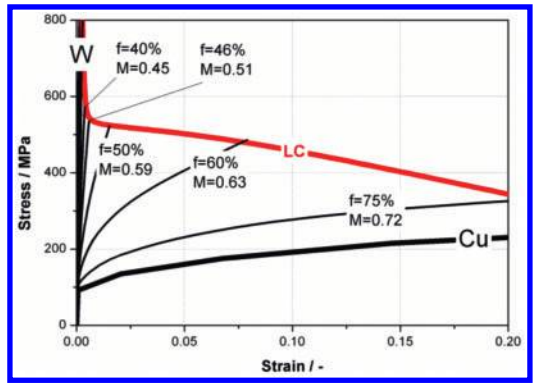


Figure 6. Calculated stress-strain curves of the W/Cu composite for different compositions and according matricities (f = volume fraction of Cu, M = matricity of Cu). LC = limit curve at which the averaged first principal stress in the W-phase reaches 800 MPa.

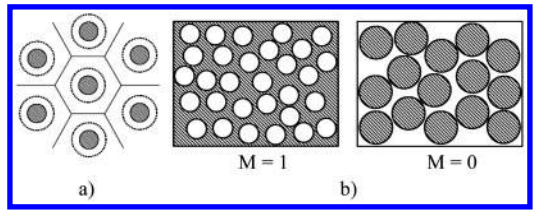


Figure 7. Independence of the volume fraction f and matricity M (schematically) of the shaded phase. a): Change of the volume fraction at constant matricity. b): Change of the matricity from M = 1 to M = 0 at constant volume fraction.

If the functionality of a sample requires limited plastic deformation during application, the loading limitation of the W/Cu composite is the yield stress of the Cu-phase. For this purpose, the averaged von Mises stress in the Cu-Phase is compared to the yield stress of Cu (=95 MPa) during the loading of the embedded cells. Figure 5 shows the calculated stress-strain curves of the W/Cu composite combined with the limit curve, which defines the state, where the averaged von Mises stress in the Cu-phase reaches the critical value (yield stress of copper) of 95 MPa. Because of the averaging of all integration points, which belongs to the Cu-phase, the limit curve admits some plastic deformation of the composite.

As expected, the deformation limit of the W/Cu composite depends on the volume fraction of the Cu-phase (Figure 5): For low copper volume fractions up to 40%, there exists nearly no change in the limit stress. For Cu volume fractions above 40% the limit stress (on the LC) decreases strongly. Overall, for the given requirements, the max. allowed strain of the W/Cu composite is limited to ~0.32%. For application, comparatively high stresses at comparatively high strains are feasible for a copper volume fraction in the range of 46%.

On the other hand, if plasticity in the Cu-phase of the W/Cu composite is tolerable but fracture of the brittle W-phase must be avoided in operation, the tensile strength of this phase (because of the assumed brittle behaviour) is the limitation. For this purpose the averaged first principal stress in the W-Phase is compared with the tensile strength of W (=800 MPa) during the loading of the embedded cells. According to Figure 5, Figure 6 shows the calculated stress-strain curves of the W/Cu composite and the limit curve, which defines the position where the averaged first principal stress in the W-phase reaches the critical value (tensile strength of W) of 800 MPa. As can be seen in Figure 6, the stress limit of the W/Cu composite depends again on the volume fraction of the Cu-phase: For low copper volume fractions up to 46%, there exists a broad decrease in the limit stress at low strains. For copper volume fractions in the range of 50%–75%, the limit stress changes linearly from ~500 MPa to ~300 MPa with large differences in the respective strains. In all cases, the yield stress of the copper phase is surmounted. Similar results were found in Schmauder & Weber & Reuschel & Willert, were this model was applied to an Al/TiO_2 composite.

Although, there exists a linear relation between the volume fraction f and the matricity M as experimentally found for different interpenetrating microstructures, these both microstructural parameters are independent. This is shown schematically in Figure 7.

In Figure 7a) the volume fraction of the shaded phase changes without any modification of the matricity of the white phase and therefore without change of the matricity of the shaded phase. In Figure 7b) the volume fraction of both phases in both rectangles is identical, but the matricity of the shaded phase changes from M = 1 (left) to M = 0 (right) and, therefore, for a given phase volume fraction the deformation behaviour of interpenetrating microstructures can be designed only by the variation of the matricity M. In the following, the matricity of the copper phase is varied at constant copper volume fraction of $f_{Cu} = 50\%$. According to Figure 5, Figure 8 shows the calculated stress-strain curves of the W/Cu composite combined

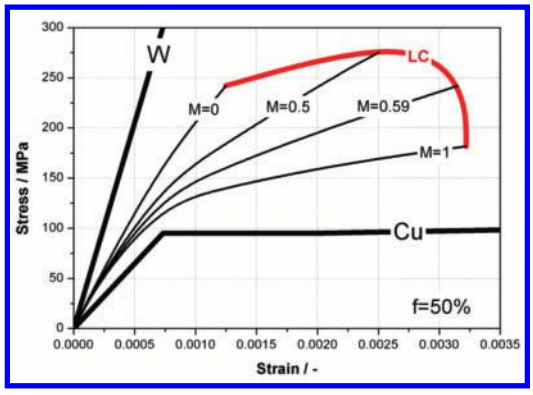


Figure 8. Calculated stress-strain curves of the W/Cu composite for a Cu volume fraction of f = 50% at different matricities M of the Cu-phase. LC = limit curve at which the averaged von Mises stress in the Cu-phase reaches 95 MPa.

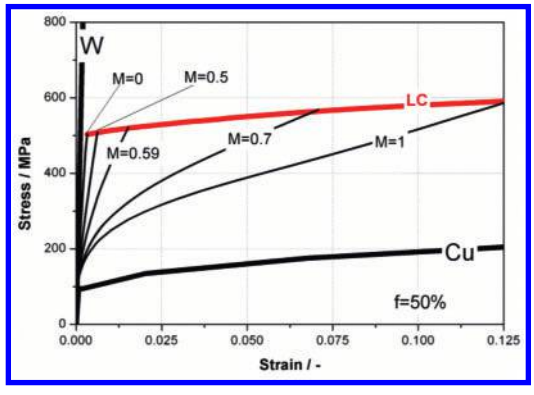


Figure 9. Calculated stress-strain curves of the W/Cu composite for a Cu volume fraction of f = 50% at different matricities M of the Cu-phase. LC = limit curve at which the averaged first principal stress in the W-phase reaches 800 MPa.

with the limit curve, which defines the state, where again the averaged von Mises stress in the Cu-phase reaches the critical value (yield stress of copper) of 95 MPa. After a slight increase from M = 0 to M = 0.5 (M = 0 denotes, that W is the pure matrix and Cu is the pure inclusion), the limit curve decreases rapidly at M > 0.5, where the copper phase plays more and more the role of the matrix. The highest strength at comparable strain are found for a Cu matricity M = 0.5.

According to Figure 6, Figure 9 shows for a given volume fraction of copper (f = 50%) the calculated stress-strain curves of the W/Cu composite combined with the limit curve, which defines the state, where the averaged first principal stress in the W-phase reaches the critical value (tensile strength of W) of 800 MPa. As can be seen in Figure 9, with increasing Cu matricity M, the limit curve allows more and more deformation at increasing strength. But again, in all cases, the yield stress of the copper phase is exceeded and plastic deformation occurs in the W/Cu composite. If plasticity is tolerable, the most suitable composition (high strength at high strain) is found at M = 1.

2.4 *Elastic properties*

Finally, the calculated elastic properties like Young's modulus E and Poisson's Ratio μ are shown in Figure 10. Here, E and μ are plotted vs. the volume fraction of copper for different W/Cu compositions, respectively. Because the Young's Modulus of W is higher and its Poisson's Ratio is lower than of Cu, the Young's Modulus E and the Poisson's Ratio μ of the W/Cu composite decreases and increases with increasing volume fraction f of Cu, respectively.

It is clearly seen, that there exists a nonlinear relation between both elastic properties and the volume fraction of Cu. The rule of mixture based on both limit volume fractions (f = 21% and f = 75%) would overestimate especially the Young's Modulus of the W/Cu interpenetrating microstructure.

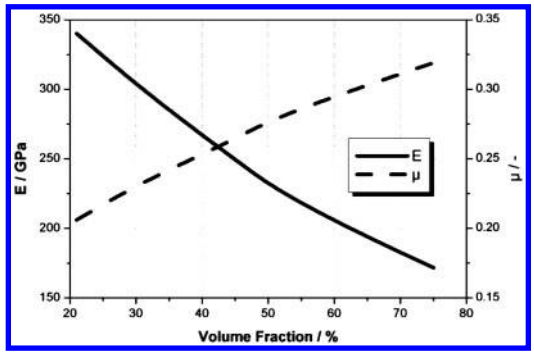


Figure 10. Correlation between volume fraction of Cu and the Young's Modulus E and Poisson's Ratio μ of the W/Cu composite.

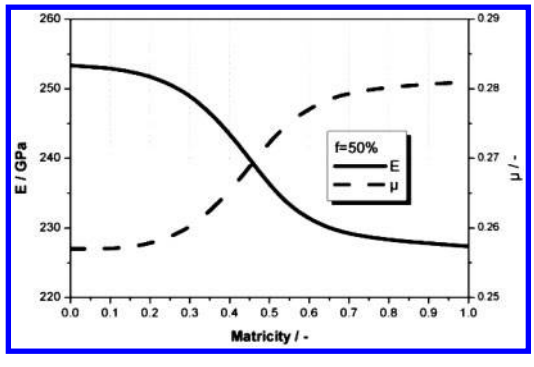


Figure 11. Correlation between the matricity of Cu and the Young's Modulus E and Poisson's Ratio μ of the W/Cu composite for a Cu volume fraction of f = 50%.

As mentioned above, the matricity of an interpenetrating microstructure is a powerful parameter to design materials with specific properties, especially in the plastic regime. But also the elastic properties are influenced by this parameter. In Figure 11, again the Young's Modulus E and the Poisson's Ratio μ are

shown as a function of the matricity of Cu for a giv-ven Cu volume fraction f = 50%.

An increasing matricity M of Cu means, that the Cu phase plays more and more the role of the matrix while the W-phase can more and more be regarded as the inclusion phase. Hence, with increasing M, the Cu properties predominate the composite behaviour and the values of E and μ tend towards the Cu-values, therefore, E and μ decreases and increases, respectively, with increasing M. Particular between M = 0.3 and M = 0.7 a clear change of E and μ can be detected. Comparable characteristics were also found for the plastic regime, where the hardening of the W/Cu composite changes dramatically between M = 0.5 and M = 0.7 (Figure 9).

3 CONCLUSION

The self-consistent matricity model was applied to systematically predict the elastic-plastic material properties of a full range of W/Cu compositions. In addition, a damage criterion based on the critical normal stresses and on the von Mises stress is applied. The results in the case of W/Cu (with one elastic and one elastic-plastic phase) can be summarized as follows.

Besides the volume fraction f, the matricity M of an interpenetrating microstructure, which describes the mutual circumvention of both phases influences the stress-strain behaviour of the investigated W/Cu composite especially in the range between M = 0.5 and M = 0.7 (M = matricity of Cu). It was found, that in experiments there exists nearly a linear relation between the matricity M and the volume fraction f. However, in principle, both microstructural parameters can be regarded to be independent.

If yielding of Cu is defined as damage criterion, the total deformation of the composite is limited to ~0.3% for $f_{Cu} = 50\%$. If fracture of the brittle W-phase should be avoided, the total composite deformation is limited to ~20%. As expected, also the elastic properties E and μ depend on the composition of the W/Cu composite: With increasing volume fraction of Cu, E decreases and μ increases, respectively.

It was also shown, that for a constant volume fraction of Cu ($f_{Cu} = 50\%$) the elastic-plastic behaviour of the W/Cu composite can be designed by varying the matricity of the copper phase. Considering a brittle damage criterion (no fracture of the W phase), the total deformation of the W/Cu composite is reduced to 12.5% but at much higher stresses as before. Concerning the elastic properties E and μ, a strong change was found in the range between $M_{Cu} = 0.3$ and $M_{Cu} = 0.7$ at $f_{Cu} = 50\%$.

Thus, the self-consistent matricity model is a powerful model to describe the elastic-plastic properties of interpenetrating microstructures and to design and adapt material properties for specific applications.

ACKNOWLEDGEMENT

This work was provided by the *Deutsche Forschungsgemeinschaft (DFG)* under contract Schm 746/12-1 and 12-2 in the frame of the *Schwerpunktprogramm Gradientenwerkstoffe* and under contract Schm 746/25-1 in the frame of the *Schwerpunktprogramm Erweiterung der Formgebungsgrenzen bei der Umformung*. This support is gratefully acknowledged. The experimental results on W/Cu composites were provided from the group of Prof. J. Rödel/Darmstadt.

REFERENCES

Dong, M. & Schmauder, S. 1996a. Modeling of Metal Matrix Composites by a Self-Consistent Embedded Cell Model, *Acta metall. mater. 44*: 2465–2478.

Dong, M. & Schmauder, S. 1996b. Transverse Mechanical Behaviour of Fiber Reinforced Composites – FE Modelling with Embedded Cell Models, *Computational Materials Science 5*: 53–66.

Jedamzik, R. & Neubrand, A. & Rödel, J. 1997. Electrochemical Processing and Characterisation of Graded Tungsten/Copper Composites. G. Kneringer, P. Rödhammer und P. Wilhartitz (eds), Metallwerk Plansee, Reutte, *in Proceedings of the 15th International Plansee Seminar, Vol.1*: 1–15.

Leßle, P. & Dong, M. & Soppa, E. & Schmauder, S. 1998. Simulation of Interpenetrating Microstructures by Self-Consistent Matricity Models, *Scripta mater. 38*: 1327–1332.

Poech, M.-H. & Ruhr, D. 1993. *Prakt. Met. Sonderband. 24*: 385–391.

Sautter, M. 1995. Modellierung des Verformungsverhaltens mehrphasiger Werkstoffe mit der Methode der Finiten Elemente, *Dissertation, Universität Stuttgart*

Schmauder, S. & Dong, M. 1996c. Vorhersage der Festigkeit von Verbundwerkstoffen, *Spektrum der Wissenschaft 11*: 18–24.

Schmauder, S. & Weber, U. & Hofinger, I. & Neubrand, A. 2001. Modelling the Deformation Behaviour of W/Cu Composites by a Self-Consistent Matricity Model, 1st Course: Composite Materials, *Proceedings Int. on Advanced Material Science and Technology,* August 23–27, 1999, University of Ancona, Jesi: 63–74.

Schmauder, S & Mishnaevsky, L.J. 2009. Micromechanics and Nanosimulation of Metals and Composites. Springer-Verlag, Berlin, Heidelberg.

Schmauder, S. & Weber, U. & Reuschel, A. & Willert, M. 2011. Simulation of the Mechanical Behaviour of Metal Matrix Composites, *Materials Science Forum Vol. 678*: 49–60.

Zahl, D.B. & Schmauder, S. & McMeeking, R.M. 1994. Transverse Strength of Metal Matrix Composites Reinforced with Strongly Bonded Continuous Fibers in Regular Arrangements, *Acta metall. mater. 42*: 2983–2997.

Research and Applications in Structural Engineering, Mechanics and Computation – Zingoni (Ed.)
© 2013 Taylor & Francis Group, London, ISBN 978-1-138-00061-2

Determination of effective elastic constants of two phase composites

O. Bulut, N. Kadioglu & S. Ataoglu
Istanbul Technical University, Faculty of Civil Engineering, Istanbul, Turkey

M. Yuksek & E. Sancak
Marmara University, Faculty of Technical Education, Istanbul, Turkey

ABSTRACT: The objective of the present study is to determine the mechanical properties of the composite materials formed in two types. The first includes small particles in a matrix while the second involves thin fibers. During calculations a fictitious, homogeneous, linear-elastic and isotropic single material which is named as effective material is considered. The base of the theoretical calculation depends on the equality of the strain energies of the composite and the effective material under the same state of stress. Considering hydrostatic tension and simple torsion, the Bulk modulus and the shear modulus of the effective material have been calculated as a function of the concentration ratio, and the elastic constants of the components. Some experiments are also achieved for comparison. The volume ratio of the matrix is much bigger compared to the particles or fibers. This means that the present study deals with experiments for the low concentration ratios.

1 INTRODUCTION

In continuum mechanics, it is assumed that materials have a continuous volume without any hole and cover the all area of this volume. In the model presented here, the atomic structure of the material is ignored since the interatomic distances are very small compared to the dimensions of the body. However, some latest works prove that the micro-structure of a material and the interactions between them affect the macro-scale properties of the body. In other words, the mechanical properties of a material which are macro-properties of it are closely related to the micro-structure of it.

In this study, to observe the results of some changing in micro-structure on macro-scale properties, composites, including very small particles or very thin fibers in a matrix, are considered. So, this study serves to understand of the behavior of the composites at the same time. Composite materials are chosen for designing frequently due to their strength or other advantages.

Here, the particles and the fibers have at least one dimension in micro-level. The materials of both of the matrix and inclusions are considered as homogeneous, linear-elastic and isotropic. The volume concentration which is inclusion volume to total volume ratio is very small in considered composites. So, there are no interactions between them. Furthermore, inclusions distribute in the matrix homogeneously. Besides, the elastic constants of matrix material are very lower than those of fibers or particles.

Under the mentioned assumptions, a representative volume element (RVE) can be defined (Hashin, 1962). This volume represents the whole composites and it is different for the cases of the particles or fibers. It has two geometrical shapes, spherical and cylindrical, according to the type of composites and consists of two parts for both of them. The first part is matrix which has the greater volume and the second is inclusion which can be a single particle or a single fiber. The inclusions are assumed as a spherical and a cylindrical body, respectively. In another saying, matrix having spherical form includes particle and matrix in cylindrical geometry includes fiber. As it is stated in the mentioned article, it is assumed that the RVE is equivalent to a single effective body which has the same geometry with the RVE.

In this study, hydrostatic tension problem has been considered for the spherical RVE and for the equivalent effective body to obtain the effective Bulk modulus. Furthermore, simple torsion problem has been solved for the cylindrical RVE and its equivalence. This process is based on the equating the total strain energies of the RVE to that of the associated effective body.

2 DETERMINING OF THE EFFECTIVE BULK MODULUS ANALYTICALLY

2.1 *Strain energy of a spherical body in the state of hydrostatic tension*

A spherical body having radius b is loaded hydrostatic pressure τ_0 (Fig. 1). For convenience, the spherical coordinates (r, θ, φ) has been used for the solution.

The problem is spherically symmetric and whole quantities are independent from θ and φ. Displacement vector $\mathbf{u}$ has only radial component u_r. In spherical

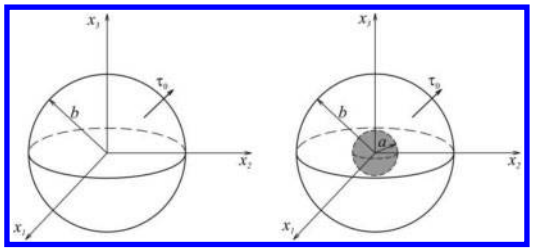


Figure 1. Spherical Bodies.

coordinates, nonzero components of the strain tensor $\boldsymbol{\varepsilon}$ are

$$\mathbf{u} = u_r \mathbf{e}_r \tag{1}$$

$$\varepsilon_{rr} = \frac{\partial u_r}{\partial r}, \varepsilon_{\theta\theta} = \varepsilon_{\varphi\varphi} = \frac{u_r}{r} \tag{2}$$

where ∂ shows the partial differential, $\mathbf{e}_r$ is the unit vector along the radial direction.

Using the constitutive equations in the theory of elasticity and considering the expressions (1) and (2) the nonzero components of the stress tensor are obtained as

$$\begin{aligned} \tau_{rr} &= (\lambda + 2\mu)\frac{\partial u_r}{\partial r} + 2\lambda\frac{u_r}{r} \\ \tau_{\theta\theta} &= \tau_{\varphi\varphi} = \lambda\frac{\partial u_r}{\partial r} + 2(\lambda + \mu)\frac{u_r}{r} \end{aligned} \tag{3}$$

where λ and μ are Lamé's constants. The equilibrium equations in terms of displacement vector is

$$(\lambda + 2\mu)\nabla\nabla\cdot\mathbf{u} - \mu\nabla\times\nabla\times\mathbf{u} = 0 \tag{4}$$

while the body forces are neglected (Malvern, 1969 & Sadd, 2005). Here, ∇ is the del operator and in spherical coordinates it is stated as (Moon & Spencer, 1961)

$$\nabla = \frac{\partial}{\partial r}\mathbf{e}_r + \frac{1}{r}\frac{\partial}{\partial\theta}\mathbf{e}_\theta + \frac{1}{r\sin\theta}\frac{\partial}{\partial\varphi}\mathbf{e}_\varphi \tag{5}$$

If the displacement vector given in the expression (1) is used in the expression (4) then

$$\frac{\partial}{\partial r}\left(\frac{\partial u_r}{\partial r} + 2\frac{u_r}{r}\right) = 0 \tag{6}$$

is obtained. This is a differential equation in the type of Euler-Cauchy. Then, the radial component of the displacement vector is obtained as

$$u_r = Ar + \frac{B}{r^2} \tag{7}$$

where A and B are the unknown constants. This solution is valid on the whole body so that at $r = 0$ the solution must be finite. This concludes that B is zero. The other boundary condition says that surface traction vector $\boldsymbol{t}$ is equal to $\tau_0\varepsilon_r$ on the boundary $r = b$. Writing these, using (2), (3) and (7), and using the outer normal of the boundary as $\boldsymbol{e}_r$

$$\begin{aligned} &t = \tau\cdot n = \tau_0\mathbf{e}_r \\ &\varepsilon_{rr} = \varepsilon_{\theta\theta} = \varepsilon_{\varphi\varphi} = A \\ &\tau_{rr} = \tau_{\theta\theta} = \tau_{\varphi\varphi} = A(3\lambda + 2\mu) = 3KA \\ &A = \frac{\tau_0}{3\lambda + 2\mu} = \frac{\tau_0}{3K} \end{aligned} \tag{8}$$

will be obtained. Here, K is the Bulk modulus and is stated as

$$K = \frac{3\lambda + 2\mu}{3} \tag{9}$$

Finally the total strain energy U accumulated on this body can be written using equation below.

$$U = \frac{1}{2}\int_V \tau_{ij}\varepsilon_{ij}dV \tag{10}$$

Here dV is the differential volume element which has to be written in spherical coordinates. When this integral is evaluated using the equations (2), (8) and (10), the result is obtained as

$$\begin{aligned} U &= \frac{1}{2}\int_{\varphi=0}^{2\pi} d\varphi\int_{\theta=0}^{\pi}\sin\theta d\theta\int_{r=0}^{b} r^2\left(\frac{\tau_0^2}{3K}\right)dr \\ &= \frac{2}{3K}\pi b^3\tau_0^2 \end{aligned} \tag{11}$$

The total volume of the sphere having radius b is

$$V = \frac{4}{3}\pi b^3 \tag{12}$$

So, if the expression (11) is re-written, then the strain energy comes as

$$U = \frac{1}{2K}V\tau_0^2 \tag{13}$$

2.2 *Strain energy of a spherical body including the co-centered spherical particle in the state of hydrostatic tension*

Here a spherical body having radius b including a spherical particle with radius a, centered on the same origin is considered (Fig. 1).

Using the expression (7), the displacement field for particle and matrix can be written as

$$u_r^P = A^P r + \frac{B^P}{r^2} \quad , 0 \le r \le a \tag{14}$$

$$u_r^M = A^M r + \frac{B^M}{r^2} \quad , a \le r \le b \tag{15}$$

Here, the letter "P" and "M" indicate the particle and the matrix, respectively. At $r=0$, the displacement must be finite so it is required that

$$B^P = 0 \tag{16}$$

The components of the strain and stress can be written using (14), (15) and (16) for particle and matrix, separately such that they are similar in the previous considered problem. There are three unknown A^P, A^M and B^M so three boundary conditions to determine them are

$$\tau_{rr}^M = \tau_0 \quad \text{at } r=b \tag{17}$$

$$u_{rr}^M = u_{rr}^P \quad \text{at } r=a \tag{18}$$

$$\tau_{rr}^M = \tau_{rr}^P \quad \text{at } r=a \tag{19}$$

If these conditions are written using the obtained stress and displacement components three equations occurs. These are

$$\left(3K^M\right)+B^M\left(-\frac{4\mu^M}{b^3}\right)=\tau_0 \tag{20}$$

$$A^M(a)+B^M\left(\frac{1}{a^2}\right)-A^P(a)=0 \tag{21}$$

$$A^M\left(3K^M\right)+B^M\left(-\frac{4\mu^M}{a^3}\right)-A^P\left(3K^P\right)=0 \tag{22}$$

The volume concentration of the included particle, c, is defined as the ratio of the volume of particle (V^P) to the volume of the total body (V). This is written as

$$c=\frac{V^P}{V}=\frac{(4/3)\pi a^3}{(4/3)\pi b^3}=\frac{a^3}{b^3} \tag{23}$$

Furthermore, if a constant D is used instead of (B^M/a^3) in the equations (20), (21) and (22), then these three equations can be solved for the unknown constants as

$$D=\tau_0\frac{K^M-K^P}{4\mu^M[K^M+(K^P-K^M)c]+3K^MK^P} \tag{24}$$

$$A^P=\tau_0\frac{4\mu^M+3K^M}{3\{4\mu^M[K^M+(K^P-K^M)c]+3K^MK^P\}} \tag{25}$$

$$A^M=\tau_0\frac{4\mu^M+3K^P}{3\{4\mu^M[K^M+(K^P-K^M)c]+3K^MK^P\}} \tag{26}$$

Now, the strain energy accumulated on the whole body can be written in terms of Bulk moduli, shear moduli and concentration ratio. To do this, the equation (10) is used for the two parts and the summation of results gives the energy. Here, the integrals are gotten over φ and θ from 0 to 2π and from 0 to π for both of the parts, respectively. The radius is changed from 0 to a for particle and from a to b for matrix. Using the stress and strain components, the equations (24), (25) and (26), and the expressions which are

$$4\pi\frac{b^3-a^3}{3}=V(1-c) \tag{27}$$

$$B^M=Da^3 \tag{28}$$

the total strain energy is calculated as

$$U=\frac{9}{2}[VcK^P(A^P)^2+VK^M(A^M)^2(1-c)] +6V\mu^MD^2c(1-c) \tag{29}$$

2.3 *Determining the effective bulk modulus*

The strain energy written in the expression (13) can be considered as the energy of effective material which must be equivalent to the RVE whose total strain energy was obtained in the expression (29). If these two strain energy are equated and rearranged for K^*, which is the effective Bulk modulus, then the result will be

$$\frac{1}{K^*}=\frac{1}{\tau_0^2}\{9[cK^P(A^P)^2+(1-c)K^M(A^M)^2] +12c(1-c)\mu^MD^2\} \tag{30}$$

Hashin used two materials for matrix and particle whose Bulk moduli are

$$K^M=418511.77MPa,\ K^P=172368.93MPa \tag{31}$$

Here, the variation of the Bulk modulus of composite materials obtained with these materials with respect to volume concentration is given in Figure 2.

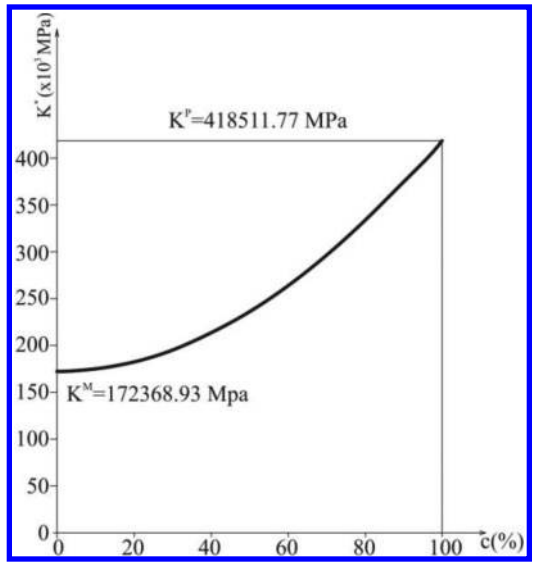


Figure 2. The variation of the Bulk modulus of composite including particle vs. volume concentration.

3 CALCULATION OF THE EFFECTIVE SHEAR MODULUS

3.1 *Simple torsion of a cylindrical body*

A single cylindrical body whose height and radius are h and b, respectively, has been considered (Fig. 3). There is a constant distributed moment m which is applied to this cylinder at both ends in x_3 direction which is the axis of the body. $M_0 = m\pi b^2$ is the total moment acting on both top and bottom surfaces. For convenience, the cylindrical coordinates (r, φ, z) will be used. The components of the stress tensor are zero except $\tau_{r\varphi}$, $\tau_{\varphi r}$, $\tau_{\varphi z}$ and $\tau_{z\varphi}$ in the cylindrical coordinates. Here, all unknowns of the problem are independent of φ and displacement vector has only u_φ component. A differential element having the height dz, and radius r is considered (Fig. 3).

$M_z + dM_z$ and M_z represent the resulting torsion moments at the top and bottom surfaces of this differential element, respectively. Let $\tau_{z\varphi}$ denotes the shear stress acting on the bottom surface. The resultant of this stresses is M_z. If this relation is written

$$M_z(r,z) = \int_{\varphi=0}^{2\pi} d\varphi \int_{r=0}^{b} \xi^2 d\xi \tau_{z\varphi}(\xi, z) \tag{32}$$

is obtained. Calculating r derivative of equation (32) gives

$$\tau_{z\varphi}(r,z) = \frac{1}{2\pi r^2}\frac{\partial M_z}{\partial r} \tag{33}$$

Additionally, the moment balance along the x_3 axis gives the equation below.

$$\tau_{r\varphi}(r,z) = -\frac{1}{2\pi r^2}\frac{\partial M_z}{\partial z} \tag{34}$$

These two shear stress expressed in (33) and (34) can be also written in terms of displacement components by using the relations between strains and displacements in cylindrical coordinates and using Hooke's Law as below.

$$\tau_{z\varphi} = \mu\frac{\partial u_\varphi}{\partial z} \quad , \quad \tau_{r\varphi} = \mu\left(\frac{\partial u_\varphi}{\partial r} - \frac{u_\varphi}{r}\right) \tag{35}$$

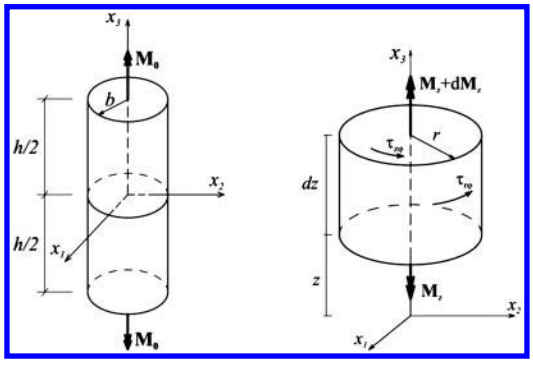


Figure 3. The cylindrical body and a differential element from that.

Using (33)–(35)

$$\frac{1}{2\pi r^2}\frac{\partial M_z}{\partial r} = \mu\frac{\partial u_\varphi}{\partial z} \tag{36}$$

$$-\frac{1}{2\pi r^2}\frac{\partial M_z}{\partial z} = \mu\left(\frac{\partial u_\varphi}{\partial r} - \frac{u_\varphi}{r}\right) \tag{37}$$

are found. Calculating r derivative of (36) and z derivative of (37), the following differential equations is obtained for M_z.

$$\frac{\partial^2 M_z}{\partial r^2} - \frac{3}{r}\frac{\partial M_z}{\partial r} + \frac{\partial^2 M_z}{\partial z^2} = 0 \tag{38}$$

The solution of this equation for this equation is

$$M_z = Cr^4 + B \tag{39}$$

M_z should vanish for $r = 0$ (Love, 1944 & Barber, 2004). Then, B becomes zero. M_z must be equal to M_0 for $r = b$. Writing this, the other constant is obtained as

$$M_z(r=b) = M_0 = m\pi b^2 \;\rightarrow\; C = \frac{m\pi}{b^2} \tag{40}$$

Substituting this into (39) and using this into the equations (33) and (34), the shear stresses obtained as well.

$$\tau_{r\varphi} = 0, \; \tau_{z\varphi} = \frac{2mr}{b^2} \tag{41}$$

So, the shear strain different from zero is also obtained using Hooke's Law as

$$\gamma_{z\varphi} = \frac{2mr}{\mu b^2} \tag{42}$$

The total strain energy accumulated in this cylinder can be calculated as

$$U = \int_{\varphi=0}^{2\pi} d\varphi \int_{z=0}^{h} dz \int_{r=0}^{b} \tau_{z\varphi}\gamma_{z\varphi} r dr = \frac{\pi h m^2}{\mu} \tag{43}$$

3.2 *Simple torsion of a cylindrical body including a coaxial cylindrical fiber*

In this subsection, the strain energy of a cylindrical body including a coaxial cylindrical fiber will be calculated under simple torsion (Fig. 4). The total torsion moment is divided to two parts. These parts M^M, M^F are gotten by the matrix and fiber, respectively.

The previous solution given in (39) for single cylinder can be used in here. For the fiber, the moment and nonzero shear stress and strain are written as

$$M_z^F = C^F r^4, \; \tau_{z\varphi}^F = \frac{2C^F r}{\pi} = \mu^F \gamma_{z\varphi}^F \tag{44}$$

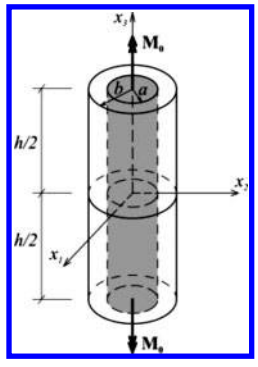


Figure 4. The cylindrical body including fiber.

Here, r may change from zero to a. For the matrix which has the geometry of hollow cylinder, the moment is

$$M_z^F = C^F r^4 + D^F \tag{45}$$

The shear stress and strain on that are the same as those in fiber totally except being the superscripts M. The total torsion moment on the surface due to these shear stresses is

$$\begin{aligned} &\int_0^a 2\pi\tau_{z\varphi}^F r^2 dr + \int_a^b 2\pi\tau_{z\varphi}^M r^2 dr = M_0 \quad \rightarrow \\ &C^F a^4 + C^M (b^4 - a^4) = M_0 \end{aligned} \tag{46}$$

This is the first equation for C^F, C^M and D^M constants. The common boundary for the matrix and fiber is at $r = a$. On that, surface traction vectors are equal for both matrix and fiber. This gives

$$C^F = C^M \frac{\mu^F}{\mu^M} \tag{47}$$

The solution of (46) and (47) are obtained as (Bulut, 2013)

$$\begin{aligned} C^F &= \frac{M_0 \mu^F}{\mu^F a^4 + \mu^M (b^4 - a^4)} \\ C^M &= \frac{M_0 \mu^M}{\mu^F a^4 + \mu^M (b^4 - a^4)} \end{aligned} \tag{48}$$

The strain energy is calculated as

$$U = \frac{b^4 m^2 \pi h}{a^4 (\mu^F - \mu^M) + b^4 \mu^M} \tag{49}$$

3.3 *Determining the effective shear modulus*

If the expression obtained in (43) which may be thought as effective shear modulus in the condition of changing μ to μ^* is equated to the expression (49), and the concentration ratio c is defined as (a^2/b^2) then the expression for the effective shear modulus will be obtained as

$$\mu^* = \mu^P c^2 + \mu^M (1 - c^2) \tag{50}$$

4 EXPERIMENTS

In order to compare the previous analytical results, the experiments of cylindrical composite samples having fibers whose radius in in micro level under simple tension have been realized. Here, polyester and Kevlar fiber are used as matrix and fibers, respectively.

Firstly, in order to determine the properties of used polyester or matrix material, cylindrical samples without any fiber have been molded. The radii and the heights of the samples are about 22 mm and 185 mm. A mold was manufactured to obtain the samples. When the samples were prepared, cobalt and methyl-ethyl-ketone (MEK) were used in the percentage of weight ratio of %0.05 and %0.25, respectively. To avoid of cracks or deformations on the samples due to the exothermic reactions causing thermal stresses were why the weight ratio of the hardener was low.

As the second step, the cylindrical composite samples which included 1% and 1.5% fibers with respect to the volume ratio have been prepared.

All samples have waited for a month and they have been put in an oven for post curing.

The simple tension tests have been realized by Instron 8802. The Young's moduli have been obtained from the stress-strain diagram of the test of these samples. Furthermore, a digital micrometer has been used for calculating the Poisson's ratios. The stress-strain curves of polyester sample without fiber and the samples including 1% and 1.5% fibers have been obtained. The slopes of the tangent to the initial portion of the curves have given the Young's moduli. These have been obtained as

$$\begin{aligned} E^M &= 1820 MPa \\ E_1^* &= 1832.6 MPa \\ E_{1.5}^* &= 1860.9 MPa \end{aligned} \tag{51}$$

Here, E_1^* and $E_{1.5}^*$ are shown the Young's moduli of the samples including 1% and 1.5% fibers, respectively.

The Poisson's ratios have been calculated as

$$\upsilon^M = 0.27\,,\ \upsilon_1^* = 0.25\,,\ \upsilon_{1.5}^* = 0.23 \tag{52}$$

5 COMPARISON OF THE ANALYTICAL AND EXPERIMENTAL RESULTS

Because of the geometry of the experimental samples, the results obtained from experiments have been compared with the analytical solution which is given in (50). To use this relation, the shear moduli of the matrix and fibers must be obtained.

The Young's modulus and the Poisson's ratio of Kevlar fibers have been gotten from the literature as

$$E^F = 10^5 MPa\,,\ \upsilon^F = 0.33 \tag{53}$$

Table 1. The results and errors.

Vol. ratio	μ_t (MPa)	μ_d (MPa)	Error (%)
%1	720.223	733.04	1.78
%1.5	724.832	756.46	4.36

The shear moduli of the matrix and fiber can be calculated from the expressions (51), (52) and (53) by using

$$\mu = \frac{E}{2(1+\upsilon)} \tag{54}$$

So, these are

$$\mu^M = 716.535MPa\,,\ \mu^F = 37593.98MPa \tag{55}$$

The shear moduli of the composites including 1% and 1.5% fibers can be calculated using the equation (50) as

$$\mu_{t1}^* = 719.688MPa\,,\ \mu_{t1.5}^* = 724.832MPa \tag{56}$$

The shear moduli of associated composites obtained experimentally are

$$\mu_{d1}^* = 733.04MPa\,,\ \mu_{d1.5}^* = 756.46MPa \tag{57}$$

The subscript t shows the results from theoretical solution whilst the letter $d$defines the experimental results.

Obtained results have been shown in Table 1.

As it can be shown here, the mean value of the error between analytical and experimental solution is %3.07.

The variation of the value of the shear modulus of composites with respect to volume concentration obtained by analytically and experimentally has been graphed in Figure 5.

6 RESULTS

In this study, the Bulk modulus of composites including particles and the shear modulus of composites including fibers have been obtained in terms of elastic constants of matrix and particle or fiber and the volume concentration, analytically. Although

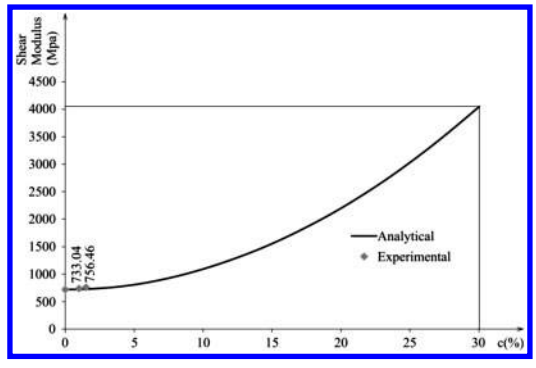


Figure 5. The variation of the shear modulus with volume ratio.

experiments have not been realized yet for preceding composite, the analytical results are in accordance with the experimental results in Hashin's article (Hashin, 1962).

The difference in this study is that the expressions of elastic constants for composites having long thin cylindrical fibers have been obtained. So, for a constant volume concentration value, a constant single value can be obtained for an associated composite.

The drawn graph shows accordance so that experimental results for the latter prove that the analytical solution is acceptable.

ACKNOWLEDGEMENT

The authors would like to thank Research Fund of Istanbul Technical University for the supports.

REFERENCES

Barber, J. R. 2004. Elasticity. New York: Academic Publishers.

Bulut, O. 2013 (expected). An Application of the theory of elasticity in micromechanics (PhD Dissertation). Istanbul: ITU, Graduate School of Science Engineering and Technology.

Hashin, Z. 1962. The elastic moduli of heterogeneous materials. *Journal of Applied Mechanics*, 29: 143–150.

Malvern, L. E., 1969. Introduction to the continuous medium. USA: Prentice-Hall.

Moon, P. & Spencer, D. E. 1961. Field theory handbook. Berlin: Springer-Verlag.

Love, A. E. H. 1944. A treatise on the mathematical theory of elasticity. New York: Dover Publication.

Sadd, M. H., 2005. Elasticity: theory, applications, and numerics. USA: Elsevier.

Research and Applications in Structural Engineering, Mechanics and Computation – Zingoni (Ed.)
© 2013 Taylor & Francis Group, London, ISBN 978-1-138-00061-2

Strain induced product properties of magneto-electric composites

J. Schröder, M.-A. Keip & M. Labusch
Institute of Mechanics, Department of Civil Engineering, Faculty of Engineering, University of Duisburg-Essen, Essen, Germany

D.C. Lupascu
Institute for Materials Science, Department of Civil Engineering, Faculty of Engineering, University of Duisburg-Essen, Essen, Germany

ABSTRACT: This paper deals with the computational homogenization of magneto-electric composites consisting of piezoelectric and piezomagnetic phases. Applying a computational homogenization scheme we calculate the effective magneto-electric coupling coefficients which arise as strain-induced product properties. The numerical procedure is based on the Finite Element Method, used for the discretization of a substructure of the heterogenous microscale. After analysing a periodic composite, we discuss the applicability of the homogenization procedure for the calculation of the effective properties of particulate magneto-electric composites obtained from experimental measurements.

1 INTRODUCTION

The magneto-electric (ME) coupling effect has attracted special attention during the last decades. Materials exhibiting coupling between magnetic and electric fields allow for many new intelligent applications, for instance as magnetic-field sensors or electric-write magnetic-read memories (Eerenstein et al. 2007). The latter application would combine the advantages of Ferroelectric and Magnetoresistive Random Access Memories (FeRAM and MRAM, respectively) resulting in a Magneto-Electric Random Access Memory (MERAM). Such device could be realized by using materials that possess both spontaneous magnetization and polarization coupled to one another (Bibes and Barthélémy 2008). Since these materials exhibit at least two distinct ferroic states (ferroelectricity and ferromagnetism, often accompanied by ferroelasticity) they belong to the class of ME multiferroics. In recent years, ME multiferroics have been studied intensively, see e.g. Schmind (1994), Schmind (2008). Works which discuss the basic experimental observations and also present theoretical investigations of the underlying phenomena are given by e.g. Cheong and Mostovoy (2007) and Khomskii (2009). Since the coupling between the two ferroic quantities in intrinsically multiferroic materials is in general weak, the range of possible applications is still quite narrow, c.f. Hill (2000). Furthermore, the obtainable ME coupling is limited as pointed out by Brown et al. (1968) who discuss an upper bound of the possible ME coefficient formulated in terms of the magnetic permeability and the electric permittivity. Thus, the design of ME composite materials becomes relevant, see e.g. Nan (1994), Eerenstein et al. (2006), Nan et al. (2008), Srinivasan (2010), Wang et al. (2010), Priya et al. (2007), Ryu et al. (2002). Such composite structures consist of individual electroactive and magnetoactive phases and the ME coupling enters the material as a *product property* (van Suchtelen 1972). A product property can be defined as a property of the composite which is not present in none of the composite phases, but which arises as product of the interaction between the individual phases. In an ME composite the interaction between the two phases is driven by strain: on the one hand, an applied electric field induces a deformation of the electroactive material which is transferred to the magnetoactive material. The deformation of the magnetoactive material then induces a magnetic reaction. On the other hand, an applied magnetic field deforms the magnetic phase which then induces strain-driven polarization in the electric phase. The latter phenomenon is often termed the direct ME effect, while the former describes the converse ME effect, see e.g. Wang et al. (2010).

In contrast to single-phase multiferroics, composite structures can show very pronounced ME coupling. Experiments on sintered granular composites and laminate structures have been performed and an ME coefficient of up to 90 V/cm *Oe* has been observed in the range of the electro-mechanical resonance. This is three to five orders of magnitude higher than the coupling observed in a typical single-phase material (Fiebig 2005). The production processes of ferromagnetic/ferroelectric heterostructures are manifold and can be optimized by nanotechnological methods, see e.g. Ramesh and Spaldin (2007) and Martin

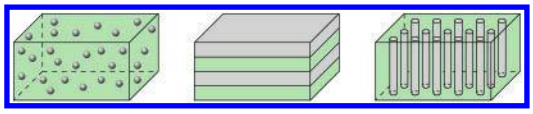


Figure 1. Typical ME composites: 0-3, 2-2, and 1-3 composite.

et al. (2010). Some typical composite structures are depicted in Figure 1.

As a convention, we will denote the type of the composites as follows. The first number indicates the spatial connectivity of the magnetoactive phase and the second number indicates the connectivity of the electroactive phase.

The determination of the effective behavior of ME composites is therefore of great interest. In this context, homogenization methods play an important role for the description of micro-heterogeneous materials since they allow for the characterization of material properties on different scales. Many theoretical investigations have been conducted in order to study the effective behavior of ME composites. The work Harshé et al. (1993b) presents a micro-mechanical approach for the estimation of the ME effect in 3-0 and 0-3 composites. Similar to that, Harshé et al. (1993a) discuss the effective response of 2–2 laminate composite structures. Huang and Kuo (1997) and Srinivas et al (2006) determine the effective properties of ME composites with ellipsoidal inclusions by using a Mori-Tanaka method. For the determination of the effective behavior by using a self-consistent approach see Srinivas and Li (2005). Camacho-Montes et al. (2009) calculate the ME coefficient of 1–3 composites on the basis of asymptotic homogenization. In the work Bichurin et al. (2003) the ME effect of 2–2 structures is analyzed in the low-frequency range. Corresponding results for electro-mechanical resonance are given in Bichurin et al. (2003). For an overview see Bichurin et al. (2010). In Nan et al. (2005) 1–3 and 2–2 ME composites are analyzed with regard to magnetic-field induced electric polarization. The influence of the mechanical boundary condition on the ME effect is discussed in Shi et al. (2004).

The present paper aims at the numerical characterization of ME composites based on computational homogenization. We will derive a numerical procedure based on the Finite Element Method in order to compute the overall ME coefficient of two-phase composites consisting of piezoelectric and piezomagnetic phases, cf. also Lee et al. (2005). The method will be applied to the computation of the effective ME properties of idealized microstructures as well as of realistic microstructures obtained from experiments. The outline of the paper is as follows. In chapter 2 the theoretical framework will be provided where the procedure for the determination of the effective properties will be discussed in detail. In chapter 3 the effective response of several composites including ideal and realistic microstructures will be computed. Chapter 4 closes the paper with a short conclusion.

2 THEORETICAL FRAMEWORK

In the following chapter, the continuum-mechanical framework for the simulation of ME materials is described briefly. We will start with writing down the fundamental balance equations and the underlying kinematical assumptions, whereby we restrict ourselves to small deformations such that the geometric linear theory can be applied. The numerical method for the determination of the overall constitutive response will be discussed, where we confine our attention to the computation of the ME coupling coefficients. After that, we will write down the periodic boundary conditions. Finally, we outline the constitutive relations of the individual phases of the composite, which respectively exhibit the piezoelectric and piezomagnetic coupling.

2.1 *Magneto-electro-mechanical boundary value problem and scale transition*

Let the body under consideration be denoted as $\mathcal{B} \subset \mathbb{R}^3$ and parameterized in space with coordinates $\mathbf{x}$. Then, the basic kinematical quantities are given by the linear strain tensor, the electric field, and the magnetic field defined by

$$\varepsilon = \nabla^s \mathbf{u}, \quad \mathbf{E} = -\nabla\phi, \quad \text{and} \quad \mathbf{H} = -\nabla\varphi, \tag{1}$$

respectively. Herein, $\mathbf{u}$, ϕ, and φ denote the displacement field and the scalar electric and magnetic potential. The fundamental balance equation are given by the balance of linear momentum

$$\nabla \cdot \boldsymbol{\sigma} + \mathbf{f} = \mathbf{0}, \tag{2}$$

the Gauß's law of electrostatics

$$\nabla \cdot \mathbf{D} = q \tag{3}$$

and the Gauß's law of magnetostatics

$$\nabla \cdot \mathbf{B} = 0, \tag{4}$$

where we have introduced the Cauchy stress tensor σ, the vector of body forces $\mathbf{f}$, the vector of dielectric displacements $\mathbf{D}$, the density of free charge carriers q and the vector of the magnetic induction $\mathbf{B}$.

In order to compute the effective response of the ME composite we analyze a representative volume element (RVE) of the actual body, which has to be imagined as periodically embedded into a higher scale macroscopic continuum. The RVE is driven by boundary conditions that arise as a consequence of macroscopic fields. These boundary conditions have to be *energetically consistent* and can be derived by exploring a *scale transition* between the scales. For this purpose, we first decompose the microscopic fields into constant macroscopic fields $\overline{\bullet}$ and fluctuation parts $\widetilde{\bullet}$ as

$$\boldsymbol{\xi} = \overline{\boldsymbol{\xi}} + \widetilde{\boldsymbol{\xi}} \quad \text{with} \quad \boldsymbol{\xi} := [\boldsymbol{\varepsilon}, \boldsymbol{\sigma}, \mathbf{E}, \mathbf{D}, \mathbf{H}, \mathbf{B}]\,. \tag{5}$$

Energetic consistence is then ensured by postulating a generalized macrohomogeneity condition of the form

$$\overline{\boldsymbol{\sigma}} : \dot{\overline{\boldsymbol{\varepsilon}}} + \overline{\mathbf{D}} \cdot \dot{\overline{\mathbf{E}}} + \overline{\mathbf{B}} \cdot \dot{\overline{\mathbf{H}}} = \frac{1}{V} \int_{\mathrm{RVE}} (\boldsymbol{\sigma} : \dot{\boldsymbol{\varepsilon}} + \mathbf{D} \cdot \dot{\mathbf{E}} + \mathbf{B} \cdot \dot{\mathbf{H}}) \, dv \,, \tag{6}$$

in this context we refer to Schröder (2009), Schröder and Keip (2010), (2011), (2012) or Keip and Schröder (2011). Periodic boundary conditions that fulfill this condition are

$$\begin{aligned} \widetilde{\mathbf{u}}(\mathbf{x}^+) = \widetilde{\mathbf{u}}(\mathbf{x}^-) \quad &\text{and} \quad \mathbf{t}(\mathbf{x}^+) = -\mathbf{t}(\mathbf{x}^-) \,, \\ \widetilde{\phi}(\mathbf{x}^+) = \widetilde{\phi}^-(\mathbf{x}^-) \quad &\text{and} \quad Q(\mathbf{x}^+) = -Q(\mathbf{x}^-) \,, \\ \widetilde{\varphi}(\mathbf{x}^+) = \widetilde{\varphi}(\mathbf{x}^-) \quad &\text{and} \quad \zeta(\mathbf{x}^+) = -\zeta(\mathbf{x}^-) \,, \end{aligned} \tag{7}$$

where $\mathbf{x}^+$ and $\mathbf{x}^-$ denote points on the opposite faces of a periodic unit cell. After the solution of the boundary value problem, we can compute the homogenized macroscopic response by averaging over the microscopic fields over the RVE. In a more general case, the macroscopic quantities hace to be defined in terms of surface integrals. For simplicity we restrict ourselves to suitable volume averages as

$$\begin{aligned} \overline{\boldsymbol{\varepsilon}} &= \frac{1}{V} \int_{\mathcal{B}} \boldsymbol{\varepsilon} \, dv, \quad \overline{\boldsymbol{\sigma}} = \frac{1}{V} \int_{\mathcal{B}} \boldsymbol{\sigma} \, dv \\ \overline{\mathbf{E}} &= \frac{1}{V} \int_{\mathcal{B}} \mathbf{E} \, dv, \quad \overline{\mathbf{D}} = \frac{1}{V} \int_{\mathcal{B}} \mathbf{D} \, dv \\ \overline{\mathbf{H}} &= \frac{1}{V} \int_{\mathcal{B}} \mathbf{H} \, dv, \quad \overline{\mathbf{B}} = \frac{1}{V} \int_{\mathcal{B}} \mathbf{B} \, dv \,. \end{aligned} \tag{8}$$

For a more general definition of macroscopic quantities in terms of suitable surface integrals we refer to Schröder (2009).

2.2 *Constitutive framework and effective ME coefficient*

For the analysis of the effective ME behavior of the composite, we suppose a linear piezoelectric and a linear piezomagnetic material response of the individual phases on the microscale. To be specific, we consider the phases to be transversely isotropic and use the constitutive framework proposed in Schröder and Gross (2004) such that each phase is characterized by a preferred direction denoted by the vector $\mathbf{a}$. This preferred direction can be imagined as the fixed direction of remanent polarization and magnetization of the two ferroic phases. Without going into detail we write down the constitutive behavior for each of the two phases as

$$\begin{aligned} \boldsymbol{\sigma} &= \mathbb{C} : \boldsymbol{\varepsilon} - \mathbf{e}^T \cdot \mathbf{E} - \mathbf{q}^T \cdot \mathbf{H} \\ -\mathbf{D} &= -\mathbf{e} : \boldsymbol{\varepsilon} - \boldsymbol{\epsilon} \cdot \mathbf{E} - \boldsymbol{\alpha}^T \cdot \mathbf{H} \\ -\mathbf{B} &= -\mathbf{q} : \boldsymbol{\varepsilon} - \boldsymbol{\alpha} \cdot \mathbf{E} - \boldsymbol{\mu} \cdot \mathbf{H} \end{aligned} \tag{9}$$

where $\mathbb{C}$, $\boldsymbol{\epsilon}$, $\boldsymbol{\mu}$, $\mathbf{e}$, $\mathbf{q}$, and $\boldsymbol{\alpha}$ denote the constant material moduli of the individual phase. Here, it has to be emphasized that for each of the two phases the ME coupling modulus is zero: $\boldsymbol{\alpha} \equiv \mathbf{0}$. However, the overall macroscopic ME modulus of the composite $\overline{\boldsymbol{\alpha}}$ is in general non-zero since it is activated by the electric- or magnetic-field induced deformation of the microstructure. This macroscopic property is defined as

$$\overline{\boldsymbol{\alpha}} = \frac{\partial \overline{\mathbf{B}}}{\partial \overline{\mathbf{E}}} = \left[\frac{\partial \overline{\mathbf{D}}}{\partial \overline{\mathbf{H}}} \right]^T . \tag{10}$$

3 NUMERICAL EXAMPLES

The following chapter contains two numerical examples for the calculation of the ME coefficient. In detail, we consider an idealized three-dimensional RVE as well as a two-dimensional part of a real microstructure obtained from an experiment. First, in order to verify the performance of the implemented model, the strain-induced ME coefficient of the 3D ideal RVE is compared to results from the literature. After that the formulation is applied to the discretized morphology of a sample of a real microstructure. Here we will analyze if the numerical results coincide with the coupling behavior obtained from experimental measurements. All computations will be performed in consideration of periodic boundary conditions.

3.1 *Ideal 3D microstructure*

In order to verify the model we will compare the results of the model to data from the literature given by the work of Lee et al. (2005). In this contribution, a periodic RVE with a piezomagnetic matrix consisting of cobalt ferrite ($CoFe_2O_4$) and a piezoelectric cylindrical inclusion consisting of barium titanate ($BaTiO_3$) is considered. The preferred directions of the two phases are assumed to point into the positive vertical direction. Figure 2 shows an illustration of the discretized RVE. The material parameters of the two phases are taken from Lee et al. (2005) and listed in table 1.

For validation of the results two numerical examples with 40% and 60% volume fraction of the inclusion are performed. For the computation we consider a macroscopic electric field $\overline{E}_3$ which is applied to the RVE using periodic boundary conditions. Since the preferred directions of both materials are oriented in x_3-direction, a pronounced coupling as a result of the applied field is activated: due to the electric field, the piezoelectric inclusion reacts with an elongation which is transferred to the piezomagnetic matrix. The deformation then leads to a magnetic reaction of the piezomagnetic matrix. This strain-induced ME coupling can be quantified by determining the quotient of the magnetic induction and the electric field following (10). For this purpose, the volume average of the magnetic induction $\overline{B}_3$ is determined by using (8). The calculation was carried out for the two volume fractions of the piezoelectric inclusion. The resulting

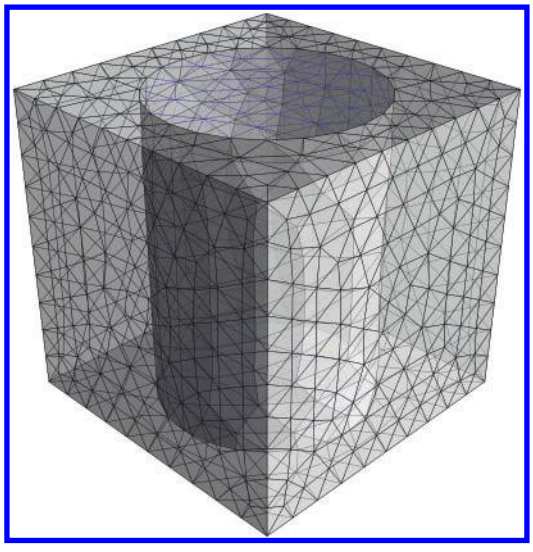


Figure 2. Piezomagnetic cube with piezoelectric cylindrical inclusion of the periodic microstructure.

Table 1. Material parameters for $BaTiO_3$ and $CoFe_2O_4$.

Parameter	$BaTiO_3$	$CoFe_2O_4$
$\mathbb{C}_{11}\ [\frac{N}{mm^2}]$	$16.6 \cdot 10^4$	$28.6 \cdot 10^4$
$\mathbb{C}_{12}\ [\frac{N}{mm^2}]$	$7.7 \cdot 10^4$	$17.3 \cdot 10^4$
$\mathbb{C}_{13}\ [\frac{N}{mm^2}]$	$7.8 \cdot 10^4$	$17.05 \cdot 10^4$
$\mathbb{C}_{33}\ [\frac{N}{mm^2}]$	$16.2 \cdot 10^4$	$26.95 \cdot 10^4$
$\mathbb{C}_{44}\ [\frac{N}{mm^2}]$	$4.3 \cdot 10^4$	$4.53 \cdot 10^4$
$\epsilon_{11}\ [\frac{mC}{kVm}]$	$112 \cdot 10^{-4}$	$0.8 \cdot 10^{-4}$
$\epsilon_{33}\ [\frac{mC}{kVm}]$	$126 \cdot 10^{-4}$	$0.93 \cdot 10^{-4}$
$\mu_{11}\ [\frac{N}{kA^2}]$	5	-590
$\mu_{33}\ [\frac{N}{kA^2}]$	10	157
$e_{31}\ [\frac{C}{m^2}]$	-4.4	0
$e_{33}\ [\frac{C}{m^2}]$	18.6	0
$e_{15}\ [\frac{C}{m^2}]$	11.6	0
$q_{31}\ [\frac{N}{kAmm}]$	0	$5.803 \cdot 10^2$
$q_{33}\ [\frac{N}{kAmm}]$	0	$6.997 \cdot 10^2$
$q_{15}\ [\frac{N}{kAmm}]$	0	$5.5 \cdot 10^2$

ME-coefficients arise as $\alpha_{33}^{40\%} = 2.671 \cdot 10^{-9}$ [s/m] and $\alpha_{33}^{60\%} = 2.503 \cdot 10^{-9}$ [s/m] for 40% and 60% volume fraction, respectively. This is in good agreement with the results from Lee et al. (2005).

3.2 *Realistic 2D microstructure*

In the second example, we analyze the ME behavior of a real composite microstructure. The morphology of the ME composite consists of a piezoelectric matrix ($BaTiO_3$) with embedded particulate piezomagnetic inclusions ($CoFe_2O_4$), where the surface

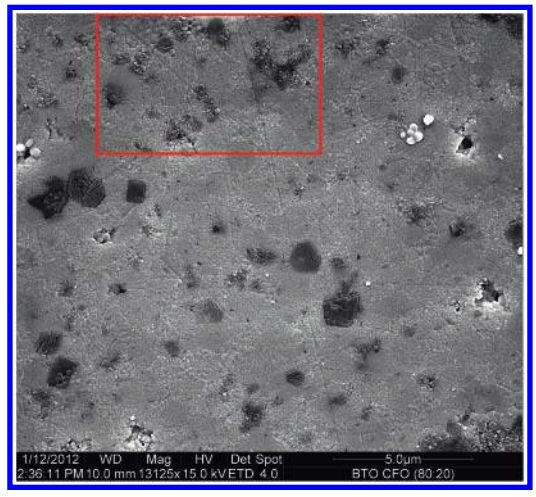


Figure 3. The real microstructure obtained by microscopy.

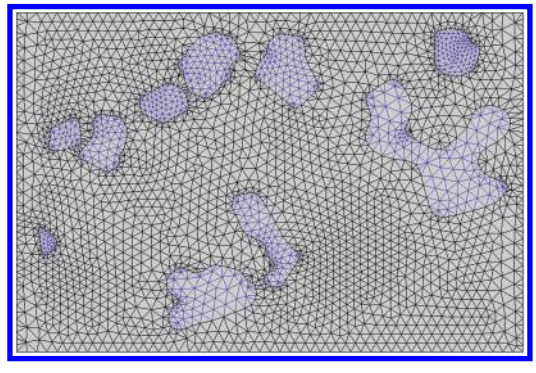


Figure 4. The discretized part of the real microstructure.

fraction of the piezomagnetic inclusions can be constituted with 16%; it is depicted in Figure 3. The experimental microstructure was discretized with triangular finite elements with quadratic shape functions and the preferred directions of the two phases are assumed to point in positive x_2-direction. The discretized microstructure is depicted in Figure 4.

In order to analyze the ME coefficient of the microstructure we apply an external electric field in positive vertical direction under plane-strain conditions. Analogously to the three-dimensional example, the deformation of the piezoelectric matrix is transferred to the piezomagnetic particles, so that a magnetic induction is generated. The resulting distributions of the microscopic electric field E_2, dielectric displacement D_2, magnetic field H_2, and magnetic induction B_2 are depicted in Figures 5 and 6.

By using (8) for the magnetic induction $\overline{B}_2$ together with (10) we obtain the effective ME coefficient $\alpha_{22} = 3.893 \cdot 10^{-11}$ [s/m]. This is not in agreement with the measurements of Etier et al. (2012), who measured an effective ME coefficient of $\alpha_{22} = 4.4 \cdot 10^{-12}$ [s/m]. This deviation might be

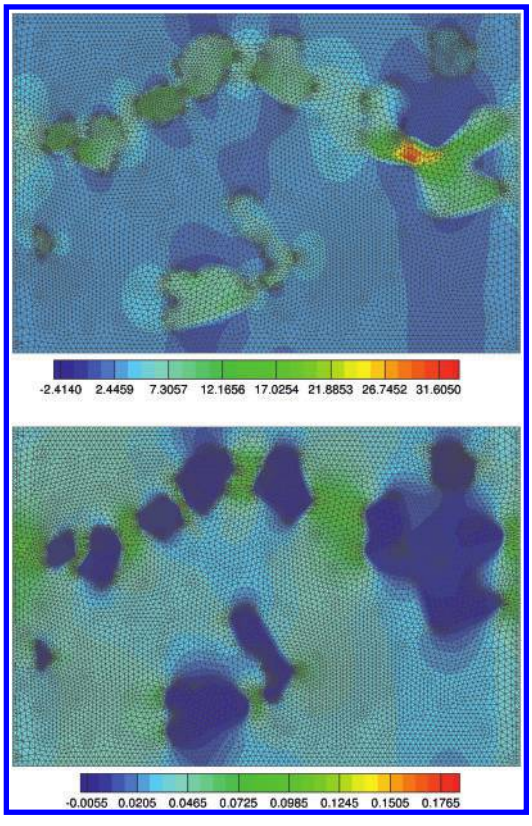


Figure 5. Distribution of the electric fields and dielectric displacement in x_2-direction.

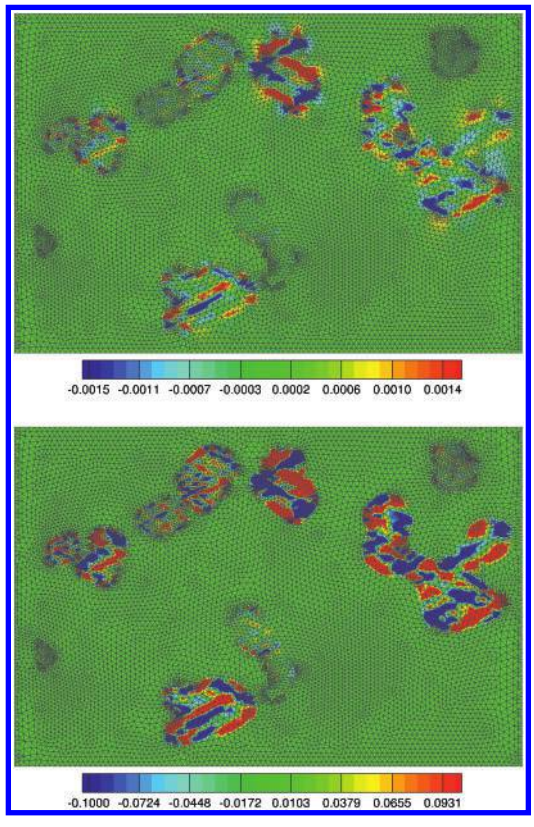


Figure 6. Distribution of the magnetic fields and magnetic induction in x_2-direction.

explained by the fact that we have assumed an ideal microscopic microstructure in which the preferred directions of the two materials point in vertical direction. In the experiment such situation is very hard to achieve since the composite has to be polarized so that the resulting remanent polarization network will differ from the ideal assumption. Furthermore, we have assumed fully activated piezoelectric and piezomagnetic coupling in the individual phases of the composite. This can be constituted as an ideal assumption as well. Both assumptions will not be fulfilled in the experiment. Another influence may arise from the two-dimensional approximation of the originally particulate three-dimensional microstructure.

4 CONCLUSION

In the present paper, the strain-induced magneto-electric coupling of two-phase magneto-electric composites consisting of piezoelectric barium titanate and piezomagnetic cobalt ferrite is analyzed numerically. First we verified the formulation by comparing the magneto-electric coefficient of a fiber-matrix composite to data from the literature. After that the formulation was applied to the computation of the magneto-electric coupling behavior of a realistic microstructure obtained from an experiment. We considered a two-dimensional discretization of the morphology of the composite microstructure. The computed magneto-electric coupling coefficient is in insufficient agreement with the coefficient obtained in the experiment. This deviation was explained by the assumption of a complete uni-directional, ideal polarization of the piezoelectric matrix and magnetization of the piezomagnetic inclusions, respectively. Such ideal situation can hardly be realized in an experiment. In order to describe the behavior of realistic magneto-electric composites more accurately the definition of different orientations for multiple parts of the microstructure should be implemented. This can be achieved by simulating the electric polarization process.

REFERENCES

Bibes, M. & A. Barthélémy (2008). Multiferroics: Towards a magnetoelectric memory. *Nature Materials* 7(6), 425–426.

Bichurin, M., D. Filippov, V. Petrov, V. Laletsin, N. Paddubnaya, & G. Srinivasan (2003, October). Resonance magnetoelectric effects in layered magnetostrictive-piezoelectric composites. *Physical Reviews B 68*(13), 132408.

Bichurin, M., V. Petrov, S. Averkin, & E. Liverts (2010, March). Present status of theoretical modeling the magnetoelectric effect in magnetostrictive-piezoelectric

nanostructures. Part I: Low frequency and electromechanical resonance ranges. *Journal of Applied Physics 107*(5), 053904.

Bichurin, M., V. Petrov, & G. Srinivasan (2003, August). Theory of low-frequency magnetoelectric coupling in magnetostrictive-piezoelectric bilayers. *Physical Reviews B 68*(5), 054402.

Brown, W. F., R. Hornreich, & S. Shtrikman (1968). Upper bound on the magnetoelectric susceptibility. *Physical Review 168*(2), 574–577.

Camacho-Montes, H., F. Sabina, J. Bravo-Castillero, R. Guinovart-Díaz, & R. Rodríguez-Ramos (2009, February). Magnetoelectric coupling and cross-property connections in a square array of a binary composite. *International Journal of Engineering Science 47*(2), 294–312.

Cheong, S.-W. & M. Mostovoy (2007). Multiferroics: a magnetic twist for ferroelectricity. *Nature Materials 6*(1), 13–20.

Eerenstein, W., N. D. Mathur, & J. F. Scott (2006). Multiferroic and magnetoelectric materials. *Nature 442*(7104), 759–765.

Eerenstein, W., M. Wiora, J. Prieto, J. F. Scott, & N. Mathur (2007, May). Giant sharp and persistent converse magnetoelectric effects in multiferroic epitaxial heterostructures. *Nature Materials 6*(5), 348–351.

Etier, M., Y. Gao, V. V. Shvartsman, D. C. Lupascu, J. Landers, & H. Wende (2012). Magnetoelectric properties of $0.2cofe_2o_4$-$0.8batio_3$ composite prepared by organic method. *Proceedings of the European Conference on the Applications of Polar Dielectrics*, 1–4.

Fiebig, M. (2005, April). Revival of the magnetoelectric effect. *Journal of Physics D: Applied Physics 38*(8), R123–R152.

Harshé, G., J. Dougherty, & R. E. Newnham (1993a). Theoretical modeling of 3-0/0-3 magnetoelectric composites. *International Journal of Applied Electromagnetics in Materials 4*, 161–171.

Harshé, G., J. Dougherty, & R. E. Newnham (1993b). Theoretical modeling of multilayer magnetoelectric composites. *International Journal of Applied Electromagnetics in Materials 4*, 145–159.

Hill, N. (2000). Why are there so few magnetic ferroelectrics? *Journal of Physical Chemistry B 104*, 6694–6709.

Huang, J. H. & W.-S. Kuo (1997). The analysis of piezoelectric/piezomagnetic composite materials containing ellipsoidal inclusions. *Journal of Applied Physics 81*(3), 1378–1386.

Keip, M.-A. & J. Schröder (2011). Effective electromechanical properties of heterogeneous piezoelectrics. In B. Markert (Ed.), *Advances in Extended and Multifield Theories for Continua*, Volume 59 of *Lecture Notes in Applied and Computational Mechanics*, pp. 109–128. Springer Berlin, Heidelberg.

Khomskii, D. (2009). Classifying multiferroics: Mechanisms and effects. *Physics 2*, DOI:10.1103.

Lee, J. S., J. G. Boyd, & D. C. Lagoudas (2005). Effective properties of three-phase electro-magneto-elastic composites. *International Journal Of Engineering Science 43*(10), 790–825.

Martin, L., Y.-H. Chu, & R. Ramesh (2010). Advances in the growth and characterization of magnetic, ferroelectric, and multiferroic oxide thin films. *Materials Science and Engineering: R: Reports 68*(46), 89–133.

Nan, C.-W. (1994, Sep). Magnetoelectric effect in composites of piezoelectric and piezomagnetic phases. *Phys. Rev. B 50*, 6082–6088.

Nan, C.-W., M. I. Bichurin, S. Dong, D. Viehland, & G. Srinivasan (2008). Multiferroic magnetoelectric composites: Historical perspective, status, and future directions. *Journal of Applied Physics 103*(3), 031101.

Nan, C.-W., G. Liu, Y. Lin, & H. Chen (2005, May). Magnetic-field-induced electric polarization in multiferroic nanostructures. *Physical Review Letters 94*(19), 197203–1–4.

Priya, S., R. Islam, S. Dong, & D. Viehland (2007, September). Recent advancements in magnetoelectric particulate and laminate composites. *Journal of Electroceramics 19*(1), 147–164.

Ramesh, R. & N. Spaldin (2007). Multiferroics: progress and prospects in thin films. *Nature Materials 6*(1), 21–29.

Ryu, J., S. Priya, K. Uchino, & H. E. Kim (2002, August). Magnetoelectric effect in composites of magnetostrictive and piezoelectric materials. *Journal of Electroceramics 8*(2), 107–119.

Schmid, H. (1994). Multi-ferroic magnetoelectrics. *Ferroelectrics 162*, 317–338.

Schmid, H. (2008). Some symmetry aspects of ferroics and single phase multiferroics. *Journal of Physics: Condensed Matter 20*(43), 434201.

Schröder, J. (2009). Derivation of the localization and homogenization conditions for electro-mechanically coupled problems. *Computational Materials Science 46*(3), 595–599.

Schröder, J. & D. Gross (2004). Invariant formulation of the electromechanical enthalpy function of transversely isotropic piezoelectric materials. *Archive of Applied Mechanics 73*, 533–552.

Schröder, J. & M.-A. Keip (2010). A framework for the two-scale homogenization of electro-mechanically coupled boundary value problems. In M. Kuczma and K. Wilmanski (Eds.), *Computer Methods in Mechanics*, Volume 1 of *Advanced Structured Materials*, pp. 311–329. Springer, Berlin, Heidelberg.

Schröder, J. & M.-A. Keip (2011). Multiscale modeling of electro-mechanically coupled materials: homogenization procedure and computation of overall moduli. In M. Kuna and A. Ricoeur (Eds.), *IUTAM Symposium on Multiscale Modelling of Fatigue, Damage and Fracture in Smart Materials*, Volume 24 of *IUTAM Bookseries*, pp. 265–276. Springer, Netherlands.

Schröder, J. & M.-A. Keip (2012). Two-scale homogenization of electromechanically coupled boundary value problems. *Computational Mechanics 50*, 229–244.

Shi, Z., C.-W. Nan, J. Liu, D. Filippov, & M. Bichurin (2004, October). Influence of mechanical boundary conditions and microstructural features on magnetoelectric behavior in a three-phase multiferroic particulate composite. *Physical Reviews B 70*(13), 134417.

Srinivas, S. & J. Y. Li (2005, September). The effective magnetoelectric coefficients of polycrystalline multiferroic composites. *Acta Mechanica 53*(15), 4135–4142.

Srinivas, S., J. Y. Li, Y. C. Zhou, & A. K. Soh (2006, February). The effective magnetoelectroelastic moduli of matrix-based multiferroic composites. *Journal of Applied Physics 99*(4), 043905.

Srinivasan, G. (2010). Magnetoelectric composites. *Annual Review of Materials Research 40*, 1–26.

van Suchtelen, J. (1972). Product properties: a new application of composite materials. *Philips Research Reports 27*, 28–37.

Wang, Y., J. Hu, Y. Lin, & C.-W. Nan (2010). Multiferroic magnetoelectric composite nanostructures. *Nature Asia-Pacific, Asia Materials 2*, 61–68.

Research and Applications in Structural Engineering, Mechanics and Computation – Zingoni (Ed.)
© 2013 Taylor & Francis Group, London, ISBN 978-1-138-00061-2

Microstructural image-based modelling of weld failure

O. Barrera & A.C.F. Cocks
Department of Engineering Science, University of Oxford, UK

E. Tarleton
Department of Materials, University of Oxford, UK.

ABSTRACT: This paper deals with the constitutive modelling of one of the phenomena affecting welding failure: Hydrogen Embrittlement (HE). The focus of the HE model is on dissimilar weld interfaces in AISI8630/IN625. Fractography of dissimilar weld interfaces in AISI8630/IN625 shows that cracks propagate in a carbides (M_7C_3)-rich region called the "featureless" region located on the Nickel side of the weld. Our model takes into account the effect of hydrogen on the material behaviour as the result of a combined HELP (Hydrogen Enhanced Local Plasticity) and HID (Hydrogen Induced Decohesion) mechanism where: (i) hydrogen enhanced dislocation mobility promotes a reduction of the flow stress in the matrix and the development of dislocation structures at the M_7C_3 carbides which increases the stress on the particles; and (ii) the presence of hydrogen also results in a reduction in the cohesive strength of the carbide/matrix interface. Here TEM images of the carbides-rich region are converted into a finite element mesh through an image-based mesh generation scheme. Simulations of the response of these structures show that in regions where the hydrogen content is high, the cohesive strength decreases, and microcracks form at the carbide-matrix interface that lead to microvoid formation. The amount of deformation then increases in a localized region adjacent to the region where (a) hydrogen content is high and (b) the carbide/matrix interface has debonded. As deformation proceeds the pores enlarge and link to form cracks which generate the failure surface.

1 INTRODUCTION

1.1 *Hydrogen embrittlement in dissimilar weld interfaces*

Dissimilar metal butter-welded joints are commonly used by the oil and gas industries to join a range of structural components such as valves, connectors or manifolds to carbon steel pipes, as they allow a welded connection between high strength hardenable carbon forged steel or non-hardenable pipe line steel to Nickel alloy components. A series of catastrophic failures of AISI 8630 steel/IN625 Nickel alloy dissimilar-metal welds has highlighted the need for further investigations on the role of hydrogen on the fracture process of the components (Fenske 2010).

One of the outstanding issues in hydrogen cracking of welds is to link micromechanical processes to the macroscopic fracture behaviour of the system. Recent TEM and SEM studies (Fenske 2010) have revealed detailed information about the microstructure in the vicinity of the fusion boundary of 8630/625 dissimilar welds and the fracture morphologies which alternates between a flat cleavage-like morphology and a highly irregular cratered structure. Figure 1 (Kitaguchi & Lozano-Perez 2012) shows a simplification of the interface microstructure of a 8630/625 dissimilar weld, (Beaugrand et al. 2009, Dodge et al. 2012), i.e. at the interface between the steel and the buttering. Three major regions can be distinguished:

a. The heat affected zone (HAZ) in the parent steel side close to the interface consists of a fine decarburised zone. This zone is mostly ferritic.

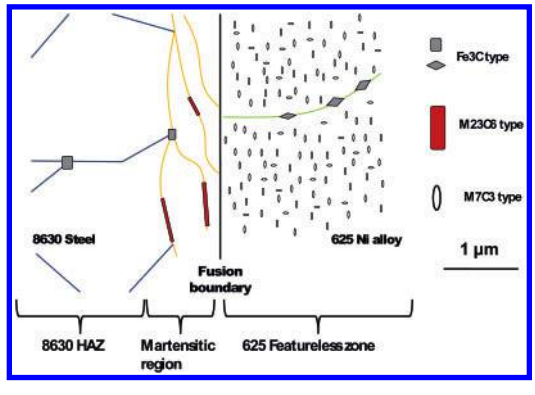


Figure 1. Schematic summary of interface microstructure 8630/625 showing the different types of precipitates that are present.

b. A martensitic iron rich region (about 1 μm wide) on the steel side close to the fusion boundary. This zone exhibits a BCT structure.
c. A FCC carbide (M_7C_3)-rich region (about 20 μm wide) in the nickel side, previously wrongly identified as a "featureless zone", that plays an important role in the macroscopic fracture behaviour of the system in a hydrogen environment. The volume fraction has been estimated to be about 15% and the dimension of the major axis of the carbides is about 40 nm as seen in Fig. 3. Fig. 2 (Dodge & Mililtitsky 2012) shows a fractured sample of an AISI8630/IN625 dissimilar weld exposed to a hydrogen rich environment. The crack path with respect to the interface structure of Fig. 1 is shown in Fig. 2, which has sections within (a) the HAZ, (b) the martensitic region and (c) the featureless zone. Despite the crack initiation location not being precisely identified (Fenske 2010, Beaugrand et al. 2009, Dodge et al. 2012) and is still subject to debate, there is general agreement that the presence of M_7C_3 carbides in the "featureless zone" provides a low energy path for crack propagation.

The fracture morphology of this region consists of terrace-cleavage or quasi cleavage features (Fig. 2). More in-depth studies of this type of fracture have revealed that the planes along which the cracks propagate are not known cleavage planes. The planes contain ridges that are almost parallel to the crack propagation path. These ridges are related to sub-surface intense and highly localized deformation bands (Martin 2011). The fracture surface appears to be generated by ductile processes, enhanced and localized to well defined slip bands by hydrogen (Martin et al. 2011). The fracture morphology within the featureless zone, which is produced only in the presence of hydrogen, is consistent with a hydrogen-induced decohesion (HID) mechanism along the M_7C_3-matrix interface succeeded by strain localization between the particles (HELP). This suggests that the effect of hydrogen on the material toughness is a result of a synergistic effect of HELP and HID mechanisms: (i) with hydrogen enhancing dislocation mobility, promoting softening and strain localization; (ii) and the combined effect of increased stress on the M_7C_3 carbides due to the enhanced plastic deformation and the effect of hydrogen on the interface cohesive properties promoting decohesion at the particle/matrix interface. In this paper we use the model developed by Barrera & Cocks (2013) in which preliminary analyses carried out on a unit cell representing the matrix/carbide system are discussed. The results showed that the HELP and HID mechanisms act synergistically. When the combined HELP+HID mechanism occurs, microcracks form at the matrix/carbide interface due to a decohesion process followed by localization of plastic flow responsible for the link-up of the micro-cracks.

Here we generate an image-based mesh of the featureless region (Figure 1) in order to explore the model presented in Barrera & Cocks (2013) when dealing with the real microstructure of the carbides-rich

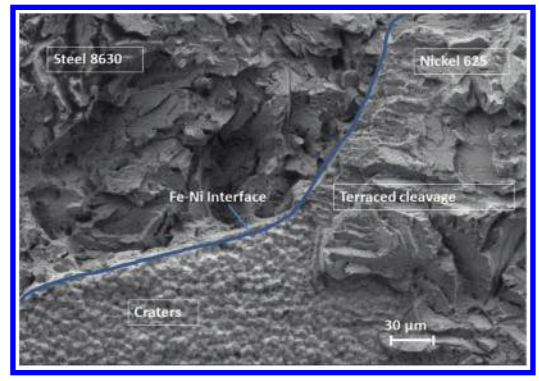


Figure 2. SEM image of fracture morphology of interface microstructure 8630/625 showing different morphologies: "Craterlike" and terraced cleavage-type.

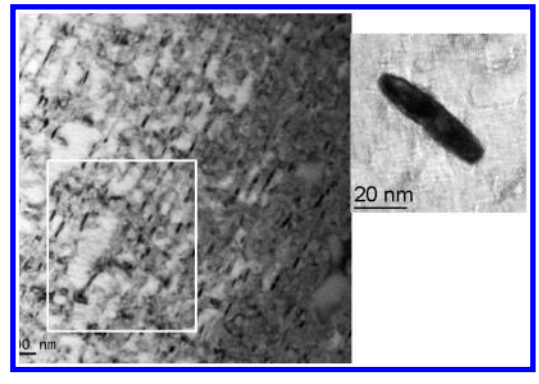


Figure 3. TEM image of the featureless zone schematically shown in Fig. 1.

region. The TEM image of the multi-carbide region in Fig. 3 is converted into a finite element mesh. A layer of cohesive elements is then assigned at the carbide/matrix interface to allow investigations of the deformation and decohesion processes (Tarleton et al. 2012).

2 CONSTITUTIVE MODELLING OF THE FEATURELESS REGION

We use the experimental observations discussed in the introduction to guide the development of models which simulate the effect of hydrogen on the material response in the carbide-rich region of Fig. 3. These observations suggest that cracks nucleate at the interface of the M_7C_3 particles in the featureless zone under the high stresses generated locally. These interfacial cracks link with each other and the main crack through localised, intense, plastic deformation. Central to the development of the model is the use of a cohesive modelling approach (CZM). Cohesive elements can be imagined as interface elements with a thickness close to zero embedded in continuum elements. Fracture

occurs at the interface between the CZM and continuum elements. One of the key properties of CZM is the definition of the traction-separation (T-δ) law. In this paper a cohesive element formulation is proposed in which the T-δ law is a function of hydrogen content and the plastic deformation of the surrounding material. We assume a single bilinear relationship in which the traction increases linearly to a peak value σ_c and then decreases to zero at an opening δ_c. We assume that the initial stiffness and critical displacement δ_c are not influenced by the hydrogen, but the cohesive strength depends on both the hydrogen content and the local accumulated plastic strain; i.e.

$$\sigma_c = \sigma_c^0 \Phi(c) - \alpha \mu_m f_p^{1/2} \epsilon^p \tag{1}$$

where σ_0^c is the cohesive strength in the absence of hydrogen and $\Phi(c)$ is a function of the hydrogen concentration, c. Here we assume a simple linear relationship for $\Phi(c)$: $\Phi(c) = (\xi - 1)c + 1$ where $\xi < 1$ is a softening parameter. The second term in eq. 1 arises from consideration of the short range stress generated on a particle from prismatic dislocation loops punched out from the particle to accommodate the inelastic strain, where α is a constant, μ_m is the shear modulus of the matrix, f_p is the volume fraction of the carbides and ϵ^p the effective plastic strain. This model has been implemented as a user element (UEL) in the commercial finite element code Abaqus (Barrera & Cocks 2013). Following Liang & Sofronis (2003) we also assume that the constitutive response of the matrix is a function of the hydrogen content. We assume an isotropic model in which the yield strength σ_Y is given by:

$$\sigma_Y = \sigma_0^H \left(1 + \frac{\epsilon^p}{\epsilon^0}\right)^{\frac{1}{n}} \tag{2}$$

where $\sigma_0^H = \Psi(c)\sigma_0$ is the initial yield strength in the presence of hydrogen that decreases with increasing hydrogen concentration. $\Psi(c)$ is a monotonically decreasing function of hydrogen concentration. ϵ^0 is the initial yield strain in the absence of hydrogen, ϵ^p is the plastic strain and n is the hardening exponent which is considered not to be affected by hydrogen. For simplicity, we will ignore swelling due to introduction of hydrogen into a material. Eq. 2 has been implemented as a UMAT user routine in Abaqus (Barrera & Cocks 2013).

3 IMAGE-BASED MESH GENERATION OF THE FEATURELESS REGION

Here the aim of the work is to model the multi-carbide "featureless" region in Fig. 3 by using an image-based approach. Tarleton et al. (2012) developed and implemented an algorithm capable of converting a binary image of the microstructure into a finite element mesh. The algorithm is currently capable of generating a 2D mesh. Let us consider an image of a single ellipsoidal carbide surrounded by matrix material as shown in the higher magnification of Fig. 3; the image is reconstructed in such a way that the particle is identified by a polygon. Salient pixels forming the polygon vertices need to be identified first and pixel connectivity is then used in order to reproduce each polygon as seen in Fig. 4. The geometry is then used to generate a finite element mesh in Fig. 5 by using the Abaqus python scripting interface. A layer of cohesive elements is then assigned at the carbide/matrix interface (Fig. 6) in order to study in detail the micromechanical processes associated with hydrogen embrittlement within the featureless region. In Fig. 7 we show the RVE highlighted in Fig. 3. Fig. 8 shows the FEM mesh of this RVE which contains 113 carbides. Fig. 9 shows a higher magnification of the lower left corner of Fig. 8. The mesh consists of 46,300 plain strain elements (CPE4) and 2,900 cohesive-user defined elements. The carbides shown in black are modelled as linear elastic with a Young's modulus of 400 GPa and Poisson's ratio of 0.3. The matrix is represented by blue elements in Fig. 8. The constitutive response is

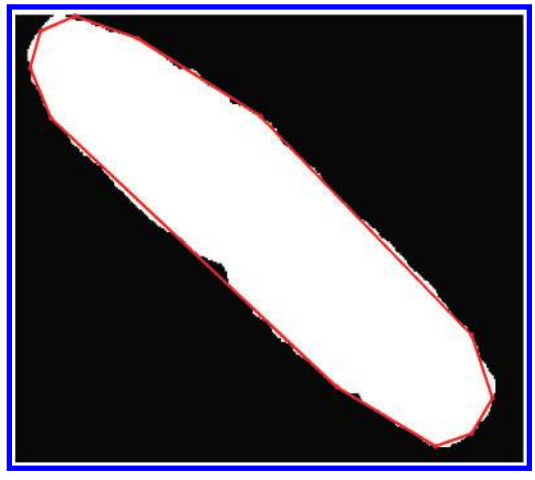


Figure 4. TEM image after processing and polygon representing the geometry of the carbide in Fig. 3.

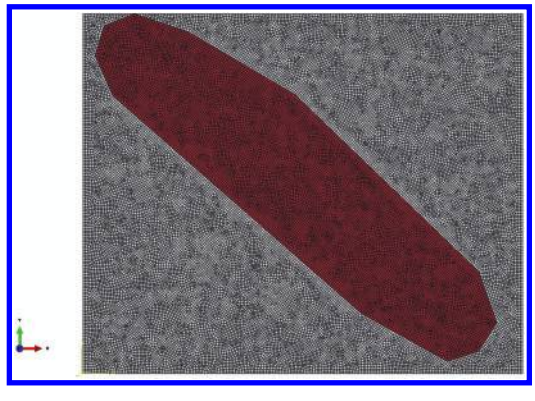


Figure 5. Finite element mesh of the single carbide of Fig. 3.

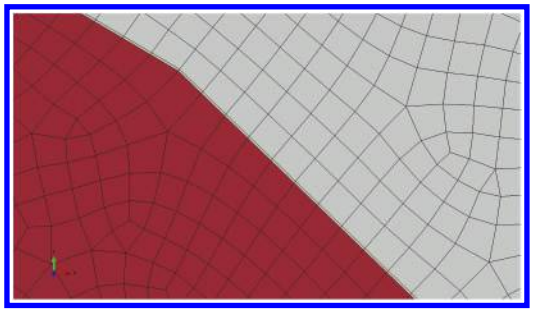


Figure 6. An higher magnification of Fig. 5 showing a layer of cohesive elements at the carbide/matrix interface.

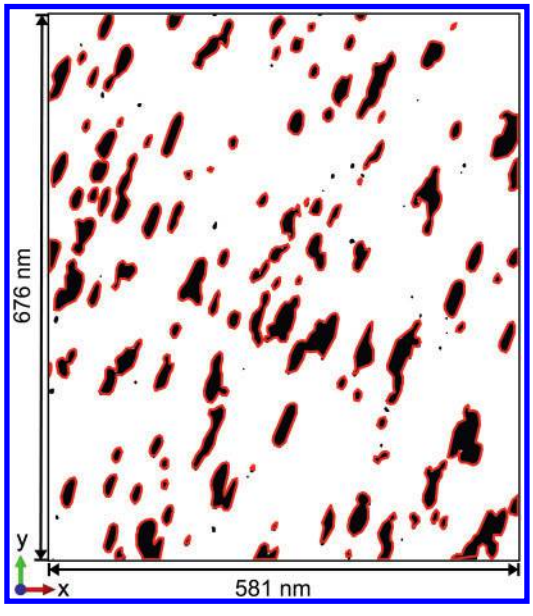


Figure 7. Representative volume element (RVE) of the "featureless" region in Fig. 3. The binary TEM image with carbides shown in black can be approximated by a set of polygons shown in red.

described in eq. 2, the initial yield strength (in the absence of hydrogen) σ_c^0 is 200 MPa, which reduces to 40 MPa at the maximum hydrogen content. Young's modulus is equal to 200 GPa and the hardening exponent $n = 10$. The cohesive user elements are shown in their damaged shape in Fig. 8. These elements are assigned at the carbide/matrix interface to simulate the evolution of the decohesion phenomenon occurring during the deformation process. The damage variable d is also shown in Fig. 8. Damage $d = 0$ corresponds to an undamaged interface, i.e. the carbide has not de-bonded from the matrix, $d = 1$ represents complete failure of the interface i.e. carbides are effectively substituted by pores (white spaces in Fig. 8). The cohesive law parameters are: stiffness $K = 200$ MPa/nm, failure displacement $\delta_c = 2$ nm. The cohesive strength of the UEL in the absence of hydrogen σ_0^c is equal

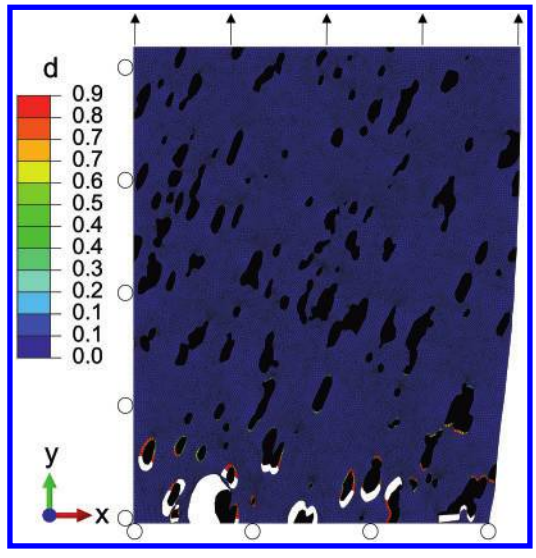


Figure 8. Finite element mesh of the RVE of Fig. 7. The figure shows the deformed mesh at the macroscopic uniaxial strain $\epsilon = 1.4$. The coloured contours give the extent of damage development, d at the carbide/matrix interface. Some cohesive elements have failed with local plastic deformation resulting in separation of the matrix from the carbides creating the white regions in the figure. The deformation is scaled by a factor of 4 for clarity.

to 200 MPa. σ_c (eq. 1) will decrease with increasing hydrogen content and due to the fact that hydrogen enhanced dislocation mobility promotes the development of dislocation structures at the M_7C_3 carbides which increases the stress on the particles; the FE analysis does not give this contribution to the local stress. We take this into account by reducing the apparent macroscopic cohesive strength. This is described by eq. 1 (Barrera & Cocks 2013).

4 DISCUSSION

The aim of the paper is to investigate the role of the hydrogen in the micromechanical failure process occurring in the "featureless zone" of the dissimilar weld interface in AISI8630/IN625. As discussed in Sec. 1 the "featureless" region shown in Fig. 3 plays a major role in the fracture behaviour of this type of interface. The reason is the presence of a fine distribution of high atomic number M_7C_3 carbides. The volume fraction has been estimated to be 12%. The carbides show an ellipsoidal shape and the dimension of the major axis varies from 20 nm–40 nm as seen in Fig. 3. The RVE in Fig. 8 is subjected to displacement boundary conditions such that the macroscopic uniaxial strain is increased at a constant rate up to 1.4%. We apply a gradient of hydrogen content $c = 1 - \frac{y}{L}$. We assume that the hydrogen in the normal interstitial sites (i.e. matrix) is in equilibrium with the hydrogen at the carbide/matrix interface. In the area where the

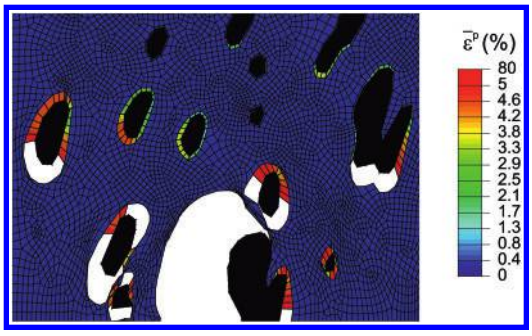


Figure 9. Higher magnification of the lower left corner of Fig. 8.

hydrogen is highly localized (i.e. lower part of Fig. 8) (i) the cohesive strength of the interface is also reduced as summarized in Eq. 1 and (ii) the material softens as consequence of Eq. 2. Therefore there are two phenomena occurring:

(i) The presence of the hydrogen facilitates the decohesion process (HID). In those regions where the carbide-matrix interface is weak, the debonding mechanism of the carbides from the matrix is shown in Fig. 8. Effectively, as a result of the deformation process due to the loading conditions and the hydrogen content, the carbides decohere from the matrix forming pores (if complete decohesion occurs d = 1) or the interface becomes damaged (i.e. partial decohesion $0 < d < 1$). The larger carbides tend to fail completely becoming pores and the smaller carbides experience partial debonding.

(ii) The presence of hydrogen enhances localization of plastic flow (HELP) in those areas where (a) the hydrogen concentration is high (i.e. material softens) and (b) the carbide-matrix interface has debonded. Fig. 10 shows the distribution of the equivalent plastic strain at the end of the deformation process. Softening occurs in the area where high concentration of hydrogen is present (i.e. lower part of Fig. 9). A macroscopically ductile process is also confirmed by the necking region in Fig. 9. As the material deforms, small microvoids (of the size of the carbides or less) form. As the deformation process proceeds the pores enlarge and link to form a crack. Cracks then link up due the highly localized plastic flow. At this point the fracture process can be very fast and can generate a fracture surface that might appear brittle, i.e. reasonably flat with the detailed cavitation process not evident on micrograph at the scale of that shown in Fig. 2, and plastic flow confined to a thin localized band which can occasionally terminate creating wisps on the failure surface. This phenomenon could explain the presence of the "terraced cleavage like" fracture surface of Fig. 2 which show evidence of wisps on the surface.

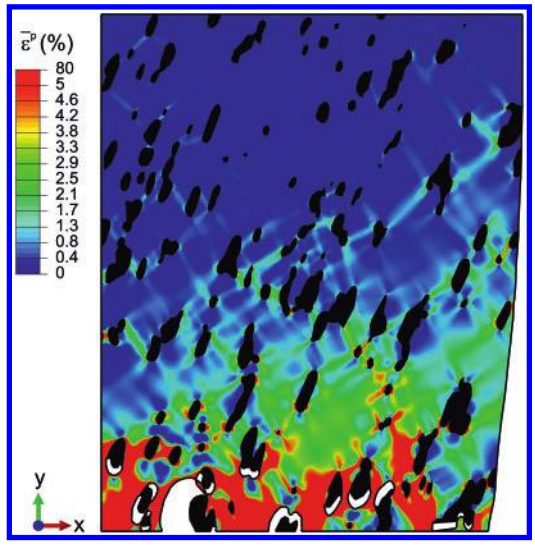


Figure 10. Equivalent plastic strain evolution of RVE in Fig. 8.

5 CONCLUSIONS

A model of the failure process of a dissimilar AISI8630/IN625 weld has been proposed. The model developed here is based on a classical continuum mechanics formalism. The scale of the particles is such, however, that the interaction of the particles with discrete dislocations and the dislocation structures generated around the particles must be taken into account in determining the constitutive response of the matrix and interface region. The work presented in this paper is based on experimental observations of the microstructure and fracture morphology that reveal that cracks nucleate at the interface of the M_7C_3 particles in the "featureless zone" under the high stresses generated ahead of a crack tip succeeded by strain localization between the particles linking these interfacial cracks with each other. The combined effect of hydrogen on the material toughness is a result of a synergistic effect of HELP and HID mechanisms: (i) with hydrogen enhancing dislocation mobility, promoting softening and strain localization; (ii) and the combined effect of increased stress on the M_7C_3 carbides due to the enhanced plastic deformation and the effect of hydrogen on the interface cohesive properties promoting decohesion at the particle/matrix interface. We simulate (1) the failure process at the interface of the M_7C_3 particles and the matrix by use of a cohesive modelling approach (CZM) whose T-δ law is a function of hydrogen content and the plastic deformation of the surrounding material. We also assume (2) that the constitutive response of the material is a function of the hydrogen content. (1) and (2) have been implemented in UEL and UMAT subroutines in Abaqus. The results show that in regions where the hydrogen content is high, the cohesive strength decreases and

microcracks occur that might lead to microvoid formation. The amount of deformation then increases in a localized region adjacent to the region where (a) the hydrogen content is high and (b) the carbide/matrix interface has debonded. As deformation proceeds the pores enlarge and link to form cracks and the intense localized plastic flow links-up the cracks and microcracks formed at adjacent carbides. The failure surface then consists of planes of intense plastic deformation, connected by small regions of decohesion around the particles, which is consistent with the morphology of failure surfaces (Fig. 2) generated as the result of crack growth through the featureless zone.

ACKNOWLEDGEMENTS

This research is supported by the Seventh Framework Programme (European Commission), Mintweld project: reference number 229108.

REFERENCES

Barrera O., Cocks A.C.F. (2013). Computational modelling of hydrogen embrittlement in welded structures. *Phil Mag*, to appear.

Beaugrand V.C.M., Smith S.L., Gittos M.F. (2009). Hydrogen embrittlement of 8630M/625 subsea dissimilar joints: factors that influence the performance. *Proceedings of the 28th International Conference on Ocean, Offshore and Arctic Engineering OMAE2009 Honolulu, Hawaii, USA*.

Dodge M.F. & Milititsky M. (2012). Private communications.

Dodge M.F., Dong H.B., Milititsky M., Barnett R.P., Marques V.F., Gittos M.F. (2012). Environment-induced cracking in weld joints in subsea oil and gas systems – PART I. *Proceedings of the 31st International Conference on Ocean, Offshore and Arctic Engineering OMAE2012 Rio de Janeiro, Brazil*.

Fenske, J.A. (2010). Microstructure and hydrogen induced mechanism in iron-nickel weldments. *PhD thesis: University of Illinois at Urbana-Champaign*.

Kitaguchi H. & Lozano-Perez S. (2012). Private communications.

Liang Y. and Sofronis P. (2003). Toward a Phenomenological Description of Hydrogen-Induced Decohesion at Particle/Matrix Interfaces. *Journal of Mechanics and Physics of Solids*, 51, 1509–1531.

Martin M.L. (2011). On the formation and nature of quasi-cleavage fracture surfaces in hydrogen embrittled steels. *Acta Materialia*, 59, p. 1601.

Martin M.L., Robertson I.M., Sofronis P. (2011). Interpreting hydrogen-induced fracture surface in terms of deformation processes: A new approach. Acta Materialia 59, p. 3680.

Tarleton E., Charalambides M.N, Leppard C. (2012). Image-based modelling of binary composites. *Computational material science*, 64, 183–186.

Research and Applications in Structural Engineering, Mechanics and Computation – Zingoni (Ed.)
© 2013 Taylor & Francis Group, London, ISBN 978-1-138-00061-2

Flame straightening application on structural steels: Effects on mechanical and fracture properties

R. Lacalle, J.A. Álvarez, D. Ferreño, J. Portilla, E. Ruiz, B. Arroyo & F. Gutiérrez-Solana
University of Cantabria, Santander, Spain

ABSTRACT: In this paper, the influence of the flame bending procedure on the microstructure of three very different structural steels (S235 JR, S460 ML and S690 QL, respectively), widely used for the construction of metallic structures, is analysed. The consequences of the heat treatment on the mechanical and fracture properties were characterised through tensile, micro-hardness Vickers and Charpy impact tests; in addition, some elastic-plastic fracture tests were performed on precracked Charpy specimens manufactured with the S235 JR steel. The relationship between the microstructural features and the material mechanical and fracture behaviour was studied in depth in all cases. For a proper understanding of the microstructural consequences of this straightening heat treatment, it was necessary to develop a Finite Element numerical model.

1 INTRODUCTION

The flame straightening (or flame bending) technique is widely used for the control of geometric distortions or tolerance deviations in steel parts caused by the manufacturing or welding processes; it is also used to repair damaged elements; nevertheless, many aspects of the process remain as uncertainties: the question of the effects induced by the heating process on the microstructure and, as a consequence, on the mechanical and fracture properties is currently an important open issue (Avent 1989, 1992, 1995, 1998, 2000). The present contribution analyses the influence of the flame bending procedure on the material properties of three very different structural steels (S235 JR, S460 ML and S690 QL, respectively), widely used for the construction of metallic structures for buildings or bridges. First, the microstructural and metallurgical changes induced by the flame heating were studied; then, the mechanical properties were assessed. Finally, the influence of the bending process on the fracture properties was determined.

2 OBJECTIVES OF THE RESEARCH

To the knowledge of the authors of the present paper, little research has specifically addressed the influence of the flame bending technique on the microstructure and mechanical or fracture properties of steels. For these reasons, the experimental scope of the present contribution was designed with the purpose of analysing the influence of the heat straightening process on three very different structural steels: S235 JR, SA460 ML and S690 QL. In order to fully understand the microstructural changes that take place in the material as a consequence of the surface heating caused by the flame, a Finite Elements (FE) numerical model was developed. Only through a numerical technique is it possible to take into account the many factors participating in the process (material properties, heat flux of the flame, trajectory and speed of the torch, location of the material point to be analysed, etc.).

3 MATERIALS

The three following structural steel grades (EN 10025 2004) were studied in this research: S235 JR, S460 ML and S690 QL. The microstructure of S235 JR and S460 ML consists of ferrite and perlite whereas S690 QL steel shows a microstructure of bainite and tempered bainite. The specified chemical compositions of the steels (EN 10025 2004) are included in Table 1. For the microstructural analysis of the consequences induced by the flame heat treatment, the material specific Fe-C phase diagram should be considered. For this reason, it is necessary to take into consideration the changes induced by the alloying elements (Baik 1961) of the three materials analysed on the basic Fe-C diagram.

Table 1. Specified chemical composition (% wt.) of the steels analysed in the research (EN 10025 2004).

Grade	C	Mn	Si	Ni	S	Cr	P
S235JR	≤0.17	≤1.40	–	–	≤0.035	–	≤0.035
S460ML	≤0.16	≤1.70	≤0.6	≤0.8	≤0.02	≤0.3	≤0.025
S460ML	≤0.2	≤1.70	≤0.80	≤2.0	≤0.010	≤1.5	≤0.20

4 EXPERIMENTAL RESULTS

4.1 *Chemical composition*

The chemical compositions of the three steels studied are given in Table 2. The comparison between these results and the limits of the material specification (Table 1) shows that the chemistry satisfies in all cases what is established there.

4.2 *Microstructure*

S235 JR steel: In Figure 1, two micrographs showing the microstructure of the non-heated S235 JR steel at two different depths in the plate (0.5 and 10 mm, respectively) can be appreciated. In Figure 2, two micrographs (with different magnification), taken from a depth of 0.5 mm, show the microstructure of the heated S235 JR steel. Two relevant microstructural effects were detected: first, Figure 2(a), the grain has experienced a noticeable refinement: (from $20 \pm 4\,\mu m$ to $14 \pm 4\,\mu m$). Second, tertiary cementite precipitates are appreciated in some grain boundaries, see Figure 2(b).

S460 ML steel: In Figure 4, two micrographs taken from a depth of 0.5 mm, show the microstructure of the non-heated S460 ML steel. A combination of proeutectoid ferrite (white) and perlite (black) can be clearly seen, In this case, the elongated non-symmetrical disposition of grains created by the rolling process is evident even in this near-to-surface micrograph. Concerning the microstructure of the flame treated S460 ML steel, a micrograph obtained at a depth of about 0.5 mm is shown in Figure 4. The alteration of the morphology of the grains is highlighted in this image; moreover, larger non uniformity is present in the grain size distribution. These features are a consequence of the recrystallization induced by the flame heating process.

S690 QL steel: The microstructure of the non-heated S690 QL steel can be seen in Figure 5 (this micrograph was taken at a depth of 15 mm). A combination of bainite and ferrite constitutes the microstructure of this material, in accordance with what is expected (see above). Although the maximum temperature reached during the heating in this case is only 688°C, the material has undergone a second tempering, superimposed on the original one, (Fig. 6a). No

Table 2. Chemical composition of the S235 JR, S460 ML and S690 QL steels (% wt.).

Grade	C	Mn	Si	Ni	S	Cr	P
S235 JR	0.13	0.72	0.20	<0.085	0.016	0.02	0.016
S460 ML	0.12	1.57	0.45	<0.085	<0.012	0.04	0.014
S690 QL	0.18	1.23	0.29	<0.085	<0.010	0.02	<0.012

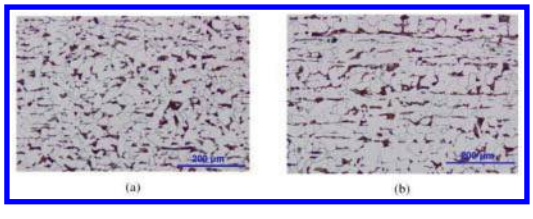


Figure 1. Micrographs showing the microstructure of the non-heated S235 JR steel at two different depths in the plate: (a) 0.5 mm, (b) 10 mm.

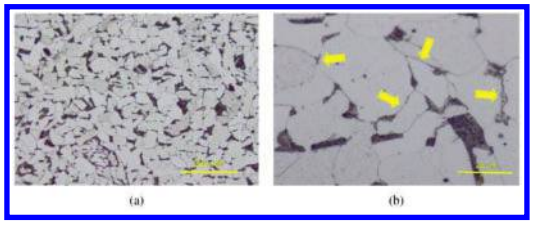


Figure 2. Micrographs showing the microstructure of the heated S235 JR steel (approximate depth of 0.5 mm).

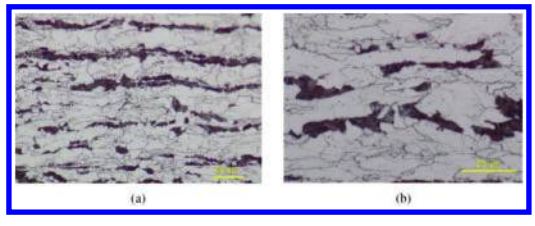


Figure 3. Micrographs showing the microstructure of the non-heated S460 ML steel at an approximate depth of 0.5 mm.

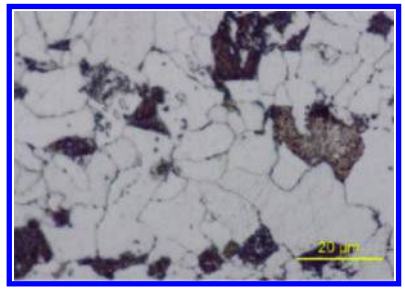


Figure 4. Micrograph showing the microstructure of the heated S460 ML steel at an approximate depth of 0.5 mm.

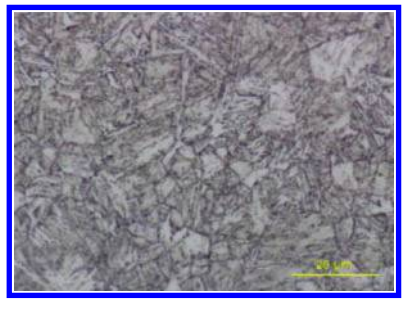


Figure 5. Micrograph showing the microstructure of the non-heated S690 QL steel at an approximate depth of 15 mm.

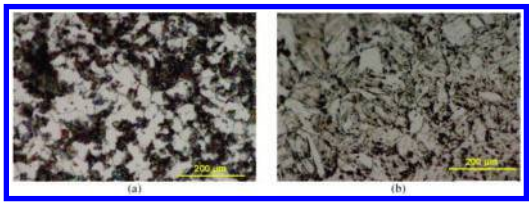


Figure 6. Micrographs showing the microstructure of the heated S690 QL steel at an approximate depth of: (a) 0.5 mm, (b) 5 mm.

Table 3. Summary of the results of the Vickers hardness tests.

Material	As received	After heating	Variation (%)
S235 JR	147 ± 6	147 ± 11	0
S460 ML	198 ± 4	172 ± 11	−13
S690 QL	291 ± 7	215 ± 21	−26

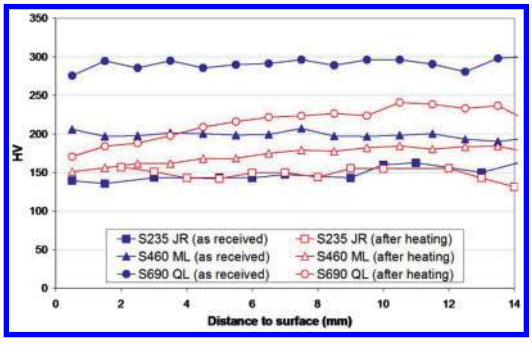


Figure 7. Results of the Vickers tests performed through the thickness of the plates, prior to and after heating, for each steel grade.

modification in the grain size or shape is appreciated, which is consistent with the fact that the maximum temperature is below T_{Ac1}.

4.3 *Mechanical characterisation*

Vickers hardness tests: The tests were performed across the thickness of the specimen below the surface heated by the flame. The average results of these tests are summarized in Table 3 and graphically represented in Figure 7. 235 JR did not undergo any substantial change in hardness; on the other hand, both S460 ML and S690 QL steels became softer as a consequence of the heat treatment experienced. On average, the Vickers hardness decrease in these materials is up to 13% and 26%, respectively.

Tensile tests: One non-heated specimen plus one heated specimen were obtained for each material (ASTM E8 2005). The tests were performed at room temperature (~20°C). The load vs. elongation curves were recorded up to fracture; from them, the stress

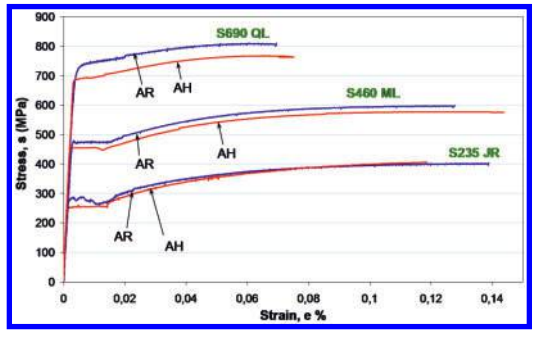


Figure 8. Stress vs. strain curves (as received and flame heated condition).

Table 4. Relevant results obtained from the Charpy characterization.

Material	Property	As received	After heating	Variation (%)
S235 JR	$S_{Y\ (0.2\%)}$ (MPa)	284	247	−13.0
	S_U (MPa)	402	410	2.0
	e_U (%)	13.8	11.8	−14.5
S460 ML	$S_{Y\ (0.2\%)}$ (MPa)	469	455	−3.0
	S_U (MPa)	597	576	−3.5
	e_U (%)	12.7	14.4	13.4
S690 QL	$S_{Y\ (0.2\%)}$ (MPa)	732	688	−6.0
	S_U (MPa)	809	767	−5.2
	e_U (%)	6.9	7.5	8.7

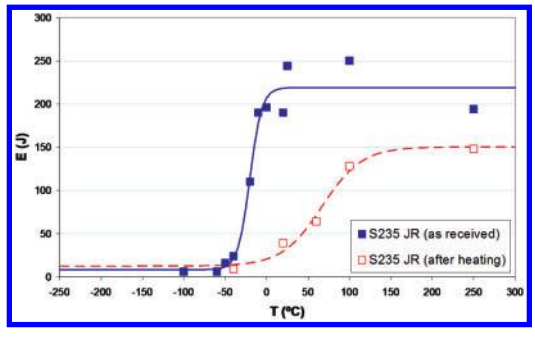


Figure 9. CVN curves (energy vs. temperature) for S235 JR steel (as received and after heating condition).

vs. strain (engineering variables) curves, represented in Figure 8, were calculated; the main mechanical parameters (Table 4). The curves clearly show that the influence of the flame heating on the mechanical response is strongly material dependent: following the same tendencies that were appreciated in the previous section, the flame treatment hardly modifies the properties of S235 JR steel, whereas the change in the other materials varies from moderate (S460 ML) to noticeable (S690 QL).

Fracture characterisation: The experimental results, expressed in terms of the absorbed energy vs. test temperature (ASTM E23 2005), are included in Figure 9

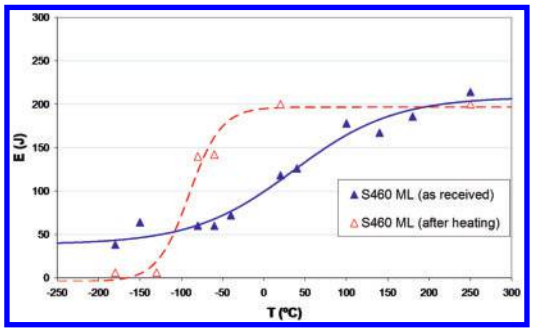


Figure 10. CVN curves (energy vs. temperature) for S460 ML steel (as received and after heating condition).

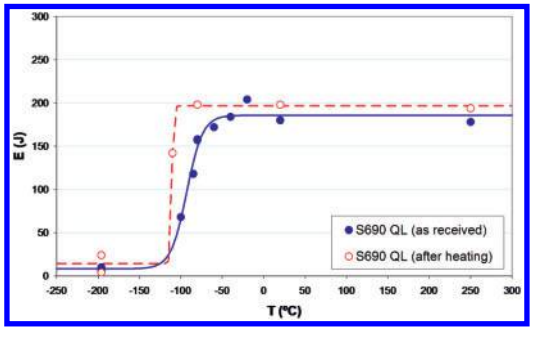


Figure 11. CVN curves (energy vs. temperature) for S690 QL steel (as received and after heating condition).

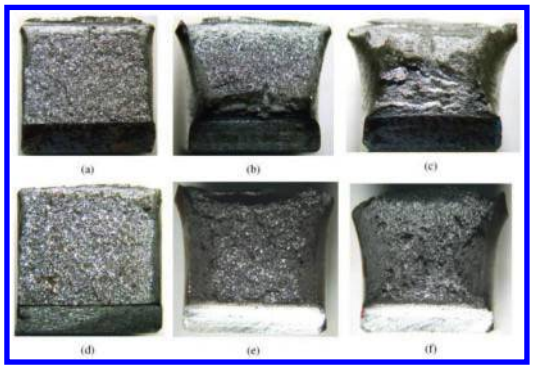


Figure 12. Macrographs showing the fracture surfaces of the S235 JR CVN specimens. As received condition: (a) −50°C, (b) 20°C, (c) 250°C. Flame heated condition: (d) −40°C, (e) 60°C, (f) 100°C.

(S235 JR), Figure 10 (S460 ML) and Figure 11 (S690 QL). To facilitate the subsequent analysis, the CVN curves were fitted to a hyperbolic tangent curve.

The curves included in Figures 9 to 11 clearly show that the influence of the flame heating on the fracture response is, again, strongly material dependent. The S235 JR steel has undergone a marked embrittlement as a consequence of the flame heating. The influence of

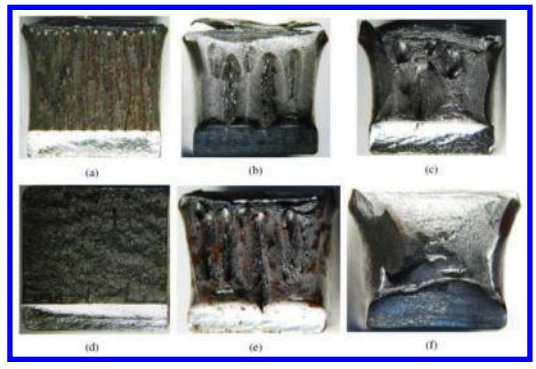


Figure 13. Macrographs showing the fracture surfaces of the S460 ML CVN specimens. As received condition: (a) −150°C, (b) 40°C, (c) 140°C. Flame heated condition: (d) −135°C, (e) −60°C, (f) 250°C.

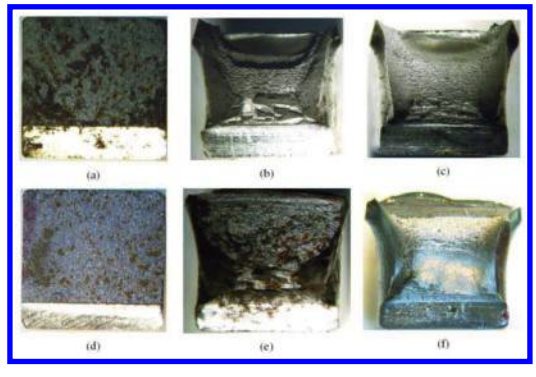


Figure 14. Macrographs showing the fracture surfaces of the S690 QL CVN specimens. As received condition: (a) −196°C, (b) −60°C, (c) 20°C. Flame heated condition: (d) −196°C, (e) −110°C, (f) 250°C.

the flame on the S460 ML steel is certainly more complex (Fig. 10) as a complete modification in the shape of the curve occurred. Finally, the fracture behaviour of the S690 QL grade hardly modified as a consequence of the flame heating process (Fig. 11). Some representative macrographs of the fracture surfaces can be appreciated in Figure 12 (S235 JR), Figure 13 (S460 ML) and Figure 14 (S690QL).

Extended characterisation of the S235 JR steel: The S235 JR steel has undergone a noticeable embrittlement as a consequence of the flame heating. To analyse this feature, the J-integral as an energy release rate (Anderson 1995, Kanninen 1985) has been used in this research (ASTM E1820 2005). In this sense, two S235JR CVN specimens (one in the as-received condition and the other in the flame treated condition) were precracked through fatigue (to induce the presence of an initial sharp crack, a_0) and subsequently tested at room temperature in three-point bending; the fracture resistance curves, which are represented in Figure 15, were obtained. The curves highlight the significant difference in fracture response between the original and the heat treated S235 JR material.

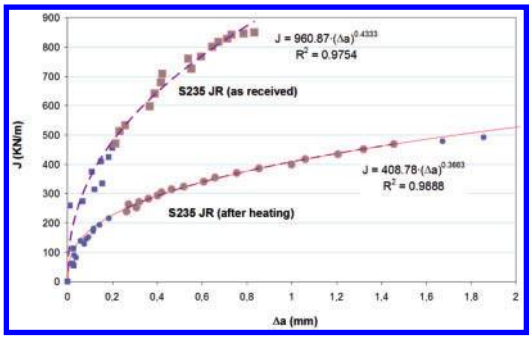


Figure 15. Fracture resistance curves (J-integral vs. crack extension, Δa) obtained for the S235 JR steel comparing the as received response with the flame treated behaviour.

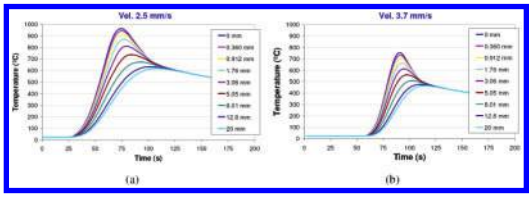


Figure 16. Finite Elements temperature vs. time curves as a function of the depth in the plate. (a) 2.5 mm/s (S235 JR and S460 ML steels); (b) 3.7 mm/s (S690 QL steel).

5 ANALYSIS AND DISCUSSION OF EXPERIMENTAL RESULTS

5.1 *S235 JR steel*

As shown by the Finite Element results (ANSYS 2011), Figure 16 (a), this material remains at a temperature higher than ~750°C ($T_{AC1} = 714$°C; $T_{AC3} = 846$°C) for at least 10 seconds in the 3 mm band closest to the surface. This process, which may be considered as an "intercritical annealing", causes the partial dissolution of pearlite which, in turn, as a result of the subsequent cooling, may lose its laminar (banded) structure (Fig. 2a) previously appreciated in the original microstructure (Fig. 1a). A second appreciable aspect is caused by the high temperature reached, exceeding $T_{AC3} = 846$°C, by the material in the 2 mm band nearest the surface. This process results in the transformation of the existing phases in austenite, this phenomenon being known as a "full annealing". A third point to notice here is the formation of "tertiary cementite" as a result of the cooling conditions to which the material is subjected. As shown by the FE model, see Fig. 16(a), the cooling rate below 600°C is very slow at any depth, thus enabling the formation of such a microstructure; indeed, the time for the temperature to decrease from 600°C to 400°C is substantially longer than 100s. This feature is shown in Figure 2b.

5.2 *S460 ML steel*

As demonstrated above, this steel shows a strongly deformed microstructure because of the rolling process, Fig. 3(a). The consequences of the heating experienced by the steel depend on the temperature reached. As the upper surface band of the plate exceeded the temperature $T_{Ac1} = 704$°C, the material was subjected to an intercritical or full annealing treatment, depending on whether the steel reached the temperature $T_{Ac3} = 859$°C. These two treatments lead to the formation of austenite as well as the recrystallization of ferrite, Figure 4.

The profile of Vickers tests in Figure 7 shows that there is no noticeable change in hardness with the depth in the as-received condition. The heated material, in turn, shows a tendency to a softer behaviour in the proximity of the surface; this can be explained as a consequence of the recrystallization induced by the flame heating process which is particularly intense on the surface of the plate. The consequences of the recrystallization also become evident when comparing the tensile response of the material in the as-received condition and after heating. These features are reflected in the fracture response of the material, as can be seen in Figure 10, when an improvement in fracture toughness is evident in the treated material as compared with the original condition.

5.3 *S690 QL steel*

As indicated above, the speed of the torch in this case was significantly higher than the other steels. This fact results in a lower maximum temperature and different cooling patterns. The analysis represented in Figure 16(b) states that, as no point in the plate has reached the temperature T_{AC1}, this martensitic-bainitic material was subjected to a tempering heat treatment.

Figure 7 shows that this material has undergone an intense change in hardness due to the flame heating. This has its corresponding counterpart in the tensile characterisation. This behaviour is perfectly reasonable in view of the second tempering detected in the microstructural investigation. Nevertheless, the fracture response is only slightly affected by the changes in microstructure.

6 CONCLUSIONS

As can be appreciated, the influence of the flame straightening procedure on the microstructure, mechanical or fracture behaviour clearly depends on the nature of the steel receiving this sort of heat treatment. These results provide clear evidence that it is not possible to determine a priori the consequences of the heat straightening on a specific steel; rather, they must be experimentally obtained on a case by case basis. Regardless of this, the experimental results reported in this study allow different families of steels to be distinguished and, from this, the following set of general recommendations to be stated: In general, when

the critical (T_{Ac3})/intercritical (between T_{Ac1} and T_{Ac3}) temperature is reached, the subsequent cooling rate must be controlled to avoid the formation of martensite. In addition, in order to prevent the formation of tertiary cementite in low carbon ferritic-pearlitic steels, low cooling rates below 650°C must be avoided.

The conventional treatises recommend not exceeding the critical temperature of dissolution of pearlite to avoid the possible harmful consequences of the flame straightening treatment. The literature, however, makes no reference to the particular characteristics of the material or heat treatment such as cooling rate. This work has revealed the importance of these and other aspects and how, in some cases, the general recommendations lead to undesirable results.

REFERENCES

Anderson, T.L. 1995. *Fracture Mechanics, Fundamentals and Applications*, second ed., CRC Press.

ANSYS user's manual. 2011. Release 14.

ASTM E8-04. 2005. Standard Test Methods for Tension Testing of Metallic Materials. In: *Annual Book of ASTM Standards*, vol 03.01. ASTM, Philadelphia.

ASTM E23-01. 2005. Standard test methods for notched bar impact testing of metallic materials. In: *Annual Book of ASTM Standards*, vol. 03.02 [section 3]. ASTM, Philadelphia.

ASTM E1820-01. 2005. Standard Test Method for Measurement of Fracture Toughness. In: *Annual Book of ASTM Standards*, vol. 03.02 [section 3]. ASTM, Philadelphia.

Avent, R.R. 1989. Heat-Straightening of Steel: Fact and Fable. J. Structural Eng. 115 (11): 2773–2793.

Avent, R.R. 1992. Designing Heat Straightening Repairs, *Proc. Nat. Steel Constr Conf*, American Institute for Steel Construction (AISC).

Avent, R.R. 1995. Engineered heat straightening comes of age. *Mod Steel Constr* 35 (2): 32–39.

Avent, R.R, Mukai, DJ & Robinson, PF. 1998. Heat-Straightening Repairs of Damaged Steel Bridges, A Technical Guide and Manual of Practice. Report No FHWA-IF-99-004, Federal Highway Administration, USA.

Avent, R.R. & Mukai, D.J. 2000. Heat-Straightening Rolled Shapes, A Technical Guide and Manual of Practice. *J Structural Eng* 126 (7): 755–763.

Bain, E. C., & Paxton, H. W. 1961. Alloying Elements in Steel, *American Society for Metals*.

EN 10025. 2004. *European structural steel standard EN 10025: 2004.*

Kanninen, M.F. & Popelar, C.H. 1985. *Advanced Fracture Mechanics*, Oxford University Press.

Research and Applications in Structural Engineering, Mechanics and Computation – Zingoni (Ed.)
© 2013 Taylor & Francis Group, London, ISBN 978-1-138-00061-2

Statistically similar RVE construction based on 3D dual-phase steel microstructures

L. Scheunemann, D. Balzani, D. Brands & J. Schröder
Institute of Mechanics, Faculty of Engineering, University Duisburg-Essen, Essen, Germany

D. Raabe
Department of Microstructure Physics and Alloy Design,
Max-Planck-Institut für Eisenforschung GmbH, Düsseldorf, Germany

ABSTRACT: This contribution presents a method to construct three-dimensional Statistically Similar RVEs (SSRVEs) for the simulation of the mechanical response of dual-phase steel (DP steel). DP steels have enhanced material properties such as high ductility and high strength compared to conventional steels. Since these properties originate in the microstructure of the material, it should be incorporated in the numerical calculations in order to account for these microstructural effects. This can be accomplished by using the FE^2 – method, however for an efficient computation SSRVEs with a reduced complexity compared to the real microstructure have to be defined. These SSRVEs still represent the mechanical response of the material accurately. The method for the construction of SSRVEs is based on a least-square functional considering suitable statistical measures describing the inclusion morphology of the real microstructure. In numerical examples, the mechanical response of the SSRVE is compared to the response of the real microstructure.

1 INTRODUCTION

Advanced high strength steels enable engineering applications where both, high strength and high damage tolerance are required such as encountered in the fields of mobility, manufacturing and safety. One specific type of such materials is dual phase steel. Here, the improved material properties originate from the interaction of the individual constituents in the microstructure, which is composed of a soft ferrite matrix with hard martensite inclusions, cf. N. Peranio and Raabe (2010). Thus, the direct incorporation of the microstructure into the model is desirable, which can be achieved using direct micro-macro approaches, such as the FE^2 method, see e.g. C. Miehe (1999), W. Brekelmans (1998), Schröder (2000). In the context of this method, a microscopic boundary value problem is solved at each evaluation point of the macroscopic boundary value problem, with a RVE reflecting the real microstructure on the microscale. These require commonly very complex discretizations if a RVE is chosen as a direct representation of a real material microstructure due to the complex morphology of the microstructure itself. A way to obtain more efficient calculations using this scheme is the application of Statistically Similar RVEs (SSRVEs), see Balzani et al. (2010), J. Schröder (2011), which have a lower complexity than the aforementioned RVEs taken directly from real microstructures but which still represent the mechanical response of the material accurately. The construction of the SSRVEs is based on the assumption that selected statistical measures describing the microstructure morphology of the real material are similar to statistical measures describing the SSRVE. Some possible descriptors are the basic scalar-valued parameters, see Ohser and Mücklich (2000), such as the volume fraction and integral of mean curvature, furthermore higher order statistical measures as the n-point probability function and lineal path function. The spectral density has been shown to be correlated to the two-point probability function, see Parzen (1992). In previous studies for two-dimensional SSRVEs, see Balzani et al. (2010), it has been found that certain statistical measures show a better performance for the application in this method than others, see J. Schröder (2011). Hence, in our construction method, the volume fraction, spectral density and lineal path function are chosen as appropriate statistical measures to describe the microstructural morphology. A method for the determination of substructures that are statistically similar to more complex two-phase microstructures has been proposed in Povirk (1995) where a least-square functional is minimized taking into account the power spectral densities of the real microstructure and the substructure with a fixed inclusion geometry. From here, the basic idea for the construction method of the SSRVEs is the minimization of a least-square functional considering the aforementioned appropriate statistical measures for

the SSRVE and the real microstructure. For the construction of 3D SSRVEs a parameterization of the inclusion morphology using different numbers of rotationally non symmetric ellipsoids is incorporated. The minimization problem is carried out applying a differential evolution algorithm for global optimization using the optimization package Mystic, see M.M. McKerns et al. (2011). Numerical examples are given to show the performance of the method.

2 STATISTICALLY SIMILAR RVES

In Finite-Element simulations based on the FE^2 approach, the boundary value problem on the microscale is built up by a RVE. This RVE commonly is determined by the smallest possible subvolume of a microstructure which is still able to represent the macroscopic mechanical response of the complete microstructure. However, this smallest possible substructure of a material is usually still too complex for efficient FE^2 calculations due to the large number of degrees of freedom originating from the discretization of the complex morphology of the microstructure. The basic idea in this context is to replace the RVE by a periodic microstructure composed of periodically arranged unitcells, see Figure 1.

The effort of calculating the complete periodic microstructure can then be reduced to only computing the periodic unitcell, if periodic boundary conditions are applied.

A least-square functional is formulated considering suitable statistical measures describing the morphology of the inclusion phase of the real microstructure and the SSRVE. This functional is minimized to obtain a SSRVE which emits the lowest error in statistical measures compared to the real microstructure. We consider the general minimization problem

$$\gamma^\star = \operatorname{argmin}\left[\mathcal{L}(\gamma)\right] \quad \text{with} \tag{1}$$

$$\mathcal{L}(\gamma) = \sum_{i=1}^{nsm} \omega_i \left[\mathcal{P}_i^{real} - \mathcal{P}_i^{SSRVE}(\gamma)\right]^2 \tag{2}$$

wherein $\mathcal{P}^{real}$ and $\mathcal{P}^{SSRVE}$ denote the suitable statistical measures describing the inclusion morphology computed for the real microstructure and the SSRVE.

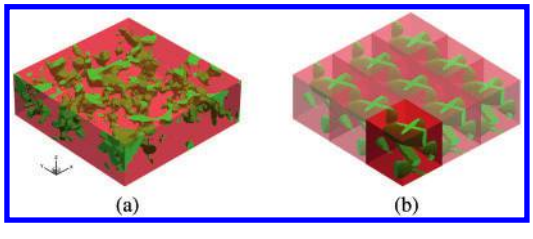


Figure 1. Schematic illustration of the basic concept, red indicating the matrix phase, green indicating the inclusion phase: (a) usual RVE with arbitrary inclusion morphology and (b) periodic microstructure with SSRVE.

The total number of statistical measures taken into account is described by *nsm* and ω represents the weighting factor of the individual statistical measures. The morphology of the inclusion phase of the SSRVE is described by a parameterization vector γ, which will be explained in Section 2.3. $\gamma^\star$ is considered the representation of the real microstructure.

2.1 *Statistical measures*

There exists a large number of statistical measures to describe the morphology of a single phase in a multiphase material, an overview can be found in Mücklich (2000). In our case we seek for measures to describe the inclusion phase in a two-phase matrix-inclusion composite, such as a DP steel. A very basic but yet important measure is the volume fraction defined by

$$\mathcal{P}_V = \frac{V_I}{V} \tag{3}$$

where V_I and V denoting the volume of the inclusion phase and the volume of the total composites, respectively. This parameter has been shown to play an important role in the method, cf. Balzani, Brands, Schröder & Carstensen 2010) and has to be considered to obtain satisfying results. A further statistical measure is the spectral density which is defined by the multiplication of the discrete Fourier transformation with its conjugate complex

$$\mathcal{P}_{SD}(n_x, n_y, n_z) := \frac{1}{2\pi N_x N_y N_z} \left|\mathcal{F}(k_x, k_y, k_z)\right|^2 \tag{4}$$

with the discrete Fourier transformation given by

$$\mathcal{F}(n_x, n_y, n_z) := \sum_{k_x=1}^{N_x} \sum_{k_y=1}^{N_y} \sum_{k_z=1}^{N_z} \exp\left(2\pi i \left(\frac{n_x\ k_x}{N_x} + \frac{n_y\ k_y}{N_y} + \frac{n_z\ k_z}{N_z}\right)\right) \chi(k_x, k_y, k_z). \tag{5}$$

The maximal number of pixels in each dimension of the considered binary data set are given by N_x, N_y and N_z, and the indicator function χ is defined by

$$\chi(k_x, k_y, k_z) := \begin{cases} 1 \text{ if point } x \text{ is in incl. phase} & (6) \\ 0 \text{ else} & (7) \end{cases}$$

with the point $x(k_x, k_y, k_z)$ in the binary data set. The coordinates in frequency domain are n_x, n_y and n_z. The spectral density captures periodicity information of a microstructure and is related to the two-point probability function, see Parzen (1992). It is considered a measure of higher order compared to the scalar valued basic parameters.

The lineal path function is another measure of higher order giving information about the probability

that line segments with different lengths and orientations are entirely located in one phase of the material. A complete computation of a lineal path function is expensive, therefore we use a template containing a certain number of line segments with distinct orientations which are analyzed instead of the whole set of possible line segments. The lineal path function is computed based on the indicator function

$$\lambda := \begin{cases} 1 \text{ if } \overrightarrow{\boldsymbol{x_1 x_2}} \text{ is in inclusion phase} & (8) \\ 0 \text{ else,} & (9) \end{cases}$$

with the line segment $\overrightarrow{x_1 x_2}$. For periodic and ergodic microstructures, the lineal path function is calculated by

$$\mathcal{P}_{LP}(m,k,l) := \frac{1}{N_x N_y N_z} \sum_{p=1}^{N_x} \sum_{q=1}^{N_y} \sum_{o=1}^{N_z} \lambda \qquad (10)$$

with $\lambda := \lambda(p+m, q+k, o+l)$ and (m,k,l) defining the oriented line segments in the template.

2.2 *Proposed method*

The outlined statistical measures cover important information about the morphology of the inclusion phase of the microstructure. With these measures in hand, the least-square functional for the minimization process is obtained as

$$\mathcal{L}(\gamma) = \omega_V \left(\mathcal{P}_V^{real} - \mathcal{P}_V^{SSRVE}(\gamma)\right)^2 \qquad (11)$$

$$+ \omega_{SD} \sum_{k_x,k_y,k_z} \left(\mathcal{P}_{SD}^{real} - \mathcal{P}_{SD}^{SSRVE}(\gamma)\right)^2 \qquad (12)$$

$$+ \omega_{LP} \sum_{p,q,o} \left(\mathcal{P}_{LP}^{real} - \mathcal{P}_{LP}^{SSRVE}(\gamma)\right)^2 \qquad (13)$$

with the weighting factors $\omega_V = 1$, $\omega_{SD} = 1$ and $\omega_{LP} = 1000$, which were found to give reasonable results.

2.3 *Parameterization of inclusion phase morphology of SSRVEs*

For the parameterization of the inclusion phase in the SSRVE, a varying number of non rotationally symmetric ellipsoidal inclusions is chosen. One ellipsoidal inclusion is described by a set of nine parameters $[x_c\ y_c\ z_c\ \psi\ \theta\ \phi\ r_1\ r_2\ r_3]$, which are defined as described in Figure 2. The first three entries x_c, y_c and z_c describe the center point of the inclusion, the Euler angles ψ, θ and ϕ measure a rotation of the coordinate system of the ellipsoid and r_1, r_2 and r_3 define the radii of each semi axis of the ellipsoid. Depending on the number of ellipsoidal inclusions in the SSRVE, the vector γ contains one data set for each ellipsoidal inclusion.

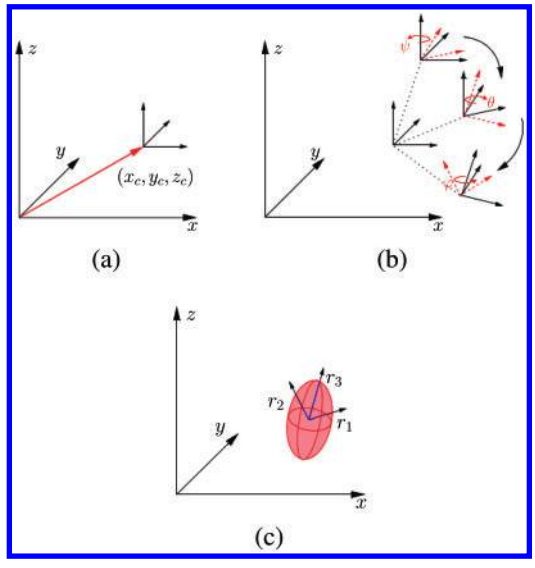


Figure 2. Illustration of parameterization of one ellipsoidal inclusion in SSRVE: (a) center coordinates of ellipsoid, (b) rotation by Euler angles, (c) radii on semi axis.

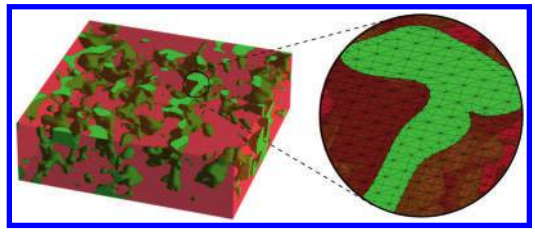


Figure 3. Reconstruction of DP steel microstructure and discretization.

3 NUMERICAL EXAMPLES

For a representation of a real DP steel microstructure, four 3D SSRVEs with different numbers of inclusions are generated. The reconstruction of a DP steel microstructure is obtained from 3D EBSD FIB-based serial sectioning measurements, cf. M. Calcagnotto and Raabe (2010), carried out in coorporation with the Max Planck Institut für Eisenforschung, Düsseldorf, for details on the method see e.g. N. Zaafarani (2006). Details of the serial sectioning and 3D reconstruction method has been described by S. Zaefferer (2008). Figure 3 shows the microstructure which was discretized with 8.5 mio. dof and 10-noded tetrahedrons, the structure measures $15.9 \times 16.45 \times 5$ micrometers. The size of the SSRVEs is calculated on the basis of the statistical measures of the real microstructure. Since the lineal path function captures length information, it can conflict with the measure of volume fraction, if the size of the SSRVE is not chosen large enough. In this contradicting case, in the minimization process, the size of

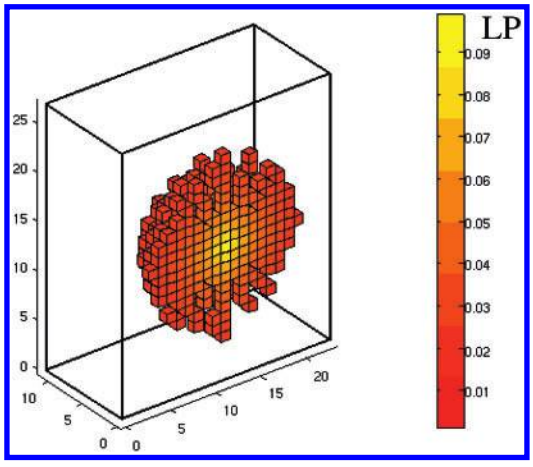


Figure 4. Illustration of lineal path function for a lower threshold of 2% probability.

the average ellipsoidal inclusion in the real microstructure, estimated from the lineal path function, would be larger than the volume fraction allows the inclusion to be. The average size of an ellipsoidal inclusion is estimated using a threshold of 2% probability, excluding small probabilities, to obtain an average ellipsoidal inclusion. The corresponding lineal path function representing the average ellipsoidal inclusion can be seen in Figure 4. Calculating the volume of this ellipsoid based on the measurements of the semi axes, V_{aver}, the size of a cubic SSRVE can be determined for the desired number of inclusions, respectively, by

$$\mathcal{P}_V^{real} = \frac{n_{inc}\, V_{aver}}{V^{SSRVE}}, \tag{14}$$

$$\rightarrow l_x = l_y = l_z = \sqrt[3]{\frac{n_{inc}\, V_{aver}}{\mathcal{P}_V^{real}}}. \tag{15}$$

For an analysis of the performance of the method, SSRVEs with one, two, three and five inclusions are constructed using the method described. The minimization process is carried out using the parallel optimization environment Mystic, cf. M.M. McKerns et al. (2011). Figure 5 shows the obtained SSRVEs and the corresponding error measures in the statistical measures are summarized in table 1.

A decrease of the errors of the statistical measures with increasing number of inclusions is clearly detectable from Table 1. The increase of complexity in the morphology of the microstructure leads to a closer fit of the statistical measures to the ones of the real microstructure. The performance regarding the mechanical response of the SSRVEs compared to the real microstructure is tested in four basic virtual experiments, tension in x-direction, tension in z-direction, shear of xz-plane in x-direction (xy) and shear of yz-plane in y-direction (yx). For comparative means, a

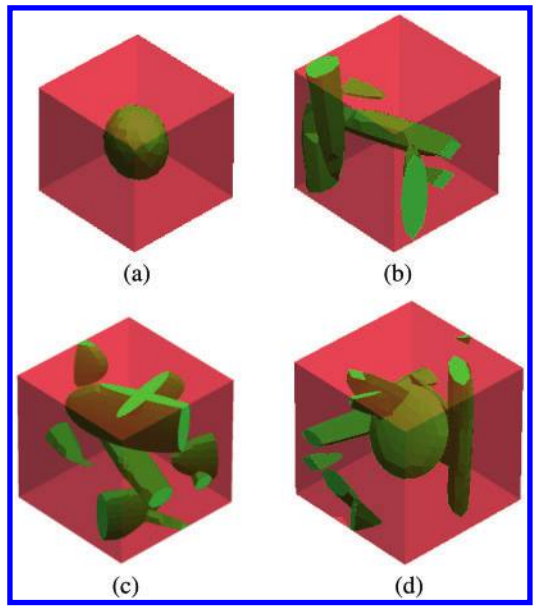


Figure 5. SSRVEs constructed for DP steel microstructure with (a) $n_{inc} = 1$, (b) $n_{inc} = 2$, (c) $n_{inc} = 3$ and (d) $n_{inc} = 5$.

Table 1. Error in statistical measures of calculated SSRVEs.

SSRVE	$\mathcal{L}[10^{-2}]$	$\mathcal{L}_V[10^{-4}]$	$\mathcal{L}_{SD}[10^{-3}]$	$\mathcal{L}_{LP}[10^{-4}]$
$n_{inc} = 1$	8.432	485.29	4.5	0.31
$n_{inc} = 2$	0.98	32.07	3.5	0.031
$n_{inc} = 3$	0.53	3.37	3.3	0.017
$n_{inc} = 5$	0.38	3.03	2.0	0.015

relative error measure is calculated for each virtual experiment by

$$\tilde{r}_j = \sqrt{\frac{1}{n}\sum_{i=1}^{n}\left[r_j^{(i)}\right]^2} \tag{16}$$

with

$$r_j^{(i)} = \frac{\bar{\sigma}_{j,i}^{real} - \bar{\sigma}_{j,i}^{SSRVE}}{\bar{\sigma}_{j,i}^{real}}, \tag{17}$$

j indicating the virtual experiment, the individual and total number of evaluation point i and n, respectively and $\bar{\sigma}$ being the macroscopic stress. An overall average error is computed by

$$\tilde{r} = \sqrt{\frac{1}{4}\left(\tilde{r}_x^2 + \tilde{r}_z^2 + \tilde{r}_{xy}^2 + \tilde{r}_{yx}^2\right)}. \tag{18}$$

Figure 6 shows the errors of the mechanical response of the SSRVEs compared to the real microstructure. For the tension test in x-direction, all

Table 2. Error in [%] of mechanical response for virtual experiments comparing SSRVEs to real microstructure and number of elements in discretization.

SSRVE	n_{ele}	$\tilde{r}_x$	$\tilde{r}_z$	$\tilde{r}_{xy}$	$\tilde{r}_{yx}$	$\tilde{r}$
$n_{inc}=1$	2851	5.3	4.6	5.5	5.5	5.24
$n_{inc}=2$	5015	0.5	3.6	4.4	4.4	3.60
$n_{inc}=3$	18835	0.5	1.8	1.5	1.3	1.36
$n_{inc}=5$	20413	0.5	2.1	2.6	2.6	2.13

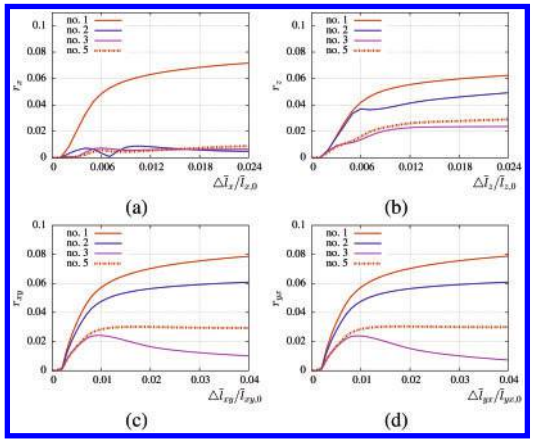


Figure 6. Error of mechanical response for virtual experiments: (a) tension x-, (b) tension in z-direction, (c) shear of xz plane in x-direction and (d) shear of yz plane in y-direction.

SSRVEs except for the single inclusion one can represent the real microstructure response accurately. For the tension test in z-direction, a separation of the curves for the SSRVEs with one and two inclusion while the other two remain lowest with the SSRVE with three inclusions having a slightly lower error. In the shear tests the error of SSRVE no. 3 emits the lowest error.

The summary of the results in Table 2 shows a decrease in the mechanical error in most virtual experiments with increase of number of inclusions, SSRVEs with three and five inclusions both having an overall error around 2%, the SSRVE with three inclusions even having a lower error, $\tilde{r}=1.36$, than the one with five inclusions. Increasing the number of inclusions from one to two inclusions leads to a large descent in the mechanical error, which was also seen for the statistical measures. A further increase of the number of inclusions up to three leads to a lower mechanical error. Increasing the number of inclusions to five does not improve the mechanical error although the error in the statistical measures decreased. Looking at the number of elements used to discretize the SSRVEs, an increasing value n_{ele} can be found with increasing number of inclusions in the SSRVE. From Figure 5, it can be found that the increase from three to five inclusions does not lead to an obvious increase of visible complexity, only slightly more elements for a discretization were needed.

4 CONCLUSION

A method for the construction of 3D SSRVEs is proposed using the volume fraction, spectral density and lineal path function to describe the morphology of the inclusion phase. From the here presented results, it can be seen that with increasing complexity of the SSRVE, i.e. increasing number of inclusions in the SSRVE, a lower error measure in the statistical measures and also, for an increase up to three inclusions, a lower error in the mechanical results can be seen. A further increase to five inclusions leads to a lower error in the statistical measures, however, no decrease in the mechanical error can be detected. This finding leads to the assumption that for the characterization of the real microstructure, the statistical measures chosen to represent the real microstructure are reasonable but not perfectly complete, since some hidden information may remain undetected. Thus, the incorporation of more statistical measures to represent the microstructure can be promising. Possible candidates are Minkowski functionals, which carry further statistical information.

REFERENCES

Balzani, D., D. Brands, J. Schröder, & C. Carstensen (2010). Sensitivity analysis of statistical measures for the reconstruction of microstructures based on the minimization of generalized least-square functionals. *Technische Mechanik 30*, 297–315.

C. Miehe, J. Schröder, C. G. B. (1999). Computational homogenization analysis in finite plasticity. simulation of texture development in polycrystalline materials. *Computer Methods in Applied Mechanics and Engineering 171*, 387–418.

J. Schröder, D. Balzani, D. B. (2011). Approximation of random microstructures by periodic statistically similar representative volume elements based on lineal-path functions. *Archive of Applied Mechanics 81*, 975–997.

M. Calcagnotto, D. P. & D. Raabe (2010). Orientation gradients and geometrically necessary dislocations in ultrafine grained dual-phase steels studied by 2D and 3D EBSD. *Mater. Sc. Engin. A 527*, 2738–2746.

M.M. McKerns, L. Strand, T. S., A. Fang, & M. Aivazis (2011). Building a framework for predictive science. *Proceedings of the 10th Python in Science Conference*.

N. Peranio, Y.J. Li, F. R. & D. Raabe (2010). Microstructure and texture evolution in dual-phase steels: Competition between recovery, recrystallization and phase transformation. *Mater. Sc. Engin. A 527*, 4161–4168.

N. Zaafarani, D. Raabe, R. N. S., F. Roters, & S. Zaefferer (2006). Three-dimensional investigation of the texture and microstructure below a nanoindent in a cu single crystal using 3D EBSD and crystal plasticity finite element simulations. *Acta Materialia 54*, 1863–1876.

Ohser, J. & F. Mücklich (2000). *Statistical analysis of microstructures in materials science*. J Wiley & Sons.

Parzen, E. (1992). *Statistical processes*. Holden-Day, San Francisco, CA.

Povirk, G. (1995). Incorporation of microstructural information into models of two-phase materials. *Acta Metallurgica Et Materialia 43/8*, 3199–3206.

S. Zaefferer, S. W. D. R. (2008). Three-dimensional orientation microscopy in a focused ion beam-scanning electron microscope: A new dimension of microstructure characterization. *Metal. Mater. Trans. A 39A*, 374–389.

Schröder, J. (2000). *Homogenisierungsmethoden der nichtlinearen Kontinuumsmechanik unter Beachtung von Stabilitätsproblemen*. Habilitationsschrift, Bericht aus der Forschungsreihe des Instituts für Mechanik (Bauwesen), Lehrstuhl I.

W. Brekelmans, R. Smit, H. M. (1998). Prediction of the mechanical behaviour of nonlinear heterogeneous systems by multi-level finite element modeling. *Computer Methods in Applied Mechanics and Engineering 155*, 181–192.

Research and Applications in Structural Engineering, Mechanics and Computation – Zingoni (Ed.)
© 2013 Taylor & Francis Group, London, ISBN 978-1-138-00061-2

A study of local mechanical properties of 304L SS welded joints subjected to cyclic straining using depth-sensing instrumented indentation

Duyi Ye & Feng Mi
Institute for Process Equipments, Zhejiang University, Hangzhou, China

Xiaoxia Yin
Institute for Architecture Design, Huaxin Consulting Co., Ltd, Hangzhou, China

ABSTRACT: In this paper, a series of experiments including low-cycle fatigue tests, depth-sensing indentation measurements, optical microscopy examinations, etc. were carried out to study the local mechanical properties and microstructures in particular zones of 304L SS welded joints subjected to cyclic straining. An analytical algorithm proposed by Dao et al. was utilized to estimate the basic mechanical properties (E, σ_y and n) in various regions of the welded joints from the indentation load-displacement data. It is shown that in the as-welded condition, the weld metal has a higher strength but lower stiffness and plasticity than does the base metal, while the material within HAZ exhibits a significant gradient of the mechanical properties. A strain amplitude-dependent variation in the local mechanical properties in particular joint regions was also obtained for the cyclically deformed welded joints. Optical microscopy examinations show that the microstructure in particular regions of 304L SS welded joints is not only decided by the metallurgical condition resulting from the welding process, but also determined by the strain amplitude applied during cyclic deformation.

1 INTRODUCTION

In welded structures, welded joints are generally known as potential 'weakest links' due to weld defects or microstructural in-homogeneities which bring about the local changes in the mechanical properties and thus result in difficulties in fatigue strength analysis of welded structures, since the stress distribution and crack behavior in welded joints are strongly dependent on the mechanical in-homogeneity (Filacchioni et al. 2002, Lee et al. 2007, Kim et al. 2007). Accordingly, comprehensive understanding of the local mechanical properties in welded joint zones, including the weld metal (WM), heat-affected zone (HAZ) and base metal (BM), as well as their variations during fatigue loading is of vital importance for the design of the welded structures against fatigue failure.

So far, a variety of methods for determining the local mechanical properties of welded joints have been developed. One of the widely applied methods is microhardness measurement that can determine the transverse profiles of the deformation resistance across the joints (Naderi et al. 2008, James et al. 2009). The conventional microhardness testing, however, can only provide qualitative data instead of further information regarding the basic mechanical properties such as Young's modulus, yield stress, strain hardening exponent, etc in welded joint zones. These basic mechanical parameters are essential for the fatigue strength analysis of welded joints subjected to cyclic external forces (Fuchs & Stephens 1980). For this reason, methods to characterize joint zone properties based on uni-axial tension test using mini- or micro-specimens have been developed in recent years (Rafal et al. 2009, Fuller et al. 2008, Rao et al. 2010). It has been found (Fuller et al. 2008), however, that preparing isolated mini-tensile specimens from the welded joints is frequently connected with certain difficulties and restrictions in practical applications due to the small-size of joint zones. For instance, in most cases the size of the HAZ does not exceed fractions of millimeter, and, additionally, its shape often makes it difficulties to produce an isolated specimen for tensile testing. It has also been indicated (Rafal et al. 2009, Boroński 2006) that the tensile tests using isolated mini-specimens can not take into account the interaction of welded joint zones on each other during the joint loading. This interaction may significantly affect the mechanical behavior of welded joints especially in the case of time-altering loadings as cyclic straining.

Depth-sensing indentation (DSI) technique, developed over the last decade, has been regarded as a power tool for the mechanical measure of small-volume materials or engineering surfaces (Giannakopulos & Suresh 1999). Much recent research (Giannakopulos & Suresh 1999, Oliver & Cheng 1984, Dao et al. 2001, Ye et al. 2007) also led to the development of numerous analytical methods for estimating the basic mechanical properties such as Young's modulus, yield stress, strain hardening exponent, etc. from the indentation load-displacement data. Among these analytical methods, an analytical

algorithm proposed by Dao et al (Dao et al. 2001) has been regarded as the representative one due to its more accordant estimations with the measured mechanical properties (Ye et al. 2011, 2012). Since DSI has various merits in practical applications, such as less destructive, quick to perform, and only a relatively small piece of material is required in testing, it provides a promising method for determining the local mechanical properties of welded joints. This is the motive of the present research work to apply the depth-sensing indentation tests and combine with Dao et al's analytical algorithm to study the local mechanical properties of 304L SS welded joints subjected to low-cycle fatigue (LCF) loadings so as to develop a local mechanical properties-based approach for the fatigue strength analysis of welded components under alternative service conditions.

2 EXPERIMENTAL DETAILS

The material used in the present study was 304L stainless steel (SS). Its actual chemical composition in weight percent was listed in Table 1. Solution-annealed base plate of 304L SS, 18 mm in thickness, was joined along the plate rolling direction by manual metal arc welding using 316L SS and Inconel 182 electrodes. The configuration of the joint groove was double-V shaped and the weld was completed in 15 passes with a voltage of 24V, a current of 100 A. Subsequent to welding, the weldments were examined, non-destructively, by X-ray to ensure their soundness. Cylindrical specimens having 12 mm gauge length and 10 mm diameter were cut from the acceptable weldments in such a way that they contained portions of the base metal, heat-affected zone and weld metal.

Experiments for the present study consist mainly of (1) room-temperature constant amplitude low-cycle fatigue (LCF) tests of 304L SS welded joint specimens, and (2) depth-sensing indentation measurements in particular zones of the fatigue failure joint specimens. Details of experimental procedures are described as follows.

Fully reversed total-axial-strain-controlled LCF tests were conducted at room temperature in air on 304L SS as-welded joint specimens using a MTS 810 servohydraulic testing system. Tests were conducted at various strain amplitudes in the range of $\pm 0.5\%$ to $\pm 1.2\%$ at a constant total strain rate of $4 \times 10^{-3}\ s^{-1}$. In this study the fatigue life (N_f) of welded joint specimens is defined as the number of cycles required to reduce the maximum stress (σ_{max}) to a value of 3/4 times the peak value experienced during previous cycles.

Table 1. Chemical compositions (wt. %) of the material investigated.

C	Mn	Si	S	P	Cr	Ni	Mo	Cu	N
0.03	2.0	0.75	0.03	0.045	18.7	10.15	0.07	0.19	0.1

Samples for the depth-sensing indentation measurements were sectioned to the required size along the longitudinal direction of both the as-welded and fatigue failure 304L SS joint specimens comprising the WM, HAZ and BM zones. The cut sections were then polished using different grads of emery papers. Final polishing was done using a diamond compound ($1\ \mu m$ particle size) in the disc polishing machine. To reveal the microstructure, the polished samples were etched for 30 s in a solution containing 70% HNO_3. Depth-sensing indentation measurements were performed using a dynamic ultra microhardness tester (Shimadzu DUH201S) equipped with a Vickers diamond indenter. In this study, a maximum indentation load of 500 mN and a dwell-time of 15 s were utilized. Throughout the indentation tests, the loading rate was kept at 200 mN/min. Taking into account the in-homogeneity of the local mechanical response in welded joint zones, indentation measurements were performed as the following ways. In the case of the as-welded joint sample, an indentation array consisting of 5×30 measures that contained portions of the base metal, heat-affected zone and weld metal was utilized. The mean results for each equivalent position were then calculated. In the case of fatigue failure joint specimens, at least 15 indentations were measured at randomly selected places in each joint zone to provide statistical representative results. During indentation testing, both the indentation load (P) and displacement (h) were continuously recorded as an indenter was driven into the sample (loading segment) and then withdrawn from it (unloading segment). The raw data were then used to construct the indentation load-depth ($P-h$) curves.

Microstructures in particular zones of both the as-welded and fatigue failure 304L SS joint specimens were observed by optical microscopy (OM). In this study, a quantitative measurement of the ferrite/martensite content in particular joint zones was also performed using a commercial magnetic instrument (MP30 Ferriscope), in which at least 11 measurements for each joint zone were recorded.

3 RESULTS

3.1 *Mechanical property distributions across the as-welded 304L SS joint zones*

Five lines of indents along the longitudinal direction of the as-welded 304L SS joint sample were illustrated in Figure 1. This figure also allowed us to identify the BM, HAZ and WM regions as well as their approximate dimensions. In Figure 1, a much less size of the indent compared to the dimension of the individual joint zone was observed, indicating thereby that the indentation load-depth ($P-h$) curve measured in this study is exactly an indication of the local elasto-plastic response of the joint zone materials. Figure 2 presents typical $P-h$ curves measured in the BM, HAZ and WM regions, respectively. For the sake of clarity, only one curve for each joint zone was presented in this

figure. As it is seen in Figure 2, not only the magnitude but also the shape of $P-h$ curves changes significantly with the joint zone, indicating that for the present 304L SS welded joint, the indentation response is highly sensitive to the details of the metallurgical condition resulting from the welding process.

In terms of the above experimental $P-h$ curves, the basic mechanical properties (σ_y, n and E) in particular zones of the as-welded 304L SS joint sample can be estimated using Dao et al's analysis algorithm. Figure 3 shows the estimated mechanical properties (σ_y, n and E) plotted as a function of the measured positions across the welded joint regions, where each data point represents an average of 5 values and error bar are ± 1 standard deviation. As it is seen in this figure, various mechanical parameters (σ_y, n and E) exhibit relatively little variation in BM and WM regions, but significant variation within HAZ. In comparison to the base metal, the weld metal shows a higher yield stress (σ_y) and strain hardening exponent (n) but a lower Young's modulus (E), while the material within HAZ exhibits gradient-distribution mechanical properties. The significant variation in the local mechanical properties across the joint is mainly attributed to the welding-altered microstructures in welded joint zones, which will be analyzed in the subsequent section.

3.2 *Fatigue mechanical properties in particular zones of 304L SS welded joints*

Figure 4 shows typical indentation load-depth ($P-h$) curves measured in the base metal, heat-effect zone and weld metal of the 304L SS joint specimens cycled to failure at two representative low and high strain amplitudes ($\pm 0.5\%$ and $\pm 1.2\%$). As it is seen in this figure, with increased strain amplitudes, the curvature of the loading curves tends to increase, as a whole, while the contact depth at the maximum load and the residual depth after complete unloading exhibit decreasing characteristics for various joint regions investigated. The above observations indicate that for the 304L SS welded joints under investigation the indentation response is also highly sensitive to

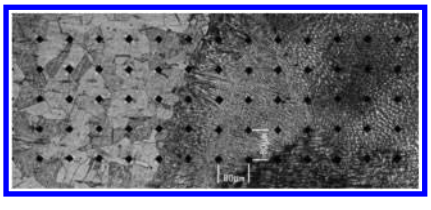


Figure 1. Optical micrograph of indentation impressions across the as-welded 304L SS joint regions.

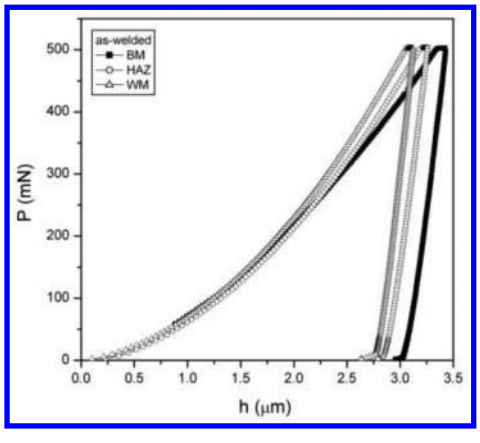


Figure 2. Typical indentation load-depth ($P-h$) curves in particular zones of as-welded 304L SS joint sample.

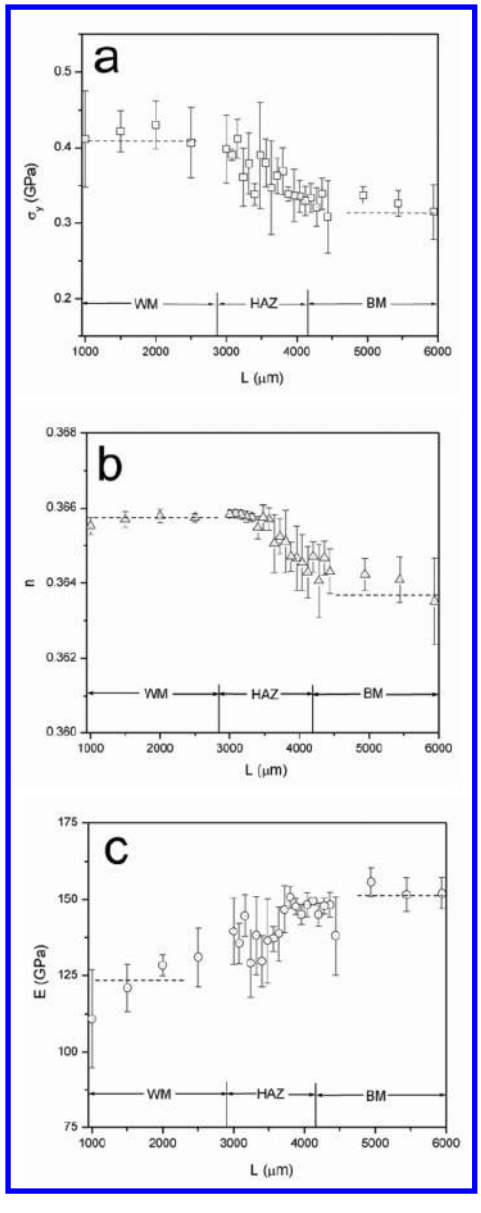


Figure 3. Distributions of the basic mechanical properties across the as-welded 304L SS joint regions: (a) yield stress (σ_y); (b) strain hardening exponent (n); (c) elastic modulus (E).

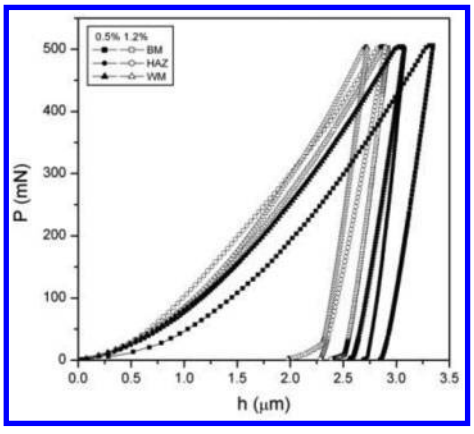


Figure 4. Typical indentation load-depth ($P-h$) curves in particular zones of fatigue failure 304L joint specimens.

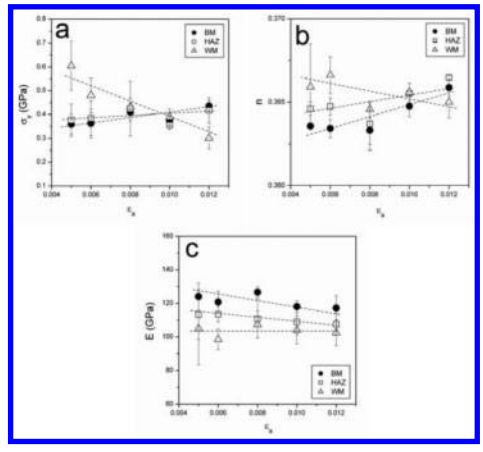


Figure 5. Dependence of the basic mechanical properties on the applied strain amplitudes: (a) yield stress (σ_y); (b) strain hardening exponent (n); (c)Young's modulus (E).

the strain amplitude applied during low-cycle fatigue loadings.

In this study, the basic mechanical properties (σ_y, n and E) in three different zones of fatigue failure joint specimens were also estimated using Dao et al's analysis algorithm combined with the measured $P-h$ curves. Figure 5 shows the values of σ_y, n and E plotted as a function of the applied strain amplitude in the base metal, heat-effect zone and weld metal, where each data point represents an average of 15 values and the error bars are ± 1 standard deviation. This figure reveals that with increasing strain amplitudes, the yield stress (σ_y) and strain hardening exponents (n) display increase in both BM and HAZ regions but decrease in WM region, while Young's modulus (E) exhibits decreasing characteristic in various joint regions investigated. This strain amplitude-dependent variation in the basic mechanical properties in particular joint zones essentially results from the strain amplitude-dependent variation in the microstructures in the welded joints during cyclic straining, which will also be discussed subsequently.

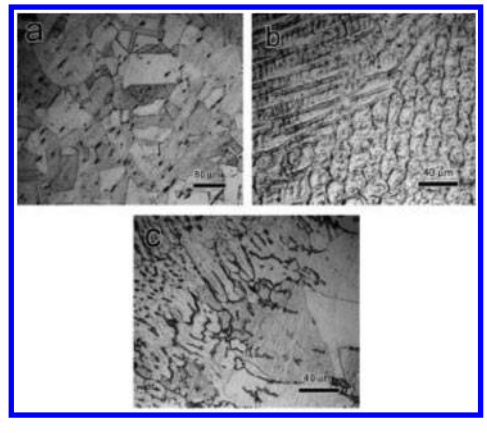


Figure 6. Microstructures in particular zones of the as-welded 304L SS joint sample: (a) base metal; (b) weld metal; (c) interfacial region close to HAZ.

3.3 *Microstructures in particular zones of 304L SS welded joints in both as-welded and cyclic straining conditions*

In order to seek for the micromechanisms responsible for the variation in the local mechanical properties of the present 304L SS welded joints, microstructural examinations were performed in particular zones of both the as-welded and fatigue failure joint specimens.

Figure 6 shows the optical micrographs of the base metal, weld metal and their interfacial regions close to HAZ of 304L SS joint sample in the as-welded condition. Note in Figure 6a that the microstructure of the base metal consists of equiaxed austenitic grains with small amount of δ – ferrite in the form of stringers. The weld metal exhibits a fine duplex austenite-ferrite microstructure (Figure 6b), where δ – ferrite with cellular and dendritic morphologies has been clearly observed. In addition, extensive precipitations of carbides and oxides are also visible preferentially on the boundaries between the austenite and ferrite phases. In Figure 6c, the microstructure of the interfacial region close to HAZ is predominantly vermicular or intercellular, although ferrite stringers are occasionally observable in some of the austenite grains.

Figure 7 summarizes representative microstructures in particular regions of fatigue failure 304L SS joint specimens tested at low and high strain amplitudes ($\pm 0.5\%$ and $\pm 1.2\%$). At low strain amplitude of 0.5%, the austenitic grains in the base metal contain a few slip bands (Figure 7-1a). Additionally, martensitic phase appeared as blocks or islands are also visible in some austenitic grains. In weld metal discrete slip bands with one slip system are found in the majority of the grains (Figure 7-1b). In the interfacial regions close to HAZ, small dark needles assumed to be deformation-induced martensite are

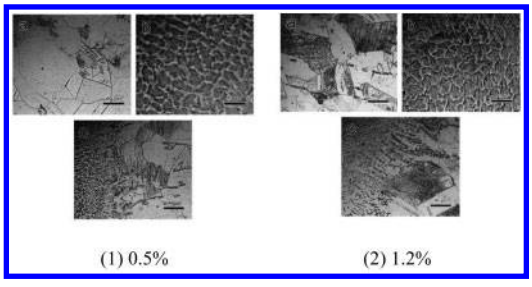


Figure 7. Microstructures in particular zones of the fatigue failure 304L SS joint specimen tested at 0.5% and 1.2%: (a) base metal; (b) weld metal; (c) interfacial region close to HAZ.

also observed (Figure 7-1c). At high strain amplitude of 1.2%, in addition to the localized single slip bands, multiple slip modes with intersecting bands on different planes, penetrating the whole grains, are found commonly in both the base metal (Figure 7-2a) and weld metal (Figure 7-2b) as well as their interfacial regions close to HAZ (Figure 7-2c). In some austenitic grains the slip bands become unrecognizable due to their high density in the base metal. Meanwhile, martensite with different morphologies and distributions has also been, more or less, observed over several austenite grains.

The above microstructural observations indicate that for the present 304L SS welded joints the microstructure in welded joint zones is not only decided by the metallurgical condition resulting from the welding process, but also determined by the strain amplitude applied during cyclic straining.

4 DISCUSSIONS

As indicated (Sireesha et al. 2000), during welding some metallurgical changes, such as (a) segregation during solidification, (b) distribution of elements during phase changes, and (c) precipitation of secondary phase particles, take place in welded joint zones. In the case of austenitic stainless steel (SS) weldments, owing to the non-equilibrium rapid solidification condition in welding process, the peak temperature in fusion zone is much higher than the upper limit of phase balance between δ – ferrite and γ – austenite (Folkhard 1984). Because of high cooling rate in the fusion zone, the possibility of ferrite to austenite transformation is low and some ferrites are remained at grain boundaries. According to Fuller et al (Fuller et al. 2008), presence of δ – ferrite at grain boundaries may prohibit grain growth and decrease the grain size. Consequently, in the present 304L SS welded joint the incomplete phase transformation during welding results in the formation of the observed a fine duplex austenite-ferrite microstructure in the weld metal region (see Figure 6b). With increasing distance from the fusion boundary, the cooling rate tends to decrease due to the thermal gradient between the joining faces and electrodes. The reduced cooling rate leads to decreasing the amount of grain boundary ferrite, which results in the formation of a partially mixed zone with a higher semicontinuous δ – ferrite content near the interface close to HAZ, as seen in Figure 6c, where the vermicular or intercellular ferrite structure is mostly because of the effects of dilution from the base metal. As it has been indicated (Folkhard 1984, Bhanu et al. 1990, Sharifitabar et al. 2011), in austenitic SS weldements the formation of δ – ferrite is an important aspect to take into account for their mechanical behavior. The δ – ferrite was found to induce an increased number of dislocation sources which act as barriers to the mobile dislocations and cause an increase in the deformation resistance (Lee et al. 2007). Several reports (Rho et al. 1998 & Hong et al. 2002) also revealed the deleterious effect of increased δ – ferrite content on resistance of fracture of weld metals. The cause was traced to the tendency for cracks to propagate preferentially along the δ – ferrite or δ/γ interface. In this study, magnetic measurements indicated the amount of the average δ – ferrite in the weld metal region to be about 2.4% and in the base metal region to be about 1.4%. The higher percentage of ferrite content in the WM region, with its many transformed phase boundaries, is believed to offer a greater resistance to plastic flow than does the relatively coarser austenitic structure of the base metal, which may be responsible for the higher local strength and strain hardening capacity in the weld metal than in the base metal, as seen in Figures 3a and 3b. Additionally, the carbide precipitations formed at grain boundaries and within grains in the weld metal will also contribute to the increase in the local strength due to the interactions between dislocations and precipitates during deformation. Since δ – ferrite is basically different from austenite matrix in its crystallography and chemical composition, stress concentration may occur at the δ/γ interface owing to strain incompatibility (Fuller et al. 2008). The high stress concentration at δ/γ interfaces promotes microcrack initiation and results in the reduction in the local stiffness. Accordingly, in the present 304L SS welded joint, the higher volume fraction of ferrite in the WM region may also become a primary factor responsible for the observed reduction in the stiffness property in the weld metal, as shown in Figure 3c, since the larger amount of δ – ferrite provides more δ/γ interfaces that imply more possible sites for crack initiation. In this study, a significant gradient of the local mechanical properties has also been observed within HAZ (see Figures 3a, 3b and 3c), which is thus mostly associated with the microstructure gradient resulting from the inhomogeneous metallurgical changes during welding process. The severe property gradient in HAZ also suggests that the tensile test using mini- or microspecimens extracted from the welded joint regions, as mentioned previously, can only provide an averaged mechanical measurement of the entire HAZ due to the fact that the dimension of the micro-tensile specimen is usually much larger than the size of the microstructure. In other words, the instrumented indentation-based

mechanical testing would provide a more reasonable approach for studying the local mechanical properties of welded joints.

As shown in the present study, the microstructure in particular regions of 304L SS welded joints undergoes strain amplitude-dependent change during low-cycle fatigue loadings. With increased strain amplitudes, both the number of micro-shear bands and activated slip systems showed increase in welded joint zones (see Figure 7). Additionally, more and thicker deformation-induced martensite was also observed at the intersections of the slip bands especially in the base metal. In this study, magnetic measurements in particular zones of the fatigue failure joint specimens revealed that with increase in strain amplitude, the volume fraction of martensite displayed increase in the base metal, but slight decrease in the weld metal. Since micro-shear band boundaries and martensite formations both impede dislocation motion and lead to a strengthening effect (Lee et al. 2007), with increasing strain amplitudes, the increase in the number of micro-shear bands and the volume fraction of martensite transformation gives rise to the increase in the local strength and strain hardening capacity in the base metal, as seen in Figures 5a and 5b. On the other hand, numerous previous investigations (Bhanu et al. 1990) also showed that at high strain amplitude, the dislocation structure in the weld metal tended to wall and cell arrangements. Since cellur structure provides a larger mean free path for dislocations, softening may take place in the weld metal in this case. Accordingly, in this study, as the applied strain amplitude increased, the decrease in the local strength and strain hardening capacity in the weld metal, also shown in Figures 5a and 5b, is mostly associated with the softening of the material resulting from annihilation of dislocations or arrangement of dislocations into cells/subgrains during cyclic straining. The nucleation of microcracks/microvoid at δ/γ interfaces during cyclic straining, as well as their increase in the number with increased strain amplitudes, will be responsible for the strain amplitude-dependent degradation in the local stiffness of the present joint region materials (see Figure 5c).

5 CONCLUSIONS

(1) The indentation response is highly sensitive to the details of the metallurgical condition resulting from the welding process. For the present investigated welded joint, not only the magnitude but also the shape of $P-h$ curves changes significantly with the joint zone.
(2) The weld metal has a higher yield stress (σ_y) and strain hardening exponent (n) but a lower Young's modulus (E) than does the base metal, while the material within HAZ exhibits a significant gradient of the mechanical properties.
(3) In the as-welded condition, the microstructure of the base metal consists of equiaxed austenitic grains with small amount of δ – ferrite. The weld metal exhibits a fine duplex austenite-ferrite microstructure. The microstructure of the interfacial region close to HAZ is predominantly vermicular or intercellular. The above microstructural features play an important role in deciding the local mechanical properties in different joint zones.
(4) With increasing strain amplitudes, the yield stress (σ_y) and strain hardening exponents (n) display increase in both BM and HAZ regions but decrease in WM region, while Young's modulus (E) exhibits decreasing characteristic in various joint regions investigated.
(5) The microstructure in particular regions of 304L SS welded joints undergoes strain amplitude-dependent change during low-cycle fatigue loadings, which is essentially responsible for the strain amplitude-dependent variation in the local mechanical properties of the present welded joints.

REFERENCES

Boro, D. Ski, 2006. *Cyclic material properties distribution in laser-welded joints. Int. J. Fatigue* 28: 346–354.

Dao, M. N.Chollacoop, K.J.Van Vliet, et al., 2001. *Computational modeling of the forward and reverse problems in instrumented sharp indentation. Acta Mater.* 49: 3899–3918.

Filacchioni, G., Montanari, R., Tata, M.E., Pilloni, L. 2002. *Structural and mechanical properties of welded joints of reduced activation martensitic steels. J. Nucl. Mater.* 307–311:1563–1567.

Fuchs, H.O., Stephens, R.I. 1980, Metal Fatigue in Engineering, first ed., A Wiley-Interscience publication, New York.

Giannakopulos, A.E., S. Suresh, 1999. *Determination of elastoplastic properties by instrumented sharp indentation. Scripta Mater.* 40: 1191–98.

James, M.N., Ting, S.-P., Bosi, M., H.lomband, Hattingh, D.G. 2009, *Residual strain and hardness as predictors of the fatigue ranking of steel welds. Int. J. Fatigue* 31: 1366–1377.

Kim, Jin Weon, Kyoungsoo Lee, Lee, Jong Sung Kim, Thak Sang Byun, 2009. Local mechanical properties of Alloy 82/182 dissimilar weld joint between SA508 Gr. 1a and F316 SS at RT and 320°C. *J. Nucl. Mater.* 384: 212–221.

Oliver, W.C., G.M. Cheng, 1984. *Improved technique for determining hardness and elastic modulus using load and displacement sensing indentation experiments. J. Appl. Phys.* 84: 1284–93.

Rao, D., J. Heerens, G. Alves Pinheiro, J.F. dos Santos, N. Huber 2010. *On characterisation of local stress–strain properties in friction stir welded aluminium AA 5083 sheets using micro-tensile specimen testing and instrumented indentation technique. Mater. Sci. Eng. A* 527: 5018–25.

Woei-Shyan Lee, Chi-Feng Lin, Chen-Yang Liu, Chin-Wei Cheng, 2007. *Effects of strain rate and welding current mode on microstructural properties of SUS 304L PAW welds. J. of Mater. Processing Technol.* 183: 183–193.

Ye, D., S. Matsuoka, N. Nagashima, 2007. *Determination of fatigue mesoscopic mechanical properties of an austenitic stainless steel using depth-sensing indentation (DSI) technique. Mater. Sci. Eng.A* 456: 120–129.

Research and Applications in Structural Engineering, Mechanics and Computation – Zingoni (Ed.)
© 2013 Taylor & Francis Group, London, ISBN 978-1-138-00061-2

Biological tissue mechanics with fibres modelled as one-dimensional Cosserat continua. Applications to cardiac tissue in healthy and diseased states

K. Sack & S. Skatulla
Department of Civil Engineering, University of Cape Town, South Africa

C. Sansour
Division of Materials, Mechanics, and Structures, The University of Nottingham, UK

ABSTRACT: Classically, the elastic behaviour of biological tissues is modelled using anisotropic strain energy functions which are supposed to capture the averaged behaviour of the matrix and the fibres. The strain energy function can be derived via representation theorems for anisotropic functions as shown in Wang (1970), Zheng (1994) and Holzapfel (2004). Alternatively, a superimposed continuum approach can be adopted where the matrix is considered as an isotropic material but the fibres are taken as superimposed one-dimensional continua (Karšaj[1], Sansour, & Sorić 2008). The latter approach allows for the inclusion of any number of families of fibres. In either case the state of stress in the fibres is one-dimensional and is parallel to the fibre tangent. Hence, fibre thickness is not a parameter in the formulation. Biological tissues, however, exhibit strong variations in fibre thickness defining different fibre hierarchies where the thickness can have a significant influence. This is especially true in inhomogeneous bending and shear-related states of stress.

To overcome this shortcoming, in this paper the approach of superimposed continua is extended. While the matrix is still considered as an isotropic continuum, the fibres are modelled as one-dimensional Cosserat continua. Hence, bending and shearing of fibres, in addition to stretching, become meaningful and fibre thickness becomes a material parameter.

The muscle fibres are enmeshed in a collagen network. Both, the fibre and the collagen material, are associated each with individual strain energy functions which are combined within a homogenization approach. In this way, a three-dimensional state of stress and strain of the complex myocardial tissue can be addressed. Presently, only the linear elastic representation for the strain energy function of the muscle fibre tissue are considered.

1 INTRODUCTION

Cardiovascular disease is the leading cause of death in the developed world accounting for 40% of all human mortality. Modelling the mechanical behaviour of the heart to improve our understanding of cardiovascular disease has been a scientific endeavour for the last 30 years. The proliferation of inexpensive high performance computing power has enabled more sophisticated simulation tools that can facilitate and guide the development of modern therapies.

Fundamental to this endeavour is the understanding and accurately describing the material and mechanical behaviour of the cardiac tissue is of great importance. Over the last 15 years constitutive models have introduced phenomenological properties as a means overcome the complex structure on a macro and micro scale (Costa et al. 2001), (Schmid, H.H. 2006) and (Holzapfel and Ogden 2009). This approach usually incorporate a large number of material parameters. A problem with this approach is the shortage of experimental data suitable for detailed parameter estimation. Increasing attempts to include the micro-structural influences directly have emerged with the hope that this will reduce, albeit not remove, the dependency on material parameters and the complicated strategies used to approximate them.

To date, the leading strain invariant-based stored energy functions only include limited micro structure considerations. Nothing has yet emerged to include an actual micro-structure on a kinematics level that influence macro-deformations in a coupled-physics behaviour.

Adopting the work of Sansour & Skatulla (2008), which successfully illustrated the increased accuracy of a three-dimensional Cosserat micro-structure in deformations of fibre orientated sheets, into the description of cardiac tissue is the objective of this paper. We consider the material response to be obtained by a homogenisation scheme superimposing

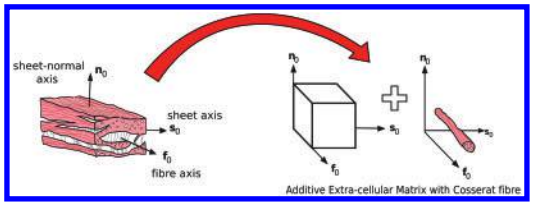


Figure 1. The material properties of cardiac tissue can be modelled as additive contributions from the extra-cellular matrix and Cosserat fibres.

the material behaviour of fibre/fibre bundles, modelled as Cosserat rods, and extra-cellular matrix, modelled as an isotropic elastic material.

2 DEFORMATION AND STRAIN

Let the deformation $\phi(\boldsymbol{X},t)$ be a mapping from the reference state of the body $\mathcal{B}$ with $\boldsymbol{X}\in\mathcal{B}$ to the current configuration at a specific time $\mathcal{B}_t$. If $\boldsymbol{X}$ and $\boldsymbol{X}$ are the respective coordinates of the reference state $\mathcal{B}$ and the current configuration $\mathcal{B}_t$, then the deformation gradient is given by:

$$\boldsymbol{F}=\mathrm{Grad}(\boldsymbol{x}) \tag{1}$$

Where Grad is the gradient operator acting with respect to the reference configuration $\boldsymbol{X}$. Given $\vartheta^i, i=1,2,3$, the co-variant curvilinear coordinate system parametrizing $\mathcal{B}$, we define, $\boldsymbol{G}_i$, the co-variant tangent vectors spanning the tangent space $\mathcal{TB}$ by:

$$\boldsymbol{G}_i=\frac{\partial \boldsymbol{X}}{\partial \vartheta^i} \tag{2}$$

In the classical Cosserat continuum every material point P is assigned a rotational field independent of displacements, enriching the continuum with additional degrees of freedom. We can express this rotational field $\boldsymbol{R}\in SO(3)$ explicitly (Sansour and Skatulla 2008):

$$\boldsymbol{R}(\vartheta^i,t)=1+\frac{\sin|\boldsymbol{\gamma}|}{|\boldsymbol{\gamma}|}\boldsymbol{\Gamma}+\frac{\cos|\boldsymbol{\gamma}|}{|\boldsymbol{\gamma}|^2}\boldsymbol{\Gamma}^2 \tag{3}$$

where $\boldsymbol{\gamma}$ denotes the rotation vector and $\boldsymbol{\Gamma}(\vartheta^i,t)\in so(3)$ is a skew a skew symmetric tensor with $\boldsymbol{\gamma}$ as its axial vector.

The *Cosserat* continuum features two strain measures. The first *Cosserat* strain tensor is a stretch-like tensor given by:

$$\boldsymbol{U}(\vartheta^i,t)=\boldsymbol{R}^T\boldsymbol{F} \tag{4}$$

where it should be noted, that unlike it's classical counterpart, is not symmetric in general. The second *Cosserat* strain measure is a change of curvature strain tensor given by:

$$\boldsymbol{K}(\vartheta^i,t)=-\frac{1}{2}\boldsymbol{\epsilon}:(\boldsymbol{R}^T\boldsymbol{R}_{,i})\otimes\boldsymbol{G}_i \tag{5}$$

For the purpose of modelling one dimensional Cosserat rods, consider a one-dimensional fibre continuum mapped by the coordinate $s=s(\vartheta^i)$. As such the fibre is assumed to be embedded in three dimensional space. The fibre deformation gradient is given by:

$$\boldsymbol{F}^{(s)}=\frac{\partial \boldsymbol{x}}{\partial \vartheta^i}\frac{\partial \vartheta^i}{\partial s}\otimes\hat{\boldsymbol{V}}_F=\boldsymbol{v}_F\otimes\hat{\boldsymbol{V}}_F \tag{6}$$

where $\boldsymbol{V}_F$ denotes a co-variant vector in fibre direction and $\hat{\boldsymbol{V}}_F$ its contra-variant equivalent. The fibre direction in the current configuration is expressed by $\boldsymbol{v}_F=\boldsymbol{F}\boldsymbol{V}_F$. In this sense, $\boldsymbol{F}^{(s)}$ is the projection of the deformation gradient $\boldsymbol{F}$ in direction of the fibre. A corresponding structural tensor is written as $\boldsymbol{M}_F=\boldsymbol{V}_F\otimes\hat{\boldsymbol{V}}_F$ representing the one-dimensional fibre continuum allowing us to alternatively express $\boldsymbol{F}^{(s)}=\boldsymbol{F}\boldsymbol{M}_F$

Similarly, we find associated strain measures $\boldsymbol{U}^{(s)}$ and $\boldsymbol{K}^{(s)}$, respectively, for the *Cosserat* fibre continuum:

$$\begin{aligned}\boldsymbol{U}^{(s)} &= \boldsymbol{R}^T\boldsymbol{F}^{(s)}=U_1^{(s)}\boldsymbol{V}_F\otimes\hat{\boldsymbol{V}}_F+\ldots\\ &\quad U_2^{(s)}\boldsymbol{A}_1\otimes\hat{\boldsymbol{V}}_F+U_3^{(s)}\boldsymbol{A}_2\otimes\hat{\boldsymbol{V}}_F \qquad (7)\\ \boldsymbol{K}^{(s)} &= -\frac{1}{2}\boldsymbol{\epsilon}:\boldsymbol{R}^T\frac{\partial\boldsymbol{R}}{\partial\vartheta^i}\frac{\partial\vartheta^i}{\partial s}\otimes\hat{\boldsymbol{V}}_F=\\ &= K_1^{(s)}\boldsymbol{V}_F\otimes\hat{\boldsymbol{V}}_F+\ldots\\ &\quad K_2^{(s)}\boldsymbol{A}_1\otimes\hat{\boldsymbol{V}}_F+K_3^{(s)}\boldsymbol{A}_2\otimes\hat{\boldsymbol{V}}_F \qquad (8)\end{aligned}$$

where $\boldsymbol{A}_i$ are the unit vectors defining the cross-fibre orientations in the reference configuration such that $(\boldsymbol{V}_F,\boldsymbol{A}_1,\boldsymbol{A}_2)$ spans an orthonormal basis.

3 VARIATIONAL PRINCIPLE

As a first approach of the theory we explore the use of a linear constitutive law, allowing us to determine if the model can suitable capture deformation in the small strain strain range before investigating the computationally demanding requirements of testing a nonlinear constitutive based model.

We look at establishing a stored energy function relating to the fibrous material and the extra cellular matrix $\psi(\boldsymbol{U},\boldsymbol{K})$ as an additive function of the two material components as follows:

$$\psi=v_m\psi_{matrix}(\boldsymbol{U})+v_f\psi_{fibre}(\boldsymbol{U}^{(s)},\boldsymbol{K}^{(s)}) \tag{9}$$

where v_m and v_f are the respective volume fractions for the matrix and fibre components, such that $v_m+v_f=1$. Additionally, we define ψ_{fibre} as a decoupled function of the two fibre Cosserat strain measures.

$$\psi_{fibre}(\boldsymbol{U}^{(s)},\boldsymbol{K}^{(s)})=\psi_I(\boldsymbol{U}^{(s)})+\frac{l^2}{12}\psi_{II}(\boldsymbol{K}^{(s)}) \tag{10}$$

where linear hyperelastic material behaviour is assumed for both, the fibre and the matrix continuum, and l is the so called *characteristic length* of the underlying micro-structure. Assuming symmetry in cross fibre directions, they can be expressed as:

$$\begin{aligned} \psi_I(\boldsymbol{U}^{(s)}) &= \frac{1}{2}\left(EAU^{(s)2}_1 + GAU^{(s)2}_2 + GAU^{(s)2}_3\right) \\ \psi_{II}(\boldsymbol{K}^{(s)}) &= \frac{1}{2}\left(GJK^{(s)2}_1 + EI_2K^{(s)2}_2 + EI_2K^{(s)2}_3\right) \end{aligned} \quad (11)$$

where E is Young's modulus G is the shear modulus, J and I_2 are the second moments of area corresponding to torsion and bending and A is the cross sectional area of the fibre bundle. In this sense, the characteristic length, l, is incorporated directly in the cross sectional area, $A = \frac{\pi l^2}{4}$ and the second moments of area $I_2 = J/2 = \frac{\pi l^4}{32}$.

This allows us to express a variational principle as:

$$\delta\Psi = \int_{\mathcal{B}} \{\boldsymbol{n} : \delta\boldsymbol{U} + \boldsymbol{m} : \delta\boldsymbol{K}\}\, \mathrm{d}V - W_{ext} \quad (12)$$

where the force stress tensor, $\boldsymbol{n}$ and the couple stress tensor, $\boldsymbol{m}$, given by:

$$\begin{aligned} \boldsymbol{n} &= v_m \frac{\partial \psi_{matrix}}{\partial \boldsymbol{U}} + v_f \frac{1}{A}\frac{\partial \psi_I}{\partial \boldsymbol{U}} \\ \boldsymbol{m} &= v_f \frac{1}{A}\frac{l^2}{12}\frac{\partial \psi_{II}}{\partial \boldsymbol{K}} \end{aligned}$$

are work conjugate to $\boldsymbol{U}$ and $\boldsymbol{K}$ respectively. Note that the contributions from the fibre have been normalized by the cross sectional area.

4 APPLICATION TO CARDIAC TISSUE

A regularly functioning, healthy heart is consists mainly of myocardial fibres, occupying roughly two thirds of the volume (Cleutjens 1996), and an extracellular matrix (ECM). The ECM has various components, most notably collagen fibrils: composed 85% of type I, 11% type III and 3% type V (Caulfield and Janicki 1997), which are responsible for the structural support and contributes to the mechanical stiffness of the problem. Other minor components include elastin, various cells and proteins as described in Weber et al. (1988) and Jugdutt (2003).

In a regular cardiac cycle, the heart undergoes four distinct phases: passive filling, isovolumetric contraction, ejection and isovolumetric relaxation. When analysing the pressure-volume relation of the left ventricle, these four cycles form a closed loop. This initial research will focus on modelling the passive filling stage, whereby the left ventricle volume cavity and internal pressure increases to accommodate the inflow of oxygenated blood. In this phase the healthy cardiac tissue performs as a nonlinear hyperelastic orthotropic material (Usyk, Mazhari, & McCulloch 2000).

4.1 *Calibration*

To model the fibres as Cosserat 1D rods embedded in a 3D ECM space, we will need to be able to separate the material properties into their respective components. While there is experimental data available for cardiovascular tissue; most notably Demer and Yin (1983) and Dokos et al. (2002), who performed biaxial and shearing properties respectively, the data sets proved unsuitable for linear model parameter calibration due to the highly nonlinear material behaviour.

Rather, we calibrated our model using a previously verified model of the rat left myocardium that employed the orthotropic based relations. Calibration employed specific computational experiments investigating simple tension, pure shear and four point bending, where appropriate Dirichlet boundary conditions are applied restraining displacement and rotational fields. The latter only applies for the Cosserat continuum-based approach. We are able to calibrate our model parameters for both the linear, isotropic ECM and the Cosserat fibre in the small strain range.

The samples of comparison tissue specimens were composed utilizing the constitutive implementation of Usyk et al. (2000). The strain energy function is expressed as:

$$\Psi_{Usyk} = C\frac{(e^Q - 1)}{2} + C_{compr}(J\ln J - J + 1) \quad (13)$$

with $Q = b_{ff}E^2_{ff} + b_{ss}E^2_{ss} + b_{nn}E^2_{nn} + b_{fs}(E^2_{fs} + E^2_{sf}) + b_{fn}(E^2_{fn} + E^2_{nf}) + b_{ns}(E^2_{ns} + E^2_{sn})$.

This treats cardiac tissues as nonlinear, orthotropic and nearly incompressible. Herein, E_{ij} are the components of the *Green* strain tensor $\mathbf{E}$. The parameters b_{ij} are constants which determine the contribution of each strain component to the strain energy:

Table 1. Strain energy function coefficients for Usyk-based model.

Parameter	Value
b_{ff}	2.8
b_{ss}	1.0
b_{nn}	1.0
b_{fs}	6.4
b_{fn}	1.0
b_{ns}	1.0

The indices refer to components aligned with fibre axis, f, sheet axiss s, and sheet-normal axis, n. Additionally the scaling parameters for healthy tissue $C = 1$ kPa and $C_{comp} = 100$ kPa were used. For more details on this model and it's calibration, one can consult (Legner et al. 2013).

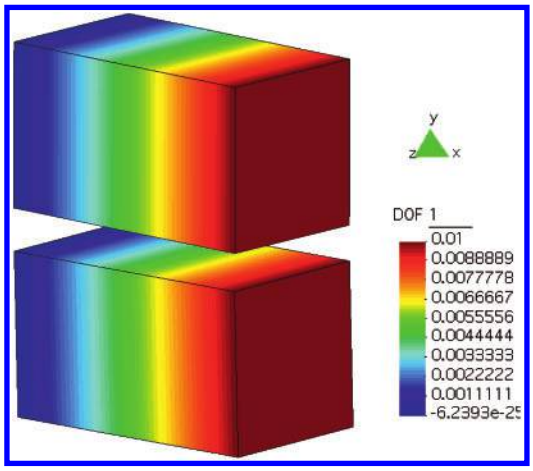


Figure 2. Deformation of Usyk-based (upper) and Cosserat (lower) for simple extension. Three of the six surface were unconstrained, allowing for extension in the direction of loading and contraction in orthogonal directions, while still enforcing a point of zero deformation.

4.2 *Initial results*

The corresponding Cosserat based model was successfully calibrated in each experiment (simple tension, pure shear and four-point bending) to within a tolerance of 0.05% of comparable stresses (or in the case of bending, with midpoint deflection). Figure 2 shows the deformation result of the Usyk-based and Cosserat based materials after calibration.

The following parameters are a result of the healthy tissue calibration:

Table 2. Material properties for Cosserat based constitutive law, modelling healthy cardiac tissue.

Parameter	Symbol	Fibre	EC matrix
Axial stiffness	E (kPa)	10.82	7.10
Shear Stiffness	G (kPa)	4.49	2.37
Characteristic length	l	0.59	–

It should be noted that the condition of near incompressibility is assumed for the isotropic ECM, as such Poisson's ration ν is modelled as 0.4999. This allows us to calibrate for only E_{ECM} and calculate G_{ECM} accordingly.

Following a myocardial infarction, the cardiac tissue experiences ischemia. The subsequent changes in tissue state and behaviour can be categorized into various stages: Acute, necrotic, fibrotic and remodelling. In the early phase of the infarct healing (acute ischemia), the tissue experiences a decrease in passive mechanical properties in the infarcted region (Holmes et al. 2005). The initial healing phase before necrosis was deliberately chosen as the micro structure of the cardiac tissue is mostly unchanged, removing the need for altering the volume ratios. To simulate this in

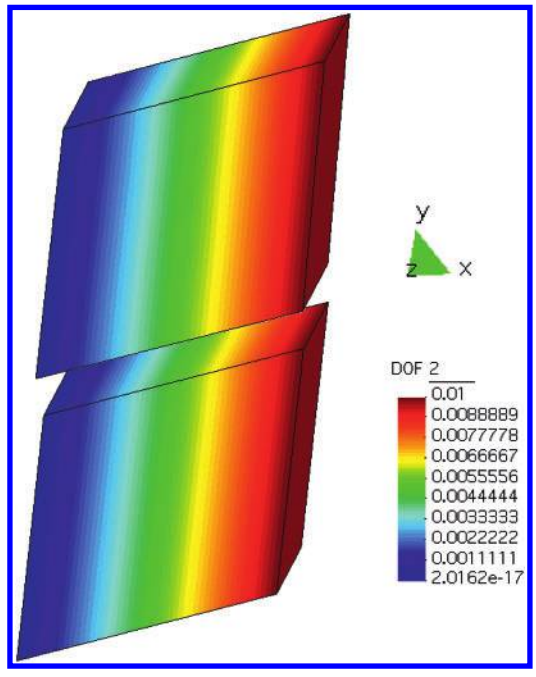


Figure 3. Shear deformation of Usyk-based (upper) and Cosserat (lower) for the pure shear experiment. Only the deformation in the direction of the applied shearing force is presented as the other deformation are trivial.

our comparison specimens, we employ the approach of Kortsmit et al. (2012), where the scaling coefficient in the Usyk formulation is reduced accordingly to $C = 0.44$ kPa.

The calibration of the Cosserat model applied to the above mentioned diseased state followed the same procedure as the healthy state and produced the following parameters:

Table 3. Material properties for Cosserat based constitutive law, modelling cardiac tissue in diseased state.

Parameter	Symbol	Fibre	EC matrix
Axial stiffness	E (kPa)	4.10	3.22
Shear Stiffness	G (kPa)	2.03	1.07
Characteristic length	l	0.851	–

In figure 3 the deformation results of the Usyk-based and Cosserat based materials are presented, for the model's calibration in the diseased state.

5 DISCUSSION

It was found through the calibration process that enforcing boundary conditions on the rotational degrees of freedom is essential to establish a well defined generalized continuum.

Mention must be made to the increase in the calibrated Cosserat characteristic length, l, from the healthy to diseased state. As the stress components in 12 have been normalized with respect to A, the primary function of l is to scale the stiffness contributions associated with flexure. In the case of calibration for bending, the weakened diseased material is especially susceptible to bending deformation and l subsequently compensates.

An interesting case to explore would be in the later stages of healing, where the diseased tissue microstructure changes. A significant portion of the cardiomyocytes would have decayed through necrosis and the volume content of the extra cellular matrix increases, with a rising contribution from collagen (Jugdutt & Amy 1986), making the infarct *stiffer*. As the volume fractions in the Cosserat continuum are explicit in the formulation it would allow for more realistic physical representation of the material, directly.

Application of the Cosserat fibre-based anisotropy model to the heart would require $\boldsymbol{V}_F$ defined for each material point $P(\xi, \eta, \theta)$. With respect to geometric boundary conditions along with displacement restraints one would apply to the base of the LV, our proposed approach also allows direct enforcement of rotational boundary conditions restraining the twist of the left ventricle. This enables the rest of the domain to experience more realistically the complex deformation modes including stretching, shearing, twisting and bending.

6 CONCLUSIONS

This initial investigation into the feasibility of using the Cosserat continuum to model cardiac tissue, illustrates the successful capability in capturing the material response in the small strain deformation range.

The linear model is not suitable to realistically capture the deformation behaviour of biological tissue which is characterized by large strains, and must be replaced with a nonlinear, preferably exponential form of (11).

The future investigation of this work, lies in the implementation of the nonlinear model, capable of capturing larger strain deformations and the application to more realistic geometries.

REFERENCES

Caulfield, J. B. & J. S. Janicki (1997). Structure and function of myocardial fibrillar collagen. *Technology and Health Care 5*(1), 95–113.

Cleutjens, J. P. (1996). The role of matrix metalloproteinases in heart disease. *Cardiovascular research 32*(5), 816–821.

Costa, K. D., J. W. Holmes, & A. D. McCulloch (2001). Modelling cardiac mechanical properties in three dimensions. *Philosophical Transactions of the Royal Society A 359*, 1233–1250.

Demer, L. L. & F. C. P. Yin (1983). Passive biaxial mechanical properties of isolated canine myocardium. *Journal of Physiology 339*, 615–630.

Dokos, S., B. H. Smaill, A. A. Young, & I. J. LeGrice (2002). Shear properties of passive ventricular myocardium. *American Journal of Physiology – Heart and Circulatory Physiology 283*, H2650–H2659.

Holmes, J. W., T. K. Borg, & J. W. Covell (2005). Structure and mechanics of healing myocardial infarcts. *Annual Review of Biomedical Engineering 7*, 223–253.

Holzapfel, G. A. & R. W. Ogden (2009, Sep 13). Constitutive modelling of passive myocardium: a structurally based framework for material characterization. *Philosophical Transactions of the Royal Society a-Mathematical Physical and Engineering Sciences 367*(1902), 3445–3475.

Holzapfel, G. A. (2004). *Encyclopedia of Computational Mechanics*, Chapter Computational Biomechanics of Soft Biological Tissue. John Wiley & Sons.

Jugdutt, B. I. & R. W. Amy (1986). Healing after myocardial infarction in the dog: changes in infarct hydroxyproline and topography. *Journal of the American College of Cardiology 7*(1), 91–102.

Jugdutt, B. I. (2003, Sep 16). Ventricular remodeling after infarction and the extracellular collagen matrix: when is enough enough? *Circulation 108*(11), 1395–403.

Karšaj[1], I., C. Sansour, & J. Sorić (2008). Numerical modelling of fibre reorientation at soft tissue.

Kortsmit, J., N. H. Davies, R. Miller, J. R. Macadangdang, P. Zilla, & T. Franz (2012). The effect of hydrogel injection on cardiac function and myocardial mechanics in a computational post-infarction model. *Computer Methods in Biomechanics and Biomedical Engineering* (ahead-of-print), 1–11.

Legner, D., S. Skatulla, J. MBewu, R. R. B. Reddy, C. Sansour, N. Davies, & T. Franz (2013). Studying the influence of hydrogel injections into the infarcted left ventricle using the element-free galerkin method. *International Journal for Numerical Methods in Biomedical Engineering*. Under review.

Sansour, C. & S. Skatulla (2008). A non-linear cosserat continuum-based formulation and moving least square approximations in computations of size-scale effects in elasticity. *Computational Materials Science 41*, 589–601.

Schmid, H.H. (2006). Myocardial material parameter estimation—a comparative study for simple shear. *Journal of biomechanical engineering 128*(5), 742.

Usyk, T., R. Mazhari, & A. McCulloch (2000). Effect of laminar orthotropic myofiber architecture on regional stress and strain in the canine left ventricle. *Journal of Elasticity 61*, 143–164. 10.1023/A:1010883920374.

Wang, C.-C. (1970). A new representation theorem for isotropic functions. *Archive for Rational Mechanics and Analysis 36*(3), 166–197.

Weber, K., J. Janicki, S. Shroff, R. Pick, R. Chen, & R. Bashey (1988). Collagen remodeling of the pressure-overloaded, hypertrophied nonhuman primate myocardium. *Circulation research 62*(4), 757–765.

Zheng, Q. (1994). Theory of representations for tensor functions—a unified invariant approach to constitutive equations. *Applied Mechanics Reviews 47*(11), 545–587.

Research and Applications in Structural Engineering, Mechanics and Computation – Zingoni (Ed.)
© 2013 Taylor & Francis Group, London, ISBN 978-1-138-00061-2

Buckling analysis of thin composite plates reinforced by carbon nanotubes (CNTs) using finite strip methods (F.S.M)

M. Pazoki & M. Azhari
Department of Civil Engineering, Isfahan University of Technology, Isfahan, Iran

A. Heidarpour
Department of Civil Engineering, Monash University, Australia

ABSTRACT: Due to high mechanical strength, Carbon Nanotubes (CNTs) as single walled carbon nanotubes, are being considered as Nano scale fibers to enhance the performance of polymer composite materials. An improvement of the physical properties of polymer Nano-composites, based on Carbon Nanotubes (CNTs), is devoted to a good dispersion and strong interactions between the matrix and the filler. Theoretical studies indicate that the tensile modulus of multi-walled nanotubes may reach 1 TPa.In the present study, the composite rectangular thin plate reinforced with Single-Walled Carbon Nanotubes (SWCNTs) is subjected to axial and biaxial loads and the critical buckling load of plate is calculated using Classical Plate Theory (CPT). Finite Strip Method (F.S.M) is employed to derive buckling equations. The Mori-Tanaka method is further used to calculate the effective elastic modulus of composites having aligned oriented straight CNTs. Furthermore the effect of CNTs agglomeration is investigated when CNTs are dispersed non- uniformly in the polymer matrix. The effects of aspect ratio and the edge conditions on the critical buckling load are also considered.

Keywords: Buckling, Mori-Tanaka, Nano composite, Carbon Nanotubes (CNTs), Finite Strip Method

1 INTRODUCTION

Since the discovery of carbon nanotubes(CNTs) by Ijima in 1991 (Iijima, 1991), several research works have been conducted by using CNTs in different areas of science and technology. Nowadays, due to the increasing need for materials with different mechanical properties, the use of Nano materials including Nano composites has been extended into the industry. These composites consist of two phases: the matrix phase and the phase composed of Nano-scale morphologies. Good mechanical and thermal properties of these materials could have important effects on the composite strength. Among the Nano-materials, Carbon nanotubes (CNTs) are noticeable. Due to lower resistance of the matrix phase relative to the reinforced phase, when the plate undergoes different loads the loads are transferred to the reinforcement phase (Yakobson et al., 1996, Yu et al., 2000, Zhang et al., 2002).

Griebel et al. compared experimentally the effect of aligned CNTs in polymer reinforcement (Griebel and Hamaekers, 2004). They concluded that for a constant compressive force, if the direction of nanotube axis is parallel to the force direction, the polymer composite would have higher resistance against the exerted force. Also, if the compressive force is perpendicular to nanotube axis, the composite longitudinal modulus would be improved slightly compared to bare polymer matrix. In the case of non-directional compressive loads, randomly arranged nanotubes will give better invariant modulus in comparison to the aligned ones (Griebel and Hamaekers, 2004). Formica et al. studied the vibrational properties of carbon nanotube reinforced composites (CNTRC) by means of an equivalent continuum model and Shelby-Mori-Tanaka approach (Formica et al., 2010).

Alibeigloo (Alibeigloo, 2012) continued the research by investigating the buckling of functionally graded Nano-composites aligned by SWCNTs subjected to uniaxial and biaxial in-plane loadings based on the first-order shear deformation theory (FSDT).

Hitherto, there is no available theoretical study investigating the buckling of plates reinforced by randomly oriented CNTs using finite strip method. In this paper, considering the enhanced mechanical properties of carbon nanotubes, buckling analysis of composite plates reinforced with randomly oriented CNTs are investigated. For the buckling analysis of plates under in plane loads and different boundary condition, the finite strip method (FSM) is used. FSM was developed by Cheung (Cheung, 1976). This method is efficient for plate analysis of all loading and support conditions. Finite strip method is based on the harmonic functions where the plate is divided into limited strips. Comparison of the present results for the plate

buckling coefficient for 0% volume fraction of CNTs (0% CNTs) with those obtained by other theoretical studies have shown the good accuracy of the present method.

2 THEORETICAL METHOD

2.1 *Eshelby-Mori-Tanaka method*

In the present study, the Eshelby-Mori-Tanaka method is used to determine the properties of the composites reinforced with carbon nanotubes. This method is based on the Eshelby equivalent inclusion idea and the average stress method (Mori and Tanaka, 1973, Benveniste, 1987). Therefore, the following equation expresses the tensor of effective elastic moduli $\mathbf{D}^*$:

$$\mathbf{D}^* = (V_m \mathbf{E}_m + V_{CNT} (\mathbf{E}_{CNT}^T \mathbf{A}))^T (V_m \mathbf{I} + V_{CNT} \mathbf{A})^{-1} \quad (1)$$

Where, $\mathbf{V}_m$ and $\mathbf{V}_{CNT}$ represent the volume fractions of matrix and CNTs phase, respectively. Also, $\mathbf{E}_m$ and $\mathbf{E}_{CNT}$ are the tensors of elastic moduli for each phase, $\mathbf{I}$ is the demonstrator of the fourth-order unit tensor and $\mathbf{A}$ is the partial concentration factor ($\varepsilon_{CNT} = A\varepsilon_m$), where ε_{CNT} and ε_m are the strain matrices for each phase and $\mathbf{A}$ is given by the following equation such that:

$$\mathbf{A} = (\mathbf{I} + \mathbf{S}^T \mathbf{E}_m^{-T} (\mathbf{E}_{CNT} - \mathbf{E}_m))^{-1} \quad (2)$$

In Eq. (2) $\mathbf{S}$ is the fourth-order Eshelby tensor (Eshelby and Eshelby, 1957), which is expressed as:

$$S_{ijkl} = \frac{5\nu - 1}{15(1-\nu)} \delta_{ij}\delta_{kl} + \frac{4 - 5\nu}{15(1-\nu)} (\delta_{ik}\delta_{jl} + \delta_{il}\delta_{jk}) \quad (3)$$

in ν is Poisson's ratio of matrix phase.

2.2 *Composites reinforced with randomly oriented, straight CNTs*

Figure 1 shows the orientation of straight CNT nanotubes in two different coordinate systems denoted by angles α and β. The global (X_1, X_2, X_3) and local (X_1', X_2', X_3') coordinate systems are shown in Figure 1.

The transformation matrix components a_{ij} forms a relationship between global and local coordinate systems such that:

$$e_i = a_{ij} e_j \quad (4)$$

In which, the transformation matrix $\mathbf{a}$ is obtained from:

$$\mathbf{a} = \begin{bmatrix} \cos\beta & -\cos\alpha\sin\beta & \sin\alpha\sin\beta \\ \sin\beta & \cos\alpha\cos\beta & -\sin\alpha\cos\beta \\ 0 & \sin\alpha & \cos\alpha \end{bmatrix} \quad (5)$$

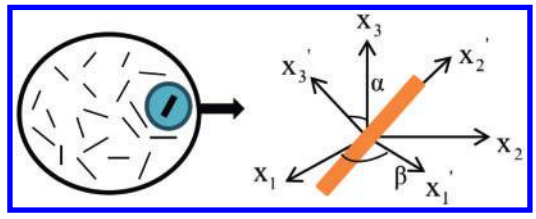


Figure 1. Randomly oriented carbon nanotubes.

Carbon nanotubes are distributed in matrix by a probability density function P(α, β) in which the overall probability is unit:

$$\int_0^{2\pi} \int_0^{\pi/2} P(\alpha,\beta) \sin\alpha d\alpha d\beta = 1 \quad (6)$$

For plenary randomly oriented CNTs with uniform distribution in the matrix volume P(α, β) is equal to $\pi/2$.

According to Eshelby-Mori-Tanaka method, the relations between the CNTs strain (ε_{CNT}) and stress (σ_{CNT}), and the matrix stress (σ_m) are (Huang et al., 2004):

$$\begin{cases} \boldsymbol{\varepsilon}_{CNT}(\alpha,\beta) = \mathbf{A}(\alpha,\beta)^T \boldsymbol{\varepsilon}_m = \mathbf{A}(\alpha,\beta)^T C_m^{-T} \boldsymbol{\sigma}_m \\ \boldsymbol{\sigma}_{CNT}(\alpha,\beta) = \mathbf{E}_{CNT}^T \mathbf{A}(\alpha,\beta)^T \boldsymbol{\varepsilon}_m = (\mathbf{E}_{CNT}^T \mathbf{A}(\alpha,\beta)^T C_m^{-1})^T \boldsymbol{\sigma}_m \end{cases} \quad (7)$$

where $\mathbf{A}(\alpha, \beta)$ is expressed by Eq. 2. Thus, the average strain and stress of randomly oriented CNTs in matrix are given by:

$$\begin{cases} \{\varepsilon_{CNT}\} = (\int_0^{2\pi} \int_0^{\pi/2} P(\alpha,\beta) \mathbf{A}(\alpha,\beta) \sin(\alpha) d\alpha d\beta)^T \varepsilon_m \\ \{\sigma_{CNT}\} = (\int_0^{2\pi} \int_0^{\pi/2} P(\alpha,\beta) (\mathbf{A}(\alpha,\beta)^T C_m^{-1}) \sin(\alpha) d\alpha d\beta)^T \sigma_m \end{cases} \quad (8)$$

Finally, according to the Eshelby-Mori-Tanaka method, the relations between average stress and strain of isotropic composites can be written as:

$$\begin{cases} \boldsymbol{\sigma} = f_m \boldsymbol{\sigma}_m + f_r \boldsymbol{\sigma}_r \\ \boldsymbol{\varepsilon} = f_m \boldsymbol{\varepsilon}_m + f_r \boldsymbol{\varepsilon}_r \end{cases} \Rightarrow \boldsymbol{\sigma} = \boldsymbol{D}^* \boldsymbol{\varepsilon} \quad (9)$$

This indicates that the composite reinforced with randomly oriented (and straight) CNTs is isotropic.

3 BUCKLING ANALYSIS

3.1 *Displacement field*

The Kirchhoff theory is used to investigate thin plates. In this theory, the out-of-plane displacements of the plate, w, is expressed as:

$$w_{ij} = \sum_{i=1}^{4} \sum_{i=1}^{m} (N_i(x) Y_j \delta_{ij}) \quad (10)$$

in which, δ is the nodal displacement vector, Y_j is the longitudinal term which is given by:

$$Y_j(y)=\sin\left(\frac{\lambda_j y}{L}\right)\qquad \lambda_j=j\pi \tag{11a}$$

when both ends are simply supported, and

$$Y_j(y)=\sin\frac{\lambda_j y}{L}-c_j\sinh\frac{\lambda_j y}{L},\quad \lambda_j=\frac{4j+1}{4}\pi,\quad c_j=\frac{\sin\lambda_j}{\sinh\lambda_j} \tag{11b}$$

when one end is simply supported and the other is fixed, and

$$Y_j(y)=\sin\frac{\lambda_j y}{L}-\sinh\frac{\lambda_j y}{L}-c_j\left(\cos\frac{\lambda_j y}{L}-\cosh\frac{\lambda_j y}{L}\right)\qquad \lambda_j=\frac{2j+1}{2}\pi,\quad c_j=\frac{\sin\lambda_j-\sinh\lambda_j}{\cos\lambda_j-\cosh\lambda_j} \tag{11c}$$

when both ends are fixed.

In Eqs. 11, L is the length of strip and $j=1,2,\ldots,m$. In Eq. 10, N_i is the Hermitian transverse shape functions expressed as

$$\begin{cases} N_1(x)=1-3\bar{x}^2+2\bar{x}^3 & N_2(x)=x(1-2\bar{x}+\bar{x}^2) \\ N_3(x)=3\bar{x}^2-2\bar{x}^3 & N_4(x)=x\left(\bar{x}^2-2\bar{x}\right) \end{cases}\qquad \bar{x}=x/b \tag{12}$$

where b is width of strip.

3.2 *Total potential energy* Π

The total potential energy of the plate is defined as summation of strain energy and the work done by the applied load. The strain energy $\boldsymbol{U}$ for each strip of the plate is given by:

$$U_f=\frac{1}{2}\{\delta_f\}^T\left[K_f\right]\{\delta_f\} \tag{13}$$

where the elements of the stiffness matrix $[K_f]$ are obtained from:

$$\left[K_{f\,ij,mn}\right]=\iint_\Omega\left[B_f\right]_{ij}^T\left[D_f\right]\left[B_f\right]_{mn}dxdy \tag{14}$$

in which $\mathbf{B_f}$ is the strain matrix and the vector $\{\varepsilon_f\}$ can be expressed as

$$\{\varepsilon_f\}=\left[B_f\right]\{\delta_f\} \tag{15}$$

In Eq. (14) $\mathbf{D_f}$ represents the elastic matrix given by:

$$\left[D_f\right]=\frac{Eh^3}{12(1-\nu^2)}\begin{bmatrix}1 & \nu & 0\\ \nu & 1 & 0\\ 0 & 0 & (1-\nu)/2\end{bmatrix} \tag{16}$$

The work done by the applied load can be written as:

$$V_p=\frac{1}{2}\{\delta_f\}^T\left[K_g\right]\{\delta_f\} \tag{17}$$

in which the geometric matrix $[K_g]$ for each strip is defined as:

$$\left[K_{g\,ij,mn}\right]=\iint_\Omega\left[B_g\right]_{ij}^T\left[\sigma_g\right]\left[B_g\right]_{mn}dxdy \tag{18}$$

where σ_g is the in-plane stress matrix determined by:

$$\left[\sigma_g\right]=\begin{bmatrix}\sigma_x & \sigma_{xy}\\ \sigma_{xy} & \sigma_y\end{bmatrix} \tag{19}$$

3.3 *Eigenvalue equation*

Using the principle of virtual work minimization of the total potential energy results in the eigenvalue equation such that

$$\left(\left[K_f\right]-\sigma_0\left[K_g\right]\right)\{\delta\}=\{0\} \tag{20}$$

in which σ_0 is the buckling parameter.

4 ILLUSTRATION

In this study, Polystyrene and SWCNTs are matrix and reinforcement phase of composite plate, respectively. The Young's modulus of polystyrene and SWCNTs are assumed to be $E_m=1.9$ GPa and $E_{CNT}=1$ TPa, respectively and the Poisson's ratio for both of them is taken as $\nu=0.3$.

Many scholars have attempted to analyze the buckling of plates by different numerical methods such as the finite strip method (Mizusawa, 1993) and exact solution (Hosseini-Hashemi et al., 2008).

Table 1 shows the local buckling coefficients of plates under various loadings and boundary conditions while the magnitude of the length to width (a/b) ratio is equal to 1. The buckling coefficients have also been compared with the finite strip method (Mizusawa, 1993) and the exact solution (Hosseini-Hashemi et al., 2008).

By comparison of the present results with the results obtained by F.S.M and exact solution method for uniaxial and biaxial load, it can be seen that the method proposed in this paper is accurate for 0% CNTs (Table 1). Due to high modulus elasticity of carbon nanotubes, the local plate buckling coefficients is increase when the volume fraction of carbon nanotubes increases.

Table 2 presents the results for buckling of the plates with different boundary conditions under uniaxial loading where the length to width ratios (a/b) is assumed to be 1. It can be seen that the use of reinforcing CNTS is effective for increasing the loading of the plate and results in the increase of plate strength.

Figures 2 and 3 depict the variations of the local buckling coefficient (K) of composite plates under uniaxial pressure with different volume fractions of CNTs and various length to width ratios (a/b). The boundary conditions are assumed to be simply supported (Fig. 2) or fully clamped (Fig. 3).

Table 1. Local buckling coefficient for uniaxial and biaxial load.

	Boundary condition	F.S.M Mizus. (1993)	Exact Hosse. (2008)	0%CNTs	1%CNTs	5%CNTs	10%CNTs
Uniaxial load	SSSS	4	4	4	5.6	12.01	20.23
	CSCS	6.74	6.74	6.744	9.42	20.25	34.11
	CSSS	4.84	4.84	4.854	6.78	14.58	24.55
	CSFS	2.39	2.39	2.39	3.38	7.17	12.08
	SSFS	2.36	2.36	2.37	3.34	7.19	12.12
	SCSC	7.69	–	7.69	10.76	23.13	38.96
	CCCC	10.08	–	10.08	14.1	30.3	51.02
Biaxial load	SSSS	2	2	2	2.79	6	10.11
	CSFS	1.14	1.14	1.15	1.61	3.74	5.84
	SSFS	1.05	1.05	1.064	1.48	3.19	5.38
	CCCC	–	–	5.316	7.43	15.94	26.85

Table 2. Local buckling coefficient for general boundary conditions.

Boundary condition	0%CNTs	1%CNTs	5%CNTs	10%CNT
CCSC	8.38	11.73	25.14	42.33
CCCS	8.07	11.28	24.24	40.87
CSCF	4.38	6.12	13.21	22.27
CCCF	4.59	6.42	13.84	23.32
CFCF	3.92	5.49	11.82	19.91
SSSC	5.74	8.02	17.24	29.03
SSSF	1.40	1.96	4.26	7.18
SCSF	1.66	2.32	5.03	8.48
SFSF	0.95	1.33	2.88	4.86

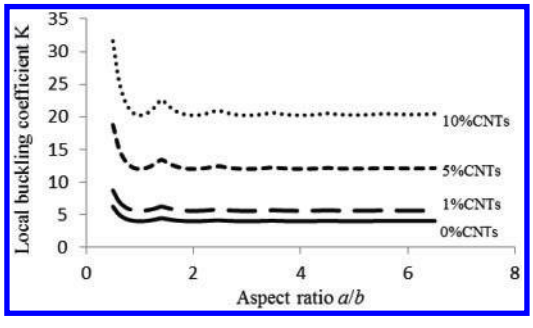


Figure 2. Local buckling Coefficient for simply condition.

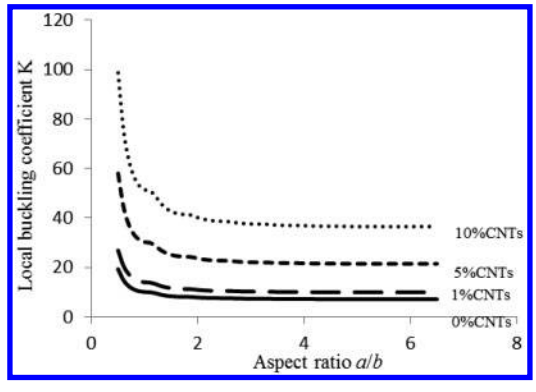


Figure 3. Local buckling Coefficient for clamped condition.

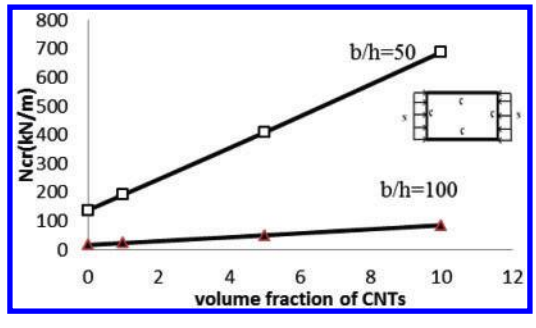


Figure 4. Critical buckling load for clamped plate.

It can be seen from Figures 2 and 3 that the local buckling coefficient decrease when the length to width ratio of the plate increase. From the other side, it can be easily seen that CNTs can considerably increase the plate resistance against buckling.

The effect of the value of the width to thickness ratio (b/h) on the buckling of composite plates is shown in Figure 4. It can be seen that the critical buckling load (N_{cr}) of the fully clamped composite plate increases when the volume fraction of CNTs increase or when the value of width to thickness ratio decreases.

5 CONCLUSIONS

In this study the buckling analysis of thin plates reinforced with randomly distributed single-walled carbon nanotubes (SWCNTs) using the finite strip method was investigated. To obtain the elastic modulus of the composite plates, Mori-Tanaka theory was employed. This theory proposes an analytical method to obtain the internal stress of the composite plates. It was shown that when the volume fraction of carbon nanotubes in

the composite plates increases, the stiffness and critical buckling load of the composites increase which is due to the high modulus elasticity of carbon nanotubes. Also, it has been shown that by reducing the width to thickness ratio and the critical buckling load increases.

REFERENCES

Alibeigloo, A. 2012. Static analysis of functionally graded carbon nanotube-reinforced composite plate embedded in piezoelectric layers by using theory of elasticity. *Composite structures*.

Benveniste, Y. 1987. A new approach to the application of Mori-Tanaka's theory in composite materials. *Mechanics of materials,* 6, 147–157.

Cheung, Y. K. 1976. Finite strip method in structural analysis.

Eshelby, J. D. & Eshelby, J. 1957. The determination of the elastic field of an ellipsoidal inclusion, and related problems. *Proceedings of the Royal Society of London. Series A. Mathematical and Physical Sciences,* 241, 376–396.

Formica, G., Lacarbonara, W. & Alessi, R. 2010. Vibrations of carbon nanotube-reinforced composites. *Journal of Sound and Vibration,* 329, 1875–1889.

Griebel, M. & Hamaekers, J. 2004. Molecular dynamics simulations of the elastic moduli of polymer–carbon nanotube composites. *Computer methods in applied mechanics and engineering,* 193, 1773–1788.

Hosseini-hashemi, S., Khorshidi, K. & Amabili, M. 2008. Exact solution for linear buckling of rectangular Mindlin plates. *Journal of Sound and Vibration,* 315, 318–342.

Huang, Y. Y., Hwang, K.-C. & Gao, H. 2004. The effect of nanotube waviness and agglomeration on the elastic property of carbon nanotube-reinforced composites. *Urbana,* 51, 61801.

Iijima, S. 1991. Helical microtubules of graphitic carbon. *nature,* 354, 56–58.

Mizusawa, T. 1993. Buckling of rectangular Midlin plates with tapered thickness by the spline strip method. *International Journal of Solids and Structures,* 30, 1663–1677.

Mori, T. & Tanaka, K. 1973. Average stress in matrix and average elastic energy of materials with misfitting inclusions. *Acta metallurgica,* 21, 571–574.

Yakobson, B. I., Brabec, C. & Bernholc, J. 1996. Nanomechanics of carbon tubes: Instabilities beyond linear response. *Physical review letters,* 76, 2511–2514.

Yu, M. F., Files, B. S., Arepalli, S. & Ruoff, R. S. 2000. Tensile loading of ropes of single wall carbon nanotubes and their mechanical properties. *Physical review letters,* 84, 5552–5555.

Zhang, P., Huang, Y., Geubelle, P., Klein, P. & Hwang, K. 2002. The elastic modulus of single-wall carbon nanotubes: a continuum analysis incorporating interatomic potentials. *International Journal of Solids and Structures,* 39, 3893–3906.

Research and Applications in Structural Engineering, Mechanics and Computation – Zingoni (Ed.)
© 2013 Taylor & Francis Group, London, ISBN 978-1-138-00061-2

Identification of nonlinear hyperelastic material parameters for healthy myocardial tissue via an inverse method based on modelling the passive filling stage of the cardiac cycle

M. Essack & S. Skatulla
CERECAM and the Department of Civil Engineering, University of Cape Town, South Africa

ABSTRACT: In order to fully comprehend the function of biological tissue in the context of the canine left ventricle, it is required that proper material parameters are identified that govern the materials behaviour according to a particular set of constitutive laws. For the purposes of this research, the passive filling stage of the cardiac cycle is modelled with a non linear hyperelastic orthotropic material law (Usyk, Mazhari, & McCulloch 2000). Inherent to this constitutive law are eight material parameters namely A, A_{compr} and b_{ij}, where i, j $\in$ (1, 2, 3). In order to calibrate the material parameters of this model to experimental data, or any patient specific application for that matter, a nonlinear optimization algorithm in the form of the Bounded Levenberg-Marquardt algorithm, with the additional option of a line search is implemented in the in-house modelling software SESKA. In order to test the algorithm implementation, pseudo experimental data are generated with a set of assumed to be true parameters for a canine ellipsoidal left ventricle geometry. Consequently, the implemented algorithms ability to converge towards this true set of parameters from a number of different initial starting points is tested. For the case of the conventional Bounded Levenberg-Marquardt algorithm implementation, material parameters converge quickly towards the true values provided that the initial guess for parameters is close enough to the true set. However, for initial parameter guesses that are far from the true values, parameters may converge to a ridge in the cost function, which does not represent a minimum in the cost function surface. Furthermore, when the conventional Levenberg-Marquardt algorithm is combined with a line search, parameters are more likely to converge towards a local minimum within a well defined range, regardless of whether the initial parameter guess is good or not. However, it should be noted that the line search does not assure convergence of material parameters to a global minimum in the cost function, it just prevented convergence of parameters towards ridges in the cost function.

1 INTRODUCTION

In order to fully comprehend the function of biological tissue in the context of the left ventricle, it is required that proper material parameters are identified that govern the materials behaviour according to a particular set of constitutive laws.

Despite continued progress in the treatment of infarcted myocardium within the left ventricle, current treatments continue to be challenged to consistently improve myocardium function for extended durations. Improved approaches for myocardium repair rests upon the ability to more fully comprehend and simulate its functions. Consequently, appropriate material parameters need to be derived for both healthy and infarcted myocardium within the left ventricle.

Although it is the ultimate objective of this line of research to identify material parameters for both the healthy and diseased states of the left ventricle, this paper is limited to only the healthy case. In addition, only the passive filling phase of the left ventricle cardiac cycle is considered, and the associated passive material parameters that govern this phase of the cardiac cycle.

Many methods have been proposed in order to identify the material properties of passive myocardium, however, this research shall focus on a fairly new field, involving updating methods of inverse modelling (Avril, Bonnet, Bretelle, Grdiac, Hild, Ienny, Latourte, Lemosse, Pagano, Pagnacco, & Pierron 2007). Such methods involve the computation of displacement, strain, stress, pressure or volume fields numerically (i.e. using computer simulations), using initial estimates or guesses for material parameters defined in the particular constitutive law chosen. The actual constitutive material parameters are then identified by minimizing a cost function, which compares available strain, displacement, stress, pressure or volume measurements from experimental testing, to the corresponding results simulated via an FEM analysis.

In addition, minimization of the cost function is conducted via the use of an optimization algorithm. Since the number of material parameters that need to be identified within the passive filling stage of the

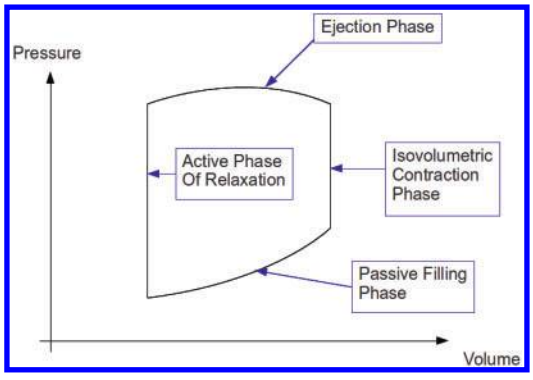


Figure 1. Idealized representation of the left ventricle cardiac cycle.

cardiac cycle is small, it was deemed adequate to utilize a local, gradient based algorithm based on the Levenberg-Marquardt algorithm (Marquardt 1963), with the option of an additional line search algorithm, in order to ensure convergence of parameters to at least a local minimum of the cost function, within a predefined range (Yu 2004). This algorithm is implemented in the in-house modelling software SESKA, which is also used to generate the required simulated data fields that are core to the cost function.

Consequently, this paper shall outline the portions of the cardiac cycle that have been modelled, followed by an exploration of what inverse modelling entails. Next, methods for material parameter identification shall be explored, followed by an outline of the conventional Levenberg-Marquardt and modified Levenberg-Marquardt algorithms implemented in SESKA. Finally, the results of numerical simulations of the passive filling stage of a ellipsoidal canine left ventricle geometry shall be presented, followed by a discussion of key observation of the behaviour of the optimization algorithm in terms of its convergence properties towards a unique set of material parameters.

2 MODELLING THE CARDIAC CYCLE

Figure 1 is an illustration of an idealized cardiac cycle, which is similar to what would be simulated via a computational analysis. In addition, figure 2 is an illustration of the idealized canine ellipsoidal left ventricle model, which was constructed using the preprocessing software GID, and was used for all numerical simulations in this paper. In addition, the left ventricle model is disrcretized with sixty six particles, and comprises of sixty six tetrahedral elements.

It is clear from figure 1 that the cardiac cycle is split into various phases. In the following section only the passive filling stage of the cardiac cycle shall be explained (Niederer & Smith 2009). In addition, the constitutive model that is implemented in the cardiac mechanics module of SESKA, in order to simulate the passive filling phase shall be introduced.

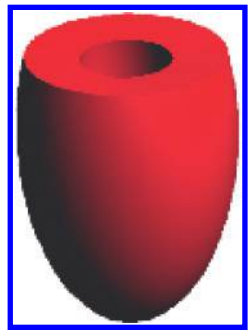


Figure 2. Ellipsoidal left ventricle geometry.

2.1 *Passive filling*

This is the first phase of the cardiac cycle and is also referred to as diastole. In this phase the left atrium and the mitral valve open, allowing blood to fill the ventricle. Consequently, the left ventricle cavity volume increases and the pressure increases as more blood causes the ventricle to inflate. During this phase, healthy myocardial tissue is modelled as a non linear hyperelastic orthotropic material (Usyk, Mazhari, & McCulloch 2000).

3 MATERIAL PARAMETER IDENTIFICATION

In the previous section, the passive filling phase of the cardiac cycle was explained, as well as the constitutive law that is implemented in the cardiac mechanics module of SESKA in order to simulate it.

Within the passive filling phase of the cardiac cycle, the behaviour of myocardial tissue is simulated using a non linear hyperelastic orthotropic material model with the following strain energy function (Usyk, Mazhari, & McCulloch 2000).

$$W = A(e^{Q} - 1)/2 + A_{compr}\Big\{ det[U]\,ln(det[U]) - det[U] + 1)\Big\} \quad (1)$$

Where:

$$Q = b_{11}\hat{E}_{11}^2 + b_{22}\hat{E}_{22}^2 + b_{33}\hat{E}_{33}^2 + b_{12}(\hat{E}_{12}^2 + \hat{E}_{21}^2) + b_{13}(\hat{E}_{13}^2 + \hat{E}_{31}^2) + b_{23}(\hat{E}_{23}^2 + \hat{E}_{32}^2) \quad (2)$$

Firstly, E_{ij} (i,j $\in$ (1,2,3)) are components of the Green strain **E**, and the right stretch tensor is denoted by U.

From the strain energy function illustrated by equation 1, it is clear that the behaviour of healthy myocardial tissue within the passive filling stage depends on eight material parameters, namely; A, A_{compr}, and b_{ij}, where i,j $\in$ (1,2,3). However, the stiffness of the myocardial tissue is primarily governed by parameters A and A_{compr}. Consequently, parameters b_{ij} which govern the anisotropy of the material are neglected from

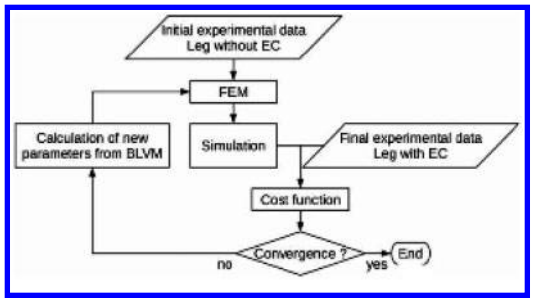


Figure 3. Schematic of updating methods of inverse modelling.

the numerical optimization, and only the main stiffness parameters; A and A_{compr} are optimized for during the passive filling of the cardiac cycle.

Consequently, parameters A and A_{compr} are identified via an inverse method which shall be explained briefly in the following section.

3.1 *Inverse modelling*

Identification of constitutive parameters A and A_{compr} was conducted using numerical simulations (using SESKA) in combination with experimental measurements of kinematic field variables, i.e. pressure, volume data relating to the passive filling stage of the cardiac cycle. This method of parameter identification is referred to as an updating method of inverse modelling (Avril, Bonnet, Bretelle, Grdiac, Hild, Ienny, Latourte, Lemosse, Pagano, Pagnacco, & Pierron 2007). The basic schematic of updating methods of inverse modelling is illustrated in figure 3.

For the purposes of this paper, pseudo experimental data for the passive filling stage of the cardiac cycle is generated, instead of using actual data, as the objective is to ascertain whether the optimization algorithm (which shall be explained in detail later in this paper) performs as required. This pseudo experimental data is generated using a set of assumed to be true material parameters for the constitutive law found in literature (Usyk, Mazhari, & McCulloch 2000).

Finally, an important component of updating methods of inverse modelling is that an objective cost function, that is to be minimized, must be formulated, and the nature of this cost function shall be explained in the following sections.

3.1.1 *Choice of an objective cost function*

The cost function to be minimized can be constructed from the simulated and targeted volumes at each pressure step of the passive filling stage of the cardiac cycle (Avril, Bonnet, Bretelle, Grdiac, Hild, Ienny, Latourte, Lemosse, Pagano, Pagnacco, & Pierron 2007). This cost function is illustrated in equation 3 below.

$$J^2(\boldsymbol{\theta}) = \frac{1}{2}\sum_{i=0}^{i=N-1}\left[\left(V_i^e - V_i^s(P_i;\boldsymbol{\theta})\right)^2\right] \quad (3)$$

Where V_i^e and $V_i^s(P_i;\boldsymbol{\theta})$ represent the experimentally measured and simulated left ventricle cavity volumes, taken at a particular pressure step P_i within the passive filling phase and given a certain set of material parameters $\boldsymbol{\theta}$.

Minimization of the cost function (equation 3) is conducted using an optimization algorithm, therefore allowing material parameters to be derived. Such optimization algorithms shall be explored in the following section.

3.2 *Choice of optimization algorithm*

The minimization of equation 3 involves the use of a non linear optimization algorithm. Since the number of material parameters that need to be identified within the passive filling stage of the cardiac cycle is small, it was deemed adequate to utilize a local, gradient based algorithm based on the Bounded Levenberg-Marquardt algorithm or BLVM (Levenberg 1944), with the option of an additional line search algorithm (Yu 2004), in order to ensure convergence of parameters to at least a local minimum of the cost function, within a predefined parameter range.

3.2.1 *The standard non-linear bounded Levenberg-Marquardt algorithm*

The standard non-linear bounded Levenberg-Marquardt algorithm flexibly updates the material parameters between the Gradient descent and Gauss Newton update methods (Gavin 2011), based on the following parameter update equation. ($\boldsymbol{\delta\theta}$).

$$\left[\boldsymbol{J}^T\boldsymbol{J} + \lambda \mathrm{diag}\left(\boldsymbol{J}^T\boldsymbol{J}\right)\right]\boldsymbol{\delta\theta} = \mathbf{J}^{\mathbf{T}}\left[\left(\mathbf{V}^{\mathbf{e}} - \boldsymbol{V}^{\boldsymbol{s}}(\boldsymbol{\theta})\right)\right] \quad (4)$$

In equation 4 above, λ is a positive scalar. It is clear that for large values of λ the Levenberg-Marquardt parameter update tends to that produced by the Gradient Descent method. However, for small values of λ the Levenberg-Marquardt parameter update tends to that produced by the Gauss Newton method. Consequently, the algorithm exhibits fast convergence of the material parameters ($\boldsymbol{\theta}$) towards a local minimum. Also, $\boldsymbol{V}^s(\boldsymbol{\theta})$ represents a vector of simulated cavity volumes produced via an FEM analysis, and $\boldsymbol{V}^e$ represents a vector of experimentally measured cavity volumes corresponding to the same pressure step P_i in the passive filling stage of the cardiac cycle. In addition, $\boldsymbol{\theta}$ represents a vector of material parameters pertaining to the constitutive law utilized (Usyk, Mazhari, & McCulloch 2000). Furthermore, the right hand side of equation 4 represents the cost function gradient vector, whose components ($\frac{\partial J^2(\boldsymbol{\theta})}{\partial \theta_i}$) represent the gradient of the cost function ($J^2(\boldsymbol{\theta})$) with respect to a particular material parameter θ_i.

In addition, $\boldsymbol{J}$ is the Jacobian matrix, which represents the sensitivity of the simulated field (volume fields in the context of this research) to small perturbations in the material parameters. The Jacobian can be approximated numerically using finite differences

(equation 5) or alternatively using a higher order difference (equation 6), the later ensuring better numerical stability of the algorithm at smaller parameter increments, in other words it approximates the Jacobian matrix accurately upto a term of order equal to h^2, where h represents a small perturbation in θ_i. Consequently, the second Jacobian implementation results in a better conditioned Jacobian matrix. In addition, the second Jacobian implementation is constructed specifically for modelling the cardiac cycle, because it appeared that the first order finite differences Jacobian matrix was ill conditioned even at larger parameter perturbations of 10^{-3}. Also, in equation 5 and 6 below the jth element of $\boldsymbol{\delta\theta}_j$ is the only non zero element and is set to a value of $\epsilon_2(1+|\theta_i|)$ (Gavin 2011), where ϵ_2 is some small value, say 10^{-6}.

$$J_{ij} = \frac{V_i^s(P_i;\boldsymbol{\theta}+\boldsymbol{\delta\theta}_j) - V_i^s(P_i;\boldsymbol{\delta\theta}_j)}{\|\boldsymbol{\delta\theta}_j\|} \tag{5}$$

Or alternatively;

$$J_{ij} = -\frac{V_i^s(P_i;\boldsymbol{\theta}+2\boldsymbol{\delta\theta}_j) - 4V_i^s(P_i;\boldsymbol{\theta}+\boldsymbol{\delta\theta}_j)}{2\|\boldsymbol{\delta\theta}_j\|} - \left\{ \frac{V_i^s(P_i;\boldsymbol{\delta\theta}_j)}{2\|\boldsymbol{\delta\theta}_j\|} \right\} \tag{6}$$

Consequently, a new set of material parameters can be found by solving the set of linear equations represented by equation 4, and adding this new parameter update to the old set of parameters, as illustrated in equation 7 below.

$$\theta_{\mathrm{i}}^{\mathrm{new}} = \theta_{\mathrm{i}} + \delta\theta_{\mathrm{i}} \tag{7}$$

Next, meaningful parameter constraints are applied to the new parameter vector, such that the inequality in equation 8 below holds true, thus giving a new set of material parameters for the iteration.

$$\theta_{\mathrm{i}}^{\mathrm{min}} < \theta_{\mathrm{i}}^{\mathrm{new}} < \theta_{\mathrm{i}}^{\mathrm{max}} \tag{8}$$

where θ_i^{min} represents the lower range of θ_i, and θ_i^{max} represents its upper range.

Finally the cost function (equation 3) is evaluated at the new set of material parameters $J^2(\boldsymbol{\theta}^{\mathrm{new}})$, and compared to the value at the old set of parameters $J^2(\boldsymbol{\theta}^{\mathrm{old}})$.

If the new cost function value is less than the old, then the parameters are in fact moving in a descent direction, towards a local minimum, hence λ is decreased by a factor of eleven (Gavin 2011), and the new set of material parameters replaces the old set for the next iteration of the algorithm. If the new cost function is greater than the old, then λ is increased by a factor of nine (Gavin 2011), and the old parameters are kept for the next iteration of the algorithm.

However, the main disadvantage of this algorithm is that the parameter values tend to oscillate endlessly,

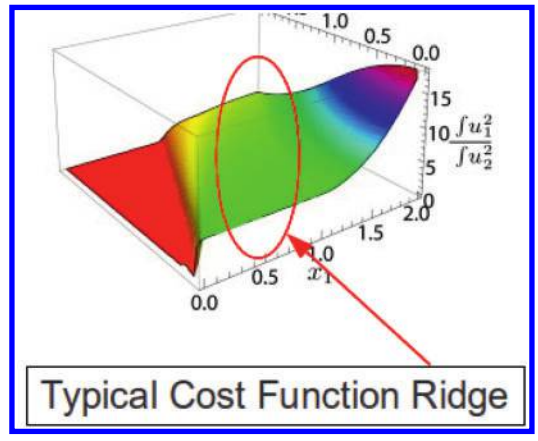


Figure 4. Illustration of a typical ridge in a cost function surface.

if a ridge in the cost function is obtained (Dubuis, Avril, Debayle, & Badel 2011). A ridge is a portion of the cost function surface where the absolute value of the maximum component of the cost function gradient vector ($|\max(\frac{\partial J^2(\boldsymbol{\theta})}{\partial \boldsymbol{\theta}})|$) is close to zero, but does not represent a local minimum in the cost function. Such a surface can be compared to an inflection point in a two dimensional function. Consequently, if the cost function values on such a surface are small (i.e. close to zero) it may appear that the algorithm has converged to a local minimum, however, this set of parameters does not correspond to those which would minimize the cost function represented in equation 3. Figure 4 illustrates a typical ridge in a cost function of two variables.

Consequently, in order to avoid the problems associated with cost function ridges, an additional formulation of the conventional Levenberg-Marquardt algorithm (Yu 2004) was considered, which incorporates a line search. The additional line search was proposed in order to assist the algorithm in avoiding convergence to parameters that would produce a ridge in the cost function, where its gradient is close to zero. The details as to how this line search algorithm is incorporated into the Levenberg-Marquardt algorithm shall be discussed in the following section of this paper.

3.2.2 *Modified Levenberg-Marquardt algorithm*

This modified Levenberg-Marquardt algorithm accepts an initial guess of material parameters $\boldsymbol{\theta}$, then calculates the parameter update $\boldsymbol{\delta\theta}$ and a new parameter set $\boldsymbol{\theta}^{\mathrm{new}}$ according to equation 4 and 7 respectively. Parameter constraints are then applied according to equation 8 giving a set of new parameters for the iteration. The cost function (equation 3) is then computed at this new set of parameters and compared to that at the initial set. If the new cost function is less than the old, then λ is decreased by a factor of eleven. However, if the cost function at the new set of parameters is greater than that with the old set, then instead of increasing λ by a factor of nine (as in the conventional Bounded

Levenberg-Marquardt algorithm), a line search is initiated to ensure that a final new parameter $\boldsymbol{\theta}_{i+1}^{new}$ is calculated such that the cost function value is always moving in a descent direction, hence ensuring that the algorithm always converges to a local minimum in the cost function surface, within a predefined parameter range.

The line search works by accepting the parameter update calculated via equation 4 (i.e. $\boldsymbol{\delta\theta}$), and using it as a descent direction. Next, a new step size η_{i+1} is computed using a regula falsi or secant procedure as illustrated in equation 9 below.

$$\eta_{i+1} = \eta_i - \frac{\eta_i - \eta_{i-1}}{J^2(\boldsymbol{\theta}^i) - J^2(\boldsymbol{\theta}^{i-1})} J^2(\boldsymbol{\theta}^i) \tag{9}$$

Where;

$$\boldsymbol{\theta}^i = \boldsymbol{\theta} + \eta_i \boldsymbol{\delta\theta} \tag{10}$$

$$\boldsymbol{\theta}^{i-1} = \boldsymbol{\theta} + \eta_{i-1} \boldsymbol{\delta\theta} \tag{11}$$

Note that for equation 9, $\eta_0 = 0$ and η_1 must be chosen such that the following inequality holds true.

$$\eta_1 < \min\left[\max\left(\left|\frac{\theta_i^{max} - \theta_i}{\delta\theta_i}\right|\right), \max\left(\left|\frac{\theta_i^{min} - \theta_i}{\delta\theta_i}\right|\right)\right] \tag{12}$$

If the above inequality does not hold true for η_1 (which is the maximum step size) then the step size η_1 shall move parameters to a new set that lies outside the specified parameter range, thus equation 9 no longer holds. If the equality represented in equation 12 holds true, then a new parameter ($\boldsymbol{\theta}^{i+1}$) is then calculated as follows.

$$\boldsymbol{\theta}^{i+1} = \boldsymbol{\theta} + \eta_{i+1} \boldsymbol{\delta\theta} \tag{13}$$

Next the value of the cost function (equation 3) is then evaluated at the new material parameter $J^2(\boldsymbol{\theta}^{i+1})$ and compared to the initial value of the cost function at the initial set of parameters $J^2(\boldsymbol{\theta})$. The line search iteration is terminated if the new cost function is less than the initial value multiplied by a factor ϵ_3 (which is set to a default value of 0.9), in other words, the line search has found a new descent direction that moves the parameters towards those which would produce a local minimum in the cost function. In this case the new parameter $\boldsymbol{\theta}^{i+1}$ is used as the starting parameter for the next iteration of the Levenberg-Marquardt type algorithm.

4 BENCHMARKING AND TESTING OF ALGORITHM IMPLEMENTATIONS

4.1 *Generation of Pseudo experimental data*

Both optimization algorithms explored in the sections above are implemented in C++ in the in-house modelling software SESKA. For the purpose of testing each optimization algorithm, pseudo experimental data was generated for an ellipsoidal canine left ventricle model (figure 2), which was constructed using the preprocessing software GID. Table 1 lists the set of assumed to be true parameters, for the non linear hyperelastic orthotropic material model (equation 1), used to simulate myocardial tissue of the canine left ventricle. The simulated pressure, volume, data (figure 5) for the passive filling stage of the cardiac cycle, obtained using the above set of true material parameters was taken as the experimental data for testing purposes.

Table 1. True material parameter values used to generate experimental data.

Parameter	Value
A	0.88 kPa
A_{compr}	150 kPa
b_{11}	−6
b_{22}	−5
b_{33}	9
b_{23}	12
b_{13}	12
b_{12}	−6

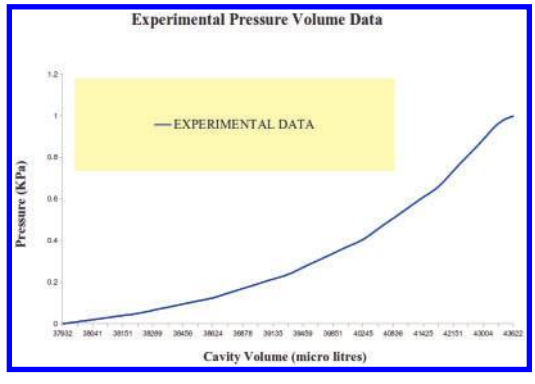


Figure 5. Pseudo experimental data for the passive filling stage of the cardiac cycle.

Table 2. Initial parameter guesses.

Parameter	Case 1	Case 2	Case 3
A (kPa)	0.11	0.5	1.0
A_{compr} (kPa)	51	200	230

4.2 *Testing tegime*

Simulations were first run using the conventional Bounded Levenberg-Marquardt algorithm with three different starting parameters (table 2), and then separately using the modified Levenberg-Marquardt Algorithm with the same three different initial starting

parameters. Bear in mind that only parameters A and A_{compr} were optimized for, hence parameters b_{ij} are excluded from table 2, as they are the same as those values in table 1 for each simulation run.

4.3 *Results and discussion of numerical simulations*

Before the results of numerical simulations are presented, a few definitions from earlier on in this paper shall be revised in order to facilitate better understanding of the results and discussions presented in the following sections. Firstly, $J^2(\boldsymbol{\theta}^{\text{final}})$, and $|\max(\frac{\partial J^2(\boldsymbol{\theta}^{\text{final}})}{\partial \boldsymbol{\theta}^{xtfinal}})|$ represent the cost function value and the absolute value of the maximum component of the cost function gradient vector (respectively) at the final set of material parameters $\boldsymbol{\theta}^{\text{final}}$. If both $J^2(\boldsymbol{\theta}^{\text{final}})$, as well as $|\max(\frac{\partial J^2(\boldsymbol{\theta}^{\text{final}})}{\partial \boldsymbol{\theta}^{xtfinal}})|$ are close to zero (i.e. less than 10^{-7}) then the final set of material parameters produced a local minimum in the cost function. However, if $J^2(\boldsymbol{\theta}^{\text{final}})$ is large (i.e greater than or equal to 10^{-2}, and $|\max(\frac{\partial J^2(\boldsymbol{\theta}^{\text{final}})}{\partial \boldsymbol{\theta}^{xtfinal}})|$ is close to zero (i.e. less than 10^{-7}) then the final set of material parameters produced a ridge in the cost function.

4.3.1 *Conventional bounded Levenberg-Marquardt algorithm*

Referring to table 2, the first set of initial material parameters was taken as $A = 0.11$ KPa and $A_{compr} = 51$ kPa. After nine iterations of the algorithm, parameters converged to $A = 0.645$ kPa and $A_{compr} = 300$ kPa, at which point the $J^2(\boldsymbol{\theta}^{\text{final}})$ was 10^{-8}, and $|\max(\frac{\partial J^2(\boldsymbol{\theta}^{\text{final}})}{\partial \boldsymbol{\theta}^{xtfinal}})|$, had a value of 10^{-7}. Consequently, it appears that the algorithm converged to a local minimum in the cost function. This set of parameters is however not a global minimum, as it is already known that the parameters that produce a global minimum in the cost function are $A = 0.88$ kPa and $A_{compr} = 150$ kPa.

For the next calculation, initial material parameters were taken as $A = 0.5$ kPa and $A_{compr} = 200$ kPa (table 2). After 40 iterations of the algorithm, the algorithm exited without a converged set of parameters, as the maximum number of iteration was set as twenty multiplied by the number of parameters. The final set of parameters was $A = 0.7$ kPa and $A_{compr} = 170$ kPa and $J^2(\boldsymbol{\theta}^{\text{final}})$ was 10^{-2}, at which point $|\max(\frac{\partial J^2(\boldsymbol{\theta}^{\text{final}})}{\partial \boldsymbol{\theta}^{xtfinal}})|$ had a value of 10^{-9}. Consequently, it appears that the algorithm has found a ridge in the cost function, as the maximum cost function gradient component is near zero, whereas, the value of the cost function is comparatively larger, and it this ridge that prevents the conventional Levenberg-Marquardt algorithm from moving in a consistent descent direction towards a local minimum.

Finally, the initial material parameters were taken as $A = 1.0$kPa and $A_{compr} = 230$ kPa. After six iterations of the algorithm, parameters converged to $A = 0.88$ kPa and $A_{compr} = 150$ kPa, at which point $J^2(\boldsymbol{\theta}^{\text{final}})$ was 10^{-12}, and $|\max(\frac{\partial J^2(\boldsymbol{\theta}^{\text{final}})}{\partial \boldsymbol{\theta}^{xtfinal}})|$ had a value of 10^{-10}. Consequently, it appears that the algorithm converged to a global minimum in the cost function. This set of parameters is a global minimum, as it is already known that the parameters that produce a global minimum in the cost function are $A = 0.88$ kPa and $A_{compr} = 150$ kPa. Table 3 is a summary of the results discussed in the section above. Finally, figure 6 illustrates a plot of the simulated pressure volume curves for each set of final parameters represented in table 3.

Table 3. Initial parameter guesses and final parameters found based on the conventional bounded Levenberg-Marquardt algorithm.

Parameter	Case 1	Case 2	Case 3
A^{initial} (kPa)	0.11	0.5	1.0
$A^{\text{initial}}_{\text{compr}}$ (kPa)	51	200	230
A^{final} (kPa)	0.645	0.7	0.88
$A^{\text{final}}_{\text{compr}}$ (kPa)	300	170	150
$J^2(\boldsymbol{\theta}^{\text{final}})$	10^{-8}	10^{-2}	10^{-12}
$\lvert\max(\frac{\partial J^2(\boldsymbol{\theta}^{\text{final}})}{\partial \boldsymbol{\theta}^{\text{final}}})\rvert$	10^{-7}	10^{-9}	10^{-10}
Result	Local Minima	Cost Function Ridge	Global Minima

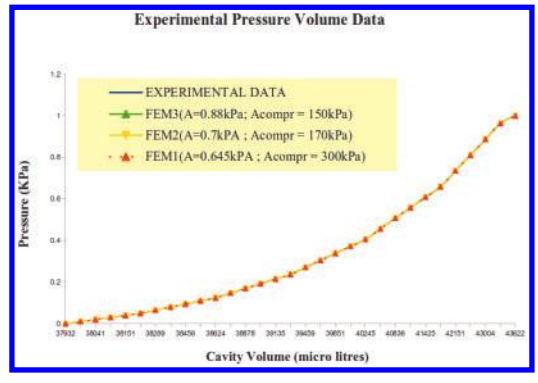


Figure 6. Plot of experimental and simulated pressure volume curves.

4.3.2 *Modified Levenberg-Marquardt algorithm*

Starting at an initial set of material parameters of $A = 0.11$ kPa and $A_{compr} = 51$ kPa (from table 2). After four iterations of the algorithm, parameters converged to the same local minimum of $A = 0.645$ kPa and $A_{compr} = 300$ kPa, which is also found by the standard Levenberg-Marquardt algorithm, and consequently $J^2(\boldsymbol{\theta}^{\text{final}})$ was also 10^{-8}, and $|\max(\frac{\partial J^2(\boldsymbol{\theta}^{\text{final}})}{\partial \boldsymbol{\theta}^{xtfinal}})|$ also had a value of 10^{-7}. Consequently, this seems to illustrate that the set of parameters, $A = 0.645$ kPa and $A_{compr} = 300$ kPa definitely produces a local minimum in the cost function.

Table 4. Initial parameter guesses and final parameters found based on Modified Levenberg-Marquardt algorithm.

Parameter	Case 1	Case 2	Case 3
A^{initial} (kPa)	0.11	0.5	1.0
$A^{\text{initial}}_{\text{compr}}$ (kPa)	51	200	230
A^{final} (kPa)	0.645	0.88	0.88
$A^{\text{final}}_{\text{compr}}$ (kPa)	300	150	150
$J^2(\boldsymbol{\theta}^{\text{final}})$	10^{-8}	10^{-8}	10^{-12}
$\lvert\max(\frac{\partial J^2(\boldsymbol{\theta}^{\text{final}})}{\partial \boldsymbol{\theta}^{\text{final}}})\rvert$	10^{-7}	10^{-7}	10^{-10}
Result	Local Minima	Global Minima	Global Minima

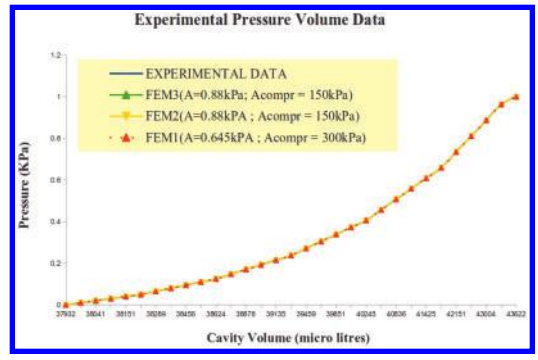


Figure 7. Plot of the experimental and simulated pressure volume curves.

Next, a new calculation was initiated with an initial set of material parameters of $A = 1.0$ kPa and $A_{compr} = 230$ kPa (from table 2). As was the case for the standard Levenberg-Marquardt algorithm, parameters converged to $A = 0.88$ kPa and $A_{compr} = 150$ kPa, and consequently $J^2(\boldsymbol{\theta}^{\text{final}})$ was also 10^{-12}, and $|\max(\frac{\partial J^2(\boldsymbol{\theta}^{\text{final}})}{\partial \boldsymbol{\theta}^{xtfinal}})|$ also had a value of 10^{-10}. Consequently, this example again illustrates the ability of the algorithm to converge consistently to the global minimum, provided that the initial guess for material parameters is good, i.e close to the true set which would produce a global minima in the cost function.

For the final calculation, initial material parameters are $A = 0.5$ kPa and $A_{compr} = 200$ kPa (table 2). After 10 iterations, the algorithm exited with a converged set of parameters of $A = 0.88$ kPa and $A_{compr} = 150$ kPa. At this final set of parameters $J^2(\boldsymbol{\theta}^{\text{final}})$ was 10^{-8}, and $|\max(\frac{\partial J^2(\boldsymbol{\theta}^{\text{final}})}{\partial \boldsymbol{\theta}^{xtfinal}})|$ had a value of 10^{-7}. Consequently, whereas material parameters tended to oscillate within a cost function ridge for the conventional bounded Levenberg-Marquardt algorithm, the line search was able to move the parameters away from this ridge, and in a descent direction, ensuring that the material parameters converged to a local minimum within a predefined parameter space. In this case the parameters that the algorithm converges to do in fact produce a global minimum in the cost function, however, it is important to note, that the line search simply ensures convergence to a local minimum, and does not always ensure convergence to a global minimum within a predefined parameter space. Table 4 below summarizes the results discussed in the section above. Finally, figure 7 illustrates a plot of the simulated pressure volume curves for each set of final parameters represented in table 4.

5 CONCLUSIONS

For the purposes of this research, the passive filling stage of the cardiac cycle was modelled with a non linear hyperelastic orthotropic material law (Usyk, Mazhari, & McCulloch 2000). Inherent to this constitutive law are eight material parameters namely A, A_{compr} and b_{ij}, where i, j $\in (1, 2, 3)$. In order to calibrate these material parameters for the canine left ventricle geometry, to experimental data, or any patient specific application for that matter, a non-linear optimization algorithm in the form of the Bounded Levenberg-Marquardt algorithm, with the additional option of a line search is implemented in the in-house modelling software SESKA.

In order to test the algorithm implementation, pseudo experimental data was generated with a set of assumed to be true parameters for the canine ellipsoidal left ventricle geometry. Consequently, the implemented algorithms ability to converge towards this true set of parameters from a number of different initial starting points was tested.

For the case of the conventional Bounded Levenberg-Marquardt algorithm implementation, it is found that parameters converged quickly towards the true values, provided that the initial guess for parameters is close enough to the true set. However, for initial parameter guesses that are far from the true values it is noticed that parameters may converged to a ridge in the cost function, which does not represent a minimum in the cost function surface.

However, using the modified Levenberg-Marquardt algorithm, which incorporates a line search, assisted the algorithm in always converging to a set of parameters, within a well defined range, which produces a local minimum in the cost function, regardless of whether the initial parameter guess was good or not. However, it should be noted that the line search did not assure convergence to a global minimum in the cost function, it just prevents convergence of parameters towards ridges in the cost function, in fact, the use of the line search illustrated the presence of multiple local minima of the cost function within the defined parameter space.

Consequently, due to the existence of multiple minima within a predefined parameter range, it would be prudent to test the uniqueness of any one particular set of parameters derived via the conventional or modified Levenberg-Marquardt type algorithms. One way of testing the uniqueness of a solution would be to make use of a non parametric boot strapping technique (Sun, Sacks, & Sellaro 2003).

Finally, in this paper only the passive filling stage of the cardiac cycle has been modelled for the case of healthy myocardial tissue. However, the optimization algorithms presented in this paper are intended to be applied to the remaining portions of the cardiac cycle (isovolumetric contraction, ejection and relaxation, as illustrated in figure 1) in order to provide a means of calibrating material parameters for any patient specific cardiac model to patient specific data, for the case of both healthy, and diseased myocardium.

REFERENCES

Avril, S., M. Bonnet, A. Bretelle, M. Grdiac, H. Hild, P. Ienny, L. Latourte, D. Lemosse, S. Pagano, E. Pagnacco, & F. Pierron (2007). Overveiw of identification methods of mechanical parameters based on full-feild measurements. *Journal of Experimental Mechanics 48*, 438–402.

Dubuis, L., S. Avril, J. Debayle, & P. Badel (2011). Identification of material parameters of soft tissue in the compressed leg. *Computer Methods in Biomechanics and Biomedical Engineering 1*, 1–9.

Gavin, H. (2011). The levenberg-marquardt method for nonlinear least squares curve fitting problems. *Computer Methods in Biomechanics and Biomedical Engineering 2*, 289–97.

Levenberg, K. (1944). A method for the solution of certain non-linear problems in least squares. *The Quarterly of Applied Mathematics 9*, 164–168.

Marquardt, D. (1963). An algorithm for least-squares estimation of nonlinear parameters. *Journal of the Society for Industrial and Applied Mathematics 11*, 431–441.

Niederer, S. & N. Smith (2009). The role of the frank-starling law in the transduction of cellular work to whole organ pump function: A computational modeling analysis. *PLoS Comput Biol 5*, 1–5.

Sun, W., M. Sacks, & T. Sellaro (2003). Biaxial mechanical response of bioprosthetic heart valve biomaterials to high in-plane shear. *Journal of Biomechanical Engineering 125*, 372–380.

Usyk, T., R. Mazhari, & A. McCulloch (2000). Effect of laminar orthotropic myofiber architecture on regional stress and strain in the canine left ventricle. *Journal of Elasticity 61*, 143–164.

Yu, Z. (2004). On the global convergence of a levenberg-marquardt method for constrained nonlinear equations. *Journal of Applied Mathematics and Computing 11*, 431–441.

Research and Applications in Structural Engineering, Mechanics and Computation – Zingoni (Ed.)
© 2013 Taylor & Francis Group, London, ISBN 978-1-138-00061-2

Numerical properties of second order integration algorithms for plasticity models

M. Jahanshahi
Department of Civil Engineering, School of Science and Engineering, Sharif University of Technology, International Campus, Kish Island, Iran

ABSTRACT: Investigating the behavior of materials in plastic limit is very important in different fields of engineering. Due to the simplicity of implementation and numerical stability, implicit types of algorithms are conventionally used to deal with plasticity problems. The backward Euler method as a first order accurate algorithm has proven very efficient for integrating the rate form of differential equations governing the behavior of different plasticity models. However, it is desirable to have algorithms with superior performance and quadratic rate of convergence compared with backward Euler method. Many second order integration algorithms have been proposed in the literature which are majorly focused on metal plasticity with isochoric dominant behavior in post yielding range and various types of hardenings. The J_2 plasticity model can be mentioned as a good example. It is also possible to present second order algorithms for material models with pressure sensitive behavior such as soil and concrete. The aim of this work is to present a comparison between classical backward Euler method and second order algorithms that are proposed in the literature for different types of plasticity models. The efficiency of algorithms is investigated through iso-error maps and error graphs.

1 INTRODUCTION

The evolution of implicit integration algorithms dates back to the pioneering work of Wilkins (1964). The algorithm that he developed was actually a backward Euler type of algorithm for the integration of first order ordinary differential equations as a function of time. Backward Euler algorithm has been used successfully in the work of many authors and has proven its applicability in many research and commercial Softwares. Midpoint rule algorithm was first proposed in the work of Ortiz & Popov (1985). They also presented a method for investigating the stability of this type of algorithm which was later modified and corrected in the work of Simo & Govindjee (1991). Double step algorithms as known today were introduced by Simo (1998), but were not elaborated until recently. Artioli et al. 2007a used double step methods for linear hardening and a type of nonlinear hardening in some detail, Artioli et al. 2007b. Jahanshahi (2012a) modified second order integration algorithms to account for generalized form of isotropic hardening and formulated a variant of double step integration scheme for nonlinear hardening, Jahanshahi (2012b).

Single step algorithms for plasticity models with different types of nonlinearities are well developed in the literature. The complexity that arises in deriving the algorithmic setup and tangent operators for double step algorithms makes it hard to apply them for arbitrary hardening rules. However, considering the fact that double step algorithms are second order accurate and thus have better convergence properties compared with the classical backward Euler method makes them appealing in various engineering applications.

The aim of this work is to present a rather brief discussion on the formulation of double step integration algorithms for plasticity models with general isotropic and kinematic hardening. Tangent operators and an investigation of numerical properties are presented as well. The behavior of algorithms is compared with backward Euler method as benchmark and the convergence history is studied through iso-error maps and error graphs.

The paper is organized as follows. In section 2 the time continuous model based on which double step integration algorithms are developed is presented. The formulation of integration algorithms as well as the enforcement of consistency condition is discussed in section 3. In section 4 tangent operators that are essential for quadratic rate of convergence are discussed briefly. Finally in section 5 the behavior of algorithms is investigated using numerical examples. Efficiency and accuracy of algorithms are studied through iso-error maps and error graphs.

2 TIME CONTINUOUS MODEL

In this work we consider an associative von Mises plasticity with nonlinear isotropic and kinematic hardening within the infinitesimal range. If the stress and strain

tensors are split into deviatoric and volumetric parts we can write

$$\boldsymbol{\sigma} = \boldsymbol{s} + p\mathbf{1} \qquad \text{with} \qquad p = \frac{1}{3}\text{tr}(\boldsymbol{\sigma}) \tag{1}$$

$$\boldsymbol{\varepsilon} = \boldsymbol{e} + \frac{1}{3}\theta\mathbf{1} \qquad \text{with} \qquad \theta = \text{tr}(\boldsymbol{\varepsilon}) \tag{2}$$

$$p = \kappa\theta \tag{3}$$

where tr is the trace operator, $\mathbf{1}$, $\boldsymbol{s}$, $\boldsymbol{e}$, p and θ are, respectively, the second order identity tensor, the deviatoric stress and strain tensors, the volumetric stress and strain terms and finally κ is the bulk modulus.

Based on the splitting mentioned above, the equations of the model can be written as:

$$\boldsymbol{s} = 2G(\boldsymbol{e} - \boldsymbol{e}^p) \tag{4}$$

$$\boldsymbol{\xi} = \boldsymbol{s} - \boldsymbol{\beta} \tag{5}$$

$$f = \|\boldsymbol{\xi}\| - \sqrt{\frac{2}{3}}K(\bar{e}^p) \tag{6}$$

$$\dot{\boldsymbol{e}}^p = \gamma\boldsymbol{n} \tag{7}$$

$$\dot{\boldsymbol{\beta}} = \frac{2}{3}H'(\bar{e}^p)\gamma\boldsymbol{n} - \gamma b\boldsymbol{\beta} \tag{8}$$

$$\dot{\bar{e}}^p = \sqrt{\frac{2}{3}}\gamma \tag{9}$$

$$\gamma \geq 0, \quad f \leq 0, \quad \gamma f = 0 \tag{10}$$

where G is the shear modulus, $\boldsymbol{e}$ is the total deviatoric strain, $\boldsymbol{e}^p$ is the plastic strain whose trace is zero, $\boldsymbol{\xi}$ is the relative stress, $\boldsymbol{\beta}$ is the center of yield surface in stress deviator space (back stress, f is the von Mises yield function, $\boldsymbol{n}$ is the normal to the yield surface, $\bar{e}^p$ is the equivalent plastic strain, the functions $K'(\bar{e}^p)$ and $H'(\bar{e}^p)$ are called the isotropic and kinematic hardening modulus respectively and b is the material constant. Finally, equations (10) are the so called Kuhn-Tucker conditions.

The kinematic hardening as prescribed by equation (8) is of nonlinear type due to the presence of the extra term $-\gamma b\boldsymbol{\beta}$. If this term is omitted the kinematic hardening becomes linear as it is widely used in the literature. Moreover, nonlinear forms can be considered in the definition of $K'(\bar{e}^p)$ and $H'(\bar{e}^p)$ in which a saturation hardening term of exponential type can be appended to linear terms, Simo & Hughes (1998). The forms employed in this work are

$$h(\bar{e}^p) = \overline{K}_\infty - \left[\overline{K}_\infty - \overline{K}_0\right]\exp(-\delta\,\bar{e}^p) + \overline{H}'\,\bar{e}^p$$

$$\begin{aligned} K(\bar{e}^p) &= \beta\, h(\bar{e}^p) \\ H(\bar{e}^p) &= (1-\beta)\, h(\bar{e}^p), \quad \beta \in [0,1] \end{aligned} \tag{11}$$

where, $\overline{K}_\infty$, $\overline{K}_0$, δ and $\overline{H}'$ are material constants and β provides a modulation between pure kinematic ($\beta = 0$) and pure isotropic ($\beta = 1$) hardening.

3 INTEGRATION ALGORITHMS

The loading history over the interval $[0, T]$ is divided into N subintervals. An intermediate time interval is therefore represented by $\Delta t = t_{n+1} - t_n$. The midpoint instant $t_{n+\alpha}$ for each subinterval $[t_n, t_{n+1}]$ is chosen such that $t_n \leq t_{n+\alpha} \leq t_{n+1}$ and

$$\alpha = \frac{t_{n+\alpha} - t_n}{\Delta t} \tag{12}$$

Given the variables $\{\boldsymbol{s}_n, \boldsymbol{e}_n, \boldsymbol{e}^p_n, \boldsymbol{\beta}_n, \bar{e}^p_n\}$ at time t_n and the deviatoric strain $\boldsymbol{e}_{n+1}$ at time t_{n+1}, the objective is to compute the variables at time t_{n+1}.

The difference between second order integration algorithms lies in the way the governing differential equations are integrated. In single step algorithms usually a midpoint rule is applied to midpoint instant $t_{n+\alpha}$ while in double step algorithms the return mapping procedure is performed twice per time interval, first at $t_{n+\alpha}$ and then at t_{n+1}. In the first step, a backward Euler integration is performed over the subinterval $[t_n, t_{n+\alpha}]$. The results are extrapolated to time instant t_{n+1} and projected onto the yield surface if necessary, Artioli et al. 2007a.

It was mentioned that applying a backward Euler method over the subinterval $[t_n, t_{n+\alpha}]$ constitutes the first step. Therefore the algorithmic setup for the first step can be formulated as follows.

$$\begin{aligned} &\boldsymbol{e}^p_{n+\alpha} = \boldsymbol{e}^p_n + \lambda_1\boldsymbol{n}_{n+\alpha} \\ &\boldsymbol{s}_{n+\alpha} = 2G(\boldsymbol{e}_{n+\alpha} - \boldsymbol{e}^p_{n+\alpha}) \\ &\boldsymbol{\beta}_{n+\alpha} = \frac{1}{1+b\lambda_1}\left(\boldsymbol{\beta}_n + \sqrt{\frac{2}{3}}\Delta H_{n+\alpha}\boldsymbol{n}_{n+\alpha}\right), \; \Delta H_{n+\alpha} = H(\bar{e}^p_{n+\alpha}) - H(\bar{e}^p_n) \\ &\boldsymbol{\xi}_{n+\alpha} = \boldsymbol{s}_{n+\alpha} - \boldsymbol{\beta}_{n+\alpha} \\ &\bar{e}^p_{n+\alpha} = \bar{e}^p_n + \sqrt{\frac{2}{3}}\lambda_1, \; \lambda_1 = \Delta t\,\gamma_{n+\alpha} \end{aligned} \tag{13}$$

If the kinematic hardening is linear it is sufficient to set b to zero in equation $(13)_3$. It is initially assumed that the evolution of variables over the time interval $[t_n, t_{n+\alpha}]$ is elastic and if the trial values violate the consistency condition a plastic correction is employed. Based on the elastic hypothesis the trial step is

$$\boldsymbol{e}^{p,\text{trial}}_{n+\alpha} = \boldsymbol{e}^p_n$$

$$\begin{aligned} &\boldsymbol{s}^{\text{trial}}_{n+\alpha} = \boldsymbol{s}_n + 2G\Delta\boldsymbol{e}_{n+\alpha}, \; \Delta\boldsymbol{e}_{n+\alpha} = \boldsymbol{e}_{n+\alpha} - \boldsymbol{e}_n \\ &\boldsymbol{\beta}^{\text{trial}}_{n+\alpha} = \boldsymbol{\beta}_n \\ &\boldsymbol{\xi}^{\text{trial}}_{n+\alpha} = \boldsymbol{s}^{\text{trial}}_{n+\alpha} - \boldsymbol{\beta}^{\text{trial}}_{n+\alpha} \\ &\bar{e}^{p,\text{trial}}_{n+\alpha} = \bar{e}^p_n \end{aligned} \tag{14}$$

If the trial relative stress violates the consistency condition, i.e. if

$$\left\|\boldsymbol{\xi}^{\text{trial}}_{n+\alpha}\right\| - \sqrt{\frac{2}{3}}K\left(\bar{e}^{p,\text{trial}}_{n+\alpha}\right) > 0 \tag{15}$$

a plastic correction according to the following equations should be applied.

$$
\begin{aligned}
&\boldsymbol{e}^{p}_{n+\alpha} = \boldsymbol{e}^{p,\text{trial}}_{n+\alpha} + \lambda_1 \boldsymbol{n}_{n+\alpha} \\
&\boldsymbol{s}_{n+\alpha} = \boldsymbol{s}^{\text{trial}}_{n+\alpha} - 2G\lambda_1 \boldsymbol{n}_{n+\alpha} \\
&\boldsymbol{\beta}_{n+\alpha} = \frac{1}{1+b\lambda_1}\left(\boldsymbol{\beta}^{\text{trial}}_{n+\alpha} + \sqrt{\frac{2}{3}}\Delta H_{n+\alpha}\boldsymbol{n}_{n+\alpha}\right) \\
&\boldsymbol{\xi}_{n+\alpha} = \boldsymbol{\zeta}_{n+\alpha} - \left(2G\lambda_1 + \frac{\sqrt{2/3}}{1+b\lambda_1}\Delta H_{n+\alpha}\right)\boldsymbol{n}_{n+\alpha} \\
&\bar{e}^{p}_{n+\alpha} = \bar{e}^{p,\text{trial}}_{n+\alpha} + \sqrt{\frac{2}{3}}\lambda_1
\end{aligned}
\tag{16}
$$

where $\boldsymbol{\zeta}_{n+\alpha}$ is defined as follows.

$$
\boldsymbol{\zeta}_{n+\alpha} = \boldsymbol{s}^{\text{trial}}_{n+\alpha} - \frac{1}{1+b\lambda_1}\boldsymbol{\beta}^{\text{trial}}_{n+\alpha} \tag{17}
$$

The plastic multiplier λ_1 is calculated by enforcing the consistency condition at time instant $t_{n+\alpha}$. The procedure is schematically shown in figure 1.

As the second step, the results of the first step are extrapolated to time instant t_{n+1}, Artioli et al. 2007a. If it is assumed that the evolution of variables over the time interval $[t_n, t_{n+1}]$ is linear, then the extrapolation can be performed by expressing the quantities at time instant t_{n+1} in terms of the quantities at time instants t_n and $t_{n+\alpha}$. The variables obtained in this way constitute the trial state for the second step. Therefore the trial state can be written as

$$
\begin{aligned}
&\boldsymbol{e}^{p,\text{trial}}_{n+1} = \frac{1}{\alpha}\boldsymbol{e}^{p}_{n+\alpha} - \frac{1-\alpha}{\alpha}\boldsymbol{e}^{p}_{n} \\
&\boldsymbol{s}^{\text{trial}}_{n+1} = \frac{1}{\alpha}\boldsymbol{s}_{n+\alpha} - \frac{1-\alpha}{\alpha}\boldsymbol{s}_{n} \\
&\boldsymbol{\beta}^{\text{trial}}_{n+1} = \frac{1}{\alpha}\boldsymbol{\beta}_{n+\alpha} - \frac{1-\alpha}{\alpha}\boldsymbol{\beta}_{n} \\
&\boldsymbol{\xi}^{\text{trial}}_{n+1} = \frac{1}{\alpha}\boldsymbol{\xi}_{n+\alpha} - \frac{1-\alpha}{\alpha}\boldsymbol{\xi}_{n}
\end{aligned}
\tag{18}
$$

$$
\bar{e}^{p,\text{trial}}_{n+1} = \frac{1}{\alpha}\bar{e}^{p}_{n+\alpha} - \frac{1-\alpha}{\alpha}\bar{e}^{p}_{n}
$$

Similar to the first step, a plastic correction as specified by the following equations would be required if the trial relative stress $\boldsymbol{\xi}^{trial}_{n+1}$ violates the yield condition.

$$
\begin{aligned}
&\boldsymbol{e}^{p}_{n+1} = \boldsymbol{e}^{p,\text{trial}}_{n+1} + \lambda_2 \boldsymbol{n}_{n+1} \\
&\boldsymbol{s}_{n+1} = \boldsymbol{s}^{\text{trial}}_{n+1} - 2G\lambda_2 \boldsymbol{n}_{n+1} \\
&\boldsymbol{\beta}_{n+1} = \frac{1}{1+b\lambda_2}\left(\boldsymbol{\beta}^{\text{trial}}_{n+1} + \sqrt{\frac{2}{3}}\Delta \bar{H}_{n+1}\boldsymbol{n}_{n+1}\right) \\
&\boldsymbol{\xi}_{n+1} = \boldsymbol{\zeta}_{n+1} - \left(2G\lambda_2 + \frac{\sqrt{2/3}}{1+b\lambda_2}\Delta \bar{H}_{n+1}\right)\boldsymbol{n}_{n+1} \\
&\bar{e}^{p}_{n+1} = \bar{e}^{p,\text{trial}}_{n+1} + \sqrt{\frac{2}{3}}\lambda_2
\end{aligned}
\tag{19}
$$

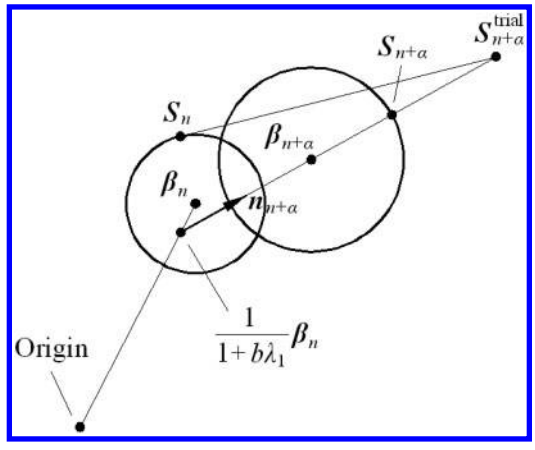


Figure 1. Stress updating procedure for the first step, Jahanshahi (2012b).

The plastic multiplier λ_2 is calculated by enforcing the consistency condition at time instant t_{n+1}. A detailed description of the stress updating procedure outlined above can be found in Jahanshahi (2012b).

4 TANGENT OPERATOR

In order to preserve the quadratic rate of convergence of the Newton-Raphson method used to solve the elastoplasticity problem under consideration, the tangent operator should be consistent with the corresponding integration algorithm. For single step algorithms such as backward Euler method or midpoint rule it is rather trivial to derive the corresponding tangent operator. However for double step algorithms, the procedure of deriving tangent operator can be tedious and complex depending on the type of nonlinearity being used (linear/nonlinear isotropic/kinematic hardening).

It can be shown that in the case of linear kinematic hardening and general form of isotropic hardening ($b = 0$) the tangent operator takes the following form, Jahanshahi (2012a).

$$
\begin{aligned}
&\mathbf{C}^{ep} = \kappa \mathbf{1}\otimes\mathbf{1} \\
&+2G\left[\left[1-A-\left(1-\bar{A}\right)C\right]\left(\boldsymbol{I}-\frac{1}{3}\mathbf{1}\otimes\mathbf{1}\right)\right. \\
&-\left[\left(\bar{A}-\bar{B}\right)C-\left(A-B\right)\right]\boldsymbol{n}_{n+\alpha}\otimes\boldsymbol{n}_{n+\alpha} \\
&-\left(1-\bar{A}\right)\left(D-C\right)\boldsymbol{n}_{n+1}\otimes\boldsymbol{n}_{n+1} \\
&\left.-\left[\left(\bar{A}-\bar{B}\right)\left(D-C\right)\left(\boldsymbol{n}_{n+1}:\boldsymbol{n}_{n+\alpha}\right)-\bar{C}\right]\boldsymbol{n}_{n+1}\otimes\boldsymbol{n}_{n+\alpha}\right]
\end{aligned}
\tag{20}
$$

where $\boldsymbol{n}_{n+\alpha}$ and $\boldsymbol{n}_{n+1}$ are respectively the outward normals to the yield surface at time instants $t_{n+\alpha}$ and t_{n+1}. A to D and $\bar{A}$ to $\bar{C}$ are parameters which are defined as follows.

$$
A = \frac{2G\lambda_1}{\left\|\boldsymbol{\xi}^{\text{trial}}_{n+\alpha}\right\|},\quad B = \left[1+\frac{H'(\bar{e}^{p}_{n+\alpha})+K'(\bar{e}^{p}_{n+\alpha})}{3G}\right]^{-1} \tag{21}
$$

$$C = \frac{2G\lambda_2}{\left\|\xi_{n+1}^{\text{trial}}\right\|},\quad D = \left[1 + \frac{H'(\bar{e}_{n+1}^{p}) + K'(\bar{e}_{n+1}^{p})}{3G}\right]^{-1} \tag{22}$$

$$\bar{A} = \frac{1}{\left\|\xi_{n+\alpha}^{\text{trial}}\right\|}\left(2G\lambda_1 + \sqrt{\frac{2}{3}}\Delta H_{n+\alpha}\right) \tag{23}$$

$$\bar{B} = \left[1 + \frac{H'(\bar{e}_{n+\alpha}^{p})}{3G}\right]B \tag{24}$$

$$\bar{C} = \frac{H'(\bar{e}_{n+1}^{p}) - H'(\bar{e}_{n+1}^{p,\text{trial}}) + K'(\bar{e}_{n+1}^{p})}{3G}B \tag{25}$$

If the kinematic hardening is of nonlinear type ($b \neq 0$) the procedure that is required to derive $\mathbf{C}^{ep}$ is more involved. One can refer to Jahanshahi (2012b) for an elaboration.

5 NUMERICAL EXAMPLES

In this section, iso-error maps and a numerical example are used to investigate the behavior of the double step integration algorithm compared with backward Euler method. Both algorithms have been implemented into a C++ program based on standard concepts in finite element analysis, Bathe (1996).

The elastic properties of material are taken as $E = 7000$ MPa, $\nu = 0.3$, and the material constants are $\overline{K}_\infty = 35$ MPa, $\overline{K}_0 = 30$ MPa, $\delta = 0.1$, $\overline{H}' = 280$ MPa, $\beta = 0.8$ and $b = 1$.

5.1 *Iso-error maps*

Iso-error maps are extensively employed by researchers as a procedure to systematically assess the accuracy of a proposed algorithm. In the literature, iso-error maps are generated by applying a set of normalized strains in principal directions. A detailed description be found in Simo & Hughes (1998).

The iso-error maps corresponding to point **C** of the yield surface in figure 2 are shown in figures 3 and 4 and are generated for $\alpha = 0.5$.

The error range for each iso-error map is divided into 10 error levels. Regarding figure 3, it can be concluded that the accuracy of backward Euler method as a first order accurate algorithm is quite acceptable showing low error levels for large time steps. It also should be emphasized that the simplicity of implementation as well as the efficiency with regard to computational effort make this algorithm numerically attractive.

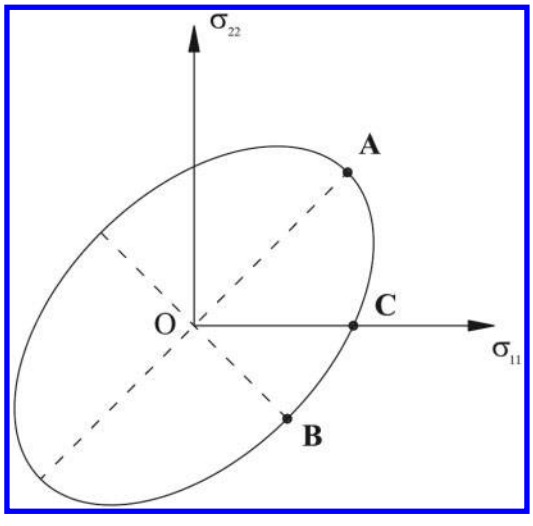


Figure 2. Plane strain yield surface. Points for iso-error maps.

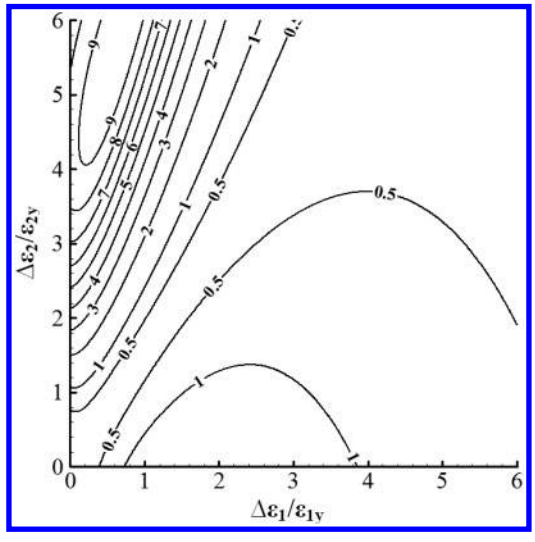


Figure 3. Iso-error maps for point **C** of the yield surface using backward Euler method, Jahanshahi (2012b).

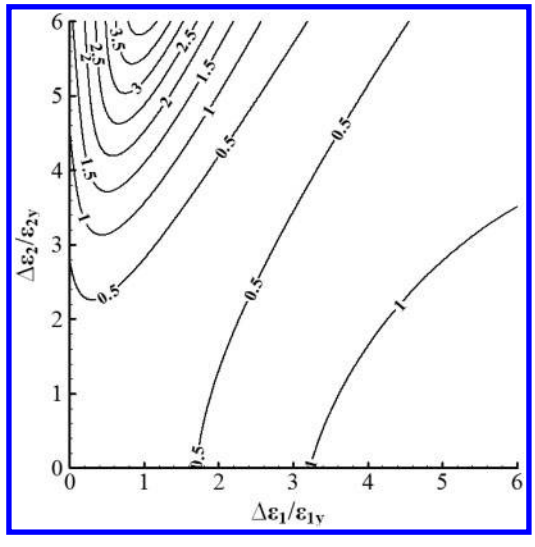


Figure 4. Iso-error maps for point **C** of the yield surface using double step algorithm, (Jahanshahi 2012b).

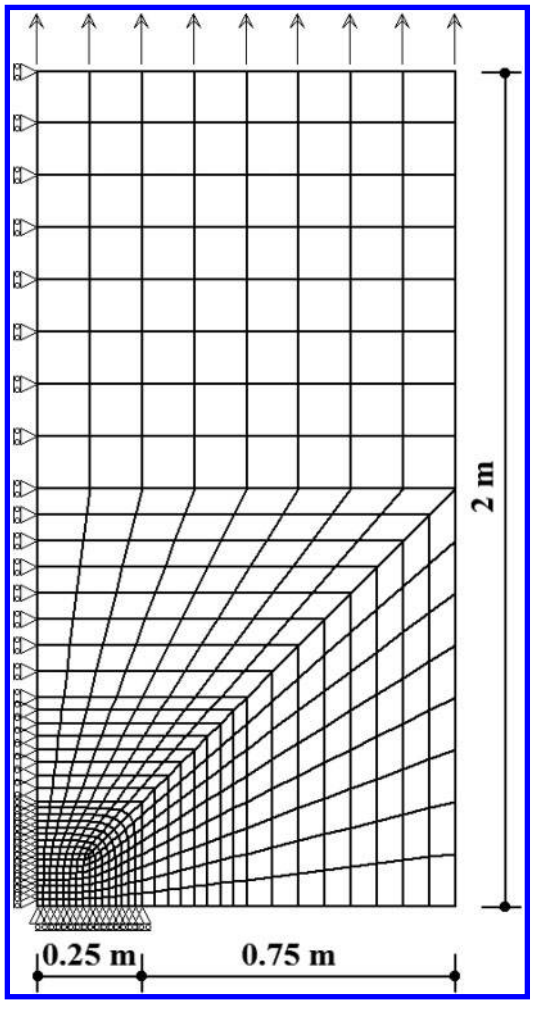


Figure 5. Finite element model for one quarter of double-notched plate, Jahanshahi (2012b).

Comparing figures 3 and 4 one can see that the maximum error using backward Euler method is 9% while for the double step algorithm it is 4.2%. A literature survey shows that for proportional loading (points **A** and **B** in figure 2) the maximum error and the difference between maximum error values from the backward Euler method and the double step algorithm are lower than the case of non-proportional loading presented here. Based on this observation it can be conferred that the double step algorithm has a superior performance compared with backward Euler method.

5.2 *Double-notched plate subject to cyclic load*

A plate with two symmetrical notches in plane strain condition is considered as a numerical example to investigate the performance of the double step integration algorithm briefly discussed in previous sections, Jahanshahi (2012b). The finite element model for one quarter of the plate is shown in figure 5. A total of

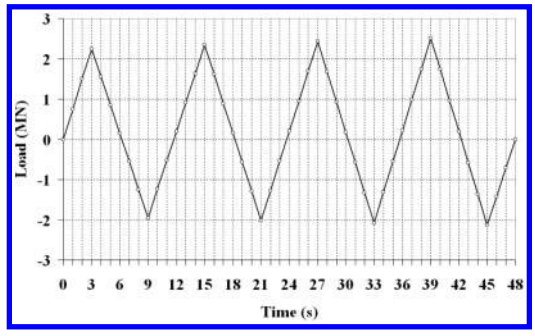


Figure 6. Variation of cyclic load applied to double-notched plate, Jahanshahi (2012b).

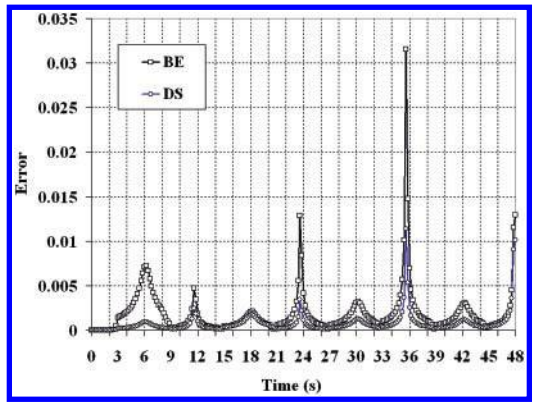


Figure 7. Error graph for BE and DS algorithms applied to double-notched plate with cyclic load and $\alpha = 0.8$, Jahanshahi (2012b).

512 quadrilateral plane strain elements with 4 integration points and linear displacement interpolation along each direction are used to model the plate. The variation of point loads that are applied to indicated nodes is shown in figure 6. The loading program comprises of four cycles of tension and compression and it takes 4 s. For the first cycle, the intensity of load increases to 2.25 MN at $t = 3$ s and drops to -1.95 MN at $t = 9$ s. In subsequent cycles, the maxima of load increases gradually both in tension and compression. In the last cycle it increases to the maximum of 2.50 MN at $t = 39$ s and drops to the minimum of -2.15 MN at $t = 45$ s. Finally, the value of load increases again until it becomes zero at $t = 48$ s.

An error graph is provided in figure 7 to compare the results of algorithm for $\alpha = 0.8$. BE and DS in this figure refer respectively to backward Euler method and double step algorithm. The residual stresses that remian in plate after completing the loading program are shown in figure 8. Regarding the error graph the following observations can be made:

- The maximum error for the double step algorithm is 64 percent lower than the maximum error for backward Euler method.

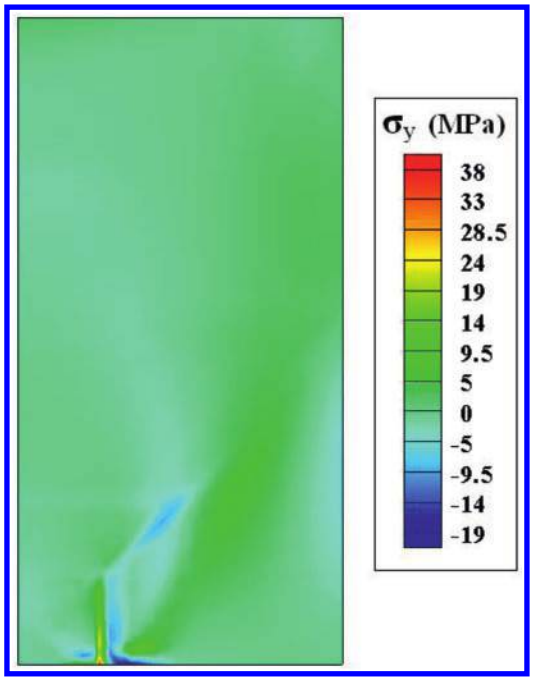


Figure 8. Residual stresses in double-notched plate. Jahanshahi (2012b).

- In addition to maximum error, the error of double step algorithm is lower than the backward Euler method at all points during the loading program.

6 CONCLUSIONS

Second order integration algorithms have been shown by many authors to have better convergence properties compare with backward Euler method. In this paper a double step integration scheme is presented for linear/nonlinear isotropic and kinematic hardening. Based on numerical examples it was shown that the behavior of this type of algorithm is superior to backward Euler method. It should also be emphasized that the number of numerical operations that have to be performed also increases but this extra computational effort is offset by using large time steps.

Numerical experience shows that under sever loading conditions where most parts of the medium under consideration plasticize, the double step algorithm demonstrates its efficiency compared with classical methods such as the backward Euler method. However under moderate loading conditions where only small parts of the medium enter the plastic limit the difference between the two methods might not be very noticeable.

REFERENCES

Artioli, E., Auricchio, F. & Beirão da Veiga, L. 2007a. Generalized midpoint integration algorithms for J_2 plasticity with linear hardening. *International journal of numerical methods in engineering* 72: 422–463.

Artioli, E., Auricchio, F. & Beirão da Veiga, L. 2007b. Second order accurate integration algorithms for von-Mises plasticity with a nonlinear kinematic hardening mechanism. *Computer methods in applied mechanics and engineering* 196: 1827–1846.

Bathe, K.J. 1996. *Finite element procedures*. New York: Prentice-Hall.

Jahanshahi, M. 2012a. Second order integration algorithms for J_2 plasticity with generalized isotropic/kinematic hardening. *Asian journal of civil engineering* 13(2): 203–232.

Jahanshahi M. 2012b. Numerical assessment of a double step integration algorithm for J_2 plasticity with Armstrong-Frederick evolution of back stress. *Scientia Iranica; Transactions A: civil engineering* 19(5): 1168–1179.

Ortiz, M. & Popov, E.P. 1985. Accuracy and stability of integration algorithms for elastoplastic constitutive relations. *International journal of numerical methods in engineering* 21: 1561–1576.

Simo, J.C. 1998. Topics on the numerical analysis and simulation of plasticity. In P.G. Ciarlet & J.L. Lions (eds), *Handbook of numerical analysis* 4. Amsterdam: Elsevier.

Simo, J.C. & Govindjee, S. 1991. Non-linear B-stability and symmetry preserving return mapping algorithms for plasticity and visco-plasticity. *International journal of numerical methods in engineering* 31: 151–176.

Simo, J.C. & Hughes, T.J.R. 1998. *Computational inelasticity*. New York: Springer Verlag.

Wilkins, M.L. 1980. Calculation of elastic-plastic flow. In Adler et al. (eds), *Methods of computational physics* 3. New York: Academic Press.

7. Numerical modelling, FEM modelling

Research and Applications in Structural Engineering, Mechanics and Computation – Zingoni (Ed.)
© 2013 Taylor & Francis Group, London, ISBN 978-1-138-00061-2

A layered shell element for the thermal analysis of plates exposed to non-uniform heating

A.E. Jeffers
University of Michigan, Ann Arbor, MI, USA

ABSTRACT: This paper describes a heat transfer element that has been formulated to model the 3D thermal response of plates subjected to non-uniform heating. Unlike existing elements, the present formulation uses a combination of finite element and control volume techniques to discretize the plate into layers that are each characterized by a temperature field that is lumped at the mid-section of the layer. In plane, the temperature field is interpolated from nodal values as quadratic. Although a combination of finite difference and finite element approximations is used, the element equations are in a form that can readily be implemented in a finite element code. Verification studies demonstrate that the element exhibits excellent accuracy and rapid convergence. Comparisons to continuum elements illustrate that the proposed element also results in considerable cost savings. The element also facilitates the transfer of temperature data to a structural analysis because both models utilize the same mesh.

1 INTRODUCTION

As illustrated in Figure 1, the simulation of structures in fire involves three sequentially coupled processes: 1) a fire analysis to determine the thermal boundary conditions at the structural surface, 2) a conduction heat transfer analysis to determine the temperatures in the structure, and 3) a structural analysis to determine the force-deformation response of the structure. For structural design, research has historically focused on post-flashover fire exposures, in which the fire behavior is described in terms of a uniform gas temperature. This assumption is valid for most building structures, in which compartments are relatively small and the fuel distribution is fairly uniform. However, fully developed compartment fire models have been questioned due to their inability to capture fire spread that occurs naturally in large, open compartments (Stern-Gottfried et al. 2010).

As a result, significant efforts are underway to study structural response under non-uniform fire exposures, including the coupling of structural models to computational fluid dynamics codes (Chen et al. 2011, Tondini et al. 2012). The coupling of a high-resolution fire simulation to a low-resolution structural model poses a number of challenges due to the severe disparities in spatial and temporal scales between the various models (Prasad & Baum 2005), as shown in Figure 1.

One of the primary challenges to studying structural response under non-uniform heating is that there is no direct way to model the thermal response of the structure in a way that is compatible with the finite elements that are typically used in structural analysis (Jeffers and Sotelino 2009). Consequently, an analyst must conduct a high-resolution heat transfer analysis using computationally expensive continuum elements and perform an intermediate calculation to resolve the temperature data to a form that is compatible with the structural elements (i.e., frame and shell elements) that are used to evaluate the mechanical response of the structure. This approach involves excessive computational costs, making the simulation approach impractical for most engineering applications.

To overcome the limitations of current techniques for modeling heat transfer in structures, this paper introduces a novel heat transfer finite element for evaluating the thermal response of non-uniformly heated plates. Using the approach of Jeffers & Sotelino (2009), a combination of finite element and control volume methods are used to discretize the temperature field in the plate heat transfer element. In particular, temperatures over the plate's thickness are modeled in high-resolution using a finite difference grid while temperatures in plane are modeled in low-resolution using quadratic interpolation functions. The result is a layered plate heat transfer element that is capable of capturing the complete 3D thermal response. The formulation emphasizes compatibility between the thermal and structural models because the heat transfer element uses the same layering technique that is used in mechanics-based plate and shell elements to model distributed plasticitity (Ramm & Matzenmiller 1988, Buchter et al. 1994, Wriggers et al. 1996). The resulting element efficiently simulates the 3D thermal response while facilitating the transfer of data between the thermal and structural models due to the compatibility between the finite element meshes.

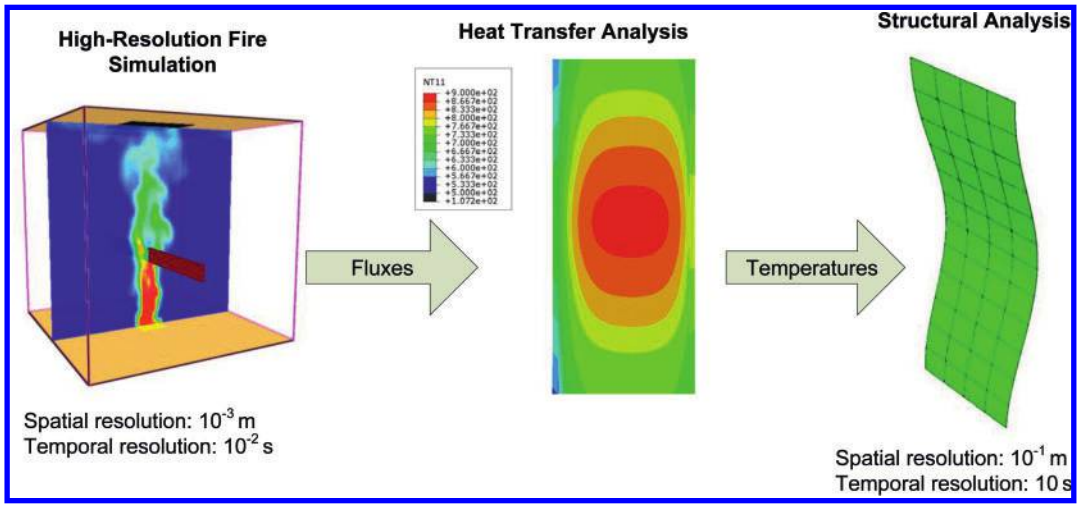


Figure 1. Transfer of thermal data across disparate scales in modeling structures in fire.

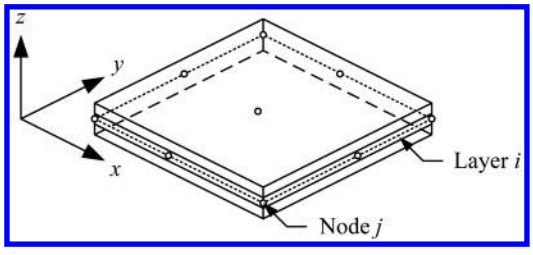


Figure 2. Plate transfer heat element.

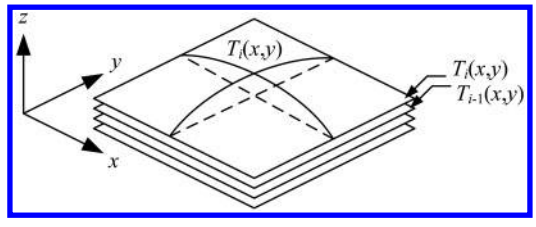


Figure 3. Quadrature temperature field in layer i.

This paper provides a summary of the element formulation and results of the verification studies that were conducted to evaluate the plate heat transfer element. Additional details can be found in the paper by Jeffers (2013).

2 ELEMENT FORMULATION

As illustrated in Figure 2, the plate heat transfer element is discretized into n layers. The thickness t_i of layer i is assumed to be relatively small such that the temperature field is lumped in each layer. As a result, the temperature field in layer i is reduced to a 2D temperature field that varies only in plane, as illustrated in Figure 3. A combination of finite element and control volume techniques can be employed to arrive at a set of equations that account for heat transfer across the layers in the element.

In particular, the weak form of the governing energy conservation equation in layer i is given as

$$\int_{V_i}\left[\rho C\frac{\partial T}{\partial t}-\frac{\partial}{\partial x}\left(k\frac{\partial T}{\partial x}\right)-\frac{\partial}{\partial y}\left(k\frac{\partial T}{\partial y}\right)-\frac{\partial}{\partial z}\left(k\frac{\partial T}{\partial z}\right)\right]dV_i=0 \qquad (1)$$

where ρ = mass density, C = specific heat, k = conductivity, T = temperature, t = time, and V_i = volume of layer i.

Because the thickness of layer i is relatively small, it can be assumed that the temperature gradient $\partial T/\partial z$ is approximately zero over the depth of the layer. Thus, the 3D temperature field $T(x, y, z, t)$ is replaced by a 2D layer temperature $T_i(x, y, t)$ that only varies in plane (Figure 3). To satisfy the energy balance, however, additional terms must be introduced into the governing equation to account for heat transfer by conduction from the adjacent layers $i-1$ and $i+1$. Thus, Equation 1 becomes

$$\int_{V_i}\left[\rho C\frac{\partial T_i}{\partial t}-\frac{\partial}{\partial x}\left(k\frac{\partial T_i}{\partial x}\right)-\frac{\partial}{\partial y}\left(k\frac{\partial T_i}{\partial y}\right)-Q\right]dV_i + \int_A\left(k\frac{\partial T}{\partial z}\right)\Big|_{i-}dxdy-\int_A\left(k\frac{\partial T}{\partial z}\right)\Big|_{i+}dxdy=0 \qquad (2)$$

The first term in Equation 2 results from substituting the layer temperature $T_i(x, y, t)$ into Equation 1 while the remaining terms account for the flux that enters the bottom and top surfaces of layer i by conduction from the adjacent layers. Symbols $i-$ and $i+$ represent the boundaries between layers (i.e., at $i-1/2$ and $i+1/2$, respectively). Note that heat transfer by conduction occurs normal to the element's xy plane and therefore the energy flow is integrated over plate's area A.

The heat transfer by conduction from the adjacent layers can be approximated as finite differences, i.e.,

$$\left(k\frac{\partial T}{\partial z}\right)\Big|_{i-} = k_{i-}\left(\frac{T_i - T_{i-1}}{z_i - z_{i-1}}\right), \left(k\frac{\partial T}{\partial z}\right)\Big|_{i+} = k_{i+}\left(\frac{T_{i+1} - T_i}{z_{i+1} - z_i}\right), \quad (3)$$

where k_{i-} and k_{i+} = effective conductivities at the layer interfaces, which are calculated by averaging the thermal resistances of adjacent layers (Jaluria & Torrance 2003). In Equation 3, z_i is the location at which the layer temperature is lumped in the z-direction. For interior layers, z_i coincides with the mid-height of the layer. For exterior layers, z_i coincides with the surface of the element to provide greater accuracy in modeling the thermal boundary conditions at the element's surface (Jaluria & Torrance 2003).

Note that Equation 2 only applies to interior layers in which heat is transferred by conduction from an adjacent layer. For exterior layers (i.e., the layers at the top and bottom surface of the plate), the appropriate boundary conditions must be applied to simulate prescribed temperature, flux, convection and/or radiation boundary conditions. These terms are given by Jeffers (2013).

The finite element method is applied to Equation 2 by assuming that the temperature field $T_i(x, y)$ in layer i is interpolated from the nodal temperatures $\mathbf{T}_i$ using element shape functions $\mathbf{N}$, i.e.,

$$T_i(x, y) = \mathbf{N}\,\mathbf{T_i}. \quad (4)$$

As shown in Figure 3, a quadratic temperature field is assumed here, resulting in a nine-node heat transfer element.

Equation 4 is substituted into Equation 2, and the Galerkin finite element method is employed. After some manipulation, the governing equations for an interior layer i are given by

$$\mathbf{c_i}\dot{\mathbf{T}}_\mathbf{i} + \mathbf{k_i}\mathbf{T_i} - \left(\mathbf{k_{i-}}\mathbf{T_{i-1}} + \mathbf{k_{i+}}\mathbf{T_{i+1}}\right) = \mathbf{r_i}, \quad (5)$$

Where

$$\mathbf{c_i} = \int_A \mathbf{N}^T \rho C t_i \mathbf{N} dxdy \quad (6)$$

$$\mathbf{k_i} = \int_A \mathbf{N_{,x}}^T k t_i \mathbf{N_{,x}} dxdy + \int_A \mathbf{N_{,y}}^T k t_i \mathbf{N_{,y}} dxdy + \mathbf{k_{i-}} + \mathbf{k_{i+}} + \mathbf{h_i} \quad (7)$$

$$\mathbf{k_{i-}} = \int_A \mathbf{N}^T \frac{k_{i-}}{z_i - z_{i-1}} \mathbf{N}^T dxdy \quad (8)$$

$$\mathbf{k_{i+}} = \int_A \mathbf{N}^T \frac{k_{i+}}{z_{i+1} - z_i} \mathbf{N}^T dxdy \quad (9)$$

$$\mathbf{h_i} = \int_S \mathbf{N}^T (h + h_r)\mathbf{N} dS \quad (10)$$

$$\mathbf{r_i} = \int_S \mathbf{N}^T q_s'' dS + \int_S \mathbf{N}^T (hT_\infty + h_r T_{sur}) dS \quad (11)$$

In Equations 5–11, t_i = thickness of layer i; $\mathbf{N}_{,x}$ and $\mathbf{N}_{,y}$ = derivatives of the shape function matrix with respect to x and y, respectively; h = convection heat transfer coefficient and T_∞ = fluid temperature (for a convection boundary condition); h_r = linearized radiation heat transfer coefficient and T_{sur} = temperature of surroundings (for a radiation boundary condition); q_s'' = surface flux (for a prescribed flux boundary condition).

For exterior layers, Equation 5 is modified to include the appropriate boundary conditions specified at the top or bottom surface of the plate. For a prescribed flux, the following term is added to $\mathbf{r_i}$:

$$\mathbf{r_{qb}} = \int_A \mathbf{N}^T q_b'' dxdy. \quad (12)$$

For a convection boundary condition, the following terms are added to $\mathbf{k_i}$ and $\mathbf{r_i}$, respectively:

$$\mathbf{h_b} = \int_A \mathbf{N}^T h \mathbf{N} dxdy, \ \mathbf{r_{hb}} = \int_A \mathbf{N}^T h T_\infty dxdy. \quad (13)$$

For a radiation boundary condition, the following terms are added to $\mathbf{k_i}$ and $\mathbf{r_i}$, respectively:

$$\mathbf{h_{rb}} = \int_A \mathbf{N}^T h_r \mathbf{N} dxdy, \ \mathbf{r_{hrb}} = \int_A \mathbf{N}^T h_r T_{sur} dxdy. \quad (14)$$

Equation 5 represents the temperature in layer i, which is dependent on the temperatures in the adjacent layers $i-1$ and $i+1$. The governing equations for the entire element are obtained by assembling the n layers (with temperatures described in terms of m nodal temperatures) over the element's domain. The resulting element has $n \times m$ degrees of freedom. After assembly, the element equations have the form

$$\mathbf{c}\dot{\mathbf{T}} + \mathbf{k}\mathbf{T} = \mathbf{r} \quad (15)$$

where $\mathbf{c}$ = heat capacity matrix, $\mathbf{k}$ = conductivity matrix, $\mathbf{r}$ = an array of thermal loads, $\mathbf{T}$ = an array of nodal temperatures, and $\dot{\mathbf{T}}$ = first derivative of temperatures with respect to time. Note that, although a combination of finite element and control volume methods were used in the element formulation, the governing equations in Equation 15 are in a form that can readily be implemented into a finite element program.

3 VERIFICATION

The element was implemented in *ABAQUS* (2010) as a user-defined element to verify the element formulation. A series of verification cases were devised to evaluate the element's accuracy in simulating various cases of non-uniform heating.

Two cases are shown here to demonstrate the element's ability to simulate 2D and 3D heat transfer. Both cases consider a rectangular steel plate

with dimensions 2 m, × 1 m, × 10 cm. The steel was assumed to have density $\rho = 7{,}833\ \text{kg/m}^3$, conductivity $k = 54$ W/m-K, and specific heat $C = 465$ J/kg-K. Material properties were assumed to be independent of temperature. Results from the proposed heat transfer element were compared to high-resolution finite element analyses conducted in *ABAQUS* using linear 2D and 3D continuum elements.

3.1 *Two-dimensional heat transfer*

To evaluate the heat transfer over the section, the plate was given an initial temperature of 0°C and the top surface was instantaneously fixed at 100°C, while the remaining surfaces were maintained at 0°C. The nature of the heating induced a temperature field that varied in two dimensions over the cross-section. The shell element was assigned seven layers over the depth, and a convergence study was carried out to determine the influence of increasing the number of elements along the width of the plate.

Mid-surface temperatures were evaluated at times $t = 10$ s, 50 s, 170 s, and at steady state (i.e., $t = 10{,}000$ s). Figure 4 shows the results at steady state. Under the prescribed boundary conditions, the temperature varies non-uniformly. From Figure 4, it can be seen that the shell element converges rapidly, with excellent agreement achieved with eight elements over the width of the plate.

To better illustrate the level of accuracy achieved by the shell model, the L_2-norm error was calculated for each mesh. These errors are given in Table 1 at various times. Initially, the temperature gradient is quite significant, resulting in somewhat large errors at $t = 10$ s. As time progresses, the temperature profile smoothes out and the quadratic shell element provides an improved prediction of the thermal response. The data in Table 1 indicates that excellent accuracy is achieved with as few as eight elements over the width, with errors less than three percent for times greater than 50 s.

Simulation times were recorded for various finite element meshes to demonstrate the efficiency of the new heat transfer element. The converged finite element solution was based on a 2D heat transfer analysis conducted in *ABAQUS* using four-node continuum elements. The high-resolution model used rectangular elements that were 1 cm × 1 cm. Consequently, the 2D heat transfer analysis required 1,111 temperature degrees of freedom (DOFs). The analysis using the shell elements involved a 3D analysis of the plate with elements arranged in four meshes: 1 × 1, 2 × 2, 4 × 4, and 8 × 16. The corresponding numbers of degrees of freedom are given in Table 2 along with the recorded simulation times. Note that the simulation times for the shell models were on the same order of magnitude as the high-resolution 2D finite element analysis.

3.2 *Three-dimensional heat transfer*

To study the element's ability to capture a temperature field that varies in three dimensions, an analysis was conducted for a plate subjected to a non-uniform surface flux. The plate was given an initial temperature of 0°C and then heated by the boundary conditions illustrated in Figure 5. In particular, one-fourth of the top surface of the plate was subjected to a prescribed flux of 30 kW/m^2 while the remainder of the top surface was cooled by convection, with the fluid temperature $T_\infty = 0$°C and a heat transfer coefficient

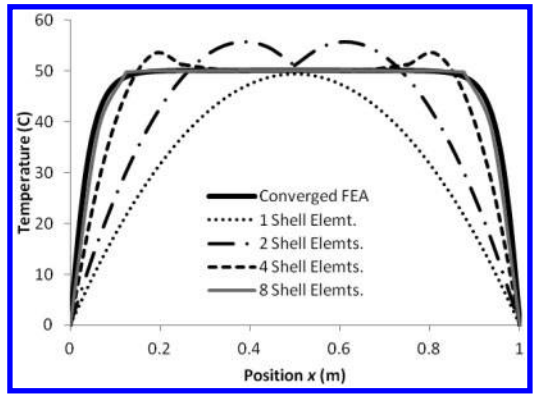


Figure 4. Mid-surface temperature at steady state for plate subjected to 2D heating of cross-section.

Table 1. L_2-norm errors for 2D heating of cross-section.

Number of Elements	Time (s)			
	10	50	170	10,000
1	34.4	37.4	36.5	35.5
2	30.9	27.6	26.0	25.0
4	20.9	13.3	11.6	10.7
8	17.1	3.0	2.7	2.4

Table 2. Simulation timesfor 2D heating of cross-section.

Analysis	Number of DOFs	Total CPU Time (s)
2D FEA	1,111	1.2
Shell Element		
1 × 1	63	0.6
2 × 2	175	0.6
4 × 4	567	0.6
8 × 16	3,297	2.3

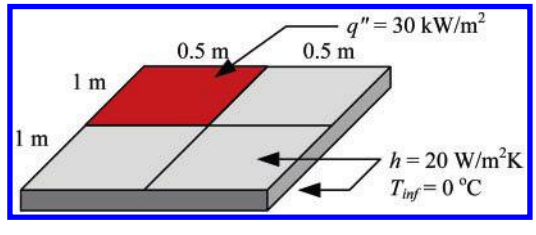


Figure 5. Boundary conditions for 3D heat transfer case.

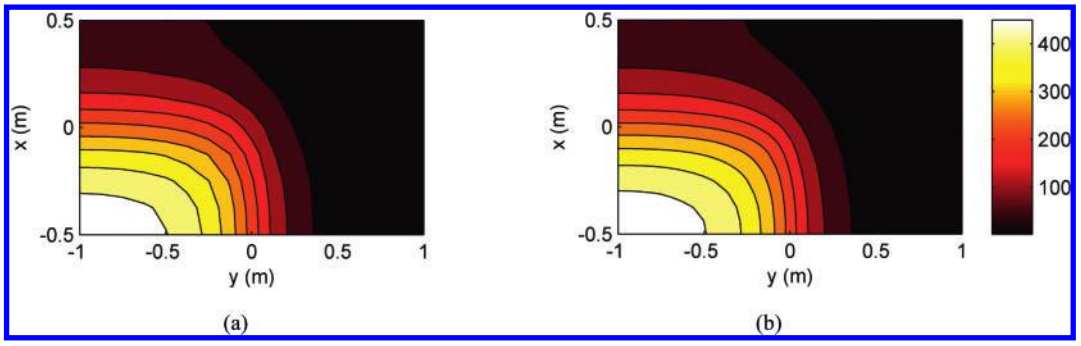


Figure 6. Steady-state temperature contours at the mid-surface of the plate, (a) 4 × 8 elements, and (b) 8 × 16 elements.

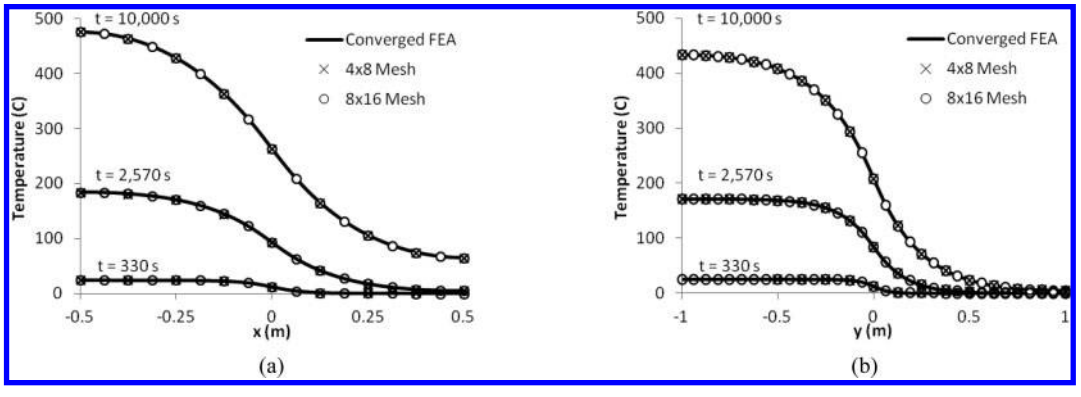


Figure 7. Comparison of mid-height temperatures at various times, (a) y = −0.75 m, and (b) $x = 0.25$ m.

$h = 25\ \mathrm{W/m^2K}$. The bottom surface of the plate was cooled by the same convective boundary condition. The sides of the plate were treated as insulated. Note that the temperatures are non-uniform over the thickness of the plate as well as along the surface under this heating.

The shell elements were arranged in two meshes: 4 × 8 and 8 × 16. The temperature contours calculated at the mid-surface at steady state are presented in Figure 6 for the two meshes of plate heat transfer elements. Qualitative comparisons between Figure 6 and results computed using a high-resolution mesh of continuum elements indicated good agreement in the predicted thermal response.

To better assess the accuracy of the analyses, temperatures were plotted along two paths at the mid-surface of the plate: 1) along $y = -0.75$ m, and 2) along $x = -0.25$ m. These results are shown in Figures 7a and 7b, respectively, for times $t = 330$ s, 2570 s, and 10,000 s. Note that the results from the plate heat transfer element agree very well with the high-resolution finite element analysis.

Simulation times were recorded in Table 3 for each analysis to provide a means of assessing the efficiency of the shell model. From the data presented in Table 3, it is clear that the shell element offers substantial savings in computational costs, with the 8 × 16 mesh requiring 2.6 s whereas the high-resolution finite element analysis required several minutes to run. It is important to realize that these savings would be magnified when larger and more complex structural systems are analyzed.

Table 3. Simulation times for 3D heat transfer.

Analysis	Number of DOFs	Total CPU Time (s)
3D FEA	223,311	830.7
Shell Element		
4 × 8	1,071	1.3
8 × 16	3,297	2.6

4 CONCLUSIONS

In this paper, a novel heat transfer element was formulated to provide an accurate and efficient means for predicting the temperature field in non-uniformly heated shells. The formulation used a combination of finite element and control volume techniques to discretize the temperature field into 2D layers that were coupled by a finite difference approximation of the transverse flux. While the element uses a combination of techniques, the layers can be assembled into

a set of element equations that are in a form that can readily be implemented into a finite element analysis. The present study focused on a nine-node quadratic element, although the formulation is valid for linear elements as well. On-going research is being done to extend the formulation to shells with more complex (i.e., curved) geometries.

Two verification examples were presented here to demonstrate the capabilities of the proposed element. The results indicate that the element rapidly converges with the use of more elements. While not shown here, more layers can be used to provide greater accuracy in predicting large thermal gradients over the depth of the element.

Comparisons to high-resolution finite element analyses demonstrate that the shell element presented here offers substantial cost-savings in the 3D analysis of plates subjected to non-uniform heating. These savings will be amplified when the heat transfer element is coupled with a mechanics-based shell element to perform thermo-structural analyses of non-uniformly heated structures. In addition to offering significant computational savings, the element also greatly simplifies that transfer of data from the heat transfer analysis to the structural analysis because the element's mesh is compatible with existing elements for distributed plasticity analysis of shells.

REFERENCES

ABAQUS (v. 6.10) 2010. Providence, RI: Dassault Systemes Simulia Corporation.

Buchter, N. et al. 1994. Three-dimensional extension of nonlinear shell formulation based on the enhanced assumed strain concept. *International Journal of Numerical Methods in Engineering* 37: 2551–2568.

Chen, L. et al. 2011. FDS and Abaqus coupling toolkit for fire simulation and thermal and mass flow prediction. In M. Spearpoint (ed.), *Proceedings of the 10th International Symposium on Fire Safety Science*: 1465–1477, London.

Jaluria, Y. & Torrance, K.E. (2nd ed.) 2003. *Computational Heat Transfer*. New York: Taylor and Francis.

Jeffers, A.E. 2013. Heat Transfer Element for Modeling the Thermal Response of Non-Uniformly Heated Plates. *Finite Elements in Analysis and Design* 63: 62–68.

Jeffers, A.E. & Sotelino, E.D. 2009. Fiber Heat Transfer Element for Modeling the Thermal Response of Structures in Fire. *Journal of Structural Engineering* 135: 1191–1200.

Prasad, K. & Baum, H. 2005. *Fire Structure Interface and Thermal Response of World Trade Center Towers, Federal Building and Fire Safety Investigation of the World Trade Center Disaster*, NIST NCSTAR 1-5G, National Institute of Standards and Technology, Gaithersburg, MD.

Ramm, E. & Matzenmiller, A. 1988. Consistent linearization in elasto-plastic shell analysis. *Engineering Computations* 5: 289–299.

Stern-Gottfried, J. et al. 2010. Experimental review of the homogeneous temperature assumption in post-flashover compartment fires. *Fire Safety Journal* 45: 249–261.

Tondini, N. et al. 2012. Development of an interface between CFD and FE software. In M. Fontana et al. (eds.), *Proceedings of the 7th International Conference on Structures in Fire*: 459–468, Zurich, Switzerland.

Wriggers, P. et al. (1996). A comparison of three-dimensional continuum and shell elements for finite plasticity. *International Journal of Solids and Structures* 33: 3309–3326.

Research and Applications in Structural Engineering, Mechanics and Computation – Zingoni (Ed.)
© 2013 Taylor & Francis Group, London, ISBN 978-1-138-00061-2

Co-rotational FEM for fast geometrically nonlinear static and dynamic algorithms

D. Marinkovic
Department of Structural Analysis, Berlin Institute of Technology, Germany
Faculty of Mechanical Engineering, University of Nis, Serbia

M.W. Zehn
Department of Structural Analysis, Berlin Institute of Technology, Germany

ABSTRACT: The Finite Element Method (FEM) is the dominant tool in the field of structural analysis. Typical engineering tasks imply "off-line" FEM computations with high accuracy set as the primary simulation objective. However, in many areas of applications, such as Multi-Body System (MBS) dynamics or virtual reality simulators, high numerical efficiency with respect to time becomes an aspect of similar importance as the accuracy itself. Furthermore, adequate modeling in the field of the applications mentioned requires the consideration of geometrically nonlinear effects. As a response to those requirements, the authors propose a simplified co-rotational FEM formulation, the essence of which is to account for rigid-body rotation on the element level. The development is briefly presented for solids and shells. A set of examples have been chosen to demonstrate the features of the proposed FEM formulation.

1 INTRODUCTION

A number of methods have been developed with the aim of predicting the physical behavior of deformable objects with very high level of accuracy. The finite element method (FEM), as the dominant tool in the field of structural analysis, has deservedly gained the reputation of the 'state-of-the-art method'. Typical engineering tasks require models and computations that provide an authentic representation of the real world. The solutions are obtained through "off-line" FEM computations with the accuracy set as the primary simulation objective. For small deformations and displacements a linear analysis is conducted. For larger deformations and displacements, particularly rotations, rigorous geometrically nonlinear FEM formulations are used, which involve a significantly larger numerical effort compared to the linear analysis.

However, in many areas of application, such as MBS-FEM integration (Zehn 2005) or virtual reality simulators (Erleben et al. 2005), the efficiency of computing nonlinear deformational behavior becomes an objective of similar or maybe even greater (real-time simulators) importance than the accuracy itself. For computation of multi-body system dynamics over longer time-intervals and with geometrical nonlinearities included, so-called co-simulations (MBS-FEM) based on commercially available software packages can be used (Kalmykov et al. 2001, Busch & Schweizer 2010). This, however, requires a rather expensive data transfer in each time-step of numerical integration as well as synchronization of different software products (with different types of data storage, structure and solver), which implies rather long computational times with numerical instability as a potential problem as well. Similarly, FEM software packages do offer means to conduct computations for different types of virtual reality simulators, but with computational times much longer than required for the purpose of simulations at interactive frame rates. Hence, both the mentioned applications impose the strong demand for rather efficient computations with geometrical nonlinearities included.

This paper offers a simplified co-rotational FEM formulation designed to response to the challenges of the aforementioned and similar applications. The essence of the formulation is given for solid and shell elements and several examples are provided to give an idea of achievable results.

2 THE IDEA BEHIND THE PROPOSED CO-ROTATIONAL FEM FORMULATION

The linear FEM is highly efficient and numerically stable but accurate only for rather small deformations and displacements. Rigorous nonlinear FEM offers high accuracy of predicted deformational behavior, but is significantly slower than the linear FEM and the numerical stability of computation may also be an issue.

The co-rotational FEM proposed by the authors is supposed to combine the advantages of both approaches. The general idea behind the formulation arises from the principles of incorporating flexible bodies in Multi-Body-System (MBS) dynamics. To achieve high computational efficiency, the overall motion of a flexible body in an MBS program is decomposed into large rigid-body motion and a small deformation described with respect to the body-fixed reference frame. This local reference frame is actually attached to the body and performs the same rigid-body motion as the body itself. Hence, it excludes large rotation from the motion, thus allowing extraction of the deformable motion (in the average sense), which might be, on the other hand, just a small portion of the overall motion.

The idea is simply extended so that each element of the finite-element assemblage is assigned a local reference system, with respect to which the behavior of the element remains entirely linear. In this manner, deformations of a body, characterized by large local rotations of sub-domains with respect to the remaining of the body, are easily handled. The approach permits the computation of the linear stiffness matrices of single elements in a step prior to simulation. Over the course of simulation, it is necessary to extract the rigid-body motion of each element and use it to update the element stiffness matrices and to compute the internal forces. Hence, the numerical effort is significantly reduced and the numerical stability is notably improved compared to the rigorous geometrically nonlinear FEM, with the accuracy somewhat but for many purposes not significantly reduced.

3 THE CO-ROTATIONAL FEM WITH SOLID ELEMENTS

3.1 *Handling the translational degrees of freedom*

Solid elements result from discretization of structural elements viewed as continua. The mutual property of solid elements is that they describe the displacement field by means of nodal translations as degrees of freedom. Typical representatives of this group of finite elements are tetrahedral and hexahedral elements.

The linear tetrahedral element is well-known for its rather stiff behavior, which accounts for its disadvantage. Its major advantage, on the other hand, is the ability to mesh any geometry. The description of this finite element is widely available in literature (e.g. (Bathe 1997)) and, for the sake of brevity, it is not given here, but the element is used to elaborate the proposed co-rotational formulation. The very essence of the formulation is computation of the internal forces of the element, $\{F_e\}$ according to the following expression:

$$\{F_e\} = \mathbf{R}_e \mathbf{K}_e \left(\mathbf{R}_e^{-1} \{x_e\} - \{x_{0e}\} \right) \quad (1)$$

where $\{x_e\}$ and $\{x_{0e}\}$ are the current and initial element configurations (i.e. nodal coordinates), respectively, $\mathbf{R}_e$ is the rigid-body rotational matrix and $\mathbf{K}_e$ the linear element stiffness matrix. It will be worthwhile to give the interpretation of this equation by means of Figure 1. The first term in the parenthesis on the right-hand side of the equation yields the current element configuration rotated back to the original element orientation. Observing Figure 1, that configuration is obtained when the deformed element is rotated backwards through $\mathbf{R}_e^{-1}$. Thus, the entire term in the parenthesis gives the rotation-free nodal displacements. Multiplied with the linear element stiffness matrix, $\mathbf{K}_e$, the element internal (elastic) forces with respect to the original element configuration are obtained. Finally, what remains is to rotate the internal forces to the current element configuration, which is achieved by multiplication with the element rotational matrix, $\mathbf{R}_e$.

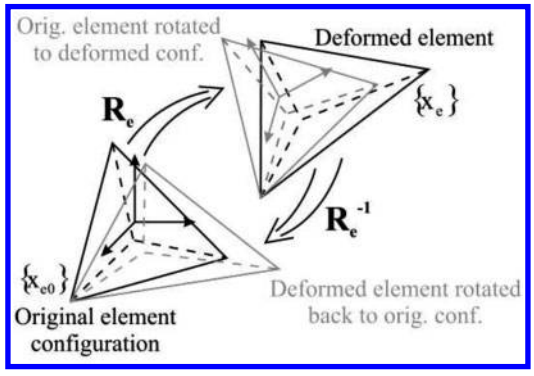


Figure 1. Decomposition of element's motion into rotation and deformation.

Finally, it should be noted that, regarding the linear tetrahedral element, there is a unique matrix that transforms the initial element configuration into the current one. Polar decomposition of this matrix yields the rotation matrix $\mathbf{R}_e$. With other element types, a kind of averaged rotation matrix has to be computed for the presented approach.

3.2 *An example with the tetrahedral element*

An example is given below to demonstrate the achievable accuracy with the simplified co-rotational approach. The considered structure is a part of a Volkswagen car's sliding door hinge. The boundary conditions are defined as fixed nodes over the surface of the holes designed for the hinge pin and a rather large excitation force, the direction of which can be seen in Figure 2. The depicted boundary conditions resemble the case when a car door opens quickly and hits against the bump stops. The induced force is large enough to cause large, geometrically nonlinear deformations. The deformation can be visually inspected in Figure 3 from different perspectives. It should be emphasized that the deformation is inspected in Figure 3 from different perspectives. It should be emphasized that the deformation is depicted in its actual size, i.e. with the deformation scaling factor equal to 1.

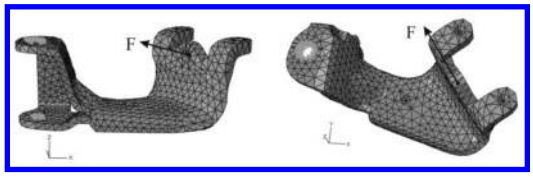


Figure 2. FEM model of a sliding door hinge (courtesy of VW).

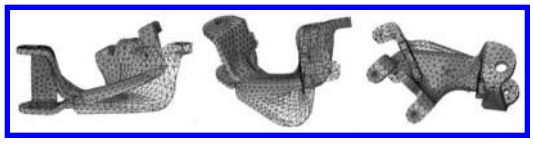


Figure 3. Deformed door hinge from different perspectives (scaling factor equals 1).

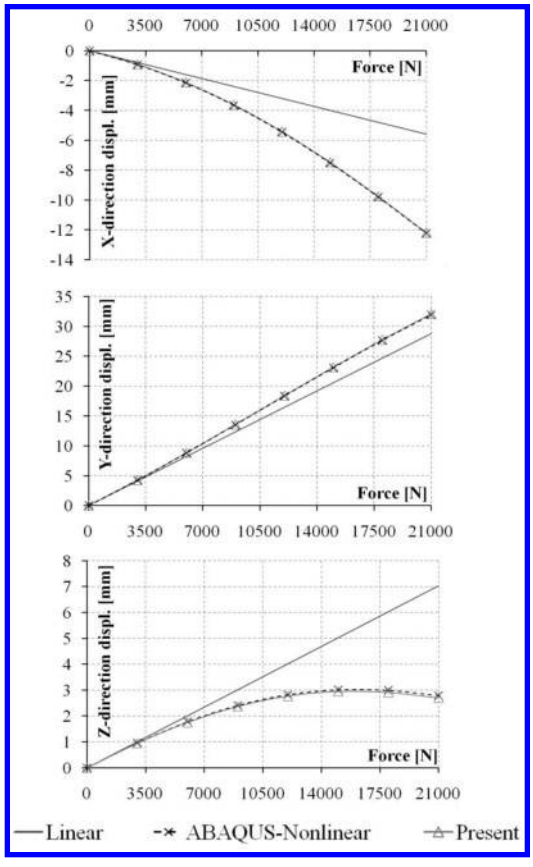


Figure 4. Global displacements of the point of force application.

The diagrams in Figure 4 shows very high agreement of the results obtained by the presented method and by the rigorous geometrically nonlinear computation conducted in ABAQUS.

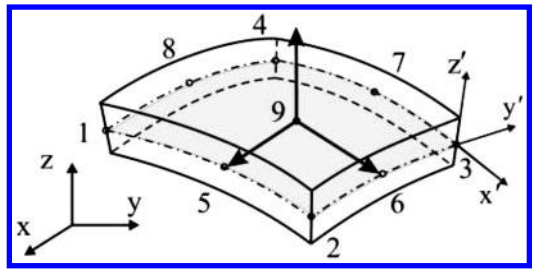


Figure 5. 9-node degenerate shell element.

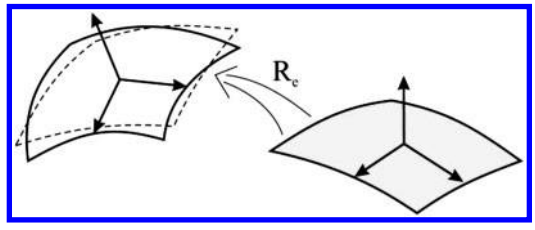


Figure 6. Decomposition of shell motion into rotation and deformation.

4 IMPLEMENTION OF A SHELL ELEMENT INTO THE CO-ROTATIONAL FORMULATION

4.1 *Handling the rotational degrees of freedom*

The efficient simulation of global deformational behavior of thin-walled structures is driven by the recognition that the nature of their global behavior allows condensation of the complex 3D field to the essential ingredients of the structural response described by a 2D approach. For this purpose, the authors use recently developed 9-node degenerate shell element (Marinkovic 2007) (Fig. 5).

The degenerate shell element has 3 translations and 3 rotations at each of the 9 nodes in the global coordinate system (x, y, z). The translations are handled in exactly the same manner as in the case of solid elements. To determine an average rotation of the element, an element local reference frame is introduced as depicted in Figure 5. The reference frame is determined by the element mid-node (node 9) and the mid-side nodes 5 and 6. The same nodes are used in both the original and the current configuration. As a matter of fact, one may define a tetrahedron by using those nodes and a point along the axis obtained by a cross-product of axes $\vec{v}_{95}$ and $\vec{v}_{96}$. This allows the use of exactly the same procedure as for the tetrahedral element to extract the rotation matrix.

The update of the rotational degrees of freedom is where the actual complexity with the shell element resides within a geometrically nonlinear formulation. The rotations do not share the same properties with the translations and cannot be simply rotated as it is done with the translations. Instead, the incremental rotations computed in each time-step are used to update the shell normals at each node. This is done by computing the

incremental rotation matrices of the shell normals as (Argyris 1982):

$$\mathbf{Q} = \mathbf{I} + \frac{\sin\gamma}{\gamma}\mathbf{S} + \frac{1}{2}\left(\frac{\sin\gamma}{\gamma}\right)^2 \mathbf{S}^2 \tag{2}$$

$$\text{with } \gamma = \sqrt{\theta_1^2 + \theta_2^2 + \theta_3^2} \tag{3}$$

$$\text{and } \mathbf{S} = \begin{bmatrix} 0 & -\theta_3 & \theta_2 \\ \theta_3 & 0 & -\theta_1 \\ -\theta_2 & \theta_1 & 0 \end{bmatrix} \tag{4}$$

where θ_1, θ_2 and θ_3 are the 3 incremental global rotations at the node. The rotation matrix $\mathbf{Q}$ is further used to update the orientation of the shell normal. By means of the inverse of the element rotation matrix, $\mathbf{R}_e^{-1}$, the updated normal is rotated back to the original configuration and the local 2 rotations are determined and used to compute the internal moments with respect to the original configuration. Finally, the internal moments are rotated to the current configuration using $\mathbf{R}_e$. Once both the internal forces and moments are computed and the element stiffness matrix is updated by means of rotation matrix, a static or dynamic computation may proceed.

4.2 *An example with the shell element*

A rather simple example is given below in order to compare the results by the rigorous geometrically nonlinear FEM and by the presented co-rotational FEM. In the original configuration, the considered structure's geometry is flat (50 × 30 × 3 mm) and considering the boundary conditions and the load, it could have been described as a plate (Fig. 7). The material is steel.

However, upon the deformation has been initiated, the behavior of the considered structure is actually that of a shell and the membrane effects gain more on importance as the deformation proceeds. The force of F = 12 kN is chosen so that significant geometrically nonlinear effects are observable in structural behavior. The deformation can be visually assessed in Figure 8 from different perspectives. Again, the deformation is shown in its actual size (scaling factor set to be 1) with both the initial and deformed configuration depicted.

The resulting displacements in the global x- and z-directions are summarized in the form of diagrams given in Figure 9. The z-displacement of the point of force application exceeds 25 mm, which is more than a half of the structure's length. The geometrically nonlinear effects are obvious in the obtained results. One may notice somewhat larger differences in the nonlinear results obtained with shell elements compared to the differences in the nonlinear results obtained with the tetrahedral element (Fig. 4). This fact is worth of discussion. There are a couple of reasons for this. Actually, one of the reasons has already been mentioned. Namely, the linear tetrahedral element has the unique rotation matrix, which describes the rotational motion of the element accurately. This is not the case with the full biquadratic shell element, i.e. in this case the matrix describing the rigid-body rotation is an averaged rotation matrix and this aspect certainly affects the accuracy. An additional reason should be sought in the differences in the shell element formulation used by the authors and the one from ABAQUS. The shell element from ABAQUS is an 8-node element with reduced integration and an hourglass control. The element applied here is the full biquadratic element with full integration implemented. Those differences in the element formulations actually lead to small differences in linear results as well, whereas the tetrahedral elements are identical and yield identical linear results.

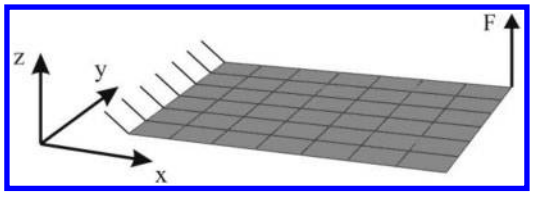


Figure 7. One-side clamped thin-walled structure with static load.

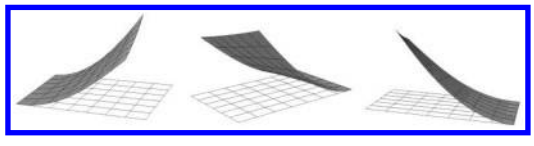


Figure 8. Deformed shell structure.

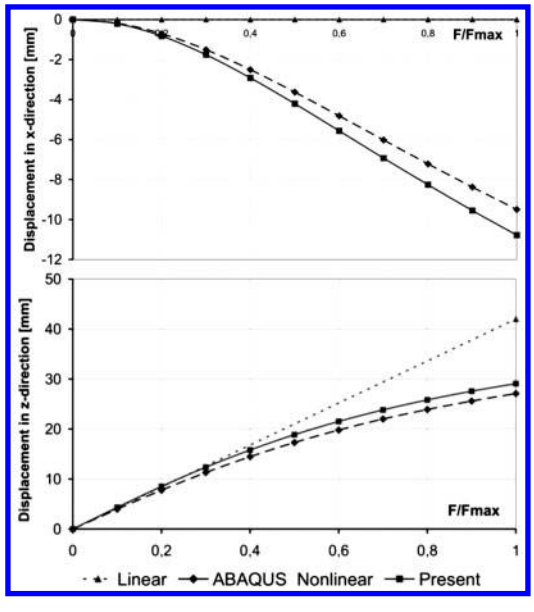


Figure 9. Global displacements of the point of force application.

5 FIELDS OF APPLICATION

The presented co-rotational FEM formulation offers a combination of the features originating from the linear and geometrically nonlinear FEM. It is more efficient and stable than the rigorous geometrically nonlinear FEM and covers geometrical nonlinearities up to a great extent. The authors use this formulation in a combination with an iterative preconditioned conjugate gradient solver. The solver provides further means to perform a "trade-off" between the accuracy and numerical effort by simply limiting the number of iterations in the solver. The solver is also a good choice for dynamic computations. Namely, the efficiency of the iterative solver can be noticeably improved by a reasonable choice of the starting vector of the iterative process. This is particularly interesting in dynamics with the system of equations solved for nodal velocities. The nodal velocities typically do not change dramatically within a time-step and, therefore, a good choice would be to take the nodal velocities from the previous time-step as a starting vector for the iterative solver in the next time-step. This improves the numerical efficiency of simulation as fewer iteration steps are needed to arrive to the solution.

With those features, the presented FEM formulation may find its application in all the systems where high numerical efficiency and consideration of geometrical nonlinearities are required and where a trade-off between the accuracy and computational efficiency may also be an option. Consideration of elastic structures in MBS dynamics is typically resolved in modal space, which intrinsically covers only linear deformations. However, adequate simulations of many structures require consideration of geometrical nonlinearities in order to reach a reasonable accuracy. An example of such a structure is the rear car axle shown in Figure 10. The crank arms of the axle may perform an average rotation of up to 15° over the course of the axle's deformation caused by a fast change of the car's driving direction. Simulation of such a deformation by means of a linear model yields results of insufficient accuracy for the prediction of the turning curve of the car.

Another interesting field of application is in virtual-reality simulators. A distinctive example of such a simulator would be a surgery simulator, particularly for the laparoscopic surgery. It is a type of surgery that minimizes the damage to surrounding tissue caused by reaching the location of intervention. Very difficult conditions (no direct contact with the operation site, 2D "on-screen" surgery monitoring, limited movability of surgery tools) give rise to a relatively high rate of surgeon errors with less experienced surgeons performing laparoscopic surgeries and, hence, adequate training tools are needed. They require plausible real-time simulation of internal organs' behavior. In this application, the real-time requirement has obviously the highest priority, while the accuracy requirement is not defined in terms of numbers and may be jeopardized as long as the on-screen behavior appears realistic to human perception. In many commercially available devices this goal is achieved by means of the simplest approach, namely the mass-spring systems, to realize geometrically nonlinear real-time simulations. The formulation presented in this paper offers a more sophisticated approach to simulate internal organs' deformation (Fig. 11) and still realizable in real-time.

In the entertainment industry, there is an ever growing tendency to use physics-based animation in order to achieve a higher degree of realism. In this field, the graphics requirements are always on the high end of achievable with the current hardware technology and, hence, highly efficient solutions are also sought for the background physics. The presented co-rotational FEM can also find its application in this field. Figure 12 shows deformations of a dog model over the



Figure 10. A model of a rear car axle used by VW for MBS dynamics.



Figure 11. Screen-shots from a real-time simulation of liver deformations determined by the presented co-rotational FEM.

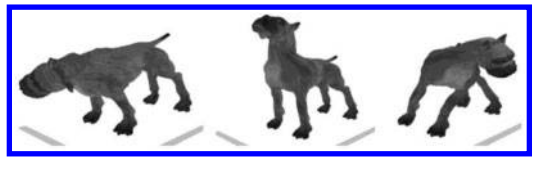


Figure 12. Screen-shots from an interactive simulation with a dog model.

course of an interactive simulation computed with the presented approach.

6 CONCLUSIONS

The paper presents the fundamental idea of the simplified co-rotational FEM formulation that covers geometrical nonlinearities by accounting for rigid-body rotation on the element level. It has been demonstrated that the method combines the advantages of the linear and geometrically nonlinear FEM. It permits performing a great deal of computation prior to the simulation, thus offering high numerical efficiency and stability. Regarding the accuracy, the limit of application of the presented approach depends on the requirements in the field of application and on the character of deformation. Rather high accuracy can be expected in the cases where local rotations dominate in the geometrically nonlinear behavior, while strains remain small. Deformational behavior with larger strains involved would require modification of the presented approach.

The formulation has been presented for solid and shell elements, the latter being more demanding due to the rotational degrees of freedom. Computing an average element rotation is an ambiguous issue for most elements. The linear tetrahedron is one of the rare elements with a unique rotation matrix. This is the major reason why this element yields very high agreement between the results obtained with this formulation and the results obtained by the rigorous geometrically nonlinear FEM. More attention should be given to the aspect of element rotation in the future work.

Several possible fields of application have been briefly discussed. The list includes MBS dynamics and the applications where interactive dynamics is required. However, this list is definitely not exhaustive. The features of modern hardware render this approach even more attractive, as the applied solver offers great parallelization potential. To take the full advantage of hardware's computation power, the computation could be switched from CPU to GPU (graphics processing unit), as modern GPUs contain a number of processors and give a massive floating-point computation power expressed in teraflops (10^{12} floating-point operations per second). This would certainly expand the list of possible applications of the presented approach.

REFERENCES

Argyris, J. H. 1982. An excursion into large rotations, *Computer Methods in Applied Mechanics and Engineering* 32: 85–155

Bathe, K. J. 1996. *Finite Element Procedures*, New York: Prentice Hall

Busch, M. & Schweizer, B. 2010. MBS/FEM co-simulation approach for lubrication problems. *Proc. Appl. Math. Mech.* 10:729–732

Erleben, K., Sporring, J., Henriksen, K. & Dohlmann H. 2005. *Phyisics-Based Animation*, Canada: Charles River Media

Kalmykov, I., Burger, M. & Dehning, C. 2001. Application for MBS-FEM coupling with MpCCI using automotive as example, *NAFEMS Seminar 'The Role of CAE in System Simulation', November 2011.* Wiesbaden

Marinkovic, D. 2007. *A new finite composite shell element for piezoelectric active structures*, Duesseldorf: VDI

Zehn, M. 2005. MBS and FEM: A Marriage-of-Convenience or a Love Story?, *BENCHmark, Int. Magazine for Eng. Design & Analysis*: 12–15

Research and Applications in Structural Engineering, Mechanics and Computation – Zingoni (Ed.)
© 2013 Taylor & Francis Group, London, ISBN 978-1-138-00061-2

Finite element modelling of shear tab connections including damage simulation

A. Mirzaei & C.A. Rogers
McGill University, Montréal, Canada

R. Tremblay
École Polytechnique de Montréal, Montréal, Canada

ABSTRACT: A common approach to connect steel beams to columns is to use shear tabs. Numerous laboratory test programs of these connections have been completed; however, the development of finite element models that accurately capture their behaviour lags behind. A series of full-scale lab tests were carried out at McGill University on "standard" and "non-standard" shear tab connections. The results from these tests were used in the development of a finite element model that is capable of simulating the response of the connection under load; predict the ultimate resistance and the progression of failure. The intent is to use the model for the future evaluation of shear tabs under extreme loading conditions such as combined axial and vertical forces. Previous finite element modelling of shear tabs lacked damage simulation capability, did not include the effect of weld tearing, and as such often overestimated the connection resistance. This paper will summarize the development of a finite element simulation model and provide a comparison with the laboratory results.

1 INTRODUCTION

1.1 *Shear tabs*

Single plate beam web connections, also known as shear tabs or fin plates, are one of the more common simple connections used in the steel construction industry. Shear tab connections are typically specified due to their cost efficiency, as well as ease of fabrication and installation on the construction site. They are usually used to connect girder beams to columns and secondary beams to girders. The connecting plate is welded to the supporting member in the fabrication shop. The connection between the supported beam's web and the steel plate is made by means of field-installed bolts.

1.2 *Research program*

The current design procedure used for shear tabs in Canada (CISC, 2010) is based on the research carried out by Astaneh (1989) and Astaneh et al. (1989); it has not been further developed. This approach is only applicable to shear tabs with one vertical row of 2 to 7 bolts connected to a rigid support (e.g., the flange of a W section column) or a flexible support (e.g., the web of a column or a girder) by using E49 fillet welds and A325 bolts. The current Canadian approach does not cover the usage of multiple vertical rows of bolts or the use of configurations with more than 7 bolts per vertical row. The size and thickness of the shear tab is further limited due to design restrictions. The existing design approach also does not address the application of combined shear and axial forces on the connection.

The objective of the global research project involves the development of shear tab design and detailing provisions to be used in Canada. It comprises full-scale laboratory testing and finite element (FE) modelling. The advantage of using finite element simulation is that the load level can easily be changed and more cases can be investigated in less time and with less cost compared to full-scale testing. The FE models described herein will be used in future studies to investigate the performance of the same shear tab connections under extreme loading conditions such as an axial plus gravity loading scenario. The validity of the FE models was verified by using data obtained from full-scale testing.

2 FULL-SCALE LAB TESTING

2.1 *Overview*

A series of full-scale laboratory tests was carried out by Marosi et al. (2011a, b) at McGill University on "standard" and "non-standard" shear tab connections subjected to gravity loads. Data collected from the tests were used to calibrate the FE models capable of simulating the test procedure and predicting the performance and ultimate shear resistance of the same tested shear tab connections.

2.2 *Test setup*

The test configuration used by Marosi et al. is shown in Figure 1 and its functionality schematic is illustrated in Figure 2. The shear tabs were shop welded to a W360x196 ASTM A992 Grade 50 ($F_y = 345$ MPa) column which was secured to the strong floor, minimizing column movement and rotation. The shear tabs, ASTM A572 Grade 50 ($F_y = 345$ MPa) hot rolled plate, were fillet welded on both sides using a flux-cored arc welding (FCAW-G) process along with an additional shielding gas (CO_2) and an E71T (480 MPa) electrode. An ASTM A992 Grade 50 ($F_y = 345$ MPa) test beam (Table 1) was used to transfer the forces from the actuators to the connection. A 12 MN actuator was responsible to create the main shear force in the connection. To eliminate friction and permit free rotation between the actuator head and the test beam's top flange a half steel cylinder, steel plate and roller system was used. The end of the beam was attached to a 269 kN actuator which limited the vertical displacement in order to control the rotation of the connection. ASTM A325 snug tight bolts, placed at a 76 mm spacing both vertically and horizontally (when applicable), were used to connect the shear tab to the test beam. A lateral bracing system was used which simultaneously allowed the test beam to displace vertically without lateral movement as illustrated in Figure 1. A target rotation of 0.02 rad for the W310 and 0.015 rad for the W610 and W920 beam connections at the predicted ultimate shear resistance was used for the loading protocol. A displacement based loading approach was used in which the relative displacement rate of the two actuators was controlled to attain the target rotation. A range of instrumentation was used to measure vertical, horizontal and rotational movements of the shear tab, test beam and column. To monitor the change in strain throughout the steel plate, strain gauges were installed on the shear tabs. The connection shear force was determined based on the data from load cells attached to the actuators. Table 1 contains a summary of the six test configurations that that were modelled in ABAQUS; additional information on the testing can be found in Marosi et al. (2011a, b).



Figure 1. Test setup used for Test #2 (Marosi et al. 2011a,b).

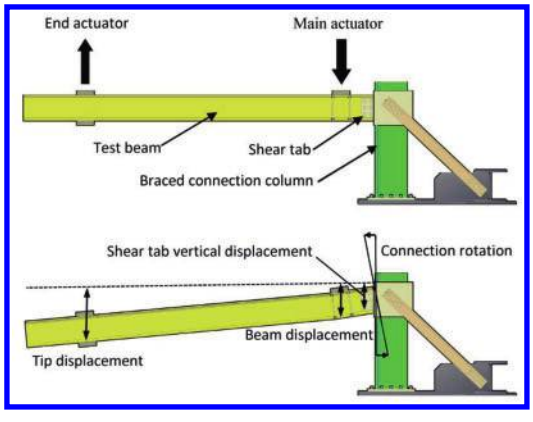


Figure 2. General schematic of the test functionality.

3 MATERIAL PROPERTIES

3.1 *Coupon testing and simulation*

In order to obtain an accurate FE simulation, material properties were determined by performing coupon tests on specimens cut from the plates and beams used for the connection tests by Marosi et al. Four coupons were extracted from the beam's flanges, three from the web, and three for each shear tab specimen. The

Table 1. Shear tab specimens tested by Marosi et al. (2011a, b).

Test No.	Shear tab size mm	Beam size	Bolt size mm	Row and number of bolts	Fillet weld size mm
1	228 × 89 × 6	W310 × 60	19	1 × 3	6
2	228 × 165 × 10	W310 × 60	19	2 × 3	6
7	456 × 102 × 8	W610 × 140	22	1 × 6	6
8	456 × 178 × 16	W610 × 140	22	2 × 6	10
13	760 × 102 × 10	W920 × 223	25	1 × 10	6
15	760 × 178 × 22	W920 × 223	25	2 × 10	14

results from the coupon tests were available in terms of engineering stress-strain curves. Since the FE package (ABAQUS) requires true stress-strain curves as an input, the coupon tests were modelled in ABAQUS such that the material model could be accurately calibrated with the test information. Tests were not conducted for the bolt material property; the nominal properties were converted into true stress and strain input instead. For the fillet welds, the same elastic and plastic data from the corresponding shear tab specimen were used, but with different damage parameters that were calibrated with the shear tab test data.

3.2 *Damage simulation*

The results from testing showed that the performance of the shear tabs was dependent on the ductility of the steel plate and the strength of the connecting weld. In tests where the weld started to tear, the shear tab continued to carry shear force until a point at which either cracks developed in the plate itself between the bolt holes or the weld was excessively fractured. For shear tabs in which the ultimate resistance was governed mainly by net area plate fracture with no tearing in the welds, the FE models without damage simulation could still approximate the ultimate shear resistance with reasonable accuracy. In contrast, for shear tabs that experienced weld tearing, the FE model without damage simulation overestimated the shear resistance and stiffness of the connection. Based on this initial observation a damage model was deemed essential for shear tab FE simulation since the failure mode is not necessarily known a priori.

The material damage simulation model is illustrated in Figure 3. At the onset of loading the material behaves elastically until it reaches point 1 (yielding point). Subsequently, the material experiences plastic deformation until it reaches point 2 at the ultimate stress level. At this point the damage parameter (D) is incorporated in the analysis. A ductile damage for metals initiation criterion was utilized, which is a function of triaxiality, fracture strain and strain rate. Determination of the damage parameters requires accurate measurement of the fractured coupons and recorded data of the post ultimate behaviour; therefore, for simplicity it was assumed for different levels of triaxiality that the fracture strain is 0.21 at a strain rate of 0.01/s. The damage initiation criterion controls when damage initiates and has no effect on the material unless equipped with damage evolution capability. Damage evolution controls the stiffness degradation parameter (D) by using an energy approach which is based on the fracture energy required for failure. Beyond point 2, through to point 3, the D parameter increases, leading to stiffness degradation (softening) of the material. At point 4, $D = 1.0$ which means the stiffness is absent, and as such the material cannot develop any stress. Generally steel never reaches point 4, therefore another parameter called the maximum stiffness degradation is used to determine where the material fails; it can be determined based on the post ultimate coupon test information. In cases where the data was not available a maximum stiffness degradation of 0.5 was used. Once D reaches its specified limit, an option exists to remove the degraded elements from the global stiffness matrix or to keep them in the system although having a degraded stiffness. Element removal results in a modification to the global system stiffness and gives the ability to redistribute stresses in the connection to compensate for the loss of stiffness, at weld fractures for example (Simulia, 2011).

As an example, Figure 4 shows the effect of the damage model in the simulation of a coupon extracted from the shear tab specimen used in Test #2; Figure 5 shows the corresponding stress-strain curve.

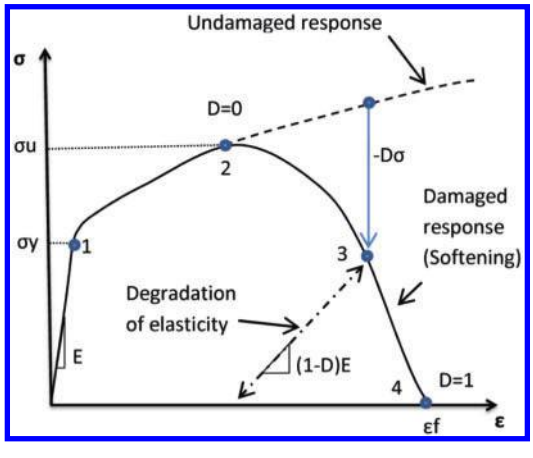


Figure 3. Schematic representation of the damage model.

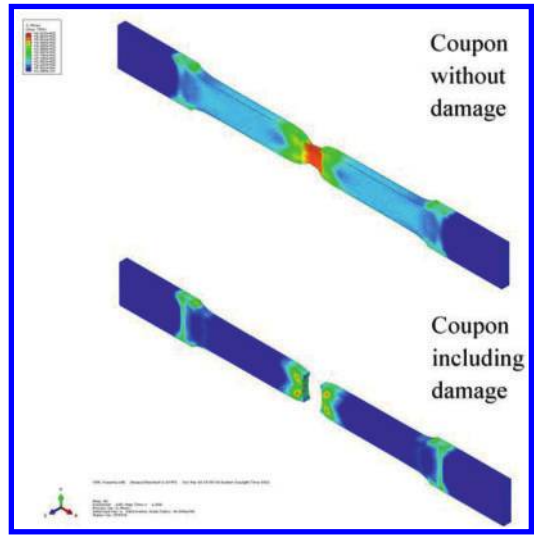


Figure 4. Comparison of Mises stress in a coupon simulation including and excluding damage.

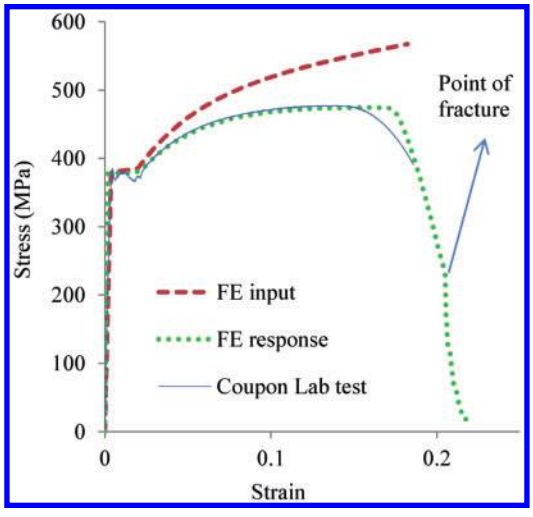


Figure 5. Stress-strain curve of coupon (damage included).

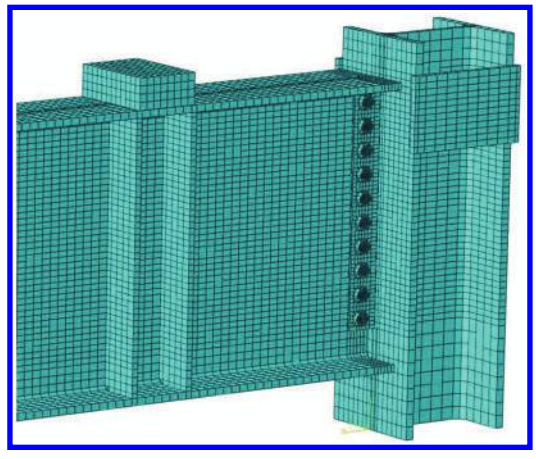


Figure 6. Global part assembly and mesh design of the FE model of Test 13 before load application.

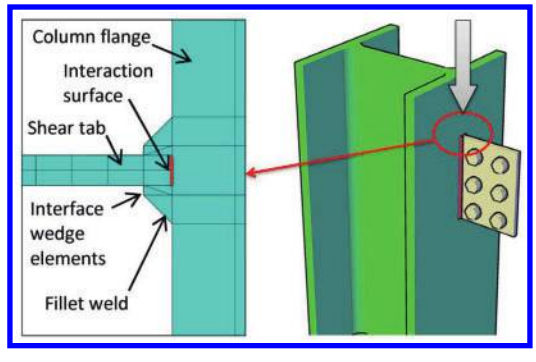


Figure 7. Mesh design representation at the interface of the shear tab with the connecting fillet weld.

4 CONNECTION FINITE ELEMENT MODEL

4.1 *General simulation strategy*

A 3D solid finite element model was used for simulation, which includes the beam, column, shear tab, bolts, washers, welds and load blocks (Figure 6). The different components of the test setup modelled in ABAQUS were assumed to be homogeneous and deformable solids. For mesh design, two different element types were used for modelling. An 8-node cubic 3D element with full linear integration (C8 element) was used to model most parts except for locations where the geometry conditions had curvature involved (such as the bolts or the curve between the flange and web of the beam). A 6-node linear triangular prism 3D element (C3D6 element) was used to model these geometric conditions. The lateral brace mechanisms used in the full-scale testing were simulated by applying a boundary condition to the beam flanges to prevent lateral displacements but allow for other degrees of freedom to displace and rotate. The loading generated from the main actuator and tip actuator was applied as a displacement boundary condition to the load blocks that have a frictionless interaction defined at their interface with the beam's flange. The load block had the feature to rotate freely as it displaces to simulate the half cylinder–roller system used for applying the main load in the lab tests.

To allow for weld tearing, the mesh assembly in Figure 7 was used. The problem with classical FE models is that all the components are usually modelled as one individual part, which would result in shared nodes between the shear tab, weld and supporting member. This would limit the ability to capture the shear tab separation from the column and would result in incorrect stresses in the weld leading to over-estimated shear resistance of the connection. To resolve this issue the steel plate, including an interface layer of 2 wedge elements on each side, was assembled as a separate part distinct from the column. The interface layer of wedge elements, which physically would be part of the weld, was tied with a tie constraint to the fillet weld. A contact interaction was also used between the vertical edge of the plate and the column flange which included a separation allowance. By using this technique and applying the damage properties to the shear tab and weld, tearing simulation was made possible. Once damaged, the weld was able to tear resulting in separation of the shear tab on top and a more accurate compression stress distribution at the bottom of the shear tab due to contact with the column. The thickness of the wedge layer was minimized while still satisfying mesh quality requirements. By utilizing damage and weld tearing in the simulation, the final deformed shape of the FE models showed significant improvement in the failure progression of the connection compared to preliminary FE models which lacked these features.

The element removal feature was used for the fillet weld properties in all tests, but was not used in the shear tab mesh for some tests. Removing an element from a mesh that is part of an interaction property (such as a contact) causes numerical instability. The software

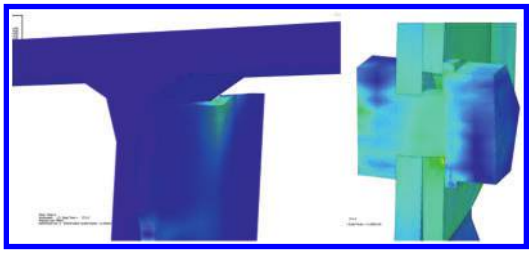


Figure 8. Cross sectional view of the contact between the shear tab and the test beam (left), stress distribution in a bolt (right).

was still capable of reassigning the interaction surfaces after element removal but the procedure would not always be executed to completion due to numerical instability. Initial modelling attempts included the element removal feature in the plate but when numerical instabilities occurred it was itself removed, while the stiffness degradation was kept functional. Using the damage modelling in the simulation increased the running time but resulted in a more realistic behaviour of the connection as compared with laboratory tests.

4.2 *Contact interactions*

The FE model included many contact interactions. These contacts were assigned tangential behaviour with a friction coefficient of 0.3 and normal behaviour with separation allowance; all were defined as surface-to-surface contacts. Bearing simulation at bolt surfaces was achieved by the contact between a bolt's outer surface and the surface of the inner hole on the beam web and the shear tab. The diameter used for the bolt was the same as the diameter of the hole on the shear tab. The reason for selecting the same diameter is that in the FE model the 2 mm space gap between the bolts with the holes cannot exist due to continuity of the interaction surfaces. Since each bolt was assembled as an individual part in the FE assembly, this technique allowed for stability of the assembly at the initial stage of the analysis. Figure 8 shows a cross section of a bolt from the FE model for Test #1. The contour shows the von Mises stress distributed inside the bolt which is caused mainly due to shear stress.

Other contacts simulated were: contact between the shear tab and the beam web, washers with the shear tab, and the shear tab with the column flange. Additional contacts that were observed during lab testing were also embedded in the models such as the contact of the top of the shear tab with the curve between the beam flange and web (Figure 8). Based on observations during testing tearing of the fillet welds was influenced by the contact between the top of the shear tab and this region of the beam.

5 RESULTS

The FE models were capable of simulating the behaviour and progressive damage observed in the six shear tab tests by Marosi et al. Most of the FE model analyses where able to run completely but some terminated at just over 90% of the testing procedure due to numerical instabilities after damage evolution. Figure 9 compares the final deformed shape of the shear tab specimen of Test #1 with its corresponding FE model (bolts have been removed to show the plate deformation). The shear tab experienced flexural and shear plastic yielding between the bolt line and the fillet weld. Weld tearing can be observed on top of the shear tab in both the model and test. Figure 10 demonstrates net area failure simulation in the FE models, which in this case was combined with weld fracture. During testing cracks developed in the shear tab between the four centre bolt holes. The same damage progression was observed in the FE model (with damaged element removal capability), which demonstrates the ability of the model to simulate net area failure.

The shear tab vertical displacement and connection rotation versus the shear force were selected as the

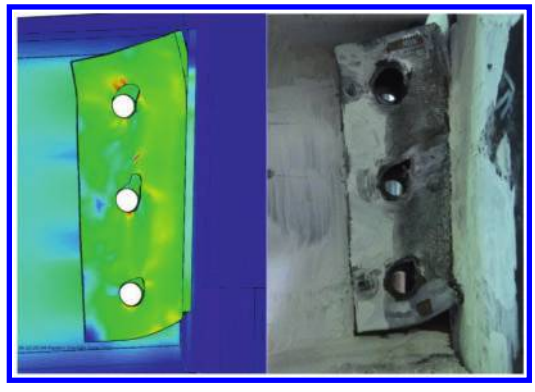


Figure 9. FE simulation vs. lab test result of Test 1.

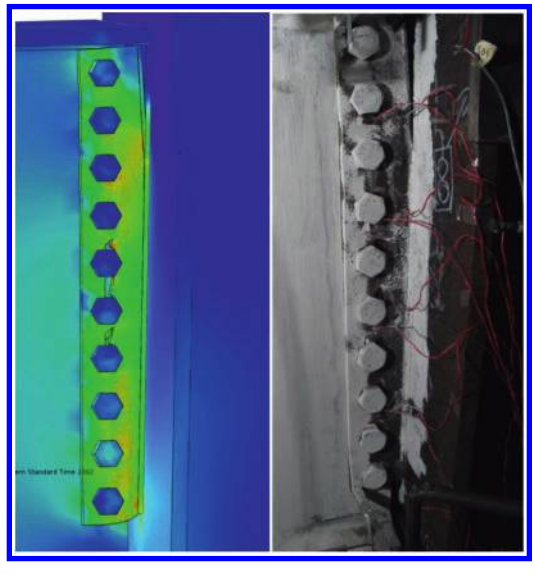


Figure 10. FE simulation vs. lab test result of Test 13.

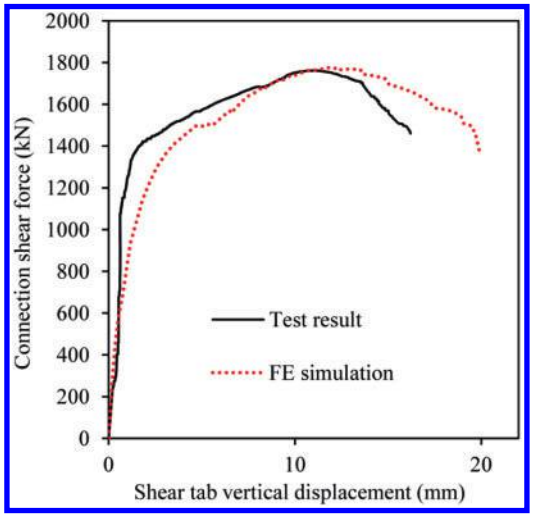


Figure 11. Response curves obtained from Test 13.

Table 2. Comparison of the FE simulation shear resistance with test results conducted by Marosi et al. (2011a, b).

Test No.	Predicted kN	Lab result kN	FE simulation kN
1	297	363	374
2	424	513	517
7	737	961	969
8	1476	1735	1745
13	1531	1762	1778
15	3515	3489*	3617

*Actuators reached maximum stroke prior to connection failure

criteria for comparing the response from FE simulation with the lab test results. Figure 11 demonstrates the response curves of Test #13. Some alterations are observed in the deformation due to the simulation technique, slippages between the components during the testing process, errors in the instrumentation, equipment, etc. Nevertheless, in terms of connection shear resistance the FE models were able to predict the ultimate shear resistance of the connection with a very good accuracy. Table 2 contains a listing comparing the predicted (by hand calculation), tested and FE simulated shear resistance of the test configurations. The predicted shear resistance was calculated based on Marosi et al.'s modified AISC (2005) extended shear tab method using a resistance factor, ϕ, of 1.0 and actual material properties from coupon testing. The predicted shear resistances underestimated the measured resistances of the connections whereas FE simulation results are all very close to the experimental results.

6 CONCLUSION

A series of finite element models representing six full-scale shear tab tests were created to replicate the laboratory testing procedure and connection configuration. The simulation strategy with appropriate material properties and equipped with a damage model was able to simulate weld tearing and net area fracture of the connections. The results showed the capability of ABAQUS to closely match the shear tabs behaviour observed in previous test programs, which has provided confidence in the models and their potential use for the evaluation of other loading scenarios.

ACKNOWLEDGEMENTS

The authors would like to thank ADF Group Inc. and DPHV Structural Consultants for their generous technical and financial support as well as the Natural Sciences and Engineering Research Council of Canada.

REFERENCES

AISC 2005. *Manual of steel construction, 13th Edition*, American Institute of Steel Construction; Chicago.

Astaneh, A. 1989. Demand and supply of ductility in steel shear connections. *Journal of Constructional Steel Research* 14: 1–19.

Astaneh, A., Call, S.M., McMullin, K.M. 1989. Design of single plate shear connections. *American Institute of Steel Construction Engineering Journal* 26(1): 21–32

CISC 2010. *Handbook of steel construction, 10th Edition*. Canadian Institute of Steel Construction; Toronto.

Marosi, M., Tremblay, R., Rogers, C.A. 2011a. Behaviour of single and double row bolted shear tab connections and weld retrofits. Research Report Dept. of Civil Eng. & Applied Mechanics, McGill University, Montreal, Canada.

Marosi, M., D'Aronco, M., Tremblay, R., Rogers, C.A. 2011b. Multi-row bolted beam to column shear tab connections. *6th European Conference on Steel and Composite Structures;* Budapest, Hungary. 555–560.

Simulia 2011. *Abaqus 6.11 Analysis User's Manual Volume III: Materials:* Sec 23.2.

Research and Applications in Structural Engineering, Mechanics and Computation – Zingoni (Ed.)
© 2013 Taylor & Francis Group, London, ISBN 978-1-138-00061-2

Nonlinear static and dynamic analysis of an electrically-actuated microbeam modelled by means of the strain gradient elasticity theory

Pierpaolo Belardinelli & Stefano Lenci
Department of Civil and Building Engineering, and Architecture, Polytechnic University of Marche, Ancona, Italy

ABSTRACT: The main goal of this work is to investigate the static and the dynamic behaviour of an electrically-actuated microbeam modelled by means of the strain gradient elasticity theory. Considering the nonlinearities due to the mid-plane stretch and of the applied electric force, a numerical solution for the static response is obtained by the differential quadrature method including also the features introduced by the non-classical continuum theory. A parametric analysis confirms the well-known hardening effect generated by a tensile applied axial load and highlights the variation of the deflection with respect to the high-order material parameters. We propose an approximate model, for the electric force acting on the microbeam, using the Chebyshev method. An accurate model, so that the error is spread smoothly over the domain, is then analysed with a single-degree-of-freedom model. Particular attention is paid to find the influence of the high-order length scale material parameters, introduced by the non-classical theory, that progressively modify the oscillating behaviour.

1 INTRODUCTION

Control and design of Micro-electro-mechanical systems (MEMS) is, nowadays, a fundamental step in widely different engineering fields. Other than mechanical application, as micro switches, micro-electromechanical silicon resonators (Mestrom, Fey, van Beek, Phan, & Nijmeijer 2008), biological and biomedical applications have become field of particular interest with widespread use in a variety of activities.

The mechanical modeling of an electrically-actuated microbeams, is, often, based on the classical mechanics (Abdel Rahman, Younis, & Nayfeh 2002). Recently, the modeling in microstructures is moving towards the non-classical continuum theories (Kahrobaiyan, Asghari, Rahaeifard, & Ahmadian 2011). The deformation, when the characteristic length is on the micro scale order, has been shown to be size dependent (Yang, Chong, Lam, & Tong 2002), and high-order elastic theories can catch this phenomena. The non-classical approach increments the order of the governing differential equations introducing high-order length scale material parameters (Fleck & Hutchinson 1997, Mindlin & Tiersten 1962). This work wants to apply the modified strain-gradient elasticity proposed by (Lam, Yang, Chong, Wang, & Tong 2003) at an electrically-actuated clamped-clamped microbeam.

Other aim of this work is to derive an alternative, more efficient, method to approximate the electric actuation. Although with few terms of a Taylor series we cannot achieve an uniform error, we want to show, using the Chebyshev method, how to limit the error into a specified constrains. The purpose is, thus, to formulate an expression that can be successfully applied in all prescribed domains with a limited and reduced approximation error. The work done in (Younis, Abdel-Rahman, & Nayfeh 2003) shows a comparison between a more complicated exact solution and the Taylor series approximation. The method of differential quadrature, introduced by Bellman (Bellman, Kashef, & Casti 1972) is here used to analyse the static behaviour of the electromechanical model. It works approximating all the partial derivatives by a weighted linear sum of the function values at given discrete points. We also investigate, in the last section of the paper, on the discretized dynamical problem with a Galerkin procedure, evaluating the single-degree-of-freedom response as function of different parameters.

2 PROBLEM FORMULATION

The strain energy density (here named s), considering the strain-gradient elasticity theory, is a function both of the strain tensor ε_{ij} and of the second-order deformation gradient tensor η_{ijk}, defined respectively as:

$$\varepsilon_{ij} = \frac{1}{2}\left(u_{i,j} + u_{j,i}\right), \quad \eta_{ijk} = u_{k,ij}, \tag{1}$$

being u_i the components of the displacement vector. The Einstein's notation for partial derivatives is used. Considering the variation of the strain energy:

$$\delta s = \frac{\partial s}{\partial \varepsilon_{ij}}\delta\varepsilon_{ij} + \frac{\partial s}{\partial \eta_{ijk}}\delta\eta_{ijk}, \tag{2}$$

we can identify, as suggested in (Mindlin 1965), the Cauchy stress tensor $\sigma_{ij} = \partial s / \partial \varepsilon_{ij}$ and of the double stress tensor $\tau_{ijk} = \partial s / \partial \eta_{ijk}$.

The double stress tensor and the second-order deformation gradient can be recasted in such a way that:

$$\delta s = \sigma_{ij}\delta\varepsilon_{ij} + \tau^{(0)}_{ijk}\delta\eta^{(0)}_{ijk} + \tau^{(1)}_{ijk}\delta\eta^{(1)}_{ijk} + \tau^{a}_{ijk}\delta\eta^{a}_{ijk} \tag{3}$$

where with the apexes ^{s} and ^{a}, $^{(0)}$ and $^{(1)}$, are indicated the symmetric and antisymmetric, trace and traceless parts of the tensors. The second-order virtual work density can be rearranged using the dilatation gradient γ_i, the deviatoric stretch gradient $\eta^{(1)}_{ijk}$ and the symmetric part of the rotational gradient χ^s_{ij}, which are defined by:

$$\gamma_i = \varepsilon_{mm,i},$$
$$\eta^{(1)}_{ijk} = \frac{(\varepsilon_{jk,i} + \varepsilon_{ki,j} + \varepsilon_{ij,k})}{3} - \frac{\delta_{ij}(\varepsilon_{mm,k} + 2\varepsilon_{mk,m})}{15} \tag{4}$$

$$- \frac{[\delta_{jk}(\varepsilon_{mm,i} + 2\varepsilon_{mi,m}) + \delta_{ki}(\varepsilon_{mm,j} + 2\varepsilon_{mj,m})]}{15}, \tag{5}$$

$$\chi^s_{ij} = \frac{1}{2}(e_{ipq}\varepsilon_{jp,q} + e_{jpq}\varepsilon_{ip,q}). \tag{6}$$

δ_{ij} is the Kronecker delta and e_{ijk} the Levi-Civita alternating tensor, see Section 2.2 of (Lam, Yang, Chong, Wang, & Tong 2003) for details.

By the previous developments, the first variation δs of the strain energy becomes

$$\delta s = \sigma_{ij}\delta\varepsilon_{ij} + p_i\delta\gamma_i + \tau^{(1)}_{ijk}\delta\eta^{(1)}_{ijk} + m^s_{ij}\delta\chi^s_{ij} \tag{7}$$

where the conjugate static terms σ_{ij}, p_i, $\tau^{(1)}_{ijk}$, m^s_{ij} are defined by the constitutive functions (Zhao, Zhou, Wang, & Wang 2012):

$$\sigma_{ij} = 2\mu\left(\varepsilon_{ij} + \frac{\nu}{1-2\nu}\varepsilon_{mm}\delta_{ij}\right), \tag{8}$$

$$p_i = 2\mu l_0^2\gamma_i, \tag{9}$$

$$\tau^{(1)}_{ijk} = 2\mu l_1^2\eta^{(1)}_{ijk}, \tag{10}$$

$$m^s_{ij} = 2\mu l_2^2\chi^s_{ij}. \tag{11}$$

l_n $(n = 0; 1; 2)$ are the material length parameters related, respectively, to p_i, $\tau^{(1)}_{ijk}$ and m^s_{ij}; ν is the Poisson's ratio and μ the Lamé's second parameter.

We use the extended Hamilton's principle, to get the equations of motion for an electrically-actuated slender microbeam:

$$\delta\int_{t_1}^{t_2}(T - \Pi + W_{nc} + U_e)\,dt = 0, \tag{12}$$

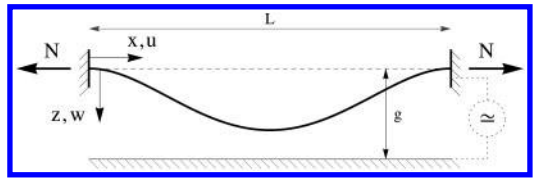


Figure 1. 1-D model for the electrically-actuated microbeam.

where T and Π are the kinetic and the elastic energy, while W_{nc} and U_e represent the non-conservative energy and the electric potential energy stored in the parallel plate capacitor. The kinetic energy of the beam in its variational form, being u and w the longitudinal and the transversal displacements (see Figure 1), is given by:

$$\delta T = \int_0^L \rho A\,(\dot{u}\delta\dot{u} + \dot{w}\delta\dot{w})\,dx \tag{13}$$

The dot is used to represent time differentiation. Integrating by parts in time with the assumption that the true and the varied paths coincide at t_1 and t_2 ($\delta u(x,t_1) = \delta u(x,t_2) = 0$ and $\delta w(x,t_1) = \delta w(x,t_2) = 0$) we have:

$$\delta T = -\rho A\int_0^L (\ddot{u}\delta u + \ddot{w}\delta w)\,dx. \tag{14}$$

The variation δW_{nc} due to the mechanical damping c, is expressed by:

$$\delta W_{nc} = \int_0^L (-c\dot{w})\,\delta w dx. \tag{15}$$

The variational form of the electric energy in a parallel plate capacitor reads (Fargas Marques, Costa Castello, & Shkel 2005):

$$\delta U_e = -\frac{1}{2}\int_0^L \left(\frac{\varepsilon_0\varepsilon_r bV^2}{(g-w)^2}\delta w\right)dx. \tag{16}$$

The elastic energy variation is represented by the volume integral of the strain energy density given in (7):

$$\delta\Pi = \int_V \left(\sigma_{ij}\delta\varepsilon_{ij} + p_i\delta\gamma_i + \tau^{(1)}_{ijk}\delta\eta^{(1)}_{ijk} + m^s_{ij}\delta\chi^s_{ij}\right)dV. \tag{17}$$

The mechanical problem, associated to the analysed slender microbeam, is formulated under the assumption of the nonlinear Euler-Bernoulli theory. Considering a second order axial stretch, the only non-null component of the strain tensor is:

$$\varepsilon_{xx} = \frac{\partial u}{\partial x} + \frac{1}{2}\left(\frac{\partial w}{\partial x}\right)^2 - z\frac{\partial^2 w}{\partial x^2} \tag{18}$$

in which the last term on the right hand side of the equation represents the deformation curvature of the beam. The higher-order deformations are given by (4, 5, 6) using ε_{xx}:

$$\begin{aligned}
&\gamma_x = \varepsilon_{xx,x} = \frac{\partial^2 u}{\partial x^2} + \frac{\partial w}{\partial x}\frac{\partial^2 w}{\partial x^2} - z\frac{\partial^3 w}{\partial x^3},\\
&\gamma_z = \varepsilon_{xx,z} = -\frac{\partial^2 w}{\partial x^2},\\
&\eta^{(1)}_{xxx} = \frac{2}{5}\varepsilon_{xx,x}, \qquad \eta^{(1)}_{xxz} = \eta^{(1)}_{zxx} = \eta^{(1)}_{xzx} = \frac{4}{15}\varepsilon_{xx,z},\\
&\eta^{(1)}_{xyy} = \eta^{(1)}_{xzz} = \eta^{(1)}_{yxy} = \eta^{(1)}_{yyx} = \eta^{(1)}_{zxz} = \eta^{(1)}_{zzx} = \frac{1}{5}\varepsilon_{xx,x},\\
&\eta^{(1)}_{yyz} = \eta^{(1)}_{yzy} = \eta^{(1)}_{zyy} = -\frac{1}{15}\varepsilon_{xx,z}, \qquad \eta^{(1)}_{zzz} = -\frac{1}{5}\varepsilon_{xx,z},\\
&\chi^s_{xy} = \chi^s_{yx} = \frac{1}{2}\varepsilon_{xx,z}.
\end{aligned} \tag{19}$$

The higher-order stresses component acting on the beam can be found inserting (19) into the constitutive functions (9, 10, 11); moreover for the only non-zero term in Cauchy stress tensor we have:

$$\sigma_{xx} = E\left(\frac{\partial u}{\partial x} + \frac{1}{2}\left(\frac{\partial w}{\partial x}\right)^2 - z\frac{\partial^2 w}{\partial x^2}\right). \tag{20}$$

with E the Young's modulus (Akgoz & Civalek 2011).

The variational form of the elastic energy, after an integration along the thickness and the width of the beam, using primes to indicate spatial derivatives, becomes:

$$\begin{aligned}
\delta\Pi = \int_0^L &[D_1 w''\delta w'' + D_2 w'''\delta w''' +\\
&+EA\left(u' + \frac{1}{2}w'^2\right)(\delta u' + w'\delta w') + D_3(u'' + w'w'')\times\\
&\times(\delta u'' + w''\delta w' + w'\delta w'')]\,dx
\end{aligned} \tag{21}$$

with:

$$\begin{aligned}
&D_1 = EI + \mu A\left(2l_0^2 + \frac{8}{15}l_1^2 + l_2^2\right),\\
&D_2 = \mu I\left(2l_0^2 + \frac{4}{5}l_1^2\right), \qquad D_3 = \mu A\left(2l_0^2 + \frac{4}{5}l_1^2\right).
\end{aligned} \tag{22}$$

After some parts integrations, we get the governing equations of motion; we can also specify the boundary conditions in such way that all the terms due to the integrations by parts vanish. The equations:

$$w = w' = 0 \quad \text{at} \quad x = 0, L \tag{23}$$

and

$$w'' = 0 \quad \text{at} \quad x = 0, L. \tag{24}$$

are respectively the classical (equation (23)) and non-classical (equation (24)) transverse boundary conditions, associated with the microbeam clamped at both edges. For the longitudinal direction we take

$$u(0,t) = 0 \quad \text{and} \quad u(L,t) = LN_0 \tag{25}$$

for the classical boundary conditions, while

$$\left(u' + w'^2/2\right)' = 0 \quad \text{at} \quad x = 0, L \tag{26}$$

are the higher order ones.

Using equations (14, 15, 16, 21), separating the transverse and longitudinal equation and, finally, condensing the longitudinal equation of motion into the vertical equation, as frequently used in slender microbeam with negligible longitudinal inertia (Rega 2004), we have:

$$\begin{aligned}
&\rho A\ddot{w} + c\dot{w} + D_1 w^{iv} - D_2 w^{vi} =\\
&= EA\left(N_0 + \frac{1}{2L}\int_0^L w'^2 dx\right)w'' + \frac{\varepsilon_0\varepsilon_r b V^2}{2(g-w)^2}.
\end{aligned} \tag{27}$$

2.1 *Dimensionless problem*

Introducing the following dimensionless variables:

$$w^* = \frac{w}{g}, \quad x^* = \frac{x}{L}, \quad t^* = \sqrt{\frac{\rho A L^4}{D_1}}t, \tag{28}$$

the dimensionless form for the governing equation is:

$$\begin{aligned}
&\frac{\partial^4 w^*}{\partial x^{*4}} - \alpha_3\frac{\partial^6 w^*}{\partial x^{*6}} + c\frac{\partial w^*}{\partial t^*} + \frac{\partial^2 w^*}{\partial t^{*2}} =\\
&= \left(N + \alpha_1\int_0^1\left(\frac{\partial w^*}{\partial x^*}\right)^2 dx^*\right)\frac{\partial^2 w^*}{\partial x^{*2}} + \frac{\alpha_2 V^2}{(1-w^*)^2}.
\end{aligned} \tag{29}$$

The previous equation takes into account, through the parameter N, an externally applied load, while the geometric nonlinearity due to the axis elongation is also considered by means of the integro-differential term. The associated dimensionless boundary conditions are:

$$w^* = \frac{\partial w^*}{\partial x^*} = \frac{\partial^2 w^*}{\partial x^{*2}} = 0 \quad \text{in} \quad x^* = 0, 1. \tag{30}$$

The dimensionless constants and parameters in (20) are defined as follows:

$$\begin{aligned}
&\alpha_1 = \frac{EAg^2}{2D_1}, \quad \alpha_3 = \frac{D_2}{D_1 L^2}, \quad c = \frac{\hat{c}L^4}{\sqrt{\rho A L^4 D_1}},\\
&N = \frac{EAN_0 L^2}{D_1} \qquad \alpha_2 V^2 = \frac{bL^4\varepsilon}{2D_1 g^3}V^2,
\end{aligned} \tag{31}$$

where $V(t) = V_{dc} + V_{ac}(t)$ is the applied electric voltage.

In the following sections we work with dimensionless variables avoiding the upper stairs for the sake of simplicity.

3 SOLUTIONS APPROACH

Neglecting all time dependences in (29), we get the steady state problem:

$$w_s^{iv} - \alpha_3 w_s^{vi} - \left[N + \alpha_1 \int_0^1 {w'_s}^2 dx\right] w_s'' = \frac{\alpha_2 V_{dc}^2}{(1-w_s)^2}, \quad (32)$$

where $w_s = w_s(x)$ is the nondimensional static transversal deflection. The static boundary conditions are:

$$w_s = w_s' = w_s'' = 0 \quad \text{at} \quad x = 0, 1. \quad (33)$$

We solve numerically the static problem with the differential quadrature method approximating the derivative of the function at a specific grid point by a linear weighted summation of all the grid point values over the whole computational domain.

In order to solve the problem given by equations (29, 30), we look for a solution that is the sum of a static (w_s) and a dynamic (w_d) response of the system:

$$w(x,t) = w_s(x) + w_d(x,t). \quad (34)$$

Now we look for an optimal approximation series of the last term on the right side of equation (29), containing the dynamic term at the denominator. We write:

$$\frac{\alpha_2 V^2}{(1 - w_d/(1-w_s))^2} = \alpha_2 V^2 \sum_{k=0}^{\infty} \tilde{c}_k P_k \quad (35)$$

in which $\tilde{c}_k$ are the series coefficients, and $P_k = P_k\left(\frac{w_d}{(1-w_s)}\right)$ are the series polynomials. A classic approach consists of using the Taylor series expansion ($P_k = \left(\frac{w_d}{1-w_s}\right)^k$), which is characterized by a very small error around the center of the expansion. The alternative applied in this work is represented by the use of the Chebyshev polynomials ($P_k \propto \cos\left(k \arccos\left(\frac{w_d}{1-w_s}\right)\right)$), spreading smoothly the error over the domain. Using (34) and retaining up to the third order ($k = 3$) term in the power series (35) we have:

$$\begin{aligned} &w_s^{iv} + w_d^{iv} - \alpha_3 w_s^{vi} - \alpha_3 w_d^{vi} + c\dot{w}_d + \ddot{w}_d + \\ &- \left[N + \alpha_1 \int_0^1 \left({w'_s}^2 + 2w'_s w'_d + {w'_d}^2\right) dx\right](w_s'' + w_d'') = \\ &= \frac{\alpha_2 (V_{dc}^2 + 2V_{dc}V_{ac} + V_{ac}^2)}{(1-w_s)^2} \sum_{i=0}^{3} \frac{c_i}{(1-w_s)^i} w_d^i, \end{aligned} \quad (36)$$

where the coefficient c_n for $n = 0, 1, 2, 3$ are combination of the coefficients for the same order in w_d of the Chebyshev polynomials.

4 REDUCED-ORDER MODEL

Substituting (32) into (36), we get:

$$\begin{aligned} &w_d^{iv} - \alpha_3 w_d^{vi} - \alpha_1 \int_0^1 \left({w'_s}^2 + 2w'_s w'_d + {w'_d}^2\right) dx\, w_d'' + \\ &- N w_d'' - \alpha_1 \int_0^1 \left(2w'_s w'_d + {w'_d}^2\right) dx\, w_s'' + c\dot{w}_d + \ddot{w}_d = \\ &= \alpha_2 \left(2V_{dc}V_{ac} + V_{ac}^2\right) \eta_0 + \alpha_2 \left(V_{dc}^2 + 2V_{dc}V_{ac} + V_{ac}^2\right) \times \\ &\times \left(w_d \eta_1 + w_d^2 \eta_2 + w_d^3 \eta_3\right) \end{aligned} \quad (37)$$

with $\eta_i = \frac{c_i}{(1-w_s)^{i+2}}$ for $i = 0, \ldots, 3$.

We discretize the continuous problem using the Galerkin decomposition method in order to rule out the spatial dependence in (37), we then assume:

$$w_d(x,t) = \sum_{i=1}^{\infty} \phi_i(x) u_i(t). \quad (38)$$

The spatial functions ϕ_i are picked up in the set of the linear undamped modal shapes. They are the solution of the eigenvalue problem given by (37) assuming an harmonic motion of the form $w_d(x,t) = \phi_n(x) e^{i\omega t}$ and neglecting the terms involving l_n ($i = 0, 1, 2$) and V_{ac}. In this problem the eigenfunction ϕ_n and the eigenvalue ω_n are respectively the nth vibrating mode and its natural (circular) frequency. For the i-th degree of freedom we have:

$$\begin{aligned} &\ddot{u}_i + c\dot{u}_i + K_i u_i + \sum_j C_{ij} u_i u_j + \sum_{j,k} E_{ijk} u_i u_j u_k = \\ &= F_{0i} + F_{1i} u_i + \sum_j F_{2ij} u_i u_j + \sum_{j,k} F_{3ijk} u_i u_j u_k + \\ &+ \sum_{j,k,m} F_{4ijkm} u_i u_j u_k u_m. \end{aligned} \quad (39)$$

To save space the expressions of the coefficients are not reported here, however, they can be easily obtained substituting (38) into (37), multiplying for the function ϕ_i and integrating from 0 to 1.

5 NUMERICAL EXAMPLES

Investigating on the variation of the maximum dimensionless deflection of the microbeam, we can see the nonlinear response of the device increasing the value of $\alpha_2 V_{dc}^2$. In figure 2 it is shown the influence of the parameter involved in the high order elastic theory, namely α_3. Inside this parameter we found the three material length l_n, that underlying the size dependence of material deformation behaviour at the microscale. An increasing value of α_3 moves the curves towards high values of $\alpha_2 V_{dc}^2$ and so staving off the risk of the instability in pull-in regime. The plot display also

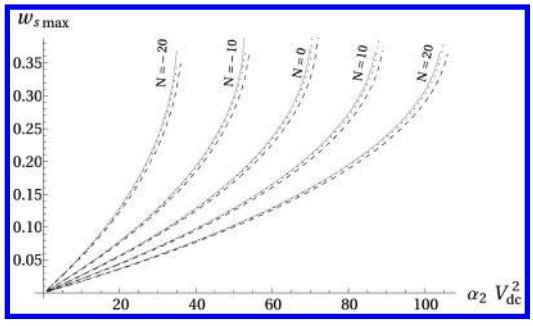


Figure 2. Variation of the maximum dimensionless deflection $w_{smax} = w_s(x = 1/2)$ for different values of axial load. The solid line curve has $\alpha_3 = 0$, while the dotted and the dashed refer respectively to $\alpha_3 = 10^{-6}$ and $\alpha_3 = 10^{-5}$.

Table 1. Hardening effect of α_1 parameter. Data refers on maximum nondimensional deflection with null axial load, $\beta = 0$, $\alpha_3 = 10^{-4}$.

$\alpha_2 V^2$	$\alpha_1 = 0$	$\alpha_1 = 3$	$\alpha_1 = 10$
50	0.168997	0.166576	0.161647
70	0.32668	0.295722	0.262641

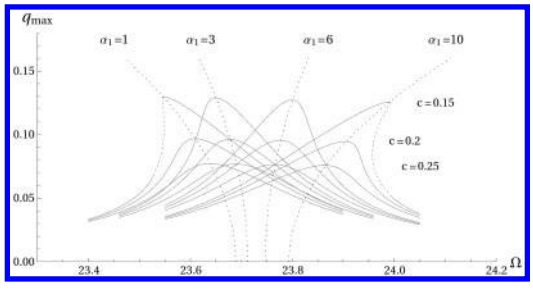


Figure 3. Variation of the nonlinear response for different α_1. The microbeam parameters are $\alpha_3 = 10^{-5}$, $\alpha_2 V_{dc}^2 = 25$, $N = 10$.

the influence of the axial load in both cases of compression and stretch loads. The parameter α_1 is, for a small values of l_n, proportionally to the square of the ratio between the initial gap g and the thickness h. Increasing this parameter there is an hardening effect that moves the pull-in limit towards higher values of $\alpha_2 V_{dc}^2$, as reported in table 1.

Regarding the dynamics, we report some results obtained from both the Runge Kutta numerical integration and the homotopy analysis method (Qian, Ren, Lai, & Chen 2012).

The considered system can present a flexible nonlinear behaviour, since both softening and hardening responses can be found by varying α_1, as shown in figure 3. The figure illustrates the frequency-response curves for different values of mechanical damping and a dynamic voltage of $V_{ac} = 0.1\cos(\Omega t)$. It is also shown, by means of the dotted back-bone curves, that the bending behaviour changes from soft to

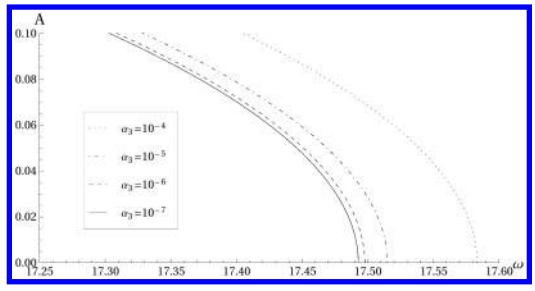


Figure 4. Variation of the nonlinear response for different α_3. Others parameters are: $\alpha_2 V_{dc}^2 = 25$, compressive axial load $N = -10$, $\alpha_1 = 0$.

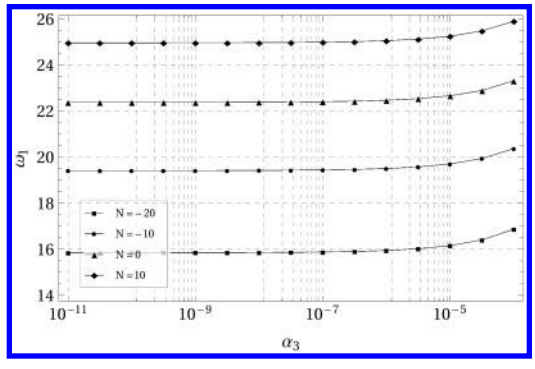


Figure 5. Variation of the first eigenfrequency ω_1 with respect to α_3 for different values of axial load. $\alpha_2 V_{dc}^2 = 0$.

hard increasing α_1. The comparison of the numerical and the analytical back-bone shows an excellent agreement. We investigate on the influence of α_3, the parameter generated by the use of the strain-gradient elasticity theory in the beam modeling. In figure 4, several back-bone curves obtained for different values of α_3, show the variation of the nonlinear frequency responses due to the high-order length scale parameters. It is shown how the influence decreases progressively for low values of α_3. The variation of the first eigenfrequency with respect to α_3 for different values of axial load is shown in figure 5. The plot shows how the influence on ω_1 is reduced decreasing the value of α_3.

6 CONCLUSIONS

We have obtained, by the use of the extended Hamilton's principle, the equation of motion and the corresponding boundary conditions for a clamped-clamped electrically-actuated microbeam, moving from the classical theory of the microbeams. With a modified strain-gradient elasticity theory, applied to a MEMS device, we have studied the influence of the high-order parameters. The static solution has been solved by the differential quadrature method, showing that the non-classical theory modifies the

response. Attention has been focused on the modeling of the nonlinear electric actuation term, involving a new procedure based on the Chebyshev method. The approximation obtained by this method reduces the error at the boundary of the prescribed domain.

Also the dynamic behaviour presents this dependence, as shown by means of both the numerical Runge Kutta results and the homotopic analytical approximated solution. The dynamic analysis has also highlighted, in the nonlinear regime, a multi-stable dynamic behaviour of the device.

REFERENCES

Abdel Rahman, E. M., M. I. Younis, & A. H. Nayfeh (2002). Characterization of the mechanical behavior of an electrically actuated microbeam. *Journal of Micromechanics Microengineering 12*(6), 759–766.

Akgoz, B. & O. Civalek (2011). Strain gradient elasticity and modified couple stress models for buckling analysis of axially loaded micro-scaled beams. *International Journal of Engineering Science 49*(11), 1268–1280.

Bellman, R., B. Kashef, & J. Casti (1972). Differential quadrature: A technique for the rapid solution of nonlinear partial differential equations 1. *Journal of Computational Physics 10*, 40–52.

Fargas Marques, A., R. Costa Castello, & A. M. Shkel (2005). Modelling the electrostatic actuation of mems: state of the art 2005. Technical report, Polytechnic University of Catalugna.

Fleck, N. & J. Hutchinson (1997). Strain gradient plasticity. Volume 33 of *Advances in Applied Mechanics*, pp. 295–361. Elsevier.

Kahrobaiyan, M. H., M. Asghari, M. Rahaeifard, & M. T. Ahmadian (2011). A nonlinear strain gradient beam formulation. *International Journal of Engineering Science 49*, 1256–1267.

Lam, D., F. Yang, A. Chong, J. Wang, & P. Tong (2003). Experiments and theory in strain gradient elasticity. *Journal of the Mechanics and Physics of Solids 51*(8), 1477–1508.

Mestrom, R., R. Fey, J. van Beek, K. Phan, & H. Nijmeijer (2008). Modelling the dynamics of a mems resonator: Simulations and experiments. *Sensors and Actuators A: Physical 142*(1), 306–315.

Mindlin, R. (1965). Second gradient of strain and surface-tension in linear elasticity. *International Journal of Solids and Structures 1*(4), 417–438.

Mindlin, R. & H. Tiersten (1962). Effects of couple-stresses in linear elasticity. *Archive for Rational Mechanics and Analysis 11*, 415–448.

Qian, Y., D. Ren, S. Lai, & S. Chen (2012). Analytical approximations to nonlinear vibration of an electrostatically actuated microbeam. *Communications in Nonlinear Science and Numerical Simulation 17*(4), 1947 – 1955.

Rega, G. (2004). Nonlinear vibrations of suspended cables – part 1: Modeling and analysis. *Applied Mechanical Review 57*(6), 443–478.

Yang, F., A. Chong, D. Lam, & P. Tong (2002). Couple stress based strain gradient theory for elasticity. *International Journal of Solids and Structures 39*(10), 2731–2743.

Younis, M., E. Abdel-Rahman, & A. Nayfeh (2003). A reduced-order model for electrically actuated microbeam-based mems. *J. Microelectromechanical Systems 12*(5), 672–680.

Zhao, J., S. Zhou, B. Wang, & X. Wang (2012). Nonlinear microbeam model based on strain gradient theory. *Applied Mathematical Modelling 36*(6), 2674–2686.

Research and Applications in Structural Engineering, Mechanics and Computation – Zingoni (Ed.)
© 2013 Taylor & Francis Group, London, ISBN 978-1-138-00061-2

Peak shear stress distribution in finite element models of concrete slabs

E.O.L. Lantsoght, C. van der Veen & J.C. Walraven
Concrete Structures, Delft University of Technology, Delft, The Netherlands

A. de Boer
Ministry of Infrastructure and the Environment, Utrecht, The Netherlands

ABSTRACT: For the evaluation of existing slab bridges in the Netherlands, the governing shear stress resulting from composite dead load and live loads is determined from a finite element model. It is necessary to determine over which length (expressed as a multiple of the effective depth) the peak shear stress can be distributed for comparison to the design shear capacity. To answer this question, a numerical model is compared to an experiment. A continuous reinforced concrete slab, representing a half-scale slab bridge, is tested under a concentrated load. The support consists of 7 bearings equipped with load cells, measuring the reaction force profile, that can be compared to the stress profile determined in the finite element model. The comparison of measured reaction force profiles over the support to finite element models results in a research-based distribution width that replaces the rules of thumb that were used until now.

1 INTRODUCTION

1.1 *Existing bridges in the Netherlands*

As a result of the expansion of the Dutch road network in the post-war years, a large number of bridges are reaching the end of their original service life. Within the current bridge stock, 60% of the structures were built before 1975. More specifically, a large number of the Dutch existing reinforced concrete bridges in the road network are short span solid slab bridges. Since the construction of these bridges, the traffic loads have increased significantly, resulting in heavier live load models in EN 1991-2:2003 (CEN, 2003) than in the previously used national code. Also, the prescribed shear capacity is more conservative in the recently implemented EN 1992-1-1:2005 (CEN, 2005) than in the former Dutch NEN 6720:1995 (Normcommissie 351001, 1995).

As a result, 600 slab bridges are found to be shear-critical when assessed with the Eurocodes. Upon inspection, these bridges did not show signs of distress (Walraven, 2010). This indicates that slab bridges possess of additional sources of bearing capacity that are not taken into account in the concrete design codes. In slabs, one of the major sources of additional capacity is the slab's ability for transverse load redistribution (Lantsoght et al., 2012c).

1.2 *Quick Scan approach and finite element models*

The large number of solid slab bridges that are identified as shear-critical requires a systematic approach. In a preliminary general assessment the database of slab bridges is screened in order to identify the bridges requiring a more detailed analysis. For this purpose, a fast, simple and conservative tool is required: the "Quick Scan" method (Lantsoght et al., 2012b, Lantsoght et al., 2012a). The first "Quick Scan" sheets are developed by Dutch engineering firms for the Ministry of Infrastructure and the Environment in the mid-2000s. The goal was to develop a spreadsheet-based approach that automatically evaluates the entire database and helps to identify the structures needing further assessment. The output of the Quick Scan sheet at a considered cross-section is a "unity check" value: the ratio between the design value of the applied shear stress resulting from the loads (composite dead loads and live loads) and the shear resistance as prescribed by the code.

1.3 *Interpretation of peak shear stresses*

For those bridges that are identified by the Quick Scan method as needing a more detailed assessment, the calculation is based on a finite element model. The spreadsheet-based method from the Quick Scan corresponds to a hand-calculation method, using conservative assumptions and only studying a selected set of cross-sections.

When using a linear finite element analysis, the loading consists of the composite dead load (self-weight of the structure and weight of the wearing surface) and the live loads as defined by Load Model 1 from EN 1991-2:2003. The results of the calculation at the face of the support is a shear stress distribution over the entire width of the support.

For assessment, the resulting shear stress at the support needs to be compared to the shear capacity as

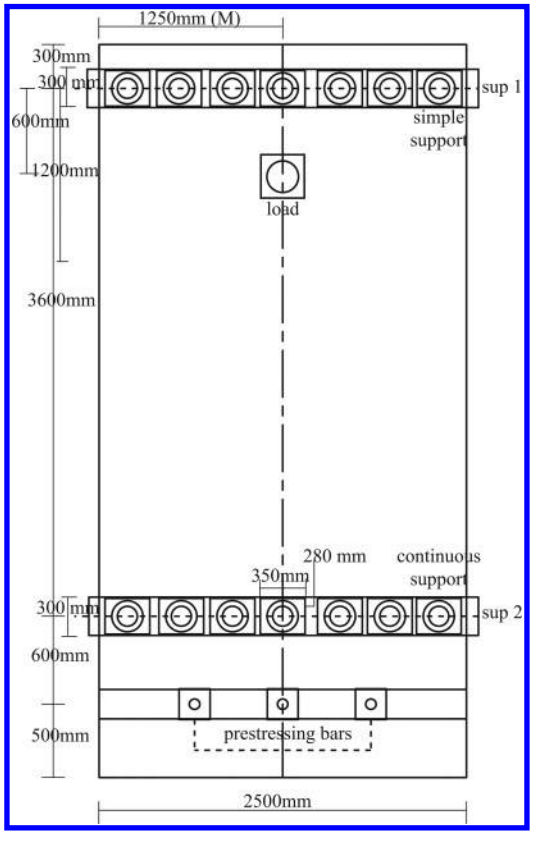


Figure 1. Top view of setup of S25T1.

prescribed by the code (eg. $v_{Rd,c}$ from EN 1992-1-1:2005). As this shear stress is now a distribution over the width, in practice a certain width is defined over which the peak shear stress can be distributed. The resulting average shear stress is then used for comparison to the shear capacity. The distribution width is typically determined based on rules of thumb and local practice. In The Netherlands, a multiple of the effective depth to the longitudinal flexural reinforcement, d_l, is used.

2 DESCRIPTION OF EXPERIMENT

2.1 *Test setup*

To study the shear capacity of slab bridges under wheel loads, a comprehensive series of experiments was carried out at Delft University of Technology. In a first series (Lantsoght et al., 2011), 18 slabs and 12 slab strips were tested under a concentrated load near to the support. In a second series, an additional 8 slabs were tested under a combination of a concentrated load near to the support and a line load. To study the distribution of the peak shear stress over the support, experiment S25T1 from the second series (Fig. 1), loaded with a concentrated load only, is analysed. The slab size was 5 m × 0.3 m × 2.5 m, representing a half-scale continuous solid slab bridge. Each support line consisted of 7 steel bearings equipped with load cells and hinges. On top of the steel bearings, a steel strip of 100 mm × 15 mm × 2500 mm was placed as well as 7 strips of N100 felt of 100 mm × 280 mm × 5 mm (Prochazkova and Lantsoght, 2011). The 300 mm × 300 mm concentrated load was placed in the middle of the width near to the simple support (Fig. 1).

2.2 *Specimen properties*

The main longitudinal reinforcement of S25 consisted of φ20 mm bars at 125 mm spacing, and the transverse flexural reinforcement consisted of φ10 mm bars at 125 mm spacing. The effective depth to the longitudinal reinforcement was $d_l = 265$ mm. Thus, S25 had a longitudinal reinforcement ratio $\rho_l = 0.996\%$ and a transverse flexural reinforcement ratio $\rho_t = 0.258\%$.

Normal strength concrete class C28/35 with a maximum aggregate size of 16 mm was used. The cube concrete compressive strength at the age of testing (170 days) was $f_{c,cube} = 58.57$ MPa and the tensile splitting strength was $f_{ct} = 4.47$ MPa.

2.3 *Description of experiment*

Failure occurred for a maximum concentrated load of $P_u = 1461$ kN. After the experiment, mostly longitudinal cracks were observed on the bottom of the slab (Lantsoght, 2012), as well as some punching damage. Remarkably, on the side faces no cracks were visible, not even flexural cracks.

2.4 *Reaction forces in experiment*

At the simple support line, 7 load cells were used to measure the reaction force continuously during the experiment. For the current study, 9 levels of the applied loading in increments of 10% of the ultimate load (up to 90% of the ultimate load on the slab) are used. The final interval from 90% of ultimate load to 100% of the ultimate load is not considered because the occurring failure cracking cannot be represented correctly by a linear finite element model. The measured reaction forces in the load cells are graphically represented in Figure 2.

3 DESCRIPTION OF FINITE ELEMENT MODEL

3.1 *Model assumptions*

The experiment is simulated in Diana, Release 9.4.4 (TNO DIANA, 2012). The slab was modeled as shell elements and the supports were modeled as 3D solid elements (Fig. 3). In between the solid elements and the shell elements, interface elements representing the layer of felt were used. For the model, 40% of orthotropy was assumed. The load was modeled as

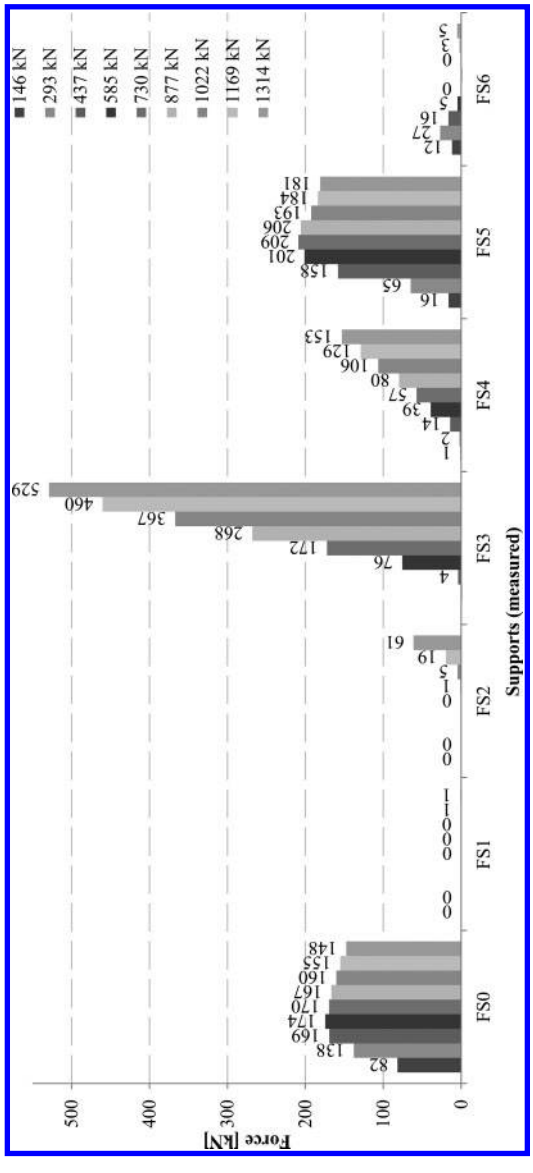


Figure 2. Measured reaction forces at 9 intervals of 10% of the ultimate concentrated load.

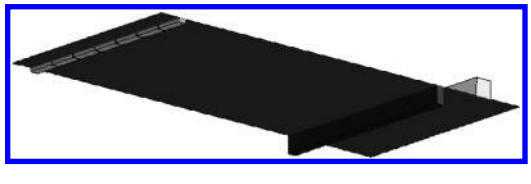


Figure 3. Overview of the finite element model.

300 mm × 300 mm, as in the experiment. The slab was not resting on all support bearings due to initial geometric imperfections. Based on the measurements of the reaction forces in the supports, a phased activation of the supports was implemented into the model.

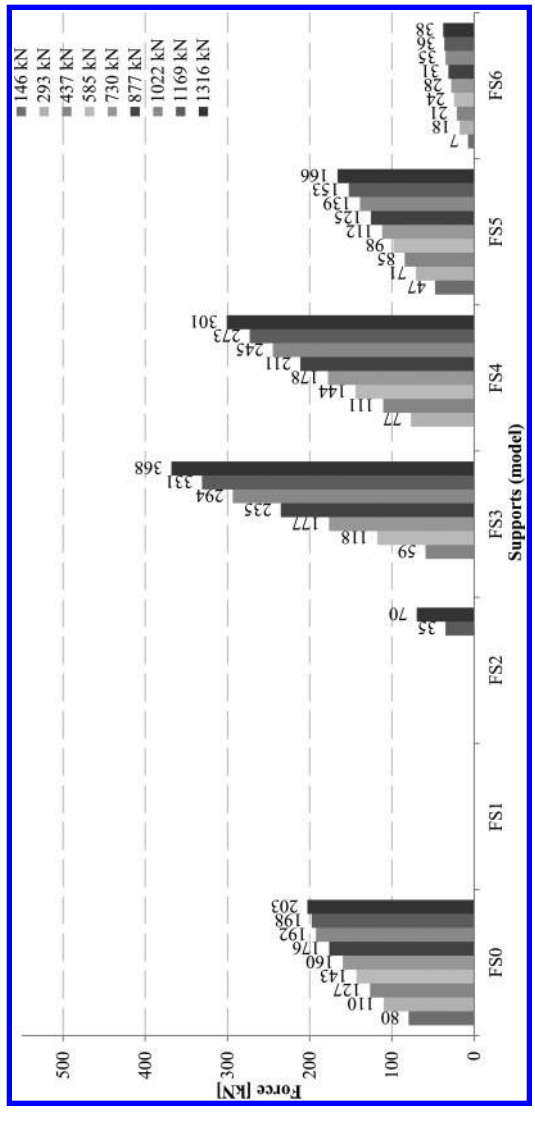


Figure 4. Reaction forces at 9 intervals of 10% of the ultimate concentrated load, using phased activation of the supports.

3.2 *Verification of model results*

Before the result of the finite element model can be used for comparison to the experiments, the measured reaction forces at the load cells are used to check if the model represents the experiment satisfactorily. The measured reaction forces as shown in Figure 2 can be compared to reaction forces in the model. The same 9 intervals of the applied load are considered. The resulting reaction forces from the model can be found in Figure 4. These results indicate that the performance of the finite element model is satisfactory and that the model can be used to study the distribution width of the peak shear stresses.

4 SHEAR STRESS ANALYSIS

4.1 *Shear stress distribution in experiment*

To determine the shear stress over a distribution width that equals a multiple of the effective depth d_l, the results of the measured reaction forces are translated into shear stresses. Two levels of the ultimate load are considered: 585 kN (40% of the ultimate load) and 1314 kN (90% of the ultimate load). The method is illustrated for a concentrated load of 1314 kN. The reaction forces are measured at discrete locations along the slab width. To distribute the reaction force over $2d_l$ and $4d_l$, it is assumed that the reaction force is distributed uniformly over the corresponding influence length of the support (Fig. 5, Fig. 6). The distance $2d_l$ or $4d_l$ is assumed around the center of the middle load cell (FS3), which is located at the middle of the slab width.

The total applied reaction force, $F_{tot,2d}$ over $2d_l$ is:

$$F_{tot,2d} = FS3 + \frac{86\text{ mm}}{358\text{ mm}}(FS2 + FS4) = 580\text{ kN} \quad (1)$$

The shear stress τ_{2d} over $2d_l$ can thus be defined as:

$$\tau_{2d} = \frac{F_{tot,2d}}{2d_l^2} = \frac{580\text{ kN}}{2(265\text{ mm})^2} = 4.13\text{ MPa} \quad (2)$$

A similar approach is used to determine the applied reaction force $F_{tot,4d}$ over $4d_l$:

$$F_{tot,4d} = FS3 + \frac{351\text{ mm}}{358\text{ mm}}(FS2 + FS4) = 739\text{ kN} \quad (3)$$

Similarly, the shear stress τ_{4d} over $4d_l$ can thus be defined as:

$$\tau_{4d} = \frac{F_{tot,4d}}{4d_l^2} = \frac{739\text{ kN}}{4(265\text{ mm})^2} = 2.63\text{ MPa} \quad (4)$$

At 40% of the ultimate load (585 kN) the largest reaction force occurs at load cell FS5 (Fig. 2). A similar procedure as described for a load of 1341 kN is followed, but now the distribution is considered around FS5. Assuming a distribution of $2d_l$, a total force $F_{tot,2d} = 212$ kN is found, resulting in a shear stress $\tau_{2d} = 1.51$ MPa. Assuming a distribution of $4d_l$, a total force $F_{tot,4d} = 244$ kN is found, resulting in a shear stress $\tau_{4d} = 0.87$ MPa.

4.2 *Shear stress distribution in finite element model*

When the results from the finite element model are analyzed, the shear stress over the distribution width can be determined from two methods:

1. By integrating the shear stresses over the considered distribution width to determine the shear force at the support, which is then divided by the distribution width and the effective depth, and

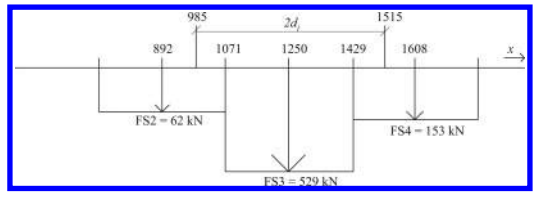


Figure 5. Method for determining the shear stress over $2d_l$ around the peak of the measurement. x-axis along width, distances in [mm].

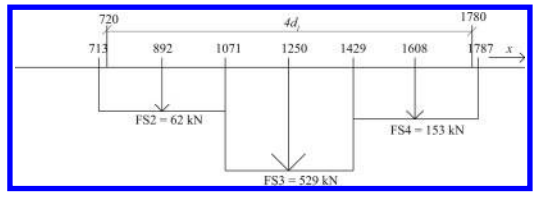


Figure 6. Method for determining the shear stress over $4d_l$ around the peak of the measurement. x-axis along width, distances in [mm].

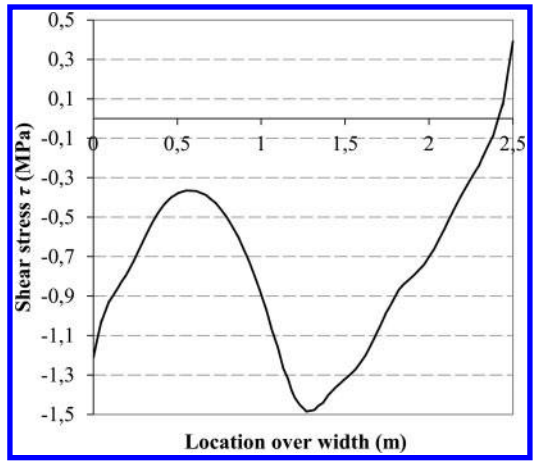


Figure 7. Shear stress distribution at the support in the finite element model.

2. Based on the reaction forces in the discrete supports, this approach is similar to the interpretation of the experimental results (Fig. 5, Fig. 6).

At a concentrated load of 585 kN, the stress distribution at the support in the finite element model is shown in Figure 7. Integrating the shear stress over $2d_l$ results in $\tau_{2d} = 1.30$ MPa and integrating over $4d_l$ results in $\tau_{4d} = 1.10$ MPa.

In Figure 4, the reaction forces in the load cells at the support at a concentrated load of 585 kN are given. The peak reaction force is found in FS4. If the method as described for the measured reaction forces is used around the peak for FS4, then $F_{tot,2d} = 196$ kN and the shear stress over $2d_l$ is found to be $\tau_{2d} = 1.39$ MPa. For a distribution over $4d_l$, the total load $F_{tot,4d} = 356$ kN and the shear stress $\tau_{4d} = 1.27$ MPa.

Table 1. Overview of results for comparison of experimental shear stress over $2d_l$ and $4d_l$ to the finite element model.

	585 kN		1314 kN	
Concentrated load Shear stress	τ_{2d} (MPa)	τ_{4d} (MPa)	τ_{2d} (MPa)	τ_{4d} (MPa)
Measurements	1.51	0.87	4.13	2.63
Model, integrating stresses	1.30	1.10	3.28	2.70
Model, reaction forces	1.39	1.27	3.25	2.60

4.3 *Comparison of distributions*

For the concentrated load at 90% of the ultimate load, a similar approach is followed for the results of the finite element model as discussed for 585 kN in §4.2. An overview comparing the results in the experiment to those from the finite element model is given in Table 1 for 40% of the ultimate experimental load (585 kN) and 90% of the ultimate load (1314 kN). The results in Table 1 show that distributing the peak shear stress over $4d_l$ gives a conservative estimate of the shear stress in the finite element model as compared to the shear stress based on the reaction forces in the experiment. The results in Table 1 also show similar results for both approaches to determine the shear stress based on the results in the finite elements program.

4.4 *Resulting unity check*

In the Quick Scan approach, the decision whether or not the considered bridge needs further investigation is based on the resulting unity check value. For the evaluation of the resulting shear stresses from the finite element model, a comparison to the shear capacity from EN 1992-1-1:2005 is provided:

$$v_{Rd,c} = 0.12k\left(100\rho_l f_{ck}\right)^{1/3} = 0.12\times1.87\left(0.996\times28\text{MPa}\right)^{1/3} = 0.68\text{MPa} \quad (5)$$

$$v_{min} = 0.035k^{3/2}f_{ck}^{1/2} = 0.035\times1.87^{3/2}\times28^{1/2} = 0.47\text{MPa} \quad (6)$$

The design shear stress is the maximum of v_{min} and $v_{Rd,c}$ and is thus $v_{Rd,c} = 0.68$ MPa. This value can be compared to the shear stress over $2d_l$ and $4d_l$, for example at 40% of the experimental ultimate load based on the results from integrating the stresses over the support in the finite element model. In that case, the unity check over $2d_l$ equals 1.91 and over $4d_l$ equals 1.62.

The resulting unity checks indicate the large inherent conservatism in the code as compared to the experimental result, as noted previously in the slab shear research (Lantsoght et al., 2013b). Also, the unity checks show that using a distribution width over $4d_l$ leads to a smaller underestimation of the capacity, and is thus to be preferred.

4.5 *Comparison to Quick Scan results*

To complete this study, a comparison between the Quick Scan results and the unity check based on a linear finite elements approach is briefly described (Lantsoght et al., 2013a) for an existing solid slab bridge.

The Quick Scan approach results in unity checks for 3 cross-sections, while the finite element results can be used to verify every cross-section in the studied spans.

For the considered case, the governing cross-section in the Quick Scan is at support 2-3 (Lantsoght et al., 2012a), resulting in a unity check of 1.02. If the results from the finite element model are used, the shear force at $2.5d_l$ from the support (Rijkswaterstaat, 2012) is found to be 278 kN/m. The shear capacity is determined by the lower bound of the shear stress v_{min} and results in $V_{min} = 451$ kN/m. The unity check is then 0.62.

This comparison shows that the goal of the finite element model – to be a more selective assessment tool than the Quick Scan method – is met. This observation is reflected by a smaller unity check value.

4.6 *Discussion*

In the experiments a flat slab is supported with steel bearings equipped with load cells and hinges. This support condition is different from the practical case of an existing solid slab bridge. In a real bridge, an edge beam is cast onto the slab, which results in an even better distribution of the load over the support. The choice of the distribution width to be $4d_l$ is thus a conservative approach.

5 CONCLUSIONS

For the assessment of existing reinforced concrete solid slab bridges in the Netherlands, the first approach is a spreadsheet-based calculation, the Quick Scan. If a bridge fails to meet the criteria of the Quick Scan, a more refined analysis needs to be carried out by means of a finite element analysis.

When interpreting the results from the finite element analysis for assessment, the key question is how to distribute the peak stress from the shear stress distribution over the support to obtain the design shear stress.

In this paper it is shown that the peak shear stress at the support can be distributed over a width of $4d_l$ and that conservative results are still obtained. The resulting shear stresses over $4d_l$ are smaller than the resulting shear stresses over $2d_l$ and thus, when the results are compared to the design shear stress from Eurocode 2, smaller unity checks result. This shows the improved selection capacity of the assessment method when using the distribution width of $4d_l$.

A case study of an existing bridge shows that the resulting unity check according to the Quick Scan is larger than the unity check resulting from a finite element analysis. This result shows that the Quick Scan

performs well as a coarse selection tool, and that using a finite element model leads to a more precise and less conservative result.

ACKNOWLEDGEMENTS

The authors wish to express their gratitude and sincere appreciation to the Dutch Ministry of Infrastructure and the Environment (Rijkswaterstaat) for financing this research work.

REFERENCES

CEN 2003. Eurocode 1: Actions on structures – Part 2: Traffic loads on bridges, EN 1991:2-2003.

CEN 2005. Eurocode 2 – Design of Concrete Structures: Part 1-1 General Rules and Rules for Buildings. EN 1992-1-1:2005.

Lantsoght, E. O. L. 2012. Tests of reinforced concrete slabs subjected to a line load and a concentrated load. Delft University of Technology.

Lantsoght, E. O. L., de Boer, A. & van der Veen, C. 2013a. Notitie: Berekening schuifspanning plaatexperimenten.

Lantsoght, E. O. L., van der Veen, C. & Gijsbers, F. B. J. 2012a. Achtergrondrapport bij spreadsheet. Delft University of Technology.

Lantsoght, E. O. L., van der Veen, C. & Walraven, J. 2011. Experimental Study of Shear Capacity of Reinforced Concrete Slabs. ASCE Structures Congress. Las Vegas, NV.

Lantsoght, E. O. L., van der Veen, C. & Walraven, J. C. 2012b. Shear assessment of solid slab bridges. ICCRRR 2012, 3rd International Conference on Concrete Repair, Rehabilitation and Retrofitting. Cape Town, South Africa.

Lantsoght, E. O. L., van der Veen, C. & Walraven, J. C. 2012c. Shear capacity of slabs and slab strips loaded close to the support. ACI SP-287, Recent Development in Reinforced Concrete Slab Analysis, Design and Serviceability, 5.1-5.18.

Lantsoght, E. O. L., van der Veen, C. & Walraven, J. C. 2013b. Shear in One-way Slabs under a Concentrated Load close to the support. ACI Structural Journal, (in press).

Normcommissie 351001 1995. NEN 6720 Technische Grondslagen voor Bouwvoorschriften, Voorschriften Beton TGB 1990 – Constructieve Eisen en Rekenmethoden (VBC 1995). Delft, The Netherlands: Civieltechnisch centrum uitvoering research en regelgeving, Nederlands Normalisatie-instituut.

Prochazkova, Z. & Lantsoght, E. O. L. 2011. Material properties – Felt and Reinforcement For Shear test of Reinforced Concrete Slab. Delft University of Technology.

Rijkswaterstaat 2012. Richtlijnen Beoordeling Kunstwerken – beoordeling van de constructieve veiligheid van een bestaand kunstwerk bij verbouw en afkeuren.

TNO DIANA 2012. Users Manual of DIANA, Release 9.4.4. Delft, The Netherlands.

Walraven, J. C. 2010. Residual shear bearing capacity of existing bridges. fib Bulletin 57, Shear and punching shear in RC and FRC elements; Proceedings of a workshop held on 15–16 October 2010 Salò, Lake Garda, Italy.

Research and Applications in Structural Engineering, Mechanics and Computation – Zingoni (Ed.)
© 2013 Taylor & Francis Group, London, ISBN 978-1-138-00061-2

Elimination of slip-locking in composite beam analysis by using a meshfree method

R.E. Erkmen
Centre for Built-Infrastructure Research, School of Civil and Environmental Engineering, University of Technology, Sydney, Australia

ABSTRACT: Composite beams that consist of two different components juxtaposed with a shear connection find widespread applications, especially in the floor system and bridge design. The interlayer slip between the two components significantly affects the behaviour of the composite beams, and therefore mathematical models that consider the interlayer slip is adopted in their analysis. In the numerical analysis of composite beams inconsistencies in the shape functions of the transverse and longitudinal displacement fields may cause oscillations in the slip field and reduction in the accuracy of the results known as slip-locking. In order to eliminate slip-locking, matching field strategy is adopted herein by using a meshfree method in which shape functions of the longitudinal displacement fields are obtained from the derivatives of shape functions of the transverse displacement fields. Continuous blending method is modified in order to impose the boundary conditions.

1 INTRODUCTION

It is well know that interlayer slip between the components of composite beam-columns significantly affects the structural response. A mathematical model that considers the interlayer slip was initially developed by Newmark *et al.* (1951), in which two Euler-Bernoulli beams are connected by assuming that vertical separation does not occur between the two components. Subsequently, several displacement-based finite element formulations were developed e.g., Arizumi *et al* (1981). In order to prevent slip-locking in finite element analysis of composite beams consistent interpolation strategy was employed in Dall'Asta and Zona (2002), in which additional internal nodes are needed. An advantage of the meshfree methods e.g., Belytschko *et al* (1994) over the finite element method is that the polynomial order of the shape functions is not directly associated with the number of the nodes used, and at each integration point the shape functions of a displacement field can be produced to exactly match with the derivatives of the shape functions of another displacement field in order to eliminate locking in multi-field problems. This approach was first introduced in Donning and Liu (1998) within the context of Reproducing Kernel Particle Method (RKPM) to alleviate shear-locking.

On the other hand, the finite element method has several advantages over the mesh-free methods; computation and integration of approximation functions are less costly; imposition of the boundary conditions is simpler; and computation of the reaction forces is easier. In order to benefit from the advantages of both methods several coupling techniques have been proposed so that mesh-free and FE methods can be used jointly. Among these methods the continuous blending method introduced in Huerta and Mendez (2000) can produce shape functions that satisfy the Kronecker delta property at the nodes.

Erkmen and Bradford (2010) used the matching field approach to develop a locking free composite beam-column analysis method, in which the continuous blending method is also modified in order to be able to impose the boundary conditions directly at the specified nodes. In this study, results of Erkmen and Bradford (2010) are discussed and the numerical example shows that slip-locking in the composite beam-column behaviour can be totally eliminated using meshfree methods.

2 COMPOSITE BEAM-COLUMN ANALYSIS

2.1 *Kinematics*

Basic kinematic assumptions adopted in this paper were initially presented by Newmark et al. (1951) based on which the member is composed of two Euler-Bernoulli beam components, which are referred herein as beams 1 and 2. The composite cross-section is thus represented as $A = A_1 + A_2$, where A_1 and A_2 are the cross-sections of beams 1 and 2, respectively. The displacement field consists of the vertical displacement v of the reference axis and the longitudinal displacements w_1 and w_2 of the centroids of beams 1 and 2, respectively. The slip at the interface between the two components of the composite beam is denoted as Γ which is due to the difference in longitudinal

displacements w_1 and w_2, and the rotation of both Euler-Bernoulli beam cross-sections v', i.e.

$$\Gamma = w_2 - w_1 + hv', \tag{1}$$

where h is the distance between the centroids of beams 1 and 2, and $(\,)' = \mathrm{d}(\,)/\mathrm{d}x$. Strain expressions in each component can be determined by using the Euler-Bernoulli beam kinematics, hence in terms of the extensions w_1' and w_2' and the curvature v'' due to bending deformations as

$$\varepsilon_1 = w_1' - (y - h_1)v'', \tag{2}$$

$$\varepsilon_2 = w_2' - (y - h_2)v'', \tag{3}$$

2.2 *Variational formulation*

The total potential energy functional based on the deformations described in the Newmark's model can be written as

$$\Pi = \tfrac{1}{2}E_1A_1\int_L w_1'^2\mathrm{d}x + \tfrac{1}{2}E_2A_2\int_L w_2'^2\mathrm{d}x + \tfrac{1}{2}(E_1I_1 + E_2I_2)\int_L v''^2\mathrm{d}x + \tfrac{1}{2}\beta b\int_L (w_2 - w_1 + hv')^2\mathrm{d}x - \Pi_{ext} \tag{4}$$

where, L is the total span of the composite member, E_1 and E_2 are the modulus of elasticity for components 1 and 2 respectively, I_1 and I_2 are the second moments of area of the beams with respect to the principal axes of each cross-section passing through the centroids, β is the elastic stiffness of the shear connection (force/length^3) which is the uniformly distributed longitudinal shear stress across the width of the interface surface b per unit slip and Π_{ext} is the work done by the external forces. By using the first variation of the functional in Eq. (4), a Galerkin weak form can be obtained for the numerical analysis.

3 ELEMENT-FREE GALERKIN METHOD

Shape functions for the transverse displacement field v in Eq. (4) can be generated by using the moving least squares (MLS) approximation procedure, based on which the approximation of the transverse displacement field can be written as

$$v^a(x) = \sum_{i=1}^{n^\rho}\Phi_i(x)v_i, \tag{5}$$

where $i \in I^\rho$ denote the nodes within the meshfree analysis domain Ω^ρ, n^ρ is the number of nodes considered in the approximation of the displacement field, Φ_i are the shape functions and v_i are the nodal parameters which in general do not directly provide nodal displacements, i.e. $v_i \neq v^a(x_i)$. Details of the shape function calculations can be found in several resources.

3.1 *Elimination of slip locking by using the matching field approach*

The shape functions generated in Eq. (5) can also be used for the longitudinal displacement fields, i.e.

$$w_1^a(x) = \sum_{i=1}^{n^\rho}\Phi_i(x)w_{1i} \tag{6}$$

$$w_2^a(x) = \sum_{i=1}^{n^\rho}\Phi_i(x)w_{2i}, \tag{7}$$

in which w_{1i} and w_{2i} are the unknown nodal displacement parameters and in general, they do not directly provide nodal displacements, i.e. $w_{1i} \neq w_1(x_i)$ or $w_{2i} \neq w_2(x_i)$. Consequently, the approximate slip field $\Gamma^a(x)$ can be obtained by substituting Eqs. (5), (6) and (7) into Eq. (1). In order to show that oscillations may occur in the approximate slip field, the longitudinal displacement fields can be alternatively expressed as

$$w_1^a(x) = \sum_{i=1}^{n^\rho}\sum_{j=1}^{n^\rho}\Phi_{j,x}(x)b_{ij} + r_1(x) \tag{8}$$

$$w_2^a(x) = \sum_{i=1}^{n^\rho}\sum_{j=1}^{n^\rho}\Phi_{j,x}(x)c_{ij} + r_2(x), \tag{9}$$

in which $r_1(x)$ and $r_2(x)$ are residual functions to recover the approximations in Eqs. (6) and (7). The residual functions can be selected such that coefficients b_{ij} and c_{ij} in Eqs. (8) and (9) can be associated with the nodal parameters w_{1i} and w_{2i} by using n^ρ conditions as

$$\sum_{j=1}^{n^\rho}\Phi_{j,x}(x_k)b_{ij} = \Phi_i(x_k)w_{1i}, \tag{10}$$

$$\sum_{j=1}^{n^\rho}\Phi_{j,x}(x_k)c_{ij} = \Phi_i(x_k)w_{2i}, \tag{11}$$

where x_k are the coordinates of nodes within the support domain of weight functions whose peak point is at node $j \in I^\rho$. From Eqs. (1), (5), (8) and (9), the slip expression can be obtained as

$$\Gamma^a(x) = \sum_{j=1}^{n^\rho}\Phi_{j,x}(x)\Gamma_j + r(x), \tag{12}$$

in which $\Gamma_i = \sum_{j=1}^{n^\rho}(c_{ij} - b_{ij} + hv_j\delta_{ij})$ and $r(x) = r_2(x) - r_1(x)$ were used and δ_{ij} is the Kronecker delta operator. By using Eqs. (10) and (11), the nodal slip values can be written as

$$\Gamma^a(x_k) = \sum_{j=1}^{n^\rho}\Phi_{j,x}(x_k)\Gamma_j. \tag{13}$$

On the other hand, the residual function $r(x)$ does not necessarily vanish in between nodes which is the

source of oscillations in the slip field in Eq. (12). This can be shown by using Eq. (10) and (11), from which the coefficients b_{ij} and c_{ij} can be written as

$$b_{ij} = w_{1i} \sum_{p=1}^{n^\rho} \mathbf{D}_{ip} \mathbf{C}^{-1}_{pj} \tag{14}$$

$$c_{ij} = w_{2i} \sum_{p=1}^{n^\rho} \mathbf{D}_{ip} \mathbf{C}^{-1}_{pj}, \tag{15}$$

where

$$\mathbf{D} = \begin{bmatrix} \Phi_1(x_1) & \dots & \Phi_1(x_{n^\rho}) \\ . & \dots & . \\ \Phi_n(x_1) & \dots & \Phi_n(x_{n^\rho}) \end{bmatrix}, \tag{16}$$

$$\mathbf{C} = \begin{bmatrix} \Phi_{1,x}(x_1) & \dots & \Phi_{1,x}(x_{n^\rho}) \\ . & \dots & . \\ \Phi_{n,x}(x_1) & \dots & \Phi_{n,x}(x_{n^\rho}) \end{bmatrix}. \tag{17}$$

The residual function $r(x)$ can be obtained as (Erkmen and Bradford 2010)

$$r(x) = \sum_{i=1}^{n^\rho} \left[\sum_{j=1}^{n^\rho} \Phi_j(x)\delta_{ij} - \Phi_{j,x}(x) \sum_{p=1}^{n^\rho} \mathbf{D}_{ip} \mathbf{C}^{-1}_{pj} \right] \left(w_{2i} - w_{1i} \right) \tag{18}$$

Since shape functions $\Phi_j(x)$ are one order higher than their derivatives $\Phi_{j,x}(x)$, the residual function $r(x)$ shown in Eq. (18) does not vanish at any point x for any $\mathbf{D}$ or $\mathbf{C}$ unless $w_{2i} - w_{1i} = 0$ which is the cause of oscillations between nodes. On the other hand, for stiff connection limit, i.e. $\beta \to \infty$, Eq. (12) should vanish, i.e., $\Gamma^a(x) \to 0$ which in general requires the residual function to vanish i.e. $r(x) \to 0$. This enforces a spurious constraint on the approximate longitudinal displacement fields which can be stated as

$$w_2{}^a(x) - w_1{}^a(x) = \sum_{j=1}^{m-1} p_j(x) d_j, \tag{19}$$

where $p_j(x)$ are monomial basis functions (e.g. $p_1(x) = 1$, $p_2(x) = x, \dots, p_{m-1}(x) = x^{m-2}$) and d_j are coefficients. Thus, in order for the interface slip to vanish the highest order terms in the approximate longitudinal displacement fields $w_1^a(x)$ and $w_2^a(x)$ should cancel each other as stated by the condition in Eq. (19). This spurious constraint on the approximate longitudinal displacement fields causes poor or delayed convergence. The slip-locking behaviour can be alleviated by using the matching field approach, in which case the derivatives of the approximation functions $\Phi_i(x)$ are selected as the approximation functions of the longitudinal displacement fields, i.e.

$$w_1{}^a(x) = \sum_{i=1}^{n^\rho} \Phi_{i,x}(x) q_{1i} \tag{20}$$

$$w_2{}^a(x) = \sum_{i=1}^{n^\rho} \Phi_{i,x}(x) q_{2i}, \tag{21}$$

where q_{1i} and q_{2i} are the nodal parameters and in general, they do not directly provide nodal values, i.e. $q_{1i} \neq w_1(x_i)$ or $q_{2i} \neq w_2(x_i)$. It can be verified that using $b_{ij} = q_{1j}\delta_{ij}$ and $c_{ij} = q_{2j}\delta_{ij}$ in Eqs. (8) and (9) produce Eqs. (20) and (21), respectively in which case the residual functions in the approximate longitudinal displacement fields vanish, i.e. $r_1(x) = r_2(x) = r(x) = 0$.

4 TREATMENT OF BOUNDARY CONDITIONS

4.1 *Continuous blending method*

The shape functions produced by using the procedure described in section do not necessarily satisfy the Kronecker delta property at the nodes, i.e. $\Phi_i(x_j) \neq \delta_{ij}$, which complicates the imposition of the essential boundary conditions. In the continuous blending method, incomplete bases of primitive functions $N_j(x)$, which provide unity at the boundary nodes, i.e. $N_j(x_j) = 1$, are introduced at the prescribed region Ω^h. The nodes associated with these primitive functions are the boundary nodes (or the nodes that are connected to finite elements) i.e., $j \in I^h$ and are different from the meshfree nodes, i.e. $j \notin I^\rho$. Mesh-free functions $\tilde{\Phi}_i(x)$ complement these primitive functions and together they satisfy the polynomial reproducing conditions which can be written by using the shifted basis as

$$\sum_{i=1}^{n^\rho} \tilde{\Phi}_i(x) \mathbf{p}(x_i - x) + \sum_{j=1}^{n^h} N_j(x) \mathbf{p}(x_j - x) = \mathbf{p}(0), \tag{22}$$

where n^h is the number of the primitive functions. The nodes associated with these functions can be covered by or can be out of the support domain Ω^h of the primitive functions $N_j(x)$. By using Eq. (22), complementing meshfree functions $\tilde{\Phi}_i(x)$ can be calculated as

$$\tilde{\Phi}_i(x) = \left[\mathbf{p}^{\mathrm{T}}(0) - \sum_{j=1}^{n^h} N_j(x) \mathbf{p}^{\mathrm{T}}(x_j - x) \right] \mathbf{M}^{-1} \mathbf{B}_i, \tag{23}$$

The transverse displacement field in the interface region can be written as

$$v^a(x) = \sum_{i=1}^{n^\rho} \tilde{\Phi}_i(x) v_i + \sum_{j=1}^{n^h} N_j(x) \alpha_j. \tag{24}$$

where α_j denotes the displacement parameters of the boundary nodes. From Eq. (23), it can be verified that $\tilde{\Phi}_i(x_j) = 0$ at the boundary nodes $j \in I^h$ and by using Eq. (24) and $N_j(x_j) = 1$, the displacement parameters α_j can be shown to be equal to the transverse displacements at the nodes, i.e. $\alpha_j = v(x_j)$. Thus, the transverse displacements at the boundary nodes can be directly specified or the transverse displacements at the nodes

that are connected to finite element nodes can be identified as α_j. By using the matching field approach the longitudinal displacement fields can be approximated as

$$w_1^a(x) = \sum_{i=1}^{n^o} \tilde{\Phi}_{i,x}(x) q_{1i} + \sum_{j=1}^{n^h} N_{j,x}(x) \psi_{1j} \tag{25}$$

$$w_2^a(x) = \sum_{i=1}^{n^o} \tilde{\Phi}_{i,x}(x) q_{2i} + \sum_{j=1}^{n^h} N_{j,x}(x) \psi_{2j}, \tag{26}$$

in which ψ_{1j} and ψ_{2j} are the longitudinal displacement parameters associated with the boundary nodes $j \in I^h$. However, in general $\tilde{\Phi}_{i,x}(x_j) \neq 0$ and $N_{j,x}(x_j) \neq 1$ and thus the boundary conditions can not be directly applied to the longitudinal displacement fields at the boundary nodes. In order to be able to satisfy Kronecker delta property for both transverse displacement and the longitudinal displacement fields at the boundary nodes (or the nodes that are connected to finite elements) continuous blending method should be modified.

4.2 *Modification of the continuous blending method*

In addition to the primitive functions $N_j(x)$, a new set of primitive functions $R_j(x)$ is introduced in the support domain of the primitive functions Ω^h which satisfy $R_{j,x}(x_j) = 1$ and $R_j(x_j) = 0$. Also, the primitive function $N_j(x)$ is required to satisfy $N_{j,x}(x_j) = 0$ in addition to the previously required Kronecker delta property, i.e. $N_j(x_j) = 1$. By using the primitive functions the polynomial reproducing condition based on the shifted basis can be written as

$$\sum_{i=1}^{n^o} \tilde{\Phi}_i(x) \mathbf{p}(x_j - x) + \sum_{j=1}^{n^h} N_j(x) \mathbf{p}(x_j - x) + \sum_{j=1}^{n^h} R_j(x) \frac{\mathrm{d}\mathbf{p}(x_j - x)}{\mathrm{d}x} = \mathbf{p}(0), \tag{27}$$

It should be noted that the contribution of the primitive function $R_j(x)$ in the reproducing conditions is similar to a C^1 finite element formulation. From Eq. (27) complementing meshfree shape functions $\tilde{\Phi}_i(x)$ can be written as

$$\tilde{\Phi}_i(x) = \left[\mathbf{p}^{\mathrm{T}}(0) - \sum_{j=1}^{n^h} N_j(x) \mathbf{p}(x_j - x) - \sum_{j=1}^{n^h} R_j(x) \frac{\mathrm{d}\mathbf{p}(x_j - x)}{\mathrm{d}x} \right] \mathbf{M}^{-1} \mathbf{B}_i \tag{28}$$

in which matrices **M** and **B** can again be obtained from moving least-squares approximation (Erkmen and Bradford 2010). The approximation of the transverse displacement function in the support domain Ω^h of the primitive functions can be written as

$$v^a(x) = \sum_{i=1}^{n^o} \tilde{\Phi}_i(x) v_i + \sum_{j=1}^{n^h} N_j(x) \alpha_j + \sum_{j=1}^{n^h} R_j(x) \beta_j, \tag{29}$$

where α_j and β_j denote the displacement parameters of the boundary nodes, i.e., $j \in I^h$. By using Eq. (28), it can be verified that $\tilde{\Phi}_i(x_j) = \tilde{\Phi}_{i,x}(x_j) = 0$ at the boundary nodes $j \in I^h$. Thus, from Eq. (29) it can be shown that parameters α_j are equal to the transverse displacement at the nodes, i.e. $\alpha_j = v^a(x_j)$, since $N_j(x_j) = 1$ and $R_j(x_j) = 0$. On the other hand parameters β_j are equal to the rotations at the node, i.e. $\beta_j = v^a_{,x}(x_j)$ since $\tilde{\Phi}_{i,x}(x_j) = 0$, $N_{j,x}(x_j) = 0$ and $R_{j,x}(x_j) = 1$. Therefore, the transverse displacements or the rotations at the boundary nodes can be directly specified or the transverse displacements and the rotations at the nodes that connected to finite element nodes can be identified as α_j and β_j respectively. The longitudinal displacement fields can be interpolated by using the derivatives of the approximation functions used in Eq. (29) as

$$w_1^a(x) = \sum_{i=1}^{n^o} \tilde{\Phi}_{i,x}(x) q_{1i} + \sum_{j=1}^{n^h} N_{j,x}(x) \psi_{1j} + \sum_{j=1}^{n^h} R_{j,x}(x) \zeta_{1j} \tag{30}$$

$$w_2^a(x) = \sum_{i=1}^{n^o} \tilde{\Phi}_{i,x}(x) q_{2i} + \sum_{j=1}^{n^h} N_{j,x}(x) \psi_{2j} + \sum_{j=1}^{n^h} R_{j,x}(x) \zeta_{2j} \tag{31}$$

in which ψ_{1j}, ψ_{2j}, ζ_{1j} and ζ_{2j} are the longitudinal displacement parameters associated with the boundary nodes $j \in I^h$. Since $\tilde{\Phi}_{i,x}(x_j) = 0$, $N_{j,x}(x_j) = 0$ and $R_{j,x}(x_j) = 1$, the parameters ζ_{1j} and ζ_{2j} associated with the boundary nodes are equal to the respective longitudinal displacements at the boundary nodes, i.e. $\zeta_{1j} = w_1^a(x_j)$ and $\zeta_{2j} = w_2^a(x_j)$. Thus, the longitudinal displacements at the boundary node can also be directly specified or the longitudinal displacements at the node that are connected to finite element nodes can be identified as ζ_{1j} and ζ_{2j}.

5 APPLICATIONS

The evidence of slip-locking and the performance of the proposed method are illustrated for simply-supported boundary conditions, in which, total span of the composite beam-column is selected as $L = 10$ m and the cross-sectional and material properties for components 1 and 2 used in Eq. (5) are selected as $E_1 = 200 \times 10^3$ MPa, $A_1 = 6000\,\mathrm{mm}^2$, $I_1 = 1122 \times 10^2\,\mathrm{mm}^4$, $E_2 = 26 \times 10^3$ MPa, $A_2 = 7104\,\mathrm{mm}^2$ and $I_2 = 124 \times 10^6\,\mathrm{mm}^4$. Slip stiffness parameter β is varied between $2.16\,\mathrm{N/mm}^3$ and $216\,\mathrm{N/mm}^3$ for an effective surface width of $b = 200$ mm which correspond to $\alpha L = 25$ and $\alpha L = 250$, respectively where αL is a dimensionless slip stiffness parameter.

$$\alpha = \sqrt{\beta b \left[1/(E_1 A_1) + 1/(E_2 A_2) + h^2/(E_1 I_1 + E_2 I_2) \right]}. \tag{32}$$

For the simply supported beam shown in Figure 1 (i.e., $w_2(0) = v(0) = v(L) = 0$), 11 equally distributed nodes and 200 integration points are used. Polynomial basis used in the MLS procedure is quadratic, i.e. $m = 3$ and

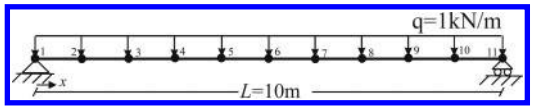


Figure 1. Simply supported beam under uniform load.

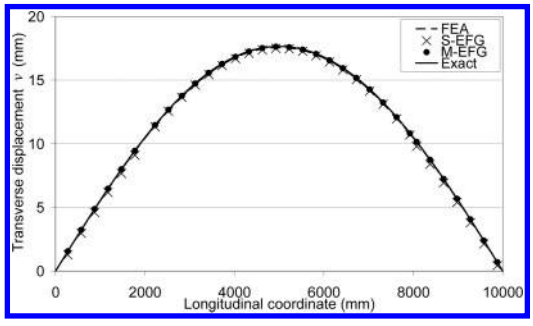


Figure 2. Displacement v for $\alpha L = 25$.

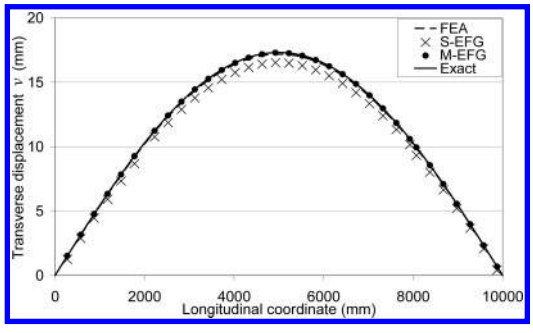


Figure 3. Displacement v for $\alpha L = 250$.

the support domain of the weight function is selected as $d_s = 4500$ mm.

The interface regions are selected between nodes 1 and 3 at the left end, and between nodes 9 and 11 at the right end. The primitive functions associated with nodes 1 and 11 are selected as

$$N_j(x) = \left[2\left(\frac{x-x_k}{x_j-x_k}\right) - \left(\frac{x-x_k}{x_j-x_k}\right)^2 \right] \left[1 - \left(\frac{x-x_j}{x_j-x_k}\right)^2 \right]^4 \quad (33)$$

where $j = 1$ and $k = 3$ at the left end and $j = 11$ and $k = 9$ at the right end.

Since the selected primitive functions satisfy $N_j(x_j) = 1$ at both ends, the boundary conditions can directly be applied for the transverse displacement field v, i.e. $\alpha_1 = v(0) = 0$ and $\alpha_{21} = v(L) = 0$.

When the same approximation functions are used for the longitudinal displacement fields w_1 and w_2, the results are referred as S-EFG to indicate the standard EFG analysis. When the derivatives are used as the shape functions of the longitudinal displacement fields, the results are referred as M-EFG to indicate matching field approach in which case an additional primitive function has to be introduced in the interface region.

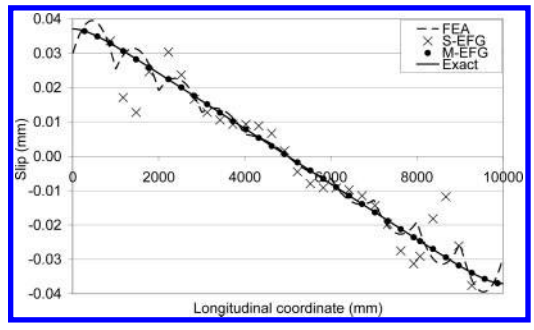


Figure 4. Slip for $\alpha L = 25$.

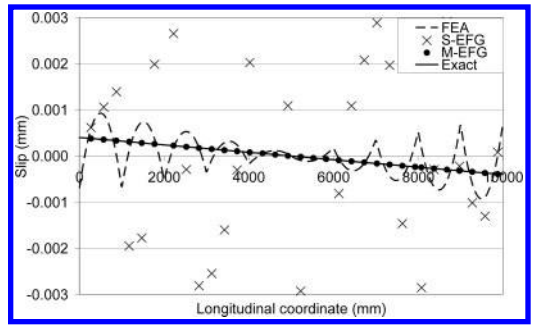


Figure 5. Slip for $\alpha L = 250$.

In order to be able to fix the longitudinal displacement w_2 at the left end the second primitive function is selected as

$$R_j(x) = \left[x_k - x + \frac{(x-x_k)^2}{x_j-x_k} \right] \left[1 - \left(\frac{x-x_j}{x_j-x_k}\right)^2 \right]^4, \quad (34)$$

where $j = 11$ and $k = 9$. The second primitive function $R_j(x)$ and its derivatives $R_{j,x}(x)$ are shown in Figs. 2d and e respectively.

It can be verified that $R_{j,x}(x_j) = N_j(x_j) = 1$ and $R_j(x_j) = N_{j,x}(x_j) = 0$. Since the shape functions for the longitudinal displacement fields are the derivatives of the shape functions of the transverse displacement field v, the boundary conditions can directly be imposed for the longitudinal displacement field w_2, i.e. $\zeta_{21} = w_2(0) = 0$. It should be noted that approximation functions together with the primitive function $N_j(x)$ form a partition of unity, where as similar to a C^1 FE formulation, primitive function $R_j(x)$ does not contribute to the partition of unity. Fig. 2 and 3 shows numerical analysis results for the transverse displacements and slip fields for slip stiffness parameters $\alpha L = 25$ and $\alpha L = 250$, respectively. For comparison purposes the results of the simplest Finite Element which is based on the cubic interpolation of the transverse displacement field v and the linear interpolation of the longitudinal displacement fields w_1 and w_2 is used and denoted herein as (FEA). Ten elements are used for the finite element analysis. The error in the strain energy is obtained by using an exact solution. In

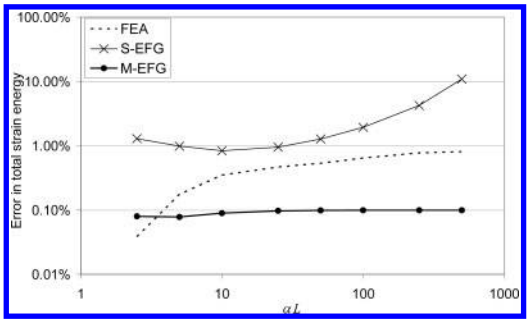


Figure 6. Error in strain energy versus αL.

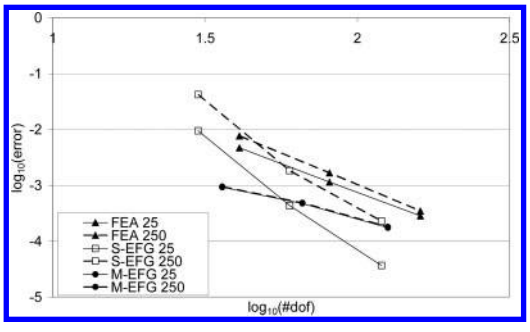


Figure 7. Convergence based on strain energy.

Figs. 2 and 3 it can be observed that when the dimensional connection stiffness parameter is changed from $\alpha L = 25$ to $\alpha L = 250$ S-EFG shows a stiffer behaviour comparison to other solutions. Locking behaviour can be observed in Fig. 4 and 5 in which slip results of the S-EFG solution show oscillations. On the other hand M-EFG results match with the exact results for both $\alpha L = 25$ and $\alpha L = 250$. Figure 6 shows the effect of slip stiffness on the strain energy error for S-EFG, M-EFG and FEA based on 11 node solutions. It can be verified that when the slip stiffness increases the error in the total strain energy increases for both S-EFG and FEA. On the other hand, error in M-EFG results is not affected by the slip stiffness.

Also, in Fig. 7 convergence rates based on the normalized errors in total strain energy are shown and compared for $\alpha L = 25$ and $\alpha L = 250$ by using 11, 21 and 41 node solutions in which all other parameters are kept constant including the span of the interface region. By comparing the slopes in Fig 7, it can be verified that S-EFG converges faster than the others however its convergence rate is slightly reduced for the stiffer connection. When the connection stiffness increases the accuracies of FEA and S-EFG results decrease, however the accuracy and the convergence rate of M-EFG results are not affected.

6 CONCLUSIONS

Displacement based numerical formulations suffer from slip-locking when used for the analysis of composite beams. The main problem is that for stiff connections slip results may be erroneous due to severe oscillations. In this study matching field approach was adopted which eliminates oscillatory behaviour due to slip-locking and the error estimates remain independent of the slip stiffness parameter. On the other hand, in order to be able to impose the boundary conditions, an efficient technique is developed by modifying the continuous blending method when the matching field approach is adopted.

REFERENCES

Arizumi, Y., Yamada, S, & Kajita T. 1981. Elastic-plastic analysis of composite beams with incomplete interaction by finite element method. *Comput Struct*; 14:543–462

Belytschko, T., Lu, Y.Y. & Gu, L.L. 1994. Element-free Galerkin methods. *Int J Numer Methods Engrg*; 37(2):229–256

Donning, B.M & Liu W.K. 1998. Meshless methods for shear-deformable beams and plates. *Comput Methods Appl Mech Engrg*; 152:47–71

Dall'Asta, A. & Zona, A. 2002. Non-linear analysis of composite beams by a displacement approach. *Comput Struct;* 80: 2217–2228

Erkmen, R.E. & Bradford, M.A. 2010. Elimination of slip-locking in composite beam-column analysis by using the element-free Galerkin method. *Comput Mech*; 46:911–924.

Huerta, A. & Fernandez-Mendez S. 2000. Enrichment and coupling of the finite element and the meshless methods. *Int J Numer Meth Engrg*; 48: 1615–1636

Newmark, N.M, Siess, CP & Viest IM. 1951. Tests and analysis of composite beams with incomplete interaction. *Proc Soc Exp Stress Anal*; 9(1):75–92

Research and Applications in Structural Engineering, Mechanics and Computation – Zingoni (Ed.)
© 2013 Taylor & Francis Group, London, ISBN 978-1-138-00061-2

Nonlinear analysis of semi-rigid steel frames subjected to blast or fire

A. Heidarpour
Department of Civil Engineering, Monash University, Australia

ABSTRACT: The behaviour of steel structures subjected to extreme actions such as fire or blast has become an important research area in structural engineering. This paper presents an innovative methodology to describe the nonlinear behaviour of steel structures subjected to extreme actions such as heating phase of a compartment fire or blast. The methodology is based on a non-discretisation semi-analytical formulation of a generic cross-section with elastic and plastic parts which allow for the spread of yielding to be modelled. The model incorporates large displacement and material nonlinearity effects whilst it considers the yielding and development of catenary action affects with an increase in the temperature. Each steel element is assumed to be restrained at its two ends with translational and rotational springs while the variations of the stiffness and yield strength at various load cases are simulated using empirical retention functions given elsewhere. The strain-rate effect is considered when the structure is subjected to explosion. The proposed methodology is shown to agree well with solutions given by ABAQUS finite element modelling.

1 INTRODUCTION

2 MECHANICAL PROPERTIES OF STEEL

Based on fire tests under transient or steady-state conditions of heating, a number of empirical models have been proposed for the material properties of steel and concrete at elevated temperature. Lie (1992) proposed a useful bilinear curve, with a small transition between the linear portions, to represent the stress-strain curve at elevated temperatures. The curve consists of two separate equations as

$$\sigma = \begin{cases} E_s.\varepsilon_e & \varepsilon \le \varepsilon_p \\ \left(c_1\varepsilon_e + c_2\right)\sigma'_y - c_3\,\sigma'^2_y \,/ E_s & \varepsilon > \varepsilon_p, \end{cases} \quad (1)$$

in which

$$\varepsilon_p = \frac{c_2\sigma'_y - \dfrac{c_3\sigma'^2_y}{E_s}}{E_s - c_1\sigma'_y} \quad (2)$$

The coefficients in Eq. (1) are taken as $c_1 = 12.5$, $c_2 = 0.975$ and $c_3 = 12.5$. In Eqs.(1) and (2), E_s is the elastic modulus of the steel and σ'_y is the yield stress. In the case of having blast loading, the strain-rate effect of steel material is considered such that (Perzyna, 1966)

$$\sigma'_y = \left[1 + \left(\frac{\dot{\varepsilon}^{pl}}{\gamma}\right)^m\right]\sigma_y \quad (3)$$

While at elevated temperatures, the mechanical properties of steel are obtained from

$$\frac{E_s}{E_0} = \begin{cases} 1 + \dfrac{T}{2000\ln(T/1100)} & 0 \le T \le 600^\circ\mathrm{C} \\ \dfrac{690\,(1 - T/1000)}{T - 53.5} & 600^\circ\mathrm{C} \le T \le 1000^\circ\mathrm{C} \end{cases} \quad (4)$$

and

$$\frac{\sigma'_y}{\sigma_0} = \begin{cases} 1 & 0 \le T \le 215^\circ\mathrm{C} \\ \dfrac{905 - T}{690} & 215^\circ\mathrm{C} \le T \le 905^\circ\mathrm{C} \end{cases} \quad (5)$$

in which E_0 and σ_0 are the modulus of elasticity and yield strength of steel material at ambient state.

3 THEORETICAL FORMULATION

The normal strain at a typical steel cross-section can be represented by (Fig. 1)

$$\varepsilon_t = \varepsilon_m + \left(y - \bar{y}\right)\kappa \quad (6)$$

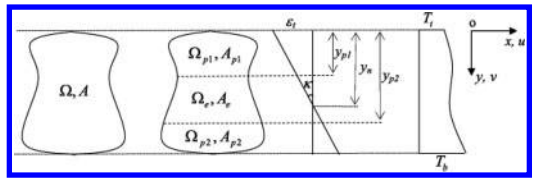


Figure 1. Cross-section and strains: (a) Steel cross-section before loading. (b) Steel cross-section after loading. (c) Total strain diagram. (d) Thermal profile over the cross-section.

The alternative forms of Eq. (6) are

$$\varepsilon_t = \varepsilon_e + \varepsilon_\theta \quad \text{and} \tag{7}$$

$$\varepsilon_t = (y - y_n)\kappa \tag{8}$$

In Eqs.(6) to (8) $\bar{y}$ is the location of the elastic centroid of the steel section below the local reference level,which is assumed to be coincident with the top fibre of the steel cross-section, y_n is the location of the neutral fibre, ε_m, ε_e and ε_θ are the appropriate membrane, mechanical and thermal strains which are obtained from

$$\varepsilon_m = \frac{\mathrm{d}u}{\mathrm{d}x} + \frac{1}{2}\left(\frac{\mathrm{d}v}{\mathrm{d}x}\right)^2, \quad \varepsilon_\theta = \Theta T(x,y), \quad \varepsilon_e = \varepsilon_t - \varepsilon_\theta \tag{9}$$

For a given cross-section Ω, the magnitude of the total axial force and internal bending moment can be obtained from

$$N_{\text{int}} = N_e + \sum_{i=1,2} N_{pi} \quad \text{and} \quad M_{\text{int}} = M_e + \sum_{i=1,2} M_{pi} \tag{10}$$

in which the subscripts "e" and "pi" indicate the internal actions which act on the elastic part (Ω_e) and on each of the two plastic parts (Ω_p) of the cross-section, respectively and are determined from

$$N_e = \int_{A_e} \sigma \mathrm{d}A_e \quad , \quad N_{pi} = \int_{A_{pi}} \sigma \mathrm{d}A_{pi} \quad \text{and} \quad (i = 1,2) \tag{11}$$

$$M_e = \int_{A_e} \sigma y \mathrm{d}A_e \quad , \quad M_{pi} = \int_{A_{pi}} \sigma y \mathrm{d}A_{pi} \quad (i = 1,2) \tag{12}$$

Substituting Eqs.(1) and (7) into Equation (11) leads to

$$N_e = \left(\overline{E_s B_e} - y_n \overline{E_S A_e}\right)\kappa - N_{eT} \tag{13}$$

$$N_{pi} = c_1\left[\left(\overline{SB}_{pi} - y_n \overline{SA}_{pi}\right)\kappa - N_{pTi}\right] \quad (i = 1,2) \tag{14}$$

where thermal section properties are defined as

$$\overline{E_s B_e} = \int_{A_e} E_s y \mathrm{d}A_e \quad , \quad \overline{E_s A_e} = \int_{A_e} E_s \mathrm{d}A_e \tag{15}$$

$$\overline{SB_{pi}} = \int_{A_e} y\sigma'_y \mathrm{d}A_{pi} \quad , \quad \overline{SA_{pi}} = \int_{A_{pi}} \sigma'_y \mathrm{d}A_{pi} \quad (i = 1,2) \tag{16}$$

and

$$N_{eT} = \Theta \int_{A_e} E_s T \mathrm{d}A_e \tag{17}$$

$$N_{pTi} = \int_{A_{pi}} \sigma'_y \left[\Theta T - \frac{c_2 - c_3 \sigma'_y / E_s}{c_1}\right] \mathrm{d}A_{pi} \quad (i = 1,2) \tag{18}$$

The location of the neutral axis y_n can be determined by substituting Eqs. (13) and (14) into Eq. (10) so that

$$y_n = \frac{\overline{E_s B_e} + c_1 \sum_{i=1,2} \overline{SB}_{pi} - \left[N_{\text{int}} + N_{eT} + c_1 \sum_{i=1,2} N_{pTi}\right] \Big/ \kappa}{\overline{E_s A_e} + c_1 \sum_{i=1,2} \overline{SA}_{pi}} \tag{19}$$

The magnitudes of the internal moment M_{int} in Eq. (10) can be obtained from Eqs. (1),(7) and (12) such that

$$M_{\text{int}} = \left(\frac{\omega_A \omega_I - \omega_B^2}{\omega_A}\right)\kappa + \left(\frac{\omega_B}{\omega_A}\right)\left[N_{\text{int}} + N_T\right] - M_T \tag{20}$$

where

$$N_T = N_{eT} + c_1 \sum_{i=1,2} N_{pTi} \, , \quad M_T = M_e + c_1 \sum_{i=1,2} M_{pTi} \tag{21}$$

and ω_A, ω_B and ω_I depend on the mechanical properties of the steel material which is given by

$$\omega_A = \overline{E_s A_e} + c_1 \sum_{i=1,2} \overline{SA}_{pi} \qquad \omega_B = \overline{E_s B_e} + c_1 \sum_{i=1,2} \overline{SB}_{pi}$$

$$\omega_I = \overline{E_s I_e} + c_1 \sum_{i=1,2} \overline{SI}_{pi} \tag{22}$$

where

$$\overline{E_s I_e} = \int_{A_e} E_s y^2 \mathrm{d}A_e \quad , \quad \overline{SI_{pi}} = \int_{A_e} \sigma'_y y^2 \mathrm{d}A_e \tag{23}$$

In Eq. (21) M_e and M_{pTi} are obtained from

$$M_{eT} = \Theta \int_{A_e} y E_s T \mathrm{d}A_e \tag{24}$$

$$M_{pTi} = \int_{A_{pi}} y\sigma'_y \left[\Theta T - \frac{c_2 - c_3 \sigma'_y / E_s}{c_1}\right] \mathrm{d}A_{pi} \quad (i = 1,2) \tag{25}$$

Equation (20) can then be rearranged so that the curvature κ at a cross-section is written as a function of the internal actions in the form

$$\kappa = \beta_1 (M + M_T) - \beta_2 (N + N_T) \tag{26}$$

in which the flexibility coefficients β_1 and β_2 are

$$\beta_1 = \frac{\omega_A}{\omega_A \omega_I - \omega_A^2} \quad \text{and} \quad \beta_2 = \frac{\omega_B}{\omega_A \omega_I - \omega_A^2}. \tag{27}$$

Using the equilibrium of the steel element in its deformed configuration, the magnitude of the internal bending moment M_{int} is written as a function of

bending moment, shear force and axial force at the left side of the element such that

$$M_{\text{int}}(x) = M_0 + R_0(x - u_0 - u) + N_0(\bar{y} - v_0 + v) - \int_{u0}^{x-u_0-u} (q_s - q_e + f_{id})(x - u - \zeta)\,d\zeta \quad (28)$$

in which u_0 and v_0 are the axial and vertical deformation at $x = 0$ respectively and u and v are the axial and transverse displacement fields along the steel element, respectively. In Eq. (28) f_{id} is the total inertia and damping forces which is given by

$$f_{id} = f_i + f_d = \left(\frac{m}{\Delta t} + \gamma\xi\right)\left(\frac{v_{t+\Delta t} - v_t}{\beta \Delta t} - \frac{\dot{v}_t}{\beta}\right) - \left[\frac{m}{2\beta} - \Delta t\left(1 - \frac{\gamma}{2\beta}\right)\xi\right]\ddot{v}_t \quad (29)$$

in which $\gamma = \frac{1}{2}$ and $\beta = \frac{1}{4}$ (or $\frac{1}{6}$ are the coefficients corresponding to the average acceleration method (or linear acceleration method), m is the mass per unit length of the steel element and $\ddot{v}$ and $\dot{v}$ are the local acceleration and velocity respectively, while ξ is a damping coefficient which represents the resistance to transverse velocity. In addition, the axial force equilibrium of the deformed configuration of the steel element leads to

$$N_{\text{int}} = N_0 \cos\theta - \left[\int_{u0}^{x-u_0-u} (q_s - q_e + f_{id})\,d\zeta - R_0\right]\sin\theta \quad (30)$$

The relationship between the slopes at the ends of the element can be numerically found by integration of the curvature in Eq. (26) so that

$$\theta_L - \theta_0 = \frac{L}{2}\sum_{j=1}^{n_G} \overline{w}_j \kappa(x_j) \quad (31)$$

Similarly, the difference in the deflections at two ends of element can be determined from Eq. (31) such that

$$v_L - v_0 = \frac{L}{2}\sum_{j=1}^{n_G} \overline{w}_j \theta(x_j) \quad (32)$$

in which

$$\theta(x_j) = \theta(x_{j-1}) + \frac{1}{2}(x_j - x_{j-1})\sum_{k=1}^{n_G} \overline{w}_k \kappa(x_k) \quad (j=1,..,n_G) \quad (33)$$

In Eqs. (31) to (33), n_G is the number of integration points in the Gauss-Legendre integration technique; $x_j \in [0, L]$ is the designation evaluation point and $\overline{w}_j$ is the associated weighting factor. Using Eqs.(6) to (9) the relationship between the axial deformations at the two ends of the steel element can be expressed as

$$u_L - u_0 = \frac{L}{2}\sum_{j=1}^{n_G} \overline{w}_j \left\{[\bar{y} - y_n(x_j)]\kappa(x_j) - \frac{1}{2}[\theta(x_j)]^2\right\} \quad (34)$$

in which $y_n(x_j)$ is the location of the neutral axis at $x = x_j$ given by Eq. (19).

At the end of the member,

$$N_0 = k_0 u_0 \quad , \quad N_L = -k_L u_L \quad (35)$$

$$M_0 = r_0 \theta_0 \quad , \quad M_L = -r_L \theta_L \quad (36)$$

and since the vertical deflection of the ends of the element is zero ($v_0 = v_L = 0$) and so $N_0 = N_L$ which produces,

$$M_L = M_0 + R_0(L - u_0 - u) - \int_{u0}^{L-u_0-u} (q_s - q_e + f_{id})(L - u - \zeta)\,d\zeta \quad (37)$$

For this boundary value problem, substituting Eqs. (35) to (37) into Eqs. (31) to (34) leads to a system of three equations which must be solved simultaneously for M_0, R_0 and N_0; this is done herein using the mathematical package MAPLE (2008). Since the deflection v in Eq. (28) is unknown a priori, the solution procedure is iterative. The following steps illustrate the solution methodology:

Step 1. The initial values of M_0, R_0 and N_0 are determined using an elastic analysis in which the yielded domain Ω_p at each Gauss_Legendre point $x = x_j$ is taken as zero, and the deflection is set initially as zero.

Step 2. Updated values of y_{p1} and y_{p2} (Fig. 1) at each cross-section $x = x_j$ are determined using von Mises' yield criterion at elevated temperature given by

$$\sigma^2 + 3\tau^2 = \sigma_y'^2 \quad (38)$$

in which σ is the normal stress produced by the axial force and bending moment, τ is the shear stress produced by the shear force and σ_y' is the yield stress (Eq. (5)). On a given cross-section, Eq. (38) defines the parts of it which have yielded.

Step 3. The magnitude of the slope, transverse and axial deformations at each cross-section $x = x_j$ are determined from Eq. (31) to (34).

Step 4. The mechanical properties of each cross-section at the locations $x = x_j$ are found from Eqs. (15), (16), (22),(23) and (27).

Step 5. Substituting the updated values of y_{p1} and y_{p2}, as well as the updated values of the displacement field and the mechanical properties at a cross-section determined in Steps 2 to 4 into Eqs. (31), (32) and (34) leads to a new system of three equations which are solved to find updated values of M_0, R_0 and N_0.

Step 6. Steps 2 to 5 are repeated until a convergence criterion is satisfied. Herein, convergence is deemed to have been achieved when

$$\frac{\|\mathbf{P}_n\| - \|\mathbf{P}_{n+1}\|}{\|\mathbf{P}_n\|} < \varepsilon_{tol} \tag{39}$$

in which $\|\mathbf{P_n}\|$ represents the Euclidean norm, n is the iteration number, ε_{tol} is a predetermined convergence tolerance and

$$\mathbf{P} = \langle M_0 \quad R_0 \quad N_0 \rangle \tag{40}$$

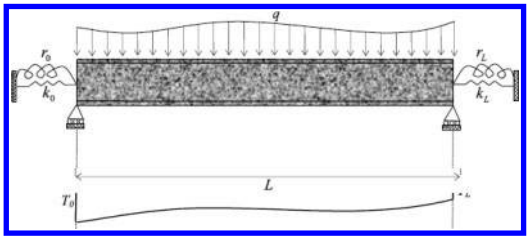


Figure 2. Steel beam subjected to a typical distributed and thermal loads.

4 ILLUSTRATION

4.1 *Example 1*

The numerical model developed in the previous section is used to investigate the behaviour of a generic steel beam at elevated temperatures as depicted in Fig. 2. The results have also been validated using ABAQUS (2008) modelling. For the analysis, the beam has a length $L = 8$ m, and it is subjected to a sustained uniformly distributed load of $q = 30$ kN/m which includes its self-weight. The steel section is chosen to be a UB $457 \times 152 \times 60$ with an elastic modulus $E_0 = 200$ GPa and yield strength $\sigma_0 = 300$ MPa at 20°C. The cross-sectional thermal regime is defined by a linear variation of temperature from the bottom fibre of T_b to the top fibre of βT_b, and this is taken as constant along the member. The end restraint stiffnesses are defined as

$$k_0 = k_L = \mu_c \left(\frac{E_s A_0}{L} \right), \quad r_0 = r_L = \mu_c \left(\frac{E_s I_0}{L} \right) \tag{41}$$

The efficiency of the proposed model has been evaluated by comparing its solutions with those of ABAQUS

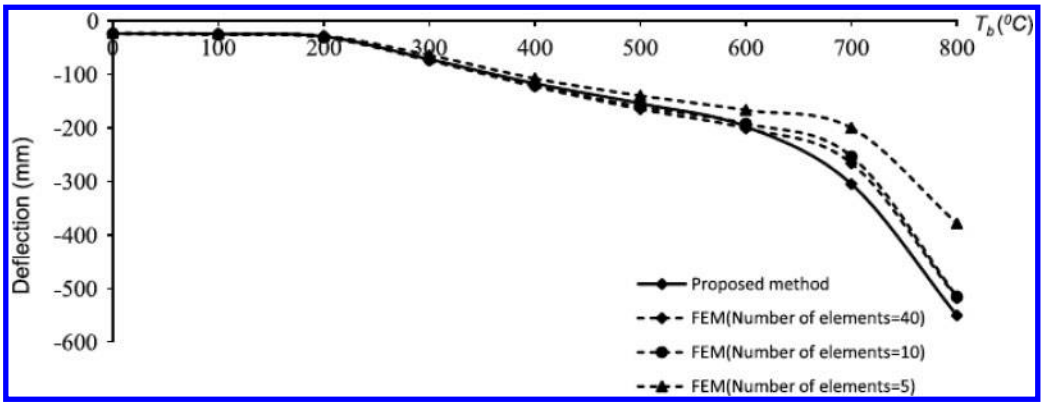


Figure 3. Deflection at mid-span given by proposed model compared to FEM ($\mu_c = 0.1$, $\beta = 1.0$).

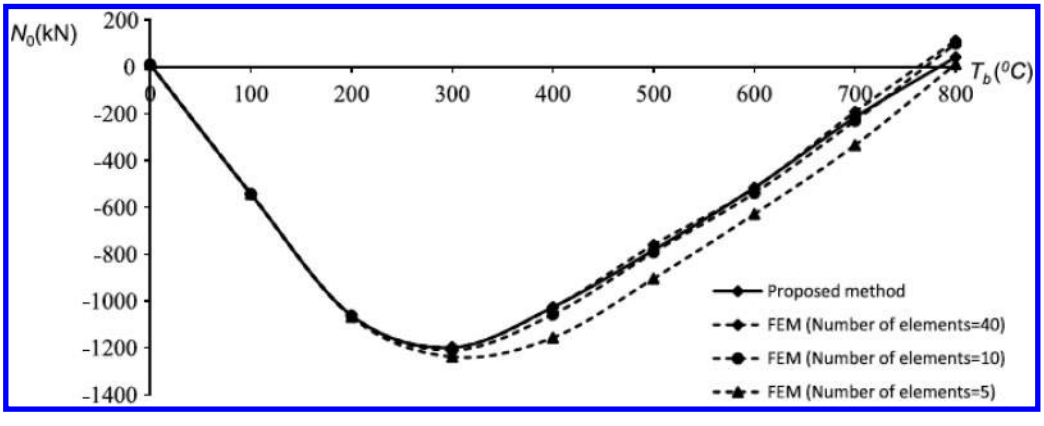


Figure 4. The magnitude of axial force N0 given by proposed model compared to FEM ($\mu_c = 0.1$, $\beta = 1.0$).

(2008) modelling of the beam in Figs. 3–5. These figures indicate that the proposed non-discretisation model which uses one 'element' with 8 Gauss-Legendre points ($n_g = 8$) agrees well with the finite element results as the number of elements increases; the agreement with the solution with 40 elements is good and this shows that the computational effort for obtaining accurate solutions from the proposed model is significantly less than that of the finite element method.

4.2 *Example 2*

The semi-analytical mechanical-based formulation developed in the previous section has been used to investigate the behaviour of a generic straight steel beam subjected to an explosion. The I-shaped steel cross-section is an Australian 610UB125, with the mechanical properties of the steel material being taken as $E_s = 200$ GPa and $\sigma_y = 300$ MPa in which the stress–strain relationship is represented by Eq. (1). The length of the steel member is $L = 6$ m and it is further assumed that the steel member is subjected to a uniformly distributed gravity load of $q_g = 30$ kN/m. (including self-weight), as well as to the blast load represented by a uniformly distributed overpressure $q_e(t) = q_0\overline{q}(t)$ in which q_0 is its intensity and $\overline{q}(t)$ is a typical normalised overpressure time–history for a gas–air mixture in a vented confined explosion initially proposed by Smith and Hetherington (1994) and later idealized by Izzuddin et al. (2000), as shown in Fig. 6. Figs. 7–9 show the variation of vertical reaction R_0, axial force N_0 and deflection at mid-span of the steel beam with respect to time ($\mu_c = 1.0$), given by the present model in comparison to the solution of ABAQUS (2008) while a good agreement is achieved. More details can be found in the papers published by author (Heidarpour and Bradford, 2009 & 2011).

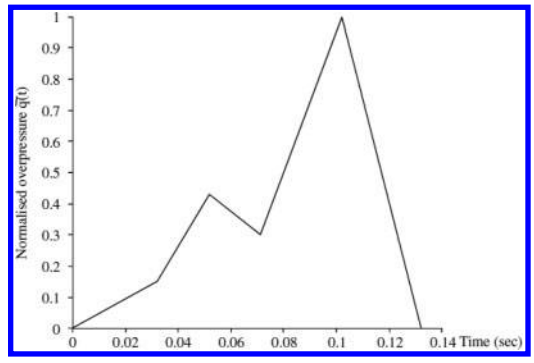


Figure 6. Variation of normalised overpressure over time.

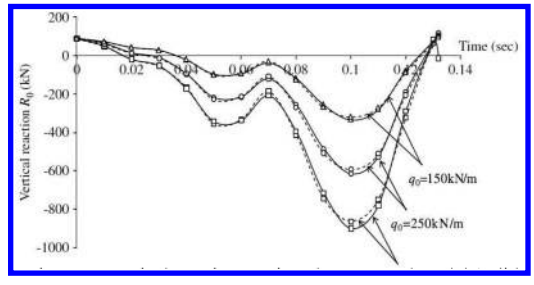


Figure 7. Vertical reaction R0 given by proposed model (solid curves) compared to finite element model (broken curves).

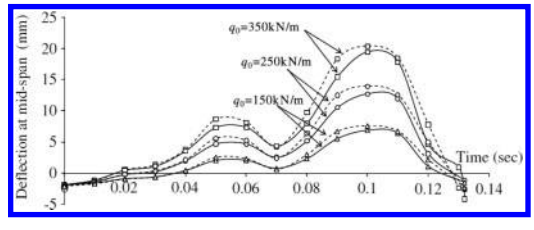


Figure 8. Deflection at mid-span given by proposed model (solid curves) compared to finite element model (broken curves).

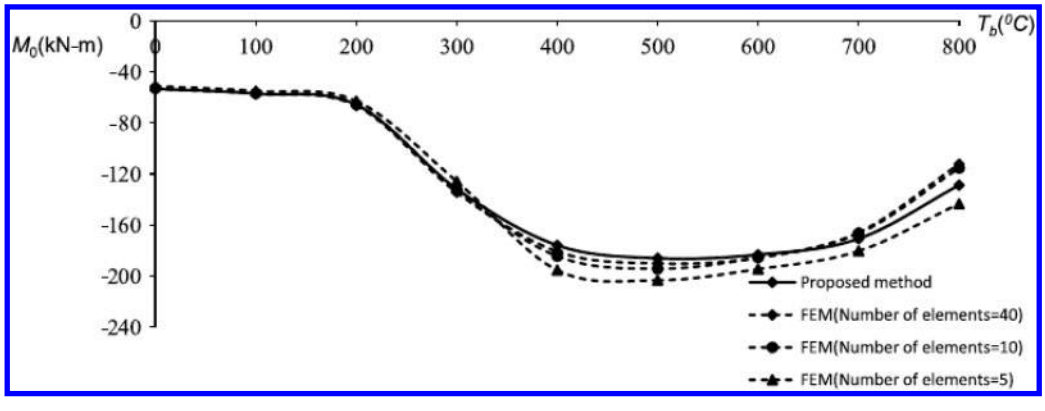


Figure 5. The magnitude of bending moment M0 given by proposed model compared to FEM ($\mu_c = 0.1$, $\beta = 1.0$

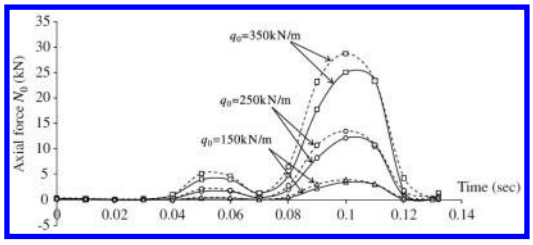


Figure 9. Axial force N0 given by proposed model (solid curves) compared to finite element model (broken curves).

5 CONCLUSION

The non-linear behaviour of an isolated beam–column steel element subjected to blast and fire loading was presented in this paper using a generic semi-analytical non-discretisation mechanical-based method, for which the steel member was restrained at its two ends by translational and rotational springs that represent semi-rigid joints in a frame. The formulation of the model allowed the geometric and material non-linearities, as well as the rate dependent effect of the steel material, to be considered accurately while it further allowed the statical and kinematic boundary conditions to be satisfied exactly. The non-linear solution was expedited by an iterative scheme in terms of three unknowns.

The model proposed in the paper was validated against the finite element model using ABAQUS, and good agreement was achieved. The scope of the formulation was illustrated by reporting a study of a steel member subjected to an explosion and fire, which demonstrated the variation of reactions as well as the displacements with different magnitudes of the blast loading or temperature. The solution was obtained using only one 'element', and is very efficient computationally. This model has the potential to be used in structural analysis and design.

ACKNOWLEDGEMENT

The work presented in this paper was supported by Australian Research Council through a discovery project (DP1096454) awarded to the author.

REFERENCES

ABAQUS FEA, Simulia(Providence, RI, USA); 2008.

HEIDARPOUR,A. & BRADFORD, M.A. 2009. Generic nonlinear modelling of restrained steel beams at elevated temperatures. *Engineering Structures*, 31: 2787–2796.

HEIDARPOUR,A. & BRADFORD, M.A. 2011. Bema-column element for non-linear dynamic analysis of steel members subjected to blast loading. *Engineering Structures*, 33: 1259–1266.

IZZUDDIN, B.A., SONG, L., ELNASHI, A.S. & DOWLING, P.J. 2000. An integrated adaptive environment for fire and explosion analysis of steel frames — Part II: verification and application. *J Construct Steel Res*,53:87–11.

LIE, T.T. editor. Structural fire protection. New York, NY: ASCE; 1992.

Maplesoft Inc.Maple 12. Maplesoft. Waterloo (Ontario, Canada); 2008.

PERZYNA, P. 1966. Fundamental problems in viscoplasticity. *Adv Appl Mech*,9,343–77.

SMITH, P.D., HETHERINGTON, J.G. 1994. Blast and ballistic loading of structures, vol. 80. Oxford (UK): Butterworth-Heinemann.

Standards Australia, AS4100-1998 Steel structures, Sydney; 1998.

Research and Applications in Structural Engineering, Mechanics and Computation – Zingoni (Ed.)
© 2013 Taylor & Francis Group, London, ISBN 978-1-138-00061-2

Coupling different FE-models for the calculation of the thermo-mechanical behavior of ultra high performance concrete components under high temperature load

M. Siemon, D. Hosser & J. Zehfuß
Institute of Building Materials, Concrete Construction and Fire Protection (iBMB)
Technische Universität Braunschweig (Institute of Technology), Braunschweig, Germany

ABSTRACT: Although many commercial finite element programs are capable of coupling the thermal and mechanical calculation, the definition for an appropriate model for both calculations yields to several problems, especially in fire protection engineering. Due to high spatial and temporal temperature gradients, the resolution of the mesh has to be very high at edges and areas of a structure applied with fire load. This usually leads to problems in the mechanical calculation where a graded mesh results in deformed element geometries and convergence problems. An evenly spaced high resolution mesh on the other hand leads to excessive computational time consumption. By combining two different finite element models for the thermal and thermomechanical calculation with a transfer program, the contradictory mesh discretization requirements can be solved. As a second advantage, both models can be optimized for their purpose, the thermal or thermomechanical calculation. In this paper, this procedure is presented by an example of a simple geometry ultra high performance concrete column. Utilization of UHPC allows for the design of slight building components and small cross-sections when compared to traditional concrete components. When it comes to fire protection, these aspects yield to disadvantageous behavior under fire load. In this case, the assessment of the coupled thermomechanical approach using advanced finite element methodologies is capable of determining the behavior of such building components.

1 INTRODUCTION

This paper deals with the problems that occur in the field of fire protection engineering when utilizing state-of-the-art finite element software to calculate the thermomechanical behavior of building components. Although several powerful tools and solutions are existing for a huge amount of problems, there is a need of customization and freedom in defining constitutive material models as well as the general problem of contradictory meshing requirements for the thermal and thermomechanical calculations. In a lot of cases, this yields to the need of high computational resources, the occurrence of convergence problems or compromises in the formulation of the constitutive material model to meet the constraints of the utilized software. The approach presented in this paper is the transfer of the temperature values for defined spatial and temporal points from a microscale mesh (thermal calculation) to a macroscale mesh (thermomechanical calculation). As finite element methodologies are node-based, a main boundary condition is the coincidence of the nodes in spatial and temporal dimensions where the information needs to be transfered. This excludes nonconformal meshes when the usage of interpolation functions is not wanted. Here, the temperature as a scalar value is a simple variable as there are no directional informations like for displacements, flows or velocities. A comparable methodology is used in the field of computational fluid dynamics solvers, e.g. FDS (McGrattan, McDermott, Hostikka, & Floyd 2010) in cases where large volumes with comparable small details like ventilation openings leads to the demand of a coarse spatial resolution for the general volume and a high resolution at the openings.

2 PROBLEM AND MOTIVATION

2.1 *Special constitutive functions*

In the field of fire protection engineering, the fire scenario as the thermal loading of a building component is described via temperature-time curves as depicted in figure 1. These curves describe the environmental temperature due to a fire. The usual approach for the determination of the exposition of a building component is the definition of a heat flux W/m^2 derived from convective and radiative heat transfer conditions based on experimental results. These conditions, together with the temperature-time curves as environmental temperatures $\theta_{env,t}$ are then applied as Neumann boundary conditions to the assessed thermal problem. The

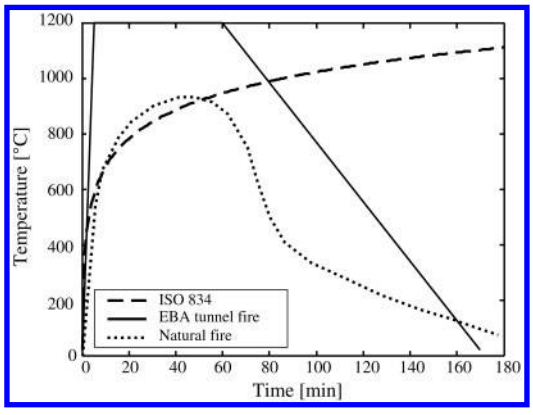


Figure 1. Temperature-time curves used in fire protection engineering.

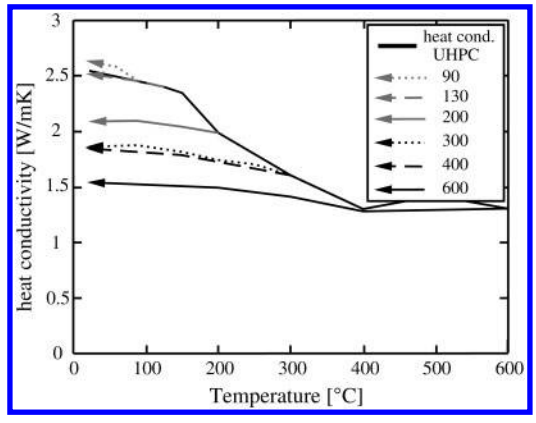


Figure 2. Heat conductivity of UHPC for heating and cooling Phase.

calculation is done after equation 1, equation 2 and equation 3.

$$\dot{h}_c = \alpha_c \cdot (\theta_{env} - \theta_\Gamma), \tag{1}$$

$$\dot{h}_r = \Phi \cdot \varepsilon_m \cdot \varepsilon_f \cdot \sigma \cdot [(\theta_{env} + 273)^4 - (\theta_\Gamma + 273)^4], \tag{2}$$

$$\dot{h_\Gamma} = \dot{h}_c + \dot{h}_r, \tag{3}$$

The depicted functions are then applied as boundary conditions to solve the Fourier equation shown in 4. The initial value for $\theta_{\Gamma,t=0}$ is usually defined as a starting condition (e.g. $\theta_{\Gamma,t} = 20°C$). The material parameters density $\rho(\theta)$, specific heat capacity $c_p(\theta)$ and heat conductivity $\lambda(\theta)$ are functions of the temperature. Like the stress-strain relationship for the mechanical analysis, these functions were derived from experiments and called constitutive material model. The resulting nonlinear partial differential equation is usually solved the finite element methodology, Newton-Raphson iteration for the linearization of the system of equations and explicit/implicit transient analysis in the temporal axis, e.g. described in Bathe (2002) or Zienkiewicz & Taylor (2000).

$$\rho c_p \frac{\partial \theta}{\partial t} - \lambda \cdot \frac{\partial^2 \theta}{\partial x^2} \cdot \frac{\partial^2 \theta}{\partial y^2} = -\dot{h_B}, \tag{4}$$

The calculation of temperature values is a basic function of many finite element solvers, as well as the consideration of the nonlinearity of the factors ρc_p and λ. As it can be seen in figure 1, the natural fire temperature curve contains a heating phase and a cooling phase. If you want to consider different thermal material behavior in those phases, a lot of FE solvers do not allow to define the material behavior in such a detailed manner. Recent research on ultra high performance croncrete showed a path dependency of the temperature dempendent heat conductivity. Figure 2 shows the temperature dependent heat conductivity of an assessed ultra high performance concrete for the heating phase (continous black line) and for the cooling phase for different reached maximum temperatures.

The consideration of this material behavior is important when the behavior of building components exposed to natural fires is the point of interest. In this case, the coupling of a self-developed heat solver with full access to all program internals with a consolidated and validated structural solver can be required.

2.2 *Contradictory meshing constraints*

A second problem is the different requirement for the mesh discretization for the thermal and the thermo-mechanical analysis. As a rule-of-thumb, the German guideline for fire protection engineers (Hosser 2009) recommends an element discretization according to the expected temperature gradient with maximum edge dimensions of 2 to 3 cm and edge to edge ratios larger than 1:2. As it can be seen in figure 1, the heating velocity of the design temperature curves can reach values up to 240 K/min for the EBA tunnel fire design curve (EBA 1997). This yields to the demand of strongly graded meshes and small element dimensions when modeling a concrete cross-section. Meshing the whole 3-dimensional model in appropriately small elements yields to non suitable computational times due to the large number of DOFs. The violation of the aforementioned meshing criteria on the other hand leads to convergence problems due to bad elementation or bifurcation phenomena resulting in unrealistic displacements for single nodes as shown in figure 3.

The standard behavior of a low-resolution mesh for thermal analysis in fire protection engineering is shown in figure 4 for a one-dimensional heat conduction problem. This example is taken from a calculation of the transient temperature development in 6 cm depth of a concrete tunnel shell exposed to the EBA fire curve (see figure 1). The low-resolution mesh was the maximum economic discretization for a following thermomechanical analysis of the whole tunnel shell utilizing solid elements whereas the high-resolution mesh shows the discretization needed to calculate the temperatures without numerical problems.

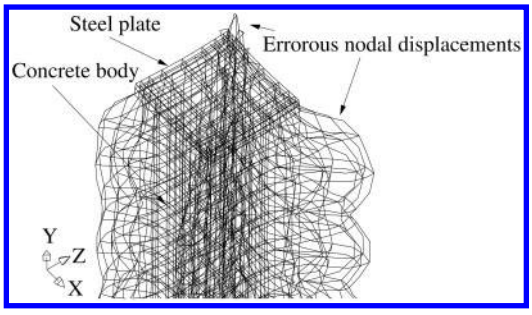


Figure 3. Bifurcation phenomena at the corners of a 4-side fire exposed column.

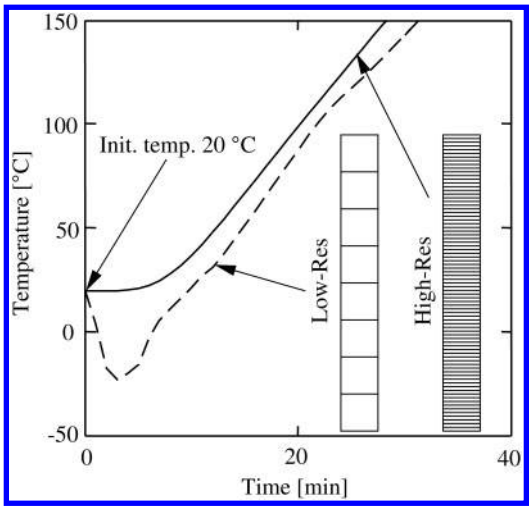


Figure 4. Transient temperature development for different mesh resolutions in the first 40 min.

3 MULTI-MESH APPROACH

In this paper, the advantages of the software DIANA (deWitte & Wijtze 2005) in modeling discrete reinforcement and passing user-supplied subroutines for the definition of the constitutional material behavior in the thermomechanical analysis should be used without the loss of flexibility for the thermal analysis. To avoid the problems explained in section 2, a multi-mesh approach with a microscale mesh for the thermal analysis and a macroscale mesh for the thermomechanical analysis was chosen. This approach is possible when meeting several requirements and basic estimates. Due to the uncertain nature lying in the description of fire scenarios, the design fire curves as depicted in figure 1 are applied over the complete height or length of a building component. This assumption leads to a simplification of the thermal analysis where only the cross-section of a building component needs to be analyzed depending on the edges exposed to fire, e.g. a column centered in the compartment exposed from four sides or a beam located at the ceiling which is usually assumed to be exposed from one or three sides. The resulting temperature field is then transferred to the FE-model defined for the thermomechanical calculation and adapted over the whole height or length (in case of a 3-dimensional mesh).

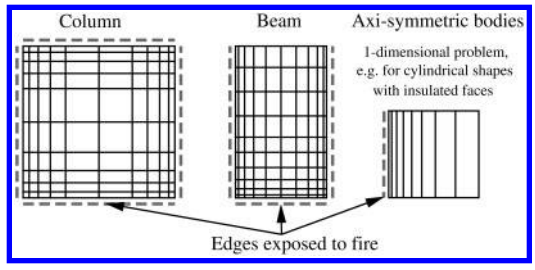


Figure 5. Different cross-sections discretized for thermal analysis.

3.1 *Microscale thermal analysis*

The temperature field needed for the analysis of the building component is calculated under consideration of the forementioned simplifications with a 2-dimensional model. For concrete members, most cross-sections are primitive shapes like squares and rectangles which are easily discretized with graded meshes concerning the exposed temperature boundary conditions. Examples for the most common cases are depicted in figure 5.

For the thermal analysis as the first step of the analysis process, there are two main conditions when setting up the FE-model. The discretization of the temporal domain (timesteps) has to fit the requirements of the following thermomechanical analysis, i.e. being the same or a multiple of the timesteps of the thermomechanical analysis. The other condition is the need of writing out the temperature values for every timestep at every point of interest (nodes of the cross-section of thermomechanical analysis) defined with global x-y-coordinates that need to comply with the coordinates of the nodes for one 'sliced' cross-section of the 3-dimensional thermomechanical model. A graphical overview of these basic conditions is shown in figure 7.

For usual problems in fire protection engineering, the compliance with this conditions is given because the thermal analysis usually needs a finer mesh as well as a finer temporal discretization. Additionally, the need for mesh and time step refinement due to large spatial and temporal temperature gradients is correlated with changes in displacements, which yields to an accordance of the requirements of numerical solving techniques for both analysis. In advance to figure 7, when utilizing an equidistant 3-dimensional mesh with 20-nodes elements, temperature values for every timesteps at the coordinates are written as corner node values for the 8-node main layer after the following rule $x \rightarrow [0 : x]$ with $\Delta x = \frac{x}{el_x}$ and $y \rightarrow [0 : y]$ with $\Delta y = \frac{y}{el_y}$. The edge nodes of the bottom layer are derived with the following rule $x \rightarrow [\frac{\Delta x}{2} : x - \frac{\Delta x}{2}]$ with $\Delta x = \frac{x}{el_x}$ and $y \rightarrow [\frac{\Delta y}{2} : y - \frac{\Delta y}{2}]$ with $\Delta y = \frac{y}{el_y}$.

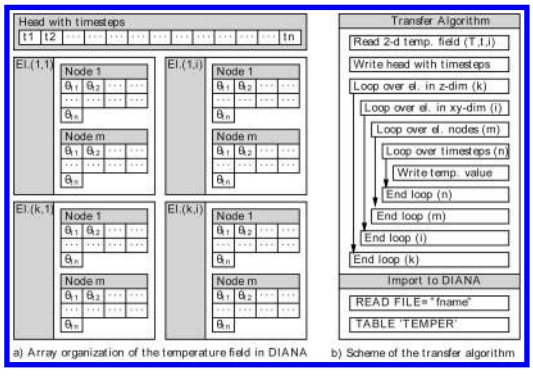


Figure 6. Required format for readable temperature field for DIANA.

The values for the middle layer nodes are then copied from the bottom corner nodes, with $z = \frac{z}{el_z} \cdot 0.5$.

3.2 *Combining Micro- and Macroscale*

The algorithm of a transfer program is based on the element formulation chosen for the thermomechanical model. This chapter shows the implementation of a transfer algorithm for a specific problem with the FE-software DIANA as thermomechanical solver and the assessement of a concrete column using 3-dimensional solid elements. In this case, the model for the thermomechanical calculation is based on a 20-node isoparametric element with quadratic interpolation functions (see deWitte & Wijtze (2005)). The discretization for the upstream 3-dimensional thermal analysis is derived from this mesh and based on linear isoparametric brick elements. Because the conditions mentioned in section 3.1 allow the free choose of a thermal solver, the setting of the ANSYS thermal analysis is not otherwise specified. For the following explanation, it is assumed that there exist valid temperature information for every timestep and every node following the conditions explained in section 3.1 grounding on a sufficiently fine mesh and an appropriate solver. The required input format for temperature fields in DIANA is shown in figure 6.

The first part of the temperature table as input file for DIANA is the head section containing the timesteps in seconds. The following blocks contain the temperature values for each element in ascending order. Each element block exists of temperature-time information for every node. In contrast to figure 6a, there is no seperation between the single nodes, i.e. the temperatures for node 1 are written for all timesteps in ascending temporal order, followed by the values for node m. The temperature table does not distinct between cross-section elements and height/length elements as shown in figure 6a, but this is easily done as the first $x \cdot y$ elements define the bottom layer with the mid-height of $z = \frac{z}{el_z} \cdot 0.5$ of the 3-dimensional model. When the temperature-time values for the xy-dimension are sortet by the transfer algorithm, the loop over the z-dimension simply copies the values of the cross-section (see figure 6b for the general explanation of the transfer algorithm). This methodology is only valid if the assumptions of section 3 are met. As shown in figure 7, $el_{x,y,z}$ is the number of elements in the x,y or z-direction, x and y are the cross-section dimensions and z is the height or length of the building component.

Table 1. Basic data of the assessed UHPC columns

Parameter	Value	further inform.
Cross-section area	$300 \cdot 300\,mm^2$	–
Column height	$3.7\,m$	–
Reinf. geom.	$8 \cdot 20\,mm$ diam.	–
Reinf. mat.	BST500	(Eurocode2 2006)
Comp. str. at 20°C	about $155\,MPa$	det. at iBMB
Tens. str. at 20°C	about $15\,MPa$	(Scheydt et al. 2012)
Mech. load	$1800\,kN$	–
Eccentricity	7.5 and $15\,mm$	–
Fire load	ISO 834	(ISO834 1999)

4 UTILIZATION FOR A SPECIFIC PROBLEM

4.1 *Ultra high performance concrete columns*

The thermal analysis was done utilizing a 2-dimensional graded ANSYS model with temperature-dependend material parameters for the heat conductivity $\lambda(\theta)$, the desity $\rho(\theta)$ and the specific heat capacity $c_p(\theta)$ which were derived from experiments (Hosser, Kampmeier, & Hollmann 2012). The thermal calculation in this context had two functions. The first function was a validation calculation of the derived contitutive functions from small-scale experiments with the experimental results of the large-scale column tests. As a second function, this calculation was the base for the following thermomechanical calculation of the column behavior under fire exposure and mechanical load.

The thermomechanical model contains of 3-dimensional solid elements already described in section 3. In addition to the concrete body, the load charging steel plate made of S235 was also modeled as a direct exposure of the column face with the mechanical load would lead to numerical problems due to the softening behavior under temperature influence. As a second advantage, the consideration of the steel plate leads to a more realisticaly modeling of the experiments. The reinforcement was modeled with discrete elements especially developed for modelling reinforced concrete components, assuming a perfect bond between reinforcement and concrete body. The capabilities of modelling discrete reinforcement is one of the main advantages of DIANA when it comes to FE-calculation of reinforced concrete components. Table 1 gives an overview of the experimental and numerical setup as well as further information on the used parameters.

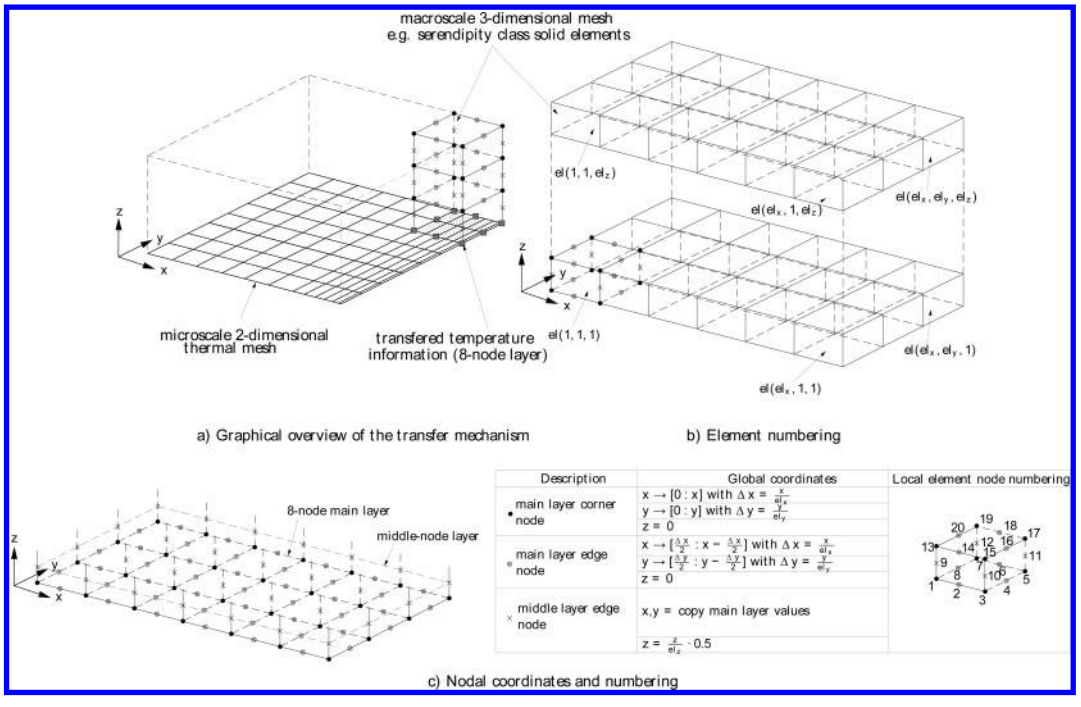


Figure 7. Graphical overview of the transfer mechanism.

In addition to table 1, all heat transfer conditions are derived from the Eurocode2 (2006). For a further look on the utilized material model and the contitutive stress-strain-temperature behavior of the concrete, take a look at the report of the research program 1182 which will be published this year.

4.2 *Results*

As shown in figure 8, the calculated temperatures show good compliance to the measured temperatures for different depths of the cross-section. The derived constitutive functions for the thermal material parameters can be viewed as a good approach to describe the temperature-dependend thermal behavior of UHPC. Furthermore, the gained temperature-time values are proven as a good basis for a following thermomechanical calculation.

The results of the coupled thermomechanical calculations with DIANA are shown in figure 9. As it can be seen, the general behavior can be reproduced by the calculation, although the experiments show smaller dispacements over the time. For fire engineering problems, the failure time of an assessed component is the main design value as it is important to ensure a minimum duration required by standards and codes.

As depicted in figure 9, the calculated failure times are slightly shorter than the ones derived from the experiments, underestimating the load-bearing capacity under fire exposure about 3 up to 10 min. The failure of the column in the calculation is usually at the

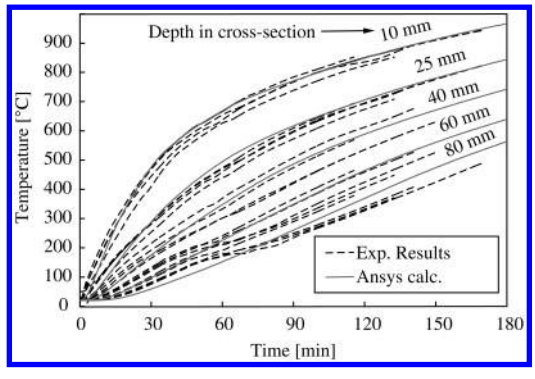


Figure 8. Calculated temperatures compared with experimental results.

point of convergence problems due to large displacements violating the agreeability constraints. As it is depicted in figure 9, the experimentally derived failure times of about 140 min for an eccentricity of 15 mm and 173 min for an eccentricity of 7.5 mm are slighlty underestimated by the calculation (10 min and 3 min). Due to the complex setup of the problem, resulting in physical and geometrical nonlinearities, the determined discrepancies in the failure time are comparable small. Hence, the method presented in this paper is generally capable of calculating the thermomechanical behavior of reinforced concrete building components exposed to fire.

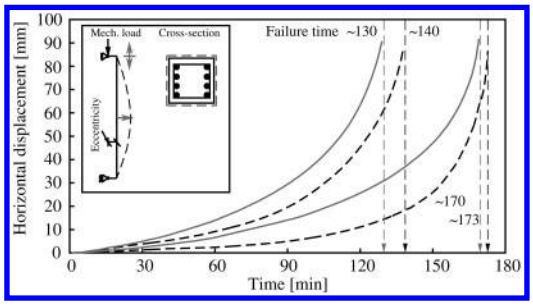


Figure 9. Calculated displacements and failure times.

5 CONCLUSION

Due to specific problems and shortcomings when utilizing standard FE-solvers in the field of fire protection engineering, the presented methodology offers a simple and effective solution combining different solvers and different meshes for the assessment of temperature-dependent behavior of reinforced concrete components avoiding usual shortcomings. Those shortcomings are contradictory meshing requirements for the thermal and thermomechanical calculation and the need for modeling complex contitutive functions describing the material behavior of modern concrete mixtures exposed to fire (see figure 2). The possibility of DIANA to read a temperature-time table offers the utilization of additional and specialized solvers for the thermal analysis and transfer of the derived values with a transfer algorithm. Another benefits is the possibility to use previously calculated temperature values without the need of a new thermal analysis. The standard approach of a combined usage of one mesh would yield to an increase of DOFs and as a result the additional need of computational time due to the 3-dimensional approach. This is avoided by relying on a fine discretization of the cross-section only when it is needed (thermal calculation). A main disadvantage is the confinement to primitive cross-section and building component geometries and the need of a static mesh which suspends the possibility of adaptive mesh refinement techniques of modern FE-software. Another point is the loss of the possibility for a mutual coupling of thermal and thermomechanical behavior, e.g. the simulation of cracking behavior which yields to a reduced heat conduction at this location. For standard fire protection engineering problems, this is theoretical problem as the uncertainties in modeling the fire scenario are high and a smeared (and isotropic) approach lowering the heat conductivity for fire-damaged concrete is generally capable of describing the temperature development quite well, as it can be seen in figure 8.

ACKNOWLEDGMENT

The authors would like to acknowledge the German Research Foundation (DFG) for the support of the research project 'Theoretische und experimentelle Untersuchungen zu Ermittlung und Optimierung des Brandverhaltens von ultra-hochfestem Beton' (Theoretical and experimental studies for determining and optimizing the fire behavior of ultra high performance concrete) in the priority program 1182.

REFERENCES

Bathe, K.-J. (2002). *Finite-Elemente-Methoden* (2 ed.). Berlin; Heidelberg: Springer-Verlag.

deWitte, F. C. & P. K. Wijtze (2005). *DIANA – Finite Element Analysis: Element Library* (release 9 ed.). Delft, The Netherlands: TNO DIANA BV.

EBA (1997). Richtlinie über anforderungen des brand- und atastrophenschutzes an den bau und betrieb von eisenbahntunneln des eisenbahn-bundesamts.

Eurocode2 (2006). Eurocode 2: Design of concrete structures – part 1–2: General rules – structural fire design; german version en 1992-1-2:2004.

Hosser, D. (2009). Leitfaden Ingenieurmethoden des Brandschutzes: Technischer Bericht vfdb TB 04-01. Altenberge and Braunschweig.

Hosser, D., B. Kampmeier, & D. Hollmann (2012). Behavoir of ultra high performance concrete (uhpc) in case of fire. In *Ultra-High Performance Concrete and Nanotechnology in Construction: 3rd International Symposium on UHPC and Nanotechnology for High Performance Construction Materials*., Kassel, Germany, pp. 573–582.

ISO834 (1999). Iso/tc 92 fire safety: Fire-resistance tests – elements of building construction – part 1: General requirements.

McGrattan, K., R. McDermott, S. Hostikka, & J. Floyd (2010). Fire dynamics simulator (version 5), user's guide. Nist special publication 1019-5, National Institute of Standards and Technology, USA and VTT Technical Research Centre, Finland.

Scheydt, J., O. Millon, H. S. Müller, & K. Thoma (2012). Entwicklung eines brandbeständigen ultrahochfesten betons für hochdynamische beanspruchungen (engl.: Development of a fire resistant and ultra high performance concrete for highly dynamic load). Beton- und Stahlbetonbau Heft 5, 289–301.

Zienkiewicz, O. & R. Taylor (2000). *The Finite Element Method, Volume 2: Solid Mechanics* (5 ed.). Woburn, MA, USA: Butterworth-Heinemann.

Research and Applications in Structural Engineering, Mechanics and Computation – Zingoni (Ed.)
© 2013 Taylor & Francis Group, London, ISBN 978-1-138-00061-2

FE modelling of semi-rigid flush end plate joints with concrete-filled steel tubular columns

A. Ataei & M.A. Bradford
Centre for Infrastructure Engineering and Safety, School of Civil and Environmental Engineering, The University of New South Wales, Sydney, Australia

ABSTRACT: A semi-rigid beam-to-column composite blind bolted connection is modelled using ABAQUS software. The composite beam is connected to the concrete-filled square column using blind bolts, and the model simulates a connection in hogging bending moment. Partial shear connection is considered, as well as the non-linear material properties of all constitutive components. All connection components were taken as roughly the same size as used in the experiments against which the method is calibrated, and the model does not need recourse to empirical push test data. The technique can be used to model connections easily, resulting in rapid and reliable solutions.

1 INTRODUCTION

Flush end plate joints in a connection between a composite beam and a concrete-filled square tubular column are an attractive design solution in low-rise composite framed buildings, because the semi-rigid nature of the joint allows for resistance against lateral forces without the need for diagonal bracing. However, facilitating a joint of this type can be problematic because the inside of the hollow tube is not readily accessible, and this has led to the use of "blind bolting" as a design solution.

Whilst necessary for validation purposes, experimental studies of composite connections are expensive and time-consuming and, as a result, considerable research momentum is gathering on using numerical simulations for connections. Early work on the numerical simulation of composite beams and joints including stud shear connectors was reported by Kalfas & Pavlidis (1997), Kim *et al.* (1999) and Bahaari & Sherbourne (2000). More recently, Mirza & Uy (2010, 2011) have reported the numerical modelling of composite joints that contain blind bolts. Despite bespoke numerical models such as those of Pi *et al.* (2006) and Liu *et al.* (2012) being computationally attractive, most research has focused on using commercial software packages such as ABAQUS and ANSYS, because of their flexibility in modelling all of the components in a composite joint. The advantages of this flexibility are often negated by their computational intensity, leading to slow convergence to the correct solution and, as a consequence, most models have focused on two-dimensional modelling rather than on three-dimensional studies.

In order to provide a robust and efficient means for modelling flush end plate joints in composite connections containing concrete-filled steel tubes with blind bolting, the present paper presents a three-dimensional modelling using ABAQUS software. It augments the studies presented by Mirza & Uy (2010, 2011) and, importantly, models the complex situation of cracked concrete in negative bending by a simple elastic-perfectly yielded representation. The modelling is benchmarked against the extensive testing of connections with blind bolting reported by Loh *et al.* (2006), and is shown to provide an efficacious technique for conducting parametric studies, so as to develop design guidance in this fast-evolving application in composite construction.

2 BENCHMARK EXPERIMENTAL RESULTS

Loh *et al.* (2006) presented a comprehensive set of experiments on composite connections. In this work, one non-composite and five semi-rigid composite beam to column connections were tested under symmetric loading, with the composite beams being connected to the tubular columns using blind bolts. Two rows of M20 Grade 8·8 blind bolts attached flush end plates to the columns, and to which the steel beams were connected (Fig. 1). Composite action was achieved between the steel beam and concrete slab by stud shear connectors welded through the profiled steel decking. The tests were designed to simulate an internal composite beam-to-column connection typical of a low-rise building system. In the tests, the variables were the degree of shear connection, the shear stud spacing and the area of reinforcement. Tables 1 and 2 summarise the dimensions and components in the experimental programme.

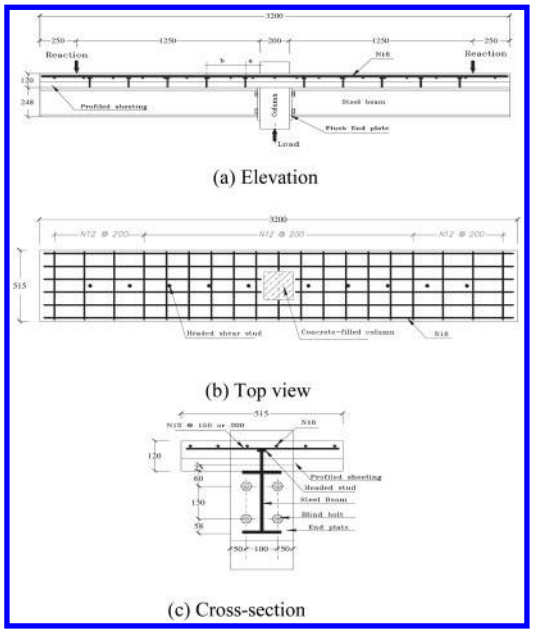


Figure 1. Composite joint tested by Loh *et al.* (2006).

Table 1. Variables in tests of Loh *et al*. (2006)

	CJ1	CJ2	CJ3	CJ4	CJ5
Reo. bars	4ϕ16	4ϕ16	4ϕ16	2ϕ16	6ϕ16
Reo. ratio	1·30%	1·30%	1·30%	0·65%	1·90%
a(mm)*	100	140	300	140	100
b(mm)*	265	480	800	480	160

*a = distance of first connector from column face
b = stud spacing

Table 2. Constants in tests of Loh *et al*. (2006)

Property	Value
Slab thickness (mm)	120
Slab width (mm)	515
Profiled sheeting	Lysaght Bondek
Column	200×200×9
Steel beam	250 UB 25·7
End plate thickness (mm)	10
Blind bolt	Hollow-Bolt M20
Stud shear connectors	19×100 mm

3 FINITE ELEMENT MODEL

3.1 *Material properties*

For the ABAQUS modelling, the actual stress-strain curves determined by Loh *et al.* (2006) were used for the shear connectors, steel beam, reinforcement, profiled sheeting and blind bolts. These are shown in Fig. 2, which also shows the piecewise linear representation of these curves for input into the ABAQUS model.

Concrete in compression and tension was represented using the damaged plasticity model in ABAQUS. For concrete in compression, the curve of Carreira & Chu (1985) is used, for which the stress-strain relationship is linear when the stress is less than $0.35f_c$, and

$$\sigma_c = \frac{f_c\gamma(\varepsilon/\varepsilon_c)}{\gamma - 1 + (\varepsilon/\varepsilon_c)^{\gamma}} \quad (1)$$

thereafter, in which

$$\gamma = (f_c/32{\cdot}4)^3 + 1{\cdot}55, \quad (2)$$

$\varepsilon_c = 0{\cdot}002$, f_c is the mean cylinder compressive strength and is in units of MPa.

For concrete in tension, the stress-strain relationship is linear until concrete cracking, after which the concrete is assumed to be perfectly plastic. This simplistic model circumvents several difficulties encountered in FE modelling and improves the rate of convergence, as vindicated with the close agreement between the numerical model and the tests of Loh *et al.* (2006).

3.2 *Element types*

Three-dimensional solid elements were used to model the bare and composite connections. 8-node solid elements with reduced integration (C3D8R) were used to mesh and simulate all components, except for the steel reinforcing bars. These elements lead to more precise and reasonable results and they avoid the shear locking difficulties encountered using other elements such as C3D8I. For the reinforcing bars, a two-node linear truss element (T3D2) was chosen. A typical FE model of a composite joint is shown in Fig. 3.

3.3 *Modelling of shear studs and bolts*

In the present study, the stud shear connector is included in the analysis discretely, in deference to other studies which model the shear connection using non-linear springs whose load-slip response must be defined from empirical push-test results. The shear connector meshing is shown in Fig. 4.

Most researchers have modelled blind bolts with axial and shear springs, with the axial and shear forces carried by these springs being defined based on the shear and tensile strengths of the bolts, with the pretension being neglected. ABAQUS provides an option for that allows for the pretension being included simply, in which the bolt is divided lengthwise into two, defining a surface on which the pretension is applied. The pretension is then applied in the bolts using the "bolt load" module, and this option was used in the present study. Fig. 4 illustrates the meshing of blind bolt. All components were modelled, except the threads on the shank and ledges. The head and nut of the bolts were assumed to connect completely to the shank.

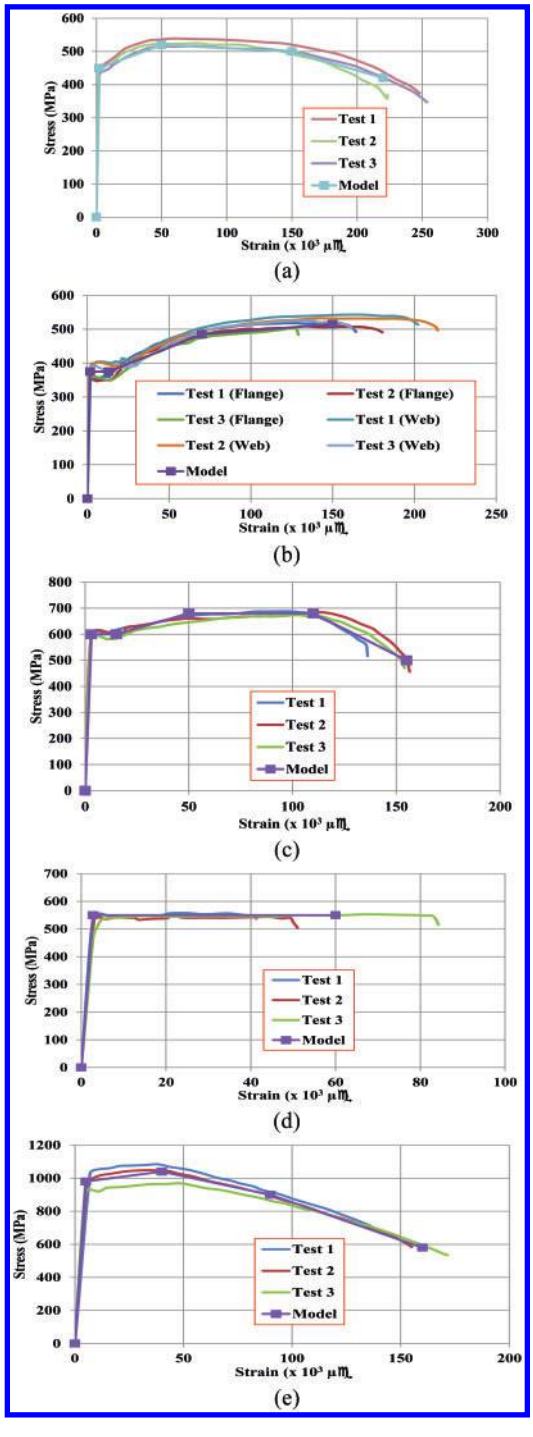


Figure 2. Test and adopted curves: (a) stud connector; (b) steel beam; (c) reinforcing bars; (d) profiled sheeting; (e) blind bolts.

3.4 *Load application*

Loading was applied in two steps. First, the pretension was applied to the blind bolts and the joints were then loaded, at which state the bolts were subjected to the pretension. Mirza and Uy (2011) have pointed out that Riks' technique is needed to capture any unloading in the non-linear analysis, and so the GENERAL method and modified RIKS method were used for the first step and second step respectively. A static concentrated load was applied at the centre of the CFST column, as was done in the tests.

In FE modelling, correct representations of the boundary conditions are essential since slightly different boundary conditions can produce significantly different results. For the simulation in this paper, the boundary conditions were taken as being exactly the same as in the tests, with the column being allowed to move in the vertical direction and with the flanking ends of the beams having roller supports.

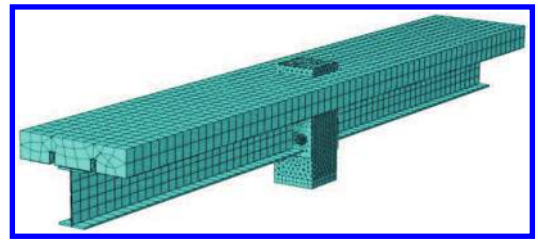


Figure 3. Finite element model of a composite joint.

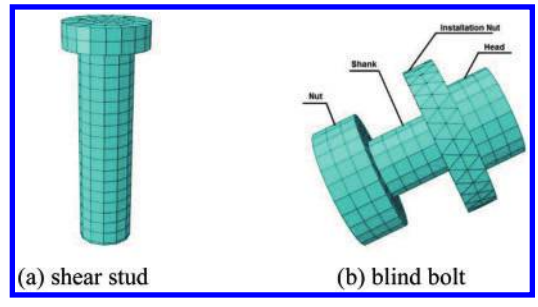


Figure 4. FE meshing of connector components

3.5 *Contact modelling*

One of the most important aspects of modelling is simulation of the contact interaction between components. There are various materials in composite connections which interact with each other, and the results of the FE analysis depend on the accurate modelling of the contact interaction between these materials. The interactions between these materials were treated in ABAQUS in the following way.

Experiments reported elsewhere show there is no separation between the head of the bolt and the flush end plate in a composite connection, and also between the nut of the bolt and the inner face of the steel column. Therefore, the TIE option was used for connecting these components which leads to their having the same displacements. The TIE option was also used for the steel beam and flush end plate because of the welding of these two components together.

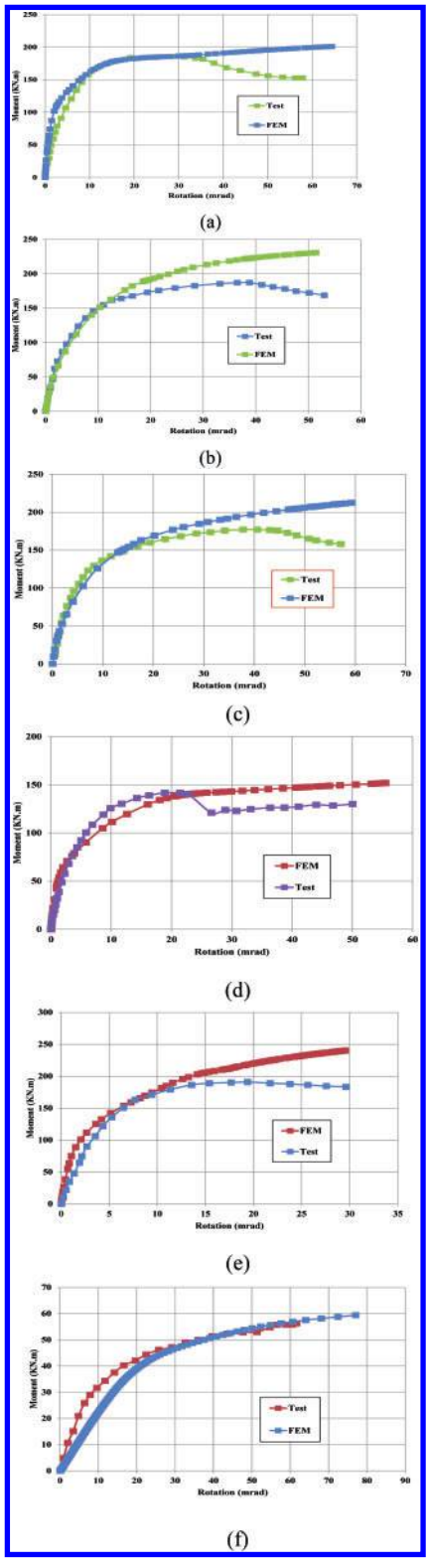


Figure 5. Comparison of FE model and tests for moment-rotation response. (a): test 1, (b): test 2, (c): test 3, (d):test 4, (e): test 5; (f): test 6.

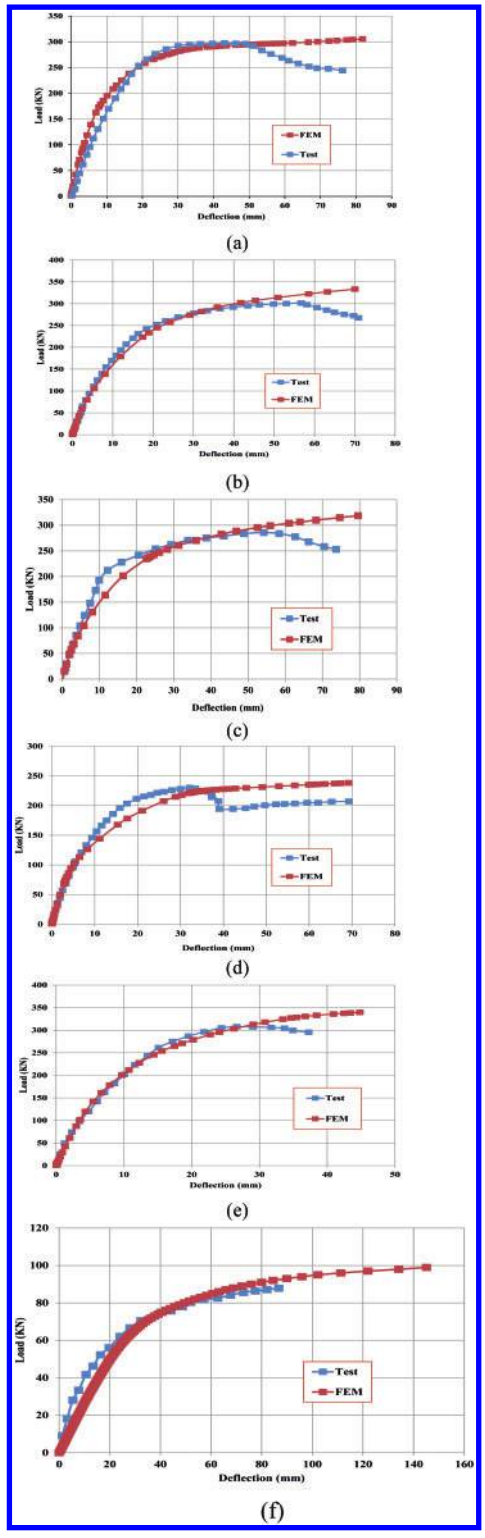
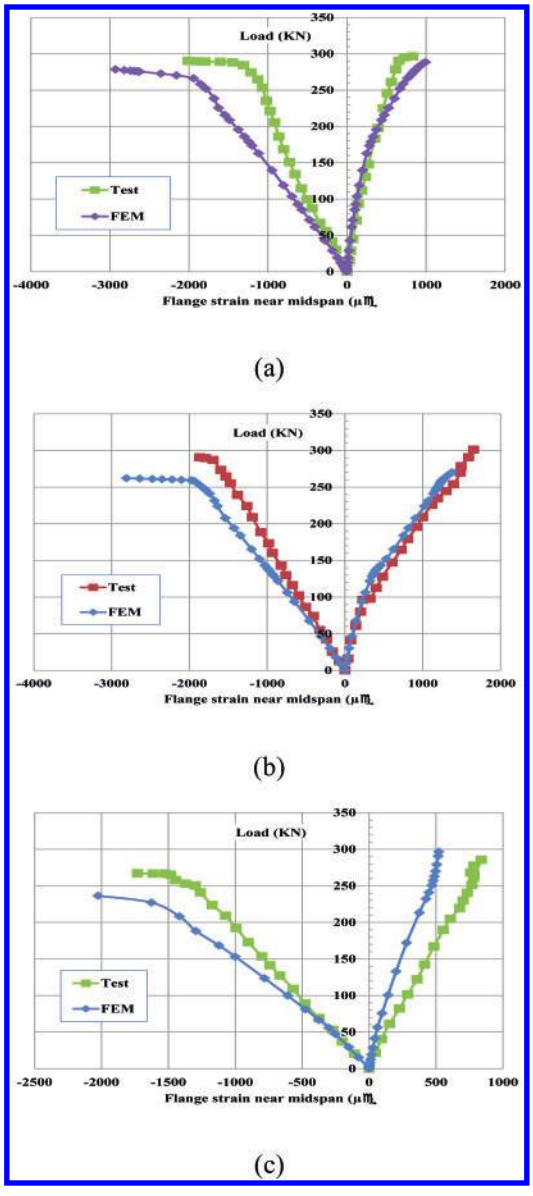


Figure 6. Comparison of FE model and tests for load-deflection response. (a): test 1, (b): test 2, (c): test 3, (d):test 4, (e): test 5; (f): test 6.

In order to simulate the interaction between the top flange of the steel beam and the lower part of the profiled steel sheeting, surface-to-surface contact interaction with a coefficient of friction of 0·1 was adopted, in which the top flange and the profiled sheeting were considered as master and slave surfaces respectively. The same interaction was used to model the interaction between the profiled sheeting and the lower part of the concrete slab. Because headed stud connectors are through-welded to the top flange, the TIE option was used.

As noted earlier, the shank and head of the stud shear connectors were simulated in the FE model. The studs and concrete slab were considered as being embedded and host regions respectively. Gil *et al.* (2013) have pointed out that if the headed studs in a composite joint are embedded in the slab, the model is able to capture the deformation of the concrete. Tahmasebinia *et al.* (2012, 2013) have also adopted this procedure. In this research, only the top part of the shank and head were embedded into the host region (concrete slab) to facilitate reliable convergence. Reinforcement was also embedded into the slab, with the slab being the host region and the bars being an embedded region. This technique connects these two different components and prevents slip between them. Interac-



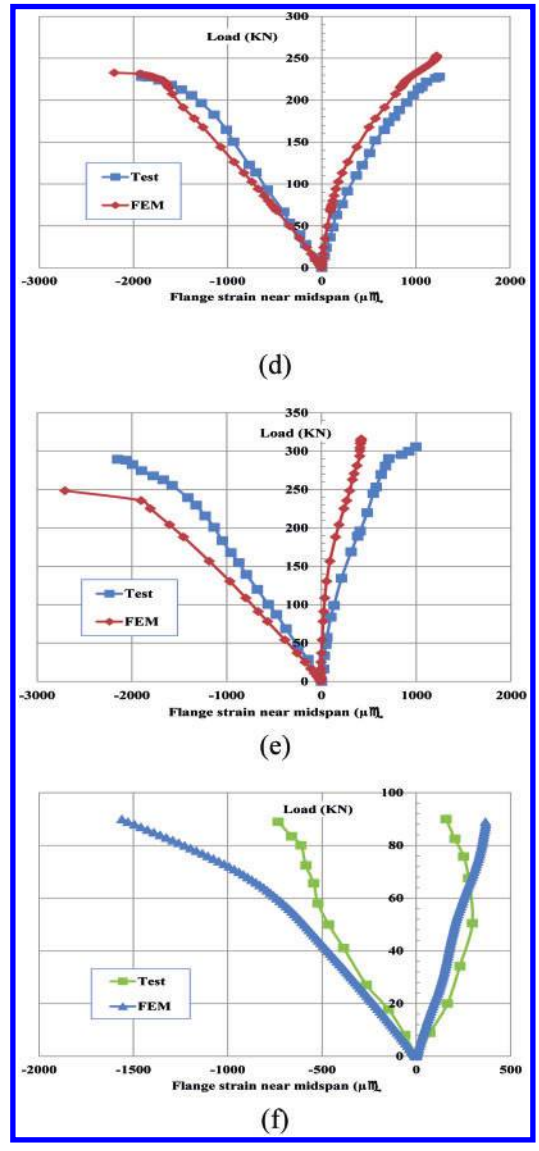


Figure 7. Comparison of FE moel and tests for top and bottom steel strain response. (a): test 1, (b): test 2, (c): test 3, (d):test 4, (e): test 5; (f): test 6.

tion of the concrete and inner faces of the steel tubular column was simulated as a surface-to-surface contact interaction with a coefficient of friction of 0·25.

4 COMPARISON OF TESTS AND FE MODEL

A most important consideration for a FE model is its validation with physical tests. In order to achieve this, the results of the ABAQUS-based FE modelling are compared herein with the experimental results of Loh *et al.* (2006). In this comparison, the moment versus rotation response was modelled, and the results are given in Figs. 5(a) to 5(e) for the five composite connections tested and in Fig. 5(f) for the connection with a bare steel beam. It can be seen that the agreement is very good for much of the range of response, with the discrepancies with large rotations (greater than 15 mrad) probably being attributable to the simplistic modelling of the cracked concrete. The evolution of the curves progressed rapidly using the ABAQUS model described in Section 3.

The load versus deflection response was also modelled, and the results are given in Figs. 6(a) to 6(e) for the five composite connections tested and in Fig. 6(f) for the connection with a bare steel beam. Again, the agreement can be seen to be satisfactory, except for deflections exceeding around 45 mm, for which concrete cracking in negative bending is dominant.

Finally, Loh *et al.* (2006) measured the strains in the top and bottom of the steel section 100 mm from the face of the columns. These were also determined using the ABAQUS model, with the results being given in Figs. 7(a) to 7(e) for the five composite connections tested and in Fig. 7(f) for the connection with a bare steel beam. The results can be seen to be in good agreement.

5 CONCLUSIONS

An efficient finite element modelling using ABAQUS has been developed to simulate the structural response of semi-rigid flush end plate joints with concrete-filled steel tubular columns. The modelling is simplified in its treatment of concrete in tension as quasi elastic-plastic, and it has the facility to handle the stud shear connectors in a discrete fashion rather than by the use of springs and empirical push test data. The technique was shown to be accurate when compared with comprehensive test data reported elsewhere, and it provides an efficacious means for structural modelling in order to develop much-needed design guidance for this application of composite structures technology.

ACKNOWLEDGEMENT

The work in this paper was supported by the Australian Research Council through an Australian Laureate Fellowship (FL100100063) awarded to the second author.

REFERENCES

Bahaari, M.R. & Sherbourne, A.N. 2000. Behavior of eight-bolt large capacity endplate connections. *Computers and Structures* 77(3):315–325.

Carreira, D.J. & Ku, K.H. 1985. Stress-strain relationship for plain concrete in compression. *Journal of the American Concrete Institute* 82(6):797–804.

Gil, B., Goñi, R., & Bayo, E. 2013. Experimental and numerical validation of a new design for three-dimensional semi-rigid composite joints. *Engineering Structures* 48: 55–69.

Kalfas, C. & Pavlidis, P. 1997. Load-slip curve of shear connectors evaluated by FEM analysis. In *Composite Construction, Conventional and Innovative, International Conference Innsbruck*. Zurich: IABSE.

Kim, B., Wright, H.D., Cairns R. & Bradford, M.A. 1999. The numerical simulation of shear connection. In M.A. Bradford *et al.* (eds), *Mechanics of structures and materials; Proc. 16th ACMSM, Sydney 8–10 December 1999*. Rotterdam: Balkema.

Liu, X., Bradford, M.A. & Erkmen, R.E. 2013. Nonlinear inelastic analysis of steel-concrete composite beams curved in-plan. Submitted for publication.

Loh, H.Y., Uy, B. & Bradford, M.A. 2006. The effects of partial shear connection in composite flush end plate joints. Part I – experimental study. *Journal of Constructional Steel Research* 62(4):232–246.

Mirza, O. & Uy, B. 2010. Parametric studies of behaviour of composite beam-column flush end plate connections subjected to low probability, high consequence loading. In: B. Young (ed), *Tubular Structures XIII, 13th International Symposium on Tubular Structures*. Hong Kong.

Mirza, O. & Uy, B. 2011. Behaviour of composite beam-column flush end-plate connections subjected to low-probability, high-consequence loading. *Engineering Structures* 33(2):642–662.

Pi, Y.-L., Bradford, M.A. & Uy, B. 2006. Second order nonlinear analysis of steel-concrete composite members. I: Theory. *Journal of Structural Engineering, ASCE* 132(5):751–761.

Tahmasebinia, F., Ranzi, G., & Zona, A. 2012. Beam tests of composite steel-concrete members: A finite element model. *International Journal of Steel Structures* 12(1): 37–45.

Tahmasebinia, F., Ranzi, G., & Zona, A. 2013. Probabilistic three-dimensional finite element study on composite beams with steel trapezoidal decking. *Journal of Constructional Steel Research* 80:394–411.

Research and Applications in Structural Engineering, Mechanics and Computation – Zingoni (Ed.)
© 2013 Taylor & Francis Group, London, ISBN 978-1-138-00061-2

Development and testing of a technique for the simulation of the rock cutting process

M.J. Mikl, R. Tichy & W. Ecker
Materials Center Leoben Forschung GmbH

T. Antretter
Institute of Mechanics, Montanuniversitaet Leoben

G. Pittino
Chair of Subsurface Engineering, Montanuniversitaet Leoben

ABSTRACT: This study presents a method for the numerical simulation of the rock cutting process, with the focus on the setup of the model and the description of the material. The aim is to obtain the loads on the pick for different pick geometries and modes of cutting. A quasi-isotropic and quasi-homogeneous rock type is chosen and described with a damage-plasticity constitutive law, which is implemented in the commercial finite element package Abaqus. The constitutive law is extended by a user-subroutine to account for the changing material behavior during the cutting process. The potentially fatal mesh distortion is avoided by the removal of critically damaged elements from the calculation with another user-subroutine. Fine discretization allows the adequate resolution of the contact area and therefore modeling of the effects of different pick geometries and modes of cutting. Additionally, infinite elements are applied as boundary conditions to reduce the model size and calculation time significantly and to prevent any undesirable shock wave reflections in the explicit analysis. It is shown that with the developed method different modes of cutting and pick geometries can be evaluated and compared.

1 INTRODUCTION

1.1 *Principles of excavation*

Roadheaders are widely used for excavation and mining purposes but high material strengths limit their usability (Tockner 1999). Nowadays a challenge is to extend their field of application to harder and more abrasive rock materials. The forces on the pick are of great importance and determine wear and especially the efficiency of the machine. Additionally the cutting capability is naturally limited by the weight of the machine, which makes the reduction of reaction forces by optimizing the process parameters rewarding. (Tockner 1999).

The cutting capability of a pick under certain cutting parameters is tested with the cutting test shown in fig.1. It consists of a rock specimen and one pick that is dragged through the specimen at a certain velocity, attack angle and cutting depth. The cutting test allows to determine the ability of a pick to cut out a certain amount of rock material and is performed to find the cutting parameters that maximize the excavated material and minimize the resulting forces (Tockner 1999).

Fig.2 shows the principle of cutting and the predominant forces. Variation of pick geometry, cutting depth or attack angle will result in an alteration of these forces and determine the efficiency of the process (Tockner 1999). In brittle materials cutting is a stepwise phenomenon of separation and removal of a large segment, the so called chip (Chiaia 2001). The mechanisms of rock cutting follow the principle of indentation (Kou et al. 1999). For spherical and conical indenters these mechanisms are summarized and

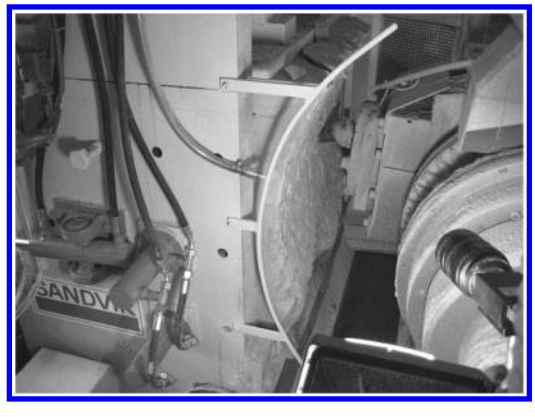


Figure 1. Picture of cutting test (Source: Sandvik Mining and Construction GmbH).

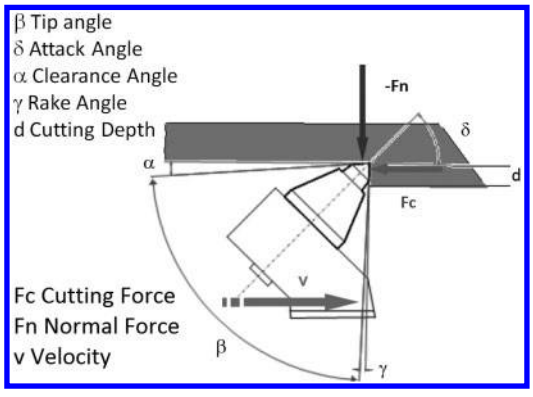


Figure 2. Scheme of the cutting test (Source: Sandvik Mining and Construction GmbH).

analyzed comprehensively by (Chiaia 2001). Directly under the indenter a hydrostatic stress state evolves causing the material to fail only due to crushing and fragmentation mechanisms. In the close surroundings large strains emerge and tensile cracks are formed but in a further distance the material behaves elastically. While blunt indenters form Hertzian cone cracks that propagate with increasing load, sharp indenters lead to the formation of penny shaped cracks and splitting. (Chiaia 2001) further states that with increasing load the fracture behaviour of a blunt object transitions into that of a sharp one. Depending on the rake angle the fracture propagation is either driven by tensile stresses or crushing, which makes the contact zone a determinant for the cutting (Chiaia 2001).

1.2 *Numerical approaches for excavation modeling*

Su & Akcin (2009) point out that rock cutting experiments are currently the most powerful method to characterize the tool-rock interaction. However, they are costly and time consuming.Numerical simulations represent one way to reduce these costs. Su & Akcin (2009) and Lunow & Konietzky (2009) regard particle methods adequate due to their ability of modeling heterogenity. Liu et al. (2002) consider FEM with coupled fracture models most promising and showed together with Kou et al. (1999) the possibility of modeling heterogenity with statisitcal material models. This approach allows the use and adaption of well elaborated constitutive equations available in FEM programs. Liu et al. (2004) point out the importance of an adequate material model and Saksala (2010) additionally mentions the importance of a special treatment of the boundary. Saksala (2010) uses dashpots to suppress energy refelction at the boundary but states that this approach works poor in multiaxial applications. Cho et al. (2010) introduce infinite transmitting boundary conditions to overcome the size limit of the model and maintain fine discretization to calculate rock fragmentation with disc cutters. The problem of potential large mesh distortions arising in the FEM simulation of an excavating cutterhead is solved by Shen et al. (2009) using an arbitrary langrangian eulerian method and by Cho et al. (2010) using element deletion. In a subsequent Cho et al. (2013) perform the numerical optimization of disc cutter spacing and relate the work to the mass of deleted elements as measurement for efficency.

2 THEORETICAL FRAMEWORK

2.1 *General aim*

A procedure is suggested to model rock cutting with the explicit FEM and evaluate the reaction forces on a pick for different cutting parameters and pick geometries. The focus is on the development of the method and its ability to simulate rock cutting. For this purpose the adequate constitutive equations and the adequate discretization are necessary. The zone of pick-rock interaction is crucial for cutting and must be discretized finely enough to resolve the pick geometry and the domain must be embedded such that boundary effects are eliminated.

2.2 *Constitutive equations*

The constitutive equations used, base on the plastic-damage model for concrete by Lubliner et al. (1989) extended by Lee & Fenves (1998). A yield function $F(\underline{\underline{\sigma}})$ in the three-dimensional principal stress space is required in order to identify the stress tensor $\underline{\underline{\sigma}}$ which is critical when inelastic deformation or failure initiates. When eq. (1) is fulfilled, the stress state causes inelastic deformation or failure. Additionally the consistency condition eq. (2) must be fulfilled to ensure that the stress state stays on the yield surface during plastic deformation.

$$F(\underline{\underline{\sigma}}) = 0 \tag{1}$$

$$\dot{F}(\underline{\underline{\sigma}}) = 0 \tag{2}$$

$$F = \frac{1}{1-\alpha(r_\sigma)}(\overline{q} - 3\alpha(r_\sigma)\overline{p} + \beta(\tilde{\epsilon}_c^{pl}, \tilde{\epsilon}_t^{pl}, r_\sigma)\langle\hat{\overline{\sigma}}_{max}\rangle - \gamma\langle-\hat{\overline{\sigma}}_{max}\rangle - \overline{\sigma}_c(\tilde{\epsilon}_c^{pl}) = 0 \tag{3}$$

$\overline{p}$ is the hydrostatic pressure, $\overline{q}$ is the Mises equivalent effective stress and α can be expressed in terms of r_σ, the ratio of initial equibiaxial compressive yield stress to initial uniaxial compressive yield stress. The function β denotes the ratio of the actual uniaxial compressive strength $\overline{\sigma}_c(\tilde{\epsilon}_c^{pl})$ to the actual uniaxial tensile strength $\overline{\sigma}_t(\tilde{\epsilon}_t^{pl})$. γ depends on the ratio of the slopes of the tensile and the compressive meridians in Haigh-Westergaard coordinates. $\hat{\overline{\sigma}}_{max}$ is the maximum principal effective stress, where $\langle . \rangle$ denotes the

Macaulay brackets. The compressive and tensile accumulated plastic strains are denoted by $\tilde{\epsilon}_c^{pl}$ and $\tilde{\epsilon}_t^{pl}$. They are zero at the initiation of failure or inelastic deformation. The constitutive equation can be used to model softening as well as hardening. This means that all parameters which are functions of the compressive and tensile accumulated plastic strains $\tilde{\epsilon}_c^{pl}$ or $\tilde{\epsilon}_t^{pl}$ can change during calculation. The elastic behavior is linear (Simulia 2012).

A different tensile and compressive behavior is modeled using the concept of damage-plasticity separated into tensile and compressive terms. This allows material subjected to tensile failure to stil bel able to bear compression.

$$d_t = d_t(\tilde{\epsilon}_t^{pl}) \tag{4}$$

$$d_c = d_c(\tilde{\epsilon}_c^{pl}) \tag{5}$$

$$d = d(d_t(\tilde{\epsilon}_t^{pl}), d_t(\tilde{\epsilon}_c^{pl})) \tag{6}$$

$$E^{el} = (1-d)E_0^{el} \tag{7}$$

The damage parameters d_t and d_c (eqs. 4,5) are tensile and compressive damage respectively and are combined in a total damage factor d (eq. 6) to degrade the elastic stiffness E^{el} during calculation according to eq. (7). The constitutive equations are therefore adequate to model tensile and compressive damaging and softening or stiffening separately as well as a combination of both. While eqs. (4–5) are user-specified linear functions, eq. (6) is defined in Simulia (2012).

2.3 *Modifications of the constitutive equations*

The constitutive equations are supplemented with a user subroutine. The status of an element (active or inactive in the calculation) as well as material behavior can be changed during the calculation accoring to additional equations. Within this work only the status and the dilation of the material are modified according to eqs. (8–9).

$$s(d_t) = \begin{cases} 1 & \text{if } d_t < d_t, crit \\ 0 & \text{else} \end{cases} \tag{8}$$

$$\phi(\tilde{\epsilon}_c^{pl}) = \begin{cases} \phi & \text{if } \tilde{\epsilon}_c^{pl} < \tilde{\epsilon}_{c,crit}^{pl} \\ 0.02 \cdot \phi & \text{else} \end{cases} \tag{9}$$

The status $s(d_t)$ determines the existence of an element. Changing the status from 1 to 0 indicates the removal of an element from the calculation. $\phi(\tilde{\epsilon}_c^{pl})$ characterizes the dilation of the material and determines the volumetric change due to plastic deformation. It is made adjustabled and set to a low value at $\tilde{\epsilon}_{c,crit}^{pl}$ to avoid unrealistic swelling due to plastic strain.

3 FINITE ELEMENT MODELING

3.1 *Strategy for the elimination of boundary effects*

When the region of interest is small compared to the surrounding medium, actions in the region of interest do not affect the surrounding, making it negligible. However a reasonable distance to the surrounding must be kept. A fine discretization and this reasonable distanceare mutually exclusive when the number of elements shall not increase excessively. To maintain fine discretization where it is needed, without an excessive number of elements on the one hand and without having to deal with numerical artefacts caused by the close boundary on the other hand, the discretized domain can be embedded into so-called infinite elements. This way the surrounding is regarded as unbounded or infinite medium and can be approximated by defining the infinite elements with decay functions over a semi-infinite domain. In dynamic analyses where classical boundary conditions (BCs) would reflect energy back into the domain, infinite elements suppress unrealistic reflection of shockwaves at the domain boundaries (Simulia 2012).

The benefit of infinite elements in explicit analyses is investigated by comparing their behavior against two other modeling approaches. Those are modeling with classical BCs by fixing degrees of freedom and modeling with classical BCs including a constrained discretization discontinuity. The latter allows reduction of elements in the model at positions where coarse discretization is acceptable. The three modeling approaches are compared in three corresponding models. Subjecting the cubic specimen to a time dependent pressure load induces a stress wave travelling through the material. Analyzing the time-dependency and behavior of the stress wave, especially at the boundary and the discretization discontinuity, allows a distinct comparison and choice of the modeling approach. The material is described using the constitutive equations eqn. (1–9).

3.2 *Evaluation of the boundary modeling*

In fig.3 the maximum principal stress with respect to the uniaxial tensile strength at every position along the three cubic test specimens is shown at different times. For simplicity this is further called the stress wave. Fig.3a shows the evolving stress wave in the specimen with classical BCs, while fig.3b shows it in the specimen with classical BCs including a constrained discretization discontinuity and fig.3c shows the stress wave in the domain embedded in infinite elements. The stress waves are plotted at given timesteps after the start of the calculation. The time discretization follows according to the stability requirements for explicit analyses and allows to completely observe the stress wave at any time of the simulation.

It can be clearly seen in fig.3 that the choice of boundary conditions and discretization strongly affects the results. The simulation with classical BC leads to a reflection of a stress wave at the boundary

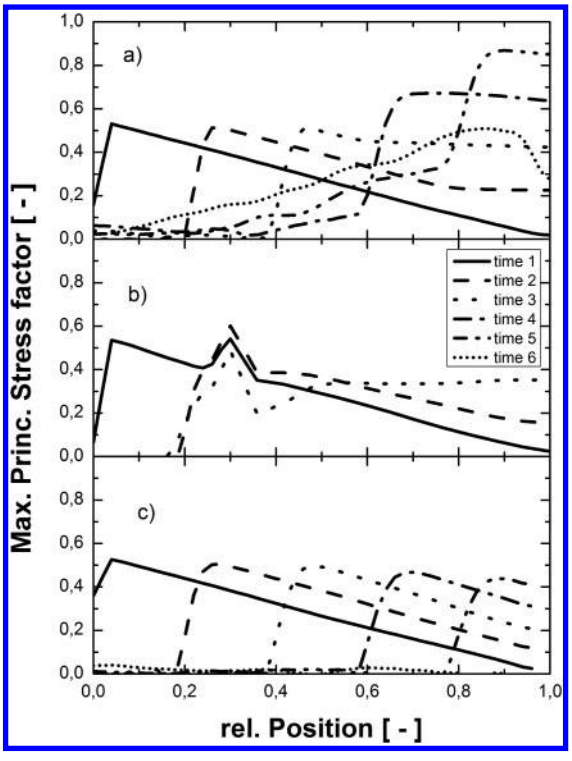


Figure 3. Wave experiment in a discretized domain with a) classical BCs b) classical BCs and discretization discontinuities and c) infinite elements.

(fig.3a). The interference of the reflected wave with the incoming one leads to stress peaks that could fulfill the failure criterion at the boundary and cause damage. In an unbounded domain this effect does not occur. In fig.3b it is evident that the stress wave is partly reflected at the constrained discretization discontinuity at position 0.3 which causes immediate interference and a pronounced stress peak at this position. Due to the resulting interferences a further analysis of the stress-wave after "time 3" is futile. In fig.3c the effect of infinite elements is shown. They replace BCs so that the incoming stress wave can continue without being reflected thus causing interferences. They so inhibit these numerical artefacts and are adequate to model a fine discretized domain within an infinite surrounding.

3.3 *Cutting simulations*

For the cutting simulations two different pick geometries, modeled as displacement-controlled rigid bodies, were used. The first is semi-spherical and the second conical with a height-to-radius ratio of 2. The attack angle was 45 degrees and the cutting depth was either 5 or 10 mm. The material is described according to the constitutive eqn. (1–9). Infinite elements were used to embed the domain and symmetry BCs were used to halve the problem size.

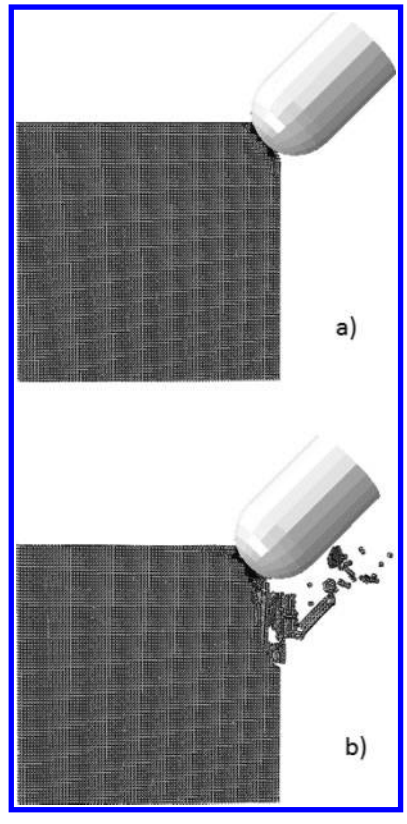


Figure 4. Three-dimensional cutting experiment with a semi-spherical pick at a) 5 mm cutting depth and b) 10 mm cutting depth.

4 RESULTS

4.1 *Results of the cutting simulations*

The cutting simulations yield the load displacement curves in fig.6 and fig.7. The corresponding picture of the cutting model is shown in fig.4 and fig.5 respectively. Each pick geometry and cutting position is evaluated separately for the cutting force and the normal force. The external work can be put in relation to the volume of the removed elements as Cho et al. (2013) did, but this is not adequate in the case of cutting with chipping. First of all it would neglect material that chips off, and second a smaller element size would lead to an increase of the work to removed volume ratio, making the efficiency dependent on the elment size. The direct comparison of the results is set aside because this determination of the efficiency is not satisfactory.

In fig.4a it is evident, that crushing can be modeled when the semspherical pick is pressed onto the surface at minor cutting depths. Fig.6a shows the corresponding force-displacement curve. In absence of sufficiently high shear or tensile stresses the force further increases and normal and cutting force are equivalent. High hydrostatic stresses increase the reaction force on the pick but will prefer crushing over

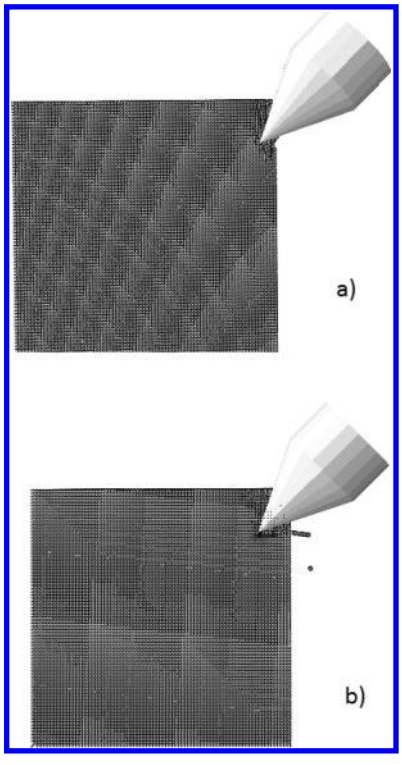


Figure 5. Three-dimensional cutting experiment with a conical pick at a) 5 mm cutting depth and b) 10 mm cutting depth.

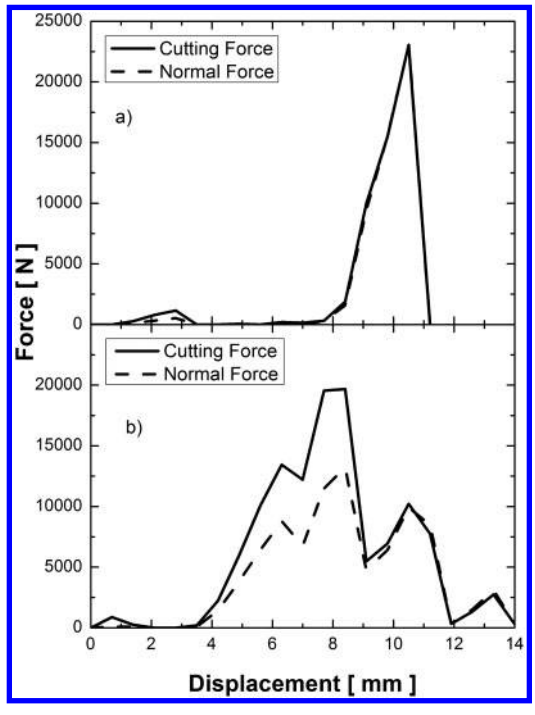


Figure 6. Force-displacement curve of the cutting experiment with a semi-spherical pick at a) 5 mm cutting depth and b) 10 mm cutting depth.

chipping and therefore indicate ineffective cutting. Additionally it can be seen that the forces are temporarily zero. This is caused by the removal of elements directly under the pick which causes the pick to lose contact.

Higher cutting depths favor chipping which can be seen in fig. 4b and in the corresponding force-displacement curve in fig. 6b where the cutting force is higher than the normal force. The chip forms due to tensile stresses in the specimen perpendicular to the cutting direction and surface. Fracture induced by only tensile stresses is favored over fracture accompanied by compressive stresses and chipping is prefered over crushing due to its higher efficiency (Tockner 1999). The high ratio of uniaxial compressive strength to uniaxial tensile strength makes tensile failure much more effective.

In fig.5a a very sharp pick pressed onto the specimen at low cutting depth is shown. The corresponding forces see in fig.7a obtained in the calculation are low due to the characteristics of sharp indenters (Chiaia 2001). The positive rake angles and the very sharp pick yields undercutting and tensile fracture as mentioned by (Chiaia 2001). The very low cutting force and the lower normal force suggest, that few elements are compressed hydrostatically and the major failure mode is due to tensile or shear stresses. The normal force is partly negative which indicates undercutting.

Cutting at higher cutting depth with the conical pick is shown in fig.5b with the corresponding forces in in fig.7b. The observed tendencies are the same as for lower cutting depths because the geometrical relations do not change for increasing the cutting depth. However they do not fully match, which shows the mesh dependency of the simulation when only few elements are in contact with the pick. For both calculations the forces temporarily become zero because the pick is losing contact when elements directly underneath it are deleted.

5 CONCLUSIONS

Within this work a method to simulate rock cutting with an explicit finite element analysis is developed and evaluated. An elaborate set of constitutive equations is extended with an element deletion subroutine to overcome large mesh distortions. It is shown that the treatment of the boundary is of great importance. The introduction of elements with decay functions over a semi-infinite domain (infinite elements) allow to suppress unrealistic reflection of energy back into the domain. The method is then tested by performing calculations where different picks are pressed onto specimens at different positions. It is shown that the process of fracture under high compression as well as chipping can be modeled with the developed modeling approach. Also the effect of different pick geometries

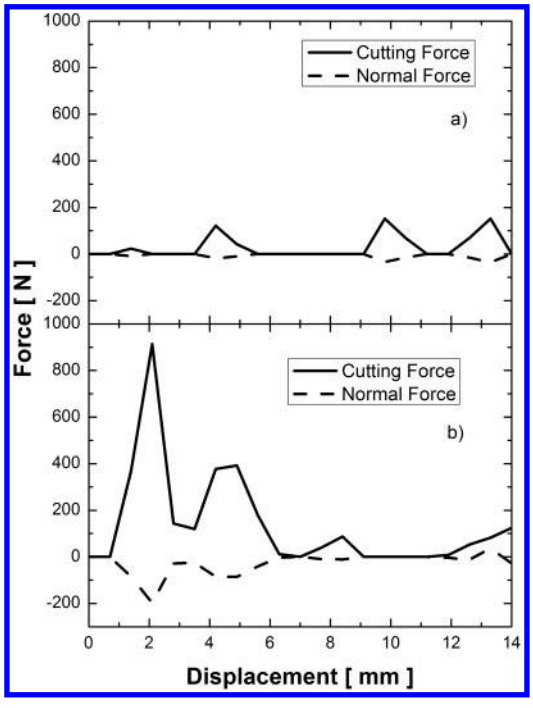


Figure 7. Force-displacement curve of the cutting experiment with a conical pick at a) 5 mm cutting depth and b) 10 mm cutting depth.

and cutting depths can be evaluated. However, direct comparison of the efficiency proves to be difficult due to the combination of chipping and element removal in the simulation. While the basic mechanisms of cutting are accessible with the proposed method, further work has to be put into the development of an adequate criterion to calculate and compare the efficiencies when cutting parameters are changed. Additionally the sensitivity of the model to the discretization must be investigated.

ACKNOWLEDGMENTS

Financial support by the Austrian Federal Government (in particular from the Bundesministerium fuer Verkehr, Innovation und Technologie and the Bundesministerium fuer Wirtschaft und Arbeit) and the Styrian Provincial Government, represented by Oesterreichische Forschungsfoerderungsgesellschaft mbH and by Steirische Wirtschaftsfoerderungsgesellschaft mbH, within the research activities of the K2 Competence Centre on "Integrated Research in Materials, Processing and Product Engineering" is gratefully acknowledged.

REFERENCES

Chiaia, B. (2001). Fracture mechanisms induced in a brittle material by a hard cutting indenter. *International Journal of Solids and Structures* 38(4445), 7747–7768.

Cho, J.-W., S. Jeon, H.-Y. Jeong, & S.-H. Chang (2013). Evaluation of cutting efficiency during tbm disc cutter excavation within a korean granitic rock using linear-cutting-machine testing and photogrammetric measurement. *Tunnelling and Underground Space Technology 35*(0), 37–54.

Cho, J.-W., S. Jeon, S.-H. Yu, & S.-H. Chang (2010). Optimum spacing of tbm disc cutters: A numerical simulation using the three-dimensional dynamic fracturing method. *Tunnelling and Underground Space Technology 25*(3), 230–244.

Kou, S., P.-A. Lindqvist, C. Tang, & X. Xu (1999). Numerical simulation of the cutting of inhomogeneous rocks. *International Journal of Rock Mechanics and Mining Sciences 36*(5), 711–717.

Lee, J. & G. Fenves (1998). Plastic damage model for cyclic loading of concrete structures. *Journal of Engineering Mechanics 124*(8), 892–900.

Liu, H., S. Kou, P.-A. Lindqvist, & C. Tang (2002). Numerical simulation of the rock fragmentation process induced by indenters. *International Journal of Rock Mechanics and Mining Sciences 39*(4), 491–505. *Numerical Methods in Rock Mechanics*.

Liu, H., S. Kou, P.-A. Lindqvist, & C. Tang (2004). Numerical studies on the failure process and associated microseismicity in rock under triaxial compression. *Tectonophysics 384*(14), 149–174.

Lubliner, J., J. Oliver, S. Oller, & E. Onate (1989). A plasticdamage model for concrete. *International Journal of Solids and Structures 25*(3), 299–326.

Lunow, C. & H. Konietzky (Eds.) (2009, 9–11 September). *Zweidimensionale Simulation der drckenden und der schenidenden Gesteinszerstrung*, Ruhr University Bochum. 2nd International Conference on Computational Methods in Tunneling: Aedificatio Publishers, 1–4.

Saksala, T. (2010). *Numerical Modelling of Rock Fracture in Percussive Drilling*. Ph. D. thesis, Tampere University of Technology.

Shen, J., X. Jin, Y. Li, & J. Wang (2009). Numerical simulation of cutterhead and soil interaction in slurry shield tunneling. *International Journal for Computer-Aided Engineering and Software 26*(8), 985–1005.

Simulia (2012). Abaqus 6.12 documentation. *www.simulia.com*.

Su, O. & N. A. Akcin (2009, January). Numerical simulation of rock cuttability. *Proceedings of the International Conference on Rock Joints and Jointed Rock Masses, Tucson, Arizona, USA 35*, 1–6.

Tockner, J. (1999). *Untersuchung der leistungsbestimmenden Parameter fr die mechanische Gewinnung von Festgestein mit Rundschaftmeieln an Teilschnittmaschinen*. Ph. D. thesis, University of Leoben.

Research and Applications in Structural Engineering, Mechanics and Computation – Zingoni (Ed.)
© 2013 Taylor & Francis Group, London, ISBN 978-1-138-00061-2

Material influence on the strength of aluminium column web in tension

G. Sarracco, G. Brando & G. De Matteis
Department of Engineering and Geology, University "G. d'Annunzio" of Chieti-Pescara, Italy

ABSTRACT: The current paper presents the first results of an ongoing research activity which aims at investigating the behaviour of aluminium beam-to-column joints. In particular, a wide parametric study, developed on the basis of reliable FEM numerical models and carried out in order to determine the influence of the used alloy on the strength of aluminium column web in tension, is described. In a first phase, the calibration process is implemented in order to validate, on the basis of experimental tests retrieved by literature, the proposed models. Then, alloys characterized by different hardening and ductility are analysed, in order to understand their influence on the resisting mechanisms of the studied component. Finally, the obtained outcomes are interpreted for providing suitable formulations to be adopted in Codes and Guidelines.

1 INTRODUCTION

In the design process of every metal structure particular care must be devoted to the joints. On the one hand, their performance is strongly affected by the intersection and overlap of stresses deriving from converging members. On the other hand, the limited ductility of certain components could give rise to undesired behaviours that must be properly controlled, in particular when the structure is located in strong earthquake prone zones.

With regard to beam-to-column connections, it would be important, for analysis purposes, to characterize the joints by proper moment-rotation relationships (M-Φ) able to reproduce their behaviour in both the linear and the non-linear field (see figure 1). To this aim, the well known component method is currently adopted in Eurocode 3 (EC3, 2003) for steel structures. This method basically allows to obtain the strength and the stiffness of the whole joint by determining, through the application of proper formulations, based on experimental and numerical studies, the mechanical features of the fundamental components.

This is also the general approach currently indicated by Eurocode 9 (EC9, 2007) and other Guidelines, such as the recent Italian CNR-DT 208 (2011), dealing with aluminium alloy structures. For some components, i.e. the ones that can be modelled by T-stubs, formulations traditionally given for steel have been properly adapted through the use of some corrective factors which have been calibrated on the basis of experimental and numerical analysis (De Matteis et al. 2000, 2009, 2012[b]). On the contrary, due to the lack of exhaustive studies in literature, other components have been considered by simply proposing the same expressions used for steel.

Considering the increasing interest on the aluminium employment for realizing new structures

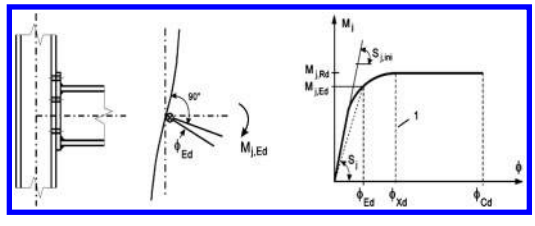


Figure 1. Beam-to-column joint modelling according to EC3.

(De Matteis et al., 2012[a]), as well as the peculiarity of the material itself with respect to steel, further studies are therefore necessary, as the above assumption seems to lead to a rough evaluation of the actual joint strength.

In front of this necessity, the current study, developed in the framing of an ongoing research activity focused on the interpretation of the behaviour of aluminium beam-to-column joints, aims at providing reliable formulations for a correct interpretation of the behaviour of the "column web in tension" component.

In particular, a wide parametric analysis, based on reliable FEM numerical models validated on the basis of experimental tests available in literature, is carried out, in order to highlight the influence of the of the used alloys features, on the strength of the considered component.

2 STATE OF THE ART

Apart from possible buckling phenomena, provided the iso-resistance of metal materials, both column web in tension and compression components behave in the same manner. This aspect allows to retrieve a large

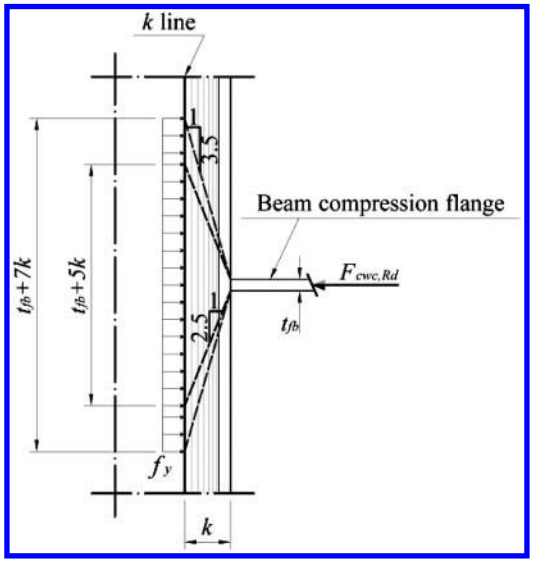


Figure 2. Linear stress distributions through the column web in compression according to Graham et al. (1959).

number of studies in literature which are the basis of the current Codes formulations.

The first researches were developed during the late fifties by Graham et al. (1959), who carried out tests on a simplified specimen of a flange-to-column joint, given by a plate in compression, acting as a beam flange, welded to the flange of a column profile (see figure 2).

The authors established that the maximum strength $F_{cwc,Rd}$ of a steel column web in compression component, when instability phenomena are avoided, is given by eq. (1)

$$F_{cwc,Rd} = f_y t_{wc}\left(t_{fb} + 7k\right) \tag{1}$$

where f_y is the yield stress of the column material, t_{wc} and t_{fb} are the column web and the beam flange thicknesses, respectively, k is the sum of the column flange thickness (t_{fc}) and the fillet root radius (r_c) and identifies the distance between the outer face of the flange and the longitudinal line, lying on the web, on which crashing may develop (henceforth called k line). The above equation results by the assumption of a linear distribution of the compressive stresses, trough the column web, characterized by a 3.5:1 slope.

In the same work, also on the basis of other experimental tests carried out on real complete beam-to-column joints specimens, the Authors recognized that the presence of the beam web, not explicitly considered in their first tests, could reduces the stress distribution inclination to 2.5:1. Hence, the final recommended design value for the strength of the column web in compression has been expressed according to eq. (2).

$$F_{cwc,Rd} = f_y t_{wc}\left(t_{fb} + 5k\right) \tag{2}$$

On the basis of another experimental activity, always focused on steel coupons similar to the ones shown in Figure 2, Aribert et al. (1981) developed a theoretical model able to give a more rigorous interpretation of the two previous equations. They empirically determined the stress distribution at different load steps, by measuring the strains by means of strain-gauges and video extensometers, so to identify three specific strength levels. The first corresponds to the elastic limit state, which is assumed to be attained when the early plasticity arises into the specimens. The corresponding force was given according to eq. (3).

$$F_{cwc,el} = f_y t_{wc}\left(t_{fb} + 2{,}3k\right) \tag{3}$$

The second force level $F_{cwc,pl}$, representing the plastic limit state, was given by eq. (4)

$$F_{cwc,pl} = f_y t_{wc}\left(t_{fb} + 5k\right) \tag{4}$$

The third strength level, corresponding to the section failure (ultimate limit state) was provided by eq. (5).

$$F_{cwc,u} = f_y t_{wc}\left(t_{fb} + 7k\right) \tag{5}$$

Therefore, the Authors obtained, by experimental observations, the same ultimate strength given in eq. (1), but they attributed it to the full exploitation of the strain hardening of the base material.

At the beginning of eighties, Witteveen et al.(1982) carried out some experimental tests in order to determine the moment capacity of both un-stiffened welded and bolted steel beam-to-column joints. For welded specimens they found that the column web in compression can be characterized by the following strength:

$$F_{cwc,Rd} = f_y t_{wc}\left[t_{fb} + 5\left(t_{fc} + r_c\right)\right] \tag{6}$$

On the other hand, for bolted end plate connections, the following expression was provided:

$$F_{cwc,Rd} = f_y t_{wc}\left[t_{fb} + 2\sqrt{2}\ a + 2t_p + 5\left(t_{fc} + r_c\right)\right] \tag{7}$$

where a represents the throat thickness of fillet weld connecting the beam flange to the end plate and t_p is the end plate thickness.

In both the above expressions, the stress distribution was assumed to be linear with an inclination of 45° through both the weld and the end-plate, whereas it was supposed to vary linearly with a slope of 2.5:1 (about 22°) in the column web. It is worth of being noticed that eqs. (6) and (7) are currently provided by EC3, where the expressions given in the square parentheses are defined as effective length (b_{eff}) and represent the portion of the "k line" in which the yielding stresses develop.

With regard to aluminium beam-to-column joints, experimental and numerical activities, aimed at predicting the yielding strength of column web in tension,

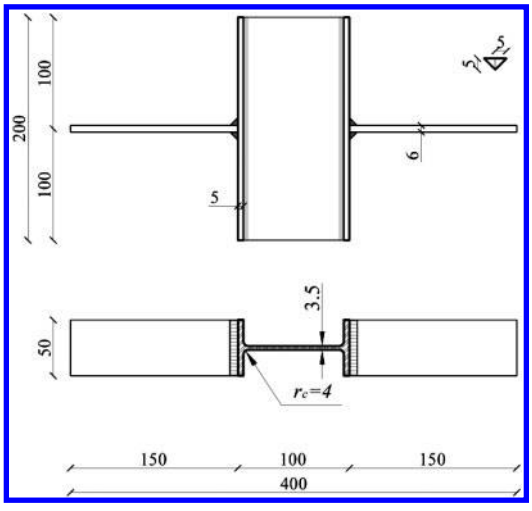


Figure 3. Geometrical dimensions of the specimens tested by Matusiak (1999).

Table 1. Parent material of tested specimens (Matusiak,1999): mean value of mechanical features.

Joint component	Dir.	$f_{0.2}$ (MPa)	f_u (MPa)	$f_{0.2}/f_u$ (MPa)	ε_u (MPa)
Plate	||	304.5	313.5	1.03	0.064
Profile I-100, web	⊥	262.7	281.6	1.07	0.068
Profile I-100, flange	||	268.9	283.4	1.05	0.061

have been described in Matusiak (1999). Specimens made of the EN AW 6082-T6 alloy, whose mechanical features are described in table 1 with regard to the parent material, were investigated.

Their geometry is depicted in figure 3.

The experimentally observed failure mode consisted in a column web fracture along the "*k* line", similar to that expected for steel. For this reason, the Authors proposed the following elastic strength (eq. 8)

$$F_{cwt,el} = t_w b_{eff,el} f_{0.2} \tag{8}$$

Therefore the same base formulation fixed for steel, given in eq. (7), was assumed, with the yielding strength of steel replaced by the conventional elastic strength of aluminium ($f_{0.2}$). The effective length $b_{eff,el}$ was assumed according to eq. (9).

$$b_{eff,el} = t_{pl} + 2\sqrt{2}a + 3.4(t_f + r) \tag{9}$$

In this case a linear distribution of 1.7:1 slope was considered for stresses, which is lower than the one considered for steel in (7), but is higher than the one considered in (3) for the elastic strength of steel.

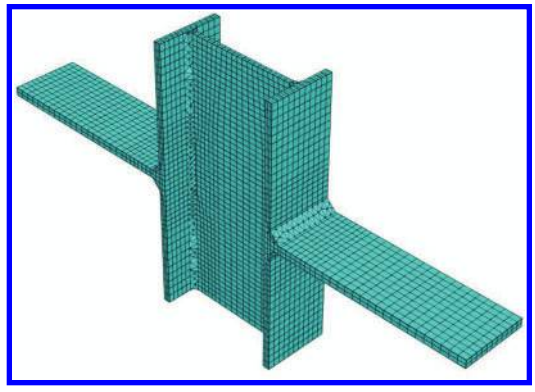


Figure 4. The proposed FE numerical model.

3 THE PROPOSED NUMERICAL MODEL

3.1 *Basis*

A numerical model of a simple aluminium flange-to-column joint has been set up on the basis of the tests carried out by Matusiak (1999) at the NTNU University of Trondheim (Norway). The reliability of the proposed model has been proved by ascertaining that the obtained numerical results fit well the experimental ones. Then, a parametric analyses, has been implemented.

The experimental tests are related to three equal samples, whose geometry has been already shown in Figure 3. The specimens were subjected to an increasing tensile force up to the failure, acting on two plates (equivalent to the beam flanges) welded to the flanges of a I-100 profile, acting as a column.

3.2 *Model Description*

The geometry of the above tested specimens has been modelled by using the ABAQUS FEM non linear software (Hibbitt et al. 1997). The three-dimensional 8-node hexahedral finite elements C3D8R, with reduced integration, have been adopted for meshing all the parts, except the ones representing the weld seams. For the latter, the 4-node linear tetrahedral elements (C3D4) have been used in order to prevent hourglass control problems (see figure 4).

Particular care has been spent in the model meshing algorithm: three elements have been set along the column flanges thickness, while two elements have been imposed transversally to the column web. A more refined mesh has been imposed in the proximity of the plate-to-column flange connection, to account for the higher stresses and strains expected in this zone. Totally, 8534 finite elements, with an average dimension of 4 mm, and 9647 nodes have been used.

As the numerical results could be mesh affected, in order to validate the adopted meshing algorithm, a sensitivity analysis has been performed. To this purpose, the previously described geometry has been also meshed with the same finite elements, but with a halved average size (2 mm instead of 4 mm).

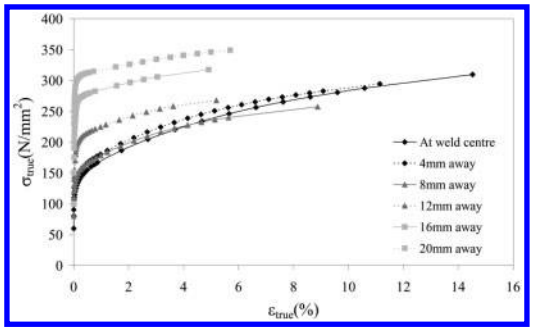


Figure 5. Experimental stress-strain curves of the heat affected material.

As far as the material modelling is concerned, the mechanical features previously described in Table 1 for the parent material have been imposed in terms of true stress-true strain. As far as the heath affected zone is concerned, the true stress-true strain relationships shown in figure 5 have been assumed depending on the distance by the weld seams, according to Matusiak (1999).

In order to simulate the same boundary condition imposed during the experimental tests, the nodes belonging to the free edges of one of the two external plates have been rigidly constrained to a reference point with all the degrees of freedom restrained. Nodes belonging to the free edges of the other plate have been tied to another reference point where all the displacements have been restrained except the one perpendicular to the column flange plane. Along this direction the reference point itself has been subjected to a controlled displacement linearly increasing up to the attainment of the ultimate strain in the specimen. A standard analysis procedure has been implemented and both the mechanical and the geometrical non linearity have been taken into account.

As it is possible to observe by the comparison of Figure 6.a and Figure 6.b, the deformed shapes corresponding to the collapse of both the experimental and the numerical specimens are very similar. Moreover, as revealed by Figure 6.c, the obtained numerical force-displacement relationships, for both the assumed meshes, are depicted and compared with the three curves obtained by tests.

The numerical and experimental results are in good agreement, thus proving the reliability of the implemented modelling process. Moreover the fact that the differences between the two numerical curves are almost negligible allows to state that the less refined meshed model is also reliable for carrying out parametric analyses without jeopardizing the trustworthiness of the obtained results.

4 THE PARAMETRIC ANALYSIS

The mechanical behaviour of aluminium joints is strongly dependent by the mechanical features of the

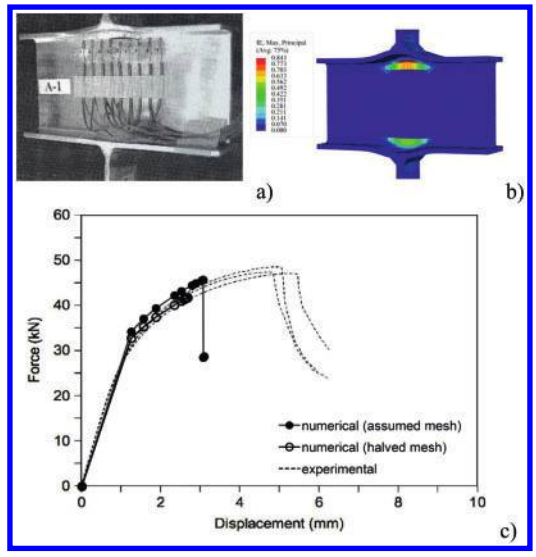


Figure 6. Numerical vs. experimental results: a) The specimen tested by Matusiak (1999), b) Inelastic strain of the numerical model before failure and c) force-displacements curves.

adopted alloys. In fact, as it is known, contrarily to steel, aluminium is characterized, in a different way according to the amount of alloyed elements, by a large strain hardening and a limited ductility. These peculiarities determine the modalities by which possible resisting mechanisms, such as stress distributions inside the components, can occur in the joint and therefore have to be investigated in order to understand their influence.

To this purpose, a parametric analysis has been carried out by imposing the 48 material different constitutive relationships shown in figure 7 to the model presented in previously, for which the presence of the heat affected zone has been neglected.

These have been obtained consistently to the Ramberg-Osgood relationship (Ramberg & Osgood 1943, Mazzolani 1995) given in eq. (10), by fixing the conventional yielding strength f_0 to a value of 250 MPa and by varying the material ultimate strain (ε_u) and the corresponding stress (f_u).

$$\varepsilon = \frac{\sigma}{E} + \left(\frac{\sigma}{B}\right)^{n_p} \tag{10}$$

In detail hardening parameter n_p equal to 5, 6, 8, 10, 15, 20, 30, ∞ have been imposed and, for each value, ductility levels (ε_u) of 4, 8, 12, 16, 20, 24 have been assumed. In this way, eight different families composed by six stress-strain relationships, each one characterized by a different ductility (for a totality of forty-eight constitutive low), have been obtained.

The numerical results obtained by the analysis have been interpreted by checking, for each loading level, both the stress and the strain distributions in the joint. For the sake of example, in Figures 8.a the Mises stress

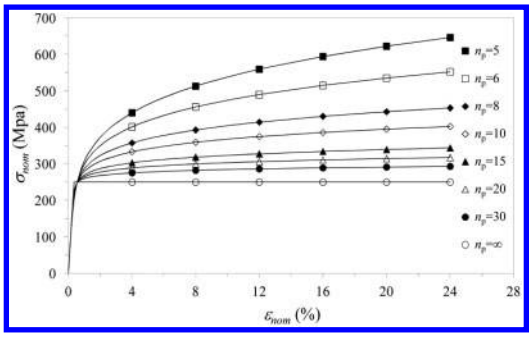


Figure 7. Nominal stress-strain curves for a ultimate strain ε_u=24 assumed in the parametric analysis.

distribution along the "k-line" at the failure attainment is shown for a material characterized by a hardening parameter n_p =30 and a variable ultimate strain (ε_u). It is possible to observe that as the material ductility increases, a larger distribution of plastic stresses is given. Analogously, when the ductility is kept constant, by increasing the strain hardening the slope of the stress distribution through the column web raises (see figure 8.b). Therefore both material characteristics, n_p and ε_u, affect significantly the component strength.

The integral of the above stress distributions represents the maximum strength of the column web in tension. Therefore, when divided by both the reference strength of the base material and the web thickness, it provides a conventional measure of the effective length to be used in equation (7). It is to be highlighted that as reference strength, contrarily to steel, for aluminium the ultimate strength of the base material appears to be more appropriate, allowing to account implicitly for the effect of hardening.

The new formulation for the effective length of the column web in tension has been therefore proposed (see eq. 11) by considering a correction factor β to be introduced in the formulation of the effective length given for steel according to eq. (7).

It has been calibrated so that the ultimate strength $F_{u,num}$ obtained by numerical analyses can be expressed by the following expression:

$$F_{u,num} = f_u \cdot t_w \cdot b_{eff,alu} = \\ = f_u \cdot t_w \cdot \left[t_{pl} + 2\sqrt{2}a_b + 2\beta\left(t_{fc} + r_c\right)\right] \quad (11)$$

The proposed effective length for aluminium joint $b_{eff,alu}$ by means of the β factor takes into account the actual slope (β:1) of the stress distribution in the web, due to the material parameters ε_u and n_p.

The results obtained for the forty-eight studied alloys are represented by the curves plotted in Figure 9., which are well fitted by the by the surface given in figure 10.

The latter has been expressed according to the following expression:

$$\beta(\varepsilon_u, n_p) = \xi(\varepsilon_u) \cdot \eta(n_p) \quad (12)$$

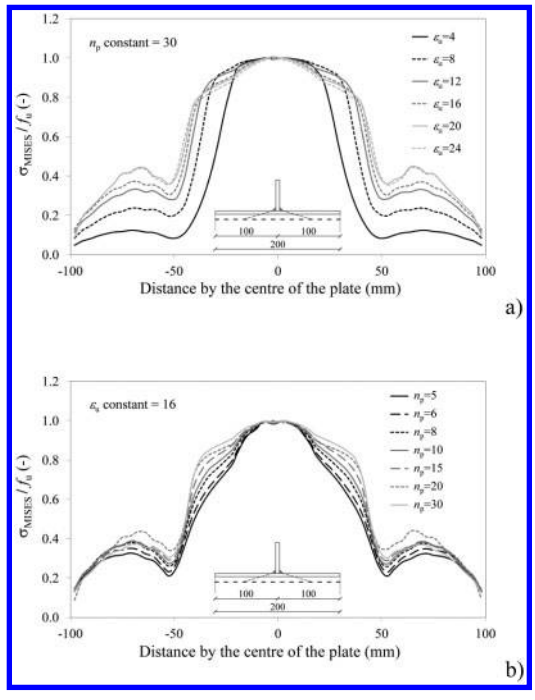


Figure 8. Mises stress distribution for a material with a) n_p =30 and variable ε_u and with b) ε_u =16% and variable n_p.

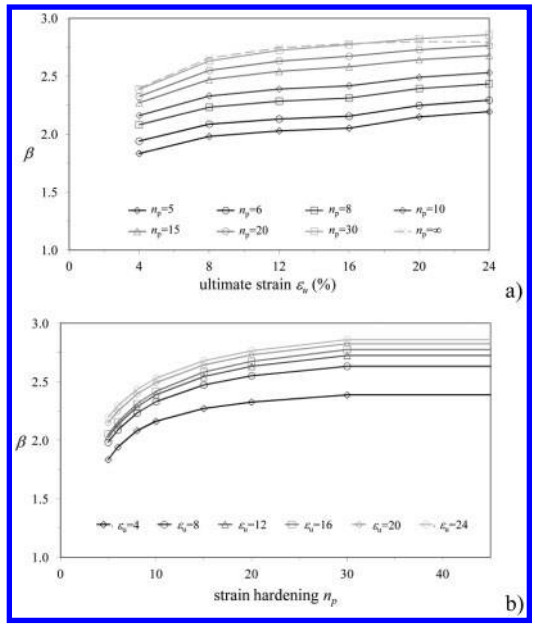


Figure 9. β correction factor as function of a) ultimate strain ε_u and b) strain hardening n_p.

in which

$$\xi(\varepsilon_u) = 0.21 \cdot \ln(\varepsilon_u - 1.6) + 2.2 \quad (13)$$

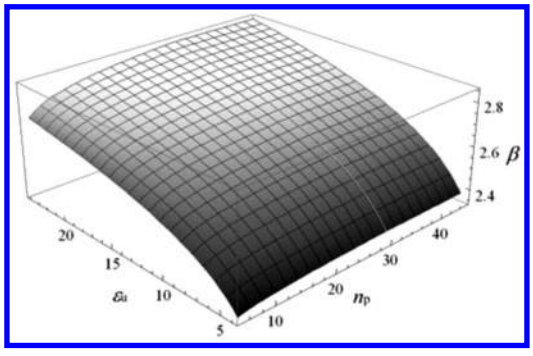


Figure 10. β correction factor: combined effect of ε_u n_p.

and

$$\eta(n_p) = \min\left[1.00\ ; \frac{0.31 \cdot \ln\left(n_p^{2/3} - 2\right) + 2.23}{2.86}\right] \qquad (14)$$

CONCLUSIONS

In the current paper, a parametric analysis aimed at investigating the influence of the base material features on the strength of aluminium column web in tension has been carried out.

In a first stage, a reliable FEM numerical model has been set up. This has been calibrated on the basis of useful experimental tests retrieved by literature.

Then 48 different constitutive models, obtained on the basis of the Ramberg-Osgood relationship, once the ductility and the strain hardening have been properly varied, have been imposed, in order to understand how the component strength is influenced by such parameters.

Static non linear analyses have been run, giving back results that put into evidence that the formulation provided by EC3 is not conservative if applied *sic et simpliciter* to the studied aluminium component.

As a consequence, a suitable β correction factor, to be adopted for properly modifying the effective length given by Eurocode 3 for the strength calculation, has been outlined.

These results are therefore to be intended as a proposal to be included in Codes and Guidelines focused on the use of aluminium structures.

REFERENCES

Aribert, J.M., Lauchal, A., Nawawy, O.I. 1981, Elastic-Plastic Modelization of the Resistance of a Column in the Compression Region. Construction Metallique, No. 2. (in French).

CNR-DT 208/2011, Istruzioni per la Progettazione, l'Esecuzione ed il Controllo di Strutture di Alluminio (in Italian), Roma, 8 november 2011.

De Matteis, G., Mandara, A., Mazzolani, F.M. 2000, T-stub aluminum joints: Influence of behavioural parameters. Computers and Structures, 78 (1), pp. 311–327.

De Matteis, G., Brescia, M., Formisano, A., Mazzolani, F.M. 2009, Behaviour of welded aluminium T-stub joints under monotonic loading. Computers and Structures, 87 (15–16), pp. 990–1002

De Matteis, G., Brando, G., Mazzolani, F.M. 2012a, Pure aluminium: An innovative material for structural applications in seismic engineering. Construction and Building Materials, 26 (1), pp. 677–686.

De Matteis, G., Naqash, M.T., Brando, G. 2012b, Effective length of aluminium T-stub connections by parametric analysis. Engineering Structures, 41, pp. 548–561.

EN 1993-1-8, Eurocode 3, Design of steel structures – Part 1–8: Design of joints, CEN, 2003.

EN 1999-1-1, Eurocode 9, Design of aluminium structures – Part 1-1: General structural rules, CEN, 2007.

Graham, J.D., Sherbourne, A.N., Khabbaz, R.N. 1959, Welded Interior Beam to Column Connections. American Institute of Steel Construction, Chicago, Ill.

Hibbitt, Karlsson and Sorensen, 1997, ABAQUS, Theory Manual, Version 5.7.

Matusiak M. 1999, Strength and Ductility of Welded Structures in Aluminium Alloys., Ph.D. Thesis, Departement of Structural Engineering. Norwegian University of Science and Technology (NTNU).

Mazzolani, F.M. 1995, Aluminium alloy structures, 2nd ed. London: E & FN Spon.

Ramberg, W. and Osgood, W.R. 1943, Description of stress-strain curves by three parameters, NACA Techn. No. 902.

Witteveen, J., Stark, J.W.B., Bijlaard, F.S.K., Zoetemeijer, P. 1982, Welded and Bolted Beam-to-Column Connections. ASCE Journal of the Structural Division, Vol. 108, No. ST2, Proc. Paper 16873, pp. 433–455.

8. Impact, blast, damage mechanics, damage modelling

Research and Applications in Structural Engineering, Mechanics and Computation – Zingoni (Ed.)
© 2013 Taylor & Francis Group, London, ISBN 978-1-138-00061-2

Interaction forces between huge cargo vessels and quay walls

M. Bahr & V. Sigrist
Institute of Concrete Structures, TUHH – Hamburg University of Technology, Hamburg, Germany

ABSTRACT: The berthing maneuver of huge cargo vessels causes high reaction forces. To avoid damages to the ship and the quay walls, rubber fender systems are installed to absorb the kinetic energy of the berthing vessel. In order to analyse the entire berthing maneuver it is essential to understand the mechanics of a berthing vessel and to determine the force-deflection behavior of the rubber fenders in real conditions. Therefore, rather small rubber fenders are tested. The results of these tests can be applied to bigger identically built fenders.

1 INTRODUCTION

It is complex to determine the forces which are transferred from a container ship to a quay wall. There are several reasons for high reaction forces, such as wind pressure upstream, heavy sea or the kinetic energy of the berthing vessel. This paper aims at contributing to the theoretical treatment of the force transmission in case of berthing. During berthing the kinetic energy of the ship has to be absorbed by the quay wall, especially by the fender system. To absorb the kinetic energy of the vessel the fender has to have the right size and shape. There is a big range of different types of fenders to fulfill exactly the requirements for every dimension of vessel and quay wall. In the following the mechanical principles of a berthing ship will be explained and the kinetic impact energy will be determined. Afterwards, experimental and theoretical investigations are outlined that include the testing of fenders and the analysis of the results. In the tests the fender is compressed and unloaded with a constant loading velocity and the reaction forces and displacements are measured and the stored and dissipated energy is determined. Finally the similitude theory is used to transform the results to fenders of bigger size which leads to the conclusion that the reaction force of a huge cargo vessel at berthing can be extremely high.

2 BERTHING IMPACT ENERGY

To analyse the impact energy of a berthing vessel it is necessary to subdivide the berthing procedure at first. Usually the berthing maneuver does not proceed with the vessel lying in parallel to the quay wall (Fig. 1). Initially, the ship hits the first fender with its bow or stern so that the ship's kinetic energy is partially lost. Then the ship turns around its center of mass until it hits another fender with the other end. It can be

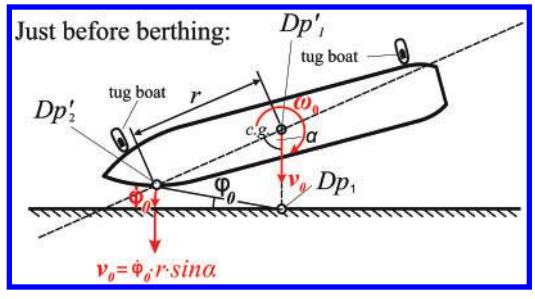


Figure 1. State (a) – geometry just before berthing.

assumed that the velocity vector does not have a component parallel to the waterfront structure because the berthing maneuver is assisted or totally controlled by tugs (Gaythwaite 1990). An angular motion ω_0 of the ship can be disregarded unless external forces such as wind, water current or tug thrust do appear (Gaythwaite 1990). The kinetic energy of the berthing vessel is mainly absorbed by the fender system but also by the ship's hull and the waterfront structure. (Gaythwaite 1990) and (PIANC 2002) refer to a method to determine the energy E_f which has to be absorbed by a fender at first contact. Based on the equation of translational energy E, the energy E_f can be determined to:

$$E_f = E\,C_e\,C_m\,C_s\,C_c = \frac{1}{2}\,m\,v_0^2\,C_e\,C_m\,C_s\,C_c \qquad (1)$$

Gaythwaite (1990) and PIANC (2002) specify the different factors of Eq. 1 as follows:

- Mass m [t]
  Ship mass.
- Vessel's velocity normal to the pier v_0 [m/s]
  The velocity v_0 depends on the shipload as well as on the berthing conditions. Under very difficult conditions a huge vessel berths with a maximum velocity of about 0.2 m/s. The berthing velocity v_0

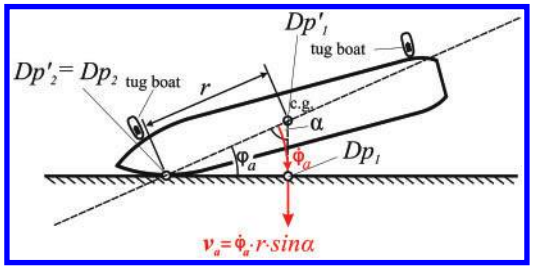


Figure 2. State (b) – geometry in the course of berthing.



Figure 3. Experimental assembly.

has a pronounced influence on the kinetic energy as the energy is proportional to the velocity squared.

- Eccentricity coefficient C_e
  Though formulas for the eccentricity coefficient can be found in the literature, no derivation is given. For this reason C_e is explained here:
  The first contact of the ship and the pier takes place at a point Dp_2 eccentrical to the center of mass $c.g.$ (Fig. 2). In order to determine the impact energy at Dp_2 the rotational energy of the vessel with the angular motion $\dot{\varphi}_a$ around Dp_2 has to be taken into consideration.
  Hence, the kinetic energy of the ship is multiplied by the eccentricity coefficient C_e:

$$C_e = \frac{k^2 + r^2 \cos^2\alpha}{k^2 + r^2} \qquad (2)$$

  where:
  k = radius of gyration of the vessel's mass about its $c.g.$ [m]
  r = distance between the $c.g.$ and the point of impact [m]
  α = angle between the vector of velocity v_0 and the line between the point of contact and the centre of mass [°]

  C_e usually ranges from 0.5 to 0.8. The eccentricity coefficient is calculated with help of the rigid body mechanics by considering eccentrical berthing in 2 states: (a) just before berthing; (b) in the course of berthing. Both states are shown in the Figures 1 and 2. The infinitesimal translatoric motion at the point of contact D_{p2} perpendicular to the shore line has to be considered as a rotational motion with the angular velocity $\dot{\varphi}_0$ and with the corresponding radius r (Fig. 1). This especially applies to long vessels.

  The eccentricity coefficient can be derived with the law of conservation of energy and the parallel axes theorem. Hence, the rotational energy of point Dp'_2 around point Dp_1 in state (a) has to be equated with the rotational energy of point Dp'_1 around point Dp_2 in state (b).

- Virtual mass coefficient C_m
  The virtual mass coefficient C_m accounts for the added mass due to entrained water. There are several suggestions to determine the mass of the water to be moved along with the ship. For C_m the default values are as follows:
  for small under-keel clearance: $C_m = 1.5$
  for large under-keel clearance: $C_m = 1.8$.

- Softness coefficient C_s
  A rather small part of the impact energy is absorbed by the ship's hull. For hard fendering and large ocean-going vessels C_s ranges from 0.9 to 1.0 while the value for soft fendering is 1.0.

- Configuration coefficient C_c
  The configuration coefficient accounts for the damping of the pier. C_c ranges from 0.9 to 1.0 depending on the type of structure to which the vessel is berthing.
  Especially in the case of closed piers (for example vertical sheet pile walls) part of the energy is dissipated because the water between the wall and the approaching vessel cannot drain off quickly enough from around and under the vessel.

3 FENDER MECHANICS

3.1 *Experimental investigation*

In the course of this research fender tests are carried out. For experimental and technical reasons rather small fenders are investigated.

In Fig. 3 the experimental assembly for testing a fender is shown. The tested version is a Cone Fender and is 0.4 m high and has a diameter of 0.5 m at the bottom. The fender is compressed and unloaded with a constant deformation velocity. First the fender is deformed to the maximum allowable value as stated in the product data sheet. Afterwards, the fender is unloaded again. Force and deformation are measured and displayed grafically. Figure 4 exemplarily shows the reaction force as a function of the deformation of the fender. The characteristics of the curve can be attributed to the material properties and the fender geometry.

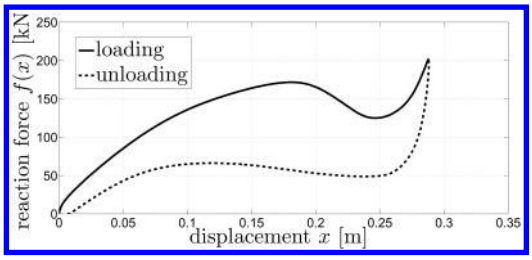


Figure 4. Loading behavior of a small Cone Fender.

During compression the reaction force is higher than during unloading which may be explained with the elastic after-effect. According to (Gerthsen & Vogel 1997) the elastic after-effect is defined as follows:

If an elastic material after loading needs some time to decrease, the material possesses an elastic after-effect. This is exactly what characterizes the fender's relaxation.

Immediately after the load piston is run up, it is measured that the fender has become smaller. At the very end of the phase of unloading ($x < 0.015$ m), the fender is out of touch with the piston and no reaction force is acting anymore (Fig. 4). The original size is not attained within the duration of the run but it rather takes several hours. Regardless of how many runs are executed, there is no accumulating plastic deformation of the fender.

3.2 *Theoretical analysis*

Each type of fender has a characteristic load and deflection behavior.

The integration of the load-deflection relationship yields the mechanical work or the absorbed energy $E(x)$ of the fender, respectively.

As shown in Fig. 4 the tested fender has a nonlinear characteristic and an elastic after-effect. This implies that the energy which is absorbed by the fender during compression is partially returned to the vessel and partially dissipated within the material (PIANC 2002). Both curves (loading and unloading) form a hysteresis. The area between those two curves is the dissipated energy, the part of energy which is not returned back to the vessel. The area under the unloading curve is the stored energy to push the vessel back.

The stored energy and the progression of the hysteresis depend on the deflection x as a result of the magnitude of the impact energy.

Hence, the potential energy $E(x)$ in the equation of motion attains in the phase of loading other values than in the phase of unloading. The potential energy $E(x)$ of the fender in the phase of loading is equal to the absorbed energy while the potential energy $E(x)$ in the phase of unloading is the stored energy, the difference of the absorbed and dissipated energy.

Eq. 3 is the equation of motion, whereas it is assumed, that the ship as well as the waterfront structure do not absorb energy, that means $C_s = 1$ and $C_c = 1$.

By integrating the equation of motion the law of conservation of energy is obtained (Eq. 4).

$$C\,m\,\ddot{x} + f(x) = 0 \tag{3}$$

where:

$f(x)$ = measured reaction-force [kN]
C = $C_e\,C_m\,C_s\,C_c$ [1]
m = ship mass [t]
$\ddot{x} = \frac{d^2x}{dt^2}$ = acceleration [m/s^2]

$$C\,\frac{m\,\dot{x}^2}{2} + E(x) = const = E \tag{4}$$

where:

$E(x)$ = potential energy [kNm]
$\dot{x} = \frac{dx}{dt}$ = velocity [m/s]

The sum of both terms in Eq. 4, here the addition of the kinetic and the potential energy, remains constant. The velocity of the berthing maneuver can be derived from Eq. 4:

$$\dot{x} = \sqrt{\frac{2}{C\,m}(E - E(x))} \tag{5}$$

This expression for the velocity is only be used for the process of berthing and for the duration of compression, respectively. The virtual mass factor C_m increases significantly when the ship is pushed back.

4 TRANSFER OF THE RESULTS

Experimental investigations of fenders for large ocean-going ships are not easy to realise, because of their large size and weight. The transportation is rather challenging and huge and powerfull testing devices are required. It is simpler to test small fenders and to transfer the results to identically built bigger size fenders.

The basis for the transfer of the results is the similitude theory. The evidence of physical similarity of two systems can be adduced by using the equation of motion. In the following the small fender is defined as system 1 and the bigger size fender is defined as system 2. Two systems are physically similar if the equation of motion of system 1 can be transferred to system 2 (Worthoff & Siemes 2012). In other words: If the equation of motion of system 1 is multiplied with a scalar λ and the result is the equation of motion of system 2, both systems are physically similar.

Therefore the system transformation is determined with the following skaling transformation to examine if the equation of motion remains invariant (Landau & Lifschiz 1962).

$$x_2 = \delta\,x_1 \tag{6}$$

$$t_2 = \beta\,t_1 \tag{7}$$

$$m_2 = \gamma\,m_1 \tag{8}$$

For a larger ship with the mass m_2, C has to be recalculated and is denoted as C' in the following.

Hence, Eq. 8 can be written by using the coefficients C and C' as follows:

$$C' m_2 = \gamma C m_1 \tag{9}$$

$$\Leftrightarrow \; M_2 = \gamma M_1 \tag{10}$$

Finally, the equation of motion of system 1 (Eq. 3) becomes the equation of motion of system 2 (Eqs. 11 or 12) with the derivatives:

$$\gamma M_1 \frac{d^2}{d(\beta^2 t_1^2)}(\delta x_1) + f_2(\delta x_1) = 0 \tag{11}$$

$$\Leftrightarrow \; \frac{\gamma\,\delta}{\beta^2} M_1 \frac{d^2}{dt_1^2} x_1 + f_2(\delta x_1) = 0 \tag{12}$$

The dynamic part of the bigger size system is determined by multiplying the dynamic part of the small system with the following factor:

$$\lambda = \frac{\gamma\,\delta}{\beta^2} \tag{13}$$

In the next step the reaction-force $f_2(\delta x_1)$ can be derived from $f_1(x_1)$.

Therefore the deformation of system 1 and of system 2, respectively, are calculated by using the principle of virtual displacements.

The deformation of system 1 is calculated as a function of the force $f_1(x_1)$, the deformation of system 2 as a function of the force $f_2(\delta x_1)$. If both equations are solved for the forces $f_1(x_1)$ and $f_2(\delta x_1)$ and afterwards the ratio of the forces is formed (Eq. 14) it is demonstrated that the ratio posesses the order 2 concerning the scaling of lenght.

$$\frac{f_2(\delta x_1)}{f_1(x_1)} = \left(\frac{x_2}{x_1}\right)^2 = \delta^2 \tag{14}$$

where:
$\delta =$ scaling of lenght

The equation of motion of system 1 can only be transformed to the equation of motion of system 2 if the ratio of the forces fullfilles Eq. 14.

To merge Eqs. 13 and 14, λ must additionally be defined as follows:

$$\lambda = \delta^2 \tag{15}$$

$$\Rightarrow \; \delta^2 = \frac{\delta\,\gamma}{\beta^2} \tag{16}$$

Eq. 16 points out that the scaling of mass γ and the scaling of length δ can be selected without restrictions. The scaling of time β follows as soon as γ and δ are set.

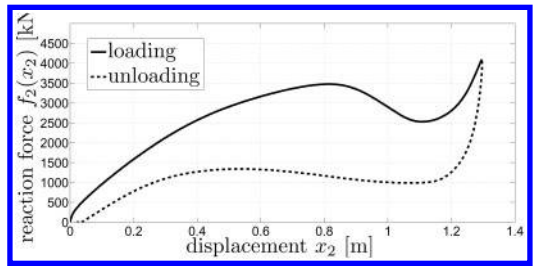


Figure 5. Behavior of fender 2 during loading and unloading.

Using Eqs. 13, 14 and 15, Eq. 12 results in:

$$\frac{\gamma\,\delta}{\beta^2} M_1 \frac{d^2}{dt_1^2} x_1 + \delta^2 f_1(x_1) = 0 \tag{17}$$

$$\Leftrightarrow \; \lambda M_1 \frac{d^2}{dt_1^2} x_1 + \lambda f_1(x_1) = 0 \tag{18}$$

If Eq. 18 is divided by λ, the equation of motion of system 1 is obtained, which means that the equation of motion remains invariant and the two systems are physically similar.

Eqs. 6 and 14 transform the load-deflection relationship of the tested small fender to a bigger size Cone Fender. The result is shown in Fig. 5.

The bigger fender (fender 2) is 1.8 m high and has a diameter of 2.25 m at the bottom.

Hence, this fender is 4.5-times bigger than the tested one and is able to withstand a very high kinetic energy.

The ratio of the reaction forces δ^2 of two systems (Eq. 14) and the principle of work and energy yields the ratio of energy:

$$\frac{f_2(x_2)}{f_1(x_1)} \frac{\Delta x_2}{\Delta x_1} = \left(\frac{x_2}{x_1}\right)^2 \frac{\Delta x_2}{\Delta x_1} = \frac{E_2(x_2)}{E_1(x_1)} = \delta^3 \tag{19}$$

With the ratio of the reaction forces δ^2 and the ratio of erergies δ^3 the following example can be treated:

The big fender is able to absorb a kinetic energy which is caused by a container vessel of the 6th generation with a length of about 395 m, a mass m_2 of about 250000 t and a berthing verlocity of $v_0 = 0.17$ m/s.

In this case the maximum reaction-force is obtained by Fig. 5 or from Eq. 20:

$$f_2 = f_1\,\delta^2 = 200 \cdot 4.5^2 = 4050 \text{ kN} \tag{20}$$

The ratio of energy and Eq. 5 imply that the velocity of a large ship progresses as follows:

$$\dot{x}_2 = \sqrt{\frac{2}{C_2\,m_2}(E_1 - E_1(x_1))\,\delta^3} \tag{21}$$

Figure 5 shows the velocity in the course of loading and unloading of a big fender. Although it is not quite correct to use the virtual mass factor C_m for the velocity of unloading, C_m remains fixed in the example to get a better understanding of the fender's potential energy.

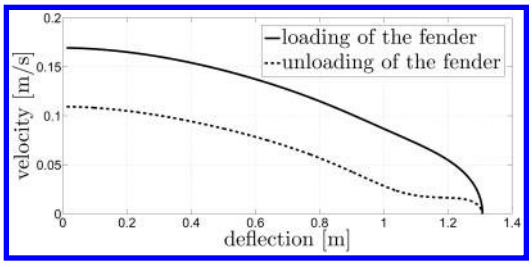


Figure 6. Velocity of the fender deflection.

5 SUMMARY AND CONCLUSION

In the previous sections it is shown how the results of the experimental investigations of small fenders can be transferred to identically built bigger size fenders.

An example for a berthing container vessel of the 6th generation illustrates that the maximum reaction force can be very high.

REFERENCES

Gaythwaite, J. (1990). *Design of marine facilities for the Berthing, Mooring, and Repair of Vessels*. VAN NOSTRAND REINHOLD Co. Ltd.

Gerthsen & Vogel (1997). *Gerthsen Physik*. Springer-Verlag.

Landau & Lifschiz (1962). *Lehrbuch der theoretischen Physik*. Akademie-Verlag Berlin.

PIANC (2002). *PIANC – Guidelines for the design of fender systems: 2002*. International Navigation Association.

Worthoff & Siemes (2012). *Grundbegriffe der Verfahrenstechnik, 3., vollstaendig ueberarbeitete Auflage*. WILEY-VCH Verlag GmbH & Co. KGaA.

Research and Applications in Structural Engineering, Mechanics and Computation – Zingoni (Ed.)
© 2013 Taylor & Francis Group, London, ISBN 978-1-138-00061-2

Response of a building envelope system to near field blast events

H.D. Hidallana-Gamage, D.P. Thambiratnam & N.J. Perera
Science and Engineering Faculty, Queensland University of Technology, Brisbane, Australia

ABSTRACT: This paper presents the methodology, numerical analysis and the initial findings of the research work conducted by the authors towards the safe and efficient design of building facades and their components to blast loads. Building facades using Laminated Glass (LG) windows are studied by considering their superior blast resistance compared to the other techniques used in building facades. The effects of support conditions on the blast response of LG windows are examined in the paper by varying the thickness of the structural sealant joints. The results from numerical analyses indicate that the LG panels with thick sealant joints undergo larger deformations absorbing higher blast energy compared to those with thinner sealant joints. The increase in the thickness of sealant joints causes significant reduction of the stresses close to the supports of LG panels improving their performance under blast loads.

1 INTRODUCTION

External facades forming a building envelope is the most vulnerable component in a building to blast loads. Glass facades are the most popular types among the building owners and architects for their architectural features and the aesthetical aspects. However, it is evident that more than 80–90% of injuries caused by blast loads are due to flying glass fragments and façade pieces (Muller & Wanger, 2006). If the building façade disintegrates, the blast pressure will enter the building causing injuries to the occupants and even structural collapse. Building facades should therefore be designed for a credible blast event to minimize, if not eliminate there consequences.

Research has investigated blast resistant window systems, as well as retrofit techniques to strengthen existing facades. Four different techniques commonly used in such building facades are window films, window catcher systems, laminated glass (LG) windows (or panels) and ballistic windows. Window films and catcher systems are especially used to retrofit existing windows. Window films are cheap, but usually the life span is less, as they degrade when exposed to the Ultraviolet (UV) light. On the other hand, window catcher systems affect the appearance of a building as they are attached inside the building façade. Ballistic windows are capable of resisting very high loads and are usually used in bullet resistant windows. However, they are very expensive and also transfer high loads to the window frames. LG windows are energy absorbing and the most popular because of their capability to withstand high blast loads. This paper therefore illustrates the blast response of building facades using LG windows.

LG is made of several glass panes that are interconnected using one or more interlayers. Different glass types such as annealed, heat-strengthened or tempered glass are used in LG windows where the polyvinyl butyral (PVB) is usually used as the interlayer material. LG windows are mounted to the window frames using structural sealant joints. LG provides superior blast resistance compared to normal glass as the interlayer holds the glass panes even after the glass cracks. It has been shown that the post-crack load carrying capacity of a LG panel is considerably higher than that at the pre-crack phase (Cormie et al., 2009).

Design standards such as American Society for Testing and Materials F 2248-09 (ASTM F 2248-09, 2010) and Unified Facilities Criteria 3-340-02 (UFC 3-340-02, 2008) are used for designing glazed facades to blast loads. However, both standards are conservative as they are based on simplified single degree of freedom analysis. The ASTM F 2248-09 neglects the effects of interlayer in the analysis, while the UFC 3-340-02 is limited to design of monolithic thermally tempered glass. The UK Glazing Hazard Guide (UK Glazing Hazard Guide, 1997) considers both pre and post-crack load carrying capacity of LG and hence provides a more realistic design approach compared to the previous standards. However, it was established for only few window sizes available in the UK and is restricted to military use. This emphasizes the requirement for a rigorous and reliable analytical procedure to investigate the behaviour of building facades with LG windows to blast loads.

2 METHODOLOGY AND NUMERICAL ANALYSIS

2.1 *Methodology*

This research was initiated to investigate the behaviour of building facades with LG windows, and study the

influence of controlling parameters such as material and geometric properties, support conditions and energy absorption to establish a framework for their design for a credible blast event. The developed framework will optimize the building envelope as well as the structural framework of the building while providing adequate blast resistance. Following tasks are conducted during this research in order to achieve the desired outcomes.

1. Develop a rigorous analytical procedure for reliable design of building facade systems and components for the effects of near field blast events
2. Investigate the effects of facade size, glass pane thickness, interlayer thickness, bed width and thickness of structural sealant joints and the type of secondary supports using parametric studies to enhance the blast resistance, system performance and safety
3. Parametric study on properties of glass, interlayer and structural sealant materials to enhance the performance under blast loading
4. Investigate the performance of different facade systems such as Double Skin Facades (DSFs), Cable Net Facades (CNFs) and alternative combined systems using the outcome of abovementioned studies

2.2 *Numerical analysis*

Numerical analysis with finite element (FE) codes is a feasible method to analyse the response of LG windows under extreme loads. FE codes with explicit capabilities such as LS DYNA, ABAQUS ANSYS and EUROPLEXUX FE have been used to analyse their behaviour under blast and impact loads. The authors have developed and validated a FE based procedure to analyse LG windows under blast loads with LS DYNA FE code. Both three and two dimensional (3D and 2D) LG models are presented incorporating different material models. In the 3D LG models glass panes and interlayer are modelled with 3D solid elements using material model 110 for glass while using material model 24 for the interlayer. In the 2D LG models the whole LG panel is modelled with 2D shell elements using material model 32. In both 3D and 2D LG models the structural sealant joints are modelled with 3D solid elements using material model 24.

It was observed that the 3D LG models provide more accurate results and can be used to investigate the effects of geometric and material properties of different façade components. On the other hand, the 2D LG models provide reasonably accurate results consuming less computational time compared to the 3D LG models, and hence can be used to investigate the global behaviour of large façade panels. The 3D LG models are used in this paper to investigate the effects of support conditions of LG panels by varying the thickness of the structural sealant joints.

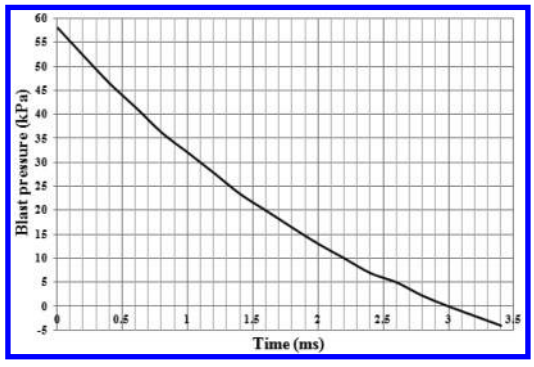


Figure 1. Blast pressure time-history curve.

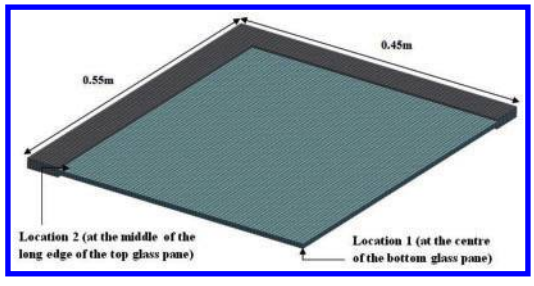


Figure 2. 3D view of the FE model.

3 EFFECTS OF STRUCTURAL SEALANT JOINTS

3.1 *Description of the case study*

(Kranzer et al., 2005) conducted experiments on LG panels with 1.1 m width, 0.9 m height and 7.5 mm thickness (3 mm annealed glass + 1.52 mm PVB + 3 mm annealed glass) under different blast loads. The numerical modelling techniques used in this paper had been validated using the results from one of them involving a free field blast test (FX005) and were presented in a previous research work. The experiment was conducted under a blast load with a maximum positive blast pressure of about 58kPa and positive load duration of about 3 ms. The blast pressure time-history curve of the experiment is shown in Figure 1.

The experiments were carried out according to (BS EN 13541, 2001) which states that the test panels should be clamped using rubber strips having about 50 mm width and 4 mm thickness. BS EN 13541: 2001 states that the thickness of rubber strips should be in the range of 3–5 mm. However, FE analyses were carried out by taking the thickness of the rubber strips as 3, 4, 5 and 6 mm to investigate the effects of thickness of these strips on the behaviour of the LG panel. The 3D LG model mentioned in section 2.2 was used in the FE analysis where one-quarter of the test panel was modelled by considering symmetry conditions. The blast load was applied uniformly on the top glass pane and the 3D view of the FE model is shown in Figure 2. Material properties required in the FE analysis for glass, PVB and the rubber sealant were obtained

Table 1. Material properties of glass, PVB and rubber sealant

Material property	Glass	PVB	Sealant
Density (kg/m^3)	2500	1100	1100
Young's modulus (MPa)	72000	530	2.3
Poisson's ratio	0.22	0.485	0.495

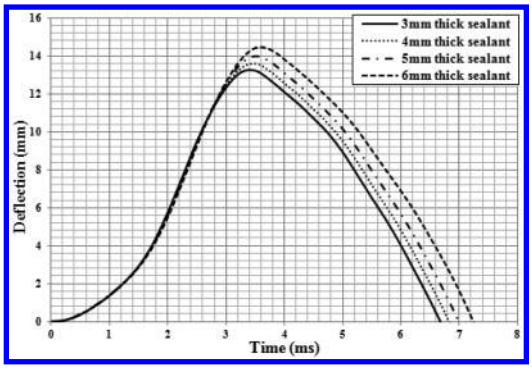


Figure 3. Deflection-time history curves at the centre for different thicknesses of sealant joints.

from the literature and are given in Table 1. (Hooper et al., 2012) mentioned that dynamic breaking strength of annealed glass can be about 80 MPa under blast loads, and was taken as the tensile strength (T) of the glass during the FE analyses.

3.2 *Results and discussion*

Results from FE analysis for deflections and principal stresses at critical locations as well as the total energy absorption of the FE models are presented. It could be noted that all the deflections presented in this paper are those normal to the plane of the LG panel at its initial stage. Figure 3 illustrates the variation of the deflection at the centre of the LG panel for different thicknesses of the structural sealant joints. Maximum deflection corresponding to LG panel with 3 mm thick sealant joints is 13.25 mm. It increased to 13.62, 13.98 and 14.45 mm when the thicknesses of the sealant joints are taken as 4, 5 and 6mm respectively. The increases in the maximum deflections are about 2.8, 5.5 and 9.1% respectively compared to that of LG panel with 3 mm thick sealant joints. It is clear that the increase in the thickness of the sealant joints increases the flexibility of the LG panels allowing them to undergo large deformations.

Figure 4 illustrates the variation of the deflection at the middle of the long edge of the top glass pane (refer location 2 in Fig. 2) for different thicknesses of the sealant joints. Maximum deflections occurred at about 4.5 ms in each case and there is a significant increase in those with the increase in the thickness of the sealant joints. The lowest maximum deflection, which is about 0.26 mm, occurs for the LG panel with

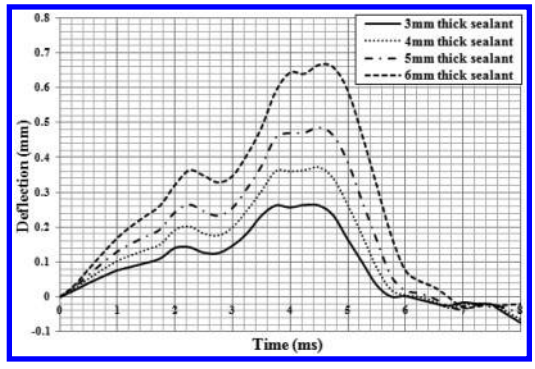


Figure 4. Deflection-time history curves at the middle of the long edge of the top glass pane (at location 2) for different thicknesses of sealant joints.

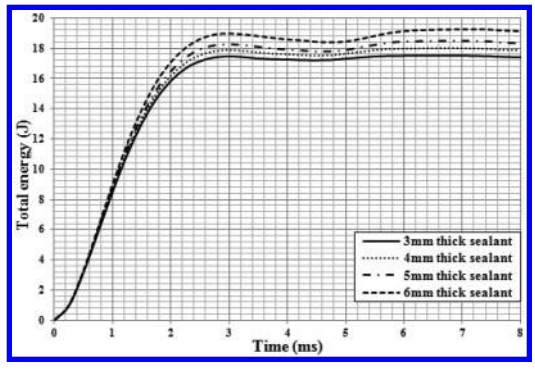


Figure 5. Total energy-time history curves for different thicknesses of sealant joints.

3 mm thick sealant joints. It increased to about 0.37, 0.49 and 0.67 mm when the thicknesses of the sealant joints are taken as 4, 5 and 6 mm respectively. The increases in the maximum deflections are about 42, 88 and 158% respectively compared to the value obtained for the LG panel with 3 mm thick sealant joints.

Figure 5 illustrates the total energy-time history curves for different thicknesses of sealant joints. The total energy increases rapidly until about 3 ms which is equal to the positive load duration of the blast load, and then becomes a constant value thereafter for each case. It is clear that the total energy absorbed by the FE models increases with the increase in the thickness of the sealant joints. The total energy absorbed by the LG panel with 3 mm thick sealant joints is about 17.46J. It increased to about 17.98, 18.5 and 19.25J when the thicknesses of the sealant joints are taken as 4, 5 and 6 mm respectively. The increases in the total energy are about 3, 6 and 10.3% respectively compared to the value obtained for the LG panel with 3 mm thick sealant joints.

Figure 6 compares the maximum principal stress variations at the centre of the bottom glass pane (refer location 1 in Fig. 2) for the LG panels with 3 and 6 mm thick sealant joints. The peak maximum principal stresses obtained from the FE models of those

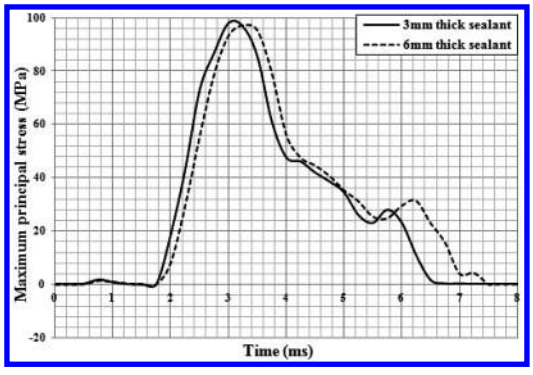


Figure 6. Maximum principal stress variations at the centre of the bottom glass pane (location 1).

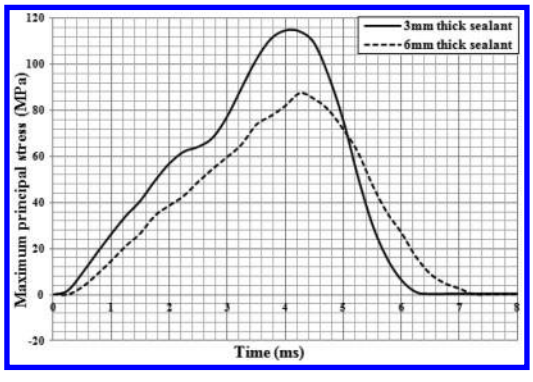


Figure 7. Maximum principal stress variations at the middle of the long edge of the top glass pane (location 2).

LG panels are 98.5 and 97.5 MPa respectively. Both occurred at about 3.1–3.4 ms and there is about 1% reduction in the peak maximum principal stress for the LG panel with 6 mm thick sealant joints compared to that with 3 mm thick sealant joints.

Figure 7 compares the maximum principal stress variations at the middle of the long edge of the top glass pane (refer location 2 in Fig. 2) for the LG panels with 3 and 6 mm thick sealant joints. The peak maximum principal stresses occurred at about 4.1–4.3 ms and corresponding values for LG panels with 3 and 6 mm thick sealant joints are about 116 and 88 MPa respectively. There is a significant reduction (about 24%) in the peak maximum principal stress for the LG panel with 6 mm thick sealant joints compared to that with 3 mm thick sealant joints. LG panel with 6 mm thick sealant joints undergoes excessive movements at the supports (as observed in Fig. 4) and hence causes a reduction in the tensile stresses along the edges of the top glass pane.

Even though a quarter of the LG panel was used for the FE analysis, maximum principal stress contours were plotted for the whole LG panel as shown in Figures 8–11. Maximum principal stress variations on the bottom glass pane at 3.25 ms for the LG panels with 3 and 6 mm thick sealant joints are shown in Figures 8 and 9 respectively. Stress variations at the middle of

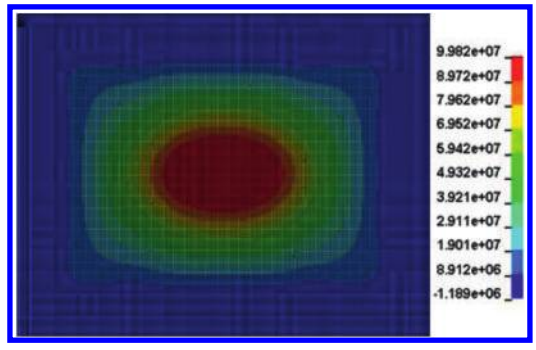


Figure 8. Maximum principal stress variation on the bottom glass pane at 3.25 ms for the LG panel with 3 mm sealant joints.

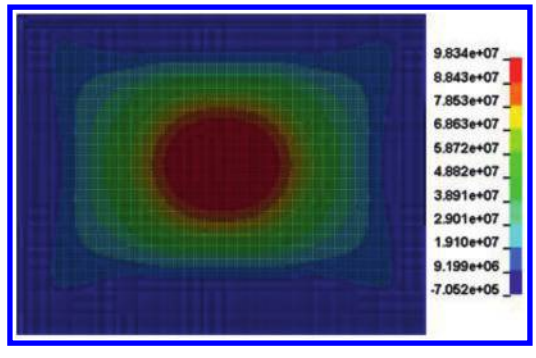


Figure 9. Maximum principal stress variation on the bottom glass pane at 3.25 ms for the LG panel with 6 mm sealant joints.

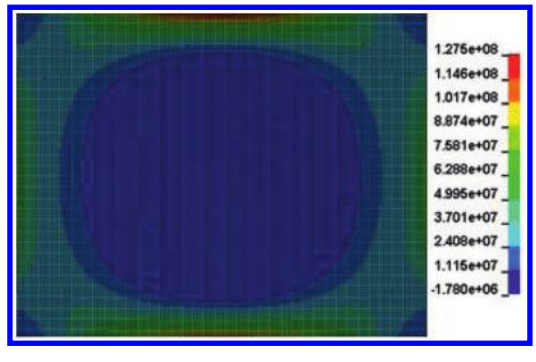


Figure 10. Maximum principal stress variation on the top glass pane at 4.25 ms for the LG panel with 3 mm sealant joints.

the bottom glass pane are similar in both figures, but the LG panel with 6 mm thick sealant joints shows an increase in stress distribution towards the supports.

Maximum principal stress variations on the top glass pane at 4.25 ms for the LG panels with 3 and 6 mm thick sealant joints are shown in Figures 10 and 11 respectively. It is clear that there is a significant reduction in the maximum principal stress along the edges of the LG panel with 6 mm thick sealant joints.

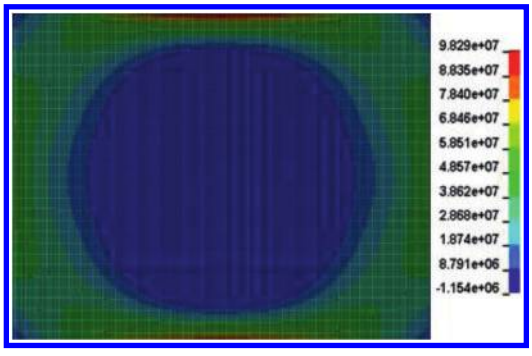


Figure 11. Maximum principal stress variation on the top glass pane at 4.25 ms for the LG panel with 6 mm sealant joints.

This might be due the increase in stress distribution throughout the perimeter of the LG panel with 6 mm thick sealant joints, than gathering the stresses into critical regions as observed in the LG panel with 3 mm thick sealant joints.

4 CONCLUSIONS

The results form FE analyses indicate that the increase in the thickness of the sealant joints causes an increase in the maximum deflection as well as the energy absorption of the LG panels. LG panels with thick sealant joints have freedom to undergo larger deformations at the joints reducing the stresses close to their supports and hence provide superior blast resistance compared to those with thinner sealant joints. It is evident that the increase in the thickness of sealant joints or the flexibility at the supports of LG panels increases their performance under blast loads. The authors therefore believe that the cable net facades with LG windows will further improve their performance as the cable net can itself undergo large deformations, and this will be investigated in the later part of the present research.

REFERENCES

ASTM F 2248-09: 2010. Standard Practice for Specifying an Equivalent 3-Second Duration Design Loading for Blast Resistant Glazing Fabricated with Laminated Glass. West Conshohocken, PA: ASTM International.

BS EN 13541: 2001. Glass in Building – Security Glazing – Testing and Classification of Resistance against Explosion Pressure. London: British Standards Institution.

Cormie, D., Mays, G. & Smith, P. 2009. *Blast Effects on Buildings*: Thomas Telford Services Ltd.

Hooper, P. A., Sukhram, R. A. M., Blackman, B. R. K. & Dear, J. P. 2012. On the Blast Resistance of Laminated Glass. *International Journal of Solids and Structures* 49: 899–918.

Kranzer, C., Gürke, G. & Mayrhofer, C. 2005. Testing of Bomb Resistant Glazing Systems: Experimental Investigation of the Time Dependent Deflection of Blast Loaded 7.5 mm Laminated Glass. *Glass Processing Days 2005*, August 2005. Germany.

Müller, I. R. & Wanger, M. 2006. Computation of Blast Resistant Window and Facade Constructions, August 2006.

UFC 3-340-02: 2008. Structures to Resist the Effect of Accidental Explosions. Washington DC: US Department of Defense.

UK Glazing Hazard Guide: 1997. Glazing Hazard Guide, Cubicle Stand-Offs, Tables and Charts. SAFE/SSG. Explosive Protection. London. SSG/EP/4/97.

Research and Applications in Structural Engineering, Mechanics and Computation – Zingoni (Ed.)
© 2013 Taylor & Francis Group, London, ISBN 978-1-138-00061-2

Impact velocity and initial length influence on the crushing behaviour of TWCF open section members under axial impact

M. Kotełko & R.J. Mania
Łodź University of Technology, Department of Strength of Materials, Łódź, Stefanowskiego, Poland

M. Jankowski
Design & Research Center OKB, Brójce, Bukowiec, Rokicińska, Poland

ABSTRACT: The paper is devoted to the study of transition between progressive dynamic buckling and global bending failure of axially loaded open section steel columns subjected to the compressive impact force. Channel and top hat section are under investigation. An influence of the column initial length and impact velocity on the crushing behaviour (failure mode) is investigated. The analysis is performed on the basis of FE simulations and mainly experimental tests. The tests are realized on the drop hammer rig. Results of impact crushing tests carried out at different impact velocities on specimens of different length are presented. The impact tests are performed with the impact energy up to 5 kJ and impact velocity up to 10 m/s. Experimental results are compared with the results of the analytical calculations of critical (transition) buckling length based on the simplified theoretical model. The results are presented in load – time diagrams and failure patterns. Some conclusions concerning an influence of the impact velocity upon the final mode of failure related to the energy absorption capability of columns are derived.

1 INTRODUCTION

Dynamic buckling response of thin-walled structural members subjected to impact, axial compressive load has been investigated extensively by many researchers. In recent years some research have been carried out into the transition from progressive local buckling to global bending failure mode in thin-walled columns (bars) under axial impact. Such a transition is observed in the stage of collapse of relatively long bars and at impact velocities higher than a certain 'critical' one. Determination of 'limit' or 'critical' values of bar's length and impact velocity is still an open question. Since a transition from local progressive buckling to global bending leads to a significant decrease of energy absorption capability, the determination of a threshold criterion between those two failure modes is of crucial importance.

Experiments carried out on axially impacted circular tubes by Alves and Karagiosova (2004) and channel – section columns by Teramoto (2004) show, that the critical buckling length depends on initial impact velocity and material parameters. Research into analytical solutions of the problem was carried out by Alves and Karagiosova (2004), who proposed three theoretical models of dynamic buckling of circular tubes subjected to axial compressive force. There are three different theoretical "rod models" proposed, namely; the Euler buckling model (Fig. 1a), the three-link model (Fig.1b) and the "two-phase deformation model" taking into account inertia effects and allowing one to analyze an influence of initial velocity on the critical buckling length. The models have been derived for the circular tube. Two first models were adopted by Kotełko and Mania (2012) for the case of an arbitrary open section column, who presented results of preliminary impact tests of open section members.

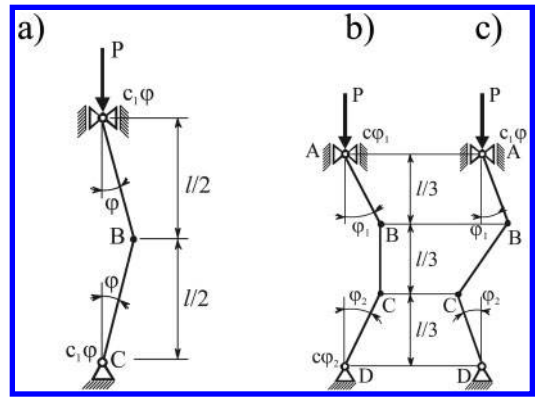


Figure 1. Collapse modes of "rod" models […]: a) – Euler buckling mode ($L^1_{cr(}$) , b) – three-link failure mode I. ($L^2_{cr(}$), c) – three-link failure mode II. ($L^3_{cr(}$).

These models are shown in Fig.1 with the notation of critical lengths corresponding to them. Table 1. shows relations describing those three cirical lengths.

Table 1. Critical buckling lengths

No	
1	Euler dynamic buckling mode: $L_{cr}^1 = \sqrt{\frac{6E_r I}{A\sigma_0}}$
2	Three-link first dynamic buckling mode: $L_{cr}^2 = 3\sqrt{\frac{E_r I}{A\sigma_0}}$
3	Three-link dynamic second buckling mode: $L_{cr}^3 = \sqrt{\frac{15E_r I}{A\sigma_0}}$

Where: A – sectional area, I - sectional moment of inertia, E – Young modulus, E_t - tangent modulus, σ_0 - yield stress.

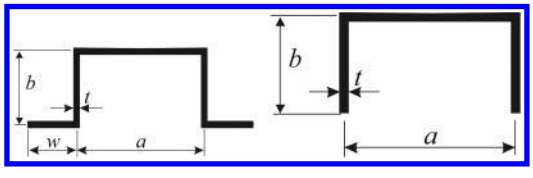


Figure 2. Open section members under investigation.

Detailed derivations are given by Kotełko and Mania (2012).

The aim of the present study was the experimental investigation into an influence of impact velocity and initial length of open section columns shown in Fig.2, subjected to axial impact, upon their crushing behaviour (failure mode and energy absorption capability). Additionally, experimental validation of FE simulations and mainly verification of analytical models mentioned above, are carried out.

2 EXPERIMENTAL TESTS

2.1 *Experimental stand*

Experiments were carried out on the drop hammer rig (Fig. 3), which consists of the impactor of changeable mass, hoisting mechanism and release mechanism of the hammer as well as additional springs, which allow one to increase the energy of impact. The springs are driven by the separate driving system. All mechanisms are controlled by a special computer program. The measuring system consists of piezoelectric force transducer, displacement transducer and accelerometer.

2.2 *Specimens*

Dimensions of specimens (columns), which have been tested are shown in Table 2. Impact tests were carried out on steel specimens of different a/b ratio and different length from 250 to 500 [mm], as well different impact velocities from 4 to 10 [m/s]. Wall thickness of

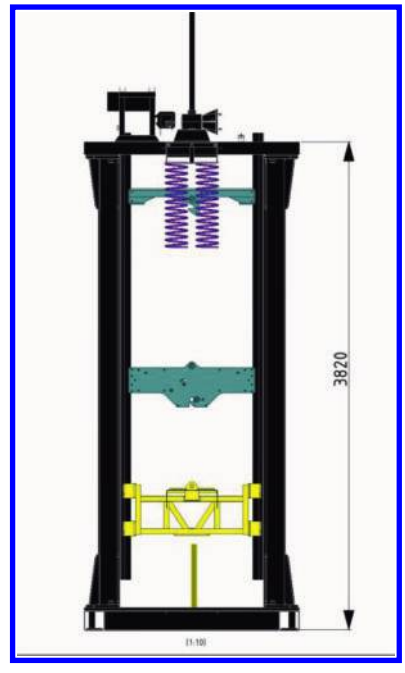


Figure 3. Experimental stand – drop hammer rig.

Table 2. Dimensions of specimens

No –	Not. –	a mm	b mm	w mm	L_{cr}^1 mm	L_{cr}^2 mm	L_{cr}^3 mm
1	A1	60	60	–*	306	374	483
2	B1	90	45	–	223	273	352
3	C1	135	45	–	236	289	373
4	D1	60	45	–	220	270	345
5	A2	60	60	15	352	431	557
6	B2	90	45	12	265	324	419
7	C2	135	45	12	282	346	447
8	D2	60	45	12	257	305	425
9	P1	75	37.5	–	173	211	273
10	P2**	30	30	8	182	222	287

* channel sections ($w = 0$)

all columns was $t = 1$ mm, except P2, were wall thickness was 0.6 mm. Altogether about 50 impact tests were carried out. All specimens were clamped in two parallel plates (situated in grooves made by milling machine) and spot welded , as shown in Figure 4.

Material data: $\sigma_0 = 286$ MPa (eccept P2), $E = 194000$ MPa, $E_t = 3000$ MPa, $\sigma_0 = 165$ MPa (for P2).

2.3 *Results of impact tests*

The results of tests indicate, that in most cases the progressive buckling mechanism was observed, even for long columns, of lengths much greater , than critical values shown in Table 1. However, in some cases global bending was observed and collapse modes were similar to the "rod" models shown in Figure 1. In some



Figure 4. Lay-out of the specimen.



Figure 5. Specimen P1, $L = 275$ mm > L_{cr}, a) $-v = 4$ m/s, b) $-v = 6$ m/s.

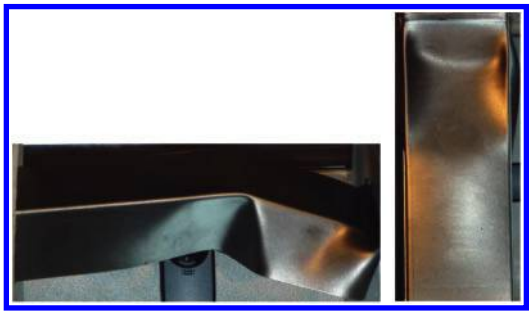


Figure 6. Specimen P1, $L = 375$ mm , quasi-dynamic test – $v = 600$mm/min.

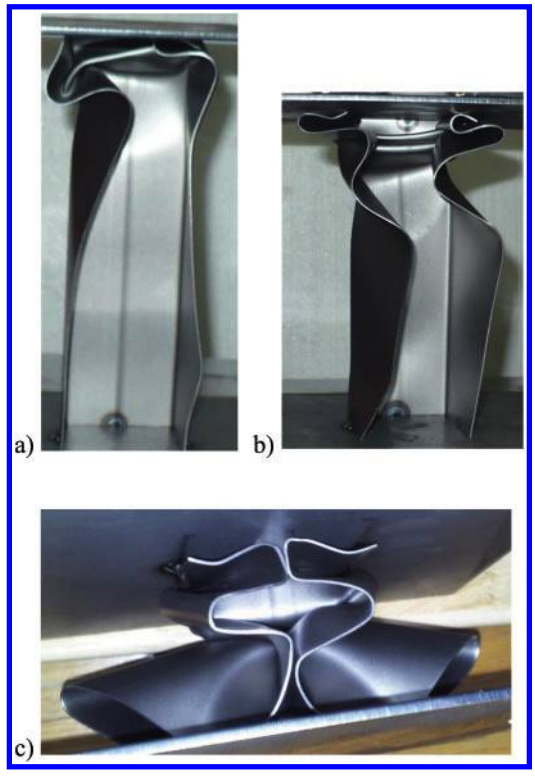


Figure 7. Specimens A1, $L = 250$ mmm: a) $-v = 4.5$ m/s, b) -v = 6 m/s, c) $-v = 9.5$ m/s.



Figure 8. Specimen B1, $v = 8$ m/s: a) $-L = 200$ mm, b) $-L = 300$ mm.

cases an anomalous failure mode was observed, similar to that reported by Teramoto (2004).

Figure 4 shows failure modes of specimens P1 (channel section, $a/b = 2$) for two different impact velocities. For lower velocity (Fig. 4a) the response is similar to the theoretical Euler buckling mode, but the column length is greater than L_{cr}^3. For the higher velocity the anomalous response is observed (Fig. 4b). The failure mode of the same specimen P1 at the impact velocity v = 4 m/s is compared with FE simulation result (Fig. 5). The agreement is satisfactory. The applied FE model and detailed simulation results for specimens P1 and P2 are reported by Kotełko & Mania (2012).

In order to illustrate the influence of loading velocity upon the failure mode, Figure 5 shows the failure mode of the specimen P1 under quasi-dynamic loading velocity. At this velocity the failure mechanism is nearly the same as under the static load. It was reported in details by Kotełko & Mania (2012). The influence of impact velocity upon the failure mode of specimens



Figure 9. Specimen D2, $L = 400$ mm, $v = 8$ m/s.

A1 is shown in Figure 7. All three failure modes can be classified as progressive buckling.

As was mentioned, only in some particular cases the global bending failure mode was observed, namely for channel sections B1 ($a/b = 2$). Figure 8 shows failure modes for two specimens: of length $L < L_{cr}$, were progressive buckling was observed and of length $L_{cr}^2 < L < L_{cr}^3$, were global bending mode II was observed.

In the case of top hat sections no global bending failure mode was recorded, even for the longest columns (Fig. 9). However, in that case for columns of $a/b \geq 1.5$, the failure mode, which may be classified as interaction of flexural-torsional and progressive buckling mode (Fig. 10) was observed.

The influence of a failure mode (progressive buckling or global bending) upon the load – versus time diagram and subsequently – upon the energy absorption capability , is show in Figure 11 and 12. As was mentioned, the global bending failure leads to the deterioration of the energy absorption capability (steep gradient of the first peak of load-time diagram).

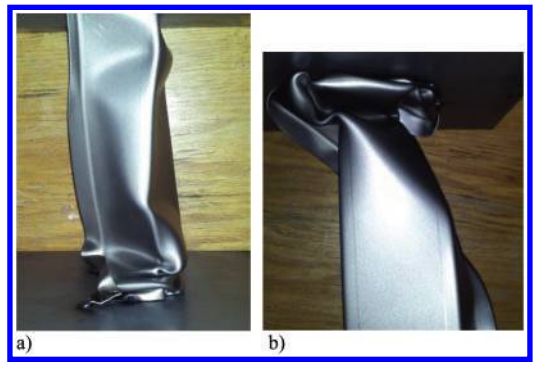


Figure 10. Specimen D2, $v = 8$ m/s, a) $-L = 250$ mm, b) $L = 400$ mm.

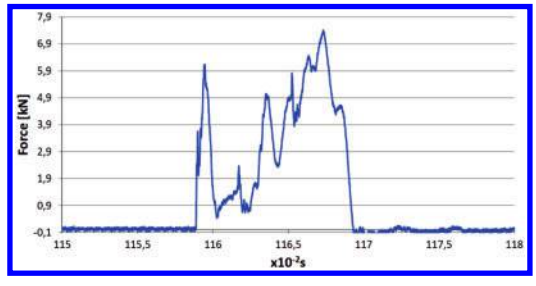


Figure 11. Load-time diagram of specimen B1, $L = 200$ mm $v = 8$ m/s (progressive buckling).

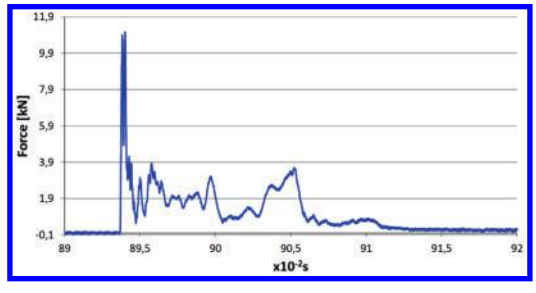


Figure 12. Load-time diagram of specimen B1, $L = 300$ mm, $v = 8$ m/s (failure mode II).

3 FINAL REMARKS

The "rod" model proposed by Alves & Karagiosova (2004) occurred to be not entirely adequate for open section members. The critical buckling length for dynamic buckling was not in a satisfactory agreement with the results of experiments.

In the case of channel section there are no clear indications into limit buckling length; in some cases an anomalous response against impact load is reported

In the case of top hat sections only the progressive buckling failure mode was observed. Additionally, in some cases, an interaction of progressive buckling and flexural-torsional buckling was recorded.

More clear indications of the threshold criterion (or criteria) of the transition between progressive buckling and global bending can be obtained from further research which would take into account larger diversity of impact velocities and dimensions. Also impact tests at different impact mass have to be performed in order to investigate inertia effects.

ACKNOWLEDGMENTS

This research has been conducted within the activity of the project N N501 215438 'Load-capacity and energy absorption in thin-walled structures under dynamic loading', funded by the Ministry of Science and Higher Education of Poland.

REFERENCES

Alves M. & Karagiosova D.: Transition from progressive buck-ling to global bending of circular shells under axial impact – part I: Experimental and numerical observations. *Int. J. of Solids and Struct.*, v. 41, 2004, pp. 1565–1580

Alves M. & Karagiosova D.: Transition from progressive buck-ling to global bending of circular shells under axial impact – part II: Mathematical model. *Int. J. of Solids and Struct*., v. 41, 2004, pp. 1581–1604

Kotełko M. & Mania R.J.: Quasi-static and dynamic axial crushing of TWCF open-section members, *Int. Journal of Thin-Walled Struc*., v.61, Dec. 2012, pp. 115–120

Kotełko M. & Mania R.J. : Investigation into different collapse modes of twcf open section members under axial impact, *Proc. of ICTWS'2012*, Glasgow December 2012, pp. 391–399

Teramoto S.S. & Alves M.: Buckling transition of axially impacted open shells. *Int.J. of Impact Eng., v.30, 2004*, pp. 124–12

Research and Applications in Structural Engineering, Mechanics and Computation – Zingoni (Ed.)
© 2013 Taylor & Francis Group, London, ISBN 978-1-138-00061-2

Computational modelling of reinforced concrete wall subjected to transformer tank rupture

M.A. Seman & M.A. Nasly
Civil Engineering & Earth Resources, Universiti Malaysia Pahang, Malaysia

Y.T. Feng
Civil & Computational Engineering Centre, Swansea University, Wales, UK

Z.M. Jaini
Civil & Environmental Engineering, Universiti Tun Hussein Onn Malaysia, Malaysia

ABSTRACT: Transformer is one of the vital equipment to provide reliable electricity. The worst of the transformer explosion may lead to the major blackout. Transformer explosion maybe due to, lack of maintenance or the problems inside itself. In the past, transformers were adjacent to each other and without a wall in between at substation. Nowadays, constructing reinforced concrete wall between transformers is in practice as protection precaution. Finite Element Method (FEM) software is used due to the capability of analyzing and simulating reinforced concrete structure subjected to high rate and short duration dynamic loading. The simulation results reveal the crack propagation behavior is identical for the different blast modes. The cracks start to occur at the bottom of the wall on the transformer side. Later follows with the crack propagations on the other side at about one third of the wall height in the curve shape.

1 INRODUCTION

Electric substation is the place where transformers are installed in order to transform the electric voltage from high to low level or otherwise before can be distributed to the respective customer. Typically, there are more than one transformers operating at one time to supply the electricity. These transformers are located adjacent to each other within the required distance. As a protection precaution, a wall is constructed in between the transformers. For comparison, in Brazil initially substations were operating for some years without a wall in between transformer (Duarte, 2004). Probably due to transformer fire at one of the substation, the firewall is constructed later. In the studies revealed, the wall can start to collapse after just one hour. In fact, the wall is designed for 4 hours fire resistance. This is because, the energy releases by the transformer explosion and the subsequent effect of fire did not take into consideration during the design stage.

This study presents the simulation result of the potential damage of the reinforced concrete wall due to transformer tank rupture. Three blast modes based on the point of transformer tank rupture are used for the modeling. Although, there is no direct experimental result available yet to validate the numerical result, the previous field test provided indirect result for the comparison.

2 TRANSFORMER TANK RUPTURE

In general, transformer explosions are originated from broken-down insulations, which may be caused by over load switching, lightning surges, deterioration of insulations, low level and moisture or acid contamination in the transformer oil. Inside the transformer, with the high temperature and energy released by the arc, the insulation oil will be decomposed to highly explosive gasses, mainly Hydrogen and Acetylene. This decomposition process will generate pressure inside the transformer tank until the tank cannot withstand and the tank rupture will be occurred (Surasit, 2008, Chille et al., 1998, GexCon, 2007).

According to the investigation report of Power Transformer Tank Rupture and Mitigation by the task force of IEEE Power Transformer Subcommittee, when the explosion happens, transformer is able to release arc energy between 1 MJ up to 147 MJ (IEEE, 2010). In the research works done by Sergi, it is discovered, for a 100 MJ electrical arc inside the oil, the first MJ creates 2.3 m^3, of explosive gas. The other 99 MJ add only 2 m^3. Obviously any electrical arc is very dangerous whatever its energy (SERGI, 2008).

The point of tank rupture will be varies for each transformer, normally occurred at the weakest point of the rectangular tank (IEEE, 2010), which is can be at; main cover to tank wall flange-welded joint; tank wall

corner-welded joint; tank wall to base plate-welded joint; high stress points at throats and large penetrations through the tank plate; and high stress at end of stiffeners where the end reaction force transmitted to the tank plate. Therefore, different blast modes are based on the point of rupture.

3 BLAST PRESSURE ANALYSIS

Detonation of high explosives usually produces an ideal blast wave, which is symmetrical. The pressure generated at distance R from the center of explosion originally at the ambient pressure, then instantaneously reach to peak pressure decay to ambient pressure. The resulting pressure can be described by the modified Friedlander equation, which is dependent on time. This equation allows some freedom to customize the pressure profile for any explosion at various distances from the source (Baker, 1973).

The Trinitrotoluene (TNT) mass equivalent used to model the effect of the explosion that the energy released is equated to the mass of TNT, where the impact will give the equivalent amount of damage. Once the equivalent is assumed, the variation of overpressure and impulse will be determined according to a graph or related equation (Philips et al., 1994). For the transformer tank rupture, the highest arc energy reported is used to calculate TNT equivalent masses (W_{TNT}) for further blast analysis.

$$W_{TNT} = \frac{explosion\ energy}{4.6MJ\ kg^{-1}} x\ efficiency\ factor \quad (1)$$

The blast scaling laws have been established since all blast parameters are primarily on the amount of energy released by a detonation in the form of a blast wave and distance from the explosion. The scaling law provides parametric correlations between a particular explosion and a standard charge of the same substance (Ngo et al., 2007).

Angle of incident is one of the factor affect the blast load on structural component. The angle of incident is the angle between outward normal to the direct vector from the explosive charge (Remennikov, 2007). This method is used to determine the blast load at the point of interest on the surface of the wall as stated in Equation 2.

$$Actual\ effective\ distance, R = \sqrt{{R_G}^2 + h^2} \quad (2)$$

3.1 *Blast calculation*

TM5-1300(UFC 3-340-02) – Structure to resist the effect of the accidental explosion by US Army Technical Manual (US Department of the Army, 1990) is used to predict the blast pressure on the structure. The scaled graph of the positive shock wave parameters for a hemispherical TNT explosion on the surface at sea level is used for the important parameters such as; peak reflected over pressure (P_r), peak over pressure (P_{so}), blast arrival time (t_a), positive phase duration (t_o) and blast velocity of wave front (U). With the data provided from the graph, the dynamic wind blast (P_q) as stated by Ngo is calculated by used Equation 3 (Ngo et al., 2007).

$$P_q = \frac{5{P_{so}}^2}{2(P_{so} + 7P_a)} \quad (3)$$

Kingery-Bulmash developed equations to predict air blast and it is widely accepted to predict free-field pressure and loads on structures (Kingery & Bulmash, 1984). The equation takes realistic approach and assuming an exponential decay of pressure in time as in the Equation 4.

$$P_t = P_{so}\left[1 - \frac{t - t_a}{t_o}\right] exp\left[-\frac{b(t - t_a)}{t_o}\right] \quad (4)$$

where P_t is the pressure at time t (kP_a); P_{so} is the peak incident pressure (kP_a); t_o is the positive phase duration (msec); b is the decay coefficient (dimensionless); and t_a is the arrival time (msec).To fully utilize the equation above, Equation 5 is used (Lam et al., 2004).

$$b = Z^2 - 3.7Z + 4.2 \quad (5)$$

3.2 *Pressure distribution*

The mapping method (Jaini & Feng, 2010) is used for the blast pressure distribution on the wall surface, where the arrival time (t_a) is used as the identification for the grouping purpose. In the computation sheet, the arrival time (t_a) for certain angles of incident will have a closer value. From these parameters, the different hemispherical radius can be mapped on the wall surface. The average value of blast pressure is taken for each groups based on the closest group of the arrival time (t_a). Figure 1 shows 18 different blast pressure time histories according to the blast energy of 147 MJ. The distance is 1 m from the center of explosion. Only the positive blast pressure phase is considered in this study. For each blast mode, on the blast pressure area, the blast pressure time history will be imposed accordingly.

There are three blast modes are assessed in the study, where the tank rupture is assumed to be occurred at; Blast mode A-at the bottom of the transformer tank; Blast mode B-at the height of 2.5 m from the bottom of the transformer tank; and Blast mode C-at the top of the transformer tank which is 4.4 m from the bottom of the transformer tank as shows respectively in Figures 2, 3 and 4.

4 COMPUTATIONAL MODEL

Elfen, a finite element package developed by Rockfield Software Limited in Swansea, UK (Rockfield) is used for the simulation in this research work. This

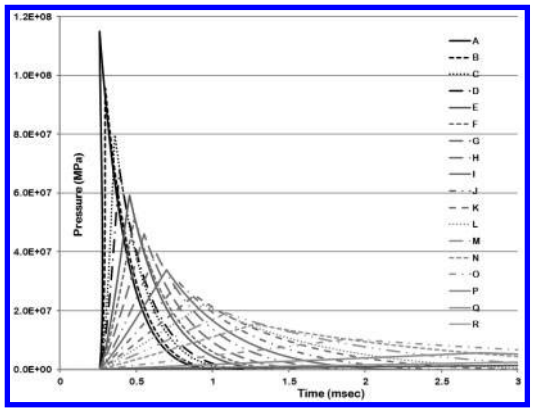


Figure 1. Blast pressure time history (P_t).

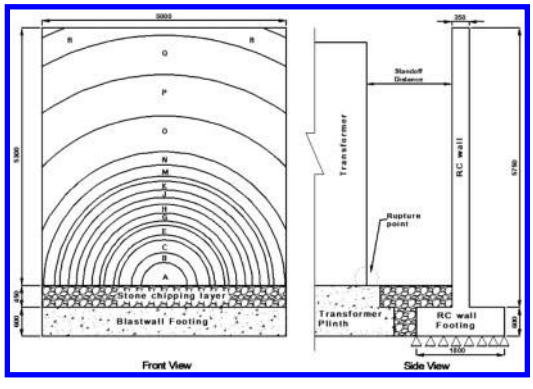


Figure 2. Blast pressure distribution for Blast mode A.

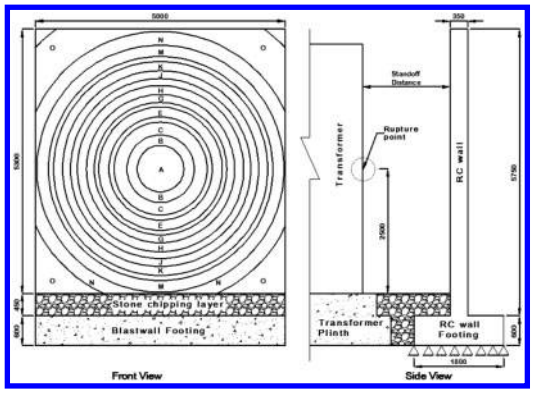


Figure 3. Blast pressure distribution for Blast mode B.

is because, Elfen has capability of analyzing and simulating the reinforced concrete structure subjected to high rate and short duration dynamic loading (Jaini & Feng, 2010, May et al., 2006).

The full scale of reinforced blast wall constructed by Tenaga Nasional Berhad (TNB) is modeled in Elfen. The wall constructed with Grade 30 (f_{cu} =30 N/mm^2) concrete and high yields steel (f_y =410 N/mm^2) bars. It is consists the reinforcement of 12 mm and 16 mm

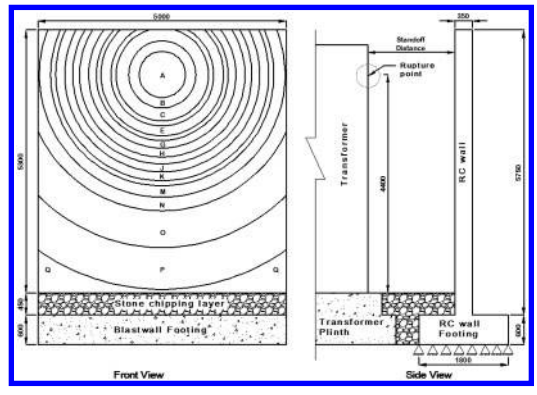


Figure 4. Blast pressure distribution for Blast mode C.

radius steel bars. The bars arrangement is 150 mm center to center with 25 mm reinforced cover. For the footing, both horizontal and vertical reinforcement arrangement used 16 mm bars. However for wall structure, only vertical arrangement used 16 mm bars.

Three-dimensional continuums with four-noded solid tetrahedral are used for both concrete and steel, where the size of 50 mm unstructured meshes is used. 3D beam elements with an elasto-plastic property are used to model reinforcement bars, and a perfect bond condition is assumed between the concrete and bars.

The Mohr-Coulomb criterion is used for the plastic strain of concrete, where it ranges between 0 to 100,000 s^{-1} and the tensile strength from 2.73×10^6 to 60.18×10^6 N/m^2. The implementation of this compression elacto-plastic material includes a cut-off tension in the form of complete Rankine tensile corner with fracture. According to the previous research work (Jaini & Feng, 2010), there is no explicit softening law included for tensile strength, while indirect softening does result from the degradation of cohesion. Fracture energy plays an important role to determine crack propagation. The fracture energy for concrete volume is taken between 75 and 100 N/m. For steel, the hardening properties are range from 0 to 0.0223 s^{-1} of plastic strains and the tensile strength in the range from 2.5×10^8 to 6.3×10^8 N/m^2. The Von-Mises criterion is applied for steel and utilized the backward Euler stress update algorithms. This rate independent model implemented in form of a nonlinear isotropic hardening form, where piecewise linear hardening is specifies using hardening material and hardening properties.

5 RESULT AND DISCUSSION

The computational result from this study revealed the propagation of the crack, fracture and displacement pattern at the specific time once blast load is applied on the structure. The crack propagation for all blast modes clearly shows, after the impact load is applied, the cracks start to occur at certain time instances at the bottom of the blast wall on the billet side (transformer side). This follows later with the cracks on the die

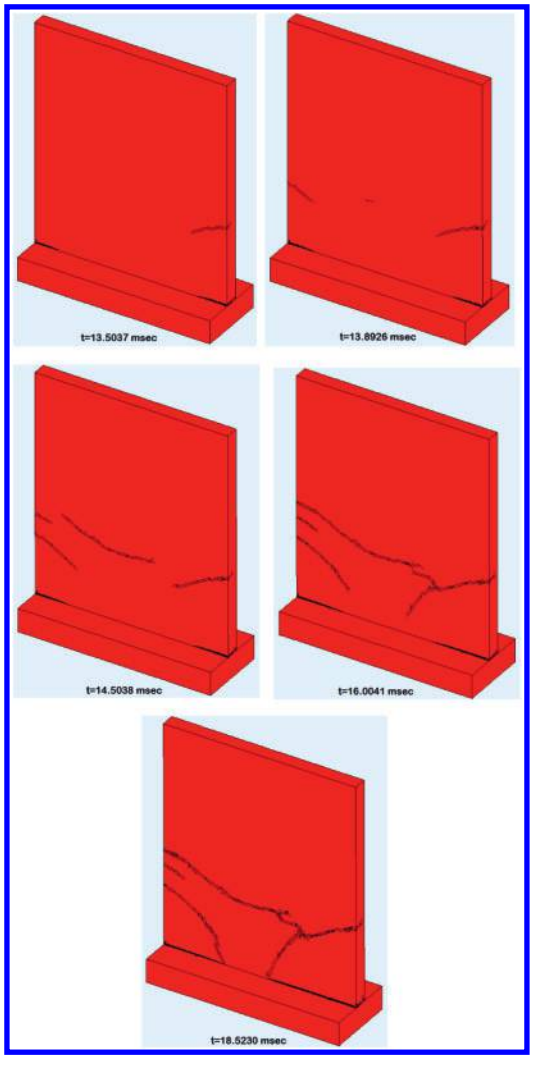


Figure 5. Crack propagations (Blast mode B).

side (other side) at about one third of the wall height. The propagations of the cracks then continue to move downwards to the center of the blast wall at the bottom part in the curvy shape. It is clearly discovered, the Blast mode B gives the worst scenario due to the transformer tank rupture at certain height. Figure 5 shows the crack propagation for Blast mode B, where clearly stated at the time instance when the crack start to appear. At the end of the simulation up to approximately 18 msec, the maximum displacements recorded are 22.51 mm, 24.05 mm and 17.29 mm for Blast mode A, B and C respectively.

Although there is no attempt yet done on the exact type on the wall as simulated, the earlier test shows a favor agreeable based on the blast loading map and the post impact on the reinforced concrete wall (Culberston, 1997). The crack patterns show a similarity.

6 CONCLUSION

Finite element analysis of reinforced concrete wall with strip footing subjected to transformer tank rupture is presented. The behavior and crack pattern of the reinforced concrete wall obtained from the present study is acceptable. This is because, the mapping method and the assumption for the Elfen package used for this simulation have already proved in the previous research work. Where the simulation result shows the same crack pattern and behavior in comparison to the experimental work. Besides, the blast test done on reinforced concrete wall shows similarity in the crack pattern after the blast impact.

REFERENCES

Baker, W. E. (1973) *Explosions in Air*, University of Texas Press.

Chille, F., et al. (1998) Containment of blast phenomena in underground electrical power plants. *Advances in Engineering Software*, 29, 7–12.

Culberston, J. (1997) Case Study Relating Blast Effect Tests To The Events of April 19, 1995 Alfred P.Murrah Federal Building Oklahoma City, Oklahoma. Armanent Directorate Wright Laboratory Eglin Air Force Base.

Duarte, D. (2004) A performance overview about fire risk management in the Brazilian hydroelectric generating plants and transmission network. *Journal of Loss Prevention in the Process Industries*, 17, 65–75.

Gexcon (2007) Transformer explosions.

Ieee (2010) Investigation Report Power Transformer Tank Rupture and Mitigation Houston, Texas, Task Force of IEEE Power Transformer Subcommittee

Jaini, Z. M. & Feng, Y. T. (2010) Computational Simulation if Reinforced Concrete Slab Subjected to Blast Loading. *18th UK Conference on Computational Mechanics (ACME-UK)*. Southampton.

Kingery, C. N. & Bulmash, G. (1984) Airblast Parameters from TNT Spherical Air Burst and Hemispherical Surface Burst. *Report ARBL-TR-02555, U.S. Army BRL, Aberdeen Proving Ground, MD*.

Lam, N., et al. (2004) Responce Spectrum Solutions for Blast Loading. *Electronic Journal of Structural Engineering*, 4.

May, I. M., et al. (2006) Reinforced concrete beams under drop-weight impact loads. *Computers & Concrete*, 3, 79–90.

Ngo, T., et al. (2007) Blast Loading and Blast Effects on Structures – An Overview. *EJSE International*, 76–91.

Philips, H., et al. (1994) *Explosions in the process industries*, Institution of Chemical Engineers, Rugby.

Remennikov, A. M. (2007) The state of the art of explosive loads characterisation. *AEES*. The Australian Earthquake Engineering Society.

Rockfield ELFEN Explicit User Manual Version 3.8. Technium, Swansea, UK.

Sergi (2008) Transformer Protector -The only solution against transformer explosions. Acheres, France, Sergi France.

Surasit, P. (2008) Fire Supression Failure Analysis On Substation Transformer Case Study Of Metropolitan Electricity Authority. Safety Department, Metropolitan Electricity Authority (MEA),Bangkok, Thailand.

Us Department of the Army, N., and Air Force (1990) TM 5-1300, The Design of Structures to Resist the Effects of Accidental Explosions.

Research and Applications in Structural Engineering, Mechanics and Computation – Zingoni (Ed.)
© 2013 Taylor & Francis Group, London, ISBN 978-1-138-00061-2

Blast test and numerical simulation of point-supported laminated glass curtain wall

S. Chen, C.G. Zhu & G.Q. Li
State Key Laboratory for Disaster Reduction in Civil Engineering, Tongji University, Shanghai, China

Y. Lu
The University of Edinburgh, Kings Buildings, Edinburgh, UK

ABSTRACT: To investigate the blast resistance of point-supported laminated glass curtain wall, 9 site blast tests were carried out, considering 2 types of glass thickness and 6 different TNT charges from 0.4 kg to 30 kg. The overpressure and displacement were measured and the failure mode was observed. The tests demonstrated that the overpressure suddenly increased and quickly decayed within a few milliseconds; the displacement response of the glass curtain wall increased with the increase in TNT charge and decreases with the increase of the glass thickness; the final failure mode was featured by tearing off of PVB at the support of the laminated glass panel while the glass shards still adhered to the PVB. Nonlinear dynamic finite element simulation agrees well with the results from the blast tests. Severe stress concentration has been predicted at the rim of the support holes and leads to the failure at these supports, and this also agrees with the failure mode observed from the blast test.

1 INTRODUCTION

Blast loading has recently been considered in the design of glass curtain wall for concerns over the fact that high-speed flying shard from glass curtain wall is one of the main reasons to cause the casualties in the event of a blast (Norville 2006, Morison 1999). To ensure appropriate design consideration, it is necessary to thoroughly understand the blast performance of glass curtain wall. In the literature, a certain number of numerical simulations on glass curtain wall subjected to blast loading have been reported (Dharani & Wei 2002, Krauthammer & Altenberg 2004, Deng & Jin 2009]. Dharani & Wei (2002) used a 3-D nonlinear finite element model to predict the failure probability of laminated architectural glass subjected to blast loading. Martin et al. (2012) reviewed the applicability of smeared model, layered shell model and 3D solid model in simulating the failure of the glass as well as of the interlayer and found that layered shell model is efficient. Tao (2011) studied the dynamic responses of monolithic and laminated glass by the indoor blast simulator and found that there are almost no spatters after the failure of laminated glass while monolithic glass was broken and the glass fragments splashed. On the other hand, however, few experimental studies have been published, due apparently to the complexities involved in conducting a blast test of this kind.

A series of field blast tests has recently been conducted on four-point-supported laminated glass curtain walls. An associated finite element simulation study has also been carried out to check against the test observations. This paper presents the test programme and the main results. The numerical model and some of the comparisons are also described and discussed.

2 BLAST TEST

2.1 *Test specimen*

The specimens in this test were a type of laminated glass consisting of two layers of tempered glasses and a layer of polyvinyl butyral (PVB) with dimension of 1000 mm × 1000 mm. Each specimen was four-point-supported, as shown in Figure 1. In each test, four glazing panels were installed as shown in Figure 2, and the one in the left upper corner was instrumented for response measurements. Two different glass thicknesses of 8 mm and 10 mm, respectively, were used, while the thickness of the PVB remains the same of 1.14 mm. The tests consisted of 2 stages, as summarized in Table 1. In the first stage, eight sets of blast tests with small charges were performed and no obvious damage was observed. In the second stage, a larger charge of 30kg TNT was detonated to load the specimens to failure, and thus obtaining the failure patterns. Table 2 lists the parameters of each TNT charge. In all tests, the explosive charge was placed at a fixed standoff distance of 5 m (See Fig. 2).

2.2 *Instrumentation*

Thirteen pressure transducers CY-YD-205 were installed on a steel panel fixed in a reinforced concrete frame having the same standoff distance with the glazing specimens. Figure 3 shows the layout of the pressure transducers. Five displacement transducers BWG4-100 were installed one of the glazing specimens, located on the left upper corner as

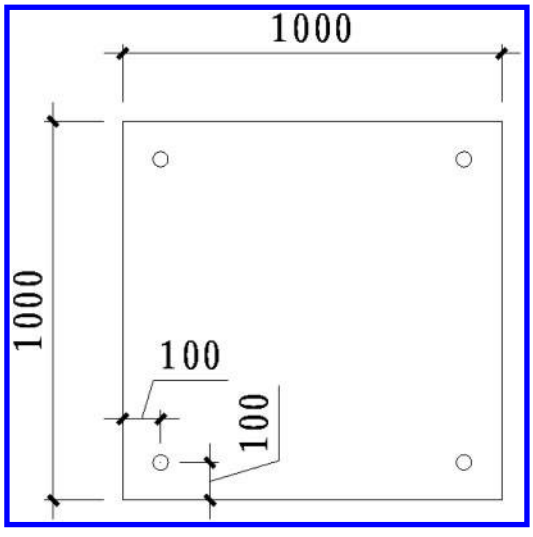


Figure 1. Dimensions of the specimen.

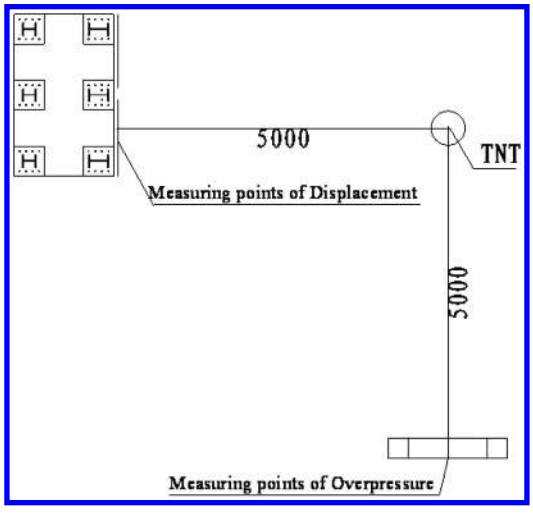


Figure 2a. Layout of blast test.



Figure 2b. Photo of blast test.

Table 2. Parameters of one TNT block.

Density/ g·cm^{-3}	length/ cm	width/ cm	thickness/ cm	weight/ g
1.63	5	5	10	400

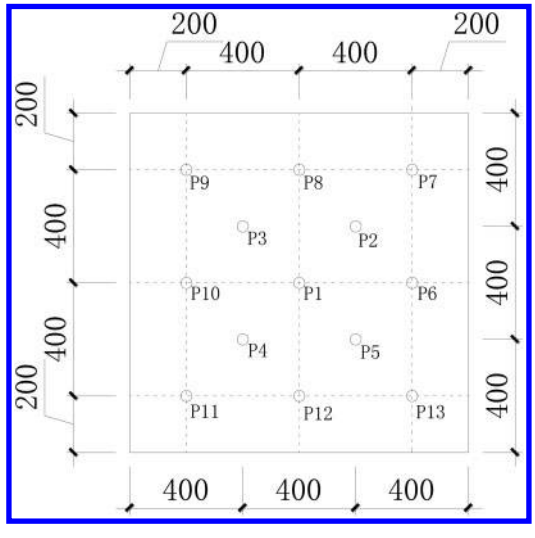


Figure 3. Arrangement of overpressure transducers.

Table 1. Summary of test groups.

Laminated Glass Specifications				
8 mm + 1.14 mm + 8 mm	10 mm + 1.14 mm + 10 mm	TNT Charge/kg	Standoff distance/m	Stage
B8-1	–	0.4	5	First stage – no visible damage
B8-2	B10-1	0.6	5	
B8-3	B10-2	0.8	5	
B8-4	B10-3	1.0	5	
–	B10-4	1.2	5	
–	B10-5	30	5	Failure stage

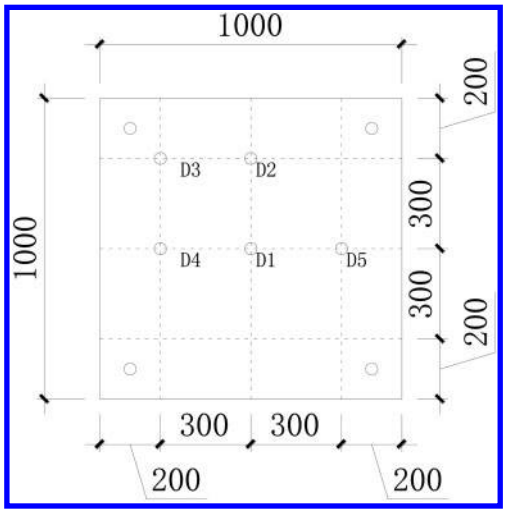


Figure 4. Arrangement of displacement transducers.



Figure 5. Failure at the support hole in case B10-5.

mentioned earlier, to measure the typical displacement responses of the specimens, as shown in Figure 4.

3 TEST RESULTS

3.1 *Failure modes*

The laminated glasses exhibited no visible damage after the stage 1 tests. Failure occurred when they were subjected to the stage 2 test. The failure mode of such four-point-supported glass curtain wall subjected to blast loading was featured by the tearing off of PVB at the supported areas while the glass shards still adhered onto the deformed PVB. This is clearly seen from Figure 5. Such a failure pattern illustrates clearly a significant advantage of the laminated glass for blast resistance.

3.2 *Overpressure measurement*

Overpressure-time curves at point P1, P8 and P12 of case B8-4 and case B10-5 are shown in Figure 6 and Figure 7, respectively. The Overpressure-time curves show a classical pattern in that there is a steep increase of the overpressure in the beginning and this is followed by a quick decay phase within a short duration of about several milliseconds.

The maximum, minimum and mean values of the 13 peak overpressures of each test set are listed in Table 3. It is obvious that the peak overpressure increases with the increase of the TNT charge.

The curves of point P1 in Figure 6 and Figure 7 have two peaks. The second peak appears to be the Mach stem that occurs when the reflected wave catches up with the incident wave and forms a third wave front.

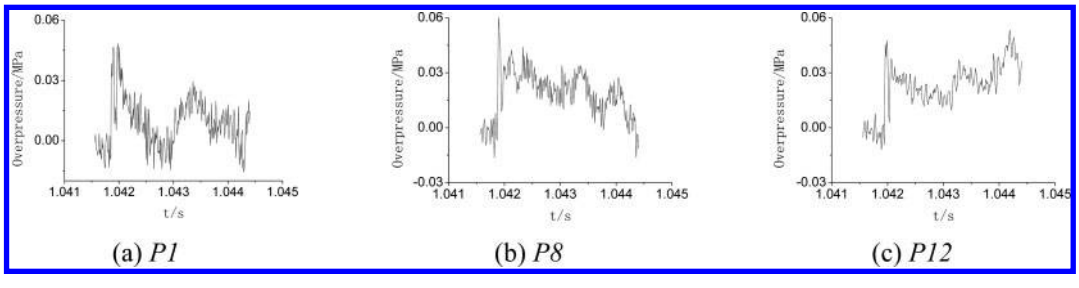


Figure 6. Overpressure-time curves for case B8-4 (TNT = 1.0 kg).

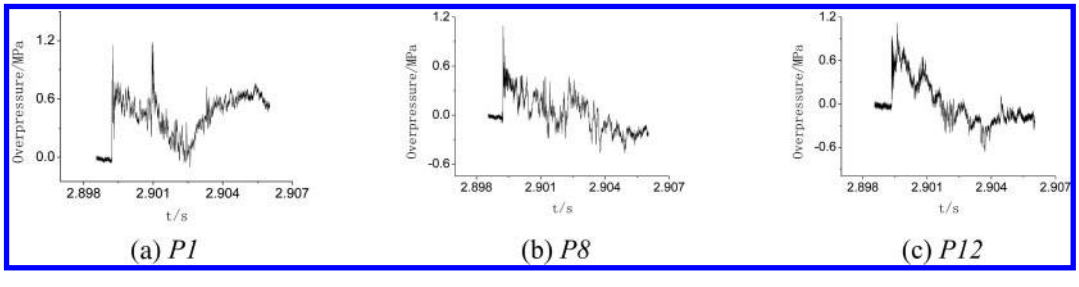


Figure 7. Overpressure time history curves for case B10-5 (TNT = 30 kg).

3.3 *Displacement response*

Typical displacement-time curves at point D1 for different cases are given in Figure 8. It can be observed that the laminated glass specimens mainly responded in the elastic range during the tests with small TNT charges (see Fig. 8a, b), whereas the specimens failed with a large residual displacement when subjected to the large TNT charge, as shown in Figure 8(c).

The maximum center displacement at point D1 of all the test cases are listed in Table 4 and the relationship between the maximum displacement and the TNT charge weights is shown in Figure 9. It can be observed that, for the same properties of the glazing panels the displacement response increases with the increase in the amount of TNT charge; an increase of the thickness of the glass improved the blast resistance behavior of the point-supported glass curtain wall.

4 NUMERICAL SIMULATIONS

4.1 *Finite element model*

Software ANSYS/LSDYNA is used for this simulation. Considering the symmetry, a quarter of a laminated glazing panel is modeled as shown in Figure 10 and symmetric constraints are imposed. SOLIDE164 elements are employed to model the glass and PVB. The glass is considered as elastic brittle material with an ultimate tensile strength of 84 MPa. The PVB is considered as visco-elastic material and a strain failure criterion is adopted with an ultimate strain of 1.0. The material properties are listed in Table 5 (after Wei (2010)). The blast load is idealized as a linear decaying curve.

Software A.T.BLAST is employed to calculate the peak overpressure and duration for the linear decayed curve. Table 6 shows a comparison between the peak overpressures from software prediction and the mean overpressures obtained from the blast tests (listed in Table 3). From the comparison, the overpressures from A.T. BLAST agree well with the test results. Thus, the peak overpressure and duration as obtained from the predictions were adopted for the numerical simulations and applied on the surface of the outer glass ply in the simulation.

Table 3. Peak overpressure for different test sets.

Case	TNT Charge/ kg	Peak Overpressure/kPa		
		Max	Min	Mean
B8-1	0.4	54.2	27.3	37.26
B8-2	0.6	59.4	30.3	45.57
B8-3	0.8	88.5	48.0	59.3
B8-4	1.0	62.2	44.5	55.34
B10-4	1.2	75.2	51.1	58.2
B10-5	30	1154.2	944.5	1064.4

*Case B10-2 did not collect any useful data of overpressure; the TNT charge weight of case B10-1 and case B10-3 are same to the case B8-2 and case B8-4 respectively, and the overpressures of the case B8-2 and case B8-4 are listed in the Table.

Table 4. Maximum displacement of the glass panel center D1.

Cases	TNT Charge/kg	Displacement/mm
B8-1	0.4	−5.612
B8-2	0.6	−8.936
B8-3	0.8	−12.238
B8-4	1.0	−14.771
B10-1	0.6	−6.683
B10-2	0.8	−9.670
B10-3	1.0	−11.762
B10-4	1.2	−13.174
B10-5	30	−82.4

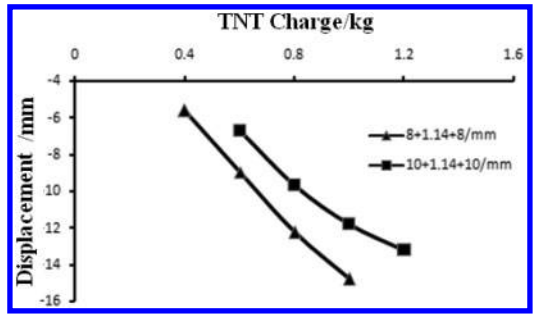


Figure 9. TNT charge-center displacement curve.

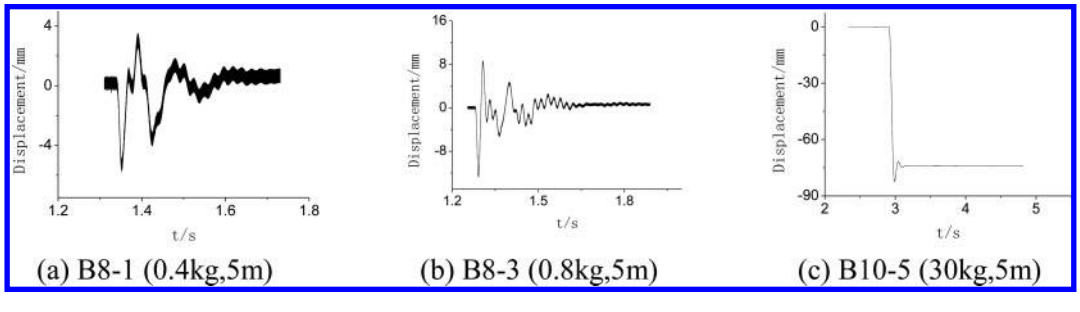


Figure 8. Time history of the center displacement.

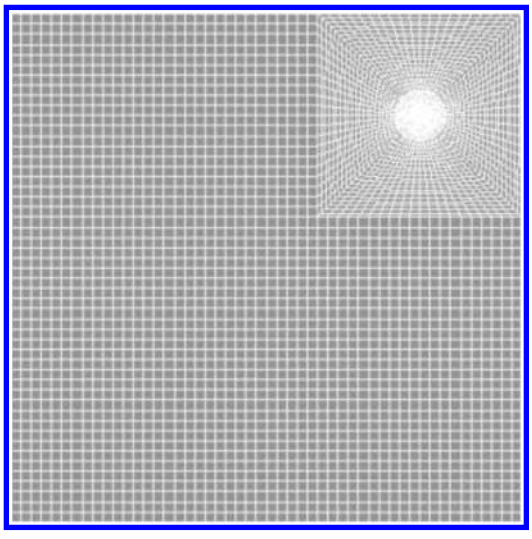


Figure 10. Finite element model.

Table 5. Material Properties.

Materials	Properties
Glass	Young's modulus, E = 72 GPa; mass density, $\rho = 2560\ kg/m^3$; Poisson's ratio, $\nu = 0.22$
PVB	Short term modulus,$G_0 = 1.1$ MPa; long time modulus, $G_\infty = 0.69$ MPa; bulk modulus, K = 10.63 MPa; mass density, $\rho = 1100\ kg/m^3$; decay factor, $\beta = 12.6\ s^{-1}$;

Table 6. Comparison of peak overpressure from tests and predictions.

TNT Charge/kg	Peak overpressure/kPa			Time/ ms
	Test	A.T. BLAST	Difference	
0.4	37.26	39.78	6.76%	2.06
0.6	45.57	49.16	7.88%	2.21
0.8	59.3	57.57	−2.92%	2.3
1.0	55.34	65.43	18.23%	2.36
1.2	58.2	72.88	25.22%	2.41
30	1064.4	1014.01	−4.73%	1.74

* Difference=(A.T. Blast results – Test results)/ Software results.

4.2 *Simulation results*

The center displacements from the simulation are compared with the test results in Table 7. The difference between the simulation results and the test results is less than 35%. The stress contour of case B10-5 is shown in Figure 11. Severe stress concentration is observed around the rim of the support hole.

The numerical simulation shows that damage initiates at the rim of the support and the final failure mode is the fracture of glass and tearing off of PVB extending from the support hole, as shown in Figure 12

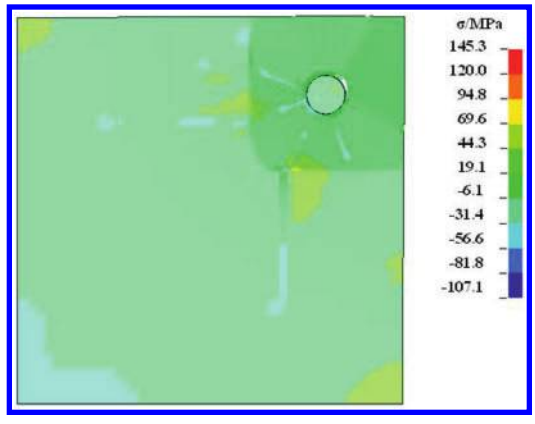


Figure 11. Stress contour (Case B10-5).

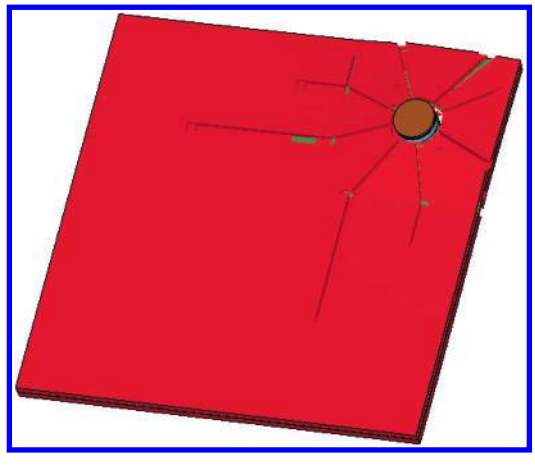


Figure 12. The failure of B10-5.

Table 7. Comparison of maximum center displacements from simulation and test.

TNT Charge/kg	8 mm + 1.14 mm + 8 mm			10 mm + 1.14 mm + 10 mm		
	Test results	Software results	Difference	Test results	Software results	Difference
0.4	−5.612	−6.165	9.85%	–	–	–
0.6	−8.936	−7.978	−10.72%	−6.683	−5.540	−17.1%
0.8	−12.238	−9.447	−22.81%	−9.670	−6.684	−30.88%
1.0	−14.771	−10.877	−26.36%	−11.762	−7.720	−34.36%
1.2	–	–	–	−13.174	−8.700	−33.96%

* Difference = (Software results – Test results)/ Test results.

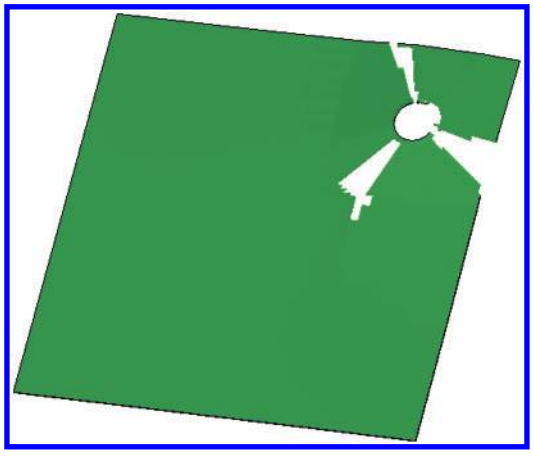


Figure 13. The failure of PVB of B10-5.

and Figure 13 respectively. This phenomenon agrees favourably with the test results.

5 SUMMARY

This paper investigates the blast resistance of pointed-supported laminated glass curtain wall. Main findings of this study are summarized as follows:

1) The overpressure curve has characteristics of an instantaneous rise, followed by a rapid decay and a relatively short positive phase.
2) Displacement response of the glass curtain wall increases with the increase of TNT charge; the increase of the glass thickness is useful to reduce the displacement response and increase the blast-resistance of the point-supported glass curtain wall.
3) The final failure mode may be characterized by the tearing off of PVB at the support hole while the glass shards still adhered on the PVB.
4) The difference between displacement response obtained by numerical simulation and blast test is less than 35%, which verified the effectiveness of the numerical model.

ACKNOWLEDGEMENT

The authors would like to acknowledge the financial support from National Science Foundation of China (51278365) and State Key Laboratory for Disaster Reduction in Civil Engineering in China (SLDRCE10-B-10).

REFERENCES

Deng, R, Jin X., Chen, J & Ding, J. 2009. Three Dimensional Numerical Simulation for Blast Analysis of Glass Curtain Wall. *Development and Application of High Performance Computing*, 26(1): 35–39. (in Chinese)

Dharani L R, Wei J, Ji F S. 2002. 'Failure analysis of laminated architectural glass panels subjected to blast loading.' 7th International Conference on Structures Under Shock and Impact. Montreal, Canada. Southampton. WIT Press, May 2002. pp. 37–46.

Hooper P. 2011, Blast performance of silicone-bonded laminated glass, PhD dissertation, Imperial College, UK.

Martin Larcher, George Solomos, Folco Casadei, Norbert Gebbeken 2012. Experimental and numerical investigations of laminated glass subjected to blast loading. International Journal of Impact Engineering, 39 (1): 42–50.

Krauthammer T, Altenberg A 2004. Negative Phase Blast Effects on Glass Panels. International Journal of Impact Engineering, 24: 1–17.

Morison C 1999. Response of glazed facades to blast loading, MSc dissertation, University of Westminster, UK.

Norville H. Scott, Edward J. Conrath 2006, Blast-Resistant Glazing Design. Journal of Architectural Engineering, Vol. 12(3): 129–136.

Tao Zhixiong 2011. Explosive Dynamic Response and Design Method of Explosion Resistance for Glass Curtain Wall, PhD dissertation, Tongji University,:51–74. (in Chinese)

Wei Ya 2010. Study on the Responses of Point-supported Glass Curtain Wall Subjected to Blast Loads. MSc dissertation, Tongji University: 82–83. (in Chinese)

Research and Applications in Structural Engineering, Mechanics and Computation – Zingoni (Ed.)
© 2013 Taylor & Francis Group, London, ISBN 978-1-138-00061-2

Thermodynamics-based constitutive modeling of coupled dissipative phenomena in engineering materials

H. Egner, W. Egner & M. Ryś
Institute of Applied Mechanics, Cracow University of Technology, Cracow, Poland

ABSTRACT: In the present paper a general phenomenological model, based on the irreversible thermodynamics, is formulated and used to describe the multi-dissipative material under the assumption of small strains. Two examples are presented: (1) modeling of thermo-plastic coupling in AISI L6 steel subjected to fatigue tests in non-isothermal conditions, and (2) thermodynamics-based modeling of coupling between plasticity, damage and phase transformation in 316L stainless steel at cryogenic temperatures.

1 INTRODUCTION

The increasing demands for high performance materials require the adequate constitutive modeling, as well as the appropriate predictions of the overall failure mechanisms under complex thermo-mechanical loading. When engineering materials classified as elastic-plastic are subjected to external loading, the material degradation connected with slip rearrangements of crystallographic planes through dislocation motion is observed at the macro-scale as plastic behavior. Another dissipative phenomenon is the development of micro-cracks and micro-voids. The nucleation, growth and interaction of these micro-defects under external loads result in a deterioration process on the macro-scale and, as a consequence, change of the constitutive properties of the material.

If the elastic-plastic-damage material is loaded so that not only inelastic strains develop, but also the temperature is changed, then thermo-elasticity, thermo-plasticity and thermo-damage are encountered, while not only the temperature itself but also the heating rate makes a significant impact on parameters that determine carrying capacity at elevated temperatures.

When FCC metals and alloys are loaded at very low temperatures another dissipative phenomenon is observed, which is plastic strain induced transformation from the parent phase (γ) to the secondary phase (α') . The phase transformation process leads to creation of two-phase continuum, where the parent phase coexists with the inclusions of secondary phase. Experimental results indicate the correlation between decreasing damage rate and increasing martensite content.

2 GENERAL MODEL OF DISSIPATIVE MATERIALS BASED ON IRREVERSIBLE THERMODYNAMICS

2.1 *Basic assumptions*

Continuum mechanics approach, applied in the present work, provides the state and evolution equations in the framework of thermodynamics of irreversible processes. The material heterogeneity (on the micro- and meso-scale) is smeared out over the representative volume element (RVE) of the piece-wise discontinuous material. The true distribution of micro-changes within the RVE, and the correlation between them are measured by the change of the effective constitutive properties.

In the case of infinitesimal deformation the total strain can be expressed as the sum of the elastic, ($\boldsymbol{\varepsilon}^E$), inelastic ($\boldsymbol{\varepsilon}^I$), and thermal strain ($\boldsymbol{\varepsilon}^\theta$).

The irreversible rearrangements of the internal structure can be represented by a group of state variables describing the current state of material microstructure: $\{\Lambda^k\}$, $k = p, d, ph, \ldots$ (p meaning plastic, d – damage, ph – phase change etc), where Λ^k may be scalars, vectors or even rank tensors. Another group of state variables consists of internal (hidden) variables corresponding to the modifications of loading surfaces: $\{h^k\} = \{r^k, \alpha^k_{ij}, l^k_{ijpq}, g^k_{ijpqmn}, \ldots\}$, where r^k is related to isotropic expansion of the loading surface, α^k_{ij} affects translatoric displacements of the loading surface, l^k_{ijpq} is a hardening tensor which includes varying lengths of axes and rotation of the loading surface, and g^k_{ijpqmn} describes changes of the curvature of the loading surface (distortion) related to k-th dissipative phenomenon (cf Egner, 2012). The complete

set of state variables $\{V_{st}\}$ reflecting the current state of the thermodynamic system consists of observable variables: elastic strain tensor $\boldsymbol{\varepsilon}^E$ and absolute temperature θ, and two groups of microstructural $\{\Lambda^k\}$ and hardening $\{h^k\}$ state variables:

$$\{V_{st}\} = \{\varepsilon_{ij}^E, \theta; \Lambda^k; h^k\},\ k=p, d, ph,\ldots \tag{1}$$

2.2 *Equations of the model*

By the use of state variables (1) the Helmholtz' free energy of the material can be written as a sum of elastic (*e*), plastic (*p*), damage (*d*), phase change (*ph*) etc. terms (cf Abu Al-Rub & Voyiadjis, 2003):

$$\rho\psi = \rho\psi(V_{st}) = \sum_{j=1}^{n} \rho\psi^j,\ \ j = e, p, d, ph,\ldots \tag{2}$$

The following state equations express the thermodynamic forces conjugated to state variables (1):

$$\sigma_{ij} = \frac{\partial(\rho\psi)}{\partial\varepsilon_{ij}^E}, s = -\frac{\partial\psi}{\partial\theta} \tag{3}$$

$$-Y^k = \frac{\partial(\rho\psi)}{\partial\Lambda^k}, H^k = \frac{\partial(\rho\psi)}{\partial h^k} \tag{4}$$

In the above equations s is specific entropy, Y^k stand for thermodynamic forces conjugated to microstructural state variables Λ^k, whereas H^k are hardening forces conjugated to hidden state variables h^k. To derive the kinetic equations the existence of several dissipation potentials F^k is assumed, corresponding to each k-th microstructural rearrangement (due to plastic flow F^p , damage growth F^d , phase change F^{ph} etc.) and defined independently but partly coupled.

The kinetic equations for state variables can be obtained by the use of the generalized normality rule (cf Chaboche, 1997; Egner, 2012):

$$\dot{\varepsilon}_{ij}^I = \sum_{k=1}^{n} \dot{\lambda}^k \frac{\partial F^k}{\partial\sigma_{ij}} = \dot{\lambda}^p \frac{\partial F^p}{\partial\sigma_{ij}} + \dot{\lambda}^d \frac{\partial F^d}{\partial\sigma_{ij}} + \dot{\lambda}^{ph} \frac{\partial F^{ph}}{\partial\sigma_{ij}} + \ldots \tag{5}$$

$$\dot{\Lambda}^k = \sum_{i=1}^{n} \dot{\lambda}^i \frac{\partial F^i}{\partial Y^k} = \dot{\lambda}^p \frac{\partial F^p}{\partial Y^k} + \dot{\lambda}^d \frac{\partial F^d}{\partial Y^k} + \dot{\lambda}^{ph} \frac{\partial F^{ph}}{\partial Y^k} + \ldots \tag{6}$$

$$-\dot{h}^k = \sum_{i=1}^{n} \dot{\lambda}^i \frac{\partial F^i}{\partial H^k} = -\left(\dot{\lambda}^p \frac{\partial F^p}{\partial H^k} + \dot{\lambda}^d \frac{\partial F^d}{\partial H^k} + \dot{\lambda}^{ph} \frac{\partial F^{ph}}{\partial H^k} + \ldots\right) \tag{7}$$

where $\dot{\lambda}^i$ are non-negative consistency multipliers and n is a number of dissipative phenomena, taking place in the material. For rate-independent problems the consistency multipliers may be calculated from the consistency conditions $\dot{f}^k = 0$, $k = 1,2,\ldots,n$.

The parameters $\dot{\lambda}^i$ are assumed to obey the classical Kuhn-Tucker loading/unloading conditions.

Table 1. State variables and thermodynamic forces for 2M1C model.

State variable	Conjugated force
ε_{ij}^E(elastic strain)	$\sigma_{ij} = E_{ijkl}(\theta)\varepsilon_{kl}^E$
θ(temperature)	s
$\alpha_{ij}^{(1)}$ (kinematic hardening)	$X_{ij}^{(1)} = \frac{2}{3}(C_{11}(\theta)\alpha_{ij}^{(1)} + C_{12}(\theta)\alpha_{ij}^{(2)})$
$\alpha_{ij}^{(2)}$ (kinematic hardening)	$X_{ij}^{(2)} = \frac{2}{3}(C_{22}(\theta)\alpha_{ij}^{(2)} + C_{12}(\theta)\alpha_{ij}^{(1)})$
$r^{(1)}$ (isotropic hardening)	$R^{(1)} = b_1(\theta)Q_1(\theta)r^{(1)}$
$r^{(2)}$ (isotropic hardening)	$R^{(2)} = b_2(\theta)Q_2(\theta)r^{(2)}$

3 MODELLING OF COUPLING BETWEEN DISSIPATIVE PHENOMENA IN ENGINEERING MATERIALS

3.1 *Thermo-viscoplastic coupling in AISI L6 hot work tool steel*

In this analysis the 2M1C model derived by Cailletaud & Sai (1995) and identified by Velay et al. (2006) to describe the elasto-viscoplastic behaviour of AISI L6 steel at different (but constant) temperatures, is extended to account for the effect of temperature change (nonisothermal conditions). The set of state variables and corresponding thermodynamic conjugated forces is given in Table 1.

Total strain is partitioned into an elastic, inelastic and thermal components: $\varepsilon_{ij} = \varepsilon_{ij}^E + \varepsilon_{ij}^I + \varepsilon_{ij}^\theta$, while inelastic strain can be partitioned itself in two different strain mechanisms: $\varepsilon_{ij}^I = A_1(\theta)\varepsilon_{ij}^{(1)} + A_2(\theta)\varepsilon_{ij}^{(2)}$.

The equations of the 2M1C model for isothermal case are in details presented in Velay et al. (2006). However, in nonisothermal conditions additional terms proportional to temperature rate appear in the evolution equations for thermodynamic conjugate forces, due to temperature-dependence of the material characteristics ($k = 1,2$; $l = 1,2$; $k \neq l$):

$$\dot{\sigma}_{ij} = (\dot{\sigma}_{ij})_{\dot{\theta}=0} - [-\frac{\partial E_{ijpq}}{\partial\theta}(\varepsilon_{pq} - \varepsilon_{pq}^I) + \frac{\partial\beta_{ij}}{\partial\theta}(\theta - \theta_0) + \beta_{ij}]\dot{\theta} \tag{8}$$

$$\dot{X}_{ij}^{(k)} = (\dot{X}_{ij}^{(k)})_{\dot{\theta}=0} + \frac{2}{3}(\frac{\partial C_{kk}}{\partial\theta}\alpha_{ij}^{(k)} + \frac{\partial C_{kl}}{\partial\theta}\alpha_{ij}^{(l)})\dot{\theta} \tag{9}$$

$$\dot{R}^{(1)} = (\dot{R}^{(1)})_{\dot{\theta}=0} + (\frac{\partial b_1}{\partial\theta}Q_{1\infty} + b_1\frac{\partial Q_{1\infty}}{\partial\theta})(1 - e^{-2\mu p^*})r^{(1)}\dot{\theta} \tag{10}$$

$$\dot{R}^{(2)} = (\dot{R}^{(2)})_{\dot{\theta}=0} + (\frac{\partial b_2}{\partial\theta}Q_2 + b_2\frac{\partial Q_2}{\partial\theta})r^{(2)}\dot{\theta} \tag{11}$$

3.1.1 *Discussion of results*

The numerical procedure based on the extended 2M1C model was built and verified for the isothermal case by comparing with the results presented in Velay et al. (2006). Good agreement was achieved.

Next the anisothermal fatigue test was subjected to numerical analysis, according to the strain and temperature controlling presented in Figure 1. A reversed strain cycles were considered with temperature changes taking place at the maximum total strain

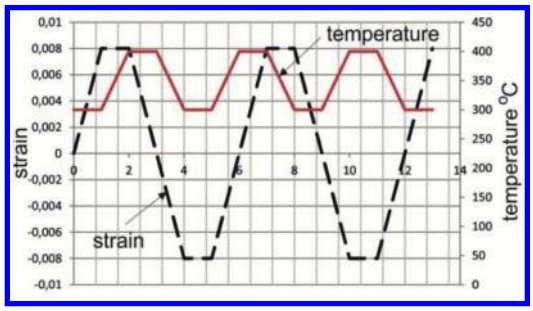


Figure 1. Anisothermal fatigue test: strain and temperature change.

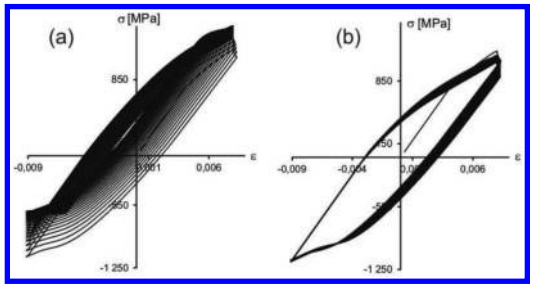


Figure 2. Hysteresis loops for (a) case 1; (b) case 2.

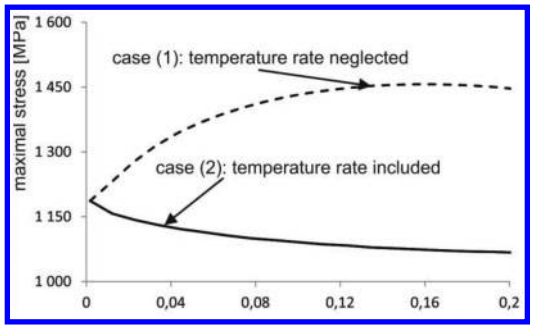


Figure 3. Evolution of maximal stress versus cumulated plastic strain for both cases.

(from low to high temperature) and at the minimum strain (from high to low temperature). During strain change the temperature is kept constant. Two cases were compared: (1) temperature rate terms in kinetic equations (8)-(11) neglected, and the influence of temperature changes accounted for only by changing material characteristics (case 1); (2) all temperature rate terms included (case 2). The stress-strain loops for both cases are presented in Figure 2a, b. Qualitatively different results were obtained: without temperature rate terms the response exhibits cyclic hardening due to unreasonable shift of hysteresis loops along the stress axis, while including additional temperature rate terms allows to preserve stable behavior (cyclic softening is observed). The results are confirmed in Fig. 3 showing the evolution of maximal stress versus cumulated plastic strain.

3.2 *Modeling of coupled dissipative phenomena in 316L stainless steel at cryogenic temperatures*

The RVE based constitutive model presented in the paper is based on the following assumptions:

- two-phase material is composed of the elastic-plastic-damage austenitic matrix and brittle martensitic platelets,
- current damage state, both in austenitic matrix and in martensitic inclusions, is described by the use of the second-order classical damage tensors,
- rate independent plasticity is applied,
- small strains are assumed,
- mixed isotropic/kinematic plastic hardening affected by the presence of martensite fraction is included,
- the material obeys the associated flow rule,
- isothermal conditions are considered.

The current state of the material in isothermal conditions is described by the following set of state variables: $\{V_{st}\} = \{\varepsilon_{ij}^E; D_{ij}^{\gamma}, D_{ij}^{\alpha'}, \xi; \alpha_{ij}^p, r^p\}$, where the elastic strain tensor ε_{ij}^E is the observable variable; D_{ij}^{γ} and $D_{ij}^{\alpha'}$ are second order tensors describing the current state of ductile damage in austenitic matrix and brittle damage in martensitic inclusions, respectively, ξ stands for the scalar variable reflecting the current state of phase transformation; α_{ij}^p and r^p denote internal variables related to kinematic and isotropic hardening of the material. The total material degradation in the RVE is described by the damage tensor $\mathbf{D}^{avg}$, being a superposition of the ductile part $\mathbf{D}^{\gamma}$ and brittle part $\mathbf{D}^{\alpha'}$. In general, one can introduce a function $m(\xi)$, such that $m(0) = 0$ and $m(1) = 1$, to define a general mixture rule: $D_{ij}^{avg} = [1 - m(\xi)]D_{ij}^{\gamma} + m(\xi)D_{ij}^{\alpha'}$.

The Helmholtz free energy of the material can be written as a sum of elastic (E), inelastic (I) and chemical (CH) terms:

$$\rho\psi = \rho\psi(V_{st}) = \rho\psi^E + \rho\psi^I + \rho\psi^{CH} \tag{12}$$

In the present model the following functions for $\rho\psi^I$ and $\rho\psi^E$ are assumed:

$$\rho\psi^I = 1/3C^p(\xi)\alpha_{ij}^p\alpha_{ij}^p + \\ + R_{\infty}^p(\xi)\{r^p + \frac{1}{b^p(\xi)}\exp[-b^p(\xi)r^p]\} \tag{13}$$

$$\rho\psi^E = 1/2\varepsilon_{ij}^E E_{ijkl}(\mathbf{D}^{avg})\varepsilon_{kl}^E \tag{14}$$

Term $\rho\psi^{CH}$ in Equation (12) represents the chemically stored energy:

$$\rho\psi^{CH} = [1 - n(\xi)]\rho\psi_{\gamma}^{CH} + n(\xi)\rho\psi_{\alpha'}^{CH} \tag{15}$$

The terms $\rho\psi_{\gamma}^{CH}$ and $\rho\psi_{\alpha}^{\prime CH}$ are the chemical energies of the respective phases, cf. Hallberg et al. (2010). This internally stored energy is different for the two phases and it will affect the generation of heat during phase transformation, as well as the transformation itself. Symbol $n(\xi)$ denotes a function similar to $m(\xi)$.

Since the $\gamma \to \alpha'$ phase transformation does not affect the elastic properties of the material, in the Equation (14) $E_{ijkl}(\mathbf{D}^{avg})$ stands for the current elastic stiffness tensor affected only by damage. Adopting the strain equivalence principle (cf. Lemaitre 1992), the current elastic stiffness is related to the initial stiffness of the undamaged material, E^0_{ijkl}, by the use of damage effect tensor $M_{ijkl}(\mathbf{D}^{avg})$ (cf Cordebois & Sidoroff 1983) in the following way: $E_{ijkl}(\mathbf{D}^{avg}) = M^{-1}_{minj} E^0_{mnkl}$. On the other hand, it is assumed here that damage does not affect plastic hardening properties, therefore, in Equation (13) the material parameters: $R^p_\infty(\xi)$, $C^p(\xi)$, and $b^p(\xi)$ depend on the current state of phase transformation only.

By eliminating all the reversible processes from the Clausius-Duhem inequality, the following state equation which expresses the thermodynamic force conjugated to the observable state variable is obtained:

$$\sigma_{ij} = \frac{\partial(\rho\psi)}{\partial \varepsilon^E_{ij}} \tag{16}$$

In addition, the forces conjugated to other state variables are postulated in a similar form to (16):

$$-Y^\gamma_{ij} = \frac{\partial(\rho\psi)}{\partial D^\gamma_{ij}}, -Y^{\alpha'}_{ij} = \frac{\partial(\rho\psi)}{\partial D^{\alpha'}_{ij}} \tag{17}$$

$$Z = \frac{\partial(\rho\psi)}{\partial \xi} = \frac{\partial(\rho\psi')}{\partial \xi} + \frac{dn}{d\xi}(\rho\psi^{CH}_{\alpha'} - \rho\psi^{CH}_{\gamma}) \tag{18}$$

$$X^p_{ij} = \frac{\partial(\rho\psi)}{\partial \alpha^p_{ij}} = \frac{2}{3} C^p(\xi)\alpha^p_{ij} \tag{19}$$

$$R^p = \frac{\partial(\rho\psi)}{\partial r^p} = R^p_\infty(\xi)\{1 - \exp[-b^p(\xi) r^p]\} \tag{20}$$

In the above equations Y^γ_{ij} and $Y^{\alpha'}_{ij}$ stand for the ductile and brittle part of the elastic strain energy release rate, respectively (cf. also Kintzel et al., 2010).

In Equations (18)–(20) Z is the chemical force for phase transformation, and X^p_{ij} and R^p are the plastic hardening forces.

The constitutive law (16) under isothermal conditions includes the plastic, irreversible damage and transformation strains:

$$\sigma_{ij} = E_{ijkl}(\mathbf{D}^{avg})\left(\varepsilon_{kl} - \varepsilon^p_{kl} - \varepsilon^{id}_{kl} - \xi\varepsilon^{bs}_{kl}\right) \tag{21}$$

where $\boldsymbol{\varepsilon}^p$ is the plastic strain tensor, $\boldsymbol{\varepsilon}^{id}$ is the irreversible damage strain tensor, and $\boldsymbol{\varepsilon}^{bs} = 1/3\Delta\upsilon\mathbf{I}$ denotes the free deformation called bain strain, expressed in terms of the relative volume change $\Delta\upsilon$. It is assumed that the mesoscopic strain tensor $\boldsymbol{\varepsilon}^{bs}$ is obtained by integrating the microscopic eigen-strain tensor $\boldsymbol{\varepsilon}^{bs}_\mu$ over the RVE (cf. Garion et al. 2006).

The Clausius-Planck inequality takes therefore the following form:

$$\begin{aligned}&\sigma_{ij}\dot{\varepsilon}^I_{ij} - \rho\dot{\psi} = \sigma_{ij}\dot{\varepsilon}^p_{ij} - X^p_{ij}\dot{\alpha}^p_{ij} - R^p\dot{r}^p \\ &+(\sigma_{ij}\varepsilon^{bs}_{ij} - Z)\dot{\xi} + \sigma_{ij}\dot{\varepsilon}^{id}_{ij} + Y^\gamma_{ij}\dot{D}^\gamma_{ij} + Y^{\alpha'}_{ij}\dot{D}^{\alpha'}_{ij} \geq 0\end{aligned} \tag{22}$$

As it can be seen from (22), the quantity $Q = \sigma_{ij}\varepsilon^{bs}_{ij} - Z$ is conjugated to the transformation rate $\dot{\xi}$ and can be treated as a thermodynamic force that drives the phase front through the material.

3.2.1 *Evolution of state variables*

It is assumed here, after Lemaitre (1992), that ductile damage and phase transformation mechanisms are governed by plasticity with a single dissipation potential F: $F(J_{cf}, V_{st}) = F^p + F^{d\gamma} + F^{tr}$ and normality rule involving only one plastic multiplier, $\dot{\lambda}^p$, determined from the consistency condition. The equations involving the dissipation potentials take the form:

$$\dot{\varepsilon}^p_{ij} = \dot{\lambda}^p \frac{\partial F^p}{\partial \sigma_{ij}}, \; \dot{D}^\gamma_{ij} = \dot{\lambda}^p \frac{\partial F^d}{\partial Y^\gamma_{ij}}, \; \dot{\xi} = \dot{\lambda}^p \frac{\partial F^{tr}}{\partial Q} \tag{23}$$

$$\dot{\alpha}^p_{ij} = -\dot{\lambda}^p \frac{\partial F^p}{\partial X^p_{ij}}, \; \dot{r}^p = -\dot{\lambda}^p \frac{\partial F^p}{\partial R^p} \tag{24}$$

The irreversible strain ε^{id}_{ij} related to damage evolution is here neglected.

In such approach the ductile damage and the phase transformation progress only when there is plastic flow. Similarly, beyond damage threshold there is no plasticity without a corresponding increase in damage, and beyond phase transformation threshold there is no plasticity without a corresponding increase in martensite content.

Plastic potential F^p is here equal to von Mises type yield surface:

$$F^p = f^p = J_2[\widetilde{\sigma}_{ij} - \widetilde{X}^p_{ij}(\xi)] - \sigma_y - \widetilde{R}^p(\xi) = 0 \tag{25}$$

where

$$\widetilde{\sigma}_{ij} = M_{ikjl}(\mathbf{D}^{avg})\sigma_{kl}, \; \widetilde{X}^p_{ij} = M_{ikjl}(\mathbf{D}^{avg})X^p_{kl} \tag{26}$$

$$\widetilde{R} = R/\left(1 - D^{avg}_{eq}\right), \; D^{avg}_{eq} = \sqrt{D^{avg}_{ij} D^{avg}_{ij}} \tag{27}$$

are the effective variables. The relevant potential of damage dissipation reads (cf. Egner & Skoczen, 2010):

$$\begin{aligned}&F^{d\gamma} = 1/2 C_{ik} Y^\gamma_{kl} C_{ij} Y^\gamma_{ij} \\ &\times\sqrt{\frac{(\widetilde{s}_{mn} - \widetilde{X}^p_{mn})L_{mnpq}(\mathbf{D}^{avg})(\widetilde{s}_{pq} - \widetilde{X}^p_{pq})}{(\widetilde{s}_{rs} - \widetilde{X}^p_{rs})(\widetilde{s}_{rs} - \widetilde{X}^p_{rs})}} - B^{d\gamma} = 0\end{aligned} \tag{28}$$

where
$L_{ijkl}(\mathbf{D}^{avg}) = M^{-1}_{ijmn}(\mathbf{D}^{avg}) M^{-1}_{mnkl}(\mathbf{D}^{avg})$, $\mathbf{C}$ is a tensor that defines the material properties related to texture, and $B^{d\gamma}$ denotes the barrier force for damage, and $\mathbf{s}$ is the deviatoric stress.

The phase transformation dissipation potential is assumed here in a simple form:

$$\begin{aligned}&F^{tr} = A(\theta, \boldsymbol{\sigma}, \dot{\boldsymbol{\varepsilon}}^p)Q \\ &\times\sqrt{\frac{(\widetilde{s}_{mn} - \widetilde{X}^p_{mn})L_{mnpq}(\mathbf{D}^{avg})(\widetilde{s}_{pq} - \widetilde{X}^p_{pq})}{(\widetilde{s}_{rs} - \widetilde{X}^p_{rs})(\widetilde{s}_{rs} - \widetilde{X}^p_{rs})}} - B^{tr} = 0\end{aligned} \tag{29}$$

where $A(\theta, \boldsymbol{\sigma}, \dot{\boldsymbol{\varepsilon}}^p)$, in general, is a function of temperature, stress state and strain rate, and B^{tr} is the barrier force for phase transformation. For rate independent plasticity, isothermal process and small stress variations function A may be treated as a constant value.

By taking into account relations (23) and (25), the following plastic flow rule is obtained:

$$\dot{\varepsilon}_{ij}^p = \frac{\partial f^p\left(\widetilde{\boldsymbol{\sigma}}, \widetilde{\mathbf{X}}, \widetilde{R}\right)}{\partial \widetilde{\sigma}_{kl}} \frac{\partial \widetilde{\sigma}_{kl}}{\partial \sigma_{ij}} \dot{\lambda}^p \tag{30}$$

Plastic hardening variables evolve according to (24) and (25):

$$\dot{\alpha}_{ij}^p = \dot{\varepsilon}_{ij}^p\,, \quad \dot{r}^p = \dot{\lambda}^p / (1 - D_{eq}^{avg}) \tag{31}$$

Ductile damage rate is governed by the relation resulting from (23) and (28):

$$\dot{D}_{ij}^{\gamma} = C_{ik}(\boldsymbol{\varepsilon}^p) Y_{kl}^{\gamma} C_{lj}(\boldsymbol{\varepsilon}^p) \dot{p} H(p - p_D) \tag{32}$$

where p_D denotes damage threshold, and $\mathbf{C}(\boldsymbol{\varepsilon}^p)$ represents texture induced anisotropy of damage (cf. Egner & Skoczen, 2010).

By taking into account (23) and (29) the evolution of phase transformation variable takes the form:

$$\dot{\xi} = A\, \dot{p} H[(p - p_{\xi})(\xi_L - \xi)] \tag{33}$$

In the above equation p_{ξ} stands for the phase transformation threshold (to trigger the formation of martensite), while ξ_L is a limit of martensite evolution, above which the martensitic transformation rate is considered equal to zero. The consistency multiplier $\dot{\lambda}^p$ is obtained from the consistency condition:

$$\frac{\partial f^p}{\partial \sigma_{ij}}(\dot{\sigma}_{ij} - \dot{X}_{ij}) + \frac{\partial f^p}{\partial R}\dot{R} + \frac{\partial f^p}{\partial D_{ij}^{avg}}\dot{D}_{ij}^{avg} + \frac{\partial f^p}{\partial \xi}\dot{\xi} = 0 \tag{34}$$

Martensite inclusions are subjected to brittle damage described by the second order damage tensor $\mathbf{D}^{\alpha\prime}$. According to Litewka & Debinski (2003) the deterioration of brittle material structure due to applied load can be described by damage evolution equation expressed in the form of tensorial function, $D_{ij}^{\alpha\prime} = f_1 \delta_{ij} + f_2 \sigma_{ij}$. Two multipliers, f_1 and f_2, are scalar-valued functions of the stress tensor invariants. The first term represents the isotropic damage and the second one accounts for the oriented damage due to different effects of the stress tensor.

Evolution of thermodynamic forces

The evolution equations for thermodynamic conjugated forces are obtained by taking time derivatives of equations (16)–(20):

$$\dot{\sigma}_{ij} = E_{ijkl}\dot{\varepsilon}_{kl}^E + \frac{\partial E_{ijkl}}{\partial D_{pq}^{avg}}\varepsilon_{kl}^E \dot{D}_{pq}^{avg} \tag{35}$$

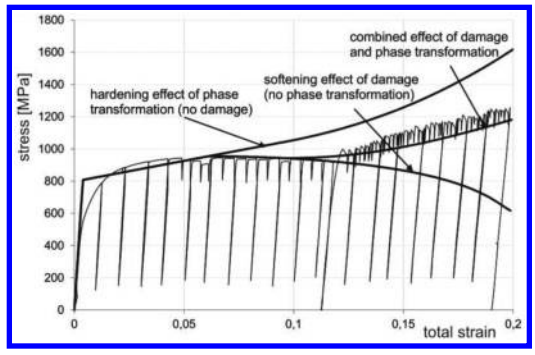


Figure 4. Numerical simulations of stress-strain curve.

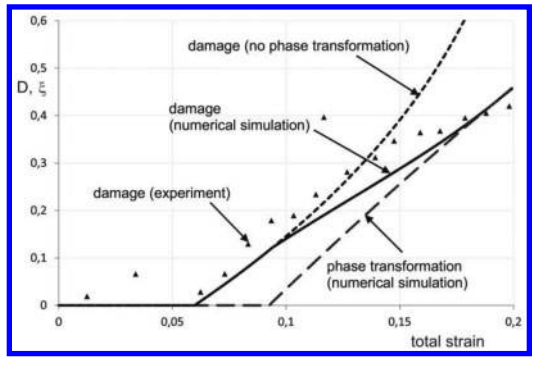


Figure 5. Numerical simulation of damage evolution.

$$\dot{X}_{ij}^p = \frac{2}{3}C^p(\xi)\dot{\varepsilon}_{ij}^p + \frac{1}{C^p(\xi)}\frac{\partial C^p}{\partial \xi}X_{ij}^p\dot{\xi} \tag{36}$$

$$\dot{R}^p = b^p(R_{\infty}^p - R^p)\dot{r}^p + \left[\frac{1}{R_{\infty}^p(\xi)}\frac{\partial R_{\infty}^p}{\partial \xi}R^p + (R_{\infty}^p - R^p)r^p\frac{\partial b^p}{\partial \xi}\right]\dot{\xi} \tag{37}$$

Functions $C^p(\xi)$ and $R_{\infty}^p(\xi)$ were derived via Mori-Tanaka homogenization in Garion et al. (2006).

3.2.2 *Discussion of results*

Accounting for three dissipative phenomena: plasticity, damage and phase transformation in the present constitutive model allows to obtain a satisfactory reproduction of the experimental stress-strain curve for 316L stainless steel subjected to uniaxial tension at cryogenic temperatures (see Fig. 4).

Another effect captured by the present model consists in the interaction between the increasing amount of the secondary (martensitic) phase and decreasing rate of damage (Fig. 5). Before the phase transformation threshold is reached, purely ductile damage develops. In agreement with the experimental observations, this stage exhibits accelerated character of damage rate. With the appearance of phase transformation a significant drop of damage rate is observed.

4 CONCLUSIONS

- The general constitutive model of dissipative material, based on thermodynamics of irreversible processes with internal state variables was presented.
- The model was used to investigate the influence of temperature rate on the response of the constitutive model when cyclic fatigue tests in nonisothermal conditions are simulated. The significant differences in results were obtained when the temperature rate terms, usually neglected in constitutive modeling, were included into the rate equations of thermodynamic hardening forces.
- The new, thermodynamically based constitutive model of stainless steel at cryogenic temperatures, accounting for coupling between ductile damage in austenite, brittle damage in martensite and phase transformation was also presented.

ACKNOWLEDGEMENT

This work has been supported by the National Science Centre through the Grants No. N N501 228540 and 2011/03/B/ST8/05132.

REFERENCES

Abu Al-Rub, R.K. & Voyiadjis, G.Z. 2003. On the coupling of anisotropic damage and plasticity models for ductile materials. *Int. J. Solids Struct*. 40: 2611–2643.

Cailletaud , G. & Sai, K. 1995. Study of plastic/viscoplastic models with various inelastic mechanisms. *Int. J. Plasticity* 11: 991–1005.

Chaboche, J.L. 1997. Thermodynamic formulation of constitutive equations and application to the viscoplasticity and viscoelasticity of metals and polymers. *Int. J. Solids Struct.* 18: 2239–2254.

Cordebois, J.P. & Sidoroff, F. 1983. Damage induced elastic anisotropy, In J.P. Boehler (ed.), *Mechanical Behavior of Anisotropic Solids*, Martinus Nijhoff, Boston, 761–774.

Egner, H. & Egner, W. 2013. Modeling of Coupled Dissipative Phenomena in Engineering Materials. In H. Altenbach & S. Kruch (eds), *Advanced Materials Modeling for Structures*, Springer 2013 (in press).

Egner, H. 2012. On the full coupling between thermoplasticity and thermo-damage in thermodynamic modeling of dissipative materials. *Int. J. Solids Struct.* 49: 279–288.

Egner, H., Skoczen, B. 2010. Ductile damage development in two-phase materials applied at cryogenic temperatures. *Int. J. Plasticity* 26: 488–506.

Garion, C., Skoczen, B., Sgobba, S. 2006. Constitutive modelling and identification of parameters of the plastic strain induced martensitic transformation in 316 L stainless steel at cryogenic temperatures. *Int. J. Plasticity*, 22, 7, 1234–1264.

Hallberg, H., Hakansson, P., Ristinmaa, M. 2010. Thermomechanically coupled model of diffusionless phase transformation in austenitic steel. *Int. J. Solids Struct*. 47: 1580–1591.

Kintzel, O., Khan, S., Mosler, J. 2010. A novel isotropic quasi-brittle damage model applied to LCF analyses of Al2024. *Int. J. Fatigue*, 32, 12: 1948–1959.

Lemaitre, J. 1992. A course on damage mechanics. Springer-Verlag, Berlin, New York.

Litewka, A., Debinski, J. 2003. Load-induced oriented damage and anisotropy of rock-like materials. *Int. J. Plasticity*, 19, 2171–2191.

Velay, V., Bernhart, G., Penazzi, L. 2006. Cyclic behavior modeling of a tempered martensitic hot work tool steel. *Int. J. Plasticity* 22: 459–496.

Research and Applications in Structural Engineering, Mechanics and Computation – Zingoni (Ed.)
© 2013 Taylor & Francis Group, London, ISBN 978-1-138-00061-2

Heterogeneous structures studied by an interphase elasto-plastic damaging model

G. Giambanco, G. Fileccia Scimemi & A. Spada
Department of Civil, Environmental, Aerospace and Materials' Engineering,
University of Palermo – Palermo, Italy

ABSTRACT: Heterogeneous materials present a mechanical response strongly dependent on the static and kinematic phenomena occurring in the constituents and at their joints. At the mesoscopic level the interaction between the units is simulated by mean of apposite mechanical devices such as the zero thickness interface model where contact tractions and displacement discontinuities are the primary static and kinematic variables respectively. In heterogeneous materials the response also depends on joint internal stresses. The introduction of internal stresses brings to the interphase model or an enhancement of the classical zero-thickness interface. With the term 'interphase' we shall mean a layer separated by two physical interfaces from the bulk material or a multilayer structure with varying properties and several interfaces. Different failure conditions can be introduced for the physical interfaces and for the joint material. The interphase model has been implemented in an open-source research-oriented finite element analysis program for 2D applications.

1 INTRODUCTION

The mechanical response of all those structures that are constituted by heterogeneous materials is dependent by different static and kinematic phenomena occurring in each constituent and at their joints. Material degradation due to nucleation, growth and coalescence of microvoids and microcracks is usually accompanied by plastic deformations as decohesion and sliding that cause strain softening and induced anisotropy.

The mesoscopic approach is by now the most diffused technique to understand this kind of materials, because it overcomes the problems associated with the strong simplifications that have to be introduced when the macroscopic approach is applied. In particular, with the mesoscopic approach all the material constituents are modelled individually and their interactions are regulated by using appropriate devices able to reproduce the inelastic phenomena that usually occur at the physical interfaces. In the last decades zero-thickness interface elements (ZTI) have been applied in several engineering applications due to their simple formulation and to their easiness to be implemented in finite element codes.

The interface constitutive laws are expressed in terms of contact tractions and displacement discontinuities which are considered as generalized joints strains. In order to model the nonlinear behaviour caused by plastic deformations and damage evolution the constitutive laws of the interface elements are formulated making use of concepts borrowed by theory of Plasticity and Continuum Damage Mechanics.

In many cases the structural response depends also on internal stresses and strains within the joint. It is sufficient to think to the fracture that appears in the middle of masonry blocks caused by the horizontal tangential contact stresses between the mortar and the block when a masonry assembly is subjected to a pure compressive load. These tangential stresses cannot be captured by the classical ZTI model. Therefore, the usual assumption used in zero-thickness interface elements, where the response is governed by contact stress components, may require a correction by introducing the effect of the internal stresses into the analysis. This enhancement of the ZTI is known as interphase model, for the first time proposed by Giambanco and Mròz (2001).

The interphase element has been formulated by authors as a new contact element and introduced in a scientific oriented finite element code. Patch tests have been carried out in elasticity to investigate the numerical performance and convergence of the element. All the results are shown in the paper written by Giambanco el al. (2012). In particular, in that paper is shown how strategies such as the Reduced Selective Integration or the Enhanced Assumed Strain methods are necessary to avoid shear locking effects of the element.

In this work the interphase element is implemented for nonlinear applications by introducing separate limit conditions for the joint bulk material and for the physical interfaces. The overall model is thermodynamically consistent and the flow rules are derived by applying the Lagrangian method. With the aim to show

the effectiveness of the model the interphase constitutive laws have been implemented in an open-source research-oriented finite element analysis program for 2D applications and by using the Selective Reduced Integration.

2 GENERAL ASSUMPTIONS AND THERMODYNAMICS

Let us consider, in the Euclidean space $\Re^3$ referred to the orthonormal frame $(O, \mathbf{i_1}, \mathbf{i_2}, \mathbf{i_3})$, a structure formed by two adherents Ω^+, Ω^- connected by a third material Ω in contact with the two bodies by means of the two physical interfaces Σ^+ and Σ^- respectively, as in Figure 1.

It is assumed that the thickness h of the joint is small if compared with the characteristic dimensions of the bonded assembly.

The boundary of the two adherents is divided in the two parts $\Gamma_u^{\pm}$ and $\Gamma_t^{\pm}$, where kinematic and loading conditions are specified respectively.

The joint interacts with the two adherents through the following traction components:

$$\mathbf{t}^{\pm} = t_1^{\pm}\mathbf{e}_1 + t_2^{\pm}\mathbf{e}_2 + t_3^{\pm}\mathbf{e}_3 \tag{1}$$

which can be considered as the external surface loads for the joint.

In Equation 1 $\mathbf{e}_1$, $\mathbf{e}_2$ and $\mathbf{e}_3$ are the unit vectors of the local reference system, with $\mathbf{e}_3$ oriented along the normal to the middle surface Σ and directed towards the adherent Ω^+. The joint can be regarded as an interphase model. It is assumed that the fibers inside the interphase and directed along $\mathbf{e}_3$ are maintained rectilinear during the deformation process. In view of this hypothesis the interphase displacement field $\mathbf{u}$ can be easily obtained from the displacement $\mathbf{u}^+$ and $\mathbf{u}^-$ of the interfaces Σ^+ and Σ^-, thus

$$\mathbf{u}(x_1,x_2,x_3) = \left(\frac{1}{2}+\frac{x_3}{h}\right)\mathbf{u}^+(x_1,x_2) + \left(\frac{1}{2}-\frac{x_3}{h}\right)\mathbf{u}^-(x_1,x_2) \tag{2}$$

with x_1, x_2 and x_3 the Cartesian coordinates in the orthonormal frame $(O, \mathbf{e}_1, \mathbf{e}_2, \mathbf{e}_3)$.

Since the thickness of the joint is generally small if compared to the characteristic dimensions of the adherents, we can assume the strain state ε uniform along the $\mathbf{e}_3$ direction and given by:

$$\boldsymbol{\varepsilon}(x_1,x_2) = \frac{1}{h}\int_{-h/2}^{h/2} \nabla^s \mathbf{u}(x_1,x_2,x_3)\,dx_3 \tag{3}$$

Substituting the Equation 2 we have:

$$\boldsymbol{\varepsilon}(x_1,x_2) = \frac{1}{2h}\left([\mathbf{u}]\otimes\mathbf{n} + \mathbf{n}\otimes[\mathbf{u}]\right) + \frac{1}{2}\nabla^s\left(\mathbf{u}^+ + \mathbf{u}^-\right) \tag{4}$$

where $[\mathbf{u}] = \mathbf{u}^+ - \mathbf{u}^-$, $\mathbf{n}$ is the unit normal vector to the interphase plane and ∇^s is the symmetric gradient operator defined as $\nabla^s = \frac{1}{2}\left(\nabla + \nabla^T\right)$.

Let us note that in the interphase model the joint curvatures generated by displacement field (2) and the related flexural effect are neglected.

Equilibrium equations are derived by applying the principle of virtual displacements (PVD) that asserts that the external work produced by the contact tractions equals the internal work developed in the joint. According to the hypothesis of a constant strain state, by applying the divergence theorem and assuming that $\Sigma = \Sigma^+ = \Sigma^-$, the PVD leads to the following local equilibrium relations of the interphase model:

$$\begin{aligned} &\mathbf{t}^+ - \boldsymbol{\sigma}\cdot\mathbf{n} + \frac{h}{2}div\boldsymbol{\sigma} = \mathbf{0}; \\ &\mathbf{t}^- + \boldsymbol{\sigma}\cdot\mathbf{n} + \frac{h}{2}div\boldsymbol{\sigma} = \mathbf{0} \end{aligned} \qquad on\ \Sigma, \tag{5}$$

$$\mathbf{m}\cdot\boldsymbol{\sigma} = \mathbf{0} \qquad on\ \Gamma. \tag{6}$$

The basic kinematical hypotheses are the additive decomposition of total strain in the internal (i) and contact (c) parts and, for the contact strain only, a further decomposition in elastic (e) and inelastic (p) parts:

$$\boldsymbol{\varepsilon} = \boldsymbol{\varepsilon}^i + \boldsymbol{\varepsilon}^c \tag{7}$$

$$\boldsymbol{\varepsilon}^c = \boldsymbol{\varepsilon}^{ce} + \boldsymbol{\varepsilon}^{cp} \tag{8}$$

with

$$\boldsymbol{\varepsilon}^i = \mathbf{A}\boldsymbol{\varepsilon}\mathbf{A} \tag{9}$$

being $\mathbf{A} = \mathbf{I} - \mathbf{n}\otimes\mathbf{n}$ the unit second order tensor.

In order to comply with thermodynamic requirements, the interphase Helmholtz free energy is introduced in the following form:

$$\begin{aligned} \Psi\left(\boldsymbol{\varepsilon}^i,\boldsymbol{\varepsilon}^c,\boldsymbol{\varepsilon}^{cp},\boldsymbol{\omega},\xi_d,\xi_p\right) &= \Psi^i\left(\boldsymbol{\varepsilon}^i,\boldsymbol{\omega},\xi_d\right) + \\ &+\Psi^c\left(\boldsymbol{\varepsilon}^c,\boldsymbol{\varepsilon}^{cp},\xi_p\right) + \Psi^{i,c}\left(\boldsymbol{\varepsilon}^i,\boldsymbol{\varepsilon}^c,\boldsymbol{\varepsilon}^{cp},\boldsymbol{\omega}\right) \end{aligned}; \tag{10}$$

where Ψ^i and Ψ^c represent the free energies related to the internal and contact parts of the strain state respectively and Ψ^{ic} is the mixed term of the free energy

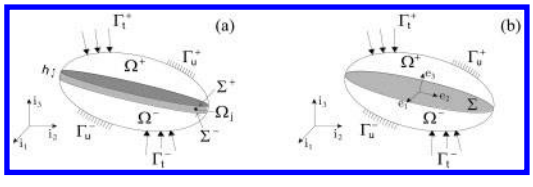


Figure 1. (a) Mechanical scheme of a third body interposed between two adherents; (b) Interphase mechanical scheme.

which takes into account the co-presence of the contact and internal strains. ξ_d and ξ_p are the damage and plastic internal variables, respectively.

The principle considered for developing the constitutive laws is that damage occurs in the bulk material, therefore the damage tensor ω appears in the two terms of the total free energy that are functions of the internal strains also. In this way the constitutive model takes into account the onset of microvoids and fractures along the thickness of the joint. On the other hand, debonding of the joint from the adherents, sliding and fractures developing on surfaces parallel to the middle plane of the interphase are modelled using elastoplasticity and the inelastic contact strains ε^{cp} are the related internal variables.

In this work a single scalar damage variable ω governs the loss of stiffness of the bulk material. It ranges from 0 to 1, with the inferior and superior limits having the meaning of a pristine and a fully damaged bulk material, respectively.

The explicit expression of the components of the free energy is given below:

$$\Psi^i = \frac{1}{2}(1-\omega)\left[\lambda\,\mathrm{tr}^2\left(\boldsymbol{\varepsilon}^i\right)+2\mu\boldsymbol{\varepsilon}^i:\boldsymbol{\varepsilon}^i\right]+ -h_d\left[\xi_d+\ln\left(1-\xi_d\right)\right] \tag{11}$$

$$\Psi^c = \frac{1}{2}\left[\lambda\,\mathrm{tr}^2\boldsymbol{\varepsilon}^{ce}+2\mu\boldsymbol{\varepsilon}^{ce}:\boldsymbol{\varepsilon}^{ce}\right]+\frac{1}{2}h_p\xi_p^2 \tag{12}$$

$$\Psi^{i,c} = (1-\omega)\lambda\,\mathrm{tr}\left(\boldsymbol{\varepsilon}^i\right)\mathrm{tr}\,\boldsymbol{\varepsilon}^{ce} \tag{13}$$

where λ and μ are the Lamè's constants, h_d is a material parameter which governs the softening response associated to the damage onset and growth, and h_p is a material parameter specifying isotropic hardening/softening interface response.

3 STATE EQUATIONS AND FLOW RULES

In order to derive the interphase constitutive equations, the second principle of thermodynamics, taking into account also the balance equation (first principle) can be applied in the form of the Clausius-Duhem inequality. This inequality for isothermal purely mechanical evolutive process reads as

$$D = \boldsymbol{\sigma}:\dot{\boldsymbol{\varepsilon}}-\dot{\Psi}\geq 0 \tag{14}$$

where D is the interphase dissipation (for unit surface) or net entropy production.

From the assumed form of the Helmholtz free energy its general rate has the following expression:

$$\dot{\Psi} = \left(\frac{\partial\Psi^i}{\partial\boldsymbol{\varepsilon}^i}+\frac{\partial\Psi^{i,c}}{\partial\boldsymbol{\varepsilon}^i}\right):\dot{\boldsymbol{\varepsilon}}^i+\left(\frac{\partial\Psi^c}{\partial\boldsymbol{\varepsilon}^c}+\frac{\partial\Psi^{i,c}}{\partial\boldsymbol{\varepsilon}^c}\right):\dot{\boldsymbol{\varepsilon}}^c+ +\left(\frac{\partial\Psi^c}{\partial\boldsymbol{\varepsilon}^{cp}}+\frac{\partial\Psi^{i,c}}{\partial\boldsymbol{\varepsilon}^{cp}}\right):\dot{\boldsymbol{\varepsilon}}^{cp}+\left(\frac{\partial\Psi^i}{\partial\omega}+\frac{\partial\Psi^{i,c}}{\partial\omega}\right):\dot{\omega}+ +\frac{\partial\Psi^i}{\partial\xi_d}\dot{\xi}_d+\frac{\partial\Psi^c}{\partial\xi_p}\dot{\xi}_p \tag{15}$$

Particularizing Equation 14 for a purely elastic incremental deformation process ($\mathbf{P}^{cp}=\mathbf{0}$, $\dot{\omega}=\dot{\xi}_d=\dot{\xi}_p=0$), assuming the decomposition of the stress state similar to that used for the strain state

$$\boldsymbol{\sigma}=\boldsymbol{\sigma}^i+\boldsymbol{\sigma}^c, \qquad \text{being} \qquad \boldsymbol{\sigma}^i=\mathbf{A}\boldsymbol{\sigma}\mathbf{A} \tag{16}$$

and considering the adopted expressions of the free energy parts (Eqs. 11–13), the elastic stress-strain equations can be derived, thus

$$\sigma^i = (1-\omega)\left\{\lambda\left[\mathrm{tr}\left(\boldsymbol{\varepsilon}^i\right)+\mathrm{tr}\left(\boldsymbol{\varepsilon}^c-\boldsymbol{\varepsilon}^{cp}\right)\right]\mathbf{A}+2\mu\boldsymbol{\varepsilon}^i\right\} \tag{17}$$

$$\sigma^c = \lambda\left[(1-\omega)\,\mathrm{tr}\left(\boldsymbol{\varepsilon}^i\right)+\mathrm{tr}\left(\boldsymbol{\varepsilon}^c-\boldsymbol{\varepsilon}^{cp}\right)\right](\mathbf{I}-\mathbf{A})+ +2\mu\left(\boldsymbol{\varepsilon}^c-\boldsymbol{\varepsilon}^{cp}\right) \tag{18}$$

$$\chi_p = h_p\xi_p \tag{19}$$

$$\chi_d = h_d\frac{\xi_d}{1-\xi_d} \tag{20}$$

$$\zeta = \frac{1}{2}\left[\lambda\,\mathrm{tr}^2\left(\boldsymbol{\varepsilon}^i\right)+2\mu\boldsymbol{\varepsilon}^i:\boldsymbol{\varepsilon}^i\right]+\lambda\,\mathrm{tr}\left(\boldsymbol{\varepsilon}^i\right)\mathrm{tr}\left(\boldsymbol{\varepsilon}^c-\boldsymbol{\varepsilon}^{cp}\right) \tag{21}$$

where χ_p and χ_d are the static variables conjugate of the internal variables ξ_p and ξ_d respectively, and ζ the thermodynamic force conjugate of the damage variable ω.

Making use of the elastic strain-stress equation and of the previous positions, the final expression of the instantaneous dissipation is obtained:

$$D = \boldsymbol{\sigma}^c:\dot{\boldsymbol{\varepsilon}}^{cp}-\chi_p\dot{\xi}_p-\chi_d\dot{\xi}_d+\zeta\dot{\omega}\geq 0\,. \tag{22}$$

In order to regulate the activation of each dissipative mechanism, two different yield functions are defined in the space of the proper static variables, namely:

$$\Phi_p\left(\boldsymbol{\sigma}^c,\chi_p\right)\leq 0, \qquad \Phi_d\left(\zeta,\chi_d\right)\leq 0 \tag{23}$$

where Φ_p is the classical plastic yield function specifying the elastic contact domain assumed convex and Φ_d is the damage activation function also assumed convex.

The activation of each dissipation mechanism can be effectively described by a variational formulation which is represented by the generalized principle of maximum intrinsic dissipation:

$$\max_{\boldsymbol{\sigma}^c,\chi_p,\chi_d,\zeta}\left(\boldsymbol{\sigma}^c:\dot{\boldsymbol{\varepsilon}}^{cp}-\chi_p\dot{\xi}_p-\chi_d\dot{\xi}_d+\zeta\dot{\omega}\right) \tag{24}$$

subject to the constraints (Eq. 23). The Kuhn-Tucker conditions of the maximum constrained problem provide the plastic and damage evolution laws of the interphase:

$$\dot{\boldsymbol{\varepsilon}}^{cp}=\dot{\lambda}_p\frac{\partial\Phi_p}{\partial\boldsymbol{\sigma}^c}; \qquad \dot{\omega}=\dot{\lambda}_d\frac{\partial\Phi_d}{\partial\zeta} \tag{25}$$

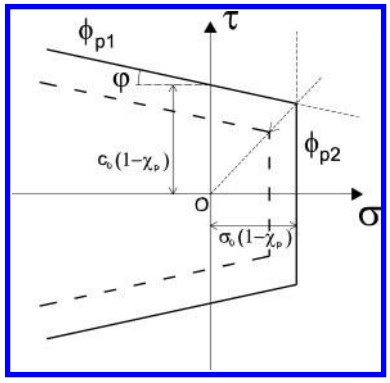


Figure 2. Plastic yield conditions represented in the stress space.

$$-\dot{\xi}_p = \dot{\lambda}_p \frac{\partial \Phi_p}{\partial \chi_p}; \quad -\dot{\xi}_d = \dot{\lambda}_d \frac{\partial \Phi_d}{\partial \chi_d} \tag{26}$$

$$\Phi_p\left(\boldsymbol{\sigma}^c, \chi_p\right) \le 0, \quad \dot{\lambda}_p \ge 0, \quad \dot{\lambda}_p \Phi_p\left(\boldsymbol{\sigma}^c, \chi_p\right) = 0 \tag{27}$$

$$\Phi_d\left(\zeta, \chi_d\right) \le 0, \quad \dot{\lambda}_d \ge 0, \quad \dot{\lambda}_d \Phi_d\left(\zeta, \chi_d\right) = 0 \tag{28}$$

being $\dot{\lambda}_p$ and $\dot{\lambda}_d$ the plastic and damage multiplier, respectively.

In the present study the elasto-plastic convex domain is defined by the intersection of the classical Mohr-Coulomb bilinear function with a tension cut-off:

$$\Phi_{p1}\left(\boldsymbol{\sigma}^c, \chi_p\right) = \left|\boldsymbol{\tau}^c\right| + \sigma^c \tan\varphi - c_0\left(1-\chi_p\right) \tag{29}$$

$$\Phi_{p2}\left(\boldsymbol{\sigma}^c, \chi_p\right) = \sigma^c - \sigma_0\left(1-\chi_p\right) \tag{30}$$

where τ^c and σ^c are the tangential stress vector and the normal stress component of the contact stresses, φ is the friction angle, c_0 and σ_0 the cohesion and tensile strength of the virgin interfaces.

The two yield functions are depicted in Figure 2. The following four zones can be distinguished:

I elastic zone: $\Phi_{p1} < 0,\ \Phi_{p2} < 0$
II plastic activation in shear: $\Phi_{p1} = 0,\ \Phi_{p2} < 0$
III plastic activation in tension: $\Phi_{p1} < 0,\ \Phi_{p2} = 0$
IV plastic activation in tension and shear (corner): $\Phi_{p1} < 0,\ \Phi_{p2} < 0$.

The damage activation function is linear and the first activation occurs when the thermodynamic force reaches the relative threshold value ζ_0:

$$\Phi_d\left(\zeta, \chi_d\right) = \zeta - \zeta_0\left(1-\chi_d\right) \tag{31}$$

4 NUMERICAL APPLICATIONS

The interphase model presented in Sections 2 and 3 has been implemented in an open-source research-oriented finite element analysis program for 2D applications. With the aim to run a step-by-step integration, flow rules have been rewritten as discrete laws. The implicit backward-Euler difference method was applied to obtain results within the time step $[t_n, t_{n+1}] \subset [0, \quad T]$. In particular the nonlinear solution at time t_{n+1} has been calculated by means of an elastic prediction – plastic and/or damaging correction procedure. The interphase element has four nodes and zero-thickness. The integration of the stiffness matrix has been solved by applying the Reduced Selective Integration method, that is two Gauss are used for the integration in the direction normal to the interphase plane while one Gauss point is used in the tangential one.

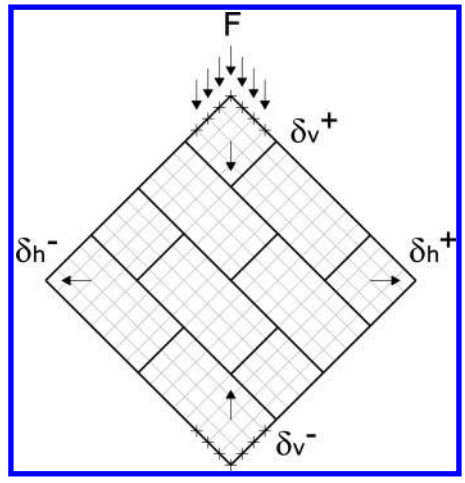


Figure 3. Diagonal compression test on a masonry panel: finite element model.

The numerical applications presented in this work regard diagonal compression test on a cylindrical masonry specimen and a masonry vault loaded by a monotonic increasing load. All numerical examples have been carried out under the hypothesis of plane stress state.

4.1 *Diagonal compression test on masonry*

A diagonal compression numerical test has been carried out on a masonry panel and compared with the experimental results obtained in laboratory. With reference to Figure 3, the specimen is made of four courses of sandstone blocks with calcium-cement mortar. It has a squared shape with a length of 67 cm for each side. A single block is 33 cm long and 16 cm high. The mortar layer has a thickness of 1 cm. A total number of 256 plane stress 2D solid elements and 72 interphase elements has been used to create the finite element model.

The mechanical variables for blocks and mortar and the parameters used for the finite element model are reported in Table 1.

The test has been run with 400 steps under displacement control. At each step the values of the total vertical load F and the displacement discontinuities $\delta h = \delta h^+ + \delta h^-$ and $\delta v = \delta v^+ + \delta v^-$, in horizontal and vertical direction respectively, have been evaluated and reported in the load-displacement curves of

Table 1. Parameters used for diagonal compression test.

Parameter	Brick	Mortar
E (MPa)	11141.67	37000
v	0.25	0.14
c_0 (MPa)	–	5.0
σ_0 (MPa)	–	1.0
ζ_0 (MPa)	–	10^{-5}
φ (°)	–	35
h_p	–	0.04
h_d	–	0.001

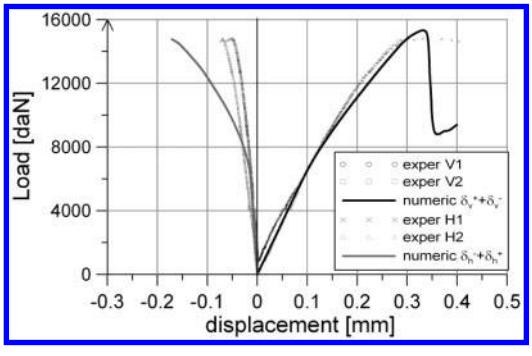


Figure 4. Load-displacement curves: comparison between numerical and experimental results.

Figure 4. A good agreement has been obtained with experimental results.

Figure 5 finally shows a comparison between the collapse experimental and numerical configurations. A very good agreement can be observed, even if the numerical model is not able to simulate the fracture inside the blocks because an elastic behavior was chosen for bricks.

4.2 *Cylindrical masonry vault*

The second example evaluates the structural response of a cylindrical masonry vault.

The results of the numerical analysis have been compared to the experimental work of Failla et al. (2004) who tested a vault made of 24 courses of calcarenite ashlars stones ($21 \times 36 \times 16\,cm^3$). Each course is separated by a mortar layer of average thickness h equal to 2.5 cm. The vault is 118 cm long, 16 cm thick and of internal radius equal to 260 cm. The imposts form an angle of 30° with the horizontal plane (Fig. 6). The vault has been subjected to a uniform load applied onto the seventh course of stones. The test has been performed under displacement control until the formation of four hinges has been reached.

The structure has been numerically implemented as a bi-dimensional arch, 118 cm wide. Each stone has been discretized with a 4×8 plane stress solid elastic elements (4-noded). The radial joints have been modeled using eight interface elements (4-noded).

To adhere to the experimental protocol, the numerical analysis has been carried out in displacement control.

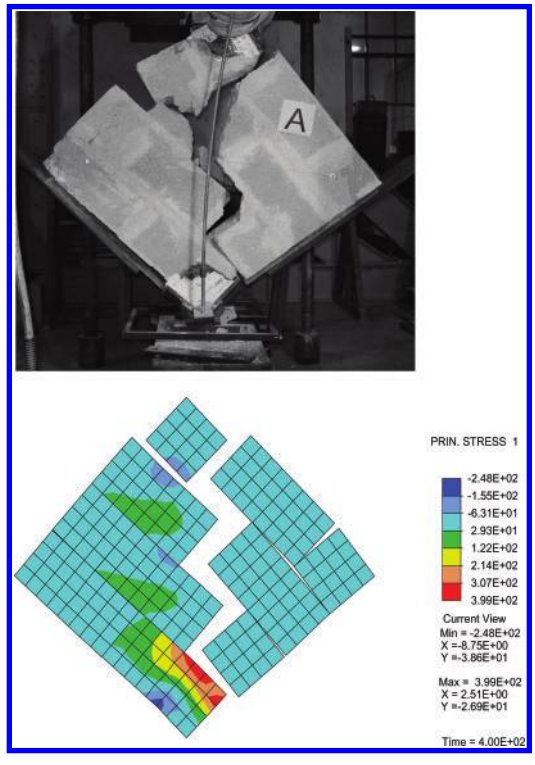


Figure 5. Comparison between numerical and experimental collapse configurations.

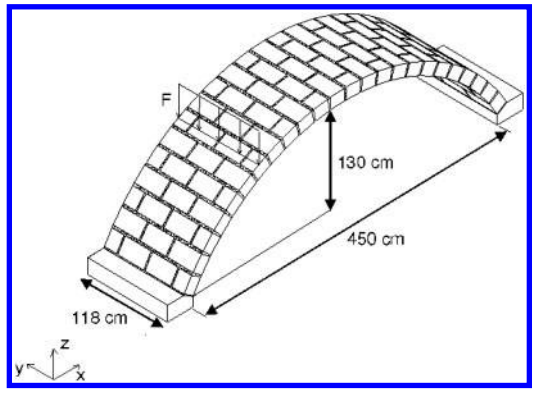


Figure 6. Tridimensional view of the vault.

The load-displacement curve, in comparison with experimental one, is reported in Figure 7. It is clear as the numerical model is able to catch the same stiffness, peak load and residual force of the experimental test. Figure 8 shows instead the final configuration of the vault after the formation of the hinges.

5 CONCLUSIONS

The present paper deals with the mesomodelling of heterogeneous structures by means of interphase elements, that can be considered as an enhancement of

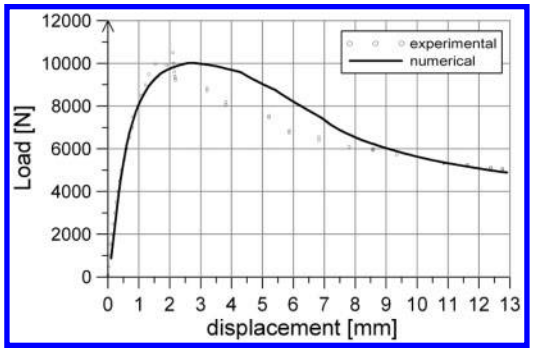


Figure 7. Load-displacement curve of the test on the vault.

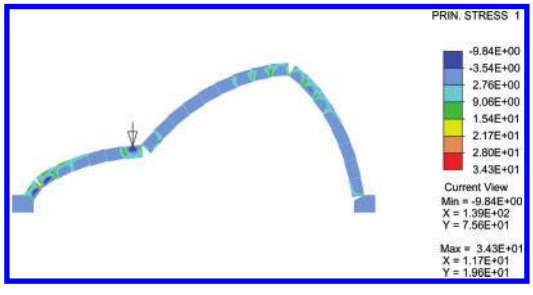


Figure 8. Collapse mechanism of the vault.

the common interface elements. Separate failure conditions have been considered for the bulk material and for contact tractions. An isotropic damage model has been used to model the nonlinear response of the bulk material, while an elastoplastic bilinear domain governs the evolution of plasticity for contact tractions. The interphase model has been written in the framework of a thermodynamically consistent theory. State equations and flow rules have been derived and rewritten in a discrete form to be suitable to be used for finite element implementation. Two numerical applications on masonry structural elements have been conducted.

Ongoing and future efforts are devoted to the introduction of plastic activation functions on the physical interfaces between mortar and block, and to the possibility to introduce a new damage model to catch horizontal fractures also.

ACKNOWLEDGEMENTS

The authors acknowledge the financial support given by the Italian Ministry of Education, University and Research (MIUR) under the PRIN09 project 2009XWLFKW_005, "A multiscale approach for the analysis of decohesion processes and fracture propagation".

REFERENCES

Alfano, G. & Crisfield, M.A. 2001. Finite element interface models for the delamination analysis of laminated composite: mechanical and computational issues. *Int. Journ. Num. Meth. Engrg.* 50: 1701–1736.

Alfano, G. & Sacco, E. 2006. Combining interface damage and fiction in a cohesive-zone model. *Int. Journ. Num. Meth. Engrg.* 68: 542–582.

Einav, I., Houlsby, G.T. & Nguyen, G.D. 2007. Coupled damage and plasticity models derived from energy and dissipation potentials. *Int. Journ. Solids Struct*. 44: 2487–2508.

Failla, A., Cottone, G. & Giambanco, G. 2004. Numerical modeling of masonry structures reinforced by FRP plate/sheets. In Proceedings of the: *Fourth International Seminar on Structural Analysis of Historical Constructions*, *Padova, 10–13 November 2004*. Padova, Italy.

Giambanco, G. & Mroz, Z. 2001. The interphase model for the analysis of joints in rock masses and masonry structures. *Mechanica* 36 (1): 111–130.

Giambanco, G., Rizzo, S. & Spallino, R. 2001. Numerical analysis of masonry structures via interface models. *Comput. Methods Appl. Mech. Engrg*. 190: 6493–6511.

Giambanco, G., Fileccia Scimemi, G. & Spada, A. 2012. The interphase element. *Comp. Mech*. 50 (3): 353–366.

Lofti, H.R. & Shing, P.B. 1994. Interface model applied to fracture of masonry structures. *Journ. Struct. Eng.* (ASCE) 120 (1): 63–80.

Lourenco, P.B. & Rots, J. 1997. Multisurface interface model for analysis of masonry structures. *Journ. Engrg. Mech*. 123 (7): 660–668.

Parrinello, F., Failla, B. & Borino, G. 2009. Cohesive-frictional interface costitutive model. *Int. Journ. Solids Struct.* 46: 2680–2692.

Sacco, E. & Lebon, F. 2012. A damage-friction interface model derived from micromechanical approach. *Int. Journ. Solids Struct.* 49 (26): 3666–3680.

Spada, A., Giambanco, G. & Rizzo, P. 2009. Damage and plasticity at the interfaces in composite materials and structures. *Comput. Methods Appl. Mech. Engrg.* 198: 3884–3901.

William, K., Rhee, I. & Shing, B. 2004. Interface damage model for thermomechanical degradation of heterogeneous materials. *Comput. Methods Appl. Mech. Engrg.* 193: 3327–3350.

Research and Applications in Structural Engineering, Mechanics and Computation – Zingoni (Ed.)
© 2013 Taylor & Francis Group, London, ISBN 978-1-138-00061-2

A coupled local-nonlocal framework for modeling hydraulic fracturing in the Karoo

D.Z. Turner
Department of Civil Engineering, Stellenbosch University, Stellenbosch, South Africa

ABSTRACT: A great deal of debate over whether or not to allow hydraulic fracturing in the Karoo (in order to improve hydrocarbon production; making natural gas an economical local alternative energy source) has been waged with very little emphasis on scientific investigation. In particular, little is known about the transport of contaminants used in the process through the fractured formation. Many of the surfactants used to enable greater water penetration during fracturing can contain toxic chemicals, but the probability of underground water resource contamination by these chemicals has not been widely studied. This is partially due to a lack of modeling tools that can address such a complex engineering problem. This work presents a new computational framework for modeling hydraulic fracturing with the following features: a non-local representation of solid mechanics in which cracks are naturally part of the solution, a locally mass conserving, edge-based finite element model for flow and transport, and a general local-nonlocal coupling that includes loosely and strongly coupled algorithms. This framework is capable of modeling a number of stages during the fracturing process including the initial perforation of the reservoir, the fracture itself, leakoff in the vicinity of the fracture, poroelastic response, damage modified permeability, as well as transport of species through the damaged matrix. It is intended that this framework be used to assess the probability of contamination for a given fracturing scenario and to discover ways to improve the fracturing process to reduce the associated risk. An overview of the numerical formulation will be given as well as some numerical illustrations.

1 INTRODUCTION

Whether or not to allow hydraulic fracturing in South Africa's Karoo region has been widely debated. The amount of shale gas stored in the subsurface of this region is estimated to be able to provide over 400 years worth of the entire country's energy needs. Conversely, aggressive drilling techniques like hydraulic fracturing have the potential to pollute underground water resources. While many welcome the economic benefits of harvesting natural gas, they fear the loss of the Karoo's most vital water supply. Unfortunately, many of the policy decisions regarding fracturing in the Karoo are being made with little scientific investigation. This is primarily due to a lack of the tools necessary to carry out these types of investigations. This work presents a framework for modeling hydraulic fracturing that can be used to evaluate the efficacy of using this technique in the Karoo and estimate the probability of groundwater contamination.

Modeling hydraulic fracture (including flow, deformation, damage, and chemical species transport) involves a number of challenging aspects, for example discontinuities in the displacement field, strong gradients in concentration, fast acting reactions, and physically complex flow behavior, and evolving material properties (just to name a few). In order to build a framework capable of incorporating these aspects, the following components were selected according to the features they provide:

- Solid modeling based on the Peridynamic Theory, which naturally incorporates cracks as part of the solution
- Flow and transport modeling using control volume finite elements, since this discretization scheme is mass conserving
- Effective stress treatment of pore pressure to incorporate the influence of the fracturing fluid on the geologic media
- Damage modified permeability to model the effects of degredation of the porous material on the flow characteristics
- Loose physics coupling for algorithmic stability and for decomposing time scales (enabling sub-cycling of physics)
- Analytic fields for material properties to provide for user-specified material models
- And a control volume based stencil for the peridynamic horizon that facilitates transfer of information between the flow/transport and deformation discretizations.

2 FORMULATION

We present here the basic formulation for this coupled framework in terms of the peridynamic theory, control volume finite elements, and the alterations required to couple the various discretizations into one coherent model.

2.1 *Peridynamics*

Although the peridynamic theory can be generalized to more sophisticated solid modeling (including plasticity, complex material behavior, etc., for references see (Silling 2000, Silling 2007, Silling & Askari 2005, Silling & Lehoucq 2008)), to simplify the initial implementation, we shall employ a linear elastic, quasi-static, state-based peridynamic formulation. We assme that inertial terms may be neglected and that the geologic material performs as perfectly elastic until failure. In a more sophisticated presentation of this framework, these assumptions can be relaxed.

Consider a neighborhood $\mathcal{H}$ of a material point $\mathbf{x}$ of radius δ (called the *horizon*) that includes all other material points for which a non-zero force interaction exists. If we denote another material point in this horizon as $\mathbf{x}$' then the governing equation for state-based peridynamics can be written

$$\int_{\mathcal{H}_x} \{\underline{\mathbf{T}}[\mathbf{x},t]\langle \mathbf{x}'-\mathbf{x}\rangle - \underline{\mathbf{T}}[\mathbf{x}',t]\langle \mathbf{x}-\mathbf{x}'\rangle\}\, \mathrm{d}V_{\mathbf{x}'} + \mathbf{b}(\mathbf{x},t) = 0 \tag{1}$$

where $\mathbf{T}$ is the force vector state field that defines the force interaction between two points $\mathbf{x}$ and neighbor $\mathbf{x}'$ and $\mathbf{b}(\mathbf{x},t)$ is the usual volumetric force. If we assume that the force between these neighbors acts along the vector pointing from $\mathbf{x}$ to $\mathbf{x}'$, denoted $\mathbf{M}$, we can evaluate $\mathbf{T}$ as a scalar coefficient times this unit vector

$$\mathbf{T}[\mathbf{x},t] = \tilde{t}\mathbf{M} \tag{2}$$

This scalar coefficient, $\tilde{t}$, is computed as

$$\tilde{t} = \frac{-3p}{m}x + \beta e^d \tag{3}$$

where p is the peridynamic pressure, m is the weighted volume, x is the distance magnitude between the two points in the reference configuration, β is a material parameter and $e^d = e - \theta x/3$ is the deviatoric extension scalar state field ($e = y - x$, y is the distance magnitude between the points in the deformed configuration and θ is the dilatation of the material).

2.2 *Control volume finite elements*

Unlike traditional finite elements, that require special modification to ensure local conservation of mass, control volume finite element schemes are locally mass conserving by construction (Martinez 2006). This is due to the degrees of freedom for velocity being based on the flux over each surface of the control volume rather than a nodal velocity. A good introduction to control volume finite elements can be found in (Voller 2009). Not only are control volume finite elements advantageous from the perspective of mass conservation, but they also provide robustness in several realistic scenarios that traditional finite elements do poorly. For example, along boundaries where the material properties change drastically, often spurious oscillations occur in node based schemes like finite elements. This is not the case for control volume finite elements which can be used along these boundaries without loss of accuracy or advanced stabilization schemes.

2.3 *Effective stress principle*

This framework includes the influence of two factors on the crack propagation caused by hydraulic fracturing. The first is the force of the fluid in the crack (after the initial perforation stage) and the second is the pore fluid pressure caused by fracturing fluid penetrating the region of material in the vicinity of the crack. The relative magnitude of these effects with respect to each other will vary according to the injection parameters. A high flow rate injection into a low permeability material will have very little leakoff, as such the fluid force in the crack will completely characterize the driving mechanism. Conversely, a slow injection into a highly permeable material will result in extensive penetration of the fluid beyond the crack surfaces effecting the response of the material in these regions.

A modification of the peridynamic theory to account for pore fluid pressure was presented in (Turner 2012). To account for the influence of pore pressure in the leakoff region of the hydraulic fracture, the peridynamic pressure p is augmented with the pore fluid pressure p_f such that the peridynamic pressure includes both a dilatational term and pore fluid pressure term

$$p = -k\theta + \gamma p_f \tag{4}$$

where γ is the fluid pressure coefficient and k is the bulk modulus. Depending on the definition of γ one can recover various forms of effective stress. For example if $\gamma = 1$, the resulting formulation closely resembles the classical effective stress principle of Terzaghi or Biot (Terzaghi 1943, Biot 1941, Biot & Willis 1957).

2.4 *Bond aligned fluid forces*

Fluid forces on the surface of the crack as it propagates are represented by bond aligned fluid forces. Since the peridynamic model is discretized into cells having only a single node as the crack surface evolves (that represents the centroid of the cell), there is no means by which to evaluate a normal vector on the surface. As such, one cannot simply convert the fluid pressure into

a force on that surface. In this framework we assume that the fluid forces act in the direction **M** defined by the bonds between neighbors. This applies to bonds that are broken as well. The magnitude of the fluid force $\tilde{f}$ is computed as

$$\tilde{f} = \frac{3p_f}{m}x \tag{5}$$

In this way, the driving force of the fluid pressure is applied to the residual for each cell according to the accumulation of the force relationship with each neighbor and a fluid force with each neighbor that persists even when the bond is broken.

2.5 *Damage modified permeability*

Damage is incorporated in the flow model via the damage modified permeability approach (Turner 2011) whereby the permeability of the porous matrix degrades according to the damage field computed in the peridynamic analysis. If the pristine permeability of the porous matrix is $\tilde{k}$ the damage modified permeability $\hat{k}$ is written

$$\hat{k} = (1.0 - d)\tilde{k} + d\bar{k} \tag{6}$$

where $\bar{k}$ is the permeability of a fully damaged material (representative of flow through a crack). The damage field from the peridynamic analysis is computed as the percentage of broken bonds for a given cell. Damage is zero for a pristine cell and one for a cell with all of its bonds broken. Figure 1 gives a representation of this model from the undeformed and damaged perspectives.

2.6 *Coupling aspects*

As an initial implementation the various physics of this framework are coupled via loose coupling using either a Gauss-Seidel approach or Jacobi iterations. In both of these methods, the residuals are evaluated in lock-step manner such that the control volume fluid calculation is advanced, the fluid pressure is passed to the peridynamic calculation, the peridynamic calculation is advanced and the resulting damage is passed to the fluid model. More sophisticated coupling algorithms are currently under investigation.

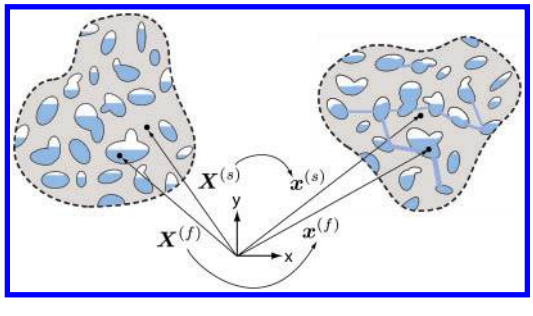


Figure 1. Pictorial description of the damage modified permeability model.

3 NUMERICAL EXAMPLES

3.1 *Breakdown pressure for constant flow rate injection*

To test the efficacy of this framework, initial simulations were performed to evaluate how well the proposed framework captures the breakdown pressure during a constant flow rate injection. In this scenario a subsection of the borehole is modeled as a plate in plane strain. The plate can be conceptualized as a slice of the material in the immediate vicinity of the borehole. The outer boundary of the plate is treated as the far-field and the inner boundary as the surface of the borehole which is pressurized by injection. The boundary condition consist of a constant mass flux into the borehole and lithostatic pressure conditions on the far-field boundary.

The complete process for this simulation can be broken down into several stages. In the first stage, the borehole pressurizes leading to dilation of the borehole. Eventually the material surrounding the borehole cracks leading to penetration of the fracturing fluid. Initially, the porous material is given a low permeability which degrades due to the presence of cracks. The fracturing fluid then flows into the regions of high permeability created by the cracks leading to crack propagation. Ultimately, due to increased volume in the cracks and less resistance to flow through the cracks the pressure profile drops substantially. The drop in pressure is indicative of the completion of fracturing. The ultimate pressure is known as the breakdown pressure.

The results of this simulation are shown in Figure 2 and Figure 3. Figure 2 shows the fluid pressure, fluid velocity and damage profile for a particular instance during the simulation just prior to breakdown. Figure 3 shows the breakdown pressure for two values of the bond critical stretch. The bond critical stretch

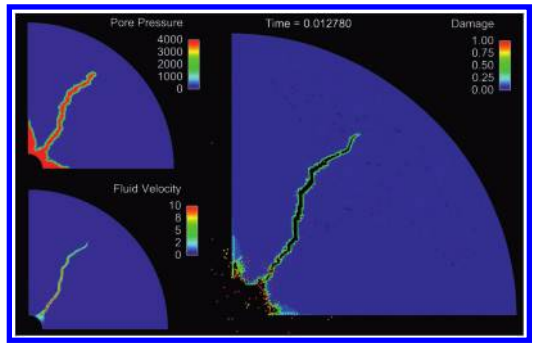


Figure 2. Snapshot of breakdown pressure prototype simulation. The top left image shows the fluid pressure, the bottom left image shows the fluid velocity and the right image shows the damage profile.

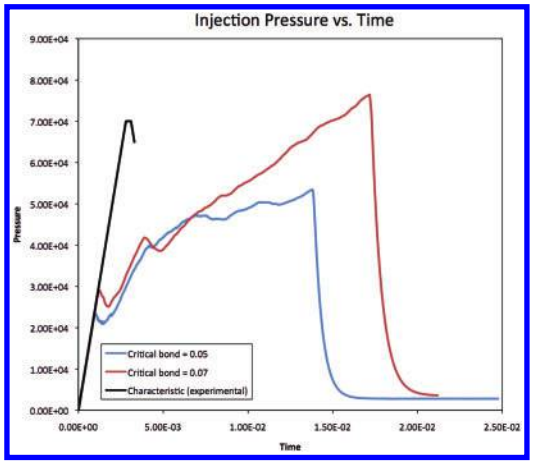


Figure 3. Breakdown pressure for various bond critical stretch values.

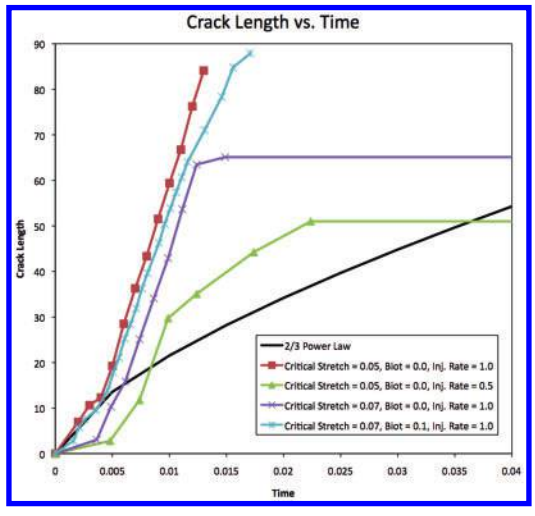


Figure 4. Crack length vs. time.

is representative of the ultimate strain the material. Note that the initial pressure profile increases linearly as expected, but the time of breakdown cannot easily be identified. Although the results capture the initial stages of the injection process, the ultimate ability of the material to resist damage propagation is overestimated as indicated by the lack of a distinct breakdown pressure. This is most likely due to the relationship between leakoff and crack penetration for a particular material. If the injection rate is high for a low permeability material, very little leakoff will occur. For a high permeability material with low injection rate, the fracturing fluid will permeate through a large portion of the material in the vicinity of the crack. This can have a large effect on the breakdown process causing aberrencies in the results such as those shown above.

3.2 *Crack propagation*

The proposed framework was also investigated with regards to the rate at which the cracks propagate in time. Depending on the injection parameters, the resulting cracks will either propagate enough to relieve the stress in the material resulting in a state of equilibrium or continue to race through the material with an infinite growth rate. Simulations were performed to evaluate the nature of crack propagation for the proposed framework.

Figure 4 shows the crack length vs. time for the injection simulations described above. Note that only in the initial stages does the crack propagate according to the 2/3 power law as predicted. Later stages in the simulation show cracks propagating in large increments or racing through the domain in one step. Further investigation is required to determine if modification of the time step or other simulation parameters will lead to closer correspondence with the 2/3 power law.

3.3 *Hydraulic fracturing in the Karoo*

This example illustrates the potential for this framework to evaluate the risk of underground water contamination from surfactants used in hydraulic fracturing. Given information such as the depth of the water table, the composition of the subsurface layers and associated material properties, as well as the nature of the groundwater currents, one can use the proposed framework to estimate the probability that contaminants introduced via the fracturing process will infiltrate underground water resources. The full capabilities of the proposed framework are employed for this problem: Propagation of the crack is modeled using the bond aligned fluid force method. The effects of leak-off are accounted for with the effective stress implementation. The injection behavior of the fluid is modeled using control volume finite elements as well as the transport of the contaminant. Finally, degradation of the permeability of the porous solid is captured via the damage modified permeability approach.

The domain of this problem is shown in Figure 5 by the dashed black line. A snapshot of the results from the simulation is shown in Figure 6. At the bottom of the domain, an initial perforation is placed to represent the damage that would have occurred in the initial stages of fracturing. This was done by preventing bonds from forming near a localized region of the injection. A constant pressure was applied to the surfaces of the perforation and lithostatic pressure was applied to the top of the domain. It was assumed that the concentration of the contaminant in the fracturing fluid was 1.0. This is of coarse not representative of the actual composition of a standard fracturing fluid, but can be treated as a worst case scenario. An advection velocity was used to represent underground currents such that the transport of the contaminant through the domain was characterized by diffusion and advection.

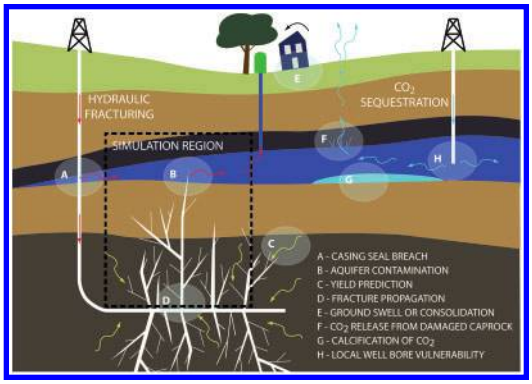


Figure 5. Cartoon showing domain of hydraulic fracturing simulation.

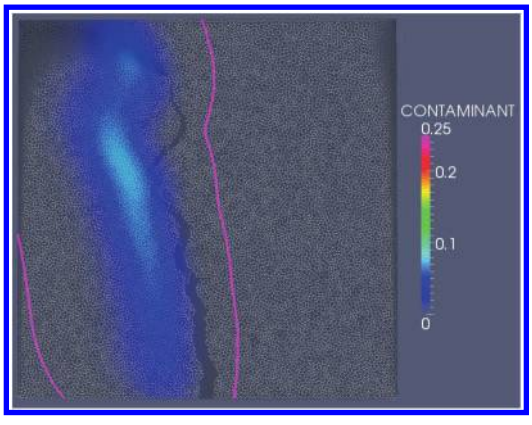


Figure 6. Snapshot of hydraulic fracturing simulation showing the concentration of contaminant as it is transported through the damaged domain.

4 DISCUSSION

Clearly, these initial simulations have not been experimentally validated, but rather illustrate the potential for this framework to model such a complex process under realistic conditions. In order for this framework to be applied effectively in decision making regarding hydraulic fracturing activities in South Africa's Karoo region an extensive study of the actual subsurface conditions must be performed. It is intended that in future works each component of the proposed framework will be verified through numerical investigation (mesh refinement studies, comparison with analytic or manufactured solutions) and validated with whatever experimental data is available. In addition, we intend to perform experiments to fill in the gaps where necessary.

Development of the numerical framework will continue as well, in particular with regards to assimilation of disparate time scales representing the various physics involved. Fracture propagation in porous media happens on a much faster timescale than the transport of the contaminants. These initial simulations were performed using a lockstep coupling by which each physics executes one step, variables are then passed, and the process is repeated for a certain time step until convergence is reached. This can be expensive computationally unless some type of subcycling is introduced. Also, the computational mesh used for each physics is identical (overlay) which aids in the transfer of data between peridynamics and the control volume finite elements, but in many cases requires much more refinement than is necessary.

5 SUMMARY

This work presents a coupled local-nonlocal framework for modeling hydraulic fracturing that can be used to predict the probability of subsurface water resource contamination. The framework consists of using peridynamics to model deformation and damage, control volume finite elements to model flow and transport, an effective stress principle to capture leak-off effects, damage modified permeability to represent the degradation of the porous material's resistance to flow, and bond aligned fluid forces to apply the driving mechanism of the fluid forces on the surfaces of the crack as it propagates. A number of simulations are presented that illustrate the potential of this framework. This work highlights the need for further experimental investigation of these processes to provide information with which to validate the model. It is intended that this work serve as a basis for further development of this framework to be used in numerical studies of hydraulic fracturing in the Karoo and other plays where groundwater contamination is a critical issue.

ACKNOWLEDGMENTS

This work was funded by Sandia National Laboratories (through the Lab Directed Research and Development Fund) and the Institute for Structural Engineering at Stellenbosch University.

REFERENCES

Biot, M. A. (1941). General theory of three dimensional consolidation. *Journal of Applied Physics 12*, 155–164.

Biot, M. A. & P. G. Willis (1957). The elastic coefficients of the theory of consolidation. *Journal of Applied Mechanics 24*, 594–601.

Martinez, M. J. (2006). Comparison of Galerkin and control volume finite element for advection–diffusion problems. *International Journal for Numerical Methods in Fluids 50*, 347–376.

Silling, S. A. (2000). Reformulation of elasticity theory for discontinuities and long-range forces. *Journal of the Mechanics and Physics of Solids 42*, 175–209.

Silling, S. A. (2007). Peridynamic states and constitutive modeling. *Journal of Elasticity 88*, 151–184.

Silling, S. A. & E. Askari (2005). A meshfree method based on the peridynamic model of solid mechanics. *Computers and Structures 83*, 1526–1535.

Silling, S. A. & R. B. Lehoucq (2008). Convergence of peridynamics to classical elasticity theory. *Journal of Elasticity 93*, 13–37.

Terzaghi, K. (1943). *Theoretical Soil Mechanics*. New York:Wiley.

Turner, D. Z. (2011). The damage modified permeability model: capturing flow and crack propagation in heterogenous porous media. *ASME International Mechanical Engineering Congress & Exposition*.

Turner, D. Z. (2012). A nonlocal model for fluid-structure interaction with applications in hydraulic fracturing. *International Journal for Computational Methods in Engineering Science & Mechanics. in-press*.

Voller, V. R. (2009). *Basic Control Volume Finite Element Methods for Fluids and Solids*. New Jersey, USA: World Scientific.

Research and Applications in Structural Engineering, Mechanics and Computation – Zingoni (Ed.)
© 2013 Taylor & Francis Group, London, ISBN 978-1-138-00061-2

Tensile and compressive buckling of shear deformable damaged beams

S. Caddemi, I. Caliò & F. Cannizzaro
Dipartimento di Ingegneria Civile ed Ambientale, University of Catania, Italy

ABSTRACT: In this work the static stability analysis of the Timoshenko beam in presence of an arbitrary number of concentrated cracks is studied. The governing differential equations are formulated by modelling the cracks as a concentrated reduction of the flexural stiffness, accomplished by the use of Dirac's delta distributions. The adopted model allowed the formulation of exact closed form solutions of the buckling modes and the buckling load equation for an arbitrary number of cracks and under different boundary conditions able to account for the shear deformability. The presented closed from solutions, besides the classical compressive buckling, is also able to capture the tensile buckling phenomenon, i.e. damaged columns subjected to a tensile axial load. The influence of multiple cracks on the stability of shear deformable beams, particularly under the action of tensile loads, has never been assessed in the literature and is here addressed on the basis of an extensive parametric analysis.

1 INTRODUCTION

The problem concerning the analysis of damaged beams has received considerable attention in the specific literature and interesting developments have been recently proposed in the last few years with regard to the adopted models, the analysis methods and closed-form solutions for particular structural problems.

The interest of the scientific community towards the mentioned problem is strongly motivated by the influence that damage might play in several engineering problems. In particular, the case of concentrated cracks have been studied by providing expressions for a diffused stiffness reduction in the vicinity of the crack (Christides and Barr, 1984; Sinha et al., 2002; Chondros et al., 1998; Liebowitz and Claus, 1968). Concentrated cracks have been also modelled, according to a macroscopic approach, as an equivalent rotational spring that allows a rotation discontinuity interpreted as the crack effect on the response (Gounaris and Dimarogonas, 1988; Ostachowicz and Krawczuk, 1991; Paipetis and Dimarogonas, 1986). The effect of a single concentrated crack on the response of a straight beams has been mostly evaluated under the hypothesis that the crack remains open during the loading process, implying a linear behaviour. Particularly, when damage occurrence along the beam span is not restricted to a single crack appearance, the equivalent spring approach shows to be suitable for determining competitive procedures and closed form solutions.

Among the engineering problems involving straight beams, particularly important is the loss of stability of the equilibrium configuration due to buckling caused by axial loads in columns under different boundary conditions. It has been widely proved that the presence of concentrated cracks can cause a considerable decrement of the buckling loads as well as modification of the relevant buckling modes. The stability of single and multiple cracked columns has been studied both for the Euler-Bernoulli (Anifantis and Dimarogonas, 1983; Wang et al., 2004; Li, 2001; Gurel 2007) and the Timoshenko (Takahashi, 1999; Li, 2002; Fan and Zeng, 2003) models, with the particular purpose, in the latter case, of assessing the influence of the shear deformability of the column. To the authors' knowledge, all the studies, focussed on the buckling of cracked columns, consider the action of compressive loads, except that reported in (Zapata-Medina et al., 2010) where the buckling behaviour of a single cracked shear deformable column has been captured by means of a classical approach in presence also of a tensile load. In (Aristizabal-Ochoa, 2005) it has been stated that the tensile buckling occurs also in slender beams and, moreover, that the tensile buckling loads are not necessarily the mirror images of the compression counterparts. However, it seems that when rubber bearing isolators are subjected to tensile loads, they reach cavitation before the tensile buckling occurs (Kelly, 2003). In any case, the influence of shear deformation might play a fundamental role, since the tensile buckling load can decrease significantly and be comparable to the compressive buckling.

The contribution of the present work is intended towards the formulation of closed form solutions for buckling modes and buckling load equations of shear deformable columns, affected by an arbitrary number of cracks, able to capture also the buckling phenomenon under the action of tensile loads.

So far, the authors have studied extensively the Euler-Bernoulli beam within different contexts in presence of an arbitrary number of cracks, providing closed form solutions (Caddemi and Caliò, 2008, 2009, 2012). The latter studies provided encouraging results based on the adoption of generalized functions (distributions) to model both flexural and shear stiffness reductions due to different causes (Biondi and Caddemi, 2007; Caddemi et al. 2012).

Aim of this paper is applying the distributional model to shear deformable columns with multiple cracks for evaluating their influence on tensile and compressive buckling. The adopted integration procedure leads to explicit closed-form solutions for the buckling modes and the buckling load equations of the Timoshenko column under different boundary conditions.

2 THE GOVERNING EQUATIONS FOR THE STABILITY OF THE TIMOSHENKO BEAM WITH MULTIPLE CRACKS

In this section a model of Timoshenko beam showing multiple discontinuities in the rotation function is presented, and its capability of describing the influence of concentrated cracks is shown. In particular the governing equations of the latter model will be formulated in presence of an axial load N to study the stability of such a beam.

Multiple singularities in the rotation functions, due to the presence of internal rotational springs at x_{γ_i}, $i=1,\dots,n_\gamma$, with $0 \le x_{\gamma_i} \le L$, can be modelled as reductions of the reference flexural stiffness by means of the adoption of the well known Dirac's delta $\delta(x)$ distribution, as follows (Biondi and Caddemi, 2007):

$$\begin{aligned} E(x)I(x) &= E_0 I_0 \left[1-\sum_{i=1}^{n_\gamma} \overline{\gamma}_i \delta(x-x_{\gamma_i})\right] \\ G(x)A(x) &= G_0 A_0 \end{aligned} \tag{1}$$

where E_0I_0 and G_0A_0 are the flexural and shear stiffnesses and $\overline{\gamma}_i$ are parameters describing the flexural stiffness reduction associated to the concentrated rotational singularities.

The stiffness reduction introduced in the model adopted in Eq. (1) can be considered equivalent to the effect produced by concentrated cracks if a suitable correspondence with the crack depth is adopted (Caddemi and Caliò, 2008, 2009).

For simplicity, by considering the dimensionless coordinate $\xi = x/L$, and indicating with the apex the differentiation with respect to ξ, the governing differential equations of the Timoshenko beam, by accounting for the singularities introduced in Eqs.(1), take the following form:

$$\begin{aligned} &\left[\left[1-\sum_{i=1}^{n_\gamma} \gamma_i \delta(\xi-\xi_{\gamma_i})\right]\varphi'(\xi)\right]' = \\ &= br^2\left[u'(\xi)+\varphi(\xi)\right]+\sigma^2\left[u'(\xi)+\varphi(\xi)\right] \end{aligned} \tag{2}$$

$$br^2\left[u'(\xi)+\varphi(\xi)\right]'+\sigma^2\varphi'(\xi)=0 \tag{3}$$

In Eqs.(2),(3), the normalized displacement function $u(\xi)$, the rotation function $\varphi(\xi)$ and the normalised axial load $\sigma^2 = N L^2/E_0I_0$ have been introduced. Furthermore, in Eqs.(2),(3), the dimensionless singularity parameters $\gamma_i = \overline{\gamma}_i/L$, and the shear stiffness parameter br^2, with $b = G_0/E_0$ and $r^2 = L^2A_0/I_0$, have been introduced.

After some mathematical manipulation Eqs.(2),(3) are written as follows:

$$\varphi'(\xi) = \left[\sigma^2 u(\xi) + b_1\xi + b_2\right]\left[1+\sum_{i=1}^{n_\gamma} \lambda_{\gamma_i}\,\delta(\xi-\xi_{\gamma_i})\right] \tag{4}$$

$$u'(\xi) = \frac{1}{H(\xi)}\left[-\frac{\sigma^2}{br^2}\varphi(\xi)+\frac{b_1}{br^2}\right]-\varphi(\xi) \tag{5}$$

where the dimensionless parameters $\lambda_{\gamma_i} = \gamma_i/(1-A\gamma_i)$ have been introduced. The latter quantities λ_{γ_i} will be considered in this work as damage parameters since they can be easily related to the crack depth according to classical crack models as shown in (Caddemi and Caliò, 2009).

The governing equations of the Timoshenko beam in presence of multiple cracks provided by Eqs.(4),(5) can be, however, reduced to a single equation by means of differentiation of Eq.(5), substitution of Eq.(4), and after simple algebra, providing the following expression for $u^{II}(\xi)$:

$$\begin{aligned} u^{II}(\xi)+\overline{\sigma}^2 u(\xi) = &-\hat{\sigma}^2\left[b_1\xi+b_2\right]+ \\ &-\sum_{i=1}^{n_\gamma} B\left[u(\xi_{\gamma_i})\right]\delta(\xi-\xi_{\gamma_i}) \end{aligned} \tag{6}$$

with the following positions:

$$B\left[u(\xi_{\gamma_i})\right] = \hat{\sigma}^2\left[\sigma^2 u(\xi_{\gamma_i})+b_1\xi_{\gamma_i}+b_2\right]\lambda_{\gamma_i} \tag{7}$$

$$\hat{\sigma}^2 = 1+\frac{\sigma^2}{br^2} \quad , \quad \overline{\sigma}^2 = \hat{\sigma}^2\sigma^2 \tag{8}$$

Explicit expressions for the normalised deflection function $u(\xi)$ can be obtained by integration of Eq.(6) as outlined in the following section.

3 EXACT SOLUTION OF THE STABILITY GOVERNING EQUATIONS

The general solution of Eq.(6) is given by the solution of the corresponding homogeneous equation, $u_h(\xi)$ and a particular integral $u_p(\xi)$ as follows:

$$\begin{aligned} u(\xi) &= u_h(\xi)+u_p(\xi) = \\ &= \hat{C}_3\sin\overline{\sigma}\xi+\hat{C}_4\cos\overline{\sigma}\xi+u_p(\xi) \end{aligned} \tag{9}$$

where $\hat{C}_3$, $\hat{C}_4$ are integration constants. We seek a particular integral $u_p(\xi)$ to be determined such that Eq.(6) is verified. The particular integral is found as follows:

$$\begin{aligned} u_p(\xi) = &-\frac{1}{\overline{\sigma}}\sum_{i=1}^{n_\gamma} B\left[u(\xi_{\gamma_i})\right]\sin\overline{\sigma}(\xi-\xi_{\gamma_i})U(\xi-\xi_{\gamma_i})+ \\ &+c_1\sin\overline{\sigma}\xi+c_2\cos\overline{\sigma}\xi+C_1\xi+C_2 \end{aligned} \tag{10}$$

c_1, c_2, C_1, C_2 being integration constants. The general solution of Eq.(6) can be written, in view of Eqs.(9),(10) and (7), as follows:

$$u(\xi) = C_1\xi + C_2 + C_3 \sin\bar{\sigma}\xi + C_4 \cos\bar{\sigma}\xi + \\ -\sum_{i=1}^{n_\gamma}\left[\bar{\sigma}\, u(\xi_{\gamma_i}) - \bar{\sigma} C_1 \xi_{\gamma_i} - \bar{\sigma} C_2\right]\lambda_{\gamma_i} \sin\bar{\sigma}(\xi - \xi_{\gamma_i}) \tag{11}$$

where the positions $C_3 = c_1 + \hat{C}_3$ $C_4 = c_2 + \hat{C}_4$ have been introduced.

According to Eq. (11) the deflection function $u(\xi)$, at the generic abscissa ξ, depends on the response at the preceding sections, where concentrated cracks occur, in terms of deflection $u(\xi_{\gamma_i})$, $\xi_{\gamma_i} < \xi$. The latter circumstance requires the evaluation of $u(\xi_{\gamma_i})$, for $\xi_{\gamma_i} < \xi$, by making use of the same Eq. (11), which can be rewritten in explicit closed form expression as follows:

$$u(\xi) = C_1 f_1(\xi) + C_2 f_2(\xi) + C_3 f_3(\xi) + C_4 f_4(\xi) \tag{12}$$

The functions $f_j(\xi), j = 1, ..., 4$, introduced in Eq.(12), in view of Eq. (11), assume the following expressions:

$$f_1(\xi) = \xi \quad , \quad f_2(\xi) = 1 \\ f_3(\xi) = \sin\bar{\sigma}\xi + \\ \quad -\sum_{i=1}^{n_\gamma} \bar{\sigma}\, f_3(\xi_{\gamma_i})\lambda_{\gamma_i} \sin\bar{\sigma}(\xi - \xi_{\gamma_i}) U\left(\xi - \xi_{\gamma_i}\right) \tag{13} \\ f_4(\xi) = \cos\bar{\sigma}\xi + \\ \quad -\sum_{i=1}^{n_\gamma} \bar{\sigma}\, f_4(\xi_{\gamma_i})\lambda_{\gamma_i} \sin\bar{\sigma}(\xi - \xi_{\gamma_i}) U\left(\xi - \xi_{\gamma_i}\right)$$

The solution in terms of rotation function $\varphi(\xi)$ can be obtained by substituting $u^I(\xi)$ into Eq.(5), as follows:

$$\varphi(\xi) = C_1 g_1(\xi) + C_2 g_2(\xi) + C_3 g_3(\xi) + C_4 g_4(\xi) \tag{14}$$

where

$$g_1(\xi) = -(1/\hat{\sigma}^2) f_1^I(\xi) - (1/\hat{\sigma}^2)(\sigma^2/br^2) = -1 \\ g_2(\xi) = -(1/\hat{\sigma}^2) f_2^I(\xi) = 0 \\ g_3(\xi) = -(1/\hat{\sigma}^2) f_3^I(\xi) \\ g_4(\xi) = -(1/\hat{\sigma}^2) f_4^I(\xi) \tag{15}$$

Eqs.(12)–(15) represent the sought closed-form solution of the governing Eqs.(2),3) and will be exploited to evaluate the buckling load of the Timoshenko beam in presence of multiple cracks.

4 THE EXPLICIT EXPRESSION OF THE BUCKLING LOAD EQUATION OF MULTI-CRACKED SIMPLY SUPPORTED COLUMNS

The buckling load equation can be derived for Timoshenko columns with multiple cracks by simply imposing the standard boundary conditions, including the general case of rotational and translational spring supports. In this section, the closed form solution presented in Eqs.(12)–(15) are adopted to treat the case of simply supported Timoshenko columns. The buckling load equations are derived and numerically solved in order to obtain the critical loads of the considered multi-cracked columns and the corresponding modes. The presented buckling load equations are able to capture the behaviour in both cases of compression and tension axial loads. The two cases are recovered for positive and negative values of the solutions, respectively.

The boundary conditions of the simply supported Timoshenko column are:

$$u(0) = 0 \ , \ \varphi^I(0) = 0 \ , \ u(1) = 0 \ , \ \varphi^I(1) = 0 \tag{16}$$

The four integration constants can be obtained, by imposing the conditions in Eqs.(16), as follows:

$$C_2 = 0 \quad , \quad C_4 = 0 \\ C_1 + C_3[\sin\bar{\sigma} - \sum_{i=1}^{n_\gamma} \bar{\sigma}\lambda_{\gamma_i} f_3(\xi_{\gamma_i}) \sin\bar{\sigma}(1 - \xi_{\gamma_i})] = 0 \tag{17} \\ C_3[\bar{\sigma}^2 \sin\bar{\sigma} - \sum_{i=1}^{n_\gamma} \bar{\sigma}^3 f_3(\xi_{\gamma_i})\lambda_{\gamma_i} \sin\bar{\sigma}(1 - \xi_{\gamma_i})] = 0$$

The last of Eqs.(17) leads to the following buckling load equation for the simply supported Timoshenko beam in presence of multiple cracks:

$$\sin\bar{\sigma} - \bar{\sigma} \sum_{i=1}^{n_\gamma} f_3(\xi_{\gamma_i})\lambda_{\gamma_i} \sin\bar{\sigma}(1 - \xi_{\gamma_i}) = 0 \tag{18}$$

Once the smallest solution $\bar{\sigma}_{cr}$ of Eq.(18) is obtained, the value of the first critical load $\sigma_{cr}^2 = N_{cr} L^2/(E_0 I_0)$ can be inferred by the definition $\bar{\sigma}^2 = [1 + \sigma^2/(b\, r^2)]\sigma^2$, given by Eq.(8), as follows:

$$\frac{\sigma_{cr}^4}{br^2} + \sigma_{cr}^2 - \bar{\sigma}_{cr}^2 = 0 \tag{19}$$

Solution of Eq.(19) leads to the following values for the compression (positive value) ${}^{+}\sigma_{cr}^2$ and tension (negative value) ${}^{-}\sigma_{cr}^2$ critical load parameters:

$$\left.\begin{aligned} {}^{+}\sigma_{cr}^2 &= {}^{+}N_{cr} L/(E_0 I_0) \\ {}^{-}\sigma_{cr}^2 &= {}^{-}N_{cr} L/(E_0 I_0) \end{aligned}\right\} = \frac{br^2}{2}\left[-1 \pm \sqrt{1 + \frac{4}{br^2}\bar{\sigma}_{cr}^2}\right] \tag{20}$$

Furthermore, once the tensile ${}^{-}N_{cr}$ and the compressive ${}^{+}N_{cr}$ critical loads have been evaluated, the relevant buckling modes are determined by means of the evaluation of the integration constants by solving Eqs.(17) and substituting in Eq.(12).

5 NUMERICAL APPLICATIONS

The presented closed form expressions of the buckling modes and the buckling load equations allow an



Figure 1. A simply supported column with two cracks at symmetric cross-sections.

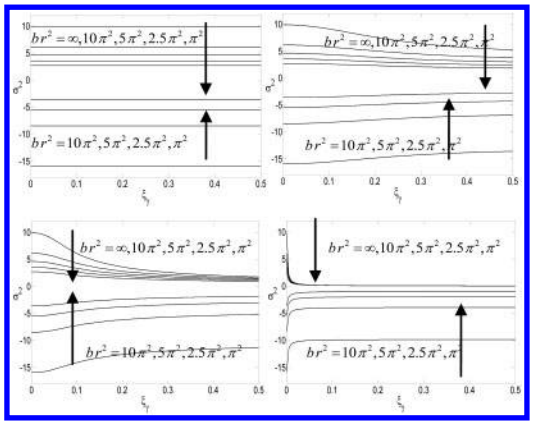


Figure 2. Critical load parameters ${}^{-}\sigma^2_{cr}$, ${}^{+}\sigma^2_{cr}$ versus crack position ξ_γ for different values of shear stiffness $br^2=\infty,\ 10\pi^2,\ 5\pi^2,\ 2.5\pi^2, \pi^2$ for the simply supported column with two cracks in Fig. 1: a) $\lambda_\gamma=0$; b) $\lambda_\gamma=0.2$; c) $\lambda_\gamma=1$; d) $\lambda_\gamma=100$.

extensive parametric analysis of columns with multiple cracks by accounting for the influence of the shear deformability. This section aims at new results regarding the influence of multiple cracks on the buckling under both tensile and compressive axial loads. The parametric analysis has been conducted by plotting graphs of the buckling load parameter σ^2 and the buckling shapes for different number, position and intensity of the cracks and analysing the sensitivity with regard to the shear deformability of the column.

It is shown how the tensile buckling load is very sensitive to the shear deformability in comparison to the compressive case.

The buckling behaviour of a simply supported column with two cracks occurring at symmetric cross-sections, as depicted in Fig. 1, is analysed. The critical load parameters versus the crack position ξ_γ along the column axis is plotted in Fig. 2 for different values of the shear stiffness and the crack intensity.

The results for the simply supported column with two cracks are reported in compact form in Fig. 3 where the surfaces representing the tensile ${}^{-}\sigma^2_{cr}$ and the compressive ${}^{+}\sigma^2_{cr}$ buckling load parameters versus the crack position and the crack intensity parameter are reported for different values of the shear stiffness. The buckling shapes for the case of double cracked simply supported column are reported in Fig. 4.

The novelty of the proposed procedure with respect to the others, available in the literature, lies in the capability of capturing the effect of the presence of an arbitrary number of multiple cracks by means of closed

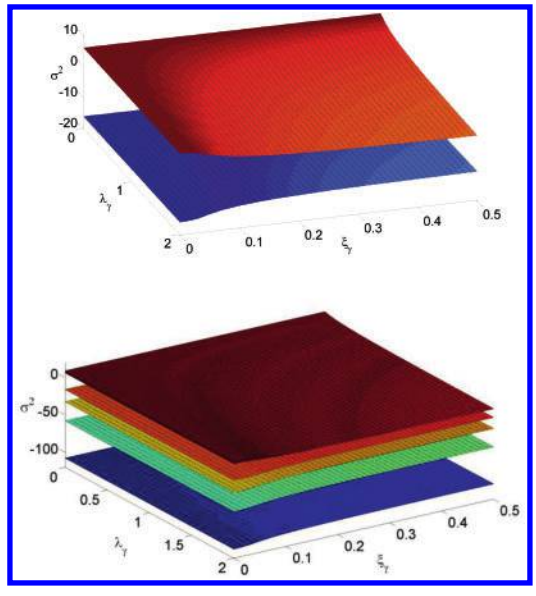


Figure 3. Critical load parameters ${}^{-}\sigma^2_{cr}$, versus crack position ξ_γ and intensity λ_γ for the simply supported column with two cracks in Fig. 1 for different values of shear stiffness: a) $br^2=\pi^2$; b) $br^2=10\,\pi^2,\ 5\,\pi^2, 2.5\,\pi^2, \pi^2$.

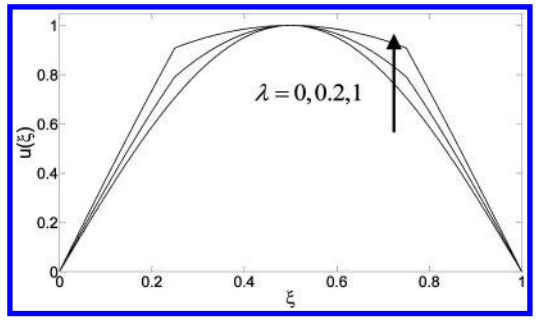


Figure 4. Compressive and tensile buckling shapes for the simply supported column with two cracks in Fig. 1 for crack intensity parameter $\lambda_\gamma=0,\ 0.2,\ 1$, for crack position $\xi_\gamma=0.25$.

form solutions able to obtain also results concerning the tensile buckling phenomenon. No additional computational cost with respect to the classical undamaged case is required. Hence, finally, since to date extensive analyses for cases with multiple cracks are not available in the literature, in Figs.5-7 the case of simply supported column with an increasing number of cracks has been treated. In particular, in Figs.5,6 results in terms of buckling load and shapes, respectively, for $n_\gamma=5,\ 10$ cracks are reported. While in Fig. 7 the surfaces representing the tensile ${}^{-}\sigma^2_{cr}$ and the compressive ${}^{+}\sigma^2_{cr}$ buckling load parameters versus the crack intensity parameter λ_γ and the number n_γ of the cracks, uniformly spaced along the span, are reported.

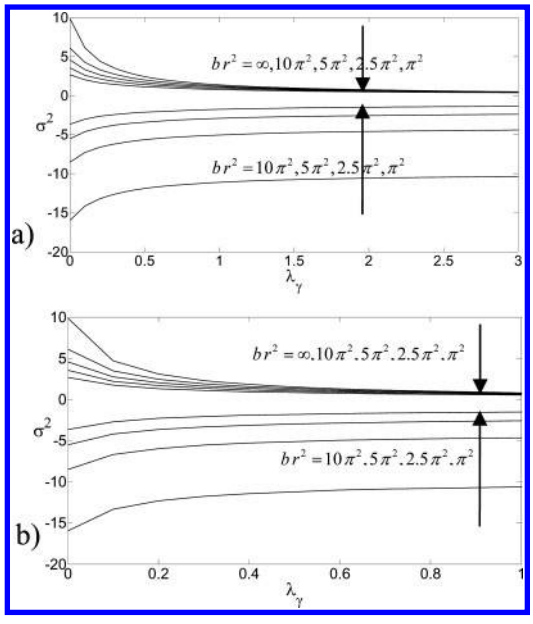


Figure 5. Critical load parameters ${}^{-}\sigma_{cr}^2$, ${}^{+}\sigma_{cr}^2$ versus the crack intensity parameter λ_γ for a simply supported column with multiple n_γ cracks, uniformly spaced along the span, for different values of shear stiffness $br^2=\infty,\ 10\pi^2,\ 5\pi^2, 2.5\pi^2, \pi^2$: a) $n_\gamma=5$; b) $n_\gamma=10$.

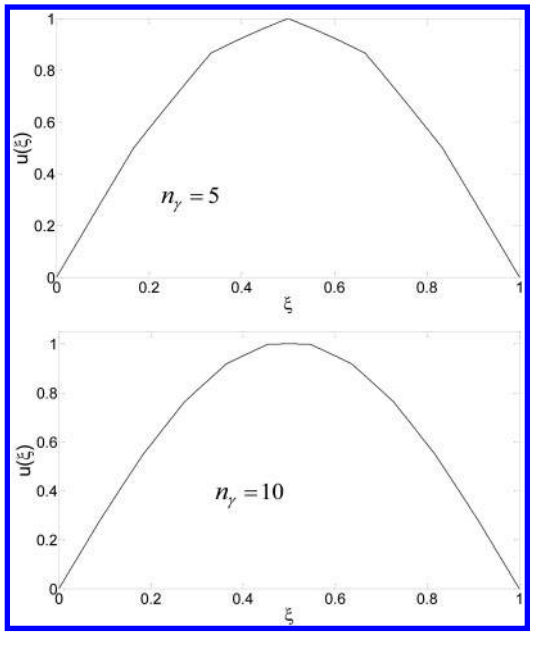


Figure 6. Compressive and tensile buckling shapes for a simply supported column with multiple $n_\gamma=5,\ 10$ cracks, uniformly spaced along the span, for crack intensity parameter $\lambda_\gamma=1$.

6 CONCLUSIONS

In this work a contribution towards the understanding of the buckling phenomenon of shear deformable damaged columns, in presence of compressive and tensile loads, has been provided. The damage has been considered in the form of multiple cracks modelled as a concentrated flexural stiffness reduction of the column that has been accounted for, in the governing equations, by means of Dirac's delta distributions. An integration procedure leading to closed form solutions of the buckling modes and the buckling load equations has been presented. The proposed explicit solutions concerning the buckling of shear deformable columns, accounting for the presence of an arbitrary number of cracks, represents a novel achievement in the specific literature. Moreover, study of the tensile buckling phenomenon of multi-cracked columns has been possible in this work, for the first time, by means of the proposed explicit solutions. Extensive parametric analyses for multi-cracked simply supported and clamped-clamped columns have been conducted and no additional difficulty with respect to undamaged columns is introduced. The model adopted in this work for the concentrated crack does not account for any influence on the local shear deformability. This latter aspect, however particularly significant in the tensile buckling phenomenon, is not trivial and is currently under investigation.

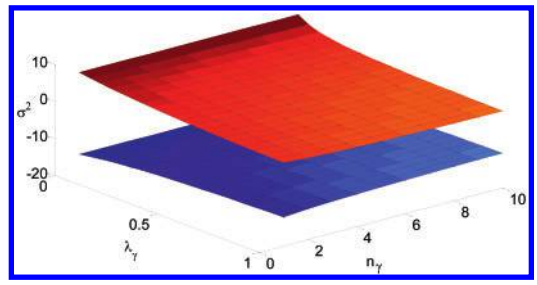


Figure 7. Critical load parameters ${}^{-}\sigma_{cr}^2$, ${}^{+}\sigma_{cr}^2$ versus the intensity λ_γ and the number n_γ of cracks, uniformly spaced along the span, for the simply supported column for the shear stiffness $br^2=\pi^2$.

REFERENCES

Anifantis N., Dimarogonas A., 1983, Stability of columns with a single crack subjected to follower and vertical loads. *International Journal of Solids and Structures* 19, 281–291.

Aristizabal-Ochoa, J.D., 2005, Discussion on "Tension buckling in multilayer elastomeric bearings" by James M. Kelly. *Journal of Engineering Mechanics* ASCE 131, 106–108.

Biondi, B. & Caddemi, S. 2007. Euler-Bernoulli beams with multiple singularities in the flexural stiffness. *European Journal of Mechanics A/Solids* 26: 789–809.

Caddemi, S., Caliò, I., 2008. Exact solution of the multi-cracked Euler-Bernoulli column. *International Journal of Solids and Structures* 45(16), 1332–1351.

Caddemi, S., Caliò, I., 2009. Exact closed-form solution for the vibration modes of the Euler–Bernoulli beam with multiple open cracks. *Journal of Sound and Vibration* 327, 473–489.

Caddemi, S., Caliò, I., 2012. The influence of the axial force on the vibration of the Euler-Bernoulli beam with an arbitrary number of cracks. *Archive of Applied Mechanics* 82(6), 827–839.

Caddemi, S., Caliò, I., Cannizzaro, F., 2012. Closed-form solutions for stepped Timoshenko beams with internal singularities and along-axis external supports. *Archive of Applied Mechanics* doi:10.1007/s00419-012-0704-7.

Chondros, T.J., Dimarogonas, A.D. and Yao, J., 1998. A continuous cracked beam vibration theory. *Journal of Sound and Vibration* 215(1), 17–34.

Christides, S., Barr, A.D.S., 1984. One-dimensional theory of cracked Bernoulli-Euler beams. *International Journal of Mechanical Sciences* 26(11/12), 639–648.

Fan, S.C., Zheng, D.Y., 2003. Stability of a cracked Timoshenko beam column by modified Fourier series. *Journal of Sound and Vibration* 264, 475–484.

Gounaris, G., Dimarogonas, A.D., 1988. A finite element of a cracked prismatic beam for structural analysis. *Computers and Structures* 28, 309–313.

Gurel, M.A., 2007. Buckling of slender prismatic circular columns weakened by multiple edge crack. *Acta Mechanica* 188, 1–19.

Kelly, J.M., 2003. Tension buckling in multilayer elastomeric bearings. *Journal of Engineering Mechanics* ASCE 129(12), 1363–1368.

Li, Q.S., 2001. Buckling of multi-step cracked columns with shear deformation. *Engineering Structures* 23, 356–364.

Li, Q.S., 2002. Buckling of an elastically restrained multi-step non-uniform beam with multiple cracks. *Archive of Applied Mechanics* 72, 522–535.

Liebowitz, H., Claus Jr., W.D.S., 1968. Failure of notched columns. *Engineering Fracture Mechanics* 1, 379–383.

Ostachowicz, W.M., and Krawczuk, C., 1991. Analysis of the effect of cracks on the natural frequencies of a cantilever beam. *Journal of Sound and Vibration* 150(2), 191–201.

Paipetis, S.A., and Dimarogonas, A.D., 1986. *Analytical Methods in Rotor Dynamics*. Elsevier Applied Science, London.

Sinha, J. K., Friswell, M.I., and Edwards, S., 2002. Simplified models for the location of cracks in beam structures using measured vibration data. *Journal of Sound and Vibration* 251(1), 13–38.

Takahashi, I., 1999. Vibration and stability of non-uniform cracked Timoshenko beam subjected to follower force. *Computers and Structures* 71, 585–591.

Wang, C.Y., Wang, C.M., Aung, T.M., 2004. Buckling of a weakened column. *Journal of Engineering Mechanics* ASCE 130, 1373–1376.

Zapata-Medina, D.G., Arboleda-Monsalve, L.G., Aristizabal-Ochoa, J.D., 2010. Static stability formulas of a weakened Timoshenko column: effects of shear deformations. *Journal of Engineering Mechanics* ASCE 136(12), 1528–1536.

9. Fracture, fatigue

Research and Applications in Structural Engineering, Mechanics and Computation – Zingoni (Ed.)
© 2013 Taylor & Francis Group, London, ISBN 978-1-138-00061-2

The use of the theory of critical distances in fracture and structural integrity assessments

S. Cicero, V. Madrazo, I. Carrascal & T. García
Universidad de Cantabria, Santander, Spain

ABSTRACT: There are many situations where the structural integrity of a given component or structure is determined by the presence of defects acting as stress risers. Moreover, these defects are not necessarily cracks, which can be analysed using fracture mechanics concepts, but they may be notch-like defects (e.g., mechanical damage, fabrication defects, corrosion defects, holes…). In such cases, the application of ordinary fracture mechanics assessments may lead to overconservative results, so that it is important to define methodologies for the fracture and structural integrity assessment of components containing notches or any other kind of stress riser. This paper presents the capacities of the Theory of Critical Distances (TCDs) for the assessment of this kind of situations, gathering and summarising the results obtained by the authors in a wide range of materials. The results show how the TCDs provides reasonable results for the prediction of both the apparent fracture toughness and the load-bearing capacity. It also increases the accuracy of the structural integrity assessments performed using Failure Assessment Diagrams.

1 INTRODUCTION

1.1 *The theory of critical distances*

The Theory of Critical Distances (TCDs) is essentially a group of methodologies, all of which use a parameter (the critical distance, L) when performing fracture and fatigue assessments (Taylor (2007). The critical distance, in fracture assessments is defined by:

$$L = \frac{1}{\pi}\left(\frac{K_c}{\sigma_0}\right)^2 \tag{1}$$

K_c is the material fracture toughness and σ_0 is a characteristic material strength parameter named the inherent strength, usually larger than the material ultimate tensile strength (σ_u) that requires calibration.

As shown in Taylor (2009), the most important methodologies included within the TCDs are:

Figure 1. Stress-distance curve at the defect tip, and definition of the PM and LM methodologies.

a) The Point Method (PM): it establishes that fracture occurs when the stress reaches the inherent strength (σ_0) at a certain distance from the defect tip, L/2 (Equation 2):

$$\sigma\left(\frac{L}{2}\right) = \sigma_0 \tag{2}$$

b) The Line Method (LM): it assumes that fracture occurs when the average stress along a certain distance, 2L (starting from the defect tip), reaches the inherent strength, σ_0. Therefore, the LM expression is:

$$\frac{1}{2L}\int_0^{2L}\sigma(r)dr = \sigma_0 \tag{3}$$

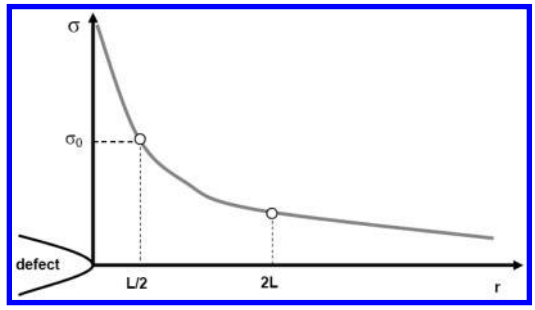


Figure 1. Stress-distance curve at the defect tip, and definition of the PM and LM methodologies.

Figure 1 shows an example of both methodologies:

c) The Imaginary Crack Method (ICM): it considers an imaginary crack at the defect tip, and failure occurs when a critical value of the stress intensity factor, K_c is reached. The length of the crack is, precisely, L.

d) Finite Fracture Mechanics (FFM): In this approach the failure is predicted using a balance of energies, analogously to Griffith (1920), but assuming finite

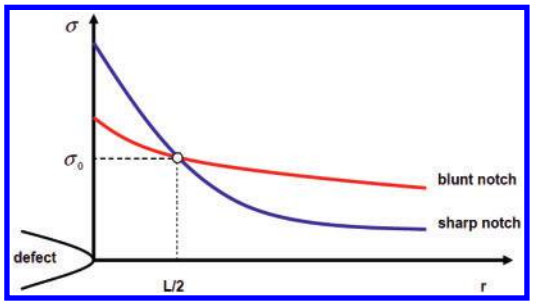


Figure 2. Obtaining of L and σ_0.

crack propagations (Δa, instead of da). The failure stress can be expressed as:

$$\sigma_f = \sqrt{\frac{G_c E}{\pi\left(a+\frac{\Delta a}{2}\right)}} = \frac{K_c}{\sqrt{\pi\left(a+\frac{\Delta a}{2}\right)}} \quad (4)$$

The most suitable value for Δa is 2L.

There is a relatively simple way to obtain L and σ_0 for a certain material, based on the PM. It consists in performing fracture tests on two specimens with different types of defects (e.g., sharp and blunt defect). The specimens can then be modeled at fracture with finite elements, obtaining the corresponding stress fields at the defect tip (Figure 2). The stress-distance curves cross each other at a point with coordinates L/2 and σ_0 (Taylor 2007, Cicero et al. 2012a, Madrazo et al. 2012, Cicero et al. in press).

Whichever the methodology used, one of the key aspects of the TCDs is that it can be applied to any kind of stress riser, not only to cracks, so it extends the fracture analysis of fracture processes far beyond the capacities of ordinary fracture mechanics, whose application to non-sharp defects (i.e., cracks) generally leads to overconservative results.

Once the TCDs and its different methodologies have been explained, the next sections are focused on the different applications of this theory when performing fracture and structural integrity analyses.

2 PREDICTIONS OF LOAD-BEARING CAPACITY

2.1 *Linking the TCDs to the load-bearing capacity*

The TCDs allows the load bearing capacity of a structural component containing any kind of stress risers to be estimated. For this purpose it is necessary only to apply the equations defining any of the different methodologies included within the TCDs. For example, Equation (1) must be applied in the case of the PM, or Equation (3) in the case of the LM.

2.2 *Experimental validation of load-bearing capacity predictions*

As an example, in Cicero et al. (2012b) there is a wide application of the PM on the fracture analysis of 38 different specimens made of Al7075-T651, combining different types of loads (tensile vs. bending) and defects (U-shaped notches, V-shaped notches, circular holes, etc). Figure 3 compares the predictions provided by the PM to the experimental results, revealing accurate results in most of the tested specimens.

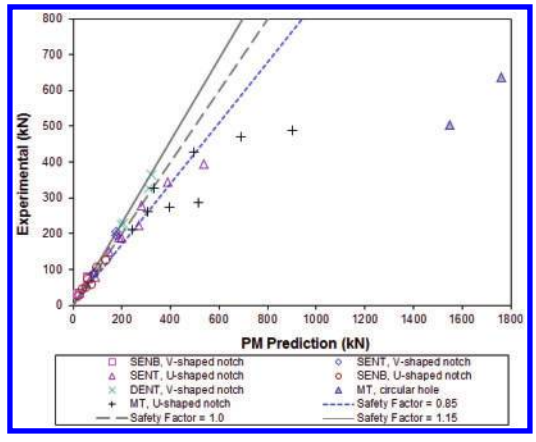


Figure 3. Comparison between the experimental results and the load-bearing capacity predictions provided by the PM.

Details concerning the limitations of this kind of predictions, as well as the justification of those inaccurate predictions shown in Figure 3, may be consulted in Cicero et al. (2012b). Here, it is sufficient to say that the strict application of the TCDs provides good results as long as the relation between the notch radius and the critical distance (ρ/L) is lower than 20. This ratio is known as the Neuber number (Taylor 2011).

The literature presents many other examples validating the application of the TCDs to perform load-bearing capacity predictions (e.g., Taylor 2007).

3 PREDICTIONS OF APPARENT FRACTURE TOUGHNESS

3.1 *Linking the TCDs to the apparent fracture toughness, K_{IN}*

The TCDs, in its different versions, allows the apparent fracture toughness (K_{IN}) of any material to be predicted in notched conditions, which is generally higher than the fracture toughness observed in cracked conditions. For this propose, it is necessary to consider the stress distribution on the notch tip. One commonly used expression is that provided by Creager & Paris (1967), Equation 5, for U-shaped notches, which is equal to that ahead of the crack tip but displaced a distance equal to ρ/2 along the x-axis:

$$\sigma(r) = \frac{K_I}{\sqrt{\pi}} \frac{2(r+\rho)}{(2r+\rho)^{3/2}} \quad (5)$$

where K_I is the applied stress intensity factor for a crack with the same dimensions as the notch being

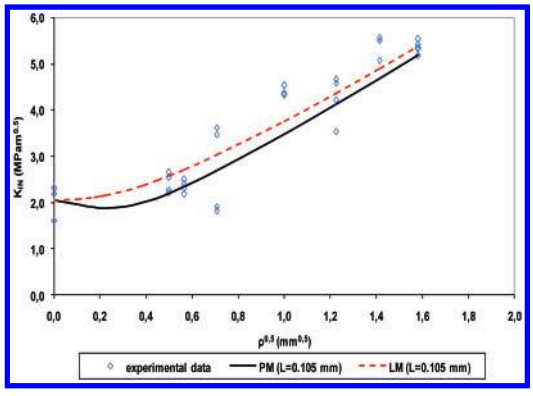


Figure 4. Comparison between experimental results and the TCDs (PM and LM) predictions of K_{IN}. PMMA.

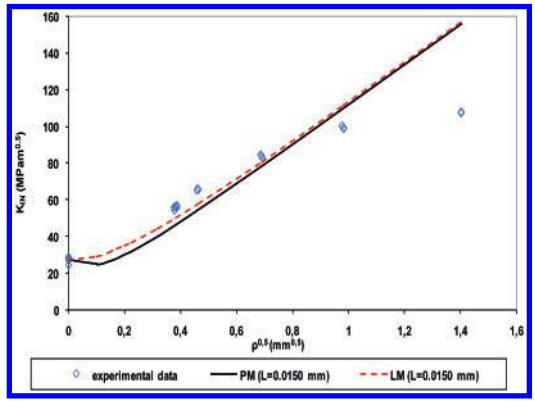


Figure 5. Comparison between experimental results and the TCDs (PM and LM) predictions of K_{IN}. Al7075-T651 (LT).

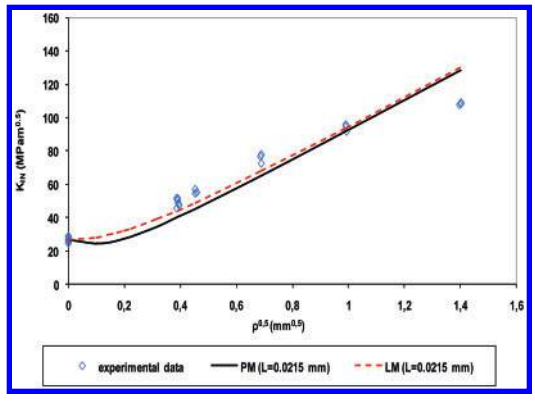


Figure 6. Comparison between experimental results and the TCDs (PM and LM) predictions of K_{IN}. Al7075-T651 (TL).

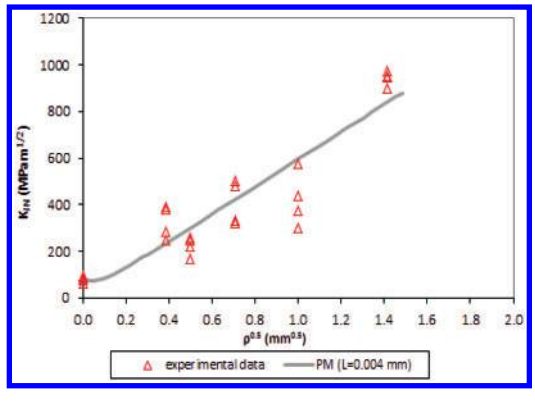


Figure 7. Comparison between experimental results and the TCDs (PM and LM) predictions of K_{IN}. Steel S275JR (−50°C).

analysed, and ρ is the notch radius. Then, combining Equation 5 and the different methodologies of the TCDs, the corresponding expressions of the apparent fracture toughness can be easily obtained. In the case of the PM, this gives:

$$K_{IN} = K_C \frac{\left(1+\frac{\rho}{L}\right)^{3/2}}{\left(1+\frac{2\rho}{L}\right)} \quad (6)$$

In the case of the LM, the expression is even simpler:

$$K_{IN} = K_C \sqrt{1+\frac{\rho}{4L}} \quad (7)$$

Once K_{IN} is determined, the fracture analysis of an existing notch in a material whose fracture toughness is K_c is transformed into an equivalent fracture analysis of an existing crack in a material whose fracture resistance is K_{IN}. Therefore, the analysis is reduced to Equation 8:

$$K_I = K_{IN} \quad (8)$$

Again, K_I is the applied stress intensity factor solution for a crack (with well-known existing solutions for a wide variety of geometries, e.g. BS7910 2005, FITNET FFS 2008), and K_{IN} is the so- called apparent fracture toughness.

3.2 *Experimental validation of K_{IN} predictions*

The K_{IN} predictions provided by the TCDs have been applied to a number of very distinct materials: polymer PMMA (Cicero et al. 2012a), aluminum alloy Al7075-T651 with two different orientations, TL and LT (Madrazo et al. 2012), and two structural steels, S275JR and S355J2 at −50°C and −150°C respectively (Cicero et al., in press).

The corresponding comparisons between the prediction of K_{IN} and the experimental results are shown in Figures 4–8. These figures represent the apparent fracture toughness as a function of the square root of the notch radius, which is a common representation in notch assessments (Taylor 2007), given that it clearly shows the notch effect on fracture resistance and also because the notch radius is included in a square root in K_{IN} predictions (Equation 7) or nearly (Equation 6).

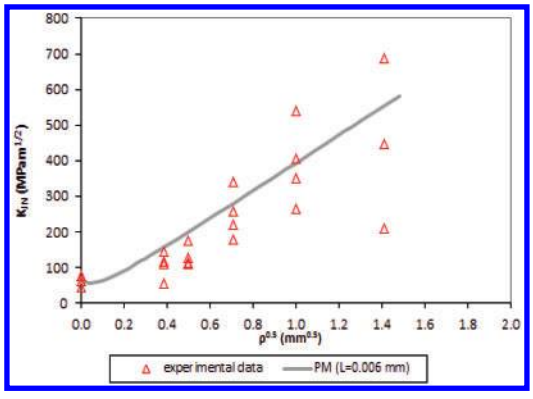


Figure 8. Comparison between experimental results and the TCDs (PM and LM) predictions of K_{IN}. PMMA.

From the results shown above, it is clear that the TCDs provides accurate predictions of the apparent fracture toughness. Again, details concerning the limitations of this kind of predictions may be consulted in Cicero et al. (2012a), Madrazo et al. (2012), Cicero et al. (in press).

4 COMBINING THE TCD WITH FAILURE ASSESSMENT DIAGRAMS

4.1 *Failure Assessment Diagrams*

Failure Assessment Diagrams (FADs) constitute one of the main engineering tools for the assessment of fracture-plastic collapse processes in cracked components (e.g., Anderson 1991, FITNET FFS 2008). These diagrams present a simultaneous assessment of both fracture and plastic collapse processes by using two normalised parameters, K_r y L_r, whose expressions are:

$$K_r = \frac{K_I}{K_C} \tag{9}$$

$$L_r = \frac{P}{P_L} \tag{10}$$

P being the applied load and P_L being the plastic collapse load. Therefore, L_r evaluates the structural component situation against plastic collapse, and K_r evaluates the component against fracture. Once the component assessment point is defined through the coordinates (K_r,L_r), it is necessary to define the component limiting conditions. With this purpose, the Failure Assessment Line (FAL) is defined, so that in case the assessment point is located between the FAL and the coordinate axes, the component is considered to be under safe conditions, whereas if the assessment point is located above the FAL, the component is considered to be under unsafe conditions. The critical situation (failure condition) is that in which the assessment point lies exactly on the FAL. Figure 9 shows an example with the different possible situations. In any

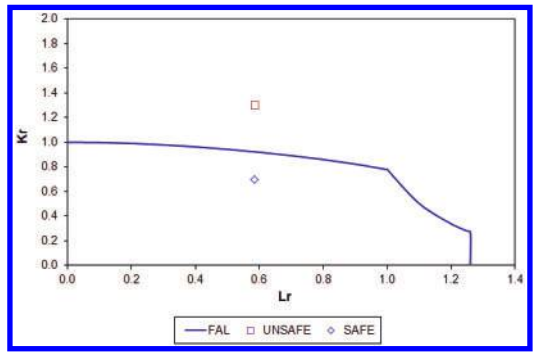


Figure 9. FAD analysis showing two possible situations: safe conditions; unsafe conditions.

case, a key point concerning FADs is that they allow fracture assessments to be performed for the whole range of plasticity levels, from linear-elastic fracture mechanics up to plastic collapse. This has particular importance when assessing notches, given that this kind of defects generate an increase in the non-linear phenomena occurring in the material (e.g., Cicero et al. 2012a), and fracture analyses based on Equation (8) would not take into account this fact (and thus would not be accurate).

4.2 *Combining the TCDs and FADs*

Now, if it is intended to perform structural integrity assessments on notched components using the FAD methodology, it is necessary to define both K_r and L_r for this particular case. Considering the fracture analysis of a notch presented above (Section 3.1), the K_r parameter would be:

$$K_r = \frac{K_I}{K_{IN}} \tag{11}$$

K_{IN} may follow the different solutions provided by the TCDs (e.g., Equation 6 or Equation 7).

In order to complete the FAD analysis, it is necessary to define the L_r parameter, which depends on the plastic collapse load (see Equation 10). Plastic collapse occurs through the yielding of the remnant section, so that in a perfectly plastic material it may be defined by the material yield stress and the defect dimensions, with no influence of the radius existing on the defect tip. In other words, at plastic collapse, the defect does not act as a stress riser, it reduces the resistant section, so that the plastic collapse does not depend on the notch tip and it is (ideally) the same for notches and cracks (which are actually notches whose notch radius tends to zero) (e.g., Miller 1988, Cicero et al. 2008). Therefore, the definition of L_r for notches is exactly the same as that defined for cracks, with P_L well known solutions provided by the literature.

If this methodology is compared to the assessment of notches as if they were cracks (a conservative practice), this correction would produce a reduction of

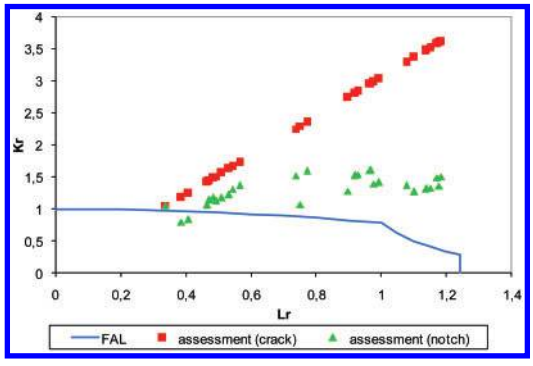


Figure 10. FAD assessment of PMMA notched specimens (K_{JC} value corresponding to a 95% confidence level).

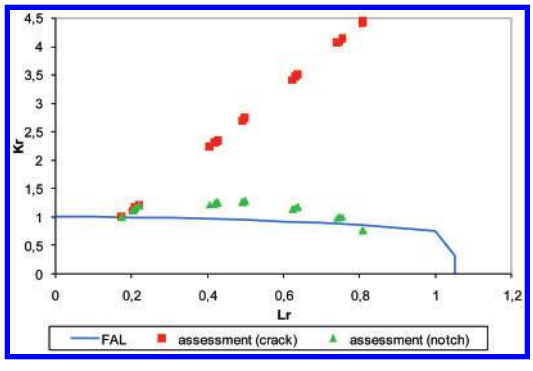


Figure 11. FAD assessment of Al7075-T651 specimens (K_{JC} corresponding to a 95% confidence level). LT orientation.

the K_r parameter and, then, a vertical displacement (downwards) of the assessment point.

In order to apply and validate the methodology here proposed, it is necessary to determine the corresponding K_c and L values for the materials being analysed. K_c can be directly obtained from the test results of the cracked specimens. A common engineering practice in FAD assessments is to consider a characteristic value associated to a given confidence level, when a probabilistic approach is pursued (e.g., 95% confidence level).

4.3 *Experimental validation*

Figures 10–14 gather, respectively, the results obtained for PMMA, Al7075-T651, and steels S275JR (−50°C) and S355J2 (−150°C), when performing a FAD assessment of fracture notched specimens made of these materials. The figures show a comparison between the analysis of notches without any consideration of the notch effect, and the analysis performed following the methodology proposed in this paper (thus, considering the notch effect). The expressions defining the FAD have been taken from the FITNET FFS (2008), Option 1, whereas the K_I and P_L solutions have been taken from Anderson (1991). The notch correction applied in the analyses was the one provided by the PM (Equation 7).

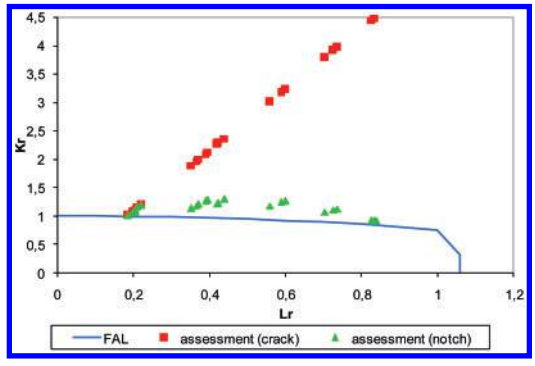


Figure 12. FAD assessment of Al7075-T651 specimens (K_{JC} corresponding to a 95% confidence level). TL orientation.

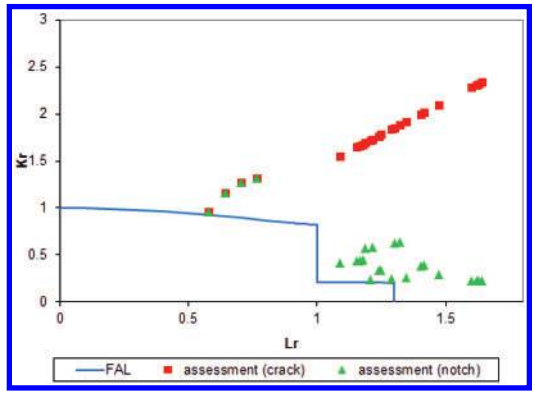


Figure 13. FAD assessment of S275JR specimens at −50°C (K_{JC} value corresponding to a 95% confidence level).

It can be observed how the assessment points (at failure) of the specimens when there are no notch corrections are located, in many cases, far from the critical condition defined by the FAL. This means that the failure load predictions derived from the FAD analysis would have been much lower than the actual ones (showing the conservatism of this type of analysis). However, once the notch corrections have been applied, the corresponding assessment points are located very close to the FAL, providing much closer predictions to the failure loads.

Here, it should be noted that in the case of the PMMA and the Al7075-T651 the fracture toughness was measured in terms of K_{IC}, providing K_{IN} values in notched conditions when using Equation 7, whereas for the two analysed steels the fracture resistance was measured in terms of K_{Jc} (ASTM E1820-11 2011), providing K_{JN} values through Equation 7. It can also be observed how the assessment points appears grouped together, each group corresponding to a given notch radius and, then, to a certain level of conservatism (the larger the notch radius, the further away the points from the FAL and, then, the higher the conservatism).

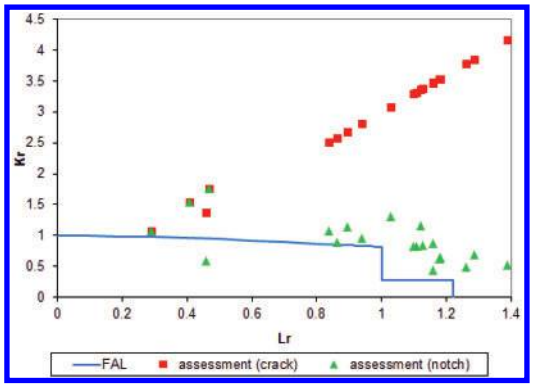


Figure 14. FAD assessment of S355J2 specimens at −150°C (K_{JC} value corresponding to a 95% confidence level).

5 CONCLUSIONS

This paper has presented the main applications of the TCDs, and its corresponding methodologies (e.g., PM and LM), to structural integrity assessments: a) the estimation of the load-bearing capacity by the direct application of the different methodologies included within the TCDs; b) the estimation of the apparent fracture toughness, which may be used in fracture assessments by direct comparison to the applied stress intensity factor; c) the combination of the TCDs with FADs, which allows notched components within the whole range of plasticity levels to be assessed, from linear-elastic conditions up to plastic collapse situations.

Experimental data covering different types of materials (PMMA, Al7075-T651, S275JR and S355J2) have also been presented, validating the above-mentioned applications, and demonstrating how the TCDs can be applied to the assessment of notched components, providing safe, accurate results.

REFERENCES

Anderson, T.L. 1991. *Fracture mechanics: fundamentals and applications*. Florida: CRC Press.

ASTM E1820-11. 2011. *Standard test method for measurement of fracture toughness*. Philadelphia: American Society for Testing and Materials.

BS 7910: 2005. 2005. *Guide to methods for assessing the acceptability of flaws in metallic structures*. London: British Standards Institution.

Cicero, S. et al. 2008. *Structural integrity assessment of components subjected to low constraint conditions*. Engineering Fracture Mechanics 75: 3038–3059.

Cicero, S. et al. 2012a. *Analysis of notch effect in PMMA by using the Theory of Critical Distances*. Engineering Fracture Mechanics 86: 56–72.

Cicero, S. et al. 2012b. *On the Point Method load-bearing capacity predictions in Al7075-T651structural components containing stress risers*. Engineering Failure Analysis 26: 129–138.

Cicero, S. et al. 2013. *On the notch effect in load bearing capacity, apparent fracture toughness and fracture mechanisms of polymer PMMA, aluminium alloy Al7075-T651 and structural steels S275JR and S355J2*. Engineering Failure Analysis 29: 108–121.

Creager, M. & Paris, C. 1967. *Elastic field equations for blunt cracks with reference to stress corrosion cracking*. International Journal of Fracture 3:247–252.

FITNET Fitness-for-Service (FFS) Procedure – Volume 1. 2008. Geesthacth: GKSS Forschungszentrum.

Griffith, AA. 1920. *The phenomena of rupture and flow in solids*. Philosophical Transactions of the Royal Society of London A 221:163–198.

Madrazo, V. et al. 2012. *On the point method and the line method notch effect predictions in Al7075–T651*. Eng Fract Mech 79: 363–379.

Miller, A.G. 1988. *Review of limit loads of structures containing defects*. International Journal of Pressure Vessels and Piing 32: 197–327.

Taylor, D. 2007. *The theory of critical distances: a new perspective in fracture mechanics*. Amsterdam: Elsevier.

Taylor, D. 2011. *Applications of the theory of critical distances in failure analysis*. Engineering Failure Analysis 18: 543–549.

Research and Applications in Structural Engineering, Mechanics and Computation – Zingoni (Ed.)
© 2013 Taylor & Francis Group, London, ISBN 978-1-138-00061-2

Fracture mechanics as an improvement of fatigue life assessment in orthotropic bridge decks

W. Nagy, H. De Backer & Ph. Van Bogaert
Ghent University, Ghent, Belgium

ABSTRACT: Orthotropic bridge decks are widely used in long span steel bridges since they are extremely light weighted when compared with the load carrying capacity. In the past, fatigue life problems have sometimes been overlooked during design. Nowadays, approaches for fatigue design have reached their limits resulting in conservative design leading to overestimating the necessary dimensions. An improved fatigue life assessment method is thus necessary. One possibility is to start using fracture mechanics. These techniques have many advantages since they form a more in-depth analysis. This implies that an entire crack propagation can be evaluated. If the case study of the Temse bridge in Belgium is evaluated, a crack length of 461,703 mm is found while a crack length of 600 mm was detected in reality. Although the results show the effort of fracture mechanics, improvements are still necessary such as implementing residual stresses into the model.

1 INTRODUCTION

Although fatigue in steel constructions is the most important form of fracture, it is the least understood behaviour because of its complexity. In the past, fatigue life problems have sometimes been overlooked during design. Fatigue as a failure mode first came to light in the mid-nineteenth century with Wöhler's research work in Germany on the premature failure of railroad axles at stresses below the elastic limit (Polák, J. 2003). His work is still used in the form of SN-curves. The problem however is that these curves should be updated for every project where a different design approach or installation procedure is used. Of course, this is mostly not the case leading to a misunderstanding of the fatigue behaviour of the detail being studied. Additionally, the Palmgren-Miner method is used to calculate the lifetime of that detail. The most important advantage of this method is its simplicity while giving a good indication of the remaining lifetime. However, this method is not very accurate because the load history and the load sequences do not have any effect on the fatigue behaviour. These design imperfections lead to overestimating the dimensions when considering orthotropic bridge deck plates.

Orthotropic bridge decks are widely used in long span steel bridges since they are extremely light weighted when compared with the load carrying capacity and are therefore durable and very efficient. These types of bridge decks consist out of a complex network of closed trapezoidal longitudinal stiffeners and transverse web stiffeners welded to a deck plate (Fig. 1).

Because of the latter, various complex welding operations cause multiple fatigue problems across the bridge deck. To investigate the complex fatigue behaviour, other methods are needed besides the traditional way of fatigue calculation. Therefore, a more in-depth analysis is used: fracture mechanics. This method is well known in the aerospace, marine and automobile sector because it can evaluate the crack behaviour in detail. Also a much larger dataset will be available for estimating the total fatigue lifetime or even a more realistic evaluation for the remaining lifetime of existing bridges.

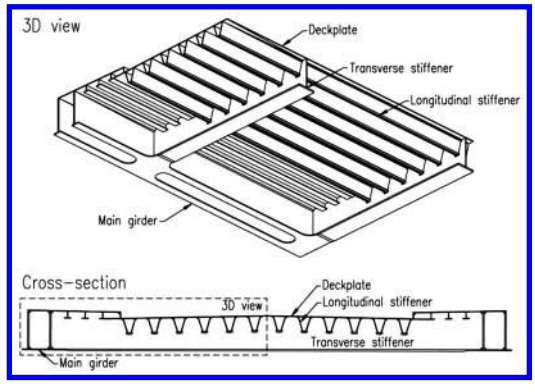


Figure 1. Cross-section and 3d view of an orthotropic bridge deck.

2 DESCRIPITION OF THE PROBLEM

In the past 10 years, several fatigue problems have been observed in several orthotropic bridge decks across Europe. Especially in the Netherlands, where many of



Figure 2. The Temse bridge across the river Scheldt (Belgium).



Figure 3. Movable part of the Temse bridge.



Figure 4. Orthotropic deck plate of the Temse bridge.

these bridge decks were constructed (Maljaars, J. et al. 2012). An example in Belgium described in this article, is the Temse bridge across the river Scheldt (Figs 2–4). Fatigue problems are mostly due to the lack of understanding of the fatigue behaviour. Additionally, the traffic intensity and also the traffic loads increased a lot since the construction of these bridge decks. But even recent constructed bridges could develop fatigue cracks (Maljaars, J. et al. 2012). This confirms that a more in-depth analysis is needed. In addition, fatigue cracks often initiate at the weld root. So, in the case of a stiffener-to-deck plate connection with closed stiffeners, the crack would propagate without any possible detection through visual inspection. Therefore, the fatigue crack would only be visible when there is already considerable damage.

3 CASE STUDY

An example of an orthotropic bridge deck with a poor fatigue behaviour is the Temse bridge across the river Scheldt in Belgium. This bridge is part of an important transport route for heavy lorries to the port of Antwerp.



Figure 5. Longitudinal crack through the deck plate at a stiffener-to-deck plate connection (left), multiple welds intersecting at the crack location (right).

The Temse bridge was built in 1955. Initially, the movable part had an aluminium deck plate. After many repairs, the movable part however was rebuilt in 1994 using a steel orthotropic plated deck (Fig. 4).

The deck plate of this movable part of the bridge is 12 mm thick and the stiffeners are 8 mm thick. The overall dimensions of the traffic lane are 53,90 m by 7,00 m. The trapezoidal stiffeners are 350 mm high and 300 mm wide on top and 90 mm width of the lower soffit. The distance between the longitudinal stiffeners equals 300 mm.

In 2004, a 600 mm long crack was detected in the stiffener-to-deck plate detail mid-span between two crossbeams (Fig. 5). The main reason for this crack is the occurrence of multiple welds intersecting one another (Van Bogaert, Ph. & De Backer, H. 2008, Nagy, W. et al. 2012). In addition, these welds were not chamfered and even the in the design demanded lack of penetration can be questioned here. In this particular case, the crack propagated through the deck plate starting from the weld root. Even when the crack had penetrated the deck surface, still no visible damage could be detected at the through because of the location of the crack initiation. With these cracks, there is already sufficient damage when the crack front occurs at the deck surface. A this stage, the crack is not stable anymore and propagates proportionally. Because the crack front occurs close to the high traffic loads, the crack has been repaired immediately (Van Bogaert, Ph. & De Backer, H. 2008).

4 ANALYTICAL STUDY

4.1 *General*

To verify the fatigue problem in detail, a more sophisticated method is needed instead of the traditional

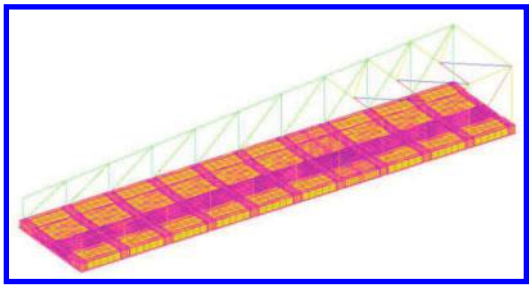


Figure 6. Large FEM-model of the Temse bridge.

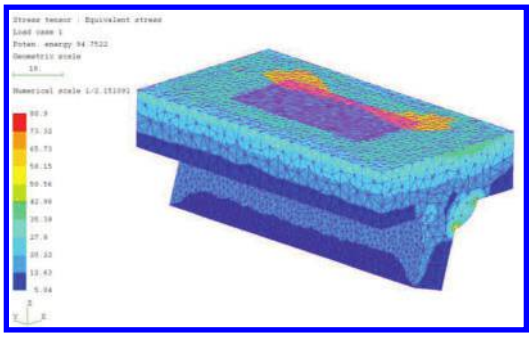


Figure 7. Von Misses stresses of the detailed small-scale model.

SN-curves and the Palmgren-Miner hypothesis as already explained. Therefore, the use of fracture mechanics could give a more detailed and improved look at the problem. To analyse the stiffener-to-deck plate connection detail, a FEM-model was developed in the finite element software Samcef. The advantage of using such software, is the ability to evaluate several fracture mechanics parameters and the crack propagation as well. This is done with an XFEM (eXtended Finite Element Method) method. With this method, the crack growth can be assessed without re-meshing the model in the vicinity of the crack. Although this is a very helpful tool, it needs a huge amount of computation time and power. Especially when the model is complex or when large cracks need to be evaluated.

4.2 *FEM-model*

In a first stage, a FEM-model is built of the whole movable part of the Temse bridge (Fig. 6). This is done with shell elements and beams. Although this model reflects the real behaviour of the structure well, a more detailed model is needed for studying the fracture mechanics parameters. Therefore, a more detailed small-scale model is constructed consisting of volume elements (Fig. 7).

To relate both models, the displacements and rotations are taken from the first model and introduced on the boundaries of the detailed model. This also implies that the big model is reduced to only the detail being studied, and that the computation time decreases.

4.3 *XFEM-model*

4.3.1 *Manual model*

Two possible ways to assess the fatigue life of welded connections with an XFEM-model exist. The first option is to insert a certain number of crack fronts in the weld corresponding to the crack front detected in a damaged detail of a construction. For this case study, an initial elliptical crack of 1 mm (both axes) was inserted at the weld root and perpendicular to the bridge deck (Fig. 9). The choice of this initial crack length could have a great influence on the total fatigue life of the structure. Depending on the welding detail, used construction technologies, lifetime of the structure, etc. an initial crack between 0,1 mm and 1 mm is often chosen (Polák, J. 2003, Nagy, W. et al. 2012). The reason why a 1 mm crack is assumed for this case study relies on a microscopic study of present weld details of a stiffener-to-deck plate connection (De Backer, H. 2006). The difference between several manufacturers is also taken into account.

After the fracture mechanics parameters are gathered from this initial crack, several other crack fronts could be evaluated with incrementing dimensions. An important parameter to evaluate is the stress intensity factor (SIF). This parameter can be used to evaluate the crack growth and its lifetime using one of the many crack propagation laws. In this case, the traditional Paris law is used:

$$\frac{da}{dN} = C \cdot \Delta K_I^{\,m} \tag{1}$$

where C and m are material properties and ΔK_I represents the stress intensity factor for mode I cracks. For structural steel C equals 3.10^{-13} [N, mm] and m equals 3 [−] (Maljaars, J. et al. 2012). For the assessment of existing (old) steel bridges, $C = 4.10^{-13}$ and $m = 3$ could be used (Kühn, B. et al. 2008).

Knowing the SIF-values for a certain number of crack fronts, it is possible to simulate the geometrical depended parameter $f(a)$ from equation 2:

$$\Delta K_I = f(a) \cdot \Delta\sigma \cdot \sqrt{\pi \cdot a} \tag{2}$$

In this equation $\Delta\sigma$ represents the applied stress range at the crack front and a the crack length. The geometrical parameter $f(a)$ not only depends on the crack length a, but also on the overall dimensions of the bridge deck. Therefore, once this parameter is evaluated for a particular bridge deck geometry and weld detail, this could be used for several other bridges with comparable dimensions.

Finally in order to get more realistic results, the Paris law could be expanded with the threshold value of the SIF-value:

$$\frac{da}{dN} = C \cdot (\Delta K_I^{\,m} - \Delta K_{th}^{\,m}) \tag{3}$$

This threshold value lies between 61 and 80 N/mm$^{3/2}$ for structural steel (Maljaars, J. et al. 2012, Kühn, B. et al. 2008).

From equation 3 it is now possible to evaluate the total fatigue life of the detail being studied:

$$N_f = \int_{a_i}^{a_f} \frac{da}{C \cdot (\Delta K_I{}^m - \Delta K_{th}{}^m)} \tag{4}$$

or:

$$N_f = \int_{a_i}^{a_f} \frac{da}{C \cdot ((f(a) \cdot \Delta\sigma \cdot \sqrt{\pi \cdot a})^m - \Delta K_{th}{}^m)} \tag{5}$$

4.3.2 *Automatic model*

A second and more accurate option to evaluate the crack front is with an automatic crack propagation method using the full advantage of the XFEM possibilities. Generally, the principle is the same as with the manual method. At first, an initial crack is placed in the model. After that, the XFEM-model uses the Paris law in order to propagate the crack automatically according to the path which uses the least energy to crack:

$$\frac{da}{dN} = C \cdot \left(\Delta K_I{}^{eff}\right)^m \tag{6}$$

The SIF-value in this equation is a function of $\Delta K_I, \Delta K_{II}, \Delta K_{III}, \theta_p$ (bifurcation angle) and the used material.

Besides the SIF-values and the fatigue lifetime, this method also gives the crack propagation path in a complex three-dimensional way. This is a great advantage in evaluating the weld geometry and their resulting cracks. The only disadvantage of this method is the computational effort. This method only gives accurate results if the mesh is sufficient fine enough around the crack front. Therefore, only relative small cracks could be evaluated with this method.

5 RESULTS

Before the XFEM analysis, a FEM analysis is done of the orthotropic bridge deck of the Temse bridge. Figure 7 illustrates the Von Misses stresses in the geometrical detail of the weld, while Figure 8 represents the third principal stresses of a cross section of the detail midspan two crossbeams.

Figure 8 also indicates a zone of compression at the weld root, which is the location of the initial crack for the XFEM calculation. Therefore, the crack propagation is due to compression and not tension.

According to a traditional fatigue analysis of this bridge deck (De Backer, H. et al. 2006), a total fatigue life of 23,8 years is observed. This incredibly small result indicates that it is obvious that a crack length of 600 mm was detected after 10 years of service life. One of the reasons of this poor result relies on the fact that only a very thin surface layer of 8 mm is used. And as Figure 5 indicates, the deck is already damaged at the crack location in a way that no load dispersion could be possible.

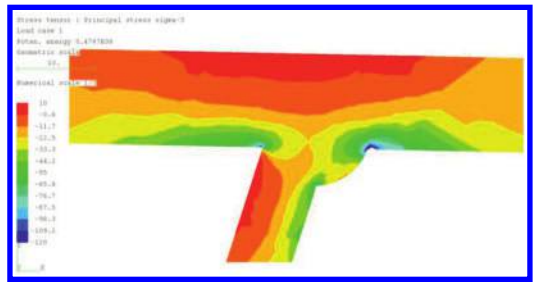


Figure 8. Third principal stresses of a cross-section of the detailed small-scale model.

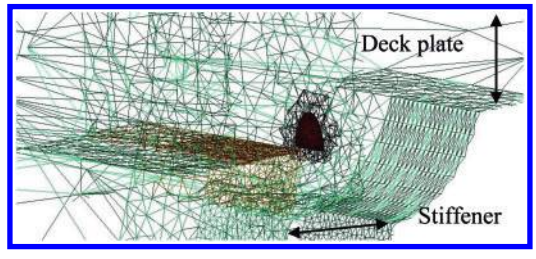


Figure 9. Initial semi-elliptical crack length of 1 mm on both axes.

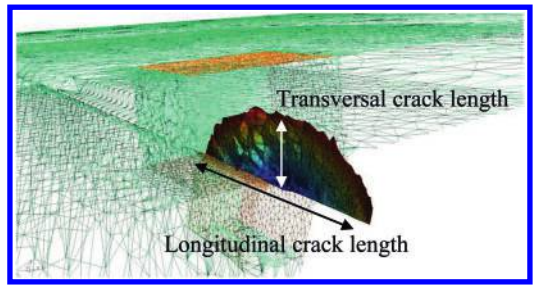


Figure 10. Large crack length developed through the deck plate.

5.1 *Manual XFEM-model*

The calculations with the manual XFEM method are done with an initial semi-elliptical crack length of 1 mm as already explained (Fig. 9). In addition, several other cracks with incremented dimensions are evaluated like the larger crack front in Figure 10.

Concerning the applied stresses, model 4 is used conform the Eurocodes (Structural Eurocodes 2010). This implies that a traffic distribution is used with five characteristic lorries. Figure 11 illustrates the location of the corresponding axle loads in relation with the crack location. As a result, Figure 12 and Figure 13 illustrate the SIF-values for all the crack geometries being studied. A best-fit curve could be found representing the formulation for the geometrical parameter $f(a)$. Therefore, all the SIF-values are known for every crack length and different axle loads. It is also visible

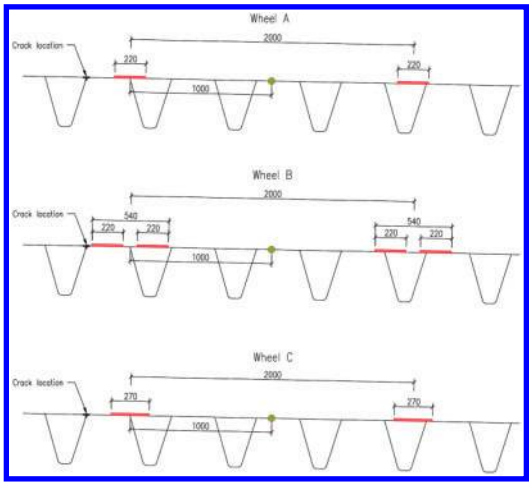


Figure 11. Position of the axle loads in relation with the crack location.

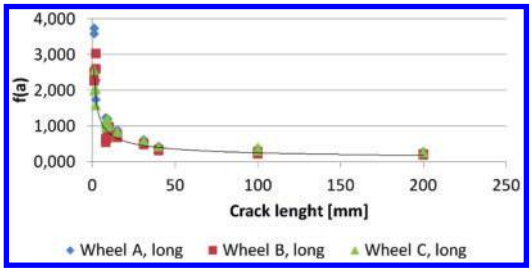


Figure 12. Geometrical parameter $f(a)$ for the longitudinal crack propagation.

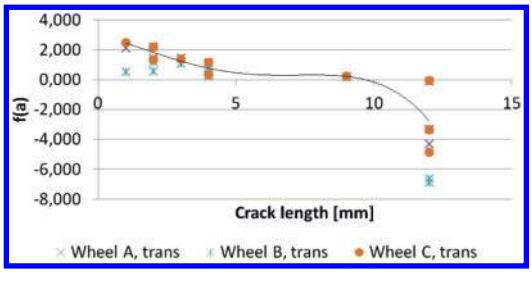


Figure 13. Geometrical parameter $f(a)$ for the transversal crack propagation.

that the crack would propagate much faster in the longitudinal direction and not so fast in the transversal. The crack only propagates much faster transversally, when the crack front counters the tensile zone of Figure 8. This indicates that the crack first propagates longitudinal through the weld before propagating through the deck plate, which confirms the problem of visual inspection of fatigue cracks.

It is known that during the past service live of 10 years, where the crack propagated until the crack length of 600 mm, an approximate load cycle history is equal to:

$$N = 10 years \cdot 250 days \cdot 2800 \frac{lorries}{day} = 7 \cdot 10^6 \qquad (7)$$

The corresponding fatigue crack with these load cycles could be derived from equation 2 and 3:

$$a = \sum_i C \cdot ((f(a_i) \cdot \Delta\sigma_i \cdot \sqrt{\pi \cdot a_i})^m - \Delta K_{th}{}^m) \cdot dN \qquad (8)$$

With this equation, a longitudinal fatigue crack length of 461,703 mm could be found for the 7.10^6 lorries and 10 years of service life. This is smaller than the 600 mm detected in real life, but it must be said that a FEM-model is still an ideal environment with no inhomogeneities. In addition, this model does not take into account any residual stresses, which are most likely present in the weld. Especially because multiple welds intersect at the crack location (Fig. 5) and the welds are not chamfered or treated at the surface to reduce any residual stresses.

5.2 *Automatic XFEM-model*

As with the manual method, an initial crack length of 1 mm was chosen. Although only a small crack propagation of several mm could be simulated due to the heavy computation time, a clear indication of the crack propagation patch becomes visible. The crack seems to propagate through the weld itself and not through the deck plate. This is not so peculiar because the largest stresses are within the weld throat itself and not in the deck plate (Fig. 8). Why the crack path is different for the crack in real life could be for the same reasons of the manual calculations. Residual stresses have a great influence on the crack initiation stage and also on the crack propagation.

6 CONCLUSIONS

It becomes clear that fracture mechanics as an improvement of the fatigue life assessment in orthotropic bridge decks has many advantages. In the traditional fatigue calculations, there are too many assumptions and simplifications to get accurate results. Especially when different geometries or construction technologies are used. Fracture mechanics on the other hand makes it possible to evaluate every detail separately, this being less conservative. In addition, once a particular detail is properly studied, a geometrical parameter $f(a)$ imposes itself. Therefore, other similar details could be evaluated without doing an intensive FEM and XFEM calculation.

Application of this method to the case of the Temse bridge in Belgium, resulted in a crack length of 461,703 mm after a service life of 10 years. Compared to the 600 mm of crack length found in reality, this is a good result although a bit optimistic. A possible

explanation is that the model does not take any residual stresses into account. The implementation of such stresses in the model could be an improvement for further research.

REFERENCES

De Backer, H., Van Bogaert, Ph. & Outtier, A. 2006. Fatigue cracks in orthotropic decks: possible alternatives. *Proc. 6th international Symposium Steel Bridges, Prague, 2006*: 1–10.

De Backer, H. 2006. *Optimalisatie van het vermoeiingsgedrag van het orthotroop brugdekconcept door verbeterde dispersie van de verkeersbelasting.* Universiteit Gent.

Kühn, B., Lukic, M., Nussbaumer, A., Günther, H.-P., Helmerich, R., Herion, S., Kolstein, M.H., Walbridge, S., Androic, B., Dijkstra, O. & Bucak, Ö. 2008. *Assessment of Existing Steel Structures: Recommendations for Estimation of Remaining Fatigue Life*. JRC-ECCS.

Maljaars, J., van Dooren, F. & Kolstein, H. 2012. Fatigue assessment for deck plates in orthotropic bridge deck. *Steel Construction 5*, No. 2: 93–100.

Nagy, W., De Backer, H. & Van Bogaert, Ph. 2012. Crack propagation in a stiffener-to-deckplate connection of an orthotropic steel bridge deck. *Proc. 19th European Conference on Fracture*. *Kazan, Russia*: 2012.

Polák, J. 2003. *Comprehensive Structural Integrity.* Volume 4: *Cyclic Loading and Fatigue*. Elsevier Ltd.

Structural Eurocodes 2010. *Eurocode 1: Actions on structures – Part 2: Traffic loads on bridges.* EN 1991-2:2003/AC:2010 2010

Van Bogaert, Ph. & De Backer, H. 2008. Early fatigue damage and repair of steel orthotropic plated bridge deck. *Proc. 5th European Conference on Steel and Composite Structures. Graz, Austria 2008*: 851–856.

Research and Applications in Structural Engineering, Mechanics and Computation – Zingoni (Ed.)
© 2013 Taylor & Francis Group, London, ISBN 978-1-138-00061-2

Analogies in the fracture mechanisms of concrete and ice

B. Chiaia, A.P. Fantilli & B. Frigo
Politecnico di Torino, Torino, Italy

ABSTRACT: The existence of a single model, capable of describing the fracture behaviour of both concrete and ice, is investigated in the present paper. More precisely, the fracture energy of concrete, and the fracture toughness of ice as well, are herein predicted through a new size effect law. As in the evaluation of crack pattern of reinforced concrete ties and beams, the proposed approach reveals that a "golden ratio" (i.e., the number $\phi = 1.61803$) plays a fundamental role in the fracture mechanisms of brittle and quasi-brittle materials. In other words, it can be argued that the centrality of golden section in the field of concrete and ice structures has profound physical meanings. Indeed, it can bring together the aesthetic of nature and architecture, where golden section frequently recurs, and the equilibrium of stress flow in solid bodies. This aspect is finally confirmed by the results of different experimental campaigns performed on concrete beams, tested in three point bending, and on ice sheets.

1 INTRODUCTION

As is well known (Rilem TC QFS 2004), size effect is an important aspect of cracked members made of plain or lightly reinforced concrete. It affects some mechanical properties (i.e., tensile strength, shear strength, fracture energy, etc.) because of the non-homogeneous character of the material and the occurrence of fractures.

A wide literature on size effect has considered the decrease of material strength, and the increase of fracture energy, with structural size. Weibull (1939) defined size effect as the result of statistical distribution of defects inside the material, whereas Bazant (1984) adopted an engineering approach based on the energy release rate. More recently, Carpinteri et al. (1995) combined the statistical and energetical approaches within the framework of fractal geometry, which permitted to take into account the intimate nature of energy dissipation during fracture propagation. As a result, the following Multifractal Scaling Law (MFSL) can be assumed for the fracture energy (Carpinteri & Chiaia 1996):

$$\frac{G_F}{G_{F\infty}} = \left(1 + \frac{l_{ch}}{D}\right)^{-1/2} \tag{1}$$

where G_F = nominal fracture energy; D = external characteristic structural size; $G_{F\infty}$ = nominal asymptotic fracture energy ($D \to \infty$); l_{ch} = internal microstructural length.

According to Eq.(1), fracture energy, and consequently fracture toughness, increase with the dimension D of the specimen, up to the asymptotic value $G_{F\infty}$. Several experimental analyses, performed on concrete an ice, seem to confirm the reliability of such law. Although concrete is a man-made material while ice is natural material, they show granular size depending behaviour and present a structurally similar brittle response. Thus, the mechanical properties of concrete and ice show, at different scales, some typical peculiarities of a fractal, characterized by scale invariant fractal porosity (Carbone et al. 2010, Carpinteri & Chiaia 1996).

Nevertheless, to apply the MFSL in brittle and quasi-brittle materials, the parameters $G_{F\infty}$ and l_{ch}, which cannot be measured through direct specific tests, have to be computed by using a best-fitting algorithm. Obviously, the regression procedure is more statistically reliable if the experimental measures of G_F are performed on a wide size range. In other words, a high number of tests are required to use correctly the MFSL (Carpinteri et al. 1995), as well as the Bazant's (1984) size effect law.

A new size-effect model is therefore introduced in the present paper with the aim of predicting the fracture energy of concrete, and the fracture toughness of ice, starting from few tests performed on a single scale. In the opinion of the authors, such a model should be based on the golden ratio, which recurs in the size effect of crack pattern of concrete ties and beams.

2 THEORETICAL AND EXPERIMENTAL OBSERVATIONS ON CRACK SPACING

As stated by Fantilli & Chiaia (2013), if the crack spacing of reinforced concrete (RC) member increases with

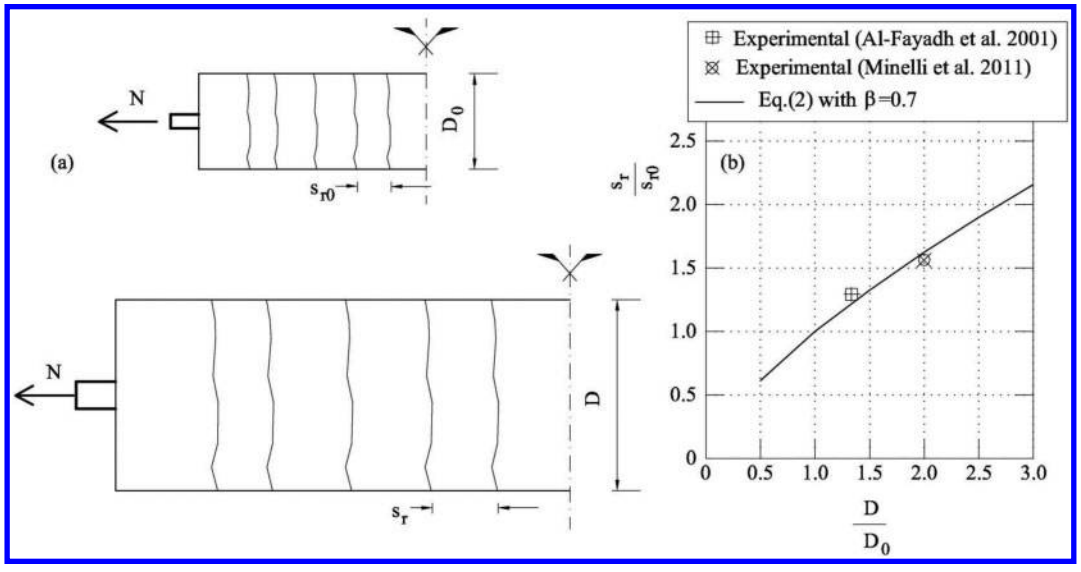


Figure 1. The tests performed by Minelli et al. (2011) and Al-Fayadh et al. (2001): (a) Geometry of the scaled specimens; (b) Comparison between the measured crack spacing and the proposed size effect law.

the size, a size effect law having the form of a power function (Rilem TC QFS 2004) can be introduced:

$$\frac{s_r}{s_{r0}} = \left(\frac{D}{D_0}\right)^{\beta} \tag{2}$$

where D_0 = reference dimension; D = dimension at a generic scale; s_{r0} = average distance between cracks in the reference member; s_r = average distance between cracks at a generic scale; and β = exponent that has to be defined by fitting experimental and/or numerical data. According to the model proposed by Fantilli & Chiaia (2013), when the geometrical dimensions of the RC member are doubled (i.e., $D/D_0 = 2$), transfer length and crack distances increase of a factor ϕ (i.e., $s_r/s_{r0} = \phi = 1.61803$), and therefore $\beta \cong 0.7$. In mathematics, ϕ is generally known as the golden ratio, or the divine proportion.

Results of different experimental campaigns validate the tension stiffening model by Fantilli & Chiaia (2013). This is the case of the ties tested by Minelli et al. (2011), and made with four different types of cement-based composites. As shown in Fig.1a, cracking has been investigated at two scales (i.e., $D_0 = 50$ mm, and $D = 100$ mm). In this case, the ratio between the average values of crack distance (i.e., $s_{r0} = 72.3$ mm when $D_0 = 50$ mm, and $s_r = 113$ mm when $D = 100$ mm) is very close to the golden ratio ϕ. As a matter of fact, the point of coordinates $D/D_0 = 2$ and $s_r/s_{r0} = 113$ mm/72.3 mm, as measured by Minelli et al. (2011), is adjacent to the curve given by Eq.(2) (with $\beta = 0.7$) and depicted in Fig.1b. In the same Figure, also the point of coordinates $D/D_0 = 80$ mm/60 mm = 1.33 and $s_r/s_{r0} = 132.5$ mm/102.5 mm [referred to the high strength concrete ties tested by Al-Fayadh et al. (2001)] is close to the proposed size effect law.

The previous observations can be extended to the RC beams depicted in Fig.2a (Swamy & Qureshi 1971). The first group of four beams have geometrical dimensions equal to half those of the largest beams. In all the beams, the average crack distances in the constant moment zone have been registered (i.e., $s_{r0} = 69.5$ mm at reference scale D_0, and $s_r = 113$ mm when $D/D_0 = 2$). Also in these beams, when the ratio $D/D_0 = 2$, the tests give $s_r/s_{r0} \cong \phi$, and therefore the above experimental bending results are correctly predicted by Eq.(2) with $\beta = 0.7$ (see Fig.2b).

3 EXPERIMENTAL OBSERVATIONS ON THE FRACTURE OF CONCRETE AND ICE

Similarly to the crack spacing of reinforced concrete ties and beams, the fracture energy of concrete, and the fracture toughness of ice, increase with the structural size. Some experimental campaigns, performed on both the materials and described in the following sections, evidenced such behaviour.

3.1 *Tests on concrete beams*

The procedure proposed by Rilem TC-50 FCM (1985) is generally used to evaluate the fracture energy of cement-based composites. Perdikaris & Romeo (1992) adopted such procedure in an experimental campaign performed on concrete beams. Specifically, the notched specimens depicted in Fig.3a, and tested in three point bending, were investigated at different scales. Table 1 shows the geometrical properties of these samples.

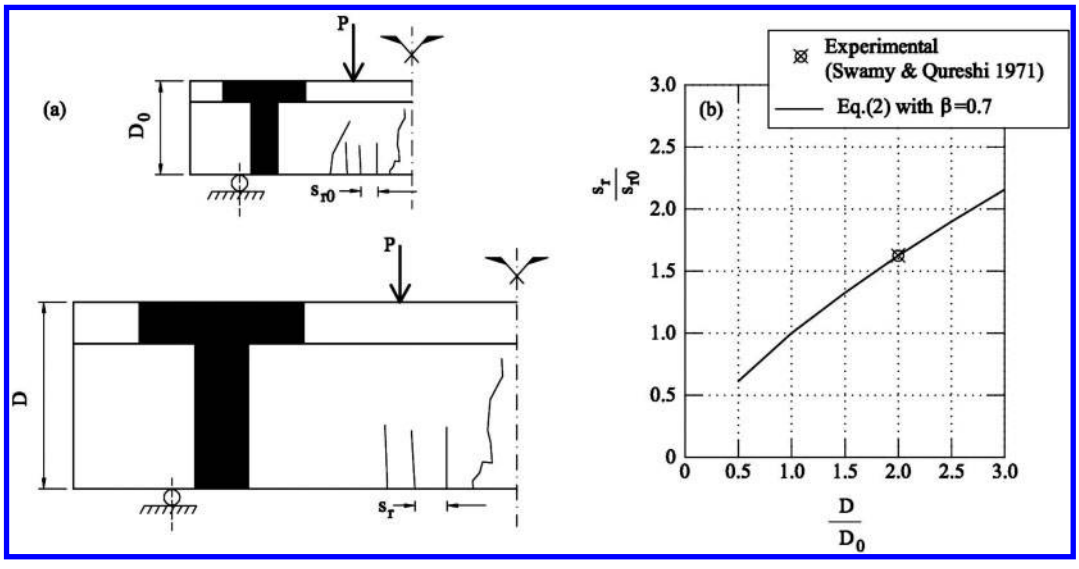


Figure 2. The tests performed by Swamy & Qureshi (1971): (a) Geometry of the scaled specimens; (b) Comparison between the measured crack spacing and the proposed size effect law.

Table 1. Three point bending tests on concrete beams (Perdikaris & Romeo 1992).

SF	concrete	H mm	L mm	a/H	B mm	G_F N/m
1	C1	63.5	254	0.3	127	76
2	C1	127	508	0.3	127	94
4	C1	254	1016	0.3	127	117
1	C2	63.5	254	0.3	127	69
2	C2	127	508	0.3	127	82
4	C2	254	1016	0.3	127	118

The beams were cast with two different concrete mixtures: C1 is a normal strength concrete (f_c = concrete strength = 35 MPa, E_c = elastic modulus = 33 GPa), whereas C2 is a high strength concrete (f_c = 75 MPa, E_c = 40 GPa). In both the concretes, the maximum aggregate size is 6.4 mm.

The external load P (Fig.3a) was applied by means of a servo-hydraulic testing machine, so that the peak was reached in approximately 10 minutes. Local LVDTs were also adopted to measure deflection η in the midspan of the specimen. Fig.3b shows a complete load midspan deflection curve measured in a single beam, and used to evaluate G_F. To be more precise, the value of fracture energy can be experimentally measured through the following formula (Hillerborg 1985):

$$G_F = \frac{W}{B(H-a)} \tag{3}$$

where, W = total amount of absorbed energy (i.e., the area below the measured load-deflection curve).

An increase of G_F with the size factor SF, which varies from 1 to 4, can be observed in Table 1. Nevertheless, such variation differs from that measured in the crack spacing of RC ties and beams. As reported in Fig.1 and Fig.2, crack distance becomes ϕ times higher when the geometrical dimensions of the specimen are doubled. Here, fracture energy shows the same increase only when $SF = 4$ (see Table 1). This difference can be ascribed to the geometry of the beams adopted in the three point bending tests (Fig.3b). In fact, only the height H, the notch a, and the span L of the beam were scaled. Conversely, the width B of the cross-section was kept constant, and equal to 100 mm, for all the specimens.

Finally, the size effect on G_F seems to be the same for both the types of concrete. Indeed, as observed by Perdikaris & Romeo (1992), at all the scales the fracture energy of higher strength concrete mix (C2) is either similar or slightly lower than that of the lower strength mix (C1).

3.2 *Tests on ice plates*

Ice is a porous medium consisting of air and a random assemblage of grains of solid water. It could be generated from metamorphosis of snow or direct freezing of water. In Nature, several types of ice, having different physical and mechanical properties, can be observed (e.g., sea and saline ice, equi-axed granular, macro-crystalline S1 and columnar S2 freshwater ice, glaciers, etc.). In all the cases, density can vary from 800 to 917 kg/m^3.

To investigate the fracture properties of ice, a set of samples are herein taken into consideration (Fig.4). The specimens, generally called base-edge-notched reverse-tapered plate (Mai et al. 1975, Defranco & Dempsey 1994, Dempsey et al. 1995), are those of the

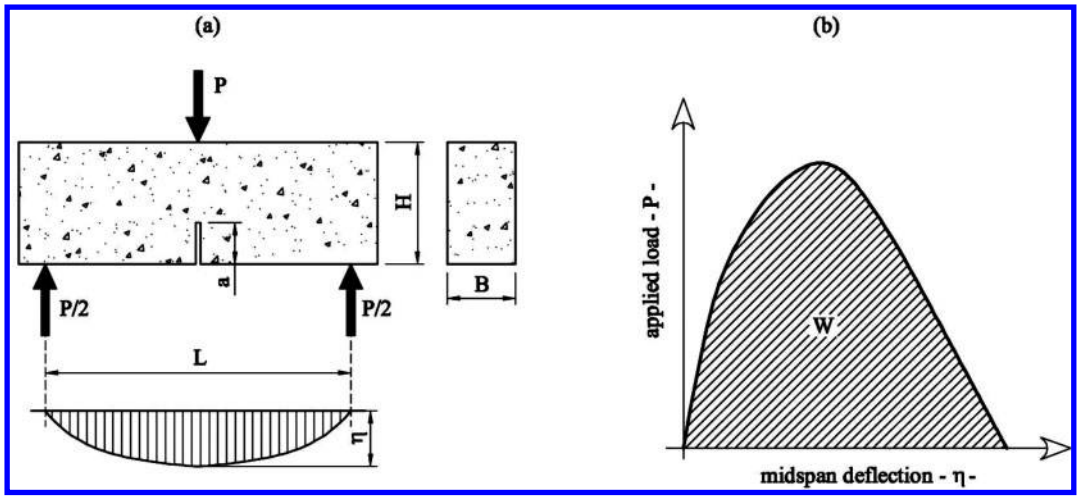


Figure 3. Three point bending tests on concrete beams (Rilem TC-50 FCM 1985): a) Geometrical dimensions of the specimens; b) Typical applied load vs. midspan deflection diagram.

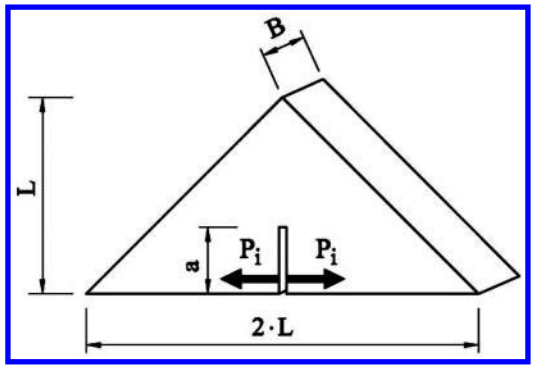


Figure 4. *In-situ* base-edge-notched reverse-tapered plate tests on S1 ice (Dempsey et al. 1999a).

Table 2. *In-situ* base-edge-notched reverse-tapered plate tests (Dempsey et al., 1999a).

SF	ice	L m	a m	a/L	B m	K_Q kPa m$^{0.5}$
1	RT1	1.41	0.43	0.3	0.5	97
2	RT7	3.18	0.99	0.3	0.5	193
1.5	RT8	3.20	0.99	0.3	0.5	144
7.3	RT6	10.36	20.8	0.3	0.5	186
20.3	RT9	28.64	8.98	0.3	0.5	297

in-situ experimental campaign performed by Dempsey et al. (1999a, 1999b) on S1 freshwater lake ice of Spray Lakes Reservoir (Alberta – Canada). The aim was to investigate the size effect on fracture toughness by testing several plates, whose geometry (see Table 2) varies from laboratory to structural-scale (1.41 m < L < 28.64 m).

S1 freshwater ice is a secondary congregation ice that usually grows under, or on, the primary ice (the first thin layer to form) or snow. It is typically composed by massive irregularly shaped crystals extended on vertical, or near vertical, c-axes (Michel & Ramseier 1971). The physical and mechanical properties of Spray Lakes Reservoir ice have been measured by Dempsey et al. (1999a) at Clarkson University.

The plates were cut from the parent ice sheet, having uniform and stable thickness ($B = 0.5$ m), by using chainsaws. The test temperatures were above −5°C, and the ambient weather did not affect the ice sheet thickness during the tests. In this campaign, Dempsey et al (1999a) consider the thickness B of the specimens not scaled. In fact, due to the crystalline microstructure of ice, it is necessary to have a 2D similarity to compare each specimen tested. Moreover, according to van Vliet & van Mier (1998), in quasi-brittle fracture tests, measurements do not depend on the length of the crack front.

The load P_i (see Fig. 4) was applied by means of flatjack loading device, controlled by a servo-hydraulic control system coupled with a displacement measuring gauge located on the crack (Shapiro et al. 1979). The specimen size and the loading rate are scaled to consider the homogeneity of the ice during the tests. In fact, as the specimen size increases, the material behaviour is expected to become more homogeneous, and eventually the length of the fully developed process zone will be lower in comparison with the specimen size (Dempsey et al. 1999a).

As no standard test exists, the theory of Linear Elastic Fracture Mechanics is generally applied to freshwater ice. Accordingly, the critical stress intensity factor K_{Ic} is generally substituted by K_Q (Dempsey 1991):

$$K_Q = K_{apparent}^{initiation} = K_I\left(a, \rho, P_Q\right) \tag{4}$$

where K_Q, which symbolically represents the assumptions involved and the lack of a standard test, also

depends on the crack tip radius ρ, and on the maximum load P_Q.

When the load P_i is applied on the crack surfaces by a flatjack, the fracture toughness K_Q can be easily evaluated through the following equation (Dempsey et al. 1999a):

$$K_Q = f\left(\frac{a}{L}\right)\frac{P_i}{w\,h}\sqrt{\pi\,a} \tag{5}$$

where w and h = width and thickness of the flatjack, respectively; and $f(a/L)$ = function defined by Dempsey et al. (1995).

For each plate, the related values of K_Q are reported in Table 2. As for the fracture energy of concrete specimens, the fracture toughness of ice increases with the size factor SF. To be more precise, K_Q becomes ϕ times higher when the geometrical dimensions of the specimen are scaled with a size factor $SF = 4$.

4 SIZE EFFECT AND GOLDEN RATIO

Similarly to crack spacing, if the fracture energy of concrete and the fracture toughness of ice specimens increase with the size, a size effect law having the form of a power function (Rilem TC QFS 2004) can be introduced:

$$\frac{G_F}{G_{F0}} = \frac{K_Q}{K_{Q0}} = \left(\frac{D}{D_0}\right)^{\beta} = SF^{\beta} \tag{6}$$

where, G_{F0} (or K_{Q0}) = average fracture energy (or fracture toughness) measured in the reference member ($SF = 1$); G_F (or K_Q) = average fracture energy at a generic scale ($SF \neq 1$); and β = exponent that has to be defined by fitting experimental data. According to the experimental results reported in the previous sections, when $SF = D/D_0 = 4$, fracture energy of concrete, and fracture toughness of ice, increase of a factor ϕ (i.e., $G_F/G_{F0} = K_Q/K_{Q0} = \phi$), and therefore $\beta \cong 0.35$.

The new model for fracture energy and toughness can be used to predict the experimental data previously described. In the case of concrete beams (Fig.5), the proposed size effect law of fracture energy [i.e., Eq.(6) with $\beta = 0.35$] seems to be in good agreement with the results obtained by Perdikaris & Romeo (1992). This is true for both normal strength concrete (C1 in Fig.5) and high strength concrete (C2 in Fig. 5).

Similarly, the fracture toughness of the reverse-tapered plates, tested by Dempsey at al. (1999a) and made with S1 freshwater ice, varies according to the proposed size effect law. As Fig.6 shows, Eq.(6) with $\beta = 0.35$ gives a reasonable approximation of K_Q also in the case of large specimens (i.e., $SF = 20$).

In the same figures, also the results of MFSL have been reported. The fracture energy of concrete predicted by Eq.(1) is in good agreement with both the experimental data and results of the proposed size effect law (Fig.5). Whereas, the fracture toughness of ice seems to be better evaluated by Eq.(6) with $\beta = 0.35$, especially at large scales.

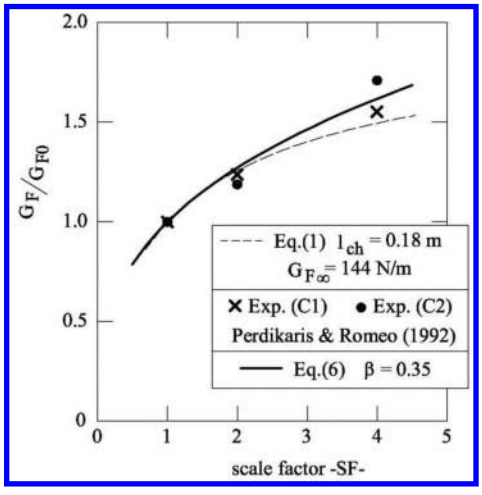


Figure 5. Comparison between the measured fracture energy of concrete and the proposed size effect law.

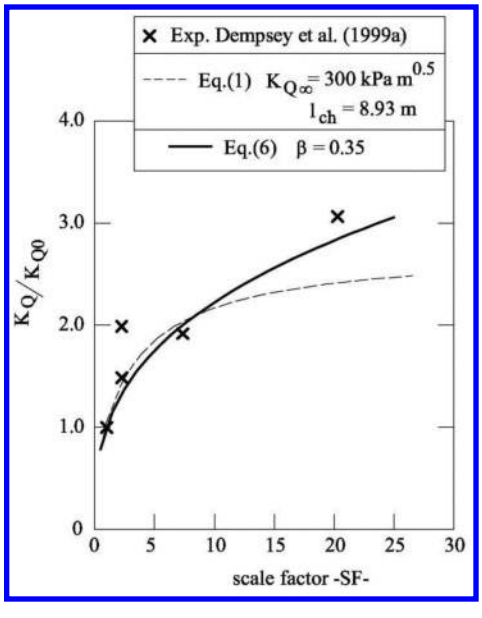


Figure 6. Comparison between the measured fracture toughness of ice and the proposed size effect law.

5 CONCLUSIONS

A new size effect law for the fracture energy and the fracture toughness of quasi-brittle materials has been presented. From the comparison between the results of the proposed model and some experimental data, the following conclusions can be drawn:

- Similarly to the crack pattern of reinforced concrete ties and beams, the golden ratio also recurs in the fracture mechanism of ice and concrete.
- A single size effect law can be used for the fracture energy of concrete and the fracture toughness of ice.

– With respect to the traditional size effect models, the proposed law can predict G_F, and K_Q with good accuracy, by using a reduced number of tests.

Nevertheless, only two quasi-brittle materials (i.e. concrete and ice) have been investigated in the present paper. Future works should therefore consider the behaviour of other materials, such as rocks, in order to generalize the effectiveness of the proposed size effect law.

REFERENCES

Al-Fayadh, S., Engström, B., and Magnusson J. 2001. Cracking Behaviour of Reinforced Concrete Tensile Members. *Report of RILEM TC 147-FMB, Tension of Reinforced Concrete Prisms – Round Robin Analysis and tests on Bond*. Rilem: 1–121.

Bazant, Z.P. 1984. Size effect in blunt fracture: concrete, rock, metal. *ASCE Journal of Engineering Mechanics* 110(4): 518–535.

Carbone, A., Chiaia, B., Frigo, B., and Türk, C. 2010. Snow metamorphism: a fractal approach, *Physical Review E* 82(036103): 1–5.

Carpinteri, A. & Chiaia, B. 1996. Size effects on concrete fracture energy: dimensional transition from order to disorder. *Materials and Structures* 29(189): 259–266.

Carpinteri, A., Chiaia, B., and Ferro, G. 1995. Size effects on nominal tensile strength of concrete structures: multifractality of material ligaments and dimensional transition from order to disorder. *Materials and Structures* 28(6): 311–317.

Defranco, S.J. & Dempsey, J.P., 1994. Crack propagation and fracture resistance in saline ice. *Journal of Glaciology* 40: 451–462.

Dempsey, J.P. 1991. The fracture toughness of ice. In S.J. Jones, R.F. McKenna, J. Tillotson, and I.J. Jordaan (eds.), *Ice-Structure Interaction,* Springer-Verlag, Berlin: 109–145.

Dempsey, J.P., Adamson, R.M. and Defranco, S.J. 1995. Fracture analysis of base-edge-cracked reverse-tapered plates. *International Journal of Fracture* 69: 281–294.

Dempsey, J.P., Defranco, S.J., Adamson, R.M. and Mulmule, S.V. 1999a. Scale effects on the in-situ tensile strength and fracture of ice. Part I: Large grained freshwater ice at Spray Lakes Reservoir, Alberta. *International Journal of Fracture* 95: 325–345.

Dempsey, J.P., Adamson, R.M. and Mulmule, S.V. 1999b. Scale effects on the in-situ tensile strength and fracture of ice. Part II: First-year sea ice at Resolute, N.W.T. *International Journal of Fracture* 95: 347–366.

Fantilli, A.P. & Chiaia, B. 2013. The golden ratio in the crack pattern of reinforced concrete structures. *ASCE Journal of Engineering Mechanics* (in press).

Hillerborg, A. 1985. The theoretical basis of a method to determine the fracture energy GF of concrete. *Materials and Structures* 18 (4): 291–296.

Michel, B. & Ramseier R. (1971). Classification of River and Lake Ice. *Canadian Geotechnical Journal*. 8(1): 35–45.

Minelli, F., Tiberti, G., and Plizzari, G.A. 2011. Crack Control in RC Elements with Fiber Reinforcement. In C.-M. Aldea & M. Ekenel (eds.), *ACI Special Publication SP-280: Advances in FRC Durability and Field Applications*.

Perdikaris, P.C. & Romeo, A. 1992. Effect of size and compressive strength on the fracture energy of plain concrete. In Z.P. Bazant (ed.). *Proceedings of the First International Conference on Fracture Mechanics of Concrete Structures, FRAMCOS 1*, Breckenridge (USA): 550–555.

RILEM TC 50 FCM 1985. Determination of fracture energy of mortar and concrete by means of three-point bend tests on notched beams. *Materials and Structures* 18(106): 285–290.

Rilem TC QFS 2004. Quasibrittle fracture scaling and size effect – Final report. *Materials and Structures* 37: 547–568.

Shapiro, L.H., Hoskins, E.R., Nelson, R.D. and Metzner, R.C. 1979. Flatjack methods of in-situ measurements of the mechanical properties of sea ice. *ASME Journal of Energy Resources Technology* 101: 196–202.

Swamy, R. N. & Qureshi, S.A. 1971. Strength, Cracking and Deformation Similitude in Reinforced T-beams Under Bending and Shear. *ACI Journal Proceedings* 68 (3): 187–195.

Van Vliet, M.R.A. & Van Mier, J.G.M. 1998. Experimental and numerical investigation of size/scale effects in concrete fracture. In R. De Borst and E. Van der Giessen (eds.), *Material Instabilities in Solids*. John Wiley & Sons, Chichester: 185–206.

Weibull, W. 1939. A Statistical Theory for the Strength of Materials. *Swedish Royal Institute for Engineering Research*, Stockholm.

Research and Applications in Structural Engineering, Mechanics and Computation – Zingoni (Ed.)
© 2013 Taylor & Francis Group, London, ISBN 978-1-138-00061-2

An investigation of the double torsion geometry using peridynamics

T.H. Becker
Department of Mechanical and Mechatronic Engineering, University of Stellenbosch, South Africa

D.Z. Turner
Department of Civil Engineering, University of Stellenbosch, South Africa

ABSTRACT: The Double Torsion (DT) technique is a powerful experimental method for fracture parameter characterisation of brittle materials. One of the distinguishing features is that the geometry, in principle, provides a crack length independent test configuration. This attractive feature allows for the propagation of relatively long cracks in a highly controlled manner in exceptionally brittle materials (compared to compact tension and single edge notched beam geometries). Despite this salient feature, the DT technique is challenging to model computationally using traditional approaches (cohesive elements, extended finite elements, analytically enriched finite elements). Presented is an investigation of the DT geometry with the use of peridynamics to model the fracture of brittle materials. Peridynamics (a non-local theory of continuum mechanics based on an integro-differential equation without spatial derivatives) overcomes several of the challenging aspects of modelling the DT geometry. For example, discontinuities are naturally part of the solution, the crack path can be arbitrary, and the formulation is robust for a wide variety of material properties. This paper aims to investigate the DT technique using peridynamics by comparing numerical results with experimental data in terms of the obtained load, displacement and cracking behaviour in order to evaluate the efficacy of this approach for fracture test geometry analysis.

1 INTRODUCTION

The Double Torsion (DT) technique is a powerful testing configuration that facilitates fracture investigations of highly brittle materials, such as glass (Fuller 1979), and quasi-brittle materials such as rock (Ciccotti 2001), concrete (Tait 1987) and nuclear graphite (Becker 2011). The distinguishing feature of this technique is that the Stress Intensity Factor (SIF) is, as a first approximation, independent of crack length. This allows for the propagation of relatively long cracks in a highly controlled manner, compared to conventional compact tension (CT) and single edge notched beams (SENB).

The DT technique, however, is yet to be standardized and several question remain regarding the validity of a crack length independent geometry. Corrections to the technique have been proposed, which include Leevers' analytical large deflection correction (Leevers 1985), Chevaliers' experimentally based geometry correction (Chevaliers 1996) and Ciccotti's Finite element based correction factors (Ciccotti 2000a, 2000b). To date, none of the proposed corrections have been widely accepted in the literature and the utilization of the DT technique is predominantly based on experience. Contributing to the limited use of the DT technique is that the specimen geometry is challenging to model computationally using traditional approaches such as cohesive elements, XFEM or analytically enriched finite elements. The crack tip geometry is complex as both high tensile and compressive regions are present.

Presented in this paper is an alternative method to investigate the DT geometry using peridynamics. Peridynamics allows for the modelling of fracture and, as opposed to traditional formulations for solid mechanics (which are based on spatial partial derivatives), is integral based. As such, incorporation of cracks into the solution is much more natural. Peridynamics has been shown effective for a number of applications including membranes, reinforced concrete, carbon fibre reinforced composites, and hydraulic fracturing. The development of the peridynamic theory and some applications are presented in (Silling 2000, Silling 2007, Silling & Askari 2005, Silling & Lehoucq 2008, Turner 2013).

2 THE DOUBLE TORSION TECHNIQUE

The DT geometry essentially comprises a rectangular plate that is loaded in a four point bending configuration at one end across a notch (Figure 2). The specimen can be considered as two halves around the cracked portion, which deform independently. Subjected only to small torsional deformations, the stiffness of each

half is a function of its cross-section and length. As a result, the stiffness of each half is a function of the crack length. If assumed that the unbroken ligament remains completely rigid, a linear compliance relationship is obtained (Evans 1972)

$$C(a)=\frac{y}{P}=\frac{3W_m^{\ 2}}{Wd^3\mu}a \tag{1}$$

where, P and y are the applied load displacement at the load point respectively, μ is the shear modulus, W the specimen width and w_m the moment arm.

The actual crack profile in the DT geometry is curvilinear and therefore a crack front inclination is defined by $c=\Delta a/d$, where Δa is the crack extension difference between the upper and lower surface of the test specimen (Figure 2). Noteworthy is that the crack front shape and inclination is said not to change over the length of the specimen (Evans 1972).

Accordingly, the strain energy release rate, G, and hence the equivalent stress intensity factor (using $K=\sqrt{EG}$) can be calculated using (Williams and Evans 1973)

$$G_I=-\frac{dU}{dA}=\frac{P^2}{2d}\frac{dC}{da}=\frac{W_m^{\ 2}P^2}{2\mu Wd^4\psi} \tag{2}$$

where, U is the total strain energy, A the crack extension surface area and ψ a thickness correction given as a function of $W/d4$.

Noteworthy in Eq. (2) is the crack length independent strain energy release rate (or equivalent stress intensity factor), which allows for the aforementioned stable crack propagation in highly brittle materials.

3 PERIDYNAMIC THEORY

The peridynamics model presented in this work is the most basic implementation of the peridynamic theory. Considered is quasi-static deformation of the DT specimen as a linear-elastic solid (with bond breaking to represent the crack). Employed is a state-based rather than bond-based approach to the implementation of peridynamics.

Consider a neighbourhood H depicted in Figure 2 of a material point x of radius δ that includes all other material points for which a non-zero force interaction exists. If we denote another material point in this horizon as x' then the governing equation for state-based peridynamics can be written

$$\int_H \left\{T[x,t]\langle x'-x\rangle - T[x',t]\langle x-x'\rangle\right\}dV_{x'}+b(x,t)=0 \tag{3}$$

where, $T[x,t]$ is the force vector state field that defines the force interaction between two points x and neighbor x'. If we assume that the force between these neighbours acts along the vector pointing from x to x' denoted M, we can evaluate T[x,t] as a scalar coefficient times its unit vector

$$T[x,t]=\tilde{t}M \tag{4}$$

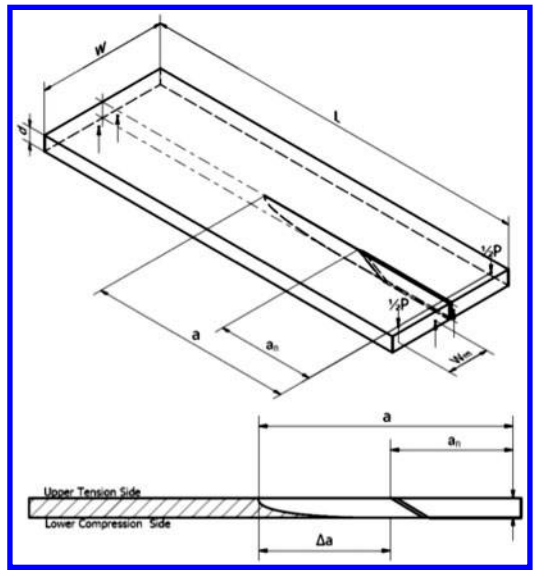


Figure 1. Schematic of the DT specimen geometry. L, W and d are the specimen length, width and thickness respectively, a the crack length and a_n the Notch Length.

This scalar coefficient, $\tilde{t}$, is computed as

$$\tilde{t}=\frac{-3p}{m}\bar{x}+\beta e^d \tag{5}$$

where p is the peridynamic pressure, m is the weighted volume, $\bar{x}$ is the distance magnitude between the two points in the reference configuration, β is a material parameter and $e^d=e-\theta\bar{x}/3$ is the deviatoric extension scalar state field ($e=\bar{y}-\bar{x}$, $\bar{y}$ is the distance magnitude between the points in the deformed configuration and θ is the dilatation of the material). In the discrete form, the governing equation above can be written as

$$\sum_{i=1}^{N}\left\{T[x,t]\langle x'-x\rangle - T[x',t]\langle x-x'\rangle\right\}\Delta V_{xi'}+b(x,t)=0 \tag{6}$$

where N is the number of neighbours and $\Delta V_{xi'}$ is the discretized cell volume of neighbour i. This way, equilibrium is evaluated for each cell on the basis of the force contribution from each neighbour. Damage is incorporated in this model via a critical stretch for each bond. Once the critical stretch is reached for a particular bond, that bond is treated as broken and contributes no force to the neighbouring cells. Once bonds are broken, it is assumed that they cannot be re-established.

4 METHODOLOGY

The DT geometry was modelled assuming Polymethylmethacrylate (PMMA) properties as $\mu=1.52$ GPa for the shear modulus and $k=2.13$ GPa for the bulk modulus (Kourtesis1997). The specimen size was set as $3W{:}W{:}0.04W$ for $L{:}W{:}d$ respectively,

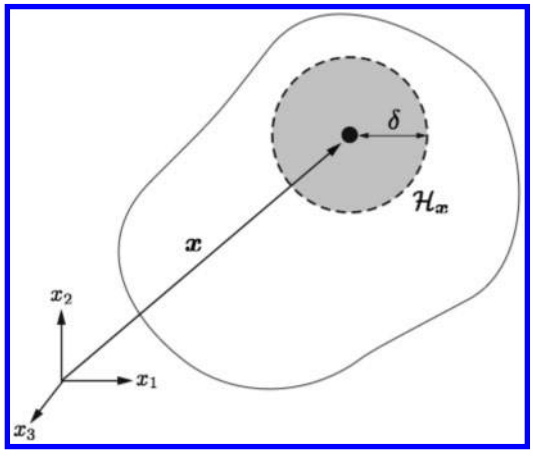


Figure 2. The peridynamic horizon of the material point at location x. The diameter of the spherical neighborhood is δ. All other material points within this horizon have a non-zero force interaction with point x.

where W was taken as 50 mm. The notch length $a_n = W/5$ and the notch inclination was set to $c = 0$.

The results were computed using a parallel software package developed in c++ by the authors that is built on the Trilinos framework (Trilinos 2013).

For each of the results presented, the damage was calculated as the ratio of the number of broken bonds to the number of original bonds for each element. Note that for a perfectly aligned crack that propagates along an element boundary, the damage for elements along this crack will be 0.5 as only the bonds along one side of the element will be broken. An arbitrary value of 1 millistrain was used for the critical stretch. When computing iterations for the equilibrium calculations, if a bond's stretch exceeds the critical stretch, the bond is removed from the neighbourhood (as if broken) and the iteration is restarted. Restarting the iterative solver after bond breaking is not always necessary, but it prevents the solver from diverging if the crack propagates over a large distance in a single step. Damage was also restricted to a zone of width 1 mm from the centreline of the domain, to ensure that the crack did not deviate from the centre due to asymmetry. It is worth noting, that future work will relax this constraint to investigate possible sensitivities to crack deviation from the centre.

4.1 *Boundary conditions*

The boundary conditions applied consist of a prescribed displacement of small sets of elements on the outer edge of the flanges (on each side of the notch) and on a set of elements near the vicinity of the notch as well to create an applied torque to each flange in opposing directions (as indicated in Figure 2) so that $W_m = 0.4W$. Displacement was restricted in the x and y direction (Figure 3) at one node to ensure that the boundary value problem is well posed.

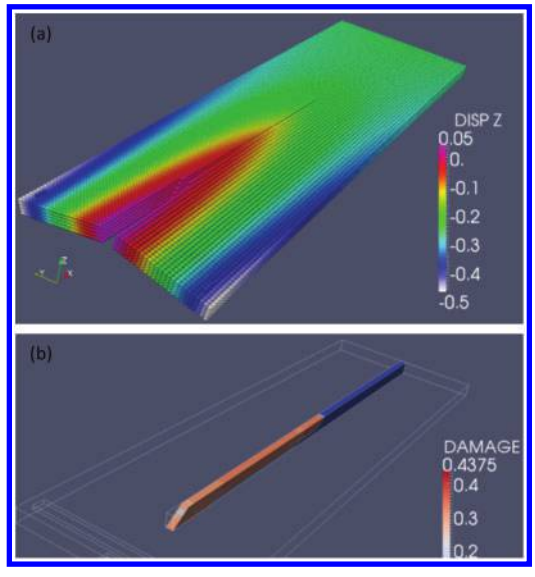


Figure 3. (a) Out of plane displacement map (in z) at time step 30 for the coarse mesh. (b) Crack propagation modelled as damage (only the central region of the domain is shown in the figure).

4.2 *Mesh sensitivity*

A simple mesh refinement study was performed to verify that no mesh sensitivity exist between computed results. A coarse mesh consisted of 5 elements through the thickness and an element diameter of 1.0mm. The medium mesh had 7 elements through the thickness and an element diameter of 0.6mm. The fine mesh had 8 elements through the thickness and an element diameter of 0.25mm. Number of elements for the course, medium and fine mesh are 59, 197 and 299 thousand respectively.

5 RESULTS

Snapshots of the computed results are shown in Figure 3. The top portion of the figure shows the out of plane displacement. The bottom portion of the figure shows the profile of the crack as it propagates down the centre of the domain (most of the domain has been removed to show the profile of the crack). The resulting curvilinear profile of the crack at the crack front shows excellent correspondence with the experimental results. Figure 4 shows the experimental profile superimposed on the computational results. Agreement between the two results was obtained for the entirety of the simulation, including the later stages in which the crack extends fully from the top to the bottom of the domain.

Figure 5 shows the crack length vs. time step, which shows a linear growth of the crack as expected. There is slight variation from the linear profile as in some steps the crack propagates further than predicted, however, this was typically followed by a slowing of the crack

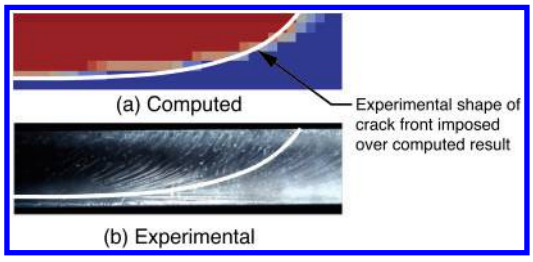


Figure 4. Comparisons of the (a) computed and (b) experimentally obtained crack front profiles.

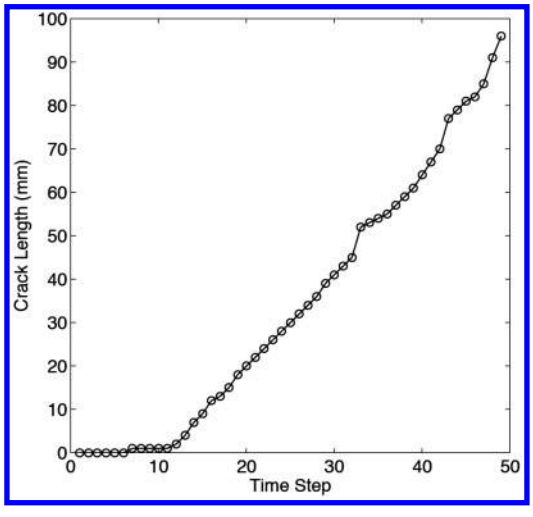


Figure 5. Crack length vs. time calculated as the distance of the furthest damaged cell from the origin of the notch.

growth in proceeding steps. A controlled growth of the crack, even for brittle materials is one of the advantages of the DT technique, which is clearly captured, in the simulated result.

Figure 6 illustrates a near constant applied force necessary to maintain a stable crack growth. These results illustrate the behaviour of the DT geometry. The predicted profile of the force vs. crack length curve is linear until the crack begins to propagate (suggesting the specimen behaves linear elastically). Once the crack begins to propagate, the predicted profile is a constant force, as the specimen can no longer withstand an increasing load due to the damage.

It is worth noting that the computed results in Figure 6 compare well with the experimental results in terms of a constant load state while the crack propagates, however, deviations during the initial stages exist. This deviation is largely due to the difference in the notch geometries being employed for the experimental and computed results (the experimental notch geometry is based on $c = 4$ inclination). As such, the constant force profile is delayed until the crack forms the characteristic curvilinear, full thickness crack font profile (whereas in the experiments the angled surface of the notch already closely matched the final profile of the crack).

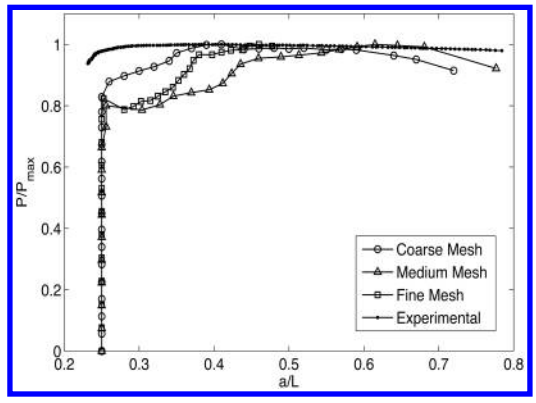


Figure 6. Force vs. crack length for meshes of various mesh sizes compared to experimental results.

Discrepancies, between the mesh sizes may also be attributed to the formation of the crack font where the mesh size effects the rate of achieving the constant crack front profile. Interesting to note though is that all geometries achieve the constant load curve over the middle of the specimen length.

6 CONCLSUIONS

It is clear that peridynamic modelling shows tremendous potential to simulate crack propagation for the DT technique, which in other contexts such as finite elements is quite difficult to accomplish. In particular, the shape of the crack front as it propagates is captured. A number of other features have also been simulated by the peridynamic theory including a (near) constant force profile as the crack advances in length.

This preliminary study into the use of peridynamics for modelling DT highlights the importance of further investigation on topics such as the convergence of the results with mesh refinement, alteration of the bond damage model, and using this method for alternative materials.

ACKNOWLEDGEMENTS

The second author was supported by the Institute for Structural Engineering at Stellenbosch University. Their support is greatfully acknowledged.

REFERENCES

Becker, T. H., Marrow T.J., Tait R.B. (2011). An Evaluation of the Double Torsion Technique. *Experimental Mechanics* 51, 1511–1526

Chevalier J., De Aza A. H. , Gremillard L. , Zenati R., Fantozzi G. (2001). Slow crack growth in zirconia ceramics: from the single crystal to the composites. *Materials Engineering* 12,159–178

Ciccotti M., Gonzato G., Mulargia F. (2000a). The double torsion loading configuration for fracture propagation: an

improved methodology for the load-relaxation at constant displacement. *International Journal of Rock Mechanics and Mineral Science* 37, 1103–1113

Ciccotti M. (2000b) Realistic finite-element model for the double torsion loading configuration. *Journal of the American Ceramics Society* 83, 2737–2744

Ciccotti M., Negri N., Gonzato G., Mulargia F. (2001) Practical application of an improved methodology for the double torsion load relaxation method. *International Journal of Rock Mechanics and Mineral Science* 38, 569–576

Evans A. G. (1972) A method for evaluating the timedependent failure characteristics of brittle materials—and its application to polycrystalline alumina. *Journal Materials Science* 7,1137–1146

Fuller, E. R. (1979). An evaluation of double-torsion testing analysis. Fracture mechanics applied to brittle materials, ASTM STP 678. *American Society for Testing and Materials*

Kourtesis G., Renwick G. M., Fischer-Cripps A. C., Swain M. V. (1997) Mechanical property characterization of a number of polymers using uniaxial compression and spherical tipped indentation tests. *Journal of Material Science* 32, 4493–4500.

Leevers P. S. (1986). Large deflection analysis of the double torsion test. *Journal of Material Science Letter* 5,191–192.

Silling, S. A. (2000). Reformulation of elasticity theory for discontinuities and long-range forces. *Journal of Mechanics and Physics of Solids* 42, 175–209.

Silling, S. A. (2007). Peridynamic states and constitutive modeling. *Journal of Elasticity* 88, 151–184.

Silling, S. A. & E. Askari (2005). A meshfree method based on ther peridynamic mode of solid mechanics. *Computers and Structures* 83, 1526–1535.

Silling, S. A. & R. B. Lehoucq (2008). Convergence of peridynamics to classical elasticity theory. *Journal of Elasticity* 93, 13–37.

Tait R. B., Garrett G. G. (1986). In situ double torsion fracture studies of cement mortar and cement paste inside a scanning electron microscope. *Cement and Concrete Res* 16(2), 143–155

Trilinos (2013). The Trilinos Project. Sandia National Laboratories. *http://trilinos.sandia.gov/*.

Turner (2013). A nonlocal model for fluid-structure interaction with applications in hydraulic fracturing. *International Jounral for Computational Methods in Engineering Science & Mechanics*. Accepted.

Williams D. P., Evans A. G. (1973) A simple method for studying slow crack growth. *Journal of Testing and Evaluation* 1, 264–270

Research and Applications in Structural Engineering, Mechanics and Computation – Zingoni (Ed.)
© 2013 Taylor & Francis Group, London, ISBN 978-1-138-00061-2

Propagation of non-planar pressurized cracks from a borehole

J.A.L. Napier
Department of Mining Engineering, University of Pretoria, South Africa
Department of Civil Engineering, University of Minnesota, Minnesota, USA

E. Detournay
Department of Civil Engineering, University of Minnesota, Minnesota, USA
CSIRO Earth Science and Resources Engineering, Australia

ABSTRACT: The in-situ stress field plays a crucial role in determining the orientation and shape of fractures that are initiated from a borehole. The paper outlines some investigations into the initial propagation of fractures from a pressurized borehole in both two-dimensional and three-dimensional cases. This has specific importance in understanding the stress field orientation and highlights some important contrasts between two and three-dimensional simulations of fracture propagation.

1 INTRODUCTION

Knowledge of the in-situ stress field is critical for mine planning and for designing underground excavations. One technique to measure the stress at depth is hydraulic fracturing; it consists of injecting water from a packed-off interval to create a fracture that propagates from the borehole. The fluid pressure-time record during propagation and eventually closure of the fracture after injection has stopped is then interpreted to extract information about the in-situ stress. However, only the least compressive in-situ stress σ_3^0can reliably be deduced from such a test; it is equated to the fluid pressure at which the fracture closes. Our current inability to deduce more information from the pressure-time record actually stems from the lack of a comprehensive model that can be used to simulate the 3D propagation of a crack, including fracture turning and warping if the borehole is inclined to the principal in-situ stress directions.

This paper presents the results of numerical simulations involving the propagation of the two wings of a fracture, which initially were longitudinal edge cracks aligned parallel to the borehole axis. The cracks are here assumed to be uniformly pressurized, i.e., the flow of water in the crack is not presently simulated. The numerical algorithm, RIFT (Napier, 2011), is based on the displacement discontinuity method (Crouch & Starfield, 1983) which only requires element mesh tessellation of the crack surface for problems involving homogeneous elastic infinite or semi-infinite domains. In RIFT, the three-dimensional crack surface is built up using flat, triangular or quadrilateral, displacement discontinuity elements with having constant, cubic or bi-quadratic strength. The displacement discontinuity formulation leads to a linear system of equations that relates the unknown displacement jumps in each element to the given tractions along the crack. The stress intensity factors are determined from the displacement discontinuities of the tip elements located next to the crack edge.

2 PLANE STRAIN FRACTURE PROPAGATION

A simplifying assumption that is often made in attempting to simulate propagation of fractures in a brittle material is to assume that the propagation path occurs in a representative plane section with respect to the local crack front edge as shown in Figure 1. In this case the x-axis is the outward tangent to the crack front edge, the y-axis is normal to the crack surface at the crack front and, by implication, the z-axis is parallel to the crack edge and points out of the plane in Figure 1. A suitable crack growth algorithm must be devised to determine the growth path direction and the stress state that matches the strength of the material. For brittle fracture in tension, the material strength is assumed to be determined by the Mode I fracture toughness, K_{Ic}. The simplest strategy that can be used to determine the growth path direction is to perform a direct search at a series of points located at a fixed distance, r, from the crack tip as shown in Figure 1. The hoop stress component $\sigma_{\theta\theta}$ is evaluated at each point (r,θ) and the maximum value $\sigma^*_{\theta\theta}$ is inferred using a suitable interpolation scheme to determine the optimum angle θ^* (see, for example, Napier & Hildyard, 1992). The crack path is then assumed to be a flat line segment joining the current tip and the point (r,θ^*). An analytic expression for the growth direction can be determined from the classic asymptotic crack tip expansions for a square

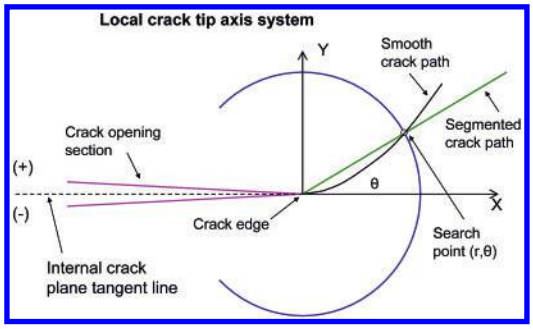


Figure 1. Crack tip axis system to define the crack front growth direction θ with respect to the current crack edge.

root crack tip opening and slip displacement discontinuity distribution (this scheme is adopted, for example, by Thomas & Pollard, 1993). In this case, the crack displacement discontinuity components Δu_x and Δu_y at a distance ε from the crack edge are defined by the difference in the displacement components $u_x(-\varepsilon, y)$ and $u_y(-\varepsilon, y)$ as $y \to \pm 0$ on the (+) and (−) sides of the crack as depicted in Figure 1. Specifically,

$$\Delta u_x = u_x(-\varepsilon, 0^+) - u_x(-\varepsilon, 0^-), \tag{1}$$

$$\Delta u_y = u_y(-\varepsilon, 0^+) - u_y(-\varepsilon, 0^-). \tag{2}$$

The relationships between the limiting shear and opening displacement discontinuity components are given in terms of the stress intensity factors K_I and K_{II} by

$$\Delta u_x = [8(1-\nu^2)/E]K_{II}\sqrt{\varepsilon/2\pi} \tag{3}$$

and

$$\Delta u_y = [8(1-\nu^2)/E]K_I\sqrt{\varepsilon/2\pi}, \tag{4}$$

respectively where E is Young's modulus and ν is Poisson's ratio. From the asymptotic crack tip stress fields (Lawn, 1993), the hoop stress component $\sigma_{\theta\theta}$ can be shown to be given by

$$\sigma_{\theta\theta}(r,\theta) = \cos^2(\theta/2)\{K_I\cos(\theta/2) - 3K_{II}\sin(\theta/2)\}/\sqrt{2\pi r}. \tag{5}$$

Differentiating Equation (5), provides the angle θ^* at which $\sigma_{\theta\theta}$ attains a maximum value as

$$\sin(\theta^*) = \rho(1-3\sqrt{1+8\rho^2})/(1+9\rho^2), \tag{6}$$

$$\text{where } \rho = K_{II}/K_I;\ K_I \neq 0. \tag{7}$$

If the fracture propagates in the direction θ^*, the incipient value of the mode I stress intensity factor K_I^* in the new direction is inferred to be

$$K_I^* = \cos(\theta^*/2)\{K_I(1+\cos\theta^*) - 3K_{II}\sin\theta^*\}/2. \tag{8}$$

Fracture propagation is assumed to proceed under the condition that $K_I^* = K_{Ic}$. In the construction of a crack growth algorithm, it is necessary to assume that the crack will advance by a specified distance, g, which, in the absence of a full crack tip velocity model, has to be viewed as a user parameter. Continued growth or halting of growth will be determined by the problem specific details of the boundary or crack surface loading. Tensile crack propagation at each active crack tip is considered to be locally stable if, under fixed loading stresses, a small advance, δs, at each crack tip position results in a decrease in the mode I stress intensity factor at each crack tip. Specifically, crack growth is assumed to be stable if

$$\partial K_I / \partial s < 0 \tag{9}$$

at each active crack tip.

In the limiting case where $K_I \to 0$in Equation 6 (mode II shear only),

$$\theta^* = \sin^{-1}\left[\frac{-\sqrt{8}K_{II}}{3|K_{II}|}\right] \sim 70.53° \text{ if } K_{II} < 0\ . \tag{9}$$

In this case, from Equations (5) and (8), the absolute value of the maximum hoop stress is given by

$$|\sigma_{\theta\theta}^*| = (2/\sqrt{3})|K_{II}|/\sqrt{2\pi r}. \tag{10}$$

It is important to note however that the corresponding maximum value of the asymptotic radial tensile stress component σ_{rr} within the crack surface (position $x = -\varepsilon; y = 0$ in Figure 1), is given by

$$\sigma_{rr} = 2|K_{II}|/\sqrt{2\pi\varepsilon}. \tag{11}$$

The singularity coefficient in Equation (11) is notably greater than in Equation (10) and, consequently, the asymptotic crack propagation would therefore be expected to initiate from within the crack surface and at right angles to the crack surface, rather than at the incipient angle given by Equation (9). This result appears not to have been noted in previous analyses of crack kinking (Cherepanov, 1968, Cotterell & Rice, 1980).

In general, the maximum tensile stress crack growth direction determination procedure outlined above will result in the construction of a kinked crack path trajectory comprising piecewise flat crack segments that are joined end to end. In extreme cases this can result in the initiated crack segment having a relatively large residual mode II shear component, Δu_x, at the crack tip which may, in turn, result in subsequent spurious oscillations of the simulated crack growth path. A more exact specification of the conditions required for smooth crack propagation (Cherepanov, 1979) is that at the crack tip,

$$K_{II} = 0 \text{ and } K_I = K_{Ic}. \tag{12}$$

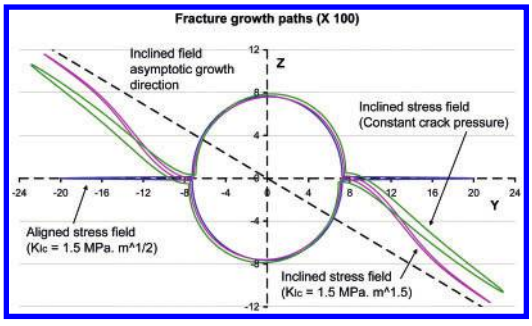


Figure 2. Superimposed fracture growth paths from the edge of a circular hole with starter cracks perpendicular to and tilted at 60 degrees with respect to the minimum principal field stress, σ_3^0. The volume-controlled growth paths are compared to the growth path that is found with constant pressure loading in the hole and within the cracks. (Axis scales in cm).

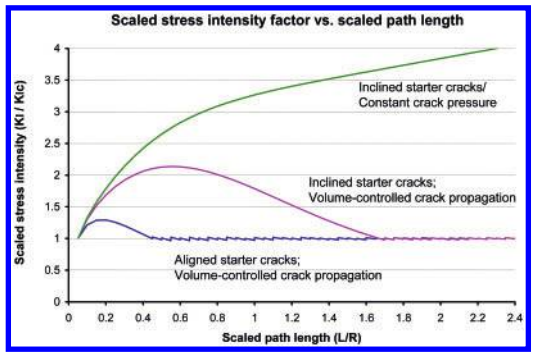


Figure 3. Comparison of Mode I stress intensity values at the crack tip (scaled to the assumed fracture toughness) plotted against the mean fracture path from each edge of the borehole, scaled to the borehole radius. (The three cases considered are respectively: (a) the starter cracks are perpendicular to the direction of the minimum principal field stress component, (b) the starter cracks are inclined at 60 degrees to the direction of the minimum principal field stress component, (c) as for case (b) but the pressure in the propagating cracks is constant).

If it is further demanded that the crack path be smooth (no kinks; see Figure 1) then it is possible to develop a theory that allows the crack radius of curvature to be determined at the successive crack tip positions (Cherepanov, 1979, Cotterell & Rice, 1980). However, this theory is still incomplete in the case of a three-dimensional crack front where double curvature of the front may generally occur and where Mode III loading may lead as well to the segmentation of the crack front (Napier, 2011). In the present paper the "first order" direction theory expressed essentially by Equations (6) and (8) above will be employed with the proviso that the crack increment advance step size g is sufficiently small to ensure that residual K_{II} values along the current crack front are "small" relative to the dominant values of K_I at the crack front.

3 PLANE STRAIN FRACTURE PROPAGATION FROM A CIRCULAR BOREHOLE

Consider next the case of a borehole section of nominal radius $R = 75$ mm centered on the origin in a y-z coordinate axis system as shown in Figure 2. The x-axis in this case is taken to be aligned to the borehole axis and the hole has an initial internal pressure, P_0. It is assumed that two initial edge cracks of length g = 0.375 mm exist at opposite points on the hole diameter where $z = 0$ in Figure 2. The subsidiary principal field stress components in the plane section of the hole are assumed to be $\sigma_3^0 = \sigma_{zz} = -10$ MPa and $\sigma_2^0 = \sigma_{yy} = -20$ MPa respectively. It is further assumed that the initial pressure P_0 is adjusted to a level where the stress intensity factor at the tips of the edge cracks reaches a postulated nominal fracture toughness, $K_{Ic} = 1.5\,\text{MPa.m}^{1/2}$, of the surrounding rock. In this analysis, the borehole circumference is simulated with 60 flat line segment displacement discontinuity elements. The surrounding rock is assumed to have a Young's modulus, $E = 72000$ MPa and a Poisson's ratio, $\nu = 0.2$.

Fracture growth is controlled by adjusting the total crack and borehole opening volume in a series of constant increments until it is found that $K_I \geq K_{Ic}$ at one or more of the active crack tips. Additional elements of length g are then connected to the active crack tips, in the appropriate advance directions calculated from Equation 6, and the element assembly is solved iteratively to satisfy the current opening volume constraint by adjusting the applied borehole and internal crack pressures. Alternatively, if it is found that the Mode I stress intensity factor increases at a particular crack tip when a new growth element is added to the tip, the total opening volume constraint value is "frozen" and successive crack elements are then introduced until the active crack tip stress intensity factors do not exceed the specified toughness parameter. (This allows the model to accommodate what is effectively an unstable growth phase).

The resulting fracture paths for three cases where fracture propagation initiates at the borehole edges in the plane $z = 0$ are shown in Figure 2. In the first case, the minimum principal stress is parallel to the z-axis and, in the remaining two cases, is tilted at an angle of 30 degrees to the z-axis. The Mode I stress intensity factors at each crack tip, scaled to the fracture toughness, are plotted in Figure 3 as a function of the crack path length, L, scaled by the borehole radius, R. It is observed that for the volume-controlled propagation cases there is an initial phase of "unstable" fracture growth where the stress intensity factor increases when the opening volume is held constant followed by "stable" crack propagation in the sense that the crack opening volume must be increased incrementally to maintain the advancing crack tip stress intensity at the magnitude of the assumed fracture toughness. In the case of constant pressure loading, the fracture propagation is "unstable" with the Mode I stress intensity

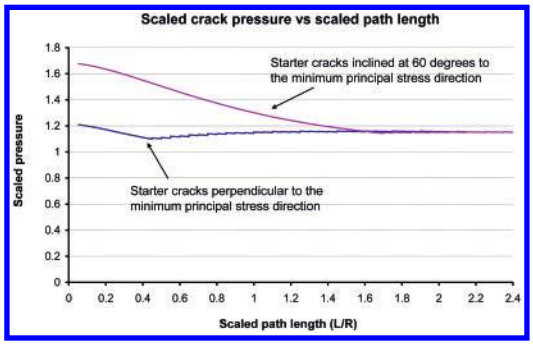


Figure 4. Comparison of the scaled crack pressure as a function of the scaled fracture path length for: case (a) the starter cracks are perpendicular to the direction of the minimum principal field stress component and case (b) the starter cracks are inclined at 60 degrees to the direction of the minimum principal field stress component.

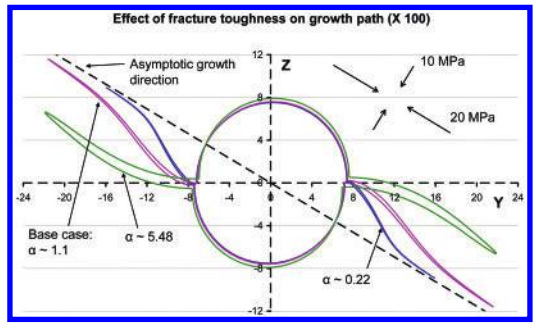


Figure 5. Comparison of crack growth paths for three values of the fracture toughness and the corresponding values of the dimensionless parameter α. (Axis scales in cm).

factor progressively increasing at each crack tip (see Figure 3). The constant pressure crack path in Figure 2 is observed to deviate significantly from the corresponding volume-controlled crack path in the inclined stress field.

The scaled crack and borehole surface pressure is shown in Figure 4 for the aligned and tilted stress fields respectively as a function of the evolving crack path length. The pressure is scaled by the minimum principal field stress value, σ_3^0. During the unstable crack growth phase, the pressure is observed to fall and then to increase steadily as the fracture length is increased. It is notable as well that the initial pressure for the tilted stress field case is significantly greater that for the case of the aligned stress field.

The alignment of the crack path trajectory to the asymptotic growth direction (corresponding to the direction perpendicular to the minimum principal field stress) is controlled by the dimensionless parameter α defined by (Mogilevskaya *et al*, 2000)

$$\alpha = K_{Ic} / S_0 \sqrt{R} \tag{13}$$

where S_0 represents the far-field deviatoric stress. For the field loading relevant to the present example in Figure 2,

$$S_0 = \left|\sigma_2^0 - \sigma_3^0\right| / 2 = 5 \text{ MPa.} \tag{14}$$

Fracture paths for the cases where $K_{Ic} = 0.3$ MPa.m$^{1/2}$ and $K_{Ic} = 7.5$ MPa.m$^{1/2}$ respectively are compared to the base case $K_{Ic} = 1.5$ MPa.m$^{1/2}$ in Figure 5. The corresponding values of the parameter α computed from equation 13 are 0.22, 5.48 and 1.10 respectively and indicate that for "small" values of α the growth path approaches the asymptotic growth direction more rapidly.

4 THREE-DIMENSIONAL FRACTURE PROPAGATION

4.1 Aligned stress field

The construction of a propagating crack front in three dimensions requires additional assumptions to be made to determine the growth advance distance at each point i on the crack front, located at an arc length position t_i measured from some appropriate initial point on the crack front. Whereas it is implicit that the stress intensity is uniform at each point along the crack front in the plane strain case (i.e. the out of plane direction in Figure 1), this assumption is no longer necessarily valid for a three-dimensional crack front advance (Napier, 2002). It is unclear, in fact, exactly how the crack front shape should be evolved to maintain the condition that $K_I = K_{Ic}$ at every point along the incrementally advanced crack front. The provisional assumption is made therefore that the advance distance at each point along the crack front will be scaled by a defined "growth potential metric", F_i, that is evaluated at selected points along the crack front. This metric may be chosen, for example, to be the estimated stress intensity factor of the incipient front advance, as in Equation 8. In the present study, F_i, is defined to be the maximum tensile hoop stress $\sigma^*_{\theta\theta}$ evaluated in a direct search at a fixed distance, ε, ahead of each position t_i along the current crack front. The value of F_i is determined in a local $x-y$ plane, as shown in Figure 1, where the x-axis is the outward crack tangent vector, the y-axis is the local normal vector to the crack surface at the crack front and the z-axis is the tangent direction parallel to the crack edge (see as well Napier, 2011).

The new crack front offset g_i from the existing crack front point i is determined according to the simple assumption that

$$g_i = \frac{F_i}{F_{\max}} g_{\max}, \tag{15}$$

where $g_{\max}$ is a user-specified maximum allowed advance distance and where $F_{\max} = \max[F_i]$ within

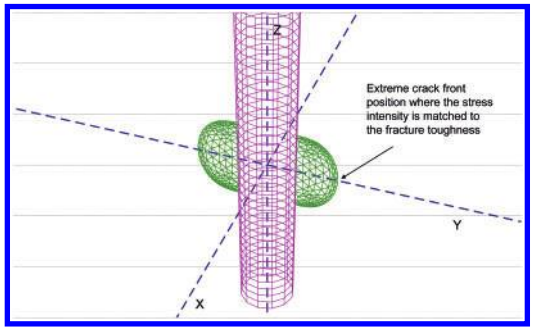


Figure 6. Fracture profile with a short fracture initiation length along the borehole wall. ($H_0/R = 0.267$).

a selected set of sampled positions along the current crack front. It is convenient as well to choose a threshold advance, g_c which can be expressed as

$$g_c = \gamma g_{\max}, \tag{16}$$

and where $0 < \gamma \leq 1$. In the subsequent simulations it is assumed that $\gamma = 0.5$.

The advanced crack front must then be constructed from a suitable element tessellation joining the old front and the new front offset positions. In the simulations presented in this paper, it is assumed that the bridging elements are triangular and that the displacement discontinuity values are constant within each element. (The element influence functions are described in Napier and Malan, 2007). The following simple procedure, based on the structure of Equation (4), is used to estimate the Mode I stress intensity factors at the mid points of the crack front element edges:

$$K_I = \frac{E\Delta u_y}{8(1-\nu^2)}\sqrt{\frac{2\pi}{\varepsilon + f_c\sqrt{A}}}. \tag{17}$$

In equation (17), f_c is an empirically chosen "correction factor" and A is the area of the local edge triangular element. It is found empirically that for constant strength, triangular displacement discontinuity elements $f_c = 0.5$ is an appropriate choice for the correction factor although there is some scatter in the estimated values with errors of ~5 percent.

It is assumed that the borehole radius, $R = 75$ mm as for the circular hole considered in Section 3. The borehole is represented as a truncated cylindrical crack of length H (where $H/R = 18.67$) and comprises rectangular displacement discontinuity elements as shown in Figure 6. The borehole axis is aligned to the z-axis coordinate direction as shown in Figure 6. The compressive principal field stress magnitudes in the x, y and z directions are set initially to 10 MPa, 20 MPa and 50 MPa respectively. The fracture is allowed to initiate from the surface of the borehole along a line of length H_0, parallel to the borehole axis in the y-z plane. Figure 6 illustrates the development of two planar fracture surfaces in the y-z plane on each side of the hole after 8

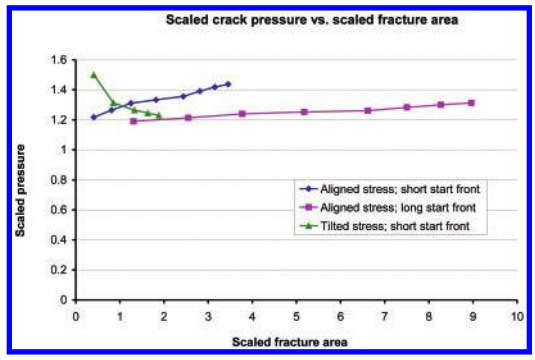


Figure 7. Evolution of scaled crack pressure as a function of the scaled fracture area to maintain an estimated match of the crack front stress intensity to the nominal fracture toughness.

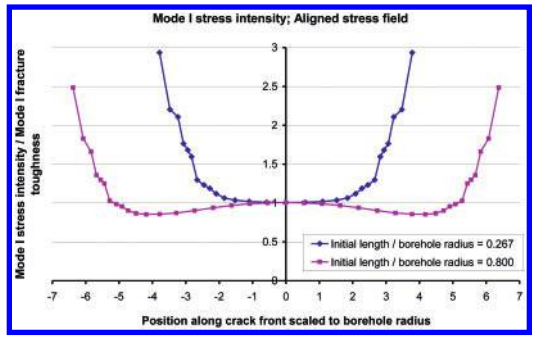


Figure 8. Mode I stress intensity variation along the crack front edge after 8 growth steps for (a) short fracture initiation length ($L_0/R = 0.267$) and (b) long fracture initiation length ($L_0/R = 0.800$).

growth steps for the case where $H_0/R = 20/75 \sim 0.267$. In each growth step, the borehole and crack pressure is adjusted to match the nominal fracture toughness $K_{Ic} = 1.5$ MPa.m$^{1/2}$ before determining the new crack front position. It is important to note that the fracture toughness is matched only at the extreme outer crack front positions in Figure 6 and, as noted before, is not necessarily uniform along the entire crack front. Figure 7 indicates the corresponding crack pressure values (designated by the label "aligned stress; short start front") scaled to the minimum principal stress magnitude σ_3^0 plotted against the total fracture area of both wing cracks scaled to the nominal cross sectional area of the borehole. A second case was analysed with a longer start crack length, $H_0/R = 60/75 = 0.8$. The corresponding evolution of the crack pressure as a function of the developed fracture area is shown in Figure 7. These results suggest that the initial fracture growth is stable in the sense that the pressure and the fluid volume have to be increased in order to propagate the cracks. This is in distinct contrast to the cases analysed in plane strain in section 3 and the pressure profiles shown in Figure 4.

The Mode I stress intensity values along the developed crack front of the wing cracks developed in the region y > 0 (Figure 6) are shown for the two cases

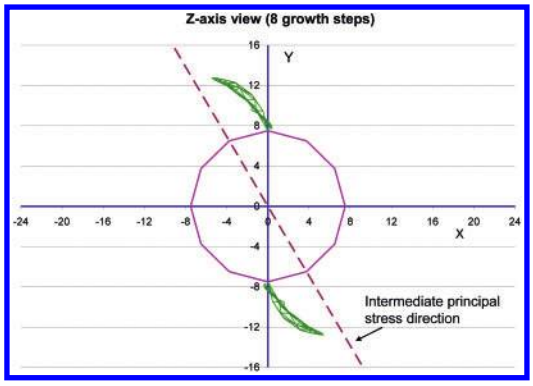


Figure 9. View along borehole axis of fracture surface evolution for tilted stress field.

of fracture growth from the short and long initiation lengths respectively in Figure 8. The distribution of the stress intensity values shows that although the nominal toughness is matched (as required) at the central position, it is in detail characteristically different for the short and long initiation length cases and exceeds the nominal toughness at the upper and lower extremities of the developed front with respect to the z-axis direction (see also, Figure 6). This suggests that the shape of the developed crack surface shown in Figure 6 (and the similar extended profile found for the case of the long initial crack length) must be treated with some caution.

4.2 Inclined stress field

The simulation of the fracture initiation from the short start length case was repeated for the case of an inclined stress field rotated about the z-axis as shown in Figure 9 where the z-axis view of the developed wing cracks after 8 growth steps are shown. The corresponding evolution of the crack pressure as a function of the scaled crack area is included in Figure 7 for the first 5 growth steps. It is of particular interest to note that the initial fracture growth now appears to be unstable in contrast to the two cases where the minimum principal stress field is perpendicular to the developing wing cracks.

It is significant to note that in this case, the stress intensity factor at the outer crack front mid-point was found to fall below the nominal toughness value after growth step 3 and ad hoc estimates of the average stress intensity values had to be made in order to estimate the appropriate crack opening pressure. This complex behaviour of the evolving crack front stress intensity profile is a critical feature of three-dimensional fracture growth simulation.

5 CONCLUSIONS

The stress field orientation plays a crucial role in determining the trajectories of fractures that are initiated from a borehole. It is of particular interest that the stability of three-dimensional fracture propagation may not match that of the plane strain case, depending on the initial fracture length along the edge of the borehole. It is noted further that there are a significant number of unresolved issues relating to the determination of the evolutionary shape of a three-dimensional crack front.

REFERENCES

Cherepanov, G.P. 1979. *Mechanics of Brittle Fracture*. New York. McGraw-Hill.

Cotterell, B. and Rice, J.R. 1980. Slightly curved or kinked cracks. *International Journal of Fracture*. 16(2): 155–169.

Crouch, S.L. and Starfield, A.M. 1983. *Boundary Element Methods in Solid Mechanics*. London: George Allen & Unwin.

Lawn, B. 1993. *Fracture of Brittle Solids*. Second Edition. Cambridge: Cambridge University Press.

Mogilevskaya, S.G., Rothenburg, L. and Dusseault, M.B. 2000. Growth of pressure-induced fractures in the vicinity of a wellbore. *International Journal of Fracture*. 104: L25–L30.

Napier, J.A.L. and Hildyard, M.W. 1992. Simulation of fracture growth around openings in highly stressed, brittle rock. *J.S. Afr. Inst. Min. Metall.* 92: 159–168.

Napier, J.A.L. 2002. Crack edge collocation for the direct computation of stress intensity factors using the displacement discontinuity method. *South African Journal of Science.* 98: 481–485.

Napier, J.A.L. and Malan, D.F. 2007. The computational analysis of shallow depth tabular mining problems. *J.S. Afr. Inst. Min. Metall.* 107: 725–742.

Napier, J.A.L. 2011. Explicit discontinuity modeling of deep mine stope face and pillar foundation failure. Paper 11–476. In *45th US Rock Mechanics/Geomechanics Symposium, 26–29 June 2011*. San Francisco.

Thomas, A.L. and Pollard, D.D. 1993. The geometry of echelon fractures in rock: implications from laboratory and numerical experiments. *Journal of Structural Geology* 15: 323–334.

Research and Applications in Structural Engineering, Mechanics and Computation – Zingoni (Ed.)
© 2013 Taylor & Francis Group, London, ISBN 978-1-138-00061-2

Hydraulic fracture simulation: Comparison with exact solutions

C. Detournay, P.A. Cundall & B. Damjanac
Itasca Consulting Group, Inc., Minneapolis, USA

ABSTRACT: Hydraulic fracturing is a technique to stimulate gas and oil-bearing rock layers through the creation of large cracks in the reservoir by injection of fluid from a borehole. The Particle Flow Code (*PFC*) and the new lattice based *HF simulator* are two coupled fluid-mechanical codes capable of modeling fracture initiation and propagation, including slip and opening along joints in a pre-existing Discrete Fracture Network (DFN). A new efficient coupled fluid-mechanical scheme (MIF) has been devised as part of the *HF simulator* design and development.

In the paper, we use a simple framework, and *PFC* as a test bed, to demonstrate the ability of the MIF scheme to capture important fluid-mechanical mechanisms associated with fluid injection in a fracture. Two example problems are considered: fluid injection at a fixed rate into a pre-existing crack, and linear fracture propagation along a pre-existing joint. The numerical solution for pressure and aperture evolution with time is compared to analytical solutions for the two examples. Different mesh resolutions are considered and it is shown that the trends of the analytical solution can be captured satisfactorily with a relatively coarse mesh and small model size.

1 INTRODUCTION

Hydraulic fracturing is a technique to stimulate gas and oil-bearing rock layers through the creation of large cracks in the reservoir by injection of fluid from a borehole. Recently, this technique has become critical to unlock the enormous reserve of gas contained in large deposits of shales throughout the world. However, numerical models that were developed to design hydraulic fracturing treatments for conventional reservoirs are not applicable for the stimulation of gas shales. Indeed, these models generally assume propagation of a single planar fracture in a homogenous elastic medium, and are not capable of accounting for the many discontinuities present in the shales that interact with the hydraulic fracture. The work presented in this paper documents a first step to developing a new generation of numerical models, which are freed of the restrictions of most previous models.

The particle flow code *PFC* (Itasca, 2008) and the more specialized, computationally efficient lattice based *HF simulator* (Damjanac et al., 2013) are two coupled fluid-mechanical codes capable of modeling fracture initiation and propagation, including slip and opening along joints in a pre-existing discrete fracture network (DFN).

An important aspect of any numerical development is the ability to compare model predictions with exact solutions. In the paper, we use a simple framework and *PFC* as a test bed to demonstrate the ability of the numerical scheme to capture important fluid-mechanical mechanisms associated with fluid injection in a fracture. Two example problems are considered: fluid injection at a fixed rate into a non-propagating crack, and linear fracture propagation along a pre-existing joint. The numerical solution for pressure and aperture evolution with time is compared to analytical solutions for the two examples. Different mesh resolutions are considered and it is shown that the trends of the analytical solution can be captured satisfactorily with a relatively coarse mesh and small model size.

2 NOTATION CONVENTION

By convention in the text below, R represents the discretization length used in the numerical model (i.e., distance between contacts in a *PFC* model or nodes in a lattice model) and a is the joint aperture. Also, K_R is rock bulk modulus, and K_F is (apparent) fluid bulk modulus. The quantities k_R and k_J are one-dimensional stiffness in the model (in units of force/displacement) associated with the rock and the joint, respectively. In addition, κ_F is the joint permeability factor (parallel plate model), expressed as $\kappa_f = 1/12\mu$, where μ is the dynamic viscosity of the fluid. Δt is the (explicit) time step increment.

Finally, a unit model thickness is considered in the discussion, and A is the apparent area of the joint element (in the order of R in a 2D model of unit thickness).

3 MIF SCHEME

The MIF scheme (Mechanical Incompressible Fluid) (Cundall, 2011) is a new coupled fluid-mechanical

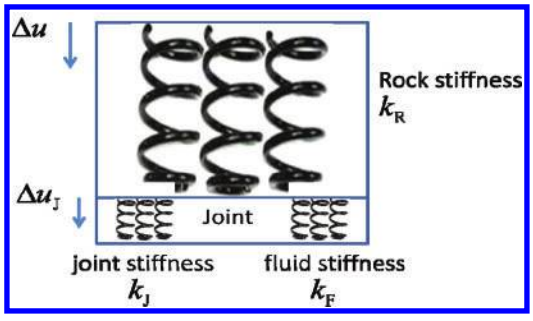


Figure 1. Schematic of a rock element the size of the resolution with embedded fluid-filled joint – normal direction.

algorithm to model the mechanisms associated with hydraulic fracturing and/or fluid injection in pre-existing joints. The scheme is applicable to situations in which the rock compressibility is much larger than that of the fluid. One of the main advantages of the scheme, compared to the algorithms currently implemented in Itasca codes, is the larger explicit time steps required for numerical stability.

We note that fluid pressure is defined at contacts in a *PFC* model (springs in a lattice), and flow occurs in pipes, which are linear entities connecting the contacts. Fluid compressibility is assumed to be very small compared to the rock.

The MIF scheme is described by considering an element of rock of a dimension equal to the discretization length, R, that includes a single joint. Figure 1 illustrates the mechanical arrangement in the normal direction. Fluid and rock stiffness in the plot are related to fluid and rock bulk modulus: $k_F = K_F A/a$, and $k_R = K_R A/R$. Also, typically $k_F >> k_R$.

The combined joint normal stiffness, k_C is $(k_J + k_F)$, and the total element stiffness, k_T is

$$k_T = \frac{k_R k_C}{k_R + k_C} \tag{1}$$

In one time step, Δt, an increment of relative displacement for the element, Δu gives rise to a force increment of

$$\Delta F = k_T \Delta u \tag{2}$$

And a joint displacement of

$$\Delta u_J = \frac{\Delta F}{k_C} \tag{3}$$

The increment in fluid pressure is $\Delta P = \Delta u_J k_F / A$; after some substitution, it is expressed as

$$\Delta P = \frac{\Delta u\, k_R}{A} \frac{k_F}{k_F + k_R + k_J} \tag{4}$$

If $k_F >> k_R$, the fluid pressure increment approaches

$$\Delta P \rightarrow \Delta u\, k_R / A \tag{5}$$

Thus, the fluid pressure increments depend only on rock spring stiffness, and the mechanical time-step is not affected by the presence of the fluid.

The apparent fluid modulus (used in the flow part of the model) is also modified as follows. Consider a fluid "displacement" increment Δu_F (derived from a flow imbalance, ΣQ in the joint), which is imagined to be injected in a series with the fluid spring, k_F at each fluid time-step. The increment in fluid force is then

$$\Delta F_F = \frac{(k_J + k_R)k_F}{k_J + k_R + k_F} \Delta u_F \tag{6}$$

The pressure increment $\Delta P = \Delta F_F / A$ approaches

$$\Delta P \rightarrow \frac{\Delta u_F (k_R + k_J)}{A} \tag{7}$$

when $k_F >> k_R$. Thus, in the limit of $k_F >> k_R$, the fluid "sees" an apparent bulk modulus of

$$K_F = \frac{a}{A}(k_R + k_J) \tag{8}$$

This apparent fluid bulk modulus is much smaller than a true fluid bulk modulus, allowing much longer fluid time-steps.

Finally, the lattice spring force is incremented as a result of fluid displacement arising from the flow calculation, as follows:

$$\Delta F = \frac{\Delta u_F\, k_R\, k_F}{k_R + k_J + k_F} \tag{9}$$

In the limit $k_F >> k_R$,

$$\Delta F \rightarrow \Delta u_F k_R \tag{10}$$

The stable fluid time-step in the MIF scheme (*PFC* test bed) is taken as:

$$\Delta t = 0.25 \frac{\lambda^3}{\kappa_f K_R} \tag{11}$$

where $\lambda = R/a$. For comparison, the fluid time-step in the existing (compressible fluid) scheme is (Itasca, 2008):

$$\Delta t = \frac{\lambda^2}{\kappa_f K_f} \tag{12}$$

For most practical applications: K_R and K_f are of the same order of magnitude, and thus, the denominators in (7) and in (8) are also of the same order. Compared to previous schemes, the "gain" in fluid time-step magnitude is directly proportional to λ, a number typically much larger than 1.

In the existing scheme, the stable mechanical-step is typically smaller than the stable fluid-step. In the new scheme, uniform density scaling is applied by giving the mechanical time-step a value equal to that of the fluid. (In this technique, inertial masses are multiplied by a factor, such that the computed mechanical time-step is equal to the fluid time-step. Gravitational masses are unaffected.)

4 INJECTION IN A PRE-EXISTING CRACK

We consider the two-dimensional problem of fluid injection at a constant rate into a pre-existing crack of constant length, embedded in an elastic medium of negligible permeability and large extent. The problem has been analyzed by Garagash and Detournay (1998), who also derived a semi-analytical solution. The numerical solution obtained using the new scheme is compared to the semi-analytical results, which were provided by the authors in the form of a spreadsheet.

4.1 *Semi-analytic solution*

The crack half length is$L$, and the constant injection rate is Q_0. The effective net pressure inside the crack is given by the difference between fluid pressure inside the crack, p and compressive far-field stress component normal to the crack σ:

$$p_e = p - \sigma \tag{13}$$

The initial crack loading (effective net pressure p_e) is assumed to be zero, and the crack has an initial opening a_0. The origin of reference axis is at the crack center (fluid inlet), and the x-axis points to the right along the crack. The following dimensionless variables are used: $\hat{x} = x/L$, $\hat{t} = t/t^*$, $\hat{p} = (p-\sigma)/p^*$, $\hat{a} = a/a_0$ where characteristic time t^* and pressure p^* are given for the plane stress case, as:

$$t^* = \frac{12\mu}{E'}\left(\frac{L}{a_0}\right)^3 \quad p^* = E'\frac{a_0}{L} \tag{14}$$

with $E' = E/(1-\nu^2)$, E is Young modulus, and ν is Poisson ratio. Also, the dimensionless fluid flux at the inlet (plane stress case) is:

$$\hat{Q} = \frac{12\mu}{E'}\frac{L^2}{a_0^4}Q_0 \tag{15}$$

The semi-analytical solution assumes that there is no lag at the crack tip; it gives the evolution of $\hat{p}$ and $\hat{a}$ as a function of $\hat{t}$ at equidistant points along the crack.

4.2 *Simulation data*

The elastic macro-properties for the crack are 6 GPa for Young modulus, and 0.3 for Poisson ratio. The crack length (2 L) is 11 m. Fluid viscosity is 10^{-3}Pa-s, and fluid flux at the inlet is 0.266 m^2/s (dimensionless fluid flux for the full crack is 200π). Initial fracture aperture is 0.4 mm. The joint stiffness is zero. Also initial stress σ is zero, and so is initial pressure p_0 inside the crack.

4.3 *PFC models*

The *PFC* models for the simulations are 43 m wide and 36.5 m high. The models use a hexagonal packing of balls, and two rows or rectangular packed balls along the line of the crack. Two different resolutions are considered for the models: the coarse model, shown in Figure 2, uses a ball radius of 0.5 m, and a ball radius three times smaller is used in the fine model.

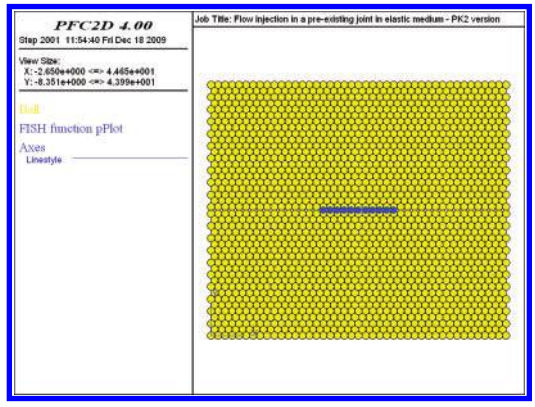


Figure 2. Ball assembly for coarse model.

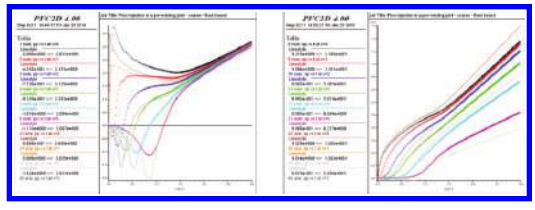


Figure 3. $\hat{p}$ versus $\hat{t}$ (left) and $\hat{a}$ versus $\hat{t}$ (right): comparison between analytical (gray) and numerical (color) predictions at selected monitoring points – coarse model.

Fixed (roller) boundary conditions are used in the simulations. The local x-axis is along the crack line, and the origin is at the inlet. Monitoring points are selected at six locations along the crack: x = 0, 1, 2, 3, 4 and 5 m.

4.3.1 *Elastic micro properties for the simulations*

The contact shear and normal stiffness for the ball assembly are derived from relationship between elastic macro-properties and micro-properties for a hexagonal packing (Alassi, H.T., 2008), i.e., $k_n = E/(\sqrt{3}(1-\nu))$, and $k_s = k_n(1-3\nu)/(1+\nu)$.

The calibration was verified successfully by conducting a dry compression test using the ball assembly shown in Figure 1, and checking the overall elastic model response.

4.3.2 *Coarse model results*

Comparison between numerical and analytical predictions for dimensionless pressure and aperture at selected points along the crack are shown in Figure 3. The numerical results for pressure and aperture evolution with time show trends similar to those predicted by the analytic solution for no lag. In particular, the effective net pressure shows a characteristic non-monotonic behavior, which occurs because the crack re-opens ahead of the (zero net pressure) fluid front. Note that problem results interpreted in their dimensionless

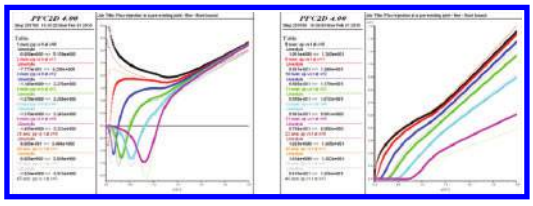


Figure 4. $\hat{p}$ versus $\hat{t}$ (left) and $\hat{a}$ versus $\hat{t}$ (right): comparison between analytical and numerical predictions at selected points – fine model.

form are not necessarily restricted to the particular set of data used to derive them; in particular, the occurrence of a negative dimensionless net pressure $\hat{p}$ does not always imply that fluid pressure is negative; it all depends on the actual level of confining stress σ.

As shown, there is an initial increase in net pressure at the inlet, followed by a decrease as the crack reopens progressively and the fluid progresses to the tip, and by a further increase as the full crack opens and an asymptotic solution is reached. Indeed, for sufficiently large values of $\hat{t}$ (when a non-zero net pressure acts along the full crack length), the rate of increase of net pressure becomes constant. The (constant) asymptotic rate can be evaluated by reasoning that Griffith's aperture solution applies at those large times.

The numerical values of pressure and aperture are within the expected analytical bounds. In addition, there is a reasonable match between analytical and numerical time prediction at negative peak net pressure; this shows that the new scheme is able to adequately estimate the problem time-scale.

4.3.3 *Fine model results*

The fine model has the same overall size and crack length as the coarse model, but with three times the number of balls in both the x- and y-directions. The numerical and analytical predictions for dimensionless pressure and aperture at selected points along the crack are shown in Figure 4.

The results in Figure 3 show a better fit with the analytical solution than those reported in Figure 2 for the coarse model, indicating convergence of the numerical predictions to the analytical solution for finer model discretization. A close-up view of displacement vectors near the crack is shown at the end of the simulation in Figure 5.

5 FRACTURE PROPAGATION ALONG A PRE-EXISTING JOINT

The two-dimensional problem of injection of a viscous fluid at a constant rate in a planar fracture with zero toughness is considered for this example. The medium is elastic and of large extent. The problem is similar to the one considered for early times in Example 1; however, particular focus is given here to the study of fracture propagation. The numerical results are compared with the zero toughness solution of Adachi and Detournay, 2002.

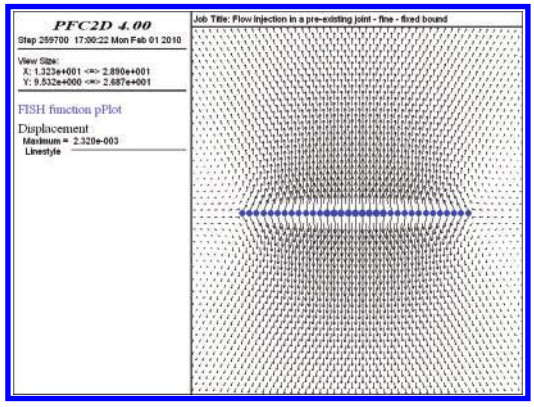


Figure 5. Displacement vectors in the vicinity of the crack at the end of the simulation – fine model.

5.1 *Analytic solution*

We use the same notation convention as in Example 1. The dimensionless variable $\hat{x}$ is introduced as $\hat{x} = \frac{x}{L}$ where L is the instantaneous half-length of the fracture (see (12), below).

The first order approximation of the zero toughness plane stress solution is (see Adachi, 2001; Adachi and Detournay, 2002, Detournay, 2004):

$$\begin{aligned} p - \sigma &= \varepsilon(t) E' \Pi_{mo}(\hat{x}) \\ a &= \varepsilon(t) L'(t) \Omega_{mo}(\hat{x}) \\ L &= \gamma_{mo} L'(t) \end{aligned} \tag{16}$$

where, by definition:

$$L' = \left(\frac{E' Q_0^3 t^4}{12\mu} \right)^{\frac{1}{6}} \quad \varepsilon = \left(\frac{12\mu}{E' t} \right)^{\frac{1}{3}} \quad \gamma_{mo} = 0.616 \tag{17}$$

The functions Π_{mo} and Ω_{mo} have a closed form expression; values tabulated at 80 regular $\hat{x}$ intervals were provided in the form of spreadsheet by the authors, and are used for the comparisons documented in this paper.

5.2 *Simulation data*

The elastic macro-properties for the crack are 6 GPa for Young modulus, and 0.3 for Poisson ratio. Fluid viscosity is 10^{-3} Pa-s, and fluid flux at the inlet is 4 10^{-4} m^2/s. Initial fracture aperture is 1 micron. Also initial stress $\sigma$is zero, and so is initial pressure inside the crack.

5.3 *PFC model*

The *PFC* models for the simulations are similar to those considered in the previous example. Fixed (roller) boundary conditions are considered. Fluid is injected at the center of the crack line for a total of

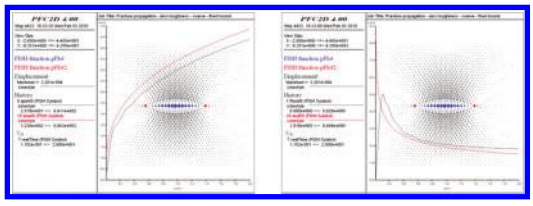


Figure 6. a/a_0 (left) and net pressure (right) versus time at injection point – comparison with analytical solution – coarse model.

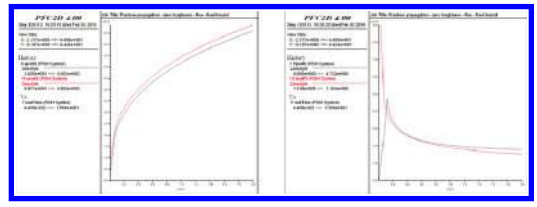


Figure 9. a/a_0 (left) and net pressure (right) versus time at injection point – comparison with analytical solution fine model.

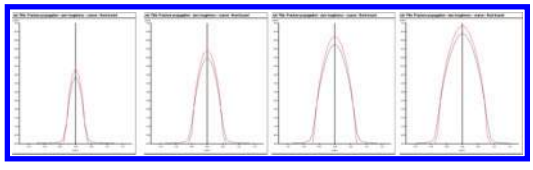


Figure 7. a/a_0 versus x at t = 5 s, 10 s, 15 s and 20 s – comparison with analytical solution (red) – coarse model.

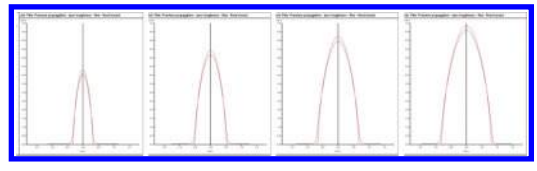


Figure 10. a/a_0 versus x at t = 5 s, 10 s, 15 s and 20 s – comparison with analytical solution (red) – fine model.

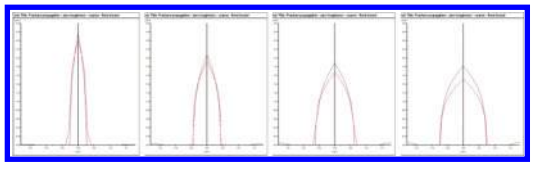


Figure 8. p_e versus x at t = 5 s, 10 s, 15 s and 20 s – comparison with analytical solution (red) – coarse model.

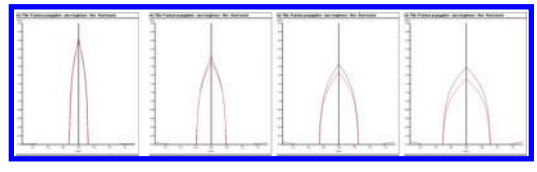


Figure 11. p_e versus x at t = 5 s, 10 s, 15 s and 20 s – comparison with analytical solution (red) – fine model.

20 sec. Pressure and aperture at the inlet are monitored during the simulation. Also, fracture aperture and pressure are recorded at four intervals in time (t = 5, 10, 15 and 20 sec), and the numerical predictions are compared to the zero toughness analytical solutions.

5.3.1 *Coarse model results*

Numerical values of relative aperture a/a_0 and net fluid pressure p_e at the inlet are plotted versus simulation time in Figure 6.

The net pressure in the fracture is represented by blue (positive) and red (negative) dots, and displacement vectors at the end of the simulation are also shown in the figure. The difference between numerical and analytical aperture values does not appear to grow significantly with time on Figure 5 (left plot).

The numerical estimate for relative aperture a/a_0 is plotted versus distance along the crack line and compared to the analytical solution at four different times in Figure 7.

The maximum relative error on aperture at the end of the simulation is about −6.6%. Net pressure from the simulation is plotted versus distance along the crack line and compared to the analytical solution at four different times in Figure 8; negative net pressure values, that develop necessarily to satisfy equilibrium, are not represented in the figure (only positive values are represented).

The numerical estimate for maximum aperture is *smaller* than the analytical value in Figure 6, and the estimate for maximum net pressure is *larger* than the theoretical value in Figure 7; this behavior is consistent with the approximation of finite size and fixed boundary conditions for the model used for the simulations.

5.3.2 *Fine model results*

The simulations are repeated with the fine model. The model has the same overall size as the coarse model, but with three times the number of balls in both the x- and y-directions. Numerical values of relative aperture a/a_0 and effective net pressure p_e at the inlet are plotted versus simulation time in Figure 9.

The maximum relative error on aperture at the end of the simulation is about −3.8% (compared to −6.6% for the coarse model case). The numerical estimate for relative aperture a/a_0 is plotted versus distance along the crack line, and compared to the analytical solution at four different times in Figure 10.

Net pressure predicted from the simulation is plotted versus distance along the crack line and compared to the analytical solution at four different times in Figure 11 (positive values shown).

5.3.3 *Fluid volume conservation*

Numerical and analytical value of injected fluid volumes are calculated from the area under the aperture curves, and compared to the product of fluid injection rate times and elapsed fluid time at the end of the 20-sec simulations. The relative error is about 3% for the coarse model and less than 1% for the fine

one. The numbers show that the fluid volume is conserved with good accuracy under the assumption of fluid incompressibility (in the MIF scheme, the fluid is only approximately incompressible, see (8)).

5.3.4 *Timing test*

To estimate computational efficiency, we ran the Example 1 simulations with the coarse grid using the MIF and the scheme currently used in *PFC2D* for simulations of hydro-mechanical coupling. A small modification was made to let the current *PFC2D* scheme use the same (linear) contact law as the MIF scheme.

The fluid-mechanical simulation was run for a total injection time of 0.1 s. The computational time on an Intel Dual Core 2.53 GHz machine is 143.8 sec. for the current *PFC2D* scheme, and 2.8 sec. for the new scheme. The MIF scheme is about 52 times faster than the current *PFC2D* scheme for this particular problem and specific computer.

6 CONCLUSIONS

Numerical simulations were performed, using *PFC* as a testbed to evaluate the accuracy and calculation speed of the new fluid-mechanical scheme (MIF) for application to hydraulic fracturing. Two examples were considered: fluid injection in a pre-existing fracture, and fracture propagation in a medium with zero toughness. The numerical results were compared to existing analytical and semi-analytical solutions. The results documented in the paper show that the numerical solutions have the same behavior as the analytical ones, and that the results converge to the infinite domain solutions when the discretization length is decreased (the impact of the size of the computational domain has not been investigated in this paper).

Timing tests were run on one of the coupled fluid-mechanical examples and it was shown that for that particular case, the new proposed scheme was 50 times more computationally efficient that former scheme.

REFERENCES

Adachi, J. I. (2001) *Fluid-driven fracture in permeable rock*. Ph.D. thesis, Univ. of Minnesota, Minneapolis.

Adachi, J. I. and E. Detournay (2002). Self-similar solution of a plane-strain fracture driven by a power-law fluid. *Int. J. Numer. Analyt. Meth. Geomech.*, 26(6), 579–604.

Alassi Haitham Tayseer (2008) Modeling reservoir geomechanics using discrete element method: Application to reservoir monitoring. Doctoral Theses at NTNU, 2008:233.

Cundall, P.A. (2011) Lattice method for modeling brittle, jointed rock. Continuum and Distinct Element Numerical Modeling in Geomechanics. Sainsbury, Hart, Detournay & Nelson (eds.) ISBN 978-0-9767577-2-6.

Damjanac, B., C. Detournay, P. Cundall and Varun. Three-Dimensional Numerical Model of Hydraulic Fracturing in Fractured Rock Masses. HF2013. Submitted.

Detournay, E. (2004) Propagation Regimes of Fluid-Driven Fractures in Impermeable Rocks. *International Journal of Geomechanics*, DOI: 10,1061/(ASCE)1532-3641 4:1(35).

Garagash D. and E. Detournay (1998) Injection of fluid into a joint. Unpublished document.

Itasca Consulting Group, Inc. (2008) *PFC2D* (Particle Flow Code in 2 Dimensions), Version 4.0. Minneapolis: Itasca.

Research and Applications in Structural Engineering, Mechanics and Computation – Zingoni (Ed.)
© 2013 Taylor & Francis Group, London, ISBN 978-1-138-00061-2

Optimisation of the Double Torsion geometry

S.P. Goqo
Department of Mathematics and Applied Mathematics, North-West University, Potchefstroom, South Africa

S. Skatulla
CERECAM, Department of Civil Engineering, University of Cape Town, Cape Town, South Africa

T.H. Becker
Department of Mechanical and Mechatronic Engineering, Stellenbosch University, Stellenbosch, South Africa

ABSTRACT: The Double Torsion (DT) geometry is a test specimen configuration that facilitates for fracture investigations in highly brittle materials and is well-known to produce a stress intensity factor that is independent of crack length. This feature allows for the propagation of relatively long cracks in a highly controlled manner in exceptionally brittle materials. However, the DT geometry is yet to be standardised and to date many questions remain regarding optimal specimen dimension, load point deflections, and out of plane deformations. This paper aims to investigate the DT geometry using the Finite Element methodology in order to obtain an optimum specimen geometry that can be utilised in fatigue threshold and other fracture mechanics related investigations.

1 INTRODUCTION

The Double Torsion (DT) geometry is a test specimen configuration that facilitates for fracture investigations in highly brittle materials. The novelty of the DT technique lies in the property of a constant stress intensity factor (SIF) regime during crack propagation (Attia 2010), which is considered to produce a crack length independent geometry by achieving a constant stress intensity factor (SIF) regime (Attia 2010). As such, the DT geometry is commonly used when testing highly brittle materials such as rocks (Yoshitaka 2012), glass and ceramics (Lewis 1981) and nuclear graphite (Becker 2011a) for example. Furthermore, the technique is practical for situations where crack length measurements are not always possible (such as in high temperature test conditions) due to the fact that the SIF is crack length independent and no crack length measurements are required during testing (Attia 2010).

To date, however, several questions remain regarding the technique. The crack length independent SIF is not completely undisputed within the fracture mechanics community, as deviations from the crack length independent SIF have been observed (Fuller 1979, Baskaran 1985, Ebrahimi 1999, Ciccotti 2000a & Chevalier 2001, Becker 2011b).

The development of the DT technique is credited to the work undertaken by Outwater and Gerry (1969), Kies and Clark (1969) and William and Evans (1973). The load is applied in a four-point bend configuration at the one end (as shown in Figure 1), where the crack propagates through the centre of the specimen.

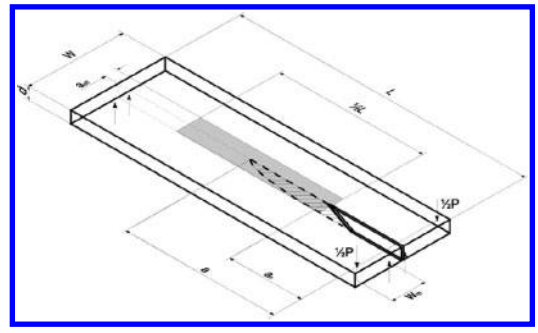


Figure 1. The DT layout and load configuration, (Becker 2011b).

The loading configuration is such that each specimen half, separated by the crack, is loaded in torsion. It is assumed that the compliance of the specimen is linearly dependent on the length of each torsion bar (i.e. the crack length) and that the unbroken ligament remains rigid during loading (Becker 2011b). This assumption, however, has been found to have implications on the crack length independent SIF; the deformation of the un-cracked ligament has been shown not to remain rigid (Becker 2011b) and large deflections at the load point result in a non-linear torsional compliance (Leevers et al.). Further reading on the DT geometry can be found by (e.g. Becker 2011a, Tait 1987, Evans 1972).

Several attempts have been formulated to model the geometry using the Finite Element (FE) method. Examples include Trantina (2006) who investigated

the DT geometry using a three-dimensional finite element model. An agreement was found between numerical and analytical obtained SIF over the middle of the specimen $0.18 < a/L < 0.78$ (for a specimen geometry $W = 3$). The work of Ciccotti et al. (Ciccotti 2000b & Ciccotti 2001) formulated a series of correction factors for a range of specimen geometry configurations to correct the deviations to the analytical solution.

Furthermore, Attia (2010) performed a three-dimensional FE analysis, evaluating for the optimum thickness of the DT geometry, and observed deviations between FE model and experimental data. The deviations have been attributed to the curvilinear crack front, which is typically modelled as a straight crack front in the FE environment.

These studies have however not investigated an overall optimum specimen geometry ratio that allows for a crack length independent geometry. Presented in this paper is the optimisation of the DT geometry which provides a crack length independent geometry. It is the aim to contribute to the understanding of the DT geometry and the use of this novel test configuration.

2 THE DOUBLE TORSION GEOMETRY

Figure 1 shows the DT geometry layout and the aforementioned loading configuration.

A linear compliance is obtained by assuming that the unbroken ligament remains rigid and only the cracked ligaments deform under torsion (Fuller 1979)

$$C(a) = \frac{y}{P} = \left(\frac{3w_m^2}{Wd^3\mu}\right)a \tag{1}$$

where y is the deflection caused by load P, w_m is the moment arm, d is the specimen thickness, W is the specimen width and μ is the shear modulus.

The strain energy release rate G is related to the derivative of compliance (mode I) assuming the crack extension area remains constant during crack propagation i.e., $dA = d \cdot da$. This leads to

$$G = -\left(\frac{dU}{dA}\right) = \frac{P^2}{2d}\frac{dC}{da} \tag{2}$$

where, U denotes the total strain energy release rate. According to Williams and Evans (1973), the relationship between the SIF (mode I) and the energy release rate is given by

$$K_I = \sqrt{EG} = PW_m\sqrt{\frac{3(1+\nu)}{Wd^4\Psi(d,W)}} \tag{3}$$

where Ψ is a thickness correction factor given by

$$\Psi(\tau) = 1 - 0.6302\tau + 1.20\tau e^{-\frac{\pi}{\tau}} \tag{4}$$

and $\tau(d, W) = 2d/W$ (Attia 2010).

As aforementioned, the crack front profile in the DT geometry is curvilinear. A crack front inclination

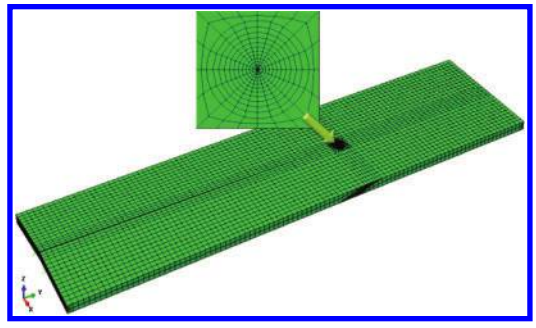


Figure 2. DT specimen meshed with quadrilateral hexahedral elements. A zoomed area around the crack tip showing a ring of element is also shown. Include is also specimen axis, x-axis the width, y-axis the length and z-axis the thickness of the specimen.

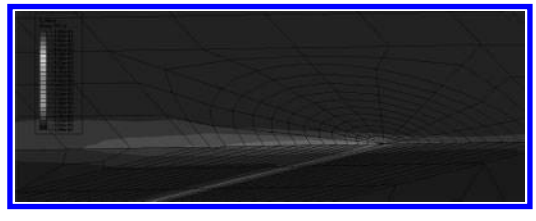


Figure 3. Inclined crack tip showing deformation stress, which signifies the crack opening.

is approximated by $c = \Delta a/d$, where Δa is the crack extension difference between the upper and lower surface of the test specimen (Becker 2011b). Furthermore, note that the SIF (in Eq. 3) is independent of crack length. It is this feature that allows for stable crack propagation in brittle materials.

3 FINITE ELEMENT MODEL

The DT geometry is analysed using ABAQUS version 6.10. In order to obtain optimum specimen geometry nine geometry configurations are considered. These include three different length to width ratios ($L/W = 2$, 3 and 4) and three different thicknesses to width ratios ($d/W = 0.06$, 0.08 and 0.1) where $W = 50$ mm. Each test geometry was analysed at five different crack length ratios ($a/L = 0.25$, 0.38, 0.5, 0.62, 0.75) generating 45 models in total.

3.1 *Mesh*

Each model simulated the entire DT geometry obtaining an average number of 6047 quadratic hexahedral elements (Figure 2). The mesh is refined mesh near the crack tip using a concentrated mesh with collapsed elements as illustrated along a vertical long-axis cross-section in Figure 3. This allows a better description of the strain field near the crack tip and has been validated against analytical solutions (Trantina 2006). Numerical solution values of the associated SIF are calculated using the contour integral method. The computed J-integral is converted to an equivalent SIF using

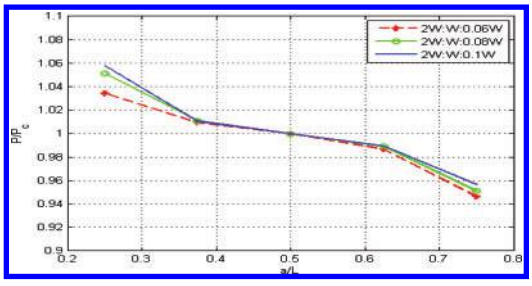


Figure 4. Normalised force vs crack length comparison of thickness of Length $L = 2W$.

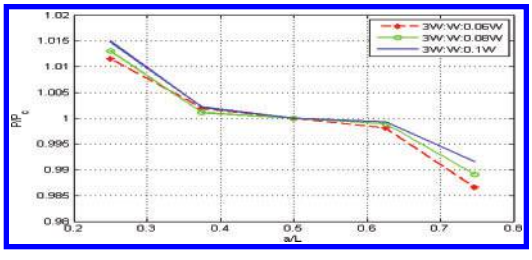


Figure 5. Normalised force vs crack length comparison of thickness of Length L = 3W.

Eq. (3) where J-integral is equivalent to G. A mesh refinement study was undertaken to ensure convergence of the numerical solutions.

3.2 *Boundary conditions*

The boundary conditions of the model assumed that the nodes near the loading points are constrained in the y direction and at the far side in the x, y direction (Figure 2).

To simulate the experimental setup of a four-point loading configuration a force couple is applied at one far end of the specimen. The resulting torsional moment is scaled to obtain a SIF equivalent to the $K_{IC} = 46.8\,\text{MPa}\sqrt{mm}$ (the fracture toughness of the PMMA).

In order to simulate a more realistic crack tip configuration, an inclined crack front of $c = 4$ was used (Figure 3). Contact was defined between the crack surfaces as tangential behaviour with 0.5 friction coefficient for rough surfaces.

3.3 *Evaluation of the crack length independent SIF*

The output parameters obtained for each model are the load point displacement y and the applied moment to obtain a SIF equal to that of the aforementioned PMMA fracture toughness. The applied moment can be seen as a concentrated load P with moment arm length w_m in Eq. (3). Since the SIF, i.e. K_I, is only a function of P in Eq. (3), it is possible to evaluate a crack length independent SIF only using P, normalised to P_c (the load at $a = 0.5L$).

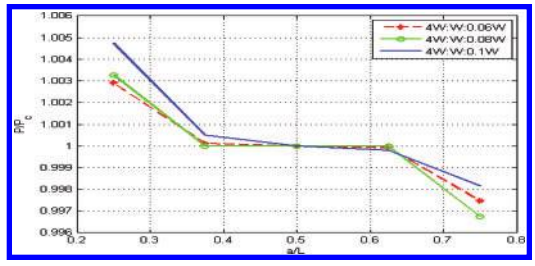


Figure 6. Normalised force vs crack length comparison of thickness of Length L = 4W.

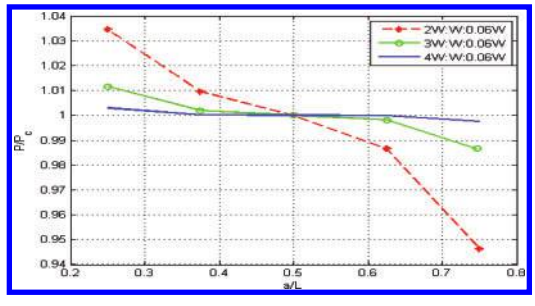


Figure 7. Normalised force vs crack length comparison of thickness of Length $L = 2W$.

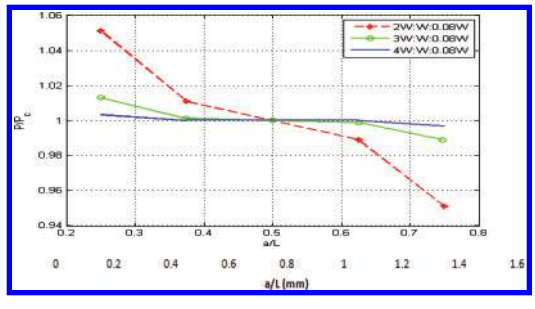


Figure 8. Normalised force vs crack length comparison of thickness of Length $L = 2W$.

4 RESULTS

Figures 4, 5 and 6 show the normalised force vs. crack length results for three different specimens length ratios of $2W$, $3W$ and $4W$ respectively.

Similarly, Figure 7, 8 and 9 show the normalised force vs. crack length results for three different specimen thickness ratios of $0.06W$, $0.08W$ and $0.01W$ respectively.

From Figures 4, 5 and 6 it can be seen that a thinner specimen configuration yields a more crack length independent geometry. Figure 5 for example, $L = 3W$, shows a relatively constant SIF between the range $0.37W$ to $0.75W$. Comparing Figures 7, 8 and 9, the thinner specimen configuration $d = 0.06W$ shows the constant SIF over middle of the specimen.

From Figures 7, 8 and 9 it can be seen that the specimen that is closest to producing constant SIF lies between $L = 3W$ and $L = 4W$ thickness.

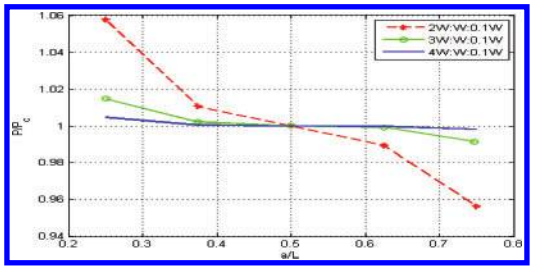


Figure 9. Normalised force vs crack length comparison of thickness of Length $L = 2W$.

Based on these two comparisons, involving length and thickness of the specimen geometries, respectively, we propose that the optimum specimen geometry should be of order $3.5W{:}W{:}0.06W$.

5 CONCLUSION

This paper investigated an optimum specimen geometry using nine different specimen geometry configurations. The analysis is undertaken in the FE environment to obtain a relationship between the SIF and crack length. An ideal specimen would yield a crack length independent SIF.

It is found that a thinner specimen results in producing constant SIF. It is found that a thinner specimen results in producing constant SIF. It is found that a thinner specimen produces a more constant SIF regime. Similarly, It was also observed that the longer specimen results in a more constant SIF regime. This is in agreement with Trantina (2006) and Tait (1987) who suggested that the SIF remains constant over $0.18 < a/L < 0.78$ range.

A comparison of the results suggests that an optimum specimen geometry exists around 3.5W:W:0.06W.

ACKNOWLEDGEMENT

The first author would like to acknowledge support from CERECAM.

REFERENCES

Attia M. S., Mahmoud A. S., Megahed M. M., Radwan A. A. (2010). Numerical investigations of the stepped double torsion fracture toughness specimen. *Engineering Fracture Mechanics* 77, 3359–3367

Baskaran S. Bhaduri S. B., Hasselman D. P. H. (1985). Effect of crystallites on subcritical crack growth and strain-rate sensitivity of strength of cordierite glass-ceramics. *AM Ceram Soc* 68, 112–119

Becker T. H. Tait R. B., Marrow T. J. (2011). Damage, crack growth and fracture characteristics of nuclear grade graphite using the double torsion technique. *Journal of Nuclear Material.* 32–43

Becker T. H., Marrow T. J., Tait R. B. (2011). An Evaluation of the Double Torsion Technique. *Experimental Mechanics 51, 1511–1526.*

Chevalier J. De Aza A. H., Gremillard L., Zenati R., Fantozzi G. (2001). Slow crack growth in zirconia ceramics: from the single crystal to the composites. *Mater Eng* 12. 159–178

Ciccotti M. Gonzato G., Mulargia F., (2000a) The double torsion loading configuration for fracture propagation: an improved methodology for the load-relaxation at constant displacement. *Rock Mechanics and Mining Sciences* 37, 1103–1113.

Ciccotti M. (2000b). Realistic Finite-Element Model for the double torsion loading configuration. *J. Am. Ceram. Soc*., 83, 2737–44.

Ciccotti M., Negri N., Gonzato G., Mulargia F. (2001). Practical application of an improved methodology for the double torsion load relaxation method. *Int J Rock Mech Min Sci* 38, 569–576

Ebrahimi M. E. Chevalier J., Fantozzi G. (1999) Slow crack-growth behavior of alumina ceramics Materials 15, 142–147.

Evans A. G. (1972). A method for evaluating the time dependent failure characteristics of brittle materials – and its application to polycrystalline alumina. *Journal of Material Science* 7, 1137–1146

Fuller J. R. (1979). An evaluation of the double-torsion testing analysis. Fracture mechanics applied to brittle materials, ASTM STP 678. *American Society for Testing and Materials*

Hyunwook K. Manfred N. P., (2011). Development of a double-torsion fracture test to predict channelized crack behaviors of asphalt concrete. *Construction and Building Materials.*

Kies J. A., Clark A. B. J. (1969). Fracture propagation rates and times to fail proof stresses in bulk glass. In: P. L. Pratt, editor. *Proceedings of the second International Conference on Fracture; 1969 Apr 13–18; Brighton, England. London: Chapman and Hall Ltd.;* p. 483–491

Lewis M. H. Karunaratne B. S. B. (1981) Determination of High-Temperature KI-V Data for Si-Al-O-N Ceramics. *American Society for Testing and Materials*, 13–32.

Madjoubi M. A. Hamidouche M., Bouaouadja N., Chevalier J., Fantozzi G. (2007). Experimental evaluation of the double torsion analysis on soda-lime glass. *J Material Science* 83, 2737–2744.

Moustafa N. A. Niek D., Cees J. K., Albert J. F. (2012) The influence of pigments on the slow crack growth in dental zirconia. *Dental Materials* 28, 410–415.

R. FullerJr E. (1979). An evaluation of double-torsion testing analysis. Fracture mechanics applied to brittle materials, ASTM STP 678. *American Society for Testing and Materials*

Tait R. B. Fry P. R., Garrett G. G. (1987). Review and Evaluation of the Double-Torsion Technique for Fracture Toughness and Fatigue Testing of Brittle Materials. *Experimental Mechanics* 15, 14–22.

Trantina G. G., Johnson C. A. (2006). Subcritical crack growth in Boron-Doped SiC. *American Ceramic Society* 58, 44

Williams D. P., Evans A. G., (1973). A simple method for studying slow crack growth. *J Test Eval* 1, 264–270

Yoshitaka N. Kazuya M., Naoki H.c, Tetsuro Y., Katsuhiko K., Philip M. B. (2012) Influence of relative humidity on fracture toughness of rock: Implications for subcritical crack growth. Solids and Structures 49, 2471–2481

Research and Applications in Structural Engineering, Mechanics and Computation – Zingoni (Ed.)
© 2013 Taylor & Francis Group, London, ISBN 978-1-138-00061-2

An experimental validation of residual stresses in weld clad pipelines

G. Schnier, J. Wood & A. Galloway
JW Analysis, UK

ABSTRACT: The nature and distribution of residual stresses are invariably critical for fatigue life with dissimilar material joints often inducing high tensile residual stresses. A fatigue-resistant concept of weld cladding process pipelines, producing compressive residual stresses, is under investigation to examine how these stresses may be influenced. Simplified weld cladding simulations have successfully illustrated the development and distribution of residual stresses through the joint. The study has highlighted the importance of accurate material data for clad and substrate materials with current analysis assumptions in a simple thick-walled pipe discussed. Experimental validation, using ICHD, measured residual stresses with depth on weld clad specimens, resulting in good correlation between simulation and experiment for a nickel-chromium-based superalloy clad on low alloy carbon steel as discussed. Future work, including a full 3D representation of the cladding process and a comparison of residual stress measurement methods, are also discussed.

1 INTRODUCTION

Residual stresses are typically described as the stresses in a body post-manufacture with no external loading or constraints present. Depending on the nature of these residual stresses, they can be beneficial or detrimental to the fatigue life of a component. It has been found that many machining processes induce tensile residual stresses which in turn shorten fatigue life. Tensile residual stresses also arise in dissimilar joints and can be as high as yield for the materials in question. From a fatigue perspective, it is desirable to maintain compressive residual stresses to increase fatigue strength, particularly at the surface of a component where operational stresses are often at their highest.

Residual stresses are elastic and self-equilibrating in nature and arise from various mechanisms in the case of dissimilar weld cladding: a surface "heat-treatment effect" due to materials varying with temperature affecting cooling rates and constraint levels, a "pre-heat shrink-fit effect" accounting for effective shrinking of the cladding relative to the substrate affected by material and temperature dissimilarity and "spatial and temporal variation" of the clad deposition process and subsequent cooling causing changes in microstructure through phase transformation and chemical reactions.

This paper presents results from initial simplified 2D models validated with experimental residual stress measurements and discusses the progression to a full 3D model. As will be shown, pipeline weld cladding and dissimilar material joints in general will also display significant discontinuity stresses at the interface between the dissimilar materials. Fatigue cracking may therefore occur sub-surface.

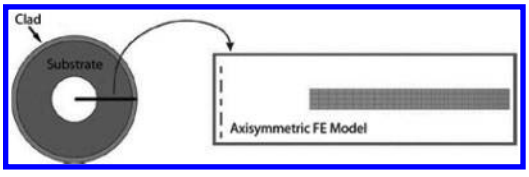


Figure 1. Axisymmetric FE Model.

2 DISSIMILAR JOINT SIMULATION

The weld clad pipeline model currently takes the form of a thermal transient stress analysis of a two-dimensional axisymmetric finite element model (Fig. 1). A simplified process of an entire clad layer being deposited onto the outer diameter of a pre-heated thick-walled pipe at melt temperature at time $t = 0$ seconds has been employed as an initial study. This modelling technique assumes that there is no variation in temperature or stress field in the axial and hoop directions as a function of time. The entire component was then subjected to slow cooling on the inner and outer surfaces using a convective heat transfer coefficient $h = 10\,\mathrm{W/m^2K}$ and a bulk temperature of 25°C, with latent heat effects being neglected. The *CAX4T* Abaqus element type was utilised with bi-linear displacement and temperature shape functions.

The radial edges of the model were insulated to simulate no axial heat transfer and plane strain conditions applied on the radial lines (Fig. 2).

Although this model is a simplification of a process with spatially and temporally varying deposition, it is representative of methods such as evaporative deposition or spray coating followed by sintering. In the following sections it will be shown however that it also

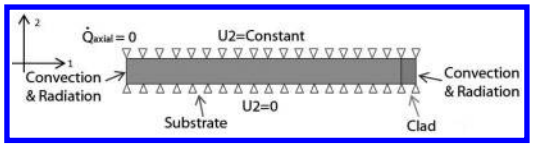


Figure 2. Axisymmetric Model Boundary Conditions.

provides good correlation to experimental measurements for the spatially and temporally varying weld deposition process used.

An elastic-perfectly plastic material model was assumed with temperature dependent thermal and mechanical material properties. Focus was placed on coefficient of thermal expansion, specific heat, thermal conductivity, Young's modulus and yield stress. These properties primarily govern the modelling of the thermal event, degree of constraint and therefore the development of residual stresses (Ahmed et al. 2007), with further contributing factors discussed in the reference given. Poisson's ratio and emissivity were assumed to remain constant. The nature of residual stresses differs depending on the state of a component, as discussed by Withers and Bhadeshia, with misfit resulting from different parts, phases and regions highlighted as the key characteristic influencing residual stresses (Withers & Bhadeshia 2001). Phase transformations in steels have been shown to influence residual stress development in X70 pipeline steel (Onsoien et al. 2010) for example.

Figure 3 shows a large discontinuity in the stress distribution in the vicinity of the low alloy carbon steel substrate and clad interface for both pre-heat and material combinations, with a change from compressive to tensile stresses. At the idealised interface between the substrate and clad there is a step change in the stresses with the nickel-chromium-based superalloy clad showing a reduction in residual stress, which remains significantly tensile throughout the clad. The form of residual stress graph for the nickel-chromium-based superalloy clad is indicative of yielding and reflects the elastic-perfectly plastic model used.

The stainless steel clad simulation results on the other hand show a further increase in residual stress in the clad, which is unexpected and is contrary to the experimental results obtained, which show a similar value of residual stress throughout the clad but compressive in nature.

3 EXPERIMENTAL VALIDATION

3.1 *Background*

Incremental centre hole drilling (ICHD) is a relaxation technique used for residual stress measurement through the measurement of local displacement in the vicinity of a drilled hole (ASTM International 2008). Material removal through the drilling of a hole into a component allows the consequent movement of remaining material to be measured and residual stresses to be deduced. This occurs most commonly

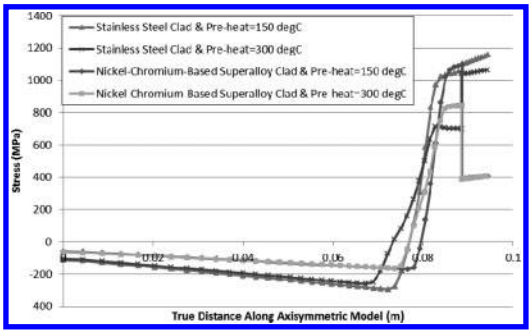


Figure 3. Cladding Simulation: Hoop Stress Comparison.

through the application of a strain gauge to obtain strain values throughout the material removal process, which can be converted into stress values. Through the drilling of the hole, additional stresses can be induced, however the application of high-speed air-driven turbines operating at speeds up to 400,000 rpm (Grant et al. 2006) minimises this effect.

3.2 *Hole-drilling method*

Specialised three element strain gauge rosettes are applied to the surface after appropriate surface preparation techniques. The method of surface preparation is dependent on the initial roughness of the surface and could require machining prior to finishing with fine grain sandpaper. Wiring and balancing of the gauges follows the laying of the gauge after which the fixture can be applied to the component by means of cementing the detachable legs prior to assembling the drilling kit.

Strain readings are then recorded at incremental depths, with accuracy of the readings decreasing with increasing depth due to the travelling further from the applied strain gauge on the surface. The maximum depth to which strain readings can be used for the purpose of residual stress measurements is to one half of the diameter of the drilled hole (Grant et al. 2006).

Residual stress measurements were obtained for both cylindrical and rectangular specimens. On the cylindrical specimens, gauges were installed at the centre of the outer diameter of the component at two diametrically opposed circumferential locations to demonstrate variability in cladding and measurement process. For the rectangular specimens, gauges were applied along the centre-line to allow effects of global bending to be deduced.

3.3 *Strain measurement conversion*

Three main conversion methods exist for the conversion of strain measurements, namely the Equivalent Uniform Stress (EUS), Power Series and Integral methods (Schajer 1988). Schajer notes that the EUS and Power Series are approximations of the Integral method, which provides the most acceptable interpretation of uniformly varying residual stresses through

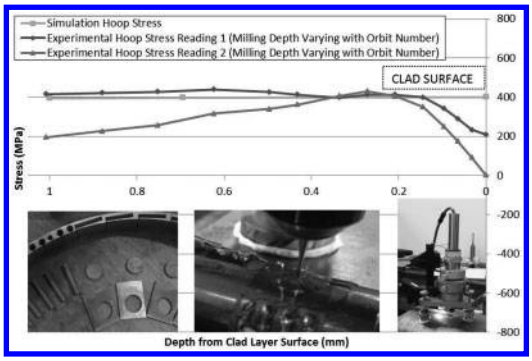


Figure 4. Simulation & Experimental Results Comparison: Nickel-Chromium-Based Superalloy Clad & Pre-heat Temperature = 150°C (EDM extraction of thermal property testing specimens & residual stress measurement equipment also shown).

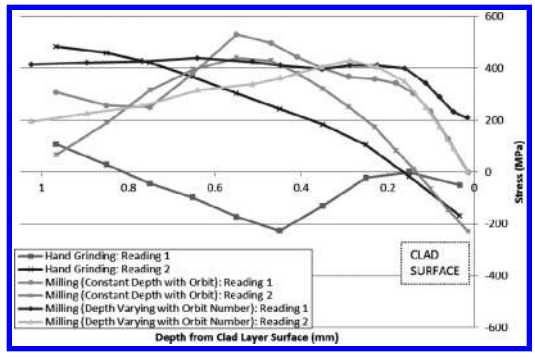


Figure 5. Nickel-Chromium-Based Superalloy Clad: Residual Hoop Stress Measurements: Surface Preparation Technique Comparison.

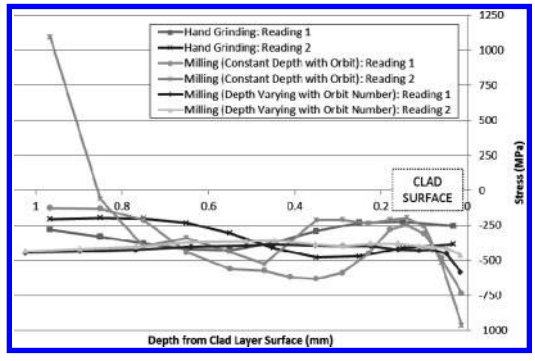


Figure 6. Stainless Steel Clad: Residual Stress Measurements: Surface Preparation Technique Comparison.

applying the least smoothing of results and is therefore applied as the standard calculation procedure for residual stresses using ICHD.

4 RESULTS

Figure 4 shows good agreement between the nickel-chromium-based superalloy cladding simulation results and experimental measurements using ICHD. The two sets of experimental results are for two different diametrically opposed positions on the centre of the cylindrical specimen. The difference in the experimental results is indicative of the effect of process variability. The reduction in both sets of experimental results over the first 200 microns will largely be due to the machining of the weld profile to provide a flat surface for strain gauging.

4.1 *Comparison of surface preparation techniques*

Three surface preparation techniques were used in preparation for applying the strain gauge. The first was the use of a hand-held compressor driven stone grinder followed by fine finishing using P400 fine sand paper. The second technique was CNC milling at 500 rpm using 10 μm increments to a depth of 0.5 mm for the nickel-chromium-based superalloy clad and 0.7 mm for the stainless steel due to varying clad profiles. Lastly surface preparation using a PC-controlled machine tool beginning at 16 μm per orbit, decreasing to 8 μm and finally 2 μm for the final two orbits was applied to minimise machining effects.

From the results shown for a nickel-chromium-based superalloy clad pipe, it can be seen that in comparing hoop stress values for the three surface preparation techniques the hand grinding technique gives a highly inaccurate representation (Fig. 5). Results for the milling and PC-controlled surface preparation techniques produce a greater degree of correlation as would be expected, with discrepancies arising especially close to the surface however.

Focus is placed on hoop stress values in the following discussion as this stress component presents the greatest contribution to the final stress state.

The results shown for the stainless steel clad pipe (Fig. 6) show a greater variation in the CNC surface preparation method with alarming gradients shown in one milling measurement. This is most probably due to user technique, however the requirement for careful surface preparation is clear.

Overall, the residual stress values for the stainless steel clad material provide a tighter band of results with greater uniformity of stresses over the 1 mm depth shown. From these results, it can be concluded that there are greater effects due to process variability in the case of nickel-chromium-based superalloy clad.

4.2 *Errors associated with ICHD*

As mentioned in the previous sections, errors arising through the ICHD method can heavily influence strain readings and hence residual stress values. Strain measurement errors can also arise due to user technique, instrumentation errors and additional strains induced through material removal, while hole measurement errors in both the depth and diameter, tapering of the hole and any roundness in the bottom of the hole can influence calculated stress values. Differences can also

arise from using different strain gauge types which was the case in the last surface preparation technique of milling depth varying with orbit depth.

Furthermore, errors can arise from deviations in hole roundness and eccentricity errors in the location of the hole with respect to the strain gauge along with material constant errors arising from Young's modulus and Poisson's ratio values applied in the strain-to-stress conversion process (Schajer & Altus 1996).

4.3 *Additional considerations*

An area that requires careful consideration with regards to residual stresses is that of machining. Any machining of the component after cladding will modify the self-equilibrating residual stress distribution in a thin surface layer and for this reason care must be taken to ensure that any beneficial compressive residual stresses effects are not removed by such an operation. Machining can induce tensile residual stresses, which may also increase stress-corrosion cracking susceptibility in some materials, while also decreasing fatigue life. This was emphasised in a study in 1969 (Paxton & Procter 1969), highlighting the need for careful consideration of machining processes, through experimental procedures, to ensure an acceptable residual stress state while maintaining adequate corrosion resistance. Investigation into electro-polishing is underway to determine whether this technique, minimising stress state adjustment, can provide further increased accuracy.

Another aspect which could alter surface residual stresses is that of the thermal environment present at the surface during cooling.

Optimal depth increments have been discussed for differing strain gauge rosette radii and hole radii (Stefanescu et al. 2006). Arbitrary values were applied in this study due to the lack of measuring such precise increments, however in future it would be recommended that a method of determining and measuring such incremental values is employed with reference to the work noted above.

5 DISCUSSION ON INFLUENCING RESIDUAL STRESSES

5.1 *Pre-heat temperature*

The effect of pre-heating the substrate to a specified uniform temperature before commencing with the joining process was investigated using two temperature values. The purpose of pre-heating the substrate serves as a method of reducing the heat sink effect and a higher pre-heat would be expected to reduce residual stress levels. A higher preheat however will also increase the pre-heat shrink-fit effect referred to in the introductory section of this paper.

Results show that a lower pre-heat temperature for stainless steel clad specimens results in a higher residual stress level, desirable both economically and for fatigue purposes, however in the case of the nickel-chromium-based superalloy a lower residual stress occurred with a lower pre-heat temperature.

5.2 *Substrate geometry*

The investigation of substrate geometry effects suggests that there are no great variations in residual stresses in the clad pipe and rectangular specimen. Results for low alloy carbon steel clad with stainless steel on the cylindrical and rectangular specimens at a pre-heat temperature of 300°C in particular demonstrated that equal residual stress levels are attainable in both geometries providing the thermal transient event is maintained for the differing substrate geometry.

5.3 *Post-weld stress relief*

Post-weld stress relief was unsuccessful for the nickel-chromium-based superalloy clad case, thought to be due to the large mismatch in material properties between these materials. Results for stainless steel clad demonstrate a significant decrease in residual stress values post-stress relief, as well as an almost equi-biaxial stress field further beneficial to fatigue life. The stainless steel and low alloy carbon steel are both high-strength materials with similar metallurgical structure and material property values for CTE and yield stress. However, clearly in the case of stainless steel clad stress relief is not desirable as it would lower the high level of beneficial compressive residual stresses.

6 CONCLUSIONS

A simplified 2D simulation model of cylindrical dissimilar weld clad process pipeline specimens has shown good agreement with experimental residual stress measurements for nickel-chromium-based superalloy clad on low alloy carbon steel. The lack of agreement for a stainless steel clad has prompted an experimental programme to determine more accurate temperature dependent mechanical property data to increase residual stress representation in the FE model. Published data availability, even for wrought material, in this case was very limited neglecting the phase change present in stainless steel clad and substrate materials assuming instead a linear extrapolation beyond 400°C.

Simulation models using a step change in material properties at an idealised interface employ a significant approximation to reality. Studies (not reported herein) reveal a variation in elemental composition and grain structure across such junctions, reflected in micro- and nano-hardness measurements. It is likely therefore that other properties used in such simulations will also show a transition (albeit over a relatively short distance). This will have the effect of reducing discontinuity stresses and eliminating any theoretical singularities that may be picked up with very fine finite element meshes.

Experimental residual stress measurements concluded that surface preparation techniques are critical to ensure that the residual stress state in a component is not further altered prior to measurement, therefore rendering harsh hand grinding unacceptable. Additional sources of error were discussed and the sensitivity of readings with user technique highlighted.

Lastly a discussion on influencing residual stresses revealed that a lower pre-heat temperature was more beneficial in the stainless steel and low alloy carbon steel combination, however this was not found to be the case for nickel-chromium-based superalloy and low alloy carbon steel. Substrate geometry effects were found to be negligible and so residual stresses should be attainable in both the cylindrical and rectangular specimens at similar values, while stress relief was unsuccessful in the case of nickel-chromium-based superalloy cladding, although achievable with stainless steel clad material. Experimental variability in the cladding process revealed a much greater effect in the case of nickel-chromium-based superalloy cladding in diametrical measurements and along the centre line of the clad plate.

7 FURTHER WORK

Although acceptable representations of the residual stress states in the dissimilar joint were obtained for the nickel-chromium-based superalloy clad, it is important that the model is developed to include a more accurate representation of all relevant temperature dependent material properties. This will provide a better representation of the measured results for a stainless steel clad. In addition, although a simple axisymmetric idealisation has shown good agreement with experiment for the nickel-chromium-based superalloy clad, a 3D model taking into account both spatial and temporal process variation is underway. Sequential deposition of the clad material is currently being investigated in the 2D model and this feature of the process will also be included in the 3D simulation.

It is recognised that it is important in such simulations to capture the thermal behaviour of the joining process (Smith et al. 2011) and so calibration of the 3D simulation will be carried out using extensive temperature information obtained during the cladding process, which also reflects the weld inter-pass temperature used.

Further work is also underway to examine the use of functionally graded material properties in dissimilar joints in an effort to reduce the level of sub-surface discontinuity stresses whilst retaining the benefit of any compressive residual stresses that may result in the clad layer. The metallurgy of the joint will also be further examined with emphasis placed on the influence of weld parameters on joint metallurgy.

Due to limitations of ICHD it would be desirable to develop finite element models calibrating the residual stress state further into the component. Alternatively the deep-hole drilling method could be investigated providing residual stress measurements to depths of up to 750 mm (VEQTER 2013). Further investigation of surface preparation techniques will allow the curvature of cylindrical specimens to be accounted for such that gauges will be laid on a rounded surface as opposed to the milled surface being completely flat.

REFERENCES

Ahmed, R. et al., 2007. Residual Strain Measurements in Thermal Spray Cermet Coatings via Neutron Diffraction. *Journal of Tribology*, 129(2), p.411.

ASTM International, 2008. Standard Test Method for Determining Residual Stresses by the Hole-Drilling Strain-Gage Method. *ASTM E837-08e1*.

Grant, P.V., Lord, J.D. & Whitehead, P.S., 2006. *Measurement Good Practice Guide No . 53 – Issue 2 The Measurement of Residual Stresses by the Incremental Hole Drilling Technique*,

Onsoien, M.I., M'Hamdi, M. & Akselsen, O.M., 2010. Residual Stresses in Weld Thermal Cycle Simulated Specimens of X70 Pipeline Steel. *Welding Journal*, 89, p.127–s–132–s.

Paxton, H.W. & Procter, R.P.M., 1969. The Effects of Machining and Grinding on the Stress-Corrosion Cracking Susceptibility of Metals and Alloys. *American Society of Tool and Manufacturing Engineers*, EM68-520.

Schajer, G. S., 1988. Measurement of Non-Uniform Residual Stresses Using the Hole- Drilling Method . Part I — Stress Calculation Procedures. *Journal of Engineering Materials and Technology*, 110(October), pp.338–343.

Schajer, G. S. & Altus, E., 1996. Stress Calculation Error Analysis for Incremental Hole-Drilling Residual Stress Measurements. *Journal of Engineering Materials and Technology*, 118(1), pp.120–126.

Smith, M.C., Smith, A.C. & Wimpory, R., 2011. *Review of the NeT Task Group 1 Single Weld Bead on Plate Benchmark Round Robin*,

Stefanescu, D. et al., 2006. Improvements in Residual Stress Measurement by the Incremental Centre Hole Drilling Technique. *Experimental Mechanics*, 46(4), pp.417–427.

VEQTER, 2013. Deep-Hole Drilling. *VEQTER Ltd.* Available at: http://www.veqter.co.uk/residual-stress-measurement/deep-hole-drilling [Accessed February 11, 2013].

Withers, P. & Bhadeshia, H.K.D.H., 2001. Residual stress: Part 2 – Nature and origins. *Materials Science and Technology*, 17, pp.366–375.

Research and Applications in Structural Engineering, Mechanics and Computation – Zingoni (Ed.)
© 2013 Taylor & Francis Group, London, ISBN 978-1-138-00061-2

Assessment of fracture toughness in strain hardening cement-based composite (SHCC) made from fine and coarse sand

S.C. Paul & G.P.A.G. van Zijl
Stellenbosch University, South Africa

ABSTRACT: This paper investigates the effect on fracture toughness of matrices intended for strain hardening cement based composite (SHCC), using very fine sand (size up to 0.3 mm, subsequently referred to as FS) and local coarse sand (size up to 2.36 mm and 1.7 mm, CS). ASTM E-399 was followed for measuring fracture toughness of the matrices. A series of characterising tests are also reported, including 100 mm cube compressive strengths, 100 × 200 mm cylinder responses for the E-moduli and flexural strength from 100 × 100 × 500 mm notched beams tested in three point bending. The matrix fracture toughness K_{IC} was determined from the flexural response of the FS and CS beams together with the observed crack propagation in both matrices. The maximum value for K_{IC} was found to be 1.12 MPa.m$^{1/2}$ and 0.95 MPa.m$^{1/2}$ respectively for the CS and FS mortar matrices, compressive strengths of 32 MPa (CS) and 36 MPa (FS), and E-moduli of 17 GPa for both FS and CS. Finally, by performing direct tensile tests on both FS and CS matrices containing maximum 2.2% and 2% by volume of polyvinyl alcohol (PVA) fibres, the formation of multiple cracks were verified for both sand types. The purpose of the study was to determine the influence of the particle size on the fracture toughness as well as the relevant parameter of the SHCC matrix. The potential of using more realistic sands as aggregate in these high performance cement-based materials is shown by the results of the research presented in this paper.

1 INTRODUCTION

In the last twenty years much research has been conducted on high performance cementation materials such as strain hardening cement-based composites (SHCC) and of most importance was the improvement of structural durability. Structural durability depends on the performance of materials under various circumstances and until now such knowledge is limited. Much research is needed to fill these gaps, especially due to lack of understanding of the micromechanical behaviour of SHCC. Pseudo strain hardening (PSH) is one of the most important characteristics of SHCC, associated with multiple, fine cracks. Due to this crack control, higher strain and stress can also be found in SHCC (Li et al. 2002, Sahmaran et al. 2008, and Paul & van Zijl, 2012b). In SHCC, PSH can be achieved by inclusion of relatively low volumes of micro fibres (polyethylene (PE), polyvinyl alcohol (PVA), etc.). Good dispersion of micro fibres in SHCC is essential and depends on the particle size, as large particles push and displace the fibres in a random way (Liu et al. 2011).

An important requirement for multiple crack formation is steady-state cracks rather than Griffith type of cracks. The latter lead to fibre breakage or premature pull-out from the matrix and as a result, brittle failure of structures occurs (Li, 2003). A sufficient amount and homogeneous distribution of fibres provides enough reinforcement to bridge cracks and transfer the load to the next weakest point in the matrix. This usually requires a relatively low fracture toughness of the matrix to ensure that the energy required for fibre pull-out exceeds the crack tip toughness by a sufficient margin.

The common practise is to use very fine sand (FS) (particle size less than 0.3 mm) in SHCC as the main aggregate (Li, 1993, Wittmann et al. 2009, and Adendorff et al. 2009) together with a large volume of cement and fly ash. Special attention is needed in processing this kind of FS and therefore introducing coarse sand (CS) in SHCC could be a cost-effective alternative. However, the increased particle size leads to higher fracture toughness of the matrix (Paul & van Zijl 2013a), posing a challenge to retaining the multiple crack formation.

In SHCC the fine cracks offer significant potential of structural durability by retarding ingress of deleterious substances under service conditions, for instance by protection of embedded reinforcing steel in concrete. This paper is limited to the fracture toughness of SHCC matrix made from both FS and CS together with PSH behaviour in direct tensile testing as well as in flexural testing. Part of this work has already been published in Paul & van Zijl (2013a, 2013b) and is part of the durability assessment of SHCC in a large scale

research project carried out at Stellenbosch University and further inputs will be reported on in subsequent proceedings.

2 POTENTIAL OF SHCC

SHCC originated in 1990 for its extraordinary performance of high ductility as well as strength (Li and Wang 1990, Li 1992, 1993) relative to conventional concrete. Higher ductility of concrete is an important protection mechanism of structures against tensile action in hazardous environments, seismic action, wind load, tidal load, etc. Typically ultimate strain values of normal concrete (NC) range between 0.015–0.02%, while more than 4% strain can be obtained for SHCC (Sahmaran et al. 2008, Paul and van Zijl 2013,b). Until now SHCC has been used in several countries as a repair material for bridge decks, tunnels, retaining walls and offshore structures. Full scale SHCC structures are not yet generally constructed and the reasons behind it may be the high material cost and limited information available on SHCC performance as a relatively new material.

3 FRACTURE TOUGHNESS TEST

In most materials the failure mechanism of crack development can be examined by fracture mechanics. However the fracture mechanics of quasi brittle materials like concrete is not yet clearly understood due to the complexity of concrete, and its properties depending on many factors. The fracture toughness of concrete provides a quick assessment of the safety of a concrete structure at the post cracking stage.

Cracks in concrete structures are major sources of reduced durability of the structures. They allow quick entry of liquids and gases which may for instance lead to corrosion of the embedded steel. A damage zone starts to form in the structure when the tensile strain in the structure exceedes the concrete capacity. Using a numerical technique like the finite element method, and experimental tests such as to characterise the stress-crack mouth opening displacement (CMOD) curve (see Figures 1 and 2), it is possible to analize the damage zone and structural behaviour theoretically (Hillerborg 2004).

The CMOD of a flectural specimen (Figure 1) is used to calculate the fracture toughness of concrete. According to the recommendations by ASTM E399-09, each specimen is verified under certain conditions. To establish valid matrix toughness, conditional results of K_{IC} need to be calculated from the Load-CMOD curve. In the Load-CMOD curve a best-fit straight line first needs to be drawn to obtain the slope of the curve ($\tan\theta$) after which a second best-fit line with compliance 5% greater than that of the initial line needs to be drawn. If the maximum flexural load (P_{max}) falls in between these two lines, the matrix toughness can be calculated using the P_{max} value. If the P_{max} value falls outside these two lines, the load must be calculated using the second straight line connecting

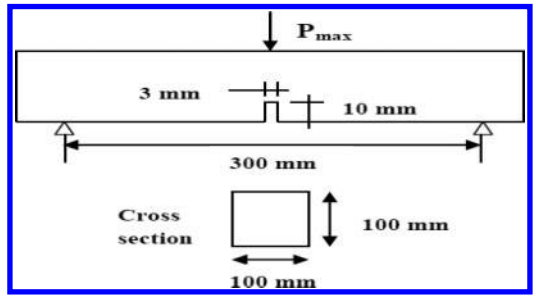


Figure 1. Flexural test for fracture energy.

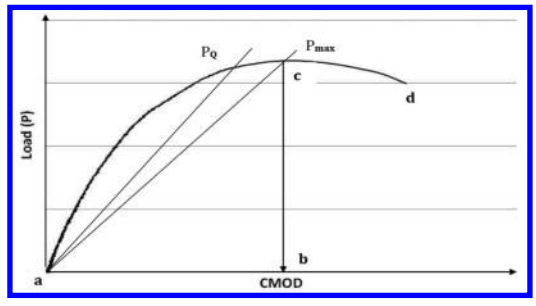


Figure 2. Calculation of fracture energy from the flexural specimen response.

point on the curve (P_Q). For the details see Figure 2. Furthermore, if the ratio of $P_{max}/P_Q < 1.1$, P_Q will be used to calculate K_Q otherwise the test is invalid. To recheck the validity of K_{IC}, it is also necessary to check that $2.5(K_Q/\sigma_y)^2 < b$ as well as the specimen ligament (d-a), where σ_y is the yield strength, b is the specimen width, d is the specimen depth and a is stable crack growth. If the above condition is satisfied the K_Q is valid and is equivalent to K_{IC} (ASTM E399-09). The reason of aforementioned test validity may be because this test method and equations are empirical, i.e. correlated from many experimental results to give reasonable results of K_{IC} despite the simple nature of the test method. Eqs (1) to (3) are used to calculate K_{IC} for both the mortar and SHCC specimens.

$$K_{IC} = \frac{3P_{max}S}{2bd}\sqrt{\pi a_1}F(x) \quad (1)$$

where P_{max} is the valid peak load
S is the specimen loading span
b is the width of beam
d is the depth of beam
a_1 is the effective critical crack length $= a_0 +$ stable crack growth at peak load

$$F(x) = \frac{1}{\sqrt{\pi}}\frac{1.99 \quad x(1 \quad x)(2.15 \quad 3.93x + 2.7x^2)}{(1+2x)(1 \quad x)^{3/2}} \quad (2)$$

$$x = \frac{a_1}{d} \quad (3)$$

Table 1. Materials used in this study.

Materials	FS, CS 1 (kg/m^3)		FS, CS 2 (kg/m^3)	
	SHCC	Mortar	SHCC	Mortar
Cement	450		390	
Fly-ash	670		670	
Sand	550		550	
Water	395		390	
Fibre	28.6, 26	–	26	–
SP	2.7, 3.6	–	3.6	–
VA	1.13	1.35	1.35	1.35
AEA	0.45	0.45	0.45	0.45

Table 2. The flow value and mechanical properties of the matrixes at 28 days (CoV (%) in brackets).

Type		Flow (mm)	f_{cu} (MPa)	E-mod (GPa)
FS-SHCC	1	170–200	39 (4%)	20 (12%)
	2	200–230	29 (5%)	13 (22%)
CS-SHCC	1	170–200	35 (2%)	18 (4.4%)
	2	195–225	25 (2%)	14 (7%)
FS-Mortar	1	200	36 (4%)	17 (0.1%)
	2	205	32 (7%)	17 (11%)
CS-Mortar	1	220	32 (6%)	17 (9%)
	2	225	29 (3%)	15 (11%)

Finally the matrix crack tip toughness J_{tip} can be calculated from K_{IC} and matrix modulus of elasticity (E_m) value as follows

$$J_{tip} = \frac{K_{IC}^2}{E_m} \quad (4)$$

4 EXPERIMENTAL METHODOLOGY

4.1 *Materials compositions*

The compositions of materials used in this study are shown in Table 1. CEM I 52.5 cement together with class F Fly ash were used as binder of the matrix. ASTM F95 graded fine Phillippi sand with maximum size of 0.3 mm was used as FS and local sand with maximum particle size up to 2.36 mm (in mix 1) and 1.7 mm (in mix 2) were used as CS. Dynamo Sp1 super plasticizer (SP), viscous agent (VA), air-entraining agent (AEA) and PVA fibre ($L_f = 12$ mm and $d_f = 0.04$ mm) were also used in this study.

4.2 *Specimen specifications*

In determining the matrix fracture toughness 22 beam specimens with dimention of $100 \times 100 \times 500$ mm^3 were prepared from both FS and CS. Another set of 16 specimens were prepared from FS-SHCC and CS-SHCC to compare the matrix toughness with and without fibre. Both mortar and SHCC cubes (100 mm) and cylinders (100 mm diameter, 200 mm long) were also made to determine the compressive strength and E-moduli of the matrices. From both SHCC mixes small dumbbell shaped specimens with a cross section of $30 \pm 2 \times 16 \pm 2$ mm^2 in the 80 mm gauge length were made for the direct tensile test.

4.3 *Specimen preparation and testing*

After mixing both mortar and SHCC, small slump flow was measured as given in Table 2. All specimens were demoulded after 48 hours, after which specimens were kept in a water curing tank at 21 ± 3°C until the testing day (28 days). In case of dumbbell specimens, the total curing period was 7 days, after which specimens were air dried until the 14 days of testing. All flexural beams were notched (3 mm width and 10 mm length) at the bottom surface before testing as is shown in Figure 1.

A Z250 Zwick materials testing machine was used to perform flexural and direct tensile tests. For determining the compressive strength and E-modulus, a contest materials testing machine was used. In case of the flexural test, a constant position control rate of 0.005 mm/s was maintained for all specimens while for the direct tensile test, a constant deformation rate was 0.0075 mm/s. In the dumbbell specimen the gauge length was 80 mm for measuring the tensile strain of the SHCC matrix.

The fracture energy obtained from the area under the stress vs CMOD curve has been shown to be a simple and accurate method (Byung-Hwan et al 1999). The fracture energy was calculated as the area under the ac curve in Figure 2 (where on the y axis stress calculated using equation provided for the three point bending test was used instead of load) where c is the ultimate stress point. The stress vs CMOD curve represents the total amount of energy absorbed by the specimen before failure in flexure. The area under the curve depicts energy per unit volume, absorbed by the whole specimen. It is worth mentioning that failure of the mortar specimen in the flexural test was sudden after reaching the ultimate stress. So the point d was not considered to calculate the fracture energy as the matrix behaviour is completely different after reaching the point c. Simpson's rule was used to calculate the area under the ac curve.

5 EXPERIMENTAL FINDINGS

5.1 *Compressive strength and E-modulus properties of the matrixes*

The 28 days mechanical properties of compressive strength (f_{cu}), E-modulus (E-mod) of the mortar and SHCC matrixes with their coefficient of variations (CoV) are shown in Table 2. In both cases, mix 2 of mortar and SHCC show higher slump flow than the mix 1. Mix 2 has lower f_{cu} and E-mod values than

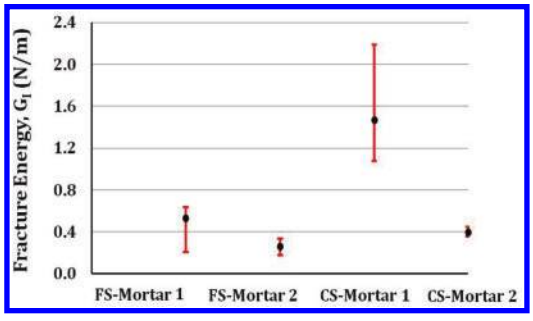


Figure 3. Variation of fracture energy (G_I) obtained from FS-Mortar and CS-Mortar matrix.

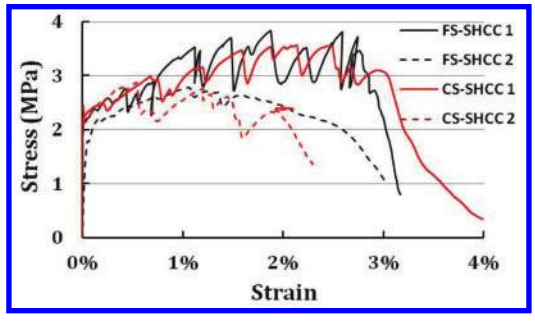


Figure 4. Stress-strain response of SHCC specimens in direct tensile test.

Table 3. Matrix fracture toughness (K_{IC}), crack tip toughness (J_{tip}) and fracture energy (G_I).

Type		K_{IC} (MPa.m$^{1/2}$)	J_{tip} (J.m^2)	G_I (N/m)
FS-Mortar	1	0.824	0.04	0.53
	2	0.95	0.053	0.26
CS-Mortar	1	1.12	0.080	1.47
	2	1.02	0.074	0.40
FS-SHCC	1	1.87	0.18	–
	2	2.48	0.48	–
CS-SHCC	1	1.61	0.15	–
	2	2.15	0.33	–

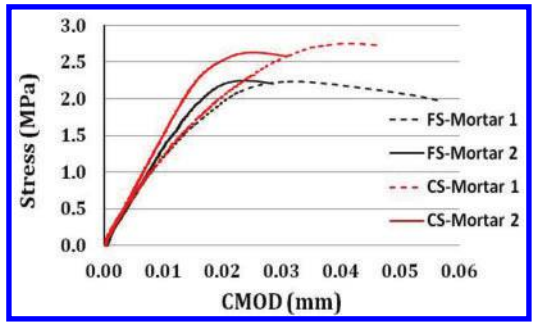


Figure 5. 28 days flexural testing response of mortar specimens.

mix 1, ascribed to the higher water-binder ratio of mix 2.

5.2 *Fracture energy of the matrix*

Figure 3 illustrates the variations of fracture energy for two different matrix types for both FS and CS-Mortar. In both matrices, mix 2 has lower fracture energy than mix 1. Higher variation of fracture energy was observed in both mix 1 matrices. Also, CS causes a higher fracture energy of the matrix.

5.3 *Fracture and crack tip toughness of the matrix*

Whether strain hardening is achieved depends strongly on the matrix toughness, as expressed by the crack tip toughness J_{tip}, and on the bond τ between the matrix and fibres. No direct measurement of J_{tip} has been attempted in this study. Eqs. 1 to 4 together with E-mod obtained for different matrices were used to calculate fracture and crack tip toughness. Matrix fracture toughness together with the crack tip toughness and fracture energy of the matrices are shown in Table 3.

From Table 3 it is clear that the fibres in the matrix lead to higher K_{IC} and J_{tip} values. Since the K_{IC} value is related to the P_{max} (in eq 1), lower P_{max} values of FS-Mortar have corresponding lower K_{IC} values than the CS-Motar. However in SHCC higher P_{max} values of FS-SHCC cause higher values of K_{IC} and J_{tip}than the CS-SHCC. Note that, in the test validity check (section 3), 10 out of 11 specimens from FS-Mortar and 7 out of 11 specimens of CS-Mortar satisfied the conditions mentioned in section 3. The CoV was also higher in case of CS-Mortar. In SHCC, almost all the FS-SHCC and CS-SHCC specimens satisfied the conditions.

5.4 *Direct tensile test response of SHCC specimens*

Figure 4 shows the typical stress-strain curve obtained from the direct tensile test of SHCC dumbbell specimens at 14 days. Note that these are typical individual responses and not average or best responses. The average ultimate tensile strengths of 3.61 MPa and 2.67 MPa were found for FS-SHCC 1 and 2. In case of CS-SHCC 1 and 2 maximum 3.64 MPa and 2.76 MPa ultimate tensile strengths were found. Maximum 3.4% tensile strain was observed for FS-SHCC 1 at 14 days and minimum 1.52% was observed for CS-SHCC 2. A lower number of cracks and larger crack widths were found in CS-SHCC compared to FS-SHCC. More detailed results of tensile strength and strain can be found in Paul & van Zijl (2013b).

5.5 *Flexural test response of mortar and SHCC specimens*

As it has already mentioned, the beam specimens were used to determine the G_I and K_{IC} values. Flexural testing of the notched beam specimens were performed. Figures 5 and 6 show the stress vs CMOD responses of the mortar and SHCC specimens. Note that these are

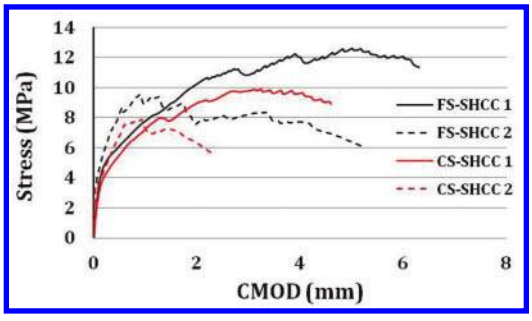


Figure 6. SHCC specimens under flexural stress vs CMOD.

Table 4. 28 days ultimate flexural strength (f_{fl}) of mortar and SHCC matrix.

Type		FS f_{fl} (MPa)	FS CoV (%)	CS f_{fl} (MPa)	CS CoV (%)
Mortar	1	2.34	10	3.41	9.4
	2	2.43	5.36	2.62	1.8
SHCC	1	11.5	8.5	9.24	6.65
	2	10.36	6.81	7.47	10.04

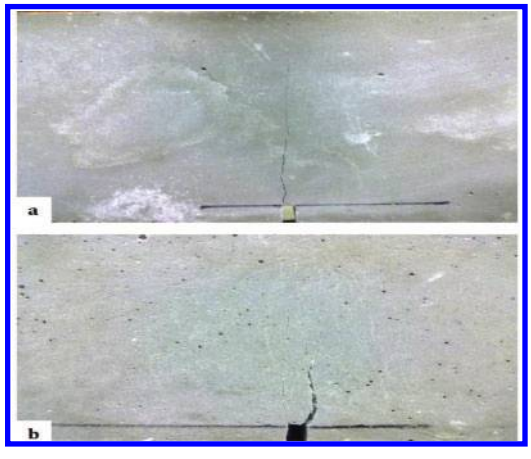


Figure 7. Crack growth in Mortar (a) and SHCC (b) specimens during flexural test.

typical individual responses and not average or best responses. In case of the mortar, specimens with CS show higher flexural strength (see Figure 5) than the FS specimen and for SHCC matrix it is vice versa. It can be explained by the presence of different particle sizes in CS than the FS which improve the matrix interlocking behaviour. Typically aggregate locking actions provide the crack bridging capacity in plain concrete, but additional crack bridging actions are introduced by adding fibres to concrete (Li et al. 1993). Table 4 shows the ultimate flexural strength (average and CoV (%)) of both mortar and SHCC matrices.

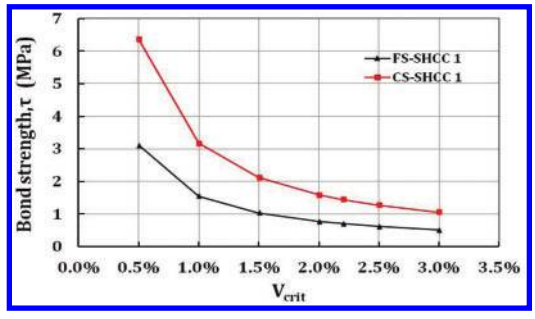


Figure 8. Bond strength vs critical fibre volume.

5.6 *Crack growth in mortar and SHCC specimens*

In most of the mortar specimens, only one crack (see Figure 7a) in the notched vicinity appeared close to the ultimate state and after that specimen failed abruptly. On the other hand, in SHCC specimens multiple cracks were observed in the vicinity of the notches and beyond (see Figure 7b).

5.7 *Bond strength of SHCC matrix*

For a particular mix of SHCC the bond strength (τ) was calculated for FS and CS-SHCC 1 by using the 28 days tensile strength, as well as E-mod and J_{tip} values from FS and CS-Mortar 1. Details of the calculation procedures can be found in Paul & van Zijl 2013a. The results obtained for τ with respect to V_{crit} are shown in Figure 8. No direct test was performed to calculate the τ values. The shown τ values are lower for an increase in fibre volume. Also CS shows higher bond than FS. This higher bond strength of CS leads to fibre breakage in the CS SHCC specimens and results in lower strain and number of cracks. To achieve higher strain and multiple cracking behaviour of SHCC, lower bond strength of the matrix is required so that fibres do not break, but rather pull out from the matrix.

6 CONCLUSIONS AND RECOMMENDATIONS

To achieve multiple cracking and PSH behaviour of SHCC, a matrix with low fracture toughness of the matrix relative to fibre pull-out resistance is required. The fracture properties of the SHCC matrix produced from two different types of sand and two different mixes have been reported in this paper. The outcome of this study may contribute to the knowledge of typical fracture toughness of SHCC matrices and may also help to predict the PSH behaviour for different particle sizes in the matrix. Based on the results of this study, the following conclusions can be made:

PSH behavior can be achieved with local CS. However, the larger particle size of CS leads to higher fracture toughness of the matrix. For both CS-Mortar and CS-SHCC higher fracture toughness and lower E-moduli were found. Higher crack tip toughness was found for the CS matrices than for the FS matrices.

Using fibre in both types of mortar matrices increased the fracture and crack tip toughness significantly since the crack growth rate in SHCC specimen is much lower than the mortar specimen.

Lower ultimate strain was found in direct tensile and flexural tests for CS-SHCC than for FS-SHCC.

CS-Mortar shows higher flexural strength than FS-Mortar.

The higher bond strength in CS matrices also leads to reduced ultimate strain and number of cracks, but wider crack widths in CS-SHCC.

In future studies single fibre pull out tests will be performed to determine the fibre bond strength on these FS and CS matrices to validate the results obtained from the indirect test. Several other issues are currently under scrutiny to understand the SHCC behaviour correctly in different applications, like critical fibre volume, fibre orientation, influence of local sand and cement replacement materials. These research results will be reported in subsequent publications.

REFERENCES

Adendorff, C.J., Boshoff, W.P. and van Zijl, G.P.A.G. 2009. Crack characterisation in SHCC: towards durability assessment, *Advances in cement based materials.* van Zijl and Boshoff (eds), CRC press, pp.215–221.

ASTM E399-09. 2010. Standard Test Method for Linear-Elastic Plane-Strain Fracture Toughness *KIc* of Metallic Materials.

Byung-Hwan, O., Seung-Yup, J. & Hyung-Kyun, B. 1999. Prediction of fracture energy of concrete, *KCI Concrete Journal.* Vol. 11, No.3.

Hillerborg, A. 2004. The theoretical basis of a method to determine the fracture energy G_F of concrete, *Matriaux et Constructions.* Vol. 18, No. 106.

Li, V.C., Wang, Y. And Backer, S. (1990). Effect of inclined angle bundling and surface treatment on synthetic fiber pull-out from a cement matrix. *Composites*, Vol. 21(2), 132–140.

Li, V.C., Stang, H. & Krenchel, H. 1993. Micromechanics of crack bridging in fibre-reinforced concrete. *Materials and Structures.* Vol. 26, pp. 486–494.

Li, V.C., Wu, C., Wang, S., Ogawa, A. & Saito, T. 2002. Interface tailoring for strain-hardening polyvinyl alcohol engineered cementitious composite (PVA-ECC). *ACI Materials J.* 99(5), 463–472.

Li, V.C. 2003. On Engineered Cementitious Composites. *Journal of Advanced ConcreteTechnology.* 1(3), pp.215–230.

Liu, J., Li, C., Liu, J., Du, Z. & Cui, G. (2011). Charecterization of fibre distributions in steel fibre reinforced cementatious composites with low water-binder ratio. *Indian Journal of Engineering & Materials Sciences.* Vol. 18, pp. 449–457.

Paul, S.C. & van Zijl, G.P.A.G. 2013a. Mechanical behaviour of strain hardening cement-based composites (SHCC) based on micromechanical design. *Advances in Cement and Concrete Technology in Africa.* January 28–30, Johannesburg, South Africa.

Paul, S.C. & van Zijl, G.P.A.G. 2013b. Strain hardening cement based composite (SHCC) with fine and coarse sand under tensile load and chloride attack. *In Proceedings 8th Int. Conf. on Fracture Mechanics of Concrete and Concrete Structures.* March 10–14, Toledo, Spain.

Sahmaran, M., Li, M. and Li, V.C. 2007. Transport properties of engineered cementitious composites under chloride exposure. *ACI Materials Journal.* November–December, V. 104, No.6.

Sahmaran, M., Li, V.C. & Andrade, C. 2008. Corrosion resistance performance of steel-reinforced engineered cementitious composite beams. *ACI Materials Journal.* May–June, V. 105, No.3.

Wittmann, F.H., Zaho, T., Tian, L., Wang, F. and Wang, L. 2009. Aspect of durability of strain hardening cement-based composites under imposed strain. *Advances in Cement-based Materials.* van Zijl and Boshoff (eds), CRC press, pp.173–179.

Research and Applications in Structural Engineering, Mechanics and Computation – Zingoni (Ed.)
© 2013 Taylor & Francis Group, London, ISBN 978-1-138-00061-2

Polymeric facades: fatigue performance of pultruded panel connections

P. T. Gates, Prof. T. J. Ibell, Dr. A. P. Darby & Dr. M. Evernden
University of Bath, Bath, England

ABSTRACT: The long-term performance of pultruded structural angle sections has been investigated through a campaign of fatigue testing. Equal angle sections have served to represent the connected element of Glass Fibre Reinforced Polymer (GFRP) façade panels. Suitable design limits on maximum recommended transverse strain at connections in the pultrusion have been established. Characteristic behaviour pertinent to application of GFRP pultrusions in facades is reported. The existence of a strain threshold in pultruded connections, below which fatigue does not occur over 100,000 cycles, has been revealed.

1 INTRODUCTION

1.1 *Polymeric facades*

Replacing a building's façade offers the prospect of improving the whole life performance of the building. This presents the opportunity to exploit the properties of advanced composite materials for maximum benefit. 'Upwards and outwards' retrofit, where extending floor slabs yields extra floor area, is permitted by a lightweight replacement façade, without the need for significant structural retrofit or to underpin foundations.

It is paramount to resolve how the connections in a façade system of glass fibre reinforced polymer (GFRP) can enable it to meet the many requirements of an integrated building envelope. The permanent action acting on light, self-supporting GFRP panels is small, however wind and occupancy loading impart significant imposed actions. Therefore, whilst creep deflection is often a significant consideration for structural GFRP design, quantifying fatigue performance is a higher priority for validating the ideology of polymeric facades.

Much existing research focuses on fatigue when stresses are in the principal fibre direction. (Salvia et al. (1997), Salvia & Vincent (1996), and Tong (2002).) However, this is not necessarily the critical stress direction in cladding connection situations. The unidirectional nature of pultruded glass fibre reinforcement yields a scenario of critical stresses at the panel interfaces, occurring in the weaker, secondary fibre direction. The fatigue-testing programme presented examines the performance of pultruded angles compatible with 'long-edge' panel connections.

1.2 *Testing of pultruded angle sections*

Six structural angle sections have served as the subject of experimental investigation. Two different pultruded profiles of equal angle sections have stood to represent the edge returns found to occur in abundance on prototype designs (Fig. 1) developed to form the connection assembly on a polymeric façade. Component testing of representative elements has avoided the need for whole panel fabrication. Testing methodology and loading parameters have been selected to profile how damage propagates in such an element, and how the performance of the represented connection type would endure the lifetime service of a polymeric façade.

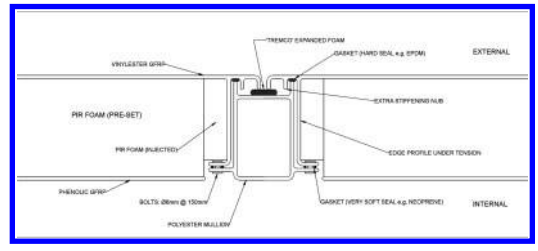


Figure 1. Façade scheme developed as a design platform for research. Suitable designs revealed an abundance of return angles in the pultrusions.

The aim of the testing campaign presented is to establish the general behaviour and response of a suitable connection scheme. A large volume of data is generated when monitoring fatigue testing of the type undertaken. The data capture and analysis options considered to best describe the structural behavior exhibited are discussed, and the chosen numerical procedures employed are justified.

2 METHODOLOGY

2.1 *Test rig set-up*

The angle section is situated in the test rig housing as shown in Figure 2. The prepared specimen is secured

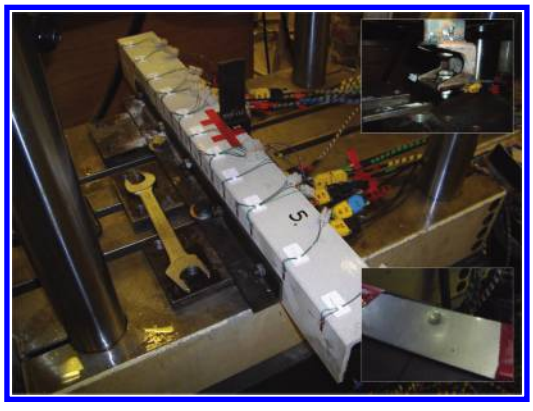


Figure 2. Prepared specimen situated in fatigue test rig set-up.

in place by the horizontal clamps and bolts, which pass through the specimen and grip the rails. The bolt-holes in the rails were drilled as low clearance and the bolt-holes in each specimen were filed out in-situ to yield as low clearance as possible and mitigate slipping and slack developing in the system. The rails are bolted securely to the fixed rig base.

In the arrangement shown in Figure 2 the clamped flange represents the façade panel face, and the free horizontal flange, gripped at a single discrete location, represents the edge return of a pultruded panel with a discrete mechanical connection. The flange is not drilled at this location, as testing is not intended to generate data concerned with stresses around bolts in pultruded GFRP. There is existing comprehensive literature available addressing such behavior (Turvey (2011), Turvey & Cooper (2004), Turvey & Wang (2008).)

The protective steel tabs at the load application point prevent localised damage in the composite. Taping to secure these using electrical tape proved the most efficient means that did not result in tabs breaking free; other tapes that could not stretch, tore away, and epoxy bonding of tabs fractured immediately upon commencement of cyclic loading. The gripper was clamped securely onto the horizontal flange and the crosshead brought down and clamped to the fin plate of the custom welded gripper. All cyclic loading commenced from a neutral displacement position at zero load. Cycling was conducted under displacement control at 1 H_z. The limits of displacement selected corresponded to maximum critical transverse strain measured on the material. (As shown in Table 1.)

2.2 *Preparation of angle sections*

Two different sized sections were tested at lengths of 500 mm. A total of six specimens were prepared and strain-gauged as shown in Figure 2.

There are two important parameters associated with strain gauge location and how the specimen is situated in the test rig. The gauge-offset distance from the inferred apex of the angle cross-section: this distance

Table 1. Specimen information.

Specimen	Flange (mm)		Max. strain ($\mu\varepsilon$)	% Stiffness retained
	l	*t*		
S1	75	6.4	3,000	37
S2	75	6.4	2,000	38
S3	100	9.5	3,000	42
S4	100	9.5	2,000	44
S5	75	6.4	1,100	100
S6	75	6.4	1,100	100

*l is flange length measured externally and t is flange thickness



Figure 3. Parameter for the gripped length of flange on angle section specimen.

was 30 mm for the larger section and 20 mm for the small section. This ratio is the same as that of the angle section leg thicknesses. The gripped length of flange element when clamped into the test rig rails was 60 mm for the larger section and 45 mm for the smaller section. This parameter is illustrated by figure 3 and is specified to be in the same ratio as the structural angle leg lengths.

The strain gauges applied captured the state of strain at increments along the specimen length, on the upstand element of the section; i.e. once the stress has passed around the root radius. The sampling rate for data logging chosen is 10 Hz. Throughout the duration of a test, the response of the specimen can be monitored, and the way the fatigue load is 'shared out' along the member length can be appreciated. The manner in which damage propagates along the element can also be assessed. The most important quantifiable connection property established is the connection stiffness, and the manner in which it diminishes.

2.3 *Data collection and processing*

Data from up to 17 channels, for strain, load and stroke (displacement) had to be recorded at a sufficient sampling rate to monitor behaviour of the specimen at all parts of the load cycle, and be able to represent some form of index relating to the performance of the specimen over the entire programme of loading.

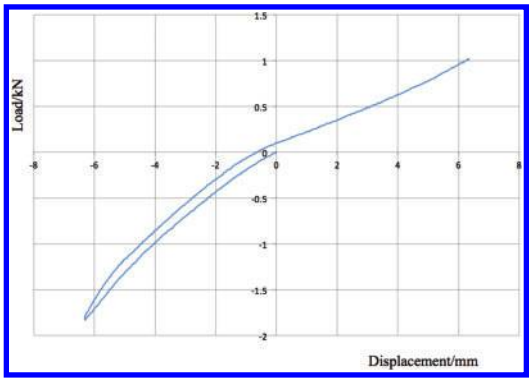


Figure 4. Typical response of connection to final linear ramp.

The average value of the stresses, strains, loads and displacements, recorded over a specific number of cycles in a fatigue programme, is zero. Another means to produce an index that can continuously depict the performance of the connection is therefore necessary. Under displacement control the resistive load is proportional to the specimen connection stiffness.

Applying a Route Mean Square (RMS) numerical procedure to the load data collected over a fatigue programme affords a continuous measure of the stiffness of the connection, and therefore, how the specimen response diminishes. A further benefit is that the procedure can reduce the amount of data by 100 times. If the RMS of loads and strains recorded over every 10 cycles (i.e. 100 data points) is assessed, the RMS load, or RMS strain at a certain strain gauge location can be presented as a continuous function of time with 100 times fewer data points. The time step, in this case, increased to 10 seconds. The RMS strain at each discrete gauge location along the specimen is a measure of how hard the material is working at that location.

3 RESULTS

3.1 *Specimen and loading parameters, and connection stiffness retained*

S1-S4 were cycled 10,000 times and S6 and S8 100,000 times. The % Stiffness retained, shown in the last column of Table 1, is inferred from the initial and final linear load ramps conducted. Figure 4 shows a typical load displacement graph for the final ramp. In contrast to the graph in Figure 5 for a typical initial linear ramp, it can be seen that post fatigue test, the connection specimen retains greater stiffness at the extents of its imposed displacement. This is more noticeable for the negative displacement in Figure 4, which corresponds to the external angle surfaces being in tension, and inner root in compression. The importance in the capacity of the RMS Load parameter to represent the stiffness of the connection over the whole range of imposed waveforms during the intervening fatigue cycling can be appreciated.

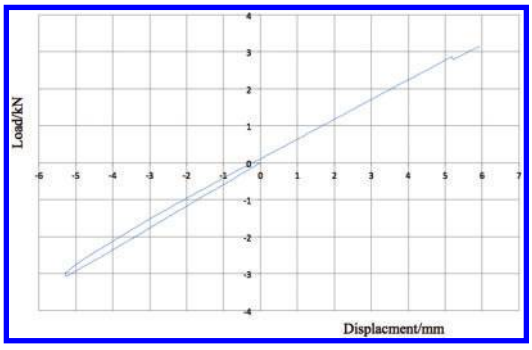


Figure 5. Typical response of connection to initial linear ramp.

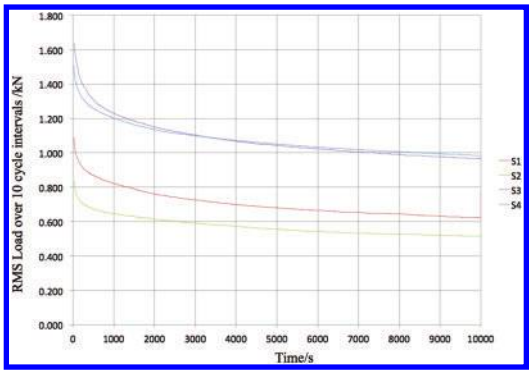


Figure 6. Plot of RMS load profiles for specimens S1-S4.

3.2 *Profiles for diminishing stiffness*

Testing at the levels of strain selected serves important function in understanding both the initiation, and propagation of damage in the connection component. The nature in which damage accumulates in the specimens can be seen in Figure 6.

The RMS Load is an arbitrary measure of stiffness, which has been established by others as proportional to, and a good measure of, damage in the composite material (Elmahi et al (1995) and Lemaitre & Desmorat (2005)).

It can be seen in Figure 6 that the two specimens of smaller section size, S1 and S2, appear to reduce in stiffness a similar amount, and follow a similar pattern of decay, despite the max state of stress and strain being initially much higher for S1. (3,000 $\mu\varepsilon$ for S1, as opposed to 2,000 $\mu\varepsilon$ for S2.)

The larger specimens, S3 and S4, behave quite differently. These specimens, which provide a greater resistive load to the imposed displacements, appear to be more sensitive to the imposed maximum cyclic strain. The specimen S3 which was subject to a higher cyclic displacement and critical strain (of 3,000 $\mu\varepsilon$), decays more rapidly than specimen S4, and in fact also ends up offering less resistance to the driving displacements than S4 does after 10,000 cycles. The case for the larger section specimens is perhaps more what was expected: the programme of larger displacements

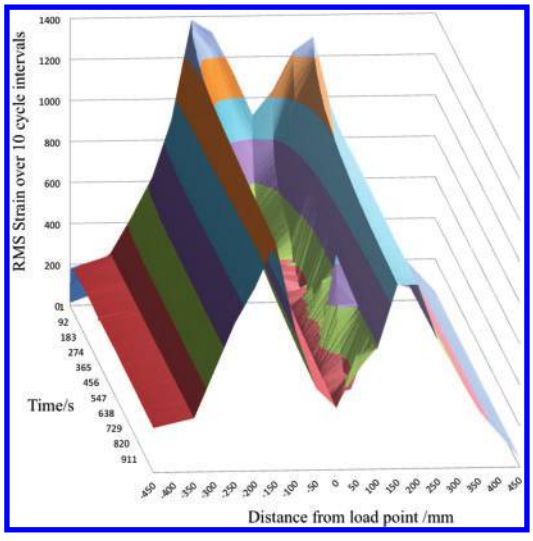


Figure 7. Plot of RMS Strain for the 1000 mm length specimen.

imposed is of greater detriment to the conservation of stiffness.

Specimens S3 and S4 appear to commence at a close state of RMS load. This could be evidence of initial damage having been caused by the monotonic loading (conducted at 1 mm/min, to the same maximum strain and displacement as that observed in cycling,) before the fatigue programme commenced.

Figure 6 portrays smooth curves indicative of a gradual decline in stiffness with progression of damage occurring at a steady rate. The continuous nature of this decay is exploited in Section 4 where the behaviour is modelled numerically.

3.3 *Profile for distribution of damage*

A plot for RMS strain in Figure 7 offers further insight into how damage propagates in a specimen. The specimen represented in this figure was tested in addition to S1-S6 under displacement control at a maximum transverse cyclic strain of 2,500 $\mu\varepsilon$. It can be appreciated that the specimen endured damage during the initial linear ramp, which has resulted in a reduced RMS Strain value at the central portion of the specimen from the very first cycle.

Figure 7 shows that this specimen exhibited initial damage followed by subsequent degradation behaviour in line with that previously observed for S1-S4. It can also be appreciated how the full length of the specimen is working to resist the load. This is an important finding from the 1,000 mm length specimen test, with implications on how cumulative action from adjacent connections on a façade panel could manifest itself. At a state of initial max strain imposed in the cyclic loading of 2,500 $\mu\varepsilon$, the influence of the imposed displacements was still just felt at the extents of a 1,000 mm span.

A further important finding indicated by the plot is that the cracked zone becomes weaker (or the crack gets deeper) where initiated, but does not spread any wider.

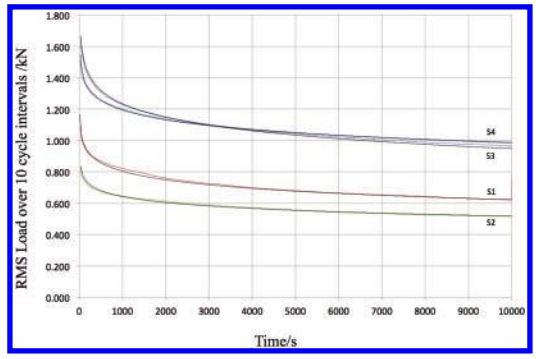


Figure 8. Plot of RMS Load for S1-S4 showing log law based curve-fitting relationships.

4 DISCUSSION

The three-dimensional response of the pultruded connections represented by the stiffness degradation curves is associated with onset of damage at levels of critical transverse strain as low as 2000 $\mu\varepsilon$.

These findings are in line with the findings of El-Assal & Khashaba (2007) who assessed the fatigue performance of pultruded rods under torsional loading as well as bending. It was found that torsional fatigue programmes resulted in a strength half that compared to specimens subjected to pure bending.

The torsion emanating in each longitudinal direction from a discrete connection point initiates damage at a lower transverse stress state than that initiated by plane flexure. Torsion, arising through stresses at connections, is verified to be of detriment to the interfacial bond of pultruded composites, under both quasi-static loading, and fatigue loading.

RMS load has served as a useful index of performance of the connection specimens, representing stiffness over the whole range of displacements from the imposed waveform. The continuous nature of the plot as a function against time permits further analysis techniques which employ 'curve fitting' to measure decay behaviour.

The form of the log law relationship adopted for the model is shown in Equation 1, and the values of the co-efficients, Φ and Ψ, for specimens S1-S6 are shown in Table 2.

$$RMS\ Load = \Phi - \Psi \ln(t) \quad (1)$$

It is of interest whether an RMS Load profile for a specimen displaying no fatigue could have been produced at a higher imposed max transverse strain than those at 1,100 $\mu\varepsilon$. In seeking to determine whether this is the case, the value Ψ, which signifies degradation in stiffness, or accumulation of damage, is examined in relation to the maximum imposed initial transverse strain. It can be seen that the green line plotted in Figure 9 suggests that Ψ is very sensitive to strain

Table 2. Ψ and Φ values for S1-S6.

Specimen	Ψ	Φ
S1	0.079	1.350
S2	0.054	1.018
S3	0.124	2.091
S4	0.090	1.814
S5	0.001	0.349
S6	0.001	0.349

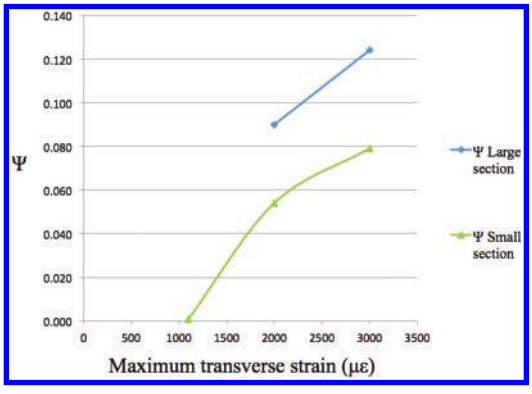


Figure 9. Ψ values, as a function of maximum imposed transverse strain.

near the threshold of onset of damage, even under displacement control testing such as that undertaken. (The gradient of this line is much steeper near $\Psi = 0$.) The implication of this finding is that though a damage threshold exists, if exceeded, the rate at which damage propagates is very sensitive to the loading parameters. Therefore, whilst a certain amount of damage over 10,000 cycle fatigue programme could be deemed acceptable, it is recommended that connection components are designed to retain full stiffness. There is no evidence to suggest a zero damage fatigue programme could have been achieved with any greater maximum transvers strain than that applied (of 1,100 με). The larger section size would appear to possess the same kind of limit on damage initiation if the same trend were observed. (Denoted by the blue line on the plot in Figure 9.)

5 CONCLUSIONS

At a maximum transverse strain of 1,100 με full connection specimen stiffness was retained after a 100,000 cycle fatigue programme. Specimens tested to fatigue loading parameters of high stress and strain (S1-S4) have demonstrated how the stiffness, or performance, of a connection component diminishes over 10,000 cycles.

The response of a pultuded GFRP angle element to a discrete mechanical connection load has been investigated through observation of the RMS strain at intervals along the section length throughout a fatigue-loading programme. This behavior is key to informing good design practice when considering cumulative action of adjacent connections on a façade panel.

The RMS strain profiles produced have revealed the nature of damage propagation. Specimens that suffered an initial amount of damage deteriorated further by cracks that perpendicularly bisected the direction of transverse strain. These cracks became progressively deeper, but not wider over the duration of the fatigue-loading programme.

The onset of damage accumulation at maximum cyclic transverse strains lower than that expected from testing reported concerning purely flexural fatigue, has evidenced a strong influence of torsion on the connection performance.

Testing has shown that though a threshold of damage accumulation does exist for transverse strain in fatigue loading of connections. The rate of damage accumulation once this limit is exceeded is very sensitive to the loading parameters, and the performance quickly diminishes with increasing maximum transverse strain.

The quantitative findings presented above relate to the specific design and fibre architecture of the pultrusions tested. The absolute values in the threshold of critical transverse strain determined will only be appropriate for these pultrusions. It is recommended however, that a factor of safety to be placed on the limit of max transverse strain in design, should be in line with that considered for ultimate failure though quasi-static loading on a façade, owing to the nature of the behaviour established through this testing campaign.

REFERENCES

El-Assal, A.M. & Khashaba, U.A. 2007. Fatigue analysis of unidirectional GFRP composites under combined bending and torsional loads. *Composite Structures* 79:599–605

Elmahi, A., Berthelot, J.M. & Brillaud, J. 1995. Stiffness reduction and energy-release rate of cross-ply laminates during fatigue tests. *Composite Structures* 30:123–30

Lemaitre, J. & Desmorat, R. 2005. *Engineering damage mechanics: ductile, creep, fatigue and brittle failures*: Springer.

Salvia, M., Fiore, L., Fournier, P. & Vincent, L. 1997. Flexural fatigue behaviour of UDGFRP experimental approach. *International Journal of Fatigue* 19:253–62

Salvia, M & Vincent, L. 1996. Modelling of flexural fatigue behaviour in UD glass-fibre-reinforced polymer. *Compos. Sci. Technol.* 56:797–802

Tong, J. 2002. Characteristics of fatigue crack growth in GFRP laminates. *International Journal of Fatigue* 24:291–7

Turvey, G.J. 2011. Experimental evaluation of bolt pull-through in pultruded glass-fibre-reinforced polymer plate. *Proceedings of the Institution of Civil Engineers-Structures and Buildings* 164:307–19

Turvey, G.J. & Cooper, C. 2004. Review of tests on bolted joints between pultruded GRP profiles. *Proceedings of the Institution of Civil Engineers-Structures and Buildings* 157:211–33

Turvey, G.J. & Wang, P. 2008. An FE analysis of the stresses in pultruded GRP single-bolt tension joints and their implications for joint design. *Computers & Structures* 86:1014–21

Research and Applications in Structural Engineering, Mechanics and Computation – Zingoni (Ed.)
© 2013 Taylor & Francis Group, London, ISBN 978-1-138-00061-2

Experimental evaluation of the fretting fatigue behavior of high-strength steel monostrands

J. Winkler
Department of Civil Engineering, Technical University of Denmark, Kongens Lyngby, Denmark
ATKINS Denmark A/S, Copenhagen, Denmark

C.T. Georgakis & G. Fischer
Department of Civil Engineering, Technical University of Denmark, Kongens Lyngby, Denmark

ABSTRACT: In this paper, the fretting fatigue behavior of pretensioned high-strength steel monostrands is investigated. A method based on the digital image correlation (DIC) technique was used to quantify the relative movement between individual wires along the length of the monostrand. The experimental data indicate that the interwire movement due to transverse deformations is highest at the neutral axis of the monostrand. The results show that the midspan and the anchorage of the monostrand are the two locations where the combination of tensile strains and the interwire friction is the most unfavorable. Moreover, the paper provides relevant information about the monostrand bending stiffness and the extent of relative displacement between core and outer wires of the monostrand undergoing flexural deformations. The results presented herein are of special interest for the fatigue analysis of modern stay cable assemblies where fretting constitutes the main mechanism of the fatigue life reduction.

1 INTRODUCTION

Parallel monostrand stay cable systems are frequently subjected to transverse vibrations due to wind and traffic (Gimsing & Georgakis 2012). The stay vibrations may lead to substantial relative movements between the monostrand wires (fretting) in the free span of the tendons and local bending stresses in the anchorage regions. The fretting mechanism leads to damage resulting from small amplitude displacements between the contacting surfaces of adjacent wires. These interwire movements significantly reduce the life expectancy of the cable and, consequently, the service life of the supported structure. Recent bending tests on high-strength steel monostrands axially pretensioned to 45% of the ultimate tensile strength (UTS) (Fig. 1) have shown that wire failures due to fretting and high localized bending stresses were concentrated in the cable anchorage and at the midspan (Wood & Frank 2010, Winkler et al. 2011). Modern cable anchorage systems often feature technologies that significantly reduce local bending effects and, therefore, fretting may often constitute the main mechanism of the fatigue life reduction. However, due to lack of data on the fretting fatigue performance of steel monostrands subjected to transverse deformations, the life expectancy of stay cables has not been evaluated in sufficient detail to date (Jensen et al. 2007).

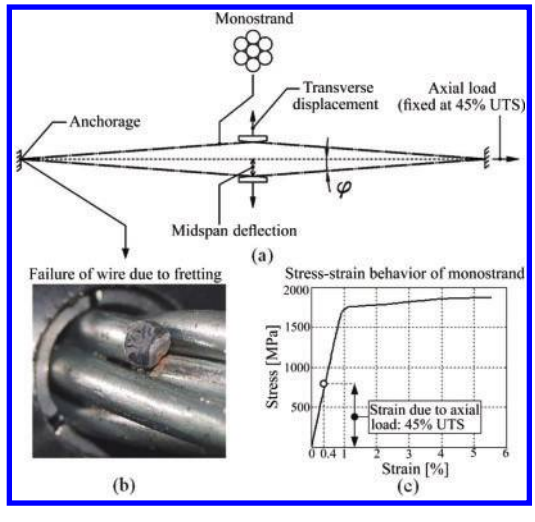


Figure 1. Schematic sketch of test setup (a), wire failure due to fretting (b) and stress-strain behavior of monostrand (c).

1.1 *Fretting fatigue of steel cables*

An important consideration in the fatigue analysis of steel cables is the fretting behavior of a monostrand. During bending tests on high-strength steel monostrands a hysteresis was observed in the

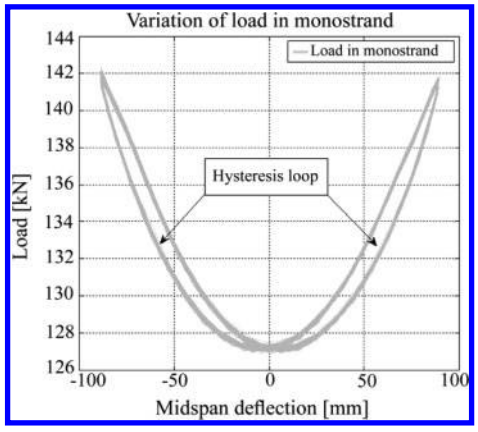


Figure 2. Variation of axial load and monostrand hysteresis.

load-displacement diagram (Fig. 2) (Rodríguez & Olabarrieta 2010, Winkler et al. 2011).

This was an indication that the monostrand experienced some form of internal energy dissipation which is likely a result of interwire movements. The interwire movement will accelerate the crack initiation, propagation and final failure of steel wires due to fretting. Fretting is an important degradation mechanism for steel cables and has been described previously (Hobbs & Raoof 1994). However, the relative movement between strand wires has been found difficult to deduce from strain gauge measurements. To date, there is no information about the distribution of the interwire movement along the length of the monostrand and the extent of the relative displacement between core and outer wires of the monostrand undergoing flexural deformations. The fretting problem is not yet fully clarified and, in the absence of relevant experimental data, it is difficult to draw reliable conclusions from purely analytical approaches.

In this paper, the fretting fatigue behavior of pretensioned high-strength steel monostrands is investigated. A method, based on the digital image correlation (DIC) technique was used to quantify the relative movement between individual wires along the length of the monostrand, leading to a more in-depth understanding of the underlying fretting fatigue mechanism.

2 METHODLOGY

2.1 *Materials and test setup*

An experimental investigation was carried out on high-strength steel monostrands with 5.1 m length and of 15.7 mm nominal diameter subjected to cyclic transverse deformations. The specimens consisted of two layers of galvanized round wires helically spun together. The monostrands were of low relaxation grade, waxed and PE coated. The ultimate tensile strength of the monostrand was 1860 MPa (279 kN) (Fig. 3).

To assess the fretting fatigue performance of a monostrand, a test rig that can simulate flexural effects

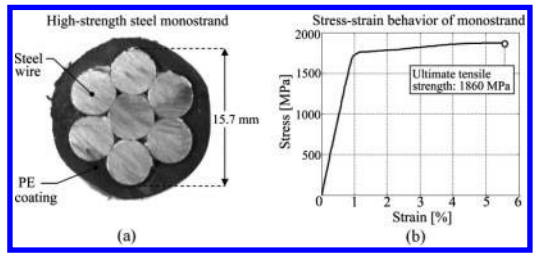


Figure 3. Cross section (a) and ultimate tensile strength of the monostrand (b).

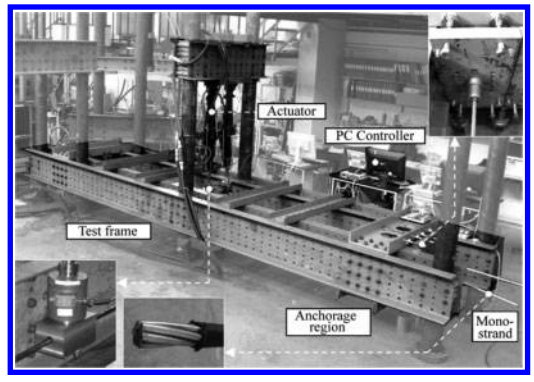


Figure 4. Test rig for monostrand bending tests.

was devised, so that the fatigue behavior of the monostrand with emphasis on relative wire movements could be investigated (Fig. 4). Full details of the cable specimens and testing arrangements have been described by Winkler et al. (2011) and therefore only a summary is presented herein. The high-strength steel monostrand was stressed to 45% of the UTS. The transverse deformation was applied by a hydraulic actuator attached to a deflection collar at the monostrand. With this setup, monostrand wires were subjected to varying degrees of bending, resulting in fretting-induced local stress and strain concentrations.

2.2 *Measurement technique*

Information on the extent of interwire movements corresponding to local curvatures is required to assess damage in the monotrands and estimate the remaining fatigue capacity of the cable. For this purpose, a digital image correlation (DIC) technique was employed as a tool for quantifying the interwire movement and measurement of individual wire strains along the length of the monostrand.

The applicability of the image analysis technique to measure local cable deformations was demonstrated previously by Winkler et al. (2012), with good agreement found between the wire strains measured using image analysis and those measured by conventional strain gauges (Fig. 5).

Details of the measurement technique were described earlier by Winkler et al. (2012), hence, the

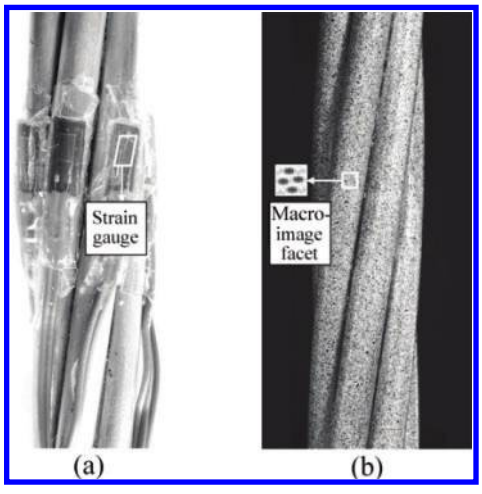


Figure 5. Conventional strain gauge measurement (a) and optical measurement based on DIC (b).

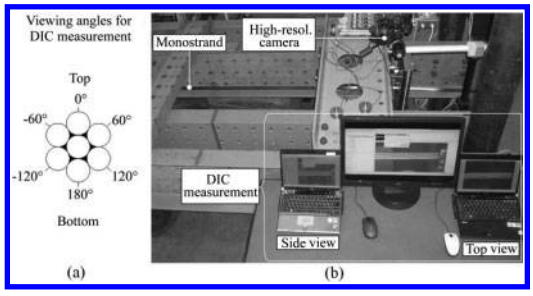


Figure 6. Viewing angles (a) and setup for the DIC analysis (b).

information provided here is intended only as a brief summary.

Image analysis involved capturing a reference image of the monostrand surface in its undeformed state. As the load was applied, additional images were collected. The deformation and the strain of the documented surface were computed using a post-processing algorithm. The post-processing algorithm of the photogrammetry software involved a stage-wise analysis, in which each stage consisted of one image resulting in a description of displacements occurring on the surface of the monostrand.

A high-resolution SLR camera with interchangeable lenses was used for image acquisition. The camera was controlled remotely from a computer where the collected images in JPG format were stored for processing with a commercially available photogrammetry software (Fig. 6b).

The orientation sketch of the monostrand with the different viewing angles used for capturing of the photogrammetric data is shown in the Figure 6a. The distance from the camera to the monostrand specimen was 35 cm.

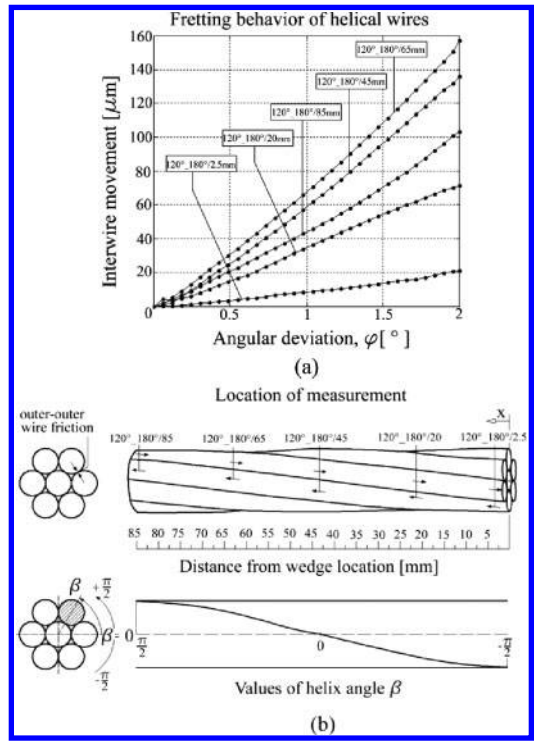


Figure 7. Fretting behavior of wires due to applied midspan deflection (a) and location of measurement (b).

3 RESULTS

3.1 *Interwire movement of outer wires of the monostrand*

The relative displacement of the outer wires was measured along the lay length of the monostrand (Fig. 7b). The DIC extensometers were placed on wires at 120° and 180° (120°–180°) and angular deviations φ between 0° to 2.0° were investigated. The interwire movement due to midspan deflection is plotted for each angular deviation φ and the measured response of the wires is shown in the diagram below (Fig. 7a).

The interwire movement (fretting) occurs as the radial forces in the monostrand are no longer high enough to prevent relative displacement between the individual wires due to the transverse deformation. The diagram in Fig. 7a shows that, depending on the value of helix angle b, the relative movement of wires will increase or decrease. The helix angle b varies along the lay length of wire from $-p/2$ to $+p/2$ and it can be seen that parts of the same wire slipped more while others slipped less. This is due to the fact that the Coulomb frictional forces acting on the wires are the smallest in the region of neutral axis ($b = 0$). Consequently, the slippage at $b = 0$ will be the highest. A similar fretting behavior has been observed in transmission line conductors (Papailiou 1997). It was also noticed that the failure due to fretting does not occur in the bending plane, where the bending stresses are highest, but

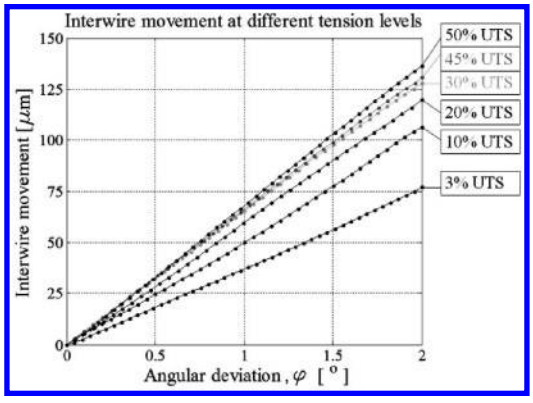


Figure 8. Interwire movement at different tension levels.

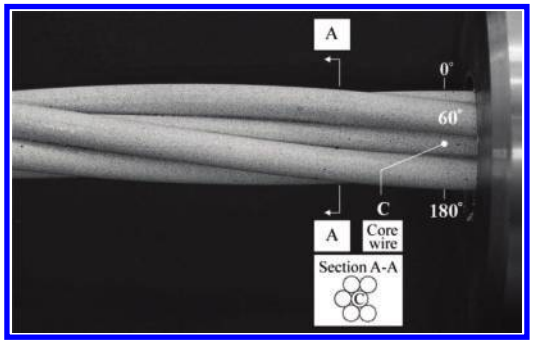


Figure 9. Strand specimen for the optical measurement of the core-outer wire relative displacement.

in the area where the combination of bending stresses and the tangential frictional forces is most unfavorable (Raoof 1991).

In addition, the interwire movement was measured at different tension levels ranging from 10% to 50% of the UTS (Fig. 8). The measurement was taken at the location of b = 0.

The diagram in the Fig. 8 indicates that the interwire movement increases with an increase of the tension load level in the monostrand. It can be also noticed that the difference of the interwire movement between 30% and 50% of UTS is negligible. Hence, the fatigue tests performed at a lower axial load levels (e.g. 30% of UTS) seem not to be more critical for the evaluation of fretting fatigue performance of the monostrand.

3.2 *Relative movement between core and outer wires of the monostrand*

The photogrammetry system enabled measurement of the relative movement between core and outer wires of the monostrand undergoing flexural deformation. For this test, the outer wire at 120° was removed allowing visual access to the core wire "C" and the 6-wire strand was pretensioned to an equivalent axial load level (45% of UTS) (Fig. 9).

The DIC extensometers were placed on the core wire "C" and the outer wires at 60° and 180° (Fig. 10b)

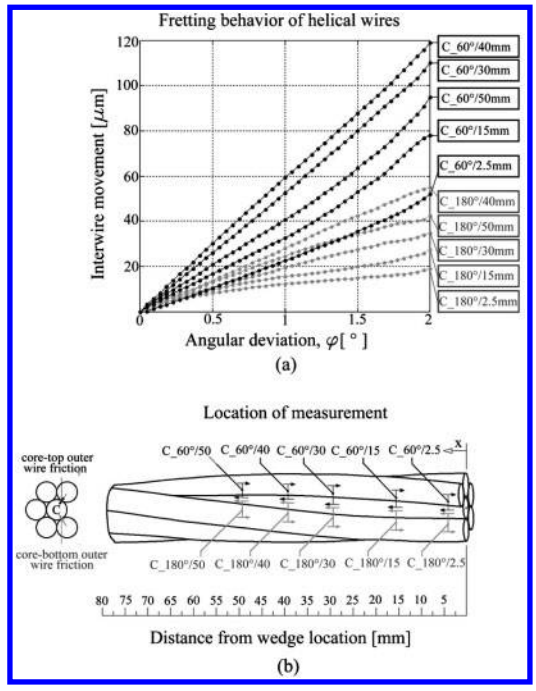


Figure 10. Fretting behavior of 6-wire strand specimen due to applied midspan deflection (a) and location of measurement (b).

and the ranges from 0° to 2.0° of angular deviations f were investigated. The interwire movement due to the midspan deflection obtained from the extensometers C_60° and C_180° are presented for each angular deviation (Fig. 10a).

Note the unequal interwire movement of bottom and top wires with respect to the core wire (Fig. 10a). It can be also seen that the bending-induced relative displacement between outer wires (Fig. 7a) is higher than the one between core and outer wires.

3.3 *Distribution of the interwire movement along the length of the monostrand*

It was possible to capture the interwire movement along the length of the monostrand by relocating the camera in the test rig (Fig. 11). The photogrammetry system enabled documentation of the side part of the monostrand from the anchorage to the midspan. The DIC extensometers measured the relative displacement between the core and outer wire at different angular deviations φ.

The experimental data show that the midspan and the anchorage of the monostrand are the two locations where the combination of the tensile strains and the interwire friction is the most unfavorable (Fig.12).

Aside from the anchorage region and the loading point most of the length of the monostrand showed a uniform tensile strain. Hence, the fatigue behavior of the strand in the free length (Fig. 12) is governed by the axial and frictional forces induced in the monostrand due to applied transverse deformation.

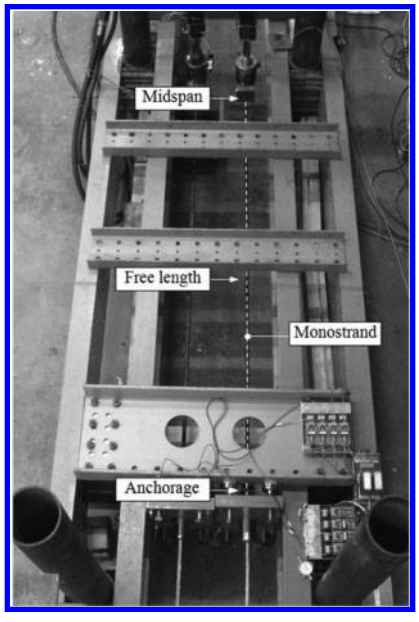


Figure 11. Test rig for the measurement of interwire movement.

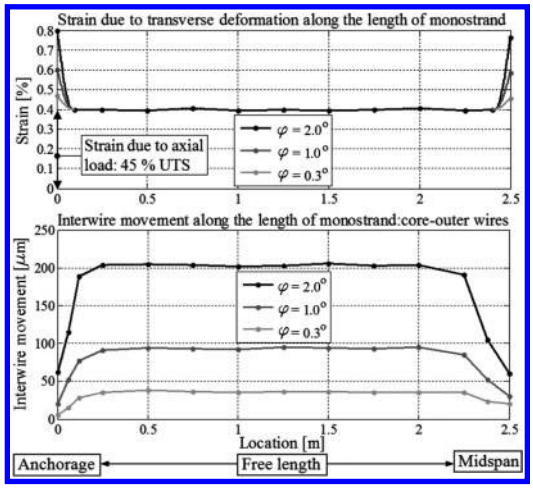


Figure 12. Distribution of the interwire movement and strain along the length of the monostrand.

3.4 *Transverse stiffness of the monostrand*

The transverse stiffness was measured at angular deviations of $\phi = 0°$, $1.0°$, $1.5°$ and $2.0°$. A linear least-square fit was used to plot the average measured stiffness for tension load levels ranging from 30 kN to 140 kN (10% to 50% UTS) (Fig. 13a).

The difference in stiffnesses (the vertical shift in the linear fit) is caused by an increase in tension load due to the applied midspan deflection (Fig. 13b) together with changes in the interwire movement.

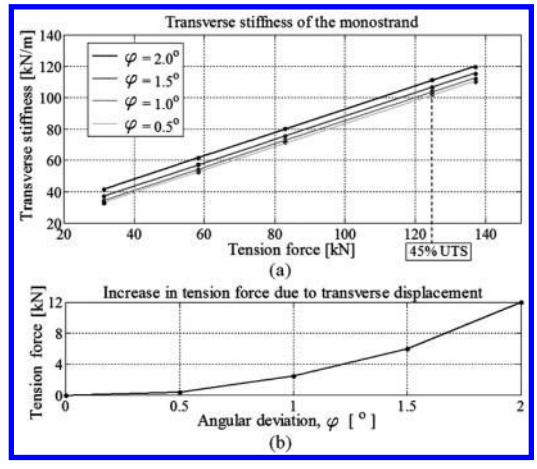


Figure 13. Measured transverse stiffness of the monostrand (a) and increase in tension force due to midspan deflection (b).

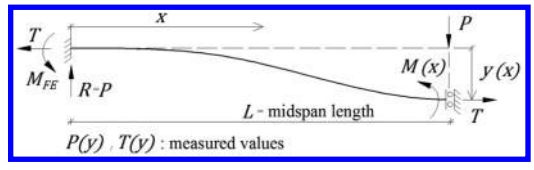


Figure 14. Free body diagram of the deformed monostrand.

3.5 *Bending stiffness of the monostrand*

The monostrand comprised of individual wires can be modeled as an elastic tension strut. The measurement of the bending moment in cables with a small diameter is not accurate enough for a direct validation of the theoretical models (Gourmelon 1992) and a similar problem was encountered in this study. However, it was possible to measure the midspan deflection and the corresponding vertical and tensile force in the monostrand. Consequently, the effective bending stiffness EI_{eff} of the monostrand was estimated from the numerical model described below.

3.5.1 *Description of the numerical model*

The monostrand was modeled as tension strut carrying an axial load and subjected to bending (Fig. 14).

Equation 1 defines the moment equilibrium equation for the deformed monostrand:

$$M(x) = R \cdot x - T \cdot y(x) - M_{FE} \tag{1}$$

where R = reaction at the left support; P = vertical force; T = tensile force; y(x) = transverse displacement at x; and M_{FE} = moment at the left support.

Substituting the relationship between moment and curvature, the vertical reaction for a symmetric loading condition, and defining the parameter $\lambda = \sqrt{T/EI}$, yields the governing equation:

$$\frac{\partial^2}{\partial x^2} y(x) - \lambda^2 \cdot y(x) = -\frac{R}{EI} \cdot x + \frac{M_{FE}}{EI} \tag{2}$$

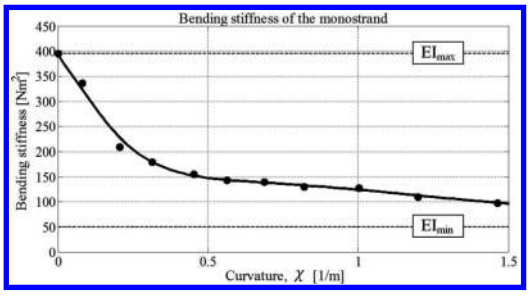


Figure 15. Effective bending stiffness of monostrand.

The general solution for the Equation 2 is of form:

$$y(x) = e^{\lambda \cdot x} \cdot A + e^{-\lambda \cdot x} \cdot B - \frac{M_{FE}}{T} + \frac{R \cdot x}{T} \quad (3)$$

The constants A, B and the unknown moment M_{FE} can be found by exploiting the boundary conditions:

$$A = \frac{M_{FE} \cdot \lambda - R}{2 \cdot EI \cdot \lambda^3}; B = \frac{R}{2 \cdot EI \cdot \lambda^3} + \frac{M_{FE}}{2 \cdot EI \cdot \lambda^2}; M_{FE} = \frac{(-1+e^{\lambda \cdot L}) \cdot R}{(1+e^{\lambda \cdot L}) \cdot \lambda}$$

Consequently, the constants and the moment are of the form:

$$A = \frac{M_{FE} \cdot \lambda - R}{2 \cdot EI \cdot \lambda^3}; B = \frac{R}{2 \cdot EI \cdot \lambda^3} + \frac{M_{FE}}{2 \cdot EI \cdot \lambda^2}; M_{FE} = \frac{(-1+e^{\lambda \cdot L}) \cdot R}{(1+e^{\lambda \cdot L}) \cdot \lambda}$$

3.6 *Estimation of the effective bending stiffness*

The effective bending stiffness EI_{eff}, indicated by the dots in the Figure 15, was determined by solving Equation 3 for the set of measured values: $y(L)$, $T(y(L))$, $R(y(L))$. The EI_{eff} was calculated for the displacements corresponding to the range of curvatures χ between 0 and 1.5 1/m (Fig. 15).

Figure 15 shows the variable bending stiffness of the high-strength steel monostrand over the monostrand curvature χ for the tension level of 40% UTS. EI_{max} (solid body assumption) and EI_{min} (full slippage of wires) constitute the upper and lower bound of the bending stiffness. One can see a significant reduction (55%) in the EI at the range of χ between 0 and 0.25 1/m. Note that the presented results are only applicable to single-strand bending. With an increased section size, the amount of the interwire movement might vary. It is recommended that further testing be performed on a multi-strand stay cable assembly to establish the correlation between the single and multi-strand bending response.

4 CONCLUSIONS

In this paper, the fretting fatigue behavior of pretensioned high-strength steel monostrands was investigated. A method, based on the DIC technique was used to quantify the relative movement between individual wires along the length of the monostrand.

The experimental data indicate that the interwire movement due to transverse deformations is the highest at the neutral axis of the monostrand. Moreover, the results show that the midspan and the anchorage of the monostrand are the two locations where the combination of tensile strains and the interwire movement is the most unfavorable.

The presented data show that the interwire movement increases with an increase of the tension load level in the monostrand. However, the difference of the interwire movement between 30% and 50% of UTS is relatively small.

Finally, the effective bending stiffness EI_{eff} of the monostrand was estimated from the numerical model showing the reduction in stiffness of 55% at the range of χ between 0 and 0.25 1/m.

REFERENCES

Gimsing, N. J. & Georgakis, C. T. 2012. *Cable Supported Bridges: Concept and Design*, 3rd edition, New Jersey: John Wiley & Sons, 544–547.

Gourmelon, J.P., Brevet, P. & Siegert, D. 1992. Failure mechanisms in rotating bending fatigue on 7-wire strands. *IABSE workshop, Madrid 1992: Length effect on fatigue of wires and strands*. Vol. 66, 251–258.

Hobbs, R. E. & Raoof, M. 1994. Mechanism of fretting fatigue in steel cables, *Int. J. Fatigue*, 16(4), 273–280.

Jensen, J.L., Bitsch, N. & Laursen, E. 2007. Fatigue Risk Assessment of Hangers on Great Belt Bridge, *Proc. 7th ISCD, Vienna, 10–13 December 2007.*

Papailiou, K.O. 1997. On the bending stiffness of transmission line conductors, *IEEE Transactions on Power Delivery*, 12(4), 1576–1588.

Raoof, M. 1991. Methods for analysing large spiral strands, *J. Strain Anal. Eng.*, 26(3), 165–174.

Rodríguez, G. & Olabarrieta, C. J. 2010. Fatigue testing with transverse displacements in stay cable systems, *Proc. 3rd fib International Congress, Washington, May 29–June 2 2010.*

Winkler, J., Fischer, G. & Georgakis, C.T. 2012, Localized bending fatigue behavior of high-strength steel monostrands, *Proc. 6th IABMAS, Stresa, 8–12 July 2012.*

Winkler, J., Fischer, G., Georgakis, C.T. & Kotas A. 2011. A preliminary bending fatigue spectrum for steel monostrand cables, *J. IASS*, 52(4), 249–255.

Wood, S. & Frank, K.H. 2010. Experimental investigation of bending fatigue response of grouted stay cables, *J. Bridge Eng.*, 15, 123–130.

10. Wind loading, robustness, progressive collapse, tall buildings

Research and Applications in Structural Engineering, Mechanics and Computation – Zingoni (Ed.)
© 2013 Taylor & Francis Group, London, ISBN 978-1-138-00061-2

Revised wind loading for linear and non-linear design of cooling towers

Hans-Jürgen Niemann
Ruhr-Universität Bochum, Department of Civil and Environmental Engineering, Bochum, Germany

Wolfgang Hubert
Niemann & Partner Consultants, Bochum, Germany

ABSTRACT: Natural draught cooling towers provide the most cost-effective technology for cooling the condenser circuit of thermal power plants. The tower is constructed as a reinforced concrete shell supported by a ring of columns. Wind effects dominate the structural safety regarding the reinforcement for tensile meridional and ring stresses, and for shell buckling. The wind pressures fluctuate randomly in time constituting a broadband stochastic excitation to the structure. Additionally, neighbouring buildings interfere with the flow, deforming the mean pressure distribution and providing additional turbulent energy to the excitation. For design calculations, various equivalent static loads have been adopted in the past. More recently, a method was developed to identify the momentary pressure distributions which generate the peak structural response for any leading structural response. The load identified in this manner is particularly useful for non-linear calculations of structural failure.

1 INTRODUCTION

Cooling towers provide the heat sink at the cold end of thermal power plants. Various cooling techniques are in use: The cooling airstream inside the tower is driven either artificially by a fan (forced draft), or by natural thermal updraft (Natural Draught Cooling Tower, NDCT) or by a combination of both (Hybrid Cooling Towers, HCT). NDCT cooling towers provide the most cost-effective technology because no additional power is required. The warm water coming from cooling the condenser is discharged into the water distribution of the cooling tower. The droplets falling down from the water distribution into the basin release the residual process heat via evaporation and convection to the ambient air. Warming up the air induces an updraft in the NDCT providing a continuous heat flow into the atmosphere. In this manner, cooling towers protect rivers or lakes, used otherwise for cooling, from overheating.

The NDCT is constructed as a reinforced concrete shell supported by a ring of columns. Ring beams at the lower and upper end of the shell stabilize its circular cross-section of the shell. Figure 1 shows the NDCT Tower Niederaussem in Germany designed in 1998. With this cooling tower, the enormous height of 200 m was reached for the first time. It is remarkable that the minimum wall thickness was not more than 22 cm. NDCTs even beyond 200 m are presently under construction in China.

The important actions are due to dead-weight, wind, temperature change, foundation settlements, and concrete shrinkage. Designing for the limit state of

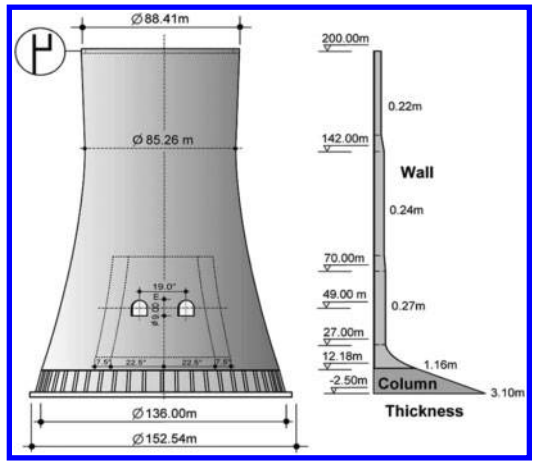


Figure 1. The 200 m Natural Draught Cooling Tower at the Power Plant Niederaussem, built from 1999 to 2001.

structural integrety, the combination of wind inducing tensile stresses plus dead-weight inducing compressive stresses is critical. In 1965, 3 NDCTs failed because of tensile failure of the vertical reinforcement in the lower part of the shells, during a "severe westerly wind". From the findings by the Committee of Inquiry (CEGB Report 1966), three main issues may be inferred:

(1) The maximum tensile membrane stress at the windward meridian, being the difference of two stresses nearly numerical equal, is very sensitive to wind uplift;

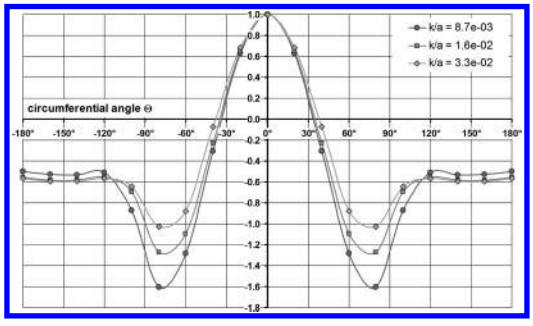


Figure 2. Pressure distribution around the circumference of a cooling tower model for different wind rib roughness.

(2) The wind pressures should be based on realistic pressure coefficients and an adequate gust wind speed;
(3) Sufficient structural safety cannot be achieved by a global safety factor but requires partial safety factors.

The collapse at Ferrybridge stimulated in the following years research efforts in areas such as shell theory and numerical calculation methods, material behaviour, structural safety, and – last not least – wind engineering.

2 THE NATURE OF THE WIND LOAD

Wind pressures act on the external and internal surfaces of the shell. They fluctuate randomly in space and time constituting a broadband stochastic excitation process. The mean of the process is defined as the average taken over 10 min. The fluctuations superimposed on the mean, are caused by the turbulence of the natural wind, and by vortices generated as the flow separates from the tower surface. Additionally, neighbouring buildings of comparable size interfere with the flow, deforming the distribution of the mean pressure on the tower surface and adding at the same time to the random excitation, eventually increasing the shell stresses.

Figure 2 shows a typical distribution of the variation of the mean external wind pressure at the circumference of a cooling tower model. The pressure, w_e is referred to the mean velocity pressure, q(z) at the same level.

At stagnation, the pressure is $w_e/q(z) = 1$. As the flow passes downstream along the contour, the flow velocity increases to a maximum and the pressure drops to a minimum. Behind it, the pressure rises again and, accordingly, the flow in the boundary layer is decelerated gradually until the velocity reaches zero. At this stage, the flow separates from the tower surface. The two separation points at each side mark the beginning of the wake behind the cylinder. The pressure rise which can be attained depends on surface roughness: when the surface is rough, the pressure rise is low as well as the magnitude of the pressure minimum.

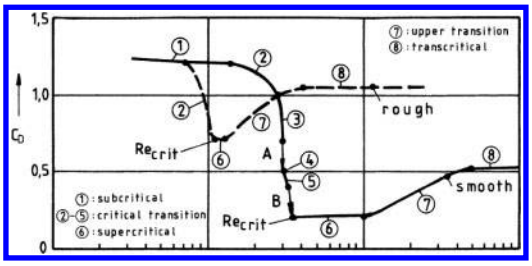


Figure 3. The flow regimes of circular cylinders with smooth and rough surface.

The total wind force resulting from this pressure distribution is however high. In both regards the opposite applies to a smooth surface. On the other hand, the wind uplift, i.e. the maximum of the tensile meridional force at stagnation, is more or less proportional to the modulus of the pressure minimum. Therefore, high surface roughness reduces the meridional stresses in the shell, although it goes along with a high total wind force. This is due to the specific load carrying behaviour of the shell structure (Niemann et al. 1972). For this reason, the majority of NDCTs in Germany is equipped with wind ribs.

Reynolds number Re, the surface roughness, the aspect ratio defined by (total height H)/(mean diameter d_m), and the profile of the wind flow are the dominating parameters for the pressure distribution. Turbulence scale and intensity are less important for the features of the mean flow.

Most of what we know about the flow around cooling towers is owed to research on the flow around circular cylinders performed in wind tunnel experiments (Fage, Warsap 1930; Roshko 1961, Schewe 1983, Wieselsberger 1921). The experiments have demonstrated the strong effect of Reynolds number on the flow regimes. Figure 3 depicts this effect on the dragforce coefficient, c_D of a circular cylinder. The drag varies considerably at Re-numbers up to 10ˆ6; it becomes independent of Re in the transcritical range. If the surface is rough, the critical pressure drop is less pronounced and the flow reaches the transcritical range at lower Re. One important result from Figure 3 is that at transcritical Reynolds numbers, the effect of Re on flow separation and subsequently on the pressure minimum has vanished. However, the effect of surface roughness – by wind ribs or distributed sand grain roughness – is still present.

At design wind speeds, the Reynolds number of high cooling towers, e.g. the NDCT Niederaussem is typically $Re_{full-scale} = 40 \cdot 98/15 \cdot 10\text{-}6 = 3 \cdot 10\text{ˆ}8$. For a smooth surface, it is beyond the range of wind tunnel experiments. This so-called Reynolds number disparity between the wind tunnel experiment and the full-scale flow was at that time a major source of ambiguity and posed one of the challenges encountered in determining the wind load for cooling towers. It was overcome by pressure measurements at full scale towers which were performed mainly in Germany, France, USA, and China. Figure 4 shows the effect of surface

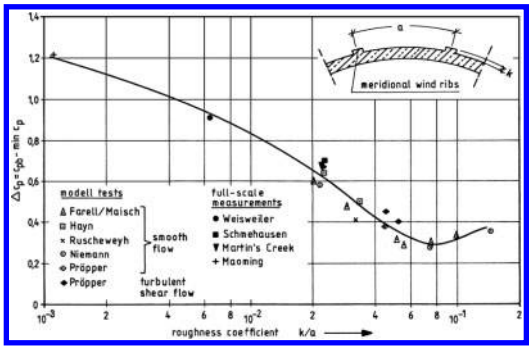


Figure 4. Influence of surface roughness on the pressure rise coefficient at transcritical Reynolds numbers.

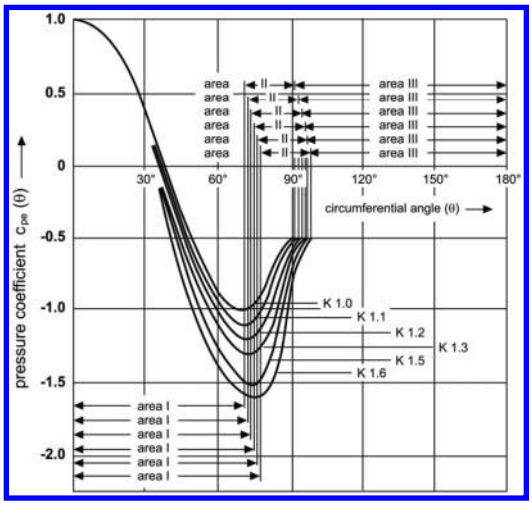


Figure 5. Pressure distributions for design of NDCTs in the VGB guideline BTR 2010 for Structural Engineering of Cooling Towers (VGB-R 610 2010).

roughness by wind ribs on the coefficient for the pressure rise from the minimum to the wake pressure at transcritical Re.

This result permitted to introduce realistic pressure distributions considering surfaces with and without wind ribs. They are applied as the basis of equivalent static wind loads for design. Figure 5 shows the regulation adopted in (VGB-R 610 2010).

A further result was that the transcritical full-scale pressure distribution can be simulated at much lower wind tunnel Reynolds numbers by increasing the surface roughness of the wind tunnel model.

3 WIND LOAD FOR DESIGN

3.1 *The gust response factor approach – equivalent static wind pressures for cooling towers*

In the detailed design calculations, the effect of the randomly fluctuating part of the wind pressures is in general taken into account by a static load. It is equivalent in the sense that its effect equals the real, most adverse gust load effect on the leading internal forces. It goes back to A.G. Davenport's gust response factor concept, in which the equivalent wind force F_w is based on the mean wind force, F_{wm}, amplified according to the effect of the fluctuating load component by the gust response factor G (Davenport 1967).

$$F_w = G \cdot c_f \cdot A \cdot q_{m_m} \tag{1}$$

in which c_f = aerodynamic force coefficient; A = loaded area; q_m = mean velocity pressure of the undisturbed flow. For NDCTs, the design calculations can only be based on wind pressures, not on resulting wind forces. The equivalent static wind load is given for external and internal pressures, w_e and w_i by (VGB-R 610 2010)

$$w_e(z,\theta) = c_{pe}(\theta) \cdot \varphi \cdot F_I \cdot q_p(z) \tag{2}$$

$$w_i = c_{pi} \cdot F_I \cdot q_p(H) \tag{3}$$

in which z – height above ground; Θ – peripheral angle; c_{pe}, c_{pi} – pressure coefficients at the external and internal shell surface; φ – dynamic response amplification due to resonance to turbulence; F_I – response amplification by flow interference with neighbouring buildings or structures; q_p – peak velocity pressure; H – tower height. In Equation 2, the external pressure at height z is proportional to the velocity pressure at the same height whereas the pressure coefficients c_{pe} are independent of z. The internal pressures, Equation 3, are constant over periphery and height; they are dominated by the velocity pressure at the tower top, q_p(H). Their contribution to resonant stress amplification is negligible.

In this formulation, the increase of the internal forces caused by the pressure fluctuations is included in the peak velocity pressure, q_p. The pressure coefficients are those of the mean pressures, s. Figure 5; they do not reflect peak pressures. The peak velocity pressure, q_p is derived from the gust response factor of a leading response. Since the resonant effect of the pressure fluctuations is small, it is allowed for separately by the dynamic factor, φ which is the ratio of total to the quasi-static gust response factors:

$$\varphi = {}^{G}/_{G_Q} \tag{4}$$

Then, merely the quasi-static gust response has to be calculated, and the co-variance method can be utilized (Niemann et al. 1996). The most important wind load effect is the meridional tension max n_{xx} at stagnation, where $\Theta = 0°$. It is rather constant in the lower third of the shell height. In this region maximum reinforcement is necessary. The peak velocity pressure is therefore derived from the gust response factor of n_{xx}. In this context, a simplified consideration may be applied for relating the meridional tensile force to the velocity pressure: (1) n_{xx} is proportional to the wind

Table 1. Gust wind profile parameters for NDCTs.

Tower Height	α	G_Q	α'	$q_p(10)/q_m(10)$
flat, open terrain with low vegetation, category II, roughness length 0.05 m				
120 m	0.16	1.831	0.110	2.25
200 m		1.766		
flat terrain without obstacles, category I, roughness length 0.01 m				
120 m	0.12	1.707	0.085	1.93
200 m		1.643		

force moment; (2) the diameter d and the aerodynamic force coefficient c_f are constant over the tower height. Then

$$G_Q = \frac{\int_0^H c_f \cdot d \cdot q_p(z) \cdot z \cdot dz}{\int_0^H c_f \cdot d \cdot q_m(z) \cdot z \cdot dz} \tag{5}$$

The profiles of the mean and peak velocity pressure are

$$q_m(z) = q_m(10) \cdot \left(\frac{z}{10}\right)^{2\alpha} \tag{6}$$

$$q_p(z) = q_p(10) \cdot \left(\frac{z}{10}\right)^{2\alpha'} \tag{7}$$

The exponent, α of the mean wind profile is well documented and defined in codes. The exponent, α' of the peak wind profile is smaller than α. It reflects a gust wind profile and depends on the gust averaging time. The values of α' are chosen for NDCTs as depicted in Table 1. The peak and mean values of the wind force moment are calculated from Equation 5, resulting for given G_Q in the ratio q_p/q_m. This factor is finally introduced in Equation 7.

The advantage of deriving the equivalent static load in this manner is that it is applicable to all customary tower dimensions. However, in addition to the design for tensile meridional stresses, more requirements have to be met such as sufficient hoop reinforcement, or sufficient wall thickness for the buckling safety of the shell. One equivalent static load may not cover all important stresses in all structural parts of the tower. In particular, the peaks of the tensile hoop force and of bending are sometimes underestimated. The internal pressure w_i produces circumferential compression, superimposed on the tension due to external pressure and reduces hoop tension. Therefore, two wind load cases have to be considered namely w_e and $(w_e + w_i)$ whichever is more harmful.

3.2 *Most adverse, momentary pressure distributions – the LRC-method*

A more precise wind load may become necessary, e.g. when the load-bearing capacity of an existing tower has to be investigated, or when strong interference has to be considered. For this task, an alternate approach consists of identifying, out of the randomly fluctuating wind pressures at the loaded surface, an extreme wind load distribution which produces the worst load effect (Kasperski 1988). Considering a wind load effect S, the peak can be written as a superposition of the mean, S_m, with the rms response, σ_S, amplified by the peak factor k_{Sp}:

$$S_p = S_m + k_{Sp} \cdot \sigma_S \tag{8}$$

The mean wind pressures for calculating the mean response are

$$w_m(z, \theta) = c_p(\theta) \cdot q_m(z) \tag{9}$$

The rms response is obtained by loading the structure with the rms-pressures. However, the effect of the pressure at a loading point depends on the correlation between pressure and response fluctuations. It can be shown that the weighting factor is exactly the correlation coefficient ρ_{pS} between the pressure and the response considered. The load has been termed LRC load since it is based on the **L**oad **R**esponse **C**orrelation. The gust load distribution for calculating the rms response σ_S is then (Niemann 1998, also the following Equations 10 to 12)

$$\Delta w(z, \theta) = \sigma_p(z, \theta) \cdot \rho_{pS}(z, \theta) \tag{10}$$

The LRC can be obtained by calculation when the vector of the mechanical influence coefficients, a, are known and the covariance matrix of the pressures, Cov(p) has been measured in a wind tunnel test. The response variance is then

$$\sigma_S^2 = \underline{a} \cdot \underline{Cov(p)} \cdot \underline{a}^T \tag{11}$$

where T indicates a transposed vector. The load response correlation required in Equation 10 is

$$\underline{\rho_{pS}} = \frac{1}{\sigma_S} \cdot \underline{a} \cdot \underline{diag(\sigma_p)} \cdot \underline{\rho_p^T} \tag{12}$$

An alternative is to measure the LR correlations in wind tunnel tests. For load-response-correlation tests, an elastic model is needed for measuring the response, e.g. in terms of strains. This method has been developed and frequently used for identifying interference factors. Figure 6 shows a cooling tower model for measuring strains and pressures simultaneously.

Pressure distributions for the isolated 200 m tower are depicted in Figure 7. The pressure coefficients at the 130 m level are normalized by the mean velocity pressure at that level. Three pressure distributions are considered: The mean pressures have a typical distribution with a maximum coefficient of 1 at stagnation, −1.4 at the minimum and −0.5 in the wake. The equivalent gust wind pressures are greater at this level by a constant factor of 1.9. The LRC-load has a higher value at stagnation and lesser values in the suction region. The meridional internal force n_{xx} at stagnation due to the LRC-load is 5% smaller than calculated with the equivalent static load according to the BTR.



Figure 6. Elastic wind tunnel model for Load Response Correlation tests.

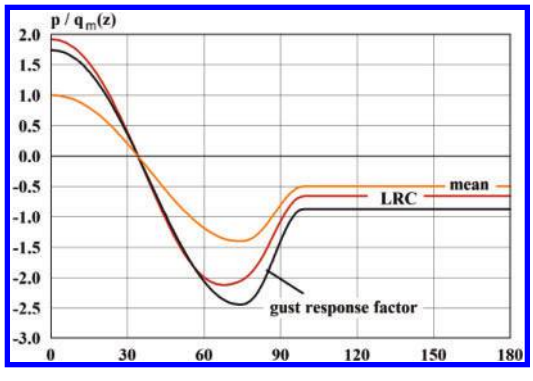


Figure 7. Comparison of external pressures p/q_m at a 200 m NDCT at the 130 m level.

4 APPLICATION TO INTERFERENCE EFFECTS

An example is presented of an NDCT in a strong interference situation where the extreme wind load effects are evaluated on the basis of most adverse, momentary pressures distributions. The LRC load is obtained by calculation. Measurements of time histories of wind pressures were conducted in the Boundary Layer Wind Tunnel at the Ruhr University Bochum. Mechanical influence coefficients relating a structural response to the surface pressures are derived from an FE model of the cooling tower.

The cooling tower is relatively slender having an aspect ratio of about 1.9. The roughness of the exterior shell surface, originating from formwork ribs and additional wind ribs, is classified by the pressure distribution curve K1.1 (Fig. 5).

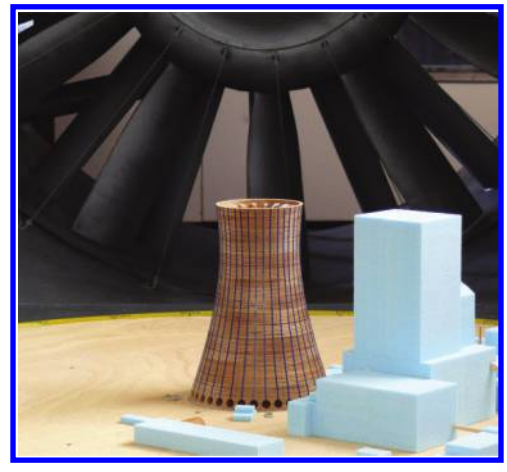


Figure 8. Wind tunnel model of a cooling tower in a strong interference situation.

A rigid pressure model was made at a scale of 1:400. It is equipped with 118 pressure tabs in total which are arranged in 5 sections with 18 pressure tabs for measuring the highly varying external pressures and several additional pressure tabs for measuring internal pressures simultaneously. Figure 8 shows the wind tunnel model of the NDCT with neighboring buildings. As it can be seen the boiler house and the cooling tower are of same height and in a very close configuration.

In order to evaluate the correlation coefficient ρ_{pS} between the pressure and the response considered the measured wind pressures have to be extended to the grid of the FE model. For this first step in the subsequent calculations a special interpolation and approximation scheme is used and the plausibility of the interpolation is controlled.

Based on such time histories of surface pressure distributions the evaluation of the load response correlations (Eqns. 11–12) and generation of most adverse pressure distributions from the mean and the gust wind load distribution is practicable. Measurements and subsequent calculations are done for the isolated cooling tower as well as for the interference configuration (Fig. 8). To identify decisive interference situations the wind rose is investigated in a step size of 10 degree.

Influence coefficients are provided for the shell forces. For each reaction force in each element an LRC wind load is generated for the upper and lower extreme value as well as for the two wind load cases w_e and $(w_e + w_i)$ and the corresponding force value is calculated. In case of a symmetric reinforcement the extreme values around the circumference in a particular height are of interest.

For the isolated tower the maximum meridional tensile force is identified at stagnation ($\Theta = 0°$) in a height $z/H = 0.38$ due to the net wind load. The corresponding LRC load is shown in Figure 9. The peak velocity

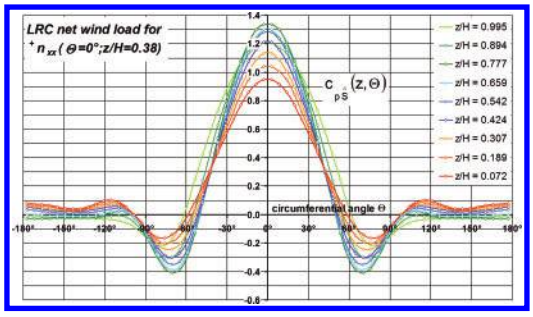


Figure 9. LRC wind load inducing the maximum meridional tensile force for the isolated tower: ${}^{+}n_{xx}(\Theta = 0°; z/H = 0.38)$.

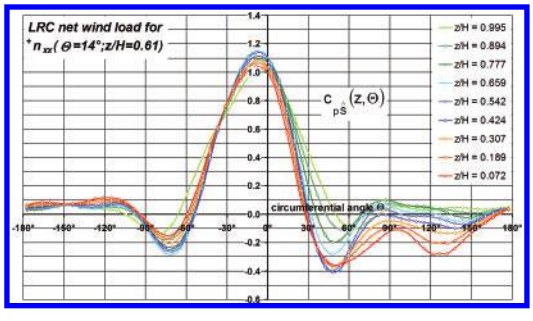


Figure 10. LRC wind load inducing the maximum meridional tensile force due to interference: ${}^{+}n_{xx}(\Theta = 14°; z/H = 0.61)$.

pressure at tower height H is used as reference leading to a varying pressure coefficient at stagnation in contrast to the formulation used in the VGB guideline (Eqn. 2, Fig. 2).

Analyzing interference effects the maximum meridional tensile force is found for a wind direction resembled in Figure 8. In contrast to the isolated case it occurs not at the circumferential angle equal to the wind direction ($\Theta = 0°$) but is shifted slightly to the left side. Beyond that it is also shifted to an upper part of the shell, $z/H = 0.61$. This is an important fact because the beneficial effect of the dead weight is decreased. The corresponding LRC load is shown in Figure 10.

With this example it could be shown that the LRC wind loads can be derived from measured pressure time histories. Time and effort for the wind tunnel tests, the determination of the mechanical influence coefficients and last but not least the calculations to generate the LRC wind loads are bearable for practical application. The wind load inducing extreme effects in the shell is determined more realistic and therefore also more suitable especially for nonlinear stress calculations.

ACKNOWLEDGEMENT

The wind tunnel tests were accomplished in the Boundary Layer Wind Tunnel Laboratory at the Ruhr University Bochum, Prof. Dr.-Ing. R. Hoeffer. The mechanical influence factors have been provided for this study by ZERNA Planen & Pruefen GmbH, Bochum. The collaboration with both partners is gratefully acknowledged.

REFERENCES

Central Electricity Generating Board 1966. *Report of the Committee of Inquiry into Collapse of Cooling Towers at Ferrybridge*, 1 November, 1965.

Davenport, A.G. 1967. Gust Loading Factors. *Journal of the Structural Division, ASCE* 93: 11–34.

Fage, A.; Warsap, J.H. 1930. The effect of turbulence and surface roughness on the drag of a circular cylinder. *Reports & Memoranda No. 1283*. London: ARC.

Kasperski, M. 1988. Identifikation bemessungskritischer Lastanteile aus stochastischen Prozessen am Beispiel der Naturzugkühltürme unter Windbelastung (Identification of critical load distributions for wind loading). *Technisch-wissenschaftliche Mitteilungen Nr.88-6*. Ruhr-Universität Bochum: Inst. f. Konstruktiven Ingenieurbau.

Niemann, H.-J.; Peter, H. L.; Zerna, W. 1972. Naturzugkühltürme im Wind – Der Einfluß der Oberflächenrauhigkeit auf die Beanspruchung des Schalentragwerkes (Effect of surface roughness on the wind-induced shell stresses of NDCTs). *Beton- und Stahlbetonbau* 67(6): 121–129.

Niemann H.-J.; Flaga A.; Höffer R.; Hölscher, N.; Kasperski M. 1996. Structural response to wind loads. In W.B. Krätzig & H.-J. Niemann (eds), *Dynamics of Civil Engineering Structures*: 245–280. Rotterdam: Balkema.

Niemann, H.-J. 1998. Wind load modelling in the analysis of very high cooling towers. In J.D. Riera & A.G. Davenport (eds), *Wind Effects on Buildings and Structures*: 201-208. Rotterdam: Balkema.

Roshko, A. 1961. Experiments on the flow past a circular cylinder at very high Reynolds number. *Fluid Mechanics* 10: 345–356.

Schewe, G. 1983. On the force fluctuations acting on a circular cylinder in cross-flow from subcritical to transcritical Reynolds numbers. *Fluid Mechanics* 133: 265–285.

VGB-R 610 2010. *Structural Design of Cooling Towers*. Essen: VGB Power Tech e.V.

Wieselsberger, C. 1921. Neuere Feststellungen über die Gesetze des Flüssigkeits- und Luftwiderstands. *Physikalische Zeitschrift* 22: 321–328.

Research and Applications in Structural Engineering, Mechanics and Computation – Zingoni (Ed.)
© 2013 Taylor & Francis Group, London, ISBN 978-1-138-00061-2

Wind-tunnel investigations of pressure distribution over high-rise buildings

M. Cwik & M.A. Gizejowski
Warsaw University of Technology, Warsaw, Poland

A.M. Goliger
Council for Scientific and Industrial Research, Pretoria, South Africa

ABSTRACT: This paper deals with the wind-tunnel investigations of high-rise buildings. In the first part, an overview of the developments in model testing, as well as the future trends, have been discussed. Particular emphasis has been placed on methods of evaluating wind loads of high-rise structures. The second part provides a description of the research, conducted at the wind-tunnel of the Council for Scientific and Industrial Research, in Pretoria, South Africa. The aim of this research was to determine pressure distribution over the façade of 208 m high Warsaw Trade Tower building. Wind tunnel tests were a part of a wider research project which also includes full-scale measurements and numerical simulations (CFD, FEM), in order to examine the possibility of application of wind action simulations in structural health assessment of high-rise buildings. An overview of this research project and expected results are described in the third part.

1 INTRODUCTION

A realistic determination of environmental effects is essential to ensure an economic and safe design of structures. Within these effects, wind and seismic actions constitute the most critical aspect of the design of high-rise buildings.

Methods of evaluating wind loads of specific structures can be grouped into: 1) full-scale measurements; 2) model tests (BLWT – boundary-layer wind-tunnel tests) and 3) numerical simulations (CFD – computational fluid dynamics).

Generally full-scale measurements provide the most reliable results. Nevertheless, costs of research and difficulties in implementation, to infinite variety of situations, are high in comparison with other methods.

Despite of tremendous development and great potential of numerical simulations, there are still many issues which foreclose harnessing of this method without validating the results with one of the other methods.

It seems that for now the boundary-layer wind-tunnel tests are most suitable for the evaluation of wind actions on structures.

2 OVERVIEW OF BLWT TESTING

2.1 *Background*

Baker (2007) suggested a categorization of the history of wind engineering into five periods, namely: 1) traditional (up to 1750); 2) empirical (1750–1900); 3) establishment (1900–1960); 4) growth (1960–1980) and 5) modern (1980-present).

These periods, related originally to the entire discipline of wind engineering aptly fit to history of model testing. In the following section only the modern period will be described briefly, in terms of the developments in the boundary-layer wind-tunnel testing.

2.2 *Recent developments*

Most developments in the wind-tunnel testing of high-rise buildings took place in the last 30 years. The main reason for that was the significant progress in measuring technology. Efforts of scientists began in 1970s, led in 1980s to the development of high frequency base balance (H-FBB) (Tschanz & Davenport 1983). This method is used primarily for high-rise buildings tests. Next milestone was the development of synchronous multi-channel pressure sensors (SM-PSS) at the turn of the 1980s and 1990s (Cermak 2003). Both of these technologies are widely implemented till present. In the meantime researches on aeroelastic wind-tunnel testing of high-rise buildings were conducted. During this period a number of advanced and increasingly larger BLWTs have been designed and constructed.

Developments in the wind-tunnel testing during this period, enhanced significantly the height limits of buildings. BLWTs became fundamental tools for designing the high-rise buildings. The importance and impact of wind-tunnel investigations of high-rise buildings are best illustrated by a quote of the structural engineer of Burj Dubai, Bill Baker (Skidmore, Owings & Merrill): "In the old days, wind tunnels

were for confirmation of forces, not to tell you what the building would look like. We virtually designed [the tower] in a wind tunnel," (ENR 2006).

On the other hand there is an ongoing scientific debate regarding the inability of evaluating extreme pressures for very small areas by using wind-tunnel technology.

2.3 *Future*

Modern buildings become taller and wind effects, related to their shape, become critical design aspect. This brings designers closer to the wind-tunnels, where using the iteration process, building's shape can be optimized. It seems that this trend will prevail in the future.

Another noticeable tendency is the design and construction of increasingly larger BLWT. For instance in 2008 in Southwest Jiaotong University a BLWT with a test section of 22.5 m wide, 36 m long and 4.5 m high was put into use (Li et al. 2009).

Noticeable is also the supporting role of the wind-tunnel testing in development of the computational fluid dynamics (CFD) simulations. Recent developments in the CFD methods enable to combine them with wind-tunnel tests and validate results obtained using both methods.

Nevertheless, despite of the increasing role of CFD simulations and due to economic limitations of full-scale measurements, wind-tunnel testing remains the essential tool in predicting wind effects on high-rise buildings.

3 WIND-TUNNEL TESTS OF WARSAW TRADE TOWER

3.1 *Aim and scope of the research*

The aim of the research was to evaluate average pressure distribution over the façade of a Warsaw Trade Tower building under certain wind conditions. Warsaw Trade Tower (WTT), formerly Daewoo Center, building which is 208 m high (184 m excluding the spire) is currently the third tallest building in Poland (Fig. 1). It is used mainly for commercial offices purpose. The building was constructed during 1997–1999. The structure consists of a covered exterior steel framed tube lateral system and an interior reinforced-concrete core. It is 52 × 27 m in plan. The shape of the building reminds semi-cylinder with flat western façade and with cuboids intersecting the curved rest of the façade. The building is located in the northwest part of city centre. The nearest surroundings are 9% built-up, with buildings exceeding 15 m. The analyzed area can be characterized as a terrain between category III and IV, according to PN-EN 1991-1-4.

The scope of the study included determination of wind pressure values at 117 measuring points distributed over all façades of the model. Measurements covered the full range of wind azimuths. Research has been conducted at a Boundary-Layer Wind-Tunnel (BLWT) located at the Council for Scientific and



Figure 1. Warsaw Trade Tower (WTT) building.



Figure 2. CSIR boundary-layer wind-tunnel.

Industrial Research (CSIR), in Pretoria, South Africa (Fig. 2).

3.2 *BLWT at CSIR*

CSIR's boundary-layer wind-tunnel was established in the early 1980s. Since then several improvements were

introduced to the instrumentation and the data acquisition system. Modern instrumentation includes, among others, new pressure measuring system.

CSIR's BLWT is an open-circuit type with a boundary-layer development length of 18 m and a cross-section of 2 m by 1 m with a turntable of 1.8 m diameter. Wind-tunnel is equipped with a single centrifugal fan powered by a thyristor-controlled 75 kW variable-speed motor which allows obtaining variable air speeds of up to 22 m/s. The inlet area consists of 50 mm tripping wall and four 250 mm high × 100 mm wide triangular spires.

SM-PSS system, used for pressure measurements, is based on the RAD3200 system manufactured by Scanivalve Corp. It allows to measure, at the same instance of time, pressure at 32 points with a frequency of reading the same transducer of 625 Hz. 1-dimensional hot-wire anemometers are used to measure flow speed. Reference dynamic pressure is obtained from a pressure transducer connected to a pitot-tube which is attached at height of 740 mm above centre of the turntable. Reference static pressure is obtained from the pressure tapping in the roof above the model, slightly at the back. Analogue readings are converted into digital format and transferred to the computer measuring system. Software based on Scanivalve's RAD, and adopted for boundary-layer wind-tunnel tests, is responsible for archiving and post-processing of the data.

3.3 *Model*

The building model and its immediate surroundings were constructed at a geometric scale of 1:500. WTT model was about 40 cm height with a cross-section of 10 × 6 cm. It was divided into 11 horizontal measuring sections and one additional point located centrally at the horizontal surface of the roof. Each of 11 levels included from 7 up to 12 measuring points. In total pressure readings were carried out in 117 points located over the external surfaces of the model. After conducting measurements it was found that, due to the technical problems, data corresponding to point 2 at level 10 and points 5 and 6 at level 11 for all azimuths became corrupt and has been excluded from further analysis. Consequently from the initial 117, only 114 points were taken into account.

The surrounding model contained an area of the city within a radius of 450 m around the WTT building. Model included all the objects higher than 3 m. The overall number of structures in the analyzed area exceeded 250. In accordance to the terrain elevation measurements it was assumed that the area has a constant altitude.

3.4 *Testing*

Initially, measurements of the horizontal wind profile were conducted. Wind speed profile was measured in front of the wind-tunnel turn table. Readings have been taken for full-range of heights with a step of 25 mm,

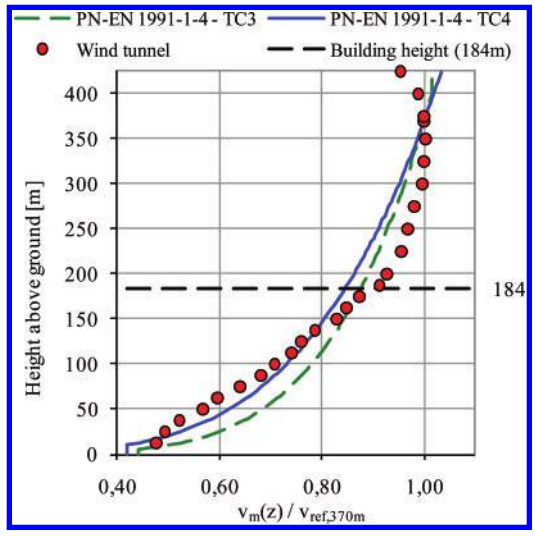


Figure 3. Comparison of wind speed profiles from tunnel tests and PN-EN 1991-1-4:2008 for TC III and IV.

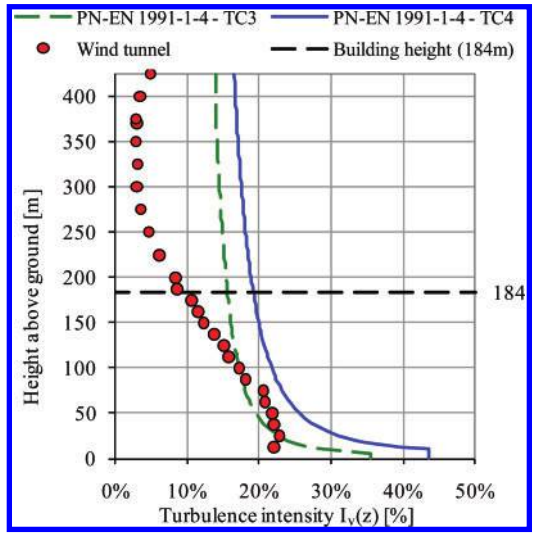


Figure 4. Comparison of turbulence intensity profiles from tunnel tests and PN-EN 1991-1-4:2008 for TC III and IV.

between 25 and 400 mm and a step of 50 mm from 450 up to 850 mm. Additional measurements were taken for the height of 740 mm which corresponds to the position of the pitot-tube. Each measurement cycle consisted of 24576 readings at a frequency of 625 Hz.

A comparison between the results and the power-law wind speed profiles as well as the logarithmic turbulence intensity profiles, corresponding to terrain categories III and IV from National Annex and code PN-EN 1991-1-4:2008, is shown in Figures 3, 4.

It can be noted that the wind speed profiles obtained in the wind-tunnel tests are fairly similar to those stipulated in the design codes. Below 100 m the wind-tunnel flow is slightly lower. Above that level, the speed is

increasing and is slightly higher than the code profile. Turbulence intensity profile in lower parts up to 125 m shows good fit. Differences between profiles increase with height.

Subsequently, pressure measurements for a full range of wind azimuths, with basic step of 20° have been carried out. Additionally, having considered the most frequent wind directions in Warsaw, for the azimuths between 250° and 290° a step of 5° has been applied. Consequently, measurements included 25 wind directions.

Each measuring cycle, for a specific level and wind azimuth, consisted of 24576 readings at a frequency of 625 Hz. The mean wind speed at a height of 740 mm was of 11.9 m/s. Assuming the full-scale wind speed derived from PN-EN 1991-1-4:2008, for terrain category III at height of 370 m, equal to 35 m/s, the wind speed scale was equal to 1:2.9. Taking into account the geometric scale of 1:500 and wind speed scale of about 1:2.9, the time scale was equal to about 1:170. Therefore the tunnel sampling frequency of 625 Hz corresponds to 3.68 Hz at full scale, so each of 39.3 seconds cycle corresponds to 111.4 minutes sampled at a time interval of 0.272 seconds. All statistical calculations have been performed using a program developed by the authors in Visual Basic for Applications in Excel. Before carrying out statistical calculations, filtering of electrical spikes and removing of influence of standing wave have been performed.

Finally, measurements of the wind speed at a location corresponding to the position of the weather station in the full-scale, were carried out. These were carried out for 35 wind directions. (The weather station in full-scale measurements was located in 1/3 distance between the lowest and the highest point of the upper edge of western façade 2 m, above interior edge of the parapet wall of the roof at height of 181.5 m above ground.) These measurements were done in order to the correlation of the results obtained in wind-tunnel tests, CFD simulations and full-scale measurements.

3.5 *Results*

The variations of wind speed and turbulence intensity, at a location corresponding to the weather station, are shown in Figure 5. Wind speed ratio was calculated as a ratio of wind speed at weather station to the undisturbed wind speed measured for the same height in the horizontal profile measurements. The wind speed ratio varies from 0.22 to 0.94. The results indicate a significant decrease of wind speed at weather station localization for wind azimuth from 220° up to 320° with minimum for 260° which correspond to wind direction perpendicular to western façade equal to 256°. Two peaks for azimuth 200° and 330° which corresponds to wind direction of 60° and 70° for western façade can be observed. Clear decrease of wind speed and increase of turbulence intensity related to deflection of wind direction from western façade are observed for wind azimuth from 0° up to 180°.

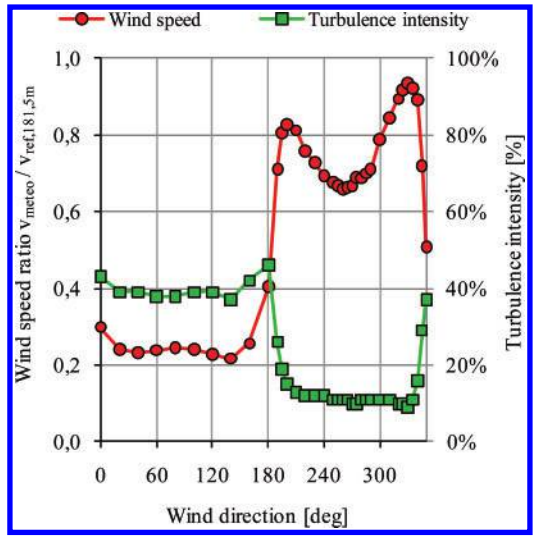


Figure 5. Variation of wind speed and turbulence intensity at weather station localization with wind azimuth.

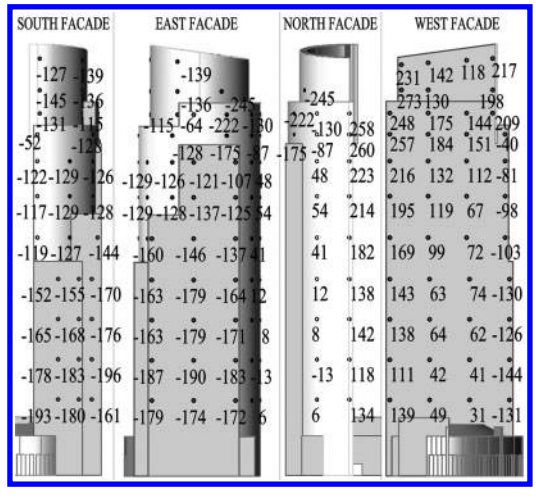


Figure 6. Average wind pressure over WTT facades.

Average values of the external pressure over building façade, shown in Figure 6, were calculated for wind speed of 24.2 m/s at height of 181.5 m (363 mm in model scale) and direction of 320°. All results are given in Pa. Wind speed and direction correspond to results obtained in full-scale measurements.

The average wind pressure varies between −245 and 273 Pa. Positive pressures occur for the most of the western and northern facades. For southern and eastern facades as well as for southern vertical edge of western façade and upper parts of the northern façade negative pressure values are observed. Lowest negative values were recorded in the upper parts of the northern façade. Highest positive values are observed at upper parts of the edge of western and northern facades. Average value of pressure at the roof is of 150 Pa.

The validation of the pressure values and wind speeds corresponding to the location of the weather station, using CFD simulations was carried out by Sitek et al. (2013). Both sets of the results indicate a fair degree of convergence.

4 STRUCTURAL HEALTH ASSESSMENT

Most of the high-rise buildings are designed to fulfill their function between 50 to 100 years or even more. At all time structures should remain safe, serviceable and durable. Obviously it is impossible to fulfill these requirements without appropriate maintenance. Apart of the standard maintenance activities it is necessary to undertake periodic inspections of structures. In Poland such compulsory inspections have to be carried out every 5 years and each time after the occurrence of an extreme action. Inspections should provide information on the condition of the building and answer the question whether the building is safe to further use or not.

Due to the possibility of fatigue, corrosion as well as the deterioration caused by other phenomena – comprehensive inspections require access to all components of a structure. These activities introduce interruptions in the utilization of various areas of the building. This will have financial implications, particularly in the case of high-rise buildings used for commercial purposes (e.g. removal of finishing elements and reconstruction, compensations for stoppages etc). Furthermore, among the others disadvantages, such inspections are time-consuming and sometimes introduce significant technical challenges.

These problems may result in limiting or adjusting the scope of inspections to suit the needs of specific buildings and their occupants. This situation can be considered as inappropriate and requiring the development of relevant solutions. The need for a quick, reliable, non-disruptive and inexpensive testing method is apparent.

One has to consider that it is almost impossible to access and evaluate every part of a structure. The principle of the proposed solution is not to examine the structure itself but rather to examine and analyze its response to a known loading. A comparison of the theoretical and measured responses would then constitute the indicator of structural condition. The above discussion suggests a solution in terms of a Structural Health Monitoring (SHM) system, which currently many of the high-rise buildings are being equipped with. General principles of SHM are based on three steps: continues measurements of the structure's behavior and environmental effects, analyses of the data which is obtained, and alerting when results extend beyond assumptions. The SHM appears to be a sufficient solution to evaluate the condition of a building. However, the cost of assembly and maintenance of such systems is relatively high and even more costly for existing buildings. In most cases, there are no reasons for conducting continues measurements for each and every high-rise building.

Proposed solution is not intended to replace the standard inspection process. The objective is to periodically evaluate general condition of a high-rise building and to evaluate the possible need of performing the comprehensive inspection. Structural health assessment can be described in 5 steps as follows.

Step 1. Full-scale measurements. Evaluation of the physical displacement of a structure using global navigation satellite system (GNSS) devices mounted on a building's roof. Simultaneously measurements of wind speed, direction and other meteorological quantities using weather station also mounted on building's roof. The results will represent the physical response of the structure subjected to specific wind loads.

Step 2. Wind-tunnel tests. Evaluation of pressure distribution over the building façade. Test conditions and calculations should correspond to those obtained in the full-scale measurements. The results would provide information on wind loading at specific points, which resulted in building's response, as measured in full-scale.

Step 3. CFD simulations. Evaluation of pressure distribution over the entire building's façade. Simulation conditions should correspond to those obtained in full-scale and wind-tunnel tests. Validation of the results to be carried out using the wind-tunnel data. The results will represent the estimation of a wind loading, over the entire building's façade, which resulted in the response, as measured in full-scale.

Step 4. FEM calculations. Evaluation of theoretical displacement of the structure caused by wind loads obtained in CFD simulations. The result would represent the theoretical response of the structure subjected to wind loads, which correspond to those observed in full-scale measurements.

Step 5. Analysis of the results. Comparison of theoretical (derived from FEM) and physical (measured in full-scale) displacements of the structure.

Similar approach was proposed by Chmielewski et al. (2009) who presented results of comparison of theoretical and measured response of the Stuttgart TV Tower. The assumption of the research was that the changes in the first natural frequency may indicate potential damage of the tower. The difference between methods is that Chmielewski et al. (2009) compared natural frequencies. Proposed method is based on comparison of displacements which is considered to be a more suitable approach in reference to high-rise buildings.

Authors expect to obtain a fair degree of similarity in theoretical and physical displacements of high-rise buildings which are in a good structural condition, and clear differences for buildings with structural deficiencies.

Clear advantages of the proposed structural health assessment system are: the non-destructive and non-disruptive testing, relatively low costs and ease of implementation. The biggest problem lies in the dependence on the weather, i.e. the required magnitude of wind loading which will introduce considerable displacement of the building. Nevertheless, reliable

system of measuring displacements of high-rise structures, subjected to low magnitude winds, using GNSS technology was presented by Breuer et al. (2002).

The wind-tunnel investigation of WTT building, presented in the current paper, forms a part of the research project to examine the possibility of application of the structural health assessment process.

5 CONCLUSIONS

The paper provides a brief historical outline of the developments as well as the future trends in wind-tunnel investigations of high-rise buildings.

The process of evaluating the mean wind pressures over the façade of a high-rise building (Warsaw Trade Tower), with the use of boundary-layer wind-tunnel technology, is presented. Wind-tunnel located at the CSIR in Pretoria, South Africa, which was used in the current research, is described. Comparisons of wind speed and turbulence intensity profiles measured in the wind-tunnel and those derived from Eurocodes are discussed. Results of the mean values of wind pressure over the building façade as well as the wind speed and turbulence intensity at the roof of the building are presented and discussed.

An overview of the research project, related to the use of wind engineering technology, as a tool to identify potential structural deterioration of high-rise buildings, is described. Assumptions of the proposed method are based on a comparison of theoretical and physical displacements of structures. The method involves the use of: wind-tunnel testing, CFD simulations, FEM calculations and full-scale measurements (including particular use of GNSS measurements). The expected results are also described.

ACKNOWLEDGEMENT

This paper is a review of the wind-tunnel tests, undertaken at the advanced stage of a PhD research study of the first co-author carried out at the WUT and CSIR. Part of the research, related to the wind-tunnel testing, has been carried out at CSIR.

The scientific interaction between the CSIR and WUT was undertaken within the framework of the SA/Poland Agreement on Cooperation in Science in Technology. The authors would like to express their appreciation to the South African National Research Foundation (NRF) and the Ministry of Science and Higher Education in Poland, for the financial support of this research partnership. Most of the wind-tunnel measurements were carried out by Mr Ters van Wyk of CSIR.

REFERENCES

Baker, C.J. 2007. Wind engineering – past, present and future. *Journal of Wind Engineering and Industrial Aerodynamics* 95(2007): 843–870.

Breuer, P., Chmielewski, T., Gorski, P. & Konopka, E. 2002. Application of GPS technology to measurements of displacements of high-rise structures due to weak winds. *Journal of Wind Engineering and Industrial Aerodynamics* 90(2002): 223–230.

Cermak, J.E. 2003. Wind-tunnel development and trends in applications to civil engineering. *Journal of Wind Engineering and Industrial Aerodynamics* 91(2003): 355–370.

Chmielewski, T., Breuer, P., Gorski, P. & Konopka, E. 2009. Monitoring of tall slender structures by GPS measurements. *Wind and structures,* Vol. 1, No. 5 (2009): 401–412.

ENR 2006. Final Height of 'On-Deck' Tallest Tower Shrouded In Secrecy by Peter Reina & Nadine Post. *Engineering News-Record*.

Li, M., Liao, H. & Zheng, S. 2009. A new extreme large boundary layer wind tunnel at Southwest Jiaotong University. In *Proceedings of the Seventh Asia-Pacific Conference on Wind Engineering (APCWE-VII), Taipei, 8–12 November 2009*.

PN-EN 1991-1-4:2008, Eurocode 1: Actions on structures – Part 1–4: General actions – Wind actions (in Polish). PKN, Warsaw 2008.

Sitek, M.A., Cwik, M., Goliger, A.M. & Gizejowski, M.A. 2013. Computational fluid dynamics simulations and validation of results. In *Proceedings of the 5th International Conference on Structural Engineering, Mechanics and Computation (SEMC 2013), Cape Town, 2–4 September, 2013* (in prep.)

Tschanz, T. & Davenport, A.G. 1983. The base balance technique for the determination of dynamic wind loads. *Journal of Wind Engineering and Industrial Aerodynamics* 13(1983): 429–439.

Research and Applications in Structural Engineering, Mechanics and Computation – Zingoni (Ed.)
© 2013 Taylor & Francis Group, London, ISBN 978-1-138-00061-2

Probabilistic models for design of structures against wind loads

J.V. Retief & C. Barnardo-Viljoen
Stellenbosch University, Stellenbosch, South Africa

M. Holicky
Czech Technical University in Prague, Prague, Czech Republic

ABSTRACT: Much effort has been expended on the proper probabilistic representation of strong wind loading mechanisms; effective design procedures that are sufficiently operational, yet essentially capture variability and uncertainty; achievement of sufficient levels of reliability consistently over the range of design situations through calibration. There is nevertheless an acute need to improve probability models for strong winds in order to address specific needs. Capturing the complexity of the geographical distribution of the strong wind climate in deriving suitable probability models to serve as basis for stipulation of design values is one such a need. In this paper, the conditions in South Africa is used as a case to consider proper probabilistic representation of strong winds across a complex and diverse geography and climate. Based on a set of extreme value models and climatic strong wind characterization, a procedure is demonstrated for deriving characteristic values as distributed across a region, with dispersion properties on which design values are based per region. This provides the key components of the probabilistic modeling of strong winds are represented in a cohesive and systematic manner, for use in the calibration of reliability based operational design procedures.

1 INTRODUCTION

Wind loading represents an important class of action that needs to be provided for in structural design. The variable nature of the occurrence of strong wind conditions is a critical aspect of this type of structural loading that can only be treated probabilistically. Much effort has therefore been expended on the proper probabilistic representation of strong wind loading mechanisms. The probability models form the basis for effective design procedures that are sufficiently operational, yet essentially capture variability and uncertainty to achieve sufficient levels of reliability consistently over the range of design situations through calibration.

In spite of the attention received, there is still an acute need to improve probability models for strong winds in order to address specific needs. A specific need for instance is to improve the representation of the strong wind climate and probability models for a specific region, making use of the latest series of observations.

Certain classes of structure such as modern light steel structures are particularly sensitive to extreme environmental actions such as wind loading. For the design of important structures, very high levels of reliability is required; extreme wind loads at very low probabilities of occurrence need to be considered.

Design for wind loading can broadly be divided into the natural environmental processes and the conversion of the free field wind into wind pressure loading on the structure. Natural wind conditions are predominantly modeled by time variant probability models representing the stochastic nature of strong wind conditions. Probability modeling of the wind pressure loading process is predominantly a time invariant representation of uncertainties of predicting wind pressure conversion and distribution across the structure.

This paper is concerned with probability models for the natural conditions related to wind loading on structures. The loading process nevertheless needs to be taken into account in setting up appropriate probability models for the natural strong wind occurrence.

Two extreme cases can be identified for the probabilistic modeling of natural time variant strong wind occurrence: In the case of very important structures with high consequences of structural failure, extreme wind with very low probabilities of occurrence needs to be determined. For standardized design procedures, robust probability models for strong wind are required on which effective and optimal reliability based design wind load values can be based.

In both cases, the probability models can be constrained by limited data, as compared to the probabilities associated by the relevant levels of reliability.

Complementary information on strong wind processes such as the nature of the strong wind generating process can play an important role to improve the quality of the models by revealing unknown sources of

uncertainty. Climate change provides a serious challenge to proper probability modeling of strong wind (Retief et al 2013). The relationship between wind generating processes and strong wind occurrences is of critical importance to project future trends in terms of climate change modeling.

2 GENERAL WIND LOAD PROBABILITY REPRESENTATION

2.1 *Extreme value probability models*

The extreme values (maximal or minimal) in a population of a certain size are random variables and their distribution is extremely important for the theory of structural reliability. The General Extreme Value (GEV) distribution covers three types of distribution of extreme values that are usually denoted as types I, II and III. Each of the types has two versions – one for the distribution of minimal values, the second for the distribution of maximal values. All these types of distribution have a simple exponential shape and are convenient to work with.

The extreme value distribution of type I, which is commonly called the Gumbel distribution, is described in detail by Equations (1) and (2) (Holicky 2009). The distribution parameters are the shape coefficient α and the mode β which are related to the population paramters for the mean (μ) and standard deviation (σ) as given by Equation (3).

$$F(x) = EXP(-EXP(-y)) \tag{1}$$

$$y = (x - \beta)/\alpha \tag{2}$$

$$\alpha = \sigma\sqrt{6}/\pi \qquad \beta = \mu - 0.577\alpha \tag{3}$$

In a similar way as type I Gumbel distribution, type II distribution, the so-called Fréchet distribution, and type III distribution, the so-called Weibull distribution, are defined by exponential functions. All three types of distribution complement each other with regard to possible values of the skewness s. Each type covers a certain area of skewness, as shown in Figure 1.

Types I and II of the extreme values distribution are often applied in the description of quantities of which the maximal values are studied (wind actions), and type III distribution is applied for quantities of which the minimal values are studied (e.g. strength and other material properties).

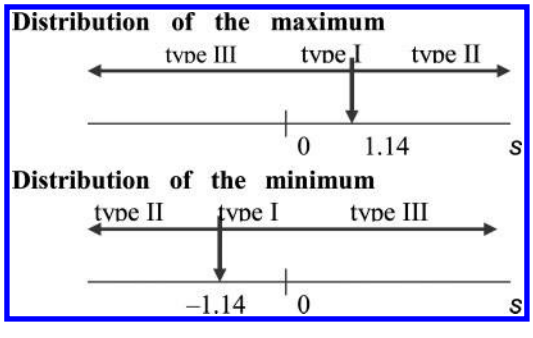


Figure 1. Types of distributions of extreme values with skewness s.

However, it should be mentioned that both these distributions have relatively high skewness ($\alpha \geq 1.14$) and should be applied with a caution. Long term experience shows (Holicky 2009) that when the available data indicate a low skewness ($s$close to zero) then the Gumbel distribution may lead to conservative estimates of extremes and the General Lognormal (three-parameter) distribution may provide a better approximation.

2.2 *Wind load probability model*

The wind pressure on a structure may generally be written as the combination of the time variant effect of the wind velocity v or Q_{Ref} and the time invariant processes given in Equation (4). The variables are defined in Table 1, together with listing of typical distribution values; ρ is the deterministic value of the air pressure.

$$Q = 0{,}5\rho v^2 c_r c_a c_g c_d = Q_{\mathrm{Ref}} c_r c_a c_g c_d \tag{4}$$

Where ρ is the air density and v the wind speed, with other basic variables defined in Table 1; representative distribution values are also tabulated:

2.3 *Design values for wind load*

Assuming a Gumbel distribution for the wind load, expressions can be formulated for the design value (Q_d) and characteristic value (Q_k) of the wind load in terms of the mean value (μ_Q), the target level of reliability (β_T), the coefficient of variation of the wind load (w_Q) and the annual pressure ($w_{Q,Ref}$), the ratio of reference period to design life N (typically 50) (Holicky 2009).

By stipulating the characteristic value of wind load at the 2% probability level, the ratio of characteristic to mean value is given by Equation (5).

$$Q_k/\mu_Q = 1 - w_Q\,(0.45 + 0{,}78\,\ln(-\ln(0.98))) \tag{5}$$

The ratio of design to mean wind load value is given by Equation (6). The partial load factor γ_Q can be

Table 1. Representative distribution parameters and time dependence for wind load.

Symbol	Variable	Time Dep.	Mean	CoV w_o
Q_{Ref}	Annual pressure extreme	Yes	0.8–1.0	0.25
c_r	Terrain roughness	No	0.8–1.0	0.15
c_a	Aerodynamic shape	No	1.0	0.20
c_g	Gust effects	No	1.0	0.15
c_d	Dynamic effects	No	1.0	0.15

obtained from the ratio of design to characteristic value as shown by Equation (7).

$$Q_d/\mu_Q = 1 - w_Q F_1 + w_{Q,\mathrm{Ref}} F_2 \quad (6a)$$

$$F_1 = 0.45 + 0{,}78\ln(-\ln(\Phi(-0.7\beta_T))) \quad (6b)$$

$$F_2 = 0.78\ln(N) \quad (6c)$$

$$\gamma_Q = Q_d / Q_k \quad (7)$$

Based on the parameter values listed in Table 1 to obtain w_Q whilst parametrically varying the values for $w_{Q,Ref}$, indicative values for the characteristic wind load from Equation (5) and the partial load factor (γ_Q) from Equation (7) are shown in Table 2 to for typical target reliability (β_T) values used in Eurocode and South African standards.

The inverse of the characteristic value ratio (~0.5) should be compared with the indicative relative mean of $0.8 \times 0.8 = 0.64$ from Table 1. The relative sensitivity of the partial factor (and the design value from Equation (7)) to the variability of the annual pressure extreme can be observed from these indicative results.

3 STRONG WIND MODELS FOR SOUTH AFRICA

Updating the probability models for strong winds for South Africa serves as an illustration of the process of the application of these models as input to reliability based design models.

3.1 *Observations and records*

The specific nature of strong wind for structural design needs to be taken into account when extracting observations form general climatic records (Kruger et al 2011). Since only annual maximum wind speed is extracted for further analysis, quality assessment of the records is of critical importance. The recording period is of critical importance, due to the low probabilities for which the models are to be applied.

Due to boundary layer effects on strong wind loading, the height of observation and exposure of the weather station are critical factors influencing the quality of the observation. General terrain roughness, topography and upwind obstructions over extensive distances may have directional influences on the observations.

The density of coverage of the network of weather station has an important bearing on the geographic resolution of the strong wind records. Sufficiency of coverage is related to climatic and topographic characteristics of the region.

Table 2. Indicative values for characteristic wind load and partial load factors.

$w_{Q,Ref}$		0.20	0.25	0.30
Q_k/μ_Q		1.99	2.06	2.14
γ_Q	$\beta_T = 3{,}8$	1.55	1.62	1.69
	$\beta_T = 3{,}0$	1.32	1.39	1.45

3.2 *Related climatic information*

The relationship between strong winds and the related climatic conditions provides useful information to complement the statistical treatment of observations (Kruger et al 2012). The weather conditions under which strong winds are generated are of critical importance for example to differentiate between synoptic scale events and meso scale thunderstorms in terms of turbulence of the wind.

Mixed climate conditions need to be taken into account in probabilistic modeling of strong winds (Kruger et al 2010). Significant under-estimation of strong winds can occur if differentiation of strong wind mechanisms is not taken into account (Kruger et al 2012).

3.3 *Strong wind datasets*

The strong wind record of the present wind design maps for South Africa are based on 14 weather stations with a record length ranging from 18 to 43 years, with an average period of 26 years. However, from a quality audit, these records were rejected for further analysis (Kruger et al 2011). Analysis is now based on a network of 172 new generation of automatic weather stations (AWS) deployed since 1990. From a quality audit, 74 AWS records are selected mainly on the basis of at least ten years of recording.

The main features of the dataset of strong wind records are:

- Recording periods limited to 10 – 18 years
- Improved geographical distribution
- Identification of strong wind mechanism associated with each occurrence

3.4 *Strong wind climate*

The main features of the strong wind climate as shown in Figure 2 can be summarized as (Kruger et al 2010):

- The strong wind climate shows a complex geographical distribution;
- Two dominant strong wind mechanisms (frontal and thunderstorm) with several secondary conditions that can be identified;
- Mixed climate conditions with both frontal and thunderstorm wind occurs is prevalent over large areas;
- There is limited agreement between gust and hourly mean strong wind distribution.

Strong wind generating mechanisms and its geographical distribution need to be taken into account in compiling probability models for wind speed.

3.5 *Representative strong wind models*

Since design is primarily based on static equivalent wind load, gust wind models are considered in

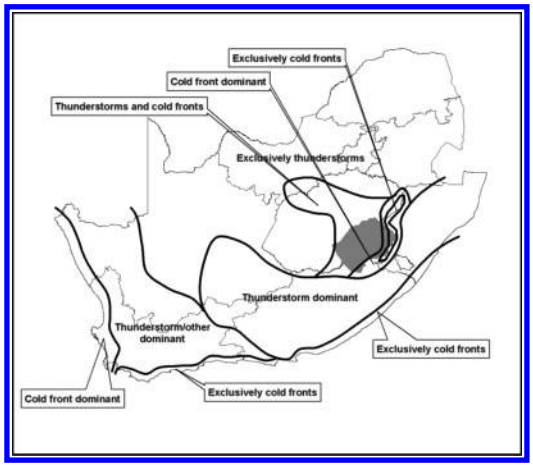


Figure 2(a). Strong wind mechanisms for gusts.

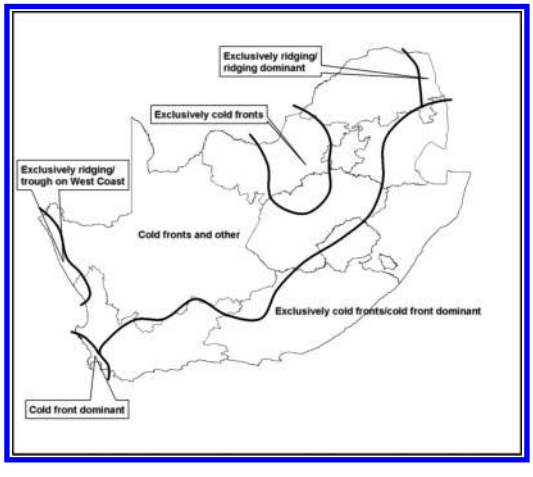


Figure 2(b). Strong wind mechanisms for hourly mean wind.

assessing probability models for South Africa. Various probability models are employed by Kruger et al (2013) to take account of short record lengths and mixed strong wind climate effects. Gumbel models are however sufficient to illustrate the main features of the South African strong wind climate.

Representative probability models for the three main metropolitan centers of the country are given in Figure 3, based on parameters summarized in Table 3.

In addition to indicating strong wind characteristics for significant regions of the country, Figure 3 is also representative of upper and lower ranges of strong wind probability distributions. It also represents the two main strong wind generating mechanisms of synoptic scale frontal wind and meso scale thunderstorms. Strictly speaking Cape Town should be classified as "mixed climate" although the second mechanism is also of synoptic scale; it is therefore not as significant as cases where the mixed climate derives from frontal and thunderstorm events.

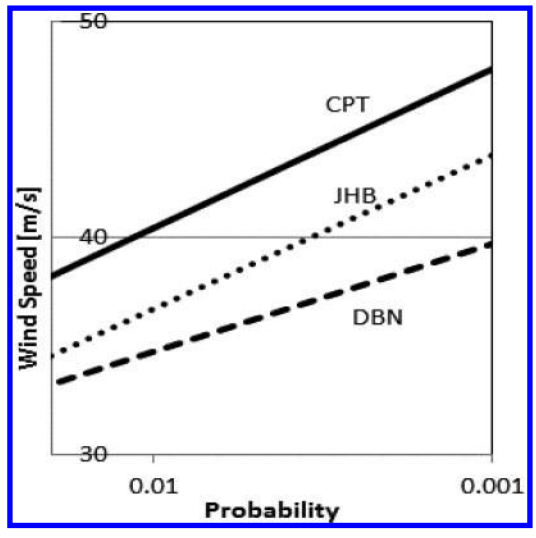


Figure 3. Representative strong wind probability models for Cape Town (CPT), Johannesburg (JHB) and Durban (DBN).

Table 3. Summary of distribution parameters.

DATA/PARAMETER	JHB	DBN	CPT
Record period (y)	14	16	16
Mean $\bar{x}$ (m/s)	24.4	26.1	27.7
Standard Deviation s	3.94	2.76	4.08
Dispersion α	3.07	2.16	3.18
Mode β	22.6	24.8	25.8
Skewness	0.77	1.01	0.75
Thunderstorm (TS) or Synoptic scale (SS)	TS	SS	SS

The range of strong wind values are characterized by its relative vertical position, as related to the mode (β) and slope of the graph, related to the shape parameter (α) or dispersion for the Gumbel distribution. Frontal winds cover the full range, with high values for both the mode and the dispersion for Cape Town and low values for Durban respectively; thunderstorms are generally characterized by larger dispersion such as for Johannesburg.

3.6 *Regional effects*

An indication of geographical effects can be obtained by comparing the probability models for the three main centers given Figure 3 to their respective regions.

Wind maps are conventionally expressed in terms of characteristic values at an exceedance probability of 0.02 per annum, or approximately the expected 50 year extreme value. It is therefore convenient to normalize the distribution to the characteristic wind speed for each location (V-0.02) as shown in Figure 4.

Differences in slope of the normalized graphs reflect differences in the dispersion parameter value

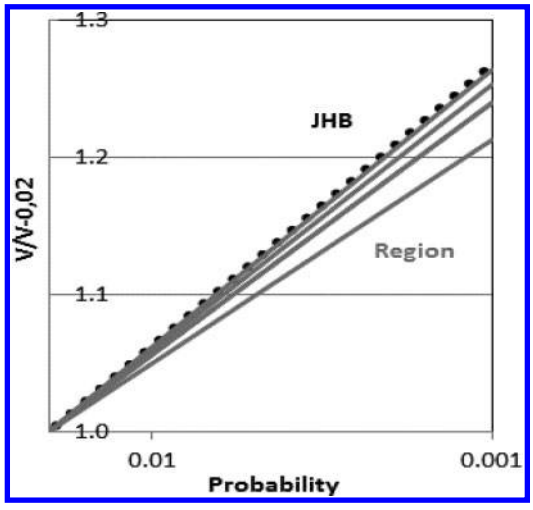


Figure 4(a). Comparison of normalized strong wind probability models for Johannesburg (JHB) and regional locations.

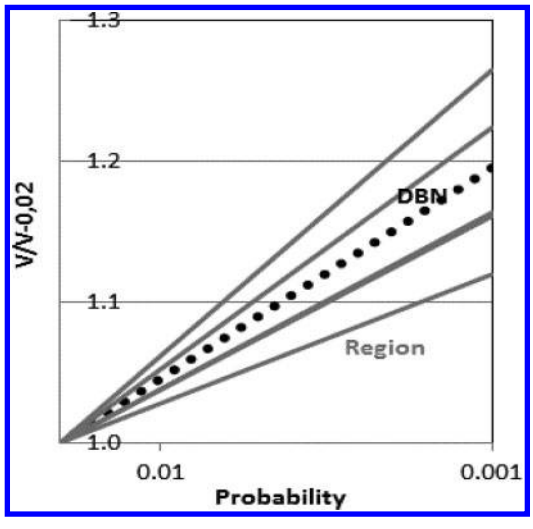


Figure 4(b). Comparison of normalized strong wind probability models for Durban (DBN) and regional locations.

(α) for the respective locations. Different regional features for the three regions can be related to the local strong wind climate and other geographical factors.

The graphs for regional locations lie relatively close below the Johannesburg graph, probably reflecting the homogeneity of thunderstorm wind.

The regional graphs are scattered widely around that for Durban; this is probably due to the effects of synoptic wind close to the coastline, with thunderstorms becoming the main source of strong wind from a small distance inland. The upper graph is however quite similar to the graph for Johannesburg.

In spite of the fact that strong wind is predominately generated by synoptic conditions, the scatter of the normalized graphs is the widest of the three regions. This can probably be ascribed to the topography of the

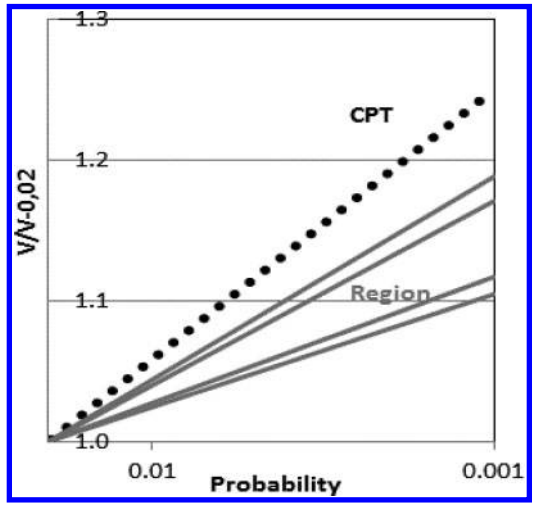


Figure 4(c). Comparison of normalized strong wind probability models for Cape Town (CPT) and regional locations.

region and the occurrence of frontal and other synoptic conditions causing strong winds.

3.7 *Applied probability model*

The strong wind climate of South Africa is complex due to the large geographical area covered and the diverse basic climate from which strong winds derive. Strong winds are generated from thunderstorms or various synoptic scale conditions, or mixed climate combinations of these mechanisms.

The agreement of the upper limits of the wind speed normalized to the characteristic wind speed for the three main metropolitan centers of the country however provides the basis for modeling dispersion conservatively.

An envelope of the dispersion of strong winds describing the quantile wind speed as a function of the annual exceedance probability can be described by a Gumbel function of the upper limit of the sets shown in Figure 4. The parameters for this Gumbel function V_{Disp} are $\alpha = 0.09$; $\beta = 0.65$; with a mean $\mu_{Disp} = 0.70$ and standard deviation $\sigma_{Disp} = 0.115$ as obtained from Equation (1).

The quantile wind speed V_P at exceedance probability P is then obtained as the product of V_{Disp} and the characteristic wind speed $V_{0.02}$ as given by Equation (8):

$$V_P = V_{0.02} V_{Disp} \tag{8}$$

The geographic distribution of V_P can be obtained by taking the value of $V_{0.02}$ for a given location from the map of characteristic wind speed from the map for South Africa presented by Kruger et al (2013).

Similar assessment needs to be done to confirm that this procedure is sufficient for other regions; alternatively to identify regions that need special treatment or exclusion from such simplified basis for design procedures.

4 CONCLUSIONS

Appropriate procedures for design wind loading to achieve the required levels of performance determined from the principles of structural reliability requires the representation of strong wind in terms of suitable probability models.

In an example it is demonstrated how the geographical distribution of strong winds can be represented in the form of a characteristic wind speed map, whilst the dispersion on which calibration of design procedures are based can be represented by conservative modeling of dispersion for a diverse range of strong wind climatic conditions.

Extension of this approach to include all the regions identified from previous investigations will provide for the compilation of a comprehensive map of characteristic wind speed. Furthermore, calibration of design procedures can be based on regional dispersion models for the whole region.

REFERENCES

Holický, M. (2009) Reliability analysis for structural design. SUN PRESS, Stellenbosch. ISBN 978-1-920338-11-4.

Kruger, AC, Goliger AM, Retief JV and Sekele S. (2010), "Strong wind climatic zones in South Africa", *Wind & Structures*, **13**(1), 37–55.

Kruger AC, Retief JV, Goliger AM (2011). *An updated description of the strong wind climate of South Africa.* 13th International Conference on Wind Engineering. Amsterdam.

Kruger AC, Goliger AM, Retief JV, Sekele SS (2012). Clustering of extreme winds in the mixed climate of South Africa. *Wind & Structures*, **15**(2) 87–109.

Kruger AC, Retief JV, Goliger AM (2013). Strong wind in South Africa: Mapping of updated statistics. SAICE Journal, in press.

Retief JV, Barnardo-Viljoen C, Van der Klashorst E and Diamantidis D (2013). *Extreme actions and climate change.* 11th International Conference of Structural Safety and Reliability, Columbia University, New York.

Research and Applications in Structural Engineering, Mechanics and Computation – Zingoni (Ed.)
© 2013 Taylor & Francis Group, London, ISBN 978-1-138-00061-2

Computational fluid dynamics simulations and validation of results

M.A. Sitek, M. Cwik & M.A. Gizejowski
Warsaw University of Technology, Warsaw, Poland

A.M. Goliger
Council for Scientific and Industrial Research, Pretoria, South Africa

ABSTRACT: Wind flow influence on a high-rise building is analyzed. The research covers full-scale tests, wind-tunnel experiments and numerical simulations. In the present paper computational model used in simulations is described and the results, which were obtained, are compared with wind tunnel data.

1 INTRODUCTION

Many high-rise buildings with complicated geometry are currently built in Poland. In the last few years several of them were constructed in the centre of Warsaw. This new situation requires a modern approach to design. Dynamic influence of wind on smaller buildings is typically negligible and, if relevant, can be incorporated into the loading in terms of a static load combined with a dynamic magnification factor. Dynamic influence becomes important when tall structures are taken into consideration. Greater precision of computations during the design process is necessary. Wind gusts frequency can be close or equal to natural frequency of a building and cause resonant effect. Recently introduced Polish code PN-EN 1991-1-4:2008 covers this subject to a wider extent than the previous one, but still the guidelines for designers are not sufficient for all structures.

The influence of wind loads on structures can be assessed by full-scale measurements, boundary-layer wind tunnel tests and numerical simulations. Full-scale tests give the most reliable results, but they are also expensive and time consuming. Currently wind tunnel tests are considered to be the primary method in the determination of loadings for tall buildings. However, computational fluid dynamics (CFD), which has been a focus of many researchers (e.g. Huang, Li & Xu 2006, Dagnew et al. 2009, Bitsuamlak & Simiu 2010, van Hooff et al. 2011) will become the future alternative. The advantages of CFD are numerous e.g.: computations are cheaper, faster and provide an opportunity to modify the model and to test more variants. The computations are made in the whole domain therefore give more useful information. Furthermore, the results can be presented in a form of advanced visualizations. Although the numerical models cannot generate exactly the same results as those obtained in wind tunnel tests, they are generally in good agreement.

The most common approach to solve equations of motion is to use spatial or time averaging of pressure and velocity fields. This results in a set of Reynolds Averaged Navier-Stokes equations (RANS). This concept requires turbulence modeling which sometimes introduces significant errors to the solution. The advantage is that the computational mesh doesn't have to be as dense as in direct solution methods and require smaller computational resources. RANS methods are widely used in CFD software, ANSYS/Fluent among others.

There is no turbulence model that is generally acknowledged and suitable for every problem. One of the most popular models is a two-equation k-ε model (Launder & Spalding 1972) along with its latter modifications: renormalization group theory, RNG (Yakhot & Orszag 1986) and realizable (Shih et al. 1995). Both are recommended, over the standard model, because of their successful performance in many problems.

2 THE SCOPE OF THE PAPER

Present study is a part of a research project (Cwik et al. 2009, Cwik et al. 2012) concerning wind action on a 208 m high Warsaw Trade Tower building, shown on Figure 1, which is located in a central but undeveloped part of Warsaw. The project covers: full-scale measurements, wind tunnel tests and numerical simulations.

The main goal is to examine the possibility of application of wind action simulations in structural health assessment of high-rise buildings. Another aim is to perform a comparative analysis of the results and to verify the recommendations of the Polish design code.



Figure 1. Warsaw Trade Tower (WTT) building.

Considering the scope of this project, it is the first such comprehensive attempt on this topic in Poland.

This paper presents preliminary results of CFD simulations and their validation through a comparison with experimental data from wind tunnel tests (Cwik et al. 2013). Initial conditions (mean velocity and turbulence intensity) for the computations are taken from the experiment and they correspond to wind direction 320°. A convergence analysis for various grids is performed to assess the best grid density in this particular problem. Mean pressure coefficient distribution over building's façade is obtained and compared with the wind tunnel measurements. In addition mean wind speed at the site corresponding to the location of the weather station is checked. Percentage error of mentioned quantities, with respect to the experimental data, is also given.

3 NUMERICAL MODEL

3.1 *Computational domain*

The geometry and mesh of the computational model are created in Abaqus. Then an input file is imported

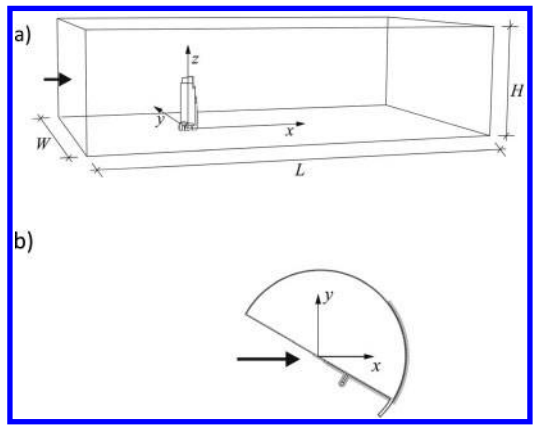


Figure 2. a) Geometry of the computational domain and b) top view of the building. Wind direction is indicated schematically with an arrow.

to ANSYS/Fluent 14.0, where RANS equations are solved.

The dimensions of the computational domain are adopted so that the cross-section of the domain is the same as the cross-section of the tunnel. The upstream length is chosen to equal $2h$, downstream length – $5h$, where h is building's height. Therefore the dimensions are $L \times H \times W = 2.7\,\text{m} \times 1\,\text{m} \times 2\,\text{m}$ (Fig. 2). A Cartesian coordinate system is chosen with coordinates: x – on ground plane, along wind direction, y – on ground plane, perpendicular to wind direction, z – perpendicular to ground plane. The geometry of the building model is simplified and the structures surrounding WTT are omitted. Building dimensions are the same as the dimensions of the model from experiment, which was made in a scale of 1:500.

The domain is discretized with an unstructured tetrahedral mesh. Cell sides are aligned with the contours of the building and domain boundary. The building has a fairly complex geometry and the grid used is fine enough to model the details. Three cases of grids are considered – coarse, medium and fine. Coarse mesh has 409706, medium – 694850, and fine – 1844736 cells.

3.2 *Solver configuration*

It is assumed that RANS equations are time independent. They are solved using RNG $k - \varepsilon$ turbulence model. Default ANSYS/Fluent model constants are adopted: $C_{mu} = 0.0845$, $C_{1\varepsilon} = 1.42$, $C_{2\varepsilon} = 1.68$.

Coupled pressure-based algorithm is chosen as a method for pressure-velocity coupling. Spatial discretisation gradient is based on the least squares cell. Pressure interpolation is standard. The convection and viscous terms are modeled with second-order discretisation schemes. Hybrid initialization is chosen as the solution initialization method. The solution convergence is monitored by checking the values of scaled residuals, following each iteration. The computations are completed when the difference for two consecutive

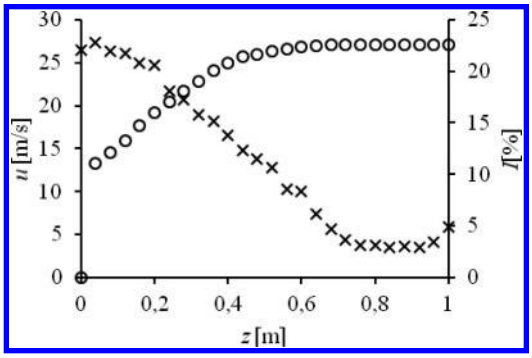


Figure 3. Mean velocity u (ooo) and turbulence intensity I ($\times\times\times$) inlet profiles.

iterations is smaller than 10^{-5} for continuity, 10^{-6} for x-velocity, 10^{-5} for turbulent kinetic energy and 10^{-5} for turbulence dissipation rate.

3.3 *Boundary conditions*

At the inlet of the domain, profiles of mean wind velocity, turbulent kinetic energy and turbulence dissipation rate are defined. Values of mean wind velocity u as well as turbulence intensity I are those derived from tunnel test measurements. Profiles of these two parameters are shown on Figure 3. Turbulent kinetic energy is calculated from $k = 1.5(uI)^2$ and the turbulence dissipation rate is established from $\varepsilon = C_\mu^{3/4} k^{3/2} / z\kappa$, where turbulence viscosity constant equals $C_\mu = 0.09$ and von Karman constant is $\kappa = 0.42$.

Wall boundary conditions are used to model ground and building surfaces, with standard wall functions (Blocken et al. 2007). No-slip boundary condition is enforced.

On the top and sides of the domain the same boundary condition is prescribed. Because tunnel test is being modeled in CFD, then according to recommendations found in literature (Tominaga et al. 2008), these boundaries should be represented as no-slip walls.

The flow exit is modeled by outflow boundary condition which corresponds to a fully developed flow, where the velocity is constant in the flow direction and the diffusion gradients in x-direction, for all flow variables are zero. There are no values to provide at this kind of boundary in ANSYS/Fluent.

4 NUMERICAL RESULTS

4.1 *Grid convergence*

Three aforementioned grids are checked for convergence. Figure 4 depicts static pressure along a vertical line on south-west façade passing through points nr 2 between levels 1 and 9.

It can be seen that with an increase in grid density the solution is converging. Therefore the finest mesh is chosen for further analyses. Although it requires more computational resources than medium mesh, it enables to obtain more accurate pressure distribution on the building façade and therefore better agreement of the results.

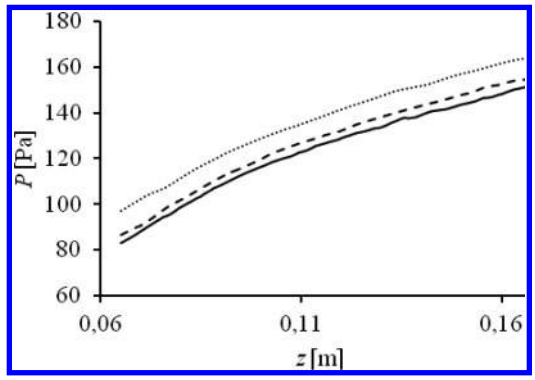


Figure 4. Comparison of static pressure for three meshes: coarse (…), medium (- - -) and fine (—) along a vertical line on south-west façade passing through points nr 2 between levels 1 and 9.

4.2 *Comparison of numerical and experimental results*

One specific wind direction of 320^0 (Fig. 2b) is selected from full-scale tests for validation of numerical modeling. Values of velocity at weather station location and pressure coefficient distribution are compared with wind tunnel data. Locations of the sensors on the building model are shown on Figures 5a)–b).

The weather station is located on the south-west side of the roof, 182 m above ground, as shown on Figure 5a. Mean wind speed measured in full-scale at this point is equal to 21.5 m/s. From numerical computations value of 22.2 m/s is obtained, which accounts for a good approximation.

Further evaluation of the results concentrates on establishing values of mean pressure coefficient on building façade. This parameter is fundamental in engineering design process. Pressure coefficient is calculated as $C_p = (P - P_{ref})/0.5\rho u_{ref}^2$, where: P – local static pressure, P_{ref} – reference static pressure, ρ – air density ($\rho = 1.25\,\mathrm{kg/m^3}$), u_{ref} – reference wind velocity at height 370 m ($u_{ref} = 27.34\mathrm{m/s}$). In order to compute the pressure coefficient with an adequate precision, the reference pressure must be established very carefully (Montazeri & Blocken 2013). The location of reference point corresponds to the pitot-tube position in the experiment. The sensor was located right above the building model at the height of 740 mm, which corresponds to the full-scale reference height of 370 m.

Figure 6 depicts change of static pressure along a vertical line passing through the origin of coordinate system xyz. The reference point is located in a flow field undisturbed by the building model and reference pressure equals to about 36.12 Pa.

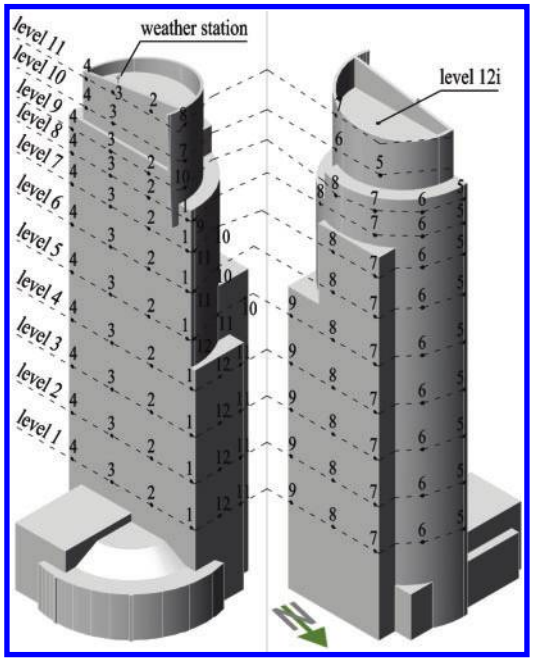


Figure 5a. Location of pressure measuring points on south-west (left) and north-east (right) facades. Weather station position.

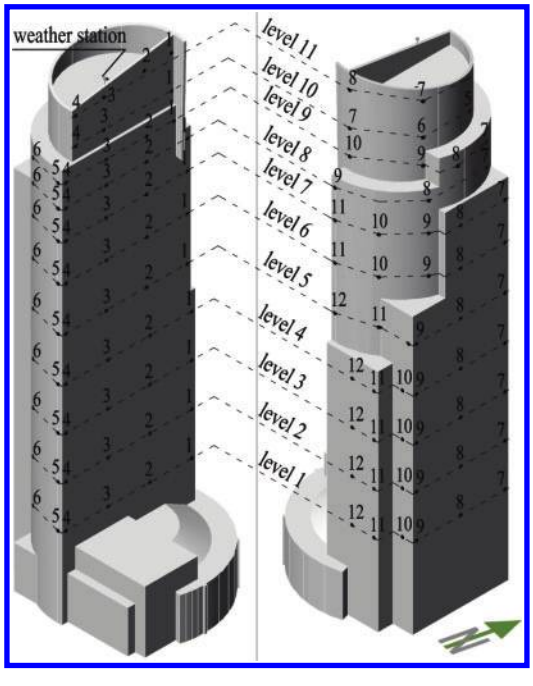


Figure 5b. Location of pressure measuring points on north-west (left) and south-east (right) facades.

Figures 7a)–d) show contour plots of mean pressure coefficient distribution on model façades obtained from calculations.

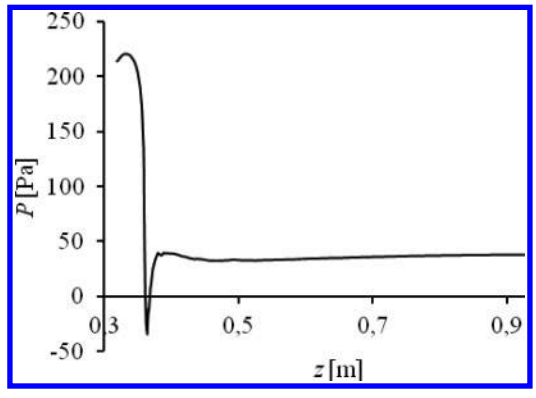


Figure 6. Static pressure along global coordinate z.

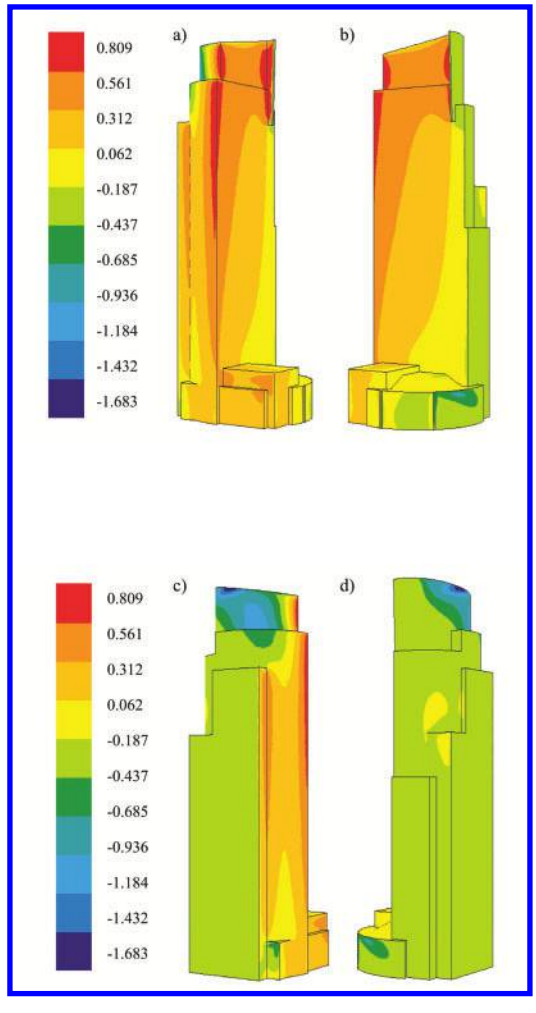


Figure 7. Contour plots of mean pressure coefficient distribution on building façades.

Comparison with wind tunnel results is shown on Figures 8–10. Three representative sets of measuring points are chosen. Sensors nr 2 and 3 are located on windward façade and points nr 8 on leeward façade.

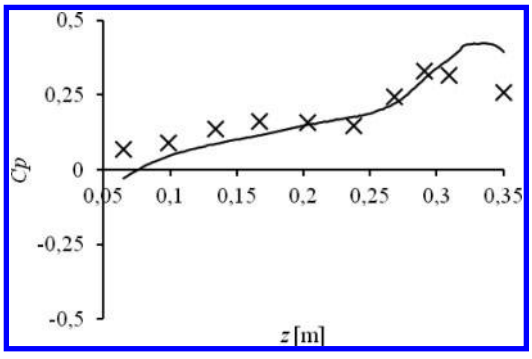


Figure 8. Mean pressure coefficient at points nr 2 between levels 1–11. Solid line – numerical results, ××× – experimental results.

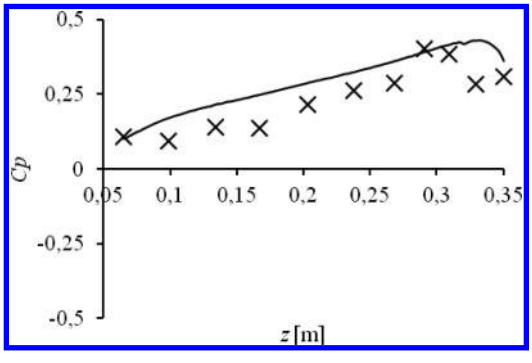


Figure 9. Mean pressure coefficient at points nr 3 between levels 1–11. Solid line – numerical results, ××× – experimental results.

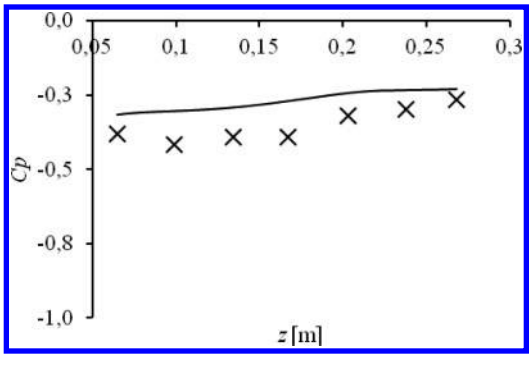


Figure 10. Mean pressure coefficient at points nr 8 between levels 1–7. Solid line – numerical results, ××× – experimental results.

5 DISCUSION AND FURTHER RESEARCH

Horizontal velocity at the weather station location is slightly higher than measured in the wind tunnel, but the difference is only 3%.

Numerical values of C_p make up for a better estimation in higher parts of the model. Moreover, error is smaller in central regions of the façades than near the edges. As an oblique wind direction is considered, divergence of results is similar on all facades. The average difference of the coefficient at windward façade between point levels 1 to11 equals 17% for points nr 2 and 34% for points nr 3. At leeward façade, for points nr 8 between levels 1–7, it is equal to 23%. Deviation in max value of C_p on windward façade is equal to 3%. Minimum value on leeward façade differs by 27%.

The differences in experimental and numerical results can be caused by a number of factors. Present investigation is of a preliminary nature and there are some simplifications made. Geometry of the model consists of an isolated building. Changes will be made in this respect to concentrate on the modeling of the surrounding structures. Moreover, in the current analysis steady state conditions were assumed. RANS simulations are known to have limitations, because they use only spatial averaging and are unable to imitate properly effects of flow fluctuations in time. Following analyses will consist of using Large Eddy Simulation (LES) which uses time averaging and is said to be more accurate, but also requires more computational resources.

In addition, further research will include: influence of various wind directions on the flow around the building, fluid-structure interaction analysis (building's roof displacements due to wind gusts) along with comparison with the data obtained from Global Navigation Satellite System (GNSS) measurements and also the influence of the high-rise building on other buildings in its vicinity.

6 CONCLUSIONS

Numerical results of CFD simulations of wind loading on a high-rise building are presented and compared to data from wind tunnel experiments. Computational setting, including: geometry, boundary conditions, discretisation of the domain as well as solver configuration, is chosen.

The paper concentrates on pressure coefficient distribution over building's façades and wind mean speed at the weather station location. The analysis shows that CFD prediction of the considered quantities agrees well with wind tunnel results.

A more detailed investigation will be carried out in the future.

ACKNOWLEDGEMENT

The authors would like to express their gratitude to the Council for Scientific and Industrial Research, Pretoria, South Africa, where the wind tunnel tests were carried out.

This paper was made possible due to the financial support of the South African National Research Foundation and the Ministry of Science and Higher Education in Poland.

REFERENCES

Bitsuamlak G., Simiu E. 2010. CFD's potential applications: a wind engineering perspective. In: *The Fifth International Symposium on Computational Wind Engineerin*g, Chapel Hill, North Carolina, USA, 23–27 May 2010.

Blocken B., Stathopoulos T., Carmeliet J. 2007. CFD simulation of the atmospheric boundary layer: wall function problems. *Atmospheric Environment* 41(2): 238–252.

Cwik M., Gizejowski M.A., Goliger A.M. 2009. Wind loadings of structures – a review of wind characteristics, wind-tunnel testing, in-situ measurements, computer modeling and code estimation procedures. In Obrebski J.B., Przybylo W. (ed.) *Lightweight structures in civil engineering. Contemporary problems. Proceedings of the XV International Seminar of IASS Polish Chapter LSCE*. Warsaw, 4–5 December, 2009.

Cwik M., Gizejowski M.A., Goliger A.M., Sitek M. 2012. Wind pressure loading for tall buildings. A case study of Warsaw Trade Tower. In Obrebski J.B., Przybylo W. (ed.) *Lightweight Structures in Civil Engineering. Contemporary problems. Proceedings of the XVIII International Seminar of IASS Polish Chapter LSCE.* Warsaw, 7 December 2012.

Cwik M., Gizejowski M.A., Goliger A.M. 2013. Wind tunnel investigations of pressure distribution over high-rise buildings In *Proceedings of the 5th International Conference on Structural Engineering, Mechanics and Computation*, Cape Town, 2–4 September 2013 (in prep.)

Dagnew A.K., Bitsuamlak G.T., Merrick R. 2009. Computational evaluation of wind pressures on tall buildings. In: *11th Americas Conference on Wind Engineering*, San Juan, Puerto Rico, 22–26 June 2009.

Huang S., Li Q.S., Xu S. 2006. Numerical evaluation of wind effects on a tall steel building by CFD. *Journal of Constructional Steel Research*. 63: 612–627

Launder B.E., Spalding D.B. 1972. *Lectures in mathematical models of turbulence*. London. Academic Press.

Montazeri H., Blocken B. 2013. CFD simulation of wind-induced pressure coefficients on buildings with and without balconies: Validation and sensitivity analysis. *Building and Environment* 60: 137–149.

Shih T.-H., Liou W.W., Shabbir A., Yang Z., Zhu J. 1995. A new k-ε eddy-viscosity model for high Reynolds number turbulent flows – model development and validation. *Computers Fluids*. 24(3): 227–238.

Tominaga Y et al. 2008. AIJ guidelines for practical applications of CFD to pedestrian wind environment around buildings. *Journal of Wind Engineering and Industrial Aerodynamics*. 96: 1749–1761.

van Hooff T., Blocken B., Aanen L., Bronsema B. 2011. A venturi-shaped roof for wind-induced natural ventilation of buildings: Wind tunnel and CFD evaluation of different design configurations. *Building and Environment*. 46: 1797–1807

Yakhot V., Orszag S.A. 1986. Renormalization group analysis of turbulence: I basic theory. *Journal of Scientific Computing*. 1(1): 1–51.

Research and Applications in Structural Engineering, Mechanics and Computation – Zingoni (Ed.)
© 2013 Taylor & Francis Group, London, ISBN 978-1-138-00061-2

Equivalent static wind loads for structures with non-proportional damping

N. Blaise & V. Denoël
Department of Architecture, Geology, Environment and Constructions, Structural Engineering Division, University of Liège, Liège, Belgium

T. Canor
F.R.S.-FNRS, National Fund for Scientific Research, University of Liège, Liège, Belgium

ABSTRACT: Usually, wind structural design is often carried out by a recourse to the concept of equivalent static wind loads. The main advantage of such loadings is to reproduce, with static analyses, the same extreme structural responses as those resulting from a formal buffeting analysis. This paper proposes an asymptotic method for the computation of equivalent static wind loads for structures with non-proportional damping in a modal framework. This method is based on recent results obtained with asymptotic expansion of the modal transfer matrix of such structures. The method is illustrated on a wind-sensitive high building mitigated with a Tuned Mass Damper (TMD) or a Tuned Liquid Column Damper (TLCD). Each damping device produces a different level of coupling allowing to study the convergence of the proposed method. For a similar level of mitigation, the TMD introduces more coupling than the TLCD does. Relative errors on structural responses (displacements, internal forces) are critically analysed.

1 INTRODUCTION

Over the last years, methods have been derived to compute equivalent static wind loads for structures with quasi-static (Davenport 1967, Holmes 1988, Kasperski 1992) or resonant behaviour (Holmes 1996, Zhou, Gu, & Xiang 1999, Chen & Kareem 2001, Blaise & Denoël 2013), analysed in nodal or modal basis. Equivalent static wind loads are derived to produce, with static analyses, the same extreme structural responses as those obtained with formal dynamic analyses. In the modal basis, such static loadings are defined as weighted combinations of inertial loads. An inertial load statically applied to the structure produces a deflection affine to the corresponding mode shape. The control of dynamic response of wind-sensitive structure such as wide-span roofs or bridges and high-rise buildings may be achieved using damping devices, e.g. tuned mass damper as well as tuned liquid dampers. These damping devices are source of non-proportional damping and consequently, the modal damping matrix and the modal transfer matrix are no longer diagonal. In this case, the dynamic analysis in the modal basis enables to reduce the size of the system, M-modes $\ll N$-degrees of freedom, but not to decoupled the modal equations. Rayleigh (1945) has proposed a decoupling approximation that neglects these off-diagonal elements of the modal damping matrix due to their relative smallness compared with the diagonal ones. Recently, an asymptotic expansion of the modal transfer matrix has been proposed by Denoël & Degée (2009) in a deterministic framework and then extend to a stochastic context (Canor, Blaise, & Denoël 2012), that enables to avoid full transfer matrix inversions for all frequencies.

For structures with non-proportional damping, this paper further extends the formulation of the asymptotic expansion to the weighting coefficients necessary to derive equivalent static wind loads with the inertial loads. The proposed method is formulated with the by-products resulting from the application of the asymptotic expansion of the modal transfer matrix.

The method is illustrated with a realistic example and a detailed analysis of the asymptotic convergence of both modal amplitudes and weighting coefficients of the inertial loads is performed.

2 BUFFETING WIND ANALYSIS

We consider a stationary Gaussian random loading $\mathbf{p}_{tot}(t)$, representing wind actions, although the concepts could be generalized to other loadings. For convenience the loading is split into a mean part $\boldsymbol{\mu}_p$ and a fluctuating part $\mathbf{p}(t)$

$$\mathbf{p}_{tot} = \boldsymbol{\mu}_p + \mathbf{p}. \tag{1}$$

The dynamic motion $\mathbf{x}(t)$ of a linear structure loaded by this random excitation, in the nodal basis, is obtained by solving the equation of motion

$$\mathbf{M}\ddot{\mathbf{x}} + \mathbf{C}\dot{\mathbf{x}} + \mathbf{K}\mathbf{x} = \mathbf{p} \tag{2}$$

where $\mathbf{M}$, $\mathbf{C}$ and $\mathbf{K}$ are $N \times N$ mass, damping and stiffness matrices, respectively. Contributions to the damping matrix are the structural $\mathbf{C}_s$, concentrated $\mathbf{C}_c$ (due to damping devices) and aerodynamic damping $\mathbf{C}_a$ matrices. The structural responses $\mathbf{r}(t)$ (nodal displacements, internal forces or reactions) are considered here to be expressed as linear combinations of the nodal displacements

$$\mathbf{r} = \mathbf{O}\mathbf{x} \tag{3}$$

where $\mathbf{O}$ is a matrix of influence coefficients, typically known from the FE model. The structural response of a given linear dynamic system can be computed using a small number M of normal modes of vibrations ($M \ll N$) characterized by mode shapes $\mathbf{\Phi}$ (Clough & Penzien 1993). These modes are normalized to have unit generalized masses. Using the modal superposition principle, the equation of motion (2) is written as

$$\ddot{\mathbf{q}} + \mathbf{D}\dot{\mathbf{q}} + \mathbf{\Omega}\mathbf{q} = \mathbf{g} \tag{4}$$

where $\mathbf{q}(t)$ ($\mathbf{x} = \mathbf{\Phi}\mathbf{q}$) is the vector of modal coordinates, $\mathbf{g}(t) = \mathbf{\Phi}^{\mathrm{T}}\mathbf{p}(t)$ is the vector of generalized forces, $\mathbf{\Omega}$ is a diagonal matrix containing generalized stiffnesses (equal, in this case, to the squared circular frequencies) and $\mathbf{D} = \mathbf{\Phi}^{\mathrm{T}}\mathbf{C}\mathbf{\Phi}$ is the modal damping matrix. The frequency domain formulation of the equation of motion in the modal basis is obtained by a side-by-side Fourier Transform of (4)

$$\mathbf{Q} = \mathbf{H}\mathbf{G} \tag{5}$$

where $\mathbf{Q}(\omega)$ and $\mathbf{G}(\omega)$ are respectively the Fourier transforms of $\mathbf{q}$ and $\mathbf{g}$. The modal transfer matrix $\mathbf{H}(\omega)$ is defined by

$$\begin{aligned} \mathbf{H} &= \left(\mathbf{\Omega} - \omega^2\mathbf{I} + i\omega\left(\mathbf{D}_d + \mathbf{D}_o\right)\right)^{-1} \\ &= \left(\mathbf{I} + \mathbf{H}_d\mathbf{J}_o\right)^{-1}\mathbf{H}_d \end{aligned} \tag{6}$$

where $\mathbf{D}_d$ and $\mathbf{D}_o$ are built as $D_{d,ij} = D_{ij}\delta_{ij}$ (diagonal elements) and $D_{o,ij} = D_{ij}(1 - \delta_{ij})$ (off-diagonal elements) where δ_{ij} denotes the Kronecker-delta function and $\mathbf{H}_d(\omega) = (\mathbf{\Omega} - \omega^2\mathbf{I} + i\omega\mathbf{D}_d)^{-1}$, $\mathbf{J}_o(\omega) = i\omega\mathbf{D}_o$. The asymptotic expansion of the modal transfer matrix (6) for small off diagonal elements (Denoël & Degée 2009) gives

$$\mathbf{H}_k = \mathbf{H}_d + \sum_{i=1}^{k} (-1)^i \left(\mathbf{H}_d\mathbf{J}_o\right)^i \mathbf{H}_d \tag{7}$$

where k is the approximation order of the transfer function. The psd matrix of the modal coordinates $\mathbf{S}^{(q)}(\omega)$, is obtained by

$$\mathbf{S}^{(q)} = \mathbf{H}\mathbf{S}^{(g)}\mathbf{H}^* \tag{8}$$

where the superscript * denotes the conjugate transpose operator and where $\mathbf{S}^{(g)}(\omega)$ is the psd matrix of the generalized Gaussian forces. The kth approximation of the psd matrix of the modal displacements (8) is obtained by

$$\mathbf{S}^{(q_k)} = \mathbf{S}^{(q_d)} + \sum_{i=1}^{k} \mathbf{\Delta S}^{(q_i)};\ \mathbf{S}^{(q_d)} = \mathbf{H}_d\mathbf{S}^{(g)}\mathbf{H}_d^* \tag{9}$$

where $\mathbf{S}^{(q_d)}$ ($k = 0$) is the psd matrix in the uncoupled system and the successive correction terms $\mathbf{\Delta S}^{(q_i)}$ are expressed in a general recurrence relation

$$\begin{aligned} \mathbf{\Delta S}^{(q_i)} &\overset{i=1}{=} -\left(\mathbf{H}_d\mathbf{J}_o\mathbf{S}^{(q_d)} + \mathbf{S}^{(q_d)}\mathbf{J}_o^*\mathbf{H}_d^*\right) \\ &\overset{i>1}{=} -\left(\mathbf{H}_d\mathbf{J}_o\mathbf{\Delta S}^{(q_{i-1})} + \mathbf{\Delta S}^{(q_{i-1})}\mathbf{J}_o^*\mathbf{H}_d^*\right) \\ &\quad -\mathbf{H}_d\mathbf{J}_o\mathbf{\Delta S}^{(q_{i-2})}\mathbf{J}_o^*\mathbf{H}_d^* \end{aligned} \tag{10}$$

with $\mathbf{\Delta S}^{(q_0)} = \mathbf{S}^{(q_d)}$. In the following, the covariance matrix $\mathbf{C}^{(q_k)}$ of the modal coordinates, is calculated by integration (along the circular frequencies) of the corresponding psd matrix

$$\mathbf{C}^{(q_k)} = \int_{-\infty}^{+\infty} \mathbf{S}^{(q_k)}\, d\omega = \mathbf{C}^{(q_d)} + \sum_{i=1}^{k} \mathbf{\Delta C}^{(q_i)} \tag{11}$$

where k denotes one of the aforementioned methods, namely (i) the exact approach ($q_\infty \equiv q$), (ii) the decoupling approximation ($q_0 \equiv q_d$), (iii) the proposed approximation with k correction terms.

The structural design needs envelope values (minimum and maximum) of the structural responses which are computed here as expected values of extrema on 10-minute observation windows. The envelope ($\mathbf{r}^{min}$, $\mathbf{r}^{max}$) is defined as

$$\mathbf{r}^{k,min} = -\mathbf{g}^k \circ \boldsymbol{\sigma}^{r_k};\ \mathbf{r}^{k,max} = \mathbf{g}^k \circ \boldsymbol{\sigma}^{r_k} \tag{12}$$

where $\boldsymbol{\sigma}^{r_k}$ is the standard deviation of the structural response, $\mathbf{g}^k$ is the peak factor derived from Rice's formula (Rice 1945) and $\circ$ denotes the Hadamard product operator. The kth approximation of standard deviations of the structural responses are derived from the corresponding covariance matrix of the modal displacements using

$$\boldsymbol{\sigma}^{r_k} = \sqrt{diag\left(\mathbf{\Upsilon}\mathbf{C}^{(q_k)}\mathbf{\Upsilon}^{\mathrm{T}}\right)} \tag{13}$$

where $\mathbf{\Upsilon} = \mathbf{O}\mathbf{\Phi}$ is the matrix of modal structural responses with υ_{im} the value of the ith structural response in the mth mode and *diag* is a matrix operator that keeps only the diagonal of the matrix. For the

structural design, the maximum value of the jth structural response is given by the following formula with a CQC approach:

$$r_j^{k,max} = g_j^k \left(\sum_{m=1}^{M} \sum_{n=1}^{M} \upsilon_{jm} \upsilon_{jn} \sigma_{mn}^{q_k} \right)^{1/2} = g_j^k \frac{\sum_{m=1}^{M} \sum_{n=1}^{M} \upsilon_{jm} \upsilon_{jn} \sigma_{mn}^{q_k}}{\sigma_j^{r_k}} \quad (14)$$

where $\sigma_{mn}^{q_k} = \sigma_{mn}^{q_d} + \sum_{i=1}^{k} \Delta\sigma_{mn}^{q_i}$ is the covariance between the mth and nth modes, formally obtained with (11), or more efficiently with an approximate relation (Denoël 2009).

3 EQUIVALENT STATIC WIND LOAD

The static analysis under an equivalent static wind load (ESWL) $\mathbf{p}_j^{e,k}$ associated with the jth response reproduces the maximum dynamic response $r_j^{k,max}$ obtained with a classical buffeting analysis:

$$\mathbf{r}_j^{e,k} = \mathbf{A}\mathbf{p}_j^{e,k} \text{ with } r_{jj}^{e,k} = r_j^{k,max} \quad (15)$$

where $\mathbf{r}_j^{e,k}$ is a vector of structural responses under the jth ESWL and $\mathbf{A} = \mathbf{O}\mathbf{K}^{-1}$ is a matrix of influence coefficients.

Inertial forces are defined as inertial load excitation that produce the dynamic displacement from (2) under a static analysis, i.e.

$$\mathbf{x} = \mathbf{\Phi}\mathbf{q};\ \mathbf{K}\mathbf{x} = \mathbf{\Psi}\mathbf{q} \quad (16)$$

where $\mathbf{\Psi} = \mathbf{K}\mathbf{\Phi}$ is the matrix of inertial forces with $\boldsymbol{\psi}_m$ the inertial force associated with the mth modal shape. Chen & Kareem (2001) have proposed to derive ESWL from combinations of these inertial forces using adequate weighting coefficients.

What is discussed next is the formulation of these weighting coefficients with corrections terms if the system is coupled. The matrix of modal structural responses may be also computed with the inertial forces as

$$\mathbf{\Upsilon} = \mathbf{A}\mathbf{\Psi};\ \upsilon_{jm} = \mathbf{a}_j \boldsymbol{\psi}_m, \quad (17)$$

and the introduction of (17) into (14) gives

$$r_j^{k,max} = a_j g_j^k \sum_{m=1}^{M} \left(\frac{\sum_{n=1}^{M} \upsilon_{jn} \sigma_{mn}^{q_k}}{\sigma_j^{r_k}} \right) \boldsymbol{\psi}_m = a_j g_j^k \sum_{m=1}^{M} \left[\frac{\sigma_j^{r_d}}{\sigma_j^{r_k}} W_{jm}^d \boldsymbol{\psi}_m + \sum_{i=1}^{k} \Delta W_{jm}^i \boldsymbol{\psi}_m \right]$$

where the weighting factors W_{jm}^d and ΔW_{jm}^i are expressed by

$$W_{jm}^d = \frac{\sum_{n=1}^{M} \upsilon_{jn} \sigma_{mn}^{q_d}}{\sigma_j^{r_d}};\ \Delta W_{jm}^i = \frac{\sum_{n=1}^{M} \upsilon_{jn} \Delta\sigma_{mn}^{q_i}}{\sigma_j^{r_k}}.$$

The kth approximation of the static loading, $\mathbf{p}^{e,k}$, is described as a summation of two contributions: (a) a scaling of the equivalent loading that would be obtained if the system was uncoupled, $\mathbf{p}^{e,d}$ and (b) a corrective equivalent loading, $\Delta\mathbf{p}_j^k$, resulting from the non-proportionality of damping:

$$\mathbf{p}_j^{e,k} = \left[\alpha_j^k \mathbf{p}_j^{e,d} + \Delta\mathbf{p}_j^{e,k} \right] = g_j^k \sum_{m=1}^{M} W_{jm}^k \boldsymbol{\psi}_m \quad (18)$$

$$\mathbf{p}_j^{e,d} = g_j^d \sum_{m=1}^{M} W_{jm}^d \boldsymbol{\psi}_m \quad (19)$$

$$\Delta\mathbf{p}_j^{e,k} = g_j^k \sum_{m=1}^{M} \sum_{i=1}^{k} \Delta W_{jm}^i \boldsymbol{\psi}_m \quad (20)$$

where $\alpha_j^k = (g_j^k \sigma_j^{r_d})/(g_j^d \sigma_j^{r_k})$ is a scaling coefficient and the kth approximation of the weighting coefficients W_{jm}^k is derived from

$$W_{jm}^k = \alpha_j^k W_{jm}^d + \sum_{i=1}^{k} \Delta W_{jm}^i \quad (21)$$

which well extends the formulation $W_{jm}^k = W_{jm}^d$ corresponding to the case where modal coupling is neglected. Notice also that α_j degenerates in $\alpha_j = 1$ for $k = 0$.

4 ILLUSTRATION

A 76-story, 306 m tall building is analysed under wind actions. This structure is a numerical example used in (Xu, Samali, & Kwok 1992) to study the mitigation of the along-wind response of structures using a tuned liquid column damper (TLCD) instead of a tuned mass damper (TMD). The structural model is a 10 lumped-mass cantilever model with 11 nodes and the finite element (FE) model is an assembly of classical 2-D beam elements with two DOFs per node (rotation and horizontal displacement). The proposed method is illustrated on this structure, with each damping device, keeping the first four modes for the modal analysis. The TMD or the TLCD are connected to the top floor of the building and are tuned to match the fundamental frequency of the structure. Both structures (with TMD or TLCD) have similar natural frequencies equal to 0.16, 0.19, 0.57 and 1.33 Hz. Figure 1 depicts the horizontal components of the first two modes and the corresponding inertial forces. A one-dimensional Gaussian velocity turbulence field is considered. The longitudinal turbulent component v of the velocity field is modeled by the spectrum of longitudinal turbulence proposed by Davenport (1961). The spanwise coherence function of v between two points of the tower separated by a height l is modelled by a decreasing exponential. Structural, TMD, TLCD and wind load spectrum data are not reported here for sake

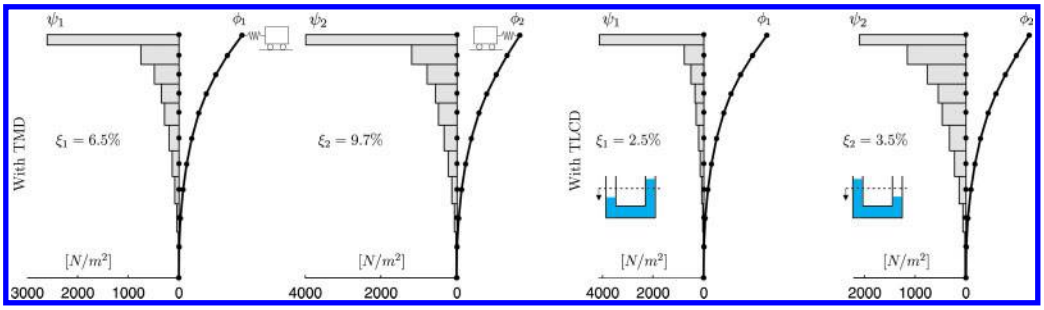


Figure 1. First two modal horizontal components (normalized to have a top displacement equal to 10 cm) and inertial horizontal forces per wind area. Each circle represents the nodes of the FE model. For each figure, the left and the right illustrate results for the structure with TMD and with TLCD, respectively.

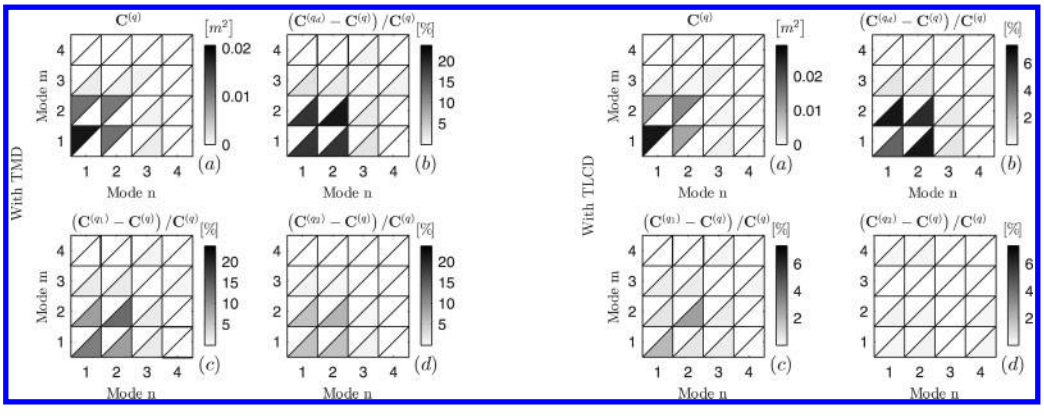


Figure 2. (a) Exact covariance matrix of the modal coordinates $\mathbf{C}^{(q)}$ (b) and relative error for different approximations $\mathbf{C}^{(q_d)}$, (c) $\mathbf{C}^{(q_1)}$ and (d) $\mathbf{C}^{(q_2)}$. Relative errors are expressed with respect to $\mathbf{C}^{(q)}$. For each square, the upper left corner correspond to positive value and the lower right corner to negative value.

of conciseness but may be found in (Xu, Samali, & Kwok 1992). In a unidimensional turbulence model, a linearized expression of the zero-mean fluctuating applied force at the ith level $p_i(t)$ is adopted as

$$p_i = C_{a,i} v_i \tag{22}$$

in which $C_{a,i}$ reads

$$C_{a,i} = \frac{\overline{W}_{10}}{\overline{V}_{10}} \sqrt{6K_0} C_d A_i \left(\frac{H_i}{10}\right)^{\alpha} \tag{23}$$

where $\overline{W}_{10}$, $\overline{V}_{10}$ K_0, C_d, A_i, H_i and α are the mean wind pressure at 10 meters, the mean wind velocity at 10 meters, the surface drag coefficient, the drag coefficient, the surface exposed to wind, the height of the ith level and the exponent coefficient, respectively. The aerodynamic damping is taken into account and therefore a diagonal aerodynamic damping matrix $\mathbf{C}_a$ is added to the structural $\mathbf{C}_s$ and concentrated damping $\mathbf{C}_c$ to constitute the total damping matrix $\mathbf{C} = \mathbf{C}_s + \mathbf{C}_c + \mathbf{C}_a$. The index of diagonality (see Horn & Johnson 1945) defined as $\rho(\mathbf{D}) = \sigma[\mathbf{D}_d^{-1}\mathbf{D}_o]$ where $\sigma[\,\cdot\,]$ is the spectral radius is an indicator of the diagonal dominance of $\mathbf{D}$. A low value indicates that the off-diagonal terms are small compared to the diagonal ones. The structure without damping device but considering the non proportional aerodynamic damping has an index equal to 0.02 and the classical decoupling approximation may be applied. Because of the TMD (resp. TLCD) the index of diagonality increases to 1.72 (resp. 1.03) and the classical decoupling approximation can not be formulated anymore. A larger diagonal index for the structure with TMD rather than with the TLCD, indicates that the solution with the decoupling approximation has a larger discrepancy with the reference solution ($k = \infty$). The reference covariance matrix ($k = \infty$) of modal coordinates and the relative error for the different approximations are represented in Figure 2. Concerning modes 1 and 2 the proximity of their natural frequencies and the similarities of mode shapes induce dynamic coupling (Denoël 2009) and high modal correlation coefficients equal to 0.78 and 0.5, respectively with TMD or TLCD. Figure 2-(b) on the left indicates that neglecting off-diagonal terms of the damping matrices, induces a maximum error of -23% on the variance of mode 2. The proposed method with first and second order correction terms offers a reduction of this error down to -14% and -6%, respectively. Figure 2-(b) on the right indicates that the decoupling approximation, induces a

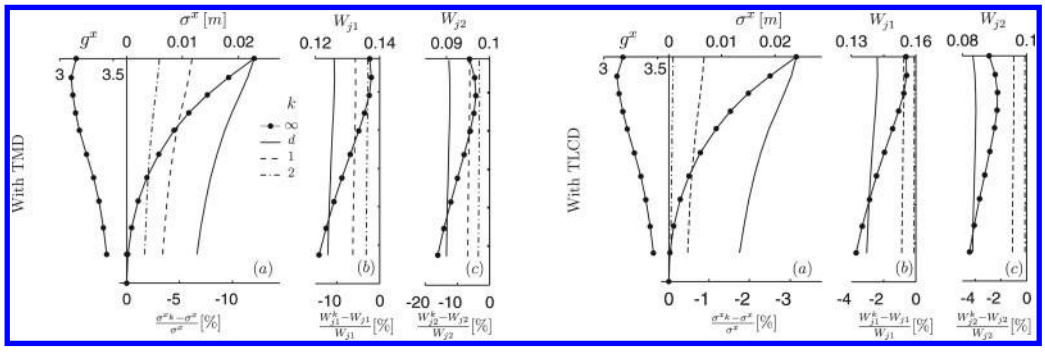


Figure 3. Results for the structural displacements. The upper axis, corresponding to reference values ($k = \infty$), is associated with lines with circles. The lower axis, corresponding to relative errors, is associated with solid ($k = d$), dashed ($k = 1$) and dashed-dot ($k = 2$) lines. (a) On the left, the peak factors and on the right standard deviations. (b) Weighting coefficients of the first and (c) the second inertial force for each structural displacement.

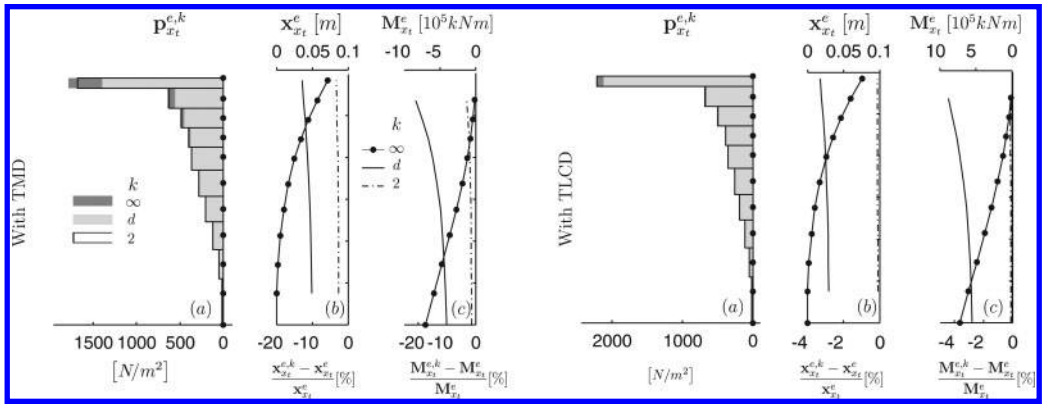


Figure 4. Equivalent static analysis associated with maximisation of the top displacement x_t. (a) Reference equivalent static wind load (grey patch) and those obtained with the decoupling approximation (lighter patch) and the proposed method with second order correction (line). (b) Reference equivalent static displacement and (c) reference equivalent static bending moments. Same conventions of Figure 3 applied for the lower and upper axis.

maximum error of -7.3% on the covariance between mode 1 and 2. Addition of the first and second correction terms reduces this error down to -1.9% and -0.25%, respectively. For the three approximations, the errors are the most significant for the group of correlated modes (1 and 2). Comparison of these relative errors on the covariance matrix for two levels of non proportionality (quantified by $\rho(\mathbf{D})$) shows that the proposed method with second order (or more) correction terms have to be considered for the structure with TMD while only the first correction term may be sufficient for the structure with TLCD. Figure 3-(a) depicts the peak factors and standard deviations of nodal horizontal displacements obtained with the reference approach. On the right is also represented the relative errors for each displacement, for the first three approximations. The decoupling approximation leads to underestimations of the displacements up to -12% (resp. -3%) for the structure with TMD and TLCD. With only the first correction term of the proposed method, these extreme underestimations are divided by two (resp. by three). The second order approximation provides underestimations less than -3% (resp. $\simeq 0\%$) and therefore this order of approximation is used for the computation of equivalent static wind loads. In both cases, for the decoupling approximation, relative errors on the peak factors are less than 2% and therefore are not represented. For each structural displacement, Figure 3-(b) and -(c) illustrate the weighting coefficients for the first and second inertial force, respectively. As expected, the relative errors and the convergence are similar to those associated with the evaluation of the standard deviations of the structural displacements. The structural displacement at the top is chosen for the illustration of the proposed method. Figure 4-(a) depicts the reference equivalent static wind loads ($k = \infty$) and those obtained with the decoupling approximation ($k = 0$) and with second order correction terms ($k = 2$). Underestimations of the reference loadings occur with the decoupling approximation and a second order approximation is necessary to correctly fit the reference static loadings. The largest underestimations of the loadings are located at the top of the structure. Figure 4-(b)

illustrates the static displacement under the reference ESWL. For the structure with the TMD, the decoupling approximation produces underestimations up to −12% while with the first two correction terms, relative errors are reduced down to −3%. Figure 4-(c) shows the static bending moments under the reference ESWL. The decoupling approximation produces underestimations up to −21% which are reduced to −1.5% with the first two corrections terms. For the TLCD, as expected, relative errors are smaller than those obtained for the structure with TMD. Levels of errors for the static displacements and static bending moments are similar to those reported for the weighting coefficients, see Figure 3.

5 CONCLUSIONS

High-rise buildings may be excited by the wind loading resulting in unacceptable level of displacements, internal forces or stresses. For such cases, among other solutions, damping devices are usually used to mitigate the wind response of such structures. These damping devices may be tuned mass or liquid column dampers and introduce non-proportional damping. A new method consisting in the asymptotic expansion of the modal transfer matrix enables to avoid full transfer matrix inversion. This work developed further the method for the establishment of equivalent static wind loads. The new method is illustrated with a 306 m tall building tower with (a) a tuned mass damper and (b) a tuned liquid column damper. Introduction of the TMD produces a larger index of diagonality, $\rho = 1.72$, in comparison with $\rho = 1.03$ for the structure with the TLCD. Major results are listed below:

1. the asymptotic method with two corrections terms offers an accurate estimation of the response, while the reference solutions are obtained with full inversion of the transfer matrix;
2. expressions of the asymptotic expansion of the weighting coefficients of inertial forces have been derived in order to compute equivalent static wind load;
3. the decoupling approximation can not be stated for the structure with TMD. Indeed, too large underestimations occur for the structural displacements −12% and for the evaluation of the equivalent static wind load. Static analysis produces large underestimations of the static displacements and static bending moments;
4. for the structure with the TLCD, the decoupling approximation may be stated if relative errors smaller than −5% are acceptable. Otherwise, the proposed method with two correction terms produces solutions that are nearly identical to the reference ones;
5. for this structure, peak factors dot not vary significantly between the coupled and uncoupled system;
6. if ESWLs are used for the envelope reconstruction problem (Blaise & Denoël 2013), the decoupling approximation produces large errors on the bending moments under the ESWL that maximizes the top displacement. This justifies the use of the proposed method to ensure reliability when using equivalent static wind loads in a structural design.

REFERENCES

Blaise, N. & V. Denoël (2013). Principal static wind loads. *Journal of Wind Engineering and Industrial Aerodynamics 113*, 29–39.

Canor, T., N. Blaise, & V. Denoël (2012). Efficient uncoupled stochastic analysis with non-proportional damping. *Journal of Sound and Vibration 331*(24), 5283–5291.

Chen, X. Z. & A. Kareem (2001). Equivalent static wind loads for buffeting response of bridges. *Journal of Structural Engineering-Asce 127*(12), 1467–1475.

Clough, R. W. & J. Penzien (1993). *Dynamics of structures* (2nd edition ed.). New-York: McGraw-Hill.

Davenport, A. G. (1961). The application of statistical concepts to the wind loading of structures. *Proceedings of the Institute of Civil Engineers 19*, 449–472.

Davenport, A. G. (1967). Gust loading factors. *In: Proceedings of the American Society of Civil Engineers. Journal of Structural Division 93*(3), 11–34.

Denoël, V. (2009). Estimation of modal correlation coefficients from background and resonant responses. *Structural Engineering And Mechanics 32*(6), 725–740.

Denoël, V. & H. Degée (2009). Asymptotic expansion of slightly coupled modal dynamic transfer functions. *Journal of Sound and Vibration 328*(1-2), 1–8.

Holmes, J. D. (1988). Distribution of peak wind loads on a low-rise building. *Journal Of Wind Engineering and Industrial Aerodynamics 29*(1-3), 59–67.

Holmes, J. D. (1996). Along-wind response of lattice towers – iii. effective load distributions. *Engineering Structures 18*(7), 489–494.

Horn, R. A. & C. R. Johnson (1945). *Matrix Analysis*. Cambridge University Press, Cambridge, United Kingdom.

Kasperski, M. (1992). Extreme wind load distributions for linear and nonlinear design. *Engineering Structures 14*(1), 27–34.

Rayleigh, J. W. S. L. (1877, re-issued 1945). *The Theory of Sound*, Volume 1. New York: Dover Publications.

Rice, S. (1945). Mathematical analysis of random noise. *Bell System Technical Journal 24*, 45–156.

Xu, Y. L., B. Samali, & K. C. S. Kwok (1992). Control of along-wind response of structures by mass and liquid dampers. *J. Engineering Mechanics 118*(1), 20–39.

Zhou, Y., M. Gu, & H. Xiang (1999). Alongwind static equivalent wind loads and responses of tall buildings. part ii: Effects of mode shapes. *Journal of Wind Engineering and Industrial Aerodynamics 79*(1-2), 151–158.

Research and Applications in Structural Engineering, Mechanics and Computation – Zingoni (Ed.)
© 2013 Taylor & Francis Group, London, ISBN 978-1-138-00061-2

Robustness of structures: State of art

Seema
Jaypee University of Information Technology, Waknaghat, Solan, H.P, India

N. Baldassino & R. Zandonini
University of Trento, Trento, Italy

ABSTRACT: Vulnerability of structures to progressive collapse and mitigation of the effects of local damages are topics widely discussed inside the scientific community. The progressive collapses that recently occurred due to terrorist attacks and the consequent huge loss of human lives, pointed towards the need for a new design criteria. A criteria that aims to design robust structures, i.e. structures able to withstand exceptional loads without being damaged to the extent disproportionate to the original cause. Event control, specific local resistance, redundancy, design of key elements, compartmentalization and detailing rules are some of the preventive strategies proposed by the recent studies and design standards. In this paper, the main facets of this problem are briefly illustrated. The approaches recommended by the standards, and in particular by the EN 1991-1-7, are presented.

1 INTRODUCTION

Progressive collapse of a building or part of it, caused by localized damage as a consequence of accidental actions, is a relatively rare event. The increasing frequency of terrorist attacks aimed at civilian and military targets and the consequent significant losses viz. economic and human lives caused by them, have highlighted the need to consider, more appropriately and rationally, the vulnerability of the buildings to progressive collapse. It requires a certain criteria to mitigate the effects of a localized damage.

The current design approaches, although based on probabilistic criteria, are not generally able to ensure an adequate level of security against local damage which can even lead to progressive collapse of the structure (Fig. 1). The first reason being that design guidelines are usually applied on a local level only (check of cross-sectional forces or element stability). Structural safety, therefore, is accounted for the local level only. The global safety, i.e., the safety against the collapse of the entire system or a major part thereof, is not only a function of the safety of all the individual elements against local failure but also of the system response to local failure. Different systems will respond differently to local failure. Such methods when applied to non-robust structures will produce unsafe designs. The other reason may be low probability of occurrence and the unpredictability of events, the difficulty in the retrieval of data regarding the scope of action and identification of an acceptable probability of collapse. These lead to the neglect of accidental actions during the design considerations (Starossek, 2006). Thus point out the need to identify new design criteria for robust structures.



Figure 1. Ronan Point, London, U.K. (1968).

A localized damage may result in progressive collapse extended to the whole or part of the structure. In such a case, the structure is not able to reach new stable equilibrium configurations or lacks the structural requirements such as strength, ductility, stability, continuity and redundancy. Development of chain reactions characterized by the activation of large displacements and deformations, separation of structural elements, redistribution of internal stresses, dynamic effects resulting from collapse are possible consequences of localized damage. In these circumstances,

the response of a structural system should be determined by non-linear dynamic analysis in the time domain, considering the variety of possible scenarios. The operational difficulties and the inability to predict in advance all possible causes initiating a progressive collapse, imposes the identification of design criteria to mitigate the effects. The aim of design is therefore realization of "Robust" structures for which the effects of damage are not disproportionate to the initiating event. The other possible strategies for prevention against progressive collapse are: event control, elements and connections designed for specific local resistance, redundancy, design of key structural elements, alternate load paths, compartmentalization, detailing rules for ductility and recommendations on the construction details and practices.

A small kitchen gas explosion in mid storey at Ronan Point in Canning Town, London in 1968 (Fig. 1) (Griffiths et al., 1968) has led to a catastrophic partial collapse of the building. This incident had prompted numerous efforts to develop structural design criteria for progressive collapse resistance. As an outcome, results of numerous studies were published in the seventies. This was also reflected in regulations with the introduction of specific projects aimed at creation of robust structures. During the eighties and nineties, the interest on this particular issue took a backseat. The terrorist activities leading to tragedies of Alfred P. Murrah Federal Building in Oklahoma in 1995 (Fig. 2), U.S. embassies in Nairobi and Dar-Es-Salam in 1998 and more recently the collapse of World Trade Centre Towers New York in 2001 (Corley, 2004), have provided impetus for research on improved building practices and design procedures to control the likelihood of progressive collapse.

This paper, dealing with the structural strength, analyzes the possible strategies for prevention of progressive collapse. Initially, the paper analyzes at general level, and then discusses in detail and in particular the design philosophy proposed in EN 1991-1-7 (Eurocode-1, 2006).

2 PREVENTION OF PROGRESSIVE COLLPAPSE – THE STRATEGY

The term robustness is commonly used with different meanings in different sectors of technological sciences (control theory, statistical inference, decision making, and programming). In civil engineering, in the context of structural systems subjected to exceptional hazards, the uncertainty associated with the structure, and the consequences of the hazard plays a prominent role in measuring structural robustness (Maes et al., 2006). A consensus meaning of the term is variously used as a synonym for stability, ductility, redundancy and resistance to complete collapse.

According to EN 1991-1-7 (Eurocode-1, 2006), the robustness is defined as "The ability of the structure to withstand events like fire, explosions, impact or consequences of human error, without being damaged to an extent disproportionate to the original cause". According to this definition, robustness is intended as intrinsic property of the structure and is explicitly linked to the concept of disproportionate collapse while recognizing that total collapse is an acceptable outcome from a hazard. "Resistance to collapse" is a property that is influenced by numerous conditions including the structural features and possible actions (Starossek, 2005). Robustness of structures varies widely with varying degree of actions while resistance to collapse may not be required for every structure. The distinction between "robustness" and "resistance to collapse" is defined so that the analysis and design strategies are differentiated according to the probability of occurrence of the event, extent of damage, structural response and consequences of collapse or, in other words, the level of risk. In relation to the latter, the lines of prevention can be grouped into two categories:

1) Within the contained levels of risk, the objective to confer "robustness" to the structure can be achieved by simple design and minimum requirements for ductile performance of structural elements and connections. Additional safeguards may be obtained through horizontal and vertical ties (tying), providing alternate load paths (bridging the gap), and design of key structural elements;
2) For high levels of risk, verification of the "resistance to collapse" against possible scenarios characterized by intensity, location and extent of the damage event is necessary. From this point of view, robustness can be achieved through the redundant design of structures and elements. Structure should be able to undergo limited damage, preventing the activation of chain reaction (performance-based design). The techniques that may be employed consist of redundancy, alternate load paths (bridging), design of key structural elements (key elements), control of events and compartmentalization.

A better understanding of the lines of prevention can be obtained starting from the definition of general likelihood of collapse. Given the generic accidental event 'E' characterized by a probability '$P(E_i)$', the local damage 'D' is the consequence of accidental event 'E_i', characterized by a probability '$P(D/E_i)$', and the probability of progressive collapse 'C' resulting in damage 'D', '$P(C/D \cap E_i)$'. The probability of progressive collapse of the structure, '$P(C)$' can be expressed as (Ellingwood & Dusenberry, 2005):

$$P(C) = P(C / D \cap E_i) \bullet P(D / E_i) \bullet P(E_i) \quad (1)$$

The probability of progressive collapse must be limited to an acceptable value. This is suggested by limiting the second variable in (1). The three probabilities discussed in (1) can be limited at three levels:

1. Event control i.e. reducing the probability of the event E_i, $P(E_i)$;
2. Local damage (range of type of structures characterized by low sensitivity to the damage, assured

requirements of specific local resistance), limiting the probability of local damage D as a consequence of event E_i, $P(D/E_i)$;

3. Progressive collapse (statically indeterminate structures, alternative load paths), limit the probability of progressive collapse resulting in the localized damage D caused by the event E_i, $P(C/D \cap E_i)$;

The first operating line, which provides for the adoption of preventive measures aimed at limiting the accidental action, is classified as non-structural. Direct as well as indirect design methods can be used to work on the local damage and the progressive collapse. The direct design methods are based on specific local resistance of structural elements i.e. structural response against accidents and the capability of the structure transferring the loads in case of "removal" of structural elements. The indirect design methods ensure minimum level of strength, ductility and structural continuity or minimum levels of robustness.

For contained levels of risk, the use of (1) can lead to operational difficulties. The adoption of equation independent of the type of accidental event can simplify the problem. In this case (1) assumes the simplified expression (Ellingwood & Dusenberry, 2005):

$$P(C) = P(C/D) \bullet P(D) \quad (2)$$

Prevention techniques in this case ensure the transfer of loads through "alternate paths" to avoid the propagation of the event. This can be achieved through the design of continuous structures, statically indeterminate and ductile.

3 STRUCTURAL ROBUSTNESS AND GLOBAL NORMS

The first regulations regarding the progressive collapse were based on studies conducted following the collapse of the Ronan Point in 1968. The concept of structural design to be implemented in a way that damages are not disproportionate to the cause of initiating event was introduced by the UK in 1976 by building regulations. Later it was 'Approved document A' to realize the concepts indicating the design criteria based on tying the horizontal and vertical elements, identification of alternative load paths by bridging the gaps and design of key structural elements. Later prevention strategies were implemented, modified and supplemented by major design codes on metal structures, masonry, timber and concrete. The use of these prescription rules and study of response of structures affected by accidental actions designed in compliance with these requirements have provided with the upgraded version of the documents. The recent version of this document is available as 'Approved document A' published in 2004 with amendments.

In the United States the basic concept regarding the progressive collapse were published through legislation in 1972 in the document ANSI A.58.1. Later these concepts were developed and published in extensive first version of the ASCE-7 document on general design requirements in 1982 which have been upgraded over the years. The basic concepts were similar to that adopted in the UK which were refined by normative documents relating to different materials and the codes regarding the structural design. A significant contribution to this subject was made by US government agencies like Interagency Security Committee (ISC), General Services Administration (GSA), Department of Defense (DoD), Federal Emergency Management Agency (FEMA) which have published specific documents related to progressive collapse. Similarly, for other places like Canada, Australia and New Zealand, the methodology regarding the design criteria of robust structures is analogous to that of the UK and the US.

The studies with research papers and the subsequent normative laws provide the basic criteria for the design of robust structures. With these as reference point, most of the regulations and codes have adopted the same design philosophy and methodological approach. The same observation applies to the Eurocode in EN 1991-1-7 that specifically deals with the issues related to the structural design in the presence of accidental actions. However, the 'Approved document A' and EN 1991-1-7 follow the same approach, the latter proposes an extensive discussion of accidental actions and the corresponding methodologies for analysis.

4 ROBUSTNESS AND EN 1991-1-7

The prevention strategies identified by EN 1991-1-7 initiates with the general principles of design provided by EN 1990. It states that the structure must be designed so as to ensure adequate fire resistance, accidental actions, human error so that the effects are not disproportionate to the cause. Ensuring these, the chances of collapse are limited signifying an acceptable level of structural sustainability which is economically justifiable. With this consideration, it becomes necessary to consider the accidental actions in the planning stages. Including this aspect EN 1991-1-7 provides for the classification of buildings into three consequence classes (CC) characterized by low (CC1), medium (CC2) and high (CC3) consequences of failure. The division of the buildings in these classes depends on the type and use of the building, number of storey and extensions plans. In each of the consequences classes, the method of analysis and prevention strategies vary. The consequences classes are:

1) Consequence Class 1 (CC1): There are no specific considerations against accidental actions except that the required structural design is in accordance with the criteria set by EN 1990 – EN 1999;
2) Consequence Class 2 (CC2): The recommended design analysis based on simplified static equivalent actions that can reproduce the accidental actions and respect the prescriptive detailing requirements;

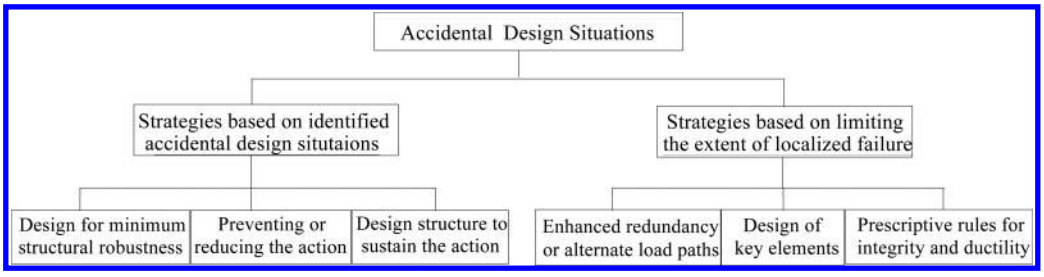


Figure 2. Strategies for accidental design situations as per EN 1991-1-7.

3) Consequence Class 3 (CC3): An examination and study of possible scenarios and if necessary, implementation of hazard analysis and non-linear analysis in dynamic range.

Along with the consequences classes, additional definitions are considered by EN1991-1-7 to define the strategic lines for prevention of accidental actions. Considering the randomness of the accidental events which cannot be established in advance for all possible scenarios, EN1991-1-7 has broadly classified the accidental actions into identifiable and unidentifiable actions as shown in Fig. 2. Factors such as the probability of occurrence of action, the consequences of its occurrence, the possibility of using preventive measures and the level of acceptable risk for deciding the set of accidental actions qualify as identifiable actions. Apart from the case of earthquake and fire, which are dedicated to specific parts of Eurocodes, EN1991-1-7 explicitly considers the identifiable actions of explosions and impact. In the case of impact, the actions considered due to vehicles, forklifts, trains, ships and helicopters as a result of abrupt maneuvers landing. For explosions and impact, it proposes representation of actions, operational criteria and risk analysis wherever necessary.

The preventive measures suggested in case of identified actions are:

1) Control of events such as:
   – reduction of the probability of occurrence of action at a level considered acceptable;
   – controlling of intensity of the action through structural identification;
2) Measures to protect the structure can limit the effects of accidental actions;
3) Structural Identification
   – identification and design of key structural elements;
   – use of materials and design of structural elements with adequate levels of ductility;
   – Redundant structures ensure the redistribution of load through alternate load paths.

The preventive measures depend on the peculiarity of the action like intensity or mode of action, characteristics of the structure and the consequence of the collapse.

In case of unidentified accidental actions, the choice of prevention strategies should mitigate the potential failure. The ultimate goal of the design and construction of structures shall be to survive in partial or whole for a time sufficient to evacuate the building and the area surrounding it. The strategies suggested are:

1) Design key elements, on which the stability of the structure depends to sustain the effects of model accidental action (suggested value for buildings is 34 kN/m^2);
2) Design the structure so that the localized damage will not endanger the stability of the whole or part of it;
3) Apply the prescriptive rules of detailing to provide acceptable level of robustness for the structure.

In this specific case for structures, EN 1991-1-7 divides and specializes prevention strategies in four consequences classes (CC1-CC3) as follows:

1) Consequence Class 1 (CC1): Design for normal use in accordance with the criteria of the Eurocodes 0-9;
2) Consequence Class 2a (CC2a): In addition to the requirements for consequence class 1, inclusion of horizontal ties in the case of framed structures (Fig. 3) and anchoring systems on the floors in the case of load-bearing masonry structures;
3) Consequence Class 2b (CC2b): For load-bearing masonry and framed structures, in addition to the requirements for consequence class 1, inclusion of horizontal ties (Fig. 4) corresponding to each vertical column or bearing wall. Alternatively, the building shall be so designed that the "removal" of any column does not affect the stability of the whole structure and that the damage does not exceed a limit deemed acceptable (acceptable limit suggested: damaged area of the floor adjacent to the element "removed" less than 15% of the total area);
4) Consequence Class 3 (CC3): In depth analyses are suggested that include risk analysis. The complexity and the degree of depth of analysis will depend on the particular problem analyzed. Intervention strategies may be structural (design structure and its elements for adequate levels of resistance, via the alternate load paths) or non-structural (reduction of the probability of occurrence of the action, its intensity and consequences of the collapse).

From the design viewpoint, it is important to note that the specific criteria for dimensions are provided

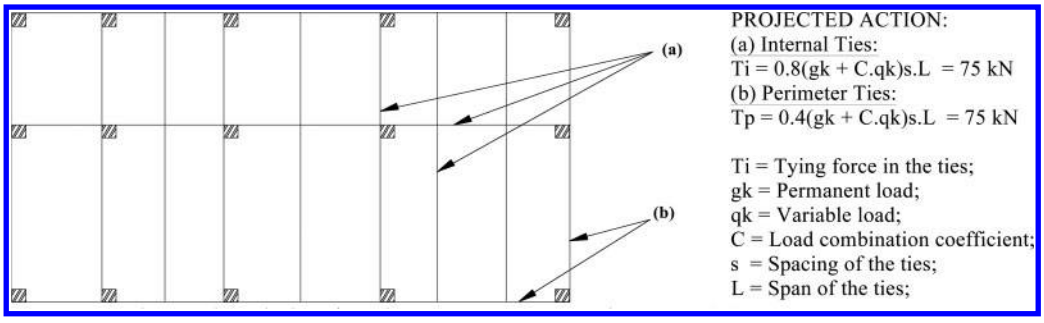


Figure 3. Horizontal tying of members as per Consequence Classes 2a and 2b as per EN 1991-1-7.

only to the classes 2a and 2b (Fig. 4). The objective of these design requirements is to give the structure a minimum level of robustness, which ensures the development of resistant mechanisms to enable the transfer of stresses, in the case where the redundancy is less. For consequence class 3, however, possible intervention strategies are indicated to the particular problem analyzed.

The risk analysis for consequence class 3 (CC3) may be conducted at qualitative, and where the importance of the problem makes it necessary, also at quantitative level. The need for possible action against the progressive collapse is dependent on the adoption of risk acceptance criteria. In this respect the EN 1991-1-7 provides only limited guidance, delegating the choice to the engineer. If necessary, the measures of mitigation of the risk may consist in:

- Attenuation of events implemented by aid either structural or non-structural;
- Event control;
- Design of structures characterized by reserves of strength, stiffness and redundancy;
- Reduction in the levels of damage by controlled collapse.

5 ROBUSTNESS AND DUCTILITY

A complete understanding and fulfillment of required ductility and available ductility is a key step which accompanies several advantages for the system. Economical advantages, avoiding a brittle damage which in turn gives more escaping time and dissipation of more energy with less damage are the major advantages that are achieved with careful design of ductile system. Thus ductility should be quantified at same level as strength and stiffness. For a structural system, ductility is quantified as its ability to undergo large deformations after initial yielding without any significant reduction in the ultimate strength. Ductility in a system can be achieved by enabling the joints to provide large rotations, so that membrane forces can be activated allowing a redistribution of internal forces. Thus an adaptive structure is created which keeps sufficient strength even under exceptional loading and large deformations.

Research till date has exploited ductility as an essential tool for systems when subjected to seismic forces. This has resulted in seismic design standards where, ductility requirements for joints are formulated in terms of deemed to satisfy rules i.e. provided that certain design requirements are met, the joint may be assumed to behave in a ductile manner sufficient enough to ensure a safe structural behaviour. However, here a big question arises whether the seismic design rules are adequate for protective design methods against progressive collapse? Studies have shown that with seismic detailing, the damage due to blast can be significantly reduced. A case study of terrorist bombing of the Alfred P. Murrah Federal Building in Oklahoma City in 1995 is such an interesting case to evaluate this point. The building at the time of design and construction phase was in accordance with the prevalent regulations. Later, the seismic standards were included and updated. Researchers had commented that if the building would have been designed according to the present seismic regulations, it would have performed better by minimum of 50% to a maximum of 80% depending upon the seismic structural measures adopted, leading to less damage and causalities (Corley 2004). But, conclusively, it can be stated that the seismic regulations are not equivalent to the blast effects or impact or fire loads and is one of the cases to be considered under extreme loading conditions. Some guidance is available in literature regarding the nature of occurrence and effects of blasts overpressures and fire loads and some recommendations are also available to include them into design. But consistent experimental verification, numerical assessment and codified literature are the requirements so that these can be implemented and such extreme events as progressive collapse can be prevented.

6 CONCLUSION

This paper focuses on the problem of structural design in the presence of accidental actions. In the absence of specific structural requirements, the damage due to the accidental actions can lead to the development of chain reactions with a consequent collapse of the whole or part the structure. Therefore, establishing the

importance of accurate, sustainable but economically feasible prevention strategies is crucial.

The probability of failure resulting from accidental actions is influenced by the type of event (intensity, mode of collapse), the local damage caused by these event and the structural response. From the structural point of view, the probability of failure can be limited by acting on the accidental events, by means of control of events, the local damage by design of structures with limited sensitivity to the damage and provided with appropriate performance requirements and, ultimately, on statically indeterminate structures by providing continuity and ductility to the structural system. Studies and research on the subject have been accompanied by the development of codes and regulatory requirements which, although different in different countries when compared at local level, have a common approach to the philosophy and methodology. To better analyze the design strategy, the last part of the work was devoted to an analysis of EN 1991-1-7 (Eurocode-1, 2006).The regulations are normative in nature and lack consistent experimental and numerical verification.

According to EN 1991-1-7 (Eurocode-1, 2006), the characteristics of the consequence classes classify the accidental actions and guides the choice of prevention techniques from progressive collapse. These can range from simple design specifications to real strength and ductility requirements, depending on the event type and structural response. From the computational point of view, simplified analyses by forces equivalent to the actions or more sophisticated analysis is non-linear dynamic range are recommended.

At the conclusion of the work, it is important to note that although the prevention strategies against the progressive collapse are well outlined, these are not yet adequately translated into design specifications/ guidelines. The peculiarity of each problem in terms of accidental action and structural response makes it difficult to identify structural design criteria of general validity. The problem is further complicated by the lack of experimental data; the complexity of the numerical analysis necessary for the study of the structural response and the multiplicity of possible scenarios. Instead the definition of rules aimed to acquire the minimum strength and robustness achieved through requirements such as continuity and structural ductility seems more feasible. In that regard, efforts are required in terms of both numerical and experimental study. Studies and research on this specific issue are currently underway. The same authors of this paper are involved in a research project that seeks to identify requirements for minimum ductility for beam-column joints of composite steel and concrete structures as a tool for the prevention of the progressive collapse.

ACKNOWLEDGEMENT

This work was developed as part of a research project funded by the Research Fund for Coal and Steel (RFCS) of the European Economic Community.

REFERENCES

Building Regulations 2000 – *Approved Document A – Structures, Approved Document A – Amendments* 2004 – The Stationary Office, 2004.

Corley, W. G., Lessons learned on Improving Resistance of Buildings to Terrorist Attacks, *Journal of Performance of Constructed Facilities*, Vol. 18, n. 2, pp. 68–78, May, 2004.

Ellingwood, B. R., Dusenberry, D. O., Building Design for Abnormal Loads and Progressive Collapse, *Computer-Aided Civil and Infrastructures Engineering*, Vol. 20, pp. 194–205, 2005.

EN 1990, Eurocode – *Basis of Structural Design*, CEN European Committee for Standardization, April 2002.

EN 1991-1-7, Eurocode 1 – *Actions on Structures – Part 1–7: General Actions – Accidental actions*, CEN European Committee for Standardization, July 2006.

Griffiths, H., Pugsley, A., Saunders, O., *Report of the Inquiry* into the Collapse of Flats at Ronan Point Canning Town, Her Majesty's Stationery Office, London, 1968.

Maes, M. A., Fritzsons, K. E. and Glowienka, S., Structural Robustness in the Light of Risk and Consequence Analysis, *Structural Engineering International*, Vol. 16, n. 2, pp. 101–107, May 2006.

Seema, *"Robust Structures by Joint Ductility", Ph.D. Thesis*, University of Trento, Italy, March 2009.

Starossek, U., and Wolff, M., "Design of collapse-resistant structures," *Workshop on Robustness of Structures, Watford, UK, November, 28–29, 2005*.

Starossek, U., Progressive Collapse of Structures: Nomenclatures and Procedures, *Structural Engineering Internationl*, Vol. 16, n. 2, pp. 113–117, May 2006.

Research and Applications in Structural Engineering, Mechanics and Computation – Zingoni (Ed.)
© 2013 Taylor & Francis Group, London, ISBN 978-1-138-00061-2

Performance-based plastic design of earthquake resistant tall building frames

W.-C. Liao
National Taiwan University, Taipei, Taiwan

M.R. Bayat
Englekirk & Sabol Structural Engineers, Los Angeles, California, USA

S.C. Goel
University of Michigan, Ann Arbor, Michigan, USA

ABSTRACT: Seismic design of tall building frames poses special problems because of factors such as, participation of higher modes, P-Delta effects, column design, etc. Current code practice does not yield very satisfactory designs. In recent years a design methodology, which accounts for structural inelastic behavior directly and practically eliminates the need for any assessment or iteration after initial design, has been developed. The method is called Performance-Based Plastic Design (PBPD). It is a complete design method that considers factors such as determination of appropriate design lateral forces, member strength hierarchy, selection of desirable yield mechanism, and target drift right from the beginning of the design process. This paper will briefly present the methodology. Design examples of tall steel and RC moment frames are included along with results of inelastic static and dynamic analyses under severe ground motions to demonstrate the merits of the PBPD method.

1 INTRODUCTION

Tall buildings have become a solution to the increasing population of cities on the urban landscape. However, the design of these tall buildings in seismically active regions may require more work beyond a traditional design based on elastic analysis and force reduction factors.

Design codes, such as the International Building Code (ICC 2006), were mainly developed for application to low and medium-rise buildings. In addition, they use elastic analysis with force reduction factors for strength design which may not be adequate for tall buildings where higher modes of vibration contribute significantly to seismic response. Moreover, no guidance is provided as to how to get the initial starting design or how to make changes during iteration to achieve the intended performance.

The objective of this paper is to present a performance-based practice developed by Goel and his associates at the University of Michigan for the seismic design of high-rise buildings. This method is called Performance-Based Plastic Design (PBPD). The design concept uses pre-selected target drift and yield mechanism as key performance objectives. This method has been successfully applied to steel MF, BRBF, EBF, STMF, and CBF (Goel & Chao 2008). Results of extensive inelastic static and dynamic analyses have proven the validity of the method. In all cases, the frames developed the desired strong column-weak beam yield mechanisms as targeted, and the story drifts/ductility demands were well within the selected design values, thus meeting the selected performance objectives. Comparisons of responses with corresponding baseline frames designed by current practice have consistently shown superiority of the proposed methodology in terms of achieving the desired behavior. An overview of the PBPD method and examples of a 20 story steel moment frame and a 20 story RC moment frame are briefly presented in the paper.

2 WEAKNESS OF CURRENT CODE PRACTICE FOR TALL BUILDINGS

Seismic design of tall building frames poses special problems because of factors such as, participation of higher modes, P-Delta effects, column design, etc. Current code practice, which is primarily based on elastic analysis, does not yield very satisfactory designs. In the current U.S. seismic design practice it is common to obtain design base shear from code-specified spectral acceleration assuming the structures to behave elastically, and reducing it by force reduction factor, R, depending upon available ductility of the structural system. This strength demand is increased according to the importance of specific structures by using an occupancy importance factor, I. After selecting the member sizes for required strengths as obtained from elastic analysis, the calculated drift at design forces is multiplied by a deflection amplification factor, C_d, and kept within specified limits (generally

in the order of 2%). Appropriate detailing provisions are followed in order to meet the expected ductility demands. When struck by severe ground motions, however, the structures designed by such procedures have been found to undergo inelastic deformations in a somewhat "uncontrolled" manner. The inelastic activity, which may include severe yielding and buckling of structural members and connections, can be unevenly and widely distributed in the structure. This may result in rather undesirable and unpredictable response, sometimes total collapse, or difficult and costly repair work at best.

While the above design practice has served the profession rather well in the past, societal demands are pushing the practice to achieving higher levels of performance, safety and economy including life cycle costs. Los Angeles Tall Building Structural Design Council and similar organization in San Francisco have recommended alternative design procedures for tall buildings based on inelastic behavior, albeit requiring extensive iterations to arrive at the desired design.

For the practice to move in that direction, design factors such as, determination of appropriate design lateral forces and member strength hierarchy, selection of desirable yield mechanism, and structure strength and drift etc., for specified hazard levels should become part of the design process right from the start.

3 PERFORMANCE-BASED PLASTIC DESIGN (PBPD) METHOD

3.1 *PBPD concept*

The PBPD method uses pre-selected target drift and yield mechanism as key performance objectives. These two design parameters are directly related to the degree and distribution of structural damage, respectively. The design base shear for a specified hazard, which is generally given as design spectrum in the codes, is calculated by equating the work needed to push the structure monotonically up to the target drift to the energy required by an equivalent EP-SDOF to achieve the same state (Fig. 1). Also, a new distribution of lateral design forces is used, which is based on relative distribution of maximum story shears consistent with inelastic dynamic response results (Chao et al. 2007). Plastic design is then performed to detail the frame members and connections in order to achieve the intended yield mechanism and behavior. Thus, determination of design base shear, lateral force distribution, and plastic design are three main components of the PBPD method.

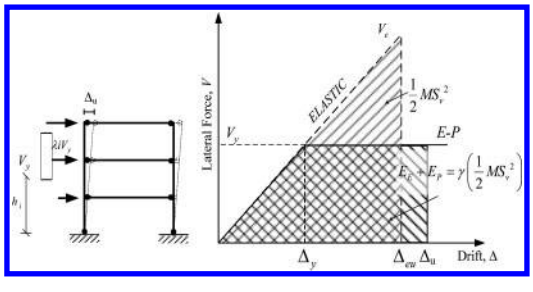


Figure 1. PBPD concept.

3.2 *Determination of design base shear*

Determination of the design base shear for given hazard level is a key element in the PBPD method. It is calculated by equating the work needed to push the structure monotonically up to the target drift to that required by an equivalent elastic-plastic single degree of freedom (EP-SDOF) system to achieve the same state. Assuming an idealized E-P force-deformation behavior of the system, the work-energy equation can be written as:

$$(E_e + E_p) = \gamma\left(\frac{1}{2}MS_v^{\,2}\right) = \frac{1}{2}\gamma M\left(\frac{T}{2\pi}S_a g\right)^2 \quad (1)$$

where E_e and E_p are, respectively, the elastic and plastic components of the energy (work) needed to push the structure up to the target drift. S_v is the design pseudo-spectral velocity; S_a is the pseudo spectral acceleration; T is the natural period; and M is the total mass of the system. The energy modification factor, γ, depends on the structural ductility factor (μ_s) and the ductility reduction factor (R_μ), and can be obtained by the following relationship:

$$\gamma = \frac{2\mu_s - 1}{R_\mu^{\,2}} \quad (2)$$

Because of their simplicity, spectra proposed by Newmark and Hall (1982) were used to relate the ductility reduction factor, R_μ, and the structural ductility factor, μ_s, for EP-SDOF. It should be mentioned that for this purpose any inelastic spectra for EP-SDOF systems can be used as preferred, such as by Miranda and Bertero (2004).

The work-energy equation can be re-written in the following form

$$\frac{1}{2}\left(\frac{W}{g}\right)\cdot\left(\frac{T}{2\pi}\frac{V_y}{W}g\right)^2 + V_y\left(\sum_{i=1}^{N}\lambda_i h_i\right)\theta_p = \frac{1}{2}\gamma\left(\frac{W}{g}\right)\cdot\left(\frac{T}{2\pi}S_a g\right)^2 \quad (3)$$

or

$$\left(\frac{V_y}{W}\right)^2 + \frac{V_y}{W}\left(h^*\cdot\frac{\theta_p 8\pi^2}{T^2 g}\right)\theta_p - \gamma S_a^{\,2} = 0 \quad (4)$$

The admissible solution of Equation (4) gives the required design base shear coefficient, V_y/W:

$$\frac{V_y}{W} = \frac{-\alpha + \sqrt{\alpha^2 + 4\gamma S_a^{\,2}}}{2} \quad (5)$$

where α is a dimensionless parameter given by,

$$\alpha = \left(h^*\cdot\frac{\theta_p 8\pi^2}{T^2 g}\right) \quad (6)$$

The term θ_p represents plastic component of the target drift ratio, and

$$h^* = \sum_{i=1}^{N} (\lambda_i h_i) \tag{7}$$

As mentioned earlier, Equation (5) for V_y was derived by assuming ideal elastic-plastic (E-P) force-deformation behavior and "full" hysteretic loops for the system. That is characteristic of a number of ductile steel framing systems, such as MF, EBF, STMF, and BRBF. For systems that do not posses such hysteretic property, such as steel braced frames with buckling type braces or RC frames, some modification is warranted.

Based on consideration of the effect of degrading hysteretic behavior on peak (target) displacement, Investigators have studied the effect of degrading hysteretic behavior of SDOF systems on resulting peak displacements. The results show that the peak displacements are larger than those of systems with non-degrading hysteretic behavior in short period range, but are about equal for longer periods. Approximate expressions have been proposed for modification factors to account for this effect, e.g., factor C_2 in FEMA 440 (2006). Thus, the target design drift for a given structural system with degrading hysteretic behavior can be divided by the C_2 factor which will give design target drift for an equivalent non-degrading system. The design base shear can then be calculated by using this modified target drift and Equation (5).

3.3 *Lateral force distribution*

Traditionally, vertical distribution of design lateral forces in modern building codes has been based on elastic fundamental mode response of MDOF systems. Modifications have been made in the basic equations to account for effects, such as contribution of higher modes. Chao et al. (2007) proposed a modified lateral force distribution mainly derived by empirical fit with results from a variety of common structural systems as shown in Equation (8).

$$F_i = (\beta_i - \beta_{i+1}) \cdot \left(\frac{w_n h_n}{\sum_{j=1}^{n} w_j h_j} \right)^{0.75T^{-0.2}} V_y \tag{8}$$

where F_i is the design lateral force at level i, the terms w and h represent seismic weight and height above the base, and V_y is the total base shear. β_i is the ratio V_i/V_n, termed as shear distribution factor.

4 ADVANTAGES OF DESIGN OF TALL BUILDINGS BY USING PBPD METHOD

The PBPD method not only accounts for structural inelastic behavior directly but also considers factors such as determination of appropriate design lateral forces, member strength hierarchy, selection of desirable yield mechanism, and target drift right from the beginning of the design process. Thus, advantages of design of tall buildings by using PBPD method can be summarized as below:

- Assure strong column/weak beam design reached because the yielding mechanism is preselected and all non designated yielding members (columns) are designed by capacity design approach considering an entire "column tree" instead of single joints.
- P-Delta effect is included in the determination of required moment capacity of beams, particularly for the 20-story RC SMF, in order to provide necessary strength to counter the overturning due to gravity loads.
- The higher mode effects are considered in a more representative distribution of lateral design forces used in PBPD design, which is based on relative distribution of maximum story shears consistent with inelastic dynamic response results.

5 DESIGN EXAMPLES

5.1 *20-story steel moment frame*

An example of a tall steel moment frame is presented in this section. This 20-story frame was the subject of extensive analytical study as part of the SAC Steel Research Program (Gupta & Krawinkler 1999). The frame was re-designed by the PBPD method as outlined in the preceding sections. The resulting design and its responses under static pushover and dynamic time-history analyses due to selected set of ground motions are compared with those of the original SAC frame.

The framing plan of the structure is shown in Figure 2. Since the original SAC frame was designed according to UBC (1994), same loading and other design parameters were used for redesign of the frame by PBPD method. The story heights are 5.5 m for the

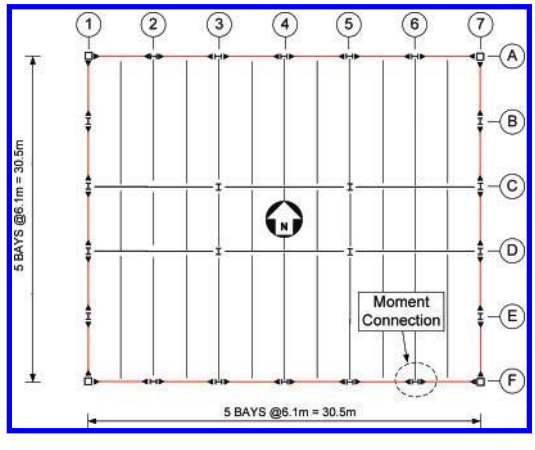


Figure 2. Floor plan of the LA 20-story SAC building.

Table 1. Design parameters for 20-story steel PBPD frame.

Design parameters	10% in 50 years Hazard (2/3MCE)	2% in 50 years Hazard (MCE)
S_a	0.36 g	0.54 g
T(sec.)	2.30	2.30
Yield Drift Ratio	1.0%	1.0%
Target Drift Ratio	2%	3%
Inelastic Drift Ratio	1%	2%
μ	2.0	3
R_μ	2.0	3
γ	0.75	0.438
α	0.942	1.884
V/W	0.094	0.037
Design Base Shear	5098 kN (governs)	2033kN

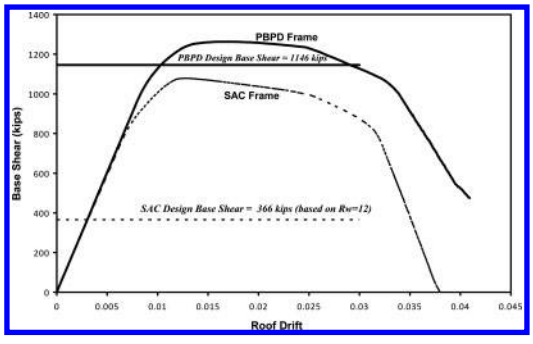


Figure 3. Comparison between pushover curves of PBPD frame and SAC frame.

first story and 4 m for all others. The PBPD procedure as described in the preceding sections was used to redesign the 20-story SAC frame. The important design parameters are given in Table 1. The target yield mechanism is sway mechanism similar to the one shown in Figure 1. Grade 50 steel was used. More details can be found elsewhere (Bayat 2010).

Nonlinear static (pushover) and dynamic (time-history) analyses were carried out for the SAC and PBPD frames by using Perform-3D program (CSI 2007). A lumped "gravity column" was added which enables the model to capture the P-Delta effect as well as the contribution of all gravity columns in the response of the structure. Strength degradation of moment-rotation behavior of plastic hinges and panel zone deformations were also modeled.

Figure 3 shows base shear versus roof drift plot of the two frames from the pushover analysis. The PBPD frame has somewhat greater ultimate strength than the SAC frame. The design base shear for SAC frame is significantly smaller than its ultimate strength because for steel moment frames, the design is generally governed by drift. As targeted in the design, absence of plastic hinges in columns of the PBPD frame (except at the bases) can be noticed. In contrast, significant plastic hinging in the columns of the SAC frame in lower stories is observed, which is also reflected in the

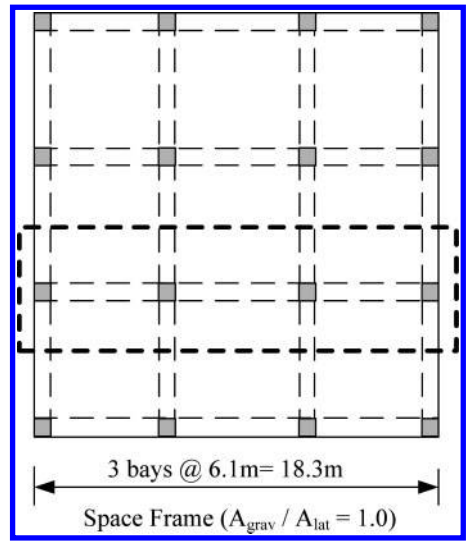


Figure 4. Floor plan of the 20-story RC space moment frame building.

differences in deformed shape of the two frames, i.e., concentration of drift in the lower stories of the SAC frame. Also, plastic rotations in the beams and column bases at 3.5% roof drift are significantly smaller in the PBPD frame as compared with those in the SAC frame.

Inelastic dynamic analyses of both frames were carried out by using 10/50 and 2/50 SAC ground motions for LA site (Somerville et al. 1997). The results showed superior behavior of the PBPD frame under 10/50 as well as 2/50 hazard levels. No unexpected plastic hinging was observed in the columns of the PBPD frame, whereas significant plastic hinging was observed in the SAC frame columns under both sets of ground motions (Bayat 2010). Moreover, collapse of the SAC frame was seen for three ground motions, namely LA30, LA35, and LA36. Even though those ground motions caused large story drifts in the PBPD frame, but the structure did not lose stability.

5.2 *20-story RC special moment frame*

RC structures present special challenge due to their complex and severely degrading ("pinched") hysteretic behavior. While development of the PBPD method for RC structures is currently in progress, results from the study so far have been most promising. An example of a 20-story RC moment frame structure is briefly presented in this section. This baseline space frame was designed to comply with the requirements of ASCE 7-05 and ACI 318-05 (Haselton & Deierlein 2007). It was redesigned by the modified PBPD method by using the FEMA 440 (2006) C_2 factor approach as mentioned in Section 3.2. More details can be found elsewhere (Liao & Goel 2010).

Typical floor plan is shown in Figure 4, and important design parameters are given in Table 2. For

Table 2. Design parameters for 20-story PBPD RC moment frame.

Design parameters	10% in 50 years Hazard (2/3MCE)	2% in 50 years Hazard (MCE)
S_a	0.3 g	0.45 g
T(sec.)	3.36	3.36
C_2	1	1
Yield Drift Ratio	0.5%	0.5%
Target Drift Ratio	2%	3%
Inelastic Drift Ratio	1.5%	2.5%
μ	4	6
R_μ	4	6
γ	0.4375	0.3056
α	0.662	1.103
V/W	0.055	0.054
Design Base Shear	1135 kN (governs)	1103kN

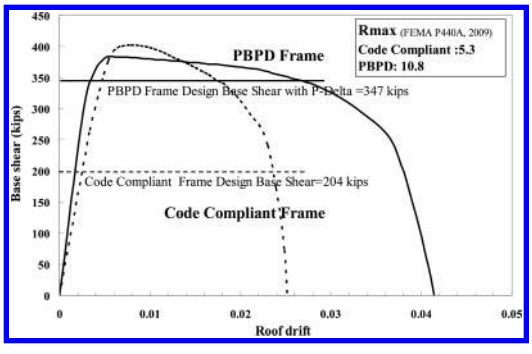


Figure 5. Pushover curves for PBPD and code compliant 20 story RC moment frames.

response evaluation purposes the baseline code compliant frame and the PBPD frame were subjected to inelastic pushover and time-history analyses by using Perform 3D as well.

It should be mentioned that P-Delta effect was not included in Equation (18). That is the way design of beams of the PBPD steel frame was performed. However, due to strength degradation at beam plastic hinges it was found necessary to include P-Delta effect in the determination of required moment capacity of beams for the 20-story RC frame. That was accomplished by adding "P-Delta lateral force" to the basic design force, F_i, in Equation (8). Force F_{i-PD} can be taken equal to $P_i\theta_u$, where P_i represents the tributary gravity load at floor level i and θ_u the target design drift ratio which is assumed constant for design purposes. Their influence on the total lateral design force can be clearly noticed as it has significant effect on the required frame strength.

The pushover curves for the two frames in Figure 5 show that even though the design base shear for the baseline is smaller than that of the PBPD frame, the ultimate strength of the two are almost equal. That is mainly due to the fact that the design of the baseline

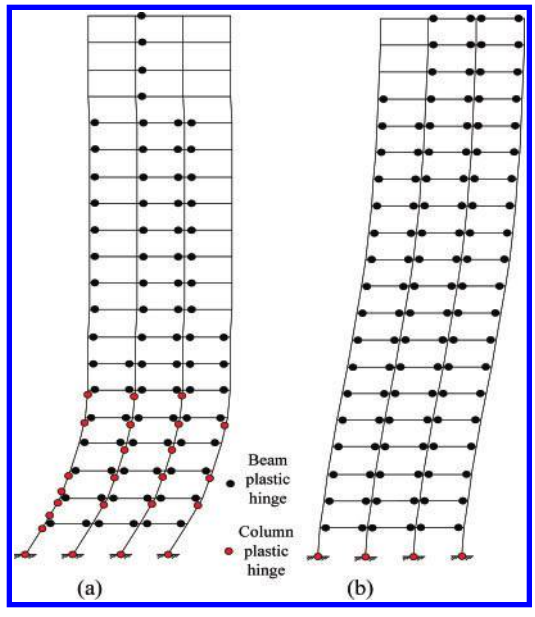


Figure 6. PH locations at 2.5% roof drift, (a) Code compliant frame, (b) PBPD frame; Pushover Analysis.

frame is governed by drift which requires major revision of the member sizes after they have been designed for strength. That iteration step is not needed in the PBPD method.

Figure 6 shows the deformed shape and location of plastic hinges of the two frames at 2.5% roof drift. Formation of plastic hinges in the columns and story mechanism in the lower part of the baseline frame can be clearly noticed. In contrast, there are no unintended plastic hinges in the columns of the PBPD frame, resulting in more favorable deformed shape and yield pattern as targeted in the design process.

The comparison of maximum interstory drifts of the baseline and PBPD frames obtained from time-history analyses using appropriately scaled ground motion records representative of 2/3 MCE and MCE hazard levels can be found in Figure 7. For clarity and brevity only the mean values of maximum interstory drifts are shown here. The results show that the mean maximum interstory drift ratios of the PBPD frames are well within the corresponding target values, i.e., 2% for 2/3 MCE and 3% for MCE. Moreover, the story drifts of the PBPD frames are more evenly distributed over the height as compared with those of the baseline frame where undesirable "softness" in the lower stories is evident, which is caused mainly by plastic hinges in the columns. Formation of plastic hinges in the columns and story mechanism in the lower part of the baseline frames can be clearly noticed. In contrast, there are no unintended plastic hinges in the columns of the PBPD frame, resulting in more favorable deformed shape and yield pattern as intended in the design process.

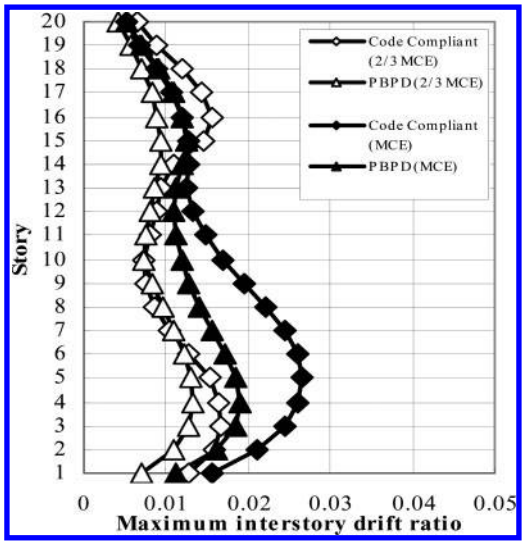


Figure 7. Comparison of maximum interstory drifts by time-history analyses of code complaint and PBPD frames for 2/3 MCE and MCE hazard levels.

6 SUMMARY AND CONCLUSION

The PBPD method is a direct design method which uses pre-selected target drift and yield mechanism as key performance objectives. The examples of 20-story steel and RC moment frames as presented in this paper showed that the method is especially advantageous for tall frames where the cumbersome and lengthy iterative process in current design practice can be completely eliminated, while leading to excellent performance as targeted.

REFERENCES

Bayat, Mohammad Reza. Performance-Based Plastic Design of Earthquake Resistant Steel Structures Concentrically Braced Frames, Tall Moment Frames, Plate Shear Wall Frames. Thesis (Ph.D.)–University of Texas at Arlington, 2010

Chao, S.-H., Goel, S. C., and Lee, S.-S., "A Seismic Design Lateral Force Distribution Based on Inelastic State of Structures." Earthquake Spectra, V. 23, No. 3, 2007, pp. 547–569

CSI, "PERFORM-3D v.4.0 User Manual." Computers & Structures Inc, 2007

FEMA, "Quantification of Building Seismic Performance Factors (ATC-63 Project)," FEMA P695, Federal Emergency Management Agency, Washington D.C., 2009

FEMA, "Improvement of Nonlinear Static Seismic Analysis Procedures." FEMA 440, Federal Emergency Management Agency, Washington D.C., 2006

Goel, S.C., and Chao, S.-H., "Performance-Based Plastic Design: Earthquake Resistant Steel Structures." International Code Council, 2008

Gupta, A. and Krawinkler, H., "Seismic Demands for Performance Evaluation Steel Moment Resisting Frame Structures." Report No. 132, The John A. Blume Earthquake Engineering Center, Dept. of Civil and Env Eng., Stanford University, 1999

Haselton, C.B., and Deierlein, G.G. "Assessing Seismic Collapse Safety of Modern Reinforced Concrete Frame Buildings." Report No.156, John A. Blume Earthquake Engineering Center, Dept. of Civil and Env Eng., Stanford University, 2007

ICC, "International Building Code (IBC2006)," International Code Council, 2006

Liao, W.-C. and Goel S. C., "Performance-Based Plastic Design of Earthquake Resistant Reinforced Concrete Moment Frames", Technical Report No. UMCEE 10-01, University of Michigan, Ann Arbor, MI, 2010, 206 pp.

Miranda, E. and Bertero, V. V., "Evaluation of Strength Reduction Factors for Earthquake-Resistant Design." Earthquake Spectra, Vol. 10, No. 2, 2004, pp. 357–379

Newmark, N. M., and Hall, W. J., "Earthquake Spectra and Design," Earthquake Engineering Res. Inst., El Cerrito, California, 1982

Somerville, P. G., Smith, M., Punyamurthula, S., and Sun, J. "Development of Ground Motion Time Histories for Phase 2 of the FEMA/SAC Steel Project." Report No. SAC/BD-97/04, SAC Joint Venture, Sacramento, CA., 1997

Uniform Building Code. International Conference of Building Officials, Whittier, CA., 1994

Research and Applications in Structural Engineering, Mechanics and Computation – Zingoni (Ed.)
© 2013 Taylor & Francis Group, London, ISBN 978-1-138-00061-2

Parametric study of pyramid-like tubular structure

Gin-Show Liou & Heng-Chih Kuo
Department of Civil Engineering, National Chiao Tung University, Hsin-Chu, Taiwan

ABSTRACT: Framed-tube structure is a generally used structural type for tall buildings. Its basic form is closely spaced columns connected with deep spandrel beams at the periphery of building structure. This structural type is very efficient for resisting horizontal (wind) load. However, Shear lag phenomenon is the main cause to reduce the effectiveness of tubular structure. Therefore, reducing shear lag effect become a challenge to design a framed-tube structure. The paper will study the behaviors of pyramid-like tubular structure, which could effectively soothe the shear lag problem.

1 INTRODUCTION

Due to urban development and economic necessity, tall building becomes an solution for the concentration of population. As the building is getting taller, the technique to withstand the horizontal loadings induced by earthquake and wind is more demanding. To resist the horizontal loading, many structural systems are available such as large-scale bracing, core, diagrid, outrigger, framed tube structures and others as explained by Ali and Moon (2007).

Among these structure forms, framed tube structure has the advantage of arranging all the resisting component at the perimeter of the building. This makes the components more efficient to resist the overturning moment caused by horizontal loading. The concept of tubular structure was first proposed by Khan and Amin (1973). However, the disadvantage of tubular structure is the shear-lag problem. The shear lag will reduce the efficiency of the components. Therefore, bundle tubular structure is introduced as explained by Ali and Moon (2007) in order to relieve the problem of shear lag. Wang (2012) has presented the typical shear lag phenomenon in Fig. 1 for a 3×3 bundle tubular structure with some modular tubes curtailed at the heights of 400 m and 800 m. In the figure, symbol I is relative moment of inertia of cross sections of spandrel beam. However, for the higher story, Singh and Nappal (1994) have shown that negative shear lag will occur. The typical negative shear lag phenomenon is shown in Fig. 2 for the 3×3 bundle tubular structure by Wang (2012). This means that the axial stress of the interior column in the flange frame is larger than that of the exterior column. By observing Figs. 1 and 2, one can conclude that as the moment of inertia of cross section of spandrel beam (I) becomes larger, the effect of shear lag will be reduced. As the effect of shear lag is diminishing, the tubular phenomenon becomes more apparent. This can be observed in Fig. 3. In the figure, the vanishing of shear lag effect, as seen in Figs. 1 and 2, will make the horizontal stiffness of the building larger. This means the lateral displacement of the building subjected to horizontal loading is reduced.

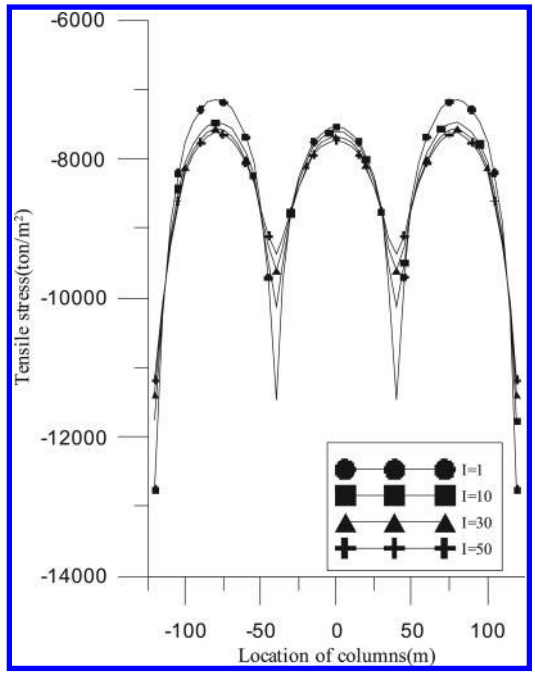


Figure 1. Typical shear lag phenomenon for compressional flange frame at height 0 m (Wang 2012).

In order to mitigate the shear lag problem, a pyramid-like tubular structural form is suggested for tall buildings. The pyramid-like tubular structure is defined as the tubular structure with gradually reduced floor area through the height of floor. Since the floor area is reduced through the height, the periphery columns have to be inclined accordingly. The inclined

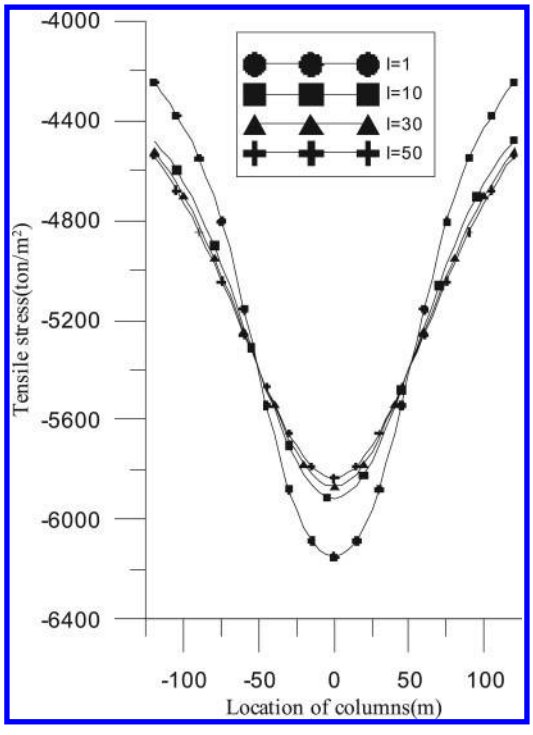


Figure 2. Typical negative shear lag phenomenon for compressional flange frame at height 200 m (Wang 2012).

columns can balance part of horizontal load directly. This could also mitigate the shear lag problem.

The paper will investigate the behavior of the pyramid-like tubular structure by changing the relative stiffness of spandrel beams to periphery column, and the effectiveness of the structure type for withstanding horizontal load. Also, the shear lag phenomenon for the structural type will be discussed. The analysis program SAP 2000 will be employed to model and analyze the structures. In the analysis model, only 3-D beam elements are used and rigid zone at beam-column joints is assumed.

2 NUMERICAL ANALYSIS

In order to study the behavior of pyramid-like tubular structure, the building structure shown in Fig. 4 is assumed. In the figure, the base of the structure is 240 m × 240 m and the height is 1200 m. This means the inclination of columns at periphery of the structure is 1/10 in the horizontal x and y directions. The story height is 5 m. This leads to 240 stories for the structure. The building code of Taiwan (2006) is adopted to calculate the horizontal wind load. The wind pressure on the building is shown in Fig. 5. In the figure, the wind pressure is calculated by assuming 5% damping ratio for the structure.

Computer program SAP2000 is employed to model the pyramid-like structure. In the model, only beam

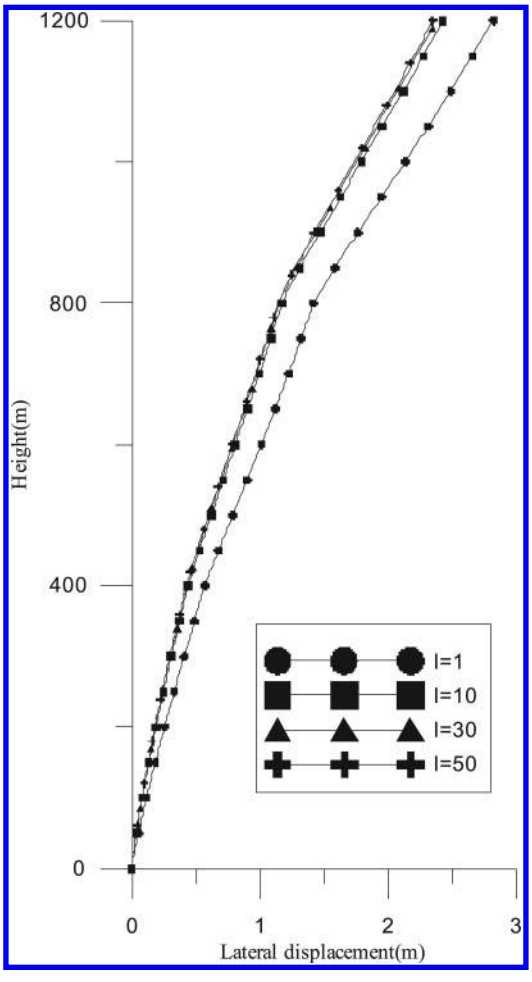


Figure 3. Typical lateral displacement (Wang 2012).

element is used to model columns and spandrel beams, rigid diaphragms for all the floors are assumed, and the option of rigid zones at beam-column connections is selected. The members for the four corner columns are circular tubes with 200 cm in diameter and 6 cm, 8 cm or 10 cm in thickness. The members for the other periphery columns are 100 cm × 50 cm rectangular tube with 6 cm, 8 cm or 10 cm in thickness. In order to keep total area of corss sections of columns constant at periphery of the structure, the spacing of the columns is 3 m for the thickness 6 cm, the spacing of the columns is 4 m for the thickness 8 cm, and the spacing of the columns is 5 m for the thickness 10 cm. Three types of member are selected for the spandrel beams. The cross sections of the three types of beams are shown in Fig. 6. Therefore, one totally has 9 cases (3 different cross sections of spandrel beams times 3 different spacing of periphery columns) to be studied. In the study, the vertical loading (gravity loading) is not taken into account. Therefore, only periphery columns and spandrel beams are modeled in Fig. 4 to resist the horizontal wind pressure shown in Fig. 5.

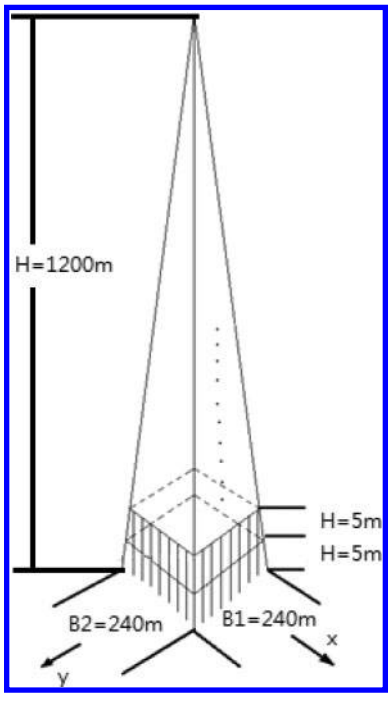


Figure 4. Pyramid-like tubular building structure.

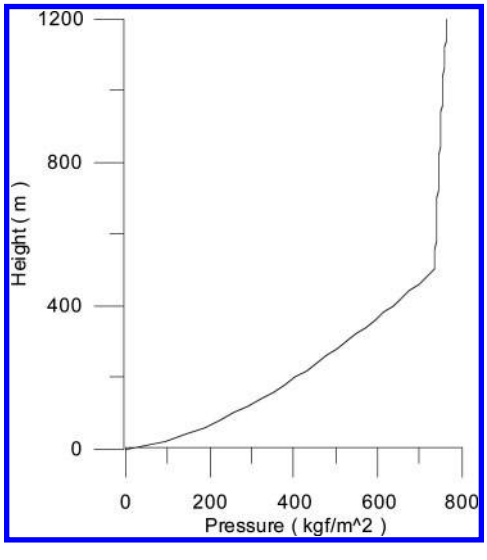


Figure 5. Design wind pressure by building code of Taiwan (2006).

The lateral displacement due to the wind load of Fig. 5 is shown in Fig. 7. In the figure, the symbol 3 m-1 represents the case with 3 m column spacing and spandrel beam type No. 1 of Fig. 6, and the other similar symbols (3 m-2…etc.) represent the corresponding cases. From Fig. 7, one can observe the phenomenons as follow:

(1) Stiffer spandrel beam will make the lateral displacement smaller. For examples, the sways for

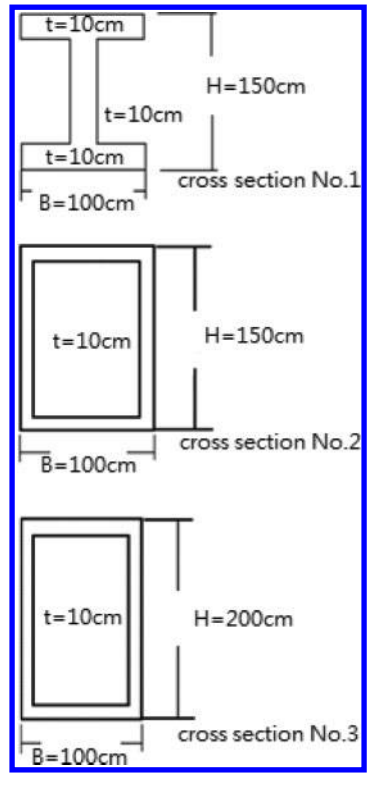


Figure 6. Cross sections of spandrel beams.

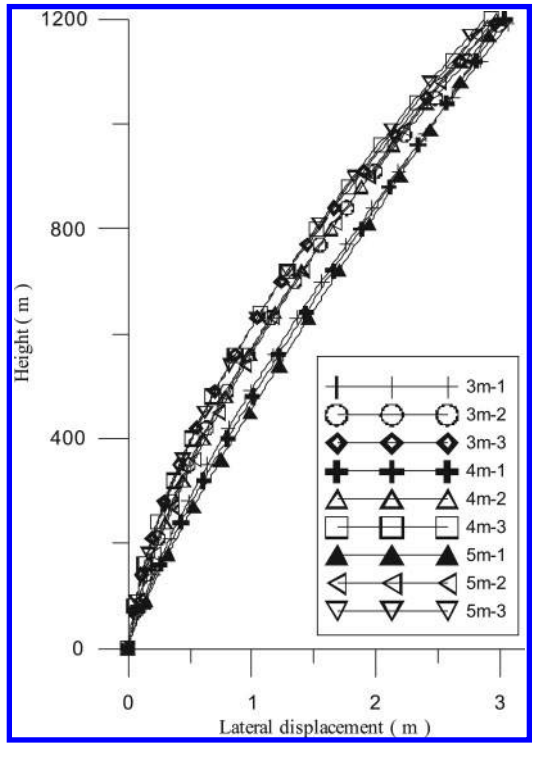


Figure 7. Lateral displacement due to wind load.

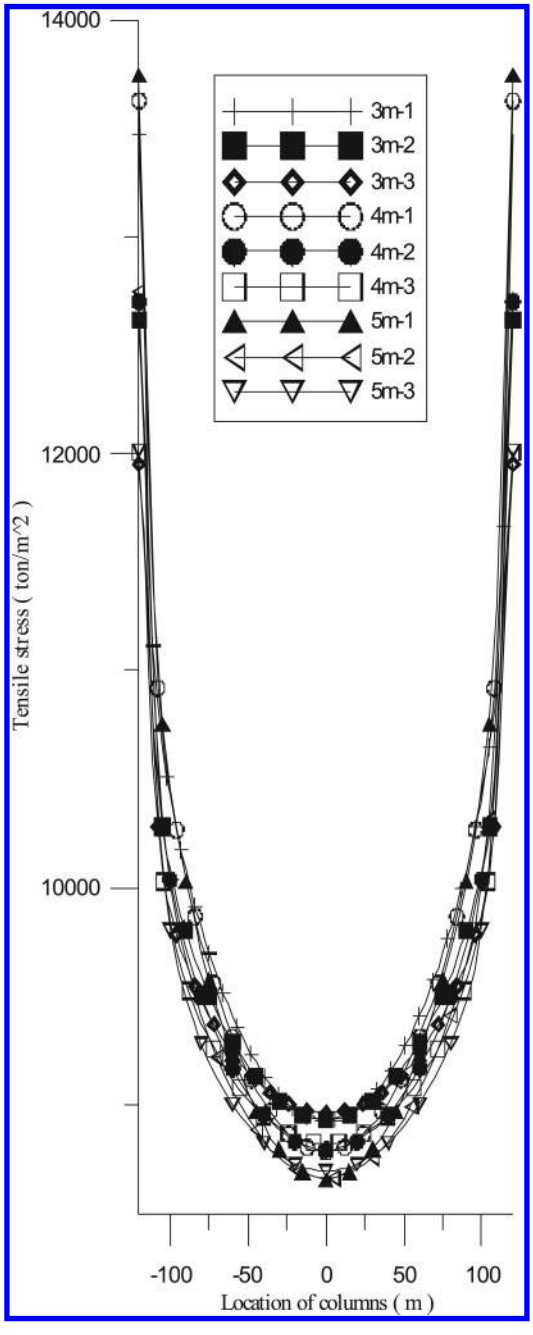


Figure 8. Tensile stress of columns of flange frame at height 0 m (1st story).

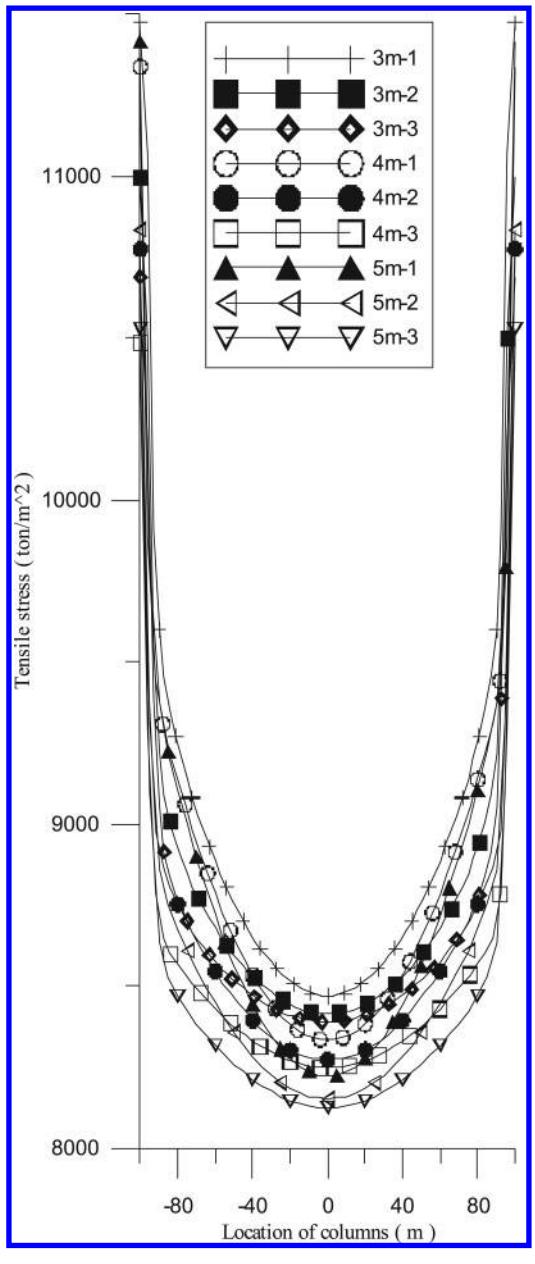


Figure 9. Tensile stress of columns of flange frame at height 200 m.

the cases 3 m-3, 4 m-3 and 5 m-3 are smaller, while compared to the corresponding cases 3 m-2, 4 m-2 and 5 m-2, and 3 m-1, 4 m-1 and 5 m-1, respectively.

(2) If the column area is more evenly distributed around the periphery, the sway is smaller. For examples, results for the case 3 m-1 is smaller than that for the cases 4 m-1 and 5 m-1.

(3) However, the maximum lateral displacement at top of the building structure seems entangled for the 9 cases.

Fig. 8 shows the tensile stress of the columns of flange frame at height 0 m. In the figure, one can see that the curves for shear lag phenomenon can be divided into 3 groups for the 3 types of spandrel beams shown in Fig. 6 respectively. For stronger spandrel beam, the shear lag effect is lesser. For example, the shear lag phenomenon is lightest for the strongest

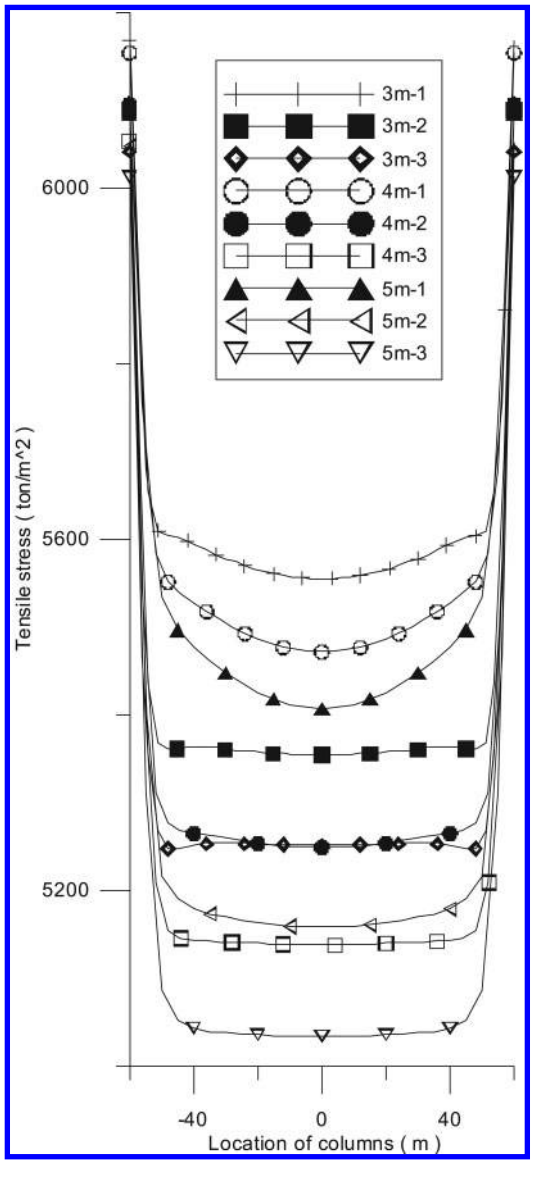


Figure 10. Tensile stress of columns of flange frame at height 600 m.

spandrel beam (Type No. 3 in Fig. 6). However, the effect of evenly distributed column area seems not so obvious to reduce shear lag phenomenon. This can be observed by comparing the results for cases of 3 m spacing to that for the corresponding cases of 4 m and 5 m spacings.

Figs. 9 and 10 show the tensile stress of columns at heights 200 m and 600 m respectively. From these two figures, one can observe that negative shear lag phenomenon does not occurs for all 9 cases. As a matter of fact, there is no negative shear lag observed along the height of the building, as one examines all the column stress. This could be the effect of inclination of columns.

3 CONCLUDING REMARKS

The pyramid-like structural type is suitable for super tall building. It has the advantages to effectively reduce shear lag phenomenon along periphery columns and lateral displacement along the height of building. Also, this structural type can be easily combined with other structural forms, e.g. large scale bracing and outrigger structures, to resist horizontal wind load.

ACKNOWLEDGMENTS

The work is partly sponsored by National Science Council of Taiwan. The support is greatly appreciated.

REFERENCES

Ali, Mir M. & Kyoung, Sun Moon 2007. Structural Developments in Tall Buildings: Current Trends and Future Prospects, *Architectural Science Review* Vol 50.3: 205–223.

Building code of Taiwan. 2006.

Connor, J.J. & Pouangare, C.C. 1991. Simple Model for Design of Framed-Tube Structures, *Journal of Structural Engineering*, ASCE, 117(12): 3623–3644.

Khan, F.R. & Amin, N.R. 1973. Analysis and design of framed tube structures for tall concrete buildings, *The Structural Engineer*, Vol. 51: 85–92.

Singh, Y. & Nagpal, A.K. 1994. Negative Shear Lag in Framed-Tube buildings, *Journal of structural Engineering*, ASCE, 120(11): 3105–3121.

User's manual of SAP 2000. 2000.

Wang, C.C. 2012. Parametric study of bundle tubular structures, *Master Thesis (In Chinese)*.

Research and Applications in Structural Engineering, Mechanics and Computation – Zingoni (Ed.)
© 2013 Taylor & Francis Group, London, ISBN 978-1-138-00061-2

More optimal seismic design of highrise structures using nonlinear analysis techniques

S.A. Ashrafi
Thornton Tomasetti, New York, NY, USA

ABSTRACT: It is a well-known feature of dynamic response of highrise structures that their seismic response, including the distribution of strength and deformation requirements, is very different from low-rise structures. Most design codes allow for or require the use of modal analysis techniques to allow the design to capture the effects of higher modes present in the response. However, buildings are typically designed to undergo significant nonlinearity during a design level strong earthquake. These nonlinearities change the value and distribution of the strength and displacement demands in ways that can be very different than what linear modal analysis implies. Nonlinear dynamic analysis allows for capturing the expected behavior of the building and designing accordingly. The result can be safer and more optimal design of the structure. This paper will discuss how the design of a tall building can change as a result of using nonlinear analysis in the context of performance based design.

1 INTRODUCTION

Most building design codes rely on a force-based seismic design approach. In this approach, some prescribed seismic forces are calculated for a building and the building elements are proportioned to have sufficient strength and stiffness to carry these forces. As the design for most structures relies on significant nonlinearity during strong seismic events, the prescribed forces are reduced compared to elastic demands.

For short buildings, a single mode in each direction can be considered to comprise most of the dynamic response. On the other hand, several modes can be present in the response of highrises, with different relative importance in deflections and internal forces at different levels of the building. Using a single reduction factor to modify all the responses makes the implicit assumption that the nonlinearity affects all the modes similarly, and that initiation of nonlinearity in the structure only changes the amplitude of the force and displacement demands, not their distribution.

Nonlinear dynamic analysis gives the tool to the designer to study the actual expected response of a structure to any given set of ground motions, not relying on simple assumptions to estimate the effects of nonlinearity. There have been several studies looking at such effect. For example, see Klementec et al. 2007, Moehle et al. 2011, Fry et al. 2010, and Zekioglu et al. 2007. However, one important fact about nonlinear analysis is that it needs an initial design with a given distribution of strength and stiffness. The nonlinear dynamic analysis then becomes largely a verification process for that initial design. Part of the reason for this common approach is the level of effort required in modeling and analyzing a proper nonlinear model of a structure, and the large computational and time costs associated with a nonlinear analysis.

There are several ways in which the nonlinear analysis approach can be used for the design. The first approach is to design the building using standard codes, and then perform nonlinear analysis to verify that the structure meets its performance criteria. This is most often the way nonlinear analysis is used.

The second approach is to design the building using the standard code approach, but for a service level seismic force. Then nonlinear analysis can be used to check the adequacy of the design for higher levels of ground shaking, and if necessary, the design can be updated. This approach has the advantage that it does not fully design the structure based on some fictitious loads, but rather, uses realistic loads at service level and then allows the designer to increase stiffness and strength at various locations as required to achieve satisfactory performance for extreme events. The downside is that there is no guidance provided in how best to modify the building properties to achieve a satisfactory and also optimal design. Similarly, it does not provide any direction for proportioning the structure at the service level. The desired design philosophy in terms of how various components have to be proportioned relative to each other is not clear, beyond proportioning members for strength based on linear analysis results.

The third approach id to use nonlinear analysis in the context of performing parametric studies within the range of the design parameters for a specific project to allow finding the near optimal solution that satisfies the performance criteria. There are many parameters to look at, such as moment and shear at various floors,

internal forces of members, drifts and deflections. Also, these parameters can be looked at in the terms of average demands, maximum demands, standard variation of the demands, and in general, fragility of various responses. Therefore, it might be hard to find what combination of these parameters should be part of the optimization processand what their relative weights are. However, the nonlinear parametric study will help clarify the effect of various design choices and let the designer achieve a near optimal design based and the cost and benefits for any design choice.

The last approach clearly provides room for maximum efficiency in design and flexibility for the designer. It is also the option with the maximum computational costs. However, given the potential gains in a design, an intelligent adoption of this approach early in the design process could allow for a much better overall design. In addition, a group of such studies can be used to draw broader lessons regarding proper design principles to guide the initial design and the parametric study for different structural systems.

2 CASE-STUDY OF THE EFFECTS OF NONLINEARITY

Effects of nonlinearity on structural response and variations in the response as a result of parametric changes in the strength of various components are studied for a sample 150 m tall concrete core structure. Strength of the walls and link beams are variedproportionally and the effects on the response are studied.

The structure is studied subject to seven pairs of ground motions representing high seismic demand. Expected properties are used for the concrete and steel reinforcement in lieu of the minimum specified properties since the goal is to capture the realistic structural response. The strength of steel and concrete in the analysis models are 484 MPa and 52 MPa, respectively. This study is performed using a concrete core as the sole lateral system of the structure.

Perform 3D program is used for nonlinear analysis (CSI, 2011). Walls are modeled using fiber elements. The fiber elements allow for cracking of concrete under tension and incorporate confinement effects in compression, in addition to accounting for yielding of the rebars. Moment hinges are used to capture nonlinearity in link beams. Since structural elements are allowed to yield and crack explicitly, no additional modifications are used to adjust wall stiffness, as would be the case for linear models. Energy dissipation is modeled through a combination of modal damping to model the ever-present low-amplitude damping, and explicit modeling of nonlinearity within elements. Based on the data on ambient damping of structures of similar height and construction, a modal damping ratio of 2% is selected for the nonlinear models (CTBUH 2009).

The core models have walls that are 1.1 m wide at the base and narrow down to 0.6m at the top. However, the nonlinear capacities of the wall elements and link beams are varied between the models. The strongest nonlinear model (Model 1) has 2% reinforcement at the base with 2.5% reinforcement at the corners. The reinforcement is reduced through the height, ending with 1% reinforcement at the top. The link beams have diagonal reinforcement and are considered to have strength similar to the maximum capacity allowed for link beams per ACI code (ACI, 2008). Table 1 shows the variations in the amount of reinforcement in the models. As the nonlinear strength of the structure is limited by the capacity of link beams and tension capacity of the walls, the reduction in reinforcement is also a good estimate for reduction in strength as long as the limiting force types do not change.

Table 1. Description of models.

Model	Description
Model 1	Baseline nonlinear model
Model 2	25% reduction in wall and link beam reinforcement compared to Model 1
Model 3	50% reduction in wall and link beam reinforcement compared to Model 1
Model 4	67% reduction in wall and link beam reinforcement compared to Model 1

All the four case study models have roughly the same initial period of 3.3s in both principal directions because the initial period is mostly a factor of the core wall and link beam geometry, not the amount of reinforcement and hence strength provided in the model. Here lies one weakness of relying fully on linear models for design. Whereas the four models will have very different behaviors under the same dynamic loading, linear models are incapable of capturing such differences or providing guidance as to which model provides the best seismic behavior.

3 PARAMETRIC STUDY RESULTS

Models are analyzed using seven sets of ground motions. Because of the variation of the response depending on the individual ground motion being considered, a statistical measure of each response, such as mean, or mean plus one standard deviation, is typically used for evaluation of the performance of the structure. Here, average values are used for comparison.

For tall buildings, large modal mass and response spectrum values for higher modes result in significant contribution of higher modes to the seismic response. This phenomenon is well understood for linear models (Smith & Coull 1991, Taranath, 2005). For the first mode in each principal direction, the equivalent forces all act in the same direction. As a result, story shear forces and overturning moments increase monotonically from top to the base of the structure. The effective moment arm defined as the base overturning moment divided by base shear would be about 2/3 of the height for a linear first mode.

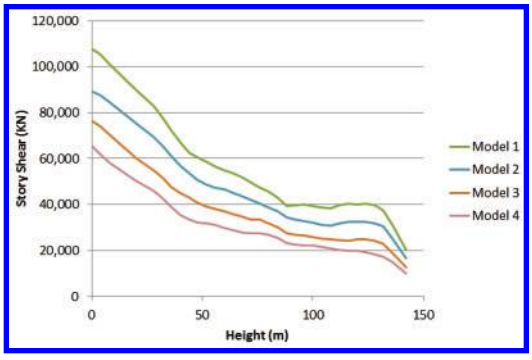


Figure 1. Mean story shear forces throughout the building height.

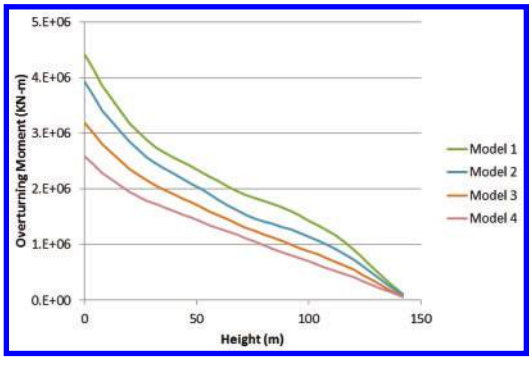


Figure 2. Mean story overturning moment throughout the building height.

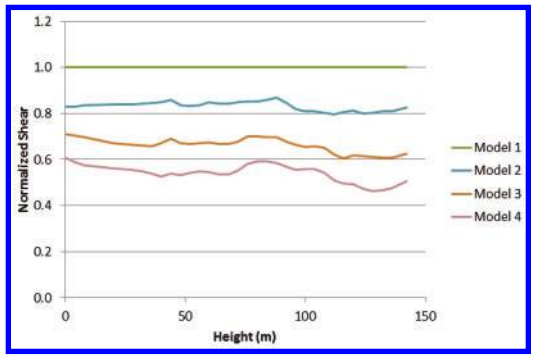


Figure 3. Normalized story shear throughout the building height.

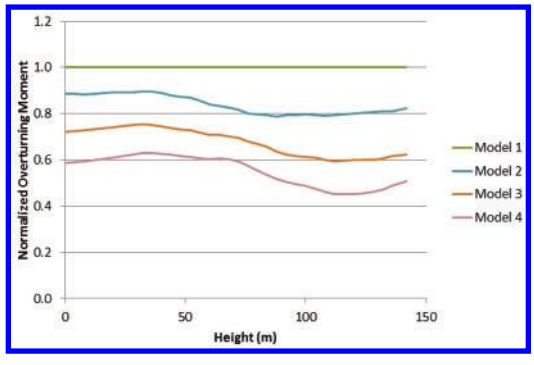


Figure 4. Normalized story overturning moment throughout the building height.

For the second mode in a direction, the structure tends to move one way at the top and another way lower in the structure. Because the effective forces on the structure act in opposite directions through the height, the story shears and overturning moments do not increase monotonically and the effective moment arms is lower for higher modes. Also, the ratio of the shear forces in some upper floors to the base shear is higher than what it would be for the first mode. In addition, the high curvature mode shape result in high interstory drift contributions. The same observations can be made regarding the third and higher modes in any direction. Therefore, the first mode is expected to dominate the base overturning moments and roof displacements. The higher modes are expected to make a meaningful difference to the base shear, as well as story shear forces, overturning moments, and story drifts in upper stories.

Figures 1 and 2 show the story shears in X direction and the corresponding overturning moments about the Y axis in the models. Figures 3 and 4 show the same results, as normalized to the results of Model 1. As expected, reduction in strength of the structural elements generally results in reduction of structural forces. When comparing to results from linear models, the reduction in overturning moment is expected to be more than that in shear (See Ashrafi 2013). That is because the strength of the core is mostly governed by a plastic hinge close to the base .A reduction in first mode response due to such plasticity will not affect the shear forces from the higher modes as much and these higher mode shear forces could be a significant part of the total shear. However, when comparing the nonlinear models, the reduction in shear forces does not show a substantially different trend than the reduction in overturning moment. An interesting observation from Figures 3 and 4 is that the reduction in forces in the structure does not correspond to a simplistic definition of the reduction of strength. For example, Model 4 has 1/3 the reinforcement of Model 1. However, its shear and bending forces are 45–60% of Model 1. The reason is the yielding in such a structure with many elements does not occur all at once. Rather, different elements at different locations in plan and height yield at different times. As a result, any global force deflection curve (such as story overturning moment vs. lateral movement) will be a gradually softening curve, as opposed to an elastic perfectly plastic curve. Therefore, Model 4 can reach a force larger than 1/3 that of Model 1, albeit at a different deformation level.

Figures 5 and 6 represent the variation of average and maximum story drifts. In general, reduction of structural strength leads to higher peak drift, but this trend does not monotonically hold at all the elevations or for all strength levels. Figure 5 seems to indicate

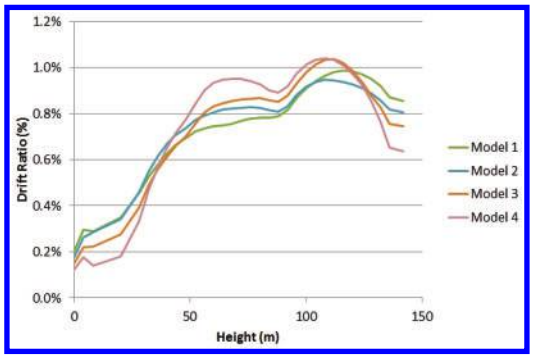


Figure 5. Mean drift ratios throughout the building height.

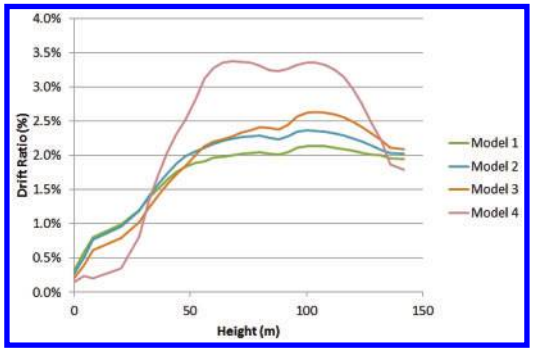


Figure 6. Maximum drift ratios throughout the building height.

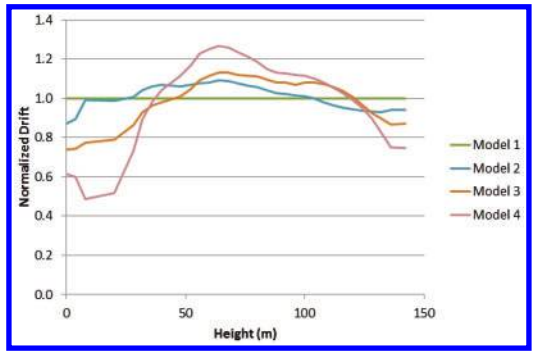


Figure 7. Normalized mean drift ratio throughout building height.

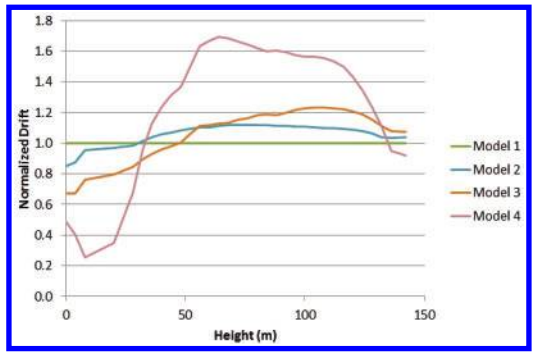


Figure 8. Normalized maximum drift ratio throughout building height.

relative insensitivity of mean drift responses for models with a wide range of strengths. However, Figure 6 shows that when looking at maximum drifts, Model 4 is clearly separated from the other models and exhibits much higher deformations. The maximum displacement here provides information on the sensitivity of the results to variations in ground motion. Given the inherent uncertainty in ground motions, it is important to be cognizant of the probability distribution of the response values, as opposed to just the mean values. Whereas the savings in design can lead to choosing Model 2 or Model 3 instead of Model 1 as the desired design, Model 4 is clearly a risky design where the building seems to have passed a threshold for stability of the results. The final design decision depends on the performance and design targets, but it is this parametric nonlinear analysis that allows for understanding of the full meaning of the design choices, and hence an optimal design to achieve the design goals. Figures 7 and 8 that show mean and maximum drift values, normalized to the values for Model 1, are important in their own right. A comparison with Figures 3 and 4 shows that varying the strength of the elements affect the distribution of drift values more than those of shear or overturning moment. The normalized shear and bending values are roughly uniform for each model, suggesting little change in distribution of these forces. On the other hand, Figures 7 and 8 show very non-uniform curves, indicating more drifts in mid-height floors, but less close to the top and base of the structure.

Overall, it can be seen that variations in strength affect distribution of forces and displacement, but not in a uniform manner. Parametric studies using nonlinear analysis allow for understanding of the design tradeoffs and informed selection of the right design for the project.

4 CONCLUSIONS

Linear analysis can only use the initial stiffness of the structure. Given a set of seismic ground motions and assumption of a reduction factor for the forces, it will provide unique required strength values for all the structural members. The designer's hands will be tied to change those design strength values. Under a strong earthquake, the actual demands on the structure could end up being quite different.

The study here illuminates how models with the same linear properties could have very different dynamic responses. Some of the conclusions from this study are:

1. Linear models cannot distinguish between models with similar initial stiffness but different strength levels. In nonlinear models, final deformations and

internal forces of the structure depend on elastic stiffness properties as well as force capacities. The designer can adjust both sets of parameters to achieve the design goals. Relying solely on linear analysis procedures limits the designer to adjusting the stiffness of the members and designing for the forces, as reduced by a reduction factors. Linear analysis method is simply incapable of providing any direction for a more optimal and efficient design. Using nonlinear analysis results gives the designer more flexibility for a proper seismic design.

2. Using nonlinear analysis to confirm the adequate seismic performance of building designed using linear procedures is beneficial. However, only a design based on the results of parametric nonlinear study of the structure has the potential to guide the designer towards the most rational and optimal design given the response parameters of interest. Nonlinear analysis expands the available design options and significantly improves reliability of the prediction of structural demands. Instead of changing stiffness and designing for the obtained forces, the designer can play with strength and stiffness values within the entire structure. The design can push forces away from elements that have undesirable response or expensive design and toward elements with more desirable response. The full interplay between different performance targets and the tradeoffs involved in terms of cost, reliability, and response of various components of the structure are not fully clear until nonlinear behavior of the structure is parametrically studied.
3. Nonlinear studies of various types of structures can provide a general understanding of the interplay between design parameters for each type of building. Such efforts are encouraged as they would provide guidance to the designer and allow for a more targeted parametric study for each individual project, incorporating the broad lessons from previous studies.

REFERENCES

ACI 318-08 Standard: Building Code Requirements for Structural Concrete (318-08) and Commentary, Farmington Hills, MI: American Concrete Institute, 2008.

Ashrafi SA, Nonlinear Dynamic Analysis As a Tool for More Optimal Seismic Design of Tall Buildings, Structural Engineering International, 2010, in press.

CSI, Perform 3D User Guide, Computers and Structures, Berkeley, California, 2011.

CTBUH, Recommendations for the Seismic Design of High-rise Buildings. Chicago, IL: Council on Tall Buildings and Urban Habitat; 2008.

Fry JA, Hooper JD, Klemencic R, Core Wall Case Study Design for Pacific Earthquake Engineering Research/California Seismic Safety Commission, Structural Design of Tall and Special Buildings, 19, 61–75, 2010

Klemencic R, Fry JA, Hooper JD, Morgen BG, Performance-Based Design Of Ductile Concrete Core Wall Buildings—Issues To Consider Before Detailed Analysis, Structural Design of Tall and Special Buildings, 16, 599–614, 2007

Moehle J, Bozorgnia Y, Jayaram N, Jones P, Rahnama M, Shome N et al. PEER 2011/05 Report, Case Studies of the Seismic Performance of Tall Buildings Designed by Alternative Means , July 2011.

Smith BS, Coull A. Tall Building Structures: Analysis and Design. New York: Wiley; 1991.

Taranath BS. Wind and Earthquake Resistant Buildings: Structural Analysis and Design. CRC Press; 2005.

Zekioglu A, Willford M, Jin L, Melek M, Case Study Using the Los Angeles Tall Buildings Structural Design Council Guidelines: 40-Storey Concrete Core Wall Building, Structural Design of Tall and Special Buildings, 16, 583–597, 2007.

Research and Applications in Structural Engineering, Mechanics and Computation – Zingoni (Ed.)
© 2013 Taylor & Francis Group, London, ISBN 978-1-138-00061-2

Progressive collapse prevention of drive-in steel storage racks

Siddharth Yadwad & Lip H. Teh
University of Wollongong, Wollongong, Australia

ABSTRACT: Unlike residential and commercial buildings, a more effective and rational approach to preventing progressive collapse in storage racks is to sacrifice the bay where a local failure initiates. The cost of a confined collapse of one bay is insignificant compared to the cost of a progressive collapse. This paper investigates the use of fuse connectors between the portal beams and the uprights of typical drive-in steel storage racks for preventing a local collapse in a bay from propagating to adjacent bays. Through nonlinear dynamic analysis, it identifies the topology and conditions where fuse connectors may be effective.

1 INTRODUCTION

Steel storage racks are widely used to store consumer and industrial goods. There are two primary types of steel storage racks: selective racks and drive-in racks (DIRs). DIRs are characterised by topologies that enable forklift trucks to drive into the rack structure to deposit or retrieve pallets on a 'first in, last out' basis. A layout of a typical DIR is provided in Figure 1.

DIRs are composed of upright members laced together by frame braces in the direction perpendicular to the aisle (cross-aisle direction), and by portal beams in the direction parallel to the aisle (down-aisle direction). Portal beams are installed only at the top of the uprights, and vertical down-aisle bracing (called spine bracing) is confined to either the rear of the rack in the case of a single entry DIR, or to the middle plane in the case of a double entry DIR. Sometimes the entire storage space of one bay is sacrificed for spine bracing, and the rest becomes a drive-through rack. Pallets are stored on rail beams, which are connected to the uprights in the cross-aisle direction via support brackets. The members composing DIRs are typically cold-formed, thin-walled open steel sections.

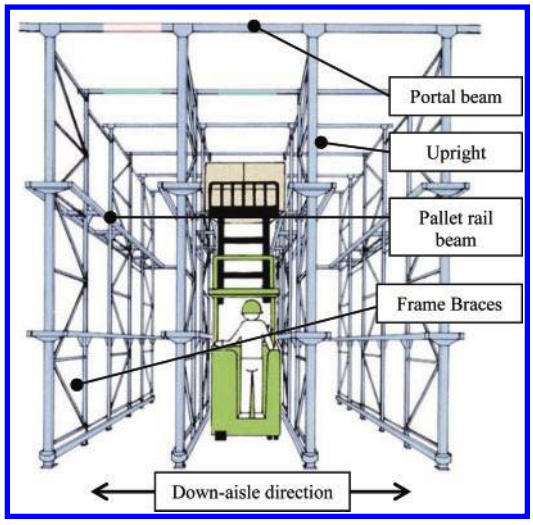


Figure 1. Diagrammatic representation of a typical steel DIR (HR Largertechnik 2010).

DIRs are particularly susceptible to collapse due to their loading process, tight design and topology. Collapses are often initiated by a localised upright failure resulting from accidental overloading or impact from forklift trucks (Gilbert & Rasmussen 2009). In some cases, the redistribution of load associated with the localised failure can produce a progressive failure mechanism, resulting in disproportionate collapse of the rack. Many such collapses have occurred worldwide, with the cost of damaged goods, repairs and lost production estimated to total more than ∈500 million in Europe alone in 2003 (Coutinho 2008).

McConnel and Kelly (1983) studied the progressive collapse of selective steel storage racks, concluding that the axial pull-out strength of the connection between the pallet beam and the upright (the "beam end" connection) largely determined whether a collapse would be progressive or confined. In cases where progressive collapse occurred, the beam end connections remained intact, and in cases where the collapse of the rack was confined, the beam end connections were found to have failed.

The tendency of a beam end connection to fail is dependent on the tensile force developed in the portal beam and the capacity of the connection in axial tension. The tension developed in the portal beam following the localised collapse of an upright was explained by McConnel & Kelly (1983) as an effect of the 'joint rotation' mechanism: a downward translation of the damaged upright that draws the adjacent uprights inwards, causing a rotation of the

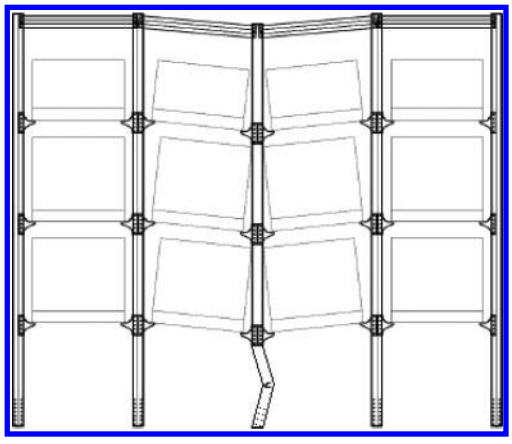


Figure 2. Joint rotation mechanism in a DIR following a localised upright failure, based on McConnel & Kelly (1983).

pallet beams. This mechanism was also noted to occur in DIRs (Gilbert 2010), an illustration of which is provided in Figure 2.

A proposed measure to prevent the occurrence of disproportionate collapse in DIR structures is the installation of fuse connectors; connections that are designed to fail under a certain tensile force or displacement. Fuse connectors would be installed between the portal beams and the uprights, acting as beam end connectors. In principle, if an upright is to fail, the tensile forces developed in the portal beams attached to it would cause failure of the fuse connectors, disengaging the portal beams from the uprights in the adjacent bays. This would inhibit progressive collapse, confining the collapse to one bay on either side of the initially damaged upright.

Of course, the failure of uprights is not the only reason tensile forces develop in the portal beams. Tension in portal beams will also develop under normal operating conditions including design loading, component misfit and ordinary accidental impacts. As such, it is important to ensure that fuse connectors do not fail under the tensile forces associated with these design actions.

This paper establishes whether fuse connectors may be feasibly applied for the prevention of progressive collapse in a DIR by comparing the smallest peak tensile forces experienced by the portal beams leading to progressive collapse against the largest tensile forces experienced by the same beams under normal operating conditions. Based on the premise of McConnel & Kelly (1983), in order for fuse connectors to be feasibly applied, the tensile forces found to occur in the DIR portal beams following the localised failure of an upright must be substantially larger than those found to occur under normal operating conditions.

2 DIR CONFIGURATIONS ANALYSED

A number of DIR configurations were analysed over the course of the present research, of which DIR3, DIR4 and DIR5 best represent the findings. These configurations vary only in their spine bracing arrangements. The upright spacing in the down-aisle direction is 1475 mm, and the vertical spacing between pallet rail beams is 1250 mm. Down-aisle views of these configurations are shown in Figure 3, Figure 4 and Figure 5.

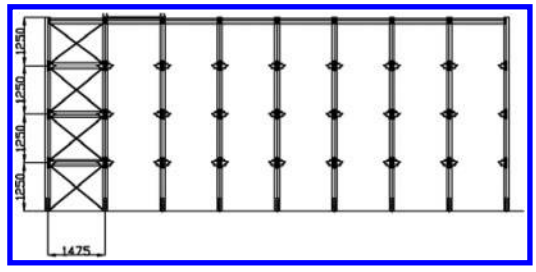


Figure 3. DIR3 – One spine bracing module *at the back* of one end bay.

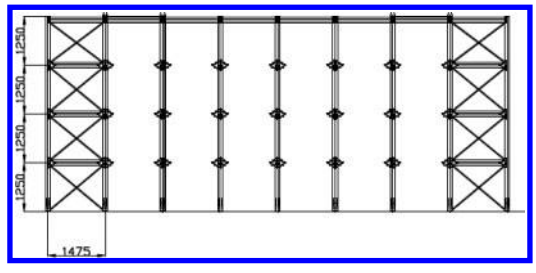


Figure 4. DIR4 – Two spine bracing modules, one *at the back* of each end bay.

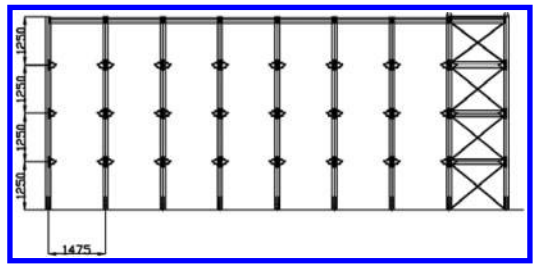


Figure 5. DIR5 – A 'Drive-Through Rack' where one entire end bay is sacrificed to accommodate bracing between every pair of uprights.

3 ANALYSIS OF DIR UNDER NORMAL OPERATING CONDITIONS

3.1 *Ordinary design loading and out-of-plumb*

Nonlinear static analysis was employed in studying the behaviour of DIRs under ordinary design loading and out-of-plumb. The provisions of the Australian Standard AS 4084-1993 (Standards Australia 1993) were used to define the magnitude of the out-of-plumb forces and the load factors for the ultimate limit state. A number of loading configurations were considered,

with the largest portal beam tensile forces found to occur in DIRs that are fully loaded.

3.2 *Ordinary accidental impact loading*

Minor accidental impacts between forklift trucks and DIR uprights are a common occurrence and are therefore considered to be a normal operating condition. Two separate methods were used to evaluate the response of DIRs following an accidental impact. The first considered a static equivalent force, with the magnitude consistent with the approach described in European Standard EN15512 (CEN 2009). The impact location used was in accordance with FEM 10.2.07 (FEM 2002), which specifies that the impact force must be applied at the location in the DIR that will produce the critical case of the action being determined; in this case the portal beam tensile force.

The second approach is a dynamic method employed by Ng et al. (2009) and refined by Gilbert (2010). Using this method, a transient impact load was applied to the DIR at various locations. For any given topology, the impact location that produced the largest portal beam tensile force was taken to be the critical case.

4 ANALYSIS OF DIRS FOLOWING A LOCALISED UPRIGHT FAILURE

4.1 *Modelling residual upright capacity*

Transient inelastic dynamic analysis was used to simulate the response of DIR structures following the localised failure of an upright. A procedure that is consistent with the progressive collapse simulation methodologies described by Marjanishvili (2004) and Marjanishvili & Agnew (2006) can be summarised as follow:

1. The axial force and bending moment at a particular location of the to-be-damaged upright are determined by performing a nonlinear static analysis under design loading conditions.
2. A portion of the damaged upright is removed from the model and replaced with the equivalent reaction forces as determined in Step 1.
3. A transient nonlinear inelastic dynamic analysis is performed in which the equivalent reaction forces are reduced over time as illustrated in Figure 6. The response of the remaining DIR structure is evaluated to determine whether any components fail as a result of this initial failure.
4. If a member is found to fail, it is deleted from the model and replaced with equivalent reaction forces that vary according to the response hysteresis recorded in Step 3 up to failure. After failure, the reaction forces are reduced to zero over a short time.
5. In the event that failure occurs in an upright outside the cross-aisle plane of the initial failure, a progressive collapse is taken to have occurred and the analysis is terminated. The peak portal beam tensile force during the analysis is recorded.

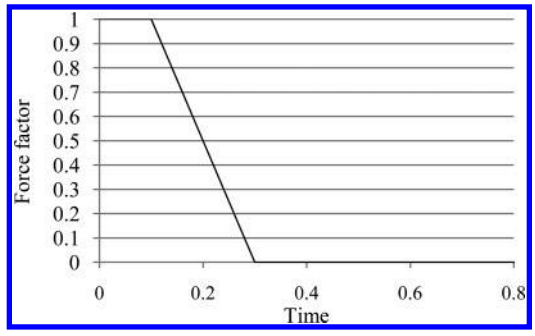


Figure 6. Reduction of initial reaction forces over time, used to model the initial local failure of an upright.

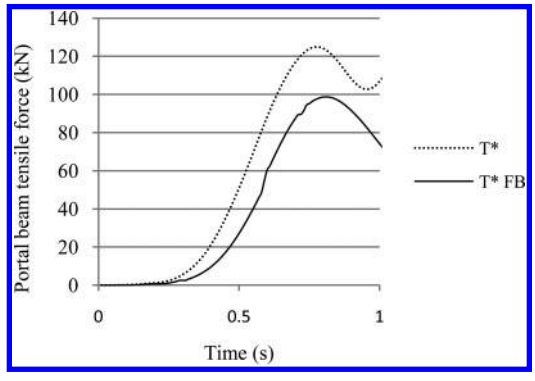


Figure 7. Response hysteresis illustrating the effect of incorporating the residual resistance of a failed upright on the portal beam tensile force.

The preceding procedure assumes that failed uprights disappear from the structure. However, in reality, they continue to provide some resistance in the upward and downward directions. The residual resistance of the failed upright is modelled in the present work using frictional contact elements that produce a force of constant magnitude in the opposite direction to the upright's displacement (either downwards or upwards). Where the residual resistance was more than 10% of the original member capacity, a significant reduction in the magnitude of the peak portal beam tensile force was noted, as shown in Figure 7.

In Figure 7, T* denotes the portal beam tensile force in a model that did not incorporate residual resistance. T^*_{FB} is the portal beam tensile force observed in a model incorporating the 'frictional damper' element with a residual resistance in both directions equal to 10% of the member capacity.

4.2 *Behaviour of DIRs following a localised upright failure*

The behaviour of a DIR following the localised failure of an upright is most conveniently explained by considering it in each of the primary directions of the structure, i.e. the cross-aisle plane and the down-aisle plane. Figure 8 shows a section of an analysed DIR

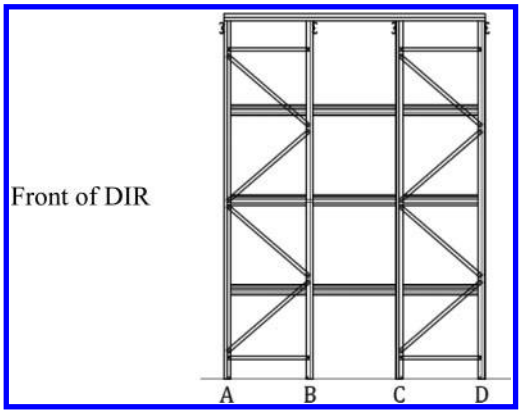


Figure 8. Elevation of a DIR in the cross-aisle plane.

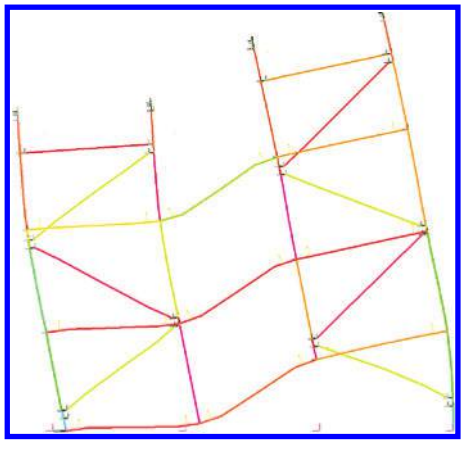


Figure 9. Load transfer to upright C, facilitated by the formation of shear and axial forces in the pallet rail beams.

in the cross-aisle plane where a localised upright failure would occur. The initially damaged upright in this case is marked 'A' with subsequent uprights labelled 'B' to 'D'.

Following the failure of upright 'A', the pallet load it previously supported in axial compression is transferred to upright 'B'. This load transfer is facilitated by the cross-aisle braces and pallet rail beams. Upright 'B' then fails due to the increased axial compression. The frame consisting of upright 'A' and 'B' then translates downward, resulting in deflection of the pallet rail beam and the formation of tensile forces in the attached portal beams.

The pallet load originally supported by uprights 'A' and 'B' distribute to the corresponding uprights in the adjacent bays and to upright 'C'. Load transfer to upright 'C' is facilitated by shear and axial forces in the pallet rail beams, as can be visualised from Figure 9.

It should be noted that the failure of an upright in the same cross-aisle plane is not considered to be a progressive collapse in the present work.

The portal beam tensile forces, in addition to producing an increase in axial compression in the adjacent

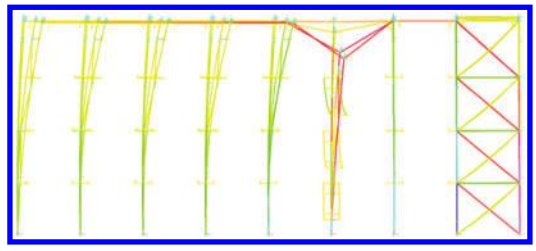


Figure 10. Load transfer to uprights in adjacent cross-aisle planes via portal beam tensile forces.

Table 1. Maximum portal beam tensile forces associated with ordinary impact and ordinary design loading/out-of-plumb.

	Maximum portal beam tensile force (kN) – normal operating conditions	
Configuration	Ordinary impact	Ordinary design loading & out-of-plumb
DIR3	5.03	0.28
DIR4	6.28	0.68
DIR5	4.33	0.54

uprights, also cause large bending moments. The combined actions may cause failure of the uprights, which is considered to be a progressive collapse. In some cases, upright 'C' may fail prior to the failure of the uprights in adjacent cross-aisle planes, however the load transfer mechanism remains the same.

Load transfer to the uprights in adjacent cross-aisle planes (bays) is facilitated by the formation of tensile forces in the portal beams between the uprights, as illustrated in Figure 10.

5 PORTAL BEAM TENSILE FORCES UNDER NORMAL CONDITIONS AND FOLLOWING A LOCALISED UPRIGHT FAILURE

The tensile force that develops in a portal beam is dependent on the pallet weights, the location of the portal beam and the applied loading condition. The primary concerns were to establish the portal beams in which the largest tensile forces occurred, and the variation of portal beam tensile forces within the structure under normal operating conditions and following an upright failure.

Accidental impact load cases analysed using the dynamic approach described in Section 3.2 were found to produce the largest tensile forces of all the normal operating conditions as shown in Table 1.

Therefore, the minimum strength required by a fuse connector for a given DIR may be established by analysing the structure for accidental impacts. In all cases analysed, the largest tensile forces were found to develop in the portal beams connected to the impacted upright. The largest tensile forces associated with

Table 2. Peak portal beam tensile forces in DIRs.

Cross-aisle plane where damage is initiated	One spine bracing module DIR 3	Two spine bracing modules DIR 4	Drive-through rack DIR 5
1	(0.22)*	(0.23)*	(1.73)*
2	(2.80)	(6.25)*	10.49
3	(3.20)	(5.96)*	17.53
4	6.33	16.71	20.71
5	9.32	14.39	24.99
6	6.71	16.71	24.99
7	8.52	(5.96)*	25.84
8	7.67	(6.25)*	N/A
9	(0.22)*	(0.23)*	N/A

*No progressive collapse.

design loading and out-of-plumb, on the other hand, were found to occur in braced bays, however the magnitudes of these forces were significantly smaller than those associated with ordinary accidental impacts.

It was noted that larger peak portal beam tensile forces occurred following upright failure in DIRs with topological features that increase the down-aisle stiffness of the structure. These include spine braces in DIRs and braced bays in Drive-Through Racks (DTRs). The inclusion of these features was not found to result in larger portal beam tensile forces under normal operating conditions.

Peak portal beam tensile forces exceeding those in the ordinary impact load case were found to occur in some, but not all, of the DIR structures in which upright failure was simulated. Table 2 shows the peak portal beam tensile forces that develop following upright failures in DIR3, DIR4 and DIR5. A bracketed number means that the force is lower than the largest in the rack developed under normal operating conditions (with factored design loads).

From Table 2, it can be seen that the largest peak portal beam tensile forces are developed in DIR5, which is the drive-through rack. The peak portal beam tensile forces in DIR3 were significantly smaller and, in some cases, less than the maximum portal beam tensile forces found to occur under normal operating conditions.

The reason behind the significant difference in peak portal beam tensile forces can be explained by considering the DIR as two separate 'sub-structures' on either side of the failed upright in the down-aisle direction. In cases where the 'sub-structure' attached to the portal beam had a higher down-aisle stiffness, the peak portal beam tensile force was found to be larger. An example of this phenomenon can be observed in the case of DIR5. A failure of the upright in the centre cross-aisle plane produces a very high stiffness 'sub-structure' at the braced end, and a very low stiffness 'sub-structure' at the unbraced end. Progressive collapse analysis shows the peak tensile forces developed in the portal beams connected to the braced region to be about 25% larger than those in the portal beams connected to the unbraced region, as shown in Figure 11 for post progressive collapse responses.

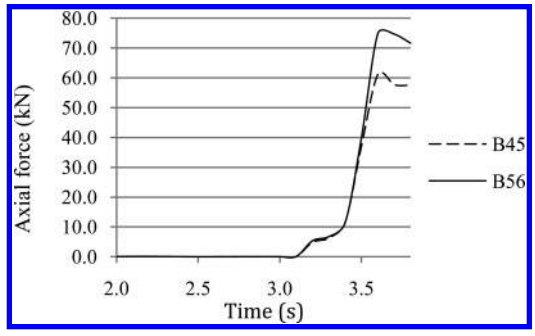


Figure 11. Comparison of tensile forces post progressive collapse – portal beams connected to high (B56) versus low (B45) stiffness 'sub-structures'.

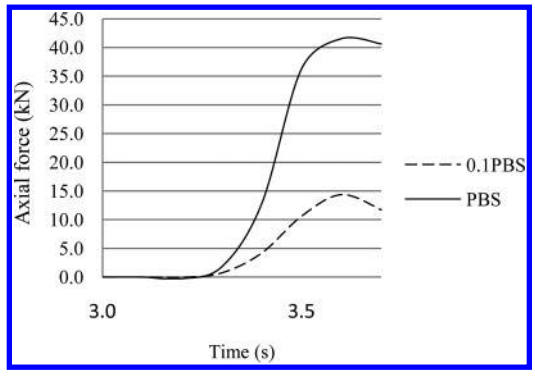


Figure 12. Effect of fuse connector stiffness on portal beam tensile force following upright failure.

6 ANALYSIS OF DIRS INCORPORATING FUSE CONNECTORS

To incorporate fuse connectors into models of DIR structures, 25-mm long 'fuse' elements were inserted at each portal beam end connection. The structural properties of the fuse elements were taken to be the same as the portal beams, however, if a specified tensile force was exceeded, the element would disappear from the model. For each DIR, the fuse strength was taken to be 110% of the largest portal beam tensile force developed under the normal operating conditions (factored loads).

The axial stiffness of the fuse connectors has an effect on the tensile forces developed in the portal beams following a localised upright failure. As the stiffness was decreased, the peak portal beam tensile force decreased. This phenomenon is illustrated in Figure 12, where the axial stiffness of the fuse connector is expressed as a ratio of the axial stiffness of the portal beam, PBS. For this purpose, fuse behaviour was disabled to allow post progressive collapse analysis.

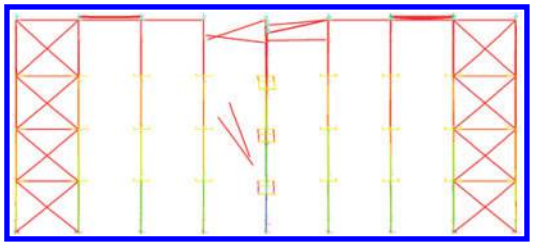


Figure 13. Confined collapse following failure of an upright in a model of DIR4 incorporating fuse connectors.

In the present analyses, where the fuse connector axial stiffness was equal to the axial stiffness of the portal beam, the portal beam tensile forces measured were the same as those in the DIR model that did not include fuse connectors.

In cases where the portal beam tensile force incurred by an upright failure exceeded the fuse connector strength, the fuse connector disengaged the portal beam from the upright, confining the collapse. An example of a confined collapse due to the incorporation of fuse connectors into DIR4 is provided in Figure 13.

7 CONCLUSIONS

The application of fuse connectors, based on the premise of McConnel & Kelly (1983), to prevent progressive collapse in DIRs is feasible under certain conditions only. DIR topologies can be designed so as to increase the magnitude of the peak portal beam tensile forces which develop following an upright failure, relative to those which develop under normal operating conditions.

The most effective arrangement would be to sacrifice both end bays entirely for the installation of spine braces between every pair of uprights.

Accidental fork-lift truck impact was found to be the normal operating condition in which the largest portal beam tensile forces tend to occur, and as such may be used for specifying the minimum strength that a fuse connector must have.

For a DIR with a low down-aisle sway stiffness, which may be unavoidable in practice, a different type of fuse connector is required as described during the conference's oral presentation.

REFERENCES

Coutinho, G. 2008. Numerical simulation of the seismic behaviour of steel storage pallet racking system. Instituto superior tecnico, Universidade Tecnica De Lisboa, Lisbon, Portugal.

European Committee for Standardisation (CEN) 2009, Steel static storage systems – Adjustable pallet racking systems – Principles for structural design. European Committee for Standardisation (CEN), Brussels, Belgium.

Fédération Européenne de la Manutention (FEM) 2011, The design of drive in and drive through racking (FEM 10.2.07), West Midlands, UK.

Gilbert, B.P. 2010. The behaviour of steel drive-in racks under static and forklift impact forces. PhD Thesis, The University of Sydney, Sydney, Australia.

Gilbert, B.P. & Rasmussen, K.J.R. 2009. Finite Element modelling of steel drive-in rack structures. Research Report No. R901, Centre for Advanced Structural Engineering at The University of Sydney, The University of Sydney, Sydney, Australia.

HR Lagertechnik 2010. Drive-in racks, viewed 20 April 2010, <http://www.hr-lagertechnik.de/index.php?id=85>.

Marjanishvili, S.M. 2004. Progressive Analysis Procedure for Progressive Collapse. *Journal of Performance of Constructed Facilities* 18(2): 79–85.

Marjanishvili, S. & Agnew, E. 2006. Comparison of Various Procedures for Progressive Collapse Analysis. *Journal of Performance of Constructed Facilities* 20(4): 365–374.

McConnel, R.E & Kelly S.J. 1983. Structural aspects of the progressive collapse of warehouse racking. *The Structural Engineer* 61A(11): 343–347.

Ng, A.L.Y, Beale, R.G. & Godley, M.H.R. 2009. Methods of Restraining Progressive Collapse in rack structures. *Engineering Structures* 31(7): 1460–1468.

Standards Australia 1993. AS4084 – Steel storage racking, SAI Global, Sydney, Australia.

Research and Applications in Structural Engineering, Mechanics and Computation – Zingoni (Ed.)
© 2013 Taylor & Francis Group, London, ISBN 978-1-138-00061-2

Assessment of column removal time for progressive collapse evaluation of high rise structures

O.D. Stephen
School of Civil Engineering, University of Leeds, UK

D. Lam
School of Engineering, Design and Technology, University of Bradford, UK

V.V. Toropov
School of Civil Engineering, University of Leeds, UK

ABSTRACT: Sudden removal of column has been the basis for progressive collapse assessment in existing literatures, codes and design guidelines around the world. This provision is based on the fact that a structure should be capable of bridging over a loss column in case of any eventuality probably due to any unforeseen event like impact, blast, or explosions. The response of the structure for progressive collapse assessment depends on how 'sudden' a column is lost. The time lapse at which a column is removed significantly affects the stress redistribution within the structural system and the joint displacement response. This paper investigates the response of moment resisting frame structure to varying time of column loss. Selective time points ranging from 0.001 to 0.5 was used for this investigation and it was observed that the rate of column removal affects the structural response. It is observed that structural stability begins at 0.2 seconds, beyond this time up to 0.5 seconds, the dynamic effect diminishes to static response.

1 INTRODUCTION

Progressive collapse is characterised by chain transmission of localised failure initiated by damage of critical structural members. This could result to partial or total collapse of the structure depending on the magnitude of the abnormal load relative to the ultimate carrying capacity of the structure. Damage of single or multiple load bearing members (Columns, walls etc.) could trigger complex redistribution of stresses within the structural system which may exceed the magnitude initially assumed at the conceptual design stage. [1] Impact, blast, extreme fire or explosions on a structural system could trigger progressive collapse. In view of this, the structure seeks a new equilibrium state which involves a complex transmission of stresses via the joints to other connecting structural members. This process takes place within a fraction of a second and this may results to partial or total collapse of the structure.

Research interest in progressive collapse has been attributed to the disproportionate collapse of Ronan Point Building in the United Kingdom. [2,3] This event as reported by some researchers [4,5] was triggered by domestic gas explosion at the 18th floor of a 22 storey building apartment in 1968 in London. The collapse of this building is referred to disproportionate collapse when the magnitude of collapse is compared to the triggering event. [5] Other highly publicised collapses are: Alfred Murrah Building in 1995 and the world trade centre in 2001 due to terrorist activities. These landmark events stimulated research in progressive collapse assessment particularly in the United States which resulted in the development of current design guidelines used around the world. [6,7] Application of these guidelines, merits and demerits has been reviewed by some researchers in existing literature. [8, 9]

Different modelling techniques are adopted in existing literature for progressive collapse investigation. These affects the results and conclusion. [10]–[12] However, each modelling technique depends on the column removal time. The time lapse at which a column is removed for assessment defines how 'sudden' the structure responds to the dynamic effects of the triggering event. This paper is aimed at evaluating the effect of time lapse of column removal on structural responses using moment resisting frame structure. The Internal forces in the beams and columns, and the joint displacements were investigated to study the extent to which these design variables are affected by sudden column loss. SAP 2000 finite element code was used for these investigations. [13]

2 OBJECTIVES

The objectives of this investigation is outlined below; the time points used ranges from 0 to 0.5 seconds

- To determine the effect of column removal time on beam responses during progressive collapse
- To determine the effect of column removal time on the adjacent columns
- To determine the joint displacement response due to different rates of column removal time.

3 DESCRIPTION OF MODEL

Figure 1 and Figure 2 represents the elevation and plan view of the model used for this investigation. It is a 10 storey moment resisting frame structure having a span of 6m along the y-axis and a span of 4.5 m along the x-axis. An assume 3.5 m floor to floor height was used in building the model. Section size of 305 × 305 × 198UC was used from the ground floor to the fourth floor, 254 × 254 × 167UC from the fifth to seventh floor and 203 × 203 × 60UC from the eight floors to the roof. The foundation base is assumed to be fixed. The beam section along the y-axis was 406 × 140 × 39UB while along the x-axis was 305 × 127 × 37UB.

A slab thickness of 130 mm was assumed for this investigation while the unit weight of concrete is 23.6 kN/m^3. The perimeter wall loading of 15 kN/m was applied on the external frame excluding the roof structural elements. The slab span one-way in x-direction and the tie beams are assumed not been effective in resisting gravity load. The plan view of the model shown in figure two indicates the relative column positions before column removal.

The dynamic loading condition is based on the provision of GSA 2003 as shown in equation (1) and (2). A factor of 2.0 as shown in equation (1) accounts for the dynamic effects which is an amplification factor recommended in GSA 2003 design guideline and the acceptance criteria is based on the demand capacity ratio as defined in equation (3) for static analysis.

For static analysis procedure:

$$N = 2 \times (DL + 0.25LL) \quad (1)$$

For dynamic analysis procedures:

$$N = DL + 0.25LL \quad (2)$$

where N is the loading, DL is the dead load and LL is the live load.

$$DCR = AF/CE \quad (3)$$

AF is the acting or applied stress resultants on a member or connection which could either be moment, axial force or shear. CE is the ultimate un-factored capacity of the member or connection which could be moment, axial force and shear for assessment.

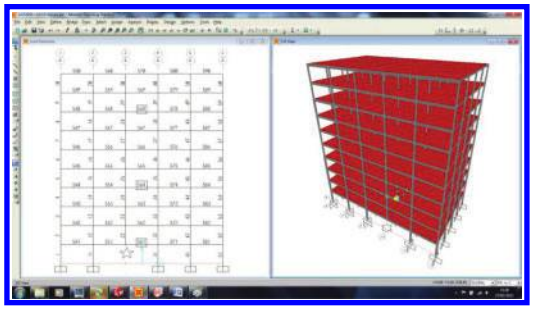


Figure 1. 3D model used for a case study.

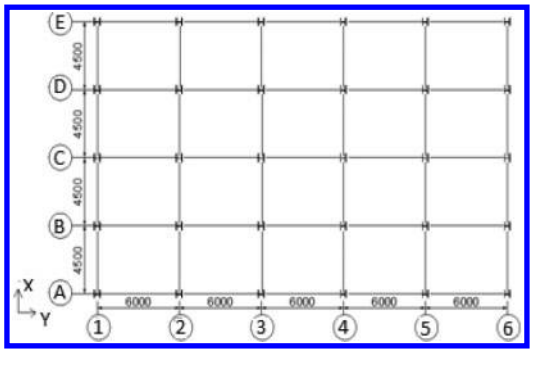


Figure 2. Plan view of the model.

4 ANALYSIS PROCEDURE

The column internal forces and the gravity loading are defined by the time history function path of PVM and N respectively as shown in figure 3. The stability period is represented with S_t, while the column removal time is represented by R_t. Column removal time points ranging from $0.001 \leq R_t \leq 0.5$ s was used for this investigation. The stability period (S_t) is assumed to be 3 seconds and this was used throughout the analysis while varying the column removal time (R_t). The GSA loading condition defined by equation (2) was used for this study. To model sudden column removal, the removed column is replaced by the internal forces; that is the axial force (P), shear force (V)

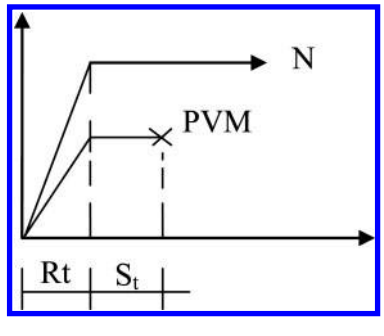


Figure 3. Loading history function.

and moment (M). The internal forces and the gravity loading are assumed to stabilise after three seconds when it gets to the maximum values.

5 ANALYSIS CASES

Three analysis cases were investigated and each case is described briefly below.

5.1 *Description of case one – Beam responses*

The perimeter column (Col 21) located on grid A-3 as shown on the elevation and plan view of Figure 1 and 2 was removed suddenly at varying time. The response of first floor beam (BM 561), the fourth floor beam (BM 564) and the eight floor (BM 568) as shown on the elevation of figure 1 were studied at each column removal time. Internal forces in the beams: Shear (V), moment (M) and axial forces (P) that determines the equilibrium state were studied when the column was removed suddenly at varying time. The results are presented in figure 4 to 6.

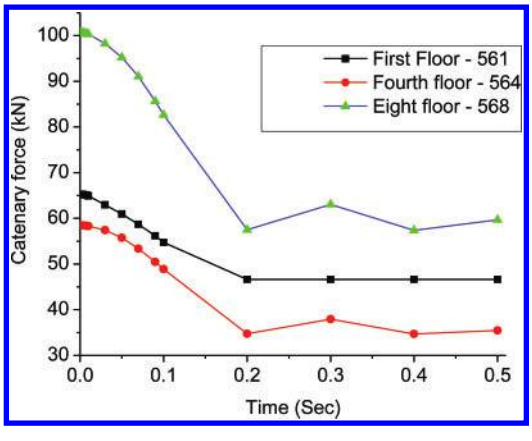


Figure 4. Maximum catenary force vs time.

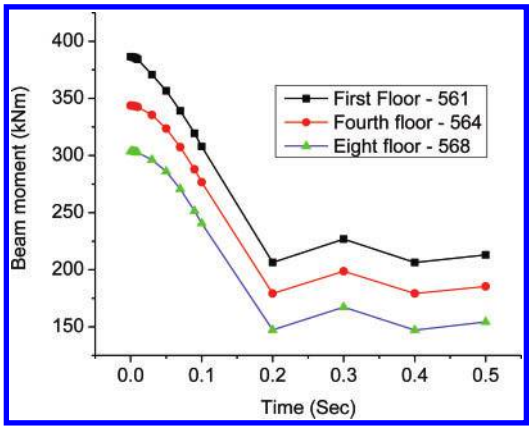


Figure 5. Maximum moment vs time.

5.2 *Description of case two – Column responses*

Four adjacent columns at different positions were investigated due to sudden column removal. The corner column located on grid A1 was removed to investigate the behavior of adjacent columns: Column on grid B1 (Col B1) and grid A2. (Col A2). The edge column located on grid A3 was removed suddenly and the behavior of the column on grid A4 (Col A4) was studied. Similarly, the interior column located on grid C4 was removed while the response of the column at grid 5C (Col 5C) was studied. The maximum internal forces (PVM) due to the varying time lapse for all the cases were compared as shown in Figure 7 to Figure 9.

5.3 *Description of case three – joint responses*

These investigations were carried to investigate how sudden column removal time affects joint behavior using displacement response. The corner column located on grid A-1 was removed based on time points between $0.001 \leq R_t \leq 0.5$ s and the maximum displacement was recorded. Similar procedure was

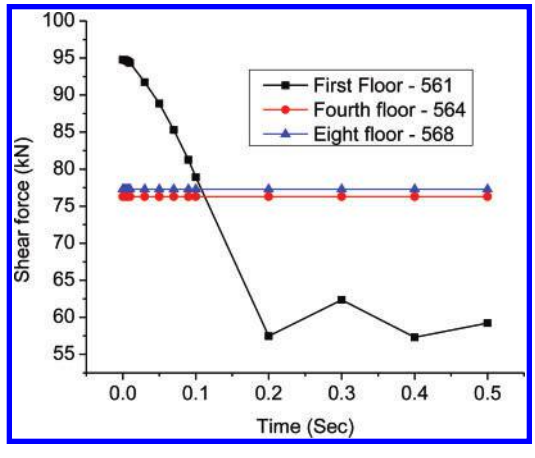


Figure 6. Maximum shear force vs time.

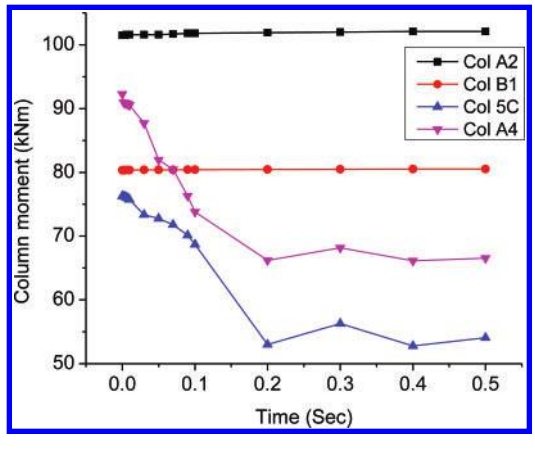


Figure 7. Maximum moment vs time.

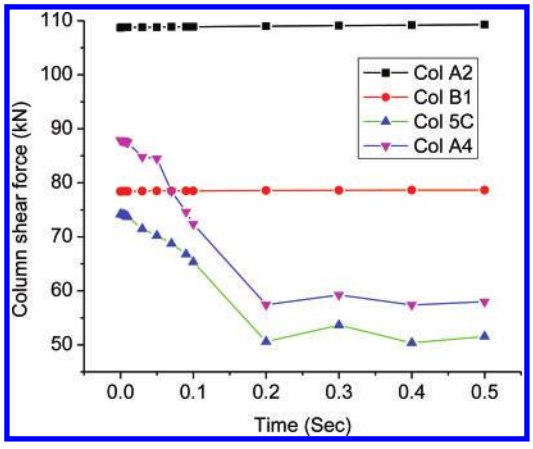


Figure 8. Maximum column shear force vs time.

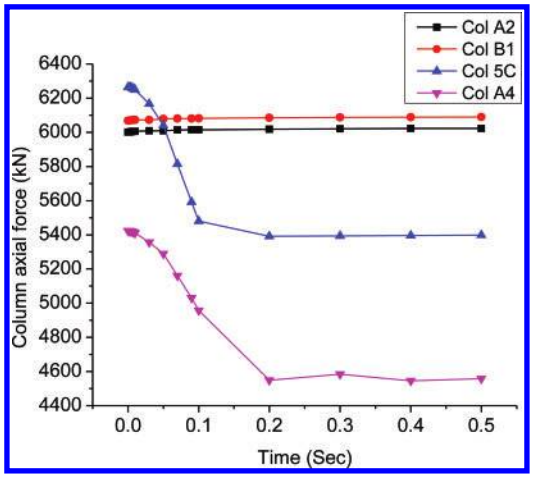


Figure 9. Maximum axial force vs time.

repeated by removing column located on grid A-3, and the interior column located at grid 4-C as shown on the layout of the building of figure 2. The maximum displacement at these joints at varying column removal time was recorded. The relative response of the joints due to varying column removal time is shown in figure 10.

6 DISCUSSION OF RESULTS

6.1 *Beam responses – Catenary action*

Axial responses of the beams at the first floor (Beam 561), fourth floor (Beam 564) and the eight floor (Beam 568) are shown in figure 4 to 6 below. Comparing the results, varying the time at which a column is removed significantly affect the beam behavior particularly at the first floor as shown through Figure 4 to 6. Most importantly, it is observed that significant changes in the axial forces occurred within the range $0.001 \leq R_t \leq 0.1$ seconds.

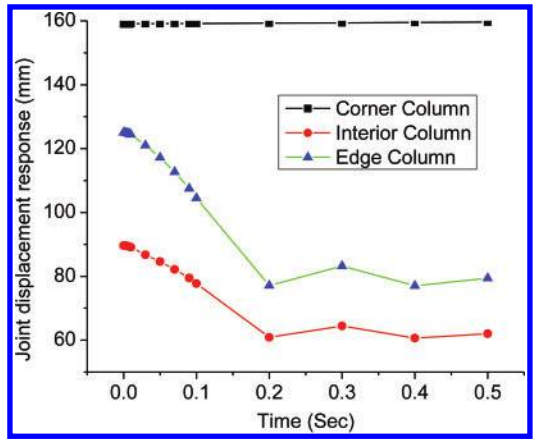


Figure 10. Maximum joint displacement vs time.

For the range $0.1 \leq R_t \leq 0.2$ s, sudden drop in response occurs in the axial force (P), Shear force (V) and the Moment (M). The structure begins to stabilize to static response beyond 0.2 seconds. Relative responses of the beams considered indicates that the catenary response at the eight floor is more critical with a maximum value of 101 kN followed by the first floor (65 kN) and the fourth floor having a value of 58 kN.

6.2 *Beam responses – Moment*

It is observed as in figure 5 that changes in column removal time significantly affect the moment responses of beam elements. Comparing the moment responses of Beam 561, Beam 564 and Beam 568, as shown in figure 5 below, it is observed that at 0.2 seconds, the moment in the beams begins to stabilize at the same pattern to a stable equilibrium state. A turning point from dynamic to static response begins at 0.2 seconds. The maximum beam moment at the first floor is 386 kNm, at the fourth floor is 342 kNm and at the eight floor is 303 kNm.

From 0.001 to a maximum of 0.1, the moment changes gradually at the time points considered, from 0.1 to 0.2, the changes are more significant. Maximum moment in beams increases in the order Beam 561, Beam 564 and Beam 568. Despite the fact that the load applied on the beams is the same, it is evident from Figure 5 that beam location significantly determines the response of the beam element to sudden column removal time and the critical beam for moment response occurs at the first floor.

6.3 *Beam responses – Shear force*

The shear force response in the beams at the first floor (Beam 561) fourth floor (Beam 564) and the eight floors (Beam 568) are shown in figure six. Comparing the beam response, the maximum shear force for the beams considered increases in the order Beam

568, Beam 564 and Beam 561 exhibiting the maximum response to sudden column loss time lapse. It is observed that Beam 561 and Beam 568 are not significantly affected by sudden column loss despite changes in column removal time from 0.001 to 0.5seconds. However, this is not the case for the first floor beam (Beam 561).

It is observed that structural stability begins at 0.2seconds, beyond this time, the dynamic response diminishes to static response. The maximum shear force at the first floor, fourth and eighth floor are: 94.9 kN, 76.3 kN and 77.3 respectively. The critical response for shear force occurs at the first floor.

6.4 *Column responses – Moment*

The maximum moment response at the adjacent columns (Col A2, Col B1) due to varying time of corner column removal, response of adjacent column (Col 5C) due to removal of interior column and the response of adjacent column (Col A4) due to perimeter column removal are shown in Figure 7. It is observed that the removal of the corner does not affect the response of the adjacent column significant. The adjacent column due to the removal of the perimeter column is more critical relative to that due to removal of corner and interior column. However, it is important to note that the response significantly depends on the mode of load distribution adopted for the model.

6.5 *Column responses – shear forces*

The time at which a column is removed suddenly does not affect the maximum shear force response of Col A2 and Col B1 significantly. However, sudden removal of column significantly affect the response of the interior and perimeter column as shown in figure 8.

From 0.001 to 0.1 seconds, gradual decrease in the maximum shear force occurs as column removal time was increased. From 0.1 to 0.2 intervals, shear force decrease linearly. From 0.2 seconds to 0.5 seconds, the dynamic effect of column removal time on the maximum shear force begins to diminishes to static response.

6.6 *Column response – Axial force*

Figure 9 shows the axial structural response of interior column (Col 5C), edge column (Col 4A) and adjacent columns (Col A1, Col B1) to varying time lapse. From 0.001 to 0.1 seconds, there is a gradual decrease in the axial force due to varying time lapse of adjacent column removal as shown in Figure 9.

The dynamic response is significant between $0.001 \leq R_t \leq 0.1$ s, and a sudden drop between $0.1 \leq R_t \leq 0.2$ s. The structure seeks stability to a static equilibrium state from $0.2 \leq R_t \leq 0.5$ s within the range considered. Beyond 0.2 seconds, a stability begins within the columns with minimal variation in response to axial force.

6.7 *Joint responses due to varying time of column loss*

Joint displacement responses due to the removal of corner column, perimeter column and interior column at varying time are shown in figure 10. The maximum joint displacement path is similar. From 0.1 to 0.2 seconds, an approximate linear response is observed in the displacement response for all the three joints. Although, below 0.1, the behavior is slightly parabolic with the maximum displacement of 160 mm. Joint sensitivity to varying column removal time occurs at the edge column removal point relative to the joint at the corner and interior column removal position. Beyond 0.2seconds, the structure seeks stability to a static response and varying column time does not have significant effect on the joint response.

7 ANALYSIS SUMMARY

Time lapse at which structural members are removed for progressive collapse assessment affect member response and the entire structural system. However, the response depends on the position of the structural member been considered and the direction of load distribution either one way or two way. Generally, considering the range $0.001 \leq R_t \leq 0.5$ s used for this investigation, it was observed that $0.2 < R_t \leq 0.5$ s does not accurately capture the dynamic response due to sudden column loss. it is observed that significant dynamic response occurs when the column removal time ranges from $0.001 \leq R_t < 0.1$

Furthermore it was observed that within the range of $0.2 < R_t \leq 0.5$ s the internal forces stabilize to a static equilibrium state such that the dynamic influence of sudden column removal does not affect the response of the structural system significantly. Beyond 0.2 seconds, the internal forces are unaffected by the time lapse at which a column is removed.

In conclusion, how sudden a column is removed affects the response of the structure and the internal forces that determine the equilibrium state under progressive collapse scenario. To account for the dynamic effect effectively, column removal time range of $0.001 \leq R_t < 0.1$ s is recommended. Further investigation is recommended to assess the exact time point that relates to the dynamic amplification factor of 2.0 recommended in GSA 2003 design guidelines. The behavior of structural elements under progressive collapse scenario depends on the location of the member within the structural system. Critical joint response occurs at the top of the removed corner column while the least response occurs at the interior joint.

REFERENCES

[1] Stephen, D., J. Ye, and D. Lam (2012) "Progressive Collapse Evaluation of High Rise Steel Structures due to Sudden Loss of Structural Members". In *10th International Conference on Advances in steel Concrete Composite and Hybrid Structures*. Singapore,

[2] Ellingwood, B.R. and D.O. Dusenberry (2005), "Building Design for Abnormal Loads and Progressive Collapse". Computer-Aided Civil and Infrastructure Engineering, **20**(3): p. 194–205.
[3] England, J., J. Agarwal, and D. Blockley (2008), The vulnerability of structures to unforeseen events. *Computers and Structures*, **86**(10): p. 1042–1051.
[4] Mohamed, O. (2006), Progressive Collapse of Structures: Annotated Bibliography and Comparison of Codes and Standards. *Journal of Performance of Constructed Facilities,* **20**(4): p. 418–425.
[5] Nair, R. (2006), Preventing Disproportionate Collapse. *Journal of Performance of Constructed Facilities*, **20**(4): p. 309–314.
[6] (GSA 2003) General Service Administration in Progressive collapse Analysis and Design Guidelines, USA.
[7] (DOD 2005) Department of Defence, in Design of Building to Resist Progressive Collapse, USA.
[8] Marjanishvili, S. (2004) Progressive Analysis Procedure for Progressive Collapse. *Journal of Performance of Constructed Facilities*, **18**(2): p. 79–85.
[9] Marjanishvili, S. and E. Agnew (2006), Comparison of Various Procedures for Progressive Collapse Analysis. *Journal of Performance of Constructed Facilities*, **20**(4): p. 365–374.
[10] Kim, H.-S., J. Kim, and D.-W. An (2009), Development of integrated system for progressive collapse analysis of building structures considering dynamic effects. *Advances in Engineering Software*, **40**(1): p. 1–8.
[11] Stephen, D., J. Ye, and D. Lam (2011). Realistic Modelling of High Rise Steel Structures subjected to progressive collapse. *in Thirteenth International Conference on Civil, Structural amd Environmental Engineering Computing.* Civil Comp Press, Stirlingshire UK.
[12] Pujol, S. and J. Paul Smith-Pardo (2009), A new perspective on the effects of abrupt column removal. *Engineering Structures*, **31**(4): p. 869–874.
[13] (SAP 2000), Integrated Software for Structural Analysis & Design: Berkeley, California, USA.

Research and Applications in Structural Engineering, Mechanics and Computation – Zingoni (Ed.)
© 2013 Taylor & Francis Group, London, ISBN 978-1-138-00061-2

Rotational capacity of concrete slabs and its influence on tensile membrane action in the framework of robustness analysis

D. Gouverneur, R. Caspeele & L. Taerwe
Ghent University, Department of Structural Engineering, Ghent, Belgium

ABSTRACT: Robustness of structures primary received significant attention 40 years ago following the famous collapse of the apartment building in Ronan Point (UK), and recent terrorist attacks at several locations were an unfortunate reminder of the potential fatal risks in case of initiation of progressive collapse. In order to investigate the strength reserve in concrete slabs subjected to large deformations, an experimental large-scale test series was established involving the testing of continuous, longitudinally restrained, reinforced concrete slab strips exposed to a simulated accidental failure of the central support and subsequent vertical loading until collapse. In case a support of such a statically indeterminate concrete specimen is removed, tensile membrane forces can be activated at large deflections. This effect was found to increase the load-carrying capacity considerably compared to predictions obtained from small deformation theories neglecting membrane forces. Further, the collapse of the specimens was ultimately induced by the tensile failure of the reinforcement bars in the cracked regions over the supports while being exposed to a plastic rotation. It is well established that such nonlinear effects are important to recognize as the development of plastic hinges influences the capacity of the structure to absorb energy and withstand extreme loads. The rotation of the sections over the supports created the necessary deformations to allow for the effect of catenary behaviour. As such, an appropriate modelling of the rotational capacity is of crucial importance when performing a failure analysis of concrete slabs subjected to tensile membrane action. The details of the test set-up are explained and some experimental data (among which those related to rotation angles) are discussed here. Finally, the results will be evaluated with numerical FEM analyses and the influence of the rotational capacity of the specimen on tensile membrane action will be assessed.

1 INTRODUCTION

Interest in the robustness of concrete structures emerged simultaneously to the partial collapse of the apartment building at Ronan Point (UK) in 1968 (Yi et al. (2008)). Due to this dramatic accident, extensive research associated with the progressive collapse of structures has been established. In addition, the bombing attacks on American buildings at several locations and the terrorist attacks on the World Trade Center in New York and the Pentagon in Washington in 2001 triggered a renewed interest in this research topic.

It has long been recognized that the development of membrane action can considerably increase the load-displacement response of concrete structures (Westergaard & Slater (1921) and Ockleston (1955)). Figure 1 illustrates a typical load – deflection curve taken from Park (1964).

Considering a rectangular slab panel with perfect edge restraints against lateral displacement, it was observed that compressive membrane action is induced due to restraining the outward movement along the slab edges in the early part of the loading phase. This may offer a much higher flexural load than the maximum load predicted by Johansen's Yield Line Theory (1962). After the maximum flexural load has been reached in point B, the load-displacement graph shows a rapid decrease of the supported load with increasing deflection as a result of the reduction of compressive membrane forces. Further, near point C, membrane forces being in the central part of the slab reach the stage where they change from compression to tension. The slab boundary restraints start to resist inward movement of the edges. Accordingly, cracks extend over the full thickness of the slab and the yielding of steel reinforcement is established due

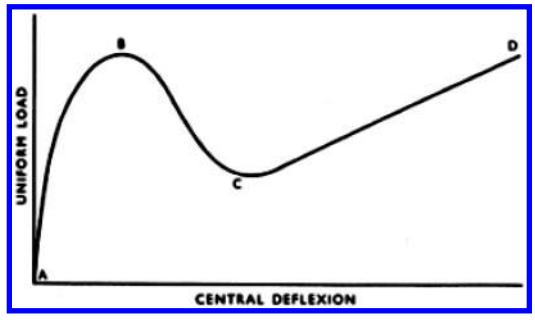


Figure 1. Load-deflection curve of a slab with full edge restraint according to Park (1964).

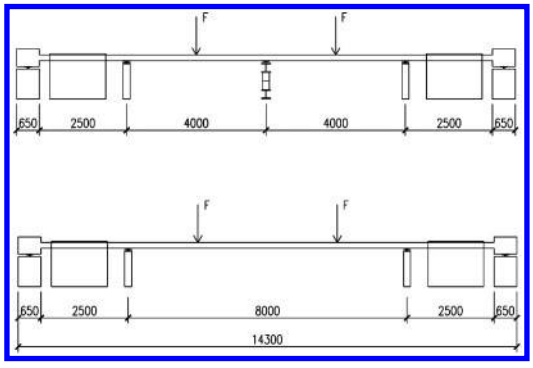


Figure 2. Loading scheme before (top) and after (bottom) removal of the central support.

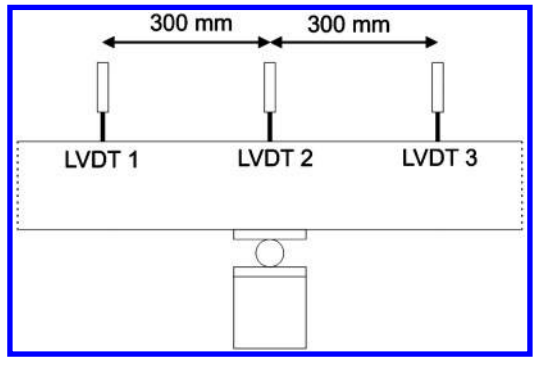


Figure 3. Detail for measurement of rotation angles.

to the elongation of the slab surface. It is observed that beyond point C the reinforcement acts as a tensile membrane that enables carrying the load under increasing deflections. The carried load increases for a second time until the reinforcement finally starts to fracture at point D. Already in 1964, Park stated that knowledge of the region CD in Figure 1 is of importance, since a snap through will occur in point B unless the tensile membrane strength of the reinforcement is high enough to absorb the load.

The main interest of research in the past decades has been in compressive membrane action. However, a few attempts towards tensile membrane action are reported in literature such as Brotchie & Holley (1971), Regan (1975) and Guice et al. (1989). Guice et al. (1989) state that the behaviour of reinforced concrete slabs is not entirely understood, in particular when large deflections occur. Researchers involved in case studies of failures in reinforced concrete slabs noted that an improved theoretical knowledge is necessary to characterise the behaviour of slabs under excessive loading.

2 EXPERIMENTAL INVESTIGATION

2.1 *Test set-up*

In order to investigate the tensile membrane action under accidental events in more detail, an experimental test set-up has been developed as illustrated in Figure 2. The configuration basically consisted of a 160 mm thick and 1800 mm wide reinforced concrete slab strip. The total length of the specimen was 14.30 m with the distance between the inner supports and the central support being 4 m, changing to one span of 8 m at the removal of the support (simulating an accidental situation).

A detailed description of the test set-up for a first experimental large-scale test is available in Gouverneur et al. (2013). This slab specimen was exposed to an artificial failure of the central support and subsequent vertical loading until collapse. However, the slab was reinforced with continuous longitudinal reinforcement bars. Further, a second reinforced concrete slab strip differing only in the reinforcement arrangement based on a more realistic situation of reinforcement curtailment according to the Eurocode EN 1992-1-1 (2004) was tested.

Besides, the rotation angles for this second test were measured by use of displacement transducers (LVDTs) at both inner supports as illustrated schematically in Figure 3.

3 NUMERICAL MODELLING

3.1 *General*

Creating a finite element model to study the large deformation behaviour of reinforced concrete structures implicates a lot of care in the definition of material models, mesh definition and boundary conditions. In the present study, an advanced finite element software (TNO Diana) was used to perform the analysis.

3.2 *Geometry and meshing*

As a result of the symmetry of the specimen regarding its geometry and loading, only half of the specimen was modelled. The geometrical nonlinearity was taken into account by a total Lagrange approach. Eight-node quadrilateral isoparametric plane stress elements (CQ16M) based on quadratic interpolation and Gauss integration were used to model the concrete elements. For the reinforcement, one dimensional fully embedded bar reinforcement (truss elements) were applied with perfect bond between the reinforcement and the neighboring concrete elements. Strains for the reinforcement are calculated based on the surrounding concrete elements.

3.3 *Loading and boundary conditions*

The loading procedure was applied in accordance with the laboratory tests by making use of a phased analysis. Initially, self-weight as well as the service load were applied. The obtained stresses and strains were transmitted to the next phase within which the elements

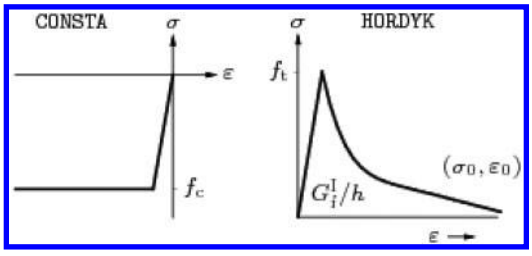


Figure 4. Material stress-strain behaviour: Concrete in compression (left), Concrete in tension (right).

of the central support were deactivated in order to simulate the removal of the central support. Further, self-weight as well as a displacement controlled load until the rupture of the reinforcement bars over the supports were applied. Interface as well as spring elements (with values based on the obtained measurement data) provided the vertical boundary conditions at the slab's ends.

3.4 *Material models*

The concrete compressive behaviour was implemented as a bi-linear stress-strain relationship as illustrated in Figure 4 (left). A Hordijk tension softening model and a total strain fixed crack model was adopted for concrete in tension (see Fig. 4 (right)).

For reinforcing steel, a multi-linear stress-strain relationship in accordance with laboratory testing on reference specimens was applied with a mean value of the ultimate strain $\varepsilon_u = 8.5\%$. Further, the strain hardening hypothesis together with the Von Mises plastic criterion was used.

4 RESULTS

4.1 *Validation of the model*

Figure 5 illustrates the load-displacement curves of slab 1 (continuous reinforcement) and slab 2 (curtailed reinforcement) measured during the laboratory testing in comparison with the numerical simulations.

Both the laboratory tests and numerical simulations showed that the development of tensile membrane actions can indeed significantly increase the load-carrying capacity of a slab strip in accidental situations when very large displacements occur (branch 1-2 of curve in Fig. 5). FE modelling is able to predict this increase in the load-carrying capacity due to tensile membrane forces. The load-displacement curves until the rupture of the top reinforcement bars over the inner supports (Point 2, Fig. 5) were calculated within a reasonable tolerance and showed good agreement with the laboratory tests.

4.2 *Influence of steel ductility (slab 1)*

The plastic deformation capacity of reinforced concrete structures depends mainly on the ductility of the

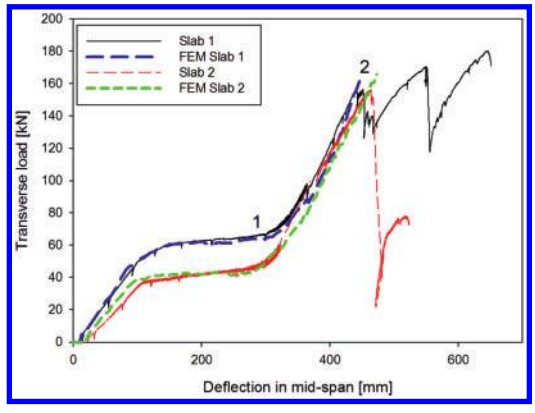


Figure 5. Load-displacement curves of slab 1 and slab 2 in comparison with numerical analyses.

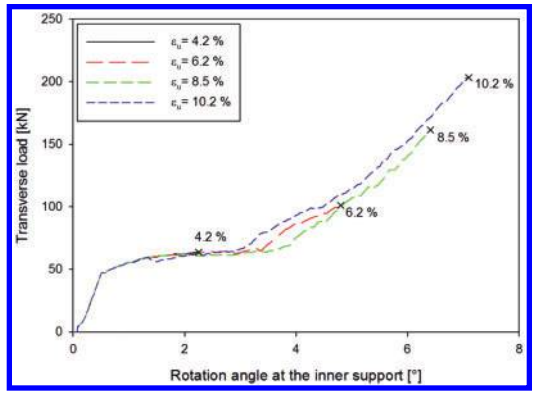


Figure 6. Load-rotation angle relationship for slab 1: influence of the ultimate strain of the reinforcing bars.

steel reinforcement. If linear elasticity is considered in the design of an element, there exists also a linear relationship between the curvature and bending moment in each section. However, in reality only the first part of the loading range can be considered to be linear. In case the yielding moment is exceeded, large cracks form and the moment-curvature relationship becomes non-linear. After yielding of the reinforcement bars, the deflections increase rapidly until either the concrete crushes or the steel ruptures. The influence of the ultimate strain of the reinforcement steel on the rotation capacity is investigated in this section. Figure 6 illustrates a parametric study of the rotation angles over the inner supports for slab 1. The stress-strain relationship of the reinforcement was modeled in accordance with tensile tests on the reinforcement bars differing only in the ultimate strain (4.2%, 6.2%, 8.5% and 10.2%) at an ultimate tensile strength of 605 MPa.

It was observed that the ultimate rotation capacity and the point of rupture of the reinforcement bars are highly influenced by the ultimate strain capacity of the reinforcement. The results of the parameter study are summarized in Table 1.

Table 1. Influence of the ultimate reinforcement strain on the rotation angle and ultimate load.

Ultimate reinforcement strain ε_u	Ultimate load F_u	Ultimate rotation angle θ_u
4.2%	63 kN	2.25°
6.2%	101 kN	4.80°
8.5%	162 kN	6.41°
10.2%	203 kN	7.10°

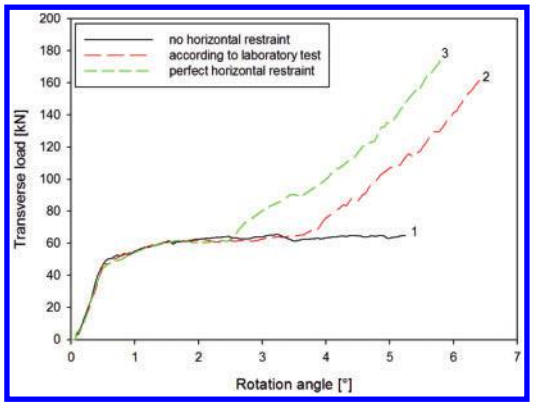


Figure 7. Influence of horizontal restraint conditions (slab 1).

4.3 *Influence of horizontal supports (slab 1)*

The influence of the horizontal restraint conditions for slab 1 is provided in Figure 7.

In total three cases of horizontal restraint were analyzed: (1) no horizontal restraint, (2) horizontal restraint according to laboratory testing taking the actual horizontal movement of the restraining concrete blocks into account as a load-dependent spring constant, (3) perfectly restrained edge beams against inward movement.

It was found that in case no horizontal restraint was present (Curve (1), Fig. 7) no increase in the load-rotation capacity could be obtained. As a consequence of the absent horizontal restraint, the reinforcement yields under the applied load without any increase in load until the reinforcement starts to rupture.

Further, Figure 7 illustrates that an increase in the horizontal stiffness caused the displacements associated with the perfect horizontal support (Curve 3) to be smaller compared to the case of the laboratory test at the same load level. Thus, the horizontal spring constant plays an important role when assessing the influence of tensile membrane action on the overall structural response.

4.4 *Influence of curtailment*

Figure 8 illustrates the load-rotation curve for slab 2 (curtailed reinforcement). Note that for this test also experimental results for the rotation capacity were

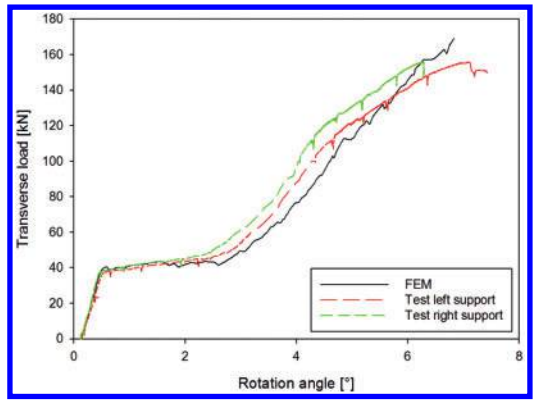


Figure 8. Numerical and experimental results for the load-rotation angle relationship for slab 2.

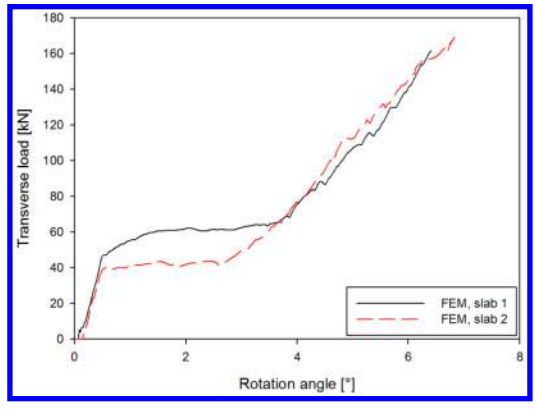


Figure 9. Numerical results for the load-rotation angle relationship of slabs 1 and 2.

available (see Fig. 3 for the measurement arrangement).

It was found that for this particular reinforcement arrangement the FE model shows still to be consistent and the results demonstrate a good agreement with the experiments. For the laboratory test an ultimate plastic rotation of 6.30° (right support) and 7.07° (left support) is obtained at a load of 155 kN (maximum load prior to the rupture of the top reinforcement bars). These values correspond to the numerically calculated ultimate plastic rotation of 6.83° at 169 kN.

In addition, a comparison of the numerical results of both slabs is provided in Figure 9.

It was observed that the predicted ultimate load as well as the ultimate plastic rotation for slabs 1 and 2 were approximately equal.

The results of the ultimate load and rotation angle obtained from the experimental investigation as well as the numerical results for slab 1 and 2 are provided in Table 2.

Hence, it can be concluded that the influence of curtailment on the ultimate rotation angle θ_u is rather limited.

Table 2. Influence of the reinforcement curtailment on the rotation angle.

Ultimate reinforcement strain ε_u	Ultimate load F_u	Ultimate rotation angle θ_u
Test left support, slab 2	155 kN	7.07°
Test right support, slab 2	155 kN	6.30°
FEM slab 2	169 kN	6.83°
FEM slab 1	162 kN	6.41°

5 CONCLUSION

The paper presents a novel real-scale test set-up. Some experimental results as well as a numerical verification are provided. It has been demonstrated that the development of tensile membrane actions can indeed significantly favour the load-carrying capacity in accidental situations of a slab strip when very large displacements occur. On the basis of the realized experimental investigations, it can be concluded that for this particular test arrangement, a loss of the central support did not cause the specimens to fail under gravity load. Note that slab 2 was not explicitly designed for this accidental event as the moment in mid-span changes sign as soon as the central support artificially fails. The central bottom region of the specimen, that was originally designed to be in compression, changes to tension which implies a severe alteration of the structural system as only 50% of the flexural reinforcement was provided due to the applied curtailment rules in case of slab 2.

Based on the realized numerical analysis it can be concluded that FE modelling is able to predict the increase in the load-carrying capacity due to tensile membrane forces as well as the development of the rotation angles over the inner supports. The load-rotation curve until the rupture of the reinforcement bars as well as the ultimate transverse load was simulated within a reasonable tolerance. Further, the influence of the ultimate reinforcement strain, the horizontal support conditions and the reinforcement curtailment was investigated. It was shown that the ductility of the reinforcement bars is of crucial importance with respect to rotational angles and ultimate load.

The development of the load-rotation relationship was similar for slabs 1 and 2 and the ultimate load capacity as well as the ultimate rotational angles were almost the same for both slabs and as such the effect of curtailment was found negligible with respect to the strength just prior to the rupture of the top reinforcement bars over the supports.

REFERENCES

Brotchie, J.F. & Holley, M.J. 1971. Membrane action in slabs. *ACI Publication SP-30; Cracking deflection and ultimate load of concrete slab systems, pp. 345–377.*

EN 1992-1-1. 2004. *Eurocode 2: Design of concrete structures, European standard*. Brussels: CEN.

Gouverneur, D., Caspeele, R. & Taerwe, L. 2013. Experimental investigation of the load-displacement behaviour under catenary action in a restrained reinforced concrete slab strip. *Engineering Structures* (in press).

Guice, L.K., Slawson, T.R & Rhomberg, E.J. 1989. Membrane analysis of flat plate slabs. *ACI Structural Journal* 86(1): 83–92.

Johansen, K.W. 1962. *Yield-Line Theory*. London: Cement and Concrete Association.

Ockleston, A.J. 1955. Load Tests on a 3-Story Reinforced Concrete Building in Johannesburg. *The Structural Engineer* 33(10): 304–322.

Park, R. 1964. Tensile membrane behaviour of uniformly loaded rectangular reinforced concrete slabs with fully restrained edges. *Magazine of Concrete Research* 16(46): 39–44.

Regan, P.E. 1975. Catenary Action in Damaged Concrete Structures. *ACI Publication SP-48; Industrialization in Concrete Building Construction, pp. 191–224.*

Westergaard, H.M. & Slater, W.A. 1921. Moments and Stresses. *ACI Journal* 17(2): 415–539.

Yi, W.-J., He, Q.-F. & Kunnath, S.K. 2008. Experimental Study on Progressive Collapse-Resistant Behavior of Reinforced Concrete Frame Structures. *ACI Structural Journal* 105(4): 433–439.

Research and Applications in Structural Engineering, Mechanics and Computation – Zingoni (Ed.)
© 2013 Taylor & Francis Group, London, ISBN 978-1-138-00061-2

The impact of fire scenario to the collapse of a tall structure

S. Selamet
Bogazici University, Istanbul, Turkey

ABSTRACT: The aim of this study is to investigate the effect of the fire load to a tall structure and draw conclusions for a more robust structural design. If a building is not properly designed and constructed to withstand potentially catastrophic events due to risk factors posed by fires, such disasters can nullify the benefits gained from green construction. Leadership in Energy and Environmental Design (LEED) developed by the U.S. Green Building Council and other international certification organizations. One common aspect of most of these certification systems is a lack of consideration for the impact of risks such as fire hazard on sustainability. In order to design sustainable tall structures, their robustness against extreme fire scenarios must be adequately satisfied. In this study, a generic tall structure is modeled using the finite element software LS-Dyna. The two-dimensional model consists of line elements (beams and columns) as well as the shell elements (concrete deck). To simulate the building collapse, the explicit dynamic analysis is used with proper surface-based contact configurations.

1 INTRODUCTION

The progressive collapse behavior of tall buildings has been intensively studied after the collapse of World Trade Center Towers in 2001 (Hoffman, 2004, Gross, 2005). A sensitivity analysis of a moment resisting and a dual system steel frame due to a column loss is conducted by Kim et al. (2011) and they concluded that the beam yield strength is the most critical design parameter. A detailed three-dimensional composite floor structure with shear connections is modeled by Sadek et al. (2008) and Alashker et al. (2010). One-floor composite structure is suddenly subjected to a column loss and it is observed that the tensile forces in the composite floor are carried by the metal deck. Further, the effect of shear connection capacity is found to be limited. A similar observation is made by Yu et al. (2009). A comprehensive three-dimensional model of the eight-story Cardington steel frame building is created by Kwasniewski (2010). The nonlinear dynamic behavior is analyzed due to column loss at different locations and due to increased gravity loading. The dynamic behavior of a 20 story steel building is investigated due to column loss with several different column locations by Fu (2009). Izzuddin et al. (2008) and Vlassis et al. (2009) laid out a theoretical groundwork for steel frames due to a sudden column loss. A steel building might also collapse due to an extreme event such as fire. The underlying mechanisms of tall buildings when subjected to fire have been previously investigated by Lange et al. (2012). It was found that the main cause of collapse is the outward and inward deflection of the columns above and below the heated floor. These columns are called as 'pivot columns'. Sun et al. (2012) investigated the vulnerability of steel braced frames and the development of plastic hinges at elevated temperatures.

In light of the described previous research on this subject, the main objective of this study is the assessment of the structural response of a 49 story steel high-rise structure due to ISO834 fire. It is intended to provide a better understanding of the effect of fire loading leading to the collapse mechanism of a high-rise structure. For all case studies, 3 floors are heated simultaneously at different floor locations and regions (asymmetric vs. symmetric heating). The commercial finite element code LS-Dyna is used as the analysis tool for the uncoupled thermo-mechanical dynamic response of the structure. Simulations are carried out using the Central Difference explicit time integration scheme. Geometric nonlinearity in terms of large displacements and rotations are taken into account. Material nonlinear response is considered through the use of a bi-linear constitutive model. The steel yield stress and stiffness of the material vary at elevated temperatures according to Eurocode provisions. The high-rise steel frame consists of steel beams and columns modeled with 2-node 1D (line) finite elements and composite floors modeled with 4-node shell 2D finite elements. In order to cut down the computational expense, the beam and columns are not modeled with shell elements, which could have accurately captured the local buckling effects during fire as discussed by Selamet & Garlock (2012). The structural load carrying system of the high-rise structure is assumed to be a moment resisting frame. Perimeter (primary) beams are connected to each other and to columns with rigid (moment) connections, the secondary beams and the bracing members have pinned connections.

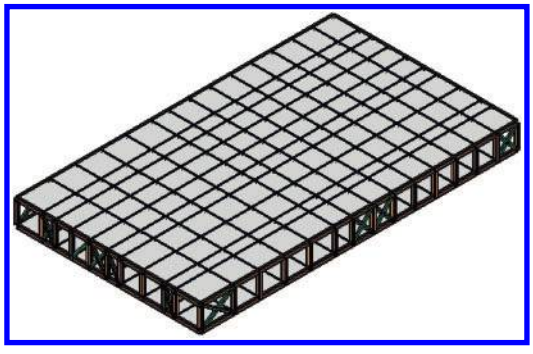


Figure 1. The floor structure of the tall building model.

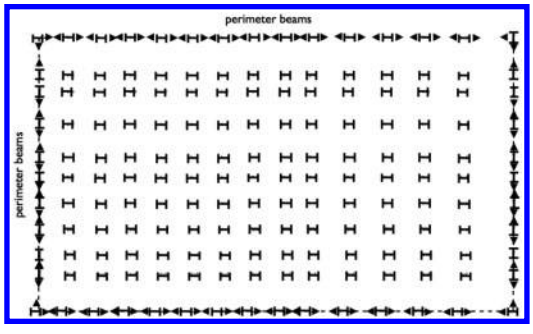


Figure 2. The column orientations for moment frame design.

2 TALL BUILDING STRUCTURE

2.1 *Design*

The tall steel structure is first modeled in ETABS, widely used structural engineering software. The steel frame sections (i.e. primary and secondary beams, bracings and columns) are designed with a combined earthquake and gravity load according to ASCE\SEI 7-10 seismic loading provisions (ASCE 2010). The prototype composite floor layout is based on Chase Tower (formerly known as BankOne) in Chicago, IL and it consists of secondary beams, primary beams, lateral bracings and 10 cm thick concrete slab with full composite action with the secondary beams. The building has 50 m by 29 m floors with a total height of 179 m. The model deflection calculations takes account the contribution of the concrete slab to the flexural stiffness; however this contribution is neglected for steel design calculations as a conservative approach. The height of each floor is 3.6 m and the member size of the columns is decreased at every 10th floor. Figure 1 and Figure 2 show the extruded view of a typical steel floor and the column orientations, respectively. The beam member sizes are shown in Table 1. The connections between the primary and secondary beams are idealized as pinned connections and the perimeter (primary) beams are connected with moment connections as part of the moment frame design. The bracings are modeled as truss elements. The prototype composite floor shown in Figure 1 is replicated for the upper floors.

Table 1. The structural steel member sizes.

Structural member	Steel section
Primary beam	W24 × 146
Secondary beam	W14 × 34
Lateral bracings	W14 × 120
Column (1–10th)	W24 × 335
Column (11–20th)	W24 × 306
Column (21–30th)	W24 × 207
Column (31–40th)	W24 × 146
Column (41–49th)	W24 × 103

2.2 *Gravity and earthquake loads for design*

The dead load is assumed to be the self-weight of the steel members and the superimposed dead load, which is estimated to be 3.6 kN/m^2. The superimposed dead load includes the weight of the light-weight concrete and the other structural elements such as partitions. The live load is assumed to be 2.4 kN/m^2, which is typical for an office building according to ASCE 7-10. The steel members are assumed to carry the gravity load depending on their tributary areas. The first natural period of the tall building is calculated as $T_d = 2.6174$ sec. Both the modal response spectrum analysis and the equivalent lateral force analysis methods are used for the earthquake design. Los Angeles CA region is taken as a basis for both methods. The response modification R and the occupancy importance I factors are taken as 8 and 3, respectively. The 0.2 sec (S_s) and the 1.0 sec (S_1) spectral accelerations are found as 2.1226 sec and 0.7837 sec, respectively. The base shear coefficient is calculated by ETABS as $C_w = 0.177$.

3 FINITE ELEMENT MODEL IN LS-DYNA

3.1 *Model description*

The geometry of the entire tall building model in ETABS is imported to LS-Dyna for uncoupled thermo-mechanical analysis with various fire scenarios, which requires an explicit dynamic scheme with highly nonlinear material behavior as well as large displacements. The Hughes-Liu beam elements and Belytschko-Tsay shell elements are employed in the model. The shell elements only provide additional stiffness to the building as a diaphragm. A rigid body is placed on the base to provide contact surface for the collapsed floors as seen in Figure 3. The gravity loading defined in the design is applied by using *LOAD BODY Z command for 6 seconds to ensure that no significant inertial (dynamic) forces are created before the fire starts. The reactions due to dead and live loads at the base are validated with the ETABS results. In order to simulate

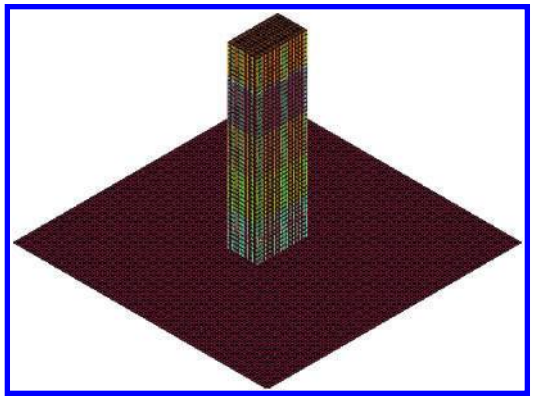


Figure 3. The tall building model in LS-Dyna with rigid base.

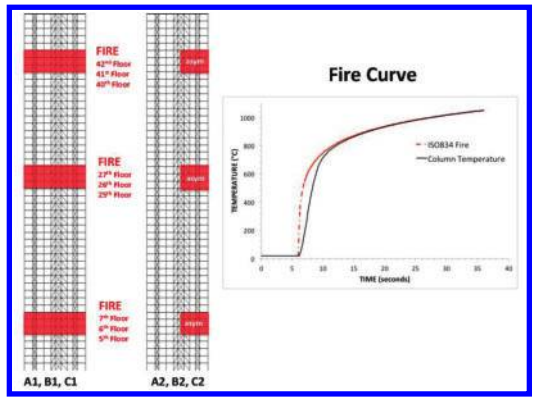


Figure 4. The fire location and progression in the tall building.

Table 2. Temperature dependent properties of steel.

T (°C)	20	100	300	500	600	700	900	1100
ρ (kg/m^3)	7850	7850	7850	7850	7850	7850	7850	7850
E (GPa)	200	200	160	120	62	26	13.5	4.5
σ_y (MPa)	345	345	345	269	162	79	21	4.3
ν	0.3	0.3	0.3	0.3	0.3	0.3	0.3	0.3
E_t/E	0.01	0.01	0.01	0.01	0.01	0.01	0.01	0.11
$\alpha(\times 10^{-5})$ (1/°C)	1.23	1.25	1.33	1.41	1.45	1.49	1.34	1.46

Table 3. Properties of the concrete slab.

ρ (kg/m^3)	E (GPa)	σ_y (MPa)	ν –	E_t (GPa)	Failure strain –
1750	24.8	27.6	0.2	24.8×10^{-2} 0.05	

progressive collapse, the contact interactions are introduced between the shells, beams and the rigid surface with *CONTACT GENERAL command. The steel material in the heated floors is defined as temperature dependent with *MAT ELASTIC PLASTIC THERMAL command. This material type does not have a failure limit state. Due to this limitation, the steel material for the other (not heated) floors is defined as temperature independent with *MAT PIECEWISE LINEAR PLASTICITY.

The temperature dependent material strength and stiffness of the steel sections and the material properties of the concrete slab are given in Table 2. A simple bilinear stress-strain relationship (constant E_t) is assumed, which is based on Eurocode 3 (CEN 2001). Since the concrete is not heated in the model, only ambient temperature material properties are used as seen in Table 2. For simplicity, no reinforcement bars are modeled for the concrete material. The temperature dependent thermal expansion coefficient α of steel is taken from Eurocode 3.

Table 4. Fire scenarios.

Label	Floor location	Fire spread
Case A1	5th–7th	Symmetrical
Case B1	25th–27th	Symmetrical
Case C1	40th–42nd	Symmetrical
Case A2	5th–7th	Asymmetrical
Case B2 25th–27th	Asymmetrical	
Case C2 40th–42nd	Asymmetrical	

3.2 *Gravity loading and fire scenarios*

A total of 6 fire scenarios are investigated, which are illustrated in Figure 4 and defined in Table 4. In conducting these scenarios, the aim is to understand the effect of the fire location (bottom, middle or top floors) and the fire spread (symmetric or asymmetric). For all cases, the steel building is gradually (quasi-statically) loaded with the dead load and the live load for 6 seconds. No oscillations are observed during the gravity loading, which validates that the loading remained static. The unprotected column members are heated with ISO834 fire curve as seen in Figure 4 (CEN 2001). The fire curve is applied at 6 seconds soon after the gravity load is applied. For computational efficiency, the fire curve is scaled to range only to 36 seconds as shown in Figure 4. Within the period, the kinetic energy of the system is carefully monitored in order to get a quasi-static behavior of the building during the thermal loading. The steel temperatures are calculated using lumped mass method with four-sided heating with convective heat transfer coefficient $h = 25$ W/m^2 °C and emissivity $\varepsilon = 0.5$. No fire protection is applied to the columns. ISO834 fire curve and the lumped column temperature are shown in Figure 4. The temperatures are directly applied to the nodes without a heat transfer analysis in LS-Dyna (uncoupled thermo-mechanical analysis). For Cases A through C, three columns at 5th–6th–7th floors, 25th–26th–27th floors and 40th–41st–42nd floors are heated uniformly considering a symmetrical collapse (A1, B1

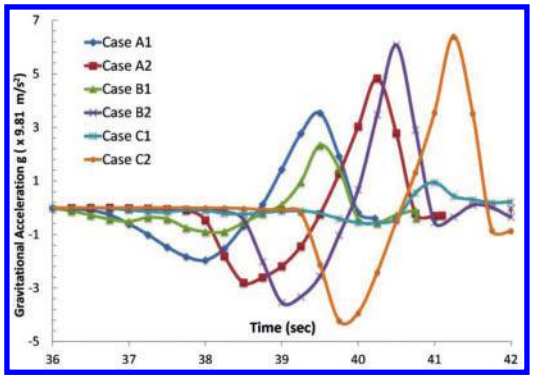


Figure 5. Rigid body acceleration of the entire building in the vertical direction.

and C1), respectively. For Cases 4 through 6, only half of the regions at 5th–6th–7th floors, 25th–26th–27th floors and 40th–41st–42nd floors are heated (A2, B2 and C2), respectively. Hence, the asymmetrical collapse is expected. After the plastic deformations of the structural members in the fire-applied floor, the gravity loading is scaled 5 times until 40 seconds to initiate collapse.

4 OBSERVATION AND RESULTS

4.1 *Collapse characteristics*

Figure 5 clearly shows the distinct collapse characteristics of the tall steel building. The collapse initiates soon after the fire application is over at around 36 seconds. At the onset of the collapse, the building has downward (negative) acceleration in g-units. But as the collapse progresses, the acceleration reserves the sign as the lower floors resist the impact and the downward motion slows down. The severity of the collapse is larger for the asymmetric fires. In general a fire in the lower floors causes the collapse initiation to occur slightly earlier. Further, the asymmetric collapse causes the building to lean over to one side and more debris is spread to a larger area on the rigid base as seen in Figure 6. This is a great concern in urban areas with high density of tall buildings in the neighboring regions. It is also observed that the asymmetric collapse in the lower floors causes an overturning moment, which tears apart the base columns and the shell elements in the cool (not heated) region.

4.2 *Column axial forces*

To analyze the behavior of the tall building at the collapse instant, the axial stress development of the three corner columns observed as shown in Figure 7. The heated column is compared to the (pivot) columns right below and above the heated region. Figures 8 through 10 show the axial stress development in these columns for Cases A, B and C, respectively.

In addition, the temperature dependent yield stress capacity of the columns is plotted. Note for some pivot

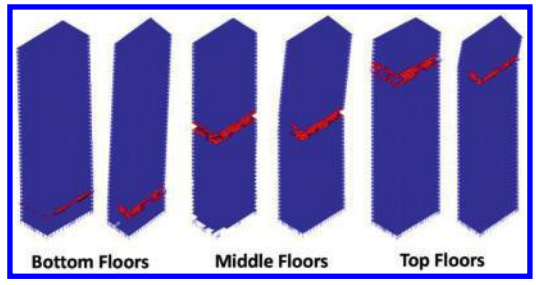


Figure 6. The collapse initiation for all cases. The heated floors are in red (lighter color).

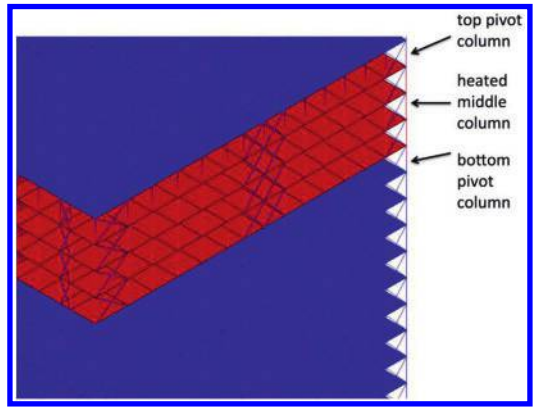


Figure 7. The location of the heated and pivot corner columns in the tall building for all cases.

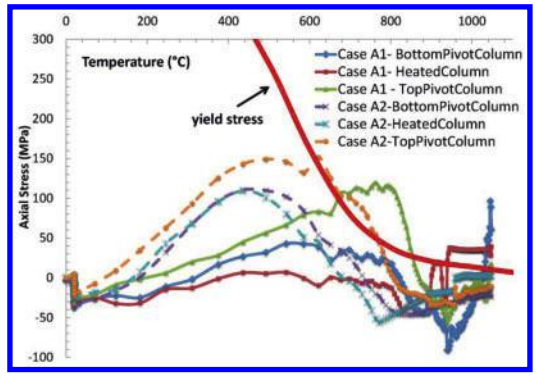


Figure 8. Column axial stress-temperature history for bottom floors fire (Cases A1 and A2).

columns, the axial stress surpasses the yield stress at some instances, which is expected since these pivot columns stay at ambient temperature. As seen in Figure 8, the initial compressive (negative) stress in the column due to gravity is considerably low. This is expected since the model is specially designed for lateral (earthquake) resistance of a large earthquake. It is observed that the heated column carries a minimum load whereas the pivot columns go into tensile action to the outward movement of the floors due to expansion.

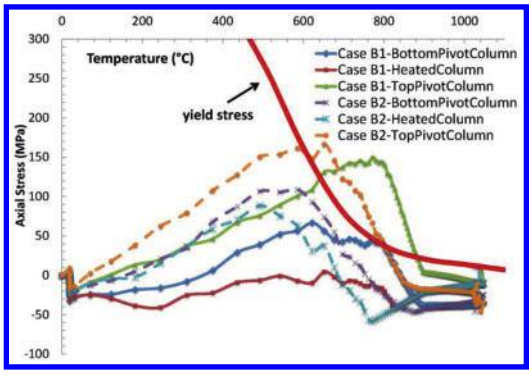


Figure 9. Column axial stress-temperature history for middle floors fire (Cases B1 and B2).

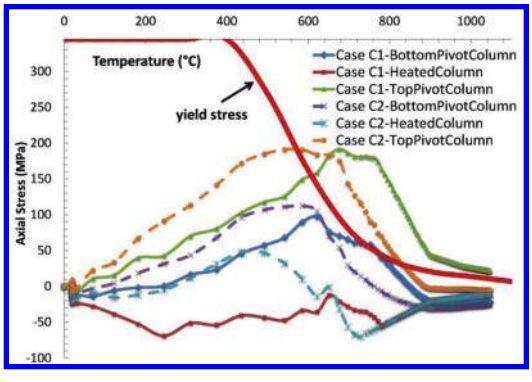


Figure 10. Column axial stress-temperature history for top floors fire (Cases C1 and C2).

The top pivot column carries the maximum load until it fails first at around 800°C. The difference between the symmetric and asymmetric collapse is seen in the magnitude of these stresses. Further, for the asymmetric case, the sudden drop in column stresses is seen at around 600°C.

Figures 9 and 10 show the same trend but the heated column has larger compression and the pivot columns have larger tension. This can be explained by the visual inspection in Figure 6. In Cases C1 and C2 with the heated top floors, the building leans over towards the corner region more than the other cases, which causes the stresses to differ significantly larger between the pivot and heated columns.

5 CONCLUSION

This study presents the ongoing research on the collapse mechanisms of tall steel buildings with symmetric and asymmetric fire conditions and various fire floor locations. The observations suggest that the asymmetric heating causes the steel building to collapse by leaning on the side that corresponds to the heated floor region. It also suggests that a building designed even for a large earthquake is not resistant to weakened floors due to the imposed ISO834 fire. In general, an asymmetric fire spread causes more damage to the building and the building collapse initiates earlier when compared to a symmetrical fire spread. The fire location seems to change the collapse behavior only slightly. In all cases, the pivot columns below and above the heated regions go into tension due to the lateral expansion of the floors. The author intends to expand the study by adding the *MAT EROSION command for the heated steel members. Furthermore, a finer meshing in the beam members will enable to capture a possible buckling behavior.

ACKNOWLEDGEMENTS

This research is funded by Bogazici University Scientific Research Project (BAP) No. 7122: 13A04P1. All opinions, findings and conclusions expressed in this paper are the authors' and do not necessarily reflect the policies and views of BAP.

REFERENCES

Alashker, Y., El-Tawil, S., Sadek, F. 2010. Progressive collapse resistance of steel-concrete composite floors. *Journal of Structural Engineering ASCE* 136 (10): 1187–1196.

ASCE 2010. ASCE/SEI 7-10 Minimum Design Loads for Buildings and Other Structures (1st Edition). Reston: Virginia.

CEN 2001. Eurocode 3: Design of steel structures Part 1.2: General Rules Structural fire design ENV 1993-1-2:2001. Brussels: Belgium.

Fu, F. 2009. Progressive collapse analysis of high-rise building with 3-D finite element modeling method. *Journal of Constructional Steel Research* 65: 1269–1278.

Gross, J.L. & McAllister, T.P. 2005. Structural fire response and probable collapse sequence of the World Trade Center Towers. Federal building and fire safety investigation of the World Trade Center disaster (NIST NCSTAR 1-6), *NIST*. Gaithersburg: Maryland.

Hoffmann, C., Popescu, V., Kilic, S. A., Sozen, M. 2004. Modeling, simulation, and visualization: The Pentagon on September 11th. *Computing in Science & Engineering (CISE)* 6(1): 52–60.

Izzuddin, B.A., Vlassis, A.G., Elghazouli, A.Y., Nethercot, D.A. 2009. Progressive collapse of multi-storey buildings due to sudden column loss – Part I: Simplified assessment framework. *Engineering Structures* 30: 1308–1318.

Kim, J., Park, J-H., Lee, T-H. 2011. Sensitivity analysis of steel buildings subjected to column loss. *Engineering Structures* 33: 421–432.

Kwasniewski, L. 2010. Nonlinear dynamic simulations of progressive collapse for a multistory building. *Engineering Structures* 32: 1223–1235.

Lange, D., Roeben, C., Usmani, A. 2012. Tall building collapse mechanisms initiated by fire: Mechanisms and design methodology. *Engineering Structures* 36: 90–103.

LSTC 2012. LS-DYNA Keyword User's Manual Volume I & II version 971. Livermore: California.

Sadek, F., El-Tawil, S., Lew, H.S. 2008. Robustness of composite floor systems with shear connections: Modeling, simulation, and evaluation. *Journal of Structural Engineering ASCE* 134(11): 1717–1725.

Selamet, S., & Garlock, M. 2012. Plate buckling strength of steel wide-flange sections at elevated temperatures. *Journal of Structural Engineering ASCE* doi: 10.1061/(ASCE)ST.1943-541X.0000769.

Sun, R., Huang, Z., Burgess I.W. 2012. The collapse behaviour of braced steel frames exposed to fire. *Journal of Constructional Steel Research* 72: 130–142.

Vlassis, A.G., Izzuddin, B.A., Elghazouli, A.Y., Nethercot, D.A. 2009. Progressive collapse of multi-storey buildings due to failed floor impact. *Engineering Structures* 31: 1552–1534.

Yu, M., Zha, X., Ye, J. 2010. The influence of joints and composite floor slabs on effective tying of steel structures in preventing progressive collapse. *Journal of Constructional Steel Research* 66: 442–451.

Research and Applications in Structural Engineering, Mechanics and Computation – Zingoni (Ed.)
© 2013 Taylor & Francis Group, London, ISBN 978-1-138-00061-2

Behavior of tall buildings under blast loading with direct simulation method

Feng Fu
School of Engineering and Mathematical Sciences, City University, London, Northampton Square, London

ABSTRACT: In this paper, a 3-D numerical model with the direct simulation of blast load is proposed to study the real behavior of a 20-storey tall building under the blast loading. The modeling techniques are discussed in details. In the analysis, a typical package bomb charge was simulated to be detonated on the 12th floor. The corresponding dynamic response of structure was studied. The method to enhance the robustness of the buildings is also recommended.

1 INTRODUCTION

Recently, the special design requirement of buildings against blast load becomes more and more important for the safety of the occupants. The UK SCI publication 244[1] provides a guidance on the design of commercial and public buildings where there is a requirement to provide protection against the effects of explosions caused by the detonation of explosives. In United States, FEMA 426 [2] provides the design measurements to reduce physical damage to the structural and non-structural components of building and related infrastructures during conventional bomb attacks, as well as attacks using chemical, biological and CBR agents. Kambouchev *et al.* [3] discussed the nonlinear compressibility effects in fluid-structure interaction and their implications on the air-blast loading of structures Blanc et al. [4] discussed empirical method to estimate the blast loading.

However, due to the huge cost, it is almost impossible to investigate the response of the multi-story buildings against blast loads with full-scale experimental tests. Therefore, advanced numerical tools such as the finite element method become the main approach for the related research. The analysis and design of structures subjected to blast loads require a detailed understanding of blast phenomena and the dynamic response of various structural elements. Some numerical modeling has been done in the past decades. Børvik et al. [5] investigated if a pure Lagrangian formulation could be applied to determine the structural response in a specified blast load problem. Luccioni et al. [6] performed a detailed analysis of the structural failure of a reinforced concrete building caused by a blast load. However, most of the current numerical modeling research is involved with massive computational time and the model is difficult to build due to its complexity. Therefore, for designers, it is imperative to establish a simple modeling method to study the detailed behavior of the building after the blast denotation.

To solve this problem, in this paper, using ABAQUS [7], a 3-D finite element model representing a 20-storey building was built to perform the blast analysis. A simplified direct simulation method of blast load is applied here. The proposed method can apply the blast loads directly on the frames and the floors of the building. The nonlinear material behaviour and dynamic effects are also included in the simulation. The proposed method requires substantially less computational effort as compared to other direct numerical simulations. Based on this model, detailed response of the multi-storey buildings is also discussed. The measures to increase the robustness of the high-rise building in the future design are also recommended.

2 3D FINITE ELEMENT MODEL

As shown in Fig. 1, a three-dimensional finite element model was created by Fu [8] using the ABAQUS [7] package. It replicatesa20-Storey steel composite building with the grid spacing of 7.5 m in both directions. The main lateral stability of the building is provided by cross bracings in the exterior frame at the four facades. The floor height is 3 m for each floor. The slab thickness is 130 mm. All the structural steel members are using grade S355 steel. The columns are British universal column UC356X406X634 for ground floor to level 6, UC356X406X467 for level 7to level 13, UC356X406X287 for level 14 to level 19. All the beams are British universal beam UB533X210X92. The cross bracings are British circular Hollow section CHCF273X12.5. The section properties are shown in Table 1. The section sizes of the structural steel members were determined followed the capacity design principles of British standards [9],[10].

All the beams and columns were simulated using *BEAM elements. The Slabs were simulated using the four node *Shell elements. Reinforcements were represented as a smeared layer in each shell element using the *REBAR elements and were defined in both slab

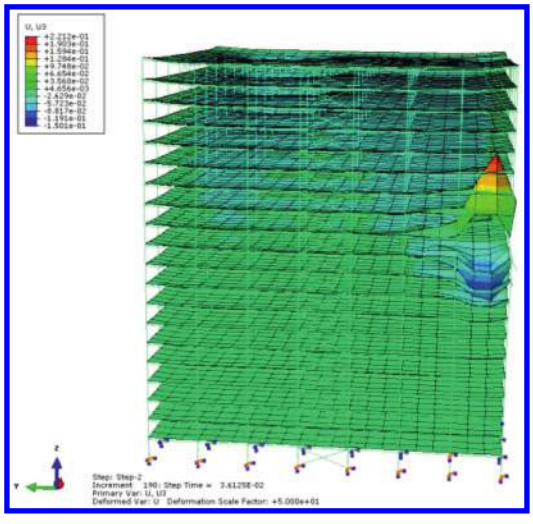


Figure 1. Isotropic view (blast detonated at level 12, deformation samplified).

directions. The beam and shell elements were then coupled together using rigid beam constraint equations to give the composite action between the beam elements and the concrete slabs. The detailed description of the modeling technique is shown in Fu[8]. The nonlinear behaviour and dynamic effects of the material due to blast or impact loading are also considered in the simulation which is determinated based on [1].

As it is discussed in [1][2], to precisely evaluate the shock propagation around the structure and the structure's response, using a fluid-structure interaction method is possible. However, it will generate big models. Another possibility is to use the empirical model to compute the load on the structure. This solution is computational effective and is used in this paper with the program ATBLAST [11]. A subroutine program with Visual BASIC language is designed by the author, which can transfer the blast load profile worked out by ATBLAST [11] to the 20-storey prototype model built in ABAQUS. In the simulation, the blast load was applied as an area load working directly on the slabs and line load directly on the beams and columns with all the related information as shown in Fig. 2. For the applied blast loading, the time of arrival and load duration are all different due to their distance to the blast charge locations. Therefore, the propagation of the blast wave was also simulated. Therefore, the response of the 20 storey prototype building can be evaluated.

There are many ways in which an explosive device may deliver an attack. As it is stated in [1], there are several conventional devices like Vehicle bombs, Package bombs, Mortar bombs, Culvert bombs and Incendiary devices. In this paper, the scenario of Package bombs is selected for the study, as this type of attack is more difficult to be prevented than other attack scenarios such as vehicle bombs.

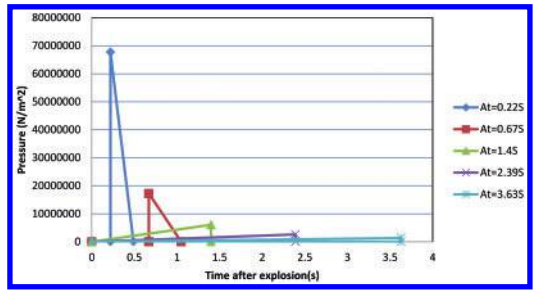


Figure 2. Blast overpressure profile at different Arrival time (At) of the proposed analysis model.

3 RESPONSE OF THE BUILDING UNDER BLAST LOAD

Using general purpose program ABAQUS, the response of the prototype building under the blast load is assessed here using a nonlinear dynamic analysis method with 3-D finite element technique. The loads are computed as dead loads (which is the self-weight of the floor) plus 25% of the live load in accordance with the acceptance criteria outlined in GSA guidelines [12].

The static analysis with the dead and live load loaded to the building was conducted in the first second as a static step. After this step, a blast load of 15 kg TNT is detonated at location of column A1 on level 12 as it is shown in Fig. 1. This is to simulate the typical charge weight for a package bombs indicted in SCI 244 [1] table 6.1 occurs inside an office building. Fig. 6 is the Pressure of distributed blast load on element surface at different selected time. It clearly shows the blast wave pressure propagating from the charging location to the adjacent structural members on level 12.

The simulations were conducted with 5% mass damping. In the analysis, the internal forces, such as axial force, shear force, bending moment, displacements and rotations for each of the members involved in the scenario are recorded. To facilitate the following discussion, the columns and beams are designated as follows according to the grid line shown in [8]. For instance, Column C1 stands for the column at the junction of grid C and grid 1. Beam E1-D1 stand for the beam on grid 1 starting from grid E to grid D.The response of the structure was extracted from the 3-D finite element model. And the results are shown in the following sections.

3.1 *Shear force comparisons of columns at different location*

The car bomb attack happened in Oklahoma City in 1995 shows that, except the failure of the column where the bomb was detonated, the adjacent columns were also sheared off. Fig. 3 is the shear force response of the column B1on level 12 which is adjacent to the blast charge location. It can be seen that at time 1.01S, the shear force of the column reach a peak value

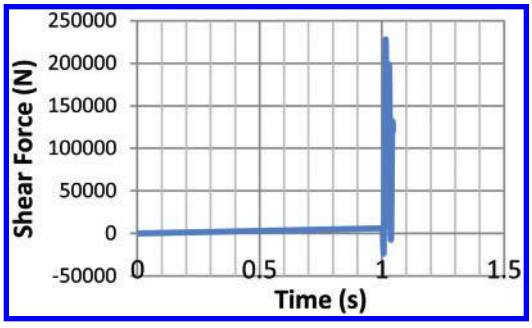


Figure 3. Shear force of column B1 at level 12.

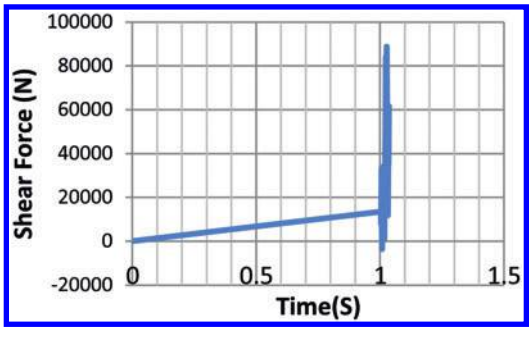


Figure 4. Shear force of column B2 at level 12.

220 kN. As this shear force is quite large, so it could not be ignored. Therefore, one way to mitigate the collapse of the building is to enhance the shear capacity of the column.

The shear forces of columns at other locations are chosen for the study as well, as it is shown in Fig. 4. It can be seen that, with the increasing of the distance, the response of the column decreased dramatically, the effect of the blast loading become quite small, can be ignored.

3.2 *Axial force comparisons of columns at different location*

In order to investigate the axial force of the columns, the columns at different location are chosen for the studies. Fig. 5 is the axial force response of the column B1on level 12. It can be seen that at time 1.006 s, the compressive force of the column reached a peak value −1200 kN, after that the force started to decrease until it become in tension.

The axial force of the columns at different location is shown in Fig. 6. It is the response of the column D4 at level 12. Following the principle of the scaling law. It can be seen that, compared with column A1 at level 12, the axial forces of D4 was almost kept unchanged after the blast charge.

3.3 *Collapse potential of the building*

It is well known that the columns play an important role in the prevention of the collapse of the building.

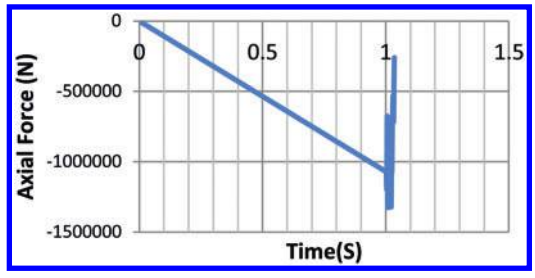


Figure 5. Axial force of column C1 at level 12.



Figure 6. Axial force of column D4 at level 12.

Following Progressive collapse analysis and design guidelines [12], the collapse potential of the building is checked here starting from the columns. From numerical analysis, it can be seen that, the three columns A1, B1 and A2 (due to symmetry, the force in B1 and A2 are identical)at level 12 near the blast charge location started to yield. However, a manual checking in accordance to BS5990 [9] is made, it shows that the maximum axial force, bending moment and shear force obtained from the analysis does not exceed the capacity of the columns, the three columns did not fail, nor did the adjacent columns. Therefore, no collapse of the whole building was triggered.

3.4 *Discussion of Analysis*

The above analysis shows that, the blast load decreases dramatically with the increasing of the distance, beyond certain distance, the effect of blast pressure can be ignored. It can also be seen that, one way to prevent the progressive collapse of the building under blast load is to enhanced shear capacity and increase the ductility of the column. For the buildings designed using the current design guidance, the small scale blast such as the package bomb will normally cause localized structural member damage, and it hardly triggers the collapse of the whole building, as long as the alternative path can be provided for the load to be redistributed.

4 CONCLUSIONS

In this paper, the numerical simulation of a tall building under a 15 Kg package bomb is conducted. The

dynamic behavior of the building is studied in details. The robustness of the tall building under the blast load is studied. The main conclusions are made as follows:

1. The Alternative Path Method ignores the huge shear force applied to the column due to the blast loading. Therefore, when using the APM method to evaluate the robustness of the building, the shear capacity of the column should also be checked.
2. To prevent the progressive collapse of the building under blast load, the shear capacity and of the column need to be enhanced.
3. For the buildings designed using the current design guidance, the small scale blast such as the package bomb will normally cause localized structural member damage, and it hardly triggers the collapse of the whole building, as long as the alternative path can be provided for the load to be redistributed.

REFERENCES

[1] E YANDZIO, M GOUGH, Protection of Buildings against Explosions. SCI PUBLICATION 244, (1999)

[2] Risk Management series, reference manual to mitigate potential terrorist Attacks against buildings, FEMA426, Dec 2003

[3] N. Kambouchev, L. Noels, and R. Radovitzky, Nonlinear compressibility effects in fluid-structure interaction and their implications on the air-blast loading of structures, J. Appl. Phys. 100, 063519 (2006)

[4] G. Le Blanc, M. Adoum, V. Lapoujade, External blast load on structures – Empirical approach, 5th European LS-DYNA Users conference.

[5] T. Børvik, A.G. Hanssen, M. Langseth and L. Olovsson, Response of structures to planar blast loads – A finite element engineering approach Computers& Structures, Volume 87, Issues 9-10, May 2009, Pages 507–520

[6] B. M. Luccioni, R. D. Ambrosini, R. F. Danesi, Analysis of building collapse under blast loads, Engineering Structures, Volume 26, Issue 1, January 2004, Pages 63–71

[7] ABAQUS theory manual, (2003) Version 6.7Hibbitt, Karlsson and Sorensen, Inc. Pawtucket, R.I.

[8] F Fu, Progressive collapse analysis of high-rise building with 3-D finite element modelling method, Journal of Constructional Steel Research, Vol. 65,2009, pp1269–1278

[9] British Standards Institution. BS 5950: Structural use of steelwork in buildings, Part 1: Code of practice for design — rolled and welded sections, London (UK).

[10] British Standards Institution. BS 8110, Structural use of concrete, Part 1: Code of practice for design and Construction London (UK).

[11] ATBLAST 2.0, Applied Research Associates, 2000

[12] GSA. Progressive collapse analysis and design guidelines for new federal office buildings and major modernization projects. The U.S. General Services Administration; 2003.

Research and Applications in Structural Engineering, Mechanics and Computation – Zingoni (Ed.)
© 2013 Taylor & Francis Group, London, ISBN 978-1-138-00061-2

A modal property analysis of linked tall buildings using a matrix model

K.T. Tse & J. Song
Department of Civil and Environment Engineering, The Hong Kong University of Science and Technology, Hong Kong, P.R. China

ABSTRACT: In order to study the effect of link on modal properties of linked tall buildings, a 3-D analytical matrix-form model of linked tall building that can consider varied locations and numbers of links is introduced. Then the effect of stiffness of link is investigated by parametric analysis. The results show that the link can decrease the natural periods of antisymmetric mode of linked twin buildings significantly, i.e. can stiffen the structure. In addition, the mode shapes of these antisymmetric modes could be changed from a linear form to a hyperbolic form, which is rather different from the ones of single building and should be received researchers' and designers' attentions.

1 INTRODUCTIONS

With the development of cities, there is a trend that increasing tall buildings are erected in a relatively close proximity owing to inadequate available land in urban area, especially in some metropolises, which gives a possibility to connect these adjacent buildings horizontally. Consequently, more and more tall buildings in close proximity are designed as linked buildings all over the world, such as the Petronas Twin Towers in Kuala Lumpur and Marina Bay Sands Hotel in Singapore.

Compare to regular isolated tall buildings, the dynamic properties of which have been analyzed comprehensively and thoroughly, there are only limited researches that have done for linked tall buildings. Xie & Irwin (1998, 2001) divided the mode shape of whole complex including several towers connected by sky-bridges into the mode shape of each substructure to calculate the wind-induced responses. For seismic response analysis, Zhang & Xu (1999) derived an analytical model for two adjacent buildings connected by viscoelastic dampers vibrating in one translational direction, i.e., one-dimensional (1D) motion. The coupling effect of dampers was introduced by modeling each damper as the Voigt model with axial stiffness and damping. Lim (2009) and Lim et al. (2011) reduced a complex with two towers connected by a skybridge to a six-degree-of-freedom model at the elevation of skybridge. This model provides a better understanding about the structural coupling of link by assuming that the first six mode shapes of linked buildings can be fitted by power functions. Lim also summarized that the effect of link on the structural coupling between towers can be sorted as two aspects: on one hand, the axial stiffness of link tends to synchronize the motion of two towers along the direction of link, which is similar to Zhang & Xu's the model; on the other hand, the bending stiffness may synchronize the motion of sway perpendicular to the link and torsion of two towers simultaneously.

However, it should be noted that due to recent trend of irregular or elongated building shapes, the mode shape of isolated buildings could be significantly three-dimensional (3D) coupled and nonlinear, let alone the one of linked buildings, which could be more complicated for the effect of link. So without a careful investigation the characteristics of mode shape of linked tall buildings, it should be cautious when using Lim's method to predict wind-induced vibration of linked tall buildings. In addition, this simplified model just addresses the case with one link at a given elevation. In real case, the links could cover a succession of floors or at several separate floors. Apparently, the whole system of two linked buildings by no means can be lumped at one location to form a six-degree-of-freedom model.

In view of the forgoing discussion, it is crucial to develop an analytical model of linked tall building that can take account the 3-D structural coupling caused by link and can deal with the case with links at a succession of floors or at several separate floors. Therefore, a 3-D analytical matrix-form model of linked tall building allowing for structural coupling of links at a succession of floors or at several separate floors was developed in this paper. To evaluate the accuracy of the proposed model, a case of linked buildings was modelled by finite element method (FEM) model and by the analytical matrix-form model, then the modal properties of the complex was calculated by the analytical model to compare to "exact" ones obtained by FEM model. Subsequently, a systematic parametric analysis was conducted to examine the effect of axial stiffness and bending stiffness of link on the modal properties.

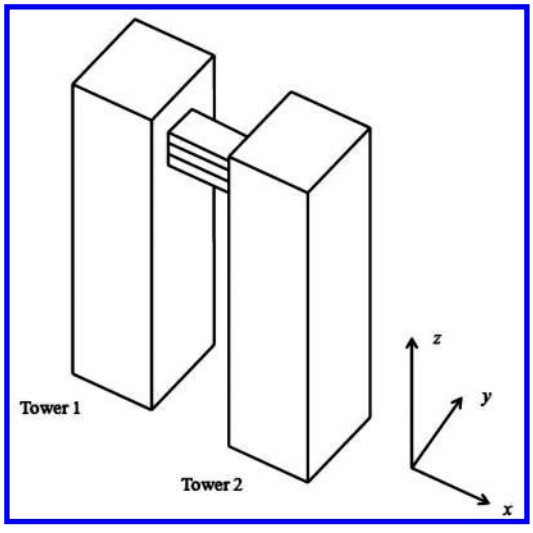


Figure 1. Isometric view of one case of linked buildings and definition of coordinate.

2 MODELLING OF STRUCTURAL COUPLING EFFECT OF LINK

A 3-D analytical model of linked buildings that can take into account the effect of structural coupling of link is outlined in this section briefly. Fig. 1 is a drawing of two twin tall buildings (tower 1 and 2) connected by *n*-floor links. Each tower with *m* floors can be modelled by lumped mass system having three dynamic degrees of freedom, i.e. sway motions along x and y and torsional motion along z, at the elevation of each floor. Each link can be modelled by a link beam with three degrees of freedom at each end.

In order to study structural coupling effect of link, the sub-matrix of structural property of each sub-part, i.e. two towers and link system, should be formed at first. The structural-property matrices of tower can be obtained by FEM model easily. If we do not consider the effect of link here, given the mass and stiffness matrices of each tower, we can easily assemble them as

$$\mathrm{M}_{tower} = \begin{bmatrix} M_1 & & & & & \\ & M_1 & & 0 & & \\ & & J_1 & & & \\ & & & M_2 & & \\ & 0 & & & M_2 & \\ & & & & & J_2 \end{bmatrix}_{6m\times 6m} \quad (1)$$

$$\mathrm{K}_{tower} = \begin{bmatrix} K_{1xx} & 0 & K_{1x\theta} & & & \\ 0 & K_{1yy} & K_{1y\theta} & & 0 & \\ K_{1x\theta}^T & K_{1y\theta}^T & K_{1z\theta} & & & \\ & & & K_{2xx} & 0 & K_{2x\theta} \\ & 0 & & 0 & K_{2yy} & K_{2y\theta} \\ & & & K_{2x\theta}^T & K_{2y\theta}^T & K_{2\theta\theta} \end{bmatrix}_{6m\times 6m} \quad (2)$$

where M_1, M_2, J_1, and J_2 are mass matrix and moment of inertial of tower 1 and 2, and mass matrix of links,

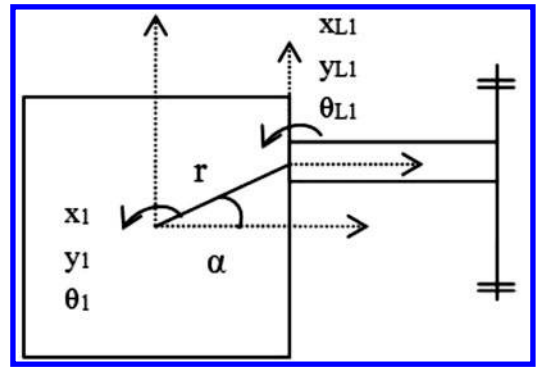


Figure 2. Relationship between link and tower in plan.

respectively; K_{trs} ($t = 1$ or 2, s, $r = x$, y or θ) is the stiffness matrix of tower t. For each tower, the centers of mass and stiffness of each floor are assumed to be coincident with the geometric center of each floor to eliminate the static and dynamic coupling within each building so that the structural coupling effect of link can be show more clearly and directly.

In order to take the structural coupling effect of link into account, the structural-property matrices of link should be formed and then the total matrices can be obtained by assembling them into the above tow matrices in Eq. 1 and 2. Assuming that link can be simulated by a fixed-fixed beam without the stiffness of out-plane, the stiffness matrix of link K_{link} for the deformation of two ends of link $\{\mathrm{x}_{L1}, \mathrm{x}_{L2}, \mathrm{y}_{L1}, \mathrm{y}_{L2}, \theta_{L1}, \theta_{L2}\}^T$ can be expressed as (Przemieniecki, 1985)

$$K_{link} = \begin{bmatrix} k_a & -k_a & 0 & 0 & 0 & 0 \\ -k_a & k_a & 0 & 0 & 0 & 0 \\ 0 & 0 & 12k_b & -12k_b & 6k_b l & 6k_b l \\ 0 & 0 & -12k_b & 12k_b & -6k_b l & -6k_b l \\ 0 & 0 & 6k_b l & -6k_b l & (4+\beta)k_b l^2 & (2-\beta)k_b l^2 \\ 0 & 0 & 6k_b l & -6k_b l & (2-\beta)k_b l^2 & (4+\beta)k_b l^2 \end{bmatrix} \quad (3)$$

where x_{Lt}, y_{Lt} and θ_{Lt} ($t = 1$ or 2) are deformations of end of links in the two translational directions and torsional directions along axis z; l is the length of link; axial stiffness $k_a = EA/l$; bending stiffness $k_b = EI'/l^3$, in which $\mathrm{I}' = I/(1+\beta)$, $\beta = 12\mu EI/(GAl^2)$; μ is a correction factor, for rectangular beam, $\mu = 1.2$.

It should be noted that the above stiffness matrix K_{link} is formed at the point connecting main towers and link. In order to assemble it to the total stiffness matrix, it should be transferred to the mass center of the related floor. According to the relationship shown in Fig. 2, the stiffness matrix of link for the deformation of mass center of tower can be derived as

$$K'_{link} = HK_{link}H^T \quad (4)$$

where H is the transformation matrix.

$$H=\left[\begin{array}{ccc|cc} 1 & -r_1\sin\alpha_1 & & & \\ & 1 & r_1\cos\alpha_1 & 0 & \\ & & 1 & & \\ \hline & & & 1 & r_2\sin\alpha_2 \\ 0 & & & 1 & -r_2\cos\alpha_2 \\ & & & & 1 \end{array}\right]_{6\times 6} \quad (5)$$

The above stiffness matrix K'_{link} is only for one link. Then the stiffness matrix for all links K_L can be formed by assembling all stiffness matrices of link as

$$K_L = K'_{link} \otimes U_n \quad (6)$$

where U_n is $n \times n$ unite matrix; $\otimes$ is Kronecker tensor product.

Now stiffness matrices of all subparts have been evaluated, then stiffness matrix K_{total} of this linked complex can be assembled as

$$K_{total} = K_{tower} + EK_L E^T \quad (7)$$

where E is a whole location matrix to show the relationship of connection between link and of towers,

$$E = diag\left(E_1, E_1, E_1, E_2, E_2, E_2\right)_{6m\times 6n} \quad (8)$$

here, E_t ($t = 1$ or 2) is a location matrix to show relative location relationship between links and each tower. Taking tower 1 for example, $E_1 = [e_1, e_2, \ldots, e_p, \ldots, e_n]_{m\times n}$, each e_p is a vector as

$$e_p = \{0 \quad \cdots \quad 1 \quad \cdots \quad 0\}^T \quad (9)$$

Since one link is only connected with one story of tower 1, elements of e_p are zero except the ith element equal to one, which mean that the ith floor of tower 1 is connected with the pth link. For example, if there are three links connected with tower 1 at the top three floors, E_1 can be formed as

$$E_1 = \begin{bmatrix} 0 & 0 & 0 \\ \vdots & \vdots & \vdots \\ 1 & 0 & 0 \\ 0 & 1 & 0 \\ 0 & 0 & 1 \end{bmatrix}_{m\times 3} \quad (10)$$

Lumping the mass of link to the connected floors of two towers equally, the total mass matrix M_{total} can be expressed as

$$M_{total} = M_{Tower} + M_L = M_{Tower} + \frac{1}{2}\times E\times\left[diag\left(1,1,r^2,1,1,r^2\right)\otimes M_L\right]\times E^T \quad (11)$$

In this way, the mass and stiffness matrices for the whole system are formed and hence then structural model properties such as frequencies and mode shapes can be calculated directly by eigenvalue analysis based on the equation of undamped free vibration

$$M_{total}\ddot{D} + K_{total}D = 0 \quad (12)$$

where D is displacement response vector, $D = \{D_{1x}, D_{1y}, D_{1\theta}, D_{2x}, D_{2y}, D_{2\theta}\}^T$, and $D_{ts} = \{d_{ts1}, d_{ts2}, \ldots, d_{tsm}\}^T$ ($t = 1$ or 2, s, $r = x$, y or θ).

Table 1. Natural periods calculated by the analytical model and FEM model.

	Natural period (s)					
Mode	1	2	3	4	5	6
Matrix model	4.182	4.182	3.368	1.779	1.656	1.553
FEM model	4.184	4.184	3.334	1.779	1.675	1.553
Difference (%)	−0.03	−0.03	1.02	−0.02	−1.15	−0.03

3 VERIFICATION OF THE ANALYTICAL MODEL

To evaluate the accuracy of the above analytical model of linked tall buildings, it is necessary to simulate the same complex with a detailed finite element model to capture comprehensive structural properties and then calculate "exact" modal properties of structure. In this section, therefore, an example of linked tall buildings with two identical towers is simulated by finite element method (FEM). Each tower is a 40-storey, 160 m tall reinforced concrete framed-tube structure with a uniform square floor plan of 30 m by 30 m throughout its height. At the top two floors, there is a two-story link with span of 15 m and width of 18 m.

Tab. 1 shows the comparison of natural periods of the two approaches, i.e. matrix-form method and FEM. Clearly, the natural periods hardly show noticeable differences between the two methods, which gives compelling evidence that the matrix-form model of linked buildings can provide satisfied accuracy as FEM. As we all know that one of drawbacks of FEM for dynamic analysis is its time-consuming calculation. As a result, for the subsequent analysis we can replace the time-consuming FEM model with the analytical matrix-form model, which can save a lot of time and improve efficiency of analysis remarkably.

4 PARAMETRIC ANALYSIS AND DISCUSSION

In order to examine the effect of stiffness of link on the modal properties of linked tall buildings, a parametric analysis is conducted in this section.

As in section two, we assume that the link has stiffness of out-plane and just has axial stiffness k_a and bending stiffness k_b in the horizontal plane.

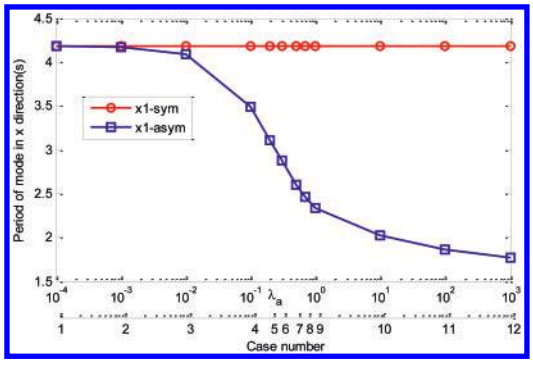


Figure 3. The effect of axial stiffness on periods of the first two modes in x direction.

According to Huang (2001), two relative values of stiffness are introduced

$$\lambda_a = \frac{k_a}{k_{e,b}} \qquad \lambda_b = \frac{k_b}{k_{e,t}} \tag{13}$$

where k_a is axial stiffness of link; $k_{e,b}$ is equivalent lateral stiffness of tower below the link, i.e., the required force applied at the level of link to make the tower sway one unite displacement at this level; similarly, k_b is bending stiffness of link; $k_{e,t}$ is equivalent torsional stiffness of tower below the link, i.e., the required torque applied at the level of link to make the tower rotate one unite degree at this level.

Even though the axial stiffness of links usually is correlated with bending stiffness of link somehow, we here study the effect of these two independently. And from the above derivation it is evident that dynamic motion in x direction is decoupled from those in the y and θ direction. We can, therefore, analyze them independently. Meanwhile, the axial stiffness of link k_a just affects the motion in x direction and the horizontally bending stiffness of link k_b just has an effluence on the motion in y and θ direction. So in the subsequent parametric analysis, the effect of k_a on the modal properties in x direction and the effect of k_b on the modal properties in y and θ direction are analyzed independently.

4.1 *The effect of axial stiffness of link k_a*

The axial stiffness of link, working as a spring to connect two objects, will tend to synchronize the motion of two towers in x direction. In order to study its effect on modal properties, 12 cases of axial stiffness of link, as shown in Fig. 3, are selected and then modal analysis is conducted for each case to obtain the structural frequencies and mode shapes in x direction.

It can be seen from Fig. 3 that the periods of symmetric mode, i.e. mode x1-sym, remains unchanged with the increase of axial stiffness, while the one of antisymmetric mode, i.e. mode x1-asym, decrease with the increase of axial stiffness. The reason for this can be explained by Fig. 4. The mode shapes of x1-sym

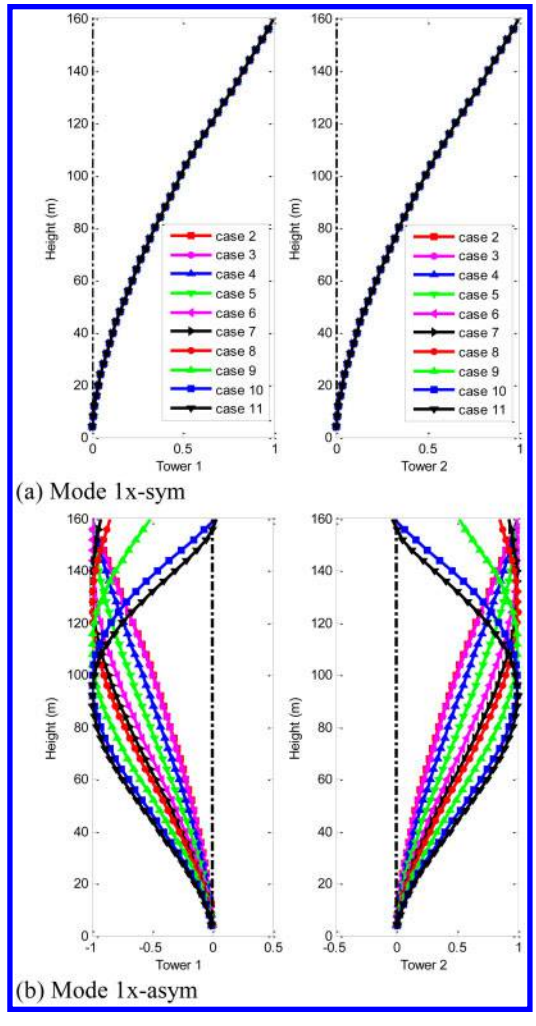


Figure 4. The effect of axial stiffness on mode shapes of the first two modes in x direction.

of two towers are symmetric so that there is no relative deformation between two towers. In other words, the link just sways with tower simultaneously and resultantly, has no effect on mode shape and frequency. For mode x1-asym, however, the mode shapes are antisymmetric so that there is relative deformation between two towers. This relative deformation will make link work as a spring to synchronize the deformation, which leads to the increase of stiffness of total structure and hence decrease the structural periods.

In addition, it should be noted that the axial stiffness has a significant effect on the nonlinearity of antisymmetric mode shape. As can be seen, when the stiffness is relatively small as in cases 2-5, the mode shape can be approximated by a straight line, while with the increase of stiffness, mode shapes of case 7 and 8 show noticeable curvature and for next cases such as 9 and 10, mode shapes already vary from an approximate linear function to a hyperbolic one.

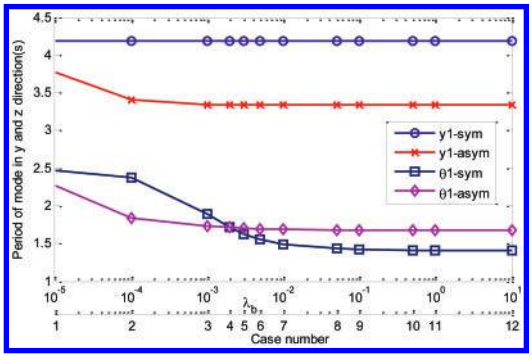


Figure 5. The effect of bending stiffness on periods of the first four modes in y and θ direction.

4.2 *The effect of bending stiffness of link k_b*

Similar to the axial stiffness, bending stiffness of link also can synchronize the motion of two towers in y direction. Moreover, as derived in section 2, this synchronization is coupled in y and θ direction. As the bending stiffness of link can limit the motion in y and θ direction, the modal analysis in these two directions is analyzed simultaneously.

The frequencies and mode shapes of the first 4 modes in y and θ direction are presented in Fig. 5 and 6. Compare to the ones in x direction, the mode shapes are more complicated so that we examine the first four modes one by one.

(1) *The first symmetrical sway mode in y (y1-sym)*
Obviously, the link has no effect on the mode shape and the frequency of this mode as the frequencies of this mode remain unchanged and the mode shapes are identical to a symmetric form in y direction, as shown in Fig. 6a. This is the corollary of symmetrical mode as the link just sways with the two towers and has no effect on structural motion. As a result, there is no coupling between y and θ direction for this mode.

(2) *The first antisymmetric sway mode in y (y1-asym)*
For all cases this mode shows a dominant antisymmetric mode shape in direction y, as shown in Fig. 6b. Apparently, even small bending stiffness of link such as $\lambda_b = 10^{-5}$ in case 1 can bring noticeable torsion motion, which means even small bending stiffness could cause moderate coupling of motion between y and θ for this mode. With the increase of bending stiffness, the natural period shows a trend of decrease from the beginning. However, it hardly goes on dropping once $\lambda_b \geq 10^{-3}$. For each component of mode shapes, Fig. 16b shows that the bending stiffness only has negligible effect on the y component of mode shape, whereas the portion of θ component rises with the bending stiffness from case 1 to case 3, i.e., the bending stiffness will enhance the coupling of motion between y and θ direction of this mode. After case 3, i.e. $\lambda_b \geq 10^{-3}$, however, the mode shape keeps almost identical,

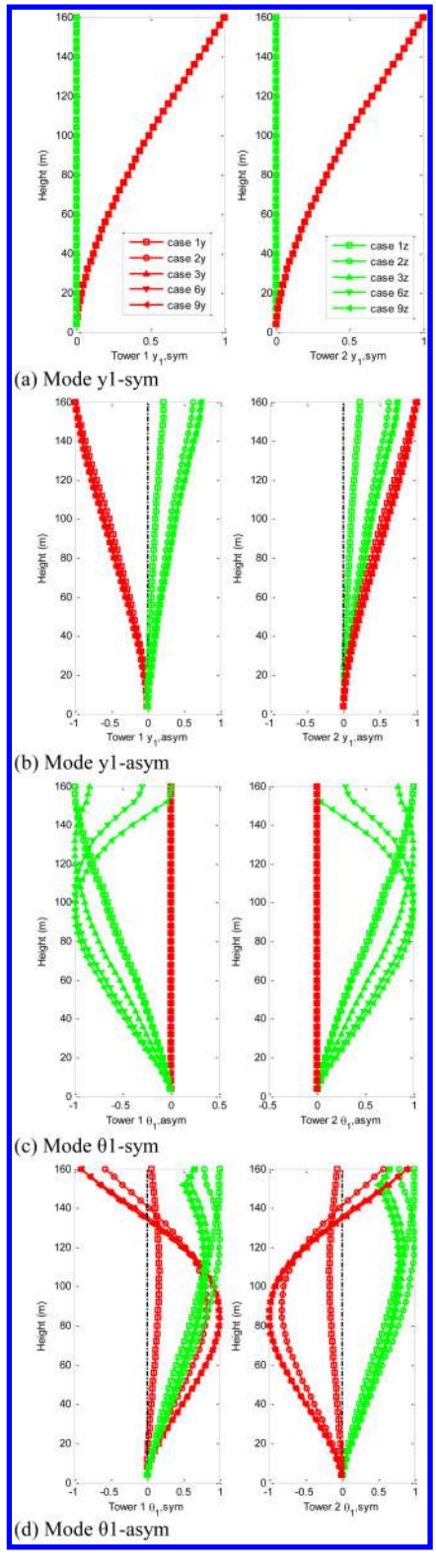


Figure 6. The effect of bending stiffness on mode shapes of the first four modes in y and θ direction.

which means that the additional increase of stiffness will not change the mode shape any more. In addition, even though its proportion will increase with the stiffness, the linearity of θ component hardly varies with the stiffness. We can conclude, therefore, that the bending stiffness will hardly change the linearity of this mode shape, for both y component and θ component

(3) *The first antisymmetric torsion mode in θ (θ1-sym)*

The period of this mode decrease remarkably with the bending stiffness, which means the stiffness can stiffen this mode significantly. For all cases, as can be seen in Fig. 6c, this mode just shows torsional motion in θ direction and the one in y direction is negligible. The reason for this is that antisymmetric torsional motion of two towers will lead to an equivalent symmetrical motion in y direction. Similar to the discussion on above section, link has no effect on symmetrical motion of two towers so that the y component of this mode shape maintain static as shown in Fig. 6c. On the other hand, the bending stiffness does affect the antisymmetric mode shape in θ direction, making it change from a linear form, such as in case 1 and 2, to a hyperbolic form, such as in the case after case 8, with the increase of bending stiffness.

(4) *The first antisymmetric sway mode in θ (θ1-asym)*

The period of this mode decreases dramatically from case 1 to case 3 and afterward, it almost keeps constant with the increase of stiffness. As can be seen in Fig. 6d, this mode shows a dominant symmetric motion in θ direction. With the increase of stiffness, the proportion of motion in y direction increase to a considerable part for the mode. As for the linearity of mode shape, the θ component of mode shape in the case with minor stiffness, such as $\lambda_b = 10^{-3}$ in case 3, is an approximate linear form. With the increase of bending stiffness, the linearity decrease dramatically. The y component of this mode varies more dramatically. It varies from a similar hyperbolic form, e.g. in case 1, to a typical second order mode shape, which shows a change the sign of mode in some elevation of height.

5 CONLUSIONS

A 3-D analytical matrix-form model of linked tall building that can consider varied locations and numbers of links is developed in this paper to investigate the effect of stiffness of link on model properties.

The results of parametric analysis show that although the link hardly shows noticeable effect on the modal properties of symmetrical modes, the periods of antisymmetric mode will decrease with the increase of stiffness of link. Moreover, the mode shape of antisymmetric mode will change remarkably from an approximately linear form to a hyperbolic form, which means that it could be inadvisable to blindly assume linear or power-function form of mode shape.

REFERENCES

HUANG, K. 2001. Static, seismic and wind-resistant analysis of linked two towers. Zhejiang University, Hangzhou.

LIM, J. 2009. Structural coupling and wind-induced response of twin tall buildings with a skybridge. COLORADO STATE UNIVERSITY.

LIM, J. et al. 2011. Modeling of structural coupling for assessment of modal properties of twin tall buildings with a skybridge. *Journal of Wind Engineering and Industrial Aerodynamics,* 99: 615–623.

PRZEMIENIECKI, J. S. 1985. *Theory of matrix structural analysis.* Dover Publications.

XIE, J. & IRWIN, P. A. 1998. Application of the force balance technique to a building complex. *Journal of wind engineering and industrial aerodynamics,* 77: 579–590.

XIE, J. & IRWIN, P. A. 2001. Wind-induced response of a twin-tower structure. *WIND STRUCT INT J.* 4: 495–504.

ZHANG, W. S. & XU, Y. L. 1999. Dynamic characteristics and seismic response of adjacent buildings linked by discrete dampers. *Earthquake engineering & structural dynamics,* 28: 1163–1185.

11. Bridge engineering, bridge girders

Research and Applications in Structural Engineering, Mechanics and Computation – Zingoni (Ed.)
© 2013 Taylor & Francis Group, London, ISBN 978-1-138-00061-2

Composite steel-concrete cable-stayed bridges: Developments and future trends

J.J. Oliveira Pedro
Technical University of Lisbon, Civil Engineer – GRID, Consulting Engineers, Portugal

A.J. Reis
Technical University of Lisbon, Technical Director – GRID, Consulting Engineers, Portugal

ABSTRACT: Composite cable-stayed bridges are elegant and efficient solutions. Today, they are the most adopted solution for 400–600 m span range. Design developments of composite cable-stayed decks are resumed. Particular reference is made to medium-span road and railroad composite decks and to truss decks. Slenderness of the decks, material quantities of stays cables and decks are referred to. Future trends of composite cable-stayed bridges are at last discussed. Particular reference is made to the prospective developments in the field of structural materials, cables, and bridge concepts.

1 DESIGN DEVELOPMENTS

Cable-stayed structures are elegant and efficient solutions for bridges. In the last fifty years the range of these bridges has been steadily increasing and today they are the mostly adopted solution for medium and long-spans, reaching 1000–1200 m spans.

The increase on span required lighter and more resistant deck cross-sections. Steel decks adopting box-girder cross-sections made by orthotropic panels are suitable for very long spans. For cable-stayed bridges with spans up to 600 m, and possibly to 700 m, composite steel-concrete decks may be considered as the most efficient and competitive solution, as confirmed by the variety of composite steel-concrete decks built in the last years (Fig. 1).[1,2,3,4]

1.1 *Design of long-span roadway bridges*

Modern long-span composite decks adopted a simple deck (Fig. 2). Reducing the space between stay-cables, slender lateral main girders directly suspended by closely spaced cables, were feasible. Closely spaced floor-beams provided support for a slender and lighter slab. Deck slenderness, defined as the length/depth ratio of the main span, has been very much increased. Modern designs adopt thin and lighter decks, inducing savings in the deck, cables, piers and foundations. Field bolted splices provided fast and simple connections between almost identical modules, ensuring maximum repetition of pre-fabricated deck components and construction procedures.[3] These concepts have been applied to the majority of composite cable-stayed bridges with main-spans exceeding 200 m, built over the last twenty years by the balanced cantilever construction method.

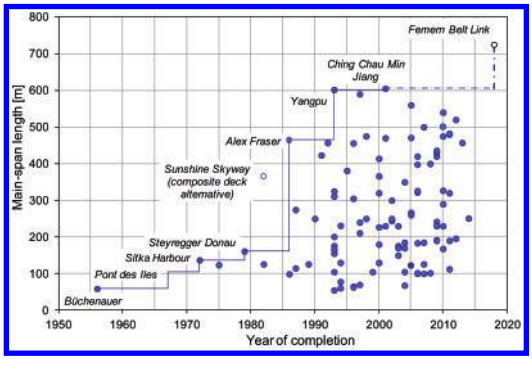


Figure 1. Composite cable-stayed span length evolution.[6]

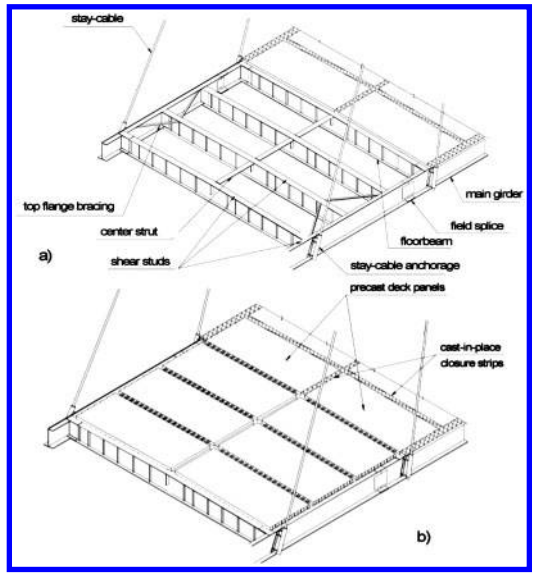


Figure 2. Typical composite cable-stayed decks: a) steel section detail and b) concrete slab executed with precast panels.[5]

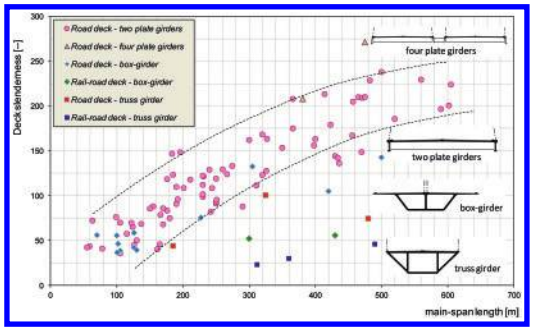


Figure 3. Deck slenderness (main-span length/deck depth) vs. main-span length, for composite cable-stayed bridges.[6]

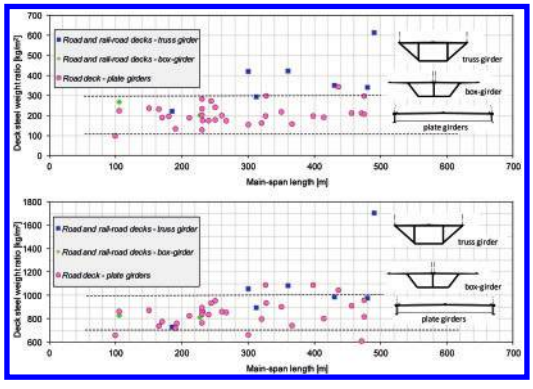


Figure 4. a) Deck steel weight ratio and b) deck self-weight ratio, per square meter of the deck, vs. main-span length.[6]

The study of the main features of road and railway composite cable-stayed bridges built all over the world led to some significant conclusions.[6] With respect to the deck slenderness (Fig. 3):

- For roadway girder decks, values grow up from 75 to 225 with the increasing on span length; slenderness tends to be approximately constant for spans over 500 m long;
- Out of this range, the four-girder deck of the Ting Kau Bridge has a very high slenderness of 271.
- Slenderness of railway decks is much lower, with typical values below 50, due to deformability restrictions imposed by functional requirements.

With respect to the deck self-weight:

- The structural steel weight ratio per square meter of the deck is between 125 kg/m^2 and 300 kg/m^2, with an average value of 213 kg/m^2 (Fig. 4a);
- The average deck self-weight ratio per square meter of the deck is 850 kg/m^2 (considering the weight of the structural steel and of the concrete slab), and typical values are between 700 kg/m^2 and 1000 kg/m^2 (Fig. 4b).

With respect to the stay-cables steel weight:

- steel weight ratio of the stays per square meter of the deck increases with the main-span length, according with the boundaries of stay-cables catalogues[7] for steel, composite and concrete cable-stayed decks (Fig. 5a);
- Plotting in the same graphic the steel weight of the stays per deck square meter, for the composite cable-stayed bridges, results are quite dispersed;
- Railroad decks present always stay's weight ratio much higher than the values recorded for road decks, due to greater deck dead and live loads;
- Assuming a equivalent main-span length for road bridges with an asymmetrical single tower equal to twice the real main-span length (Fig. 5b) stay's steel weight ratios per deck square meter are much better fit;
- A quadratic trend-line is almost over the average line proposed for composite decks with long spans in the stay-cables catalogues[7] (Fig 5b).

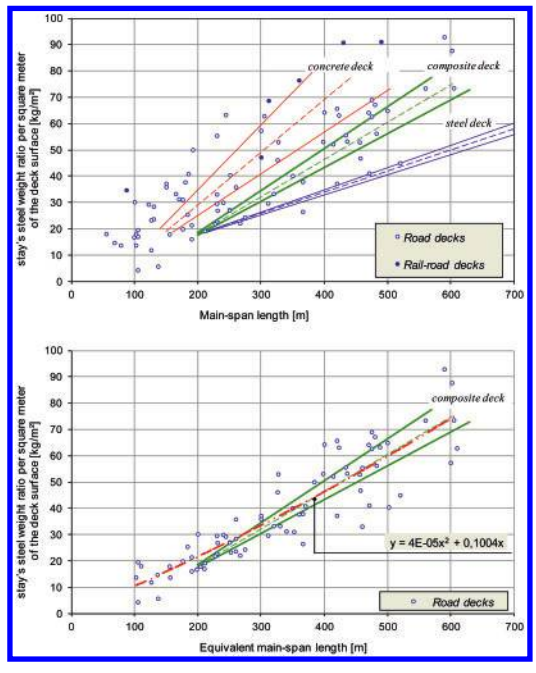


Figure 5. Cables steel weight ratio per square meter of the deck vs. a) main-span length; b) equivalent main-span length.[6]

1.2 *Design of medium-span roadway bridges*

For spans up to 250 m, cable-stayed bridges compete with box-girder bridges and arch bridges, and they are rarely economical for these spans lengths. However, a cable-stayed bridge with slender deck may be desirable in an urban environment for aesthetics or due to difficulties of positioning the deck supports. These aspects may favour the cable-stayed solution, not only in the transposition of rivers and canals, but also on very wide road and railways. Other factors supporting a cable-stayed solution are: 1) aesthetic due to transparency of the structure, resulting from the reduction on the number of piers and increased slenderness of the deck, and 2) reduction the traffic constraints during the execution.

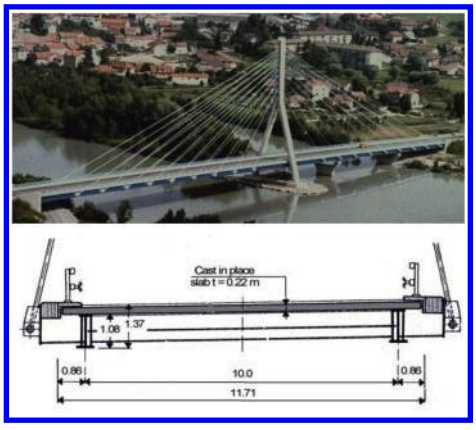


Figure 6. Seyssel Bridge, France.[10].

For medium-spans the usual symmetric cable-stayed layout with a three-span straight deck and two towers, is not very often the best solution. Asymmetric solutions with a single tower or with a curved deck may be more appropriate to overcome local and environment constraints.[8]

Design of medium-span composite cable-stayed bridges has allowed simple deck solutions erected by fast construction methods, like decks composed by two plate girders lateral suspended. The concrete slab on the top is still supported by closed spaced floor-beams, like the Saint-Maurice Bridge (Switzerland, 1986) and the Seyssel Bridge (France, 1987, Fig. 6). Built in the end of the eighties, these two bridges have a structural asymmetric layout. The first bridge consisting of two decks located at the exit of tunnels, with the towers built over the tunnels and suspending 99 m long spans, with two planes of three stays, 24 m apart at the deck level.[9] The second bridge has a more classical configuration, with a single tower suspending a 115 m long main-span and three side spans of 35.2 m, with two plans of nine stays at each side.[10]

Decks with lateral suspension have nevertheless a major drawback, due to the visual impact of two plans of stays. The axial suspension of the deck improves aesthetics but requires a deck with higher torsional rigidity, namely a box-girder cross-section. The Arena Viaduct[11] (Spain, 1993, Fig. 7), with five 105 m inner spans, and the Alzette River Bridge[12] (Luxembourg, 1994, Fig. 8), with two side spans 130 m long, are good examples of medium-span cable-stayed bridges in an in-plan curved road alignment, with an axial suspension.

The Arena cable-stayed deck was built using an unusual method. Each span was fully executed on the ground, including concreting the slab, and raised up to a height of 30 m by lifting deck segments of around 2600 tons. Each span was then welded to the previous one. Only after erecting all the deck, the steel masts were put in place and the six axial stays were installed on each side of the masts.[11]

Balanced cantilever construction method leads normally to longer construction time. For medium-span

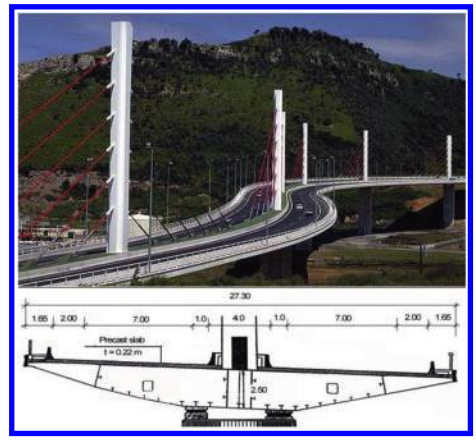


Figure 7. Arena Viaduct, Spain.[11].

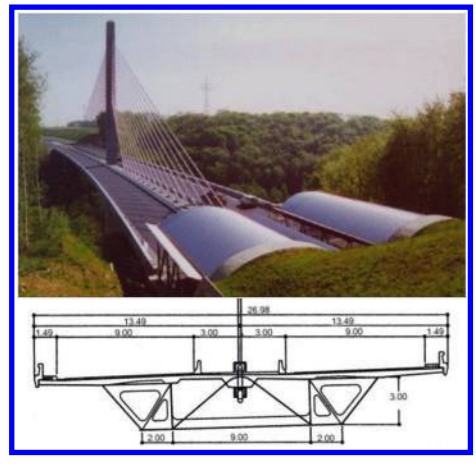


Figure 8. Alzette River Bridge, Luxemburg.[12].

bridges incremental launching or erection by cranes and temporary supports has been used, as in the Seyssel and Alzette River Bridges; the steel decks were launched using temporary supports, and the slabs were casted-in-place using mobile formworks supported on the steel structures.

A special reference should also be made to several medium-span cable-stayed bridges built by the incremental launching method in Finland, as the Tähtiniemi and Utsjoki Bridges, with main-spans of 165 m 155 m. The same method was used in the particular asymmetric Kemijoki Bridge (Fig. 9) with a composite box-girder deck with inclined struts supporting the cantilevers, and a 126 m main-span suspended by two axial plans of stays.[13]

1.3 *Design of composite cable-stayed truss decks*

The design of cable-stayed bridges with composite truss decks allows superstructures to be lighter than traditional prestressed concrete box-girders and less deformable than steel or composite plate girder decks. By anchoring the stays at the top slab level, the

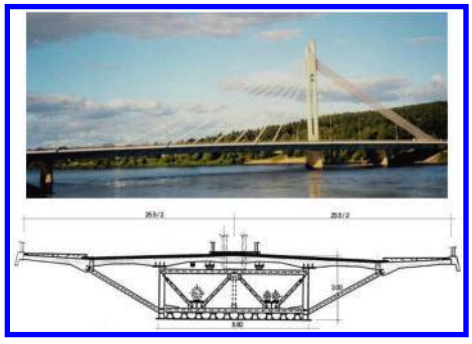


Figure 9. Kemijoki Bridge, Finland.[13].

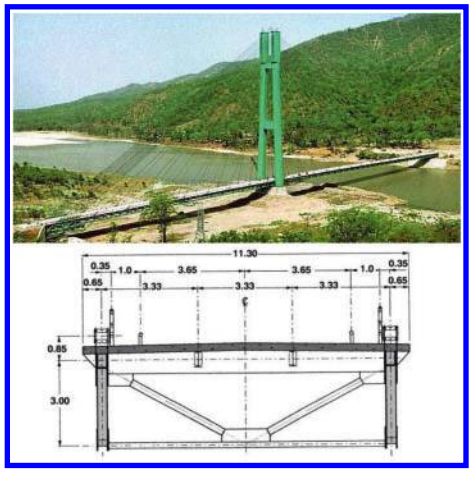


Figure 10. Karnali Bridge, Nepal.[14]

stays horizontal compression component is transmitted directly to the slab, since the truss girders are relatively flexible in the longitudinal direction compared to the axial rigidity of the slab. This feature of the deck is actually important for a composite deck, since it reduces the effects of shrinkage and creep of the concrete slab, as in the longitudinal direction each lattice girder acts as a "harmonium", allowing the deformations and reducing internal forces due to time dependent effects.

Karnali Bridge [14] (Nepal, 1993, Fig. 10) was the first cable-stayed road bridge with a composite truss deck. This outstanding structure has a 325 m lateral span, suspended by a single tower (deck slenderness approximately 100). To reduce deck deformability two lattices Warren girders 3 m deep were adopted.[14]

For rail and railroad bridges, a stiff deck is needed to ensure train's operation requirements. Truss girder decks are widely adopted in suspension bridges and in some cable-stayed bridges. In particular, composite steel-concrete truss decks combine high stiffness with relative low weight, using the concrete slabs to provide the proper circulation platforms. Composite truss decks were adopted in the Øresund Bridge (between Sweden and Denmark, 2000, Fig. 11), and more

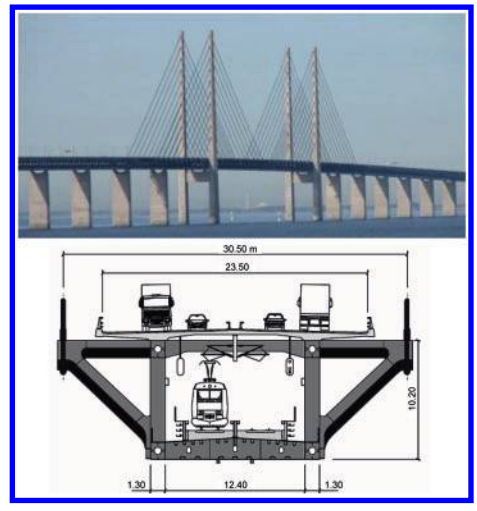


Figure 11. Øresund Bridge, Sweden/Denmark.[15]

recently in the Mercosur Bridge, over the Orinoco River (Venezuela, 2011).

The 490 m span Øresund Bridge,[15] adopted a deck with two vertical steel trusses, with a concrete slab on the top for the roadway. At the bottom level, a continuous orthotropic steel deck supports two ballast boxes for high-speed lines. The construction used deck steel segments pre-fabricated in Spain and transported by ship to Sweden, where the slab was pre-casted. Handling operations of these elements, 120 m to 140 m long, and weighting up to 6200 tons, were carried out with a crane mounted on a barge. Deck segments were placed on temporary supports and welded. Later, the stays were installed and temporary supports were removed to new positions.[16]

The 360 m long span Mercosur railroad Bridge[17] adopted also a composite steel-concrete Warren truss girder deck, with 10 m between truss joints, and upper and lower cross-beams 3.33 m apart. However, unlike the other examples, axial suspension was adopted, with two planes of stay-cables 0.80 m apart, and the deck steel framing of the side spans were erected by incremental launching. Afterwards, the concrete slab was casted in place and stays were installed and tensioned. The 120 m steel central part of the main-span, weighting 2400 tons, was then lifted from a barge by four strand jacks located on the existing cantilevers. The main-span slab was finally poured in several steps.[17] These two decks are relatively deep, with steel structures 10.2 m and 11.6 m height, which correspond to slenderness of only 48 and 28. Additionally, the self-weight and structural steel of these decks are higher than the values for double plate girder road composite decks (Fig. 4a).

But, all these bridges adopted longitudinal trusses with vertical diagonals. Three-dimensional tubular diagonals can also be used, as it was first done in the Europa Bridge[18] (Portugal, 2004, Fig. 12). This highway deck, with a 186 m long main-span, is axially suspended by two plans of stays fixed to a single mast

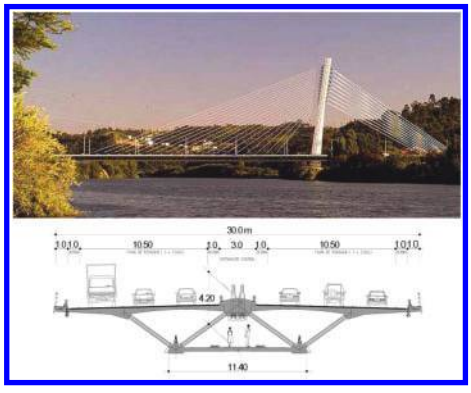


Figure 12. Europa Bridge, Portugal.[18].

located on the left bank of the river. The mast inclined 8° towards the side spans is retained by two layers of backstays externally anchored to the transition pier blocks. The specificity of this composite deck truss, with steel tube diagonals, comes not only from the steel elements joints to the concrete slabs, but also from shear deformability and effects of local concentrated bending moments introduced on the slab at the joints. The deck is a 3D composite truss 4.2 m deep and 30 m wide, made of high strength steel tubes with joints spaced at 3.75 m, and two concrete slabs prestressed in the transversal and longitudinal directions.

Steel plates enclosed by reinforced concrete were used at the upper truss nodes. These plates not only transfer the vertical forces from the slabs, but also balance the forces between the diagonal tubes that converge on the node, and transmit the horizontal forces to the concrete slabs. On the lower node between 3.75 m long segments, two "teeth" plates were used, perfectly matched to each other, to ensure the direct transmission of vertical and horizontal internal forces. The bridge deck was designed to be executed with precast segments with the pre-casting yard located on the left bank, and the precast segments (3.75 m length), weighing up to 150 tons, transported in the river by a barge, were lifted vertically to the deck. After deck assembling and longitudinal prestressing applied, the overhangs of the deck slab were cast in-place and a second phase of transversal pre-stressing was applied.

2 FUTURE TRENDS

2.1 *In the field of materials*

The use of precast slab panels with concrete strengths up to 70 to 100 MPa is gradually increasing for very long-span composite cable-stayed bridges. To reduce weight ribbed slab sections between floor-beams have been recently adopted.[1] Lightweight aggregate concrete (LWAC) was also used in at least one composite cable-stayed deck. The *Grenland* Bridge (Norway, 1996) adopted slabs of LWAC in the 305 m long main-span.[19]

The use of steel grades S420 and S460 has much increased in recent years. New steels allow the design of steel girders, floor-beams and stay anchors more compact and with thinner plates. However, the use of these steels has no significant advantage for fatigue resistance. The recent introduction of even higher steel grades in bridge construction, such as the S690 and S700, may be explored in the future.[20]

2.2 *In the field of cables*

Cables made of CFRP have been proposed to reduce weight and diameter, as they combine very high resistance with a self-weight lower than steel. However, their time dependant behaviour is still not well known, axial deformability is much higher, and CFRP stay-cables are costly compared to steel stays.

Cable forces in service are usually limited to 45% of its ultimate guaranteed resistant strength (FGUT). Few solid justifications have been given to continue using this limit, imposed to prevent the negative consequences of the fatigue stresses, and the local bending stresses in the anchorage of the first large-diameter stay-cables. For a characteristic combination of loads, the Eurocode 3, part 1-11 allows cable forces up to 50% of FGUT, if vibration damping devices are adopted at anchorages. In addition, during cables installation, the first strands may have installed forces up to 60% FGUT, provided after stressing the remaining strands of a cable work in the limit of 55% FGUT.

The assessment of stay-cable fatigue stresses needs also to be carried out for the service conditions (considering both the axial stresses and the bending stresses near the anchorages, due to angular deviations caused by catenary effects, wind forces and erection imperfections). The French recommendations[21] propose a simple method valid for road bridges, limiting the cables axial stress variation to 70 MPa for the passage of the fatigue vehicle LM3 of the Eurocode 1-Part 2.

2.3 *In the field of design*

In the field of design of composite steel-concrete cable-stayed bridges several new solutions have been recorded over the years, in some cases only with architectural aspects, but in other cases technically innovative. Both types of developments are important, since the public interest in cable-stayed bridges is, to a large extent, also a result of its high aesthetics quality. The recent *Boyne* and *Suir River* Bridges (Ireland, 2003 and 2009), *Sirhowy River* Bridge (Wales, 2005), *Berliner* Bridge (Germany, 2005), *Alcide de Gasperi* Bridge (Italy, 2005) and *Korabelny* Bridge (Russia, 2011), are good examples of medium-span composite cable-stayed bridges, following these principles. New bridges of the same type, such as the *Signature* Bridge (India, 2014), are under construction or being designed.

In the field of rail and railroad decks, composite solutions can also play an important role. In the future, this is certainly an area of composite cable-stayed bridge developments, as shown by the recent

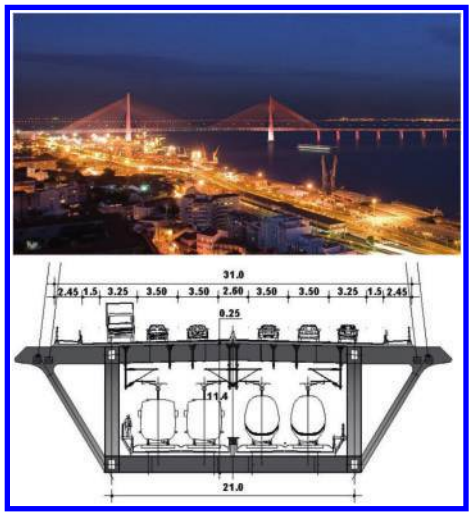


Figure 13. Preview of the Third Tagus River Crossing Bridge, in Lisbon.[22,23].

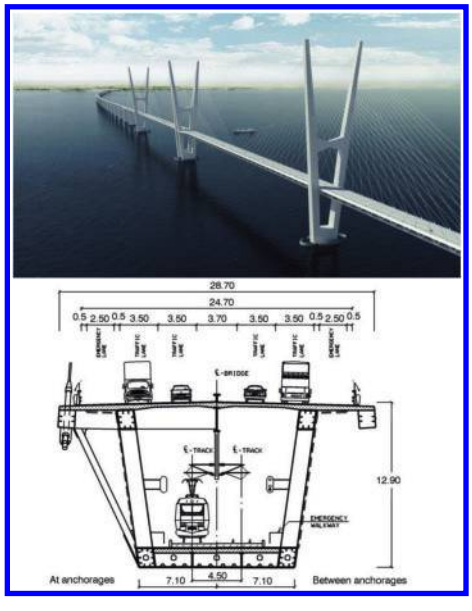


Figure 14. Preview of the Femern Belt Bridge, between Germany and Denmark.[24].

studies for the *Third Tagus River Crossing* Bridge in Lisbon[22,23] (Fig. 13), as well for the bridge connecting the *Fehmern Belt*[24] between Germany and Denmark (Fig. 14).

REFERENCES

[1] Taylor, P. 2001. What are the limiting criteria governing the maximum span of composite cable-stayed bridges? *State of the Art in Technology and Analysis – Proc. 3rd Intern. Meeting on Composite Bridges*, Madrid, p.43–54.

[2] Svensson, H. 1999. The Development of Composite Cable-Stayed Bridges. *Cable-Stayed Bridges: Past, Present and Future. IABSE Conf. Proc*, Malmö, p. 352–361.

[3] Taylor, P. 1994. Composite cable-stayed bridges. *Intern. Conf. AIPC-FIP Proc. Vol.1*. Deauville, p.185–198.

[4] Pedro, J.J.O.; Reis, A.J. 2010. Nonlinear analysis of composite steel-concrete cable-stayed bridges. *Engineering Structures* 32 (2010), p.2702–2716.

[5] Hague,S.T. 2003. Steel/concrete composite design for long span bridges. *TRB 2003 annual meeting*.

[6] Pedro,J.J.O. 2007. *Structural analysis of composite cable-stayed bridges.* Ph. D Thesis. Technical University of Lisbon (in Portuguese), 426 p.

[7] Freyssinet, 1994-1999. *Stay-cables Catalogue.* September 1999 and May 1994.

[8] Reis, A. *et al.* 1999. Cable-Stayed Bridges for Urban Spaces. *Cable-Stayed Bridges: Past, Present and Future. IABSE Conf. Proc*., Malmö, p.106–115.

[9] SZS, 1987. Ponts sur le Rhône à Saint Maurice. *Construire en Acier, N°10*.

[10] Virlogeux,M. *et al.* 1985. Projet et Construction du Pont de Seyssel. *Bulletin de Ponts Métalliques, N° 12*, p.73–96.

[11] Arenas, J.; Pantaleón, M. 1992. Puentes mixtos atirantados. *Puentes mixtos: Estado actual de su tecnología y análisis - Comunicaciones y Mesas Redondas de las Primeras Jornadas Intern*. Barcelona.

[12] Biwer, R. *et al.* 1994. Cable-stayed bridge upon Alzette. *Intern. Conf. AIPC-FIP Proc.Vol.1*. Deauville, p.413–420.

[13] Vähääho, J. *et al*. 1996. The Cable-stayed bridges in the Finnish lake and river landscape. *IABSE 15th Congress Report*. Copenhagen, p.171–177.

[14] Arzoumanidis, S.; Kunihiro, M. 1994. The Carnali River Bridge. *Intern. Conf. AIPC-FIP Proc. Vol.1*. Deauville, p.395–404.

[15] ASO Group, 1999. *The Øresund Bridge*. May 1999, 39p.

[16] Sörensen, L.T.; Thorsen, N.E. 1999. The Øresund Bridge, Erection of the Cable-Stayed Span. *Cable-Stayed Bridges: Past, Present and Future. IABSE Conf. Proc*. p.465–475.

[17] Humpf,K.; Schiele, I. 2009. Puente Mercosur – Truss Girder Bridge across the Orinoco. *IABSE Conf. Proc.* Bangkok.

[18] Reis,A.; Pedro,J.J.O. 2004. The Europe Bridge in Portugal: concept and structural design. *ELSEVIER Journal of Constructional Steel Research n° 60*, p.363–372.

[19] Fergestad, S.; Jordet, E. 2000. The economic potential of LWAC in 4 different major bridges. *Proc.2nd Intern. Symp. Structural Lightweight Aggregate Concrete*. Kristiansand, Norway, p. 355–364.

[20] IABSE, 2005. Use and Application if High-Performance Steels for Steel Structures. *IABSE Structural Engineering Documents, n° 8.* 152p.

[21] SETRA, 2001. *Haubans. Recommandations de la commission interministérielle de la précontrainte*. 198p.

[22] GRID, SA, 2009. *Third Tagus River Crossing: Main Bridge – Base Case Design* (in Portuguese).

[23] Reis, A.J. 2008. Composite bridges: Options and design issues. *Proc. 7th Intern. Conf. Steel Bridges*, p.I-3–I-28.

[24] Femern Sund Baelt 2010. Fehmarnbelt Link – Technical Solution: Cable-Stayed Bridge. *www.fehmarnlink.com/uk*, accessed in 15-11-2010.

Research and Applications in Structural Engineering, Mechanics and Computation – Zingoni (Ed.)
© 2013 Taylor & Francis Group, London, ISBN 978-1-138-00061-2

Analysis of steel and steel-concrete bridge girders through a higher order beam model

R.F. Vieira, F.B. Virtuoso & E.B.R. Pereira
Department of Civil Engineering, Architecture and Georesources, Instituto Superior Técnico, Universidade Técnica de Lisboa

ABSTRACT: The three-dimensional analysis of steel and composite steel-concrete bridges in practice engineering is usual performed using shell finite element models. Although these models allow to accurately consider a broad range of structural phenomena: geometric and material nonlinearities, non-linear dynamic and static analysis, the analysis of results becomes cumbersome, being also difficult to separate structural phenomena. A higher order beam model with the displacement field properly enriched to capture three-dimensional effects is presented in this paper as an alternative to shell finite elements. The higher order beam model considers the corresponding displacement field to be defined by a set of linear independent approximation functions defined over the cross-section. A consistent criterion for uncoupling the beam deformation modes based on a non-linear eigenvalue problem is adopted in order to render the model âŁœusableâŁž from an engineering perspective, allowing the definition of uncoupled higher order modes of the cross-section, e. g. cross-section warping and distortion. The presented higher order beam model is applied to the static and dynamic analysis of bridges, focusing on the cross-section warping behaviour and on the linear stability phenomena involving local and global buckling modes.

1 INTRODUCTION

The use of thin-walled beam models are successful alternatives for the analysis of bridges despite the widespread use of an increasingly finite element technology.

In fact, several beam models that include the classic cross-section deformation modes of warping, shear-lag and distorsion have been applied to bridge analysis, (Maisel 1982, Boswell & Zhang 1984, Kermani & Waldron 1993). Moreover, towards a more accurate representation of the cross-section three-dimensional structural behaviour, cross-section deformation modes of higher order were considered through a refinement of the beam displacement field approximation over the cross-section, (Paavola 1990, Razaqpur & Li 1991, Tesar 1996, Bogensperger 2000). However, the criteria for the definition of such deformation modes is dependent on *ab-initio* cross-section structural hypotheses, narrowing the applicability of the corresponding beam models.

The Generalised Beam Theory developed by (Schardt 1989) which has been further extended through additional formulations, (Möller 1982, Dinis, Camotim, & Silvestre 2006) to consider more general cross-sections and surpass some initial restrictions has been successfully applied to the analysis of stability phenomena and also to the analysis of bridges, (Schrade 2010).

A thin-walled higher order beam model to the analysis of steel and composite steel-concrete bridges is presented in this paper. This higher order beam model is properly enriched through a representative set of orthogonal displacement modes, which are obtained from a non-linear eigenvalue problem in order to represent the thin-walled structural behaviour.

The model has the advantage of providing a clear understanding and an adequate consideration of the structural phenomena involved, due to its uncoupling modal characteristic, benefitting from the simplicity of a one-dimensional model.

The higher order thin-walled beam model is applied to (i) the static analysis of a steel bridge girder by including appropriate higher order deformation modes; (ii) a linear stability analysis considering local and global buckling modes and (iii) the dynamic analysis of a bridge girder submitted to an eccentric moving load including the cross-section warping.

2 HIGHER ORDER THIN-WALLED BEAM FORMULATION

The thin-walled structural behaviour is obtained through the reduction of the corresponding three-dimensional elasticity formulation to a set of one-dimensional equilibrium equations written in terms of the displacement field **u** as follows:

$$\mathbb{D}\,\mathbf{C}\,\mathbb{D}^{*}\,\mathbf{u} + \mathbf{p} - \rho\ddot{\mathbf{u}} = 0 \qquad (1)$$

where $\mathbb{D}$ and $\mathbb{D}^{*}$ represent, respectively, the equilibrium and the compatibility differential operators, **p** represents the load vector and ρ the mass density.

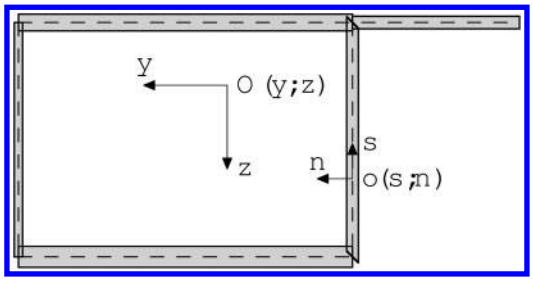


Figure 1. Approximation functions for a cross-section element.

The cross-section layout considered in this formulation corresponds to a set of rectilinear wall segments forming a generic shape, being considered to have both a flexural and a membrane structural behaviour. For the flexural behaviour, it is assumed that the elements are sufficiently "thin" in order to consider valid the *Kirchhoff* formulation and hence neglect the shear deformation on the planes perpendicular to the middle surface.

For an accurate representation of the cross-section structural mechanics the displacement field is approximated by a set of linearly independent functions defined over the thin-walled cross-section as follows:

$$\mathbf{u} = \mathbf{B}(s,n)\,\tilde{\mathbf{u}}(x) \tag{2}$$

where $\mathbf{u} = [u_x,\ u_s,\ u_n]^t$ and $\tilde{\mathbf{u}}(x) = [\tilde{\mathbf{u}}_x,\ \tilde{\mathbf{u}}_s,\ \tilde{\mathbf{u}}_n]^t$, being adopted the reference frame $O(x,s,n)$ represented in Fig. 2.

The approximation functions are defined in matrix $\mathbf{B}(s,n) = \mathbf{B}_0(s,n) + \mathbf{B}_1(s,n)\,\partial_x$ where $\mathbf{B}_0$ and $\mathbf{B}_1$ are given by:

$$\mathbf{B}_0(s,n) = \begin{bmatrix} \boldsymbol{\phi}^t & \cdot & \cdot \\ \cdot & \boldsymbol{\psi}^t & -n\boldsymbol{\chi}^t_{,s} \\ \cdot & \cdot & \boldsymbol{\chi}^t \end{bmatrix} \tag{3}$$

$$\mathbf{B}_1(s,n) = \begin{bmatrix} \cdot & \cdot & -n\boldsymbol{\chi}^t \\ \cdot & \cdot & \cdot \\ \cdot & \cdot & \cdot \end{bmatrix} \tag{4}$$

The vector subscript $(,s)$ stands for the component derivatives in the variable s and ∂_x represents the derivative of the corresponding components in the axial direction (d/dx).

The displacement field of the cross-section middle surface is thus approximated in the three spatial directions (x,s,n) through sets of approximation functions, $\boldsymbol{\phi}$, $\boldsymbol{\psi}$ and $\boldsymbol{\chi}$, respectively, which can globally (at a section level) be defined as follows:

$$\begin{aligned} \boldsymbol{\phi}^t &= [\phi_1(s),\cdots\phi_p(s)],\ \mathbf{u}_x = [u_{x1}(x),\cdots u_{xp}(x)]^t \\ \boldsymbol{\psi}^t &= [\psi_1(s),\cdots\psi_q(s)],\ \mathbf{u}_s = [u_{s1}(x),\cdots u_{sq}(x)]^t \\ \boldsymbol{\chi}^t &= [\chi_1(s),\cdots\chi_r(s)],\ \mathbf{u}_n = [u_{n1}(x),\cdots u_{nr}(x)]^t \end{aligned} \tag{5}$$

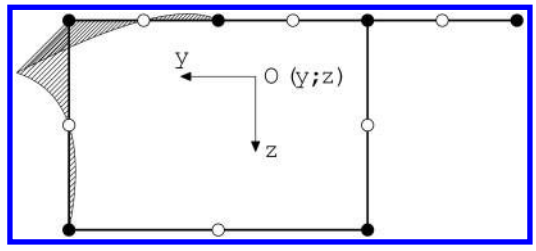


Figure 2. Approximation functions for a cross-section element.

with p, q, and r degrees of freedom for the x, s and n direction, respectively. The corresponding amplitudes are the unknowns $\mathbf{u}_x$, $\mathbf{u}_s$ and $\mathbf{u}_n$.

In order to properly capture the three-dimensional behaviour of thin-walled structures, the approximation can be refined either by increasing the degree of the approximation functions or by increasing the discretization at a cross-section level. A quadratic function for the axial displacement is represented in figure 2.

Substituting the displacement field approximation (2) into the equilibrium equations defined in equation (1) and weighting the result by the same approximation functions, the following one-dimensional equilibrium equation is obtained:

$$\int_A \mathbf{B}^t \left(\mathbb{D}\,\mathbf{C}\,\mathbb{D}^*\,\mathbf{B}\tilde{\mathbf{u}}(x) + \mathbf{p} - \rho\mathbf{B}\,\ddot{\tilde{\mathbf{u}}}(x)\,dA \right) = 0 \tag{6}$$

Considering the differential operator $\mathbb{D}$ decomposed into one part defining transverse derivatives and other defining a derivative along the beam axis and performing the integration of Eq. (6) over the cross-section, the following beam governing equations are obtained,

$$\mathbb{K}_4\,\partial_x^4\mathbf{u} + \mathbb{K}_2\,\partial_x^2\mathbf{u} + \mathbb{K}_1\,\partial_x\mathbf{u} + \mathbb{K}_0\,\mathbf{u} - \mathbb{M}\,\ddot{\mathbf{u}} = 0 \tag{7}$$

where the coefficient matrices $\mathbb{K}_4$, $\mathbb{K}_2$ $\mathbb{K}_1$ and $\mathbb{K}_0$ are defined in (Vieira 2010).

The analysis of the three-dimensional behaviour of thin-walled structures through the higher order beam model can be enhanced by refining the displacement field projection. However, if the resulting governing equations are not properly uncoupled, the result is a tangled set of equations that, despite representing the elasticity formulation of the problem, do not allow a clear physical interpretation of the structural phenomenon. The procedure of uncoupling is therefore essential to the usability of the higher order beam model.

A concept of uncoupling has been put forward in (Vieira 2010, Vieira, Virtuoso, & Pereira 2013) by considering the eigenvalue problem associated with the differential equations of the model, Eq. (7). A set of uncoupled deformation modes is obtained from the eigenvectors, retrieving the classic theories and defining deformation of higher order.

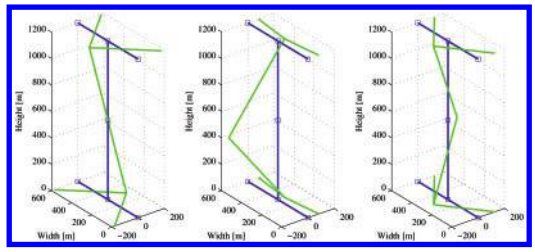


Figure 3. I section out-of-plane higher order modes.

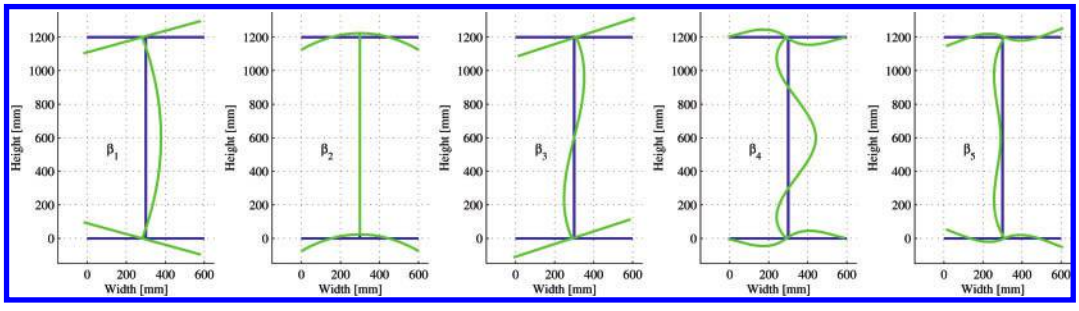


Figure 4. I section in-plane higher order modes.

3 APPLICATIONS TO BRIDGE ANALYSIS

The higher order thin-walled beam model is applied to the static and dynamic analyses of a bridge girder, highlighting its applicability in reproducing the three dimensional structural behaviour.

3.1 *Cross-section higher order modes*

The cross-section analysis towards the definition of uncoupled deformation modes is a key feature of the beam model. The cross-section analysis of a steel plated beam (I shaped) having a web with dimensions $1200 \times 20\,mm^2$ and equal flanges of dimensions $600 \times 50\,mm^2$ is performed. The cross-section is divided into 6 elements (two elements per flange and two elements for the web), being the displacement field for each element approximated by linear Lagrange functions for the thin-walled in-plane displacements and by Hermite functions for the displacements normal to the thin-wall middle surface. The displacement modes obtained from the eigenvalue uncoupling procedure are depicted in figures 3 and 4 for the out-of-plane and in-plane components (β_1 to β_4), respectively.

3.2 *Static analysis*

A cantilever beam with $5\,m$ long subjected to an eccentric tip load of $100\,kN$, which is represented in figure 5 is analysed. The displacement modes of the cross-section are represented by the orthogonal modes defined by the warping modes represented in figures 3, being the transverse deformation of the cross-section neglected. A numerical solution for the beam model

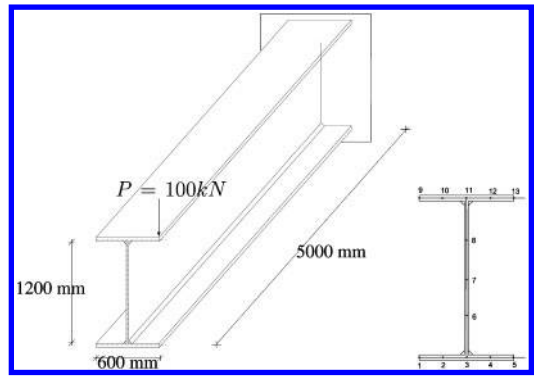


Figure 5. Steel cantilever beam.

was obtained within the framework of the finite element method by approximating the amplitudes of the displacement modes.

The beam stress field is computed taking in account the modal amplitudes distributions obtained and the corresponding deformation modes. The stress components are evaluated in a mesh of sampling points, being represented in figure 6 the membrane axial stresses at the beam upper flange; these stresses have maximums at the full fixed support, decaying along the beam axis towards its free end.

A comparison between the developed thin-walled beam model and a shell finite element model implemented in (Abaqus 2006) was performed, being verified a satisfactorily agreement of results both in terms of displacements and stresses.

The longitudinal distribution of the thin-walled middle surface stresses are plotted for the bottom

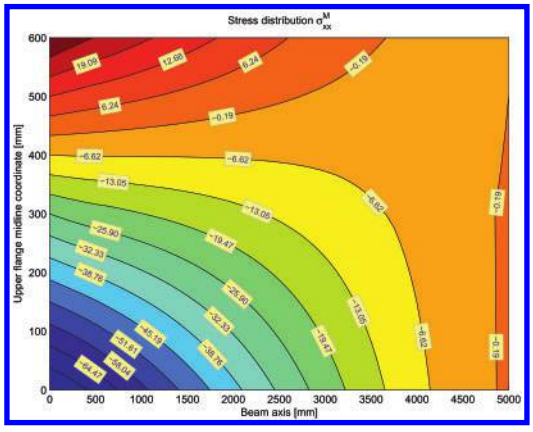


Figure 6. Steel plated I section, stresses in upper flange.

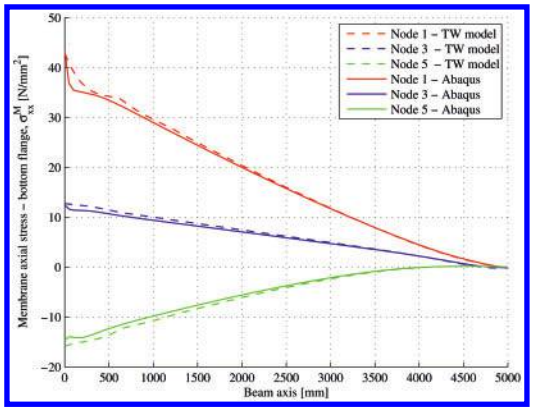


Figure 7. Steel plated I section, σ_{xx}^{M}.

Table 1. Membrane stress comparison, $\sigma_{xx}^{M}, (N/mm^2)$.

	node 1		
(mm)	TW-model	Abaqus	Classic theory
0	42.85	43.40	45.19
1250	27.40	26.68	24.24
2500	15.98	15.75	16.27
3750	6.09	6.14	8.17
5000	0.06	0.00	0.00

flange and for the axial component in figure 7 (alignments corresponding to nodes 1, 3 and 5 represented in figure 5.

The stresses obtained from classic theory were also compared with the stresses obtained through the higher order model (TW-model) and from Abaqus, being the corresponding results presented in table (1) and (2).

3.3 *Buckling analysis*

The linear governing equations for a configuration that is "disturbed" from the fundamental path are obtained

Table 2. Membrane stress comparison, $\sigma_{xx}^{M}, (N/mm^2)$.

	node 6		
(mm)	TW-model	Abaqus	Classic theory
0	3.12	2.87	
1250	3.35	3.49	
2500	3.37	3.51	3.21
3750	3.69	3.73	
5000	0.29	−0.04	

by considering the contribution of the corresponding non-linear geometric terms in addition to the equilibrium defined by Eq. (7), being the resulting equation written as follows,

$$\mathbb{K}_4\,\tilde{\mathbf{u}}'''' + \left(\mathbb{K}_2 - \mathbb{K}_2^G\right)\tilde{\mathbf{u}}'' + \left(\mathbb{K}_1 + \mathbb{K}_1^G\right)\tilde{\mathbf{u}}' + \mathbb{K}_0\,\tilde{\mathbf{u}} = 0 \quad (8)$$

where $\mathbb{K}_2^G$ and $\mathbb{K}_1^G$ represent geometric matrices.

A linear buckling analysis is performed through the solution of Eq. (8) towards the evaluation of the corresponding bifurcation loads by making use of the beam model uncoupling criteria. To this purpose Eq. (8) is rewritten in the orthogonal displacement modes, allowing to identify the thin-walled structural behaviour, in particular the buckling modes "activated" by the applied loads through the corresponding fundamental path; in fact, the geometric matrices remain coupled in the orthogonal modes, which allows to identify for each buckling phenomenon the involved cross-section displacement modes.

The buckling modes are therefore defined through linear combinations of orthogonal displacement modes of the cross-section. The bifurcation loads corresponding to either global or local buckling modes are obtained from (8) by considering a suitable selection of displacement modes for the cross-section.

A linear stability analysis of an element with an I shaped cross-section submitted to a uniform compressive stress is presented. The displacement basis functions that correspond to the cross section rotations, translations and out-of-plane warping are considered for the global stability analysis, whereas the in-plane distortional displacement modes represented in figure 4 are considered for the local stability analysis.

The analysis of the linear stability equations allows to conclude that the transverse distortion, β_1, is coupled with the flexure along the cross-section weak axis through the corresponding transverse displacement, v, and to the web flexure mode, β_4 of an higher eigenvalue. Hence for a local buckling analysis, the in-plane distortional mode is defined as follows,

$$\mathbf{u}_{LB_1} = \begin{bmatrix} v & \beta_1 & \beta_4 \end{bmatrix}^t \quad (9)$$

Rewriting Eq. (8) for the displacement modes defined by Eq. (9) and considering a solution of

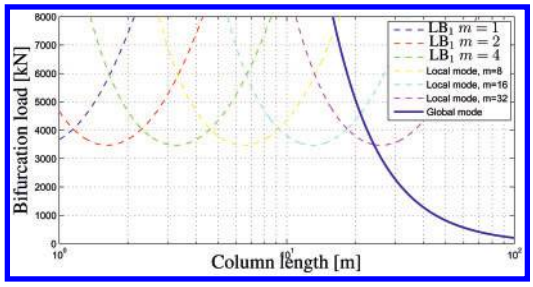


Figure 8. I section, distortional buckling mode, analytical model.

trigonometric functions with the same wavelength for all modes, which is a commonly adopted hypothesis for local buckling modes, (Allen & Bulson 1980), the buckling load is obtained through the solution of the following eigenvalue problem,

$$(\mathcal{K}_{LB_1} - P\mathcal{K}_G)\,\mathbf{u}_{0,LB_1} = \mathbf{0} \tag{10}$$

where the matrices $\mathcal{K}_{LB_1}$ and $\mathcal{K}_G$ are given as follows,

$$\mathcal{K}_{LB_1} = \mathbf{K}_{4,LB_1}(m\pi/L)^4 + \mathbf{K}_{2,LB_1}(m\pi/L)^2 + \mathbf{K}_{0,LB_1} \tag{11}$$

$$\mathcal{K}_{G_{LB_1}} = (\mathbf{K}_{G_1,LB_1} + \mathbf{K}_{G_2,LB_1})(m\pi/L)^2 \tag{12}$$

The bifurcation loads for the distortional buckling of the I section are plotted in figure 8 for several half-length waves. The minimum bifurcation load obtained for the local buckling is almost a constant value for different half lengths, $P_{cr} \cong 3470\,kN$.

The buckling analysis that considers the interaction between the local and the flexural mode that corresponds to the rotation around the y axis is performed by considering

$$\mathbf{u}_{FL+LB_1} = [\ \theta_y \quad v \quad \beta_1 \quad \beta_4\ ]^t \tag{13}$$

The linear stability equations are written for the degrees of freedom defined in 13, considering a solution of trignometric terms with the same wavelength for the global and the local buckling mode. The bifurcation loads for the interaction of flexural and local buckling modes are represented in figure 9.

A numerical stability analysis considering a finite element formulation for the higher order thin-walled beam model is performed in order to consider the possibility of different wavelengths for the local and global buckling mode. The finite element model considers all of the orthogonal modes defined by the eigenvalue analysis for the cross section displacement modes.

The bifurcation loads obtained numerically from the finite element model are represented in figure 10, being compared with: (i) the analytical results obtained from Eq. (10) and (ii) the results obtained from a linear

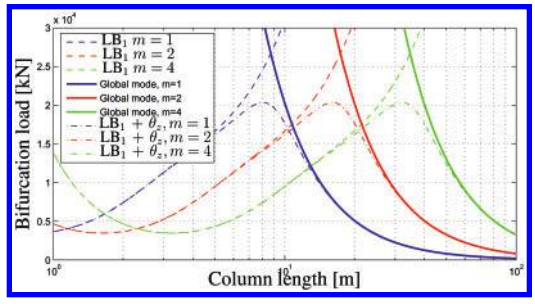


Figure 9. I section, distortional buckling mode, analytical model.

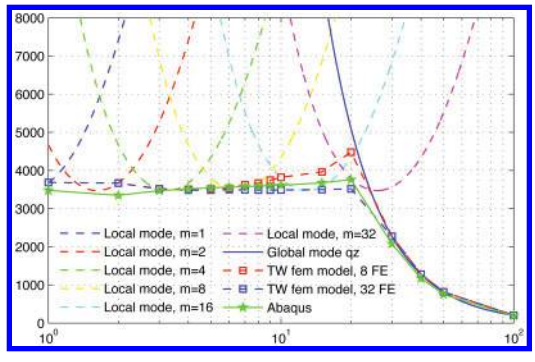


Figure 10. I section, global and distortional buckling modes; comparison between analytical and numerical model and .

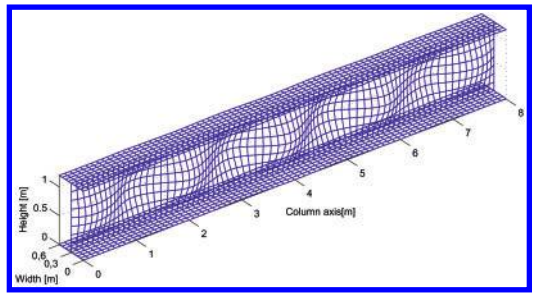


Figure 11. Buckling mode obtained from one-dimensional fem, $L = 8000\,mm$.

buckling analysis of a three-dimensional shell finite element performed in (Abaqus 2006). The results obtained either analytical or numerically through the proposed formulation are in a good agreement with the results obtained from (Abaqus 2006).

The buckling mode obtained from the one dimensional finite element model is represented in figure 11.

3.4 *Dynamic analysis*

The thin-walled beam model is applied to the dynamic analysis of a 3 span continuous bridge girder, with spans of 30m+40m+30m and a double T cross-section, submitted to an eccentric load $e = 2.5\,m$ as represented in figure 12.

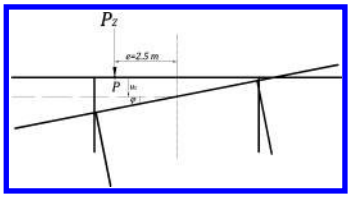


Figure 12. Sketch of the point P for the double-T section.

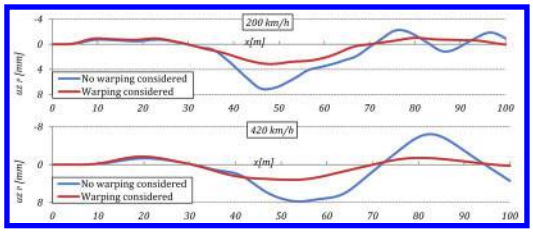


Figure 13. Dynamic influence line of the displacement u_z^P.

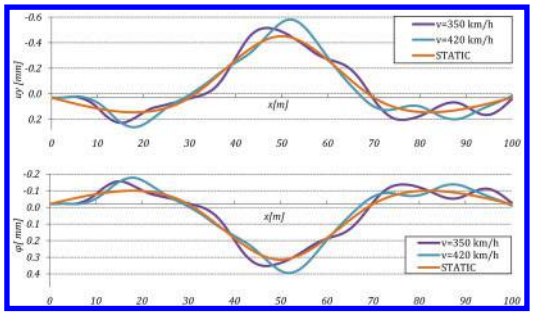


Figure 14. Comparison of static and dynamic influence lines of the displacement φ.

The dynamic influence line of the vertical displacement of point P is represented in figure 13 for the velocity of 200 km/h and 400 km/h, with $P_z = 1000\,kN$. The cross-section warping is considered in the analysis, being its influence evaluated through the vertical displacement of the cross-section; the relevance of the warping stiffness in evaluating the dynamic displacements for cross-sections with an open profile is highlighted by the results obtained.

The dynamic amplification of the displacement was evaluated by comparing the vertical displacement of the central mid-span obtained from a static and a dynamic analysis. The dynamic influence lines for the displacements u_y and φ of the cross-section are represented and compared with the static displacements in figure 14; the amplification factors obtained for the transverse displacement and torsion of the cross-section for a velocity of 350 km/h are respectively 1.13 and 1.11 and for a velocity of 420 km/h 1.24 and 1.27

Notice that a maximum train speed of 350 km/h corresponds to a design speed of 420 km/h, being the dynamic increment related to this speed quantified as 24% and 27%, for u_y and φ, respectively.

4 CONCLUSIONS

A higher order thin-walled beam model applied to the analysis of a bridge girder was presented. The model relies on the approximation of the displacement field over the cross-section by a set of linearly independent basis functions to accurately represents the three-dimensional behaviour of thin-walled structures.

The model has successfully represented the structural behaviour of a bridge girder both in static and in a dynamic analysis; the comparison with the results obtained from a shell finite model was sufficiently accurate.

The beam model is therefore considered a possible method of analysis for bridge girders, having the advantage of enhancing the interpretation of the structural phenomena involved due to its modal characteristic.

REFERENCES

Abaqus (2006). *Abaqus*. SIMULIA Dassault Systèmes.

Allen, H. G. & P. S. Bulson (1980). *Background to buckling*. McGraw-Hill.

Bogensperger, T. (2000). *Erweiterte Stabtheorie und der gevoutete Trager im Bruckenbau*. Ph. D. thesis, TU – Graz, Austria.

Boswell, L. & S. Zhang (1984). The effect of distortion in thinwalled box spine beams. *International Journal of Solids and Strucutres 20*, 845–862.

Dinis, P., D. Camotim, & N. Silvestre (2006). GBT formulation to analyse the buckling behaviour of thin-walled members with arbitrarily branched open cross-sections. *Thin-Walled Structures 44*(1), 20–38.

Kermani, B. & P. Waldron (1993). Analysis of continuous box girder bridges including the effects of distortion. *Computers and Structures 47*(3), 427–440.

Maisel, B. I. (1982). Analysis of concrete box beams using small computer capacity. *Cement and Concrete Association*. Möller, R. (1982). *Zur Berechnung prismatischer Strukturen mit beliebigem nicht formtreuem Querschnitt*. Ph. D. thesis, TU – Darmstadt. (in German).

Paavola, J. (1990). *A study of curved thin-walled girders*. Ph. D. thesis, Helsinki University of Technology.

Razaqpur, A. & H. Li (1991). Thin-walled multicell box-girder finite element. *Journal of Structural Engineering 117*(10), 2953–2971.

Schardt, R. (1989). *Verallgemeinerte Technische Biegertheorie*. Springer-Verlag. (in German).

Schrade, W. (2010). Anwendung der verallgemeinerten technischen biegetheorie in der ingenieurpraxis. *Stahlbau 79*, 127–135.

Tesar, A. (1996). Shear-lag in the behaviour of thin-walled box bridges. *Computers and Structures 59*(4), 607–612.

Vieira, R. (2010). *A higher order thin-walled beam model*. Ph. D. thesis, Universidade T'ecnica de Lisboa, Instituto Superior T'ecnico.

Vieira, R. F., F. B. Virtuoso, & E. B. R. Pereira (2013). A higher order thin-walled beam model including warping and shear modes. *International Journal of Mechanical Sciences 66*, 67–82.

Research and Applications in Structural Engineering, Mechanics and Computation – Zingoni (Ed.)
© 2013 Taylor & Francis Group, London, ISBN 978-1-138-00061-2

Full-scale testing of concrete deck slabs under fatigue-causing axle loads

G. Borkowski, K. Thoma & P. Roos
Lucerne University of Applied Sciences and Arts – Competence Centre Structural Engineering, Horw, Switzerland

ABSTRACT: The conservation of existing structures including maintenance, assessment and, if necessary, strengthening is a current challenge for engineers. For the evaluation of the load carrying capacity and the remaining service life, detailed knowledge of the load bearing behavior especially due to proceeding fatigue damage is required. In this paper, concrete deck slabs of hollow box girder bridges subjected to vehicle axle loads are examined.

The paper presents first test results from a large-scale experiment on a concrete deck slab specimen under cyclic loading. The test specimen has a span of 12m and a width of almost 6m. The axle loads (Swiss Code loads) are simulated using three hydraulic cylinders, which act one after another. First, the experimental procedure is presented. Second, the experimentally determined bending moments, strains and curvatures in the deck slab are shown. These results are calculated with an in-house software tool and they are compared with results from a 3D FE-Model based on nonlinear material behavior.

Finally, it is discussed how the load bearing behavior of the deck slab changes due to proceeding fatigue damage in the structure. This research project aims at contributing towards a better judgment of whether the service life of a bridge can be reached or strengthening is necessary.

1 INTRODUCTION

1.1 *Initial Situation*

The construction of prestressed concrete bridges started in the 1940s and reached its peak in the 1960s. By that time, the need for new bridges was increasing and the prestressing technology was extensively being taken advantage of. Today, increasing traffic loads and serious durability problems require regular inspections of the bridges. Since the planned service life of most of these bridges has not been reached, it is often more economical to maintain and strengthen, rather than replace them.

In 2009 a study on segmental bridges built between 1958 and 1976 was published (Buschmayer, W. et al. 2009). The study shows that almost 90% of the reviewed bridges exhibited cracks or damaged coupling joints and strengthening would be necessary. The question arises whether global or local strengthening of such bridges is really necessary or whether corrosion protection might be sufficient.

If strengthening is necessary, first it needs to be determined what stresses are acting on the bridge and what type of failure is decisive: Failure by reaching the bearing load or fatigue.

1.2 *Research Objectives*

In general, existing bridges are assessed using presently valid design loads. Due to constantly increasing traffic loads, the design loads in the present design standards are considerably higher than the design loads, which were used at the time of construction of the bridges. This means that often the requirements for the ultimate limit state and the service limit state cannot be met. Even when using detailed numerical calculations with sophisticated models, the resistances of the structures are frequently found to be much smaller than the design actions (Borkowski, G., Sigrist, V., 2012).

For the assessment of existing bridges, fatigue requirements often govern. In many cases these requirements cannot be met because the methods in the design standards are based on strongly conservative assumptions. The research project presented in this paper seeks to address these issues.

Large-scale bending tests on slabs are used to analyze their load-bearing behaviour. In these tests, segments of bridge slabs are cyclically loaded until their bending reinforcement fails due to fatigue.

Three hydraulic jacks are used to simulate recurring vehicle crossings. The applied vehicle loads meet the size and geometrical specifications given in the relevant Swiss standard (SIA 261, 2003).

The aim of the research project is to provide monitoring methods for determining and assessing the damage process cause by fatigue. Further, it is planned to incorporate the gained knowledge in the relevant design standards.

2 EXPERIMENTAL INVESTIGATIONS

2.1 *Specimen*

The investigations focus on determining the load transfer within deck slabs. The test setup is based on the

cross-sectional geometry and reinforcement detailing of older bridges. Further, the bending reinforcement is designed so that fatigue damage occurs after three to four million test load cycles (s. Tab. 1). The specimen dimensions can be seen in Figure 1.

The specimen represents the top slab of a box girder. As the bottom slab is missing in the test setup, the transverse stiffness of a box girder is reproduced with six prestressed (50 kN each) threaded rods (Figure 1–4). The test specimen is mounted on four 0.5 MN hydraulic jacks, so that its position can be adjusted during the test if necessary.

2.2 *Experiment set-up*

The load is applied with three hydraulic jacks, which successively load the specimen. Therefore, during one load cycle the three jacks are applied one after another. Following the provisions given in the relevant Swiss standard (SIA 261, 2003), a transverse beam distributes each jack load to two load distribution plates. The transverse spacing between the plates is 2 m (Figure 1) and corresponds to the distance between the two point loads of an axle load as stipulated by the code. The 270 kN load applied by each jack corresponds to the characteristic value of this axle load. In the longitudinal direction the distance between the jacks is 2.4 m (Figure 3). The load history of one cycle is shown in Figure 5. As can be seen, the loads are applied successively, but a minimal load of 30 kN is always maintained at each jack so as to ensure that the testing equipment is never completely unloaded during the test.

Besides the continuous load and deformation measurements at the locations of the jacks, the vertical deformations of the test specimen at 16 locations and the force in the prestressed transverse rods are measured every five hours for 20 seconds. This means that the specimen deformations due to at least five full load cycles (fictitious vehicle crossings) can be measured (Figure 5).

Table 1. Reinforcement in the specimen slab.

	Reinforcement	
Layer	Ø [mm]	Spacing [cm]
Top transversal	14	20
Bottom transversal	10	20
Top longitudinal	10	20
Bottom longitudinal	14	20

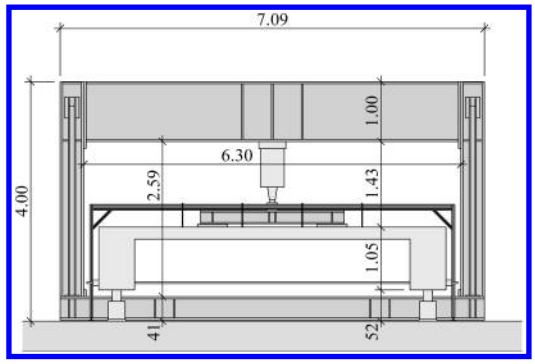


Figure 2. Cross section of the experiment set-up.

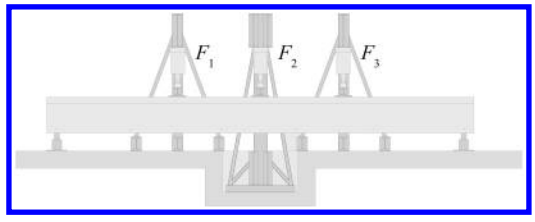


Figure 3. Longitudinal section of the experiment set-up.

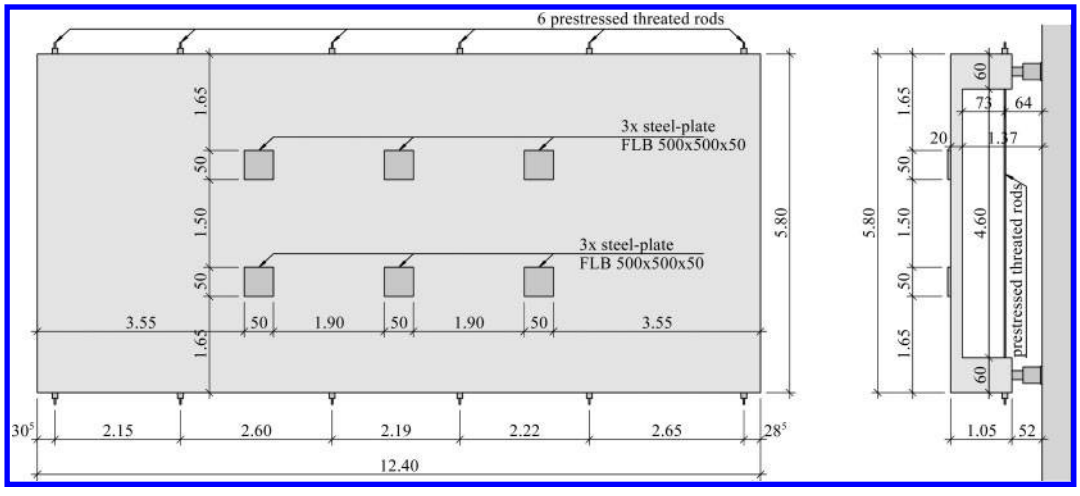


Figure 1. Specimen, left: top view, right: cross section.



Figure 4. Photo of the experiment set-up.

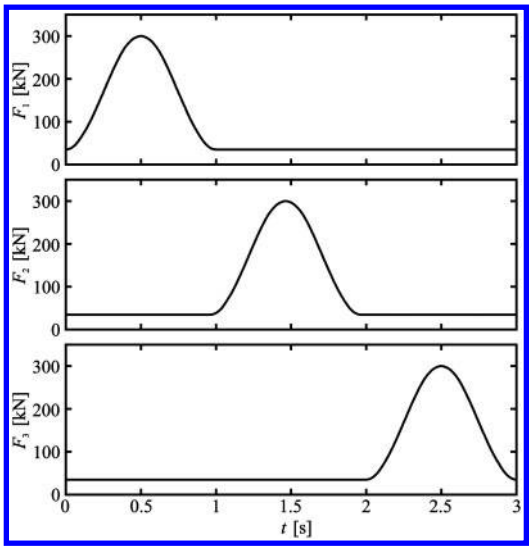


Figure 5. Load history for one cycle.

After every 500 thousand (500 k) cycles the loading process is interrupted. During these breaks the surface deformations on the upper and lower slab face are measured with a hand-held mechanical strain gauge (measurement accuracy 1/1000 mm). The measurements are carried out three times on one half of the slab. Thereto each jack is loaded separately up to 300 kN and put into deformation control mode, while the other two jacks are maintained at 30 kN. The crack pattern is recorded at each load application so that the cracking progress is documented after every 500k cycles (Figure 6).

With a program especially designed for this purpose, which is based on the layer model for slabs according to (Kollegger, J., 1991, CEB, 2008, Seelhofer, H. 2009, Urweider, T., 2012,), the cross-sectional strains, curvatures, steel stresses and bending moments in the slab can be determined from the deformation measurements taken with the hand-held mechanical strain gauge.

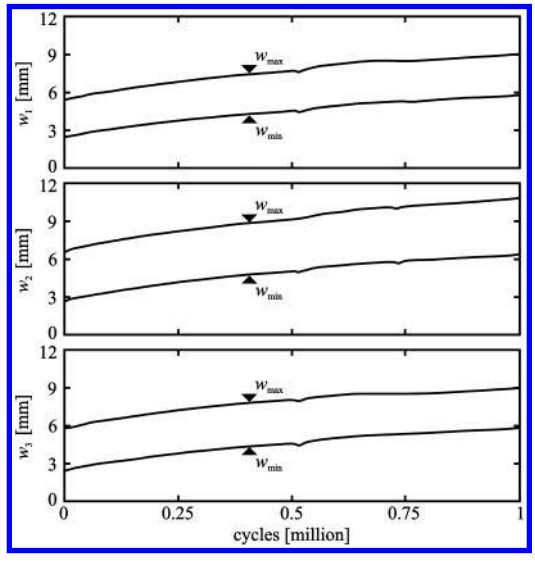


Figure 6. Vertical slab displacement vs. load cycles up to 1 million cycles.

Thereto, each layer is assumed to have a plane stress state, which is determined with the Cracked Membrane Model according to (Kaufmann, W., 1998).

3 RESULTS

3.1 *Measurements*

At the time of submission of this paper, a total of one million load cycles have been applied to the specimen. At present, only results from the load level of 500 k cycles can be presented as the mechanical strain gauge measurements are taken and evaluated every 500 k cycles.

Figure 6 shows the recorded vertical slab deformations below each of the three jacks. The envelopes of the maximal and minimal deformation values are shown. The figure shows to which extent the test specimen exhibits residual deformations due to cyclic loading. It can also be seen that the specimen stiffness relative to the load is almost constant.

Figure 7 shows the initial cracks and the crack pattern established after 500 k cycles. The top and bottom face of one half of the slab is shown. It is clearly visible that the cyclic loading caused a progression of the cracks. The cracks progressed in both the longitudinal and transverse direction of the slab, which indicates an enhancement of the global load-bearing action in the slab.

3.2 *Nonlinear FE-Calculations*

The deck slab was designed and verified with a nonlinear three-dimensional Finite Element (FE) Model. The results of the model allowed the determination of the right amount of reinforcement necessary to achieve

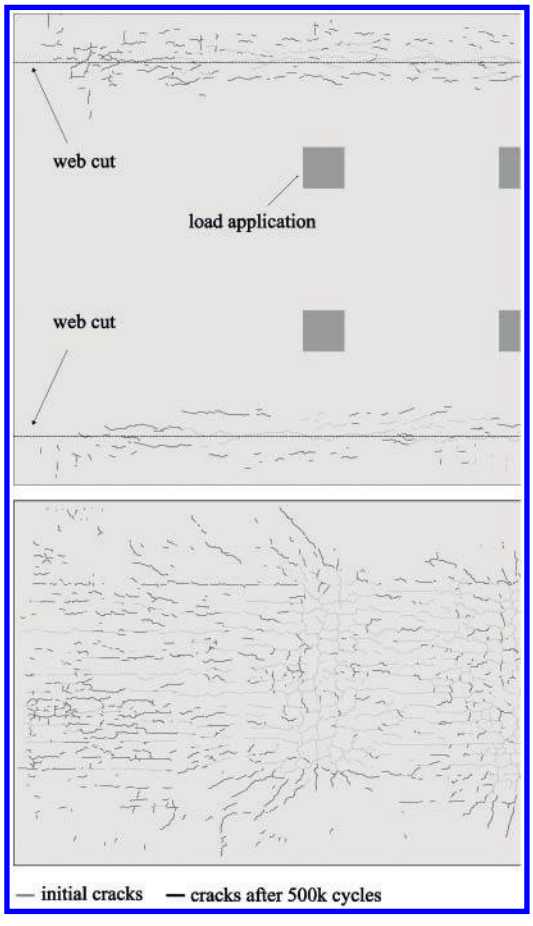


Figure 7. Cracks in one half of the deck slab; top: top view of the slab, bottom: bottom view of the slab between the webs.

the desired stress level in the reinforcement of the specimen. Through computational reassessment of the specimen during testing it is possible to check the model assumptions regarding the stress levels in the reinforcement to ensure that fatigue relevant stresses are developing.

Further, during the course of the test it is possible to determine to which extent the FE model needs to be adapted so that it can account for the progressive damage of the test specimen. Hence, from this model the necessary stiffness adjustments due to fatigue damage can be deduced for general recalculations of existing bridges.

The FE Model uses shell elements (Figure 8, Sofistik 2010). Bilinear material behaviour is assumed for the reinforcing steel. For the concrete in the compression zone non-linear material behaviour is adopted, while the tensile concrete is modelled according to Hillerborg et al. (Hillerborg et al. 1976). The material constants are determined during the course of the test and can be directly entered into the FE Model. The following figures show the calculated bending moments about the transverse and longitudinal axes

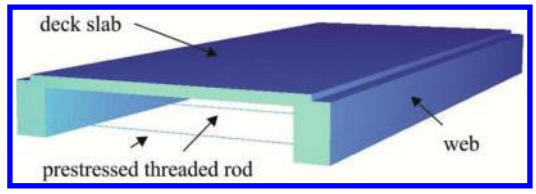


Figure 8. FE-Model.

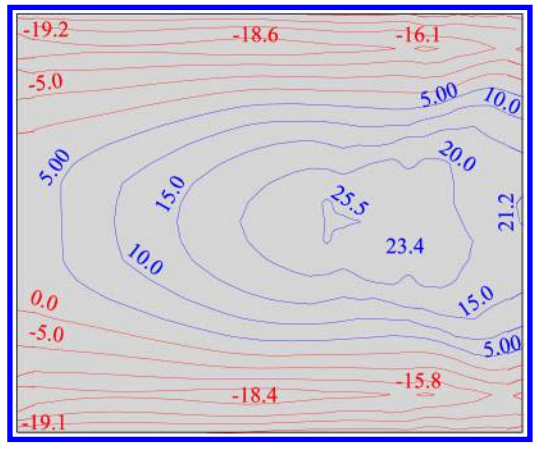


Figure 9. Calculated bending moments about the longitudinal axis.

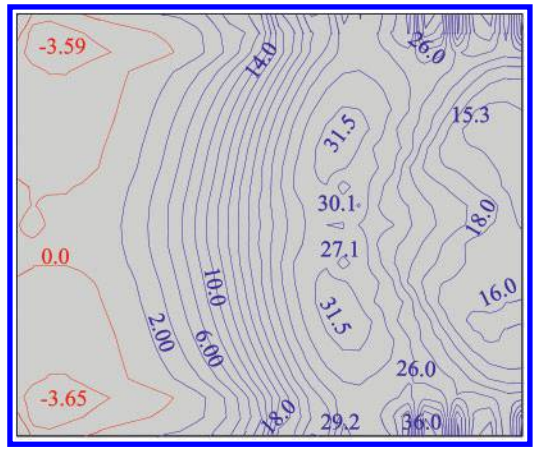


Figure 10. Calculated bending moments about the transversal axis.

(Figure 9 and 10). On both figures only one half of the slab is shown.

It can be seen that the calculated stress resultants correspond well with the stress resultants determined from the measurements (Figure 11 and 12). This means that the values obtained from the initial design describe the effective behaviour well and that the desired stress levels are being reached in the bending reinforcement of the test specimen. Further, the FE calculations can provide information for locations of the test specimen,

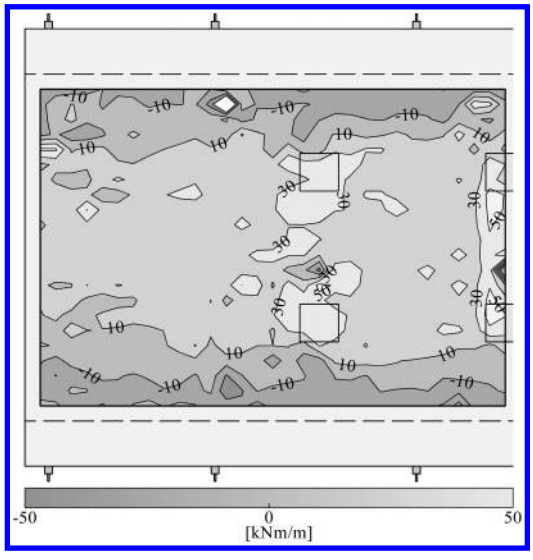


Figure 11. Bending moments about the longitudinal axis.

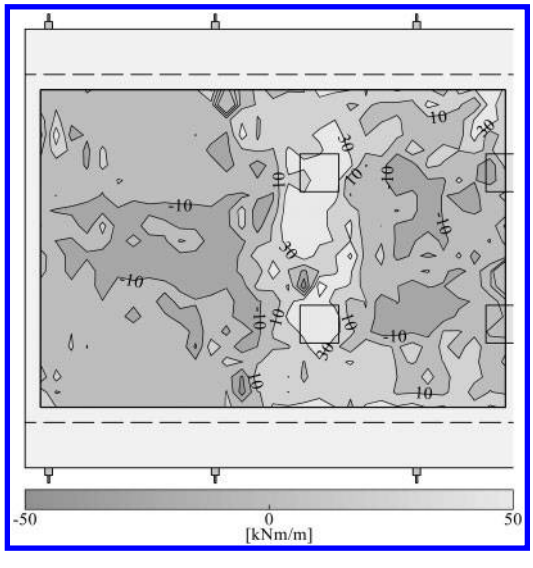


Figure 12. Bending moments about the transversal axis.

where no measurements are being carried out, e.g. the stress levels in the bending reinforcement in the web.

3.3 *Stress state of the Reinforcement*

Based on the measurements carried out on the test specimen and on the in-house software tool, the bending steel stresses can be determined for each reinforcement layer of the specimen. The following three figures show the stresses after 500 k load cycles in the top transverse reinforcement (Figure 13), the bottom transverse reinforcement (Figure 14) and the bottom longitudinal reinforcement (Figure 15).

These stresses can only be determined experimentally in regions with target studs on the top and bottom

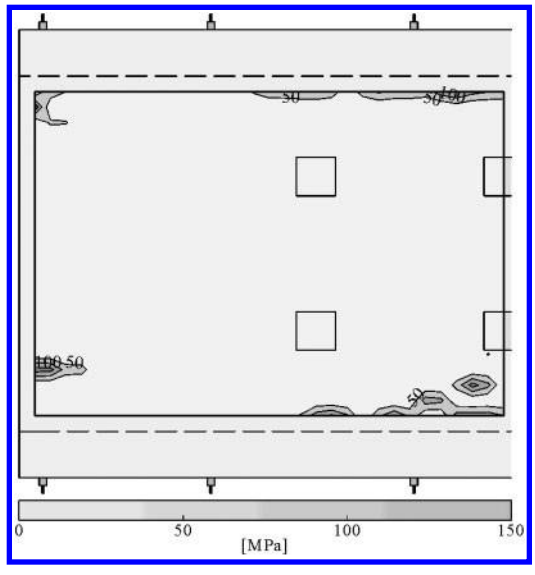


Figure 13. Stresses in the top reinforcement in transversal direction after 500 k cycles.

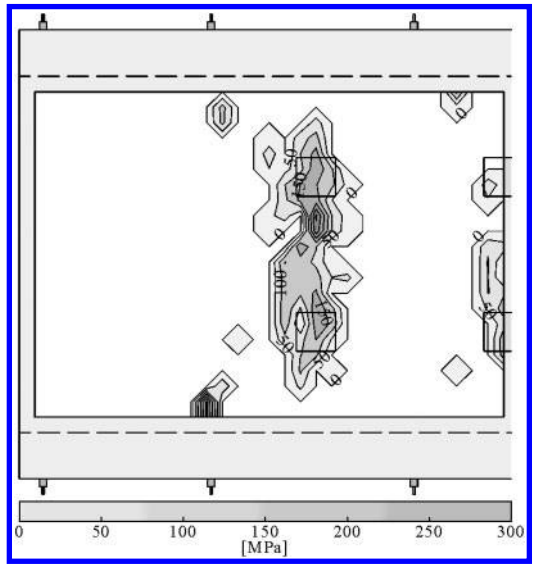


Figure 14. Stresses in the bottom reinforcement in transversal direction after 500 k cycles

face of the slab. This means that the steel stresses due to negative bending moments at the flange-web intersection cannot be determined. These values have to be provided by the FE model.

As can be seen in the figures, the bottom reinforcement in the transverse and longitudinal direction is subjected to stresses equal to 200 MPa. As the transverse negative moment at the flange-web intersection dies down rapidly, relatively low stress levels are measured experimentally. However, if the FE Model is used to determine the steel stresses, steel stresses of

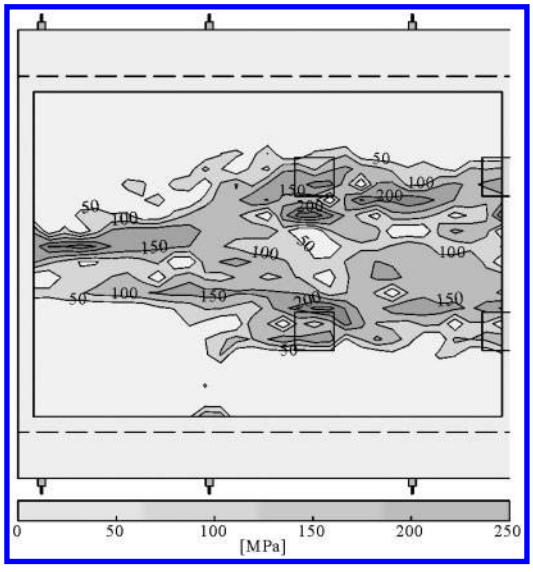


Figure 15. Stresses in the bottom reinforcement in longitudinal direction after 500 k cycles

170 MPa are found in the transverse reinforcement above the web.

As there is hardly any stress present in the reinforcement in the unloaded state, fatigue relevant stress amplitudes equal to 200 MPa and 170 MPa can be assumed.

4 CONCLUSIONS AND FURTHER RESEARCH

The present research work comprises the execution and evaluation of large-scale tests on bridge deck slab members, which are subjected to fatigue relevant stress levels caused by vehicle axle loads. First, the general testing program is presented. The test specimen is described and the loading sequence is explained.

Further, the components of the measuring program are presented and it is shown which data can be gained from the measurements. Then the experimentally determined stress resultants are compared with the results from non-linear FE calculations and a good agreement is found. Finally, the stress levels in the slab bending reinforcement are illustrated.

By means of the experiment and the evaluation program it is possible to illustrate the load bearing behaviour in the slab due to fatigue damage. It is planned to carry out at least three further tests on identical test specimens. These test specimens will be preloaded with tensile and compressive forces in the longitudinal and transverse direction, in order to be able to represent effects such as longitudinal and transverse bending in the span and support regions of the bridge.

FE calculations will be carried out to simulate the load bearing behaviour in the case of fatigue damage.

The knowledge gained from this research project is intended to be incorporated in the Swiss Standard for the assessment of existing structures. On this basis, the load bearing reserves of existing bridges can be more accurately determined and evaluated, in order to prevent unnecessary strengthening measures.

ACKNOWLEGEMENTS

The authors thank the Swiss Federal Roads Office (ASTRA) for financing the project. This project is also being assisted by the University of Applied Science in Rapperswil under the supervision of Prof. Dr. techn. sc. A. Kenel.

REFERENCES

Buschmayer, W., Roder, C., Gusia. 2009. Erfahrungen bei der Beurteilung der Dauerhaftigkeit vorgespannter Bewehrung von älteren Spannbetonbrücken. *Bautechnik Vol. 86*

Borkowski, G., Sigrist, V. 2012. Computational Assessment of Prestressed Concrete Bridges. *18th IABSE Conference Seoul*

CEB Comité Euro-International du Béton. 2008. Practitioners' Guide to Finite Element Modeling of Reinforced Concrete Structures. *bulletin state of the art report No. 45*

Hillerborg, J., Modeer, M., Peterson, P. E. 1976. Analysis of Crack Formation and Growth in Concrete by Means of Fracture. Mechanics and Finite Elements. *Cement and Concrete No. 6*

Kaufmann, W., 1998. Strength and Deformations of Structural Concrete Subjected to In-Plane Shear and Normal Forces. *Institut für Baustatik und Konstruktion ETH Zürich Nr. 12'711*

Kollegger, J. 1991. Algorithmus zur Bemessung von Flächentragwerkelementen unter Normalkraft- und Momentenbeanspruchung. *Beton- und Stahlbetonbau 86 p. 114ff*

Seelhofer, H. 2009. Ebener Spannungszustand im Betonbau: Grundlagen und Anwendungen. *Institut für Baustatik und Konstruktion ETH Zürich Nr. 18'486*

Sofistik, 2010.,*Finite-Elemets-Software. Vers. 2010*

Swiss Code SIA 261, 2003. Actions on Structures. *Swiss Society of engineers and architects*

Urweider, T., 2012. Plattenschnittkräfte auf Basis von Setztdeformetermessungen. *Master-Thesis, Lucerne University of Applied Sciences and Arts*

Research and Applications in Structural Engineering, Mechanics and Computation – Zingoni (Ed.)
© 2013 Taylor & Francis Group, London, ISBN 978-1-138-00061-2

Cable stressing sequence of an asymmetrical cable stayed bridge

John R.B. Anderson
SMEC South Africa (Pty) Ltd, Cape Town, South Africa

ABSTRACT: This paper describes the cable stressing sequence for an asymmetrically rock anchored cable stayed pedestrian bridge at Tshelimnyama. The bridge crosses the N3 highway near Durban and was built for the South African National Roads Agency SOC Ltd (SANRAL). During the construction period various stressing sequences were analyzed with the aim of limiting the erection engineering effort and the construction risks. The final solution was found after a number of iterations and used the structures' self-weight to partially stress the most critical cables. Importantly this limited the forces on the temporary support cables and reduced the jacking forces needed to stress the permanent cables.

1 INTRODUCTION

1.1 *Introduction*

This paper describes the cable stressing sequence for an asymmetrically rock anchored cable stayed pedestrian bridge at Tshelimnyama on the N3 near Durban built for the South African National Roads Agency SOC Ltd (SANRAL). During construction various stressing sequences were analyzed with the aim of limiting the erection engineering effort and risks. After a number of iterations the final solution used the structure's self-weight to partially stress the most critical cables. Importantly this limited the forces on the temporary support cables and reduced the required jacking forces needed to stress the permanent cables resulting in an overall cost saving to the client.

1.2 *The bridge*

The bridge is a two span structure with a total length of 89.75 m, a main span length of 55.75 m and a back span length of 34.0 m. The 3.2 m wide deck is constructed from reinforced and prestressed concrete and is supported by 10 sets of stay cables. A 32 m long inclined, twin legged structural steel tower that is pinned at its base supports the cables by means of spade and fork connections.

Because the tower leans, the structural systems needs lateral restraint. The end of the bridge deck is therefore integral with the southern abutment which is anchored into the rock with twelve rock anchors. The first pair of cables (C1) on the bridge connects the tower to the rock anchored abutment. This connection to a rigid point provides much of the stiffness in the structural system and limits the deflection of the deck due to asymmetrical dead and live loads. As a result the C1 cable carries far higher loads than any of the other cables.

1.3 *The problem*

The method of erecting the tower and the associated temporary works design was a fundamental part of the project. In its final state the tower is held in position by the balanced forces in the back span and main span

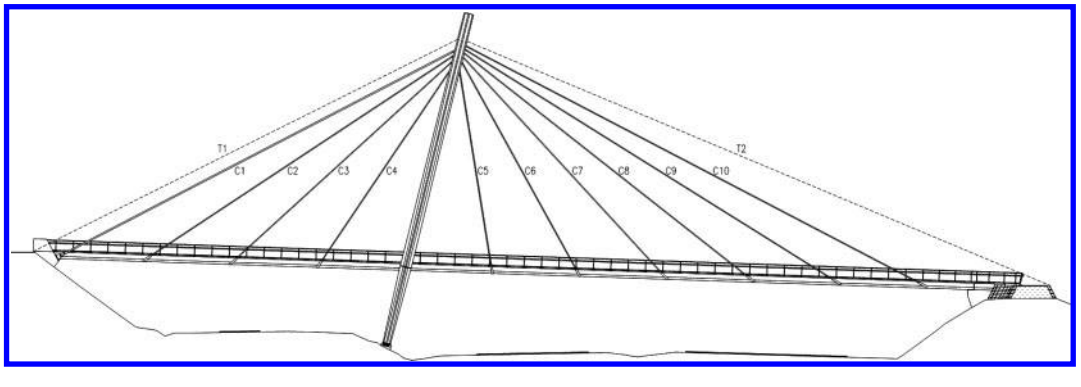


Figure 1. Bridge elevation and cable annotation.

stay cables. However, because the tower is pinned at its base, it was necessary to temporarily support it during the installation of the permanent stay cables.

The challenge became the design of temporary works because it required the detailed modeling of the installation and stressing of the permanent stay cables. In such instances it is considered impractical for a contractor to take full responsibility for the temporary works design. This is because he would have to employ an experienced bridge engineer to model the complete structural system. In the context of the South African construction market, and the low capital value of the project, this is not considered a practical expectation.

This paper highlights that the most appropriate temporary works solutions are not always found when the engineer and contractor are separated by their contractual roles. To this end the benefits of collaboration between the designer and the contractor are documented.

2 ORIGINAL STRESSING SEQUENCE

Early on in the design process it was decided to construct the deck section of the bridge on staging. Cantilever construction was considered to be impractical for the proposed structural system. In terms of the cable stressing sequence the design team's proposed method was led by the fact that the C1 cable provided the necessary stiffness to the structural system and carried the highest load.

The construction drawings required the C1 cable be installed first and nominally stressed by the self-weight of the tower structure and by whatever temporary supports the contractor proposed. As a fixed length cable the intent was that the C1 cable would control the top of tower position whilst the remaining cables were installed and stressed.

It was required that the cables adjacent to the tower be then installed and stressed to 25% of the design stress. Working outwards from the tower this process was repeated for each pair of back span and main span cables. Finally the C1 cable was to be stressed to 25%.

The intent of this process was to start by removing the slack from the cables and to get some stiffness into the structural system before the cables were sequentially stressed to their design forces. By starting with the cables adjacent to tower more vertical force was initially added to the tower than lateral force. This helped reduce the movements at the top of the tower during the stressing sequence.

The next iteration followed the same sequence now stressing the cables to 90% of their design forces. A final stressing pass to get the forces up to the target values was allowed to achieve the desired vertical alignment of the deck section.

Although the stressing sequence was considered logical in the end it was flawed on two accounts. The first was that stressing sub-contractors prefer to put as much force as they can into a cable to reduce the number of stressing operations. This said, generally cables have to be stressed in at least two operations to ensure that the correct deck alignment is achieved.

The contractor's cable choice of cable and anchorage system is also an important variable that can affect the stressing sequence. In some cases the cables anchorage assemblies need to be activated by a minimum force for safety reasons. This force can be as much as 30% of the cable's ultimate force.

The second more important flaw was that the stressing sequence did not account for the temporary works. During the conceptualization of the structure it was judged that the bidding contractors would each have a preferred means of providing temporary support to the tower. Fully detailing a temporary works solution was therefore ruled out. However, the interaction between the temporary works and the cable stressing sequence was fundamental. This was identified at the onset of the contractor's temporary works design when a set of temporary cables attached to the top of the tower were proposed.

3 TEMPORARY WORKS DESIGN

3.1 *General arrangement*

The temporary works proposal used two sets of temporary cables to stabilize the tower, by connecting the top of the tower to fixed points onto either side of the bridge. The T1 cables consisted of two cables connecting the top of the tower to the fixed abutment by means of a temporary steel anchorage assembly. The T2 cable followed a similar arrangement and connected the top of the tower to a temporary micropiled concrete structure at the other end of the bridge.

It was important that the force in the temporary cables could be varied if required. The contractor, Freyssinet and the design team therefore came up with a system of connecting the strands to steel connection boxes that then connected to a stress bar which was fixed into the anchorage assemblies. By stressing the stress bar the forces in the support system were then easily controlled.

A temporary steel support frame was detailed for the steel anchorage boxes to ensure that the stress bar was not subject to bending or shear stresses. Refer to figure 2.

3.2 *Permanent Cable system*

In any stressing sequence the cable supplier's requirements for stressing the cables are an important factor. In this case Freyssinet's H1000 cable system was used. The cables are made up of 15.7 mm galvanised and coated mono-strand housed within an uPVC sheath.

The C1 cables utilised spade and fork connections. A fixed anchorage was detailed at the top of the tower and an adjustable fork at the fixed abutment. An important constraint was that a minimum force was required to safety activate the anchorages in the assembly.



Figure 2. Steel anchorage assembly and support frame.



Figure 3. Jacking assembly on adjustable fork.



Figure 4. RAB type Anchorage assembly.

The C2 to C10 cables had fixed spade and fork assemblies that top of the tower and adjustable anchorages at the deck anchorages. It was impractical for the strands to be jacked individually and a jack that grabbed the whole anchorage assembly was needed to stress all strands equally. Freyssinet's RAB anchorage with a threaded collar was therefore used.

4 ANALYSIS MODELS

Using temporary cables attached to the top of the tower meant that as the permanent cables were installed the forces in the temporary cable changed. Similarly when the temporary cables were released the forces in the permanent cables changed. The temporary works cables where therefore included in the analysis model to review the stressing sequence.

It was also important to check that the temporary works were designed with sufficient redundancy to allow for the event of a temporary support cable breaking. This was checked with an impact analysis to calculate the magnified forces in the system due to a sudden failure of a cable.

When the original stressing sequence was analyzed with the temporary stays, the maximum force in T1 reached 578 kN. The main concern became designing the temporary anchorages to restrain this force and the construction risks associated with a cable out scenario.

As mentioned the cable C1 provides much of the stiffness to the structural system and in the bridge's final state its design force is significantly larger than the other cables. The challenge was that C1 could not be stressed unless the other cables were already in place. Without the internal cables there was essentially nothing to restrain the tower and therefore nothing to jack against.

A further issue was that the contractor initially wanted to stress the cables to close to 100% of the design load. However, the implication was that after the installation of cables C2 to C10 the temporary T1 cable was highly stressed. This sequence also required that T1 cable had to be re-stressed continuously to keep the top of the tower in the correct position. The consequence of the tower moving was that the tolerances in the permanent cable lengths could be exceeded.

5 FINAL SEQUENCE

Although various alternative stressing methods were tested for the purposes of this paper the final solution is explained.

The crux of the final sequence was to stress the C1 cable to its full force as soon as possible whilst the T1 cable remained in place. To get the full force into C1 all of the back-span and main span cables had to be in place. However if they were stressed to the design force the result was the increase in force in T1. The answer to the problem came from using the structure's dead weight to fully stress C1.

In summary the final construction sequence first involved installing the permanent stay cables (C2 to C10) and the stressing them to a nominal force. This required minimal effort and control from the contractor and was carried out relatively quickly. The main C1 cable was then installed and stressed to a force of 800 kN and the temporary T1 cables were removed. With the C2 to C10 cables installed the necessary restrain to jack against was present. The deck staging



Figure 5. Completed structure.

was then removed. The deck deflected downwards by up to 80 mm before the C2 to C10 cables were stressed to the design forces bringing the deck back up to the required alignment.

The initial C1 target force of 800 kN was found by an iterative process that limited the final force in the C1 cable after the release of the deck formwork and the C2 to C10 cable stressing to 1100 kN.

The above sequence greatly reduced the forces in the temporary cables, thus minimizing the construction risks. The maximum T1 force was limited to 217 kN increasing the redundancy in the temporary works design.

The cable forces and deck displacements where monitored closely on site during the stressing operation to check the structure's behaviour. The stressing sequence analysis proved to be accurate, with additional stressing required on only four of the cables to ensure correct the deck displacement.

In review the stressing sequence process required a significant amount of additional analysis and design work. The design actions on the tower and deck elements had to be checked at each stage of construction. This led to the formwork between C1 and C2 remaining in place till the completion of the stressing operations to limit the bending moments in the deck section.

6 CONCLUSIONS

This project highlights that, on certain structures, the temporary works design cannot be divorced from the detailed erection engineering. In the case of cable stayed structures the load effects on the temporary works change through the erection sequence. As a result collaboration with the design engineer is essential to accurately model the behaviour of the permanent structure and the load effects on the temporary works components. These type of projects could be considered by clients to be let rather as design and construct type projects using the EPC suite of the FIDIC documentation as an example due to the substantial amount of interaction between the designer and contractor.

The construction process also highlighted that the constraints of contractor's proprietary cable system and jacking methods have to be carefully understood when considering the erection methods.

The final stressing sequence used worked well in that it reduced the construction risks, simplified the erection engineering and saved significant time. It is considered that using the structure's dead weight to stress the cable stays is an effective method, especially for pedestrian bridges.

ACKNOWLEDGEMENTS

The author acknowledges the client, the South African National Roads Agency SOC Ltd (SANRAL), for permission to publish this paper.

REFERENCES

PTI DC45.1-07. Recommendations for stay cable design, testing and installation, Fifth Edition

Research and Applications in Structural Engineering, Mechanics and Computation – Zingoni (Ed.)
© 2013 Taylor & Francis Group, London, ISBN 978-1-138-00061-2

Design curves for stiffened flanges used in steel box girder bridges

P.S. Ferreira
Polytechnic Institute of Setubal, Escola Superior de Tecnologia do Barreiro and ICIST, Setubal, Portugal

F. Virtuoso
Technical University of Lisbon, Instituto Superior Técnico, DECivil-ICIST, Lisbon, Portugal

ABSTRACT: This paper presents a design method for stiffened flanges used in steel box girder bridges based on a set of design curves that take into account all relevant parameters regarding the ultimate strength of stiffened flanges, including the real boundary conditions for the in-plane displacements at the edges. These design curves were developed and calibrated based on the results obtained with nonlinear analysis using the semi-analytical and finite element methods and they were validated by comparison with the results of experimental tests in accordance with the target failure probability of the European standard EN-1990. Finally, it is presented a comparison between the ultimate strength obtained using the proposal design curves with that obtained using the nonlinear analysis and the current bridge design rules.

1 INTRODUCTION

National standards with design rules for stiffened flanges used in steel box girder bridges were almost non-existent until the early nineteen seventies. These design rules were based on the elastic critical stress (σ_{cr}) obtained by the linear buckling theory of plates with some correction factors to take into account the favorable effect of the postcritical strength reserve (ECCS Committee8 1976).

Research work to establish new design rules for plated structures was strongly increased in the early nineteen seventies as a result of well known accidents during construction involving box girder bridges (Galambos 1998). Although the behavior and strength of stiffened plates have been extensively studied over the last forty years, there are still some inconsistencies and gaps between the results of some studies and the results obtained through the design rules established in the European and American standards (EN-1993-1-5 2006, AASHTO-LRFD-BDS 2007), which are usually adopted by the bridge designers to solve the problem of predicting the ultimate strength of stiffened plates.

As the current design rules laid down in the European and American standards do not recognize the effect of boundary conditions for the in-plane displacements at the edges to obtain the ultimate strength of stiffened plates, the use of these design rules can give inaccurate results and in some cases against safety.

This paper presents a design method for stiffened flanges used in steel box girder bridges based on a set of design curves that take into account all relevant parameters regarding the ultimate strength of stiffened flanges, including the real boundary conditions for the in-plane displacements at the edges. These design curves were developed and calibrated based on the results obtained with nonlinear analysis using the semi-analytical and finite element methods and they were validated by comparison with the results of experimental tests in accordance with the target failure probability of the European standard EN-1990 (2002). Finally, it is presented a comparison between the ultimate strength obtained using the proposal design curves with that obtained using the nonlinear analysis and the current bridge design rules.

2 PROBLEM DESCRIPTION

The most widely used bridge structural elements that resort to the use of steel plates are the plate and box girders. Steel plates used in these structural elements are outstand flanges, internal flanges and webs.

Outstand flanges have a free longitudinal edge and they are used as upper and lower flanges of the plate girders and narrow top flanges in open top box girders of composite sections. Internal flanges are used as bottom flanges of box girders and wide top flange in closed box girders of steel sections. In wide flanges and webs of considerable height it is common to use longitudinal stiffeners to reduce the problems associated with the effects of buckling.

The study of the behavior and strength of steel plates with longitudinal stiffeners is very complex because they depend on a large number of variables, such as the shape and amplitude of the initial geometric imperfections, the residual stresses, the boundary

conditions for the in-plane and out-of-plane displacements, the load conditions and the geometric and material data. Recent numerical studies (Ferreira 2012, Braun 2010) showed that the behavior and strength of steel plates are very sensitive to in-plane displacements boundary conditions and the European and American standards (EN-1993-1-5 2006, AASHTO-LRFD-BDS 2007) do not provide a definition and clear guidance for the proper use of the simplified rules available to designers. These rules may give considerable errors, particularly when applied to the safety verification of stiffened plates where the transverse in-plane displacements at longitudinal edges cannot be considered as uniform (in-plane displacements perpendicular to the longitudinal edges constrained to remain straight).

In European standard (EN-1993-1-5 2006) the resistance assessment of webs and internal flanges with longitudinal stiffeners used in steel box girder bridges is performed through the same criterion and independent of the in-plane displacement boundary conditions of the plate. Just apparently both elements may have the same in-plane displacement boundary conditions. Indeed, the webs are usually connected to flanges that possess sufficient rigidity to consider uniform the in-plane displacements at longitudinal edges, while the flanges are connected to webs that usually do not provide this type of constraint and it is more conservative to consider free the in-plane displacements at longitudinal edges, as shown in the work of Ferreira & Virtuoso (2011) through a comparison between numerical and experimental results.

The design proposal presented in this paper for stiffened flanges aims to fill a gap in the current European bridge design rules, which should not be applied to stiffened plates with the fully free transverse in-plane displacements at longitudinal edges.

3 DESIGN PROPOSAL

3.1 *General*

The design proposal is a model based on design curves (arithmetic expressions) describing the influence of all relevant parameters on the ultimate strength of stiffened flanges used in steel box girder bridges. It was developed and calibrated based on the results obtained with the semi-analytical and finite element methods and it was validated by comparison with the results of experimental test in accordance with the target failure probability of EN-1990 (2002).

These design curves consider that the plate is subject to compressive longitudinal direct stress with a stress ratio higher than 0.5 (lower compressive longitudinal stress to the higher compressive longitudinal stress ratio, $\psi > 0.5$), the transverse stiffeners provide rigid support lines, the longitudinal stiffeners are fully effective and equally spaced and the plates have the longitudinal in-plane displacements constrained to remain straight at loaded edges (transverse edges) and the other in-plane displacements fully free. This design model does not consider the effects of local buckling of the stiffener elements and tripping of the stiffener. These effects can be avoided by adopting minimum values for the geometric properties of the longitudinal stiffeners as used in European and American standards (EN-1993-1-5 2006, AASHTO-LRFD-BDS 2007).

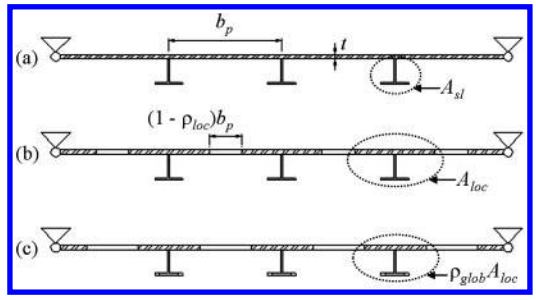


Figure 1. Reduction of the cross-sectional area of a stiffened plate in the design proposal: (a) the gross cross-sectional area, (b) the effective local cross-sectional area and (c) the effective cross-sectional area.

3.2 *Design procedure*

The design proposal is a design approach based on the reduced section concept, where the mean compressive stress at peak load (or ultimate strength σ_u) of a stiffened plate is estimated through the yield strength of the effective cross-sectional area according to

$$\frac{\sigma_u}{f_y} = \rho_{glob}\frac{A_{eff,loc}}{A} \tag{1}$$

where f_y = yield stress; ρ_{glob} = global reduction factor; $A_{eff,loc}$ = effective local cross-sectional area which takes into account the local buckling effects; and A = gross cross-sectional area of the stiffened plate.

From Equation 1 it can be noted that the effective cross-sectional area ($A_{eff} = \rho_{glob} \cdot A_{eff,loc}$) which takes into account the local and global buckling effects is obtained by reducing the cross-sectional area of the stiffened plate in two different steps, as illustrated in Figure 1.

In the first step the effect of local buckling in the panels between longitudinal stiffeners is taken into account and an effective width of these panels is adopted to obtain an effective local cross-sectional area ($A_{eff,loc}$) according to

$$A_{eff,loc} = \sum_{i}^{n_{st}+1}\left(\rho_{loc,i}b_{p,i}\right)t_i + n_{st}A_{sl} \tag{2}$$

where n_{st} = number of longitudinal stiffeners; ρ_{loc} = the local reduction factor; b_p = width of the panels between longitudinal stiffeners; t = plate thickness; and A_{sl} = gross cross-sectional area of a single longitudinal stiffener (without the contribution of the plate). The local reduction factor (ρ_{loc}) takes into account the favorable effects from postcritical strength reserve and the unfavorable effects of the initial imperfections

and it is defined for each panel between longitudinal stiffeners by

$$\rho_{loc} = \frac{\lambda_{p,norm} - 0.055(3+\psi)}{\lambda^2_{p,norm}} \leq 1 \quad (3)$$

where $\lambda_{p,norm}$ = relative slenderness of the panels. For a relative slenderness of the panels lower than 0.673 the local reduction factor should be considered equal to 1. Equation 3 is the same criterion used in European standard (EN-1993-1-5 2006).

In the second step, which takes into account the effect of global buckling in the stiffened plate, a global reduction factor (ρ_{glob}) is considered to reduce the effective local cross-sectional area ($A_{eff,loc}$). The global reduction factor is given by

$$\rho_{glob} = \max(\chi_c ; \rho_{p,\infty}) \quad (4)$$

where χ_c = reduction factor for the column buckling behavior; and $\rho_{p,h}$ = reduction factor for the plate buckling behavior estimated for a long stiffened plate (stiffened plate where the elastic critical stress σ_{cr} no longer depends of the plate length a).

Column buckling behavior is considered in stiffened plates with insignificant postcritical resistance. This behavior is modeled by removing the supports along the longitudinal edges of the plate and considering the cross-section of the column equivalent to the plate composed of a single stiffener with an effective width of the adjacent panels to the stiffener. The reduction factor for the column buckling behavior is obtained by

$$\chi_c = \min\left(0.66^{\lambda_{c,norm}}; \frac{1}{\phi_c + \sqrt{\phi_c^2 - \lambda^2_{c,norm}}}\right) \leq 1 \quad (5)$$

where $\lambda_{c,norm}$ = relative slenderness of the equivalent column; and ϕ_c = parameter that depends on the initial imperfections, the relative slenderness of the equivalent column ($\lambda_{c,norm}$), the relative flexural stiffness of the stiffened plate γ (second moment of area of the stiffened plate I_{st} to the second moment of area for bending of the plate corrected by the effect of the Poisson coefficient ($bt^3/[12(1-\nu^2)]$) ratio) and the number of longitudinal stiffeners (n_{st}).

The first term in Equation 5 ($0.66^{\lambda c,norm}$) is the critical criterion in stiffened flanges with low values of equivalent column relative slenderness ($\lambda_{c,norm}$) and it is equal to the reduction factor established in the American standard (AASHTO-LRFD-BDS 2007) for the column buckling behavior of stiffened plates. The other term in Equation 5 is the determinant criterion in stiffened plates with intermediate and high values of equivalent column relative slenderness ($\lambda_{c,norm}$) and it is equal to the reduction factor established in the European standard (EN-1993-1-5 2006) for the column buckling behavior of stiffened plates with an improvement that takes into account the relative flexural stiffness of the stiffened plate (γ) and the number of longitudinal stiffeners (n_{st}).

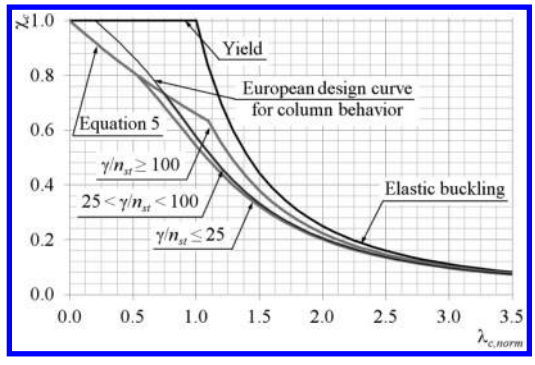


Figure 2. Reduction factor for the column buckling behavior obtained using the design proposal.

Figure 2 presents the reduction factor for the column buckling behavior (χ_c) obtained using the design proposal. It is also shown the yield, the elastic buckling and the European standard criteria. An equivalent geometric imperfection of 1/400 of the plate length (a) was used.

Plate buckling behavior is considered in stiffened plates with postcritical resistance. The design proposal uses this type of behavior to define the minimum ultimate strength of the stiffened plate, which is estimated considering a long plate. The reduction factor for the plate buckling behavior of a long stiffened plate is obtained by

$$\rho_{p,\infty} = \begin{cases} \dfrac{1}{4\xi} \leq 1 & for \quad \lambda_{p,norm} \leq 2\xi \\ \dfrac{1}{\lambda_{p,norm}} - \dfrac{\xi}{\lambda^2_{p,norm}} \leq 1 & for \quad \lambda_{p,norm} > 2\xi \end{cases} \quad (6)$$

where $\lambda_{p,norm}$ = relative slenderness of the stiffened plate; and ξ = parameter that depends on the compressive longitudinal stress ratio (ψ), the panel slenderness λ_p (width of the panels between stiffeners b_p to the plate thickness t ratio), the relative cross-sectional area δ (cross-sectional area of the stiffeners without any contribution of the plate $n_{st}A_{sl}$ to the cross-sectional area of the plate (bt) ratio), the relative flexural stiffness of the stiffened plate (γ) and the number of longitudinal stiffeners (n_{st}).

The reduction factor for the plate buckling behavior estimated for a long stiffened plate (ρ_p, ∞) is governed by the parameter ξ and Equation 6 becomes the well-known criterion proposed by Winter when this parameter is equal to 0.22. Based on the geometric parameters of the stiffened flanges identified in the survey of stiffened flanges used in real steel box girder brides presented in Ferreira (2012) the minimum and maximum values of the parameter ξ are 0.19 and 0.64 respectively.

Figure 3 presents the reduction factor for the plate buckling behavior of a long stiffened plate (ρ_p, ∞)

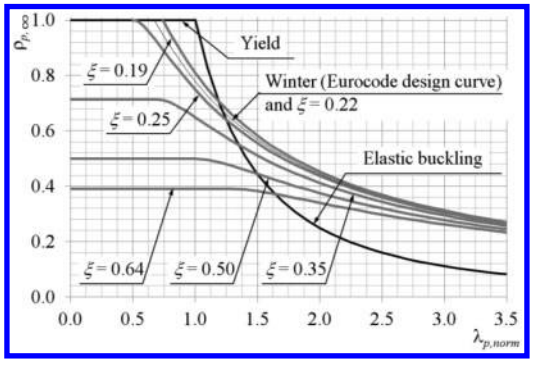


Figure 3. Reduction factor for the plate buckling behavior obtained using the design proposal with different values of the parameter ξ.

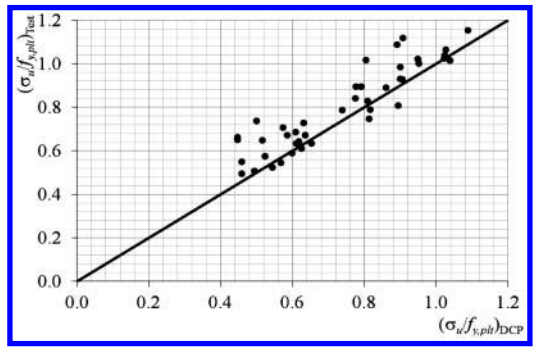


Figure 4. Ultimate strength results obtained by the design proposal (DCP) against the test results (Test).

obtained using the design proposal with different values of the parameter ξ. It is also shown the yield, elastic buckling and Winter criteria.

Figure 3 shows that the application of the design proposal results in a lower ultimate strength (σ_u) of the stiffened flange with fully free in-plane displacements at longitudinal edges than that obtained by the current European bridge design rules, which is consistent with the results obtained using nonlinear finite element simulations and with the results of experimental tests presented in the works of Ferreira & Virtuoso (2010, 2011).

The complete definition of the procedures and variables used in the design proposal can be found in the work of Ferreira (2012).

3.3 *Statistical evaluation*

In order to ensure that the design proposal for assessing the resistance of longitudinally stiffened compression flanges used in steel box girder bridges is safe and economical to use as a design rule, a statistical evaluation using experimental test results within the framework of a probabilistic reliability theory in accordance with EN-1990 (2002) should be carried out.

The target of this statistical evaluation is to establish the numerical value for the partial safety factor (γ_M) to be used in the design proposal. The use of this partial safety factor in the design proposal is achieved by replacing the yield stress f_y by f_y/γ_M in Equation 1. As the definition of the partial safety factors is a responsibility of each European country (Nationally Determined Parameter) the establishment of a minimum numerical value for this partial safety factor is extremely important for the national standards bodies.

In this work a reliability class RC2 and a consequence class CC2 (EN-1990 2002) were considered, which corresponds to a minimum value for the reliability index of 3.8 associated with a 50 year reference period, as defined in the background documents to support the implementation, harmonization and further development of design rules for plated structural elements (Johansson 2007).

The test results used to evaluate the partial safety factor were obtained from the experimental test programs conducted at the Research Institute of Industrial Science and Technology (RIST) in the Republic of Korea, carried out by Choi et al. (2009), the Pontifícia Universidade Católica of Rio de Janeiro (PUC-Rio) in Brazil, carried out by Ghavami (1994), the National Maritime Research Institute (NMRI) in Japan, carried out by Tanaka & Endo (1988), and the University of Manchester (UM) in the United Kingdom. The experimental test program at UM has been divided into two phases, the first was carried out by Horne & Narayanan (1976) and the second was carried out by Horne et al. (1977).

It was not possible to use all the available test results because fourteen tests were carried out on specimens with amplitude values for the initial geometric imperfections outside the range considered in the design rules. Thus, only 42 of the 56 available test results were used for the statistical evaluation. The specimens T5 and T6 from RIST, the specimens P1R, P2T and P2R1T from PUC-Rio and the specimens 1, 14, 12, D22, D21, E23, E21, PF2 and SW6 from UM were excluded from the statistical evaluation.

Figure 4 presents the comparison between the ultimate strength results obtained by the design proposal with the test results. From the analysis of Figure 4 it can be noted that the design proposal provides viable and conservative results. A coefficient of variation of 11.2% for the comparison between the ultimate strength obtained by the design proposal and the test results shows a slightly larger scatter, but in the safety side.

According to EN-1990 (2002) and with the purpose of obtaining economic design models it is possible to divide the total test population into appropriate subsets. These subsets should be associated with parameters that have the greatest influence on the scatter. A total of 5 subsets were considered taking into account the following geometric parameters: the plate aspect ratio (ratio between the length a and the width b of the plate), the panel slenderness (λ_p), the relative cross sectional area (δ) and the relative flexural stiffness (γ); and the different specimen buckling behaviors. To consider the variability of the geometric and material

Table 1. Minimum values of the partial safety factor for the subsets of tests.

Subsets	Test program	Number of specimens	γ_M
1	RIST	13	1.09
2	RIST	3	0.74
3	NMRI	10	1.11
4	UM	14	1.10
5	UM	2	1.21

properties in the probabilistic model of the resistance the following variation coefficients were taken into account (Johansson et al 2007): 0.07 for the yield stress; 0.03 for the plate thickness; 0.01 for the plate length; and 0.01 for the plate width.

In Table 1 are presented the minimum values of the partial safety factor (γ_M) for the subsets of tests obtained by statistical evaluation according to the probabilistic reliability theory established in EN-1990 (2002).

From the analysis of Table 1 it can be verified that a numerical value of 1.10 for the partial safety factor ($\gamma_M = 1.10$) is consistent with the experimental test results, which is the recommended numerical value for the partial factor for resistance of members to instability assessed by member checks (γ_{M1}) on bridges (EN-1993-2 2006). Just the subset 5 shows a significant difference for the partial safety factor of 1.10. This is however not a serious indication because this subset is not representative, since it has a small numbers of tests.

3.4 *Comparison with nonlinear analysis and current bridge design rules*

The comparison between the ultimate strength (σ_u) obtained using the design proposal with that obtained using nonlinear analyses and current bridge design rules established in the European and American standards (EN-1993-1-5 2006, AASHTO-LRFD-BDS 2007) was performed considering 20 stiffened flanges. The 20 stiffened flanges were obtained based on two types of cross-sections, SF1 and SF2, and considering for each cross-section the plate aspect ratio ϕ ($= a/b$) ranging from 0.5 to 5.0 at intervals of 0.5. Both cross-sections have five longitudinal equally spaced and single sided stiffeners, the stiffened flanges with the cross-section SF1 have a relative flexural stiffness γ ($= 12I_{st}(1-\nu^2)/(bt^3)$) of 65 and the stiffened flanges with the cross-section SF2 have a relative flexural stiffness γ of 130. All stiffened flanges have a relative cross-sectional area δ ($= A_{sl}/(bt)$) of 0.5, plate slenderness λ_{plt} ($= b/t$) of 150 and panel slenderness λ_p ($= b_p/t$) of 25.

The nonlinear analyses were performed using the semi-analytical model presented in the work of Ferreira (2012) and considering a yield stress (f_y) of 355 Nmm^{-2}, Young's modulus (E) of 2.1×10^5 Nmm^{-2} and Poisson's coefficient (ν) of 0.3.

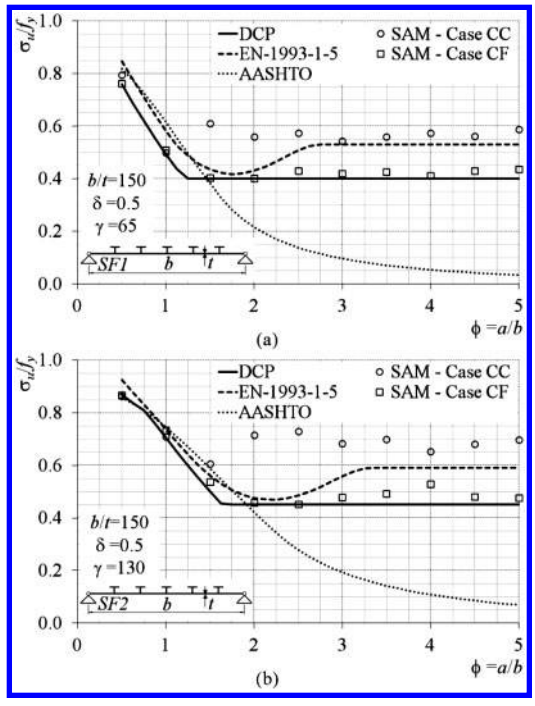


Figure 5. Comparison between the ultimate strength obtained by the design proposal (DCP), the semi-analytical model (SAM) and current bridge design rules for the stiffened flanges with the cross-section: (a) SF1 and (b) SF2.

The stiffened flanges were considered simply supported under longitudinal uniform compression (σ) with the following two cases for the in-plane displacement boundary conditions: in-plane displacements perpendicular to the edges constrained to remain straight in all edges (case CC) and in-plane displacements perpendicular to the edges constrained to remain straight at loaded edges and free at unloaded edges (case CF).

Figure 5 presents the comparison between the ultimate strength (σ_u) obtained by the design proposal, the semi-analytical model and current bridge design rules. Figure 5a shows the ultimate strength for the stiffened flanges with the cross-section SF1 and Figure 5b shows the ultimate strength for the stiffened flanges with the cross-section SF2. The results are presented in terms of normalized strength (mean compressive stress at peak load σ_u to the yield stress f_y ratio) for different values of the plate aspect ratio ϕ ($= a/b$).

From the analysis of Figure 5 it can be noted that the ultimate strength (σ_u) obtained by the design proposal presents a much better agreement with the nonlinear analysis results obtained by the semi-analytical model considering the case CF for the in-plane displacement boundary conditions than the ultimate strength obtained by the current bridge design rules. This observation is particularly clear in the case of long plates, where the design rules established by the European standard leads to nonconservative results and

the design rules established by the American standard leads to extremely conservative results.

4 CONCLUSIONS

From this study the main conclusions can be summarized as follows: (i) the ultimate strength (σ_u) obtained using the design proposal is in agreement with the test results and the main differences are in the safety side, (ii) the numerical value of the partial safety factor (γ_M) for the design proposal is 1.10, (iii) the ultimate strength obtained using the design proposal is in close agreement with the results obtained using the semi-analytical models considering fully free in-plane displacements at longitudinal edges and (iv) it presents a much better agreement with the results obtained using the semi-analytical model considering fully free in-plane displacements at longitudinal edges than the ultimate strength obtained with the current bridge design rules.

The design proposal predicts the ultimate strength (σ_u) in a quick and simple way and provides viable and conservative results, which thus proves its usefulness as a design tool.

ACKNOWLEDGEMENTS

This work was carried out in the framework of the research activities of ICIST, *Instituto de Engenharia de Estruturas, Território e Construção* and was funded by FCT, *Fundação para a Ciência e Tecnologia*.

REFERENCES

AASHTO-LRFD-BDS. 2007. *AASHTO LRFD Bridge Design Specification*. Washington: American Association of State Highway and Transportation Officials.

Braun, B. 2010. *Stability of steel plates under combined loading*. PhD thesis. Stuttgart: University of Stuttgart.

Choi, B. & Hwang, M. & Yoon, T. & Yoo, C. 2009. Experimental study of inelastic buckling strength and stiffness requirements for longitudinally stiffened panels. *Engineering Structures* 31: 1141–53.

ECCS Committee8. 1976. *Manual on Stability of Steel Structures*. ECCS publication 22. Brussels: ECCS.

EN 1990. 2002. *Eurocode – Basis of structural design*. Brussels: European Committee for Standardization.

EN-1993-1-5. 2006. *Eurocode 3 – Design of Steel Structures – Part 1-5: Plated Structural Elements*. Brussels: European Committee for Standardization.

EN-1993-2. 2006. *Eurocode 3 – Design of Steel Structures –Part 2: Steel Bridges*. Brussels: European Committee for Standardization.

Ferreira, P. 2012. *Stiffened compression flanges of steel box girder bridges: postbuckling behaviour and ultimate strength*. Ph.D thesis. Lisbon: Instituto Superior Técnico, Technical University of Lisbon.

Ferreira, P. & Virtuoso, F. 2011. Efeito do tipo de restrição nos bordos longitudinais no comportamento e resistência de placas metálicas em pontes. In L. Simões da Silva, P. Cruz, N. Lopes, J. Fernandes, and A. Baptista (ed.), *Proceedings of the 8th Conference on Steelwork Construction, Guimarães, 24-25 November 2011.* Coimbra: CMM and University of Minho. (in Portuguese)

Ferreira, P. & Virtuoso, F. 2010. Collapse load of box flanges with longitudinal stiffeners under uniform compression: comparative study of EC3 and AASHTO LRFD bridge design rules with nonlinear finite element analysis. In N. Yardimci, B. Aydöner, Y. Gür'es, and C. Yorgun (ed.), *Proceedings of the International Symposium on Steel Structures: Culture & Sustainability, Istanbul, 21-23 September 2010*. Istanbul: TUCSA and ECCS.

Galambos, T. 1998. *Guide to Stability Design Criteria for Metal Structures*. New York: John Wiley & Sons, Inc.

Ghavami, K. 1994. Experimental study of stiffened plates in compression up to collapse. *Journal of Constructional Steel Research* 28: 197–221.

Horne, M. & Montague, P. & Narayanan, R. 1977. Influence on strength of compression panels of stiffener section, spacing and welded connection. *ICE Proceedings* 63: 1–20.

Horne, M. & Narayanan, R. 1976. Ultimate capacity of longitudinally stiffened plates used in box girders. *ICE Proceedings* 61: 253–80.

Johansson, B. & Maquoi, R. & Sedlacek, G. & Müller, C. & Beg, D. 2007. *Commentary and worked examples to EN 1993-1-5 "Plated Structural Elements"*. Joint Report EUR 22898 EN, Luxembourg: Joint Research Centre and ECCS.

Tanaka, Y. & Endo, H. 1988. Ultimate strength of stiffened plates with their stiffeners locally buckled in compression. *Journal of the Society of Naval Architects of Japan* 164: 456–67. (in Japanese)

Research and Applications in Structural Engineering, Mechanics and Computation – Zingoni (Ed.)
© 2013 Taylor & Francis Group, London, ISBN 978-1-138-00061-2

Fatigue life assessment of existing motorway bridge

L. D'Angelo, A. Nussbaumer, M.-A. Fénart & A.-G. Dumont
Ecole Polytechnique Fédérale de Lausanne, ENAC-LAVOC, Switzerland

ABSTRACT: The aim of this paper is to provide a fatigue-life assessment of an existing composite steel-concrete bridge within Switzerland. The Venoge bridgeis a 219 meters length, four spans, four girder composite bridge, situated on the Geneva-Lausanne Swiss motorway. Stress response influence lines at fatigue critical details are characterized with a refined three-dimensional (3-D) Finite Element (FE) model that takes into account the effective transverse load repartition and the cracking of the concrete slab; the model is further validated using strain gauge measurements. Real traffic simulations are run to get the effective traffic histograms on the bridge. Weigh in Motion (WIM) data from the Denges station (1 km from the bridge) are used as input for the simulations. The effective slow lane position over the bridge section is taken in account and future traffic increase is considered. The fatigue failure probability of the bridge at a critical location under the long-term effect of highway traffic is calculated by defining a limit state function for fatigue reliability analysis. The results show that fatigue is not a concern for the Venoge bridge, even though particular attention has to be paid to future change in traffic lane configurations which could require re-consideration of the fatigue critical details.

1 INTRODUCTION

Reliable consideration of infrequent loads (rare extreme loads) is a technical challenge in the fatigue-life assessment of motorway bridges. In fatigue analysis, the proper evaluation of these extreme loads which lie near the fatigue constant amplitude limit (CAFL) is of fundamental importance. A small error in the load definition can result in a significant error in estimation of the bridge fatigue life. Weigh-in-motion (WIM) technology combined with traffic simulation tools is a solution to the problem.

WIM devices can capture static vehicle axle weights, which allow for characterization of traffic demands. Collected WIM data provide information on the frequency distribution of total gross weight, axle group weight, and axle distance. Prior to recent years, probabilistic approaches were used to find rare extreme load events and extrapolate them to longer time periods (i.e. one recorded week extrapolated to 120 years) (Bailey, 1996) (Crespo-Minguillón & Casas, 1997) (Meystre & Hirt, 2006); however, recent improvements in data storage, traffic simulators, and WIM technologies provide a deeper understanding of extreme load events (recorded traffic data of one or more years).

In this study, a traffic simulation software (AIMSUN (TSS Transportation Simulation System, 2011)) is coupled with Monte-Carlo Simulations (MCS) and finite element (FE) analysis to assess fatigue life of an existing motorway bridge within Switzerland. The chosen bridge is located on the A1 Swiss Motorway between the high population areas of Lausanne and Geneva and hereafter referred as the Venoge bridge.

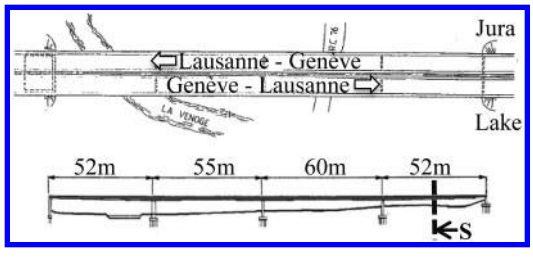


Figure 1. Venoge bridge: in plain view and elevation.

The Venoge bridge consists of two identical independent bridges (one for each direction) with a 219 meter length divided in four spans (see Figure 1). Each bridge was constructed in 1961 with two girders and then enlarged in 1995 to four girders (see Figure 2). Due to symmetry, only the bridge with traffic in the Lausanne-Geneva direction is considered in this study.

Two fatigue critical locations within the bridge are identified by inspection: 1) the stiffener weld attachment at the girder lower flange (location B in Figure 2) at the middle of the first span (FAT 56 according to EN 1993-1-9 table 8.4 (Eurocode EN 1993, 2005)); and 2) the cover plate weld attachment at the girder lower flange (location C in Figure 2) at the middle of the first span (FAT 40 according to EN 1993-1-9 table 8.5 (Eurocode EN 1993, 2005)). Due to the slow lane location over the enlarged bridge section (girders A and B in Figure 2), the majority of traffic is supported by girder B; therefore, detail 1 was chosen as the critical location for the fatigue failure analysis in this study.

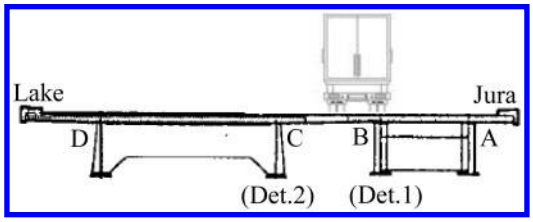


Figure 2. Bridge's section at the first mid-span: candidate fatigue critical locations.

2 FATIGUE RELIABILITY ANALYSIS

2.1 *Problem definition*

This section discusses the framework for the fatigue reliability analysis of the Venoge bridge, under the long-time effect of highway traffic. Due to the inherent randomness of traffic loading and detail fatigue strength, a probabilistic model has to be established. Probability of fatigue failure is associated with the evaluation of a limit state function that correlates the fatigue resistance and the fatigue loading for the considered critical fatigue detail.

Fatigue tests of structural steels for variable amplitude (VA) stress ranges, show that if the maximum stress range $\Delta\sigma_{max}$ stay below the CAFL of EN 1993-1-9 standard bilinear fatigue strength curves, then the life of a structural detail tends to be infinite; this observation can be used for the following verification:

$$\Delta\sigma_{max} \leq \Delta\sigma_D \tag{1}$$

Given that the stress time history at the fatigue critical detail is a stochastic process, the maximum stress range $\Delta\sigma_{\max}$ turns out to be a random variable. Regarding fatigue resistance, the CAFL value is also considered as a random variable. By considering these two random variables, a fatigue failure probability function can be defined as follows:

$$P_f = \int_{g(x,\boldsymbol{\theta}_g)\leq 0} f_{\mathbf{X}}(x,\boldsymbol{\theta}_f)dx \tag{2}$$

where $\mathbf{X} = (\Delta\sigma_D, \Delta\sigma_{\max})$ is a two-dimensional vector of random variables with continuous joint density function $f_{\mathbf{X}}(x,\boldsymbol{\theta}_f)$, where x is a realization of the random vector and $\boldsymbol{\theta}_f$ is a vector of distribution parameters. Failure is defined in terms of a limit-state function $g(x,\boldsymbol{\theta}_g) = \mathbf{X}_1 - \mathbf{X}_2$, where $\boldsymbol{\theta}_g$ is the vector of limit-state function parameters. The fatigue failure probability P_f can be related to the reliability index β as follows:

$$P_f = \mathrm{F}(-\beta) \tag{3}$$

where F is the cumulative distribution function of a standard normal distribution.

In this analysis EN 1993-1-9 double slope (m = 3, k = 5) standard fatigue strength curves are used. According to Table 8.4 in (Eurocode EN 1993, 2005), the considered fatigue critical detail is classified as FAT 56. The $\Delta\sigma_D$ can be regarded as a random variable modeled by a lognormal distribution with mean value μ_{RI} of 4.257 and standard deviation σ_{RI} of 0.113 (Technical European Convention for Constructional Steelwork – TC6, 1985); the parameters of the $\Delta\sigma_{max}$ probability distribution can be estimated through the following steps(details are given later in Section 3):

1. Randomly generate bridge load time-history samples by using the traffic simulation software and WIM -Swiss Automatic Road Traffic Data Collection (SARTC) database
2. Compute the stress-time response samples, at the fatigue critical location, using FE analysis;
3. Compute the stress-range spectrum samples, at the fatigue critical location, using the rain flow counting method;
4. Estimate the maximum stress range $\Delta\sigma_{max}$ probability distribution parameters, by using MCS.

2.2 *Reliability analysis – FORM method*

Once the probability distribution parameters of the random variables have been defined, then the problem structure is implemented in a Matlab code using the FERUM open source toolbox (Bourinet, Mattrand, & Dubourg, 2009). The fatigue reliability problem of Equation (1) is transformed from the original space of random vector $\mathbf{X}$ to a standard normal space. Following the failure probability P_f and the related reliability index β are estimated using the First-Order Reliability Method (FORM).

3 PROBABILISTIC LOAD MODEL

3.1 *Highway traffic simulation*

In order to get a realistic time-history of bridge crossing vehicles, traffic simulations were developed in the EPFL LAVOC laboratory, using the AIMSUN software. This software enables simulation of traffic flow in a road network, with the possibility to set up vehicle specifications and lane characteristics, to include driver behavior models in the software catalogue and to analyze different traffic scenarios (i.e. accidents, lane closures).In the first version of the traffic model, a linear highway network with a 3 km length,2000 vehicles per hours per lane (vph/pl) total capacity and 120 km/h speed limit was modeled; bridge is considered as a single point in the network. Following classes of vehicles were introduced in the software catalogue:

- Six classes of light vehicles (from motorbike to delivery vehicles);
- Thirteen classes of heavy vehicles with gross vehicle weight (GVW) higher than 10 tons (Table A.2 in (Meystre & Hirt, 2006));
- Two classes of heavy vehicles with GVW lower than 10tons (coaches, buses and trucks, road trains and articulated vehicles);

Since the lateral distribution of heavy vehicles on the bridge section is not currently known, a

conservative hypothesis was made: all the heavy vehicles of more than 10 tons detected by WIM circulatein the slow lane.

A statistical study based on data from Swiss Automatic Road Traffic Data Collection (SARTC) in Préverenges station (A1 Lausanne-Geneva direction, 2008) and from WIM in Denges station (A1 Lausanne-Geneva direction, 2008), was carried out to determine the class, the free flow speed distributions and the average time allocation for each vehicle class; Denges 2008 WIM database was chosen because it is the most recent available complete database.

Traffic simulation is based on origin-destination (O/D) matrices representing a standard week from year 2008; probability distribution of heavy cars was calibrated in terms of vehicle flow, by using empirical measurements for year 2008.

As it was aforementioned, a typical week of 2008 was simulated, as well as a forecasted week for 2012, assuming a 13.3% growth rate of traffic (3.3% per year), calculated from SARTC data of 2012. Simulated data (vehicle class, speed, and bridge crossing time)were used as input for fatigue analysis.

3.2 *Weekly stochastic stress response*

Simulated data for a typical week of 2008 (or forecasted week of 2012) were coupled to vehicle total length (TVL), vehicle axle spacing (AVS),vehicle gross weight (GVW) and vehicle axle load (AVW) information recorded by the WIM Denges station over the year 2008, in order to build the bridge traffic loading time history. Only heavy vehicles with a GVW over than 10 tons were involved in the calculation because lighter vehicles give a negligible contribution to the bridge fatigue damage. Simulation of one-week continuous traffic was performed using AIMSUN traffic simulator.

The simulation output is a bridge crossing-time sheet, which gives information on vehicle class, speed and arrival time. One sample of the bridge loading time history for a typical week of 2008 (or forecasted week of 2012) was calculated through the following steps:

1) The TVL and GVW histograms from WIM database were fit to standard probability distributions for each vehicle class;
2) TVL and GVW were randomly generated for each crossing vehicle by using fitted probability distributions generated at point 1);
3) the AVS and AVW histograms from WIM database were fit to the AVS-TVL and AVW-GVW relationship equations for each vehicle class, and;
4) the AVS and AVW were randomly generated for each crossing axle using equations

Generation of two hundred loading time-history samples was performed following the above steps. A3-D refined FE model of the bridge, which takes into account the effective transverse load repartition and the cracking of the concrete slab, was used to compute the nominal stress range influence line at the critical fatigue location (detail 1 in Figure 2); the FE model was calibrated and validated using experimental results from bridge static tests (Burdet, 1997). MSC/Nastran (MSC Software, 2012) was used for the analysis. The $\Delta\sigma_{norm}$ influence line and the loading time-history samples were then used to compute two hundred weekly stress response samples Tw_j both for a typical week of 2008 and for a forecasted week of 2012 (see Figure 3).

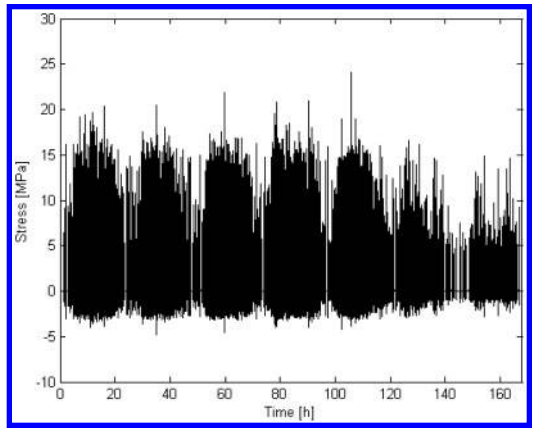


Figure 3. Sample of traffic-induced time stress response Tw_{2012}.

3.3 *Probability distribution of the maximum stress ranges*

3.3.1 *No traffic growth*

A rain flow counting algorithm and MCS were used to determine time invariant $\Delta\sigma_{max}$ probability distribution parameters at the failure critical location (detail 1 in Figure 2), assuming no future traffic evolution.

Two-hundred $Tw_{2012,j}$ were computed at the critical structural detail and two-hundred samples of $\Delta\sigma_{2012,j}$ were then obtained by application of a rain flow counting algorithm. Following, the generalized extreme value (GEV) probability distributions family was considered to model the upper bound of each stress range sample.

Type III GEV distribution (log-Weibull distribution with location parameter $\zeta = 0$) was fit to data using MLE. The scale parameter, λ_{lW}, is 3.39 and the shape parameter, k_{lW}, is 57.76. To visually assess the goodness of fit, the fitted probability density function (PDF) and the fitted cumulative distribution (CDF) function are shown in Figures 4 and 5.

3.3.2 *Linear traffic growth pattern*

Considering that the highway traffic may increase in the future, a time-dependent $\Delta\sigma_{max}$ probability distribution was computed assuming that distribution parameters have a linear growth pattern (conservative hypothesis). Using the approach described in section 3.3.1 two different $\Delta\sigma_{max}$ GEV probability distributions were estimated from $\Delta\sigma_{2008,j}$ and

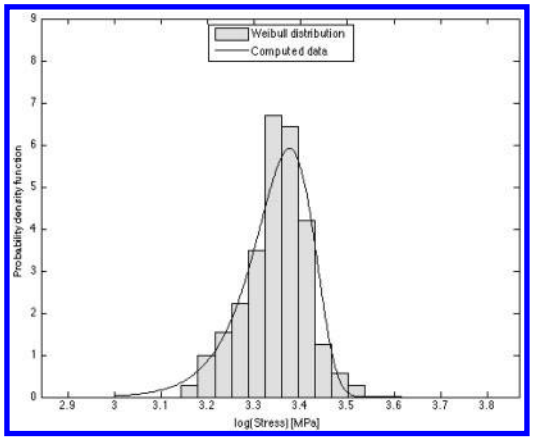


Figure 4. PDF of the $\Delta\sigma_{max2012}$ random variable.

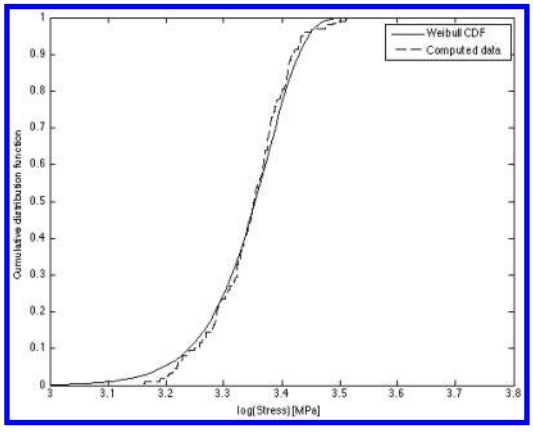


Figure 5. CDF of the $\Delta\sigma_{max2012}$ random variable.

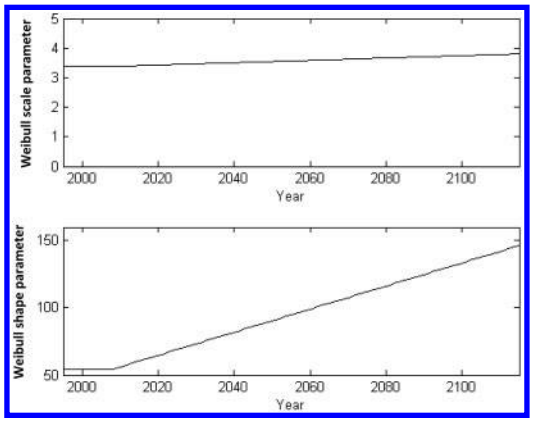


Figure 6. Time evolution of $\Delta\sigma_{max}$ distribution parameters.

$\Delta\sigma_{2012,j}$ samples. Following, the slope of the time-dependent $\Delta\sigma_{max}$ probability distribution parameters were calculated by linear interpolation.

As shown in Figures 6 and 7, no traffic growth was assumed between 1995 and 2008.

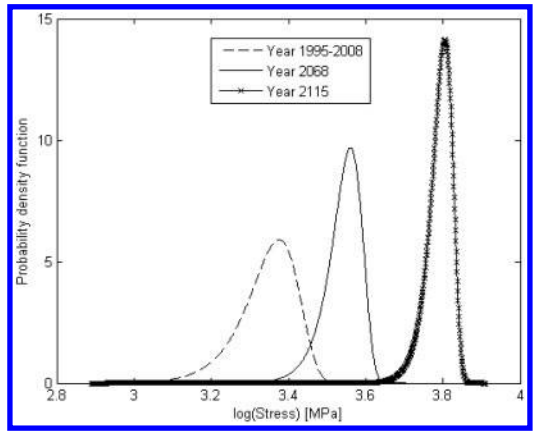


Figure 7. PDF of the time-dependent $\Delta\sigma_{max}$ random variable.

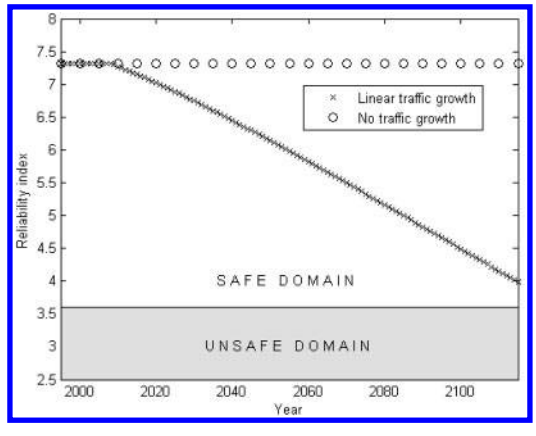


Figure 8. Fatigue reliability index evolution.

4 RELIABILITY ANALYSIS RESULTS

On the basis of the limit-state equation defined in Equation (2) and of the probabilistic load model defined in Section 3, the failure probability P_f at the fatigue critical location and the related reliability index β were computed for two considered future traffic evolution scenarios. Assuming no future traffic growth, the reliability index β at the end of the bridge design-life is equal to 7.31 (corresponding to a failure probability P_f lower than 0.0001%). When assuming a linear traffic growth pattern (see Section 3.3.2) the reliability index β at the end of the bridge design-life is 3.98 (corresponding to a failure probability P_f of 0.0035%). For reference, a target reliability index value of 3.6 is recommended from article C6 in (Eurocode EN 1990, 2001) for 120 year design life where inspections are not planned. The value of the computed β at the end of the 120 year design life is higher than the reference value, as shown in Figure 8.

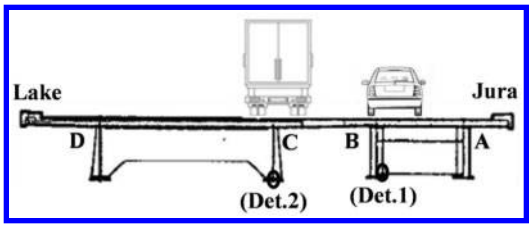


Figure 9. Future lane change.

5 TRAFIC SIMULATION DEVELOPMENTS AND POTENTIAL FOR FUTURE ADVANCES

While the AIMSUN software allows for generation of realistic traffic in a road network, the first version of the traffic model (the version used herein) is limited to linear network simulation with all heavy vehicles placed in the slow lane and it needs a post processing to include vehicle lengths, weights and axle spacing. Future versions of the model under development will overcome these limitations and allow simulation of special events like a lane closure or the opening of a new highway exit. The lateral positioning of heavy vehicles is being studied using video recording: collected data will be used to define realistic vehicle lateral distribution on the bridge section.

Particular attention has to be paid to these "special" events because they could require the re-consideration of the fatigue critical locations and or re-definition of the limit state function. A lane configuration change as shown in Figure 9, would result in FAT 40 detail 2 as the critical fatigue location and require a re-definition of the limit state function in terms of accumulated damage (given that a considerable amount of cycles could be higher than the CAFL).

The reliability analysis framework set up in this paper and the realistic traffic simulator constitute two powerful tools to perform fatigue reliability analysis of road bridges for any future traffic evolution scenario and for several special events simulation.

6 CONCLUSIONS

In this paper a framework for the fatigue reliability analysis of a highway bridge has been formulated in terms of a limit state function that describes the relationship between the fatigue strength of a selected critical detail and the maximum stress range. The framework has been applied to the Venoge bridge within the A1 Swiss Motorway. A traffic simulator tool, WIM database, and FE analysis were combined to compute the time-stress response at the fatigue critical location. MCS has been used to define parameters of the maximum stress-range probability distribution. Finally, the fatigue failure probability and a related reliability index are calculated at the end of the bridge design life. The results show that fatigue is not a concern for the Venoge bridge over the considered 120 year design life, evident by a reliability index greater than the target reliability index (3.98 compared to a target value of 3.6, see again Figure 8). Particular attention is needed however, for future changes in traffic lane configuration, which could require re-consideration of fatigue critical locations and re-definition of limit state function.

REFERENCES

Bailey, S. F. (1996). *Basic principles and load models for the structural safety evaluation of existing road bridges*. Ecole Polytechnique Fédérale de Lausanne.

Bourinet, J. M., Mattrand, C., & Dubourg, V. (2009). A review of recent features and improvements added to FERUM softwares (ICOSSAR'2009). *10th International Conference on Structural Safety and Reliability*. Osaka.

Burdet, O. (1997). *Pont sur la Venoge (VD) côté Jura , après la solidarisation, Rapport d'essai de charge statique*. Lausanne.

Crespo-Minguillón, C., & Casas, J. (1997). A comprehensive traffic load model for bridge safety checking. *Structural Safety*, 19(4), 339–359.

Eurocode EN 1990. (2001). Basis of structural design. Bruxelles: European Committee for Standardization.

Eurocode EN 1993. (2005). Design of steel structures - Part 1-9: Fatigue. Bruxelles: European Committee for Standardization.

Meystre, T., & Hirt, M. A. (2006). Evaluation de ponts routiers existants avec un modèle de charge de trafic actualisé, Mandat de recherche AGB 2002/005. Lausanne: Office Fédérale des Routes (OFROU).

MSC Software. (2012). MSC Nastran Quick Reference Guide. Santa Ana: MSC Software.

Technical European Convention for Constructional Steelwork – TC6. (1985). Recommendations for the fatigue design of steel structures.

TSS Transportation Simulation System. (2011). Aimsun Version 6.1 User's Manual. Barcelona: TSS Transportation Simulation System.

Research and Applications in Structural Engineering, Mechanics and Computation – Zingoni (Ed.)
© 2013 Taylor & Francis Group, London, ISBN 978-1-138-00061-2

Comparing two types of fatigue and tsunami resisting medium span bridges

Ph. Van Bogaert
Ghent University, Belgium

ABSTRACT: Two alternatives of medium span steel railway bridges have been considered to be reinforced from common design conditions to resist tsunami load. The tropical cyclone method is being used to assess the effect of tsunami impact. Verification demonstrates that the effects of surge impact and the post-wave action are different for a plate girder and truss type bridge. This also applies to the effect of the debris force and overturning of the train vehicles. For moderate span, the plate girder bridge needs far less reinforcement than the truss bridge and is easier to adapt. A discussion about the scale effect is also added.

1 INTRODUCTION

1.1 *Tsunami resistance*

Although this type of disaster has been known throughout history, the major disasters of the last decades have made tsunami waves again a relevant accidental load for structures. This paper does not aim at closely simulating the effects of tsunami waves or define approaches for that purpose. It merely tries to discuss a conceptual question, whether two types of medium-span bridges are able to resist both frequent loading conditions, such as fatigue as well as an accidental situation, caused by an average tsunami impact. This problem was initiated by a steel fabricator who was asked to deliver such a comparison for a pacific railway company, renewing its oldest bridges. The results of this comparison are delivered in this paper and may show a somewhat surprising result.

1.2 *Bridge replacement conditions*

Since the railway company was replacing more than 40 bridges of various spans, the present study needed to focus on one particular span range. For this, a typical bridge of 38.1 m span has been considered. In addition, the railway loading corresponds to LM 71 according to Eurocode 1 (EN 1991-2 2003), including the requirements for fatigue resistance.

The bridges to be replaced are mostly dating from the late 19th or early 20th century, and although they have been well kept, they are showing major corrosion. In addition, the design loads are unknown and there may be doubt whether these structures comply with the requirements of modern train vehicles. Fig. 1 shows a typical bridge of the truss-type. Other bridges have plain web girders. It may be noticed that only few bridges have ballast track, wooden sleepers being mostly fixed to the steel structure.



Figure 1. Typical truss girder bridge with wooden sleepers.

2 TSUNAMI LOAD

2.1 *Tropical cyclone method*

Various methods have been developed quantify the effect of tsunami loads on buildings. The method described by in (Yeh 2007), seems at present the most complete, since it distinguishes the various origins of this type of load. This method was derived from the effect of tropical cyclones. It involves the hydrostatic force, the hydrodynamic drag, the surge impingement effect, as well as the buoyancy and debris forces. The latter forces do not necessarily occur simultaneously with other effects, since they show a delay compared to the actual impact (Yamamoto et al 2006).

2.2 *Hydrostatic force*

The equivalent hydrostatic force acting on a plain panel of width b and height h_w is given by equation 1. In this expression h is the height of the tsunami

wave, whereas ρ is the water density and g the gravity acceleration.

$$F_h = \rho g \left(h - \frac{h_w}{2} \right) b\, h_w \quad (1)$$

Elementary quantification of the tsunami force increase the value of h up to 2.5 or 3 times the actual height of the tsunami wave. In the tropical cyclone method, other parameters are used.

2.3 *Hydrodynamic drag*

The effect of the wave speed is found through the hydrodynamic flow force of equation 2. In this A is

$$F_d = \frac{1}{2} \rho\, C_d\, A\, u_p^2 \quad (2)$$

the projected area perpendicular to the direction of flow, C_d is the drag coefficient and u_p is the flow velocity. The drag coefficient depends on the shape and roughness of the object. For a rectangular shape this coefficient equals approximately 2 (Fujima et al 2009). To determine the flow velocity, it may be assumed that the tsunami wave progresses on a river and constitutes a shallow water waver. The velocity of this type of waves can be found from equation 3.

$$u_p = \sqrt{g\, d_s} \quad (3)$$

2.4 *Surge impingement force*

This is the hydrodynamic force of the leading edge of the tsunami wave. It is determined using equation 4. Herein C_I is the impingement factor and h the

$$F_I = C_I\, \rho\, g\, h^2 \quad (4)$$

In literature (Palermo et al 2008a, b) a value of 4.5 for C_I may be found. According to some authors this value is conservative and overestimates the impingement force.

2.5 *Buoyancy force*

The buoyancy force is an uplift effect due to the sudden rise of the water level below the structure. It is found from equation 5 in which V is the water

$$F_B = \rho\, g\, V \quad (5)$$

volume displaced by the bridge itself. In the case of the open, ballastless structures being discussed, the value of V is rather low and the buoyancy is limited. In fact, it is totally being compensated by the structure's dead weight.

2.6 *Debris force*

This force is caused by water-borne objects, such as boats, vehicles and driftwood, hitting the bridge. There are various methods to determine this force. Among them is the stiffness approach, which is recommended for driftwood. The debris force becomes

$$F_{debris} = C_M\, u_p \sqrt{;\, k\, m} \quad (6)$$

C_M being a mass coefficient, u_p the flow velocity, k the effective stiffness and m the mass of the debris. A reasonable value for C_M is 2 and k equals 2.4 MN/m. The Honolulu building code gives a value of 455 kg for the mass m (Santo et al 2010).

Table 1. Tsunami pressures.

Effect		Pressure
Hydrostatic	F_h	24.53 kN/m^2
Hydrodynamic drag	F_d	49.05 kN/m^2
Surge impingement	F_I	198.65 kN/m^2
Initial impact	F_{1L}	198.65 kN/m^2
Post impact	F_{1P}	73.58 kN/m^2

2.7 *Combination of tsunami effects*

The previously mentioned effects do not occur simultaneously during tsunami impact. Two phases should be distinguished : the initial impact and the post wave impact. During the initial impact, the surge impingement force is possible accompanied by the debris force, according to equation (7), whereas subsequently the combination of hydrostatic force, hydrodynamic force, buoyancy and debris force can act together, according to equation 8.

$$Phase\ 1: \ F_I + F_{debris} \quad (7)$$

$$Phase\ 2: \ F_h + F_d + F_B + F_{debris} \quad (8)$$

In this study, the tsunami height has been assumed to reach 4.5 m according to (Shoh et al 2007) the wave velocity being 7 m/s. Obviously, more extreme values may be considered. These assumptions render the pressures mentioned in table 1 and the resulting combinations.

3 PLATE GIRDER BRIDGE

3.1 *Initial design*

If no tsunami load is considered, the various effects are dead weight, permanent rail loading, vertical and horizontal train loading and wind. The analysis of the FE model shown in Figure 2, reveals that fatigue is the critical condition. This is explained by the large proportion of the variable load, since the dead loads are rather small.

The numerical model clearly shows the main girders and crossbeams, which are at the distance of 3.81 m and are connected to the vertical stiffeners. The open

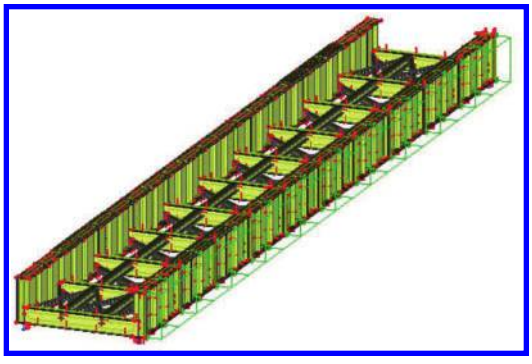


Figure 2. FE-model of plate girder bridge.

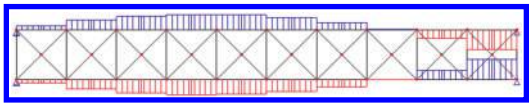


Figure 3. Lower bracing.

deck structure also contains stringers below the rails. The latter are uninterrupted at the intersection with the crossbeams.

3.2 *Adapting to resist tsunami effects*

Applying tsunami loads to the plate girder alternative shows that the critical situation occurs when the wave hits the main girder closest to the sea. This means that the opposite girder is not subjected to the wave impact. This condition is more important than the simultaneous action of wave impact on the reduced section of the second, land side girder and post impact force on the seaside girder.

The plate girder structure must be equipped with heavy horizontal bracing, since the seaside girder receives large compression, whereas the landside girder shows large tensile force. The horizontal bracing, including the normal forces is shown in Figure 2.

As can be seen in figure 3, the distribution of normal forces in the edge beams is not symmetrical. This is due to the fact that the horizontal restraining of displacements by the bearings is statically indeterminate, as the horizontal reactions influence the normal forces in the edge beams.

The most important result from tsunami loading is the heavy bending and possible crippling of the girder web. This has resulted in adding 1 or 2 vertical stiffeners to reduce the bending effect. As shown in Figure 4a, one additional stiffener does not resolve the problem, since the panel width equals its height and the panel is too large. In Figure 4b with two additional stiffeners, the ratio of width to height has been reduced sufficiently.

In addition, the local impact load of debris also necessitates reducing the panel length. The effect on plate stresses is shown in Figure 4c. However, after failure of this panel, the plate girder bridge remains

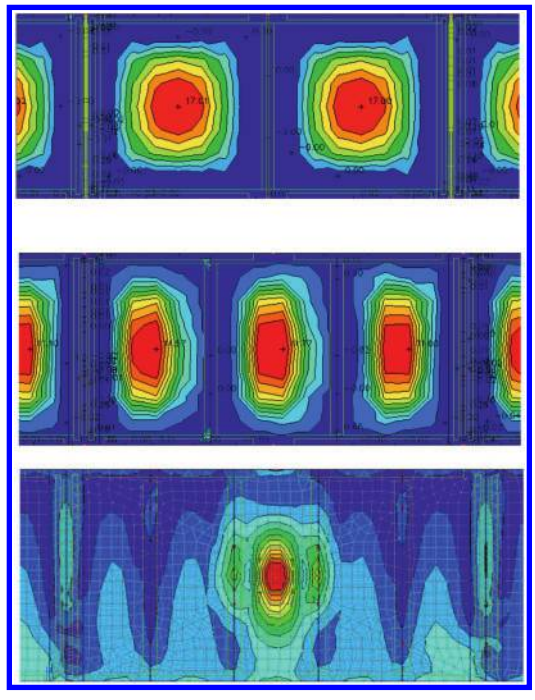


Figure 4a, b, c. Web plate stresses caused by surge load with 1 (a), and 2 (b) additional stiffeners and by debris force (c).

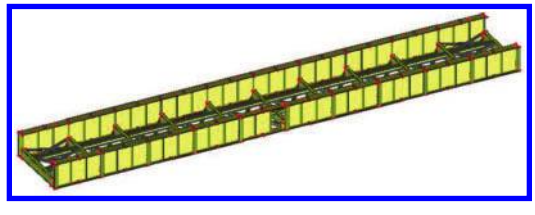


Figure 5. Bridge model with 1 plate panel failed.

capable to resist railway loading, this being verified by a numerical model with one panel being cut out as in Figure 5.

To conclude the case of the plate girder bridge, the case of simultaneous railway and tsunami loading has also been considered. However, the train loading will take a ψ-factor equaling 0.5. In this case, the additional stiffening becomes somewhat heavier. In particular, the intermediate stiffeners, which are simple vertical plates, are subjected to bending with respect to a horizontal axis.

The concept of using simple plate stiffeners for intermediate ones and more heavy stiffeners, including flanges at the location of crossbeams, shown both in Figure 6 (left and right) may seem old, yet it continues to be sensible, since the first type is easier to fabricate than the latter. Figure 6 shows for both types the stress state in case of simultaneous railway and tsunami load. It can be noticed that the plate stiffeners receive almost no contribution to resistance from the web plate.

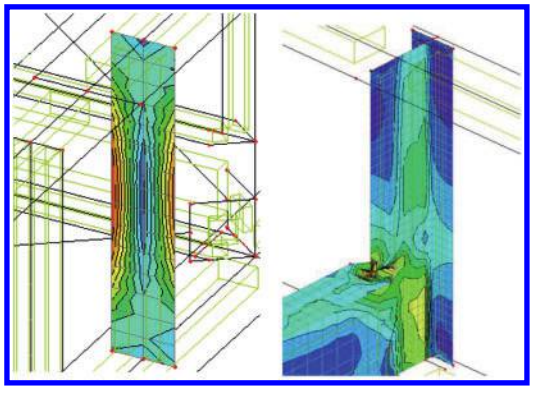


Figure 6. Plate and flange-type vertical stiffener.

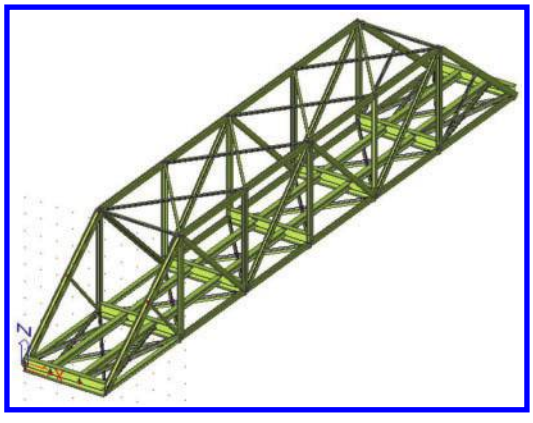


Figure 7. Truss bridge model.

4 TRUSS BRIDGE

4.1 *Initial design*

As in the former case, the design without tsunami load again shows that fatigue resistance is the critical condition. The stringers are being reinforced to resist the stress variations and crossbeams, which are at 6.1 m distance, also are determined by fatigue conditions, the category corresponding to 80 MPa.

As for the truss members, the second diagonal, as shown in Figure 7 is the most critical for fatigue.

The upper edge member is determined by buckling conditions at ultimate limit state, rather than fatigue resistance.

4.2 *Effects of tsunami load*

Calculations demonstrate that the tsunami load has maximum effect if the surge impingement hits the landside truss girder and the post-impact effects are acting on the seaside truss member. Again, the lower bracing becomes much heavier compared to the initial design and additional bars are needed. The outer diagonal members are subjected to heavy out-of-plane bending, since they act as a portal frame, together with

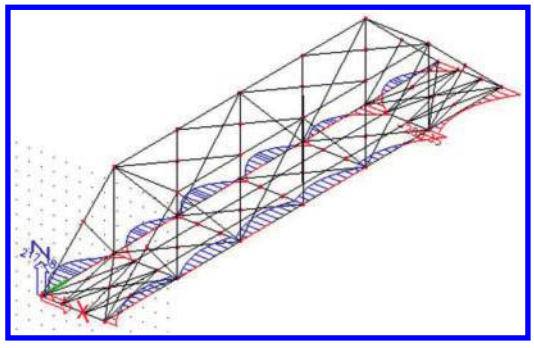


Figure 8. Lateral bending of lower truss member.

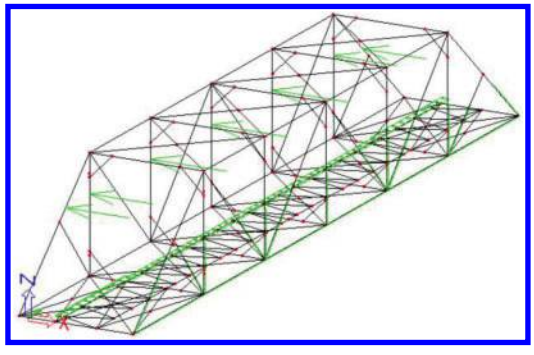


Figure 9. Truss bridge with debris force on members.

the edge crossbeams. These effects are due to global distortion of the truss bridge.

In addition, the seaside lower edge member becomes heavily compressed, a non-existing situation for the initial design. This causes a stability problem for the member, which needs excessive increase of the cross-section stiffness. The edge member is also subjected to bending, which is an unusual condition for normal truss bars. This is shown in Figure 8.

A particularly difficult problem is the debris force, causing concentrated loads on the vertical or diagonal members. Obviously, most members are indispensable and the strategy adopted for the plate girder bridge no longer applies. Hence, these members required larger reinforcement.

The combination of simultaneous train load and tsunami is more complicated for this truss bridge. As the rail vehicle is obstructing the impact of the wave, the vehicle is subjected to the surge. In these conditions, the vehicle will overturn and immediately hit the truss diagonal and vertical bars. This condition has also been considered, the loading case being shown in Figure 9.

In order to improve the distribution of loads, the width of the bridge needs to be increased, in this case up to 6.1 m. This results in higher resistance to horizontal loads.

As a result of the combined action of tsunami and railway load and the overturning of the rail vehicle is the need to add sloping bars in the edges of the portal

frames constituted of the vertical truss bars and bracings. This can also be seen in Figure 9. These additional bars are needed to resist the large bending moments at the frame angles, caused by the distortion effect.

5 DISCUSSION OF REINFORCEMENTS

5.1 *Plated girder bridge*

In this and the following sections, the overview of reinforcement of sections, due to tsunami loads are being discussed. For the case of the plated girder bridge, subjected to tsunami load without railway loading, the following members are affected.

- the longitudinal stringers are unaffected and continue to function as in the original;
- all crossbeams show sufficient resistance, apart from the edge crossbeam, which changes from HEA to HEB 700 profile;
- the primary lower bracing must be reinforced consistently from HEA 120 to HEM 220 profiles, as well as the bolted connections. However the height of secondary bars changes slightly from 100 to 120 mm.

If both the railway and tsunami loading are acting on the plated girder bridge, the following adaptations are necessary:

- the longitudinal stringers are still functioning in their original version;
- all crossbeams show sufficient resistance, apart from the edge crossbeam, which changes from HEA to HEB 700 profile;
- the primary lower bracing must be reinforced consistently from HEA 120 to HEM 240 profiles, as well as the bolted connections. However the height of secondary bars changes slightly from 100 to 120 mm

It should be remembered that debris force is critical for the web plate and will cause local damage.

5.2 *Truss bridge*

The difference between the original, fatigue resistant truss bridge and the structure, resisting to tsunami load alone, without railway loading can be summarized as follows:

- the longitudinal stringers have sufficient resistance in both cases, although the last sections near the bridge ends are heavier;
- summarized as follows:
- the edge crossbeams have to be increased, whereas normal crossbeams are satisfactory;
- the lower edge truss member needs considerable reinforcement from HEA 240 to HEM 500, also because it shows compression force instead of uniform tension;
- the upper edge truss member continues satisfying the requirements;
- the upper bracing as well as the lower bracing members become considerably heavier;
- the end portal frames and extreme diagonal bars are to be reinforced considerably.

If the same loading conditions are combined with the debris force, the following additional design revisions are necessary:

- the type of profile of the edge crossbeam needs serious revision, since a closed section of 750 mm width is needed;
- this also applies to the lower edge truss member, for which a closed section 750*300 mm becomes necessary;
- all diagonal truss members need serious reinforcement, although a change of type of profile is unnecessary;

Obviously the latter is due to the concentrated debris force, acting independently on the diagonal bars. If the combined effects of tsunami and train loading are considered, the following additional revisions proved to be necessary:

- the type of profile of all stringers needs to be changed to closed sections of 400*380
- the upper truss member also requires a hollow cross section of 300*300
- the first and last diagonal and vertical members must be changed to hollow section profiles of 600*600
- most importantly, the total width of the bridge should be increased to at least 6.1 m.

As a result of this, the tsunami and railway load resistant plate girder bridge's steel mass increases by 26%. In the case of the truss bridge adaptations to resist an identical combination, steel weight will increase by 80%, which further increases to 105% if debris force must be resisted.

5.3 *Scale effects*

The former calculations show that the plate girder alternative is more capable to be adapted to tsunami loading. However, the calculations concern a 38.1 m span bridge.

Should the span of the bridge be larger than the value being considered, under normal conditions a truss bridge should become more advantageous. The length of individual members increasing, the number of fatigue loading cycles should decrease. This particularly is in favour of the truss alternative.

Concerning the effect of tsunami loading, the height of a plate girder bridge will increase with the span, obtaining a larger impact surface for the surge wave. In addition, the span of the vertical stiffeners increases and the higher impact pressure, acting on longer stiffeners, will introduce larger stresses in these members. This will cause heavier reinforcement of the plate girder bridge.

In case of a truss bridge, the increase of span will necessarily require larger resistance of all members. The effect of tsunami will act on somewhat larger areas, although compared to the former case this size effect clearly is moderate. The same applies to the debris force and the train car overturning loads.

Consequently, the increase of steel mass for the plate girder will increase with the span more rapidly than for the truss alternative, which may very well reduce below 80 or 105%.

6 CONCLUSIONS

Two alternatives of medium span steel railway bridges have been considered to be adapted from common design conditions to resist tsunami load. These examples clearly demonstrate this aim certainly proved to be realistic.

Large uncertainty continues to exist about the magnitude of tsunami loads. The surge wave height and speed is a fundamental issue and some assumptions had to be made. In addition the debris force may be discussed, since it has large impact on both bridge types.

A plate girder bridge seems to be loaded by tsunami effects in a totally different way than the truss alternative. In the first case, the surge impact acts directly on the seaside girder, the landside girder being still unloaded. For the truss alternative the most critical condition corresponds to having initial impact on the landside truss and post-impact effect on the seaside girder.

Simulations for a 38.1 m span bridge have shown that the condition of tsunami loading, combined with railway loads will increase the steel mass by 26%, mainly due to adding vertical stiffeners of the girder webs and reinforcing the bracing. For the alternative of a truss bridge, the mass increase moves up to 105%. This demonstrates that the plate girder bridge performs better than the alternative.

Obviously, larger span bridges will show different results, and it is expected that gradually the truss bridge will perform much better.

REFERENCES

Eurocode EN 1991(2003). Eurocode 1 Actions on Structures – Part 2 Traffic loads on bridges. CEN-Brussels

Fujima,K., Achmad, F., Shigihara, Y., Mizutani, N. (2009) Estimation of tsunami force for rectangular structures. *Journal of Disaster Research* 4, n˚6.

Palermo, D., Nistor, I. (2008a). Tsunami-induced loading on structures. *Structure* march 2008, pp 10–13.

Palermo, D., Nistor, I. (2008b) Understanding tsunami risk to structures, a Canadian perspective. *Science of Tsunami Hazards* 27(4) pp 1–11.

Santo,J., Robertson, I. (2010). Lateral loading on vertical structural elements due to a tsunami bore. Research Rept Univ. of Hawai.

Yamamoto,Y., Takanashi,S., Hettrarachi,S., Samarawickrama,S. (2006). Verification of the destruction mechanism of structures in Sri Lanka and Thailand due to the Indian Ocean tsunami. *Coastal Engineering Journal*, JSCE 48(2) pp 117–146

Yeh, H. (2007). Design tsunami forces for onshore structures. *Journal of disaster research*, 2(6) pp 531–532

Research and Applications in Structural Engineering, Mechanics and Computation – Zingoni (Ed.)
© 2013 Taylor & Francis Group, London, ISBN 978-1-138-00061-2

Are short span reinforced concrete bridge girders cost effective?

T.N. Haas & D. Smith
Department of Civil Engineering, Stellenbosch University, South Africa

ABSTRACT: This study investigated the cost effectiveness of steel girders compared to the conventional reinforced concrete girders used in bridge construction in South Africa. The investigation considered an existing bridge which required widening as a result of increased traffic flow in close proximity to an industrial area. The consulting engineer specified the same reinforced concrete cross sections for the 10 m abutment and 22 m central span girders to maintain uniformity with the existing bridge. To determine the cost effectiveness of this approach, steel girders were designed for only the 10 m abutment span based on the relevant South African codes of practice. The analysis was conducted for non-composite as well as composite action between the steel girder and the reinforced concrete bridge deck. Based on the steel sections obtained a cost comparison was performed. The investigation revealed that for generally available off the shelf I-sections in South Africa, steel girders are an economically viable option, even when considering corrosion treatment. For the 10 m span, the composite girder construction proved to be more economical compared to the reinforced concrete beam over a 5 year periods. However, for the same period, the non-composite girders were economical for 2 years out of the 5 year period. Thus, bridge designers should consider steel girders as an option during the conceptual design stage for short spans, i.e. up-to 10 m in length. A survey was also conducted amongst senior bridge design engineering professionals to determine the apathy towards using steel sections as girders in bridge construction.

1 INTRODUCTION

Highway bridge elements in South Africa are usually constructed of reinforced concrete (RC). These elements include; bridge decks, girders, piers and the foundations. It is understandable that all of these elements, except for the girders, are constructed with RC since the members are in compression. When live and dead loads are applied to the bridge deck, it causes the section above the neutral axis of the girder to be in compression and the remainder of the cross section to be in tension. Thus, any material which is economically viable can be used to construct bridge girders.

For many years engineering professionals have debated which material is more economical in highway bridge construction. To emphasize this point, approximately 97% of highway bridges in the Western Cape in South Africa are constructed with RC girders, Viljoen (2012). This uncertainty led to this investigation to determine whether RC or structural steel would be better suited in highway bridge construction with particular emphasis on bridge girders. Most highway bridges in South Africa consist of two central spans and two abutment spans. The central spans are approximately 22 m long while the abutment spans are approximately 10 m long. A bridge, which required widening, in the Kuilsriver area in the Western Cape with these dimensions was used for the analysis. The widening of the existing bridge was necessitated due to the significant increase in the housing development which led to a corresponding increase in traffic volumes during peak hours.

In many countries around the world, structural steel sections are commonly used as bridge girders. However, in South Africa this is not the case. There are many factors which affect the material choice used in bridge construction. Some of the most important factors include, but not limited too, are:

- Abutment span
- Location
- Experience of the bridge engineer working with structural steel
- Cost of the structural steel and the availability of larger off the shelf steel sections
- Environmental factors
- Time constraints
- Safety requirements
- Standardized RC sections used by provincial road agencies and consulting engineers
- Norm?

To answer the aforementioned question, this investigation considered the responses of a survey completed by senior structural engineering professionals. The aim of the survey was to determine why engineering professionals are reluctant to use structural steel as bridge girders. In addition, steel girders were also analyzed and designed to perform a cost analysis to determine whether off the shelf steel sections can be used as bridge girders for abutment spans. The analysis

Table 1. Average level of agreement why composite bridge construction is not used in South Africa.

Question	% level of agreement
Required off the shelf steel sections not available	20%
Steel bridge girders are too expensive	80%
Installation of steel bridge girders are expensive	30%
High cost of maintenance	80%
Concrete beams have become the norm	70%
Steel bearing are expensive	40%
Shear connectors are expensive	40%
Aesthetic appeal	50%
Steel girders have the potential to buckle laterally	20%

considered transportation costs, corrosion treatment costs and composite construction.

2 SURVEY

A survey questionnaire, developed by Smith (2010), was sent to numerous companies who specialize in highway bridge construction to determine the reason(s) why RC girders are predominantly used in highway bridge construction. The survey questionnaire was designed as a web based survey where the respondents had to indicate their level of agreement to the questions. An explicit requirement was that only experienced bridge / structural engineering professionals complete the survey questionnaire. Only 10 responses were obtained from the survey. From the survey it was established that the respondents had an average of 21 and 16 years of experience in structural engineering and bridge design, respectively. Based on the average years of experience of the respondents, the authors felt confident that only experienced professionals took part in the survey. The authors also felt confident that the responses would be similar if a wider audience were sought. Some of the important results from the survey are now presented in Table 1.

Based on the survey we notice that the apathy toward using steel girders in bridge construction are that; steel girders as too expensive, the high cost of maintenance, concrete girders have become the norm and the aesthetic appeal of the concrete girders. The latter two factors are based on the designer's and/or client's appreciation and not on economic considerations. The first two factors however need to be investigated to have a sound economic base. The authors believe that these factors are solely based on past experience and not on a cost analysis per project.

3 PRICE INDICE OF STRUCTURAL STEEL

It is common knowledge that the price of steel fluctuates significantly over time. Erling (2012), from the

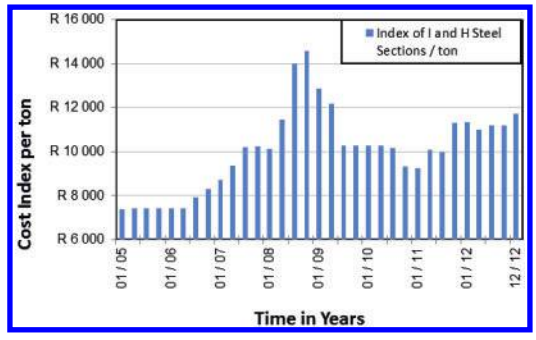


Figure 1. Cost index of steel per ton since January 2005.

Southern African Institute of Steel Construction was approached to determine the accuracy of this claim. Erling provided data which is presented in Figure 1 to monitor the price fluctuations of I and H sections since 2005.

Figure 1 shows that during 2005 the price index of steel ("raw" cost) remained constant and steadily increased from mid-2006. During 2008 the price of steel dramatically increased to a record high of approximately R14 600 per ton. Thereafter the price of steel experienced a significant decrease to stabilize at approximately R10 800 per ton during 2009 to 2012. Figure 1 shows the that the price of steel does indeed fluctuate significantly over time and that it is imperative to conduct a cost analysis to provide the client with the most affordable cost for the project.

4 DESCRIPTION OF BRIDGE

The existing reinforced concrete bridge deck is supported on two 22 m simply supported central span girders and two 10 m simply supported abutment span girders. The existing bridge had a width of 8.6 m which allowed for a single carriageway in both directions. Due to the increase in traffic volumes the existing bridge was widened to allow for a dual carriageway in both directions. To maintain conformity with the existing bridge the design engineer used RC sections for all the new elements.

5 BRIDGE LOADING

The existing bridge is located in the vicinity of an industrial area which accommodates unusually heavy traffic loading. Therefore the bridge needed to be designed for all possible traffic loads as specified in the "Code of Practice for the Design of Highway Bridges and Culverts in South Africa", TMH 7, Parts 1 to 3. TMH 7 specifies that the bridge be designed for the following load cases namely:

- NA loading – normal loading on the bridge
- NB loading – abnormal loading on the bridge
- NC loading – super loading on the bridge

Table 2. Summary of the traffic loading.

	Traffic loading		
	NA	NB	NC
SF (kN)	186	238	198
BM (kNm)	466	481	495

The maximum shear force (SF) and bending moments (BM) were obtained for the abutment spans. Based on the requirements of Kayser and Nowak (1989), wind loads were ignored from this study as it is not significant in short to medium span bridges. No allowance was made for impact and dynamic effect as specified in clause 2.6.1.3 of TMH 7. From clause 2.2.6 of TMH 7, 3 notational lanes are required for an 8.6 m wide carriageway. To determine the maximum SF and BM for each type of loading, the appropriate material and partial factors were applied to the uniform distributed loads on the abutment spans. The material factor for steel was obtained as 1.1 while the partial factors for NA, NB and NC loading are 1.5, 1.2 and 1.2, respectively.

6 RESULTS OF THE MAXIMUM SHEAR FORCE AND BENDING MOMENT

6.1 *SF and BM due to traffic loading*

The individual maximum SF and BM for each type of traffic loading are presented in Table 2.

From Table 2, we notice that the maximum SF and BM due to traffic loading are 238 kN and 495 kNm, respectively. We also notice that the maximum SF and BM are obtained from different loading conditions. An interesting observation is that the SF differs by 21.8% while the BM differs by 5.6% between the three loading conditions. The maximum SF and BM varied by less than 2% from the design engineers results.

6.2 *SF and BM due to bridge deck*

Before the girders could be designed, the dead loads due to the asphalt, concrete deck and girders were required. An asphalt thickness of 50 mm together with a density of 22.0 kN/m^3 and 1 m strip was used to determine the SF and BM, while a slab thickness of 245 mm with a density of 25.5 kN/m^3 was used for the concrete deck. Using a material load factor of 1.2, the maximum SF and BM for the 10 m span was obtained as 44 kN and 110 kNm.

6.3 *SF and BM due to girders*

The dead load of the abutment girders was also required before the beams could be designed. The final steel sizes were achieved after an iterative approached was employed to obtain the optimal steel section for composite and non-composite action.

Table 3. Maximum SF and BM

	$SF_{MAXIMUM}$ (kN)	$BM_{MAXIMUM}$ (kNm)
Non-composite action	289	623
Non-composite action	287	618

Table 4. Summary of beams obtained.

	Span	Section	Shear Connectors
Non-Composite Action	L = 10 m W = 1.0 m	533 × 210 × 122 I-section	N/A
Composite Action	L = 10 m W = 1.0 m	457 × 191 × 89 I-section	19 mm ϕ studs with 0.5 m spacing

6.4 *Maximum SF and BM*

The maximum SF and BM due to traffic and dead loads for the abutment beams are presented in Table 3.

7 DESIGN OF STEEL GIRDERS

The steel girders were designed according to the South African National Standard, SANS 10162-1 of 2005 and the Southern African Steel Construction Handbook (2005). To achieve the most economical steel sections, the beams were designed to be laterally supported. This could be achieved if a groove of equivalent width of the top flange is recessed at the bottom of the concrete deck.

For further economy, the beams were also designed for composite and non-composite action based on clause 17 of SANS 10162-1. To achieve a proper composite connection shear connectors were designed to resist the horizontal shear that form between the concrete and the steel sections.

7.1 *Summary of steel beams*

The most economical steel sections which satisfy both Ultimate Limit State and Serviceability Limit State requirements for non-composite and composite action are shown in Table 4. The design of the abutment girders were controlled by Serviceability Limit State requirements, i.e. deflection criteria.

7.2 *Cost of the steel sections for the abutment spans*

Numerous steel suppliers were contacted to provide quotations for off the shelf steel I-sections. The suppliers were limited to a 10 kilometre radius from the site to minimize transportation costs. Of the suppliers contacted only one could provide a detailed cost history of these sections since 2007. As the

supplier has branches nationally and their prices were cheaper than the other suppliers, their data was used for the analysis. I-sections are stocked in 9 m and 13 m lengths. 13 m I-sections needed to be purchased even though the abutment spans were 10 m long.

7.3 *Protective steel treatment*

It is important to protect steel from corrosion to prevent the sections from experiencing a reduction in its load carrying capacity, Kayser, (1989). Corrosion on steel sections is not uniform which leads to further uncertainty of the section's performance. In the study various commercial corrosion treatment options were considered over the design life of the bridge. Hot dipped galvanizing was found to be the most economical method of preventing corrosion on steel sections. Using information supplied from the Hot Dip Galvanized Association of Southern Africa (HDGASA) and the recommendation from Wilmot, a 150 μ m zinc coating is sufficient to protect the steel sections for 50 years. The current cost of hot dipped galvanizing steel sections is approximately R6 250 per ton. The authors could not obtain accurate prices from suppliers for hot dipped galvanizing steel since 2007. To obtain a cost history backdated to 2007, a 10% depreciation was applied to the current cost of hot dipped galvanizing.

7.4 *Cost of shear connectors*

Shear connectors are required to provide a composite action between the concrete and steel girders. Based on the design requirements, a total of 40 shear connectors of 19 mmϕ × 100 mm are required. The total cost to attach shear connectors to the top flange of the I-section was R1 440 based on 2012 prices. A 10% depreciation was applied to obtain cost estimates backdated to 2007.

7.5 *Transportation cost*

The average cost of transporting I-sections to site is approximately R450 per ton based on 2012 prices. A 10% depreciation was again applied to obtain cost estimates backdated to 2007.

8 RESULTS AND DISCUSSION

The RC beams were cast 8 kilometres off-site and needed to be transported on a lowbed to site. Since the project commenced in 2009, the contractor provided cost estimates from this time. A 10 % depreciation was applied to the RC girders to obtain a cost history for 2007 and 2008.Figure 2 shows the total cost inclusive of transportation and installation of the RC girder obtained from the contractor.

Superimposed on Figure 2 is the cost of the I-sections over a 5 year period inclusive of galvanizing, transportation and shear connectors were necessary.

Figure 2 shows a dramatic escalation in the cost of steel at the beginning of 2008. This confirms the steel cost index from Figure 1. It is observed that a composite steel girder is more economical compared to an RC beam. Since 2008, the cost difference between RC and composite steel girders increased on a yearly basis. This proves that composite construction of the abutment girders are more economical compared to RC beams.

When non-composite girder construction is considered, we notice that RC abutment beams are more economical compared to off the shelf steel sections until the mid-2009. After 2009, the non-composite construction becomes more economical with an increasing cost difference between RC and steel girders.

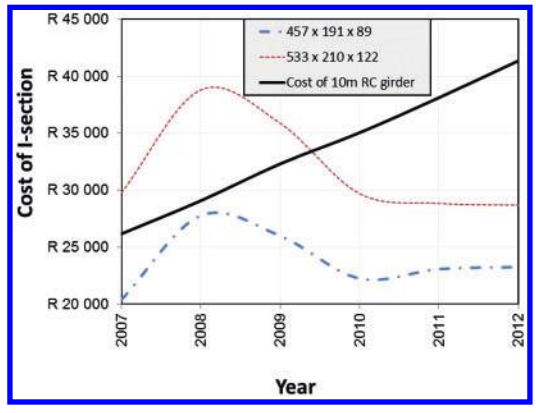


Figure 2. Girder costs.

Table 5. Total cost saving.

Year	Total cost saving for composite construction	Total cost saving for non-composite construction
2007	R115 602	R72 077
2008	R26 186	R194 359
2009	R126 578	R70 918
2010	R255 978	R107 130
2011	R300 845	R185 708
2012	R361 929	R253 374

9 CONCLUSIONS

Although the accuracy of the estimated total cost of steel girders could be questioned, the results show that using steel girders in short span bridge construction is a viable option and needs to be considered. As shown in Figure 2, it is important for design engineering professionals to conduct a cost analysis to provide the client with the most economical design. For the two abutment spans, a total of 20 beams were required. Based on this number of beams, the total cost saving is presented in Table 5 for composite and non-composite construction.

The shaded cells identifies that steel girder construction is more economical. From Table 4 it is clear that steel girders in short span bridge construction is a viable option.

REFERENCES

Committee of State Road Authorities, TMH7, Part2 1, 2 and 3, *Code of practice for the design of highway bridges and culverts in South Africa*.

Erling, S. 2012. *Personal communique*.

Hot Dip Galvanizers Association of Southern Africa. *Hot Dip Galvanized Information Sheet No.8, Corrosion of Zinc – Corrosivity of Atmospheres.*

Kayser, J.R. and Nowak, A.S., 1989. *Reliability of corroded steel girders. Structural Safety*. 6: 53–63.

Smith, D. 2012. *An investigation into the lack of usage of composite steel sections as bridge girders in South Africa*, Final year project, Stellenbosch University.

South African National Standard. 2005. *The structural use of steel – Part 1: Limit –state design of hot rolled steelwork (SANS 10162-1)*. Groenkloof: Standards South Africa.

Southern African Institute for Steel Construction. 2008. *Southern African Steel Construction Handbook*. Johannesburg.

Viljoen, H. 2012. *Personal communique.*

Wilmot, B. 2013. *Personal communique.*

Research and Applications in Structural Engineering, Mechanics and Computation – Zingoni (Ed.)
© 2013 Taylor & Francis Group, London, ISBN 978-1-138-00061-2

Effect of constraint in-plane displacement conditions for the unloaded edges of stiffened flanges used in steel box girder bridges

P.S. Ferreira
Polytechnic Institute of Setubal, Escola Superior de Tecnologia do Barreiro and ICIST, Setubal, Portugal

F. Virtuoso
Technical University of Lisbon, Instituto Superior Técnico, DECivil-ICIST, Lisbon, Portugal

ABSTRACT: This paper presents a computational semi-analytical model for the post-buckling analysis and ultimate strength prediction of stiffened plates under longitudinal uniform compression. The possibility of considering fully free in-plane displacements at longitudinal edges (or unloaded edges) is the innovation of this model over existing models, where these displacements are assumed constrained to remain straight. Comparisons between the semi-analytical model results and nonlinear finite element model results are presented in order to discuss the effect of in-plane displacement boundary conditions on behavior and design of stiffened flanges used in steel box girder bridges. This study shows that the in-plane displacement boundary conditions for the unloaded edges significantly influence the post-buckling behavior and ultimate strength of stiffened flanges and this problem cannot be neglected in the definition of the design rules.

1 INTRODUCTION

Recent work in the field of semi-analytical methods used for the nonlinear analysis and design of stiffened plates with buckling problems have shown an important and alternative tool that provide an efficient and understandable response (Paik et al. 2008, Brubak & Hellesland 2008).

Nowadays two computational programs use the semi-analytical method to analyze the post-buckling behavior of plates and to predict their ultimate strength. The computer program ALPS/ULSAP (Paik & Thayamballi 2003), which uses a semi-analytical method previously known as the incremental Galerkin method (Ueda et al. 1987) and the computer program PULS (Bycklum 2002) developed at Det Norske Veritas (DNV) and accepted as general buckling code for ship and offshore platform structures as part of the DNV specifications (DNV-RP 2002).

The existing semi-analytical models are restricted to stiffened plates supported by rigid transverse and longitudinal girders. This type of arrangement is typical in ship, aircraft, tanks and offshore platform structures where it is assumed that the analyzed stiffened plate is simply supported and the in-plane displacements perpendicular to the edges are constrained to remain straight in all edges. Generally, in bottom flanges of steel box girder bridges there are no neighboring panels in the longitudinal edges to provide this kind of constraint and it is more conservative to consider the longitudinal edges with fully free in-plane displacements that are characteristic of edges free from stresses.

This paper presents a computational semi-analytical model for the post-buckling analysis and ultimate strength prediction of stiffened plates under longitudinal uniform compression. The possibility of considering fully free in-plane displacements at longitudinal edges (or unloaded edges) is the innovation of this model over existing models. Comparisons between the semi-analytical model results and nonlinear finite element model results are presented in order to discuss the effect of in-plane displacement boundary conditions on behavior and design of stiffened flanges used in steel box girder bridges.

2 METHOD OF ANALYSIS

2.1 *General*

In order to validate the results obtained by the semi-analytical model that was developed, all nonlinear simulations were performed using the semi-analytical method and the finite element method.

The simulations with both methods were performed considering a yield stress (f_y) of 355 Nmm^{-2}, Young's modulus (E) of 2.1×10^5 Nmm^{-2} and Poisson's coefficient (ν) of 0.3.

The stiffened flanges were considered simply supported under longitudinal uniform compression (σ) with the following two cases for the in-plane displacement boundary conditions: in-plane displacements perpendicular to the edges constrained to remain straight in all edges (case CC) and in-plane displacements perpendicular to the edges constrained to remain

straight at loaded edges and free at unloaded edges (case CF).

Unless otherwise indicated an equivalent geometric imperfection, including the geometric imperfections and residual stresses in accordance with European standard (EN-1993-1-5 2006), was considered for the initial imperfection. Amplitude of 1/400 of the minimum between the length and width of the half-wave of the imperfection mode was considered for the equivalent geometric imperfection with a global imperfection mode shape. For a local imperfection mode shape the same principle was considered, with amplitude of 1/200.

2.2 *Implementation of the semi-analytical method*

The semi-analytical method uses the two nonlinear fourth order partial differential equations of the large deflection theory, the equilibrium and compatibility equations derived by von Kármán in 1910 (Timoshenko & Woinowsky-Krieger 1959) for perfect plates and extended to plates with initial imperfections by Marguerre (1937). The method is called semi-analytical because in a first step an analytical solution for the Airy stress function (F) is obtained solving the compatibility equation. Trigonometric series for the out-of-plane displacements (w) and for the initial imperfections (w_0) are adopted, which satisfy the boundary conditions.

In a second step approximate solutions for the unknown amplitudes (q) of the out-of-plane displacements are obtained solving the equilibrium equation using a variational method. Based on the approximate solutions for the unknown amplitudes of the out-of-plane displacements, the kinematic and constitutive relations and the yield criterion it is possible to analyze the post-buckling behavior and to predict the ultimate strength of plates.

The computational implementation of the semi-analytical model developed in the framework of this study uses the Rayleigh-Ritz method to solve the equilibrium equation and it was implemented using the programming language of Mathematica6 (Wolfram 2007). The initial imperfections (w_0) and out-of-plane displacements (w) considered in the computational semi-analytical model, which satisfy the boundary conditions for simply supported plates, are given as follow

$$w_0 = \sum_{m=1}^{\infty}\sum_{n=1}^{\infty} q_{0,mn} \sin\frac{m\pi x}{a}\sin\frac{n\pi y}{b} \tag{1}$$

$$w = \sum_{m=1}^{\infty}\sum_{n=1}^{\infty} q_{mn} \sin\frac{m\pi x}{a}\sin\frac{n\pi y}{b} \tag{2}$$

where m = number of half-waves in the longitudinal direction; n = number of half-waves in the transverse direction; q_0 = prescribed amplitudes of the initial imperfection; q = unknown amplitudes of the out-of-plane displacement; a = plate length; b = plate width; x = longitudinal coordinate; and y = transverse coordinate. The xy plane coincides with the plate mid-surface. Figure 1 illustrates an overview of the semi-analytical model developed.

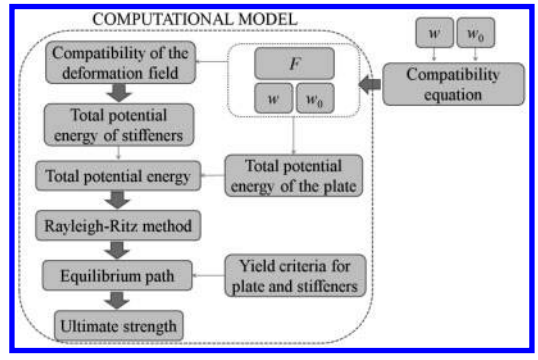


Figure 1. Overview of the semi-analytical model developed.

The stiffened plate analysis through this semi-analytical model is achieved considering the separate analyses of the plate and the stiffeners. Plate and stiffeners are modeled as an isotropic plate and as beam elements, respectively.

The compatibility equation for the isotropic plate used in the first step of the semi-analytical model to obtain the analytical solution for the Airy stress function (F) is expressed as

$$w_0 = \sum_{m=1}^{\infty}\sum_{n=1}^{\infty} q_{0,mn} \sin\frac{m\pi x}{a}\sin\frac{n\pi y}{b} \tag{1}$$

The stiffener deformations are defined through the compatibility of the deformation field between the isotropic plate and the beam elements considering the stiffener curvature (κ_{sl}) equal to the longitudinal plate curvature for bending ($-w_{,xx}$) and the stiffeners strain (ε_{sl}) equal the longitudinal plate membrane strain (ε_x^m) at their intersection. The strain of the stiffener is evaluated at transverse stiffener location (y_{sl}) and the general expression is given by

$$\varepsilon_{sl}(z) = \left[\varepsilon_x^m - (z - z_{st})w_{,xx}\right]_{y=y_{sl}} \tag{4}$$

where z = height coordinate measured from the plate mid-surface; z_{st} = geometric centre of the cross-section composed of the plate and the stiffeners.

The transverse (or lateral) displacements and the torsional rotation of the stiffeners are accounted for in the total potential energy of stiffeners. By compatibility the angle of twist (θ) and the transverse displacement at the shear centre of the single stiffener (v_{sc}) are defined as

$$\theta = w_{,y} \tag{5}$$

$$v_{sc} = -w_{,y} z_{sc} \tag{6}$$

where z_{sc} = coordinate z of the shear centre of the single stiffener.

The local buckling effect of the stiffener elements is not considered in the response. This assumption is reasonable if the local buckling problems in the stiffener elements are prevented by satisfying minimum requirements for the stiffener geometric properties as established in the European standard (EN-1993-1-5 2006). These minimum requirements are used in the standards because the collapse of stiffened plates by local buckling of the stiffeners (lateral torsional buckling of the stiffener or local buckling of the stiffener elements) may exhibit a very unstable response.

This semi-analytical model enables to take into account the initial imperfections, cases CF and CC for the in-plane displacement boundary conditions, the interaction between local and global buckling, the geometric nonlinearity and in an approximate way, the material nonlinearity associated with the stiffness reduction after reaching the yield in the extreme fiber of the plate. The von Mises yield criterion was assumed for the plate and the stiffeners.

The plate yield criterion was defined for the sum of membrane and bending stresses at one-quarter of the plate thickness. This criterion allows for the formation of plasticity through the possibility of an additional strength after yielding in outer fibers in order to take into account in an approximate way for the material nonlinearity.

The stiffener yield criterion was defined by the yield stress, in tension or compression, at the location of the maximum stiffener stress. This criterion gives conservative ultimate strength predictions for global buckling cases when the stiffener extreme fibers are compressed.

The computational semi-analytical model developed has the following assumptions: the plate has a width b, length a and uniform thickness t, it is possible to consider one or more longitudinal stiffeners positioned symmetrically or eccentrically about the middle plane of the plate, the material is considered isotropic and linear elastic, characterized by Young's modulus E, Poisson's coefficient ν and yield stress f_y and the stiffened plate is subject to uniform compression σ in the longitudinal direction.

The complete definition of each step and the procedures of the semi-analytical model developed can be found in Ferreira (2012).

2.3 *Finite element modeling*

The commercial program ADINA (Bathe 2006) was used to perform the nonlinear simulations by the finite element method. The program uses a large displacement/small strain with a Total Lagrangian formulation. The stiffened flanges were modeled using a four-node shell element for the plate and the stiffeners. This type of element allows for finite strains due to in-plane displacements (membrane) and out-of-plane displacements (bending). A collapse analysis was performed in the full range behavior of the stiffened flanges, including the post-buckling regime and assuming a von Mises yield criterion.

The nodes of each stiffener at loaded edges were connected with rigid links in order to assure their planar rotation about the supported edge. For the plate edges with in-plane displacements constrained to remain straight it was used a constraint for all nodes of the edge to ensure a uniform in-plane displacement.

The material behavior for all elements was modeled assuming elasto-plastic behavior with linear strain hardening. A value of Young's modulus/100 was adopted for the yield branch, in accordance with European standard (EN-1993-1-5 2006).

3 RESULTS AND DISCUSSIONS

3.1 *Post-buckling behavior*

To study the effect of boundary conditions for the in-plane displacements at unloaded edges on behavior and to compare the results obtained by the semi-analytical model with the results obtained by the finite element program ADINA a stiffened flange with five longitudinal equally spaced symmetric stiffeners, relative cross-sectional area δ (cross-sectional area of the stiffeners without any contribution of the plate A_{sl} to the cross-sectional area of the plate (bt) ratio) of 0.5 and relative flexural stiffness γ (second moment of area of the stiffened plate I_{st} to the second moment of area for bending of the plate corrected by the effect of the Poisson coefficient ($bt^3/[12(1-\nu^2)]$) ratio) of 65 was considered. The stiffened flange has a plate aspect ratio ϕ (ratio between the length a and the width b of the plate) of 5, plate slenderness λ_{plt} (ratio between the width b and the thickness t of the plate) of 150 and panel slenderness λ_p (ratio between the width of the panels between stiffeners b_p and the thickness t of the plate) of 25.

The reasons for choosing this stiffened flange are due to the fact that it is possible to validate the present model for the simplest case of stiffened plates with symmetric stiffeners, slender plates have a considerable post-critical resistance, which enables to study the effect of boundary conditions for the in-plane displacements on post-buckling and the panels between the stiffeners do not have problems of local buckling which reduces the number unknown amplitudes in the semi-analytical model.

The q_{21} was the unknown amplitude for the out-of-plane displacements assumed to be non-zero in the semi-analytical model. Two cases of initial imperfections were considered in the analysis: (i) an ideally perfect flange ($w_0 = 0$) and (ii) an equivalent geometric imperfection with the shape of the critical buckling mode ($m = 2$ and $n = 1$) with an amplitude ($q_{0,21}$) of $b/400$.

Figure 2 presents the three dimensional view of the critical buckling mode obtained from the semi-analytical model.

The elastic critical buckling stress (σ_{cr}) and the critical buckling mode obtained by the semi-analytical model illustrated in Figure 2 are in exact agreement

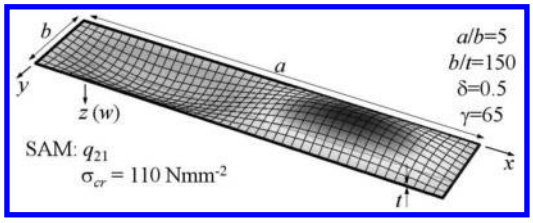


Figure 2. Three dimensional view of the critical buckling mode obtained from the semi-analytical model developed.

with the theoretical analysis exposed in reference works (Timoshenko & Woinowsky-Krieger 1959, Allen & Bulson 1980). Although Figure 2 presents an apparent mesh of elements the critical buckling mode of the semi-analytical was generated through a three-dimensional plot based on single unknown amplitude (q_{21}).

Figures 3–4 presents the comparison between the equilibrium paths obtained by the semi-analytical model and nonlinear finite element simulations for the stiffened flange considering the cases CC and CF for the in-plane displacement boundary conditions. Figure 3 shows the equilibrium path for the perfect flange and Figure 4 shows the equilibrium path for the imperfect flange. The equilibrium paths are presented in terms of normalized load (longitudinal compression σ to the yield stress f_y ratio) as a function of the normalized total deflection (ratio between the sum of out-of-plane displacement w and initial imperfection w_0 with the plate thickness t).

The load-deflection responses and the ultimate strength (σ_u) obtained by the semi-analytical model shown in Figures 3–4 are in close agreement with the finite element results for both cases of modeling the in-plane displacements at unloaded edges.

The main differences between the results obtained with the semi-analytical model and the nonlinear finite element simulations occur in large out-of-plane displacements at the end of the load-deflection response. This can be explained by the facts that the nonlinear finite element simulations allow an increase in load and the progressive extension of plastification after local yielding of the stiffened plate, while in the semi-analytical model the plastification is accounted for through the yield criterion in an approximate way and the nonlinear finite element simulations use a large number of degrees of freedom, which allow to consider the interaction between displacement modes while in the semi-analytical model only single unknown amplitude for the out-of-plane displacements was used.

Nevertheless, the differences between the semi-analytical model and the nonlinear finite element simulations for the ultimate strength are less than 4% in the flange with fully free in-plane displacements at unloaded edges (case CF) and about 1% in the flange with uniform in-plane displacements at unloaded edges (case CC). These small differences can be reduced with an increase in the number of unknown amplitudes for the out-of-plane displacements.

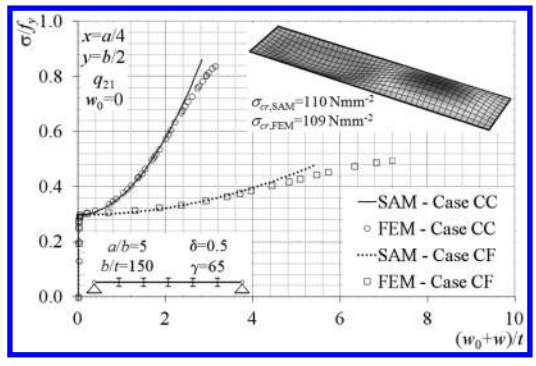


Figure 3. Comparison between the equilibrium paths obtained by the semi-analytical model (SAM) and nonlinear finite element simulations (FEM) for the perfect flange.

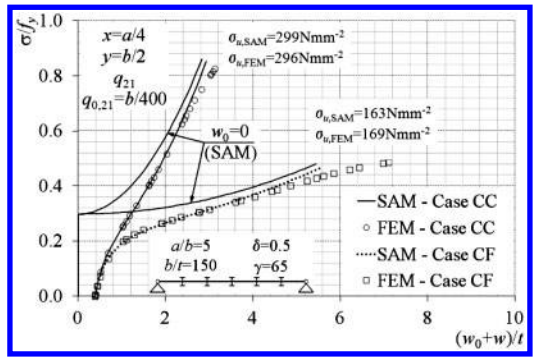


Figure 4. Comparison between the equilibrium paths obtained by the semi-analytical model (SAM) and nonlinear finite element simulations (FEM) for the imperfect flange.

Based on these results it can be verified that the post-buckling behavior and the ultimate strength differs considerably according to the in-plane displacement boundary conditions at unloaded edges. In fact with the condition of fully free in-plane displacements at the unloaded edges, the transverse stresses are significantly reduced and consequently the stiffness of the plate also decreases. This point is particularly important for plates with higher post-critical resistance.

As expected, the elastic critical buckling stress (σ_{cr}) does not depend on the in-plane displacement boundary conditions at unloaded edges.

3.2 *Ultimate strength*

The effect of boundary conditions for the in-plane displacements at unloaded edges on ultimate strength was studied considering further 20 stiffened flanges. The results obtained by the semi-analytical model were also compared with the results obtained by the finite element program ADINA. The 20 stiffened flanges were obtained based on two types of cross-sections, SF1 and SF2, and considering for each cross-section the plate aspect ratio $\phi(=a/b)$ ranging from 0.5 to 5.0 at intervals of 0.5. Both cross-sections have five longitudinal

equally spaced and single sided stiffeners, the stiffened flanges with the cross-section SF1 have a relative flexural stiffness γ ($=12I_{st}(1-\nu^2)/(bt^3)$) of 65 and the stiffened flanges with the cross-section SF2 have a relative flexural stiffness γ of 130. All stiffened flanges have a relative cross-sectional area δ ($=A_{st}/(bt)$) of 0.5, plate slenderness λ_{plt} ($=b/t$) of 150 and panel slenderness λ_p ($=b_p/t$) of 25.

In order to evaluate the ultimate strength of the stiffened flanges the following cases of equivalent geometric imperfections were considered: the shape of the first, second and third local buckling modes considered separately (cases 1–3), the shape of the first, second and third global buckling modes considered separately (cases 4–6), the combination of the local and global buckling modes with a local mode leading the imperfection (case 7) and the combination of the local and global buckling modes with a global mode leading the imperfection (case 8). In order to take into account the stiffener eccentricity the imperfection amplitude was considered with both signs (positive for imperfections in the direction of stiffeners and negative for imperfections toward the plate) for symmetrical buckling modes. The buckling modes were obtained by a linearized buckling analysis of the same stiffened flange without initial imperfection. The ultimate strength of the stiffened flange was considered as the minimum strength obtained by the several cases of equivalent geometric imperfection.

The leading imperfection in combined buckling modes was considered with the full amplitude value and the accompanying imperfection was considered with its amplitude value reduced to 70%, in accordance with European standard (EN-1993-1-5 2006).

Figures 5–6 show the comparison between the ultimate strength (σ_u) obtained by the semi-analytical model and nonlinear finite element simulations for the stiffened flanges considering the cases CC and CF for the in-plane displacement boundary conditions. Figure 5 shows the ultimate strength for the stiffened flanges with the cross-section SF1 and Figure 6 shows the ultimate strength for the stiffened flanges with the cross-section SF2. The results are presented in terms of normalized strength (mean compressive stress at peak load σ_u to the yield stress f_y ratio) for different values of the plate aspect ratio ϕ ($= a/b$).

The ultimate strength (σ_u) obtained by the semi-analytical model shown in Figures 5–6 are in close agreement with the finite element results for both cases of modeling the in-plane displacements at unloaded edges. This remark, which is based on results for the total of twenty stiffened flanges, strengthens the remark stated above based on results for one stiffened flange.

Based on results presented in Figures 5–6 it can be noted that the ultimate strength (σ_u) is similar for both cases of in-plane displacement boundary conditions in stiffened flanges with plate aspect ratio equal to or less than 1 ($\phi \leq 1$). In stiffened flanges with plate aspect ratio greater than 1 ($\phi > 1$) the ultimate strength tends to constant values for the case CF

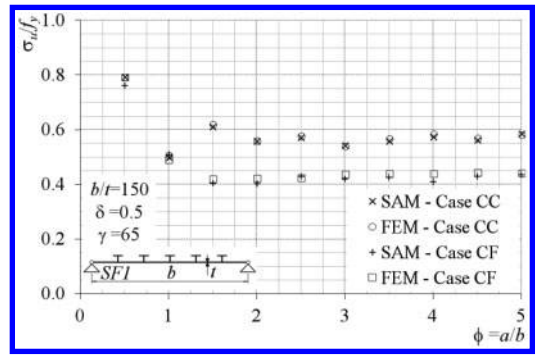


Figure 5. Comparison between the ultimate strength obtained by the semi-analytical model (SAM) and nonlinear finite element simulations (FEM) for the stiffened flanges with the cross-section SF1.

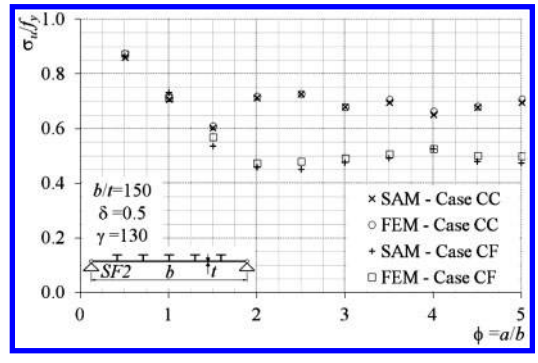


Figure 6. Comparison between the ultimate strength obtained by the semi-analytical model (SAM) and nonlinear finite element simulations (FEM) for the stiffened flanges with the cross-section SF2.

of in-plane displacement boundary conditions, it has a pronounced increase after reaching the minimum value for the case CC of in-plane displacement boundary conditions and it is considerably higher for the case CC of in-plane displacement boundary conditions than for the case CF.

These remarks show that the evaluation and definition of the type of constraint for the in-plane displacements at unloaded edges of stiffened plates is a very important issue to estimate a correct value for the ultimate strength. In European standard (EN-1993-1-5 2006) the ultimate strength of webs and internal flanges with longitudinal stiffeners used in steel box girder bridges is obtained through the same condition and this condition is independent of the in-plane displacement boundary conditions of the plate. Just apparently both elements may have the same in-plane displacement boundary conditions. Indeed, the webs are usually connected to flanges that possess sufficient rigidity to consider uniform the in-plane displacements at longitudinal edges, while the flanges are connected to webs that usually do not provide this type of constraint and it is more conservative to consider free the in-plane displacements at longitudinal

edges, as shown in the work of Ferreira & Virtuoso (2011) through a comparison between numerical and experimental results.

So if the design rules defined in the European standard are set for the case CF of in-plane displacement boundary conditions, a very conservative value may be obtained for the ultimate strength of webs with higher values of plate aspect ratio. If the design rules defined in the European standard are set for the case CC, an unsafe value may be obtained for the ultimate strength of flanges with higher values of plate aspect ratio.

4 CONCLUSIONS

From this study the main conclusions can be summarized as follows: (i) the results obtained by the computational semi-analytical model are in close agreement with the nonlinear finite element results for both cases of modeling the in-plane displacements at unloaded edges, (ii) the semi-analytical model prove to have a clear potential to provide reasonably accurate solutions require only a short computer time, (iii) the boundary conditions for the in-plane displacements at unloaded edges significantly influence the post-buckling behavior and the ultimate strength of plates and (iv) the design rules of stiffened plates cannot neglect the in-plane displacement boundary conditions of the plate.

ACKNOWLEDGEMENTS

This work was carried out in the framework of the research activities of ICIST, *Instituto de Engenharia de Estruturas, Território e Construção* and was funded by FCT, *Fundação para a Ciência e Tecnologia*.

REFERENCES

Allen, H. & Bulson, P. 1980. *Background to Buckling*. New York: McGraw-Hill.

Bathe, K. 2006. *ADINA System Documentation*. Massachusetts: ADINA R&D Inc.

Brubak, L. & Hellesland, J. 2008. Strength criteria in semi-analytical, large deflection analysis of stiffened plates in local and global bending. *Thin-Walled Structures* 46: 1382–1390.

Bycklum, E. 2002. *Ultimate strength analysis of stiffened steel and aluminium panels using semi-analytical methods*. Ph.D. thesis. Trondheim: Norwegian University of Science and Technology.

DNV-RP. 2002. *Recommended Practice DNV-RP-C201 – Buckling Strength of Plated Structures*. Høvik: Det Norske Veritas.

EN-1993-1-5. 2006. *Eurocode 3 – Design of Steel Structures – Part 1–5: Plated Structural Elements*. Brussels: European Committee for Standardization.

Ferreira, P. 2012. *Stiffened compression flanges of steel box girder bridges: postbuckling behaviour and ultimate strength*. Ph.D thesis. Lisbon: Instituto Superior Técnico, Technical University of Lisbon.

Ferreira, P. & Virtuoso, F. 2011. Efeito do tipo de restrição nos bordos longitudinais no comportamento e resistência de placas metálicas em pontes. In L. Simões da Silva, P. Cruz, N. Lopes, J. Fernandes, and A. Baptista (ed.), *Proceedings of the 8th Conference on Steelwork Construction, Guimarães, 24–25 November 2011*. Coimbra: CMM and University of Minho. (in Portuguese)

Marguerre, K. 1937. The apparent width of the plate in compression, *Technical Memorandum 833*. Washington: National Advisory Committee for Aeronautics.

Paik, J. & Kim, B. & Seo, J. 2008. Methods for ultimate limit state assessment of ships and ship-shaped offshore structures: Part II stiffened panels. *Ocean Engineering* 35: 271–280.

Paik, J. & Thayamballi, A. 2003. *Ultimate Limit State Design of Steel-Plated Structures*. Chichester: John Wiley & Sons Ltd.

Timoshenko, S. & Woinowsky-Krieger, S. 1959. *Theory of Plates and Shells*. New York: McGraw-Hill.

Ueda, Y. & Rashed, S. & Paik, J. 1987. An incremental Galerkin method for plates and stiffened plates. *Computers & Structures* 27: 147–56.

Wolfram, S. 2007. *Mathematica Documentation Center*. Champaign: Wolfram Research, Inc.

Research and Applications in Structural Engineering, Mechanics and Computation – Zingoni (Ed.)
© 2013 Taylor & Francis Group, London, ISBN 978-1-138-00061-2

Buckling resistance with combined shear of steel curved bridge girder webs

Ph. Van Bogaert
Ghent University, Belgium

ABSTRACT: The web curvature of a closed-section girder is gradually increased, to assess the influence of this curvature on the shear buckling resistance. Various types of numerical analysis have been used, from linear elastic, up to material and geometric nonlinear analysis, including imperfections of various amplitudes. The results show that web curvature increases the shear buckling resistance and the webs are mildly sensitive to imperfections. These conclusions are similar to those already found for bending stresses. Further steps in the research, as the effect of residual stress, are also being discussed.

1 INTRODUCTION

1.1 *Curved Bridge Panels*

This paper continues on previous research concerning the buckling resistance of curved bridge girder panels. It has been shown (Van Bogaert 2012) that in spite of the more shell-like behaviour, the curvature of bridge girder webs may increase the buckling resistance. This has been found through a model of a closed-section bridge girder in which the web curvature is increased gradually until the cross-section is close to a circle. During this previous research, nonlinear material and geometric response as well as the influence of critical imperfections of variable amplitude have been considered. However, residual stresses have not been included and the type of loading of the numerical models was mainly bending. This paper further develops the research in case shear is the main type of loading.

1.2 *Simulation tool*

A numerical model has been used, consisting of a closed box section, including diaphragm stiffeners at a distance equal to the box section height. The latter are required to prevent distortion.

A fine meshing is needed and the entire girder could not be simulated. This required limiting the model to the central part of the girder, although it should comprise several panels, since edge effects should be excluded. As the girder height was taken 3 m, the model comprises 7 fields of 3 m length and thus it represents about one third of the actual length of the girder. The boundary conditions of the model include edge bending moments and shear forces, equivalent to the stress states at the appropriate sections in the entire girder. The latter have been calculated from simple beam theory and distributed accordingly among the nodes of the edge sections. This vertical force corresponds to the reaction of bridge crossbeams, fixed to the main girders at the location of the diaphragms. These reactions may be expressed in a dimensionless manner as their individual value times the girder height divided by the applied bending moment, this ratio equals 0.0233 in the case of the model. The model mentioned has almost flat web plates. There is a slight curve, corresponding to a radius of curvature of 100 m. This allows parametric variation of the radius down to 1.65 m. However, the upper- and lower flanges have identical thickness, distinctly higher than the webs and the most curved section certainly is different from a circular tube. It is believed that these sections are relevant for the behaviour of curved panels and plates of bridge structures.

Table 1. Elastic buckling moments.

Radius (m)	100	15	9	5	3	1.65
$M_{E,crit}$ (kNm)	54630	78467	102733	148033	215542	366107
$\sigma_{E,crit}$ (MPa)	126	182	356	594	912	1503

2 RESULTS BUCKLING BY NORMAL STRESS

2.1 *Linear elastic buckling*

Calculations have resulted in values for elastic buckling loads, or elastic critical stresses. Table 1 summarizes the values of the critical bending moments, as a function of the circle segment rise to height ratio.

The critical bending moment can also be transformed to a critical elastic compression stress. The latter is obtained by multiplying the normal bending stress at the location of the top of the buckling mode, by the critical multiplier. For this, the mode shapes have been analyzed more closely.

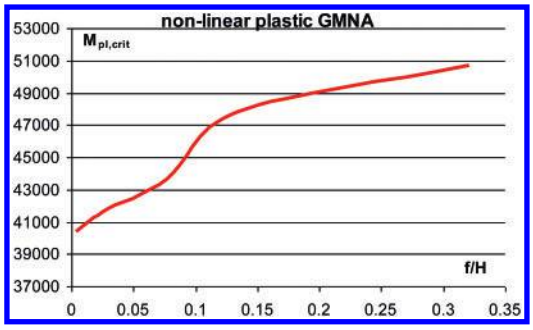


Figure 1. Nonlinear calculations results for bending moments.

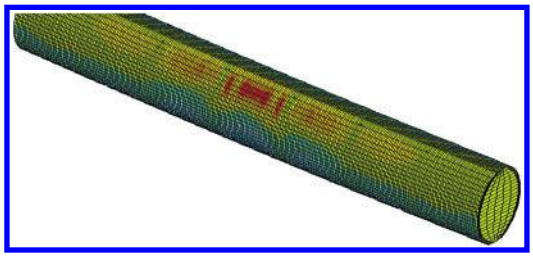


Figure 2. Nonlinear buckling – plasticity areas.

Both the critical stress and the bending moment are increasing with the web curvature. This is unexpected, since no other stress components than horizontal normal stress is appearing. Obviously the linear analysis is unable to adequately describe the buckling phenomenon.

For this reason a nonlinear plastic analysis has been conducted, including large deformation. A simple plastic law, excluding strain-hardening was used. The incremental load strategy has been used, during which the load step was optimized.

2.2 *Elastic-plastic results*

The formerly mentioned models have been used during plastic analysis, including nonlinear displacements. A simple plastic law, excluding strain-hardening was used. The incremental load strategy has been used, during which the load step was optimised. The values of these ultimate bending moments have been plotted in fig. 1. Similar to the results from elastic calculations, the load carrying capacity is increasing with the web.

However, the increase is distinctly less (1.25 instead of 6.7) then for elastic buckling. Displacements rise towards the upper flange with increasing curvature (see fig. 2). This demonstrates that the beam is acting more in a shell-like manner, the most compressed part of the shell circumference having higher resistance. Plastic buckling then occurs close to the area of change in plate thickness, in the thinner part.

2.3 *Imperfections*

Imperfections have large influence on buckling problems of thin-walled members. This is mostly true

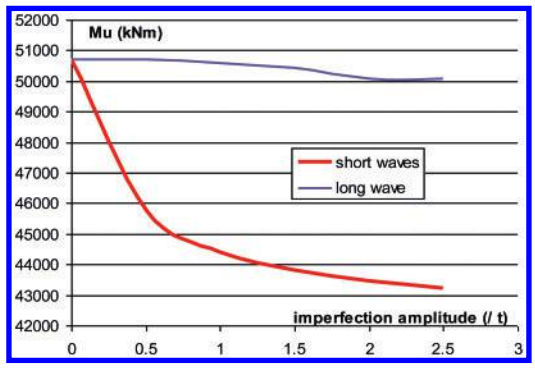


Figure 3. Ultimate bending moments with imperfections.

for shells and membranes, where meridional and circumferential compression occurs.

Some codes (EN 1993 – 2004) recommend identifying the shape of imperfections to the fundamental elastic buckling mode. However, this mode shape may well be improbable, since imperfections and tolerances are due to lack of flatness and fabrication processes. Therefore two types of imperfections have been introduced, the first one corresponding to the code and the second being more reasonable. In addition, the imperfection amplitudes have been varied.

Results of this type of GMNIAnalyses have shown that imperfections of bended curved panels have moderate influence on the failure bending moment. The short-wave imperfection type, corresponding to the elastic buckling mode shape is the most critical one. This is demonstrated in fig. 3.

The results may be compared to the use of classical web crippling procedures, similar to lateral buckling. The latter results in M_u =31743 kNm or 62.6% of the value for a perfect web to 73.5% of the case with the largest imperfection amplitude of 2.5-times the web thickness.

3 CURVED SHEAR PANELS

3.1 *Numerical model*

An identical model is being used to introduce large shear in the webs of varying curvature. However, the boundary conditions were changed to perfect clamping of one side and vertical support. Since the effects of pure shear are to be found, vertical forces have been introduced at sufficient distance from the clamped section, to avoid any local effects.

Hence, the vertical loads have been applied at the second stiffening diaphragm, which basically causes a shear force of 3000 kN and a clamping moment of 18000 kNm, considerably smaller than in the case of bending.

3.2 *Elastic buckling load*

Similar as for the panels subjected to bending, the mode shape changes gradually with increasing web

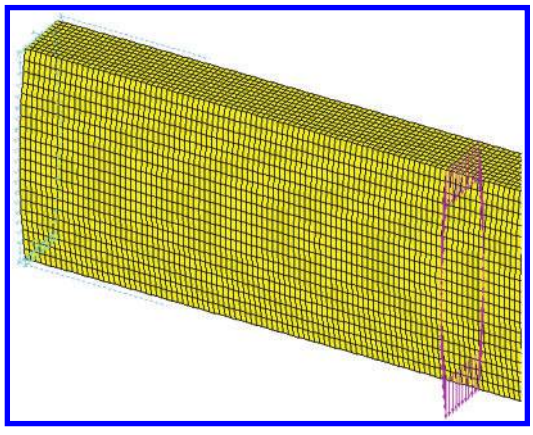


Figure 4. Load and boundary conditions of model.

Table 2. Elastic buckling moments.

Radius (m)	100	15	9	5	3	1.65
$V_{E,crit}$ (kN)	8116	13019	17340	24860	34234	50581
τ_{Ecrit} (MPa)	70.01	112.3	149.6	214.5	295.3	436.3

curvature. In fig. 5a (top) and 5b (bottom) the mode shapes corresponding to almost flat and almost cylindrical alternatives are shown. Obviously, for a flat web, a single sloping wave pattern is found, as expected. As the web curvature increases, the wave rapidly becomes double, one above the other and then gradually shifts from the first panel to the second one between vertical diaphragms.

Table 2 summarizes the results of the critical shear forces. It may be noticed that the critical shear force increases rapidly with the web curvature.

However, with exception of the value corresponding to the radius of curvature of 1.65 m, all critical shear stresses are in the elastic condition. The critical shear force increases by a factor of 6.23, which is close to the case of bending normal stresses.

Even if the critical shear stress remains elastic, elastic buckling forces do not correspond to the actual failure condition, since the web slenderness reaches 167 and plasticity may truncate the results. Hence, further plastic analysis is indispensable, including nonlinear material law and large displacements.

3.3 *Nonlinear plastic stability*

A simple plastic law, excluding strain-hardening was used. The incremental load strategy has been applied, during which the load step was optimized.

The results show that failure mostly occurs through constant shear plasticity, combined with normal stress in the clamping area. The effect of clamping gradually becomes less important as the web curvature increases. Results of the failure load are summarized in table 3 and the graph of fig. 6.

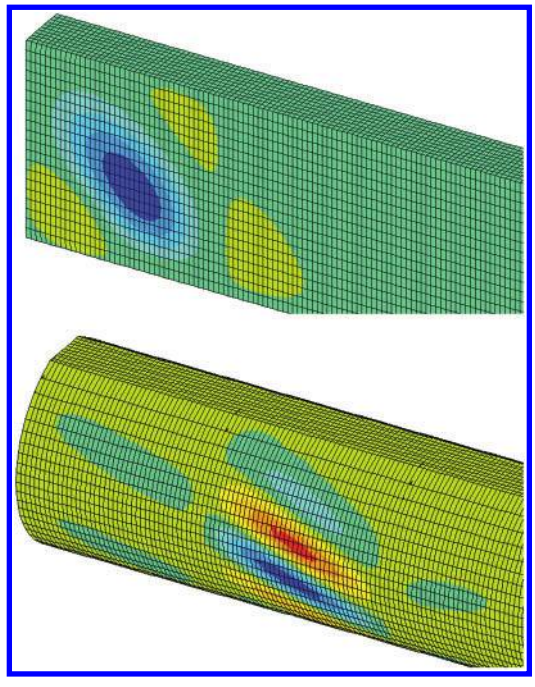


Figure 5. a and b. Elastic mode shapes (top : flat web, bottom curved web).

Table 3. Plastic failure shear load.

Radius (m)	100	15	9	5	3	1.65
VE,crit (kN)	10827	11945	12712	13004	13487	14971

An interesting result concerns the case of flat webs, where the plastic failure load is larger than the elastic buckling value. This is due to the post-critical capacity of the structure, which cannot be found from elastic theory. This appears only in nonlinear plastic analysis, causing larger failure load.

The graph of fig. 6 also shows that the increase of the failure load with curvature first rises rapidly, followed by a slower evolution. This has also been found in the former results concerning normal bending stress. The effect may be explained by the fact that a minor curvature already introduces vertical stabilizing stress and this does not contribute to a large extent beyond the first appearance of this stress state.

During the load increase, the horizontal displacements of some parts of the web may tend to reverse sign. This can be noticed in the graph of fig. 7 which shows the horizontal displacement, in this case at the single wave where plastic phase has been reached. The reversal of these deformations (limited to 3 mm) may be typical of this event.

3.4 *Imperfections*

The GMNA-procedure of paragraph 3.3 does not take into account the effect of imperfections of the

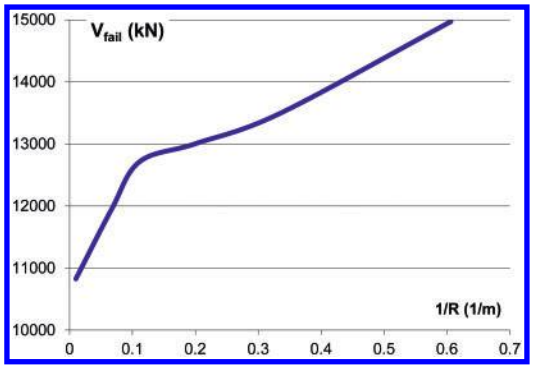


Figure 6. Failure shear load from nonlinear analysis.



Figure 7. Horizontal displacement during plastic phase.

Table 4. Imperfection amplitude according to EN 1993-1-6.

Quality Class	excellent	high	normal
$\Delta w_{0,eq,1}$	9.2 mm	14.72 mm	23 mm

structure, in particular local or general geometric errors. In the case of shell behaviour, the latter can substantially reduce the buckling resistance.

However, it may be expected that the influence of imperfections is milder than in the case of bending stresses. The effect of eccentric transmission of compression stress must be more critical than for shear. This is can be explained by the example of a buckling column, wherein normal force causes the stability issue, rather than eccentric shear, the latter introducing straightforward bending.

Since the imperfection shape, complying with the fundamental elastic buckling mode is the most critical, this type of imperfection has been introduced in the models. The amplitude has been varied by considering fractions of the web thickness. However, the amplitude is considerably larger than the values corresponding to those of EN 1993-1-6 for shells, which have been summarized in table 4.

The normally accepted amplitude corresponds to 1.28-times the web plat thickness. In the present analysis considerably larger amplitudes have been considered.

The results of the GMNIA have been assembled in the graph of fig. 8, in terms of the failure shear load.

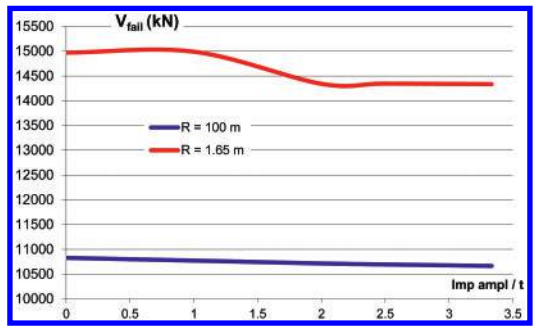


Figure 8. GMNIA failure load versus imperfection amplitude.

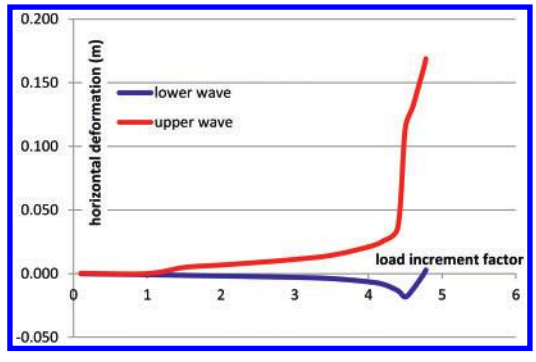


Figure 9. Horizontal web deformation of 2 buckling waves

The graph shows the evolution of the load with varying amplitudes for the two extreme cases of almost flat webs and curved webs close to cylindrical shape. Clearly, this demonstrates that imperfection amplitudes well above normal values do practically not influence the failure load.

The latter confirms the aforementioned understanding of imperfection-sensitivity for structural parts, subjected to shear. This diagram may be compared to fig. 3, where the influence of imperfections is substantial.

Evidently, the largest horizontal deformation appears in the maximum imperfection amplitude area. Fig. 5 already demonstrated that for large curvature, the width of the imperfection is rather small and may consist of a double buckle. This is found again in the GMNIAnalysis. It seems characteristic that The lower wave, as in fig. 5b, is tending to reverse change as the failure load is reached, whereas the upper wave continues its deformation in an identical direction. This is shown in the graph of fig. 9, where horizontal deformations of both waves are represented. The deformation of the upper wave is much larger than the lower one. The graph applies to the almost circular cross-section.

The vertical deformations of the waves follow closely those of the diaphragm of the vertical load. Obviously, the diaphragm section shows larger vertical displacement. Again, the values for the lower wave are considerably smaller than for the upper wave. This is shown in fig. 10.

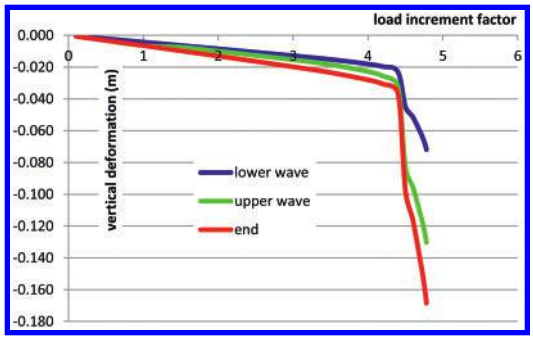


Figure 10. Vertical deformations of web waves and diaphragm.

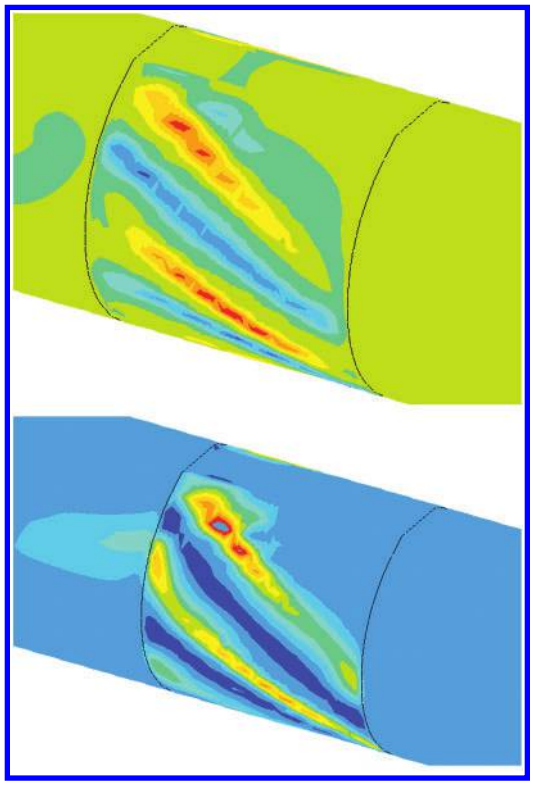


Figure 11a and b. Normal stresses (top) and shear stress (bottom) before failure.

The results of GMNIA for stresses near the failure condition should also be considered. Both the results for normal and shear stress may be considered.

The most relevant results are shown in fig. 11. Normal longitudinal stresses, as well as shear stresses are represented. Both stress types are heavily influenced by the imperfections introduced in the model. The narrow waves of the buckling mode shape directly determine the pattern of normal longitudinal stress distribution. This direct relation may be expected since local bending is introduced. However the effect of imperfections on the distribution of shear stress is less evident. Fig 11 clearly demonstrates that the maximum values of shear do not necessarily correspond to the area of maximum imperfection amplitude. In fact, as curvature increases, the maximum shear area shifts from the web centre towards the upper side of the web, near to the connection with the girder flange. All this confirms the former conclusion, that imperfections are less critical for shear loading than for bending or normal force.

A final verification may be to compare the loading condition to the use of simple bending formulas. For the flat web alternative, the slenderness reaches 167, well beyond class 3, the load carrying capacity thus being limited by web buckling. Failure occurs for a load of 10827 kN. The ultimate loads, corresponding to slenderness category 2 and 3 respectively are 13312.5 kN and 11716.2 kN. These quantities demonstrate that the failure by complete plasticization is close to the result from GMNAnalysis.

4 FURTHER DEVELOPMENTS

4.1 *Residual stress*

In the former, the effect of residual stress has not been taken into account. Nevertheless, the comparison between flat web girders and curved members is relevant, since the effect of residual stress due to welding and cold forming is expected to be similar for both situations.

Obviously, the curving of the webs is obtained by cold forming and this introduces meridional stress in the webs. This may reduce the shear failure load and further research should clarify the influence. In addition, welding stresses will have similar effect for both cases, the processes and developed heat being similar.

4.2 *Experimental verification*

The numerical results will have to be confirmed by experiments, allowing verification of the predicted values. Tests with scaled models are being considered. However, scaled models are generally too perfect and the introduction of imperfections should be considered thoroughly. In addition, the test setup will inevitably include both bending and shear loading.

At present, scaled model tests of plastic material are being considered, since this material easily allows curving of the webs. In addition, the material properties have been closely determined in the past. However, clamping of the model end is difficult to guarantee in tests. Therefore, a symmetrical model with central support and identical edge loading is being considered at present.

5 CONCLUSIONS

It was implied that, from various numerical simulations, the curvature of webs of bridge girders may

increase their buckling resistance, in spite of a more shell-like behaviour. This has been found through a model of a closed-section bridge girder in which the web curvature is increased gradually until the cross-section is close to a circle. However, the upper- and lower flanges have higher thickness than the webs and continue having higher contribution to the load carrying capacity.

Linear elastic calculations show considerable increase of the critical shear force, whereas non-linear plastic simulations show a similar tendency, however in a weakened manner. The influence of imperfections of a critical type, corresponding to the mode shape, verified during GMNIAnalysis, confirms that the curved webs are not highly sensitive to imperfections, even for amplitudes larger than normal fabrication quality.

REFERENCES

Eurocode EN 1993-1 (2004). Eurocode 3: Design of steel structures Part 1–1 : General rules and rules for buildings. CEN-Brussels

Eurocode EN 1993-1-6 (2007). Eurocode 3 : Design of steel structures Part 1–6 : Strength and stability of shells structures. CEN-Brussels

Van Bogaert,Ph. , Buckling resistance of steel curved bridge girder webs. In *Innovative Infrastructures Towards Human Urbanism.* Report on the 18th Congress of IABSE Seoul 2102 pp 326–327 + CDRom.

Research and Applications in Structural Engineering, Mechanics and Computation – Zingoni (Ed.)
© 2013 Taylor & Francis Group, London, ISBN 978-1-138-00061-2

The weathering steel bridges maintenance practice in Poland

M. Lagoda & T. Wierzbicki
Road and Bridge Research Institute, Warsaw, Poland

ABSTRACT: The weathering steel was quite often used for constructing bridges in Poland in the past. The main weathering steel bridges volume origins from the eighties of the last century. These structures are made from original Polish steel 12HNNbA. Some aspects of weathering steel itself and its history of invention are presented. During the service life some troubles in their behavior, which slightly differs from anticipated one, have occurred. Since then some administrative restriction has been put on use weathering steel in bridge construction. The paper describes day-to-day maintenance practice as well as results of investigations carried on some structures. Some results of tests on weathering resistant steel 12HNNb used for a span of railway bridge laid in the South and two highway bridges in Central Poland are presented in the paper. Worth underlying is the fact that every of those structures have different main girder structure – box, plate and T beam girders.

1 INTRODUCTION

1.1 *The origin of weathering steel*

Since the corrosion was regarded as the most severe problem in steel bridge structure maintenance, engineers were searching for the corrosion resistant material. Since the thirties of the previous century, it is believed that weathering steel might cause great savings on bridge building and maintenance.

The first documented use of weathering steel process occurred during the revolutionary war (1775–1783), when gunsmiths protected the surface of rifle and pistol barrels with a thin coat of iron oxide. This process, known as "browning" involved treating the exposed steel surfaces with chemicals to form a corrosion-resistant layer (McDad et al. 2000).

There are some tales on the first ideas of the weathering steel developing. One story says that during a London bridge demolishing, proceeded in the middle of the nineteenth century, it was discovered that some parts of the structure were in much better condition then the others. Chemical analysis showed that the well preserved structures have the 0,2% copper addition. This fact gave the idea to D. M. Buck, who reported in 1910 (or 1913 according to other sources) that carbon steel containing 0,2 % or more of copper had from 1,5 to 4 times the atmospheric resistance of carbon steel with a residual copper content. The most significant differences were found in severe industrial atmospheres, and the least improvement occurred in rural atmospheres (McDad et al. 2000), (Czyrski 1988). It was found out however that the copper presence in steel is valuable if the amount is being kept between 0,05% to 0,2%. Further copper presence increasing (over the 0,6%) does not affect atmospheric resistance, but has very negative impact on yield resistance and steel weldability. Later studies by various investigators pointed to beneficial effects from the inclusion of 2%, or less, of certain common alloying elements. Phosphorus, silicon, nickel and chromium appeared to provide atmospheric corrosion resistance to carbon steel.

The first major commercial application of weathering steel came in 1933, when it was used to build coal hopper cars. The first use of steel sheets in a building occurred in 1939 and in highway bridges in 1935. Later the wide use of the weathering steel can be observed in electrical transmission towers, guard rails and mainly in the architectural applications. Especially the last use of weathering steel made this material popular and gained public acceptance.

1.2 *Polish weathering steel*

Since weathering steels were introduced in USA, which was called corten steel there and gave the name for the whole weathering steels family, many countries were trying to adopt the idea of corrosion resistant steel in their own laboratories. Poland was between them as well, and some original steels were elaborated. In 1956 the Lenin Steelworks (Sendzimir Steelworks) has worked out the 10H steel, which was the first Polish weathering steel. This material was used for the coal miners cars only. In 1964 the next generation of weathering steels 10HA (copper, phosphorus and chromium steel) was introduced. This steel was used for railway

Table 1. Chemical composition of the 12HNNbA steel (TWT 1988).

Element	Composition [%]
C	0.09–0,14
Mn	0.60–1.00
Si	0.30–0.60
P	max. 0.0035
S	max. 0.0035
Cr	0.70–1.10
Ni	0.30–0.60
Cu	0.30–0.55
Nb	0.015–0.035
Al	0.06–0.15

cars. In 1971 the Institute for Ferrous Metallurgy has finished the research activity on the structural weathering steels and five new materials were put on the market, together with two welding materials dedicated for that material. This were 10HAV, 10HNAP, 12PJA, 12H1JA and 12HNNbA and welding wires SpG1Ncu and SpG2S1Ncu.

One of these steel grades were used for constructing the very first bridge structure in Poland. In 1975 the highway viaduct was erected as a part of trans European road E8 in Poznan, western Poland. The bridge structure, made of 7 10HAV steel girders was the composite one with five spans. The viaduct is kept in service till today, but the steel surface was painted shortly after the erection. Although the structure is still in service, the 10HAV was not intended for bridge structure erection. As this steel has relatively high, among the weathering steels, yield limit (390 MPa) and high tensile strength (510–650 MPa), it was intended to build mainly structures for mining industry, railway cars, steel containers and general building structures. The steel grade intended for bridges mainly was the 12HNNbA steel. This material is quite sophisticated one from the metallurgical point of view, and is composed from three main elements. These are copper, chromium and nickel. This steel has very positive plastic properties, which are high toughness in temperatures between +20°C and −40°C, high fracture toughness and good weld ability.

Those properties have made the structural engineers build some bridges in Poland in the eighties and early nineties of the previous century. These structures are presented later in this paper.

2 POLISH WEATHERING STEEL BRIDGES AT GLANCE

2.1 *General remarks*

First of all it must be stated that weathering steels were never the primary structural material in Polish bridge engineering. A few bridges, which were erected can not be compared to the structures made in the Czech Republic (former Czechoslovakia), Germany or other western European countries, not mentioning USA nor Japan. Moreover nobody has decided for this material in bridge engineering for the last twenty year. The reason for that is, that there is a practice in Poland to care about initial construction costs, not counting future savings on maintenance or traffic delays costs paid by road users. It was not mentioned here yet, but the 12HNNbA steel used to be 20% more expensive then ordinary structural steel. This extra cost was compensated with maintenance cost within the lifetime of the structure. The reason for refrain from using weathering steel could be slightly different way of designing details, which could allow for patina growing and preserving. Further some problems with weathering steel in Polish structures are presented.



Figure 1. General view of the Zakroczym Bridge.

2.2 *The Zakroczym bridge*

The road bridge is located in route of the National Road No 7 leading from Chyzne to Gdansk, which is one of the primary importance for Polish road network. The bridge was built in form of two independent structures, each leading single traffic direction placed on the isolated supports. The structure is built as a continuous box girder with the span 75.0 m+4×95,0 m+75,0 m. the box girder high is 2,7 m. The bridge was put in service in 1990 (the Gdansk direction) and 1992 (the other way). The bridge can be seen at the Figure 1.

2.3 *The Nur bridge*

The road bridge was constructed as the composite one with four steel plate girders and composite concrete slab. The girders were made of 12HNNbA steel and were left uncoated. The structure is situated in rural, non-aggressive atmosphere. The bridge structure was erected in 1987. This structure is pictured at the Figure 2.

2.4 *The Kaczawa bridge*

The bridge over the Kaczawa river in Prochowice is situated in the south-west part of Poland. This is the railway bridge located on the secondary railway line and was put out of service recently. The one span (27,0 m) structure was built in the late nineties of the



Figure 2. General view of the Nur Bridge.



Figure 3. General view of the Kaczawa Bridge.



Figure 4. General view of the DK 7 viaduct.

previous century. The span carries one railway track and is composed of two 12HNNbA steel plate girders 1,965 m high. The Kaczawa bridge is shown at the Figure 3.

2.5 *The DK 7 viaduct*

The local road viaduct over the DK 7 is situated just around 20 km away the Zakroczym bridge. The superstructure is made of two 12HNNbA steel plate girders (0,96 m high) and the concrete composite slab. The total length of the bridge structure is 77,70 m



Figure 5. General view of the DK 7 ecological viaduct.



Figure 6. General view of the Kanal Zeranski bridge.

and is composed of three spans 22,4+32,0+22,4 m. The viaduct was erected in the beginning of nineties XX century. This bridge structure is presented at the Figure 4.

2.6 *The DK 7 ecological viaduct*

This road viaduct built the same time as the Zakroczym bridge was made to allow wild life exist in the environments of the busy road. The structure is 117,60 m long, six spans 15,13+3x21,36+20,24+15,56. This is again composite structure with six 12HNNb steel plate girders in a cross section. This viaduct is presented at the Figure 5.

2.7 *Kanal Zeranski bridge*

The bridge built in mid-nineties, last century located in Warsaw. There is a continuous three span structure 27,10+38,00+27,14 m of total 92,28 m length. The cross section consists of four 10HNPA steel plate girders with variable high from 1,27 to 2,45 m over the supports. the bridge is located in a weak urbanized area, however the locals made the road authorities to paint the outer surface of the girders, as they were unlikely to see “rusty” bridge, which was addressed negative in terms of aesthetics. The bridge can be seen at Figure 6.



Figure 7. General view of the Kepno viaduct.

2.8 *Kepno viaduct*

This structure is a railway viaduct, which carries the rail track over the most busy road in Poland. This is one span structure, with the span length 15,0 m. The cross section consists of two steel plate girders 2,30 m high. There is an orthotropic deck, made, together with the girders, of 12HNNbA steel. This structure's view is presented at Figure 7.

3 THE EXPERIENCE GAINED THROUGH WEATHERING STEEL USE FOR BRIDGE STRUCTURES

3.1 *General*

As mentioned the weathering steel is not the popular structural material in Polish bridge engineering. In general the most common structural material is the concrete. If the steel is chosen the most common is the conventional S355J2 with the paint anticorrosion protection. The reason for avoiding the weathering steel is unknown. The truth is, that the former bridge designing Standard did not include the weathering steel for the material catalogue. On the other hand there were some information on temporary ban on its use in USA and German bridge engineering. Though that problem was promptly solved and the steel is widely used in both countries the suspicious atmosphere in national bridge engineering did not disappeared.

3.2 *The common problems*

The biggest problem, which faced structure administrator was, similarly to all over the world owners, preserving of the patina layer. One of the commandment in steel structure designing, and in the case of weathering steel in particular, is to avoid zones were the debris and moisture can be accumulated. That needs careful detailing. The structures were detailed in a very conservative way, the way the structures made in conventional approach. That means that the shape they made it allows for accumulation debris and destroying patina. Quite a serious problem were the devastation as well, which destroyed patina directly or through devastation of drainage system, which washed out the patina from the steel surface. There is a problem if let say aesthetic nature as well. There are often opinions meet that the bridge, although new one is already destroyed (corroded). Though this attitude is going to be changed shortly probably, as the growing non-bridge structures number utilise weathering steel for the façade for decorative purposes.

3.3 *The results of the investigation*

There were detailed investigation made on the three Polish bridges – the Zakroczym bridge, the Nur bridge and the Kaczawa bridge.

The investigation scenario was moreover similar in all three cases, however the Zakroczym bridge was under special surveillance including inside temperature and humidity monitoring, due to its extraordinary box cross section. There was a dedicated automatic monitoring system installed. It was to register the climate condition inside and outside the box girder. For nearly two years, five gauges measuring humidity and ten measuring temperature (half of them were measuring the steel surface temperature and half the air temperature) every ten minutes was monitoring and recording measured values. The cyclical structure assessment revealed that one of the steel of one bridge span did not create proper patina layer neither after three years of service nor after five years since it was produced. The girder surface was covered with thick, brittle layer of corrosion products, which were tearing apart exposing bare steel surface, which was not protected with the patina again. The specimens were examined in periodical time space, so there is a possibility to trace the particular value variation in the time.

The investigation revealed two main reasons of the steel behavior.

Firstly the steel sheets had some rolling defects, There were traces of non metallic material linear overlaps seen under the microscopic examination. They were met all over the steel sheet surface. These technological defects with no doubt explain the reason of the noticed delamination of the corrosion products found inside the girder box.

The defects found in the weathering steel structure do not explain however, why the dense, protective patina made of the corrosion products do not cover the steel surface despite exposing steel surface for few years. According to the literature and normal practice happens after a year or two. The reason for that was discovered thanks to the previously described monitoring activity. It appeared that since October 1994 till May 1995 the steel surface was practically permanently wet. In such thought condition the patina has no chance to grow. So it was the microclimate inside the box girder, which did not allow patina to cover the steel surface with the proper, protective patina.

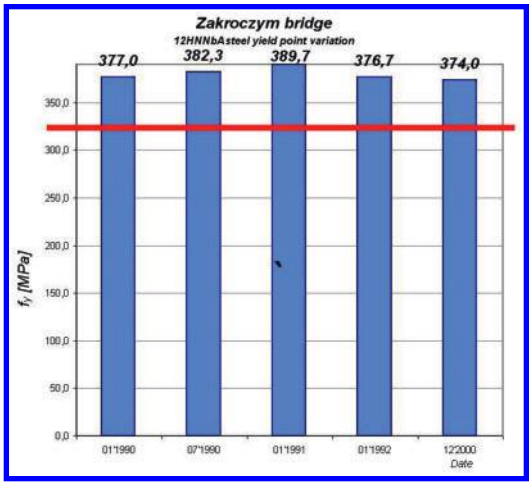


Figure 8. Psychical yield point variation at Zakroczym bridge.

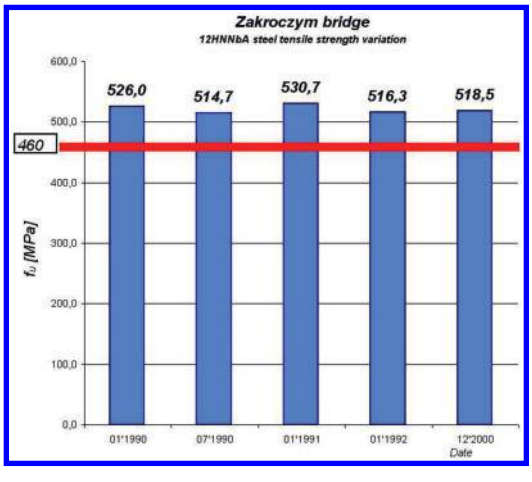


Figure 9. Tensile strength variation at Zakroczym bridge.

Anyway in case of all three brides, the investigation covered the weathering steel specimens strength testing, visual testing and metallographic investigation. And the strength test included: bending test, strength test, Charpy test both the natural and artificially matures specimens. All the specimens were prepared from the original weathering steel taken from the bridge structures at the excessive steel sheets. That means that the sample steel was under the same mature circumstances and was exposed for the same weathering conditions like the steel of the bridge.

It must be stated that all the experiments were positive in every case in terms of strength capacity. The steel despite 20 years of service was in very good condition, with no signs of cracks, excessive corrosion or any damage. All the results like psychical yield point, tensile strength, bending strength, percentage reduction of area elongation value and impact resistance were far above the limits required by the temporary production conditions (TWT 1988).

The red lines on the drawings represents the minimal values required by the (TWT 1988). In case of psychical yield point this is 325 MPa and in case of tensile strength this is 460 MPa. The other structures gave the similar results.

The only problem with the structural material was recorded in case of the Zakroczym bridge. There were two problems in fact. The first problem found in this structure was the insufficient durability of the orthotropic deck. The cracks in longitudinal ribs welded joints were found after the 18 years of service. The first idea was to blame excessive corrosion of weathering steel elements, which caused the water leakage and further destroy. Albeit the owner was trusted in this explanation there were some research activity raised to find out the reason for damage.

The other was a problem, described already, of never appearing patina inside the box girder, which lead to excessive corrosion loses. In that case, the bridge owner was forced to paint the inner surfaces of the box girder in the most destroyed sections (Wierzbicki 2012).

4 CONCLUSION

As a general conclusion one may states that the weathering steel in Polish railway and road bridges, after over twenty years of service performers reasonably well. All the strength investigations show that the structural material is strong and does not ageing. There were some problems observed in one of the bridges, with extraordinary construction (box girder with orthotropic deck) and as a result the avoidance of using this solution in weathering steel bridges is advised.

REFERENCES

Czyrski W., Stale konstrukcyjne trudno rdzewiejace, Wydawnictwa Akcydensowe, Warsaw, 1988.

McDad B., Laffrey D, C., Dammann M., Medlock R. D., Performance of Weathering Steel in TxDOT Bridges, Report on 0-1818 Project, Texas 2000.

TWT/2.1/90/88 Tymczasowe Warunki Techniczne dla blach ze stali trudno rdzewiejacej 12HNNbA.

Wierzbicki T. Ksztaltowanie konstrukcji mostowych ze stali HPS, w tym stali Trudno rdzewiejacych w aspekcie ich trwalosci. IBDiM Warsaw, 2012.

Research and Applications in Structural Engineering, Mechanics and Computation – Zingoni (Ed.)
© 2013 Taylor & Francis Group, London, ISBN 978-1-138-00061-2

Study on high speed railway prestressed continuous rigid frame bridges

Jun-Qing Lei & Kun Zhang
School of Civil Engineering, Beijing Jiaotong University, Beijing, China

ABSTRACT: For high-speed railway prestressed concrete bridge, to control the deflection of the bridge as the standard, studying the key technologies of the bridge design and construction, finite element methods to calculate and analyze the Static characteristics of the beam bridge. The design of the main consideration load as: weight, temperature gradient, the settlement of bearing, the second phase load bearing (uniformly distributed load), moving load on the influence of the bridge deflection in the same bridge design provides technical reference. The construction monitoring procedure of the five-span continuous rigid frame bridge (80 m+3×145 m+80 m) of Wenzhou-Fuzhou high-speed railway, the way of construction monitoring, simulation calculation, calculation of elevation, and measurements of elevation and stress are introduced in this paper, and controlling situation of alignment and stress of the bridge is emphatically analyzed. Also, comparative analysis on the influence of changes of bulk density and elastic modulus of concrete on the final bridge line is made, which comes a conclusion that the change of bulk density of concrete is more effective. So field test of influence parameters of the final bridge line is recommended besides the calculation analysis to reduce the difference between theoretical elevation and actual elevation. Finally, this paper concludes the situation of calculation analysis and construction monitoring: formwork erected with relative elevation method can remove temporary load's effect and effects of stochastic factors and can get a smooth final bridge line; a better theoretical elevation can be calculated if parameters are corrected according to field tests. The controlling measures such as adjusting the Elevation and Control weight are taken for the construction, in accordance with the results of the analysis in order to ensure that the stresses and alignments of the beam can meet the relevant code requirements at each construction stage and the bridge is completed successfully. The reference information is provided to the another bridge.

Keywords: high-speed railway; Strain and Stress; linear control; Continuous rigid frame bridge; Construction monitoring; Influencing factors of alignment; Deflection deformation

1 INSTRUCTIONS

In recent years, with the pre-stressed technology and the transportation development, pre-stressed concrete continuous rigid-frame bridge with its construction is simple, economic and reasonable cost, comfortable and maintenance costs low unique advantage is becoming more and more applications. To ensure the continuous steel bridge design bridge is in good agreement with the linear and the structural is safety in the construction process, construction supervision is more and more attention. Construction of long-span bridge structure is aimed at monitoring the construction process through the various parts of the bridge structure, deformation, strain, stress monitoring and control, to ensure that the bridge structure during construction and bridge closure precision, linear and internal forces after the structure meet the design requirement.

White Horse River Bridge, located in Wenzhou-Fuzhou express railway Ningde section, across the White Horse River Bay, the main bridge for the cross-hole layout for the 80 m+3×145 m+80 m of large-span continuous rigid frame bridge (see Figure 1).



Figure 1. Bridge overall layout.

Design live load is used China- live load and ZK load line for the two-lane I-class railway passenger and freight lines were designed driving speed of 200 km/h, set aside 250 km/h speed conditions. The main beam uses three approaches the pre-stressed concrete box girder structure, longitudinal entire pre-stressed. Box single box single form, the control of the high beam are: side supports of straight line segments and cross-side cross in the Department to 4.5 m, side cross-section of a long line 8.3 m (including end-to-side bearing beam center 0.8 m); Bridge box girder bottom width 7.5 m, roof width 13 m. Wenzhou-Fuzhou White Horse Creek Bridge High-speed Railway Bridge Total Beam 157, Closure has 5, the bridge girder construction of ma

2 THEORY OF CONSTRUCTION MONITORING

2.1 *Construction Monitoring Ideas*

According to the continual rigid frame bridge's construction characteristic, the segments have been completed for the error can't be adjusted, and not completed segment of the state and the accurate simulation, and the completed segment of the error has nothing to do. This decided that the continual rigid frame bridge's construction control should be in the prediction that namely the accuracy for a given beam elevation end of the formwork. First, it is assumed that the structure is the ideal state of structure parameters various structural parameters are designed according to specifications or drawings of value, given the ideal state of pre-cast high to guide the construction of the superstructure.

When carries on the beam section formwork erection elevation computation, the main provider of each beam section to be poured around the end section of the height difference, absolute elevation as reference, to have complete section for stress and elevation measurement, when appears the stress and the predicted value do not tally, should analyze possibly has error's reason, the parameter identification, fixed structure parameters of calculation, construction segmental ideal. If appear displacement calculated results and actual displacement value deviation of elevation, there are fixed.

In the bridge deck height control, we should aim to ensure smooth deck, not one-sided pursuit of the theory of individual node level. When the construction of a process or beam segment elevation after pouring deviation value and the theoretical value after the occurrence, without force in the next paragraph immediately adjust the beam over, but should identify the features of Control error occurred reason, the later calculation of cantilever deflection when casting an amendment, when in the next few beam section of the cantilever pouring all late even beam deviation will gradually corrected elevation. Finally into bridge may have many practical elevation and beam design elevation error, but the overall linear deck is smooth.

2.2 *Simulation computations*

In the present stage construction the bridge simulation computational method mainly includes: orderly-erecting analysis method, inversion analytic method and un-stressing condition computation method.

The greatly cross continual rigid frame bridge usually uses cantilever cast-in-place construction method, the construction cycle is long, connected the parameter like loss of pre-stress, the concrete shrinkage continuous variation with the time and so on to be big to the construction control influence, therefore, it uses orderly-erecting analysis method to be more suitable.

The structure of discrete except in simulated stress of the pier top, cross-sectional layout of the measuring point and thin wall pier, the other is the main beam by beam segment is divided, full bridge were divided into 234 finite elements, the main beam 202 units Each cantilever casting segment as a unit, each continuous 0# block pier Department is divided into eight units, rigid frame pier Department 0# block is divided into 12 units, piers divided into 8 units. Support the construction process simulation for the temporary support, the main beam and pier use master-slave nodes the connection. When modeling the following assumptions: full-pre-stressed girder structures; does not consider the ordinary steel bar participation structure stress; pier cap bottom and constraints into account by the consolidation.

2.3 *Elevation determination*

Main beam linear control most direct and effective way is the measured value on the theoretical values to determine the box after correction segment elevation model legislation. Various errors caused by changes in the elevation and girder can be corrected by adjusting the girders during so that the main beam close alignment as possible after the bridge design of linear fit.

Box girders during the theoretical calculation formula for:

$$H_n^i = H^i + f_y^i + f_n^i \tag{1}$$

where H_n^i is the n construction stage i node formwork elevation; $H^i$is the i node design elevation; f_y^i is the i node camber; f_n^i is the i node from the n construction stage to the bridge total deflection.

As the material properties, load error, temperature changes, shrinkage and creep and relaxation tendons and other factors, the situation has some differences with the calculated. So have to constantly fixed girders during theory on. Elevation of the box the actual legislation:

$$H_n^i = H^i + f_y^i + f_n^i + f_g + \Delta f^i \tag{2}$$

where H_n^i is the i node elevation of the actual legislation f_g is the Hanging Basket elastic deformation; Δf^i is according to observations and cantilever deflection deformation of the trend adjustment to determine the value of the deflection.

Elevation of the actual legislation calculation, if the measured value and the theoretical values deviate from the small, and find out the law of deviation from the value, then the legislation can be more accurate elevation model is given; if deviation values larger or irregular, you need to by linear regression theory and gray theory to analyze and predict. White Horse River Bridge span continuous rigid frame full-bridge formwork camber curve in Figure 2.

From the Fig. 2 can see, in 12# pier or 13# pier on both sides of the arch value difference is bigger, in the near side of the cross-camber side span of almost the double camber, which mainly due to downward deflection in the span much higher than the second side span,

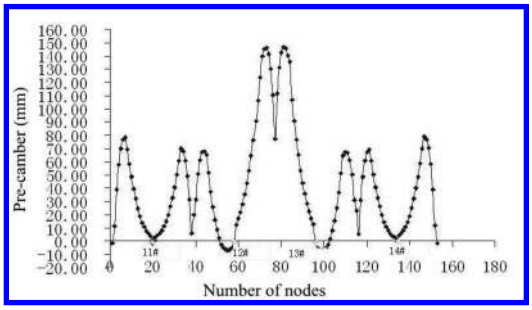


Figure 2. Bridge formwork camber curve.

the late creep across the impacts that are relatively large, these had decided when mid-span formwork erection must throw the high certain value. 11 pier# or 14# pier both ends of the camber is basically the same. For both ends of each pier Camber is then decreased, in the near Closure camber also reduces the time, this is because in the vicinity of Closure beam, post-weight is not caused by the accumulation of the beam segment under its Flexible, on the contrary will occur up rebound phenomenon because of the rigidity of a large fold.

2.4 *Density and elastic modulus of concrete*

In bridge deck construction and operational phases of impact parameters of more linear, but in general include geometric and material parameters in these two areas. The geometrical and material parameters are closely related with the construction, pre-calculated value and actual value of their existence often some differences, so when construction monitoring is necessary to analyze these differences impact on the linear. According to various parameters influence quantity size, modeling predicted ahead of time to adjust, so as to meet the design goals linear bridge.

The earlier period computation mainly involves to the concretes bulk density, elastic modulus of concrete, concrete shrinkage and creep coefficient, pre-stressed parameters, temperature field, main pier foundation settlement parameters of the 6 areas. The following analysis focused on bulk density and elastic modulus of concrete changes in the span is the elevation changes of the node.

2.4.1 *Concretes bulk density change to bridge linear influence*

In the bridge design, concrete bulk density and elastic modulus values according to specifications, but in actual construction of concrete and reinforced concrete density of sand and cement ratio of closely related. Despite the continuous bridge construction, each segment is used the same gravel concrete materials and water-cement ratio, but all segments of the concrete mixing and pouring is separate, so the differences will still exist. Based on past experience shows that construction monitoring: weight error is less than 5%. To bridge balance basis, beam weight change on the main beam linear in Table 1.

Table 1. Beam weight change on the main beam linear.

Beam weight changes /%	Δh/mm		
	A	B	C
5%	0.19	−6.72	−4.24
3%	0.13	−4.06	−2.55
0	0	0	0
−3%	−0.08	3.92	2.52
−5%	−0.14	6.59	4.21

* Note: ① h for the node elevation changes, the same; ② A, B, C respectively, cross-border, sub-side span, location across the span; ③ Figures in the table are representations on the deflection, that under the negative deflection, the same below.

Table 2. Beam weight change on the main beam linear.

E/MPa	Δh/mm		
	A	B	C
3.35×10^4	−0.55	3.19	−1.64
3.35×10^4	−0.45	2.64	−1.34
3.35×10^4	−0.36	2.09	−1.05
3.35×10^4	−0.25	1.52	−0.77
3.35×10^4	−0.17	1.02	−0.5
3.35×10^4	−0.09	0.51	−0.25
3.35×10^4	0	0	0

As can be seen from Table 1, the maximum beam weight change 5% change in the maximum deflection of the bridge 6.72 mm, so the change of beam re-alignment of the bridge obviously.

2.4.2 *The elastic modulus of concrete on the bridge of linear*

In the early design and review process of calculation, concrete elastic modulus values according to standard requirements for the bridge, the main beam is used C60 grade concrete. So, when calculated in accordance with design specifications to take concrete elastic modulus 3.65×10^4 *MPa*. However, non-linear concrete material, the elastic modulus changes with time, during the construction process, the coagulation of the elastic modulus of concrete by the impact of age and conservation does not necessarily meet the design specification to the reference value.

As can be seen from Table 2, the bridge is the change of elastic modulus of the bridge alignment is not very obvious, the biggest change to 3.19 mm.

3 ANALYSIS OF THE ACTUAL STRESS OF CONCRETE

3.1 *Effect of the Shrinkage and Creep Strain*

Concrete creep and concretes applied stress related, under the working stress, concrete elastic strain and creep strain and stress is linear. Therefore, as long as the total stress does not exceed 50% of concrete

strength in batches produced by the strain imposed by the stress superposition principle can be used. Situation for uninstall or load shedding, D. 1943 McHenry reversible creep theory proposed, will consider imposing load unload set, it generates the same time the creep load is applied in disguise, etc. creep generated, but in the opposite direction. The concretes test sample's experimental showing principle of superposition tallies very well to the basic continuous variation.

3.2 *Effect of the Temperature*

After the strain gauges embedded in concrete, the deformation occurred simultaneously with the deformation of concrete. As the concrete and the strain gauge thermal expansion coefficients of different, so when the temperature changes, strain gauges have the same passive deformation with concrete, by now the strain gauge received the concretes one kind of binding force (i.e. temperature strength), when temperature increment, the strain gauge receives the compressed stress, otherwise receives the tensile stress. The temperature elevates or reduces, will bring cantilever beams in free to elongate or shorten. This elongation or shortening the body does not produce stress in the beam changes, but the change in beam length will be embedded in the main beam reflected on the sensor, the sensor out from the concrete stress test points, including elongation of concrete caused by temperature changes or shortened.

4 MONITORING AND ANALYSIS

4.1 *Elevation Monitoring*

Elevation measurement points set in front of each block in the line, laying a 2~3 cm reinforced above the concrete. To minimize the effect of temperature, the White Horse Creek Bridge, the deflection of cantilever construction observation time normally scheduled for around 7:00 in the morning.

As the pre-stressed concrete continuous rigid frame bridge elevation observed before and after the task is to reflect the process or a specific period of time the actual deflection of the main beam changes, the elevation of the observations should be conducted before and after the procedure. Cantilever construction of the bridge, each of Cantilever Beam conditions to carry out four kinds of linear control of observations, that is, ① hanging basket in place, ② after concrete pouring, ③ tension pre-stressed steel beam before, ④ pretensile stress of steel beam is completed.

According to the method of continuous rigid-frame bridge white river Wenzhou-Fuzhou railway construction process of the deck elevations, the theoretical calculation and the actual result tallies basically, the differential value control in 5 cm, linear changes in the overall smooth main beam.

Can be learned from the previous plan, the actual level of control over the White Horse River bridge

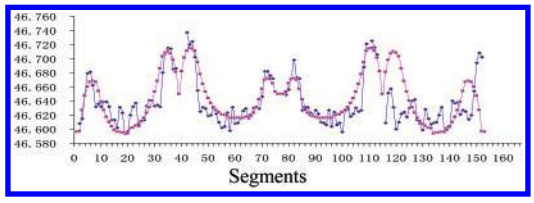


Figure 3. Measured elevation and design of the top flange should be compliance with high contrast chart.

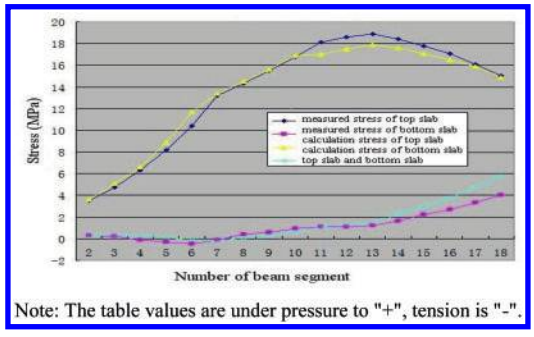


Figure 4. Caption Measured and calculated stress ratio.

is consistent with the overall design of the expected elevation linear. But because of 14 pier construction quickly, for the second side failed to timely adjust across elevation design elevation, the expected linear slightly lower than expected elevation design. And the corresponding 11 of control is perfect, good control of the line. Another Pier 12 and Pier 13 on both sides of cantilever segmental construction of elevation control in line with the design elevation.

4.2 *Stress Monitoring*

The main beam of stress and strain tests were selected in each cross-section of the fulcrum around 1/4 cross in the middle section. Beam test at the Department of the section of the roof, laid the floor of observation points, observation embedded devices (embedded concrete strain gauge steel strings). Standard beam section of each course of construction, on cradle in place, concrete pouring is completed, pre-stressed tension is complete, and on cradle mobile observation points in four operating conditions the stress test.

Each T cantilever both sides each three test section, decorate besides cantilever root 2 section 8 points, decorate the other section are six test points, a total of 40 test points. The bridge has four T-frame, total $4 \times 40 = 160$ test points. Strain sensors embedded in concrete are arranged horizontally in the direction of the bridge. Near the main pier construction phase of a cross-section measured stress values compared with the calculated values shown in Figure 4.

From the Figure 4, the measured cross section various stages of stress and stress calculation in good agreement, basically the same trend, only a slight departure from some, less than the maximum difference in 2 MPa. Error for many reasons: ① the

selection of design parameters (such as: the material properties, density and characteristic parameters); ② Construction Status Determination (working load, elastic modulus of concrete, concrete shrinkage and creep, pre-stress losses, temperature and other parameters) and measurement differences in the environment; ③ test equipment laying position, when the tension of the pre-stressing tendon closer position and test instruments, it will produce local stress concentration, the impact on test results. In general, this test is entirely reasonable, the error in a reasonable range.

5 CONCLUSIONS

(1) Concrete bulk density and elastic modulus of concrete is a continuous rigid frame bridge a greater impact on linear factors. Changing in bulk density of concrete is relatively linear effects on the more apparent. When linear control must carry on the key monitoring and the analysis to it, suggests when the computation analysis does the scene experiment to the linear influence parameter.

(2) The relative elevation method for setting formwork can eliminate the temporary load, and other random factors, obtained control of linear flow. Elevation of the legislation setting out the process, focus on the beam temperature difference changes, the measurement of time as we choose the temperature more stable periods, as short as possible formwork time.

(3) In large-span continuous rigid frame bridge construction monitoring, suggested by the structural parameters according to the standard according to the measured values, then complete the segment of the measured elastic modulus of concrete and the shrinkage coefficient to amend the method of calculating the model parameters to achieve the computing model and the actual structure of the line, in order to better predict the level of construction formwork.

(4) Stress monitoring results with the calculated error of close to 2 MPa, in addition to the scene of some random factors, the more the main reason is that individual tensioning tendons relative position and test equipment too close, and the calculation used to model creep and shrinkage the actual difference between the creep caused by the situation. There is no very consistent with China's actual situation creep model to study a better reflect the actual creep model is very necessary.

ACKNOWLEDEMENT

The authors wish to acknowledge the support and motivation provided by Scientific Research and Development Program of Ministry of Railways of China (NO.2006G010-A). At the same time, it has been supported and provided financial aid by National 863 program of Ministry of Science and Technology, contract number: 2008AA11Z102. At the same time, it has been supported and provided financial aid by National Natural Science Foundation of China, contract number: 50878020 and 51178042.

REFERENCES

Code for Design on Reinforced and Prestressed Concrete Struture of Railway Bridge and Culvert (TB10002.3-2005) [M]. Beijing: China Communication Press

Lichu Fan and Guanghui Xu. 2008. Bridge Engineering (Volume 1) [M]. Beijing: China Communication Press

Yuhui Fu, Chen Yanjiang and Sun Peng. 2006. Analysis of temperature influence on long-span continuous rigid frame bridge construction control [J]. Journal of Harbin University of Commerce(Natural Sciences Edition), 22(3).

European International Concrete Committee CEB-F1 Mode Specifications

Junqing Lei. 1999. Cantilevered bridge construction and design. Beijing: People's Traffic Press,

Anbang Gu. 2005, Bridge construction inspection and control. Machinery Industry Press.

Research and Applications in Structural Engineering, Mechanics and Computation – Zingoni (Ed.)
© 2013 Taylor & Francis Group, London, ISBN 978-1-138-00061-2

Experimental study on hybrid FRP-concrete bridge superstructure

Y.L. Wang, J.H. Ran, Y.Y. Li & M.M. Cao
School of the Civil Engineering, Dalian University of Technology, Dalian, China

ABSTRACT: The concept of the hybrid FRP-concrete design was exploited in a new type of bridge superstructure system. The proposed hybrid bridge superstructure was designed as a simply supported, 10 m singlespan, one-lane bridge. The bridge superstructure consists of two bridge decks and each deck is comprised of four Fiber Reinforced Polymer (FRP) box sections combined with a thin layer of concrete in the compression zone. This new design was proposed to reduce the initial costs and increase the stiffness of FRP composite structure. This paper presents the results from the experimental study on a one-third scale model of the hybrid FRP-concrete bridge superstructure. The scale model was subjected to four-points loading to simulate the truck load. The test results indicate that the proposed bridge model meets the stiffness requirement and has an significant reserve strength.

1 INTRODUCTION

A major concern for many bridge superstructures is the significant reduction in durability and life expectancy caused by the corrosion of the reinforcing steel and the corresponding deterioration of the concrete. These problems are accelerated by the application of de-icing salts in cold area. The corrosion will eventually cause enough damage to warrant a superstructure replacement or retrofit (Robbins 2002). According to the U.S. National Bridge Inventory, nearly 27 percent of 590,000 public bridges were either structurally deficient or functionally obsolete as of 2003. The U.S. Department of Transportation (DOT) estimates the average annual cost to improve bridge conditions for the 20-year period of 1998–2017 to be $10.6 billion in 1997 dollars (Kitane & Aref 2004, Kitane et al. 2004). The similar situation exists in China. These facts imply that it is imperative to develop and construct bridge systems that have long-term durability and require low maintenance.

As one of the solutions to this problem, structural applications of fiber reinforced polymer (FRP) composites have recently been attractive in the civil engineering community due to their superior material properties such as high corrosion resistance, high specific strength, and high specific stiffness. In terms of initial costs, FRP composites are still too expensive to compete with other conventional materials used in civil engineering applications. To make the best use of materials and reduce the initial costs, combinations of FRP and conventional materials have recently been investigated by a number of researchers (Mirmiran 2001). The advantages of the combined or hybrid structural systems include the cost-effectiveness and the ability to optimize the structural section based on material properties of each constituent material. According to Mirmiran (2001), the most effective use of FRP composites in civil structural applications is in the form of a hybrid construction with concrete.

Among the bridge maintenance items at U.S. DOT, bridge decks are ranked No.1 maintenance priority (Brailsford et al. 1995). Therefore, the concept of the hybrid FRP-concrete structural system was applied to bridge superstructure in this study. The primary objectives of this study were to propose a conceptual design of a hybrid FRP-concrete bridge superstructure, and to examine its performance under live loads by experimental investigation.

2 PROPOSED HYBRID FRP-CONCRETE BRIDGE SUPERSTRUCTURE SYSTEM

Although many configurations of the hybrid FRP-concrete bridge superstructure are possible, a conceptual design of the hybrid bridge superstructure shown in Figure 1a, where supports and substructures are not shown, was chosen. A prototype bridge was designed as a simply supported, single-span, one-lane bridge with a span length of 10 m. Geometrical parameters of the cross sections in Figure 1b were determined based on numerous finite-element analyses. The cross section of the bridge is comprised of 8 box sections, each of which has a layer of concrete in the compression zone. E-glass woven fabric reinforcement and vinyl ester matrix were selected as constituents for the GFRP laminate. In this study, the ratio of the area of concrete to the total area in the cross section is 0.4.

The bridge design is based on the traditional plank bridge concept, in which a number of individual beams

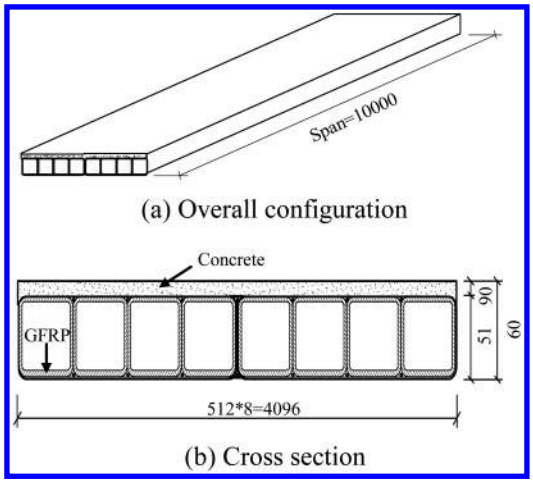


Figure 1. The proposed hybrid bridge superstructure (units in mm).

are placed side by side to create a bridge. The advantages of this concept include: (1) corrosion resistance for steel-free design; (2) initial costs reduction due to the effective use of concrete; (3) lightweight; (4) reduction of local deformation under concentrated loads that is found to be a problem in all-composite bridge; (5) no joints between decks and girders (the girders are the decks); (6) significant understanding of the bridge behaviour can be obtained by testing of individual beams; (7) the concept is well understood by bridge engineers.

Four beams make up a bridge deck with a width of 2,048 mm. The prototype bridge consists of two bridge decks. The 2,048 mm wide bridge deck can be easily transported to site on a standard truck and assembled into a bridge using simple field joints.

The design concept is similar to the concept proposed by Van Erp et al. (2002). However, there are several distinctnesses, including: (1) without utilization of CFRP due to its expensive price and lack of source in recent years in China; (2) usage of normal concrete instead of polypropylene fiber reinforced concrete; (3) the ways of assembling between two decks, and among GFRP beams in the bridge deck.

3 EXPERIMENTAL PROGRAM

3.1 *Material*

Two types of bidirectional E-glass woven fabric with a weight of 600 g/m^2, (0°/90°) and (±45°), were selected as the primary continuous reinforcement of FRP laminates. In these fabrics, fibers in 0° and 90° or +45° and −45° directions have the same weight (300 g/m^2). Vinyl-ester resin, Swancor 901, was chosen as the matrix. Vinyl-ester resins are typically used when high durability, thermal stability and extremely high corrosion resistance are required; therefore, they are very suitable for civil engineering structures.

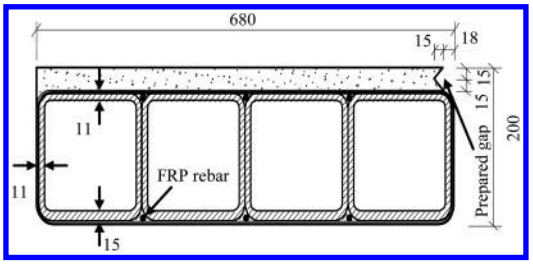


Figure 2. Cross section of 1/3 scaled hybrid bridge deck (units in mm).

Due to the size of the test specimen, coarse aggregates with maximum size of 10 mm were used in the concrete. The compressive strength of the concrete on the day of test is 51 MPa. Young's modulus of the concrete will be slightly smaller than the normal concrete due to the use of small size coarse aggregates.

3.2 *Test specimen*

The test specimen is a one-third scale model of the 10 m hybrid FRP-concrete bridge superstructure shown in Figure 1. As mentioned above, the bridge superstructure consists of two same bridge decks. Figure 2 shows the cross section of one bridge deck. The specimen (FRP part only) was fabricated at Harbin Composites Corp. of China. The box sections were fabricated by the hand lay-up process at present stage. The top flange and the webs of each box section had the same fiber architecture, which consisted of 13 layers of woven fabric reinforcement. However, the bottom flange consisted of 19 layers of woven fabric to increase the global stiffness of the section. Stacking sequences of the top and bottom flanges were $[(0°/90°)_3, (\pm45°)_2, (0°/90°)_2, (90°/0°), (\mp45°)_2, (90°/0°)_2]$, $[(0°/90°)_3, (\pm45°)_2, (0°/90°)_2, (90°/0°), (\mp45°)_2, (90°/0°), (0°/90°)_3, (90°/0°)_3, (90°/0°)_2]$, respectively. The fiber volume fraction of the FRP part is about 0.3.

The eight individual box beams were fabricated firstly. Secondly, by combining two sets of 4 box beams each using vinyl-ester resin and chopped strand mat (CSM), 2 sections with a width of approximately 680 mm were created. Thirdly, the tw2 sections were wrapped individually with a laminate having a $[(0°/90°)_2]_s$ laminate construction to strengthen the transverse stiffness of the sections. Fourthly, concrete was cast on the top surfaces of the two sections, forming the hybrid FRP-concrete bridge decks (shown in Figure 2). Finally, the 2 bridge decks were assembled together, forming the proposed hybrid bridge superstructure (shown in Figure 1). The connecting details for the 2 bridge decks are shown in Figure 3. High quality vinyl-ester resin and CSM were also used to bond the FRP parts (webs). Mortar/epoxy mortar was selected to fill the prepared gaps of the bridge decks. And FRP rebar was adopted to fill the gap at the bottom surface of the bridge superstructure. Additional FRP laminate was added to the bottom of the bridge

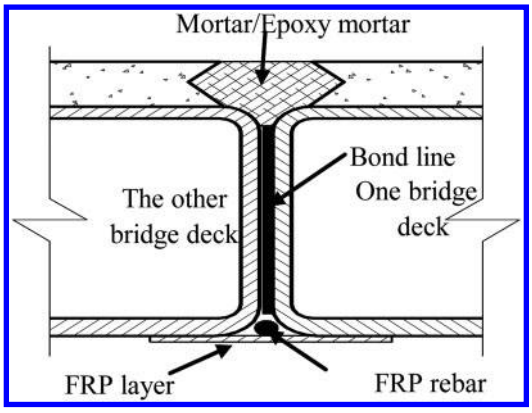


Figure 3. Connecting details for two bridge decks.

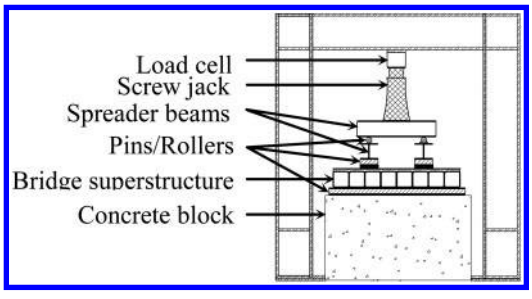


Figure 4. Experimental setup.

superstructure to give the structure some transverse stiffness. In real bridge assembling, FRP layer and FRP rebar will be neglected for simple operation.

3.3 *Test setup and apparatus*

The test setup is shown in Figure 4. Loads were applied vertically at four points on the top surface of the test specimen by three spreader beams and the screw jack supported by the top beam of a reaction frame. The load configuration simulates the two heaviest axles of the standard truck load (total 5 axles) specified in the Chinese Bridge Design Specifications (JTG D6-2004). In the specifications, the design truck load is a live load and has 5 axles. And the two heaviest axles are specified as 140 kN each, where one axle is 1.4 m away from the other. Each axle has two tires that are 1.8 m apart center-to-center, and each tire area has a length of 0.6 m and a width of 0.2 m. For the 1/3 scale model, this design truck load becomes two axles of 15.56 kN, 0.467 m apart. Two tires of axle are 0.6 m apart, and each tire area is 0.2 m long and 0.067 m wide.

The test specimen was simply supported by concrete blocks with a support length of 0.2 m at each end. To protect the bottom surface of the specimen from damage, rubber pads were placed between test specimen and the pin/roller at two ends of the specimen. Figure 5 shows the positions of the displacement and strain measurement to be acquired during the experiment.

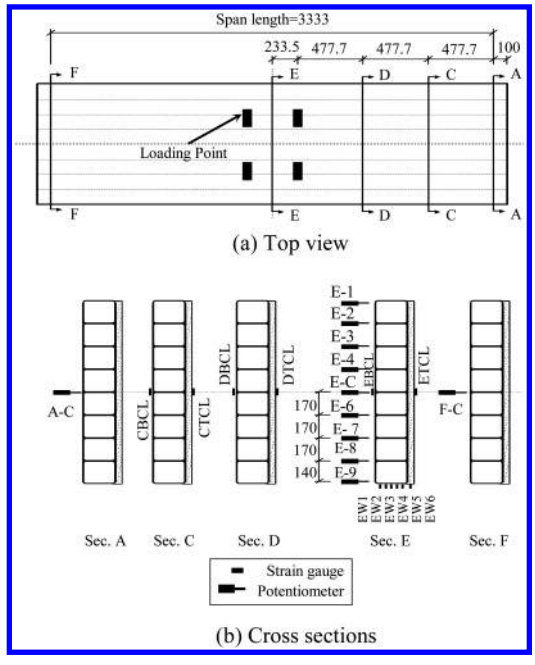


Figure 5. Instrumentation layout (units in mm).

3.4 *Test Procedures*

The hybrid FRP-concrete bridge specimen was tested by flexural and off-axis flexural loadings (shown in Figure 6) firstly. These tests were performed by force control, and the maximum load of 3 times the scaled truck load (93.3 kN) was applied. In the tests, displacement and strain were measured. Then the hybrid bridge model was tested in flexure to failure to examine its ultimate strength and failure modes. The strength test was also performed by force control, and it was divided into two steps. In the first step (Step I), a cyclic force profile was used with the amplitude gradually increased. For each cycle, the force ranged from 0 to a predetermined amplitude, and three cycles were applied for each amplitude to examine the deflection stability. In the second step (Step II), force was increased monotonically until the test specimen failed.

4 TEST RESULTS AND DISCUSSIONS

4.1 *Flexural Test*

No sound of cracking of either the concrete or GFRP was heard during the flexural test. Visual inspection after the test revealed no cracking in the surface of the test specimen. Figure 7 shows the force-displacement relationship obtained at E-C (see Figure 5 for the location). It can be concluded that the obtained force-displacement response is very much linear and has a good repeatability for the hybrid bridge specimen. The deformed shapes of the bottom surface are described in Figure 8. From this figure, we can see that the

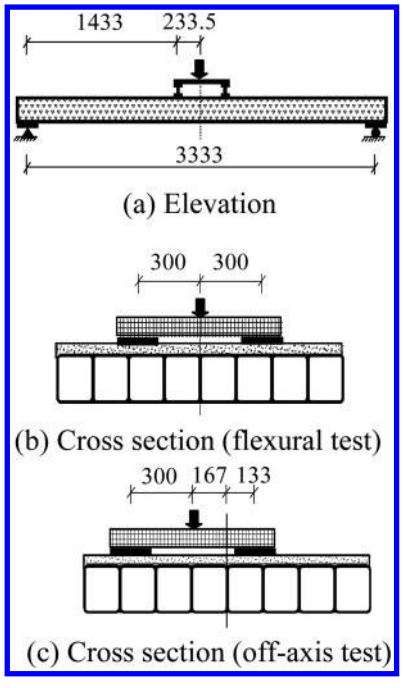


Figure 6. Loading configurations (dimensions in mm).

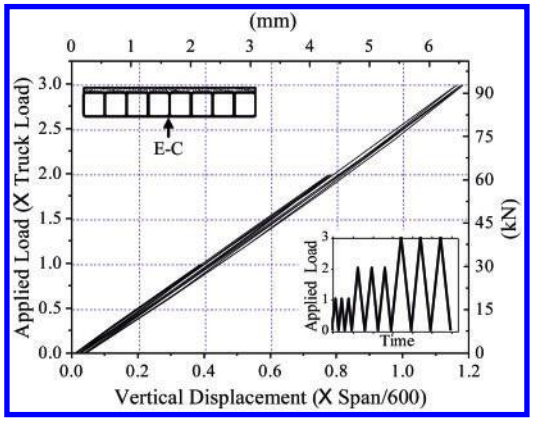


Figure 7. Force versus displacement at E-C (flexural test).

deformed shapes of bottom surface at midspan section (section E) are nearly linear, which indicates that the hybrid bridge specimen has adequate transverse stiffness and the 8 box beams can work together as a plate.

It is specified in the Chinese Bridge Design Specifications (JTG D6-2004) that the maximum deflection under live loads is smaller than $L/600$ (L = span length). The live load for this check is design truck load. As the span length of the test specimen is 3.333 m, the maximum deflection under truck load has to be smaller than $L/600 = 5.555$ mm. Deflection due to truck load measured at E-C is

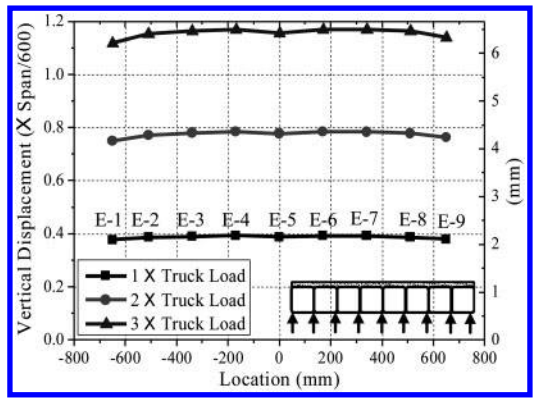


Figure 8. Deformed shapes of bottom surface at section E (flexural test).

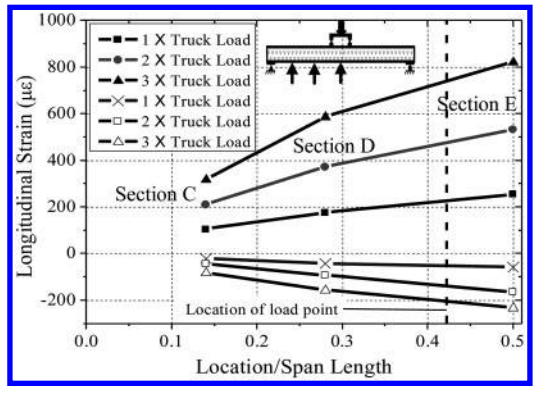


Figure 9. Longitudinal strain obtained at bottom and top center (flexural test).

$2.16\,\text{mm} = 0.39 \times L/600$. The hybrid bridge specimen well satisfied the Chinese live load deflection specification.

Longitudinal strain variations along the centerline of the bottom and top surface and over the height on the exterior web are shown in Figures 9 and 10. Figure 9 shows that longitudinal strain variations along the centerline of the bottom and top surface appear to have a good regularity with the expected results. Figure 10 shows that the bending theory for small strain can apply—i.e., the plane section before deformation remains plane after deformation. And the concrete layer is in the compressive zone, which is designed to utilize concrete effectively

4.2 *Off-Axis Flexural Test*

The screw jack and spreader beams were then moved off the centreline by 167 mm, so that the jack could apply an off-axis load, as shown in Figure 6(c). 167 mm was the largest eccentricity in the real traffic condition. Applied load history was the same as that used for the symmetrical flexural test. No sound of cracking of either the concrete or GFRP was heard during the experiment. Visual inspection after the test

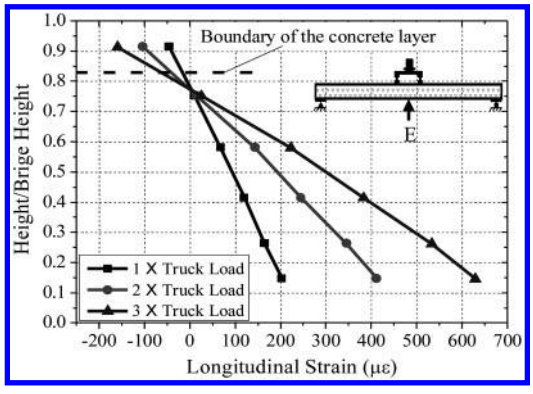


Figure 10. Longitudinal strain obtained on exterior web at section E (flexural test).

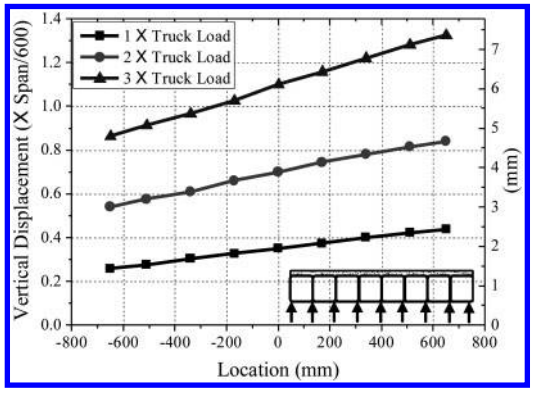


Figure 11. Deformed shapes of bottom surface at section E (off-axis test).

revealed no cracking in the surface of the test specimen. The obtained deformed shapes of the bottom surface are shown in Figure 11. Eight box sections acted together under such a load and the bonding between box sections was strong enough to keep them together. This design appears to have excellent section torsional resistance.

4.3 *Strength Test*

Figure 12 shows force-displacement responses obtained at E-C during the strength tests (Step I and II). At the load of near 16 × truck load in step II, there was a medium loud noise. It is regretted that visual inspection was not conducted in time. So the noise may be caused by the cracking of the interface between FRP and concrete or the cracking of concrete under the loading points. And at this point, the slope of force-displacement curve changes slightly. The load was 8.8 times the Chinese Bridge Design requirement of 1.4(1 + IM) × truck load for live loads in the strength limit state, where IM = dynamic load allowance, and has a value of 0.3 in this case.

The load path from Step II shows that the loading path is nearly linear until the specimen failed. A global

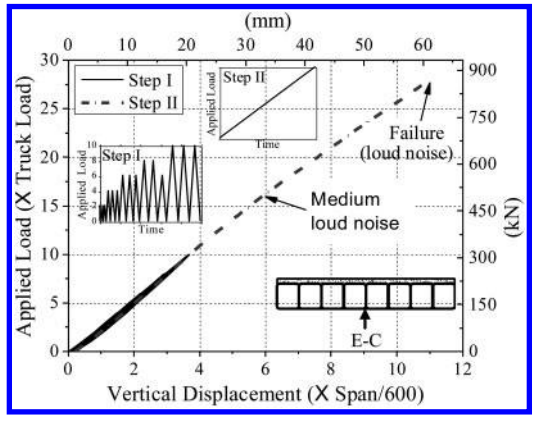


Figure 12. Force versus displacement at E-C (strength test).

failure as shown in Figure 13 occurred at 28 × truck load, which is 15.4 times the 1.4(1 + IM) × truck load. Crushing of concrete in compression near the loading points defines flexural collapse of test specimen. However, the FRP part was found to be intact. This can be described as follows. As concrete failed, large deflection occurred immediately due to the low stiffness of FRP part in comparison to the hybrid specimen, along with instantaneous reduction of the load for the quick increase of deflection, and the combined compression capacity of the FRP top flange and the residual strength of the concrete enable the specimen to carry the residual load. After unloading the residual load, the deflection of the specimen almost came back. The failure was sudden due to the nature of the concrete. However, the obtained failure mode is considered to be favorable because it did not lead to collapse of the entire bridge and the bridge can be retrofitted easily by the replacement of the concrete layer.

5 CONCLUSIONS

The experimental study presented here shows the feasibility of the proposed hybrid FRP-concrete bridge superstructure. The main features of the proposed design include: (1) the efficient use of the concrete layer in the compressive zone to increase the system stiffness, and to reduce the FRP composites and initial costs; (2) the effective implementation of aggregate coating to ensure composite action of the FRP and concrete; (3) the effective ways of assembling between two decks, and among FRP box beams in the bridge deck; and (4) the use of box sections to provide significant torsional stiffness for the cross section.

As is often the case with FRP composite bridges, the design of the proposed bridge superstructure is stiffness-control. It has been proved that the proposed hybrid bridge can be designed to meet the live load deflection requirement of Chinese Bridge Design Specifications and to have significant reserve strength (15.4 times design requirement). Therefore, the depth

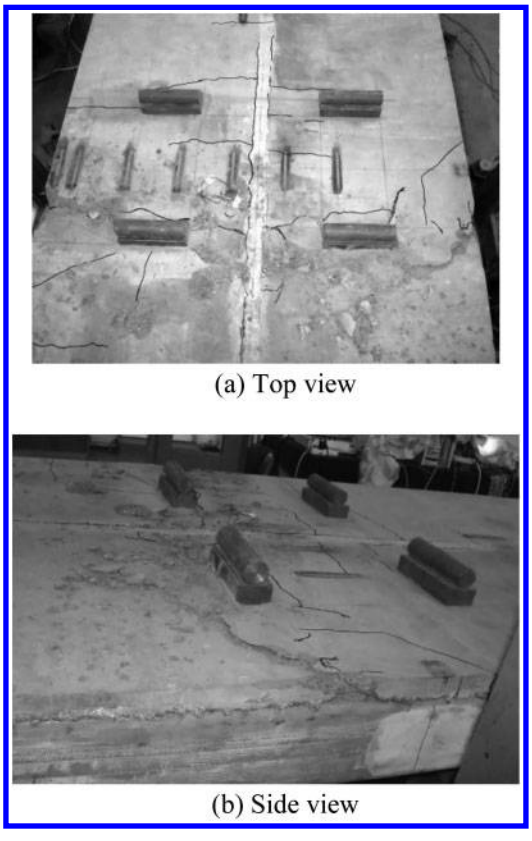


Figure 13. Failure of test specimen.

of the bridge may be increased so that the same flexural rigidity can be achieved with less material and the strength can be used more efficiently.

The concept of the hybrid design—using different materials where they perform best—is a very prudent way to design a structure. A combination of FRP composites and concrete is especially promising in civil infrastructure applications. Although the proposed hybrid FRP-concrete bridge superstructure may not be close to an optimal design, it gives an example of the hybrid design in a bridge superstructure application

ACKNOWLEDGMENTS

The authors gratefully acknowledge the financial support provided by the National Key Basic Research Program of China (Project No. 2012CB026200), the Natural Science Foundation of China (Project No. 50908030) & the National Key Technologies R&D Program of China (Project No. 2011BAJ09B00 & 2011BAK02B00).

REFERENCES

Berg, A.C. 2004. Analysis of a Bridge Deck Built on U.S. Highway 151 with FRP Stay-In-Place Forms, FRP Grids, and FRP Rebars. *MS thesis of University of Wisconsin-Madison*, Madison, USA.

Brailsford, B., Mikovich, S.M. & Hopwood, T. 1995. Definition of Infrastructure Specific Markets for Composite Materials. *Report for Project P93-121/A573*. Evanston: Northwestern University.

Kitane, Y. & Aref, A.J. 2004. Hybrid FRP-Concrete Bridge Deck and Superstructure. In M. El-Badry (ed.), *Proc. 4th international conference on Advance Composite Materials in Bridges and Structures*, Calgary, Alberta, Canada, 1–8 July.

Kitane, Y., Aref, A.J. & Lee G.C. 2004. Static and Fatigue Testing of Hybrid Fiber-Reinforced Polymer-Concrete Bridge Superstructure. *Joural of Composites for Construction*, ASCE, 8(2), 182–190.

Mirmiran, A. 2001. Innovative Combinations of FRP and Traditional Materials. In J.G.Teng (ed.), *Proc. the International Conference on FRP Composites in Civil Engineering*, Vol. II, Hong Kong, China, 4–6 December, New York: Elsevier Science Ltd..

Robbins, V.W. 2002. Design of a Steel Free Bridge Deck System. *Report for the Midwest Transportation Consortium*, the Bridge Engineering Center at Iowa State University, Ames, USA.

Van Erp, G.M., Heldt, T., Mccormick, L., Carter, D. & Tranberg, C. 2002. An Australian Approach to Fibre Composite Bridges. In D. Carter (ed.), *Proc. the International Composites Conference ACUN4*, Sydney, Australian, 11–13 October 2002.

12. Lightweight structures, roof systems, membranes, cables, bars, rods, struts

Research and Applications in Structural Engineering, Mechanics and Computation – Zingoni (Ed.)
© 2013 Taylor & Francis Group, London, ISBN 978-1-138-00061-2

Design of tension components according to Eurocode 3 Part 1-11

K. Kathage
Deutsches Institut für Bautechnik (DIBt), Berlin, Germany

ABSTRACT: This paper deals with the design rules of Eurocode 3 Part 1-11 (EN 1993-1-11) for tension components. The paper covers tension rod systems, prefabricated steel and stainless steel wire rope systems and cable systems using prestressing steel. These systems include the corresponding end connectors or anchorages as well as clamps and saddles. The design rules rules of EN 1993-1-11 are explained and introduced. If necessary the relevant reference to additional supporting documents (eg. European technical approvals or assessments) is given.

1 INTRODUCTION

Eurocode 3 Part 1-11 (EN 1993-1-11) covers the design of tension components made of steel or stainless steel which are adjustable and replaceable. The scope comprises different types of tension components which are subdivided into the three groups A, B and C according to Table 1.

Products of group A are used for simple and aesthetic architectural solutions for bracings and suspensions of filigree steel, steel-glass and timber structures.

Products of group B are used for masts, aerials and bridges, bridge hangers, suspension of membrane, steel, steel-glass and timber and roof structures, cable nets and bracings.

Products of group C are mainly used as stay cables for bridges (steel, composite or suspension bridges) or other superior suspended structures.

Additional information concerning the design of tension components according to EN 1993-1-11 is provided by Kathage & Misiek (2012).

Table 1. Groups of tension components

Group	Tension Component
A	Tension rod system: Round steel or stainless steel bars with threads and fork end connectors
B	Steel and stainless steel wire rope system: Spiral strands, locked coil strands and strand ropes including end connectors, clamps and saddles
C	Cable system using prestressing steel: Parallel wire strands, bundles of parallel wires or strands including anchorages and saddles

2 GROUP A: TENSION ROD SYSTEMS

Tension rods are made of steel or stainless steel. Most prefabricated tension rod systems have fork end connectors made of forged or cast materials. The tension rods are threaded into the fork end connectors which are connected to the corresponding gusset plates by pins (Fig. 1).

The design value of the tension resistance has to be determined according to EN 1993-1-1 in combination with EN 1993-1-8. The resistance is the minimum value of either the tension resistance of the fork end connector (including the pin and the corresponding gusset plate) or the tension rod itself.

In this paper only the determination of the tension resistance $F_{Rd,TRod}$ of the tension rod is given. The design value is determined similar to the design value of the tension resistance of bolts. It is the minimum value of the resistance of the threaded part and the unthreaded part of the tension rod.



Figure 1. Typical tension rod system

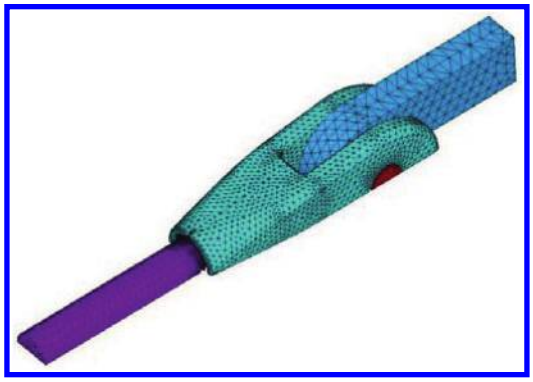


Figure 2. FE model of fork end connector

The design value $F_{Rd1,TRod}$ of the threaded part is determined according to EN 1993-1-8, Table 3.4 as follows:

$$F_{Rd1,TRod} = \frac{0.9 \cdot f_{ub,k} \cdot A_S}{\gamma_{M2}} \quad (1)$$

Where $f_{ub,k}$ = characteristic value of tensile resistance of tension rod, A_S = cross section of threaded part.

The recommended partial safety factor is $\gamma_{M2} = 1.25$. For tension rods with cut threads which are manufactured in a non-series process the value according to equation (1) has to be multiplied by 0.85.

The design value $F_{Rd2,TRod}$ of the unthreaded part is determined according to EN 1993-1-1, section 6.2.3 as follows:

$$F_{Rd2,TRod} = \frac{f_{yb,k} \cdot A}{\gamma_{M0}} \quad (2)$$

Where $f_{yb,k}$ = characteristic value of yield resistance of tension rod, A = cross section of unthreaded part.

The recommended partial safety factor is $\gamma_{M0} = 1.0$.

The minimum value min $\{F_{Rd1,TRod}; F_{Rd2,TRod}\}$ is the design tension resistance $F_{Rd,TRod}$ of the tension rod.

The design tension resistance $F_{Rd,ForkEndConnector}$ of the fork end connector (including the pin and the corresponding gusset plate) can be determined according to EN 1993-1-8, section 3. The procedure is described by Kathage (2003) and by Kathage et al (2011).

Since the determination of the design tension resistance of fork end connectors gives quite conservative results, the design tension resistance of prefabricated tension rod systems is determined in many cases by FE analysis or by tests. A typical FE model is shown in Fig. 2.

In the case of tests a European technical approval or European technical assessment is recommended as basis for the design.

For the ultimate limit state it shall be verified that

$$\frac{F_{Ed}}{F_{Rd,GroupA}} \le 1 \quad (3)$$



Figure 3. Fork socket with pin.

Where F_{Ed} is the design tension load and $F_{Rd,GroupA} = min\ \{F_{Rd,TRod}; F_{Rd,ForkEndConnector}\}$ the design tension resistance of the entire tension rod system.

For fatigue design of tension rod systems the rules given in EN 1993-1-9 shall be taken into account. The fatigue strength curves of fork end connectors made of cast materials shall be determined by tests. Usually the objective of these tests is to verify the detail category 50 (fatigue resistance $\Delta\sigma_c = 50$ N/mm^2 for $2 \cdot 10^6$ load cycles) according to EN 1993-1-9.

3 GROUP B: STEEL AND STAINLESS STEEL WIRE ROPE SYSTEMS

3.1 *General*

Tension components according to group B of EN 1993-1-11 and Table 1 are for instance steel or stainless steel wire ropes with metal or resin filled sockets (Fig. 3), swaged sockets, swaged fittings with thread, U-bolt grips or eye loops with swaged aluminium ferrule. The wire ropes may be deviated by saddles and may be connected to each other by clamps.

The materials of wires, ropes and end connectors have to fulfill the requirements of the European product standards given in section 3 of EN 1993-1-11. For steel wires a maximum nominal strength of 1770 N/mm^2 (round wires) respectively 1570 N/mm^2 (Z-wires) is recommended and for stainless steel wires a maximum nominal strength of 1450 N/mm^2.

According to section 4 of EN 1993-1-11 steel wire ropes have a corrosion protection system that should be as follows:

- Corrosion protection of individual wires,
- Corrosion protection of the interior by inner filling,
- Corrosion protection of the outer surface by sheathing or painting.

For stainless steel wire ropes no information about the corrosion resistance of the different stainless steel alloys is given in EN 1993-1-11.

Additional corrosion protection is required at end connectors, saddles and clamps.

The modulus of elasticity for the different types of wire ropes is given in Table 3.1 of EN 1993-1-11.

Unfortunately no values for the creep elongation of steel and stainless steel wire ropes are given in EN 1993-1-11. Normally creep elongation has to be taken into account for the design of stainless steel wire ropes with permanent loads of more than 40%.

3.2 *Design of steel and stainless steel wire rope systems*

3.2.1 *Ultimate limit state*

For the ultimate limit state the verification of sufficient design resistance is similar as to equation (3). It shall be verified that

$$\frac{F_{Ed}}{F_{Rd,GroupB}} \le 1 \tag{4}$$

Where F_{Ed} is the design tension load and $F_{Rd,GroupB}$ is the design tension resistance of the prefabricated steel or stainless steel wire ropes including end connectors.

The design tension resistance $F_{Rd,GroupB}$ of the prefabricated wire rope shall be determined with the recommended partial safety factor $\gamma_R = 1.0$ as follows:

$$F_{Rd,GroupB} = \min\left\{\frac{F_{uk}}{1.5 \cdot \gamma_R}; \frac{F_k}{\gamma_R}\right\} \tag{5}$$

where F_{uk} is the characteristic value of the breaking strength and F_k the characteristic value of the proof strength of the entire prefabricated wire rope.

F_{uk} is determined as follows in N:

$$F_{uk} = F_{\min} \cdot k_e = K \cdot d^2 \cdot R_r \cdot k_e \tag{6}$$

Where F_{min} is the minimum breaking force [N] of the wire rope itself (without end connector), k_e is the loss factor given in Table 2 for some types of end connectors, K is the minimum breaking force factor, R_r is the tensile strength of the wire rope [N/mm^2] and d is the diameter of the wire rope [mm].

K, d and R are specified in the relevant product standard EN 12385-2.

The loss factor should be determined by tension tests (Fig. 4). In this case a European technical approval or European technical assessment is recommended as basis for the design.

The characteristic value of the proof strength F_k can not be calculated but only determined by tests according to Fig. 4. However, normally it is not relevant for the design.

Table 2. Loss factors k_e.

End connector	k_e
Metal filled socket	1.0
Resin filled socket	1.0
Swaged socket	0.9
Swaged fitting with external thread	0.9
Eye loops with swaged aluminium ferrule	0.9
U-bolt grip	0.8



Figure 4. Tension test of wire rope with fork socket

3.2.2 *Serviceability limit state*

EN 1993-1-11, section 7 gives the relevant design criteria for the serviceability limit states. Provided that fatigue design is necessary it shall be verified for the serviceability limit state that

$$\frac{\sigma_{Ek}}{f_{SLS}} \le 1.0 \tag{7}$$

Where

$$\sigma_{Ek} = \frac{F_{Ek}}{A_m} \tag{8}$$

σ_{Ek} is the characteristic value of the stress determined by dividing the characteristic value of the tension force F_{Ek} by the metallic cross section A_m

f_{SLS} = upper stress limit for service conditions

$f_{SLS} = 0.50 \cdot k_e \cdot f_{uk}$ for fatigue design with bending stresses and

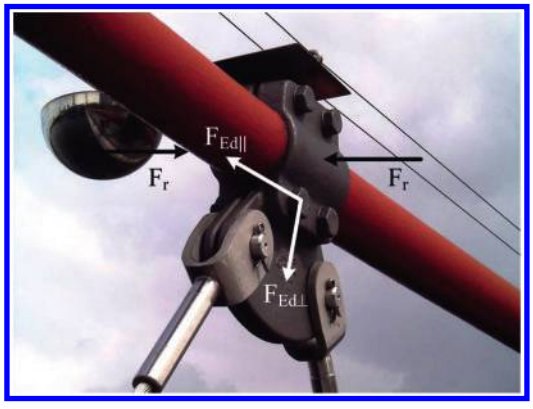


Figure 5. Clamp with corresponding forces.

$f_{SLS} = 0.45 \cdot k_e \cdot f_{uk}$ for fatigue design without bending stresses
f_{uk} = characteristic value of tensile resistance of wire rope

The stress limitation for the construction phase according to EN 1993-1-11 section 7 is already covered by the ultimate limit state design for the construction phase and thus not relevant.

3.3 *Design of clamps*

Clamps are used to connect wire ropes to each other. They transmit longitudinal forces (Fig. 5).

Slipping of clamps shall be verified as follows:

$$F_{Ed\,//} \leq \frac{(F_{Ed\,\perp} + F_r) \cdot \mu}{\gamma_{M,fr}} \tag{9}$$

$F_{Ed//}$ *und* $F_{Ed\perp}$ are the components of the design loads parallel and perpendicular to the wire rope. F_r is the radial clamping force, μ is the friction factor (unfortunately no value is given in EN 1993-1-11) and $\gamma_{M,fr} = 1.65$ is the recommended partial safety factor. Normally F_r can not be calculated, thus in most cases the design resistance of the slipping force is determined by tests. In this case a European technical approval or European technical assessment is recommended as basis for the design.

Transverse pressure could reduce the design tension resistance of the clamped wire rope. The transverse pressure due to the forces F_r and $F_{Ed\perp}$ should meet the following requirement:

$$\frac{q_{Ed}}{q_{Rd}} \leq 1 \tag{10}$$

Where

$$q_{Ed} = \frac{F_{Ed\perp} + F_r}{d' \cdot L_2} \tag{11}$$

$$q_{Rd} = \frac{q_{Rk}}{\gamma_{M,bed}} \tag{12}$$



Figure 6. Pylon with saddle

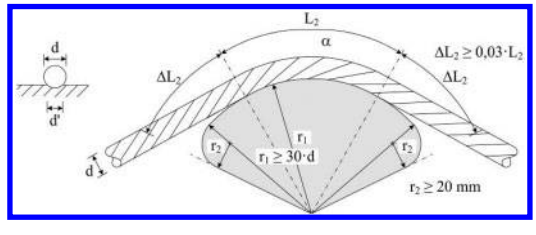


Figure 7. Curvature of a wire rope over a saddle

d' is the contact width and d the rope diameter and $0{,}6\ d \leq d' \leq d$ according to Fig. 7.
L_2 is the clamping length (Fig. 7), q_{Rk} is the limit value of the transverse pressure according to Table 6.4 of EN 1993-1-11.
$\gamma_{M,bed} = 1.0$ is the recommended partial safety factor.

Clamps shall be designed for a force equal to 1.15 times the proof strength F_k of the secondary tension component clamped to the main tension component.

3.4 *Design of saddles*

Saddles are used as support for steel and stainless steel wire ropes with curvature (eg. pylon with saddle; Fig. 6 and Fig. 7).

The transverse pressure of wire ropes with curvature over a saddle could reduce the design tension resistance of the rope. The design resistance of wire ropes with curvature over a saddle can be determined by tests. If the geometrical requirements according to Fig. 7 and section 6.3.1 of EN 1993-1-11 are met the influence of the transverse pressure on the tension

resistance of the rope at the saddle may be neglected for saddles without additional clamps.

Slipping of wire ropes on a saddle without additional clamps shall be verified with the *Euler-Eytelwein*-formula as follows:

$$\frac{F_{Ed1}}{F_{Ed2}} \le e^{\left(\frac{\mu \cdot \alpha}{\gamma_{M,fr}}\right)} \tag{13}$$

Where $F_{Ed1} > F_{Ed2}$; F_{Ed1} and F_{Ed2} are the design values of the tension forces on the left and the right side of the saddle, μ is the friction factor (unfortunately no value is given in EN 1993-1-11), α is the angle according to Fig. 7 and $\gamma_{M,fr} = 1.65$ is the recommended partial safety factor.

If equation (13) can not be satisfied, additional clamps are necessary. In this case equation (13) shall be modified as follows:

$$\frac{F_{Ed1} - \frac{k \cdot F_r \cdot \mu}{\gamma_{M,fr}}}{F_{Ed2}} \le e^{\left(\frac{\mu \cdot \alpha}{\gamma_{M,fr}}\right)} \tag{14}$$

The factor k is normally 2.0 if full friction between the saddle grooves and the clamp may be taken into account, otherwise $k = 1.0$.

If the geometrical requirements according to Fig. 7 and section 6.3.1 of EN 1993-1-11 are met the transverse pressure due to radial clamping forces F_r shall be determined as follows:

$$q_{Ed} = \frac{F_r}{d' \cdot L_2} \tag{15}$$

The requirements of equation (10) shall be verified. q_{Rd} shall be determined according to equation (12).

Saddles shall be designed for a force equal to 1.1 times the breaking strength F_{uk} of the wire rope.

3.5 *Vibrations and fatigue design*

EN 1993-1-11, section 8 gives some general information how to limit wind induced vibrations of wire ropes (eg. by using damping devices) and how to estimate possible risks. However, this information is not sufficient for the design for wind induced vibrations.

Fatigue of steel and stainless steel wire ropes usually occurs at end connectors, saddles or clamps. The detail category for fatigue design of these construction details (wire rope incl. end connector or saddle or clamp) should be determined by tests. For fatigue design of spiral strands and locked coil strands with sockets and mainly axial fatigue action bilinear fatigue strength curves are given in section 9.2 of EN 1993-1-11. These curves are for fluctuating tension loads with or without bending due to wind and rain. The detail categories refer to a fatigue resistance $\Delta\sigma_c$ for $2 \cdot 10^6$ load cycles. For spiral strands and locked coil strands with metal or resin filled sockets the detail category 150 may be used for design ($\Delta\sigma_c = 150\ \mathrm{N/mm^2}$). Additional protective measures are required to minimize bending at end connectors.

At least one test with $2 \cdot 10^6$ load cycles, $1.25 \cdot \Delta\sigma_c$ and an upper stress limit of $0.45 \cdot \sigma_{uk}$ for each diameter of the tension component (incl. end connector) is recommended according to EN 1993-1-11 Annex A section A.4 in order to verify the fatigue strength curves mentioned above. No failure of the end connectors should occur. The fatigue resistance of end connectors, clamps and saddles should be higher than the fatigue resistance of the corresponding wire ropes.

4 GROUP C: CABLE SYSTEMS USING PRESTRESSING STEELS

Cable systems using prestressing steels like parallel wire strands and bundles of parallel wires or strands are usually used as stay cables or main cables for bridges (suspension bridges, steel or composite bridges). These group C products need a special anchoring and an appropriate corrosion protection system (Fig.8).

In fact cable systems using prestressing steels can not be designed according to EN 1993-1-11 because the design resistance for static loads as well as the design for fatigue loads is not really covered by EN 1993-1-11. Tests with the corresponding anchorages are necessary to determine the design tension resistance and the design fatigue resistance.

The fatigue strength curves for group C tension components given in EN 1993-1-11 section 9.2 can not be used for design because there is no information concerning the anchorage available.

Only the breaking strength F_{uk} of group C tension components can be determined according to EN 1993-1-11 section 6.2 as follows:

$$F_{uk} = A_m \cdot f_{uk} \tag{16}$$

Where A_m is the metallic cross section and f_{uk} the tensile strength of the tension component.

For the serviceability limit state section 3.2.2 of this paper applies accordingly.

Instead of EN 1993-1-11 the fib recommendation bulletin 30 (2005) Acceptance of stay cable systems using prestressing steels" should be used for the corrosion protection, static and fatigue tests and the determination of the design resistance. This recommendation covers tests for tension components with anchorages as well as tests for saddles.

The design concept of EN 1993-1-1, section 6.2 and section 9 can be used for the necessary verifications, provided the design resistances are determined according to the fib recommendation.

However, a European technical approval or European technical assessment is recommended as basis for design.



Figure 8. Anchorage of bundle of parallel strands.

5 CONCLUSIONS

The design rules according to EN 1993-1-11 for the three different types of tension components of the product groups A, B and C according to EN 1993-1-11 are presented. This paper shows that for all product groups a determination of the design resistance only by calculation is not usual or possible. This applies for instance to the determination of the design resistance of the end connectors and anchorages. The design of group C products, which are cable systems using prestressing steels and which are mainly used for bridges is not possible according to EN 1993-1-11. For these products and in the case where tests are necessary a European technical approval or European technical assessment is recommended as basis for the design.

REFERENCES

EN 1993-1-1:2005 + AC:2009. Eurocode 3: Design of steel structures – Part 1 – 1: General rules and rules for buildings

EN 1993-1-8:2005 + AC:2009. Eurocode 3: Design of steel structures - Part 1 – 8: Design of joints

EN 1993-1-9:2005 + AC:2009. Eurocode 3: Design of steel structures - Part 1 – 9: Fatigue

EN 1993-1-11:2005 + AC:2009. Eurocode 3: Design of steel structures - Part 1 – 11: Design of structures with tension components

EN 12385-2:2002 + A1:2008. Steel wire ropes – Safety – Part 2: Definitions, designation and classification

fib recommendation bulletin 30. 2005. Acceptance of stay cable systems using prestressing steels. Lausanne: International Federation for Structural Concrete (fib).

Kathage, K. 2003. European technical approvals for prefabricated tension rod systems. Proceedings of the international conference on advances in structures (ASSCCA'03). Sydney, Australia, 22–25 June 2003, Volume 1, 95–100. Rotterdam: Balkema.

Kathage, K., Misiek, T. and Ummenhofer, T. 2011. Zugstäbe und ihre Anschlüsse. Stahlbaukalender 2011, 461–501. Berlin: Ernst & Sohn.

Kathage, K. and Misiek, T.2012. Bemessung und Konstruktion von Zuggliedern nach DIN EN 1993-1-11. Stahlbau 81 (2012), Heft 4, 324–331. Berlin: Ernst & Sohn.

Kathage, K. and Misiek, T.2012. Bemessung von Zuggliedern nach DIN EN 1993-1-11 – Grenzzustände der Gebrauchstauglichkeit. Stahlbau 81 (2012), Heft 8, 621–623. Berlin: Ernst & Sohn.

Research and Applications in Structural Engineering, Mechanics and Computation – Zingoni (Ed.)
© 2013 Taylor & Francis Group, London, ISBN 978-1-138-00061-2

Extraordinary possibilities using fabric to form concrete structures

J.J. Orr, T.J. Ibell, A.P. Darby & M. Evernden
BRE Centre for Innovative Construction Materials, University of Bath, Bath, England

ABSTRACT: Concrete, our most widely used construction material, is a fluid that offers the opportunity to economically create structures of almost any geometry. Yet this unique fluidity is seldom capitalised on, with concrete instead being cast into rigid prismatic moulds to create high material use structures with large carbon footprints. This paper will demonstrate how replacing conventional orthogonal moulds with a flexible system comprised primarily of high strength, low cost fabric sheets, can utilise the fluidity of concrete to create extraordinary possibilities for highly optimised, architecturally interesting, building forms.

1 INTRODUCTION

The language and technology of concrete construction has changed dramatically over the past two thousand years – from dome of the Pantheon, through its renaissance in the 1800s, and up to the work of Nervi and other modern masters of this fluid material. Throughout this, concrete has been cast almost exclusively into wooden or steel moulds to create prismatic elements. Nervi noted that:

> *'although reinforced concrete has been used for over a hundred years and with increasing interest during the last few decades few of its properties and potentialities have been fully exploited so far …the main cause of this is a trivial technicality: the need to prepare wooden forms' (Nervi, 1956)*

This triviality pervades the minds of Engineers even today, with increased cost being associated with concrete structures that deviate from the use of flat panels of timber or steel as formwork. Despite this, concrete remains one of the most widely used man made materials in the world, with global production of cement approaching 3.4×10^9t in 2011 (USGS, 2011).

Cement accounts for a large proportion of the world's raw material expenditure, reaching nearly 33% of the total in 2008 (Orr, 2012). Although concrete has a relatively low embodied energy (Hammond and Jones, 2011) its rate of consumption means that cement manufacture alone is estimated to account for some 5% of global CO_2 emissions (Orr, 2012).

Against a backdrop of carbon dioxide emissions reduction targets, a recognition of the impact construction has on the environment and an increasing client focus on sustainability, design philosophies centred around the need to put material where it is required are becoming increasingly desirable.

Recent research has shown that for concrete structures, large reductions in embodied carbon can be achieved simply by replacing conventional orthogonal moulds with lightweight, high strength, low cost sheets of fabric. This 'flexible formwork' not only provides environmental benefits, but also provides a new form of architecture for concrete structures.

The architectural delight of fabric formed concrete is an additional advantage to the material savings achieved through the structural optimisation processes that are made possible by the use of a flexible mould.

Research undertaken at the Building Research Establishment Centre for Innovative Construction Materials (BRE CICM) at the University of Bath has shown that by following simple optimization routines and casting concrete into a flexible mould, material

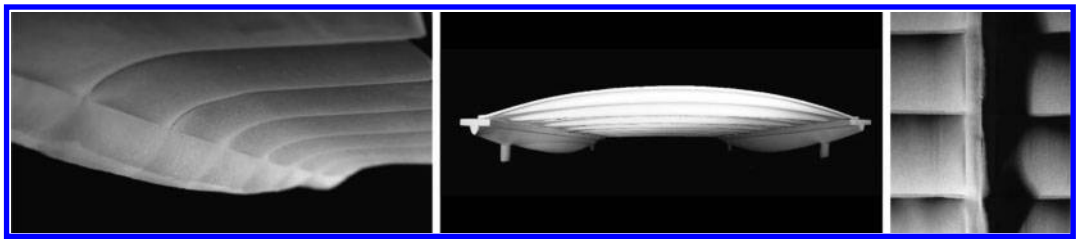


Figure 1. Possibilities with fabric formwork.

savings of up to 40% can be achieved in reinforced concrete beams (Orr, 2012, Orr et al., 2011, Orr et al., 2012c). This figure is supported by additional work showing similar reductions in material use when casting steel reinforced concrete beams.

In addition to significant material use reductions, research at the BRE CICM has demonstrated that fabric formwork can provide concrete with enhanced durability when compared to concrete cast against an impermeable surface. Significant reductions in carbonation depth and chloride ingress have been recorded (Orr et al., 2012a).

From this, it is apparent that the use of fabric formwork can provide:

- Material use reductions by replacing conventional orthogonal structures with non-prismatic, structurally efficient, alternatives;
- Enhanced durability by the provision of a permeable formwork system;
- New forms of concrete architecture.

Flexible formwork therefore has the potential to facilitate the change in design and construction philosophy that will be required for a move towards a less material intensive, more sustainable, construction industry.

2 HISTORY

The genesis of fabric formwork can perhaps be found in very early work with reinforced concrete structures, as shown in Gustav Lilienthal's patents for reinforced concrete flooring systems from the late 19th Century (Lilienthal, 1899). In the 1930s, fabric formwork became a popular method for underwater concrete construction, and remains so today.

It was, however, the introduction in the late 1960s of synthetic, high strength, fabrics that led to a second phase in fabric formwork. Initiated by architects such as Miguel Fisac, the new technique was used to create increasingly complex shapes (Fisac, 1969).

More recently, pioneering architectural research been undertaken by Professor Mark West (University of Manitoba), Professor Remo Pedreschi (Edinburgh University) and Kenzo Unno, amongst many others.

A primary research interest at the BRE CICM has been to marry the architectural achievements of fabric formwork with a desire to produce low-carbon concrete structures. This has been achieved by considering the design process afresh. In doing so, numerous challenges and exciting opportunities have been created, some of which are described in this paper.

Much of the latest research in this field was presented at the BRE CICM in June 2012, as described by Orr et al (2012c).

3 STRUCTURAL BEHAVIOUR

By replacing orthogonal concrete moulds with a system formed of flexible sheets of fabric it is possible

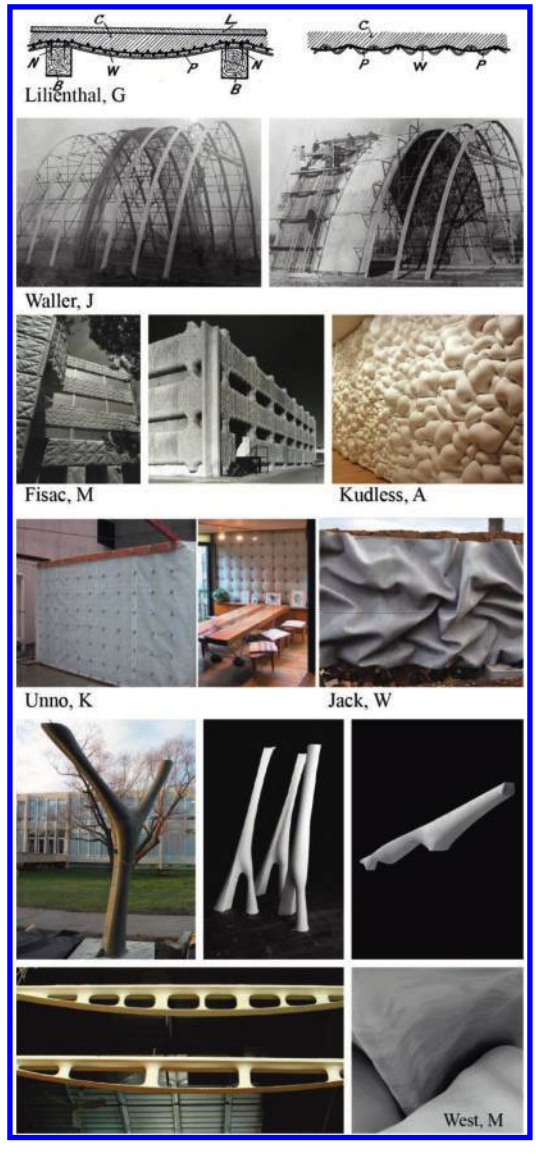


Figure 2. Fabric Formwork. Top to Bottom: Gustav Lilienthal, James Waller, Miguel Fisac, Andrew Kudless, Kenzo Unno, Walter Jack and Mark West. Figure after (Orr, 2012).

to construct optimised, variable cross section concrete elements that can provide material savings of up to 40% (Orr, 2012) when compared to an equivalent strength prismatic member.

The principle behind the design of beams using fabric formwork is illustrated in Figure 3. This process of optimization has been applied at the BRE CICM by the authors to over thirty beam specimens of varying spans and loading conditions (Garbett, 2008, Bailiss, 2006, Orr, 2012).

In essence, the optimisation process ensures that at each section along the length of the beam, the resistance of the beam (in flexure, shear, torsion and so on, R_d) matches the requirements of the design envelope

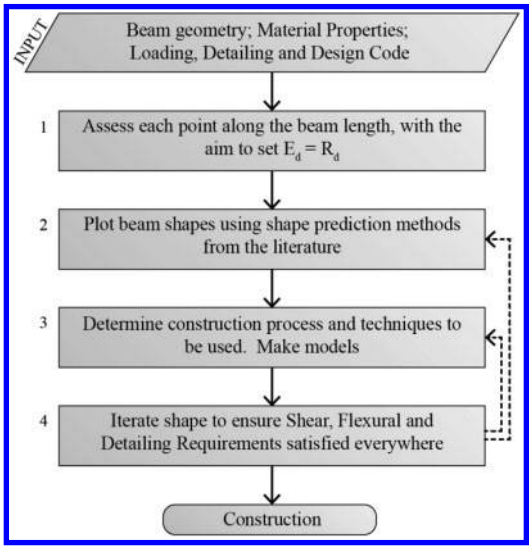


Figure 3. A design process for fabric formed beams.

(E_d). This simple principle of setting $R_d = E_d$ can create complex shapes – which can then be constructed using the flexible fabric mould.

Although much structural testing has focused on beams, this optimisation process (and fabric formwork) can be used for many other structural forms (as seen in work presented in Orr et al (2012c)).

3.1 *Flexure*

The flexural design of reinforced concrete relies primarily on the assumption that plane sections before bending remain plane after bending. This assumption forms the basis of most design codes and has been verified through extensive testing to provide a straightforward design method that gives generally unambiguous results (Bentz et al., 2006).

As optimized structures are usually not prismatic the applicability of this approach is not immediately apparent. However, work by Maki and Kuenzi (1965) and later by Davies et al (1973), as well as work by the authors showing accurate predictions of the fleuxural strength of non-prismatic beams (Orr, 2012), suggests that it is an acceptable approach for elements with moderate tapers.

The design process logically leads to elements with inclined reinforcement, and in much of the literature the theoretical contribution of this inclined bar is used in the calculation of shear capacity. However, the effective utilization of such an inclined bar has not been shown experimentally (Orr et al., 2012b).

3.2 *Shear*

There are a number of contributing factors by which a reinforced concrete beam can carry shear, as described in Figure 4. The relative importance of each

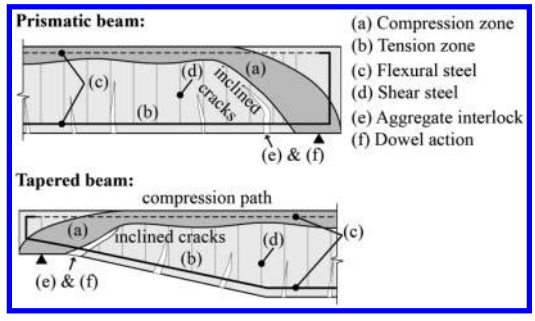


Figure 4. Contributing factors to shear resistance in tapered and prismatic section.

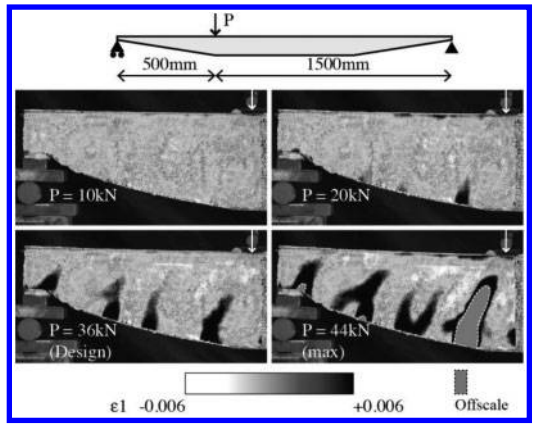


Figure 5. Digital image correlation monitoring the shear behaviour of non-prismatic beams in shear.

factor for prismatic sections is discussed in more detail elsewhere (Kotsovos, 2007, Jelic, 2002).

In the steel reinforced section, cracks form when the principal tensile stress in the concrete exceeds its tensile capacity, and inclined cracks typically propagate from the tension face of the member towards the neutral axis as the applied loads are increased. In sections that taper towards their supports, it is imaginable that the interaction of these diagonal cracks with the path of the compression force that reaches the supports is perhaps more critical.

Premature failures in shear were recorded in some early optimized beam tests, primarily designed using the empirical provisions of BS 8110 (1997).

A test program undertaken by the authors, described by Orr et al (2012b) has begun to address the provision of a design method for tapered beams that does not result in non-conservative capacity predictions and can be used in practice. Using digital image correlation to monitor concrete strains in 21 tapered beams during loading (Figure 5), a better understanding of the behavior of such sections is being developed. This research has shown good results when either a modified Compressive Force Path method, or a strut and tie model, is used.

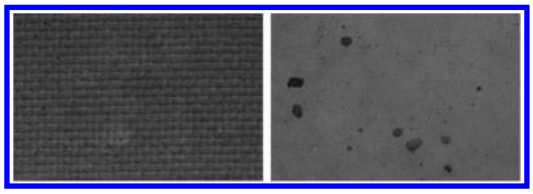


Figure 6. Comparison of concrete cast in a fabric (left) and timber (right) mould.

3.3 *Shape predictions*

Accurate shape predictions for fabric cast concrete elements (beams, column, shells and so on) are essential. Scale models (using plaster) have been successful, and new techniques have simply replaced physical models with virtual ones. Methods used include simple spreadsheets which predict the hydrostatic shape of the fluid filled fabric (mathematically explained by Iosilevski (2010)) to more complex computer programs that can automate the entire process (Veenendaal, 2008).

4 DURABILITY

By allowing water and air to be expelled from a concrete element as it cures, permeable formwork systems such as fabric formwork provide concrete with improved durability due to its denser microstructure and reduced water:cement ratio in the cover zone (Mccarthy et al., 2001). Changes in the surface appearance of such concrete can be seen in Figure 6.

Commercially available permeable formwork systems require the fixing of both permeable and draining layers to the inside of conventional structural formwork. The use of a single flexible fabric formwork system for the creation of optimised, durable structures therefore offers real advantages for designers and contractors.

In addition to tests considering structural behaviour, work at the BRE CICM has made use of accelerated testing methods to determine the effect of the permeable mould on durability.

To date, carbonation, chloride ingress, surface hardness and sorptivity tests have been undertaken, comparing permeably- and impermeably-cast concrete samples. In addition, scanning electron microscopy has been used to compare the cement contents at the surface of the cast samples.

Carbonation testing, undertaken using NordTest NT 357 (1989), exposed concrete cubes cast against fabric and steel surface to carbonation in a chamber of 4% CO_2 for up to 180 days (representing 25 years in service). Chloride ingress testing was undertaken in a similar manner, using a sodium chloride solution with a chloride concentration 5.3 times that of Atlantic seawater. Full details of the tests and their results are provided by Orr et al (2012a). A summary of the improvements seen in this work is presented in Table 1.

Table 1. Summary of durability testing (after (Orr, 2012)) representing tests undertaken on 300 concrete samples.

Test undertaken	Recorded improvement using fabric formwork
Carbonation	**50%**
(Coefficient of Carbonation – (Nordtest, 1989))	
Chloride ingress	**42%**
(Chloride Penetration Parameter, K_{cr} – (Nordtest, 1995))	
Surface hardness	up to **13%**
(Rebound Hammer – (BS EN 12504-2 (2001))	

4.1 *Discussion*

Based on experimental and analytical work undertaken at the BRE CICM it is premised that by casting concrete into a fabric mould three effects which serve to improve the durability of the fabric cast concrete occur as air and water are expelled from the mould:

- Finer material collects in the surface zone as water is expelled from the cast surface, resulting in a more tortuous surface (see Hall and Hoff (2002)) with fewer interconnected pores;
- A greater concentration of cement particles (or a reduction in the *water:cement* ratio) at the surface may result in smaller pores to both constrict the flow of gases through the structure of the concrete and provide sites for the formation of Friedel's salt;
- The macroscale surface texture provided to the concrete gives the fabric cast face a greater specific surface area when compared to the timber or steel cast face.

The Carmen-Kozeny equation has been used to begin to describe the relationships between porosity, permeability and specific surface area for fabric cast concrete, but further testing is required to confirm the precise effect of fabric formwork on the internal structure of concrete.

Faced with environmental effects, fabric cast concrete shows a number of advantages. A harder surface, as measured using a rebound hammer, suggests locally increased cement content. An increased cement content at the surface is also suggested in data from Scanning Electron Microscopy (Energy-dispersive X-ray spectrography) undertaken on small concrete samples (Orr, 2012).

A greater concentration of cement particles at the surface could have the combined effect of constricting the flow of gases through the structure of the concrete (hence providing the resistance to carbonation seen above), while also providing ample sites for the formation of Friedel's salt (which slows the ingress of chlorides). In addition a reduction in the volume of large pores at the surface (as suggested by sorptivity tests) provides a less permeable surface for both carbonation and chloride ingress. These processes thus further retard the corrosion process. Increased chloride binding by this higher cement content also prevents

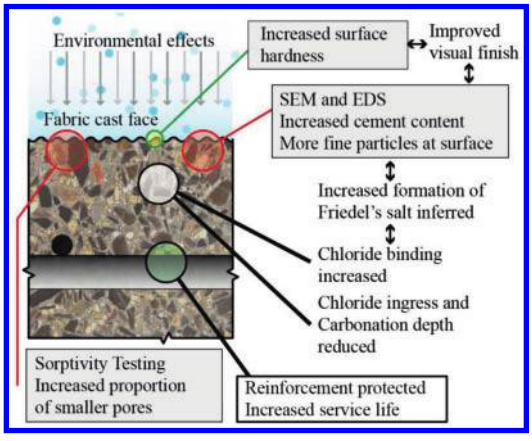


Figure 7. Web of durability advantages found through the use of fabric formwork as a permeable concrete mould.

depassivation of the steel, which is thus better protected. This web of potential advantages for fabric formed concrete is illustrated in Figure 7.

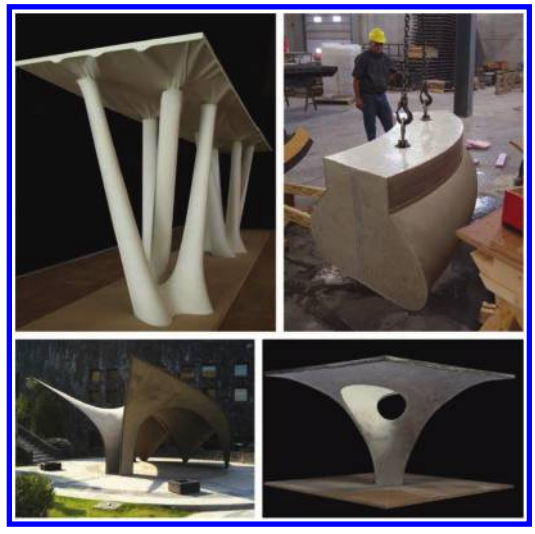


Figure 8. A sample of recent fabric formwork projects (images courtesy, clockwise from top left: (West and Araya, 2012, Araya and West, 2012, Belton, 2012, Bhooshan and El Sayed, 2012).

5 ARCHITECTURAL POSSIBILITIES

In addition to the important structural and durability-based advantages of fabric formwork, further possibilities are found in architecture.

In teaching, fabric formwork has been successfully used at multiple Universities as a means to consider not only how Engineers and Architects undertake efficient design, but also to 're-think' how concrete itself should be used as a structural material.

In practice, the use of fabric formwork in 'real' projects is, at present, quite limited. Examples, shown in Figure 8 include a Women's hospital in Winnipeg, Canada, (by Professor Mark West and Mr Ronnie Araya) shell structures, flat slabs, and columns. All of these elements have been designed and constructed using a flexible fabric mould.

6 CONCLUSIONS

This paper has summarised some of the recent research undertaken at the University of Bath. Not only is it demonstrated that fabric formwork can be used to create optimised, low carbon concrete structures, but it is also shown that the use of fabric formwork facilitates significant improvements in surface durability.

In addition, where the concrete surface is required to provide a visual finish, conventional approaches such as increases in cement content may be avoided through the use of fabric formwork. Instead, the use of a flexible formwork provides both durability and visual benefits.

The majority of testing described here has made use of just one fabric, and further work is currently underway to determine the relative advantages of other available materials in the hope of finding the optimum material that can combine flexibility, a low creep modulus, high strength and a small pore size with low cost.

By designing optimised concrete structures, significant savings in material use can be achieved, with concomitant reductions in both embodied carbon and construction cost. Fabric formwork not only provides a simple means by which such structures can be cast, but by allowing excess pore water to bleed from the surface of the concrete the resulting element is both durable and beautiful. Fabric formwork thus offers exciting opportunities for engineers and architects in the move towards a more sustainable construction industry.

7 FUTURE WORK

This paper has outlined just some of the work undertaken in the field of flexible formwork. Challenges remain – including the issue of shear behavior in elements with complex shapes, the provision of a full analysis and shape prediction computer model that can be used in industry, and solving some remaining construction difficulties.

Areas of future work for fabric formwork include the application of prestressing to the optimization process, the design and practical construction of flat slabs, permanent formwork systems and precast elements for entire building structures. In addition, the use of low-carbon concretes as an alternative to ordinary Portland cement concretes is an area that could lead to even greater savings in the embodied carbon of fabric formed concrete structures.

REFERENCES

Araya, R. & West, M. 2012. Flat sheet fabric moulds for double curvature precast concrete elements. *In:* Orr, J. J., *et al.* (eds.) *Second International Conference on Flexible Formwork* University of Bath: Bath.

Bailiss, J. 2006. *Fabric-formed concrete beams: Design and analysis.* MEng MEng, University of Bath.

Belton, S. 2012. Digital formfinding and fabrication. *In:* Orr, J. J., *et al.* (eds.) *Second International Conference on Flexible Formwork.* University of Bath: Bath.

Bentz, E. C., Vecchio, F. J. & Collins, M. P. 2006. Simplified compression field theory for calculating shear strength of reinforced concrete elements. *ACI Structural Journal,* 103, 614–624.

Bhooshan, S. & El Sayed, M. 2012. Sub-division surfaces in architectural form finding and fabric forming. *In:* Orr, J. J., *et al.* (eds.) *Second International Conference on Flexible Formwork.* University of Bath: Bath.

BSI 1997. BS 8110-1. *Structural use of concrete – Part 1: Code of practice for design and construction.*

BSI 2001. BS EN 12504-2. *Testing concrete in structures — Part 2: Non-destructive testing — Determination of rebound number.* BSI.

Davies, G., Lamb, R. S. & Snell, C. 1973. Stress distribution in beams of varying depth. *The Structural Engineer,* 51, 421–434.

Fisac, M. 1969. Centro de Rehabilitación para la Mutualidad del Papel, Prensa y Artes Gráficas. Madrid: Fundacion Miguel Fisac.

Garbett, J. 2008. *Bone growth analogy for optimising flexibly fomed concrete beams.* MEng MEng, University of Bath.

Hall, C. & Hoff, W. D. 2002. *Water transport in brick, stone and concrete,* London, Spon Press.

Hammond, G. P. & Jones, C. I. 2011. Embodied energy and carbon in construction materials. *Proceedings of the Institution of Civil Engineers: Energy,* In Press.

Iosilevskii, G. 2010. Shape of a soft container under hydrostatic load. *Journal of Applied Mechanics,* 77, 3.

Jelic, I. 2002. *Behaviour of reinforced concrete beams: A comparison between the CFP method and current practice.* PhD, Imperial College London.

Kotsovos, M. D. 2007. Concepts Underlying Reinforced Concrete Design: Time for Reappraisal. *ACI Structural Journal*, 104, 675–684.

Lilienthal, L. W. G. 1899. *Fireproof Ceiling*. USA patent application.

Maki, A. C. & Kuenzi, E. W. 1965. Deflection and stresses of tapered wood beams. Madison, Wis: Forest Products Laboratory, Forest Service, US Department of Agriculture.

McCarthy, M. J., Giannakou, A. & Jones, M. R. 2001. Specifying concrete for chloride environments using controlled permeability formwork. *Materials and Structures,* 34, 566–576.

Nervi, P. L. 1956. *Structures*, FW Dodge Corp.

Nordtest 1989. NT BUILD 357. *Concrete, repairing materials and protective coating: Udc carbonation resistance.*

Nordtest 1995. NT BUILD 443. *Concrete, hardened: Accelerated chloride penetration.* Nordtest.

Orr, J. J. 2012. *Flexible formwork for concrete structures.* PhD, University of Bath.

Orr, J. J., Darby, A. P., Ibell, T. J. & Evernden, M. 2012a. Durability enhancements using fabric formwork. *fib symposium: Concrete structures for Sustainable Community.* Stockholm.

Orr, J. J., Darby, A. P., Ibell, T. J., Evernden, M. C. & Otlet, M. 2011. Concrete structures using fabric formwork. *The Structural Engineer,* 89, 20–26.

Orr, J. J., Darby, A. P., Ibell, T. J., Lava, P. & Debruyne, D. 2012b. The shear behaviour of non-prismatic concrete beams determined using digital image correlation (submitted for publication). *In:* Dirckx, J. (ed.) *5th International Conference on Optical Measurement Techniques for Structures and Systems 2012.* Antwerp, Belgium.

Orr, J. J., Evernden, M., Darby, A. P. & Ibell, T. J. 2012. Proceedings of the Second International Conference on Flexible Formwork. The Second International Conference on Flexible Formwork, 27th–29th June 2012c Bath, UK. University of Bath.

USGS. 2011. *Minerals Information* [Online]. US DoI, USGS. Available: http://minerals.usgs.gov/minerals/ [Accessed 01/01 2013].

Veenendaal, D. 2008. *Evolutionary optimisation of fabric formed structural elements.* Masters, University of Delft.

West, M. & Araya, R. 2012. Recent fabric formwork construction projects. *In:* Orr, J. J., *et al.* (eds.) *Second International Conference on Flexible Formwork.* University of Bath: Bath.

Research and Applications in Structural Engineering, Mechanics and Computation – Zingoni (Ed.)
© 2013 Taylor & Francis Group, London, ISBN 978-1-138-00061-2

The Porsche Pavilion in the Autostadt Wolfsburg, Germany

H. Pasternak & T. Krausche
IPP Braunschweig/Cottbus and University of Technology, Chair of Steel and Timber Structures, Cottbus, Germany

ABSTRACT: The Porsche Pavilion is an innovative stainless steel construction using the principle, often used in ship and car design, as an advantage for building a light but stiff structure. The Pavilion is a one of a kind and outstanding construction that you can find. It fits right in the existing parts of the Autostadt within the lagoon landscape and was built in only eight months. With its curving lines and exiting bends the structure is an extraordinary work which was designed by Henn architects, Munich. The monocoque has a good balance between material and support structure. The stiffness is achieved by the upper and lower side sheathing plates and the intermediate formers. Also the roof shell has no joints and a smooth surface. The assembling of the structure requires a large time and effort cost due to many welds which are necessary to connect all section to one large shell.

1 INTRODUCTION

The Autostadt near the Volkswagen factory in Wolfsburg, Germany, was established in June 2000 by the Volkswagen Group. The Autostadt is the interface between customer and company [1]. On 28 hectares of hills and lakes, visitors are invited to a journey into the world of mobility. The pavilions of Volkswagen, Audi, SEAT, Škoda, Lamborghini are situated in the park. Each of the pavilions expresses its own brand philosophy via its architecture.In June 2012 the new Porsche pavilion with the dimensions of approximately $50 \times 35 \times 10$ [m] [length × width × height] opened. The construction time was 8 months for approximately 1400 m^2 floor area. In a unique combination of functionality and design, visitors can experience the philosophy and values of the traditional sports car brand [1].

2 ARCHITECTURAL CONCEPT

The unique shape of the roof (Fig. 1) creates a new focal point in the park and lagoon landscape which is a protected space. In line with the Porsche tradition of lightweight construction, the spatial envelope based on a monocoque design forms the self-supporting structural system. A stainless steel surface, combined with dynamically elegant lines, clearly alludes to Porsche automobile styling [1].

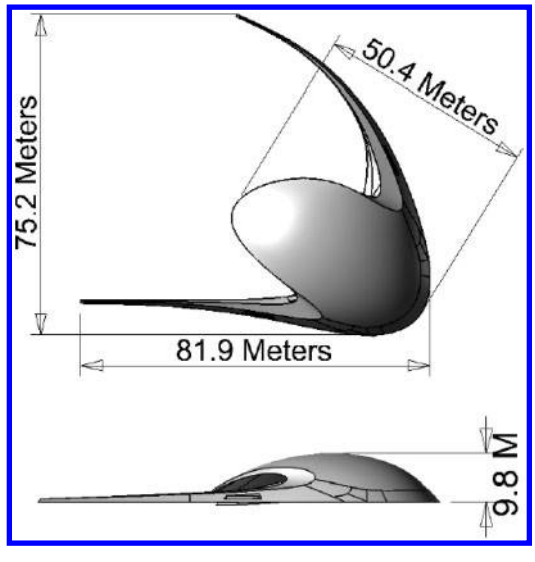


Figure 1. Upper view and elevation, dimensions[3].

3 BUILDING DESIGN

3.1 *Foundation and concrete construction*

This building part is built out of reinforced concrete C 35/45 except for the inner wall axis 1 (C45/55). Due to the soil conditions in the Autostadt, the foundation is constructed on a 50 cm thick surface. The roof parts consist of the polygon shell and the roof shell (monocoque) supported on a concrete construction. Both roofs will be supported by the wall (axle 1) and the lisenes (axle 2–9) (Fig. 2). While the monocoque is fitted on top with prestressed steel connected to the concrete, the supports for the polygon shell are on the side with shear lugs out of rolled profiles.

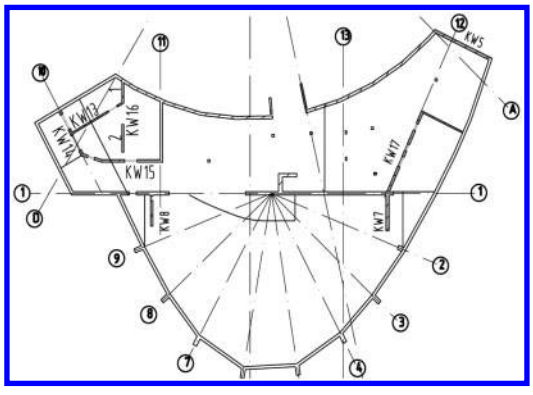


Figure 2. Ground plan concrete construction [2].

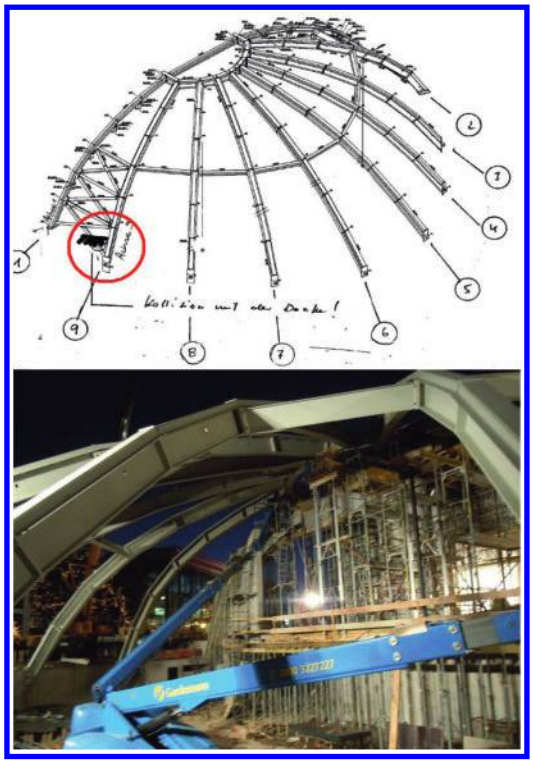


Figure 3. Top – Polygon shell 3-D drawing [2], bottom – Polygon shell during construction.

3.2 *Polygon shell*

The supporting structure is formed by 10 radially arranged steel arches out of steel S355 (HEA 700) with a rise of about 1.70 m – 1.80 m. The floor plan related spans (end support wall – bearing wreath) are from 12,09 m to 17,50 m (Fig. 3). On top of the longitudinal axes of the steel beams there are trapezoidal steel sheets. Normal to the loading direction, the sheet metal is relatively soft and can take as little curvatures perpendicular to the beads. The trapezoidal sheets are

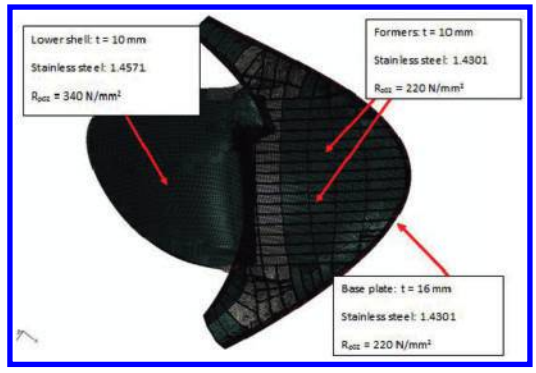


Figure 4. Upper shell, plate thickness and material.

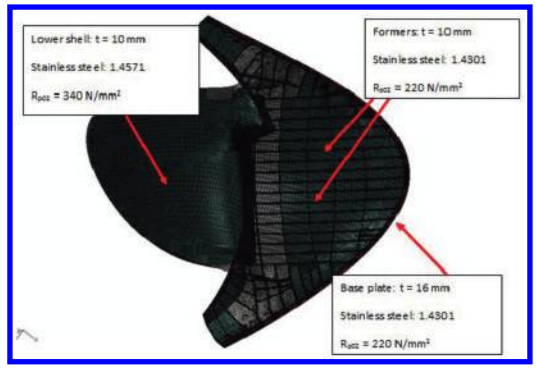


Figure 5. Lower shell, plate thickness and material.

hung on the top flange, and thus act generally as a single span. To reduce the bending of the arches there are square to axis of the free cross section in arc centre cross members (IPE 500) placed. For the presentation of the vehicles inside there are several loads such as large beamers and loudspeakers provided. Considering that on top of the polygon shell is the monocoque, there is according to the verifier [4] wind forces are expected of $\pm 0.15\,\mathrm{kN/m^2}$ because of the ventilated shells.

3.3 *Roof shell – Monocoque*

The monocoque is a construction principle you find nowadays in the machine building industry. Usually the factoring is used with cars, airplanes or ships. This type of structure has a space forming shell which will carry the loads instead of the traditional beam construction. Apparently with this type of design the whole roof is very light compared to its stiffness. The stiffness is achieved by the upper and lower side sheathing plates and the intermediate formers as you can find in a ship. The higher design expenses and manufacturing cost are the reason why this type of structure is not used more often. The whole monocoque is built out of stainless steel. While the inner parts such as the formers is stainless steel WNR 1.4301 with a yield strength of $f_{yk} = 220\,\mathrm{N/mm^2}$ the cover

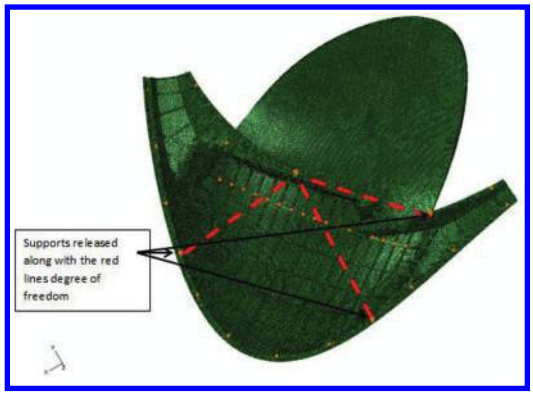


Figure 6. Boundary conditions for the resolution of the concentration of stress.

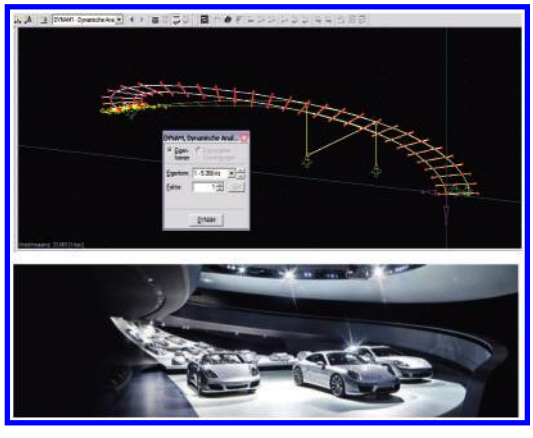


Figure 7. Top: Model of the ramp, bottom: Showroom with ramp in the background [1].

panels are WNR 1.4571 $f_{yk} = 340\,N/mm^2$. Fig. 4 and Fig. 5 show the different usage of the material and plate thickness. Basically, the monocoque is built out of 10 mm thick plates. Only in more highly stressed parts, such as the middle of the upper shell due to the cantilever arm, plates of 12 mm thickness are used. The base plate is made out of 16 mm plates. The plate thickness at the supports is 50 mm.

Due to the seamless and thereby highly statically indeterminate monocoque, it was required to reduce stress out of forced stress, such as temperature load, if possible to support the structure without constraints. In Fig. 6 the yellow dots show the supports with elastomeric bearings. All bearings are free to move except for the bearings at the red dashed line. The middle point was used as a fixed point with no horizontal movement. The other bearings along the red dashed line are movable along the line. Each bearing has a specific solution as a mounting part consisting of a base plate, tension rod and elastomeric bearing.

For verification of the calculation of the structure the FEM program ABAQUS® was used. Moreover plate buckling was analyzed according to [5]. A special significance during design was the load case wind.



Figure 8. Assembly of stainless steel sheets in the factory.

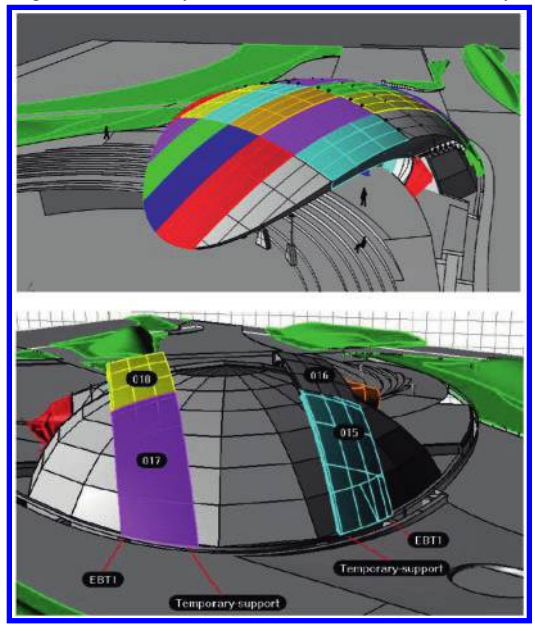


Figure 9. Top – Sections and building stages, bottom -Stage two [3].

To form the wind realistically on the model the wind was implemented based on the wind report [4]. Hereby there were 12 different wind directions (0°, 30°, …, 330°) examined.



Figure 10. Stage three – cantilever arm with temporary support.

3.4 *Ramp*

In the staging area, a ramp made of steel S355 was built as a link between the basement and ground floor (Fig. 7). The unwound ramp length is about 25 m and is designed as a double-curved pipe with 2 rolled sections as the main support members. The construction is divided into eight elements, which are connected via torsion partition plates. In the region of the third and fourth element, the ramp is supported. As supports, rolling steel beams are constructed out of S235. The ramp is designed for an audience.

4 CONSTRUCTION AND ASSEMBLY

The monocouque structure is built out of 56 prefabricated sections. All stainless steel sheets were cold formed and welded together (Fig. 8) in the factory at the plant of "Ostseestaal GmbH" in Stralsund and were transported to the site in Wolfsburg. To ensure a trouble-free mounting of the parts, measurements were taken.

On site, there were three stages of construction. Firstly, the vertical sections were placed. After the vertical parts the sections were placed above the Polygon shell (Fig. 9). The third stage was the cantilever arm (Fig. 10). Every section was elevated by a crane of 400 tons on hoisting eyes and brought into position. All sections were welded together on site. Before the structure could support its own weight, it was temporarily supported. As the last step, the deflection of the key points in the structure, such as the end of the cantilever arm, were checked in comparison with the calculation. The differences were within a construction practice range and were considered safe.



Figure 11. Final view [1].

5 CONCLUSIONS

The Porsche pavilion is a unique building consisting of a monocoque roof and a substructure (Fig. 11).

This type of roof is light compared to its stiffness. On the other hand you have higher design expenses and manufacturing costs. The innovative design was a challenge for all participants of the projects.

ACKNOWLEDGEMENTS – MAIN PROJECT PARTNERS

Client:	Dr.-Ing. h.c. F. Porsche AG, Stuttgart
Architect:	Prof. G. Henn, Architekten, Munich
Design:	Prof. M. Schlaich, sbp, Berlin (general); CSI, Groningen, Netherlands (moncoque); DBT Ingenieursozietät, Frankfurt/M. (ramp)
Construction:	Kümper & Schwarze, Wolfenbüttel (concrete); Temme Stahlbau, Bad Lauchstädt (polygon shell); Ostseestaal, Stralsund (monocoque); Ahlgrimm GmbH, Steinsberg (ramp)
Verification:	Prof. H. Pasternak, ipp, Braunschweig/Cottbus

REFERENCES

[1] http://www.autostadt.de

[2] Approval and execution planning, sbp, Berlin, 2011–12

[3] Execution planning, CSI, Groningen (Netherlands), 2012

[4] Wind tunnel tests for the roof, Wacker Ingenieure, Birkenfeld, 2011

[5] DIN EN 1993-1-5:2010-12 Plated structures

Fig. 3 bottom, Fig. 4–6, Fig. 7 top, Fig. 8, Fig. 10 were done by Prof. Pasternak and co-workers.

Research and Applications in Structural Engineering, Mechanics and Computation – Zingoni (Ed.)
© 2013 Taylor & Francis Group, London, ISBN 978-1-138-00061-2

Computational model for simulation of rigid foldable origami structures

J.D. van der Woerd, R. Chudoba & J. Hegger
Institute of Structural Concrete, RWTH Aachen University, Germany

ABSTRACT: The paper presents a flexible and efficient modeling approach of the folding of crease patterns. The development of the model has been motivated by the need to provide support for targeted design and efficient manufacturing of shell structures exploiting the origami technique. This type of structures is becoming increasingly popular in many engineering disciplines and has been referred to as origamics.

In the present work the folding technique is used to produce spatial structures from continuously reinforced thin-walled cementitious composite plates without the need to construct curved spatial formworks. In order to support the targeted design and manufacturing of folded concrete (oricrete) structures a numerical model has been formulated and implemented. By defining different types of constraints the model can be used for several purposes. In this paper we exemplify the application of the model for the simulation of the folding and the manufacturing processes.

1 INTRODUCTION

The folding technique inspired by the traditional japanese art of origami has been used for ages to produce diverse shapes and forms of a sheet of paper. The correspondence between the crease pattern and the final shape of the product has attracted mathematicians and engineers since decades and is still a subject of ongoing research (Hull 2002, Lang 2009, Wang-Iverson 2011). Applications of the origami concepts in engineering disciplines have been realized in architecture (Sorguc et al. 2009), medicine (Kuribayashi et al. 2006) and mechanical engineering (Onal et al.).

Rigid origami, a subdomain of origami, is especially interesting for technical applications e.g. deployable mechanisms (Künstler & Trautz 2011). In rigid origami only rotations along the creases are allowed (Tachi 2010). The individual facets remain rigid and are not imposed to any deformation at any stage of the folding process. Examples for rigid foldable crease patterns are shown in an unfolded state in Fig. 1 and in folded state in Fig. 2.

By modifying the crease pattern or solely adjusting its parameters different geometrical forms can be achieved. The dependency of crease pattern and final form is only for a few cases obvious so that the design and production process of rigid foldable origami structurs calls for a computer-aided support for the simulation of the folding process. The load bearing behaviour of the final spatial structure is also impacted by the layout of the crease pattern (Trautz & Ayoubi 2011). The zero-extension condition has been used in Schenk and Guest (2011) to study the stiffness properties of the folded sheets.

Examples of models for rigid origami simulation have been reported recently by Tachi (2009). In Chudoba et al. (2013) a modeling framework for rigid origami has been proposed, formulated as an optimization problem with several types of optimality criteria and equality constraints. In the present work

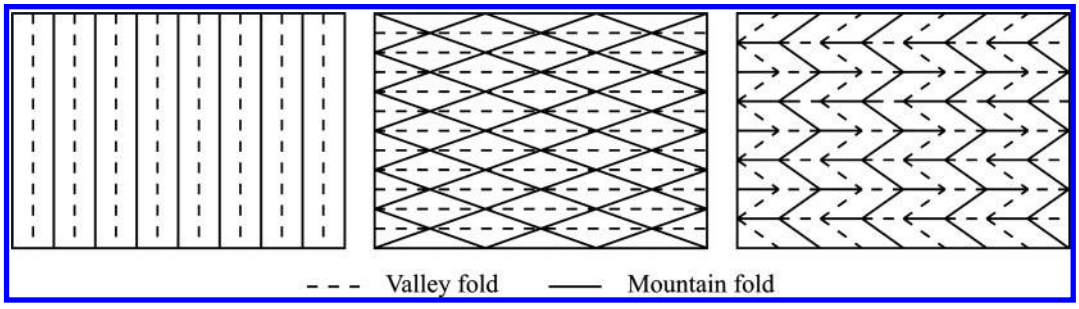


Figure 1. Rigid foldable crease patterns before folding: a) parallel folding b) Yoshimura-Pattern c) Miura-Ori-Pattern.



Figure 2. Rigid foldable crease patterns after folding: a) parallel folding b) Yoshimura-Pattern c) Miura-Ori-Pattern.

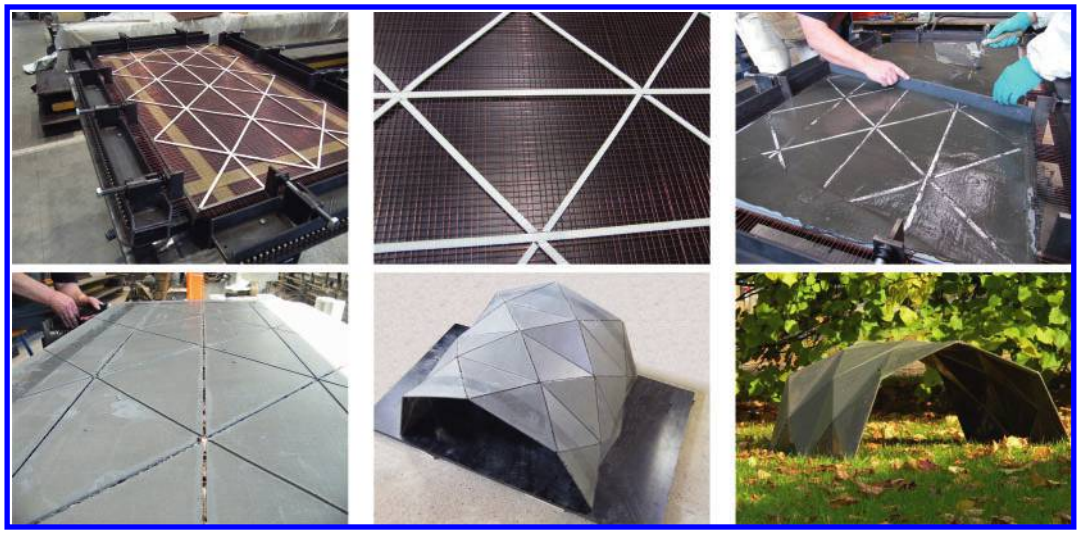


Figure 3. Production of a prototype with crease pattern introduced using linear spacers (top row), manual folding of the concreted plate and its fixation in the target shape with grout (bottom row).

we focus on the equality constraint derived from the kinematics of a rigid foldable crease pattern. The application for simulation of the folding process and for the development of folding devices is shown.

The paper is organized as follows: In Sec. 2 the oricrete method is introduced as an application of folding principle in structural concrete. The method is exemplified with the description of a realized prototype. In Sec. 3 the mathematical model is derived and its implementation is presented. Afterwards in Sec. 4 examples are shown applying the model for simulation of folding and the design of a lifting device for manufacturing.

2 FOLDING TECHNIQUE APPLIED TO CONCRETE PLATES

A crease pattern is introduced into the concrete plate using linear spacers. The continuity of the plate is provided by the textile reinforcement bridging the crease lines. After folding and reaching the desired shape the crease lines are filled with grout and the structure is fixed. By using this method spatial structures can be produced without the need to construct spatial formwork.

As a reinforcement flexible, continuous high-performance materials such as carbon and AR-glass textile fabrics are used. Textile reinforced concrete exhibits high strength and ductile behavior (Konrad & Chudoba 2009, Hegger & Voss 2008). Due to the non-corrosiveness of the textile reinforcement, no extra cover is required for its protection. Consequently, its properties can be highly exploited in thin-walled spatial and shell structures (Scholzen et al. 2012, Ehlig et al. 2012). This fact opens up the the space for the shape optimization of light-weight shell structures (Ramm & Mehlhorn 1991).

In order to demonstrate the manufacturing concept and to test its feasibility a prototype of a folded cementious shell has been produced using the Yoshimura crease pattern. Fig. 3 shows the production steps starting from the formwork with installed linear spacers and the reinforcement grid. The plate had the thickness of 6 mm and dimensions 120 × 80 cm. In spite of the simplicity and manual and improviced production, the example has shown the potential of the folding in combination with the continuous flexible reinforcement.

However, the production of the prototype has clearly emphasized the need for new concepts and

infrastructure both in the design and in the manufacturing of elements folded from a crease pattern. In order to achieve an acceptable quality and precision, concepts for the folding equipment need to be developed and exact information on the position of individual control nodes during the folding process is required. For supporting this task the use of a mathematical model is a must.

3 MATHEMATICAL MODEL

3.1 *Basic considerations*

In the following formulation of the mathematical model only crease patterns with triangular facets have been considered. Even for the simple triangular form of the facets, the design space for folded structures is large. By adding additional constraints assuring planarity of the facets, the model can be used for quadrilateral and polygonal facets.

In the folding of rigid facets the thickness of the facets has to be considered (Tachi 2011). Since the size of the oricrete plates is small and the textile reinforcement has certain flexibility, we can neglect the thickness in the model.

Regarding the crease pattern as a pin-jointed framework of the crease lines, the folding process can be modeled using kinematic equations preserving constant length of the crease lines at any stage of folding.

The model is presented in the following steps: In Sec. 3.2 the mathematical representation of the crease pattern is defined. The constant length constraint is introduced in Sec. 3.3 and additional kinematic constraints for controlling the folding process in Sec. 3.4 are added. In Sec. 3.5 the Newton-Raphson method is used for solving the system of quadratic equations and the implementation of the model is shown in Sec. 3.6

3.2 *Representation of the crease pattern*

Let us introduce a crease pattern as an enumerated set of nodes

$$\mathcal{N} \coloneqq \{i,\ i = 1 \dots N\} \tag{1}$$

and the crease lines as an enumerated set of node pairs connected by crease lines

$$\mathcal{L} \coloneqq \{l \to (i,j)\,,\ l = 1 \dots L, \wedge\, i,j \in \mathcal{N}\}\,. \tag{2}$$

In the initial configuration the position of a crease pattern node i is prescribed by a vector

$$\boldsymbol{x}_i^0 = \left\{ \begin{array}{ccc} x_i^0 & y_i^0 & 0 \end{array} \right\}^T. \tag{3}$$

with the z_i coordinate set to zero.

The vector along a crease line between two nodes i and j in the initial configuration is defined as

$$\mathbf{v}_l^0 = \boldsymbol{x}_j^0 - \boldsymbol{x}_i^0. \tag{4}$$

The displacement of a node i in an intermediate configuration t is denoted as

$$\boldsymbol{u_i}(t) = \left\{ \begin{array}{ccc} u_x & u_y & u_z \end{array} \right\}^T, \tag{5}$$

so that the current position of the node at time t can be written as

$$\boldsymbol{x}_i(t) = \boldsymbol{x}_i^0 + \boldsymbol{u}_i(t). \tag{6}$$

The corresponding vector between the nodes (i,j) at an intermediate state of folding t is expressed as

$$\mathbf{v}_l(t) = \boldsymbol{r}_j(t) - \boldsymbol{r}_i(t),\ (i,j) \in \mathcal{V}. \tag{7}$$

The unknown displacements are assembled in the global vector

$$\boldsymbol{U} = \{\boldsymbol{u}_1, \boldsymbol{u}_2 \dots \boldsymbol{u}_N\}^T. \tag{8}$$

3.3 *Constant length constraint*

By introducing the constant length constraint of a crease line a geometrically non-linear model reflecting the kinematics as a system of quadratic equations is obtained. In the initial configuration the length of a crease line l in an intermediate configuration t is evaluated as the norm of the crease line vector introduced in (Eq. 4)

$$\ell_l^0 \coloneqq \left\|\mathbf{v}_l^0\right\|. \tag{9}$$

Correspondingly, the length of a crease line l in an intermediate configuration t is expressed using the norm of the instantaneous vector (Eq. 7) as

$$\begin{aligned} \ell_l(t) &\coloneqq \|\mathbf{v}_l(t)\| \\ &= \|\boldsymbol{r}_j(t) - \boldsymbol{r}_i(t)\| \\ &= \left\|\boldsymbol{r}_j^0 + \boldsymbol{u}_j(t) - \boldsymbol{r}_i^0 - \boldsymbol{u}_i(t)\right\| \\ &= \left\|\mathbf{v}_l^0 + \boldsymbol{u}_j(t) - \boldsymbol{u}_i(t)\right\|. \end{aligned} \tag{10}$$

The length of all crease lines must remain constant during the folding process so that we require that:

$$\ell_l^0 = \ell_l(t). \tag{11}$$

In particular, the initial length (Eq. 9)

$$\ell_l^0 = \sqrt{\mathbf{v}_l^{0T}\mathbf{v}_l^0} \tag{12}$$

is set equal to the instantaneous length (Eq. 10), with t parameter omitted:

$$\ell_l = \sqrt{\begin{array}{c}\mathbf{v}_l^{0T}\mathbf{v}_l^0 + 2\mathbf{v}_l^{0T}\boldsymbol{u}_j - 2\mathbf{v}_l^{0T}\boldsymbol{u}_i + \\ +\boldsymbol{u}_j^T\boldsymbol{u}_j - 2\boldsymbol{u}_j^T\boldsymbol{u}_i + \boldsymbol{u}_i^T\boldsymbol{u}_i\end{array}}. \tag{13}$$

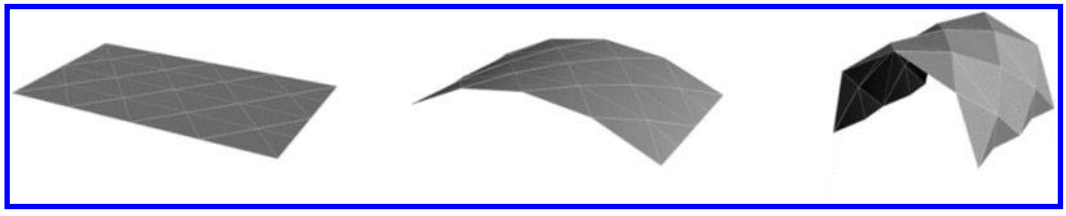


Figure 4. Simulation of folding process of the prototype by applying the model.

The constant-length constraint (Eq. 11) for a single crease line l is then obtained as

$$G_l^{(\ell)} = 2\mathbf{v}_l^{0T}\boldsymbol{u}_j - 2\mathbf{v}_l^{0T}\boldsymbol{u}_i \tag{14}$$

$$+\,\boldsymbol{u}_j^T\boldsymbol{u}_j - 2\boldsymbol{u}_j^T\boldsymbol{u}_i + \boldsymbol{u}_i^T\boldsymbol{u}_i = 0. \tag{15}$$

By applying the length-constraint to all crease lines and boundary edges of the crease pattern a system of L quadratic equations with unknown $3N$ nodal displacements assembled in the vector $\boldsymbol{U}$ is obtained in the form:

$$\boldsymbol{G}^{(\ell)}(\boldsymbol{U}) = 0 \tag{16}$$

3.4 *Kinematic constraints*

Since the constant length constraint is not sufficient for obtaining a solvable system of equations, we need $K = 3N - L$ additional constraints. Several types of kinematic constraints can be added to the model in order to provide more control over the folding and the geometrical details in the target configuration of the folded elements. They are particularly useful for the explicit specification of the boundary shapes and for the simulation of the manufactoring process. The kinematic link constraints are assembled into the vector $\boldsymbol{G}^u(\boldsymbol{U}, t)$.

3.5 *Solving by Newton Raphson technique*

In case that the total number of constraints $L + K$ is equal to the number of degrees of freedom $3N$ the model is fully constrained and can be effectively solved using standard Newton-Raphson iteration scheme. The length constraints and the kinematic constraints constitute a complete system of nonlinear equations

$$\boldsymbol{G}(\boldsymbol{U}, t) = \left\{ \begin{array}{c} \boldsymbol{G}^{(\ell)}(\boldsymbol{U}) \\ \boldsymbol{G}^{(u)}(\boldsymbol{U}, t) \end{array} \right\} = 0. \tag{17}$$

The linearized form of the system is obtained using the Taylor expansion around an admissible configuration at the instance of time

$$\boldsymbol{G}(\boldsymbol{U}) = \boldsymbol{G}(\boldsymbol{U}_t) + \left.\frac{\partial \boldsymbol{G}}{\partial \boldsymbol{U}}\right|_t \Delta\boldsymbol{U} + O^n(\boldsymbol{U}) = \boldsymbol{0}. \tag{18}$$

Neglecting higher-order terms an iterative scheme can be constructed in the form:

$$\begin{aligned} \left.\frac{\partial \boldsymbol{G}(\boldsymbol{U})}{\partial \boldsymbol{U}}\right|_k \Delta\boldsymbol{U}_{k+1} &= -\boldsymbol{G}(\boldsymbol{U}_k) \\ \boldsymbol{U}_{k+1} &= \boldsymbol{U}_k + \Delta\boldsymbol{U}_{k+1}. \end{aligned} \tag{19}$$

3.6 *Implementation*

The model has been implemented within a modeling framework using the high-level, scripting language Python together with the environment for scientific computing bundled in the Enthought Tool suite (Enthought 2013) provided as open source code. The model is accessible on the open-source management platform github.com (oricrete 2013).

In Fig. 4 the model is used to simulate the folding of the prototype shown in Sec. 2.

4 APPLICATION OF THE MODEL

For supporting the design process of the oricrete method from Sec. 2 the mathematical model is used for two tasks within this section:

- Simulate the folding of a given crease pattern,
- Simulate the manufacturing of the folded structure using explicitly imposed kinematic conditions including the lifting device for folding and identify its control parameters.

Different kinematic constraints have to be defined and implemented to use the model for these purposes.

4.1 *Folding simulation*

The simplest type of direct kinematic control of crease pattern nodes can be introduced using constraint equation linking several degrees of freedom in the form:

$$G^{(u)} := a_1 u_1 + a_2 u_2 + \ldots a_K u_K - \bar{u}(t) = 0 \tag{20}$$

where a_i are the coefficients and $\bar{u}(t)$ is the prescribed displacement. As an example of a direct kinematic control of crease pattern nodes consider

$$G_1^{(u)} := u_1 = 0, \quad G_{23}^{(u)} := u_2 - u_3 = 0 \tag{21}$$

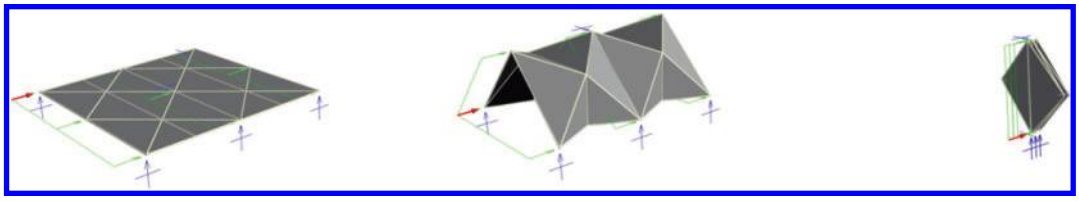


Figure 5. Direct kinematic control of crease pattern nodes: Oricrete simulation of Yoshimura crease pattern from unfolded to flat folded configuration.

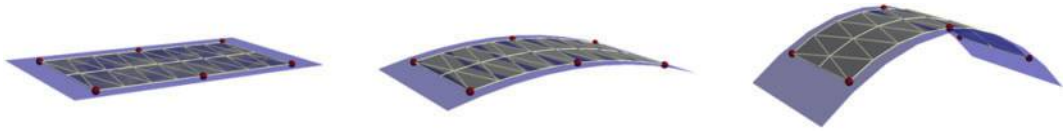


Figure 6. Kinematic control of crease pattern nodes due to deformation of a surface: Oricrete simulation of Yoshimura crease pattern.

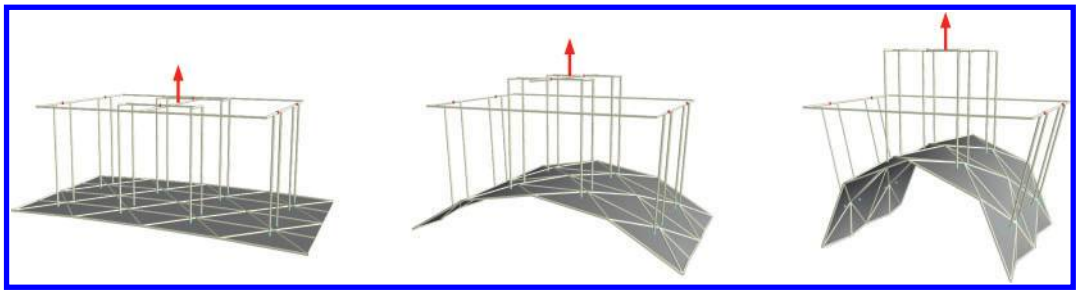


Figure 7. Simulation for designing a lifting device : Folding of the vault with 4×2 Yoshimura crease elements.

with G_1^u representing a fixed support and G_{23}^u linking two displacements together, respectively. The use of the link constraints is exemplified using the vault example in Fig. 5 by enforcing the nodes at the left-hand edge of the pattern to stay in a vertical plane.

It is also possible to attach selected crease pattern nodes to surfaces. The surface can either represent a fixed support or change its properties over time and control the folding. An example of attaching selected nodes to a single curved surface is shown in Fig. 6

4.2 *Design of a lifting device for the folding process*

For the design of simple folding equipment two additional kinematic constraints representing elements of a lifting device are defined.

- Grab points x_{ijk} on the facet with the nodes i, j, k. The position within the triangular facet is specified using the barycentric coordinates

$$\boldsymbol{G}_{(3)}^{(u)} = L_i \boldsymbol{x}_i + L_j \boldsymbol{x}_j + L_k \boldsymbol{x}_k - \boldsymbol{x}_{ijk} = 0. \qquad (22)$$

  The newly introduced node $\boldsymbol{x}_{ijk}$ can be involved in other constraints or optimality conditions.
- Sliding lines and sliding surfaces that can be used to limit the movement so that it remains on a given line ($\boldsymbol{x}_l$ on $l \in \mathcal{L}$) or a surface defined by a level set function $G^{(u)}(\boldsymbol{x}_s) = 0$.

By combining and adding these constraints to a crease pattern a raising gadget can be constructed as shown in Fig. 7.

CONCLUSIONS

We have described the formulation and implementation of a numerical model for simulation of rigid foldable origami structures. By using examples we have shown different strategies for choosing and introducing folding constraints for two different use cases:

- simulation of the folding process
- support for the design of the lifting device realizing the folding process

Further applications of the simulator include the structural analysis of the folded structure and identification of a crease pattern reproducing a desired shape. However these use cases would go beyond the scope of this paper and will be presented elsewhere.

ACKNOWLEDGEMENTS

The work was supported by the Deutsche Forschungsgemeinschaft in the framework of the priority program 1542, project No. CH276/3-1. This support is gratefully acknowledged.

REFERENCES

Chudoba, R., J. van der Woerd, & J. Hegger (2013). Oricrete: Modeling support for design and manufacturing of folded concrete structures. Advances in Engineering Software (submitted).

Ehlig, D., F. Schladitz, M. Frenzel, & M. Curbach (2012). Textilbeton – Ausgefu¨hrte Projekte im U¨ berblick. Beton- und Stahlbetonbau 107(11), 777–785. Enthought, I. (2013). Enthought Scientific Computing Solution.

Hegger, J. & S. Voss (2008). Investigations on the bearing behaviour and application potential of textile reinforced concrete. Engineering Structures 30(7), 2050–2056.

Hull, T. (2002). Origami : Third International Meeting of Origami Science, Math, and Education. Natick MA: A K Peters.

Konrad, M. & R. Chudoba (2009). Tensile behavior of cementitious composite reinforced with epoxy impregnated multifilament yarns. International Journal for Multiscale Computational Engineering 7(2), 115–133.

Künstler, A. & M. Trautz (2011). Wandelbare Faltungen aus biegesteifen Faltelementen. Bautechnik 88(2), 8693.

Kuribayashi, K., K. Tsuchiya, Z. You, D. Tomus, M. Umemoto, T. Ito, & M. Sasaki (2006). Selfdeployable origami stent grafts as a biomedical application of ni-rich TiNi shape memory alloy foil. Materials Science and Engineering: A 419(12), 131–137.

Lang, R. J. (2009). Origami 4: Fourth International Meeting of Origami Science, Mathematics, and Education. A K Peters.

Onal, C., R. Wood, & D. Rus. Towards printable robotics: Origami-inspired planar fabrication of threedimensional mechanisms. In 2011 IEEE International Conference on Robotics and Automation (ICRA).

oricrete (2013). Oricrete: Tool for modeling of folding and manufacturing of thin-walled concrete structures. http://github.com/simvisage/oricrete.

Ramm, E. & G. Mehlhorn (1991). On shape finding methods and ultimate load analyses of reinforced-concrete shells. Engineering Structures 13(2), 178–198.

Schenk, M. & S. D. Guest (2011). Origami folding: A structural engineering approach. In Proceedings of the Fifth International Meeting of Origami Science, Mathematics, and Education, Boca Raton FL, pp. 291–303. CRC Press.

Scholzen, A., R. Chudoba, & J. Hegger (2012). Dünnwandiges Schalentragwerk aus textilbewehrtem Beton. Beton- und Stahlbetonbau 107(11), 767–776.

Sorguc, A., I. Hagiwara, & S. Selcuk (2009). Origamics in architecture: a medium of inquiry for design in architecture. METU Journal of the faculty of architecture 26(2), 235–247.

Tachi, T. (2009). Simulation of rigid origami. In Proceedings of the Fourth Internatinal Meeting of Origami Science, Mathematics, and Education, Natick MA, pp. 175–187. A K Peters.

Tachi, T. (2010). Geometric consicerations for the design of rigid origami structures. In Proceedings of the International Association for Shell and Spatial Structures (IASS) Symposium 2010, Shanghai, China.

Tachi, T. (2011). Rigid-foldable thick origami. In Proceedings of the Fifth International Meeting of Origami Science, Mathematics, and Education, Boca Raton FL, pp. 253–264. CRC Press.

Trautz, M. & M. Ayoubi (2011). Das Prinzip des Faltens in Architektur und Ingenieurbau. Bautechnik 88(2), 7679.

Wang-Iverson, P. (2011). Origami 5: Fifth International Meeting of Origami Science, Mathematics, and Education. Taylor & Francis.

Research and Applications in Structural Engineering, Mechanics and Computation – Zingoni (Ed.)
© 2013 Taylor & Francis Group, London, ISBN 978-1-138-00061-2

Performance analysis of a membrane roof project

E.F. Nunes & J.B.M. de Sousa Jr.
Federal University of Ouro Preto, Ouro Preto, MG, Brazil

B. Baier
University of Duisburg Essen, Essen, Germany

A.M.S. de Freitas
Federal University of Ouro Preto, Ouro Preto, MG, Brazil

ABSTRACT: This paper presents a qualitative investigation of the membrane roof project efficiency, in a preliminary stage of work, based on numerical and experimental data. The first stage involved the optimization procedure of the structural system of the original model under the action of load. The second stage comprised the experimental investigation of the membrane material behaviour within the structure in order to analyze the geometry of the flattened membrane. The working process adopted broadened the understanding and the evaluation of this system pointing out possibilities of improving its performance and minimizing failures during the preliminary stage of the design.

1 INTRODUCTION

This work is a qualitative investigation of the membrane roof project performance, considering a particular situation.

Structural membranes are based on the concept of surface structures with minimum thickness and weight, which withstand loads developing only tensile stress in their own plane. The three-dimensional stability of the investigated structures is a result of the geometry (double curvature in opposite directions, being referred to as anticlastic curvatures) and by the pre-stress applied at its boundaries (planar tensile forces). In addition they also work together and continuously with the support system (e.g., masts, cables, trusses, arches) allowing the development of complex buildings with large spans, low weight, high strength, fast construction process.

These structures are characterized by high complexity presenting great challenges during design and constructive process. Membranes take on forms according to the forces acting on them, similar to cable nets. They are flexible when compared to rigid-type systems such as shells, even if the working loads are within the elastic state, i.e. they present nonlinear geometric behavior (Lewis 2003), making it difficult to be analyzed by traditional methods and processes.

The designing process generally includes the stage of form finding, search for three-dimensional equilibrium of the membrane surface for certain stress distribution and boundary conditions, not considering the material behavior (Wagner 2005), the system static analysis and the patterning procedure (flattening of the three-dimensional surface for its manufacturing).

The wind is generally considered the critical load requiring a careful analysis of its action. Accurately evaluate the distribution of wind loads and their effects on membrane structures is a complex task due to the geometry and behavior of these structures and particularities of the wind load (Pauletti 2003). So, it is essential to have good information about the dynamic effects of wind in these structures, usually obtained in wind tunnel experimental tests, in order to conduct the analysis.

The material used for membranes treated herein as structural fabric, presents high strength and low weight, but, it also displays a complex behavior under tensile forces and needs to be tested.

Moreover, membrane surfaces, such as the steel components of the support system, are pre-fabricated. The surfaces, compounded of flat panels joined by seam, are just assembled and tensioned on site, which restricts major changes of its geometry.

In Brazil, architects and engineers deal with the typical challenges of this system, the uncertainties of the evaluated data and the limitations of the numerical programs used. So, it is usual to adopt simplifications in numerical simulations that could generate methodological flaws in design procedure, making the analysis less accurate and hindering performance of these structures.

These particularities reassure the motivations for investigating the efficiency of a project, trying to understand the strategies used to achieve the structural

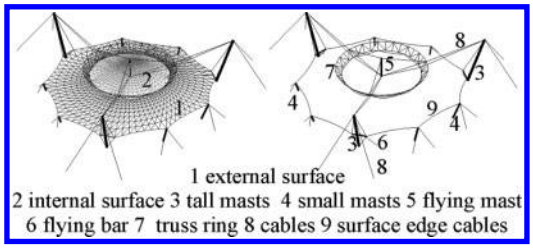


Figure 1. Membrane roof project (Nunes 2008).

efficiency of the system and the procedures that contribute to improve the structural and building performance of these structures.

1.1 *Project that guides the preliminary analysis*

The reference project for this study is the membrane roof project for the amphitheater at Federal University of Ouro Preto (UFOP) developed during the author's master research which is referred here as A1 or original model (~2000 m2), (Fig. 1).

Its system arrangement is characterized by combination and cooperation between membranes and supporting system in a pre-tension state. The supporting system is comprised of three tall masts, small masts and the spatial support system, with hinged joints. The spatial support system is formed by the spatial arrangement of the flying mast and truss ring, within a continuous net of cables forming a stable volume in space (Tensegrity principle). This model has two anticlastic membrane surfaces, with different shapes and behavior. The cone shaped external surface is fixed, while the inner surface is retractable and comprised of nine saddle shape modules arranged in a radial way. The upper part of the inner surface rests on the top of the flying mast while the base lies over the truss ring. The external surface is anchored on the truss ring, on the top of small masts and on flying bars which are hung by cables connected to the top and the base of tall masts (Nunes, 2008).

2 OPTIMIZATION PROCESS

2.1 *Variables that guided the preliminary analysis*

The first stage of the qualitative analysis comprised the optimization procedure of the structural system of the A1 model. It covered modelling and simulation of the structural system under load actions.

A set of variables (number of masts, the cable configuration and geometry of the surface) were analyzed leading to changes in the structural system arrangement and membrane geometry of the A1 model, and thus originating models with different geometries. These models were assembled in analysis cases according to the investigated variables.

The influence of the number of masts which hold the spatial support system was evaluated in the first case of analysis (Fig. 2). Configurations have also

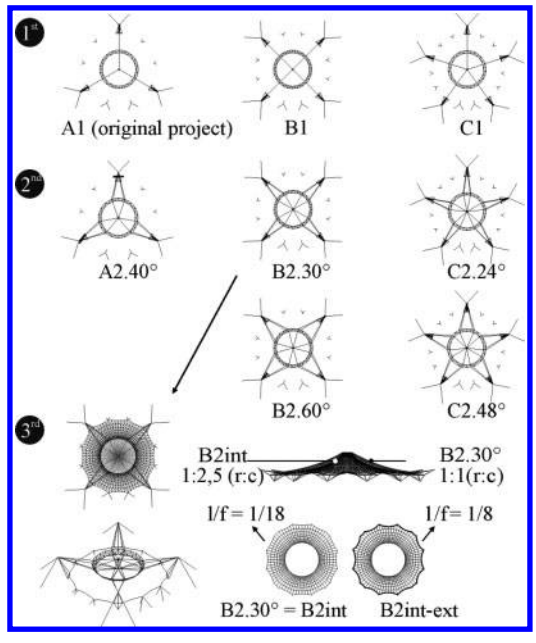


Figure 2. Cases of analysis (Nunes 2012).

been proposed with four and five tall masts originating B1 and C1 models. A pair of cables was arranged perpendicularly to the truss ring anchors in each tall mast.

The arrangement of cables that hold the flying mast and truss ring was investigated in the second case of analysis (Fig. 2). In the new cable configuration, two pairs of cables were anchored in three, four and five tall masts. It was verified the models whose angle between the pair of cable is defined by one module (A2-40°, B2-30°, C2-24° models) and two modules of the inner surface (B2-60°, C2-48° models).

The model whose spatial support system is held by two pairs of cables that are anchored in four masts (B2-30° model) was also subject of evaluation of the membrane surface geometry, shown in the third case of analysis (Fig. 2). An increase over the surfaces' curvatures was proposed. So, the pre-tensioning ratio (r:c) applied in the radial (r) and circumferential (c) directions of the inner surface was changed, originating B2int model. Then, it was also altered the ratio (f/l) of the rise of the curvature (f) and the length (l) between bottom anchor points over the outer surface, generating B2int-ext model.

2.2 *Preliminary analysis procedures and methods*

This investigation was carried out by the preliminary analysis of each model under loads and the compared study of them. The analyses were conducted in three stages: surface form finding, three-dimensional modeling of the system and preliminary analysis of the system.

The A1 model was initially defined according to physical model. So, the pre-tension forces applied to

its forms of equilibrium (represented by cable nets), in the form finding procedure, sought to approximate curvatures of cable nets to the ones of the physical model. The surface stress field of other models maintained the proportionality of A1 model surfaces, and was determinate by the pre-tension applied to the cable net elements and edge cable curvatures.

In the form finding procedure, the forms of equilibrium were carried out using Force Density Method and the software Densalfa (Oliveira 2003). Then, they were converted into surfaces and connected to the support system components, using a graphics platform (AutoCAD ®). The geometri-cally non-linear static analysis of this three-dimensional model was conducted using the Finite Element Method and Straus7 software.

The membrane material type IV (Mehler 2008) was chosen for preliminary analysis, considering its behavior as isotropic and linear. The Elastic modulus had as reference values presented by Meeß-Olsohn (2004).

The load of wind and rain were considered in these preliminary analyses. The rain load was calculated considering the water pressure of 0.01m over the surface. There was no planned wind tunnel testing. So, the wind load simulation had as reference the procedure laid down by Brazilian standard (NBR 1988) and the pressure coefficients resulted from models of membrane structures subjected to wind tunnel tests performed by Vilela (2011).

In order to perform the mapping of the wind coefficients above the surface, it was considered the tested models whose surface angle was similar to the approximate angles of the model surfaces. Then, the surfaces of the models were circumferentially sectored in accordance to the angles of the tested models. Afterwards, the wind directions were defined, i.e. global directions (−X, Y, −Y, −Y2) and local directions (in relation to surface anchor points: perpendicular to the anchor point, mid-span, and fourth portion of the span).

The dynamic pressure resultant of wind pressure calculation was multiplied by wind pressure coefficients values and applied perpendicularly to the surfaces of the models as mapping, to identify the pressures acting in surface geometry, as determined by wind directions.

The preliminary simulation of models was conducted by two performance evaluations.

The first one comprised the membrane evaluation which was based on allowable stresses, applying real load and having pre-tension values recommended by experience (Koenen 2009). It was also considered the range in which the membrane material can behave fairly linear way (Koch 2004).

The influence of magnitude and duration of long-term and short-term loads were verified. The maximum stress in the membrane surfaces under the wind action (short-term load) was limited to 25% of the material directions tensile strength; and pre-tension (long-term load) was limited to 5% of the material directions tensile strength. So, surface cutting patterns and material directions (weft and warp) considerations are required to this evaluation.

The second evaluation involved the steel support system. It was based on combination of actions, according to the American standard (AISC 2010). The following combination of actions was evaluated: 1,2D + 1,6Wdead load; W- wind; R- rain; PT-pre-tension).

The performance factor (load/ resistance) considered to the support system components was approximately 80%. The calculations performed had aimed a preliminary specification/ dimensioning of the models' support system components for their comparison, not being strictly accurate.

For the preliminary analysis and comparison of all models the same loads were considered and the same pre-tension was applied on membrane surfaces and edge cables in all models. The pre-tension applied to support system cables may change in each model, allowing to evaluate the level of pre-tension of these cables and to calculate the dimensions of the components of the support system required to support loads in each model involved.

2.3 *Preliminary analysis results*

The pre-tension applied, the surface stress field, the mass/total area and displacements of components of the models were evaluated. The wind was the critical load observed, and the most unfavorable directions were noticed directly or near anchor points of the surface causing great suction forces.

In the first case of analysis (A1, B1, C1 models), a progressive reduction of pre-tension applied to the support system cables by increasing the number of masts was observed, although these models showed similar mass/area relation. These configurations were characterized by great flexibility, since system arrangements did not offer significant restraint to displacements of support system and membrane surfaces.

The arrangement of cables proposed in the second case (A2-40°, B2-30°, C2-24° models) allowed better integration of components and increased the whole system stiffness, helping to reduce the displacements of components especially on the windward side. So, the importance of spatial arrangement of cables, reducing load path, were observed. It was observed that pre-tension applied to the support system cables also reduced progressively by increasing the number of tall masts, but the magnitude of pre-tension increased 100%. Increasing the angle between pair of cables that hold spatial support system (B2-60°, C2-48° models) helped to maximize support system stiffness, but it caused a significant raise of pre-tension magnitude applied to support system cables and the mass/area of models.

The models of the first and second cases showed similar stress distribution. In the external surface, high stress concentration was observed surrounding truss ring on the leeward side and near bottom anchor points on the leeward and windward sides. In the internal surface, the highest concentration of stress occurred only at the top of the surface surrounding the top ring,

mainly on the windward side; around this area a more homogeneous stress field with lower magnitude predominated; areas of higher stress occurred near surface anchorage points at truss ring on the windward side.

The changes of surface geometry in the third case of analysis increased membrane surface stiffness and its load bearing ability, as well as the global stability of the structural system. Greater curvatures required lower forces for the membrane surface to be in equilibrium and withstand loads, causing a significant reduction of pre-tension applied to support system cables and of system mass/area.

Among the evaluated models, C2-48° and B2int-ext showed the most favorable conditions for system equilibrium, besides having similar system mass and pre-tension magnitude applied to cables. The performance of C2-48° model resulted in large number of masts and new cable configuration. The optimal performance of B2int-ext model derived from the global stability achieved with structural system arrangement and membrane geometry. In this model, the membrane stiffness enabled support system arrangement with smaller number of masts, greater integration between components and more evenly stress distribution on membranes.

3 EXPERIMENTAL INVESTIGATION

In the first stage of qualitative analysis the form of equilibrium of the membrane was evaluated, i.e., a continuous three-dimensional surface whose definition does not consider the behavior of the material.

Thus, in the second stage of this investigation the geometry of the flattened membrane was evaluated considering the influence of material behavior.

This investigation was guided by the experimental tests of the material (biaxial test and seam tests) and the preliminary analysis of the model B2int-ext. The tests were performed at Laboratory for Lightweight structures Essen, University Duisburg-Essen, Essen, Germany, using the material PES/PVC (FR1400 Mehatop F – type IV), (Mehler 2008).

3.1 *Membrane structure that guided the tests*

This investigation had as reference the characteristics (geometry and stress field) of the external surface of B2int-ext model (Fig. 3).

Radial cutting patterns were proposed, which are aligned to surface principal curvatures. Thus, the directions of the material, warp and weft, follow radial and circumferential directions, respectively.

The trajectories of maximum stress were observed in surface circumferential direction (weft direction) on the leeward direction (caused by suction forces), and did not exceed 25% of selected material tensile strength (Fig. 3). Regarding pre-tension level, the maximum stress predicted in the surface circumferential direction (weft direction) did not exceed 5% of the selected material strength), (Fig. 3).

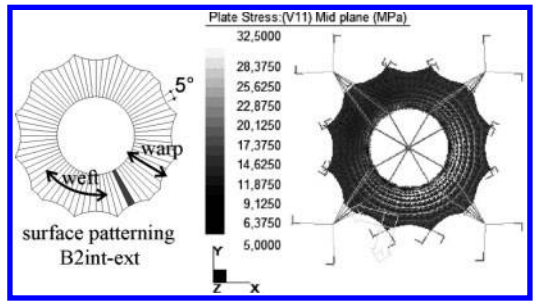


Figure 3. B2int-ext model -geometry/stress field (Nunes 2012).

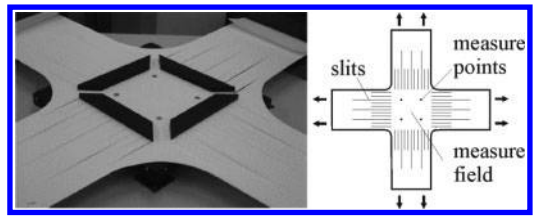


Figure 4. Biaxial test (Nunes 2012).

3.2 *Procedures and methods*

Aiming to simulate the material behavior under loads that act in the structure, the biaxial test was performed. This test is carried out under a temperature of 23°C, with cross-shaped specimen with arms extended toward material directions (warp and weft), which are cut to ensure stress transfer equally to material. Moreover, the forces are applied simulta-neously in both specimen directions of membrane material (Fig. 4).

The biaxial test was conducted according to proposed load ratio, i.e., the magnitude and duration of the loads that acts long term and short term in structure, described in a series of loads applied in warp and weft. It was performed as follows: initially the material was tensioned up to pre-tension level in both directions, maintaining a constant load. Then, the directions of warp and weft were subjected to alternated load cycles (mean and maximum values of critical load), that were intercalated with steps of constant load, simulating membrane pre-tensioning.

The influence of orientation of the material threads and of the angle between adjacent flat panels in the seam was evaluated by the seam biaxial test (Fig. 5).

The approximated angle of the cutting patterns in the investigated surface is 5°. So, threads of material (warp, weft) present a relatively small rotation compared to the seam.

In order to compare and evaluate the effect of this angle over the joint of panels by the seam, tests were performed at angles of 0°, 4° and 8°. In the first test the warp direction is parallel to seam axis, and thus, the material directions are aligned to the flow of forces. In the other tests, the warp was rotated at 2° and 4° to seam axis. In addition, the seam of specimens was performed by hot welding with overpass of 8 cm.

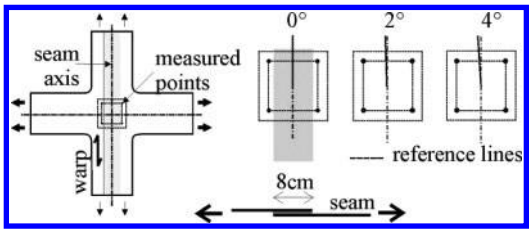


Figure 5. Seam biaxial test (Nunes, 2012).

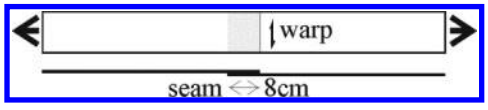


Figure 6. Uniaxial seam test (Nunes, 2012).

The pre-tension, mean and maximum values of the critical load were considered in the seam biaxial tests. The material was initially tensioned at pre-tension level in both directions. The warp direction remained constant throughout the test. The weft has been loaded in several load cycles (50% and 100% of critical load), that were in-terspersed with steps of constant load. The specimens were marked with measuring points and reference lines to favor material behavior observation.

It was also verified the temperature effect in the seam performance. So, the uniaxial seam tests were performed at angle of 0° between panels (warp parallel to seam) at the following temperatures: 23°C, 70°C and −10°C.

The seam strength was evaluated through the analysis of five specimens, considering load applied in the weft direction (transversal to seam), using specimens of 10 cm in width and seam overlap of 8cm (Fig. 6).

3.3 *Experimental analysis results*

The analysis and interpretation of tests' results were conducted according to information provided by the Laboratory, the observations and the photographic record of the tests.

The analyses of the stress and deformations that resulted of maximum load (predicted on the evaluated structure) obtained from biaxial test guided the evaluation of the elastic constants of the material.

In this preliminary investigation, the Elastic moduli (warp and weft directions) were obtained by linear adjustment of stress-strain longitudinal curves of the maximum load cycles. The stresses and strains in the warp and weft directions were replaced by their range, according to Blum (2002). The Poisson ratios (transverse deformation in the weft direction caused by the load in the warp direction, and vice-versa) were also calculated through linear adjustment of transversal deformation curve as a function of longitudinal deformation curve, as determined by Alvim & Pauletti (2004).

A small difference between the stiffness of the warp and weft was observed, i.e., there is a tendency on the material to present isotropic behavior based on the characteristics of the evaluated structure and load ratio. Moreover, these Elastic moduli had lower magnitude than Elastic modulus assumed in the preliminary analysis, something to be considered in the refined analysis.

Theoretically, Poisson's ratio for isotropic elastic materials does not exceed the value of 0.5. However, in this analysis, these ratios exceeded this value. According to MSAJ/M-02-1995, the threads and coating are not unified. So, when threads are tensioned, changes in the wave of threads, known as crimp interchange, are observed, causing geometric deformation. As a result, the material elongation and shrinkage could be associated not only to elastic deformations, but also to geometric ones as it was observed.

The analyses of the stress and deformations that derived from loads that prevail during the structure life time (mean load predicted) guided the calculation of the compensating values (adjustment values used to reduce or increase the dimensions of the flat panels according to the stretching and shrinking of the material). They were evaluated considering not only material deformations, but also cutting patterns geometry and stress distribution on membrane surface. This procedure sought to contribute to minimize the differences between the form of equilibrium and the real shape, reducing material wrinkles in such a way that the surface achieves the proposed form under pre-tension during its life time.

Analyzing the results of the seam biaxial tests, it was observed that the deformation magnitude of material (warp and weft directions) between adjacent flat panels in the seams of the evaluated angles was similar. However, comparing the lines on specimens (the beginning and during the tests), it was observed the distortion of the material. Increasing the angle between panels and the applied loads, the material distortion (shear deformation) became more intense. This behavior results from sliding movement and rotation between threads, caused by different forces acting on material directions, and thread orientation in relation to force direction, confirming the importance of limiting the angle between panels.

In the uniaxial seam tests under the temperature of 23°C, the seam breaking strength showed a higher value than the material tensile strength. The failures at the end of the seam prevailed with fabric breaking parallel to seam, which reveals high strength of seam. Reducing the temperature (−10°C) the seam breaking strength showed a small decrease comparing to test at 23°C, but still showed similar value to the material strength. The material was brittle and failures at the edge of the material prevailed. Increasing temperature (70°C) there was a significant reduction in the seam performance (approx. 50% of material strength), which is reversible with the decrease of temperature. The PVC coating softened, reducing adhesion. These analyses made it possible to observe coating behavior and its influence in seam strength, confirming the importance of evaluating seam width and weld

manufacturing process mainly in tropical regions such as Brazil.

4 CONCLUSION

The qualitative analysis of the membrane roof project, based on numerical and experimental data, make it possible to broad the understanding and the evaluation of this system, helping to minimize failures during the preliminary stage of design.

The first stage involved the optimization procedure of the structural system of the original model under the load action. This stage of study was conducted by the definition of a set of variables (related to support system arrangement and membrane geometry) to analyze the structural system of the original model, as well as by analysis methods and the performance evaluations.

The proposed procedure permitted to predict the global behavior of each model as a trend and to carry out the comparison of the models (original model and the ones originated by the proposed variables), refining and improving the geometry of the original model.

The set of variables, gradually added in each case of analysis, contributed to greater integration between components, increasing the stiffness of the whole structure. Thus, it was verified that enhancing three-dimensional stability of the whole system and membrane stiffness, as well as improving organization and joint work among all components in pre-tension state can reduce support system and membrane displacements, making possible to withstand external loads with low system mass, and thus achieving optimal performance of these structures.

The experimental analysis, in the second stage, showed that membrane material has also a flexible structure, that is, it withstands forces by movement and or deformation of threads. These movements can be observed in the deformation and or distortion of material and are influenced by fabric weaving, orientation and stiffness of material threads, as well as magnitude and duration of loads, time and temperature. Thus, to control the movements of material under load action and to improve the construction performance of these structures, the geometry of flat panels should be adjusted, according to the evaluation of the material behavior in the context of the structure.

The working procedure adopted also demonstrated that the optimal performance of these structures is a result of an optimization process that involves the analysis of three-dimensional geometry and arrangement of all components (membrane and support system) under load action, as well as the analysis of the geometry of the membrane surface formed by flat panels considering the material behavior. This procedure also leads to the best force path and appropriated use of materials.

ACKNOWLEDGEMENTS

Prof. Dr. Jochen Menkenhagen, for providing favorable conditions for the development of this work and for resources to experimental tests in the University Duisburg-Essen/ Essen Labor. Dr Reinhold Koenen, for orientation in numerical and experimental analysis, sharing great knowledge and experience. Mr. Saxe and Mr. Homm (Essen Labor), for information, valuable suggestions in experimental analysis and for conducting the material tests. Mr. Robert Schwetz and Mehler Texnologies team, for receptivity, and assignment for material sample tests. Harry Buskes (Carpro), for gentle preparation of materials for tests. Vinicius Oliveira, the kind assignment of Densalfa software. Capes, Fapemig and Fundação Gorceix, for providing the resources for this research.

REFERENCES

American Institute of Steel Construction, Inc. AISC. 2010.

Alvim, R. A. A.; Pauletti, R. M. O. 2004. Experimental evaluation of the mechanical proprieties of the structural fabrics. In: *Jornadas Sud-Americanas de Ingenieria Estrutural,* Mendonza, may (in Portuguese).

Blum, R. 2002 Evaluation method for the elastic moduli. *Tensinews*, Brussels, Newsletter n.3, p.3, sep.

Koch, K. 2004. *Membrane Structures-Innovative Buildind with Film and Fabric*. Munich: Prestel Verlag,

Koenen, R. 2009. *Skript Leichtbau*. Institut für Metall- und Leichtbau. Universität Duisburg-Essen. Editors: Dipl. Ing. Jan Peter Hartmann & Dr.Ing Reinhold Koenen 11/13/2009: Design of lightweight shell structures – Master course, out.2011- fev.2012. Lecture handout/ notes.

Lewis, W. 2003. *Tension structures: form and behavior*. London: Thomas Telford Publishing.

Meeß-Olsohn, L. 2004. *Textegrity – Textiles and tensegrity*. Dissertation, Universität Essen,

Mehler Texnologies. 2008. Valmex structures. *Products data*. V314/ 03/2008.

Membrane Structures Association of Japan. MSAJ/M-02-1995. *Testing method for elastic constants of membrane materials*.

Nunes, E.F. 2008. *Tensile structures: elements and cables associated to membranes*. Master dissertation. Federal University of Ouro Preto, Ouro Preto (in Portuguese).

Nunes, E.F. 2012. *Qualitative investigation of the performance of a structural membrane roof project*. Doctoral thesis. Federal University of Ouro Preto, Ouro Preto (in Portuguese).

Oliveira, V. M. B. 2003. *Analysis and design of fabric tensile structure roofs*. Doctoral thesis. Federal University of Rio de Janeiro, COPPE/ UFRJ. Rio de Janeiro, (in Portuguese).

Pauletti, R. M. O. 2003. *História, análise e Projeto das Estruturas Retesadas*. Tese de Livre docência. Escola Politécnica da Universidade de São Paulo. São Paulo.

Specification for structural steel buildings. Brazilian Association of Technical Norm. NBR 6123 – 1988. *Wind pressures on buildings*. Rio de Janeiro, (in Portuguese).

Vilela, C.A.B.S. 2011. *Wind static action in tensile structures*. Doctoral thesis in Civil engineering. Department of Civil engineering and Environment. University of Brasília, Brasília (in Portuguese).

Wagner, R. 2005. *On the design process of tensile structures*. In: OÑATE, E.; KRÖPLIN, B. (eds). Textile Composites and Inflatable Structures. Netherlands: Springer. p.1-16.

Research and Applications in Structural Engineering, Mechanics and Computation – Zingoni (Ed.)
© 2013 Taylor & Francis Group, London, ISBN 978-1-138-00061-2

Collapse behaviour of double-layer grid structures in steel

J.M. Adams & A. Zingoni
University of Cape Town, Cape Town, South Africa

ABSTRACT: The propensity of Double-Layer Grid (DLG) structures to fail suddenly, without warning, has contributed to their reduced popularity in industry. To identify DLG pre-critical yielding behaviour and increases in DLG post-critical structural resistance, which represent improvements to conventional DLG failure behaviour, a structural and geometric parametric study was undertaken of DLG symmetric collapse under distributed loading. The parametric study additionally served to identify and characterize DLG plastic failure and collapse behaviour for structures representative of those employed in practice. Finite element analysis with the Abaqus code was employed for the structural collapse analysis; the displacement-controlled analysis method was verified against a previously undertaken experimental analysis of DLG collapse. DLG geometric configurations with reduced bottom chord densities were found to be an easily implementable means of achieving stable pre-critical plastic displacement; the extent of pre-critical plastic displacement was comparable to that achieved by employing over-sized and 'soft' compression members.

1 INTRODUCTION

Flat double-layer grid (DLG) structures are efficient modular structural systems which span in two or more directions and consequently develop their resistance in three dimensions. For unobstructed roofing applications, DLG structures offer many structural, constructional and aesthetic advantages over alternative planar structures. DLG structures, however, have been observed to have a propensity for sudden collapse behaviour, as witnessed in the collapse of the Hartford Coliseum roof structure in 1978 (Parke 1988). An investigation of DLG collapse behaviour was consequently undertaken to identify if improvements to DLG collapse behaviour could be achieved through specific combinations of common structural and geometric DLG parameters (Adams 2012); pre-critical yielding behaviour and post-critical increases in DLG resistance were considered to represent improvements over conventional DLG collapse behaviour; for both cases the initiation of DLG failure is identifiable prior to collapse.

2 PREVIOUS RESEARCH

Research into the collapse behaviour of DLG structures has largely been conducted with two experimental aims in view. Initial studies, such as those presented by Schmidt et al. (1976, 1982), Collins (1981) and Saka & Taniguchi (1994) focused on establishing the collapse behaviour of DLG structures. Due to the unfavourable nature of this established behaviour, and collapses in industry, subsequent studies as presented by Parke (1988), Mwakali (1990) and El-Sheikh & McConnel (1993) focused on improving DLG structure collapse behaviour.

The highly nonlinear behaviour of structural collapse has resulted in most authors adopting physical model testing as their primary means of analysis. Experimental modelling of DLG structures has highlighted their sensitivity to structural and geometric imperfections, as observed in the divergence from symmetry in DLG failure and the variability of experimental results.

Studies into DLG collapse behaviour have additionally been accompanied by numerical collapse analysis; notable examples of such studies include the work of Collins (1981), Parke (1988), Mwakali (1990), El-Sheikh & McConnel (1993) and Saka & Taniguchi (1994). Numerical collapse analysis of DLG structures has been conducted largely through use of idealized strut implementations of DLG behaviour; Saka & Taniguchi (1994) are the exception who investigated DLG critical behaviour using a buckling analysis method.

The use of idealized strut implementations of member behaviour for the numerical analysis of DLG structures has not allowed for the continuous behaviour of DLG collapse to be established. The effect of the grid restraint on individual member behaviour has also not been captured. Furthermore, the idealized strut implementations have not accounted adequately for the effects of member bending resistance and joint rotation in the post-critical regime where changes to DLG geometry result in structures whose structural resistance can no longer be assumed to be comprised of axial stiffness only.

3 PROBLEM STATEMENT

Despite the propensity of DLG structures to fail suddenly, only limited and inconsistent results describing DLG structure failure and collapse behaviour are available. A parametric study, where the results would allow for the identification of trends in pre-critical DLG yielding behaviour and post-critical increases in DLG resistance, was therefore required.

4 METHOD

In order to identify trends in DLG collapse behaviour, results covering the full design spectrum of DLG collapse behaviour were required; the large number of analysis cases was to be developed with structural finite element (FE) analysis. The numerical method of analysis to be employed was developed and validated through comparison with published experimental results. The case of distributed loading was considered as this is consistent with the loading commonly assumed in roof structure design. Corner supports were employed to limit the effect of boundary conditions on DLG behaviour.

4.1 *Numerical analysis*

The numerical method employed for the finite element analysis of DLG structures, with the Abaqus code, was a quasi-static, geometry and material nonlinear, incremental and iterative, displacement controlled analysis (Simulia 2010). A novel application of the distributing couple element was used for the application of uniformly distributed load in a displacement controlled analysis[1]. As DLG structure failure behaviour is characterized by the compression failure of individual members, a half-sine geometric (bow) imperfection was introduced into the initial geometry of all member groups, which could potentially experience compression in the DLG elastic regime; geometric imperfections were applied in the vertical plane to negate their effect on symmetry. Member imperfections were introduced to avoid problems associated with bifurcation in the numerical analysis.

4.2 *Validation*

The comparison of the numerical results, from FE analysis, with the experimental results of Collins (1981) showed a good correlation for the entire failure path (Figure 1); the numerical analysis method was consequently considered to be validated.

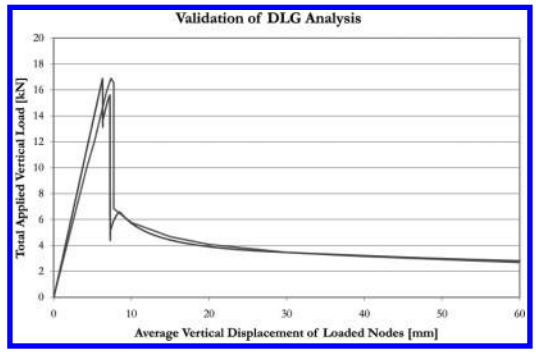


Figure 1. Validation of FE results for SOS DLG collapse through comparison with the experimental results of Collins (1981). Load redistribution between adjacent chord members was evident prior to collapse for the numerical model results.

The validation of the numerical method for the square-on-square (SOS) DLG configuration under point loading was extended to the following additional cases:

- Semi-rigid connections
- Uniformly distributed loading
- Diagonal-on-square DLG configuration

The validation of the structural parameterization employed was achieved through the consideration of DLG scale, a DLG scale of up to × 10 was considered. A maximum error between numerical results and predicted results for flexural, shear and yielding collapse mechanisms of 0.6% and 1.25% was observed when evaluating critical load and energy applied to DLG respectively; this was considered to be an acceptable error.

To increase computational efficiency and to enforce symmetric failure, one quarter of the complete DLG geometry was considered for the parameter study. A maximum error between numerical results for both numerical model representations of <3.0% was observed with respect to the energy applied to the DLG; this more significant error was attributed to deviations from a symmetric failure path for the full DLG model and was consequently not considered to be associated with the use of symmetry in the model.

4.3 *Investigation method*

Following the validation of the numerical DLG collapse analysis method, a parametric study was developed which allowed for the full design spectrum of DLG behaviour to be established. The DLGs selected for analysis (Figure 2) were limited to the cases of SOS and DOS configurations with: cornice edge detail; simple corner supports; aspect ratio of 1.0; circular hollow section (CHS) members of steel grade S355; 9 × 9 and 7 × 7 modules for the SOS and DOS DLG configurations respectively.

[1]Application of distributed load in a displacement controlled analysis was achieved as follows: a continuum distributing couple linked a control node with the reference nodes; reference nodes were located directly below the top intersection nodes on the DLG; link connector elements were defined between the reference nodes and the DLG top nodes; equation constraints were defined to equate the horizontal displacements of the reference nodes and the DLG top intersection nodes. This allowed for the force associated with a single displacement boundary condition at the control node to be distributed equally to all the DLG top intersection nodes.

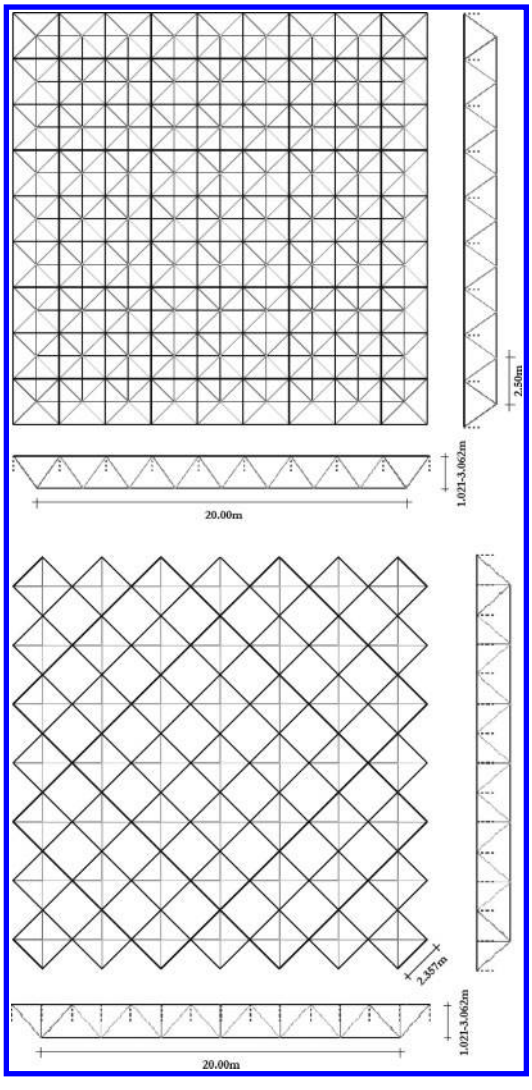


Figure 2. 20×20 m, SOS (top) and DOS (bottom) DLGs with cornice edge detail. Member groups used for analysis included top chords, bottom chords, web members and support members (four web members at each corner support). DLGs were supported at the four bottom corner nodes.

DLG member sizes were based on a design in accordance with the relevant European Standards (CEN 2003, 2005). This was undertaken such that DLGs analyzed were representative of DLG structures employed in practice; elastic, perfectly plastic material behaviour was employed.

DOS DLG geometry and section sizes were scaled to achieve an equivalent span distance for both SOS and DOS DLGs; span:depth was maintained constant between SOS and DOS DLGs by adjusting the DOS web angle. A DOS DLG with fewer modules than the SOS DLG was selected to maintain the number of load points and web member angles approximately equivalent between SOS and DOS DLGs of equal span; an odd number of top modules were selected to allow for a symmetric displacement field.

Parameterization of the DLG structures aimed to capture the complete behaviour of the structure so that the effect of scale on structural behaviour could be accurately accounted for. The parameters considered included: Span:Depth; Web:Top Chord Resistance; Chord Area Ratio; and Connection Stiffness.

Parameter values were selected which defined the typical structural and geometric ranges employed in industry. For the purpose of the parametric study, the parameter values selected were varied concurrently so that the full interaction of parametric behaviour could be observed in the results; in total 480 individual structures were analyzed.

To account for member instability and yielding behaviour, member resistance was parameterized in terms of A/λ^2 (where: A = member cross-section area, λ = member slenderness ratio) such that member resistance to instability and yielding was varied proportionally. Connection stiffness was defined, with respect to individual member capacity, between pinned and fixed bounds.

The following parameters were considered:

- DLG Configuration: SOS, DOS
- Span:Depth: 6:5, 11:3, 19:6
- Connection Stiffness: 0% (pinned), 33%, 66% and 100% (fixed)
- Web:Top Chord Resistance: 33%, 50%, 66%, 83% and 100%
- Chord Area Ratio: 50%, 66%, 83% and 100%

5 RESULTS

The nonlinear collapse analysis of the DLG structures, of SOS and DOS configuration, allowed for the failure and collapse behaviour of such structures to be observed under uniformly distributed loading. DLG behaviour resulting from the collapse analyses was divided into three regimes for the purpose of comparison: pre-critical behaviour (comprising of linear elastic and plastic behaviour); critical behaviour; and post-critical behaviour. DLG behaviour was initially identified and categorized; trends in structural behaviour were then established through comparison of post-processed representations of DLG load-displacement responses (Adams 2012). Critical and post-critical behaviour was observed to vary as a result of failure mechanism (critical behaviour), collapse mechanism (post-critical behaviour) and as a direct result of the variation of structural and geometric parameters.

5.1 *Pre-critical behaviour*

Pre-critical behaviour was dominated by plastic yielding behaviour of DOS DLG configurations. Significant plastic deformation of SOS DLGs was not observed; this was attributed to the denser layout of bottom chord members in SOS DLGs relative to DOS

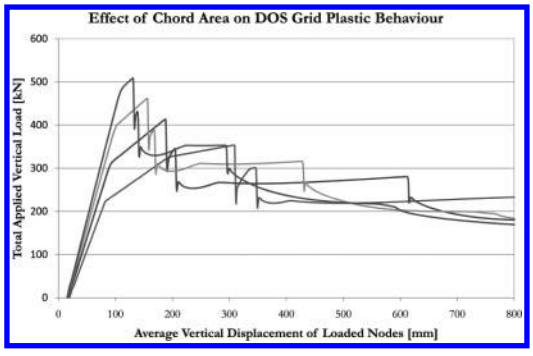


Figure 3. Variation of DOS DLG load-displacement behaviour for increasing values of the Chord Area Ratio parameter (bottom to top).

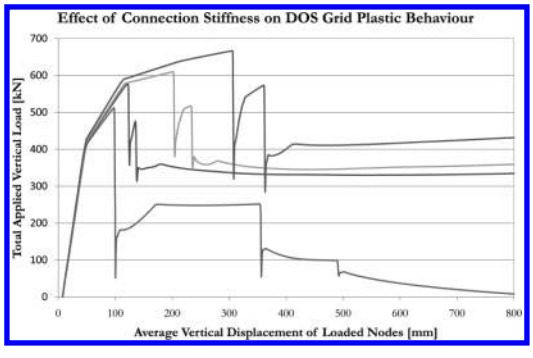


Figure 4. Variation of DOS DLG load-displacement behaviour for increasing values of the Connection Stiffness parameter (bottom to top).

DLGs. Plastic behaviour of DOS DLGs was assessed by comparing plastic and critical energy fractions; these fractions were represented by the integral of the load-displacement responses for DLG plastic and pre-critical regimes respectively.

DLG pre-critical behaviour, observed in the results of DLG collapse analysis, was summarized as follows:

- DOS DLGs were less stiff than comparable SOS DLGs.
- DLG stiffness increased for increasing values of the Connection Stiffness and Chord Area Ratio parameters.
- DLG stiffness decreased for increasing values of the Span:Depth parameter.
- Web members did not affect DLG flexural stiffness.
- DOS DLG configurations allowed for the development of significant nonlinear behaviour prior to the onset of DLG failure.
- Initiation of DLG plastic deformation was inversely proportional to the Chord Area Ratio parameter (Figure 3).
- Stability of DLG plastic deformation was dependent on the avoidance of shear and flexure failure mechanisms; plastic deformation consequently increased with Connection Stiffness (Figure 4) and Web:Top Chord Resistance parameters.

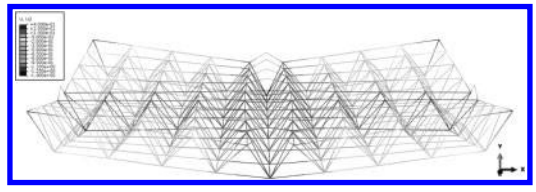


Figure 5. Flexural failure of SOS DLG, with vertical displacement field superimposed.

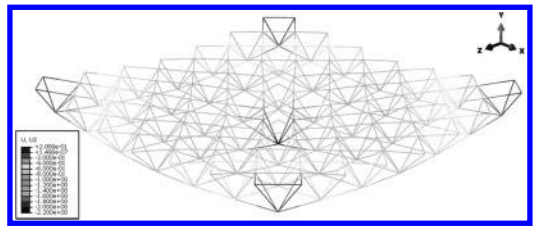


Figure 6. Flexural failure of DOS DLG, with vertical displacement field superimposed.

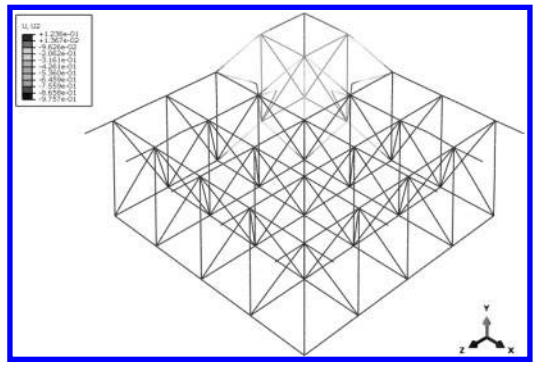


Figure 7. Shear failure and collapse of SOS DLG, with vertical displacement field superimposed.

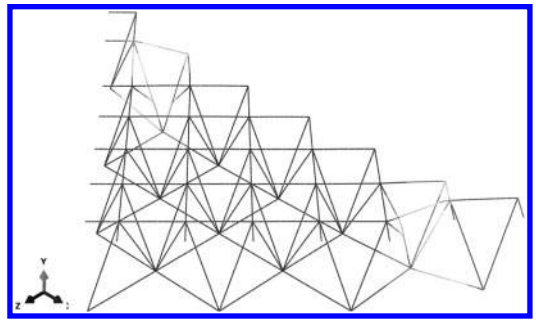


Figure 8. Shear failure and collapse of DOS DLG, with vertical displacement field superimposed.

5.2 *Critical behaviour*

Critical behaviour of DLG structures was observed to be dependent on flexural failure (Figures 5–6) and shear failure mechanisms (Figures 7–8) which were in turn dependent on Web:Top Chord Resistance and Span:Depth parameters. DLG critical resistance was

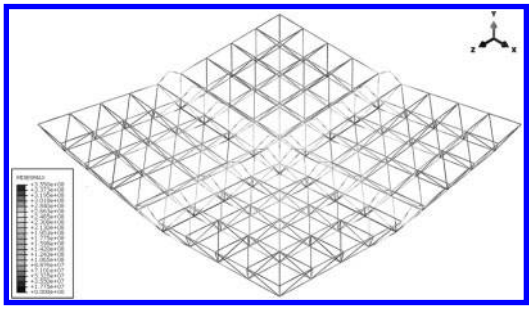


Figure 9. Flexural collapse of SOS DLGs was characterized by the development of plastic hinges in two directions across the DLG; an equivalent displacement field cannot develop for DOS DLG configurations. Max. von Misses Stresses are shown superimposed on the deformed geometry.

observed to be further dependent on Chord Area Ratio and Connection Stiffness parameters.

DLG critical behaviour, observed in the results of DLG collapse analysis, was summarized as follows:

- Shear failure of DLGs resulted in significant reductions to structural efficiency in comparison to similar DLGs which failed in flexure.
- Shear failure was observed to be dependent on Web:Top Chord Resistance, Connection Stiffness and Span:Depth parameters.
- SOS DLGs were observed to be more susceptible to shear failure than DOS DLGs due to the increased flexural resistance of SOS DLGs.
- Web:Top Chord Resistance and Connection Stiffness parameters were observed to have the most significant effect on critical load for DLGs which failed in shear.
- Chord Area Ratio, Span:Depth and Connection Stiffness parameters were observed to have the most significant effect on critical load for DLGs which failed in flexure.

5.3 *Post-critical behaviour*

The collapse of DLG structures was frequently observed to be consistent with the initial failure mechanism, although significant interaction of web, top and bottom chord member failure was also observed. Three principle collapse behaviours were identified: shear collapse (Figures 7–8), flexural collapse (Figure 9) and flexural failure with post-critical shear collapse interaction. The displacement field associated with flexural collapse was not developable for DOS DLGs due to the orientation of top chord members relative to supports. Post-critical behaviour was assessed in terms of the average post-critical load resistance and the ratio of average post-critical:critical resistance.

DLG post-critical behaviour, observed in the results of DLG collapse analysis, was summarized as follows:

- Shear collapse of DLGs was characterized by only nominal post-critical residual strength.
- Improved post-critical resistance was observed for increasing values of the Connection Stiffness parameter.
- More rapid decreases in DLG post-critical resistance resulted from reductions of the Span:Depth parameter.
- Slender top chord members resulted in sudden collapse with only nominal post-critical load resistance.
- DOS DLGs were generally observed to collapse more quickly than similar SOS DLGs.
- Flexural collapse of SOS DLGs resulted in significant, sudden decreases in DLG post-critical resistance.
- Initiation of flexural collapse was dependent on Web:Top Chord Resistance and Chord Area Ratio parameters.
- Flexural failure and post-critical shear collapse interaction was generally characterized by a gradual decrease in load resistance.

6 DISCUSSION

The results presented are for the case of symmetrical failure. In 'real' DLG structures symmetrical failure is not observed due to the sensitivity of such structures to imperfections. The results presented, therefore, provide a means of evaluating the effects of the identified structural and geometric parameters in an idealized DLG failure.

The failure of the DLG structures considered was observed to be followed by increased post-critical resistance in only a few instances and a trend in such behaviour was not established. Although exceeding the critical load of all the other structures considered results in collapse, the post-critical behaviour observed is indicative of the nature of collapse. The design of DLG structures should consequently avoid global shear failure, which results from the failure of web members adjacent to supports, as global shear failure is characterized by a sudden decrease in load resistance. Initial flexural failure followed by interaction with web member failure was observed to result in the most gradual decrease in DLG load resistance; such a collapse mechanism is consequently preferred as the failure is characterized by multiple non-critical member failures.

DLGs, with low values of the Bottom:Top Chord Area parameter, demonstrated significant nonlinear behaviour prior to failure, this therefore represents a notable improvement to DLG failure behaviour. The significant yielding behaviour observed for DOS structures was believed to be equally as effective as the use of 'soft' chord members or over-designed top chord members in improving pre-critical and critical behaviour, presented by Parke (1988). The less dense distribution of bottom chord members in the DOS configuration is an effective and simple means of introducing pre-critical yielding behaviour in DLG structures

which provides warning of structural damage prior to structural collapse.

SOS DLGs were observed to demonstrate the preferred post-critical behaviour; however, DOS DLGs were observed to demonstrate the preferred DLG pre-critical behaviour. The most significant concern regarding the behaviour of DLG structures has been their propensity to fail without warning; DOS DLGs consequently represent the most suitable DLG configuration considered for corner supported DLG structures.

7 CONCLUSION

Nonlinear analysis of SOS and DOS DLG structures was successfully undertaken to determine global pre-critical yielding and critical behaviour. Bifurcation behaviour, at a member level, was accounted for by applying initial geometric imperfections. Distributed loading was applied to the DLG structures in a displacement controlled analysis; the effect of grid restraint and connection restraint on member behaviour was accounted for.

The behaviour of DOS DLG configurations with low values of the Bottom:Top Chord Area Ratio parameter, were shown to exhibit significant stable nonlinear pre-critical behaviour resulting from the yielding of bottom chord members. The DOS DLG configuration, and potentially other DLG configurations, with less dense bottom chord arrangements, therefore represent attractive structural configurations for design purposes, provided dominant loading is applied in one direction only.

Connection Stiffness and Span:Depth parameters were observed to have the greatest effect on DLG post-critical behaviour. A general improvement in post-critical behaviour was observed for increasing values of the Connection Stiffness and Span:Depth parameters; slender top chord members were observed to result in sudden DLG collapse behaviour.

REFERENCES

Adams, J.M. 2012. Collapse behaviour of double layer grid structures in steel. Cape Town: University of Cape Town.

CEN. 2002. Eurocode 1: Actions on structures – Part 1-1: General actions – Densities, self-weight, imposed loads for Buildings. Brussels: European Committee for Standardization.

CEN. 2005. Eurocode 3: Design of Steel Structures – Part 1-1: General rules and rules for buildings. Brussels: European Committee for Standardization.

Collins, I.M. 1981. Collapse analysis of double-layer grids. Guildford: University of Surrey.

El-Sheikh, A. & McConnel, R. 1993. Experimental study of behaviour of composite space trusses. *Journal of Structural Engineering* (119) 747–766.

Mwakali, J.R. 1990. The collapse behaviour of double-layer space trusses incorporating eccentrically loaded tee-section members. Guildford: University of Surrey.

Parke, G. A. R. 1988. The behaviour of space trusses incorporating novel compression members. Guildford: University of Surrey.

Saka, T. & Taniguchi, Y. 1994. Buckling behaviour of square-and-diagonal double-layer grid. *Journal of Structural Engineering* (120) 1088–1102.

Schmidt, L. C., Morgan, P. R. & Clarkson, J. A. 1976. *Journal of the Structural Division, Proceeding of the American Society of Civil Engineers* (102) 1479–1492.

Schmidt, L., Morgan, P. R. & Hanaor, A. 1982. Space trusses with brittle-type strut buckling. *Journal of the Structural Division, Proceeding of the American Society of Civil Engineers* (108) 1325–1335.

Simulia, 2010. Abaqus analysis user's manual version 6.10. Providence: Simulia Corp.

Research and Applications in Structural Engineering, Mechanics and Computation – Zingoni (Ed.)
© 2013 Taylor & Francis Group, London, ISBN 978-1-138-00061-2

Behavior of composite bar structures: Theory and examples

J.B. Obrębski
Faculty of Civil Engineering, Warsaw University of Technology, Warsaw, Poland

ABSTRACT: The present author has elaborated complex theory for straight bars with any type of Cross-Sections (CSs) – in it homogenous and composite, too. There, was proposed, that for the bars with full – compact Cross-Section (CS), can be calculated geometrical characteristics, identically as in theory of thin-walled bars (TWBs), when the CS is modeled as set of closed tubes located each into the other (see short paper). The tubes can be of composite character with different materials concentrated in longitudinal strips located along theirs circuit. With such geometrical characteristics of full CSs is possible much more exact calculation of bars in range till now known rather in theory of TWBs. Both papers, short and full, form one whole.

1 INTRODUCTION

The paper are shows some examples of calculations for composite straight bars under combined loading. It tries to present in one place summary of created unconventional possibilities for designing of different composite bar structures. On example of simply supported bar (Fig. 1) with seven similar rectangular CSs, were compared normal stresses, cores and mechanical behavior. The six of them have identical external dimensions, but other dislocation of two materials: steel and timber. There, were presented some drawings showing position of indifferent axes (where normal stresses are equal zero) and area of calculated the CSs' cores (short paper, Fig. 3). Values of normal stresses are presented in proper tables.

For calculation of CSs warping (warping functions) and position of shearing centers, they were divided in two different manners for sets of five or six closed thin-walled, homogenous (steel or timber) or composite (having steel and timber). In consequence it gives a little different effects and results.

For strength calculations were used: own program MBK and MS Excel. The calculations are based on

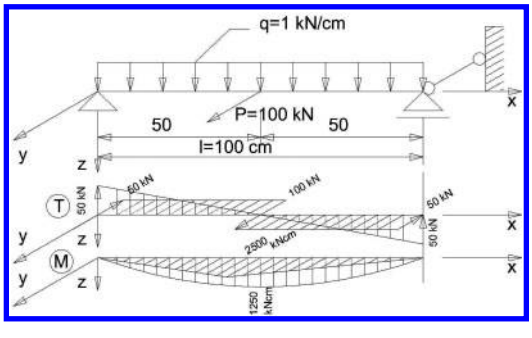


Figure 1. Scheme of investigated bar, loadings and diagrams of shearing forces and bending moments.

mentioned own theory (Obrebski 1991, 1997), next extended in some large papers published in LSCE books (1995–2012). Together both manuals forms one portion of knowledge concerning static and dynamic analyses in range of first and second order including instability of the bars which can interacting with surrounding media (dumping, aerodynamics, elastic multi-parametrical foundation etc.). There, can be straight bars with any type of CSs composed from some materials in it full and thin-walled o open or closed with one- or multi-circular and open closed. Moreover short review of previous author's researches (including SEMC), related to different aspects of strength calculations for composite straight bars are given, too.

The paper presents rather comparison of behavior considered seven similar simply supported bars. In the future works is foreseen extension of investigations on instability of such single bars and on space bar structures built from many composite bars.

In author's theory are defined "reduced principal axes" of CS, for which are equal zero some next geometrical characteristics (static moments and centrifugal moments of inertia – all reduced):

$$\overline{A} = \oint d\overline{A} \quad \& \quad d\overline{A} = \left(\frac{E_1}{E}\right)\delta\, ds = \left(\frac{E_1}{E}\delta\right) ds = \overline{\delta}\, ds \quad \& \quad \overline{\delta} = \left(\frac{E_1}{E}\delta\right) \tag{1}$$

Some essential formulae of applied theory are quoted in next chapters, only.

2 INVESTIGATED BAR

Comparative strength analyses are performed for short bar with length 100 cm, Fig. 1. There, is given external loading acting in two principal planes of bar CS. Continuous uniform loading q is given in vertical plane of symmetry and horizontal force P = 100 kN in half of CS height. The calculations were done for seven

prismatic bars with constant rectangular CS. Six CSs have external dimensions 10 × 12 cm, and the seventh is bigger – 12 × 12 cm. The first CS is made from steel, but six next besides steel (E = 205 GPa, E_1 = 225.27 GPa; G = 80 GPa; ν = 0.281) have inclusions of timber with area of its CS from 24 cm^2 up to 80 cm^2 (E = 10 GPa, G = 63 GPa; ν = 7). The all CSs are symmetrical with regard to vertical z axis The CSs A & C are bisymmetrical, (see short paper, Figs 2, 3).

3 GEOMETRICAL CHARACTERISTICS

There, key-matter is definition of so called geometrical characteristics for CS. As the first is defined reduced area:

$$\bar{I}_i = \oint (\eta_j)^2 d\bar{A}, \quad i, j=2, 3 \ \wedge \ i \neq j, \tag{2}$$

where $\bar{\delta}$ = new reduced thicknesses of the bars walls.

Similarly are defined reduced moments of inertia:

$$\bar{S}_2 = \bar{S}_2 = \bar{S}_{\hat{\omega}} = \bar{I}_{23} = \bar{I}_{2\hat{\omega}} = \bar{I}_{3\hat{\omega}} = 0 \ . \tag{3}$$

$$\bar{I}_{23} = \oint \eta_2 \eta_3 d\bar{A}, \quad \bar{I}_{\hat{\omega}} = \oint (\hat{\omega})^2 d\bar{A}, \quad \bar{I}_{j\hat{\omega}} = \oint \eta_j \hat{\omega} d\bar{A}, \quad j=2,3$$

where η_i = coordinates. Obtained in this way geometrical characteristics for considered CSs are shown in Table 1. Next, in Table 2 are given positions of reduced center of gravity, shearing center and arm of the force P generating torsion moment M_1.

As follow from Table 1, by much dense division of CS on tubes (5 on 10), is slightly changing only sectorial moment of inertia (last column). Similarly, as follow it from Table 2, by much dense division of CS on tubes (5 or 10), slightly changes torsion rigidity K_s from 87.3 % to 88% (last column). There, theoretical solution is regarded as exact.

Table 1. Basic geometrical characteristics of CSs.

Type of cross-section	A cm^2	$\bar{A}$ cm^2	$\bar{I}_2$ cm^4	$\bar{I}_3$ cm^4	$\bar{I}_{\hat{\omega}}$ cm^6
A	120	120.00	1440.00	1000.00	145.09
A10*	120	120.00	1440.00	1000.00	146.97
Ba	120	62.9268	289.24	524.39	1962.73
Bb	120	62.9268	289.24	524.39	881.02
C	120	43.9024	805.85	594.15	84.49
C10*	120	43.9024	805.85	594.15	85.17
Da	120	36.2927	526.76	553.56	8541.25
Db	120	36.2927	526.76	553.56	9503.46
Ea	120	85.7561	1101.04	954.34	21075.83
Eb	120	85.7561	1101.04	954.34	12796.86
Fa	120	97.1707	1117.78	969.56	21564.46
Fb	120	97.1707	1117.78	969.56	14091.47
Ga**	144	121.1707	1415.33	1697.56	48506.33
Gb**	144	121.1707	1415.33	1697,56	24937.10

*Division on 10 tubes. **Division on 6 tubes.

Table 2. Torsion rigidity of full rectangular CS type A by different modeling.

Type of model for cross-section	Ks kN cm^2	Exactness %
Theoretical, exact solution	16 023 100	100
CS A modeled as 5 tubes	13 929 133	87.3
CS A modeled as 10 tubes	14 109 447	88.0

4 "TRADITIONAL" CALCULATIONS

The calculations were started from trivial determination of graphs for internal forces – shearing T and bending moments M, (see Table 1). All seven compared calculations were led for following bending moments (in vertical and horizontal planes): $M_2 = ql^2/8 =$ 1250 kN cm, $M_3 = Pl/4 = ql^2/4 =$ 2500 kN cm.

Determination of internal forces associated with torsion needs of knowledge about position of shearing centre (see chapter 5.3). The normal stresses for each kind of bar should be calculated as follow:

$$\sigma_1 = \frac{E_1}{E}\left(\frac{T_1}{A} - \frac{M_3\eta_2}{\bar{I}_3} + \frac{M_2\eta_3}{\bar{I}_2} + \frac{B\hat{\omega}}{\bar{I}_{\hat{\omega}}}\right) \ . \tag{4}$$

There last term describes torsion. Traditionally, by strength calculations for compact CSs, the fourth term

Table 3. Torsion rigidity Ks in particular tubes of CSs type A, B & C.

Tube No	CS A kN cm^2	CS Ba kN cm^2	CS Bb kN cm^2	CS C kN cm^2
Cross-sec.	13929133	217669	3110858	7888746
Tube 1	7840800	122527	2314286	7840800
Tube 2	3969000	62023	18225	31255
Tube 3	1633333	25524	705600	12862
Tube 4	450000	7032	5556	3543
Tube 5	36000	562	66666	283
Tube 6	525			

Table 4. Torsion rigidity Ks in particular tubes of CSs type D & E.

Tube No	CS Da kN cm^2	CS Db kN cm^2	CS Ea kN cm^2	CS Eb kN cm^2
Whole CS	347249	118780	891658	169300
Tube 1	299303	62015	576596	62015
Tube 2	31255	36317	236983	54017
Tube 3	12862	15507	74251	46020
Tube 4	3543	4536	3543	6597
Tube 5	283	403	283	648

Table 5. Torsion rigidity Ks in particular tubes of CSs type F & G.

Tube No	CS Fa kN cm^2	CS Fb kN cm^2	CS Ga kN cm^2	CS Gb kN cm^2
Cross-sec.	895426	280823	1430005	302324
Tube 1	576596	117754	855047	99368
Tube 2	236983	92302	388845	82843
Tube 3	74251	66939	144438	66354
Tube 4	7032	3543	38172	49930
Tube 5	562	283	3375	3543
Tube 6			125	283

is neglected. In such case, we have indifferent axis which for each type of CS has other inclination.

In turn, in the Table 6 are given positions of cores for particular CSs. Here, turn the attention different shape and area of each core. The coordinates of its corners were determined according to formulae:

$$z_0 = -\frac{\overline{i_2}^2}{e_3}, \qquad y_0 = -\frac{\overline{i_3}^2}{e_2},$$

where e_2 & e_3 = coordinates of the points where a longitudinal force is applied (external corners of the CS); y_0 & z_0 = coordinates of the points in which indifferent axis crosses the reduced principal axes;

$$\overline{i_2}^2 = \frac{\overline{I_2}}{A}, \qquad \overline{i_3}^2 = \frac{\overline{I_3}}{A},$$

are squares of reduced radiuses of inertia for particular CSs, Obrebski 1991, 1997.

In the Table 8, are compared deflections of particular bars depending on reduced moment of inertia.

5 TORSION IN INVESTIGATED BARS

According to theoretical derivations follows, that torsion moment M_1 is calculated with regard to shearing centre. For its determination is needed knowledge of warping of considered CS. In this moment appears necessity to modeling full – compact homogenous or composite CSs as built from some tubes located one into the other, Obrebski 1991, 1997, 2012. So, it is assumed division of CSs on generally 5 tubes, treated from this moment as thin-walled. But shearing centre, moments of inertia, center of gravity (reduced, too) are calculated as common for whole CS. Here, geometrical characteristics are calculated as sums of similar values, but calculated for particular tubes.

Especially in this paper, are shown three possible methods of CSs division. Version "a" assumes existence of closed composite tubes – built here from steel and timber. Version "b" assumes homogenous closed thin-walled tubes, only (short pap. Fig. 3). Each closed tube is represented by middle line forming closed circuits, with length L (Table 10) and with double area of closed tubes: $\Omega = 2 \times A$ (Table 9).

The warping of the each homogenous rectangular closed tube used in CS type A was calculated according to the following formula, Obrebski (1991):

$$K = a \times b \frac{b-a}{a+b}, \qquad (5)$$

Table 6. Position of vertexes in CS cores.

Node	coordinates	A cm	B cm	C cm	D cm	E cm	F cm	G cm
1	y	0	0	0	0	0	0	0
	z	−2	−1.69	−3.06		−1.95	−1.72	−1.78
2	y	1.67	1.67	2.71	3.05	2.23	2	2.8
	z	0	0	0	0	0	0	0
3	y	0	0	0	0	0	0	0
	z	2	1.4	3.06		2.38	2.17	2.15
4	y	−1.67	−1.67	−2.71	−3.05	−2.23	−2	−2.8
	z	0	0	0	0	0	0	0

Table 7. Comparison of areas in CSs.

Area of:	CS units	A	B	C	D	E	F	G
Whole CS	cm^2	120	120	120	120	120	120	120
Steel	cm^2	120	60	40	32	84	96	120
	%	100	50	33.33	26.67	70	80	83.33
Timber	cm^2	0	60	80	88	36	24	24
	%	0	50	66.67	73.33	30	20	16.67
Core of CS	cm^2	6.66	2.34	16.56	15.32	9.62	7.77	11.007
	%	5.55	1.95	13.80	12.77	8.02	6.47	7.64

Table 8. Calculated vertical deflections in middle bars span, only [cm] (q = 0.1 kN/cm).

CS:	A	B	C	D	E	F	G
Defl. cm	1.54	7.67	2.75	4.21	2.01	1.98	1.56

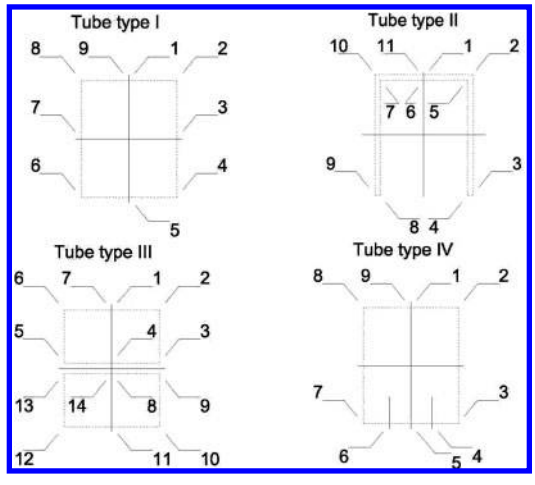


Figure 2. Four applied different types of thin-walled closed tubes and its characteristic points.

Table 9. Area Ω – double area of closed tube circuit.

Type of CS	Ω [cm^2] in particular tubes with number 1	2	3	4	5	6
A	198	126	70	30	6	
Ba	198	126	70	30	6	
Bb	90	90	42	42	10	10
C	198	126	70	30	6	
Da	198	126	70	30	6	
Db	31.5	140	80	36	8	
Ea	198	126	70	30	6	
Eb	31.5	27.5	23.5	48	12	
Fa	198	126	70	30	6	
Fb	39.5	31.5	23.5	30	6	
Ga**	242	162	98	50	18	2
Gb**	38.5	32.5	26.5	20.5	30	6

**Division on 6 tubes.

Table 10. Length L of closed tube circuit.

Type of CS	L [cm] in particular tubes with number					
	1	2	3	4	5	6
A	40	32	24	16	8	
Ba	40	32	24	16	8	
Bb	28	28	20	20	12	12
C	40	32	23	16	8	
Da	40	32	24	16	8	
Db	64	34	26	18	10	
Ea	40	32	24	16	8	
Eb	64	48	48	22	14	
Fa	40	32	24	16	8	
Fb	62	50	38	16	8	
Ga**	44	36	28	20	12	4
Gb**	67	57	47	37	16	8

**Division on 6 tubes.

Table 11. Location of geometrical centre, shearing centre of CSs & torsion moment (for A & C $M_1 = 0$).

Type of cross-section	η_0 cm	η_{Ak} cm	η_P cm	P kN	M_1 kN cm
Ba	−2.7209	−3.9053	−6.6262	100.00	−662.62
Bb	−2.7209	−0.0234	−2.7443	100.00	−274.43
Da	−1.1532	−8.4308	−9.5840	100.00	−958.402
Db	−1.1532	−8.8908	−10.0440	100.00	−1004.4
Ea	−0.599	−8.9796	−9.5786	100.00	−957.86
Eb	−0.599	−9.0479	−9.6469	100.00	−964.691
Fa	−0.7048	−8.7784	−9.4832	100.00	−948.322
Fb	−0.7048	−6.8350	−7.5398	100.00	−753.984
Ga**	−0.5652	−8.8354	−9.4006	100.00	−940.061
Gb**	−0.5652	−7.5396	−8.1048	100.00	−810.481

*Division on 10 tubes. **Division on 6 tubes.

where K = value of warping function in corner of each rectangular tube, a = value o half width of particular closed rectangular tube, b = value of half high of particular closed rectangular tube. For remaining tubes, homogenous and composite ones, was used the formula in its general shape (6) Obrębski 1991:

$$\hat{\omega}(s) = \hat{\omega}_A + \omega(s) - \Omega\frac{l}{L} \quad \& \quad l = \int_0^s \frac{ds}{G\delta}, \quad L = \oint \frac{ds}{G\delta}, \qquad (6)$$

where $\hat{\omega}(s)$ = value of calculated warping for closed tube; $\hat{\omega}_A$ = value of warping in starting point (s = 0); $\omega(s)$ = warping calculated for opened CS. By means of above formulae and program MS Excel, were calculated values of warping function in characteristic points of each particular tube (Table 7).

As the last step in calculations presented in this paper, are positions of shearing centers for each type of CS defined by two coordinates:

$$\eta_{zA'} = \frac{\bar{I}_{3\hat{\omega}}}{\bar{I}_2}, \qquad \eta_{yA'} = \frac{\bar{I}_{2\hat{\omega}}}{\bar{I}_3}. \qquad (7)$$

where $\bar{I}_{2\hat{\omega}}$ & $\bar{I}_{3\hat{\omega}}$ = warping-centrifugal reduced moment of inertia of the CS. All geometrical characteristics, including above formulae, are calculated as

Table 12. Values of B and M_ω on dependence on Ks and coefficient α (for CSs type A & B is $B = M_\omega = 0$).

Type of cross-section	Ks kNcm^2	α 1/cm	B kNcm^2	M_ω kNcm
Ba	217669	0.070164	−4713	−331.31
Bb	3110858	0.395906	−346	−137.21
Da	347249	0.042482	−10962	−479.20
Db	118780	0.023555	−17662	−502.20
Ea	891658	0.043336	−10765	−478.93
Eb	169300	0.024234	−16663	−482.35
Fa	895426	0.042933	−10746	−474.16
Fb	280823	0.029743	−11443	−376.99
Ga**	1430005	0.036175	−12313	−470.03
Gb**	302324	0.023198	−14341	−405.24

*Division on 10 tubes. **Division on 6 tubes.

Table 13. Part of particular tubes in carrying of torsion moment (for CSs type A & C $M_1 = 0$).

Type of CS	in whole CS	Part of torsion moment in tube number					
		1	2	3	4	5	6
Ba	−662.62	−372	−188	−77	−21	−1.7	
Bb	−274.43	−204	−1.6	−62	−0.5	−5.9	−0.05
Da	−958.40	−826	−86	−35	−9	−0.7	
Db	−1004.4	−524	−307	−131	−38	−3.4	
Ea	−957.86	−619	−254	−79	−3.8	−0.3	
Eb	−964.69	−353	−307	−262	−37	−3.6	
Fa	−948.32	−610	−250	−78	−7.4	−0.6	
Fb	−753.98	−316	−247	−179	−9.5	−0.8	
Ga**	−940.06	−562	−255	−94	−25	−2.2	−0.08
Gb**	−810.48	−266	−222	−177	−133	−9.5	−0.76

**Division on 6 tubes.

the sums of n similar, determined for each (i) particular tube. In few tables below, are given some results of calculation of torsion bars rigidity and generated by them in task internal forces. This matter is here without comments.

It is interesting to know, what part of torsion moment carry particular tubes. It is proportional to torsion rigidity K_s of particular tubes with regard to torsion rigidity of whole CS (compare Table 13).

After determination of shearing centre, warping function $\hat{\omega}$, sectorial moment of inertia $\bar{I}_{\hat{\omega}}$, and bimoment B, we can use for calculation of normal stresses, full version of formula (3). Results for particular CSs are given in Tables 14–19. There is omitted table with normal stresses σ_x in external corners of CS type A (as homogenous built from steel).

Shearing stresses in general case should be calculated according to formula (8), where last term gives influence of torsion (bending-torsion moment).

$$\tau_{1s} = \tau_O - \frac{1}{\delta}\left(\frac{T_z\widetilde{S}_3}{\bar{I}_3} + \frac{T_y\widetilde{S}_2}{\bar{I}_2} + \frac{M_{\hat{\omega}}\widetilde{S}_{\hat{\omega}}}{\bar{I}_{\hat{\omega}}}\right). \qquad (8)$$

For the reason of limited volume of this paper, in tables 20 & 22 are given the flows of τ_o, only.

In presented bars type A & C, horizontal force P has not giving any torsion. In result in Table x torsions were equal zero. Therefore, in Table 22, below are shown

Table 14. Comparison of normal stresses σ_x in external corners of CS type B.

CS	Pt corn.	pt nr	Tube nr	y cm	z cm	σ_x(B) kN/cm^2	σ_x (M$_i$) kN/cm^2	σ_x kN/cm^2
B	A			5	2.72			35.596
	B			−5	2.72			−12.078
	C			−5	−3.28			−38.008
	D			5	−3.28			9.666
Ba	(A)*	3	1	4.5	2.72	−45.41	33.21	−12.20
	(B)*	7	1	−4.5	2.72	45.41	−9.69	35.71
	(C)*	8	1	−4.5	−2.78	−13.01	−33.46	−46.47
	(D)*	2	1	4.5	−2.78	13.01	9.44	22.45
Bb	(A)*	3	3	4.5	2.22	−1.72	31.05	29.33
	(B)*	5	3	−4.5	2.22	1.72	−11.85	−10.13
	(C)*	6	3	−4.5	−2.78	−0.81	−33.46	−34.27
	(D)*	2	3	4.5	−2.78	0.81	9.44	10.25

*Parentheses contain closest corners of the cross-section.

Table 15. Comparison of normal stresses σ_x in external corners of CS type C.

CS	Pt corn.	pt nr	Tube nr	y cm	z cm	σ_x (B) kN/cm^2	σ_x (M$_i$) kN/cm^2	σ_x kN/cm^2
C	A			5	6	0	30.345	30.345
	B			−5	6	0	−11.732	−11.732
	C			−5	−6	0	−30.345	−30.345
	D			5	−6	0	11.732	11.732
Ca	(A)*	3	1	4.5	5.5	0	27.47	27.47
	(B)*	7	1	−4.5	5.5	0	−10.40	−10.40
	(C)*	8	1	−4.5	−5.5	0	−27.47	−27.47
	(D)*	2	1	4.5	−5.5	0	10.40	10.40

*Parentheses contain closest corners of the cross-section.

Table 16. Comparison of normal stresses σ_x in external corners of CS type D.

CS	Pt corn.	pt nr	Tube nr	y cm	z cm	σ_x(B) kN/cm^2	σ_x(M$_i$) kN/cm^2	σ_x kN/cm^2
D	A			5	7.15		39.55	39.55
	B			−5	7.15		−5.606	−5.606
	C			−5	−4.85		−34.083	−34.083
	D			5	−4.85		11.08	11.08
Da	(A)*	3	4	4.5	1.15	−36.18	23.06	−13.12
	(B)*	7	4	−4.5	1.15	36.18	−17.58	18.60
	(C)*	8	4	−4.5	−4.35	−24.68	−30.64	−55.32
	(D)*	2	4	4.5	−4.35	24.68	10.01	34.69
Db	(A)*	3	3	4.75	6.90	−48.65	37.83	−10.82
	(B)*	5	3	−4.75	6.90	48.65	−5.07	43.58
	(C)*	6	3	−4.75	−4.60	−42.17	−32.36	−74.53
	(D)*	2	3	4.75	−4.60	42.17	10.54	52.71

*Parentheses contain closest corners of the cross-section.

shearing stresses flows, possible to appear in particular tubes.

6 FURTHER PLANNED NUMERICAL TESTS

Separate matter appears with global analysis of large complicated space bar structures, which can be built from homogenous and composite bars having any type of CSs including full and thin-walled. It can concern

Table 17. Comparison of normal stresses σ_x in external corners of CS type E.

CS	Pt corn.	pt nr	Tube nr	y cm	z cm	σ_x(B) kN/cm^2	σ_x(M$_i$) kN/cm^2	σ_x kN/cm^2
E	A			5	6.60		20.59	20.59
	B			−5	6.60		−5.61	−5.61
	C			−5	−5.40		−19.23	−19.23
	D			5	−5.40		6.97	6.97
Ea	(A)*	3	4	4.5	6.10	−13.03	18.71	5.68
	(B)*	7	4	−4.5	6.10	13.03	−4.86	8.16
	(C)*	8	4	−4.5	−4.90	−10.21	−17.35	−27.56
	(D)*	2	4	4.5	−4.90	10.21	6.22	16.43
Eb	(A)*	3	3	4.75	6.35	−36.61	19.65	−16.96
	(B)*	5	3	−4.75	6.35	36.61	−5.23	31.38
	(C)*	6	3	−4.75	−5.15	−27.15	−18.29	−45.44
	(D)*	2	3	4.75	−5.15	27.15	6.59	33.74

*Parentheses contain closest corners of the cross-section.

Table 18. Comparison of normal stresses σ_x in external corners of CS type F.

CS	Pt corn.	pt nr	Tube nr	y cm	z σ_x(B) cm	σ_x(M$_i$) kN/cm^2	σ_x kN/cm^2	kN/cm^2
F	A			5	6.70		20.39	20.39
	B			−5	6.70		−5.39	−5.39
	C			−5	−5.29		−18.81	−18.81
	D			5	−5.29		6.97	6.97
Fa	(A)*	3	4	4.5	6.20	−12.92	18.54	5.62
	(B)*	7	4	−4.5	6.20	12.92	−4.66	8.26
	(C)*	8	4	−4.5	−4.79	−9.75	−16.96	−26.71
	(D)*	2	4	4.5	−4.79	9.75	6.24	15.99
Fb	(A)*	3	3	4.75	6.45	−27.28	19.46	−7.82
	(B)*	5	3	−4.75	6.45	27.28	−5.03	22.25
	(C)*	6	3	−4.75	−4.79	−9.30	−17.61	−26.91
	(D)*	2	3	4.75	−4.79	9.30	6.89	16.19

*Parentheses contain closest corners of the cross-section.

Table 19. Comparison of normal stresses σ_x in external corners of CS type G.

CS	Pt corn.	pt nr	Tube nr	y cm	z cm	σ_x(B) kN/cm^2	σ_x(M$_i$) kN/cm^2	σ_x kN/cm^2
G	A			6	6.56	14.63	14.63	
	B			−6	6.56	−3.04	−3.04	
	C			−6	−5.43	−13.64	−13.64	
	D			6	−5.43	4.04	4.04	
Ga	(A)*	3	4	5.5	6.06	−8.06	13.45	5.39
	(B)*	7	4	−5.5	6.06	8.06	−2.74	5.32
	(C)*	8	4	−5.5	−4.93	−6.06	−12.46	−18.52
	(D)*	2	4	5.5	−4.93	6.06	3.74	9.80
Gb	(A)*	3	3	5.75	6.31	−23.77	14.04	−9.73
	(B)*	5	3	−5.75	6.31	23.77	−2.89	20.88
	(C)*	6	3	−5.75	−5.06	−9.62	−12.94	−22.56
	(D)*	2	3	5.75	−5.06	9.62	4.00	13.62

*Parentheses contain closest corners of the cross-section.

e.g. single- and multi-layer bar coverings: flat, different vaults and domes, too. So, future works should be related to such structures.

The second domain of planned comparative calculations, using as a basis presented above geometrical characteristics, is instability of composite bars under combined external loading. It was proved by author together with J.Tolksdorf, that in such situations we

Table 20. Shearing stresses flow τ_o in particular tubes of CSs type A, B and C.

Type of CS	Tube No	from M1 kN/cm	from Ti & Mω kN/cm	Resulting kN/cm
A	Tube 1	0.00	1.920	1.920
	Tube 2	0.00	1.536	1.536
	Tube 3	0.00	1.183	1.183
	Tube 4	0.00	0.852	0.852
	Tube 5	0.00	0.512	0.512
Ba	Tube 1	−1.883	0.159	−1.724
	Tube 2	−1.498	0.895	−0.602
	Tube 3	−1.110	0.868	−0.242
	Tube 4	−0.714	0.482	−0.231
	Tube 5	−0.285	0.113	−0.172
Bb	Tube 1	−2.268	1.985	−0.283
	Tube 2	−2.268	−0.026	−2.295
	Tube 3	−1.482	1.021	−0.460
	Tube 4	−1.482	−0.008	−1.490
	Tube 5	−0.588	0.325	−0.263
	Tube 6	−0.588	−0.001	−0.589
C	Tube 1	0.00	2.935	2.935
	Tube 2	0.00	0.0036	0.0036
	Tube 3	0.00	0.0020	0.0020
	Tube 4	0.00	0.0008	0.0008
	Tube 5	0.00	0.0001	0.0001

Table 21. Shearing stresses flow τ_o in particular tubes of CSs type D and E.

Type of CS	Tube No	from M_1 kN/cm	from Ti & Mω kN/cm	Resulting kN/cm
Da	Tube 1	−4.172	2.257	−1.915
	Tube 2	−0.685	0.0516	−0.633
	Tube 3	−0.507	0.0320	−0.475
	Tube 4	−0.326	0.0162	−0.310
	Tube 5	−0.130	0.0043	−0.126
Db	Tube 1	−16.648	2.827	−13.821
	Tube 2	−2.194	0.057	−2.136
	Tube 3	−1.639	0.036	−1.603
	Tube 4	−1.065	0.018	−1.047
	Tube 5	−0.426	0.005	−0.421
Ea	Tube 1	−3.128	2.049	−1.079
	Tube 2	−2.020	2.144	0.123
	Tube 3	−1.139	1.278	0.138
	Tube 4	−0.127	0.007	−0.120
	Tube 5	−0.051	0.002	−0.049
Eb	Tube 1	−11.218	1.680	−9.538
	Tube 2	−11.193	1.756	−9.436
	Tube 3	−11.159	1.913	−9.245
	Tube 4	−0.783	0.015	−0.768
	Tube 5	−0.308	0.004	−0.303

can determine certain “critical surface” dependent in general case on multi parameters.

7 CONCLUSIONS

For the reason of limited volume of this paper some essential information are only enclosed. Calculated shearing stresses were here omitted. The paper shows possibility to calculate for composite bars some parameters and quantities proper rather up to the moment for TWBs: shearing centre, warping of CS and warping stresses.

Table 22. Shearing stresses flow τ_o in particular tubes of CSs A and C [kN/cm].

Tube No	when $M_1 = 1$ & CS A kN/cm	when $M_1 = 1$ & CS C kN/cm
Tube 1	0.00284	0.005
Tube 2	0.00226	3.14E-5
Tube 3	0.00167	2.33E-5
Tube 4	0.00108	1.5E-5
Tube 5	0.00043	5.99E-6

It is shown, that in five cases on seven, appears strong torsion, which by traditional analyses will be not considered at all. In consequence appears significant warping stresses, which extremely modify image of resulting stresses. In this case the shapes of warping function, longitudinal displacements and σ_x are not limited by plane surface, but are rather a complicated surface, difficult to draw. Torsion in some cases generates concentration of stresses in selected corners of the particular CSs.

After calculation, it can be observed, that proposed approach to modeling of the bars for σ_x gives rather excellent results. In the case of shearing stresses in the moment, are some questions: method of calculation is much more complicated; especially calculation of τ_o is rather laborious; obtained results well describe torsion, but are rather fare from traditional. The last problem needs much more time for recognition and observation.

REFERENCES

Obrębski, J.B. 1991, 1999. *Thin-walled elastic straight bars*. Warsaw. OWPW.

Obrębski, J.B. 1997. *Strength of Materials*. Warsaw, Micro-Publisher.

Obrębski, J.B. 2001. On the mechanics and strength analysis of composite structures. (Invited paper) In A. Zingoni (ed.), *Structural Engineering, Mechanics and Computation*, Cape Town, 2-4.04.2001, Elsevier Sc. Ltd, Amsterdam-London-New York – Oxford – Paris–Shannon – Tokyo:161–172.

Obrębski, J.B. 2007. Torsion in analysis of space bar frames – review and discussion. (Inv. Paper). In A. Zingoni (ed.) Third Int. Conf. *Structural Engineering, Mechanics and computations*. 10–12 September 2007, Cape Town, South Africa, abstr.: 49–50 + CD ROM.

Obrębski, J.B. 2010. Own theory for thin-walled straight bars: Development and investigations. In A. Zingoni (ed.) **4-th Int. Conf. *Advances and Trends in Structural Engineering, Mechanics and Computation*, 6–8 September 2010, Cape Town, South Africa**. Inv. lecture:146 (abst.)+CD ROM.

Obrębski, J.B. 2012. Examples of stresses calculation for composite bars under combined load. *Mechanik*, 7, 2012: +CD.

Obrębski, J.B. 2012. Some observations on Mechanical behavior of bars wit composite cross-sections. In W. Przybylo & J. Obrebski (Eds). *Lightweight Structures in Civil Engineering*. 7 December 2012. MP. Warsaw, Poland: 110–121.

Research and Applications in Structural Engineering, Mechanics and Computation – Zingoni (Ed.)
© 2013 Taylor & Francis Group, London, ISBN 978-1-138-00061-2

A method for reconstructing the shape of highly flexible, slender objects from distributed strain measurements

M.D. Todd
Department Structural Engineering, University of California, San Diego, La Jolla, CA, USA

C.J. Stull
AET-6, Los Alamos National Laboratory, Los Alamos, NM, USA

M. Dickerson
3 Phoenix Inc., Chantilly, VA, USA

ABSTRACT: This paper presents a method for determining three-dimensional global displacement (for arbitrarily-sized deformation but "small" strain) of thin rod/tether-like structures from a limited set of scalar strain measurements. The approach is rooted in Cosserat rod theory with the adoption of a material-adapted reference frame and a localized linearization approach that facilitates an exact local basis function set for the displacement as well as the material frame evolution itself. The solution set is shown to be robust to potential singularities from vanishing bending and twisting angle derivatives and from vanishing measured strain. Validation of the approach is performed through comparison with finite element simulations of a tube-like structure subjected to arbitrary deformations. The average root mean square reconstruction error of 0.01%–1% of the total length, for reasonably low sensor counts. Analysis of error due to extraneous noise sources and boundary condition uncertainty shows how error scales with those effects. The algorithm involves relatively simple operations, the most complex of which is square matrix inversion, lending itself to potential low-power embeddable solutions for structural monitoring applications requiring shape reconstruction. Experimental verification will also be shown in the presentation accompanying this paper.

1 INTRODUCTION

There are a number of applications where it is desirable to monitor long, slender, highly flexible structures such as cables, tethers, long rods, or any such system which has one dimension's length scale dimension substantially greater than any other dimension's length scale. Such systems share the common kinematic behavior of arbitrarily large deformation (bending, twisting, rotating) while experiencing relatively small (linear, elastic) strain. Euler initiated the first formal study of such objects (the elastica), followed by more modern theories (Love 1909, Cosserat & Cosserat 2001, Bishop 1975, Reisner 1981, Langer & Singer 1996).

In the monitoring applications of interest, a common objective is to obtain the displacement of the these structures from distributed measurements of some kind, whether the measurements are acceleration (requiring integration), direct non-contact measures of displacement (such as with laser vibrometry), or indirectly through distributed local measures of a kinematically-related quantity, such as strain. This last approach comprises the scope of the present paper. The main challenge in this class of monitoring problems lies in obtaining a reasonable inverse model that converts a finite number of local strain measurements into global displacement estimations. For small displacements of certain structural models (beams, plates), classical theory can be directly inverted, but no such viable method currently exists for long, highly deformable objects. This paper presents a kinematic model rooted in Cosserat theory and introduces a material basis reference frame to describe the deformation more precisely in a way that measurable strain metrics are calculable from the theory. Then, under local linearization assumptions, the resulting displacement/material frame evolution equations are integrated in terms of the strain metrics to obtain global displacement. The approach is validated against several full finite element displacement simulations of a pipe undergoing arbitrarily large deflections in this paper, and validation against an experimental hose test bed will be presented at the conference accompanying this paper.

2 KINEMATIC MODEL

2.1 *Geometry, kinematics, and strain measure*

Figure 1 shows the relevant geometry. Under the assumption that the neutral axis of the object does not

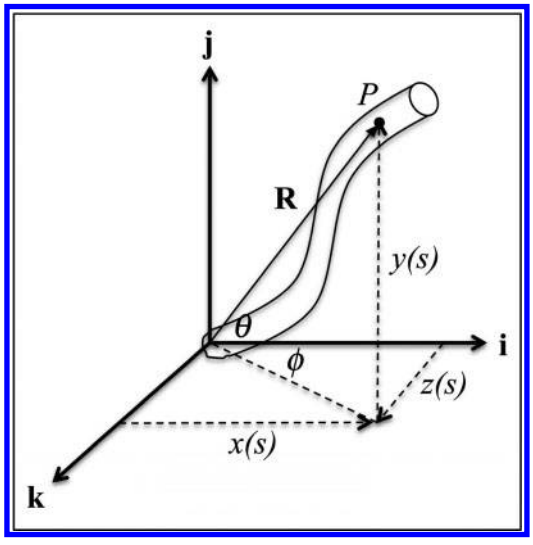


Figure 1. Fundamental geometry description of the deformed structure.

stretch appreciably, a point P on the neutral axis of the object in the deformed state may be located by the vector **R** in an inertial reference frame **i-j-k** by a pitch angle θ in the **i-j** plane and a yaw angle ϕ deviation from the **i-j** plane, each parameterized by the arc length variable s:

$$\mathbf{R}(s)=\underbrace{\left(\int_0^s \cos\theta(p)\cos\phi(p)\,dp\right)}_{x(s)}\mathbf{i}+\underbrace{\left(\int_0^s \sin\theta(p)\,dp\right)}_{y(s)}\mathbf{j}+\underbrace{\left(\int_0^s \cos\theta(p)\sin\phi(p)\,dp\right)}_{z(s)}\mathbf{k} \tag{1}$$

While the vector **R** may successfully locate P on the neutral axis through the two angle functions, it is insufficient in describing the material deformation about P, which is what generates strain. Recourse is made to a reference frame that somehow evolves with the deformed structure; one such common frame is the Frenet frame, consisting of a tangent **T**, normal **N**, and binormal **B** vector set. However, as Todd et al. (2013) discussed in earlier work, the Frenet frame suffers discontinuities, because it is not evolve according to the material's actual physical twisting and bending, but rather with the kinematic curvature and torsion. As a consequence, the Frenet frame **N** and **B** vectors can suddenly switch sign at inflection points, causing apparent (but not real) strain discontinuity in the model; since inflection points aren't known a priori, this is an undesirable restriction on use. Instead, a true material-referenced frame may be used by rotating the **N** and **B** vectors into **U** and **V** vectors through the actual local material rotation $\sigma(s)$. Figure 2 shows the relevant geometry at an arbitrary cross section, where the **U** and **V** vectors rotate with the material, and

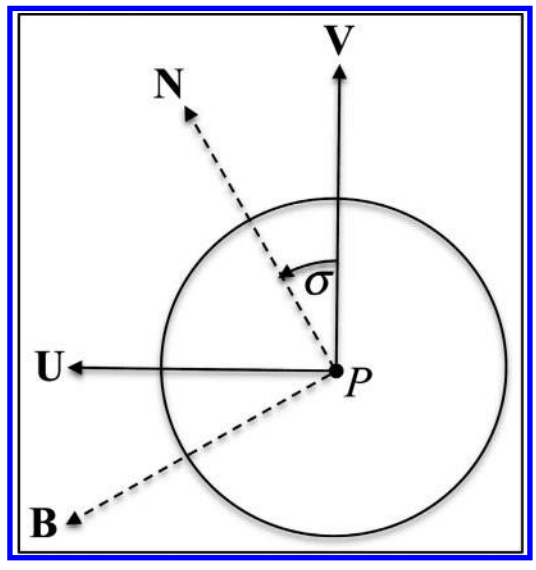


Figure 2. A material twist angle $\sigma(s)$ relating **N** and **B** vectors to material-referenced **U** and **V** vectors.

the difference between their current orientation and the Frenet frame orientation is $\sigma(s)$.

The same tangent vector **T** is retained; only the cross section is rotated, which is where the discontinuity potential is. This choice of material frame guarantees that the pitch angle θ defines the projection of **V** into **j**, or $\mathbf{V}\cdot\mathbf{j}=\cos\theta$. Using this definition and the Frenet-Serrat equations governing the Frenet frame evolution, a new set of equations may be derived for the material frame:

$$\begin{bmatrix}\mathbf{R}'\\ \mathbf{T}'\\ \mathbf{V}'\\ \mathbf{U}'\end{bmatrix}=\begin{bmatrix}0 & 1 & 0 & 0\\ 0 & 0 & \theta' & \phi'\cos\theta\\ 0 & -\theta' & 0 & -\phi'\sin\theta\\ 0 & -\phi'\cos\theta & \phi'\sin\theta & 0\end{bmatrix}\begin{bmatrix}\mathbf{R}\\ \mathbf{T}\\ \mathbf{V}\\ \mathbf{U}\end{bmatrix} \tag{2}$$

where a prime mark indicates differentiation with respect to s, and the relationships between material twist σ, traditional curvature κ, and torsion τ are given by

$$\begin{aligned}\kappa\sin\sigma&=\phi'\cos\theta\\ \kappa\cos\sigma&=\theta'\\ \sigma'&=\tau+\phi'\sin\theta\end{aligned} \tag{3}$$

The angles θ and ϕ clearly are embedded in the relationships. The last of Equations (3) shows the explicit relationship between material rotation rate and torsion; the two are not equal, and the additional term is what helps to accommodate discontinuities.

Figure 3 shows a representative curve with the **U**, **V**, **N**, and **B** vectors superimposed at several locations along it. At all inflection points, the Frenet (**N,B**) frame suddenly flips direction, while the material-referenced frame (**U,V**) smoothly follows material

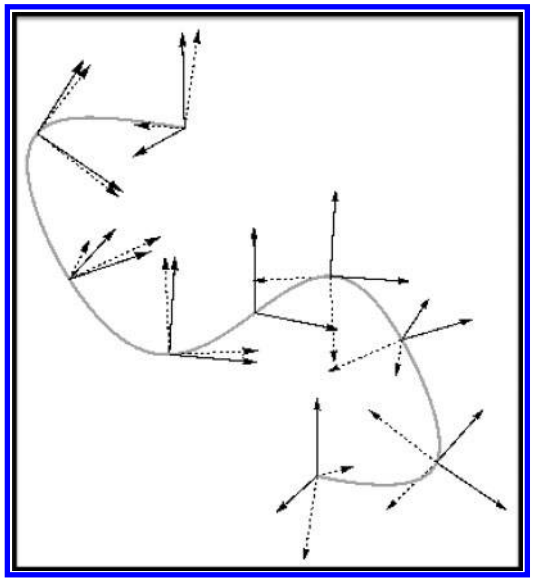


Figure 3. A curve showing the (**U**, **V**) frame (solid lines) and the (**N**, **B**) frame (dashed lines) as they evolve around the curve.

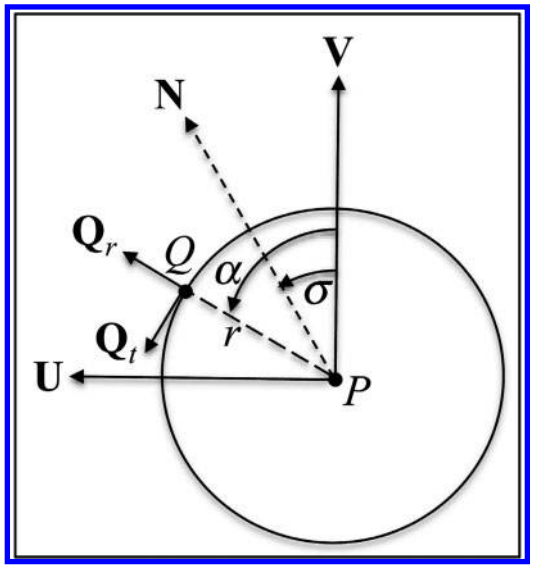


Figure 4. Cross-sectional geometry locating an arbitrary surface point Q for calculation of strain.

rotation. The Frenet frame leads to ambiguous (and thus indeterminate) strain measurements at such points of discontinuity.

Now a measure of strain may be computed from this kinematic model. Given the one-dimensional geometry of the class of objects under consideration, only strains due to changes in the s-coordinate are assumed non-negligible. Figure 4 shows the cross-sectional geometry at an arbitrary location s relative to the centerline point P and an arbitrary point on the surface of the object, Q. Since most strain measurements are obtained by a surface-mounted gage, the figure reflects this, although the theory doesn't require this; the radial distance r of the point Q relative to point P should be thought of as an arbitrary distance locating the strain point relative to P, oriented through the angle a relative to. The components of strain (the strain vector, since the rest of the components of the tensor in this formulation are zero) in the three directions **T**, **U**, and **V** may be computed by differentiating the vector locating Q relative to P:

$$\begin{aligned}\boldsymbol{\varepsilon} &= \mathbf{r}'_{Q/P} \\ &= \left(r\cos\alpha\mathbf{V} + r\sin\alpha\mathbf{U}\right)' \\ &= -r\alpha'\sin\alpha\mathbf{V} + r\cos\alpha\mathbf{V}' + r\alpha'\cos\alpha\mathbf{U} + r\sin\alpha\mathbf{U}' \\ &= \left(-r\cos\alpha\theta' - r\sin\alpha\phi'\cos\theta\right)\mathbf{T} \\ &\quad -r\sin\alpha\tau\mathbf{V} + r\cos\alpha\tau\mathbf{U} \\ &= \left(-r\cos\alpha\theta' - r\sin\alpha\phi'\cos\theta\right)\mathbf{T} + r\tau\mathbf{Q}_t\end{aligned} \tag{4}$$

where Equations (2) were used to substitute for the material frame derivatives and material continuity was imposed, i.e., changes in the location angle α must equal changes in material twist σ. For a surface-mounted strain gage at point Q, a more useful vector space is spanned by **T** (out of the page) and $\mathbf{Q}_t$, as shown in Figure 4. A gage can only be mounted in some orientation that is a combination of **T** and $\mathbf{Q}_t$ (radial direction mounting is impossible, obviously), so this transfer from (**U**,**V**) into ($\mathbf{Q}_r$,$\mathbf{Q}_t$) is represented in the final line of Equations (4).

Equation (4) is very easily interpreted in its final form, where the strain is clearly decomposed into bending strain (the **T** component) and torsional strain (the $\mathbf{Q}_t$ component). For a strain gage arbitrarily mounted, assuming an orientation angle μ from the **T** direction, the scalar strain expected at the point Q is given by

$$\begin{aligned}\varepsilon = &-r\cos\mu\cos\alpha\theta' - r\cos\mu\sin\alpha\phi'\cos\theta \\ &+r\sin\mu\tau\end{aligned} \tag{5}$$

Equation (5) is a very general model predicting the scalar strain that a surface-mounted gage would be expected to see, in terms of all the relevant kinematic parameters. The torsion τ has a highly complex, nonlinear relationship with the two angles (not explicitly shown here), so orientating a gage that is insensitive to torsion by choosing $\mu = 0$ would simplify Equation (5) to

$$\varepsilon = -r\cos\alpha\theta' - r\sin\alpha\phi'\cos\theta \tag{6}$$

As shown in the next subsection, this (final) model form, while still a nonlinear relationship between strain and kinematic displacement angles, nonetheless facilitates an approach that leads to a viable solution. Now that Equations (2) and (6) relate displacement and strain, respectively, to the kinematic variables, the solution will be proposed by combining multiple strain measurements at each cross section and local linearization.

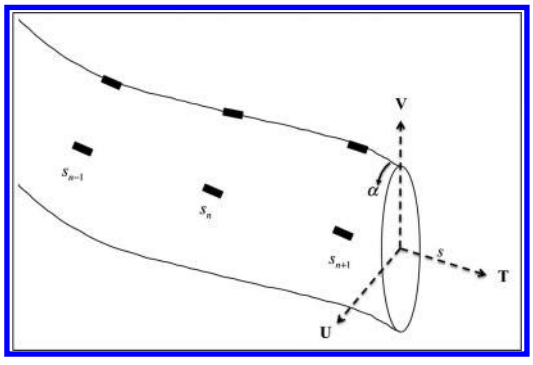


Figure 5. Assumed arrangement of discrete strain gages.

2.2 *Solution method*

The first assumption is that a finite set of discrete strain measurements is available from gages placed at locations $s = s_n$, $n = 1 \ldots N$, at multiple circumferential locations α_m, $m = 1 \ldots M$. The case of $M = 2$ is shown in Figure 5, which is the minimum number of circumferential independent readings required, as will now shown. From Equation (6), then, the strain at each gage is given by

$$\varepsilon_{n,m} = -r\cos\alpha_m \theta_n' - r\sin\alpha_m \phi_n' \cos\theta_n \tag{7}$$

and it is straightforward to show that at each cross sectional station n where two gages are located,

$$\begin{aligned} \frac{\sin\alpha_2 \varepsilon_{n,1} - \sin\alpha_1 \varepsilon_{n,2}}{\sin(\alpha_1 - \alpha_2)} &= r\theta_n' \equiv e_{n,1} \\ \frac{-\cos\alpha_2 \varepsilon_{n,1} + \cos\alpha_1 \varepsilon_{n,2}}{\sin(\alpha_1 - \alpha_2)} &= r\phi_n' \cos\theta_n \equiv e_{n,2} \end{aligned} \tag{8}$$

where it is clear that the two circumferential locations cannot be chosen 0 or π radians apart (across from each other). The second assumption made now is that, if the structure's curvature changes between from any location n to its nearest locations is small compared to the spacing between sensor locations, the strain is locally constant in the n-th so-called "neighborhood". This means the strain combinations $e_{n,1}$ and $e_{n,2}$ are constant, so the first of Equations (8) may be directly integrated to find

$$\begin{aligned} \theta_n &= a_n + (e_{n,1}/r)s \\ &\approx a_n + (e_{n,1}/r)s_n \end{aligned} \tag{9}$$

where a_n is a constant of integration, and the second line is a zero-order Taylor series approximation of θ_n about $s = s_n$, which will allow for Equations (2) to be solvable. So, with θ_n determined locally by Equation (9) and using Equations (8), the system of Equations (2), for the n-th cross-section, may be written

$$\begin{bmatrix} \mathbf{R}_n' \\ \mathbf{T}_n' \\ \mathbf{V}_n' \\ \mathbf{U}_n' \end{bmatrix} = \begin{bmatrix} 0 & 1 & 0 & 0 \\ 0 & 0 & \frac{e_{n,1}}{r} & e_{n,2}/r \\ 0 & -\frac{e_{n,1}}{r} & 0 & -\frac{e_{n,2}}{r}\tan\theta_n \\ 0 & -\frac{e_{n,2}}{r} & \frac{e_{n,2}}{r}\tan\theta_n & 0 \end{bmatrix} \begin{bmatrix} \mathbf{R}_n \\ \mathbf{T}_n \\ \mathbf{V}_n \\ \mathbf{U}_n \end{bmatrix} \tag{10}$$

where everything in the matrix is a constant for that n-th cross section. Equations (10) may be solved exactly analytically, the solution in particular for the n-th displacement vector $\mathbf{R}_n(s)$ is given by

$$\begin{aligned} \mathbf{R}_n(s) = {} & \frac{\mathbf{c}_{n,2} r e_{n,1} + \mathbf{c}_{n,1} r e_{n,2} + \mathbf{c}_{n,4}\gamma_n^2}{\gamma_n^2} \\ & + \left(\frac{\delta_n e_{n,2}\left(-\mathbf{c}_{n,1} e_{n,1} + \left(\mathbf{c}_{n,2} + \delta_n \mathbf{c}_{n,3}\right) e_{n,2}\right)}{\gamma_n^2} \right) s \\ & + \left(\frac{\delta_n e_{n,2}\left(\mathbf{c}_{n,1} e_{n,1} - \mathbf{c}_{n,2} e_{n,2}\right) + \mathbf{c}_{n,3}\left(e_{n,1}^2 + e_{n,2}^2\right)}{\gamma_n^3} \right) r\sin\left(\frac{\gamma_n s}{r}\right) \\ & - \left(\frac{\mathbf{c}_{n,2} e_{n,1} + \mathbf{c}_{n,1} e_{n,2}}{\gamma_n^2} \right) r\cos\left(\frac{\gamma_n s}{r}\right) \end{aligned} \tag{11}$$

where the $\mathbf{c}_{n,j}$ are vector constants of integration and

$$\begin{aligned} \gamma_n &= \sqrt{e_{n,1}^2 + \left(1 + \delta_n^2\right) e_{n,2}^2} \\ \delta_n &= \tan\theta_n \end{aligned} \tag{12}$$

with θ_n given by Equation (9). Similar expressions are found for $\mathbf{T}_n$, $\mathbf{U}_n$, and $\mathbf{V}_n$.

The total number of unknowns in the solution, given by the combination of Equations (9), (11), and (12) is $13N$, with $12N$ coming from the three components of the four vector quantities and N more from θ_n. Table 1 summarizes all the continuity and boundary conditions imposed to make the solution unique. In general, continuity is imposed in each kinematic variable (the four vector quantities and θ_n) at each segment boundary, defined to be s_n* in the table, and five remaining boundary conditions are drawn from some combination of those five same variables. In general, the choice of s_n* is made to coincide with the midpoint between s_n and s_{n+1}, although the choice could be any value in that range.

With the problem now completely determined and unique, Equation (11) explicitly provides the Cartesian coordinates of the three-dimensional displacement of the structure at any point along it within a neighborhood of the n-th cross-section; these individual "local" solutions are just added over their respective ranges of validity using Heaviside functions $u()$ to obtain the global displacement for any s:

$$\mathbf{R}(s) = \sum_{n=1}^{N} \mathbf{R}_n(s)\left[u\left(s - s_{n-1}^*\right) - u\left(s - s_n^*\right)\right] \tag{13}$$

Table 1. Summary of constraints imposed to make solution unique.

Condition or constraint description	Number of imposed constraints
Continuity in $\mathbf{R}_n$: $\mathbf{R}_n = \mathbf{R}_{n+1}$ at some s_n*	$3N$-1
Continuity in $\mathbf{T}_n$: $\mathbf{T}_n = \mathbf{T}_{n+1}$ at some s_n*	$3N$-1
Continuity in $\mathbf{U}_n$: $\mathbf{U}_n = \mathbf{U}_{n+1}$ at some s_n*	$3N$-1
Continuity in $\mathbf{V}_n$: $\mathbf{V}_n = \mathbf{V}_{n+1}$ at some s_n*	$3N$-1
Continuity in θ_n: $\theta_n = \theta_{n+1}$ at some s_n*	N-1
Any five boundary conditions	5
TOTAL	$13N$

Close inspection of Equation (11) shows that a possible singularity might occur if both measured strains were zero, or $e_{n,1} = e_{n,2} = 0$. However, evaluating the limit of the solution in this condition reveals that

$$\lim_{e_{n,1},e_{n,2}\to 0} \mathbf{R}_n(s) = \mathbf{c}_{n,4} + \mathbf{c}_{n,3}s \tag{14}$$

which is a smooth, continuous result. Thus, in any practical algorithm, either Equation (11) or (14) would be used as the basis function selected for the displacement at each neighborhood n, depending on the tolerances of the measured strains to zero.

Finally, in the case of purely planar (two-dimensional) deformation, where $\tau = 0$ (and thus $\phi = 0$), the strain model reduces to

$$\varepsilon_{n,m} = -r\cos\alpha_m\theta'_n \tag{15}$$

Since the dependence upon ϕ is eliminated, technically only one strain reading is required at each cross section ($M = 1$). However, since it is not generally known a priori where the plane of bending is, it is advantageous to retain two strains at each cross and only computing the strain measure $e_{n,1}$ to ensure a more robust solution. If the plane of bending is known a priori, in contrast, then only a single strain is required, as $e_{n,1}$ is not needed, with the only constraint that it not be placed at a circumferential direction corresponding to the initial **B** direction. The planar bending simplification of Equation (11) is

$$\mathbf{R}_n(s) = \mathbf{c}_{n,4} + \mathbf{c}_{n,2}\frac{r\left(1-\cos\left(e_{n,1}s/r\right)\right)}{e_{n,1}} + \mathbf{c}_{n,3}\frac{r\sin\left(e_{n,1}s/r\right)}{e_{n,1}} \tag{16}$$

and this solution is also easily shown in the limit of vanishing $e_{n,1}$ to be Equation (14), so no singularities are present in the planar version either. Thus, the two-dimensional solution is a natural subset of the full three-dimensional version, and no separate theories distinguishing between the two classes of problems is required.

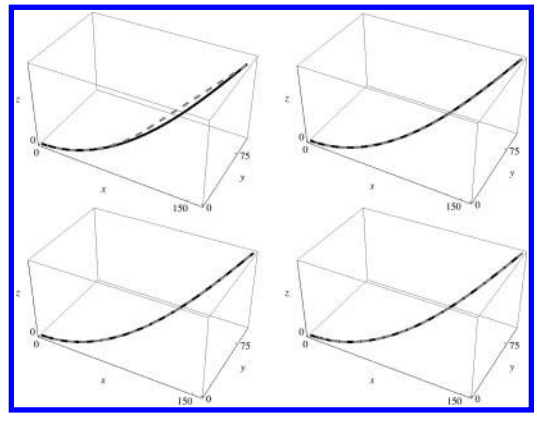


Figure 6. Comparison of exact finite element simulation (black solid line) and shape reconstruction approach (gray dashed line) of the first simulation shape, for, left-to-right then top-to-bottom, $N = 2, N = 5, N = 10$, and $N = 20$ sensor locations.

3 MODEL VALIDATION EXAMPLES

3.1 *Validation via finite element simulations*

The proposed model was validated by using finite element-based simulation of the large deformation of a hollow steel cylinder with a length of 212 m, inner diameter of 20 cm, and outer diameter of 30 cm. The material constants were chosen consistent with linear elastic theory, with a Young's modulus of 200 GPa and Poisson's ratio of 0.3. Abaqus S4R general-purpose shell elements were employed to model this structure, given their superior capability and computational efficiency in modeling large-scale bending and torsional behavior. Two three-dimensional deformations were simulated, and strains in the **T**-direction were retained at $\alpha = 0$ and π, each averaged over 1 cm of elements to simulate the average gage length of many types of strain gages.

Figure 6 shows the results for the first shape, which only contained one substantial change in curvature. The exact centerline of the hollow cylinder, as simulated by Abaqus, is shown as a solid black line, while the reconstructed shape from the algorithm presented in Section 2 is shown as a gray dashed line, for different numbers of sensor locations N. For this first shape, even for just N = 2 (4 total sensors), fairly good reconstruction is observed, with an average (over the total length) rms error of about 7 m (3% of the length); this error decreases quite rapidly, and for $N = 20$ (40 total sensors), the average rms error is only 1 mm. The spacing between each pair of sensors along s was chosen to be uniform over the 212 m (i.e., the spacing is about $212/N$ m).

Figure 7 shows results for a substantially more complex shape. This complexity inherently degrades detection performance compared to the previous test shape; the same sensor count will not result in the same reconstruction performance here. Nonetheless, with about 50 sensor locations, only a few cm of rms

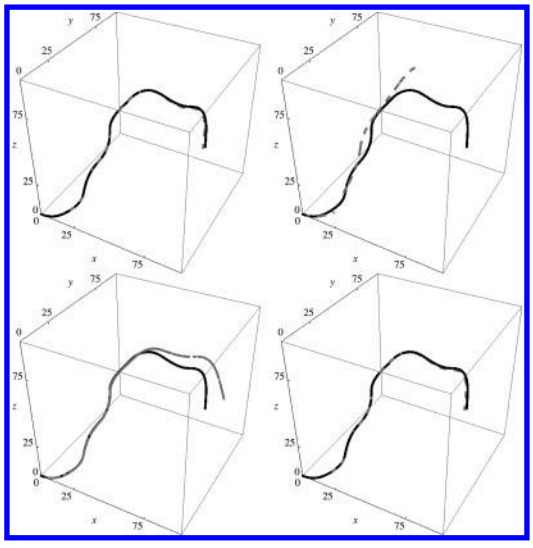


Figure 7. Comparison of exact finite element simulation (black solid line) and shape reconstruction approach (gray dashed line) of the second simulation shape, for, left-to-right then top-to-bottom, $N = 2$, $N = 5$, $N = 10$, and $N = 20$ sensor locations.

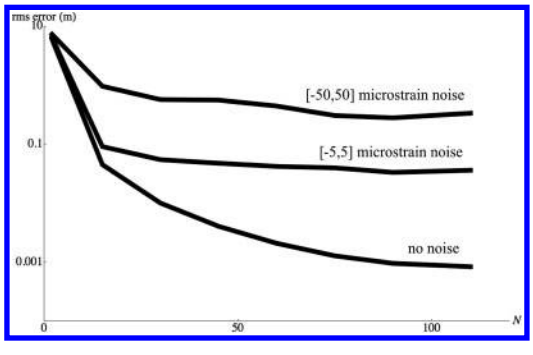


Figure 8. RMS error for the first simulation shape for various noise levels as a function of sensor locations N.

error—approximately 0.01% of the total length—is observed.

3.2 *Noise robustness*

In practical applications, the measurements of strain from a real sensor array contain noise, and additionally other sources of external uncertainty can corrupt the algorithm's performance. To address robustness, Monte Carlo simulations on both shapes were performed with uniform noise added at both the $[-5,5]$ microstrain and $[-50,50]$ microstrain levels. The resulting rms errors are shown, as a function of N, for the first shape in Figure 8 and the second in Figure 9. As expected, the reconstruction performance is degraded, although eventually the noise saturates the

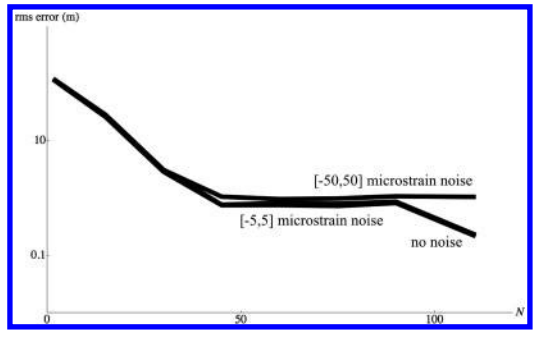


Figure 9. RMS error for the second simulation shape for various noise levels as a function of sensor locations N.

performance, as the error does not appear to decrease with additional sensors past a certain point.

4 SUMMARY AND ACKNOWLEDGEMENT

This paper proposed a method for obtaining the global three-dimensional displacement of rod-like from discrete strain measurements. The method is rooted in Cosserat rod theory using a material-adapted reference frame whose evolution equations are locally linearized in segments and subsequently solved analytically. The solution set was shown to be robust to singularities and was validated with two finite element models of a 212 m hollow steel tube undergoing significant three-dimensional deformation. Depending on the number of measurement points and shape complexity, average rms errors from tens of m down to a few mm were obtained. Preliminary noise tolerance studies showed the rms error trends with extraneous noise due to measurement uncertainty.

This work was performed under an Office of Naval Research (ONR) Small Business Technology Transfer (STTR) Program contract #N00014-10-C-0200.

REFERENCES

Bishop, R. L. 1975. There is more than one way to frame a curve. *American Mathematics Monthly* 82(3): 246–251.

Cosserat, E. & Cosserat, F. 2001. *Theorie des Corps Deformables*. Paris: Herman.

Kawakubo, S. 2007. Kirchoff elastic rods in three-dimensional space forms. *J. Mathematical Society of Japan* 60(2): 551–582.

Langer, J. and Singer, D. 1996. Lagrangian aspects of the Kirchoff elastic rod. *SIAM Review* 38(4): 605–618.

Love, A. E. H. 1909. *A Treatise on Mathematical Theory of Elasticity*, New York: Dover.

Reisner, E. 1981. On finite deformations of space-curved beams. *J. Applied. Mathematics and Physics* 32: 723–744.

Todd, M. D., Stull, C. J., and Dickerson, M. 2013. "A local material basis solution approach to reconstructing the three-dimensional displacement of rod-like structures from strain measurements," *ASME J. Applied Mech*., doi: 10.1115/1.4023023.

Research and Applications in Structural Engineering, Mechanics and Computation – Zingoni (Ed.)
© 2013 Taylor & Francis Group, London, ISBN 978-1-138-00061-2

Rod-in-tube buckling – Comparative analysis of numerical and test results

V.S. Tikhonov
Weatherford Int, Moscow, Russia

O.S. Bukashkina
Weatherford Int, St.-Petersburg, Russia

ABSTRACT: Buckling is considered to be a deleterious phenomenon because it can cause locking-up of a drillstring in a wellbore. Notwithstanding the numerous works devoted to numerical analysis and experimental investigations, the problem of buckling continues to be the urgent one. It is explained by the fact that the results of many numerical analysis correlate badly to the results of the laboratory experiments conducted with a rod-in-tube simulating drillstring in a wellbore. Present investigation tries to explain the character of these distinctive features on the basis of the improved dynamic model of a drillstring. The model includes effects of wellbore wall stiffness and multicomponent friction, it accounts for initial rod curvature and other factors. The analysis is made on the basis of the DYNTUB software, which allows carrying out numerical simulation of nonlinear 3D dynamics for long drillstring in the 3D well. The results of the laboratory experiments performed by McCann & Suryanarayana (1994) are used as the basis for comparison. The simplified analytical expressions developed in the paper to evaluate buckling loads are additional proofs of correct analysis. The results of the work allow to understand better the nature of buckling and to predict better the objectionable effects occurring in drilling.

1 INTRODUCTION

Buckling of compressed sections of the drillstring and coiled tubing is typical for horizontal and inclined intervals of wells at extended reach drilling. The buckling may lead to undesirable effects:

- Crooking of the well from the direction of drilling;
- Decreased axial load transferred to the bit up to the drillstring lockup;
- Failure of the drill pipes under action of bending moment at contact points of connectors with the wellbore wall.

The main areas of buckling investigation are related to development of analytical expressions to calculate buckling loads, numerical simulation methods and small-scale tests of the rod-in-tube samples modeling the drillstring in the wellbore. Their detailed overview was presented by Hajianmaleki et al. 2012. Despite numerous investigations in this area, there is still no understanding of the process behavior. It is in many ways due to inconsistency of the rod-in-tube test results. The actual rod behavior during buckling is strongly affected by such "fine" factors as friction, rod length, initial curvature, etc.

The paper describes these variables impact based on DYNTUB software analysis that simulates the time-domain dynamics of the drillstring (Tikhonov et al. 2006, Tikhonov & Safronov 2011). This software is efficient for simulating various drillstring operation regimes (Tikhonov et al. 2013). However its verification by comparison with the results obtained using conventional analytical expressions for critical sinusoidal and helical buckling forces (Wu & Juvkam-Wold 1993) and experimental data revealed rather poor accuracy. To understand the reason, DYNTUB software was specially upgraded to compare the simulation results with the rod-in-pipe buckling test results.

The comparison is based on the results of the laboratory experiments performed by McCann & Suryanarayana (1994). The authors obtained the rod-in-tube test results with high reproducibility. The paper was the first to recognize poor correlation of the common buckling loads formulae with experimental results and state one of the primary reasons of poor accuracy as neglecting the hoop component of the friction force. It is curious but long after the above paper had been published other researchers still failed to consider the friction force effects and kept on using the same formulae introduced by Dawson & Paslay (1984). Only 2–3 years ago Gao & Miska (2009, 2010) again paid attention to the friction phenomenon during buckling.

This paper provides a brief description of DYNTUB model and represents the results of numerical simulation for the compressed rod in horizontal tube analysis vs the friction factor, rod length and initial curvature. Comparative analysis of the numerical simulation and test results is carried out. The results are supported with simplified expressions for sinusoidal and helical buckling loads.

2 MATHEMATICAL MODEL OF THE ROD DYNAMICS

The detailed description of the mathematical model of drillstring dynamics in the 3D well was provided by Tikhonov et al. 2010. It is a set of equations for lateral, axial and torsional motion of the rod. The specified model was upgraded for the purpose of buckling test result analysis:

- The multicomponent friction model was improved;
- The bottomhole stiffness was introduced, which allowed to enhance the efficiency of the algorithm for the axial force acting on the rod at kinematic loading of the top end;
- The initial curvature of the rod was considered.

To describe the rod motion in the tube, introduce the righthand coordinate system *OXYZ* with *OX* axis connected with the tube center line and *OY* axis directed along the normal to the tube wall (Fig. 1). For straight-line tube, the equations of motion for the uniform rod in projections on *OXYZ* axes are as follows (Tikhonov et al. 2010):

$$m\ddot{x} = -Q' + f_x, \tag{1}$$

$$m^*\ddot{\mathbf{r}} = Q\mathbf{r}'' - EI(\mathbf{r}'' + j\boldsymbol{\kappa}_0)'' + j[M(\mathbf{r}'' + j\boldsymbol{\kappa}_0)]' + \mathbf{f}_\mathbf{n}, \tag{2}$$

$$\rho I_p \ddot{\Psi} = M' + \mu, \tag{3}$$

where $\mathbf{r} = y + jz$; x, y and z are projections of the rod center line onto *OX*, *OY* and *OZ,* respectively; m = rod mass per unit length; *AE*, *EI* and *GI p* are axial, bending and torsional stiffness of the rod; ρIp = moment of inertia relative to the rod axial line; $Q = AE(x' - 0.5|\mathbf{r}'|^2$ = axial compressive force; ψ = torsion angle; $M = GI_p\Psi'$ = torque; $\boldsymbol{\kappa}_\mathbf{0} = \kappa_{y0} + j\kappa_{z0}$, κ_{y0} and $j\kappa_{z0}$ are projections of the rod initial curvature vector $\boldsymbol{\kappa}_\mathbf{0}$ onto axes *OY* and *OZ*; $\mathbf{f_n} = fy + jf_z$; f_x, f_y and f_z are projections of the external force $\mathbf{f_n}$ per unit length onto axes *OX*, *OY* and *OZ*; μ = external torque per unit length; $j = (-1)^{1/2}$; the prime means a derivative with respect to rod arc length s, and the point is derivative with respect to time t; bold type means the complex variable (vector in *OYZ* plane), which real part is the vector projection on axis *OY*, and imaginary part is the projection on axis *OZ*.

Major components of external force$_\mathbf{f}\mathbf{n}$ include weight per unit length w, and vectors of normal contact force $\mathbf{p}$ and friction force $\mathbf{f_t}$ per unit length (Fig. 1).

Assume that the absolute value of p vector of the normal contact force $\mathbf{p}$ is determined by tube wall deformation $\Delta = \sqrt{y^2 + z^2} - \delta$ and $p(\Delta)$ dependence is quadratic-elastic (Fontaine et al. 2002), where δ = gap between the tube wall and the rod.

A multicomponent friction model was developed for the complex motion of the rod in the wellbore and axial movement with simultaneous rotation around mass center and wellbore center line, Tikhonov et al. (2012). Neglecting the force of rolling friction, represent the components of the sliding friction force as

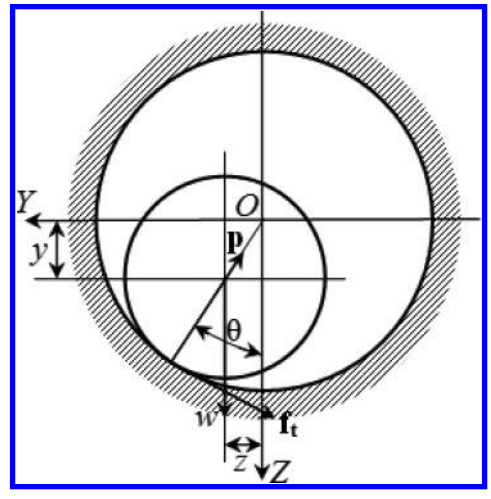


Figure 1. Coordinate system and external forces acting on the rod.

projections on axis *OX*, f_x and on the tangent to the wellbore wall in *OYZ* $\mathbf{f_t}$ plane:

$$f_x = k_a \frac{\dot{x}}{v}, \quad \mathbf{f_t} = k_\theta \frac{\mathbf{v_\theta}}{v}, \tag{4}$$

where k_a and k_θ are friction factors in axial and circumferential directions, respectively; $\mathbf{v_\theta}$ = vector of relative circumferential velocity of the rod, which absolute value is the ratio of the difference between the hoop velocities of the rod surface points relative to its center of mass and wellbore center line to their sum, $v_{\theta m}$; $v = \sqrt{\dot{x}^2 + (v_{\theta m}/\gamma)^2}$; γ = factor of transition zone width from sliding to rolling friction in the zone of low speed v_θ.

All the above considered, the external forces vector:

$$\mathbf{f_n} = w\sin\alpha - p\mathbf{r}/|\mathbf{r}|\left(1 - jk_\theta v_\theta / v\right), \tag{5}$$

where α = inclination angle of the tube axis relative to the vertical.

The boundary conditions for the Equations (1)–(3) are defined by the specified displacement of end points in the cross-sectional plane of the tube, fixity conditions (hinge/cantilever) as well as loading conditions at compression and torsion. Assume the following:

1) Rod compression is achieved under kinematic load of the top end with the specified velocity vg, $\dot{x}(L, t) = v_g(t)$, where L is the rod length;
2) The bottom end of the rod elastically supports on the bottomhole: $Q(0, t) = \lambda x(0, t)$, where λ = stiffness of the bottomhole;
3) The torque in the bottom end $M(0, t) = 0$;
4) The top end is fixed to prevent rotation: (in general rotating rod buckling case, the condition determining variation of angular velocity of the top end in time).

The solution method for the set of Equations (1)–(3) is described in detail by Tikhonov et al. (2010) and

consists in approximation of partial derivatives with respect to length s by finite differences and in integrating of the net set of ordinary differential equations derived in this way with the explicit scheme.

3 ANALYSIS OF NUMERICAL SIMULATION RESULTS

The results of the aluminium rod test in a horizontal wellbore performed by McCann & Suryanarayana (1994) were used as a basis for comparative analysis:

- Outer rod diameter = 6.3754 mm;
- Inner tube diameter = 38.15 mm;
- Rod length, $L = 3.683$ m;
- Hoop friction factor = 0.331;
- Loading speed = 0.1016 mm/sec.

The rod ends are fixed in hinges in the bottom surface of the tube.

Figure 2 shows load curves of the rod as the bottom load vs top displacement.

The curves marked with geometric figures are borrowed from McCann & Suryanarayana (1994) for eight different tests (as rescaled from inch-lbs to mm-N). The curve marked with a solid line was calculated by DYNTUB. For the largest part of the top distance range, the difference between the load curves does not exceed 15%. At the same time there is a rather large difference between the curves at the initial loading phase, correlating with elastic deformation of the rod. However, simple calculations demonstrate that the value of the theoretical slope of the curve in this phase,

$$\frac{\partial Q(L)}{\partial x_g} = \frac{AE}{L} = 6.067 \text{ N/m},$$

is far from the slope evaluated based on the test results and is close to the calculated value.

Upon completion of the elastic deformation phase, there is a transition from the straight-line to sinusoidal shape of the rod. According to the test data, the sinusoidal buckling load is 70 N and according to the numerical simulation results – 76 N. The conventional value of the sinusoidal buckling load by Dawson & Paslay (1984),

$$Q_{\sin} = 2\sqrt{\frac{EIw}{\delta}} = 35.7 \text{ N}, \quad (6)$$

is significantly lower than both these values. This formula derivation process does not consider friction.

The formula (A-7) for sinusoidal buckling load calculation with allowance for friction is given in the Appendix. In compliance with it, $Q_{\sin} = 59.6$ N at the friction factor of 0.331 (Fig. A-1). This formula has been derived for deduced buckling while the test was performed with $L = 3.683$ m rod close to the sinusoidal buckling $l = 3.228$ m. It is natural that in this case the boundary conditions will act the essential part for the rod shaping. This can be demonstrated by comparison of the load curves for L, $2L$, $3L$ and $4L$ rods (Fig. 3).

It is obvious that with increase of the rod length the sinusoidal buckling load tends to decrease reaching 53 N at the fourfold length of the rod. Periodic drops of the bottom load (points A, B1-B2, C1-C2-C3, the last is not shown) which occur with increase of top displacement, are typical for generation of successive turns of helix near the rod ends and propagating to its middle. With the minimum length of the rod, $L \sim l$, there is almost no drop of the bottom load. Immediately after helical buckling the rod assumes a spring shape and the bottom load is steadily growing. With increase of the rod length such growth settles only upon turns development along the whole length of the rod.

Note that in the process of turns generation the helical buckling load does not change much, it is within 59–64 N. For comparison, the helical buckling load by Dawson & Paslay (1984)

$$Q_{\text{hel}} = 2\sqrt{\frac{2EIw}{\delta}} = 50.5 \text{ N}. \quad (7)$$

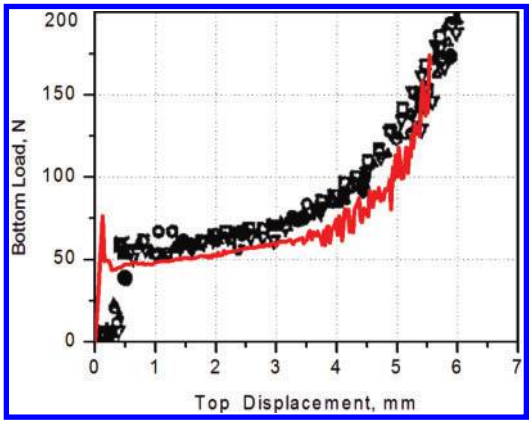


Figure 2. Experimental vs calculated load curves.

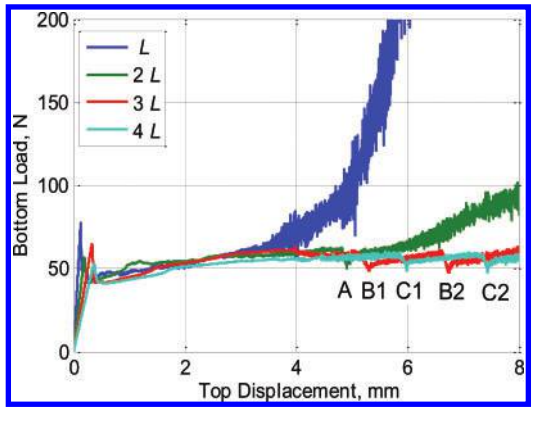


Figure 3. Influence of the rod length on the load curve.

Table 1. Comparative analysis of buckling loads for various rod lengths.

Buckling Load, N	Experiment (L)	Numerical simulation L	$2L$	$4L$	Formula
$Q_{\sin}$	70	76	57	53	60
Q_{hel}	79	79	63	59	51

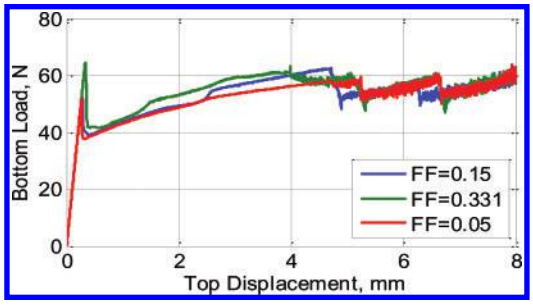


Figure 4. Influence of the friction factor on the load curve.

The results of the comparative analysis of the sinusoidal and helical buckling loads for various rod lengths at friction factor 0.331 are shown in the Table.

Figure 4 shows the load curves plotted for various friction factors of triple rod length, $3L$. It is obvious that with decrease of the friction factor the sinusoidal buckling load also decreases tending to the conventional value $Q_{\sin}$ (6). Meanwhile the helical buckling load remains almost constant.

In the investigation of the effect of the initial bending, the initial shape of the rod was given in the form of a sine wave:

$$z_0 = A \sin \frac{2\pi n s}{L},$$

where $A =$ amplitude of the sine; $n =$ the number of sine waves along the length of the rod. In this case $\kappa_{y0} = z_0''$, $\kappa_{z0} = 0$.

Figure 5 shows the load curve for the threefold length of the rod, $3L$, bent of the three sinusoids shape ($n = 3$) with the amplitude $A = 1$ mm.

As shown from Fig. 5, the initial bending significantly increases the sinusoidal buckling load. A similar effect was observed at a buckling of the straight-line rod in curved wellbore (Wu & Juvkam-Wold 1995).

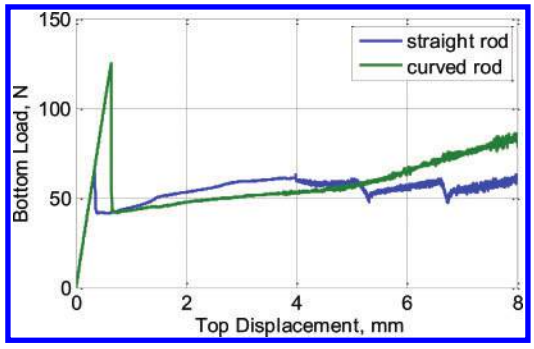


Figure 5. Influence of initial bending on the load curve.

4 CONCLUSIONS

1) The comparative analysis results confirmed DYNTUB software capability and feasibility for drillstring buckling analysis.
2) With increase of the friction factor, sinusoidal buckling load increases and helical buckling undergoes minor changes. As a result, with rather high friction factor, sinusoidal buckling load can exceed helical buckling load. This conclusion alters the existing understanding of sinusoidal and helical buckling relation.
3) The load curve character for rod buckling essentially depends on the rod length due to boundary conditions effect. It shall be considered when performing buckling experiments.
4) Subject to initial rod bending, sinusoidal buckling load increases and helical buckling load undergoes slight changes.
5) The derived simplified formulae of sinusoidal and helical buckling loads with allowance for friction can be used for improvement of buckling load values for practical drilling operations.

REFERENCES

Dawson, R. & Paslay, P.R. 1984. Drillpipe buckling in inclined holes. *Journal of Petroleum Technololgy* October: 1734–1738.

Fontaine, E., et al. 2002. Modeling of riser contact – friction problems. *Proc. Offshore Technology Conf., OTC 14157, Houston, TX, 6–9 May*.

Gao, G. & Miska, S. 2009. Effects of boundary conditions and friction on static buckling of pipe in a horizontal well. *SPE Journal* 14(4): 782–796.

Gao, G. & Miska, S. 2010. Effects of friction on post-buckling behavior and axial load transfer in a horizontal well. *SPE Journal* December: 1110–1124.

Hajianmaleki, M., et al. 2012. Buckling analysis of drill strings in inclined wellbores using the explicit finite element method. *ASME 2012 Intern. Mechanical Congress & Exposition, IMECE2012-89638, Houston, TX, 9–15 November*.

McCann, R.C. & Suryanarayana, P.V.R. 1994. Experimental study of curvature and frictional effects on buckling. *Proc. Offshore Technology Conf., OTC 7568, Houston, TX, 2–5 May*: 511–521.

Tikhonov, V.S. & Safronov, A.I. 2011. Analysis of postbuckling drillstring vibrations in rotary drilling of extended-reach wells. *Trans ASME. Journal of Energy Resources Technology* 133 (December): 043102-1-8.

Tikhonov, V.S., et al. 2006. Method of dynamic analysis of rod-in-hole buckling. *Proc. Conf on Engng. Systems design and Analysis, ESDA2006-95059, Torino, Italy, 4–7 July*.

Tikhonov, V.S., et al. 2013. Dynamic model for stiff string torque and drag. *Proc. SPE/IADC Drilling Conf. and Exhibition, SPE/IADC 163566, Amsterdam, The Netherlands, 5–7 March*.

Tikhonov, V.S., et al. 2010. Development of mathematical model, numerical scheme and algorithm for calculation of contact force acted on drill string. Dynamic statement. *Report (unpubl.), Weatherford Co, Moscow, Russia*: 57 p.

Tikhonov, V.S., et al. 2012. Multi-component friction testing of full-scale drill pipe specimen. *Proc.4th Intern. Conf. on Tribology & Design, Kos, Greece, 3–5 September*: 65–76.

Wu, J. & Juvkam-Wold, H.C. 1993. Helical buckling of pipes in extended reach and horizontal wells. *Trans ASME. Journal of Energy Resources Technology* 115 (September): 190–195.

Wu, J. & Juvkam-Wold, H.C. 1995. The effect of wellbore curvature on tubular buckling and lockup. *Trans ASME. Journal of Energy Resources Technology* 117 (September): 214–218.

APPENDIX – DERIVATION OF FORMULAE FOR DEVELOPED BUCKLING WITH ALLOWANCE FOR FRICTION

Assume that at the sinusoidal buckling, the rod rests on the bottom wall of the tube and bends in a shape of a sinusoid with the period, within which the compression force can be considered constant. Then according to the Langrange-Dirichlet theorem, any equilibrium rod bending shape can be determined subject to minimal energy functional with all possible movements, preset limitations of its buckling in the tube and boundary conditions. Total rode bending energy is composed of elastic bending energy, work of axial load, weight and friction force. In this case the energy functional can be represented as:

$$J_{\sin} = \int_0^l \left[\begin{array}{l} 0.5EI(y''^2 + z''^2) - 0.5Q(y'^2 + z'^2) \\ + w\sin\alpha(\delta - y) + k_\theta w\delta|\theta|\cos\theta \end{array} \right] ds, \quad \text{(A-1)}$$

where $\theta = \theta_0 \sin(2\pi x/l)$ is rod axis offset angle relative to vertical (Fig. 1); θ_0 = amplitude of sinusoid.

Coordinates y and z with sinusoidal buckling:

$$y = \delta\cos\theta, z = \delta\sin\theta. \quad \text{(A-2)}$$

With medium low values of the angle $\theta_0 < 1$ the Equations (A-2) can be approximately represented in the form of the series expansion:

$$y = \delta\left(1 - 0.5\theta_0^2 \sin^2\frac{2\pi x}{l}\right), z = \delta\theta_0 \sin\frac{2\pi x}{l}\left(1 - \frac{\theta_0^2}{6}\sin^2\frac{2\pi x}{l}\right). \quad \text{(A-3)}$$

Substituting y, z (A-3) as well as their derivatives in the Equation (A-1) and integrating, we'll get the expression for the rod energy functional with sinusoidal buckling:

$$J_{\sin} = \frac{EI\delta\pi^4\theta_0^2}{l^3}(4 + 3\theta_0^2) - \frac{Q\delta\pi^2\theta_0^2}{l} + 0.25wl\theta_0\left(\theta_0 + \frac{8k_\theta}{\pi}\right)\sin\alpha. \quad \text{(A-4)}$$

At the critical point of transition from the straight-line to sinusoidal rod shape $J_{\sin} = J_s$, where J_s = energy of the straight-line shape. It is obvious that $J_s = 0$, and $J_{\sin} = 0$ respectively. Then based on the Langrange-Dirichlet theorem, we'll get two conditions:

$$\frac{\partial J_{\sin}(Q,\theta_0,l)}{\partial\theta_0} = 0 \text{ (a)}, \frac{\partial J_{\sin}(Q,\theta_0,l)}{\partial l} = 0 \text{ (b)}, \quad \text{(A-5)}$$

Transformation of the system composed of three equations: $J_{\sin} = 0$ (A-4), (A-5a) и (A-5b) results in equation in angle $\theta 0$:

$$-4.5\mu\theta_0^4 + 3\theta_0^3 + 4\mu\theta_0^2 - 8\mu = 0, \quad \text{(A-6)}$$

where $\mu = 2k_\theta/\pi$.

The solution of the Equation (A-6) determines the angle θ_0 corresponding to the minimal energy of rod sinusoidal buckling. The determined θ_0 value can be used for calculation of sinusoidal buckling load with allowance for friction:

$$Q_{\sin} = k_{\sin}(\mu)\sqrt{\frac{EIw\sin\alpha}{\delta}}, \quad \text{(A-7)}$$

where the sinusoidal buckling factor is

$$k_{\sin} = \sqrt{\frac{(4 + 3\theta_0^2)[\theta_0 + \mu(4 - \theta_0^2)]}{\theta_0}}. \quad \text{(A-8)}$$

Without friction, $\mu = 0$, functional $J_{\sin}$ does not depend on angle θ_0 and factor $k_{\sin}$ (A-8) assumes a value of 2 similar to those derived by Dawson & Paslay (1984).

Sinusoid period

$$l = \pi\sqrt[4]{\frac{4EI\delta\theta_0(4 + 3\theta_0^2)}{w\left(\theta_0 + \frac{8\mu}{\pi}\right)}}. \quad \text{(A-9)}$$

Helical buckling energy:

$$J_{\text{hel}} = \int_0^\ell \left[\begin{array}{l} 0.5EI(y''^2 + z''^2) - 0.5Q(y'^2 + z'^2) \\ + w\sin\alpha(\delta - y) \end{array} \right] ds, \quad \text{(A-10)}$$

where $y = \delta\cos(2\pi x/\ell)$, $z = \delta\sin(2\pi x/\ell)$; ℓ – helix pitch.

At the critical point of transition from the sinusoidal to helical rod shape $J_{\text{hel}} = J_{\sin}$. Then, making expression $J_{\sin}$ (A-1) equal to J_{hel} (A-10), integrating and using conditions resulting from Langrange-Dirichlet theorem, similar to the above calculations we'll get the equation for angle θ_0 corresponding to

rod helical shape. The expression for helical buckling force with allowance for friction is as follows:

$$Q_{\text{hel}} = k_{\text{hel}}(\mu)\sqrt{\frac{EIw\sin\alpha}{\delta}}. \qquad \text{(A-11)}$$

The dependence of the sinusoidal and helical buckling coefficients, k_{sin} and k_{hel}, on the friction factor, μ, is shown in Figure A-1. It shall be noted that with increase of the friction factor the helical buckling coefficient k_{hel} decreases, and with $\mu > 0.139$ the helical buckling energy becomes lower than the sinusoidal buckling energy. In this case the helical buckling load will be lower than the sinusoidal buckling load.

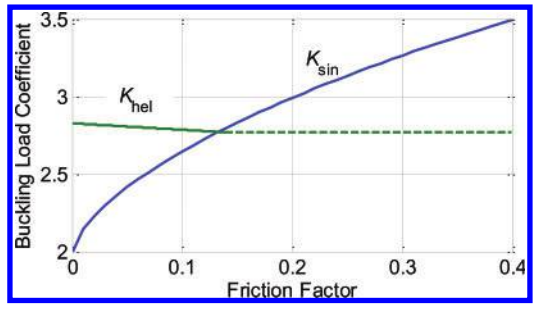


Figure A-1. Dependence of the sinusoidal and helical buckling coefficients on the friction factor.

Research and Applications in Structural Engineering, Mechanics and Computation – Zingoni (Ed.)
© 2013 Taylor & Francis Group, London, ISBN 978-1-138-00061-2

On load drop phenomenon in axially compressed elasto-plastic columns

L. Kwasniewski
Warsaw University of Technology, Warsaw, Poland

ABSTRACT: The phenomenon of Finite-Disturbance Buckling instability (FDB), i.e. sudden critical load drop, is commonly associated with buckling of thin elastic cylindrical and spherical shells but rarely related with buckling of columns. Ziolkowski & Imielowski's (2011) recent experimental study, revealing appearance of FDB in aluminum columns with slenderness remaining within a specific range only, raises questions about its physical sources and mechanism. The present study is a continuation of the work of Kwasniewski & Ziolkowski (2013) which provided a theoretical explanation and quantitative evaluation on the phenomenon of finite-disturbance buckling of columns with rectangular cross-section made of linearly elastic-perfectly plastic material. Here an effort is focused on effects resulting from cycling loading and unloading performed in the post-buckling regime and generating residual stress distributions. The results from FE numerical simulations are compared with experimental evidence.

1 INTRODUCTION

Different post-buckling behavior scenarios are often attributed to specific classes of structures such as columns, shells or plates. The post-buckling response of structures has strong implications on their load carrying capacity, imperfection sensitivity, and structural safety and has an important bearing on today's design procedures.

Ziolkowski & Imielowski's (2011) recent experimental study, revealing appearance of FDB in aluminum columns with slenderness remaining within specific range only, raises questions about its physical sources and mechanism. The present study is the continuation of the work of Kwasniewski & Ziolkowski (2013) which provided a theoretical explanation and quantitative evaluation on the phenomenon of finite-disturbance buckling of columns undergoing elasto-plastic deformation and expressing itself in the form of critical load drop. A simplified, analytical model of buckling of linearly elastic-perfectly plastic column with rectangular cross-section was developed to explain the phenomenon of sudden load drop appearing in the columns with slenderness remaining in the neighborhood of critical slenderness, Kwasniewski & Ziolkowski (2013). The theoretical study was accompanied by a numerical investigation using finite element (FE) models built of brick and shell elements, dedicated for two selected FE code packages.

The present study is focused on effects of cycling loading and unloading performed in the post-buckling regime and generating residual stress distributions. The paper presents comparison of numerical results for the simplified problem defined in the previous paper for analytical consideration. The results of numerical studies are compared with experimental data. In the present study attention is focused on the effect of Return Point Memory (RPM) and the effect of generated residual stress distributions on the character of post-buckling equilibrium paths. Considered case was investigated numerically based on the FEM models formulated in the previous study of Kwasniewski & Ziolkowski (2013).

2 SIMPLIFIED COLUMN MODEL

2.1 *Idealized column*

The considered case refers to the theoretical example of idealized column with critical slenderness $\lambda = \lambda_0$, i.e. critical stress σ_{cr} is equal to the yield stress σ_Y. The problem was investigated analytically in Kwasniewski & Ziolkowski (2013) but without consideration of subsequent post-buckling loading and unloading stages. For this case a prismatic strut with a rectangular cross-section made of elastic–perfectly plastic material, is considered. The idealization is due to the material, which can be considered as a limit case for the materials with a clear plastic plateau and a small "knee" that is a small difference between the proportional and the yield limits, Galambos (1988). The present study is focused on analysis of the return point memory (RPM) and the effect of residual stresses on the equilibrium path, Gere & Goodno (2009). This is the case in which loss of strength will be greater than in real materials with a nonlinear stress-strain relationship and strain hardening, but the mechanism of the phenomenon will be the same, i.e., nonuniform increase of stresses in the cross-section due to simultaneous bending and axial loading within the inelastic range. Majority of

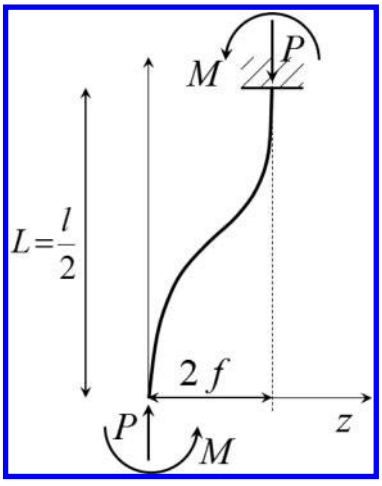


Figure 1. Schematic view of column deformation, boundary conditions and loading.

investigated problem parameters such as geometrical dimensions, loading conditions, material parameters values are taken the same as those identified for specimen tested by Ziolkowski & Imielowski's (2011). The only major difference is that instead of Ramberg-Osgood material model, linear elastic–perfectly plastic material model has been adopted with the bilinear characteristics of $\sigma-\varepsilon$ and with material data: yield stress $\sigma_Y = 189$ MPa, Young modulus E = 63300 MPa, Poisson ratio v = 0.45. Due to problem symmetry only half of the specimen has been considered in numerical simulations, Figure 1. The cross-section is rectangular with the following dimensions taken for numerical calculations: width b = 19.98 mm, height h = 5.88 mm, total length l = 195.18 mm. The applied boundary conditions result in column effective slenderness $\lambda = \lambda_0 = 57.49$ ($\sigma_{cr} = \sigma_Y$). The column maximum lateral deflection takes place in its middle height and is denoted by $2f$. It is assumed that the post-buckling bending results in linear distribution of strains in the column cross-sections, i.e. satisfies classical assumption on planar sections. In Kwasniewski & Ziolkowski (2013) two FEM models of buckling column were prepared one composed of shell and of solid elements. Subsequently relevant numerical tasks for one loading-unloading cycle have been solved using two FEM commercial codes ABAQUS, Abaqus (2007) and LS-DYNA®, Hallquist (2007).

The numerical results are compared with predictions of a simplified analytical model recalled succinctly in the next section of this work and with the experimental results.

2.2 *Simplified analytical model of FDB*

In order to understand essential features of FDB instability in columns a relatively simple analytical model of column buckling was formulated in Kwasniewski & Ziolkowski (2013). The key result predicted by this model, i.e. buckling and post-buckling equilibrium deformation path of a column exhibiting FDB is schematically presented in Figure 2. On x-axis of Figure 2 there are placed values of normalized axial contraction $\Delta l/\Delta l_{cr}$ of effective length of the column. The Δl_{cr} denotes the yield contraction, here corresponding also to Euler's buckling contraction ($\sigma_{cr} = \sigma_Y$). On y-axis there are values of normalized loading parameter σ/σ_Y, where $\sigma = P/A$; P is compressive loading force. In order to make the present paper self-contained, the simplified analytical model relations are presented succinctly below. At any moment and in any location of the column the axial force P and the bending moment M must satisfy global equilibrium equation, Figure 1

$$\mathrm{Pf} - \mathrm{M} = 0 \tag{1}$$

It is convenient to divide column post-buckling behavior into two phases of deformation. The phase I is characterized by condition $\sigma_2 \le 2\sigma_Y$, where σ_2 is the maximum negative tensile stresses increment due to bending, on the convex side of the middle cross-section. The moment M_I and axial force P_I, in the middle of the column, resulting from combined compression and bending, i.e. with asymmetric distribution of stresses in the cross-section, can be expressed as follows, Kwasniewski & Ziolkowski (2013)

$$P_I = \sigma_y bh - \frac{1}{2}\sigma_2 b\left(\frac{h}{2} + z_0\right) \tag{2}$$

$$M_I = \frac{1}{6}\sigma_2 b\left(\frac{h}{2} + z_0\right)(h - z_0) \tag{3}$$

z_0 denotes a distance from the cross-section centroid to the fiber undeformed by bending. Upon substitution of (2) and (3) into (1), it becomes

$$\sigma_y h 2f - \sigma_2 f\left(\frac{h}{2} + z_0\right) - \frac{1}{3}\sigma_2\left(\frac{h}{2} + z_0\right)(h - z_0) = 0 \tag{4}$$

At moderate lateral deflections, when the buckled column shape can be well approximated with sine function, σ_2 can be expressed as, Kwasniewski & Ziolkowski (2013)

$$\sigma_2 = \frac{\mathrm{E}\pi^2 \mathrm{f}}{\mathrm{L}^2}\left(\frac{\mathrm{h}}{2} + \mathrm{z}_0\right) \tag{5}$$

One can determine z_0 as a function of lateral deflection f, by solving constraint relation (4) after replacing σ_2 with the aid of (5). Subsequently $\mathrm{P_I}$ and $\mathrm{M_I}$ can be expressed in terms of f. In the present study, the most unfavorable material characteristic is considered, regarding FDB instability. When column is made of material exhibiting strain hardening (e.g. aluminum), the additional bending strength can origin from stress increase in a part of the cross section already in plastic range of deformation. Thus axial load drop will be smaller in such a case.

The phase II begins, when the value of stress σ_2 is equal or greater than $2\sigma_Y$. Then, the axial force P_{II} and the moment M_{II} in the middle of the buckling column can be expressed as, Kwasniewski & Ziolkowski (2013)

$$P_{II} = \sigma_y bh - \frac{\sigma_2 b}{2}\left(\frac{h}{2}+z_0\right) + \frac{(\sigma_2 - 2\sigma_y)b}{2}\left(\frac{h}{2}-z_1\right) \tag{6}$$

$$M_{II} = \frac{\sigma_2 b}{6}\left(\frac{h}{2}+z_0\right)(h-z_0) - \frac{\sigma_2 - 2\sigma_y}{6} b\left(\frac{h}{2}-z_1\right)(h+z_1) \tag{7}$$

where z_1 denotes a distance of a fiber, closest to the cross-section centroid in which tensile stress increment reached $2\sigma_Y$. The following relation must be satisfied upon the assumption of flat cross sections in bending, Kwasniewski & Ziolkowski (2013)

$$z_1 = \frac{2\sigma_y}{\sigma_2}\left(\frac{h}{2}+z_0\right) - z_0. \tag{8}$$

The value of z_0 as a function of lateral deflection f in the phase II of buckling deformation can be determined, by solving equilibrium equation (1) after substituting into it (6), (7), and (8).

The strut tracing subsequent equilibrium states, i.e. subjected to ideal constraints, changes its length at the time of buckling, as the result of interaction between two effects. On the one hand, there is a reduction of the distance between the end cross-sections (the chord) caused by bending (treated as positive), and calculated from the known formula, Timoshenko & Gere (1961), valid for small deflections

$$2\Delta l_1 = 2\int_0^L L\left(\frac{dz}{dy}\right)^2 dy \tag{9}$$

where L denotes the effective length of the column. On the other hand, an opposite effect takes place in the form of (negative) growth of the total fiber length. In the case considered here, because of the symmetry, both the upper and the middle cross-sections (see Fig. 1) remain in a horizontal position, and all the fibers change their lengths in the same way. Distribution of the strain along the length of a selected fiber is not uniform, for the strain increments at the ends of the fibers (for a half of the bar) are different because of the shift of the rotation axis. In the case of elastic buckling, the rotation axis keeps the centroid position, the strain distribution is asymmetrical, and the fiber elongation due to bowing does not take place. This change of the fiber's length (negative for extension) was approximated in Kwasniewski & Ziolkowski (2013) by

$$2\Delta l_2 = -2\int_0^L \epsilon_m dy = -\frac{2z_0 L\epsilon_2}{\left(\frac{h}{2}+z_0\right)}. \tag{10}$$

where ϵ_2 is the absolute value of the maximum tensile strain (increment). The mean strain is different from zero and is

$$\epsilon_m = \frac{\epsilon_U + \epsilon_M}{2} = \frac{z_0}{\left(\frac{h}{2}+z_0\right)}\epsilon_2. \tag{11}$$

where ϵ_U and ϵ_M are strains at the fiber ends, in the upper and middle cross-sections respectively. In the case of sine approximation for deformed axis, the shortening of the column along the y-axis can be expressed with the formula

$$2\Delta l = 2\Delta l_1 + 2\Delta l_2 = \frac{\pi^2 f^2}{L} - \frac{4\pi^2 f z_0}{L}. \tag{12}$$

Closed form solutions for P_I, P_{II}, M_I, M_{II} are unavailable to the author, hence in order to reach some tangible results, computer program MathCAD was used to effectively determine solutions of nonlinear constraint relations in phase I and II. Results of this computation in the form of equilibrium path of buckling column are shown in Figure 2. They very clearly illustrate the source and the essence of FBD instability. The point P_{12} in Figure 2 indicates a transition between Phase I and II, as defined previously. The 40% load drop, marked in Figure 2 as a difference between P_{crU} and P_{crD}, can be considered as a sort of limiting case, as columns with the same geometry but made of material with strain hardening exhibits lesser drop. The phenomenon of FDB in the considered simplified case is associated with three effects occurring simultaneously, Kwasniewski & Ziolkowski (2013). These are the post-buckling load drop accompanied by the rod's elongation, and the contraction due to bowing in the first post-buckling phase, just after buckling. The load drop is due to the unsymmetrical distribution of strain increments caused by buckling (bowing) in plastified regions represented by middle and end cross-sections for a fixed column. Unsymmetrical means that the rotation axis is not in the centroid position. The load drop is directly caused by nonuniform stress distribution in the cross-section, magnified by perfect plasticity, which does not allow for positive (compressive) stress increments (when $\lambda = \lambda_0$). The asymmetry of strain distribution in the (middle and end) characteristic cross-sections also causes unbalanced strain variation along the fibers, with negative (elongation) average strain and total fiber elongation. This effect is accompanied by the cord contraction due to bending of the axis. The cord contraction is nonlinearly dependent on the magnitude of the axis deformation and dominates for larger deflection when the bar's overall chord shortens. Therefore, after buckling, a rod equipped with the ideal restrains allowing the adoption of successive positions of equilibrium, would experience a simultaneous decrease in strength (axial load drop) and a reduction of shortening (elongation). This behavior is reflected by a specific shape of the secondary equilibrium path with negative increments of both, the

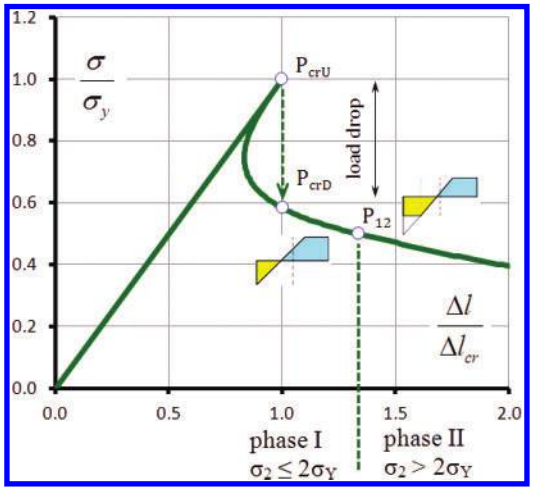


Figure 2. Equilibrium path for an ideal column with intermediate slenderness, Kwasniewski & Ziolkowski (2013).

load and the vertical displacement (captured by analytical and ABAQUS solutions), Figure 2. The load drop is indicated by the ordinate difference between two points P_{crU} and P_{crD}, representing two equilibrium states, for the strait and deflected bar. The equilibrium state represented by P_{crD} refers to the situation where both mentioned before effects: shortening of the chord and elongation of fibers, are balanced so the distance between characteristic cross-sections, upper and middle, is the same as at the critical state depicted by P_{crU}. The arrow between points P_{crU} and P_{crD} show a transition experienced during an experiment controlled by displacement.

2.3 *FE models*

Figure 3 shows FE model built of solid elements, applied in the calculations using LS-DYNA code. Numerical model represents only upper half of the column. The imposed boundary conditions reflect fixing conditions present during actual buckling experiments and symmetry of the investigated problem. The load was applied as a forced vertical displacement of the upper end. In the sequel of this study LS-DYNA code computations were performed employing solver with implicit solution algorithm (BFGS) dedicated for static analyses, Hallquist (2007). A variant case of basic buckling problem was examined with geometrical imperfection in the form of a small initial curvature defined by a sine function with the maximum amplitude of 0.001 mm (on both sides in the direction of buckling).

2.4 *Loading vs. unloading*

Figure 4 shows equilibrium paths obtained using FE solid model and LS-DYNA calculations for the considered simplified column with critical slenderness. The loading is applied as a prescribed displacement of the

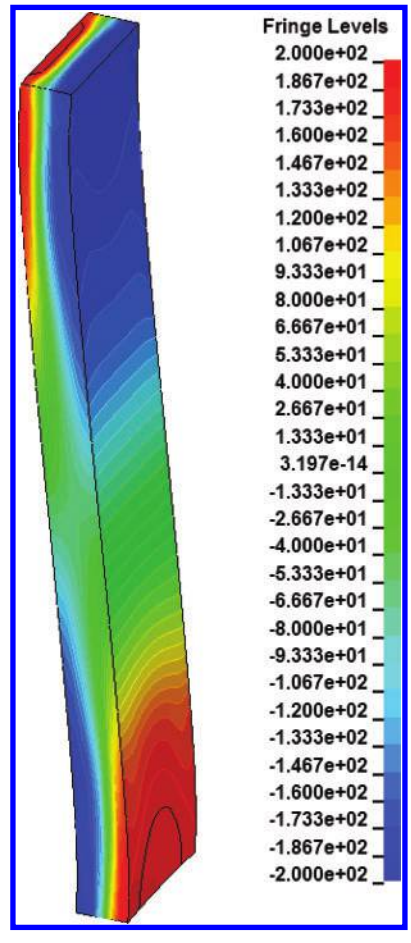


Figure 3. Contours of normal stress for the phase II deformation. FE solid element model.

upper end. The regular loading is accompanied by two unloading steps, identified with the numbers 1 and 3 in Figure 4 and followed by repeated loading marked as steps 2 and 4. The unloading is performed until the original length of the strut is reached so it covers also tensioning, leading to generation of additional residual stress. As it can be seen from Figure 4 the repeated loading (steps 2 and 4) follow different paths than unloading (steps 1 and 3), creating typical hysteresis loops, but the meeting points on the principal equilibrium path, identified as return point memory RPM1 and RPM2, are the same for loading and unloading paths. After reaching the RPM the behavior of the strut follows the principal equilibrium path until the prescribed displacement is reduced again.

Figure 5 shows normal stress and Figure 6 effective plastic strain distributions for four selected equilibrium states, three marked with triangles at the paths presented in Figure 4, and forth corresponding to RPM1. Figures 5 and 6 depict evolution of plastic regions in the vicinity of upper and middle cross-sections, where bending due to buckling is the largest.

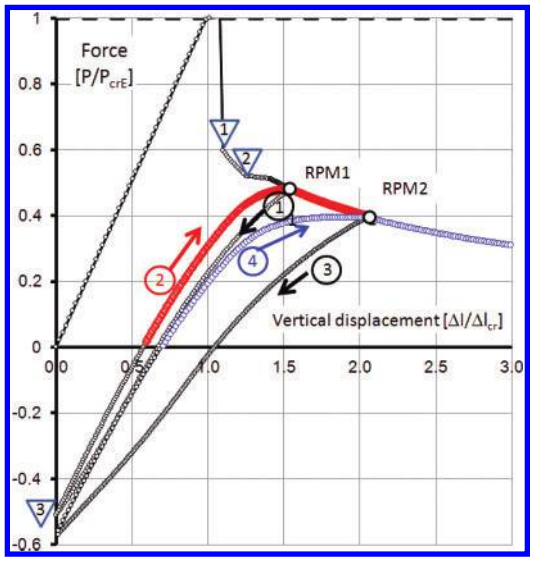


Figure 4. Equilibrium paths for alternate loading and unloading, obtained using FE solid model and LS-DYNA calculations.

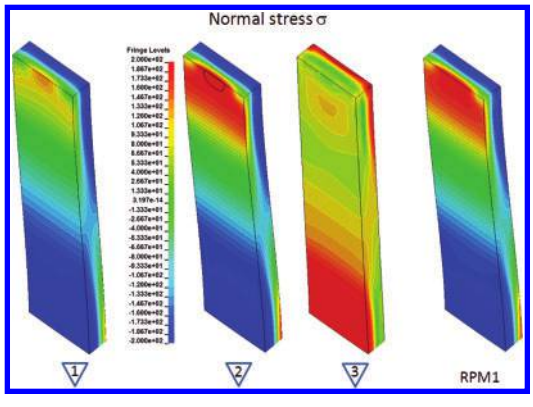


Figure 5. Contours of normal stress for four selected equilibrium states indicated in Figure 4.

There is also visible variation of normal stress distribution in both cross-sections during successive loading and unloading. Presented numerical results for 3D FE models provide a good complement to the experimental data and give a good insight in the mechanism of considered FDB phenomenon.

Figure 7 shows two selected segments of equilibrium paths presented in Figure 4 for repeated loading steps 2 and 4. Only segments for compression are shown, starting from the state for which P = 0. Additionally, the curves are translated to the origin of the coordinate system to represent a potential compressive test on a column which before the test was subjected to successive loading and unloading, reaching beyond the elastic range. Such a column possesses some permanent deformation and self-equilibrated residual stresses. Thus it can be stated that the curves shown in Figure 7 depict a performance of a column with

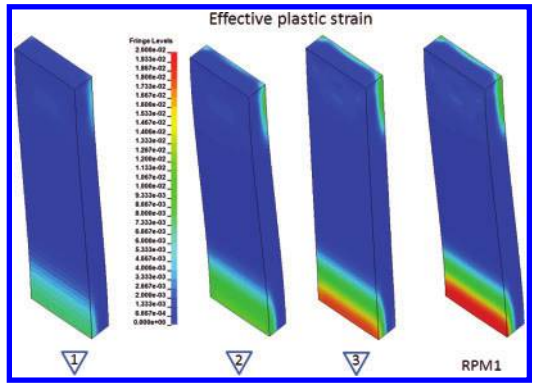


Figure 6. Contours of effective plastic strain for four selected equilibrium points indicated in Figure 4.

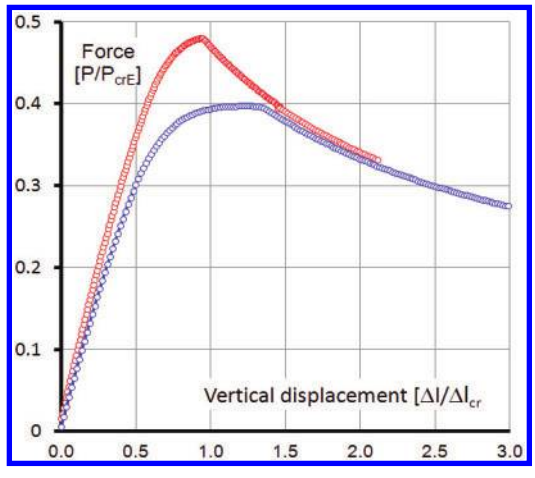


Figure 7. Segments of equilibrium paths for alternate loading and unloading, obtained using FE solid model and LS-DYNA calculations.

imperfection and residual stresses, during a compressive test. The difference between curves in Figure 7 comes from different loading history resulting in the different level of residual stress.

Due to assumed material model and because of the extensive unloading reaching to the original length of the column, the considered case is extreme. In real columns such large reduction of critical loading is rear.

3 COMPARISON WITH EXPERIMENT

Qualitative comparison of the numerical results with experimental data is presented in Figure 8. The experimental data was obtained by Ziolkowski & Imielowski's (2011) for an aluminum column with slenderness $\lambda = 53$. Except the length, the actual column differ from the numerical FE model mainly in terms of material which shows strain hardening and nonlinear transition between elastic and plastic ranges. Even though compared cases differ and additionally

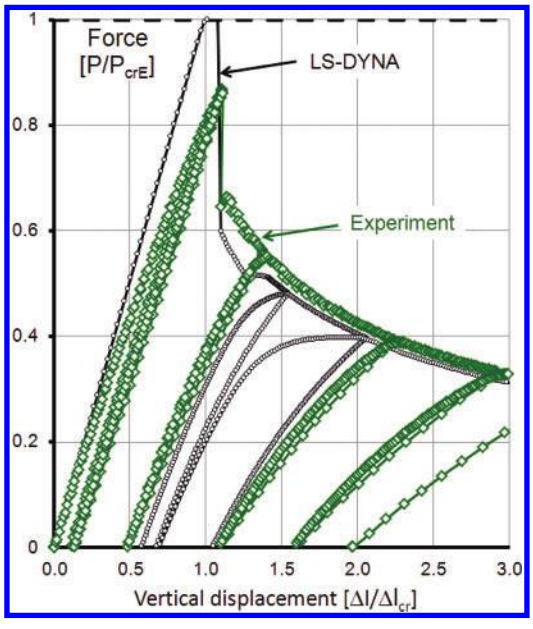


Figure 8. Comparison of equilibrium paths for numerical and experimental data Ziolkowski & Imielowski's (2011).

the experimental data is subjected to some uncertainties, both curves in Figure 8 show many similarities. The main difference is for pre-buckling phase, where the actual column shows bigger reduction of critical loading and also more nonlinear behavior comparing to the performance of the ideal FE model.

4 SUMMARY

Besides imperfection the effect of residual stress is recognized as one of the main features reducing critical loading of actual columns. Even though residual stresses can have many different sources, such as manufacturing, their quantitative effect on compressive behavior maybe similar as it is in the case of imperfections. The residual stress reduces critical loading and leads to more nonlinear response in the pre-buckling phase. To analyze this phenomenon quantitatively, first they have to be included in the computational model. The theoretical residual stress distribution is well known for beams with simple cross-sections, subjected to elastic-plastic bending. In the cases considered here residual stresses are generated through successive loading – unloading, reaching tension. The results were obtained using FE model built of solid elements which enable tracing stress and strain distributions through the column's cross-section. The numerical results were partially verified and validated. The verification was performed through comparison with analytical solutions for loading phase. The validation included quantitative comparison with experimental data for an actual column with similar characteristics. Presented methodology shows potential for further qualitative investigation of effects of residual stress on buckling of metal columns.

ACKNOWLEDGEMENTS

The author wishes to thank Andrzej Ziolkowski D.Sc. for making available the experimental results, presented in the paper. These results were obtained as a part of the research project supported by Polish Ministry of Science and Higher Education, Grant PB N50104131/2765 "The analysis of critical and post-critical states of structures under conservative and non-conservative loads. Experimental and theoretical investigation, verification of existing design codes".

REFERENCES

Abaqus 2007. Abaqus user's manual, ABAQUS Ine, Dassault Systèmes, Rhode Island, USA.

Galambos T.V. 1988. Guide to stability design criteria for metal structures, 4th Edition, Wiley.

Gere J.M., Goodno B.J. 2009. Mechanics of materials, 7th Edn., Cengage Learning, Stamford.

Hallquist J.O. 2007. LS-DYNA Keyword User's Manual-Version 971, Livermore Software Technology Corporation.

Kwasniewski L., Ziolkowski A., (2013) Simplified analytical model and numerical simulations of finite-disturbance buckling of columns, International Journal of Non-Linear Mechanics, 51 (2013): 121–131.

Timoshenko S.P., Gere J.M. 1961. Theory of elastic stability. McGraw-Hill, New York.

Ziolkowski A., Imielowski S. 2011. Buckling and Post-buckling Behaviour of Prismatic Aluminium Columns Submitted to a Series of Compressive Loads, *Experimental Mechanics*, Springer (51) 8: 1335–1345.

Research and Applications in Structural Engineering, Mechanics and Computation – Zingoni (Ed.)
© 2013 Taylor & Francis Group, London, ISBN 978-1-138-00061-2

Eulerian formulation for an extensible elastic rod

A. Huynen
F.R.I.A., F.R.S.-FNRS, National Fund for Scientific Research, Bruxelles, Belgium
Department of Civil Engineering, University of Minnesota, USA

E. Detournay
Department of Civil Engineering, University of Minnesota, USA

V. Denoël
Structural Engineering, Department of Architecture, Geology, Environment and Constructions, University of Liege, Belgium

ABSTRACT: This paper reformulates the governing equations of an extensible elastic rod by reference to a given spatial curve. This Eulerian formulation is motivated by the need to solve efficiently the constrained elastica problem encountered in many medical and engineering applications, in which a thin rod is inserted in a tortuous conduit. The Eulerian reformulation of the equations hinges on the restatement of the rod local equilibrium in terms of derivatives with respect to the curvilinear coordinate associated with the reference curve and the description of the rod deflection as a perturbation of this curve. The originality of the proposed formulation lays in the axially unconstrained character of the resulting system such that the determination of the rod configuration between two fixed points reduces to the resolution of a classical boundary value problem.

1 INTRODUCTION

The general problem of a slender elastic body constrained to deform inside a straight or sinuous conduit is widely encountered in medical and engineering applications. Examples include the insertion of miniature instruments into blood vessels for the treatment of vascular and cerebrovascular pathologies (e.g. abdominal and thoracic aortic aneurism, stroke) as well as the endoscopic examination of internal organs (e.g. colonoscopy, fibroscopy, rhinoscopy), see for instance Schneider (2003). Another application concerns the petroleum industry which relies on several kilometers long drillstrings to transmit the axial force and torque necessary to drill the rock formations and reach deep hydrocarbon reservoirs (Inglis 1988, Sampaio 2008). The assessment of the energy loss along the drill string, known as the *torque and drag problem*, plays an essential role in drilling and well design as the friction appearing at the contacts between the drillstring and the borehole may dramatically increase the costs or, even, be a limiting factor in some configurations (Mason and Chen 2007). The identification of the number of contacts between the rod and the conduit (e.g. blood vessel or borehole) as well as their position and extent constitutes the central concern of this relatively broad class of problems. The nonlinearities associated with the large deflection of the rod and the unilateral contact condition as well as the *a priori* unknown number of contacts, however, make the use of conventional numerical tools rather inefficient. Additionally, the commonly adopted division of the problem in rod segments bounded by two contacts (Chen & Li 2007, Denoël 2008) requires to solve the governing equations on domains which are initially unknown and, therefore, leads to the establishment of integral constraints on the unknown length of a rod forced to go through fixed points in space. Finally, the assessment of the unilateral contact condition, which requires in principle the comparison of two curves parametrized by distinct curvilinear coordinates (e.g. the rod centroid and the conduit axis), prove to be a rather intensive computational task.

To circumvent the above-mentioned difficulties, an Eulerian reformulation of the rod governing equations is proposed and the strategy initiated by Denoël & Detournay (2011) for the planar elastica is generalized to three-dimensional configurations and extensible rods. Modeling the elastic body by means of the special Cosserat rod theory, its deflection is described as a perturbation of a reference curve (e.g. the conduit axis) while the rod local equilibrium is formulated within the Eulerian reference frame associated with this curve. Consequently, the determination of the rod configuration between two adjacent contacts reduces to the resolution of a classical boundary value problem for which, in addition to the axial components of the internal force and moment at one end, the rod

eccentricity as well as its inclination with respect to the reference curve are prescribed at both extremities of the domain.

The originality of the proposed formulation lays in the axially unconstrained character of the resulting system. Indeed, as the reference curve is substituted for the domain of the problem, the unstressed length of the rod is not prescribed and, therefore, freely evolves as a result of the loading. This particular aspect is encountered in various additional applications in which the length of the domain is *a priori* unknown or susceptible to self-adjustment such as the continuous casting process, the extrusion of plastic through a draw plate or the laying of cables and pipelines. We will refer to the ability of the proposed method to handle this particular class of axially unconstrained problems, as *self-feeding*.

2 PROBLEM DEFINITION & GOVERNING EQUATIONS

The canonical problem considered in this paper consists in the determination of the deformed configuration adopted by an extensible rod forced to go through two fixed points in space and subjected to a known external loading (e.g. weight, applied torque and tension at an extremity). Consequently, the length of the rod, which satisfies the boundary conditions and is in equilibrium with the external loading, is unknown.

To solve this problem, let us define the right-handed orthonormal basis $\{e_k\}$ for the Euclidean space $\mathbb{E}^3$ and denote by $R(S) = X_k\, e_k$ the position vector of the point lying on the reference curve $\mathscr{C}$ at S. The arc-length parameter S, referred to as the Eulerian coordinate, identifies a *section* along $\mathscr{C}$ which consists of all points whose reference positions are on the plane perpendicular to the reference curve at S. For the sake of clarity, the parametrization of this curve is assumed to be natural such that $\mathscr{C}$ is said to be unit-speed (Pressley 2010).

Having defined the global $\{e_k\}$–basis, the position vector of the rod cross section centroid with curvilinear coordinate s is denoted by $r(s) = x_k\, e_k$. The parameter s, which is referred to as the (natural) Lagrangian coordinate in contrast to the Eulerian coordinate S, identifies the rod cross section in its unstressed configuration $r^0(s)$. To fully characterize the spatial configuration of the rod, one has to additionally supply this space curve $\mathscr{E}$ with a pair of orthonormal vectors $d_1(s)$, $d_2(s)$ characterizing the configuration of a pair of orthogonal material lines of the section (Antman 2005). The rod is therefore entirely defined by the three-vector valued functions

$$[s_a, s_b] \ni s \mapsto \boldsymbol{r}(s),\, \boldsymbol{d}_1(s),\, \boldsymbol{d}_2(s) \in \mathbb{E}^3 \tag{1}$$

with $s = s_a$ corresponding to the origin of the canonical problem located at $S = S_a$, and $s = s_b$ corresponding to its extremity located at $S = S_b$, see Figure 1(a).

The cross section orientation is then naturally described by its normal $d_3(s) = d_1 \times d_2$ such that the resulting triplet of *directors* $\{d_k(s)\}$ constitutes a right-handed orthonormal basis for $\mathbb{E}^3$ for each cross section s. The rod change of shape is measured by the twist and stretch vectors, $u = u_k\, d_k$ and $v = v_k\, d_k$, which are defined as

$$\mathrm{d}_s \boldsymbol{d}_k = \boldsymbol{u} \times \boldsymbol{d}_k \qquad \mathrm{d}_s \boldsymbol{r} = \boldsymbol{v} \tag{2}$$

respectively. Their components in the directors basis, u_k and v_k, are referred to as strain variables.

Considering only local interactions between adjacent cross sections of the rod and defining the internal force $F(s) = F_k\, d_k$ and moment $M(s) = M_k\, d_k$, the conservation of linear and angular momenta yields (Antman 2005)

$$\mathrm{d}_s \boldsymbol{F} + \boldsymbol{f} = 0 \tag{3}$$

$$\mathrm{d}_s \boldsymbol{M} + \mathrm{d}_s \boldsymbol{r} \times \boldsymbol{F} = 0 \tag{4}$$

where $f(s) = w\, e_3$ is the body force per unit reference length with w the rod specific weight.

For an unshearable rod of circular cross section made of linearly elastic material, the components of the internal force and moment are related to the strain variables by means of the following constitutive equations

$$\boldsymbol{M}(s) = EI\,(u_1\, \boldsymbol{d}_1 + u_2\, \boldsymbol{d}_2) + GJ\, u_3\, \boldsymbol{d}_3 \tag{5}$$

$$\boldsymbol{F}(s) = F_1\, \boldsymbol{d}_1 + F_2\, \boldsymbol{d}_2 + EA\,(\alpha - 1)\, \boldsymbol{d}_3 \tag{6}$$

with the bending stiffness EI, the torsional stiffness GJ and the axial stiffness EA. To close the formulation, one must additionally consider the material restraint $v(s) = \alpha\, d_3$ which expresses that the centroid tangent vector is aligned with the normal to the rod cross section and where the stretch $\alpha(s) > 0$.

2.1 *Parametrization of the rotation group SO(3)*

The use of six components for the directors d_1 and d_2 may appear clumsy since these components are subject to three orthonormality constraints. The introduction of unit quaternions to parametrize the three-dimensional rotation group $SO(3)$ is an alternative to the habitual Euler angles subject to gimbal lock (Kuipers 1999). It is motivated by the desire to resort to a regular representation of the rotation tensor.

According to Euler's rotation theorem, the orientation of the triplet of directors $\{d_k(s)\}$ can be defined by specifying its rotation about the unit axis of rotation a through the angle ω with respect to the global $\{e_k\}$–basis. The set $\{\omega, a\}$ can advantageously be replaced by the so-called quaternion $\mathbf{g}(s) = (g_0, g_1, g_2, g_3)^T$ with $\|\mathbf{g}\| = 1$ and whose components are defined as

$$g_0(s) = \cos(\omega/2) \qquad \boldsymbol{g}(s) = \sin(\omega/2)\, \boldsymbol{a} \tag{7}$$

(Kuipers 1999). Additionally to being regular, the quaternion components vary continuously as the orientation changes.

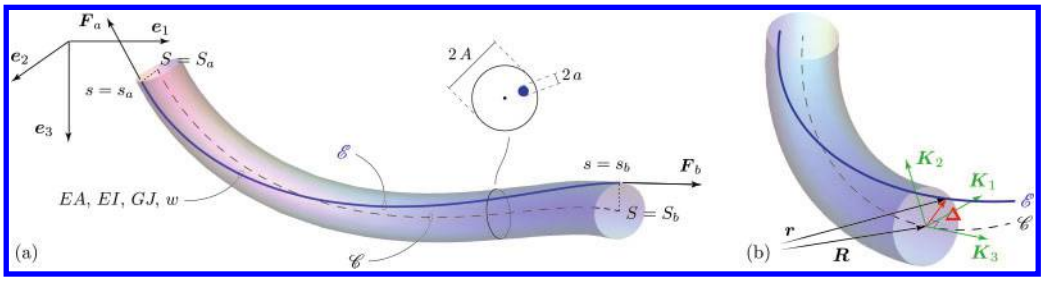


Figure 1. (a) Description of the canonical problem, and (b) Decomposition of the position vector $r(s) = R(S) + \mathbf{\Delta}(S)$. For the sake of readability, the region in which the solution is expected be found is represented (for the constrained problem, this region corresponds to the conduit centered on the reference curve).

2.2 *Shortcomings of the Lagrangian formulation*

As already emphasized in the introduction, the canonical problem under consideration consists in a two points boundary value problem for which the rod location and inclination are prescribed at both extremities s_a and s_b of the domain. However, as the parametric coordinates of the rod $x_k(s)$ in the absolute reference frame $\{e_k\}$ are given by

$$x_k(s) = x_k(s_a) + \int_{s_a}^{s} \mathrm{d}_s \boldsymbol{r} \cdot \boldsymbol{e}_k \, \mathrm{d}s \tag{8}$$

with $\mathrm{d}_s r = v$, the boundary conditions associated with the canonical problem reduce to a set of three integral constraints on the unknown length of the rod forced to go through two fixed points in space. These stiff isoperimetric constraints result in ill-conditioned equations requiring an excessive amount of iterations, provided that convergence is reached, which worsens with decreasing bending stiffness (Denoël & Detournay 2011).

For the constrained problem, a further difficulty is related to the assessment of the unilateral contact condition which ensures that the computed deformed configuration of the rod is contained within the conduit. This constraint indeed requires the evaluation of the distance Δ between the reference curve (*i.e.* the conduit axis), parametrized as

$$X_k(S) = X_k(S_a) + \int_{S_a}^{S} \mathrm{d}_S \boldsymbol{R} \cdot \boldsymbol{e}_k \, \mathrm{d}S \tag{9}$$

in the absolute reference frame $\{e_k\}$, and the rod cross section centroid $\mathscr{E}$ given in Equation (8). As these two curves are parametrized by two distinct curvilinear coordinates (S and s respectively), this task turns out to be computationally intensive.

Finally, the ill-conditioning of the governing equations for small flexural rigidity, the existence of spurious solutions associated with curling of the rod as well as the demand for increasing accuracy of the solutions with decreasing clearance, are sources of various additional complications or other bottlenecks, with the consequence that the Lagrangian formulation of the problem is particularly ineffective and laborious to solve.

3 EULERIAN FORMULATION

To circumvent the above-mentioned shortcomings of the Lagrangian formulation and on account of the nature of the problem, which is characterized by relatively close spatial curves $\mathscr{C}$ and $\mathscr{E}$, the proposed formulation hinges on the introduction of the *eccentricity vector* $\mathbf{\Delta}(S)$, characterizing the rod deflection with respect to the reference curve. The description of the problem is further expressed in terms of the Eulerian coordinate S rather than the natural Lagrangian coordinate s of the rod. As presented in Figure 1(b), the position vector of the rod cross section centroids $r(s) = x_k\, e_k$ can, naturally, be expressed as

$$\boldsymbol{r}(s) = \boldsymbol{R}(S) + \mathbf{\Delta}(S) \tag{10}$$

where the position vector of the reference curve $R(S) = X_k\, e_k$ is known, and the eccentricity vector is perpendicular to $\mathscr{C}$, *i.e.* $\mathrm{d}_S R \cdot \mathbf{\Delta} = 0$. The former expression describes the rod configuration as a perturbation of the reference curve, such that the eccentricity vector can be interpreted as a measure of the rod deflection and rotation with respect to $\mathscr{C}$ in the *section* of curvilinear coordinate S.

From now on, derivatives of scalar and vector valued functions with respect to the Eulerian coordinate S will be denoted by the apposition of a prime while derivatives with respect to the Lagrangian coordinate s are explicitly specified.

3.1 *Definition of the reference curve*

With each point of the reference curve, one may associate a triplet $\{K_j(S)\}$ constituting a right-handed orthonormal basis with $K_3 = R'$ defined as the unit vector tangent to $\mathscr{C}$. The orientation of this triplet can be defined through a unit quaternion $\mathfrak{Q}(S)$ specifying its rotation with respect to the global $\{e_j\}$–basis. Additionally imposing the component of this rotation about K_3 to be null, one has

$$\mathfrak{Q}(S) = (Q_0, Q_1, Q_2, 0)^T \tag{11}$$

with $Q_0^2 + Q_1^2 + Q_2^2 = 1$. This arbitrary definition of $Q_3(S) = 0$ simply reflects that the reference curve

needs only to be specified through the inclination of its tangent vector $\boldsymbol{K}_3(S)$ on the global axes; in other words the possible rotation of a pair of vectors spanning the plane perpendicular to the reference curve is irrelevant. An alternative definition of the unit quaternion $\mathfrak{Q}(S)$ would be to specify its components such that the triplet $\{\boldsymbol{K}_j(S)\}$ coincides with the Frenet basis attached to the reference curve. However this would lead to uniqueness and continuity issues for reference curves with vanishing curvature.

As a result of the previous definition, the pair $\{\boldsymbol{K}_1, \boldsymbol{K}_2\}$ constitutes an orthonormal basis for the plane perpendicular to the reference curve in which the eccentricity vector reads

$$\boldsymbol{\Delta}(S) = \Delta_1 \boldsymbol{K}_1 + \Delta_2 \boldsymbol{K}_2 \tag{12}$$

with $\Delta_1 = \Delta \cos\beta$ and $\Delta_2 = \Delta \sin\beta$. The components of the position vector in the global basis may, therefore, be expressed as

$$x_1(s) = X_1 + \Delta_1\left(1 - 2Q_2^2\right) + 2\Delta_2 Q_1 Q_2 \tag{13}$$

$$x_2(s) = X_2 + 2\Delta_1 Q_1 Q_2 + \Delta_2\left(1 - 2Q_1^2\right) \tag{14}$$

$$x_3(s) = X_3 - 2Q_0\left(\Delta_1 Q_2 - \Delta_2 Q_1\right) \tag{15}$$

in which each variable is a function of the Eulerian coordinate S and where the X_j's are obtained by integration of the reference curve local inclination expressed in terms of the quaternion components $Q_j(S)$.

3.2 *Definition of the rod*

By analogy with the definition of the reference curve and for reasons that will become clear in the following section, the orientation of the rod cross section is described by means of two unit quaternions

$$\mathbf{q}(s) = (q_0, q_1, q_2, 0)^T \qquad \mathbf{t}(s) = (t_0, 0, 0, t_3)^T \tag{16}$$

representing two successive rotations and such that the quaternion corresponding to the total rotation is given by the quaternion product $\mathbf{g}(s) = \mathbf{q} \cdot \mathbf{t}$. This parametrization of the rotation tensor allows to uncouple the attitude of the director $d_3(s)$ from the rotation of the section about this director.

Expressing the directors in terms of the unit quaternion $\mathbf{g}(s)$, one may compute their derivatives $\mathrm{d}d_k/\mathrm{d}s$ and identify the components of the twist vector, $u = u_k\, d_k$, in the directors basis.

3.3 *Jacobian of the mapping*

To complete the reformulation of the local equilibrium (3–4) within the reference frame associated to $\mathscr{C}$, one has to further express the natural derivatives $\mathrm{d}\cdot/\mathrm{d}s$ in terms of derivatives with respect to the Eulerian curvilinear coordinate $\mathrm{d}\cdot/\mathrm{d}S$. The function $s(S)$, which maps the Eulerian coordinate of the reference curve on the Lagrangian coordinate of the rod, is therefore introduced. Considering the definition (2) of the centroid tangent vector $\mathrm{d}\boldsymbol{r}/\mathrm{d}s$ in terms of the stretch vector components and applying the chain rule differentiation, the Jacobian $s'(S)$ of this transformation can be expressed as

$$\frac{\mathrm{d}s}{\mathrm{d}S} = \pm \left\|\boldsymbol{R}' + \boldsymbol{\Delta}'\right\| / \|\boldsymbol{v}\| \tag{17}$$

where the positive sign is selected in order to prevent the appearance of parasitic solutions associated with curling of the rod. This expression emphasizes that the origin of the drift existing between the two curvilinear coordinates is two-fold: (i) the eccentricity between the rod and the reference curve, and (ii) the stretch $\|v\| = \alpha$ of the rod itself.

Defining the function $J_1(S) = 1/s'$ as the Jacobian of the inverse mapping $S(s)$, *i.e.* from the Lagrangian to the Eulerian coordinate, one may compute its successive derivatives using the following recursive relation

$$J_k(S) = \left.\frac{\mathrm{d}^k S}{\mathrm{d}s^k}\right|_{s=s(S)} = J'_{k-1}\, J_1 \tag{18}$$

for $k > 1$.

3.4 *Rod attitude*

The next step in the Eulerian reformulation of the problem consists in rewriting the quaternion $\mathbf{g}(s)$, representing the directors orientation, in terms of the quaternion $\mathfrak{Q}(S)$, expressing the reference curve local inclination, and the components (Δ_1, Δ_2) of the eccentricity vector in the section S.

Using expressions (13–15) for the position vector components and the definitions of the directors $\{d_k\}$ in terms of the quaternion $\mathbf{g} = \mathbf{q} \cdot \mathbf{t}$ in the kinematic relation (2), one may obtain the following set of equations

$$2\alpha\, q_0\, q_2 = J_1\, \boldsymbol{r}' \cdot \boldsymbol{e}_1 \tag{19}$$

$$-2\alpha\, q_0\, q_1 = J_1\, \boldsymbol{r}' \cdot \boldsymbol{e}_2 \tag{20}$$

$$\alpha\left(2q_0^2 - 1\right) = J_1\, \boldsymbol{r}' \cdot \boldsymbol{e}_3 \tag{21}$$

with the stretch $\alpha > 0$ and where the uncoupling between the representation of d_3 attitude and the rotation of the section about this director has been advantageously used. Solving this set of equations, one may relate the Lagrangian quantities $q_j(s)$ function of the rod curvilinear coordinate s to the Eulerian quantities $Q_j(S)$ and $\Delta_1(S)$, $\Delta_2(S)$ function of the reference curve curvilinear coordinate S.

3.5 *The excess of twist*

Finally, the second quaternion $\mathbf{t}(s)$ characterizing the rotation of the rod cross section about the director $d_3(s)$ cannot be related to the eccentricity vector and, therefore, to the Eulerian quantities $\Delta_1(S)$ and $\Delta_2(S)$. The angle $\varphi(S)$ is consequently introduced such that $t_0 = \cos(\varphi/2)$ and $t_1 = \sin(\varphi/2)$ with

$$\varphi_{,s} = J_1\,\varphi' \qquad \varphi_{,ss} = J_1^2\,\varphi'' + J_2\,\varphi' \tag{22}$$

and where $\varphi_{,s}$ can be interpreted as the internal torsion or the excess of twist of the rod. Similarly, additional Lagrangian quantities appearing in the conservation of linear and angular momenta, such as the internal force $\boldsymbol{F}(s)$ or the stretch $\alpha(s)$, are re-written as functions of the Eulerian coordinate and their derivatives are evaluated using the same scheme.

3.6 *Boundary conditions*

In conclusion, one obtains a mixed order system of six ODE's involving exclusively Eulerian quantities. This system being first order in the components $F_k(S)$ of the internal force, second order in the angle $\varphi(S)$, and third order in the components $\Delta_k(S)$ of the eccentricity vector, a total of eleven boundary conditions is required.

In addition to the rod eccentricity and inclination with respect to the reference curve, which must be prescribed at both extremities of the boundary value problem, the axial component of the internal force and the torque need to be specified at one extremity of the domain. The eccentricity vector $\boldsymbol{\Delta}(S)$ and its derivative $\boldsymbol{\Delta}'(S)$ are, therefore, imposed at both $S = S_a$ and $S = S_b$ while the stretch $\alpha(S)$ as well as the angle $\varphi(S)$ and its derivative $\varphi'(S)$ are prescribed at either $S = S_a$ or $S = S_b$, depending on the nature of the problem under consideration.

4 NUMERICAL IMPLEMENTATION

To solve numerically the resulting nonlinear boundary value problem, a collocation method has been implemented. Defining a partition π of $[S_a, S_b]$ constituted of N subintervals, we seek an approximate solution $(\boldsymbol{\Delta}^*, \varphi^*, F^*)$ such that

$$\boldsymbol{\Delta}^* \in \mathcal{P}_{k+3,\pi} \cap C^2[S_a, S_b] \tag{23}$$

$$\varphi^* \in \mathcal{P}_{k+2,\pi} \cap C^1[S_a, S_b] \tag{24}$$

$$\boldsymbol{F}^* \in \mathcal{P}_{k+1,\pi} \cap C^0[S_a, S_b] \tag{25}$$

where $k \geq 3$ is the number of collocation points per subinterval and $\mathcal{P}_{n,\pi}$ is the set of all piecewise polynomial functions of order n on the partition π. For reasons of efficiency, stability, and flexibility in order and continuity, B-splines are chosen as basis functions while collocation is applied at Gaussian points (Ascher et al. 1979).

The unknown B-splines coefficients are then determined by solving the nonlinear system of 6 kN collocation equations and imposing the 11 boundary conditions. This method has been implemented in MATLAB using the nonlinear solver `fsolve` as well as the *Spline Toolbox* (De Boor 2005) to evaluate the B-splines and their derivatives.

5 APPLICATION

As an implementation of the proposed formulation, we consider the progressive twisting of a clamped-clamped beam subject to its specific weight w as well as a prescribed tension T, see Figure 2(a). The particularity of the present loading, which results from the Eulerian reformulation of the problem, is that the unstressed length of the rod ℓ^0 is actually not prescribed but freely evolves as the loading progress (c.f. *self-feeding*); the length L of the straight reference curve remaining however constant.

The response diagram presented in Figure 2 pictures the twist angle $\varphi(L)$, imposed at the rod extremity, versus the dimensionless stretched length $(\ell - L)/L$ for various values of the loading parameter $\Gamma = T/wL$. This diagram was obtained for a unitary distance between supports, *i.e.* $L = 1$, and a specific weight $w = 10$ while the rod stiffnesses were chosen such that $EI = 4\,GJ/3 = EA/255 = 1$. These relations as well as the deformed configurations graphed in the figure were obtained using the numerical implementation presented in the previous section with $k = 5$ gaussian points in each of the $N = 15$ uniformly spaced subintervals.

Observe that, while the number of helical waves in the deformed configuration clearly increases with the imposed end rotation $\varphi(L)$, foldings in the relation between the end rotation and the dimensionless stretched length are triggered by the development of additional helical waves in the rod deformed configuration. Eventually, material flows inside the domain either for compressive axial force (buckling) or insufficient tensile force (regarding the imposed end rotation) as more rod is required to maintain the equilibrium state.

6 CONCLUSIONS

The Eulerian reformulation of the equations governing the three-dimensional deflection of an extensible rod has been achieved by (i) the introduction of the eccentricity vector $\boldsymbol{\Delta}(S)$, characterizing the rod deflection with respect to a given reference curve, (ii) the uncoupling of the attitude of the rod centroid tangent vector form the rotation of the cross section about it, and (iii) the expression of the rod local equilibrium in terms of derivatives with respect to the reference curve curvilinear coordinate. The originality of the proposed

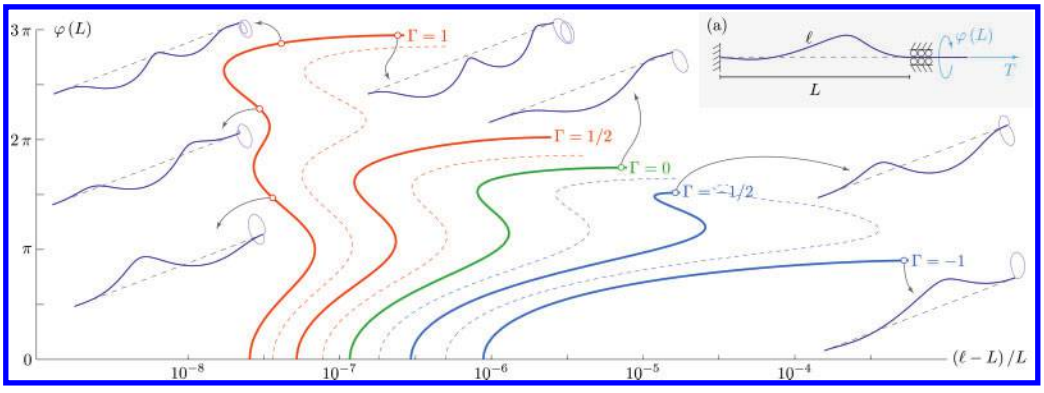


Figure 2. Response diagram of a clamped-clamped beam subject to progressive twisting as well as its specific weight $w = 10$ and a prescribed tension T. The imposed end rotation $\varphi(L)$ is plotted as a function of the dimensionless stretched length $(\ell - L)/L$ for various values of the loading parameter $\Gamma = T/wL$ and a unitary distance between support $L = 1$; the rod stiffnesses were chosen such that $EI = 4GJ/3 = EA/255 = 1$.

formulation, which resolves in one stroke a series of issues that afflict the classical Lagrangian approach (isoperimetric constraints and potential contact detection with the wall of a conduit), lays in the *self-feeding* character of the resulting system as the unstressed length of the rod is subject to self-adjustement in response to the loading. Finally, the response of a clamped-clamped beam subject to progressive twisting is obtained using the proposed formulation and its numerical implementation.

ACKNOWLEDGEMENT

The authors acknowledge the National Fund for Scientific Research of Belgium for its support.

REFERENCES

Antman, S. (2005). *Nonlinear problems of elasticity*, Volume 107. Springer Verlag.

Ascher, U., J. Christiansen, & R. D. Russell (1979). A collocation solver for mixed order systems of boundary value problems. *Mathematics of Computation* *33*(146), 659–679.

Chen, J.-S. & C.-W. Li (2007). Planar elastica inside a curved tube with clearance. *International Journal of Solids and Structures 44*(18-19), 6173–6186.

De Boor, C. (2005). *Spline toolbox for use with MATLAB: user's guide, version 3*. MathWorks.

Denoël, V. (2008). Advantages of a semi-analytical approach for the analysis of an evolving structure with contacts. *Communications in Numerical Methods in Engineering 24*(12), 1667–1683.

Denoël, V. & E. Detournay (2011). Eulerian formulation of constrained elastica. *International Journal of Solids and Structures 48*(3-4), 625 – 636.

Inglis, T. (1988). *Directional drilling*, Volume 2. Springer.

Kuipers, J. (1999). *Quaternions and Rotation Sequences: A Primer With Applications to Orbits, Aerospace, and Virtual Reality*. Princeton Univers. Press.

Mason, C. & D. Chen (2007). Step changes needed to modernise T&D software. In *SPE/IADC Drilling Conference*.

Pressley, A. (2010). *Elementary Differential Geometry*. Springer London.

Sampaio, J. H. B. (2008). *Drilling Engineering*. Curtin University of Technology, Department of Petroleum Engineering.

Schneider, P. (2003). *Endovascular skills: guidewire and catheter skills for endovascular surgery*. CRC Press.

Research and Applications in Structural Engineering, Mechanics and Computation – Zingoni (Ed.)
© 2013 Taylor & Francis Group, London, ISBN 978-1-138-00061-2

Some results of experimental investigations of thin-walled bars

J.B. Obrębski
Faculty of Civil Engineering, Warsaw University of Technology, Warsaw, Poland

ABSTRACT: The present author has elaborated complex theory for general analysis of space bar structures, composed from straight bars including any type of Cross-Sections (CSs) – in it compact, thin-walled and composite, too. Specially, theory for thin-walled straight bars (TWBs) has some assumptions, which accuracy was verified experimentally. Moreover, in literature we can find, that sometimes calculated results are dramatically different from reality. So, it can be concluded, that especially computer analysis is certain simulation, only (Pruki R.P. & Lopez P.M. SEMC-2001). More adequate results to reality can be obtained after its verification or calibration by experiments. The author by himself and in cooperation with his co-worker has perform some wide series of experiments over TWBs, described below.

1 INTRODUCTION

So, the author perform by himself and in cooperation with Z. Urbaniak, P. Flont, S. Wichniewicz, N. Jankowska, M.E. El Awadi (Egypt) some series of experiments for thin-walled structures: cantilevers under combined loading – bended eccentrically; instability effects also by loading bar by pure bimoment; transmission of torsion forces (bimoment and bending-torsion moment) through plane nodes connecting 2 or 3 TWBs and some simple experiments for presentation for students during lectures. The attention is there focused on some examples of visible bimoment influence on instability of thin-walled bars (TWBs).

Shown photographs and drawings presents observed effects. In the light of these experiments, the bimoment is evidently real internal force, very dangerous for structures, which should be seriously considered by designing objects composed of TWBs. The paper presents mainly experiments performed in years 1988–1992 and elaborated partially a little latter. Some observations concerning considered phenomena were quoted in author's books. The others materials were not published up to the moment.

Especially valuable are results of measurements done by electro-resistance methods and different approaches to elaboration of obtained results.

Moreover, are compared results of investigations presented in the book of A.I. Strielbitska & G.I. Jewsiejenko and the other measurements done much later by A. Glinicka – all concerning of some thin-walled elements used by designing of civil engineering structures. In all mentioned examples, are pointed visible influences of applied methods and input data to numerical analyses, on quality of obtained results.

To comparative analyses, including experiments, were used large brazen models: cantilevers – for bending-torsion loadings (Figs 1, 2, 5, 6), short bar

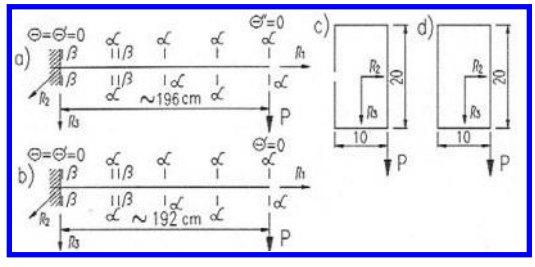


Figure 1. Scheme of the cantilevers with free end a), planar constrained displacements b); loading system for **TWB**s with rectangular **C**Ss: open c), closed d).

for loading by pure bimoment (Figs 7, 8) and simple frames (Figs 9, 11). All these models were having rectangular **CS**s with approximate dimensions 10×20 cm.

2 CANTILEVERS UNDER COMBINED LOADING

2.1 *Applied models and measuring method*

There, was investigated cantilever beams behaviour under bending-torsion loading with schemes given in Figures 1, 2. As specimens were used natural scale brazen **TWB**s with approximate dimensions $10 \times 20 \times 196$ cm, with wall thicknesses 0.5 mm, 1.5 mm and 2.5 mm. Strains in two **CS**s β-β, displacements in **CS**s α-α and load capacity of the bar were measured. Moreover, behaviour of the beam was observed and documented carefully.

2.2 *Observed effects*

There, 17 bars were investigated. Out of these, 13 with a vertical position (as in Figs 1, 2) and rectangular

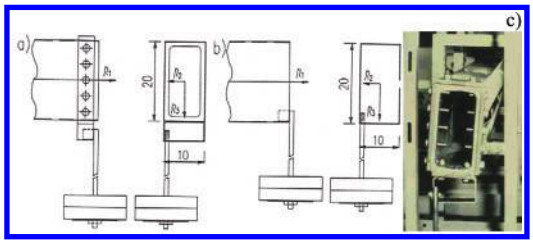


Figure 2. Scheme of the loading system for cantilevers – TWBs: planar constrained displacements a), c) and free end b).

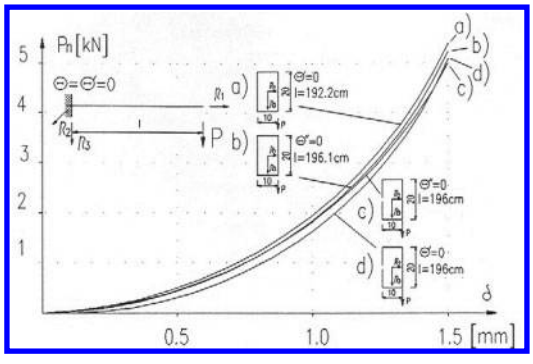


Figure 3. Diagrams of P_n dependent on wall thickness δ.

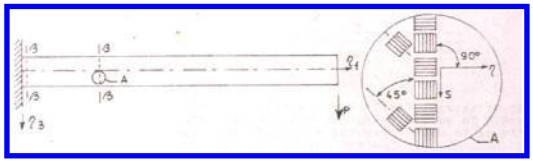


Figure 4. Allocation of electro-resistance tissue (paper) sensors (detail A), Obrebski (1994, 2009).

CS (with Urbaniak, 1992, 2009) and 4 with a horizontal orientation (together with Flont, 1995)). In all of the above experiments, before bar damage (breaking) some waves appeared at the fixed end (Figure 2c, 5) on both bar sides and in the bottom wall. Some waves appear at loaded bar end, too, where longitudinal displacements were constrained by a rigid cork, Figure 2c. Development of waves during this type of experiments was observed, too.

In the Figure 5d are compared four similar bars with identical wall thickness. Two of the bars have an open **CS** and the opposite loaded end is totally free, or constrained by a cork. Similarly, the other two bars with a closed **CS** have the opposite end free or constrained by a cork, too. The different distances of breaking from the fixed end on the bottom wall and its inclination are interesting, Figure 6a-d. Here we should remember that for open type **CS**s, warping stresses are much higher. Also, the distribution of normal longitudinal stresses for bars with open and closed **CS**s is dramatically different.

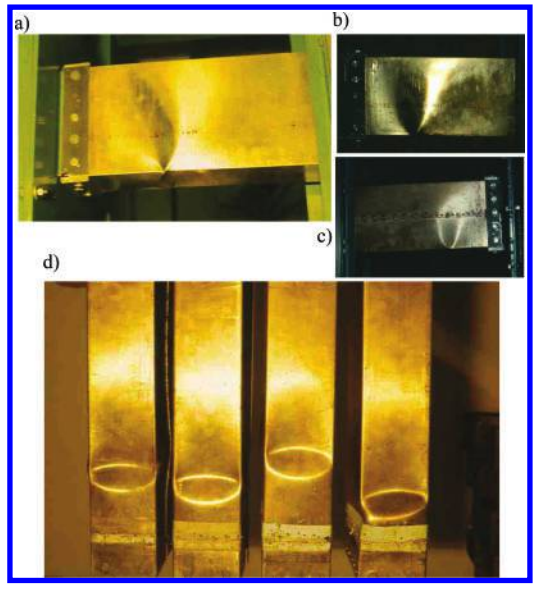


Figure 5. View of hinge (breaking point) of cantilever beams with planar constrained fixed end a); waves on lower wall and on both sides of the bar b, c); four cases of bars (Fig. 1) seen from down (wall thickness $\delta = 0.5$ mm) d).

Table 1. Calculated analytically and measured experimentally bimoments B and bending-torsion moments M_ω.

		B	M_ω
Model	Obtained	kN cm^2	kN cm
Model 21	analytically	831.82	−10.1908
	measured	848.475	−2.175
Model 22*	analytically	−4.826	2.189
	measured	9.65	3.35

*Errors in range of calculation accuracy.

2.3 *Elaboration of experimental results*

Strains were measured experimentally by electro-resistance method. Then were calculated: a) bimoment B and bending-torsional moment M_ω, shown in the Table 13 (method proposed by Obrębski (1994). There, were applied closed formulae:

$$B = \oint \sigma_1 \hat{\omega}\, d\bar{A} \quad , \quad M_{\bar{\omega}} = \oint \tau\, d\hat{\omega} \quad , \tag{1}$$

where σ_1 = normal stresses, $\hat{\omega}$ = warping function, τ = flow of shearing stresses, $\bar{A}$ = reduced area of CS.

Next, by MS Excel were calculated geometrical characteristics of **CS**s, normal stresses, shearing stresses, principal strains and stresses, angle of shape deformation. Some selected results are presented in the Tables 2 to 9.

It is interesting, what shows Table 1, that on basis of known experimentally obtained strains, were calculated B & M_ω with satisfying accuracy. This tests were

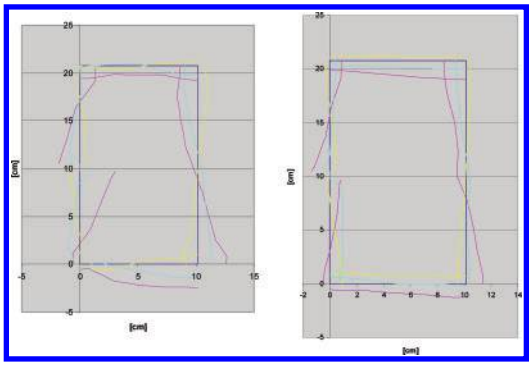


Figure 6. Diagrams of strains (black lines – shape of **CS**, red – longitudinal, yellow – cirquital, green – inclined) in **CS** β-β: 2 cm & 55 cm from fastening (Fig. 1).

Table 2. Experimental data for CS $\eta = 2$ cm.

Model & BC (type)		σ_x kN/cm^2	σ_s kN/cm^2	τ_{xs} kN/cm^2	γ_{xs} degrees
11 $\Theta = 0$ (open)	max.	6.665	3.110	2.346	**0.032**
	min.	−8.442	−2.173	−2.086	−0.028
12 $\Theta = 0$ (closed)	max.	4.953	4.862	0.909	0.012
	min.	−5.241	−1.489	−2.518	**−0.034**
13 $\Theta = 0$ (open)	max.	8.668	4.491	0.542	0.007
	min.	−2.479	0	−1.683	−0.023
14 $\Theta = 0$ (closed)	max.	4.659	1.715	−0.988	0.012
	min.	−4.756	−0.719	−0.988	−0.013

Table 3. Experimental data for CS $\eta = 55$ cm.

Model & BC (type)		σ_x kN/cm^2	σ_s kN/cm^2	τ_{xs} kN/cm^2	γ_{xs} degrees
11 $\Theta = 0$ (open)	max.	3.673	0.421	1.430	0.019
	min.	−4.966	−2.339	−1.478	**−0.020**
12 $\Theta = 0$ (closed)	max.	3.804	0.680	2.069	**0.028**
	min.	−3.499	−1.028	−0.904	−0.012
13 $\Theta = 0$ (open)	max.	3.226	0.409	2.000	0.027
	min.	−3.377	−0.727	−0.511	−0.007
14 $\Theta = 0$ (closed)	max.	4.390	1.462	0.588	0.008
	min.	−2.815	0.183	−0.628	−0.008

Table 4. Experimental data for CS $\eta = 2$ cm.

Model & BC (type)		σ_1 kN/cm^2	σ_2 kN/cm^2	Angle ϕ_n degrees
11 $\Theta = 0$ (open)	max.	6.791	1.912	44.325
	min.	−1.086	−8.442	−42.896
12 $\Theta = 0$ (closed)	max.	5.904	0.965	43.379
	min.	−1.454	−4.201	−39.939
13 $\Theta = 0$ (open)	max.	8.748	4.357	29.462
	min.	0	−2.510	−31.405
14 $\Theta = 0$ (closed)	max.	4.692	1.681	42.420
	min.	−0.678	−4.760	−43.235

Table 5. Experimental data for CS $\eta = 55$ cm.

Model & BC (type)		σ_1 kN/cm^2	σ_2 kN/cm^2	Angle ϕ_n degrees
11 $\Theta = 0$ (open)	max.	3.673	1.66E-16	44.920
	min.	−0.683	−4.968	−43.624
12 $\Theta = 0$ (closed)	max.	3.810	0.573	40.030
	min.	−0.196	−3.516	−40.817
13 $\Theta = 0$ (open)	max.	3.226	0.113	44.572
	min.	−0.395	−3.377	−44.641
14 $\Theta = 0$ (closed)	max.	4.532	1.436	42.678
	min.	−1.624	−5.488	−38.414

Table 6. Results of calculation by FEM by means of ROBOT v.16, for CS $\eta = 2$ cm.

Model & BC (type)		σ_x kN/cm^2	σ_x %	τ_{xs} kN/cm^2	τ_{xs} %
11 $\Theta = 0$ (open)	max.	5.807	87.12	0.07	0.31
	min.	−5.999	71.06	−0.006	0.31
12 $\Theta = 0$ (closed)	max.	4.207	84.93	0.005	0.53
	min.	−4.208	80.13	−0.005	0.19
13 $\Theta = 0$ (open)	max.	5.129	59.16	0.006	1.05
	min.	−5.129	206.88	−0.004	0.28
14 $\Theta = 0$ (closed)	max.	4.325	92.82	0.005	−0.49
	min.	−4.324	90.91	−0.005	0.49

Table 7. Results of calculation by FEM by means of ROBOT v.16, for CS $\eta = 55$ cm.

Model & BC (type)		σ_x kN/cm^2	σ_x %	τ_{xs} kN/cm^2	τ_{xs} %
11 $\Theta = 0$ (open)	max.	4.319	117.58	0.001	0.049
	min.	−4.459	89.80	−0.001	0.047
12 $\Theta = 0$ (closed)	max.	3.126	82.16	0.001	0.038
	min.	−3.126	89.31	−0.001	0.089
13 $\Theta = 0$ (open)	max.	3.378	95.52	0.001	0.03
	min.	−3,378	89.42	−0.001	0.14
14 $\Theta = 0$ (closed)	max.	3.025	68.91	0.001	0.13
	min.	−3.025	93.08	−0.001	0.12

Table 8. Results of analytical approach by means of MS Excel, for CS $\eta = 2$cm.

Model & BC (type)		σ_x kN/cm^2	σ_x %	τ_{xs} kN/cm^2	τ_{xs} %
11 $\Theta = 0$ (open)	max.	6.148	92.23	0.352	15.014
	min.	−6.163	73.01	−0.107	5.146
12 $\Theta = 0$ (closed)	max.	6.611	133.47	0.371	40.845
	min.	−6.536	124.47	−0.501	19.911
13 $\Theta = 0$ (open)	max.	5.288	61.00	0.363	66.890
	min.	−5.286	213.22	−0.113	6.744
14 $\Theta = 0$ (closed)	max.	6.764	145.18	0.823	−89.328
	min.	−6.671	140.24	−2.2E-7	2.2E-5

repeated later by Jankowska (2006) and than exploited by investigation of plane TW frames.

3 TRANSMISSION OF TORSION FORCES THROUGH NODES

3.1 *Reason and method of measurements*

The problem of computer analysis of space frames taking into consideration of bimoments, too, was numerically investigated by some authors. There, can be mentioned e.g. works by J. Rutecki [18], J.H. Argyris and D. Radaj (1971), R. Dziewolski (IASS, Kielce 1973), Obrebski [8, 9, 13, 15, 17] (1985, 1991), K. Grygierek (Ph.D. dissertation, Gliwice, 2003), and C. Szymczak et al. (2003).

There, still is serious question about real behaviour of space bar frames. Therefore, N. Jankowska (2006) in she's Ph.D. dissertation (supervised by J.B.Obrebski), has investigated 8 models of simple thin-walled frames, type L, T and Y (Figs 6, 7). The frames were composed of the 2 or 3 **TWB**s, made of the brass, connected with one central node, only. By both ends of each bar, in distance of 2.5 cm were glued 25 electro-resistance rosettes. There was applied very modern in that time electronic bridge of the firm VISHAY, system 5000, Figure 3c. All together, were investigated 32 **CS**s, in it most of them placed by central node.

Table 9. Results of analytical approach by means of MS Excel, for CS $\eta = 55$ cm.

Model & BC (type)		σ_x kN/cm^2	σ_x %	τ_{xs} kN/cm^2	τ_{xs} %
11 $\Theta = 0$	max.	4.373	119.07	0.342	23.89
(open)	min.	−4.348	88.29	−0.101	6.81
12 $\Theta = 0$	max.	3.342	87.83	0.228	11.01
(closed)	min.	−3.308	94.53	−0.205	22.62
13 $\Theta = 0$	max.	3.483	107.97	0.352	17.60
(open)	min.	−3.478	102.97	−0.107	20.93
14 $\Theta = 0$	max.	3.677	83.74	0.448	76.17
(closed)	min.	−3.425	121.65	−2.1E-7	3.3E-5

3.2 *Some results and its evaluation for series of thin-walled frames*

Jankowska [2] has presented proper diagrams of shearing and normal stresses (e.g. Figure 9b), and calculated among the other, internal forces, associated

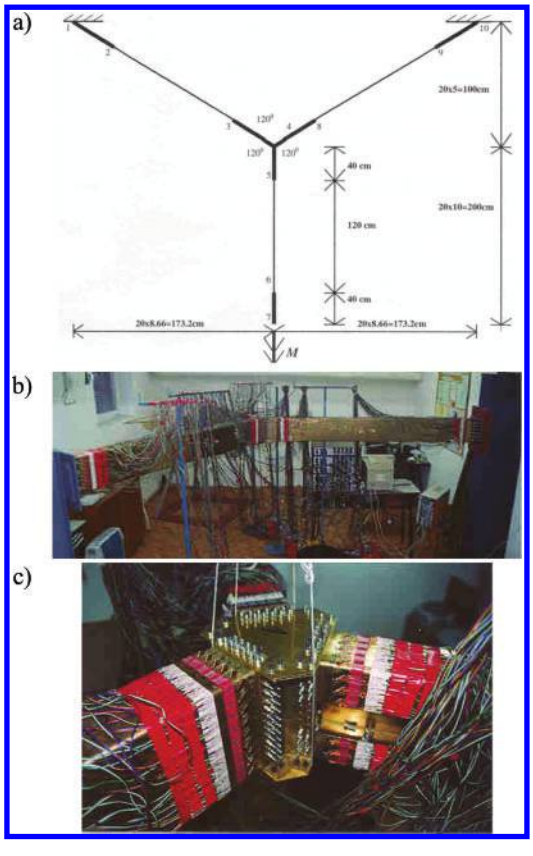


Figure 7. Scheme of frame type Y a); general view b); node of the frame c) Jankowska (2006).

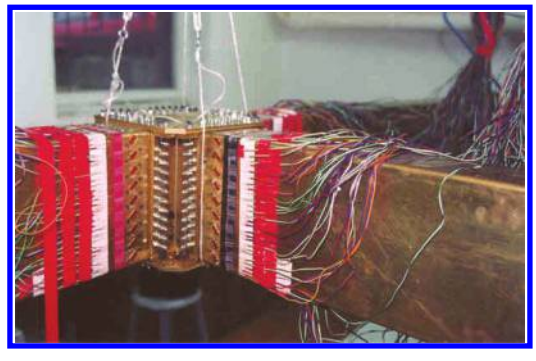


Figure 8. Node of frame type T with sensors for electro-resistance measurements.

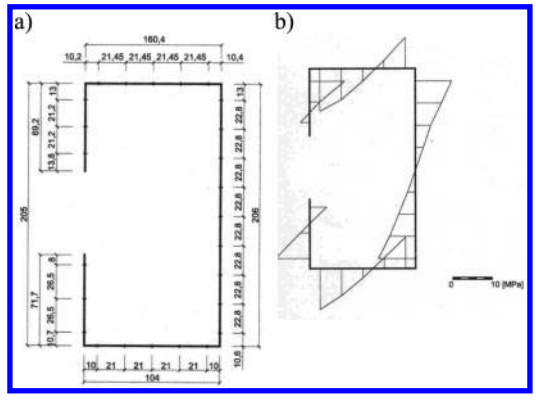


Figure 9. Location of rosettes in one of the **CS**s a); diagram of measured normal stresses [2] b).

Table 10. Measured bimoments in central nodeof frames (Jankowska 2006).

Frame type	Number of sheets	C-active CS kN cm^2	%	B-passive CS kN cm^2	%	E-passive CS kN cm^2	%
L1	1	−1364	100	−455	33.35		
L2	2	−1355	100				
L3	3	−1259	100				
T1	1	−1495	100	−285	19.06	287	19.19
T2	2	−1390	100	−261	18.77	−241	17.99
T3	3	−1339	100	−241	17.99	222	16.57
Y1	1	−1413	100	−322	22.79	259	18.33
Y2	2	−1333	100	−285	21.38	223	16.73

with torsion: B – bimoment and $M_{\hat{\omega}}$ – bending-torsion moment, according to formulae (1), by method proposed by J.B. Obrębski.

Some next results are given in the Table 10. So, the transmission of bimoment through node is from 16.57% to 33.35 and its dependence on node rigidity was confirmed. It is important, that similar observation concerning of bimoments transmission, obtained numerically by super-elements technique, was reported by C.Szymczak et al., too.

4 STABILITY OF THIN-WALLED BARS LOADED BY PURE BIMOMENT

4.1 *Applied models an method of measuring*

In this type of experiments, the short bar was loaded by pure bimoment only, Figure 10a. There, pure bimoment was applied at the bottom end of the bar. At the top of the specimen, in each case was applied a rigid cork to constrain longitudinal displacements and to stiffen the whole mode (Fig. 10b). Also, three different types of longitudinal slits were applied: in the middle, in one quarter of the wider wall and in the bar corner (Fig. 10c). Moreover, three wall thicknesses were applied: 0.5 mm, 1.0 mm, 1.5 mm.

Waves appeared along the longitudinal slit, at a certain value of bar loading P. The value of force P when waves appeared, was noted as critical loading by bimoment B. Beside slit edge waving, certain rotations of the top end of the bars were observed. So, when bimoment is applied, torsion appears. In this series of experiments, without any doubt, waves and critical loading were the result of pure bimoment application, only. So, it all confirms the thesis that bimoment is significantly responsible for wavy effects on side walls and along slits, too Fig. 4a.

4.2 *Some obtained results*

In the Figure 10c are shown a few diagrams of compared curves obtained experimentally and theoretically (Obrębski 1997). Especially for model with thin bar walls, accuracy of calculated results seems to be enough.

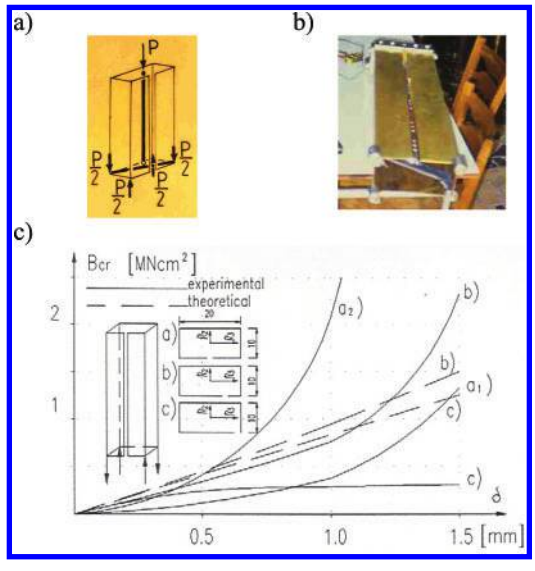


Figure 10. Scheme of experiment for critical bimoment a); planarly constrained displacements by strong steel cork at top b); loading system by pure bimoment at bottom bar end a,b); diagrams of measured and calculated critical bimoments c).

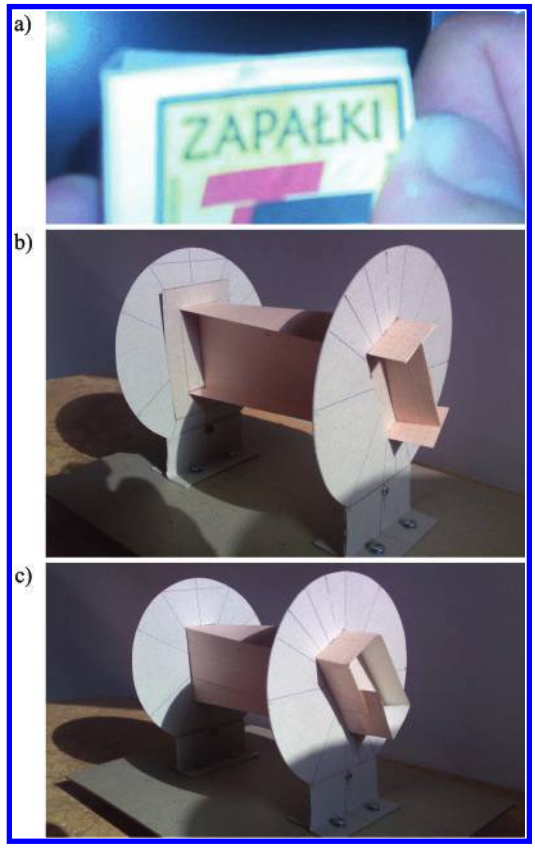


Figure 11. Three simple experiments with torsined models: match box a), I cross-section and strongly lipped open cross-sections.

5 EXPERIMENTS FOR DIDACTIC PURPOSES

There, were performed some very simple experiments, which each student can do at home. They show, the phenomena, which are computed by means of theory. It is interested, that model in the Figure 11b represents closed tube . . .

6 CONCLUSIONS

The more important conclusions are listed below. For wider information and literature, please, see to Obrębski (2009).

□ Bimoment is real internal force as longitudinal force, shearing force, bending and torsion moments, and can be calculated their critical values including combined loadings.

□ Bimoment can be measured experimentally, especially for open **CS**s.

□ In bars torsion always appears together with bimoment and bending-torsion moment.

□ Any type of loading and combined loading can lead to the critical state of bar behaviour.

□ Circuital normal stresses for **TWB**s can reach up to 98.17%, ($\eta = 2$ cm) & 11.4–47.1%, ($\eta = 55$ cm) of longitudinal normal stresses (see Tabl. 2, 3).

□ Shearing stresses for **TWB**s can reach $6.25 \div 67.92\%$, ($\eta = 2$ cm, Table 2) & $13.41 \div 61.99\%$, ($\eta = 55$ cm, Table 3) of longitudinal normal stresses.

□ In investigated cantilevers the angles of shape deformation (non-dilatation strain) for open **CS**s reach up to $-0{,}034^0$ and for closed **CS**s $+0.032^0$ (93,20% when $\eta = 2$ cm or 71,45% when $\eta = 55$ cm – of similar angles for closed **CS**s, Tables 2, 3). In Vlasov's theory (1940 & 1959) it was assumed zero!

□ The analytically obtained stresses were for cantilever bars close to experimental ones, than similar calculated by FEM (compare Tables 6–9).

□ Calculation of critical forces is possible for composite bars, under combined loading, too Obrebski (1991, 1997, 2001, 2008).

□ Many effects observed in behaviour of **TWB**s, considered in standards by means of certain coefficients, can be calculated simply by author's theory.

□ Assumptions and possibilities of theory of **TWB**s elaborated by Obrebski (1989, 1991, 1997, 2008) seem to be well confirmed by experiments, much better than in the others mentioned below.

□ So, computer algorithms together with good theory, are giving the best solutions.

In this paper only the more important remarks and conclusions are presented. It should be pointed out that nowadays, in standards, torsion and bimoment are almost completely neglected. There is a strong tendency to eliminate stresses calculation from the dimensioning process. It seems to be highly dangerous. **Investigations are continued.**

REFERENCES

Flont, P. 1995. *Badania doswiadczalne stanu odksztalcenia i naprezenia pewnej klasy pretów cienkosciennych*. (M.Sc. dissertation – supervisor J.B. Obrębski). Warsaw University of Technology, Warsaw.

Jankowska, N. 2006. *Influence of nodes deformations on internal forces in thin-walled frames*. (In Polish, doctor dissertation – supervisor J.B.Obrębski), Warsaw University of Technology, Warsaw.

Jastrzebski, P. & Mutermilch, J. & Orlowski W.1985 *Strength of Materials* (In Polish), Arkady, 1985 (Vol.1), 1986 (Vol.2), Warsaw.

Kollbrunner C.F. & Hajdin N. 1975. *Dünnwandige Stäbe*. Vol. 1,2. Berlin, Heidelberg, New York, Springer.

Magnucki, K. & Szyc, W. 1997. *Structures with Thin-Walled Open CSs* (In Polish). Publ.House of Wyzszej Szkoly Pedagogicznej im. T.Kotarbinskiego w Zielona Góra.

Murray, N.W. 1984. Introduction to the Theory of Thin-Walled Structures. Oxford Eng.Sc. Ser.

Mutermilch J. & Kociolek A. 1972. *Strength and Stability of Thin-Walled Bars with Open Cross-Sections*. (In Polish), Warsaw, WPW.

Obrębski J.B. 1989. Second-order and second-approximation theory in the statics and dynamics of thin-walled straight bars. *Thin-Walled Structures*, Appl.Sc.Publ. 8,1989: 81–97.

Obrębski J.B. 1991 & 1999. Thin-Walled Elastic Straight Bars (In Polish), (lect. notes), Warsaw, WPW: pp. 452.

Obrębski J.B. & Urbaniak Z. & ElAwady M.E. 1992. On designing of the thin-walled bars in the light of theory and experiments. In Int. IMEKO-GESA Symp. on *Risk Minimisation by Experimental Mechanics*, Düsseldorf, FRG.

Obrębski J.B. 1994. Experimental estimation of bimoment and bending-torsional moment (In Polish), in XVI Symp.on *Experim.Mech. of Solids*, Jachranka, Poland: 249–252.

Obrębski, J.B. 1997. Uniform criterion for geometrical unchengeability and for instability of structures. In Proc. of the Intern. Conf. on *Stability of Structures*. Zakopane, Poland.

Obrębski, J.B. 1997. *Strength of Materials* (In Polish, lecture notes of Warsaw Univ. of Techn.), Micro-Publisher J.B. Obrębski Wydawn. Naukowe, Printed by AGAT, Warsaw.

Obrębski J.B. & Szmit R. 2000. Dynamics and dynamical stability of tall buildings, (Invited lecture). Int. Conf. ICSSD, Taipei, Taiwan: 85–94.

Obrębski J.B. 2001. On the mechanics and strength analysis of composite structures. (Invited paper). In A. Zingoni (ed.), SEMC, Cape Town, 2-4.04.2001, Elsevier Sc. Ltd., Amsterdam-(..), 2001, 161–172.

Obrębski J.B. 2003. Advantages of 3D-Time Space Description for dynamical analysis of structures, (Invited paper). In Int. Conf. IASS-APCS, Taipei, Taiwan, 2003: 40–41+CD-ROM.

Obrębski J.B. 2009. Review of own complex researches related to bar structures. In XIV LSCE - *Lightweight Structures in Civil Engineering – Contemporary Problems*, Local Seminar of IASS Polish Chapter, Warsaw, 5 December, 2008: 87–128.

Rutecki, J. 1957. *Strength of Thin-Walled Structures*. (In Polish), Warsaw, PWN.

Vlasov, V.Z. 1940 & 1959. *Thin-walled elastic bars* (In Russian), Moscow.

Obrębski, J.B. 2012. Examples of stresses caalculation for composite bars being under combined loading. *Mechanik*, 7/2012: 602 +CD. WAT.

Obrębski, J.B. 2012. Some observations on mechanical behavior of bars with composite cross-sections. In W. Przybylo & J. Obrębski (eds.). Lghtweight Structures in Civil Engineering, LSCE 2012: 110–121.

13. Plates, shells, laminated composite structures, sandwich structures

Research and Applications in Structural Engineering, Mechanics and Computation – Zingoni (Ed.)
© 2013 Taylor & Francis Group, London, ISBN 978-1-138-00061-2

Bending and buckling of circular sandwich orthotropic plates with corrugated cores

K. Magnucki & M. Walachowski
Institute of Applied Mechanics, Poznan University of Technology, Poznan, Poland

E. Magnucka-Blandzi
Institute of Mathematics, Poznan University of Technology, Poznan, Poland

ABSTRACT: The subject of the study is a circular sandwich plate with corrugated main core and three-layer faces. The cores of the faces are made of homogeneous isotropic polyurethane foam. The plate is a thin-walled structure with three cores: one main – in the middle, and two others – internal layers of faces and four sheets. The corrugation of the main core is along the radius. The field of displacements, strains, and stresses are formulated basing on the Zig-Zag hypothesis. The system of partial differential equations of equilibrium for the circular sandwich plate is derived based on the principle of stationary total potential energy. Moreover, for verification of the results a Finite Element Model (FEM – ANSYS – system) for the plate is formulated. The bending and buckling analysis was carried out to determine the critical load and buckling shape. Comparison of the results obtained in the analytical and numerical (FEM) analysis is shown in figures.

1 INTRODUCTION

Sandwich structures are well-known since the mid of 20th century. Modelling and design of these structures was a basic problem. Elastic constants for corrugated cores of the sandwich structures were elaborated by Libove & Hubka (1951). Objective basic researches for sandwich structures were intensively conducted in further decades. Allen (1969) elaborated fundamental monograph for sandwich structures. Noor et al (1996) and Vinson (2001) presented a review of selected problems of sandwich structures. Strength and stability problems of sandwich structures are the subject of contemporary studies. Carrera (2003) elaborated a review of theories for multilayers plates and shells. Carlsson et al (2001) elaborated the elastic stiffnesses of corrugated core sandwich. Analytical modeling and FEM calculations of sandwich structures were presented by Steeves & Fleck (2004), Talbi et al (2009), Kazemahvazi & Zenkert (2009), Seong et al (2010), Jasion et al (2012), Magnucka-Blandzi et al (2012) and Magnucki et al (2013). Modeling and analysis of buckling problems of circular sandwich plates were presented by Jasion et al (2012), Luo et al (2004), Luwu & Changjun (1992), Pawlus (2006), (2008) and Wang & Chen (2003).

The subject of the paper is a circular sandwich plate composed of seven layers: two outer flat sheets, two inner flat sheets, two isotropic polyurethane foam cores of the faces and one main corrugated core (Fig. 1). The plate is under a uniform pressure p_0 or uniform distributed radial compression load of intensity N_r^0.

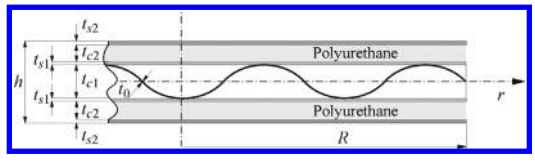


Figure 1. Scheme of the circular sandwich plate.

The analytical and numerical FEM analyses for axisymmetric bending or buckling of the plate are presented.

2 ANALYTICAL STUDY

2.1 *Analytical model*

The assumption: the straight line – normal to the middle plane of the plate before bending, does not remain straight and normal after axisymmetric bending, but becomes a broken line (Fig. 2).

The hypothesis makes a basis for formulation of the field of displacements, strains and stresses. Displacements are as follows:
the outer sheets of thicknesses t_{s1}

$$u(r,z) = -t_{c1}\left[\zeta\frac{dw}{dr} \pm \psi_1(r) \pm x_2\psi_2(r)\right], \tag{1}$$

the polyurethane foam cores of faces – t_{c2}

$$u(r,z) = -t_{c1}\left\{\zeta\frac{dw}{dr} \pm \psi_1(r) - \psi_2(r)\left[\zeta \pm \left(\frac{1}{2} + x_1\right)\right]\right\}, \tag{2}$$

the inner sheets of thicknesses t_{s2}

$$u(r,z) = -t_{c1}\left[\zeta \frac{dw}{dr} \pm \psi_1(r)\right], \tag{3}$$

the main core of thickness t_{c1}

$$u(r,z) = -t_{c1}\zeta\left[\frac{dw}{dr} - 2\psi_1(r)\right]. \tag{4}$$

The upper sign is related to upper layers, and lower sign is related to lower layers. The following dimensionless coordinate and parameters are introduced:

$$\zeta = \frac{z}{t_{c1}}, \quad x_1 = \frac{t_{s1}}{t_{c1}}, \quad x_2 = \frac{t_{c2}}{t_{c1}}, \quad x_3 = \frac{t_{s2}}{t_{c1}}. \tag{5}$$

Moreover, two dimensionless functions are defined:

$$\psi_1(r) = \frac{u_1(r)}{t_{c1}}, \quad \psi_2(r) = \frac{u_2(r)}{t_{c2}}. \tag{6}$$

Strains for each layer of this circular plate are defined as follows:

$$\varepsilon_r = \frac{\partial u}{\partial r}, \quad \varepsilon_\varphi = \frac{u}{r}. \tag{7}$$

Stresses for each layer of this circular plate are defined as follows.

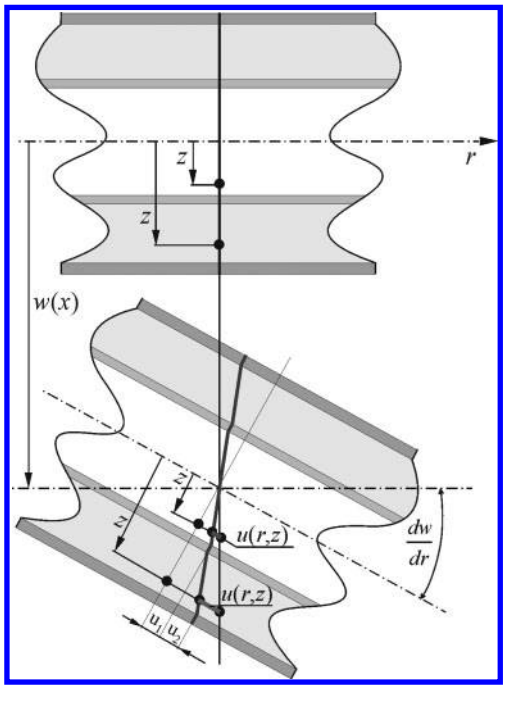


Figure 2. The hypothesis of deformation of the normal to the middle plane of the circular sandwich plate.

the flat sheets

$$\sigma_r = \frac{E}{1-\nu^2}\left(\varepsilon_r + \nu\varepsilon_\varphi\right), \quad \sigma_\varphi = \frac{E}{1-\nu^2}\left(\varepsilon_\varphi + \nu\varepsilon_r\right), \tag{8}$$

$$\tau_{rz} = \tau_{r\varphi} = 0, \tag{9}$$

the cores of the faces

$$\sigma_r = \frac{E_{c2}}{1-\nu_{c2}^2}\left(\varepsilon_r + \nu\varepsilon_\varphi\right), \quad \sigma_\varphi = \frac{E_{c2}}{1-\nu_{c2}^2}\left(\varepsilon_\varphi + \nu\varepsilon_r\right), \tag{10}$$

$$\tau_{rz} = G_{c2}\gamma_{rz}, \quad \tau_{r\varphi} = 0, \tag{11}$$

the main core

$$\sigma_r = \frac{E_r^{(c1)}}{1-\nu_{c2}^2}\left(\varepsilon_r + \nu\varepsilon_\varphi\right), \quad \sigma_\varphi = E_\varphi^{(c1)}\varepsilon_\varphi, \tag{12}$$

$$\tau_{rz} = G_{rz}^{(c1)}\gamma_{rz}, \quad \tau_{r\varphi} = 0, \quad \nu_r = 0, \quad \nu_\varphi = \nu. \tag{13}$$

Elastic constants for corrugated core are elaborated similarly to the ones presented by Libove & Hubka (1951) and Kazemahvazi & Zenkert (2009).

2.2 *Equations of equilibrium*

The elastic strain energy of the plate is a sum of energy of the following layers: two outer sheets, two face polyurethane cores, two inner sheets and one main corrugated core

$$U_\varepsilon = 2U_\varepsilon^{(os)} + 2U_\varepsilon^{(fc)} + 2U_\varepsilon^{(is)} + U_\varepsilon^{(mc)}. \tag{14}$$

The work of the load

$$W = 2\pi\int_0^R\left[p_0 w(r) + \frac{1}{2}N_r^0\left(\frac{dw}{dr}\right)^2\right]rdr. \tag{15}$$

From the theorem of stationary total potential energy

$$\delta\left(U_\varepsilon - W\right) = 0, \tag{16}$$

one obtains three equilibrium equations:

$$\Re_{10}(w) - \Re_{11}(\psi_1) - \Re_{12}(\psi_2) = Q_r(r) - N_r^0\frac{dw}{dr}, \tag{17}$$

$$\Re_{20}(w) - \Re_{21}(\psi_1) - C_{\psi 1}\psi_1(r) = 0, \tag{18}$$

$$\Re_{30}(w) - \Re_{31}(\psi_1) - \Re_{32}(\psi_2) + C_{\psi 2}\psi_2(r) = 0, \tag{19}$$

where the differential operators are composite, for example

$$\Re_{10}(w)= D_{c1}\left[C_{w101}\Im_0(w)+\frac{1-\nu^2}{6}\Im_1(w)\right]+D_{c2}C_{w102}\Im_0(w) \quad (20)$$

and

$$\Im_0(w)=\frac{d}{dr}\left[\frac{1}{r}\frac{d}{dr}\left(r\frac{dw}{dr}\right)\right], \quad (21)$$

$$\Im_1(w)=\tilde{E}_r^{(c1)}\frac{1}{r}\frac{d}{dr}\left(r\frac{d^2w}{dr^2}\right)-\tilde{E}_\varphi^{(c1)}\frac{1}{r^2}\frac{dw}{dr}. \quad (22)$$

2.3 *Analytical solution*

The circular plate of radius R with clamped edge is under a uniform pressure p_0 or uniform distributed radial compression load of intensity N_r^0 (Fig. 3).

The equilibrium equations (17), (18) and (19) for the plate are approximately solved assuming the three unknown functions in the following forms

$$w(r)=w_a\left[1-2\left(\frac{r}{R}\right)^2+\left(\frac{r}{R}\right)^4\right], \quad (23)$$

$$\psi_1(r)=\psi_{1a}\left[\frac{r}{R}-\left(\frac{r}{R}\right)^3\right],\ \psi_2(r)=\psi_{2a}\left[\frac{r}{R}-\left(\frac{r}{R}\right)^3\right], \quad (24)$$

where: w_a, ψ_{1a}, ψ_{2a} – parameters of the functions.

Substituting these expressions into (17), (18) and (19), one obtains the deflection and the critical load in complicated forms.

Example. The corrugation of the core consist of circular arcs – semicircles (Fig. 4).

Data for the plate: $R=1000$ mm, $h=39.7$ mm, $R_0=10$ mm, $t_0=0.5$ mm, $t_{c1}=20.5$ mm, $t_{s1}=0.6$ mm, $t_{c2}=8$ mm, $t_{s2}=1$ mm, $E_{c2}=50$ MPa, $\nu_{c2}=0.2$, $E=200$ GPa, $\nu=0.3$.

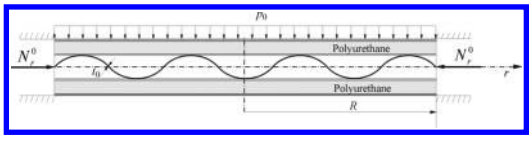


Figure 3. Scheme of the load of the plate.

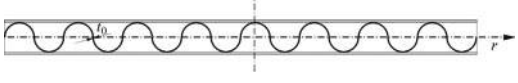


Figure 4. Scheme of the corrugated core.

3 NUMERICAL – FEM STUDY

3.1 *FEM model*

The FEM model was built as the shell structure and body structure. The main core, the outer sheets and the inner sheets were modelled as the shell structure. The polyurethane foam cores of faces were modelled as the body (Fig. 5).

The model was built as the axial symmetrical, thanks to that only the one fourth of the plate were taken into account (Fig. 6).

The mesh for each part was built as the quadrilaterals and the sizing was decided as the 50 mm for each elements (Fig. 7).

The contact between the parts were defined as the bounded.

The boundary conditions for the circular sandwich plate were defined on the edge of the plate (Fig. 8). The horizontal displacements and X, Y, Z rotation were blocked.

The uniform presser p_0 was added on the top surfaces (Fig. 9), and the uniform distributed radial

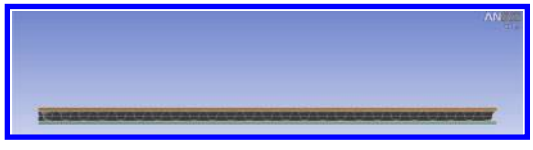


Figure 5. Model of the plate.

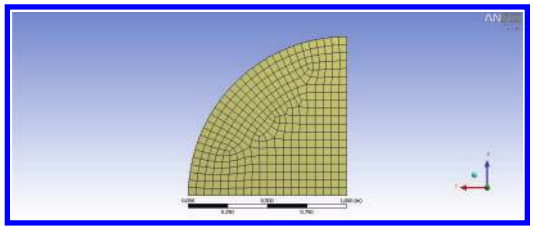


Figure 6. Axial symmetrical model.

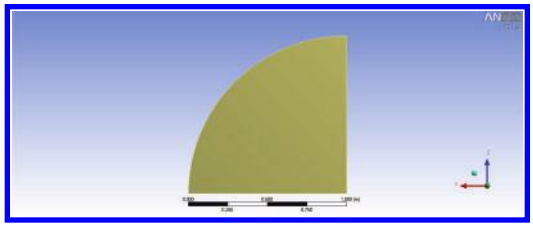


Figure 7. Quadrilaterals mesh.

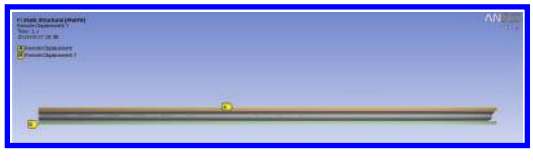


Figure 8. Edge of the plate.

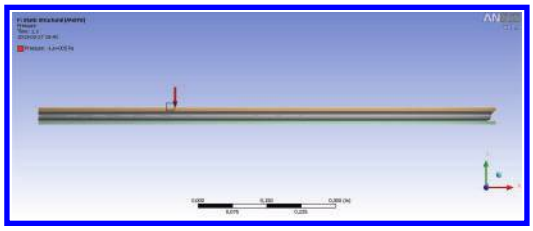


Figure 9. The uniform presser p_0.

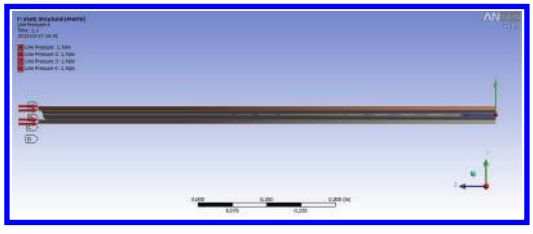


Figure 10. The uniform distributed radial compression load of intensity N_r^0.

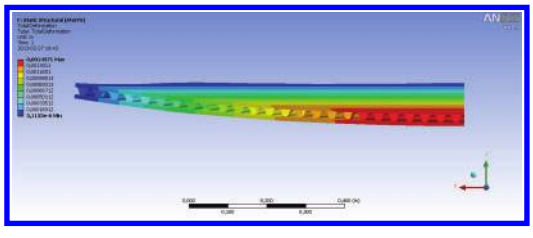


Figure 11. Total deformation.

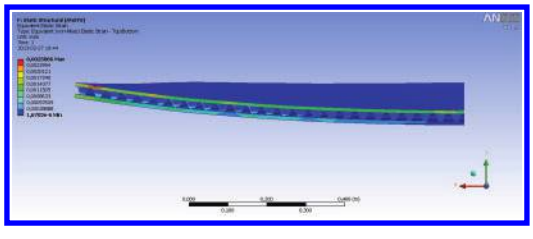


Figure 12. Equivalent elastic strain.

compression load of intensity N_r^0 was added on the edge of sheets (Fig. 10).

3.2 *Numerical – FEM calculations*

FEM calculations were divided for two analysis. First one the static structural analysis, and the second one lineal buckling analysis.

Total deformation (Fig. 11), equivalent elastic strain (Fig. 12) and equivalent stress (Fig. 13) were calculated in the static structural analysis. The uniform pressure p_0 and uniform distributed radial compression load of intensity N_r^0 were considered.

In the lineal buckling analysis only the uniform distributed radial compression load of intensity N_r^0 was considered. Total deformation was calculated in lineal

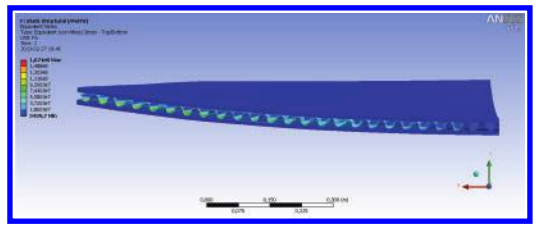


Figure 13. Equivalent stress.

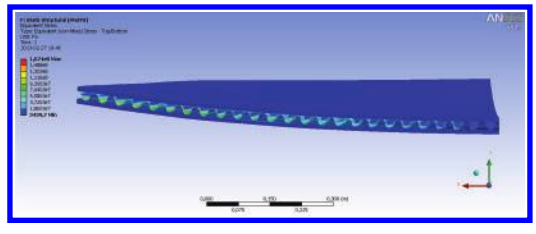


Figure 14. First mode of total deformation.

buckling analyse. The first mode of total deformation is presented (Fig. 14).

Results of numerical FEM Calculations are following:

Total deflection

$$w_a^{(FEM)} = 0.00149\ m$$

$$w_a^{(ANALYT)} = 0.00119\ m$$

The critical load

$$N_a^{(FEM)} = 1107.5\ \frac{kN}{m}$$

$$N_a^{(ANALYT)} = 1240.7\ \frac{kN}{m}$$

4 CONCLUSION

The subject of a study is the variety of classic sandwich plate. The mathematical and numerical models of the plate are presented, as well as the results obtained by these methods. The shirring effect is a sum of shirring of the main core and the polyurethane core of the outer layers. The bending and critical forces are closely related to the shirring effect.

REFERENCES

Allen H.G. 1969. *Analysis and Design of Structural Sandwich Panels.* Oxford, London, Edinburgh, New York, Toronto, Sydney, Paris, Braunschweig: Pergamon Press.

Carlsson L.A., Nordstrand T., Westerlind B. 2001. On the elastic stiffnesses of corrugated core sandwich, *Journal of Sandwich Structures and Materials* 3: 253–267.

Carrera E. 2003. Historical review of zig-zag theories for multilayers plates and shells. *Applied Mechanics Reviews* 56(3): 287–308.

Jasion P., Magnucka-Blandzi E., Szyc W., Magnucki K. 2012. Global and local buckling of sandwich circular and beam-rectangular plates with metal foam core. *Thin-Walled Structures* 61: 154–161.

Kazemahvazi S., Zenkert D. 2009. Corrugated all-composite sandwich structures. Part 1: *Modeling. Composite Science and Technology* 69: 913–919.

Libove C., Hubka R.E. 1951. *Elastic constants for corrugated-core sandwich plates*. National Advisory Committee for Aeronautics. Technical Note 2289, Washington: NACA.

Luo JZ, Liu TG, Zhang T. 2004. Three-dimensional linear analysis for composite axially symmetrical circular plates. *International Journal of Solids and Structures* 41: 3689–3706.

Lu-wu H, Chang-jun C. 1992. The buckled states of annular sandwich plates. *Applied Mathematics and Mechanics* 13(7): 623–628.

Magnucka-Blandzi E., Kuligowski P., Krus M., Magnucki K. 2012. Elastic buckling of a sandwich rectangular plate with three-layer faces. In: J. Loughlan, D.H. Nash & J. Rhodes (eds.), *Proc. of the 6-th Intl Conference on Coupled Instabilities in Metal Structures*, CIMS, Glasgow, 3–5 December. 611–618.

Magnucki K., Jasion P., Krus M., Kuligowski P., Wittenbeck L. 2013. Strength and buckling of sandwich beams with corrugated core. *Journal of Theoretical and Applied Mechanics* 51(1): 15–24.

Noor, A.K., Burton W.S., Bert C.W. 1996. Computational models for sandwich panels and shells. *Applied Mechanics Reviews* 49(3): 155–199.

Pawlus D. 2006. Solution to the static stability problem of three-layered annular plates with a soft core. *Journal of Theoretical and Applied Mechanics* 44(2): 299–322.

Pawlus D. 2008. Approach to evaluation of critical static loads of annular three-layered plates with various core thickness. *Journal of Theoretical and Applied Mechanics* 46(1): 85–107.

Seong D.Y., Jung C.G., Yang D.Y., Moon K.J., Ahn D.G. 2010. Quasi-isotropic bending responses of metallic sandwich plates with bi-directionally corrugated cores. *Materials and Design* 31: 2804–2812.

Steeves CA, Fleck NA. 2004. Collapse mechanisms of sandwich beams with composite faces and a foam core, loaded in three-point bending. Part I: analytical models and minimum weight design. *International Journal of Mechanical Sciences* 46: 561–583.

Talbi N., Batti A., Ayad R., Guo Y.Q. 2009. An analytical homogenization model for finite element modelling of corrugated cardboard. *Composite Structures* 88: 280–289.

Vinson J.R. 2001. Sandwich structures. *Applied Mechanics Reviews* 54(3): 201–214.

Wang H-J, Chen L-W. 2003. Axisymmetric dynamic stability of sandwich circular plates. *Composite Structures* 59: 99–107.

Research and Applications in Structural Engineering, Mechanics and Computation – Zingoni (Ed.)
© 2013 Taylor & Francis Group, London, ISBN 978-1-138-00061-2

Modeling and simulation of large amplitude vibrations of layered composite and smart structures

R. Schmidt, M.N. Rao & T.D. Vu
RWTH Aachen University, Institute of General Mechanics, Germany

ABSTRACT: This paper presents a numerical study on dynamics of layered composite and smart structures. The shell element is based on the Reissner-Mindlin first-order shear deformation theory and strain-displacement relations are valid for small strains but finite rotations. The electromechanical coupling is considered by introducing three additional electrical degrees of freedom for each electrode pair. Nonlinear transient analysis is carried out for a layered angle-ply cylindrical shell and a smart piezolaminated composite plate. The present simulations are compared with those obtained by finite element analyses based on first-order transverse shear deformation moderate or refined von Kármán-type theories in earlier literature.

1 INTRODUCTION

Modeling and numerical simulation of both the nonlinear dynamic response of layered composite structures and of adaptive structures with integrated distributed control capabilities has attracted considerable research interest in recent years. While geometrically linear theories for structures with piezoelectric layers and associated numerical methods have been developed by a number of authors, geometrically nonlinear problems have been treated considerably less in literature.

Most of the available papers treat the nonlinear transient response of composite structures with simplified geometrically nonlinear theories based either on the first (Reddy (1983), Reddy & Chandrashekara (1985), Palmerio et al. (1990), Ganapathi & Vardhan (1996), Klosowski et al. (1996), Sansour et al. (1997), Pellicano et al. (2002)), or third-order (Khdeir et al. (1989)) transverse shear deformation theory, using the refined von Kármán-type or moderate rotation theories. Concerning nonlinear vibrations of adaptive structures, Yi et al. (2000) used solid elements for geometrically nonlinear analysis of sensor voltage output of surface bonded patches on beams, plates and shells. Mukherjee & Chaudhuri (2005) analyzed nonlinear vibrations of piezolaminated beams by adopting von Kármán-type nonlinearity in the framework of first-order shear deformation theory. Marinkovic et al. (2009) investigated geometrically nonlinear vibrations of active thin-walled structures using a degenerated shell element. Nonlinear transient analysis, vibration control of smart isotropic or composite laminated beams, plates and shells with integrated piezoelectric actuator and sensor layers was considered in our previous works (Lentzen & Schmidt (2005a, b)) accounting for moderate rotations in the framework of first-order shear deformation theory. Schmidt & Vu (2009) and Vu (2011) considered the refined von Kármán-type nonlinearity in the framework of third-order shear deformation hypothesis to analyze nonlinear vibrations of smart structures.

The present paper deals with geometrically nonlinear transient analysis of composite laminated structures and adaptive structures in the framework of the first-order transverse shear deformation theory (FOSD). The theory and the finite element method account for full geometrical nonlinearity, thus they account for arbitrary, finite rotations. The finite rotation theory (FRT) finite element formulation developed by Lentzen (2009) and extended to nonlinear vibration analysis in Schmidt et al. (2010) is applied and further extended to dynamic analysis of composite plates and shells with integrated piezoelectric layers and patches. For comparative purposes, finite element methods with the refined von Kármán-type (RVK) and the moderate rotation first-order shear deformation (FOSD MRT) shell theories (Schmidt & Reddy (1984), Palmerio et al. (1990), Kreja et al. (1997), Lentzen et al. (2007)) are also used.

The developed composite piezolaminated shell element is deployed in a few numerical examples dealing with large amplitude vibrations of composite and adaptive structures in the geometrically nonlinear range of deformation.

2 FINITE ROTATION SHELL THEORY AND FINITE ELEMENT METHOD

Concerning the underlying theory and finite element method, the present paper is based on the FOSD shell theory for small strains and finite rotations of Habip (1965) and the FE implementation of Gruttmann & Wagner (2006) and Lentzen (2009).

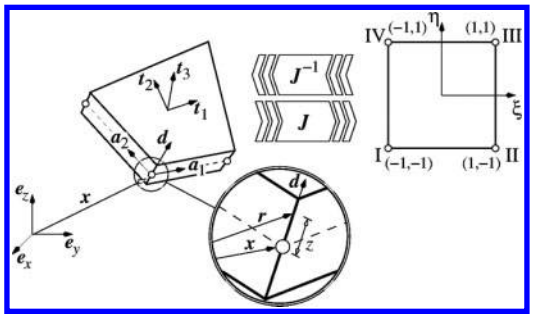


Figure 1. Definition of the coordinate systems in the FRT-element.

Figure 1 shows the four-node element with the global $\mathbf{e}_i$, the local $\mathbf{a}_\alpha$, the natural $\xi-\eta$ and the orthonormal material $\mathbf{t}_i$ coordinate systems. The position vector to the reference surface in the initial configuration at node I is denoted as $\mathbf{x}_I$.

Figure 1 also shows that a linear displacement field is assumed by introducing the inextensible director d which is a unit vector perpendicular to the reference surface in the undeformed configuration. For the FOSD or Reissner-Mindlin hypothesis, the position vector r to an arbitrary point on the director at the position (ξ,η) is described as

$$\boldsymbol{r}=\boldsymbol{x}(\xi,\eta)+z\boldsymbol{d}(\xi,\eta) \tag{1}$$

where z denotes the thickness coordinate ranging from the bottom to the top of the considered shell.

In the framework of this hypothesis, the Green strain-tensor components for fully nonlinear finite rotation strain-displacement relations are obtained as (see Habip (1965))

$$\begin{aligned}
\varepsilon_{\alpha\beta}&=\overset{0}{\varepsilon}_{\alpha\beta}+\zeta\overset{1}{\varepsilon}_{\alpha\beta}+\zeta^2\overset{2}{\varepsilon}_{\alpha\beta}\\
\varepsilon_{\alpha 3}&=\overset{0}{\varepsilon}_{\alpha 3}+\zeta\overset{1}{\varepsilon}_{\alpha 3}\\
\varepsilon_{33}&=0
\end{aligned} \tag{2}$$

where

$$\begin{aligned}
\overset{0}{\varepsilon}_{\alpha\beta}&=\frac{1}{2}\left(\bar{\boldsymbol{x}}_{,\alpha}\cdot\bar{\boldsymbol{x}}_{,\beta}-\boldsymbol{x}_{,\alpha}\cdot\boldsymbol{x}_{,\beta}\right)\\
\overset{1}{\varepsilon}_{\alpha\beta}&=\frac{1}{2}\left(\bar{\boldsymbol{x}}_{,\alpha}\cdot\bar{\boldsymbol{d}}_{,\beta}+\bar{\boldsymbol{x}}_{,\beta}\cdot\bar{\boldsymbol{d}}_{,\alpha}-\boldsymbol{x}_{,\alpha}\cdot\boldsymbol{d}_{,\beta}-\boldsymbol{x}_{,\beta}\cdot\boldsymbol{d}_{,\alpha}\right)\\
\overset{2}{\varepsilon}_{\alpha\beta}&=\frac{1}{2}\left(\bar{\boldsymbol{d}}_{,\alpha}\cdot\bar{\boldsymbol{d}}_{,\beta}-\boldsymbol{d}_{,\alpha}\cdot\boldsymbol{d}_{,\beta}\right)\\
\overset{0}{\varepsilon}_{\alpha 3}&=\frac{1}{2}\left(\bar{\boldsymbol{x}}_{,\alpha}\cdot\bar{\boldsymbol{d}}-\boldsymbol{x}_{,\alpha}\cdot\boldsymbol{d}\right)\\
\overset{1}{\varepsilon}_{\alpha 3}&=\frac{1}{2}\left(\bar{\boldsymbol{d}}_{,\alpha}\cdot\bar{\boldsymbol{d}}-\boldsymbol{d}_{,\alpha}\cdot\boldsymbol{d}\right).
\end{aligned} \tag{3}$$

Here ζ denotes the thickness coordinate and an overbar indicates the deformed configuration. Due to thinness of the regarded plates and shells the components $\overset{2}{\varepsilon}_{\alpha\beta}$ and $\overset{1}{\varepsilon}_{\alpha 3}$ are neglected.

There are no kinematical restrictions with respect to the range of rotations. The director is assumed to be inextensible and the rotations are parameterized with the Rodriguez formulation. In order to overcome various types of locking, the ANS procedure suggested by Bathe & Dvorkin (1985), Hughes & Tezduyar (1981) combined with EAS (Lentzen (2009)) has been used.

2.1 *Electric potential distribution*

For this finite element, the electric potential is assumed to vary quadratically through the thickness by introducing three electrical degrees of freedom per layer

$$\varphi(\zeta)=\overset{0}{\varphi}+\zeta\overset{1}{\varphi}+\zeta^2\overset{2}{\varphi} \tag{4}$$

where φ denotes the electric potential.

The above mentioned electrical degrees of freedom are converted into the electric potential on the lower electrode, in the middle of the piezoelectric layer and on the top electrode, respectively, denoted by $\bar{\varphi}$, $\overset{m}{\varphi}$ and $\overset{+}{\varphi}$. The conversion is performed by inverting the following matrix-vector representation of the boundary conditions.

$$\begin{Bmatrix}\bar{\varphi}\\ \overset{m}{\varphi}\\ \overset{+}{\varphi}\end{Bmatrix}=\begin{pmatrix}1 & \bar{\zeta} & \bar{\zeta}^2\\ 1 & \overset{m}{\zeta} & \overset{m}{\zeta}^2\\ 1 & \overset{+}{\zeta} & \overset{+}{\zeta}^2\end{pmatrix}\begin{Bmatrix}\overset{0}{\varphi}\\ \overset{1}{\varphi}\\ \overset{2}{\varphi}\end{Bmatrix} \tag{5}$$

leading to

$$\begin{Bmatrix}\overset{0}{\varphi}\\ \overset{1}{\varphi}\\ \overset{2}{\varphi}\end{Bmatrix}=\frac{1}{k_1}\begin{pmatrix}\overset{m}{\zeta}\overset{+}{\zeta}t_1 & -\bar{\zeta}\overset{+}{\zeta}t_2 & -\overset{m}{\zeta}\bar{\zeta}t_3\\ \left(\overset{+}{\zeta}+\overset{m}{\zeta}\right)t_3 & \left(\overset{+}{\zeta}+\bar{\zeta}\right)t_2 & \left(\overset{m}{\zeta}+\bar{\zeta}\right)t_3\\ t_1 & -t_2 & -t_3\end{pmatrix}\begin{Bmatrix}\bar{\varphi}\\ \overset{m}{\varphi}\\ \overset{+}{\varphi}\end{Bmatrix} \tag{6}$$

$$\text{where } k_1=-\overset{m}{\zeta}\overset{+}{\zeta}t_1-\overset{+}{\zeta}\bar{\zeta}t_2-\bar{\zeta}\overset{m}{\zeta}t_3, \tag{7}$$

$$t_1=\left(\overset{+}{\zeta}-\overset{m}{\zeta}\right),\ t_2=\left(\overset{+}{\zeta}-\bar{\zeta}\right),\ t_3=\left(\bar{\zeta}-\overset{m}{\zeta}\right). \tag{8}$$

2.2 *Constitutive equations*

The mechanical and electrical quantities are coupled to each other by two linear constitutive relations describing the direct and the converse piezoelectric effect, respectively,

$$\begin{aligned}
\{D\}&=[e]\{\varepsilon\}+[\delta]\{E\}\\
\{S\}&=[c]\{\varepsilon\}-[e]^T\{E\}
\end{aligned} \tag{9}$$

where $\{S\}$ denotes the stress vector, $\{\varepsilon\}$ the strain vector, $\{D\}$ the electric displacement vector and $\{E\}$ the electric field vector:

$$\{S\}=\begin{Bmatrix}\sigma_{11}\\ \sigma_{22}\\ \tau_{12}\\ \tau_{23}\\ \tau_{13}\end{Bmatrix},\{\varepsilon\}=\begin{Bmatrix}\varepsilon_{11}\\ \varepsilon_{22}\\ 2\varepsilon_{12}\\ 2\varepsilon_{23}\\ 2\varepsilon_{13}\end{Bmatrix} \qquad (10)$$

$$\{D\}=\begin{Bmatrix}D_1\\ D_2\\ D_3\end{Bmatrix} \text{ and } \{E\}=\begin{Bmatrix}E_1\\ E_2\\ E_3\end{Bmatrix}.$$

Further $[\mathrm{e}]=[d][c]$ and $[\mathrm{e}]^T=[c][d]^T$, where $[c]$ denotes the elasticity matrix for anisotropic material, $[d]$ the piezoelectric constant matrix and $[\delta]$ the dielectric constant matrix

$$[c]=\begin{bmatrix}c_{11}&c_{12}&c_{13}&0&0\\ c_{12}&c_{22}&c_{23}&0&0\\ c_{13}&c_{23}&c_{32}&0&0\\ 0&0&0&c_{44}&c_{45}\\ 0&0&0&c_{45}&c_{55}\end{bmatrix}=\begin{bmatrix}[C_1]&0\\ 0&[C_2]\end{bmatrix}, \qquad (11)$$

$$[d]^T=\begin{bmatrix}0&0&d_{31}\\ 0&0&d_{31}\\ 0&0&0\\ 0&d_{15}&0\\ d_{15}&0&0\end{bmatrix} \text{ and } [\delta]=\begin{bmatrix}\delta_{11}&0&0\\ 0&\delta_{22}&0\\ 0&0&\delta_{33}\end{bmatrix}.$$

2.3 *Variational formulation*

The finite element developed by Lentzen (2009) is based on the shell element of Gruttmann & Wagner (2006) and extended with the electromechanical coupling. In the present element a displacement based variational principle is chosen in order to reduce the number of internal variables. The variational formulation reads

$$\int_V \left(\boldsymbol{S}:\delta\boldsymbol{\varepsilon}-\boldsymbol{D}\cdot\delta\boldsymbol{E}\right)dV=\int_A\left(\boldsymbol{T}\cdot\delta\boldsymbol{\upsilon}+Q\,\delta\varphi\right)dA +\int_V\left(\rho(\boldsymbol{b}-\ddot{\boldsymbol{\upsilon}})\right)\cdot\delta\boldsymbol{\upsilon}\,dV \qquad (12)$$

where S is the second Piola-Kirchhoff stress tensor, D is the electric displacement vector, $\boldsymbol{\varepsilon}$ is the Green-Lagrange strain tensor, E is the electric field vector, $\delta\boldsymbol{\upsilon}$ is the virtual displacement vector, T is the traction vector on the boundary, Q is the surface related charge density, ρ is the mass density, b is the body force density and $\ddot{\boldsymbol{\upsilon}}$ is the acceleration vector. Here a total Lagrangian approach is adopted.

The variation of the Green-Lagrange strain tensor components are

$$\begin{aligned}\delta\overset{0}{\varepsilon}_{\alpha\beta}&=\frac{1}{2}\left(\delta\bar{\boldsymbol{x}}_{,\alpha}\bullet\bar{\boldsymbol{x}}_{,\beta}+\bar{\boldsymbol{x}}_{,\alpha}\bullet\delta\bar{\boldsymbol{x}}_{,\beta}\right)\\ \delta\overset{1}{\varepsilon}_{\alpha\beta}&=\frac{1}{2}\left(\delta\bar{\boldsymbol{x}}_{,\alpha}\bullet\bar{\boldsymbol{d}}_{,\beta}+\delta\bar{\boldsymbol{x}}_{,\beta}\bullet\bar{\boldsymbol{d}}_{,\alpha}+\bar{\boldsymbol{x}}_{,\alpha}\bullet\delta\bar{\boldsymbol{d}}_{,\beta}+\bar{\boldsymbol{x}}_{,\beta}\bullet\delta\bar{\boldsymbol{d}}_{,\alpha}\right) \qquad (13)\\ \delta\overset{0}{\varepsilon}_{\alpha 3}&=\frac{1}{2}\left(\delta\bar{\boldsymbol{x}}_{,\alpha}\bullet\bar{\boldsymbol{d}}+\bar{\boldsymbol{x}}_{,\beta}\bullet\delta\bar{\boldsymbol{d}}\right).\end{aligned}$$

with $\bar{x}=x+\upsilon$, it follows that $\delta\bar{x}_{,\alpha}=\delta\upsilon_{,\alpha}$. The variation of the director and its linearization developed by Gruttman & Wagner (2006) has been used.

2.4 *The system matrices and vectors*

The electric field is assumed to be homogeneous over the electrode and exists only in transverse direction. In addition to the mechanical degrees of freedom at each node, three electrical degrees of freedom have to be introduced per electrode pair.

After introducing the shape functions to interpolate mechanical and electrical quantities, the generalised displacements $\{q\}$ and electric potential $\{\varphi\}$, integrated constitutive matrices $[H_1]$ for the elastic material, $[H_2]$ for the piezoelectric constants, $[H_3]$ for the dielectric constants, and the following set of equations can be derived on element level from the variational formulations

$$\begin{bmatrix}[M_{qq}]&0\\ 0&0\end{bmatrix}^e\begin{Bmatrix}\{\ddot{q}\}\\ \{\ddot{\varphi}\}\end{Bmatrix}^e +\begin{bmatrix}[K_{qq}]&[K_{q\varphi}]\\ [K_{\varphi q}]&[K_{\varphi\varphi}]\end{bmatrix}^e\begin{Bmatrix}\{\Delta q\}\\ \{\Delta\varphi\}\end{Bmatrix}^e=\begin{Bmatrix}\{f_q\}\\ \{f_\varphi\}\end{Bmatrix}^e \qquad (14)$$

where

$$\begin{aligned}[K_{qq}]^e&=[K^\sigma]^e+\int_{\Omega^e}[B_q]^T[\mathrm{H}_1][B_q]\,d\Omega,\\ [K_{q\varphi}]^e&=[K_{\varphi q}]^{eT}=\int_{\Omega^e}[B_q]^T[\mathrm{H}_2][B_\varphi]\,d\Omega, \qquad (15)\\ [K_{\varphi\varphi}]^e&=\int_{\Omega^e}[B_\varphi]^T[\mathrm{H}_3][B_\varphi]\,d\Omega.\end{aligned}$$

The incremental stiffness matrix $[K_{qq}]$ is the only matrix containing the geometrical nonlinear stiffness $[K^\sigma]$. Further $[K_{q\varphi}]$ denotes the electromechanical coupling matrix, $[K_{\phi\varphi}]$ is the piezoelectric capacity matrix, $[M_{qq}]$ is the mass matrix, $\{f_q\}$ is the vector containing the nodal forces, moments and in-balance forces, $\{f_\varphi\}$ is the vector containing the nodal charges and in-balance charges, $[B_q]$ is the strain-displacement matrix and $[B_\varphi]$ is the electric field matrix.

3 NUMERICAL EXAMPLES

3.1 *Angle-ply cylindrical shell subjected to impulsive internal pressure*

This numerical example deals with a two layer angle-ply [−45°/45°] clamped cylindrical shell as shown in Figure 2 subjected to impulsive internal pressure in form of a step load. The material properties of the shell are taken as $E_{11} = 7.5e6$ psi, $E_{22} = 2.0e6$ psi, $\nu_{12} = 0.25$, $G_{12} = G_{13} = G_{23} = 1.25e6$ psi, $\rho = 1.0\,\text{lb} \cdot \text{s}^2/\text{in}^4$.

Here, simulations of the dynamic behavior of the cylindrical shell corresponding to two different finite element methods, FOSD MRT and FOSD FRT are carried out. Following Reddy & Chandrashekara (1985), for this example, one quadrant of the shell was modeled. An equivalent density of nodes and the Newmark method was used in both FOSD FRT and FOSD MRT theories.

Figure 3 shows the predictions of deflections at the center of the shell with different time steps for both theories. The present results are compared with those given in the existing literature by Reddy & Chandrashekara (1985) using FOSD RVK theory. Figure 4 and 5 show the velocity and accelerations of the cylindrical shell at the center, respectively. It can be observed that the responses predicted by FOSD FRT, MRT and RVK are remarkably different from each other.

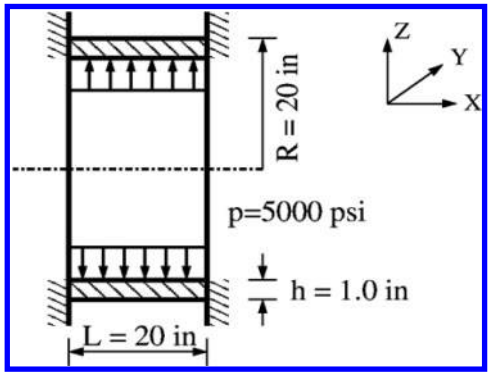


Figure 2. Clamped angle-ply cylindrical shell.

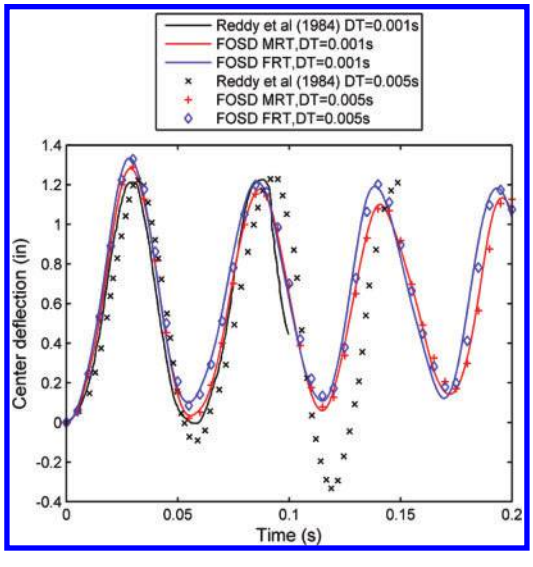


Figure 3. Center deflection of the clamped cylindrical shell.

3.2 *Two edge simply supported piezolaminated composite plate*

The numerical example considered here is the two sides hinged composite piezolaminated plate as shown in Figure 6. The transient behavior of the structure is simulated when an input voltage in form of a harmonic

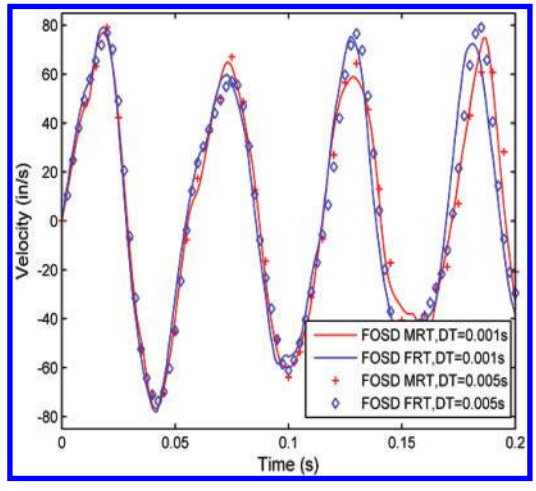


Figure 4. Velocity at the center of the clamped cylindrical shell.

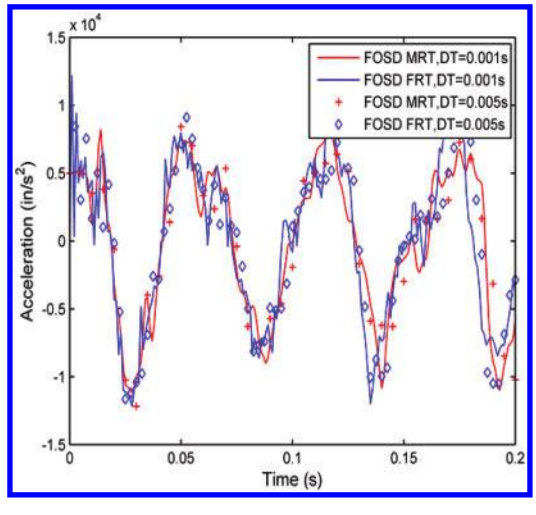


Figure 5. Acceleration at the center of the clamped cylindrical shell.

time function is applied to the two actuator layers. The middle layer is a graphite-epoxy T300/976 layer with the fiber orientation of 90° covered by two PZT G1195 layers.

The in-plane dimensions are 40×40 mm. The thickness of the PZT layers is 0.15 mm each and that of the composite layer is 0.2 mm. The material properties of the graphite-epoxy are taken as $E_{11} = 150$ GPa, $E_{22} = 9$ GPa, $\nu_{12} = \nu_{23} = 0.3$, $G_{12} = 7.1$ GPa, $\rho = 3.95$ g/cm^3 and those of the PZT are taken as $E = 63$ GPa, $\nu = 0.3$, $e_{31} = 2.286$e-05 Cmm^{-2}, $\rho = 7.85$ g/cm^3.

Here, the actuator layers are subjected to electric voltage in sine form with the amplitude of 300 V and a frequency of 100 Hz. The PZT layers are oppositely polarized, which results in moments that are uniformly distributed over the edges of the piezolayers. The response at the mid-point of the structure is observed over a time period of 0.05 s. The linear and nonlinear predictions of FOSD FRT are obtained by the Newmark method with a time step 10^{-5} s. From Figure 7, it can be seen that both the linear and nonlinear prediction of the dynamic response of the structure yield oscillations driven at the frequency of excitation. The amplitudes predicted by the nonlinear simulation are lower than those of the linear simulation because of the stress stiffening due to the von Kármán effect in the geometrically nonlinear range of deformation.

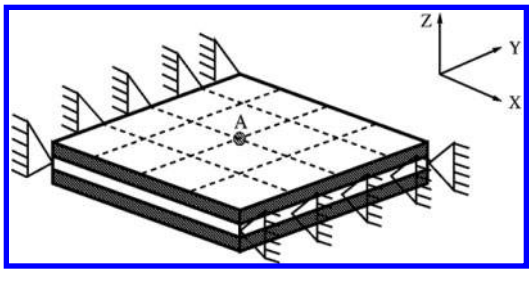


Figure 6. Two edge simply supported piezolaminated plate.

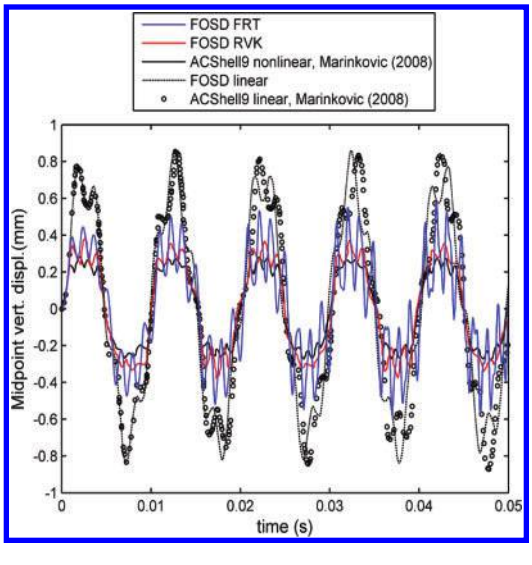


Figure 7. Mid-point vertical displacement to harmonic electric excitation.

The present predictions (FOSD FRT) are compared to those in the existing literature given by Marinković et al. (2009), in which a degenerated 9-node active shell element (ACShell9) obtained through the degeneration process from a 27-node solid element was used and by Vu & Schmidt (2011), in which FOSD RVK theory was used. The amplitudes predicted by FOSD FRT are much higher than those obtained by the degenerated element.

4 CONCLUSIONS

In this paper, large amplitude vibrations of a two layered angle-ply composite cylindrical shell with impulsive internal pressure and a two edges simply supported piezolaminated plate with harmonic electric excitation have been examined by different nonlinear models (FOSD FRT, FOSD MRT). The present simulations show that due to the thinness of the considered smart structures FRT is necessary in many cases.

REFERENCES

Bathe, K.J. & Dvorkin, E. 1985. A 4-node plate bending element based on Mindlin/Reissner theory and a mixed interpolation. *Int. J. Num. Meth. Eng.* 21: 367–383.

Ganapathi, M. & Vardhan, T.K. 1996. Large amplitude vibrations of circular cylindrical shells. *Journal of Sound and Vibration* 192: 1–14.

Gruttmann, F. & Wagner, F. 2006. Structural analysis of composite laminates using a mixed hybrid shell element. *Computational Mechanics* 37: 479–497.

Habip, L.M. 1965. Theory of elastic shells in the reference state. *Ing.-Archiv* 34: 228–237.

Hughes, T.J.R. & Tezduyar, T.E. 1981. Finite elements based upon Mindlin plate theory with reference to the four-node isoparametric element. *Int. J. Num. Meth* 48: 587–596.

Khdeir, A. A., Reddy, J. N., & Frederick, D. 1989. A study of bending, vibration and buckling of cross-ply circular cylindrical shells with various shell theories. *International Journal of Engineering Science* 27(11): 1337–1351.

Klosowski, P., Schmidt, R. & Reddy, J.N. 1996. Nonlinear transient analysis of composite laminates undergoing moderate rotations. *Journal of Applied Mathematics and Mechanics* 76: 369–372.

Kreja, I. & Schmidt, R. 1997. Finite elements based on a first-order shear deformation theory with applications to the analysis of composite structures. *Int. J. Nonlinear Mech.* 32: 1123–1142.

Lentzen, S., Klosowski, P. & Schmidt, R. 2007. Geometrically nonlinear finite element simulation of smart piezolaminated plates and shells, *Smart Mater. Struct.* 16: 2265–2274.

Lentzen, S. & Schmidt, R. 2005a. Nonlinear finite element modleing of vibration control of piezolaminated composite plates and shells. *Smart Structures and Materials: Damping and Isolation; Proc. of SPIE,* Bellingham, WA (USA): paper 5716–16.

Lentzen, S. & Schmidt, R. 2005b. Large amplitude vibrations and model sensing of intelligent thin piezolaminated structures. *Proc. of 6 th European Conference on Structural Dynamics*, Paris , France: 1569–74.

Lentzen, S. 2009. Nonlinearly coupled thermopiezoelectric modelling and FE simulation of smart structures, *PhD Thesis, RWTH Aachen University, Fortschritt-Berichte VDI* 20: 419.

Marinković, D., Köppe, H. & Gabbert, U. 2009. Aspects of modeling piezoelectric active thin-walled strucutres. *Journal of Intelligent Material Systems and Structures*: 1835–1844.

Mukherjee, A. & Chaudhary, A.S. 2005. Nonlinear dynamic response of piezolaminated smart beams, *Computers and Strucutres* 83: 1289–1304.

Palmerio, A.F., Reddy, J.N. & Schmidt, R. 1990. On a moderate rotation theory of elastic anisotropic shells. *Part 1: th*eory, *Part 2: FE analysis . Int. J. Non. Mech.* 25: 687–714.

Pellicano, F., Amabilli, M. & Paidoussis, M.P. 2002. Effect of geometry on nonlinear vibration of circular cylindrical shells, *Int. J. Non. Mech.* 37: 1181–1198.

Reddy, J.N. & Chandrashekara, K. 1985. Geometrically nonlinear transient analysis of laminated, doubly curved shells. *Int. J. Nonlinear Mech*. 20(2): 79–90.

Reddy, J.N. 1983. Geometrically nonlinear transient analysis of laminated composite plates. *AIAA Journal* 21: 621–629.

Sansour, C., Wriggers, P. & Sansour, J. 1997. Nonlinear dynamics of shells: theory, finite element formulation, and integration schemes. *Nonlinear Dynamics* 13: 279–305.

Schmidt, R. & Reddy, J.N. 1988. A refined small strain and moderate rotation theory of elastic anisotropic shells, *ASME J. Appl. Mech.* 55: 611–617.

Schmidt, R. & Vu, T.D. 2009. Nonlinear dynamic FE simulation of smart piezolaminated structures based on first- and third-order transverse shear deformation theory, *Advanced Materials Research*: 1313–1316.

Schmidt, R. Tiranasavasdi, S. & Vu, T.D. 2010. Finite rotation finite element analysis of layered composite plates and shells. *Advance and Trends in Structural Engineering, Mecahncis and Computation (Ed. Zingoni),* Capetown: 481–486.

Vu, T.D. & Schmidt, R. 2011. Nonlinear transient FE analysis of piezolaminated structures. *82 nd Annual meeting of International Assocaition of Applied Mathematics and Mechanics (GAMM),* Graz, 11(1): 297–298.

Vu, T.D. 2011. Geometrically nonlinear higher-order shear deformation FE analysis of thin-walled smart structures. *PhD Thesis, RWTH Aachen University.*

Yi, S., Ling, S.F. & Ying, M. 2000. Large deformation finite element analyses of composite structures integrated with piezoelectric sensors and actuators. *Finite Elem. Anal. Des.* 35: 1–15.

Research and Applications in Structural Engineering, Mechanics and Computation – Zingoni (Ed.)
© 2013 Taylor & Francis Group, London, ISBN 978-1-138-00061-2

Simplified modelling of stiffened panels for simultaneous static and dynamic optimisation

L. Weiß, H. Köke & C. Hühne
Institute of Composite Structures and Adaptive Systems,
DLR German Aerospace Center, Braunschweig, Germany

ABSTRACT: In this paper a novel simplified structural modelling approach for stiffened panels is presented. It specifically addresses structural response of aircraft fuselage components made from Carbon Fibre Reinforced Plastics (CFRP). The proposed method considers structural modelling requirements necessary for structural optimisation with respect to system response under simultaneous static and dynamic loads. The standard explicit Finite Element (FE) solver LS-Dyna is utilised, providing the framework to regard statics and dynamics as well as non-linearities by material, large deformation and contact. The simplified model is fundamentally composed of shell, beam, and discrete elements. Simulating the structural collapse behaviour of thin-walled CFRP sections under bending load the detailed model provides input parameters for the discrete elements. Furthermore, skin-frame-interaction attributes immanent to the present fuselage configuration are reviewed and considered by idealised deformation characteristics. Finally, the present approach is verified through analyses of the detailed model. The results illustrate the benefits of model simplification. Replacing detailed shell model features by beam and non-linear spring elements significantly reduces computational effort. At the same time the accuracy deduction is acceptable considering topological optimisation requirements.

1 INTRODUCTION

Research and technology projects on aircraft fuselage pursue the application of lightweight materials to endeavour improved structural efficiency. Especially thermoset fibre reinforced plastics (FRPs) comply with the designer's need for excellent specific material properties. Structural designs applying such composite materials need to satisfy the authorities airworthiness code for 'equivalent level of safety' EASA (2003).

Due to plastic deformation capacity of state-of-the-art metallic fuselage designs, those certification requirements are achieved almost naturally by the design's intrinsic energy absorption capabilities. In contrast to metallic materials, thermoset FRPs exhibit brittle fracture behaviour when loaded beyond their elastic limits. Thus energy absorption by plastic deformation is unsatisfactory limited. Considering FRP constitutive non-linearities in dynamic loading conditions at early design stages, however, induce alternative principles of energy absorption.

At early design stages only static or quasi-static loads are accounted for in the structural layout. If at all, common engineering practice simplifies dynamic loading conditions for consideration in the initial phase of the design process. Such, dynamic structural behaviour (e.g. energy absorption characteristics) of composite design is an inappropriate result of static structural layout. This suggests that composite fuselage design requires simultaneous consideration of static and dynamic loading conditions at the preliminary design stage. An appropriate optimisation procedure is essential for determining an efficient structural layout. Following Eschenauer (2006) the proposed optimisation scheme depicted in figure 1 consists of three constituents: a structural analysis, an optimisation model, and an optimisation algorithm.

A typical approach of structural optimisation for severe dynamic objectives applies a detailed continuum FE model in association with metamodelling schemes as studied in Fang et al. (2005). Usually, the required detailed continuum FE model is not available in the initial phase of the design process. Alternatively discrete modelling techniques are applied. Appropriate representation of the governing collapse mode is their uniting feature. Analytical or hybrid modelling has been proposed by Wittlin and Lackey (1983) in order to obtain floor pulse characteristics of transport aircraft in hard landings. To represent the response to severe dynamic load of a metallic frontal impact structure of a car Lust (1992) and Hamza and Saitou (2005) apply spring-mass-models for sizing optimisation. Multibody modelling with rigid-flexible links is used by Ambr'osio and Dias (2007) for road vehicles and Pereira et al. (1997) for train vehicles. In the later case shape optimisation is carried out based on the structural response. Discrete modelling for topology optimisation is developed by Pedersen (2004) for metallic structures, and by Hajela and Lee (1997) and Bisagni et al. (2002) for composite structures respectively. Recently, Waimer et al. (2010) developed

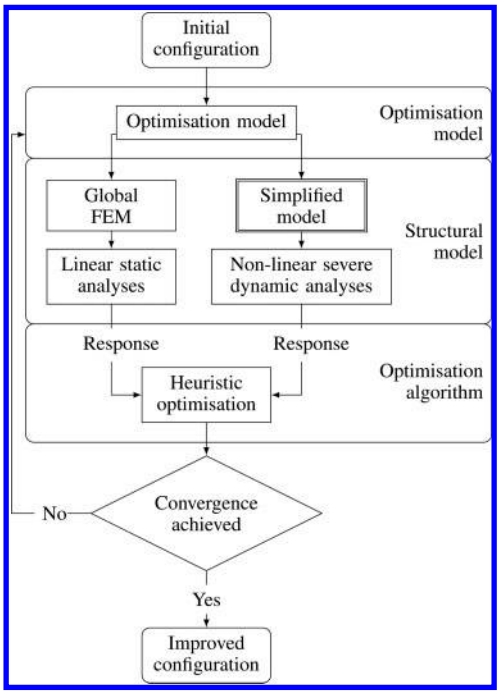


Figure 1. Optimisation scheme indicating the relevance of simplified modelling.

a method placing macro elements within a fuselage shell model to obtain the kinematic response of fuselage cross sections subjected to typical severe dynamic loads.

Most promising, however, appears the simplified modelling approach suggested by Liu and Day (2008) with respect to the obtained accuracy in relation to the computation time saved. It is verified for aluminium frame structures based on analytical formulations of plastic hinge development in impact loaded structures. Nevertheless, it contains inspiring features such as adjustable non-linear springs.

Yet, current discrete modelling techniques are applied either to metallic structures forming plastic hinges due to bending deformation or to axially loaded composite structures. In this paper a novel simplified structural modelling approach for stiffened CFRP panels is presented. As such it classifies in between spring-mass models and kinematic models.

Reconsidering the integration of the simplified modelling technique within the proposed topological optimisation scheme, the requirements remain open.

In essence there are two essential prerequisites:

1. elapsed computer time per calculation less than 60 seconds
2. less than 20% deviation on severe dynamic indicees such as displacement or energy absorption.

Where displacement implies significance on collapse mechanism and deformation pattern prediction, energy absorption indicates the suitability of an obtained solution.

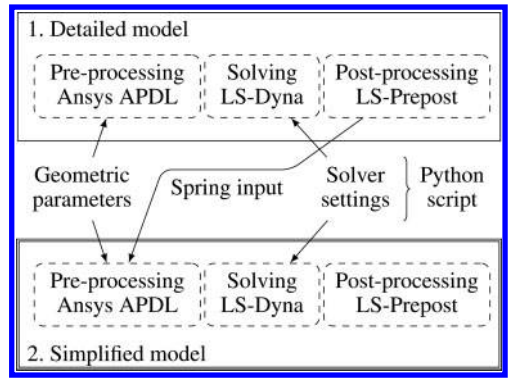


Figure 2. Shared data and data handling between models.

With the optimisation framework set, the aim of this paper is to propose a simplified modelling approach for stiffened CFRP panels. The following sections will guide the reader starting from the analysis of a detailed model via the examination of the governing collapse mechanism to the derivation of discrete element characteristics. This data is put forward to the simplified model as depicted in figure 2. Results of relevant indices are compared for both models before conclusions on the proposed modelling scheme complete this paper.

2 DETAILED MODEL

The detailed model describes a generic arrangement of aircraft composite fuselage design. The modelled section features a skin, stringers (longitudinal supports), frame (circumferential supports), and the interconnecting clips. It represents a 6° angular sector of an 650 mm wide circular configuration with 1800 mm radius. Such, it features roughly 16.5k elements. Except the aluminium rivets, the model entirely consists of CFRP components.

The corresponding material properties for standard aluminium (MAT1) and T700 carbon fibre/2510 epoxy prepreg (MAT54) are summarised in table 1 as published in Feraboli et al. (2011). Shells of type Belytschko-Tsay (ELFORM 2) are used to mesh the mid-surface geometry with an average size of 10 mm element edge length. Shell elements on the clip geometry are refined to an average edge length of 5 mm. Table 2 shows the stacking sequences and respective section properties of the individual parts. Beam elements of type Hughes-Liu (ELFORM 1) of 5 mm diameter are in place to connect the clips with the frame and the skin which are actually riveted. For the present approach rivet failure is assumed of negligible influence for the global deformation pattern, as will be shown later. Thus, an idealised modelling is applied using a solid circular cross-section with linear elastic properties.

However, as large deformations are considered parts may get in contact during the featured calculation time. Thus, three different contact definitions are

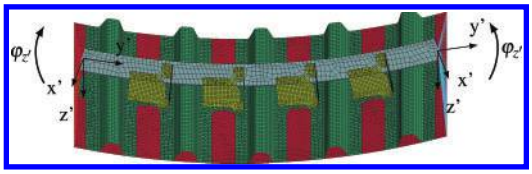


Figure 3. Detailed model with its constituents: skin (red), stringer (green), frame (grey), clips (yellow), and nodal rigid bodies on either side.

Table 1. Material properties of aluminium and CFRP. Subscripts T and C denote tension and compression respectively.

Property	Symbol	Value
Aluminium		
Density	ρ_{Alu}	2.78 g/cm^3
Modulus	E	70.0 GPa
Poisson's ratio	ν	0.33 –
CFRP		
Density	ρ_{CFRP}	1.52 g/cm^3
Modulus in 1-direction	E_1	127.00 GPa
Modulus in 2-direction	E_2	8.41 GPa
Shear modulus	G_{12}	4.21 GPa
Minor Poisson's ratio	ν_{21}	0.02049 –
Strength in 1-direction	X_T	2200.0 MPa
Strength in 1-direction	X_C	1470.0 MPa
Strength in 2-direction	Y_T	48.9 MPa
Strength in 2-direction	Y_C	199.0 MPa
Shear strength	S_{12}	154.0 MPa
Cured ply thickness	t	0.1667 mm

Table 2. Stacking sequences and resulting laminate thickness for individual parts ($[]_S$ denotes symmetry plane).

Part	Stacking sequence	Thickness mm
Skin	[45/-45/0/90/-45/45/90/0/-45/45]	1.667
Stringer	$[45/-45/0/90]_S$	1.334
Frame	[45/-45/0/90/-45/45/90/0/-45/45]	1.667
Clip	[45/-45/0/90/-45/45/90/0/-45/45]	1.667

set between the individual parts. First, stringers are tied to the skin with a TIED_NODES_TO_SURFACE algorithm. Second, AUTOMATIC_SURFACE_TO_SURFACE contacts are established between clip and frame, clip and stringer as well as frame and stringer. And third, an AUTOMATIC_SINGLE_SURFACE contact is defined in case of frame failure and subsequent shell contact under large deformations.

Nodal rigid bodies are utilised to apply boundary conditions to the near and far end of the modelled section. The boundary conditions are defined with respect to local coordinate systems (see figure 3). The near end is fixed in all degrees of freedom (DOFs) except the rotation about the local z-axis where a rotational displacement of 2.75° is prescribed as shown in figure 4. The same applies to the far end except the nodal rigid body is allowed to displace freely across the local y-z-plane. Furthermore, the nodes along the curved free

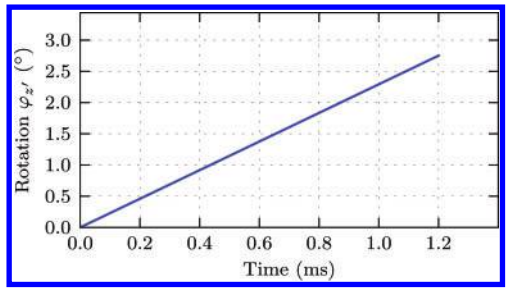


Figure 4. Prescribed rotational displacement applied at both ends of the section.

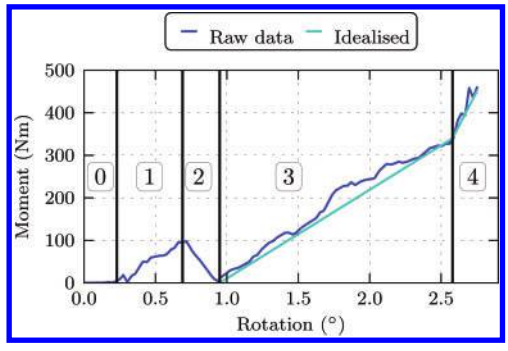


Figure 5. Bending moment about global z-axis vs. rotation response of frame section. The cyan curve shows the idealised spring characteristic used for model simplification. Numbers 0–4 denote stages as described in section 3.

edges of the skin and stringer shells are fixed in the global z-direction.

3 COLLAPSE MECHANISM

Due to the curved shape and the rotational displacement applied the frame is under compression forming a closing hinge. Closing hinge describes a deformation pattern where the curvature of a the structure increases upon load application. In total, five stages are determined in the evolution of the deformation mechanism as emphasised in figure 5.

(0) As the results are obtained from an explicit calculation with a time integration scheme, time elapses in the 'initial stage' until the entire structure is loaded. Since the section for response retrieval is located at central position (see figure 6) the far ends have already been rotated before a bending moment is obtained.

(1) In the 'elastic stage' the fuselage section deforms in a linear elastic manner with the frame displacing towards the skin. Therefore, the clips are under compression transferring the load onto the skin, which locally deforms.

(2) As the calculation progresses beyond 0.69° rotation the 'twisting stage' is initiated, with the clip walls starting to deform out-of-plane allowing the frame to twist and bend out of its initial planar shape. This distortion is eventually restrained by the clips holding the frame back.

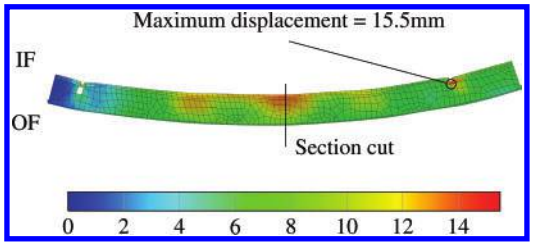


Figure 6. Contours of resultant displacement in global coordinates of frame. Element deletion indicates material failure progressing from inner flange (IF) radius towards outer flange (OF). The left side is globally constrained.

(3) In the 'buckling stage' the overall deformation increases resulting in local buckling on the inner flange of the frame (see figure 6). Induced by the inner flange buckling the frame's web and outer flange buckle locally. Deformation continues until the initial clearance between frame and stringer is entirely closed and the parts are getting in contact, with the frame then partially resting on the stringer.

(4) At 2.58° rotation the 'failure stage' of the progressing collapse mechanism is reached. It culminates in material failure initiation at the inner flange radius and failure progression towards the frame's web.

However, the observed deformation pattern is entirely based on relative part stiffness. The collapse mechanism outlined is only true for the geometry, material properties, and boundary conditions specified. With one of them being subject to modification different collapse modes may be observed.

4 DISCRETE ELEMENT CHARACTERISTICS

For the simplified modelling it is crucial to determine representative discrete element characteristics. In order to obtain those the frame and the clips are examined in detail. The section plane functionality in LS-Prepost assists that approach. It is used to perform section cuts of the model for analysis. The section cuts are fixed to the model and not fixed in space which is important when large deformations are present. Such, the bending moment of the frame is used to define the behaviour of rotational springs, and the axial forces of the clip are obtained to specify the performance of discrete beams.

The rotational spring characteristic is directly derived from figure 5. The response of stages 3 and 4 is idealised by a bi-linear law representing the bending moment vs. rotation characteristic. The first part is governed by the frame deformation whereas the increased stiffness of the second part results from the frame getting in contact with the stringers.

The discrete beam input for the frame-skin-interaction is evaluated locally at the clips. The axial force components are then applied to the respective DOF of the discrete beam. The graphs in figure 7 depict the idealised piecewise linear laws. The relation in x-direction is extended in order to account for

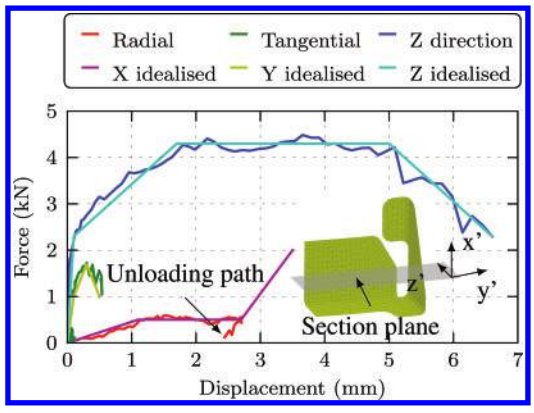


Figure 7. Force vs. displacement characteristics for the clip obtained from the detailed model. The lighter colours denote the idealised representatives forwarded to the simplified model.

the contact between frame and stringer as described in stage three of the collapse mechanism. As a first assumption the contact stiffness is estimated to be equal to the modulus of the curve's unloading part.

As the idealised relations are obtained from resultant responses they are defined in the first quadrant. This, however, describes the response to tensile load only. To account for compressive loading, all idealised relations are extended into the third quadrant by symmetry operation to the point of origin.

5 SIMPLIFIED MODEL

At early stages of the design process simplified modelling approaches are common practise. Inspired by the global finite element modelling technique (GFEM) applied in aircraft industry the proposed method uses beam and shell elements. Similar to the detailed modelling the shells are of type Belytschko-Tsay and the beams are of type Hughes-Liu. In addition, discrete beams replace the clips for translational coupling of frame and skin, as shown in figure 8. Different to the detailed model, the discrete elements are not located between the stringers but in fact share nodes with stringer beams. This modelling assumption is made to reduce number of elements to a minimum. Such, it features 43 elements only.

However, figure 9 illustrates the nodal coupling defined at the hinge positions. The DOFs of each individual node triple are coupled or conditioned according to table 3. The numerical code denotes $0 =$ free, $-1 =$ coupled, $1 =$ constrained, and $2 =$ fixed. Fixed and free refers to DOFs in global coordinates. Upper case *d* denotes the application of discrete beams (ELFORM 6, MAT119), whereas upper case *s* denotes the use of discrete springs (MATS04). Constrained describes a nodal constraint using the CONSTRAINED_NODE_SET keyword. Coupled refers to the application of discrete elements of either non-zero length for the translational springs coupling the frame to the skin or zero length for the translational

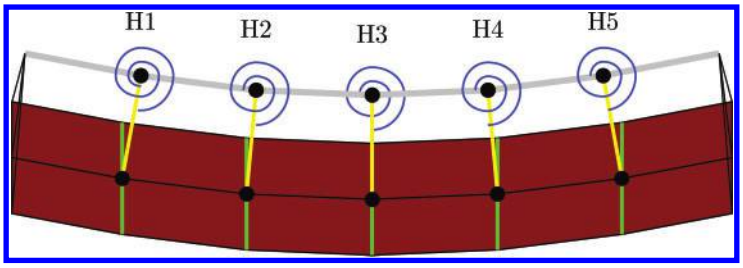


Figure 8. Simplified model with its constituents: skin (red), stringer (green), frame (grey), rotational springs (blue), discrete beams (yellow), and nodal rigid bodies on either side. H1-5 denote hinge positions.

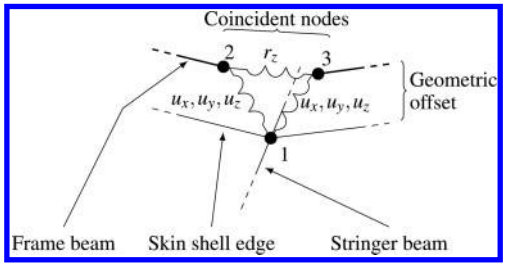


Figure 9. DOF coupling with discrete elements. Node numbering specified for interaction matrix 3.

Table 3. Interaction matrix for DOF coupling and conditioning. The numerical code reads as: free (0), coupled (−1), constrained (1), and fixed (2). Compare figure 9 for node numbering. -1^d denotes discrete beam and -1^s denotes spring element.

Global DOF		nodes 1-2	nodes 1-3	nodes 2-3
translation in x	u_x	-1^d	-1^d	1
translation in y	u_y	-1^d	-1^d	1
translation in z	u_z	-1^d	-1^d	1
rotation about x	r_x	0	0	2
rotation about y	r_y	0	0	2
rotation about z	r_z	0	0	-1^s

rotational non-linear springs acting between the frame nodes only.

In relation to the detailed model material properties and section definitions for the shell elements remain the same. In contrast linear elastic properties (MAT1) are assigned to the beam elements. It is assumed that all contribution to structural response beyond the elastic limit such as buckling and failure may be lumped in distinct positions evenly distributed along the frame. Hence, the sections in between act linear elastic. Yet, only homogenised properties may be specified in MAT1. The classical laminate theory (CLT) is used to obtain the desired properties according to Kollár and Springer (2003). For the stringer the elastic properties used are $E_{stringer} = 48.6$ GPa and $\nu_{stringer} = 0.314$. The elastic properties of the frame are $E_{frame} = 43.4$ GPa and $\nu_{frame} = 0.387$ accordingly.

Finally, with respect to the detailed model, nodal rigid bodies transfer the characterised boundary conditions to the structure.

Table 4. Comparison of results from both models.

Parameter	Detailed model	Simplified model	Difference (%)
Displ. global (mm)	7.02	6.85	2.5
Displ. hinge 5 (mm)	3.54	3.08	14.9
Displ. hinge 4 (mm)	3.54	3.29	7.6
Displ. hinge 3 (mm)	3.70	3.59	3.1
Displ. hinge 2 (mm)	3.51	3.67	4.4
Displ. hinge 1 (mm)	3.67	3.96	7.3
Absorbed energy (J)	125.8	159.1	20.9
Computer time (s)	2316	2	99.9

6 RESULTS AND COMPARISON

The results of this study are summarised in table 4. LS-Dyna version 971 in double precision mode is utilised for all calculations. The timing information provided are based on the usage of an dualcore i7 CPU M620 machine at 2.67 GHz with 4 CPUs specified for the calculation runs.

Comparing the computer time used for the solution of the detailed and simplified model significant savings are obvious.

Examining the timing information provided for the detailed model, the element processing holds about 92% and the contact algorithm about 7% of the total CPU time. Simplifying the model towards a minimal amount of elements and omitting contact definitions contributes substantially.

Displacements and energy absorption are relevant indices in severe dynamic structural response. Therefore the resultant displacement at the hinge positions as well as the global deformation are compared. Surveying all displacements, the discrepancies are indeed less then 15% which is well within the range initially specified. Figure 10 contains the chronological sequence of the overall displacement of both, the detailed and the simplified model which are in adequate agreement. This, however, proofs the assumption of lumping non-linear structural response in distinct positions right.

Comparing the overall energy absorption featured in figure 11 reveals moderate agreement. Between 3–5 mm global resultant displacement the energy response diverges. This displacement range coincides with the twisting stage outlined in section 3. Yet, the

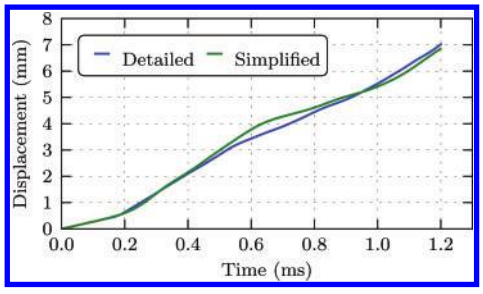


Figure 10. Comparison of the global resultant displacement at the nodal rigid body master nodes.

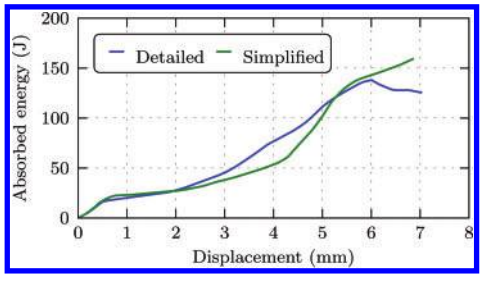


Figure 11. Comparison of overall energy absorption.

offset is recovered up to the failure stage where graphs separate again. The difference on energy absorption between the detailed and the simplified model is 20.9% at termination time. Although being more then initially sepcified, this offset is still acceptable considering the requirements of simultaneous static and dynamic optimisation. Hence, particular attention is to be paid on the failure stage with respect to further verification of the proposed method.

7 CONCLUSIONS

This paper established a novel simplified structural modelling approach for stiffened panels. The results illustrate the benefits of model simplification and findings are summarised as:

1. Representing skin-frame-interaction as well as collapse modes immanent to CFRP fuselage constituents by idealised deformation characteristics is a feasible approach.
2. All contribution to structural response beyond the elastic limit such as buckling and failure may be lumped in distinct positions evenly distributed along the frame.
3. Replacing detailed shell model features by beam and discrete elements significantly reduces computational effort. At the same time the accuracy deduction is acceptable considering system response optimisation requirements.

ACKNOWLEDGEMENTS

The authors wish to express their gratitude to AIRBUS Operations GmbH for supporting this work. The present work benefited from the input of Dr Dieter Hachenberg, Dr Lars Fiedler, and Mr Lars Margull who provided valuable assistance and thoughtful comments to the undertaking of the research summarised here.

REFERENCES

Ambrósio, J. & J. Dias (2007). A road vehicle multibody model for crash simulation based on the plastic hinges approach to structural deformations. *International Journal of Crashworthiness 12*(1), 77–92.

Bisagni, C., L. Lanzi, & S. Ricci (2002, March-April). Optimization of helicopter subfloor components under crashworthiness requirements using neural networks. *Journal of Aircraft 39*(2), 296–304.

EASA (2003). Certification specifications for large aeroplanes cs-25. European Aviation Safety Agency.

Eschenauer, H. A. (2006). Structural behaviour and optimal layout of light constructions. *Archive of Applied Mechanics 75*, 441–457.

Fang, H., M. Rais-Rohani, Z. Liu, & M. Horstemeyer (2005). A comparative study of metamodeling methods for multiobjective crashworthiness optimization. *Computers & Structures 83*, 2121–2136.

Feraboli, P., B. Wade, F. Deleo, M. Rassaian, M. Higgins, & A. Byar (2011). Ls-dyna mat54 modeling of the axial crushing of a composite tape sinusoidal specimen. *Composites Part A: Applied Science and Manufacturing 42*(11), 1809–1825.

Hajela, P. & E. Lee (1997). Topological optimization of rotorcraft subfloor structures for crashworthiness considerations. *Computers & Structures 64*(1–4), 65–76. Computational Structures Technology.

Hamza, K. & K. Saitou (2005, May). Design optimization of vehicle structures for crashworthiness using equivalent mechanism approximations. *Journal of Mechanical Design 127*, 485–492.

Kollár, L. P. & G. S. Springer (2003). *Mechanics of Composite Structures*. Cambridge University Press.

Liu, Y. & M. L. Day (2008). Bending collapse of thin-walled circular tubes and computational application. *Thin-Walled Structures 46*(4), 442–450.

Lust, R. (1992). Structural optimization with crashworthiness constraints. *Structural and Multidisciplinary Optimization 4*, 85–89.

Pedersen, C. (2004). Crashworthiness design of transient frame structures using topology optimization. *Computer Methods in Applied Mechanics and Engineering 193*(6-8), 653–678.

Pereira, M. S., J. A. C. Ambrósio, & J. P. Dias (1997). Crashworthiness analysis and design using rigid-flexible multibody dynamics with application to train vehicles. *International Journal for Numerical Methods in Engineering 40*(4), 655–687.

Waimer, M., D. Kohlgrüber, D. Hachenberg, & H. Voggenreiter (2010, October 25–28). The kinematics model – a numerical method for the developement of a crashworthy composite fuselage design of transport aircraft. In *Sixth triennial international aircraft fire and cabin saftey research conference*, Atlantic City, New Jersey.

Wittlin, G. & D. Lackey (1983, April). Analytical modeling of transport aircraft crash scenarios to obtain floor pulses. Contractor report 166089, Nasa.

Research and Applications in Structural Engineering, Mechanics and Computation – Zingoni (Ed.)
© 2013 Taylor & Francis Group, London, ISBN 978-1-138-00061-2

Finite element vibration analysis of pole structures made of advanced composite materials

G.-D. Kim & S.-Y. Lee
Department of Civil Engineering, Andong National University, Andong-Si, Gyeongsangbuk-Do, South Korea

ABSTRACT: The dynamic analysis of poles made of advanced composite materials is carried out for different length-thickness ratios and layup sequences. The numerical results using ABAQUS obtained for plates and shells are in good agreement with those reported by other investigators. The new results for laminated composite pole structures in this study mainly show the effect of the interactions between the radius-length ratio and other various parameters. The effect of fiber angles of long composite poles also investigated. Key observation points are discussed and a brief design guideline is given.

1 INTRODUCTION

With the advancement of technology in composite materials, applications of laminated composites to pole structures are advantageous because of their light weight, high specific stiffnesses and high specific strengths. However, laminated poles with a long length may result in a significant change of the dynamic characteristics during various external loading. Therefore, it is essential to study the effect of fiber angles and geometries simultaneously on the frequency of layered poles.

Numerous theories exist for laminated composite plates or structures. Many these theories were developed originally for thin shells and are based on the Kirchhoff-Love kinematic hypothesis (Sanders, 1963). However, these classical theories are inadequate to describe accurately the kinematic behavior of anisotropic composite shells. The first-order shear deformation theory (FSDT) has been extended by other investigators to deal with those problems (Kraus, 1967; Sanders, 1059; Zukas and Vinson, 1971). In general, a first order shear deformation theory can describe easily and accurately the kinematic behavior of a thin composite structure (Reddy, 2004). The composite pole types can be practically applied to wind turbine towers. Polyzois et al. (2009) studied static and dynamic characteristics of multi-cell jointed glass fiber-reinforced polymer (GFRP) wind turbine towers.

In this paper, we performed a finite element analysis based on FSDT to analyze the free vibration of laminated poles with a long length. Very little research has been studied to identify the interaction between vibrations and layup sequences for long composite pole type structures. The length-thickness ratio and layup sequence of laminated poles with different geometries could play a dominant role in determining and efficiently controlling the dynamic characteristics of the composite structure without causing a change in its material properties. Numerical examples are focused on the changes in natural frequencies for different radius-length ratios, layup sequences, shapes of the cross-section and interactions between these parameters.

2 BASIC THEORY

In the laminated structures, the stiffness properties are function of the normal coordinate. In Figure 1 a cross-section of laminated plate composed of N layers is presented. A linear elastic properties of the anisotropic layers are characterized by the tensor of elasticity C_{ijkl}. In many applications, it can be assumed that calculations of shell stiffness properties can be performed neglecting the differences in spatial and shell mid-surface metrics. In this case, the Hook's law for each layer can be written by

$$S_{ij} = C_{ijkl} E_{kl} \tag{1}$$

Since the present formulation is based on the natural coordinate reference frame, we introduce here an explicit transformation scheme between natural coordinates and the global coordinate system, to obtain a natural coordinate based constitutive equation. The stress tensor in the natural coordinate can be written as follows:

$$\tilde{S}_{ij} = \tilde{C}_{ijkl} \tilde{E}_{kl} = \tilde{J}_0 \mathbf{T} \tilde{D}_{ijkl} \mathbf{T}^{\mathrm{T}} \tilde{E}_{kl} \tag{2}$$

where $\tilde{J}_0$ is the determinant of the Jacobian matrix and $\tilde{D}_{ijkl}$ is the constitutive matrix for orthotropic materials with the material angle θ. The transformation matrix $\mathbf{T}$ in Eqation 2 is given by Han *et al.* (2004). The strain energy U can be expressed by

$$U = \frac{1}{2} \int_A \int_{-h/2}^{h/2} \tilde{C}_{ijkl} \tilde{E}_{ij} \tilde{E}_{kl} \, d\xi_3 \, dA \tag{3}$$

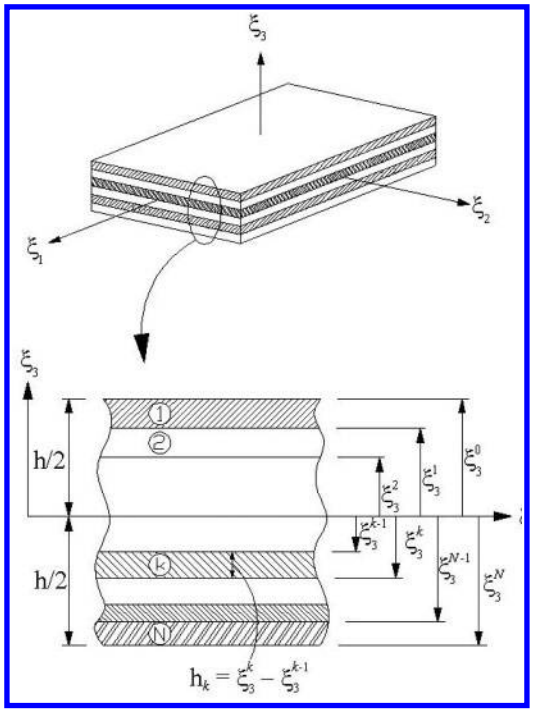


Figure 1. Cross-section of laminated plate composed of N layers.

After integration, throughout the thickness, the strain energy can be obtained in terms of shell quantities: stress resultants and couples and laminated shell stiffness characteristics

$$A_{\alpha\beta\gamma\delta}, B_{\alpha\beta\gamma\delta}, D_{\alpha\beta\gamma\delta} = \int_{-h/2}^{h/2} \tilde{C}_{\alpha\beta\gamma\delta}(1, \xi_3, \xi_3^2)\, d\xi_3 \quad ,$$
$$A_{\alpha 3\beta 3} = k_s \int_{-h/2}^{h/2} \tilde{C}_{\alpha 3\beta 3}\, d\xi_3 \quad . \tag{4}$$

The Reissner's value of 5/6 is used as the transverse shear correction factor in the FE formulation based on the first shear deformation theory.

The shell element displays resultant forces acting on a laminate which are obtained by integration of stresses through the laminate thickness. In this study, we impose the plane state on the natural constitutive equation of Equation 2 before forming the equivalent constitutive equation. The constitutive relations of the composite laminate are as follows:

$$\begin{Bmatrix} N_{\alpha\beta} \\ M_{\alpha\beta} \\ Q_{\alpha 3} \end{Bmatrix} = \begin{bmatrix} A_{\alpha\beta\gamma\delta} & B_{\alpha\beta\gamma\delta} & 0 \\ B_{\alpha\beta\gamma\delta} & D_{\alpha\beta\gamma\delta} & 0 \\ 0 & 0 & A_{\alpha 3\beta 3} \end{bmatrix} \begin{Bmatrix} \tilde{E}^m_{\gamma\delta} \\ \tilde{E}^b_{\gamma\delta} \\ \tilde{E}^s_{\beta 3} \end{Bmatrix} \tag{5}$$

3 FINITE ELEMENT MODEL

In the current study, the ABAQUS program was used to develop finite element models for simulating the structural behavior of laminated composite poles. The poles tested had an average height of 5.00 m from the base.

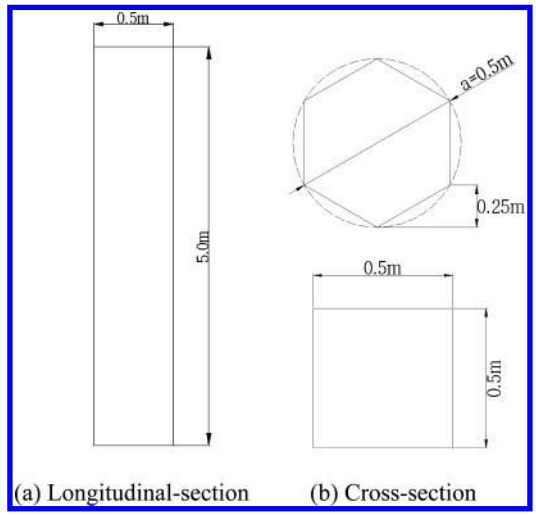


Figure 2. Two type test models.

The sectional properties are shown in Figure 2. Each ply of the laminates has equal thickness. The material properties of the plies are $E_1 = 40.0E_2$, $G_{12} = 0.5E_2$, $G_{23} = 0.6E_2$ $G_{13} = 0.5E_2$, and Poisson's ratio = 0.25. The produced natural frequencies are normalized. Figure 3 shows finite element laminated composite models using different element types in ABAQUS program. The mass density is assumed for convenience to have a unit value. The boundary conditions are free-clamped supported such as a cantilever beam.

4 NUMERICAL EXAMPLES

4.1 *Quadrangle poles*

Table 1∼3 show non-dimensional natural frequencies of quadrangle poles for different layup sequences and length-thickness ratios (a/h). It can be observed from the tables that the use of different layup sequences (symmetry or anti-symmetry) has a negligible effect on the laminated poles, regardless of the fiber angles and length-thickness ratios. On the other hand, the induced frequency for the same layup sequence is strongly dependent on the fiber angle, especially for $[0/90]_s$ and $[15/-75]_2$.

4.2 *Hexagon poles*

Table 4∼6 show non-dimensional natural frequencies of hexagon poles for different layup sequences and length-thickness ratios (a/h). The produced natural frequencies for hexagon poles show a similar trend with those of quadrangle poles. The highest frequency occurs for the laminate with a layup sequence of [0/90/90/0] or [0/90/0/90] because its stiffness is greater than that of the others. The differences between the layup sequences for different fiber angles depend on many geometrical parameters such as shape of the cross-section, length-to-thickness ratio, and boundary conditions.

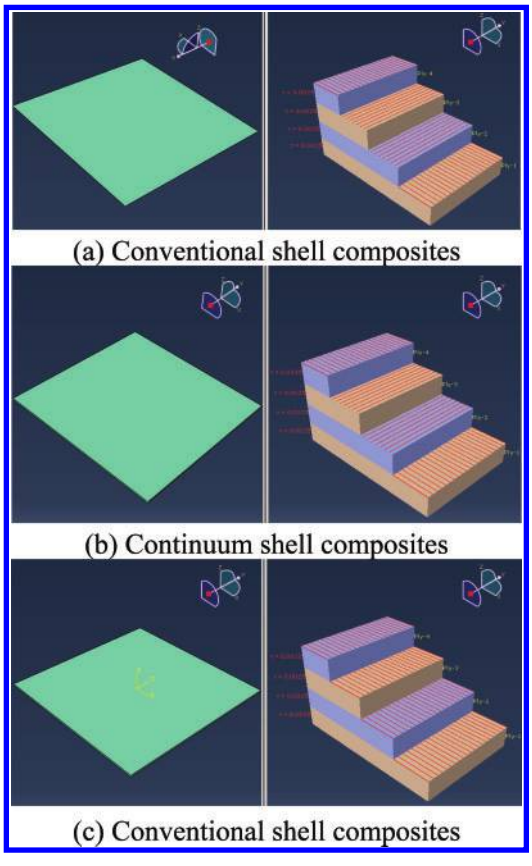


Figure 3. ABAQUS modeling of laminated composites.

Table 1. Non-dimensional natural frequencies for different layup sequences (quadrangle, a/h = 5.0)

Mode	[0/90]s	[15/-75]s	[30/-60]s	[45/-45]s	[60/-30]s
	Symmetry layup sequence				
I	0.239	0.158	0.108	0.096	0.108
II	0.537	0.617	0.672	0.604	0.673
III	0.954	0.888	0.850	1.201	0.852
IV	1.634	1.875	1.852	1.718	1.856
	Anti-symmetry layup sequence				
I	0.230	0.153	0.106	0.095	0.109
II	0.537	0.615	0.661	0.600	0.676
III	0.930	0.868	0.850	1.194	0.841
IV	1.634	1.872	1.825	1.707	1.858

4.3 *Mode shapes*

Figures 5∼6 show the mode shapes of symmetric cross-ply laminated quadrangle and hexagon poles with free-clamped ends. Each figure represents (a) symmetric vertical bending, (b) symmetric horizontal bending, (c) torsional, and (d) antisymmetric horizontal bending modes, respectively. As shown in the figures, some peculiar and complex mode shapes are produced due to the combined effect of both shapes of the cross-section of and layup stacking sequences.

Table 2. Non-dimensional natural frequencies for different layup sequences (quadrangle, a/h = 10.0)

Mode	[0/90]s	[15/-75]s	[30/-60]s	[45/-45]s	[60/-30]s
	Symmetry layup sequence				
I	0.476	0.311	0.214	0.190	0.213
II	1.062	1.203	1.327	1.195	1.324
III	1.886	1.752	1.679	2.398	1.683
IV	3.235	3.660	3.651	3.397	3.645
	Anti-symmetry layup sequence				
I	0.466	0.306	0.211	0.189	0.215
II	1.062	1.204	1.310	1.191	1.331
III	1.856	1.724	1.683	2.389	1.667
IV	3.234	3.661	3.612	3.384	3.656

Table 3. Non-dimensional natural frequencies for different layup sequences (quadrangle, a/h = 50.0)

Mode	[0/90]s	[15/-75]s	[30/-60]s	[45/-45]s	[60/-30]s
	Symmetry layup sequence				
I	0.951	0.619	0.425	0.377	0.424
II	2.116	2.377	2.634	2.375	2.628
III	3.754	3.481	3.325	4.786	3.332
IV	6.441	7.227	7.243	6.746	7.225
	Anti-symmetry layup sequence				
I	0.941	0.613	0.421	0.377	0.426
II	2.116	2.379	2.614	2.371	2.639
III	3.721	3.450	3.335	4.776	3.312
IV	6.440	7.235	7.195	6.734	7.250

Table 4. Non-dimensional natural frequencies for different layup sequences (hexagon, a/h = 5.0)

Mode	[0/90]s	[15/-75]s	[30/-60]s	[45/-45]s	[60/-30]s
	Symmetry layup sequence				
I	0.215	0.139	0.094	0.083	0.095
II	0.585	0.667	0.582	0.521	0.586
III	0.896	0.791	0.896	1.197	0.898
IV	1.761	1.911	1.585	1.459	1.595
	Anti-symmetry layup sequence				
I	0.205	0.134	0.093	0.083	0.095
II	0.585	0.666	0.572	0.517	0.586
III	0.868	0.770	0.897	1.191	0.887
IV	1.761	1.877	1.561	1.447	1.593

5 SUMMARY AND CONCLUSION

A technique based on the first-order shear deformation plate theory is developed to analyze the static and free vibration behavior of pole structures made of laminated composite materials. The usage of composite for poles could be an attractive approach from the practical point of view, not only because it has high stiffness but also because we can avoid the undesirable corrosion occurred in steel structures.

The technique is then implemented for quadrangle and hexagon poles of various layup sequences and end conditions to compare the results obtained

Table 5. Non-dimensional natural frequencies for different layup sequences (hexagon, a/h = 10.0)

Mode	[0/90]s	[15/-75]s	[30/-60]s	[45/-45]s	[60/-30]s
	Symmetry layup sequence				
I	0.428	0.274	0.186	0.165	0.187
II	1.161	1.305	1.150	1.032	1.152
III	1.774	1.559	1.773	2.392	1.777
IV	3.497	3.755	3.131	2.891	3.139
	Anti-symmetry layup sequence				
I	0.417	0.268	0.184	0.164	0.187
II	1.161	1.306	1.135	1.026	1.154
III	1.739	1.529	1.778	2.382	1.761
IV	3.497	3.699	3.095	2.875	3.139

Table 6. Non-dimensional natural frequencies for different layup sequences (hexagon, a/h = 50.0)

Mode	[0/90]s	[15/-75]s	[30/-60]s	[45/-45]s	[60/-30]s
	Symmetry layup sequence				
I	0.855	0.543	0.370	0.329	0.371
II	2.315	2.585	2.283	2.053	2.287
III	3.530	3.096	3.521	4.774	3.528
IV	6.972	7.451	6.220	5.754	6.231
	Anti-symmetry layup sequence				
I	0.844	0.537	0.367	0.328	0.371
II	2.315	2.588	2.266	2.046	2.289
III	3.492	3.062	3.531	4.761	3.507
IV	6.972	7.381	6.178	5.732	6.230

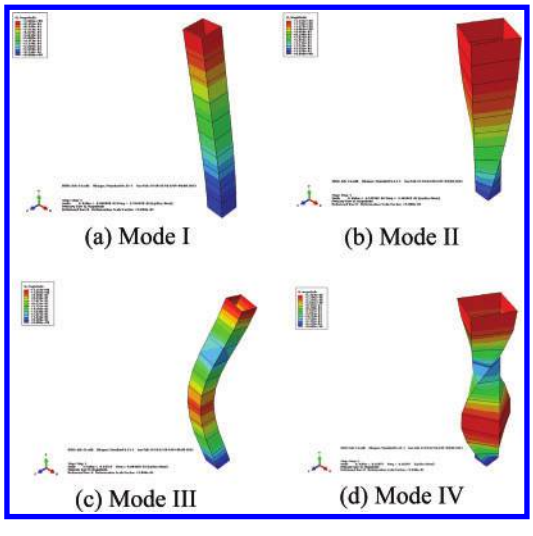


Figure 4. Mode shapes of quadrangle laminated composite poles (0/90/90/0).

from different length-to-thickness ratios. It is observed that the use of different layup sequences make little difference regardless of fiber angles, but the produced frequencies for different fiber angles become significant for various length-to-thickness ratios.

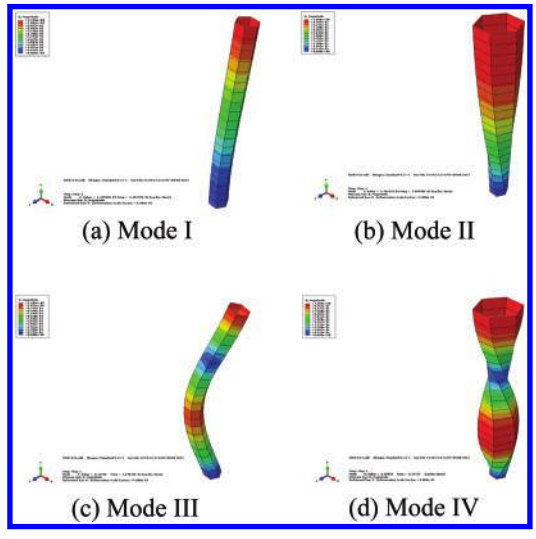


Figure 5. Mode shapes of hexagon laminated composite poles (0/90/90/0).

For composite poles with the closed section, e.g., quadrangle or hexagon box, the significance could be greater, because it is not only the properties of the materials but also the sectional properties of the member that makes large contributions to the overall behavior of the structure. The results of this study may serve as a benchmark for future guidelines in designing composite pole structures. But our parametric study is only an example and more studies should be carried out for individual design cases.

ACKNOWLEDGMENT

This research was supported by Basic Science Research Program through the National Research Foundation of Korea (NRF) funded by the Ministry of Education, Science and Technology (No. 2012R1A1A1014722).

REFERENCES

Dimos, J.P. & Ioannis, G.R. & Nibong, U. 2009. Static and dynamic characteristics of multi-cell jointed GFRP wind turbine towers. *Composite Structures*, 90: 34–42.

Han, S.C. & Kim, K.D. & Kanok-Nukulchai, W. 2004. An element-based 9-node resultant shell element for large deformation analysis of laminated composite plates and shells. *Structural Engineering and Mechanics*, 18(6): 807–829.

Kraus, H. 1967. *Thin elastic shells*, Willy, New York.

Reddy, J.N. 2004. *Mechanics of Laminated Composite Plates and Shells: Theory and Analysis*, CRC Press, New York.

Sanders, J.L. Jr. 1959. *An improved first approximation theory of thin shells*, NASA TR-R24.

Sanders, J.L. Jr. 1963. Nonlinear theories for thin shells Q. *Applied Mathematics*, 21: 21–36.

Zukas, J.A. & Vinson, J.R. 1971. Laminated transversely isotropic cylindrical shells. *Journal of Applied Mechanics*, 38: 400–407.

Research and Applications in Structural Engineering, Mechanics and Computation – Zingoni (Ed.)
© 2013 Taylor & Francis Group, London, ISBN 978-1-138-00061-2

Experiments on fatigue behaviour of sandwich panels

Harald Nelke & Jörg Lange
Institut für Stahlbau und Werkstoffmechanik, Technische Universität Darmstadt

ABSTRACT: Sandwich structures are widely used in structural engineering. Sandwich panels for building construction differ strongly from sandwich structures in mechanical engineering: The core material is lighter, the face sheets are thinner and the panel width is greater. So far applications for these sandwich panels are limited to installations where static or quasi-static loads occur. In this paper primary results of high-cycle fatigue behaviour are presented for the core materials polyurethane (PU) and mineral wool (MW). The tests are carried out on a three-point-bending test setup. Samples measure 168 cm × 70 cm × 20 cm. The following failure types are observed: Shear failure (MW), Wrinkling (PU & MW) and indentation of face sheet (PU). By comparing the cyclic results to the static tests, it can be pointed out that the face sheet failures are related to a cyclic damage of core material in compression.

1 INTRODUCTION

The advantages of sandwich panels in structural engineering are obvious. They are light in weight and combine a core which is structural member and thermal insulation. And most important, they are cost effective in production and easy to mount. Two different types of core material are examined in this paper: Mineral wool (MW) and polyurethane foam (PU). Mineral wool is incombustible and can be fully recycled. Polyurethane is lighter, cheaper and better in insulation than mineral wool, but only flame retardant.

Sandwich panels are automatically fabricated in production lines: Coils deliver the steel for both face sheets on which the mineral wool has to be glued whereas the polyurethane glues on its own. Detailed information about the production process, constructional solutions and mounting can be found in Pöoter(2010). Sandwich panels are used as wall or roof panels. The thickness normally varies between 40 mm and 200 mm. This paper focuses on wall panels of 200 mm. The face sheets are usually made out of steel with a minimum yield strength of $f_{y,k} = 220$ MPa. The thickness is typically between 0.4 mm and 1.0 mm. The construction and calculation of sandwich panels is regulated in Europe according to EN 14509.

On structural point of view sandwich panels can be assessed according to the sandwich theory formulated in Stamm & Witte (1974). A brief derivation and more information about sandwich panels is given in Lange & Berner (2010). This theory states that sandwich elements with planar or quasi-planar face sheets can be divided into two structural parts: The face sheets act as a two-point cross section and take over the bending moment whereas the core carries all the shear force. Typical failure modes are: Wrinkling or yielding of face sheets, shear or compression failure of the core and delamination between face sheet and core.

Under normal conditions static or quasi-static loads dominate in structural engineering. But there is number of applications where loading occurs cyclic and the fatigue strength becomes important. Indeed, sandwich structures have already been used for applications requiring resistance to cyclic loads such as offshore structures, wind energy converters, shipbuilding or aerospace. One of the most renowned systems is probably the Sandwich Plate System (SPS) (Kennedy 2007). But all these sandwich structures differ strongly from sandwich panels used in building construction. Mostly the face sheet material is different[1] the ratio of face sheet thickness to element width is far higher and the core material is much denser (compare e.g. Mathieson & Fam 2011, Kennedy 2007, Roosen 2005, Sharma, Narasimha Murthy, & Krishna 2004, Burman 1998).

Mineral wool as core material in fatigue tests has almost not been investigated. Buska, Lybye, & Maciulaitis (2008) analysed the effect of point loads on mineral wool boards. In their studies the mineral wool is not included in a sandwich construction, but it works as a pure insulation board on flat roofs which are usually loaded for service reasons only.

2 EXPERIMENTAL SETUP

The experiments can be regarded as pretests to examine in which way sandwich elements perform under cyclic load. The test setup is a three-point-bending test with 140 cm of inner length and 168 cm of outer length

[1] E.g. fibre reinforced polymers instead of steel.

(figure 1). Loads were applied via a Schenck servo hydraulic testing machine for tension with a maximum load of 200 kN (figure 2).

The samples measured 168 cm × 70 cm × 20 cm (length × width × thickness). The local conditions limited the length and the width to the chosen values (see figure 2). The thickness of 20 cm results from the maximum thickness which is usually produced. The maximum thickness is necessary since the testing machine worked at its minimum level of force: Smaller elements might not have withstand the minimum loads.

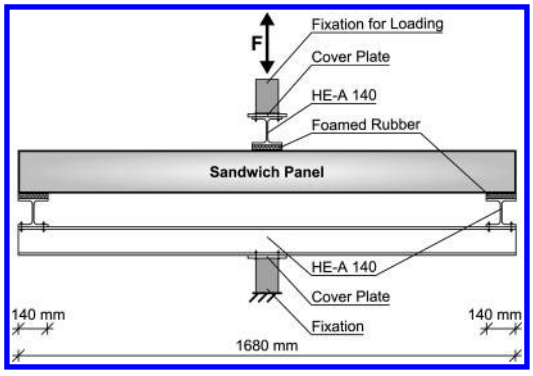


Figure 1. Three-Point-Bending Test: Schematic Test Setup.



Figure 2. Three-Point-Bending Test: Photograph of the Test Setup.

The samples were cut out of whole elements measuring 6,00 m × 1,00 m (MW) and 6,00 m × 1,10 m (PU) respectively. Samples with a core of rock wool originate from tested elements (Six-Point-Bending-Test for wrinkling failure) and were cut out by hand with a jig saw. Samples with a core of polyurethane foam originate from brand new elements and were cut out manually with a band saw.

Table 1 lists the profiling and the main material properties of tested samples. Material properties for samples with mineral wool as core material were fully determined according to EN 14509. For samples with a core of polyurethane foam instead, material properties from the same product line but from a different batch had to be used. But still, they were determined according to EN 14509. So the material properties for samples with a core of PU can only serve as an estimate. A "positive" orientation means that the bottom side during production is placed in the compression area whereas a "negative" orientation stands for the opposite.

The samples were subjected to cyclic loads according to table 2. Where possible, the maximum load was increased by 15% after the given number of cycles. The capabilities of the hydraulic system limited the frequencies f. The frequencies were chosen as high as possible.

3 EXPERIMENTAL RESULTS

In table 2 the maximum number of cycles is given when the sample failed. Figures 3 to 7 show the failure

Table 1. Material Properties of Tested Samples

Sample	Core Material	Orientation	Top	Bottom	t_{Top} mm	$t_{Bot.}$ mm	e mm	G kN	ρ_C kg/m^3	f_{Cc} MPa	$f_{Cc}(10\,\%)$ MPa	f_{Cv} MPa	σ_w MPa
S-1	MW	Positive	l	l	0.51	0.51	200.1	0.39	120.7	0.097	–	0.067	166
S-2	MW	Positive	l	l	0.51	0.51	200.1	0.39	120.7	0.097	–	0.067	166
S-3*	PU	Negative	l	ml	0.38	0.43	202.3	0.18	37.6	0.126	0.162	0.101	131
S-4*	PU	Positive	ml	l	0.43	0.38	202.3	0.18	37.6	0.126	0.162	0.101	196
S-5*	PU	Positive	ml	l	0.43	0.38	202.3	0.18	37.6	0.126	0.162	0.101	196

l: lined
ml: micro lined
e: Sample thickness minus mean face sheet thickness
f_{Cc}: Compressive strength of core material, MW: ultimate strength, PU: at elastic limit/at 10% relative displacement
f_{Cv}: Shear strength of core material
σ_w: Wrinkling stress
∗: Material properties from a different batch

Table 2. Test Procedure

Sample	F_{max} kN	F_{min} kN	F_m kN	F_a kN	R –	$\sum$N cycles	f Hz
S-1	9.9	1.1	5.5	4.4	0.11	440	1.0
S-2	5.0	1.0	3.0	2.0	0.20	109,000	3.0
	5.8	1.0	3.8	2.4	0.17	210,000	3.0
	6.6	1.0	3.8	2.8	0.15	310,000	3.0
	7.6	1.0	4.3	3.3	0.13	410,000	2.5
	8.7	1.0	4.9	3.9	0.11	424,000	2.0
S-3	11.0	1.0	6.0	5.0	0.09	16,155	1.0
S-4	11.0	1.0	6.0	5.0	0.09	30,000	1.0
	12.7	1.0	6.8	5.8	0.08	60,000	1.0
	14.5	1.0	7.8	6.8	0.07	65,000	1.0
	16.7	1.0	8.9	7.9	0.06	65,155	1.0
S-5	12.7	1.0	6.8	5.8	0.08	60,000	1.4
	14.5	1.0	7.8	6.8	0.07	229,648	1.4



Figure 3. S-1: Wrinkling.

modes[2]. The wrinkling failure (S-1, S-4, S-5) and the shear crack failure with delamination (S-2) are typical failure modes of sandwich elements under static loads[3]. In contrast, the failure of S-3 (indentation of face sheet) is similar to wrinkling failure, but has not been observed in static tests yet.

During the tests the samples S-3, S-4 and S-5 had not shown any kind of damage such as cracks or delamination until failure. Sample S-1 was immediately near its bearing capacity and showed heavy deformations allover. The development of damage was observable for sample S-2. The delamination of both face sheets

[2] Note that in figure 3 and 4 the edges of face sheets are still capped with a silver tape which was necessary for mounting.

[3] E.g., wrinkling failure is normally enforced in a six-point-bending test on full elements, shear failure in a four-point-bending test on short beams (both according to EN 14509).



Figure 4. S-2: Shear Crack with Face Delamination (Both-Sided).

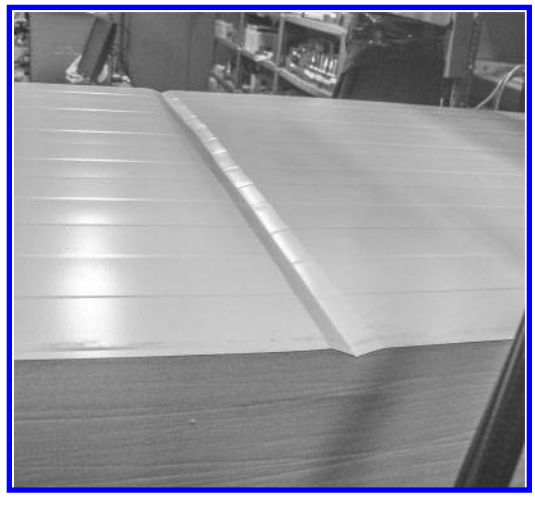


Figure 5. S-3: Indentation of Face Sheet.

increased slowly with an ongoing number of cycles. The shear crack appeared at about 350,000 cycles.

4 CALCULATION OF STRESSES

The loads and stresses from the fatigue test were compared to the results from the static tests to classify the results. As mentioned before the results from static tests for the samples S-3 to S-5 were obtained from a different batch. So variations in production are not covered within the comparison.

The static system of the test setup is a simply supported beam with a point load in the middle (figure 8). The span length cannot be clearly identified since the foamed rubber at both supports changed its characteristic during the tests. At the beginning it was still



Figure 6. S-4: Wrinkling.



Figure 7. S-5: Wrinkling.

stiff so that the supports were not fully under compression: A gap could be recognized of about half of the support width. With ongoing number of cycles the length of the gap first decreased and then disappeared at about 100,000 cycles. So in the calculations, there is a differentiation between two span lengths: Assuming a triangular distribution, the span length arises to approximately 145 cm for half of the support width under compression (N < 100,000 cycles) and to approximately 149 cm for a completely compressed support (N ≥ 100,000 cycles). For these two span lengths the following calculation is carried out.

The compressive stress, the shear stress and the normal stress in the upper face sheet are calculated for both, the maximum applied load and the cyclic load. All stresses are compared to the strength from the static tests (compare table 1) by calculating the stress-strength-ratio[4]. Table 3 shows the results. The stress

[4] For PU the compressive strength of core material (f_{Cc}) at elastic limit is chosen.

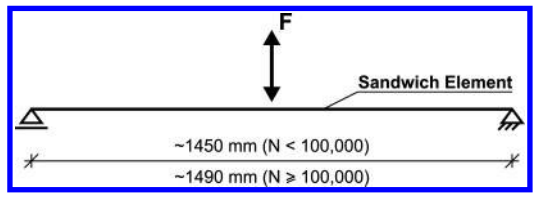


Figure 8. Three-Point-Bending Test: Static System.

ratios which might cause failure are printed in bold. The stresses are calculated according to the sandwich theory (Stamm & Witte 1974). The notation is oriented according to EN 14509.

$$\sigma_c = \frac{F_{max}}{B \cdot L_S} \qquad \Delta\sigma_c = \frac{\Delta F}{B \cdot L_S} \tag{1}$$

$$\eta_{\sigma_c} = \frac{\sigma_c}{f_{Cc}} \qquad \eta_{\Delta\sigma_c} = \frac{\Delta\sigma_c}{f_{Cc}} \tag{2}$$

$$V_u = \frac{F_{max}}{2} + \frac{G \cdot L}{L_E \cdot 2} \qquad \Delta V_u = \frac{\Delta F}{2} \tag{3}$$

$$\tau = \frac{V_u}{B \cdot e} \qquad \Delta\tau = \frac{\Delta V_u}{B \cdot e} \tag{4}$$

$$\eta_v = \frac{\tau}{f_{Cv}} \qquad \eta_{\Delta v} = \frac{\Delta\tau}{f_{Cv}} \tag{5}$$

$$M_u = \frac{F_{max} \cdot L}{4} + \frac{G \cdot L^2}{L_E \cdot 8} \qquad \Delta M_u = \frac{\Delta F \cdot L}{4} \tag{6}$$

$$\sigma_f = \frac{M_u}{e \cdot B \cdot t_{top}} \qquad \Delta\sigma_f = \frac{\Delta M_u}{e \cdot B \cdot t_{top}} \tag{7}$$

$$\eta_{\sigma_w} = \frac{\sigma_f}{\sigma_w} \qquad \eta_{\Delta\sigma_w} = \frac{\Delta\sigma_f}{\sigma_w} \tag{8}$$

With:

$L = 1450$ mm	(Span length, N < 100,000)
$L = 1490$ mm	(Span length, N ≥ 100,000)
$L_E = 1680$ mm	(Element length)
$B = 700$ mm	(Element width)
$L_S = 140$ mm	(Width of HE-A 140)

5 DISCUSSION OF RESULTS

Samples S-1 and S-4 withstood only a few hundred cycles in their maximum load range. The maximum load, not the cyclic load, is close to or even above the failure strength in static tests. Therefore the maximum loads are examined as well. Nevertheless, the failures were caused by cyclic load since the samples would had broken otherwise after one cycle.

Samples S-1, S-4 and S-5 failed in the same way; they all wrinkled. But table 3 shows that actually the stress-strength-ratios of differential normal stress in the upper face sheet were less than 50 % whereas

Table 3. Comparison of Cyclic to Static Results

Sample	F_{max} kN	ΔF kN	σ_c MPa	$\Delta\sigma_c$ MPa	η_{σ_c}	$\eta_{\Delta\sigma_c}$	τ MPa	$\Delta\tau$ MPa	η_v	$\eta_{\Delta v}$	σ_f MPa	$\Delta\sigma_f$ MPa	η_{σ_w}	$\eta_{\Delta\sigma_w}$
S-1	9.9	8.8	0.101	**0.090**	104%	**92%**	0.037	0.031	54%	47%	51	45	31%	27%
S-2	8.7	7.7	0.089	0.079	91%	81%	0.032	**0.027**	48%	**41%**	46	40	28%	24%
S-3*	11.0	10.0	0.112	**0.102**	89%	**81%**	0.039	0.035	39%	35%	75	67	53%	47%
S-4*	16.7	15.7	0.170	**0.160**	135%	**127%**	0.060	0.055	59%	55%	100	93	51%	48%
S-5*	14.5	13.5	0.148	**0.138**	117%	**109%**	0.052	0.048	51%	47%	89	83	46%	42%

σ_c; $\Delta\sigma_c$: Compressive stress due to F_{max}; ΔF
τ; $\Delta\tau$: Shear stress due to F_{max}; ΔF
σ_f; $\Delta\sigma_f$: Normal stress in face sheet due to F_{max}; ΔF
η: Stress-strength-ratio
*: Material properties from a different batch for comparisons with static strength (η-values)

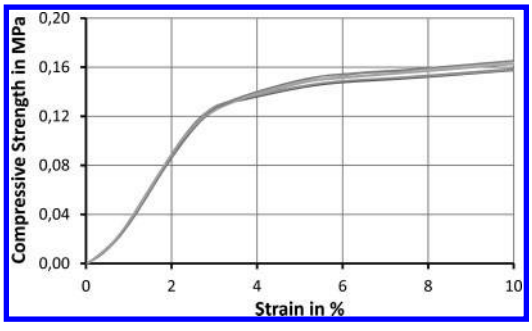


Figure 9. Compressive Strength Test of Core Material (PU).

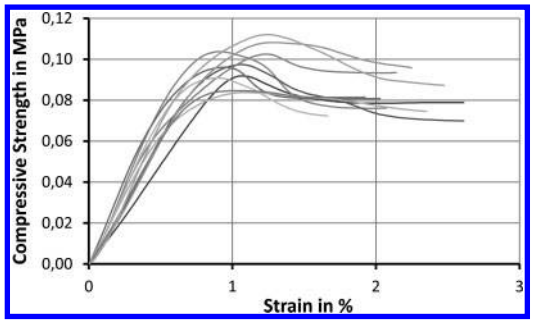


Figure 10. Compressive Strength Test of Core Material (MW).

the stress-strength-ratio for differential compressive stress was 92%, 127% and 109 % respectively. So it is assumed that the high level of compressive stress and, additionally for sample S-4 and S-5, the 60,000 cycles on lower load levels damaged the range in the middle where the load was applied. Due to this damage the continuous elastic support for the face sheet was reduced and therefore the face sheet wrinkled.

For samples S-1 (MW), S-4 and S-5 (both PU) the stress-strength-ratio for compressive stress even exceeded 100 %. Nevertheless, the samples did not fail immediately. The static compressive strength was determined from a test item measuring 10 cm × 10 cm. In the cyclic test the sample was much larger so that a three dimensional stress state could spread out which led to higher strength. For sample S-4 the stress-strength-ratio even reached 127 %, for sample S-5 still 109 %. There again the three dimensional stress state increased the compressive strength, but the characteristic stress-strain relation for PU shows another helping effect: After the elastic limit is reached (at about 3 %) the compressive strength still increases with a lower slope (figure 9). So exceeding the elastic limit will not lead to immediate failure. For MW the stress-strain relation for compression is totally different (figure 10): After the elastic limit and thereby the compressive strength is reached the curves decrease.

The failure mode for sample S-3 is similar to S-1, S-4 and S-5. There again the face sheet failed. It did not wrinkle though. Instead of that, the face sheet was pressed into the foam of PU. Looking at the stress-strength-ratios reveals that again a high level of differential compressive stress was reached. With 81 % the differential compressive stress (and with 89 % the maximum compressive stress, too) are still in the elastic range. There again this stress level damaged the range in the middle where the load was applied. Since the applied stress-strength-ratio was lower the damage might not spread as far as in samples S-4 and S-5 and in the adjacencies the foam was still strong enough to prevent the face sheet from lifting. Indeed, a video analysis watched in slow motion revealed that in sample S-4 the foam softened at first and afterwards the face sheet was lifted up (figure 11). The dark part in this figure indicates the flange of HE-A 140 in the middle of the sample.

Only Sample S-2 failed in shear. The damage underneath the location of load application[5] was not the decisive factor although the stress-strength-ratio for differential compressive stress reached 81% (as high as for sample S-3). On the one hand, the stress-strength-ratio for differential normal stress was quite low (24%). On the other hand, the face sheets started to delaminate due to the influence of shear from the beginning on. Regarding the shear crack in the mineral wool itself, it is assumed that a combination of shear

[5] From early on in the test, some cracks in the mineral wool were visible which slowly increased in length.

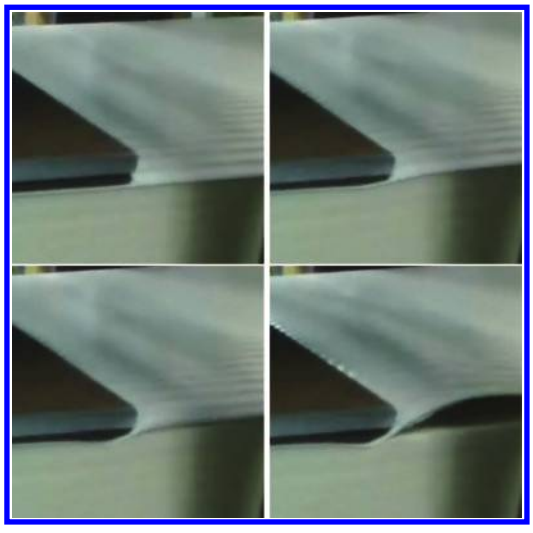


Figure 11. Sample S-4: Sequence of Failure.

crack and a loss of glue between the face sheet and the mineral wool encouraged the failure.

6 SUMMARY AND OUTLOOK

The sandwich system has many benefits in structural engineering. Sandwich panels used in building construction differ from sandwich structures in mechanical engineering since the insulation plays a decisive role for use as building envelope. So far the fatigue behaviour of these panels had not been studied yet. The main characteristics of sandwich panels are the thin face sheets (normally made out of steel), the light core material and a relative large thickness due to insulation.

A three-point-bending test was chosen for test setup. Due to local conditions the size of the samples was limited to 168 cm × 70 cm × 20 cm (length × width × thickness). The samples were loaded according to results of the static tests. After a certain number of cycles was exceeded (30,000 to 100,000 cycles) the initial cyclic load was increased by increasing the maximum load by 15%. The maximum number of cycles varied between a couple of 100 and over 400,000 depending on load and core material. Three failure modes occurred: Two known ones from static tests (shear failure with delamination of face sheet for MW and wrinkling of face sheet for PU and MW) and a new one similar to wrinkling (indentation of face sheet for PU).

Differential stresses from the cyclic load were calculated and compared to the static results. The mineral wool sample obviously failed in shear on account of a combination of loss of adhesive bond leading to delamination of both face sheets and a shear crack in the core material. It was pointed out that the samples where wrinkling and the indentation appeared failed for the same reason: Due to cyclic load, the compression strength of the core material was decreased and hence, the core material could not provide enough elastic support to prevent the face sheet from instability.

The presented tests form the basis to evaluate fatigue behaviour of sandwich panels in detail. The basic results are given to set up a test series: Fundamental failure modes are described, for different load levels the maximum number of cycles is determined (for both core materials) and the reasons for failure are discussed. Variations of span length, width, profiling of face sheet, producer and static system should now be tested. The following step will be the development of a mathematical model with the obtained results.

REFERENCES

Burman, M. (1998). *Fatigue Crack Initiation and Propagation in Sandwich Structures: Report No. 98-29*. Ph. D. thesis. ISSN 0280-4646.

Buska, A., D. Lybye, & R. Maciulaitis (2008). Effect of Dynamic Load on Value of Point Load of Mineral Wool Boards. *Materials Science – Medžitagotyra 14*(3), 268–272.

EN 14509 (2007-02). Self-supporting double skin metal faced insulating panels – Factory made products – Specifications.

Kennedy, S. (2007). Das Sandwich-Platten-System (SPS): Sandwich Plate System (SPS). *Stahlbau 76*(7), 455–464.

Lange, J. & K. Berner (2010). Sandwichelemente im Hochbau. In U. Kuhlmann (Ed.), *Stahlbau Kalender 2010*, pp. 643– 699. Berlin: Ernst & Sohn.

Mathieson, H. & A. Fam (2011). GFRP-Polyurethane Sandwich Panels under Reversed Bending Fatigue. In L. Ye, P. Feng, and Q. Yue (Eds.), *Advances in FRP Composites in Civil Engineering: Proceedings of the 5th International Conference on FRP Composites in Civil Engineering (CICE 2010), Sep 27–29, 2010, Beijing, China*, pp. 164–167. Springer.

Pöter, H. (2010). Bausysteme aus Stahl für Dach und Fassade. Technical Report 558, Stahl-Informations-Zentrum.

Roosen, D. (2005). Fatigue behavior of sandwich foam core materials: Comparison of different core materials. *Journal of advanced materials 37*(1), 38–42.

Sharma, S.C., H. N. Narasimha Murthy, & M. Krishna (2004). Interfacial studies in fatigue behavior of polyurethane sandwich structures. *Journal of Reinforced Plastics and Composites 23*(8), 893–903.

Stamm, K. & H. Witte (1974). *Sandwichkonstruktionen: Berechnung, Fertigung, Ausführung*. Wien and New York: Springer.

Research and Applications in Structural Engineering, Mechanics and Computation – Zingoni (Ed.)
© 2013 Taylor & Francis Group, London, ISBN 978-1-138-00061-2

Modeling and nonlinear FE analysis of composite shells at finite rotations

R. Schmidt, M.N. Rao & T.D. Vu
RWTH Aachen University, Institute of General Mechanics, Germany

ABSTRACT: This paper presents a numerical study on static and stability analysis of layered composite structures. The shell element is based on the Reissner-Mindlin first-order shear deformation theory and strain-displacement relations are valid for small strains but finite rotations. Finite rotations are treated by Rodrigues parameterization. Two types of examples, static analysis of a composite laminated plate with hinged edges and stability analysis of a layered cross-ply cylindrical shell are carried out in the range of geometrically nonlinear deformation. The present simulations are compared with those obtained by finite element analyses based on first-order transverse shear deformation moderate or large rotation or refined von Kármán-type theories in earlier literature.

1 INTRODUCTION

Most of the available papers treat the nonlinear static response of composite structures with simplified geometrically nonlinear theories based either on the degenerated solid approach (Stander et al. (1989), Chang & Sawamiphakdi (1981)) or on various shell theories, such as the classical Kirchhoff-Love theory (Saigal et al. (1986)), the first- (Schmidt & Reddy (1988), Palmerio et al. (1990), Brank et al. (1995), Sansour & Bednarczyk (1995)) or third-order (Reddy (1990),Tsai et al. (1991)) transverse shear deformation theory, respectively, using the refined von Kármán-type or moderate rotation theories. Very less literature can be found on the geometrically nonlinear problems dealing with large rotations (e.g. Basar et al. (1993), Masud et al. (2000), Kreja & Schmidt (2006), Arciniega & Reddy (2007)).

The present paper deals with geometrically nonlinear static and stability analysis of composite laminated structures in the framework of the first-order transverse shear deformation theory (FOSD). The theory and the finite element method account for full geometrical nonlinearity, thus they account for arbitrary, finite rotations. The finite rotation theory (FRT) finite element formulation developed by Lentzen (2009) and extended to nonlinear vibration analysis in Schmidt et al. (2010) is applied. Here we deal with geometrically nonlinear static and stability problems of composite laminated structures. The Riks–Wempner arc-length control method is used to trace equilibrium paths in the pre- and post-buckling range of deformation.

We consider standard benchmark problems of composite laminated plate and shell structures. In particular, we compare the results with those that have been obtained in our earlier paper Kreja & Schmidt (2006) and Kreja (2007) where comparative finite element analysis has been performed using a variety of geometrically nonlinear shell theories.

2 FINITE ROTATION SHELL THEORY AND FINITE ELEMENT METHOD

Concerning the underlying theory and finite element method, the present paper is based on the FOSD shell theory for small strains and finite rotations of Habip (1965) and the FE implementation of Gruttmann & Wagner (2006) and Lentzen (2009).

Figure 1 shows the four-node element with the global $\boldsymbol{e}_i$, the local $\boldsymbol{a}_\alpha$, the natural $\xi-\eta$ and the orthonormal material $\boldsymbol{t}_i$ coordinate systems. The position vector to the reference surface in the initial configuration at node I is denoted as $\boldsymbol{x}_\mathbf{I}$. The position vector $\boldsymbol{r}$ to an arbitrary point in shell space is described as

$$\boldsymbol{r} = \boldsymbol{x}(\xi,\eta) + z\boldsymbol{d}(\xi,\eta) \tag{1}$$

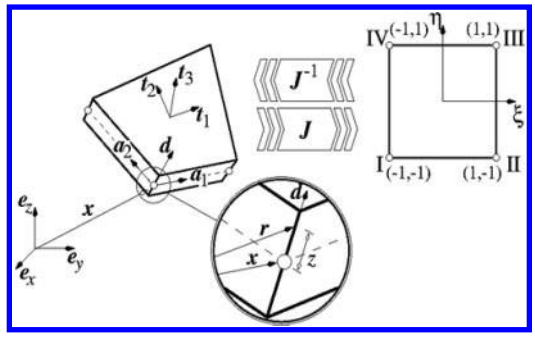


Figure 1. Definition of the coordinate systems in the FRT-element.

where z denotes the thickness coordinate ranging from the bottom to the top of the considered shell and $\boldsymbol{d}$ is the shell director.

In the framework of FOSD or Reissner-Mindlin hypothesis, the Green strain-tensor components for fully nonlinear finite rotation strain-displacement relations are obtained as (see Habip (1965))

$$\begin{aligned}
\varepsilon_{\alpha\beta} &= \overset{0}{\varepsilon}_{\alpha\beta} + \zeta \overset{1}{\varepsilon}_{\alpha\beta} + \zeta^2 \overset{2}{\varepsilon}_{\alpha\beta} \\
\varepsilon_{\alpha 3} &= \overset{0}{\varepsilon}_{\alpha 3} + \zeta \overset{1}{\varepsilon}_{\alpha 3} \\
\varepsilon_{33} &= 0
\end{aligned} \tag{2}$$

where

$$\begin{aligned}
\overset{0}{\varepsilon}_{\alpha\beta} &= \frac{1}{2}\left(\bar{\boldsymbol{x}}_{,\alpha}\cdot\bar{\boldsymbol{x}}_{,\beta} - \boldsymbol{x}_{,\alpha}\cdot\boldsymbol{x}_{,\beta}\right) \\
\overset{1}{\varepsilon}_{\alpha\beta} &= \frac{1}{2}\left(\bar{\boldsymbol{x}}_{,\alpha}\cdot\bar{\boldsymbol{d}}_{,\beta} + \bar{\boldsymbol{x}}_{,\beta}\cdot\bar{\boldsymbol{d}}_{,\alpha} - \boldsymbol{x}_{,\alpha}\cdot\boldsymbol{d}_{,\beta} - \boldsymbol{x}_{,\beta}\cdot\boldsymbol{d}_{,\alpha}\right) \\
\overset{2}{\varepsilon}_{\alpha\beta} &= \frac{1}{2}\left(\bar{\boldsymbol{d}}_{,\alpha}\cdot\bar{\boldsymbol{d}}_{,\beta} - \boldsymbol{d}_{,\alpha}\cdot\boldsymbol{d}_{,\beta}\right) \\
\overset{0}{\varepsilon}_{\alpha 3} &= \frac{1}{2}\left(\bar{\boldsymbol{x}}_{,\alpha}\cdot\bar{\boldsymbol{d}} - \boldsymbol{x}_{,\alpha}\cdot\boldsymbol{d}\right) \\
\overset{1}{\varepsilon}_{\alpha 3} &= \frac{1}{2}\left(\bar{\boldsymbol{d}}_{,\alpha}\cdot\bar{\boldsymbol{d}} - \boldsymbol{d}_{,\alpha}\cdot\boldsymbol{d}\right).
\end{aligned} \tag{3}$$

Here ζ denotes the thickness coordinate and an overbar indicates the deformed configuration. Due to thinness of the regarded plates and shells the components $\varepsilon^2_{\alpha\beta}$ and $\varepsilon^1_{\alpha 3}$ are neglected.

There are no kinematical restrictions with respect to the range of rotations. The director is assumed to be inextensible and the rotations are parameterized with the Rodriguez formulation. In order to overcome various types of locking, the ANS procedure suggested by Bathe & Dvorkin (1985), Hughes & Tezduyar (1981) combined with EAS (Lentzen (2009)) has been used.

2.1 *Variational formulation*

The finite element developed by Lentzen (2009) is based on the shell element of Gruttmann & Wagner (2006). In the present element a displacement based variational principle is chosen in order to reduce the number of internal variables. The variational formulation reads

$$\int_V \boldsymbol{S} : \delta\boldsymbol{\varepsilon}\, dV = \int_A \boldsymbol{T}\cdot\delta\boldsymbol{v}\, dA + \int_V \left(\rho(\boldsymbol{b} - \ddot{\boldsymbol{v}})\right)\cdot\delta\boldsymbol{v}\, dV \tag{4}$$

where $\boldsymbol{S}$ is the second Piola-Kirchhoff stress tensor, ε is the Green-Lagrange strain tensor, $\delta\boldsymbol{v}$ is the virtual displacement vector, $\boldsymbol{T}$ is the traction vector on the boundary, ρ is the mass density, $\boldsymbol{b}$ is the body force density and $\ddot{\boldsymbol{v}}$ is the acceleration vector. Here a total Lagrangian approach is adopted.

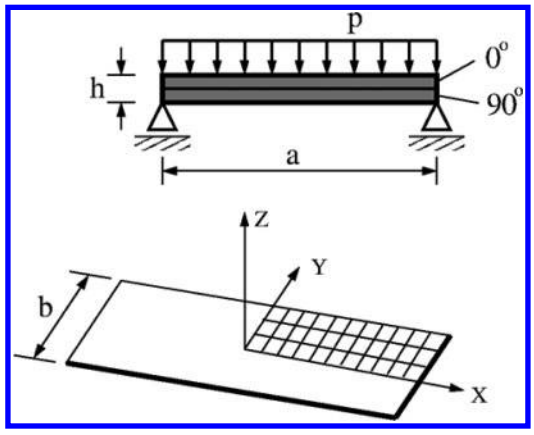


Figure 2. Two edges hinged composite laminated plate.

The variation of the Green-Lagrange strain tensor components are

$$\begin{aligned}
\delta\overset{0}{\varepsilon}_{\alpha\beta} &= \frac{1}{2}\left(\delta\bar{\boldsymbol{x}}_{,\alpha}\bullet\bar{\boldsymbol{x}}_{,\beta} + \bar{\boldsymbol{x}}_{,\alpha}\bullet\delta\bar{\boldsymbol{x}}_{,\beta}\right) \\
\delta\overset{1}{\varepsilon}_{\alpha\beta} &= \frac{1}{2}\left(\delta\bar{\boldsymbol{x}}_{,\alpha}\bullet\bar{\boldsymbol{d}}_{,\beta} + \delta\bar{\boldsymbol{x}}_{,\beta}\bullet\bar{\boldsymbol{d}}_{,\alpha} + \bar{\boldsymbol{x}}_{,\alpha}\bullet\delta\bar{\boldsymbol{d}}_{,\beta} + \bar{\boldsymbol{x}}_{,\beta}\bullet\delta\bar{\boldsymbol{d}}_{,\alpha}\right) \\
\delta\overset{0}{\varepsilon}_{\alpha 3} &= \frac{1}{2}\left(\delta\bar{\boldsymbol{x}}_{,\alpha}\bullet\bar{\boldsymbol{d}} + \bar{\boldsymbol{x}}_{,\beta}\bullet\delta\bar{\boldsymbol{d}}\right).
\end{aligned} \tag{5}$$

With $\bar{\boldsymbol{x}} = \boldsymbol{x} + \boldsymbol{v}$, it follows that $\delta\bar{\boldsymbol{x}}_{,\alpha} = \delta\boldsymbol{v}_{,\alpha}$. The variation of the director and its linearization developed by Gruttman & Wagner (2006)

$$\delta\bar{\boldsymbol{d}} = \boldsymbol{\delta w}\times\bar{\boldsymbol{d}}\ , \tag{6}$$

has been used, where $\boldsymbol{\delta w}$ is the axial vector of rotation expressed in terms of virtual rotations as

$$\delta\boldsymbol{w} = \boldsymbol{H}\delta\boldsymbol{\omega} \tag{7}$$

and $\boldsymbol{H}$ is determined as

$$\boldsymbol{H} = \boldsymbol{I} + c_1\boldsymbol{W} + c_2\boldsymbol{W}^2 \tag{8}$$

with $c_1 = \frac{1-\cos\psi}{\psi^2}$ and $c_2 = \frac{\psi-\cos\psi}{\psi^3}$,
where $\boldsymbol{W}$ is the rotation tensor and ψ is the rotation angle.

3 NUMERICAL EXAMPLES

3.1 *Asymmetric cross-ply laminated plate strip under uniformly distributed transverse load*

Here, the considered example is an asymmetric cross-ply laminated plate with hinged edges as shown in Figure 2. The geometry is defined by a = 9.0 in, b = 1.5 in, h = 0.04 in and the material properties are taken as $E_{11} = 2.0 \cdot 10^7$ psi, $E_{22} = 1.4 \cdot 10^6$ psi, $\nu_{12} = 0.3$, $G_{12} = G_{13} = G_{23} = 0.7 \cdot 10^6$ psi.

The deflection at the center of the plate is simulated by the present FOSD FRT model. Due to the

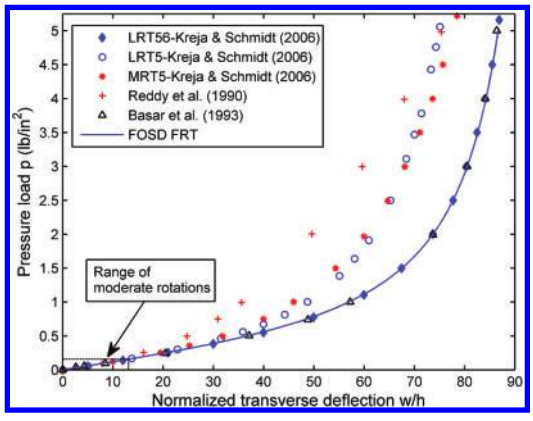


Figure 3. Normalized center deflection of the plate strip under pressure load.

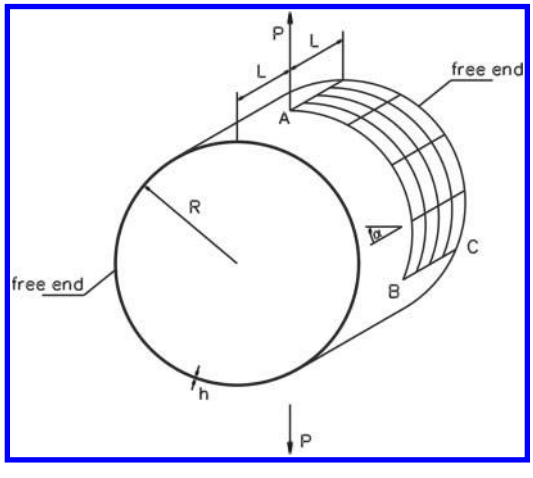


Figure 4. Cross-ply laminated short cylinder.

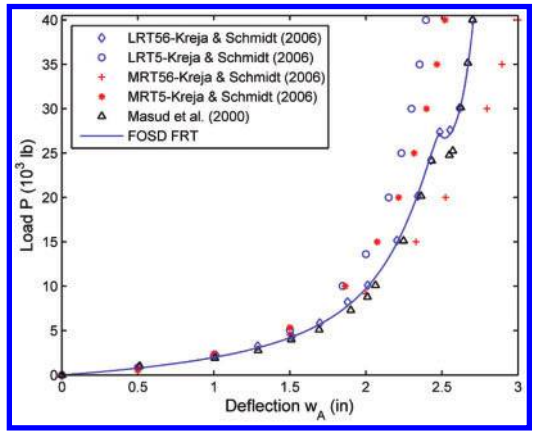


Figure 5. Radial deflection at point A for (0°/90°) plies lay-up.

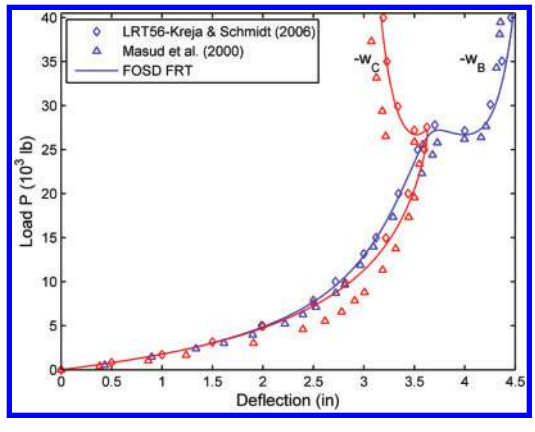


Figure 6. Radial deflection at points B and C for (0°/90°) plies lay-up.

dual symmetry of the analyzed structure, a quarter of the plate is modeled. In Figure 3 the normalized transverse deflection is compared with the existing literature given by Kreja & Schmidt (2006) (LTR56, LRT5, MRT5) together with the reference solutions of Reddy (1990) and Basar et al. (1993).

The von Kármán-type model of Reddy (1990) and the MRT5-Kreja & Schmidt (2006) model are capable of dealing with deflections in the range of moderate rotations marked in Figure 3. Our (FOSD FRT) results agree very well with those of Basar et al. (1993) and LRT56-Kreja & Schmidt (2006).

3.2 *Stretching of a composite laminated short cylinder*

The considered example is a well-known nonlinear benchmark problem of a composite laminated short open cylindrical shell stretched by two opposite point loads as shown in Figure 4. The material properties of each layer are $E_{11} = 30500$ ksi, $E_{22} = 10500$ ksi, $G_{12} = G_{13} = G_{23} = 4000$ ksi and $\nu_{12} = 0.3125$. Here two different cases of stacking sequences of the composite shell are analyzed. Due to the symmetry, only one octant of the shell is modeled using 20×32 elements (20 along the length and 32 along the periphery).

In the first simulation, the composite shell with fiber orientations (0°/90°) is analyzed. In Figure 5 the radial displacement at point A obtained from the present FE formulation is compared with reference solutions of Masud et al. (2000) and Kreja & Schmidt (2006), who use two large (LRT5, LRT56), and two moderate rotation (MRT5, MRT56) theories. The results of the present FE model (FOSD FRT) are in excellent agreement with those of the LRT56 model. The result of Masud et al. (2000) differs in the snap-through region, while the LRT5 model fails to predict the buckling phenomenon at all. As expected, the moderate rotation theories (see Librescu & Schmidt (1988), Schmidt & Reddy (1988), Palmerio, Reddy & Schmidt (1990), Kreja, Schmidt & Reddy (1997)) yield good results only in the range of moderate rotations.

Figure 6 show the radial displacements at points B and C obtained from the present simulation compared

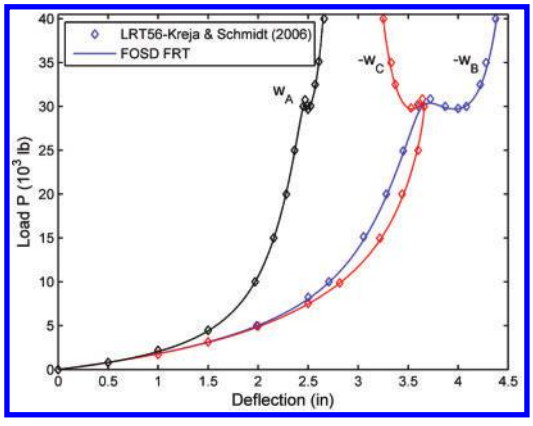


Figure 7. Radial deflection at points A, B and C for (90°/0°) plies lay-up.

with those of the existing literature. The present simulations are in very good agreement with the LRT56-Kreja & Schmidt (2006) model but differ from Masud et al. (2000), especially for point C.

In the second case, the numerical investigation is performed for the composite laminated short cylinder with lay-up (90°/0°). Figure 7 shows the radial displacements at points A, B and C, respectively. In Figure 7 the present simulations by FOSD FRT agree very well with those of LRT56-Kreja & Schmidt (2006). From Figures 3, 4 and 5, it can be observed that the snap-through load for stretching the composite laminated cylinder increases significantly, when the stacking sequence is changed from (0°/90°) to (90°/0°).

4 CONCLUSIONS

In this paper, nonlinear static analyses of a composite laminated plate strip subjected to uniform distributed load and stability analysis of cross-ply cylindrical shells with different stacking sequences are simulated by FOSD FRT model. The present simulations demonstrate the importance of the finite rotation models concerning a reliable consideration of nonlinearities.

REFERENCES

Arciniega, R.A. & Reddy, J.N. 2007. Tensor-based finite element formulation for geometrically nonlinear analysis of shell structures. *Computer Methods in Applied Mechanics and Engineering* 196: 1048–1073.

Basar, Y., Ding, Y. & Schultz, R. 1993. Refined shear deformation models for composite laminates with finite rotations, *Int. J. Solids Struct.* 30: 2611–2638.

Bathe, K.J. & Dvorkin, E. 1985. A 4-node plate bending element based on Mindlin/Reissner theory and a mixed interpolation. *Int. J. Num. Meth. Eng.* 21: 367–383.

Brank, B., Peric, D. & Damjanic, F.B. 1995. On implementation of a nonlinear four node shell finite element for thin multilayered elastic shells. *Computational. Mech.* 16: 341–359.

Chang, T.Y. & Sawamiphakdi, K. 1981. Large deformation analysis of laminated shells by finite element method. *Computers and Structures* 13: 331–340.

Gruttmann, F. & Wagner, F. 2006. Structural analysis of composite laminates using a mixed hybrid shell element. *Computational Mechanics* 37: 479–497.

Habip, L.M. 1965. Theory of elastic shells in the reference state. *Ing.-Archiv* 34: 228–237.

Hughes, T.J.R. & Tezduyar, T.E. 1981. Finite elements based upon Mindlin plate theory with reference to the four-node isoparametric element. *Int. J. Num. Meth* 48: 587–596.

Kreja, I. 2007. Geometrically non-linear analysis of layered composite plates and shells, *Habilitation Thesis, Politechnika Gdanska.*

Kreja, I. & Schmidt, R. 2006. Large rotations in first-order shear deformation FE analysis of laminated shells, *Int. J. Nonlinear Mech.* 41: 101–123

Kreja, I., Schmidt, R. & Reddy, J.N. 1997. Finite elements based on the first-order shear deformation moderate rotation shell theory with applications to the analysis of composite structures, *Int. J. Nonlinear Mech.* 32: 1123–1142.

Lentzen, S. 2009. Nonlinearly coupled thermopiezoelectric modelling and FE simulation of smart structures, *PhD Thesis, RWTH Aachen University, Fortschritt-Berichte VDI* 20: 419.

Librescu, L. & Schmidt, R. 1988. Refined theories of elastic anisotropic shells accounting for small strains and moderate rotations, *Int. J. Nonlinear Mech*. 23: 217–229.

Masud, A., Tham, C.L. & Liu, W.K. 2000. A stabilized 3-D cororational formulation for geometrically nonlinear analysis of multi-layered shells. *Comp. Mech.* 26: 1–12.

Palmerio, A.F., Reddy, J.N. & Schmidt, R. 1990. On a moderate rotation theory of elastic anisotropic shells. *Part 1: th*eory, *Part 2: FE analysis . Int. J. Non. Mech.* 25: 687–714.

Reddy, J.N. 1990. A general nonlinear third-order theory of plates with moderate thickness. *Int. Journal of Non-linear Mechanics* 25: 677–686.

Saigal, S., Kapania, R.K. & Yang, T.Y. 1986.Geometrically nonlinear finite element analysis of imperfect laminated shells. *Journal of Composite Structures* 20: 197–214.

Sansour, C. & Bednarczyk, H. 1995. The Cosserat surface as a shell model, theory and finite-element formulation. *Comput. Methods Appl. Mech. Eng.* 120: 1–32.

Schmidt, R. & Reddy, J.N. 1988. A refined small strain and moderate rotation theory of elastic anisotropic shells, *ASME J. Appl. Mech.* 55: 611–617.

Schmidt, R. Tiranasavasdi, S. & Vu, T.D. 2010. Finite rotation finite element analysis of layered composite plates and shells. *Advances and Trends in Structural Engineering, Mechanics and Computation (Ed. A. Zingoni),* Taylor & Francis Group, London, UK, CRC Press Balkema, Leiden, The Netherlands, 481–486.

Stander, N., Matzenmiller, A. & Ramm, E. 1989. An assessment of assumed strain methods in ?nite rotation shell analysis, *Eng. Comput.* 6: 58–66

Tsai, C.T., Palazotto, A.N. & Dennis, S.T. 1991. Large rotation snap-through buckling in laminated cylindrical panels. *Finite Elements in Analysis and Design* 9: 65–75.

Research and Applications in Structural Engineering, Mechanics and Computation – Zingoni (Ed.)
© 2013 Taylor & Francis Group, London, ISBN 978-1-138-00061-2

Using the polynomial annihilation edge detection for locating delamination in laminated composite plates

C. Surace & H. Darwich
Department of Structural Geotechnical and Building Engineering, Politecnico di Torino, Torino, Italy

M. Gherlone
Department of Mechanical and Aerospace Engineering, Politecnico di Torino, Torino, Italy

ABSTRACT: The problem of non-destructively detecting delamination in laminated composite plates is addressed in this article. As the presence of a delamination causes a discontinuity in the first derivative of the mode shapes, a numerical method for detecting discontinuities in smooth piecewise functions and their derivatives, based on a polynomial-annihilation technique, has been proposed and applied to the problem of damage detection and localisation in plate-like structures for which only post-damage mode shapes are available. Mode shapes of the test structure can be obtained by measuring the dynamic response on a regular grid of points on the surface of the plate. In this study, numerical simulations have been performed using the FE method of the dynamic behaviour of orthotropic multilayered composite plates with delaminations; two cases have been analysed in which the delamination considered is between different layers of the composite plate. Results indicate that further development of the technique for non-destructive testing of composite structures would be highly worthwhile.

1 INTRODUCTION

In quite recent years there has been a significant effort to employ vibration-based inspection methods for identifying various types of structural damage. Since the occurrence of damage modifies the stiffness, the mass and the damping properties of a structure, its vibrational response will also change as a result of damage occurring. By appropriately assessing the eigen-parameters of a damaged structure, it may be possible to detect, locate, and even quantify the extent of damage. One class of damage identification techniques is based on the modifications of mode shapes due to damage or, alternatively, on the changes of the mode shape second derivatives ie. curvatures. These methods appear to be more sensitive than methods based on the modal frequency changes (Doebling et al. 1996).

Most of the techniques have been mainly applied to beam-like structures but more recently the attention has been focused also on two dimensional structures such as plates or shells.

Cornwell et al. (1999) extended the technique developed by Stubbs et al. (1996), based on the decrease in modal strain energy as defined by the curvature of the measured mode, to isotropic plates. One of the drawbacks of these methods is that data from the undamaged structure are required for the necessary comparison with the data of the damaged structure.

Ratcliffe (2000) proposed the so-called 'Gapped-Smoothing Technique' that enables damage detection in beam structures by evaluating a damage index which is a function only of the modal curvature calculated for the damaged state. The advantage is that no a-priori knowledge regarding the undamaged state is required. Battipede et al. (2001), simultaneously with Yoon et al. (2001) extended the 'Gapped-Smoothing Technique' to plate-like structures, publishing the latest developments and results in (Yoon et al. 2005).

Evolving the idea of an interpolation technique that can smooth the discontinuities in the data due to delamination, Smoothing Element Analysis (SEA) has been used and a damage index, that considers the change in strain energy due to the delamination in the laminated panel, has been formulated (Gherlone et al. 2005).

In general, methods based on modal curvatures often seem to demonstrate a high level of sensitivity to damage than those based on mode shapes. Unfortunately the weakness of these methods is that as they are based on a differentiation procedure making them highly sensitive also to the presence of measurement noise. Although the displacement mode shape is generally not sufficiently sensitive to small damage (Salawu & Williams, 1994), recently new methods

based on spatial wavelet analysis have emerged as a potential way of overcoming this problem thanks to their high-resolution: Indeed, although local changes in the mode shapes due to cracks or defects are not easily detectable, it may be possible to identify singularities in the signal by applying the wavelet transform to the mode shapes. This procedure has been applied to both one (Douka et al. 2003a, Chang, & Chen, 2003, Chang & Chen, 2005) and two-dimensional structures (Douka et al. 2003b). Latterly a method based on Gaussian Process Regression has been proposed by Hensman et al. (2011) and applied to the displacement mode shape of a cracked beam to identify damage.

In this paper a new methodology to localise damage in plate-like structures for which only few post-damage mode shapes are available is proposed. It is well known that a kind of damage such as a crack or a delamination, causes a discontinuity in the rotations and consequently in the first derivatives of the mode shapes. On this basis, the Polynomial Annihilation Edge Detection (PAED) technique (Archibald et al. 2008, Saxena, 2008), a numerical method for detecting discontinuities in smooth piecewise functions and their derivatives, already applied by Surace et al. (2013, in press a,b) to the problem of damage detection and localisation in beam-like structures, has been extended to bi-dimensional case.

The specific aim of this work is to detect the presence of delaminations in composite panels; due to this kind of damage, two sub-laminates are created respectively. Consequently, especially at high frequencies, the local modes exhibit discontinuities in the rotation function where the sub-laminates are separated. For this purpose a FE model of a delaminate composite plate has been simulated and some results are given for increasing amount of noise.

2 POLYNOMIAL ANNIHILATION EDGE AND DERIVATIVE DISCONTINUITY DETECTION IN THE 2-DIMENSIONAL CASE (PAED2)

In this section formulation for detecting edges and derivative discontinuities proposed by Archibald et al. (2008) for the mono-dimensional case, will be briefly presented for the 2-dimensional case:

Let's $f(x,y)$ be a piecewise smooth function,

$$\Omega = ([a,b] \times [a,b]) \subseteq R^2 \quad (1)$$

known only on the set of discrete points,

$$S = \{(x_1,y_1),\dots,(x_j,y_i),\dots,(x_M,y_N)\} \subseteq \Omega. \quad (2)$$

The method focuses on fixing a certain dimension, for instance y, and then applying the polynomial annihilation edge detection method along each line $y = y_i$ in the set S already considered.

Starting from this fact, the study becomes mono-dimensional through the M lines corresponding to N points in S.

For $y = y_i : i = 1,\dots N$
consider the set

$$S_i = \{(x_1,y_i),(x_2,y_i),\dots,(x_M,y_i)\} \subseteq [a,b] \times \{y_i\} \quad (3)$$

The function $f(x,y_i)$ is known in this set.

Consider the γ-derivation jump discontinuity in $f(x,y_i)$ so that $\frac{\partial^{(\gamma-1)}f}{\partial x^{\gamma-1}}(x,y_i)$ are continuous in $[a,b] \times \{y_i\}$, and jump discontinuity first appears in $\frac{\partial^{(\gamma)}f}{\partial x^{\gamma}}(x,y_i)$.

It's also assumed that at any point (x,y_i) in the domain, $\frac{\partial^{(\gamma)}f}{\partial x^{\gamma}}(x,y_i)$ has a well defined one-sided limits.

Let J_γ be the set of jump discontinuities in the γ^{th} partial derivative, that is:

$$J_\gamma = \left\{(\varepsilon,y_i): \frac{\partial^{(\gamma)}f}{\partial x^{\gamma}}(x^+,y_i) \neq \frac{\partial^{(\gamma)}f}{\partial x^{\gamma}}(x^-,y_i)\right\} \quad (4)$$

The local jump of γ^{th} partial derivatives defined as:

$$\left[\frac{\partial^{(\gamma)}f}{\partial x^{\gamma}}\right](x,y_i) = \frac{\partial^{(\gamma)}f}{\partial x^{\gamma}}(x^+,y_i) - \frac{\partial^{(\gamma)}f}{\partial x^{\gamma}}(x^-,y_i).$$

An approximation to $\left[\frac{\partial^{(\gamma)}\mathrm{f}}{\partial \mathrm{X}^{\gamma}}\right](x,y_i)$ is sought that converges rapidly to zero away from the set of discontinuities.

To this end let (x,y_i) be a reconstruction point in the domain i.e. $(x,y_i) \in (a,b) \times \{y_i\}$.

For a given positive integer $m > \gamma$, a local stencil:

$$S_x^{y_i} = \{(x_j,y_i)\backslash(x_j,y_i) \in S_i\} = \{(x_1,y_i),(x_2,y_i),\dots\dots\dots,(x_{m+\gamma+2},y_i)\}, \quad (5)$$

is chosen so that

$$\min\left(\left|S_x^{+y_i}\right|,\left|S_x^{-y_i}\right|\right) > \gamma, \quad \text{with } S_x^{+y_i} = \{(x_j,y_i)\backslash(x_j,y_i) \in S_i \cap x_j x\} \text{ and } S_x^{-y_i} = S_x^{y_i}\backslash S_x^{+y_i}. \quad (6)$$

It is desirable to construct $L_{m,\gamma,S_x^{y_i}}f(x,y_i)$ to be an approximation *to* $\left[\frac{\partial^{(\gamma)}f}{\partial x^{\gamma}}\right](x,y_i)$ such that:

$$L_{m,\gamma,S_x^{y_i}}f(x,y_i) \begin{cases} \left[\frac{\partial^{(\gamma)}f}{\partial x^{\gamma}}\right](\varepsilon,y_i), & \text{if } x_j \le x,\varepsilon \le x_{j+1}, \quad y = y_i \\ & \text{for some } (\varepsilon,y_i) \in J_\gamma \\ 0 & \text{otherwise} \end{cases}$$

$$\text{for } i = 1,\dots\dots\dots,N \quad (7)$$

The γ^{th} partial derivative edge detector, and original edge detector in the case $\gamma = 0$, of order m for stencil $S_x^{y_i}$ at $y = y_i$ is then defined as:

$$L_{m,\gamma,S_x^{y_i}}f(x,y_i) = \frac{1}{q_{m,\gamma}((x,y_i))}\sum_{(x_j,y_i)\in S_x^{y_i}} c_j((x,y_i))f(x_j,y_i). \quad (8)$$

The coefficients c_j are obtained by annihilating one-dimensional polynomials of degree up to *m-1* in the x direction by solving the linear system:

$$\sum_{(x_j,y_i)\in S_x^{y_i}} c_j(x,y_i)p_l(x_j,y_i) = p_l^m(x,y_i), \quad l = 1,\dots,m \tag{9}$$

subjected to constraints:

$$\sum_{(x_j,y_i)\in S_x^{+y_i}} c_j(x,y_i)p_l(x_j,y_i) = h^{-m+\gamma}(x)\, p_l^{\gamma}(x,y_i), \quad l = 0,\dots,\gamma; \tag{10}$$

where the density h or the maximum separation distance is defined as:

$$h(x) = \max\{|x_i - x_{i-1}| : x_i, x_{i-1} \in S_x^{y_i}, \quad y = y_i\} \tag{11}$$

Here p_l, $l = 1\dots m$, is a basis of π_m, the space of all polynomials of degree $\leq m$.

In the case of $\gamma = 0$, the constraint equations are not required.

The normalizing factor $q_{m,\gamma}((x,y_i))$ is given by:

$$q_{m,\gamma}((x,y_i)) = \sum_{(x,y_i)\in S_x^{+y_i}} c_j(x,y_i).\frac{(x-x_j)^{\gamma}}{\gamma!}. \tag{12}$$

The constraints guarantee that this factor is non-zero.

The annihilation of polynomials up to degree m results in all the first m terms in the Taylor expansion of $f(x,y_i)$ becoming zero.

When the remainder of the Taylor expansion is divided by the scaling factor$q_{m,\gamma}((x,y_i))$, a high order of convergence is achieved in the smooth regions.

The polynomial edge and derivative detector may lead to false jumps when using a low order of m, while selecting a large m causes oscillations near the discontinuities.

A *min-mod limiter* over multiple stencils and orders can be used on $L_{m,\gamma,S_x^{y_i}} f(x,y_i)$ to better resolve discontinuities.

Of course the same procedure can be applied also along each line $x = x_j$ (y direction) in the set S already considered in order to localise the discontinuity with more accuracy.

3 NUMERICAL RESULTS

The method has been applied to a delaminated multilayered composite plate in order to demonstrate its effectiveness. The in-plane dimensions of the plate are 300 × 300 mm and the lower horizontal edge is clamped. QUAD4 shell elements (5 × 5 mm) have been employed to discretise the plate domain with the use of the FEM code Nastran.

The stacking sequence of the composite plate is $(0°/45°/–45°/90°)_S$ for a total thickness of 2 mm, the material of each layer is a carbon-epoxy unidirectional composite ($E_1 = 111000$ MPa, $E_2 = 7857$ MPa, $G_{12} = G_{13} = G_{23} = 3290$ MPa, $\nu_{12} = 0.33$, $\rho = 1496$ Kg/m^3). The delamination size is 20 × 20 mm and two through-the-thickness positions:

Damage case A: between 1° and 2° layer

Damage case B: between 3° and 4° layer

have been tested. The geometric centre of the delaminated area is positioned as shown in Figure 1.

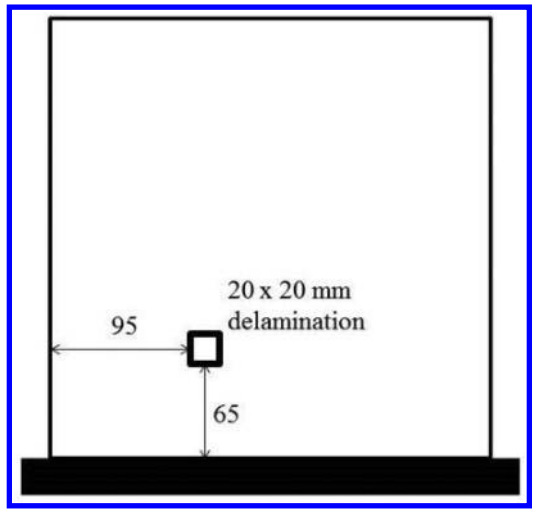


Figure 1. Delaminated multilayer composite plate.

Delaminations have been simulated using a shell element for each of the two thickness domains and attributing to them the correct offset with respect to the reference surface of the whole plate.

The first 36 mode shapes of the plate have been calculated and then to simulate the noise of experimental data white Gaussian noise was added to the data at various signal-to-noise ratios (SNR), utilising the *awgn*() MatLab function.

The PAED2 method has been applied firstly considering a grid of 61x61 points

Figures 2 and 3 illustrate indicative results for the method applied, respectively, to the first mode shape for damage case A and to the tenth mode shape for damage case B.

The subplots (a) and (b) of each figure show the contour plots of jump function approximation calculated respectively in the × and y directions for order $m = 5$ with the use of a central stencil.

In order to clearly visualise the results, a threshold t, has been applied to this function that only data greater than 70% of the maximum value are displayed.

The study reveals that the method is able to determine the location of the delamination in each case. In particular, two ridges appear in correspondence of the two sides of the rectangular delamination orthogonal to the direction in which the procedure has been applied since the discontinuity in the rotation occurs on the boundary of the delamination area

Thus in figure 2 the delamination is correctly located by employing the method with the first mode

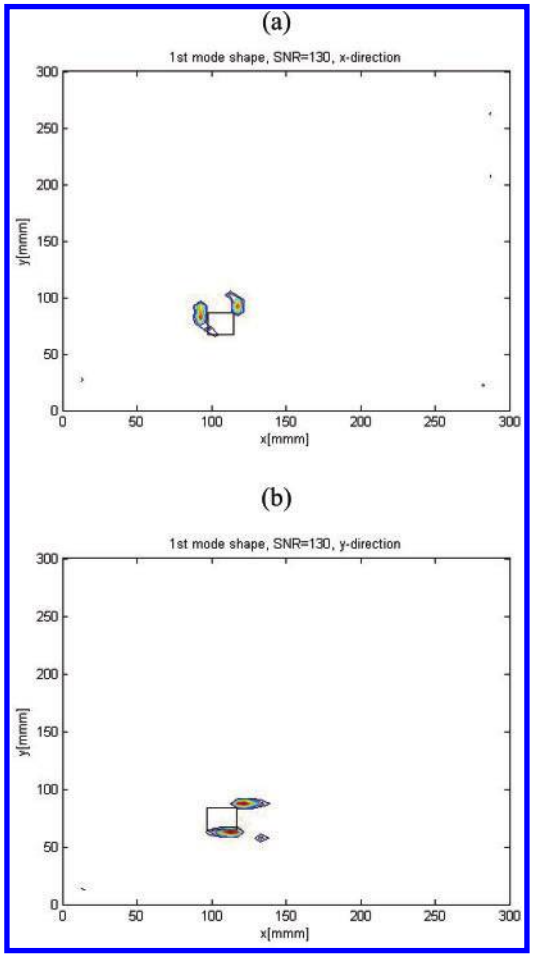


Figure 2. Contour plots of the jump function approximation in damage case A – 1st mode shape – SNR = 130. Grid: 61 × 61 (a) PAED2 method applied in x-direction; (b) PAED2 method applied in y-direction.

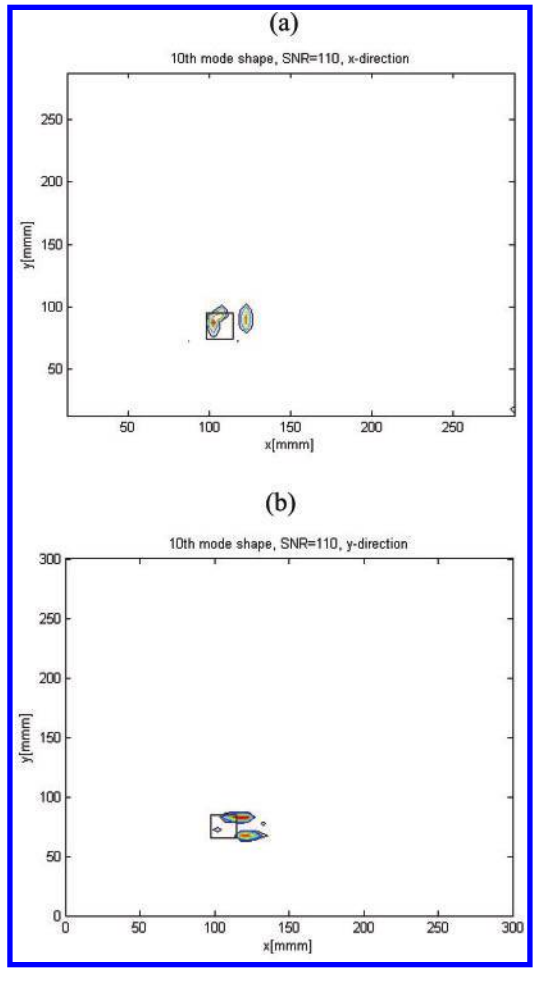


Figure 3. Contour plots of the jump function approximation in damage case B – 10th mode shape – SNR = 110. Grid: 61 × 61 (a) PAED2 method applied in x-direction; (b) PAED2 method applied in y-direction.

shape, when the maximum value of the signal to noise ratio is SNR = 130 while in figure 3 the method has been successfully applied to the 10th mode shape for a SNR = 110.

Afterwards the PAED2 procedure was applied considering a reduced grid of 31 × 31 points.

In figures 4 and 5 the results are reported for damage case B and A respectively. In particular in figure 4 the 20th mode shape polluted by a noise with SNR = 110 has been analysed while in figure 5 the 35th mode shape has been considered with a superimposed noise characterised by a SNR = 70. As the number of grid points is reduced, the method is still able to locate the damage zone but less precisely.

The analysis has been performed with all the 36 mode shapes and, in general it can be said that the modes more sensitive to delamination are the higher as they are local modes.

4 CONCLUSIONS

In this paper a numerical method for detecting discontinuities in smooth piecewise functions and their derivatives, based on a polynomial annihilation technique, has been applied to the problem of delamination detection and localisation in multilayered composite plates. This procedure is based on the fact that in correspondence of the boundary of the delamination area the rotation and hence the first derivative of the mode shapes presents a discontinuity. The performance of this methodology has been analysed with respect to simulated data using a finite element model of the plate for two cases of damage and increasing amounts of noise This method only requires post-damage mode shapes, which is very beneficial to real-world structures, as pre-damage information may not be available in many practical applications.

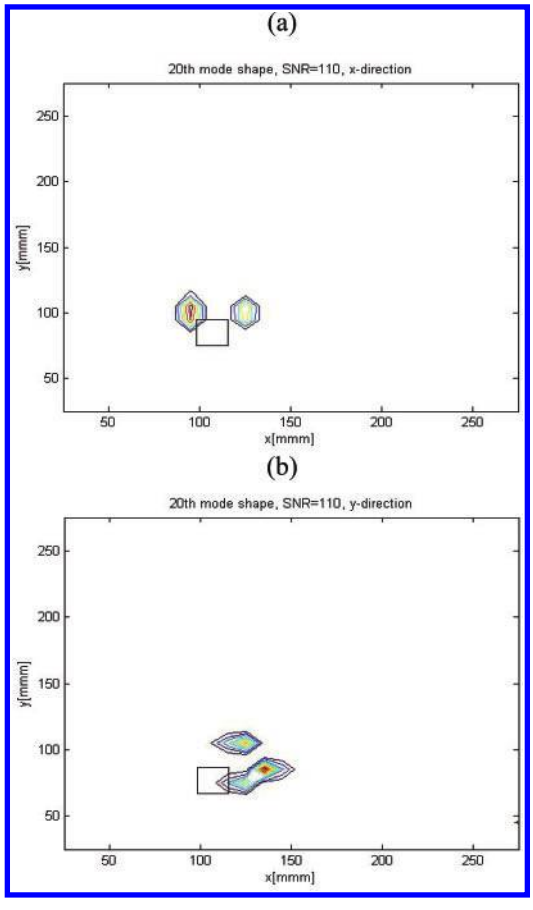


Figure 4. Contour plots of the jump function approximation in damage case B – 20th mode shape – SNR = 110. Grid: 31 × 31 (a) PAED2 method applied in x-direction; (b) PAED2 method applied in y-direction

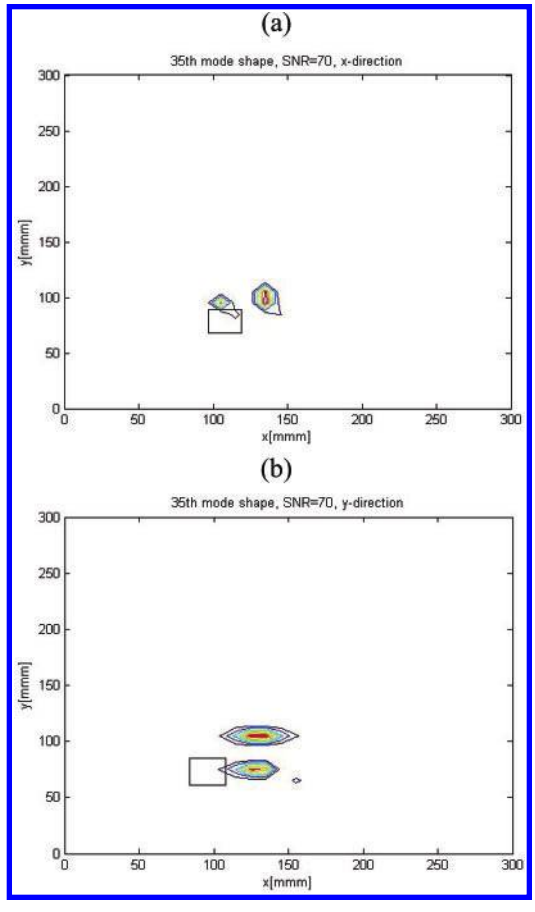


Figure 5. Contour plots of the jump function approximation in damage case A – 35th mode shape – SNR = 70. Grid: 31 × 31 (a) PAED2 method applied in x-direction; (b) PAED2 method applied in y-direction.

The approach requires a reasonably high spatial resolution of the measurement points on structures. This requirement can be addressed employing advanced measurement instrumentation, such as a scanning laser vibrometer, capable of acquiring data in a great number of observation points.

Future work would include experimental validation of the proposed method on a delaminated panel. Different numbers of sensor will be considered to investigate the influence of the sensor distribution density on the effectiveness of the proposed approach.

Finally more further research would comprise improving the derivative edge detection algorithm to make it more robust against noise.

ACKNOWLEDGEMENTS

The authors would like to thank Dr. Saxena for the useful suggestions and discussions.

REFERENCES

Archibald, R., Gelb, A. & Yoon, J. 2008. Determining the locations and discontinuities in the derivatives of functions. *Appl. Num. Math.* 58(5): 577–592.

Battipede, M., Ruotolo R. & Surace C. 2001. Damage detection of plate-like structures. Key Engineering Materials. 204–205: 27–34.

Chang, C.C. & Chen, L.W. 2003. Vibration damage detection of a Timoshenko beam by spatial wavelet based approach. *Appl. Acoustics* 64: 1217–1240.

Chang, C.C. & Chen, L.W. 2005. Detection of the location and size of cracks in the multiple cracked beam by spatial wavelet based approach. *Mech. Syst. Signal Process.* 19: 139–155.

Cornwell, P., Doebling S.W. & Farrar C. R. 1999. Application of the strain energy damage detection method to plate-like structures, *J. of Sound & Vib.* 224(2): 359–374.

Doebling, S.W., Farrar, C.R., Prime, M.B. & Shevitz, D. W. 1996. Damage identification and health monitoring of structural and mechanical systems from changes in their vibration characteristics: a literature review. *Report No. LA-13070-MS, Los Alamos National Laboratory, Los Alamos, NM.*

Douka, E., Loutridis, S. & Trochidis, A. 2003. Crack identification in beams using wavelet analysis, *Int. J. of Solids and Struct.* 40: 3557–3569.

Douka, E., Loutridis, S. & Trochidis, A. 2003. Crack identification in plates using wavelet analysis. *J. of Sound & Vib.* 270: 279–295.

Gherlone, M., Mattone, M., Surace, C., Tassotti, A., & Tessler, A. 2005. Novel Vibration-Based Methods for Detecting Delamination Damage in Composite Plate and Shell Laminates, *Key Eng. Ma*. 293–294: 289–296.

Hensman, J., Surace, C. & Gherlone, M. 2011. Detecting mode shape discontinuities without differentiation: examining a Gaussian process approach, *J. of Phys. Conf. Series, IOP Publishing* 305: 1–10.

Ratcliffe, C.P. 2000. A Frequency and Curvature Based Experimental Method for Locating Damage in Structures.*J. Vib. & Acoust.* 122: 324–329.

Salawu, O.S. & Williams, C. 1994. Damage location using vibration mode shapes, *Proc. of the SPIE, 2251, Proc. of the 12th International Modal Analysis Conference*. 933–941.

Saxena, R. 2008. High order methods for edge detection and applications. *PhD dissertation. Dept. of Mathematics and Statistics, Arizona State University.*

Stubbs, N. & Kim, J.T. 1996. Damage localization in structures without baseline modal parameters. *AIAA Journal*. 34: 1644–1649.

Surace, C., Archibald, R. & Saxena, R. 2013. On the Use of the Polynomial Annihilation Edge Detection for Locating Cracks in Beam-Like Structures. *Computers & Structures*.

Surace, C. Yan, G., Archibald, R., Saxena, R. & Feng, R.. Crack Detection using the Polynomial Annihilation Edge Detection Method. *Australian Journal of Structural Engineering* (*in press*).

Surace, C. Mattone, M., Gherlone, G. Detection and Localisation of Structural Damage Based on the Polynomial Annihilation Edge Detection: An Experimental Verification. *Key Engineering Materials (in press).*

Yoon, M. K., Heider, D., Gillespie, J. W., Ratcliffe C.P. & Crane R.M. 2001. Damage Localization using the Two-Dimensional Gapped Smoothing Method. *46th International SAMPE Symposium/Exhibition, Long Beach Convention Center, Long Beach, CA,* 46: 752–764.

Yoon, M. K., Heider, D., Gillespie, J. W., Ratcliffe C.P. & Crane R.M. 2005. Local damage detection using the two-dimensional gapped smoothing method. J. Sound and Vibration. 279: 119–139

Research and Applications in Structural Engineering, Mechanics and Computation – Zingoni (Ed.)
© 2013 Taylor & Francis Group, London, ISBN 978-1-138-00061-2

On the design of plates and stiffeners of rectangular industrial ducts

T. Thanga
Hatch Ltd, Mississauga, Ontario, Canada

K.S. Sivakumaran
Department of Civil Engineering, McMaster University, Hamilton, Ontario, Canada

B. Halabieh
BAH Enterprises Inc, Oakville, Ontario, Canada

ABSTRACT: The internal pressure and the serviceability limit determine the plate thickness and the stiffener spacing associated with industrial duct, which are currently designed based on elastic large deflection plate theory. The first part of this paper establishes relations between internal pressure and stiffener spacing recognizing the partial yielding, which may result in an economical and efficient duct system. This investigation is based on finite element analysis of long plates made of elastic-plastic steel. Based on a parametric study, the paper presents design equations for industrial plates for three different design scenarios namely; 0%, 16.5% and 33% of through thickness yielding of the plate. The stiffeners are often wide flanged steel beam sections, where one flange is connected to the side panel and the other flange is unsupported. Under suction situation, the unconnected flange is in compression and the duct panel is in tension. Since the tension flange is connected to the remaining system, the duct panel and the web may provide a partial rotational restraint to the compression flange of the stiffeners, which is often not considered in the design. The second part of the paper establishes the bending capacity of such stiffeners. This investigation discovered that the stiffener web slenderness and the overall stiffener slenderness dominate the behavior and the capacity of stiffeners of industrial ducts. The paper establishes the ranges of parameters for different failure modes and it establishes the corresponding bending strengths of the stiffened steel panels.

1 INTRODUCTION

The industrial duct systems, which are often of rectangular cross-section and transport large amounts of pressurized air or flue gases, can be considerably large steel structures. Figure 1 shows the sketch of such a duct system. The positive or negative pressure inside the ducts may be in the range of 10 to 15 kPa. The cross-section is formed by welding together thin steel plates which are stabilized by regularly spaced stiffeners. The cross-sectional dimensions of such industrial rectangular ducts may be 5–15 m. The practical spacing of the stiffeners (B) may be 1–2 m, which results in side wall plate elements with aspect ratio greater than 2, and thus the plate-stiffener system can be treated as a one-way slab system. The selection of stiffener spacing goes hand in hand with the plate thickness, which are determined by considering the allowable stress and deflection of a plate strip between stiffeners. The stress and deflection of the strip of the plate is generally calculated by utilizing the elastic large deflection plate theory which includes the bending stress and the diaphragm stress. However, a stiffened plate can carry loads beyond those causing the first yielding, occurring at the outer fibers at the stiffener locations, due to formation of plastic hinges and the resulting redistribution of stresses. In the first part of this paper, we create design charts and equations for relations between transverse pressure loads, transverse deflections, plate thickness and stiffener spacing, recognizing the benefit of yielding and the deflection limit of side walls of industrial ducts.

In view of the size and in view of the high loading, often, wide flanged structural sections are used as stiffeners, where one of flanges is weld connected to the side walls, whereas the other flange is unbraced and unsupported. When the duct is under suction (negative pressure) the unconnected/unbraced flange would be in compression and the connected flange and the side wall plate would be in tension. Under such loading, the distortional buckling of the stiffener may govern the strength of the stiffened panel. The second part of the paper concerns with the bending capacity and the design of such stiffeners, recognizing the benefits of rotational restraints provided by the duct panels and the web.

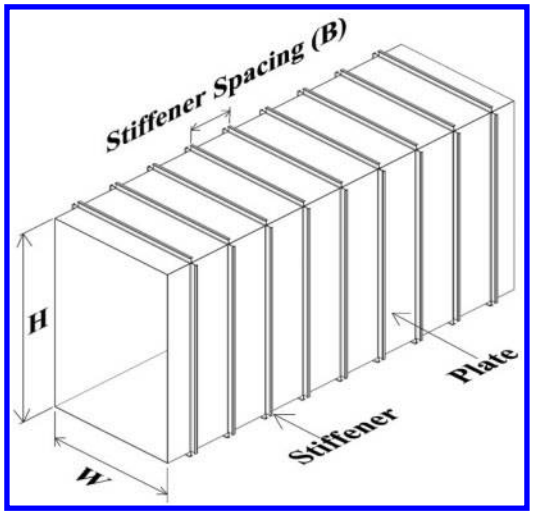


Figure 1. The sketch of a typical rectangular industrial duct.

2 THE CAPACITY OF THE SIDE WALLS (PLATE)

As shown in Figure 1, the plate element under consideration is supported by stiffeners along two of its edges and it is customary to assume that the plate is transversely and rotationally fixed supported, and in-plane held at these edges. Since the length of the plate elements (dimensions H or W) is often considerably larger than the dimension b (clear spacing between the stiffeners), these plate elements are treated as long plates. Therefore, the analysis and design of the plate elements can be based on consideration of a unit width of the plate element subjected to a pressure p. A total of 8 fundamental parameters, plate length b, thickness t, Young's modulus E, yield stress Fy, lateral pressure p, lateral deflection at mid-span δ, the total stress σ_t and the membrane stress σ_m, characterize the behavior, including the strength and the deformation, of laterally loaded plate. Note that the total longitudinal stress is the sum of the longitudinal bending stress σ_b and longitudinal membrane stress σ_m. The Poisson's ratio for a steel plate can be taken as 0.3. Without going into details, through dimensional analysis, these variables have been reduced to five non-dimensional parameters of significance that have been used in this investigation so that the results may be applied to a wider range of problems. They are; load parameter $Q = pE/(Fy^2)$, plate slenderness parameter $\beta = (b/t)(\sqrt{(Fy/E)}$, normalized deflection $\Delta = \delta/t$, normalized total stress $T = \sigma_t/Fy$, and normalized membrane stress $U = \sigma_m/Fy$. The validity (i.e. independence from scale and material characteristics) of these parameters for strength analysis, including partial yielding, was confirmed through nonlinear finite element analyses of plates (Thanga 2012).

A finite element model for the side wall plate, represented as a long plate was developed using the commercial multi-purpose nonlinear finite element program ADINA (2009). Figure 2 shows the overview of the plate under consideration. In this study, incremental nonlinear static finite element analysis was performed. In the finite element model the strip of plate was assumed to be fixed in such a manner that they cannot rotate nor pull in from two edges attached to stiffeners. The plate was subjected to increasing uniform lateral pressure p. The plate material was chosen to be carbon steel Grade A36 and assumed to be elastic-perfectly plastic material. The material properties of Grade A36 carbon steel are Elastic Modulus E = 200,000 MPa, Poisson Ratio $\upsilon = 0.3$ and Yield Strength Fy = 250 MPa. A four-node nonlinear shell element based on Mindlin/Reissner plate theory was used, which can be employed to model thick and thin general shell structures. von Mises yield criterion and isotropic hardening rule captured the yielding behavior. Furthermore, in order to simulate through thickness yielding, Newton-Cotes integration scheme with seven integration points were used in the thickness direction. From the results, the x directional stresses and strains at the support for each time step and for all integration points through thickness were obtained. The membrane stresses for each time step were calculated from the stress obtained at seven integration points through thickness. The pressure load and deflections for the case of onset of yielding at the first, second and third integration points were obtained. These correspond to 0%, 16.5% and 33% of through thickness yielding of the plate.

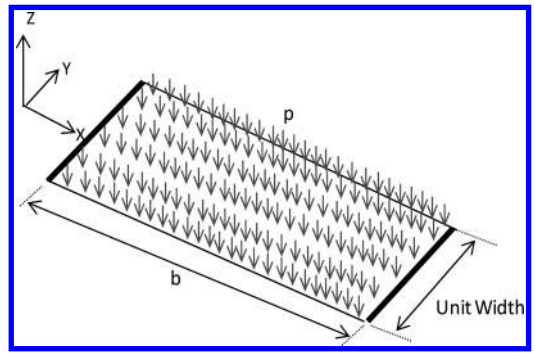


Figure 2. Side wall idealized as a long plate.

In practice, the ratio of stiffener spacing to plate thickness b/t is generally in the range of 125 to 350, thus analysis considered plate models having b/t = 125, 150, 175, 200, 225, 250, 275, 300, 325 and 350. Based on these parametric analyses, the limiting load parameters corresponding to different stages of partial yielding and the corresponding normalized peak deflections (at mid-span) and the normalized membrane stresses were established, and are graphically presented herein as Figures 3, 4, and 5. The relationship between the plate slenderness parameter $\beta = (b/t)/\sqrt{(Fy/E)}$ and the dimensionless limiting load parameter $Q = pE/(Fy^2)$, corresponding to three strength criteria, namely, onset of top fibre yielding and 16.5% and 33% of plate

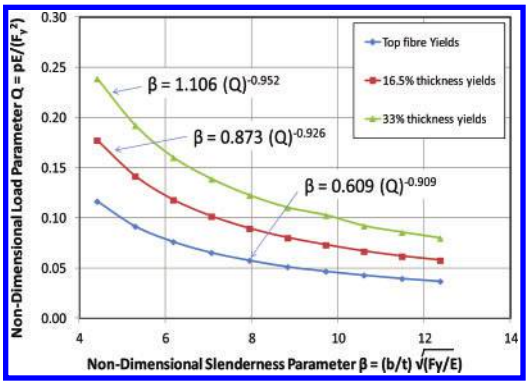


Figure 3. Load versus plate slenderness relations.

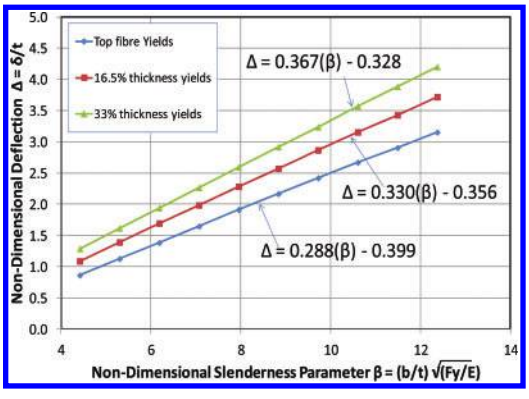


Figure 4. Deflection versus plate slenderness relations.

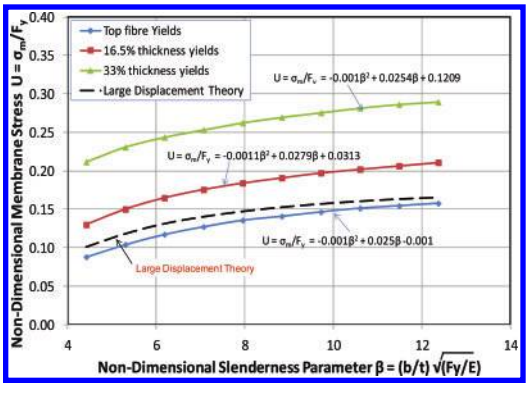


Figure 5. Membrane stress versus plate slenderness relations.

thickness yielding, are shown in Figure 3. It is evident from this figure that if the strength criterion permits plates undergoing partial yielding then the plates can carry higher lateral loads. For a given slenderness, the load resistance can be increased by approximately 55% for 16.5% partial yielding, and it can be increased by 113% by permitting 33% partial yielding. Power law based trend line equations for these plots were generated for designer's convenience and are also shown in this figure. Thus, a designer can decide on a strength criterion and choose the required slenderness (stiffener spacing) for a known load parameter. For example, if the strength criterion of 16.5% thickness yield is used to design a 5 mm thick steel (Grade A36 - Fy = 250 MPa) duct for a design internal pressure of 20 kPa (non-dimensional load parameter value of 0.064), the necessary slenderness parameter is $\beta \leq 11.13$, and the corresponding stiffener spacing is $b \leq 1575$ mm. The load corresponding to $\beta = 11.13$ at which the first yield occurs can be obtained from the graphs or through inverse relations given in Figure 3 as $Q = 0.041$, which corresponds to a pressure of 12.78 kPa. Therefore, the duct plate will not yield under service conditions, provided the service operating pressure is less than 12.78 kPa.

Figure 4 shows the relations between normalized peak deflection versus plate slenderness parameter corresponding to the three strength criteria under consideration. These relations are linear and the corresponding design equations are also given in Figure 4. The peak deflection of the plate corresponding to slenderness of the side wall plate of 11.13 at first yield can be obtained either from Figure 4 or from the relations $\Delta = 0.288(\beta) - 0.399$ as $\Delta = 2.806$. The corresponding deflection is 14.0 mm. Assuming an operating pressure of 12 kPa, the deflection at the operating pressure can be proportioned as 13.2 mm. In the design of rectangular industrial ducts under consideration, the generally accepted deflection limit is one hundredth of the stiffener spacing (b/100) or for this example 1575 mm/100 = 15.8 mm, therefore the partially yielding plate satisfies the serviceability limit. The deflection at ultimate limit state, that is when the pressure is 20 kPa or $Q = 0.064$, can be obtained either from Figure 4 plot corresponding to 16.5% yielding or from the relations $\Delta = 0.330(\beta) - 0.356$ as $\Delta = 3.317$ or 16.6 mm.

Figure 5 shows the relations between the non-dimensional membrane stress $U = \sigma_m/Fy$ and the slenderness parameter. It can be observed that the slender plates experience larger membrane stresses since such plates tend to resist the transverse loads through catenary action than bending action. It can also be observed that partial yielding causes increased membrane stresses. As presented earlier, the selection of plate thickness and stiffener spacing is based on total stress, which is the combination of the membrane stresses σ_m and the bending stress σ_b, and thus it is not really necessary to focus on the membrane stresses, except for the membrane stress σ_m in the end panel. In an interior panel, the in-plane forces due to the membrane stress σ_m are balanced by similar stresses that exist in the plates on either side of the interior plate under consideration. However, the membrane stress σ_m associated with the end panel needs to be externally resisted as the plate discontinues at the last stiffener.

3 THE CAPACITY OF THE STIFFENER

In view of the high loading and large size often, wide flanged structural sections are used as stiffeners. Figure 6 shows the general arrangement of the stiffened panel under suction and the repetitive pattern a structural engineer may consider for analysis and design of the stiffener. Under such loading, it appears that the strength of the stiffened panel may be controlled by lateral-torsional buckling of the stiffener. However, because of the constraints provided by the sidewalls, the stiffeners of the industrial duct may be treated as fully restrained against lateral translation and perhaps elastically restrained against twist. Under this scenario, the stiffener may undergo elastic or inelastic distortional buckling of the web rather than overall lateral-torsional buckling. Various researchers (Hancock, et al. 1980, Bradford and Trahair 1981, Bradford 1999) have built beam type finite elements to capture the web distortional buckling of beams. With the available plate/shell finite elements and the computing power, more precise modeling of stiffened steel plate panels can be achieved, where factors such as residual stresses and initial imperfections can be explicitly incorporated into such numerical models. Here we describe such a finite element model built for this study using Finite Element (FE) software package ADINA (2009).

The stiffeners in the duct are often equally spaced on the sides of the industrial duct. Because of the symmetry of stiffeners, only one repetitive panel as shown in Figure 6, i.e. a portion of the plate of width B with the stiffener centered on the plat strip, need to be modeled. The large deflection of laterally loaded stiffened plate panel involves in-plane and out-of-plane displacements. Therefore, shell element was used to study the behavior of the laterally loaded plate. The 4-node nonlinear shell element with the shell mid-surface nodal points was formulated with the assumptions used in the Timoshenko beam theory and the Mindlin/Reissner plate theory. The shell element used in this study can be employed to model thick and thin general shell structures, undergoing large displacement/small strains. The material model selected for the elements was elasto-plastic-multilinear material model with von Mises yield criterion, associated flow plasticity based on isotropic hardening rule. In order to capture the onset and spread of material yielding through thickness the Newton-Cotes rule with seven integration points was chosen. The Load Displacement Control (LDC) method of ADINA(2009) was used to capture the loading and unloading regions of the pressure load-lateral deflection response. The LDC method uses the load magnitude as the unknown and controls the incremental displacement from the load-displacement response. This method will terminate the computations at a user defined displacement.

Geometric imperfections may exist in plate elements of stiffened plate panels, thus the current study incorporated a double sine wave geometric imperfection. In general, the lines of web/flange intersections were defined to be straight, and either the middle line or the free edges along the length direction was defined to form a number of half sine waves. The Canadian standard for general requirements structural quality steel (CISC 2010) permits a maximum variation in straightness of the plate of 0.001 times of length of half sine wave, which was assigned here as the peak imperfection. The stiffener residual stresses were taken to be of a linear pattern with a peak compressive and tensile stresses of 0.3Fy, where Fy is the yield strength. The welding operations cause tensile stresses at the weld location and compressive stresses in adjacent areas. Staggered intermittent fillet welds are widely used in industrial ducts to connect the flange tip of the stiffener to the plate. In this analysis, a linearly varying tensile stresses (peak value of 0.5Fy) were assumed to exist in the plate to a distance of bf/6 on either side of the flange tip, where, bf is the flange width of the stiffener. Equilibrating compressive stresses were assumed to be of uniform distribution of value 0.125Fy over a distance of bf/3 on either side of the tensile stresses. The residual stresses were incorporated into the FE model as initial strains at nodal points.

Due to the severe nature of the material and geometric nonlinearities involved in the current analyses, a very dense mesh of shell elements was desirable in order to trace the nonlinear equilibrium path into the unloading regime. Based on a mesh density convergence study a dense mesh containing 5920 elements were used in the analysis. In actual physical dimensions, each element in this mesh is of size 50 mm × 20 mm. Figure 7 shows such a FE model.

The proposed finite element model was applied to an experimental study Udall (2007) conducted on such stiffened plates. To simulate the loading and the boundary condition of industrial duct, Udall (2007)

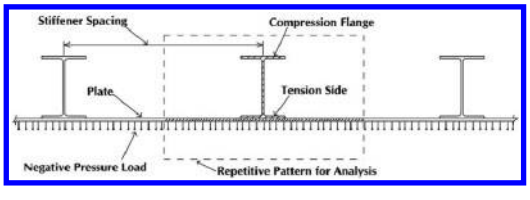


Figure 6. Configuration of an industrial duct stiffener.

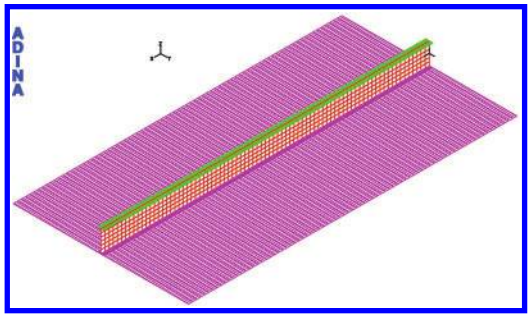


Figure 7. The finite element model of stiffener and side wall.

made a shallow box with removable top, which contained the plate and a stiffener. The box was made air tight and a vacuum pump caused suction pressure load. This arrangement simulated a single stiffener and plate between adjacent stiffeners subjected to lateral pressure. The size of the box was 4572 mm × 2438 mm in plan area and 152 mm deep. The thickness of plate was 4.76 mm and was made of ASTM 44 W steel having 300 MPa nominal yield strength. The test stiffeners were W8 × 18 wide flange sections made of A992 steel having 345 MPa nominal yield strength. W8 × 18 stiffener is considered a slender sections. The experiment was repeated two times. In the FE materials models for A992 and 44W steel grades the Young Modulus E for both grades was taken as 200 GPa, giving a corresponding yield strains of 0.001725 and 0.0015, respectively. An yield plateau was considered, and the strains at initiation of strain hardening for these steel grades were taken as 0.0345, and 0.03, respectively. The strain hardening slope E_{st} was considered to be (E/30 = 6.67 GPa). The ultimate strength of A992 and 44W steel grades were taken to be 450 MPa, and 400MPa, respectively.

The nodes along the four edges of the plate were constrained against translations and rotations, thereby creating fixed boundary conditions. The out-of-plane and in-plane lateral translation of flange and web of the stiffeners were not prevented, during the experiment and in the analysis, in order to create the case of an actual industrial duct structure. The analytical and experimental results for stiffened plate panel consisting of W8 × 18 stiffener are shown in Figure 8. The vertical and horizontal axes represent the pressure load in kPa and mid-span deflections in mm, respectively. It could be observed that the FE analysis results agree very well with the experimental results. The shapes of the curves are similar and the measured and the analytical strengths are comparable.

The failure of stiffened plate is primarily due to distortional buckling of the stiffener compression flange leading to section reaching its flexural capacity. The fundamental geometric and mechanical parameters affecting the behavior and strength of stiffener of the rectangular industrial duct are; B width of the plate (stiffener spacing), t plate thickness, h_w stiffener web height, t_w stiffener web thickness, b_f stiffener flange width, t_f stiffener flange thickness, L stiffener length, F_{ys} yield stress of stiffener material, F_{yp} yield stress of plate material, E Young's modulus of steel and M_a applied bending moment. Without going into details, through a dimensional analysis, it can be shown that the following five non-dimensional parameters, namely, β_1, β_2, β_3, β_4, M govern the behavior of a stiffened plate, where;

$\beta_1 = (b_f/t_f)\sqrt{(F_{ys}/E)}$ – stiffener flange flexural slenderness

$\beta_2 = ([h_w - 2t_f]/t_w)\sqrt{(F_{ys}/E)}$ – web flexural slenderness

$\beta_3 = (B/t)\sqrt{(F_{yp}/E)}$ – side wall plate slenderness

$\beta_4 = (L/r)\sqrt{(F_{ys}/E)}$ – stiffener overall slenderness

and M = Ma/My, where My is the yield moment capacity of the stiffened plate panel.

Eight models of stiffened plate panels each having identical dimensionless parameters $\beta_1 = 0.654$, $\beta_2 = 1.749$, $\beta_3 = 7.701$ and $\beta_4 = 7.889$ with different actual values for B, t, h_w, t_w, b_f, t_f, L, F_{ys} and F_{yp} were analyzed. The initial geometric imperfections and residual stresses were the same in all models. Figure 9 shows the non-dimensional applied bending moment (Ma/My) versus mid span vertical deflection Δ responses for all eight models. The ultimate moment can be easily obtained from these graphs, however, the Southwell plot method was used to obtain the distortional buckling moment Mcr of the stiffeners. Even though the yield moment My of these cases range between 93.4 kN.m. and 188.3 kN.m, the mean and standard deviation of normalized moments Mcr/My for all analysis models were found to be 1.138 and 0.002, respectively. Similarly, the mean and standard deviation for Mu/My of all models were found to be 1.159 and 0.002, respectively.

Therefore, it can be concluded that the dimensionless parameters identified above completely represent the behavior of stiffened plate panels associated with the industrial ducts. The impact of each of the parameters were investigated and the observations are summarized here in brief. For all intents and purposes,

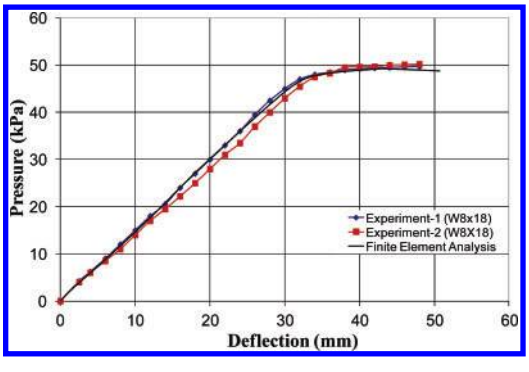


Figure 8. Pressure versus mid-span deflection of duct.

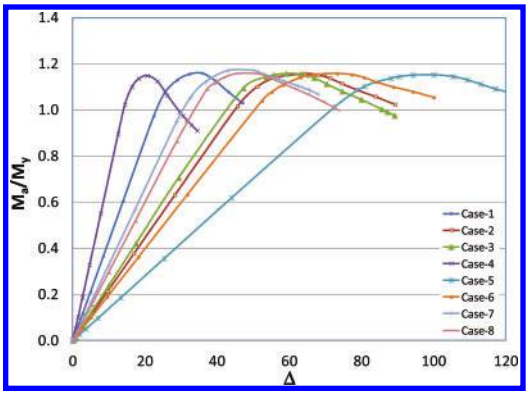


Figure 9. Normalized applied moment versus deflection.

the plate slenderness parameter β_3 did not influence the distortional buckling capacity or the flexural strength of stiffened plate panels subjected to negative pressure. Parametric studies indicated that when the stiffener slenderness parameter β_1 is less than one the system experiences distortional buckling at a moment of 1.163 My. When β_1 is greater than one, the stiffener flange experiences lo cal buckling resulting in reduced overall buckling strength and moment capacity. It was observed that most of the rolled steel sections contain compact flanges, and thus the value of stiffener flange slenderness parameter β_1 for these sections were noted to be less than 1. Therefore, it was concluded that for practical steel sections stiffener flange slenderness parameter β_1 did not influence the distortional buckling capacity or the flexural strength of stiffened plate panels subjected to negative pressure.

It was observed that the distortional buckle has a wave length (and an associated buckling moment) whose value depends on web flexural slenderness parameter β_2. It was also observed that there is a corresponding value of stiffener overall slenderness parameter, say, $\beta_{4(\text{critical})}$. There is no change in buckling moment for stiffeners having β_4 greater than the critical value $\beta_{4(\text{critical})}$. Thus, it was concluded that $\beta_4 > [\beta_{4(\text{critical})} = 3.33\ \beta_2 + 0.145]$ do not change the failure mode. It was further concluded that the stiffened plate system reaches the yield moment My, if $\beta_2 > 2$ and $\beta_4 > 3.33\ \beta_2 + 0.145$. For system having $\beta_2 < 2$ and $\beta_4 > 3.33\ \beta_2 + 0.145$ the distortional buckling moment can be established as Mcr = (1.51–0.275 β_2) My. Further details of this investigation are available in the thesis by Tharani (2012).

4 REMARKS

Based on finite element analysis of long steel plates subjected to pressure, this paper established the relations between pressure and plate slenderness parameter and between plate deflections and the slenderness parameter for three different design scenarios namely; 0%, 16.5% and 33% of through thickness yielding of the plate. Based on these results design equations have been derived for the convenience of designers of rectangular industrial ducts.

Under negative pressure (suction) situation, the unconnected flange of the stiffener of rectangular industrial duct side panels is in compression and the duct panel is in tension. The tension flange, which is connected to the duct panel, and the web may provide a partial rotational restraint to the compression flange of the stiffeners, thus the establishment of the bending capacity and the design of such stiffened steel panels are not straightforward. Finite element analysis models were built using the finite element software ADINA(2009). The finite element model included reasonable geometric imperfections and residual stresses. In order to capture the onset and spread of material yielding through thickness the Newton-Cotes rule with seven integration points was used. The Load Displacement Control (LDC) method was used to capture the loading and unloading regions of the pressure load-lateral deflection response. The finite element model was validated through comparison with experimental results. The difference between the predicted bending capacity and the measured capacity for the stiffener W8 × 18 is about 1%. Based on dimensional analysis the five non-dimensional parameters, namely, β_1, $\beta_2, \beta_3, \beta_4$, M those govern the behavior of a stiffened plate were identified. The finite element model discussed in this paper was used in a parametric study which resulted in design guidelines for such industrial ducts. However, in the interest brevity, these details are not given in this paper but may be available in future publications.

REFERENCES

ADINA , (2009), "ADINA 8.5 user manual." ADINA R & D Inc, Watertown, MA, USA.

ASCE, (1995), The Structural Design of Air and Gas Ducts for Power Stations and Industrial Boiler Applications, Air and Gas Structural Design Committee of the Energy Division of the ASCE, Reston.

Bradford, M.A., (1999), "Distortional Buckling Strength of Elastically Restrained Monosymmetric I-beams", Thin Walled Structures, Vol. 9, pp. 339–50.

Bradford, M.A., and Trahair, N.S.,(1981), "Distortional buckling of I-beams", J. Struct. Div., ASCE Vol.107 (ST2), pp. 355–370.

CISC, (2010), Handbook of Steel Construction, 10th Edition, Canadian Institute of Steel Construction, Markham, Ontario, Canada.

Hancock, G.J., Bradford, M.A., Trahair, N.S., (1980), "Web Distortion and Flexural Torsional Buckling", Journal of Structural Engineering, ASCE , Vol.106(ST7), pp. 1557–71.

Thanga, T. (2012), "Design Methods for Large Rectangular Industrial Ducts", Ph.D. Thesis, McMaster University, Hamilton, Ontario, Canada, p. xiii, p. 328.

Wang, D., EI-Sheikh, A.I., (2005), Large Deflection Mathematical Analysis of Rectangular Plates, Journal of Engineering Mechanics, ASCE, 131(8), 809–821.

Udall, J.D., (2007), "Effective Design of Stiffener on Industrial Ducts", Master Thesis, McMaster University, Hamilton, Canada.

Young, W.C., and Budynas, R.G., (2002), Roark's Formulas for Stress & Strain. 7th edition. McGraw Hill, New York.

Research and Applications in Structural Engineering, Mechanics and Computation – Zingoni (Ed.)
© 2013 Taylor & Francis Group, London, ISBN 978-1-138-00061-2

Structural behaviour of flexible straws

B. Zhang & Z. You
Department of Engineering Science, University of Oxford, Oxford, UK

ABSTRACT: The structural behaviour of flexible straws is investigated. Finite element models of conical frustum shells with reference to a real flexible straw are built and analysed. Moreover a parametric study is carried out. The results show that the collapse mechanism can vary due to different geometric configurations. The critical load which causes the snap-through is dependent of the geometric configurations as well.

1 INTRODUCTION

1.1 *Background*

Fascinating structural behaviour can be found on commonly-used utensils. A drinking straw is a thin-walled tube that a drinker uses to suck a beverage from its container. Flexible straws, or bendy straws, contains a corrugated portion that allows a kink being created and hence the flexibility. Modern flexible straws are normally made of Polypropylene (PP) and the corrugated portion has a shape shown in Figure 1.

Flexible straw belongs to a family of multi-stable thin-walled structures, such as Ping-Pong balls and a type of candy box, where inversion could occur under certain loadings. This behaviour is highly dependent on the ductility of the materials, e.g. it is impossible to push an egg, which is geometrically similar to a ping pong ball, into an inverted shape without fracturing it.

1.2 *Past Work*

1.2.1 *Snap-Through*

The snap-through behaviour is related to the flexible straw performance and is best illustrated by a 2D truss structure (Fig. 2) that consists of two identical rigid rods of length L connected with a pin joint at one end and supported by a pin joint and a roller with a horizontal linear spring of stiffness k at the other, respectively (Thompson and Hunt, 1973).

Initially, they are at an angle α to the horizontal line. When a concentrated load P is applied at the middle joint, angle α decreases to θ and the length of the spring decreases as well. The force due to the change in length of the spring is

$$F = 2kL(cos\theta - cos\alpha) \tag{1}$$

From the force equilibrium in the vertical direction, the downward force P can be written in terms of θ as

$$P = 4kL(sin\theta - cos\alpha\ tan\theta) \tag{2}$$

If we plot P against θ, the graph shown in Figure 3 is obtained. Starting at $\theta = \alpha$, the loading path is stable until the 'limit point' is reached. The model



Figure 1. The corrugated portions of flexible straws.

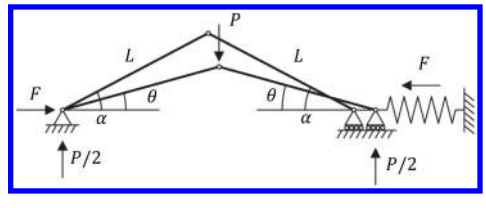


Figure 2. A basic 2D snap-through model.

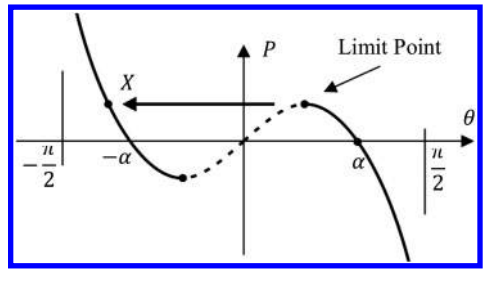


Figure 3. Plot of P againstθ in snap-through model.

snaps through to the point X. Though the path (dashed line in Figure 4) satisfies force equilibrium, they will not exist during an increasing force loading as the stability criteria cannot be met. The limit point is at $dP/d\theta = 0$, so

$$P_{cr} = 4kL[1 - (cos\alpha)^{2/3}]^{3/2} \quad (3)$$

If the load is released at point X, the model does not go back to its original shape. It follows the path back to the point at $\theta = -\alpha$, which is the second stable state of the model.

1.2.2 *Inversion of a Spherical Shell and a Egg-box*

Calladine (1985) summarised the inversion behaviour of some of the shell structures with large plastic deformations. One of his cases was the progressive inversion of a spherical shell. He proposed a plastic travelling hinge model to describe the progressive inversion behaviour of a spherical shell under downward point load.

A common egg-box consists of many close-top conical frusta which are arranged in lattice pattern. Deshpande & Fleck (2003) analysed the structural behaviour of an egg-box based on a modified plastic travelling hinge model.

As shown in Figure 4, the dash and solid lines represent the original and deformed shapes, respectively. The frustum is compressed between two frictionless rigid plates. They gave a following relationship between P and u,

$$\frac{P}{Yt^2} = \frac{2\pi tan\omega}{(2\omega - sin2\omega)^{1/2}}\left[\frac{a}{t} + \frac{u}{t}cot\omega\right]^{1/2} \quad (4)$$

It is noticed that Equation 4 is not applicable around the origin due to the assumption of the model. Hence the force that initiates the snap-through cannot be found by this model.

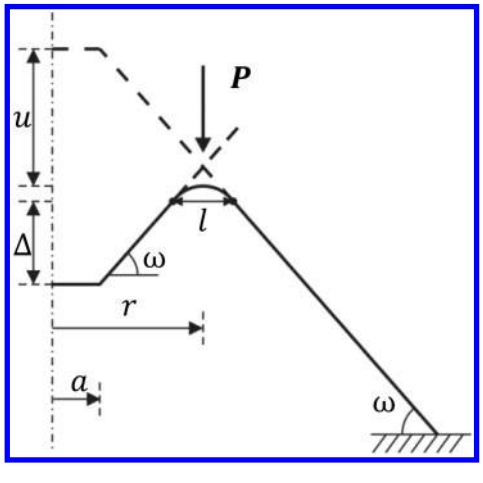


Figure 4. Cross-section of a closed-top conical frustum shell with thickness t.

1.3 *Objectives and Layout*

This paper examines the inversion behaviour of the flexible straw with the aim to utilise this feature in the design of energy absorption and multi-stable structures.

The layout of this paper is as follows. First in Chapter 2, the characteristics of flexible straws and a simplified geometrical model is presented, which are used in the subsequent analysis. Numerical analysis based on the finite element simulation is introduced in Chapter 3, followed by results and discussion in Chapter 4. Finally, final remarks and further work are given in Chapter 5, which concludes the paper.

2 GEOMETRIES

2.1 *Characteristics of a Flexible Straw*

A corrugated portion of a flexible straw shown in Figure 5a can be transformed into two states. It can shrink into that of Figure 5b, or be bent into that of Figure 5c. All of these three states are stable. The basic element of the flexible straws is a pair of conical frustum shells which are joined together. During each transformation, the deformation of the taller frustum is negligible hence it is reasonable to treat the taller frustum as a rigid body. Therefore, the deformation of the shorter frustum is considered lonely in this paper. The geometry of a frustum shell can be defined by tilting angle ω, bottom radius R_b, top radius R_t and shell thickness t, hence the height of the frustum h can be found in terms of ω, R_b and R_t, as shown in Figure 6. By observation, it was found that no distinct progressive inversion occurs during the transformation of the flexible straw, i.e. no formation of travelling hinges. It was expected that this was due to its dimensions and materials of the structure. We set out to prove this.

2.2 *Configurations for the Default Frustum and Variations*

The geometrical data of a typical flexible straw, given in Table 1, was measured and treated as a default frustum. Subsequently geometric parametric study was carried out by varying the height h, the tilt angle ω and the thickness t of the default frustum.

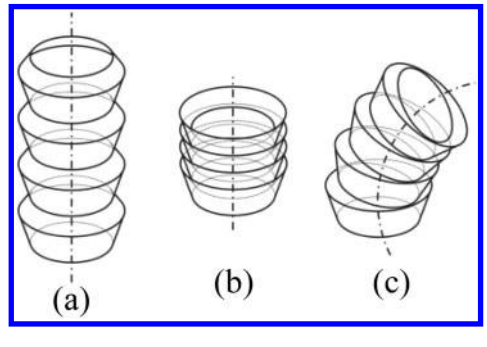


Figure 5. Three stable states of a corrugation portion of a flexible straw.

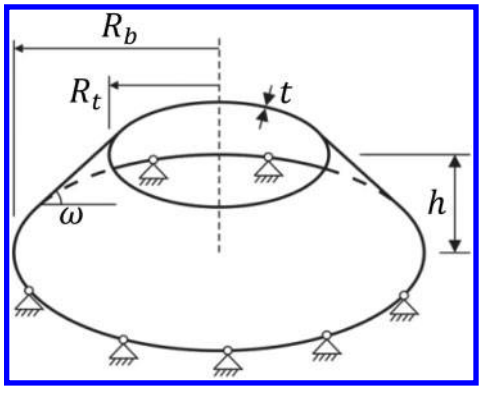


Figure 6. Configuration of a conical frustum shell.

Table 1. Typical data of the shorter frustum of flexible straws.

Dimension Type	Value & Units
Bottom Radius, R_b	2.95 mm
Top Radius, R_t	2.4 mm
Tilt Angle, ω	38.02°
Shell thickness, t	0.15 mm
Height, h	0.43 mm
Side length	0.698 mm

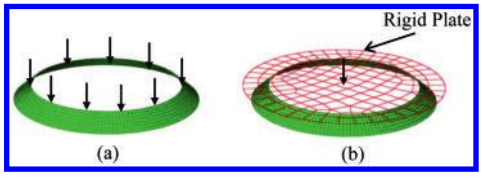


Figure 7. Two loading methods for the FE simulations.

3 NUMERICAL SIMULATION

Finite element (FE) simulations were performed using the general purpose finite element package ABAQUS Ver.6.10 (DSS 2010). A default frustum and several variations were built using shell elements according to the dimensions provided previously. The base of the frustum was constrained to have no relative displacement but free to rotate.

3.1 *Loading Methods*

In order to simulate the transformation of the shorter frustum and capture the inversion process, where a decrease in force has to be allowed in the loading history, the displacement-control loading was used in the simulations and the corresponding reaction force caused by the displacement was monitored and recorded. Two loading methods were considered: ring loading (Fig. 7a) and plate loading (Fig. 7b).

Table 2. Properties of Polypropylene (PP)

Property Name	Value & Units
Young's Modulus, E	1300 N/mm^2
Poisson's Ratio, ν	0.45
Yield Stress, σ_y	25 N/mm^2
Yield Strain, ε_y	1.9%
Density, ρ	940 kg/m^3

3.2 *Material Models*

Measuring the materials properties of this particular kind of straws is difficult. It was decided to use mean values of the PP's properties. Table 2 lists the values which are used in the simulation. The material was treated as an isotropic material. Two material models were used in the simulation: linear elastic (LE) and elastic-perfectly plastic (EPP).

3.3 *Solving Scheme*

The inversion was assumed to be a quasi-static problem, and hence no kinetic energy was associated with the problem. An implicit analysis was the best fit of the requirement. In this method, the stiffness matrix must be updated and reconstructed at each iteration due to the high non-linearity of the problems, and thus the analysis was computationally costly. An explicit analysis was used instead when the computational time was too long. In the implicit FE analysis, two nonlinear different iterative solution methods, the full Newton method and Riks method were used and the results were compared.

3.4 *Meshing*

The size of each shell element was controlled to be approximate 0.1 mm on the frustum. Hence, the default frustum had a total of 1141 shell elements. For the frusta with various tilt angles or thicknesses, the mesh has no difference from the default frustum. More elements of the same size were seeded for the frusta of various other heights accordingly.

4 SELECTED RESULTS AND DISCUSSION

4.1 *The Default Frustum*

Five simulations were carried out for the default frustum itself. The results are plotted at Figure 8.

As expected, the snap-through behaviour during the inversion has been captured in the analysis since the plots are quite similar to that shown in Figure 3.

No matter what loading method or solving scheme was used, the results were similar for same material model, which means the explicit scheme did a fair job on quasi-static simulations and the loading method did not affect the response. It is showing clearly on the graph that the critical force was larger for an LE material than that of an EPP one, given that Young's Modulus was the same. They followed the same loading path at the beginning and separated after the EPP

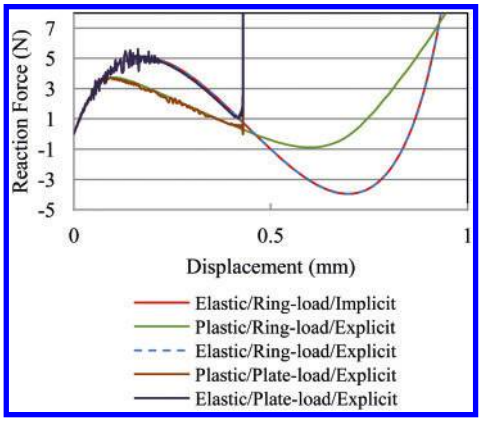


Figure 8. The default frustum results using different solving scheme.

material yielded. Afterwards, the reaction forces of EPP frusta started to drop while forces of the elastic frusta kept rising until its critical forces were reached.

For both plate-load/explicit cases, a sudden force increment to infinity was observed when the displacement was about 0.43 mm, which was the height of the frustum. This happened when the loading plate touched the bottom plane of the frustum, which could not be penetrated according to the boundary conditions.

4.2 *Frusta of Various Heights*

Including the default configuration, frusta with five different heights were analysed. The ring-load method was used for the LE material and the plate-load method was used for the EPP material.

4.2.1 *LE Material*

The results are plotted in Figure 9. Results from the Newton method and Riks method agreed well with each other at the beginning. Some of the load history started to split then. This was because the Newton method used displacement as increment while the Riks method used a varying load-factor which was modified at each iteration until convergence was achieved. The load history obtained by the Riks method indicated other possible equilibriums but was not energetically favourable in this case, and hence these paths could not exist in reality.

As the height increased, the value of the critical forces varied. The shape of the loading path changed as well. Initially, the default frustum gave a sine-like curve; as the height went larger, a rather flat zone in the force graph was formed and the zone expanded when the initial height increased. Figure 9b shows the deformed shape of the case of a 1.65 mm high frustum at point I, II and III.

4.2.2 *EPP Material*

The results are shown in Figure 10. The critical force increased as the height increased until the height reached 1.15 mm. A knuckle region was formed on the structure afterwards. A second local peak of force

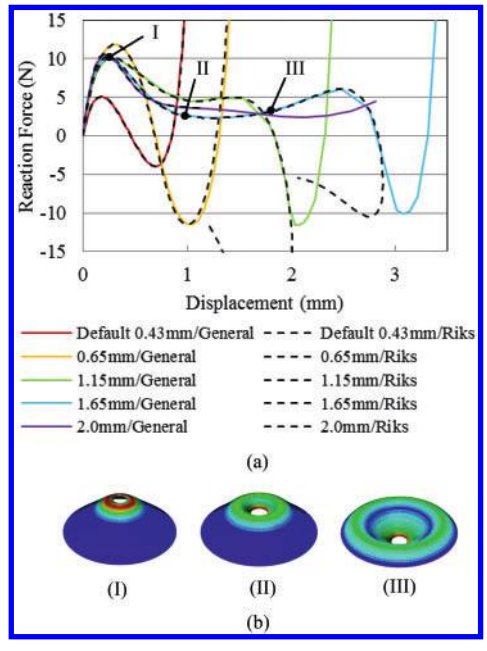


Figure 9. Results from LE frusta with various heights.

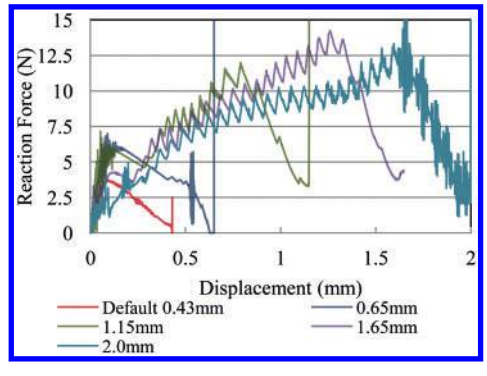


Figure 10. Results from EPP frusta with various heights.

started to appear on the graph and overtake the initial critical force. In other words, the one-off snap was replaced by two snaps at the beginning and the end, and progressive inversion in the middle of the deformation history. It is also noticed that first local force peak disappeared when the height reached 2.0 mm. Figure 11 summarises these changes of loading histories as height increased schematically. The collapse mechanism changes to different modes as the height increases.

The FE results of reaction forces within the progressive inversion region fits well with what the Deshpande & Fleck's model describes. A detailed comparison between FE results and analytic predictions is given later in this Chapter.

4.3 *Frusta of Various Tilt Angles*

Including the default configuration, frusta with five different tilt angles were analysed. They were 38.02°

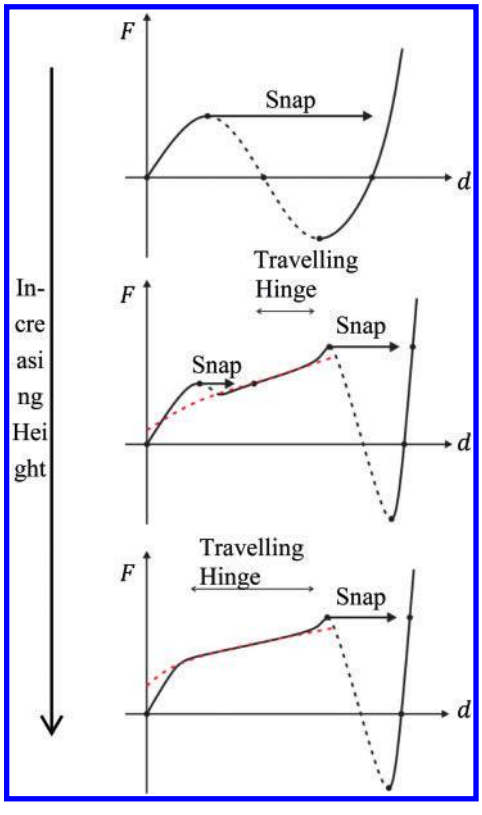


Figure 11. Schematic diagram about effects of increasing height. (Red dosh lines represent the travelling hinge model predictions).

(default), 20°, 30°, 50° and 60°. Again, the ring-load method was used for the LE material and the plate-load method was used for the EPP material.

A switch of collapse mechanism is expected before the tilt angle increases to 90°, hence the problem becomes cylindrical shell buckling under axial compressive load. It has been investigated by many people due to its widespread use in industry.

4.3.1 *LE Material*

The results are shown on Figure 12. Results from Newton method and Riks method agreed well with each other.

Figure 12 shows that the critical forces increased as the tilt angle increased. The snap-through behaviour was found on all frusta simulated. Therefore, varying the tilt angle of the frustum around current configuration, did not affect the collapse mechanism.

4.3.2 *EPP Material*

The plotted results are shown on Figure 13.

The critical force shows a clear trend of increasing as the tilt angle increases. The snap-through behaviour was found on all frusta which were simulated. Therefore, varying the tilt angle of the frustum, did not affect the collapse mechanism at current configuration.

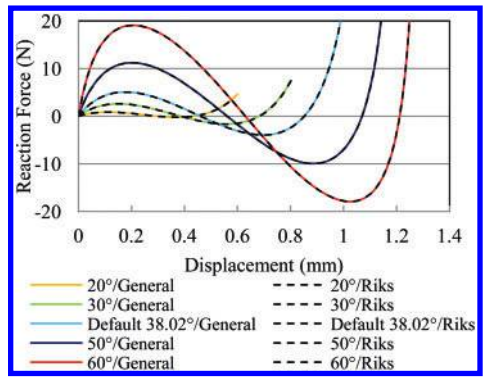


Figure 12. Results from LE frusta with various tilt angles.

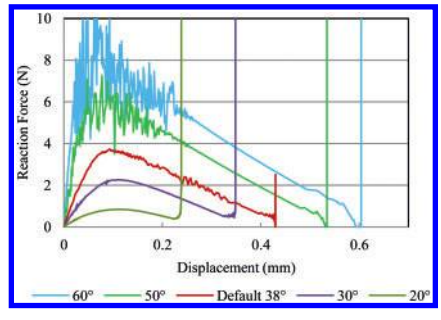


Figure 13. Results from EPP frusta with various tilt angles.

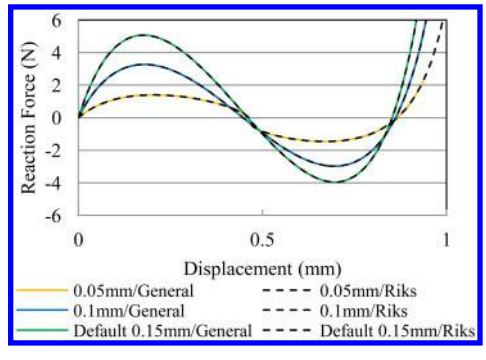


Figure 14. Results from LE frusta of various thicknesses.

The fluctuating force curves for the cases of 60° and 50° tilt angles are caused by the vibration of the frustum due to the impact of the loading plate.

4.4 *Frusta of Various Thicknesses*

Including the default configuration, frusta of four different thicknesses, 0.15 mm (default), 0.1 mm and 0.05 mm, were analysed. The ring-load method was used for the LE material and the plate-load method was used for the EPP material.

4.4.1 *LE Material*

The results are shown on Figure 14. The Newton method and Riks method agreed well with each other.

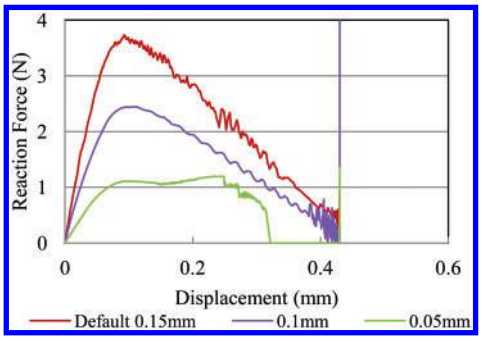


Figure 15. Results from EPP frusta of various thicknesses.

Figure 14 shows similar results comparing with Figure 12. The critical forces increased as the thickness increased. The snap-through behaviour was found on all frusta which were simulated. Therefore, varying the thickness of the frustum, did not affect the collapse mechanism at current configuration.

4.4.2 *EPP Material*

The results are shown on Figure 15. For the frustum of 0.05 mm thickness, the mesh size was reduced to 0.05 mm since the artificial strain energy of the system had to be controlled below 2% of the total internal energy to reduce the hour-glassing and shear locking effect.

It is noted that local buckling along the top circle of the frustum happened before the snap-through when the thickness reduced to 0.05 mm. This is why that the 0.05 mm frustum has rather strange force curves comparing with others. Furthermore, the sudden force drop for the frustum of 0.05 mm thickness at around 0.38 mm displacement occurred when the loading plate lost its entire contact to the frustum and the loading forces reduced to zero. This collapse mechanism for 0.05 mm thickness frustum was much more complicated than the one of the default frustum and needed further investigation.

The linear elastic material had no local buckling because the ring-load method forced top circle lines of the frusta to move downwards at the rate in the boundary condition setting. A hoop stiffener around the top edge could be added to stop the structure from buckling at this mode.

4.5 *Comparison between FE Results and Analytic Predictions*

The default frustum and its variation when height was 2.0 mm with EPP materials were chosen to be compared with the analytic predictions by Deshpande & Fleck's model. The results are plotted in Figure 16. The analytic model failed to give valid predictions for the default frustum. For the 2.0 mm high frustum, the analytic model gave fair predictions of forces during the progressive inversion but failed to give good estimate at the beginning or around the snap. In general, the analytical results are slightly larger than the FE

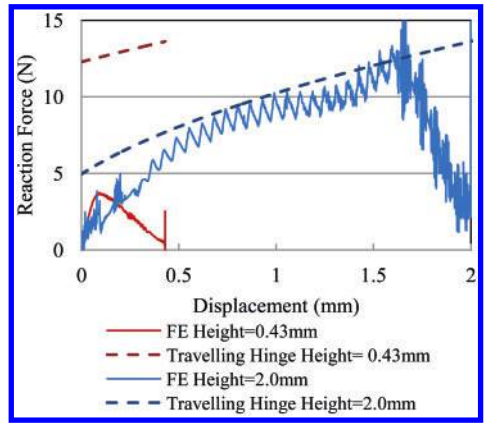


Figure 16. Comparison of FE results and Analytical Predictions.

results. This is due to the small difference of boundary conditions between my FE settings and Deshpande & Fleck's model.

5 CONCLUSIONS

In conclusion, under certain range of geometric and material configuration, the critical force for a frustum to invert can be increased by increasing the tilt angle or the thickness. The influence of height is more complex, as the collapse mechanism would switch to a different mode under certain conditions. For an EPP material, this paper demonstrates how the collapse mechanism and critical forces could change. When travelling hinge lines are formed, the force response fits well with Deshpande & Fleck's prediction. However, the plastic travelling hinges do not always form.

For a real flexible straw, the taller frustum has a larger tilt angle and a larger height compared to the shorter one, hence requires a larger critical force to snap through. The shorter frustum reaches its critical force and snaps before the taller one does, thus the corrugation could invert into a shape shown in Figure 2b.

Though only results of the FE simulation is presented in this paper, we are setting up experiments to verify the results in the future.

REFERENCES

Calladine C.R. 1985. Analysis of large plastic deformations in shell structures. *IUTAM Symposium: Inelastic Behaviour of Plates and Hells*, 5-8-1985 to 9-8-1985: 69–101.

Deshpande V.S. & Fleck N.A. 2003. Energy absorption of an egg-box material. *Journal of the Mechanics and Physics of Solids*, 51 187–208.

DSS 2011. *Abaqus Analysis User's Manual*, Version 6.10. Dassault Systèmes Simulia Corp.

Thompson J.M.T. & Hunt G.W. 1973. *A general theory of elastic stability*. John Wiley & Sons Ltd.

Research and Applications in Structural Engineering, Mechanics and Computation – Zingoni (Ed.)
© 2013 Taylor & Francis Group, London, ISBN 978-1-138-00061-2

A strain gradient Reissner-Mindlin micro-plate model obtained through an asymptotic analysis

M. Serpilli
Department of Civil and Building Engineering, and Architecture, Università Politecnica delle Marche, Italy

ABSTRACT: In this paper we derive a strain gradient plate model from the three-dimensional equations of strain gradient linearized elasticity. The deduction is based on the asymptotic analysis with respect of a small real parameter being the thickness of the elastic body we consider. The body is constituted by a second gradient isotropic linearly elastic material. The obtained model is recognized as a strain gradient Reissner-Mindlin plate model.

1 INTRODUCTION

Higher order gradient continuum theories in linear and nonlinear elasticity have recently raised the interest on many scientists, since modern technologies involving multi-scale materials exhibit size effects and a strong dependence on internal (material) lengths.

A possible generalization of Cauchy model has been proposed in the pioneering works by Mindlin (1964) and Germain (1973). In these papers, the stored deformation energy is assumed to depend not only on the strain, but also on the strain gradient. These general continua are called second gradient continua by Germain, or strain gradient continua. In strain gradient continua approaches it is necessary to generalize the concept of Cauchy contact actions, see dell'Isola et al. (2012), and the constitutive laws, see dell'Isola et al. (2009).

In recent years plate theories have found several applications in the areas of micro-mechanics and nano-mechanics. Micro-mechanical systems and nano-mechanical systems show size effects and non local behavior. The lack of an intrinsic length scale implies that this kind of phenomena cannot be captured by classical continuum theory; therefore strain gradient elasticity theories, containing length scale parameters, find their natural and appropriate application. In order to deeply understand the effect of the internal length scale parameters in strain gradient elasticity, the authors recommend, for instance, the works by Lam et al. (2003) and by Yang et al. (2002).

For what concerns with strain gradient plate theories, Lazopoulos presented the first formulation of the Kirchhoff-Love model, respectively, for plates, (Lazopoulos 2009), and shallow shells, (Lazopoulos 2011), based on the strain gradient elasticity. More recently, in Ramezani (2012), the author proposed a micro-plate model taking into account shear deformations, based on a general strain gradient elasticity theory. All those plate models have been derived by using classical variational tools.

In the present work we derive a strain gradient micro-plate model starting from the three-dimensional equations of strain gradient linearized elasticity through an asymptotic analysis. We consider a plate-like domain filled by an isotropic second gradient linearly elastic material. By defining a small real parameter ε, which represents the thickness of the plate-like domain, we apply the asymptotic expansion method, following the approach by Ciarlet (1997). Then, we characterize the leading terms of the asymptotic expansion, and the associated limit problems. The obtained model corresponds to a strain gradient Reissner-Mindlin plate model.

The asymptotic analysis is a widely used technique for the formal derivation and justification of classical theories of thin structures, starting from the classical three-dimensional elasticity, (see Ciarlet (1997), in the case of plate models). For what concerns with the derivation of plate models, it is well-known that if we apply the asymptotic methods to the classical linear or nonlinear elasticity equations, we are capable to derive only Kirchhoff-Love plate models. In order to obtain and justify the Reissner-Mindlin plate model through an asymptotic analysis or variational convergence we need to generalize the initial three-dimensional stored elastic energy. For instance, Pa-roni et al. (2007) obtain the Reissner-Mindlin plate model via Γ-convergence by adding some specific second gradient terms to the classical linear elasticity equations. Another way to proceed in the justification of Reissner-Mindlin equations is the one proposed in the pioneering work by Erbay (2000) in which the author uses the asymptotic expansion method starting from the Cosserat elasticity equations. More recently, within two different functional frameworks, Aganovič et al. (2006) and Neff et al. (2010) consider the Cosserat elasticity as "parent" model and, respectively, derive the

Reissner-Mindlin model for rods, plates and shells by means of variational and Γ-convergence arguments.

2 STATEMENT OF THE PROBLEM

In the sequel, Latin indices range in the set $\{1,2,3\}$, while Greek indices range in the set $\{1,2\}$ and the Einstein's summation convention with respect to the repeated indices is adopted.

Let $\omega \in \mathbb{R}^2$ be a smooth domain in the plane spanned by vectors $\mathbf{e}_\alpha$, let γ_0 be a measurable subset of the boundary γ of the set ω, such that length $\gamma_0 > 0$, and let $0 < \varepsilon < 1$ be an dimensionless *small* real parameter which will tend to zero. For each ε, we define

$$\Omega^\varepsilon := \omega \times (-\varepsilon h, \varepsilon h),$$
$$\Gamma_0^\varepsilon := \gamma_0 \times [-\varepsilon h, \varepsilon h], \quad \Gamma_\pm^\varepsilon := \omega \times \{\pm \varepsilon h\}.$$

Hence the boundary of the set Ω^ε is partitioned into the lateral face $\gamma \times [-\varepsilon h, \varepsilon h]$ and the upper and lower faces Γ_+^ε and Γ_-^ε, and the lateral face is itself partitioned as $\gamma \times [-\varepsilon h, \varepsilon h] = (\gamma_0 \times [-\varepsilon h, \varepsilon h]) \cup (\gamma_1 \times [-\varepsilon h, \varepsilon h])$, where $\gamma_1 := \gamma - \gamma_0$. In order to avoid inessential complications in the sequel we suppose that $\gamma = \gamma_0$, and thus $\gamma_1 = \emptyset$.

We assume that the set $\overline{\Omega}^\varepsilon$ is the reference configuration of a strain gradient linearly elastic plate of thickness $2\varepsilon h$ and middle surface $\overline{\omega}$. We study the physical problem corresponding to the mechanical behaviour of a strain gradient plate. The plate is completely clamped on $\Gamma_0^\varepsilon = \Gamma^\varepsilon$, in the sense that the boundary conditions of place, imposed to the displacements, are $u_i^\varepsilon = 0$ and $\partial_n^\varepsilon u_i^\varepsilon = 0$ on Γ_0^ε, where ∂_n^ε represents the derivative operator with respect to the unit outer normal vector (n_i^ε) along the boundary Γ_0^ε. Moreover, we supposed that the plate is subjected to body forces $(f_i^\varepsilon) : \Omega^\varepsilon \to \mathbb{R}^3$, and surface forces $(g_i^\varepsilon) : \Gamma_+^\varepsilon \cup \Gamma_-^\varepsilon \to \mathbb{R}^3$.

We finally assume that the strain gradient linearly elastic material constituting the plate Ω^ε is homogeneous and isotropic. The constitutive laws for this kind of material (see dell'Isola et al. (2009)) take the following form:

$$\sigma_{ij}^\varepsilon := \lambda^\varepsilon e_{pp}^\varepsilon \delta_{ij} + 2\mu^\varepsilon e_{ij}^\varepsilon,$$
$$p_{ijk}^\varepsilon := c_1^\varepsilon (e_{ppj}^\varepsilon \delta_{ik} + 2e_{kpp}^\varepsilon \delta_{ij} + e_{ppi}^\varepsilon \delta_{jk}) + c_2^\varepsilon e_{ppk}^\varepsilon \delta_{ij} +$$
$$+ 2c_3^\varepsilon (e_{jpp}^\varepsilon \delta_{ik} + e_{ipp}^\varepsilon \delta_{jk}) + 2c_4^\varepsilon e_{ijk}^\varepsilon + 2c_5^\varepsilon (e_{ikj}^\varepsilon + e_{jki}^\varepsilon),$$

where $(\sigma_{ij}^\varepsilon)$ is the classical Cauchy stress tensor, (p_{ijk}^ε) is the hyperstress tensor, $(e_{ij}^\varepsilon(\mathbf{u}^\varepsilon)) := (\frac{1}{2}(\partial_i^\varepsilon u_j^\varepsilon + \partial_j^\varepsilon u_i^\varepsilon))$ is the linearized strain tensor and $(e_{ijk}^\varepsilon(\mathbf{u}^\varepsilon)) := (\partial_k^\varepsilon e_{ij}^\varepsilon(\mathbf{u}^\varepsilon))$ is the gradient of $(e_{ij}^\varepsilon(\mathbf{u}^\varepsilon))$. It is important to stress out that the ratios between the second gradient elastic moduli c_k^ε and the Lamé's constants, λ^ε and μ^ε, have the dimensions of square length, i.e. $c_k^\varepsilon/\mu^\varepsilon \propto (\ell^\varepsilon)^2$. The length scale parameter ℓ^ε is a material property associated with the heterogeneity of the material and it measures the size of the internal microstructure of the material.

The displacement field $\mathbf{u}^\varepsilon = (u_i^\varepsilon)$ satisfies the following variational problem defined over the variable domain Ω^ε:

$$\int_{\Omega^\varepsilon} \left\{ \sigma_{ij}^\varepsilon(\mathbf{u}^\varepsilon) e_{ij}^\varepsilon(\mathbf{v}^\varepsilon) + p_{ijk}^\varepsilon(\mathbf{u}^\varepsilon) e_{ijk}^\varepsilon(\mathbf{v}^\varepsilon) \right\} dx^\varepsilon = l(\mathbf{v}^\varepsilon), \quad (1)$$

for all $\mathbf{v}^\varepsilon \in V(\Omega^\varepsilon)$, where

$$V(\Omega^\varepsilon) := \left\{ \mathbf{v}^\varepsilon \in H^2(\Omega^\varepsilon; \mathbb{R}^3);\ \mathbf{v}^\varepsilon = \partial_n^\varepsilon \mathbf{v}^\varepsilon = \mathbf{0} \text{ on } \Gamma_0^\varepsilon \right\},$$

and

$$l(\mathbf{v}^\varepsilon) = \int_{\Omega^\varepsilon} f_i^\varepsilon v_i^\varepsilon dx^\varepsilon + \int_{\Gamma_+^\varepsilon} g_i^\varepsilon v_i^\varepsilon d\Gamma^\varepsilon.$$

For a more general formulation of the three-dimensional strain gradient non linear elasticity theory, the reader can refer to the works by dell'Isola et al. (2009) and dell'Isola et al. (2012).

In order to perform an asymptotic analysis, we need to transform problem (1) posed on a variable domain Ω^ε onto a problem posed on a fixed domain Ω (independent of ε). Accordingly, we let

$$\Omega := \omega \times (-h, h),$$
$$\Gamma_0 := \gamma_0 \times [-h, h], \quad \Gamma_\pm := \omega \times \{\pm h\}.$$

We suppose that the thickness of the plate h^ε depends linearly on ε, so that $h^\varepsilon = \varepsilon h$. Hence, we define the following change of variables (see Ciarlet (1997)):

$$\pi^\varepsilon : x := (\tilde{x}, x_3) \in \overline{\Omega} \mapsto x^\varepsilon := (\tilde{x}, \varepsilon x_3) \in \overline{\Omega}^\varepsilon,$$

with $\tilde{x} = (x_\alpha)$. By using the bijection π^ε, one has $\partial_\alpha^\varepsilon = \partial_\alpha$ and $\partial_3^\varepsilon = \frac{1}{\varepsilon}\partial_3$.

With the unknown displacement field $\mathbf{u}^\varepsilon = (u_i^\varepsilon) \in V(\Omega^\varepsilon)$ and test functions $\mathbf{v}^\varepsilon = (v_i^\varepsilon) \in V(\Omega^\varepsilon)$, we associate, respectively, the scaled displacement field $\mathbf{u}(\varepsilon) = (u_i(\varepsilon)) : \overline{\Omega} \to \mathbb{R}^3$ and the scaled test functions $\mathbf{v} = (v_i) : \overline{\Omega} \to \mathbb{R}^3$, for all $x^\varepsilon = \pi^\varepsilon x \in \overline{\Omega}^\varepsilon$, defined by the scalings:

$$u_\alpha^\varepsilon(x^\varepsilon) = \varepsilon u_\alpha(\varepsilon)(x) \text{ and } u_3^\varepsilon(x^\varepsilon) = u_3(\varepsilon)(x),$$
$$v_\alpha^\varepsilon(x^\varepsilon) = \varepsilon v_\alpha(x) \text{ and } v_3^\varepsilon(x^\varepsilon) = v_3(x).$$

We make the following assumptions on the data, and, thus, we require that the Lamé constants and the second gradient elastic moduli satisfy the following relations:

$$\lambda^\varepsilon = \lambda, \quad \mu^\varepsilon = \mu, \quad c_k^\varepsilon = c_k, \ k \in \{1,2,3,4,5\}.$$

In terms of the internal length parameter ℓ^ε, this means that $\ell^\varepsilon := \ell$ is independent of ε, and so the actual thickness of the plate $h^\varepsilon = \varepsilon h$ is an order of magnitude smaller than the internal length ℓ^ε. As it is shown in Lam et al. (2003) and Yang et al. (2002), the influence

of the microstructure is predominant when $h^\varepsilon \ll, \ell^\varepsilon$. This assumption on the dependences of ℓ^ε and h^ε on ε is aimed at emphasizing the effect of the microstructure in the simplified model.

We can now reformulate the problem on the fixed domain Ω. The rescaled displacement field $\mathbf{u}(\varepsilon) \in V(\Omega)$ is the unique solution of the following rescaled problem:

$$\begin{aligned}&\frac{1}{\varepsilon^4}a_{-4}(\mathbf{u}(\varepsilon),\mathbf{v})+\frac{1}{\varepsilon^2}a_{-2}(\mathbf{u}(\varepsilon),\mathbf{v})+a_0(\mathbf{u}(\varepsilon),\mathbf{v})+\\&+\varepsilon^2 a_2(\mathbf{u}(\varepsilon),\mathbf{v})=l_0(\mathbf{v})+\varepsilon^2 l_2(\mathbf{v}),\end{aligned} \tag{2}$$

for all $\mathbf{v} \in V(\Omega)$, where

$$V(\Omega) := \left\{\mathbf{v} \in H^2(\Omega;\mathbb{R}^3);\ \mathbf{v} = \partial_n \mathbf{v} = \mathbf{0} \text{ on } \Gamma_0\right\}.$$

The bilinear forms a_{-4}, a_{-2}, a_0, $a_2 : V(\Omega) \times V(\Omega) \to \mathbb{R}$ depend on the scaled components of the linearized strain tensor $e_{ij}(\mathbf{u}(\varepsilon))$ and of its gradient $e_{ijk}(\mathbf{u}(\varepsilon))$.

3 ASYMPTOTIC EXPANSIONS

We can now perform an asymptotic analysis of the rescaled problem (2). Since it has a polynomial structure with respect to the small parameter ε, we can look for the solution of the problem as a series of powers of ε:

$$\mathbf{u}(\varepsilon) = \mathbf{u}^0 + \varepsilon^2\mathbf{u}^2 + \varepsilon^4\mathbf{u}^4 + \varepsilon^6\mathbf{u}^6 + \dots\ . \tag{3}$$

By substituting (3) into the rescaled problem (2), and by identifying the terms with identical power of ε, we obtain, as customary, the following set of problems, defined for all $\mathbf{v} \in V(\Omega)$:

$$\begin{aligned}&\mathcal{P}_{-4}: \quad a_{-4}(\mathbf{u}^0,\mathbf{v}) = 0,\\&\mathcal{P}_{-2}: \quad a_{-4}(\mathbf{u}^2,\mathbf{v}) + a_{-2}(\mathbf{u}^0,\mathbf{v}) = 0,\\&\mathcal{P}_{2}: \quad a_{-4}(\mathbf{u}^4,\mathbf{v}) + a_{-2}(\mathbf{u}^2,\mathbf{v}) + a_0(\mathbf{u}^0,\mathbf{v}) = l_0(\mathbf{v}),\end{aligned}$$

By solving each variational subproblem we characterize the limit displacement field $\mathbf{u}^0$ and the associated limit problem.

The displacement field $\mathbf{u}^0$ takes the following form:

$$\begin{cases} u^0_\alpha(\tilde{x},x_3) = x_3\varphi^0_\alpha(\tilde{x}),\\ u^0_3(\tilde{x},x_3) = w^0(\tilde{x}).\end{cases}$$

The above displacement field corresponds to the well-known Reissner-Mindlin kinematics assumptions for a plate, where w^0 and φ^0_α are, respectively, the transverse displacement and the free rotation of the normal fiber to the middle plane of the plate.

The limit displacement field verifies the following limit variational problems:

$$\begin{aligned}&\int_\omega \left[(C_1\partial_{\beta\beta}w^0 + C_2\partial_\beta\varphi^0_\beta)\partial_{\alpha\alpha}\eta_3 + \right.\\&+\left(c_4(\partial_{\alpha\beta}w^0+\partial_\beta\varphi^0_\alpha)+c_5(\partial_\alpha\varphi^0_\beta+\partial_\beta\varphi^0_\alpha)\right)\partial_{\alpha\beta}\eta_3+\\&\left.+\mu(\partial_\alpha w^0+\varphi^0_\alpha)\partial_\alpha\eta_3\right]d\tilde{x} = \frac{1}{h}\int_\omega q\eta_3 d\tilde{x},\\&\int_\omega \left[\left(C_2\partial_{\beta\beta}w^0 + C_3\partial_\beta\varphi^0_\beta\right)\partial_\alpha\eta_\alpha + \right.\\&+(c_4+2c_5)(\partial_{\alpha\beta}w^0+\partial_\beta\varphi^0_\alpha+\partial_\alpha\varphi^0_\beta)\partial_\beta\eta_\alpha+\\&\left.+c_4\partial_\beta\varphi^0_\alpha\partial_\beta\eta_\alpha+\mu(\partial_\alpha w^0+\varphi^0_\alpha)\eta_\alpha\right]d\tilde{x} = 0,\end{aligned} \tag{4}$$

for all $\eta_i \in V(\omega) := \{\eta \in H^1(\omega,\mathbb{R}^2)\times H^2(\omega);\ \eta = \mathbf{0},\ \partial_\nu\eta_3 = 0 \text{ on } \gamma_0\} = H^1_0(\omega,\mathbb{R}^2)\times H^2_0(\omega)$, $q(\tilde{x}) := \int_{-h}^{h} f_3(\tilde{x},x_3)dx_3 + g_3(\tilde{x},\pm h)$, and

$$\begin{aligned}C_1 &:= c_3 - \frac{(c_1-2c_3)^2}{\tilde{c}},\\C_2 &:= c_1 + c_3 - \frac{(3c_1+c_2+2c_3)(c_1+2c_3)}{\tilde{c}},\\C_3 &:= 2c_1 + c_2 + c_3 - \frac{(3c_1+c_2+2c_3)^2}{\tilde{c}},\end{aligned}$$

By integrating by parts problem (4), we obtain the following differential system:

$$\begin{cases} h(C_1\Delta-\mu)\Delta w^0 + h(C_2\Delta-\mu)\mathrm{div}\boldsymbol{\varphi}^0 = q \ \text{ in } \omega,\\ (C_2\Delta-\mu)\nabla w^0 + (C_3\Delta-\mu)\boldsymbol{\varphi}^0 + C_4\nabla(\mathrm{div}\boldsymbol{\varphi}^0) = \mathbf{0},\\ w^0 = 0,\ \ \partial_\nu w^0 = 0,\ \ \boldsymbol{\varphi}^0 = \mathbf{0} \text{ on } \gamma_0,\end{cases}$$

where $\Delta\phi := \partial_{\alpha\alpha}\phi$ is the two-dimensional Laplacian operator applied to ϕ, $\mathrm{div}\phi := \partial_\alpha\phi_\alpha$ is the divergence operator applied to $\phi = (\phi_\alpha)$, $\nabla\phi := (\partial_\alpha\phi)$ is the two-dimensional gradient operator applied to ϕ, and

$$\begin{aligned}&\mathcal{C}_1 := c_4 + C_1, \quad \mathcal{C}_2 := c_4 + 2c_5 + C_2,\\&\mathcal{C}_3 := 2\left(c_4+c_5\right), \quad \mathcal{C}_4 := c_4 + 2c_5 + C_3.\end{aligned}$$

Remark. In several works (see, for instance, Aifantis (1999)), Aifantis has proposed a simplified strain gradient isotropic linearly elastic constitutive law, in which $c_1 = c_3 = c_5 = 0$, $c_2 = \ell^2\lambda$ and $c_4 = \ell^2\mu$, where ℓ is an internal length connected to the micro-structure. The simplified strain gradient constitutive law gets the following expression:

$$\begin{aligned}&\sigma^\varepsilon_{ij}(\mathbf{u}^\varepsilon) := \lambda^\varepsilon e^\varepsilon_{pp}(\mathbf{u}^\varepsilon)\delta_{ij} + 2\mu^\varepsilon e^\varepsilon_{ij}(\mathbf{u}^\varepsilon),\\&p^\varepsilon_{ijk}(\mathbf{u}^\varepsilon) := \ell^2\partial^\varepsilon_k(\lambda^\varepsilon e^\varepsilon_{pp}(\mathbf{u}^\varepsilon)\delta_{ij} + 2\mu^\varepsilon e^\varepsilon_{ij}(\mathbf{u}^\varepsilon)).\end{aligned}$$

In this particular case the limit problem takes the following form:

$$\begin{cases} h\mu(\ell^2\Delta - 1)(\Delta w^0 + \mathrm{div}\boldsymbol{\varphi}^0) = q & \text{in } \omega,\\ \mathcal{L}^2 D\Delta\mathrm{div}\boldsymbol{\varphi}^0 = -q & \text{in } \omega,\end{cases}$$

where $D := \frac{\mu(\lambda+\mu)h^3}{3(\lambda+2\mu)} = \frac{Eh^3}{12(1-\nu^2)}$ is the classical rigidity modulus of the plate and $\mathcal{L}^2 := 12(\ell/h)^2$.

The coefficient $\mathcal{L}^2$ usually appears in strain gradient plate and beam theories and it represents the ratio between the intrinsic length of the microstructure and the actual thickness (resp. diameter) of the plate (resp. beam). Its influence is high for small thicknesses, when the intrinsic length ℓ is comparable or bigger than the thickness of the plate. Besides, it has been shown in several works Lam et al. (2003), Lazopoulos (2009) and Yang et al. (2002) that, by comparing the deflections of a classical Kirchhoff-Love plate and the deflections of a strain gradient Kirchhoff-Love plate, for large values of $\mathcal{L}^2$, the bending stiffness of the plate increases drastically.

4 CONCLUSIONS

In the present work we derive a strain gradient Reissner-Mindlin plate model by means of an asymptotic analysis starting from the equations of strain gradient linearized elasticity. We concentrate our attention to the flexural behavior, by neglecting at this stage the membrane behaviour.

As it is mentioned in the Introduction to this paper, in order to obtain the Reissner-Mindlin kinematics for a plate through the asymptotic analysis or Γ-convergence, we need to generalize the initial classical elastic energy by adding some second gradient extra terms or by using the micropolar continuum model. In our work we give another proof of the fact that, in order to formally deduce the Reissner-Mindlin plate model, it is necessary to use a different continuum model, such as the second gradient continuum model.

From a mechanical point of view, the obtained strain gradient Reissner-Mindlin plate model can be used to study the mechanical behaviour of micro-plates and nano-plates, especially by considering the reduced Aifantis strain gradient elastic material. The new model contains a material internal length scale parameter ℓ to account the microstructural effect, unlike the classical Reissner-Mindlin plate model. The presence of this additional material constant enables this model to capture size effects.

As we already claimed in Sect. 2, in the asymptotic procedure, we assume that the thickness of the plate $h^\varepsilon = \varepsilon h$ is much smaller that the internal length scale parameter $\ell^\varepsilon = \ell$. As future developments, it would be interesting to study the asymptotic behavior of the plate by considering all the other situations, for instance, $\ell^\varepsilon \ll h^\varepsilon$ or $\ell^\varepsilon \sim h^\varepsilon$, which will lead to different limit models.

At last let us explicitly point out that all the obtained conclusions are true also when the plate is clamped only on a measurable subset $\gamma_0 \times [-\varepsilon h, \varepsilon h]$ of the lateral boundary Γ^ε with length $\gamma_0 > 0$, and $\gamma_1 \neq \emptyset$.

REFERENCES

Aganović, I., J. Tambača, & Z. Tutek (2006). Derivation and justification of the models of rods and plates from linearized three-dimensional micropolar elasticity. *J. Elasticity 84*, 131–152.

Aifantis, E. (1999). Strain gradient interpretation of size effects. *Int. J. Fract. 95*, 299–314.

Ciarlet, P. (1997). *Mathematical Elasticity, vol. II: Theory of Plates*. Amsterdam: North-Holland.

dell'Isola, F., G. Sciarra, & S. Vidoli (2009). Generalized hooke's law second gradient materials. *Proc. R. Soc. A 465*, 2177–2196.

dell'Isola, F., P. Seppecher, & A. Madeo (2012). How contact interactions may depend on the shape of cauchy cuts in nth gradient continua: approach "'a la d'alembert". *Z Angew Math Phys 63*, 1119–1516.

Erbay, H. (2000). An asymptotic theory of thin micropolar plates. *Int. J. Engng. Science 38*, 1497–1516.

Germain, P. (1973). La méthode des puissances virtuelles en mécanique des milieux continus. i. théorie du second gradient. *J. Mécanique 12*, 235–274.

Lam, D., F. Yang, A. Chong, J. Wang, & P. Tong (2003). Experiments and theory in strain gradient elasticity. *J. Mech. Phys. Solids 51*, 1477–1508.

Lazopoulos, K. (2009). On bending of strain gradient elastic micro-plates. *Mech. Res. Commun. 36*, 777–783.

Lazopoulos, K. (2011). Nonlinear strain gradient elastic thin shallow shells. *Eur. J. Mech. A-Solid 30*, 286–292.

Mindlin, R. (1964). Micro-structure in linear elasticity. *Arch. Ration. Mech. Anal. 16*, 51–78.

Neff, P., K.-I. Hong, & J. Jeong (2010). The reissner-mindlin plate is the γ-limit of cosserat elasticity. *Math. Models Methods Appl. Sci. 20*, 1553–1590.

Paroni, R., P. Podio-Guidugli, & G. Tomassetti (2007). A justification of the reissner-mindlin plate theory through variational concergence. *Analysis and Applications 5*, 165–182.

Ramezani, S. (2012). A shear deformation micro-plate model based on a most general form of strain gradient elasticity. *Int. J. Mech. Sci. 57*, 165–182.

Yang, F., A. Chong, D. Lam, & P. Tong (2002). Couple stress based strain gradient theory for elasticity. *Int. J. Solids Struct. 39*, 2731–2743.

Research and Applications in Structural Engineering, Mechanics and Computation – Zingoni (Ed.)
© 2013 Taylor & Francis Group, London, ISBN 978-1-138-00061-2

Inelastic buckling of annular plates in shear

J. Becque
The University of Sheffield, Sheffield, South Yorkshire, UK

ABSTRACT: This paper presents a solution to the problem of determining the buckling load of an annular plate made of an inelastic metal and subject to pure shear loading. The solution is new in that it is based on the principles of plastic flow theory while being unaffected by the so-called 'plastic buckling paradox'. New inelastic constitutive relationships are first derived linking normal stresses and normal strains at the point of buckling, which are then incorporated into the classical Kirchhoff theory. Finally, the new model is validated against previous experimental data pertaining to the buckling of aluminium, brass and stainless steel annular plates in shear.

1 INTRODUCTION

A state of pure shear in an annular plate (Fig. 1) may for instance result from performing an in-plane torsion test, which is an established way to determine the stress-strain response of metal plates. Buckling is thereby undesirable. The problem of purely elastic buckling of an annular plate in shear was first resolved by Dean (1924). In 1989, Ore and Durban published a milestone paper, in which they studied the inelastic equivalent of the problem, using both plastic flow theory (or 'incremental theory') and plastic deformation theory. The plastic flow formulation employed in their derivations was the well-established small strain J_2 model. When comparing the predictions of flow theory with those of deformation theory for a number of realistic material properties and geometries, it was observed that the predictions using flow theory exceeded the predictions of deformation theory by factors of up to 17. After carrying out a comparison with the experimental work by Bauer (1987, 1988), who conducted tests on clamped annular plates of various geometries and material properties, Ore and Durban concluded that the predictions of flow theory were unrealistically high, while deformation theory on the other hand agreed fairly well with the experiment. This conclusion highlighted the so-called 'plastic buckling paradox' (Hutchinson 1974).

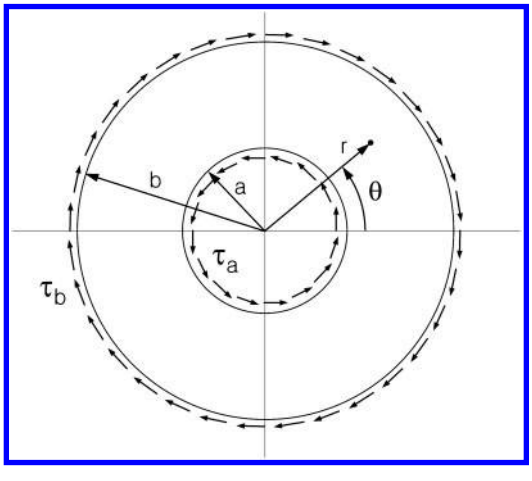


Figure 1. Annular plate in shear.

This paper revisits the problem of inelastic buckling of annular plates and proposes a model based on plastic flow theory. The plastic buckling paradox is thereby avoided by deriving the constitutive relations of an infinitesimal plate element while considering this plate element in its slightly deformed shape just past the point of local buckling. It is demonstrated that the theory leads to excellent predictions of Bauer's (1987, 1988) experimental results.

2 CONSTITUTIVE RELATIONSHIPS

Figure 2 depicts an infinitesimal element of infinitesimal thickness embedded within the plate and subject to an increment in shear stress $\dot{T}$. In this case, the plastic shear strain increment $\dot{\gamma}_p$ is linked to the shear stress increment $\dot{T}$ through the well-established equation of flow theory:

$$\dot{\gamma}_p = \frac{3}{E_p}\dot{T} = \left[\frac{3}{E_t} - \frac{3}{E_0}\right]\dot{T} \tag{1}$$

In Eq. (1), E_0 is the elastic (Young's) modulus of the material and E_t is the tangent modulus. E_t can be obtained from the stress-strain curve in uniaxial tension by determining the stiffness at an equivalent (normal) stress level $\sigma = \sqrt{3}\tau$.

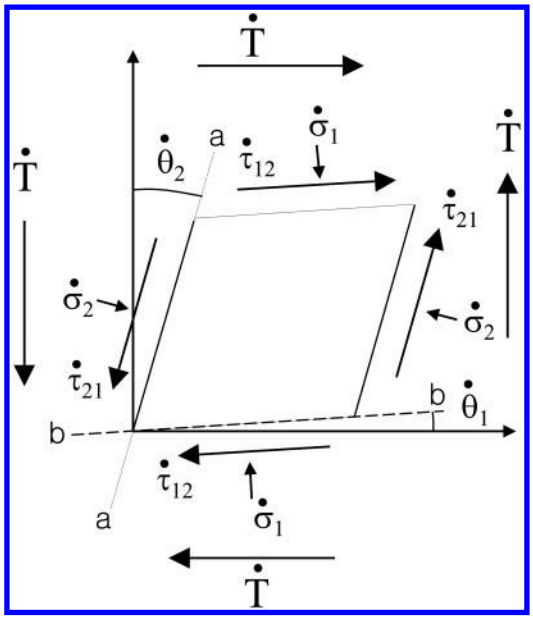


Figure 2. Infinitesimal plate element.

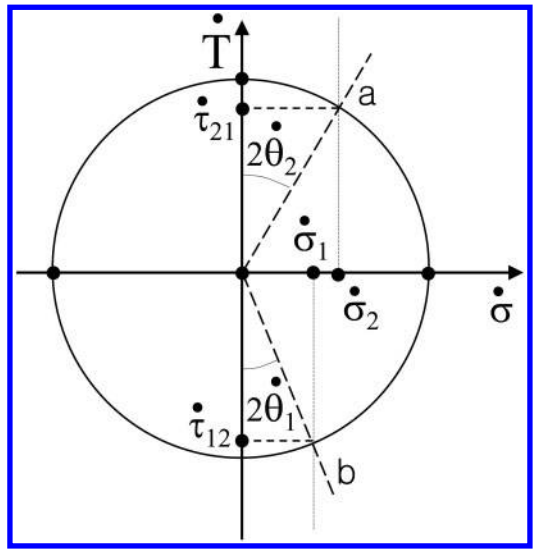


Figure 3. Mohr's circle of stress.

The above follows from the von Mises yield criterion and the concomitant definitions of equivalent stress σ_e and equivalent incremental plastic strain $\dot{\varepsilon}_{pe}$:

$$\sigma_e = \left(\sigma_x^2 + \sigma_y^2 - \sigma_x\sigma_y + 3\tau^2\right)^{1/2} \tag{2}$$

$$\dot{\varepsilon}_{pe} = \frac{2}{\sqrt{3}}\left(\dot{\varepsilon}_{px}^2 + \dot{\varepsilon}_{py}^2 + \dot{\varepsilon}_{px}\dot{\varepsilon}_{py} + \frac{1}{4}\dot{\gamma}_p\right)^{1/2} \tag{3}$$

With respect to the normal stresses, the governing opinion, as supported by, among others, Hutchinson (1974), Lubliner (1990), Bazant & Cedolin (1991) and Ore & Durban (1989), is that the normal stress and strain increments remain linked through the elastic modulus E_0 at the point of buckling:

$$\dot{\varepsilon}_1 = \frac{1}{E_0}\left(\dot{\sigma}_1 - \nu\dot{\sigma}_2\right) \tag{4}$$

$$\dot{\varepsilon}_2 = \frac{1}{E_0}\left(-\nu\dot{\sigma}_1 + \dot{\sigma}_2\right) \tag{5}$$

In other words, no plastic extension takes place. While this point of view is compatible with the Prandtl-Reuss equations (equivalent to the adoption of a flow rule associated with the von Mises surface), it leads to an overestimate of the axial stiffness of an infinitesimal plate element and is ultimately responsible for the immense mismatch between theory and experiment.

A counterargument to the above rationale can be constructed by considering the infinitesimal plate element in Fig. 2 at its transition from the initial unbuckled state into the shear buckled state. It is thereby reasonably assumed that the directions of the externally applied shear stresses remain unchanged, e.g. in Fig. 1 they remain tangential to the circumferential edges of the plate. Considering Mohr's circle of plane stress (Fig. 3), it is seen that along the rotating sides a-a and b-b of the elementary plate normal stresses $\dot{\sigma}_1$ and $\dot{\sigma}_2$ develop, which are given by:

$$\dot{\sigma}_1 = \dot{T}\sin\left(2\dot{\theta}_1\right) \approx 2\dot{T}\dot{\theta}_1 \tag{6}$$

$$\dot{\sigma}_2 = \dot{T}\sin\left(2\dot{\theta}_2\right) \approx 2\dot{T}\dot{\theta}_2 \tag{7}$$

On the other hand, since the principal directions of stress, and with them the principal directions of incremental plastic strain, remain firmly directed along the diagonals of the elementary plate during this shear stress increment, small plastic extensions necessarily have to take place along the inclined planes a-a and b-b. Their magnitude can be determined from Mohr's circle of the incremental plastic strains (Fig. 4), which in this case is a valid tool since the normal to the plate is a principal direction of plastic strain increment. It is seen that the plastic extension rates increase with the angles of rotation $\dot{\theta}_1$ and $\dot{\theta}_2$ from zero at the point of buckling to finite values at the end of the load increment. The incremental normal plastic strain $\dot{\varepsilon}_{p1}$ along b-b at the end of the load increment is thus given by:

$$\dot{\varepsilon}_{p1} = \int_0^{\dot{\theta}_1} \frac{1}{2}\left(\frac{\dot{\gamma}_p}{\dot{\theta}_1}\right)\sin(2\alpha)d\alpha \approx \frac{1}{2}\dot{\gamma}_p\dot{\theta}_1 \tag{8}$$

or, substituting Eqs. (1) and (6) into Eq. (8):

$$\dot{\varepsilon}_{p1} = \frac{3}{4E_p}\dot{\sigma}_1 \tag{9}$$

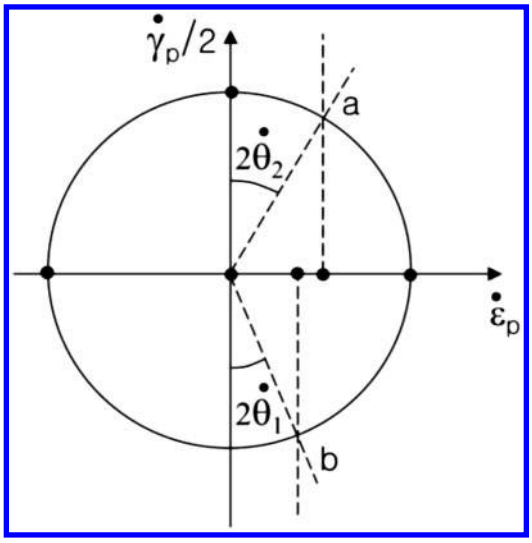


Figure 4. Mohr's circle of the incremental plastic strains.

The analogous equation for $\dot{\varepsilon}_{p2}$ is then:

$$\dot{\varepsilon}_{p2} = \frac{3}{4E_p}\dot{\sigma}_2 \tag{10}$$

Combining the incremental plastic strains given by Eqs. (1), (9) and (10) with Hooke's laws of the elastic strain increments yields the constitutive relations:

$$\dot{\varepsilon}_1 = \left[\frac{1}{4E_0} + \frac{3}{4E_t}\right]\dot{\sigma}_1 - \frac{\nu}{E_0}\dot{\sigma}_2 \tag{11}$$

$$\dot{\varepsilon}_2 = -\frac{\nu}{E_0}\dot{\sigma}_1 + \left[\frac{1}{4E_0} + \frac{3}{4E_t}\right]\dot{\sigma}_2 \tag{12}$$

$$\dot{\gamma} = \frac{(2\nu-1)E_t + 3E_0}{E_0 E_t}\dot{\tau} \tag{13}$$

3 DIFFERENTIAL EQUATIONS

The governing differential equations are derived by expressing the equilibrium of an infinitesimal plate element at the point of buckling. The very point of buckling may be seen as a limit state where, starting from the deformed plate element in Fig. 2, the angles $\dot{\theta}_1$ and $\dot{\theta}_2$ are reduced to zero while traveling back over the load history. The equilibrium equations then reduce back to the classical equations of St. Venant/Kirchoff theory, but combine with the constitutive equations (11–13), which are independent of $\dot{\theta}_1$ and $\dot{\theta}_2$ (within a small perturbation of the buckling point). For the purpose of studying an annular plate, the resulting equation is most conveniently expressed in polar coordinates r and θ (Fig. 1):

$$\begin{aligned}&\frac{1}{r}\frac{\partial^2}{\partial r^2}\left[r\left(E_{rr}\kappa_{rr} + E_{r\theta}\kappa_{\theta\theta}\right)\right] - \frac{1}{r}\frac{\partial}{\partial r}\left(E_{r\theta}\kappa_{rr} + E_{\theta\theta}\kappa_{\theta\theta}\right)\\ &+\frac{4}{r^2}\frac{\partial^2}{\partial r\partial\theta}\left(rG_{r\theta}\kappa_{r\theta}\right) + \frac{1}{r^2}\frac{\partial^2}{\partial\theta^2}\left(E_{r\theta}\kappa_{rr} + E_{\theta\theta}\kappa_{\theta\theta}\right)\\ &-\frac{\lambda}{r^2}\kappa_{r\theta} = 0\end{aligned} \tag{14}$$

where the incremental curvature changes κ_{rr}, $\kappa_{r\theta}$ and $\kappa_{\theta\theta}$ are expressed in terms of the incremental plate deflections $\dot{w}$ as follows:

$$\kappa_{rr} = \frac{\partial^2\dot{w}}{\partial r^2} \tag{15}$$

$$\kappa_{r\theta} = \frac{\partial}{\partial r}\left(\frac{1}{r}\frac{\partial\dot{w}}{\partial\theta}\right) \tag{16}$$

$$\kappa_{\theta\theta} = \frac{1}{r}\frac{\partial\dot{w}}{\partial r} + \frac{1}{r^2}\frac{\partial^2\dot{w}}{\partial\theta^2} \tag{17}$$

and:

$$E_{rr} = E_{\theta\theta} = 4E_0E_t\left(\frac{3E_0 + E_t}{9E_0^2 + 6E_0E_t + (1-16\nu^2)E_t^2}\right) \tag{18}$$

$$E_{r\theta} = \frac{16\nu E_0E_t^2}{9E_0^2 + 6E_0E_t + (1-16\nu^2)E_t^2} \tag{19}$$

$$G_{r\theta} = \frac{E_0E_t}{3E_0 + (2\nu-1)E_t} \tag{20}$$

Further to Eq. (14), λ is a load parameter which is proportional to the shear stresses in the plate:

$$\lambda = \tau_{r\theta}\frac{24r^2}{t^2} \tag{21}$$

where t is the plate thickness and the factor 24 has been introduced for convenience.

The solution method by Durban and Stavsky (1982) is followed where the incremental plate displacements $\dot{w}$ are represented as:

$$\dot{w} = \mathrm{Re}\left\{\phi(r)e^{im\theta}\right\} \tag{22}$$

where m is an integer and ϕ is a function which only depends on the radial coordinate r. Substitution of Eq. (22) into Eq. (14) yields the ordinary differential equation:

$$\begin{aligned}&E_{rr}\phi'''' + 2\left(E'_{rr} + \frac{E_{rr}}{r}\right)\phi''' + F_2\frac{\phi''}{r^2} + \left(F_1 - im\lambda\right)\frac{\phi'}{r^3}\\ &+\left(m^2F_0 + im\lambda\right)\frac{\phi}{r^4} = 0\end{aligned} \tag{23}$$

with:

$$F_0 = -r^2 E_{r\theta}'' + 2rE_{r\theta}' - 2E_{r\theta} + rE_{\theta\theta}' + (m^2 - 2)E_{\theta\theta} + 4rG_{r\theta}' - 4G_{r\theta} \quad (24)$$

$$F_1 = r^2 E_{r\theta}'' - 2m^2 rE_{r\theta}' + 2m^2 E_{r\theta} - rE_{\theta\theta}' + E_{\theta\theta} - 4m^2 rG_{r\theta}' + 4m^2 G_{r\theta} \quad (25)$$

$$F_2 = r^2 E_{rr}'' + 2rE_{rr}' + rE_{r\theta}' - 2m^2 E_{r\theta} - E_{\theta\theta} - 4m^2 rG_{r\theta} \quad (26)$$

The primes thereby indicate differentiation with respect to the radial coordinate r.

For many inelastic metals the stress-strain curve may be represented by the Ramberg-Osgood equation:

$$\varepsilon = \frac{\sigma}{E_0} + 0.002\left(\frac{\sigma}{\sigma_{0.2}}\right)^n \quad (27)$$

Where $\sigma_{0.2}$ is the 0.2% proof stress of the material and the exponent n is representative of the roundness of the stress-strain curve. By differentiating Eq. (27) and combining it with Eq. (21), the tangent modulus E_t can be expressed as an explicit function of the radial coordinate r:

$$E_t = E_0\left[1 + 0.002\frac{nE_0}{\sigma_{0.2}^n}\left(\frac{\sqrt{3}}{24}\lambda\right)^{n-1}\left(\frac{t}{r}\right)^{2(n-1)}\right]^{-1} \quad (28)$$

Through Eqs. (18–20), Eq. (28) allows the coefficients F_0, F_1 and F_2 (Eqs. 24–26) to be determined.

The boundary conditions to the problem are, along a clamped edge:

$$\dot{w} = 0, \qquad \frac{\partial \dot{w}}{\partial r} = 0 \quad (29)$$

or, along a simply supported edge:

$$\dot{w} = 0, \qquad \frac{\partial^2 \dot{w}}{\partial r^2} + \left(\frac{E_{r\theta}}{rE_{rr}}\right)\frac{\partial \dot{w}}{\partial r} = 0 \quad (30)$$

While a closed form solution of Eq. (23) is non-existent, the critical value of the load parameter λ_{cr}, associated with shear buckling of the annular plate can be determined by employing a finite differences scheme, as proposed by Ore and Durban (1989). For this purpose the radial interval between $r = a$ and $r = b$ (Fig. 1) is subdivided into N-1 equal intervals, bounded by N 'proper' nodes. A central differences scheme is here adopted, whereby two 'dummy' nodes are added outside the interval on both sides, in order to allow Eq. (23) to be expressed in its finite differences form at the boundary nodes of the interval. The values of the function ϕ at each node constitute $N + 4$ unknowns, while $N + 4$ linear equations are obtained by writing Eq. (23) in its finite differences form at each proper node and by adding two boundary conditions (Eqs. 29 or 30) at each end. In order to obtain a non-zero solution for ϕ and $\dot{w}$, the determinant Δ of the resulting system of equations needs to be zero. It is thereby noted that, while the coefficients in Eq. (23) are complex, the eigenvalues λ of the problem are real (Ore and Durban 1989). A numerical solution is obtained by calculating $\mathrm{Re}^2(\Delta) + \mathrm{Im}^2(\Delta)$ for increasing values of the load parameter λ until the smallest eigenvalue λ_{cr} is obtained. This procedure is carried out for a given plate geometry and given material properties, but needs to be repeated for a realistic range of m-values, where m indicates the number of circumferential waves of the buckling pattern. The smallest eigenvalue λ_{cr} considered over all m-values determines the critical shear buckling load.

Table 1. Material Properties

	E_0 MPa	$\sigma_{0.2}$ MPa	n –	ν –
Al	70000	36.3	4.46	0.33
ST	210000	160.9	4.9	0.30
CuZn	114400	56.1	2.4	0.33

Table 2. Comparison of theoretical and experimental results

	b mm	t mm	b/a –	M_{cr} Exp. Nm	M_{cr} Theory Nm	Theory/ Exp. –
Al	35	0.5	1.75	67.5	67.8	1.01
	35	0.5	3.04	28.8	27.4	0.95
	35	0.5	4.67	13.9	14.3	1.03
	35	1.0	1.75	195.0	187.6	0.96
	80	0.5	4.00	57.5	59.7	1.04
	80	0.5	6.95	25.1	26.1	1.04
	80	0.5	10.67	14.3	14.0	0.98
	80	1.0	4.00	200.0	176.3	0.88
	35	0.5	3.04	154.0	113.9	0.74
	35	0.5	4.67	71.0	58.4	0.82
ST	80	0.5	4.00	360.0	247.1	0.69
	80	0.5	6.96	140.0	106.1	0.76
	80	1.0	6.95	311.0	309.2	0.99
CuZn	35	0.5	1.75	193.0	157.9	0.82
	35	0.5	3.04	75.0	60.1	0.80
	35	0.5	4.67	43.5	33.4	0.77
	35	1.0	1.75	600.0	573.8	0.96
	80	0.5	4.00	146.0	101.5	0.70
	80	0.5	6.96	73.0	47.9	0.66
	80	0.5	10.67	45.0	29.1	0.65
	80	1.0	6.96	254.0	187.4	0.74
					Average	0.86
					St. Dev.	0.137

4 EXPERIMENTAL VERIFICATION

The proposed theory was verified against torsion experiments on annular plates carried out by Bauer (1987, 1988). Plates were tested with inner and outer edges clamped. Three different metals were considered: aluminium (Al), stainless steel (ST) and brass (CuZn). The material properties are given as Ramberg-Osgood parameters (see Eq. 27) in Table 1.

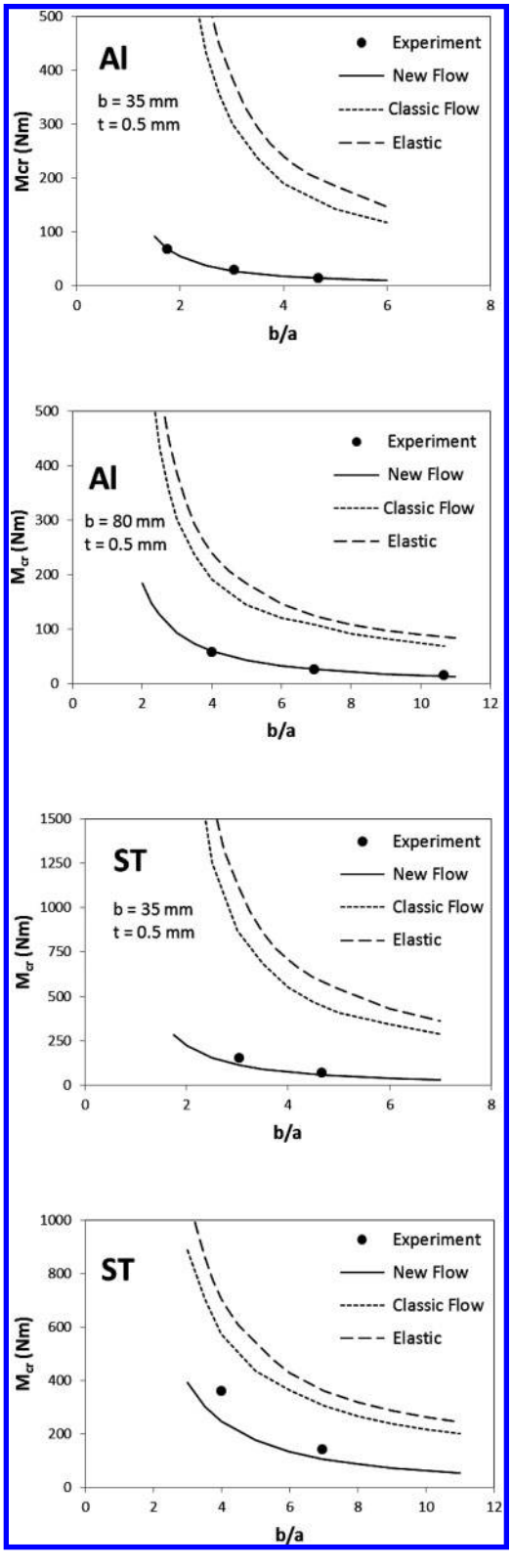


Figure 5. *continued*

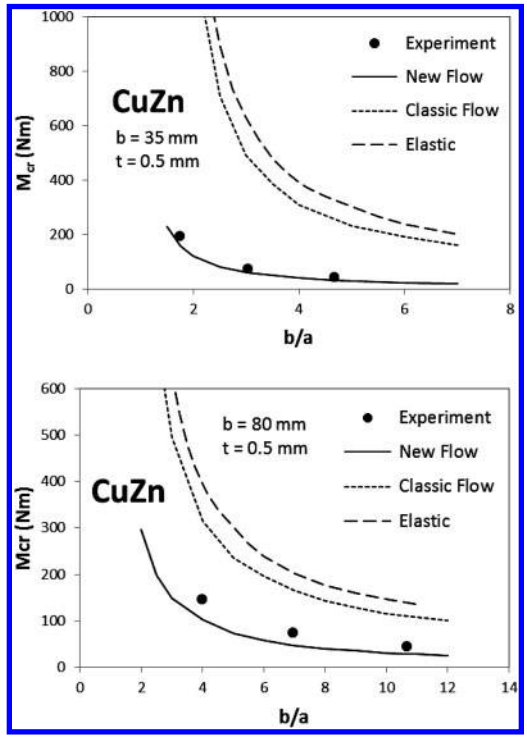


Figure 5. Comparison of theoretical and experimental results.

For each material, annular plates of widely varying geometries were tested. The onset of buckling was determined from the torsion-twist curve combined with visual observation. Table 2 makes a comparison between the experimentally observed critical (torsional) moment and the critical moment determined using the here proposed flow-based theory. Reasonably good agreement is obtained: the average ratio of the theoretical prediction to the experimental result is 0.86 with a standard deviation of 13.7%. In order to clarify and discuss the results further, a graphical representation is provided in Figure 5. First of all, a comparison between the experimental results and the elastic buckling curves clearly indicates that all plates buckle well into the inelastic range. Second, a very large discrepancy is noted between the experimental results and the predictions based on the classic interpretation of flow theory incorporating Eqs. (4–5) and detailed by Ore and Durban (1989) (labelled 'Classic Flow' in Fig. 5). On the other hand, the new approach laid out in this paper (labelled 'New Flow' in Fig. 5) matches the experiments well and yields results which are of the right order of magnitude.

5 CONCLUSIONS

A new model is proposed to describe the inelastic buckling of annular plates in shear. The model is

based on plastic flow theory ("incremental plastic theory"), but avoids the pitfalls of earlier theories by reinterpreting the plastic flow equations. In particular, incremental plastic extensions along the rotating sides of an infinitesimal plate element at the point of buckling are taken into account. The resulting plate equation, in general, requires a numerical solution. When verified against experimental data pertaining to aluminium, stainless steel and brass plates of various geometries, the proposed theory performs well, especially when compared to earlier flow-based attempts. An average ratio of the predicted buckling moment to the experimental buckling moment of 0.86 was obtained with a standard deviation of 0.137.

REFERENCES

Bauer, M. 1987. Faltenbildung beim ebenen torsionversuch. *Ingenieur-Archiv*, 57, 39–50.

Bauer, M. 1988. Ermittlung der Fließkurven von Feinblechen im ebenen Torsionsversuch. Doctoral thesis, Stuttgart University, Germany.

Bazant, Z.P. & Cedolin, L. 1991. *Stability of Structures*, Oxford University Press, Oxford, U.K.

Dean, W.R. 1924. The elastic stability of an annular plate. *Proceedings of the Royal Society A*, 106, 268–284.

Durban, D. & Stavsky, Y. 1982. Elastic buckling of polar orthotropic annular plates in shear. *International Journal of Solids and Structures*, 18, 51–58.

Hutchinson, J. W. 1974. Plastic buckling. *Advances in applied mechanics*, C-S. Yih, ed., Academic, New York, pp. 67–144.

Lubliner, J. 1990. *Plasticity theory*, Macmillan, New York.

Ore, E., and Durban, D. (1989). Elastoplastic Buckling of Annular Plates in Pure Shear. *Journal of Applied Mechanics*, ASME, 56, pp. 644–651.

Research and Applications in Structural Engineering, Mechanics and Computation – Zingoni (Ed.)
© 2013 Taylor & Francis Group, London, ISBN 978-1-138-00061-2

A novel analytical solution of orthotropic rectangular thick plate

Pan Baofeng & Liu heng
School of Civil and Hydraulic Engineering, Dalian University of Technology, Dalian, China.

ABSTRACT: Exact closed form solutions are presented for the thick plate with orthotropic properties. A novel analytical method for decoupling the governing equations of orthotropic thick plate is developed. By introducing two new functions the governing equations are converted into two independent equations. The uncoupling equations have been solved for the exact closed form solutions of orthotropic rectangular thick plate with simply supported four edges.

1 INTRODUCTION

The orthotropic plates are widely used in many fields of modern technology namely aerospace, naval, ocean and structural engineering. For the purpose of more accurate and reliable application, it is of much significance to investigate the characteristics of orthotropic plates. The present methods to solving the plate are divided into analytical approaches and numerical approaches. The Rayleigh-Ritz method is a widely agreed numerical method. Many research (Hearmon RFS 1959, Bhat RB. 1985, Dickinson SM & Di Blasio A. 1986) have extend the Rayleigh method to the solution of plates with different conditions and the obtained results are consistent with those of FME (Rossi RE & Bambill DV & Laura PAA. 1998). The analytical method of transforming a partial differential equation into an ordinary differential was also extended, shown in references (Jones R. & Milne BJ. 1976, Dalaei M. & Kerr AD. 1996, Bercin AN 1996, Sakata T. & Takahashi K. & Bhat RB. 1996). However the vibration model of orthotropic plates is more complicated than that of the isotropic plates. It is more difficult to solve the problem with the analytical method because of the increase of the number of governing equations and independent coordinates. In this paper, for decoupling multiple differential equations of high order, a novel substitution variable method is used. In section two, the novel substitution variable is determined according to the original equations, and transform the coupled equations into independent equations. In section three, using the method of separation of variables, two independent equations are solved respectively. And the result of a numerical example calculated using the novel method is shown in section four.

2 GOVERNING EQUATIONS AND DECOUPLE THE SYSTEM

Consider an orthotropic rectangular thick plate of length a,width b and uniform thickness h. The coordinate system $\{x, y, z\}$ of the rectangular plate is shown in Fig. 1.

The governing equations are given by

$$C_{11}\frac{\partial^2 w}{\partial x^2} + C_{22}\frac{\partial^2 w}{\partial y^2} - C_{11}\frac{\partial \beta_x}{\partial x} - C_{22}\frac{\partial \beta_y}{\partial y} + q = 0 \quad (1)$$

$$D_{22}\frac{\partial^2 \beta_y}{\partial y^2} + D_{66}\frac{\partial^2 \beta_y}{\partial x^2} + C_{22}\frac{\partial w}{\partial y} - C_{22}\beta_y + (D_{12} + D_{66})\frac{\partial^2 \beta_x}{\partial x \partial y} + m_y = 0 \quad (2)$$

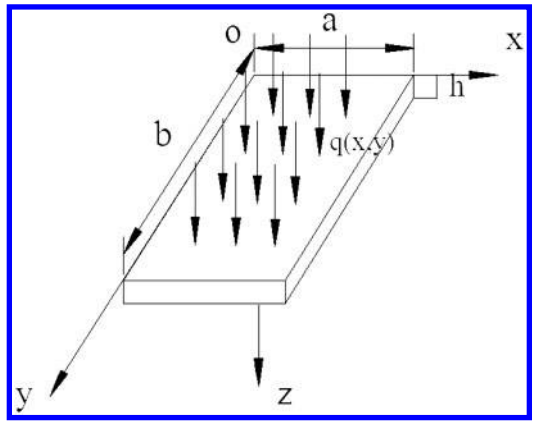


Figure 1. A rectangular plate and coordinates.

$$D_{11}\frac{\partial^2\beta_x}{\partial x^2}+D_{66}\frac{\partial^2\beta_x}{\partial y^2}+C_{11}\frac{\partial w}{\partial x}-C_{11}\beta_x+(D_{12}+D_{66})\frac{\partial^2\beta_y}{\partial x\partial y}+m_x=0 \quad (3)$$

where w is the transverse deflection of the middle surface, β_x and β_y are the rotations of a normal line due to plate bending, m_x m_y and q is the load distribution function, D_{ij} and C_{ij} are the bending stiffness and the share stiffness respectively. Defining some orthotropic stiffness parameters as:

$$\begin{aligned} D_{11} &= \frac{E_1h^3}{12(1-\upsilon_1\upsilon_2)}, & D_{22} &= \frac{E_2h^3}{12(1-\upsilon_1\upsilon_2)}, \\ D_{12} &= \frac{\upsilon_2E_1h^3}{12(1-\upsilon_1\upsilon_2)}, & D_{66} &= \frac{G_{12}h^3}{12}, \\ C_{11} &= hG_{23}, & C_{22} &= hG_{13} \end{aligned} \quad (4)$$

where E_i are the elastic modulus, G_{ij} are the share modulus, υ_{ij} are the Possion's ratios. The resultant bending moments M_x and M_y, the twisting moments M_{xy} can be obtained, namely

$$M_x=D_{11}\frac{\partial\beta_x}{\partial x}+D_{12}\frac{\partial\beta_y}{\partial y} \quad (5)$$

$$M_y=D_{12}\frac{\partial\beta_x}{\partial x}+D_{22}\frac{\partial\beta_y}{\partial y} \quad (6)$$

$$M_{xy}=D_{66}\left(\frac{\partial\beta_x}{\partial y}+\frac{\partial\beta_y}{\partial x}\right) \quad (7)$$

For decoulping the govering equations, it is assumed that

$$\beta_x=\frac{\partial F}{\partial x}+A\frac{\partial f}{\partial y} \quad (8)$$

$$\beta_y=\frac{\partial F}{\partial y}+B\frac{\partial f}{\partial x} \quad (9)$$

where A,B is undetermined coefficient. Substitution of Eq. (8) and Eq. (9) into Eq. (1) lead to the governing equation in terms of new variables as:

$$C_{11}\frac{\partial^2(w+F)}{\partial x^2}+C_{22}\frac{\partial^2(w+F)}{\partial y^2}-(C_{11}A+C_{22}B)\frac{\partial^2 f}{\partial x\partial y}-q=0 \quad (10)$$

For simplicity one can have $A=C_{22}$ and $B=-C_{11}$, then Eq. (10) has the form:

$$C_{11}\frac{\partial^2(w+F)}{\partial x^2}+C_{22}\frac{\partial^2(w+F)}{\partial y^2}-q=0 \quad (11)$$

Substitution of A and B into Eqs. (8) and (9) lead to

$$\beta_x=\frac{\partial F}{\partial x}+C_{22}\frac{\partial f}{\partial y} \quad (12)$$

$$\beta_y=\frac{\partial F}{\partial y}-C_{11}\frac{\partial f}{\partial x} \quad (13)$$

Substitution of Eq. (12) and Eq. (13) into Eq. (2) and Eq. (3) as followed:

$$\frac{\partial w}{\partial y}-\frac{\partial F}{\partial y}+\frac{D_{22}}{C_{22}}\frac{\partial^3F}{\partial y^3}+\frac{2D_{66}+D_{22}}{C_{22}}\frac{\partial^3F}{\partial x^2\partial y}=\frac{C_{12}D_{22}-C_{22}D_{12}-C_{22}D_{66}}{C_{22}}\frac{\partial^3f}{\partial x\partial y^2}+\frac{C_{11}D_{66}}{C_{22}}\frac{\partial^3f}{\partial x^3}-C_{11}\frac{\partial f}{\partial x}-m_y \quad (14)$$

$$\frac{\partial w}{\partial x}-\frac{\partial F}{\partial x}+\frac{D_{11}}{C_{11}}\frac{\partial^3F}{\partial x^3}+\frac{2D_{66}+D_{11}}{C_{11}}\frac{\partial^3F}{\partial y^2\partial x}=\frac{C_{12}D_{11}-C_{11}D_{12}-C_{11}D_{66}}{C_{11}}\frac{\partial^3f}{\partial y\partial x^2}+\frac{C_{22}D_{66}}{C_{11}}\frac{\partial^3f}{\partial y^3}-C_{22}\frac{\partial f}{\partial y}-m_x \quad (15)$$

then assume that

$$w=C_1F+C_2\frac{\partial^2F}{\partial x^2}+C_3\frac{\partial^2F}{\partial y^2} \quad (16)$$

where C_1,C_2 and C_3 are the undefined constants. Substitution into Eq. (14) and Eq. (15),

$$(C_1-1)\frac{\partial F}{\partial y}+(C_3+\frac{D_{22}}{C_{22}})\frac{\partial^3F}{\partial y^3}+(C_2+\frac{2D_{66}+D_{22}}{C_{22}})\frac{\partial^3F}{\partial x^2\partial y}=\frac{C_{12}D_{22}-C_{22}D_{12}-C_{22}D_{66}}{C_{22}}\frac{\partial^3f}{\partial x\partial y^2}+\frac{C_{11}D_{66}}{C_{22}}\frac{\partial^3f}{\partial x^3}-C_{11}\frac{\partial f}{\partial x}-m_y \quad (17)$$

$$(C_1-1)\frac{\partial F}{\partial x}+(C_2+\frac{D_{11}}{C_{11}})\frac{\partial^3F}{\partial x^3}+(C_3+\frac{2D_{66}+D_{11}}{C_{11}})\frac{\partial^3F}{\partial y^2\partial x}=\frac{C_{12}D_{11}-C_{11}D_{12}-C_{11}D_{66}}{C_{11}}\frac{\partial^3f}{\partial y\partial x^2}+\frac{C_{22}D_{66}}{C_{11}}\frac{\partial^3f}{\partial y^3}-C_{22}\frac{\partial f}{\partial y}-m_x \quad (18)$$

also for simplification it is requested that $C_1 = 1$, $C_2 = -D_{11}/C_{11}$ and $C_3 = -D_{22}/C_{22}$, so changing w into terms of F as followed:

$$w = F - \frac{D_{11}}{C_{11}}\frac{\partial^2 F}{\partial x^2} - \frac{D_{22}}{C_{22}}\frac{\partial^2 F}{\partial y^2} \tag{19}$$

subsititution Eq. (19) into Eqs. (11),(17) and (18) resulting as:

$$D_{11}\frac{\partial^4 F}{\partial x^4} + D_{22}\frac{\partial^4 F}{\partial y^4} + (\frac{C_{22}D_{11}}{C_{11}} + \frac{C_{11}D_{22}}{C_{22}}) \frac{\partial^4 F}{\partial x^2 \partial y^2} + q = 0 \tag{20}$$

$$\frac{C_{12}D_{22} - C_{22}D_{12} - C_{22}D_{66}}{C_{22}}\frac{\partial^3 f}{\partial x \partial y^2} + \frac{C_{11}D_{66}}{C_{22}}\frac{\partial^3 f}{\partial x^3} - C_{11}\frac{\partial f}{\partial x} - m_y = (\frac{2D_{66} + D_{22}}{C_{22}} - \frac{D_{11}}{C_{11}})\frac{\partial^3 F}{\partial x^2 \partial y} \tag{21}$$

$$\frac{C_{12}D_{11} - C_{11}D_{12} - C_{11}D_{66}}{C_{11}}\frac{\partial^3 f}{\partial y \partial x^2} + \frac{C_{22}D_{66}}{C_{11}}\frac{\partial^3 f}{\partial y^3} - C_{22}\frac{\partial f}{\partial y} - m_x = (\frac{2D_{66} + D_{11}}{C_{11}} - \frac{D_{22}}{C_{22}})\frac{\partial^3 F}{\partial y^2 \partial x} \tag{22}$$

Combination Eq. (21) and Eq. (22) getting the partial differential equations just including the new variable f as followed:

$$\alpha\frac{\partial^4 f}{\partial x \partial y^3} + \beta\frac{\partial^4 f}{\partial x^3 \partial y} + \gamma\frac{\partial^2 f}{\partial x \partial y} = -\Phi(m_x, m_y) \tag{23}$$

α, β, γ and $\Phi(m_x, m_y)$ defined as follow:

$$\alpha = (\frac{2D_{66} + D_{22}}{C_{22}} - \frac{D_{11}}{C_{11}})\frac{C_{22}D_{66}}{C_{11}} + (\frac{D_{22}}{C_{22}} - \frac{2D_{66} + D_{11}}{C_{11}})\frac{C_{12}D_{22} - C_{22}D_{12} - C_{22}D_{66}}{C_{22}} \tag{24}$$

$$\beta = \frac{C_{12}D_{11} - C_{11}D_{12} - C_{11}D_{66}}{C_{11}}(\frac{2D_{66} + D_{22}}{C_{22}} - \frac{D_{11}}{C_{11}}) - (\frac{2D_{66} + D_{11}}{C_{11}} - \frac{D_{22}}{C_{22}})\frac{C_{11}D_{66}}{C_{22}} \tag{25}$$

$$\gamma = (\frac{2D_{66} + D_{11}}{C_{11}} - \frac{D_{22}}{C_{22}})C_{11} - (\frac{2D_{66} + D_{22}}{C_{22}} - \frac{D_{11}}{C_{11}})C_{22} \tag{26}$$

$$\Phi(m_x, m_y) = \frac{\partial m_y}{\partial y}(\frac{2D_{66} + D_{11}}{C_{11}} - \frac{D_{22}}{C_{22}}) - \frac{\partial m_x}{\partial x}(\frac{2D_{66} + D_{22}}{C_{22}} - \frac{D_{11}}{C_{11}}) \tag{27}$$

In this section w, β_x, β_y are in terms of F, f and the system (1),(2),(3) is turned into two independent equations (20),(23). In what follows, two decoupled equations are solved respectively.

3 SOLUTION METHOD OF NEW EQUATIONS

In this section, take an orthotropic rectangular plate with four simple edges as an example. Solve (20) and (23) respectively. Lastly get the solution of the system though F and f. The boundary conditions of edges are:

$$x = \{^0_a\text{: } w = 0, M_x = 0, M_{xy} = 0 \tag{28}$$

$$y = \{^0_b\text{: } w = 0, M_y = 0, M_{xy} = 0 \tag{29}$$

substitution of (12),(13) and (19) into (28) and (29) leads to

$$(F - \frac{D_{11}}{C_{11}}\frac{\partial^2 F}{\partial x^2} - \frac{D_{22}}{C_{22}}\frac{\partial^2 F}{\partial y^2})|^{x=0}_{x=a} = 0 \tag{30}$$

$$[D_{11}\frac{\partial^2 F}{\partial x^2} + D_{22}\frac{\partial^2 F}{\partial y^2} + (D_{11}C_{22} - D_{22}C_{11})\frac{\partial^2 f}{\partial x \partial y}]|^{x=0}_{x=a} = 0 \tag{31}$$

$$(2\frac{\partial^2 F}{\partial x \partial y} + C_{22}\frac{\partial^2 f}{\partial y^2} - C_{11}\frac{\partial^2 f}{\partial x^2})|^{x=0}_{x=a} = 0 \tag{32}$$

$$(F - \frac{D_{11}}{C_{11}}\frac{\partial^2 F}{\partial x^2} - \frac{D_{22}}{C_{22}}\frac{\partial^2 F}{\partial y^2})|^{y=0}_{y=b} = 0 \tag{33}$$

$$[D_{22}\frac{\partial^2 F}{\partial y^2} + D_{11}\frac{\partial^2 F}{\partial x^2} + (D_{22}C_{11} - D_{11}C_{22})\frac{\partial^2 f}{\partial x \partial y}]|^{y=0}_{y=b} = 0 \tag{34}$$

$$(2\frac{\partial^2 F}{\partial x \partial y} + C_{22}\frac{\partial^2 f}{\partial y^2} - C_{11}\frac{\partial^2 f}{\partial x^2})|^{y=0}_{y=b} = 0 \tag{35}$$

then solve the Eq. (20) with the boundary condition (30) and (33). Use the separation of variables to obtain the general solutions for the system. It is assumed that F has the form as:

$$F(x, y) = \sum_{m=1}^{\infty}\sum_{n=1}^{\infty} X_m(x)Y_n(y) \tag{36}$$

In order to meeting the boundary condition Eqs. (30) and (33), $X_m(x)$ and $Y_n(y)$ are defined as followed:

$$X_m(x) = A_m \sin\frac{m\pi x}{a}, Y_n(y) = A_n \sin\frac{n\pi y}{b} \tag{37}$$

so Eq. (36) can be rewritten as:

$$F(x,y) = \sum_{m=1}^{\infty}\sum_{n=1}^{\infty} A_{mn} \sin\frac{m\pi x}{a} \sin\frac{n\pi x}{b} \tag{38}$$

where $A_{mn} = A_n A_m$. Certainly Eq. (38) is also required to meet Eq. (20). In order for determing A_{mn}, the load function in Eq. (20) is expressed in double sine series form:

$$q(x,y) = \sum_{m=1}^{\infty}\sum_{n=1}^{\infty} Q_{mn} \sin\frac{m\pi x}{a} \sin\frac{n\pi x}{b} \tag{39}$$

where

$$Q_{mn} = \frac{4}{ab}\int_0^a\int_0^b q(x,y) \sin\frac{m\pi x}{a} \sin\frac{n\pi x}{b} dxdy$$

substitution of Eq. (39) into (20) as:

$$\sum_{m=1}^{\infty}\sum_{n=1}^{\infty} A_{mn}[D_{11}(\frac{m\pi}{a})^4 + (\frac{C_{22}D_{11}}{C_{11}} + \frac{C_{11}D_{22}}{C_{22}}) (\frac{m\pi}{a})^2(\frac{n\pi}{ab})^2 + D_{22}(\frac{n\pi}{b})^4] \sin\frac{m\pi x}{a} \sin\frac{n\pi x}{b} = \sum_{m=1}^{\infty}\sum_{n=1}^{\infty} \sin\frac{m\pi x}{a} \sin\frac{n\pi x}{b} Q_{mn} \tag{40}$$

According to the uniqueness theorem of Fourier expansion, obtain A_{mn} as:

$$A_{mn} = Q_{mn}[D_{11}(\frac{m\pi}{a})^4 + (\frac{C_{22}D_{11}}{C_{11}} + \frac{C_{11}D_{22}}{C_{22}}) (\frac{m\pi}{a})^2(\frac{n\pi}{ab})^2 + D_{22}(\frac{n\pi}{b})^4]^{-1} \tag{41}$$

substituting Eq. (41) into Eq. (38),

$$F(x,y) = \sum_{m=1}^{\infty}\sum_{n=1}^{\infty} \frac{4}{ab}\int_0^a\int_0^b q(x,y) \sin\frac{m\pi x}{a} \sin\frac{n\pi y}{b} dxdy[D_{11}(\frac{m\pi}{a})^4 + (\frac{C_{22}D_{11}}{C_{11}} + \frac{C_{11}D_{22}}{C_{22}}) (\frac{m\pi}{a})^2(\frac{n\pi}{ab})^2 + D_{22}(\frac{n\pi}{b})^4]^{-1} \sin\frac{m\pi x}{a} \sin\frac{n\pi y}{b} \tag{42}$$

What follow using the method of separating variables to solve Eq. (23) with boundary condition. The expression in the form of the separation of variables for $f(x,y)$ is:

$$f(x,y) = \sum_{m=1}^{\infty}\sum_{n=1}^{\infty} X_m(x)Y_n(y) \tag{43}$$

also we can have:

$$\frac{\partial}{\partial x} f(x,y) = \sum_{m=1}^{\infty}\sum_{n=1}^{\infty} X'_m(x)Y_n(y) \tag{44}$$

$$\frac{\partial^2}{\partial x^2} f(x,y) = \sum_{m=1}^{\infty}\sum_{n=1}^{\infty} X''_m(x)Y_n(y) \tag{45}$$

$$\frac{\partial^2}{\partial x \partial y} f(x,y) = \sum_{m=1}^{\infty}\sum_{n=1}^{\infty} X'_m(x)Y'_n(y) \tag{46}$$

for simplification, only Eq. (46) will be used to solve the equation for f. Substitution of (42) and (46) into (31) and (34), getting the boundary function just about separations of f as followed:

$$x = \{^0_a : X'_m(x) = 0, \qquad y = \{^0_b : Y'_n(y) = 0 \tag{47}$$

in order to satisfy the condition Eq. (47), set separations of $X'_m(x)$ and $Y'_n(y)$ as:

$$X'_m(x) = B'_m \sin\frac{m\pi x}{a}, \qquad Y'_n(y) = B'_n \sin\frac{n\pi y}{b} \tag{48}$$

also we have:

$$X_m(x) = B_m \cos\frac{m\pi x}{a} + C_m$$

$$Y_n(y) = B_n \cos\frac{n\pi y}{b} + C_n$$

$$X''_m(x) = B''_m \cos\frac{m\pi x}{a} \qquad Y''_n(y) = B''_n \cos\frac{n\pi y}{b}$$

where B_m, B'_m, B''_m and B_n, B'_n, B''_n have the relationships as followed:

$$B_m = -(\frac{m\pi}{a})^{-1}B'_m = (\frac{m\pi}{a})^{-2}B''_m$$

$$B_n = -(\frac{n\pi}{b})^{-1}B'_n = (\frac{n\pi}{b})^{-2}B''_n$$

then substitute Eq. (42) and f into Eq. (32) and (35), and determine the constants in the equation about f,

$$2\sum_{m=0}^{\infty}\sum_{n=0}^{\infty} A_{mn}\frac{m\pi}{a}\frac{n\pi}{b} \cos\frac{n\pi}{b}y = \sum_{m=0}^{\infty}\sum_{n=0}^{\infty} B_{mn}[C_{22}(\frac{n\pi}{b})^2 - C_{11}(\frac{m\pi}{a})^2] \cos\frac{n\pi}{b}y - E_{mn}C_{22} (\frac{n\pi}{b})^2 \cos\frac{n\pi}{b}y + F_{mn}C_{11}(\frac{m\pi}{a})^2 \tag{49}$$

$$2\sum_{m=0}^{\infty}\sum_{n=0}^{\infty}A_{mn}\frac{m\pi}{a}\frac{n\pi}{b}\cos m\pi\cos\frac{n\pi}{b}y=\sum_{m=0}^{\infty}\sum_{n=0}^{\infty}\tag{50}$$

$$B_{mn}[C_{22}(\frac{n\pi}{b})^2-C_{11}(\frac{m\pi}{a})^2]\cos m\pi\cos\frac{n\pi}{b}y-$$

$$E_{mn}C_{22}(\frac{n\pi}{b})^2\cos\frac{n\pi}{b}y+F_{mn}C_{11}(\frac{m\pi}{a})^2\cos m\pi$$

$$2\sum_{m=0}^{\infty}\sum_{n=0}^{\infty}A_{mn}\frac{m\pi}{a}\frac{n\pi}{b}cos\frac{m\pi}{a}x=\sum_{m=0}^{\infty}\sum_{n=0}^{\infty}B_{mn}[\tag{51}$$

$$C_{22}(\frac{n\pi}{b})^2-C_{11}(\frac{m\pi}{a})^2]\cos\frac{m\pi}{a}x-E_{mn}C_{22}$$

$$(\frac{n\pi}{b})^2+F_{mn}C_{11}(\frac{m\pi}{a})^2\cos\frac{m\pi}{a}x$$

$$2\sum_{m=0}^{\infty}\sum_{n=0}^{\infty}A_{mn}\frac{m\pi}{a}\frac{n\pi}{b}\cos\frac{m\pi}{a}x\cos n\pi=\sum_{m=0}^{\infty}\tag{52}$$

$$\sum_{n=0}^{\infty}B_{mn}[C_{22}(\frac{n\pi}{b})^2-C_{11}(\frac{m\pi}{a})^2]\cos\frac{m\pi}{a}x$$

$$\cos n\pi-E_{mn}C_{22}(\frac{n\pi}{b})^2\cos n\pi$$

$$+F_{mn}C_{11}(\frac{m\pi}{a})^2\cos\frac{m\pi}{a}x$$

where B_{mn} is equal to B_nB_m, and E_{mn}, F_{mn} are not usefull. So according to the uniqueness theorem of Fourier expansion, we have:

$$2A_{mn}\frac{m\pi}{a}\frac{n\pi}{b}=B_{mn}[C_{22}(\frac{n\pi}{b})^2-C_{11}(\frac{m\pi}{a})^2]\tag{53}$$

$$-E_{mn}C_{22}(\frac{n\pi}{b})^2$$

$$2A_{mn}\frac{m\pi}{a}\frac{n\pi}{b}\cos m\pi=B_{mn}[C_{22}(\frac{n\pi}{b})^2-C_{11}\tag{54}$$

$$(\frac{m\pi}{a})^2]\cos m\pi-E_{mn}C_{22}(\frac{n\pi}{b})^2$$

$$2A_{mn}\frac{m\pi}{a}\frac{n\pi}{b}=B_{mn}[C_{22}(\frac{n\pi}{b})^2-C_{11}(\frac{m\pi}{a})^2]\tag{55}$$

$$+F_{mn}C_{11}(\frac{m\pi}{a})^2$$

$$2A_{mn}\frac{m\pi}{a}\frac{n\pi}{b}cosn\pi=B_{mn}[C_{22}(\frac{n\pi}{b})^2-C_{11}(\tag{56}$$

$$\frac{m\pi}{a})^2]\cos n\pi+F_{mn}C_{11}(\frac{m\pi}{a})^2$$

Solve Eqs. (53),(54),(55) and (56), we can obtain:

$$B_{mn}=2A_{mn}\frac{m\pi}{a}\frac{n\pi}{b}[C_{22}(\frac{n\pi}{b})^2-C_{11}(\frac{m\pi}{a})^2]^{-1}$$

$$E_{mn}=F_{mn}=0$$

So the expression in the form of double sine series for $f(x,y)$ is

$$f(x,y)=\sum_{m=1}^{\infty}\sum_{n=1}^{\infty}\frac{8mn\pi^2}{a^2b^2}\int_0^a\int_0^b q(x,y)\sin\frac{m\pi x}{a}\tag{57}$$

$$\sin\frac{n\pi y}{b}dxdy[D_{11}(\frac{m\pi}{a})^4+(\frac{C_{22}D_{11}}{C_{11}}+\frac{C_{11}D_{22}}{C_{22}})$$

$$(\frac{m\pi}{a})^2(\frac{n\pi}{b})^2+D_{22}(\frac{n\pi}{b})^4]^{-1}[C_{22}(\frac{n\pi}{b})^2-$$

$$C_{11}(\frac{m\pi}{a})^2]^{-1}\cos\frac{m\pi x}{a}\cos\frac{n\pi y}{b}$$

substitution Eq. (57) into Eq. (23), and define the relationship between m and n in Eq. (57), resulting as:

$$\alpha(\frac{m\pi}{a})^2+\beta(\frac{n\pi}{b})^2-\gamma=0\tag{58}$$

And substitution of Eqs. (42) and (57) into Eqs. (19) and (12) and (13), obtain the expression for w,β_x and β_y,

$$w(x,y)=\sum_{m=1}^{\infty}\sum_{n=1}^{\infty}(1+\frac{D_{11}}{C_{11}}(\frac{m\pi}{a})^2+\frac{D_{22}}{C_{22}}(\frac{n\pi}{b})^2)\tag{59}$$

$$\frac{4}{ab}\int_0^a\int_0^b q(x,y)\sin\frac{m\pi x}{a}\sin\frac{n\pi y}{b}dxdy[D_{11}$$

$$(\frac{m\pi}{a})^4+(\frac{C_{22}D_{11}}{C_{11}}+\frac{C_{11}D_{22}}{C_{22}})(\frac{m\pi}{a})^2(\frac{n\pi}{b})^2$$

$$+D_{22}(\frac{n\pi}{b})^4]^{-1}\sin\frac{m\pi x}{a}\sin\frac{n\pi y}{b}$$

$$\beta_x(x,y)=\sum_{m=1}^{\infty}\sum_{n=1}^{\infty}\frac{4m\pi}{a^2b}\int_0^a\int_0^b q(x,y)\sin\frac{m\pi x}{a}\tag{60}$$

$$\sin\frac{n\pi y}{b}dxdy[D_{11}(\frac{m\pi}{a})^4+(\frac{C_{22}D_{11}}{C_{11}}$$

$$+\frac{C_{11}D_{22}}{C_{22}})(\frac{m\pi}{a})^2(\frac{n\pi}{ab})^2+D_{22}(\frac{n\pi}{b})^4]^{-1}$$

$$\cos\frac{m\pi x}{a}\sin\frac{n\pi y}{b}+\sum\sum_{\alpha(\frac{m\pi}{a})^2+\beta(\frac{n\pi}{b})^2-\gamma=0}$$

$$-\frac{8C_{22}mn^2\pi^3}{a^2b^3}\int_0^a\int_0^b q(x,y)\sin\frac{m\pi x}{a}$$

$$\sin\frac{n\pi y}{b}dxdy[D_{11}(\frac{m\pi}{a})^4+(\frac{C_{22}D_{11}}{C_{11}}+\frac{C_{11}D_{22}}{C_{22}})$$

$$(\frac{m\pi}{a})^2(\frac{n\pi}{b})^2+D_{22}(\frac{n\pi}{b})^4]^{-1}[C_{22}(\frac{n\pi}{b})^2-$$

$$C_{11}(\frac{m\pi}{a})^2]^{-1}\cos\frac{m\pi x}{a}\cos\frac{n\pi y}{b}$$

$$\beta_y(x,y)=\sum_{m=1}^{\infty}\sum_{n=1}^{\infty}\frac{4n\pi}{ab^2}\int_0^a\int_0^b q(x,y)\sin\frac{m\pi x}{a} \quad (61)$$

$$\sin\frac{n\pi y}{b}dxdy[D_{11}(\frac{m\pi}{a})^4+(\frac{C_{22}D_{11}}{C_{11}}$$

$$+\frac{C_{11}D_{22}}{C_{22}})(\frac{m\pi}{a})^2(\frac{n\pi}{ab})^2+D_{22}(\frac{n\pi}{b})^4]^{-1}$$

$$\sin\frac{m\pi x}{a}\cos\frac{n\pi y}{b}+\sum\sum_{\alpha(\frac{m\pi}{a})^2+\beta(\frac{n\pi}{b})^2-\gamma=0}$$

$$\frac{8C_{11}m^2n\pi^3}{a^3b^2}\int_0^a\int_0^b q(x,y)\sin\frac{m\pi x}{a}$$

$$\sin\frac{n\pi y}{b}dxdy[D_{11}(\frac{m\pi}{a})^4+(\frac{C_{22}D_{11}}{C_{11}}+\frac{C_{11}D_{22}}{C_{22}})$$

$$(\frac{m\pi}{a})^2(\frac{n\pi}{b})^2+D_{22}(\frac{n\pi}{b})^4]^{-1}[C_{22}(\frac{n\pi}{b})^2-$$

$$C_{11}(\frac{m\pi}{a})^2]^{-1}\cos\frac{m\pi x}{a}\cos\frac{n\pi y}{b}$$

4 NUMERICAL EXAMPLE

In this section the exact solution of the *SSSS* rectangular plate is calculated by the method which is developed in this paper. The numerical example is considered, the data for the plate and load amplitude are $a=b=4\,m$, $h=0.8$, $E=343\,MPa$ and $\gamma=0.3$. The calculating result for deflection of the plate is shown in Fig. 2, where $q=2.0\times10^6\,N$. Then the exact value of maximal w is calculated shown in Table. 1, when x/a equals 0.5.

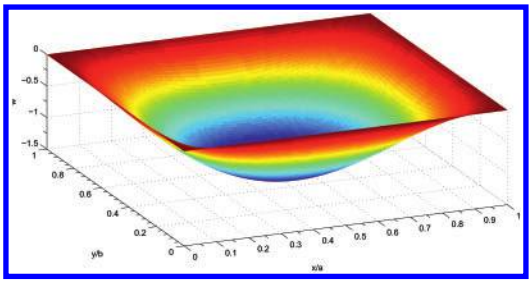


Figure 2. The result for deflection of the plate($a=b=4m$, $h=0.8$, $E=343\,MPa$, $\upsilon=0.3$ and $q=2.0E6N$).

Table 1. The exact value of maximal w for the rectangular plates with $\gamma=0.3$, $E=343\,MPa$, $y/b=0.5$

x/a	0.45	0.48	0.5	0.52	0.55
m,n = 10	−1.4492	−1.4629	−1.4655	−1.4626	−1.4492
m,n=15	−1.4490	−1.4625	−1.4651	−1.4625	−1.4490
m,n=20	−1.4490	−1.4626	−1.4652	−1.4626	−1.4490

5 CONCLUSIONS

The novel variables were introduced for simplifying the method to solving governing equations of orthotropic thick rectangular plate. The partial differential equations were decoupled into two independent ordinary differential equations. By the mean of the separation of variable exact closed form solutions for the deflection and rotation for the orthotropic rectangular plate were obtained. For this method, the accuracy of the numerical result and more cases for the orthotropic plates with different boundary conditions will be discussed to show its rationality in the future.

REFERENCES

Hearmon RFS. (1959). The frequency of fexural vibration of rectangular orthotropic plates with clamped or supported edges. *J Appl Mech. 26*, 726–728.

Bhat RB. (1985). Natural frequencies of rectangular plates using characteristic orthogonal polynomials in the Rayleigh¨CRitz method. *J. Sound Vib 102(4)*, 493–9.

Dickinson SM, Di Blasio A. (1986). On the use of orthogonal polynomials in the ReyleighCRitz method for the study of the flexural vibration and buckling of isotropic and orthotropic rectangular plates. *J Sound Vib 108(1)*, 51–62.

Rossi RE, Bambill DV, Laura PAA. (1998). Vibrations of a rectangular orthotropic plate with a free edge a comparison of analytical and numerical results. *J. Ocean Eng. 25(7)*, 521–7.

Jones R, Milne BJ. (1976). Plate characteristic functions and natural frequencies of vibration of plates by iterative reduction of partial differential equation. *J. Vib Acoustics Trans ASME 115(2)*, 177–81.

Dalaei M, Kerr AD. (1996). Natural vibration analysis of clamped rectangular orthotropic plates. *J. Sound Vib. 189(3)*, 399–406.

Bercin AN. (1996). Free vibration solution for clamped orthotropic plates using the Kantorovich method. *J Sound Vib. 196(2)*, 243–7.

Sakata T, Takahashi K, Bhat RB. (1996). Natural frequencies of orthotropic rectangular plates obtained by iterative reduction of the partial differential equation. *J. Sound Vib. 189(1)*, 89–101.

14. Renewable energy structures

Research and Applications in Structural Engineering, Mechanics and Computation – Zingoni (Ed.)
© 2013 Taylor & Francis Group, London, ISBN 978-1-138-00061-2

Wind loading on solar chimneys: from wind tunnel experiments to CFD simulation

F. Lupi & C. Borri
University of Florence, Florence, Italy

H.-J. Niemann
Ruhr-University Bochum, Bochum, Germany

ABSTRACT: The Solar Updraft Power Plant technology is a combined sun-wind energy solution for renewable energy harvesting. It is based on the natural updraft of warm air in a chimney and conversion into electric power by wind turbines at the chimney foot. The tower structure is basically a circular cylinder, which may turn into a hyperboloid at lower levels in order apply benefits of shape strengthening. The height of the tower is up to 1.5 km and it is usually designed as a thin reinforced concrete shell. A preliminary investigation of the shell response under an equivalent static wind load revealed the key role played by stiffening rings along the height. They allow a better distribution of internal forces under wind loading, reducing risk of buckling and peaks of tension at the windward side. An extensive wind tunnel investigation has been recently performed at WiSt laboratory at Ruhr-University Bochum (Germany) and at Criaciv laboratory at University of Florence (Italy). The tests highlighted a new phenomenon regarding cross-wind loads, induced by a bi-stable and asymmetric flow distribution. This is created by compartments between stiffening rings along the tower. A further insight into the flow structures is achieved by CFD simulations. Results of both experimental and numerical studies are addressed in the paper.

1 INTRODUCTION

The original idea of energy harvesting from sun and wind – by a combination of the greenhouse effect below a large collector roof and the natural updraft of the warm air in a tower – goes back to the early twentieth century (Cabanyes, 1903). The basic working principle was documented, some years later, in a publication by the German scientist Günther (Günther, 1931). The question, whether it is possible and convenient to use the updraft of air created by solar radiation input to generate electricity, was originally tested with a full-scale prototype ($h = 195$ m) by J. Schlaich and his team (Schlaich, 1995). Since then, several studies have been carried out regarding the feasibility of this new technology, namely Solar Updraft Power and, in its original name, Solar Chimney Power Plant (see, for example, SCPT 2010 and SUTPT 2012).

Basically, a Solar Chimney Power Plant consists of three elements: the collector area, the turbine(s) with coupled generator(s) as power conversion unit and the solar tower. Solar radiation heats the collector ground and consequently warms up the air inside the collector. The warm air rises up into the chimney of the plant. The driving force is the pressure difference between a column of cold air outside and a column of hot air inside the chimney. The stream of warm air turns the turbines at the chimney foot and in the power conversion unit the kinetic energy of the flow is then transformed into electric power. Figure 1 shows a recently built power plant of small size in Inner Mongolia (China). It is a 50 m tall reinforced concrete tower with a glass collector on an only one side. It is optimized for both sun and wind energy harvesting during the summer and the winter, respectively (Wei & Wu 2012).



Figure 1. Solar Heated Wind Updraft Tower in Wuhai Desert, Inner Mongolia (China).

In October 2010, the generating electricity system in Figure 1 was combined to the grid. However, the production of energy is proportional to the volume of the cylinder having the height of the tower and the diameter of the collector. For this reason, provided

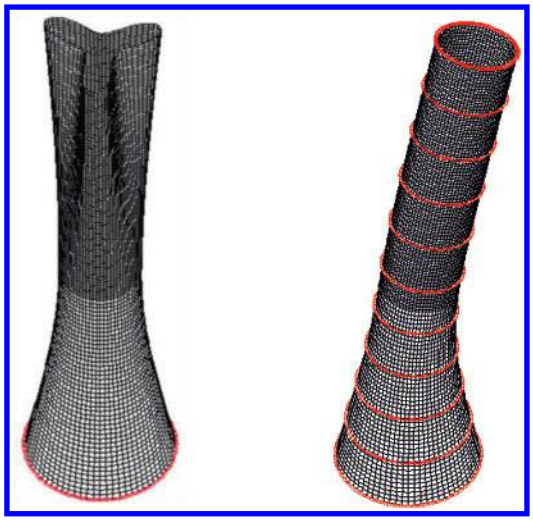


Figure 2. First natural vibration mode: without rings ($n_1 = 0.073$ Hz) and with 10 rings ($n_1 = 0.172$ Hz).

a sufficiently high solar radiation input (as it is, for example, in the great deserts), a very good efficiency of the power plant can be reached only with extra-large dimensions of the tower and/or the collector. A tower of 500 m in height can deliver about 50 MW of energy; values up to 200 MW can be achieved with structures of 1 km in height and 5 km in diameter of the collector.

2 PRELIMINARY STUDIES

Solar Towers are especially sensitive to wind, because they are ultra-high, slender and very thin shells. So, among all natural hazards, the wind action decides the structural feasibility of the tower. It comprises the mean wind load, averaged over ten minutes, the fluctuating wind load due to turbulence, the amount of resonance to turbulence, and the load induced cross-wind by vortex shedding.

A preliminary investigation on 1-km tower (predesigned by Krätzig et al. 2009) under an equivalent static wind load was performed in Lupi (2009) and discussed in Niemann et al. (2009) and Borri et al. (2010). The aims of the investigation were: 1) assess the feasibility of Solar Chimneys, with regard to the wind action, 2) find a strategy of optimization of the structure to minimize wind induced tensile stresses (reduction of steel reinforcement).

In accordance also with other authors (e.g. Krätzig et al. 2008/09/10 and Harte et al. 2007/10), it was proved that a key role in the structural design of the tower was played by stiffening rings, i.e. circular ring beams applied at the top and at various levels along the height, in order to stabilize the cross section and achieve a better distribution of internal forces. The stiffening rings guarantee a beam-like behavior at the first eigenmode (Figure 2).

One of the first issues which were studied in order to assess the feasibility of solar chimneys was the

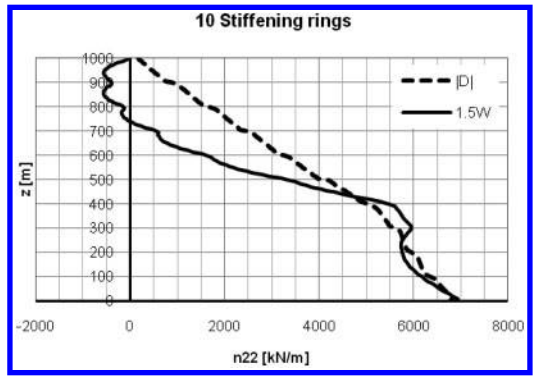


Figure 3. Meridional force n_{22} at stagnation (1-km tower with ten stiffening rings). D = self-weight induced stresses, W = wind induced stresses.

overturning of the tower by the wind action. The analysis was performed in Lupi (2009) in a combination at the ultimate limit states: D + 1.6 W, where the dead load (D) was not amplified because it is considered a favorable action, while the wind action (W) was amplified with a partial safety factor of 1.6. This value was suggested by the VGB guideline for cooling towers, in the version of 2005. In 2010, the revised version of the VGB allowed to use the factor 1.5 instead of 1.6, in line with the recommendations of the Eurocode. The results at stagnation, by using the amplification factor 1.5 for the wind action, are reported in Figure 3.

The investigation showed that the region of the tower which is more sensitive to the wind action is around 200–450 m in height, where the tensile stresses produced by the wind load at the windward side are not completely balanced by the self-weight.

Tensile stresses are caused by high peaks of tension in the shell. In the study it was noted that an increase of the stiffness of the rings beams improves the distribution of internal forces, with a consequent reduction of peaks of tension. The reason is due to the role played by the stiffening rings, which reduce the shell-like deformations of the cross section. Therefore, the distribution of internal forces in the cross section tends to be more similar to the one of a beam (linear distribution, crossing the x-axis at 90°). Since equilibrium is preserved at each level, a better distribution of internal forces, ideally tending to the one of a beam, implies reduction of peaks of tension.

In conclusion, this preliminary analysis of wind-induced global effects showed the importance of the stiffening rings in [1)] reducing the risk of overturning of the tower by the wind action, [2)] saving steel reinforcement due to the reduction of tension in the shell.

Further issues like the structural vulnerability to vortex shedding were also addressed in the feasibility analysis (Lupi 2011). In this regard, thanks to the beam-like vibration mode at a sufficiently high frequency (about 0.17 Hz for 1 km tall tower), which is ensured by the presence of the rings and the not too high aspect ratio, the critical velocity for onset of lock-in phenomena is very high (above 100 m/s).

All these promising results encouraged further investigation. In particular, the evaluation of local effects in the vicinity of the ring beams required a more sophisticated wind load model than the one suggested by the Codes, where the peak load is obtained by amplification of the mean load. Moreover, since the ring beams can be designed as circular ring beams which jut out of the structure, externally, their influence on the wind flow can have important effects. Therefore, in order to answer to these and other questions, wind tunnel tests are performed at WiSt (Ruhr-University Bochum, Germany) and at Criaciv (University of Florence, Italy). In addition to the cross-checked experimental investigation, numerical simulations have been performed on the basis of Criaciv' results by the TEE Group, Industrial Energy Department, University of Florence (Salvadori & Mattana 2013, unpublished).

3 WIND TUNNEL INVESTIGATION

The experimental investigation is performed in two wind tunnels, in order to cross-check results: the WiSt laboratory at Ruhr-University Bochum (Germany) and the Criaciv laboratory at University of Florence (Italy).

WiSt laboratory at Ruhr-University Bochum is an open circuit wind tunnel with a total length of about 17 m. The test section is 1.8 m in width and 1.6 m in height. The turbulent atmospheric boundary layer is created by three turbulent generators of Counihan type (Counihan 1969), a castellated barrier and a roughness field consisting of wooden cubes. The engine allows to attain a maximum wind speed of about 28–30 m/s. A Prandtl tube, placed at 1.3 m in height, allows to measure the dynamic pressure of the incoming flow. Temperature sensors acquire temperature during the measurements. The pressure sensors are four-active-element piezoresistive bridges. The A/D converter scans the pressures in a sample-and-hold modus, which produces simultaneous sampling of the measurements. A sampling frequency of 2 kHz is used for the measurements.

The Criaciv laboratory is an open-circuit wind tunnel located at Polo Universitario Città di Prato, which is a branch of the University of Florence. The total length is about 22 m, the tunnel has a slightly divergent shape from the inlet (in order to guarantee a constant pressure along the x-axis) and the test section is 2.4 m in width and 1.6 m in height. The atmospheric boundary layer profile which is used in these experiments is produced by three bigger turbulence generators of Counihan type and four smaller spires, followed by roughness panels with wooden cubes. The motor – with a nominal power of 160 kW – and the fan are placed at the end of the wind tunnel, followed by a T-shaped symmetric diffuser. The engine allows to attain a maximum wind speed of about 30 m/s. The pressures on the tower are measured with two different types of pressure scanners, at sampling frequency of either 250 or 500 Hz, depending on the scanner.



Figure 4. Wind tunnel model.

The model for wind tunnel tests (Figure 4) is a circular cylinder with a free-end and aspect ratio H/D ≈ 7. The cylinder is a rigid body of 1 m in height and 15 cm in diameter. In scale 1:1000, it represents a prototype of 1 km in height. Pressure taps are placed at several levels along the height and at an angular spacing of 20° in the circumferential direction. It is also possible to create an efflux inside the cylinder like in a chimney, but the most interesting results presented in the paper refer to the condition without efflux. Both external and internal pressures can be measured at each level.

The peculiarity of the model is the presence of ten circular rings along the height. They are equally spaced along the height. In the wind tunnel scale the rings are at a distance of 10 cm. The width (w) of the rings, in the wind tunnel scale is 7 mm ($w/D = 4.67*10^{-2}$). Such rings along the model reproduce the stiffening rings, previously introduced in the paper. The aerodynamic of the flow around the structure is the object of the investigation.

4 EXPERIMENTAL RESULTS

Due to the reduced scale of the model, in the wind tunnel the Reynolds number ($Re_{,WT}$) is around three orders of magnitude lower than in full-scale ($Re_{,FS}$).

$$Re_{WT} = \frac{UD}{\nu} = \frac{30*0.15}{1.5*10^{-5}} = 3*10^{5} \quad (1)$$

$$Re_{FS} = \frac{UD}{\nu} = \frac{60*150}{1.5*10^{-5}} = 6*10^{8} \quad (2)$$

Therefore, surface roughness (consisting of ribs) is applied on the model in order to attain a much higher effective Re. The concept of effective Re is described in ESDU 74030. A preliminary investigation on the circular cylinder (without rings) regarding the effect of surface roughness is performed at WiSt wind tunnel in turbulent boundary layer flow. The proper choice of surface roughness is decided with regard to a target surface pressure distribution, recommended by the VGB guideline (VGB 2010) for smooth cylinders in the transcritical range of Re.

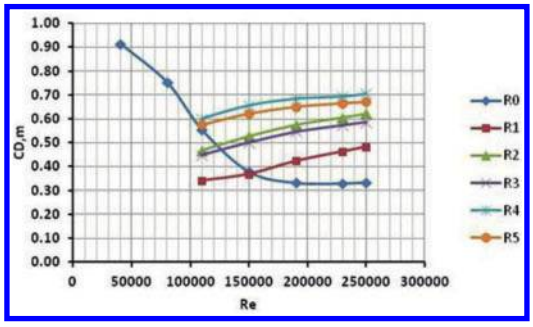


Figure 5. Mean drag coefficient versus Re. R0 = smooth cylinder, R1–R5 = rough cylinder, different distribution of ribs.

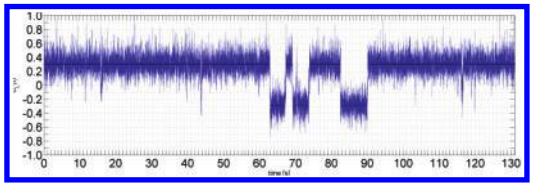


Figure 6. Time history of the lift coefficient at z/H = 0.95 (Re = 2.5*10^5, rough cylinder R1), result at WiSt wind tunnel.

Results are reported in Figure 5 in terms of mean drag coefficients. The blue curve (R0) in the graph refers to the smooth cylinder. The state of the flow ranges from the end of subcritcal to the first stage of supercritical regime. The latter is characterized by constant minimum drag, according to the classification proposed by Roshko (1961). All the other curves (named R1–R5) refer to the rough cylinder. Thanks to surface roughness and turbulence of the incoming flow, the range of Re tested in the experiments on the rough cylinder is beyond the critical Re. The target condition is well represented by the red curve (R1) at the highest Re, this is then adopted in the following analysis. Further details on Reynolds effects can be found in Lupi et al. (2012).

The tests performed on the tower with ten rings revealed a surprising effect due to the compartments created by the rings. It is a bistable flow condition, meaning that two stable states of the flow are clearly detectable in the time histories, as it is shown in Figure 6, which plots the lift coefficient at z/H = 0.95. The lift coefficient is obtained by integration of pressures in the across-wind direction.

Figure 6 proves that within each state of the bistable condition the mean lift is different from zero. Therefore, in terms of mean loads, the solar chimney exposed to wind should be designed for both mean drag and lift forces, i.e. mean forces in both the along-wind and the across-wind directions.

The existence of a not-zero mean lift force (i.e. a mean force in the across-wind direction) is due to a not symmetric mean pressure distribution. The result is rather astonishing, being the structure a circular cylinder. However, the compartments created by rings along

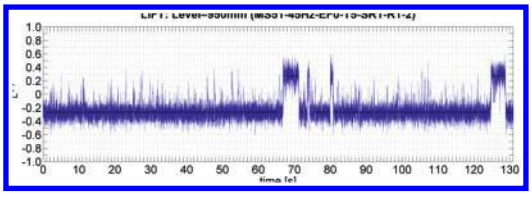


Figure 7. Time history of the lift coefficient at z/H = 0.95 (Re = 2.8*10^5, rough cylinder R1), result at Criaciv wind tunnel.

the height are responsible for a complicated flow structure, which results in not-symmetric mean pressure distribution alternated in neighboring compartments.

The cross-check of results on the same model in WiSt and Criaciv wind tunnels is decisive to assess the physical fundamentals of the phenomenon (Figure 7).

Therefore, the asymmetric mean pressure distribution, with higher suction on one side of the cylinder, must be considered an intrinsic characteristic of the observed phenomenon on the tower with rings, which is not induced by the conditions of the tests.

By the way, the bistable flow is not a completely new phenomenon in fluid dynamics. It is well known, for example, on smooth circular cylinders in smooth flow within the critical range of Re. In those conditions, transition from laminar to turbulent boundary layer occurs around the separation point and any disturbance in the flow may allow reattachment on an only one side of the cylinder. Thus, the asymmetry in the bistable flow condition is due to the formation of a laminar separation bubble on an only one side of the cylinder (Schewe, 1983). The same effect, with formation of a bubble in the wake of the cylinder, can be hypothesized also on the solar chimney. A separation bubble on an only one side of the structure produces the asymmetric load. However, it is absolutely not a laminar separation bubble in the classical sense, as described in literature on smooth circular cylinders. It cannot be, due to surface roughness applied on the cylinder surface (which promotes transition to turbulence very close to stagnation) and to turbulence of the incoming flow. Moreover, the Reynolds number of the experiment (Re = 2.5*10^5) is rather high and far beyond the critical value. In addition, in the range of Re which was possible to test in the experiments, there is not any significant dependence on Re which may suggest disappearance of the phenomenon.

This result presents several new and unknown issues regarding the flow around circular cylinders, which have also consequences for the structural design. A further proof, as well as the confirmation of formation of a separation bubble on one side of the cylinder, results from CFD simulations. It is shown in the next section.

5 CFD SIMULATIONS

CFD simulations have been performed on the basis of Criaciv' experiments by the TEE group, Industrial Energy Department (formerly known as Energy

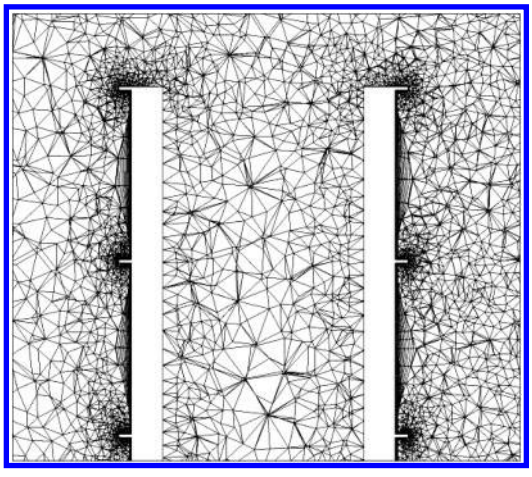


Figure 8. Detail of the mesh in the vicinity of the ring beams. Transversal cross-section.

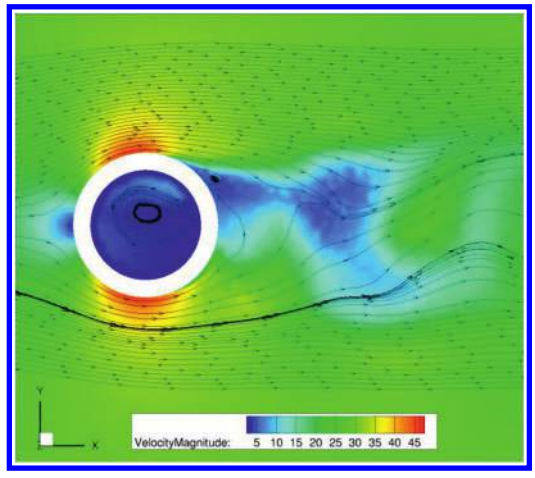


Figure 9. Horizontal cross-section, instantaneous flow velocity (magnitude, m/s) at $z/H = 0.75$.

Engineering Department "S. Stecco"), University of Florence (Salvadori & Mattana et al. 2013).

The URANS simulation is performed by using the software Ansys Fluent 14. The incompressible fluid is solved by applying Navier-Stokes equations. The time step is 0.001 s. The turbulence model is the Shear Stress Transport (SST) k-omega. This is suitable to describe separated flows on smooth surfaces and adverse pressure gradients.

In order to reproduce the conditions of CRIACIV experiments, the tunnel and also the diffusor downstream of the test section were modeled.

The boundary conditions at the inlet are the velocity profile, the turbulence intensity and the turbulent length scale. The velocity profile at the inlet is imposed like the one in Criaciv wind tunnel. The boundary conditions at the outlet are the pressure, the turbulence intensity and the turbulent length scale. No slip conditions are set to all the other surfaces.

A peculiar feature of the simulations is the high Re number ($Re = 2.8*10^7$), obtained by reducing the air viscosity of two order of magnitudes. In these transcritical conditions of Re, surface roughness on the cylinder is not necessary. Moreover, differently from wind tunnel experiments, the simulation benefits of ideal test conditions.

The research about the numerical simulation of the flow around the solar chimney is still on-going. Due to the stochastic occurrence of jumps in the time histories, a stochastic simulation like a LES should be more appropriate than a URANS. By the way, an important result is already achieved: the instantaneous flow picture in Figure 9 (horizontal cross-section at a representative level, $z/H = 0.75$), clearly confirms the asymmetry due to a separation bubble on one side of the cylinder. This is consistent with the expectations on the flow, deduced on the only basis of pressure measurements, as previously explained. The wake is not aligned on the rear of the cylinder, but it is shifted on one side. The result is rather relevant, because the numerical simulation benefits of ideal and symmetric test conditions, which could not be perfectly achieved in the wind tunnel. This confirms the physical fundamental of the phenomenon.

However, the period of time investigated in the numerical simulation (about 0.2 s) is presently too short for being representative and investigate bistable effects. Further studies are necessary.

6 CONCLUSIONS

The aerodynamic study of the flow around the solar chimney has shown several relevant features, induced by the stiffening rings along the height. The existence of a bistable not-symmetric flow around the cylindrical structure is confirmed in both experiments and simulations. Further studies are on-going, in order to investigate the three-dimensional features of the phenomenon and the wind-induced structural effects.

REFERENCES

Borri, C., Lupi, F., Niemann, H.-J., 2010. Structural optimization of solar towers to minimize wind induced effects. *Proc. of the 4th Int. Conf. Structural Engineering, Mechanics and Computation*, Cape Town, South Africa.

Borri, C., Lupi, F., Marino, E. 2010. Optimum Shell Design of Solar Updraft Towers. *Proc. 2nd Int. Conf. Solar Chimney Power Technology*, Ruhr-Universität Bochum and Bergische Universität Wuppertal:155–162.

Cabanyes, I. 1903. Las chimeneas solares (Solar chimneys). La energia eléctrica. Cited due to Wikipedia.

Counihan, J. 1969. An improved method of simulating an atmospheric boundary layer in a wind tunnel. *Atmospheric Environment* 3(2):197–214.

ESDU 74030, Mean forces, pressures and flow field velocities for circular cylindrical structures: single cylinder with two-dimensional flow, *Engineering Sciences Data Unit*, London.

Günther, H. 1931. In hundert Jahren - Die künftige Energieversorgung der Welt (In hundred years – World's future energy supply). Kosmos, Franckh'sche Verlagshandlung Stuttgart.

Harte, R., van Zij,l G.P.A.G. 2007. Structural stability of concrete wind turbines and solar chimney towers exposed to dynamic wind action. *Journal of Wind Engineering and Industrial Aerodynamics*, 95:1079–1096.

Harte, R., Graffmann, M., Wörmann, R. 2010. Progress in the Structural Design of Solar Chimneys. *Proc. 2nd Int. Conf. Solar Chimney Power Technology*, Ruhr-Universität Bochum and Bergische Universität Wuppertal:145–152, Bochum, Germany.

Krätzig, W.B., Harte, R., Wörmann, R. 2008. Large shell structures for power generation technologies. *Proc. 6th Int. Conf. IASS-IACM 2008*, Cornell University, Ithaca, NY, USA.

Krätzig, W.B., Niemann, H.-J., Harte, R., Höffer, R. 2009. Solar Updraft Power Plant with 750 m power towers and collector diameters of 3000 m to 4000 m. Internal manual, Bochum.

Krätzig, W.B., Harte, R., Montag, U., Woermann, R. 2009. From large natural draft cooling tower shells to chimneys of solar upwind power plants. In: A. Domingo, C. Lazaro (eds.), *IASS Symposium on Evolutions and Trends in Design, Analysis and Construction of Shells*. CD-Rom, University of Valencia.

Krätzig, W.B., Harte, R., Montag, U., Graffmann, M. 2010. On Structural Engineering Problems of Solar Updraft Chimneys. *Proc. 4th Int. Conf. Structural Engineering, Mechanics and Computation*, SEMC 2010, Cape Town, South Africa.

Krätzig, W.B., Gould, Ph.L., Harte, R. 2011. Shell structures for power technology. In: Mungan, I., Abel, J.F. (eds.) *Fifty years of progress for shell and spatial structures*. International Association for Shell and Spatial Structures (IASS), Madrid: 165–194.

Krätzig, W.B. 2012. Solar updraft power technology, State and advances of low-concentrated thermal solar power generation. *VGB PowerTech* 92, Vol. 11:34–39.

Krätzig, W.B. 2012. Physics, Computer Simulation and Optimization of Thermo-fluidmechanical Processes of SUPPs. *Proceedings 3rd Int. Conf. on Solar Updraft Power Tower Technology* SUTPT 2012:1–12. HUST Wuhan, China.

Krätzig, W.B., Harte R., Graffmann M., Montag U. 2013. Load response and design of Giga-towres. *CICIND Report* 29,1:55–62.

Lupi, F. 2009. *Structural behaviour, optimization and design of a solar chimney prototype under wind loading and other actions*. Master Thesis, University of Florence in cooperation with Ruhr University Bochum.

Lupi, F., Borri, C., Krätzig, W.B., Niemann, H.-J. 2011. Solar Updraft Power Plant technology: basic concepts and structural design. In *Encyclopedia Online of Life Support Systems* (EOLSS) developed under the auspices of the UNESCO, Eolss Publishers, Oxford, UK.

Lupi, F., Borri, C., Niemann, H.-J., Peil, U. 2011. Non-conventional wind loading on ultra-high Towers in Solar Updraft Power Plants. *International Journal of shell and space structures*, 52 (4):257–264.

Lupi, F., Borri, C., Niemann, H.-J. 2012. Solar Updraft Towers: the latest wind tunnel results and the current comparative studies. *6th International Symposium on Cooling Towers*, Cologne, Germany.

Niemann, H.-J., Höffer, R. 2007. Wind loading for the design of the solar tower. *Proc. 3rd Int. Conf. SEMC*, Cape Town, South Africa.

Niemann, H.-J. 2008. Prototyp eines Aufwindkraftwerks. Windeigenschaften, winderregte Schwingungen und Windlasten zur Bemessung des Stahlbetonturms. Internal report, Bochum. (in German)

Niemann, H.-J. 2009. A Refined Approach to Wind Loading for the Design of the Solar Tower. *CICIND Report*, 25(2).

Niemann, H.-J., Lupi, F., Höffer, R., Hubert, W., Borri, C. 2009. The solar updraft power plant: design and optimization of the tower for wind effects. *Proceedings of the 5th European and African Conference on Wind Engineering EACWE5*, Florence, Italy.

Niemann, H.-J. 2010. Static, quasi-static and resonant wind effects on solar towers. *2nd International Conference on Solar Chimney Power Technology* and Bergische Universität Wuppertal, Bochum.

Roshko, A. 1961. Experiments on the flow past a circular cylinder at very high Reynolds number. *Journal of Fluid Mechanics* 10 (3):345–356.

Salvadori, S. & Mattana, A., Barbanti, G. & Vita, G. 2013. CFD simulations on a Solar Updraft Tower on the basis of Criaciv' experiments, personal communication, unpublished.

Schewe, G. 1983. On the forces acting on a circular cylinder in cross-flow from subcritical up to transcritical Reynolds numbers. *Journal Fluid Mechanics* 133:265–285.

Schlaich, J (1995). The Solar Chimney, Electricity from the Sun. Edition A. Menges, Stuttgart.

SCPT 2010. *Proc. 2nd Int. Conf. on Solar Chimney Power Technology*, Ruhr-Universität Bochum and Bergische Universität Wuppertal, Bochum, Germany.

SUTPT 2012. *Proc. 3rd Int. Conf. on Solar Updraft Power Technology*, HUST, Wuhan, China.

VGB (2005) Structural design of cooling towers. Guideline VGB R 610Ue, *VGB PowerTech*, Essen.

VGB (2010) Structural design of cooling towers. Guideline VGB R 610e, *VGB PowerTech*, Essen.

Wie, Y., Wu, Z. 2012. Shed absorbability and tower structure characteristics of the Solar Heated Wind Updraft Tower Power. *Proc. 3rd Int. Conf. on Solar Updraft Power Technology* SUTPT 2012, 126–127. HUST, Wuhan, China.

Research and Applications in Structural Engineering, Mechanics and Computation – Zingoni (Ed.)
© 2013 Taylor & Francis Group, London, ISBN 978-1-138-00061-2

Stability and nonlinear behaviour of RC solar updraft towers

R. Harte
Department of Civil Engineering, University of Wuppertal, Germany,
Krätzig & Partner Civil Engineering Consultants, Bochum, Germany

ABSTRACT: Solar updraft towers will form the largest shell structures in technology. Because of their size they are extremely exposed to wind action. Many structural phenomena, like forced vibrations, static and dynamic instabilities, or damage-induced failure, will influence their safety and reliability. It makes sense to adopt the know-how from design and construction of natural draught cooling towers and transfer it to towers of solar updraft power plants. The present paper will report on typical structural design efforts to improve the load-bearing capacity of large-sized concrete shells, especially the shape optimization of the meridian, the structural safety including stability and vibrations, and nonlinear concepts to increase durability.

1 INTRODUCTION

More than 40 years of experience with natural draft cooling towers (NDCT) provide a profound insight into the response behavior of high-rise RC shell structures. Like the solar updraft tower a cooling tower shell is mainly loaded by its dead weight (*G*ravity load) G, by *W*ind action W and by ambient and service *T*emperature T. Further, in seismic active zones *E*arthquake excitations E, and in case of inhomogeneous soil conditions differential *S*ettlements S have to be considered (VGB 610 Ue 2010).

Numerical investigations have shown that the hyperbolic shape with continuous curvature is favoring the load-carrying characteristic of such shell structures. Figure 1 shows a rotational hyperboloid with its straight generators, which slope-angle β can be calculated according to (Flügge 1947). It is obvious from the sketches in Figure 1 that the shell with smaller angle β will be characterized by smaller tensile and compressive forces in the shell, thus minimizing the amount of reinforcement. This has been proved as well by numerous optimization analyses for natural draught cooling tower projects (Harte & Krätzig 2002; Krätzig et al. 2011; Noh et al. 2012).

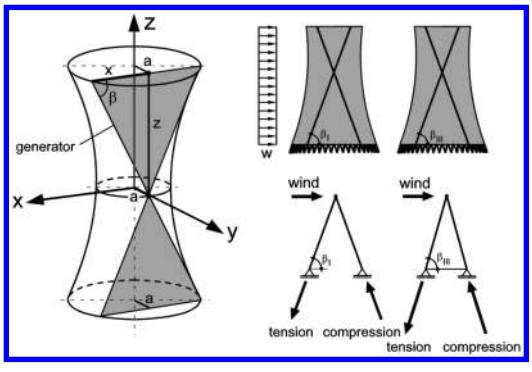


Figure 1. Principal load carrying behavior of hyperbolic shells.

From load-carrying viewpoint, solar updraft towers are extremely enlarged, over-scaled natural draught cooling tower shells, showing all problems known to cooling tower designers, as:

- high compressive stresses under *G*ravity load G, *W*ind action W and *T*emperature T,
- tendency to vertical outside cracking under G, W and T,
- high sensitivity to shell buckling instabilities under G, W and internal wind suction W_i,
- wind vibrations in the upper tower part, eventually leading to dynamic instabilities,
- a natural safety margin against seismic actions because of low 1st eigenfrequency,
- stress and thermal fatigue phenomena of the required high-performance concrete,
- durability problems to the end of life time.

Thus it makes sense to adopt the advantages of cooling tower design, i.e. the use of a hyperbolic instead of a pure cylindrical shape. Thanks to the double curvature, the structure applies the benefits of shape strengthening. Doubly curved thin shells with negative Gaussian curvature are able to resist loading acting perpendicularly to the shell surface mainly through in-plane extensional and shearing forces, the so-called membrane action. Plate and shell structures with Gaussian curvature 0 like slabs and cylinders might be dominated by bending action, characterized by transverse shear resultants, bending and twisting moments. It is well known from historical structures like pyramids and domes that structures with dominant membrane

behavior show a much better long-term stability and durability, sometimes over centuries. This principle must be adopted for cooling tower shells and even more for solar updraft towers, if the intended service life-time of more than 80 years shall be achieved.

2 STRUCTURAL BEHAVIOR

2.1 *The effect of stiffening rings*

Figure 2 shows the design study for a solar updraft tower with a total height of 500 m and diameters of 120 m at the throat and of 200 m at the base. The wall thickness increases from 0.25 m at the top to 0.60 m down to the foundation slab. The shell with shape-optimized meridian requires a classical upper edge ring and three intermediate stiffening rings.

Experienced designers of natural draught cooling towers would prefer to construct the shell without intermediate rings. In this case the wall-thickness has to be increased significantly required by globally extended instability modes and the concrete quality has to be increased to a high performance concrete of at least C 90/105.

Thus it seems to be advantageous to improve the stiffness by intermediate stiffeners. They serve three important purposes,

- to reduce the buckling lengths of the shell for sufficient safety against instability failure (Krätzig et al. 2009);
- to reduce the vibration wave length for balancing the eigenfrequencies of the shell (Borri et al. 2010; Goldack 2011);
- to constrain the meridional/shear forces in the shell due to wind towards a beam-like load-carrying behavior (Schlaich 1999; Krätzig et al. 2009; Borri et al. 2010).

The first and second purposes can be achieved with rather moderate sized cross-sections of all four stiffeners, attached on the shell outside, namely a hangover-width of 2.50 m and a thickness of 0.40 m.

The increase of the buckling safety can be observed from Figure 3. For the load combination (Gravity G + Wind W + Internal suction W_i), and for the tower design without any ring-stiffener one can clearly recognize, how the instability modes dominate the entire shell, whereas additional intermediate ring-stiffeners as arranged in Figure 2 will drive the buckling modes (as well as the vibration modes) to the lower shell region. The observable skew modal wave patterns which develop from bottom to top of the shell are a clear signal for the dominance of the (hyperbolic) shell geometry on the load response.

The third purpose requires stiffer rings in order to reduce the maximum wind tension towards the order of magnitude of the dead-load compression, an optimal design goal. These intermediate stiffening rings serve for a more cosine-like circumferential distribution of the meridional stress resultants under wind action W, as can be seen in Figure 4. With the above

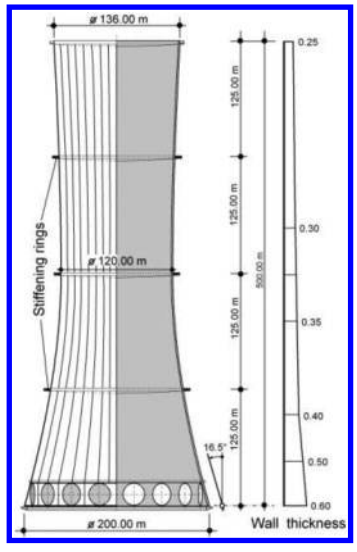


Figure 2. 500 m solar updraft tower prototype.

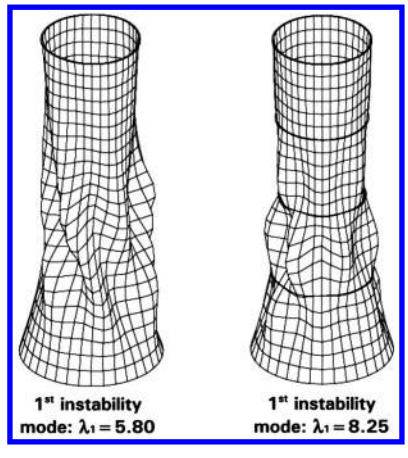


Figure 3. 500 m solar updraft tower – instability modes without and with 3 intermediate rings.

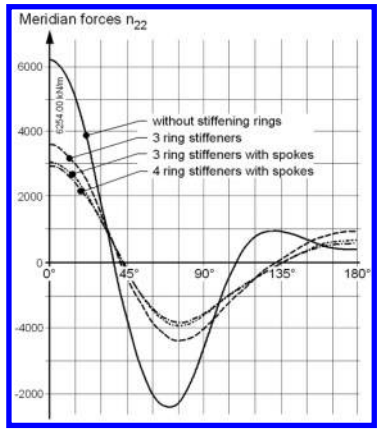


Figure 4. 500 m solar updraft tower – meridional stress resultants n_{22} due to wind action.

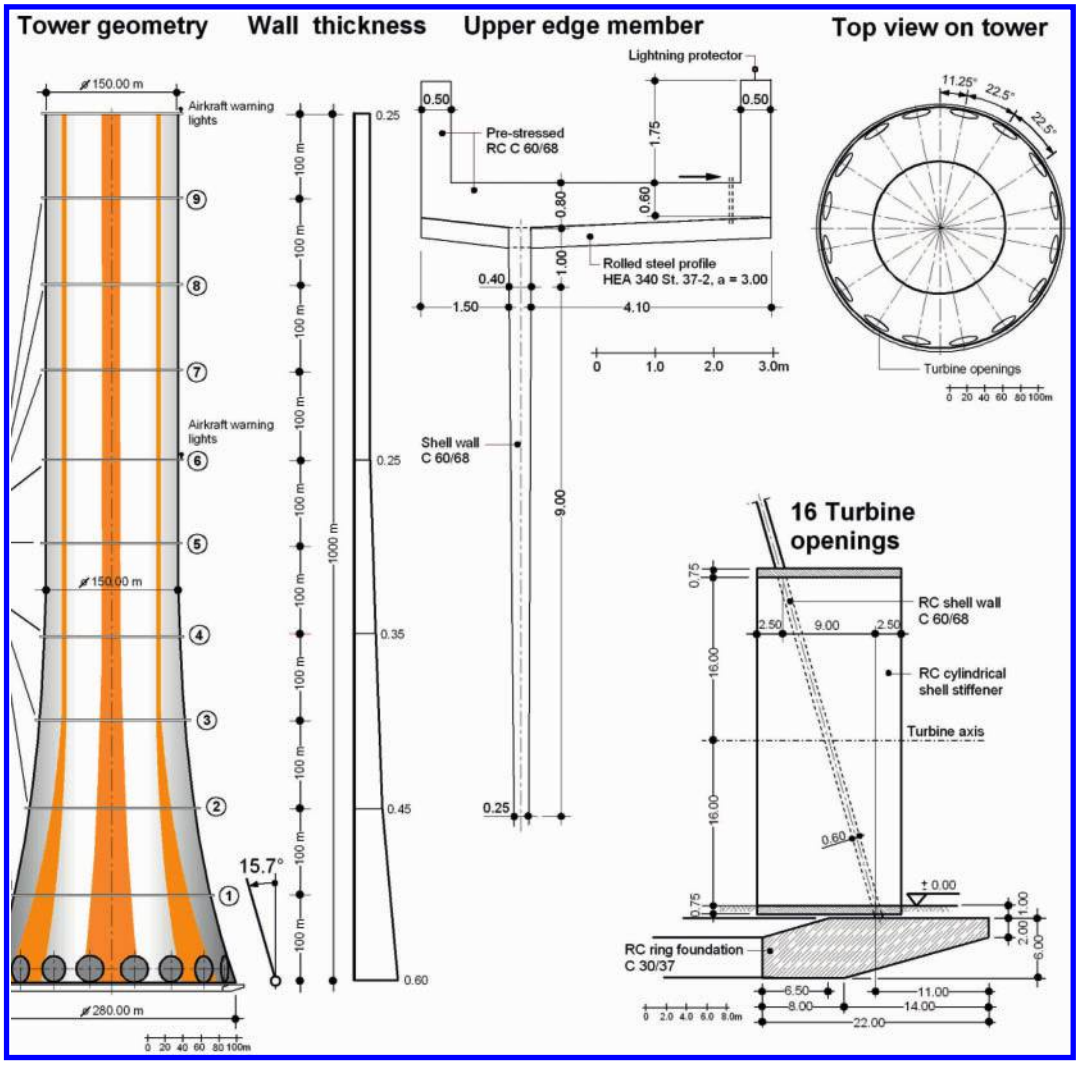


Figure 5. 1,000 m solar updraft tower pre-design by KRÄTZIG & PARTNER Civil Engineering Consultants (Harte et al. 2010).

given dimensions, the relevant tensile stress maxima can be reduced up to 2/3. Higher reductions require additional spoken wheels at the inner side of the rings, as recommended by (Schlaich et al. 2005).

2.2 *Extension to larger solar updraft towers*

The structural design of large solar updraft towers is an optimization process to compromise between several conflicting key points (Backström et al. 2008). The difficulties of the structural design of such large-sized shells are still enormous. The widening of the shell below the throat will be again shape-optimized for limitation of the shell bending and the in-plane shear.

Figure 5 presents a pre-design by KRÄTZIG & PARTNER Civil Engineering Consultants, a solar updraft power plant with a tower of 1,000 m of height. Together with a collector size of around 6,000 m of diameter this plant shall produce a peak power of 200 MW_p (equal to an annual work of ≈600 GWh/a) in regions with 2,240 MWh/a of solar irradiation. At the throat at 400 m height its shell diameter is 130 m wide, at the upper rim 145 m. Below 400 m the shell widens in a strength-optimized hyperbolic shape to a foot diameter of 260 m. The wall thickness of the shell of high-strength concrete C 70/85 varies from 0.25 m to 0.65 m. In addition to the usual upper edge ring, 9 intermediate and pre-stressed RC ring-stiffeners are fixed on the outer shell face.

16 turbo-generators are located directly on the foundation around the footing perimeter, to reduce air inflow losses and to avoid varying settlements between machinery and tower (Backström et al. 2008; Andres et al. 2010). The foundation itself is constructed as a closed ring of around 20 m of width, depending on the local soil conditions.

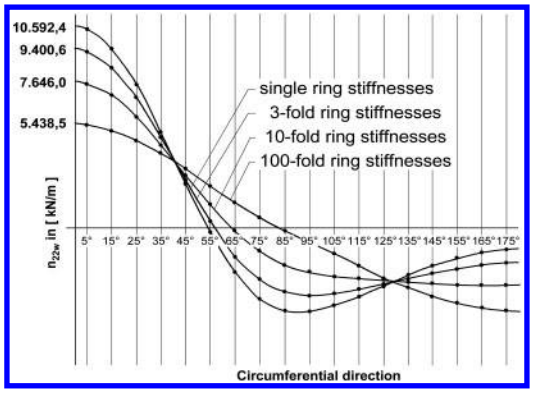


Figure 6. 1,000 m solar updraft tower at level 280 m – circumferential distribution of meridional stress resultants n_{22W} due to wind action for varying ring stiffnesses.

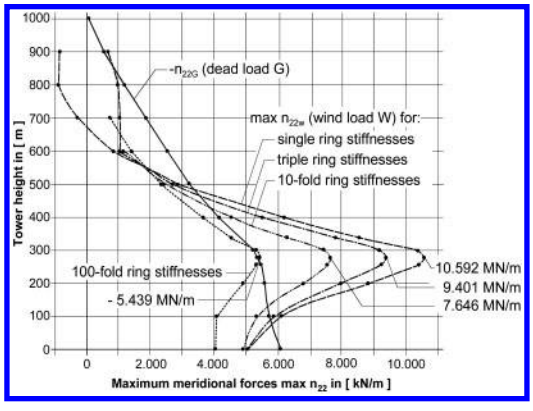


Figure 7. 1,000 m solar updraft tower – meridional stress resultants n_{22w} due to wind action versus tower height for varying ring stiffnesses.

The question is still relevant, whether a shell-like or a beam-like load-carrying characteristic will be better with respect to both structural stability and economic efficiency. The optimized shaping of the shell alone would never result in an economic tower design. In addition, the mentioned strong ring-stiffeners are required in order to constrain the meridional wind forces from shell-like distributions towards beam-like ones, and to guarantee a sufficient buckling safety.

In Figure 4 we already observed for the 500 m tower, how the wind force distributions approximate the cosine optimum, and how likewise the maximum tension stresses are reduced. Those are relevant for most of the required meridional reinforcement ratio in the cross-section.

Figure 6 elucidates the same fact again for the selected 1000 m solar updraft tower, plotting the towers response due to wind and depending on the varying stiffness of the 9 stiffening rings. The circumferential distributions of meridional wind forces at level 280 m are plotted, where the reference ring stiffness belongs to a rectangular cross-section of 0.40 m × 3.00 m, increasing from top to below over 3-fold, 10-fold finally to 100-fold values.

Figure 7 shows the maximum tensile forces from wind against tower height, again with increasing stiffness of the ring stiffeners. Compared to the compressive forces due to gravity (dead load) n_{22G} one can observe, how the tensile stresses are reduced by increasing the stiffness of the rings, likewise reducing the amount of reinforcement. But one should accentuate that any global optimization of a solar updraft tower comprises the global main dimensions, the meridional shape of the solar updraft tower as well as the stiffening rings.

The 9 intermediate ring-stiffeners constrain the structural response such that the internal lever arms are maximized, in order to keep both the tension (reinforcement) and compression (wall thickness) stresses small. Further results for the structural behavior of the stiffened 1,000 m tower shown in Figure 5 have been presented by (Borri et al. 2010).

Cost-optimized design of solar updraft towers requires thin shells because of the high costs for lifting concrete and reinforcement to great heights. But such saving will result in ring-stiffeners of increased stiffness, still an enormous construction challenge.

3 NONLINEAR DESIGN FOR DURABILITY

3.1 *Simulation method*

An economic load bearing behavior can only be achieved by use of nonlinear techniques, utilizing the increase of internal lever arms by consideration of horizontal cracking.

Up to now we have mainly treated linear elastic responses of solar updraft towers, including their instability resistance. But the constitutive behavior of RC will lead to non-linear responses (material nonlinearity), at least beyond certain wind-load intensities. Also aging of the material leads to non-linear structural response, an important aspect for the intended long life-duration of solar updraft towers of more than 80 years. In addition, in the beam-like tower structure second order effects might be activated during wind deformation (geometrical non-linearity), so any careful response study should comprise both kinds of non-linearity.

In contrast to classical linear elastic FE-technology, all applied 2D finite shell elements need to have at least a layered structure to treat material nonlinearities. This means, that each GAUSS-point of an element consists of a chain of integration sub-points, one in each layer. At these sub-points, on material point level, suitable 3D the constitutive relations of the material in question including deterioration effects have to numerically evaluated (Krätzig & Petryna 2001). The material point level, our lowest macroscopic simulation level, collects all constitutive information usually in a complete 3D environment, defined by the local base-vectors $\boldsymbol{a}_i$: $\boldsymbol{a}_1, \boldsymbol{a}_2, \boldsymbol{a}_3$.

For our RC simulations these material properties are (Krätzig 1997):

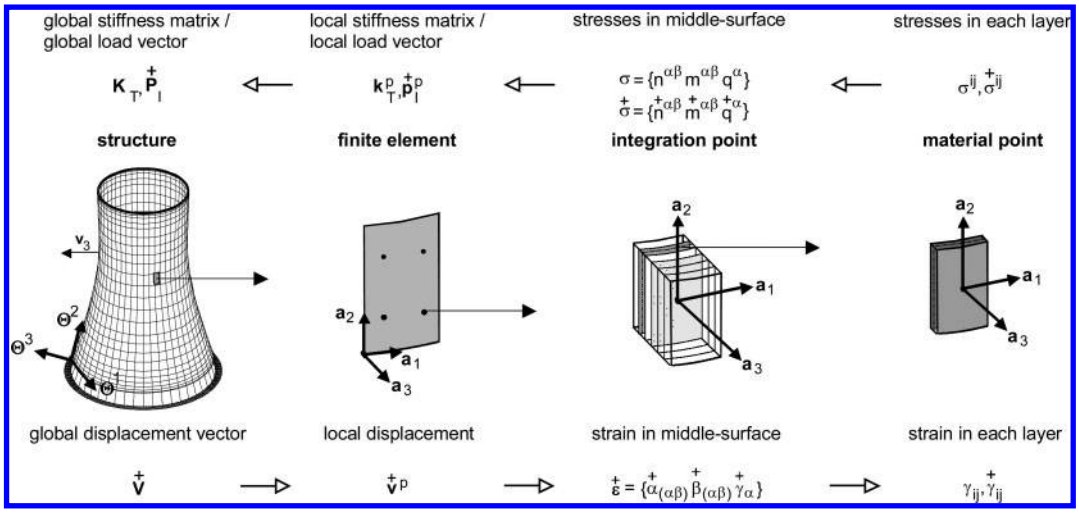


Figure 8. Layered finite shell element and multi-level simulation concept according to (Krätzig 1997; Andres & Harte 2006).

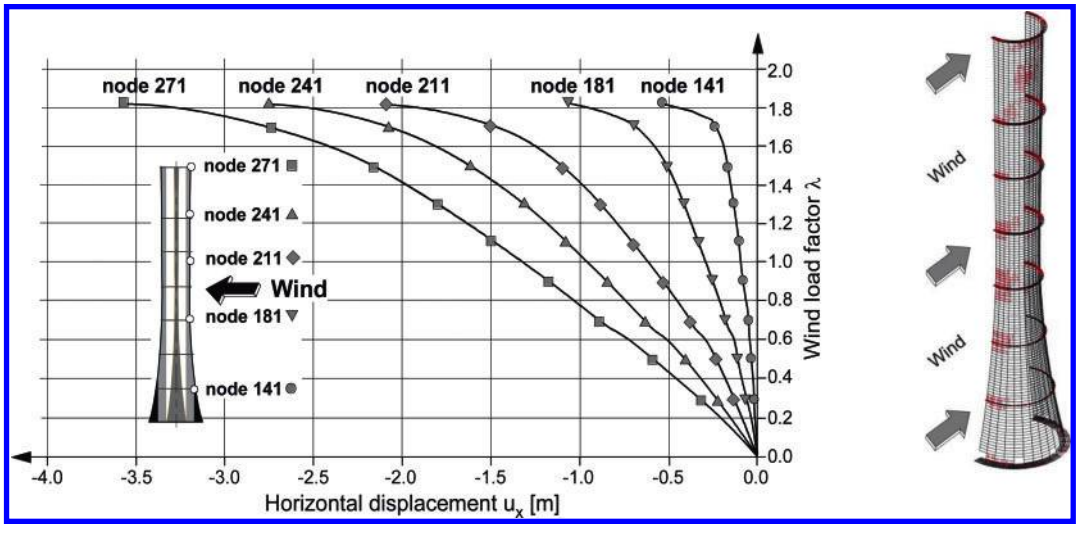


Figure 9. Non-linear displacements versus factor λ of load-combination $G + \lambda W$ for a 750 m solar updraft tower (left), and simulated crack pattern just before failure at load-level $G + 1.85W$ with max. crack-width $w = 1.8$ mm (right).

- nonlinear elastic-plastic $\sigma - \varepsilon$-behavior for concrete in compression including material micro-cracking, leading to stress release in the post-strength range,
- elastic-brittle behavior for concrete in tension with rather low tension strength leading to macroscopic crack-damage, modeled here in smeared crack manner,
- elastic-plastic material modeling for reinforcement steel,
- nonlinear inelastic bond behavior between steel and concrete, limited by inelastic slip damage.

Such nonlinear simulations are based on the tangential stiffness equation, which has to be solved incrementally with multiple iterations:

$$\boldsymbol{K}_T(\boldsymbol{V},\boldsymbol{d}) \cdot \overset{+}{\boldsymbol{V}} = \overset{+}{\boldsymbol{P}} = \boldsymbol{P} - \overset{+}{\boldsymbol{P}}_I(\boldsymbol{V},\boldsymbol{d}) \qquad (1)$$

Since $\boldsymbol{K}_T$ and $\overset{+}{P}_I$ depend on the current known deformation $\boldsymbol{V}$, the tangential stiffness equation is non-linear and thus requires iterative solution techniques for the incremental displacements $\overset{+}{V}$.

As shown in Figure 8, the final FE-analysis follows a multi-level iteration technique as described first in (Krätzig 1997). For each new load-step, the iteration starts with a new global vector of out-of-balance forces, transforming in each GAUSS-point of each element from increments of the global degrees of freedom to increments of the element degrees of freedom and finally to increments of the continuum strains at material point level. There the coded constitutive laws transform strain increments into stress

ones, after which the solution path returns back to the global structural level, to evaluate a new internal force vector $\overset{+}{P}_I$ for the next iteration step.

3.2 *Results of nonlinear simulation*

Non-linear results for another 750 m high prototype tower designed by KRÄTZIG & PARTNER (Krätzig et al. 2010) are shown in Figure 9. The nonlinear horizontal deflections of the shell at different nodes, or at different heights resp., are plotted versus the wind-load intensity factor λ, showing a max. top-deflection of approx. 3.6 m. The plot of crack evolution shows, where tensile stresses have exceeded the tensile strength of concrete and which max. crack-widths have to be expected.

Even with fast computers, such analyses require long computing time. But to study the crack evolution provides an important basis for the nonlinear improvement of the linear-elastic dimensioning of reinforcement. Thus such simulations will offer an economic, but still safe and reliable design tool for large-sized RC shells of solar updraft towers.

4 CONCLUSIONS

The beam-like load carrying characteristic has proved to be more safe and economic than the shell-like one. Thus additional stiffening rings will be inevitable. The aim of all detailed design considerations should be an operation-life of solar updraft towers of at least 80 years. Future research and development efforts have to be concentrated on the dynamic wind-structure-interaction and on a reliable prognosis of the non-linear material degradation and the resulting reduction of structural stability over life-time.

ACKNOWLEDGEMENTS

The author thanks the Volkswagen Foundation, Hanover, for financial support of the research work.

REFERENCES

Andres, M., Harte, R. 2006. Buckling of Concrete Shells: A Simplified Numerical Approach. *Journal of International Association for Shell and Spatial Structures* 47: 279–290.

Andres, M., Harte, R., Stopp, K. 2010. Soil-Structures Interaction on Large Concrete Shells. *Proc. 2nd Int. Conf. Solar Chimney Power Technology*, Ruhr-Universität Bochum and Bergische Universität Wuppertal: 173–179.

Backström, T.W. von, Harte, R., Höffer, R., Krätzig, W.B., Kröger, D.G., Niemann, H.-J., van Zijl, G.P.A.G. 2008. State and Recent Advances of Solar Chimney Power Plant Technology. *VGB PowerTech*, 88: 64–71.

Borri, C., Lupi, F., Marino, E. 2010. Optimum Shell Design of Solar Updraft Towers. *Proc. 2nd Int. Conf. Solar Chimney Power Technology,* Ruhr-Universität Bochum and Bergische Universität Wuppertal: 155–162.

Fluegge, W. 1947. Zur Membrantheorie der Drehschalen negative Kruemmung (in German), *ZAMM* 25/27: 65–70.

Goldack, A. 2011. Natural frequencies and Mode Shapes of Towers for Solar Updraft Power Plants. *Proc. 8th Int. Conf. Structural Dynamics, EURODYN 2011*, Leuven: 3575–3581.

Harte, R., Krätzig, W.B. 2002. Large-scale cooling towers as part of an efficient and cleaner energy generating technology. *Thin-Walled Structures* 40: 651–664.

Harte, R., Graffmann, M., Wörmann, R. 2010. Progress in the Structural Design of Solar Chimneys. *Proc. 2nd Int. Conf. Solar Chimney Power Technology*, Ruhr-Universität Bochum and Bergische Universität Wuppertal: 145–152.

Krätzig, W.B. 1997. Multi-level modeling techniques for elasto-plastic structural response. In D.R.J. Onate et al. (eds.) *Computational Plasticity, Part 1. Proc. 5th Int. Conf. CIMNE.* Barcelona: 457–468.

Krätzig, W.B., Petryna, Y.S. 2001. Assessment of structural damage and failure. *Arch. of Appl. Mechanics.* 71: 1–15.

Krätzig, W.B., Graffmann, M., Harte R., Montag, U. 2010. Power Towers: On structural engineering problems of solar updraft chimneys. In: Zingoni, A. (ed.). *Proc. 4th Int. Conf. SEMC2010*, Cape Town. CD-ROM.

Krätzig, W.B., Gould, Ph.L., Harte, R. (2011) Shell structures for power technology. In: Mungan, I., Abel, J.F. (eds.) *Fifty years of progress for shell and spatial structures.* International Association for Shell and Spatial Structures (IASS), Madrid: 165–194.

Noh, S.-Y., Harte, R., Lee, S.-Y. 2012. Influence of cooling tower shell shape on structural behavior. In: Harte, R., Meiswinkel, R. (eds.). *Cooling Towers. Proc. of the 6th Int. Symp. on Cooling Towers ISCT2012.* Cologne, Bergische Universität Wuppertal: 273–282.

Schlaich, J. 1999. Tension Structures for Solar Electricity Generation. *Engineering Structures* 21: 658–668.

Schlaich, J., Bergermann, R., Schiel, W., Weinrebe, G. 2005. Design of commercial solar updraft tower systems. *ASME-Journal Solar Energy Engineering*, 127: 117–124.

VGB 610 Ue:2010 (E). *Structural Design of Cooling Towers*. Technical Guideline. VGB Kraftwerkstechnik, Essen.

Research and Applications in Structural Engineering, Mechanics and Computation – Zingoni (Ed.)
© 2013 Taylor & Francis Group, London, ISBN 978-1-138-00061-2

An analysis of an optimised solar thermal chimney for desert deployment

P. Cottam
Centre for Urban Sustainability & Resilience, University College London, London, UK

P. Duffour
Department of Civil, Environmental & Geomatic Engineering, University College London, London, UK

P. Fromme
Department of Mechanical Engineering, University College London, London, UK

ABSTRACT: Renewable energy sources, including solar power, are becoming increasingly important in today's world. The Solar Thermal Chimney (STC) is a novel solar power technology which could provide a reliable large-scale power supply. However, as with all renewable energy technologies, ambient conditions (including insolation and ambient temperature) are important and thus some locations are better suited to solar power generation than others. A comprehensive STC model has been developed. It performs steady-state simulations incorporating all relevant heat transfer mechanisms, fluid shear stress and the air density lapse rate. The solar collector is simulated as a discretised, axisymmetric system composed of thermal components. This model is used, together with a simple cost model, to determine optimum system dimensions for a 100 MW STC plant at three selected sites: the Atacama Desert, Chile; Manzanares, Spain; and Arizona, USA. A tall chimney is necessary for large-scale power generation, and the significant technical challenges associated with constructing such tall, slender structures will be briefly touched upon.

1 INTRODUCTION

The solar thermal chimney – also known as a solar updraft tower or solar thermosyphon – is a large-scale solar power generation technology. It consists of a large solar collector – a transparent material supported above the ground covering a large area; a chimney located at the centre of the collector; and a turbine located at the base of the chimney. The sun heats the air beneath the collector via the greenhouse effect and the air flows through the collector and rises up the chimney under buoyancy. The turbine extracts power from the pressure difference generated by the airflow. A schematic diagram is shown in Figure 1.

The concept of extracting power from a buoyant updraft of air is not new. In 1926, Dubos proposed constructing a solar thermal chimney by affixing the chimney to a suitable mountainside and installing a solar collector at the base (Bernardes, 2010). The first large-scale research prototype of a solar thermal chimney was built in Manzanares, Spain, by German engineering consultancy Schlaich Bergermann und Partner. This solar thermal chimney had a chimney 194 m tall, a mean collector radius of 122 m and a nominal power output of 50 kW. It was built in 1981–82, and it was used for research programs before it was decommissioned in 1989 (Haaf, 1984; Haaf et al., 1983; Schlaich, 1995; Schlaich et al., 2005).

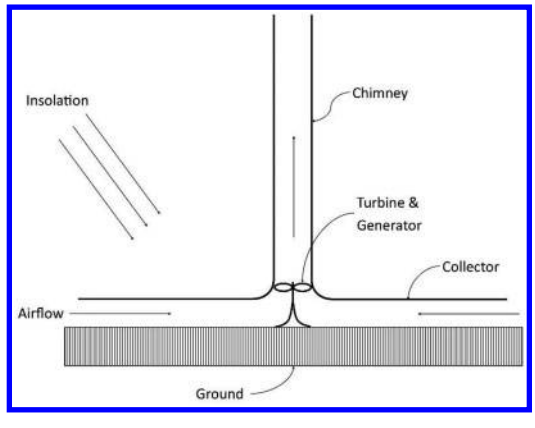


Figure 1. A schematic of the solar thermal chimney power plant.

Despite the absence of further physical prototypes, interest in solar thermal chimneys has increased and theoretical and computational modelling techniques are now well-established. Comprehensive models were developed by (Backström, 2003), (Bernardes et al., 2003) and (Pretorius et al., 2006). Studies of solar thermal chimneys using computational fluid dynamics have been produced by (Bernardes et al., 1999) and (Koonsrisuk et al., 2012). A comprehensive analysis

of system costs was produced by (Fluri et al., 2009). Cottam et al. have produced solar thermal chimney studies using a simple frictionless model with zero air density lapse rate to investigate solar thermal chimney performance for changing plant dimensions and environmental conditions (Cottam et al., 2012; Cottam et al., 2013). The model described in this paper was developed from Cottam et al.'s frictionless model.

Thermodynamic and physical models of the solar thermal chimney power plant are at an advanced stage and solar thermal chimneys can now be modelled with confidence. There are a few published models which evaluate the financial feasibility of solar thermal chimneys and projected costs vary. This paper proposes an optimisation routine which will form the foundation of an economic assessment of solar thermal chimney technology. This paper intends to evaluate the performance of solar thermal chimneys optimised for a mean power output of 100 MW at three different locations – Arizona, USA; Atacama Desert, Chile; and Manzanares, Spain.

2 COMPUTER MODELS AND METHODS

In order to assess energy-generating capacity of a solar thermal chimney power plant in different locations, two models have been developed in Matlab.

- Insolation model – predicts the annual insolation profile at a given location and altitude.
- Solar thermal chimney thermodynamical model – calculates all STC operating parameters for given environmental conditions and system size.

These models are integrated into an optimisation routine which will furnish three different configurations for an optimised STC plant, each capable of producing an annual mean power output of 100 MW. Due to differences in environmental conditions (ambient temperature and insolation), the optimised STC dimensions will be different for each location. The optimisation criteria is cost and hence a simple material cost model has been developed.

2.1 *Insolation model*

This model utilises trigonometry to calculate the profile of energy flux incident upon a particular location on the Earth's surface throughout the year. It calculates the air mass ratio to establish the attenuation of insolation through the atmosphere. It does not take into account cloud cover, and as such is seen as an over-estimate of the available solar energy. The insolation model reduces the required input variables to latitude ϕ and altitude Z_a. Note that latitudes south of the equator are denoted negative. The three locations are characterised as shown in Table 1.

2.2 *Solar thermal chimney simulation model*

The authors have developed a steady-state, incompressible flow model with axisymmetric collector flow, which calculates all STC operating parameters for given conditions and system size. It includes shear stress momentum losses in the collector and chimney and makes use of the Boussinesq approximation, which de-couples density from pressure and states that for small variations in fluid density, the density is a function of temperature only. This approximation simplifies the calculations and permits the model to use incompressible flow theory, despite the flow being driven by buoyancy.

Table 1. Characteristics of selected locations.

Location	Latitude (degrees)	Altitude (m)
Arizona, USA	32	1000
The Atacama Desert, Chile	−23	4000
Manzanares, Spain	39	500

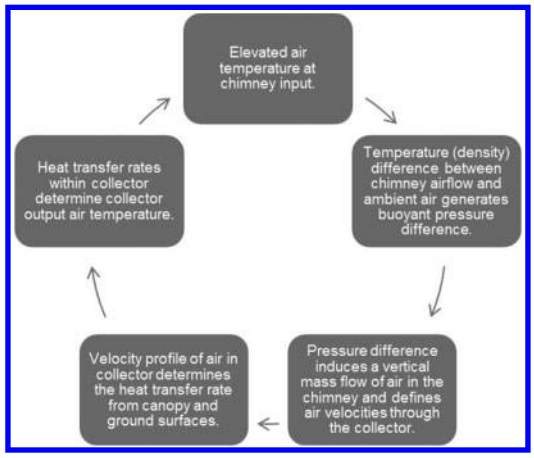


Figure 2. Implicit cyclical process for converging upon mass flow rate and collector outlet air temperature values.

This model is based largely upon the structure laid out in (Bernardes et al., 2003) with some modifications, and the heat transfer coefficient correlations are based on the relationships supplied in (Pretorius et al., 2006). An iterative algorithm is required to find the solution as the relationship of the collector output air temperature and system mass flow rate can only be expressed implicitly. Figure 2 shows the cyclical relationship which needs to be iterated in order to converge upon the solution.

The collector is modelled as a one-dimensional Boussinesq flow problem, whereby the flow from collector inlet to outlet is assumed to have radial symmetry about the chimney. The 1-D collector model is discretised and temperatures are calculated at each node for three thermal components:

- Collector canopy
- Collector air flow
- Collector ground surface

In Figure 3, energy inflows and outflows are identified for each component, where T = temperature;

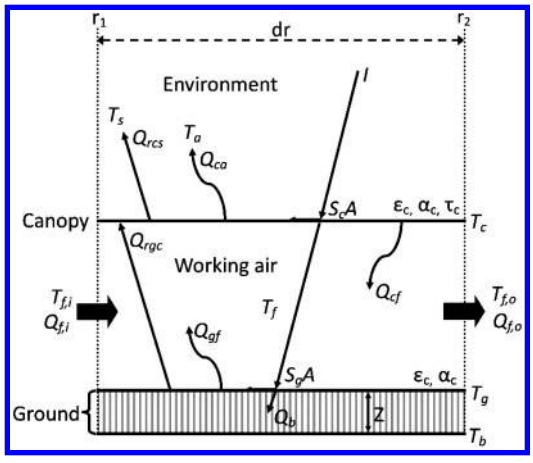


Figure 3. A discretised collector section with energy inflows and outflows.

Q = energy flux; ε = emissivity; α = absorptivity; τ = transmissivity; subscript s = sky; subscript a = ambient; subscript c = canopy; subscript f = working fluid; subscript g = ground surface; subscript b = ground at depth Z; subscript i = inlet; and subscript o = outlet. Using the First Law of thermodynamics, simultaneous energy equations are generated for each component at each node and solved via matrix methods.

The mass flow rate depends on the chimney's dimensions, the ambient temperature and the chimney inlet air condition (equal to the collector outlet air condition), and can be calculated as follows:

$$\dot{m} = \rho_{ch} A_{ch} \sqrt{\frac{2}{\rho_{ch}} \left(\int_{z_0}^{H_{ch}} (\rho_\infty - \rho_{ch}) g \, dz - \Delta p_f \right)} \tag{1}$$

where ρ_{ch} = air density within the chimney; A_{ch} = internal chimney flow area; ρ_∞ = ambient air density; g = acceleration due to gravity; z_0 = the height at which the buoyancy pressure difference is being evaluated; and H_{ch} = the total height of the chimney; and Δp_f = pressure difference due to friction. The integral term represents the pressure difference due to buoyancy. The air within the chimney is less dense than the ambient air due to the heat energy it received within the collector, and thus the collector outlet air temperature has an impact upon system mass flow rate. Solving the buoyancy difference integral requires knowledge of the rate of change of the ambient and chimney air densities with height z. The expansion of air with altitude is assumed to be isentropic and hence depends only on the air's initial condition (different for chimney air flow and ambient air) and its ratio of specific heats κ. The integrated buoyancy pressure difference equation at height z_{ch} up the chimney is presented in Equation 2. The variables α, β and γ are determined in Equations 3–5.

$$\begin{aligned} \int_{z_0}^{H_{ch}} (\rho_\infty - \rho_{ch}) g \, dz &= \frac{\alpha_\infty}{\beta_\infty(\gamma_\infty + 1)} \Big[(1 + \beta_\infty (H_{ch} - z_0))^{\gamma_\infty + 1} - (1 + \beta_\infty z_0)^{\gamma_\infty + 1} \Big] \\ &- \frac{\alpha_{ch}}{\beta_{ch}(\gamma_{ch} + 1)} \Big[(1 + \beta_{ch} (H_{ch} - z_0))^{\gamma_{ch} + 1} - (1 + \beta_{ch} z_0)^{\gamma_{ch} + 1} \Big] \end{aligned} \tag{2}$$

$$\alpha = g\rho(z_0) \tag{3}$$

$$\beta = \frac{g(\kappa - 1)}{\kappa R T(z_0)} \tag{4}$$

$$\gamma = \frac{1}{\kappa - 1} \tag{5}$$

where R = the specific gas constant for dry air. The subscripts ∞ and ch are applied to the appropriate terms of Equations 3–5, e.g. $\alpha_\infty = g\rho_\infty(z_0)$ and $\alpha_{ch} = g\rho_{ch}(z_0)$. The pressure loss due to friction is calculated using the standard theory for fluid pressure loss in a pipe, with the Darcy friction factor calculated by means of the Colebrook Equation for turbulent flow.

The turbine model remains simple, with a swept area equal to the flow area of the chimney and a constant efficiency and pressure drop ratio. Note that the solar thermal chimney utilises a Kaplan turbine extracting power from the pressure difference across it and not a wind turbine which extracts power from the kinetic energy of the flow. Equation 6 gives the power output from the turbine.

$$P = \eta_t x \Delta p_{ch} v_t A_t \tag{6}$$

where P = power output (W); η = efficiency; x = turbine pressure drop ratio; $\Delta p_{ch} = \Delta p_b - \Delta p_f$ = chimney pressure difference; v = air velocity; A = area; subscript t = turbine and subscript ch = chimney.

This model contains most of the features of those in (Bernardes et al., 2003) and (Pretorius et al., 2006). Bernardes et al. utilised a more comprehensive set of thermally-connected components to simulate the collector, including sealed water bags for heat storage, whilst Pretorius et al. included the pressure loss due to collector supports. This model includes a comprehensive simulation of pressure differences within the chimney (see Equations 1–5) and permits the simulation of solar thermal chimneys with sloping collector canopies.

This steady STC model calculates the power generated over time by calculating the monthly mean daily insolation profile using the insolation model and simulating the solar thermal chimney at half-hour intervals to produce a monthly-average daily power output profile for each STC.

2.3 *Optimisation of STC dimensions by cost*

A Matlab script optimises the STC dimensions by minimizing material cost. The associated cost model calculates prices for materials only and does not include labour, plant or financing costs. It is not intended as a full cost analysis, but rather as a metric for the optimisation procedure. All material costs are calculated assuming a 20% bulk-purchase discount. The prices per unit of material are given in Table 2.

Table 2. Material costs.

	Reinforced concrete (US$/m^3)	Transparent film (US$/m^2)	Steel C-section (US$/m)
Arizona	105.00	1.84	26.00
Atacama	85.10	1.49	21.00
Manzanares	86.80	1.52	21.40

Concrete cost based on UK direct quote.
Transparent film cost based on UK direct quote.
Steel C-section cost based on UK direct quote.
Adjustments for international price variations based on Faithful Gould Construction Parity Index (Faithful Gould, 2012).

Table 3. Optimised STC dimensions for 100 MW mean output power given location environmental conditions and local material costs.

Location	Mean insolation W/m^2	Collector radius m	Chimney height m	Energy generation MWh/a
Arizona	402	3952	1204	371.77
Atacama	427	3291	1060	265.73
Manzanares	369	3624	1151	278.31

The STC chimney height and collector radius are optimised against cost for a 100 MW power output. Collector height at input is fixed at 5 m. Collector height at output is set to $5\,\text{m} + 0.01 \times R_{coll}$. Chimney internal radius is set to $10\,\text{m} + 0.04 \times H_{ch}$. The STC's dimensions are optimised for a 100 MW power output under each location's annual mean insolation. The annual power and energy profiles from the optimised STCs were simulated and the annual energy yield from each STC design in each location was compared so that a conclusion can be reached regarding the best site for locating a solar thermal chimney and the most suitable system dimensions. The cost model utilised in the optimisation routine makes no claims to being suitable for evaluating the actual cost of constructing an STC of the optimised dimensions.

3 RESULTS & ANALYSIS

This exercise was undertaken to test the process for optimising solar thermal chimney dimensions considering both ambient conditions (insolation and ambient temperatures) and economic factors. As this was a preliminary investigation, the cost model used was greatly simplified, and considered only a cost per unit for the materials involved, which is sufficient for evaluating the optimisation procedure itself. Following this investigation, it can be concluded that the optimisation procedure performs well and that when coupled with a comprehensive cost model, it has the potential to become a powerful tool which delivers a full location-aware technical and economic analysis of an optimised

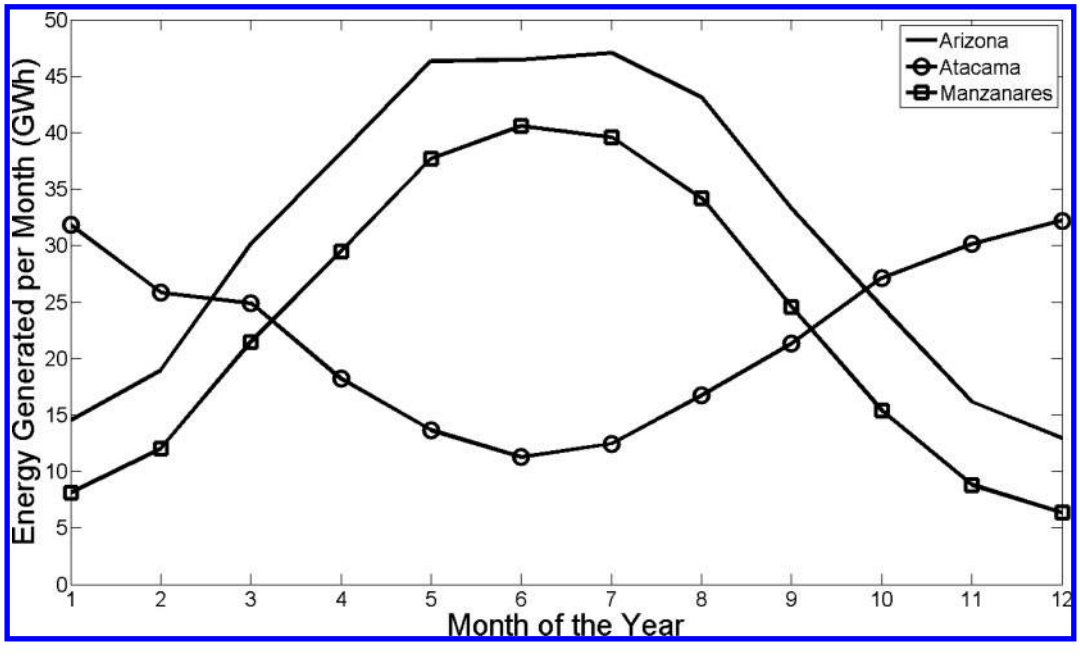


Figure 4. Monthly total energy profiles for an optimised STC rated at 100 MW in Arizona, the Atacama and Manzanares.

solar thermal chimney. In this investigation, the solar thermal chimneys were designed to deliver 100 MW at the mean insolation for each location. Table 3 gives the mean insolation, optimised collector radius and chimney height (from which other plant dimensions are calculated) and annual energy generated.

A solar thermal chimney rated to deliver 100 MW will deliver a different total of energy per year in different locations. Despite Arizona receiving a lower mean insolation than the Atacama Desert, an optimised 100 MW STC plant in Arizona will deliver 40% more energy throughout the year compared to a plant optimised to deliver the same rated power output in the Atacama. Table 3 gives the total energy generated per year for the optimised STC plant at each location, whilst the monthly total energy generation profile is shown in Figure 4.

Other factors also become important when choosing the appropriate renewable energy technology for a specific location. Solar power technologies have huge potential in areas of high solar gain, such as deserts. However, they are often criticised for the large quantities of water they consume for the regular cleaning of optical surfaces. Solar thermal chimney collectors need only be cleaned once every six months and in that time will only suffer a performance degradation of up to 12% (Haaf et al., 1983), significantly less than other solar technologies. This is particularly important given the shortage of water in the Atacama Desert.

This optimisation exercise has shown that solar thermal chimney power plants require particularly tall chimney structures in order to operate effectively (see Table 3). Furthermore, the walls of the chimney should be as thin as possible in order to reduce material usage, without endangering the structural stability of the chimney. Thin-walled structures are prone to buckling and ring stiffeners can be installed, with or without spokes, which will increase the lateral stiffness of the chimney and increase its resistance to buckling. Nevertheless, the construction of such a tall chimney still presents technical risks and uncertainties, not least concerning cost and seismic resilience. A radical reinvention of the status quo may merit investigation, particularly the concept of a fabric chimney held aloft by envelopes of lighter-than-air gas.

4 CONCLUSION

An insolation model and a solar thermal chimney model have been described. The insolation model calculates the solar flux incident upon any location after attenuation by the atmosphere, but assuming no cloud cover. The solar thermal chimney model is a 1-D incompressible Boussinesq radial-flow model using quasi-steady techniques to calculate power output profiles throughout the day and throughout the year. The impact of wall-fluid shear stress is included and particular attention is paid to the calculation of varying buoyancy pressure with altitude.

The two models were integrated in an optimisation routine with a simple material cost model to identify the location which would require the smallest material investment for a 100 MW solar thermal chimney power plant, based on the location's insolation and ambient temperature profiles and solar thermal chimney performance. The three locations studied were Manzanares in Spain, where Schlaich, Bergermann und Partner constructed a solar thermal chimney in 1982; the Atacama Desert in Chile, where there is a large unmet need for efficient and clean power generation for industrial mining and scientific consumers; and Arizona in the USA, where EnviroMission Ltd propose to construct two large-scale solar thermal chimneys. Of the three locations, Arizona in the USA delivered the greatest quantity of energy, yet the Atacama STC required the least material.

This investigation was undertaken primarily to test the optimisation procedure and integration of the insolation and STC models. A full economic analysis including life-cycle costs is required before firm conclusions can be drawn regarding Levelised Electricity Cost and profitability.

ACKNOWLEDGEMENTS

The authors wish to thank the following for their support:

- The UCL Centre for Urban Sustainability & Resilience
- Lindstrand Technologies Ltd.
- The UK Engineering & Physical Sciences Research Council

REFERENCES

von Backström, T. W. 2003. Calculation of pressure and density in solar power plant chimneys. *Journal of Solar Energy Engineering*, vol. 125, no. 1, p. 117.

Bernardes, M. A. dos S., (ed. Rugescu R. D.). 2010. *Solar Energy*. Rijeka: InTech.

Bernardes, M. A. dos S., Valle, R. M. & Cortez, M. F. B. 1999 Numerical analysis of natural laminar convection in a radial solar heater. *International Journal of Thermal Sciences*, vol. 38, pp. 42–50.

Bernardes, M. A. dos S., Voß, A. & Weinrebe, G. 2003. Thermal and technical analyses of solar chimneys. *Solar Energy*, vol. 75, no. 6, pp. 511–524.

Cottam, P., Duffour, P., Fromme, P. 2012. A Parametric Study of Solar Thermal Chimney Performance. *EuroSun 2012 Conference Proceedings*. Rijeka.

Cottam. P., Duffour, P., Fromme, P. 2013. Thermodynamic Behaviour of the Solar Updraft Tower: A Parametric Model for System Sizing. *Proceedings of Third International Conference on Solar Updraft Power Tower Technology, Applied Mechanics and Materials*, vol. 283, pp. 3–7.

Faithful Gould Ltd. 2011. *International Construction Intelligence* [online]. Available: http://www.fgould.com/uk/articles/international-construction-intelligence-q3-2011/#Parity Index [accessed 15-Mar-2013].

Fluri, T. P., Pretorius, J. P., Van Dyk, C., von Backström, T. W., Kröger, D. G. & Van Zijl, G. P. a. G. 2009. Cost analysis of solar chimney power plants. *Solar Energy*, vol. 83, no. 2, pp. 246–256.

Haaf, W. 1984. Solar Chimneys Part II: Preliminary Test Results from the Manzanares Pilot Plant. *International Journal of Solar Energy*, vol. 2, pp. 141–161.

Haaf, W., Friedrich, K., Mayr, G. & Schlaich, J. 1983. Solar Chimneys Part I: Principle and Construction of the Pilot Plant in Manzanares. *International Journal of Solar Energy*, vol. 2, pp. 3–20.

Koonsrisuk, A. & Chitsomboon, T. 2012. Mathematical modeling of solar chimney power plants. *Energy*, Article in press.

Pretorius, J. P. & Kröger, D. G. 2006. Solar Chimney Power Plant Performance. *Journal of Solar Energy Engineering*, vol. 128, no. 3, p. 302.

Schlaich, J. 1995. *The solar chimney: electricity from the sun.* Stuttgart: Edition Axel Menges.

Schlaich, J., Bergermann, R., Schiel, W. & Weinrebe, G. 2005. Design of Commercial Solar Updraft Tower Systems—Utilization of Solar Induced Convective Flows for Power Generation. *Journal of Solar Energy Engineering*, vol. 127, no. 1, p. 117.

Research and Applications in Structural Engineering, Mechanics and Computation – Zingoni (Ed.)
© 2013 Taylor & Francis Group, London, ISBN 978-1-138-00061-2

Solar energy systems under impact of aeolian sand and dust

C. Kalender-Wevers, U. Winkelmann & R. Höffer
Ruhr-Universität Bochum, Bochum, Germany

ABSTRACT: Renewable solar energy systems are situated and planned in areas, where a high solar radiation is available. Usually, these zones are desert regions and therefore a considerable amount of aeolian dust and sand transport can be expected during daily local wind and strong wind events (e.g. dust storms). The deposition and agglomeration of sand material can yield e.g. to shadowing of the solar input or to scratching of the structure surfaces materials. In this paper, the dust transport and the deposition are studied on two different solar energy systems, namely a Solar Updraft Power Plant (SUPP) and a Parabolic Trough Power Plant (PTPP). In case of the SUPP grains move over the collector surface and agglomerate at low-wind areas around and particularly behind the tower. Additionally construction parts of the glass panels may keep particles on the collector although a present sufficient threshold velocity is available. Because of the height of the collector rather fine sand/dust particles can be expected on the collector than larger sand grains. In contrast to this the troughs of the PTPP are closer to the soil bottom, so that they can collect large grains on its surfaces too. A physical wind tunnel study in combination with a numerical CFD-analysis for a single parabolic trough indicates for the deposition zones a high dependency on the orientation angle of the troughs. Both approaches are limited in terms of problem simplification and model characteristics, but give some reasonable and almost feasible results. Improvement of the models is still an ongoing work.

1 INTRODUCTION

Since last mid-century the impact of particle deposition on the output of solar energy systems were investigated. They are situated and planned in zones of the earth, where a high solar radiation is available to ensure an economical and effective energy production. Usually these areas are highly arid, semi-arid or sub-humid and belong to desert regions. The main conclusion from experiments and real measurements in past were the existent reduction of energy output due to deposition of material on the solar collectors (Mani & Pillai 2010). Since 1990 the accuracy and reliability of the performed experiments increases rapidly and the amount of considered parameters rises. But the complex interaction between different wind directions, local meteorological climate, particle type, inclination and material of the collectors and its positions within a group arrangement are still only partly investigated and understood.

Mekhilef et al. (2012) analysed the impact of dust accumulation, humidity level and the air velocity and conclude that this factors influence each other and should be considered together. El-Nashar (2009) describes in their study the effect of cleaning frequencies to the power production of a solar power plant for sea water distillation located close to Abu Dhabi. They found a high seasonal dependency of the transmittance of the collectors due to dust deposition. The lowest influence was found in January and the strongest influence was found in the summer months June, July and August, were frequently dust storms prevail. The transmittance of the class drops by monthly cleaning in that period around 10–18% and the power production decreases to 40% of the production of clean collectors. Simultaneously the development of dust risk maps for forecast the amount of expectable dust rates rises (Charabi & Gastli 2012).

These are some examples of actual research which indicates the importance of the local wind regarding the deposition of aeolian particles on solar collectors. The following chapters describe two approaches, namely physical wind tunnel and numerical CFD simulations, to model and analyse the sand and dust particle motion around two solar energy systems due to wind.

2 AEOLIAN SAND AND DUST

2.1 *Particle transport mechanism and modes*

Conventionally sand and dust are classified by their particle size, which mainly influences the wind induced motion (Tab. 1). The grains are entrained by the wind when the fluid drag and lift forces are higher than the inertial particle forces, which include vertical gravity and any cohesion between adjacent particles or surfaces (Pye & Tsoar 2009). When the wind shear force τ overcome a so called fluid threshold velocity

Table 1. Particle size and corresponding motion ranges (United nations Convention to Combat Desertification 2001).

Particle type	Particle size [mm]	Vertical height	Horizont. distance	Moving mode
Coarse sand	0.5–1.0	some cm	few m	creep
Medium sand	0.25–0.5	some 10 cm	some m	saltation
Fine sand	~0.1	some m	some km	short-term suspension
Dust	~0.01	some km	some 100 km	suspension
Fine dust	~0.001	10 km	some 1000 km	long-term suspension

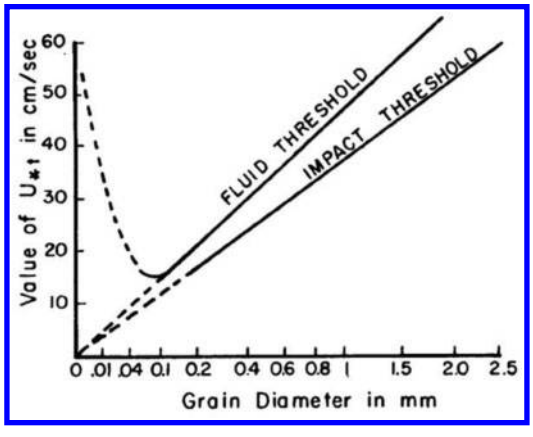


Figure 1. Required fluid threshold velocity (friction velocity) to move a particle from a sand bed (Bagnold 1954).

$u_* = (\tau/\rho_{air})^{0.5}$ corresponding to the grain diameter the particles are lifted and starts to move (Fig. 1).

Coarse sand particles creeps over the surface, medium grains starts to jump in a certain way (saltation) and fine grains are transported in suspension. The modes and trajectories are mainly influenced by the ratio between particle size, shape, settling velocity, and spin as well as wind shear stress and turbulence intensity. The larger grains settle down and deposit after a while according to their transport mode or re-enter into the air itself and inject new particles. This can results in a self-organised bed form like ripples or ridges by accumulate and sorting the jumping grains.

2.2 *The effect of local wind climate on the particle deposition*

Dust and particles, which are transported by wind, are natural and anthropogenic origin. Most solar energy systems are situated and planned in desert regions. Soil erosion due to wind occurs frequently and especially the appearance of dust/sand storms is high, e.g. Australia has about 15 dust storm days, Middle East 15–27 and North Africa around 22–27 (Pye 1987, p. 64). Dust/sand storms are defined to reduce the air visibility in eye level to less than 1000 m within 24 hours.

Beside strong wind events also the local daily wind transports fine sand and dust particles. Especially in regions, where less vegetation and urban structures slow down the wind velocity and cover the ground, the motion of dunes and soils material is well documented (Pye & Tsoar 2009). In addition daily wind can have a cleaning effect of already deposit particles. For Saudi Arabia the mean daily wind speed in 10 m height is 2–4 m/s (Rehman et al. 1994). After Figure 1 a minimum friction velocity of 0.15 m/s is necessary to move fine sand with 0.1 mm diameter. Using the logarithmic law (Eq. 1) for neutral turbulent boundary layer flow (Arya 1999) this results in a wind velocity in 10 height of 2.6 m/s, for slightly rough surface with a roughness length of $z_0 = 0.01$ m (VDI 3783-12 2000).

$$u_{10} = \frac{u^*}{\kappa} \ln\left(\frac{z+z_0}{z_0}\right) = \frac{0.15}{0.4} \ln\left(\frac{10+0.01}{0.01}\right) = 2.6\,\mathrm{m/s} \quad (1)$$

Very small dust particles can stick to a surface although the wind velocity might be high enough to move the grain. On one hand this can be caused by humidity or adhesive forces, which are very high between small particles and smooth surfaces (Goossens & van Kerschaever 1999). On the other hand the particles are so small that they are inside the laminar sublayer of the surface flow boundary layer and cannot be touched by higher velocities or turbulent eddies. Figure 1 shows this effect on the left hand side with the dashed line. The smaller the diameter the higher are the threshold velocities.

If once particles settled down they behave as obstacles for oncoming moving particles and the accumulation on the surface accelerate. On a smooth surface already settled dust particle were found to be in organised ripples systems, like described in the chapter before. Goossens & van Kerschaever (1999) found different dust coating schemes on a horizontal flat plate for different wind velocities (0.6–2.6 m/s) and show that the dust layer is less transparent during low wind velocity than during higher wind velocities, were particles starts to move over the plate. Nevertheless the older the dust-layer is the higher is the homogeneity of the particle distribution on the surface. In the end they conclude the drop of the solar cell performance due to dust deposition increase for higher wind velocities.

3 USED SIMULATION MODELS

3.1 *General simulation concept*

Two different model approaches are used in order to analyse dust and sand motion around the two solar energy systems: the physical boundary layer wind tunnel of the Ruhr-Universität Bochum and a Computational Fluid Dynamics (CFD-) simulation software. Because of the scaling requirements in the physical wind tunnel approach it is not possible to find a proper

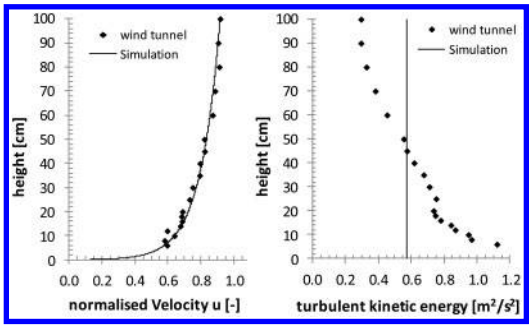


Figure 2. Boundary layer profiles in the physical wind tunnel and the used inlet conditions for the numerical simulations.

particle material for modelling suspension, deposition and saltation at the same time (Kind 1976). Therefore only velocity and pressure measurements were done and the discrete particles were considered just in the numerical approach.

In case of the PTPP physical and numerical simulations were performed and combined. The wind tunnel results are used to validate the calculated flow field as well as the pressure field. Then this validated model provides particle deposition zones. For the SUPP only numerical simulations were performed with different settings for the particle flow.

3.2 *Settings of the numerical model approach*

All numerical flow simulations are performed with a Finite-Volume Method as Reynolds-Averaged-Navier-Stokes (RANS) Simulations with the Standard k-ε turbulence model. For the approximation of the convective terms in the governing equations a second order scheme is used and the truncation error for the iterative solver is set for the maximum residuals of all equations to 10^{-6} within 1000 iteration steps. The inflow boundary conditions are modelled according to the method proposed by Richards & Norris (2011) in order to match the conditions to the performed physical wind tunnel simulations, shown in Figure 2.

Using the solved steady state flow field, discrete particles are moved with Euler-forward integration of the particle velocity in discrete points along paths through the domain (Lagrangian model). The particle velocity itself is calculated from an analytical solution of the particle momentum equation, which sums all forces acting on a spherical particle (ANSYS Inc. 2009). Equation 2 shows one of the most relevant force, the drag force, which is calculated using the Stokes-law. This includes the velocities of the fluid u_f and of the particle u_P as well as the particle diameter d_P, the dynamic fluid viscosity η and a correction factor C_{cor}, which depends on the Particle-Reynolds-Number (AEA Technology Engineering Software Ltd. 2002).

$$m_P \frac{du_P}{dt} = 3\pi\eta d_P C_{cor}(u_F - u_P) \tag{2}$$

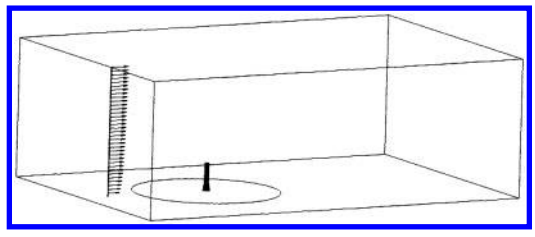


Figure 3. Numerical 3D domain of the SUPP.

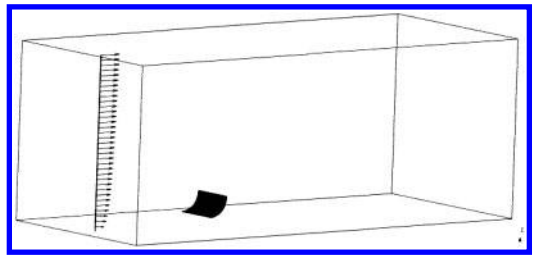


Figure 4. Numerical 3D domain of a single parabolic trough.

Additionally the stochastic "discrete droplet" model from Gosman & Ioannides (1993) is applied to calculate the turbulent diffusion of each particle due to turbulent eddies with a characteristic fluctuation velocity u_i', length ℓ_e and lifetime τ_e:

$$u_i' = \Gamma\left(\overline{u_i'^2}\right)^{1/2} = \Gamma(2k/3)^{1/2} \tag{3}$$

$$\ell_e = \left(C_\mu^{3/4} k^{3/2}\right)/\varepsilon \tag{4}$$

$$\tau_e = \ell_e/(2k/3)^{1/2} \tag{5}$$

The variable Γ denotes a normal distributed random number, k the local turbulent kinetic energy, its dissipation ε and C_μ a constant (ANSYS Inc. 2009). A certain number of idealised particles with a defined diameter distribution and density of Quartz are injected in different positions.

The geometries and meshes were generated regarding the used wind tunnel model and follow the recommendations of Franke et al. (2007). Figure 3 and Figure 4 show the domain size of each model. All meshes consist of block structured hexahedral elements and were successively refined in order to check the independency of the results regarding the mesh resolution and domain size.

3.3 *Settings of the boundary layer wind tunnel*

In the boundary layer wind tunnel the oncoming turbulent flow is generated using a Counihan-setup (Counihan 1969) and corresponds to an atmospheric wind over urban terrain with a real roughness length of $z_0 = 0.1$ m. The turntable has a diameter of 1.8 m and the height of the tunnel is 1.6 m. The measurement programme for the PTPP includes different

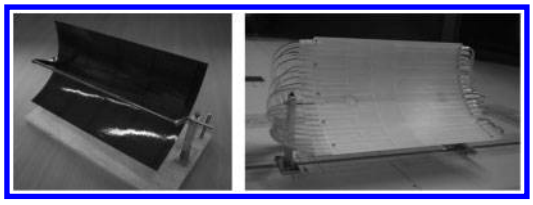


Figure 5. Left: Trough model for velocity measurements, right: trough model with pressure wholes on the surface.

wind velocities, yaw angles, orientation angles of the trough and group as well as single trough arrangements. For comparison reasons with the numerical results the single through with an approach flow with 0° is focused. Figure 5 shows the used models (scale 1:50), left for the velocity measurements with an x-hotwire anemometer and right for the surface pressure measurements.

4 AEOLIAN PARTICLES AROUND THE PTPP

4.1 *Flow field around the single trough*

The comparison of the velocity fields in front of the single parabolic trough is shown in Figure 6 exemplary for an orientation angel of 45°. The vectors are comparable in velocity magnitude, but close to the wall the wind direction of the numerical results (red) follow earlier the trough surface curve. Although the mesh consists of 2.7 Mio cells with refinement around the trough surface the mesh resolution might be not fine enough. For other orientation angles the most discrepancies can be found in the zones of recirculation. This is caused by the used turbulence model, which is not capable to predict and resolve separation eddies proper. The predicted surface pressure distribution is for the most areas partly overestimated compared to the measured pressure. This can be also explained by the used turbulence model, which was chosen due to its balance between numerical robustness and efficiency.

4.2 *Particle deposition zones on the trough*

Additional to the analysis of the flow and turbulence field around the single through, the surface inclination and the particle wall-shear zones, were particles hid the surface, from the numerical simulations were considered in order to define areas, were particle deposition on the trough can be expect. For different inclination angles the amount of particles which hits the surface are unlike.

In Figure 7 particle positions for different time steps are shown for the trough inclination of 90°. In the second time step the trough collects particles, which remains insides the vortex which occurs inside the trough.

If the wind approaches from the trough back-side almost, all particles flow overhead the tip and nearly no depositions occur. The trough-orientation follows the sun during the day and hence the directions of wind

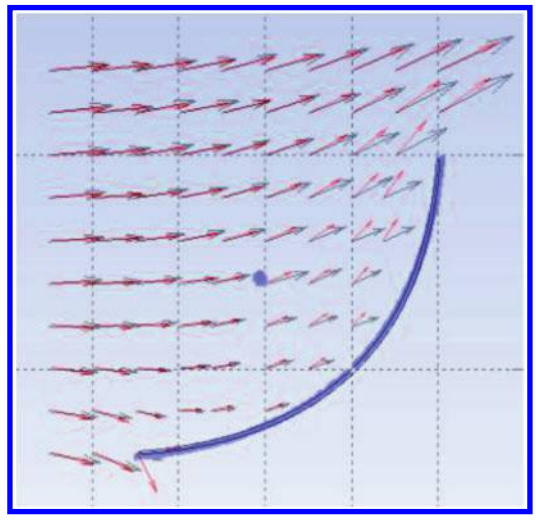


Figure 6. Velocity field in front of a single through, blue: wind tunnel measurement, red: numerical simulation.

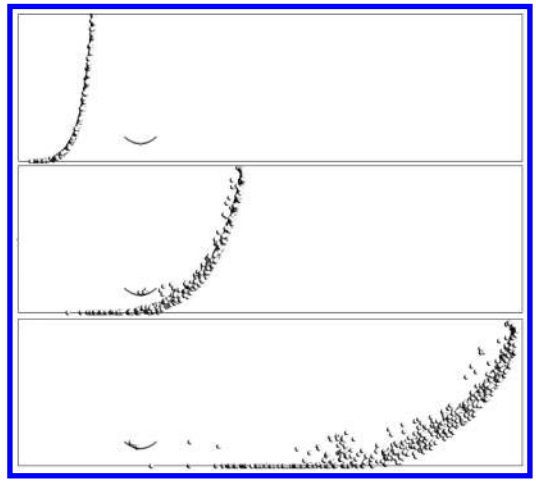


Figure 7. Particle positions in three different time steps; the particle size is scaled for visualisation purpose.

attack chances. In general, for the single through the most deposition of aeolian particles can be expect in the middle part of the surface. Close to the lateral edges the flow acceleration and the turbulence intensity prevent material settling. Usually a group arrangement of parabolic troughs builds a whole power plant with a complex flow field. Therefore the amount of settled material is most likely different for each trough in the whole arrangement.

5 PARTICLE DEPOSITION ON THE SUPP

5.1 *Simulation characteristics*

The dimensions of the SUPP are enormous with 750 m tower height and 2 km diameter of the solar collector, although this is the smallest concept of the

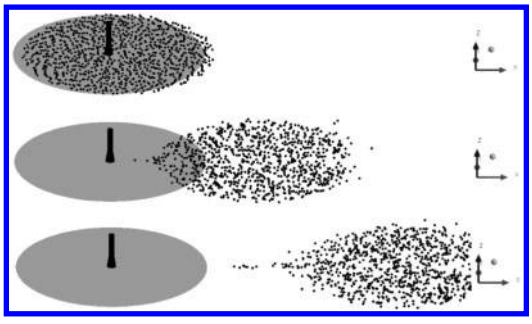


Figure 8. Particle positions on the collector surface for three different time steps; the wind comes from the left hand side.

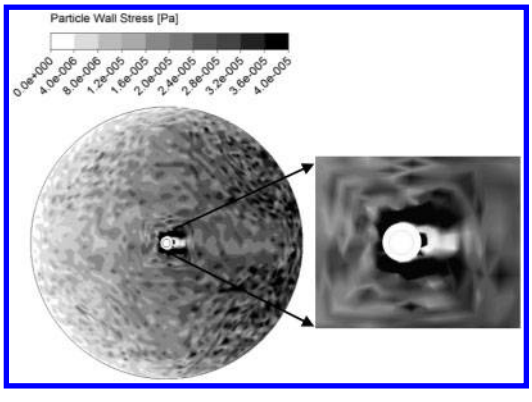


Figure 9. Mean particle wall shear stress on the collector surface, the wind comes from left the hand side.

actual designs (Harte et al. 2010). For applicability to the numerical model following simplifications and assumptions were made. The collector starts directly on the bottom, normally the height is 10 m over ground. The collector surface is almost smooth and has an ascending slope to the tower base, but the wind cannot blow under the collector or through the tower. For the inlet wind velocity a logarithmic profile is used (Fig. 3). The influence of the coriolis force, which rotates the wind angle of attack in the upper atmospheric boundary layer, is neglected.

Two scenarios are modelled: a) wind blow over an already with particles covered collector and b) wind driven particles approaching the clean collector. The interaction between the particles and the collector is modelled using a particle wall-interaction approach, which reduces the particles momentum.

5.2 *Wind over a particle-covered collector*

Figure 8 shows a first impression of particles on the collector surface which starts to move due to the wind. The particles have different diameter, which results in different particle velocities. It is not possible to model particle accumulation because of the nature of the Lagrangian particle model, but information about the particle wall shear on the collector surface can be obtained, see Figure 9. It can be seen that very close

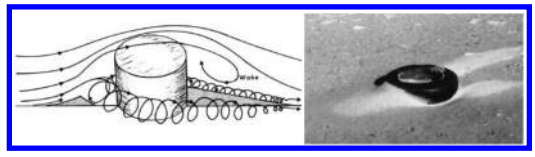


Figure 10. Flow characteristics around a cylinder (left) and resulting particle deposition (right) (Pye & Tsoar 2009).

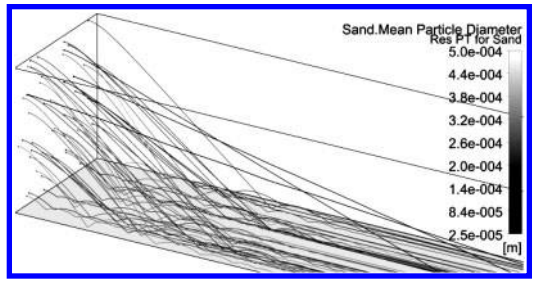


Figure 11. Particle tracks for different particle diameter.

to the tower base at the windward and lateral sides, the friction force is very high. This indicates a big amount of particles which were transported around the tower. Behind the tower, leeward, there is a white zone, were very low particle-wall interaction is found. There is a low wind recirculation behind the tower where particles settle down. Compared to Figure 10 the simulation show reasonable results, but it is obvious, that the quality of the mesh is still not high enough, because the contours in Figure 9 follow the mesh block structure (the results look slight like a cross with the tower in the centre).

5.3 *Wind driven particles approaching*

In order to identify proper boundary conditions and to save calculation time, the simulations are made without the solar tower in an empty box. Using different particle diameter the particle tracks follow the particle modes creep, saltation and suspension (Fig. 11). Still missing is the particle stop, by means of total deposition. Because of the collector height with 10 m rather fine sand and dust particles can be expect on the collector than larger sand grains (Höffer et al. 2010). Even strong winds are able to lift the coarser particles to heights about some meter, see Table 1. Because of the low velocities in the wind shadow of the tower tracked particles will settle down and accumulate. Construction parts of the collector panels can act like obstacles for the moving particles and collect them. This could yield to some local particle deposition zones, which need to be cleaned e.g. mechanically.

6 CONCLUSIONS

The impact of aeolian sand and dust particles on two solar energy systems is analysed. Two approaches were used to discover details of deposition zones on the surfaces. Numerical CFD simulations were performed for

a single parabolic through and for a simplified solar upwind power plant.

In case of the SUPP grains move over the collector surface and agglomerate at low-wind areas around and particularly behind the tower. Because of the height of the collector rather fine sand/dust particles can be expected on the collector than larger sand grains. In contrast to this the troughs of the PTPP are closer to the soil bottom, so that they can collect large grains on its surfaces too. A physical wind tunnel study in combination with a numerical CFD-analysis for a single parabolic trough indicates for the deposition zones a high dependency on the orientation angle of the troughs.

The local wind climate and the topography of the surrounding urban area play a major role for the determination of the expectedly amount of particles. To consider this before the construction can safe cleaning-costs, e.g. by choose a less dust-risky location or integrate additional windbreaks in order to reduce the amount wind transported particles.

REFERENCES

AEA Technology Engineering Software Ldt., 2002. *CFX-TASCflow: Computational Fluid Dynamics Software, Theory Documentation Version 2.12*. Canada.

ANSYS Inc., 2009. *ANSYS-CFX Solver Theory Guide, Release 12.0*. Canonsburg, PA 15317.

Arya, S.P., 1999. *Air pollution meteorology and dispersion*. New York: Oxford University Press.

Bagnold, R.A., 1954. *The Physics of Blown Sand and Desert Dunes*. Mineola, New York: Dover Publications, Inc.

Charabi, Y. & Gastli, A., 2012. Spatio-temporal assessment of dust risk maps for solar energy systems using proxy data. *Renewable Energy*, 44, 23–31.

Counihan, J., 1969. An improved method of simulating an atmospheric boundary layer in a wind tunnel. *Atmospheric Environment (1967)*, 3 (2), 197–214.

El-Nashar, A.M., 2009. Seasonal effect of dust deposition on a field of evacuated tube collectors on the performance of a solar desalination plant. *Desalination*, 239 (1–3), 66–81.

Franke, J., et al., 2007. *Best practice guideline for the CFD simulation of flows in the urban environment*. Quality assurance and improvement of microscale meteorological models. Brussels: COST office.

Goossens, D. & van Kerschaever, E., 1999. Aeolian dust deposition on photovoltaic solar cells: the effects of wind velocity and airborne dust concentration on cell performance. *Solar Energy*, 66 (4), 277–289.

Gosman, A.D. & Ioannides, E., 1993. Aspects of Computer Simulation of Liquid-Fueled Combustors. *Journal of Energy*, 7 (6), 482–490.

Harte, R., Graffmann, M., & Wörmann, R., 2010. Progress in the structural design of solar chimneys. *In:* RUB, ed. *Solar Chimney Power Technology: International Conference – Proceedings*. Ruhr-Universität Bochum, Bergische Universität Wuppertal.

Höffer, R., Wevers, C., & Görnandt, V., 2010. Transport and deposition of dust on the collector surface. *In:* RUB, ed. *Solar Chimney Power Technology: International Conference – Proceedings*. Ruhr-Universität Bochum, Bergische Universität Wuppertal.

Kind, R., 1976. A critical examination of the requirements for model simulation of wind-induced erosion/deposition phenomena such as snow drifting. *Atmospheric Environment*, 10 (3), 219–227.

Mani, M. & Pillai, R., 2010. Impact of dust on solar photovoltaic (PV) performance: Research status, challenges and recommendations. *Renewable and Sustainable Energy Reviews*, 14 (9), 3124–3131.

Mekhilef, S., Saidur, R., & Kamalisarvestani, M., 2012. Effect of dust, humidity and air velocity on efficiency of photovoltaic cells. *Renewable and Sustainable Energy Reviews*, 16 (5), 2920–2925.

Pye, K., 1987. *Aeolian dust and dust deposits*. London: Acad. Press.

Pye, K. & Tsoar, H., 2009. *Aeolian sand and sand dunes*. Berlin: Springer.

Rehman, S., Halawani, T., & Husain, T., 1994. Weibull parameters for wind speed distribution in Saudi Arabia. *Solar Energy*, 53 (6), 473–479.

Richards, P.J. & Norris, S.E., 2011. Appropriate boundary conditions for computational wind engineering models revisited. *Journal of Wind Engineering and Industrial Aerodynamics* (99), 257–266.

United nations Convention to Combat Desertification, 2001. *Global alarm: dust and sandstorms from the world's drylands*. Beijing, United Nations.

VDI 3783-12, 2000. *Environmental meteorology – Physical modelling of flow and dispersion processes in the atmospheric boundary layer – Application of wind tunnels*: Verein Deutscher Ingenieure, Beuth Verlag GmbH (VDI 3783-12).

Research and Applications in Structural Engineering, Mechanics and Computation – Zingoni (Ed.)
© 2013 Taylor & Francis Group, London, ISBN 978-1-138-00061-2

Constructability-aspects for reinforced concrete solar updraft power plants chimneys: From construction technology and logistics to schedules and costs – data-requirements for economical evaluation

L. Laußat
Bergische Universität Wuppertal, Civil Engineering Faculty, Chair of Construction Management & Economics

N. Warkus
Interdisciplinary Centre for Technical Process Management, Wuppertal, Germany

M. Helmus
Bergische Universität Wuppertal, Civil Engineering Faculty, Chair of Construction Management & Economics, Interdisciplinary Centre for Technical Process Management, Wuppertal, Germany

ABSTRACT: Up to today only a few small solar updraft power plant chimney towers have been built for evaluation reasons. In the last decades some companies tried to find investors for different mega projects with chimneys between 750 and 1,500 m and they are still doing so. But building chimneys of 500 m or more is not an everyday challenge for any construction industry in the world. Due to the needs of special climatic conditions and the availability of space for the horizontal collecting structure, solar power plants are discussed for areas far away from other industries, infrastructure and existing transportation systems, such as e.g. Western Australia, Namibia, Saudi Arabia and Arizona. But yet not one realization of these commercial intended projects has been started. This can have different reasons, e.g. economical or technological, but also commercial. The economic reasons can be divided into external factors such as the cost of construction and maintenance relative to the prices of generating power in other ways and internal factors such as perhaps the lack of plausible calculations about power output, depending on performance, efficiency and loss factors, or about energy and water needed for construction and maintenance relative to the energy generated by the plant. Technological reasons can be divided in perhaps unanswered questions about the natural hazard resistant tower design itself and those about the methods used to realize the construction work. Looking at commercial reasons, online discussions can be found, that today project development work seems to be more lucrative than project realization or that project development companies are waiting for additional subsidies. This paper gives some impressions about logistical and technological aspects of constructability of huge reinforced concrete chimneys, an important aspect, because besides all other named reasons it is crucial to know, if and how the chimney construction work as the center of the power generating project can be realized. And this knowledge also is the base for scheduling and cost calculation.

1 INTRODUCTION

1.1 *The idea of SUP*

The idea of solar updraft power (SUP) generation was first published by Cabanyes (1903). In the last decades the discussion about this "green" technology has become more popular and research started focusing these issues as could be seen in a new int. conference series (USA 2008, Germany 2010 (SCPT), China 2012 (SUTPT)). A good overview can be found under http://www.solar-tower.org.uk/.

1.2 *Review of SUPP project development*

Due to the needs of special climatic conditions and the availability of space for the horizontal collecting structure, in the last years SUP plants (SUPP) were discussed for areas with low population density, very high direct sunlight and good soil conditions for the substructure far away from other existing industries, transportation systems and infrastructure. Experts state, that only SUPP with huge chimneys (heights beginning with 0.5 km) would be commercial relevant, see e.g. Schlaich et al. 2005. Thereby SUPP-technology competes with other solar power plant technologies such as photovoltaic or concentrating solar thermal power plants (CSPP).

Yet only the construction of smaller, non-commercial research plants using subsides in

- Spain 1982 ($h_{tower} = 195$ m, A = 46 ha, <50 kW) &
- China 2010 ($h_{tower} = 53$ m, A = 6,17 m^2, ~200 kW)

are documented, whereby the 200 kW Chinese prototype in Inner Montgolia has to be seen as phase one of

three, where in ongoing phase three the SUPP shall reach 25.1 MW ($A = 2.51\,km^2$) (Chen et al. 2010). Some reports about other experimental prototypes e.g. in Botswana, Turkey, China and United Arab Emirates ($h_{tower} < 30\,m$) exist.

Today there are some discussions for SUPP with huge reinforced concrete (RC) chimneys initiated by commercial project development companies. Projects ideas are actual discussed for

- Namibia ($h_{tower} = 1.50\,km$, $A = 37\,km^2$, 400 MW),
- W. Australia ($h_{tower} = 1.00\,km$, A = ?, 200 MW),
- Saudi Arabia ($h_{tower} = 1.00\,km$, $A = 28\,km^2$, 200 MW),
- Arizona ($h_{tower} = 0.80\,km$, $A = 38\,km^2$, 200 MW),
- Spain ($h_{tower} = 0.75\,km$, A = ?, 40 MW),
- China Lan. ($h_{tower} = 0.25\,km$, $A = 1.3\,km^2$, 60 MW).

For Namibia the impact of the beginning of an investigation for a CSPP plant in 2012 on the 2008 proposal for a SUPP could not be estimated by the authors. The development of another project in Australia (New South Wales), that started 2001 ($h_{tower} = 1.0\,km$, $A = 38\,km^2$, ~200 MW), has been stopped.

The companies involved are looking for investors since several years, but there can be found some critical discussion about the commercial intention of these projects and about the assumptions used for calculating and promoting very low electricity producing costs and consequently high possible ROI. So is it e.g. possible to calculate construction costs of the SUPP today?

1.3 *Review of constructability quotations*

Schlaich 1995 states: *"… construction for a chimney about 1000 metres high … is possible without difficulty today. With the support of a German and an Indian contractor especially experienced in building cooling towers and chimneys, manufacturing and erection procedures were developed for various types in concrete … and their costs compared."* Stinnes, the initiator of the project development for Namibia, mentioned 2004: *"The structural risk* [of a tall chimney flue of 1.5 km] *is fully covered by professional insurances for design, based on the professional guarantees of Prof. Schlaich and Prof. Harte, and construction, based on the builders' insurances, so that there exists no risk for the prospective investors."* Harte et al. 2012 mention, that they think RC SUPP-chimneys (SUPPC) of max. 1.0 km can be seen as buildable today. Looking at chimney heights of 1.5 km Krätzig et al. 2013 speak of utopias.

2005 an engineering company involved in SUPP-development publicized: *"The respective structural approaches are well known and have been used in cooling towers. No special development is needed. … With the support of international contractors especially experienced in building cooling towers and towers, manufacturing and erection procedures were developed for various tower types in concrete and steel and their costs were compared. The type selected is dependent on the site. If sufficient concrete aggregate materials are available in the area and anticipated seismic acceleration is less than about one third of the earth's gravitational acceleration, then reinforced concrete tubes are the most suitable. Both conditions are fulfilled world-wide in most arid areas suitable for solar towers. Detailed statical/structural research showed that it is appropriate to stiffen the tower at several levels with cables arranged like spoked wheels within the tower, so that thinner walls can be used. This is maybe the only really new feature of solar towers compared to existing structures."* (Schlaich et al. 2005).

But is it really the same to build a 200 m cooling tower with flat surfaces and to build a 1.0 km SUPPC with overhanging stiffening-rings from a construction technology perspective? And can construction technology problems solved for high skyscrapers with floors usable as working platforms during the construction phase can be transferred to chimneys without any floors? And what about a detailed construction cost calculation reflecting these constructability aspects?

1.4 *Review of cost estimations*

Bergermann & Weinrebe 2010 point out, that the cost for the tower (without engineering and coordination) will be around 25% of the total investment costs for a SUPP and also, that *"tower costs may vary from one location to another due to availability of steel, cement or aggregates."* And so the big differences in published cost estimations are remarkable.

First cost estimations for a SUPP can be found in Schlaich 1995 for chimney height of 445, 750 and 950 m refering to German and Indian contractors with experiences in building cooling towers and chimneys. Stinnes 1997 published the results of cost estimations made by different local South African contractors for a 1.5 km RC chimney, which differ from each other with factor 3! These are followed e.g. by cost estimations for other chimney heights in Dos Santos Bernardes 2004, Schlaich et al. 2005 (some newer data can be found on their company webpage) and Fluri et al. 2009. Fluri et al. 2009 calculated costs for a 0.85 km and for a 1.0 km RC SUPPC. The newest estimations found by the authors are those in Krätzig 2012 for RC SUPPC with $h_{tower} = 0.5\,km$ and with $h_{tower} = 0.75\,km$. All these estimations are published without further breakdown of the amount and exempt from Fluri et al. 2009 nearly without giving information about the approaches. 2011 EnviroMission, one of the companies mentioned above, engaged the US contractor Hensel Phelpsw for delivering a schedule and cost estimations for the project in Arizona (EnviroMission 2011) – the results are unknown.

So yet no detailed calculations about the construction cost of RC SUPPC have been published, so that the above cost estimations could not be revised academically.

Some investigations about these differences in cost assumptions for SUPP can be found in Fluri et al. 2009. They divide the chimney cost in material cost, construction cost and transport cost. Their *"Results*

show, that previous models have underestimated the initial cost and levelised electricity cost of large-scale solar chimney power plants. … previous investigations were too optimistic … Solar Chimney power plant cost may be significantly reduced if construction materials are supplied by dedicated manufacturing facilities located on site. Additionally, these costs may be even lower when assuming the construction of multiple plants, but are unlikely to be as low as those assumed by Schlaich (2004) and Bernardes (2004)." Looking at too optimistic assumptions used for calculating levelized electricity costs, Krätzig is citated by Bonelle 2012 with the words that making such mistakes in assumptions *"illustrated the 'dangers of wishful thinking'."*

By saying *"Without humus no GreenTower"* or *"the greenhouse and humus transform the low profit updraught tower into high profit GreenTower"* Stinnes 2010 states his belief that using the space under the collector roof for agriculture is necessary to make SUPP investments commercial attractive.

At the same time different people are calling for subsidies, e.g. Bergermann & Weinrebe 2010.

1.5 *Review of construction time estimations*

Without any derivation several authors affirm, that the time needed for construction of a SUPP, including chimney, collector and aggregates etc., will be around two years (see e.g. Dos Santos Bernardes 2004 or Almasy 2011).

1.6 *Focus of the paper*

So even if companies looking for investors or for development or engineering contracts say that they were able to calculate the cost of construction already since 1995 and even if they claim in 2004 that they see no financial risks resulting from the construction of a 1.5 km high RC SUPPC, there are many reasons to do a little more research about these aspects also on academic level to find out more about the right methods and logistic concepts for doing the construction work, the time needed and the cost resulting from this work.

The intention of this paper is to identify some relevant aspects and give some estimation at the starting point of the academic research on constructability and logistic aspects for SUPPC in continuance to Helmus et al. 2010 end e.g. Strauß & Kreiner 2010.

This paper looks at some technological constructability aspects, because knowledge about the methods of construction are crucial for estimating construction costs, time needed for logistic and construction and so for economic and ecologic (e.g. energy input) valuation.

The authors will concentrate on SUPPC designs using RC structures as they seemed to be favored by the engineering companies dealing with design tasks of such chimneys (see e.g. Schlaich 1995), Schlaich et al. 2005 and Harte et al. 2012). Therefore the authors use the design concept delivered by Krätzig et al. 2009 as shown in figure 1.

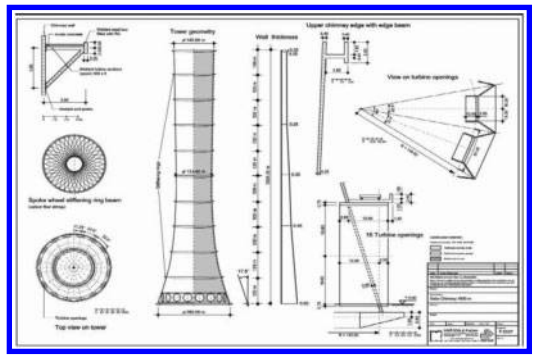


Figure 1. RC SUPPC design concept (Krätzig 2012).

2 CONSTRUCTION LOGISTIC AND CONSTRUCTABILITY ASPECTS

2.1 *Constructability aspects: Construction method*

Due to the lack of any experience building RC SUPPC is not an everyday challenge for any construction industry in the world. Various logistic and construction processes have to be evaluated, including availability of material, transport facilities, as well as building and construction technology aspects. This evaluation will lead to cost, time and resultant economic and ecological prognosis data.

Looking at constructability e.g. the following aspects have to be analyzed iteratively with the structural design of the chimney, so that loads resulting from the construction work can be considered in the static and dynamic analysis: concrete production, handling and placement method and equipment (self-climbing or crane-based), scaffold, temporary framework and formwork, vertical material transportation (cranes, elevators, pumps, helicopters, conveyor belts, winches) and additional construction safety constructions fixed at the chimney.

Helmus et al. 2010 conclude: *"Conventional concrete construction methods, with in-situ concrete and use of formwork, seem to be the only realistic and possible construction option … alternative techniques (e.g. prefabricated sections) aren't realizable."*

Some ideas can be found by analyzing technics used for high skyscraper building, pylons, water or cooling towers. The highest concrete chimney used for the cooling of conventional power plants has a height of 200 m (Niederaußem, 2000). The highest skyscraper (Burj Khalifa, Dubai, 2010) has a height of 828 m; there concrete was pumped over the first 606 m (Putzmeister 2007).

2.2 *Constructability aspects: Vertical transportation*

This assumption can also be recognized in Strauß & Kreiner 2010 or in Krätzig 2012. Latter gives an impression for some logistic aspects for equipment needed for the vertical transportation of personal and

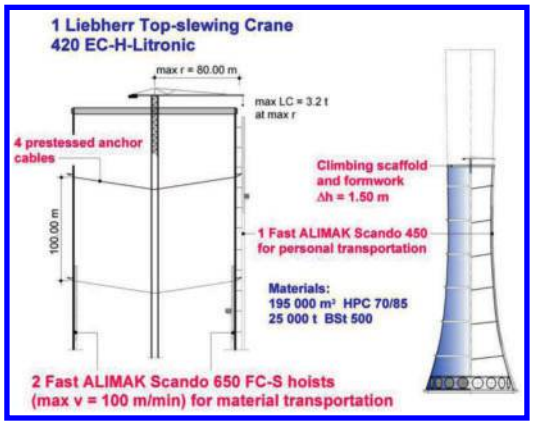


Figure 2. RC SUPPC construction concept (Krätzig 2012).

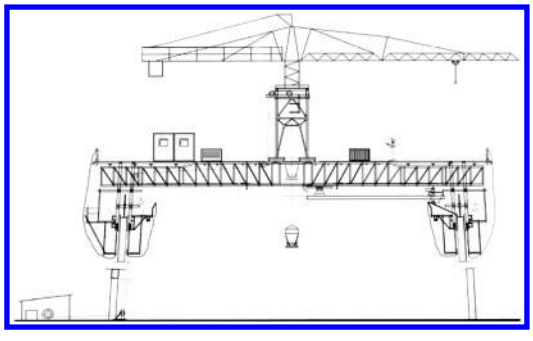


Figure 3. Concept for central crane with self-climbing working platform at the top combined with winch-systems (Gleitbau Salzburg GmbH).

material when building a 1.0 km RC SUPPC in Saudia Arabia, as shown in figure 2.

The shown Liebherr Top-slewing crane 420 EC-H has to be adapted for this purpose. Besides the tower height the length of the cable/winch system has to be considered. The max. length today is mentioned with 437 m and the max. winching speed for e.g. 5.2 to with 94 m/h (Liebherr 2012).

Another idea is to combine a central crane with a climbing platform on the top and a separate winching-system as shown in figure 3 (for smaller diameters) or the use of more than one crane (presentation to Helmus et al. 2010) is shown.

Strauß & Kreiner 2010 are thinking about *"high-speed elevators … to put huge concrete masses into position in time."* Looking at typical loads and elevating velocities, the following data could be found e.g. for the Alimak Scando 650 FC-S shown in figure 2: payload capacity 2,400–3,200 kg, speed 0–100 m/min, max. lifting height 400 m (Almiak 2012). Looking at e.g. 500 m height, once adapted for higher lifting processes, this elevator system can transport around 1 m^3 of concrete every ca. 15 minutes, assuming 2.5 min for loading, 5 min. for the way up, 2.5 min for casting and 5 min for the way back down. These are 4 m^3/h.

To make a comparison: the pumping system used for the Burj Khalifa was designed for 30 m^3/h

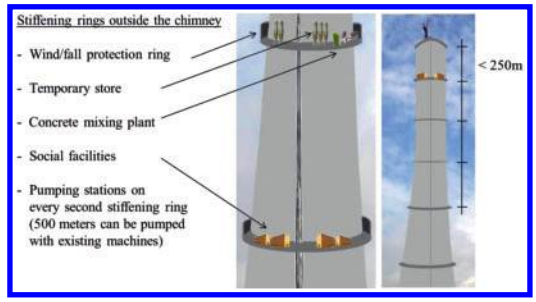


Figure 4. Working platforms at stiffening rings of a 1.5 km RC SUPPC (Presentation to Helmus et al. 2010).

(Putzmeister 2007) and Lohaus & Abebe 2010 are thinking about using two 100 mm pipes for pumping rates of 8 to 12 m^3/h for a RC SUPPC.

But this small diameter affords fine aggregate and so Lohaus & Abebe 2010 mention, that *"a new concrete concept has to be developed for the solar chimney in order to produce the type of concrete that complies with the stringent requirements of pumpability, workability and stability."*

In addition Lohaus & Abebe 2010 think about staged pumping, which requires working platforms at different levels.

So besides the working platforms which are usually combined with the self-climbing frame- and formwork at the climbing top of the chimney, there will probably be the need for additional working platforms. Perhaps the stiffening-rings of the prospected RC SUPPC-design can be used as the basis for additional platforms offering place for staged pumping, storage, for social rooms and for sanitary facilities. Or they can be even used for concrete mixing aggregates nearer to the place of concrete placement to reduce the distance for concrete pumping. The concept of several working platforms in vertical direction already has been showed related to Helmus et al. 2010 by figure 4 and is mentioned in Harte et al. 2012.

But before iteratively specifying the vertical transportation system, some more assumptions and estimates about the general resource requirement are affordable.

2.3 *Logistic aspects: Resource requirements*

Once the right place for an RC SUPP project is found, the key resources needed for construction are e.g. knowledge, skilled labor, concrete aggregate and admixtures as liquefier and retarder, cement, water, structural steel, special construction products, concrete mixing plants and pumps, climbing scaffold and formwork, cranes and elevators for personal and material transportation. Besides of these, a lot of other materials, equipment, building site facilities as well as energy and the right weather and environmental conditions for the particular work are needed.

As shown before, the construction site will probably be far away from other infrastructure, so that at least for the time of construction social and office facilities as

well as sleeping accommodations are needed. Helmus et al. 2010 assumed that for the construction work of a 1.5 km RC SUPPC a maximum of 230 employees is required doing three-shift operation.

Because as mentioned above, the only resources you can find near to the prospected sites are concrete aggregate and arid weather conditions, depending on the SUPP site chosen it would be necessary to build new roads, railway, water-pipelines, perhaps combined with seawater desalting plants, or groundwater supply wells, maybe harbors for the construction phase to bring in the required resources. So the construction logistic requirements are nearly the same as they can be found within mining projects in desert areas.

In figure 2 the amount of concrete for a 1.0 km chimney without foundation is given with 195,000 m^2 C70/85 and the amount of steel for reinforcement with 25,000 to. This is a factor of 128 kg/m^3 near to the factor of 120 kg/m^3 given by Fluri et al. 2009. The diameter of this chimney at the base is around 260 m (see figure 1). Lohaus & Abebe 2010 are calculating with 210,000 m^3, using C30/37 on the top and reaching stepwise C70/85 at the base.

They estimate around 100,000 m^3 of C25/30 or C30/37 for a ring foundation with an inner diameter of 260 m and an outer diameter of 300 m. Calculation with a steel requirement for reinforcement of 60 kg/m^3 concrete, as estimated by Fluri et al. 2009, leads to a steel requirement of 6,000 to for the foundation.

Calculating with 170 l of water per m^3 concrete, for 300,000 m^3 of concrete there is a need of 51,000 m^3 of water just for concrete production. More water is needed e.g. for the cleaning processes of aggregates. One special point is, that *"water is at least as valuable as energy in many sunny dessert countries"* (Bergermann & Weinrebe 2010). And influenced by the climatic conditions perhaps cooling of water to ice-water and flake ice will be necessary e.g. for mixing concrete, as shown by Lohaus & Abebe 2010 in their article about concrete technology aspects.

Most authors think, that climbing technology used for cooling towers can easily adapted for the RC SUPPC, but without giving answers they say, that some new developments are required for the overhanging stiffening rings.

So once the construction method is chosen, the scheduling of the project can be done iteratively with detailing construction as well as logistic tasks.

2.4 *Economic aspects: Construction time*

Lohaus & Abebe 2010 consider *"two [concrete] batching plants with a total capacity of … 2,000–2,400 m^3/day"* resulting in a minimum construction time of 50 days for the foundation, when other probably restrictive factors (e.g. capacity of pumps and trucks or other transportation systems) do not exist.

Once the construction of the chimney has started, concrete placement in sections of 1.5 m height is part of the concept shown by Krätzig 2010 (see also figure 2). Strauß & Kreiner 2010 mentioned vertical steps of 1.0 to 1.5 m as *"well established climbing technology for cooling towers"* have to be revised. Lohaus & Abebe 2010 mentioned, that using modern gliding formwork systems *"large capacity silos have been built at a concrete casting speed of 3–5 m/day"*. For RC SUPPC Lohaus & Abebe 2010 consider *"only a night-shift concrete casting of 10 hours"*, in which *"a 2 m high concrete section is assumed to be completed … The daily hours could be devoted to reinforcement installation and other related activities."*

Due to the extreme high and the long service lives of 100 to 120 years expected by Schlaich 1995, Krätzig et al. 2010 or Harte et al. 2012, Krätzig et al. 2010 postulate *"an execution quality far above the usual site level"*. So there can be doubt, if the construction velocity and technology used for cooling towers can be adapted without any change. Helmus et al. 2010 e.g. estimated three days for every 1.5 m-section in their presentation.

That means that once concrete placement for the chimney has started, a chimney of 1.0 km will consist of 1,000 m/1.5 m/section = 667 sections for casting. Calculating with 3 d/section will lead to 2,000 d and so 5.5 years assuming 7/7 d operation, calculating with 1 d/section to around 1.8 years – without foundation.

So the above mentioned estimation of a construction time of two years for the whole SUPP (incl. collector, chimney, turbines etc.) seems to be plausible only if an optimistic work cycle of 1 d per 1.5 m-section could be realized and all other work (collector, aggregates etc.) could be done parallel.

Further analysis and publishing scheduling assumptions should be done.

2.5 *Economic aspects: Construction costs*

One part of the input data for economic evaluation of an SUPP are the production costs for the chimney, that means costs for labor, material, transport, energy, machines, scaffold, framework, construction site installation etc. Some of them are depending on construction time. In 1.3 some not revisable estimates are mentioned.

E.g. Krätzig 2012 prospects that for a SUPP with a RC SUPPC ($h_{tower} = 0.75$ km, $A = 9.6\,km^2$) the production costs of the chimney will be 60.5 Mio.€ whereby the whole determined investment – neglecting costs for the land needed – will be 337.6 Mio.€. So the production costs for the chimney without the costs for engineering and testing are estimated to be nearly 18% of the whole investment. Having in mind the regular observable cost increases of mega projects, explained e.g. in Homola 1994 *("Dilemma of the first mentioned value")* or in Flyvbjerg 2009 *("Survival of the unfittest")* some more detailed cost analysis seems to be essential.

2.6 *Ecological aspects: Energy input*

It was stated, that the time needed for the energetic amortization of a SUPP construction project will be

around three years of operation. Following Almasy 2011, EnviroMission says *"the amount of carbon pollution created by the manufacture and shipment of the cement and other materials needed to build the facility* [1.0 km tower in Arizona] *will be offset after 2½ years of operation."* Detailed calculations confirming these statements couldn't be found by the authors.

3 SUMMARY

The paper shows, that even if the discussion about SUPP has taken place for decades, some basic aspects of constructability and construction logistic tasks, needed for calculating economic and ecological affects like construction time and cost, have not been subject of research in detail so far. The paper reviews some basic aspects of constructability and logistic questions with the intention to initiate further investigation needed for coming a step closer to the realization of SUPP with RC SUPPC.

REFERENCES

Almasy, S. 2011: Can hot air be the fuel of the future? CNN 10 Oct. 2011.

Alimak Hek Group AB (ed.) 2012: Alimak Scando 650 FC-S product information. http://alimakhek.com/Products/Construction-Hoists/ALIMAK-SCANDO-650-FC-S.

Bergermann, R. & Weinrebe, G. 2010: Realization and Costs of Solar Updraft Towers. In *Proc. SCPT, Bochum, 28–30 Sept. 2010:* 63–68.

Bonnelle, D. 2010: An Economically Realistic Growth Path towards Kilometric Chimneys. In *Proc. SCPT, Bochum, 28–30 Sept. 2010:* 27–34.

Bonnelle, D. 2012: Solar chimney project in Arizona: an energy budget basic check. http://publications.solartower.org.uk/200_MW_La_PAZ_SCCP_in_Arizona.pdf.

Cabanyes, I. 1903. Proyecto de motor solar. In *La Energía Eléctrica* 25 August 1903, No. 4.

Chen, Y., Yang, Y., Wei, Y., Yang, J. & Tian, Y. 2010: Solar hot air-flows power generation and its application in Wuhai Inner Montgolia. In *Energy Research and Information* 26(2) 2010: 117–121.

Dos Santos Bernardes, M. A. 2004: *Technische, ökonomische und ökologische Analyse von Aufwindkraftwerken*. Stuttgart: http://elib.uni-stuttgart.de/opus/volltexte/2004/1633/pdf/MASB_Diss.pdf.

EnviroMission Ltd. (ed.) 2011: EnviroMission Signs Hensel Phelps as US Solar Tower Contractor. In *Company Announcement Release 02 Aug. 2011*. http://www.environmission.com.au/irm/Company/ShowPage.aspx/PDFs/1299-82348792/HenselPhelpsAppointedUSSolarTowerContractor.

Fluri, T.P., Pretorius, J.P., Van Dyk, C., Von Backström, T.W., Kröger, D.G. & Van Zijl, G.P.A.G. 2009: Cost analysis of solar chimney power plants. In *Solar Energy* 83: 246–256.

Flyvbjerg, B. 2009: Survival of the unfittest: why the worst infrastructure gets build. In *Oxford Review of Economic Policy* 25(3): 344–367.

Gleitbau Salzburg GmbH (ed.): Outstanding solutions in formwork engineering. http://www.gleitbau.com.

Harte, R., Höffer, R., Krätzig, W.B., Mark, P. & Niemann, H.-J. 2012: Solare Aufwindkraftwerke: Ein Beitrag der Bautechnik zur nachhaltigen und wirtschaftlichen Energieerzeugung. In *Bautechnik* 89 (3): 173–181.

Helmus, M., Warkus, N. & Lorek, M. 2010. Solar Chimney in Southern Africa – Construction Materials and Construction Method. In *Proc. SCPT, Bochum, 28–30 Sept. 2010:* 181–188.

Homola, J. 1994: Kostenrahmen – Dilemma der erstgenannten Zahl. In DVP e.V. (ed.), *Bausteine der Projektsteuerung*. Wuppertal: DVP-Verlag.

Krätzig, W.B., Harte, R., Montag, U. & Wörmann, R. 2009: From large natural draft cooling tower shells to chimneys of solar upwind power plants. In Domingo, A. & Lazaro, C. (eds.), *Proc. of the IASS Symp., Valencia, 28 Sept.–02 Oct. 2009.*

Krätzig, W.B. 2012: Mega-Schalen der Energietechnik. *Online presentation docu., Braunschweig, 28 Nov. 2011.* http://www.ibmb.tu-braunschweig.de/tl_files/ibmb/baustoffe/Seminar%20fuer%20konstruktiven%20Ingenieurbau/Vortrag_TU%20Braunschweig_SKI_28.11.2012.pdf.

Krätzig, W.B., Harte, R., Andres, M., Eckstein, U. & Wörmann, R. 2013: Große Schalentragwerke für Energieanlagen. In Nothnagel, R. & Twelmeier, H. (eds.), *Festschrift zum 60. Geburtstag von H. Budelmann*. Berlin: Springer.

Liebherr (ed.) 2012: Turmdrehkran 420 EC-H 16. http://www.liebherr.com/CC/de-DE/region-(europe)/products_cc.wfw/id-12601-0/measure-metric?file=%7e%2fcatXmedia%2fcc-ccm%2fDocuments%2fCC_DB_420ECH16_Litronic_EN_9321-0.pdf.

Lohaus, L. & Abebe, Y.A. 2010: Concrete Concepts for Solar Chimneys. In *Proc. SCPT, Bochum, 28–30 Sept. 2010:* 135–144.

Putzmeister (ed.) 2007: Einsatzbericht Betonhochförderung am Burj Dubai – Betonpumpen mit über 400 bar Förderdruck. http://www.pmw.de/pm_online/data/BP_3893_D.pdf.

Schlaich, J. 1995: *The Solar Chimney.* Stuttgart: Deutsche Verlags-Anstalt.

Schlaich, J., Bergermann, R., Schiel, W. & Weinrebe, G. 2005. Design of commercial solar updraft tower systems – Utilization of solar induced convective flows for power generation. In *Solar Energy Engineering.* 127(1): 117–125.

Stinnes, W.W. 1997: Solar power for an arid country, Pre-Feasibility Study on a 200 MW Solar Power-Station in the Northern Cape Province of South Africa.

Stinnes, W.W. 2004: Greentower: Performance guarantees through insurance policies. In *Proc. Industrial & Commercial Use of Energy Conf., Sommerset West, 12 May 2004*.

Stinnes, W.W. 2010: Humus as the backbone of GreenTower revenues. In *Proc. SCPT, Bochum, 28–30 Sept. 2010:* 345–354.

Strauß, J. & Kreiner, A. 2010. Optimised erection technology of giga towers. In *Proc. SCPT, Bochum, 28–30 Sept. 2010:* 117–124.

Research and Applications in Structural Engineering, Mechanics and Computation – Zingoni (Ed.)
© 2013 Taylor & Francis Group, London, ISBN 978-1-138-00061-2

SHM strategies, application and measurements on tripod offshore wind energy converters within the German offshore park Alpha Ventus

W. Rücker, S. Thöns, S. Said & W. Schmid
Federal Institute for Material research and testing, BAM Berlin, Germany

ABSTRACT: Prototypes of wind turbines of the megawatt class are to be built and tested until 2008 within a German offshore wind energy test field in the North Sea (ALPHA VENTUS). To ensure a high operational reliability of offshore wind turbines with economically acceptable repair and maintenance efforts, comprehensive diagnosis and supervision concepts are required. Automatic monitoring systems will be an essential part of such concepts. Because of the fact, that during operation there will be static and dynamic interaction between the components 'structure', 'machinery' and 'blades' it is necessary to develop the monitoring techniques in an overall concept. These monitoring systems are supposed to be applied for the design and testing as well as for the operation and maintenance phases. In the paper the developed approaches for the measurement of actions and the condition monitoring of all components of an offshore wind energy plant will be shown.

1 INTRODUCTION

The need to monitor offshore wind energy converters is a result of the completely new situation for civil engineers. Buildings and structures are usually unique but now a large number of the same structures with a complex design should be built in a relative short period in a harsh environment (offshore). To avoid downtimes of the facilities due to structural defects with extensive economical consequences as well as to initiate the maintenance based on the actual condition of the structure, a permanent monitoring system will be necessary to provide these data. For a condition analysis and a continuous monitoring system of (offshore) wind energy converters the following described problems are of primary interest.

2 OBJECTIVES

The loads acting on the facility from wind and waves in a stochastic manner will be simulated in a dynamic computation and provided for further system analyses. However, the statistical description of the wind and wave is to some extent arbitrary. Furthermore there is no certainty how well the loads (in reality and/or from numerical computation) correlate with the in situ loads of the components of the wind energy converter. This relation is of great importance in the design phase (assumption of safety factors) as well as for the monitoring (up to date assessment and condition prediction). To assess the condition of all components of an offshore wind energy converter also an accompanying monitoring system for the load is necessary. A particularly important aspect is the combination of loads from wind and waves. In terms of superposition of wind and wave loads there are assumptions or estimations for dimensioning the loading capacity and for the proof of operational stability (Germanischer Loyd, 2007). Currently there is no certainty for a complete combination of the loads including the interaction of dynamic loads of all components of an offshore wind energy converter.

The determination, assessment and monitoring of the stability (ultimate limit state) of the support structures of offshore wind energy converters are of central importance. For this purpose reliable indicators for the safety monitoring and defined thresholds need to be provided. Another key task in monitoring offshore wind energy converters is the development and supply of methods with which the occurring damages can be detected, localized and their evolution monitored.

3 MAIN TASKS

From the above described aims, the development and operation of continuous monitoring systems for offshore wind energy converters have the primary tasks as follows.

3.1 *Detection of the impact*

Generally not the acting loads of wind and wave on the structure should be measured. The aim is rather to determine the effect of the acting loads as generalized stress resultants at the tower head and the pile connections in the area of the foundation. These stress resultants are compared with the determined values of the design process. This results in an improved estimation for the load approaches and also a gain in safety,

if the measured stress resultants are less than the stress resultants of the design process.

3.2 *Condition monitoring and analyses*

The Condition monitoring of offshore wind energy converters is primarily the monitoring of parameters for the serviceability limit state. The main monitored parameters are.

Inclination: For a safe operating facility the inclination limit needs to be maintained. This limit is usually permanent at about 0.5 degree, including the inclination from the production and construction. Under a dynamic load the resulting inclinations are often greater.

Deformation: The elastic deformations of the tower and the rotor must be within specified limits. In particular, a safety distance needs to be maintained between the rotor and tower. The adverse combination of loads needs to be taken into account to compute the deformations. For concrete structures the deformation under operating loads must be limited in such a way that no damage occurs. For concrete a constant elastic modulus for tension and compression can be assumed to compute the deformations. The influence of shrinking, creep and temperature has also to be taken into account.

Remaining displacements: Remaining displacements in the support structure are an indicator for a change of the loading capacity (generally a decrease) and can also lead to additional loads in the support structure. The maintained allowable threshold values result from a numerical computation of the additional possibly stresses of the support structure including the tower.

Acceleration: For a safe operating facility the accelerations at the tower head, tower shank and tower base must be within specified limits. These limits are usually given by the machine manufacturer. Also, in the VDI guideline 3834 threshold values for the acceleration are given for all parts of the facility (VDI, 2009).

Natural frequencies: The first natural frequency of the whole system "nacelle-tower-foundation-soil" from currently designed facilities is in the area of the rotor speed. The blade-passing frequency (for three blades the triple rotor frequency) is usually above the first natural frequency. For a safe operation and to avoid early fatigue the natural frequencies must have a sufficient great distance to the operational frequencies.

3.3 *Stress monitoring*

Stress monitoring of offshore wind energy converters is primarily the monitoring of parameters for the ultimate limit state. The stress monitoring of a wind energy converter has the tasks as follows.

For concrete structures a limit of tension and/or compression has to be verified. Therefore, a limit of compression for concrete is given for specified load combinations. For steel structures plastic deformations have to be avoided for characteristic loads.

Due to the proof of operational stability each component or component section must have a sufficient resistance against the effect of cyclic-dynamic loads. The proof is usually based on the Wöhler or SN curve concepts which describe the tolerable number of load cycles depending on the type of connection and the geometry of the weld by arising stress amplitudes. The life-time relevant loads will be provided with a damage equivalent load spectrum and need to be adjusted with the respective sitespecific wave and wind loads. This concerns the frequency of occurrence as well as the distribution of direction of the wind and wave events. Regarding multi-megawatt wind energy converters, the life cycle loads are orders of magnitude beyond the number of load cycles and vibration amplitudes which are usually estimated for steel structures.

The detection of damage and the damage assessment are usually distinguished in four parts: detection, localization, quantification and prediction. Currently there exists no reliable method which would solve these tasks. The presently used and developed methods are based on a change of the dynamic behavior of the structure. A numerical model solves then the so-called inverse problem to identify the location and extent of the occurring damage. Therefore it is important to install the sensors at locations of the structure where appropriate and relevant information can be obtained. These monitoring points are determined in advance either by a numerical analysis or by a-priori knowledge. For example, the monitored accelerations of the pile head can give first indications of a change of stability of the tripod foundation. Another method, which is currently tested, is the so-called "Stochastic Subspace Damage Detection" method (SSDD) (Basseville & Abdelghani et al, 2000). This method does not depend on the model as far as the damage detection is concerned. However, this method requires an adequate numerical reference model to localize and quantify damages. In various projects the SSDD-method was tested and it gave sensitive indicators for the practice of damage detection (Rücker, 2007).

Basically, the permanently monitored strains can be unused to determine local damage indicators. They can be used as pre-indicators for the damage detection prediction.

4 MEASUREMENTS ON A PROTOTYPE

The previously mentioned methods are used as an example for a prototype off an offshore wind energy converter. The prototype is a Multiibrid M5000_2 wind energy converter (Fig. 1). The hub height of the facility is 102 m, the top of the tower is at 92 m and the diameter of the rotor blades is 112 m. The mass of the tripod foundation is 500 t, the mass of the tower 350 t, the mass of the rotor 108 t, including tithe hub, and the nacelle has a mass of 194 t neglecting the rotor and the hub. The rotational speed of the rotor varies in the operating range between 5.9 and 14.8 U/man ± 10%. The nominal power of the facility is 5 MW at a nominal rotational speed of the rotor of 14.8 U/min.



Figure 1. Prototype of Multibrid M5000_2 with measurement system.

Figure 1 shows the monitoring points of the sensors on the tower and the tripod. Totally 110 strain gauges, 114 acceleration sensors and 4 inclination sensors were installed in 6 monitoring levels. Additional sensors were installed on the nacelle to monitor r the machine as well as on the rotor blades to measure the accelerations and strains. The selection and number of monitoring points on the structure were made with the tested and still developing methods based on measured values to assess the damage and load identification. Furthermore, additional monitoring points were needed, that were associated with the problem of design verification. The technical equipment for a commercial structure monitoring system operating on an offshore structure and especially the required number of sensors are derived from the analysis of the structural condition assessment. The required number of sensors can be determined on the one hand from the identification of the sensitive structural components and on the other from tracing the measurements back to the damage mechanisms of the model (e.g. Thöns & Faber, et al. (2008). Therefore, a commercial monitoring system will have a significant lower number of monitoring points.

4.1 *Monitoring the loading side*

As described above, the aim in the present case is not to measure the acting loads of the structure. The aim is rather to determine the effect of the acting loads as generalized stress resultants on the tower top and the pile connections in the area of the foundation. The stress resultants N, My and Mz are determined here

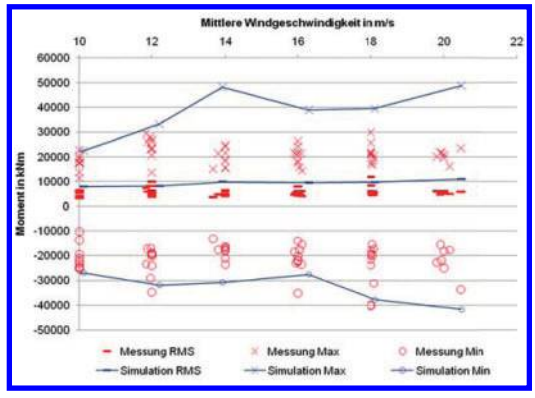


Figure 2. Comparison of measured (points) and calculated (solid line) stress resultants, exemplary for the bending moment on measurement system level 4.

Table 1. Comparison of natural frequencies determined by experiments and calculations.

Experiment	Calculation	Dev. [%]	Mode
0.4211	0.413	3.3	1.1 Bending
	0.417	2.1	1.2 Bending
	3.312	–	2.1 Bending
3.0–3.4	3.240/3.433	–	2.2 Bending

from normal stresses, which can be calculated directly from the strains. Figure 2 shows the comparison of the determined bending moment and the design bending moment on measurement system level 4 (see Figure 1). As can be seen, the design bending moment forms the envelope of the measured bending moments. The root-mean-square values (RMS value) of the monitored values are below the RMS value of the moment of the design computation with a few exceptions.

4.2 *Condition monitoring*

Tithe requirements of offshore wind turbine certification demands, inter alkali, a distance of ±5% between the natural frequencies of the structure f00,i and the excitations, i.e. operation frequencies (f_{1P}, f_{3P}, f_{6P}, …). This criterion ensures that no resonance occurs during operation. The calculated natural frequencies should thus be checked experimentally within the process of design verification before the structures are produced in a large number. Table 1 shows the results of the comparison of the first two natural frequencies of the M5000_2 on the basis of numerical and experimental modal analysis which provides information of the numerical model quality. For the numerical modal analysis monitoring data were collected over the time period of one year. A deviation of ±3% was found for the natural frequency belonging to the first bending mode.

All available acceleration measurements were analyzed for the precise identification of the behavior of

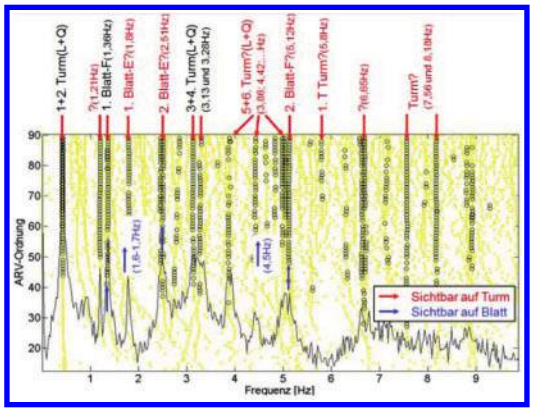


Figure 3. Frequency spectrum up to 10 Hz.

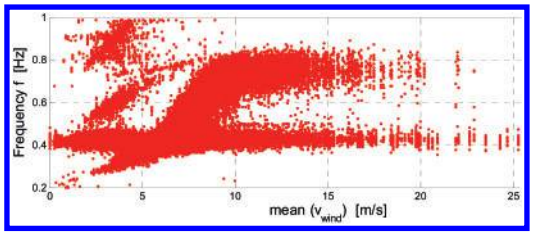


Figure 4. Measured frequencies in dependency of the mean wind speed.

the foundation, the tower and the rotor. The result is depicted in Figure 3. Up to 10 Hz more than 20 relevant frequencies have been identified which can be associated with lateral oscillations of the tower. In between there are several natural frequencies of the rotor blades. The damping is below 2% which can be concluded from the depicted spectrum.

The relevant frequencies up to 1 Hz in dependency of the wind speed are depicted in Figure 4. The first natural frequency of the tower (0.43 Hz; see the corresponding scatter band in Table 1) is passed by the excitation frequency of the rotor at about 7 m/s wind speed. The rotor frequency is constant at about 0.75 Hz for wind speeds higher than 10 m/s. Further, the triple rotor evolutions frequency can be also observed in Figure 4.

The measured inclinations of the tower at the bottom and at the top in dependency of the wind speed are shown in Figure 5. The bottom of the tower is the location for the measurement of the threshold inclination of 0.5 degrees which are defined in various guidelines. The operation mode (idle or operation) of the turbine must be considered when analyzing the inclinations. As a result, it can be seen that the inclinations in idle mode are relatively small. The inclinations increase slowly with increasing wind speed about 0.003 degrees/m/s. The maximum absolute inclinations are below 0.05 degrees. In operation mode a sudden increase of the inclinations for wind speeds higher than 5 m/s is observed. This sudden increase is correlated with passing the first natural frequency.

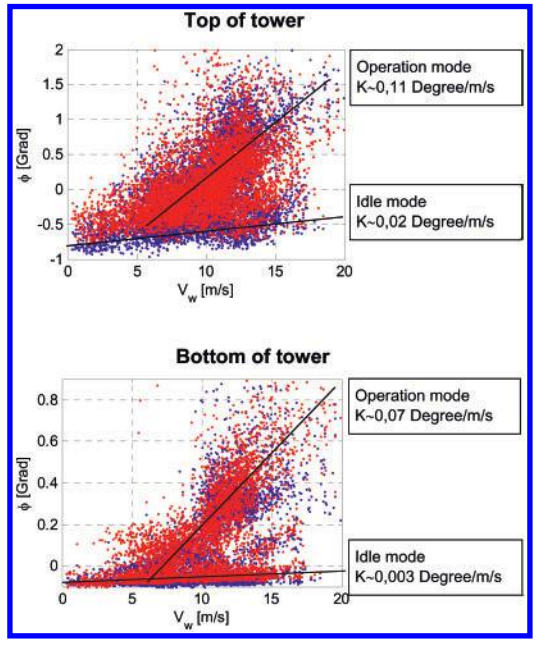


Figure 5. Correlation of inclinations with the wind speed at the bottom and at the top of the tower.

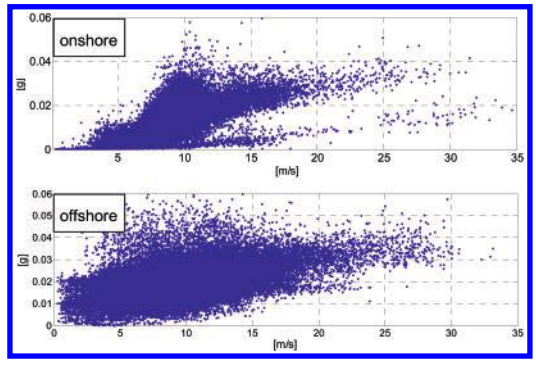


Figure 6. Correlation of accelerations with the mean wind speed on top of the tower onshore (top) and offshore (bottom).

The maximum absolute inclinations are 0.5 to 0.6 (dynamic) degrees for a wind speed of 15 m/s.

The maximum values of the accelerations at the top of the tower (onshore and offshore) in dependency of the wind speed are depicted in Figure 6. In principle the dependencies and the maximum values are very similar for onshore and offshore plants. As expected, the accelerations increase with increasing wind speeds also for onshore wind turbines. The maximum values of the accelerations at the top of the tower are about 0.4 to 0.5 m/s^2.

4.3 *Component loading monitoring*

The analyses for component loading monitoring comprise both, calculations and measurements. For the in situ measurements at the prototype of the M5000_2,

three hot spots were equipped with 24 strain gauges at each hot spot. The stress concentration factors (SCF) are calculated and compared to simulation data taking basis in a capture matrix data structure consisting of 10 min strain time series. For each of the time series 28,000 SCFs were calculated for which the mean values were consecutively determined. In this way the SCFs were analyzed for each of the four sensor chains above (HS A) and below (HS B) the weld for the hot spots 2, 3 and 4 (Figure 7).

The deviations of the mean values of the SCFs of the same hot spot are about 30%. A very good fit is found by comparing the mean values in Table 2 to calculated SCFs. A dependency of the SCFs on the wind speed is found in the lower frequency range of the M5000_2. Analyses show that in this power mode range, the dynamic hot spot strains are mostly influenced by the oscillation behavior in the area of the first natural frequency.

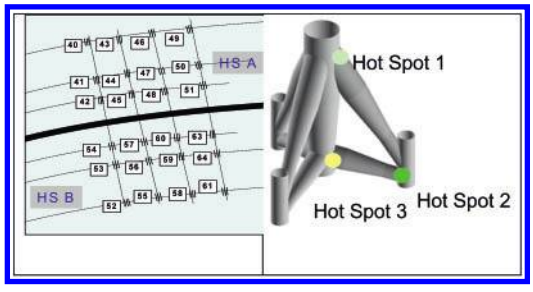


Figure 7. Sketch of strain gauge positions at hot spot (left) and location of measured hot spots on the tripod (right).

5 FURTHER DEVELOPMENTS

Deterministic behaviour has so far been assumed when performing condition assessments. In the future it is intended to utilize condition monitoring data as part

Table 2. Comparison of stress concentration factors determined by calculations and experiments.

Anschluss	Komponente	Sensorketten	SCF für Einheitslast M = 1	SCF aus Messung (Mittelwerte)
Obere Strebe-Pileguide (HS 2)	Obere Strebe	HSA	≈1.6	≈1.6
	Pileguide	HSB	≈6.4	≈6.8
Untere Strebe-Pileguide (HS 3)	Untere Strebe	HSA	≈1.1	≈1.5
	Pileguide	HSB	≈5.0	≈5.3
Zentralrohr-Untere Strebe (HS 4)	Zentralrohr	HSA	≈2.6	≈3.5
	Untere Strebe	HSB	≈1.6	≈1.4

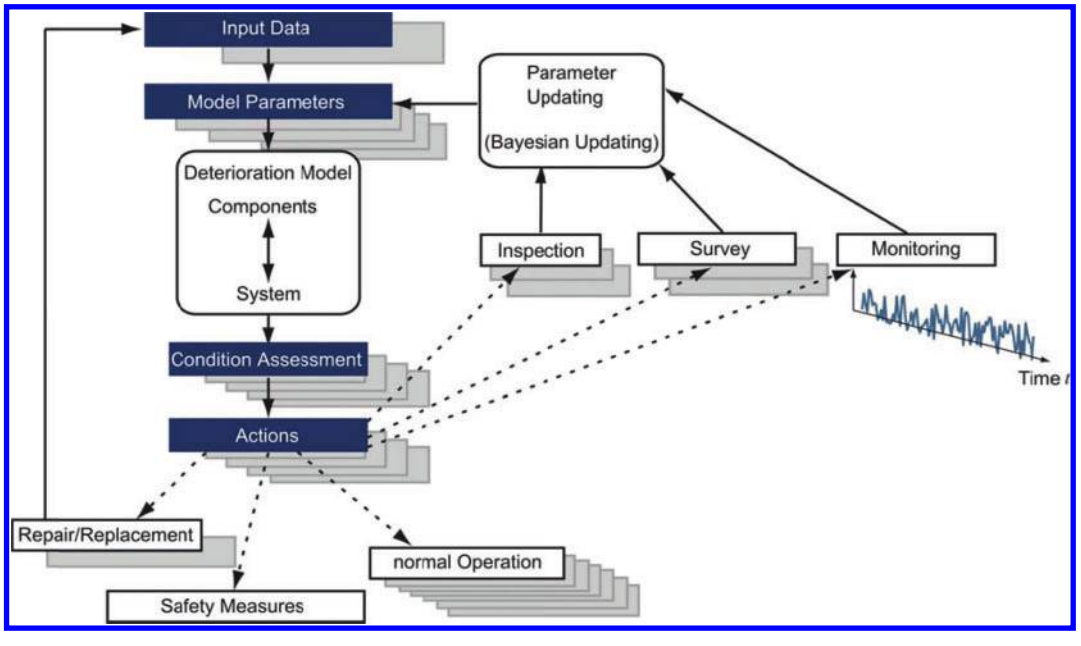


Figure 8. Concept for a reliability based condition assessment of bridges utilizing structural information (Fischer et al., 2012).

of probabilistic condition assessments. For this purpose it is necessary to develop probabilistic condition assessment models which can be updated when measurement data is available (see Figure 8 and Fischer & Schneider et al., 2012).

A probabilistic condition assessment model comprises a deterioration model of the structural components and a structural system model. These models are initialised with a-priori input data (geometry, material data, loads etc.). The models continuously provide information about the development of the reliability of the structure and its components over time.

Monitoring data and inspection results are utilized to update the parameters of the probabilistic condition assessment model using Bayesian updating. This approach makes it possible to consistently include all available information in a single model. The accuracy and information content of the collected measurement data and any other observations is explicitly taken into account when using this approach.

Through updating of the model parameters the condition assessment is also updated. This makes it possible to plan actions concerning the operation as well as monitoring activities and inspections – now conditional on the collected data. In this way the facility in combination with the monitoring system and inspections is an adaptive system which adapts to any changes. It is intended to integrate such conceptualised systems into condition monitoring systems.

6 SUMMARY

Continuous monitoring of the structural integrity as well as the serviceability of offshore wind energy converters becomes increasingly relevant due to the large number of such facilities. Implementing monitoring systems is already a requirement as part of the approval process of offshore wind energy converters. Additionally, operators utilise monitoring systems within the context of preventive maintenance planning.

The application of such conceptualised monitoring systems has been demonstrated for an existing offshore wind energy converter based on monitoring data gathered during an actual measurement campaign. The collected data allows an assessment of thee facility with respect to structural integrity, serviceability and durability. Finally, it was shown that it is possible to improve the assessment of the reliability of offshore wind energy converters based on measurement data from monitoring systems when using probabilistic methods.

REFERENCES

Basseville, M., Abdelghani, M., and Benveniste, A., 2000: Subspace–based fault detection algorithms for vibration monitoring. Automatica, 36 (1), 101–109.

Fischer, J., R. Schneider, S. Thöns, W. Rücker, D. Straub, 2012. Intelligent Structures – Reliability based condition assessment of bridges utilizing inspection and monitoring results, BAAM Federal Institute for Materials Research and Testing and Technical University Munich. Final Report (in German).

Germanischer Lloyd (GL), 2007. Guideline for the certification of offshore wind turbines, GL Hamburg, Edition 2003, reprint 2007 dpt, technology and technical data.

Rücker, W., 2007. Offshore wind energy plants – problems and possible solutions. Inn: EVACES‘07, Experimental vibration analysis for civil engineering structures, Porto, Portugal

Thöns, S., M. H. Faber, et al. (2008). Assessment and monitoring of reliability and robustness off offshore wind energy converters. ESREL 2008 and 17th SRA-Europe Conference. Valencia, Spain: 1567–1575.

VDI, 2009. Guideline 3834. Measurement and evaluation of the mechanical vibration of wind energy turbines and their components – onshore wind energy turbines with gears Issue 2009-03, VDI.

Thöns, S., et al., 2008a. Assessment and monitoring of reliability and robustness of offshore wind energy converters. In: ESREL 2008 and 17th SRA-Europe conference, Valencia, Spain.

Research and Applications in Structural Engineering, Mechanics and Computation – Zingoni (Ed.)
© 2013 Taylor & Francis Group, London, ISBN 978-1-138-00061-2

A comparative study about the effects of linear, weakly and fully nonlinear wave models on the dynamic response of offshore wind turbines

E. Marino, G. Stabile & C. Borri
Department of Civil and Environmental Engineering, University of Florence, Italy

C. Lugni
CNR-INSEAN, National Research Council, Rome
AMOS, Centre for Autonomous Marine Operations and Systems, NTNU, Trondheim, Norway

ABSTRACT: The present work aims at comparing the dynamic response of a fixed-bottom offshore wind turbine subjected to the combined wind-waves action employing different nonlinear irregular wave kinematic models. To this purpose, linear, second-order and fully nonlinear models are implemented in the hydrodynamic module of a global hydro-aero-elastic solver. All the wave models are based on the potential flow assumption. The fully nonlinear wave kinematics is reproduced both on the full simulation time and, in order to save computational time, only on some space-time subdomains within a domain decomposition strategy. This approach permits achieving a much higher accuracy in the assessment of the hydrodynamic loads keeping the global computational effort similar to the one required by linear or weakly nonlinear models. The paper represents a preliminary investigation aimed at establishing to what extend the second-order wave model can efficiently capture the system response even when the system is exposed to moderate sea states. Moreover, a comparison between the four wave models seems to reveal that some resonant oscillations of the tower are triggered by nonlinear components higher than the 2nd-order. Hydrodynamic loads associated to the four wave models are coupled with aerodynamic loads acting on the rotor of a 5-MW wind turbine. Hydro-aero-elastic calculations are performed using the NREL open-source software FAST.

1 INTRODUCTION

The development of more accurate simulation tools capable of capturing the effects of complex environmental conditions on large multi-megawatt wind turbines are strongly required within reliability-based design framework. A novel numerical package capable of predicting the nonlinear loads acting on offshore wind turbines exposed to nonlinear sea states has been recently proposed in (Marino, Lugni, & Borri 2013, Marino, Borri, & Peil 2011, Marino, Borri, & Lugni 2011). The model reproduces the structural response by coupling a fully nonlinear wave kinematic solver, (Ogilvie 1967), (Longuett-Higgins & Cokelet 1976), (Faltinsen 1977), (Grilli, Skourup, & Svedsen 1989), (Grilli & Svendsen 1990), (Nakayama 1983) and (Nakayama 1990), with a hydro-aero-elastic simulator of the entire system (Jonkman & Buhl 2005). Due to the large number of simulations required to set up a suitable probabilistic model for the design loads extrapolation, the main goal of the proposed simulation scheme was the enhancement of the model accuracy without penalizing the computational time. The computational efficiency is guaranteed by a domain decomposition strategy such that the fully nonlinear numerical wave solver is invoked only on special subdomains where nonlinear waves are expected. Whereas, on the remaining parts of the space-time domain the linear wave theory is assumed.

In this paper an irregular second-order nonlinear wave model is added according to the model proposed in (Agarwal & Manuel 2011, Agarwal & Manuel 2009). The objective is the comparison of the system response subjected to hydrodynamic loads associated with four irregular wave kinematic models: linear, second order (2nd), fully nonlinear within the domain decomposition strategy (FNL w dd), fully nonlinear over the whole space-time domain (FNL w/o dd). Each hydrodynamic model acts in conjunction with aerodynamic loads generated by a hub-height turbulent wind. Aerodynamic forces are modeled by means of the Blade Element Momentum theory (Moriarty & Hansen 2005). Hydro-aero-elastic calculations are performed with FAST (Jonkman & Buhl 2005).

The paper is structured as follows: in Section 2 the Fully Nonlinear (FNL) wave model is recalled and emphasis is placed on the domain-decomposition strategy. In Section 3 the 2nd-order irregular wave model is described. Section 4 briefly describes the baseline wind turbine model. In Section 5 the effects of the four wave models on the system response are presented and discussed.

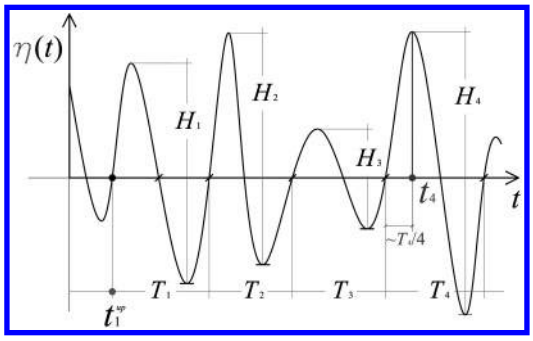


Figure 1. Sketch of the zero-crossing analysis of the free surface elevation for the estimation of the time instant at which the nonlinear event occurs. (Example with $i_b = 4$.)

2 FULLY NONLINEAR IRREGULAR WAVES MODEL

2.1 *Domain decomposition strategy*

The environmental conditions defining the loading processes the wind turbine is exposed to are characterized by the mean wind speed U, significant wave height H_s and peak spectral period T_p. The JONSWAP wave spectrum is chosen and the 2D-linear theory is used to simulate an irregular sea (Faltinsen 1990) in a global space-time domain $\mathcal{D}(t) = [x_{\min}, x_{\max}] \times [0; T_{sim}]$, where $x_{\min}$ and $x_{\max}$ are the lower and upper spatial limits of the global domain and T_{sim} is the total simulation time.

A zero-crossing analysis of the free surface elevation at the wind turbine location permits detecting the times, t_{i_b}, when a wave steepness larger than a threshold value occurs

$$t_{i_b} = t_1^{up} + T_{i_b}/4 + \sum_{h=1}^{i_b-1} T_h \tag{1}$$

where T_{i_b} is the i_b-th period corresponding to a wave steepness exceeding the minimum threshold value $ka_{\min}$ (see Figure 1); $\bar{t}^{up}$ is the vector of the zero upcrossing time instants; $\bar{T}$ and $\bar{H}$ are the arrays containing the local wave periods and wave heights, respectively. Each of these time instants, along with the spatial location of the wind turbine, corresponds to a time-space subdomain

$$\Omega_{i_b} = [x_t - \delta_1 x_t, x_t + \delta_2 x_t] \times [t_{i_b} - \delta_1 t_{i_b}, t_{i_b} + \delta_2 t_{i_b}] \tag{2}$$

on which the FNL wave model is used in place of the linear solution. $\delta_1 x_t$, $\delta_2 x_t$ and $\delta_1 t_{i_b}$, $\delta_2 t_{i_b}$ are the spatial and temporal radii of the subdomain, respectively, and x_t denotes the location of the wind turbine.

2.2 *Fully nonlinear solver: mathematical and numerical formulation*

The 2D problem governing the nonlinear propagation of gravity waves is formulated within the potential-flow assumption. For an inviscid fluid in irrotational flow, the potential function $\Phi(t,p)$ describes the velocity field at time t in each point $p \in \Omega(t)$. For an incompressible fluid, Laplace's equation is valid in the whole domain

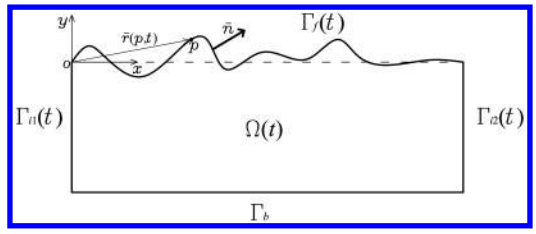


Figure 2. Two-dimensional domain of the time-depending Laplace equation.

$$\nabla^2 \Phi(t,p) = 0 \quad \forall p \in \Omega(t) \tag{3}$$

The 2D domain $\Omega(t)$ is bounded by four boundaries: inflow $\Gamma_{i1}(t)$, rigid bottom Γ_b, outflow $\Gamma_{i2}(t)$, and free-surface $\Gamma_f(t)$ (see Figure 2). On each of them, suitable boundary conditions have to be enforced. In particular, the impermeability condition $\nabla\Phi \cdot \bar{n} = 0$ is imposed on the rigid bottom, while the continuity with the linear wave kinematics has to be ensured on $\Gamma_{i1}(t)$ and $\Gamma_{i2}(t)$; finally, nonlinear kinematic and dynamic boundary conditions must be imposed on $\Gamma_f(t)$

$$\frac{\delta \bar{r}}{\delta t} = \nabla\Phi - (\nabla\Phi - \bar{v}), \quad \forall p \in \Gamma_f \tag{4}$$

$$\frac{\delta \Phi}{\delta t} = -\frac{p_a}{\rho_w} - g\eta - \left(\frac{1}{2}\nabla\Phi - \bar{v}\right)\cdot\nabla\Phi, \forall p \in \Gamma_f \tag{5}$$

where $\bar{r}$ is the position vector of the water particle p and $\eta(t)$ the free surface elevation. The operator $\delta(\cdot)/\delta t = \partial(\cdot)/\partial t + \bar{v} \cdot \nabla(\cdot)$. Depending on the values $\bar{v}(t,p)$ assumes, Eq.s (4) and (5) provide both the Eulerian and the Lagrangian description of the freesurface fluid particle, i.e.

$$\bar{v}(t,p) = \begin{cases} 0 & \text{Eulerian description} \\ \nabla\Phi(t,p) & \text{Lagrangian description} \end{cases}$$

The operator δ turns out to be either the material derivative or the partial time derivative when the Lagrangian or Eulerian description is respectively requested.

2.3 *On the transition between the linear and fully nonlinear models*

At the end sections of each spatial subdomain Ω_{i_b}, the linear wave theory is used to provide the boundary and initial conditions to the FNL solver. Coupling a linear solution with a fully nonlinear solver is formally incorrect causing numerical instabilities. The sources of inconsistency are: *a*) transition from linear to nonlinear (and vice-versa) solution; *b*) transition from Eulerian

to Lagrangian (and vice-versa) description of the free-surface evolution. Type *a*) inconsistency is faced with both a temporal ramp (for the Initial Value Problem, IVP) and damping functions at both ends of the spatial domain (for the BVP) (Dommermuth 2000, Cointe 1990). Type *b*) is addressed using ramp functions to smoothly switch in space and time $\bar{v}(t,p)$ from zero to $\nabla\Phi(t,p)$ and vice versa (see Eq.s (4) and (5)).

2.4 *The fully nonlinear solution*

The solution of the fully nonlinear time depending free-surface problem is based on a two-step Mixed Eulerian-Lagrangian (MEL) approach, which splits the problem into a kinetic and time evolution subparts.

In the Eulerian step, at a given time instant, the solution of the Boundary Value Problem (BVP) for the Laplace equation with mixed Dirichlet and Neumann boundary conditions is reformulated in an integral representation of the velocity potential (using Green's second identity). The boundary integral equation is discretized in space by means of quadratic isoparametric boundary elements (Brebbia & Dominguez 1998). We refer to (Marino, Lugni, & Borri 2013, Marino 2011) for additional details.

The Lagrangian step (time evolution) consists in the time integration of Eq.s (4) and (5) where the potential and the free-surface profile at the new time step $t+dt$ are provided. The fourth-order Runge-Kutta (RK4) algorithm is used for the time integration scheme.

3 SECOND ORDER NONLINEAR IRREGULAR WAVES

The second-order wave theory is implemented starting from the second order velocity potential. To solve Laplaces equation with nonlinear boundary conditions a perturbation approach is used (Sharma & Dean 1979). The free surface elevation $\eta(t)$ is described as a sum of a first-order term $\eta_1(t)$ and a second-order term $\eta_2(t)$. The first-order contribution comes from the sum of all the wave components used to discretize the wave spectrum

$$\eta_1(t) = \sum_{m=1}^{N} A_m cos(\omega_m t - \phi_m) \tag{6}$$

The second-order term is obtained as sum of differences and sums of frequencies as follows

$$\eta_2(t) = \eta_2^-(t) + \eta_2^+(t) \tag{7}$$

$$\eta_2^{\pm}(t) = \sum_{m=1}^{N}\sum_{n=1}^{N}[A_m A_n\{B_{mn}^{\pm} cos((\Psi_m \pm \Psi_n)\}] \tag{8}$$

In the equations above $\Psi_m = \omega_n t - \phi_m$, $\Psi_n = \omega_n t - \phi_n$. A_n, A_n, ω_n and ω_n are, respectively, the amplitude and the circular frequency of the m-th and n-th wave components. B_{mn}^- and B_{mn}^+ are the second order transfer functions (Sharma & Dean 1979).

Similarly, the second-order velocity potential is obtained as a sum of a first order and a second order term $\Phi(t) = \Phi_1(t) + \Phi_2(t)$. $\Phi_2(t)$ is defined by differences and sums of frequencies $\Phi_2 = \Phi_2^- + \Phi_2^+$, where

$$\Phi_2^{\pm} = \frac{1}{4}\sum_{m=1}^{N}\sum_{n=1}^{N}[\frac{A_m A_n g^2}{\omega_m \omega_n}\frac{cosh(k_{mn}^{\pm}(h+z))}{cosh(k_{mn}^{\pm}h)} \frac{D_{mn}^{\pm}}{(\omega_m \pm \omega_n)} sin(\psi_m \pm \psi_n) \tag{9}$$

In the above equation $k_{mn}^{\pm} = |k_m \pm k_n|$ and $D_{mn}^{\pm}$ are transfer functions (not reported here, see (Agarwal & Manuel 2011)). The horizontal particle velocity and the horizontal particle acceleration may be obtained with the second order velocity potential by taking the gradient of Φ.

3.1 *Numerical implementation*

The numerical implementation of the 2nd-order theory (as well as the first order theory) may be efficiently performed using the Inverse Fast Fourier Transform (IFFT). First-order terms, that involve single summations, require the definition of the first-order coefficients that, due to the limited space, are nor reported here, see (Agarwal & Manuel 2011).

Using the IFFT, in order to get a result compatible with the period of the simulation desired, a correct discretization of the wave spectrum is needed. Let T_{sim} and N be the simulation time and the number of samples, respectively. The time increment is $\triangle t = T_{sim}/(N-1)$, while the time vector is defined as $t_p = p\triangle t$ with $p = 0, 1, 2 \ldots, N-1$. The increment of the wave circular frequency used to discretize the wave spectrum is $\triangle\omega = 2\pi/(\triangle t N)$ and the frequency vector is defined as $\omega_m = m\triangle\omega$ with $m = 0, 1, 2, \ldots, N-1$. In this way the IFFT returns a correct result compatible with the simulation time T_{sim} and with the number of samples N.

Note that before using the IFFT to compute the 2nd-order terms, Eq. (7) is rewritten as

$$\eta_2^{\pm}(t_p) = \Re\left[\sum_{m=1}^{N}\sum_{n=1}^{N}[X_{mn}^{\pm}\exp(-i(\omega_m \pm \omega_n)t_p)]\right] \tag{10}$$

with

$$X_{mn}^{\pm} = A_m A_n B_{mn}^{\pm} exp(-i(\phi_m \pm \phi_n)) \tag{11}$$

The double summation in Eq. (10) is conveniently rewritten using only one summation. This expedient reduces significantly the computational effort.

$$\eta_2^{\pm}(t_p) = \Re\left[\sum_{j=1}^{N} Y_j^{\pm}\exp(-i(t_p\omega_j)\right] = \Re\left[\sum_{j=1}^{N} Y_j^{\pm}\exp\left(-i\left(\frac{2\pi jp}{N}\right)\right)\right] \tag{12}$$

Table 1. Key properties of the NREL 5-MW BaselineWind Turbine.

Rating Power	5 MW
Rotor Orientation, Configuration	Upwind, 3 Blades
Rotor, Hub Diameter	126 m, 3 m
Hub Height	90 m
Cut-In, Rated, Cut-Out Wind Speed	3 m/s, 11.4 m/s, 25 m/s
Cut-In, Rated Rotor Speed	6.9 rpm, 12.1 rpm
Rated Tip Speed	80 m/s
Rotor Mass	110 t
Nacelle Mass	240 t
Tower Mass	347 460 t
Pile length, diameter	30 m, 6 m
Tower top diameter, wall thickness	3.87 m, 0.019 m
Pile wall thickness, total weight	0.060 m, 187.90 t

The term within the summation in Eq. (12) is the definition of the IFFT of $Y_j^{\pm}$. The second-order Fourier coefficients $Y_j^{\pm}$ are given as follows

$$Y_j^+ = \sum_{j=m+n-1} \sum X_{mn}^+ \quad \text{and} \quad Y_k^- = \sum_{k=|m-n|+1} \sum X_{mn}^- \quad (13)$$

In the computation of Y_j^+ and Y_k^- it is necessary to consider all the pair of frequencies that yield to values of j and k included between 1 and N. The second order wave kinematics components may be evaluated using the same procedure and changing only the expression of the Fourier coefficients (Agarwal & Manuel 2011).

4 5-MW WIND TURBINE REFERENCE MODEL

The turbine model used in this study is the 5-MW Reference Wind Turbine for Offshore System Development (Jonkman, Butterfield, Musial, & Scott 2009), whose main characteristics are listed in Table 1. Further details are available in (Jonkman, Butterfield, Musial, & Scott 2009), (Kooijman, Winkelaar, & van der Hooft 2003) and their bibliography. The diameter and the wall thickness vary linearly with the tower height. The base diameter of 6 m is equal to the diameter of the monopile.

5 EFFECTS OF WAVES MODELS ON THE TURBINE RESPONSE

The following results are obtained reproducing a sea state characterized by the $H_s = 6$ m and $T_p = 9.8$ s and a mean hub-height wind speed $U = 24.00$ m/s (Faltinsen 1990). Given that this wind speed is below the cut-out level, the turbine can be either in parked configuration or in power production. The following results are limited to the parked case obtained turning the blades pitched to feather (at a pitch angle of 90°). A total simulation time of 915 s is reproduced.

The domain decomposition strategy is applied considering a steepness threshold $ka_{\min} = 0.22$ which, in the present simulation, is exceeded three times, see Table 2. The selected sea state has a mean wavelength $\lambda = 90.23$ m. The subdomain sizes are $\delta x_t/\lambda = 1.5$, $\delta_1 t_{i_b}/T_p = 14$, $\delta_2 t_{i_b}/T_p = 6$.

Table 2. Time instants and steepnesses of the nonlinear events detected in the simulation.

Number of subdomains	3
$\bar{t}_{\bar{b}}$ [s]	[251.05 475.48 799.77]
$\bar{ka}$	[0.23 0.25 0.24]

Figures 3 and 4 show time series of the hub-height longitudinal wind velocity (top panel), the wave elevations (second panel from the top) and the system response: tower-base shear (TwrBsFxt) and bending moment (TwrBsMyt) and, in the bottom panel, the tower-top fore-aft displacement (TTDspFA).

Around $t = 240$ s, see Figure 3, the FNL model with domain decomposition (FNL w dd) confirms its efficiency in capturing the actual nonlinear behavior of the waves. FNL w dd solution is in fact the same as the FNL model without domain decomposition (FNL w/o dd) that is assumed as target solution. Whereas, it is noted that the 2nd-order model underestimates the wave elevation. Approximatively at $t = 235$ s nonlinearities higher than the second order (see red or magenta curves in Figure 3) are responsible for a significant increase of TwrBsFxt and TwrBsMyt peaks. On the contrary, likewise the linear theory (blue curve), the the 2nd-order model (green curve) results inadequate because underestimates the response.

A very similar pattern is observed in Figure 4. At approximatively $t = 475$ s (center of the subdomain), an excellent agreement is observed between the FNL w dd and the target solution FNL w/o dd. This event is clearly characterized by high-order nonlinearities which make the fully nonlinear solver fundamental to properly reproduce the system response. The small differences between the FNL w dd and FNL w/o dd models observed around $t = 410$ s are caused by the ramp functions.

Peaks due to the higher order components, Figure 3 shows that the resonant vibrations of the tower, see from $t = 215$ s on, at 0.28 Hz (its first fore-aft natural frequency) is amplified and it is more persistent when the FNL models (either with or without the domain decomposition) are employed. Differences are also observed in the tower motion shown in Figure 4 (bottom panel) where again the FNL w dd is closer to the FNL w/o dd, whereas the 2nd-order model is more similar to the linear solution.

6 CONCLUSIONS

A comparison among the use of linear, weakly and fully nonlinear (with and without domain decomposition strategy) irregular wave models on the dynamic

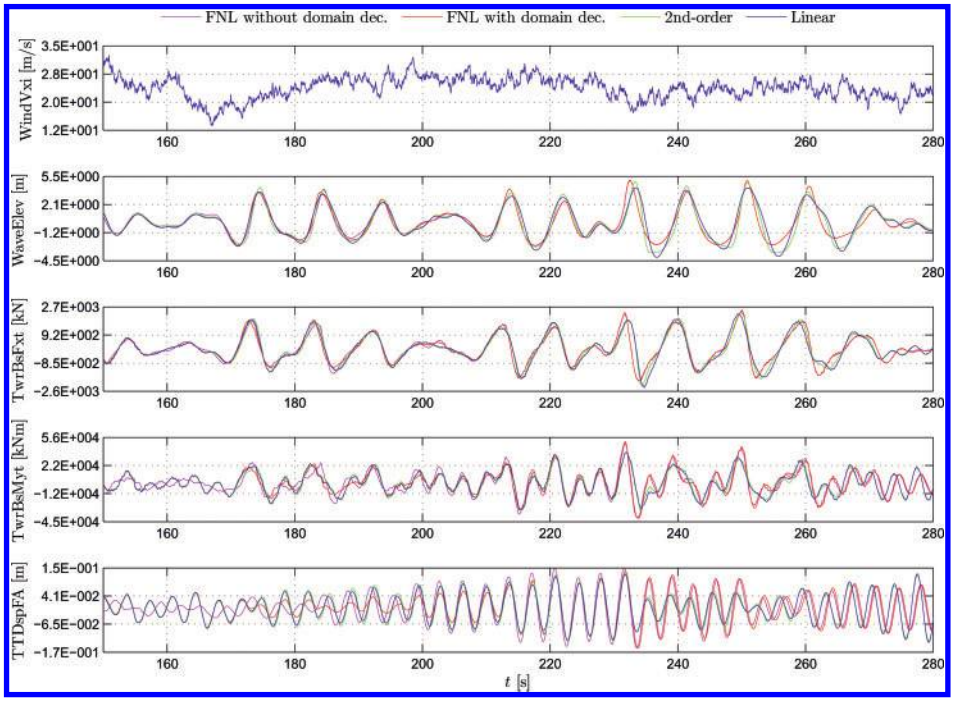


Figure 3. Time series of the hub-height longitudinal wind velocity (m/s), wave elevation (m), tower base fore-aft shear force (MN), tower base fore-aft bending moment (MNm) and tower-top fore-aft deflection (m), corresponding to the linear (blu), second-order (green), FNL with domain decomposition (red) and FNL without domain decomposition (magenta) wave kinematic models. Subdomain 1 of 3.

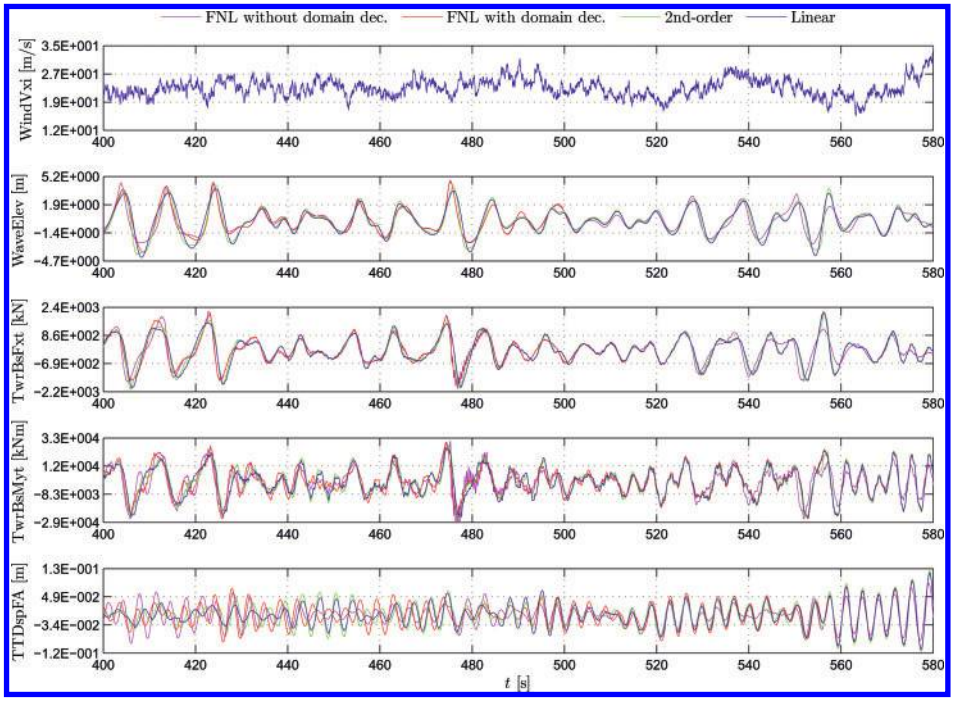


Figure 4. Time series of the hub-height longitudinal wind velocity (m/s), wave elevation (m), tower base fore-aft shear force (MN), tower base fore-aft bending moment (MNm) and tower-top fore-aft deflection (m), corresponding to the linear (blu), second-order (green), FNL with domain decomposition (red) and FNL without domain decomposition (magenta) wave kinematic models. Subdomain 2 of 3.

response of an offshore wind turbine has been presented. The main findings of this preliminary study is that 2nd-order components in the wave kinematics are often not able to reproduce the actual response of the system even for moderate sea states. Moreover, it has been shown that the domain decomposition strategy is very efficient – it permits achieving almost the same accuracy as the FNL model the target solution with a saving of about 50% in terms of computational time. (Note that this reduction can be further reduced by increasing the minimum steepness threshold used to identify the subdomains.). Further developments will improve the domain decomposition technique by coupling linear, 2nd-order and FNL solvers. This will permit a significant reduction of the transition zones further increasing the reliability of the domain decomposition approach.

ACKNOWLEDGMENTS

This work has been partially funded by the Centre of Excellence AMOS, NTNU, Norway and partially by the Flagship Project RITMARE The Italian Research for the Sea coordinated by the Italian National Research Council and funded by the Italian Ministry of Education, University and Research within the National Research Program 20112013.

REFERENCES

Agarwal, P. & L. Manuel (2009). On the modeling of nonlinear waves for prediction of long-term offshore wind turbine loads. *Journal of Offshore Mechanics and Arctic Engineering 131*(4), 041601.

Agarwal, P. & L. Manuel (2011). Incorporating irregular nonlinear waves in coupled simulation and reliability studies of offshore wind turbines. *Applied Ocean Research 33*(3), 215–227.

Brebbia, C. & J. Dominguez (1998). *Boundary Elements, An Introductory Course*. WIT Press, Boston, Southamton.

Cointe, R. (1990). Numerical simulation of a wave channel. *Engineering Analysis with Boundary Elements 7*(4), 167–177.

Dommermuth, D. (2000). The initialization of nonlinear waves using an adjustment scheme. *Wave Motion 32*, 307–317.

Faltinsen, O. M. (1977). Numerical solutions of transient nonlinear free-surface motion outside or inside moving bodies. In *Proc. of 2nd Int. Conf. Num. Ship Hydr.*

Faltinsen, O. M. (1990). *Sea Loads on Ships and Ocean Structures*. Cambridge University.

Grilli, S., J. Skourup, & I. Svedsen (1989). An efficient boundary element method for nonlinear water waves. *Engineering Analysis with Boundary Elements 6*(2), 97–107.

Grilli, S. & I. Svendsen (1990). Corner problems and global accuracy in the boundary element solution of nonlinear wave flows. *Engineering Analysis with Boundary Elements 7*(4), 178–195.

Jonkman, J. & M. Buhl (2005). FAST User's Guide. Technical Report NREL/EL-500-38230, National Renewable Energy Laboratory, Golden, CO.

Jonkman, J., S. Butterfield, W. Musial, & G. Scott (2009). Definition of a 5-mw reference wind turbine for offshore system development. Technical report, NREL.

Kooijman, H.J.T. and Lindenburg, C., D. Winkelaar, & E. van der Hooft (2003). Dowec 6 mw pre-design aeroelastic modelling of the dowec 6 mw pre-design in phatas. Technical report, DOWEC-F1W2-HJK-01-046/9 public version.

Longuett-Higgins, M. S. & E. D. Cokelet (1976). The deformation of steep surface waves on water. i a numerical method of computation. In *Proc. R. Soc. London A*, Volume 350, pp. 1–26.

Marino, E. (2011). *An Integrated Nonlinear Wind-Waves Model for Offshore Wind Turbines*. FUP, Firenze University Press.

Marino, E., C. Borri, & C. Lugni (2011). Influence of wind-waves energy transfer on the impulsive hydrodynamic loads acting on offshore wind turbines. *Journal of Wind Engineering and Industrial Aerodynamics 99*, 767–775.

Marino, E., C. Borri, & U. Peil (2011). A fully nonlinear wavemodel to account for breaking wave impact loads on offshore wind turbines. *Journal of Wind Engineering and Industrial Aerodynamics 99*, 483–490.

Marino, E., C. Lugni, & C. Borri (2013). A novel numerical strategy for the simulation of irregular nonlinear waves and their effects on the dynamic response of offshore wind turbines. *Comput. Methods Appl. Mech. Engrg. 255*, 275–288.

Moriarty, P. J. & A. C. Hansen (2005). Aerodyn theory manual. Technical report, NREL/EL-500-36881.

Nakayama, T. (1983). Boundary element analysis of nonlinear water wave problems. *International Journal for Numerical Methods in Engineering 19*(7), 953–970.

Nakayama, T. (1990). A computational method for simulating transient motions of an incompressible inviscid fluid with a free surface. *International Journal for Numerical Methods in Fluids 10*(6), 683–695.

Ogilvie, T. F. (1967). Nonlinear high-froude-number free surface problems. *J. of Engineering Mathematics 1*(3), 215–235.

Sharma, J. & R. Dean (1979). Development and evaluation of a procedure for simulating arandomdirectional second-order sea surface and associatedwave forces. *Tech. rep. ocean engineering report no. 20*.

Research and Applications in Structural Engineering, Mechanics and Computation – Zingoni (Ed.)
© 2013 Taylor & Francis Group, London, ISBN 978-1-138-00061-2

Structural health monitoring for life-cycle estimation of on-shore wind energy converters

R. Höffer, D. Hartmann, S. Lachmann, X. Liu & K. R. Leimbach
Ruhr-Universität Bochum, Faculty of Civil and Environmental Engineering Sciences, Germany

ABSTRACT: The necessity for service and health monitoring for the detection of damages of the structure of Wind Energy Converters (WEC) is science-based as the main hypothesis of this paper. A modern monitoring concept is explained and a damage detection methodology by system identification is adopted. The sensor instrumentation at a reference wind energy converter WEC is shown which forms one of the fundaments of a tailor-made automatic service and health monitoring system. Data from 3D accelerometers, displacement transducers, thermo-elements and 3D ultrasonic wind speed anemometers is continuously logged and stored in a long-term database. In a first step, spatial stress cycles are evaluated from compensated displacement time histories and used for a service strength check of the steel shaft of the WEC. Such approach permits a realistic estimate of damage accumulation and a subsequent estimation of the residual structural life time. In a second step, possible structural damages shall be detected and localized. This requires a drastic increase of the scanning density of displacement quantities. Suitable measurement solutions are described.

1 INTRODUCTION

The direct excitation of structural oscillations of a WEC is in general due to wind forces from stochastic turbulence and from the non-homogeneities of the flow in the wake of windward positioned converters in group configurations. In addition, control errors of the actuators of the blades, hunting (oscillating) of the electric generator and interactions with main fluctuations can amplify vibrations of the entire system. The susceptibility of the plants grows as the next converter generation has larger rotor diameters and hub heights. Obviously, in the future, such wind park configurations will become customary. In this context, main fluctuation due to labile energy feeding input can be more relevant than in the past. Also, investments for surveying and maintenance of wind energy plants will follow the modern concepts mentioned above. The demand of a basic concept for the service and repair that can be applied to the structure of wind turbines is that repair and/or strengthening can be planned and conducted with minimized investments and losses of service time ensuring a reliable serviceability.

Monitoring can be a qualified basis for continuous strength checking of the structure of wind converters. In recent years, structural elements of wind energy converters have been monitored in order to control and steer the blade and gear configuration during power production, to alert about dynamic overloading, and to detect dangerous conditions such as icing. New and modern monitoring concepts aim more at the identification of present or developing damages to provide an advanced estimation of the residual lifetime of the structure of the wind turbine.

To this, the applied sensor systems for periodical and/or continuous monitoring are predominantly acceleration sensors, cycle transmitters, strain-gauges, and inductive displacement transducer, where the accuracy of such systems depends strongly on the local peculiarities. Previous sensor systems have mainly been used for sensing purposes within a specified recording concept. By contrast, relatively new applications employ optical displacement detectors or radar interferometers. Both devices are mostly based at an outside reference positions adjacent to the WEC.

New research aims at the detecting of detrimental alterations of system responses including the rotor, the transmitting power train, the gear mechanism, the generator as well as its interaction with the electricity network, and the load bearing structure of a WEC. To this end, the determination of clear indications for present damages or developing deteriorations using a remote observation data base is mandatory (Volkmer et al. 2011; Lachmann et al. 2011b). A further target is the use of the sensing data for life cycle management strategies.

2 MONITORING SYSTEM

2.1 *Monitoring system and evaluation of stress resultants*

The object of this pilot application is a WEC which has been in operation for the past sixteen years. The present instrumentation concept (Höffer et al. 2012), of the monitoring system has been installed on the WEC four and a half years ago as shown on Figure 1. Following this concept six three-dimensional accelerometers, six

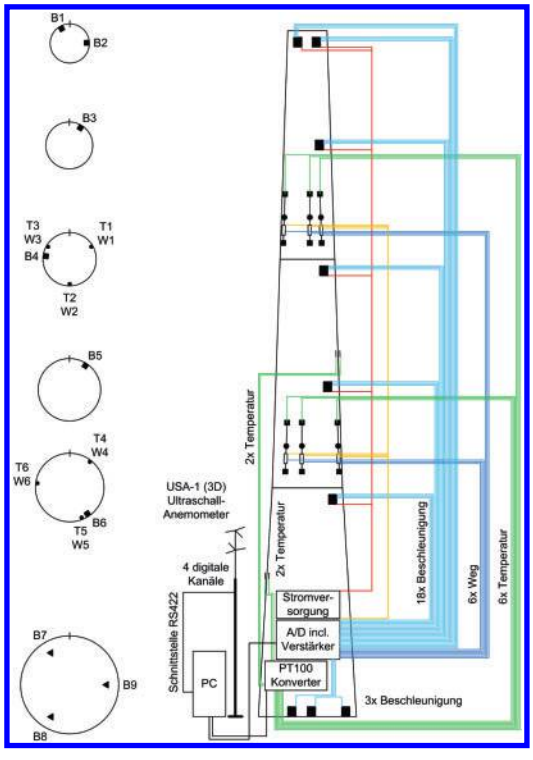


Figure 1. Schematic of the data-acquisition system.

inductive displacement transducers and ten temperature sensors have been installed on the steel tower of the WEC. The accelerometers are distributed over five levels. They mainly serve to identify the free vibration frequencies and mode shapes of the tower structure. The displacement transducers are arranged on two levels each with an angular spacing of approximately 120 degrees. Their nominal range amounts to 5 mm.

If linear material behavior is assumed, the vertical length variations, which are collected over a distance of 500 mm, can be transformed into a corresponding stress distribution of the steel tower. To eliminate the thermal effect of within the measured displacements the temperature of each round steel bar connected to the displacement transducers is measured with a surface temperature sensor. There are two additional points on different elevations on the tower equipped with inner and outer temperature sensors for measuring the temperature gradient of the tower wall.

In addition, three seismic accelerometers have been installed on the foundation. For continuous monitoring of the horizontal wind speed, the wind direction, the vertical wind component and the air temperature, a three-dimensional ultrasonic anemometer is placed on a telescopic mast at an elevation of thirteen meters above ground, adjacent to the tower. The sensing data are collected through three different dataloggers, which are connected to the on-site computer. This computer is also charged with the transfer of the measured data via a high-speed internet connection to

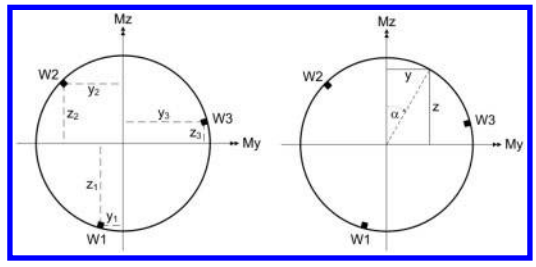


Figure 2. Definition of coordinates for stress analysis.

a remote server system. The latter resides on the remote computer, to synchronize and to transfer the data to a relational database, at which a multi-agent software technology is utilized. For interrogation purposes, the database can be easily accessed by a web-service enabling the creation of plots of various measured signals in parallel.

Signals provided by the customer interface of the wind turbine are logged synchronously such that meaningful comparisons are possible. Details included are the rotor speed in revolutions per minute of the rotor, the amount of electrical power, the azimuth angle of the rotor, the pitch angles of the rotor blades, and the wind speed measured by a cup anemometer at 67 m above ground.

The fatigue analyses (Lachmann & Höffer 2013), are conducted at two levels at elevations 21.5 m and 42.5 m, where the displacement transducers are installed. In relation to a reference length of 500 mm the strains and stresses in the tower wall can be calculated from the measured displacements following the linear elasticity theory. With a structure-embedded coordinate system (Fig. 2) having been defined, the stress plane and the fluctuating parts of the bending moments can be calculated. The fluctuating stresses in each point of the circumference of the steel tower can determined from the fluctuating bending moments.

The fluctuating normal stress, σ_N, is computed as the geometric average of the three measured stresses σ_1, σ_2, σ_3. The fluctuating bending moments can be determined from measured stresses of two sensors. The fluctuating stresses $\Delta\sigma$ at an arbitrary point on the circumference at the angle a is computed from

$$\Delta\sigma(\alpha) = \frac{\Delta My}{Iy} \cdot z(\alpha) + \frac{\Delta Mz}{Iz} \cdot y(\alpha) \qquad (1)$$

2.2 *Rainflow-analysis of fluctuating stresses*

For the analysis of the stress time series a counting procedure is applied. A classification of each single value of the time series is performed before the count of the fluctuating stresses can be performed. In the present application each class equals a bending moment of 10 kNm. On the level of elevation 42.5 m with an elastic modulus of 37899 cm^3 this equals $\Delta\sigma$ of 0.26386 N/mm^2. For the analysis of the classified stresses (Fig. 3) the specific rainflow counting method “Rainflow-HCM” (Clormann and Seeger

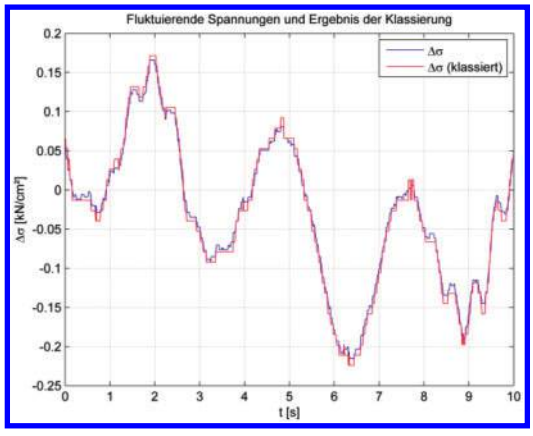


Figure 3. Computed and classified stresses.

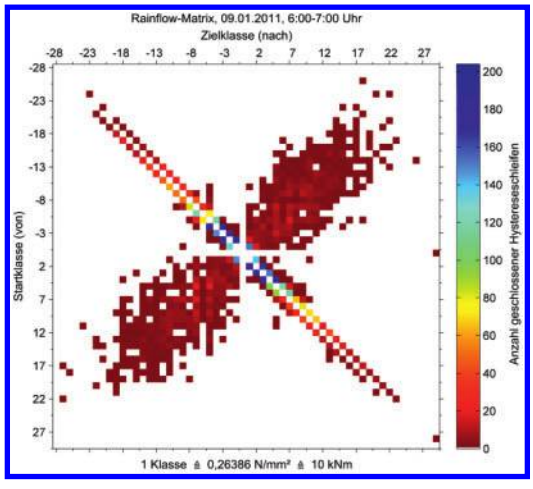


Figure 4. Result of rainflow counting for one hour.

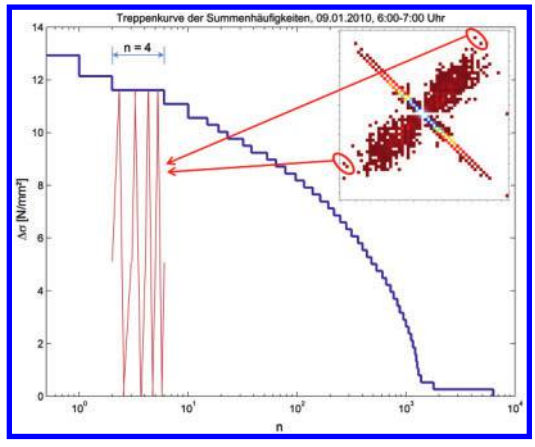


Figure 5. Diagram of accumulated summation of one hour.

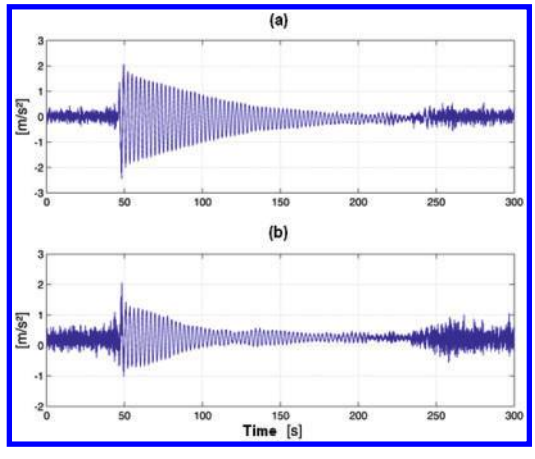


Figure 6. Measured accelerations at B1 during the impulse event: (a) forward-aft; (b) side-to-side.

1986) is used. The result of the counting procedure is in general in a quadratic format (Fig. 4). A closed hysteresis loop is arranged in the matrix by its start and target classes. A closed hysteresis loop starts in the target class, arrives and turns around in the start class and closes in the target class.

The rainflow matrix can easily be transformed into a matrix of mean values and amplitudes, which then can be used to build a spectrum of amplitudes of stress cycles. It is generally assumed that mean stresses have no significant influence on the fatigue strength of welded structures and thus can be neglected. Such an assumption is also adopted for the application of design codes for wind energy converters (Deutsches Institut für Bautechnik 2004, Germanischer Lloyd 2010) also referring to Eurocode 3, DIN EN 1993-1-9. According to the above regulatory codes the threshold value of fatigue strength for more than 10^8 load cycles must not be used. Instead, for more than 10^8 load cycles the Wöhler diagram is extended with a slope of m = 5. Figure 4 shows the result of a rainflow counting for one hour. Neglecting the average values of the rainflow matrix a stress collective is evaluated in Figure 5 which shows an incremented diagram over a time period of one hour. Four stress double amplitudes with a range of 11.6098 N/mm^2 are identified.

3 LIFE-CYCLE ASSESSMENT AFTER AN IMPULSIVE EVENT

Within the rainflow counting process of the year 2010 it was discovered that the dimensions of the rainflow matrix abruptly increased in size. The stress time histories of 11 February 2010 from 2.00 to 3.00 pm result in a 173 by 173 rainflow matrix. The residua (hysteresis loops that are not closed) are arranged in advance of the subsequent hour's worth of records. The results for the hour of 3.00 to 4.00 pm of the same day are summarized in a rainflow matrix which now has the dimension of 317 by 317 classes.

The acceleration time histories of a sample period of 300 sec duration (Fig. 6) show an exponentially decaying free vibration. At the beginning of the sample

period the facility is in a regular production process. Suddenly the structural system is subjected to a strong impulse. The wind velocity immediately before the event is about 8 m/sec, the power production of the WEC is about 200 kW. Both values are recorded at t = 45 sec of the sample period.

The acceleration amplitudes of the accelerometer B1 at an elevation of approximately 63 m (Fig. 1) are in the range of 2 m/sec^2 (Fig. 6). The tower vibration after the impulse decays exponentially for about 175 seconds, after which the facility returns to normal production mode. From the consideration of the decaying free vibration curve it is obvious that this curve cannot be responsible for the dimensional growth of the rainflow matrix. This is because in the succession of positive and negative vibration peaks each peak is numerically smaller than the previous one. The consequence of this is that while passing through the decaying vibration diagram none of the hysteresis loops can be closed. The incomplete hysteresis loops will be stored in the residuum at first appearance, until, at a later time, a new event of the same magnitude appears. At this time the hystereses that are still open can be closed. At an earlier time a corresponding impulse event must have occurred.

The high damping of the soil under the foundation restrains the effects of the impulse event to some extent.

3.1 *Comparison with measurements during two overspeed tests*

A comparison of the free vibration acceleration time history of Figure 6 with published results, for example in Devriendt et al. (2012), shows that it is a decaying free vibration after a sudden shut down of the facility. This situation occurs during the conduction of an overspeed test. Two such tests were executed on the present WEC in the course of maintenance work, on 05 October 2012 at 12.41 pm and 01.13 pm. These two overspeed tests were identified by correlating them with the SCADA data.

During the evaluation of the data of the years 2010 to 2012 several hundred impulse events of this type have been discovered in the records. Frequency of occurrence and magnitude of the stress double amplitudes qualify these events to become effective contributors to fatigue. For causing structural damage, however, several ten-thousand such events are required.

4 SYSTEM IDENTIFICATION AND DAMAGE DETECTION

The term “system identification” has been used in a broad context in the technical literature. In structural dynamics, it refers to the extraction of information about the structural behavior from measurement data, without necessarily requesting a numerical model (e.g., identification of the number of active modes or the presence of natural frequencies within a certain frequency range). However, with the increasing use of the numerical model in the analysis of the structural dynamic behavior, the system identification nowadays more often contains the development (or the improvement) of structural models from the measurements performed on the real structure using vibration sensing devices. In this paper, several important aspects are considered in the frame of system identification, including the modal identification technologies, experimentally validated finite element modeling, and its important application in health monitoring, also referred to as damage detection.

4.1 *Modal identification*

Since the WEC is measured under operational condition, the measurement of all natural excitations is impossible; the modal analysis has to be carried out based on the responses only. This modal identification method is called output-only modal analysis or operational modal analysis (OMA). There are two main groups of operational modal analysis: nonparametric methods essentially developed in frequency domain and parametric methods in time domain. In the current work, the Enhanced Frequency Domain Decomposition (EFDD) method (Brincker et al. 2001) in frequency domain and the Stochastic Subspace Identification (SSI) method (Brincker & Andersen 2006) in time domain are employed to extract the modal parameters of the WEC structure.

Table 1 lists the modal parameters of the first six bending modes of the WEC identified from a set of measurements, including three bending modes in wind direction (mode 2, mode 4 and mode 5) and three bending modes parallel to the rotation plane (mode 1, mode 3 and mode 6). By comparing the eigenfrequencies, the EFDD and SSI methods give almost identical results. However, it is very difficult to get accurate estimation of modal damping ratios under ambient loads, and also the related half-power bandwidth damping estimation method of EFDD is not very reliable. Besides, the modal damping ratios vary with the amplitude of the structural response and are influenced by the wind characteristics, which lead to the existence of aerodynamic damping. Therefore, when the accurate identification of modal damping ratios is required, complementary free vibration tests are recommended.

Table 1. Comparison of modal parameters identified by the EFDD and SSI methods.

	Frequency [Hz]			Damping ratio[%]		
	EFDD	SSI	Dev.*	EFDD	SSI	MAC
Mode 1	0.3760	0.3753	0.187	1.603	2.322	0.9668
Mode 2	0.3765	0.3779	0.370	2.252	4.685	0.9689
Mode 3	2.186	2.171	0.691	4.465	1.311	0.9229
Mode 4	2.208	2.217	0.406	3.245	3.485	0.9529
Mode 5	5.730	5.837	1.833	4.590	1.904	0.9903
Mode 6	5.819	5.857	0.649	3.426	1.997	0.9847

*Dev. = deviation [%].

The consistency of the mode shapes has been validated by the modal assurance criterion (MAC) (Allemang 2003), which takes values from 0.0 (representing no consistency) to 1.0 (representing a full consistency). High MAC values in Table 1 indicate that the modes detected by the EFDD method agree very well with those detected by the SSI method.

4.2 *Model updating*

Finite element (FE) model is increasingly used in system identification to generate the structural model matrices and to predict the structural responses. The underlying FE model customarily deviates from the real world system by approximation or even errors in the physical parameters or boundary conditions. Therefore model validation is compulsory to check the FE model through measurements. To this end, an iterative process of minimizing the defect between the model and the actual system behavior is mandatory, which is known as model updating. In continuous monitoring, the model updating is successively requested to accurately represent the current state of the real world system including damages and deteriorations. With this aim a unifying framework of model updating is developed involving efficient parameter selection method and simulation-based multi-criteria optimization.

Specifying the updating parameters is one of the most difficult yet most critical steps in the whole updating process. The number of updating parameters should be large enough to cover all the relevant uncertain parameters, but as low as possible to avoid ill-conditioning. Rather than using solely engineer's judgment, the error localization method is straightforward and more reliable for selection of updating parameters. The present error localization method bases on the concept of Equivalent Element Modal Strain Energy (EEMSE) (Zang et al. 2008) and makes use of the substructuring technique.

The updating process is dealt with as a simulation-based multi-criteria optimization problem. Formulation of the objective function involves a priori articulation of preferences and the weighted Chebyshev method (Miettinen 1999). Defects between the model and the real structure are measured by modal-domain data (eigenfrequencies and mode shapes) and space-scale-domain data (wavelet modulus), in which the latter is more damage-sensitive and specially used in the process of damage integration.

Furthermore, because the model updating constitutes a simulation-based optimization and the existing simulation software offers normally no powerful optimization tools, the Java-based optimization framework, MOPACK (Nguyen et al. 2010), is adopted in this approach and a simulation adapter is developed to integrate different simulation software into MOPACK. Due to the complexity of the optimization problem, the evolutionary algorithms (EAs) (Eiben 2002) instead of the traditional deterministic techniques have to be considered. The enhanced evolution strategy (EES) (Rechenberg 1973) and the differential evolution strategy (DE) (Storn & Price 1997), in the class of EAs, are employed in the representative numerical test, with which the effectiveness of the proposed solution concept are demonstrated.

4.3 *Damage detection*

Based on the demand of an efficient and robust non-destructive damage detection method for WECs as well as the distinct advantages of the wavelet transform, an integrated wavelet-based damage detection method is presented to accurately detect and localize incipient damage of WEC under operational condition.

The method uses the identified mode shapes as spatial signals and takes synergistic advantages of the stationary wavelet transform (SWT) and the continuous wavelet transform (CWT) (Daubechies 1992). The procedure consists of the following consecutive steps:

1. Signal decomposition. Multilevel wavelet decomposition by SWT is performed on the signal to extract details which keep track of the fluctuations in the signal.
2. Damage localization. By performing CWT on selected details and plotting the wavelet map, discontinuities on the signal can be indicated by peaks in the wavelet modulus. The possible damage position is identified by the abscissa where the line of modulus maxima progresses to fine scales.
3. Damage quantification. To find an effective criterion to quantify the damage extent, the largest wavelet modulus and the Lipschitz exponent (Mallat 2009) are considered. After comparing these two criteria, the largest wavelet modulus is preferred for quantification of small damage.

5 CONCLUSIONS

The presented method is conducted on several numerical tests and on data of an pilot experiment and the following advantages have been demonstrated:

- It is a global non-destructive evaluation technique for locating incipient damage, no prior knowledge of the damage position is required;
- The method can be performed on the large-scale in-service structures under operational condition;
- Intact modes are not necessary if the structure does not contain discontinuities or a reliable finite element model exists;
- No need of higher order modes, only the first four modes are enough for the investigated WEC for instance;
- Relatively small number of sensors are used, e.g., 19 sensors are simulated in the test case;
- Edge effect is eliminated so that damage near boundaries could also be detected;
- Influence of measurement noise on mode shapes can be measured by the indicator of normalized modal difference and reduced using statistical methods.
- The Palmgren-Miner approach in combination with Rainflow Counting of stress cycles at selected

positions of the steel shaft is used. An extension of the approach in order to detect and localize discrete structural damages requires a drastic increase of scanning density of time histories of wind forces, displacements over height, and other related operation values. First results of a conceptual study show that new, innovative sensor instrumentations are required to improve accuracy and precision of the displacement data. Respective sensor systems and measurement strategies have recently become available.

- Verification through real measurement data is of particular interest since noise or measurement errors are present in the signals, which will examine the practicality of the proposed method.
- In the future, special actuators will increasingly be employed as well to be able to instantaneously counteract excessive operational demands.

AKNOWLEDGEMENTS

The financial support of the project through the German Research Foundation DFG under the project numbers HA 1463/20-1 and HO 3286/1-2, and the kind cooperation of the operator of the reference wind converter, the public utility company DEW 21 of the City of Dortmund, is gratefully acknowledged.

REFERENCES

Allemang, R. J. August, 2003. The modal assurance criterion – Twenty years of use and abuse. *Sound and vibration* 37(8), 14–21.

Brincker, R. & Andersen, P. 2006. Understanding Stochastic Subspace Identification. *In the 24th International Modal Analysis Conference (IMAC).*

Brincker, R. Zhang, L. & Andersen, P. 2001. Modal identification of outputonly systems using Frequency Domain Decomposition. *Smart Mater. Struct*. 10, 441–445.

Clormann, H. and Seeger, T. 1986. RAINFLOW – HCM, Ein Zählverfahren für Betriebsfestigkeits-nachweise auf werkstoffmechanischer Grundlage, *Stahlbau*, Volume 55, No. 3, pp. 65–71

Daubechies, I. 1992. Ten lectures on wavelets. Philadelphia and PA: Society for Industrial and Applied Mathematics.

Deutsches Institut für Bautechnik. 2004. Richtlinien für Windenergieanlagen – Einwirkungen und Standsicherheitsnachweise für Turm und Gründung. Fassung März 2004, Berlin, Germany.

Devriendt, C., Jordaens, P. J., De Sitter, G., Guilleaume, P. 2012. Damping Estimation of an Offshore Wind Turbine on a Monopile Foundation, *EWEA Conference 2012*, Copenhagen, Denmark, 04/2012.

Eiben, A. E. 2002. Evolutionary computing: the most powerful problem solver in the universe. *Dutch Mathematical Archive*, 126–131.

Germanischer Lloyd. 2010. Richtlinie für die Zertifizierung von Windkraftanlagen, Vorschriften und Richtlinien, IV – Teil 1, GL 2010, Hrsg. Germanischer Lloyd, Hamburg.

Höffer, R., Lachmann, S. & Hartmann, D. 2012. Conceptual study on instrumentation for displacement based service strength checking of wind turbines, *The 14th International Conference on Computing in Civil and Building Engineering.* Moscow, Russia, 06/2012.

Lachmann, S. & Höffer, R. 2013. Turm- und Fundamentschwingungen einer Windenergieanlage infolge impulsartiger Erregung durch Stoppzyklen, *4. VDI-Fachtagung Schwingungen von Windenergieanlagen 2013*. Bremen, Germany, 02/2013.

Mallat, S. G. 2009. A wavelet tour of signal processing: The sparse way (3 ed.). Amsterdam and and Boston: Elsevier/Academic Press.

Miettinen, K. 1999. Nonlinear multiobjective optimization. Boston: Kluwer Academic Publishers.

Nguyen, V. V., Hartmann, D. Baitsch, M. & König, M. 2010. A distributed agent-based approach for robust optimization. *In 2nd International Conference on Engineering Optimization*.

Rechenberg, I. 1965. Cybernetic solution path of an experimental problem.

Storn, R. & Price, K. 1997. Differential evolution – a simple and efficient heuristic for global optimization over continuous spaces. *Journal of Global Optimization* 11(4), 341–359.

Volkmer, P., Mueller, F., Volkmer, D. & Schollbach, D., 2011. Zustandsueberwachung von Rotorblaettern an Windkraftanlagen zur Erkennung von Rotorblattschaeden, von Vereisungen und dynamischen Lasten. *VDI-Berichte Nr. 2123*, pp. 145–157.

Zang, C., Schwingshackl, C. & Ewins, D. J. 2008. Error localization in an FE model in model updating process using supermodels. In proceedings of ISMA 2008: International conference on noise and vibration engineering, vols. 1–8, pp. 1923–1936.

15. Cold-formed steel structures, thin-walled sections

Research and Applications in Structural Engineering, Mechanics and Computation – Zingoni (Ed.)
© 2013 Taylor & Francis Group, London, ISBN 978-1-138-00061-2

Analysis and design of perforated cold-formed steel members in compression

Z. Yao & K.J.R. Rasmussen
School of Civil Engineering, University of Sydney, Sydney, Australia

ABSTRACT: The paper presents a parametric study of the strength of a range of perforated structural sections in axial compression subjected to local, distortional, and global flexural or global flexural-torsional buckling, as well as the interactions between the modes. The sections include lipped C-sections with and without web stiffeners, Z-sections, hat sections, and storage rack upright sections. An extensive range of strength data is obtained numerically to cover the influence of the most common parameters defining perforations, including hole width, hole shape, and hole spacing. Based on the strength data, three Direct Strength Method (DSM) design options are evaluated, including two sets of proposed equations. These equations are complemented by a reliability analysis deriving appropriate resistance factors.

1 INTRODUCTION

It is common to punch holes in one or several component plates of cold-formed steel sections to allow either easy connection to other members or services to run through walls and floors.

Perforations introduce complex stress distributions which can cause early yielding during loading. The direct consequences of holes are changes in the elastic buckling modes and loads, as well as post-buckling failure modes and ultimate strengths.

To date, the design of perforated thin-walled structures has not yet been comprehensively addressed in current design standards for cold-formed steel members, such as the North American Specification (NAS) (2007) and the Australian/New Zealand Standard AS/NZS 4600 (2005). The available design provisions are usually based on the concept of the Effective Width Method (EWM), and are empirical and limited to certain cross-section configurations, hole sizes, shapes and spacings, etc.

As an alternative to the traditional EWM, the Direct Strength Method (DSM) represents an advancement in cold-formed steel design and was first adopted in Appendix I of NAS (2007), and later in Section 7 of AS/NZS 4600 (2005) for the design of non-perforated cold-formed steel columns and beams. The DSM utilises the elastic buckling loads of the gross section (i.e. $P_{cr\text{-}e}$, $P_{cr\text{-}l}$, and $P_{cr\text{-}d}$ for global, local and distortional buckling respectively) to predict the member ultimate strength, and hence provides engineers with a tool to predict the strength of members of any general cross-sectional shape. These buckling loads correspond to three strength limit states considered in the DSM, i.e. global (G) buckling or yielding, local-global (LG) buckling interaction, and distortional (D) buckling. Their respective equations for non-perforated columns are summarised as follows:

(i) Nominal global buckling strength, P_{ne}:

$$\text{For } \lambda_c \le 1.5: \quad P_{ne} = \left(0.658^{\lambda_c^2}\right) P_y \tag{1}$$

$$\text{For } \lambda_c > 1.5: \quad P_{ne} = \left(\frac{0.877}{\lambda_c^2}\right) P_y \tag{2}$$

where $\lambda_c = P_y / P_{cr\text{-}e})^{0.5}$ and $P_y = A_g F_y$.

(ii) Nominal local buckling (including local-global (LG) buckling interaction) strength, P_{nle}:

$$\text{For } \lambda_{le} \le 0.776, \quad P_{nle} = P_{ne} \tag{3}$$

$$\text{For } \lambda_{le} > 0.776, \quad P_{nle} = \left[1\text{-}0.15\left(\frac{P_{cr\text{-}l}}{P_{ne}}\right)^{0.4}\right]\left(\frac{P_{cr\text{-}l}}{P_{ne}}\right)^{0.4} P_{ne} \tag{4}$$

where $\lambda_{le} = (P_{ne}/P_{cr\text{-}l})^{0.5}$.

(iii) Nominal distortional buckling strength, P_{nd}:

$$\text{For } \lambda_d \le 0.561, \quad P_{nd} = P_y \tag{5}$$

$$\text{For } \lambda_d > 0.561, \quad P_{nd} = \left[1\text{-}0.25\left(\frac{P_{cr\text{-}d}}{P_y}\right)^{0.6}\right]\left(\frac{P_{cr\text{-}d}}{P_y}\right)^{0.6} P_y \tag{6}$$

where $\lambda_d = (P_y / P_{cr\text{-}d})^{0.5}$. The nominal design strength P_n of a column is $P_n = \min(P_{nle}, P_{nd}, \text{and } P_{ne})$.

Based on the DSM, recent studies (Tovar and Sputo, 2005, Moen and Schafer, 2011) were carried out to incorporate the effect of openings into the DSM to determine the ultimate capacity of perforated C-section columns and beams. In particular, Moen and Schafer (2011) derived a set of design equations for perforated cold-formed steel columns which

worked in harmony with the existing DSM design rules. By using the simplified methods described in (Moen and Schafer, 2009), the influence of holes was considered in the local, distortional, and global elastic buckling loads (i.e. $P_{cr\text{-}l\text{-}h}$, $P_{cr\text{-}d\text{-}h}$, and $P_{cr\text{-}e\text{-}h}$) of the columns. Six different design options were evaluated using 78 experimental and more than 200 FE simulated column data. The best-performing design option limited the LG buckling strength in Eqns. (3)–(4) to P_{ynet}, and modified the distortional buckling strength Eqns. (5)–(6) to:

$$\text{For } \lambda_d \le \lambda_{d1},\quad P_{nd} = P_{ynet} \tag{7}$$

$$\text{For } \lambda_{d1} < \lambda_d \le \lambda_{d2},\quad P_{nd} = P_{ynet} - \left(\frac{P_{ynet} - P_{d2}}{\lambda_{d2} - \lambda_{d1}}\right)\left(\lambda_{d2} - \lambda_{d1}\right) \tag{8}$$

$$\text{For } \lambda_d > \lambda_{d2},\quad P_{nd} = \left[1\text{-}0.25\left(\frac{P_{cr\text{-}d\text{-}h}}{P_y}\right)^{0.6}\right]\left(\frac{P_{cr\text{-}d\text{-}h}}{P_y}\right)^{0.6} P_y \tag{9}$$

where $\lambda_d = (P_y / P_{cr\text{-}d\text{-}h})^{0.5}$, $\lambda_{d1} = 0.561\left(P_{ynet} / P_y\right)$,

$\lambda_{d2} = 0.561\left(14\left(P_y / P_{ynet}\right)^{0.4} - 13\right)$,

$P_{d2} = \left(1\text{-}0.25\left(1/\lambda_{d2}\right)^{1.2}\right)\left(1/\lambda_{d2}\right)^{1.2} P_y$

2 PARAMETRIC STUDY

A parametric study was carried out by means of nonlinear finite element modelling in ABAQUS on 146207 perforated and non-perforated cold-formed steel columns. These simulations included five cross-section types (i.e. C, stiffened C, Z, rack, and hat sections) which were predisposed to three major buckling modes (i.e. local (L), distortional (D) and global (G)) and all the possible interactions between them (i.e. LD, LG, DG, and LDG). Table 1 summarises the section shapes, and for each predisposed failure mode the number of sections and collapse analyses, as well as the ranges of cross-sectional local and distortional slenderness and member global slenderness. The three finite element models used in the parametric study are shown in Figure 1–Figure 3, for columns predisposed to L, D, and G modes, respectively. In general, these models comprised a certain number of buckling half-wavelengths, i.e. three for local, four for distortional, and one for global failures, with the half-wavelengths calculated by the Finite Strip Method based on the gross section. Corner restraining systems were provided for the columns predisposed to local and distortional failures in order to induce the desired failure modes. Each set of corner restraints was placed between the buckling half-waves. Besides, both ends of all the columns were supported on rigid plates, and a compressive displacement was applied to the section centroid through a rigid plate. Shell elements S9R5 were used to mesh the columns.

The material properties used in the parametric studies conformed to the limits specified in the current codified DSM. The stress-strain curve was specified

Table 1. Summary of analyses in the parametric study.

Section shape	Predisposed buckling type	No. of sections	No. of collapse analyses by FEM	Slenderness: L: $\lambda_l = (P_y / P_{cr\text{-}l})^{0.5}$ D: $\lambda_d = (P_y / P_{cr\text{-}d})^{0.5}$ G: $\lambda_e = (P_y / P_{cr\text{-}e})^{0.5}$
C	L	73	20770	0.39-9.61
	D	73	20521	0.51-4.65
	G	11	28181	0.38-3.15
Z	L	71	6829	0.38-4.15
	D	70	13649	0.51-3.54
	G	23	25907	0.46-3.14
Hat	L	21	2828	0.38-3.53
	D	21	2058	0.52-3.00
	G	13	7031	0.27-3.00
Rack	L	11	920	0.31-3.02
	D	11	1064	0.50-3.00
	G	11	6375	0.30-3.01
stiffened C	L	10	634	0.22-4.67
	D	10	974	0.53-4.06
	G	10	8466	0.28-3.01

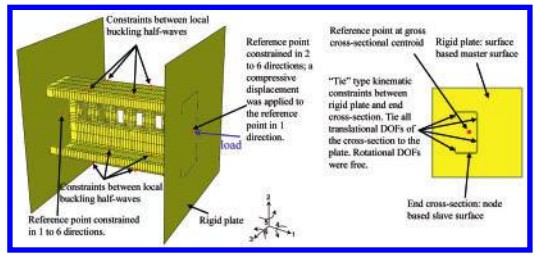


Figure 1. Boundary conditions, restraints, and loading for columns predisposed to local modes.

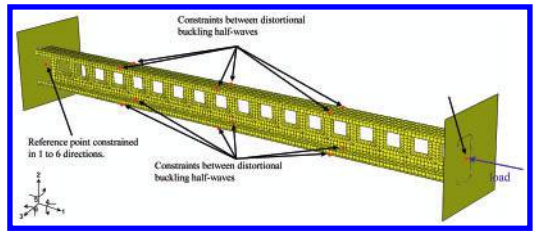


Figure 2. Boundary conditions, restraints, and loading for columns predisposed to distortional modes.

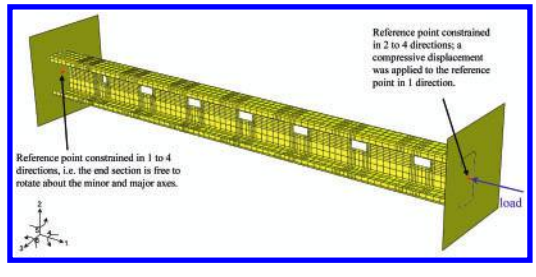


Figure 3. Boundary conditions, restraints, and loading for columns predisposed to global modes.

Table 2. Simulation-to-predicted statistics for all columns failing in different failure modes by Option 4 in (Moen and Schafer, 2011).

Section shape	Failure mode																			
	L				LG				G				D				All L, LG, G, D			
	P_m	V_p	ϕ	n	P_m	V_p	ϕ	n	P_m	V_p	ϕ	n	P_m	V_p	ϕ	n	P_m	V_p	ϕ	n
C	1.078	0.134	0.866	6923	1.031	0.106	0.855	4245	0.940	0.098	0.786	1651	1.231	0.256	0.815	3678	1.086	0.190	0.807	16497
Z	1.067	0.111	0.880	3712	1.109	0.087	0.936	784	1.040	0.045	0.903	2548	1.030	0.097	0.862	2444	1.054	0.095	0.883	9488
Hat	0.852	0.096	0.714	1414	0.952	0.204	0.691	494	1.087	0.044	0.945	137	0.866	0.169	0.664	441	0.887	0.155	0.693	2486
Rack	0.977	0.093	0.820	461	0.872	0.222	0.614	1065	0.990	0.114	0.814	383	0.913	0.093	0.767	391	0.920	0.172	0.702	2300
SC	0.950	0.106	0.787	317	1.018	0.135	0.817	143	1.024	0.067	0.878	196	1.096	0.251	0.733	245	1.016	0.174	0.773	901
All	1.043	0.142	0.830	12827	1.009	0.148	0.796	6731	1.003	0.086	0.847	4915	1.119	0.243	0.759	7199	1.047	0.174	0.796	31672
	LD				DG				LDG				All LD, DG, LDG				ALL Failure modes			
	P_m	V_p	ϕ	n	P_m	V_p	ϕ	n	P_m	V_p	ϕ	n	P_m	V_p	ϕ	n	P_m	V_p	ϕ	n
C	0.881	0.187	0.657	3157	0.836	0.174	0.636	2589	1.060	0.224	0.744	862	0.887	0.206	0.641	6608	1.029	0.213	0.736	23105
Z	0.999	0.122	0.814	4115	0.998	0.109	0.825	2989	1.064	0.159	0.827	6057	1.029	0.143	0.817	1316	1.039	0.125	0.844	22649
Hat	0.775	0.176	0.588	585	0.760	0.278	0.483	1927	0.837	0.240	0.572	964	0.784	0.256	0.520	3476	0.827	0.223	0.582	5962
Rack	0.824	0.101	0.687	137	0.880	0.180	0.663	832	0.895	0.187	0.667	900	0.883	0.181	0.665	1869	0.903	0.177	0.684	4169
SC	0.795	0.187	0.593	245	0.775	0.286	0.486	1727	0.854	0.214	0.609	800	0.800	0.260	0.526	2772	0.853	0.260	0.561	3673
All	0.929	0.172	0.708	8239	0.863	0.223	0.606	1006	1.008	0.201	0.735	9583	0.932	0.211	0.669	2788	0.993	0.199	0.726	59558

by the Ramberg-Osgood expression (Ramberg and Osgood, 1943) using n-values of $n = 5$, 10, and 20. Yield stress enhancement in the corners due to cold work was considered by using the formulae in Clause 1.5.1.2 of AS/NZS 4600.

Initial local, distortional, and global geometric imperfections were imposed on the column models, using the linear elastic buckling modes as the shapes of the geometric imperfections. The magnitudes of the local and distortional imperfections were based on the statistical information provided by (Schafer and Pekoz, 1998), and corresponded to two probabilities of exceedance, i.e. the 25th ($d/t = 0.14$ and 0.64 respectively) and 75th ($d/t = 0.66$ and 1.55 respectively) percentile values, which were used in conjunction with $L/2000$ and $L/1000$ global imperfections. Moreover, the direction of the initial geometric imperfection was explicitly considered in the FE modelling, such as "inward" and "outward" directions for local and distortional imperfections, and bow towards the web or the flanges for global imperfections. It was found that the direction of imperfection can have a profound impact on the structural response and hence the ultimate strength.

Initial residual stresses were not considered in this research, partly because it was reported by (Becque, 2008, Moen and Schafer, 2011) that their inclusion has only minimal influence on the ultimate load-carrying capacity of cold-formed structures and partly because their effect is largely accounted for by using a Ramberg-Osgood stress-strain curve.

The dimensions of the holes are such that the hole width to flat web width ratios were 0, 0.2, 0.4, 0.6 and 0.8, hole length to hole width ratios were 0.5, 1.0, 2.0, and 4.0, and clear hole spacing to hole width ratios were 1.0, 2.0, and 6.0.

3 DESIGN

The column strength database obtained from the parametric studies which involved material models defined by $n = 20$ was used in this paper to evaluate three DSM expressions: the best-performing DSM proposed by Moen and Schafer (2011), and another two methods proposed by the authors (refer to (Yao, 2013) for a total of 19 assessed methods). Statistics, including the mean (P_m) and COV (V_p) of the simulation-to-predicted strength ratios, and the resistance factor ϕ, are calculated for each design method according to the first order second moment (FOSM) reliability analysis outlined in Chapter F of the AISI Specification (NAS, 2007) with the following statistical data: LRFD reliability target index $\beta_0 = 2.5$; mean value of the fabrication factor $F_m = 1.0$ and COV $V_F = 0.05$; mean value of the material factor $M_m = 1.10$ and COV $V_M = 0.10$; representative ratio of dead load to live load $G_n/Q_n = 0.2$; representative ratios of mean dead load to nominal dead load and mean live load to nominal live load of $Q_m/Q_n = 1.0$ and $G_m/G_n = 1.05$; COVs of dead and live loads of $V_D = 0.1$ and $V_L = 0.25$; dead and live load factors of $\gamma_G = 1.2$ and $\gamma_Q = 1.5$; and $C_p = 1$.

3.1 *DSM by Moen and Schafer (2011)*

Using the best-performing DSM method (i.e. Option 4) by Moen and Schafer (2011) described in Section 1, Table 2 presents the statistics of the predictions, along with Figure 4 illustrating the simulation-to-predicted ratios ($P_{u\text{-}FEM}/P_n$) for all perforated and non-perforated columns. The results are classified by failure mode, represented by L, LG, G, D, LD, DG, and LDG.

In general, Option 4 in (Moen and Schafer, 2011) performed better than the existing DSM (results not included in this paper) in terms of a higher P_m value (0.993 vs. 0.929 by 6.89%), a smaller scatter V_p (0.199 vs. 0.212 by −6.13%), and a higher overall ϕ value (0.726 vs. 0.666 by 9.01%). This improvement is reflected in almost all individual failure modes and section types. It is particularly worth noting that the overall ϕ value for the D mode increased most

significantly by 19.0% from 0.638 to 0.759. However, the predictions by this method could not achieve $\phi = 0.85$ as prescribed in the existing DSM. Only the ϕ values for the L ($\phi = 0.830$) and G ($\phi = 0.847$) modes are reasonably satisfactory, whereas the DG mode performed worst with a ϕ value of only 0.606. In terms of section type, Z section was the only section that was just satisfactorily predicted with $\phi = 0.844$.

3.2 *Proposed method 1 – modified DSM without regression analysis*

A new method was developed based on modifying the Option 4 proposed by Moen and Schafer (2011). In particular, $P_{cr\text{-}l}$ and $P_{cr\text{-}d}$ based on gross cross-section were used instead of $P_{cr\text{-}l\text{-}h}$ and $P_{cr\text{-}d\text{-}h}$ (see Section 4 for discussion), while the distortional axial strength Eqns. (7)–(9) were modified to include the interaction with global buckling such that,

$$\text{For } \lambda_{de} \le \lambda_{d1},\ P_{nde} = P_{min} \tag{10}$$

$$\text{For } \lambda_{d1} < \lambda_{de} \le \lambda_{d2},\ P_{nde} = P_{min} - \left(\frac{P_{min} - P_{d2}}{\lambda_{d2} - \lambda_{d1}}\right)\left(\lambda_{d2} - \lambda_{d1}\right) \tag{11}$$

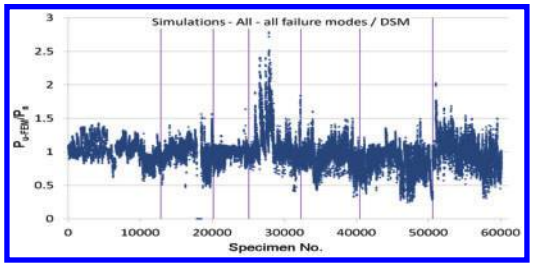


Figure 4. Simulation-to-predicted ratios for perforated columns by Option 4 in (Moen and Schafer, 2011) with classified failure modes (from left to right: L, LG, G, D, LD, DG, and LDG).

$$\text{For } \lambda_{de} > \lambda_{d2},\ P_{nde} = \left[1\text{-}0.25\left(\frac{P_{cr\text{-}d}}{P_{ne}}\right)^{0.6}\right]\left(\frac{P_{cr\text{-}d}}{P_{ne}}\right)^{0.6} P_{ne} \tag{12}$$

where $P_{min} = \min(P_{ne},\ P_{ynet})$, $\lambda_{de} = (P_{ne}/P_{cr\text{-}d})^{0.5}$,
$\lambda_{d1} = 0.561\left(P_{ynet}/P_y\right)$,
$\lambda_{d2} = 0.561\left(14\left(P_y/P_{ynet}\right)^{0.4} - 13\right)$,
and $P_{d2} = \left(1\text{-}0.25\left(1/\lambda_{d2}\right)^{1.2}\right)\left(1/\lambda_{d2}\right)^{1.2} P_{ne}$.

Besides, the local buckling (or LG interactive buckling) strength equations are,

$$\text{For } \lambda_{le} \le 0.776,\ P_{nle} = P_{ne} \le P_{ynet} \tag{13}$$

$$\text{For } \lambda_{le} > 0.776,\ P_{nle} = \left[1\text{-}0.15\left(\frac{P_{cr\text{-}l}}{P_{ne}}\right)^{0.4}\right]\left(\frac{P_{cr\text{-}l}}{P_{ne}}\right)^{0.4} P_{ne} \le P_{ynet} \tag{14}$$

where $\lambda_{le} = (P_{ne}/P_{cr\text{-}l})^{0.5}$. The global buckling strength equations are,

$$\text{For } \lambda_c \le 1.5:\ P_{ne} = \left(0.658^{\lambda_c^2}\right)P_y \tag{15}$$

$$\text{For } \lambda_c > 1.5:\ P_{ne} = \left(\frac{0.877}{\lambda_c^2}\right)P_y \tag{16}$$

where $\lambda_c = (P_y/P_{cr\text{-}e\text{-}h})^{0.5}$.

In addition, in order to achieve an overall resistance factor ϕ of about 0.85 as stipulated in the existing DSM, a penalty factor of 0.85 was applied to the final predicted strength such that,

$$P_n = 0.85 \times \min(P_{nle},\ P_{nde},\ P_{ne}). \tag{17}$$

The statistics of the predictions by Proposed Method 1 are tabulated in Table 3, along with the simulation-to-predicted ratios for all columns illustrated in Figure 5. This method performed better than Option 4 in (Moen and Schafer, 2011) primarily because it resulted in a smaller scatter in prediction

Table 3. Simulation-to-predicted statistics for all columns failing in different failure modes by Proposed Method 1 – modification to Option 4 in (Moen and Schafer, 2011) – replace D equation by DG interaction equation, use $P_{cr\text{-}l}$ and $P_{cr\text{-}d}$ based on A_g.

Section shape	Failure mode																			
	L				LG				G				D				All L, LG, G, D			
	P_m	V_p	ϕ	n	P_m	V_p	ϕ	n	P_m	V_p	ϕ	n	P_m	V_p	ϕ	n	P_m	V_p	ϕ	n
C	1.268	0.135	1.017	6923	1.227	0.124	0.997	4245	1.109	0.096	0.929	1651	1.304	0.206	0.943	3678	1.249	0.157	0.974	16497
Z	1.254	0.112	1.034	3712	1.171	0.179	0.884	1358	1.239	0.043	1.077	2548	1.126	0.090	0.948	2444	1.208	0.115	0.992	10062
Hat	0.998	0.102	0.831	1414	1.096	0.187	0.818	494	1.279	0.044	1.112	137	0.978	0.162	0.757	441	1.029	0.151	0.809	2486
Rack	1.149	0.093	0.965	461	1.056	0.182	0.793	1065	1.165	0.114	0.958	383	0.996	0.104	0.828	391	1.082	0.154	0.847	2300
SC	1.112	0.113	0.915	317	1.134	0.137	0.907	143	1.205	0.067	1.033	196	1.187	0.241	0.808	245	1.156	0.161	0.896	901
All	1.226	0.143	0.973	12827	1.181	0.157	0.920	7305	1.189	0.087	1.004	4915	1.203	0.200	0.879	7199	1.205	0.155	0.942	32246
	LD				DG				LDG				All LD, DG, LDG				ALL Failure modes			
	P_m	V_p	ϕ	n	P_m	V_p	ϕ	n	P_m	V_p	ϕ	n	P_m	V_p	ϕ	n	P_m	V_p	ϕ	n
C	0.957	0.173	0.729	3157	1.019	0.163	0.788	2589	1.243	0.214	0.887	862	1.018	0.200	0.744	6608	1.183	0.189	0.879	23105
Z	1.058	0.118	0.866	4115	1.222	0.098	1.022	2989	1.255	0.147	0.991	6057	1.186	0.150	0.934	1316	1.195	0.136	0.958	23223
Hat	0.841	0.181	0.633	585	0.965	0.240	0.659	1927	1.006	0.232	0.696	964	0.955	0.238	0.654	3476	0.986	0.207	0.713	5962
Rack	0.864	0.106	0.717	137	1.079	0.179	0.815	832	1.114	0.154	0.872	900	1.080	0.174	0.822	1869	1.081	0.163	0.836	4169
SC	0.841	0.203	0.612	245	1.019	0.237	0.699	1727	1.118	0.153	0.876	800	1.032	0.223	0.726	2772	1.063	0.213	0.760	3673
All	0.994	0.163	0.769	8239	1.074	0.197	0.788	1006	1.204	0.178	0.911	9583	1.095	0.198	0.803	2788	1.154	0.181	0.869	60132

($V_p = 0.181$ vs. 0.199). The inclusion of the DG interaction Eqns. (10)–(12) proved effective as it decreased the values of V_p for all failure modes involving the D mode (V_p for the D, LD, DG, and LDG modes decreased by 17.7%, 5.2%, 11.7%, and 11.4%, respectively). Moreover, the use of the 0.85 penalty factor raised the mean P_m and hence the resistance factor ϕ uniformly for all failure modes and section types. However, it failed to raise the overall ϕ values to 0.85 for Hat and Stiffened C sections.

3.3 *Proposed method 2 – Modified DSM with regression analysis*

Based on Proposed Method 1, a regression analysis was carried out to further improve its performance.

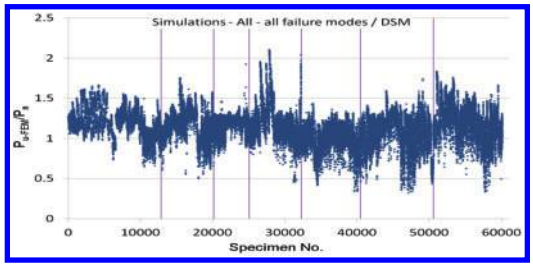


Figure 5. Simulation-to-predicted ratios for all columns by Proposed Method 1 with classified failure modes (from left to right: L, LG, G, D, LD, DG, and LDG).

Table 4. Regression analysis constants for Proposed Method 2.

a	b	c	d	e	f
9.38E-01	6.89E-02	-3.14E-02	5.76E-02	-2.20E-01	-2.46E-02
g	h	i	j	k	m
5.32E-03	1.10E-03	-2.24E-03	-6.76E-03	-7.98E-03	5.57E-02

The resulting DSM Method, i.e. Proposed Method 2, is defined as:

$$P_n = F1 \times \min(P_{nle}, P_{nde}, P_{ne}) \quad (18)$$

where F1 was obtained from a regression analysis and computed as per Eqn. (19) with all the constants defined in Table 4. The slendernesses λ_{le}, λ_{de}, and λ_c in Eqn. (19) are defined in Section 3.2, while HWF = hole width factor = hole width/flat web width, HLF = hole length factor = hole length/hole width, HSF = hole spacing factor = clear hole spacing/hole width, H = overall web width, B = overall flange width, D = overall lip width, t = thickness.

$$g \times HSF + h \times \frac{H}{t} + i \times \frac{B}{t} + j \times \frac{D}{t} + k \times \frac{H}{B} + m \times \frac{D}{B} \quad (19)$$

The statistics of the predictions and the simulation-to-predicted ratios are presented in Table 5 and Figure 6 respectively. By means of the regression factor F1, Proposed Method 2 improved the prediction significantly, demonstrated by a 15.5% decrease in the overall value of V_p. This improvement mainly came from C, Z and Hat sections, while a larger scatter in the predictions

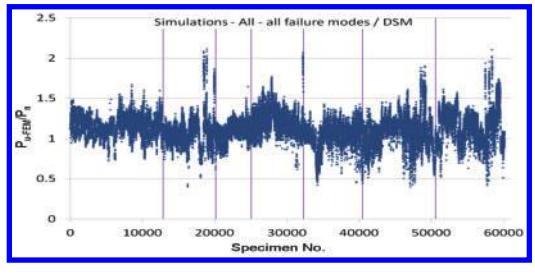


Figure 6. Simulation-to-predicted ratios for all columns by Proposed Method 2 with classified failure modes (from left to right: L, LG, G, D, LD, DG, and LDG).

Table 5. Simulation-to-predicted statistics for all columns failing in different failure modes by Proposed Method 2 – modification to Option 4 in (Moen and Schafer, 2011) – replace D eqn. by DG eqn., use $P_{cr\text{-}l}$ and $P_{cr\text{-}d}$ based on A_g, regression analyses of strengths.

Section shape	Failure mode																			
	L				LG				G				D				All L, LG, G, D			
	P_m	V_p	ϕ	n	P_m	V_p	ϕ	n	P_m	V_p	ϕ	n	P_m	V_p	ϕ	n	P_m	V_p	ϕ	n
C	1.134	0.107	0.940	6923	1.041	0.103	0.866	4245	0.994	0.082	0.842	1651	1.248	0.129	1.009	3678	1.122	0.134	0.901	16497
Z	1.180	0.098	0.987	3712	1.035	0.171	0.791	1358	1.148	0.058	0.990	2548	1.181	0.081	1.002	2444	1.153	0.106	0.956	10062
Hat	1.121	0.095	0.940	1414	1.363	0.203	0.991	494	1.233	0.078	1.048	137	1.122	0.110	0.927	441	1.175	0.157	0.916	2486
Rack	1.206	0.077	1.027	461	1.080	0.214	0.772	1065	1.065	0.088	0.899	383	1.087	0.048	0.943	391	1.104	0.159	0.858	2300
SC	1.106	0.136	0.887	317	1.068	0.114	0.879	143	1.092	0.065	0.938	196	1.286	0.255	0.854	245	1.146	0.191	0.849	901
All	1.148	0.105	0.953	12827	1.068	0.168	0.819	7305	1.090	0.097	0.912	4915	1.210	0.127	0.980	7199	1.135	0.133	0.913	32246
	LD				DG				LDG				All LD, DG, LDG				ALL Failure modes			
	P_m	V_p	ϕ	n	P_m	V_p	ϕ	n	P_m	V_p	ϕ	n	P_m	V_p	ϕ	n	P_m	V_p	ϕ	n
C	0.976	0.161	0.757	3157	0.978	0.134	0.785	2589	1.017	0.176	0.772	862	0.982	0.154	0.769	6608	1.082	0.151	0.850	23105
Z	1.062	0.090	0.894	4115	1.182	0.080	1.004	2989	1.152	0.137	0.922	6057	1.131	0.121	0.923	1316	1.140	0.115	0.937	23223
Hat	1.100	0.147	0.868	585	1.083	0.185	0.810	1927	1.214	0.237	0.832	964	1.122	0.205	0.813	3476	1.144	0.187	0.853	5962
Rack	1.053	0.108	0.871	137	1.100	0.190	0.817	832	1.251	0.151	0.983	900	1.169	0.179	0.882	1869	1.133	0.172	0.865	4169
SC	0.922	0.294	0.569	245	1.035	0.251	0.693	1727	1.111	0.243	0.753	800	1.047	0.257	0.693	2772	1.071	0.244	0.726	3673
All	1.028	0.140	0.820	8239	1.078	0.176	0.818	1006	1.152	0.173	0.878	9583	1.089	0.172	0.830	2788	1.113	0.153	0.873	60132

was associated with Rack and Stiffened C sections, as indicated by increases of 5.5% and 14.6% in the values of V_p. Moreover, the overall values of ϕ showed that all section types except Stiffened C section satisfied the prescribed value of $\phi = 0.85$. In particular, when the L, LG, G and D modes (i.e. those covered by the existing DSM) were considered in isolation, $\phi = 0.85$ was satisfied for all section types, whereas it failed to be satisfied for C, Hat and Stiffened C sections when the collection of the LD, DG and LDG modes were considered.

4 DISCUSSION

The research presented in (Yao, 2013) demonstrates that for the great majority of columns, the simplified method proposed by Moen and Schafer (2009) for calculating the elastic local buckling load accounting for the influence of holes, $P_{cr\text{-}l\text{-}h}$, produces the same buckling loads for non-perforated and perforated members. Therefore, it is not necessary to calculate $P_{cr\text{-}l\text{-}h}$ in the strength design equations, and $P_{cr\text{-}l}$ based on gross section can be used instead.

(Yao, 2013) also showed that replacing $P_{cr\text{-}d\text{-}h}$ by $P_{cr\text{-}d}$ in Option 4 of (Moen and Schafer, 2011) reduced the overall value of V_p favourably by 3.5%, although it also reduced the overall ϕ value by 2.1%. This reduced scatter in prediction was observed for a majority of individual sections and failure modes, especially for C section which showed a significant decrease of 10.8% in its overall V_p value. Therefore, considering the complexity and limitations in calculating $P_{cr\text{-}d\text{-}h}$ as per the simplified methods proposed by Moen and Schafer (2009), it is recommended to use $P_{cr\text{-}d}$ in lieu of $P_{cr\text{-}d\text{-}h}$.

Design methods generally performed worse for failure modes involving the D mode (i.e. D, LD, DG and LDG) as shown by their higher values of V_p. It has been shown that including DG interaction in the DSM distortional equations contributed significantly to the reduction of scatter in prediction related to the DG and LDG modes, and an additional regression analysis could further reduce the scatter for the D, LD, DG and LDG modes. In addition, Yao (2013) demonstrates that it is unfavourable to include LD or LDG interaction equations in the DSM because they generally result in a considerable increase in the prediction scatter and thus a decrease in the resistance factor. Future research is warranted regarding the interaction with the D mode.

It is generally true that the variation in the predictions is largely caused by interaction of buckling modes rather than the presence of holes, although it is noticed that the influence of holes to some extent depends on the section type, section dimensions, and failure modes.

Although it remains sound to base the strength on a slenderness that relates elastic buckling and yield (or strength), the statistics of the predictions by the DSM can vary significantly depending on the section type and failure mode. It is virtually impossible to achieve a uniform ϕ value for all section types and failure modes using a particular set of strength equations. From a design viewpoint, it may be preferable to select the accurate ϕ value for a specific section type and failure mode; alternatively, one may use a more conservative approach by adopting the minimum ϕ value of all failure modes for a particular section, or a less conservative approach by adopting the average ϕ value of all failure modes for a particular section.

5 CONCLUSIONS

A comprehensive parametric study was carried out using ABAQUS to determine the strengths of 146207 perforated and non-perforated cold-formed steel columns. The study included five cross-section types (i.e. C, stiffened C, Z, rack, and hat sections) and seven failure modes (i.e. L, LG, G, D, LD, DG, and LDG).

The strength database was then used to evaluate three DSM design methods, including Option 4 in (Moen and Schafer, 2011), and another two methods proposed by the authors. The best-performing method was based on modifying the Option 4 method in (Moen and Schafer, 2011) such that (i) DG interaction was included, (ii) $P_{cr\text{-}l}$ and $P_{cr\text{-}d}$ based on gross section were used, and (iii) a factor based on a regression analysis was added to improve the final design strength. This recommended method outperformed all the other methods in terms of accuracy and generality.

REFERENCES

AS/NZS:4600 2005. Cold-formed steel structures. Standards Australia, Sydney, Australia.

Becque, J. 2008. *The interaction of local and overall buckling of cold-formed stainless steel columns.* Ph.D thesis, University of Sydney.

Moen, C. D. & Schafer, B. W. 2009. Elastic buckling of cold-formed steel columns and beams with holes. *Engineering Structures*, 31, 2812–2824.

Moen, C. D. & Schafer, B. W. 2011. Direct Strength Method for Design of Cold-Formed Steel Columns with Holes. *ASCE Journal of Structural Engineering*, 137, 559–570.

NAS 2007. North American specification for the design of cold-formed steel structural members. Washington, D.C: American Iron and Steel Institute (AISI).

Ramberg, W. & Osgood, W. R. 1943. Description of stress strain curves by three parameters. National Advisory Committee for Aeronautics (NACA).

Schafer, B. W. & Pekoz, T. 1998. Computational modeling of cold-formed steel: characterizing geometric imperfections and residual stresses. *Journal of Constructional Steel Research*, 47, 193–210.

Tovar, J. & Sputo, T. 2005. Application of direct strength method to axially loaded perforated cold-formed steel studs: Distortional and local buckling. *Thin-Walled Structures*, 43, 1882–1912.

Yao, Z. 2013. *Nonlinear analysis and design of perforated thin-walled steel columns.* Ph.D thesis, University of Sydney.

Research and Applications in Structural Engineering, Mechanics and Computation – Zingoni (Ed.)
© 2013 Taylor & Francis Group, London, ISBN 978-1-138-00061-2

A semi-discretized thin-walled beam element including distortion

Michael Joachim Andreassen & Jeppe Jönsson
Technical University of Denmark, Department of Civil Engineering, Brovej, Lyngby, Denmark

ABSTRACT: An advanced thin-walled beam element including distortion of the cross section is presented. The formulation is based on a generalization of the classical Vlasov beam theory for analysis of open and closed thin-walled cross sections by including distortional displacements. The beam element formulation utilizes a semi-discretization approach in which the cross section is discretized into wall elements and the analytical solutions of the related GBT beam equations are used as displacement functions in the axial direction. Thus the beam element contains the semi-analytical solutions. In a number of related publications the authors have recently presented the semi-discretization approach and the analytical solution of the generalized beam equations. An illustrative example showing the validity and the accuracy of the developed distortional semi-discretized thin-walled beam element is given and it is shown how the novel approach provides accurate results making it a good alternative to the traditional and time consuming FE calculations.

1 INTRODUCTION

An extension of the classic beam theory is considered in this paper and in a number of companion publications published by the authors, (Jönsson & Andreassen 2011, Andreassen & Jönsson 2012b, Andreassen & Jönsson 2012a, Andreassen & Jönsson 2013, Andreassen 2012) where a novel approach to generalized beam theory is formulated. A variety of other formulations and methods taking distortional displacements into account have been proposed for analysis of both open and closed cross sections. Thus, concerning analysis of thin-walled members including distortion of the cross section there are a number of methods available among which are: (i) The use of shell finite elements in the finite element method (FEM), (Zienkiewicz & Taylor 1989), (ii) the finite strip method (FSM), (Cheung & Tham 1998), (Schafer & Ádány 2006), and (iii) the use of approximate GBT-finite beam elements known as GBT (Schardt 1966, Silvestre 2005).

In the present paper a new and alternative approach to conventional GBT is briefly presented. This novel approach to Generalized Beam Theory (GBT) involves a cross-section semi-discretization process as well as a determination of the natural cross-section eigenmodes and related axial solution functions by exact analytical solution of the related first-order GBT equations. Hereby the approach is different from the traditional GBT formulation developed by Schardt in (Schardt 1966) and (Schardt 1989). When Schardt uses the GBT equations to find distortional deformation modes the shear coupling stiffness terms are neglected. This corresponds to modal analysis with orthogonal (Rayleigh) damping in dynamic structural analysis. The solution of the shear coupled GBT equations for closed cross-sections was published by Hanf only in his thesis, (Hanf 1989). For closed (single or multi celled hollow) thin-walled cross-sections Schardt shows in his presentation of GBT in (Schardt 1989), that the theory needs a relaxation of the Vlasov assumption of negligible shear strain in order to include the warping deformation associated with the "Bredt's shear flow" around each cell. However it complicates the solution of the conventional GBT equations by introducing non negligible shear coupling terms (off diagonal) in the GBT equations. The present formulation therefore adheres to the definition of the warping function given in (Kollbrunner & Hajdin 1972), which adds the integral of the shear flow strains, see also (Jönsson 1999).

In contrast to and as a considerable advance on the traditional GBT formulation this novel finite element based semi-discretization approach to generalized beam theory (GBT) solves the fourth-order differential equations to obtain the distortional displacements for a linear beam analysis. This means that we find the analytical solution to the differential GBT equations which through the magnitude of the eigenvalues gives a much better knowledge of the length scales of the modes. This also means that we find the exact mode shapes and amplitude solutions of the reduced order GBT equations related to the discretized cross section. In contrast, the conventional GBT formulation solves the equations using the approximate engineering methods, in which the shear coupling terms are neglected, producing orthogonal axial and transverse normal stress modes. In such a case the differential equations are not solved but a weak solution may be found through introduction of the established approximate mode shapes and use of approximate modal amplitude functions.

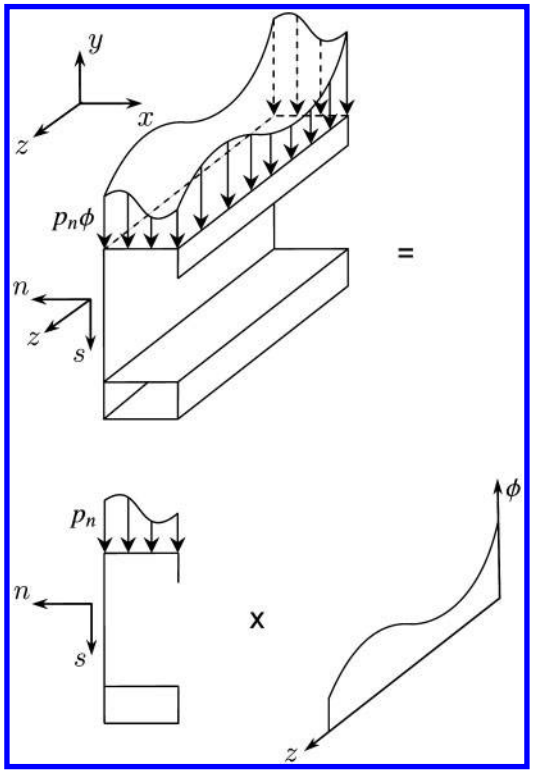


Figure 1. Global and local Cartesian reference frames and load distribution.

Thus the conventional GBT formulations uses the produced approximated modes as shape functions in a virtual work or potential energy formulation leading to approximated finite GBT beam elements and the discretization has to be performed without proper prior knowledge of the problem length scales of the individual modes.

It should be noticed that the paper is dealing with a basic generalized beam theory (GBT) and not an extended finite element formulation of an approximate beam element.

2 BEAM KINEMATICS OF A SINGLE MODE

The considered straight beam of constant cross section is described in a global Cartesian (x, y, z) coordinate system as shown in Figure 1. In the local coordinate system (z, n, s) the displacements u_n, u_s and u_z of a material point are defined as

$$u_n(s,z) = \mathrm{w}_n(s)\,\psi(z) \tag{1}$$

$$u_s(n,s,z) = \left(\mathrm{w}_s(s) - n\mathrm{w}_{n,s}(s)\right)\psi(z) \tag{2}$$

$$u_z(n,s,z) = -\left(\Omega(s) + n\mathrm{w}_n(s)\right)\psi'(z) \tag{3}$$

Here $\mathrm{w}_s(s)$ and $\mathrm{w}_n(s)$ describes the local displacements of the centerline, $\psi(z)$ is the function which describes the variation along the beam and $\Omega(s)$ describes the axial (warping) displacement mode. The local components are shown in Figure 2. The notation indicates the two dimensions of the cross section planes and the single dimension associated with the variation along the beam. The strain components associated with the given displacements are found as

$$\varepsilon_z = -(\Omega + n\mathrm{w}_n)\psi'' \tag{4}$$

$$\varepsilon_s = (\mathrm{w}_{s,s} - n\mathrm{w}_{n,ss})\psi \tag{5}$$

$$\gamma_{zs} = (\mathrm{w}_s - \Omega_{,s} - 2n\mathrm{w}_{n,s})\psi' \tag{6}$$

For a greater explanation and description see paper (Jönsson & Andreassen 2011, Andreassen & Jönsson 2012b)

3 ENERGY POTENTIAL OF A SINGLE MODE

The total potential energy of a single mode can be expressed as

$$\Pi_{tot} = \Pi_{int} + \Pi_{ext} \tag{7}$$

Here Π_{int} is the contribution from the potential energy from the internal properties, see paper (Jönsson & Andreassen 2011), and Π_{ext} is the contribution from the external loads, see paper (Andreassen & Jönsson 2012b). Introducing the strain components associated with the displacements and introducing the load variables $q_s = p_s(s)\phi(z)$, $q_n = p_n(s)\phi(z)$, $q_z = p_z(s)\phi(z)$, the total potential energy takes the following form:

$$\Pi_{tot} = \int_V \left(\tfrac{1}{2}E\varepsilon_z^2 + \tfrac{1}{2}G\gamma^2 + \tfrac{1}{2}E_s\varepsilon_s^2 - (q_z u_z + q_s u_s + q_n u_n)\right)dV \tag{8}$$

The interpolations connected to the cross section are the displacement interpolations for $\mathrm{w}_s(s)$, $\mathrm{w}_n(s)$ and Ω which is fully described in (Jönsson & Andreassen 2011). The interpolation of the cross-section loads p_s, p_n and p_z are fully introduced in (Andreassen & Jönsson 2012b). Introducing these interpolations and the calculation scheme as described in (Jönsson & Andreassen 2011, Andreassen & Jönsson 2012b) the total potential energy can be written as

$$\begin{aligned}\Pi_{tot} = \tfrac{1}{2}\int_0^L \Bigg\{ &\left[\psi\mathbf{v}_\mathrm{w}^T \;\; \psi\mathbf{v}_\Omega^T\right]'' \begin{bmatrix}\mathbf{K}^\sigma_{\mathrm{ww}} & \mathbf{0}\\ \mathbf{0} & \mathbf{K}^\sigma_{\Omega\Omega}\end{bmatrix}\begin{bmatrix}\psi\mathbf{v}_\mathrm{w}\\ \psi\mathbf{v}_\Omega\end{bmatrix}'' \\ &+\left[\psi\mathbf{v}_\mathrm{w}^T \;\; \psi\mathbf{v}_\Omega^T\right]' \begin{bmatrix}\mathbf{K}^\tau_{\mathrm{ww}} & \mathbf{K}^\tau_{\mathrm{w}\Omega}\\ \mathbf{K}^\tau_{\Omega\mathrm{w}} & \mathbf{K}^\tau_{\Omega\Omega}\end{bmatrix}\begin{bmatrix}\psi\mathbf{v}_\mathrm{w}\\ \psi\mathbf{v}_\Omega\end{bmatrix}' \\ &+\left[\psi\mathbf{v}_\mathrm{w}^T \;\; \psi\mathbf{v}_\Omega^T\right] \begin{bmatrix}\mathbf{K}^s & \mathbf{0}\\ \mathbf{0} & \mathbf{0}\end{bmatrix}\begin{bmatrix}\psi\mathbf{v}_\mathrm{w}\\ \psi\mathbf{v}_\Omega\end{bmatrix} \\ &-(\psi\mathbf{v}_\mathrm{w}^T)\mathbf{r}_\mathrm{w}\phi + (\psi\mathbf{v}_\Omega^T)'\mathbf{r}_\Omega\phi\Bigg\}dz\end{aligned} \tag{9}$$

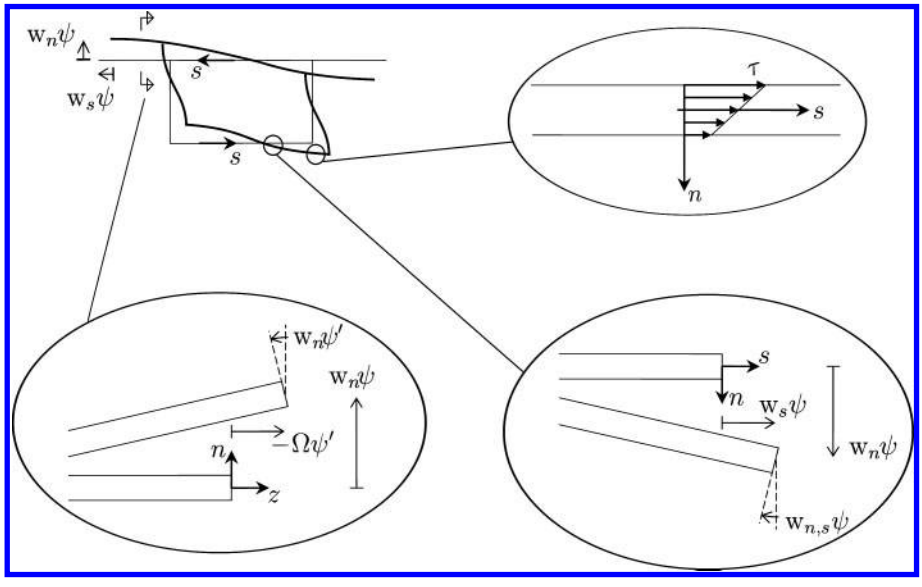


Figure 2. Local components of the displacement field and assumed shear stresses.

To get a formulation resembling a generalization of Vlasov beam theory (Vlasov 1961) the following three main steps are performed:

- In step I the shear constraint equations that bind axial and transverse modes together are introduced and at the same time equation (9) are simplified or condensed. In this process the singularity in the shear stiffness matrix related to pure axial extension is needed to be eliminated.
- In step II two eigenmodes corresponding to transverse translation of the cross section are identified and eliminated. Also a pure rotational eigenmode is identified for elimination in the next step. Furthermore the transverse displacement field is constrained, so that transverse normal strains in the middle surface of the cross section are not allowed, i.e. $w_{s,s} = 0$ is enforced, see equation (5).
- In step III the order of the coupled fourth order differential equations is reduced and the eigenvalue problem is condensed by removing singularities due pure St. Venant torsion.

This reveals the final set of (reduced order) distortional differential equations that have to be solved and the full solution along the beam obtained as

$$\begin{aligned} \mathbf{u}_w(z) &= \mathbf{V}_w[\boldsymbol{\Psi}_h(z)\,\mathbf{c} + \boldsymbol{\Psi}_p(z)\boldsymbol{\phi}] \\ \mathbf{u}_z(z) &= -\mathbf{V}_\Omega[\boldsymbol{\Psi}'_h(z)\,\mathbf{c} + \boldsymbol{\Psi}'_p(z)\boldsymbol{\phi}] \end{aligned} \tag{10}$$

For a more elaborate description see the companion papers (Jönsson & Andreassen 2011, Andreassen & Jönsson 2012b).

4 ELEMENT STIFFNESS MATRIX AND LOAD VECTOR

Now the global beam element stiffness matrix and load vector needed for the determination of the nodal element solution can be found. As the load has no influence on the stiffness contributions we use the full assembled homogeneous solution along the beam found in the companion paper (Jönsson & Andreassen 2011). We also use the homogeneous displacement modes to generate the nodal load vector.

Using the homogeneous solution vectors given in equation (79) in paper (Jönsson & Andreassen 2011) the potential energy including all the homogeneous modes in equation (9) can be written in integrated form as

$$\Pi = \tfrac{1}{2}\mathbf{c}^T(\widetilde{\mathbf{K}}\mathbf{c} - \widetilde{\mathbf{r}}) \tag{11}$$

Here $\widetilde{\mathbf{K}}$ is the stiffness matrix and $\widetilde{\mathbf{r}}$ the load vector related to the modal displacement constants $\mathbf{c}$. The stiffness matrix and the load vector are found by integration and addition of the individual sub matrix products. The stiffness matrix contributions are given i Table 1 and the two load vector contributions are given in Table 2.

4.1 *Generalized displacements*

The generalized displacements of the present GBT formulation are determined by the first variation of the potential energy, shear constrains and the multi point constraint equations, as described in paper (Jönsson & Andreassen 2011). This degree of freedom space is what we refer to as the GBT-space. As in a basic beam

Table 1. Beam element stiffness contributions enabling analytical integration.

$$\widetilde{\mathbf{K}}^{\sigma}_{\mathrm{ww}} = \overline{\mathbf{V}}^{T}_{\mathrm{w}} \mathbf{K}^{\sigma}_{\mathrm{ww}} \overline{\mathbf{V}}_{\mathrm{w}} \circ \int_0^L \overline{\mathbf{\Psi}}'' \mathbf{J} \overline{\mathbf{\Psi}}'' \, dz$$
$$\widetilde{\mathbf{K}}^{\tau}_{\mathrm{ww}} = \overline{\mathbf{V}}^{T}_{\mathrm{w}} \mathbf{K}^{\tau}_{\mathrm{ww}} \overline{\mathbf{V}}_{\mathrm{w}} \circ \int_0^L \overline{\mathbf{\Psi}}' \mathbf{J} \overline{\mathbf{\Psi}}' \, dz$$
$$\widetilde{\mathbf{K}}^{\tau}_{\mathrm{w}\Omega} = \overline{\mathbf{V}}^{T}_{\mathrm{w}} \mathbf{K}^{\tau}_{\mathrm{w}\Omega} \overline{\mathbf{V}}_{\Omega} \circ \int_0^L \overline{\mathbf{\Psi}}' \mathbf{J} \overline{\mathbf{\Psi}}' \, dz$$
$$\widetilde{\mathbf{K}}^{s} = \overline{\mathbf{V}}^{T}_{\mathrm{w}} \mathbf{K}^{s} \overline{\mathbf{V}}_{\mathrm{w}} \circ \int_0^L \overline{\mathbf{\Psi}} \mathbf{J} \overline{\mathbf{\Psi}} \, dz$$
$$\widetilde{\mathbf{K}}^{\sigma}_{\Omega\Omega} = \overline{\mathbf{V}}^{T}_{\Omega} \mathbf{K}^{\sigma}_{\Omega\Omega} \overline{\mathbf{V}}_{\Omega} \circ \int_0^L \overline{\mathbf{\Psi}}'' \mathbf{J} \overline{\mathbf{\Psi}}'' \, dz$$
$$\widetilde{\mathbf{K}}^{\tau}_{\Omega\mathrm{w}} = \overline{\mathbf{V}}^{T}_{\Omega} \mathbf{K}^{\tau}_{\Omega\mathrm{w}} \overline{\mathbf{V}}_{\mathrm{w}} \circ \int_0^L \overline{\mathbf{\Psi}}' \mathbf{J} \overline{\mathbf{\Psi}}' \, dz$$
$$\widetilde{\mathbf{K}}^{\tau}_{\Omega\Omega} = \overline{\mathbf{V}}^{T}_{\Omega} \mathbf{K}^{\tau}_{\Omega\Omega} \overline{\mathbf{V}}_{\Omega} \circ \int_0^L \overline{\mathbf{\Psi}}' \mathbf{J} \overline{\mathbf{\Psi}}' \, dz$$

Table 2. Beam element load vector contributions.

$$\widetilde{\mathbf{r}}_{\mathrm{w}} = \int_0^L \mathbf{\Psi}_h{}^T \, \phi \, dz \, \mathbf{V}^{T}_{\mathrm{w}} \mathbf{r}_{\mathrm{w}} \qquad \widetilde{\mathbf{r}}_{\Omega} = \int_0^L \mathbf{\Psi}_h'{}^T \, \phi \, dz \, \mathbf{V}^{T}_{\Omega} \mathbf{r}_{\Omega}$$

element formulation we will specify the boundary displacements at the two ends of the beam, i.e. at $z = 0$ and at $z = L$ where L is the beam length. Denoting the assembled boundary displacement vector by $\mathbf{u}_b$ we can write the following equation for the determination of the solution constants:

$$\mathbf{u}_b = \mathbf{A}\mathbf{c} \quad \Rightarrow \quad \mathbf{c} = \mathbf{A}^{-1}\mathbf{u}_b \tag{12}$$

Substituting beam boundary displacements for the solution constants into the first variation of equation (11) using equation (12) the formulation is redefined to include the end displacements in GBT-space as follows:

$$\begin{aligned} \delta\Pi &= \delta\mathbf{u}_b{}^T \mathbf{A}^{-T} \widetilde{\mathbf{K}} \mathbf{A}^{-1} \mathbf{u}_b - \delta\mathbf{u}_b{}^T \mathbf{A}^{-T} \widetilde{\mathbf{r}} \\ &= \delta\mathbf{u}_b{}^T (\mathbf{K}_e \mathbf{u}_b - \mathbf{R}_e) \end{aligned} \tag{13}$$

where $\mathbf{K}_e$ is the beam element stiffness matrix in GBT-space and $\mathbf{R}_e$ is the beam element load vector in GBT-space.

For stationarity the first variation of the potential energy must be equal to zero whereby we can write the single element equations as

$$\mathbf{K}_e \mathbf{u}_b = \mathbf{R}_e \tag{14}$$

Using a standard finite element procedure to assemble the global system we obtain

$$\mathbf{K}\mathbf{u} = \mathbf{R} \quad \Leftrightarrow \quad \mathbf{u} = \mathbf{K}^{-1}\mathbf{R} \tag{15}$$

where $\mathbf{K}$ has to be a positive definite "square" matrix and $\mathbf{R}$ is the load vector corresponding to the chosen load. However in order to achieve a positive definite matrix it is necessary to apply boundary conditions, for example as described in the next section.

5 BOUNDARY CONDITIONS AND NODAL LOADS

To introduce boundary conditions in the finite element equations (15) the simple method of adding stiff springs is chosen. The boundary stiffness contributions $\Delta\mathbf{K}_{\mathrm{FE}}$ are formulated in the unconstrained FE-space $\mathbf{u}_{\mathrm{FE}}$ corresponding to all nodal degrees of freedom and the axial derivatives of transverse components of these. Thus the beam end spring stiffness contributions $\Delta\mathbf{K}_{\mathrm{FE}}$ are transformed into GBT space by

$$\Delta\mathbf{K}_{\mathrm{GBT}} = \mathbf{T}^T \Delta\mathbf{K}_{\mathrm{FE}} \mathbf{T} \tag{16}$$

and the nodal loads (at beam element ends and intersections) are transformed from FE-space to GBT-space by the transformation

$$\Delta\mathbf{R}_{\mathrm{GBT}} = \mathbf{T}^T \Delta\mathbf{R}_{\mathrm{FE}} \tag{17}$$

Using this method quite a wide range of situations may be analyzed.

6 INTERNAL ELEMENT DISPLACEMENTS

The internal beam displacements are represented by the cross-section node displacement vectors $\mathbf{u}_z(z)$ and $\mathbf{u}_{\mathrm{w}}(z)$ as a function of the axial coordinate z. In the beam element these internal displacements are found by superposition of (a) the internal displacements induced by the nodal displacements without distributed loading and (b) the displacements induced by the loading on the beam with zero nodal displacements.

Adhering to this concept equation (18) gives us the first contribution as

$$\begin{aligned} \mathbf{u}^{(a)}_{\mathrm{w}}(z) &= \mathbf{V}_{\mathrm{w}} \mathbf{\Psi}_h(z) \, \mathbf{c} \\ \mathbf{u}^{(a)}_{z}(z) &= -\mathbf{V}_{\Omega} \mathbf{\Psi}'_h(z) \, \mathbf{c} \end{aligned} \tag{18}$$

and the second contribution is given as

$$\begin{aligned} \mathbf{u}^{(b)}_{\mathrm{w}}(z) &= \mathbf{V}_{\mathrm{w}} [\mathbf{\Psi}_h(z) \, \mathbf{c}_p + \mathbf{\Psi}_p(z) \boldsymbol{\phi}] \\ \mathbf{u}^{(b)}_{z}(z) &= -\mathbf{V}_{\Omega} [\mathbf{\Psi}'_h(z) \, \mathbf{c}_p + \mathbf{\Psi}'_p(z) \boldsymbol{\phi}] \end{aligned} \tag{19}$$

Finally the two solutions (a) and (b) can be superimposed and the semi-analytically determined internal displacement vectors can be found as

$$\begin{aligned} \mathbf{u}_{\mathrm{w}}(z) &= \mathbf{V}_{\mathrm{w}} [\mathbf{\Psi}_h(z) \, (\mathbf{c} + \mathbf{c}_p) + \mathbf{\Psi}_p(z) \boldsymbol{\phi}] \\ \mathbf{u}_{z}(z) &= -\mathbf{V}_{\Omega} [\mathbf{\Psi}'_h(z) \, (\mathbf{c} + \mathbf{c}_p) + \mathbf{\Psi}'_p(z) \boldsymbol{\phi}] \\ &\text{where } \mathbf{c} = \mathbf{A}^{-1}\mathbf{u}_b \text{ and } \mathbf{c}_p = -\mathbf{A}^{-1}\mathbf{B}\boldsymbol{\phi}. \end{aligned} \tag{20}$$

For a greater explanation and description see paper (Andreassen & Jönsson 2013).

Now we are able to find displacements, strains and stresses at any point in the beam element. In the next section an example illustrating this new approach is given.

7 EXAMPLE

In this section a simple supported lipped channel beam loaded by two point loads symmetrically placed in the

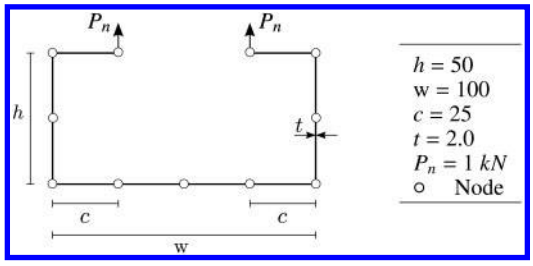


Figure 3. Geometry, in-plane discretization, parameter values and load for the lipped channel beam.

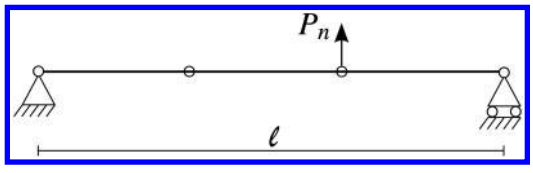


Figure 4. Geometry and discretization for a lipped channel beam consisting of 3 elements.

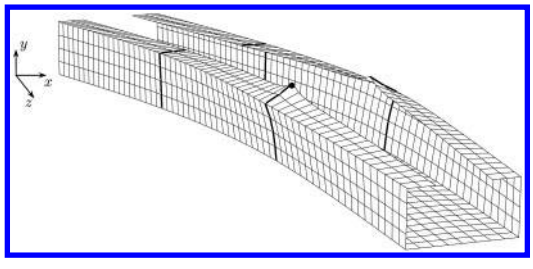


Figure 5. GBT plot of the lipped channel with point loads.

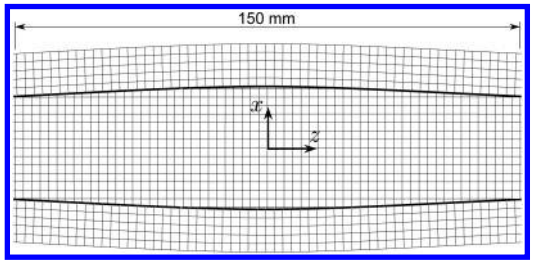


Figure 6. GBT plot of the lipped channel to shown the exponential decrease in the x-z-plane.

same cross section as shown in Figure 3 is analyzed. Nodal displacement results as well as stress distribution results of GBT are compared to those found using the commercial FE program Abaqus. A simple supported lipped channel beam with a length of 1500 mm is considered consisting of and assembled by three single beam elements of 500 mm. The end sections are constrained against transverse displacements, but otherwise free to warp (and thus also rotate). Further, one of the ends is fixed at a single node against longitudinal translation. An elasticity modulus $E = 2.1 \cdot 10^5$ MPa and a Poisson ratio of $\nu = 0.3$ have been used.

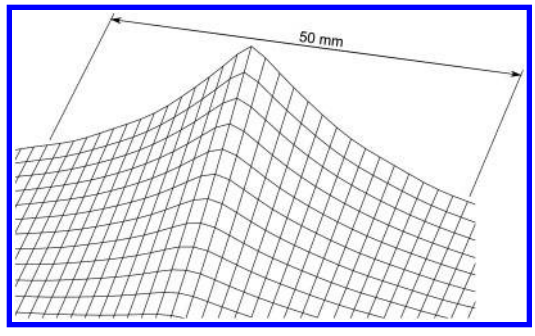


Figure 7. GBT plot of the lipped channel to shown the exponential decrease in the y-z-plane.

Table 3. Nodal displacements of GBT and FE analysis.

	GBT [mm]	Abaqus [mm]	Difference [%]
u_x	−1.424	−1.415	0.6
u_y	4.697	4.772	1.6

The results found using Abaqus are based on isotropic material and the S4 shell element with full 4 point integration. The linear elastic finite element calculations are based on a structured rectangular mesh with a side length seed of 5 mm. The cross section is fixed in the transverse directions at both ends and fixed at a single node against longitudinal translation. Using the parameters as given in Figure 3 and 4 and the full solution in equation (20) leads to the deformed configuration shown in Figure 5. Here it is seen that the global deformation is related to flexure of the beam, non-local distortional deformation of the cross section and a very local plate deformation of the lips related to the location of the point loads. Thus three length scales are represented, the global flexural beam mode as seen in Figure 5, the non-local distortional deformation of the lips as shown in Figure 6 and the local distortional plate deformation of the lip as shown in close-up in Figure 7. This example points out the importance of taking distortion into account in order to obtain a good approximation of the deformation shape. From Figure 7 it is seen that the deflection in the longitudinal z-direction decreases exponentially in the y-z-plane. It should also be noted that the deformation is so local that it is difficult to see that the surface is C^1 continuous. The decreasing non-local distortion is clear in the x-z-plot shown in Figure 6, which represents a part of the beam symmetrically about the loaded cross section. Comparing the nodal displacements of the marked node to the displacement found using a model in the commercial FE program Abaqus gives the displacement values and the corresponding deviations shown in Table 3. From Table 3 the deviation from Abaqus results of the displacement, u_x, in the horizontal direction is 0.6% while the deviation for the vertical displacement, u_y, is 1.6%. Due to the poor discretization of the cross section and

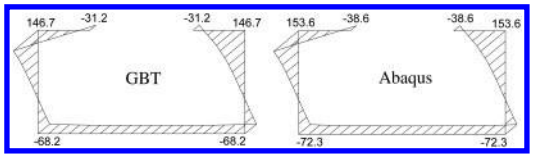


Figure 8. Comparison between the axial normal stress distributions obtained with GBT and Abaqus. All values are in MPa.

Table 4. Stress distributions of GBT and FE analysis.

	GBT [MPa]	Abaqus [MPa]	Difference [%]
σ_z	−31.2	−38.6	4.8
σ_s	492.3	481.9	2.1

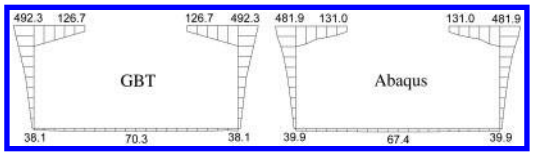


Figure 9. Comparison between the transverse bending stress distributions obtained with GBT and Abaqus. All values are in MPa.

the present approach which is based on a beam theory these deviations may also be expected.

Having compared the nodal displacement obtained with GBT and Abaqus we take a look at the stress distributions. A comparison of the membrane stresses in the z direction is shown in Figure 8. Comparing the stresses in relation to the maximum stress at the cross section a maximum deviation of 4.8% is obtained as shown in Table 4. This deviation level is expected as the chosen point is subjected to very local complex phenomena. The transverse bending stresses are shown in Figure 9. In this case a maximum deviation of 2.1% is obtained.

8 CONCLUSIONS

In this conference paper the formulation of a distortional semi-discretized thin-walled beam element is briefly presented based on a condensed presentation of the novel finite-element-based displacement approach and beam formulation published by the authors in (Jönsson & Andreassen 2011, Andreassen & Jönsson 2012b, Andreassen & Jönsson 2012a, Andreassen & Jönsson 2013, Andreassen 2012). Using the full assembled homogenous solution along the beam, the beam element stiffness matrices have been found. From the full assembled homogenous solution as well as the full assembled non-homogeneous solution the displacements of the full semi-analytical solution along the beam have been found in the context of a beam element. An illustrative example has been given including a simple supported lipped channel beam loaded by two point loads symmetrically placed in the same cross section. The chosen example show a solution which are applicable to the finite element formulation. The novel approach presented in this paper is a considerable theoretical achievement, since it without approximation gives the full analytical solution along the loaded beam for a given discretization of the cross section. Reasonable matches are obtained in all cases confirming that this new developed GBT approach provides reasonable results with a very small computational cost making it an alternative to the traditional finite element calculations and the other available methods.

REFERENCES

Andreassen, M. (2012). *Distortional mechanics of thin-walled structural elements*. Ph. D. thesis, DTU Civil Engineering, Department of Civil Engineering, Technical University of Denmark.

Andreassen, M. & J. Jönsson (2012a). Distortional buckling modes of semi-discretized thin-walled columns. *Thin-Walled Structures 51*, 53–63.

Andreassen, M. & J. Jönsson (2012b). Distortional solutions for loaded semi-discretized thin-walled beams. *Thin-Walled Structures 50*, 116–127.

Andreassen, M. & J. Jönsson (2013). A distortional semidiscretized thin-walled beam element. *Thin-Walled Structures 62*, 142–157.

Cheung, Y. & L. Tham (1998). *The finite strip method*. Boca Raton: CRC Press.

Hanf, M. (1989). *Die geschlossene Lösung der linearen Differentialgleichungssysteme der Verallgemeinerten Technischen Biegetheorie mit einer Anwendung auf die Ermittlung plastischer Grenzlasten*. Ph. D. thesis, IWMB der TU Darmstadt.

Jönsson, J. (1999). Distortional theory of thin-walled beams. *Thin-Walled Structures 33*, 269–303.

Jönsson, J. & M. Andreassen (2011). Distortional eigenmodes and homogeneous solutions of semi-discretized thin-walled beams. *Thin-Walled Structures 49*, 691–707.

Kollbrunner, C. & N. Hajdin (1972). *Dünnwandige Stäbe 1, Stäbe mit undeformierbaren Querschnitten*. Berlin, Germany: Springer-Verlag.

Schafer, B. & S. Ádány (2006). Modal decomposition for thinwalled member stability using the finite strip method. *Advances in Engineering Structures, Mechanics and Construction*, 411–422.

Schardt, R. (1966). Eine erweiterung der technischen biegelehre für die berechnung biegesteifer prismatischer faltwerke. *Der Stahlbau 35*, 161–171.

Schardt, R. (1989). *Verallgemeinerte Technische Biegetheorie*. Germany: Springer-Verlag.

Silvestre, N. (2005). *Generalized Beam Theory: New formulations, Numerical Implementation and Applications*. Ph. D. thesis, IST, TU of Lisbon, Portugal, (in Portuguese).

Vlasov, V. (1961). *Thin-walled elastic beams*. (2 ed.). Jerusalem, Israel: Israel Program for Scientific Translations.

Zienkiewicz, O. & R. Taylor (1989). *The finite element method, Basic formulations and linear problems*. (4 ed.), Volume 1. UK: McGraw-Hill Book Company.

Research and Applications in Structural Engineering, Mechanics and Computation – Zingoni (Ed.)
© 2013 Taylor & Francis Group, London, ISBN 978-1-138-00061-2

Generalised Beam Theory (GBT) for stiffened sections

G. Taig & G. Ranzi
School of Civil Engineering, The University of Sydney, Sydney, NSW, Australia

G. Piccardo
DICCA, Scuola Politecnica, University of Genova, Italy

A. Luongo
Dipartimento d'Ingegneria Civile, Edile-Architettura, ed Ambientale,
University of L'Aquila, Italy

ABSTRACT: This paper outlines the use of the Generalised Beam Theory (GBT) approach to study the structural behaviour of prismatic thin-walled members with stiffeners of arbitrary geometries. This is particular relevant for bridge applications, where the stiffeners' arrangements are usually optimized in the design. The proposed GBT procedure is expressed in the spirit of Kantorovich's semi-variational method, using the dynamic modes of an unconstrained planar frame as the in-plane conventional deformation modes. The corresponding warping deformations are then evaluated from the post-processing of these in-plane modes, thus reversing the strategy of the classical GBT procedure. Constraint conditions are applied to the stiffened plate elements to provide the rigidity exhibited by the specified stiffeners. The method used is applicable to open, closed and partially closed cross-sections. The efficiency and ease of use of the method are outlined by means of two examples, aimed to describe the linear–elastic behaviour of thin-walled members. The numerical results obtained with the proposed approach are validated against those calculated with a shell finite element model developed in Abaqus.

1 INTRODUCTION

Generalised beam theory (GBT) is an elegant method used to study the behaviour of thin-walled members. Its original formulation was proposed by Schardt (1989) which considers the thin-walled member as an assembly of plate segments which are free to bend in the plane of the cross-section. In this sense, GBT is able to capture the loss of the initial shape of the cross-section. The essence of the approach lies in the description of the displacement field as a linear combination of assumed deformation modes whose magnitudes vary along the member. Consequently GBT transforms a three-dimensional problem into a vector valued one-dimension problem.

A GBT analysis consists of two main stages: (1) the cross-sectional analysis, where the deformation modes are chosen; and (2) the member analysis, where the global response of the thin-walled member is evaluated.

Much progress has been made in this field of research since its original inception. In the 1990's, Davies and co-workers reported a number of studies on the linear-elastic and buckling behaviour of thin-walled members, e.g. (Davies & Leach 1994, Jiang & Davies 1997). Extensive work in this area has been carried out over the last decade by Camotin and his co-workers, who extended the applicability of this approach to deal with anisotropic members (Silvestres & Camotim 2002), closed or partially closed sections (Goncalves et. al 2009), finite element modelling (Dinis et. al 2007), buckling of members and frames (Basaglia et. al 2008), post-buckling-problems (Silvestre et. al 2008) and composite steel-concrete members (Goncalves & Camotim 2010). The simplification in the description of the displacement field, enabled within the GBT with the use of cross-sectional deformation modes and amplitude functions, was applied in recent years to the analyses carried out with the finite strip method (Adany & Schafer 2006) and the finite element method (Casafront et. al 2009). In very recent years, attention has been devoted to generalise Vlasov's classic hypotheses of inextensibility and shear undeformability on which GBT was initially based, e.g. (Goncalves et. al 2009, Silvestre & Camotim 2011, Jönsson & Andreassen 2011, Andreassen & Jönsson 2012).

In this context, this paper outlines the use of the GBT approach to study the structural behaviour of prismatic thin-walled members with stiffeners of arbitrary geometry. This is particular relevant for bridge applications, where the stiffeners' arrangements and geometries are usually optimized in the design. The accuracy of the proposed method is validated against a shell finite element model developed in Abaqus (ABAQUS 2008).

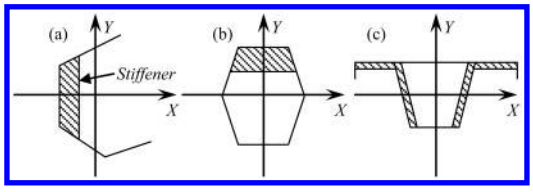


Figure 1. Generic thin-walled stiffened sections: (a) open; (b) closed; (c) partially closed.

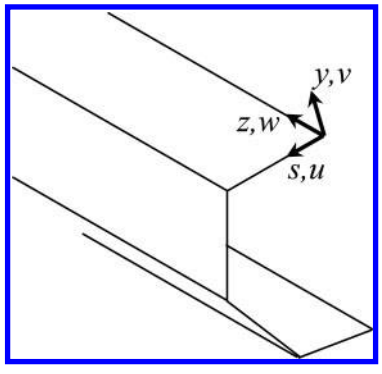


Figure 2. Displacement field.

2 BASIS OF THE GBT APPROACH

Stiffened thin-walled members with open, closed and partially closed cross-sections are considered as an assembly of plate segments (Fig. 1).

The displacement of an arbitrary point $P(s,0,z)$ on the plates mid-surface is described by:

$$\boldsymbol{u}(s,z) = u(s,z)\boldsymbol{e}_s(s) + v(s,z)\boldsymbol{e}_y(s) + w(s,z)\boldsymbol{e}_z(s) \quad (1)$$

using a three-dimensional Cartesian coordinate system, s being the curvilinear abscissa along the mid-line C, y the ordinate and z the coordinate along the member axis with unit vectors $\boldsymbol{e}_s(s)$, $\boldsymbol{e}_y(s)$ and $\boldsymbol{e}_z(s)$ and displacement components $u(s,z)$, $v(s,z)$ and $w(s,z)$ in the same triplet (Fig. 2). In the framework of GBT, Kantorovich's semi-variation method is used to describe the displacement components as a linear combination of assumed deformation modes:

$$\boldsymbol{u}(s,z) = \begin{bmatrix} \sum_{k=1}^{K} U_k(s)\varphi_k(z) \\ \sum_{k=1}^{K} V_k(s)\varphi_k(z) \\ \sum_{k=1}^{K} W_k(s)\varphi'_k(z) \end{bmatrix} \quad (2)$$

where $(')$ denotes differentiation with respect to the variable that follows. $U_k(s)$, $V_k(s)$ and $W_k(s)$ are the three components of the k-th deformation modes (with $k=1,\ldots,K$) and $\varphi_k(z)$ describes their amplitude along the member axis.

2.1 *Displacement and strain field*

The displacement of an arbitrary point $Q(s,y,z)$ lying-within the thickness of the plate can be expressed as $\boldsymbol{d}(s,y,z) = d_s(s,y,z)\boldsymbol{e}_s(s) + d_y(s,y,z)\boldsymbol{e}_y(s) + d_z(s,y,z)\boldsymbol{e}_z(s)$. Employing Kirchoff plate theory, the displacement field is described by:

$$\boldsymbol{d}(s,y,z) = \begin{bmatrix} \sum_{k=1}^{K}[U_k(s) - yV'_k(s)]\varphi_k(z) \\ \sum_{k=1}^{K} V_k(s)\varphi_k(z) \\ \sum_{k=1}^{K}[W_k(s) - yV_k(s)]\varphi'_k(z) \end{bmatrix} \quad (3)$$

The 6 component strain field is comprised of the membrane strains associated with the mid-surface of the plate and the flexural strains which are proportional to the ordinate. From Equation 3, the infinitesimal strain field $\varepsilon = \{\varepsilon_s^M,\ \varepsilon_z^M,\ \gamma_{sz}^M,\ \varepsilon_s^F,\ \varepsilon_z^F,\ \gamma_{sz}^F\}^T$ can be expressed as:

$$\boldsymbol{\varepsilon}(s,y,z) = \begin{bmatrix} \sum_{k=1}^{K} U'_k(s)\varphi_k(z) \\ \sum_{k=1}^{K} W_k(s)\varphi''_k(z) \\ \sum_{k=1}^{K}[W'_k(s) - U_k(s)]\varphi'_k(z) \\ -y\sum_{k=1}^{K} V''_k(s)\varphi_k(z) \\ -y\sum_{k=1}^{K} V_k(s)\varphi''_k(z) \\ -2y\sum_{k=1}^{K} V'_k(s)\varphi'_k(z) \end{bmatrix} \quad (4)$$

where superscripts M and F denote membrane and flexural strains respectively.

Vlasov's fundamental hypotheses for open thin-walled sections specify that the plate segments are: (i) inextensible in the tangential direction, i.e. $\varepsilon_s^M = 0$ and (ii_1) are shear indeformable in their mid-plane, i.e. $\gamma_{sz}^M = 0$. For plate segments belonging to closed loops, the second condition is relaxed and replaced with (ii_2) $\gamma_{sz}^M = constant$, in a piece-wise manner along the abscissa according to Bredt theory for torsion. The displacement components $U_k(s)$, $V_k(s)$ and $W_k(s)$ are chosen in such a way as to satisfy (i) and (ii_1), or (i) and (ii_2) where appropriate.

2.2 *Stress field*

The resulting stress field $\boldsymbol{\sigma} = \{\sigma_s^M,\ \sigma_z^M,\ \tau_{sz}^M,\ \sigma_s^F,\ \sigma_z^F,\ \tau_{sz}^F\}^T$ is composed of an active σ_a and a reactive σ_r part, i.e. $\boldsymbol{\sigma} = \boldsymbol{\sigma}_a + \boldsymbol{\sigma}_r$. In particular for plate on open branches $\boldsymbol{\sigma}_a = \{0, \sigma_z^M, \sigma_s^F, \sigma_z^F, \tau_{sz}^F\}^T$, for plates belonging to closed loops $\boldsymbol{\sigma}_a = \{0, \sigma_z^M, \tau_{sz}^M, \sigma_s^F, \sigma_z^F, \tau_{sz}^F\}^T$ and for all plates $\boldsymbol{\sigma}_r = \{\sigma_s^M, 0, \tau_{sz}^M, 0, 0,\}^T$. Assuming a linear elastic constitutive model, the stress field can be expressed as:

$$\boldsymbol{\sigma} = \boldsymbol{C}_e\boldsymbol{\varepsilon} + \boldsymbol{\sigma}_r \quad (5)$$

where $\boldsymbol{C}_e$ is the elastic matrix and is defined as:

$$\boldsymbol{C}_e = \begin{bmatrix} 0 & 0 & 0 & 0 & 0 & 0 \\ & E & 0 & 0 & 0 & 0 \\ & & G & 0 & 0 & 0 \\ & & & \frac{E}{1-\upsilon^2} & \frac{\upsilon E}{1-\upsilon^2} & 0 \\ & sym & & & \frac{E}{1-\upsilon^2} & 0 \\ & & & & & G \end{bmatrix} \quad (6)$$

2.3 *Weak form of the problem*

The principle of virtual work is used to derive the weak form of the problem which and can be expressed as:

$$\int_V \delta\boldsymbol{\varepsilon}^T\boldsymbol{\sigma}dV = \int_S \delta\boldsymbol{u}^T\boldsymbol{f}dS \tag{7}$$

where virtual quantities are denoted by $\delta(\cdot)$ and $\boldsymbol{f}(s,z) = f_s(s,z)\boldsymbol{e}_s(s) + f_y(s,z)\boldsymbol{e}_y(s) + f_z(s,z)\boldsymbol{e}_z(s)$ are the surface loads applied to the member.

Substituting Equations 3–5 into 7, the weak formulation is expressed as a function of the unknown amplitude functions $\boldsymbol{\varphi}$ as follows

$$\int_0^L(\boldsymbol{\mathcal{A}}\delta\boldsymbol{\varphi})^T\boldsymbol{T}(\boldsymbol{\mathcal{A}}\boldsymbol{\varphi})dz = \int_0^L(\boldsymbol{\mathcal{B}}\delta\boldsymbol{\varphi})^T\boldsymbol{g}dz \tag{8}$$

with differential operators $\boldsymbol{A} = [1 \;\; \partial \;\; \partial^2]^T$ and $\boldsymbol{B} = [1 \;\; \partial]^T$; the stiffness terms are grouped as follows:

$$\boldsymbol{T} = \begin{bmatrix} \boldsymbol{B} & \boldsymbol{0} & \boldsymbol{D^a} \\ \boldsymbol{0} & \boldsymbol{D^c} & \boldsymbol{0} \\ \boldsymbol{D^b} & \boldsymbol{0} & \boldsymbol{C} \end{bmatrix} \tag{9}$$

with $K \times K$ stiffness matrices $\boldsymbol{B}$, $\boldsymbol{C}$, $\boldsymbol{D^a}$, $\boldsymbol{D^b}$ and $\boldsymbol{D^c}$, whose coefficients are defined by:

$$B_{hk} = \int_{\mathcal{C}} \left[\tfrac{Et^3}{12(1-\nu^2)} V_h'' V_k''\right] ds \tag{10}$$

$$C_{hk} = \int_{\mathcal{C}} \left[EtW_hW_k + \tfrac{Et^3}{12(1-\nu^2)} V_hV_k\right] ds \tag{11}$$

$$D^a_{hk} = \int_{\mathcal{C}} \left[\tfrac{\nu Et^3}{12(1-\nu^2)} V_hV_k''\right] ds \tag{12}$$

$$D^b_{hk} = \int_{\mathcal{C}} \left[\tfrac{\nu Et^3}{12(1-\nu^2)} V_h''V_k''\right] ds \tag{13}$$

$$D^c_{hk} = \int_{\mathcal{C}} \left[Gt(U_h + V_h')(U_k + V_k') + \tfrac{Gt^3}{3} V_h'V_k'\right] ds \tag{14}$$

The loading terms are collected as:

$$\boldsymbol{g} = \begin{bmatrix} \boldsymbol{g^a} \\ \boldsymbol{g^b} \end{bmatrix} \tag{15}$$

where the coefficients included in the $K \times 1$ load vectors $\boldsymbol{g^a}$ and $\boldsymbol{g^b}$ are defined by:

$$\boldsymbol{g^a} = \int_{\mathcal{C}} f_z W_h ds \tag{16}$$

$$\boldsymbol{g^b} = \int_{\mathcal{C}} [f_s U_h + f_y V_h] ds \tag{17}$$

3 CROSS-SECTIONAL ANALYSIS

The fundamental role of the GBT cross-sectional analysis is the identification of a set of deformation modes able to adequately describe the distortion of the cross-section from its initial shape. In this study the conventional deformation modes are taken as the dynamic eigenmodes of a free planar frame representing the cross-section (Ranzi & Luongo, 2011). The dynamic analysis is carried out on a discrete model using standard finite element procedures (Bathe 2006). This leads to the following algebraic generalised eigenvalue problem

$$(\boldsymbol{K} - \lambda\boldsymbol{M})\boldsymbol{q} = \boldsymbol{0} \tag{18}$$

where $\boldsymbol{K}$ is the stiffness matrix, $\boldsymbol{M}$ the mass matrix and $\boldsymbol{q}$ is the vector of nodal displacements of the section.

3.1 *Inextensibility constraint*

Solving the eigenvalue problem in its current form results in conventional deformation modes which violates Vlasov's first fundamental hypothesis. To enforce inextensibility of the plate segments, internal constraints are introduced into the model. This is carried out following available procedures commonly used in finite element modelling (e.g., ABAQUS 2008), also applied to thin-walled structures in recent years (e.g., Casafront et al. 2009, Adany & Schafer 2008)

In local coordinates the (linearised) constraints can be written as $u_1^e - u_2^e = 0$, and in global coordinates as:

$$(u_j - u_i)\cos\alpha_e + (v_j - v_i)\sin\alpha_e = 0 \tag{19}$$

where element e joins nodes i and j and forms an angle α_e with the X-axis. In matrix form:

$$\boldsymbol{Aq} = \boldsymbol{0} \tag{20}$$

where $\boldsymbol{A}$ is an $M \times N$ matrix where M is the number of constraints (i.e one for each element) and $N > M$ is the number of *dofs* within the system; $\boldsymbol{q} = \{\quad, u_j, v_j, \theta_j, \cdots\}^T$ is an $N \times 1$ vector of nodal displacements of the section in global coordinates (X, Y).

This system of equations can be partitioned as follows:

$$[\boldsymbol{A}_m \quad \boldsymbol{A}_s]\begin{bmatrix} \boldsymbol{q}_m \\ \boldsymbol{q}_s \end{bmatrix} = \boldsymbol{0} \tag{21}$$

where $\boldsymbol{A}_s$ is an $M \times M$ invertible matrix. Therefore the M slave *dofs* $\boldsymbol{q}_s$ can be expressed in terms of the $(N - M)$ master *dofs* $\boldsymbol{q}_m$:

$$\boldsymbol{q} = \boldsymbol{R}\boldsymbol{q}_m \tag{22}$$

where:

$$\boldsymbol{q} = \begin{bmatrix} \boldsymbol{q}_m \\ \boldsymbol{q}_s \end{bmatrix} \tag{23}$$

$$\boldsymbol{R} = \begin{bmatrix} \boldsymbol{I} \\ -\boldsymbol{A}_s^{-1}\boldsymbol{A}_m \end{bmatrix} \tag{24}$$

Substituting Equation 22 into Equation 18, the eigenvalue problem with constraints can be expressed in terms of displacements of the master *dofs* $\boldsymbol{q}_m$:

$$(\boldsymbol{K}_R - \lambda \boldsymbol{M}_R)\boldsymbol{q}_m = \boldsymbol{0} \tag{25}$$

where:

$$\boldsymbol{K}_R = \boldsymbol{R}^T \boldsymbol{K} \boldsymbol{R} \tag{26}$$

$$\boldsymbol{M}_R = \boldsymbol{R}^T \boldsymbol{M} \boldsymbol{R} \tag{27}$$

3.2 *Dynamic eigenmodes and warping functions*

Solving Equation 25, the eigenvalues λ represent the squared eigenfrequencies and provide a natural ordering to the deformation modes. The in-plane deformation modes $U_k(s)$ and $V_k(s)$ from Equation 2 are chosen as the eigenvectors $\boldsymbol{q}$ and their associated shape functions.

The warping displacements $W_k(s)$ are calculated by enforcing (ii_1) nil or (ii_2) constant shear strain assumptions. The membrane shear strain can be expressed as:

$$\gamma_{sz}^M(s) = \sum_{k=1}^{K} \Gamma_k(s)\varphi_k'(z) \tag{28}$$

where:

$$\Gamma_k(s) = W_k'(s) + U_k(s) \tag{29}$$

and $\Gamma_k(s)$ is a piecewise constant function which is equal to zeros for elements lying on open branches and unknown for elements belonging to closed loops. Based on the elements displacements:

$$\Gamma_k^e = \frac{W_k^{i_2} - W_k^{i_1}}{b^e} + U_k^e \tag{30}$$

where W_k^{i1} and W_k^{i2} are the warping displacements at the near i_1 ($s = 0$) and far i_2 ($s = b^e$) nodes respectively of element e of length b^e.

For open sections the warping displacements W^i are determined by imposing for each element:

$$\Gamma_k^e = \frac{W_k^{i_2} - W_k^{i_1}}{b^e} + U_k^e = 0 \tag{31}$$

However one of the unknowns remains arbitrary and represents the uniform extension of the member. To ensure the warping of each mode is orthogonal to the extension, the remaining unknown is chosen such that the average warping of each mode is zero:

$$\int_c W_k(s)ds = 0 \tag{32}$$

For closed sections, or elements belonging to closed braches, the constants Γ_k^e are related via the constitutive law to the (unknown) tangential stress flow Q_k^j acting on the j^{th} loop. In this case Equation 31 is replaced by:

$$Gt^e \Gamma_k^e = Gt^e \left(\frac{W_k^{i_2} - W_k^{i_1}}{b^e} + U_k^e \right) = \sum_j (\pm) Q_k^j \tag{33}$$

where the sum is extended to all closed loops that element e belongs to.

Once the warping displacements have been determined, the stiffness and loading terms, $\boldsymbol{T}$ and $\boldsymbol{g}$, from Equation 8 can finally be determined.

4 MEMBER ANALYSIS

The objective of the GBT member analysis is to determine the global response of a thin-walled element. This is carried out in this study applying the finite element method to the weak form of the problem derived in Section 2.3.

4.1 *Discrete model for the member analysis*

With the finite element approach, the unknown amplitude functions $\boldsymbol{\varphi}$, expressed in terms of the member axis, are approximated by means of polynomials:

$$\boldsymbol{\varphi} \cong \boldsymbol{N}^e \boldsymbol{\varphi}^e \tag{34}$$

where $\boldsymbol{\varphi}^e$ collects the function nodal values and the adopted shape functions are specified in $\boldsymbol{N}^e$.

Substituting Equation 34 into Equation 8, the problem is transformed into the following system of linear equations for the e-th element:

$$\boldsymbol{K}^e \boldsymbol{\varphi}^e = \boldsymbol{p}^e \tag{35}$$

where $\boldsymbol{K}^e$ is the stiffness matrix, defined by:

$$\boldsymbol{K}^e = \int_0^L (\boldsymbol{\mathcal{A}}\boldsymbol{N}^e)^T \boldsymbol{T} \boldsymbol{\mathcal{A}} \boldsymbol{N}^e dz \tag{36}$$

and $\boldsymbol{p}^e$ is the vector of nodal actions, expressed as:

$$\boldsymbol{p}^e = \int_0^L (\boldsymbol{\mathcal{B}}\boldsymbol{N}^e)^T \boldsymbol{g} dz \tag{37}$$

4.2 *Constraint conditions*

Constraint conditions are applied to the stiffened plate elements to provide the rigidity exhibited by the specified stiffeners. The solution is then sought following the procedure already illustrated for the cross-sectional analysis in Equations 20–27.

5 APPLICATIONS

Numerical examples are presented in the following to illustrate the accuracy of the proposed procedure. Two simply supported thin-walled members with 1 mm thick plates, elastic modulus of 200 GPa and Poisson's ratio of 0.3 are considered. Stiffeners are placed at 0.25 m centres along their 1 m length.

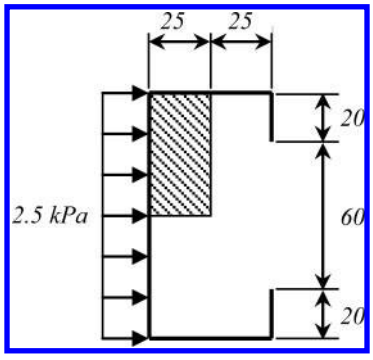


Figure 3. Stiffened lipped channel section (all dimensions are in mm).

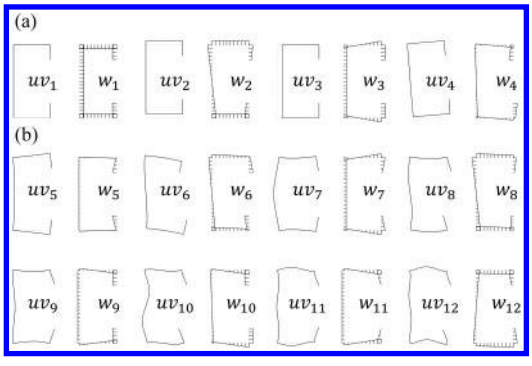


Figure 4. Lipped channel section: (a) rigid modes; (b) deformation modes.

5.1 *Lipped channel section*

The stiffened lipped channel section is depicted in Figure 3, with uniform pressure applied to the web of the section. For illustrative purposes the four rigid body modes and first eight deformation modes are presented in Figure 4.

A summary of the results is presented in Figure 5 at critical locations along the member length (i.e. where the various field outputs reach their maximum values). The results of the proposed procedure are compared to those obtained using GBT for a fully stiffened section (i.e. $\boldsymbol{\varphi}^e$ nil for all non-rigid body modes at the stiffener locations) and a shell finite element model developed in Abaqus which reflects the stiffeners' arrangement outlined in Figure 3. For clarity, the displacements have been scaled to provide a clear overview of the deformations of the section while the stresses are left unscaled to aid in comparisons between their relative magnitudes. This comparison shows a close match between the results calculated with the proposed GBT approach and Abaqus models, while the fully stiffened GBT model underestimates the deformations as expected.

5.2 *Box girder section*

The stiffened box girder section has been loaded with a uniform pressure applied to the left hand half of the top flange with one-quarter of the closed box being stiffened (Fig. 6). A summary of the cross-sectional analysis is provided in Figure 7 with the four rigid body modes and the first eight deformation modes of the section being depicted.

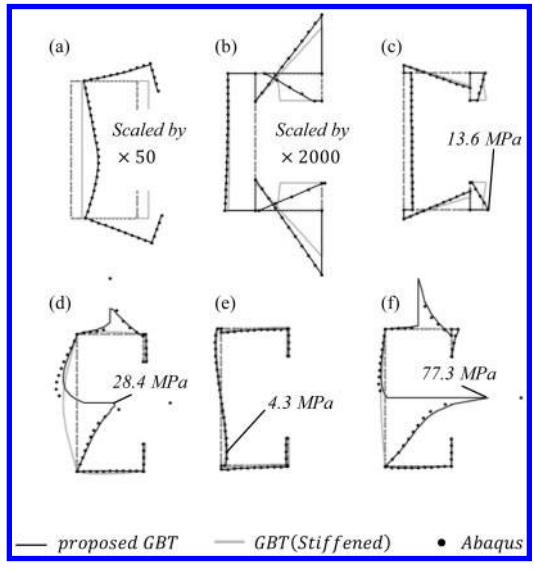


Figure 5. Lipped channel section deformations and stress distributions: (a) uv at $z = L/2$; (b) w at $z = 0, L$; (c) σ_z^M at $z = L/2$; (d) σ_z^F at $z = L/2$; (e) τ_{sz}^F at $z = 0, L$; (f) σ_s^F at $z = L/2$.

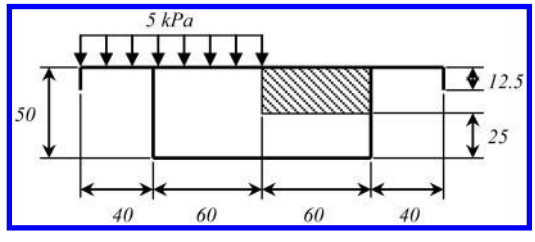


Figure 6. Stiffened box girder section (all dimensions are in mm).

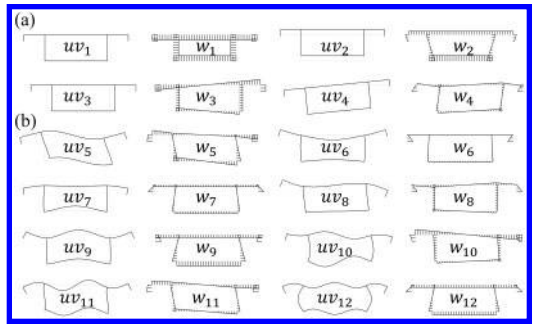


Figure 7. Box girder section: (a) rigid modes; (b) deformation modes.

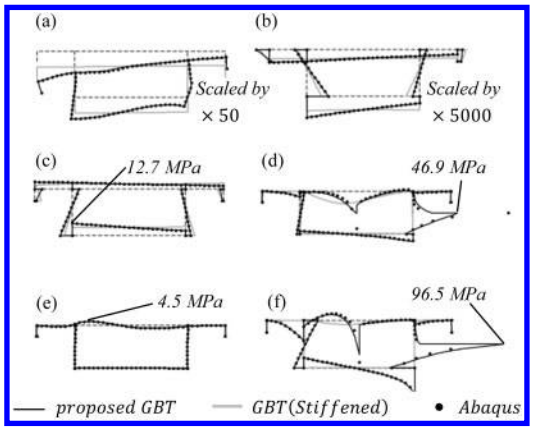


Figure 8. Box girder section deformations and stress distributions: (a) uv at $z = L/2$; (b) w at $z = 0, L$; (c) σ_z^M at $z = L/2$; (d) σ_z^F at $z = L/2$; (e) τ_{sz}^F at $z = 0, L$; (f) σ_s^F at $z = L/2$.

Comparisons of the results obtained from the three models are displayed in Figure 8, with the displacements scaled and the stresses left unscaled as in the previous example. The values obtained with the proposed GBT and the Abaqus models are in close agreement. At the edge of the stiffened regions, the section experiences large flexural stress concentrations which, in some cases, are almost an order of magnitude higher than the membrane stresses. These peak stresses are localised and dissipate within a distance equal to the depth of the section either side of the stiffener location (e.g. 450 mm $< z <$ 550 mm).

6 CONCLUSION

This paper described an approach to account for the presence of arbitrary stiffeners' arrangements and geometries in the framework of Generalised Beam Theory (GBT). With the proposed procedure, the dynamic modes of an unconstrained planar frame are used as the in-plane conventional deformation modes, from which the corresponding warping deformations are determined in a post-processing phase. Constraint conditions are applied to the stiffened plate elements to provide the rigidity exhibited by the specified stiffeners. This approach is applicable indifferently to open, closed and partially closed stiffened sections. Two numerical examples were presented to highlight the accuracy of the method, with close agreement found between the proposed GBT and a shell finite element model developed in Abaqus.

ACKNOWLEDGEMENTS

The work in this article was supported by the Australian Research Council through its Discovery Projects funding scheme (DP1096454) and by an award under the Merit Allocation Scheme on the NCI National Facility at the ANU. Part of the computational services used in this work was provided by Intersect Australia Ltd.

REFERENCES

ABAQUS (2008). *Standard User's Manual Version 6.8-1*. Hibbitt, Karlsson and Sorensen, Inc, Vols. 1–3, USA.

Adany, S. & Schafer B.W. 2006. Buckling mode decomposition of single-branched open cross-section members via finite strip method: application and examples. *Thin-Walled Structures* 44: 585–600.

Adany, S. & Schafer B.W. 2008. A full model decomposition of thin-walled, single-branched open cross-section members via the constrained finite strip method. *Journal of Constructional Steel Research* 64 (1): 12–29.

Andreassen, M.J. & Jönsson, J. 2012. Distortional solutions for loaded semi-discretized thin-walled beams. *Thin-Walled Structures* 50: 116–127.

Basaglia, C., Camotim, D., Silvestre, N. 2008. Global buckling analysis of plane and space thin-walled frames in the context of GBT. *Thin-Walled Structures* 46: 79–101.

Bathe, K.J. 2006. *Finite element procedures*. Englewood Cliffs: Prentice Hall.

Casafront, M., Marimon, F., Pastor, M.M. 2009. Calculation of pure distortional elastic buckling loads of members subjected to compression via the finite element method. *Thin-Walled Structures* 47 (6–7): 701–729.

Davies, J.M. & Leach, P. 1994. First-order Generalised Beam Theory. *Journal of Constructional Steel Research* 31: 187–220.

Dinis, P.B., Camotim, D., Silvestre, N. 2007. FEM-based analysis of local-plate/distortional mode interaction in cold-formed steel lipped channel columns. *Computers & Structures* 85: 1461–1474.

Goncalves, R., Dinis, P.B., Camotim, D. 2009. GBT formulation to analyse the first-order and buckling behavior of thin-walled members with arbitrary cross-sections. *Thin-Walled Structures* 47: 583–600.

Goncalves, R. & Camotim, D. 2010. Steel-concrete composite bridge analysis using Generalised Beam Theory. *Steel and Composite Structures* 10 (3): 223–243.

Goncalves, R., Ritto-Corrêa, M., Camotim, D. 2010. A new approach to the calculation of cross-section deformation modes in the framework of generalized beam theory. *Computational Mechanics* 46 (5): 759–781.

Jiang, C. & Davies, J.M. 1997. Design of thin-walled purlins for distortional buckling. *Thin-Walled Structures* 29 (1–4): 189–202.

Jönsson, J. & Andreassen, M.J. 2011. Distortional eigenmodes and homogeneous solutions for semi-discretized thin-walled beams. *Thin-Walled Structures* 49 (6): 691–707.

Ranzi, G. & Luongo, A. 2011. A new approach for thin-walled member analysis in the framework of GBT. *Thin-Walled Structures* 49: 1404-1414.

Schardt, R. 1989. Verallgemeinerte Technicsche Biegetheory. *Springler-Verlag*, Germany.

Silvestre, N. & Camotim, D. 2002. First-order generalised beam theory for arbitrary orthotropic materials. *Thin-Walled Structures* 40: 755–789.

Silvestre, N., Young, B., Camotim, D. 2008. Nonlinear behaviour and load-carrying capacity of CFRP-strengthened lipped channel steel columns. *Engineering Structures* 30: 2613–2630.

Silvestre, N., Camotim, D. Silva, N.F. 2011. Generalised beam theory revisited: from kinematical assumptions to the deformation mode determination. *International Journal of Structural Stability and Dynamics* 11 (5): 969–997.

Research and Applications in Structural Engineering, Mechanics and Computation – Zingoni (Ed.)
© 2013 Taylor & Francis Group, London, ISBN 978-1-138-00061-2

Cold-formed steel design and research assisted by testing

D. Dubina
"Politehnica" University of Timisoara, Romania,
Romanian Academy, Timisoara, Branch, Romania

ABSTRACT: The technical and economic efficiency of cold-formed steel structures, which usually are of thin walled sections, is strongly dependent on the ability of the designer to manage the instability problems and optimize the connection detailing. Due to complicate shapes of cold-formed steel sections, the instability interaction and non-conventional fastening technology, sometimes, it is really difficult to control such types of problems by analytical calculation procedures. On this purpose, modern design codes give the possibility to apply design methodologies assisted by testing. The paper summarizes the European codification for design and research assisted by testing and illustrates the experimental and numerical investigations carried out at the CEMSIG Research Centre of the "Politehnica" University of Timisoara, in order calibrate calculation procedures to some complex structural problems.

1 INTRODUCTION

Cold formed steel members are usually of thin walls, some times of complicate geometry and particular connecting technology. In most of cases the design of structures realized of thin walled sections is dominated by stability problems. Investigation of structural stability problems was based in early stage, e.g 18th–19th century, on experiments, which conducted to empirical solution. Later, research in the structural stability became predominantly theoretical, the extensive theoretical studies being accompanied, at most, by corroborating experiments (Singer et al, 1997), and often, even for complex structural instability problems, the design was based on theoretical assumptions only.

Experimental analysis and testing of structural solutions and calculation models is realized in laboratory or in situ. Simulation of a given problem, using test calibrated numerical models and advanced analysis is also a common research tactics. Both approaches are part of the current research and design methodologies. On this purpose, most of actual Design Codes include relevant provisions related to design assisted by testing and values for calibration of numerical models.

2 EUROPEAN CODIFICATION FRAMING

In Section 5, entitled Structural analysis and design assisted by testing of EN 1990 is stipulated that design may be based on a combination of tests and calculations and that design assisted by test results shall achieve the level of reliability required for the relevant design situation.

The statistical uncertainty due to a limited number of test results shall be taken into account.

Annex D of the code provide the statistical procedures to be applied in order to obtain experimentally the characteristic strengths, R_k, and the partial safety coefficients, γ_M to be applied in the design models in order to calculate the relevant design strengths, R_d.

EN1993-1-3, in its Section 9 it refers to the principles to apply for design assisted by testing, while in the Annex A provide standard procedures for:

- Tests on cold-formed members;
- Tests on profiled sheets and liner trays;
- Tests on structures and portions of structures;
- Tests on beams restrained by sheeting;
- Evaluation of test results to determine design values.

In principle, testing may be undertaken under any of following circumstances:

a) if the properties of steel are unknown;
b) if it is desired to take account of the actual properties of the cold-formed member or sheet;
c) if adequate analytical procedures are not available for designing the component by calculation alone;
d) if realistic data for design cannot otherwise be obtained;
e) if it is desired to check the performance of an existing structure or structural component;
f) if it is desired to build a number of similar structures or components on the basis of a prototype;
g) if confirmation of consistency of production is required;
h) if it is desired to determine the effects of interaction with other structural components;
i) if it is desired to determine the effects of the lateral or torsional restraint supplied by other components;
j) it is desired to prove the validity and adequacy of an analytical procedure;

k) if it is desired to produce resistance tables based on tests, or on a combination of testing and analysis;
l) if it is desired to take into account practical factors that might alter the performance of a structure, but are not addressed by the relevant analysis method for design by calculation.

There are available specific tests based design rules such as those for fasteners here i.e. ECCSS Publication No. 124, 2008: The testing of Connections with Mechanical fasteners in Steel Sheeting and Sections, and ECCS No. 127, 2009 – Preliminary European Recommendations for the Testing and Design of Fastenings for Sandwich Panels

The design of Storage Pallet Rack Systems, is in proportion of 80% based on tests; EN15512:2009, offers relevant procedures on this purpose.

For experimental techniques the reader may found valuable information in the General Report made by Rasmussen (2000) while a state-of-art review of experimental methods applied to study and evaluate stability for buckling of thin-walled structure is presented in the excellent book of Singer et al. (1998).

On the following, two complex structural problems approached by tests will be displayed i.e.

- Experimental evaluation of buckling imperfection coefficient for perforated rack type sections in compression;
- Experimental calibration by laboratory tests and numerical simulation of a Prescriptive Design type methodology for Wall Stud Cold Formed Steel framing house, and its validation by in situ tests.

3 EXPERIMENTAL EVALUATION OF α – IMPERFECTION COEFFICIENT FOR PERFORATED SECTIONS

3.1 *The ECBL method for calibration of the α – imperfection factor*

Since the interactive buckling approach based on ECBL method is already known (Dubina, 2001), herein the principle is summarized only. Assuming the two common mode intraction, in a thin-walled compression member, occurs by coupling of the Euler bar instability mode, $\overline{N}_E = 1/\overline{\lambda}^2$ ($\overline{\lambda}$ = relative member slenderness) and the sectional mode (e.g. distortional instability mode) $\overline{N}_L$ described by means of the reducing factor of area $N_L = Q_L$. The resulting eroded curve for coupled instability mode is $\overline{N}(\overline{\lambda}, Q_L, \psi)$ (see Figure 3).

Critical load maximum erosion (due both to the imperfections and coupling effect) occurs in the instability mode interaction point, M ($\overline{\lambda} = 1/Q_L^{0.5}$) where, the erosion factor ψ is defined as:

$$\psi = \overline{N}_D - \overline{N} \tag{1}$$

in which $\overline{N}(\overline{\lambda}, Q_L, \psi)$ is the relative interactive buckling load and $Q_L = N_L/f_y \cdot A$; A is the gross cross-section area; N_L = the ultimate capacity corresponding to local (or distortional) buckling; $\overline{N} = N/N_{pl}$ the relative axial load; N, the axial load; $N_{pl} = f_y \cdot A$, the full plastic resistance of the member; $\overline{\lambda}$ the relative slenderness of compression member.

If $\overline{\lambda} = 1/Q_L^{0.5}$ is introduced, it results an imperfection factor corresponding to the distortional-global buckling:

$$\alpha = \frac{\psi^2}{1-\psi} \frac{\sqrt{Q_L}}{1 - 0.2\sqrt{Q_L}} \tag{2}$$

Equation (2) represents the new formula of α imperfection coefficient which should be introduced in European buckling curves in order to adapt these curves to distortional-overall interactive buckling.

Even if for a few particular problems analytical procedures might be used to get the erosion factor, ψ, currently the numerical and experimental procedures are only suitable to obtain practical values. Since, anyway, a numerical procedure have to be experimentally calibrated, the experimental approach will be presented. It contains the following steps:

1. Testing of a relevant sample of compression specimens into the coupling range which is defined by the interactive slenderness, $\overline{\lambda} = 1/Q_L^{0.5}$, and also by the points of $\overline{\lambda}_L = \pm 0.1 \cdot \overline{\lambda}_L$ (Fig. 1).
2. Compute the individual value of erosion, $\psi_i = Q_i - N_{i,\exp}/N_{i,pl}$, for the i number, and the mean value of the erosion factor for all n specimens, $\psi_m = \sum_{i=1}^{n} \psi_i / n$.
3. Compute the *design value* of the erosion factor:

$$\psi_d = \psi_d + 2 \cdot s_\psi \tag{3}$$

where s is the standard deviation which is introduced in order to take into account the randomness of numerical results.
4. Compute the value of α, imperfection coefficient, using Eq. (2) using the value of ψ_d, from (3).

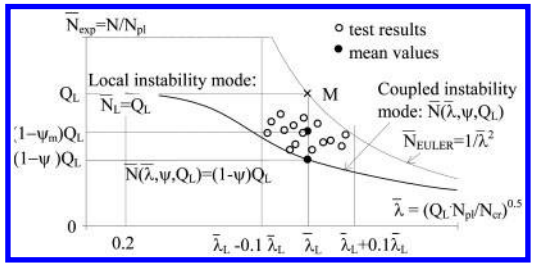


Figure 1. The ECBL model and evaluation of ψ erosion factor.

3.2 *Summary of experimental program*

The ECBL approach was applied to evaluate the α – coefficient for two pallet rack upright sections: RS125 × 3.2 and RS95 × 2.6 (Crisan et al. 2012 a, b).



Figure 2. Failure modes for distortional and interactive buckling specimens.

Table 1. Erosion coefficients.

Interactive length [mm]	Failure load [kN]	Erosion (ψ)	Interactive length [mm]	Failure load [kN]	Erosion (ψ)
RS125 × 3.2			RS95 × 2.6		
2110	296.73	0.153	1510	171.50	0.357
	296.91	0.153		169.07	0.365
	293.63	0.159		178.68	0.332
2310	276.15	0.196	1610	151.69	0.426
	274.22	0.200		160.16	0.396
	298.07	0.150		168.88	0.366
2510	265.44	0.218	1760	158.41	0.403
	269.71	0.209		149.73	0.433
	244.69	0.261		151.62	0.426
	ψ_m	0.189		ψ_m	0.389
	s	0.038		s	0.036
	ψ_d	0.265		ψ_d	0.461
	α	0.102		α	0.479

Figures 2 display selected failure modes for the tested specimens of distortional and interactive buckling length tests, while in Table 1 are presented the results obtained using the ECBL approach.

3.3 *Results*

The case of RS125 × 3.2 section is a real mode interaction case, where distortional and flexural modes are interacting, the compression reference load for erosion is the distortional ultimate load, while for RS95×2.6 section, there is no interaction of buckling modes, the erosion being caused by the effect of plastic deformations and geometrical imperfections .

In Figure 3 and Figure 4 are presented, comparatively, the buckling curves computed using the specifications of EN1993-1-1 together with the calibrated values of the α imperfection factors, obtained using the ECBL approach (considering the inertia moment of gross section (ECBL B) – solid red line and the

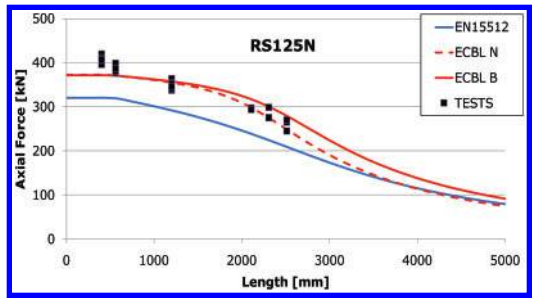


Figure 3. Buckling curve for RS125 × 3.2 section (Crisan et al.)

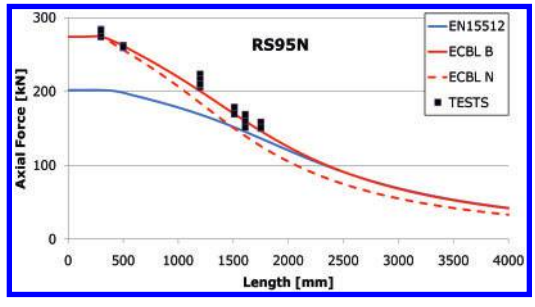


Figure 4. Buckling curve for RS95 × 3.2 section (Crisan et al. 2012).

inertia moment of the section with perforations (ECBL N) – dashed red line) and the ones obtained using the design according to EN15512:2009.

4 EXPERIMENTAL CALIBRATION OF DESIGN METHODOLGY FOR COLD-FORMED STEEL FRAMING RESIDENTIAL BUILDINGS

4.1 *Principle of prescriptive method*

For a proper design of cold-formed steel-framed houses prone to both, gravity and horizontal loadings, (e.g. wind and/or earthquake), the behavior of the shear walls has to be known.

Prescriptive Method applies for design of standardized "wall-stud" structural systems for residential low rise buildings (AISI, 1998). The principle is to compare the wall-stud capacity with corresponding gravity load demand and shear capacity of the wall-stud panels with sear demand induced by horizontal loadings. If for gravity loads the problem is quite simple, for horizontal actions, test and numerical simulations are necessary to get both shear capacity and stiffness of reference shear wall (e.g. 1m span).

Besides the structural walls, the behavior of a house is influenced, at least in the early stage of the shaking, by the non-structural elements which usually is not accounted for in the design. The non-structural finishing elements have a structural contribution that changes the vibration modes and the damping properties of the structure. So, the stiffness, resistance and ductility of cold-formed steel shear walls have to be

Series	Configuration	Cladding	Testing Method	No. Test
O		-	Monotonic	1
I		Cor. Sheet LTP20/0.5 (Ext)	Monotonic	1
			Cyclic	2
II		Cor. Sheet (Ext) Gyps Board (Int)	Monotonic	1
			Cyclic	2
III		Cross Bracing (Ext-Int)	Monotonic	1
			Cyclic	1
IV		Cor. Sheet LTP20/0.5 (Ext)	Monotonic	1
			Cyclic	2
OSB I		OSB Panels (Ext)	Monotonic	1
			Cyclic	1
OSB II		OSB Panels (Ext)	Monotonic	1
			Cyclic	1
Total number of specimens				15

Figure 5. Summary of the tested wall panels (Fulop & Dubina, 2006).

evaluated via laboratory tests and after, extended by numerical simulations.

Following, the full procedure applied to obtain reference values for shear capacity, stiffness and ductility and their validation is summarized.

4.2 *Experimental program*

4.2.1 *Tests on shear walls*

First, an experimental program on shear walls with common sheeting solutions has been carried out in order to observe the behavior and to evaluate the structural properties of different wall typologies. Each specimen series consisted of identical wall panels (3600 × 2440 mm), tested under lateral loads under monotonic and cyclic loading (Fig. 5).

The skeleton of the wall panels was made of "C" shaped cold-formed steel elements, with studs at 600mm intervals. Fixing between profiles within the wall skeleton, and between the sheeting and skeleton, was done with self-drilling screws (d = 4.8 mm).

Figure 6 displays load versus lateral displacement curves both for the monotonic and cyclic responses. Wall panels have exhibited highly nonlinear behavior.

As observed during the experiments, the lateral deformation of the panel depends on the shear deformation of the sheeting (e.g. distortion of corrugation); the deformation due to corner uplift, and, most significantly, the nonlinear deformation of the connections between the sheeting and the skeleton.

As experimental curves are nonlinear from the beginning, elastic design capacity of the panels can only be defined in a conventional way. Any assumption of an elastic design limit is to be related to a tolerable deformation within the group of connectors that are subjected to the highest forces and therefore more based on criteria of serviceability rather than strength, at the level of the entire panel. Also, there will be an important strength reserve beyond any elastic design

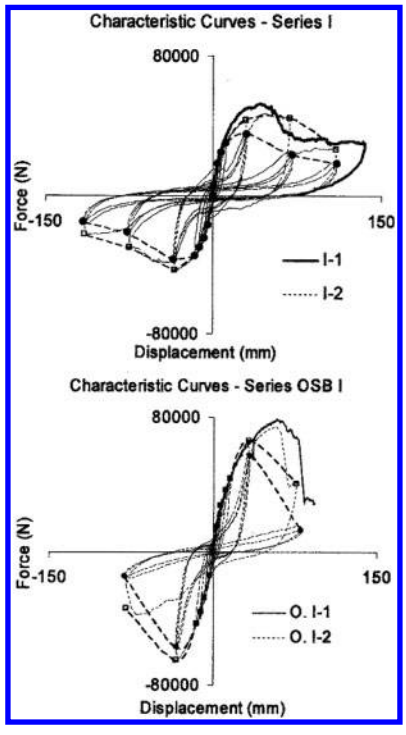


Figure 6. Experimental load versus displacement curves.

limit considered, due to the redundancy of the structural system and to the supplementary load bearing capacity of the remaining active connectors when the most loaded ones show excessive deformations or even failure.

The design strength of the panels was referred to as the minimum of the force at story drift angle 1/300 (F_{300}) and $2/3F_{max}$.

Observing comparatively the monotonic to cyclic behavior, a reduction of strength of about 10–15% can be observed in the case of cyclic loading. Hence if the design strengths of the panels are deduced based on monotonic experiments the performance will be overestimated. An important characteristic of cyclic curves is the strong pinching (a factor of 0.85 – 0.95), the source of it being the slip in the connectors at reverse loading, which implies a reduced energy dissipation. Strength degradation in consecutive loading cycles is also present as a result of accumulated damage in the panel during the loading history, leading to a significant difference between stabilized and unstabilized envelope curves.

Compared to the ones with corrugated sheeting, the failure of the OSB sheeted panels was less ductile.

4.2.2 *Tests on connections*

The second series of experiments was carried out in order to determine the mechanical properties of the connections that were identified to have a crucial effect on the behavior of the panels. Three types of screwed connection were tested, i.e. (1) connection

Table 2. Summary of Tested Connections.

Base thickness [mm]	Connected thickness [mm]	Screw diameter [mm]	Loading velocity: Slow (1 mm/min) Nr.	Slow (1 mm/min) Code	Fast (420 mm/min) Nr.	Fast (420 mm/min) Code
1.42	0.417	4.8	4 + 2	I-TP-M-V1-1,. . .,4, 6, 7	4	I-TP-M-V2-1,. . .,4
0.417	0.417	4.2	4	I-TS-M-V1-1,. . .,4	3	I-TS-M-V2-1,. . .,3

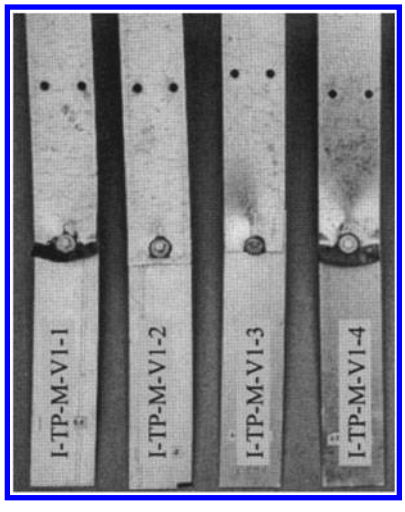


Figure 7. Experimental load versus displacement curves.

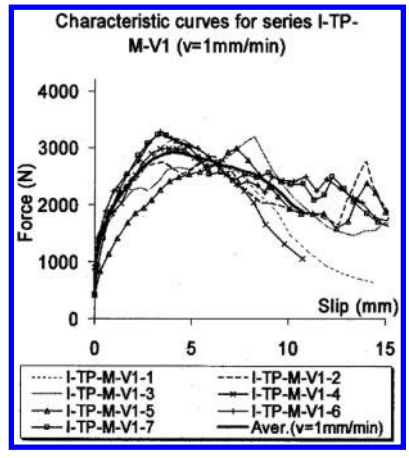


Figure 8. Experimental load versus displacement curves.

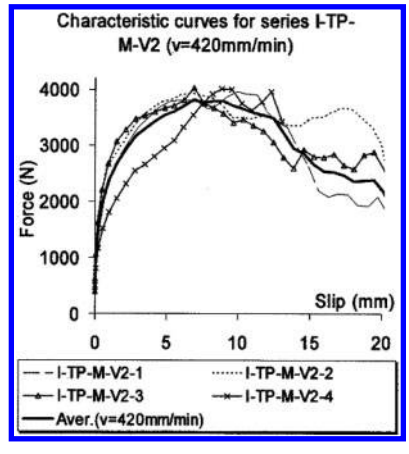


Figure 9. Experimental load versus displacement curves.

between the corrugated steel sheeting and steel profiles; (2) sheeting-to-sheeting seam connections; and (3) connections between the OSB panels and the steel profiles.

The dimensions of the specimens were chosen according to the European ECCS recommendations (1983), the dimensions of the connecting plates being 50 × 220 mm. Table 2 shows the parameters of specimens of type 1.

Figures 7 and 8 show the failure modes and the corresponding load vs. displacement curves.

The fast velocity specimens (I-TP-M-V2) have shown a similar behavior.

In the case of thin-to-thin sheet connections (Type 2), simulating seam fasteners, the failure mode was due to tilting and pulling-out of the screw. Similar failure mode was observed for seam connections during the wall panel experiments. The results are presented in Figure 9.

Figure 10 display the load-deformation curve for OSB steel specimens, while in Figure 11 is presented the corresponding failure modes.

As a general remark, these connection are not only less ductile, but also of lower strength if compared with those for sheeting-to-steel profiles.

4.2.3 *Calibration of numerical models*

Based on the component characteristics determined experimentally, a FE model was made in ANSYS in order to replicate the behavior of the entire wall panel (Fulop & Dubina, 2006).

As a first step, the wall panels of corrugated sheeting were considered because component's behavior was more homogeneous in this case.

The bars of the skeleton were modeled as elastic beam elements (BEAM4) by taking into account that these elements were not heavily deformed in the post-elastic range. The corrugated sheet was modeled as an equivalent orthotropic plate (SHELL43)

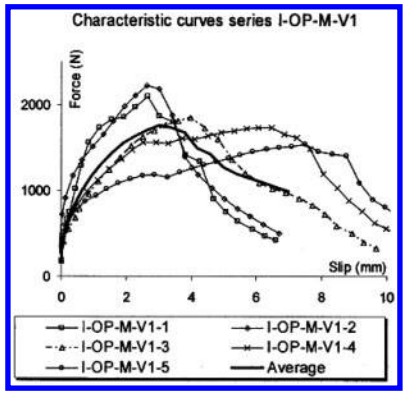


Figure 10. Experimental curves for OSB-to-steel connection.

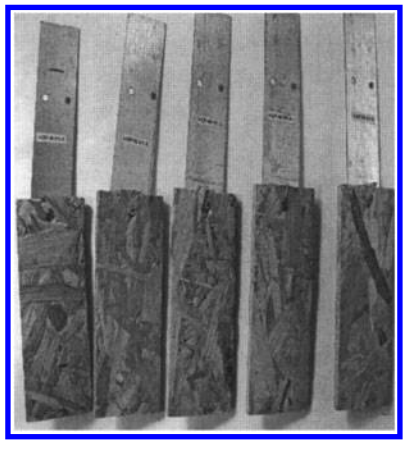


Figure 11. Failure modes for OSB-to-steel connection.

in order to take into account the fundamentally different mechanical properties of the corrugated sheet in the two principal directions and the distortion of the corrugated sheet when loaded in shear. The equivalent elastic modules (E_l – longitudinally and E_t – transversally) have been determined through preliminary modeling of a single corrugation loaded in tension in the two principal directions. The equivalent shear modulus (G_{eff}) has been calculated by taking into account the end distortion of the corrugated sheeting. Connections, both between the skeleton and the sheeting and the seam connections, were modeled using COMBIN39 elements, by considering average deformation properties of the tested connection loaded at 1 mm/min (Fig. 7).

Beside these components it is important to take into account the uplift deformation of the wall panel corners. The FE model was subjected to increasing horizontal loading at the upper part of the panel, similarly to wall panels during the full scale test. The deformation pattern and the nonlinear behavior curve obtained with the FE model was compared with the monotonic curves obtained during the wall panel experiments (Fig. 12), while Figures 13 and 14 prove the remarkable similarities in terms of deformation pattern and

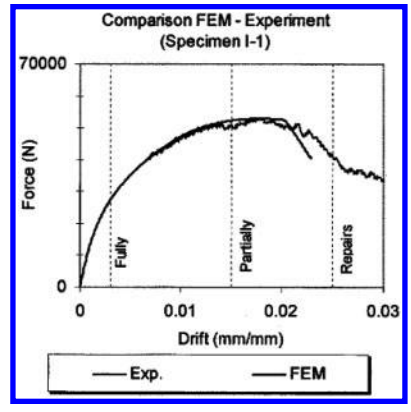


Figure 12. Behaviour curve (experimental vs. FEM–Series I).

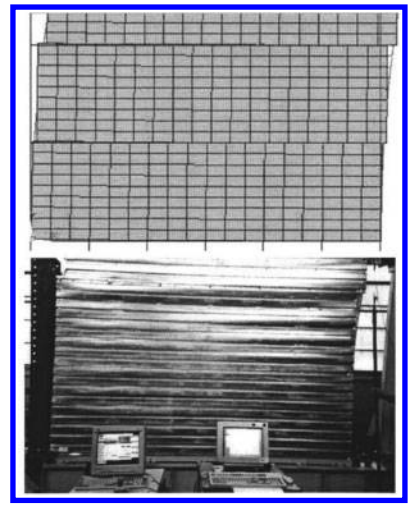


Figure 13. Comparison of deformed shape (experimental versus FEM–Series I – Fulop & Dubina, 2006).

nonlinear behavior between model and tests. By using the described FEM technique, the performance of wall panels can be evaluated, which are using the same basic materials and connection typologies but have a different geometrical configuration.

The calibrated numerical modes have enabled to characterize shear walls of same structural solutions in terms of sear capacity, stiffness and ductility (Dubina et al. 2006, Fulop & Dubina, 2006). Evidence of possibility to frame such kind of structures at least as low dissipative (e.g. $q = 1.5 - 2.0$).

4.3 *Design of house structure using "Prescriptive Method" procedure*

The structure presented in Figure 15 belongs to a two-story single family house. The dimensions of the building are 9m (axes A–D) by 10.5 m (axes 1–4), of which 1.5 m is between axes 3 and 4.

Each level is about 2.75 m high and the slope of the roof is 30°.

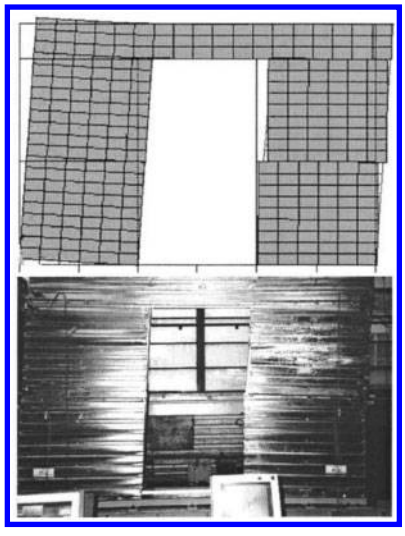


Figure 14. Comparison of deformed shape (experimental versus FEM–Series IV- Fulop & Dubina, 2006).

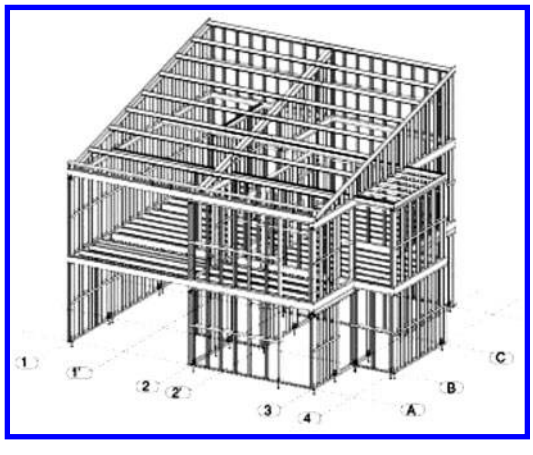


Figure 15. Steel skeleton of the structure.

The structural skeleton was made of cold-formed C-shaped profiles with a core thickness of 1.5 mm (C150/1.5) placed at 600 mm intervals. The elements of the skeleton were connected using 4.8 mm diameter self-drilling screws. The height of the C profile was 150 mm value governing the thickness of the walls. The load bearing beams in the slab are C200/1.5 profiles placed at 600 mm. The size of these profiles resulted from the condition to control the vibrations of the floor not from strength consideration. Roof purlins are Z150/1.5 profiles placed at 1200 mm intervals.

The skeleton was stiffened using 10 mm thick OSB plates fixed to both sides of structural walls. The floor diaphragms were originally designed also to be based on OSB covering. This solution has later been changed into sheathing with trapezoidal steel sheaths, both in the slab and at the level of the roof. No concrete was used in the slab.

The self-weight of the elements was evaluated to: 0.45 kN/m^2 for the roof; 0.70 kN/m^2 for the slab; 0.60 kN/m^2 for exterior and 0.20 kN/m^2 for internal walls. Other loadings for the design were determined according to the relevant Romanian standards. Live load on the slab was 1.50 kN/m^2, snow load on the roof was 1.20 kN/m^2 and wind load on the surface exposed to maximum lateral pressure was 0.4 kN/m^2

The earthquake design was based on PGA of 0.25 g.

One of the problems during the design of such a structure is the evaluation of the load bearing capacity and of the rigidity of the sheathing system of walls and slabs. For this case, the slabs can be covered with general provisions (e.g. some detailing conditions) due to the low level of stresses, but the realistic analysis for the walls is crucial. In this case, extrapolation of experimental results on shear walls was the basis to approach both shear strength and stiffness. Walls with similar skeleton sheathed on one side using identical OSB panels ($t_{OSB} = 10$ mm), with similar fixing plan (e.g. 105 mm screw intervals) and the same diameter screws ($d_{screw} = 4.2$ mm) were previously tested monotonically and cyclically. The tested panels were 2.55 m high, 3.6 m long and the ultimate load obtained from the test was $F_{max} = 69.8$ kN (or 19.4 kN/1m).

The panel's elastic rigidity was $K_{ini} = 4197$ kN/mm. The wall panels used in this case were sheathed on both sides with OSB and the corner details were strengthened compared to the tested case. The design capacity of the walls used for the construction has been evaluated to $F_{des} = 17.6$ kN/1 m. these values enabled to size the necessary length on shear walls along the main axes of the building.

4.4 *In-situ experimental validation*

Ambiental vibration tests have been performed in order to obtain a global validation of design procedure.

The dynamic properties of the building have been studied for small amplitude vibrations by measurements in the 3 stages of construction described earlier.

For each of the three stages of construction, 10 different measurement schemes with 10 velocity sensors were used and for each scheme two vibration recordings of 2 minutes duration were done with a sampling frequency of 100 Hz (Dubina et. al. 2006).

Based on the analysis of recorded vibrations, the building's modal frequencies (periods) have been estimated using two identification techniques: (i) analysis of the Fourier spectra and (ii) spectral and correlation analysis. For the estimation of the modal frequencies and corresponding damping ratios, the Eigen-system Realization Algorithm (ERA) has been used, which also validated the modal periods obtained by the above mentioned.

The first set of measurements has been done when the construction was in the stage when the skeleton of the building was almost entirely completed. The corrugated sheet of the slab was in place together with the OSB panels over it (i.e. the ones which support the finishing layers of the slab). However, the roof of the structure was not yet finished, the roof purlins included. Practically, a flexible diaphragm was

Table 3. Modal parameters obtained by FE modeling.

Stage	T_1 (s)	Type*	T_2 (s)	Type*	T_3 (s)	Type*
1	0.44	Tr	0.39	To	0.35	Lo
2	0.19	Lo	0.18	Tr	0.13	To
3**	0.33	Lo	0.31	Tr	0.23	To

* Note[1]: Tr – Tranversal, Lo – Longitudinal, To – Torsional
** Note[2]: Only the masses changed from Stage 2 to Stage 3

Table 4. Modal parameters based on the analysis of ambient vibrations (in different stages S)

	Mode 1			Mode 2			Mode 3		
S	T_1 (s)	ξ_1 (%)	Type	T_2 (s)	ξ_2 (%)	Type	T_3 (s)	ξ_3 (%)	Type
1	0.546	1.2	Lo	0.437	1.1	Tr	0.456	1.3	To
2	0.103	3.4	Tr	0.096	3.7	Lo	–	–	–
3	0.101	4.1	Tr	0.096	3.8	Lo	.072	.072	To

* Note: Vibration shapes; Tr – Tranversal, Lo – Longitudinal, To – Torsional, ξ_i – damping ratios

provided at the level of the first slab but not at the level of the roof.

The second set of measurements was done when the building skeleton was finished and most of the structural OSB panels were fixed to it. Some OSB panels, only, were still missing in the attic area. The structural part of the roof has also been finished with the outer corrugated sheath being in place. No work on the finishing (i.e. external thermal insulations, inner or outer wall finishes, slab finishing) has been undertaken at this stage.

The third set of measurements was done, before the moving in of the occupants. Therefore, all finishing has been completed but furniture has not been moved in. This can be considered the final stage of construction without live load.

Based on the analysis of the recorded vibrations the modal frequencies (periods), damping ratios and mode shapes of the structure have been identified.

Tables 3 and 4 show, comparatively, the dynamic properties numerically obtained on the structural model of the house with the shear walls sized according to "Prescriptive Method", and the in-situ measurements.

It has to be underlined that the presence of the stiffening OSB panels not only increased the rigidity of the structure considerably, but the weakest rigidity direction has been changed. The supplementary mass introduced with the finishing is counterbalanced by the stiffness increase generated by these finishing elements themselves. When live load will be added (i.e. furniture etc.) the period of vibration will slightly increase compared to the value $T_{3,St2} = 0.101$ s. Most probably the period $T_1 = 0.15$–0.2 s will be reached when the house is fully furnished. Another observation is that the damping ratio $\xi = 5\%$ is a reasonable estimate for a light-gauge steel house.

5 CONCLUDING REMARKS

Laboratory testing and numerical simulations using advanced experimentally calibrated modes are, actually, current research and design tools to be applied to solve complex structural problems of thin-walled steel structures. On this purpose, design codes offer a general guidance and some specific provisions, such as for connections. The experience and skills of structural engineer still play an important role in this matter.

The two case studies summarized in present paper, hopefully, support these concusions

REFERENCES

AISI S230-07W/S2-08: Standard for cold-formed steel framing prescriptive method for one or two family dwellings, 1998

Crisan, A, Ungureanu, V, Dubina, D. Behaviour of cold-formed steel perforated sections in compression. Part 1 – Experimental investigations, *Thin-Walled Structures, Volume 61*, 2012

Crisan, A, Ungureanu, V, Dubina, D. Behaviour of cold-formed steel perforated sections in compression. Part 1 – Numerical investigations, *Thin-Walled Structures, Volume 61*, 2012

Dubina, D. The ECBL approach for interactive buckling of thin-walled steel members, *Steel & Composite Structures,* 1 (1), 2001

Dubina, D, Fulop, L, Aldea, A, Demetriu, S, Nagy, Z. Seismic performance of cold-formed steel framed houses, *Proceedings of 5th International Conference on Behaviour of Steel Structures in Seismic Areas, STESSA,* 2006

Dubina, D. Structural analysis and design assisted by testing of cold-formed steel structures, *Thin-Walled Structures n.46,* 2008

ECCS, 1983. P21—European recommendation for steel construction: The design and testing of connections in steel sheeting and sections (replaced by ECCS 124, 2008)

ECCS Publication No124, 2008: The testing of Connections with Mechanical fasteners in Steel Sheeting and Sections

ECCS No.127, 2009 – Preliminary European Recommendations for the Testing and Design of Fastenings for Sandwich Panels

EN1990, Basis of Structural Design, 2002

EN1993-1-1 Design of steel structures – Part 1-1: General rules and rules for buildings, 2005

EN1993-1-3 Design of steel structures – Part 1-3: General rules – Supplementary rules for cold-formed members and sheeting, 2006

EN 15512 Steel static storage systems – Adjustable pallet racking systems – Principles for structural design, 2009

Fulop, L, Dubina, D. Design Criteria for Seam and Sheeting-to-Framing Connections of Cold-Formed Steel Shear Panels, *Journal of Structural Engineering, ASCE, 2006*

Rasmussen KJR. General report on experimental techniques in the testing of thin-walled structural members. *Coupled instabilities in metal structures* – CIMS2000, Lisbon, Portugal. London: Imperial College Press, 2000

Singer, J, Arbocz, J, Weller, T. Buckling Experiments, Experimental Methods in Buckling of Thin-Walled Structures, Volume 1, Basic Concepts, Columns, Beams and Plates, John Wiley & Sons, Inc., 1997

Research and Applications in Structural Engineering, Mechanics and Computation – Zingoni (Ed.)
© 2013 Taylor & Francis Group, London, ISBN 978-1-138-00061-2

On the response of cold-formed steel sections under compression

N. Baldassino, G. Torresani, & R. Zandonini
Department of Civil, Environmental and Mechanical Engineering, University of Trento, Italy

G. Manzini & F. Scavazza
Cogi srl., Calliano, Trento, Italy

ABSTRACT: This paper summarises the results of an experimental and numerical investigation performed on six series of thin-walled C-sections with intermediate and edge stiffeners. The attention focused on the response under compression and on the influence of geometrical imperfections, which significantly affect the buckling response of the member. First, compression tests allowed for determining loads and modes of failure. The influence on the collapse load of the various parameters as the material properties, the thickness, the height of the cross section and the length of the element was appraised. A comparison between the collapse deformed shape and the pattern of geometric imperfections is performed, in order to correlate the geometrical imperfections to the failure modes. The main results of FE numerical analyses performed with the software Abaqus, incorporating geometric and material nonlinearities, are also reported. The appropriateness of the specifications of the Eurocodes for modelling the geometric imperfections is finally appraised.

1 INTRODUCTION

Residential systems in thin-walled cold formed steel profiles for small and medium size buildings are well established in countries such as North America and Australia. Their peculiar characteristics such as the light weight, the high structural efficiency, the durability, the rapidity and simplicity of installation of the building equipment result in very competitive structural systems.

However, the design of these structures is fairly complex. Thin-walled cold-formed sections usually adopted tend to be very slender both globally and in the cross-sectional components. Consequently, they are subject to global, local and distortional instability, as well as to their interactions. Buckling reduces the members' load capacity, and makes design heavier, of incorporating it.

In order to develop an industrial prefabricated system, building components require studies at different level of complexity from the individual member to 2D and 3D sub-structures. The study of individual members subject to simple forces is the starting point, for it addresses their instability problems.

This paper summarises the results of an experimental and numerical investigation carried out on thin-walled C-sections with intermediate and edge stiffeners designed for an innovative housing system. The attention focused on the response under compression and on the influence of geometrical imperfections, which significantly affect the buckling response of the member.

Despite the wide literature focusing on the response of thin-walled cold formed sections under compression, only a limited number of studies investigate in detail the influence of imperfections. To the authors' knowledge, the first attempt to characterize the imperfections along the length of the element, by measuring their pattern and evaluating the periodicity was performed by Schafer and Peköz (1996, 1998). Additional studies recently carried out by Zeinoddini and Schafer (2010, 2012) focused on both the longitudinal and cross-sectional imperfections.

In the present work, the specimens' geometric imperfections were first measured in detail, by an approach similar to that used by Schafer and Peköz (1996). The subsequent experimental compression tests, enable determination of loads and modes of failure. These results allow for an appraisal of the influence on the collapse load of various parameters, such as the material properties, the thickness, the height of the cross section and the length of the element. A comparison between collapse deformed shape and the pattern of geometric imperfections is also performed, in order to correlate the geometrical imperfections to the failure modes.

The main results of FE numerical analyses carried out by means of the commercial software Abaqus, incorporating geometric and material nonlinearities are also reported in this paper, and the appropriateness of the specifications of the Eurocode 3 Part 1–5 (2006) for modelling the geometric imperfections appraised.

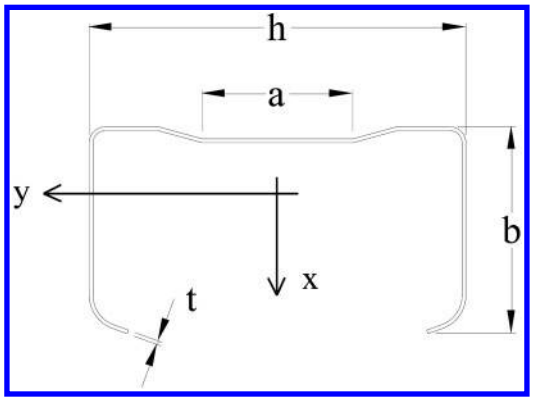


Figure 1. The investigated cross section.

2 SPECIMENS

The study focused on cold-formed channel sections with intermediate and edge stiffeners (Fig. 1). The sections are characterised by nominal web depths (h, in Fig. 1) of 100 mm, 150 mm and 200 mm, respectively. The flange width (b, in Fig. 1) is the same for all the sections. Two values of the nominal thickness, t = 1.0 mm and 1.2 mm, were selected. In summary, the study investigated six series of sections identified as A100, A150, A200, B100, B150 and B200. Letters A and B refer to the thickness of 1 mm and 1.2 mm respectively, and the following number to the nominal web depth (100 mm, 150 mm and 200 mm).

For each cross section three lengths of the specimens were considered, selected on the basis of numerical analyses carried out with the finite strip program CUFSM (Li et al., 2010). For each cross section the buckling curve was plotted and the notional lengths associated to the different forms of instability, i.e, local, distortional and global instability, were identified. The length of the specimens were hence selected so as to get a distortional buckling failure.

The three cross sections, two thicknesses and three specimen lengths for each cross section lead to a total of $3 \times 2 \times 3 = 18$ different specimen geometries. Their main dimensions and the nominal area of the cross section (A_g) are summarised in Table 1. Five specimens were tested for each geometry, in order to make a statistical appraisal. Therefore, a total of ninety specimens were tested.

Test were performed in agreement with the UNI EN 1993-1-3 (2006). At this aim, both ends of the specimen are welded to thin square plates of dimension of $220 \times 220 \times 5$ mm so that the nominal centroid of the plate corresponds to the centroid of the nominal gross section of the profile. Due to the presence of the welds, the warping of the end sections of the profile is prevented. A hole with a diameter of 8 mm driven in correspondence with the centroid of the end plates facilitates the connection to the testing rig and identifies the point of load application.

Table 1. Main dimensions of the specimens.

Cross section	Web height h	Width a	Thickness t	Gross area A_g	Length l
	mm	mm	mm	mm^2	mm
A100	100	40	1.0	215.24	300
					400
					500
A150	150	90	1.0	267.24	350
					500
					600
A200	200	140	1.0	315.24	450
					600
					750
B100	100	40	1.2	257.49	300
					400
					500
B150	150	90	1.2	317.49	350
					500
					650
B200	200	140	1.2	377.49	450
					600
					750

3 GEOMETRICAL IMPERFECTIONS

Each element presents 'physiological' geometric imperfections, as a deviation from the nominal geometry. Slender sections, such as thin-walled cold formed sections, are particularly sensitive to imperfections, which hence should be appropriately taken into account for in design. Three types of imperfections were considered:

- eccentricity of load application;
- crookedness and out-of-flatness along the length of the element;
- incomplete weld of the end-plates to the specimen.

Measures were only performed for the first two types of imperfections.The influence of the third one was investigated only numerically.

The measurement of the geometrical imperfections requires a rather complex and lengthy procedure. Therefore, measures were taken only for a part of the specimens tested in laboratory; i.e., on 36 of the 90 specimens (2 for each of the 18 geometries).

The eccentricities of the point of load application were evaluated on the two end cross sections. At this aim, the actual position of the cross sections with respect to the relevant end plate was measured. This allowed evaluating the eccentricities of the centroid of the cross sections with respect to the central hole of the plates. Random values but lower than 2 mm were obtained, as shown in Figure 2, which gathers the measures related to the bottom plate.

The imperfections of the profile along its length were gauged by connecting the specimen to the table of a milling machine (Fig. 3), at the two holes of the welded plates (so each measures were related to the hole-to-hole axis, here called z-axis).

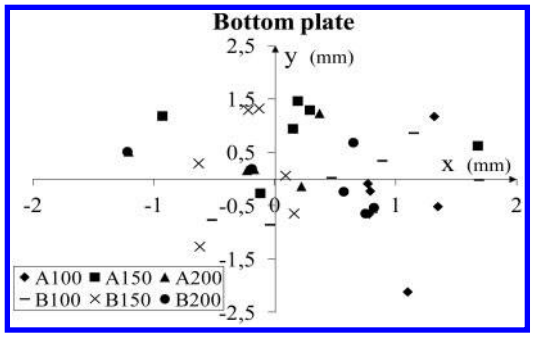


Figure 2. Eccentricities of the point of load application at the bottom plate.

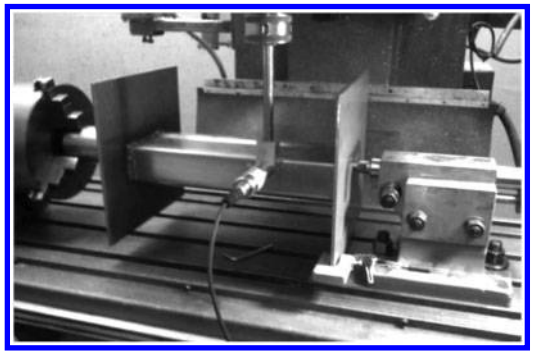


Figure 3. Measure of the out-of-straightness and out-of-flatness along the length of the element.

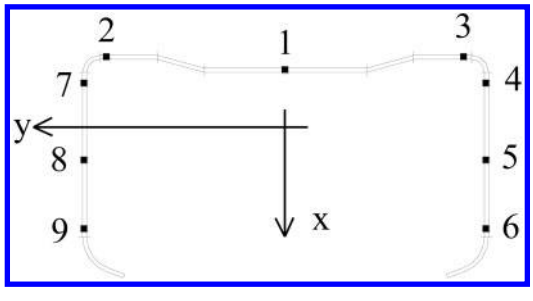


Figure 4. Points for the measurement of the imperfections.

The milling table provides a flat reference surface for measuring relative displacements. The measurement is carried out by replacing the drill bit of the milling machine with a support for a strain-gauge transducer. The transducer is held in place, while the plane of the milling machine slides; the transducer hence scans the element along a longitudinal line. A wire-sensor transducer anchored to the test specimen allows measuring z-coordinate. By synchronizing the two instruments the measure of the strain-gauge transducer was associated with the relevant section along the element. The scan operation is repeated in nine different points of the cross section, as shown in Figure 4.

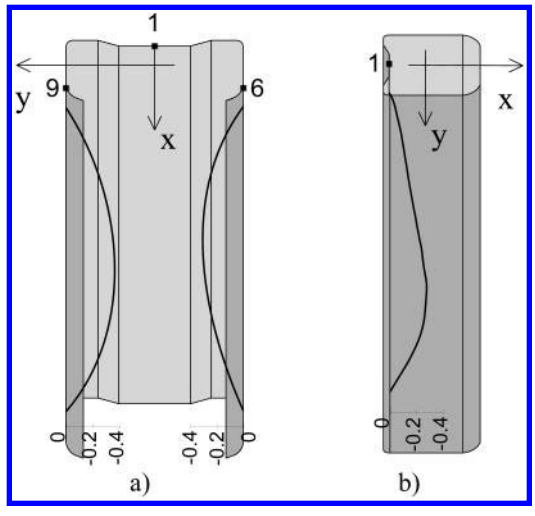


Figure 5. Geometrical imperfections: a) along lines 9 and 6; b) along line 1.

The presence of the weld at the ends of the profile prevented from taking measures along the full length of the specimen. This does not seem of actual importance: the geometry of the section near the end plates is heavily influenced by distortions induced by the welding process rather than by actual geometrical imperfections due to the fabrication process.

The procedure just described allows obtaining the transverse dimensional deviations of the cross section of the element, with respect to the nominal geometry, as a function of the longitudinal z coordinate. Examples of measured imperfections are shown in Figure 5.

It was observed that imperfections in the flanges were typically bigger than imperfections in the web, except in few cases of specimens with large web depth. In most cases the imperfection in the web had a negative sign, namely it bulged inward, that is towards the inside of the section. This trend was also typical of the imperfections of the flanges (Fig. 5)

4 TESTS RESULTS

The results of the compression tests are presented in Table 2, where the mean values of the collapse loads, their standard deviation and the β_a factor are provided. The β_a factors were computed according to EN 1993:1-3 (2006) under the assumption that the specimen is not affected by overall instability, as:

$$\beta_a = \frac{N}{A_g f_y} \quad (1)$$

where N = collapse load; A_g = cross-sectional area and f_y = steel yielding strength.

The material properties were determined by tensile coupon tests. The means values of the material properties are given in Table 3.

Table 2. Compression test results.

Cross section	Member length l	Collapse load: Mean value P	Collapse load: Standard deviation σ	β_a factor
	mm	kN	kN	
A100	300	36.986	3.101	0.67
	400	34.762	2.563	0.63
	500	35.121	1.215	0.64
A150	350	30.307	1.127	0.45
	500	30.398	0.651	0.45
	600	31.075	1.012	0.46
A200	450	32.784	2.116	0.49
	600	29.964	3.572	0.45
	750	30.125	1.225	0.45
B100	300	51.987	4.332	0.68
	400	51.858	2.812	0.68
	500	50.404	2.403	0.66
B150	350	47.165	0.604	0.50
	500	45.175	1.201	0.48
	650	45.081	2.054	0.47
B200	450	45.593	3.035	0.41
	600	48.446	0.436	0.43
	750	44.034	0.736	0.39

Table 3. Means values of the material properties.

Cross section	Yield stress f_y	Ultimate stress f_t	Elongation A
	MPa	MPa	%
A100	254.87	352.32	36.75
A150	253.62	350.32	36.00
A200	212.36	339.76	38.00
B100	295.46	385.46	30.75
B150	299.32	383.98	30.38
B200	296.91	381.70	31.13

The β_a factor, being the ratio between the experimental resistance and the plastic strength of the gross section is an index of the importance of local and distortional buckling, in terms of ultimate resistance. Table 2 shows that the β_a factor tends to decrease when the section depth increases, for both the A and B series. This clearly stresses the importance of the web slenderness on the local and distortional instability of the type of channel considered. Slight variations of β_a factor are observed between the different lengths of the profile, for the same depth of the cross section and the same thickness. This confirms that the global instability has actually little influence on the axial load capacity of these elements. As to the failure modes, the most frequent failure mode observed was by distortional buckling, in accordance with finite strip analyses carried out with CUFSM (Li et al., 2010). Only in few cases of the longer specimens of the series A200 and B200, and of the shortest specimens of the series B100 the buckling shape was closer to the local type.

Table 4. Variations of the β_a factor.

Section type	β_a Spec. A t = 1.0 mm	β_a Spec. B t = 1.2 mm	% increment
100	0.65	0.68	4.1
150	0.45	0.48	6.8
200	0.46	0.41	−11.2

A general reasonable agreement between the imperfections and the failure mode of the specimens was also observed. In particular, the imperfections of the flanges have greater influence on the collapse mode, than the imperfections of the web.

No significant influence of the eccentricity of load application is found on the collapse mode. This can be justified by the very small values of the load eccentricity (Fig. 2).

Some considerations can be done on the 'sectional degree of efficiency' associated with the increase of thickness. To this aim, reference can be made to average values of the β_a factor (Tab. 4) which incorporates the effect of the different yield strength between the test series (Tab. 3). The mean percentage variations of the β_a factor when the thickness is increased are gathered in Table 4 and should be considered in association with the average increase of 19% of the gross area for all geometries (Tab. 1). For the sections depth of 200mm the sectional efficiency appears to be significantly reduced so that the additionally material is basically not used. This result is clearly related to the yield strength parameter which is substantially higher for the B series (Tab. 3). The importance of this parameter seems even greater than assumed in the Eurocode.

5 NUMERICAL ANALYSES

The use of finite element models has become an effective and powerful tool, which enables to achieve an insight of complex problems such as those associated with the instability of thin-walled elements. The FE method was hence adopted aiming at getting a deeper insight in the response of the sections analysed in this study. In this chapter the results of the study of the influence of the imperfections are summarised.

The numerical analyses were carried out by means of the commercial software Abaqus incorporating geometric and material nonlinearities. The FE model comprised of both the profile and the welded end-plates. The end plates were assumed to be rigid while shell elements S4R with uniform size approximately equal to 4 × 4 × 4 mm were adopted for the section. Shell-to-solid coupling constraints are used to simulate adequately the plate-to-section weld.

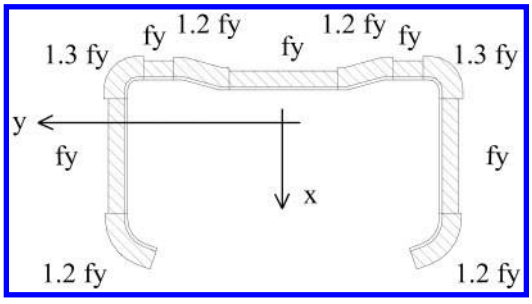


Figure 6. Yield strength and hardening effects.

The material of the specimen was modeled as elastic-perfectly-plastic. The values of the yield stress were, for each of the different cross sections, consistent with the mean values determined via tensile coupon tests (Tab. 3). The elastic modulus was assumed equal to 210000 MPa in all the analyses.

In order to take into account the material hardening in the bent zone, enhanced properties of the material in the rounded corner areas were assumed. The values of yield stress increases are related to the bending angle and were obtained from previous studies on the distribution of the yield stress along the cross section (Armani et al., 2011). In case of folds with obtuse angle, the increase is assumed to be of 20%, while in right angle folds, the increase is of 30% (Fig. 6).

The measured imperfections were incorporated in the finite element mesh. Both the eccentricities of the point of load application (Fig. 2) and the crookedness and out-of-flatness (Fig. 5) were reproduced. The incomplete weld of the edge stiffener to the end steel plate was also considered. This lack in the end connection affects the load transfer, and can be roughly seen as the source of an additional eccentricity in the first phase of loading. In absence of accurate measurement, this imperfection was investigated through a sensitivity study. The results showed their non-negligible influence on the profile response and indicate the more appropriate approach for their modeling. The lips are left completely unconnected to the steel end plates and constraints of no penetration with no friction is imposed. In addition, a thin portion of the lip is removed at both ends, so as to simulate the presence of a gap between the non-welded lip portion and the end plate, caused by the space occupied by the weld of the remaining part of the cross section.

The comparison between numerical and experimental collapse loads is presented in Figures 7 and 8, which are related to specimen A and B, respectively. For the purpose of the analysis the mean value of the experimental results is considered. A more than satisfactory agreement is apparent, with a difference in average of the order of 7%. Similar results are observed for the failure mode, for which the numerical deformed collapse shape and the experimental one match in about the 75% of the cases.

As further issue, the problem of 'standard' design imperfections was considered. The Eurocode 3 Part 1–5 (2006) provides recommendation on this aspect, i.e.,

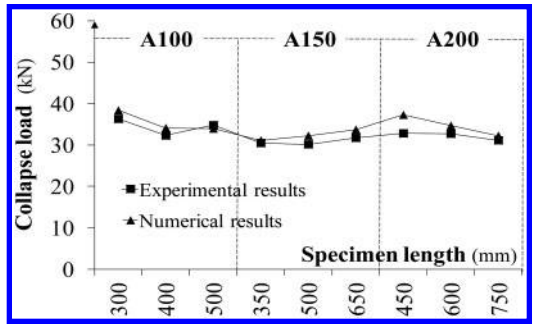


Figure 7. Experimental vs numerical results.

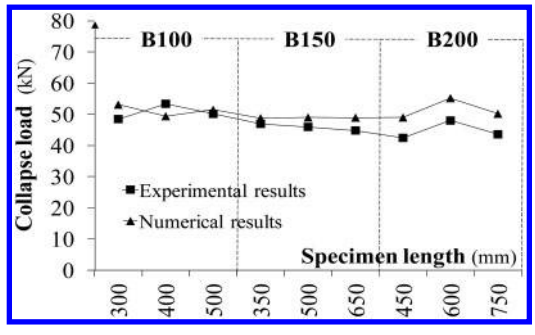


Figure 8. Experimental vs numerical results.

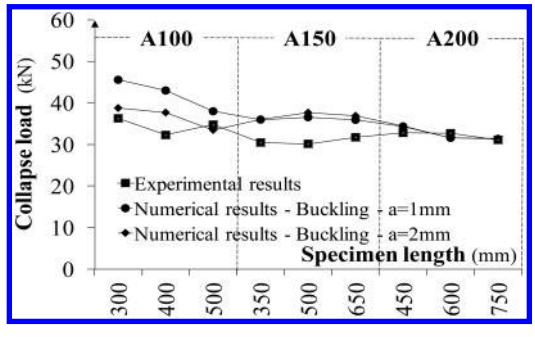


Figure 9. Experimental vs numerical results.

the first buckling shape, with an maximum amplitude equal to 80% of the geometric fabrication tolerance of the element itself, has to be assumed as initial deformed shape. Geometric imperfections in agreement with the Eurocode were then considered with the purpose of appraising the appropriateness of the code. Therefore, a buckling analysis is performed of a model comprising of the section and the end plates. The critical shape obtained is scaled as required by the Eurocode, and then entered into the model as geometric imperfection. Two values of the maximum amplitude of the imperfections (a = 1 mm and 2 mm), were considered. The eccentricity of the load application at the two ends of the specimen (Fig. 2) and material hardening (Fig. 6) were also incorporated.

Figure 9 and 10 show the results of the analyses and the comparison with the experimental outcomes.

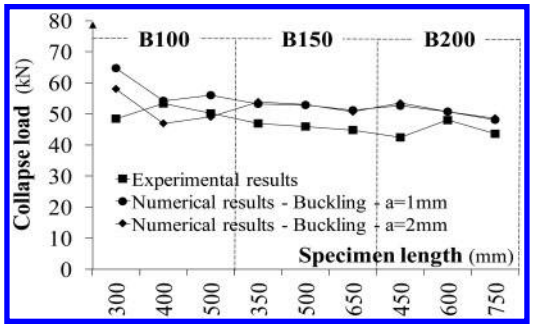


Figure 10. Experimental vs numerical results.

It is apparent that the increase of amplitude affects only the specimens of the 100 series (low depth of the cross section), while for the specimens of the 150 and 200 series the effect is negligible. In particular, in the case of the specimens of the 100 series, differences of the order of 12–13% associated with the amplitude increase are observed. For the specimens with depth of 150 mm and 200 mm, these differences are always lower than 2%. If the results of the numerical analysis are compared with the experimental outcomes, it can be noted that:

- for specimens with depth of 100 mm the imperfection amplitude of 2 mm better approximates the experimental results; the differences in collapse load are of the order of 5% for specimens A and less than 1% for specimens B;
- for specimens with depth of 150 mm the numerical analyses always noticeably overestimate the experimental collapse load, with percentage differences of the order of 17% for specimens A and of 13% for specimens B;
- for specimens with depth of 200 mm the numerical analyses overestimate the experimental collapse load in case of specimens B (differences of the order of 12%), while good agreement between numerical and experimental results is found in case of specimens of the A series.

A key factor for explaining such discrepancies is the collapse deformed shape. The collapse shapes looks alike the experimental one only in 22% of cases. This is due to the fact that the collapse in the nonlinear elasto-plastic analyses is always strongly related to the initial imperfection. If the imperfection (the first buckling shape in this case) is not representative of the actual initial deformed shape of the section, the 'numerical' collapse mode cannot match the experimental one.

6 CONCLUDING REMARKS

The paper summarises the results of a study of six geometries of cold-formed thin-walled C-sections with intermediate and edge stiffeners. Their response under compression was experimentally and numerically investigated.

The study allowed an evaluation of the influence of parameters such as the material properties, the thickness, the depth of the cross section and the length of the element on both the failure modes and the collapse load of this section type. An accurate measurement of the profiles' imperfections, i.e., load eccentricity, crookedness and out-of-flatness along the length of the element and incomplete weld of the end-plates to the specimen, made possible to extend the investigation also to the influence of these parameters. Both experimental and numerical studies confirmed the central role of the imperfections which greatly affect the profile response and stress the vital need for an accurate and reliable model for their representation. Accordingly, the Eurocode model for the geometric imperfections seems not adequate.

REFERENCES

Schafer, B.W., Peköz, T. 1996. Geometric Imperfections and Residual Stresses for Use in the Analytical Modeling of Cold-Formed Steel Members. *Proceedings of the 13th Int. Specialty Conference on Cold-Formed Steel Structures. St. Louis, Missouri, 17–18 October 1996:* 649–664.

Schafer, B.W., Peköz, T. 1998. Computational Modeling of Cold-Formed Steel: Characterizing Geometric Imperfections and Residual Stresses. *Journal of Constructional Steel Research*, 47(3): 193–210.

Zeinoddini, V.M., Schafer, B.W. 2011. Global Imperfections and Dimensional Variations in Cold-Formed Steel Members. World Scientific, *International Journal of Structural Stability and Dynamics*. 11(5): 829–854.

Zeinoddini, V.M., Schafer, B.W. 2012. Simulation of geometric imperfections in cold-formed steel members. *Proceedings of the Annual Stability Conference Structural Stability Research Council. Grapevine: Texas. April 18–21 2012*.

Eurocode 3. 2006. Design of steel structures – Part 1-5: Plated structural elements. Brussels: CEN.

Li, Z., Schafer, B.W. 2010. Buckling analysis of cold-formed steel members with general boundary conditions using CUFSM: conventional and constrained finite strip methods. *Proceedings of the 20th Int. Specialty Conference on Cold-Formed Steel Structures. St. Louis: Missouri. 3–4 November 2010.*

Eurocode 3. 2006. Design of steel structures – Part 1–3: General rules – Supplementary rules for cold-formed members and sheeting. Brussels: CEN.

ABAQUS/STANDARD User's Manual Version 6.8, Hibbit, Karlsson and Sorensen, USA 2006.

Armani, P., Baldassino, N., Zandonini, R. 2011. Study of the response of uprights of pallet racks under compression. *Proceedings of the Sixth 6th International Conference on Thin Walled Structures*. Timisoara: 5–7 September 2011: 771–778.

Research and Applications in Structural Engineering, Mechanics and Computation – Zingoni (Ed.)
© 2013 Taylor & Francis Group, London, ISBN 978-1-138-00061-2

Local and global vibration analysis of thin-walled steel frames using Generalised Beam Theory (GBT)

C. Basaglia
Structural Engineering Department, São Carlos School of Engineering, University of São Paulo, Brazil

D. Camotim
Civil Engineering Department, ICIST, Instituto Superior Técnico, Technical University of Lisbon, Portugal

H.B. Coda
Structural Engineering Department, São Carlos School of Engineering, University of São Paulo, Brazil

ABSTRACT: This paper reports the results of an ongoing investigation on the use of Generalised Beam Theory (GBT) to analyse the vibration behaviour of thin-walled steel frames. After a brief overview of the main concepts and procedures involved in performing a GBT vibration analysis, the formulation and implementation of a GBT-based beam finite element are presented, namely the determination of the finite element and frame linear and geometric stiffness matrices, as well as the frame mass matrix (incorporating the influence of the loading and frame joint configurations). Finally, in order to illustrate the application and capabilities of the proposed GBT-based finite element formulation, numerical results concerning the local, distortional and global vibration behaviour of a symmetric portal frame are presented and discussed. For validation purposes, most GBT-based results are compared with values obtained by means of shell finite element analyses carried out in the code Ansys.

1 INTRODUCTION

The thin-walled steel frames commonly used in the construction industry are often formed by members (columns, beams or beam-columns) with rather slender open cross-sections, which invariably exhibit very low torsion stiffness and a strong susceptibility to local, distortional and/or global buckling phenomena. Furthermore, given the strong mathematical similarity between the buckling and vibration analysis of structures (similar eigenvalue problems), it is just logical to expect the vibration behaviour of thin-walled frames to be also highly influenced by (i) the member cross-section (local and distortional) deformation (*e.g.*, Ahmed & Shimizu 2012), (ii) the localised displacement restraints, due to bracing systems (*e.g.*, Türker & Bayraktar 2011) and (iii) the frame joint behavioural features (*e.g.*, Sophianopoulos 2003).

Since most thin-walled steel frames are subjected to *simultaneous* static and dynamic actions (*e.g.*, the effects of heavy machinery or seismic activity), designers are faced with the need of assessing their dynamic response. Therefore, they must be equipped with numerical tools to determine the local and global frame vibration behaviour, eventually in the presence of more or less significant internal forces or moments. However, this task can only be rigorously performed currently by resorting to shell finite element analysis, a highly computer-intensive approach that (i) requires a large modelling effort (including data input and result interpretation) and, therefore, (ii) is still prohibitive for routine applications (*e.g.*, Moazed *et al.* 2012).

One very promising alternative to the above approach is the use of a one-dimensional model based on Generalised Beam Theory (GBT) – a beam theory incorporating genuine folded-plate concepts. In this context, the authors have been employing GBT-based beam finite element formulations to study the buckling behaviour of frames (*e.g.*, Camotim *et al.* 2010) – however, up until now all GBT vibration formulations dealt exclusively with isolated structural members (*e.g.*, Silvestre & Camotim 2006 and Bebiano *et al.* 2008).

The aim of this paper is to propose and validate an extension of the above GBT-based beam finite element formulations that make it possible to perform local, distortional and global vibration analyses of thin-walled steel frames. In particular, the determination of the finite element and frame linear and geometric stiffness matrices, as well as the frame mass matrix, is addressed. In order to illustrate the application and capabilities of the proposed GBT-based approach, the vibration behaviour of a load-free symmetric portal frame is first analysed. Then, since it is common practice in literature to express the static loading as a fraction of its critical buckling value, the frame buckling behaviour is studied. Finally, the vibration behaviour of the loaded frame is investigated, focusing mainly on the effect of the load magnitude

on the fundamental frequency value and mode shape nature. For validation purposes, some GBT results are compared with numerical values obtained by means of shell finite element analyses performed in the commercial code ANSYS (SAS 2009).

2 GBT VIBRATION ANALYSIS

In a GBT formulation, the cross-section displacement field is expressed as a linear combination of deformation modes, leading to a very convenient and mostly unique form of writing the member equilibrium equations – this is achieved by performing a *cross-section analysis* (Gonçalves *et al.* 2010), which allows for a much better understanding of the member structural behaviour. Figure 1 shows the dimensions and a possible GBT discretisation of the lipped channel cross-sections dealt with in this work – all frame members have elastic constants $E = 205\ GPa$ (Young's modulus) and $\upsilon = 0.3$ (Poisson's ratio). The cross-section analysis yields 15 deformation modes – the in-plane shapes of the 9 most relevant ones, *i.e.*, those contributing to the sought frame vibration modes, are also shown in Figure 1.

The GBT displacement field representation adopts the classical beam theory variable separation

$$\begin{aligned} u(x,s,t) &= u_k(s)\zeta_{k,x}(x,t) \\ v(x,s,t) &= v_k(s)\zeta_k(x,t) \\ w(x,s,t) &= w_k(s)\zeta_k(x,t) \end{aligned} \tag{1}$$

where (i) x and s are coordinates along the member axis and cross-section midline, (ii) functions $u_k(s)$, $v_k(s)$ and $w_k(s)$ provide the longitudinal, transverse membrane and transverse flexural displacements of deformation mode k, (iii) $(.)_{,x} \equiv d(.)/dx$, (iv) the summation convention applies to subscript k and (v) $\zeta_k(x,t)$ are the functions describing the variation of the deformation mode amplitudes both along the longitudinal direction and with time t.

After determining the deformation modes, the equilibrium equation system defining the dynamic problem can be readily established,

$$\begin{aligned} &C_{ik}\zeta_{k,xxxx} - D_{ik}\zeta_{k,xx} + B_{ik}\zeta_k - \\ &Q_{ik}\zeta_{k,xxtt} + R_{ik}\zeta_{k,tt} - X_{jik}(W_j^0\zeta_{k,x})_{,x} = 0 \end{aligned} \tag{2}$$

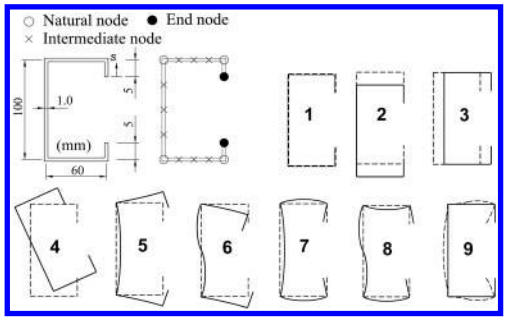


Figure 1. Lipped channel section: geometry, GBT discretisation and in-plane shape of the 9 most relevant deformation modes.

where, C_{ik} (warping displacement), D_{ik} (torsional rotations) and B_{ik} (local deformations) are cross-section modal mechanical properties, (iii) X_{jik} are geometric stiffness components associated with normal stress resultants W_j^0 due to uniform compression ($j = 1$) and/or bending ($j = 2, 3$), and (iv) R_{ik} and Q_{ik} are mass components that account for the influence of the inertia forces on the out-of-plane and in-plane cross-section displacements, and are given by (Bebiano *et al.* 2008)

$$\begin{aligned} Q_{ik} &= \rho h \int_S u_i u_k ds + \frac{\rho h^3}{12}\int_S w_i w_k ds \\ R_{ik} &= \rho h \int_S (v_i v_k + w_i w_k) ds + \frac{\rho h^3}{12}\int_S w_{i,s} w_{k,s} ds \end{aligned} \tag{3}$$

where (i) h is the wall thickness (uniform) and (ii) ρ is the material mass density (deemed uniform and equal to $7.85\ g/cm^3$ in this work).

One solution of system (2) can be found by assuming that the free vibration motions are synchronous, *i.e.*, by adopting the separation of variables

$$\zeta_k(x,t) = \phi_k(x)Y(t) \tag{4}$$

where $\phi_k(x)$ is a longitudinal shape function and $Y(t)$ is a time-dependent function satisfying the free vibration harmonic equation of motion $Y_{,tt} + \omega^2 Y = 0$, where ω is the angular frequency of vibration – thus, it may be written

$$\zeta_{k,tt} = -\omega^2 \zeta_k \tag{5}$$

The incorporation of Eq. (5) into (2) leads to the final system of equilibrium equations

$$\begin{aligned} &C_{ik}\phi_{k,xxxx} - D_{ik}\phi_{k,xx} + B_{ik}\phi_k - \\ &\omega^2(R_{ik}\phi_k - Q_{ik}\phi_{k,xx}) - X_{jik}(W_j^0\xi_{k,x})_{,x} = 0 \end{aligned} \tag{6}$$

3 FRAME ANALYSIS

In isolated members, the solution of (2) is obtained by means of a beam finite element formulation developed and implemented by Bebiano *et al.* (2008): 2-node elements with $2n$ degrees of freedom per node (n is the number of deformation modes included in the analysis) and using Hermite cubic polynomials $\psi_i(x)$ to approximate the mode amplitude functions $\phi_k(x)$ – one then has

$$\begin{aligned} \phi_k(x) = {} & \psi_1(\xi)d_{k1} + \psi_2(\xi)d_{k2} + \\ & + \psi_3(\xi)d_{k3} + \psi_4(\xi)\,d_{k4} \end{aligned} \tag{7}$$

where $d_{k1} = \phi_{k,x}(0)$, $d_{k2} = \phi_k(0)$, $d_{k3} = \phi_{k,x}(L_e)$, $d_{k4} = \phi_k(L_e)$, $\xi = x/L_e$ (L_e is the element length) and

$$\begin{aligned} &\psi_1(\xi) = L_e(\xi^3 - 2\xi^2 + \xi) \quad \psi_2(\xi) = 2\xi^3 - 3\xi^2 + 1 \\ &\psi_3(\xi) = L_e(\xi^3 - \xi^2) \quad \psi_4(\xi) = 3\xi^2 - 2\xi^3 \end{aligned} \tag{8}$$

Thus, the various sub-matrix components of the finite element linear stiffness $[K_e]$, geometric stiffness

$[G_e]$ and mass $[M_e]$ matrices are determined by means of the expressions

$$K_{ik}^{pr} = C_{ik}\int_{L_e}\psi_{p,xx}\psi_{r,xx}dx + D_{ik}\int_{L_e}\psi_{p,x}\psi_{r,x}dx + B_{ij}\int_{L_e}\psi_p\psi_r dx$$
$$G_{ik}^{pr} = W_j^0 X_{jik}\int_{L_e}\psi_{p,x}\psi_{r,x}dx \qquad (9)$$
$$M_{ik}^{pr} = Q_{ik}\int_{L_e}\psi_{p,x}\psi_{r,x}dx + R_{ik}\int_{Le}\psi_p\psi_r dx$$

where (i) subscripts $i, k = 1 \ldots n$ identify the deformation modes associated with each sub-matrix and (ii) superscripts p, $r = 1 \ldots 4$ concern the finite element degrees of freedom involved in each sub-matrix.

The overall linear and geometric stiffness and mass matrices of a given structural system are obtained by "assembling" their finite element counterparts, adopting the well-known "incidence matrix" concept. Although this constitutes a fairly trivial procedure for isolated members, its extension to frames poses several difficulties. Indeed, because the finite elements (members) connected at a frame joint exhibit different orientations, it becomes necessary to account for all the effects stemming from the need to ensure compatibility between the degrees of freedom of the connected member end cross-sections. In order to overcome these difficulties, (i) it is necessary to "transform" the modal degrees of freedom into nodal ones (generalised displacements of the point where the joint is deemed located), by means of a "joint element" concept, and (ii) constraint conditions must be imposed to enforce displacement and rotation compatibility at the connected end sections – more details can be found in the work of Basaglia *et al.* (2008, 2009).

The constraint conditions, denoted by Π_i, (i) depend on the member geometry and joint configuration, and (ii) involve i natural/intermediate nodes of the connected member end sections – these conditions read

$$\Pi_i = \{\Delta\}^T\{\phi_k\} = 0 \qquad (10)$$

where the vector $\{\Delta\}$ components are either (i) warping functions $u_k(s)$ or (ii) wall flexural functions $w_k(s)$. The particular constraint conditions considered in this work are addressed in Basaglia *et al.* (2009).

Once all the member support and joint compatibility conditions are enforced, the frame linear $[\tilde{K}]$ and geometric $[\tilde{G}]$ stiffness matrices and mass matrix $[\tilde{M}]$ are readily obtained, which are expressed in terms of "mixed" degrees of freedom: GBT modal and "conventional" nodal ones. The joint compatibility is incorporated into the stiffness matrix by means of the matrix operation

$$([\tilde{K}] - [\tilde{G}] - \omega^2[\tilde{M}]) = \\ = [\Omega]^T([K] - [G] - \omega^2[M])[\Omega] \qquad (11)$$

where (i) the tilde ($\sim$) identifies the matrices associated with joint compatibility conditions and (ii) the compatibility matrix $[\Omega]$,

$$\{d\} = [\Omega]\{\tilde{d}\}, \qquad (12)$$

contains the joint modal displacement values (*i.e.*, $u_k(s)$, $v_k(s)$ or $w_k(s)$) – $\{\tilde{d}\}$ is a "mixed" vector combining generalised displacements and GBT degrees of freedom.

After determining the frame total stiffness and mass matrices ($[\tilde{K}] - [\tilde{G}] - \omega^2[\tilde{M}]$), one (i) solves the vibration eigenvalue problem and (ii) transforms the nodal degrees of freedom (joint generalised displacements) back into GBT ones, through the operation defined in (12) – this last procedure makes it possible to obtain a fully modal representation of the frame vibration modes (*i.e.*, identify and quantify the individual contributions of the deformation modes of the various members), a feature that provides a decisive contribution towards a more in-depth understanding of the mechanical aspects involved in the local, distortional and global vibration behaviour of thin-walled frames.

4 ILLUSTRATIVE EXAMPLES

In order to validate and illustrate the application and potential of the proposed GBT-based beam finite element approach, numerical results are presented and discussed next. They concern the local, distortional and global vibration of the symmetric portal frame depicted in Figure 2(a), which is formed by three lipped channel members (A, B, C) (i) with identical cross-sections (dimensions given in Fig. 1) and (ii) made of steel ($E = 205\ GPa$ and $\nu = 0.3$). The frame has fixed column bases and joints with flange continuity. One begins by analysing the vibration behaviour of the load-free frame. Then, the buckling behaviour of the frame subjected only to uniform axial compression diagrams ($N_A = N_C = 0.83\,P$ and $N_B = 1.0P$ – see Fig. 2(b)) is analysed. Finally, the vibration behaviour of the loaded frame is investigated – the static applied loading is always expressed as a percentage of the associated critical buckling load (P_{cr}). For validation, most GBT-based results are compared with values yielded by Ansys (SAS 2009) shell finite element analyses.

The GBT analyses are based on frame discretisations into 52 finite elements, which correspond to 106 degrees of freedom for each deformation mode

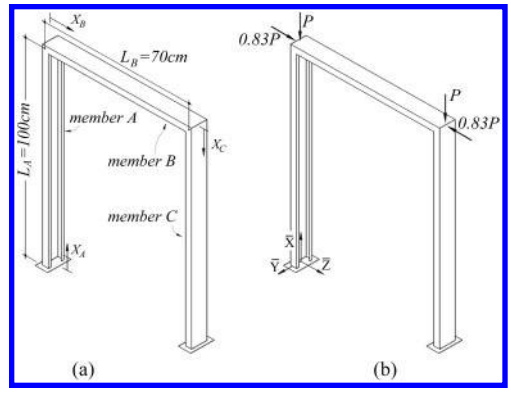


Figure 2. Symmetric portal frame: (a) geometry and (b) loading.

included in the analysis. Thus, an analysis including all *15* deformation modes stemming from the adopted GBT discretisation (see Fig. 1) involves 1590 $d.o.f.$. On the other hand, the ANSYS shell finite element analyses involve more than 16000 $d.o.f.$.

4.1 *Load-free frame vibration*

Table 1 shows the first eight natural frequencies (in rad/s), obtained by means of the GBT analysis (ω_{GBT}) and shell finite element analysis (ω_{ANSYS}). Figure 3 provides, for each of the three frame members, the amplitude functions $\phi_k(x)$ of the deformation modes that participate in the first four frame vibration modes. As for Figure 4, it displays the configurations of theses vibration modes obtained from the ANSYS shell finite element analysis. The observation and comparison between the vibration results yielded by the two numerical models prompts the following main remarks:

Table 1. GBT and ANSYS frame vibration frequencies (rad/s).

Vibration mode	ω_{GBT}	ω_{ANSYS}	Δ (%)
1	392.72	383.54	2.4
2	451.81	446.10	1.3
3	630.90	630.27	0.1
4	653.80	635.17	2.9
5	665.04	645.35	3.1
6	685.12	670.04	2.3
7	779.01	763.66	2.0
8	785.05	768.12	2.2

(i) The natural frequencies yielded by the GBT-based and ANSYS shell finite element analyses practically coincide – the maximum difference is 3.1%.

(ii) There is also a very close agreement between the GBT modal amplitude functions and the vibration mode shapes obtained from the ANSYS analysis. However, it can be easily argued that the GBT representation enables a better quantitative and qualitative insight on this frame vibration behaviour.

(iii) The local and distortional deformation modes become more relevant as the vibration mode order increase. Indeed, wile the global modes **2** and **3** are predominant in the first three vibration modes, in the fourth vibration mode prevail modes **5** and **7**.

4.2 *Frame buckling*

Figure 5 provides two representations of critical buckling mode shapes of the frame considered in this work, namely (i) GBT modal amplitude functions and (ii) ANSYS 3D views. The observation of these two sets of buckling results prompts the following remarks:

(i) The GBT and ANSYS critical loads are very similar – one has $P_{cr.GBT} = 19.25$ kN and $P_{cr.ANSYS} = 18.72$ kN (differences below 2.83 %).

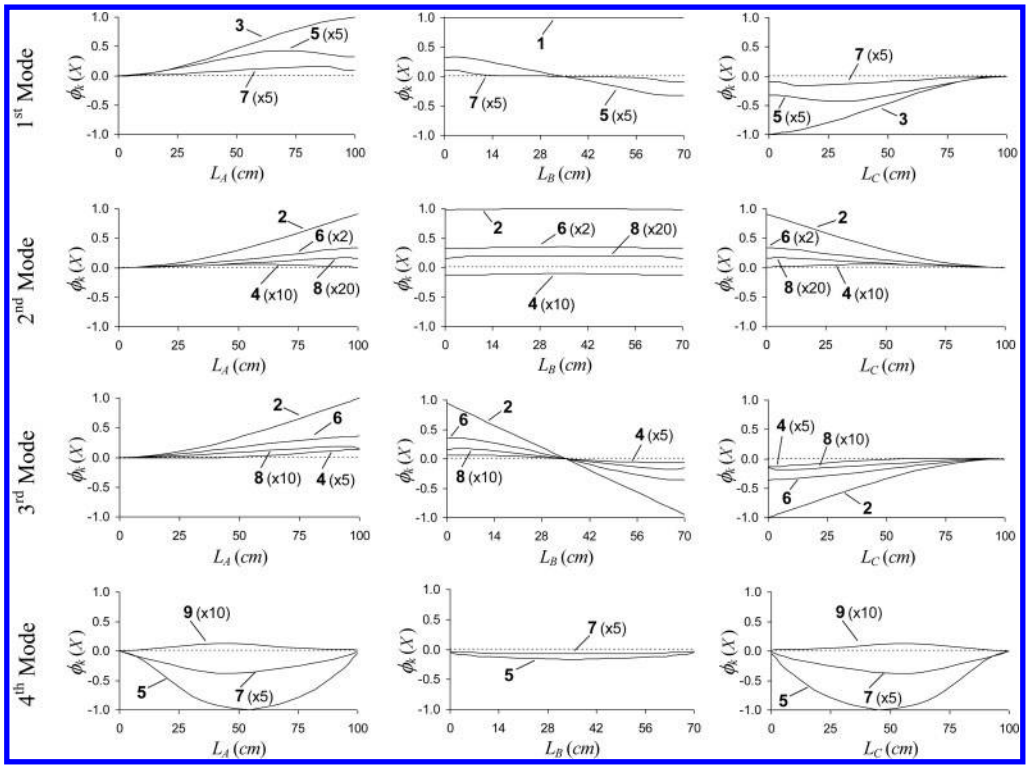


Figure 3. Modal amplitude function $\phi_k(x)$ that participate in the first four frame vibration modes.

(ii) The frame buckles in a combination of local and distortional deformation modes that (ii_1) involves the three members and (ii_2) includes contributions from the GBT deformation modes **5** (distortional) and **7** + **9** (local). The participation of mode **5** is highly dominant (75%), with the maximum values occurring at the member *B* mid-span region, but there are also non-negligible contributions from local modes **7** and **9** in the joint vicinities.

4.3 *Loaded frame vibration*

Finally, one investigates the vibration of frames subjected to uniform axial compression loads – the applied load value is defined by a parameter $P^0 \equiv W_1^0$, which is taken as fraction (α) of its critical value, *i.e.*, $P^0 = \alpha P_{cr}$. Table 2 shows the influence of the applied loading ($\alpha = 0$, 0.25, 0.5, 0.75, 0.95, 0.99) on the frame fundamental frequency ω_1. Moreover, the 3D views yielded by ANSYS and the modal amplitude functions presented in Figures 6 and 7 (three load levels) provide in-depth information on the evolution of the frame fundamental vibration mode as the applied load level increases. After observing the results presented in these figures and table, the following conclusions can be drawn:

(i) The presence of loading only cause a considerable fundamental frequency drop (*i.e.*, more than 5%) for $\alpha \geq 0.75$ – a substantial fundamental frequency drop (*i.e.*, more than 30%) occur for $\alpha \geq 0.95$.

(ii) The GBT and ANSYS fundamental frequencies are again extremely close (differences below 3.4%). Moreover, there is also excellent correlation between the fundamental vibration mode shapes provided by the ANSYS analyses and GBT modal amplitude functions.

(iii) The comparison between the modal amplitude functions for $\alpha = 0$ (see Fig. 3) and $\alpha \neq 0$, shows that the fundamental vibration mode shapes of the load-free frame and the loaded frame with $\alpha = 0.25$ are very similar. On the other hand, the fundamental vibration mode shape is considerably altered by the presence of a load level equal to $\alpha = 0.75$ – indeed, there is an increase of the contribution of the deformation modes **5** and **7**.

(iv) For $\alpha \cong 1$ the vibration mode shape changes quite drastically, approaching its critical buckling mode counterpart – indeed, for $\alpha = 0.99$ the fundamental vibration and critical buckling modes virtually coincide, as attested by the comparison with Figure 5.

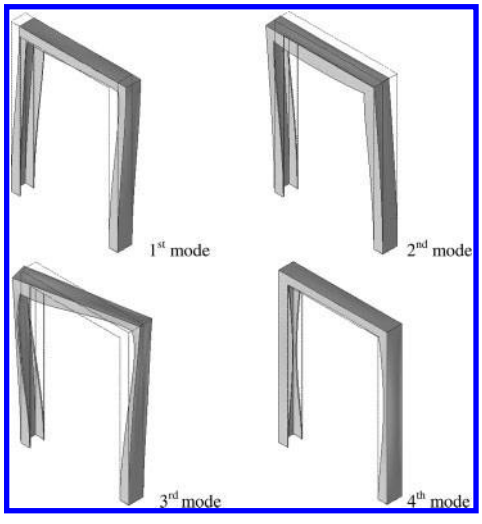


Figure 4. First four frame vibration modes obtained by ANSYS.

Table 2. Variation of the fundamental frequencies (rad/s) with α.

α	ω_{GBT}	ω_{ANSYS}	Δ(%)
0	392.72	383.54	2.4
0.25	387.69	377.58	2.7
0.50	382.31	370.44	3.2
0.75	370.13	358.32	3.3
0.95	269.21	261.43	3.0
0.99	133.94	130.30	2.8

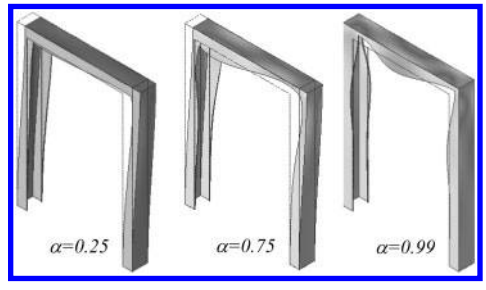


Figure 6. Fundamental vibration modes for $\alpha = 0.25$, 0.75, 0.99.

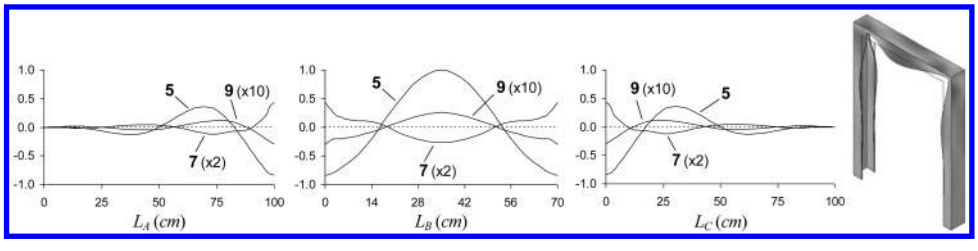


Figure 5. Frame critical buckling mode: modal amplitude functions (GBT) and three-dimensional configuration (ANSYS).

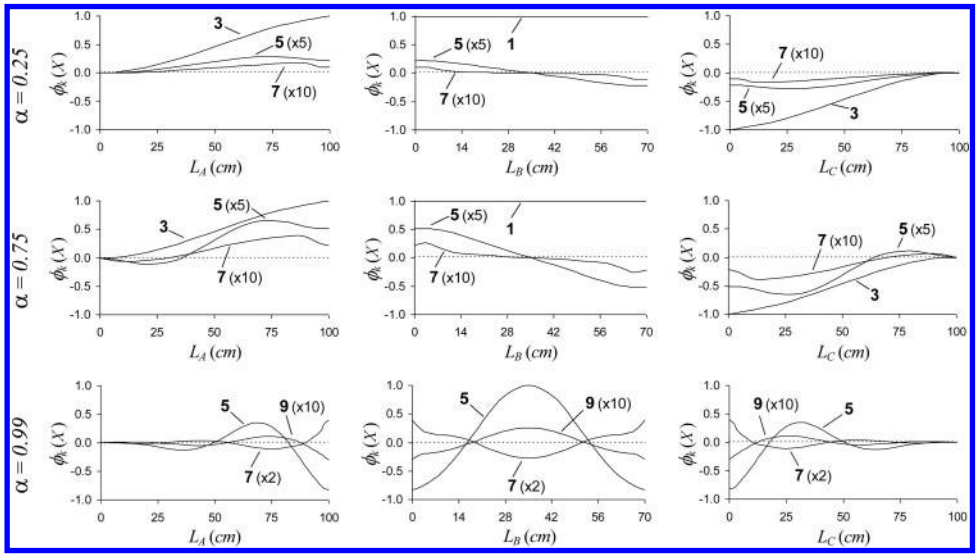


Figure 7. Modal amplitude functions $\phi_k(X)$ that participate in the fundamental vibration modes for $\alpha = 0.25, 0.75, 0.99$.

5 CONCLUSION

The paper reported the results of an ongoing investigation on the use of a GBT-based beam finite element approach to analyse the local, distortional and global vibration behaviour of thin-walled steel frames. After a very brief review of the most relevant concepts involved in performing a GBT vibration analysis, the paper described the procedures involved in obtaining the frame overall linear and geometric stiffness matrices, as well as the frame mass matrix, which incorporate the effect of the frame joints. Finally, the application and capabilities of the developed GBT-based beam finite element approach were illustrated by means of the presentation and discussion of numerical results concerning the local, distortional and global vibration behaviour of load-free and loaded symmetric portal frames – the study focused on the influence of the applied load level on the vibration frequencies and mode shapes. For validation purposes, most of the GBT-based results were compared with values obtained by means of shell finite element analyses carried out in the code ANSYS. An excellent agreement was found in all cases, despite the large difference between the numbers of $d.o.f.$ involved in the two analyses.

ACKNOWLEDGEMENTS

The financial support of *Fundação para a Ciência e Tecnologia* (FCT – Portugal), through project PTDC/ECM/108146/2008, and *Fundação de Amparo à Pesquisa do Estado de São Paulo* (FAPESP – Brazil), through project 11/15731-5, is gratefully acknowledged. The first author also acknowledges FAPESP for his postdoctoral scholarship, 2011/17557-2.

REFERENCES

Ahmed T. & Shimizu S. 2012. A study of the seismic effects on a portal frame having a hole at the beam-column connection. *Thin-Walled Structures* 52(March): 53–60.

Basaglia C., Camotim D. & Silvestre, N. 2008. Global buckling analysis of plane and space thin-walled frames in the context of GBT, *Thin-Walled Structures,* 46(1), 79–101.

Basaglia C., Camotim D. & Silvestre, N. 2009. GBT-Based local, distortional and global buckling analysis of thin-walled steel frames, *Thin-Walled Structures*, 47(11), 1246–1264.

Bebiano R., Silvestre N. & Camotim, D. 2008. Local and global vibration of thin-walled members subjected to compression and non-uniform bending. *Journal of Sound and Vibration* 315(3): 509–535.

Camotim D., Basaglia C. & Silvestre N. 2010. GBT buckling analysis of thin-walled steel frames: a state-of-the-art report, *Thin-Walled Structures*, 48(10–11), 726–743.

Gonçalves R., Ritto-Corrêa M. & Camotim D. 2010. A New Approach to the Calculation of Cross-Section Deformation Modes in the Framework of Generalized Beam Theory, *Computational Mechanics*, 46(5), 759–781.

Moazed R. Szyszkowski W. & Fotouhi R. 2009. The in-plane behaviour and FE modelling of a T-joint connection of thin-walled square tubes. *Thin-Walled Structures* 47(6–7): 816–825.

Silvestre N. & Camotim D. 2006. Vibration behaviour of axially compressed cold-formed steel members, *Steel & Composite Structures – An international Journal*, 6(3), 231–236.

Sophianopoulos D.S. 2003. The effect of joint flexibility on the free elastic vibration characteristics of steel plane frames. *Journal of Construction Steel Research* 59(8): 995–1008.

Swanson Analysis Systems Inc. 2009. Ansys Reference Manual, v.12.

Türker T. & Bayraktar A. 2011. Experimental and numerical investigation of brace configuration effects on steel structures. *Journal of Construction Steel Research* 67(May): 854–865.

Research and Applications in Structural Engineering, Mechanics and Computation – Zingoni (Ed.)
© 2013 Taylor & Francis Group, London, ISBN 978-1-138-00061-2

Moment redistribution in cold-formed steel continuous beams

C. Hui, L. Gardner & D.A. Nethercot
Imperial College London, London, UK

ABSTRACT: Cold-formed steel purlins supporting corrugated roof sheeting are often arranged to be continuous over an internal support. Economic design should be based on failure of the system, recognising the opportunity for redistribution of moments. This paper presents the findings from a numerical investigation of the degree of moment redistribution in continuous cold-formed steel zeta-section beams subjected to a Uniformly Distributed Load (UDL). Three types of nonlinear finite element analysis were validated against reported physical tests: (1) continuous two-span beams subjected to a UDL, (2) single span beams subjected to a central point load producing a moment gradient and (3) single span beams subjected to two point load producing a central region under pure bending. The interior support moments from the continuous beam models were compared with the reference moment capacities from the three-point bending models. Based on various different sections sizes, covering a range of cross-sectional slenderness, full moment redistribution with no drop-off in moment at the interior support was found to be possible only for stocky sections but not for slender sections. In the case of slender sections, local and distortional buckling caused a reduction in interior support moment prior to failure of the system. Hence a design formula is proposed to estimate the post-peak reduction of interior support moment from its initial peak, and use this reduced moment in conjunction with the full span moment to determine the load-carrying capacity of the system. Comparisons show the proposed approach to offer accurate prediction of observed system failure loads.

1 INTRODUCTION

Modern light roof construction for industrial or warehouse buildings normally comprise cold-formed steel purlins covered with sheeting. These purlins are used as secondary steelwork between the main frames. The thin-walled nature of cold-formed steel members makes them susceptible to local instabilities such as local and distortional buckling. With buckling limiting the overall load carrying capacity, the basic assumption for the application of plastic theory that the first hinge for a dual span systems can maintain its moment capacity until a mechanism is formed, is not always guaranteed. This paper reports on a study designed to provide suitable modifications to permit the basic idea of plastic theory to be applied in such cases.

Many research projects have been carried out to investigate the structural behaviour of multi-span purlin systems: Willis and Wallace (1990) conducted continuous single and triple span tests with through-fastened roof panels. Ho and Chung (2006) and Hancock et al. (1992) conducted studies to investigate the behaviour of lapped moment connections for 2-span Z sections. Gutierrez et al. (2011) investigated the connection behaviour for Z sections with slotted sleeves.

As an alternative to conducting full scale testing which can be expensive and time consuming, finite element (FE) models have been increasingly used for research into cold-formed steel. Early publications on FE modelling of cold-formed steel members were by Moreyra and Peköz (1994); since then treatments have become more robust and practical with the use of faster processing power. More recently, Haidarali and Nethercot (2011) successfully analysed FE cold-formed Z sections using ABAQUS (2006) and investigated the local/distortional buckling behaviour for Z sections subjected to pure bending.

Even though there are many reported computational analyses and physical tests on cold-formed steel, studies investigating moment redistribution in multi-span cold-formed steel systems are limited. In this paper, FE models were validated against available tests to ensure that the model can capture the local/distortional buckling behaviour and subsequent moment redistribution. The models were then used to generate a series of parametric results which have formed the basis for a proposed design approach.

2 DESIGN APPROACHES

For the two-span continuous beam shown in Fig.1, a design based on elastic principles would utilise the full cross-sectional moment capacity at the central support but not within the span. However, if redistribution of moments is utilised then there is the potential to use a greater proportion (possibly all) of the unused

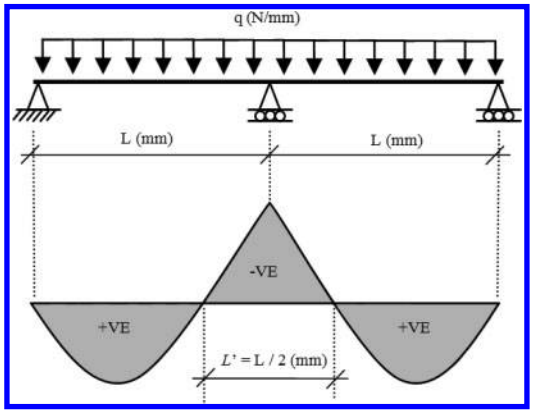


Figure 1. Elastic Bending moment diagram (BMD) for 2-span setups.

moment capacity within the span. The principle is commonly used when designing hot rolled steelwork; it has been adapted for reinforced concrete construction, composite construction and for cold-formed steel construction by recognising certain limitations in the moment-rotation relationships of cross-sections and accepting that full redistribution may not be possible.

In the ideal situation of full plastic redistribution of moments, both the bending moment at the interior support, $M_{support}$ and within the span, M_{span} reach their full cross-sectional capacity because the moment-rotation relationship for the support region is such that no significant fall off in capacity occurs before rotations develop sufficiently to allow the span moment to reach its capacity. Should this not be the case i.e. attaining full capacity within the span is accompanied by a reduction in $M_{support}$, then appropriate allowance must be made.

Thus the design issue for cold-formed steel construction is that the moment-rotation behaviour differs from the ideal arrangement of Fig 1. In cold-formed steel construction the cause is a combination of local and distortional buckling, together with some material nonlinearity.

Knowing the bending moment capacities at the span M_{span}, and supports $M_{support}$, the ultimate design load carrying capacity q for a continuous 2-span system with equal spans subjected to a UDL, can be calculated by solving Eq. 1.

$$M_{span} = \frac{\left(qL^2 - 2M_{support}\right)^2}{8qL^2} \quad (1)$$

3 FINITE ELEMENT (FE) MODELS

3.1 *Outline of different models*

To study the behavior and level of redistribution in continuous systems, for each 2-span FE model, two further single span models were used to create reference values for the interior support and span moments in the

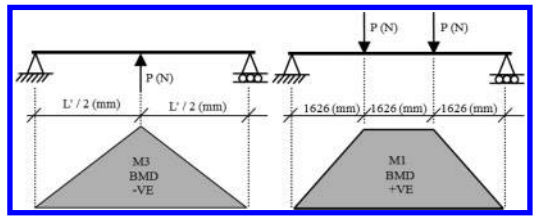


Figure 2. BMD for single span tests.

2-span model: (1) The largest sagging moment (elastically located at 0.375L from the beam ends) M_{span} was compared with a single span model subjected to uniform bending M_1 and (2) the largest hogging moment found at the interior support $M_{support}$ was compared to the maximum moment in the single span model subjected to 3-point bending M_3. Fig 2 shows the single span models used to calculate these reference moment capacities. Relevant comparisons between $M_{support}$ and M_3 were made by ensuring the beneficially sharp parabolic moment gradient observed in the 2-span system was allowed for by modifying the moment gradient in the reference single span test, as shown in the figure. The lengths of the hogging region from the 2-span models L' were used as the beam length for the 3-point bending analyses.

3.2 *FE modelling assumptions*

All FE models were developed in ABAQUS (2007) using S4R shell elements. The two-stage modified Ramberg-Osgood material model proposed by Gardner and Ashraf (2006) was used to model the gradual yielding material behaviour of the cold-formed steel members.

A two-spring model was used to replicate the restraining behaviour of common purlin-sheeting arrangements in which the sheeting is attached to the top flange. A linear translational spring was used to model the retraining behaviour provided by each fastener. A further compression-only spring was attached to the lip/flange junction to prevent any negative vertical displacement. The non-linear spring was assigned negligible stiffness in tension, but high stiffness to replicate bearing of the beam on the sheeting. Inclusion of the springs prevented the flanges buckling upwards (into the sheeting) but offered no restrictions to buckling downwards.

Geometric imperfections were included in the FE models as a superposition of local and distortional buckling modes with independent scaling amplitudes of 0.229 t and 0.099 t, respectively. The buckling shapes for both modes were decomposed using the finite strip software CUFSM (2006). The elastic buckling analysis in CUFSM adopts a constrained finite strip method which systematically increases the half-wavelength of any thin-walled member subjected to pure bending. The first two minima from the signature curve correspond to the elastic critical local and distortional buckling modes respectively. The

Table 1. Summary FE validation process.

Reference	Section type	Test type	No. tests	Mean	COV
Wang & Zhang (2008)	C	3-point bending	4	1.006	0.009
Wang & Zhang (2008)	C	Pure bending	4	0.993	0.020
Bryan & Davies (1979)	Zeta	2-span gravity	10	1.013	0.030
Bryan & Davies (1979)	Zeta	3-point bending	7	0.994	0.043
Yu & Schafer (2003)	Zed/C	Pure bending	25	1.022	0.067

individual imperfection shapes were plotted harmonically in the longitudinal direction with periods equal to their half-wavelength obtained from CUFSM.

Stiff plates ($E_{plate} = 10E_{beam}$) were modelled at the loading points and supports to eliminate any premature localised failure such as web crippling. Lateral restraints at modest spacing were adopted to prevent the system failing prematurely by lateral-torsional buckling. The loading for both single span models was applied through the centre of the stiff plates, which were tied to the beam directly. For the 2-span models, the UDL was modelled by applying a pressure load to a narrow portion of the top flange. The modified Riks method (*STATIC, RIKS) was used for all finite element models.

3.3 *FE model validation*

Prior to undertaking parametric studies, the models were first validated against various physical tests from 3 sources. Wang and Zhang (2008) completed single span pure bending and moment gradient tests for various cold-formed members including lipped channel cold-formed steel sections. Bryan and Davies (1979) carried out two studies using various zeta sections: (1) single span tests subjected to a moment gradient and (2) full scale 2-span gravity continuous tests subjected to a UDL. Yu and Schafer (2003) carried out a large number of pure bending tests comprising both lipped channel and lipped zed sections cold-formed steel members. Distortional and lateral-torsional buckling was effectively restricted by suitably located bracing.

A total of 50 comparisons between the FE models and physical tests were made. Table 1 presents a summary of the results in terms of the mean test/FE capacity and coefficient of variation (COV) for each set of tests. The overall validation results indicate excellent agreement with the largest over and under prediction being 2.2% and 0.07% respectively and minimal scatter. The buckling behaviour and the deflected shapes

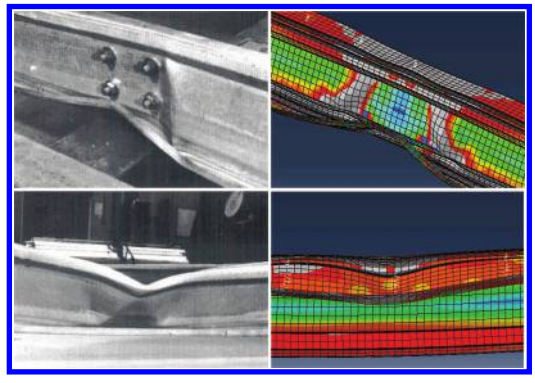


Figure 3. Typical comparison between physical FE and physical test failure modes ((a) and (b) buckling at interior support, (c) and (d) buckling in span).

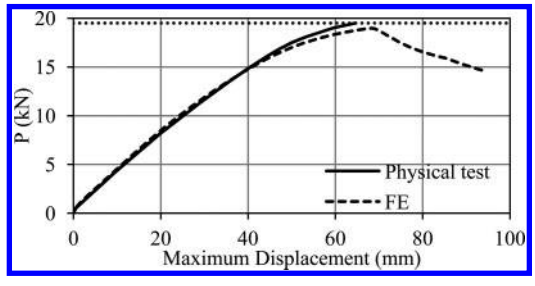


Figure 4. Typical comparison of load-displacement response between FE and physical test.

match the observed failures modes reported by Bryan and Davies (1979) and are shown in Fig. 3. The close agreement of the overall load-deformation response between a typical FE model and physical test is shown in Fig 4.

4 PARAMETRIC STUDY

4.1 *Influence of section slenderness*

Figs 5–7 and 8–10 show, respectively, the different behaviour of stocky and slender cross-sections in a two-span arrangement. For the former, behaviour accords closely with the ideal situation given by plastic theory, with full moment redistribution, the support moment $M_{support}$ being approximately M_3, and the span moment approximately M_1.A condition approximating to full redistribution occurs and the behaviour in the support region, as indicated by $M_{support}$ and approximated by M_3 occurs. However, for more slender arrangements of Fig. 8, Fig. 10 shows how the M_3 plot starts to fall very soon after reaching the maximum moment, whilst Fig. 9 shows $M_{support}$ reducing from its peak as more load is added and M_{span} builds to its maximum. The reduced $M_{support}$ corresponding to attaining the maximum M_{span} and thus the maximum moment for the system is designated αM_3.

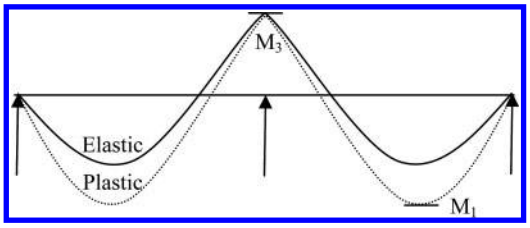


Figure 5. BMD for an ideal situation of full redistribution.

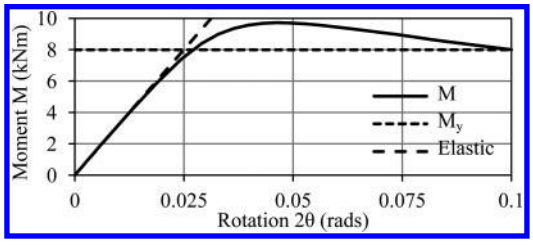


Figure 6. Typical moment-rotation (M-θ) curve for simple beams with stocky sections.

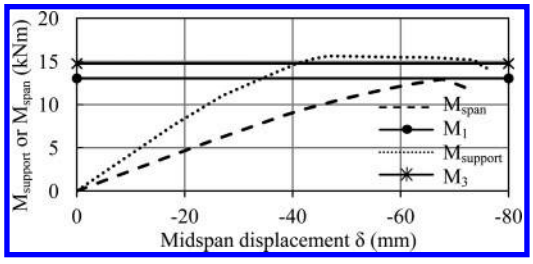


Figure 7. Typical support and span moment-midspan displacement response for stocky sections.

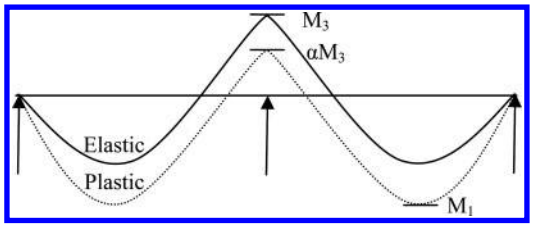


Figure 8. Typical BM redistribution behaviour for slender sections.

The proposed design method therefore utilises the plastic mechanism (redistribution) approach of EN 1993-1-3 (2006), which presumes full redistribution, but replaces the full value of the hogging moment (taken herein to be closely approximated by the M_3 value so as to recognise the beneficial effects of moment gradient) with a lesser value αM_3.

4.2 *Alpha framework*

A total of 9 zeta sections covering section depths from 125 mm to 200 mm and material thicknesses from 1.3 mm to 5 mm were analysed to cover a wide range of

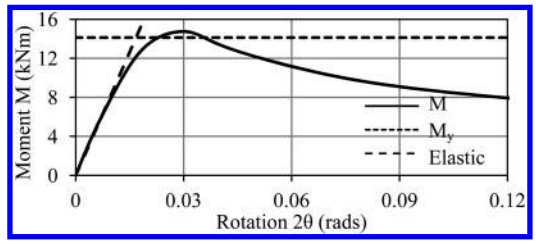


Figure 9. Typical moment-rotation (M-θ) curve for simple beams with slender sections.

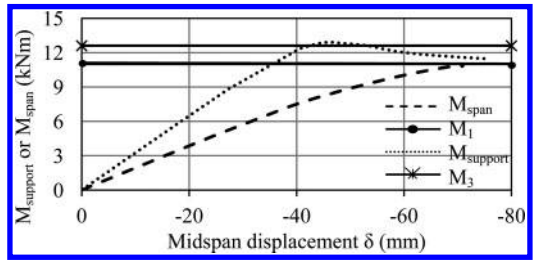


Figure 10. Typical support and span moment-midspan displacement response for slender sections.

cross-sectional slenderness. The 0.2% proof stresses, $\sigma_{0.2}$ and fastener spacing were kept constant for the study at 390 MPa and 300 mm, respectively. For each section, the following models were run: three 2-span FE models consisting of 4,6 and 8 m spans, one 4-point bending single span model with 1.667 m constant distance between point loads, and three 3-point bending single span models with 2,3 and 4 m spans. The study therefore comprised a total of 45 FE analyses.

For each 2-span model, the moment in the support region at the collapse load of the system was compared with the maximum moment from the corresponding reference moment gradient FE model. A reduction factor, α_{FEA} was defined as the ratio of these moments and is given by Eq 2, with full redistribution providing the upper bound value α_{FEA}, which is limited to unity.

$$\alpha_{FEA} = M_{support} / M_3 \qquad 0 \leq \alpha_{FEA} \leq 1 \qquad (2)$$

The cross-sectional slenderness λ_{cs} was defined as the square root of ratio of the yield strength to the elastic buckling stress. The elastic buckling stress was obtained from CUFSM. The interior support moment reduction values, α_{FEA} found from the parametric study are plotted against the cross-sectional slenderness in Fig. 11. The results are classified into their respective span lengths of 4, 6 and 8 m. It can be seen from Fig 11, that the longer spans tend to yield higher α values than shorter spans for the same section. Understanding that the amount of interior moment reduction is also influenced by the span length, a design equation is proposed to estimate α using Eq. 3.

The ultimate load q, was compared for each section between the 2-span FE model and a design load based on a combination of reference single span tests using Eq. 1. Two cases were considered when applying Eq. 1:

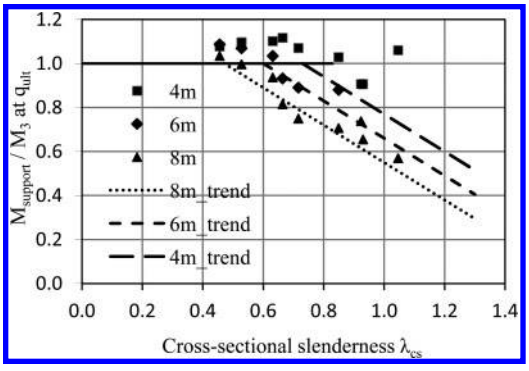


Figure 11. Support moment reduction vs. section slenderness.

(1) assuming full redistribution ($\alpha_{design} = 1$) by using M_1 and M_3 directly, and (2) allowing for a potential loss of support moment by calculating the reduction factor using Eq. 3, and applying M_1 and αM_3.

$$\alpha_{design} = -0.85\lambda_{cs} - 0.055L + 1.84 \quad (3)$$

Where L is the span length (m) and Eq. 3 is valid within the range: 4.0 m < L < 8.0 m.

Table 2 shows the ultimate loads, q from the FE analyses with 2 separate sets of design results: (1) Column q_{M1_M3} assumes α_{design} equals unity when applying M_1 and M_3 as the span and support moments for Eq. 1, and (2) column $q_{M1_\alpha M3}$ incorporates a reduction to support moment by calculating each individual α_{design} value using Eq. 3 and then applying M_1 and αM_3 as the span and support moments for Eq. 1.

Table 3 presents a summary of the two design methods and indicates that assuming full redistribution, q_{M1_M3} gives on average, a 3.2% unconservative ultimate load prediction, whereas the proposed design method which allows for a reduction in the support moment, $q_{M1_\alpha M3}$ gives on average a 2% conservative results with considerably reduced scatter. It should be notes that actual differences between the 2 predictions can be rather large, since in several cases $\alpha = 1$.

Table 2. Results of parametric study.

Section	Span (m)	q_{FEA} (kN/m)	q_{M1_M3} (kN/m)	$q_{M1_\alpha M3}$ (kN/m)
150-50	4	23.603	24.860	24.860
150-50	6	11.615	11.100	11.100
150-50	8	6.451	6.247	6.247
150-40	4	20.966	20.132	20.132
150-40	6	9.175	8.900	8.900
150-40	8	5.020	4.946	4.872
150-30	4	15.289	14.809	14.809
150-30	6	6.627	6.547	6.494
150-30	8	3.598	3.693	3.537
125-20	4	6.951	6.760	6.760
125-20	6	2.933	2.973	2.923
125-20	8	1.576	1.679	1.593
200-25	4	18.535	18.025	18.025
200-25	6	7.767	8.005	7.761
200-25	8	4.165	4.486	4.197
125-13	4	4.030	4.015	3.889
125-13	6	1.725	1.797	1.677
125-13	8	0.913	1.005	0.904
175-16	4	8.694	8.561	8.128
175-16	6	3.759	3.838	3.507
175-16	8	2.007	2.161	1.897
200-16	4	9.965	10.392	9.837
200-16	6	4.227	4.598	4.195
200-16	8	2.327	2.583	2.267
200-13	4	7.020	7.969	7.284
200-13	6	3.092	3.537	3.107
200-13	8	1.763	1.987	1.673

Table 3. Summary of alpha (α) framework.

	q_{M1_M3}/q_{FEA}	$q_{M1_\alpha M3}/q_{FEA}$
MEAN	1.032	0.980
COV	0.057	0.028

5 DISCUSSION

It is of interest to note that as arrangements become more slender so the value of $M_{support}$ at maximum load falls from its peak. Thus the design calculation using M_1 and M_3 overestimates capacity for these cases, whilst that using M_1 and αM_3 provides much closer predictions over the full range of cross-sectional slenderness, with both a mean ratio of design/FEA close to unity and low scatter. Few results are overpredicted and none by more than 5%. Thus inclusion of the α correction as obtained from Eq.3 permits the safe use of the plastic redistribution for the range of zeta sections covered.

Even though only zeta sections have been used for this study, it is expected that Eq. 3 could still be applied to other cold-formed steel sections because it incorporates the cross-sectional slenderness. Other stockier sections such as thick sections with short flanges and sufficiently deep edge stiffeners may result in α_{design} values equal to unity, whereas slender sections such as thin zed sections with no edge stiffeners would tend to yield a large reduction in central support capacity before the ultimate load has reached a peak.

6 CONCLUSIONS

Finite element modelling techniques for cold-formed steel sections have been briefly explained, giving specific ways to model the restraining behaviour of common trapezoidal sheeting methods to prevent premature buckling. The described FE models have been validated against 50 physical tests conducted by various authors. A parametric study consisting of 45 FE models for zeta sections covering a range of slenderness has been conducted to evaluate the loss of

moment at the central support in two-span continuous beams upon reaching the collapse load of the system from its peak moment capacity. The results from the study shows 2-span systems made up of slender sections at large spans could lose up to 50% of their maximum support moment at ultimate load due to a sharp loss of moment at the interior support, whereas, stocky sections can achieve full moment redistribution, since no significant reduction in the central support capacity is observed at system failure. A design formula is proposed to estimate the amount of moment redistribution for a 2-span purlin system by calculating a reduction value, α_{design} for the interior support moment at failure. The revised interior moment can be applied directly with the plastic mechanism approach of EC3. For the range of sections considered, the design approach of assuming full redistribution with the full interior support moment (i.e. $\alpha_{design} = 1$) was found to be unconservative by 3.2% on average and up to 7% for the more slender sections. However, adopting the design approach gives 2% conservative predictions on average and with a greatly reduced scatter (COV = 0.03 compared to 0.06 for αdesign = 1).

ACKNOWLEDGEMENTS

The authors are grateful to Ayrshire Metal Products for their financial and technical contributions to the project.

REFERENCES

ABAQUS. 2007. ABAQUS Version 6.7. Pawtucket, USA: Hibbitt, Karlsson & Sorensen, Inc.

Bryan, E.R., and Davies, J.M. 1979. Design basis of zeta purlins. *Department of Civil Engineering, University of Salford, report ref no. 80/132, university ref. no. LK/T2.*

CUFSM Version 3.12. 2006. Schafer, B. Department of Civil Engineering, Johns Hopkins University. http://www.ce.jhu.edu/bschafer/cufsm/

EN 1993-1-3. 2006. Eurocode 3: Design of steel structures – Part 1–3: General rules – Supplementary rules for cold formed members and sheeting. *CEN.*

Gardner, L. and Ashraf, M. 2006. Structural design for non-linear metallic materials. *Engineering Structures.* 26(6): 926–934.

Gutierrez, R., Loureiro, A., Lopez, M., and Moreno, A. 2011. Analysis of cold-formed purlins with slotted sleeve connections. *Thin-Walled Structures*. 49: 833–841.

Haidarali, M.R., Nethercot, D.A. 2011. Finite element modeling of cold-formed steel beams under local buckling or com- bined local/distortional buckling. *Thin-Walled Structures*. 49(12):1554–62.

Hancock, G.J., Celeband, M., and Healy, C. 1992. Tests on continuous purlins under downwards loading. *Proc., 11th Int. Specialty Conf. on Cold-Formed Steel Structures.* 155–179.

Ho, H.C. and Chung, K.F. 2004. Experimental investigations into the structural behaviour of lapped connections between cold-formed steel Z sections. *Thin-Walled Structures*. 42: 1013–1033

Moreyra, M.E. and Peköz, T. 1994. Finite element studies on lipped channel flexural members. *Proc., 12th Int. Specialty Conf. on Cold-Formed Steel Structures.* 57–74.

Wang, H. and Zhang, Y. 2009. Experimental and numerical investigation on cold-formed steel C-section flexural members. *Journal of Constructional Steel Research.* 65: 1225–1235.

Willis, C.T. and Wallace, T. 1990.Behaviour of cold-formed steel purlins under gravity loading. *Journal of Structural Engineering, ASCE.* 116(8): 2061–2069.

Yu, C. and Schafer, B.W. 2003. Local buckling tests on cold-formed steel beams. *Journal of Structural Engineering, ASCE.* 129(12): 1596–1606.

Yu, C. and Schafer, B.W. 2006. Distortional buckling tests on cold-formed steel beams. *Journal of Structural Engineering, ASCE.* 132(4): 515–528.

Research and Applications in Structural Engineering, Mechanics and Computation – Zingoni (Ed.)
© 2013 Taylor & Francis Group, London, ISBN 978-1-138-00061-2

Shear strengths of lipped channel beams with stiffened web openings using numerical studies

P. Keerthan & M. Mahendran
Queensland University of Technology, Brisbane, Queensland, Australia

ABSTRACT: This paper presents the details of numerical studies on the shear behaviour and strength of Lipped Channel Beams (LCBs) with stiffened web openings. Over the last couple of decades, cold-formed steel beams have been used extensively in residential, industrial and commercial buildings as primary load bearing structural components. Their shear strengths are considerably reduced when web openings are included for the purpose of locating building services. Our research has shown that shear strengths of LCBs were reduced by up to 70% due to the inclusion of web openings. Hence there is a need to improve the shear strengths of LCBs with web openings. A cost effective way to improve the detrimental effects of a large web opening is to attach appropriate stiffeners around the web openings in order to restore the original shear strength and stiffness of LCBs. Hence numerical studies were undertaken to investigate the shear strengths of LCBs with stiffened web openings. In this research, finite element models of LCBs with stiffened web openings in shear were developed to simulate the shear behaviour and strength of LCBs. Various stiffening methods using plate and LCB stud stiffeners attached to LCBs using screw-fastening were attempted. The developed models were then validated by comparing their results with experimental results and used in parametric studies. Both finite element analysis and experimental results showed that the stiffening arrangements recommended by past research for cold-formed steel channel beams are not adequate to restore the shear strengths of LCBs with web openings. Therefore new stiffener arrangements were proposed for LCBs with web openings based on experimental and finite element analysis results. This paper presents the details of finite element models and analyses used in this research and the results including the recommended stiffener arrangements.

1 INTRODUCTION

The use of cold-formed steel members in low rise building construction has increased significantly in recent times. There are many significant benefits associated with the use of lightweight cold-formed steel sections in buildings. Lipped channel and Z-sections are commonly used in low rise building construction due to their high strength-to-weight ratio, economy of transportation and handling, ease of fabrication, simple erection and installation. Figure 1 shows the use of lipped channel beams (LCB) in floor systems with circular web openings.

At present industry applications in flooring systems include openings in the web of floor joists or bearers so that building services such as electrical conduits and plumbing facilities can be located within them. Three standard opening sizes of 60, 100 and 125 mm are used with the currently available LCBs. Shear force is carried by the web element of LCB. Therefore the use of web openings in LCBs significantly reduces their shear capacity due to the reduced web area. There are many variables that affect the shear capacity of members containing web openings. They include the shape, position and size of web openings and also the web slenderness. Hence Keerthan and Mahendran (2012a,c) investigated the shear behaviour and strength of LCBs with circular web openings using experimental and numerical studies. New design equations were developed by them for the shear capacity of LCBs with web openings, which included the effects of enhanced buckling due to the rigid web-flange juncture, and post-buckling strength in shear.



Figure 1. LCBs with web openings.

Since the loss of shear capacity of LCBs was found to be as high as 70% (Keerthan and Mahendran, 2012a) when the depth of web opening to clear height ratio (d_{wh}/d_1) was 0.7, there is a need to enhance the shear capacity of LCB with web openings. A cost effective way to enhance the detrimental effects

of a large web opening is to attach suitable stiffeners around the web openings. Current cold-formed steel design standards (AISI, 2004, 2007 and SA, 2005) do not provide adequate guidelines to assist the design and construction of stiffeners for LCB floor joists with large web openings. Keerthan and Mahendran (2013) investigated the shear behaviour and strength of LiteSteel beams (OATM, 2008) with stiffened web openings using experimental and numerical studies while Sivakumaran (2008) conducted an experimental study to develop a stiffener system for cold-formed LCBs with web openings. However, limited research has been undertaken to investigate the shear behaviour of LCBs with stiffened web openings. Hence numerical and experimental studies were conducted to develop suitable stiffener arrangements for LCBs with web openings subjected to shear. This paper presents the details of finite element analysis (FEA) based studies of LCBs with stiffened circular web openings, and the results. New plate stiffener arrangements are developed for LCBs to restore the original shear capacity of LCBs without web openings based on test and FEA results.

2 EXPERIMENTAL STUDIES

This section reports the details of the web stiffening arrangements used in Keerthan and Mahendran's (2012d) experimental study. This experimental study was focused on the use of plate stiffeners with varying fastening arrangements to obtain the best fastening method. It was based on a series of primarily shear tests of simply supported LCBs with stiffened web openings subject to a mid-span load (Figure 2). Flanges were restrained by straps to eliminate the flange distortion.

Test specimens of LCBs, 250 × 75 × 1.9 LCB and 160 × 65 × 1.9 LCB, were considered in the shear tests. Three opening sizes of 60, 100 and 125 mm were selected based on the standard sizes. Plate and stud stiffeners were used with varying thicknesses and sizes and screw fastening arrangements in nine tests. Eight tests were also carried out without stiffening the web openings, giving a total of 17 tests. To simulate a primarily shear condition, relatively short test beams were selected based on two aspect ratios (shear span a/ clear web height d_1) of 1.0 and 1.5. Table 1 shows the details of test specimens while Figure 2 shows the stiffening arrangements used in this experimental study.

Stiffeners were not attached in Test Specimens 1 to 4 (Aspect ratio = 1.5). In Test Specimens 5 and 6, the web openings were reinforced with plate stiffeners based on AISI's (2004) minimum stiffening requirements. The thickness of the plate stiffener was equal to the thickness of 250 × 75 × 1.9 LCB section while the plate stiffener extended 25 mm beyond all the edges of the web openings. This provided the dimensions of 110 × 110 × 1.9 mm and 150 × 150 × 1.9 mm for the plate stiffeners of Test Specimen 5 and 6, respectively. The plate stiffener was fastened to the web of the LCB section with No.12 Tek screws at 25 mm spacing along the edges of the plate stiffener with an edge distance

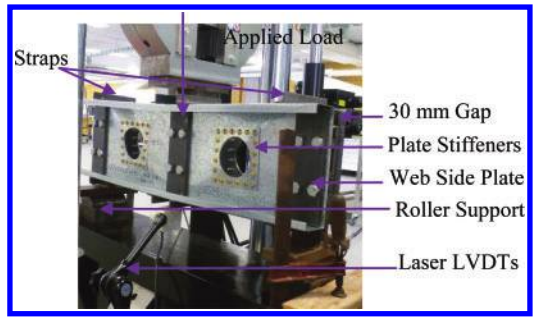


Figure 2. Experimental set-up.

Table 1. Test specimen details.

No.	LCB Sections	Aspect Ratio	d_w (mm)	d_{wh}/d_1	Type of Stiffeners	Fastening Arrangement	Stiffener Size (mm)	Shear Capacity (kN)	Shear Capacity (%)
1	250 × 75 × 15 × 1.9	1.5 0	0.00	–		–	63.0	100.0	
2	250 × 75 × 15 × 1.9	1.5	60	0.24	–		–	61.8	98.1
3	250 × 75 × 15 × 1.9	1.5	100	0.40	–		–	47.8	75.9
4	250 × 75 × 15 × 1.9	1.5	125	0.50	–		–	39.7	63.0
5	250 × 75 × 15 × 1.9	1.5	60	0.24	Plate	A1 (AISI)	110 × 110 × 1.9	65.6	104.1
6	250 × 75 × 15 × 1.9	1.5	100	0.40	Plate	A1 (AISI1	150 × 150 × 1.9	56.9	90.3
7	250 × 75 × 15 × 1.9	1.5	100	0.40	LCB Stud	A2(Optimum)	250 × 248 × 1.9	65.2	103.5
8	250 × 75 × 15 × 1.9	1.5	100	0.40	Plate	A2(Optimum)	200 × 200 × 1.9	62.7	99.5
9	250 × 75 × 15 × 1.9	1.5	125	0.50	Plate × 2	A2(Optimum)	225 × 225 × 1.9	53.7	85.2
10	250 × 75 × 15 × 19	1.5	125	0.50	Plate × 2	A2(Optimum)	225 × 225 × 3.8	62.2	99.0
11	250 × 75 × 15 × 1.95	1.0	0	0.00	–		–	55.3	100.0
12	250 × 75 × 15 × 1.95	1.0	100	0.40	–		–	34.4	62.2
13	250 × 75 × 15 × 1.95	1.0	125	0.50	–		–	28.1	50.8
14	250 × 75 × 15 × 1.95	1.0	100	0.40	Plate	A2(Optimum)	200 × 200 × 1.9	50.6	91.5
15	250 × 75 × 15 × 1.95	1.0	125	0.50	Plate	A2(Optimum)	225 × 225 × 1.9	44.2	80.0
16	160 × 65 × 15 × 1.9	1.0	0	0.00	–		–	73.8	100.0
17	160 × 65 × 15 × 1.9	1.0	100	0.63	Plate × 2	A2(Optimum)	13O × 130 × 3.8	45.3	61.4

Note: A1 – Arrangement 1, A2 –- Arrangement 2, d_{wh} = Depth of Web Opening, d_1 – Clear Height of Web. For 250 × 75 × 15 × 1.9, fyw = 515 MPa For 160 × 65 × 15 × 1.9, fyw = 515 MPa, For 250 × 75 × 15 × 1.95, fyw = 271 MPa

of 12.5 mm as shown in Figure 3(a). This stiffener arrangement was defined as "Arrangement 1" (AISI, 2004) in this paper.

To investigate the effect of using LCB stud stiffeners on the shear capacity of LCBs with web openings, Test 7 was conducted as shown in Figure 3c. Here 250 × 248 × 1.9 LCB stud stiffeners were attached to LCB specimen with 100 mm web openings. The screw fastening arrangement in Test Specimens 7 to 10 was placed with three screws on each side of the plate stiffener giving a total of 8 screws and enhanced with four additional screws in the diagonal direction giving a total of 12 screws (Arrangement 2) as shown in Figures 3b and 3c. The additional screws along the diagonal direction were located at 10 mm from the edge of the web openings. Test Specimen 10 was used to investigate the use of thicker 3.8 mm (two 1.9 mm plate stiffeners) and wider (225 mm) plate stiffeners to restore the shear capacity in the case of larger 125 mm web openings. Stiffeners were not attached in Test Specimens 11 to 13 and 16 (Aspect ratio = 1.0). In Test Specimens 14, 15 and 17, the web openings were reinforced with plate stiffeners based on Arrangement 2. Table 1 shows the ultimate shear capacities of the LCBs tested in this study. Details of experimental studies are reported in Keerthan and Mahendran (2012d).

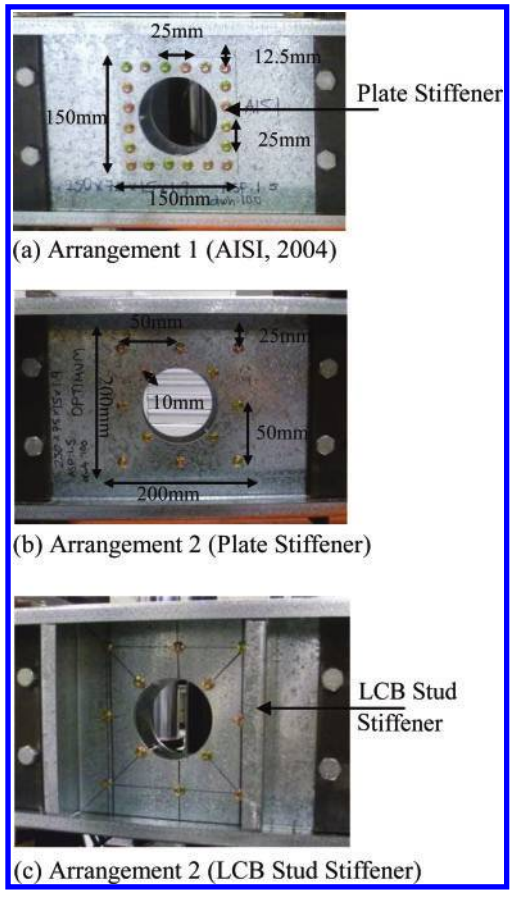


Figure 3. Stiffener Arrangements.

Test Specimen 6 only attained 90% of the shear capacity of LCB section without web openings (56.9 kN vs 63 kN). Therefore this test showed that the plate stiffeners established as per AISI (2004) recommendations are not adequate to restore the shear strengths of LCB with web openings when the ratio of depth of web opening to clear height of web (d_{wh}/d_1) is 0.40.

Experimental results (Table 1) show that by using LCB stud stiffeners with improved Arrangement 2 it was possible to attain 100% of the shear capacity of LCB without web openings (65.2 kN) in Test specimen 7 with 100 mm web openings ($d_{wh}/d_1 = 0.40$). The use of LCB stud stiffeners (Test Specimen 7, 65.2 kN) provided higher shear capacities than plate stiffeners of the same thickness (Test Specimen 8, 62.7 kN). However, LCB Stud stiffener may not be able to fully restore the shear capacity of LCBs without web openings when the depth of web opening to clear height ratio (d_{wh}/d_1) is greater than 0.40.

Tests 9 and 10 were conducted to determine the required web thickness in the case of larger 125 mm web openings. They were conducted with 1.9 mm and 3.8 mm plate stiffeners that were 225 × 225 mm wide and depth (50 mm on either side of the edge of web openings). Test Specimen 9 only attained 85% of the shear capacity of LCB section without web openings (53.7 kN vs 63 kN). However, Test Specimen 10 attained 99% of the shear capacity of LCB section without web openings (62.2 kN vs 63 kN). These tests thus show that plate stiffeners of appropriate thickness screw-fastened using Arrangement 2 were able to restore the full shear capacity of LCBs.

When compared to Test Specimens 8 and 9 (Aspect ratio = 1.5) which were identical to Test Speciemns 14 and 15, shear capacities attained in Test Specimens 14 and 15 (Aspect ratio = 1.0) were slightly lower. This slight reduction in shear capacity is a result of the optimum plate stiffener sizes being reduced for Tests 14 and 15. The aspect ratio of 1.0 meant a smaller shear panel length (a), which led to reduced distance between the web side plates and thus the optimum plate stiffener sizes had to be reduced to fit between the holding plates.

3 FINITE ELEMENT ANALYSES

This section presents the development of suitable finite element models to investigate the ultimate shear behaviour and strength of LCBs with stiffened web openings. For the numerical study, a general purpose finite element program, ABAQUS Version 6.7 (HKS, 2007), which has the capability of undertaking geometric and material non-linear analyses of three dimensional structures, was used. Finite element models were developed to simulate the actual test members' physical geometry, loads, constraints and mechanical properties in the experimental study as reported in the last section. The cross-section geometry of the finite element model was based on the measured dimensions, thicknesses and yield stresses of 17 tested LCBs. Table 1 gives the measured dimensions of the test beams made of 250 × 75 × 15 × 1.9 LCB and 160 × 65 × 15 × 1.9 LCB sections. The shell element in ABAQUS called S4R5 was used to simulate the shear behaviour of LCBs with stiffened web openings. R3D4 rigid body elements were used to simulate the restraints and loading in the finite element models of LCBs with stiffened web openings. Convergence studies showed that an element size of 5 mm × 5 mm provided an accurate representation of shear buckling and yielding deformations. To obtain accurate results, paver mesh was applied around the LCB web and stiffener openings. Figure 4 shows the geometry and finite element mesh of a typical LCB with stiffened web openings used in this numerical study.

The ABAQUS classical metal plasticity model was used in all the FE analyses. The elastic modulus and Poisson's ratio were taken as 200,000 MPa and 0.3, respectively. Simply supported boundary conditions were applied in the finite element models of LCBs with stiffened web openings. The vertical translation was not restrained at the loading point. Figure 5 shows the applied loads and boundary conditions used in the models. Shear test specimens included a 75 mm wide

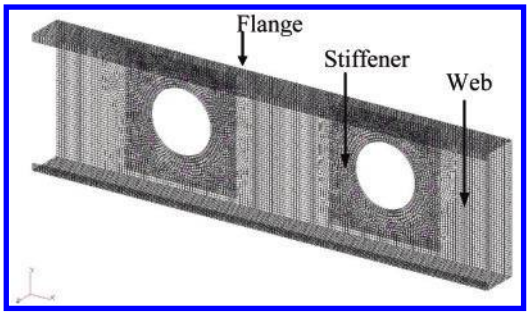


Figure 4. Geometry and finite element mesh of a typical LCB with stiffened web openings (250 × 75 × 15 × 1.9 LCB with 125 mm web openings, Aspect ratio = 1.5).

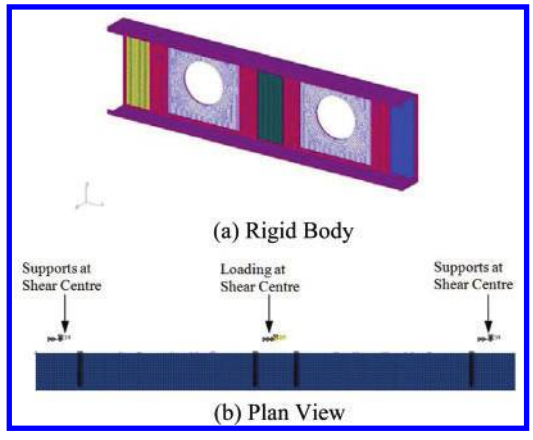


Figure 5. Applied loads and boundary conditions.

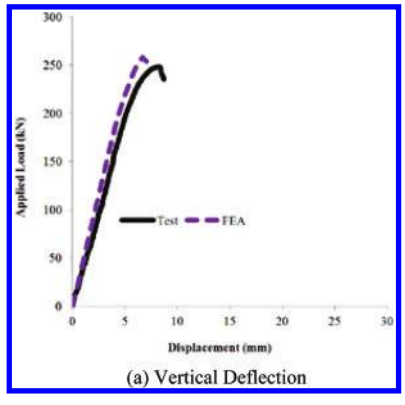


Figure 6a. Applied load versus deflections for Test specimen 10.

plate at each support to prevent lateral movement and twisting of the cross-section. These stiffening plates were modelled as rigid bodies using R3D4 elements. Simply supported boundary conditions were applied to the node at the shear centre to provide an ideal pinned support.

In Keerthan and Mahendran's (2012d) tests, there were no screw fastener failures. Therefore this observation was assumed in all the finite element analyses used here. The screw fasteners connecting the LCB to the stiffeners (Plate or LCB stud stiffeners) were not explicitly simulated in the finite element model. Instead they were simulated using perfect Tie MPCs, which makes all active degrees of freedom equal on both sides of the connection. The fabrication tolerance limit of $0.006d_1$ was used as imperfection in the numerical models of LCBs. It was decided to neglect the residual stresses in the FEA of LCBs with stiffened web openings as the effect of residual stresses on the shear capacity of LCBs with openings is less than 1% (Keerthan and Mahendran, 2012a). Experimental studies (Keerthan and Mahendran, 2012d) showed that strap failures did not occur. Considering this observation, the straps were not explicitly modelled. Instead they were simulated using suitable boundary conditions as follows at strap locations.

$$u_x = 0 \;\; u_y = 0 \;\; u_z = 1 \;\; \theta_x = 1 \;\; \theta_y = 0 \;\; \theta_z = 0$$

In the above, u_x, u_y and u_z are translations and θ_x, θ_y and θ_z are rotations in the x, y and z directions, respectively, and 0 denotes free and 1 denotes restrained.

The developed finite element models for non-linear analyses of LCBs with stiffened web openings were validated by comparing the non-linear analysis results with the results obtained from the shear tests (Keerthan and Mahendran, 2012d). This comparison was planned to establish the validity of the shell element model in the modelling of initial geometric imperfections and shear deformations, and associated material yielding. The FEA results were compared with those from testing, with particular attention given to the ultimate load, load-deflection curves and failure mechanisms. Table 2 presents a summary of the ultimate shear capacity results of LCBs with stiffened web openings from FEA and tests. The mean and COV of the ratio of test to FEA ultimate shear capacities are 0.99 and 0.01. This indicates that the finite element model developed in this study is able to predict the ultimate shear capacity of LCBs with stiffened web openings with very good accuracy. Figure 6 shows the FEA results in the form of load versus deflection for 250 × 75 × 15 × 1.9 LCB with 125 mm stiffened web openings (Test Specimen 10) and compare them with corresponding experimental results while Figure 7 shows the shear failure modes of Test Specimen 9. Figures 6 and 7 show a good agreement between the results from FEA and experiments.

Figure 6b and 7b confirms that LCBs with stiffened web openings have post-buckling strength due to the presence of tension field action.

In summary, FEA and test results in Table 2 show that plate stiffeners with dimensions equal to web opening width and depth plus 100 mm, screw fastened using Arrangement 2, are required to restore the full shear capacity of LCBs.

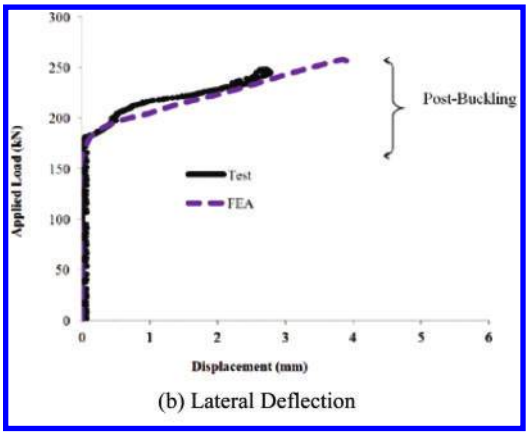


Figure 6b. Applied load versus deflections for Test specimen 10.

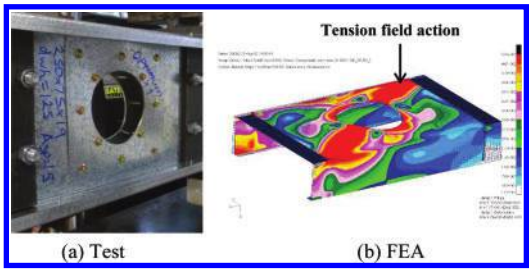


Figure 7. Failure mode of 250 × 75 × 15 × 1.9 LCB with 125 mm stiffened web openings and 225 × 225 × 1.9 mm plate stiffeners (Test specimen 9).

Table 2. Comparison of FEA and test results (aspect ratio = 1.5).

LCB section	d_{wh}/d_1	t_{stiff}/t_w	Type of Stiffeners	Fastening Arrangement	Stiffener Size (nun)	Shear capacity Test (kN)	Shear Capacity FEA (kN)	Shear Capacity (%)
250×75×15×1.9	0.00		–		–	63.0	64.0	100
250×75×15×1.9	0.24		–		–	61.8	62.0	97
250×75×15×1.9	0.40		–		–	47.8	48.3	75
250×75×15×1.9	0.50		–		–	39.7	39.9	62
250×75×15×1.9	0.24	1.0	Plate	Al (AISI)	110×110×1.9	65.6	66.0	103
250×75×15×1.9	0.40	1.0	Plate	Al (AISI)	150×150×1.9	56.9	57.5	90
250×75×15×1.9	0.40	1.0	Plate	A2(Optimum)	200×200×1.9	62.7	63.0	98
250×75×15×1.9	0.50	1.0	Plate	A2(Optimum)	225×225×1.9	53.7	54.0	84
250×75×15×1.9	0.50	2.0	Plate × 2	A2(Optimum)	225×225×3.8	62.2	64.5	101
250×75×15×1.9	0.60	2.0	Plate × 2	A2(Optimum)	250×250×3.8	–	66.0	103
250×75×15×1.9	0.70	2.0	Plate × 2	A2(Optimum)	275×250×3.8	–	58.5	91
250×75×15×1.9	0.70	2.5	Plate × 2.5	A2(Optimum)	275×250×4.8	–	66.5	104

4 SUITABLE PLATE STIFFENER SYSTEMS

In this section a suitable plate stiffener system is developed for LCBs with web openings based on test and FEA results. Although shear tests were conducted only for 250 × 75 × 1.9LCBs, it is considered that test results reported in this paper can be used to propose a suitable stiffener system that is applicable to other LCBs. FEA and test results showed that LCB stud stiffener was able to fully restore the shear capacity of LCBs without web openings when the depth of web opening to clear height ratio (d_{wh}/d_1) is equal or less than 0.40. Plate stiffeners are proposed with the following minimum dimensions based on FEA and test results. The width of the recommended plate stiffener is $d_{wh} + 100$ mm where d_{wh} is the depth of web opening while its height is lesser of clear web height (d_1) and $d_{wh} + 100$ mm. It is recommended that these plate stiffeners are fastened to LCB webs using No.12 Tek screws and Arrangement 2.

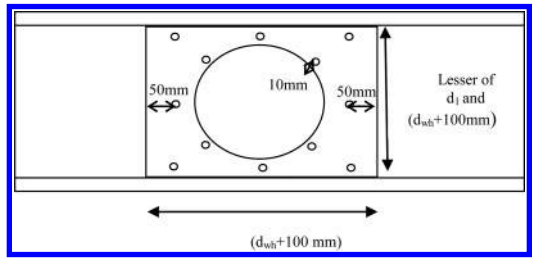


Figure 8. Effective plate stiffener system for LCBs with web openings.

It was found that the required plate stiffener thickness depends mainly on the ratio of the depth of web opening to the clear height of web ratio (d_{wh}/d_1). Therefore suitable predictive equations for the thickness of recommended plate stiffeners (t_{stiff}) were proposed based on d_{wh}/d_1 (Eqns. (1) to (3)). Eqns. (1) to (3) and associated d_{wh}/d_1 ranges were determined based on the test and FEA results reported here.

$$t_{Stiff} = t_w \qquad 0.24 < \frac{d_{wh}}{d_1} \le 0.40 \qquad (1)$$

$$t_{Stiff} = 2t_w \qquad 0.40 < \frac{d_{wh}}{d_1} \le 0.60 \qquad (2)$$

$$t_{Stiff} = 2.5t_w \qquad 0.60 < \frac{d_{wh}}{d_1} \le 0.70 \qquad (3)$$

$$w_{Stiff} = d_{wh}+100 \qquad (4)$$

$$h_{Stiff} = \text{Lesser of } d_{wh}+100 \text{ and } d_1 \qquad (5)$$

where, t_{stiff}, w_{stiff}, h_{stiff} = Thickness, width and height of plate stiffeners
d_{wh} = Depth of web openings
d_1 = Clear height of LCB web element

Since the level of fixity at the web-flange juncture of LCB is the same for the available LCBs (23% fixity level) (Keerthan and Mahendran, 2012b), Eqns. (1) to (3) are considered to be applicable to all the LCB sections.

Keerthan and Mahendran (2012b) proposed suitable equations for the shear capacity of LCBs without web openings. These equations can be used for LCBs with stiffened web openings when the improved, recommended stiffener arrangement (Arrangement 2) is used. Figure 8 shows the schematic diagram of the optimum plate stiffener arrangement for LCBs with web openings.

Keerthan and Mahendran (2013) proposed the following equation to predict the thickness of optimum plate stiffeners for hollow flange channel beams

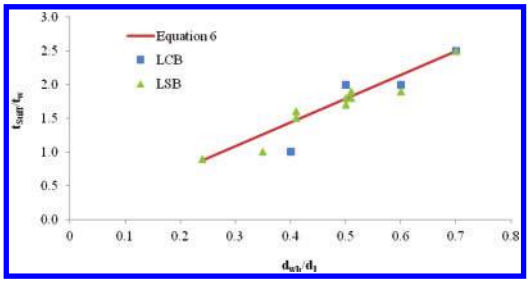


Figure 9. Optimum plate stiffener thickness to web thickness ratio (t_{Siff}/t_w) versus depth of web opening to clear web height (d_{wh}/d_1).

known as LiteSteel beams (LSB). Figure 9 includes the results of both lipped channel beams (LCB) and LiteSteel beams (LSB). It shows that Equation 6 can be also used to predict the thickness of optimum plate stiffeners LCBs.

$$t_{Siff} = \left[3.52\left(\frac{d_{wh}}{d_1}\right) + 0.035\right] t_w \qquad 0.24 < \frac{d_{wh}}{d_1} \leq 0.70 \qquad (6)$$

5 CONCLUSIONS

This paper has presented the details of a study into the shear performance and strength of lipped channel beams with stiffened web openings. Both experimental and numerical studies were conducted to develop the most suitable web stiffening arrangements for lipped channel beams with circular web openings in shear. To investigate the effects of stiffener types (plate and stud stiffeners) and sizes (thickness, width and height) and screw fastening arrangements on the shear capacities of LCBs with web openings, 17 primarily shear tests were conducted using a three point loading arrangement. Suitable finite element models were then developed and validated by comparing their results with corresponding test results. The developed nonlinear finite element model was able to accurately predict the shear capacities, load-deflection plots and failure modes of LCBs with stiffened web openings. Both numerical and experimental studies show that the plate stiffeners based on the recommendations of AISI (AISI, 2004) are not adequate to restore the shear strengths of LCBs with web openings. New plate stiffener systems with optimum sizes and screw-fastening arrangements were therefore proposed to restore the shear capacities of LCBs with web openings based on the results from both experimental and numerical studies. It was found that the width of the recommended plate stiffener is $d_{wh} + 100$ mm where d_{wh} is the web opening depth while its height is the lesser of clear web height (d_1) and $d_{wh} + 100$ mm. The required stiffener thickness was proposed as a function of the web opening depth to clear web height ratio (d_{wh}/d_1).

ACKNOWLEDGEMENTS

The authors would like to thank Queensland University of Technology for providing the necessary facilities and support to conduct this research project. They would also like to thank Mr Liam Rea and Mr Andre Dos Santos for their valuable assistance in performing the shear tests of stiffened LCBs.

REFERENCES

American Iron and Steel Institute (AISI) 2004. Supplement to the standard for cold-formed steel framing – Prescriptive method for one and two family dwellings. 2001 Edition, AISI, Washington, DC, USA.

American Iron and Steel Institute (AISI) 2007. North American specification for the design of cold-formed steel structural members. AISI, Washington, DC, USA.

Keerthan, P. and Mahendran, M. 2012a. Finite element analyses of lipped chanel beams with web openings in shear. *Proc. of the 21st International Specialty Conference on Cold-formed Steel Structures*, St. Louis, Missouri, USA. 249–263.

Keerthan, P. and Mahendran, M. 2012b. Shear buckling characteristics of cold-formed steel channel beams. *International Journal of Steel Structures, In press*.

Keerthan, P. and Mahendran, M. 2012c. Shear tests of lipped channel beams with web openings. *Proc. of the 10th International Conference on Advances in Steel Concrete Composite and Hybrid Structures*, Singapore, 171–178.

Keerthan, P. and Mahendran, M. 2012d. Shear tests of lipped channel beams with stiffened web openings, *Proc. of the 22nd Australasian Conference on the Mechanics of Structures and Materials*, Sydney, New South Wales, Australia, 819–825.

Keerthan, P. and Mahendran, M. 2013. Suitable stiffening systems for LiteSteel Beams with web openings subjected to shear. *Journal of Constructional Steel Research*. 80: 412–428.

OneSteel Australian Tube Mills, (OATM) 2008. Design of LiteSteel beams. Brisbane, Australia.

Pennock, R.W. 2001. Strength of light gauge cold-formed steel joists with web perforation. *Senior report*, University of New Brunswick, New Brunswick Canada

Sivakumaran, K.S. 2008. Reinforcement schemes for CFS joists having web openings. *Research Report*, Department of Civil Engineering, McMaster University, Ontario, Canada.

Standards Australia/Standards New Zealand (SA) 1998. Australian/New Zealand Standard AS/NZS 4100 steel structures. Sydney, Australia.

Standards Australia/Standards New Zealand (SA) 2005. Australia/New Zealand Standard AS/NZS4600 Cold-formed steel structures. Sydney, Australia.

Research and Applications in Structural Engineering, Mechanics and Computation – Zingoni (Ed.)
© 2013 Taylor & Francis Group, London, ISBN 978-1-138-00061-2

Coupled instability behavior of members with thin-walled welded box sections loaded in bending and compression

A. Taras & H. Unterweger
Graz University of Technology, Graz, Austria

S. Hafner
Ingenieurbüro Prof. Dr.-Ing. H. Bechert + Partner, Stuttgart, Germany

ABSTRACT: In this paper, the behavior of welded box sections with high local (plate buckling) and global (flexural buckling) slenderness is studied by means of numerical analysis and comparisons with code regulations. A remarkable degree of currently unused load-carrying capacity is observed for these sections and typical applications, which stems primarily from the plastic reserves and good post-buckling rotation capacity of this type of cross-section, as well as an inherent – and unnecessary-conservatism of the common design rules based on buckling reduction factors when applied to coupled instabilities.

1 INTRODUCTION

1.1 *Motivation*

The increased use of higher strength steel grades, and the consequent reduction in plate thicknesses in large bridge and building structures, has led to the need to better understand the instability phenomena affecting members with relatively thin-walled (class 3 or 4) steel cross-sections.

This paper focuses on an application of such members: welded box sections with higher plate slenderness ratios, see Figure 1, as found e.g. in (large) truss systems. A number of points must be considered when designing these members:

i. According to common design codes (e.g. the Eurocodes), the structural *analysis* of trusses with thin-walled members must take into account the bending moments due to the rotation impediments at the member ends, i.e. the classical hinged truss analysis is not applicable.
ii. In addition to this, international *design* rules for members with class 4 sections assume a rather strong interaction ("coupling") of the plate- and column buckling modes, with a full reduction to an effective (class 4) area for centric axial force even in cases where a combination with bending is present.

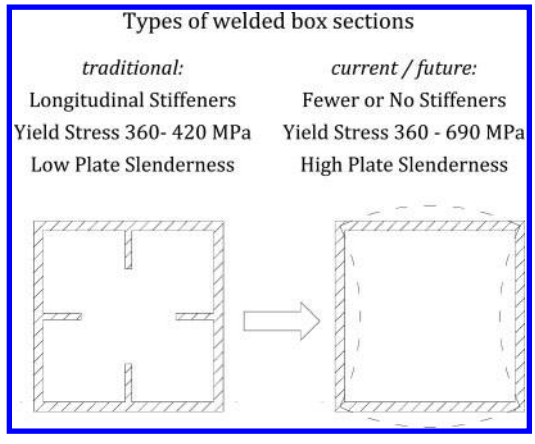


Figure 1. Types of welded box sections; increased plate slenderness due to reduced number of stiffeners and the use of higher-strength steel grades.

1.2 *Scope*

The numerical (geometrically and materially nonlinear FEM analyses with imperfections) and analytical study presented in this paper shows that the current analysis and design approaches often severely underestimate the rotational capacity and strength of the studied type of section. Preliminary recommendations are developed and the need for further experimental investigations and design rule development is highlighted.

All calculations and results presented in this paper consider internally unstiffened welded box sections of square shape (equal width and depth). Concerning the structural system, the following configurations are treated in this paper:

i. Compression members ("columns") subjected to axial force alone, with hinged ends.
ii. Beam-columns with hinged or clamped ends, subjected to variable bending moment diagrams and a compression force.

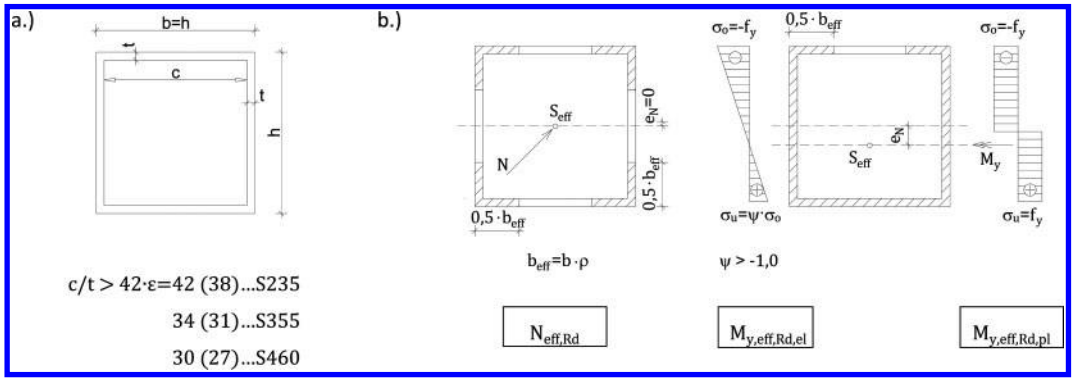


Figure 2. Studied welded box sections of cross-sectional class 4; a) limit c/t values for class 3; b) effective cross-sections and design strength values for compression and bending.

iii. A configuration as a member in a truss, with all boundary stiffnesses at the member ends thus correctly considered.

2 DETERMINATION OF THE STRENGTH OF THIN-WALLED BOX SECTIONS

2.1 *Design standards – Eurocode 3*

The strength predictions according to Eurocode 3 ("EC3", parts EN 1993-1-1 (2006) and EN 1993-1-5 (2005)) are used for comparative purposes in this paper; other international design standards only differ in details, but not in substance, from the principles used in EC3.

In EC3, a modified "Winter curve" equation (Winter, 1947) is used to determine the buckling reduction factor to be applied to rectangular plates in pure compression, see Equ. (1).

$$\rho = \frac{1}{\bar{\lambda}_p} \cdot \left(1 - \frac{0{,}22}{\bar{\lambda}_p}\right) \le 1{,}0 \qquad (1)$$

The slenderness $\bar{\lambda}_p$ is thereby calculated as the square root of the ratio between the yield stress f_y and the elastic critical buckling (bifurcation) stress σ_{cr}. In the EC3 design methodology for thin-walled cross-sections, this reduction factor is then used to determine reduced, "effective" cross-sections; see Figure 2b) for applications with pure compression or pure bending (whereby only the compressed flange is affected by buckling in the representation above). From the above rule, one can easily calculate limit values of the geometric plate slenderness c/t (b/t or h/t), which are given in parenthesis in Figure 2a) above. Interestingly, the current EC3 values used to determine whether or not plate buckling must specifically be checked (written left of the parentheses) are higher, thus creating a certain discontinuity in strength predictions.

The strength of a cross-section is finally determined by calculating the cross-sectional values (area A, section moduli W_y or W_z) of the "effective" sections and multiplying with the yield strength.

When thin walled elements are used as members under pure compression, global buckling must also be accounted for. This is done in EC3 by applying buckling reduction factors χ to the cross-sectional capacity:

$$\chi = \frac{1}{\Phi + \sqrt{\Phi^2 - \bar{\lambda}^2}} \le 1{,}0 \qquad (2)$$

with

$$\Phi = 0{,}5 \cdot \left(1 + \alpha\left(\bar{\lambda} - 0{,}2\right) + \bar{\lambda}^2\right) \qquad (3)$$

In the above equations, α is an "imperfection" factor accounting for the different buckling behaviour of different section shapes (and inherent geometric and structural imperfections), leadinf to the different so-called "European buckling curves", while the global column slenderness $\bar{\lambda}$ is calculated as the square root of the ratio between the section capacity for axial force and the Euler bifurcation load N_{cr}. For thin-walled sections, it takes on the following values:

$$\bar{\lambda} = \sqrt{\frac{A_{eff} \cdot f_y}{N_{cr}}} \qquad (4)$$

The buckling strength for axial compression $N_{b,Rd}$ is finally calculated as:

$$N_{b,Rd} = \chi \cdot A_{eff} \cdot f_y / \gamma_{M1} \qquad (5)$$

whereby γ_{M1} represents a safety factor.

If a compression member is also subjected to bending moments M_y or M_z (making it a "beam-column"), second-order effects may cause a further deterioration of the (in-plane) buckling strength. In EC3, this is taken into account (among a number of methods) by using so-called "beam-column interaction formulae". For the cases studied in this paper, with thin-walled sections and mono-axial bending, they take in the following shape:

$$\frac{N}{N_{b,Rd}} + k_{yy} \cdot \frac{N}{M_{y,eff,Rd,el}} \le 1{,}0 \qquad (6)$$

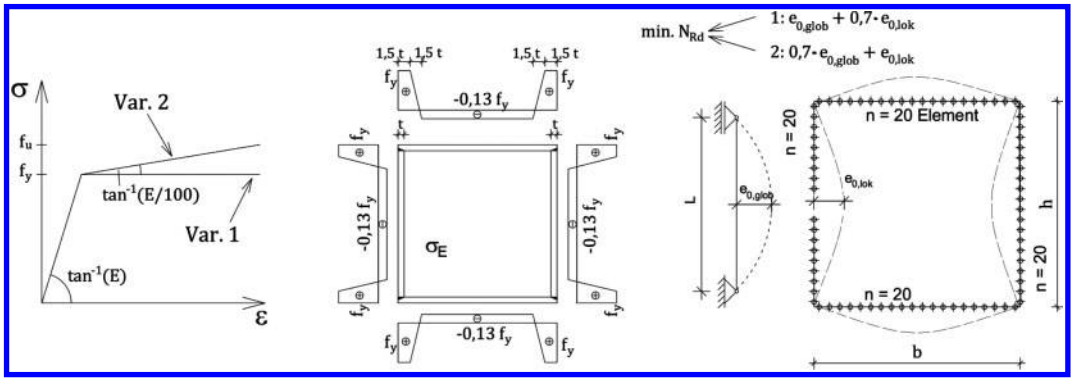


Figure 3. Numerical modelling for GMNIA calculations; stress-strain relationships; assumed residual stresses and geometric (local and global) imperfections and their combination rules; FEM discretization.

Note that the bending strength $M_{y,eff,Rd,el}$ is calculated on the basis of the effective cross-section for bending shown in Figure 2b) and an elastic cross-sectional utilization (yield in only one fibre). The interaction coefficient k_{yy} is a term that depends on both the slenderness $\bar{\lambda}$ and the bending moment diagram (factor C_m) but cannot be treated in detail here.

2.2 *Realistic strength – Numerical study*

As stated in the interaction, design procedures to determine the cross-sectional or member strength as the one described in section 2.1 assume a rather "strong" coupling between the local (plate) and gobal (flexural) buckling modes.

In order to study the realistic behavior and assess the accuracy of the EC3 design rules, a large numerical study was conducted within the scope of a graduate thesis at Graz University of Technology (Hafner, 2012). The numerical part of this work was carried out using the Finite Element Method (FEM) and the dedicated software Abaqus (Dassault Systems, 2010). The input parameters (material, geometry, imperfections) are shown in a schematic way in Figure 3 and can be described as follows:

i. A bi-linear elastic-plastic material characteristic (stress-strain relationship) was used, with and without linear strain hardening. The results shown in this paper refer to "Var. 1" above, and only to the steel grade S355.
ii. The cross-sections were discretized using 3D shell elements of type "S4R", with 4 nodes, linear isoparametric shape functions and reduced integration. 20 elements were used per each face/plate of the box sections.
iii. Imperfections of two types were considered: residual stresses σ_E as shown in the figure above and recommended by ECCS (1984), and geometric imperfections of both local and global type. The imperfection amplitude for the global buckling modes were assumed to be equal to 1/1000 of the member length, which is consistent with assumptions underlying the European column buckling curves (Beer & Schulz, 1970), while the local imperfection amplitude was calibrated – in a preliminary study – to match the Winter curve with sufficient accuracy; this led to a value of b/400, see also Rusch & Lindner (2001). Eigenmode-affine shapes were chosen for the different geometric imperfection types.

Since it is unlikely that both geometric amplitudes occur with their full magnitude at the same time, a case distinction was made, which follows rules also found in EC3. In one case, the full global imperfection was considered, in combination with 70% of the local imperfection, while in the other case the 70%/100% proportions were reversed. The lower of the two buckling resistances was considered to be relevant in the comparisons.

In summary, the chosen procedure is a Geometrically and Materially Non-linear Analysis which considers Imperfections, and is referred to as "GMNIA" in the steel structures literature and in the following figures.

3 MEMBERS IN PURE COMPRESSION – COLUMNS

The first comparison of GMNIA results with the EC3 regulations is performed for the basic case of a simply supported (hinged ends) column, under pure compression. Figure 4 shows plots representing the buckling strengths (as fraction of the EC3 cross-sectional capacity $A_{eff} \cdot f_y =$ "$N_{pl,eff,k}$") according to the GMNIA calculations, the appropriate EC3 buckling curve "b", a higher EC3 curve "a", and the Euler hyperbola. The difference between the two graphs a) and b) is given by the plate (i.e. local) slenderness $\bar{\lambda}_p$, which is 1,1 and 1,5 respectively.

The plots highlight the degree of conservatism to be found in the EC3 rules for thin-walled columns of this type. The following observations can be made:

i. Strength reserves of more than 20% were observed for the box section with $\bar{\lambda}_p$ equal to 1,1, see Figure 4a. These reserves are most visible

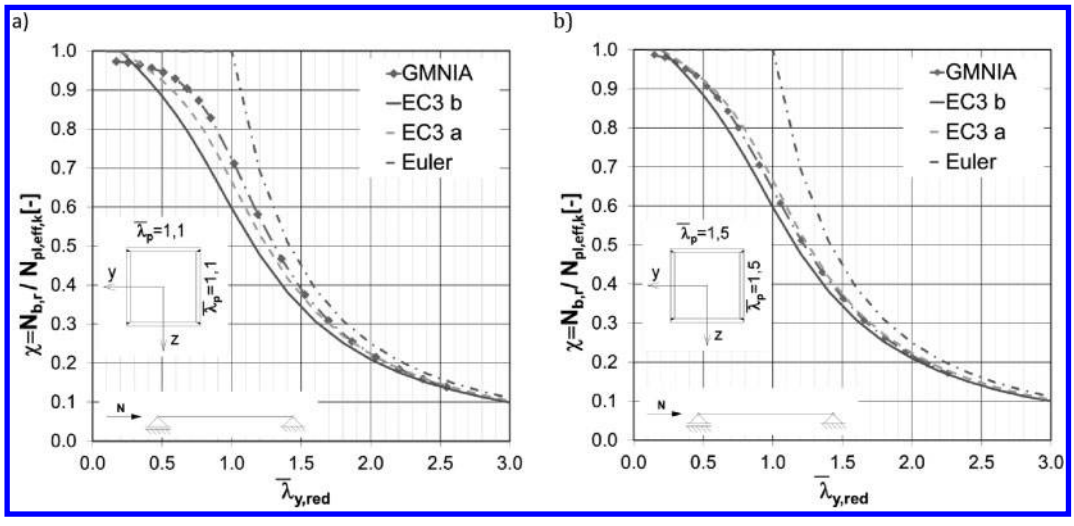


Figure 4. Buckling reduction coefficients χ for thin-walled compression members, based on the strength of the (reduced) effective cross-section, according to Eurocode 3 and the numerical GMNIA calculations.

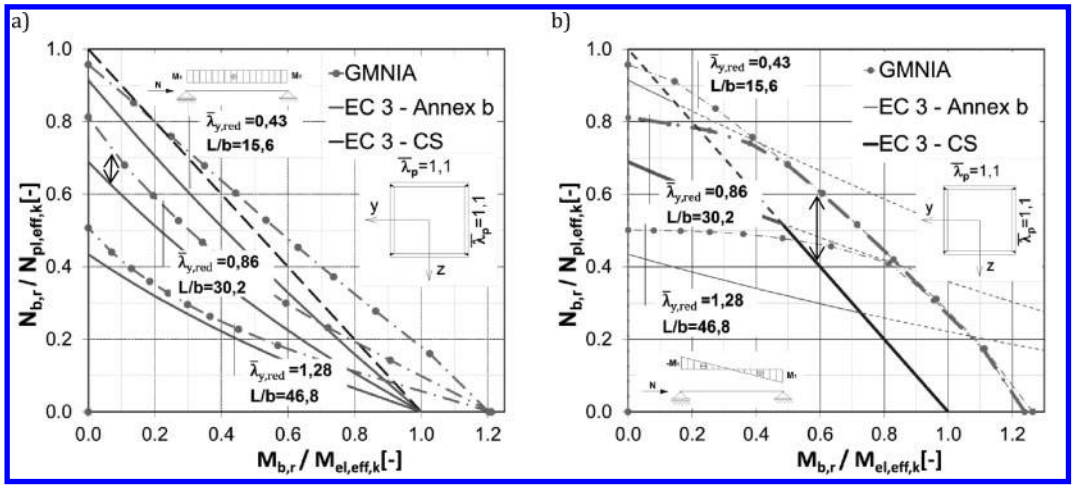


Figure 5. Buckling strengths (N-M interaction curves) for thin-walled beam-columns, according to Eurocode 3 and GMNIA calculations. a) for a uniform bending moment; b) for end moments of opposite sign.

around the "intermediate" (global) slenderness range of $\bar{\lambda}$ ($=\bar{\lambda}_{y,red}$ in the figure) of 1,0, which is the slenderness range where the combination of plasticity and elastic buckling is most felt. This is also the range where the EC3 rules most strongly assume an interaction between local and global buckling.

ii. For the member with a local plate slenderness of $\bar{\lambda}_p$ equal to 1,5 in Figure 4b, the GMNIA results fall closer to EC3 buckling curve, even though the "better" curve "a" would still describe the results better.

iii. Detzel (2006) also studied welded box sections in pure compression; she observed similar results and suggested the adoption of buckling curve "a" for the design of these sections. She attributed the inaccuracy to a combination of the "double counting" of imperfections inherent in the EC3 design process (residual stresses are included in the reduction factors for both local and global buckling and are thus counted twice) and an inaccuracy in the definition of the slenderness, which accounts for the reduced cross-section in terms of area, but not inertia.

iv. An additional explanation is given here: for columns failing in flexural buckling, the failure cross-section at the ultimate limit state is – as the name says - subjected to a lot of flexion. This bending action reduces compression in the webs and the tension-side flange, making the quantity to which the reduction is applied, i.e. the effective cross-section (for which every plate's effective

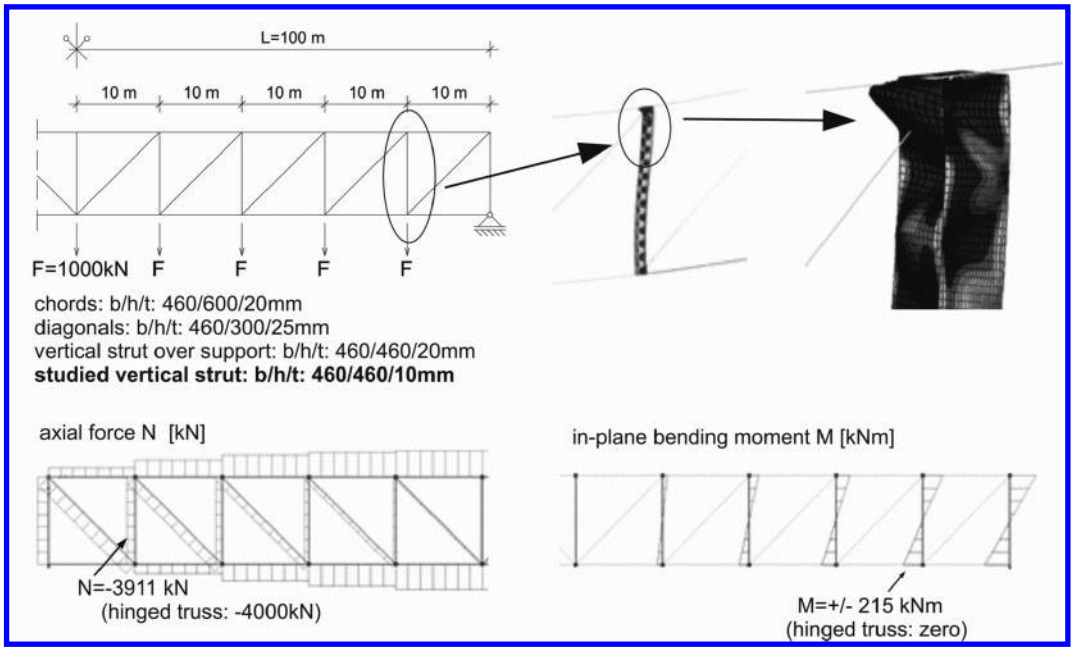


Figure 6. Case study: member in a truss; second-to-last vertical strut, subjected to compression and bending due to restraint.

width is equally reduced in a square box section) less relevant and accurate. In other words: the basis value $N_{pl,eff,k}$ is "too low" and must therefore be reduced less.

4 BEAM-COLUMNS

Members subjected to axial compression and bending were the main focus of the study presented in this paper. Among the multitude of possible bending moment diagrams and boundary conditions that can be considered for this case, Figure 5 shows two cases with linear bending moment diagrams (equal and unequal and moments of the same magnitude) and the basic case of a simply-supported beam-column.

In this case, the EC3 rules represent the interaction formulae briefly introduced in section 2.1. Again, a number of observations can be made:

i. The conservatism found to be present in the design rules for columns is obviously "carried on" in the interaction formulae design rules for beam-columns; this means that the values on the Y-axis of the plots in Figure 5 are equal to the values of χ in Figure 4a, both for the EC3 and the GMNIA curves, which makes the GMNIA N-M interaction curves plotted in Figure 5 start at a higher point than the code curves.

ii. The additional degree of conservatism that is observed in the plots of Figure 5 is given by the inaccuracy of the code rules for the bending strength (for zero axial force) of the studied square box sections.As shown in Figure 2b this bending strength is calculated on the basis of an elastic stress distribution and the EC3 effective cross-section. For the studied sections, in bending only the top flange requires the consideration of an effective width. While this reduction might be appropriate, it is obvious from the above results that the implied reduction of rotation capacity for this "class 4" section is too pessimistic: a strength approaching the plastic bending capacity was observed for the shown section with $\overline{\lambda}_p$ equal to 1,1.

iii. In order to further explain the source of this additional strength, one can use the simple model shown in Figure 2b, on the right: if the bending capacity were calculated using an effective cross-section, but with plastic utilization of the plates that are not class 4, a more realistic strength value would be calculated.

iv. Regarding the effect of the different bending moment diagrams, the example shows that the opposite-sign bending moments lead to an even higher degree of conservatism of the design rules, which can be explained by conservatism of both the interaction coefficient k_{yy} itself and the plate buckling reduction factor ρ for non-uniform compression along the plate.

5 EXAMPLE: MEMBER IN A TRUSS

To conclude this study on the behavior of thin-walled welded box sections, a case study for a "realistic" configuration of a member of this type is carried out, see Figure 6. One member in a truss (representative e.g. for a large bridge superstructure) is studied in detail,

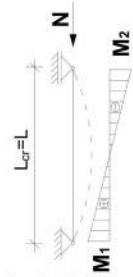
	Method 1	Method 2	Method 3	GMNIA
	 "hinged truss", N alone	 k_y=0,454 / c_{my}=0,4	 k_y=0,523 / c_{my}=0,4	Obtained Load Proportionality Factor: LPF 1,14
Utilization Buckling	**0,909**	0,896	**1,024**	Util.≈$\frac{1}{1,14}$=**0,88**
Utilization Cross-Section	0,777	**1,013**	1,013	

Figure 7. Results of the case study of Figure 6, expressed in utilizations.

using three different analysis and design methods plus a GMNIA calculation of the full truss (with the studied member sub-modeled as described in section 2.2, the rest as beam elements) for comparison. The results are summarized (in terms of utilization) in Figure 7. Briefly, the main findings are:

i The most conservative approach would be what the EC3 currently recommends: isolating the member, with its axial force and end moments, and considering it a hinged-end beam-column with its system length as buckling length.

ii However, also the use of the "real" buckling length, which is L/2 in the studied case due to the stiffness of the chords of the truss, would not significantly improve the design for this particular member, because in this case the cross-sectional resistance is dominant.

iii The most accurate design procedure for the studied case would be the "forbidden" one for trusses made of class 4 sections: an analysis and design based on a classic "hinged truss" model, i.e. neglecting the moments but considering system and buckling length to be equal.

6 CONCLUSIONS AND OUTLOOK

The study performed for this paper showed that significant strength reserves are present in the current (Eurocode) buckling design checks for thin-walled and globally slender welded box sections. Due to the increased use of sections with this characteristic of a "double slenderness", it is certainly worthwhile to expand and improve the knowledge on the actual ultimate load capacity of these sections. The plastic reserves of class 4 sections are totally unexploited at the moment, which is clearly not accurate for a variety of applications that do not require the full rotational capacity implied by the class 4 definition. Members in trusses with cross-sections of the type studied here are one clear example where increased knowledge would lead to great design economy.

REFERENCES

Beer, H., Schulz, G. 1970, Bases Théoriques des Courbes Européennes de Flambement, *Construction Métallique*, n° 3, 37–57.

Dassault Systems 2010, *Abaqus Standard, version 6.10.*

Detzel A. 2006, *Zum Gesamtstabilitätsverhalten geschweißter Rechteckquerschnitte unter Druckbelastung*. PhD thesis, Institut für Konstruktion und Entwurf, University of Stuttgart (Germany).

ECCS 1984, *Ultimate Limit State Calculation of Sway Frames with Rigid Joints,* Editor: Vogel, U., European Convention for Constructional Steelwork- TC 8, Brussels.

Eurocode 3 2005 – EN 1993-1-1, *Eurocode 3. Design of steel structures, General rules and rules for buildings*, CEN, Brussels.

Eurocode 3 2006 – EN 1993-1-1, *Eurocode 3. Design of steel structures, Plated structural elements*, CEN, Brussels.

Hafner S. 2012, *Gesamtstabilitätsverhalten geschweißter Kastenquerschnitte unter Druck und Biegung,* M.Eng. thesis, Graz University of Technology, Institute f. Steel Structures.

Rusch, A., Lindner, J. 2001, Tragfähigkeit von beulgefährdeten Querschnittselementen unter Berücksichtigung von Imperfektionen, *Stahlbau* 70, p.765–774, Ernst & Sohn, Berlin.

Winter, G. 1947. Strength of thin steel compression flanges. Reprint No. 32. Ithaca, NY, USA: Cornell University Engineering Experimental Station.

Research and Applications in Structural Engineering, Mechanics and Computation – Zingoni (Ed.)
© 2013 Taylor & Francis Group, London, ISBN 978-1-138-00061-2

Performance of reinforced web openings of cold-formed steel joists

K.S. Sivakumaran
Department of Civil Engineering, McMaster University, Hamilton, Ontario, Canada

ABSTRACT: The floor joists of Cold-Formed Steel (CFS) structures frequently require large web cut-outs, through which building services may be efficiently located. Presence of a large web opening, however, causes localized redistribution of stresses, and loss of member stiffness and cross-sectional capacities. Providing appropriate reinforcements for such openings may alleviate the adverse effects of such large web openings. The experimental investigation presented in this paper considered the flexural and shear capacities of galvanized lipped channel steel sections having circular and square web openings, and three associated reinforcement schemes. Two lipped channel sections were set face-to-face to form the test specimens. The test specimens were simply supported at their ends, and were subjected to appropriate loads. The plate reinforcement and the stud reinforcement schemes considered in the study are those recommended in the Standard for Cold-Formed Steel Framing- Prescriptive Method for One and Two Family Dwellings. This investigation shows that such reinforcement schemes are ineffective for the joists experiencing high shear. New reinforcement schemes, utilizing bridging channels, were developed for moment regions and for shear regions, and the corresponding responses were experimentally established. The new reinforcement schemes can restore the original flexural capacities and the shear capacities of such sections having large circular or square openings. Overall, it is evident from the test results that it is possible to establish cost-effective reinforcement schemes for cold-formed steel sections having large web openings. Based on this investigation, construction guidelines for web openings reinforcements for cold-formed steel joists have been proposed.

1 INTRODUCTION

The Cold-Formed Steel (CFS) members are widely used in small to medium size building construction, including family dwellings, perhaps because they are structurally efficient compared to other traditional construction materials such as reinforced concrete, masonry, and wood. The floor system of detached one- and two-family dwellings, townhouses and other attached single-family dwellings is often constructed using CFS floor joists. Typical cross section of such joists is a lipped channel shape. Large web openings may be cut-out on these floor joists in order to provide the necessary pass through space for ductwork, piping, drainage and other similar systems, while keeping the floor height to a minimum. Appropriate use of circular or non-circular web openings can enhance the aesthetic appeal and can result in cost effective construction of CFS floor systems. The depth of these large web openings, however, can be a substantial proportion of the beam depth, and introduction of such a large web opening, however, causes localized redistribution of stresses, and loss of member stiffness and loss of cross-sectional capacities. Various studies (Shanmugam & Dhanalakshmi 2001, Keerthan & Mahendran 2012, LaBoube et al. 1999) exist on the flexural, shear, web crippling strengths of CFS sections having a large web opening. The current North American cold-formed steel design standard (AISI 2007a) also provides guidelines to account for the effects of such openings. However, a cost effective way to mitigate the negative effects of a large web opening is to screw fasten appropriate reinforcements around the opening regions, so as to restore the original strength and stiffness of the member. Strategically positioned reinforcements for such openings can reestablish the overall capacity of such cold-formed steel members, and can mitigate the detrimental effects of such large web openings. Objectives of this investigation are to establish the effects of a large web opening on [a] the flexural capacity and [b] the shear capacity of cold-formed steel lipped channel shaped floor joists, and to establish constructionally effective and economical reinforcement schemes for large web openings in order to restore the original flexural and the shear capacities.

2 THE TEST SPECIMENS

This investigation focused on 203.20 mm (8″) deep 1.146 mm (43 mils) thick galvanized lipped channel cold-formed steel (CFS) joists, primarily because it is one of most widely used joists in one and two family dwellings construction in North America. The nominal

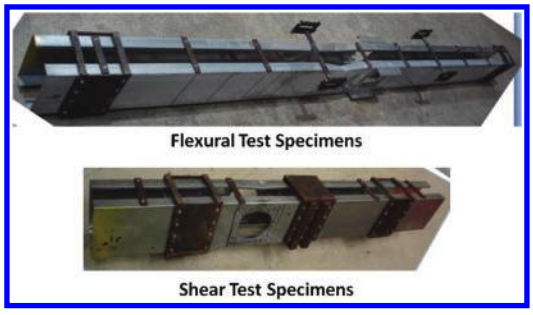


Figure 1. The test specimens.

dimensions of the section are web 203.2 mm, flanges 41.275 mm, lips 12.7 mm and thickness 1.146 mm, and these dimensions were confirmed by taking measurements at several random cross-section locations. The specified minimum yield strength of 230 MPa, whereas, the average mechanical properties based on the nine tension coupon test results are; yield stress 311 MPa, tensile strength 401 MPa, and the strain at rupture 21%. The sectional flexural strength of a fully braced section and the shear strength of the section can be established based North American cold-formed steel design standard (AISI, 2007a) and found to be 4.35 kN·m, and 8.81 kN (aspect ratio = 1.5), respectively.

The lipped channel shaped joist under consideration is a mono-symmetric section, which would experience torsional moments unless otherwise the transverse load is applied through the shear center, which is not easy to do in a single channel section as its shear center is outside of the section and does not coincide with the centroid of the section. Besides, in a joist floor system the floor loads are transmitted to the joist through its top flange. Furthermore, the top flange of the joist associated with a floor system often experience compression which may require bracing to prevent lateral torsional buckling. In a joist floor system the floor sheathing might provide such a bracing, however, the test specimens under consideration may require discrete braces. In order to alleviate such issues in this investigation two lipped channel sections were positioned face-to-face to form the test specimen assembly. Figure 1 shows such test specimens. Steel plate strips (130 × 20 × 6.4 mm) were used to tie together the compression flanges of the two sections at about 305 mm interval, and the tension flanges at every 606 mm spacing. The concentrated loads at the load point and at the supports may potentially web-cripple the cold-formed sections, prior to the projected flexural/shear failure. To prevent such a premature failure the machine load was transmitted to the test specimen through a steel bracket, as shown in Figure 1. The vertical planes of the steel brackets were fastened to the webs of the test specimens using self-drilling screws, which created gradual transfer of the concentrated loads into the web. The ends of the tests specimens were supported on similar steel brackets, which also acted as bearing plates, thereby distributing the concentrated reactions to the webs of the test specimens. In order to improve the web crippling capacities of the ends, each end of the test specimen had an overhang of more than 152 mm. With this arrangement the torsional effects are expected to be counterbalanced by each other section due to the torsional restraints that were provided at several locations namely, steel brackets at the load and the support locations and the steel plate strips in the compression flanges and at the non-bearing flanges at the load and at the support locations.

This study considered the performance of reinforced web opening in high moment zones and in high shear zones. In each case, the first part of the investigation considered the corresponding strengths of [a] sections with no openings, [b] sections with a large circular opening, and [c] sections with a large square opening. Circular opening with 127 mm diameter, and square openings with 127 mm sides were considered for the study. The size of the opening for use was determined on the basis of the space requirement for reinforcements. The opening depth considered herein is about 65% of the flat width of the web, and these openings were located at the centre of the test specimen span. Water-jet cutting was used to cut-out these large web openings. Three identical tests were done for each case. The second part of the investigation considered reinforced web openings. Three different reinforcement schemes were considered. Reinforcement Scheme – A is the AISI (2007b) specified patching scheme, where the web openings were reinforced with a solid steel plate having the same size and the shape of openings. The thickness of the steel plate was equal to the thickness of receiving section of 1.146 mm and extended 25.4 mm beyond all edges of the hole. In Reinforcement Scheme – B the web openings were patched with a CFS joist section having same size and shape of openings. The thickness of the reinforcement was equal to the thickness of receiving section of 1.146 mm and extended 25.4 mm beyond all edges of the hole. The joist reinforcement was fastened to the web of the section with No. 8 screws spaced 25.4 mm center-to-center along the edges of the patch with an outer edge distance of 12.7 mm. The reinforcement scheme C is our proposed scheme which utilizes the bridging channels. The reinforcement arrangements for high moment and high shear regions are different, and thus, the details are presented in the following sections.

3 FLEXURAL RESISTANCE OF REINFORCED WEB OPENINGS

This section discusses the flexural strength of CFS joists having a large reinforced web opening. A total of twenty seven CFS joist specimens were subjected to flexural tests. The objective of this part of the experimental investigation was to assess the effectiveness of three different reinforcement schemes for high moment zones. The flexural tests were carried

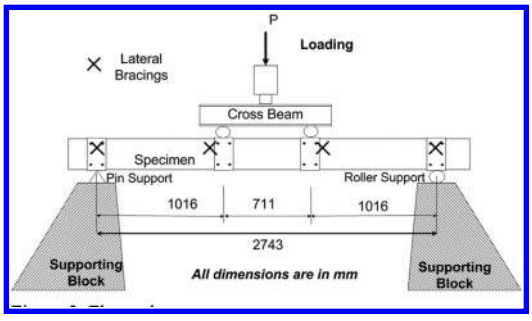


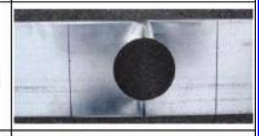
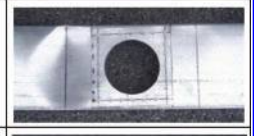
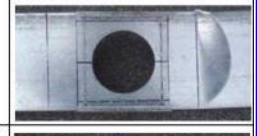
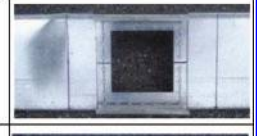
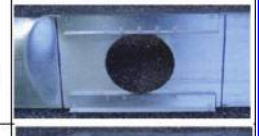
Figure 2. Flexural test setup.

out on 2,743 mm (9′) long specimens, which were simply supported at their ends, and were subjected to two equal point loads acting at equal distances from the supports. One end of the test specimens was pin-supported, whereas the other end was roller-supported. Figure 2 shows the test setup. The ends of the test specimen were laterally supported by smooth vertical rods to prevent lateral movement of the ends. Furthermore, in order to prevent lateral torsional buckling of the test specimens, lateral braces were provided at one-third span locations. A hydraulic jack having 152.4 mm stroke was used to apply a vertical downward load. A load cell having 200 kN load capacity was attached at the end of the jack to measure the total applied load. However, as shown in Figure 2 a transfer beam was used to subdivide the applied load into two equal point loads. Clear span-to-shear span ratio determines the relations between the applied shear force and the bending moments. For flexural tests such as this a clear span-to-shear span ratio within a range of 2.5 to 3.0 is recommended (Li 2002). A clear span of 2743 mm, and a shear span of 1016 mm used in the investigation give such a ratio of 2.7. For a shear span of 'a', this loading arrangement produces a uniform moment of '(P/2).a'. In the above test setup, however, load 'P/2' are applied to the specimens at the load locations, as well as at the support locations.

Table 1 summarizes the test results, which includes the moment resistances of the CFS sections with and without the reinforcements. The reduction in the flexural strength of a CFS joist section due to a large web opening (up to 65% of web height) is less than 15%. All the specimens containing reinforcement Scheme-A failed at locations other than the opening locations. Furthermore, the reinforced sections carried about 4% higher moments at the reinforced opening locations. This indicates that the steel plate reinforcement Scheme-A is capable of restoring the flexural strengths with a large web opening. Similar observations can be made on the reinforcement Scheme-B.

The investigation considered a much simpler reinforcement scheme identified herein as Scheme C, which involves screw fastening (No. 8 self-drilling screws) of bridging channels (depth 38 mm, thickness 1.146 mm) of length determined by width of the opening plus one half of the depth of the opening on either side and plus a minimum edge distance for

Table 1. Flexural resistance of reinforced web openings.

Test Series: F-N Average Moment Resistance = 4.40 kN.m (Reference Resistance)	
Test Series: F-C Average Moment Resistance = 4.13 kN.m (% Change = - 6.1%)	
Test Series: F-S Average Moment Resistance = 3.78 kN.m (% Change = - 14.1%)	
Test Series: F-CR$_A$ Average Moment Resistance = 4.59 kN.m (% Change = + 4.3%)	
Test Series: F-SR$_A$ Average Moment Resistance = 4.61 kN.m (% Change = + 4.8%)	
Test Series: F-CR$_B$ Average Moment Resistance = 4.58 kN.m (% Change = + 4.1%)	
Test Series: F-SR$_B$ Average Moment Resistance = 4.53 kN.m (% Change = + 3.0%)	
Test Series: F-CR$_C$ Average Moment Resistance = 4.62 kN.m (% Change = + 5.0%)	
Test Series: F-SR$_C$ Average Moment Resistance = 4.54 kN.m (% Change = + 3.2%)	

screws (10 mm). As a result, the total length of the reinforcements was 274 mm. The scheme-C consisted of two bridging channels, one along the top edge of the opening, and the other along the bottom edge of the opening. The bridging channels were screw fastened along the edges of the opening (12.7 mm) from the edge) at a spacing of 31.75 mm (d/4, where d is depth of the openings). The r/f scheme "C" specimens also failed outside the opening and the reinforcement. The circular and square openings with scheme "C" resisted 5% and 3% more moment, respectively, than the solid sections. Thus, the reinforcement scheme "C" is capable of restoring the original flexural strength of a CFS joist.

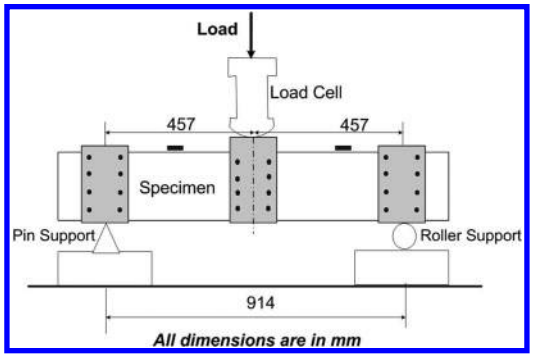


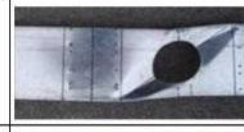
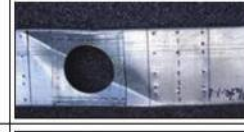
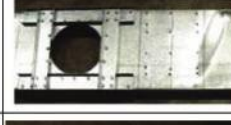
Figure 3. Shear test setup.

4 SHEAR RESISTANCE OF REINFORCED WEB OPENINGS

It is impossible to create a pure shear zone for "shear testing" because of the presence of a moment whenever there is a shear force. In practice though, a shear test is performed by creating a high shear and low moment region. Here, a 914 mm short span, with mid-span point load was considered as an appropriate test setup to achieve high uniform shear and low moments. One end of the test specimen was pin-supported, whereas the other end was roller-supported. Figure 3 shows the shear test setup. The overall load was applied at the centre of the span using the 600 kN capacity Tinius Olsen test. The test arrangement used herein results in uniform shear forces and increasing moments between the support and the load point. In reality though, short span specimen subjected to single mid-span load experiences high shear as well as high moment at the load location. Thus, this test setup simulates the high shear zones, as well as high shear-high moment conditions that exist at the over-the-support location in a continuous span joist.

Since the section is mono-symmetric, in this investigation two lipped channel sections with a length of about 1220 mm (48″) were set face-to-face to form the test specimen. Three identical tests were done for each case, thus, this part included twenty seven tests. Table 2 summarizes the test results. The reduction in the shear strength of a cold-formed steel joist section due to the presence of a large web opening (up to 65% of web height), and in the presence of high moments, may be as high as 60%. In other words, the residual shear strength of a joist with a large opening may be as low as 40%. Once agin, three types of reinforcement schemes namely, Scheme-A, Scheme-B and Scheme-C, were considered for shear tests. These reinforcements were used for both circular and square openings. The shear r/f Scheme-C is different from the flexural reinforcement Scheme-C, and it involves screw fastening (No. 8 self-drilling screws) of bridging channels [depth 38 mm, thickness 1.438 mm (54 mils)] along all four edges of the opening. Note that the bridging channels are 1.438 mm (54 mils) thick whereas the main joist section is of 1.146 mm (43 mil) thick. The shear reinforcements consisted of horizontal and vertical reinforcements. Horizontal reinforcements consisted of two bridging channels of length determined by width of the opening plus one half of the depth of the opening on both sides and a minimum edge distance for screws (10 mm). Therefore, the total length of the horizontal reinforcements was 274 mm. Vertical reinforcements included two bridging channels of length equal to the depth of the web of receiving channel 203 mm. One horizontal reinforcement was fastened along the top edge of the opening, and the other one was placed along the bottom edge of the opening. The channels were

Table 2. Shear resistance of reinforced web openings.

Test Series: S-N Average Shear Resistance = 12.43 kN (Reference Resistance)	
Test Series: S-C Average Shear Resistance = 7.43 kN (% Change = - 40.2%)	
Test Series: S-S Average Shear Resistance = 5.14 kN (% Change = - 58.7%)	
Test Series: S-CR$_A$ Average Shear Resistance = 11.52 kN (% Change = - 7.3%)	
Test Series: S-SR$_A$ Average Shear Resistance = 8.08 kN (% Change = - 35.0%)	
Test Series: S-CR$_B$ Average Shear Resistance = 12.46 kN (% Change = + 0.2%)	
Test Series: S-SR$_B$ Average Shear Resistance = 8.52 kN (% Change = - 31.6%)	
Test Series: S-CR$_C$ Average Shear Resistance = 12.95 kN (% Change = + 4.2%)	
Test Series: S-SR$_C$ Average Shear Resistance = 12.50 kN (% Change = + 0.6%)	

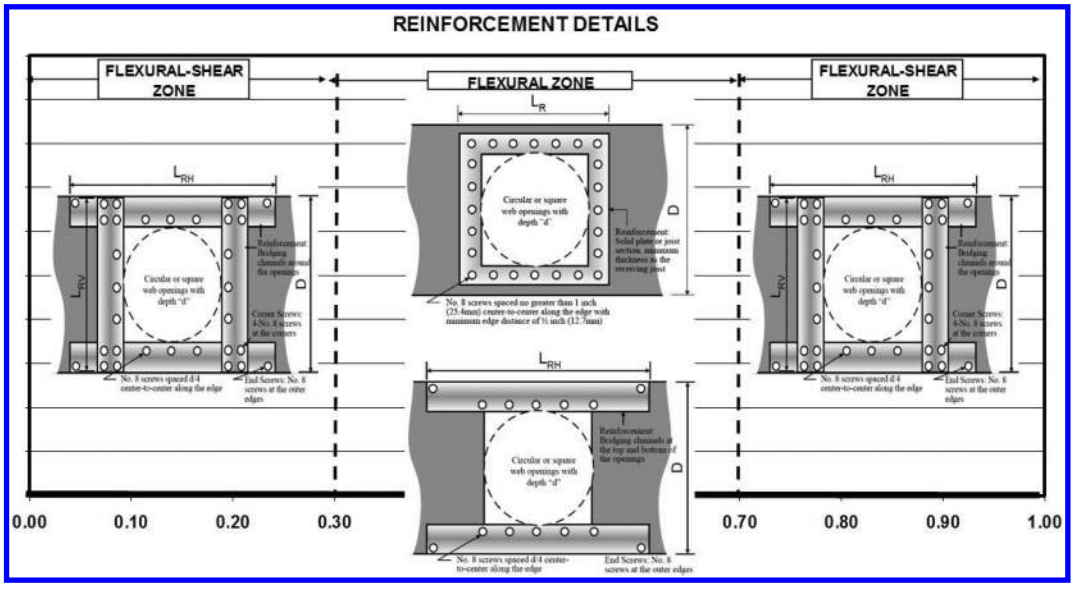


Figure 4. Recommended reinforcements details for joists with large web opening.

screw fastened at a spacing of 31.75 mm (d/4, where d is depth of the openings) close to the opening edges within the opening region, starting from the central screw. Vertical reinforcements were placed closer to the vertical edges of the openings. Four screws were fastened at the corner of horizontal and vertical reinforcements to create a joint. This system produces a Virendeel type reinforcement system.

It is evident from the test results, as presented in Table 2, the reinforcement schemes "A", and "B", established as per AISI (2007a) patching requirements, are not adequate to restore the shear strengths of joist sections with opening. It is clearly evident that the specimens with reinforcement scheme "C" failed at locations outside the reinforced opening location. Thus it may be concluded that reinforcement scheme "C", Virendeel type reinforcement system, for web opening is capable of restoring the original shear strength of a cold-formed steel joist section.

5 DISCUSSION AND RECOMMENDATIONS

Sections 3 and 4 presented the experimental flexural strength and the shear strength of cold formed steel (CFS) joist having web opening. These tests established the impact of such web opening, and they also determined the reinforcement schemes which restored the flexural strength and the shear strength, respectively. It was noted in section 3 that web opening depth up to 65 percent of web depth would reduce the flexural strength of cold-formed joist by 15 percent or in another words, CFS web with a large openings still retains a residual moment resistance of 85% of the moment resistance of the original joist. Thus, flexural reinforcement is required only when the moment at the opening location is greater than 85% of the moment resistance. Similarly, it was noted in section 4 that web opening depth up to 65 percent of web depth would reduce the shear strength of cold-formed joist by 60 % or in another words, CFS web with a large openings still retains 40% shear capacity of the original joist, thus, shear reinforcement is required when shear load at the opening location is greater than 40 percent of shear capacity.

In the experimental program, the moment and shear resistances were investigated separately and the high moment zone and the high shear zone were not defined. These zones for a joist member depend on the structural arrangement and the loading. This section establishes a definition for high moment zone and high shear zone for CFS joists. In general, the Cold-formed steel (CFS) floor joists are expected to carry uniformly distributed load imposed by the floor deck. Therefore, in the analysis and design of CFS floor joists for housing construction, it is reasonable to assume that the floor joist is subjected to uniformly distributed loads. Shear and moment variations in a floor joist having three different structural arrangements, namely, simple support, continuous support and moment optimized two-span joist were investigated. For a simply supported case the maximum shear (Vmax) occurs at the supports, and the shear forces in the mid-span region defined by 0.30 L and 0.70 L, where L is the span length, are less than 0.40Vmax. If the joist is continuous over two or more spans, then the shear forces in the mid-span region defined by 0.125 L and 0.625 L are less than 0.40Vmax, where Vmax is the corresponding maximum shear, which is higher than that for a simply supported joist. For all other structural arrangements the range under discussion is within the above two regions (example: If the joist has

an over-hang and the joist had been designed such that the moment over the support is equal to the moment at the mid-span (moment optimized two-span joist), then shear is less than 0.40Vmax in the mid-region defined by 0.18L and 0.65L). Considering these three possible structural arrangements, and considering the fact that often the shear resistance of the joist is higher than shear force, since often deflection or bending moment governs the design of such joist, it can be concluded that shear reinforcement scheme C discussed in section 4 must be provided for large openings located within 0.30L from the support. Thus, high shear zone can be defined as distance 0.3L from the supports.

Similarly, considering the moment variations in a floor joist subjected to a uniformly distributed load, if the joist is simply supported, then the maximum moment Mmax occurs at the mid-span. Focusing on the mid-span region, moments between 0.3L and 0.7L exceed 0.85Mmax. If the joist is continuous over two or more spans, then the maximum moment Mmax occurs over the support, mid-span region does not experience moments greater than 0.85Mmax. If the joist has an over-hang and the joist had been designed such that the moment over the support is equal to moment at the mid-span (moment optimized two-span joist), then the maximum moment Mmax occurs over the support and at the mid-span region at 0.41L. Focusing on the mid-span region, moments between 0.255L and 0.575L are greater than 0.85Mmax. Considering these three possible loading and structural arrangements, the mid-region between 0.3L and 0.7L, where shear force was shown to be less than 0.4Vmax, may experience moments greater than 0.85Mmax. Thus, it will suffice to provide the flexural reinforcements discussed in section 2 for large openings located in this mid-region between 0.3L and 0.7L. Figure 4 summarizes these recommendations.

ACKNOWLEDGEMENTS

Funding for this project was jointly provided by the Canadian Sheet Steel Building Institute, American Iron and Steel Institute, and the Steel Framing Alliance.

REFERENCES

AISI, (2007a), North American Specification for the Design of Cold-Formed Steel Structural Members, American Iron and Steel Institute, Washington DC, USA.

AISI, (2007b). Standard for Cold-Formed Steel Framing-Prescriptive Method for One and Two Family Dwellings. American Iron and Steel Institute, USA.

Keerthan P., Mahendran M., (2012) Shear behaviour and strength of LiteSteel beams with web openings. J Adv Struct Eng 2012;15:197–210.

LaBoube, R.A., Yu, W.W., Deshmukh, S.U., and Uphoff, C.A., (1999), Crippling Capacity of Web Elements with Openings, Journal of Structural Engineering, Vol. 125, No. 2, February, 1999.

Li, L. (2002). Strength of Cold Formed Steel Beam-Columns, MASc. Thesis., McMaster University, Hamilton, Canada.

Shanmugam, N.E., and Dhanalakshmi, M. (2001), Statte-of-Art Review and Compilation of Studies on Perforated Thin-Walled Structures, International Journal of Structural Stability and Dynamics 2001 01:01, 59–81.

Research and Applications in Structural Engineering, Mechanics and Computation – Zingoni (Ed.)
© 2013 Taylor & Francis Group, London, ISBN 978-1-138-00061-2

A linear one-dimensional model for the flexural-torsional vibrations of tapered thin-walled bars with open cross-sections

A. Andrade & P. Providência
Civil Engineering Department, University of Coimbra, INESC Coimbra, Portugal

D. Camotim
Civil Engineering Department, ICIST, Instituto Superior Técnico, Technical University of Lisbon, Portugal

ABSTRACT: The physical significance of a newly developed one-dimensional model for tapered thin-walled bars with open cross-sections is discussed by means of an illustrative example – the (undamped) free torsional motion of a family of doubly symmetric and linearly web-tapered I-section cantilevers. The shortcomings of stepped (piecewise prismatic) models, which become particularly noticeable when restrained warping plays an important part in the torsional behaviour, are highlighted. It is also shown that the approach to non-uniform torsion pioneered by Timoshenko – *i.e.*, regarding each plated component of the bar as an Euler-Bernoulli member undergoing stretching and bending –, when correctly applied to the tapered case, leads to identical results.

1 INTRODUCTION

The authors have recently developed a Vlasov-type one-dimensional (1D) model for the linear dynamic analysis of tapered thin-walled bars with open cross-sections under general monogenic loads (Andrade 2012). This paper presents, in considerable detail, a specific application of this model. The selected illustrative example, namely the (undamped) free torsional motion of a family of doubly symmetric and linearly web-tapered I-section cantilevers, serves a threefold purpose:

(i) To provide a tangible meaning for the non-standard quantities appearing in the 1D model.
(ii) To show that the approach to non-uniform torsion pioneered by Timoshenko (*i.e.*, regarding each plated component of the bar as an Euler-Bernoulli member undergoing stretching and bending), when correctly applied to the tapered case, is entirely compatible with ours.
(iii) To underscore the differences between tapered and stepped (*i.e.*, piecewise prismatic) models, regardless of the number of segments considered in the latter. In fact, stepped models exhibit a number of significant mechanical shortcomings, which are clearly pointed out.

2 A BIRD'S-EYE VIEW OF THE 1D MODEL

The most distinctive features of the developed 1D model may be summarised as follows:

(i) Thin-walled bars are basically regarded as internally constrained membrane shells.
(ii) The internal constraints extend to the tapered case the classical assumptions of Vlasov's prismatic bar theory (Vlasov 1961).
(iii) The internal constraints are treated consistently as *a priori* restrictions, of a constitutive nature, on the possible deformations of the middle surface of the bar (Podio-Guidugli 1989). The membrane forces are split additively into active and reactive parts. The reactive forces perform no work in any admissible deformation. Moreover, the constitutive dependence of the active membrane forces on the membrane strains reflects the maximal symmetry compatible with the assumed internal constraints (a special case of curvilinear anisotropy). Stress resultants are likewise split into active and reactive categories.
(iv) In tapered bars, and from the point of view of kinematics, the constraints give rise to an additional (*i.e.*, non-standard) basic membrane strain mode, which is absent in prismatic bars – its amplitude is the rate of twist. As a consequence, the model features additional stiffness terms associated with the torsional behaviour.
(v) From the point of view of statics, the counterpart of the preceding item is the contribution of the active membrane forces to the total torque, which is absent in prismatic bars.
(vi) There are exceptions to the statements in items (iv) and (v) – for instance, the additional basic strain mode and the contribution of the membrane forces to the total torque vanish in tapered bars whose middle surface is cut out from a cylindrical one.

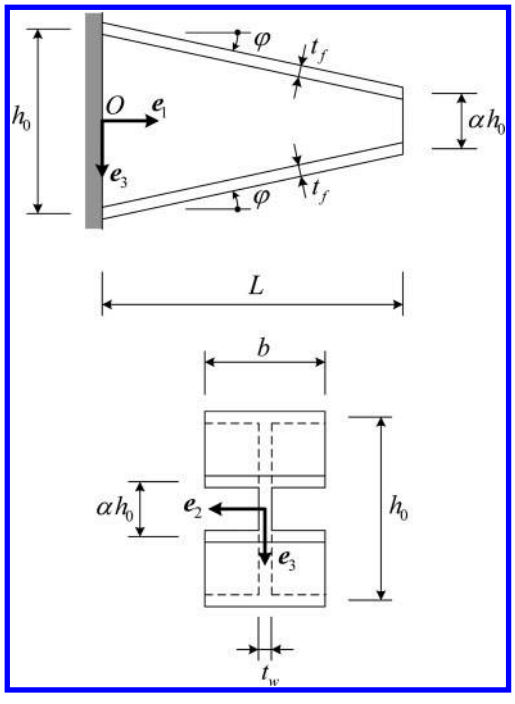


Figure 1. Illustrative example – Reference shape and support conditions.

(vii) The classical model of Vlasov for prismatic bars is obtained as a special case.

3 THE ILLUSTRATIVE EXAMPLE

To illustrate the application of the 1D model, we investigate the undamped free torsional motion of the family of doubly symmetric web-tapered I-section cantilevers whose reference shape is shown in Figure 1. The chosen inertial frame, also shown in this figure, is such that the planes containing the origin O and spanned by $\{\boldsymbol{e}_1, \boldsymbol{e}_2\}$ and by $\{\boldsymbol{e}_1, \boldsymbol{e}_3\}$ are the longitudinal planes of symmetry of the reference shape. The depth h of the web, measured between flange middle lines, varies according to the affine law

$$h(x_1) = \left[1 - (1-\alpha)\frac{x_1}{L}\right] h_0 \ , \tag{1}$$

with $0 < \alpha \leq 1$. The parameter α is referred to as the (web) taper ratio. The bar is clamped at its larger end and free at the smaller end.

4 THE MATHEMATICAL MODEL AND ITS PHYSICAL SIGNIFICANCE

4.1 *The initial-boundary value problem*

From a mathematical point of view, we will be dealing with the following initial-boundary value problem (the symbol τ denotes time, a prime denotes differentiation with respect to the longitudinal coordinate x_1 and a superposed dot represents differentiation with respect to time):

Find $\Phi_1 \in C^{4,2}[0, L] \times [0, \tau_0]$, *satisfying the partial differential equation*

$$\begin{aligned} &-\left(\tilde{E}I^*_{\omega}\,\Phi_1'' + \tilde{E}I^*_{\omega\psi}\,\Phi_1'\right)'' + \left[\tilde{E}I^*_{\omega\psi}\,\Phi_1'' + \left(GJ + \tilde{E}I^*_{\psi}\right)\Phi_1'\right]' \\ &\quad + \rho\left(I_{\omega}\ddot{\Phi}_1'\right)' - \varrho\left(I_2 + I_3\right)\ddot{\Phi}_1 = 0 \end{aligned} \tag{2}$$

on $(0, L) \times (0, \tau_0)$, *together with the boundary conditions*

$$\Phi_1(0,\tau) = 0 \qquad \Phi_1'(0,\tau) = 0 \tag{3}$$

$$\begin{aligned} &-\left(\tilde{E}I^*_{\omega}\,\Phi_1'' + \tilde{E}I^*_{\omega\psi}\,\Phi_1'\right)'(L,\tau) - \tilde{E}I^*_{\omega\psi}(L)\,\Phi_1''(L,\tau) \\ &\quad + \left(GJ(L) + \tilde{E}I^*_{\psi}(L)\right)\Phi_1'(L,\tau) \\ &\quad + \rho\, I_{\omega}(L)\ddot{\Phi}_1'(L,\tau) = 0 \end{aligned} \tag{4}$$

$$-\tilde{E}I^*_{\omega}(L)\,\Phi_1''(L,\tau) - \tilde{E}I^*_{\omega\psi}(L)\,\Phi_1'(L,\tau) = 0 \ , \tag{5}$$

$0 \leq \tau \leq \tau_0$, *and the initial conditions*

$$\Phi_1(x_1,0) = \Phi_{1.0}(x_1) \qquad \dot{\Phi}_1(x_1,0) = \dot{\Phi}_{1.0}(x_1) \ , \tag{6}$$

$0 \leq x_1 \leq L$. *In these equations,* ρ *is the (constant) mass density over the reference shape,*

$$\tilde{E} = \frac{E_1}{1 - \nu_{\text{I-II}}\,\nu_{\text{II-I}}} \tag{7}$$

is the ratio between the sole active stress component $n_{1\text{-}1}/t$ *and the corresponding membrane strain* $\gamma_{1\text{-}1}$ *for the internally constrained orthotropic membrane, and*

$$I_2 = \frac{h^3 t_w}{12} + \frac{b\,h^2}{2}\frac{t_f}{\cos\varphi} \qquad I_3 = \frac{b^3 t_f}{6\cos\varphi} \tag{8}$$

$$J = \frac{2b}{3}\left(\frac{t_f}{\cos\varphi}\right)^3 + \frac{h t_w^3}{3} \qquad I_{\omega} = \frac{b^3 h^2}{24}\frac{t_f}{\cos\varphi} \tag{9}$$

$$I^*_{\omega} = \frac{1}{24} b^3 h^2 t_f \cos^3\varphi \tag{10}$$

$$I^*_{\omega\psi} = -\frac{1}{6} b^3 h \tan\varphi\, t_f \cos^3\varphi \tag{11}$$

$$I^*_{\psi} = \frac{2}{3} b^3 \tan^2\varphi\, t_f \cos^3\varphi \tag{12}$$

are geometrical properties.■

It should be noticed that

$$I^*_{\omega\psi} = I^{*\prime}_{\omega} \qquad I^*_{\psi} = 2I^{*\prime\prime}_{\omega} = 2I^{*\prime}_{\omega\psi} \tag{13}$$

but the validity of these identities is, of course, restricted to the particular bar shape considered in this illustrative example.

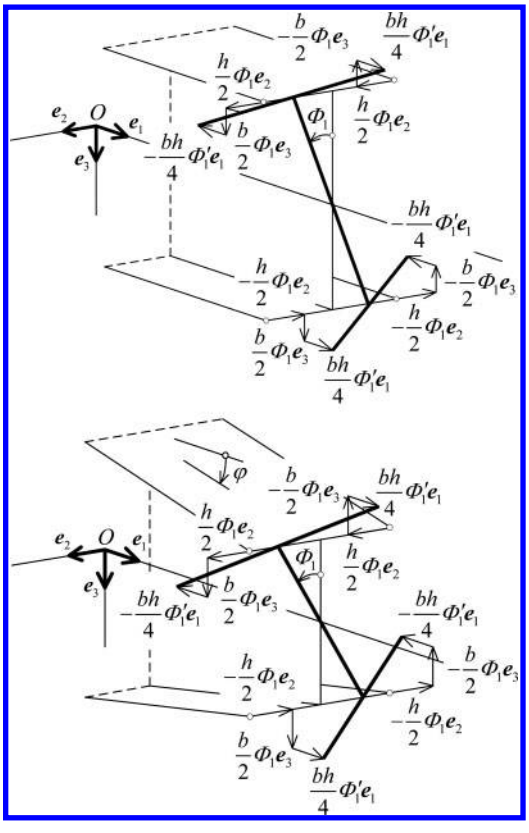


Figure 2. Contrasting the warping-torsion behaviours of prismatic and web-tapered bars – Motion of cross-section middle line.

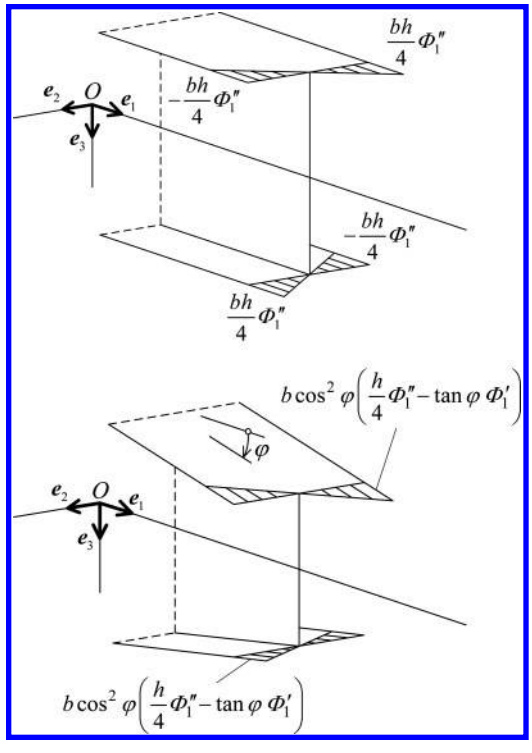


Figure 3. Contrasting the warping-torsion behaviours of prismatic and web-tapered bars – Membrane strains $\gamma_{\mathrm{I}\cdot\mathrm{I}}$.

4.2 *On the physical significance of the stiffness terms*

In an effort to gain a firm understanding of the nature of the (non-standard) stiffness terms appearing in the initial-boundary value problem 2–6, the warping-torsion behaviours of prismatic ($\alpha = 1$) and linearly depth-tapered ($0 < \alpha < 1$) doubly symmetric I-section bars is contrasted in Figures 2–7. The following facts are worthy of notice:

(i) In both cases, the Vlasov-type internal constraints, together with symmetry considerations, imply qualitatively similar motions for any given cross-section middle line (Fig. 2). However, one must not forget that in the web-tapered case the displacements along $\boldsymbol{e}_3$ are obviously *not* orthogonal to the middle planes of the flanges.

(ii) The membrane strains $\gamma_{\mathrm{I}\cdot\mathrm{I}}$ in the flanges can now be found by direct computation (Fig. 3). Comparing the ensuing strain-displacement relation for prismatic and web-tapered bars, one readily sees that the latter contains an additional term $(-\tan\varphi\,\Phi_1')$ and a common scaling factor $(\cos^2\varphi)$. These remarks also apply to the (active) membrane forces $n_{\mathrm{I}\cdot\mathrm{I}}$ in the flanges, as shown in Figure 4.

(iii) The membrane forces $n_{\mathrm{I}\cdot\mathrm{II}}$ shown in Figure 5, which have a reactive character, may be found by considering the equilibrium of a "flange slice" acted by the previously obtained membrane forces $n_{\mathrm{I}\cdot\mathrm{I}}$, as ordinarily done in standard textbooks on Strength of Materials.

(iv) The membrane forces $n_{\mathrm{I}\cdot\mathrm{I}}$ (resp. $n_{\mathrm{I}\cdot\mathrm{II}}$) are statically equivalent to a bending moment M_f (resp. shear force V_f) in each flange (Figs. 6–7). In the web-tapered case, the modified warping stiffness $\tilde{E}I_\omega^*$, calculated with the reduced flange thickness $t_f^* = t_f\cos^3\varphi$, and the non-standard mechanical property $\tilde{E}I_{\omega\psi}^*$ arise naturally in this process, thus acquiring a tangible meaning:

$$M_f = \frac{1}{6}\tilde{E}\,b^3 t_f\cos^2\varphi\left(\frac{h}{4}\Phi_1'' - \tan\varphi\,\Phi_1'\right) = \frac{1}{h\cos\varphi}\left(\tilde{E}I_\omega^*\,\Phi_1'' + \tilde{E}I_{\omega\psi}^*\,\Phi_1'\right) \tag{14}$$

$$V_f = -\frac{1}{12}\tilde{E}\,b^3 t_f\cos^3\varphi\left(\frac{h}{2}\Phi_1''' - 3\tan\varphi\,\Phi_1''\right) = -\frac{1}{h}\left(\tilde{E}I_\omega^*\,\Phi_1''' + \frac{3}{2}\tilde{E}I_{\omega\psi}^*\,\Phi_1''\right). \tag{15}$$

Observe that

$$M_f = \tilde{E}\frac{b^3 t_f}{12}\cos^2\varphi\left(\frac{h}{2}\Phi_1\right)'' \tag{16}$$

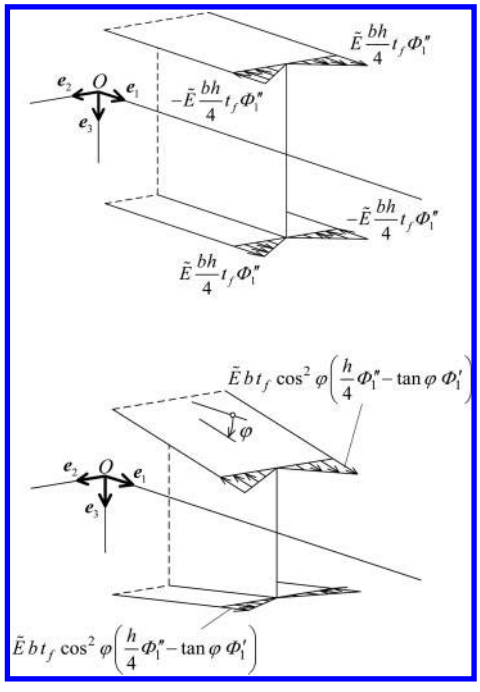


Figure 4. Contrasting the warping-torsion behaviours of prismatic and web-tapered bars – Membrane forces $n_{\mathrm{I}\cdot\mathrm{I}}$ (active).

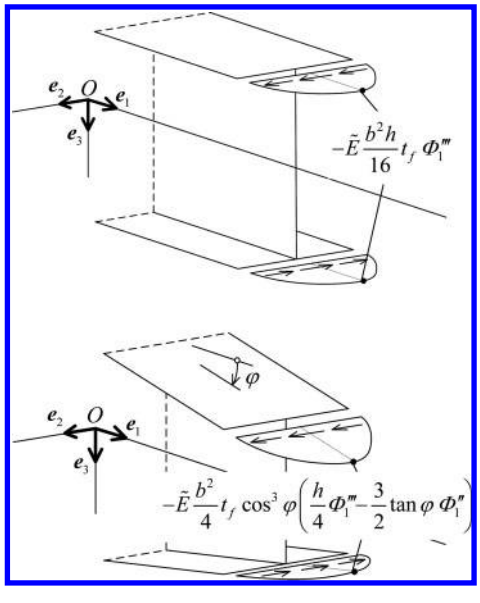


Figure 5. Contrasting the warping-torsion behaviours of prismatic and web-tapered bars – Membrane forces $n_{\mathrm{I}\cdot\mathrm{II}}$ (reactive).

$$V_f=-\cos\varphi\,M_f'\ . \tag{17}$$

We can thus look at each flange as an Euler-Bernoulli beam undergoing deflections $\pm h\,\Phi_1/2$. However, a word of caution is in order:

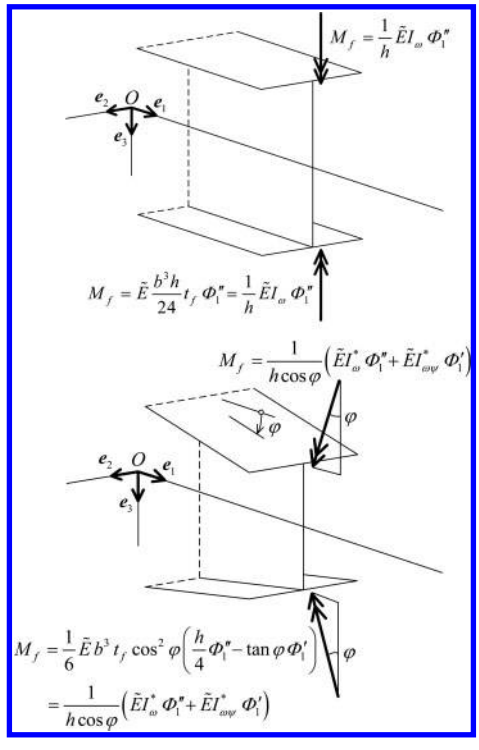


Figure 6. Contrasting the warping-torsion behaviours of prismatic and web-tapered bars – Bending moments in the flanges.

when dealing with web-tapered bars, a careful distinction must be made between derivatives with respect to x_1 and derivatives with respect to the arc length of the flange centroidal lines, whence the appearance of $\cos\varphi$ in Equations 16–17. Clearly, a stepped model, regardless of the number of prismatic segments it comprises, cannot capture the second term on the right-hand side of

$$\frac{1}{2}\left(h\Phi_1\right)''=\frac{1}{2}h\Phi_1''+h'\Phi_1'\ , \tag{18}$$

nor can it capture the factor $\cos\varphi$.

(v) In web-tapered bars, the flange bending moments have an axial component (see Fig. 6), featuring $\tilde{E}I_{\omega\psi}^*$ and $\tilde{E}I_\psi^*$, which totals

$$\begin{aligned}-2\sin\varphi\,M_f\,\boldsymbol{e}_1&=-\frac{2\tan\varphi}{h}\left(\tilde{E}I_\omega^*\Phi_1''+\tilde{E}I_{\omega\psi}^*\Phi_1'\right)\boldsymbol{e}_1\\&=\frac{1}{2}\left(\tilde{E}I_{\omega\psi}^*\Phi_1''+\tilde{E}I_\psi^*\Phi_1'\right)\boldsymbol{e}_1\ .\end{aligned} \tag{19}$$

The torque is thus given by

$$\begin{aligned}M_1&=-2\sin\varphi\,M_f+V_f\,h+GJ\,\Phi_1'\\&=-\tilde{E}I_\omega^*\Phi_1'''-\tilde{E}I_{\omega\psi}^*\Phi_1''+\left(GJ+\frac{1}{2}\tilde{E}I_\psi^*\right)\Phi_1'\ .\end{aligned} \tag{20}$$

Obviously, the contribution of the flange bending moments to the torque, absent in prismatic bars,

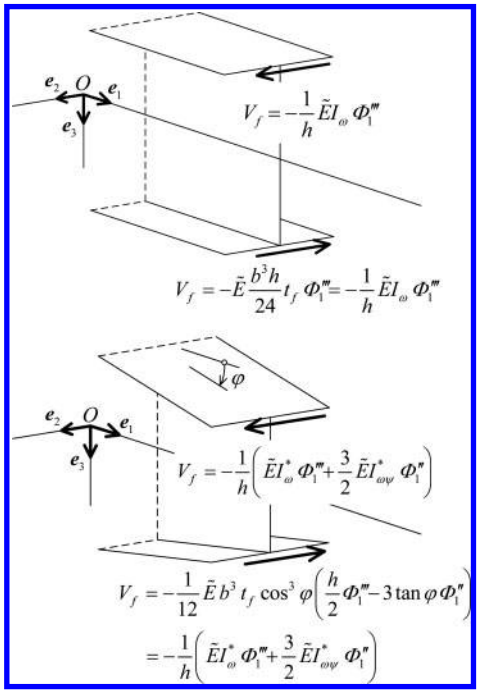


Figure 7. Contrasting the warping-torsion behaviours of prismatic and web-tapered bars – Shear forces in the flanges.

cannot be captured by stepped models. Finally, notice that

$$\cos\varphi\, M_f = \frac{1}{h}\left(\tilde{E} I_\omega^* \Phi_1'' + \tilde{E} I_{\omega\psi}^* \Phi_1'\right) = -\frac{B}{h}\,, \qquad (21)$$

where B denotes the bimoment.

4.3 *On the physical significance of the inertial terms*

The physical significance of the inertial terms $\rho I_\omega \ddot{\Phi}'_1$ and $-\rho(I_2 + I_3)\ddot{\Phi}_1$ in Equation 2 – distributed bimoment and torque, both defined per unit length of the line segment $\{O + x_1 e_1,\ 0 \le x_1 \le L\}$ – is schematically shown in Figure 8.

4.4 *The eigenproblem*

We now ignore the initial conditions and look for a very specific type of (non-trivial) solution, namely a product of two functions, one depending only on x_1 and four times continuously differentiable, and the other depending only on τ and twice continuously differentiable:

$$\Phi_1(x_1, \tau) = \phi(x_1)\, f(\tau)\ ,\quad 0 \le x_1 \le L\ ,\quad 0 \le \tau \le \tau_0\ . \qquad (22)$$

(In other words, we apply the technique of separation of variables.) The physical implication of Equation 22 is that the bar undergoes a synchronous motion. It turns out that the time dependency is harmonic, with the torsional natural frequencies k and the associated mode shapes ϕ being given by the following eigenproblem:

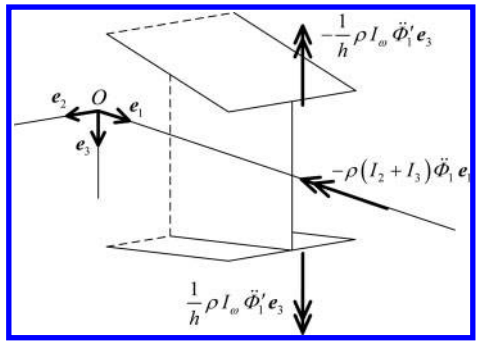


Figure 8. Resultants of the inertial forces, defined per unit length of the line segment $\{O + x_1 e_1,\ 0 \le x_1 \le L\}$.

Find $\lambda = k^2 > 0$ and $\phi \in C^4[0, L]$, with $\varphi \neq 0$, satisfying the ordinary differential equation

$$\tilde{E} I_\omega^* \phi^{(4)} + 2\tilde{E} I_\omega^{*\prime} \phi''' - GJ\,\phi'' - GJ'\,\phi' + \lambda\,\rho\left[I_\omega \phi'' + I'_\omega \phi'(\theta^1) - (I_2 + I_3)\phi\right] = 0 \qquad (23)$$

on $(0, L)$, together with the boundary conditions

$$\phi(0) = 0 \qquad \phi'(0) = 0 \qquad (24)$$

$$-\tilde{E} I_\omega^*(L)\phi'''(L) - \tilde{E} I_\omega^{*\prime}(L)\phi''(L) - \left(GJ(L) + \frac{1}{2}\tilde{E} I_\psi^*(L) - k^2\,\rho\, I_\omega(L)\right)\phi'(L) = 0 \qquad (25)$$

$$-\tilde{E} I_\omega^*(L)\phi''(L) - \tilde{E} I_{\omega\psi}^*(L)\phi'(L) = 0\ . \blacksquare \qquad (26)$$

5 SOME NUMERICAL RESULTS

Numerical results were obtained for the fundamental (lowest) torsional frequency and the corresponding normalised vibration mode of two series of cantilevers that share the geometrical and material properties

$L = 4572\,\text{mm}$	$h_0 = 554.2\,\text{mm}$	
$t_w = 11.4\,\text{mm}$	$t_f = 17.8\,\text{mm}$	
$\tilde{E} = 206.8\,\text{GPa}$	$G = 79.5\,\text{GPa}$	$\rho = 7997.4\,\text{kg/m}^3$

and differ in the width of the flanges: the cantilevers in the first series exhibit $b = 203\,\text{mm}$ (narrow flanges), while those in the second series exhibit $b = 350\,\text{mm}$ (wide flanges). In both series, the web taper ratio α varies between 0.2 and 1.0. It is worth pointing out that the non-dimensional ratio

$$\kappa_{\omega 0} = \frac{\pi}{L}\sqrt{\frac{\tilde{E} I_\omega^*(0)}{GJ(0)}} \qquad (27)$$

takes on the approximate values 1.1 and 2.0 for the cantilevers in the first and second series, respectively.

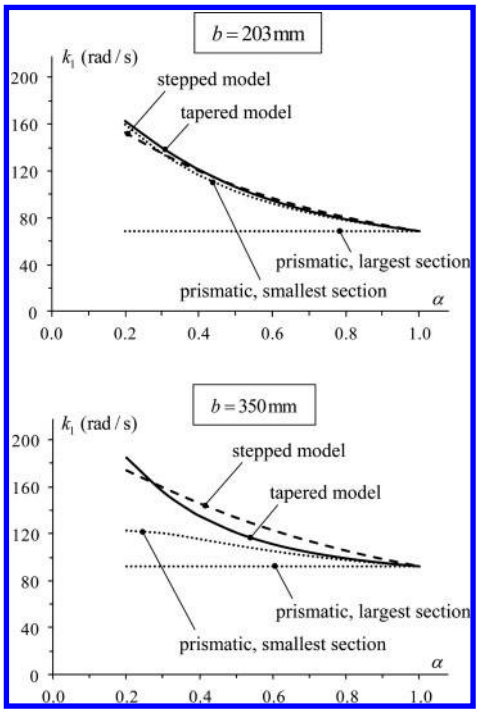


Figure 9. Illustrative example – Fundamental torsional frequency k_1 *versus* the taper ratio α.

The fundamental torsional frequency, denoted k_1, is shown in Figure 9 as a function of α (solid lines, labelled "tapered model"). The result for $b = 203$ mm and $\alpha = 0.378$, namely $k_1 = 125.1$ rad/s, is in perfect agreement with the one reported by Wekezer (1989) – Rajasekaran (1994) obtained the slightly lower value of 120.3 rad/s, which amounts to a -3.8% relative difference. If one represents the tapered cantilevers by an assembly of prismatic segments obeying Vlasov's theory and then makes the length of the segments tend to zero, one obtains the dashed lines shown in Figure 9 with the label "stepped model". For the first series ($b = 203$ mm), the solid and dashed lines are close to each other. In contrast, the two lines deviate considerably from each other in the second series ($b = 350$ mm), with the stepped model delivering higher frequencies for $0.3 < \alpha < 1.0$. Indeed, tapered and stepped models share the same inertial characteristics but exhibit different stiffnesses, as discussed in Section 4.2, and the differences in stiffness increase with $\kappa_{\omega 0}$ (*i.e.*, with the relevance of restrained warping – Andrade 2012). For reference purposes, Figure 9 also presents the fundamental torsional frequencies of prismatic cantilevers with the same length and material properties and with the largest or smallest cross-sectional dimensions, *i.e.*, with constant web depth $h_0 = 554.2$ mm or αh_0, respectively (dotted lines, labelled "prismatic, largest section" and "prismatic, smallest section"). It can be observed that the frequencies k_1 of tapered cantilevers fall outside the envelope defined by the dotted lines. According to Cywinski (2001), this fact "goes against the conventional engineering intuition, thus becoming a «paradox»". However, it must be observed that the frequencies yielded by the stepped model also fall outside that envelope (except for $\alpha < 0.3$ in the first series). In fact, since the natural frequencies depend on the relation between stiffness and inertia, it cannot be anticipated that the frequency k_1 of a tapered cantilever will always be in-between the values obtained for similar prismatic cantilevers with the largest and smallest cross-sectional dimensions. If sometimes it does not, there is nothing necessarily "paradoxical" about it.

6 CONCLUSIONS

This paper illustrated the application of the Vlasov-type 1D model developed by the authors for the linear dynamic analysis of tapered thin-walled bars with open cross-sections under monogenic loads. The selected illustrative example – (undamped) free torsional motion of a family of doubly symmetric and linearly web-tapered I-section cantilevers – allowed us (i) to offer physical explanations for the non-standard quantities appearing in the 1D model, (ii) to show that the approach to non-uniform torsion pioneered by Timoshenko (*i.e.*, regarding each plated component of the bar as an Euler-Bernoulli member undergoing stretching and bending) is entirely compatible with ours, and (iii) to point out the shortcomings of stepped (piecewise prismatic) models, which become particularly noticeable when restrained warping plays an important part in the torsional behaviour.

ACKNOWLEDGEMENTS

This work has been partially supported by the Portuguese Foundation for Science and Technology under project grant PEst-C/EEI/UI308/2011.

REFERENCES

Andrade, A. 2012. *One-Dimensional Models for the Spatial Behaviour of Tapered Thin-Walled Bars with Open Cross-Section: Static, Dynamic and Buckling Analyses*. PhD Thesis, University of Coimbra, Portugal.

Cywinski, Z. 2001. History of a "paradox" for thin-walled members with variable, open cross-section. *International Journal of Structural Stability and Dynamics* 1(1): 47–58.

Podio-Guidugli, P. 1989. An exact derivation of the thin plate equation. *Journal of Elasticity* 22(2–3): 121–133.

Rajasekaran, S. 1994. Instability of tapered thin-walled beams of generic section. *Journal of Engineering Mechanics – ASCE* 120(8): 1630–1640.

Vlasov, V.Z. 1961. *Thin-Walled Elastic Beams*. Jerusalem: Israel Program for Scientific Translation.

Wekezer, J.W. 1989. Vibrational analysis of thin-walled bars with open cross sections. *Journal of Structural Engineering – ASCE* 115(12): 2965–2978.

Research and Applications in Structural Engineering, Mechanics and Computation – Zingoni (Ed.)
© 2013 Taylor & Francis Group, London, ISBN 978-1-138-00061-2

Design models for the bolted joints of cold-formed steel pitched roof portal frames

D. Dubina & V. Ungureanu
"Politehnica" University of Timisoara, Romania
Romanian Academy, Timisoara, Branch, Romania

P. Perneş
Technical University of Cluj-Napoca, Romania

ABSTRACT: Pitched roof cold-formed steel portal frames of back-to-back built-up lipped channel sections and bolted joints are analysed in this paper. Usually, the beam-to-column and apex joints of such frames are made of gusset bracket bolted connections. Such joints, for which the bolts are installed into the webs of the C-sections trough the gusset, are partial-strength and semi-rigid. An advanced non-linear FE model has been calibrated based on relevant tests on such type of joints carried out at the CEMSIG Research Centre of the PU Timisoara. Numerical models were applied to undertake an extended parametrical study on such joints. Using these results and applying a genetic algorithm, some analytical formulas have been proposed to predict the capacity and rigidity of the joints. A portal frame was numerical tested and compared with the results obtained considering the capacity and rigidity of joints estimated with those formulas, in order to prove its effectiveness. Present paper summarizes the main phases of the study as well as the significant results.

1 INTRODUCTION

The global behaviour of cold-formed steel portal frames of bolted joints was studied experimentally by Lim (2001), Dundu & Kemp (2006), and Kwon et al. (2006). All these studies provided evidences of the crucial importance of joints performance on the global response of frames, which are semi-rigid and in almost all cases partial-strength (Lim, 2001).

An extensive experimental program on ridge (apex) and eaves knee joints of pitched roof cold-formed steel portal frames of back-to-back lipped channel sections and bolted joints was carried out at the "Politehnica" University of Timisoara. Three alternatives of joints configuration, using welded bracket elements and bolts, installed either on webs only or both on webs and flanges have been tested. Detailed results are reported by Dubina et al. (2004).

The behaviour and failure mechanisms of joints were recorded in order to evaluate their rigidity, strength and ductility. Based on experimental results, a calculation procedure, using the *component method* of EN1993-1-8:2005, was adapted to cold-formed steel joints with bolts installed both on webs and flanges (Nagy et al. 2006). Joint stiffness and moment capacity, obtained using the *component method*, were used to develop a joint model for global structural analysis.

In a second phase, two full-scale tests on cold-formed pitched-roof portal frames with bolted joints were performed (Dubina et al. 2007), with the primary objective to assess their performance under horizontal (seismic) loading, i.e. (1) horizontal load, and (2) horizontal and gravity loadings. The objective of the full-scale tests was to assess performance of pitched-roof cold-formed portal frames with moment-resisting joints under lateral loading, with particular emphasis on earthquake loading. A procedure to evaluate the ultimate design capacity of these frames, for joints with bolts both on the web and the flanges was proposed by Dubina et al. (2008).

Present paper, starting from the initial experimental results on joints with bolts on webs only, extend the investigation by numerical FEM simulations in order to calibrate analytical formulas to predict both moment capacity and stiffness of such a type of joints. At the end, *component method* design procedure is proposed and validated using the experimental results (Pernes 2012).

2 SUMMARY OF TESTING PROGRAM

In order to build realistic joint specimens, a simple pitched roof portal frame was previously designed having the following dimensions: span 12 m, bay 5 m, eaves height 4 m and roof angle 10°. The frame was subjected to loads common in Romanian, totalling approximately 10 kN/m uniformly distributed load on the rafter. The frame was analysed and designed according to EN1993-1-3:2006 provisions.

Detailed results on the behaviour of tested joints were reported by Dubina et al. (2004). The frame members are built-up sections, made of back-to-back C350/3.0 lipped-channel profiles, with the yield

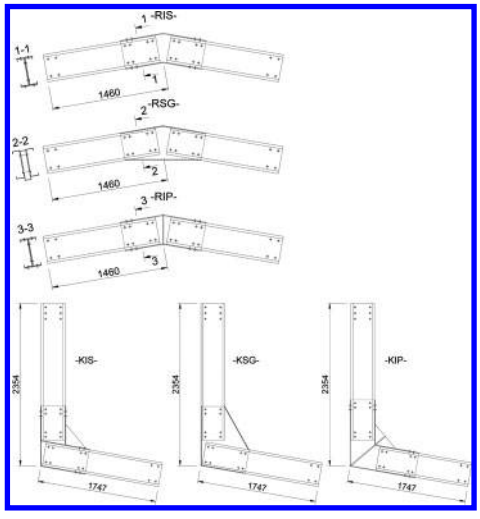


Figure 1. Ridge and knee joint specimens.

Table 1. Tested specimens

Element type	Code	Loading type
RIS (Ridge connection with I gusset profile)	RIS-FB-M	Monotonic
	RIS-FB-C1*	Cyclic: modified ECCS
	RIS-FB-C2*	Cyclic: low cycle fatigue
RSG (Ridge connection with spaced gusset)	RSG-M	Monotonic
	RSG-C1	Cyclic: ECCS procedure
	RSG-C2	Cyclic: modified ECCS
RIP (Ridge connection with I profile and end plate)	RIP-M	Monotonic
	RIP-M	Monotonic
	RIP-C1	Cyclic: ECCS procedure
KIS (Knee connection with I gusset profile)	KIS-M	Monotonic
	KIS-FB-M*	Monotonic
	KIS-FB-C*	Cyclic: modified ECCS
KSG (Knee connection with spaced gusset)	KSG-M	Monotonic
	KSG-C1	Cyclic: modified ECCS
	KSG-C2	Cyclic: low cycle fatigue
KIP (Knee connection with I profile and end plate)	KIP-M	Monotonic
	KIP-FB-M*	Monotonic
	KIP-FB-C*	Cyclic: modified ECCS

* Specimens with supplementary bolts on the flanges (FB).

strength $f_y = 350\,\mathrm{N/mm^2}$. Three joint typologies were designed, using welded bracket elements (S235, $f_y = 235\,\mathrm{N/mm^2}$) and M20 class 6.6 bolts (see Fig. 1).

The joint specimens have been tested under monotonic and cyclic loading (see Table 1).

One group of specimens (RSG and KSG) used spaced built-up gussets. In this case, bolts were provided on the webs of the C350 profile only. In the other cases, where two different details were used for connecting brackets (i.e. welded I-sections for KIS and RIS, and welded I-section with plate bisector for KIP and RIP), bolts were provided on the web only, or both on the web and the flanges. Joints where bolts were provided both on the webs and flanges were denoted by FB, as shown in Table 1.

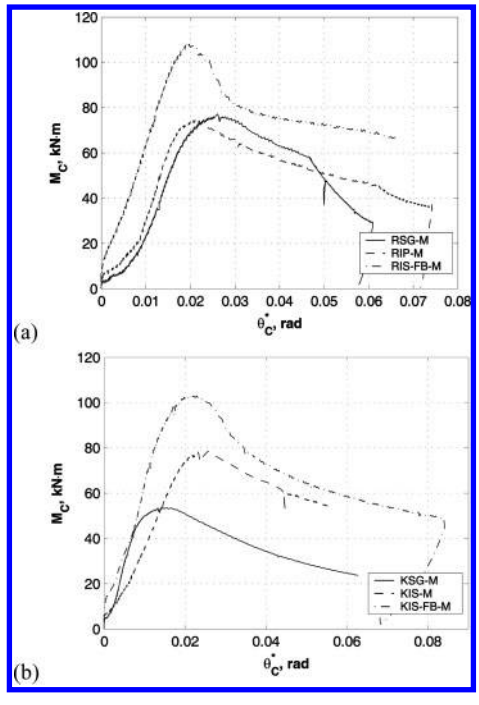


Figure 2. Comparative results from monotonic tests for (a) ridge joints and (b) knee joints.

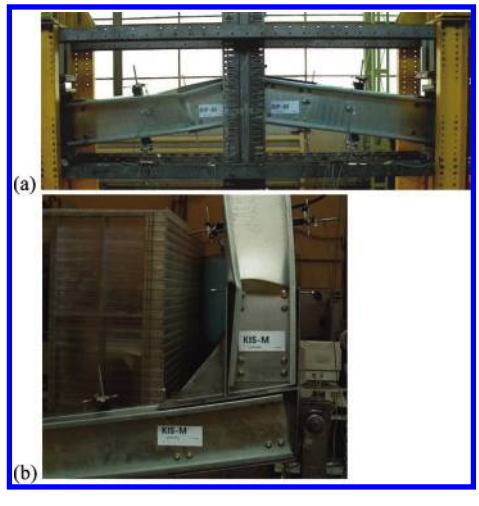


Figure 3. (a) Failure mode of RIP-M specimen; (b) Failure mode of KIS-M specimen.

Figure 2 shows comparatively the moment-rotation curves for monotonic tests, while Figure 3 shows the failure modes of some tested specimens.

3 CALIBRATION OF NUMERICAL MODELS. PARAMETRIC STUDY

Numerical models applied to simulate the behaviour of members experimentally tested have been created using the commercial FE program ABAQUS/CAE v.6.7.1 (Pernes 2012).

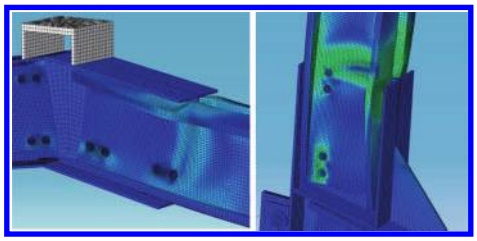


Figure 4. Failure modes obtained via numerical models: (a) RIS-M specimen; (b) KIS-M specimen.

Different element types and mesh sizes were tested in order to find the optimum number of elements from the point of view of ultimate force accuracy and, in the same time, to reduce the computational time. Rectangular 4-noded shell elements with reduced integration (S4R) were used to model the thin-walled components. For the welded brackets, bolts and nuts, 8-noded hexahedral elements with reduced integration (C3D8R) have been used. In order to create a reliable mesh, a mesh size of 8 × 8 mm for C-profiles and 12 × 12 mm for the bracket were considered to provide enough accuracy. The elements were constrained to a rectangular form using structured mesh, excepting the ones around holes for which were free mash was used. Pre-tensioning force to model the effect of bolt tightening has been introduced. A measured thickness minus zinc coating, of 2.90 mm, was considered for lipped channel profiles.

The material behaviour used for numerical modelling was in accordance with the recorded curves from tensile tests from coupons cut over the cross-section of C350/3 elements, with the following mean values for yield strength $f_y = 452.9$ N/mm^2 and $f_u = 518.16$ N/mm^2 for ultimate strength.

General contact with the following parameters have been used, i.e. (1) *normal direction* – Hard Contact; (2) *transversal direction* – a friction coefficient of $\mu = 0.3$. The load introduction and the supports were modelled to reproduce the real tests.

Some imperfections have been introduced in the models at the level of holes according to EN1090-2:2008. Nonlinear analyses were performed, using dynamic explicit steps as quasi-static, obtained by choosing time parameter so that the inertial effects on the system to be insignificant (takes into account stiffness loss due to local buckling).

The calibrated FE models reproduce the same failure mechanism in case of experimental tests, as shown in Figure 4.

Figure 5 presents the force-displacement and moment-rotation curves obtained both experimentally and numerically, for some of the joints. A good agreement can be observed between the experimental and numerical curves.

Table 2 presents the synthetically the experimental and numerical results obtained with ABAQUS computer code for three types of joints.

Based on the results obtained via numerical simulations, it can be noted that the behaviour and maximum

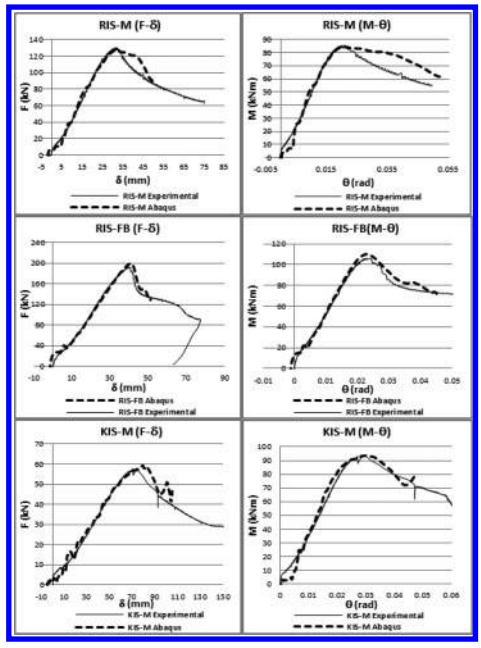


Figure 5. Force-displacement and moment-rotation curves: (a) RIS-M specimen; (b) RIS-FB specimen; (c) KIS-M specimen.

Table 2. Experimental vs. numerical results

RIS-M	F_{max} [kN]	d_{max} [mm]	M_{max} [kNm]	θ_u [rad]	$S_{j.ini}$ [kNm/rad]
Experimental	130	31.5	87.03	0.02	5071
Abaqus	126.7	31.7	84.56	0.021	5020
RIS-FB					
Experimental	193	39.1	106.3	0.023	6259
Abaqus	200	40.6	110.2	0.023	6697
KIS-M					
Experimental	58.1	74.2	92.6	0.029	4301
Abaqus	59.3	79.1	93.23	0.0283	4843

load accurately replicate the experimental tests. On the following, a parametric study has been conducted on RIS-M joints with bolts on webs only. A set of 35 numerical models have been created considering the following parameters: (1) three types of thicknesses, i.e. 2.9 mm, 2.4 mm and 1.91 mm; (2) the number and distribution of bolts (see Fig. 6).

The outputs of the parametric study are:

- long distances between the columns of bolts do not influence the maximum moment more than 2%, confirmed also by Dundu & Kemp (2006);
- if the distance between the external columns of bolts decreases, a sensitivity related to the number of bolts was recorded;
- compact columns of bolts lead to significant variation in terms of moment resistance if the number of bolts changes and, the failure is influenced by the components of the connection;
- similar conclusions can be drawn for the stiffness of joints too.

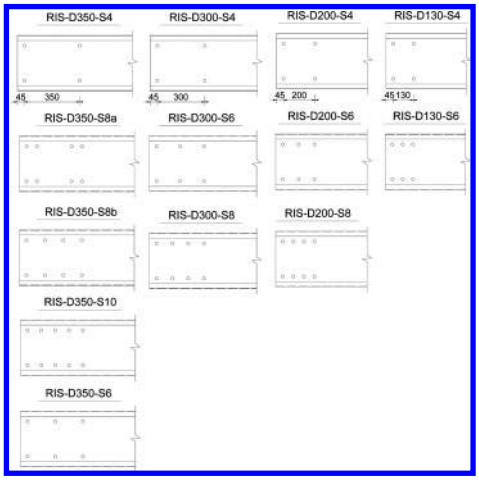


Figure 6. Number and distribution of bolts for the parametric study of RIS-M joints.

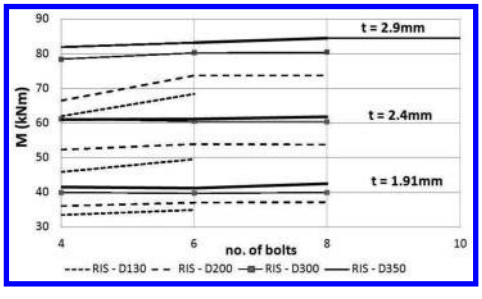


Figure 7. The influence of number of bolts on the moment resistance of joints.

Figure 7 presents the influence of number of bolts and the thicknesses of the profiles on the moment resistance of the joints, with the configurations presented in Figure 6.

According to the joints classification in terms of strength and stiffens (see EN1993-1.8:2005), the RIS joints, with bolts on webs only, are semi-rigid and partial-strength. Therefore design of light-gauge steel portal frames of the type analysed in the present paper need to account for connections flexibility.

4 THE COMPONENT METHOD

The *component method* is a general procedure for designing strength and stiffness of joints in building frames, and is implemented in EN1993-1-8:2005.

Application of the component method requires the following steps: (1) identification of the active components within the joint; (2) evaluation of the stiffness and strength of individual components; (3) = assembly of the components in order to evaluate stiffness and strength of the whole joint.

The present study investigates joints with bolts on webs (i.e. RIS-M) only, based on the conclusions of experimental and numerical program (Pernes 2012).



Figure 8. Parameters to characterise the $M^s_{j,Rd}$ component.

It was observed that bolts on the web only introduce stress concentration in the web, which causes premature local buckling failure. The following components were identified and used to model the connection strength and stiffness: (1) cold-formed steel member in bending; (2) bracket in bending; (2) local component of the beam due to stress concentration in the web around holes; (4) bolts in shear; (5) bolts in bearing with the cold-formed member; (6) bolts in bearing with the bracket.

The joint moment resistance was obtained as the minimum of moment resistance of the components:

$$M_{j,Rd} = \min\left(M^g_{j,Rd}, M^b_{j,Rd}, M^i_{j,Rd}, M^s_{j,Rd}\right) \qquad (1)$$

where: $M^g_{j,Rd}$ is the moment resistance of the bracket, $M^b_{j,Rd}$ is the moment resistance of the cold-formed steel member and was determined using measured geometrical, mechanical characteristics and effective cross-section modulus, $M^i_{j,Rd}$ is the moment resistance of the bolted connection and $M^s_{j,Rd}$ is the local component of the beam due to stress concentration in the web around holes.

It was observed that, due to the dimensions of the bracket and lipped channel profiles chosen for the experimental specimens, the moment resistance of the bracket, $M^g_{j,Rd}$, is higher than the moment resistance of the cold-formed steel member in bending, $M^b_{j,Rd}$, and both components are higher than the moment resistance of the joint obtained experimentally. Consequently, Eq. (1) becomes:

$$M_{j,Rd} = \min\left(M^i_{j,Rd}, M^s_{j,Rd}\right) \qquad (2)$$

The only major problem is to determine correctly the local component of the beam due to stress concentration in the web around holes, $M^s_{j,Rd}$.

425 numerical simulations have been done, in order to determine the influence of parameters which govern the behaviour of this component. Figure 8 presents the parameters considered in the analysis.

Based on genetic programming using Eureka Formulize software the following equation has been obtained for the component $M^s_{j,Rd}$, considering the parameters from above, i.e.:

$$M^s_{j,Rd} = \left(20t^2\left(b_c + h_c + \frac{l_c}{20}\right) + t\left(c^2 + \frac{4h^2}{125} + \frac{(h-h_c)^2}{7}\right)\right)\cdot c_n\sqrt{\frac{f_{ya}}{450}}450 \qquad (3)$$

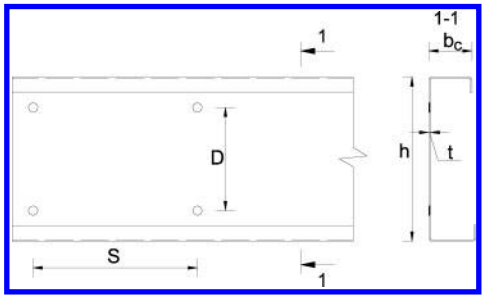


Figure 9. Details for $M^s_{j,Rd}$ component.

where
$c_n = 1 + \left(\frac{n_{b,r}}{0.17+n_{b,r}} - 0.925\right)\frac{D}{h}$ is correction coefficient
t is the thickness of the profile;
b_c is the width of the flange in compression;
h is the height of the profile;
c is the lip of the profile;
h_c is the horizontal distance between bolts, i.e. $h_c = S + 2d$ (see Fig. 9);
l_c is the vertical distance between bolts, i.e. $l_c = D + 2d$ (see Fig. 9);
d is the diameter of the of the bolt;
$n_{b,r}$ is the number of bolts on a row.

The limits of this calibrated formula are:

– cross-section (see Fig. 9):
  - $h = (250, 300, 350\,\text{mm})$
  - $0.22\,h < b < 0.35\,h$
  - $0.13\,b < c < 0.33\,b$
– connection (see Fig. 9):
  - $0.4\,h < D < h$
  - $0.4\,h < S < 0.7\,h$
– $f_y = 450\,\text{N/mm}^2$

In terms of stiffness, four components were considered to contribute to the stiffness of the connection: the bracket in bending, k_g, the cold-formed steel member in bending, k_b, the bolts on cold-formed member (shear or bearing denoted k_{br}), and bolts on the bracket (shear or bearing denoted k_{bg}), as shown in Figure 10.

Finally, the initial connection stiffness is determined as:

$$S_{j,ini} = \frac{1}{\frac{1}{k_g} + \frac{1}{k_b} + \frac{1}{k_{br}} + \frac{1}{k_{bg}}} \quad (4)$$

5 DESIGN OF PORTAL FRAMES WITH SEMI-RIGID AND PARTIAL-STRENGTH JOINTS

This chapter proposes to compare the results obtained for a full frame, using an advanced FEM model with ABAQUS and the limits obtained using beam elements

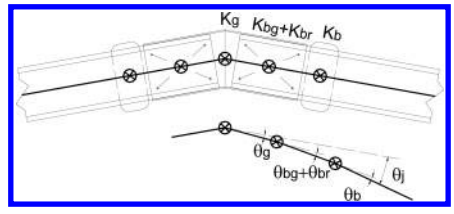


Figure 10. The components contributing to the joint stiffness.

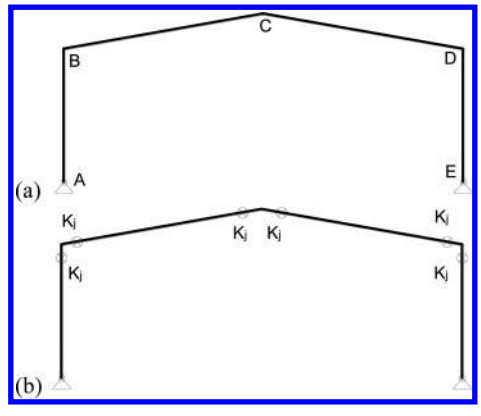


Figure 11. Beam model for (a) frame with rigid joints; (b) semi-rigid joints.

Table 3. Results for the stiffnesses of joints

	B, D		C
Node	beam	column	apex
$S_{j.ini}$ [kNm/rad]	5803	8147	5334

via SAP2000 computed code (elastic analyses), considering firstly the joints behaviour as rigid and full strength and secondly semi-rigid and partial-strength estimated with the formulas based on *component method* described previously (see Fig. 11). The frame was subjected to: (1) vertical loads only and (2) horizontal load only (Pernes 2012).

The stiffnesses of the joints presented in Figure 11(b) are calculated in Table 3, applying the formulas based on *component method* described above.

Figure 12 presents the failure mode of the frame obtained with ABAQUS software, while Figure 13 shows the force-displacement curve considering the vertical loads only.

Figure 13 presents comparatively the result obtained using ABAQUS and the ones using beam elements via SAP2000 computed code (elastic analyses), considering or not the semi-rigidity of joints. It is easy to observe that, in terms of vertical displacements the frame with continuous joints gives a vertical displacement of 66 mm, very low compared with 219 mm obtained via ABAQUS, while the frame



Figure 12. Failure mode obtained via an advanced FEM model.

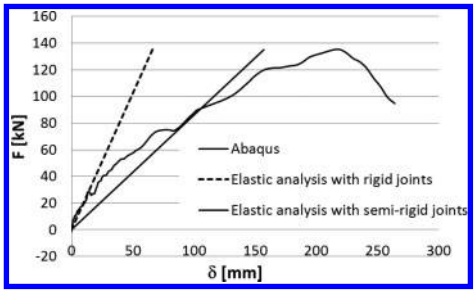


Figure 13. Force-displacement curve for vertical loads.

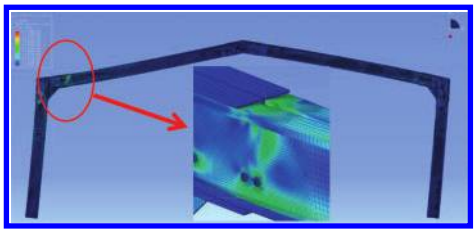


Figure 14. Failure mode obtained via an advanced FEM model.

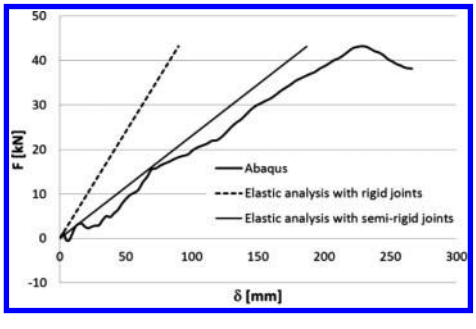


Figure 15. Force-displacement curve for horizontal loads.

with semi-rigid joints gives a vertical displacement of 157 mm.

In case of horizontal load, Figure 14 presents the failure mode for the frame obtained with ABAQUS software, while Figure 15 presents the force-displacement curve considering the horizontal load only. Figure 15 presents comparatively the result obtained using ABAQUS and the ones using beam elements via SAP2000 computed code (elastic analyses), considering or not the semi-rigidity of joints, under horizontal load only.

It is easy to observe that, in terms of horizontal displacements the frame with continuous joints gives a horizontal displacement of 90 mm, very low compared with 225 mm obtained via ABAQUS, while the frame with semi-rigid joints gives a horizontal displacement of 187 mm.

6 CONCLUSIONS

The influence of joints detailing, e.g. typology, position and number of bolts on the capacity and stiffness of cold-formed pitched roof portal frames was numerically investigated. On this purpose an advanced FEM model was experimentally calibrated and applied. Bolted joints, with bolts on web only, were parametrically studied in order to identify the active components for both moment capacity and stiffness. On this basis, *component method* design formulas have been proposed and validated.

It was confirm0ed that such type of joints are partial-strength and semi-rigid. In what concerns the influence of joints properties on the response of the frames, the semi-rigidity is more significant than partial-strength, making the frame sensitive to 2nd order effects.

REFERENCES

Dubina, D., Stratan, A., Ciutina, A., Fulop, L. & Nagy, Zs. 2004. Performance of ridge and eaves joints in cold-formed steel portal frames. *The 17th Int. Specialty Conference, Orlando, Florida, USA*, 727–742.

Dubina, D., Stratan, A. & Nagy, Zs. 2007. Full – scale testing of cold-formed steel pitched-roof portal frames of back-to-back channel sections and bolted joints. *Proc. of the Sixth International Conference on Steel and Aluminum Structures, Oxford, UK*, 931–939.

Dubina, D., Ungureanu, V. & Stratan A. 2008. Ultimate design capacity of pitch-roof portal frames made by thin-walled cold-formed members. *Proc. of the 5th International Conference on Thin-Walled Structures: Recent Innovations and Developments, Gold Coast, Australia*, Vol. 1, 387–394.

Dundu, M. & Kemp, A.R. 2006. Strength requirements of single cold formed channels connected back-to-back. *Journal of Constructional Steel Research* 62(4): 250–261.

EN1993-1-3:2006. *Eurocode 3: Design of steel structures. Part 1–3: General Rules. Supplementary rules for cold-formed thin gauge members and sheeting*. CEN, Brussels.

EN1993-1-8:2005. *Eurocode 3: Design of steel structures. Part 1–8: Design of joints*. CEN, Brussels.

Kwon, Y.B., Chung, H.S. & Kim, G.D. 2006. Experiments of cold-formed steel connections and portal frames. *Journal of Structural Engineering* 132(4): 600–607.

Lim, J.B.P. 2001. *Joint effects in cold-formed steel portal frames*. University of Nottingham, PhD Thesis.

Nagy, Zs., Stratan, A. & Dubina, D. 2006. Application of component method for bolted cold-formed steel joints. *Proc. of the International Conference on Metal Structures – ICMS2006 "Steel – A new and traditional material for building", Poiana Brasov, Romania*, 207–215.

Pernes, P. 2012. *The behaviour of bolted joint of cold-formed steel pitched roof portal frames*. PhD Thesis, Technical University of Cluj-Napoca, Romania.

Research and Applications in Structural Engineering, Mechanics and Computation – Zingoni (Ed.)
© 2013 Taylor & Francis Group, London, ISBN 978-1-138-00061-2

Tests of cold-formed steel lipped channel columns undergoing local-distortional-global interaction

B. Young
Department of Civil Engineering, The University of Hong Kong, Hong Kong, China

D. Camotim & P.B. Dinis
Civil Engineering Department, ICIST, Instituto Superior Técnico, Technical University of Lisbon, Portugal

ABSTRACT: The paper presents a test program on cold-formed steel lipped channel columns with geometries (cross-section dimensions and lengths) selected to ensure that they undergo interaction between local, distortional and global (flexural-torsional) buckling modes. The columns were compressed between fixed-ended conditions. The column ultimate loads, failure modes and load-axial shortening equilibrium path are reported. The test results obtained from this study provide clear experimental evidence of column interactive failures involving local, distortional and flexural-torsional deformations. Moreover, these test results also provide useful information for development of design rules aimed at predicting the ultimate strength of columns experiencing the triple interaction under consideration.

1 INTRODUCTION

Thin-walled cold-formed steel lipped channel columns are well known to be highly susceptible to local (L), distortional (D) and global (G – flexural or flexural-torsional) buckling. Depending on the column geometry (cross-section dimensions and length) and end support conditions, its post-buckling behaviour and ultimate strength may be significantly affected (eroded) by interactions involving the above three buckling mode types. Therefore, design codes must include procedures to adequately take into account such interaction phenomena. Out of them, local-global (LG) interaction is now quite well understood, which explains why the current specifications are able to handle it, using either the traditional Effective Width Method or the more recent Direct Strength Method (DSM). In the last decade, considerable research work was devoted to local-distortional (LD) interaction, including experimental investigations, numerical simulations and the proposal of DSM-based design approaches (Yang and Hancock 2004, Dinis et al. 2007, Silvestre et al. 2009, 2012, Kwon et al. 2009 and Young et al. 2013).

Concerning the mode interaction involving distortional and global buckling modes, namely distortional-global (DG) and local-distortional-global (LDG) interaction, the available literature is much scarcer. In the first case, there exist only a few recent numerical and experimental studies (e.g., Dinis and Camotim 2011a) and a suitable design approach is still lacking. In the case of LDG coupling, the existing research work is similarly scarce and (experimental and numerical) research work on this triple interaction was only reported in the last year (Dinis and Camotim 2011b, Dinis et al. 2011, 2012, Santos et al. 2012) and only incipient design considerations are available. One interesting preliminary conclusion from this research work was the very minor (almost inexistent) role played by the local deformations, which amounts to arguing that the DG and LDG interaction effects are qualitatively and quantitatively similar.

The objective of this work is to report the results of a well-planned experimental investigation carried out at The University of Hong Kong, aimed at assessing the non-linear (post-buckling) behaviour and ultimate strength of fixed-ended cold-formed steel lipped channel columns, affected by LDG interaction. The specimens with selected lipped channel geometries were carefully fabricated and measured (in order to acquire information on the real dimensions and initial imperfections) and then tested under uniform compression. The experimental results presented consist of initial imperfection measurements, non-linear equilibrium path (applied load vs. relevant displacements) and ultimate strengths – particular attention is paid to the characterisation of the column collapse modes, namely in order to detect the presence of local deformations. The experimental results reported are ideally suited (i) to provide evidence of the interaction effects under consideration and (ii) to provide ultimate strength data to develop and calibrate a DSM design approach for lipped channel columns experiencing LDG interaction. The future performance of a similar study involving columns displaying only DG interaction will make it possible to assess the ultimate

Table 1. Measured specimen dimensions

Specimen	Web b_w (mm)	Flanges b_f (mm)	Lips b_l (mm)	Thickness t^* (mm)	Length L (mm)
LC-1	53.5	56.7	12.5	0.985	1395
LC-2-1	57.5	61.4	12.4	0.997	1651
LC-2-2	57.6	61.4	12.5	1.001	1649
LC-3	62.6	66.2	12.5	1.001	1951
LC-4	68.7	71.0	12.5	0.976	2300
LC-5	70.8	72.3	12.2	1.193	1896
LC-6	70.9	78.3	11.9	1.203	2004
LC-7	75.7	82.9	12.0	1.194	2302
LC-8	82.1	87.7	11.8	1.171	2603
LC-9	58.0	48.2	12.8	0.983	1401
LC-10	63.3	52.6	12.7	0.989	1602
LC-11	62.7	63.9	12.4	0.987	1699
LC-12	68.5	57.3	12.8	0.986	1899
LC-13	73.2	63.3	12.4	1.204	1851
LC-14	78.4	68.4	12.5	1.174	2100
LC-15	83.3	73.4	11.9	1.176	2402
LC-16	88.5	78.3	12.3	1.204	2750

strength differences between the two column sets and, therefore, confirm or refute the above preliminary conclusion on the minor role played by the local deformations, an important issue for the development of rational design models.

2 TEST SPECIMENS

A series of cold-formed steel lipped channel columns was conducted. A total of seventeen specimens with two of the repeated specimens was tested. The column specimens were compressed between fixed ends condition. The column test specimens were brake-pressed from high strength zinc-coated grades G500 and G550 structural steel sheets having nominal 0.2% proof stresses (yield stresses) of 500 and 550 MPa, respectively. These structural steel sheets conformed to the Australian Standard AS 1397 (1993). The nominal column length ranged from 1400 to 2750 mm. The ends of the column specimens were welded to 25 mm thick steel end plates to ensure full contact between the specimen and end bearings. The test specimens had the nominal web width (b_w) ranged from 53 to 88 mm, flange width (b_f) ranged from 48 to 88 mm and a constant lip width (b_l) of 12 mm. The nominal plate thicknesses of the specimens were 1.0 and 1.2 mm. The base metal thickness (t^*) was measured by removing the zinc coating by acid-etching. The thickness of the zinc coating on one side of the section was measured as 32 μm for 1.0 mm plate thickness and 29.5 μm for 1.2 mm plate thickness. The measured inside corner radius (r_i) was 2.0 mm for all specimens. The measured cross-section dimensions and column length for each test specimen are shown in Table 1 using the nomenclature defined in Fig. 1. Furthermore, the critical local ($\sigma_{cr.L}$), distortional ($\sigma_{cr.D}$) and global ($\sigma_{cr.G}$) buckling

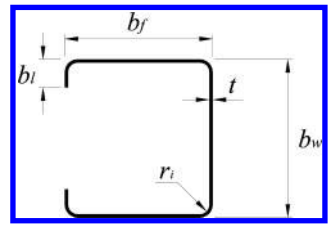


Figure 1. Definition of symbols for cold-formed steel lipped channel.

Table 2. Critical local, distortional and global buckling stresses

Specimen	$\sigma_{cr.L}$ (MPa)	$\sigma_{cr.D}$ (MPa)	$\sigma_{cr.G}$ (MPa)
LC-1	257.0	305.2	314.4
LC-2-1	225.1	254.2	254.8
LC-2-2	226.6	257.4	257.3
LC-3	194.1	214.6	213.0
LC-4	158.1	179.0	179.4
LC-5	228.0	211.6	248.3
LC-6	203.7	182.6	215.6
LC-7	177.9	161.3	189.0
LC-8	150.8	135.4	169.6
LC-9	274.2	367.5	376.7
LC-10	234.1	304.8	324.9
LC-11	197.7	231.0	257.7
LC-12	197.3	255.9	266.9
LC-13	253.0	260.6	297.4
LC-14	207.9	220.1	257.9
LC-15	183.5	180.9	218.9
LC-16	169.6	166.4	193.0

stresses are also shown in Table 2. There are nine specimens having a nominal plate thickness of 1.0 mm and labelled as LC-1, LC-2-1, LC-2-2, LC-3, LC-4, LC-9, LC-10, LC-11 and LC-12. There are eight specimens having a nominal plate thickness of 1.2 mm and labelled as LC-5, LC-6, LC-7, LC-8, LC-13, LC-14, LC-15 and LC-16.

3 MATERIAL PROPERTIES

The material properties of the column test specimens were determined by tensile coupon tests. The coupons were extracted from the centre of the flange and web in the longitudinal direction of specimens LC-1 and LC-5. The cold-formed lipped channel column specimens were fabricated from the same batch of steel for each plate thickness. Therefore, the material properties obtained from specimens LC-1 and LC-5 are expected having the same material properties for those specimens having the same nominal plate thickness.

The coupon dimensions conformed to the Australian Standard AS 1391 (2007) for the tensile testing of metals using 12.5 mm wide coupons of gauge length 50 mm. An MTS displacement controlled testing machine using friction grips was used to conduct

Table 3. Nominal and measured material properties of cold-formed steel lipped channels

Test Series	Nominal		Measured			
	t (mm)	$\sigma_{0.2}$ (MPa)	E (GPa)	$\sigma_{0.2}$ (MPa)	σ_u (MPa)	ε_f (%)
LC-1 (Flange)	1.0	550	211	597	598	10.2
LC-1 (Web)	1.0	550	216	612	619	8.7
LC-5 (Flange)	1.2	500	213	594	610	8.9
LC-5 (Web)	1.2	500	215	598	611	8.5

Note: 1 in. = 25.4 mm; 1 ksi = 6.89 MPa.

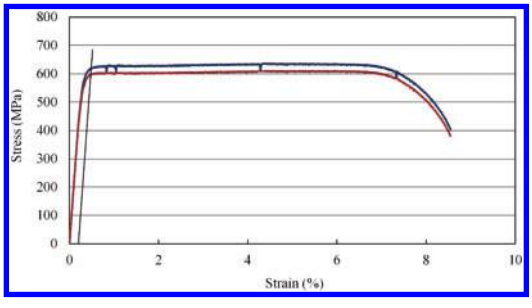


Figure 2. Stress-strain curve of cold-formed steel lipped channel specimen LC-5 in the web.



Figure 3. Column test set-up.

the coupon tests. The coupons were also tested according to the Australian Standard AS 1391 (2007). A calibrated extensometer of 50 mm gauge length was used to measure the longitudinal strain of the coupon specimens. A data acquisition system was used to record the load and the strain readings at regular intervals during the tests. The static load was obtained by pausing the applied straining for 1.5 minutes near the 0.2% proof stress and the ultimate tensile strength. This allowed the stress relaxation associated with plastic straining to take place. The nominal and measured material properties obtained from the coupon tests are summarized in Table 3. The measured values of Young's modulus (E), static 0.2% proof stress ($\sigma_{0.2}$), static tensile strength (σ_u) and elongation after fracture (ε_f) based on a gauge length of 50 mm are shown in Table 3. A stress-strain curve obtained from the coupon test for specimen LC-5 in the web is shown in Fig. 2. Both test curve and static curve are shown in the figure.

4 TEST RIG AND TEST PROCEDURE

Figure 3 shows a typical column test as well as the test rig and test set-up. A servo-controlled hydraulic testing machine was used to apply compressive axial force to the column specimens. Two steel end plates were welded to the ends of the specimen. The top end plate of the specimen was bolted to the rigid flat bearing plate, which was restrained against the minor and major axis rotations as well as twist rotations and warping. Hence, the top end of the column was fixed in position. A special bearing was used at the lower end support. Initially, the special bearing was free to rotate in any direction. The ram of the actuator was moved slowly until the bottom end plate of the specimen in full contact with the special bearing having a small initial load of approximately 1 kN. This procedure eliminated any possible gaps between the special bearing and the bottom end plate of the specimen. The bottom end plate of the specimen was bolted to the special bearing, and the bearing was then restrained from rotations and twisting by using vertical and horizontal bolts, respectively. The vertical and horizontal bolts of the special bearing were used to lock the bearing in position after full contact was achieved. Hence, the special bearing became a fixed-ended bearing. The fixed-ended bearing was considered to restrain both minor and major axis rotations as well as twist rotations and warping.

Three displacement transducers were used to measure the axial shortening of the column. Displacement control was used to drive the hydraulic actuator at a constant speed of 0.2 mm/min for all column specimens. The use of displacement control allowed the tests to be continued into the post-ultimate range. In addition, seven transducers were used to measure the deformation of the cross-section at mid-length of the column. Figure 4(a) shows the arrangement of the seven transducers. Three transducers were located in the web, where two of them located 10 mm away from the web-flange junctions and one of them located in the middle of the web. The transducer located in the middle of the web was shifted 60 mm from the mid-length of the column, as shown in Fig. 4(b). This is due to the

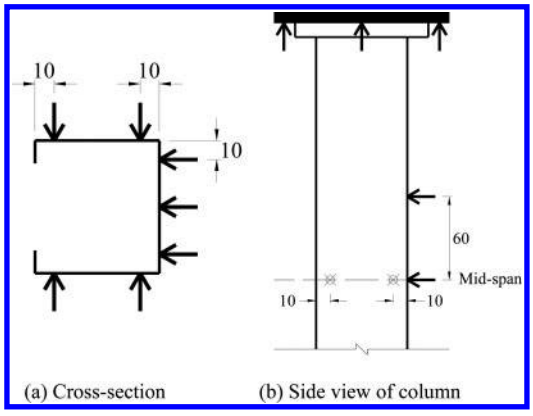


Figure 4. Location of transducers.

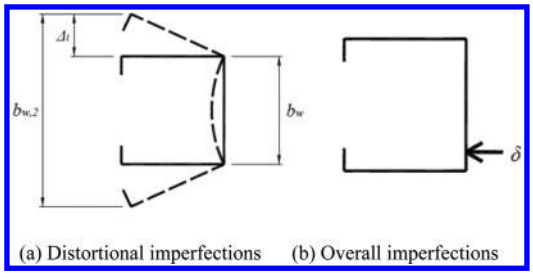


Figure 5. Initial geometric imperfection measurements.

limitation of space in the web. Local and overall buckling can be determined from these three transducers in the web. Two transducers were located 10 mm away from the web-flange junctions in the flanges. Major axis bending of the column can be determined from these two transducers. Furthermore, two transducers were located 10 mm away from the lip-flange junctions in the flanges, where distortional buckling can be identify from these two transducers. A data acquisition system was used to record the applied load and the readings of the displacement transducers at regular intervals during the tests.

5 INITIAL GEOMETRIC IMPERFECTIONS

The initial distortional and overall geometric imperfections of the column specimens were measured prior to testing. The distortional imperfections (Δ_l) were obtained by measuring the cross-section in the web width (b_w) between the web-flange junctions and also the web width ($b_{w,2}$) between the lip-flange junctions, as shown in Fig. 5(a). The measured values (Δ_l) on one side of the flange at mid-length of the columns are shown in Table 4, where positive value of Δ_l indicates outward deformations. The maximum distortional geometric imperfection was 1.78 mm inward deformation for specimen LC-8. In addition, the minor axis flexural initial overall geometric imperfections were also measured in all specimens along the web-flange longitudinal edges, as shown in Fig. 5(b).

Table 4. Measured initial distortional and overall geometric imperfections at mid-length

Specimen	Distortional imperfection $\Delta_l = (b_{w,2} - b_w)/2$ (mm)	Overall imperfection δ/L
LC-1	0.95	1/4394
LC-2-1	0.58	−1/32503
LC-2-2	0.57	−1/66891
LC-3	0.38	−1/4043
LC-4	0.81	−1/12075
LC-5	−0.17	1/29860
LC-6	0.11	−1/3586
LC-7	−0.87	−1/1888
LC-8	−1.78	−1/2927
LC-9	0.26	−1/4596
LC-10	0.10	1/15769
LC-11	0.47	−1/66891
LC-12	−0.05	−1/6501
LC-13	−0.21	−1/2974
LC-14	−1.24	−1/2756
LC-15	0.73	−1/4202
LC-16	−0.73	−1/10826

A theodolite was used to obtain readings at mid-height and near both ends of each column. The measured values at mid-height (δ), normalised with respect to the column length L, are also given in Table 4, where positive value of δ/L indicates a column curved towards the lips. The maximum overall geometric imperfection at mid-height was 1/1888 of the column length for specimen LC-7.

6 COLUMN TEST RESULTS

The experimental ultimate loads (P_{Exp}) are given in Table 5, which also provides the nature of the column failure modes – note that one test was repeated (specimen LC-2-2 is identical to the LC-2-1 one). The analysis of the experimental results presented prompts the following remarks:

(i) All specimens were found to fail in local-distortional-global interactive modes ("L + D + FT") – Figures 6 and 7 show the deformed configurations near collapse of specimens LC-4 and LC-8, respectively, providing very clear evidence of the simultaneous occurrence of local, distortional and flexural-torsion deformations.

(ii) The LDG interaction observed does not stem from the near coincidence of the local, distortional and global column critical buckling loads – Table 2 shows that the ratio between the higher and lower of the three column buckling stresses varies between 1.16 and 1.39. Instead, the interaction occurs because (ii_1) the yield stress $\sigma_{0.2}$ is "sufficiently larger" than the higher column buckling stress (it varies between 1.61 and 3.37) and (ii_2) the global buckling is never critical –



Figure 6. Interaction of local, distortional and flexural-torsional buckling for column specimen LC-4.

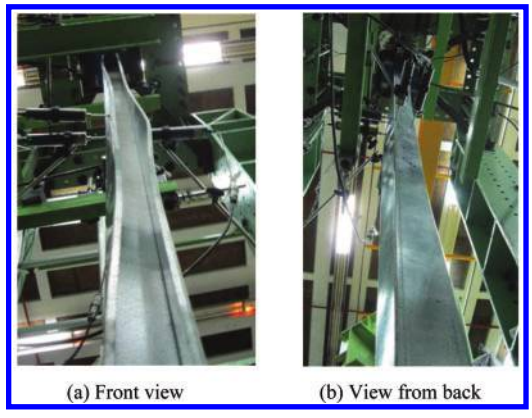


Figure 7. Interaction of local, distortional and flexural-torsional buckling for column specimen LD-8.

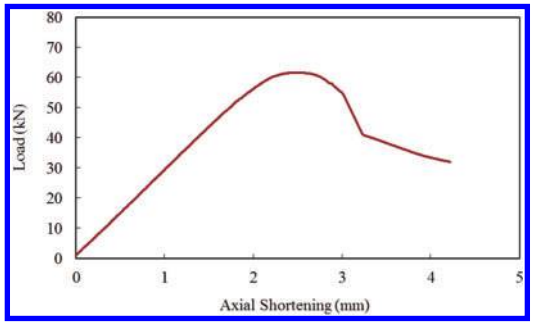


Figure 8. Load versus axial shortening curve for column specimen LC-5.

numerical studies showed that a significant ultimate strength erosion takes place when global buckling is critical (Dinis et al. 2012).

(iii) The ultimate strengths corresponding to the repeated tests with LDG interaction (specimens LC-2-1 and LC-2-2) differed by 1.3%, thus evidencing the test repeatability.

(iv) Regardless of the half-wave number exhibited by the critical distortional buckling mode, the LDG interaction involves always distortional deformation with odd-numbered half-waves – they are brought about "attracted" by the global deformations, as was already observed by Dinis et al. (2012).

Figure 8 depicts the applied load vs. axial shortening equilibrium path of specimen LC-5 – many other equilibrium paths, corresponding to various specimens and transducer measurements, were recorded and will be reported elsewhere in the near future.

7 CONCLUSIONS

An experimental investigation of cold-formed steel lipped channel columns has been presented. The columns were clearly failed by interaction of local, distortional and global buckling. Material properties of the column specimens were determined by coupon tests. The measured 0.2% proof stress of the material ranged from 594 to 612 MPa, which is considered to be high strength steel material. Initial geometric imperfections of the columns were also reported. The ultimate loads, failure modes and load-axial shortening equilibrium path of the columns provide useful

Table 5. Experimental ultimate loads and failure modes

Specimen	Experimental ultimate load P_{Exp} (kN)	Failure mode
LC-1	46.15	L + D + FT
LC-2-1	44.78	L + D + FT
LC-2-2	44.20	L + D + FT
LC-3	39.83	L + D + FT
LC-4	39.68	L + D + FT
LC-5	61.67	L + D + FT
LC-6	59.19	L + D + FT
LC-7	49.49	L + D + FT
LC-8	47.46	L + D + FT
LC-9	51.13	L + D + FT
LC-10	50.55	L + D + FT
LC-11	42.59	L + D + FT
LC-12	46.24	L + D + FT
LC-13	66.82	L + D + FT
LC-14	60.74	L + D + FT
LC-15	55.47	L + D + FT
LC-16	52.06	L + D + FT

Note: 1 kip = 4.45 kN.

information for development of design rules, in particular for columns failed by interaction of local, distortional and global buckling.

ACKNOWLEDGEMENTS

The authors are grateful to BlueScope Lysaght Singapore for supplying the cold-formed steel test specimens. The authors are also thankful to Mr Yang Jiang for his assistance during the experimental programme. The experimental work described in this paper was supported by a grant from the Research Grants Council of the Hong Kong Special Administrative Region, China (Project No. HKU719711E).

REFERENCES

Australian Standard AS1397-1993. (1993). Steel sheet and strip – hot-dipped zinc-coated or aluminium/zinc-coated. AS 1397, Standards Association of Australia, Sydney, Australia.

Australian Standard AS1391-2007. (2007). Metallic materials – Tensile testing at ambient temperature. AS 1391, Standards Australia, Sydney, Australia.

Dinis, P.B., Camotim, D. (2011a), Post-Buckling Behaviour and Strength of Cold-Formed Steel Lipped Channel Columns Experiencing Distortional/Global Interaction, Computers & Structures, 89(3-4):422–434.

Dinis, P.B., Camotim, D. (2011b), Local/Distortional/Global Mode Interaction in Simply Supported Cold-Formed Steel Lipped Channel Columns, International Journal of Structural Stability and Dynamics, 11(5):877–902.

Dinis, P.B., Camotim, D., Silvestre, N. (2007), FEM-based analysis of the local-plate/distortional mode interaction in cold-formed steel lipped channel columns, Computers & Structures, 85(19–20):1461–1474.

Dinis, P.B., Camotim, D., Batista, E., Santos, E. (2011), Local/Distortional/Global Mode Coupling in Fixed Lipped Channel Columns: Behaviour and Strength, Advanced Steel Construction – an International Journal, 7(4):113–130.

Dinis, P.B., Batista, E.M., Camotim, D., Santos, E.S. (2012), Local-Distortional-Global Interaction in Lipped Channel Columns: Experimental Results, Numerical Simulations and Design Considerations, Thin-Walled Structures, 61:2–13.

Kwon, Y.B., Kim, B.S., Hancock, G.J. (2009), Compression tests of high strength cold-formed steel channels with buckling interaction, Journal of Constructional Steel Research, 65(2):278–289.

Santos, E.S., Batista, E.M., Camotim, D. (2012), Experimental Investigation Concerning Lipped Channel Columns Undergoing Local-Distortional-Global Buckling Mode Interaction, Thin-Walled Structures, 54:19–34.

Silvestre, N., Camotim, D., Dinis, P.B. (2009), Direct strength prediction of lipped channel columns experiencing local-plate/distortional interaction, Advanced Steel Construction, 5(1):45–67.

Silvestre, N., Camotim, D., Dinis, P.B. (2012), Post-buckling behaviour and direct strength design of lipped channel columns experiencing local/distortional interaction, Journal of Constructional Steel Research, 73:12–30.

Yangm, D., Hancock, G.J. (2004), Compression tests of high strength steel columns with interaction between local and distortional buckling, Journal of Structural Engineering (ASCE), 130(12):1954–1963.

Young, B., Silvestre, N., Camotim, D. (2013), Cold-Formed steel lipped channel columns influenced by local-distortional interaction: strength and DSM design, Journal of Structural Engineering (ASCE), accepted for publication.

Research and Applications in Structural Engineering, Mechanics and Computation – Zingoni (Ed.)
© 2013 Taylor & Francis Group, London, ISBN 978-1-138-00061-2

Shear design of cold-formed steel beams using direct strength method

P. Keerthan & M. Mahendran
Queensland University of Technology, Brisbane, Queensland, Australia

ABSTRACT: This paper presents the Direct Strength Method (DSM) equations for cold-formed steel beams subject to shear. Light gauge cold-formed steel sections have been developed as more economical building solutions to the alternative heavier hot-rolled sections in the commercial and residential markets. Cold-formed Lipped Channel Beams (LCB), LiteSteel Beams (LSB) and Hollow Flange Beams (HFB) are commonly used as flexural members such as floor joists and bearers. However, their shear capacities are determined based on conservative design rules. For the shear design of cold-formed web panels, their elastic shear buckling strength must be determined accurately including the potential post-buckling strength. Currently the elastic shear buckling coefficients of web panels are determined by assuming conservatively that the web panels are simply supported at the junction between the flange and web elements and ignore the post-buckling strength. Hence experimental and numerical studies were conducted to investigate the shear behaviour and strength of LSBs, LCBs and HFBs. New Direct Strength Method (DSM) based design equations were proposed to determine the ultimate shear capacities of cold-formed steel beams. An improved equation for the higher elastic shear buckling coefficient of cold-formed steel beams was proposed based on finite element analysis results and included in the DSM design equations. A new post-buckling coefficient was also introduced in the DSM equation to include the available post-buckling strength of cold-formed steel beams.

1 INTRODUCTION

In recent times cold-formed steel members have become an increasingly integral part of the construction and building industries (see Figure 1). They have many advantages over other materials including their light weight, high strength, high quality, protection, cost-effective fabrication, accurate detailing, resistance, and non-combustibility. They are used in applications such as building frames, roof trusses, purlins and girts, floor framing and many other load bearing components.

In steel building systems, lipped channel beam (LCB), LiteSteel beam (LSB) (OATM, 2008), dogbone hollow flange beams (DHFB) and rectangular hollow flange beams (RHFB) are commonly used as flexural members, for example, floor joists, bearer and purlins. For these cold-formed steel beams to be used as flexural members, their flexural and shear capacities must be known. In this research the elastic shear buckling behaviour of such LCBs, LSBs, DHFBs and RHFBs was investigated using finite element analyses (FEA) including the effect of true support conditions at the junction between their flange and web elements. For comparison purposes, a plate girder (PG) was also considered in FEA. The results were then used to develop an equation for the elastic shear buckling coefficient of these beams and determine the corresponding ultimate shear capacity improvement based on the proposed shear capacity equations (Keerthan and Mahendran, 2010).

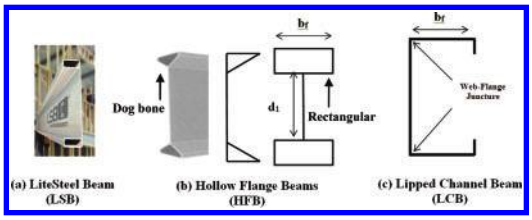


Figure 1. Hollow flange and open cold-formed steel members.

In the traditional shear design method of cold-formed steel beams, the web shear buckling performance is considered without the effect of flange rigidity. The shear strength of cold-formed steel lipped channel beams was studied by LaBoube and Yu (1978). They determined the ultimate strengths of LCBs by assuming that the web-flange juncture of LCBs was simply supported. Pham and Hancock (2009) investigated the elastic buckling behavior of unlipped and lipped channel section members subject to shear using an isoparametric spline finite strip method. They found that the flanges can have a significant influence on the shear buckling capacity of thin-walled channel sections and that lack of lateral restraint for sections with narrow flanges can lead to premature buckling of the section in a twisting and lateral buckling mode. However, they did not propose a simple equation to determine the shear buckling coefficients of lipped channel beams.

In this research, elastic buckling analyses were undertaken using suitable finite element models of LCBs, LSBs, DHFBs, RHFBs and plate girders (PG) developed based on ABAQUS. These finite element models included idealized simply supported boundary conditions and a shear flow based loading to prevent any torsional effect. Their shear buckling modes and shear buckling coefficients are presented in this paper. An improved equation for the higher elastic shear buckling coefficients of cold-formed steel beams was determined and included in the direct strength method (DSM) based design equations (Keerthan and Mahendran, 2010).

2 ELASTIC SHEAR BUCKLING ANALYSES OF HOLLOW FLANGE AND OPEN STEEL BEAMS

2.1 *Model Description*

This section presents the development of finite element models to investigate the shear behaviour of hollow flange (LSBs, DHFBs and RHFBs) and open (LCBs and PG) steel beams including their elastic shear buckling characteristics. For this purpose, a general purpose finite element program ABAQUS (HKS, 2007), which has the capability of undertaking geometric and material non-linear analyses of three dimensional structures, was used. Idealized simply supported boundary conditions were implemented in cold-formed steel beams under a three–point loading arrangement. Figure 2 shows the schematic diagram of the loading set-up used in this research. ABAQUS has several element types to simulate the shear behaviour of beams. But among those, shell element was selected for the ideal model as it has the capability to simulate the shear buckling behaviour of LiteSteel beams (LSB), lipped channel beams (LCB), dog bone hollow flange beams (DHFB), rectangular hollow flange beams (RHFB) and plate girders (PG). The shell element available in ABAQUS called S4R5 was used to model the shear behaviour of the chosen beams. This element is thin, shear flexible, isometric quadrilateral shell with four nodes and five degree of freedom per node, utilizing reduced integration and bilinear interpolation scheme. The finite element models were developed using their centreline dimensions based on the nominal external dimensions. Keerthan and Mahendran (2010) found that the effect of corners on the shear buckling behaviour of LiteSteel beam is negligible (less than 1%). Therefore in the finite element models used here, the corner radius was not included. Finite element models were created using MD PATRAN R 2.1 preprocessing facilities and then submitted to ABAQUS for the analysis. The results were also viewed using MD PATRAN R 2.1 post-processing facilities.

In the elastic buckling analyses undertaken in this study the elastic modulus (E) and Poisson's ratio (ν) were taken as 200,000 MPa and 0.3, respectively. To provide simply supported conditions for the shear

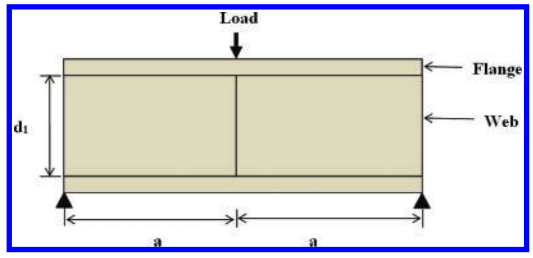


Figure 2. Schematic diagram of shear loading set-up (RHFB).

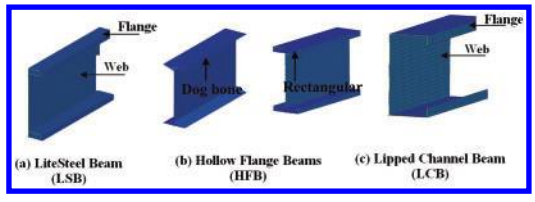


Figure 3. Geometry and finite element mesh of cold-formed steel beams.

panels of LSB, LCB, DHFB, RHFB and PG, simply supported boundary conditions were applied at the supports and the loading point (middle point).

Applied loading was based on the shear flows and forces in LCBs and LSBs to eliminate any torsional loading effects. The loading and boundary conditions used in the finite element model used in this research are similar to those used by Keerthan and Mahendran (2010, 2012) in their research on the shear buckling behaviour of LSBs and LCBs.

Figure 3 shows the geometry and finite element mesh of a cold-formed steel beam while Figure 4 shows the finite element models of LSB and plate girder (PG).

2.2 *Elastic Shear Buckling*

2.2.1 *General*

Timoshenko and Gere (1961) and Stein (1985) investigated the shear buckling stress of flat rectangular plates. Elastic shear buckling stress of a rectangular plate is given by Timoshenko and Gere (1961) as follows.

$$\tau_{cr} = \frac{k_v \pi^2 E}{12(1-\nu^2)}\left(\frac{t_w}{d_1}\right)^2 \quad (1)$$

where

d_1, t_w = Clear height and thickness of web

k_v = Shear buckling coefficient (5.34)

The shear buckling coefficient (k_v) of a plate simply supported on all four edges varies from 5.34 for a very long plate to 9.34 for a square plate. For a web element with a large depth to thickness ratio, its shear capacity is governed by its elastic shear buckling stress. The elastic critical shear buckling stress can be computed

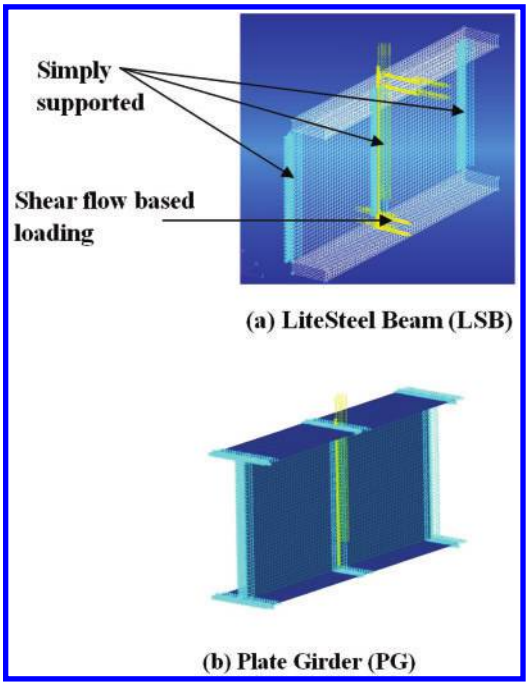


Figure 4. Ideal finite element models of steel beams.

using Equation 1 if the relevant elastic shear buckling coefficient (k_v) is known.

In the early days the web-flange juncture of cold-formed steel beams was assumed as simply supported due to lack of means to evaluate it in a rational manner. Basler (1961) assumed that the web panel of plate girders was simply supported at the web-flange juncture while LaBoube and Yu (1978) also assumed that the web panel of lipped channel beam was simply supported at the web-flange juncture. Recent research by Lee et al. (1996) has shown that the boundary condition at the flange-web juncture in practical designs is much closer to fixity for plate girders. They showed that the assumption that the web panel is simply supported at the web-flange juncture leads to a significant underestimation of the ultimate shear strength because of the underestimation of the elastic shear buckling strength of plate girders. Keerthan and Mahendran (2010) have also shown that the boundary condition at the flange-web juncture of LiteSteel beams is much closer to a fixed condition.

Keerthan and Mahendran (2010 and 2012) proposed the following simple equations based on FEA results for the determination of shear buckling coefficients of LiteSteel beams (k_{LSB}) and lipped channel beam (k_{LCB}) in terms of the shear buckling coefficients of web plates with simple-simple (k_{ss}) and simple-fixed (k_{sf}) boundary conditions. The latter case refers to web panels that have fixed conditions at the web-flange juncture and simply supported along the other two edges.

$$k_{LCB} = k_{ss} + 0.23(k_{sf} - k_{ss}) \quad (2)$$

Table 1. Comparison of shear buckling coefficients of dogbone hollow flange beams (DHFB) (Aspect ratio = 1.0 & $t_f/t_w = 1$).

No.	Section	Type	t_w	k_v
1	150 × 90 × 15 × 1.6 × 1.6	Symmetric	1.6	12.58
2	150 × 90 × 15 × 2.0 × 2.0	Symmetric	2.0	12.58
3	200 × 90 × 15 × 1.6 × 1.6	Symmetric	1.6	12.30
4	300 × 120 × 20 × 2.0 × 2.0	Symmetric	2.0	12.53
5	300 × 120 × 20 × 2.5 × 2.5	Symmetric	2.5	12.49
6	300 × 120 × 20 × 3.0 × 3.0	Symmetric	3.0	12.45
7	150 × 45 × 15 × 1.6 × 1.6	Mono Symmetric	1.6	12.57
8	150 × 45 × 15 × 2.0 × 2.0	Mono Symmetric	2.0	12.58
9	200 × 45 × 15 × 1.6 × 1.6	Mono Symmetric	1.6	12.22
10	200 × 45 × 15 × 2.0 × 2.0	Mono Symmetric	2.0	12.23

Note: $k_{ss} = 9.34$ and $k_{sf} = 12.60$ for aspect ratio of 1.0.

$$k_{LSB} = k_{ss} + 0.87(k_{sf} - k_{ss}) \quad (3)$$

$$k_{ss} = 4 + \frac{5.34}{(a/d_1)^2} \qquad \frac{a}{d_1} < 1 \quad (4a)$$

$$k_{ss} = 5.34 + \frac{4}{(a/d_1)^2} \qquad \frac{a}{d_1} \geq 1 \quad (4b)$$

$$k_{sf} = \frac{5.34}{(a/d_1)^2} + \frac{2.31}{(a/d_1)} - 3.44 + 8.39(a/d_1) \qquad \frac{a}{d_1} < 1 \quad (5a)$$

$$k_{sf} = 8.98 + \frac{5.61}{(a/d^1)^2} - \frac{1.99}{(a/d_1)^3} \qquad \frac{a}{d_1} \geq 1 \quad (5b)$$

where a = Shear span of web panel, d_1 = Clear web height and a/d_1 = Aspect ratio.

Equation 2 shows that the shear buckling coefficient of Lipped Channel beams (k_{LCB}) is closer to k_{ss} while Equation 3 shows that the shear buckling coefficient of LiteSteel beams (k_{LSB}) is closer to k_{sf}. Hence the realistic support condition of LCB at the web-flange juncture is considered to be closer to a simply supported condition while realistic support condition of LSB at the web-flange juncture is considered to be closer to a fixed supported condition.

2.2.2 *Elastic Buckling Analyses*

In order to obtain the shear buckling coefficients of both hollow flange and open steel beams, elastic buckling analyses were conducted based on the developed finite element models of DHFB, RHFB and PG with an aspect ratio (a/d_1) of 1.0 (see Figure 4). S4R5 shell elements were used with a suitable mesh size of 5 mm × 5 mm for the entire cross-section and length of steel beam sections. ABAQUS uses the subspace iteration Eigenslover in its buckling analyses. In the buckling analysis, four buckling mode shapes were considered.

Figures 5 (a) to (d) show the typical shear buckling modes of LSB, LCB, DHFB, RHFB and PG. In all the analyses here, a flange width (b_f) to clear web height (d_1) ratio more than 0.4 was used. This is because most

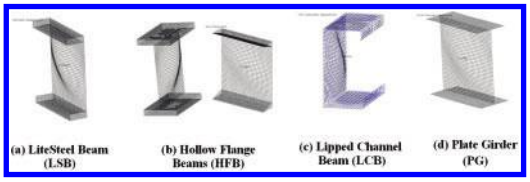


Figure 5. Shear buckling modes of steel beams (Aspect Ratio = 1.0).

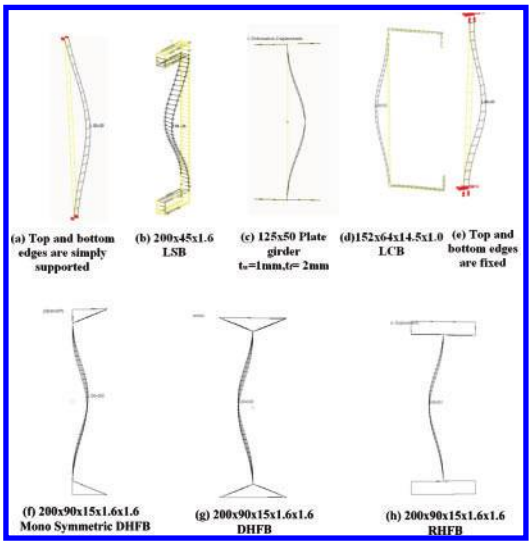


Figure 6. Shear buckling shapes (Aspect ratio = 1.0).

of the available steel sections have a b_f/d_1 ratio greater than about 0.4. Table 1 compares the shear buckling coefficients (k_v) determined from the elastic buckling analyses of dogbone hollow flange beam (DHFB) for an aspect ratio of 1.0. The web and flange thicknesses were assumed to be the same for DHFBs. The reference buckling coefficients, k_{ss} and k_{sf}, were determined by using Equations 4 and 5, respectively. Table 1 indicates that k_{DHFB} is close to k_{sf} (12.60). Hence the realistic support condition of DHFB at the web-flange juncture is considered to be closer to a fixed supported condition. Since k_{DHFB} is close to k_{sf} (12.60) with even a t_f/t_w ratio (ratio of flange to web thickness) of 1, higher t_f/t_w ratios were not considered in the analyses of DHFBs. Similar observation was also made for LSBs for which also a t_f/t_w ratio of 1 was used.

Keerthan and Mahendran (2010 and 2012) investigated the shear buckling behaviour of LSBs and LCBs using numerical studies. Shear buckling coefficient of LSBs and LCBs are given in Keerthan and Mahendran (2010 and 2012).

Figures 6 (a) to (h) show typical deformed cross-sections of buckled LSB, DHFB, RHFB, PG and LCB. This can be compared with the deformation shapes of plates with simply supported and fixed edges as shown in Figures 6 (a) and (e), respectively. This observation shows that the boundary condition at the web-flange juncture of LCBs is close to a simply supported condition while that of LSB, DHFB, RHFB and plate girder ($t_f/t_w > 2$) at the web-flange juncture is considered to be closer to a fixed supported condition.

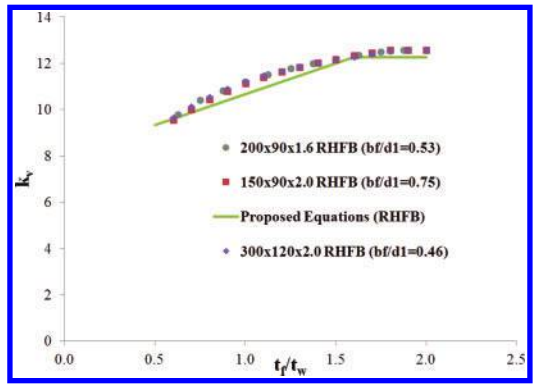


Figure 7. Shear buckling coefficients of rectangular hollow flange beams (RHFB) (Aspect ratio = 1.0).

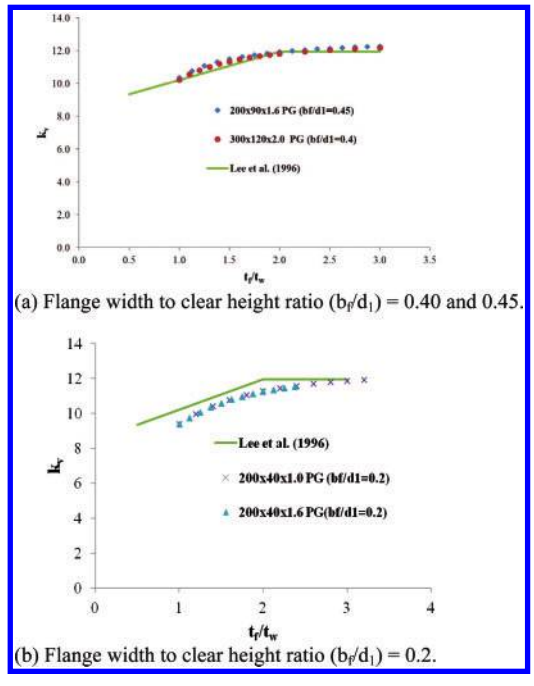


Figure 8. Shear buckling coefficients of plate girders (Aspect ratio = 1.0, Flange width to clear height ratio (b_f/d_1) = 0.20, 0.40 and 0.45.

Unlike for LCBs, LSBs and DHFBs, the effect of t_f/t_w ratio was investigated. Figure 7 shows that the elastic shear buckling coefficient of RHFB rapidly increases when this ratio increases up to 1.6. However, it did not increase much after it has exceeded 1.6. Hence it can be concluded that t_f/t_w ratio should be increased to 1.6 in order to gain about 90% fixity level for RHFBs.

Figure 8 shows that the elastic shear buckling coefficient of plate girders rapidly increases when the t_f/t_w

Table 2. Coefficient of k_n for hollow flange and open steel beams.

Section	k_n
Plate Girder (PG)	$0.8\left(1-\frac{2}{3}(2-\frac{t_f}{t_w})\right)$ $0.5<\frac{t_f}{t_w}<2.0$ $\frac{b_f}{d_1}>0.4$
Plate Girder (PG)	0.8 $\frac{t_f}{t_w}\geq 2.0$ $\frac{b_f}{d_1}>0.4$
Rectangular Hollow Flange Beam (RHFB)	$\left(0.82\frac{t_f}{t_w}-0.41\right)$ $0.5<\frac{t_f}{t_w}<1.6$ $\frac{b_f}{d_1}>0.4$
Rectangular Hollow Flange Beam (RHFB)	0.90 $\frac{t_f}{t_w}\geq 1.6$ $\frac{b_f}{d_1}>0.4$
Lipped Channel Beam (LCB)	0.23
LiteSteel Beam (LSB)	0.87
Dog Bone Hollow Flange Beam DHFB (Symmetric and Mono Symmetric)	0.90

ratio increases up to 2.0. However, it did not increase much after it has exceeded 2.0. Hence it can be concluded that the t_f/t_w ratio should be increased to 2.0 in order to gain about 80% fixity level for plate girders. Figure 8 (a) shows that the shear buckling coefficients of plate girders were similar to Lee et al.'s (1996) findings when the flange width to clear height ratio (b_f/d_1) exceeded 0.4. However, the shear buckling coefficients of plate girders were slightly different to Lee et al.'s (1996) values when the flange width to clear height ratio (b_f/d_1) was less than 0.4 (see Figure 8 (b)).

2.2.3 *Shear Buckling Coefficients*

Based on the elastic buckling analysis results, the following simple equation (Equation 6) was developed for the determination of the elastic shear buckling coefficients of both hollow flange and open steel beams. For this purpose the minimum shear buckling coefficient of LCB, LSB, DHFB, RHFB and PG from finite element analyses were used. Shear buckling coefficient equations included the effect of flange thickness to web thickness ratio (t_f/t_w) for rectangular hollow flange beams (RHFB) and plate girders (PG). The values of k_{ss} and k_{sf} for a given aspect ratio were determined from Equations 4 and 5, respectively.

$$k_v = k_{ss} + k_n(k_{sf} - k_{ss}) \tag{6}$$

where

k_v = Shear buckling coefficient of cold-formed steel beam and k_{ss}, k_{sf} = Shear buckling coefficients of plates with simple-simple and simple-fixed boundary conditions.

k_n can be obtained from Table 2 (k_n depends on the type of steel beam section).

The proposed shear buckling coefficient equation for steel beams (Equation 6) shows that the boundary condition at the flange-web juncture of LCBs is equivalent to 23% fixed condition while it shows that boundary condition at the flange-web juncture of LSBs is equivalent to 87% fixed condition. Since the level of fixity at the web-flange juncture of hollow flange and open steel beam is the same for the available steel beams, Equation 6 is applicable for all the aspect ratios. It was found that clear height to thickness ratio (d_1/t_w) does not affect the buckling coefficient of steel beams.

3 DIRECT STREGTH METHOD (DSM)

The direct strength method provides simple design procedures to determine the ultimate capacities of cold-formed steel members. Following the elastic buckling analyses and the resulting elastic buckling coefficients for the chosen hollow flange and open beams, new direct strength method equations (Equations 7 to 12) were proposed for the ultimate shear capacities of these hollow flange and open cold-formed steel beams. These equations include the accurate shear buckling coefficient that takes into account the effects of web-flange fixity. The slenderness was calculated using Equation 12.

A new post-buckling coefficient (p_n) was also introduced in the DSM equations to include the available post-buckling strength of cold-formed steel beams.

$$\frac{V_v}{V_{yw}} = 1 \qquad \lambda \leq 0.815 \tag{7}$$

$$\frac{V_v}{V_{yw}} = \frac{0.815}{\lambda} + p_n\left(1-\frac{0.815}{\lambda}\right) \qquad 0.815 < \lambda \leq 1.23 \tag{8}$$

$$\frac{V_v}{V_{yw}} = \frac{1}{\lambda^2} + p_n\left(1-\frac{1}{\lambda^2}\right) \qquad \lambda > 1.23 \tag{9}$$

where

$$V_{yw} = 0.6 f_{yw} d_1 t_w \tag{10}$$

$$V_{cr} = \frac{k_v \pi^2 E}{12(1-\nu^2)}\left(\frac{t_w}{d_1}\right)^2 d_1 t_w \tag{11}$$

$$\lambda = \sqrt{\left(\frac{V_{yw}}{V_{cr}}\right)} = 0.815\left(\frac{d_1}{t_w}\right)\sqrt{\left(\frac{f_{yw}}{E k_v}\right)} \tag{12}$$

p_n = post-buckling coefficient, For LSB, DHFB, RHFB, p_n = 0.25 and For LCB, p_n = 0.2.

Figure 9 compares the shear design curve based on the proposed DSM based shear strength equations with FEA and available experimental results of LCBs and LSBs. Both experimental and numerical analyses show that there is considerable amount of post-buckling strength for LSBs and LCBs subjected to shear, in particular for LSBs and LCBs with large clear web height to thickness (d_1/t_w) ratios. Hence post-buckling shear strength can be taken into account in the design of LSBs, LCBs, DHFB, RHFB and other cold-formed steel beams. It is clear from Figure 9 that the new shear strength equations (Eqs. 7 to 9) that include post-buckling are able to predict the shear strengths of LSBs and LCBs more accurately. Keerthan and Mahendran (2010 and 2012) found that

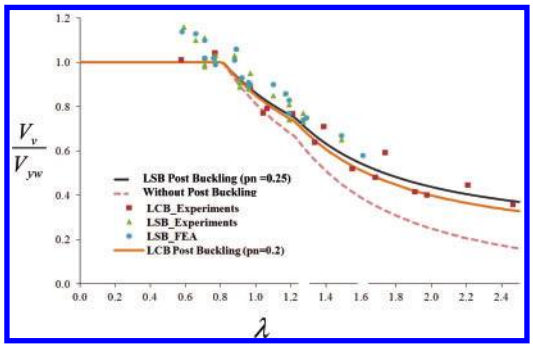


Figure 9. Comparison of shear strengths of LSBs and LCBs with DSM based design equations.

post-buckling coefficients (p_n) of LSBs and LCBs are 0.25 and 0.20, respectively based on their test and FEA results. Since the level of fixity at the web-flange juncture is the same for LSBs (87%), DHFBs (90%), and RHFBs (90%), the same post-buckling coefficient (p_n) of 0.25 can be used for LSBs, DHFBs and RHFBs.

The ultimate shear capacities of LCB, LSB, DHFB and RHFB predicted by the current design rules are very conservative as the potential post-buckling strength has also not been included while also assuming that web panels are simply supported at the web-flange juncture.

This research has shown that the currently available design guidelines in AISI (2007) and AS/NZS 4600 (SA, 2005) for the shear capacity of LCBs, LSBs, DHFBs and RHFBs can be modified to take into the effect of web to flange fixity and post-buckling strength.

4 CONCLUSIONS

This paper has presented the details of an investigation into the shear behavior and strength of hollow flange and open steel beams. Numerical analyses were conducted to investigate the shear buckling behaviour of different hollow flange (LSBs, DHFBs and RHFBs) and open (LCBs and PGs) steel beams. Currently the elastic shear buckling coefficients and strengths of web panels are determined by assuming conservatively that the web panels are simply supported at the web-flange juncture. However, it was found that the web-flange juncture in LSB, DHFB, RHFB and plate girder (PG) has some fixity. A simple equation was therefore proposed for the higher elastic shear buckling coefficient of steel beams based on finite element analysis results, and was included in the proposed ultimate shear capacity equations. The presence of post-buckling strength was also included in the proposed equations and hence they were able to predict the ultimate shear capacities of hollow flange and open cold-formed steel beams more accurately than the current design rules.

ACKNOWLEDGEMENTS

The authors would like to thank Australian Research Council for their financial support and Queensland University of Technology for providing the necessary facilities and support to conduct this research.

REFERENCES

American Iron and Steel Institute (AISI) 2007. North American specification for the design of cold-formed steel structural members. AISI, Wash-ington, DC, USA.

Basler, K. 1961. Strength of plate girders in shear. *Journal of Structural Division*, ASCE Proceedings, 87: 151–181.

OneSteel Australian Tube Mills 2008). (OATM), LiteSteel Beam publication. Brisbane, Australia.

LaBoube, R.A. and Yu, W.W. 1978. Cold-formed steel beam webs subjected primarily to shear. *Research Report*, American Iron and Steel Institute, University of Missouri-Rolla, Rolla, USA.

Lee, S.C., Davidson, J.S. and Yoo, C. 1996. Shear buckling coefficients of plate girder web panels. J*ournal of Computers and Structures*, 59: 789–795.

Keerthan, P. and Mahendran, M. 2010. Elastic shear buckling characteristics of LiteSteel Beams. *Journal of Constructional Steel Research*, 66: 1309–1319.

Keerthan, P. and Mahendran, M. 2012. Shear buckling characteristics of cold-formed steel channel beams. *International Journal of Steel Structures*. Accepted.

Hibbitt, Karlsson and Sorensen, Inc. (HKS) 2007. ABAQUS user's manual. Inc., New York, USA.

Pham, C.H. and Hancock, G.J. 2009. Shear buckling of thin-walled channel sections. *Journal of Constructional Steel Research*, 65: 578–585.

Standards Australia/Standards New Zealand (SA) 2005. Australia/New Zealand Standard AS/NZS4600 Cold-formed steel structures. Sydney, Australia.

Stein M. 1985. Analytical results for post-buckling behaviour of plates in compression and in shear. Clarendon Press, Oxford, England.

Timoshenko, S. P. and Gere, J.M. 1961. Theory of elastic stability. McGraw- Hill Book Co. Inc, New York (NY).

Research and Applications in Structural Engineering, Mechanics and Computation – Zingoni (Ed.)
© 2013 Taylor & Francis Group, London, ISBN 978-1-138-00061-2

Influence of cross-section geometry on the distortional post-buckling strength of cold-formed steel columns

A. Landesmann
Civil Engineering Program, COPPE, Federal University of Rio de Janeiro, Brazil

D. Camotim
Civil Engineering Department, ICIST, Instituto Superior Técnico, Technical University of Lisbon, Portugal

C. Basaglia
Structural Engineering Department, São Carlos School of Engineering, University of São Paulo, Brazil

ABSTRACT: This paper reports the available results of an ongoing numerical research effort and whose final goal is to assess and mechanically interpret the influence of the cross-section geometry and end support conditions on the elastic distortional post-buckling behavior and strength of cold-formed steel columns. This work deals only with simply supported columns exhibiting lipped channel, hat and zed cross-sections, which share common critical distortional buckling loads. Taking advantage of the GBT modal decomposition features, the buckling analyses are used to mechanically characterize the various column critical bucking modes. The paper presents and discusses results concerning the elastic post-critical strength of the selected column triplets, obtained from Ansys shell finite element analysis. The post-critical strength data are used to attempt identifying key parameters, in the sense that they play a pivotal role in influencing the features exhibited by the column distortional post-buckling behavior and strength.

1 INTRODUCTION

In the course of a numerical investigation on the Direct Strength Method (DSM) design, against distortional failures, of pin-ended and fixed-ended lipped channel and rack-section columns, the authors (Landesmann & Camotim 2010) literally "stumbled" on a rather unexpected finding: the current DSM design curve clearly overestimated the column ultimate strength *at room temperature* (this did not happen at all for the fixed-ended columns). This finding prompted an investigation on how the column end support condition influenced the quality of the DSM prediction of their distortional failure loads (Landesmann & Camotim 2011, 2013) – this involved (i) four end support conditions (fixed, fixed-pinned, pinned and fixed-free end sections), (ii) four cross-section shapes (lipped channels, hats, zeds and racks), (iii) a few (six or seven) mid-line dimensions per cross-section shape, selected to ensure pure buckling and failure modes, and (iv) various yield stresses, selected in order to cover a wide distortional slenderness range. The chief conclusion of the above investigation consisted of the fact that, regardless of the cross-section shape, the current DSM distortional strength curve only predicts adequately the ultimate strength of fixed columns – all the remaining column ultimate strengths were found to be more or less overestimated, a surprising feature that was (rightly) attributed to the relevant stiffening role played by the end cross-section wall bending and (mostly) warping fixity. However, another behavioral feature emerged from the this study: the wide variety of elastic post-buckling behaviors exhibited by the columns analyzed, even amongst those sharing the same cross-section shape and end support conditions – this led the authors to "pledge" that they would investigate this issue in the near future. The fulfillment of this "promise" provided the motivation for the research effort currently under way (Landesmann *et al.* 2013) and whose first fruits are reported in this paper.

The objective of this paper is two-fold. First of all, to identify and mechanically characterize a significant number of simply supported (pinned end sections that can warp freely) columns exhibiting lipped channel, zed and hat cross-sections and buckling in "pure" distortional modes, in the sense that their critical distortional buckling loads are well below their local and global counterparts, thus precluding the occurrence of relevant mode interaction effects, *i.e.*, ensuring "truly distortional" post-buckling behaviors. Taking advantage of the fact that lipped channel, hat-section and zed-section columns share the same distortional (and local) buckling behavior, each set of cross-section dimensions and length identified defines a column triplet that is eligible for the present investigation. Then, the paper addresses the elastic (distortional) post-buckling behavior and strength of the various columns identified: a representative sample of the corresponding non-linear equilibrium paths are presented, analyzed, compared and, whenever possible,

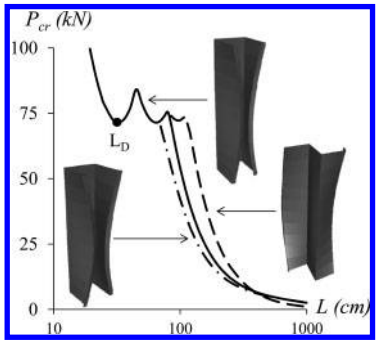


Figure 1. Curves P_{cr} vs. L concerning C-H-Z 60(6) columns with the indication of the selected lengths (L_D) and associated distortional buckling mode shapes.

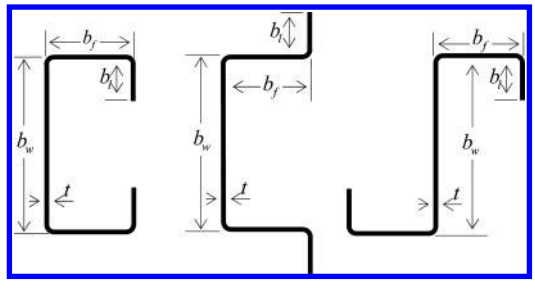
related to the buckling mode mechanical characteristics determined previously. The goal is to make an attempt to pin down key parameters (*e.g.*, cross-section dimension ratios or critical buckling mode mechanical characteristics), in the sense that they play a pivotal role in influencing the features exhibited by the column distortional post-buckling behavior and strength.

2 COLUMN GEOMETRY SELECTION

The first step consists of selecting the cross-section dimensions and lengths of the simply supported lipped channel (C), hat-section (H) and zed-section (Z) columns to be analyzed. At this stage, recall that the end cross-sections of such columns exhibit (i) null in-plane local/global displacements and torsional rotations, and (ii) free local/global rotations and warping displacements. The selection procedure involved time-consuming sequences of "trial-and-error" buckling analyses, performed with the GBT-based code GBTUL (Bebiano *et al.* 2008ab) and aimed at satisfying the following requirements: (i) columns buckling in "pure" symmetric distortional modes, this goal is achieved by ensuring, as much as possible, that the critical buckling stress (i_1) is clearly distortional and (i_2) falls considerably below the lowest local and global bifurcation stresses, (ii) cross-section dimensions not "too extreme" and involving wall proportions (*e.g.*, the web-to-flange width ratio b_w/b_f ratio) covering ranges as wide as possible and, (iii) columns lengths (iii_1) corresponding to single half-wave buckling modes and (iii_2) as close as possible to the values associated with the minimum distortional critical buckling stress, as illustrated in Figure 1 for the columns C-H-Z 60(6). Fortunately, it was possible to fulfill all the above requirements and the end product of the "trial-and-error" selection procedure are the 44 column triplets (Cs, Hs and Zs) with identical cross-section dimensions and distortional buckling lengths L_D – they are given in Table 1, where it is worth noting that (i) the columns are ordered according to the web width b_w (indicated with parenthesis) (ii) several columns share

Table 1. Column cross-section dimensions, lengths, distortional loads and elastic post-critical strengths (P_{10t}).

Cross-section (C-H-Z) $b_w/b_l/t/L_D$ *(mm)*	P_{cr} *(kN)*	P_{10t}/P_{cr} *C*	*H*	*Z*
60(1)/60/5/1.5/300	52.04	1.20	1.11	1.11
60(2)/60/5.75/1.5/300	55.48	1.17	1.08	1.10
60(3)/60/6.5/1.5/300	59.89	1.13	1.05	1.08
60(4)/60/7.25/1.5/300	65.29	1.10	1.02	1.06
60(5)/60/8/1.4/300	62.14	1.05	0.99	1.03
60(6)/60/8/1.5/300	71.68	1.06	1.00	1.21
60(7)/60/8/1.5/300	71.68	1.07	1.00	1.04
60(8)/60/8/1.6/300	82.26	1.09	1.01	1.04
60(9)/60/8/1.8/300	106.78	1.12	1.03	1.05
60(10)/60/8/2/300	136.24	1.14	1.04	1.04
60(11)/60/8/2.2/300	171.16	1.16	1.04	1.02
75/75/10/1.875/390	111.32	1.05	0.99	1.23
80(1)/40/10/2.5/260	362.16	1.43	0.88	1.13
80(2)/45/10/2.4/260	304.91	1.36	0.94	1.20
80(3)/50/10/2/310	187.64	1.20	0.92	1.13
80(4)/55/10/1.8/340	137.14	1.12	0.93	1.08
80(5)/60/10/1.7/370	111.76	1.07	0.93	1.05
80(6)/62/8/2/300	129.96	1.21	1.05	1.32
80(7)/65/10/1.6/400	90.61	1.04	0.94	1.03
80(8)/70/10/1.5/440	73.10	1.02	0.94	1.01
90/70/9.3/2.25/350	168.15	1.18	1.03	1.30
100/50/6.7/2.5/250	234.69	1.65	1.20	1.47
110(1)/55/10/3/280	408.01	1.59	1.10	1.36
110(2)/60/8/2.75/300	277.69	1.53	1.14	1.43
110(3)/60/10/2.8/310	328.03	1.46	1.06	1.36
110(4)/70/10/2.6/360	243.66	1.29	1.03	1.34
110(5)/75/10/2.4/380	189.84	1.23	1.03	1.33
110(6)/80/10/2.2/410	146.14	1.17	1.01	1.29
110(7)/85/10/2/450	110.76	1.11	1.00	1.26
110(8)/90/10/1.8/490	82.39	1.07	0.98	1.42
116/72.5/9.7/2.9/340	295.58	1.38	1.11	1.40
118/64.3/8.6/2.95/290	314.76	1.59	1.22	1.49
120(1)/75/5/2/270	76.12	1.63	1.45	1.70
120(2)/75/5/3/240	217.57	1.81	1.58	1.75
120(3)/75/5/4/220	470.60	1.77	1.63	1.74
120(4)/75/10/2/420	123.96	1.18	0.99	1.29
120(5)/75/10/3/350	315.54	1.39	1.11	1.40
120(6)/75/10/4/300	626.45	1.48	1.24	1.38
120(7)/75/20/3/570	517.35	1.12	0.86	1.08
130/65/8.7/3.25/280	386.75	1.74	1.33	1.56
140/100/10/3/430	233.89	1.34	1.15	1.45
150/80/10/3/380	284.62	1.54	1.18	1.52
160/95/10/3/430	243.10	1.43	1.18	1.51
170/100/15/3.5/540	441.13	1.28	1.00	1.34
180/95/15/4.2/480	688.30	1.50	1.09	1.42



the same b_w value and (iii) the b_w/b_f, b_w/t and b_f/b_l ratios range from 1.0 to 2.0,27.3 to 61.1 and 3.8 to 15, respectively. Table 1 also provides the (i) critical (distortional) buckling load $P_{cr.D} \equiv P_{cr}$, all obtained for $E = 210\ GPa$ (Young's modulus) and $\nu = 0.3$ (Poisson's ratio), and (ii) elastic post-critical strengthP_{10t} (this will be specifically addressed ahead in the paper).

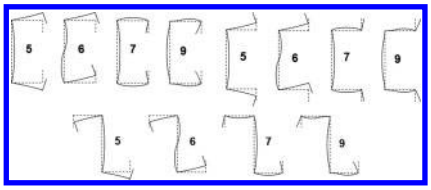


Figure 2. Configurations of the C-H-Z 110(5) column GBT deformation modes (i) **5** (symmetric distortional), (ii) **6** (anti-symmetric distortional) and (iii) **7** + **9** (web-triggered local).

3 BUCKLING MODE MECHANICAL CHARACTERIZATION

This section addresses the mechanical characterization of the critical buckling modes of the selected column triplets – the objective is to assess and quantify the natures of the deformations involved in the various column critical distortional buckling modes. This is straightforwardly done by means of GBT, taking advantage of (i) its rather unique modal features and (ii) the fact that the selected column geometries were obtained from buckling analyses carried out in the code GBTUL, which automatically provides the GBT modal decomposition of the column buckling modes (*e.g.*, Silvestre & Camotim 2002ab, Camotim *et al.* 2004, Dinis *et al.* 2006). Figure 2 displays the in-plane configurations of the C-H-Z 110(5) column GBT deformation modes that are most relevant for the present investigation, namely the (i) symmetric (**5**) and anti-symmetric (**6**) distortional modes, and (ii) two local (**7** and **9**) modes – all the remaining columns exhibit qualitatively similar deformation modes.

Figure 3 illustrates the buckled mid-span cross-section of the C 110(5) column, providing the typical contributions (percentage participation) of the GBT deformation modes (modal decomposition) to the critical buckling mode. The following conclusions can be drawn from the observation of obtained results:

(i) All critical buckling modes combine a highly dominant participation from symmetric distortion (p_5) with minor (but non negligible) contributions from web-triggered local deformations (p_7 and p_9) – p_n stands for the percentage participation of GBT deformation mode n. While the former varies in the ranges *86.0–95.4* (Cs), *87.0–97.0* (Hs) and *86.4–93.6* (Zs), the joint contribution of the latter (p_{7+9}) amounts to *3.5–12.9* (Cs), *4.3–12.2* (Hs) and 3.6 – 13.1 (Zs) – results are summarized in Landesmann *et al.* (2013). The participation of the other deformation modes never exceeds *4.5%* and is below *1.0%* in most cases.

(ii) Figure 4, which plots p_5, p_7 and p_9 against the b_w/b_f ratio for lipped channel column (which are also typical for H and Z sections), shows that there are clear (and opposite) trends concerning the variation of both p_5 and p_7 withb_w/b_f. Indeed, it is observed that p_5 (p_7) decreases (increases) as b_w/b_f grows a bit more than linearly (almost parabolic variation), which probably stems from the higher vulnerability of wider webs to local deformations. Conversely, no tendency is detected in the p_9 vs. b_w/b_f plot.

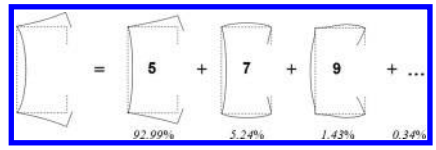


Figure 3. Illustrative GBT modal decomposition: distortionally buckled mid-span cross-section of the C 110(5) column.

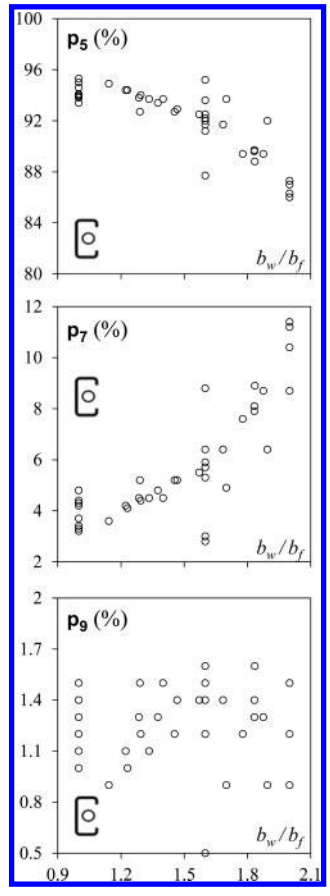


Figure 4. Variation of p_5, p_7 and p_9 with b_w/b_f for Cs columns.

4 ELASTIC POST-BUCKLING BEHAVIOR AND STRENGTH

4.1 *Numerical Model*

The column distortional post-buckling equilibrium paths were determined through geometrically nonlinear SFEA carried out in the code ANSYS (SAS 2009). The columns were discretized into SHELL181 elements (4-node shear deformable thin-shell elements with six degrees of freedom per node and full integration) – previous convergence studies showed that *5 mm* × *5 mm*

meshes provide quite accurate results, even if at the cost of a fairly high computational effort. The analyses were performed by means of an incremental-iterative technique combining Newton-Raphson's method with an arc-length control strategy. All columns exhibited (i) a linear elastic material behavior ($E = 210\,GPa$ and $\nu = 0.3$) and (ii) critical-mode (distortional) initial geometrical imperfections with small amplitudes (*10%* of the wall thickness t). Their incorporation in the columns was made automatically by means of the following procedure (*e.g.*, Dinis & Camotim 2013): (i) determination of the critical buckling mode shape, through an ANSYS SFE buckling analysis adopting exactly the same discretization/mesh employed to carry out the subsequent post-buckling analysis, which was then (ii) scaled to exhibit maximum vertical displacements along the flange-stiffener longitudinal edges equal to $0.1t$ – this buckling analysis output is then "transformed" into an input of the non-linear analysis. Following the column distortional post-buckling asymmetry first unveiled by Prola & Camotim (2002) and later also studied by Silvestre & Camotim (2006), these initial imperfections involve outward (Cs) and inward (Hs) flange-stiffener motions (those shown to lead to the lower post-buckling strengths) – obviously, this distinction makes no sense in the Z columns, since their flange-stiffener motions are always opposite (one outward and the other inward).

Concerning the modeling of the end support conditions, the membrane and bending transverse displacements were prevented at all end section nodes, while keeping the axial (warping) displacements and all the bending rotations free. To enable the load application, the rigid-body axial translation is free at both end sections – the axial compression is applied by means of a set of point loads acting on both end section nodes and increased in small increments, through the ANSYS automatic load stepping procedure.

4.2 *Results and Discussion*

These results presented and discussed consist of elastic post-buckling equilibrium paths that are then used to make a comparative assessment of the post-critical strength exhibited by the various columns. In order to illustrate the results obtained and also address the qualitative and quantitative assessment of how the column elastic distortional post-critical strength is influenced by the cross-section shape and dimensions, Figure 6 depicts the equilibrium paths of the C-H-Z 60(6) and C-H-Z 100 columns, plotting the applied load P, normalized w.r.t. P_{cr}, against $|\delta|/t$, where $|\delta|$ is the absolute value of the mid-span (maximum) flange-stiffener corner vertical displacement and t is the wall thickness (note that in the Z-section columns, $|\delta|$ always concern the flange-stiffener moving inwards). In order to achieve a more rational and meaningful comparison between the various equilibrium paths and post-critical strengths, it was decided to focus on strength values associated with $|\delta|/t = 10$, hereafter designated as P_{10t} and corresponding to the black dots drawn on the P/P_{cr} *vs.*$|\delta|/t$ curves in Figure 6.

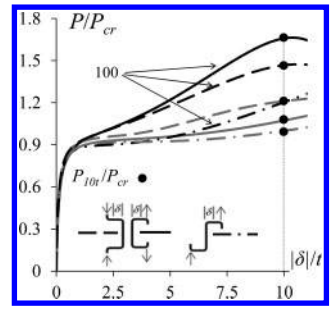


Figure 5. Elastic post-buckling equilibrium paths P/P_{cr} *vs.*$|\delta|/t$ concerning the C-H-Z 60(6)/100 columns.

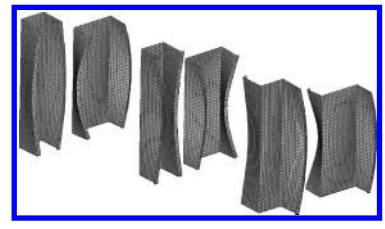


Figure 6. Post-buckling deformed configurations at $P = P_{10t}$ concerning the C-H-Z 60(6)/100 columns.

Finally, Figure 7(a) depicts the C-H-Z 60(6)/100 column deformed configurations occurring for P_{10t} on each equilibrium path displayed in Figure 6.

In order to assess the variation of P_{10t} with the columns cross-section shape and dimension concerning, Figure 8 plots P_{10t}/P_{cr} against b_w/b_f, b_w/t and b_f/b_l concerning the lipped channel columns. The close observation of the results presented in Table 1 and Figs 6 to 8 prompts the following remarks:

(i) First of all, it is worth recalling the quite visible differences between the elastic equilibrium paths P/P_{cr} *vs.*$|\delta|/t$ displayed Figure 6: the 100 columns ($b_w/b_f = 2$) exhibit considerably higher post-critical strengths than their 60(6) counterparts ($b_w/b_f = 1$).

(ii) Regardless the cross-section dimensions, the lipped channel and zed-section columns exhibit higher post-critical strengths than their hat-section counterparts (this difference is clearly visible in Figure 5).

(iii) Figure 8(a) shows that there is substantial scatter in the plots showing the variation of P_{10t}/P_{cr} with b_w/b_f, b_w/t and b_f/b_l. Indeed, these values vary between (iii_1)1.02 and 1.81 (Cs), (iii_2)0.86 and 1.63 (Hs), and (iii_3)1.01 and 1.75 (Zs) – these values confirm the assertion made in the previous item (full results are given in Landesmann *et al.*, 2013).

(iv) The comparison between the plots in Figure 8(a) provides clear evidence that, unlike their b_w/t and b_f/b_l counterparts, the b_w/b_f ratios show some correlation with the normalized column post-critical strengths P_{10t}/P_{cr}. In fact, it is observed that P_{10t}/P_{cr} generally increases with b_w/b_f.

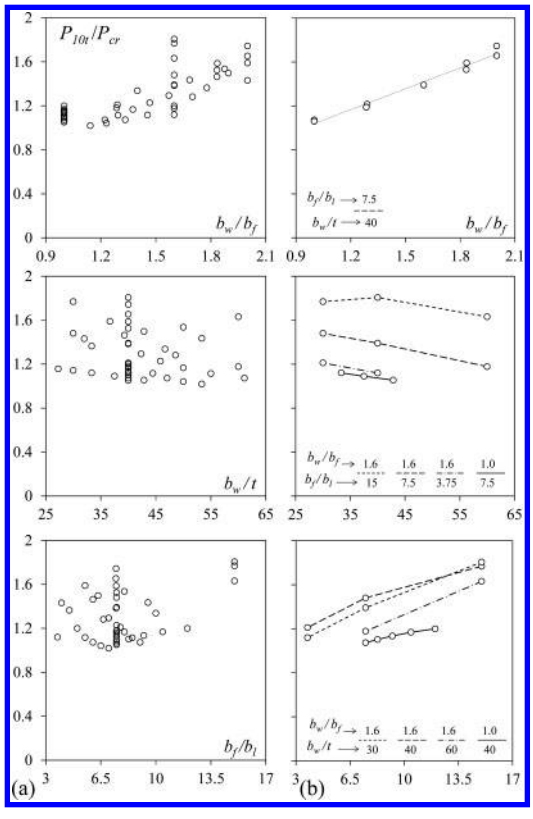


Figure 7. Variation of P_{10t}/P_{cr} with: (a) b_w/b_f, b_w/t and b_f/b_l and (b) each individual width ratio b_w/b_f, b_w/t and b_f/b_l (the remaining two are kept constant), concerning the lipped channel columns.

(v) Since the C 60(1-10) and 120(1-7) columns share the same web-to-flange width ratio (b_w/b_f equal to 1.0 and 1.60, respectively), their P_{10t}/P_{cr} values are located on the same vertical line in the P_{10t}/P_{cr} *vs.* b_w/b_f plots. The vertical dispersions exhibited by these values provide an indication of the combined influence of the b_w/t and b_f/b_l ratios, which vary within each column set. Because these vertical dispersions are much higher for $b_w/b_f = 1.6$ than for $b_w/b_f = 1.0$, it seems fair to conclude that the combined influence of b_w/t and b_f/b_l on P_{10t}/P_{cr} increases with b_w/b_f.

In an attempt to capture the influence of each individual width ratio on the column elastic distortional post-critical strength, Figure 8(b) depicts the variations of P_{10t}/P_{cr} with each of the b_w/b_f, b_w/t and b_f/b_l width ratios, while keeping the remaining two constant. The analysis of this limited amount of results suggests that:

(i) By far the best documented P_{10t}/P_{cr} variations are those associated with the b_w/b_f ratio, which involve the C 60(6)/75/80(6)/90/100/110(2)/116/118/120(7)/ 130 columns – b_w/b_f varies between 1.0 and 2.0, while $b_w/t = 40$ and $b_f/b_l = 7.50$ are kept constant (results concerning other shapes are given in Landesmann *et al.*, 2013). The variation of P_{10t}/P_{cr} with b_w/b_f follow roughly ascending straight line.

(ii) Although the variation of P_{10t}/P_{cr} with the b_w/t is poorly documented (no more than three columns sharing the same b_w/b_f and b_f/b_l combination), it seems possible to conclude that a b_w/t increase tends to slightly lower the column post-critical strength.

(iii) Lastly, the variation of P_{10t}/P_{cr} with b_f/b_l falls somewhere in between the previous two, as far as the quality of the documentation is concerned (there are five columns sharing the same b_w/b_f and b_w/t combination), the P_{10t}/P_{cr} value increases steeply with b_f/b_l.

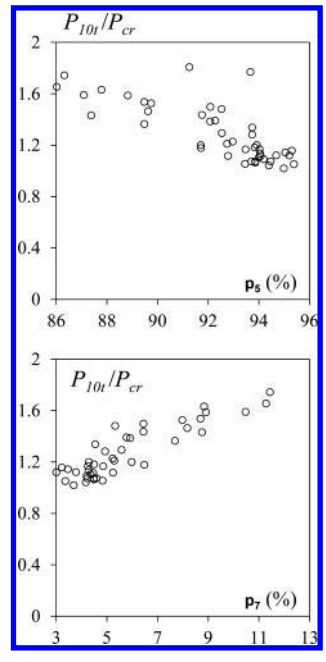


Figure 8. Variation of P_{10t}/P_{cr} with the GBT modal participations p_5 and p_7 (in the column critical buckling mode).

Finally, Figure 9 plots the P_{10t}/P_{cr} values against p_5 and p_7, *i.e.*, the participations of the GBT deformation modes **5** (symmetric distortion) and **7** (web-triggered local) on the column (distortional) critical buckling modes – recall that these modal participations were shown to exhibit some correlation with the b_w/b_f ratio. The observation of these results prompts the following remarks:

(i) There is a considerable scatter of the P_{10t}/P_{cr} values for the GBT modal participation considered. However, the least of such scatters clearly concerns local mode participations (p_7) – moreover, the corresponding P_{10t}/P_{cr} *vs.* p_7 plot shows that the presence of the local mode **7** entails a visible column post-critical strength increase (which is logical).

(ii) Naturally, the trends of the P_{10t}/P_{cr} *vs.* p_5 plots are practically the "inverse" of those exhibited by their P_{10t}/P_{cr} *vs.* p_7 counterparts, which means that now an increase in the participation of mode **5** causes a column post-critical strength drop (downward trend). Quantitatively speaking, the scatter of the P_{10t}/P_{cr} values is either (ii_1) very similar to that observed for the variation with p_7 or (ii_2) slightly above it (Cs) – in any case, the lipped channel column results still exhibit the lower scatter.

(iii) It may be safely argued that the modal participations p_5 and p_7 provide fairly good indicators of the lipped channel column post-critical strength level (p_7 slightly outperforms p_5).

5 CONCLUDING REMARKS

This paper reported the available results of a numerical research effort currently under way that aims at assessing and mechanically interpreting the influence of the cross-section geometry and end support conditions on the elastic distortional post-buckling behavior and strength of cold-formed steel columns. Regardless of the cross-section shape, it was found that, in fact, the so-called "pure distortional buckling modes" exhibit not only anti-symmetric distortional deformations (the predominant ones), but also web-triggered local deformations – moreover, the relative contribution of these deformations depends on the column cross-section shape and dimensions in a non-negligible fashion. It was observed that, generally, an increase in the presence of local deformations in the column critical (distortional) buckling mode leads to a higher post-critical strength (which seems logical, in view of the high post-critical strength reserve associated with local buckling). Finally, it was also found that more significant local deformations occur in columns exhibiting large web-to-flange width ratios, which is perfectly in line with the well-known higher vulnerability of wider webs to local buckling effects.

Concerning the correlation of the column post-critical strength with its cross-section dimension ratios and buckling mode GBT modal participations, it was found that, in the case of lipped channel columns, the variations of the (i) web-to-flange width ratio and (ii) percentage participation of the web-triggered local mode **7** provide the reasonable well the means to predict the post-critical strength change. No similar trait could be found for the hat-section and zed-section columns, for which the above correlation is visibly weaker (even if qualitatively similar). Although these preliminary findings are quite encouraging, it is undeniable that considerable further research is required before more solid conclusions can be drawn.

Finally, it is worth mentioning that the authors plan to complement the investigation reported in this paper with the performance of GBT-based elastic post-buckling analyses of several columns (*e.g.*, Silvestre & Camotim 2003, 2006 or Basaglia *et al.* 2011).

REFERENCES

Basaglia C, Camotim D, Silvestre N (2011). "Non-linear GBT formulation for open-section thin-walled members with arbitrary support conditions. *Computers and Structures*, **89**(21-22), 1906–1919.

Bebiano R, Pina P, Silvestre N, Camotim D (2008a). *GBTUL 1.0.β – Buckling and Vibration Analysis of Thin-Walled Members*, DECivil/IST, Technical University of Lisbon. (http://www.civil.ist.utl.pt/gbt)

Bebiano R, Silvestre N, Camotim D (2008b). "GBTUL A code for the buckling analysis of cold-formed steel members", *Proceedings of 19th International Specialty Conference on Recent Research and Developments in Cold-Formed Steel Design and Construction* (St. Louis, 14-15/10), R. LaBoube, W.W. Yu (eds.), 61–79.

Camotim D, Silvestre N, Gonçalves R, Dinis PB (2004). "GBT analysis of thin-walled members: new formulations and applications", *Thin-Walled Structures: Recent Advances and Future Trends in Thin-Walled Structures Technology*, J. Loughlan (ed.), Canopus Publishing Ltd., Bath, 137–168.

Dinis PB, Camotim D, Silvestre N (2006). "GBT formulation to analyse the buckling behaviour of thin-walled members with arbitrarily 'branched' open cross-sections", *Thin-Walled Structures*, **44**(1), 20–38.

Dinis PB, Camotim D (2013). "On the shell finite element buckling and post-buckling analysis of cold-formed steel members", *submitted for publication*.

Landesmann A, Camotim D (2010). "Distortional failure and design of cold-formed steel lipped channel columns under fire conditions", *Proceedings of SSRC Annual Stability Conference* (Orlando, 12-15/5), 505–532.

Landesmann A, Camotim D (2011). "DSM design of cold-formed steel columns against distortional failure: investigation on the influence of the cross-section geometry and support conditions", *USB Key Drive Proceedings of Structural Stability Research Council Annual Stability Conference* (Pittsburgh, 10-14/5).

Landesmann A, Camotim D (2013). On the direct strength method (DSM) design of cold-formed steel columns against distortional failure, *Thin-Walled Structures*, in press.

Landesmann A, Camotim D, C. Basaglia (2013). "Distortional post-buckling behavior and strength of cold-formed steel columns: how does the cross-section geometry affect it?", *USB Key Drive Proceedings of Structural Stability Research Council Annual Stability Conference* (St. Louis, 16-20/4).

Prola LC, Camotim D (2002). "On the distortional post-buckling behavior of cold-formed lipped channel steel columns", *Proceedings of SSRC Annual Stability Conference* (Seattle, 24-27/4), 571–590.

SAS (Swanson Analysis Systems Inc.) (2009). *Ansys Reference Manual* (version 12).

Silvestre N, Camotim D (2002a). "First order Generalised Beam Theory for arbitrary orthotropic materials", *Thin-Walled Structures*, **40**(9), 755–789.

Silvestre N, Camotim D (2002b). "Second order Generalised Beam Theory for arbitrary orthotropic materials", *Thin-Walled Structures*, **40**(9), 791–820.

Silvestre N, Camotim D (2003). "Non-linear Generalised Beam Theory for cold-formed steel members, *International Journal of Structural Stability and Dynamics*, **3**(4), 461–490.

Silvestre N, Camotim D (2006). "Local-plate and distortional post-buckling behavior of cold-formed steel lipped channel columns with intermediate stiffeners", *Journal of Structural Engineering* (ASCE), **132**(4), 529–540.

Research and Applications in Structural Engineering, Mechanics and Computation – Zingoni (Ed.)
© 2013 Taylor & Francis Group, London, ISBN 978-1-138-00061-2

Cold-formed steel beams of corrugated web

D. Dubina & V. Ungureanu
"Politehnica" University of Timisoara, Romania Romanian Academy, Timisoara, Branch, Romania

L. Gîlia
Technical University of Cluj-Napoca, Romania

ABSTRACT: The steel beams of corrugated web represent a relatively new structural system which emerged in the past two decades. The thin corrugated web, affords a significant weight reduction of these beams, compared with hot-rolled or welded ones. In the initial solutions, the flanges are made of flat plates, welded to the sinusoidal web sheet, requiring a specific welding technology. A new solution is proposed in this paper, in which the beam is composed by a web of trapezoidal cold-formed steel sheet and flanges of built-up cold-formed steel members (e.g. back-to-back lipped channel sections or angles with turn lips). The connections between flanges and web can be done by self-drilling screws or by spot welding. The paper summarizes the experimental and numerical investigations carried out at the CEMSIG Research Centre of the "Politehnica" University of Timisoara, in order to evaluate and validate a new technological solution.

1 INTRODUCTION

Corrugated web girders represent a relatively new structural system emerged in the past two decades especially in Germany and Austria. Increased interest of this solution was observed for the main frames of single-storey steel buildings and in steel bridges.

The main benefits of this type of elements are that the corrugated webs increase the beam's stability against buckling, which may result in a very economical design via the reduction of web stiffeners. Furthermore, the use of thinner webs results in lower material cost, with an estimated cost savings of 10–30% in comparison with conventional fabricated sections and more than 30% compared with standard hot-rolled beams. The buckling resistance of used sinusoidal corrugated sheet used for webs is comparable with plane webs of 12 mm thickness or more.

In the previously developed solutions the flanges are flat plates, welded to the sinusoidal web sheet, requiring a specific welding technology. The flanges mainly provide flexural strength to the beam with low contribution from the corrugated web, which provides the shear capacity. Failure of the web occurs by steel yielding or web buckling. Lateral-torsional buckling of the girder and local flange buckling represents other possible failure modes.

The paper presents a new technological solution of such a system, composed by webs made of trapezoidal cold-formed steel sheet and flanges of built-up cold-formed steel members (e.g. back-to-back lipped channel sections or angles with turn lips). The connections between flanges and web are made with self-drilling screws or by spot welding. It is easy to be observed that the new solution, as a whole, is 100% composed by cold-formed steel elements, avoiding the combination of two types of products, i.e. cold-formed for webs and hot-rolled for flanges. High protection to corrosion due to the fact that all components are galvanized is a major advantage. On the other hand, if the fabrication might adopt an automotive fastening technology such as cold metal transfer (CMT) welding, the production of some standardised beam series can be highly automated.

2 LITERATURE REVIEW

Significant work on girders with corrugated web was devoted to study the shear capacity. A summary of the research and development in beams with corrugated webs was reported by Elgaaly & Dagher (1990). Smith (1992) performed four tests on two girders with corrugated webs, which were welded to the flanges using intermittent welding. He found that the connection between the flange and the web is critical for the shear strength as the weld used in the test was subjected to high strength and web was easily ruptured at this point before it reached its buckling strength. He suggested that intermittent welding of the corrugated webs to the flange is not advisable.

Hamilton (1993) performed 42 tests on 21 beams, which used four different corrugation configurations and two thicknesses. Unlike Smith's (1992) specimens, the webs were continuously welded to the flanges from one side. It was found that the failure of all specimens was initiated by local buckling of one of the corrugation folds. Another conclusion was that dense corrugation profiles are more likely to fail in global shear buckling. Elgaaly et al. (1996) verified the test

results done by Smith (1992) and Hamilton (1993) using nonlinear FEM and found that the results of FEA were very close to the test results.

Luo & Edlund (1995) used non-linear finite element analysis to perform a geometrical parametric study and compared the numerical results with existing empirical and analytical formulae. They have found that the ultimate shear capacity increases proportionally with the girder depth and does not seem to be dependent on the ratio of girder length over girder depth, while the post-buckling shear capacity not only increases with the girder depth, but also appears to be dependent on the ratio of girder length over girder depth. They have also found that the corrugation depth did not seem to have much effect on the ultimate shear capacity but affected the degree of the localization of the buckling mode.

A lot of work has been done on the bending behaviour of steel girders with corrugated web. It was observed that the contribution of the web to the ultimate moment capacity of a beam with corrugated web is negligible, and the ultimate moment capacity will be based on the flange yield stress. Elgaaly et al. (1997) have performed a series of experimental and analytical studies. They have experimentally tested six specimens that had corrugated webs in the centre panel and flat panels adjacent to the support. All the specimens failed due to flange yielding followed by vertical buckling of the compression flange into the web. They found that the web did not contribute much to the bending capacity of the beam and its contribution could be neglected.

Chan et al. (2002) studied the effect of web corrugation on the bending capacity of the beam using FEM. Webs with horizontal and vertical corrugations were studied. They found that the vertically corrugated web provides a stronger support against the flange buckling than those with horizontally corrugated and flat webs. Also, the corrugation radius was investigated and found that larger corrugation radius could sustain higher bending moment.

Johnson & Cafolla (1997) have studied the effect of the vertically corrugated webs on the local buckling of the compressive flange and the flexural behaviour of beams with corrugated webs via numerically and in experimental tests. They found that the contribution of the web to flexural capacity is small.

Lindner (1990) studied by experimental tests the lateral-torsional behaviour of steel girders with corrugated webs and found that the torsional section constant I_t for a beam with corrugated web doesn't differ from that of a beam with flat web, but the warping section constant I_w is different.

The effect of the corrugation profiles of the web on the lateral-torsional buckling strength of the inelastic I-girder was also studied. Pasternak et al. (2010) presented a new proposal for Annex D of EN 1993-1-5:2006.

Moon et al. (2009, 2013) investigated the lateral–torsional buckling strength of an I-girder with corrugated steel webs under linear moment gradient by using finite element analysis. It was found that the buckling behaviour of the I-girder with corrugated steel webs differed depending on the number of periods of the corrugation. Simple equation for the moment gradient correction factor for these types of beams was suggested.

Elgaaly & Seshadri (1997) performed five tests on four different corrugation profiles. Two distinct modes of failure were observed: web crippling and web yielding. They also studied, using FEM, the interaction between partial compressive edge loading and bending or shear.

Luo & Edlund (2006) performed nonlinear finite element analysis to study the effect of four factors that influence the buckling strength of the beams, i.e.: (1) strain hardening model; (2) corner effect; (3) initial imperfections; (4) loading position. They used elastic-perfectly plastic and Ramberg-Osgood's models and found that with a Ramberg-Osgood strain-hardening model for webs, the ultimate strength of the girder is about 8-12% higher than using an elastic-perfectly plastic model. Also, the effect of the corners due to cold-forming does not have any significant effect on the ultimate strength.

Nguyen et al. (2012) investigate the moment modification factors of I-girder with trapezoidal web corrugations under moment gradient and various end restraint conditions and proposed closed-form expressions for the moment modification factors.

Another important aspect is the investigation of the stress distribution in the flange of the girders with corrugated webs (Kövesdi et al. 2012). During the experimental tests the stress distributions on different locations (i.e. flanges and web) were measured as a basis for parametric analyses.

As a final remark, a beam with corrugated web behaves similarly to a lattice girder, in which the bending moments and applied forces are transferred via flanges only, while the transverse forces are transferred through the diagonals and verticals of the lattice girder, in this case the corrugated web. The dimensioning of corrugated web beams is ruled by Annex D of the EN 1993-1-5:2006, together with specific aspects of EN 1993-1-1 and EN 1993-1-3. At the end, on the purpose of finding an analytical approach for designing such beams with corrugated web intermittently connected to the flanges, the procedure used for calculation sheathing acting as a diaphragm could be adapted (ECCS 1995). The experience, in this case, has shown the most contributing factors, both to strength and stiffness are the distortion of sheeting corrugations and seem fasteners (Fülöp & Dubina 2006).

3 EXPERIMENTAL TESTS

3.1 *Specimens and test procedure*

The experimental program was carried out at the CEMSIG Research Centre (http://cemsig.ct.upt.ro) of the "Politehnica" University of Timisoara. Five beams

Table 1. Types of specimens.

CWB-1	Standard solution: flange-to-web connection in every corrugations and uniformly distributed seam fasteners
CWB-2	Standard solution + supplementary lipped channel sections under the load application points
CWB-3	Optimized solution by adapting the flange-to-web connections according to the distribution of shear stresses (connections at each second corrugations where the shear force decreases)
CWB-4	Optimized solution by eliminating shear panels and doubling of corrugated webs in the zones with high shear forces
CWB-5	Optimized solution by adapting both the flange-to-web connections and seam fasteners to the distribution of shear stresses

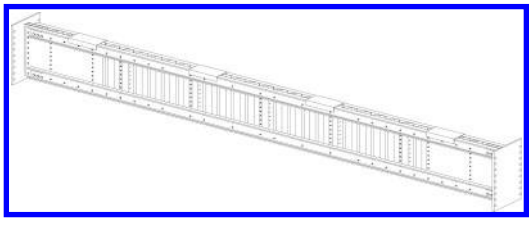


Figure 1. Configuration of the specimens.

with corrugated webs with a span of 5157 mm and a height of 600 mm have been tested (see Table 1), considering different arrangements for self-drilling screws and shear panels (Gilia 2012, Dubina et al. 2012).

Figure 1 presents the components of the CWB-1 beam with corrugated web (standard solution), i.e.:

- back-to-back lipped channel sections for flanges – 2 × C120/2.0;
- corrugated web with the corrugation depth of 43 mm and the thickness of 0.7 mm – A45/0.7;
- reinforcing shear panels – plates of 1 mm thickness and 830 mm length, at the beam ends where the shear force is maximum;
- reinforcing U150/2.0 profiles used under the load application points, to avoid excessive local deformations;
- self-drilling screws for flange-to-web connection – STP-6.3 × 25;
- self-drilling screws for shear plates to end support with a nominal diameter – STP-5.5 × 25;
- self-drilling screws as seam fasteners for corrugated webs with a nominal diameter– STT-4.8 × 20;
- bolts M12 class 8.8 for flanges to the end support connection.

Figure 2 presents the experimental arrangement. Six points bending tests, monotonically conducted, were applied for each specimen with a loading velocity of 2 mm/min.

The full-scale testing program was completed with tensile tests to determine both the material properties for beam components and the behaviour of connections.

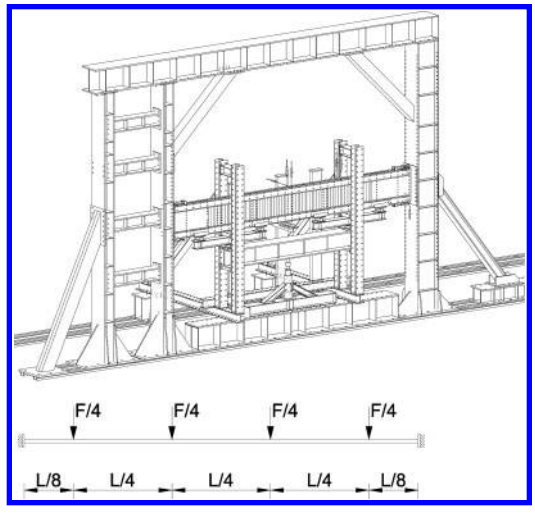


Figure 2. Experimental arrangement.



Figure 3. Deformed shape of CWB-1 beam at failure.



Figure 4. Deformed shape of the beam end shear panel.

3.2 *Test results*

3.2.1 *Beam CWB-1*

In case of the CWB-1 beam, the first deformation, which corresponds to the buckling of shear panel, appears for a displacement of 10 mm. The behaviour is ductile, with an initial stiffness of $K_{0\text{-}Exp} = 6862.2 N/mm$ and the maximum load is reached at $F_{max} = 218.9\,kN$. The collapse appears for a displacement of 58 mm. Figure 3 presents the deformed shape of the beam at collapse, while Figure 4 shows a detail of the shear panel at failure.

3.2.2 *Beam CWB-2*

In this case, the first deformation, which corresponds to the buckling of shear panel, appears for a displacement of 10 mm. The behaviour is ductile, with an



Figure 5. Deformed shape of CWB-2 beam at failure.

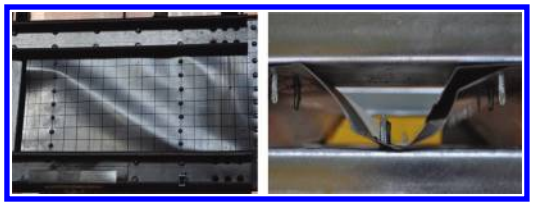


Figure 6. Deformed shape of the beam end shear panel and distortion of the web corrugation.



Figure 7. Deformed shape of CWB-3 beam at failure.



Figure 8. Distortion of the web corrugation.

initial stiffness of $K_{0\text{-}Exp} = 7831.5$ N/mm and the maximum load is reached at $F_{max} = 231.3$ kN. The collapse appears for a displacement of 54 mm. Figure 5 presents the deformed shape of the beam at collapse, while Figure 6 shows a detail of the shear panel at failure.

3.2.3 *Beam CWB-3*

For CWB-3 beam, the first deformation appears for a displacement of 15 mm, which corresponds to the buckling of shear panel and distortion of the corrugated web. The behaviour is ductile, with an initial stiffness of $K_{0\text{-}Exp} = 7184.9$ N/mm and the maximum load is reached at $F_{max} = 209.5$ kN. The collapse appears for a displacement of 62 mm. Figure 7 presents the deformed shape of the beam at collapse, while Figure 8 shows the distortion of the web corrugation.

3.2.4 Beam CWB-4

In case of this beam, the first deformation, which corresponds to the distortion of the corrugated web, appears for a displacement of 21 mm. The behaviour is ductile, with an initial stiffness of $K_{0\text{-}Exp} = 3985$ N/mm and the maximum load is reached at $F_{max} = 181.9$ kN. The collapse appears for a displacement of 164 mm. Figure 9 presents the deformed shape of the beam at collapse, while Figure 10 shows the distortion of the web corrugation.



Figure 9. Deformed shape of CWB-4 beam at failure.



Figure 10. Distortion of the web corrugation.



Figure 11. Deformed shape of CWB-5 beam at failure.



Figure 12. Distortion of the web corrugation.

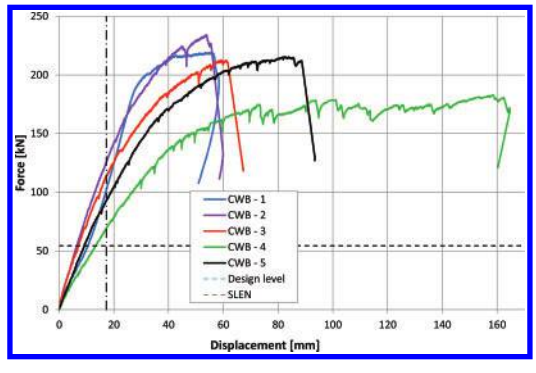


Figure 13. Load-displacement curves for the tested specimens.

3.2.5 Beam CWB-5

The first deformation corresponds to the buckling of shear panel, which appears for a displacement of 21 mm. The behaviour is ductile, with an initial stiffness of $K_{0\text{-}Exp} = 5516.2$ N/mm and the maximum load is reached at $F_{max} = 214.6$ kN. The collapse appears for a displacement of 88 mm. Figure 11 presents the deformed shape of the beam at collapse, while Figure 12 shows the distortion of the web corrugation in the region with the reduced number of screws.

Figure 13 shows comparatively, for all the five tested specimens, the load-displacement curves.

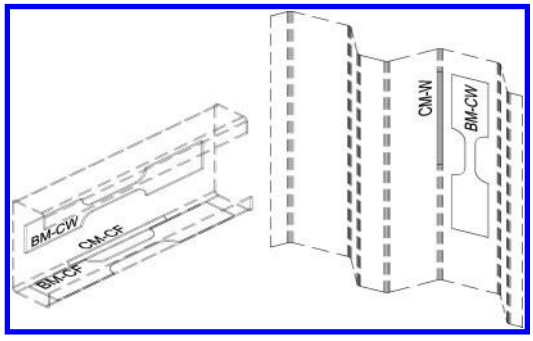


Figure 14. Samples cut from flat regions and corners.

Table 2. Yield and ultimate strengths.

Type	f_{yM} [N/mm^2]	f_{uM} [N/mm^2]	s_{fy}	s_{fu}	f_{yk} [N/mm^2]	f_{uk} [N/mm^2]
BM-CF	438.74	517.06	5.69	2.46	425.48	511.33
BM-CW	441.65	521.86	25.53	3.48	382.16	513.05
CM-CS	358.42	419.59	4.09	2.48	348.90	413.81
BM-SP	349.41	394.75	12.67	10.89	319.89	369.37
CM-F	521.64	585.07	9.89	9.69	498.60	562.49

Table 3. Types of tested connections.

Name	t_1 [mm]	t_2 [mm]	No. of tests	d_{nom} [mm]
T1-1.4	0.7	0.7	6	4.8
T2-1.7	1.0	0.7	5	4.8
T3-3.7	2.0 + 1.0	0.7	6	6.3
T4-9.0	1.0	8.0	5	5.5
T5-11.0	2.0 + 1.0	8.0	5	M12
T6-2.7	2.0	0.7	10	6.3

3.3 *Material properties and connections behaviour*

In order to determine the mechanical properties, a set of samples were cut out from the lipped channels of the flanges and corrugated web, both from the flat regions and corners, according to EN10002-1:2001 specifications, as shown in Figure 14.

Table 2 presents the mean values, standard deviations and the characteristic values for yield and ultimate strengths for the above samples.

Six types of connections were tested according to ECCS (2008), at a loading velocity of 1 mm/min, i.e. (1) T1-1.4 seam fasteners for corrugated sheets; (2) T2-1.7, seam fasteners for shear plates and corrugated sheets; (3) T3-3.7, self-drilling screws for shear plates and flanges; (4) T4-9.0, self-drilling screws for shear plates and end supports; (5) T5-11.0, bolts for flanges to end-supports; (6) T6-2.7, self-drilling screws for flanges to corrugated webs at mid-span, in order to determine the behaviour of all types of connections found in the beam (see Table 3).

4 NUMERICAL MODEL CALIBRATION AND VALIDATION

Numerical models applied to simulate the behaviour of members experimentally tested have been created using the commercial FE program ABAQUS/CAE v.6.7.1.

Rectangular 4-noded shell elements with reduced integration (S4R) were used to model the thin-walled components. CONN3D2 element types, with 2 nodes and 6 DOF per node, have been used to model the self-drilling screws and bolts. RB3D2 elements were used as rigid body for load transfer and multi-point constrain beam (MPC-Beam) for DOF coupling between groups of specified nodes.

The material behaviour used for numerical modelling was in accordance with the recorded curves from tensile tests from coupons cut over the cross-section of component elements. Self-drilling screws and bolts were introduced using CONN3D2 element type according to the mean values recorded from tests of each type of connection.

General contact with the following parameters have been used, i.e.

– Normal direction – Hard Contact;
– Transversal direction – a friction coefficient of $\mu = 0.1$.

Finally, initial imperfections according to first 3 eigen modes from a linear bucking analysis have been used.

Figure 15 presents comparatively the FEM and experimental load-displacement curves for the beam CWB-2, while Table 4 shows the initial stiffness and ultimate load obtained via numerical simulations compared to experimental results for each specimen.

Based on the results obtained via numerical simulations, it can be noted that the behaviour and maximum load accurately replicate the experimental tests.

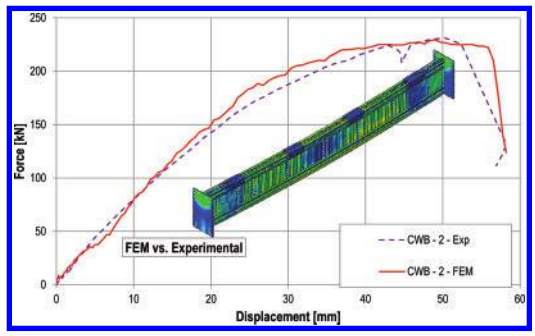


Figure 15. FEM/experimental load-displacement curves for CWB-2 beam.

Table 4. Initial stiffness and ultimate load: FEM vs. experimental results.

Beam type	$K_{0\text{-}Exp}$ (N/mm)	$K_{0\text{-}FEM}$ (N/mm)	$F_{max-Exp}$ (kN)	$F_{max-FEM}$ (kN)
CWB-1	6862.2	7721.1	218.9	225.9
CWB-2	7831.5	7834.6	231.3	229.5
CWB-3	7184.9	6819.3	209.5	205.8
CWB-4	3985.0	4932.0	181.9	223.5
CWB-5	5516.2	6594.9	214.6	216.0

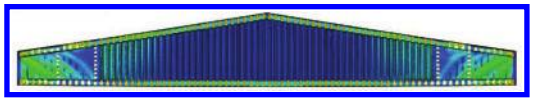


Figure 16. Stress distribution for a 12 m span beam.

On the next step, a beam of 12 m span with trapezoidal shape for the top flange has been investigated (see Fig. 16). The lateral-torsional bucking has been prevented. Similar failure modes have been obtained as in case of the tested beams, both experimentally and numerically.

5 CONCLUSIONS

A large experimental program carried out at the CEMSIG Research Centre (http://cemsig.ct.upt.ro) of the "Politehnica" University of Timisoara on five beams with corrugated webs with different arrangements for self-drilling screws and shear panels was presented.

Very good agreement can be found between beams CWB-1 and CWB-3, both in terms of initial stiffness and ultimate force. A slightly increase in stiffness can be observed in case of CWB-2 beam, due to the supplementary lipped channel sections added locally at the load application points. CWB-4 beam is the most flexible solution compared to the other four and has half initial stiffness compared to CWB-2 beam. At this level, CWB-5 beam represents the best solution in terms of optimisation.

Also, it can be underline that a very good agreement between numerical models and experimental ones have been obtained, in both failure modes and load-displacement curves.

Finally, even the results looks promising, significant work has to be done in order to investigate, validate and optimise such a solution for mass production, i.e.:

- to optimise the number of self-drilling screws used for connections;
- tests using spot welding are the next step of research; there are no differences expected at the level of global behaviour, but some are estimated in terms of strength and stiffness;
- numerical simulation of larger span beams in order to study the sensitivity to lateral-torsional buckling of such elements.

REFERENCES

Chan, C.L., Khalid, Y.A., Sahari, B.B. & Hamouda, A.M.S. 2002. Finite element analysis of corrugated web beams under bending, *Journal of Constructional Steel Research* 58(11): 1391–1406.

Dubina, D., Ungureanu, V. & Gilia, L. 2012. Cold-formed steel beams of screwed corrugated webs to the double lipped channel flanges. *ECCS TC7 – TWG 7.5 Meeting, 28-29.06.2012, Düsseldorf, Germany*.

ECCS 1995. *European recommendations for the application of metal sheeting acting as a diaphragm*. Publication P088, ECCS, Brussels, Belgium.

ECCS 2008. *The Testing of connections with mechanical fasteners in steel sheeting and sections*. Publication 124, ECCS, Brussels, Belgium.

Elgaaly, M. & Dagher, H. 1990. Beams and girders with corrugated webs, *Proceedings of the SSRC Annual Technical Session, St. Louis, MO, USA*, 37–53.

Elgaaly, M., Hamilton, R. & Seshadri, A. 1996. Shear Strength of Beams with Corrugated Webs. *Journal of Structural Engineering, ASCE* 122(4): 390–398.

Elgaaly, M., Seshadri, A. & Hamilton, R.W. 1997. Bending strength of steel beams with corrugated webs. *Journal of Structural Engineering, ASCE* 123(6): 772–782.

Elgaaly, M. & Seshadri, A. 1997. Girders with corrugated webs under partial compressive edge loading. *Journal of Structural Engineering, ASCE* 123(6): 783–791.

EN10002-1:2001. *Tensile testing of metallic materials. Method of test at ambient temperature*. CEN, Brussels.

EN1993-1-5:2006. *Eurocode 3: Design of steel structures - Part 1-5: Plated structural elements*. CEN, Brussels.

Fülöp, L. & Dubina, D. 2006. Design criteria for seam and sheeting-to-framing connections of cold-formed steel shear panels. *J. of Struct. Engineering, ASCE* 132(4): 582–590.

Gilia, L. 2012. *Structural performances of steel beams with back-to-back cold-formed lipped channel sections for flanges and corrugated web*. PhD Thesis, Technical University of Cluj-Napoca, Romania.

Hamilton, R. 1993. *Behavior of welded girders with corrugated web*. PhD Thesis, Department of Civil Engineering, University of Maine, Orono, Maine, USA.

Johnson, R. & Cafolla, J. 1997. Local flange buckling in plate girders with corrugated webs. *Proceedings of the Institution of Civil Engineers - Structures & Buildings* 12(2): 148–156.

Kövesdi, B., Jáger, B. & Dunai, L. 2012. Stress distribution in the flanges of girders with corrugated webs. *Journal of Constructional Steel Research* 79: 204–215.

Lindner, J. 1990. Lateral-torsional buckling of beams with trapezoidally corrugated webs, *Proc. of the 4th International Colloquium on Stability of Steel Structures, Budapest, Hungary*.

Luo, R. & Edlund, B. 1995. *Numerical simulation of shear tests on plate girders with trapezoidally corrugated webs*. Division of Steel and Timber Structures, Chalmers University of Technology, Göteborg, Sweden.

Luo, R. & Edlund, B. 2006. Ultimate strength of girders with trapezoidally corrugated webs under patch loading. *Thin-Walled Structures* 24: 135–156.

Moon, J., Yi, J.W., Choi, B.H. & Lee, H.E. 2009. Lateral-torsional buckling of I-girder with corrugated webs under uniform bending. *Thin-Walled Structures* 47: 21–30.

Moon, J., Lim, N.H. & Lee, H.E. 2013. Moment gradient correction factor and inelastic flexural–torsional buckling of I-girder with corrugated steel webs. *Thin-Walled Structures* 62: 18–27.

Nguyen, N.D., Han, S.R., Kim, J.H., Kim, S.N. & Kang, Y.J. 2012. Moment modification factors of I-girder with trapezoidal web corrugations under moment gradient. *Thin-Walled Structures* 57: 1–12.

Pasternak, H., Robra, J. & Kubieniec, G. 2010. New proposals for EN 1993-1-5, Annex D: Plate girders with corrugated webs. *Codes in Structural Engineering, Joint IABSE-FIB Conference, Dubrovnik, Croatia*, vol. 2, 1365–1372.

Smith, D. 1992. *Behavior of corrugated plates subjected to shear*. MSc Thesis, Department of Civil Engineering, University of Maine, Orono, Maine, USA.

Research and Applications in Structural Engineering, Mechanics and Computation – Zingoni (Ed.)
© 2013 Taylor & Francis Group, London, ISBN 978-1-138-00061-2

Post-buckling behaviour and strength of cold-formed steel lipped channel columns: when is local-distortional interaction relevant?

P.B. Dinis, D. Camotim & A.D. Martins
Civil Engineering Department, ICIST, Instituto Superior Técnico, Technical University of Lisbon, Portugal

ABSTRACT: The results of a numerical (ABAQUS shell finite element analysis) investigation concerning the relevance of Local-Distortional (L-D) interaction effects on the ultimate strength of fixed-ended lipped channel columns are presented and discussed. The columns analysed exhibit various geometries (cross-section dimensions and length) and yield stresses, selected to ensure a wide variety of combinations of the ratios between the (i) distortional and local critical buckling stresses (R), and (ii) yield and critical buckling stresses (R_y). The aim of the work is to identify the R and R_y range combinations for which the L-D interaction effects are relevant, in the sense of eroding visibly the lipped channel column ultimate strength and altering its failure mechanism. The ultimate strength erosion due to L-D interaction is assessed by comparing the numerical column failure loads with their estimates provided by the current Direct Strength Method (DSM) local and distortional strength curves – an overestimation by both curves implies the occurrence of erosion. Finally, the paper closes with some considerations on how the findings of this work may impact the DSM design of lipped channel columns undergoing different levels of L-D interaction.

1 INTRODUCTION

Most cold-formed steel members exhibit slender thin-walled open cross-sections, a feature making them highly susceptible to several instability phenomena, namely local and distortional buckling. Moreover, since several common member geometries (unrestrained length and cross-section shape/dimensions) are associated local (L) and distortional (D) buckling stresses that are not too far apart, the corresponding post-buckling behaviour (elastic or elastic-plastic), ultimate strength and failure mechanism are likely to be affected, to a larger or smaller extent, by interaction effects involving these two instability phenomena – local-distortional (L-D) interaction.

A considerable amount of research work has been recently devoted to L-D interaction, involving mostly lipped channel columns and including experimental investigations, numerical simulations and design proposals (*e.g.*, Yang & Hancock 2004, Dinis *et al*. 2007, Yap & Hancock 2011, Kwon *et al*. 2009, Silvestre *et al*. 2012, Young *et al*. 2013, Camotim *et al.* 2013). It was found that these interaction effects are relevant if the ratio between the critical distortional and local buckling stresses, denoted as $R = f_{crd}/f_{crl}$, is either (i) in the close vicinity of 1.0 (between 0.9 and 1.1) or (ii) well above 1.0, provided that the yield stress f_y is "high enough" to allow for the development of L-D interaction prior to collapse – this means that the yield-to-critical stress ratio plays a crucial role in the relevance of L-D interaction effects. However, a systematic investigation aimed at identifying the combinations of f_{crd}, f_{crl} and f_y stresses associated with non-negligible L-D coupling effects is still lacking – the only available work that addresses (partially) this issue has been reported by Dinis *et al*. (2009).

This paper presents and discusses the results of a numerical (ABAQUS shell finite element analysis – SFEA) investigation comprising 416 fixed-ended lipped channel columns that exhibit different cross-section dimensions and yield stresses, thus ensuring a wide variety of combinations concerning the stress ratios (i) $R = f_{crd}/f_{crl}$, relating the distortional and local critical buckling stresses and (ii) $R_y = f_y/f_{crmax}$, quantifying the difference between the yield stress and the non-critical of the above column buckling stresses, *i.e.*, $f_{crmax} = max\,(f_{crl}; f_{crd})$ – when f_{crd} and f_{crl} are not very close, the development of L-D interaction effects is also governed by the closeness between f_y and f_{crmax}. The aim is to identify the $R - R_y$ range combinations for which the L-D interaction effects are relevant, in the sense of eroding visibly the lipped channel column ultimate strength and altering its failure mechanism. The ultimate strength erosion due to L-D interaction is assessed by comparing the numerical column failure loads with their estimates provided by the current Direct Strength Method (DSM – Schafer 2008) local and distortional strength/design curves – an overestimation by both curves implies that erosion has occurred. Finally, the paper closes with some considerations concerning the impact of the findings reported in this work on the DSM design (ultimate strength prediction) of lipped channel columns undergoing different levels of L-D interaction.

2 BUCKLING ANALYSIS – COLUMN SELECTION

The column geometry (cross-section dimensions and length) selection to ensure the occurrence of various levels of L-D interaction was made by means of trial-and-error procedure involving the performance of buckling analysis sequences carried out in GBTUL (Bebiano *et al.* 2008), mainly due to its computational efficiency and modal nature. The selection procedure led to the cross-section dimensions (b_w, b_f, b_l, t–web/flange/lip widths and wall thickness) and lengths (L) provided in Table 1. The half-wave numbers exhibited by the critical distortional (n_d) and local (n_l) buckling modes are also included – the

Table 1. Selected column geometries and critical local/distortional buckling stresses and buckling mode half-wave numbers.

	b_w mm	b_f mm	b_l mm	t mm	L m	f_{crd} MPa	n_d	f_{crl} MPa	n_l	R
C1	160	190	10	2.45	1.55	63	2	189	–	0.33
C2	135	140	7.5	2.20	1.50	74	3	185	–	0.40
C3	135	140	7.5	1.65	1.50	52	2	110	–	0.47
C4	135	140	7.5	1.55	1.50	48	2	94	–	0.51
C5	135	140	7.5	1.40	1.50	42	2	72	–	0.58
C6	160	190	10	1.80	1.55	46	2	71	–	0.65
C7	120	110	10	2.15	0.90	184	2	263	–	0.70
C8	120	110	10	1.80	0.90	149	1	192	–	0.78
C9	120	110	10	1.60	0.90	131	1	153	–	0.86
C10	120	110	10	1.40	0.90	113	1	118	–	0.96
C11	120	80	10	1.60	1.00	189	2	178	9	1.07
C12	120	110	10	1.15	0.90	91	1	80	7	1.13
C13	120	80	10	1.40	1.00	166	2	136	9	1.22
C14	120	80	10	1.30	1.00	159	2	118	9	1.35
C15	120	80	10	1.25	1.00	153	2	119	9	1.41
C16	120	80	10	1.20	1.00	145	2	100	9	1.45
C17	120	80	10	1.10	1.00	135	2	84	10	1.60
C18	120	100	10	0.85	1.00	77	1	47	9	1.66
C19	120	100	10	0.80	1.00	73	1	41	9	1.76
C20	120	100	10	0.75	1.00	68	1	36	9	1.86
C21	120	100	10	0.70	1.00	63	1	32	9	2.00
C22	120	100	10	0.65	1.00	59	1	27	9	2.15
C23	120	100	10	0.62	1.00	55	1	25	9	2.22
C24	120	100	10	0.55	1.00	47	1	20	9	2.39

latter only when $f_{crl} < f_{crl}$. It is worth noting that the 24 fixed-ended columns ($E = 210GPa$,v $= 0.3$) (i) exhibit R values such that $0.33 < R < 2.39$ and (ii) have global critical buckling stresses much higher than their local and distortional counterparts ($f_{crg}/f_{crmax} > 7.9$), thus meaning that no interaction with flexural-torsional buckling occurs.

3 RELEVANCE OF L-D INTERACTION

This section presents and discusses the main results of the numerical investigation aimed at identifying the relevance of the L-D coupling effects. All these results were obtained by means of ABAQUS SFEA and using the elastic-perfectly plastic model adopted earlier by Dinis *et al.* 2007, 2009): (i) columns discretised into fine meshes of 4-node isoparametric shell (S4) elements with length-to-width roughly equal to 1, (ii) fixed-ended supports modelled by attaching rigid plates to the column end sections, and (iii) steel material behaviour modelled by means of Prandtl-Reuss's classical plasticity model.

It is well known that the initial geometrical imperfection shape plays a crucial role in mode interaction studies (*e.g.*, Dinis *et al.* 2007). In this work, and regardless of the stress ratio R value, all columns contained distortional initial geometrical imperfections (i) with small amplitudes (the maximum lip free edge vertical displacement is equal to 10% of the wall thickness t) and (ii) involving central half-wave outward or inward flange-lip motions - previous studies showed that outward motions are the most detrimental: they lead to the lower lipped-channel column

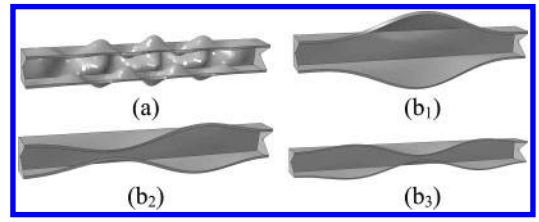


Figure 1. Initial geometrical imperfections: (a) local (multiple half-waves) and (b) distortional – (b_1) 1, (b_2) 2 and (b_3) 3 half-waves.

ultimate strengths (Dinis *et al.* 2007). Thus, when the critical buckling mode half-wave number is odd (*e.g.*, see Figs. 1(b_1) and 1(b_3)), the most detrimental imperfection corresponds to the largest number of half-wave outward flange-lip motions – when the number is even (*e.g.*, see Fig. 1(b_2)), the outward or inward shapes lead to identical ultimate strengths. Moreover, when $R > 1$ (critical local buckling) a local initial imperfection shape is also considered: its amplitude is such that the maximum mid-web flexural displacement equals 10% of wall thickness t – this imperfection "sign" is not relevant, due to symmetric nature of the column local post-buckling behaviour.

In order to cover a wide critical (L or D) slenderness range [$\lambda = (f_y/f_{cr})^{0.5}$ varying from 1.0 to 4.0 in 0.25 intervals], eleven yield stresses were considered for each imperfect column. Their maximum values ranged from 315 to 2895 MPa and involving f_{crg}/f_y always larger than 1.12. A total of 416 columns were analysed through ABAQUS SFEA (both residual stresses and corner strength effects were neglected, as they have been shown to have little impact on the column response), in order to determine their failure loads and collapse mechanisms.

The numerical ultimate strength data determined are used next to relate the R and R_y values with the relevance of the L-D interactions effects. Due to space limitations, only a representative fraction of the results obtained are presented, discussed and interpreted here – the full set of results can be found in Martins *et al.* (2013). The presentation addresses separately the identification of (i) the R limit values (closeness to 1.0) associated with "true L-D interaction", in which coupling effects gradually evolve as loading progresses (and occur regardless of the yield stress value), and (ii) the R_y limit values (large enough yield stress) required to allow the development of L-D interaction effects caused by a "secondary bifurcation" – these effects only emerge and grow as the loading nears the f_{crmax} applied stress level. The illustrative numerical results concern columns (i) C12 ($R = 1.13$), and (ii) C24 ($R = 2.39$) – no column with $R < 1.0$ is addressed in detail.

3.1 *True L-D interaction – R upper and lower limits*

After briefly presenting column C12 ($R = 1.13$ – critical local buckling) post-buckling behaviour, the relevance of the L-D interactions effects in columns with different yield stresses (R_y values) is addressed.

Figure 2(a) shows the upper portions ($P/P_{cr} > 0.5$) of the elastic-plastic P/P_{cr} vs v/t equilibrium paths (v : mid-span flange-lip corner vertical displacement) of C12 columns exhibiting (i) D or L initial imperfections and (ii) six R_y values (1.4, 2.0, 3.5, 5.5, 8.0 and ∞ – the latter corresponds to elastic behaviour). Figures 2(b), they show the deformed configurations and plastic strain distributions near collapse of columns with (i) $R_y = 2.0$ and

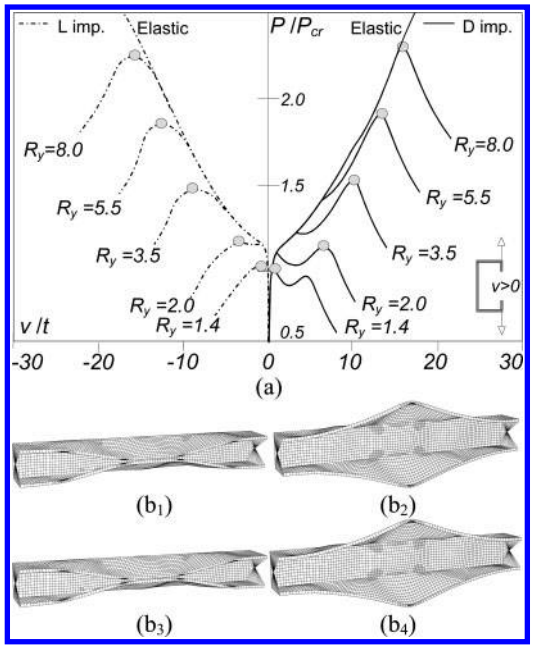


Figure 2. (a) P/P_{cr} vs v/t paths of column C12 ($R = 1.13$) with D and L imperfections, and (b) failure modes and plastic strain diagrams of the (b_1)-(b_4) $R_y = 2.0 + L$, $R_y = 2.0 + D$, $R_y = 5.5 + L$ and $R_y = 5.5 + D$ columns.

L (Fig. 2(b_1)) or D (Fig. 2(b_2)) imperfections, and (ii) $R_y = 5.5$ with L (Fig. 2(b_3)) or D (Fig. 2(b_4)) imperfections – note that the deformed configurations are amplified 10 or 2.5 times (D or L imperfections). The observation of these results prompts the following remarks:

(i) Unlike the D imperfection columns, which exhibit mid-span outward flange-lip motions, all L imperfection columns display mid-span inward flange-lip motions. This feature is due to the presence of a small amount of minor-axis bending, caused by the occurrence of effective centroid shifts towards the web (in spite of the fixed ends – Young & Rasmussen 1999). The corresponding outward web curvature "attracts" mid-span inward distortional deformations, which explains the failure modes of Figures 2(b_1) and 2(b_3).

(ii) In the columns with R_y closest to 1.0 ($R_y = 1.4$), yielding starts when the normal stress distribution is still "not too far from uniform" and, thus, precipitates a rather abrupt (imperfection-dependent) collapse.

(iii) On the other hand, in the columns with $R_y > 1.4$, first yielding occurs when normal stress distribution is already "highly non-uniform" and, thus, does not lead to an immediate failure – collapse takes place after a snap-through phenomenon and subsequent strength increase up to a limit point. As R_y increases, the snap-through becomes less pronounced (eventually barely visible) and the strength increase grows considerable-this can be confirmed by comparing the $R_y = 2.0 + D$ path with the remaining ones.

(iv) Regardless of the initial imperfections shape and R_y value, all columns with $R_y \geq 2.0$ exhibit visible L-D interaction. Moreover, note that the failure mode does not depend on R_y – *e.g.*, compare Figures 2(b_2) and 2(b_4), showing the collapse mechanisms of the $R_y = 2.0 + D$ and $R_y = 5.5 + D$ columns.

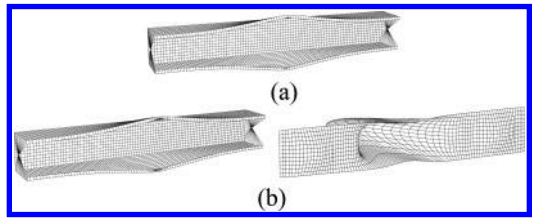


Figure 3. (a) $R = 0.78 + R_y = 1.2$ column and (b) $R = 0.86 + R_y = 1.3$ column and web deformed shapes and plastic strain diagrams at collapse.

Since L-D interaction always occurs in columns with R close to 1.0 (even if it only causes significant ultimate strength erosion for $R_y \geq 2.0$), it is important to identify when does "true L-D interaction" cease to occur, *i.e.*, the corresponding R upper and lower limits. Such limits are identified through a procedure that involves the performance of the following tasks:

(i) Select column sets with increasing and decreasing R value sequences, starting as near to 1.0 as possible, and exhibiting similar R_y values that are not too far from 1.0 (to avoid the yield stress influence).

(ii) Analyse all the columns within a set and, for each of them, observe and record the failure mode characteristics and location of the plastic strains at collapse. Only D initial imperfections are considered.

(iii) Compare the failure mode characteristics and/or collapse plastic strain patterns of the columns with similar R_y values and identify the pairs of successive R values that are associated with a change in them.

The above procedure was first adopted to identify the R lower limit associated with the presence of L-D interaction when the column critical buckling is distortional ($R < 1.0$). Figures 3(a)-(b) display the collapse modes and plastic strains of the $R = 0.78 + R_y = 1.2$ and $R = 0.86 + R_y = 1.3$ columns – note that the two column deformed shapes are amplified 3 times and the latter has its web magnified 150 times. The following conclusions can be drawn from the observation of these figures:

(i) The $R = 0.78 + R_y = 1.2$ column failure mode exhibits a perfect single-wave sinusoidal shape – there is no trace of local deformations (*i.e.*, L-D interaction).

(ii) Although barely perceptible, L-D interaction occurs near the collapse for the $R = 0.86 + R_y = 1.3$ column – the magnified deformed web shown in Figure 3(b) evidences the presence of a minute local component.

(iii) Therefore, it seems fair to argue that the emergence of L-D interaction effects takes place somewhere in between the $R = 0.78$ and $R = 0.86$ values.

A similar procedure was adopted to identify the R upper limit, which concerns columns for which critical buckling is local ($R > 1.0$). Figures 4(a)–(b) display the deformed shapes (amplified 20 times) and plastic strain diagrams of the $R = 1.41 + R_y = 1.1$ and $R = 1.35 + R_y = 1.2$ columns at the onset of collapse – note that these figures include also detailed views of the

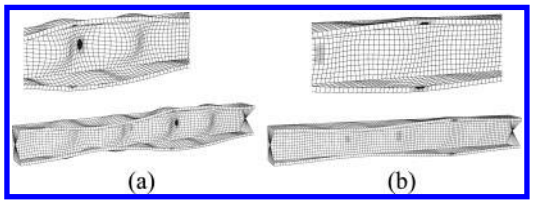


Figure 4. (a) $R = 1.41 + R_y = 1.1$ and (b) $R = 1.35 + R_y = 1.2$ column deformed shapes (with details) and plastic strain diagrams at collapse.

column region with larger outward distortional deformations. The observation of these results prompts the following remarks:

(i) Although the two failure mode configurations share the same qualitative features, namely the combination of 2 D and several L half-waves, they are quantitatively quite different. Indeed, it is very clear that the L half-waves prevail in the $R = 1.41 + R_y = 1.1$ column failure mode, while the D ones are dominant in the $R = 1.35 + R_y = 1.2$ column collapse. Since both columns have L critical buckling modes and D initial imperfections, the dominance of the L (D) deformations in the failure mode may then be attributed to the absence (presence) of L-D interaction.

(ii) The above assertion is confirmed by the plastic strain diagrams of the two columns at the onset of collapse. In the $R = 1.41 + R_y = 1.1$ column, yielding starts at the web and flange crests (*i.e.*, central areas) of the most deformed L half-wave (see detail in Fig. 4(a)), which is a clear indication of a local failure (no visible L-D interaction occurs). In the $R = 1.35 + R_y = 1.2$ column, on the other hand, yielding starts at the lip free edge regions of the mid-span cross-section (see detail in Fig. 4(b)), which is the trademark of a distortional failure – thus, L-D interaction takes place.

(iii) Thus, it may be argued that L-D interaction effects wane somewhere in between $R = 1.35$ and $R = 1.41$.

Finally, it is worth noting that (i) the above R limits are in agreement with the findings of Dinis *et al*. (2009) and (ii) Silvestre *et al*. (2012) investigated the detrimental L-D interaction effects in columns with nearly coincident L and D critical buckling stresses ($0.9 < R < 1.1$).

3.2 *Secondary bifurcation – R_y lower limits*

As mentioned earlier, L-D interaction may occur even when the L and D critical buckling stresses are far apart, *i.e.*, when R not close to 1.0. This interaction, associated with a secondary bifurcation, takes place if R_y (*i.e.*, the yield stress) is "large enough" to allow for the emergence and development of coupling before plasticity precipitates failure. Although this type of interaction may occur when $R > 1.0$ (L buckling is critical) or $R < 1.0$ (D buckling is critical), the first case is clearly more relevant, due to the higher L post-critical strength – due to space limitations, only this case is dealt with here (columns with R < 1.0 are addressed in Martins *et al.* 2013).

To illustrate the L-D interaction R_y-dependence, Figure 5(a) depicts the upper portions ($P/P_{cr} > 0.75$) of the column C24 ($R = 2.39$) elastic-plastic P/P_{cr} vs v/t equilibrium paths associated with (i) D or L initial imperfections and (ii) $R_y = 0.9,\ 1.7,\ 2.6,\ 3.8,\ \infty$. Figures

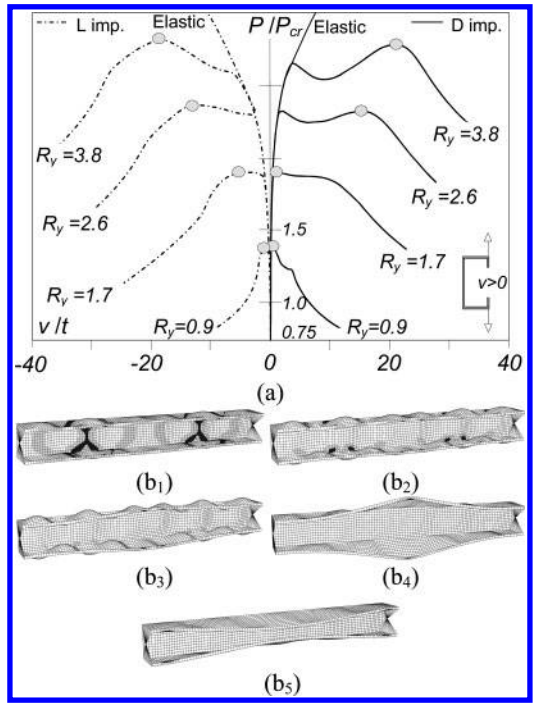


Figure 5. (a) P/P_{cr} vs v/t paths of column C24 ($R = 2.39$) with D and L imperfections, and (b) failure modes and plastic strains of the (b_1)-(b_5) R_y =0.9+D, R_y =1.7+D, $R_y = 2.6 + \mathrm{D}$, $R_y = 3.8 + \mathrm{D}$ and $R_y = 3.8 + \mathrm{L}$ columns.

5(b_1)–(b_5) show the plastic strains diagrams at the onset of collapse of columns exhibiting (i) D imperfections and $R_y = 0.9$, $R_y = 1.7$, $R_y = 2.6$ or $R_y = 3.8$, and (ii) L imperfections and $R_y = 3.8$ – the first 4 deformed shapes are amplified 20 times, and the fifth only 3 times. The observation of all these figures leads to the following comments:

(i) The $R_y = 0.9$ columns collapse abruptly with no trace of L-D interaction (see Fig. 5(b_1)).

(ii) The$R_y = 1.7$ and $R_y = 2.6$ columns exhibit local failures even in the presence of D initial imperfections (see Figs. 5(b_2)–(b_3) – no L-D interaction occurs).

(iii) Both the $R_y = 3.8$ columns with D and L imperfections exhibit L-D interaction (see Figs. 5(b_4)-(b_5)) and fail after a snap-through and subsequent applied load increase (see Fig. 5(a)). Moreover, note that, similarly to what was observed in Figures 2(a)–(b), the column with D (L) imperfections exhibits mid-span outward (inward) flange-lip motions – in the latter case, due to global bending caused by the effective centroid shift effects.

(iv) Thus, for this particular column (R value), it can be said that L-D interaction only develops if R_y is larger than a value comprised between 2.6 and 3.8. Similar investigations for columns C16 ($R = 1.45$) and C17 ($R = 1.60$) led to the determination of the following R_y lower limits for the occurrence of visible L-D interaction effects: 1.10-1.60 and 1.40-1.90. In the future, these intervals will be refined and additional ones will be obtained for other columns.

4 DIRECT STRENGTH METHOD (DSM) DESIGN

The current DSM design curves for cold-formed steel columns, defined by "Winter-type" expressions, provide mostly safe and accurate ultimate strength estimates associated with local, distortional, global and local-global interactive failures on the basis of elastic critical buckling and yield stresses – the expressions for the DSM nominal local (f_{nl}) and distortional (f_{nd}) strengths can be found, for instance, in Schafer's state-of-the-art report (2008).

The numerical ultimate strengths (f_u) obtained in the investigations reported in the previous section are now compared with the estimates provided by the current DSM local and distortional strength curves. The aim of this comparison is to assess how the combined values of R and R_y affect the ultimate strength erosion stemming from the L-D interation effects and, in particular, to provide preliminary guidelines on the relevance of such effects – due to space limitations, the results presented concern only a representative sample of the columns analysed, selected to cover the whole R range considered: columns C5-9-11-14-18-20-22-24, corresponding to $R = 0.58$-0.86-1.07-1.35-1.66-1.86-2.15-2.39. Each column was analysed with 11 distinct yield stresses, thus making it possible to cover a quite wide critical (distortional or local) slenderness range.

Figures 6(a)-(h) show the variations of f_u/f_y with λ_l or λ_d for the 8 columns listed in the previous paragraph. While for the columns buckling distortionally ($R < 1.0$) only D initial imperfections were considered, all the columns buckling locally ($R > 1.0$) were analysed with L (white circles) and D (grey circles) initial imperfections – the numerical f_u/f_y values are compared, separately, with their estimates provided the current DSM L and D strength curves. The comparative analysis of all these ultimate strength results prompts the following remarks:

(i) First of all, note that all the numerical f_u/f_y values are well aligned along "Winter-type" curves.

(ii) The DSM D curve predicts very well all the $R = 0.58$ column ultimate strengths, thus evidencing the absence of erosion due to L-D interaction effects.

(iii) The quality of the DSM D curve estimates decreases a bit for the $R = 0.86$ columns: a few overestimates in the intermediate slenderness range and practically no overestimations, reflecting the presence of just mild L-D interaction effects.

(iv) For the columns with $R > 1.0$, the first remark concerns the fact that the vast majority of the f_u values associated with L and D initial imperfections are virtually coincident, even if critical buckling is local. The few exceptions are stocky columns whose ultimate strengths are generally very well predicted by the DSM L curve, which means that they are not affected by L-D interaction (low R_y values).

(v) Secondly, practically all the most slender columns with $R > 1.0$ have failure loads clearly overestimated by the DSM L and D curves – an undeniable sign of significant L-D interaction (high enough R_y values).

(vi) Lastly, it may be concluded that, generally speaking, the ultimate strengths of the columns with $R > 1.0$ tend to be less overestimated by the DSM L curve as R increases (switch from "true L-D interaction" to "secondary bifurcation) and λ_l decreases (lower R_y values), which corresponds to less relevant L-D interaction effects (as assessed earlier) – the number of fairly accurate estimates, indicating local failures,

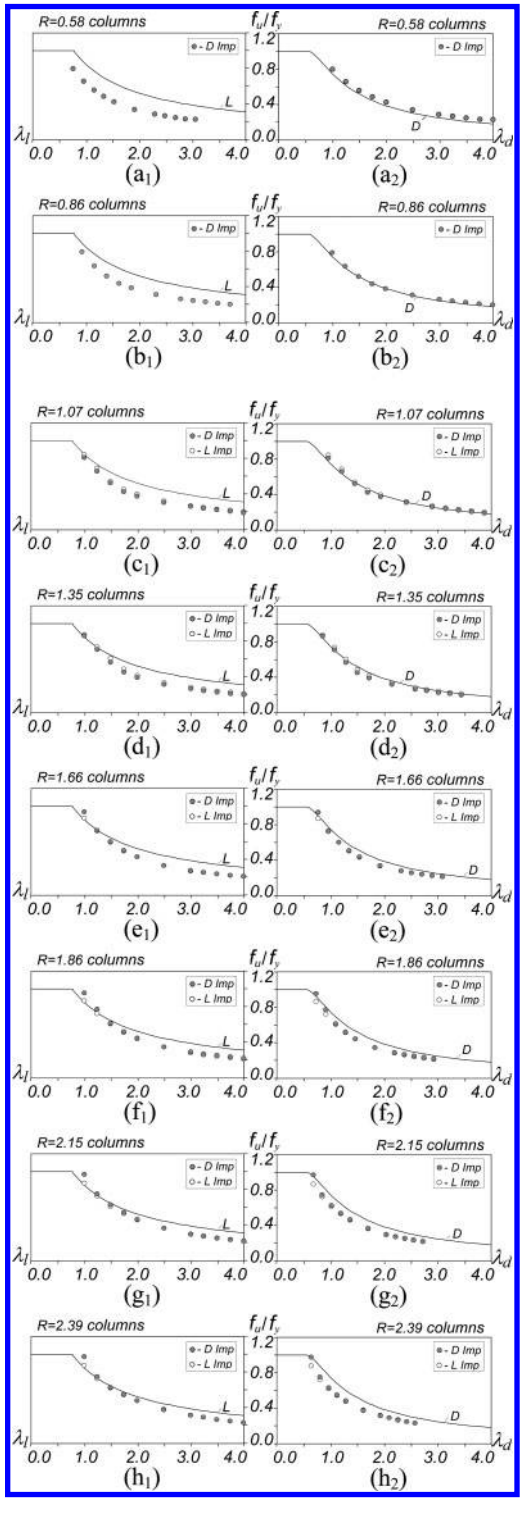


Figure 6. Variation of f_u/f_y with $(_1)\,\lambda_l$ or $(_2)\,\lambda_d$ for the (a)-(h) $R = 0.58$, $R = 0.86$, $R = 1.07$, $R = 1.35$, $R = 1.66$, $R = 1.86$, $R = 2.15$, $R = 2.39$ columns.

grows with R. Conversely, the DSM D curve provides overestimates that increase as R increases and λ_l decreases – for $R \leq 1.35$, these overestimations are invariably quite small and only become "visible" for columns with intermediate slenderness values.

5 CONCLUDING REMARKS

A numerical investigation about the relevance of L-D interaction effects on the post-buckling behaviour, ultimate strength and DSM design of fixed-ended cold-formed lipped channel columns was reported. The 416 columns analysed had cross-section dimensions, lengths and yield stresses selected to ensure a wide variety of ratios between the (i) D and L critical buckling stresses, and (ii) yield and critical buckling stresses. The ensuing results made it possible to reach preliminary (and limited) conclusions on the identification of the combinations of these ratios for which L-D interaction is relevant, *i.e.*, erodes visibly the ultimate strength of lipped channel columns and alters their failure modes. After providing numerical evidence about the presence or absence of L-D interaction, its influence on the ultimate strength erosion was assessed by comparing the numerical column failure loads with their estimates provided by the current DSM local and distortional strength curves – an overestimation by the two curves naturally implies the occurrence of more or less ultimate strength erosion.

The numerical results presented and discussed in this work, concerning lipped channel columns, provided clear evidence that cold-formed steel columns may be affected by two types of L-D interaction: (i) one associated with relatively close L and D critical buckling stresses, characterised by the simultaneous occurrence of L and D deformations since the early loading stages and denoted as "true L-D interaction", and (ii) the other stemming from a "secondary bifurcation", which occurs when the not so close L and D critical buckling stresses are well below the yield stress. However, further research is still required before it is possible to quantify adequately the relevance of the L-D interaction effects – moreover, it is also necessary to consider additional cross-section shapes.

The fruits of this ongoing investigation will help to (i) define the field of application and (ii) asses the merits of the existing DSM design methods to account for L-D interaction, proposed in quite specific/limited contexts.

ACKNOWLEDGEMENTS

The financial support of FCT (*Fundacão para a Ciência e a Tecnologia* – Portugal), through the research project PTDC/ECM/108146/2008, is gratefully acknowledged.

REFERENCES

Bebiano R, Pina P, Silvestre N & Camotim D 2008. GBTUL 1.0 β – Code for buckling and vibration analysis of thin-walled members, available at *http://www.civil.ist.utl.pt/gbt*.

Camotim D, Dinis PB, Young B & Silvestre N 2013. Local-distortional interaction in cold-formed steel columns: non-linear behaviour, ultimate strength and DSM design. In A. Zingoni (ed.), *Structural Engineering, Mechanics and Computation* (SEMC 2013 – Cape Town, 2-4/9). *Proc. 5th intern. conf.*: in press.

Dinis PB, Camotim D & Silvestre N 2007. FEM-based analysis of the local-plate/distortional mode interaction in cold-formed steel lipped channel columns. *Computers & Structures*, 85(19-20): 1461–1474.

Dinis PB, Silvestre N & Camotim D 2009. On the relevance of local-distortional interaction in the post-buckling behaviour and strength of cold-formed steel lipped channel columns. In B. Topping, L.C. Neves, R.C. Barros (eds.), *Civil, Structural and Environmental Engineering Computing* (CC 2009 – Funchal, 1-4/9), Civil-Comp Press (Stirling). *Cd-Rom Proc. 12th intern. conf.*: paper 22.

Kwon YB, Kim BS & Hancock GJ 2009. Compression tests of high strength cold-formed steel channels with buckling interaction. *Journal of Constructional Steel Research*, 65(2): 278–89.

Martins AD, Camotim D, Dinis PB & Providência P (2013). Relevance of local-distortional interaction effects in lipped channel columns. In B. Topping (ed.), *Civil, Structural and Environmental Engineering Computing* (CC 2013 – Cagliari, 3-6/9), Civil-Comp Press (Stirling). *Cd-Rom Proc. 14th intern. conf.*: in press.

Schafer BW 2008. Review: the Direct Strength Method of cold-formed steel member design. *Journal of Constructional Steel Research*, 64(7-8): 766–78.

Silvestre N, Camotim D & Dinis PB 2012. Post-buckling behaviour and direct strength design of lipped channel columns experiencing local-distortional interaction. *Journal of Constructional Steel Research*, 73(June): 12–30.

Yang D & Hancock GJ 2004. Compression tests of high strength steel channel columns with interaction between local and distortional buckling. *Journal of Structural Engineering*, 130(12): 1954–1963.

Yap DCY & Hancock GJ 2011. Experimental study of high strength cold-formed stiffened web steel sections. *Journal of Structural Engineering*, 137(2): 162–72.

Young B & Rasmussen KJR 1999. Shift of effective centroid in channel columns, *Journal of Structural Engineering*, 125(5): 524–531.

Young B, Silvestre N & Camotim D 2013. Cold-formed steel lipped channel columns influenced by local-distortional interaction: strength and DSM design. *Journal of Structural Engineering*, in press.

Research and Applications in Structural Engineering, Mechanics and Computation – Zingoni (Ed.)
© 2013 Taylor & Francis Group, London, ISBN 978-1-138-00061-2

Design of Z-section purlins under combined axial compression and bending

J. Becque
The University of Sheffield, Sheffield, South Yorkshire, UK

K.J.R. Rasmussen
The University of Sydney, Sydney, New South Wales, Australia

ABSTRACT: The paper presents a design methodology for Z-section purlins subject to combined axial compression and bending. A specific application arises when Z roof purlins are used as temporary struts in between portal frames during construction and are thus subject to compression resulting from wind loading on the frames in combination with their self-weight. In order to arrive at an economic design, the rotational restraint provided by the purlin end connections, as determined from an experimental program, is taken into account through a rational column buckling analysis. Simple span purlins, as well as purlins lapped with an adjacent span, are considered. The effects of fly-bracing and bridging are also studied.

1 BACKGROUND

As part of a fast and economical way to construct steel framed buildings, roof purlins are often counted upon during the construction phase to act as struts in between the main frames (Fig. 1).

In this situation, before the attachment of roof and wall sheeting, the purlins are subjected to an axial compressive load as a result of wind loading perpendicular to the frames (which accumulates over consecutive bays), in combination with bending moments resulting from the self-weight. Since the principal axes of a Z-section are inclined relative to the vertical, the self-weight results in biaxial bending.

Despite the fact that this only constitutes a temporary situation, it is paramount that the proposed design process is at the same time safe and economical. The latter can be achieved by incorporating the beneficial effect of the rotational end restraints provided by the connections. Three types of purlin-to-rafter connections were considered in this research (Fig. 2):

a. a purlin connected to the rafter through a cleat plate with two bolts (in what follows referred to as a 'simple connection')
b. a purlin connected to a cleat plate and lapped with an adjacent (unloaded) span (a 'continuous connection')
c. a purlin connected to a cleat plate, without lapping, but connected to the rafter by additional fly-bracing. The primary purpose of the fly-bracing is to stabilize the bottom flange of the rafter under uplift wind loading.

Single purlins as well as purlin pairs connected by bridging were considered in this research. Three different cross-sections were part of the investigation: Z200-15, Z200-19 and Z200-24. Their (nominal) geometry is detailed in Figure 3 and Table 1. All purlins were made of G450 steel to AS 1397 (2011) with a nominal yield stress of 450 MPa.

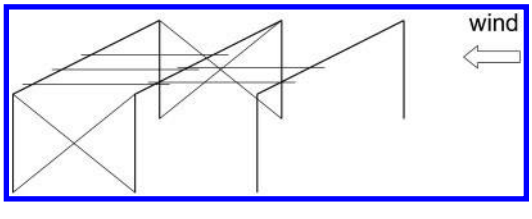


Figure 1. Purlins temporarily used as struts during construction.

2 EXPERIMENTAL PROGRAM

An experimental program was set up to measure the amount of rotational restraint provided by the three different connections previously mentioned.

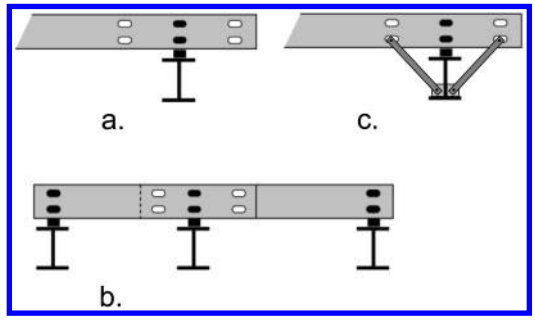


Figure 2. Purlin-to-rafter connections.

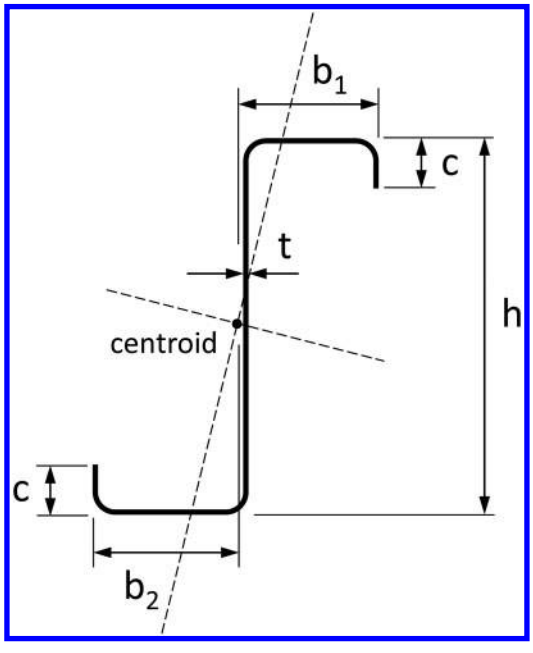


Figure 3. Cross-section geometry.

Table 1. Cross-sectional dimensions.

	h mm	t mm	c mm	b_1 mm	b_2 mm
Z200-15	203.0	1.5	16.0	74.0	79.0
Z200-19	203.0	1.9	19.5	74.0	79.0
Z200-24	203.0	2.4	21.0	74.0	79.0

The restraint was measured about both a horizontal and a vertical axis of bending. Figure 4 shows a typical test set-up. A purlin segment was bolted to a cleat plate, welded to a 360UB45 rafter stub, using two M12 grade 4.6 bolts. A 32 kN jack, placed at a distance of 0.5 m from the centerline of the connection, was then used to apply an increasing moment while maintaining the displacement rate at 0.2 mm/s.

All tests were carried out on Z200-15 purlins. Since this cross-section featured the thinnest web out of the three cross-sections considered, the tests yielded conservative values for the rotational stiffness of the connections. Three identical tests were carried out for each connection type and for each axis of rotation. Figure 5 shows the set-up used for a continuous connection, where the load was applied on a cantilever purlin, lapped over a distance of 2.2 m with an adjacent 11.5 m span. A span length of 11.5 m is the maximum length used in practical applications and therefore conservative test results were obtained for the rotational restraint of a continuous connection. Significant sagging and twisting of the purlin at mid-span was observed, even before applying any load.



Figure 4. Experimental set-up: simple connection.



Figure 5. Experimental set-up: continuous connection.

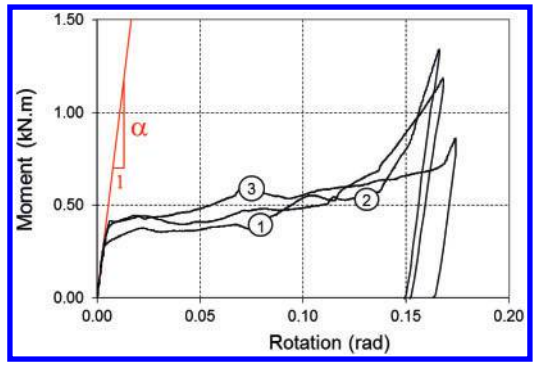


Figure 6. Moment-rotation diagram (simple connection rotating about horizontal axis).

By way of an example, Figure 6 shows the moment-rotation diagram of a simple connection about the horizontal X-axis. The initial rotational stiffness values α before slip occurred are listed in Table 2 for all tests. The standard deviations σ and the coefficients of variation V over each set of three tests are also listed. Average stiffness values are indicated by

Table 2. Calculation of (α_{Xc}, α_{Yc}); α and σ in kNm/rad.

	simple		continuous		simple + fly-brace	
	α_Y	α_X	α_Y	α_X	α_Y	α_X
Test 1	-	81.2	24.2	221	8.77	1850
Test 2	1.84	90.5	22.9	242	5.87	2823
Test 3	1.94	87.9	23.7	352	6.12	3292
α_{Xm}, α_{Ym}	1.89	86.5	23.6	272	6.92	2655
σ_α	0.071	4.80	0.66	70	1.61	736
V_α	0.037	0.055	0.028	0.26	0.23	0.28
α_{Xc}, α_{Yc}	1.33	60.9	16.6	191	4.87	1868

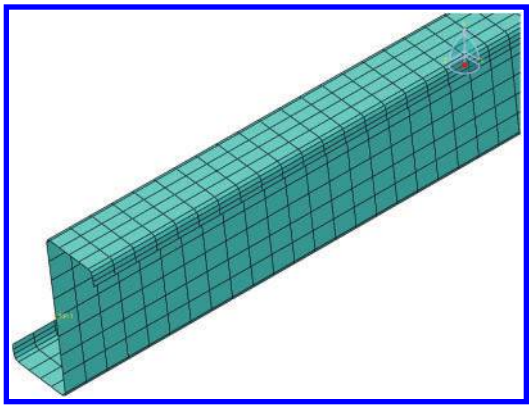


Figure 7. FE mesh.

α_{Xm} and α_{Ym}, while α_{Xc} and α_{Yc} stand for characteristic values, obtained by subtracting twice the standard deviation σ from the average.

It is seen from Table 2 that the restraint provided about the vertical Y-axis by any type of connection is rather small. Lapping the purlin with an adjacent span significantly increases the rotational restraint about a horizontal axis, while adding fly-bracing results in the most pronounced increase.

3 NUMERICAL SIMULATIONS

The finite element (FE) software package ABAQUS/CAE v6.5 was used to study (i) single purlins, and (ii) a pair of purlins with one, two or three lines of bridging, under a combination of self-weight and axial compression. Since practical span lengths range from 8.5 m to 11 m, simulations were carried out for lengths of 8.5 m, 10 m and 11.5 m, while Z200-15, Z200-19 and Z200-24 cross-sections were included.

The S4R element, a 4-node shell element with reduced integration, was used in the simulations. This element accounts for finite membrane strains and arbitrarily large rotations and is therefore suitable for large-strain geometrically non-linear analyses. A convergence study was carried out to determine a suitable mesh size. The mesh is shown in Figure 7.

Table 3. Z200-15 purlin ultimate strength axial capacities.

	Number of lines of bridging			
	0	1	2	3
L	N_u	N_u	N_u	N_u
m	kN	kN	kN	kN
8.5	6.77	6.82	6.82	6.82
10.0	4.56	5.21	5.32	5.36
11.5	3.11	4.42	4.79	4.88

The rotational end restraint provided by the connections was modeled using non-linear rotational springs with the actual moment-rotation behavior determined from the experimental program.

Geometrically non-linear analyses were carried out in two steps. In a first step, only the self-weight of the purlin was applied. In a second step, the purlin was compressed, in the presence of the self-weight, by imposing a displacement in the axial direction at one of the supports.

For purlins with bridging, the bridging was modeled as a 65 mm deep channel with 30 mm wide flanges, in accordance with typical industry practice. At both ends of the bridging channel the webs were allowed to rotate about the connecting line with the purlin web, while the flanges were left unconnected. The effect of installing bridging is illustrated in Table 3, which lists the ultimate capacities in compression in the presence of self-weight for single Z200-15 purlins and Z200-15 purlins with one, two and three lines of bridging. Not surprisingly, the effect of the bridging appears to be most beneficial for the longer 10 m and 11.5 m span purlins.

The main purpose of these FE studies was to numerically confirm the validity of the design equations proposed in Section 5 of this paper.

4 RATIONAL COLUMN ANALYSIS

In a first step towards the development of a design methodology, the stability of a Z-purlin under axial compression only, but taking into account rotational end restraints, was investigated. The problem is complicated by the fact that the rotational end restraints act about horizontal and vertical axes, while the principal bending axes of the section are inclined. In a general case, this leads to a coupling of the buckling displacements through the boundary conditions, resulting in simultaneous buckling about both principal axes, as demonstrated by Rasmussen and Trahair (2005). In order to be applicable to the problem under consideration, where different amounts of restraint may be encountered at both ends (e.g. a simple connection at one end and a lapped connection at the other end), the theory by Rasmussen and Trahair (2005) first needed modification.

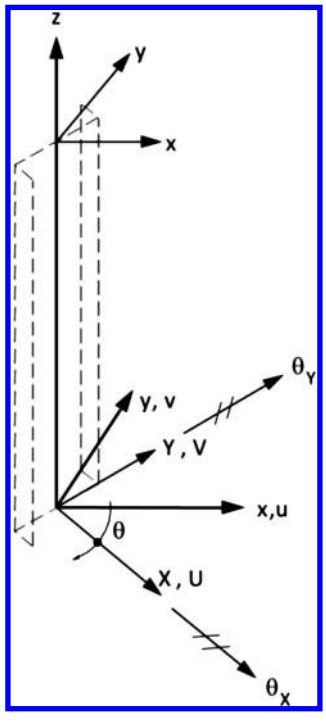


Figure 8. Coordinate systems.

Figure 8 depicts a column which is elastically restrained against rotations about oblique (X, Y)-axes, rotated over an angle θ from the principal (x, y)-axes.

At $z = 0$, the elastic external restraining moments about the X and Y axes are

$$\overline{M}_{X0} = \alpha_{X0}\theta_{X0} \qquad \overline{M}_{Y0} = \alpha_{Y0}\theta_{Y0} \tag{1}$$

where $(\alpha_{X0}, \alpha_{Y0})$ are the rotational rigidities of the supports at $z = 0$ and $(\theta_{X0}, \theta_{Y0})$ are the rotations about the X and Y axes at $z = 0$:

$$\theta_{X0} = -\left.\frac{dV}{dz}\right|_{z=0} \qquad \theta_{Y0} = \left.\frac{dU}{dz}\right|_{z=0} \tag{2}$$

Similarly, at the opposite end, $z = L$, external restraining moments about the X and Y axes are:

$$\overline{M}_{XL} = \alpha_{XL}\theta_{XL} \qquad \overline{M}_{YL} = \alpha_{YL}\theta_{YL} \tag{3}$$

where $(\alpha_{XL}, \alpha_{YL})$ are the rotational rigidities of the supports at $z = L$ and $(\theta_{XL}, \theta_{YL})$ are the rotations about the X and Y axes:

$$\theta_{XL} = -\left.\frac{dV}{dz}\right|_{z=L} \qquad \theta_{YL} = \left.\frac{dU}{dz}\right|_{z=L}. \tag{4}$$

The governing differential equations (DEs) for flexural buckling are (Timoshenko & Gere 1961; Trahair 1993):

$$(EI_y u'')'' + (Nu')' = 0 \tag{5}$$

$$(EI_x v'')'' + (Nv')' = 0 \tag{6}$$

where EI_x and EI_y are the flexural rigidities for bending about the principal x and y axes respectively and (u, v) are the principal axis displacements as shown in Figure 7. It is assumed that $EI_x \geq EI_y$.

Assuming the flexural rigidities and the internal compressive force (N) are constant along the column, the exact solution to the DEs is:

$$u = C_1 \sin\left(\frac{\sqrt{n}\pi z}{L}\right) + C_2 \cos\left(\frac{\sqrt{n}\pi z}{L}\right) + C_3 \frac{z}{L} + C_4 \tag{7}$$

$$v = C_5 \sin\left(\frac{\sqrt{en}\pi z}{L}\right) + C_6 \cos\left(\frac{\sqrt{en}\pi z}{L}\right) + C_7 \frac{z}{L} + C_8 \tag{8}$$

where and $C_1 \ldots C_8$ are arbitrary constants, and n and e are non-dimensional measures of the buckling load and the flexural rigidity (EI_x):

$$n = \frac{N_E}{N_{Ey}} \tag{9}$$

$$e = \frac{EI_x}{EI_y}. \tag{10}$$

In Eq.(9), N_E is the buckling load and N_{Ey} is the Euler load for flexural buckling about the minor y-axis without the presence of restraints:

$$N_{Ey} = \frac{\pi^2 EI_y}{L^2}. \tag{11}$$

The boundary conditions (BCs) are:

$$u = v = 0 \qquad \text{at } z = 0, L \tag{12}$$

$$\overline{M}_{X0} = M_{X0} \qquad \overline{M}_{Y0} = M_{Y0} \qquad \text{at } z = 0 \tag{13}$$

$$\overline{M}_{XL} = -M_{XL} \qquad \overline{M}_{YL} = -M_{YL} \qquad \text{at } z = L. \tag{14}$$

where (M_X, M_Y) are the bending moments about the oblique $X-$ and Y-axes.

To determine the rotations (θ_X, θ_Y), we obtain the displacements in the oblique axis directions:

$$U = u\cos(\theta) + v\sin(\theta) \tag{15}$$

$$V = v\cos(\theta) - u\sin(\theta) \tag{16}$$

and utilize:

$$\theta_X = -\frac{dV}{dz} \tag{17}$$

$$\theta_Y = \frac{dU}{dz}. \tag{18}$$

To determine the bending moments (M_X, M_Y) we obtain the bending moments (M_x, M_y) about the principal (x, y)-axes:

$$M_x = -EI_x v'' \tag{19}$$

$$M_y = EI_y u'' \tag{20}$$

and utilize:

$$M_X = M_x \cos(\theta) + M_y \sin(\theta) \tag{21}$$

$$M_Y = M_y \cos(\theta) - M_x \sin(\theta). \tag{22}$$

Equations (13, 14) can be expressed in terms of the displacements (u, v) by combining Eqs. (1–4, 19–22), where the displacement functions satisfying the DEs are given by Eqs. (7–8). On making the substitutions, the boundary conditions yield eight homogeneous equations in $C_1 \ldots C_8$ which may be arranged as:

$$[K]\{C\} = \{0\} \tag{23}$$

Non-trivial solutions are obtained by requiring:

$$\det([K]) = 0 \tag{24}$$

which produces an implicit equation in the non-dimensional buckling load n.

5 DESIGN EQUATIONS

5.1 *Single Z purlins without bridging*

It is proposed that the capacity of a single Z purlin subject to combined axial load N* and self-weight is determined from the following equation:

$$\frac{N^*}{\phi_c N_c} + \frac{M^*}{\phi_b M_{cy} \alpha_m} \le 1.0 \tag{25}$$

where ϕ_c and ϕ_b are the resistance factors applied to the ultimate capacity of the member in compression and bending, respectively. In the context of AS/NZS4600 (2005) (concurrent with the AISI (2007) guidelines for cold-formed steel): $\phi_c = 0.85$ and $\phi_b = 0.95$. N* and M* are the design values of the axial force and the mid-span (self-weight) moment, respectively. When calculating N_c, the capacity of the purlin under pure axial compression, the effect of the purlin end restraints may be brought into account by calculating the elastic Euler buckling load N_E according to the rational analysis explained in the previous paragraph.

M_{cy} is the section moment capacity about the minor principal axis. The Z200-15, Z200-19 and Z200-24 sections are thereby fully effective with respect to local buckling.

The moment amplification factor α_m in Eq. (25) is determined as:

$$\alpha_m = 1 - \frac{N^*}{N_E} \tag{26}$$



Figure 9. Z purlin in unrestrained bending.

where the Euler buckling load N_E may again be determined from a rational buckling analysis.

The proposed design equation (25) originates from the experimental observation that, in the presence of a bending moment, the cross-sections of the purlin near mid-span tend to rotate until, eventually, the minor principal axis is nearly aligned with the horizontal (Fig. 9).

The ultimate capacities obtained in the finite element models were compared to the predictions of Eq. (25) with the resistance factors set equal to 1.0. It was concluded that the proposed equation (25) results in safe predictions for all cases studied. The error is within the range of 15%–19% for the simple span purlins and within 11-18% for the purlins with one simple connection and one lapped connection. Load tables can be derived from Eq. (25) for relevant span lengths, cross-sections and end conditions and are provided in Becque & Rasmussen (2012).

5.2 *Z Purlins with bridging*

It was found that Z purlins with bridging, subject to combined self-weight and axial load, may safely be designed using the existing interaction equation of AS/NZS4600 (2005) (or AISI 2007):

$$\frac{N^*}{\phi_c N_c} + \frac{C_{mx} M_x^*}{\phi_b M_{cx} \alpha_{mx}} + \frac{C_{my} M_y^*}{\phi_b M_{cy} \alpha_{my}} \le 1.0 \tag{27}$$

The axial load capacity as determined from Eq. (27), however, should not be less than the capacity determined from Eq. (25) in the absence of bridging. M_x^* and M_y^* are obtained by projecting the design self-weight moment M* onto the principal axes x and y of the cross-section. M_{cy}, N*, N_c, ϕ_c and ϕ_b are as previously defined under Section 5.1, and C_{mx} and C_{my} may be taken as 0.85, as per AS/NZS 4600.

The effect of the rotational end restraint may be taken into account by calculating the buckling load

N_E, used to determine N_c, from the rational analysis in Section 4. The moment amplification factors α_{mx} and α_{my} are determined from Eq. (26), where N_E is taken as the Euler buckling load about the x- or the y-axis, respectively, taking into account the effect of the rotational end restraints.

In Eq. (27), M_{cx} is the member moment capacity about the major principal axis. When applying AS/NZS4600 (2005), M_{cx} is the minimum of the flexural-torsional buckling capacity, taking into account local buckling, and the distortional moment capacity M_d. M_d was calculated based on a distortional slenderness value λ_d obtained from the software package ThinWall (Papangelis & Hancock 1995) and found to be equal to 8.75 kNm for the Z200-15 section, 12.90 kNm for the Z200-19 section and 18.01 kNm for the Z200-24 section.

Eq. (27) (with $\phi_b = \phi_c = 1.0$) matches the results of the FE simulations within 0%-34%, while consistently erring on the safe side. Load tables based on Eq. (27) for Z200-15, Z200-19 and Z200-24 purlins with one, two or three lines of bridging and various span lengths and end conditions are provided in Becque & Rasmussen (2012).

6 CONCLUSIONS

This paper presents practical design equations which cover the stability of Z-section purlins under combined axial force and self-weight bending. Single purlins, as well as purlins with one or more lines of bridging were considered. The results of an experimental program are presented which aimed to measure the degree of rotational end restraint of three different connections: a simple cleat plate connection, a connection with fly-bracing and a lapped connection. It is shown how the beneficial effect of these end restraints on the purlin stability can be taken into account through a rational column buckling analysis. It is seen that significant gains in the elastic column buckling capacity can thus be obtained, ranging from 34% on average for a simply supported Z-purlin to 69% for a Z-purlin lapped at one end and more than 100% for a Z-purlin with fly-bracing at one end. When compared to detailed FE analyses, the proposed design equations are consistently safe with an average difference in ultimate capacity of 15%.

REFERENCES

ABAQUS. 2005. *ABAQUS/CAE manual, v6.5*, Hibbit, Karlsson, and Sorensen, ABAQUS Inc., Pawtucket, RI.

AISI. 2007. *North American Specification for the Design of Cold-formed Steel Structural Members, AISI-S100*, American Iron and Steel Institute, Washington DC.

AS 1397. 2011. *Continuous Hot-dip Metallic Coated Steel Sheet and Strip—Coatings of Zinc and Zinc Alloyed with Aluminium and Magnesium*, Australian Standard, Standards Australia, Sydney, Australia.

AS/NZS 4600. 2005. *Cold-Formed Steel Structures*, Australian Standard/New Zealand Standard, Standards Australia, Sydney, Australia.

Becque, J. & Rasmussen, K.J.R. 2012. The stability of Z-section purlins used as temporary struts during construction. *Journal of Structural Engineering*, doi: 10.1061/(ASCE)ST.1943-541X.0000782, Posted ahead of print 1 Dec 2012.

Papangelis, J.P. & Hancock, G.J. 1995. Computer Analysis of Thin-walled Structural Members, *Computers and Structures* 56(1):157–176.

Rasmussen, K.J.R. & Trahair, N.S. 2005. Exact and approximate solutions for the flexural buckling of columns with oblique rotational end restraints, *Thin-Walled Structures* 43, 411–426.

Timoshenko, S.P. & Gere, J.M. 1961. *Theory of Elastic Stability*, 2nd edition, McGraw-Hill, New York.

Trahair, N.S. 1993. *Flexural-torsional buckling of structures*, CRC, Boca Raton, Florida, USA.

Research and Applications in Structural Engineering, Mechanics and Computation – Zingoni (Ed.)
© 2013 Taylor & Francis Group, London, ISBN 978-1-138-00061-2

Buckling of cold-formed lipped-channel stub columns

M. Dundu
University of Johannesburg, Johannesburg, South Africa

J. Lim
Queen's University Belfast, Belfast, UK

ABSTRACT: This paper presents an experimental investigation of short cold-formed lipped-channel columns compressed between pinned ends. The short columns are subjected to pure axial compressive loading. A total of 12 column specimens are tested and the columns are categorised into three groups depending on the length and thickness. The buckling modes of failure that occurred include local buckling and distortional buckling. A comparison of the experimental results with the loads predicted by the South African standard for the design of cold-formed steelwork code (SANS 10162-2) shows that the code is not conservative enough to cater for these columns.

1 INTRODUCTION

Cold-formed lipped short columns are vulnerable to local or distortional buckling or both, because of the high width-to-thickness ratios of the web and/or flange. Local buckling (LB) occurs when the line junction of both corners do not change, with the adjoining lip, flange and web elements failing by plate flexure alone (Fig. 1(a)). Distortional buckling occurs in thin-walled channel sections when the lip-stiffened flange of the section rotates about the flange-web junction. This usually occurs if the lip stiffener does not have enough stiffness to prevent the flange from rotating. The rotation can cause the flange to either move outward (Outward distortional buckling (ODB)) or inward (Inward distortional buckling (ODB)) depending on the nature of the load, supporting system or imperfections. At ultimate failure, both rotations can be accompanied by the bending of the web (Figure 1 (b) and (c)). The wavelength of this mode of failure is in most cases between that of local and overall member buckling, which makes it a practical member length.

The aims of this paper are to investigate the behaviour (buckling failure modes) and the strength (compressive resistance) of short cold-formed lipped channel sections. According to Ziemian (2010), a short column is defined as a member that is sufficiently short so as to preclude member buckling when compressed, but sufficiently long to contain the same initial residual stress pattern as a much longer member cut from the same stock. For cold-formed steel sections, the stub-column length should be sufficiently long to exhibit local buckling as well as the effect of cold-forming on the column performance. The length of cold-formed stub columns should not be less than three times the largest dimension of the cross-section and no more than 20 times the least radius-of-gyration.

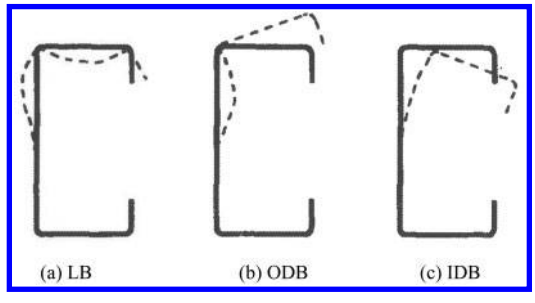


Figure 1. Local and distortional buckling modes.

Table 1. Dimensions of the columns.

Specimens (h × b × c × t)	L (mm)	r_i (mm)	r_y (mm)	3h (mm)	20r_y (mm)
300 × 75 × 20 × 2.0	500	3.00	25.7	900	514
	750	3.00	25.7	900	514
	1000	3.00	25.7	900	514
	1250	3.00	25.7	900	514
300 × 75 × 20 × 2.5	500	3.75	25.4	900	508
	750	3.75	25.4	900	508
	1000	3.75	25.4	900	508
	1250	3.75	25.4	900	508
300 × 75 × 20 × 3.0	500	4.50	25.1	900	502
	750	4.50	25.1	900	502
	1000	4.50	25.1	900	502
	1250	4.50	25.1	900	502

The cold-formed lipped sections tested are given in Table 1, and do not comply with the length provisions for a short column, determined by Ziemian (2010). In this table L is the length of the stub

Table 2. Average material properties.

Specimen	f_y (MPa)	f_u (MPa)	ε_u (%)	E (MPa)
300 × 75 × 20 × 2.0	242.79	344.88	20.37	200 766
300 × 75 × 20 × 2.5	282.26	372.20	16.86	203 058
300 × 75 × 20 × 3.0	258.94	350.42	20.35	206 308

column, h is the depth, b is the width, c is the size of the lip, t is the thickness, r_i is the internal radius and r_y is the radius of gyration of the section. To cover a wider range of lengths it was decided to test three specimens of each section size (Table 1). The 300 × 75 × 20 × 2.0, 300 × 75 × 20 × 2.5 and 300 × 75 × 20 × 3.0 are abbreviated as C2.0, C2.5 and C3.0 in Table 3, respectively.

2 MATERIAL PROPERTIES

The material properties of the cold-formed column sections were determined from coupon tests. Three longitudinal coupons were cut from the web to establish the yield stress, ultimate stress, elastic modulus and the elongation of the material. The coupons were prepared and tested according to the British Standard, BS 18. A 1195 Instron testing machine with an ultimate capacity of 100 kN was utilized to test the coupons. The tensile load was applied at a low rate of 3 mm/min. A calibrated extensometer was utilized to measure the strain. The average material properties are shown in Tables 2. In this table, f_y is the 0.2% proof yield strength, f_u is the ultimate strength, E is the elastic modulus and ε_u is the strain at fracture based on a gauge length of 50 mm. These values were established from stress – strain curves obtained from coupon tests. The 0.2% yield strengths were used to calculate the theoretical strengths of the columns.

3 TEST PROCEDURE

A total of 12 short columns were tested under pure axial compressive loading. The specimens were delivered by the manufacturer in lengths of 6 m. Each specimen was cut to a specified column length. The ends of the columns were machined flat and the load was applied at the centroid to ensure a uniform distribution of the load throughout the entire cross-sectional area of the column. The load was applied through 2 thick plates with grooves at the centre to accommodate a spherical ball, so as to simulate a pin. A Moog testing machine with an ultimate capacity of 2000 kN was used for the experimental test. To allow gradual failure of the columns, the load was applied at a rate of 2 mm/min. A schematic experimental set-up is shown in Figure 2. The testing machine measured the axial compressive load and displacement.

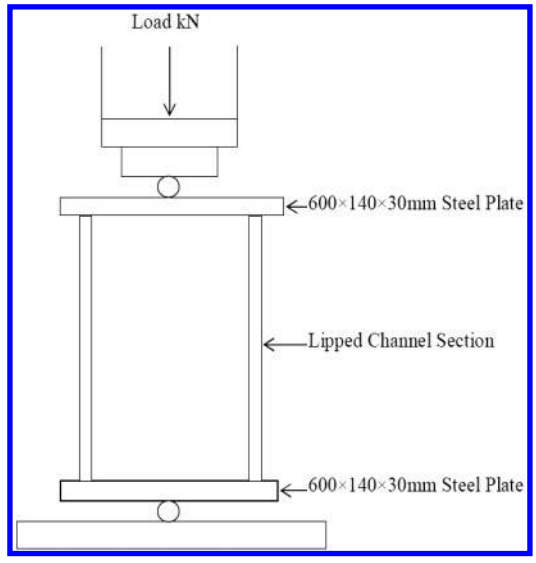


Figure 2. Schematic test setup.

Table 3. Test results.

CFS	L mm	P_{EX} kN	P_Y kN	P_{EY} kN	P_C kN	$\frac{P_{EX}}{P_Y}$	$\frac{P_{EX}}{P_{EY}}$	$\frac{P_{EX}}{P_C}$
C2.0	500	119	231	132	131	0.52	0.91	0.91
	750	114	231	132	129	0.49	0.87	0.88
	1000	110	231	132	127	0.48	0.83	0.86
	1250	115	231	132	125	0.50	0.87	0.92
C2.5	500	160	333	207	205	0.48	0.77	0.78
	750	167	333	207	202	0.50	0.81	0.83
	1000	182	333	207	197	0.55	0.88	0.92
	1250	165	333	207	192	0.49	0.79	0.86
C3.0	500	156	363	246	243	0.43	0.64	0.64
	750	161	363	246	239	0.45	0.66	0.68
	1000	178	363	246	234	0.49	0.73	0.76
	1250	146	363	246	227	0.40	0.60	0.65

4 TEST RESULTS

The experimental compressive resistance (P_{EX}), gross squash load ($P_Y = A_g f_y$), effective squash load ($P_{EY} = A_{ef} f_y$) and the buckling compressive resistance ($P_C = A_{ef} f_c$) are given in Table 3. The effective area (A_{ef}) is determined using the effective width method, where the channel lips area, the flanges area and the web area of the column are analysed separately, and P_Y and P_C are calculated using the stress conditions of $f = f_y$ and $f = f_c$, respectively. The predicted resistance values are obtained using the South African code, SANS10162-2. This code is based on the Canadian code, CAN/CSAS16.1-M01 and the North American Specification, AISI S100-07.

Table 3 shows that there is not much difference between the experimental compressive resistances of the chosen lengths of each specimen. This implies that

both lengths of columns can be classified as short. If this is the case then it is not appropriate to use the length suggested by Ziemian (2010), for these cold formed sections. In order to classify the length of these sections it is proposed to adopt the length classification for hot-rolled stub columns. According to this classification, the length of hot-rolled stub columns should not be less than $(2d + 250\,\text{mm})$ or $3d$, whichever is smaller, and not greater than $20r_y$ or $5d$, whichever is larger, where d is the depth of the shape and r_y is radius-of-gyration about the minor axis. This classification is wide enough to accommodate these sections.

Table 3 also shows the experimental buckling resistance to be almost 50% of the gross-sectional yield resistance for the $300 \times 75 \times 20 \times 2.0$ and $300 \times 75 \times 20 \times 2.5$ specimens. This percentage reduces to about 45% for the $300 \times 75 \times 20 \times 3.0$ specimens. This huge decrease in resistance clearly shows the importance of considering local and distortional buckling in such members. The effect is also seen in the corresponding effective yield and the buckling resistances. The difference in column strength between the sections tested is as a result of the different thickness, yield strengths and the magnitude of the residual stresses.

A clear trend can be seen here; the ratio of the experimental strength to the predicted strength decreases with increase in thickness of the specimen. Residual stresses tend to affect thicker sections and are responsible for the lower strength ratio of the $300 \times 75 \times 20 \times 3.0$. One other confirmation that the tested columns are actual short is that the effective yield resistance and the buckling resistance are almost the same.

A comparison of the tests results and calculated unfactored resistances shows that the SANS 10162-2 specification and its related specifications (CAN/CSA S16.1-M01 and AISI S100-07) overestimates the compressive strengths of short cold-formed lipped channel columns. On average the tests loads for the $300 \times 75 \times 20 \times 2.0$, $300 \times 75 \times 20 \times 2.5$, $300 \times 75 \times 20 \times 3.0$ specimens are 87%, 81% and 66% of the effective squash or buckling loads predicted by SANS 10162-2, respectively. For the $300 \times 75 \times 20 \times 3$, the average difference between the test results and the code predicted strength is 34%. The largest cause of this low resistance is local buckling and distortional buckling. Local buckling occurred at the end of the column in the 500 mm, 750 mm, and 1000 mm length columns and may have been initiated by the cutting process. Lam Wang and Chung (2006), and Wang, Lam and Chung (2006) found that the cutting process causes cross-section distortion and initial geometric imperfection, which in turn influences the buckling capacities of the short columns. In this investigation, Lam, Wang and Chung (2006) found the test compressive resistances of fixed ended steel stub columns, made out of $150 \times 65 \times 13 \times 1.6$ mm and $100 \times 50 \times 10 \times 1.6$ mm cold-formed lipped channels, to be 75% and 77% of the predicted resistance, calculated using the British code (BS 5950),



Figure 3. Bucking failure modes.

respectively. A similar investigation by Young and Rasmussen (1998) illustrated that design codes overestimated the strength of short cold-formed column lengths. Kwon and Hancock (1992) also found the maximum stresses in small sized lipped channel sections to range from 25% to 34% of the yield stress.

Another possible cause of the substantial low ratios of test versus predicted strengths might be the size of the lip. Specimens with a smaller effective lip size resist less load than those with a larger lip size (Known and Hancock, 1992).

5 FAILURE MODES

Two buckling modes of failure were observed from the experimental tests, namely local, and distortional buckling. Local buckling occurs when parts or portions of the section elements yield before the actual yielding of the member is achieved, and was observed in very short columns, in lengths ranging from 500 mm to 1000 mm (Figure 9(a)-(c)). The local buckling failure mode of these columns was more excessive at the ends of the columns and caused the web to buckle outwards. This failure mode is more distinct in thinner sections and the buckle of these sections seems to affect a larger area of the web than thicker sections. As indicated above the process of cutting cold-formed steel sections to form a stub column may have led to cross section distortion and initial geometric imperfection.

Distortional buckling or stiffener buckling is a mode characterized by rotation of the flange at the flange/web junction in members with edge stiffened elements (Schafer and Pekoz, 1998). Distortional buckling was observed in 1250 mm length columns. Figs. 3(d) show evidence of distortional buckling. In this figure distortional buckling is characterized by the closing up of the two flanges. This mode of failure is probably unsymmetrical because the section was distorted during the cutting process (Lam, Chung and Wang, 2006).

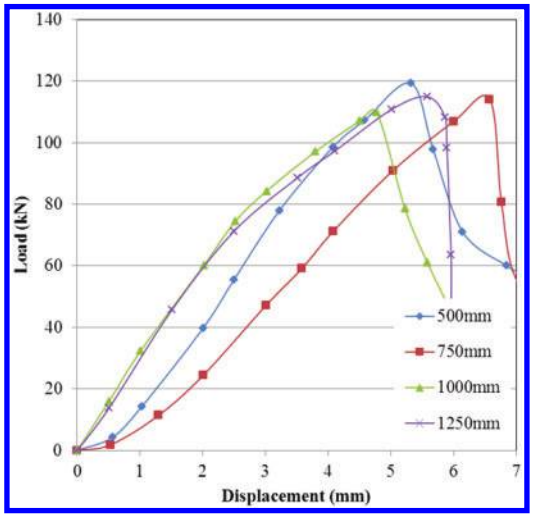


Figure 4. 300 × 75 × 20 × 2 short columns.

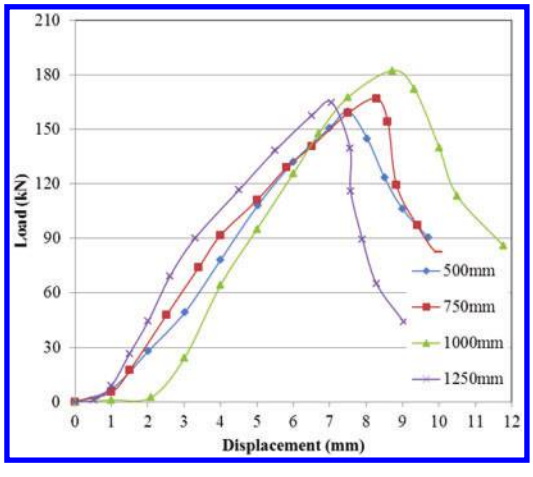


Figure 5. 300 × 75 × 20 × 2.5 short columns.

6 LOAD-AXIAL SHORTENING

The experimental load-displacement graphs for the three different sections are shown in Figure 4. The graphs are linear elastic up to the maximum load and there is little or no evidence of inelastic behaviour. For the 300 × 75 × 20 × 2 specimens, the load–axial shortening curves experience abrupt drops immediately after the ultimate loads, while for specimens 300 × 75 × 20 × 2.5 and 300 × 75 × 20 × 3.0 the load–axial shortening curve shows a smooth decrease of loads at the post-ultimate range (Figures 4-5). The abrupt drops correspond to the sudden collapse of the columns in the tests. Generally, columns with larger thickness experience less abrupt drops in load immediately after the ultimate load compared with thinner sections.

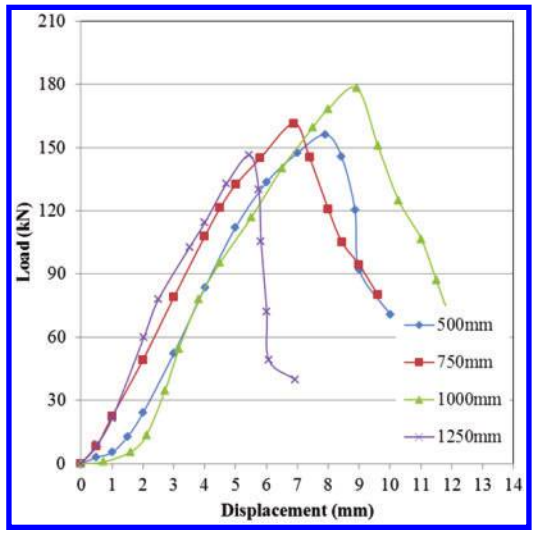


Figure 6. 300 × 75 × 20 × 3 short columns.

7 CONCLUSION

Ziemian's (2010) suggested length for short columns do not apply to these sections, however, the sections can be classified as short considering that there is little or no variation in the test strength achieved. Columns with length ranging from 500 mm to 1000 mm failed by local buckling of the web, whilst the 1250 mm column length failed by distortional buckling. The ultimate compressive resistance obtained from the test results ranged from 66–87% of the compressive resistance calculated based on SANS10162-2 and its related specifications. This implies that the design predicted strengths by the SANS10162-2 specification generally overestimated (not conservative) the design compressive strengths of the short cold-formed lipped channel columns. The predicted strengths for the 300 × 75 × 20 × 3 mm columns are much larger than the test strength. This huge difference is caused by the fact that the lips for these sections are all fully effective in resisting local buckling. Local buckling reduced the effectiveness of the lips of the 300 × 75 × 20 × 2 mm and 300 × 75 × 20 × 2.5 mm column sections.

8 ACKNOWLEDGEMENTS

The author wishes to acknowledge Nhlanhla Tshabalala, a final year Civil Engineering student, who assisted in carrying out the tests, reported in this paper and the University of Johannesburg Research Committee (URC) for sponsoring this research.

REFERENCES

AISI S100. 2007. *North American Specification for the Design of Cold-Formed Steel Structural Members*. Washington DC, USA.

BS 18. 1987. *British standard method for tensile testing of metals*. London: British Standard Institution.

BS5950-5. 1998. *Structural use of steelwork in building: Code of practice for design of cold formed thin gauge sections*. London: British Standards Institution.

CAN/CSAS16.1-M01. 2001. *Limit States Design of Steel Structures - CAN/CSA-S16-01*. Rexdale, Ontario, Canada: Canadian Standards Association.

Kwon, Y.B. & Hancock, G.J. 1992. Tests of Cold-Formed Channels with Local and Distortional Buckling. *J. Struct. Eng*. 117(7): 1786–1803.

Lam, S.S.E., Wang, X.P. and Chung, K.F. 2006. Load-carrying capacities of cold-formed steel cut stub columns with lipped C-section. *Thin-Walled Struct* 44: 1077–1083.

SANS 10162-2. 2005. *The structural use of steel, Part 2: Limit-state design of cold-formed steelwork*. Pretoria, South Africa: South Africa National Standards.

Schafer, B.W. & Pekoz, T. 1998. Computational Modelling of Cold-Formed Steel: Characterizing Geometric Imperfections and Residual Stresses. *J. Constr. Steel Res.* 47: 193–210.

Wang, X.P., Lam, S.S.E. & Chung, K.F. 2006. Cross Section Distortion due to Cutting of Cold-formed Steel Lipped C-Section. *Thin-Walled Struct*. 44(3): 271–280.

Young, B. & Rasmussen, K.J.R. 1998. Design of lipped channel columns. *J. Struct. Eng*. 124(2): 140–148.

Ziemian, R. 2010. *Guide to Stability Design Criteria for Metal Structures*. Hoboken, New Jersey, USA: John Wiley and Sons.

Research and Applications in Structural Engineering, Mechanics and Computation – Zingoni (Ed.)
© 2013 Taylor & Francis Group, London, ISBN 978-1-138-00061-2

Continuous beam tests on aluminium alloy SHS and RHS with internal stiffeners

M. Su & B. Young
Department of Civil Engineering, The University of Hong Kong, Hong Kong, China

L. Gardner
Department of Civil Engineering, Imperial College London, London, UK

ABSTRACT: The aims of this study are to generate experimental data on aluminium alloy continuous beams of square and rectangular hollow section (SHS and RHS) with internal stiffeners, as well as to assess the current design approaches for indeterminate structures using this new cross-section shape. The experimental programme comprised material tests and five-point bending tests (i.e. continuous beams over three supports) with three different loading configurations. Generally, the specimens failed by the formation of a collapse mechanism comprising three plastic hinges. Comparisons of the test results with design strengths were also carried out. The design strengths predicted by the American (2010), Australian/New Zealand(1997) and European (2007) specifications are found to be rather conservative. The plastic hinge method in Annex H of Eurocode 9 (2007) provides improved results, while the Continuous Strength Method (CSM) for indeterminate structures gives the most accurate and consistent predictions. The results reveal that both strain hardening at the cross-sectional level and moment redistribution at the global system level have significant influence on the structural performance of stocky aluminium alloy structures.

1 INTRODUCTION

Aluminium alloy structural members are being used increasingly widely nowadays owing to a range of advantageous characteristics. Ease of fabrication is one of the key benefits of aluminium alloys over steel, and should be taken into account in an economic comparison of aluminium and other metals (Mazzolani, 1994). The benefits arise from the extrusion procedure, which allows increasingly creative cross-sectional shapes to be formed.Square and rectangular hollow sections (SHS/RHS) have been widely used in a range of engineering applications, butthin-walledhollow sections are significantly affected by local buckling. In order to inhibit local buckling and utilize the cross-section more efficiently, internal cross stiffeners can be added to SHS/RHS. However, there are currently no available experimental data on either the bending or compression behaviour on this type of section.

Determination of the internal forces and moments in statically indeterminate structures cannot be achieved by statics alone, but requires knowledge of the stiffness of the structural elements, which may change during loading(e.g. through plastification).Design approaches for indeterminate structures often consider moment redistribution at the global system level, which can be addressed by means of global plastic design. Although some tests on aluminium alloy structural members subjected to bending (Langseth & Hopperstad, 1997; Faella et al., 2000; Mennink, 2002 and Su et al., 2012a) and compression (Lai & Nethercot, 1992; Moen et al., 1999; Zhu & Young, 2006; Zhu & Young 2009 and Su et al., 2012b) have been conducted, few tests on indeterminate aluminium alloy structures exist in the literature;thus a series of continuous beam tests was conducted in this study.

In the field of aluminium alloy structural member design, the design specifications of the American Aluminium Design Manual (AA, 2010), the Australian/New Zealand Standard (AS/NZS, 1997) and Eurocode 9 (EC9, 2007) are widely used. However, these specifications may lead to inaccurate capacity predictions for indeterminate structures comprising SHS/RHS with internal stiffeners due to the fact that the current design methods are (1) proposed based on traditional cross-section shapes; (2) not considering strain hardening (except Annex E in EC9) and (3) not accounting for moment redistribution(except Annex H in EC9).The continuous strength method (CSM) for indeterminate structures (Gardner et al., 2011) accounts for these factors and is described herein.

The aims of this study are to generate experimental data for aluminium alloy continuous beams of square and rectangular hollow section (SHS and RHS) with internal stiffeners, and to assess the current design approaches for indeterminate structures of this new cross-section shape.

2 EXPERIMENTAL INVESTIGATION

2.1 *Test specimens and specimen labelling*

A total of 20 continuous beam specimens of different cross-sectional geometry, defined using the symbols illustrated in Figure 1, was tested. The cross-sectional dimensions shown in Table 1 are the average measured values for each test specimen in this study. The measured material properties are also provided, which were determined by means of longitudinal tensile coupon tests. The symbols employed in Table 1 are defined as follows: E is the Young's Modulus, f_y is the material yield stress (taken as the 0.2% proof stress), f_u is the material ultimate stress, ε_u is the strain corresponding to the ultimate tensile stress of the material and F_{exp} is the total experimental ultimate load.

The specimens were labelled according to the type of material, cross-sectional dimensions and the test configuration. For example, the label "$+H50 \times 95 \times 10.5$B5I" defines a specimen of high strength aluminium alloy6061-T6, with cross-sectional dimensions of width B(50 mm) × height H(95 mm) × thickness t(10.5 mm). If the label starts with "N", it signifies that the specimen is of normal strength aluminium alloy 6063-T5. The symbol "B5I" following the dimensions refers to the five-point loading configuration, as shown in Figure 2. If a test is repeated, a letter "R" is shown in the suffix of the label. The arrangement of the cross-sectional dimensions also refers to the bending axis. In this case, the specimen $+H50 \times 95 \times 10.5$B5I was bent about the major axis, while the specimen "$+H95 \times 50 \times 10.5$B5I" was bent about the minor axis.

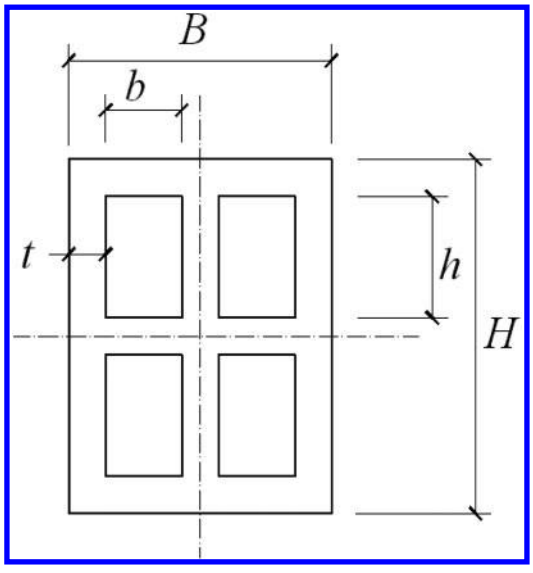


Figure 1. Definition of symbols for SHS/RHS with internal cross stiffeners.

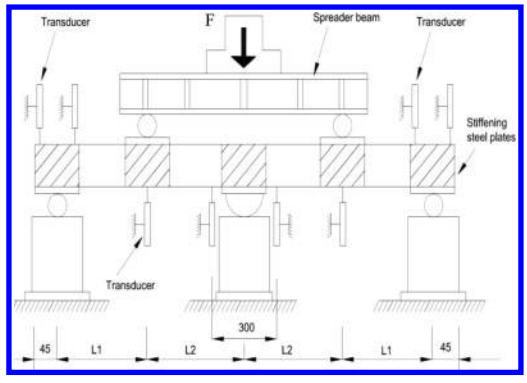


Figure 2. Schematic illustration of five-point bending configuration (dimensions in mm).

Table 1. Measured five-point bending specimen dimensions, material properties from tensile coupons and test ultimate loads.

Specimen	B (mm)	H (mm)	t (mm)	E (GPa)	f_y (MPa)	f_u (MPa)	ε_u (%)	F_{exp} (kN)
$+H70 \times 120 \times 10.5$B5I	69.9	120.0	10.30	70	192	222	8.5	678.4
$+H120 \times 70 \times 10.5$B5I	120.0	70.0	10.30	70	192	222	8.5	416.3
$+H95 \times 95 \times 4.3$B5I	95.3	95.2	4.17	66	228	236	6.0	250.4
$+N95 \times 50 \times 10.5$B5I	94.7	49.7	10.27	68	151	182	9.6	171.1
$+N50 \times 95 \times 10.5$B5I	49.7	94.6	10.28	68	151	182	9.6	329.6
$+H95 \times 50 \times 10.5$B5I	94.8	49.9	10.35	70	199	218	4.7	220.9
$+H50 \times 95 \times 10.5$B5I	49.9	94.7	10.33	70	199	218	4.7	423.8
$+H95 \times 95 \times 4.3$B5I-R	95.2	95.2	4.14	67	228	240	6.0	250.6
$+H70 \times 120 \times 10.5$B5II	69.9	120.0	10.26	70	192	222	8.5	922.7
$+H120 \times 70 \times 10.5$B5II	120.0	69.9	10.33	70	192	222	8.5	530.4
$+H95 \times 95 \times 4.3$B5II	95.3	95.2	4.17	67	228	240	6.0	319.4
$+N95 \times 50 \times 10.5$B5II	94.6	49.7	10.31	68	151	181	9.6	199.14
$+H50 \times 95 \times 10.5$B5II	49.7	94.6	10.26	70	199	218	4.7	438.9
$+H95 \times 95 \times 4.3$B5II-R	95.2	95.2	4.15	66	228	236	6.0	326.0
$+H70 \times 120 \times 10.5$B5III	69.94	120.0	10.25	69	210	238	4.6	708.2
$+H120 \times 70 \times 10.5$B5III	120.07	69.9	10.35	69	215	229	7.5	420.2
$+H95 \times 95 \times 4.3$B5III	95.27	95.2	4.15	69	208	238	7.0	274.3
$+N95 \times 50 \times 10.5$B5III	94.66	49.9	10.32	72	110	177	9.8	134.2
$+H50 \times 95 \times 10.5$B5III	49.76	94.7	10.29	70	199	218	4.7	358.4
$+H95 \times 95 \times 4.3$B5III-R	95.14	95.3	4.16	67	228	240	6.0	253.4



Figure 3. Experimental setup for five-point bending tests.

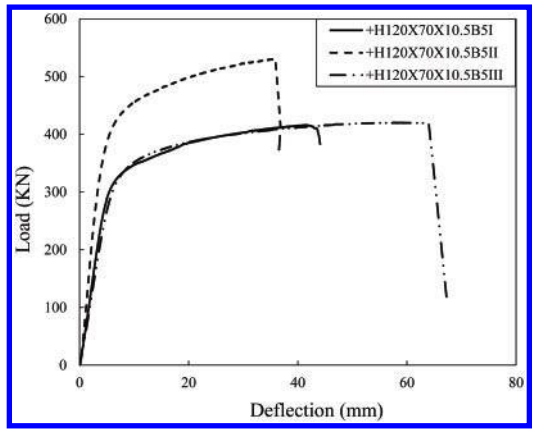


Figure 4. Typical Load-deflection curves for five-point bending tests.

2.2 *Testing procedure*

Three symmetrical five-point bending configurations (Figure 2) were employed in this study. The overall nominal length of continuous beams was 1690 mm. In loading configuration B5I, the distance between the loading points and the supports were all equal to 400 mm (L1 = $L2 = 400$ mm), while in the configurations B5II and B5III, the loads were applied at one third of the half span (L2 = 266.7 mm) and two thirds of the half span (L2 = 533.3 mm),respectively.

A 1000 kN capacity servo-controlled hydraulic testing machine was used to apply compressive force by displacement control at a constant rate of 0.8 mm/min for all tests. The specimens were loaded symmetrically at two points using a spreader beam, as shown in Figures 2 and 3.Steel rollers and a half round were employed to achieve rotationally free conditions. Steel bearing plates were placed between the specimen and loading/support points for the purpose of spreading the concentrated load. Transducers were used to measure the specimen deflection and end rotation.

2.3 *Test results and failure modes*

Generally, the specimens failed by material yielding and the formation of a collapse mechanism comprising three plastic hinges. In the case of configurations I and II, the first hinge formed at the central support and the latter two hinges formed at the loading points. Plastic hinges in the configuration III formed in a reverse sequence. Eventually all specimens fractured at the tensile flange, though in some cases, this was after the peak load, attributed to inelastic local buckling, had been attained. It should be noted that significant visual local buckling was not observed in the tests. In all cases, the ultimate loads attained in the tests were beyond the calculated loads corresponding to the occurrence of the first hinge as well as the calculated loads corresponding to the formation of the plastic collapse mechanism. Three typical load-deflection curves for the five-point bending tests, shown for specimens $+H120 \times 70 \times 10.5$B5I, $+H120 \times 70 \times 10.5$B5II and $+H120 \times 70 \times 10.5$ B5III,are given in Figure 4, while a deformed tested specimen from each loading configuration exhibiting three distinct plastic hinges is shown in Figure 5. The test results are presented in Table 1.

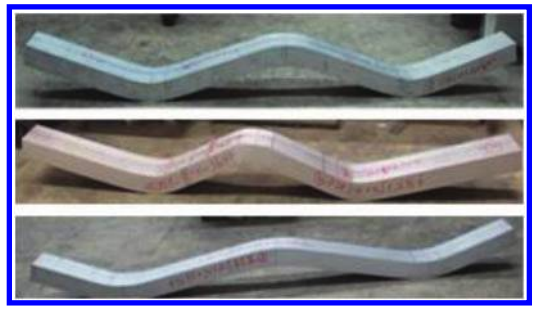


Figure 5. Tested specimens ($+N95 \times 50 \times 10.5$B5I, $+N95 \times 50 \times 10.5$B5II and $+$N$95 \times 50 \times 10.5$B5III) subjected to five-point bending.

3 COMPARISON OF TEST STRENGTHS WITH DESIGN PREDICTIONS

The experimental ultimate loads (F_{exp}) obtained from this study are compared with the design strengths predicted by the American (F_{AA}), Australian/New Zealand ($F_{AS/NZS}$) and European (F_{EC9} and F_{EC9-H}) specifications for aluminium structures. In addition, the Capacities calculated based on the CSM for indeterminate structures (F_{csm}) are also compared with the experimental ultimate loads. The predictions are all based on the measured dimensions and material properties in Table 1, while the calculation concepts for each method are summarised in Table 2, where the following symbols are used: c_{cf} and c_{cw} are the distances from the centerline of the compression flange/web group's extreme compression fibre to the cross section's neutral axis, c_{tf} and c_{tw} are the distances from the extreme tension fibre/web group's extreme tension fibre to the cross section's neutral axis, $F_c$is the local buckling stress of the flat elements in uniform

Table 2. Summary table of cross-section moment capacities and analysis methods for different approaches.

Design approach	Section capacity and analysis type	Class 1	Class 2	Class 3	Class 4
AA	Cross-section capacity	Lesser of ($M_{nc} = \mathrm{F}_c I_f/\mathrm{c}_{cf} + \mathrm{F}_b I_w/\mathrm{c}_{cw}$, $M_{nt} = \mathrm{F}_t I_f/\mathrm{c}_{tf} + \mathrm{F}_b I_w/\mathrm{c}_{tw}$), where F_c, F_b and F_t are slenderness dependent.			
	Global analysis	Elastic			
AS/NZS	Cross-section capacity	Lesser of ($W_{el}F_{bc}$, $W_{el}F_{bt}$), where F_{bc} and F_{bt} are slenderness dependent			
	Global analysis	Elastic			
EC9	Cross-section capacity	$W_{pl}f_y$	$W_{pl}f_y$	$W_{el}f_y$	$W_{eff}f_y$
	Global analysis	Elastic			
EC9- Annex H	Cross-section capacity	$\alpha\eta W_{el}f_y$	$W_{pl}f_y$	$W_{el}f_y$	$W_{eff}f_y$
	Global analysis	Plastic		Elastic	
CSM	Cross-section capacity	M_{csm} for cross-section			
	Global analysis	Plastic, but with allowance for ratio of hinge rotations. (for $\varepsilon_{csm}/\varepsilon_y < 3.6$: elastic)			

compression, F_t is the yield stress in tension, F_b is the local buckling/tensile stress of the flat elements in flexure, F_{bc} and F_{bt} are the weighted average factored limit state compressive/tensile stress in accordance with the ratio of the area of each elements, I_f and I_w are the moments of inertia of the flange/web group about the cross section's neutral axis, M_{nc} and M_{nt} are the weighted average compression/tension flexural strength, W_{pl}, W_{el} and W_{eff} are the plastic section modulus of the gross section, elastic section modulus of the gross section and elastic section modulus of the effective section, α is the shape factorη is the correction factor and ε_{csm} is the CSM strain.

The AA,AS/NZS and EC9specificationshave similar approaches for continuous beam design. The predicted failure loads are defined as when the maximum moment reaches the cross-section capacity, (i.e. the first hinge formed), following the concept of global elastic design. The mean values of the tested-to-predicted failure load ratios F_{exp}/F_{AA}, $F_{exp}/F_{AS/NZS}$ and F_{exp}/F_{EC9} are 1.80, 2.27 and 1.69,with corresponding coefficients of variation (COV) of 0.152, 0.185 and 0.153, respectively.

EC9 also gives the possibility to implement global plastic analysis as an alternative for Class 1 sections by using the plastic hinge method in Annex H (F_{EC9-H}). Besides moment redistribution, this method also takes into account strain hardening for Class 1sections. The Plastic Hinge Method in EC9 provides better agreement with the test results (mean value of $F_{exp}/F_{EC9-H} = 1.48$) and the least scatter of the predictions (COV = 0.082).

The continuous strength method (CSM) for indeterminate structures combines the merits of the traditional plastic analysis(i.e. allowing moment redistribution) and an accurate assessment of cross-section moment capacity through a deformation based approach that allows for strain hardening. In the calculation of F_{csm}, the cross-section slenderness ($\overline{\lambda}_p$) was determined by CUFSM (Li & Schafer, 2010). The material model is an elastic, linear hardening relationship where the strain hardening region is defined by the strain hardening slope (E_{sh}), given by Eq. 1. Notethat the measured ultimate strain (ε_u) from the tensile coupon tests for the comparisons made in this section. The bi-linear model has been verified by the authors against all the available coupon test material data, and it is found that the over-predictions of stress never exceed 5%. The comparison of the CSM with the results of continuous beam tests shows a mean value of 1.31 with a corresponding COV of 0.082.

$$E_{\mathrm{sh}} = \frac{f_u - f_y}{0.5\varepsilon_u - \varepsilon_y} \tag{1}$$

where $\varepsilon_y = f_y/E$ is the yield strain.

Figure 6 shows the test divided by predicted ultimate loads against section slenderness for the various design methods. The predictions of the AA, AS/NZS and EC9 specifications may be seen to be rather conservative, especially for the more stocky sections. Among the three specifications, EC9 is the least conservative while the AS/NZS specification is the most conservative. On the other hand, by allowing for moment redistribution at the global system level and accounting for strain hardening at the cross-sectional level, the two other design approaches, the plastic hinge method in Annex H of EC9 and the CSM for indeterminate structures, provide better predictions and less scatter. It can be observed in Figure 6 that the CSM offers the most accurate mean resistance, attributed to a rational exploitation of strain hardening.

4 CONCLUSIONS

A series of experiments on aluminium alloy square and rectangular hollow sections with internal stiffeners subjected to five-point bending has been presented. The specimens were of Class 1 proportions according to Eurocode 9 (2007). The experimental results were used to assess the accuracy of five design approaches: namely the American Aluminium Design Manual (2010), the Australian/New Zealand Standard(1997), Eurocode 9 (2007), the plastic hinge

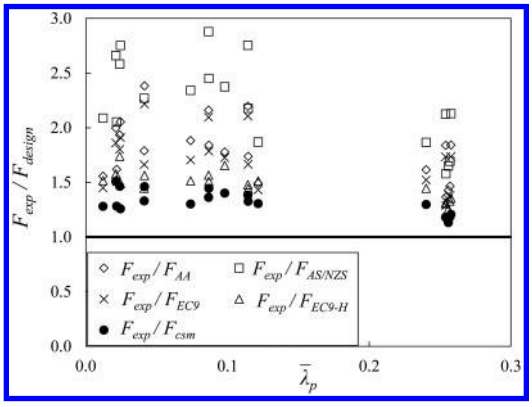


Figure 6. Comparison between the five-point bending test results and design strengths.

method in Eurocode 9and the Continuous Strength Method (CSM) for indeterminate structures. The results generally revealed that the AA, the AS/NZS and EC9standards considerably underestimate the strength of continuous beams, especially for stocky sections. As expected, the ultimate loads of the continuous beams are better predicted by the plastic hinge method (EC9)and the CSM for indeterminate structures; this is attributed to the consideration of both moment redistribution at the system level and strain hardening in the calculation of cross-section resistance. Comparing all five design approaches used in this study, the CSM for indeterminate structures yields the most accurate predictions. It should be noted that there are different configurations for indeterminate structures, but at the moment, the conclusions are only drawn based on five-point bending tests. Investigations into other indeterminate configurations are needed before reaching more general conclusions in the future.

ACKNOWLEDGEMENTS

The research work in this paper was supported by a grant from The University of Hong Kong under the seed funding program for basic research. The authors are also grateful to MrYi-Ran Li for his assistance in the experimental program as part of his final year undergraduate research project at The University of Hong Kong.

REFERENCES

Aluminum Association. 2010. *Aluminum design manual*, Washington, D.C.,

Australian/New Zealand Standard 1664. 1997. *Aluminium Structures Part 1: Limit State Design. AS/NZS 1664.1:1997*, Sydney, Australia,

European Committee for Standardization, CEN, 2007. *Eurocode 9: Design of Aluminium Structures—Part 1-1: General Rules—General Rules and Rules for Buildings. BS EN 1999-1-1:2007 + A1:2009*

Faella, C.,Mazzolani, F.M., Piluso, V. & Rizzano, G. 2000. Local buckling of aluminium members: testing and classification. *Journal of Structural Engineering* 126(3): 353–360.

Gardner, L., Wang, F. & Liew, A. 2011. Influence of strain hardening on the behaviour and design of steel structures.*International Journal of Structural Stability and Dynamics*, 11(5): 855–875.

Lai, Y.F.W. & Nethercot, D.A. 1992 Strength of aluminium members containing local transverse welds. *Engineering Structures* 14(4):241–254.

Langseth, M. & Hopperstad, O. S. 1997. local buckling of square thin-walled aluminium extrusions. *Thin-Walled Structures* 27(1):117–126.

Li, Z. & Schafer, B.W. 2010. Buckling analysis of cold-formed steel members with general boundary conditions using CUFSM: conventional and constrained finite strip methods. *Proceedings of the 20th Int;l. Spec. Conf. on Cold-Formed Steel Structures, November 2010*. St. Louis, MO.

Mazzolani, F.M. 1994.*Aluminum alloy structures 2nd.* E&FN Spon Press.

Mennink, J. 2002. *Cross-Sectional Stability of Aluminium Extrusions: Prediction of the Actual Local Buckling Behaviour.*the Netherlands

Moen, L.A., Hopperstad, O.S. & Langseth M. 1999. Rotational capacity of aluminium beams under moment gradient. I: Experiments. *Journal of Structural Engineering, ASCE* 125(8):910–920.

Su, M., Young, B. and Gardner, L. 2012a. Compression tests of aluminium alloy cross-sections. *Proceedings of the 13th International Symposium Tubular Structures* pp. 501–508 (London, 2012)

Su, M.,Young, B. and Gardner, L. 2012. Bending tests of aluminium alloy cross-sections, *Proceedings of the 13th International Symposium Tubular Structures* pp. 509–516 (London, 2012)

Zhu, J.H. & Young, B. 2006. Tests and design of aluminium alloy compression members.*Journal of Structural Engineering, ASCE* 132(7):1096–1107.

Zhu, J.H. & Young, B. 2009. Design of aluminium alloy flexural members usingdirect strength method. *Journal of Structural Engineering, ASCE* 135(5):558–566.

Research and Applications in Structural Engineering, Mechanics and Computation – Zingoni (Ed.)
© 2013 Taylor & Francis Group, London, ISBN 978-1-138-00061-2

Rational DSM design of thin-walled cruciform and angle columns

P.B. Dinis & D. Camotim
Civil Engineering Department, ICIST, Instituto Superior Técnico, Technical University of Lisbon, Portugal

ABSTRACT: This paper presents the output of an investigation on the development of more rational approaches to design pin-ended and fixed-ended equal-leg cruciform and angle columns by means of the Direct Strength Method (DSM). The key feature of these approaches consists of replacing the currently used local strength curve by genuine (i) torsional (cruciforms) or (ii) flexural-torsional (angles) ones, specifically developed for the columns under consideration and, therefore, accounting for the structural peculiarities of their cross-section shapes, formed by just four or two outstands. Moreover, the effective centroid shift effects, which have a strong impact on the pin-ended angle column ultimate strength, are also incorporated into the design approach. The merits of the developed DSM design approaches are assessed through the comparison with numerical and experimental column failure load data reported in the literature.

1 INTRODUCTION

The post-buckling behaviour and strength of cruciform and (mostly) angle columns has attracted the attention of several researchers in the past – *e.g.*, Popovic *et al* (1999), Young (2004), Ellobody & Young (2005), Rasmussen (2005, 2006), Dinis *et al.* (2010), Shifferaw & Schafer (2011), Silvestre *et al.* (2013), Trahair (2012). Some of them devoted a fair amount of work to develop rules and procedures aimed at predicting the failure loads of short-to-intermediate columns, adopting mostly local buckling concepts. Nevertheless, numerical simulations recently carried out by the authors (Dinis *et al* 2012, 2013a,b), on pin-ended and fixed-ended short-to-intermediate equal-leg cruciform and angle columns, unveiled some surprising behavioural features. It was then concluded that the column design should be based on genuine torsional (cruciforms) or flexural-torsional (angles) buckling concepts, instead of local ones. Moreover, it became clear that (i) specific design procedures, able to capture the angle column post-critical strength reserve length-dependence, were needed and (ii) that a single design approach cannot handle properly both pin and fixed-ended angle columns, due to the effective centroid shift effects.

The aim of this work is to present the output of a recent investigation on the development of more rational approaches to the Direct Strength Method (DSM – Schafer 2008) design of pin-ended (P) and fixed-ended (F) equal-leg angle and cruciform columns (Dinis *et al* 2013a,b). After briefly reviewing the most efficient DSM methodologies available to estimate these column failure loads (against "local"-global failures), namely those proposed for equal-leg angle columns by Young (2004), Rasmussen (2006) and Silvestre *et al.* (2013), the paper presents new DSM-based design approaches that take account for the structural peculiarities of the cruciform and angle cross-section shapes, formed by just four and two outstands. The key feature of the new proposals consists of replacing the current local design curves by genuine (i) torsional (cruciforms) or (ii) flexural-torsional (angles) ones, both specifically developed for the columns under consideration. The merits of these DSM design approaches are assessed through the comparison with (i) experimental load data reported in the literature and (ii) numerical failure loads obtained through ABAQUS shell finite element analyses (SFEA).

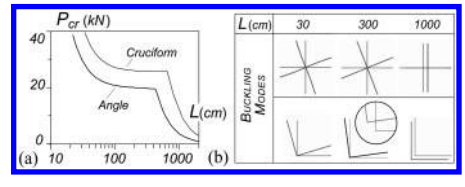


Figure 1. (a) Cruciform and angle critical buckling curve and (b) six column buckling mode shapes.

1.1 *Cruciform and angle column structural behaviour*

The peculiar behavioural features exhibited by the cruciform and angle columns are briefly addressed next – further information can be found in Dinis *et al.* (2013a,b). Particular attention is paid to the issues having higher impact on the development of the design approaches dealt with in this work.

(i) Due to the secondary warping resistance, local and torsional deformations cannot be handles similarly in cruciform columns (even if they are akin).
(ii) The ultimate strengths of P and F cruciform columns with lengths within the P_{cr} (L) curve plateau (see Fig. 1(a)) and containing torsional initial imperfections are virtually the same.
(iii) The angle column post-buckling is strongly length-dependent within the P_{cr} (L) curve plateau (see Fig. 1(a)). The shorter columns exhibit substantial

post-critical strength and little minor-axis flexure. Conversely, the longer columns exhibit minute post-buckling strength and substantial minor-axis flexure. The amount of major-axis flexure appearing in the column buckling mode (see Fig. 1(b)) was found to increase along the P_{cr} (L) curve plateau and correlate quite well with its post-buckling strength.

(iv) The angle column failure loads decrease with the length, due to lower flexural-torsional post-critical strength and higher interaction with minor-axis flexure – in the P columns, these interaction effects are further enhanced by the effective centroid shifts.

2 DIRECT STRENGTH METHOD (DSM) DESIGN

The current DSM strength/design curves for cold-formed steel columns are defined by "Winter-type" expressions that (i) were calibrated against fairly large numbers of experimental and/or numerical results and (ii) provide safe and accurate ultimate strength estimates associated with local, distortional, global and local-global interactive failures on the sole basis of elastic critical buckling (f_{crl}, f_{crd}, f_{cre}) and yield stresses. In the context of this investigation on cruciform and angle columns, the latter of which are not (yet) pre-qualified for the DSM design, the relevant nominal strengths are f_{nl} (local), f_{ne} (global) and f_{nle} (local-global) – the DSM expressions providing them can be found in Schafer (2008).

Since local and torsional deformations are akin in cruciform and angle columns, (i) both designations are often used indistinctly in the context of these columns and (ii) f_{nle} expressions are commonly used to estimate their "local"-global failure loads. However, such an approach neglects the fact that (i) torsional deformations are affected by secondary warping resistance (under warping-fixity) and (ii) angle columns buckle in flexural-torsional modes.

The most relevant design proposals for angle columns were recently revised by Silvestre *et al.* (2013), namely those proposed by Young (2004) and Rasmussen (2006). The latter developed a DSM-based approach for the design of P angle columns that incorporates explicitly the eccentricity stemming from the effective centroid shift – the strength curve depends on $\lambda_l = (f_y/f_{crl})^{0.5}$ and reads

$$f_{nl} = \rho \cdot \beta \cdot f_y \tag{1a}$$

$$\rho = \frac{A_e}{A} = \begin{cases} 1 & \text{if} \quad \lambda_l \le 0.673 \\ \dfrac{\lambda_l - 0.22}{\lambda_l^2} & \text{if} \quad \lambda_l > 0.673 \end{cases} \tag{1b}$$

$$\beta = \begin{cases} 1 & \text{if} \quad \lambda_l \le 1.22 \\ \dfrac{0.68}{(\lambda_l - 1)^{0.25}} & \text{if} \quad \lambda_l > 1.22 \end{cases} \tag{1c}$$

and accounts simultaneously for both the (i) bending effects due to the effective centroid shift, through parameter β, and (ii) "local" (flexural-torsional) buckling effects, through the effective area reduction factor ρ. Moreover, Silvestre *et al* (2013) proposed different DSM-based design approaches for P and F columns, which combine (i) Young's (2004) experimentally-based global design curve with (ii) either the current DSM local strength curve (F columns) or an empirically modified/lowered alternative curve (P columns) – these curves are expressed by

$$f_{ne} = \begin{cases} f_y \left(0.5^{\lambda_c^2}\right) & \text{if} \quad \lambda_c \le 1.4 \\ f_y \left(\dfrac{0.5}{\lambda_c^2}\right) & \text{if} \quad \lambda_c > 1.4 \end{cases} \tag{2}$$

$$f_{nl} = \begin{cases} f_y & \text{if} \quad \lambda_l \le 0.71 \\ f_y \left(\dfrac{f_{crl}}{f_y}\right)\left[1 - 0.25\left(\dfrac{f_{crl}}{f_y}\right)\right] & \text{if} \quad \lambda_l > 0.71 \end{cases} \tag{3}$$

with $\lambda_c = (f_y/f_{cre})^{0.5}$. These DSM-based design approaches were shown (i) to provide safe, accurate and reliable estimates of the available experimental and numerical failure loads, and, moreover, (ii) to outperform their most efficient predecessors: those developed by Young (2004) and Rasmussen (2006), for F and P columns. However, in spite of the quite positive performance indicators, one negative feature subsisted: the lack of a rational structural model, reflected in (i) the almost fully empirical roots of the strength curves given in Eqs. (2) and (3), and (ii) the inadequate nature of the current local DSM design curve involved in the approaches. The proposals developed in the next section aim at eradicating this negative feature.

3 NOVEL DSM-BASED DESIGN APPROACHES

Rational DSM-based design approaches for cruciform and angle columns must reflect the peculiarities of their behaviour, fully reported by Dinis *et al.* (2012, 2013a,b) and outlined in section 1.1. Thus, it may be established at the outset that the sought DSM-based design approaches must exhibit the following characteristics:

(i) Since the intermediate cruciform and angle columns fail mostly in interactive modes combining flexural (minor-axis) and torsional or flexural-torsional instability, the strength curves involved must be (i_1) the current DSM global curve and (i_2) torsional (cruciforms) or flexural-torsional (angles) strength curves, which need to be specifically developed and replace the single local strength curve in the current DSM design against local-global interactive failures.

(ii) The cruciform column torsional strength curve must take into account (ii_1) the secondary warping resistance and (ii_2) the fact that the failure loads of P and F column with initial torsional imperfections remain practically constant as the (short-to-intermediate) length grows and are unaffected by the end-support conditions – then, a single common torsional strength curve suffices for both P and F cruciform columns.

(iii) However, several flexural-torsional curves must be developed for angle columns, in order to enable capturing the progressive erosion of the column post-critical strength as its length increases within the P_{cr} (L) curve plateau – see Figure 1(a).

(iv) The effective centroid shift effects, strongly influencing the P angle column failure loads (not the F column ones), must be incorporated into

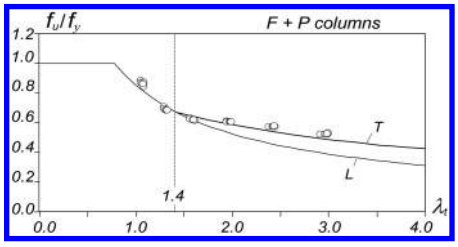


Figure 2. Variation of f_u/f_y with λ_t for F and P cruciform columns.

the design approach through a procedure or parameter that only comes into play for the P columns – exactly the idea of Rasmussen (2006) (see parameter β in Eq. (1c)). However, such procedure/parameter must reflect, as closely as possible, the length-dependence of the column flexural-torsional behaviour – Rasmussen based his parameter β on local buckling concepts.

The new DSM-based design proposals for cruciform and angle columns are presented separately and their merits will be assessed trough the comparison with (i) experimental load data reported in the literature and (ii) numerical failure loads obtained through ABAQUS SFEA, based on an existing elastic-perfectly plastic model: (ii_1) columns discretised into fine 4-node isoparametric element meshes (length-to-width ≈1.0), (ii_2) P and F support conditions modelled through rigid plates attached to the column end sections (end section secondary warping and one or both flexural rotations prevented) and (ii_3) steel constitutive law described by Prandtl-Reuss's model. Details concerning the experimental tests and numerical simulations can be found in Dinis *et al.* (2012, 2013a,b).

3.1 *Cruciform columns*

The first step involved in the proposed DSM design approach for cruciform columns consists of using the numerical failure load data concerning P and F cruciform columns with torsional initial imperfections, which fail in pure torsional modes, to search for a "Winter-type" torsional strength curve to estimate them as accurately as possible. This search was made by "trial-and-error" and, taking into account that the current DSM local strength curve provides accurate estimates for slenderness values up to about 1.4, led to

$$f_{nt} = \begin{cases} f_y & \text{if} \quad \lambda_t \le 0.776 \\ f_y \left(\frac{f_{crt}}{f_y}\right)^{0.4} \left[1 - 0.15\left(\frac{f_{crt}}{f_y}\right)^{0.4}\right] & \text{if} \quad 0.776 < \lambda_t < 1.4 \\ f_y \left(\frac{f_{crt}}{f_y}\right)^{0.2} \left[1 - 0.22\left(\frac{f_{crt}}{f_y}\right)^{0.26}\right] & \text{if} \quad \lambda_t \ge 1.4 \end{cases}, \quad (4)$$

with $\lambda_t = (f_y/f_{crt})^{0.5}$. Figure 2 compares the proposed curve with (i) the current DSM local curve and (ii) the numerical torsional failure loads. The proposed curve clearly (i) lies well above the DSM local curve in the moderate-to-high slenderness range and (ii) fits nicely the numerical torsional failure loads (differences below 3.5%).

Next, Eq. (4) is combined with the current DSM global strength curve: f_y replaced by f_{ne} in Eq. (4) to yield f_{nte} ultimate strength estimates. The merits of this DSM design approach can be assessed by looking at Figures 3(a)-(b), comparing the variations of f_u/f_{nle} and f_u/f_{nte} with λ_t, concerning the numerical (white circles – 252 simulations) and experimental (black circles- 31 tests) failure loads – also shown are the associated averages, standard deviations and maximum/minimum values. The observation of these results leads to the following conclusions:

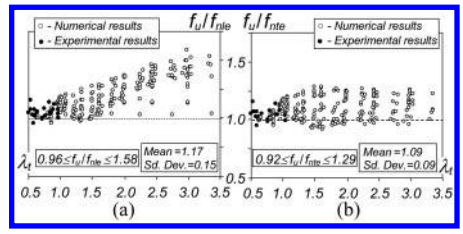


Figure 3. Variation of (a) f_u/f_{nle} and (b) f_u/f_{nte} with λ_t, for the whole set of numerical and tests results concerning the F and P columns.

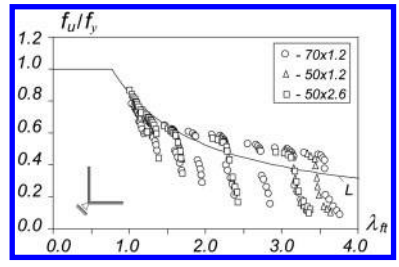


Figure 4. Variation of f_u/f_y with λ_{ft} (flexural-torsional failures).

(i) As anticipated, the f_{nte} estimates exhibit higher quality than the f_{nle} ones: ultimate-to-predicted stress ratios with (i_1) an average closer to 1.0 (1.09 *vs.* 1.17), (i_2) a smaller standard deviation (0.09 *vs.* 0.15), and (i_3) lower maximum values (1.29 *vs.* 1.58) – the obvious "trade off" was the appearance of slightly larger underestimations (0.92 *vs.* 0.96).

(ii) There are virtually no differences between the numerical ultimate-to-predicted stress ratios of the F and P columns, thus indicating that the above remarks apply to both of them.

(iii) Since the available experimental failure loads concern only quite stocky columns ($\lambda_t < 1.05$), they are equally well predicted by both DSM approaches (averages and standard deviations of 1.07/0.06).

(iv) The main differences between the f_{nte} and f_{nle} predictions concern the most slender columns, excessively underestimated by the latter. Unfortunately, there are no test results available for this slenderness range.

3.2 *Angle columns*

3.2.1 *Flexural-torsional strength curves*

A fully numerical approach is adopted to obtain "Winter-type" strength curves to predict "pure flexural-torsional failures" of equal-leg angle columns buckling in flexural-torsional modes – the failure loads of 170 columns continuously restrained against

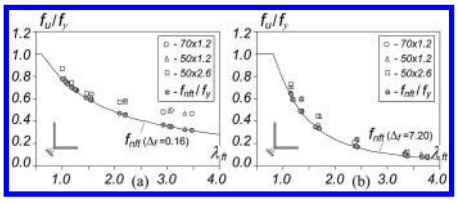


Figure 5. Proposed f_{nft} strength curves for (a) $\Delta_f = 0.16$, (b) 7.20 and numerical failure loads predicted by them.

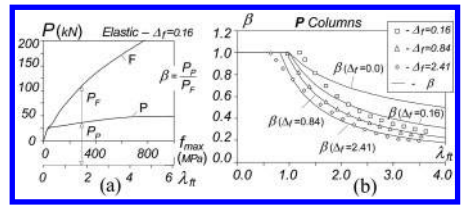


Figure 6. (a) F and P column P *vs.* f_{max} curves ($\Delta_f = 0.16$), and (b) proposed $\beta(\lambda_{ft})$ ($\Delta_f = 0.0; 0.16; 0.84; 2.41$) and fitted β values.

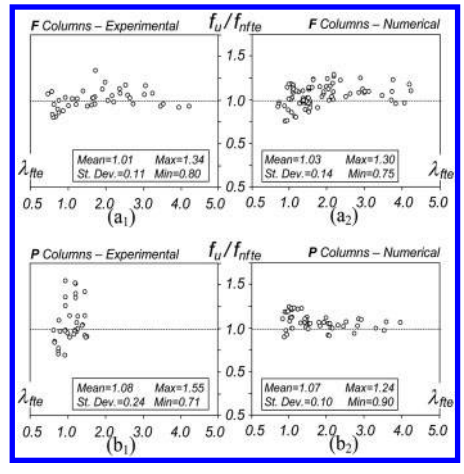


Figure 7. Variation of f_u/f_{nfte} with λ_{fte} for (a) F and (b) P angle columns: ($_1$) experimental and ($_2$) numerical results.

minor-axis flexure (forced to fail in modes combining major-axis flexure and torsion) are considered. Figure 4 shows the variation of the ultimate strength ratio f_u/f_y with λ_{ft} – also shown is the current DSM local strength curve. The huge "vertical dispersion" of the f_u/f_y values makes it easy to conclude that no single Winter-type curve can predict satisfactorily all of them. Since the "vertical dispersion" is linked to the column length, it was decided:

(i) To group the columns according to the ratio between their pure torsional (f_{bt}) and flexural-torsional (f_{crft} – critical) buckling loads – Figures 5(a)-(b) provide the variation of f_u/f_y with λ_{ft} for the columns analysed earlier sharing similar f_{bt}/f_{crft} ratios, namely 1.0016 (Fig. 5(a)) and 1.070 (Fig. 5(b)).

(ii) To propose curves to estimate flexural-torsional strengths (f_{nft}) that adopt "Winter-type" expressions and depend on a parameter a, included to capture the strength curve length-dependence – see Eq. (4). This parameter is expressed in terms of the percentage ratio Δ_f, quantifying the weakening effect of major-axis flexure on the column post-critical strength and given by $\Delta_f = [(f_{bt} - f_{crft})/f_{crft}] \times 100$.

(iii) To obtain, through a "trial-and-error curve-fitting procedure" based on the numerical failure load data, an expression for parameter a (see Eq. (5)).

3.2.2 *Effective centroid shift effects*

The strength differences between P and F columns stem from the effective centroid shift effects. Thus, a rational procedure must be found to account for them before proposing a DSM-based approach to design P columns. The procedure adopted follows Rasmussen's (2006) idea: effective centroid shift incorporated through a multiplicative parameter β that depends also on the column slenderness – the P column ultimate strength estimate is obtained by multiplying its F column counterpart (f_{nfte}) by parameter β – f_{nfte} is obtained replacing f_y with f_{ne} in the f_{nft} curves.

The search for an expression providing parameter β is based on an "elastic reduction factor" concept that accounts for the fact that both the post-buckling strength and effective centroid shift effects vary substantially with the column length. It involves the following steps:

(i) Perform elastic post-buckling analyses of geometrically identical F and P columns (same f_{bt}/f_{crft} ratio and critical-mode initial geometrical imperfections with amplitude $L/1000$) and record the evolution, as the applied load P increases, of the maximum mid-span cross-section longitudinal normal stress f_{max}. For illustration, Figure 6(a) shows the P *vs.* f_{max} curves for the F and P columns with $\Delta_f = 0.16$.

(ii) Assume that, for a given f_{max}, the difference between the F and P column applied loads (P_F and P_P) stems from the effective centroid shift effects – then, the ratio P_P/P_F provides a good approximation for the parameter β, i.e., $\beta \approx P_P/P_F$.

(iii) Relate f_{max} with the column slenderness by means of $\lambda_{ft} = (f_{max}/f_{crft})^{0.5}$, which amounts to assuming that β is the strength reduction due to the effective centroid shift effects at the "limit elastic applied load". Then, it becomes possible to develop $\beta(\lambda_{ft})$ curves, one for each Δ_f value.

(iv) Through a second "trial-and-error curve-fitting procedure", look for "Winter-type" expressions relating parameter β with λ_{ft} (see Eq. (6)). Figure 6(b) shows (iv$_1$) the β *vs.* λ_{ft} curves for $\Delta_f = 0.0$; 0.16; 0.84; 2.41, and (iv$_2$) the fitted β values (for $\Delta_f \neq 0.0$).

3.2.3 *Proposed DSM design approaches*

The proposed DSM-based approaches for the design of F and P angle columns can be cast in a unified form,

$$f_{nfte} = \begin{cases} \beta \cdot f_{ne} & \text{if} \quad \lambda_{fte} \le 0.641^{\frac{1}{a}} \\ \beta \cdot f_{ne} \left(\frac{f_{crft}}{f_{ne}}\right)^a \left[1 - 0.23\left(\frac{f_{crft}}{f_{ne}}\right)^a\right] & \text{if} \quad \lambda_{fte} > 0.641^{\frac{1}{a}} \end{cases}, \quad (4)$$

with $\lambda_{fte} = (f_{ne}/f_{crft})^{0.5}$ and

$$a = \begin{cases} 0.003\,\Delta_f^3 - 0.030\,\Delta_f^2 + 0.230\,\Delta_f + 0.400 & \Delta_f \le 4.0 \\ 1 & \Delta_f > 4.0 \end{cases}, \quad (5)$$

$$\beta = \begin{cases} 1 & \text{for } F \text{ columns} \\ (1-b)\left(\frac{1}{\lambda_{fte}^2}\right)^c \le 1 & \text{for } P \text{ columns} \end{cases}, \quad (6)$$

with

$$b = \begin{cases} 0 & \Delta_f \le 0.3 \\ 0.091\,\Delta_f - 0.027 & 0.3 < \Delta_f < 2.5 \\ 0.2 & \Delta_f \ge 2.5 \end{cases}, \quad (7)$$

$$c = \begin{cases} 0.833\,\Delta_f + 0.25 & \Delta_f < 0.3 \\ -0.009\,\Delta_f^2 + 0.047\,\Delta_f + 0.487 & 0.3 \le \Delta_f < 2.5 \\ 0.55 & \Delta_f \ge 2.5 \end{cases}, \quad (8)$$

where it is recalled that $\Delta_f = [(f_{bt} - f_{crft})/f_{crft}] \times 100$.

3.2.4 *Assessment of the proposed DSM design approaches*

Attention is now turned to assessing the performance of the proposed two DSM-based design procedures (f_{nfte} estimates), namely the DSM-F and DSM-P approaches. Figures 7(a)-(b) provide the variation of f_u/f_{nfte} (failure-to-predicted strength ratio) with λ_{fte}, for the whole set of experimentally tested and numerically analysed F and P columns – the associated averages, standard deviations, maximum and minimum values are given in Table 1, together with those concerning the proposals of Young (2004) (F columns), Rasmussen (2006) (P columns) and Silvestre *et al* (2013) (F and P columns). The observation of the results presented prompts the following remarks:

(i) The DSM-F and DSM-P procedures leads to quite accurate predictions of the experimental and numerical ultimate strengths – the f_u/f_{nfte} averages and standard deviations are (i_1) 1.04/0.12 (experimental + numerical F columns) and (i_2) 1.06/0.16 (experimental + numerical P columns).

(ii) The quality of the above performance indicators (ii_1) provides solid evidence concerning the adequacy of the reasoning behind the development of the flexural-torsional strength (F and P columns) and β *vs.* λ_{fte} (P columns) curves, and (ii_2) also indicates that the outputs of these curves reflect quite accurately the underlying structural concepts.

(iii) The comparison between the values given in Table 1 makes it possible to conclude that the proposed design approaches have performance indicators similar to those exhibited by the proposals due to Young (2004), Rasmussen (2006) and Silvestre *et al* (2013). However, it has the very important advantage of being clearly more rational – they reflect quite closely the angle column structural behaviour and, moreover, retain the current DSM global strength curve.

3.3 *Load and Resistance Factor Design (LRFD)*

The evaluation of the LRFD resistance factor ϕ associated with the proposed DSM-based approaches for angle and cruciform columns is addressed next. According to the current North American cold-formed steel specification (AISI 2007), ϕ can be calculated using the formula given in section F.1.1 of chapter F,

$$\phi = C_\phi (M_m F_m P_m)\, e^{-\beta_0 \sqrt{V_M^2 + V_F^2 + C_P V_P^2 + V_Q^2}}, \quad C_P = \left(1 + \frac{1}{n}\right)\frac{m}{m-2}, \quad (9)$$

where (i) C_ϕ is a calibration coefficient ($C_\phi = 1.52$ for LRFD), (ii) $M_m = 1.0$ and $F_m = 1.00$ are the mean values of the material and fabrication factor, respectively, (iii) β_0 is the target reliability index ($\beta_0 = 2.5$ for structural members in LRFD), (iv) $V_M = 0.10$, $V_F = 0.05$ and $V_Q = 0.21$ are the coefficients of variation of the material factor, fabrication factor and load effect, respectively, and (v) C_P is a correction factor depending on the numbers of tests (n) and degrees of freedom ($m = n - 1$). In order to evaluate ϕ for each propose procedure (DSM-F and DSM-P), it is necessary to calculate P_m and V_P (mean and standard deviation of the failure-to-predicted strength ratios f_u/f_{nfte} – the f_u values are either experimental or/and numerical.

Table 2 shows the n and ϕ values obtained for the angle column ultimate strength predictions provided by the DSM-F and DSM-P procedures applied to the total failure load data (experimental and numerical – the mean P_m and standard deviation V_P values are also given in Table 1) – also indicated are the values (i) reported by Silvestre *et al* (2013) and (ii) determined with the proposals of Young (2004) and Rasmussen (2006). It is observed that:

(i) When the whole (experimental and numerical) failure load data are considered, the resistance factors associated with each proposed DSM-based procedure are $\phi = 0.87$ for both the F and P columns. These values are almost perfectly in line with the recommendations of the North American specification for cold-formed steel compression

Table 1. Means, standard deviations and maximum/minimum values of the DSM-F and DSM-P procedures and available proposals.

	F Columns			P Columns		
	DSM-F approach	Silvestre *et al.* (2013)	Young (2004)	DSM-P approach	Silvestre *et al.* (2013)	Rasmussen (2006)
Mean	1.02	1.01	1.14	1.07	1.11	1.06
Sd. Dev.	0.13	0.12	0.17	0.16	0.20	0.21
Max	1.34	1.40	1.70	1.55	1.89	1.81
Min	0.75	0.73	0.83	0.71	0.88	0.72

Table 2. LRFD resistance factors ϕ – DSM-F and DSM-P procedures and available proposals.

	F Columns			P Columns		
	DSM-F approach	Silvestre *et al.* (2013)	Young (2004)	DSM-P approach	Silvestre *et al.* (2013)	Rasmussen (2006)
n	133	130	130	99	63	63
ϕ	0.87	0.87	0.92	0.87	0.85	0.80

members (AISI 2007 – $\phi = 0.85$) – currently not applicable to angles.

(ii) The ϕ values obtained are very similar to those reported by Silvestre *et al.* (2013) and are slightly below and above those provided by Young (2004), for F columns, and by Rasmussen (2006), for P columns.

(iii) There is solid evidence that $\phi = 0.85$ can be also recommended for cold-formed steel angle columns designed with the DSM-F and DSM-P procedures. Although this feature is shared by the proposals developed by Young (2004) and Silvestre *e t al* (2013), the structural clarity and rationality of the approaches proposed in this work is definitely an advantage.

Finally, the resistance factors associated with the proposed DSM-based procedure for cruciform columns (f_{nte}) are $\phi = 0.96$ (experimental and numerical data – $n = 283$, $P_m = 1.09$, $V_P = 0.09$). The corresponding f_{nle} value is practically the same ($\phi = 0.97$), but the f_u/f_{nle} estimates exhibit involve fairly higher average, standard deviation and maximum values (1.17-0.15-1.58 *vs.* 1.09-0.09-1.29), mostly because of the considerable overestimations in the high slenderness range.

4 CONCLUSION

This work presented the output of an investigation on the development of more rational approaches to the DSM design of P and F equal-leg cruciform and angle columns with short-to-intermediate lengths, i.e., buckling in torsional or flexural-torsional modes. After reviewing the most efficient available methods to estimate the failure loads of such members, the paper addressed the key feature of the more rational DSM approaches, i.e., the mechanical reasoning behind these proposed procedures. It is based on the fact that (i) both the F and P columns fail in interactive modes, combining minor-axis flexural and (i_1) torsional (cruciforms) or (i_2) major-axis flexural-torsional (angles) deformations, and that (ii) the above interaction is much stronger in the P angle columns, due to the effective centroid shift effects. In order to incorporate these behavioural features into the DSM design approaches, it was necessary to find efficient/accurate ways to quantify (i) the F and P column torsional (cruciforms) and flexural-torsional (angles) strength, and (ii) the P angle columns effective centroid shift effects. These tasks were performed numerically and led to the development of genuine torsional (cruciforms) and flexural-torsional (angles) strength curves, which replace the local strength curve in the traditional design against local-global interactive failure. Moreover, the numerical investigation led also to the development of curves providing a parameter able to capture the angle P column ultimate strength erosion stemming from the effective centroid shifts. Since the flexural-torsional strength curves and the new parameter were found to be heavily length-dependent, their definition included the percentage ratio between the angle column torsional and flexural-torsional buckling loads, which is able to capture the above length-dependence, essentially linked to the amount of minor-axis flexural deformations in the angle column failure modes.

The merits of the developed DSM-based design approaches were assessed trough the comparison with experimental tests results reported in the literature and numerical (Abaqus SFEA) column failure loads obtained by the authors. Both the quality and reliability of the predictions provided by the proposed design procedures were found to be very good – in particular, it was shown that the LRFD resistance factor $\phi = 0.85$, presently prescribed for member design, can also be safely adopted for the cruciform and angle columns – the latter are currently explicitly excluded from the above prescription.

REFERENCES

AISI (American Iron and Steel Institute) 2007. *North American Specification for the Design of Cold-Formed Steel Structural Members* (NAS), Washington DC.

Dinis PB, Camotim D, Silvestre N 2010. On the local and global buckling behaviour of angle, T-section and cruciform thin-walled columns and beams, *Thin-Walled Structures* 48(10–11), 786–797.

Dinis PB, Camotim D, Silvestre N 2012. On the mechanics of angle column instability. *Thin-Walled Structures* 52(March), 80–89.

Dinis PB, Green PS, Camotim D 2013a. Numerical and experimental investigation on the post-buckling behavior, ultimate strength and design of thin-walled cruciform steel columns, *USB Proceedings of SSRC Annual Stability Conference* (St. Louis, 16–20/4).

Dinis PB, Camotim D, Landesmann A 2013b. Towards a more rational DSM design approach for angle columns, *USB Proceedings of SSRC Annual Stability Conference* (St. Louis, 16–20/4).

Ellobody E, Young B 2005. Behavior of cold-formed steel plain angle columns. *Journal of Structural Engineering* (ASCE) 131(3), 469–478.

Popovic D, Hancock GJ, Rasmussen KJR. 1999. Axial compression tests of cold-formed angles. *Journal of Structural Engineering* (ASCE), 125(5), 515–523.

Rasmussen KJR. 2005. Design of angle columns with locally unstable legs, *Journal of Structural Engineering* (ASCE), 131(10), 1553–60.

Rasmussen KJR. 2006. Design of slender angle section beam-columns by the direct strength method. *Journal of Structural Engineering* (ASCE), 132(2), 204–211.

Schafer BW. 2008. Review: the direct strength method of cold-formed steel member design. *Journal of Constructional Steel Research*, 64(7–8), 766–778.

Shifferaw Y, Schafer BW. 2011. Behavior and design of cold-formed steel lipped and plain angles, *USB Proceedings of SSRC Annual Stability Conference* (Pittsburgh, 10–14/5).

Silvestre N, Dinis PB, Camotim D. 2013. Developments on the design of cold-formed Sseel angles. *Journal of Structural Engineering* (ASCE). 139(5), in press.

Trahair NS. 2012. Strength design of cruciform steel columns. *Engineering Structures* 35(February), 307–313.

Young B. 2004. Tests and design of fixed-ended cold-formed steel plain angle columns. *Journal of Structural Engineering* (ASCE) 130(12), 1931–1940.

Research and Applications in Structural Engineering, Mechanics and Computation – Zingoni (Ed.)
© 2013 Taylor & Francis Group, London, ISBN 978-1-138-00061-2

Flexural-torsional analysis of shear-deformable monosymmetric thin-walled open members – I. Closed-form solution

Mohammed Ali Hjaji
Department of Mechanical and Industrial Engineering, University of Tripoli, Tripoli, Libya

Magdi Mohareb
Department of Civil Engineering, University of Ottawa, Ottawa, Ontario, Canada

ABSTRACT: The governing field equations and boundary conditions based on a generalized Vlasov-Timoshenko beam theory are formulated using the principle of the stationary total potential energy. The formulation incorporates shear deformation effects due flexure and warping, and captures the flexural-torsional coupling in monosymmetric cross-sections. General closed-form solutions are obtained for cantilever boundary conditions. Numerical examples for the flexural-torsional coupled analysis are presented and compared with Abaqus finite element solutions. Additional comparisons are performed against non-shear deformable beam theories and the effect of transverse shear deformation is illustrated.

1 INTRODUCTION AND OBJECTIVES

Several studies investigated the coupled bending-torsional buckling of thin-walled beams. Based on the Vlasov beam theory, Friberg (1983), Leung (1991, 1992), Banerjee et al (1996), Kim et al (2007) developed the dynamic stiffness matrix in which shear deformation effects are neglected. Kollar and Pluzsik (2002) formulated the stiffness matrix for composite beams of open thin-walled sections. Kabir and Sherbourne (1999) derived a solution of thin-walled beams made from symmetric composite laminates. In their study, they neglected the effects of shear deformation and restrained torsional warping. Several studies on shear deformable beam theories have been conducted. Among them, Li et al (2004) developed the dynamic transfer matrix to formulate a solution for determining the coupled bending-torsional response of thin-walled beam under random excitations by considering the effects of warping stiffness and rotary inertia. Prokic (2006) formulated the governing equations for the coupled bending-torsional vibrations of thin-walled beams. Vo and Lee (2009) presented a general analytical solution for the study of flexural-torsional buckling and vibration analysis of open thin-walled composite beams. Jung and Lee (2003) derived a closed-form solution for both symmetric and anti-symmetric lay-up I-beam. Their solution included the effects of torsional warping and constrained warping. Kim et al. (2004) derived the exact stiffness matrices for the buckling and the elastic analysis of thin-walled beam with nonsymmetric cross-sections. Lee (2005) developed an analytical model to study the flexural behavior of thin-walled composite beams with doubly symmetric I-section subjected to distributed vertical load. The governing equations were derived from the principle of stationary potential energy are account for the ?exural response of the thin-walled composites beams. Kim and Shin (2009) derived a solution for thin-walled composite beams with monosymmetric cross-sections. Recently, Kim (2011) developed a shear deformable beam element for the coupled flexural and torsional analyses of thin-walled composite I-beams with doubly and monosymmetric cross-sections. He derived the governing equations and force–displacement relations using the principle of minimum total potential energy. His formulation captures restrained warping effects. More recently, using power series, Kim (2012) presented an explicit analytical expression for the coupled flexural-torsional analysis of thin-walled composite beams with channel section resting on elastic foundations.

To the best of author's knowledge, no study in the literature reported an analytical closed-form solution for the static transverse-torsional coupled response of thin-walled monosymmetric beams which captures shear deformation effects. Thus, the aim of the present study is to develop such a solution.

2 BASIC ASSUMPTIONS

The basic assumptions of the formulation are

1. The formulation is restricted to prismatic open thin-walled monosymmetric members,
2. Cross-section is assumed to remain undistorted (rigid) in its own plane but free to undergo warping in the longitudinal direction (Vlasov assumption),

3. The cross-section remains planar but does not remain perpendicular to the neutral axis after deformation, i.e., the transverse shear deformation of the mid-surface of the cross-section is incorporated in the formulation (Timoshenko beam assumption),
4. The deformations are assumed to remain within the elastic range of the material, and
5. Strains and rotations are assumed small.

3 KINEMATICS RELATIONS

Based on the above assumptions, the longitudinal displacement $w_p(z,s)$ and the in-plane displacements $u_p(z,s)$ and $v_p(z,s)$ of an arbitrary point $p[x(z), y(z)]$ on the mid-surface are, respectively, given by [e.g., Back and Will 1998]

$$\begin{aligned} w_p(z,s) &= w(z) + y(s)\theta_x(z) - x(s)\theta_y(z) - \omega(s)\psi(z) \\ u_p(z,s) &= u(z) - y(s)\theta_z(z) \text{ , and} \\ v_p(z,s) &= v(z) + [x(s) - x_s]\theta_z(z) \end{aligned} \tag{1-3}$$

where $w(z)$ is the average longitudinal displacement along the Z direction, $u(z)$ and $v(z)$ are the shear centre displacements along the principal X and Y axes, respectively, $\theta_x(z)$ and $\theta_y(z)$ are the rotations of the section about X and Y axes, $\theta_z(z)$ is the angle of twist of the cross-section, $\psi(z)$ is a function which characterizes the magnitude of the warping deformation, and $\omega(z)$ is the warping function of the section defined by $\omega(z) = \int_A h(z)\,dA$, where $h(s) = [x(s) - x_s]sin\alpha(s) - y(s)cos\alpha(s)$, $\sin\alpha(s) = dy(s)/ds$, $\cos\alpha(s) = dx(s)/ds$ and $\alpha(s)$ is the angle between the tangent of point p and the axis (Figure 1), $x(s)$ and $y(s)$ are the coordinates of point p, s is a curvilinear coordinate, and x_s is the coordinate of the shear center S_c along the axis of symmetry X. The tangential displacement component $\xi(z,s)$ of general point p on the mid-surface can be expressed in terms of the shear centre displacements and the rotation of the section as

$$\xi_p(z,s) = u(z)\frac{dx(s)}{ds} + v(z)\frac{dy(s)}{ds} + h(s)\theta_z(z) \tag{4}$$

4 VARIATIONAL FORMULATION

The total potential energy Π of the member is the sum of the internal strain energy U and the potential energy V of the applied forces, i.e., $\Pi = U + V$. Taking the first variation of Π and setting it equal to zero, one obtains

$$\delta\Pi = \delta U + \delta V = 0 \tag{5}$$

in which δU is the internal strain energy defined by

$$\delta U = \int_0^\ell \int_A \left[E\varepsilon_{zz}\delta\varepsilon_{zz} + G\gamma_{zs}\delta\gamma_{zs}\right]dA\,dz + \int_0^\ell GJ\theta_z'\delta\theta_z'\,dz \tag{6}$$

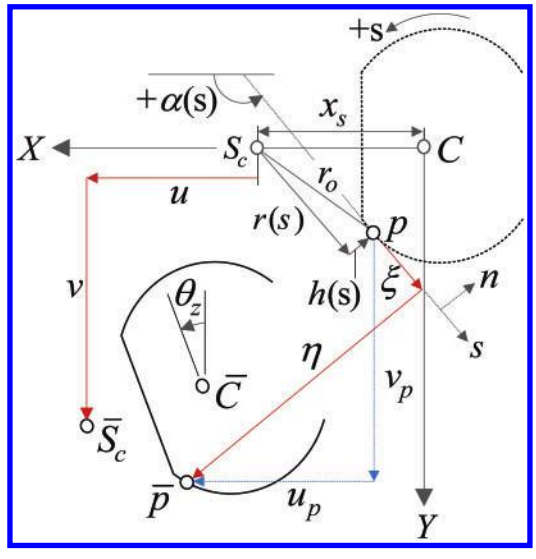


Figure 1. Coordinate systems and displacement components.

where E is the Young's modulus, G is the shear modulus, J is the St. Venant torsional constant, A is the cross-sectional area, $\varepsilon_{zz} = \partial w_p/\partial_z$ is the longitudinal strain and $\gamma_{zs} = \partial w_p/\partial_s + \partial\xi/\partial_z$ is the shear strain. All primes denote derivatives with respect to coordinate z. The potential of the applied forces δV is given by

$$\begin{aligned} \delta V = \int_0^\ell \Big[& q_z\delta w + q_x\delta u + q_y\delta v + m_z\delta\theta_z \\ & + m_x\delta\theta_x + m_y\delta\theta_y + m_w\delta\psi\Big]dz \\ & + \left[N_z\delta w\right]_0^\ell + \left[V_x\delta u\right]_0^\ell + \left[V_y\delta v\right]_0^\ell \\ & + \left[M_x\delta\theta_x\right]_0^\ell + \left[M_y\delta\theta_y\right]_0^\ell + \left[M_z\delta\theta_z\right]_0^\ell + \left[M_w\delta\psi\right]_0^\ell \end{aligned} \tag{7}$$

5 GOVERNING EQUATIONS

From Equations (1) to (4) and by substituting into energy Equations (6) and (7), and the resulting expressions into Equation (5), performing integration by parts and enforcing the orthogonality conditions; $\langle \int_A [x, y, xy, x\omega, y\omega, \omega]dA\rangle^T = \langle 0\rangle^T$, the governing field equations are given as

$$\begin{aligned} & EAw'' = -q_z\,, \\ & GD_{xx}\left(u'' - \theta_y'\right) = -q_x\,, \\ & GI_{yy}\theta_y'' + GD_{xx}\left(u' - \theta_y\right) = -m_y \\ & GD_{yy}\left(v'' + \theta_x'\right) + GD_{hy}\left(\theta_z'' + \psi'\right) = -q_y\,, \\ & -EI_{xx}\theta_x'' + GD_{yy}\left(v' + \theta_x\right) + GD_{hy}\left(\theta_z' + \psi\right) = m_x \\ & GJ\theta_z'' + GD_{hy}\left(v'' + \theta_x'\right) + GD_{\omega\omega}\left(\theta_z'' + \psi'\right) = -m_z\,, \\ & -EC_w\psi'' + GD_{hy}\left(v' + \theta_x\right) + GD_{\omega\omega}\left(\theta_z' + \psi\right) = m_w \end{aligned} \tag{9-15}$$

The relevant boundary conditions are obtained as

$$
\begin{aligned}
&\left[EAw'-N_z\right]\delta w_0^{\ell}=0,\\
&\left[GD_{xx}\left(u'-\theta_y\right)-V_x\right]\delta u\big|_0^{\ell}=0,\\
&\left[EI_{yy}\theta_y'-M_y\right]\delta\theta_y\big|_0^{\ell}=0,\\
&\left[GD_{yy}\left(v'+\theta_x\right)+GD_{hy}\left(\theta_z'+\psi\right)-V_y\right]\delta v\big|_0^{\ell}=0,\\
&\left[EI_{xx}\theta_x'+M_x\right]\delta\theta_x\big|_0^{\ell}=0,\\
&\left[GJ\theta_z'+GD_{hy}\left(v'+\theta_x\right)+GD_{\omega\omega}\left(\theta_z'+\psi\right)-M_z\right]\delta\theta_z\big|_0^{\ell}=0,\\
&\text{and }\left[EC_w\psi'+M_w\right]\delta\psi\big|_0^{\ell}=0
\end{aligned}
\tag{16-22}
$$

In the above Equations, the cross-sectional properties are defined as

$$
A, I_{xx}, I_{yy}, D_{xx}, D_{yy}, D_{hy}, D_{\omega\omega}
=\int_A\left[1, y^2, x^2, \left(\frac{dx}{ds}\right)^2, \left(\frac{dy}{ds}\right)^2, \left(\frac{dy}{ds}\right)\left(\frac{d\omega}{ds}\right), \left(\frac{d\omega}{ds}\right)^2\right]dA
$$

Equation (9) governs the longitudinal deformation of the member which is uncoupled from the remaining field equations and can be solved independently. Equations (10-11) provide the lateral deflection and related rotation, while Equations (12-15) govern the coupled transverse-torsional behaviour and associated warping deformation. The present study is focused on the closed-form solution for the response governed by the coupled transverse-torsional equations.

6 HOMOGENEOUS SOLUTION FOR COUPLED TRANSVERSE-TORSIONAL RESPONSE

The homogeneous solution of the coupled transverse-torsional equations (12-15) is obtained by setting the right-hand side of the equations to zero, i.e. $q_y(z)=m_x(z)=m_z(z)=m_w(z)=0$. The solution of the displacement functions is then assumed to take the form

$$
\begin{aligned}
\left\langle \bar{U}(z)\right\rangle_{1\times4}^{T}&=\left\langle v_h(z)\quad \theta_{xh}(z)\quad \theta_{zh}(z)\quad \psi_h(z)\right\rangle_{1\times4}^{T}\\
&=\left\langle C\right\rangle_{1\times4}^{T}e^{m_i z}\ ,\ \text{for } i=1,2,3,4
\end{aligned}
\tag{23}
$$

in which $\langle\bar{U}(z)\rangle_{1\times4}^{T}=\langle v_h(z)\ \theta_{xh}(z)\ \theta_{zh}(z)\ \psi_h(z)\rangle_{1\times4}^{T}$ is the vector of transverse and torsional displacements, and $\langle C\rangle_{i,1\times4}^{T}=\langle c_1 c_2 c_3 c_4\rangle_i$ is the vector of unknown integration constants.

From Equation (23), by substituting into Equations (12-15), rewritten in matrix form yielding

$$
\begin{bmatrix}
GD_{yy}m_i^2 & GD_{yy}m_i & GD_{hy}m_i^2 & GD_{hy}m_i\\
 & \left(GD_{yy}\right. & GD_{hy}m_i & GD_{hy}\\
 & \left.-EI_{xx}m_i^2\right) & & \\
 & Symm & G(D_{\omega\omega}+J)m_i^2 & GD_{\omega\omega}m_i\\
 & & & \left(GD_{\omega\omega}\right.\\
 & & & \left.-EC_w m_i^2\right)
\end{bmatrix}_{i,4\times4}
\times
\begin{bmatrix}
e^{m_1 z} & 0 & 0 & 0\\
0 & e^{m_2 z} & 0 & 0\\
0 & 0 & e^{m_3 z} & 0\\
0 & 0 & 0 & e^{m_4 z}
\end{bmatrix}
\begin{Bmatrix}c_1\\c_2\\c_3\\c_4\end{Bmatrix}_{i,4\times1}
=\left\{0\right\}_{4\times1}
\tag{24}
$$

A nontrivial solution is given by setting the determinant of the matrix to zero. The resulting quadratic eigen value problem is solved for the eight eigen pairs $(m_i, \{C\}_i)$. The solution of the coupled system of equation is

$$
\left\{\bar{U}(z)\right\}_{4\times1}=\left[\bar{C}\right]_{4\times8}\left[X(z)\right]_{8\times8}\left\{\bar{A}\right\}_{8\times1}
\tag{25}
$$

where $\left[\bar{C}\right]_{4\times8}=\left[\{C\}_1\ \{C\}_2\ \{C\}_3\ \{C\}_4\ \ldots.\ \{C\}_8\right]_{4\times8}$ is

where $[\bar{C}]_{4\times8}=[\{C\}_1\ \{C\}_2\ \{C\}_3\ \{C\}_4\ \ldots.\ \{C\}_8]_{4\times8}$ is the matrix of eigen vectors, $[X(z)]_{8\times8}=Diag[e^{m_1 z}\ e^{m_2 z}\ e^{m_3 z}\ e^{m_4 z}\ \ldots..\ e^{m_8 z}]_{8\times8}$ is a diagonal matrix of exponential functions, and $\{\bar{A}\}_{8\times1}$ is a vector of integration constants to be determined from the boundary conditions.

7 SOLUTION FOR CANTILEVER BEAM UNDER ENF FORCES

For a cantilever beam under tip loads $P_y(\ell)$, $M_x(\ell)$, $M_z(\ell)$ and $M_w(\ell)$, the unknown constants $\{\bar{A}\}_{4\times1}$ are determined from the boundary conditions at both ends, $z=0, \ell$

$$
\begin{aligned}
&v(0)=\theta_x(0)=\theta_z(0)=\psi(0)=0,\\
&GD_{yy}\left[v'(\ell)+\theta_x(\ell)\right]+GD_{hy}\left[\theta_z'(\ell)+\psi(\ell)\right]=P_y(\ell),\\
&EI_{xx}\theta_x'(\ell)=-M_x(\ell),\\
&GJ\theta_z'(\ell)+GD_{hy}\left[v'(\ell)+\theta_x(\ell)\right]\\
&\qquad+GD_{\omega\omega}\left[\theta_z'(\ell)+\psi(\ell)\right]=M_z(\ell)\ ,\ \text{and}\\
&EC_w\psi'(\ell)=-M_w(\ell).
\end{aligned}
$$

By substituting into the displacement fields in Equation (23), one obtains $\{\bar{A}\}_{4\times1}$ in terms of the tip loads $P_y(\ell)$, $M_x(\ell)$, $M_z(\ell)$ and $M_w(\ell)$.

Table 1. Static results for coupled lateral-torsional responses of monosymmetric cantilever.

Variable	Abaqus Beam [1]	Present Solution [2]	Vlasov Solution [3]	Diff = [1–2]/1	Diff = [1–3]/1
v_A (mm)	−65.17	−65.18	−65.16	−0.02%	0.02%
θ_z (10^3)	366.6	366.8	366.5	−0.05%	0.03%
ψ (10^{-6} rad/mm)	−101.4	−101.5	−101.4	−0.10%	0.00%

8 NUMERICAL EXAMPLES

Two examples are investigated in order to demonstrate the validity and accuracy of the present solution. In both examples, the material is assumed to be steel with $E = 200\,\text{GPa}$ and $G = 70\text{GPa}$. The analytical closed-form solution developed in the present study is applied.

8.1 *Example 1: Cantilever beam under Torsion - Coupled Lateral-Torsional Response*

A cantilever beam with monosymmetric I-section is subjected to concentrated twisting moment $M_z(\ell) = 8.0\,\text{kNm}$ applied at the cantilever free end. The dimensions of the cross-section are: flange thickness $t_f = 20\,\text{mm}$, web thickness $t_w = 15\,\text{mm}$, upper flange width $b_u = 100\,\text{mm}$, lower flange width $b_\ell = 200\,\text{mm}$ and a mid-surface height $H = 200\,\text{mm}$. The coordinate of the centroid in the direction of the principal axis of symmetry is $C_x = 77.78\,\text{mm}$ and the shear centre coordinate along the symmetry axis is $x_s = -55.56\,\text{mm}$. Section properties are;

$$A = 0.56\times10^4\,mm^2,\ I_{xx} = 15.0\times10^6\,mm^4,$$
$$J = 1.025\times10^6\,mm^4,\ C_w = 59.26\times10^9\,mm^6,$$
$$D_{xx} = 0.30\times10^4\,mm^2,\ D_{yy} = 0.60\times10^4\,mm^2,$$
$$D_{hy} = 2.667\times10^4\,mm^3 \text{ and } D_{\omega\omega} = 65.19\times10^6\,mm^4.$$

The analysis results for maximum lateral displacement v_A (point A is located at the intersection of the web and upper flange center-lines), twist angle θ_z and the warping deformation function ψ are given in Table (1) and Figure (2). Results are based on (a) the analytical closed-form solution developed in the present study, (b) Vlasov beam theory and (c) Abaqus beam solution using one-hundred B31OS beam element (≈700 dofs). Due to the mono-symmetry of the cross-section, the lateral response is fully coupled with torsional-warping response, but it is observed that the bending rotation θ_x vanishes in all three solutions. Results based on the present study are observed to exactly match those based on Vlasov theory and Abaqus beam model. It is also observed that, under the applied twisting moment, the bending rotation vanishes in all three solutions.

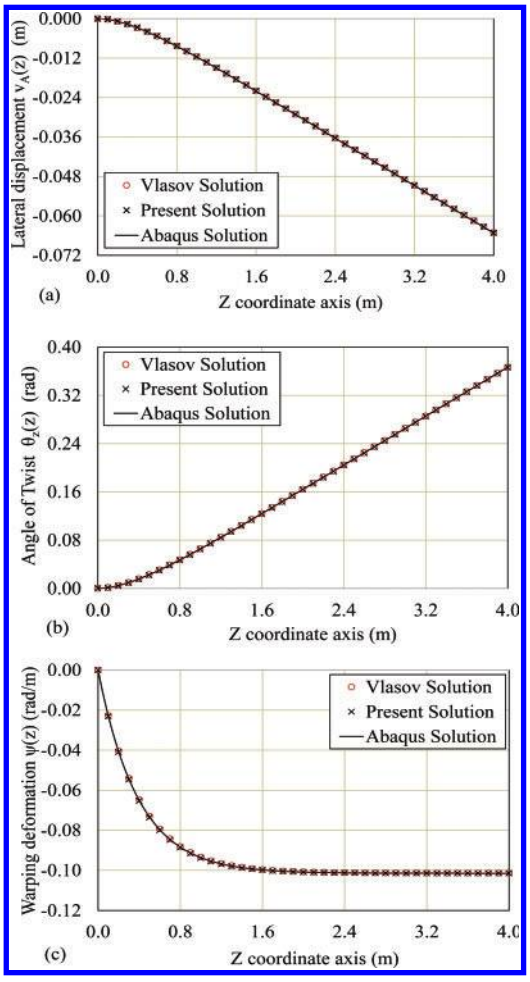


Figure 2. Static results for coupled lateral-torsional response of cantilever C-beam.

8.2 *Cantilever beam under End Transverse Forces-Shear Deformation Effect*

The purpose of this example is to demonstrate the ability of the present formulation to capture the shear deformation effects on the coupled transverse-torsional behavior of long span ($\ell = 4.8\,\text{m}$) and short span ($\ell = 1.0\,m$) cantilevers with monosymmetric channel-sections. The long cantilever is subjected to transverse force $P_y(\ell) = 4.0\,\text{kN}$ while the short cantilever is subjected to $P_y(\ell) = 80.0\,\text{kN}$ acting at the corner point A at the tip. The dimensions of the C-section are; flange thickness $t_f = 12\,\text{mm}$, web thickness $t_w = 8.0\,\text{mm}$, flange width $b = 80\,\text{mm}$ and mid-surface height $H = 200\,\text{mm}$. The coordinates of the centroid are $C_x = 21.82\,\text{mm}$, $C_y = 100\,\text{mm}$ and the coordinate of the shear centre along the axis of

Table 2. Tip deformations of cantilever C-section under transverse load.

Beam span	Variable	Abaqus Beam	Present Solution	Vlasov Solution
	v_A (mm)	−3.590	−3.787	−3.333
Short	θ_x (10_3 rad)	5.000	5.001	4.999
$\ell = 1.0\,m$	θ_z (10_3 rad)	−38.95	−39.89	−36.87
	ψ (10_6 rad/mm)	54.47	54.59	51.97
	v_A (mm)	18.50	18.54	18.43
Long	θ_x (10_3 rad)	−5.760	−5.760	−5.760
$\ell = 4.8\,m$	θ_z (10_3 rad)	13.61	13.62	13.61
	ψ (10_6 rad/mm)	−3.131	−3.124	−3.068

symmetry is $x_s = -53.12$ mm. The channel section properties are;

$$A = 35.2\times10^6\,mm^2,\ I_{xx} = 24.53\times10^6\,mm^4,$$
$$J = 0.126\times10^6\,mm^4,\ C_w = 16.92\times10^9\,mm^6,$$
$$D_{xx} = 0.192\times10^4\,mm^2, D_{yy} = 0.16\times10^4\,mm^2,$$

$$D_{hy} = 5.10\times10^4\,mm^3 \text{ and } D_{\omega\omega} = 20.77\times10^6\,mm^4.$$

Three solutions were provided based on; (i) present solution, (ii) Vlasov beam theory and (iii) Abaqus beam element model for long and short cantilever beams (Table 2). For longer span, the maximum transverse displacement $v_{\max}$, related rotation $\theta_{x\max}$, twist angle $\theta_{z\max}$ and warping deformation $\psi_{\max}$ obtained from the analytical solution developed in the present study are in excellent agreement with those based on Vlasov solution and Abaqus beam element model using 60 B31OS beam elements. For short cantilever, the present solution which captures the shear deformation effects due to bending and restraint warping predicts the transverse displacement, bending rotation, twist angle and warping deformation (a) are respectively 5.49%, 0.02%, 2.41%, and 0.22% greater than those based on the Abaqus beam element model which captured only the shear deformation due to bending. While due to the ignorance of shear deformation effects on the coupled transverse-torsional deformation, results obtained from the Vlasov theory (which ignores the shear deformation effects) are 7.16%, 0.02%, 5.34% and 4.59% lower than the corresponding results based on Abaqus beam solution.

The generalized displacements are plotted in Figure (3a-d). The transverse displacement, angle of twist and warping deformation based on the present solution demonstrate a significantly more flexible response than those obtained from the Vlasov solution but the bending rotation exactly coincided. The results based on excluding shear deformations underestimate the coupled transverse-torsional-warping response the thin-walled monosymmetric beam. Also, shear deformation effects are more significant for short beams.

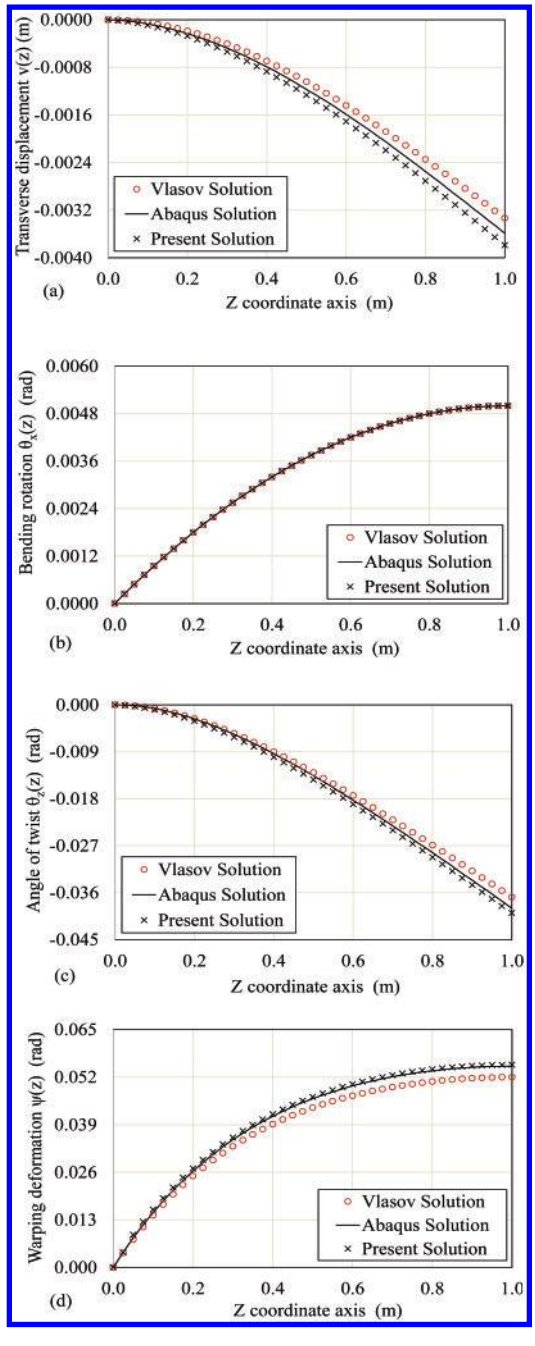


Figure 3. Response of short cantilever with a C-section under end transverse force.

9 SUMMARY AND CONCLUSIONS

1. The governing field equations and related boundary conditions were formulated for thin-walled beams of monosymmetric open cross-sections.
2. Closed-form solutions of coupled were obtained for cantilever as an example.

3. The formulation successfully captures the coupled flexural-torsional static response of monosymmetric cross-sections.
4. Numerical examples validated the accuracy of the present theory and to illustrated the shear deformation effects
5. The model provides superior predictions compared to Abaqus beam and Vlasov solutions.
6. Results show that shear deformation effects are more significant than short span beams.

REFERENCES

Banerjee, J.R., Guo, S., Howson, W. P., 1996, Exact dynamic stiffness matrix of a bending–torsion coupled beam including warping. Computers and Structures, 59: 612–621.

Chen, X. and Tamma, K. 1994, Dynamic response of elastic thin-walled structures influenced by coupling effects, Computers and Structures, 51(1): 91–105.

Friberg, P. O. 1983, Coupled vibration of beams– An exact dynamic element stiffness matrix, International Journal for numerical methods in engineering, 19: 479–493.

Leung, A.Y.T. 1991, Natural shape functions of a compressed Vlasov element, Thin-walled structures, 11: 431–438.

Leung, A.Y. 1992, Dynamic stiffness analysis of thin-walled structures, Thin-walled structures,14: 209–22.

Kim, N. et al. 2007, Stiffness matrices for flexural-torsional/lateral buckling and vibration analysis of thin-walled beam, Journal of Sound and Vibration, 299: 739–756.

Li, Jun et al. 2004, Response of monosymmetric thin-walled Timoshenko beams to random excitations, International Journal of Solids and Structures, 41(22-23): 6023–6040.

Kollar, L.P., Pluzsik, A. (2002), Analysis of thin-walled composite beams with arbitrary layup, Journal of Reinforced Plastics and Composites, 21:1423–1465.

Prokic, A. 2006, On fivefold coupled vibrations of Timoshenko thin-walled beams, Engineering Mechanics, 28: 54–62.

Jung, S. N. and Lee, J. Y., 2003, Closed Form Analysis of Thin Walled Composite I-Beams considering non-classical Effects, Composite Structures, 60: 9–17.

Kim, N.I., Lee, B. J. and Kim, M. Y., 2004, Exact element static stiffness matrices of shear deformable thin-walled beam-columns, Thin-walled Structures, 42: 1232–1256.

Kim, N., Shen, D. 2009, Coupled deflection analysis of thin-walled Timoshenko laminated composite beams, Computational Mechanics, 43: 493–514.

Kim, N.I. 2011, Shear deformable doubly- and monosymmetric composite I-beams, International Journal of Mechanical Sciences, 53 (1): 31–41.

Kim, N. I. 2012, Shear deformable composite beams with channel-section on elastic foundation, European Journal of Mechanics A/Solids, 36: 104–121.

Research and Applications in Structural Engineering, Mechanics and Computation – Zingoni (Ed.)
© 2013 Taylor & Francis Group, London, ISBN 978-1-138-00061-2

Flexural-torsional analysis of shear-deformable monosymmetric thin-walled open members – II. Finite element formulation

Mohammed Ali Hjaji
Department of Mechanical and Industrial Engineering, University of Tripoli, Tripoli, Libya

Magdi Mohareb
Department of Civil Engineering, University of Ottawa, Ottawa, Ontario, Canada

ABSTRACT: A finite element formulation is developed for the coupled flexural-torsional analysis of thin-walled open members under general forces. Based on a generalized Timoshenko-Vlasov thin-walled beam theory, and the principle of minimum total potential energy, a two-node finite element is developed with four degrees of freedom per node. The element fully captures the effects of warping stiffness, shear deformation, and the torsional-flexural coupling and is based on shape functions which exactly satisfy the homogeneous form of the equilibrium conditions. The element is demonstrated to be free from shear locking and discretization errors occurring in conventional finite element solutions. The applicability of the finite beam element is illustrated through examples. The results based on the present formulation are compared against established analytical and finite element solutions and demonstrate the accuracy and efficiency of the solution.

1 INTRODUCTION AND OBJECTIVES

Several finite element solutions investigated the coupled torsional-flexural response of thin-walled open beams. Two types of shape functions have been used; (1) approximate polynomial functions, and (2) functions based on the exact solution of the governing equilibrium equations. Most finite element formulations lie within the first type, including the work of Chen and Tamma (1994), Lee and Kim (2002a, b), Kim and Kim (2005), Voros (2008, 2009), Vo and Lee (2010) and Vo et al. (2011). Among them, Chen and Tamma (1994) used the finite element method in conjunction with an implicit-starting unconditionally stable methodology for the dynamic analysis of thin-walled open members under deterministic loads. By using linear and cubic Hermitian shape functions, Lee and Kim (2002a, 2002b) investigated the coupled free vibration of thin-walled composite beams with doubly symmetric and channel-shaped cross-sections. Lee and Lee (2004) developed a finite element model to investigate the flexural and torsional behaviour of thin-walled composite I-beams with arbitrary laminate stacking sequence using a linear combination of the one-dimensional Lagrangian interpolation function for axial displacement and the Hermite-cubic interpolation function for lateral displacements and twist angle. In their formulation, the shear deformation effects were not considered. Kim and Kim (2005) derived the coupled flexural-torsional free vibration of asymmetric thin-walled shear deformable beam using an isoparametric finite beam element.

The influence of lateral forces on the coupled flexural-torsional free vibration of thin-walled open members was studied by Voros (2008, 2009) who developed a two-noded beam element with fourteen degrees of freedom. Vo and Lee (2010) and Vo et al. (2011) studied the coupled flexural-torsional free vibration of thin-walled composite beams under constant axial forces and end moments by developing a displacement-based one dimensional finite element model. Recently, Kim (2011) developed a shear deformable beam element for the coupled flexural and torsional analyses of thin-walled composite I-beams based on an isoparametric Lagrangian interpolation formulation. More recently, Kim (2012) extended his work (Kim 2011) to investigate the coupled flexural-torsional static analysis for thin-walled channel composite beams resting on elastic foundations. Finite element solutions based on exact homogeneous solution of the dynamic equations of motion include the work of Hjaji and Mohareb (2011) and offer two advantages: (1) it eliminates the discretization errors encountered in other finite element formulations, and thus it converges to the solution using a minimum number of degrees of freedom, and (2) it leads to elements that are free from shear locking normally arising in formulations based on approximate interpolation functions. To the best of the author's knowledge, such a finite element solution not been reported for monosymmetric sections and is thus the object of this paper. The reader is referred to the companion paper for the assumptions of the formulation and a description of the kinematics of the problem.

2 VARIATIONAL FORMULATION

The total potential energy Π of the member is the sum of the internal strain energy U and potential energy V gained by the applied forces. The first variation of $\delta\Pi$ must vanish to satisfy the equilibrium condition yielding

$$\delta\Pi = \delta U + \delta V = 0 \tag{1}$$

in which the expressions for the first variation of strain energy is given by:

$$\begin{aligned}\delta U &= \int_0^\ell \int_A \left[E\varepsilon_{zz}\delta\varepsilon_{zz} + G\gamma_{zs}\delta\gamma_{zs}\right] dA\,dz + \int_0^\ell GJ\theta_z'\delta\theta_z'\,dz \\ &= \int_0^\ell \Big[\left\langle \delta\bar{U}' \right\rangle_{1\times4}^T [Y_a]_{4\times4} \left\{\bar{U}'\right\}_{4\times1} \\ &\quad + \left\langle \delta\bar{U}_s \right\rangle_{1\times4}^T [Y_s]_{4\times4} \left\{\bar{U}_s\right\}_{4\times1} \Big] dz\end{aligned} \tag{2}$$

where E is the Young's modulus, G is the shear modulus, J is the St. Venant torsional constant, A is the cross-sectional area. The primes denote derivatives with respect to coordinate z. The longitudinal strain is

$$\varepsilon_{zz} = \partial w_p/\partial z = \left\langle X_a \right\rangle_{1\times4}^T \left\{\bar{U}'\right\}_{4\times1},$$

the vector of displacement derivatives is

$$\left\langle \bar{U}' \right\rangle^T = \left\langle\, v'(z) \quad \theta_x'(z) \quad \theta_z'(z) \quad \psi'(z) \right\rangle^T,$$

the shear strain is

$$\gamma_{zs} = \partial w_p/\partial s + \partial \xi_p/\partial s = \left\langle X_s \right\rangle_{1\times4}^T \left\{\bar{U}_s\right\}_{4\times1}, \text{ and}$$

$$\left\langle \bar{U}_s \right\rangle_{1\times4}^T = \left\langle v'(z) \;\; \theta_x(z) \;\; \theta_z'(z) \;\; \psi(z) \right\rangle_{1\times4}^T.$$

in which $v(z)$, $\theta_x(z)$, $\theta_z(z)$, $\psi(z)$ are the transverse displacement, related bending rotation, twist angle and warping deformation functions, respectively.

In Equation (2),

$$[Y_s]_{4\times4} = G\int_A \left\langle X_s \right\rangle_{1\times4}^T \left\{X_s\right\}_{4\times1} dA = \begin{bmatrix} GD_{yy} & GD_{yy} & GD_{hy} & -GD_{hy} \\ & GD_{yy} & GD_{hy} & -GD_{hy} \\ & & GD_{\omega\omega} & -GD_{\omega\omega} \\ Symm & & & GD_{\omega\omega} \end{bmatrix}_{4\times4}, \text{ and}$$

$$[Y_a]_{4\times4} = E\int_A \left\langle X_a \right\rangle_{1\times4}^T \left\{X_a\right\}_{4\times1} dA + GJ = diag\left[0 \;\; EI_{xx} \;\; GJ \;\; EC_w\right]_{4\times4},$$

where I_{xx} is a moment of inertia about X axis and C_w is the warping constant.

The section properties are defined by

$$D_{yy}, D_{hy}, D_{\omega\omega} = \int_A \left[\left(\frac{dy}{ds}\right)^2, \left(\frac{dy}{ds}\right)\left(\frac{d\omega}{ds}\right), \left(\frac{d\omega}{ds}\right)^2 \right] dA,$$

where $\omega(s)$ is the warping coordinate,

$$\left\langle X_a \right\rangle_{1\times4}^T = \left\langle 0 \;\; y \;\; 0 \;\; -\omega \right\rangle_{1\times4}^T, \text{ and}$$

$$\left\langle X_s \right\rangle_{1\times4}^T = \left\langle dy/ds \;\; dy/ds \;\; d\omega/ds \;\; -d\omega/ds \right\rangle_{1\times4}^T.$$

The first variation of the potential energy δV of the applied forces is

$$\begin{aligned}\delta V &= -\int_0^\ell \left[q_y\delta v + m_x\delta\theta_x + m_z\delta\theta_z + m_w\delta\psi \right] dz \\ &\quad + \left[V_y\delta v\right]_0^\ell + \left[M_x\delta\theta_x\right]_0^\ell + \left[M_z\delta\theta_z\right]_0^\ell + \left[M_w\delta\psi\right]_0^\ell \\ &= -\left[\left\langle \delta\bar{U} \right\rangle_{1\times4}^T \{F\}_{4\times1} \right]_0^\ell - \int_0^\ell \left\langle \delta\bar{U} \right\rangle_{1\times4}^T \{Q_s\}_{4\times1} dz\end{aligned} \tag{3}$$

Equations (2–3) are obtained by; (a) substituting the displacement fields given in companion paper [Hjaji and Mohareb 2013] into first energy expressions presented in Equations (2–3), and (b) enforcing the orthogonality conditions; $\int_A [x, y, xy, x\omega, y\omega, \omega] dA = 0$. In Equation (3), $q_y(z)$ is the distributed transverse force, $m_i(z)$ for are the distributed moments about X and Z axes, $m_w(z)$ is the distributed bimoment, $V_y(z_e)$ are the transverse end forces, $M_i(z_e)$ for $i = x, z$ are the end moments about X and Z, and $M_w(z_e)$ are the end bimoments. All forces and moments are applied at beam ends ($z_e = 0, \ell$). The sign conventions of the applied forces are identical to those introduced for the end displacement fields [Hjaji and Mohareb 2013].

In line with the objective of the present paper, the present study focuses on the coupled transverse-torsional-warping response of thin-walled monosymmetric cross-sections. Consequently, neglected are the terms associated with the longitudinal response and pure flexural response along the direction of symmetry axis.

3 FORMULATION OF EXACT SHAPE FUNCTIONS

Expressions for displacement fields for the coupled field equations were derived in the companion paper [Hjaji and Mohareb 2013] as

$$\left\{\bar{U}(z)\right\}_{4\times1} = \left[\bar{C}\right]_{4\times8} \left[X(z)\right]_{8\times8} \left\{\bar{A}\right\}_{8\times1} = \left[\chi(z)\right]_{4\times8} \left\{\bar{A}\right\}_{8\times1} \tag{4}$$

in which we recall that $[\chi(z)]_{4\times8} = [\bar{C}]_{4\times8}[X(z)]_{8\times8}$, matrix $[\bar{C}]_{4\times8}$ contains the eigenvectors of the

quadratic eigenvalue problem arising from the coupled system of equilibrium equations, $[X(z)]_{8\times 8} = Diag[e^{m_1 z}\ e^{m_2 z}\ e^{m_3 z}\ \ldots\ldots\ e^{m_8 z}]_{8\times 8}$ is a diagonal matrix of the exponential functions $e^{m_i z}$ (m_i being the eigen values of corresponding eigen values), and $\{\bar{A}\}_{8\times 1}$ is a vector of integration constants to be determine from the boundary conditions of the problem., In the present treatment, the constants in $\{\bar{A}\}_{8\times 1}$ are related to the nodal displacements $\{U_N\}_{8\times 1}$ through

$$\{U_N\}_{8\times 1} = \begin{Bmatrix} \{\bar{U}(0)\}_{4\times 1} \\ \{\bar{U}(\ell)\}_{4\times 1} \end{Bmatrix}_{8\times 1} = \begin{bmatrix} [\chi(0)]_{4\times 8} \\ [\chi(\ell)]_{4\times 8} \end{bmatrix}_{8\times 8} \{\bar{A}\}_{8\times 1} = [T]_{8\times 8}\{\bar{A}\}_{8\times 1} \tag{5}$$

From Equation (9), by substituting into Equation (8), one obtains:

$$\{\bar{U}(z)\}_{4\times 1} = [\chi(z)]_{4\times 8}[T]^{-1}_{8\times 8}\{U_N\}_{8\times 1} = [H(z)]_{4\times 8}\{U_N\}_{8\times 1} \tag{6}$$

where

$$[H(z)]_{4\times 8} = [\chi(z)]_{4\times 8}[T]^{-1}_{8\times 8} = \left[\{H_{1,j}(z)\}_{8\times 1}\ \{H_{2,j}(z)\}_{8\times 1}\ \{H_{3,j}(z)\}_{8\times 1}\ \{H_{4,j}(z)\}_{8\times 1}\right]_{4\times 8}$$

is the matrix of the shape functions which exactly satisfy the homogeneous form of the coupled governing field equations.

4 FINITE ELEMENT FORMULATION

From Equation (6), by substituting into energy expressions in Equations (2) and (3), and then substituted in Equation (1), one recovers

$$[K_e]_{8\times 8}\{U_N\}_{8\times 1} = \{F_e\}_{8\times 1} \tag{7}$$

In Equation (7),

$$[K_e]_{8\times 8} = \int_0^{\ell}\left[[H'(z)]^T_{8\times 4}[Y_a]_{4\times 4}[H'(z)]_{4\times 8} + [H_s(z)]^T_{8\times 4}[Y_s]_{4\times 4}[H_s(z)]_{4\times 8}\right]dz$$

is the element stiffness matrix, and

$$\{F_e\}_{8\times 1} = \int_0^{\ell}\left[[H(z)]^T_{8\times 4}\{Q_s\}_{4\times 1}\right]dz + \left[[H(z)]^T_{8\times 4}\{Q_c(z)\}_{4\times 1}\right]_0^{\ell}$$

is the element load vector, where

$$[H_S(z)]_{4\times 8} = \left[\{H'_{1,j}(z)\}_{8\times 1}\ \{H_{2,j}(z)\}_{8\times 1}\ \{H'_{3,j}(z)\}_{8\times 1}\ \{H_{4,j}(z)\}_{8\times 1}\right]_{4\times 8}.$$

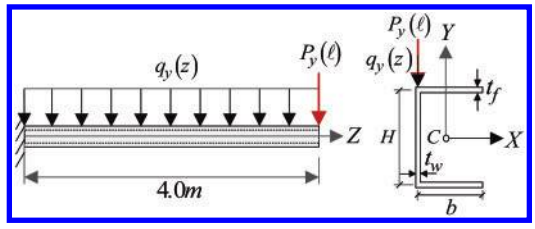


Figure 1. Cantilever C-beam under distributed and concentrated transverse forces.

Table 1. Coupled transverse-torsional static response of cantilever C-section under transverse loads.

Type of load	Variable	Abaqus beam solution	Present finite element	Vlasov solution
Concentrated	v (mm)	−20.97	−21.04	−20.87
$P_y(\ell)$	θ_x (10^{-3} rad)	7.826	7.827	7.826
	θ_z (10^{-3} rad)	52.68	52.77	52.68
	ψ (10_{-6} rad/mm)	−15.58	−15.31	−15.41
	v (mm)	−16.46	−16.49	−16.31
Distributed	θ_x (10^{-3} rad)	5.462	5.436	5.436
$q_y(z)$	θ_z (10^{-3} rad)	48.18	48.35	48.18
	ψ (10_{-6} rad/mm)	−4.758	−4.656	−4.672

5 NUMERICAL EXAMPLES AND DISCUSSION

In the following examples, material is steel are $E = 200$GPa and $G = 70$GPa. As a result of the exact shape functions derived, the present treatment eliminated mesh discretization errors is compared with additional solutions; (1) An analytical solution based on Vlasov beam theory and (2) An Abaqus B31OS beam element solution.

5.1 *Example 1: Cantilever C-beam under Torsion*

A cantilever thin-walled monosymmetric channel-section subjected to; (i) concentrated transverse force $P_y(\ell) = 4.80$ kNm applied at the cantilever free end, and (ii) uniformly distributed transverse force is considered as illustrated in Fig. (1). Section dimensions are; $t_f = 12$ mm, $t_w = 8$ mm, $b = 80$ mm, $H = 200$ mm. The coordinates of the centroid are $C_x = 21.82$ mm, $C_y = 100$ mm and the coordinate of the shear centre along the axis of symmetry is $x_s = -53.12$ mm. The section properties are; $D_{yy} = 0.16 \times 10^4$ mm^2, $D_{hy} = 5.1 \times 10^4$ mm^3 and $D_{\omega\omega} = 20.8 \times 10^6$ mm^4.

The results of nodal displacements obtained from the present finite element formulation using a single beam element are compared with Vlasov beam solution and Abaqus beam element model using one-hundred B31OS element with 700 degrees of freedom in order to achieve the solution accuracy. Table (1) provides the shows that the nodal degrees of freedom

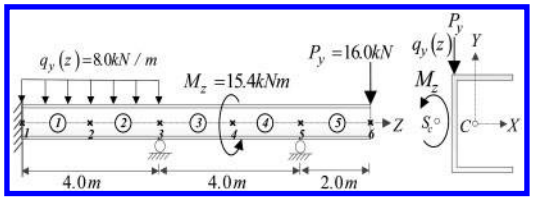


Figure 2. Continuous beam with channel-section under transverse and torsional loads.

results predicted from the present finite element using a single beam element with 8 dof are found exactly identical to the analytical closed-form solution developed in the companion paper. It is observed that the present formulations (which captures the shear deformation due to bending and warping torsion) are in excellent agreement with the results based on Vlasov beam theory (which discounts the shear deformation effects) and Abaqus beam element solution (which captures only the shear deformation due to bending) using 100 B31OS beam elements (700 dofs). Even though shear deformation effects are neglected fully in the Vlasov solution and partially in Abaqus beam solution, both solutions predict results in close agreement with the present formulation. This indicates that shear deformation effects are not significant for the present long-span beam problem.

5.2 *Example 2: Continuous Three-Span beam - Finite element formulation*

A three-span beam with the cross-section in Example 1 is subjected to three forces; concentrated transverse force $P_y(\ell) = 16.0\,kN$, concentrated twisting moment $M_z = 15.4$ kNm and uniformly distributed transverse force $q_y = 8.0\,kN/m$ is considered (Figure 3). It is required to compare the response of the continuous beam based on the finite element formulation with those based on the Abaqus beam element.

The problem is solved based on five beam elements (20 dofs). Results based on the present formulation are compared with the Abaqus solution which was able to achieve convergence based on 200 B31OS beam elements (1400 dofs). The analysis results for the nodal transverse displacement, related rotation, twist angle and warping deformation plotted against the beam axis Z are displayed in Figure (4a–d). The present solution based on five elements is in excellent agreement with that based on the Abaqus solution.

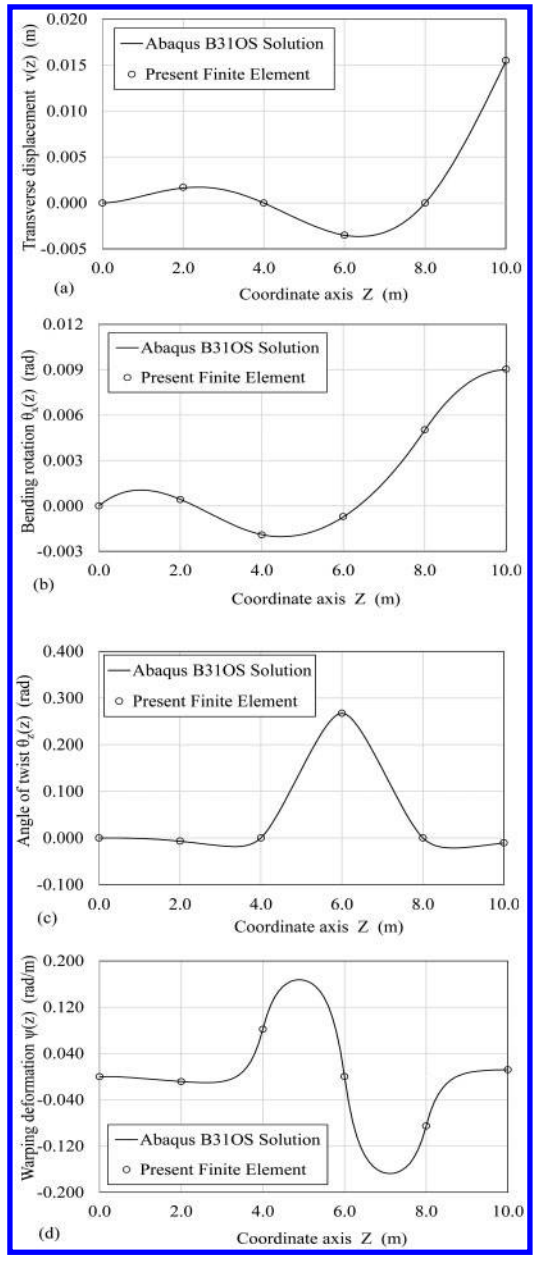


Figure 3. Static analysis for three-span monosymmetric C-beam under transverse and torsional forces.

6 SUMMARY AND CONCLUSIONS

(1) A super-convergent finite element was developed for the analysis of thin-walled members with monosymmetric sections.
(2) The element is based on a generalized Vlasov-Timoshenko beam theory which accounts for shear deformation effects due to bending and non-uniform torsion.
(3) The finite element formulation developed successfully captures the coupled flexural-torsional response of monosymmetric cross-sections.
(4) Results are in excellent agreement with Abaqus beam element at a small fraction of the computational and modeling cost.
(5) Since integration within the element is explicit, shear locking problems do not arise in the formulation.

REFERENCES

Chen, X. and Tamma, K. 1994, Dynamic Response of Elastic Thin-walled Structures Influenced by Coupling Effects, Computers and Structures, 51(1): 91–105.

Hjaji, M. A. and Mohareb, M. 2011, Steady State Harmonic Response of Doubly symmetric Thin-Walled Members-Under Harmonic Loads - Finite Element Formulation, Second International Engineering Mechanics and Materials Specialty Conference, Ottawa, Canada.

Hjaji, M. A. and Mohareb, M. 2013a, Flexural-Torsional Analysis of Shear-Deformable Monosymmetric Thin-walled open members - I. Analytical Solution, Fifth International Conference on Structural Engineering and Computation (SEMC), Cape Town, South Africa.

Hu, Y. et al. 1996, A Finite Element Model for Static and Dynamic Analysis of Thin-walled Beams with Asymmetric Cross-Sections, Computers and Structures, 61: 897–908.

Kim, N.I. 2011, Shear deformable doubly- and monosymmetric composite I-beams, International Journal of Mechanical Sciences, 53 (1): 31–41.

Kim, N. I. 2012, Shear deformable composite beams with channel-section on elastic foundation, European Journal of Mechanics A/Solids, 36: 104–121.

Kim, N. I. and Kim, M. N. 2005, Exact Dynamic/Static Stiffness Matrices of Non-Symmetric Thin-walled Beams considering coupled shear deformation effects, Thin-walled Structures, 43: 701–734.

Lee, J. and Lee, S. H., 2004, Flexural-torsional behavior of thin-walled composite beams, Thin-walled Structures, 42: 1293–1305.

Lee, J. and Kim, S. E. 2002a, Free Vibration of Thin-walled Composite Beams with I-Shaped cross-sections, Composite Structures, 55 (2): 205–215.

Lee, J. and Kim, S. E. 2002b, Flexural–torsional coupled vibration of thin-walled composite beams with channel sections, Computers and Structures, 80: 133–144.

Mei, C. 1970, Coupled vibrations of thin-walled beams of open section using the finite element method, International journal of mechanical science, 12: 883–891.

Voros, G. 2008, On Coupled Vibrations of Beams with Lateral Loads, Journal of computational and Applied Mechanics, 9 (2): 1–14.

Voros, G. M. 2009, On Coupled bending-torsional vibrations of beams with initial loads, Mechanics Research Communications, 36: 603–611.

Vo, T. P. and Lee, J. 2010, Interaction curves for vibration and buckling of thin-walled composite box beams under axial loads and end moments, Applied Mathematical Modelling, 34: 3142–3157.

Vo, T. P. et al. 2011, Vibration analysis of thin-walled composite beams with I-shaped cross-sections, Composite Structures, 93 (3-4): 812–820.

Research and Applications in Structural Engineering, Mechanics and Computation – Zingoni (Ed.)
© 2013 Taylor & Francis Group, London, ISBN 978-1-138-00061-2

Flexural strength of single channels restrained by angle cleats

G.M. Bukasa & M. Dundu
University of Johannesburg, Johannesburg, South Africa

ABSTRACT: It is common practice to restrain members in flexure using fly-bracings. In this investigation a series of channels are restrained by a purlin–angle cleat connection. The channels are subjected to a two point loading system in order to simulate a distributed load. Variable in the tests include the unbraced length between the two-point loads and the size of the channels. Failure of the channels occurred by local buckling of the compression zone of the flange and web and lateral torsional buckling of the channels between points of lateral support. The capacity reached by the channels shows that the purlin-cleat restraining system is able to resist lateral torsional buckling of the channels, and that this system can be used without including any fly bracing.

1 INTRODUCTION

Cold-formed steel channels are widely used as structural elements, especially in residential, industrial and commercial buildings. In these structures, the smaller sections are normally used as purlins and diagonal bracing elements, and the larger sections are used as the main frame. When cold-formed steel lipped channels are used as the main frame members, for example in portal frames, the channels are usually restrained against lateral torsional buckling from the top flange through an angle cleat-purlin connection. Torsional restraint is usually provided by fly bracings. This restraining system is complicated and has the disadvantages of tearing the bolted area of the top flange of the main frames if it is in tension or weakening the bearing area of the top flange, if the purlin is subjected to large downward loads.

For this reason, this study investigates a restraint that avoids the use of fly bracing and bolt-holes in the top flange of the rafter. Restraint of the beam rafter or main frame is still provided by a purlin-angle cleat connection; however the angle is long enough to connect the web of the main beam or rafter. This restraint has also the advantage of preventing the rafter and purlin's web from crippling at loading points, since it connects both elements in the web, and no drilling or welding is performed in the top flange. In addition, the moment capacities that can be achieved by these beams, with the proposed bracing, are also determined.

In all the tests carried out, the sections used are all cold-formed steel sections in order to make the structure light and all the elements of the structure are connected together by bolts only. The size of the beams investigated in this paper are $300 \times 75 \times 20 \times 2.0$ mm, $300 \times 75 \times 20 \times 2.5$ mm and $300 \times 75 \times 20 \times 3.0$ mm, and the purlin and angle cleat section are $100 \times 50 \times 20 \times 2$ mm and $100 \times 75 \times 20 \times 3$ mm, respectively. The support systems were designed to achieve simply supported end conditions in both the vertical and horizontal planes. Restraints were provided at the loading points and the beams were subjected to a two-point loading system in order to experience uniform bending in the internal span. The objectives of the tests are to examine the ability of thin cold-formed angle cleat to restrict lateral-torsional buckling and to compare the test results with unfactored resistances from the South African cold-formed steel code, SANS10162-2 (2005). This code is based on the Canadian code (CAN/CSA S16.1-M01) and the North American Specification (AISI S100-07).

2 MATERIAL PROPERTIES

The material properties were determined from the web coupons, which were cut from the $300 \times 75 \times 20 \times 2$ mm, $300 \times 75 \times 20 \times 2.5$ mm, and $300 \times 75 \times 20 \times 3$ mm sections Coupon tests from the web represent material properties of virgin steel sheet. The coupons were prepared and tested in a 100 kN capacity displacement controlled testing machine according to the guidelines provided by the British Standard, BS 18. The tensile load was applied to coupon test at a rate of 3.0 mm/min until failure.

Stress-strain relationships of the coupons were derived from the load-elongation relationship using its original cross-sectional area and the gauge length. The average yield stress (f_y), ultimate stress (f_u) and modulus of elasticity (E) of the steel in Table 1 were determined from these stress-strain curves. In compliance with SANS-10162-1 (2005), the material properties of the channels achieved the recommended ductility requirements, that is, the percentage elongation at failure exceeded 10% for a 50 mm gauge length

Table 1. Average material properties.

Specimen	f_y (MPa)	f_u (MPa)	E (GPa)
300 × 75 × 20 × 2.0	246.60	346.05	206.35
300 × 75 × 20 × 2.5	287.30	364.05	201.61
300 × 75 × 20 × 3.0	265.70	351.55	205.58

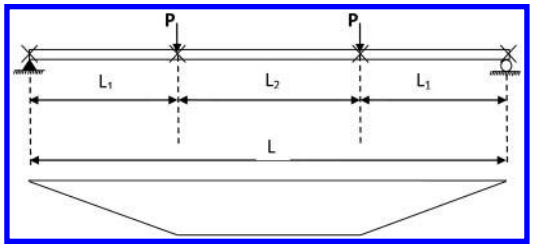


Figure 1. Restraints and support system.

Table 2. Length of tested beams.

Specimen	L (mm)	L_2 (mm)	L_1 (mm)	r_y (mm)	KL_2/r
300 × 75 × 20 × 2.0	5900	2200	1800	25.7	85.60
300 × 75 × 20 × 2.5	5900	1800	2000	25.4	70.87
300 × 75 × 20 × 2.5	5900	2000	1900	25.4	78.74
300 × 75 × 20 × 2.5	6000	2400	1750	25.4	94.49
300 × 75 × 20 × 3.0	4600	1800	1350	25.1	71.71
300 × 75 × 20 × 3.0	5900	2200	1800	25.1	87.65
300 × 75 × 20 × 3.0	6000	2400	1750	25.1	95.62

and the ratio of the specified ultimate tensile strength (f_u) to the specified yield strength (f_y) exceeded 1.08.

3 TEST PROGRAMME

3.1 *Test set-up*

A set-up was prepared to test the ability of thin cold-formed steel angle-cleats to restrain the beams from failing due to lateral-torsional buckling. The beams consisted of three different sections, namely; 300 × 75 × 20 × 2 mm, 300 × 75 × 20 × 2.5 mm and 300 × 75 × 20 × 3 mm, in order to vary the slenderness ratios, and were tested under two point loading as illustrated by the schematic diagram in Figure 1. Two-point loading provides a constant moment between the applied loads so that pure bending failure only is experienced. This loading arrangement simulates a distributed load over the entire span of the beam. The support system was designed to ensure that the beam test is simply supported, and that only lateral deflection is prevented at the ends. Lateral and torsional restraints were provided by the angle cleats at the loading points. Details of the span and points of bracing are shown in Table 2.

The middle unbraced lengths were selected based on the recommendation by Schuster (1991) on maximum unbraced length. According to this recommendation, the internal length should be greater than the maximum laterally unbraced length (L_u) for lateral-torsional buckling to occur. For a channel section the maximum unbraced length (L_u) is given by:

$$L_u = \left\{ \frac{GJ}{2C_1} + \left[\frac{C_2}{C_1} + \left(\frac{GJ}{2C_1} \right)^2 \right]^{1/2} \right\}^{1/2} \quad (1)$$

where,

$$C_1 = \frac{11.3 f_y^2 K_y^2 S_{xc}^2}{C_b^2 A \pi^2 r_y^2 E} \quad \text{and} \quad C_2 = \frac{\pi^2 E C_w}{K_t^2}$$

In Equation (1), G is the shear modulus, J is the St. Venant torsional constant, K_y is the effective length factor for bending about the minor axis, K_t is the effective length factor for torsional buckling, S_{xc} is the effective section modulus about the x-axis, the bending coefficient $C_b = 1/\omega \leq 2.5$, where, $\omega = 0.6 + 0.4\kappa$ (κ is the ratio of the smaller to the larger moment at opposite ends of the unbraced portion/segment, positive for double curvature and negative for single curvature), A is the area and C_w is the warping constant. The maximum unbraced length was derived by equating the critical elastic lateral-torsional buckling stress to the yield stress of the material.

A pair of channels was used in the test to allow interaction between the beams to occur, and to provide stability to the test set-up. This idea was selected based on previous research (Kavanagh and Ellifritt (1994), Goncalves, Malite and Javaroni (2000), and Dundu and Kemp (2006a,b)). The present investigation adopted spacing between two beams of 1.84 m from a study conducted by Dundu and Kemp (2006a, b). Two purlins, size 100 × 50 × 20 × 2 mm cold-formed sections, were used in all the tests to connect the two beams. The channels are oriented in the same direction as this offers greater stiffness than having the channels oriented in different directions (Dundu and Kemp 2006a, b).

To make the frame light-weight all members including the angle cleat are cold-formed steel members. The connection configuration of the angle cleat is shown in Figure 2. As indicated in the figure, M20 and M12 high strength bolts were used to connect the 100 × 75 × 20 × 3 mm cold-formed angle-cleat to the 300 × 75 × 20 × 3 beam channel and 100 × 50 × 20 × 2 mm purlin, respectively. The bolts used to attach angle cleat to purlin were aligned diagonally in order to generate enough rotational moment of resistance. To prevent premature local buckling failure of the beams, at the point where the load was applied, the web and the flange was stiffened using a hot-rolled steel angle, as shown in Figure 3.

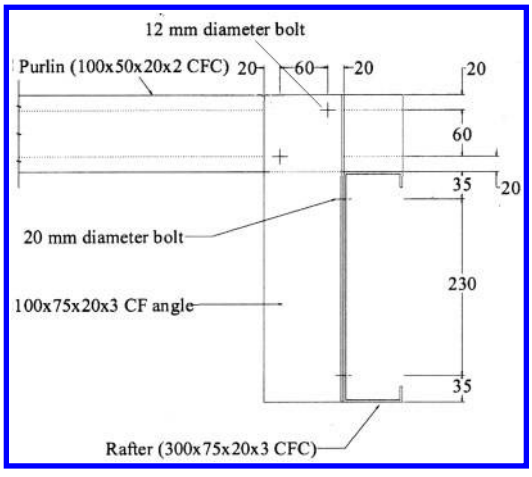


Figure 2. Angle-cleat connection.



Figure 3. Web and flange stiffener.



Figure 4. Test set-up.

3.2 *Instrumentation*

The beams were fully instrumented so that in-plane and out-of-plane deflection, strains and rotation could be measured. The measurements were recorded at the mid-span of the beams by means of a data-logging system. Two computers were used during the tests; one was used to initiate the application of the load by the Instron to the test beams, and another one to collect the readings from the data logger. In-plane and out-of-plane deflections of a beam were monitored using three linear variable differential transducers, commonly known as LVDTs. The LVDTs were installed at mid-span, since the maximum vertical and lateral deflections were expected to occur at this point.

In addition to the LVDTs in the web, a rotation gauge (also known as an AccuStar Electronic Clinometer) was installed at the centre of the web located at mid-span of the beam to monitor the rotation. Figure 5 shows the rotation gauge. The two holes of the clinometer were aligned vertically so that the output from the multimeter could read zero in the unloaded condition.

Longitudinal strains at mid-span were recorded by means of strain gauges. This was done in order to determine the moment-curvature behaviour of the beam. Two strain gauges were used for each channel; one placed inside the top flange (compression zone), and another one placed inside the bottom flange (tension zone).

3.3 *Test procedure*

Once all devices were set and calibrated, the loading procedure began. Great care was taken so that both computers start recording data at the same time. A 250 kN hydraulic Instron was used to apply a downward load to the test beam through spreader beam until its failure. The channels were subjected to equal loads. Each beam was incrementally loaded at the rate of 0.5 mm/min, so that the behaviour and failure patterns of the beam could be well observed during the test. The readings were taken after each load increment until the beams collapsed. The test was stopped once the load started falling off.

4 FAILURE MODES

The governing failure mode for all the beams tested was lateral-torsional buckling. Lateral-torsional buckling is shown in Figure 5, and was largely influenced by the length of the internal segment. In both beams the outside segments and the restraining angle cleats remained vertical. This is clear evidence that the angle cleats were able to restrain the channels. In all the $300 \times 75 \times 20 \times 3$ mm and $300 \times 75 \times 20 \times 2.5$ mm beams tested lateral-torsional buckling of the internal segment was accompanied by distortional buckling of the web, which deflected inward towards the centroid (Figure 6(a)) followed by distortional buckling of the top compression flange, which deflected upwards (Figure 6(b)). In contrast to the $300 \times 75 \times 20 \times 3$ mm and $300 \times 75 \times 20 \times 2.5$ mm channels, distortional buckling of the $300 \times 75 \times 20 \times 2$ mm caused the web to deflect outward towards the shear centre and the top compression flange to deflect inward towards the neutral axis. This behavior can be attributed to the small



Figure 5. Lateral-torsional buckling.

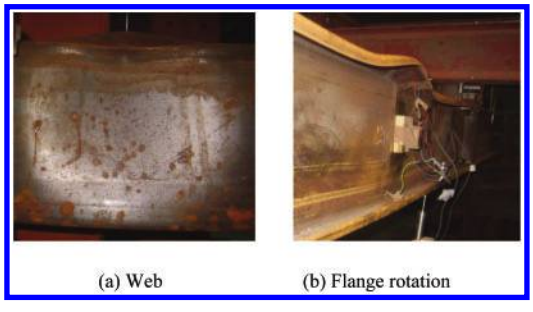


Figure 6. Distortional buckling.

thickness exhibited by the section. Considerable more distortional buckling failure of both the web and top flange were experienced in the 300 × 75 × 20 × 2 mm section because of the smaller thickness.

5 TEST RESULTS

The results of the flexural tests are shown in Table 3 In this table M_t is the maximum moment applied to the tested specimens and M_r is the buckling moment resistance, determined using the South African structural steel code, SANS 10162-2 (2005). As indicated in the introduction of this paper, this code is based on the Canadian cold-formed structural steel code, CAN-S16.1-M01, and the North American Specification, AISI S100-07. The buckling moment of resistance of the middle unbraced length is determined, based on modified section properties (effective width of compression elements) to control local buckling. The effective width concept was first proposed by Von Karman (1932) and calibrated for use by Winter (1947). An effective length factor of 1 is assumed for bending about the minor axis and a moment-gradient factor of 1 is used because of the uniform bending moment diagram.

As expected the moment capacities of all beams in Table 3 decrease with increase of the middle segment length. A comparison of the test moments and the buckling moment resistances shows the test moments of all the sections, except the 300 × 75 × 20 × 2.5 of 2.4 m length, to be larger than the buckling resistance. Significantly larger test moments are achieved by 1.8 m length of the 300 × 75 × 20 × 2.5 and 300 × 75 × 20 × 3.0 sections. In these two cases the test-to-predicted moments are 32% and 28% respectively. On average the tests moments are 16% greater than the moments predicted by SANS 10162-2 (2005). Table 3 also shows that the ratio of the test-to-predicted moments tends to be larger for sections of shorter length, and decrease as the length of the channels increases.

Table 3. Test results.

Specimen (h × b × c × t)	L_u (m)	f_y (MPa)	M_t (kNm)	M_r (kNm)	M_t/M_r
300 × 75 × 20 × 2.0	2.2	246.60	20.98	18.05	1.16
300 × 75 × 20 × 2.5	1.8	287.30	34.66	26.18	1.32
300 × 75 × 20 × 2.5	2.0	287.30	27.18	24.82	1.10
300 × 75 × 20 × 2.5	2.4	287.30	22.00	22.14	0.99
300 × 75 × 20 × 3.0	1.8	265.70	39.51	30.82	1.28
300 × 75 × 20 × 3.0	2.2	265.70	32.38	30.32	1.07
300 × 75 × 20 × 3.0	2.4	265.70	31.25	29.67	1.05

In general the test moments obtained compares favourably well of with the prediction of the South African code, SANS10161-2 (2005). The fact that the tests moments are larger than the code-predicted moments shows that the angle cleats are able to restrain lateral-torsional buckling. Even at the stage where the internal segment of the beam buckled, the angle cleat configuration remained vertical. Lateral-torsional buckling did not contribute to a significant loss of moment of resistance until distortional kicked in or took effect.

6 CONCLUSION

This paper has described tests on the lateral-torsional buckling behaviour of cold-formed channels beams, subjected to two- point loading and restrained by angle cleats. From the tests the following conclusions are made:

- The lateral-buckling strength values obtained from the tests are in all cases larger than the values predicted by the Canadian/South-Africa code of practice. The fact that the tests moments are larger than the code-predicted moments shows that the angle cleats are able to restrain lateral-torsional buckling. Even at the stage where the internal segment of the beam was buckling, the angle cleat configuration remained vertical.
- In all cases, failure of the channels occurred by a combination lateral-torsional buckling of the internal segment and distortional buckling of the web and the flange. The capacity reached by the channels shows that an angle-cleat restraining system is

able to resist lateral-torsional buckling. This means that such a system can be used without the need of fly-bracings, as is normally done in practice to restrain torsion instability.

- The connection configuration investigated is found to be better, not only because it restrains both lateral and torsional movements of the member, but, it is also acting as web stiffeners for both purlin and rafter.

ACKNOWLEDGEMENTS

The authors wish to acknowledge the University of Johannesburg Research Committee (URC) for sponsoring this research.

REFERENCES

AISI S100. 2007. *North American Specification for the Design of Cold-Formed Steel Structural Members*. Washington D.C., USA: American Iron and Steel Institute Standards.

BS 18. 1987. *British standard method for tensile testing of metals*. London: British Standard Institution.

CAN/CSAS16.1-M01. 2001. *Limit States Design of Steel Structures.* Rexdale, Ontario, Canada: Canadian Standards Association.

Dundu, M. and Kemp, A.R. 2006a. Strength requirements of single cold-formed channels connected back-to-back. *Journal of Construction Steel Research* 62: 250–261.

Dundu, M. & Kemp, A.R. 2006b. Plastic and Lateral-Torsional Buckling Behaviour of Single Cold-Formed Channels Connected Back-to-Back. *Journal of Structural Engineering*, ASCE 132: 1223–1233.

Karman, T.V. & Sechler, E.E. & Donnell, L.H. 1932. The Strength of thin plates in Compression. *Transactions, Applied Mechanics Division*, ASME 54 (5): 53–57.

Kavanagh, K.T. and Ellifritt, D.S. 1994. Design Strengths of Cold-Formed Channels in Bending and Torsion. *Journal of Structural Engineering*, ASCE 120.

Malite, M. & Javaroni, C.E. 2000. A Theoretical and Experimental analysis of Cold-Formed Steel shapes subjected to Bending-Channel and simple lipped channel. *Fifteenth International Specialty Conference on Cold-Formed Steel Structures. St. Louis, October 19–20.* Missouri, U.S.A.

SANS 10162-2. 2005. *The structural use of steel, Part 2: Limit-state design of cold-formed steelwork*. Pretoria, South Africa: South Africa National Standards.

Schuster, R. 1991. Excerpts from the new Canadian cold-formed steel design standard (it's the limit). *Conference on Trends in Steel Structures for Mining and Buildings*, Johannesburg, South Africa.

Winter, G. 1947. Strength of thin Steel Compression Flanges. *Transactions*, ASCE 112: 527–554.

Research and Applications in Structural Engineering, Mechanics and Computation – Zingoni (Ed.)
© 2013 Taylor & Francis Group, London, ISBN 978-1-138-00061-2

Single shear screwed connection tests of thin sheet steel at elevated temperatures

S. Yan
Ove Arup & Partners Hong Kong Ltd., Kowloon Tong, Hong Kong, China

B. Young
Department of Civil Engineering, The University of Hong Kong, Hong Kong, China

ABSTRACT: The design rules on screwed connections of thin sheet steel in the current International specifications for cold-formed steel structures are only applicable for ambient temperature. Up-to-date, investigation of screwed connections at elevated temperatures is quite limited. In this study, a total of 24 single shear screwed connection specimens fabricated from G550 0.42 mm, G500 1.20 mm and G450 1.90 mm thin sheet steels were conducted by transient state test method. The tests were performed at three different load levels of 25%, 50% and 75% of the failure load at ambient temperature. The critical temperature and the corresponding displacement of screwed connections were obtained from the transient state test curves. The connection strength deterioration obtained from the transient state tests was compared with that obtained from steady state tests. The critical temperatures determined by the transient state test results are slightly higher compared with those deduced from the steady state test results at similar load levels, and even higher than those from the coupon test results. Different failure modes, such as bearing, tear out, material failure and several combined failure modes were observed in the transient tests. It is found that the failure mode of the screwed connections may change as the load level increases.

1 INTRODUCTION

The use of high strength cold-formed steel structural members has increased rapidly in recent years. Cold-formed steel can provide a substantial increase in strength to weight ratio compared with thicker hot-rolled steel members (Young & Rasmussen 2000). Self-tapping screws are convenient to provide an effective means to fasten sheet metal roofing to frame members as well as connecting light gauge steel structural members together. The pull-through failures of screws in crest-fixed trapezoidal steel claddings has been numerically studied by Mahaarachchi and Mahendran (2004). Furthermore, screws can also be used as connectors in timber structures (Fragiacomo et al. 2011) and timber lightweight concrete composite floors (Jorge et al. 2010).

Screwed connection specimen tests have been conducted by Rogers and Hancock (1998 and 1999)that mainly focused on the bearing failure. Based on their test results, the Australian/New Zealand Standard (AS/NZS 2005) for cold-formed steel structures has modified the bearing factors in the design equations for tilting and bearing failure of screwed connections. However, the design rules of screwed connections in the current specifications (AS/NZS 2005; AISI 2007; EC3 2006) of cold-formed steel structures are based on investigation at ambient temperature, which means that they are not applicable to connections under elevated temperatures condition. Lu et al.(2009a and 2009b) investigated single lapped screwed connections in the temperature range from 20°C to 600°C. The reduction in screwed connection strengths and the failure modes were reported. Chen and Young (2006a and 2007) investigated the material properties of cold-formed steel at elevated temperatures. Yan and Young (2012) conducted more than one hundred screwed connections of thin sheet steels at elevated temperatures using steady state test method. It is shown that the current design rules are conservative when the reduced material properties were used to calculate the connection strengths.

The testing of a loaded structure under fire conditions can be carried out in two generic ways: (1) transient state testing; or (2) steady state testing (Wang 2002). In the transient state tests, the specimen is under a constant stress level while the temperature raise until the failure take place (Chen & Young 2006b). The transient state test method is some how closer to real fire situation compared with the steady state test method. The transient state test method has been used in experimental (Tan et al. 2007) and numerical (Young & Ellobody 2011) investigation on structural behaviour of steel and composite columns at elevated temperatures. However, the experimental investigation on the screwed connections of thin sheet steels in transient state is limited.

This paper reported a test program on single shear Screwed connections fabricated from three different thicknesses of steels tested under transient state test method. The screwed connections were investigated by varied the screw size, steel plate thickness, number and arrangement of the screws in five test series. The transient state tests were conducted at three different load levels, namely 0.25, 0.50 and 0.75 of the failure load at ambient temperature. The critical temperature is defined as the temperature that caused the failure of the specimen. The strength reduction and the failure modes of the screwed connections observed in the transient state tests were also compared with the steady state test results.

2 TRANSIENT STATE TESTS OF SCREWED CONNECTIONS

A total of 24 single shear screwed connection specimens were tested using transient state test method. The specimen design and specimen labeling are identical to those of the steady state tests conducted by Yan and Young (2012). All the screwed connection tests were conducted using the same MTS machine and test rig as those of the bolted connection tests conducted by Yan and Young (2011a). In this study, the screwed connection specimens were fabricated from the same batch of thin sheet steels as those specimens tested using the steady state test method, namely G550 0.42 mm, G500 1.20 mm, and G450 1.90 mm sheet steels. The material properties, including the 0.2% proof stresses($f_{0.2,normal}$ and $f_{0.2,T}$), tensile strengths ($f_{u,normal}$ and $f_{u,T}$), elastic moduli (E_{normal} and E_T) and ultimate strains ($\varepsilon_{u,normal}$ and $\varepsilon_{u,T}$), were obtained from normal room (ambient) temperature of 22°C to 900°C for each sheet steel. The details of the tensile coupon tests and the test results of the material properties are reported in Yan and Young (2011a).

2.1 *Load levels and heating rate*

Three different load levels were adopted in the transient state tests, namely 0.25, 0.50 and 0.75 of the failure load at ambient temperature ($P_{u,normal}$) which was obtained from the steady state tests conducted by Yan and Young (2012). As a result, the loading on each connection specimen was chosen as $0.25P_{u,normal}$, $0.50P_{u,normal}$, and $0.75P_{u,normal}$. The single shear screwed connection specimens were aiming to heat up according to the ISO Standard fire curve (EC1 2002). However, in this study, the ISO standard fire curve was not able to obtain in the first 5 – 6 minutes of the heating process due to the limitation of the heating rate on the MTS model 653.04 high temperature furnace. Therefore, the heating rate used in this study is follows: (a) The maximum heating rate of 100°C/min of the furnace was used in the first 5 minutes, and raised the temperature from 20°C to 520°C; (b) The heating rate was adjusted lower than 100°C/min in every minute, depending on the required temperature. The tests were able to follow the ISO fire curve after 5 – 6 minutes of heating.

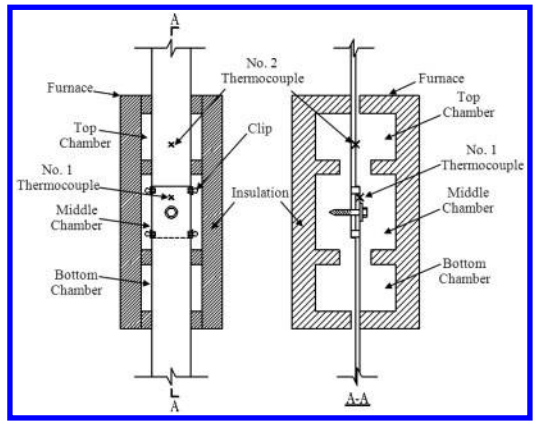


Figure 1. Position of the thermocouples.

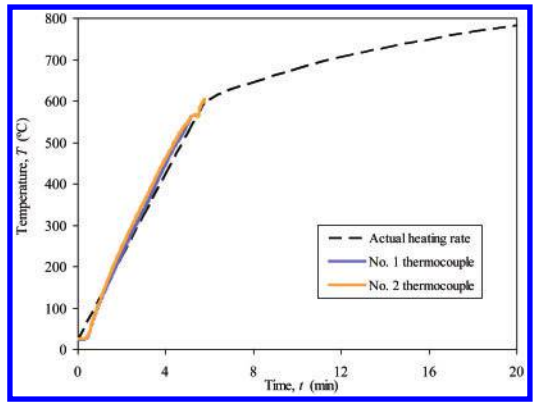


Figure 2. Measured temperature for specimen 042-190-S2-P-14.

2.2 *Transient state test procedure*

The specimens tested in the transient state were subjected to constant load while the temperature rises. The force control was used during the tests in order to maintain the load constant. The screwed connection specimen was firstly loaded to a pre-selected load level within 1 or 2 minutes. The pre-selected constant load was maintained for approximately 1 minute to ensure the load level stabilized. The temperature was then increased according to the heating rate as discussed earlier until the specimen failed or until the stroke of the hydraulic actuator reached 20 mm movement.

The temperature of the test specimen was recorded using two external thermocouples, as shown in Figure1. The thermocouple No. 1 contacted on the surface of sheet steel in the vicinity of the screws, while thermocouple No. 2 is located on the sheet steel beyond the connection overlapped region. The measured temperatures on specimen 042-190-S2-P-14 at the load level of $0.50P_{u,normal}$ recorded by these two thermocouples are shown in Figure 2, which plotted the testing time

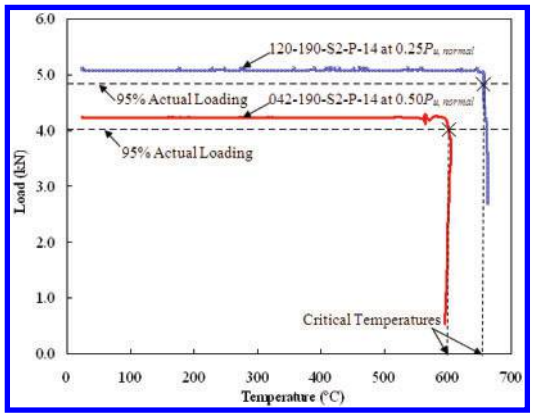


Figure 3. Definition of critical temperatures.

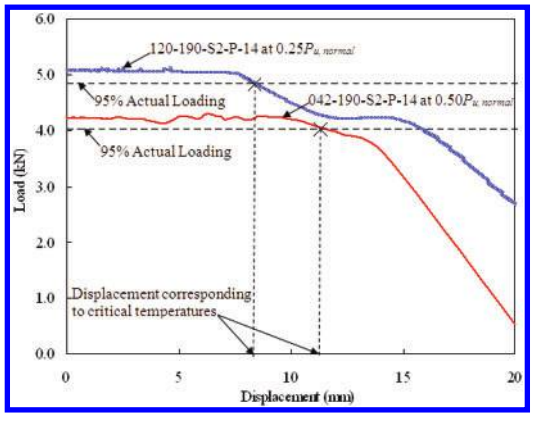


Figure 4. Definition of displacement at critical temperatures.

in minute against the temperature in degrees Celsius (°C). Due to the effect of heat convection and heat conduction, a short delay of approximately 30 seconds on the temperatures recorded by the two external thermocouples was usually observed at the beginning of the test. It is shown that the temperatures obtained from these two external thermocouples were very close to each other. Hence, the temperature inside the furnace is quite uniform. In this study, the specimen temperature was recorded by the thermocouple No. 1.

3 SCREWED CONNECTION TEST RESULTS

The critical temperature of the single shear screwed connection specimen is defined at the temperature when the load drops by 5% of the pre-selected load level from the load-temperature curve. Figure 3 shows the determination of the critical temperature of the specimens042-190-S2-P-14 at the load level of $0.50P_{u,normal}$and 120-190-S2-P-14 at the load level of $0.25P_{u,normal}$. The horizontal axis represents the specimen temperature, and the vertical axis plotted the applied load of the specimen. Figure 4 illustrated the corresponding load-displacement curves of these specimens. The displacement of the screwed connections at critical temperature can be determined from Figure 4 in which the load plotted against the displacement of the hydraulic actuator movement. Table 1 summarized the critical temperatures and the corresponding displacements of the single shear screwed connections in transient state tests. The repeated test specimens were mainly conducted at the load level of $0.50P_{u,normal}$. This is due to the fact that the critical temperatures corresponding to this load level always occur in the temperature range where the strength drops rapidly as observed in the steady state tests.

The transient state test results listed in Table 1 indicate that the critical Temperatures of screwed connections of thin sheet steels reduce as the load levels on the test specimen increases. For instance, the critical temperature dropped from 645.2°C to 357.8°C for specimen 042-190-S2-V-8, at the load levels of $0.25P_{u,normal}$ and $0.75P_{u,normal}$, respectively, as shown in Table 1. It is found that the displacements corresponding to the critical temperatures measured in any series of single shear screwed connections are much more scattered than those measured in the single shear bolted connections as reported by Yan and Young (2011b).The range of displacement for the screwed connections was measured from 2.4 mm to 14.2 mm. This may be due to the friction between the screw shank and screw holes are more vulnerable than those in the bolted connections with nuts at one end of the bolts.

4 DISCUSSION

The transient state test results of single shear screwed connections are compared with the steady state test results obtained by Yan and Young (2012), as shown in Figures 5–7. The material deterioration due to elevated temperatures for 0.2% proof stress ($f_{0.2,normal}$ and $f_{0.2,T}$) and tensile strength ($f_{u,normal}$ and $f_{u,T}$) obtained from the coupon tests (Yan & Young 2011a) for the same batch of sheet steels in this study are also shown in Figures 5–7. The temperature is plotted in the horizontal axis, whereas the vertical axis represents the normalized $f_{0.2,T}/f_{0.2,normal}$, $f_{u,T}/f_{u,normal}$ and $P_{u,T}/P_{u,normal}$. It is shown that the tendency of reduction of the screwed connection test strengths obtained from the transient state tests is similar to that from the steady state tests. The screwed connections had a distinct drop in the strengths of the critical temperatures for the load levels increased from $0.25P_{u,normal}$ to $0.75P_{u,normal}$.

The test strengths obtained from the transient state tests of single shear screwed connections of thin sheet steels are generally higher when compared with those deduced from the steady state test results at similar load levels, which represents that the critical temperatures determined by the transient state tests are generally higher than those steady state test results. The critical temperatures corresponding to the load levels of $0.25P_{u,normal}$ and $0.75P_{u,normal}$ for specimen 120-190-S2-P-14 were approximately 660°C and 550°C, respectively. However, the critical temperatures based on the steady state tests (Yan & Young

Table 1. Transient state test results of single shear screwed connections for 042-190 and 120-190 specimens.

Specimen	$P_{u,normal}$ (kN)	Load Level	Actual Load (kN)	Critical Temperature (°C)	Displacement (mm)	Failure Mode
		0.25	1.63	668.1	8.6	BT
		0.50	3.27	608.7	7.4	BT + T
042-190-S2-P-8	6.53	0.50	3.27	604.7	6.4	BT + T
		0.75	4.90	511.6	4.7	BT + T
		0.25	2.12	652.7	14.2	MF
		0.50	4.24	593.5	8.1	BT
042-190-S2-P-14	8.47	0.50	4.24	601.5	11.3	MF
		0.75	6.35	471.3	6.5	BT + T
		0.75	6.35	461.0	7.8	BT + T
		0.25	1.81	645.2	6.9	B
		0.25	1.81	618.1	7.7	B
042-190-S2-V-8	7.23	0.50	3.62	544.8	4.4	B
		0.50	3.62	520.0	4.5	B
		0.75	5.42	357.8	2.4	B + T
		0.25	2.92	592.4	5.1	MF
		0.25	2.92	612.2	5.4	MF
042-190-S4-S-8	11.68	0.50	5.84	573.7	7.2	MF
		0.47	5.49	590.9	5.9	MF
		0.75	8.76	490.0	6.9	MF
		0.25	5.09	656.0	8.4	TB + SS
		0.25	5.09	670.7	11.6	TB + SS
120-190-S2-P-14	20.37	0.50	10.19	573.6	5.7	TB + SS
		0.50	10.19	610.9	10.8	TB + SS
		0.75	15.28	550.3	12.8	TB + SS

Note: BT = Bearing failure accompanied with screw tilting; T = Tear out failure; MF = Material failure; B = Bearing failure; SS = Screw shear failure; TB = Tilting and bearing failure.

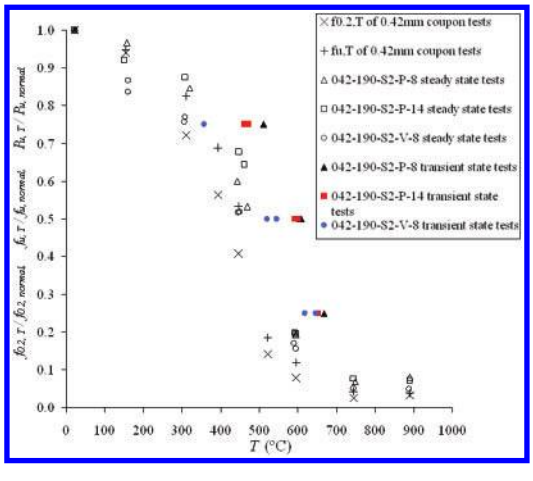


Figure 5. Comparison of transient state test results and steady state test results for 042-190-S2 single shear screwed connections.

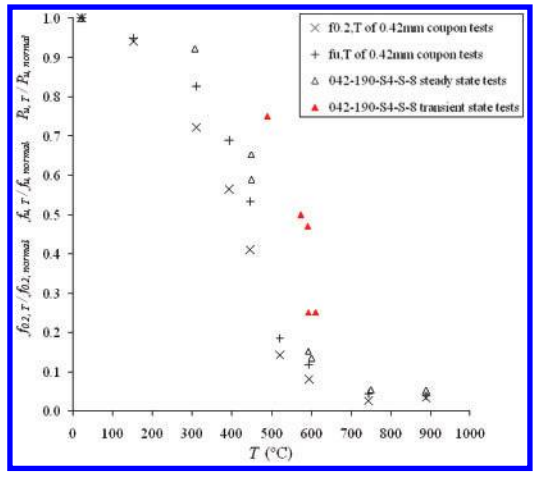


Figure 6. Comparison of transient state test results and steady state test results for 042-190-S4-S-8 single shear screwed connections.

2012) are 590°C and 443°C for the load levels of $0.22P_{u,normal}$ and $0.57P_{u,normal}$ for the same specimen 120-190-S2-P-14, respectively. The critical temperatures for specimen 042-190-S2-P-14 in the load levels of $0.25P_{u,normal}$ and $0.75P_{u,normal}$ were approximately 650°C and 465°C, whereas the corresponding critical temperatures based on the steady state tests are lower than 591°C and 447°C, respectively. The critical temperatures determined by the transient state test results of the single shear screwed connections are revealed to be even higher when compared with the coupon test results (Yan & Young 2011a), as shown in Figures 5–7.

The difference between the critical temperatures obtained from the transient state tests and that deduced from the steady state tests for the specimens assembled

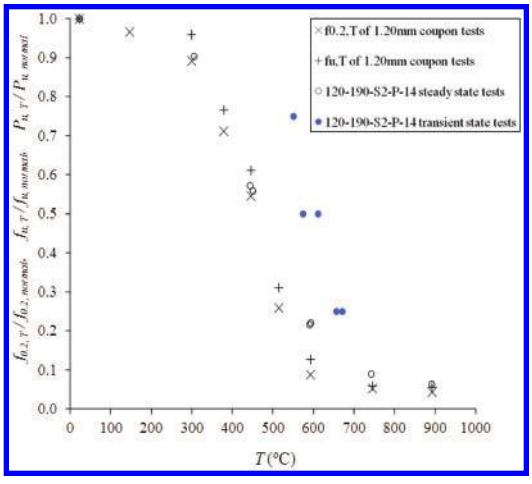


Figure 7. Comparison of transient state test results and steady state test results for 120-190-S2-P-14 single shear screwed connections.

using 1.20 and 1.90 mm sheet steels is generally larger in the high load level conditions than in the low load level conditions, as shown in Figure 7. The difference of the critical temperatures for specimen 120-190-S2-P-14 in the load level $0.25P_{u,normal}$ is approximate 70°C, and it was larger than 110°C for the load level $0.75P_{u,normal}$.

5 FAILURE MODES

Table 1 shows the failure modes of the single shear screwed connection specimens. The symbol 'BT' means the bearing failure accompanied with screw tilting which is explained in Yan and Young (2012);'B' represents the bearing failure; 'T' is the tear out failure which is specified as connection shear limited by end distance in the AISI (2007); 'SS' means the screw shear failure; and 'MF' stands for material failure as shown in Figure 8.

Some specimens failed by combined failure modes, such as the combination of tilting and bearing as well as screw shear failure 'TB+SS' for specimen 120-190-S2-P-14 for all three load levels. The combination of bearing failure accompanied with screw tilting as well as tear out failure 'BT + T' was observed for specimen 042-190-S2-P-8 at the load levels $0.50P_{u,normal}$ and $0.75P_{u,normal}$. The same failure mode 'BT+T' was also observed for specimen 042-190-S2-P-14 at the load level $0.75\ P_{u,normal}$. The combination of bearing and tear out failure 'B+T' was observed for specimen 042-190-S2-V-8 at the load level $0.75P_{u,normal}$. The specimen 042-190-S2-P-14 failed in the sheet steel beyond the overlapped connection part for material failure 'MF' at the load levels $0.25P_{u,normal}$ and $0.50P_{u,normal}$. However, bearing failure accompanied with screw tilting 'BT' instead of material failure for specimen 042-190-S2-P-14 at the load level $0.50P_{u,normal}$ was



Figure 8. Material failure (042-190-S4-S-8 at $0.25P_{u,normal}$).

observed for one of the specimen. The critical temperature for the two tests was very close to each other of approximately 600°C. The specimen 042-190-S4-S-8 failed in material for all load levels, but it is interesting to note that the same specimen was failed by net section tension in the steady state tests. The specimen 042-190-S2-V-8 was failed by bearing only at the load levels $0.25P_{u,normal}$ and $0.50P_{u,normal}$. The bearing failure accompanied with screw tilting was observed for specimen 042-190-S2-P-8 at the load level $0.25P_{u,normal}$.

It is found that the failure mode changes for some of the 042-190-S2 screwed connections when the load level increased. As mentioned earlier that the specimen 042-190-S2-V-8 failed by bearing only at the load levels $0.25P_{u,normal}$ and $0.50P_{u,normal}$. However, it is found that bearing failure in addition of tear out failure was found when the load level increases, as shown in Table 1.

6 CONCLUSIONS

The structural behaviour of single shear screwed connections of thin sheet steels at elevated temperatures was investigated. The tests were conducted using the transient state test method. Three different load levels were considered in the investigation. The critical temperatures and the failure modes were reported. The failure modes of tilting and bearing, bearing failure accompanied with screw tilting, bearing failure, tear out failure, screw shear failure, and material failure were observed in the tests. It is found that the failure mode of the screwed connections may change as the load level increases. The test results of the single shear screwed connections obtained using the transient state test method were compared with the steady state test results and the tensile coupon test results. The comparison showed a similar strength reduction tendency at elevated temperatures. However, the critical temperatures determined by the transient state test results are slightly higher compared with those deduced from the

steady state test results at similar load levels, and even higher than those from the coupon test results.

ACKNOWLEDGMENTS

The authors are grateful to BlueScope Lysaght (Singapore) Pte Ltd for providing the thin sheet steels. The research work described in this paper was supported by a grant from The University of Hong Kong under the seed funding program for basic research.

REFERENCES

American Iron and Steel Institute (AISI). 2007. *North American Specification for the design of cold-formed steel structural members*. AISI S100-2007, North American Cold-formed Steel Specification, Washington, D.C.

Australian/New Zealand Standard (AS/NZS). 2005. *Cold-formed Steel Structures*, AS/NZS 4600: 2005, Standards Australia, Australia, Sydney.

Chen, J. & Young, B. 2006a.Corner properties of cold-formed steel sections at elevated temperatures. *Thin-Walled Structures* 44: 216–223.

Chen, J. & Young, B. 2006b. Stress-strain Curves for Stainless Steel at Elevated Temperatures. *Engineering Structures* 28: 229–239.

Chen, J. & Young, B. 2007. Experimental investigation of cold-formed steel material at elevated temperatures. *Thin-Walled Structures* 45(1): 96–110.

European Committee for Standardization (EC1). 2002. *Eurocode 1 – Actions on Structures – Part 1-2: General Actions – Actions on Structures Exposed to Fire*. EN 1991-1-2:2002, Brussels.

European Committee for Standardization (EC3). *Eurocode 3 – Design of steel structures – Part 1–3: General rules – Supplementary rules for cold-formed members and sheeting*. EN 1993-1-3:2006, Brussels.

Fragiacomo, M. & Dujic, B. & Sustersic, I. 2011. Elastic and ductile design of multi-storey crosslam massive wooden buildings under seismic actions. *Engineering Structures* 33: 3043–3053.

Jorge, L.F. & Schänzlin, J. & Lopes, S.M.R. & Cruz, H. & Kuhlmann, U. 2010. Time-dependent behaviour of timber lightweight concrete composite floors. *Engineering Structures* 32: 3966–3973.

Lu, W. & Makelainen, P. & Outinen, J. 2009a. *Behaviour of Screwed Shear Sheeting Connection in Fire*. In: Application of Structural Fire Engineering. Prague, Czech Republic. p. 411–446.

Lu, W. & Makelainen, P. & Outinen, J. 2009b. Numerical Investigation of Cold-formed Steel Sheeting in Fire. In: 6th International Conference on Advances in Steel Structures 2009. The Hong Kong Institute of Steel Construction. Hong Kong, China. p. 810–817.

Mahaarachchi, D. & Mahendran, M. 2004. Finite element analysis and design of crest-fixed trapezoidal steel claddings with wide pans subject to pull-through failures. *Engineering Structures* 26: 1547–1559.

Rogers, C.A. &Hancock, G.J. 1998. Screwed connection tests of thin G550 and G300 sheet steels. Research Report No. R761. Department of Civil Engineering, the University of Sydney, Centre for Advanced Structural Engineering, the University of Sydney: Sydney.

Rogers, C.A. &Hancock, G.J. 1999. Screwed connection tests of thin G550 and G300 sheet steels. *Journal of Structural Engineering* 125(2): 128–136.

Tan, K.H. & Toh, W.S. & Huang, Z.F. & Phng, G.H. 2007. Structural responses of restrained steel columns at elevated temperatures. Part 1: Experiments. *Engineering Structures* 29: 1641–1652.

Wang, Y.C. 2002. *Steel and Composite Structures: Behaviour and design for fire safety*. Spon Press, New York.

Yan, S. & Young, B. 2011a. Tests of single shear bolted connections of thin sheet steels at elevated temperatures—Part I: steady state tests, *Thin-Walled Structures* 49: 1320–1333.

Yan, S. & Young, B. 2011b. Tests of single shear bolted connections of thin sheet steels at elevated temperatures – Part II: Transient state tests. *Thin-Walled Structures* 49: 1334–1340.

Yan, S.& Young, B. 2012. Screwed connections of thin sheet steels at elevated temperatures – Part I: Steady state tests. *Engineering Structures* 35(2):234–243.

Young, B. & Ellobody, E. 2011. Performance of axially restrained concrete encased steel composite columns at elevated temperatures. *Engineering Structures* 33: 245–254.

Young, B. & Rasmussen, K.J.R. 2000. Inelastic bifurcation of cold-formed singly symmetric columns. *Thin-Walled Structures* 36: 213–230.

Research and Applications in Structural Engineering, Mechanics and Computation – Zingoni (Ed.)
© 2013 Taylor & Francis Group, London, ISBN 978-1-138-00061-2

Finite element simulation of perforated rack sections columns

A. M. Sarmanho Freitas & M.S.R. Freitas
Federal University of Ouro Preto (UFOP), Ouro Preto, Brazil

F. T. Souza
Federal Institute of Minas Gerais (IFMG), Ouro Preto, Brazil

ABSTRACT: Industrial Storage Systems are usually built by cold-formed profiles, and their sections, called "rack section", specially designed to make assemblage easier, have perforations through their high to fit connections. This section geometry and holes induce behavior unexpected in other sections. This paper presents a theoretical-experimental analysis of buckling modes development in rack sections. This analysis is carried out by numerical analysis, using Generalised Beam Theory (GBT) and Finite Element Method (FEM) by softwares GBTul and ANSYS. The element type, mesh refinement and boundary conditions in Finite Element model are carefully developed from comparisons with Generalized Beam Theory (GBT) results to columns without holes. Once Finite Element parameters are adjusted, holes are introduced in ANSYS model. Numerical results were compared with experimental Stub Columns tests results. Experimental and Finite Element results showed good agreement, proving the Finite Element Model is suitable to predict perforated rack section stub columns behavior.

1 INTRODUCTION

Industrial Storage Systems are widely used in factories, warehouses and other places in that high storage density is needed. They are usually built by cold-formed profiles, and their sections are specially designed to make assemblage easier, called "rack section". In addiction, columns have perforations arrangements through their high to fit connections and bolts. The special rack section and the perforations sets modify the columns behavior and resistance, because they induce failure modes unexpected in other sections, as channel, for example. So, they are under local plate buckling, distortional or global buckling and these buckling modes can occur separately or under interaction.

There are several works that analyze rack systems. They are focused in global system stability and its components behavior (Freitas et al (2005, 2010), Godley (2000, 2002)). There are also recent works that consider the perforations sets (Moen & Schaffer (2008), Eccher et al, 2008), Schaffer (2012).

The existence of perforations modifies the columns behavior. This analysis is especially difficult, because available numerical tools, such as finite strip analysis (CUFSM (Schaffer & Àdáni (2006))) and generalized beam theory (GBTul (Bebiano et al (2008)) are used only to evaluate sections without holes. Thus, the analysis of a perforated rack column must be carried out using finite element analysis.

This paper shows a finite element analysis of rack sections with perforations. The purpose of this analysis is to develop a finite element model, in software ANSYS (ANSYS (2007)), which predicts the buckling load of the cold-formed perforated columns. This elastic buckling load is important to design methods, like Direct Strength Method.

The development of a finite element model must consider many important aspects, such as finite element type, mesh refinement and loading and boundary conditions. The model is often very sensitive to these parameters, and they can lead to an inaccurate finite element model.

The model consists in a stub column with fixed ends, under pure compression. In the first step, the results of column without perforations analyzed by FEM Generalized Beam Theory (GBT) were compared, in order to evaluate the finite element model suitability in buckling load prediction. So, the finite element parameters were adjusted to get good precision.

In a second moment, perforations were introduced in finite element models, using the parameters previously adjusted in first step. The results of perforated model were then compared to experimental ones.

2 FINITE ELEMENT MODEL DEVELOPMENT

In this section, a finite element model for cold-formed compressed member is developed. These analyses were carried out in order to develop and validate finite element procedure to evaluate the column without holes behavior by comparison with other numerical

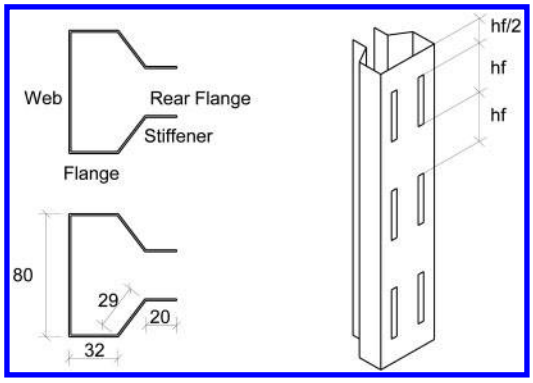


Figure 1. Section dimensions.

techniques results. Section components and dimensions are shown in Figure 1. In this stage, it was considered columns without perforations.

The finite element results were compared to GBT results in order to determine the element type, mesh refinement and boundary conditions suitable for this analysis. Eigenbuckling analysis were performed, in order to evaluate buckling load and column failure mode. There were simulated column lengths in that first buckling mode was local mode (70 mm) and distortional mode (400 mm), to evaluate model efficiency in columns affected by these phenomena.

Firstly, the element type was chosen. Three shell element types were tested to simulate the column: SHELL63, SHELL181 and SHELL281. They are similar and have the same input data. ANSYS manual indicated that SHELL63 is suitable for elastic analysis, SHELL181 is strongly indicated for plastic analysis and SHELL281 has a midside node, i.e., this element has eight nodes, while SHELL63 and SHELL181 have four nodes.

Element SHELL281, due to fact that has quadratic approximation, usually leads to better results, but increases processing time. Element SHELL181 has two options. The default option uses reduced integration, but in this work was used the full integration, due to the improvement in the results provided by its option.

Finite element type definition was based in accuracy and processing time. Results from finite element method (ANSYS) were compared to GBTul results. From these analyses, it was observed that the best element, considering the basic assumptions, was SHELL181 with full integration. This element was, then, adopted in this work.

Once the finite element type was chosen, it was analyzed the mesh refinement suitable for columns analysis, provided by comparison with generalized beam theory results. For these analyses, the manual element size set-up available in ANSYS was used. A range of element side sizes were tested, and the best results agreement was observed with element size equal to 10% web width (8.4 mm).

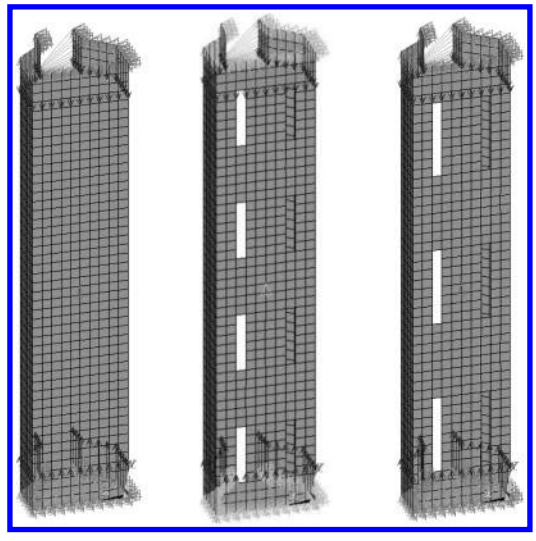


Figure 2. Finite element mesh and boundary conditions.

After choosing element type and mesh refinement, the column with pinned ends and fixed warping degree of freedom was analyzed. Consideration of this support condition is very important because it is the situation observed in experimental tests, where load plates restrict warping effects. For this analysis a generalized beam theory simulation carried out in GBTul is used as reference.

Element SHELL181 and the refinement level determined previously were used in this model. The nodes in both column extremity have translational degrees of freedom restricted in directions perpendicular to column axis, and a node in mid high column had the axial degree of freedom constrained. Loading was applied in all end nodes. The end nodes have all rotational degrees of freedom coupled, what assures that all of them will rotate equally, keeping plan extreme sections during the loading history, and the warping effects are completely restricted.

Various column lengths were simulated in ANSYS by eigen buckling analysis, in order to obtain a Buckling Load x length curve. Comparison between finite element (ANSYS) and GBT (GBTul) results shows an excellent fit between results, what indicating that the finite element procedure developed is suitable to evaluate cold formed columns behavior. Then, the model was modified to introduce perforations in the columns, to analyze its influence in columns resistance and stability. Figure 2 shows finite element meshes generated and boundary conditions for columns with and without holes.

3 EXPERIMENTAL ANALYSIS

In order to evaluate the influence of perforations is cold formed perforated stub columns, there were tested a series of specimens in the Laboratory of Structures "Prof. Altamiro Tibiriçá Dias" in Federal University

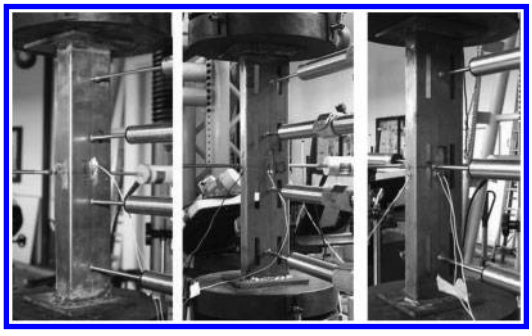


Figure 3. Specimens with and without holes positioned in testing machine.

of Ouro Preto. There were tested columns with and without holes, and their results were compared to finite element ones.

The specimens tested were stub columns with globally pinned ends and restrained warping under compression. In order to assure warping restriction and the fixed conditions, plates were welded in both extremities. The specimens were 384 mm high and section and holes dimensions is shown in Figure 1. Dimensions were chosen in order to avoid failure by material yielding and to induce the occurrence of distortional buckling. Linear finite element analysis was carried out previously to verify the specimens behavior and verify their suitability to this study.

There were tested three column types: without holes, with holes 60% web wide ($h_f = 48$ mm) and 80% web wide ($h_f = 64$ mm). The experimental tests were carried out in a Universal Testing Machine Instron Satec Series 5569. This machine permits load application velocity control and complete testing settings from specific software Partner (Instron, 2008). It was used a parallel data acquisition from HBM Spider8 and software Catman (HBM, 2003) in order to get all data needed in this analysis. Figure 3 shows the specimens with and without holes positioned in the universal testing machine.

Three specimens of each holes setup were tested, and then was determined buckling load for each one. The tests set up was defined in order to assure that specimens were under pure compression. Loadind was applied with displacement control, applied in sections mass center, and loading rate was limited to avoid abrupt collapse, letting complete phenomena observation.

Displacement transducers were positioned in columns web and rear flanges in order to determine occurrence of local or distortional modes. Strain gages were positioned in columns web and flanges, to prove the specimens are under uniform compression.

Experimental results shows, in all specimens, distortional buckling with one half wave formation. Table 1 shown experimental buckling load for each specimen and the mean value for the series. Figure 4 shows the displacements observed in specimens

Table 1. Experimental buckling loads.

h_f(mm)	L(mm)	Specimen	P_u (kN)	$P_{u\,Exp}$ (kN)	Modo
		1	41,52		
		2	40,23		
No hole	384	3	40,72	40,82	D
		1	36,75		
		2	37,00		
48	384	3	37,10	36,95	D
		1	37,89		
		2	38,66		
64	384	3	38,07	38,21	D

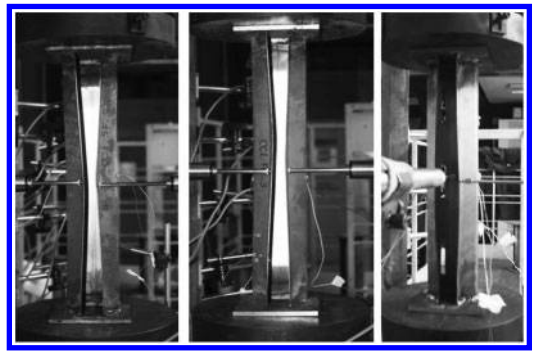


Figure 4. Distortional buckling observed in each specimen.

Table 2. Comparison between experimental and Finite Element linear buckling results.

h_f (mm)	L (mm)	$P_{u\,Exp}$ (kN)	$Mode_{Exp}$	$P_{u\,FE}$ (kN)	$Mode_{FE}$	Dif (%)
No hole	384	45,50	D1	39,7	D1	12,75
48	384	41,85	D1	37,47	D1	10,47
64	384	34,31	D1	36,38	D1	−6,03

without holes, with holes where h_f is 48 mm and where h_f is 64 mm.

4 FINITE ELEMENT LINEAR BUCKLING ANALYSIS

The finite element model presented in item 2 was used to analyze the specimens tested. The purpose of this analysis is to determine the buckling loads in order to compare to experimental results. Figure 2 shows the finite element model created.

The model was firstly used in linear buckling analysis in ANSYS. In this analysis, the buckling loads (eigenvalues) and the buckling modes were determined, and the results were compared to experimental ones. Table 2 presents the comparison between numerical and experimental results. In table 2 it can be observed that the main difference between finite element and experimental results is 12,75%, in the column without holes. This indicates that parameters such geometrical imperfections and second order effects

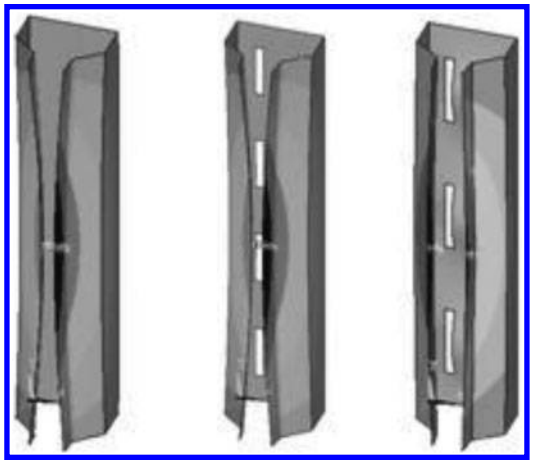


Figure 5. Distortional buckling observed in linear buckling finite element analysis.

must be considered, once they are not included in linear buckling analysis.

Despite the difference in critical loads, the linear buckling model leads to consistent buckling modes in comparison to that observed experimentally. Figure 5 shows buckling modes obtained in finite elemet analyses. It can be observed the similarity between these modes and experminental ones showed in figure 4.

5 FINITE ELEMENT NONLINEAR BUCKLING ANALYSIS

In this stage, nonlinear buckling analysis of tested specimens was carried out by ANSYS. The finite element procedure presented in item 2 was used to build the ANSYS models. For nonlinear buckling purposes nonlinear steel properties and geometrical imperfections were introduced in the model. The stress-strain relationship was introduced by a bilinear approximation. The initial imperfections were introduced by updating geometry from modes obtained in previous linear buckling analysis and amplitudes defined by specimens actual dimensions.

Results from nonlinear buckling analyses are shown in table 3. It can be observed a improvement in comparison between experimental and finite element results if results from linear buckling analysis presented in table 2 is considered. The main difference between buckling loads in nonlinear analysis is is 4,79%, observed in specimen with perforation 64 mm high. In all three specimens it can be observed improvement in numerical and experimental results fitting.

It can also be observed the nonlinear buckling analysis is efficiency in predicting buckling mode. In all specimens, it was observed the occurrence of distortional mode with one halfwave formation, which is the same mode observed experimentally. Figure 6 presents buckling modes observed in nonlinear buckling analysis.

Table 3. Comparison between experimental and Finite Element nonlinear buckling results.

h_f (mm)	L (mm)	$P_{u\,Exp}$ (kN)	$Mode_{Exp}$	$P_{u\,FE}$ (kN)	$Mode_{FE}$	Dif (%)
No hole	384	40,82	D1	39,7	D1	2,74
48	384	36,95	D1	37,47	D1	−1,41
64	384	38,21	D1	36,38	D1	4,79

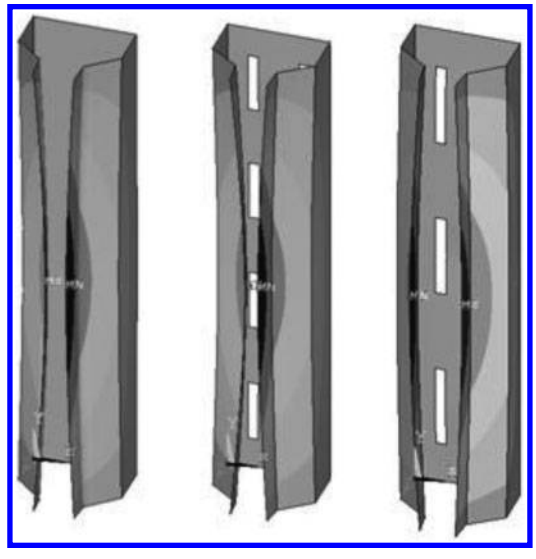


Figure 6. Distortional buckling observed in nonlinear buckling finite element analysis.

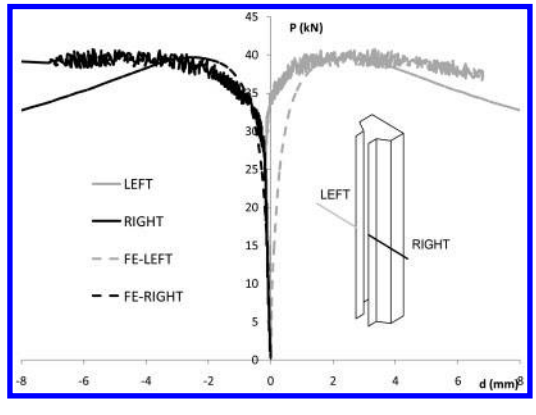


Figure 7. Displacement in column without holes mid high position in rear flanges.

The finite element nonlinear buckling analysis is also suitable to determine structural post-buckling behavior. The ANSYS finite element model was then used with this purpose, and the results comparison with experimental ones showed numerical model efficiency. Figures 7 to 9 presents the comparison between numerical and experimental displacements in column mid high position in sections rear flanges to columns

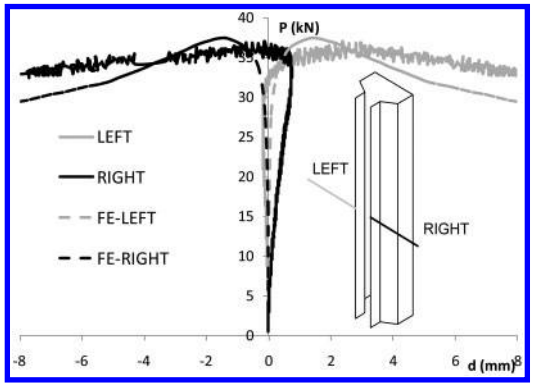


Figure 8. Displacement in column with holes 48 mm high inmid high position in rear flanges.

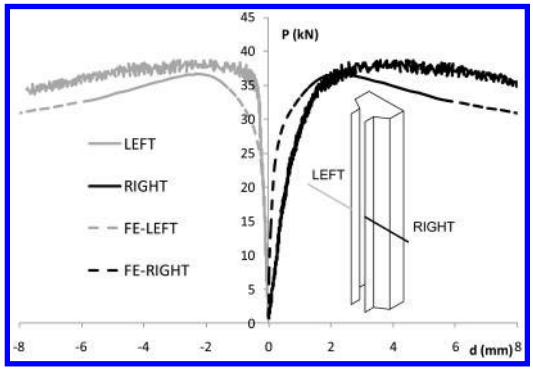


Figure 9. Displacement in column with holes 64 mm high inmid high position in rear flanges.

without perforations and with perforations 48 mm high and 64 mm high respectively. It can be observed that in all specimens the finite element model was capable to predict actual behavior, proving again its suitability to simulate cold formed columns with perforations.

It can be observed in figures 7 and 8 that transducers measured displacements indicate section closing, because left transducer indicate displacements in right directions and right transducer indicates displacements to left. Otherwise, figure 9 indicates section opening. During all loading stages, finite element displacements are close to that obtained experimentally. That shows the model suitability in post-buckling analysis of perforated rack sections columns.

6 CONCLUSIONS

The purpose of this paper is to develop a finite element procedure to simulate cold formed rack sections with perforation along their length under compression. It is used finite element commercial software ANSYS. Finite element type SHELL181 with full integration proved being suitable to this model, and meshing level was adjusted. Boundary conditions and loading applications were also developed.

The finite modeling procedure developed is suitable to analyze perforated rack sections stub columns. Comparison between finite element and experimental results indicated that the numerical model predict accurately the columns behavior and resistance.

It is observed, thus, that linear buckling analysis leads to less precise results than nonlinear buckling analysis, in that material nonlinearities, geometrical imperfections and second order effects are considered. It is also observed that nonlinear finite element model describes correctly the column post-buckling behavior. This indicates the importance of considering the nonlinear buckling analyses in cold formed steel columns, because these members high slenderness make them highly sensitive to physical and geometrical nonlinearities and initial imperfections.

ACKNOWLEDGEMENT

Authors would thank the company Águia Sistemas de Armazenagem for support this research.

REFERENCES

ANSYS, 2012. User's manual for revision 14. Swanson Analysis Systems Inc.; Houston, PA.

Bebiano R., Pina P., Silvestre N. and Camotim D. 2008. GBTUL – Buckling and Vibration Analysis of Thin-Walled Members, DECivil/IST, Technical University of Lisbon (http://www.civil.ist.utl.pt/gbt).

Eccher, G, Rasmussen, K J R, Zandonini, R. 2008. Linear elastic isoparametric spline finite strip analysis of perforated thin-walled structures. *Thin-Walled Structures*, 46(3), p. 242–260.

Freitas A.M.S., Freitas M.S.R., Souza F.T. 2005. Analysis of steel storage rack columns. *Journal of Constructional Steel Research*, 61(8), p. 1135–1146.

Freitas A.M.S., Souza F.T., Freitas M.S.R. 2010. Analysis and behavior of steel storage drive-in racks. *Thin Walled Structures*, 61(8), p. 1135–1146.

Godley M.H.R. 2002. The bahavior of drive-in storage structures. *In: Proc. of 16th International Specialty Conference on Cold-Formed Steel Structures.* Orlando, FL.

Godley M.H.R., Beale R.G., Feng X. 2000. Analysis and design of down-aisle pallet rack structures. Computers and Structures; 77(4), p. 391–401.

Hottinger Baldwin Messtechnic. 2003. Catman 4.5 Operating Manual.

Instron. 2008. Partner Operating Help - Version 8.4a.

Moen, C.D., Schaffer, B. W. 2008. Experiments on cold-formed steel columns with holes. *Thin-Walled Structures* 46, p. 1164–1182.

Schafer, B.W., Ádány, S. 2006. Buckling analysis of cold-formed steel members using CUFSM: conventional and constrained finite strip methods. *In: Proc. of 18th International Specialty Conference on Cold-Formed Steel Structures*. Orlando, FL.

Schaffer, B. W., Moen, C. D. 2011. Direct Strength Method for Design of Cold Formed Steel Columns with Holes. *Journal of Structural Engineering* 147, p 559–570.

16. Steel structures: Stability, strength, design

Research and Applications in Structural Engineering, Mechanics and Computation – Zingoni (Ed.)
© 2013 Taylor & Francis Group, London, ISBN 978-1-138-00061-2

Inelastic post-buckling GBT analysis of tubular thin-walled metal members

M. Abambres, D. Camotim & N. Silvestre
Civil Engineering Department, ICIST, Instituto Superior Técnico, Technical University of Lisbon, Portugal

ABSTRACT: After providing a brief overview of a recently developed and validated elastoplastic post-buckling Generalised Beam Theory (GBT) formulation, the paper presents and discusses illustrative numerical results concerning three tubular members exhibiting bi-linear and non-linear material behaviours. The GBT results consist of equilibrium paths, modal participation diagrams, stress contours, displacement profiles and collapse mechanisms, most of which are compared with values obtained from Abaqus shell finite element analyses. The GBT modal nature makes it possible to (i) acquire in-depth knowledge about the member behavioural mechanics at any given equilibrium state (elastic or elastic-plastic), as well as (ii) evidence the GBT computational efficiency (d.o.f. reduction of over 75%), partly due to the exclusion from the analyses of all deformation modes playing no role in a given member response.

1 INTRODUCTION

Most thin-walled metal members exhibit slenderness values leading to structural behaviours and ultimate strengths governed by interaction between plasticity and instability, which renders their rigorous analysis a complex task. This stimulates the development of more efficient design rules and methods of structural analysis. In this context, even if conventional structural design concerns mostly serviceability/ultimate limit states, a performance-based design also requires accurate member post-collapse response predictions (Hiriyur & Schafer 2005). As experimental studies are invariably scarce, alternative approaches must be sought. The most universal is performing non-linear shell finite element analyses (SFEA), involving (i) large degree of freedom (d.o.f.) numbers, (ii) time-consuming/error-prone data processing and interpretation, and (iii) nodal stress/displacement outputs, rather than modal ones (*e.g.*, stress resultants).

Generalised Beam Theory (GBT) is an alternative to the above structural analysis methods. In spite of its limited current field of application (prismatic, straight and non-perforated thin-walled bars) and dissemination, GBT is recognised as an elegant and efficient approach to analyse thin-walled members and structural systems. These traits arise mostly from its modal nature: displacement field expressed as a linear combination of cross-section deformation modes with amplitudes varying continuously along the member length. This feature makes it possible to (i) acquire in-depth insight on the member behaviour and (ii) judiciously exclude from future similar analyses those modes found to play no role in the particular behaviour under scrutiny, thus further reducing the d.o.f. number. GBT has attracted the interest of several researchers, leading to new formulations and applications concerning various types of analysis, support and loading conditions, and materials (Camotim *et al.* 2010). With a few exceptions, the material models considered were linear elastic. The first physically non-linear GBT formulations are due to Gonçalves & Camotim (2004, 2011, 2012): beam finite elements (BFE) based on J_2-flow plasticity theory aimed to perform member bifurcation, first and second-order inelastic analyses. The authors (Abambres *et al.* 2012, 2013a-c) developed and validated alternative 1st and 2nd order elastoplastic GBT formulations, also based on J_2-flow theory but differing from the previous ones in the (i) deformation mode determination and (ii) consideration of warping rotations (novel d.o.f.) – in these works, GBT was first applied to strain-hardening materials, namely stainless steel. When compared with carbon steel, stainless steel (i) has no well-defined yield point and (ii) exhibits a high non-linearity beyond the proportional limit.

The aim of this paper is (i) to present a brief overview of the materially and geometrically non-linear GBT formulation, and (ii) to illustrate its application and potential by studying the post-buckling behaviour and strength of tubular members made of perfectly-plastic, bi-linear and non-linear materials. The analyses include local and/or global initial geometrical imperfections, but neglect membrane residual stresses and corner strength effects. For validation, most GBT results (equilibrium paths, displacement profiles, stress contours, collapse mechanisms) are compared with Abaqus SFEA values. The GBT modal nature is highlighted through the presentation of modal participation diagrams.

2 GBT NON-LINEAR ELASTIC-PLASTIC FORMULATION – OVERVIEW

Only an overview of the main concepts and procedures involved in the development and implementation of the proposed GBT formulation is reported. After focusing on aspects related to kinematics and cross-section analysis, the member non-linear equilibrium equations are established and their BFE incremental solution addressed.

2.1 *Kinematics and equilibrium equations*

Consider the local coordinate system (x, s, z) shown in Figure 1(a) at each wall mid-surface of a thin-walled bar, where x, s and z are the longitudinal ($0 \le x \le L$ – member length), transverse ($0 \le s \le b$ – wall width) and through-thickness ($-t/2 \le z \le t/2$ – wall thickness) coordinates – the associated displacements are u (warping), v (transverse) and w (flexural). The GBT analysis consists of two main steps: (i) cross-section analysis and (ii) member analysis. The former leads to the deformation mode displacement profiles u_k, v_k and w_k (for mode k), along s, while the member analysis determines the modal amplitude functions $\zeta_k(x)$ – displacement profile longitudinal variations. Then, the GBT mid-surface displacement field is given by a linear combination of products between modal displacement profiles and their amplitude functions,

$$u(s,x) = u_k(s)\zeta_{k,x}(x) \qquad v(s,x) = v_k(s)\zeta_k(x) \qquad w(s,x) = w_k(s)\zeta_k(x) \tag{1}$$

where k satisfies the summation convention. The cross-section analysis adopted considers 4 deformation mode families: conventional, cell shear flow, warping shear and transverse extension. The existing analyses, considering either 3 (u, v, w) or 4 (u, v, w, θ_x – rotation about the x-axis) d.o.f. per section node, require fine discretisations to capture highly non-linear axial displacement variations along the cross-section mid-line, due to spread of yielding and/or shear deformation. This justifies the convenience of enhancing the warping representation, done here through additional nodal d.o.f. ("warping rotations"): rotations about the z-axis θ_z – one per intermediate node and more than one per natural node (independent θ_z per converging wall direction). This enables the approximation of each warping profile u_k by piecewise (in each wall segment) *cubic* polynomials, instead of piecewise linear functions (see warping shear modes in Figs. 4 and 6).

Note that the formulation keeps the GBT plane-stress assumption (null σ_{xz}, σ_{sz}, σ_{zz} stresses and γ_{xz}, γ_{sz}, ε_{zz} strains). Accordingly, the Principle of Virtual Work leads to the GBT equilibrium equations $(m, n = \{x, s\})$

$$\int_L \int_b \int_t \sigma_{mn}\delta\varepsilon_{mn}\, dz\, ds\, dx = \int_L \int_b \left[\begin{matrix}(q_x u_i)\delta\zeta_{i,x} + \\ (q_s v_i + q_z w_i)\delta\zeta_i\end{matrix}\right] ds\, dx \tag{2}$$

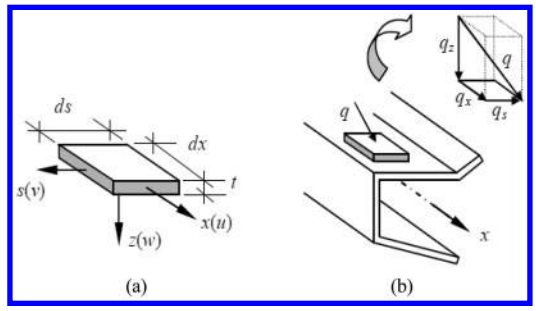


Figure 1. (a) Local coordinate system at each wall mid-surface and (b) general external distributed load $q(x, s)$.

where (i) σ_{xx}, σ_{ss}, σ_{xs} are axial, transverse and shear 2^{nd} Piola-Kirchhoff stresses, (ii) q_x, q_s, q_z are local components of a distributed load on the member mid-surface (see Fig. 1(b)), and (iii) $\delta\varepsilon_{xx}$, $\delta\varepsilon_{ss}$, $\delta\gamma_{xs}$ are axial, transverse and shear Green-Saint-Venant non-linear virtual strains, expressed in terms of the modal amplitude functions $\zeta_k(x)$ and their derivatives, through Eqs. (1).The formulation also accounts for (i) residual stresses and geometrical imperfections, and (ii) arbitrary single-parameter (λ) loadings, including concentrated forces and moments.

2.2 *Non-linear beam finite element*

The cylindrical arc-length method is adopted, involving (i) incremental equilibrium equations based on the tangent stiffness matrix K_{tan}, (ii) internal force vectors f^{int} and (iii) a path-independent iterative strategy: strain increments evaluated w.r.t. the last converged equilibrium state.

The results shown in section 3 were obtained using Hermite cubic polynomials to approximate the GBT modal amplitude functions in each BFE, *i.e.*,

$$\zeta_{k,x}^{v,w=0}(x) = \Psi_H(x)\, d_k \qquad \zeta_k^{v,w\neq 0}(x) = \Psi_H(x)\, d_k \tag{3}$$

where (i) the 1×4 Ψ_H vector stores the Hermite polynomials, (ii) d_k is the 4×1 displacement vector related to the mode k approximation, (iii) the first expression concerns only axial extension and warping shear modes ($v = w = 0$), and (iv) the second expression applies to all other modes ($v \neq 0$ and/or $w \neq 0$). After inserting the above approximations in Eq. (2) (including virtual strains), the internal and external force vectors interrelation for a generic "equilibrium configuration" ($mn = xx, ss, xs$)

$$\sum_{mn} f_{i(mn)}^{int} = \lambda \bar{f}_i, \qquad f_{i(mn)}^{int} = \int_{L_e}\int_b\int_t \sigma_{mn}\, F_{i(mn)}^{int}\, dV_e \tag{4}$$

is obtained, where (i) the ith components are 4×1 sub-vectors related to deformation mode i and (ii) $\bar{f}$ is the external force vector for a unit load parameter λ. Then, the incremental equilibrium

equation for a deformed configuration j can be established as

$$K_{\tan}\Big|_j \Delta d = \Delta\lambda\, \bar{f} \tag{5}$$

where (i) d is the displacement vector and (ii) the tangent stiffness matrix (i, p)th component, $K_{\mathrm{ip,tan}}$, is a 4×4 sub-matrix concerning deformation modes i and p, reading

$$K_{ip,\tan} = \frac{\partial f_i^{\mathrm{int}}}{\partial d_p}, \qquad \frac{\partial f_i^{\mathrm{int}}}{\partial d_{pl}} = \frac{\partial f_{i(xx)}^{\mathrm{int}}}{\partial d_{pl}} + \frac{\partial f_{i(ss)}^{\mathrm{int}}}{\partial d_{pl}} + \frac{\partial f_{i(xs)}^{\mathrm{int}}}{\partial d_{pl}} \tag{6}$$

$$\frac{\partial f_{i(mn)}^{\mathrm{int}}}{\partial d_{pl}} = \int_{L_e}\int_b\int_t \left\{ \frac{\partial \sigma_{mn}}{\partial d_{pl}} F_{i(mn)}^{\mathrm{int}} + \sigma_{mn} \frac{\partial F_{i(mn)}^{\mathrm{int}}}{\partial d_{pl}} \right\} dV_e \tag{7}$$

It corresponds to the Jacobian of the internal force vector ith component, w.r.t. the mode p displacement vector – its components are d_{pl} ($l = 1, \ldots, 4$). For any inelastic material, the stress gradients at every point read

$$\frac{\partial \sigma_{mn}}{\partial d_{pl}} = \frac{\partial \sigma_{mn}}{\partial \varepsilon_{xx}} \frac{\partial \varepsilon_{xx}}{\partial d_{pl}} + \frac{\partial \sigma_{mn}}{\partial \varepsilon_{ss}} \frac{\partial \varepsilon_{ss}}{\partial d_{pl}} + \frac{\partial \sigma_{mn}}{\partial \gamma_{xs}} \frac{\partial \gamma_{xs}}{\partial d_{pl}} \tag{8}$$

($\partial\varepsilon/\partial d_{\mathrm{pl}}$ obtained from writing the strain-displacement relations according to the FE approximations in Eq.(3)).

The stresses and their gradients ($\partial\sigma/\partial\varepsilon$) appearing in previous relations stem from the J_2-flow theory with associated flow rule, by resorting to implicit and/or explicit numerical integration schemes wherever plastic flow takes place. Then, at every Gauss point and after each arc-length iteration, one must (i) compute the elastic stress variation, from the imposed strain variation ($\Delta\varepsilon$) w.r.t. the last equilibrium state i (stresses σ_{i} and hardening parameter κ_{i}), and then (ii) check whether the final stresses ($\sigma_{\mathrm{e}} = \sigma_{\mathrm{i}} + D^e \Delta\varepsilon$) fall outside the yield surface $f\ (\sigma, \kappa_{\mathrm{i}}) = 0$. If yes, numerical integration of the incremental constitutive equations is performed to update the stresses and hardening parameter κ – the Mean-Normal and Euler-Backward methods were used to obtain the results presented in 3.2 and 3.3–3.4, respectively. Once those variables are updated, gradients $\partial\sigma/\partial\varepsilon$ are directly computed from the consistent elastoplastic constitutive matrix.

3 ILLUSTRATIVE EXAMPLES

The application of the GBT formulation for inelastic post-buckling analysis, implemented in MATLAB (MathWorks 2010), is now illustrated. The results discussed next concern 3 numerical examples involving (i) SHS and hollow flange (HF) I-section columns and (ii) a RHS beam-column. Material models with a linear elastic regime and involving different types of strain-hardening were considered, namely the (i) perfectly-plastic (PP), (ii) bi-linear (BL – linear hardening), and (iii) non-linear (NL) models. Concerning the latter, the σ-ε relation due to Quach *et al.* (2008) is adopted – it is (i) suitable for stainless steel alloys and (ii) defined by the 3 basic Ramberg-Osgood parameters (E, $\sigma_{0.2}$, n) (implementation details reported in Abambres *et al.* 2013c). For validation purposes, GBT equilibrium paths, stress contours and deformed configurations (referred to the bar mid-surface) are compared with those yielded from ABAQUS (DS Simulia 2008) SFEA.

Table 1. Illustrative examples: material properties.

Example	E (GPA)	E_{SH}	σ_0^Y (MPA)	$\sigma_{0.2}$ (MPA)	n
SHS	$E^c = 198.2$	–	390.3	$\sigma_{0.2}^c = 560$	$n^c = 8.3$
	$E^t = 198.8$			$\sigma_{0.2}^T = 586$	$n^t = 9.0$
HF I-sec (*PP & BL*)	205	$E/50$	290	–	–
HF I-sec	$E^c = 205$	–	289.5	$\sigma_{0.2}^c = 515$	$n^c = 5.2$
(*NL*)	$E^t = 208$			$\sigma_{0.2}^t = 560$	$n^t = 6.9$
RHS	200	0	450	–	–

Table 2. Illustrative examples: FE discretisation and d.o.f. numbers.

	GBT	ABAQUS		Number of d.o.f.		
Example	BFEs	SFES (x)	SFEs (s)	GBT	ABQ	GBT/ ABQ (%)
SHS	16	50	48	865	14401	6
HF I-sec	66(*)	80	62	7391	29651	24.9
RHS	50	160	36	6462	34452	18.8

*Only non-uniform (symmetric) mesh: 18 BFEs ($x < 0.35L$) + 15 BFEs ($0.35L \le x \le 0.5L$).

Table 1 shows the material properties adopted in each analysis: (i) E, E_{sh}, are the Young's modulus and strain-hardening slope (BL model), (ii) σ_0^y, $\sigma_{0.2}$, are the initial yield and 0.2% proof stresses, and (iii) n is the hardening power (NL model – 0.01% proof stress taken as the initial yield stress) – c, t denote compressive and tensile. All these (isotropic) models are employed to simulate the compressive behaviour and a $\nu = 0.3$ Poisson's ratio is assumed. Table 2 shows the numbers of (i) GBT BFEs, (ii) axial and transverse (x, s) ABAQUS SFEs, and (iii) d.o.f. involved in each model. As for the numbers of Gauss integration points per BFE wall segment direction s, z, x (Fig. 1(a)) in each GBT analysis, they are (i) (3, 3, 3) for the SHS, (ii) (4, 5, 3) for the HF I-section and (iii) (2, 5, 4) for the RHS – the SFEA involved fairly uniform S4 FE meshes, adopting the same through-thickness integration points as the GBT analyses.

After providing information about the selected GBT modes, in 3.1, the results of each analysis are addressed in 3.2–3.4. The first one concerns a fixed-ended SHS

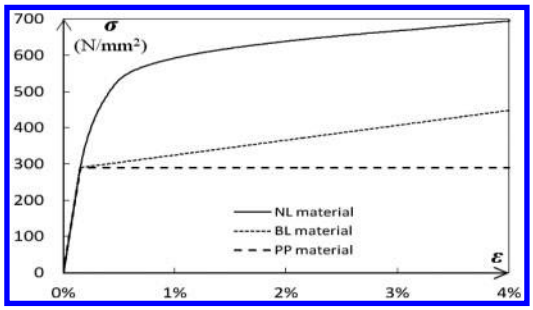


Figure 2. HF I-section column material model (stress-strain curves).

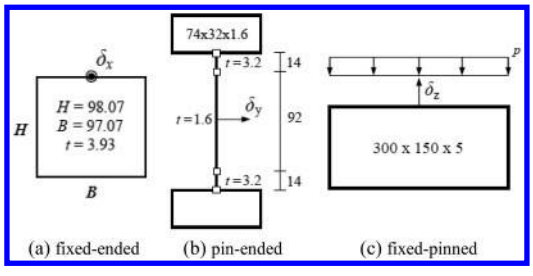


Figure 3. (a) SHS, (b) HF I-section, (c) RHS mid-line dimensions.

stub column (Fig. 3(a) – $L = 400$ mm), made of EN 1.4162 duplex stainless steel and acted by a (uniformly distributed) compressive end force $F = 102.2 \times 10^4$ λN (experimental results reported by Theofanous & Gardner 2009). The initial geometrical imperfection, akin to the 1st symmetric local buckling mode, has a $t/100$ amplitude (maximum in-plane displacement). The second problem deals with a pin-ended HF I-section column (Fig. 3(b) – $L = 1200$ mm) acted by a compressive end force $F = 100 \times 10^3$ λN – besides the end-shortening, the pinned supports allow for global flexural rotations In order to assess the impact of strain-hardening on the column behaviour and strength, analyses were carried out for PP, BL and NL material models with the same initial yield stress – Figure 2 shows their σ-ε curves. The initial imperfections combine the 1st global (flexural – $L/1000$ amplitude) and 13 half-wave local (1.18 mm amplitude) buckling modes. Lastly, a fixed-pinned (no in-plane motions) RHS beam-column (Fig. 3(c) – $L = 4000$ mm) made of a PP material is analysed, subjected to (i) a uniformly distributed vertical load acting along the full top flange ($p = 0.01$ λ N/mm^2) and (ii) an axial compression $F = 100 \times 10^3$ λN. The imperfection is akin to the 2nd local buckling mode and has amplitude equal to $t/100$.

The results shown in 3.2–3.4 correspond to the points indicated on the equilibrium path, denoted as BP (before peak), P (peak) and AP (after peak). It is also worth noting that the GBT modal participation diagrams are based on the cross-section having the maximum overall or in-plane displacement (initial imperfection not included) – each deformation mode

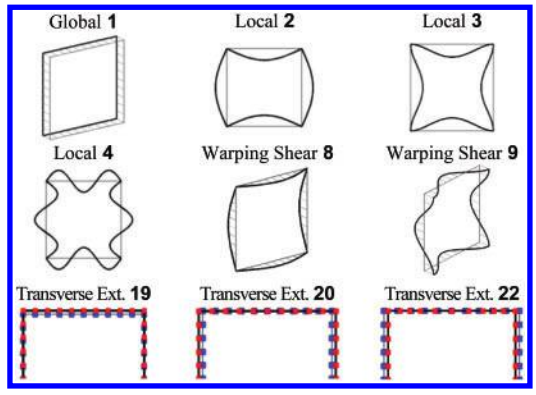


Figure 4. SHS most relevant GBT deformation modes.

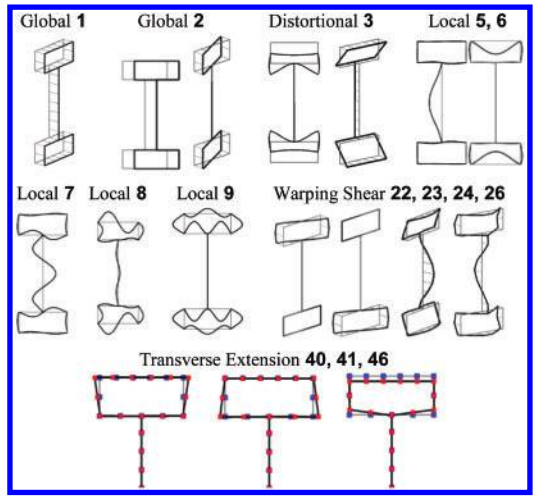


Figure 5. HF I-section most relevant GBT deformation modes.

contribution is the ratio between its maximum displacement and the sum of all such modal values, not necessarily occurring at the same point.

3.1 *GBT deformation modes*

The GBT deformation modes (**G**-global, **D**-distortional, **L**-local, **WS**-warping shear, **TE**-transverse extension and **CS**-non-global cell shear flow) included in each analysis are the following: (i) 28 modes out of 204 (1 **G**, 6 **L**, 11 **WS**, 10 **TE**), all bi-symmetric (SHS), (ii) 56 modes out of 132 (2 **G**, 1 **D**, 15 **L**, 20 **WS**, 17 **TE**, 1 **CS**), mostly symmetric w.r.t. the horizontal centroidal axis (HF I-section), and (iii) 65 modes out of 184 (2 **G**, 20 **L**, 18 **TE**, 25 **WS**), symmetric w.r.t. the vertical centroidal axis (RHS) – all these modes are renumbered sequentially, since they are just a fraction of the cross-section analysis full set. The in/out-of-plane shapes of the most relevant modes in each analysis are shown in Figures 4–6 – the discretisations adopted are shown in the symmetric TE mode half-section shapes – warping rotation d.o.f. θ_z (addressed in subsection 2.1) were used in the SHS and RHS member analyses.

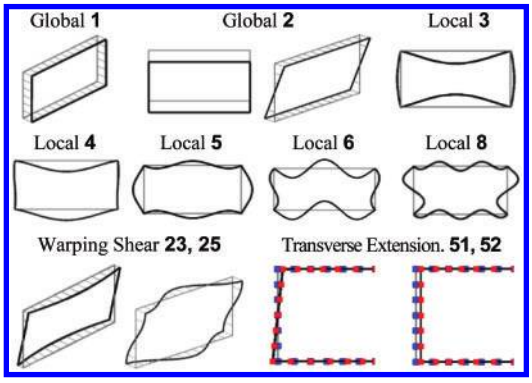


Figure 6. RHS most relevant GBT deformation modes.

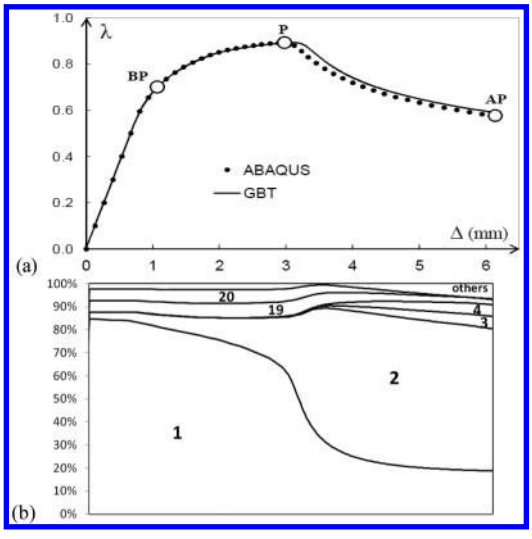


Figure 7. (a) GBT and ABAQUS equilibrium paths and (b) GBT modal participation diagram.

3.2 *SHS column*

Figure 7(a) shows the GBT and ABAQUS $\lambda(\Delta)$ equilibrium paths (Δ is the column end shortening) – the BP, P and AP λ values are: $\lambda_{GBT} = 0.701 + \lambda_{ABQ} = 0.701$ (BP), $\lambda_{GBT} = 0.893 + \lambda_{ABQ} = 0.893$(P), $\lambda_{GBT} = 0.590 + \lambda_{ABQ} = 0.577$ (AP). Fig. 7(b) shows the GBT modal participations concerning the evolution, with Δ, of the mid-span cross-section deformed shape. The following remarks are due:

(i) The agreement between the GBT and ABAQUS paths is very good (differences below 4.9%).

ii) The GBT participation diagram indicates two markedly different behaviours: (ii_1) one prior to the peak, involving mostly mode **1** (58.6–84.7%), and (ii_2) another after the peak: growth of local mode **2** (27.1–64.5%), "sweeping aside" mode **1**.

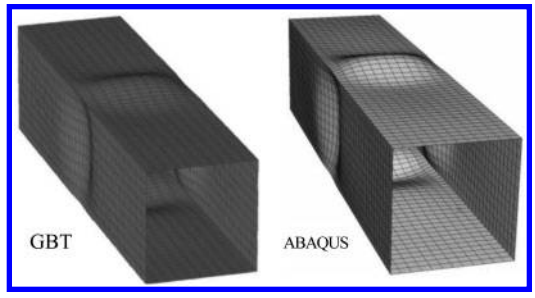


Figure 8. Column collapse mechanism (AP equilibrium state).

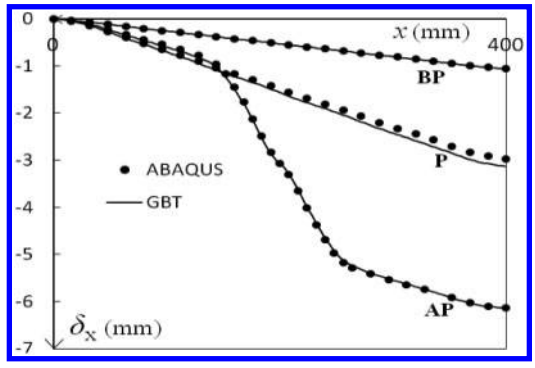


Figure 9. Axial displacement profiles of the top wall mid-point at the BP, P and AP equilibrium states.

(iii) Concerning the **TE** modes **19** and **20**, whose presence is intrinsically linked to modes **1** (Poisson effects) and **2**, it should be noted that, in spite of their small contributions (≈6% each), they play a key role. Indeed, their removal from the analysis would considerably stiffen the column behaviour since local buckling would be "artificially restrained". The post-peak participation decrease of these **TE** modes stems from elastic unloading and local deformation "localisation" very close to mid-height (see Fig. 8).

Figure 9 depicts the BP, P and AP axial displacement profiles δ_x (x) of the top wall mid-point (see Fig. 3(a)). First of all, it is readily observed that the ABAQUS and GBT results virtually coincide at the BP and AP states, and exhibit small differences at the P state. Moreover, note the linearity of the BP profile, while its P counterpart exhibits a mild non-linearity close to the column ends. At the AP state, on the other hand, δ_x exhibits three "almost linear" segments, the two outer ones with similar (small) slopes and a much steeper inner one – this axial stiffness drop occurring in the column central region stems from the plastic deformations associated with the increasing participations of the local modes **2**, **3** and **4** (see Fig. 7(b)).

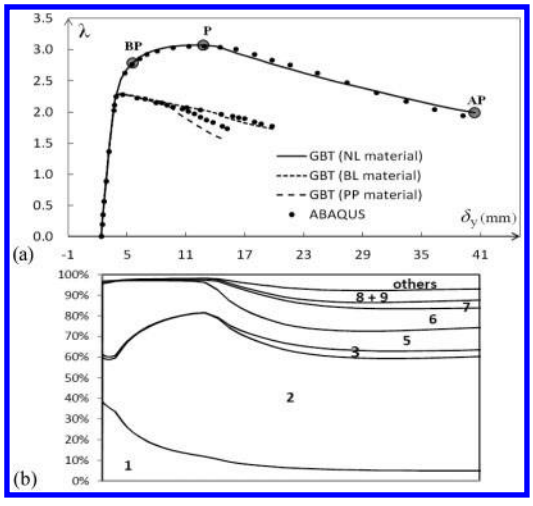


Figure 10. (a) GBT and ABAQUS equilibrium paths and (b) GBT modal participation diagram (NL column).

3.3 *HF I-section column*

Figure 10(a) shows the GBT and ABAQUS $\lambda(\delta_y)$ equilibrium paths concerning the PP, BL and NL material models (δ_y is the mid-span cross-section mid-height lateral displacement – see Fig. 3(b)). For the NL paths, the BP, P and AP applied load values are $\lambda_{GBT} = 2.79 + \lambda_{ABQ} = 2.76$ (BP), $\lambda_{GBT} = 3.08 + \lambda_{ABQ} = 3.05$ (P), $\lambda_{GBT} = 1.99 + \lambda_{ABQ} = 1.94$ (AP). As for Figure 10(b), it provides the evolution, with δ_y, of the mid-span cross-section deformed configuration (via the GBT modal participation diagram). Note that:

(i) Except for the PP material at advanced post-collapse stages, the GBT and ABAQUS curves agree very well – *e.g.*, the NL paths do not differ by more than 4%.

(ii) The PP and BL column responses prior to the later collapse stages virtually coincide (in spite of the inelastic collapse). However, the behaviour is much stiffer for the NL column ($\lambda_{u,NL} = 3.05$, $\lambda_{u,BL} = 2.28$), due to the large strain-hardening (partly responsible for the high non-linearity prior to reaching the peak load).

(iii) Figure 10(b) shows that the column behaviour exhibits relevant contributions from (iii_1) global modes **1** and **2** (21.2–69.7%), and (iii_2) local modes **5** (8.9–36.1%), **6** and **8**+**9**. Although the web-driven mode **5** dominates the local deformation in the path ascending branch (recall it participates in the initial imperfection), important contributions from the flange-driven modes **6,8** and **9** occur in the post-collapse phase – this can be attested by the failure mechanism (AP state) depicted in Fig. 11 (note the yield-line forming at the most compressed flange regions).

Figure 12 concerns the NL material response at the BP, P and AP states and shows the web mid-height lateral displacement profiles $\delta_y(x)$ (Fig. 3(b)). The agreement between GBT and SFEA results is fairly good – visible discrepancies stem mostly from differences in the initial imperfection prediction. In order to assess the material model influence, Figure 13 compares the GBT $\delta_y(x)$ profiles for $\lambda_{GBT} = 1.99$ (AP state) – it is observed that, in spite of the expected quantitative differences, they all follow the same trend (same number of half-waves).

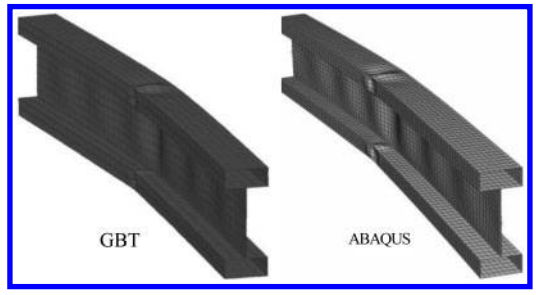


Figure 11. Column failure mechanism (AP equilibrium state).

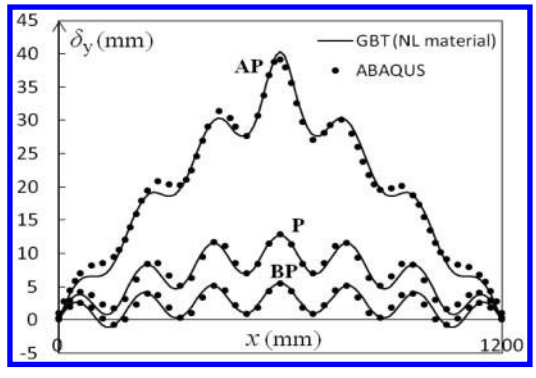


Figure 12. Cross-section mid-height lateral displacement profiles of the NL column at the BP, P and AP equilibrium states.

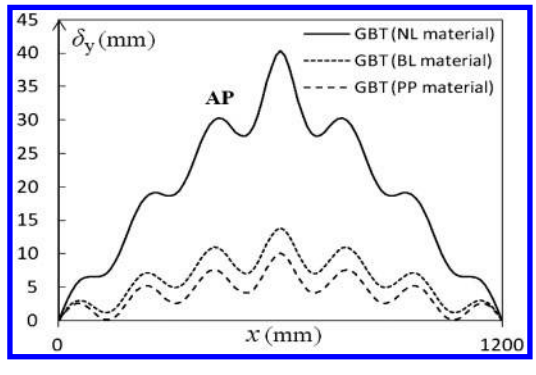


Figure 13. Cross-section mid-height lateral displacement profiles at $\lambda_{GBT} = 1.99$ for the NL, BL and PP columns.

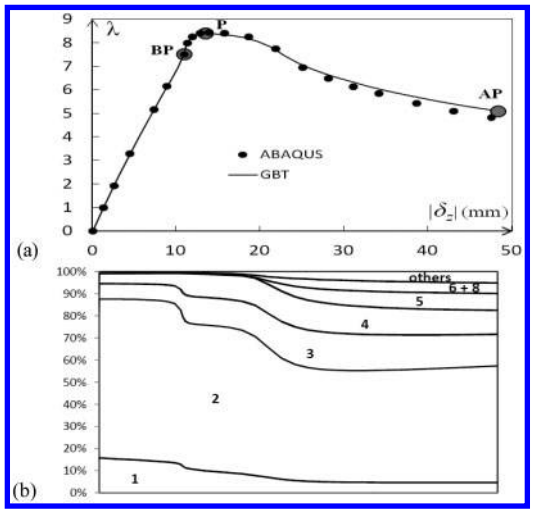


Figure 14. (a) GBT and ABAQUS equilibrium paths and (b) GBT modal participation diagram.

3.4 *RHS beam-column*

Figure 14(a) shows the GBT and ABAQUS $\lambda(|\delta_z|)$ equilibrium paths (δ_z is the mid-span top flange mid-point vertical displacement – Fig. 3(c)). The BP, P and AP λ values are $\lambda_{GBT} = 7.51 + \lambda_{ABQ} = 7.50$ (BP), $\lambda_{GBT} = 8.38 + \lambda_{ABQ} = 8.43$ (P), $\lambda_{GBT} = 5.09 + \lambda_{ABQ} = 4.81$ (AP). Figure 14(b) shows the modal participation diagram providing the evolution of the most deformed cross-section shape. It is possible to draw the following conclusions:

(i) The GBT and ABAQUS curves show a very good correlation in most of the deformation range. Even if the differences increase as loading progresses, they never exceed 6% (5% excluding the last 2 ABAQUS points).

(ii) Figure 14(b) clearly shows that the early loading stages are governed by axial extension and minor-axis bending (modes **1** and **2** – 65.7–72.7%). The local modes **3** (7.0–12.5%) and **4** (4.6–10.5%), which stem from the loaded top flange transverse bending and oppose each other in the bottom flange (Fig. 6), also have visible contributions. Lastly, mode **23** (one of the "others") captures the shear deformation associated with minor-axis bending.

(iii) In the post-peak stage there is a clear global deformation decrease (modes **1**+**2**), mostly compensated by the gradual growth, for $|\delta_z| \geq 20$ mm, of local modes **5** (web-driven – 0.3–7.6%) and **6**+**8**(1.0–4.7%). The presence of local deformation in the member yield-line mechanism can be confirmed in Figure 15.

Figure 16 compares the top flange mid-point vertical displacement profiles at the BP, P and AP states. Besides the excellent agreement between the GBT and ABAQUS outputs, note that the half-wave patterns change significantly in-between states P and AP, due to the plastic flow and elastic unloading associated with the failure mechanism. Finally, the half-column Mises stress contours depicted in Figure 17, concerning state P and evidencing excellent agreement, make

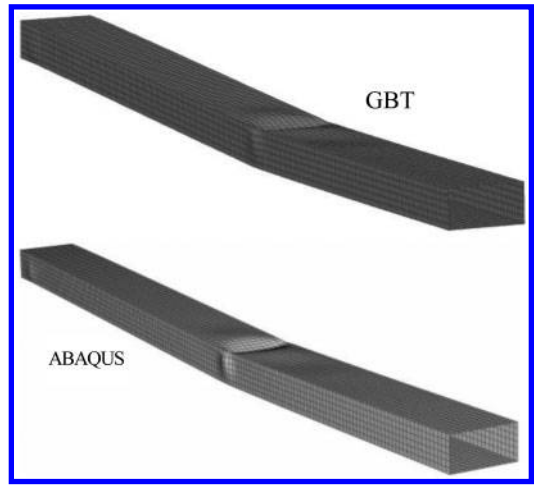


Figure 15. Member collapse mechanism (AP equilibrium state).

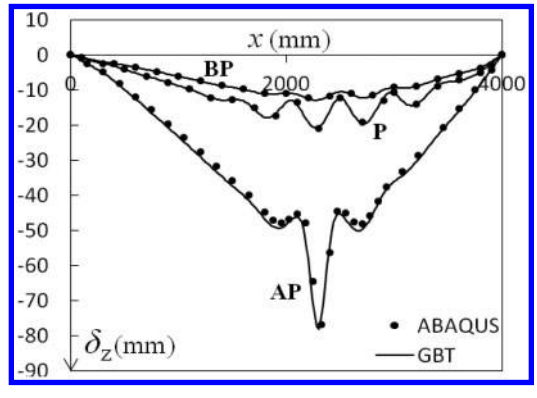


Figure 16. Vertical displacement profiles at the top flange middle point – BP, P and AP states.

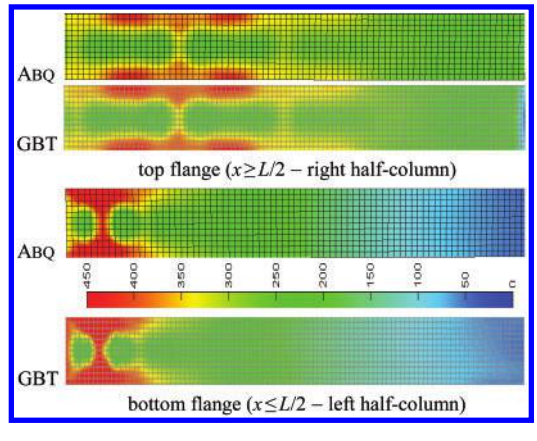


Figure 17. Mises stress (N/mm^2) contours at the P equilibrium state.

it possible to visualise the most yielded (and compressed) flange regions at collapse: the vicinities of the (i) fixed end section bottom flange ($x \leq L/2$) and (ii) most deformed cross-section top flange ($x \geq L/2$).

4 CONCLUDING REMARKS

This paper (i) provided an overview of a recently developed and validated GBT formulation to assess the inelastic post-buckling behaviour of thin-walled members, and (ii) illustrated its application and potential by presenting and discussing the analysis of several tubular members, namely a stainless steel SHS stub column, a perfectly plastic RHS beam-column and three hollow-flange I-section columns made of perfectly plastic, bi-linear and non-linear materials with identical yield stresses – the non-linear material exhibited a large strain-hardening and led to a significant strength increase. For validation purposes, most GBT results (equilibrium paths, collapse mechanisms, displacements profiles and stress contours) were compared with values yielded by ABAQUS shell finite element analyses. It was shown that the GBT analyses provide similarly accurate results, while requiring no more than 25% (16.6% on average) of the d.o.f. numbers involved in the corresponding SFEA. Moreover, it was also shown, through modal participation diagrams, that the GBT analyses provide in-depth insight on the member mechanics associated with both the elastic and elastic-plastic regimes (including the collapse mechanisms).

ACKNOWLEDGEMENTS

The authors gratefully acknowledge the financial support of Fundação para a Ciência e Tecnologia (FCT – Portugal), through project PTDC/ECM/108146/2008. The first author also acknowledges FCT for granting his doctoral scholarship SFRH/BD/43271/2008.

REFERENCES

Abambres M, Camotim D. & Silvestre N. 2012. Physically non-linear GBT analysis of thin-walled members, *submitted for publication.*

Abambres M, Camotim D. & Silvestre N. 2013a. GBT-based first-order analysis of elastic-plastic thin-walled steel members exhibiting strain-hardening, *IES Journal A: Civil and Structural Engineering* (Singapore), in press.

Abambres M., Camotim D. & Silvestre N. 2013b. GBT-based structural analysis of elastic-plastic thin-walled members, *Proceedings of SSRC Annual Stability Conference* (ST. Louis, 16–20/4).

Abambres M., Camotim D. & Silvestre N. 2013c. GBT-based elastic-plastic post-buckling analysis of stainless steel thin-walled members, *submitted for publication*.

Camotim D., Basaglia C., Bebiano R., Gonçalves R. & Silvestre N. 2010. Latest developments in the GBT analysis of thin-walled steel structures, *Proceedings of International Colloquium on Stability and Ductility of Steel Structures* (SDSS'Rio 2010, 8-10/9), E. Batista *et al.* (eds.), 33–58.

DS Simulia Inc. 2008. Abaqus Standard Manual (version 6.7–5).

Gonçalves R. & Camotim D. 2004. GBT local and global buckling analysis of aluminium and stainless steel columns, *Computers and Structures*, 82(17–19), 1473–1484.

Gonçalves R. & Camotim D. 2011. Generalised beam theory-based finite elements for elastoplastic thin-walled metal members, *Thin-Walled Structures*, 49(10), 1237–1245.

Gonçalves R. & Camotim D. 2012. Geometrically non-linear generalised beam theory for elastoplastic thin-walled metal members, *Thin-Walled Structures*, 51(February), 121–129.

Hiriyur B. & Schafer B.W. 2005. Yield-line analysis of cold-formed steel members, *International Journal of Steel Structures*, 5(1), 43–54.

MathWorks. 2010. MATLAB – The Language of Technical Computing (www.mathworks.com/products/matlab).

Quach W.M., Teng J.G., Chung K.F. 2008. "Three-stage full-range stress–strain model for stainless steels", *Journal of Structural Engineering* (ASCE), 134(9), 1518–1527.

Theofanous M. & Gardner L. 2009. "Testing and numerical modelling of lean duplex stainless steel hollow section columns", *Engineering Structures*, 31(12), 3047–3058.

Research and Applications in Structural Engineering, Mechanics and Computation – Zingoni (Ed.)
© 2013 Taylor & Francis Group, London, ISBN 978-1-138-00061-2

Direct stability analysis of steel beam-column with an elastic restraints

I. Misiunaite & A. Juozapaitis
Department of Bridge and Special Structures, Vilnius Gediminas Technical University, Vilnius, Lithuania

ABSTRACT: The paper proposes the stability analysis of beam-column with an intermediate elastic restraint and arbitrary end conditions based upon direct analysis method. The proposal accounts for the second-order effects, geometrical imperfections, material nonlinearities and interaction of bending end compression. The material nonlinearity is implemented using the concept of multiple column curves. Furthermore, paper discusses the concept of equivalent imperfections based upon generalized imperfections factor and its application for the evaluation of the geometrical and material nonlinearities. The stability verification provided by the derived governing equations, discussed and compared with the numerical values obtained from the large displacement static analysis performed by means of the finite element method code, ANSYS. On the basis of comparative study several conclusions are drawn concerning the safety and accuracy of the verification of the stability by the proposed computational method.

1 INTRODUCTION

The development of form-finding to increase efficiency and fulfill aesthetical requirements of steel structures refers to the necessity of the appropriate design methods. Many of current design codes for the stability verification alongside conventional individual member check allows advanced analysis methods known as global analysis in EN 1993-1-1 (2005) and direct analysis method in ANSI/AISC 360-10 (2010). However, despite popular use of conventional design methods in the past and present as a basis for structural analysis, the methods have their major limitations. In the conventional methods, first-order or second-order elastic analysis is carried out to analyze a behavior of a structural system. The members are isolated from the structural system between the points of restraints, and their structural verification is based upon the member strength curves and interaction formulae, which implicitly account for the effect of deformed geometry, material and geometrical imperfections. The compatibility between the isolated member and the member as the part of a structural system is implemented through the concept of the effective length factor. The direct analysis method is discussed here, as it offers an advantage to eliminate the need to calculate effective length factor verifying the structural stability of the systems. The effective length factor is a long-standing feature and generally provides a good solution in structural frame design, but its limitations and underlying assumptions are rarely satisfied in current modern structures.

Alternative methods may be necessary in order to overcome the limitations of the effective length method as well as account for the geometrical and material nonlinearities inherent in all structures. The advanced methods introduced in current design codes have the form of requirements rather than practical application. Referring to their efficiency, many research efforts have been devoted to the development of practical implementation of the advanced analysis methods.

Most of the studies pursuit of the methods to perform direct analysis and design of frame steel structures. Murat et al. (2008) considers partial base fixity using the direct analysis method for column and frames containing web-tapered members design. Kim & Choi (2001) develop a practical advanced analysis of semi-rigid frames, Kim et al. (2006) presented the advanced analysis of 3D steel frames for lateral-torsional buckling, White et al. (2006) verifies the stability of steel building frames using the 2005 AISC specifications.

Kim & Choi (2001) apply practical advanced analysis for the design of three-dimensional truss bridge. Although, there are not much studies spread in the literature which are based on attempt to analyze more complex structures. Some of them rely on the computational programs developed on the basis of the inelastic stability of beam-column elements (Landesmann & Batista 2005)

The paper presents computational method based upon elastic stability of the steel beam-column element with an intermediate elastic restraint and arbitrary end conditions, including material nonlinearities associated with residual stress, second-order effects, and geometrical imperfections. The considering calculation model reflects the structural behavior of innovative steel structures with applied supporting system which in bridge engineering refer to underdeck cable-stayed bridges and in civil engineering to

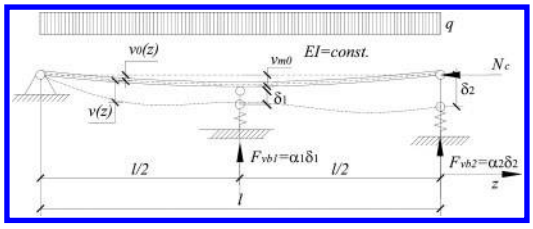


Figure 1. Calculation model of a beam-column with an intermediate elastic restraint and an elastic end support.

beam-string structures (Xue & Liu 2009). The possibility to assess structural behavior of under-deck cable-stayed bridge by applying simplified calculation models of beam-column was described by Misiunaite et al. (2012).

2 CALCULATION MODEL

The most fundamental theoretical formulation in the verification of the elastic stability of structures is the Euler formula, which defines the elastic axial buckling strength of an individual member and essentially refers to the structural analysis based on the individual member check. The theory assumes that the member is perfectly straight, behaves in-plane elastically and has a pinned ends. These assumptions all are commonly violated in real structures. In practice, elements are out-of straightness between braced points due to fabrication tolerances. Residual stresses are presented that cause inelastic behavior. Further, as a structure is loaded, deformations also occur, adding second-order forces and moments. Furthermore, it should be noted the fact that buckling always involves both an axial force and bending effects. The considering calculation model formed to implement all previously mentioned effects and moreover, the beam-column shown in Figure 1 has an intermediate restraint to cover the case when the structure is additionally supported at the mid-span, thus obtaining the semi-continuous structure. Consequently the end support assumed to be elastic to widen the applicability of the calculation model. The verification of the stability of the beam-column shown in Figure 1 performed with the approach of the Direct Analysis Method based upon nonlinear geometric elastic analysis.

2.1 *Imperfections*

Appropriate allowances shall be incorporated in the structural analysis to cover the effects of imperfections, including residual stresses and geometrical imperfections.

Residual stresses are introduced into structural shapes as a result of the production. The direct inclusion of the residual stresses in the analysis is connected with the manufacture-related approaches, which lies in the formulation of requirements that will appropriately consider all relevant factors, thus it becomes a task so complex as to be impossible. Theoretical values, for example, of the residual stresses in a shape, can be used, but this may impair the quality of the results. There are other methods based on the theoretical developments. The most important among the theoretical based methods is the one that utilizes several column strength curves. It has been included in methods proposed in many those days modern design codes. For the sake of simplicity in the proposed computational method the residual stresses are accounted by concept of equivalent geometric imperfections, with values which reflect both geometrical and material imperfections and are based on the column strength curves.

Geometrical imperfections are inherent in all structures. Small unavoidable eccentricities of loading and lack of initial straightness can be simulated mathematically by assuming an initial curvature which produces a small central deflection v_{m0}. According to equivalent geometric imperfections concept central deflection is modified on the bases of generalized imperfection factor. The generalized imperfection factor was introduced in the Perry-Robertson formula. The value of the generalized imperfection factor originally obtained by Robertson in 1925 has varied over the years and rearranged in the form of:

$$\eta = 0.001a\left(\lambda - \lambda_0\right) > 0 \tag{1}$$

where a varies from 2 to 8 depending on the shape of the section and limiting slenderness ratio:

$$\lambda_0 = 0.2\sqrt{\frac{\pi^2 E}{f_y}} > 0 \tag{2}$$

where $E =$ Elastic modulus; $f_y =$ yield strength.

Substituting Equation 2 into Equation 1 and introducing non-dimensionless slenderness:

$$\overline{\lambda} = \frac{\lambda}{\sqrt{\frac{\pi^2 E}{f_y}}} \tag{3}$$

hence:

$$\eta = \alpha\left(\overline{\lambda} - 0.2\right) \tag{4}$$

where $\alpha = 0.001a(\pi^2 E/f_y)^{1/2}$ is an imperfection factor based on the column strength curves and the multiplier 0.001 presents the maximum tolerance on elements out of straightness specified in many design codes.

The magnitude of the equivalent geometric imperfections by introducing generalized imperfection factor can be obtained:

$$v_{m0} = \alpha\left(\overline{\lambda} - 0.2\right)\frac{W}{A} \tag{5}$$

where $A =$ cross section area; $W =$ section modulus.

2.2 *Governing Equations*

The governing equations for the stability verification of the beam-column presented in Figure 1 derived considering the equilibrium by approach of moderately large displacement theory. Determining the equilibrium equations by moderately large displacement theory the structure is in equilibrium in its deformed state thus the second order effects will be accounted.

When considering simultaneous bending and compression with applying axial load N_c the deflection at z is increased by v and the differential equation of bending becomes:

$$M'' - N_c\left(v - v_0\right)'' + q = 0 \tag{6}$$

Adopting a sinusoidal function for an initial lack of straightness:

$$v_0 = v_{m0}\sin\left(\frac{\pi z}{l}\right) \tag{7}$$

and introducing:

$$k^2 = \frac{N_c}{EI} \tag{8}$$

The arbitrary solutions to the Equation 1, considering both sides of the calculation model (left: $0 \le l/z \le l/2$ and right $l/2 \le l/z \le l$) is:

$$v^{l(r)} = C_{1(5)}\sin kz + C_{2(6)}\cos kz + C_{3(7)} + C_{4(8)} + v_{part} \tag{9}$$

where superscriptions l and r indicates left and right sides of the calculation model respectively.

When the transverse distributed force is assumed to be constant and introducing:

$$n = \frac{(kl)^2}{\pi^2 - (kl)^2} \tag{10}$$

the particular solution can be taken as:

$$v_{part} = \frac{qz^2}{EIk^2} + nv_{m0}\sin\frac{\pi z}{l} \tag{11}$$

By combining Equations 3 and 5 with the boundary and continuity conditions for the beam-column with the intermediate elastic restraint and arbitrary support conditions shown in Figure 1:

$$\begin{aligned} &v^l = v^{l\,\prime\prime} = 0 \ \text{ at } z = 0, \\ &\left.\begin{aligned} v^l &= v^r = \delta_1 \\ v^{l\,\prime} &= v^{r\,\prime} \\ v^{l\,\prime\prime} &= v^{r\,\prime\prime} \end{aligned}\right\} \text{ at } z = l/2, \\ &\left.\begin{aligned} v^r &= \delta_2 \\ v^{r\,\prime\prime} &= 0 \end{aligned}\right\} \text{ at } z = l \end{aligned} \tag{12}$$

the deflection of the left and right sides of the beam-column is obtained as:

$$v^l = \frac{ql^4}{EI}\frac{1}{(kl)^2}\left[\frac{1}{(kl)^2}\left(\frac{\cos(kl/2 - kz)}{\cos kl/2} - 1\right) - \frac{F_{vb,1}}{2ql}\times\right.$$
$$\left.\times\left(\frac{\sin kz}{kl\cos kl/2} - \frac{z}{l}\right) - \frac{z}{2l}\left(1 - \frac{z}{l}\right)\right] + \delta_2\frac{z}{l} + nv_{m0}\sin\frac{\pi z}{l} \tag{13}$$

$$v^r = \frac{ql^4}{EI}\frac{1}{(kl)^2}\left[\frac{1}{(kl)^2}\left(\frac{\cos(kl/2 - kz)}{\cos kl/2} - 1\right) - \frac{F_{vb,1}}{2ql}\times\right.$$
$$\left.\times\left(\frac{\sin(kl - kz)}{kl\cos kl/2} + z/l - 1\right) - \frac{z}{2l}\left(1 - \frac{z}{l}\right)\right] + \delta_2\frac{z}{l} + \tag{14}$$
$$+nv_{m0}\sin\frac{\pi z}{l}$$

The bending moment may be expressed in terms of the displacement as:

$$M = -EIv'' \tag{15}$$

Accordingly, by Equation 15, the moments are given by:

$$M^l = \frac{ql^2}{(kl)^2}\left(\frac{\cos(kl/2 - kz)}{\cos kl/2} - 1\right) - \frac{F_{vb,1}l}{2}\frac{\sin kz}{kl\cos kl/2} \tag{16}$$

$$M^r = \frac{ql^2}{(kl)^2}\left(\frac{\cos(kl/2 - kz)}{\cos kl/2} - 1\right) - \frac{F_{vb,1}l}{2}\frac{\sin(kl - kz)}{kl\cos kl/2} \tag{17}$$

The restoring force $F_{vb,1}$ in Equations 13, 14 and 16, 17 can be taken as:

$$F_{vb.1} = EIv''' \tag{18}$$

Accordingly, by substituting Equation 18 the restoring force can be obtained as:

$$F_{vb,2} = \frac{ql}{kl}\frac{\left(1 + (kl/2)^2 - 1/\cos kl/2\right)}{kl/2 - \tan kl/2} + \frac{EI(kl)^3}{l^2\left(kl/2 - \tan kl/2\right)}\times$$
$$\times\frac{\left(\delta_1 - \delta_2/2 - nv_{m0}\right)}{l} \tag{19}$$

Elastic support at the middle of the considering beam-column shown in Figure 1 restrains its deflection to δ_1. Thus restoring force $F_{vb,1}$ can be expressed as a product of δ_1 and restraint stiffness α_1, substituting it into Equation 19 restrained deflection may be obtained as:

$$\delta_1 = \frac{ql^4}{EI(kl)^4}\frac{\left(1 + (kl/2)^2 - 1/\cos kl/2\right)}{\alpha_1/\alpha_L - 1} - \frac{\left(\delta_2/2 + nv_{m0}\right)}{\alpha_1/\alpha_L - 1} \tag{20}$$

where $\alpha_L =$ limiting restraint stiffness.

The variation with the dimensionless restraint stiffness α/α_L of the dimensionless buckling load on the bases of simply supported additionally elastically restrained compressed element was described by Trahair (2008) and the restraint stiffness expressed as:

$$\alpha_L = 16\pi^2 EI / l^3 \tag{21}$$

and was assumed to be limiting as considering element buckles in the asymmetric second mode.

Further for the sake of simplicity the limiting restraint stiffness in Equation 20 is assumed to be equal to the one obtained by Equation 21.

It follows from Equation 20 that intermediate restraint stiffness supposed to be non-equal and greater than minimum restraint stiffness, otherwise restrained deflection approach infinity and turns to unrestraint one. Furthermore, the shift from the unrestraint deflection shape to restraint one asserts between the values of 2 to 4 of the relative restraint stiffness α_1/α_L depending on slenderness parameter *kl* (Misiunaite & Juozapaitis 2012).

2.3 *Governing parameters*

All governing equations of considering structural element derived in Section 2.2 contain undetermined variable *kl*. The variable *kl* is known as slenderness parameter and may be assumed as the governing parameter performing parametric analysis of the additionally elastically restrained beam-column shown in Figure 1. The slenderness parameter relates the axial load, the flexural rigidity and the length of the structural element and may be expressed as:

$$kl = l\sqrt{\frac{N_c}{EI}} \tag{22}$$

The structural stability of the beam-column with the intermediate elastic restraint and arbitrary support conditions can be verified with the variation of slenderness parameter which for the case of buckling analysis corresponds to:

$$kl = \pi\sqrt{\frac{N_c}{N_{cr}}} \tag{22}$$

where N_{cr} = Euler critical load.

The invariable transverse distributed force q applied on an axially compressed element causes initial eccentricity which increases the stress, but does not affect the elastic stability of the considering structural element. While in case of elastic restraint, it results in a deflection dependent lateral load and a restoring force as the deflection takes place (Gambhir 2004). Thus the applied elastic restraint affects the elastic stability of the structural element. The relative restraint stiffness given in Equation 20 is assumed as one of the governing parameters and its effect on the deflection shape of the beam-column shown in Figure 1 will be considered in Section 3.2.

3 NUMERICAL IMPLEMENTATION

The derived governing equations, as a direct nonlinear solution technique is used in the analysis. The numerical procedure is straightforward in concept and implementation. The advantage of this method is its practical applicability.

3.1 *Accuracy evaluation*

The accuracy evaluation of the proposed method for the stability verification of the additionally elastically restrained beam-column element with arbitrary end conditions presented in Figure 1 performed on the bases of the finite element method by nonlinear solver of the software ANSYS. The large displacement static analysis performed and full Newton-Raphson option used for the solution. Initial sinusoidal configuration of the imperfect shape of the element simulated using B-spline which reflects to sinusoidal function.

The imperfection factor chosen on the bases of central member strength curve, due to compatibility among design codes. The central member strength curves introduced in many design codes are of similar shape and match closely (Rotter 1981). The geometric characteristics of European I-sections rely on considering member strength curve assumed on performing comparison analysis. The magnitude of the initial equivalent geometrical imperfection varies from 43.0 mm to 52.0 mm relay on slenderness of the element referring to geometric characteristics of considering shapes, as the length of the beam-column is taken 18.0 m for all cases being analyzed.

Calculation model of the beam-column element shown in Figure 1 reflects to the structural behavior of the element subjected to a compressive axial force N_c which rely on slenderness parameter and a constant distributed load q = 20 kN/m. The analysis performed for $kl = 3.0$, 4.0 and 5.0. The stiffness of the end restraint is assumed to be equal to limiting restraint stiffness and may be obtained by Equation 21. The restraint stiffness ratio α_1/α_L set to be equal to 5.0 implementing restrained deflection shape of the considering structural element.

The numerical values of the restoring force at the intermediate support, extreme bending moments and deflections for the $z = l/4$ and $z = 3l/4$ are obtained both by using governing equations derived in Section 2.3 and nonlinear solver of ANSYS. Table 1 presents the relative errors.

Table 1 shows that the proposal is safe and efficient, and that the errors obtained are in the desirable limits of accuracy.

3.2 *Verification*

Considering the beam-column element of the length of 18.0 m. shown in Figure 1 which is subjected to an axial force N_c rely on the slenderness parameter *kl*. The verification of the stability is carried out with the variation of the slenderness parameter from 2.0 to 6.0 with

Table 1. Accuracy evaluation.

Profile	Errors (Gov. Equations/ANSYS), %				
	$F_{vb,1}$	$v_{l/4}$	M_{min}	$v_{3l/4}$	M_{max}
	0.65	0.16	−3.23	−0.68	1.49
HEB 300	1.43	−1.16	−7.38	0.23	3.86
	2.48	−3.03	−13.3	1.67	7.56
	−0.01	−2.41	0.47	−2.43	−7.87
HEB 360	−0.11	−2.49	1.59	−4.49	−11.8
	−0.22	−4.38	3.05	−7.57	−14.1
	0.09	−2.52	−0.16	−2.21	−7.54
HEA 360	0.08	−3.16	−0.95	−3.59	−10.8
	0.08	−4.72	−2.00	−6.42	−12.9
	−0.34	−1.85	1.33	2.85	8.90
HEM 320	−0.80	−1.75	3.44	5.08	13.6
	−1.31	−2.25	6.21	9.23	15.3

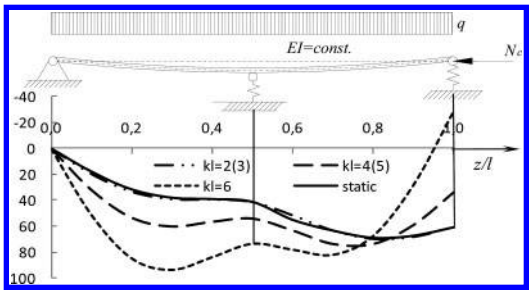


Figure 2. Verification of the deformational response of the beam-column.

increment of 1.0. The deflection and bending moment are obtained using governing equations and shown in Figures 2 and 3 respectively. The transverse distributed load is assumed to be constant with the numerical value of 20 kN/m. The geometrical and material characteristics of the considering beam-column are assumed to be equal to that of a section HEB 300 and the magnitude of the initial imperfections $v_{m0} = 43$ mm.

Figure 2 shows that the deflection shapes of the considering element with the values of the slenderness parameter 2.0 and 3.0 slightly differs from the results obtained on the bases of small displacement static theory. A sudden increase of the deflection at the slenderness parameter values of 4.0 and 5.0 indicates the element shift from the stable to unstable behavior and with the value of 6.0 it becomes unstable. The increase of slenderness parameter increases the axial response rather than flexural and the deflection shape of beam-column approaches the restraint shape of simply supported element with the intermediate elastic restraint.

Figure 3 presents the flexural response of the additionally elastically restrained beam-column element with the arbitrary end conditions presented in Figure 1. The increase of the slenderness parameter and it relying axial force in the considering beam-column element determines the increase of the extreme values

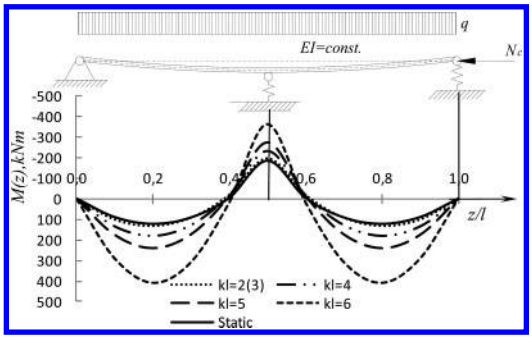


Figure 3. Verification of the flexural response of the beam-column.

of the bending moments. The significant shift of the extreme values of the bending moments at the values of 6.0 of the slenderness parameter can be assumed as the stability loss of the element.

4 CONCLUSIONS

The stability verification of the additionally elastically restrained beam-column with the arbitrary end conditions has been investigated using the finite element nonlinear solver of ANSYS in comparison with the derived governing equation with the approach of Direct Analysis Method. The analytical solution found to be in a good agreement with the results of finite element analysis.

Analysis based upon calculation model of the initially imperfect beam-column with the intermediate elastic restraint and arbitrary end conditions to reflect the behavior of more complex structures than steel frames.

The governing equations determined on the basis of the moderately large displacement theory thus accounting the effect of deformed geometry. The concept of equivalent geometrical imperfections with approach of the generalized imperfection factor is discussed. Furthermore, the modeling of initially imperfect member for the computer aided-analysis described.

Moreover, the influence of the intermediate elastic restraint on the elastic stability of the structure discussed. The governing slenderness parameter introduced to vary the axial effect on the structure and the numerical analysis carried out for the different values of slenderness parameter.

REFERENCES

An American National Standard. 2010. *American Institute of Steel Construction. Specification for Structural Steel Buildings, ANSI/AISC 360–10.*

European Standard. 2005. *Eurocode 3. Design of Steel Structures-Part1-1: General rules and rules for buildings, EN 1993-1-1.*

Eröz, M., White, D., and DesRoches, R. 2008. Direct Analysis and Design of Steel Frames Accounting for Partially Restrained Column Base Conditions. *Journal of Structural Engineering* 134(9): 1508–1517.

Gambhir, M.L. 2004. *Stability Analysis and Design of Structures*. Berlin: Springer-Verlag Press.

Kim, S-E. & Choi S-H. 2001. Practical advanced analysis for semi-rigid space frames. *International Journal of Solids and Structures* 38(50-51): 9111–9131.

Kim, S-E. & Choi S-H. 2001. Practical advanced analysis and design of three-dimensional truss bridges. *Journal of Constructional Steel Research* 57(8): 907–923.

Kim, S-E., Uang Ch-M, Choi, S-E., An, K-Y. 2006. Practical advanced analysis of steel frames considering lateral-torsional buckling. *Thin-Walled Structures* 44(7): 709–720.

Lendesmann, A. & Batista E.M. 2005. Advanced analysis of steel framed buildings using the Brazilian standard and Eurocode-3. *Journal of Constructional Steel Research* 61(8): 1051–1074.

Misiunaite, I., Daniunas, A., Juozapaitis, A. 2012. Unconventional Double-Level Structural System for Under-Deck Cable-Stayed Bridges. *Journal of Civil Engineering and Management* 18(3): 436–443.

Misiunaite, I. & Juozapaitis, A. 2012. Computational Non-Linear Buckling Analysis of an Elastically Restrained Steel Beam, in B.H.V. Topping, (ed.), *The Eleventh International Conference on Computational Structures Technology*; *Proc. Intern. Conf.*, *Dubrovnik, 4–7 September 2012*. Stirlingshire: Civil-Com-Press

Trahair, N.S., Bradford M.A., Nethercot, D.A., Gardner, L., (4 ed.). 2008. *The Behaviour and Design of Steel Structures to EC3*. New York: Taylor & Francis Press.

Rotter, J.M. 1981. A Simple Approach to Multiple Column Curves. *Metal Structures Conference. Newcastle, 11-14 May.* Vermont: ARRB Group.

White, D., Surovek, A.E., Alemdar, B.N., Chang, Ch-J., Kim, Y.D., Kuchenbecker, H. 2006. Stability Analysis and Design of Steel Building Frames Using the 2005 AISC Specification. *Steel Structures* 6: 71–91.

Xue, W., Liu, Sh., 2009. Design optimization and experimental study on beam string structures. *Journal of Constructional Steel Research* 65(1): 70–80.

Research and Applications in Structural Engineering, Mechanics and Computation – Zingoni (Ed.)
© 2013 Taylor & Francis Group, London, ISBN 978-1-138-00061-2

Stabilization of members with I-sections against flexural torsional buckling

R. Stroetmann
Technische Universität Dresden, Institute of Steel and Timber Construction, Germany

ABSTRACT: The following paper addresses the structural behavior of continuously restrained beams and beam-columns concerning flexural torsional buckling and second order effects. Beside the influence of different loadings, moment distributions and assumptions of imperfections, various restraining effects are considered. Approximate solutions for bifurcation buckling and second order analysis for calculations in practice are developed by using the energy method. The quality of the approximate solutions is reviewed by means of examples and comparisons with results of more complex FEM calculations.

1 INTRODUCTION

Stabilizing effects of adjacent structural elements are often taken into account in the verification of sufficient structural safety of beams and beam-columns (members) that are susceptible in terms of flexural torsional buckling. This is all the more required in case of increasing the slenderness and the strength of the used steel grades. The connections as well as the stabilizing elements themselves must be able to transfer the stabilization forces.

Suitable calculation models are necessary for the assessment of members and the determination of stabilization forces. On the one hand the structural behavior of the involved elements must be sufficiently accurately recorded; on the other hand the efforts for the calculation need to be limited for the practical use.

Often separate calculations for the assessment of members and stabilizing elements are carried out. For members, the use of the equivalent member methods is common, e.g. in Europe by Eurocode 3, part 1–1, chapter 6.3. For the determination of stabilization forces and moments, different calculation models with more or less major simplifications were developed in the past decades (see for example chapter 5.3.3 in EN 1993-1-1). The finding that the suitable use of these approximations is limited and that significant deviations to more accurate calculations can occur gave rise to the investigations described below.

2 STRUCTURAL BEHAVIOR OF CONTINUOUS RESTRAINT BEAMS

2.1 *Influence of shear fields*

The influence of a shear field related to the buckling load and the mode of lateral torsional buckling is illustrated by the example of a simply supported beam (Fig. 1). Figure 2 shows the buckling modes for different stiffnesses S. With increasing values S, the lateral displacement v of the upper chord decreases. At the same time the twist rotation ϑ increases. At a certain value S, the lower chord deforms in the negative y-direction in several waves. For small values S, the shape of the deformations v and ϑ can be described in good approximation by a sinusoidal half-wave. With increasing S, the deviations to this shape become larger.

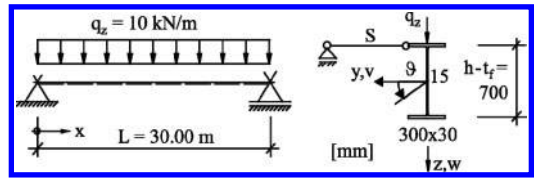


Figure 1. Simply supported beam with transverse load and shear field connecting at the top flange.

Figure 3 shows an almost linear relationship between the buckling load and the shear stiffness S. This does not apply generally and is not the case for moment distributions with different signs.

In practice, different approximations for the determination of stabilization forces on shear fields and bracing systems are common (e.g. EN 1993-1-1, chapter 5.3.3). An often used substantial simplification is to replace the beams by their compression chords (Fig. 4).

For simply supported beams with uniform distributed load q_z, lateral bow imperfections e_0 and horizontal loads q_y, the resulting stabilization force q_s can be determined by the Equations 1 and 2. The buckling load is reached, if q_s becomes infinite. From this, an approximation for α_{cr} may be deduced (Eq. 3).

$$q_s = \left(\frac{q_{y,m} + e_0 \cdot \sum P_i \cdot \pi^2 / L^2}{1 - \sum P_i / S} - q_{y,m} \right) \cdot \sin\left(\frac{\pi \cdot x}{L} \right) \quad (1)$$

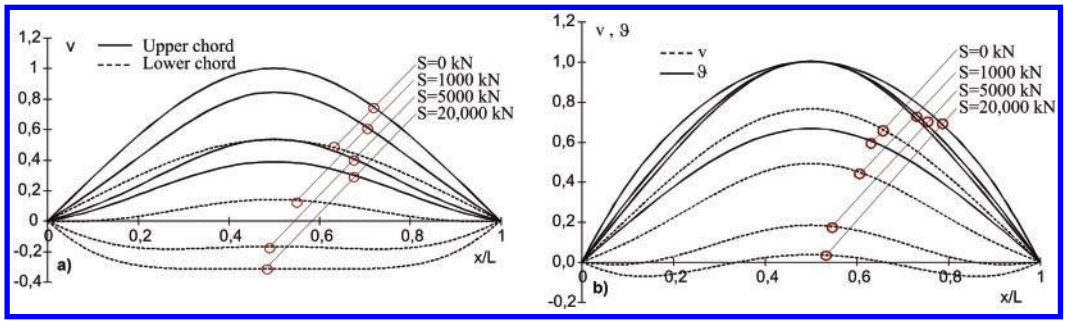


Figure 2. Standardized buckling deformations for different shear field stiffnesses S, a) Flange displacements v, b) Displacements v and twist rotations ϑ of the beam.

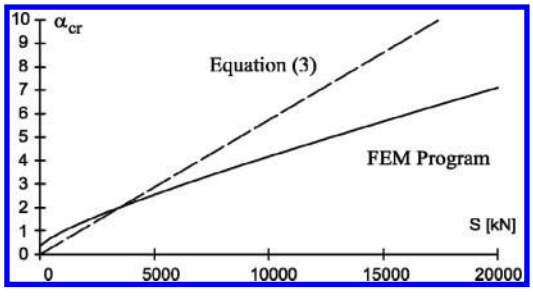


Figure 3. Buckling load calculated by FEM program and Equation 3.

$$P_i = \frac{\max M_{y,i}}{h_i - t_{f,i}} = \frac{q_{z,i} \cdot L^2}{8 \cdot (h_i - t_{f,i})} \qquad (2)$$

$$\alpha_{cr} = \frac{P_{cr}}{\sum P_i} = S \cdot \sum_i \frac{8 \cdot (h_i - t_{f,i})}{q_{z,i} \cdot L^2} \qquad (3)$$

$h - t_f$ distance of the chord axis

Figure 3 shows a diagram obtained by evaluating Equation 3 using the example in Figure 1. Neglecting the stiffness of the beam itself leads to conservative results of Equation 3 for small values S. For increasing values S, the value α_{cr} is more and more overestimated. Besides other reasons, this results from neglecting the nonlinear term due to the load q_z in combination with the twist rotation ϑ.

To show the influence of different moment distributions M_y and loads q_z on the shear field, the beam of Figure 1 was analyzed for three load cases (Fig. 5).

The stabilization loads and shear forces, its distributions and maximum values are rather different (Fig. 6).

Often the hypothesis is stated that it is conservative to simplify a variable moment distribution into a constant moment diagram with the maximum ordinate when determining the stabilizing forces. The comparison of the results for load case 3 with those from load case 1 and 2 shows that this is not generalizable.

The magnitude of the stabilization force q_s (Fig. 6) gives an idea about its influence for the design of shear fields and bracings. If, for instance, 5 to 10 beams are to be stabilized by a bracing system, this influence

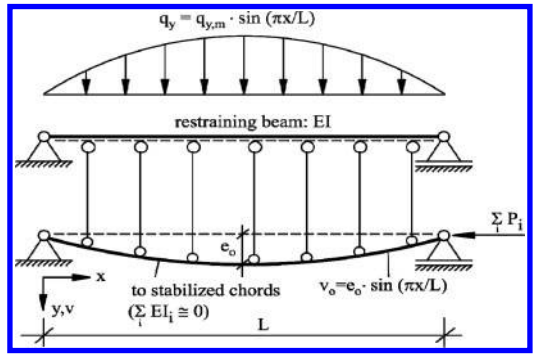


Figure 4. Approximate model to determine stabilization forces.

often cannot be considered by only a small addition to the wind load. Outer loads q_y, e.g. from wind or thrust of inclined roofs, are leading to larger deflections and increasing the stabilization forces additionally (see Eq. 1).

2.2 *Influence of different assumptions of imperfections*

For the assessment of flexural buckling of columns and frames, the formulation of equivalent loads to consider imperfections is well known. The influence of initial bow and sway imperfections in combination with compression forces may be replaced by systems of equivalent loads.

The procedure is similar for the assessment of lateral torsional buckling. In the following, the influences are clarified.

Equation 4 gives the system of coupled differential equations for a beam with doubly symmetric cross-section that is continuously restrained by a shear field. The used deflections v_g and ϑ_g, which are multiplied by bending moments M_y and cross loads q_z, are total deflections. They consist of elastic deflections and geometrical imperfections (Eq. 5). v_0 and ϑ_0 are describing the stressless initial deformed shape of the beam.

$$EI_z \cdot v''' - S \cdot (v'' - z_S \cdot \vartheta'') + (M_y \cdot \vartheta_g)'' = q_y \qquad (4a)$$

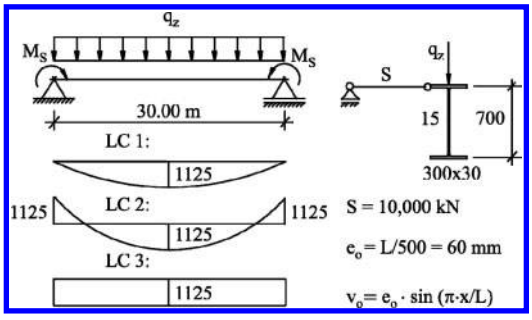


Figure 5. Structural system, imperfection and moment distributions for load cases 1 to 3.

$$EI_\omega \cdot \vartheta''' - GI_T \cdot \vartheta'' + S \cdot z_S \cdot (v'' - z_S \cdot \vartheta'') + M_y \cdot v_g'' + q_z \cdot z_q \cdot \vartheta_g = m_x \quad (4b)$$

$$v_g = v + v_0 \quad (5a)$$

$$\vartheta_g = \vartheta + \vartheta_0 \quad (5b)$$

Inserting Equation 5 into 4 and transferring the terms, which are combined with v_0 and ϑ_0, to the right side provides the equivalent loads $q_{y,0}$ and $m_{x,0}$ along the beam. For the equilibrium, additional nodal forces and moments are necessary, which are not treated here.

$$q_{y,0} = -(M_y \cdot \vartheta_0)'' = q_z \cdot \vartheta_0 - 2 \cdot Q_z \cdot \vartheta_0' - M_y \cdot \vartheta_0'' \quad (6a)$$

$$m_{x,0} = -M_y \cdot v_0'' - q_z \cdot z_q \cdot \vartheta_0 \quad (6b)$$

$$M_y = M_S + 4 \cdot M_0 \cdot (\xi - \xi^2) \quad (7)$$

with $M_0 = \frac{q_z \cdot L^2}{8}$; $\xi = \frac{x}{L}$ M_s = hogging moment

Figure 7 shows the normalized equivalent loads resulting from a sinusoidal shape of v_0 and ϑ_0 for different moment distributions. The normalization is done in terms of $q_z = 8 \cdot M_0 / L^2$ and the maximum ordinate of the respective imperfection.

From Figures 6 and 7 as well as from Equation 6 it becomes obvious that simplifying assumptions for the moment distribution and the structural behavior do not apply generally. The imperfections v_0 provides in combination with bending moments M_y torsional loads $m_{x,0}$. The maximum area of $m_{x,0}$ results from the constant bending moment. In the presence of hogging and sagging moments, the sign is changing (Fig. 7a). Twist rotations ϑ_0 lead to equivalent cross loads $q_{y,0}$. They can lead to unsafe results.

Furthermore, depending on the span length and the cross-section properties of the beam, the structural behavior for torsion can be different (parts of St. Venant torsion and warping torsion). This affects the loads and stresses of the shear field again (Friemann & Stroetmann 1998).

3 APPROXIMATE CALCULATION OF FLEXURAL TORSIONAL BUCKLING

In the following, an approximate calculation of flexural torsional buckling based on the energy method is presented. Subjects are simply supported beams and beam-columns with doubly symmetric cross-sections and continuous restraints. By using sine series for the shape of v and ϑ, matrix equations are derived, which can be easily solved by calculators,

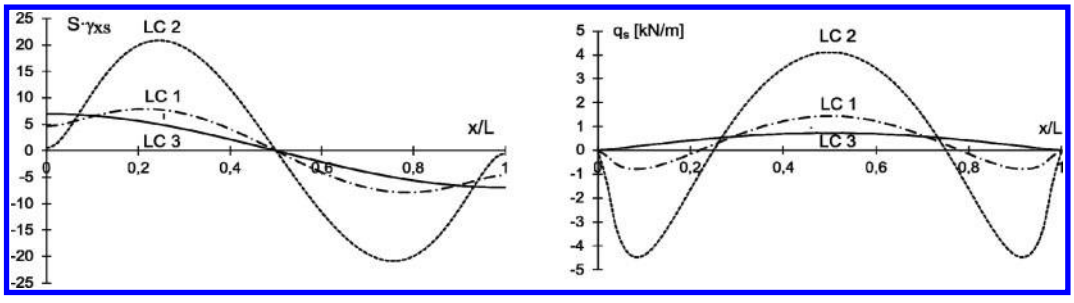


Figure 6. Distribution of shear and stabilization forces for the load cases 1 to 3 by Fig. 5.

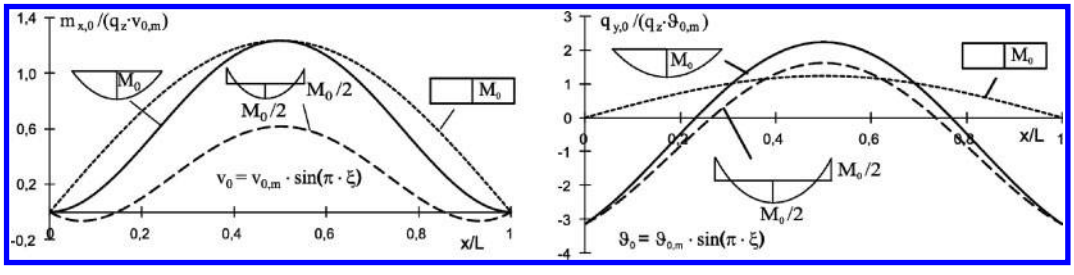


Figure 7. Equivalent torsional loads and horizontal loads for different assumptions of imperfections and moment distributions.

spreadsheets or computational software programs. The elasticity matrix considers different continuous restraining effects, whereas the stability matrix considers the normal forces, the bending moments M_y and the uniformly distributed cross load q_z. Individual parameters may set to zero to adapt to specific cases.

Five sine series terms for v and ϑ are considered in the given matrices (Fig. 8). In many cases, two sine series terms for each deformation leads to sufficiently accurate results. The user may adapt the matrix equation to a certain case and desired accuracy by eliminating columns and rows.

The Equations 8a to 8d describe the first variation of the strain energy and the potential energy (virtual work for the description of equilibrium). Inserting the sine series (Eq. 9), the moment distribution M_y (Eq. 10) and integrating over the length leads to the stiffness and stability matrices as well as to the load vector P_1 (s. Fig. 8). The indices of v and ϑ represent the number of sine half-waves over the length of the member.

$$\delta\Pi = \delta\Pi_e = \delta\Pi_g = \delta\Pi_p \tag{8a}$$

$$\begin{aligned}\delta\Pi_e = \int_L [&EI_z \cdot v'' \cdot \delta v'' + EI_\omega \cdot \vartheta'' \cdot \delta\vartheta'' + GI_T \cdot \vartheta' \cdot \delta\vartheta' \\ &+ B \cdot (v'' - z_B \cdot \vartheta'') \cdot (\delta v'' - z_B \cdot \delta\vartheta'') \\ &+ S \cdot (v' - z_S \cdot \vartheta') \cdot (\delta v' - z_S \cdot \delta\vartheta') \\ &+ c_y \cdot (v - z_C \cdot \vartheta) \cdot (\delta v - z_C \cdot \delta\vartheta) \\ &+ c_\vartheta \cdot \vartheta \cdot \delta\vartheta] \cdot dx\end{aligned} \tag{8b}$$

$$\begin{aligned}\delta\Pi_g = \int_L [&N \cdot (v' \cdot \delta v' + i_p^2 \cdot \vartheta' \cdot \delta\vartheta') \\ &+ M_y \cdot (v'' \cdot \delta\vartheta + \vartheta \cdot \delta v'') \\ &+ q_z \cdot z_q \cdot \vartheta \cdot \delta\vartheta] \cdot dx\end{aligned} \tag{8c}$$

$$\delta\Pi_p = -\int_L [q_y \cdot \delta v + m_x \cdot \delta\vartheta] \cdot dx \tag{8d}$$

$$v = \sum_i v_i \cdot \sin\left(\frac{i \cdot \pi \cdot x}{L}\right) \tag{9a}$$

$$\vartheta = \sum_j \vartheta_j \cdot \sin\left(\frac{j \cdot \pi \cdot x}{L}\right) \tag{9b}$$

$$\mathbf{M}_y(x) = M_i \cdot (1 - \xi) + M_k \cdot \xi + 4 \cdot M_0 \cdot (\xi - \xi^2) \tag{10}$$

The second order analysis follows by Equation 11,

$$(\mathbf{K}_e + \mathbf{K}_g) \cdot \mathbf{V} = \mathbf{P} = \sum \mathbf{P}_i \tag{11}$$

in which

$$\begin{aligned}&\mathbf{V}^T = [\mathbf{v}^T, \vartheta^T] = \\ &[v_1, v_2, v_3, v_4, v_5, \vartheta_1, \vartheta_2, \vartheta_3, \vartheta_4, \vartheta_5].\end{aligned} \tag{12}$$

Initial imperfections, which can be described by sine functions, can be taken into account by additional load vectors $\boldsymbol{P}_V$ (see $\boldsymbol{P}_2$ and $\boldsymbol{P}_3$ in Fig. 8).

$$\mathbf{P}_V = -\mathbf{K}_g \cdot \mathbf{V}_0 \tag{13}$$

in which

$$\begin{aligned}&\mathbf{V}_0^T = [\mathbf{v}_0^T, \vartheta_0^T] = \\ &[v_{1,0}, v_{2,0}, v_{3,0}, v_{4,0}, v_{5,0}, \vartheta_{1,0}, \vartheta_{2,0}, \vartheta_{3,0}, \vartheta_{4,0}, \vartheta_{5,0}].\end{aligned} \tag{14}$$

The calculation of the internal forces of the members and the restraining forces will implemented by means of the solution vector $\boldsymbol{V}$ and the respective equations of elasticity. This is exemplified by Equations 15 to 17. It should be noted that the accuracy of the results decreases with the order of the derivative of the deformations.

$$M_z = EI_z \cdot v'' = -EI_z \cdot \sum_i v_i \cdot \left(\frac{i \cdot \pi}{L}\right)^2 \cdot \sin\left(\frac{i \cdot \pi \cdot x}{L}\right) \tag{15}$$

$$M_\omega = -EI_\omega \cdot \vartheta'' = EI_\omega \cdot \sum_j \vartheta_j \cdot \left(\frac{j \cdot \pi}{L}\right)^2 \cdot \sin\left(\frac{j \cdot \pi \cdot x}{L}\right) \tag{16}$$

$$\begin{aligned}S \cdot \gamma_{xy} = S \cdot \Bigg[&\sum_i v_i \cdot \frac{i \cdot \pi}{L} \cdot \cos\left(\frac{i \cdot \pi \cdot x}{L}\right) - \\ &z_S \cdot \sum_j \vartheta_j \cdot \frac{j \cdot \pi}{L} \cdot \cos\left(\frac{j \cdot \pi \cdot x}{L}\right)\Bigg]\end{aligned} \tag{17}$$

For bifurcation buckling, the eigenvalues and eigenvectors can be determined by solving Equation 18.

$$(\mathbf{K}_e + \alpha_{cr} \cdot \mathbf{K}_g) \cdot \mathbf{V}_{cr} = 0 \tag{18}$$

α_{cr} is the lowest positive increasing factor when reaching the buckling load. Inserting $\boldsymbol{V}_{cr}$ into Equation 9 leads to the buckling shape v_{cr}, ϑ_{cr}.

4 EXAMPLE

The assessment and comparison of the approximate solution with a FEM calculation is done using the example of the beam in Figure 5 for the load cases 1 and 2. Because of the expected symmetrical shape of v and ϑ, only series elements with odd-numbered sine halve-waves are considered. Their numbers are varied. In the finite element calculation, the beam was divided into 50 elements. Third-order Hermite polynomials are used as basis functions for v and ϑ (Stroetmann 1999, 2011). The consideration of different load cases with various sets of shape functions allows deducing the necessary effort to get acceptable results. The results are listed in Table 1. Figure 9 shows the shear field force $S \cdot \gamma_{xs}$ as a function of the beam length. As

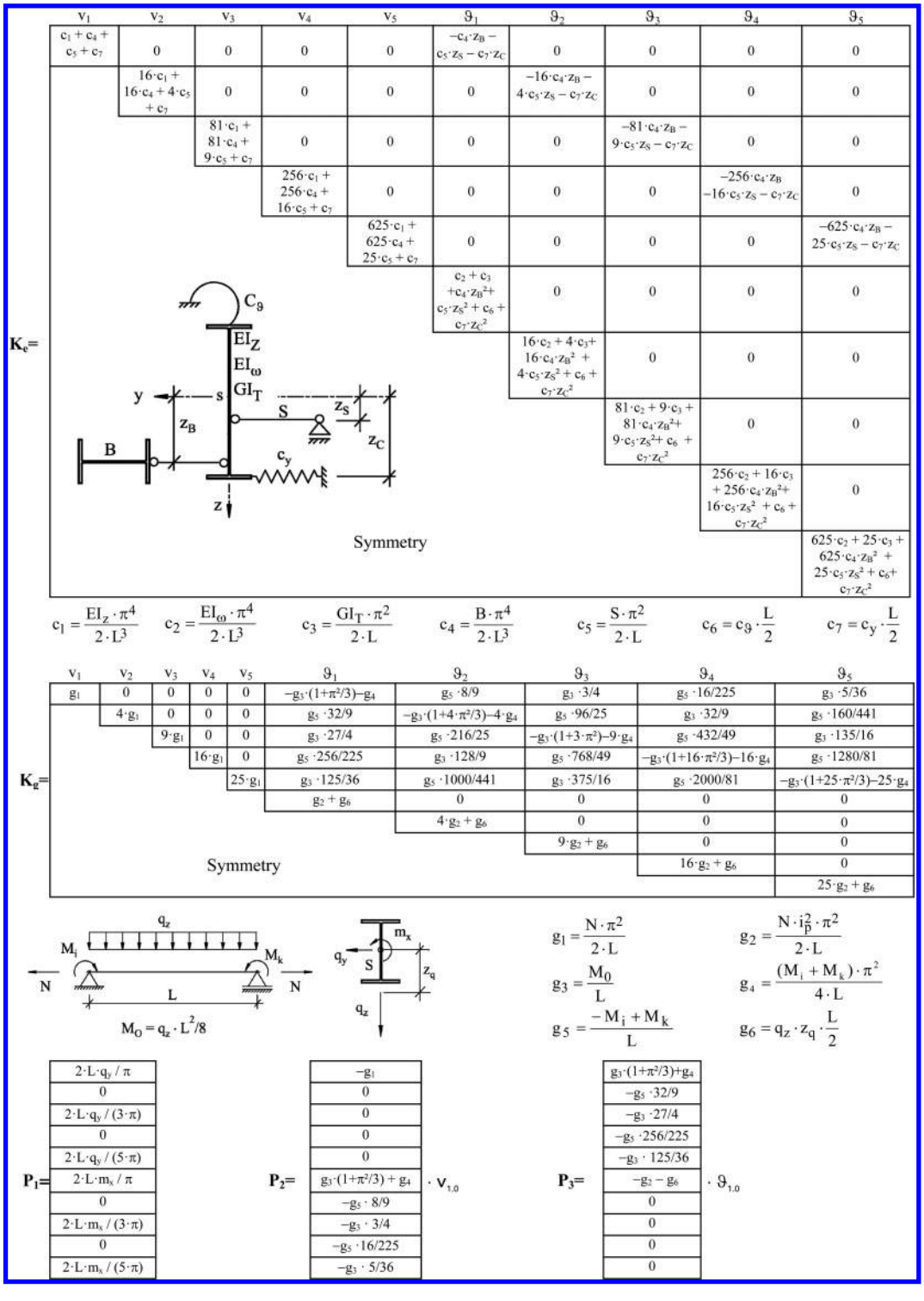


Figure 8. Stiffness matrices and load vectors for the approximate solution.

Table 1. Comparison of several results for different shape functions (system, loading, imperfection see Fig. 5).

load-case, s. Fig. 5	degree of freedom i, j /FEM	buckling load factor α_{cr} [–]	dif. [%]	deflections at midspan v [m]	dif. [%]	ϑ [–]	dif. [%]	shear diaphragm and stabilizing forces S max$\lvert\gamma_{xy}\rvert$ [kN]	dif. [%]	max q_s [kN/m]	dif. [%]
	1	4,96	18,9	−0,0174	3,0	0,0710	−1,9	7,83	−0,9	0,82	−42,7
1	1,3	4,24	1,7	−0,0167	−1,2	0,0721	−0,4	7,50	−5,1	1,64	14,7
	1,3,5	4,19	0,5	−0,0169	0,0	0,0724	0,0	7,99	1,1	1,34	−6,3
	FEM	**4,17**		**−0,0169**		**0,0724**		**7,90**		**1,43**	
	1	2,43	69,9	−0,0298	−25,9	0,115	−32,0	11,0	−47,4	1,15	−72,0
2	1,3	1,53	7,0	−0,0365	−9,2	0,156	−7,7	19,0	−9,1	4,89	19,3
	1,3,5	1,44	0,7	−0,0399	−0,7	0,167	−1,2	21,5	2,9	3,64	−11,2
	FEM	**1,43**		**−0,0402**		**0,169**		**20,9**		**4,10**	

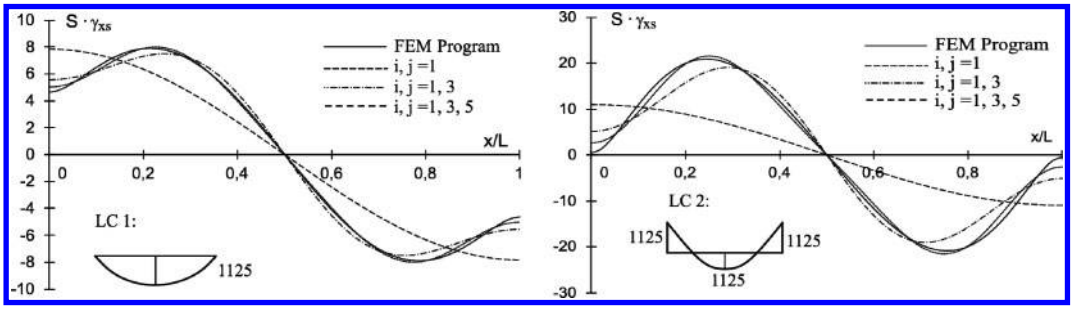


Figure 9. Comparison between the approximate solution and the FEM calculation concerning the distribution of shear diaphragm forces for the load cases 1 and 2 in Fig. 5.

expected, increasing the number of sinusoidal shape functions leads to closer approximations of the FEM results. Especially for moment distributions with hogging and sagging moments, it is obvious that a setup function with only one sine half-wave leads to inaccurate results and an overestimation of the buckling factor α_{cr}.

5 CONCLUSIONS

The presented paper describes the structural behavior of continuously restrained beams and beam-columns with the help of examples. It is shown that with typical simplifying assumptions unsafe results may be obtained for the buckling load and stabilizing forces. This is also true for the internal forces of the members. For typical cases, an approximation procedure is presented which allows to compute the buckling loads and the internal forces according to second order theory for flexural torsional buckling with moderate effort. Stabilizing forces may become significant when compared to the external loads. Besides imperfections relevant for practice, further effects such as restraints due to tangent rotations and temperature differences may increase the internal forces of the members. Therefore, the assumptions for the imperfections must be sufficiently large as well as the restraining and bracing system designed safely.

REFERENCES

Friemann, H. & Stroetmann, R. 1998. Zum Nachweis ausgesteifter biegedrillknickgefährdeter Träger. *Der Stahlbau 67* Heft 12: 936–955.

Stroetmann, R. 2010. Lateral torsional buckling of space structures with I-Beams – Structural behavior and calculation. SDSS'Rio 2010 – *International Colloquium "Stability and duc-tility of steel structures"; Proceedings Volume 2*: 587–594. *Rio de Janeiro, Brazil, September 8th–10th, 2010.*

Stroetmann, R. 1999. Zur Stabilitätsberechnung räumlicher Tragsysteme mit I-Profilen nach der Methode der finiten Elemente; *Veröffentlichung des Instituts für Stahlbau und Werkstoffmechanik der Technischen Universität Darmstadt*, Heft 61.

Research and Applications in Structural Engineering, Mechanics and Computation – Zingoni (Ed.)
© 2013 Taylor & Francis Group, London, ISBN 978-1-138-00061-2

Lateral-distortional buckling formulae for hollow tubular flange plate girders with slender unstiffened webs

M.F. Hassanein
Department of Structural Engineering, Faculty of Engineering, Tanta University, Tanta, Egypt

N. Silvestre
Department of Civil Engineering, ICIST/IST, TU Lisbon, Lisboa, Portugal

ABSTRACT: In this paper, the Lateral-Distortional Buckling (LDB) of Hollow Tubular Flange Plate Girders (HTFPGs) with slender unstiffened webs is investigated. Firstly, shell finite strip analyses are performed to have a first glance on the elastic buckling behaviour of simply supported girders under uniform bending. The numerical results clearly show the girder length range in which LDB is relevant. After these analyses, analytical models to calculate the critical LDB moment are proposed and validated by comparison with numerical values. The formulae for lateral-distortional buckling of HTFPGs are shown to be accurate and they provide the means to obtain M_{cr} values analytically without resorting to numerical tools.

1 INTRODUCTION

Members having thin-walled cross-sections are usually very slender, thus being highly susceptible to local, distortional and global buckling. One of the buckling modes that involve web distortion in I-sections is known as lateral-distortional buckling (LDB) mode. This mode is due to the simultaneous occurrence of (i) high lateral displacement and rotation of the compressed flange, (ii) low lateral displacement of the tensioned flange and (iii) distortion (transverse bending) of the web. The distortion of the web becomes even more evident if the I-section is attached to stiffer structural components such as concrete slabs in composite girders. In this case, it is designated as restrained-distortional buckling (RDB). Both LDB and RDB have been studied during the last twenty years, due to the work of several researchers. To study the RDB of I-sections, Bradford (1997) developed a model with three degrees of freedom: the twisting rotations of the restrained and unrestrained flanges and the lateral displacement of the unrestrained flange. In order to improve the twisting strength of beams with open sections and decrease their sensitivity to lateral-torsional buckling (LTB), the flat single-plated flanges have been replaced by hollow flanges. Thus, the hollow flange (HF) sections are torsionally very stiff but remain sensitive to LDB because the minor axis second moment of area of their hollow flanges slightly increases. Nowadays, the hollow tubular flange plate girder (HTFPG) with slender web shown in Figure 1 is studied. To the authors' best knowledge, the LDB of HTFPGs under bending has never been studied nor addressed in design standards. The main goal of this paper is to investigate the LDB behaviour of hollow tubular flange plate girders (HTFPGs) with slender unstiffened webs. A glance on the elastic buckling behaviour of HTFPGs with unstiffened webs is made by using shell finite strip (FS) analyses. After that, analytical models to predict the critical LDB moment are proposed and validated by comparison with numerical values.

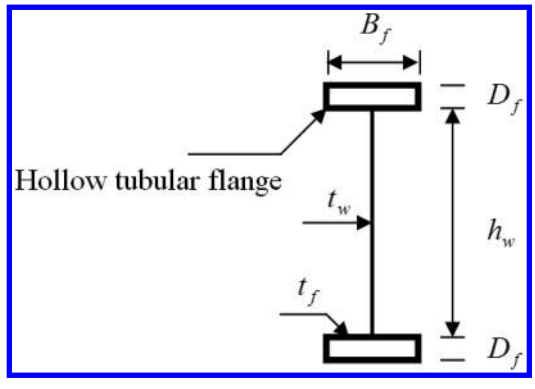


Figure 1. HTFPG geometry and dimensions.

In order to achieve these objectives, we (i) use a finite strip model in section 2, (ii) develop a simplified model with 4 degrees-of-freedom (d.o.f.) in section 3 and (iii) propose an analytical model in section 4. The HTFPG is composed of two rectangular compact flanges and a slender web as shown in Figure 1. The outside dimensions of HTFPG are also presented in Figure 1 and the corresponding mid-line dimensions of the flange are $d_f = D_f - t_f$ and $b_f = B_f - t_f$. In order to avoid the influence of several factors, we consider the simplest case regarding the load application and the support conditions: a simply supported HTFPG under uniform bending.

Table 1. Dimensions [mm] of HTFPGs used in the FSA.

Cross-section	B_f	D_f	t_f	h_w	t_w
S1	508	101.6	12.7	1500.0	10.0
S2		203.2			
S3		304.8			
S4		101.6			6.0
S5		203.2			
S6		304.8			

2 FINITE STRIP ANALYSES

In this study, we use the CUFSM software (Schafer 2010) which is based on the finite strip method (FSM). The key parameters that influence the buckling response of the HTFPGs are the following: (i) flange width-to-depth ratio (B_f/D_f), (ii) web slenderness (h_w/t_w) and (iii) span length (L). Three different flange cross-sections for the HTFPGs are used in the current study as listed in Table 1. They have the same width (B_f) and thickness (t_f) but with different depths (D_f). For the finite strip model, the web depth is fixed to $h_w = 1500$ mm. Two different web thicknesses of $t_w = 6.0$ and 10.0 mm are used, ensuring that the webs are slender. In elastic buckling analyses, the steel is considered an elastic material fully characterised by the values of Young's modulus ($E = 200 \times 10^3$ N/mm^2) and Poisson's ratio ($\nu = 0.3$).

Concerning the FS model, the cross-section is discretized with 27 nodes (10 in each flange and 9 in the web – note that there are 2 web-flange connecting nodes), 28 strips (10 in each flange and 8 along the web height), and 108 d.o.f. ($4 \times$ n, where n is the number of nodes). Despite being stiffer than the web, the flanges are also discretised with a fine mesh in order to capture the effect of local buckling. Furthermore, a stress diagram associated to major axis bending is applied to the beam end sections to produce uniform bending along its length L. In order to evaluate the influence of different buckling modes (local, lateral-distortional and lateral-torsional) on the buckling behaviour of HTFPGs under bending, it is necessary to consider a set of buckling half-wavelengths. In this study we consider a minimum length of $L_{min} = 100$ mm, a maximum length of $L_{max} = 100000$ mm, and 100 length values equally spaced in the L-logarithmic scale. The results of this study are shown in the form of curves displaying the variation of critical moment M_{cr} with L, often designated as "signature curves".

Figure 2 shows the curves $M_{cr}(L)$ obtained for the six cross-sections considered in Table 1. The following comments are due:

(i) Each curve $M_{cr}(L)$ displays a local minimum in the short half-wavelength range and a descendent branch in the moderate to long half-wavelength range. The transition between these two ranges occurs between L = 4000 and 5000 mm, depending on the cross-section geometry.

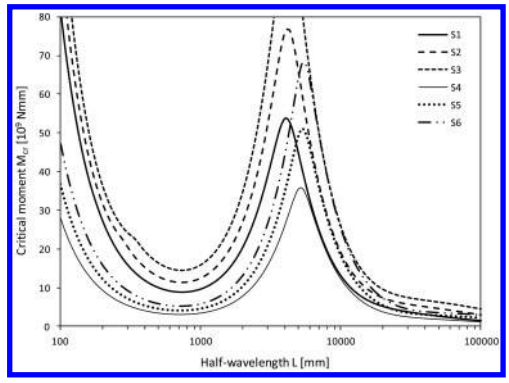


Figure 2. Variation of M_{cr} with L (single-wave FSA).

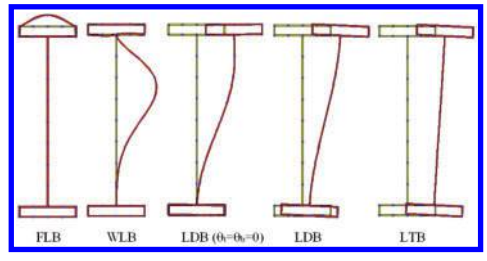


Figure 3. Buckling modes of HTFPG under bending.

(ii) In the short half-wavelength range, the descending and ascending branches of $M_{cr}(L)$ concern the local buckling (LB) mode of HTFPG. The descending branch of the S1, S2 and S3 beams is related to the local buckling of the upper plate of the top flange (FLB mode shown in Figure 3). The local minimum zone and the ascending branch of the S1, S2 and S3 beams are related to local buckling of the upper zone of the web (WLB mode shown in Figure 3). In the case of beams S4, S5 and S6, the descending and ascending branches of $M_{cr}(L)$, as well as the local minimum, concern the web local buckling (WLB). This is due to the decrease of web thickness t_w from 10 mm (S1, S2, S3) to 6 mm (S4, S5, S6), which does not influence the M_{cr} value for FLB but lowers it in the case of WLB.

(iii) Local minima of the $M_{cr}(L)$ curves occur for the same WLB half-wavelength ($L_{cr} = 705$ mm), regardless of the cross-section geometry. It means that both t_w and D_f values have no impact on the WLB half-wavelength L_{cr}.

(iv) The minimum values of the WLB moment M_{cr} (in kNm) are 8780 (S1), 11380 (S2), 14450 (S3), 3130 (S4), 4100 (S5) and 5260 (S6). Due to the decrease of t_w, the beams S4, S5 and S6 have lower WLB moment M_{cr} than the beams S1, S2 and S3. Due to the increase of flange depth D_f, the WLB moment M_{cr} increases from S1 to S3 and from S4 to S6. This increase (in absolute value) is more evident for beams S1 → S2 → S3 than for beams S4 → S5 → S6. However, and regarding the relative values, the percentage increase for

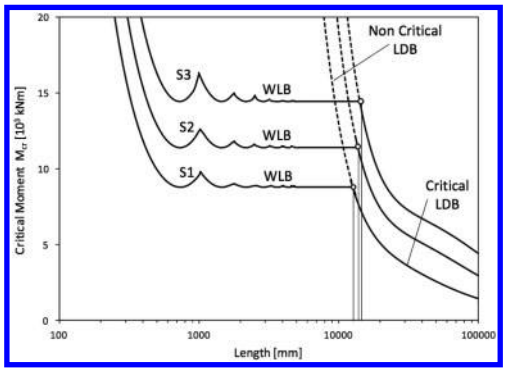


Figure 4. Variation of M_{cr} with L (multi-wave FSA).

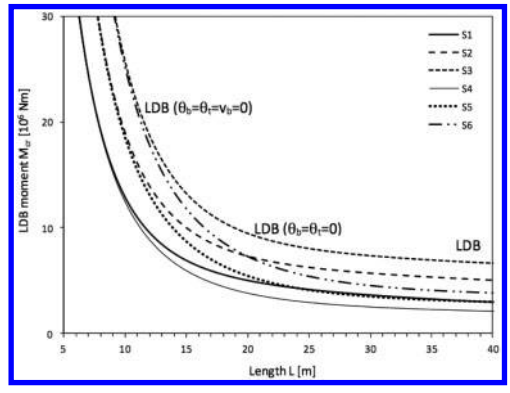


Figure 5. Variation of M_{cr} with L for LDB.

beams S1 → S2 → S3 is similar to that of beams S4 → S5 → S6.

(v) In the descendent branch of the moderate to long half-wavelength range, LDB and lateral-torsional buckling (LTB) prevail – see Figure 3. The top zone of the descendent branches corresponds to LDB modes without flange twisting ($\theta_t = \theta_b = 0$) and null displacement of the bottom flange ($v_t \neq 0$, $v_b = 0$). The middle zone of the descendent branches corresponds to LDB modes with no flange twisting ($\theta_t = \theta_b = 0$) but with movement of both flanges ($v_t \neq 0$, $v_b \neq 0$). The bottom zone of the descendent branches corresponds to LDB modes with both flange twisting ($\theta_t \neq 0$, $\theta_b \neq 0$) and lateral displacement ($v_t \neq 0$, $v_b \neq 0$). For very long half-wavelength, LTB occurs.

(vi) The considerations made before are valid for buckling modes with single half-wave. However, LB takes place for multi-wave mode. Figure 4 shows the variation of the critical buckling moment M_{cr} with the length of the HTFPG with sections S1, S2 and S3. For the beam S1, LB takes place from 1 to 19 waves and, for $L_t = 13100$ mm, changes to LDB. Qualitatively similar trend is shown by beams S2 and S3, but for transition lengths $L_t = 13900$ mm and $L_t = 14200$ mm, respectively.

(vii) The fact that LDB mode is critical for $L > L_t$ and becomes non-critical for $L < L_t$ (see the dashed parts of the curve in Figure 4), where LB mode is critical, does not mean that LDB should only be considered in design of HTFPGs for $L > L_t$. Remember that critical LB occurring for $L < L_t$ often exhibits very high post-buckling strength reserve and, therefore, the HTFPG collapse may by triggered by the non-critical LDB mode.

Figure 5 shows a portion of the curves presented in Figure 3, but only for the moderate to long HTFPGs that buckle in LDB. Concerning the influence of the cross-section dimensions on LDB of HTFPG, the following comments are due:

(i) In the steep descending branch ($L < 15$ m), characterised by LDB mode without flange twisting ($\theta_t = \theta_b = 0$), there is not too much influence of the M_{cr} value on the web thickness t_w. In fact, we see that there is almost perfect coincidence between curves S1 and S4, S2 and S5, S3 and S6. Thus, we can conclude that the M_{cr} value associated with LDB ($\theta_t = \theta_b = 0$) strongly depends on the HTFPG length L and flange depth D_f but scarcely depends on the web thickness t_w. Probably, the most influential parameter in LDB ($\theta_t = \theta_b = 0$) is the flange second moment of area about the cross-section weak axis I_{fz} and the correspondent lateral stiffness (EI_{fz}/L^2) which depends on L.

(ii) In the moderate descending branch ($15 < L < 25$ m), characterised by LDB mode without flange twisting ($\theta_t = \theta_b = 0$) but with lateral displacements ($v_t \neq 0$, $v_b \neq 0$), the web thickness influences the M_{cr} value. The web thickness affects the relative displacement between top and bottom flanges ($v_t - v_b$).

(iii) In the smooth descending branch ($L > 25$ m), characterised by LDB mode with flange twisting ($\theta_t \neq 0$, $\theta_b \neq 0$) and lateral displacements ($v_t \neq 0$, $v_b \neq 0$), we observe a pronounced difference between HTFPGs with deep flanges and shallow flanges (the difference between curves S3 and S6 is larger than that between curves S1 and S4). Thus, we can conclude that the M_{cr} value associated with LDB strongly depends on the HTFPG flange depth D_f and fairly depends on the length L and web thickness t_w. Most likely, the most influential parameter in LDB is the flange torsional constant J_f and associated twisting stiffness (GJ_f), which does not depend on L.

3 MODEL FOR LDB WITH 4 D.O.F.

From the previous FS study, we conclude that the LDB mode of HTFPGs may exhibit (i) flange rigid body movement, including twisting rotation and lateral displacement (higher for the compressed flange) and (ii) transverse bending (distortion) of the web. Thus, we present herein a simple numerical model with 4

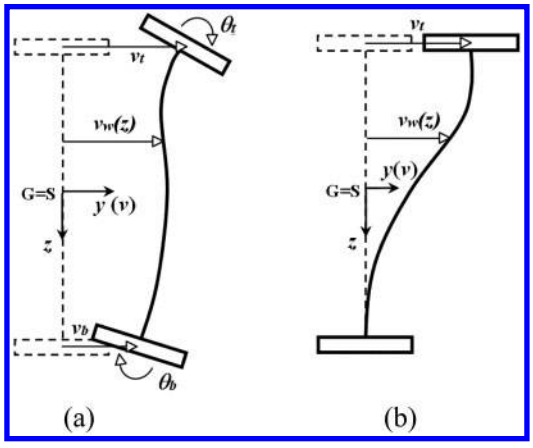


Figure 6. Models for LDB: (a) 4 d.o.f., (b) 1 d.o.f. (analytical).

degrees of freedom (d.o.f): the lateral displacements (v_t, v_b) and twisting rotations (θ_t, θ_b) of the top and bottom flanges, as seen in Figure 6(a).

The formulation presented herein resembles that proposed by Chen and Ye (2010) for LDB of I-beams. In comparison with the formulation of Chen and Ye (2010) for LDB of I-beams, a set of changes have been made in the present work to account for the hollow flanges: (i) the warping stiffness I_{fw} of the hollow flanges is included, (ii) the applied stress σ gradient along the flange depth D_f is accurately taken into account and (iii) the geometric stiffness is enlarged by the parameter (y^2+z^2) to consider the correct distance between any point of the hollow flange and its centroid. The expressions for the strain energy of the top flange, bottom flange and web are

$$U_t = \frac{EI_{fz}}{2}\int_0^L v_{t,xx}^2 dx + \frac{GJ_f}{2}\int_0^L \theta_{t,x}^2 dx + \frac{EI_{fw}}{2}\int_0^L \theta_{t,xx}^2 dx \quad (1)$$

$$U_b = \frac{EI_{fz}}{2}\int_0^L v_{b,xx}^2 dx + \frac{GJ_f}{2}\int_0^L \theta_{b,x}^2 dx + \frac{EI_{fw}}{2}\int_0^L \theta_{b,xx}^2 dx \quad (2)$$

$$U_w = \frac{Et_w^3}{24(1-\nu^2)}\int_0^L\int_{-h_w/2}^{h_w/2} v_{w,zz}^2 dz\,dx \quad (3)$$

In these equations, (i) x is the axial coordinate and (i) I_{fz}, J_f and I_{fw} are the flange minor axis second moment of area, flange torsional constant and flange warping constant, respectively. Note also that $v_t, \theta_t, v_b, \theta_b$ depend only on x while v_w depends on both x and z (coordinate along the web height). The potentials of the applied moments M, written in terms of internal stresses $\sigma(z)$, are given by

$$\Pi_t = -\frac{1}{2}\int_0^L\int_{A_t}\sigma[v_{t,x}^2 + (y^2+z^2)\theta_{t,x}^2]dA\,dx \quad (4)$$

$$\Pi_b = -\frac{1}{2}\int_0^L\int_{A_b}\sigma[v_{b,x}^2 + (y^2+z^2)\theta_{b,x}^2]dA\,dx \quad (5)$$

$$\Pi_w = -\frac{t_w}{2}\int_0^L\int_{-h_w/2}^{-h_w/2}\sigma v_{w,x}^2 dz\,dx \quad (6)$$

In these equations, (i) A_t and A_b are the area occupied by the top and bottom flanges, respectively ($dA = dzdy$) and (ii) the normal stress, considered uniform along the beam length (independent of x), is given by

$$\sigma = -\frac{M}{I_y}z \quad (7)$$

with (i) I_y being the major axis second moment of area for the whole cross-section and (ii) the vertical coordinate z varying in the ranges $-d_f - h_w/2 \le z \le -h_w/2$ (top flange), $-h_w/2 \le z \le h_w/2$ (web), $h_w/2 \le z \le h_w/2 + d_f$ (bottom flange). On the basis of the Ritz method, the following exact solutions are adopted for the top and bottom flange displacements and twisting rotations,

$$v_t(x) = A_1 \sin\left(\frac{\pi x}{L}\right) \qquad \theta_t(x) = A_2 \sin\left(\frac{\pi x}{L}\right) \quad (8)$$

$$v_b(x) = A_3 \sin\left(\frac{\pi x}{L}\right) \qquad \theta_b(x) = A_4 \sin\left(\frac{\pi x}{L}\right) \quad (9)$$

The web lateral displacement is given by

$$v_w(x,z) = v_t(x)\phi_1(z) + \theta_t(x)\phi_2(z) + v_b(x)\phi_3(z) + \theta_b(x)\phi_4(z) \quad (10)$$

with the functions $\phi_i(z)$ $(i = 1,2,3,4)$ being defined by

$$\phi_1(\eta) = 1 - 3\eta^2 + 2\eta^3$$
$$\phi_2(\eta) = (h_w + h_f)(\eta - 2\eta^2 + \eta^3) \quad (11)$$
$$\phi_3(\eta) = 3\eta^2 - 2\eta^3 \qquad \phi_4(\eta) = (h_w + h_f)(-\eta^2 + \eta^3)$$

where the non dimensional variable η reads

$$\eta = \frac{1}{2} + \frac{z}{h_w + h_f} \quad (12)$$

Note that the function $v_w(z,x)$ satisfies the compatibility between the web and the flange displacements and rotation. It is assumed that $v_w(z = -d_f/2 - h_w/2, x) = v_t(x)$, $v_{w,x}(z = -d_f/2 - h_w/2, x) = \theta_t(x)$, $v_w(z = d_f/2 + h_w/2, x) = v_b(x)$, $v_{w,x}(z = d_f/2 + h_w/2, x) = \theta_b(x)$. Introducing equations (8)–(9) and (11)–(12) in (10), we obtain the web lateral deflection v_w depending on the coordinates x and z, as well as the flange degrees of freedom (A_1, A_2, A_3, A_4). Introducing this expression and those of equations (7)–(9) into the strain energy (equations (1)–(3)) and potential of applied moments (equations (4)–(6)) and integrating over the web height, flange area and beam length, we obtain the total potential energy

$$V = U_t + U_b + U_w + \Pi_t + \Pi_b + \Pi_w \equiv V(A_1, A_2, A_3, A_4) \quad (13)$$

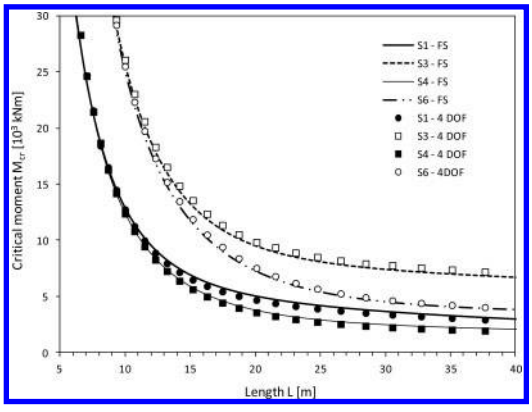


Figure 7. FS vs. 4 d.o.f. model results for LDB.

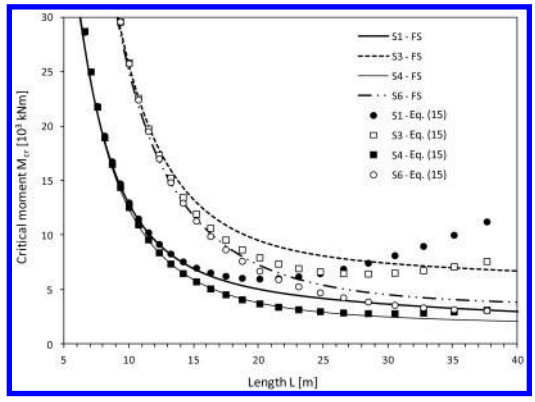


Figure 8. FS vs. Eq. (15) (1 d.o.f. model) results for LDB.

depending quadratically on the 4 parameters (A_1, A_2, A_3, A_4) and linearly on the applied moment M. Equating to zero the first derivatives of V with respect to A_i, we obtain the system of 4 equilibrium equations given by,

$$\frac{d^2V}{dA_i^2} = 0 \Leftrightarrow (K_{ij} - MG_{ij})A_j = 0 \quad i,j = 1\text{-}4 \qquad (14)$$

where K_{ij} and G_{ij} are the components of the 4×4 linear and geometric stiffness matrices [K] and [G], respectively, and A_j is the component of the 4×1 displacement vector {A}. The system in equation (14) corresponds to a fourth order eigenvalue problem and its solutions are the buckling moments M_b (eingenvalues) and buckling modes $\{A_j\}$ (eigenvectors). The 4 d.o.f. model was implemented in a symbolic computation code Maple (2009). Figure 7 shows the results obtained from the model (circles and squares) as well as the curves obtained from FS analyses – the results for S2 and S5 are qualitatively similar and are not presented in Figure 7 for the sake of simplicity and clearness of presentation. Generally, the results of the 4 d.o.f. model follow the trend of all FS curves, regardless of the HTFPG length L, web thickness t_w and flange depth D_f. This means that the model is capable of simulate the behaviour of HTFPG both for LDB ($\theta = 0$) and LDB ($\theta \neq 0$). For the HTFPGs with shallow flanges (S1 and S4), the M_{cr} values determined from the 4 d.o.f. model are slightly lower than those of FS analyses (maximum difference of 7%). For HTFPGs with deeper flanges (S3 and S6), the M_{cr} values obtained from the 4 d.o.f. model are slightly higher than the FS ones (maximum difference of 5%). In conclusion, the 4 d.o.f. model and FS results show a good agreement.

4 ANALYTICAL MODELS FOR LDB

From the previous results, we may conclude that the LDB mode for HTFPGs with moderate lengths is characterized by null flange twisting rotation ($\theta_t = 0$, $\theta_b = 0$) – see Figure 6. Thus, for HTFPGs with moderate lengths, it is possible to reduce the 4 degrees of freedom to only two (v_t and v_b) without compromising the accuracy of the solution. With this model, we can apply it to two different situations:

- LDB ($\theta_b = \theta_t = v_b = 0$): In this case, the bottom flange is fixed ($v_b = 0$) and only the top flange is allowed to displace laterally ($v_t \neq 0$). The critical moment is given by

$$M_{cr} = EI_y \cdot \frac{I_{fz}\frac{\pi^2}{L^2} + \frac{t_w^3 h_w^3}{(1-\nu^2)h^6}\frac{L^2}{\pi^2}}{ht_f(b_f + d_f) + \frac{(5h^2 - h_w^2)h_w^3 t_w}{40h^3}} \qquad (15)$$

  where $h = h_w + d_f$ is the total distance between the centroids of both flanges.
- LDB ($\theta_b = \theta_t = 0$): In this case, both flanges are free to displace laterally ($v_t \neq 0$ and $v_b \neq 0$). The critical moment is given by

$$M_{cr} = EI_y \cdot \frac{\sqrt{\frac{\pi^4 I_{fz}^2}{L^4} + \frac{2I_{fz} t_w^3 h_w^3}{(1-\nu^2)h^6}}}{ht_f(b_f + d_f) + \frac{(5h^2 - h_w^2)h_w^3 t_w}{40h^3}} \qquad (16)$$

Figure 8 displays the results determined from the Eq. (15) (1 d.o.f. model) and FS analyses. It is seen that the M_{cr} values given by Eq. (15) are generally accurate for $L < 16$ m. Obviously, this evidence agrees with the fact that LDB ($\theta_b = \theta_t = v_b = 0$) occurs in this length range. For L > 16 m (moderate to long beams), there are two distinct features. For the beams with thinner webs (S4 and S6), the analytical results become less accurate but the black squares (beam S4) and white circles (beam S6) do not diverge too much from the thin solid (beam S4) and dash-point (beam S6) curves, respectively. However, in the case of the beams with thicker webs (S1 and S3), the results become less accurate as the black circles (beam S1) and white squares (beam S3) diverge too much from the thick solid (beam S1) and dashed (beam S3) curves, respectively. We

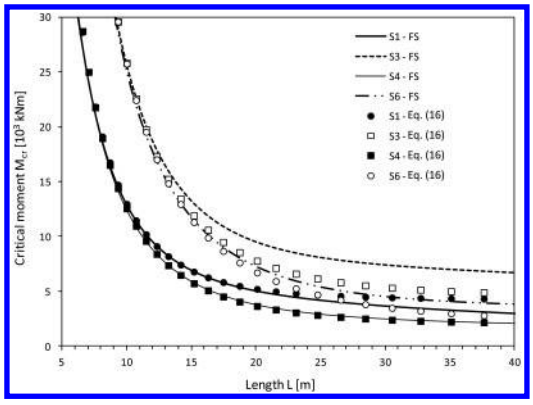


Figure 9. FS vs. Eq. (16) (2 d.o.f. model) results for LDB.

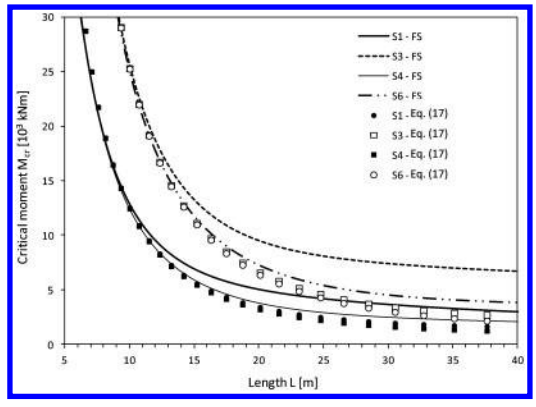


Figure 10. FS vs. Eq. (17) (Pi and Trahair 1997) results.

conclude that the analytical expression (Eq. 15) gives accurate results for beams with moderate lengths but it also gives inaccurate (non conservative) results for long beams.

Figure 9 displays the results determined from the Eq. (16) (2 d.o.f. model) as well as the curves obtained from FS analyses. It is seen that the M_{cr} values given by Eq. (16) are more accurate than those of Eq. (15). Regardless of the length, the results are very accurate for the beam S4, which has slender web and not too deep flanges. For the beam S1, which has thicker web and not too deep flanges, the results are accurate for L < 25 m (10% difference) but become overly non conservative for L > 25 m. For the beam S6, characterized by slender web and deep flanges, the results are accurate for L < 22 m (10% difference) and become fairly conservative for L > 22 m. For the beam S3, which has thicker web and deep flanges, the results are accurate for L < 16 m (10% difference) and become conservative for L > 16 m. From these comparisons, we conclude that the analytical expression (Eq. 16) gives accurate results for beams with moderate lengths and fairly good results for beams with moderate to long lengths. For beam with long to very long lengths, both flanges start to twist differently (the top flange twist further than the bottom one) and only the 4 d.o.f. model becomes the accurate one. However, an analytical formula becomes too complex and inappropriate for current practical design. For very long lengths, both twist rotations become identical and lateral-torsional buckling (LTB) takes place.

Moreover, Pi and Trahair (1997) proposed an analytical formula to determine the LDB moment of beams with hollow flanges, given by

$$M_{cr} = \sqrt{\frac{\pi^2 EI_z}{L^2}\left(\frac{2GJ_f \dfrac{Et_w^2 L^2}{(1-\nu^2)\pi^2 h_w}}{2GJ_f + \dfrac{Et_w^2 L^2}{(1-\nu^2)\pi^2 h_w}} + \frac{\pi^2 EI_w}{L^2}\right)} \qquad (17)$$

where (i) J_f is the flange torsional constant and (ii) I_z and I_w are the minor axis second moment of area and warping constant of the whole cross-section, respectively. They adapted the classical formula of LTB moment and replaced the standard torsional stiffness GJ by an effective torsional stiffness that depends not only on the flange torsional constant J_f but also on the web dimensions (h_w, t_w). Recently, Kurniawan and Mahendran (2009) used this formula to evaluate the LDB critical moment of cold-formed LiteSteel Beams. Figure 10 presents a comparison between the FS results and the M_{cr} values given by Eq. (17). It is seen that the analytical results are not sensitive to the web thickness, since the black circles and squares (beams S1 and S4) remain always quite close (the same applies for the beams S3 and S6). Due to this fact, we observe that Eq. (17) gives good predictions for moderate to long beams with thin webs (S4 and S6) but provide very inaccurate results for beams with thicker webs (S1 and S3).

REFERENCES

Bradford MA (1997). Lateral-distortional buckling of continuously restrained columns, Journal of Constructional Steel Research, 42(2), 121–139.

Chen W, Ye J (2010). Elastic lateral and restrained distortional buckling of doubly symmetric I-beams, International Journal of Structural Stability and Dynamics, 10(5), 983–1016.

Kurniawan CW, Mahendran M (2009). Elastic lateral buckling of simply supported LiteSteel beams subject to transverse loading, Thin-Walled Structures, 47(1), 109–119.

MAPLE (2009). MapleSoft, version 13, Canada, (http://www.maplesoft.com/).

Pi YL, Trahair NS (1997). Lateral-distortional buckling of hollow flange beams, International Journal of Structural Engineering (ASCE), 123(6), 695–702.

Schafer BW (2010). CUFSM - Elastic Buckling Analysis of Thin-walled Members, version 3.12, (http://www.ce.jhu.edu/bschafer/cufsm/).

Research and Applications in Structural Engineering, Mechanics and Computation – Zingoni (Ed.)
© 2013 Taylor & Francis Group, London, ISBN 978-1-138-00061-2

Modeling of force deformation characteristic of angle bracing members

M.A. Gizejowski & A.M. Barszcz
Warsaw University of Technology, Warsaw, Poland

ABSTRACT: Braced frames composed of angle diagonals are commonly used to reduce the frame drifts and to enhance the sway stability resistance. In practice, the diagonal bracing members are connected to the frame elements by direct welding or bolting through a gusset plate. Such brace systems are modeled to act as vertical trusses comprising of members that are carrying predominantly axial forces. It is justifiable therefore to use an equivalent truss element for modeling of the behavior of bracing members. This paper deals with analytical formulation of the force-deformation characteristic of a single angle brace subjected to one cycle compression. It constitutes a contribution to the development of a simple model describing the equilibrium path of imperfect compressed angles. The strut model developed herein takes into consideration the effect of brace end connections. Two different boundary conditions typical for engineering practice are dealt with, namely corresponding to braces with mono-eccentric connections and braces with bi-eccentric connections. The results of experimental program of testing the behavior of angle brace in portal subframe specimens are used for the calibration of developed analytical model of the brace behavior.

1 INTRODUCTION

Diagonals of truss bracings are traditionally designed for the pre-buckling compression or elastic tension. In case of X-type bracings, the compression diagonals are assumed to buckle and only the tension elements are considered to effectively resist sway. Brace members subjected to post-buckling compression are usually treated as ineffective and designed not to yield under tension. Such members are subjected to changing force conditions due to variable load components acting on the braced structure within the envelope prescribed by design load combinations.

Compression brace elements, after reaching their buckling strength, do not maintain the ultimate strength level, as in case of yielded tension elements. The strength drop in the post-buckling region depends upon the brace slenderness, grade of steel the member is made of and other factors among which the structural imperfections play an important role. Buckled members are subjected to straightening out under the force reversal as a result of change in variable components of load combinations. If the brace is subjected to yielding in the straightening out phase, their reloading path is somewhat different from that of unloading path and the member is not able to reach the load level corresponding to that at which the unloading has started. The behavior is a hysteretic type with its maximum force being dependent upon the amount of plastic deformations accumulated during the unloading phase.

For collapse behavior of braced frame structures and the evaluation of their strength at the ultimate limit state, the investigations of compression braces have been restricted to one cycle behavior and carried out in such a way that for different section geometry, slenderness and steel grades, a developed simple analytical model could efficiently describe the equilibrium path of imperfect member in both pre-limit and post-limit phases. Moreover, the developed models are usually able to reproduce the buckling curves from design codes in case of concentric end connections (Barszcz & Gizejowski 2007).

This paper constitutes a contribution to the development of a simple and yet accurate analytical model describing the equilibrium path of imperfect compressed angle braces. It is an extension of research work carried out by authors for members loaded in compression. Two different boundary conditions, typical for engineering practice, are dealt with, namely braces with welded fork type mono-eccentric connections (called hereafter as connections with in-plane eccentricity) and braces with bolted lap through-leg bi-eccentric connections (called hereafter as connections with out-of-plane eccentricity). Experimental program of testing the behavior of angle braces in portal subframe specimens was carried out at the Warsaw University of Technology (Barszcz 2010). Test results are used for the calibration of developed analytical model of the brace behavior.

2 ELASTIC BEHAVIOUR OF A COMPRESSED ANGLE BRACE

Let us considered a single unequal leg angle as a brace being eccentrically compressed. The eccentricity e results from the constructional details of member end connections. In a general case, the eccentricity e has to be resolved along the Cartesian principal axes

(u, v) the origin of which is at the section center of gravity C. The third principal axis is the member axis w. The principal eccentricity components are denoted $(e_u; e_v)$. There is also another useful set of axes (y, z) parallel/perpendicular to midlines of angle legs, with the same origin in the gravity center as for the principal axes (u, v). The axis x of this coordinate system coincides with the axis w of the principal coordinate system. The shear center S is placed away from the gravity center at distances u_S and v_S along the principal axes. In turn, the gravity center is located at the distances y_S and z_S from the midlines of angle legs. Considering the arbitrary point of applied axial load, being in equilibrium with the load effects of axial force N_E as well as bending moments M_{uE} and M_{vE}, the stability condition may be formulated in the well known way:

$$[S]\{\delta_b\} = \{0\} \tag{1}$$

where $[S]$ = stability matrix; $\{\delta_b\}$ = buckling shape coordinates vector.

In case of angle brace, the following stability matrix is obtained:

$$[S] = \begin{bmatrix} EI_v k_v^2 - N_E & 0 & (v_S - e_v)N_E \\ & I_u k_u^2 - N_E & -(u_S - e_u)N_E \\ \text{symm.} & & GI_T - i_S^2 N_E \end{bmatrix} \tag{2}$$

where $k_v^2 = [\pi/(\mu_v l)]^2$ and $k_u^2 = [\pi/(\mu_u l)]^2$; μ_u, μ_v = flexural buckling length factors; i_S = generalized polar radius of gyration of the eccentrically connected angle with respect to the shear center S:

$$i_S^2 = i_T^2\left(1 + \frac{e_u\beta_u + e_v\beta_v}{i_T^2}\right), \tag{3}$$

i_T = polar radius of gyration of centrically loaded angle with respect to the shear center S:

$$i_T^2 = i_u^2 + i_v^2 + u_S^2 + v_S^2, \tag{4}$$

β_u, β_v = cross-sectional properties associated with bowing effects in principal planes:

$$\beta_u = \frac{1}{I_u}\left(\int_A v^3 dA + \int_A u^2 v dA\right) - 2v_S, \tag{5}$$

$$\beta_v = \frac{1}{I_v}\left(\int_A u^3 dA + \int_A v^2 u dA\right) - 2u_S, \tag{6}$$

I_u, I_v = cross-sectional moments of inertia with respect to principal axes; I_T = uniform torsion constant; E, G = modules of elasticity and rigidity.

Equating the determinant of stability matrix to zero and its expanding gives the following algebraic equation of third degree:

$$\begin{aligned} &(N_{Fu} - N_E)(N_{Fv} - N_E)(N_T - N_E) + \\ &-(N_{Fu} - N_E)N_E^2\frac{(v_S - e_v)^2}{i_S^2} + \\ &-(N_{Fv} - N_E)N_E^2\frac{(u_S - e_u)^2}{i_S^2} = 0 \end{aligned} \tag{7}$$

where N_{Fu}, N_{Fv}, N_T = reference forces:

– N_{Fv} for flexural buckling about $v - v$ axis:

$$N_{Fv} = \frac{\pi^2 EI_v}{(\mu_v l)^2}, \tag{8}$$

– N_{Fu} for flexural buckling about $u - u$ axis:

$$N_{Fu} = \frac{\pi^2 EI_u}{(\mu_u l)^2}, \tag{9}$$

– N_T for torsional buckling about the member shear center axis:

$$N_T = \frac{GI_T}{i_S^2}. \tag{10}$$

In case of the axial force applied along the shear center axis ($e_u = u_S$ and $e_v = v_S$), the reference forces are the bifurcation ones and the critical force $N_E = N_{cr}$ is the lowest force from all the above mentioned forces:

$$N_{cr} = \min(N_{Fu}, N_{Fv}, N_T). \tag{11}$$

In case of axial force applied away from the shear center, the bifurcation forces of the above three buckling modes are coupled to produce the flexural-torsional critical forces $N_E = N_{FT,i}$ $(i = 1, 2, 3)$. Thus, the cubic Eqn. (7) must be solved for each set of reference forces N_{Fu}, N_{Fv}, N_T in order to calculate the critical force as the lowest flexural-torsional bifurcation force.

The above general approach for treating unequal leg angles is adopted hereafter for equal leg angles. Since the equal leg angle section is monosymmetric, Eqns. (1) through (10) hold for $v_S = 0$. There are two distinctive directions considered hereafter along which the axial force can be positioned. The first is along the midline of the angle leg (points S, A, B & D in Fig. 1). All the force eccentricities e associated with this direction are referred to the brace connected through one leg. Point A corresponds to the equal eccentricities about principal axes ($e_u = e_v$). Point B corresponds to the eccentricity component $e_v = 0$. Points S and D correspond to the edge points of angle legs. The other direction coincides with the principal axis u (points S, C & E in Fig. 1).

One can notice that a special case of the force application at the shear center S can be treated as a reference

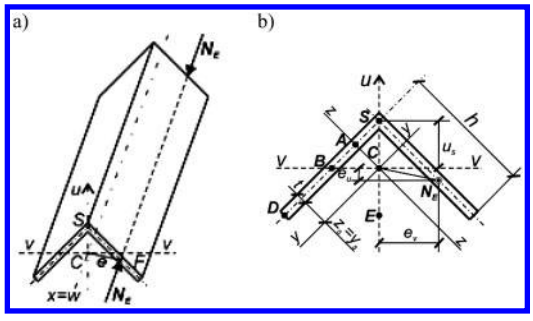


Figure 1. General notation for equal leg angle; a) member, b) cross section.

one for all the other cases of possible distinctive directions of force applications. It is clear that in this case the torsional bifurcation force does not govern the critical state. For all the angle lengths, regarding the relations between the effective length factors, the flexural mode of buckling about $v-v$ axis corresponds to the critical state when the following relationship holds:

$$I_u \mu_v^2 \geq I_v \mu_u^2 . \tag{12}$$

It might be assumed in practice that for all other eccentricities, except the range of short brace lengths, the torsional behavior might be neglected. Therefore only the member flexural buckling about $v-v$ axis could have been considered (Barszcz 2007 & 2012).

2.1 *Eccentricity out of the plane of section symmetry*

The ratio of critical force (normalized with reference to the flexural bifurcation force N_{Fv}) is evaluated numerically from Eqn. (7). In the following, three cases corresponding to force application at points A, B & D (see Fig. 1 for location of the considered points) are dealt with. It can be proven that for the force application at point S, the numerical solution of Eqn. (7) leads to the results obtained by Eqns. (8) through (10) and leading to Eqn. (11).

The numerical results of normalized critical forces are shown in Figures 2–4 with reference to force application points A, B & D, respectively.

From the presented results it is obvious that the effect of torsional behavior is in general needed to be considered for angle bracing members connected through one leg.

2.2 *Eccentricity in the plane of section symmetry*

In the stability matrix (2) and Eqn. (7) one should substitute in this case $v_S = e_v = 0$. Hence, the third term in Eqn. (7) vanishes and a quadratic algebraic equation of the following form is obtained:

$$\left(N_{Fu} - N_E\right)\left(N_T - N_E\right) + N_E^2 \frac{\left(u_S - e_u\right)^2}{i_S^2} = 0 \tag{13}$$

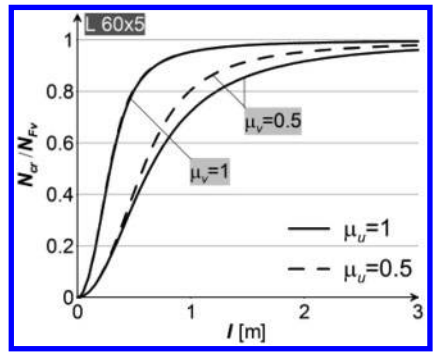


Figure 2. Normalized flexural-torsional buckling for the force application at A for different effective length factors.

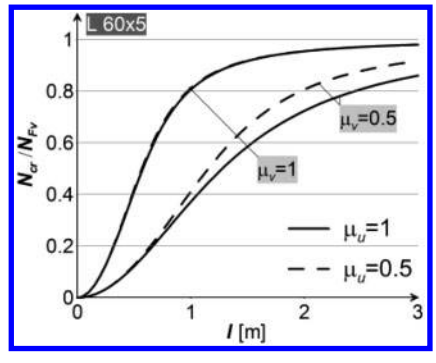


Figure 3. Normalized flexural-torsional buckling for the force application at B for different effective length factors.

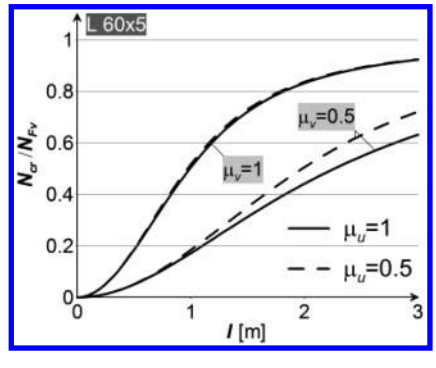


Figure 4. Normalized flexural-torsional buckling for the force application at D for different effective length factors.

As a result of canceling of the term $(N_{Fv} - N_E)$, the first in-plane flexural bifurcation force is obtained as $N_E = N_{Fv}$. The solution of Eqn. (13) leads to the remaining two flexural-torsional bifurcation forces $N_E = N_{FT,i}$ $(i = 1,2)$:

$$N_{FT,1/2} = \frac{\left(N_{Fu} + N_T\right) \pm \sqrt{\left(N_{Fu} + N_T\right)^2 - 4\kappa N_{Fu} N_T}}{2\kappa} \tag{14}$$

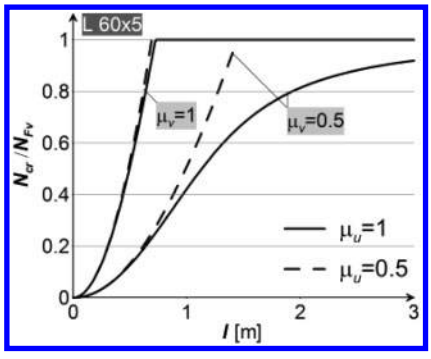


Figure 5. Normalized flexural-torsional buckling for the force application at C for different effective length factors.

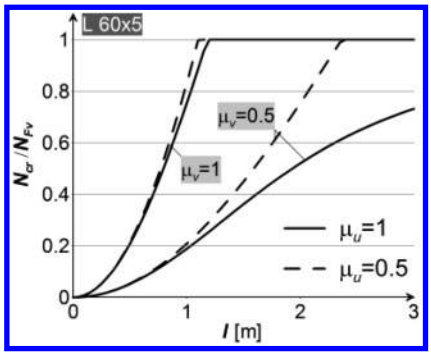


Figure 6. Normalized flexural-torsional buckling for the force application at E for different effective length factors.

where κ = dimensionless coefficient

$$\kappa = \frac{i_u^2 + i_v^2 + e_u \beta_u}{i_u^2 + i_v^2 + e_u \beta_u + u_S^2} \tag{15}$$

The critical force is therefore to be calculated as follows:

$$N_{cr} = \min\left(N_{Fv}, N_{FT,1}, N_{FT,2}\right) \tag{16}$$

Eqn. (7) is used hereafter for the similar study as it has been presented in the previous subsection. Substituting $e_v = 0$ to Eqn. (7), the resultant equation is solved for the critical force numerically for two cases corresponding to the force application at points C & E (see Fig. 1 for location of the considered points). The numerical results of normalized critical forces are shown in Figures 5 & 6 with reference to force application points C & E, respectively.

It is proven that the results obtained numerically are the same as calculated from Eqns. (13) – (14). From the presented results it is obvious that the effect of torsional behavior might be neglected for modeling of the angle brace fork-connected by welding at the member both ends.

3 PLASTIC RESISTANCE OF ANGLE SECTION

3.1 *Compression with one directional bending*

Plastic resistance of equal leg angle section for compression and bending in the plane of symmetry was given by Vayas et al. (2009) in the following form:

$$n^2 + m_v = 1 \tag{17}$$

where n = dimensionless axial force; m_v = dimensionless bending moment about $v - v$ axis:

$$n = \frac{N_E}{N_{pl}} = \frac{N_E}{A f_y}, m_v = \frac{M_{v,E}}{M_{v,pl} f_y} = \frac{M_{v,E}}{W_{v,pl} f_y}, \tag{18}$$

f_y = yield stress; A = cross section area and $W_{v,pl}$ = plastic section modulus

$$W_{v,pl} = \frac{Ah}{4\sqrt{2}}. \tag{19}$$

For bending in the other principal plane, the interaction formula can be approximated as:

$$n + m_u = 1 \tag{20}$$

where m_u = dimensionless bending moment about $u - u$ axis:

$$m_u = \frac{M_{u,E}}{M_{u,pl}} = \frac{M_{u,E}}{W_{u,pl} f_y}; W_{u,pl} = \frac{Ah}{2\sqrt{2}} = 2W_{v,pl}. \tag{21}$$

3.2 *Compression with two directional bending*

For equal angles, the limit curve for the plastic behavior can be approximated with use of the following equation:

$$m_{un}^2 + m_{vn} = 1 \tag{22}$$

where m_{un} = reduced dimensionless bending moment about $u - u$ axis

$$m_{un} = \frac{M_{u,E}}{M_{un,pl}} = \frac{M_{u,E}}{W_{u,pl} f_y (1-n)} \tag{23}$$

and m_{uv} = reduced dimensionless bending moment about $v - v$ axis

$$m_{vn} = \frac{M_{v,E}}{M_{vn,pl}} = \frac{M_{v,E}}{W_{v,pl} f_y \left(1-n^2\right)}. \tag{24}$$

If case of $n = 0$, Eqn. (22) becomes of that given by Vayas et al. (2009).

4 DIMENSIONLESS FORCE-DEFORMATION CHARACTERISTIC OF COMPRESSED ANGLE BRACES

4.1 *Analytical model*

Since the eccentrically connected brace is bent from the beginning of loading, the angle axial deformation is a superposition of axial shortening and shortening due to the bowing effect and as such can be approximated by:

$$\bar{\varepsilon} = \frac{\bar{\sigma}_E}{\psi} + \frac{8E}{3f_y}\left(\frac{f^{II}}{l}\right)^2 = \frac{\bar{\sigma}_E}{\psi} + \frac{8E}{3f_y}\left(\frac{f^{I}}{l}\frac{1}{1-\bar{\sigma}_E/\bar{\sigma}_{cr}}\right)^2 \quad (25)$$

where $\bar{\varepsilon}$ = dimensionless axial deformation; f^{II}, f^{I} = second order and first order, respectively, maximum bow coordinates; $\bar{\sigma}_E$ = dimensionless axial force corresponding to the deformation $\bar{\varepsilon}$; $\bar{\sigma}_{cr} = \sigma_{cr}/f_y$ dimensionless elastic critical force concerned with the lowest bifurcation force as it has been explained in section 2, and ψ = reduction factor equal to one in case of axial compression and compression with in-plane eccentricity while in case of compression with out-of-plane eccentricity:

$$\psi = 1 - \frac{3}{2\left(1+\bar{\lambda}^2\right)} \geq \frac{1}{4}. \quad (26)$$

Combining the elastic deformation mechanism given by Eqn. (25) with inelastic mechanisms of linear plastic-strain-hardening and nonlinear post-limit ones, the dimensionless force-deformation relationship describing the behavior of angle brace can be derived from probabilistic considerations as proposed by Barszcz & Gizejowski (2007):

$$\bar{\sigma} = \left\{\left(\frac{\bar{\sigma}_E}{\psi}\right)^{-n} + \left(1+\alpha_h\bar{\varepsilon}\right)^{-n} + \left[\frac{1}{a\left(\bar{\lambda}^2\bar{\varepsilon}\right)^m}\right]^{-n}\right\} \quad (27)$$

where $\bar{\sigma}_E/\psi$ = solution of Eqn. (25); $m = 0.5$ for centrically compressed angles and angles with eccentricity in the plane of symmetry; $m = 1.0$ for angles with the eccentricity out of the plane of symmetry; a, n = constants evaluated on the basis of experimental data; $\bar{\lambda}$ = relative slenderness ratio

$$\bar{\lambda} = \sqrt{\frac{N_{c,R}}{N_{cr}}} \quad (28)$$

and $N_{c,R}$ = class dependent section resistance in axial compression.

In case of an axially loaded member, Eqn. (25) is replaced by two separate equations, describing independent mechanisms, namely one referred to axial shortening $\bar{\sigma}_E/\psi = \bar{\varepsilon}$ and the second one – to buckling state in a neutral equilibrium $\bar{\sigma} = 1/\bar{\lambda}^2$. Equation (27) may then be transformed to that originally developed by Barszcz & Gizejowski (2007):

$$\bar{\sigma} = \left[\left(\bar{\varepsilon}\right)^{-n} + \left(1+\alpha_h\bar{\varepsilon}\right)^{-n} + \left(\frac{1}{\bar{\lambda}^2}\right)^{-n} + \left[\frac{1}{a\left(\bar{\lambda}^2\bar{\varepsilon}\right)^m}\right]^{-n}\right]^{\frac{1}{n}} \quad (29)$$

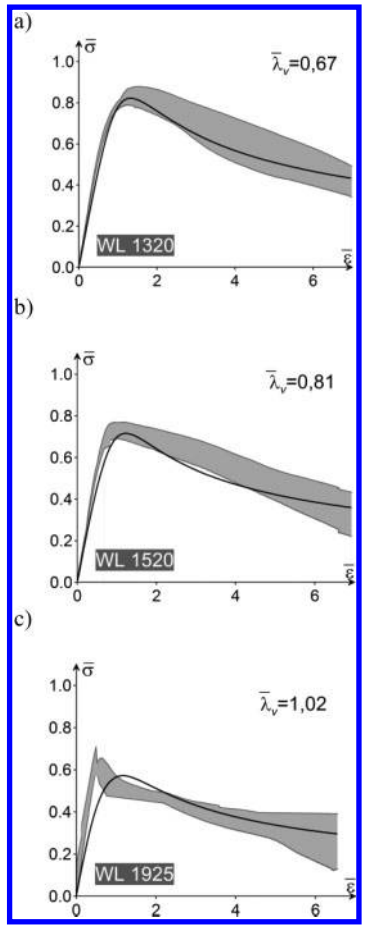


Figure 7. Comparison of experimental and analytical force-deformation curves for welded braces.

4.2 *Calibration of proposed analytical model*

Experimental investigations were carried out for subframe specimens WL with welded braces and in-pane eccentricities, and for subframe specimens BL with bolted braces and out-of-plane eccentricities.

Experiments have generally proven that angles with bolted connections are weaker, i.e. exhibit the lower

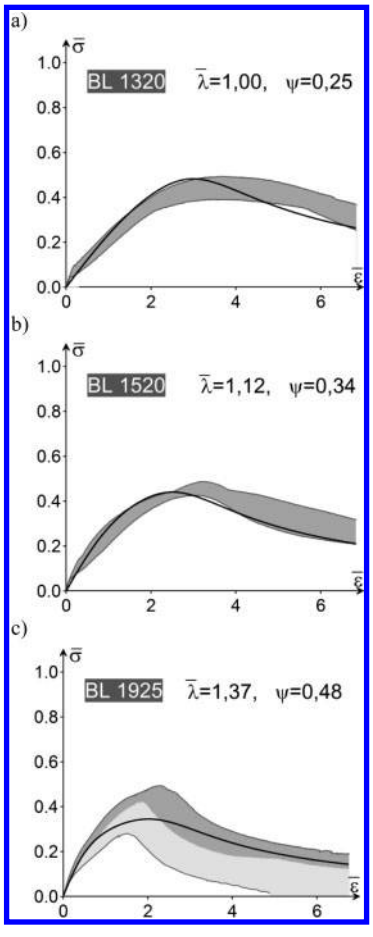


Figure 8. Comparison of experimental and analytical force-deformation curves for bolted braces.

buckling strengths and lower placement of force-deformation characteristics than those with welded connections. The calibration of model parameters was carried out considering the flexural effective length factors $\mu_v = \mu_u = 0.7$. The calibrated parameter $n = 5$ and the parameter a is the eccentricity type dependent. It is equal to 1.30 for braces with in-plane eccentricities while for braces with out-of-plane eccentricities is equal to 0.55.

Comparison of experimental force-deformation curves and analytical curves constructed with use of calibrated model parametersare presented in Figure 7 for welded angles (specimens of WL type) and in Figure 8 for bolted angles (specimens of BL type). The experimental envelope of results obtained for individual tests of each angle length and joint type is used. The area enclosed by the upper and lower boundary lines of the envelope utilized for the calibration exercise is shown in a dark grey color. The light gray color refers to the result that was regarded as less reliable. The analytical formulation developed herein when applied together with calibrated model parameters leads to a prediction of the analytical characteristics acceptable from the practical point of view for both types of welded and bolted braces.

5 CONCLUDING REMARKS

This paper presents the comprehensive study of the behavior of angle braces with fork-welded and through-leg bolted end connections. Member buckling and section resistance are discussed first, and then the modeling technique for the development of dimensionless brace force-deformation characteristic is presented.

Next, the approximate model reflecting not only the flexural behavior of angle brace is dealt with, and the way of its model parameters calibration exercise is summarized. The results of experimental investigations performed at the Warsaw University of Technology on two groups of braced subframes, namely WL and BL with braces welded and bolted, respectively, and three subgroups of different brace lengths are used for the calibration of developed model.

Finally, the validation is presented and the developed force-deformation curves with use of calibrated model parameters are compared with the envelope of experimental curves obtained for three tests in each subgroup of each group of tested specimens.

The approach presented in this paper for prediction of the force-deformation characteristic of angle braces may be used for other shapes of bracing members to create a catalogue of curves to be used in nonlinear analysis and direct design of steel braced frameworks.

REFERENCES

Barszcz, A.M. 2007. Modelling and experimental investigations of the behaviour of angle bracing strut in steel frame. In Jan Obrebski (ed.). *Lightweight Structures in Civil Engineering: Proc. of Local Seminar of IASS Polish chapter, Warsaw, 7 December 2007.* Warsaw: Micropublishing.

Barszcz, A.M. 2010. Experimental investigations of braced frame systems. *Journal of Engineering and Construction* 7: 380–384 [in Polish].

Barszcz, A.M. 2012. Investigation into the modelling of angle brace members. In Jan Obrebski (ed.), *Lightweight Structures in Civil Engineering: Proc. of Local Seminar of IASS Polish chapter, Warsaw, 7 December 2012.* Warsaw: Micropublishing.

Barszcz, A.M. & Gizejowski, M.A. 2007. An equivalent stiffness approach for modelling the behavior of compression members according to Eurocode 3. *Journal of Constructional Steel Research* 63(1): 55–70.

Vayas, I., Charalampakis, A., Koumousis, V. 2009. Inelastic resistance of angle sections subjected to biaxial bending and normal forces. *Steel Construction* 2: 138–146.

Research and Applications in Structural Engineering, Mechanics and Computation – Zingoni (Ed.)
© 2013 Taylor & Francis Group, London, ISBN 978-1-138-00061-2

Experimental and numerical research on longitudinally stiffened tapered steel plate girders subjected to shear

A. Bedynek, E. Mirambell & E. Real
Universitat Politècnica de Catalunya, Department of Construction Engineering, Barcelona, Spain

ABSTRACT: Tapered steel plate girders offer greater structural benefits than prismatic members. Their advantages include greater strength and slenderness, as well as a reduction in steel consumption. Often, they are used in long-span bridges and portal frames. In order to maintain slender webs and to reduce the consumption of steel, longitudinal stiffeners are often required.

This paper is focused on the behaviour of tapered steel plate girders with one longitudinal stiffener, subjected to shear. Four medium-scale tests of such girders were carried out and relevant experimental results are presented. Moreover, the geometrical and the structural imperfections are discussed. Based on experimental results the numerical model was validated and used in further parametric studies. The influence of the primary factors affecting the structural behaviour of tapered panels with longitudinal stiffening is studied.

Finally, a comparison of the numerical results with the results derived from EN 1993-1-5 (2006) rules (valid for prismatic members) is made. A discussion about their extended application for tapered girders is also presented.

1 INTRODUCTION

In many modern structures such as long-spans of steel bridges or industrial warehouses, girders with non-prismatic cross-section are used. Due to their trapezoidal shape, they can be better adapted to the non-uniform distribution of existing internal forces, thereby achieving greater efficiency and economy. Tapered panels are often used in large-scale structures, and are susceptible to instability problems. The most common solution to avoid local buckling and to limit their elevated slenderness is to weld additional profiles as longitudinal stiffeners. Depending on the panel slenderness and the stress distribution, these extra profiles usually have a closed cross-section (providing greater flexural and torsional rigidity in the entire panel) (Pavlovčič et al. (2007)) and, if necessary, more than one profile can be welded to the same panel, normally on the same side. Moreover, longitudinal stiffeners are most beneficial in those parts of steel panels subject to compression in order to divide large surfaces into smaller sub-panels with lower individual slenderness. In this way the problem of local buckling of the panel can be simplified to the phenomenon of local buckling in each sub-panel, which is usually more favourable.

2 EXPERIMENTAL PROCEDURE

2.1 *Geometry of tested girders*

All girders were tested as simply supported, rigid end posted, short beams with the load applied at the mid-span to consequently obtain a constant shear value. Two extra transverse stiffeners were welded on the both sides of the non instrumented web panel to ensure that shear buckling started in the instrumented one. The tested web panels are designed as slender ones in order to assure that critical shear load will be lower than the ultimate shear strength. Thanks to this, it was possible to observe the development of a diagonal tension field and post-buckling reserve.

In the laboratory tests two different geometries of tapered girders were tested. Specimens A (A1, A2) had the same dimensions and aspect ratio $\alpha = a/h_1 = 1.0$ and they varied only by the position of the longitudinal stiffener. The same scenario took place for girders B (B1, B2). Both of them have the same dimensions, the aspect ratio $\alpha = 1.5$ and they differ from each other only by the position of the longitudinal stiffener. In girders A1 and B1, longitudinal stiffener was placed horizontally in the centre of their shorter depth (Fig. 1a) and in girders A2 and B2 the stiffener was inclined in such a way that two points in the centre of the larger and smaller depths (respectively) were connected (Fig. 1b). All dimensions and corresponding symbols are presented in Table 1 and Fig. 1. The following example explains the notation of girders: A1_600_800_800_3_180_15 means a girder with the following dimensions: shortest depth $h_0 = 600$ mm, largest depth $h_1 = 800$ mm, panel length $a = 800$ mm, web thickness $t_w = 3$ mm, flange width $b_f = 180$ mm and flange (and stiffener) thickness $t_f = t_s = 15$ mm (see Table 1).

2.2 *Material properties*

All girders used in the laboratory testing were made of S235 steel. Previous standard tensile coupon tests,

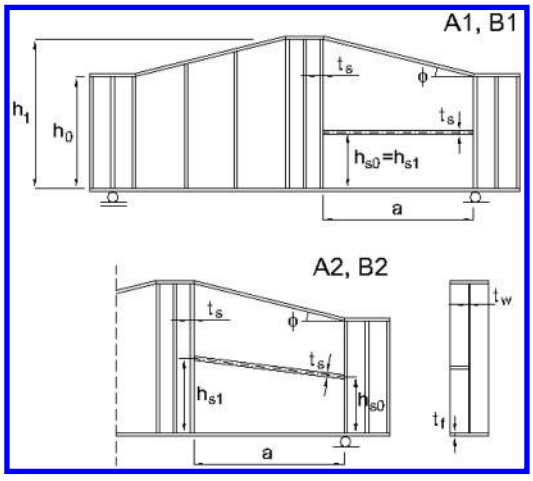


Figure 1. Geometry and symbols of the tested specimens.

Table 1. Dimensions of the tested girders.

Girder	h_0 mm	h_1 mm	a mm	t_w mm	b_f mm	t_f,t_s mm	h_{s0} mm	h_{s1} mm		$\alpha \tan(\phi)$
A1	600	800	800	3	180	15	300	300	1.0	0.25
A2	600	800	800	3	180	15	300	400	1.0	0.25
B1	500	800	1200	3	180	15	250	250	1.5	0.25
B2	500	800	1200	3	180	15	250	400	1.5	0.25

which were done for 6 specimens, allowed setting an average value of the yield stress of 300 MPa (all values between 290-322 MPa). In order to make further comparison of the numerical and experimental results, nominal values (for steel) of Young's modulus E = 210 GPa and Poisson's ratio $\nu = 0.3$ were assumed.

2.3 *Imperfections*

The web thickness of all tested girders was $t_w = 3.0$ mm and the flange (and stiffeners) thickness was $t_f = t_s = 15.0$ mm. This difference in rigidity of the connected plates and overall production process caused not only structural imperfections (flame cutting) but also considerable and visible geometrical imperfections (due to welding) observed as initial deformed shapes of the webs. This problem was observed especially in girders type B (B1, B2) due to their larger aspect ratio ($\alpha = 1.5$). Obviously, it was necessary to take into account the aforementioned factor, since previous numerical analyses proved its importance. Moreover, the presence of significant visual imperfections could possibly account for differences between experimental and numerical results.

2.4 *Test results*

Full analysis of all tested girders included 40 measurement points (24 strain gauges and 16 displacements). In this section, the most significant and representative results are presented and analysed.

For girders B1 and B2 the experimental results are shown within a limited range. Large imperfections detected in both girders made it impossible to continue the tests over a certain value of applied load (at approximately halfway to the ultimate shear resistance, both tests had to be stopped). As a result of the aforementioned initial deformed shapes, an additional horizontal force in the point of applied load occurred and started to push tested girders outside of their plane. Nevertheless, in the range where the measurements were registered, a good correlation of all results was observed.

2.5 *Load-deflection curves (A1, A2, B1, B2)*

A comparison of load-deflection curves P-δ obtained from numerical simulations and experimental tests is shown below (Fig. 2a–d). Maximum vertical displacement δ was measured at the mid-span of the girder. The correlation shown between each pair of numerical and laboratory curves is good.

2.6 *Deformed shape*

Fig. 3 shows an example of a qualitative comparison of the deformed shape of the tested panel. Here a very good correlation is also observed between experimental and numerical "buckling waves". In this case (girder A1), the upper trapezoidal sub-panel buckled first, followed by the rectangular one. Two diagonal tension fields were being created independently and they are formed as a function of their slenderness (meaning the more slender sub-panel buckles first). The darker grey tones seen in Fig. 3b are representing yielding zones, according to von Mises criterion. It may be concluded from quantitative analyses of yielding and locations where plastic hinges appeared (two flanges and longitudinal stiffener) that both subpanels may be considered separately, since the same mechanism is observed in both of them.

2.7 *Numerical model validation*

Table 2 shows experimental and numerical values of the critical shear load V_{cr} and the ultimate shear resistance V_u obtained for the tapered girders tested. Values of the numerical critical shear load $V_{cr(FEM)}$ were obtained from buckle analysis, based on the first positive eigenvalue. Experimental critical shear loads $V_{cr(test)}$ were obtained on the basis on the load-vertical displacement relationships, approximately in the point where the curve losses its linearity.

It is important to mention that all tested girders had excessive structural imperfections (manufacturers' tolerances were exceeded) which for specimens A1 and A2 led to lower ultimate shear resistance V_u comparing them to numerical equivalents (up to 11.3%). Additionally, the initial deformed shapes in girders B1 and B2 made it impossible to continue both tests

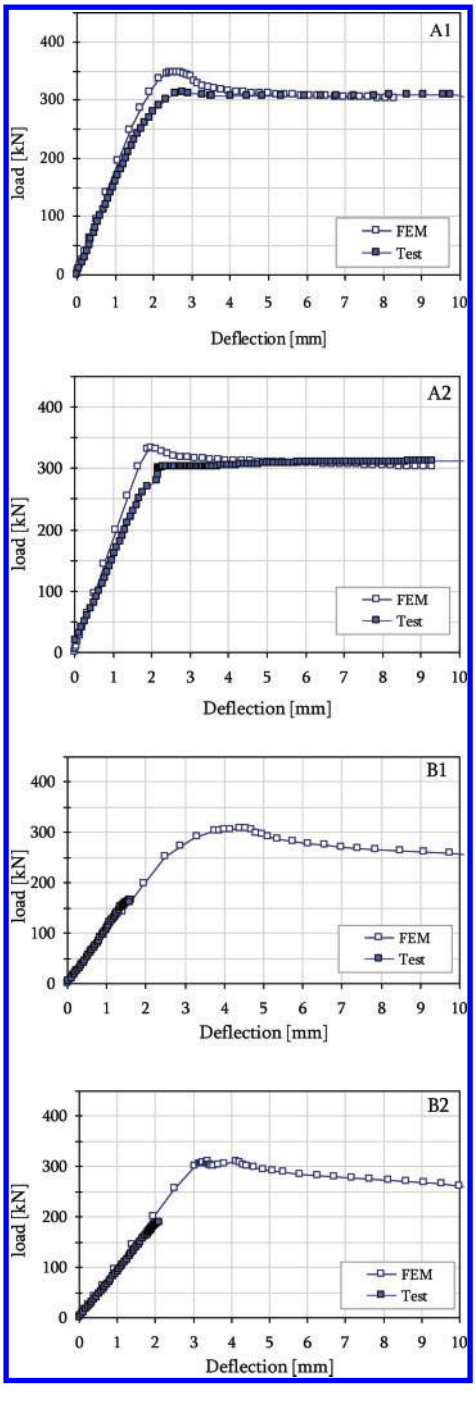


Figure 2. Numerical and experimental load-deflection curves for girders a) A1, b) A2, c) B1, d) B2.

with loads exceeding their critical shear level (see Fig. 2c–d).

For this reason, validation of the numerical model was only based on two specimens A1 and A2. Good agreement is observed between the numerical results and experimental results (see Table 2).

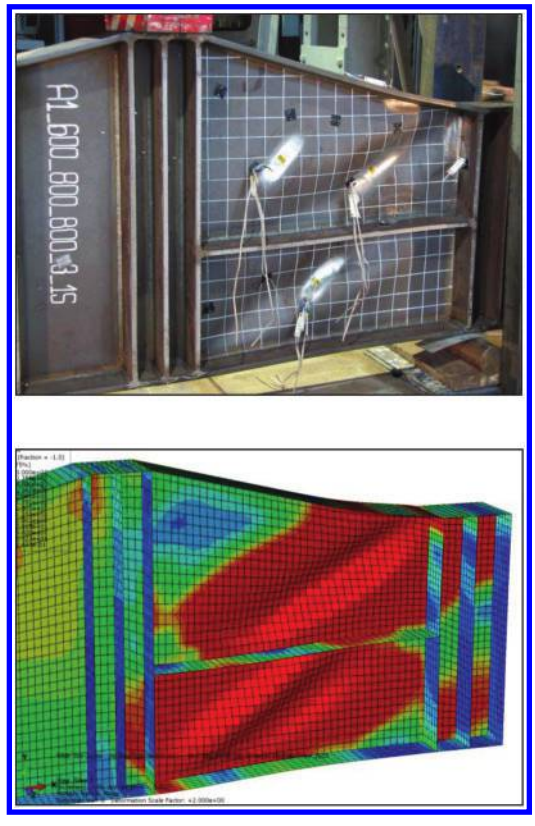


Figure 3. Qualitative comparison of deformed shape for girder A1. a) Experimental test, b) FEM model.

Table 2. Numerical and experimental results.

Girder	V_{cr_FEM} kN	$V_{cr_(test)}$ kN	Diff. %	$V_{u_(FEM)}$ kN	$V_{u_(test)}$ kN	Diff. %
A1	223.2	210.0	−6.3	347.8	312.5	−11.3
A2	295.2	270.0	−9.3	333.1	311.9	−6.8
B1	188.5	–	–	307.9	–	–
B2	280.8	–	–	310.8	–	–

The analysis of the overall behaviour of tested girders and their comparison with numerical analyses (load-deflection curves in Fig. 2a–d) show very good correlation between them, allowing us to conclude that numerical model was validated correctly.

3 PARAMETRIC STUDY

3.1 *Numerical model*

Several numerical analyses of tapered steel plate girders subjected to shear were conducted using the Abaqus code (2010). In order to reproduce the influence of large deformations that occur during the shear buckling phenomenon, 4-node shell element S4R5 was used. To deal with the geometric and material

nonlinearities (post-buckling behaviour, softening and collapse) "modified Riks" method was applied. The stress-strain relationship was based on the simplified bi-linear diagram $\sigma - \varepsilon$ with kinematic hardening and on the von Mises criterion for yield stress assumed for ductile materials.

3.2 *Material properties*

Selected material for the parametric study was S275 steel with bi-linear simplified model, yield strength of 275 MPa, Young's modulus E = 210 GPa and Poisson's ratio $\nu = 0.3$. This work is a continuation of previous analytical and numerical investigations, in which steel S275 was used (Real et al. (2010) and Bedynek et al. (2011)). In order to adapt the experimental tests on the tapered steel plate girders to the capabilities of the laboratory, steel S235 was selected.

3.3 *Geometric and structural imperfections*

Previous studies presented by Bedynek et al. (2013) for tapered plate girders with transversal stiffeners and Pavlovčič et al. (2007) for rectangular plate girders with longitudinal stiffeners concluded that plate girders are not very sensitive to the influence of structural imperfections such as residual stresses. Consequently, only geometrical imperfections are considered in this research. In order to introduce the geometrical imperfections, a scaled deformed shape from the first eigenvalue mode in buckle analysis was used (values calculated according to EN 1993-1-5 and the maximum fabrication tolerances).

3.4 *Longitudinal stiffeners*

In all analysed girders, the longitudinal stiffener has the same thickness $t_s = 15$ mm and approximately the same width $b_s = 0.5(b_f - t_w)$. The longitudinal stiffener was designed to assure enough rigidity in order to prevent the overall panel buckling. Only local buckling of sub-panels is allowed. More research about the optimum rigidity of the longitudinal stiffeners has been carried out in recent works (Pavlovčič et al. (2007) and Estrada et al. (2008)).

4 NUMERICAL RESULTS. COMPARISON WITH EN 1993-1-5

In Table 3 some of the numerical (FEM) and analytical (EN 1993-1-5) results of the ultimate shear resistance V_u are presented and compared. Additionally, in the first column, the numerical values of critical shear load V_{cr} for each girder are shown. Girders with symbol "0" do not have any longitudinal stiffener. They provide a reference value for plates having such stiffener.

Four different situations of the location of the longitudinal stiffener were studied; the values concerning to each case (Girders I-IV) are indicated in Table 3) (see Fig. 4).

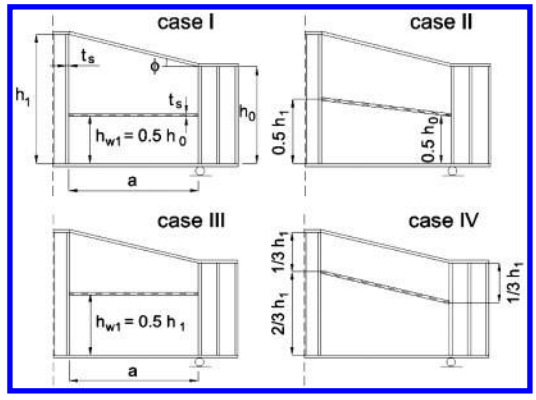


Figure 4. Four cases (I-IV) of position of the longitudinal stiffener.

Analysed girders varied by geometric parameters such as: a slope of the inclined flange (tan (ϕ) from 0.13 to 0.5), an aspect ratio (girders A: $\alpha = 1$, girders B: $\alpha = 2$ and girders C: $\alpha = 3$) and a thickness of the web ($t_w = 2$ mm and 3 mm). The thickness of both flanges and all stiffeners (transversal and longitudinal) was always $t_f = t_s = 15$ mm.

Only a specification provided by EN 1993-1-5 and commented by Johansson et al. (2007) addresses prismatic plates with various combinations of longitudinal stiffeners. In this work the attempt to adapt existing rules for non-prismatic (tapered plates) members has been made; possible limitations of their use are discussed.

The general norm for non-prismatic plates without longitudinal stiffeners proposed in EN 1993-1-5 is based on a simplification of their trapezoidal shape, reducing it to a rectangular one, assuming its larger depth h_1. The same assumption was made in this work for tapered plate girders with one longitudinal stiffener. All tested girders were examined in the mid-span, in the cross-section where the greatest bending moment occurs. The ultimate shear resistance is calculated for a rectangular plate with maximum depth h_1 and with horizontal longitudinal stiffeners (even for non-horizontal, inclined stiffeners as tested in cases II and IV) adopting depth h_{wi} for each sub-panel (see Fig. 4). Nearly all of the results obtained in this way are on the safe side, but some of them (especially cases I and IV) seem to be very conservative.

This significant underestimation of the ultimate shear load may be due to the assumption of non-prismatic sub-panels to be rectangular ones. As it is shown in Fig. 4, for cases I and IV, the trapezoidal sub-panel has a larger slenderness ratio, which could directly be the cause of the general collapse of the girder.

Each girder has been examined in two ways: as an entire panel and as separate sub-panels. According to EN 1993-1-5, from three slenderness parameters (in the case of only one longitudinal stiffener), calculated for both whole panels and sub-panels, that which gives

Table 3. Numerical and analytical (EN 1993-1-5) results.

Girder	FEM		EC3	Diff.
	V_{cr} [kN]	V_u [kN]	V_u [kN]	V_u [%]
A0_400_800_800_2_180_15	46.1	175.3	122.6	30.1
AI_400_800_800_2_180_15	86.2	201.8	135.2	33.0
AII_400_800_800_2_180_15	160.2	192.0	160.3	16.5
AIII_400_800_800_2_180_15	69.7	309.9	160.3	48.3
AIV_400_800_800_2_180_15	153.5	237.9	141.6	40.5
A0_600_1000_1000_3_180_15	98.1	294.3	207.2	29.6
AI_600_1000_1000_3_180_15	180.1	360.2	240.9	33.1
AII_600_1000_1000_3_180_15	280.8	340.3	284.7	16.3
AIII_600_1000_1000_3_180_15	184.5	335.5	284.7	15.1
AIV_600_1000_1000_3_180_15	308.1	356.9	246.4	31.0
B0_400_800_1600_2_180_15	34.4	112.5	87.6	22.0
BI_400_800_1600_2_180_15	56.7	160.6	102.9	35.9
BII_400_800_1600_2_180_15	96.6	156.9	131.0	16.5
BIII_400_800_1600_2_180_15	55.2	179.5	131.0	27.0
BIV_400_800_1600_2_180_15	130.8	158.7	108.9	31.4
B0_600_1000_2000_3_180_15	74.3	209.6	160.8	23.3
BI_600_1000_2000_3_180_15	114.5	281.8	201.3	28.6
BII_600_1000_2000_3_180_15	165.6	313.9	225.5	28.2
BIII_600_1000_2000_3_180_15	156.1	250.1	225.5	9.8
BIV_600_1000_2000_3_180_15	270.6	311.8	207.7	33.4
C0_400_800_2400_2_180_15	32.1	93.0	77.1	17.1
CI_400_800_2400_2_180_15	44.0	134.7	93.0	31.0
CII_400_800_2400_2_180_15	70.5	147.4	121.4	17.6
CIII_400_800_2400_2_180_15	47.6	132.0	121.4	8.0
CIV_400_800_2400_2_180_15	110.9	144.7	100.5	30.5
C0_600_1000_3000_3_180_15	66.0	178.9	147.5	17.6
CI_600_1000_3000_3_180_15	82.8	253.8	189.1	25.5
CII_600_1000_3000_3_180_15*	114.8	280.6	237.5	15.4
CIII_600_1000_3000_3_180_15	121.4	227.2	237.5	−4.5
CIV_600_1000_3000_3_180_15*	186.9	297.8	195.5	34.4

the higher value in the calculation of the contribution from the web should be used.

In EN 1993-1-5 (point 5.3 (5)) is stated that for webs with longitudinal stiffeners the slenderness $\bar{\lambda}_w$ should not be taken as less than (Eq.1)

$$\bar{\lambda}_w = \frac{h_{wi}}{37.4t\varepsilon\sqrt{k_{\tau i}}} \tag{1}$$

where h_{wi} and $k_{\tau i}$ refer to the sub-panel with the largest parameter $\bar{\lambda}_w$ of all sub-panels within the web panel under consideration.

The shear buckling coefficient $k_{\tau i}$ for a singular sub-panel is calculated according to the classic formulae for simply-supported rectangular plates. If the sub-panel is non-prismatic, it should also be simplified by assuming it to be a rectangular panel, using its largest depth h_{w1}.

As can be observed in Table 3, some situations seem to be more favourable than others. There is also no clear rule for the relationship between the position of the longitudinal stiffener and the ultimate shear resistance of the girder.

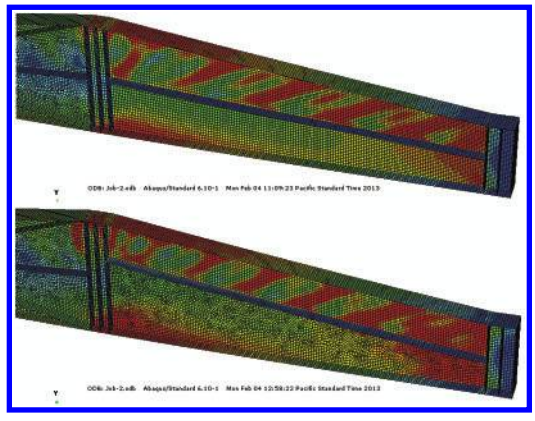


Figure 5. Mid-span section yielding: a) girder CII_600_1000_3000_3_180_15 b) girder CIV_600_1000_3000_3_180_15.

In the case of the presence of both shear forces and bending moments, two different locations for the stiffener could be considered. In the case when only shear forces are present, the optimal position of the longitudinal stiffener would be at the mid-depth of the panel, as this will reduce the slenderness ratio of the panel and will achieve similar slenderness ratios for both sub-panels.

On the other hand, if only bending moment forces are being considered, optimal results will be obtained if the longitudinal stiffener is placed in the compression zone.

In reality, all girders are subjected to both shear forces and bending moments. Therefore, the ultimate shear resistance calculation and the optimal positioning of longitudinal stiffeners are more complex, and strictly depend on the entire geometry of the panel under consideration.

On the other hand, highest values of the shear critical load were observed in cases II and IV, where the slenderness of both sub-panels was reduced and where there was not a significant disproportion between their dimensions. Nevertheless, in the cases where the higher values of the shear critical load are observed, there does not seem to be a correlation with their ultimate shear resistance.

It can also be observed that the ultimate shear resistances V_u varied in larger range for those girders, where the slope of the inclined flange is greater (girders A, up to 130%). The larger aspect ratio in girders B and C, up to 31%), the smaller inclination and the more rectangular shape of the panel explain why the position of the longitudinal stiffener plays a smaller role in the estimation of the ultimate shear resistance.

Due to their specific geometry and larger aspect ratios, two tapered girders (CII and CIV as marked with an asterisk in Table 3) did not exhibit full post-buckling shear capacity. It was observed that for those girders, ultimate shear resistance could not be achieved because of the yielding of both flanges in the cross-section where the greatest bending moment occurs (Fig. 5a–b).

5 CONCLUSIONS

The analysis of the results of experimental tests performed on four tapered steel plate girders with one longitudinal stiffener, under shear, have led to a better understanding of the structural behaviour of these girders. Parametric studies conducted have shown the importance of certain factors. In particular, further research should be focussed on the optimal arrangement of the longitudinal stiffener in order to achieve an efficient design of these girders.

The significance of this research is the applicability of EN 1993-1-5 rules for the case of tapered steel plate girders with longitudinal stiffening.

Generally speaking, an adaptation of existing procedures, for prismatic panels, can be used for non-prismatic panels with one longitudinal stiffener with the aim of determining the ultimate shear resistance of tapered steel plate girders V_u. Nevertheless, when greater precision is required, additional checks should be done. Nearly all of the values obtained for ultimate shear strength by means of the above-mentioned method are conservative and are generally underestimated (up to 48.3%). Only one exception was observed in the case of the girder CIII_600_1000_3000_3_180_15 in which the ultimate shear resistance was overestimated −4.5%. In order to avoid such differences, additional studies with a wide range of geometric parameters should be carried out.

ACKNOWLEDGMENTS

The Ministry of Science and Innovation of Spain has provided a doctoral scholarship to the first author. The authors wish to express their gratitude to the financial support provided by Spanish Ministry of Science and Innovation, as a part of the Research Project BIA2008-01897. The authors also wish to thank the Spanish Ministry of Public Works for the financial support, as a part of the Research Project 51/07 "Integral bridges".

REFERENCES

EN 1993-1-5. Eurocode 3. Design of steel structures, Part 1–5. Plated structural elements, 2006.

Pavlovčič L, Detzel A, Kuhlman U, Beg D. 2007. Shear resistance of longitudinally stiffened panels – Part 1: Tests and numerical analysis of imperfections. *Journal of Constructional Steel Research*; 63: 337–350.

Pavlovčič L, Beg D, Kuhlman U. 2007. Shear resistance of longitudinally stiffened panels – Part 2: Numerical parametric study. Journal *of Constructional Steel Research*; 63: 351–364.

Abaqus/Standard V.6.8. 2010. Simulia products. Dassault Systemes S.A.

Real E, Bedynek A, Mirambell E. 2010. Numerical and experimental research in tapered steel plate girders subjected to shear. SDSS' Rio 2010 - *International Colloquium on Stability and Ductility of Steel Structures*: Rio de Janeiro, Brazil, 8–10 September 2010: 747–754.

Bedynek A, Real E, Mirambell E. 2011. Tapered steel plate girders. Experimental and numerical investigation on shear and shear-bending interaction. *Eurosteel 2011 - 6th European Conference on Steel and Composite Structures, Proceedings*: Budapest, Hungary, August 31 – September 2: 765–770.

Bedynek A, Real E, Mirambell E. 2013. Tapered plate girders under shear: Tests and numerical research. *Engineering Structures*; 46:350–358.

Estrada I, Real E, Mirambell E. 2008. Shear resistance in stainless steel plate girders with transverse and longitudinal stiffening. *Journal of Constructional Steel Research*; 64: 1239–1254.

Johansson B, Maquoi R, Sedlacek G, Müller C, Beg D. 2007. Commentary and worked examples to EN 1993-1-5 "Plated structural elements". JRC Scientific and Technical Reports; 52–73.

Research and Applications in Structural Engineering, Mechanics and Computation – Zingoni (Ed.)
© 2013 Taylor & Francis Group, London, ISBN 978-1-138-00061-2

A new design methodology for steel hollow sections: The Overall Interaction Concept

J. Nseir, E. Saloumi & N. Boissonnade
University of Applied Sciences of Western Switzerland, Fribourg, Switzerland

ABSTRACT: This paper deals with the application of the Overall Interaction Concept (OIC) to the design of tubular cross-sections. More precisely, the concern is here to demonstrate the ability of the OIC to accurately account for the influence of local buckling on the cross-sectional carrying capacity. In this respect, extensive numerical investigations have been led, covering the various influences of i) plastic to slender cross-sectional behavior, ii) rectangular and square cross-section shapes, iii) strain-hardening effects, and iv) both simple and combined load cases. The results show that the OIC is perfectly suited to characterize the influence of local buckling on the carrying capacity, despite relying on simple application steps, namely cancelling the classification step as well as the use of the effective width method. Also, early results on the behavior of members are given, showing a potential accurate extension of the concept to members as well. Further investigations are actually under way for the derivation of a full "code-like" procedure, especially regarding interaction curves needed in the proposed design procedure.

1 INTRODUCTION

The present paper is related to the stability, resistance and design of steel hollow section members. More precisely, the behavior of sections is investigated. The intention is to improve the way the performance and the carrying capacity of tubular members are actually characterized, through the development of an original "Overall Interaction Concept" (OIC). Taking into account the resistance and stability interaction, the OIC further incorporates the effects of imperfections (non-homogenous material, residual stresses, out-of-straightness…) through the derivation of adequate "interaction curves" to accurately predict the real behavior of structural elements. The proposed concept is powerful enough to i) increase accuracy and bridge the specificities of the different materials under a unified, simple and effective basis, ii) deal with the effects of non-linear material behavior and local/global instabilities, and iii) advance consistency with the possibility of straightforwardly deal with all load cases, including combined ones (cf. Boissonnade 2013).

At present, for what regards cross-sectional instability, design codes (e.g. Eurocode 3, CEN 2005) usually characterize the sensitivity to early or late occurrence of local buckling by means of a classification of the cross-section, with respect to the b/t ratios of each wall comprised within the cross-section. Different sets of design formulae are provided, either plastic or elastic, depending on the (weakest) element having the highest class.

This concept of classes causes many practical application difficulties, such as a gap of resistance as shown in Figure 1, and almost no attempts have been made to overcome this unsatisfactory situation in a global way. In particular, the classification concept was shown to be inappropriate for hollow sections (Boissonnade 2012, Gardner 2008, Semi-Comp 2007). Figure 2 plots an example of a comparison between recommended b/t flange limits according to various standards for cold-formed hollow sections under major-axis bending moment. The observed discrepancies are so important that several b/t limit values seem questionable, to say the least.

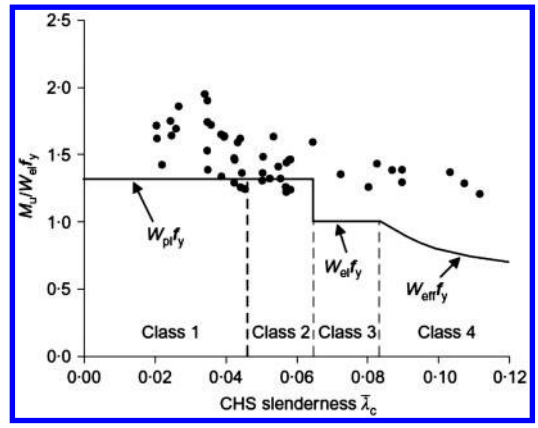


Figure 1. Circular hollow sections in bending: test results vs. concept of classes (Gardner 2008).

The aim of present research investigations is to show how the OIC can improve this situation, and

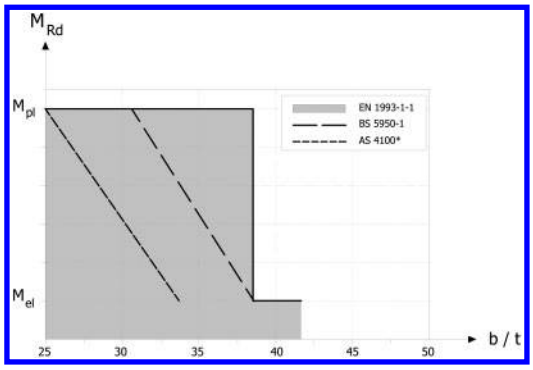


Figure 2. b/t limit values according to various design codes (cold-formed hollow sections submitted to major-axis bending).

to demonstrate that the OIC is perfectly suited to the determination of the design resistance of both hollow sections and members. Following section 2 presents the bases and features of the proposed approach, along with a first set of results for sections. Section 3 then provides results for member behavior, and actual and future research directions are addressed in section 4.

2 APPLICATION OF THE OIC TO HOLLOW SECTIONS

2.1 *Methodology – Application steps*

The proposed OIC approach first relies on the generalization of the relative slenderness concept, establishing this parameter as the key to rule the interaction between resistance and instability. The concept of relative slenderness is familiar to Structural Engineers, and is widely used nowadays to deal with flexural buckling behavior for example. It is suggested within the OIC to enlarge the field of application of this slenderness-related approach through the following generalization of the relative slenderness:

$$l_{rel} = \sqrt{\frac{R_{RESIST}}{R_{STAB}}} \qquad (1)$$

In Equation (1), R_{RESIST} represents the factor by which the actual loading has to be multiplied to reach the pure *resistance* limit, while R_{STAB} is the factor used to reach the buckling load of the ideal member (*instability* limit). Doing so allows the generalized relative slenderness taking a non-dimensional balance between the relative influences of instability and resistance, and makes it capable of dealing with combined loading situations or cross-sectional (local) instability effects (cf. Figure 3).

Once determined, this λ_{rel} value is further used in the design procedure to get into a so-called "interaction curve" and leads to the determination of a "χ" value (see Figure 4). This χ value (from analogy with Eurocode 3, CEN 2005), which may also be called "reduction factor", represents the penalty due

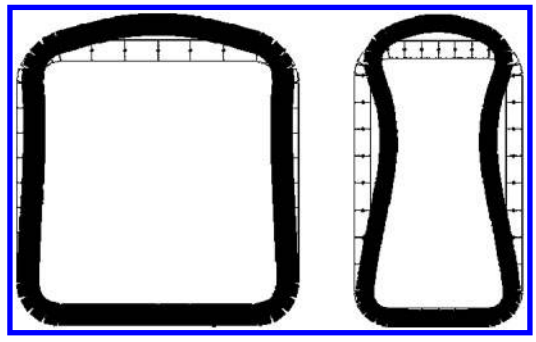


Figure 3. Local buckling of square and rectangular cross-section subjected to major-axis bending.

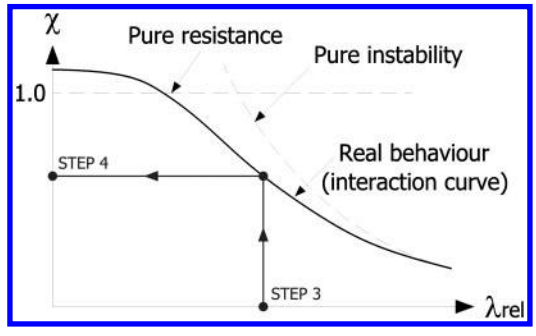


Figure 4. Resistance – instability interaction.

$$STEP\,1 : R_{RESIST}$$
$$STEP\,2 : R_{STAB}$$
$$STEP\,3 : \lambda_{rel} = \sqrt{\frac{R_{RESIST}}{R_{STAB}}}$$
$$STEP\,4 : \chi = f^{\circ}\left(\lambda_{rel}\right)$$
$$STEP\,5 : R_{REAL} = \chi \cdot R_{RESIST}$$

Figure 5. Application steps of the OIC.

to instability effects on the "pure resistant behavior"; obviously, χ can only be lower than 1.0. Then, the final resistance is evaluated as $\chi.R_{RESIST}$; Figure 5 further illustrates the proposed approach and its application steps. This rather simple procedure can be applied to many situations within Structural Engineering and become a general approach to each design situation where instability affects the resistance.

2.2 *Comparison with test results*

In an attempt to validate the pertinence of the OIC for handling the resistance-instability interaction for hollow sections, Figure 6 presents various test results collected in the literature (Kettler 2008). Its axes are "OIC-defined", i.e. the horizontal axis relates to the generalized slenderness λ_{rel} while the vertical axis reports on the cross-section reduction factor χ_{CS}.

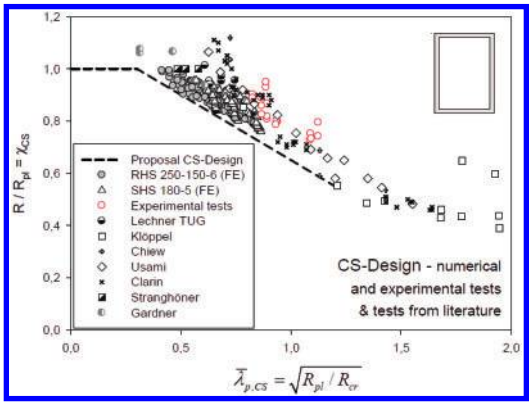


Figure 6. Cross-sectional test results (from Kettler 2008).

The OIC approach is seen to lead to highly satisfactory and consistent results, as indicated by the limited scatter observed; this is especially remarkable given the fact that some of the test results are relative to combined loading situations, such as compression with mono-axial bending.

Further, as Figure 1 experimental results show, significant over-strength may exist beyond the plastic design strength, due to a well-known conservatism in the assumption of a rigid-plastic material; this is especially true for cold-formed hollow sections. These potential resistance reserves may nevertheless be taken into account within the OIC approach in resorting to interaction curves leading to χ values above 1.0 for low relative slenderness – see Figure 4; from a mechanical point of view, this means that the OIC allows going beyond the usual perfectly-plastic behavior assumption. Numerical results presented in the next paragraph bring further evidence that this is effective and shall be accounted for.

2.3 *Numerical results*

This paragraph presents a first series of results relative to the cross-sectional behavior of tubular profiles. R_{STAB} values have been determined numerically with CUFSM (i.e. cross-sections were considered as a whole), and R_{RESIST} values have been derived by means of Eurocode 3 plastic interaction equations. Extensive numerical FE analyses have been led for the calculation of χ_{CS} values, through the use of non-linear FEM software FINELg (FINELg 2012); numerical models made of quadrangular 4-nodes plate-shell finite elements with typical features have been used (corotational total Lagrangian formulation, Kirchhoff's theory for bending). The FE-models being shown to be adequate (Boissonnade et al 2012), they have been extensively used within parametric studies and some 5500 non-linear shell numerical results have been collected – 296 tubular geometries were considered: 156 *rectangular* (RHS) + 140 *square* (SHS) hollow sections. The elastic-perfectly plastic with 2% hardening material law of Figure 7 was adopted for all

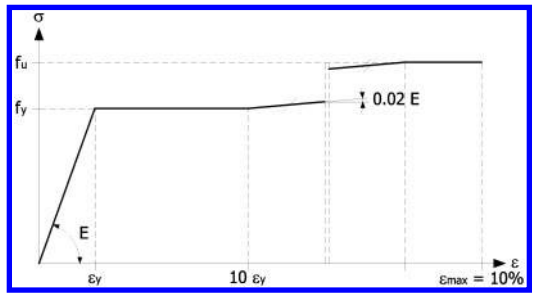


Figure 7. Stress-strain relationship adopted in FE models.

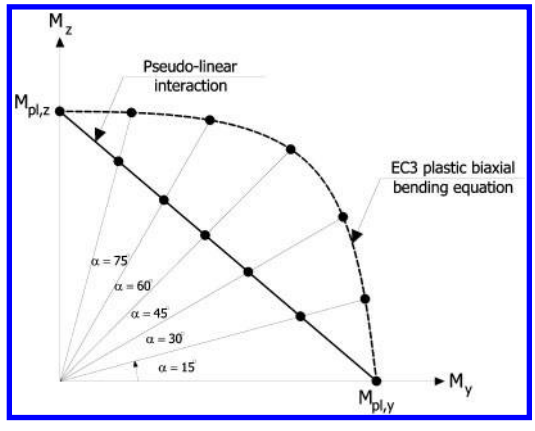


Figure 8. Stress-strain relationship adopted in FE models.

calculations, and suitable initial imperfection sets have been considered.

The numerical studies comprised the following set of parameters:

- 296 cross-section shapes (European database);
- 3 different steel grades: S235, S460, S690;
- Different loading conditions:
  - Pure compression;
  - Major-axis bending;
  - A first series of combined compression (30% of N_{pl}) and biaxial bending;
  - A second series of biaxial bending + 70% axial compression.

In order to better evidence the uniformity of the results, a distinction has been made between the different loading situations, namely with respect to the degree of biaxiality, i.e. the M_y/M_z ratio; this ratio was varied on the basis of 15° angles between plastic capacities $M_{pl,y}$ and $M_{pl,z}$ in a pseudo-linear biaxial bending interaction plot (see Figure 8).

Figures 9 and 10 show some of the obtained results, in OIC format and axes, and the proposed approach is seen to be fully appropriate, as demonstrated by the little scatters observed. It can be noticed that an increase in f_y obviously increases the relative slenderness λ_{CS} and thus decreases the χ_{CS} value, i.e. the section become more slender and prone to local buckling; a relatively small dispersion in the results is

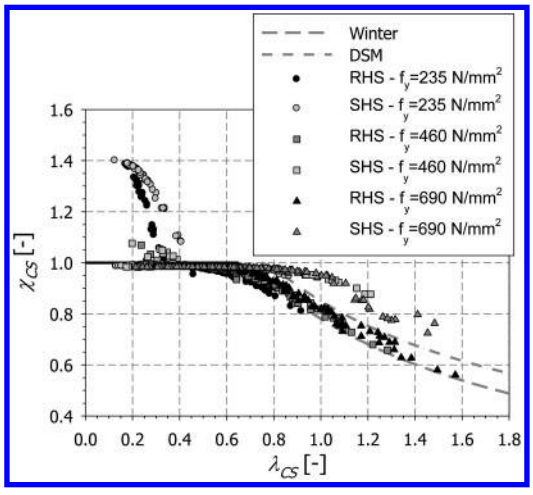


Figure 9. FE results for hollow sections under compression.

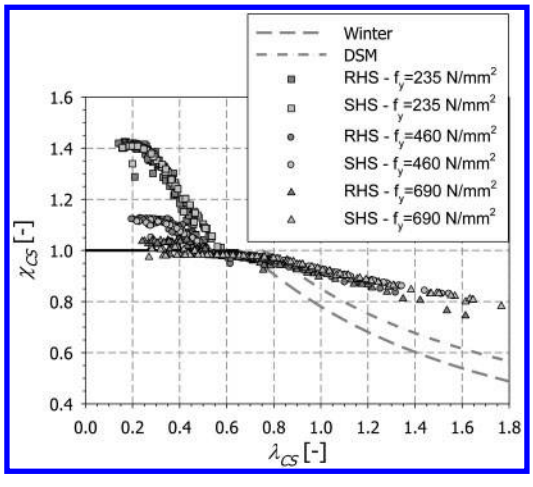


Figure 10. FE results for hollow sections under major-axis bending.

noted, though, and tendencies for slightly higher χ_{CS} values for high steel grades is observed. Too, an important level of over-strength brought by strain-hardening effects for the lowest steel grade can be noted.

As for the combined load cases, clear trends have been observed as well. For such situations, the OIC has been applied with an identical methodology as before, i.e. with R_{STAB} values numerically computed with CUFSM and R_{RESIST} values determined from the plastic $N-M_y-M_z$ equations of Eurocode 3. presents some results obtained for the 30% compression cases with yield stress $f_y = 235\,N/mm^2$. A detailed look at the results revealed that higher χ_{CS} values are reached for cases where minor axis bending takes over major axis bending, due to variations in the observed local buckling collapse modes, which obviously change with α, in addition to a certain conservatism in the $N-M_y-M_z$ plastic interaction equations adopted herein. In conclusion, the

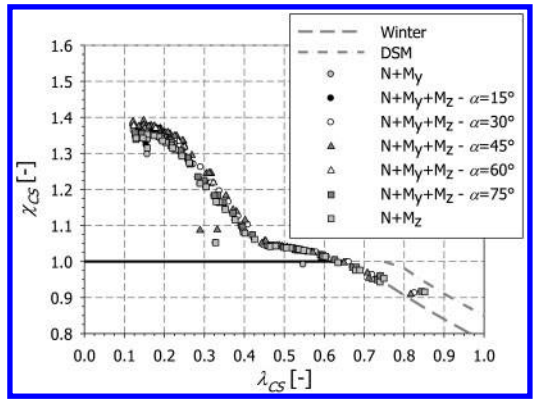


Figure 11. FE results for hollow sections under pure compression.

proposed concept is shown to be successfully applicable to tubular sections, and able to capture the mechanically-governing parameters, despite a rather simple conceptual background.

3 BEHAVIOUR OF TUBULAR MEMBERS

This section reports on the application of the OIC to *members*, with a special focus on combined load cases. Indeed, the (simple) load cases of members in compression (i.e. flexural buckling) or subjected to major-axis bending (lateral torsional buckling) immediately fit in the OIC approach, since these situations lie at the bases of the concept. For this purpose, thousands of FE-results have been reused (gathered from Ofner 1997). These numerical results are all relative to cases where local instability of the cross-section can be neglected (i.e. λ_{CS} is such that $\chi_{CS} \geq 1.0$ – Class 1 or 2 sections), and accordingly have been obtained by means of beam models – it shall be noted that the vast majority of these results is concerned with combined loading situations.

Figure 12 first shows results obtained to characterize the behavior of members with tubular sections, for $N+M_y$ cases; Figure 12 axes are here relative to *global* buckling through the *member* slenderness λ_{MB} (calculated with R_{STAB} values relative to member instability) and its associated χ_{MB} reduction factor. In this Figure, ψ stands as the ratio between applied end moments; as can be noticed, ψ can be identified as a key parameter, and a detailed analysis also showed that the M_y/N ratio can be shown to rule the differences in scatter for a given ψ value. Similar conclusions can be drawn for $N+M_y+M_z$ cases (Figure 13), however with clearer tendencies and a better level of uniformity with ψ.

These results confirm the ability of the OIC to correctly predict the response of hollow members under combined loadings. Further developments are under way to propose relevant interaction curves, on the basis of the tendencies observed.

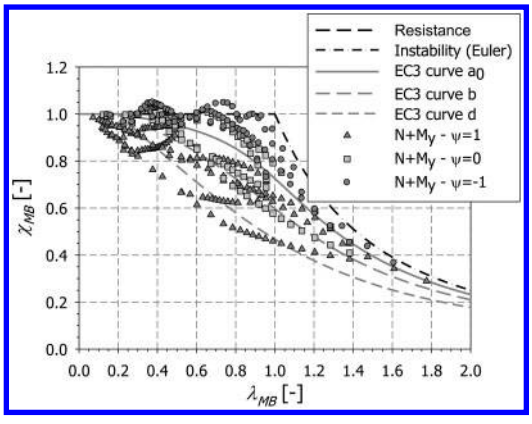


Figure 12. Results for hollow section members under combined loading ($N + M_y$).

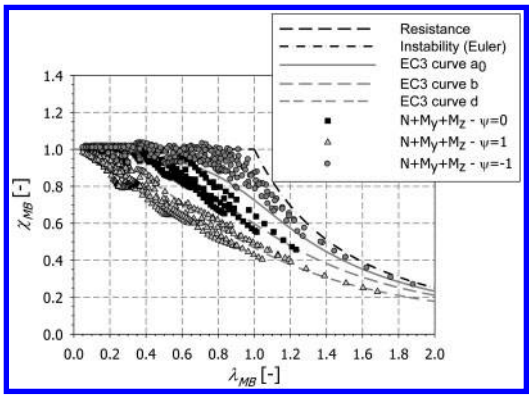


Figure 13. Results for hollow section members under combined loading ($N + M_y + M_z$).

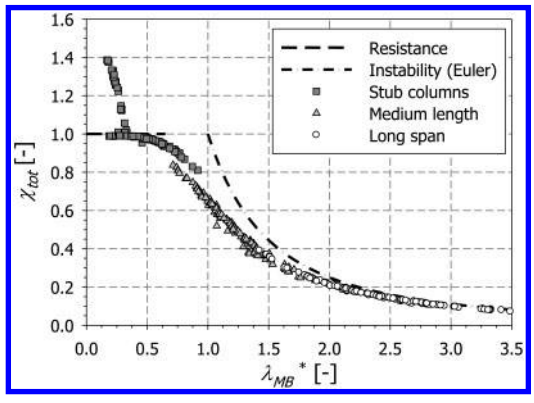


Figure 14. Results for rectangular hollow section *members* under pure compression (S235 steel).

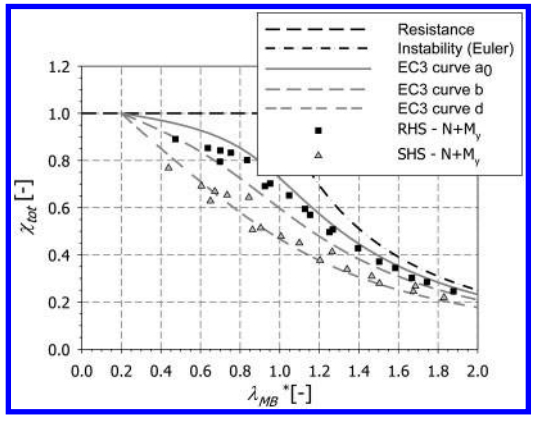


Figure 15. Results for hollow section *members* under combined loading (slender sections).

Deeper investigations also revealed that the cross-section h/b ratio plays a role on the global response of rectangular profiles. For this purpose, additional FE simulations have been performed on some 150 rectangular hollow section members (European database) submitted to axial compression only. The length of the members was varied from short to long (i.e. from stub column typical lengths to long spans leading to relative slenderness above 3.0, see Figure 14). Since some of the investigated sections were also concerned with *local* buckling (so-called "coupled instabilities"), use of a modified member relative slenderness λ^*_{MB} has been made, where R_{RESIST} is substituted by $\chi_{CS} \times R_{RESIST}$; results are plotted in Figure 14.

The observed discontinuity between the results of short length members and medium length members can be explained by the fact that the sections whose values belong to the "right side" of the stub columns' set typically have h/b ratios different from the "left side" of the medium length ones, and therefore should better be related to the values at the right end of the medium length set. This corroborates the need to resort to parameter-dependent interaction curves, rather than fixed ones as is nevertheless done in many codes for flexural buckling.

Finally, situations involving both local and global instabilities under combined load cases have been investigated, referring to SHS 250 × 250 × 5 and RHS 250 × 150 × 5 (slender) cross-sections. Both sections have been shown to exhibit an important influence of local buckling effects, with χ_{CS} values ranging from 0.4 to 0.9, depending on the load combination and on the level of web-flange interaction within local buckling modes. Use of λ^*_{MB} generalized relative slenderness has also been made, and Figure 15 depicts some of the obtained results ($N + M_y$ cases). Again, clear trends can be observed, further confirming the potential of the OIC to be relevant in such cases.

4 CONCLUSION – FUTURE DEVELOPMENTS

In the present paper, the Overall Interaction Concept has been shown to be a fully appropriate alternative to the current well-known design rules to account for the interaction between resistance and instability effects.

In particular, results on both tubular *sections* and *members* (i.e. including local and/or global instability), for simple or combined load cases have been presented.

The application of the OIC to predict the resistance of tubular cross-sections was shown to be fully appropriate, whatever the dimensions, steel grade or loading conditions. This approach is able to catch the governing parameters and to lead to consistent results, even for non-trivial situations and despite quite simple application steps. Consequently, the possibility to derive practical but accurate expressions for χ-curves exists, and is currently under completion – multiple mechanically-based expressions are foreseen, according to the trends observed for the combined load cases.

The OIC approach is actually at the core of the STSS project ("Simple Tools Sell Steel", STSS 2012), whose main objective is to develop and assess new design concepts to predict accurately the response of members made of standard and high-strength steel up to collapse (open and tubular sections). In an international effort, many related developments are conducted, involving deep, varied and extensive activities, both at the experimental, numerical, theoretical and practical level.

Besides, OIC-based investigations on high and ultra-high performance fiber concrete elements (columns and beam-columns) are currently under way. The future research directions related to an OIC approach will first be oriented towards its application to other materials, in situations where instability is of prime importance. This concerns for example members made of composite sections, stainless steel, aluminum, ultra-high performance concrete with fibers, structural glass…

Moreover, the development of new cross-sectional shapes, deliberately slender, is intended with the objective of taking the benefits from the new generation of high strength steels. Also, investigations within fire and earthquake steel design will become necessary, as a consequence of the calling off of the classification concept. Further, the OIC approach and principles, as described herein, should appreciably improve the design of specific members where coupled instabilities and/or complex solutions to implement require (partial) numerical solutions and the associated conceptual framework (e.g. tapered members, cellular beams…). Last, in the perspective of seeing the OIC embedded in various standards worldwide, the OIC should allow for a certain harmonization of standard and design habits, since relying on a general and global concept.

REFERENCES

AISC. 2005. Specification for structural steel buildings. *American Institute of Steel Construction*, Chicago, IL. ANSI/ASIC 360–05.

Bebiano, R., Pina, P., Silvestre, N. & Camotim, D. 2008. "GBTUL – Buckling and Vibration Analysis of Thin-Walled Members", DECivil/IST, Technical University of Lisbon (http://www.civil.ist.utl.pt/gbt).

Boissonnade, N., Greiner, R., Jaspart, J.P. & Lindner J. 2006. "Rules for Member Stability in EN 1993-1-1; Background documentation and design guidelines", *Eds. Mem Martins*, Portugal, E.C.C.S. – ISBN 92-9147-000-84, Vol. 119, 259 pages.

Boissonnade, N. 2011. "The Concept of Cross-section Classes in Eurocode 3 into Question", *ECCS TC8 meeting*, Lisbon, June 3rd.

Boissonnade, N. & Somja, H. 2012. "Influence of Imperfections in FEM Modeling of Lateral Torsional Buckling". *Proceedings of the Annual Stability Conference, Structural Stability Research Council*, Grapevine, Texas, April 18–21.

Boissonnade, N., Nseir, J. & Saloumi, E. 2013. "The Overall Interaction Concept: an Alternative Approach to the Stability and Resistance of Steel Sections and Members". *Proceedings of the Annual Stability Conference*, Structural Stability Research Council, St. Louis, Missouri, April 16–20.

CEN (Comité Européen de Normalisation. 2005. "Eurocode 3: Design of Steel Structures, Part 1–1: General rules and rules for buildings (EN 1993-1-1)", Brussels.

Gardner, L. 2008. "The continuous strength method". *Proc. Institution of Civil Engineers: Structures and Buildings*, vol. 161, n° 3, p 127–133.

Kettler, M. 2008. "Elastic-plastic cross-sectional resistance of semi-compact H- and hollow sections". *PhD Thesis*, Graz Technical University.

Li, Z. & Schafer, B. 2010 "Buckling analysis of cold-formed steel members with general boundary conditions using CUFSM: conventional and constrained finite strip methods." *Proceedings of the 20th Int. Spec. Conf. on Cold-Formed Steel Structures*, St. Louis, MO. November, 2010.

Non-linear finite element analysis program "FINELg". 2012. *User's Manual, version 9.3*, ArGEnCo Department, University of Liège, Greisch Info S.A., Liège, Belgium.

Ofner, R. 1997 "Traglast von Staben aus Stahl bei Druck und Biegung". *PhD Thesis*, Graz Technical University.

Semi-Comp. 2007. "Plastic member capacity of semi-compact steel sections – a more economic design (Semi-Comp)". 2007. *Final report (01/01/06 – 30/06/07)* – RFCS – Steel RTD (Contract RFS-CR-04044).

S.T.S.S. 2012. "Research project STSS – Simple Tools Sell Steel" (http://www.ims.org/2012/02/stss-simple-tools-sell-steel/).

Research and Applications in Structural Engineering, Mechanics and Computation – Zingoni (Ed.)
© 2013 Taylor & Francis Group, London, ISBN 978-1-138-00061-2

Use of the Overall Interaction Concept for the practical design of steel sections and members

N. Boissonnade, J. Nseir & E. Saloumi
University of Applied Sciences of Western Switzerland, Fribourg, Switzerland

ABSTRACT: The Overall Interaction Concept (OIC) stands as a new design approach that aims at a straightforward design check of the stability and resistance of steel members. It was developed in response to the expansion of high strength steel products, where instability has more influence and deserves specific attention, especially at the cross-sectional level. Based on the use of a generalized relative slenderness and so-called interaction curves, it applies to both open and tubular cross-sections, further includes potential non-linear material behavior (beneficial strain hardening effects, e.g. stainless steel or cold formed hollow profiles) and covers combined load cases. In addition, it can be applied in a similar manner to cross-section or to member verifications. The present paper describes the bases and features of the OIC, and its accuracy and applicability is tested against thousands of FE results, and the potential for the OIC to become an accurate and effective approach for practical design is demonstrated. Provided additional complementary developments, the OIC may appear as a powerful alternative to the current design methodologies, and serve as a basis for the next generation of standards and practical tools, especially in the frame of an increasing use of high steel grades.

1 INTRODUCTION

This paper deals with the behavior and design of steel profiles, in situations where instabilities (both local and global) play a significant role. A recently-developed new approach, the Overall Interaction Concept (OIC), is presented and detailed. Applicable to the design of both sections and members, it has been developed mainly to i) improve actual design practice, ii) increase accuracy, and iii) advance simplicity and consistency.

In particular, the research developments have been directed towards actual and future high and ultra-high strength steel grades, for which the influence of buckling is more important. Indeed, for sections made of steel whose yield stress lies above 65 ksi (S460 grades and above for Europe), many profiles fall into the slender range, yielding long and tedious calculations for the designer, and a somewhat tempered economical interest as long as all fibers of the cross-section cannot reach the yield stress at peak load.

Design codes usually characterize this sensitivity to early or late occurrence of local buckling by means of a classification of the cross-section: this consists in an additional step prior to section and member design checks, where the width-to-thickness b/t ratios of the different plates comprised within the cross-section are compared with limits provided by the code; depending on its weakest element (i.e. the one with the worst class), different sets of design formulae are provided, either plastic or elastic.

It is however nowadays commonly agreed that this concept of classes causes many practical application difficulties (Boissonnade et al. 2013, Boissonnade 2011, Gardner 2008). In particular, discrepancies and discontinuities are reported (Semi-Comp 2007, Kettler 2008), in addition to a gap of resistance that has no physical meaning (see Figure 1).

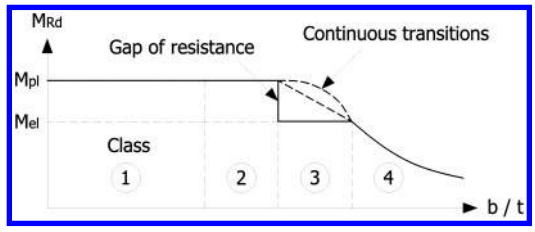


Figure 1. Classification concept according to Eurocode 3 (section in bending).

The Overall Interaction Concept detailed here is aimed at improving this situation. This approach, through the generalization of the relative slenderness concept, sets a general, simple, effective and sound framework to the design of all structural elements. Taking due account of resistance and stability phenomena, the OIC further incorporates the effects of imperfections to accurately predict the real behavior of members. Moreover, the concept is able to maintain simple application steps through the use of modern calculation tools.

Following section 2 presents the bases and features of the proposed approach, and sections 3 and 4 proposes results for sections and members, respectively. Finally, actual and future research directions are given in section 5.

2 THE OVERALL INTERACTION CONCEPT

2.1 *General concept*

The OIC aims at handling the interaction between *resistance* and *instability* ("ideal behaviors") to describe the carrying capacity of a member. On the one hand, the classical concept of *resistance* mainly characterizes the cross-sectional capacity of the member, while, on the other hand, the theory of *stability* describes the inclination of members and sections to buckle under compression stresses. In addition, the influence of imperfections (both material and geometrical imperfections) has to be taken into account.

The proposed OIC approach first relies on the generalization of the relative slenderness concept, and on establishing this parameter as the key to rule this interaction. The concept of relative slenderness is familiar to Structural Engineers, and is widely used nowadays to deal with flexural buckling behavior for example. It is suggested within the OIC to drastically enlarge the field of application of this slenderness-related approach through the following generalization of the relative slenderness:

$$\lambda_{rel} = \sqrt{\frac{R_{RESIST}}{R_{STAB}}} \qquad (1)$$

R_{RESIST} represents the factor by which the actual loading has to be multiplied to reach the pure *resistance* limit, while R_{STAB} is the factor used to reach the buckling load of the ideal member (*instability* limit). Doing so allows the generalized relative slenderness taking a non-dimensional balance between the relative influences of instability and resistance, and makes it capable of dealing with combined loading situations or cross-sectional (local) instability effects as well. Once determined, this λ_{rel} value is further used in the design procedure to get into a so-called "interaction curve" (also sometimes referred to as "buckling curve") and leads to the determination of a "χ" value (see Figure 2). This χ value (analogous to the one used in Eurocode 3, CEN 2005), which may also be called "reduction factor", represents the penalty due to instability effects on the "pure resistant behavior"; χ can obviously only be lower than 1.0. Eventually, the final resistance is evaluated as χ. R_{RESIST}; Figure 3 further illustrates the proposed approach and its application steps.

2.2 *Application to cross-sectional behavior*

The adoption of a generalized slenderness allows applying the OIC procedure to determine the resistance of slender sections. Indeed, while R_{RESIST} remains unchanged when λ_{rel} is relative to either sections or members, R_{STAB} may relate to *global* (member) buckling as well as to *local* (cross-sectional) buckling).

Therefore, the tendency of slender sections to experience early local buckling may be characterized in applying the OIC approach as well, provided that R_{STAB} corresponds to the local or distortional buckling mode of the cross-section. Usually, this is achieved through the determination of so-called critical stresses σ_{cr}, and R_{STAB} is simply set as the ratio between σ_{cr} and the actual stress on the considered wall.

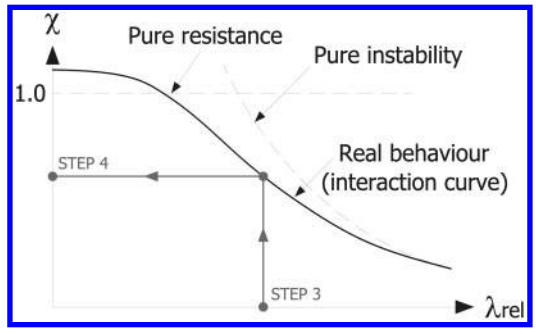


Figure 2. Resistance – instability interaction.

$$STEP\ 1: R_{RESIST}$$
$$STEP\ 2: R_{STAB}$$
$$STEP\ 3: \lambda_{rel} = \sqrt{\frac{R_{RESIST}}{R_{STAB}}}$$
$$STEP\ 4: \chi = f^{\circ}\left(\lambda_{rel}\right)$$
$$STEP\ 5: R_{REAL} = \chi \cdot R_{RESIST}$$

Figure 3. Application steps of the OIC.

It is suggested within the OIC to resort to modern, numerical tools to calculate accurate R_{STAB} values, such as CUFSM (Li & Schafer 2010) or GBTUL (Bebiano et al. 2008) for example. These (free) software not only allow for a much more accurate R_{STAB} value – usually also more favorable –, but also permit to consider the cross-section as a whole, benefiting from potential resistance reserves brought by adjacent walls restraints. Steps 3 to 5 of the design procedure (see Figure 3) then apply, however with dedicated interaction curves. This shall be seen as an important improvement brought to the current design practice that usually resorts to the effective width method for slender sections (AISC 2005): further to removing the need for classification and providing a smooth, continuous transition of the resistance from the plastic to the slender range, the method avoids the fastidious determination of effective properties.

2.3 *Combined load cases*

The OIC approach and application steps, as detailed in §2.1, remain valid whatever the loading situation considered. In particular, combined load cases (e.g. for beam-columns) can be treated as easily as simple ones, thanks to i) the use of "R-factors" as defined previously, and to ii) a generalized definition

of λ_{rel}. Moreover, if numerical evaluations of R_{RESIST} and/or R_{STAB} are contemplated, combined load cases can be afforded rather efficiently, without resorting to complex interaction equations.

2.4 *Main features of the OIC*

Further to calling off the classification concept and its many difficulties (additional step, discontinuities, complexity...), the OIC enables to keep a strong mechanical background to handle the balance between resistance and stability effects. Through a limited number of well-defined governing parameters and a simple but sound physical background, it provides practitioners with a high level of control on their design.

Simplicity arises from the definition of the generalized relative slenderness: it allows i) combined loading conditions to be treated as easily as simple ones – therefore avoiding to resort to complex interaction formulae –, ii) the use of a unique concept to characterize the resistance of sections as well as the resistance of members, and iii) the treatment of all sections shapes in a unique procedure, i.e. no distinction is made between open and tubular sections for example.

Then, the use of modern powerful analysis tools such as CUFSM, GBTUL ... provides quick and accurate results, and deeply simplifies the determination of critical stresses (or, equivalently, of R_{STAB}) as well as the resolution of so-called "coupled instabilities" problems, i.e. involving both cross-sectional (local) and member (global) instabilities.

Next, although being applied in this paper to structural steel design, the OIC remains open to any material, in particular to elements made of tomorrow's high performance materials highly susceptible to buckle (e.g. columns or beam-columns made of high performance concrete, fiber-reinforced concrete, high strength steel, composite materials...). The application to such materials is straightforward, as the bases and concept remain whatever the material considered. Particularly, materials that exhibit a high degree of nonlinearity and strain hardening (high strength steel, stainless steel, aluminum...) shall be exploited more effectively (see also Gardner et al. 2011).

Last, as already explained, resorting to the OIC approach, offering smooth and continuous transitions along the whole slenderness range, will particularly be beneficial in the frame of an increasing use of high strength steel, for which an efficient treatment of local instabilities will be crucial, especially at the cross-sectional level.

3 CROSS-SECTIONAL RESISTANCE

This paragraph presents a first series of results relative to cross-sectional behavior. Accordingly, the OIC was applied with respect to R_{STAB} values relative to *local* buckling – this was achieved with the use of CUFSM –. First, a detailed examination of the results obtained for

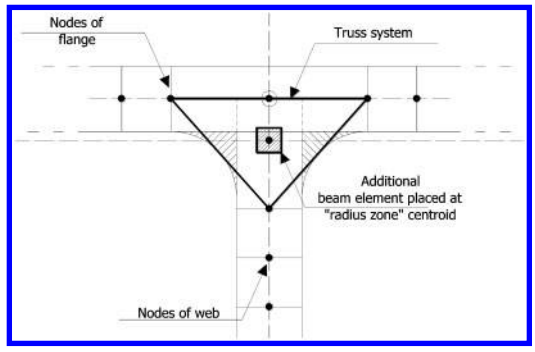


Figure 4. Shell FE-modeling detail at web-flange junction.

R_{STAB} (or σ_{cr}) values showed considerable differences between the numerically-obtained CUFSM results and the classical plate buckling theory ones (i.e. assuming ideal support conditions for webs and flanges).

Then, in order to test the adequacy of the proposed concept, a series of numerical results have been collected, by means of non-linear software FINELg, 2012. Obviously, shell models have been developed, with nowadays common features (Boissonnade et al. 2012, Boissonnade & Somja 2012).

As particular modeling features, the web-flange junction has received a careful treatment. First, an additional beam element which allows for nearly-exact cross-sectional properties was added. Then, a "truss system" was attached to the models in the web-flange junction zone, in order to keep this region nearly rigid. This ensures local buckling waves to develop as realistically as possible and an accurate characterization of the onset of buckling.

The following set of parameters has been used for this numerical study on cross-sectional resistance:

- 292 cross-section shapes (203 US + 89 European ones);
- 3 different steel grades: S235, S460, S690 for European profiles, and 36, 65 and 100 ksi steel for US profiles;
- Various load cases, from simple compression or major-axis bending to combined loading situations (predominantly $N + M_y + M_z$);

In total, more than 3 400 non-linear FE computations have been performed.

Figures 5–7 plot some of the obtained results. Their axes are "OIC-defined", i.e. the horizontal axis relates to the generalized slenderness λ_{rel}, while the vertical axis reports on the cross-section reduction factor χ_{CS}. As Figure 5 shows, an excellent level of consistency can be reached, indicated by a very limited scatter. These results demonstrate that λ_{rel} is a key parameter to rule the resistance-stability interaction and that the possibility to derive accurate and consistent equations to calculate χ values exists; such investigations are currently under development.

One may also note, for low steel grades, a rather important resistance reserve for $\lambda_{rel} < 0.3$, due to

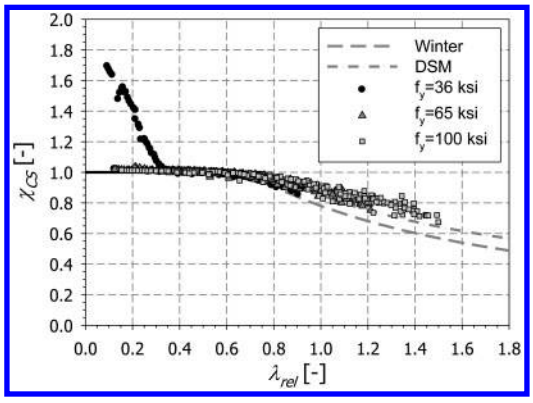


Figure 5. WF sections under compression (AISC database).

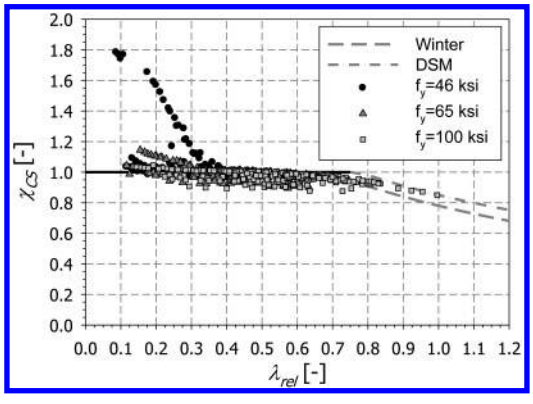


Figure 6. WF sections under major-axis bending (AISC database).

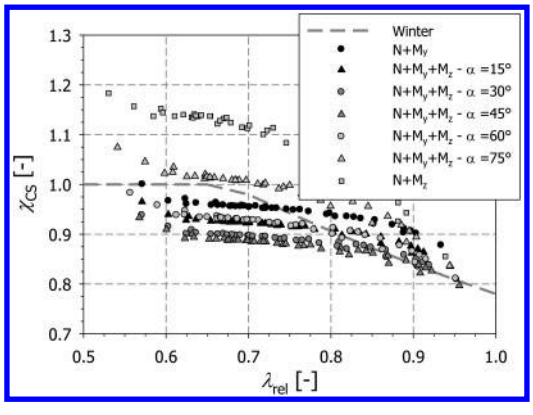


Figure 7. IPE and HEB sections under combined loading (biaxial bending with 70% compression – $fy = 460$ N/mm^2).

strain hardening effects. Similar results obtained in the same way for sections bent about the major-axis are given in Figure 6, and identical conclusions can be drawn.

Combined loading situations yielded results such as those plotted in Figure 7. In such cases, R_{STAB} values were determined numerically with CUFSM, and R_{RESIST} values have been calculated from the $N - M_y - M_z$ plastic equations of Eurocode 3. For sake of clarity, a distinction has been made between the different loading situations, with respect to the degree of biaxiality, i.e. the M_y/M_z ratio. Again clear tendencies may be emphasized, namely with respect to the degree of biaxiality as cross-sectional failure modes vary with the M_y/M_z ratio.

The application of the OIC to predict the resistance of open cross-sections is therefore seen to be fully appropriate, whatever the dimensions, steel grade or loading conditions; as presumed in the definition of a generalized relative slenderness, this approach is able to catch the governing parameters and to lead to consistent results, even for non-trivial situations and despite quite simple application steps. Consequently, the possibility to derive practical but accurate expressions for χ-curves exists, and is currently under completion (multiple mechanically-based expressions are foreseen, according to the trends observed for the combined load cases).

4 MEMBER RESISTANCE

Present paragraph now deals with *member* resistance, with a particular focus on *combined* load cases. Indeed, simply-loaded elements such as columns (flexural buckling) or beams (lateral torsional buckling) naturally fit with the OIC format, see application steps detailed in §2.

In an effort to distinguish between global and local buckling modes, a series of more than 14 000 FE results obtained by means of beam models – thus ignoring cross-sectional deformation modes – has been collected. These have been gathered from Ofner 1997 and are all relative to cases where local instability of the cross-section can be neglected (i.e. χ_{CS} is such that $\chi_{CS} \geq 1.0$ – Class 1 or 2 sections). They comprise various effects expected to have a significant influence on the member's behavior, such as different section shapes, bending moment distributions, slenderness...

Some of the results are plotted on Figure 8 under the OIC format, for members submitted to $N - M_y - M_z$ loading; it shows that as a first parameter to influence the resistance, the bending moment distribution plays a key role (ψ stands as the ratio between applied end moments: $\psi = 1$ indicates constant bending moment distribution, $\psi = 0$ triangular distribution, and $\psi = -1$ a bi-triangular pattern). It has indeed since long been shown to have a significant influence on the extent of yielding along the member (see Boissonnade et al. 2006). Also, a careful analysis of the results indicates that the M_y/N and M_z/N ratios shall be considered too as leading parameters for the derivation of appropriate interaction curves. $\chi_{MB} \geq 1.0$ results can also be pointed out, indicating a reserve of resistance up to 10%, mostly due to conservative estimates of R_{RESIST} adopted here (Eurocode 3 equations).

These results confirm the potential of the OIC approach to capture the behavior of beam-columns

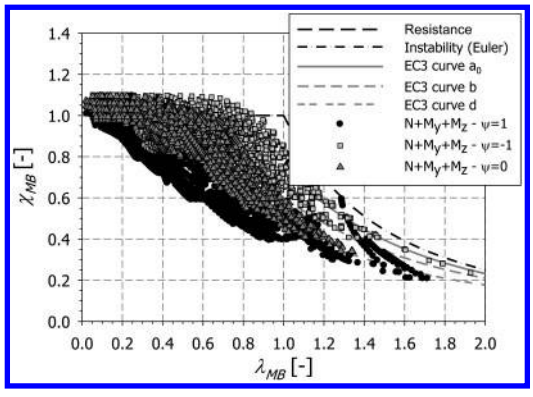


Figure 8. FE results for member under compression and biaxial bending.

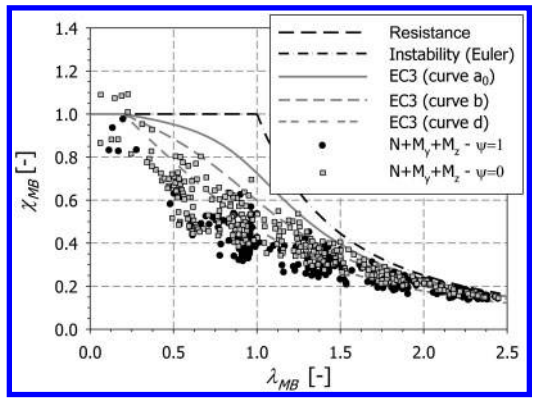


Figure 9. Members with slender sections – Global & local instabilities.

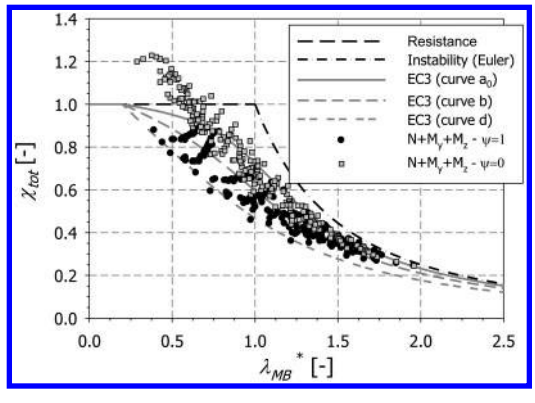


Figure 10. Members with slender sections – "DSM-like" approach.

in a straightforward manner, i.e. without resorting to so-called member interaction formulae. Provided the governing parameters are identified, the possibility to derive accurate and suitable, mechanically-based interaction curves seems obvious, and is actually under completion.

As the last and most complex structural behavior being investigated, the case of members with slender sections is addressed now, i.e. situations involving both local and global buckling – so-called "coupled instabilities". In this respect, some 2 000 non-linear shell-FE calculations with suitable sets of initial imperfections were computed for (exaggerated) slender sections, with a series of parameters as follows:

- 6 different sections defined for being slender either i) for the flange or for the web only, or ii) for both flange and web:
- 4 values of the global relative slenderness λ_{MB};
- $\psi = 1$ and $\psi = 0$ bending moment distributions;
- Various loading situations, again from simple compression or major-axis bending to combined loading situations (predominantly $N + M_y + M_z$);

All sections have been shown to exhibit an important influence of local buckling effects, with χ_{CS} values ranging from 0.4 to 0.9, depending on the load combination and on the level of web-flange interaction within local buckling modes.

Figure 9 shows the obtained results, where the horizontal axis refers to λ_{MB} – calculated from Equation (1) with an R_{STAB} value relative to global instability; χ_{tot} values reported on the vertical axis are those obtained from GMNIA shell computations, and therefore include local and global instability effects.

As can be noticed, the influence of local instability, visible at low λ_{MB} values, is often significant. Also, the complex coupling between local and global instabilities generates a rather large scatter.

These results show that additional investigations are required to provide an efficient treatment of coupled instabilities by means of the OIC. Further developments on this topic are in progress, and several ways of dealing with this coupling are actually under scrutiny, such as a "DSM-like" approach (cf. AISC 2005), where λ^*_{MB} is defined with R_{RESIST} being substituted by $\chi_{CS}.R_{RESIST}$; promising results can be shown, such as those of Figure 10.

5 CONCLUSIONS – ACTUAL AND FUTURE INVESTIGATIONS

The present paper contributed to evidence the potential for the Overall Interaction Concept to become a reliable and practical alternative to the current well-known design rules to account for the interaction between resistance and instability effects. In particular, results on both sections and members, as well as for simple or combined load cases have been presented; they demonstrate that, although being based on simple principles and with straightforward application steps, the OIC may appear as an accurate and consistent approach, and serve as a basis for the next generation of standards and practical tools, especially in the frame of an increasing use of high steel or ultra-high steel grades.

The OIC approach is actually at the core of the S.T.S.S. project ("Simple Tools Sell Steel", STSS 2012), whose main objective is to develop and assess new design concepts to predict accurately the response of members made of standard and high-strength steel up to collapse. The project focuses on cross-sectional and member resistance, materials with non-linear behavior, and on the development of new criteria to allow for plastic analysis. It will result in new practical tools and design software, and provide the scientific background for the implementation of an OIC approach in design codes.

Besides, OIC-based investigations on high and ultra-high performance fiber concrete elements (columns and beam-columns) are currently under way. Also, applications to other materials are contemplated (composite sections, stainless steel, aluminum, structural glass. . .).

As a consequence of the disappearance of the classification concept, investigations within fire and earthquake steel design are necessary. Further, the OIC approach and principles, as described herein, should appreciably improve the design of specific members where coupled instabilities and/or complex solutions to implement require (partial) numerical solutions and the associated conceptual framework (e.g. tapered members, cellular beams. . .).

REFERENCES

AISC. 2005. Specification for structural steel buildings. *American Institute of Steel Construction*, Chicago, IL. ANSI/ASIC 360–05.

Bebiano, R., Pina, P., Silvestre, N. & Camotim, D. 2008. "GBTUL – Buckling and Vibration Analysis of Thin-Walled Members", DECivil/IST, Technical University of Lisbon (http://www.civil.ist.utl.pt/gbt).

Boissonnade, N., Nseir, J. & Saloumi, E. 2013. "The Overall Interaction Concept: an Alternative Approach to the Stability and Resistance of Steel Sections and Members". *Proceedings of the Annual Stability Conference*, Structural Stability Research Council, St. Louis, Missouri, April 16–20.

Boissonnade, N. 2011. "The Concept of Cross-section Classes in Eurocode 3 into Question", *ECCS-TC8 meeting*, Lisbon, June 3rd.

Boissonnade, N., Greiner, R., Jaspart, J.P. & Lindner J. 2006. "Rules for Member Stability in EN 1993-1-1; Background documentation and design guidelines", *Eds. Mem Martins*, Portugal, E.C.C.S. – ISBN 92-9147-000-84, Vol. 119, 259 pages.

Boissonnade, N. & Somja, H. 2012. "Influence of Imperfections in FEM Modeling of Lateral Torsional Buckling". *Proceedings of the Annual Stability Conference, Structural Stability Research Council*, Grapevine, Texas, April 18–21.

CEN (Comité Européen de Normalisation. 2005. "Eurocode 3: Design of Steel Structures, Part 1–1: General rules and rules for buildings (EN 1993-1-1)", Brussels.

Gardner, L. 2008. "The continuous strength method". *Proc. Institution of Civil Engineers: Structures and Buildings*, vol. 161, n° 3, p 127–133.

Gardner, L., Wang, F. & Liew A. 2011. "Influence of strain hardening on the behavior and design of steel structures", *International Journal of Structural Stability and Dynamics*, Vol. 11, pp. 855–875.

Kettler, M. 2008. "Elastic-plastic cross-sectional resistance of semi-compact H- and hollow sections". *PhD Thesis*, Graz Technical University.

Li, Z. & Schafer, B. 2010. "Buckling analysis of cold-formed steel members with general boundary conditions using CUFSM: conventional and constrained finite strip methods." *Proceedings of the 20th Int. Spec. Conf. on Cold-Formed Steel Structures*, St. Louis, MO. November, 2010.

Non-linear finite element analysis program "FINELg". 2012. *User's Manual, version 9.3*, ArGEnCo Department, University of Liège, Greisch Info S.A., Liège, Belgium.

Ofner, R. 1997. "Traglast von Staben aus Stahl bei Druck und Biegung". *PhD Thesis*, Graz Technical University.

Semi-Comp. 2007. "Plastic member capacity of semi-compact steel sections – a more economic design (Semi-Comp)". 2007. *Final report (01/01/06 – 30/06/07)* – RFCS – Steel RTD (Contract RFS-CR-04044).

S.T.S.S. 2012. "Research project STSS – Simple Tools Sell Steel" (http://www.ims.org/2012/02/stss-simple-tools-sell-steel/).

Research and Applications in Structural Engineering, Mechanics and Computation – Zingoni (Ed.)
© 2013 Taylor & Francis Group, London, ISBN 978-1-138-00061-2

Influence of imperfections and geometrical discontinuities on the behavior of the steel towers

A.I. Dogariu & D. Dubina
"Politehnica" University, Timişoara, România

ABSTRACT: This paper analyzes the possible influence of different types of imperfections on the behavior of the steel towers. Two types of tubular towers, exposed at wind load, will be described. The first one is a wind tower of thin-walled circular section and the second one a high-mast lighting tower of polygonal cross-section. In the first case the discontinuities are due to the bolted ring stiffened joints, while in second case are the press-lapped joints. The specific technological imperfections raised from lack of evenness of joints and residual stresses caused by pressing are interacting with the usual cylindrical shell imperfection. Without experimental tests, the study offers the references for the sensitivity of such structures to imperfections and geometrical discontinuities on the buckling behavior.

1 INTRODUCTORY REMARKS

1.1 *Common applications of the steel tubular towers*

The proposed paper analyzes the influence of different types of possible imperfections on the behavior of the steel towers.

The steel towers are mostly used as supporting structures for wind turbines, lighting systems, communication technologies equipments, etc. Some of the most typical details and technological features of tubular towers, exposed at wind load, will be described.

Nowadays the society should attempt to fully exploit the most from available environmentally friendly and renewable energies sources. In this context, lately the wind power resources receive a major attention from the national and European regulations and legislation that sustain their development and permanent increase of the installed capacity. For the wind tower, the following structural concepts are used: concrete, hybrid and metallic towers, which can be lattice towers, small guyed poles or tubular towers. Even if have a higher cost, due to their structural advantages in case of large application, one can notice an significant increase in the use of the of thin-walled circular section for supporting the wind turbines.

The communication facilities as cellular worldwide networks, air traffic control, satellite reception systems, receivers and terrestrial reception antennas for radio and TV, and distribution technology for community antenna nets, have become indispensable for modern society and for the people comfort. As a direct consequence in the last decades this industry have greatly expanded, requiring a large number of supporting towers, towers which through their technological features should offer an optimal solution, both from structural and economical point of view.

An other wide used application of steel towers it's found in case of high masts lighting towers, that reach heights up to 70 m for big sports stadiums where are required high level for night shoots, and therefore considerable heights and remarkable number of floodlights. If for the before mentioned applications are used a ticker circular cross-section, in case of lighting-masts a thin polygonal cross-section is more rational to be used because of the smaller height and reduced operational loads

1.2 *Technological features*

The research studies trying to optimize the steel towers are mainly concentrated on two directions, regarding the optimization of the cross-section and element shape and the connection procedures.

The first one consists in choosing the most appropriate shape of the cross-section feasible from the technological point of view, together with the proper variation of the cross-section diameter along the height. The above parameters are dependent on the design loads magnitude and stress level, height of the structure, and the nature of the local loads effects.

Generally the tubular wind towers reaches heights over 50 m (100–140 m) supporting very heavy turbine mass, requiring large base that frequently exceed diameters of 3 m and wall thickness of 30 mm. Due to large geometrical dimensions, the 20-30 m expedition segments are obtained by rolling of the steel plates in such a way to obtain a shape of a truncated cone (see Figure 1). Each strip is welded on the longitudinal direction (see Figure 2a) and after connected with the

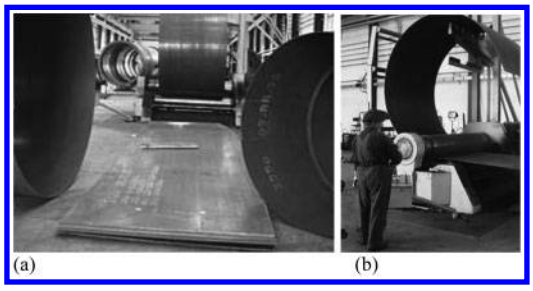


Figure 1. Steel strip fabrication: cutting (a) and rolling (b).

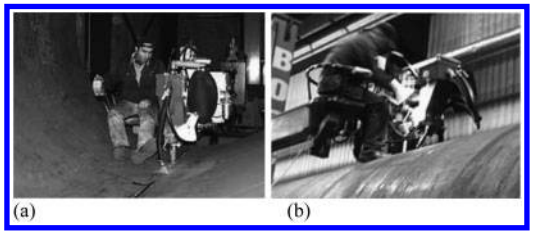


Figure 2. Welding of the tower segments.

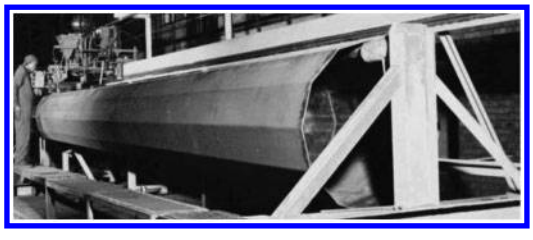


Figure 3. Cold forming of lighting-mast segments by folding the steel plates.

following next strip by a transversal circular weld (see Figure 2b) carried out by automatic MAG process.

Because of the smaller heights and reduced operational loads, compared with wind towers, the monotubular tapered steel lighting -masts have a base section that usually don't exceed 2 m in diameter and 10 mm thickness of the walls that allow to obtain the truncated cone segments polygonal cross-section by cold folding the steel sheets (see Figure 3) and subsequent external longitudinal welded along the slant.

The possibility to improve the element local behavior by longitudinal folds that acts like stiffeners allow to obtain very slender shape as well a reduce material quantity.

The second intensive investigated aspect that has a paramount importance is the segment joining method. The authors of this study believed that technology used for the connection may introduce a series of local effects with a direct influence on global behavior of the structure. In case of wind tower are traditionally used flange connection (see Figure 4) and more recent, friction connections (see Figure 5).

This connection have been studied in detail and extensively used in many applications. For both of

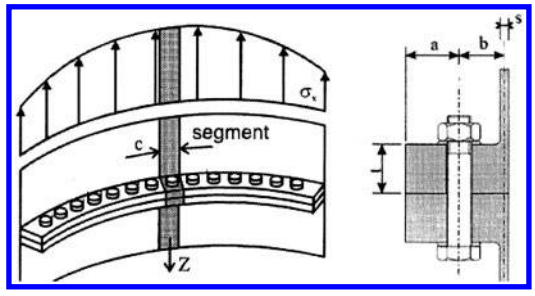


Figure 4. Calculation model for traditional bolted flange connection (L-flange / half of the T-stub connection EC3).

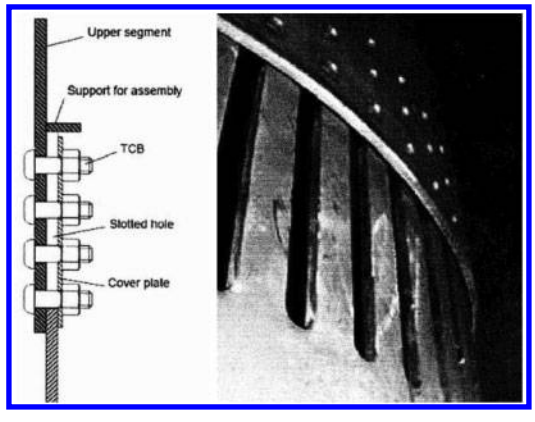


Figure 5. Friction connection between two segments using tension control bolts.



Figure 6. The high-mast lighting from "Dan Păltinişanu" soccer stadium, in Timişoara.

these connection typologies, in scientific literature, research reports and design codes, one can found: experimental results, mechanical behavior characteristics, finite element modelling strategies for numerical simulations and complete analytical models for both strength and buckling verifications. Due to this fact is very easy to control and to avoid all the undesirable effect that can introduce significant imperfection in such a way to strongly compromise the tower safety. For such connections, the EN 1993-1-6, suggest introducing the intended offset at a joint and an accidental eccentricity.

In case of lighting-mast a press-fit interference jointing is used. The connected segments (see Figure 6) act as shaft and bracket and are to be assembled at site by forced overlapping (see Figure 7).



Figure 7. The forced overlapping process of joining the shaft segments.

This type of connection technology gives unique assembly simplicity and quickness as well as a cheaper price, and is suitable when aren't imposed very sever geometric deviation (final length of the mast).

As a jointing method is very common for mechanical tools engineering, but is not so used in civil engineering applications. First important difference in application of this jointing method is the fact that in case of machining thick cylinders are used and for civil engineering structures thin-walled cylinders are used. Also the mechanical joint must be able to take and transmit the torque moment, meanwhile in structural application this connections works in bending. The reduce thickness of the segments cross-sectional walls may lead to the conclusion that the segments are forced overlapped until the cross section material yield occurrences and the hardening phenomenon. In the machining applications this connections works by friction, and was normal to initially suppose that the same working principle will be apply also for lighting-masts.

The authors of this article didn't find any available studies of this type of connection for structural application or standard rules for design and accounting the mechanical behavior, so this study will try to identify some of the possible effects that can appear due to the connection behavior. The obvious effects of cold-folding of the polygonal shape section, are residual stresses and variation of yield limit. In the same time the connection technology by the site forced cold-overlapping beside significant residual stresses and high pressure forces, may also introduce geometrical deviations and discontinuities, changes of cross-section shape, that are not described in the design rules.

2 ANALYSIS CONSIDERATIONS AND DESIGN REQUIREMENTS

2.1 *Static scheme and loading conditions*

The static scheme is the simplest thing that can be realized in structural ambit. In essence, all this supporting towers are very long vertical cantilevers subjected to wind load, operational loads, seismic load etc. These design load cases acts, more or less, as uniform distributed loads along the tower height, together with a higher concentrated horizontal force (resulted from wind or earthquake load) and gravitational self-weight force at the top of the tower, were either the wind turbines, either communication equipments or floodlights panels are position. These loads pattern induce in the structure mainly bending effects.

In order to find-out the internal forces needed for the global check of the tower capacity, in a simplified manner this types of structures may be treated, as a cantilever bar of class 4 thin circular section and it can be calculated as a 1D beam structure, with or without the account of global imperfection, using an elastic material law.

Even if the design and verification seems at first sight a simple problem, due to the complexity of curved shells behavior, refined local analysis using 3D shell models with 2D finite elements are needed, but can be limited for relevant segments only. These free body segments should be placed between two, consecutive or not, flanges that will assure the appropriate boundary condition, i.e. radial restrained. These segments must be chosen such as to contain the critical cross-sections of higher internal forces (i.e. bending moment), cross-section reduction due to the visiting door or ventilation opening, cable entry etc., or zones of expected high local imperfections due to the residual stresses, connections details and discontinuities.

2.2 *Design concepts and normalization*

The European design codes-series, by EN1993-1-6 cover the most of the resistance and stability design criteria for this types of tubular structures and by EN1993-1-8 the connection design issues. Also EN1993 part 3-1 gives specific rules for tower and masts, and some useful information can be find in EN1993-3-2 Chimneys.

Beside the general design issues stated in EN1993, other specific regulations comes to offer more detailed or more clear design methodologies and requirements for wind tower and for high-mast lighting, like IEC 61400-1 (2005-08) Wind Turbine – Part 1:Design requirements (International Electro technical Commission), respective „Technical Report number 7 – High Mast Lighting – Specification for design, manufacture, assembly, erection, painting, testing and maintenance" (The Institution of Lighting Engineers).

Because the European Standard is not permitted to include explanatory or educational materials, in European Steel Shell Buckling Recommendations (2005) which are fully compatible with EN1993-6, designers can find extended rules to cover all the arisen problems of steel tubular section.

The EN1993-6 Standard is concerned with the requirements for design against the ultimate limit states of: plastic limit (LS1), cyclic plasticity (LS2), buckling (LS3) and fatigue (LS4). The described structures are all very slender (diameter/total height ratio, ~1/25–1/35) and with thin walls (thickness/diameter ratio, ~1/100-1/150), so the buckling limit state (LS3) design criterion is the most server one. Also fatigue limit state should be considering, but is beyond the goal of this study.

From the standard procedures arise three levels of design procedures at LS3: Buckling (see Figure 8),

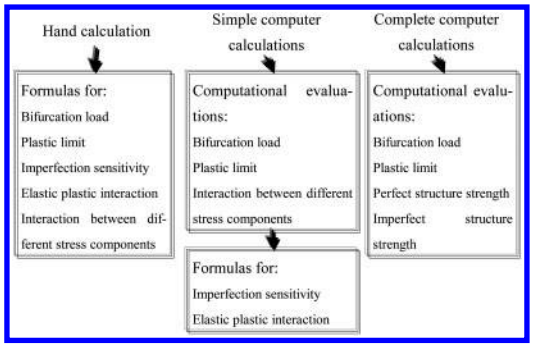


Figure 8. The alternatives to design thin curved shells.

Table 1. Types of shell analysis.

Type of analysis	Shell theory	Material law	Shell geometry
Membrane theory	membrane	not applicable	perfect
LA*	linear	linear	perfect
LBA*	linear	linear	perfect
GNA*	non-linear	linear	perfect
MNA*	linear	non-linear	perfect
GMNA*	non-linear	non-linear	perfect
GNIA*	non-linear	linear	imperfect
GMNIA*	non-linear	non-linear	imperfect

*LA – Linear elastic shell analysis, LBA – Linear elastic bifurcation analysis, GNA – Geometrically non-linear elastic analysis, MNA – Materially non-linear analysis, GMNA – Geometrically non-linear elastic analysis, GNIA – Geometrically non-linear elastic analysis with imperfections, GMNIA – Geometrically and materially non-linear analysis with imperfections.

starting from a complete hand calculation based on analytical formulas, a simple computer calculation, and a advanced complete numerical-based design.

For carrying out the various limit states LS verifications and checks are required and are available the following types of analysis, depending on considering or ignoring the material and geometrical nonlinearities and second order effects, and the introducing of equivalent geometrical imperfections.

The most common procedure, based on LBA and MNA available on most commercial software, used in practical design for buckling capacity assessment is shown in Figure 9.

The simplified procedures are rather conservative, so the most accurate and complicated in the same time is GMNIA. Even if is one of the most complex and precise design method it require the introduction of the imperfections. The most important effects are those due to geometric imperfection of shape.

2.3 *Imperfections and their expected effects*

For common design cases the EN1993-6 specify the prescribed relevant geometrical imperfection for

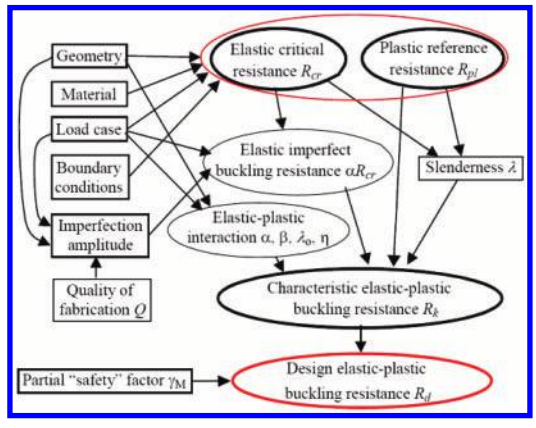


Figure 9. Buckling strength assessment using simple computer calculations.

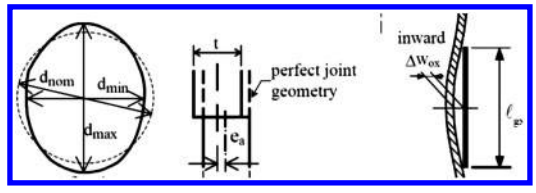


Figure 10. Geometrical imperfections prescribed by EN1993-6.

cylindrical shell, to take into account of, i.e. out-of-roundness (deviation from circularity), eccentricities (deviations from a continuous middle surface in the direction normal to the shell along junctions of plates), and local dimples (local normal deviations from the nominal middle surface) (see Figure 10).

The design impose accounting of the prescribed types of the imperfection patterns in order to fully understand and quantify their influence on buckling behavior. In case of shells even small imperfection may cause significant drop of the capacity. Depending on shell geometry and loading type, some forms of imperfection or higher amplitude imperfections strengthen and increase the buckling capacity. The assessment of the form and amplitude of the imperfection it is most important and also very difficult as specially when few or non regulation exist in this way. It is the case of forced overlapping connections of high mast lighting.

In this case the structure imperfections may raise from lack of evenness of joints, flexibilities of connections, and residual stresses caused by pressing are interacting with the usual imperfection. The available design regulations, i.e. TR 7 – High Mast Lighting, didn't make any special reference related to the connection design principle and behavior characteristics. Accounting the normative lack of information it is believed that the technology of press-fit connection should avoid appearance of any discontinuity, and the shaft could be consider as a continuum element. Even there are not available experimental results, the numerical study is based on real applications and tries to

offers the references for the sensitivity of such structures to imperfections and geometrical discontinuities on the buckling behavior.

3 NUMERICAL SIMULATIONS

3.1 *Numerical goal*

Several numerical investigation have been carried out for assessing the prescribed influence of imperfections, most of them for wind towers, and the effect of discontinuities introduced by openings. Also the authors of this paper have previously investigated the benefic behavior of the cold-folded polygonal tubular shaft for lighting mast. Even if the governing phenomenon are very complex, the capacity of this type of structures may be obtain using a very simple, rather trivial formula (1):

$$M^* = \frac{M_p}{\gamma_M}\left\{0.9241\cdot\left[\left(90\cdot\sigma_y\frac{D}{NEt}\right)^{-0.2858}\right]-0.1266\right\} \quad (1)$$

From these reasons, this study will present only the numerical simulation program dedicated to offer a qualitative view related to the overlapped connection behavior and possible modelling and influences.

Starting from the high-mast lighting from "Dan Păltinişanu" stadium from Timişoara, several connection geometries have been study to verify the above mentioned hypothesis that the connection don't introduce unfavorable effects. It is believed that because of forced overlapping appearance of any eccentricities will be avoid, but the flexibility of the connection and the state of stress will influence the behavior.

Cross section of the 55 m height mast is a regular polygon with 20 sides with wall thickness of 10 mm for the bottom segments up to 35.38 m, 8 mm up to 44.82 m and 6 mm for upper segments up to 55.00 m. The diameter varies from 1400 mm at base to 500 mm at the top.

3.2 *Finite element model*

Using ABAQUS Software 3D Shell models have been build to study the effect of the connection discontinuity.

In a first step, thirteen connection along the shaft have been numerically investigated. Three types of models have been build. An explicit contact model (T_{i-i+1}) (see Table 2) with the consideration of separate segments and two continues models. In first one (T_{const}) considering the constant thickness of the upper segment along the overlap length, and in the second one (T_{duble}) the added thickness of the two connected segments.

For the explicit model, considering that the connection work like a friction one, was supposed that the diameter misfit will cause the hardening of the sections and will introduce a uniform pressure p_n that

Table 2. Numerical models dimensions.

Model	First segment D_1	First segment D_2	First segment t	Second segment D_1	Second segment D_2	Second segment t	Overlap L
T0-1	500	536	6	518	579	6	536
T1-2	532	581	6	563	667	6	581
T2-3	579	670	6	648	734	8	670
T3-4	667	738	8	713	821	8	738
T4-5	734	825	8	798	884	10	825
T5-6	821	889	10	859	971	10	889
T6-7	884	976	10	945	1030	10	976
T7-8	971	1035	10	1003	1117	10	971
T8-9	1030	1122	10	1089	1172	10	1030
T9-10	1117	1177	10	1142	1259	10	1177
T10-11	1172	1264	10	1263	1228	10	1264
T11-12	1259	1315	10	1279	1393	10	1315
T12-13	1310	1389	10	1360	1400	10	1398

D_1 – upper cross section median diameter; D_2 – bottom cross section median diameter; t – segment thickness; L – connection (overlap) length; all dimensions are in mm

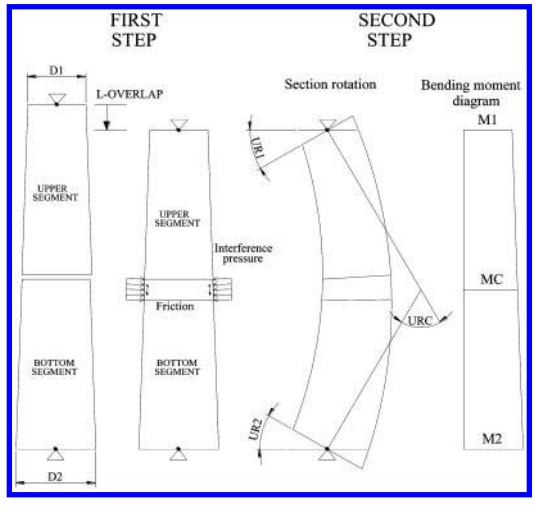


Figure 11. Numerical analysis steps and applied loads.

should facilitate the appearance of a sufficient friction force in order to assure the connection resistance and rigidity. Due to the high level of the appeared friction forces, bending behavior and failure of the connections, the friction law was neglected in the after and presented FE models results.

The segments assembly was considered double pined. The load was applied in two steps. In the first step the two segment were pressed, imposing to the upper support a displacement equal with overlap length. In the second Static Risk step an equal imposed rotation was applied at the free ends (see Figure 11).

In a second phase considering an appropriate detailing of the connection in such way offer continuity (maybe a larger overlapping lengths, more fit diameters to limit or remove the yield zones etc.), a comparison between the two continuous models

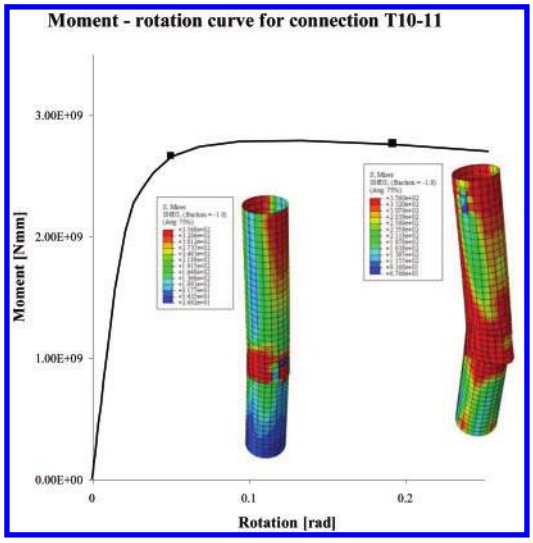


Figure 12. Numerical result for T10-11.

(i.e T_{const} and T_{duble}) accounting prescribed imperfection (i.e. out-of-roundness, local dimples) have been performed in order to emphasis the eventual behavioral differences in case of global analysis.

3.3 *Numerical results and comments*

Using the described geometrical parameters from Table 2 the moment-rotation curves shown a more flexible and less resistant behavior ($M_c = 2850$ kNm < $M_{sect} = 4200$ kNm) of the connections, fact that should be considered in the global analysis of the structures. In the Figure 12 are shown the results for model T10-11, in terms of moment-rotation $M_c - \theta_c$ (2) of the connections and failure modes. All the other models exhibits similar behavior.

These results emphases the need to clearly identify and characterize the effects of local behavior of such type of connections and to be accounted through specific imperfections that should be codified and use together with the geometrical imperfections prescribed by EN1993-6 (see Figure 10).

How it was stated before, it is believed that proper connection detail can assure a better behavior and to limit the negative effects notice based on previous numerical simulations. Further investigation will be done in this way in future studies. From this reason the next step of this study have investigated the above described continuous models.

The connection difference haven't reveal any significant behavior difference or different sensitivity at the various pattern of considered imperfections (see Figure 13). As a comment, it is believed that even if a small benefic effect have been shown in case of T_{duble} model and clearly acting like a local ring stiffener, for the global numerical analysis the two models are equal, and the T_{const} model being more simple is recommended to be used.

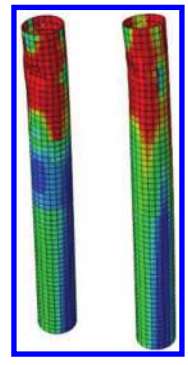


Figure 13. Comparison between T_{duble} and T_{const} failure modes.

4 FINAL REMARKS

The present study doesn't intend to offer a final and undisputed solution of the above identified problems however it can be regarded as a general guidelines, proposing a way of investigation and showing difficulties of approaching numerical solutions of these structures. Without the support of a relevant program of experimental investigations results, enabling for physical identification of problems and a base of calibration the numerical simulation provide qualitative estimation only.

Consequently, further investigations still are required in order to offer clear recommendations for maximum diameter misfit, minimum overlap length and imperfection to be considered if the recommended parameters are not respected.

REFERENCES

Abaqus User Manual 2007. Dassault Systèmes.

European Committee for Standardization. EN 1993-1-6 Design of steel structures Part 1–6 : Strength and Stability of Shell Structures.

European Shell Buckling Recommendation 2008: Buckling of steel shells European design recommendations.

HISTWIN High-strength Steel Towers for Wind Turbines, RFSR-CT-2006-00031.

International Electrotechnical Commission IEC 61400-1:2005 Wind turbines – Part 1: Design requirements.

Velikovic, M., Dubina, D., Simoes, R., Jordao, S., Rebelo, C., Marques, L. 2011. *Wind Towers: design by FEM and Technological Features*, SUSCOS training course, Coimbra.

Dogariu, A. & Dubina, D. 2011. Strehnght and stability of wind tower (ro). *AICPS Review 1-2/2011*: 72–90.

Pali Campion 2006. *Steel Columns and Masts*.

The Institution of Lighting Engineers 1996. Technical Report number 7: *High Mast Lighting – Specification for design, manufacture, assembly, erection, painting, testing and maintenance.*

Dogariu, A et all. 2010. Verification of high mast lighting from sports stadium. *Achievements and current interests in steel structures*.12th Metallic Construction National Conference: 209–220

Research and Applications in Structural Engineering, Mechanics and Computation – Zingoni (Ed.)
© 2013 Taylor & Francis Group, London, ISBN 978-1-138-00061-2

Nonlinear finite element modelling of castellated steel beams lateral torsional buckling

F.O.M. da Gama
PGECIV – Post Graduate Program in Civil Engineering, Rio de Janeiro, Brazil

L.R.O. Lima, J.G.S. Silva & P.C.G.S. Vellasco
UERJ – State University of Rio de Janeiro, Rio de Janeiro and PGECIV – Post Graduate Program in Civil Engineering, Brazil

M.M.B.R. Vellasco
PUC-Rio – Pontifical Catholic University of Rio de Janeiro, Brazil

ABSTRACT: Restrictions of space and height are often imposed to residential, commercial and industrial buildings with one, or several floors, due to aspects like regional regulations, technical, economic or aesthetic nature. In order to provide the passage of pipes and ducts with large diameter under steel girders, that normally requires great heights, sometimes leads to floors building highs with an unviable magnitude. Among others, castellated beams are a possible structural solution to overcome these obstacles. These beams are considered stability issues, since the unbraced span lengths generally reached by them are often long enough to cause instability effects. However, the substantial enhancement in the flexural strength of such members, due to the extra height coming from the manufacturing process in relation with the original profile, combined with the economy of material and utility services, ensures to the designers the attractiveness of this solution, especially when applied to large spans. The present investigation aims to develop a numerical model that calibrated with experimental results, enables the development of a parametric analysis centred on the finite element method. This analysis aimed to determine the structural behaviour of the castellated beams and their associated failure mechanisms, considering an elastic-plastic behaviour as well the geometric non-linearities. The results showed coherency and no relevant technical objections were verified, when considered the application of the castellated beams in alternative of the traditional plated beams since the advantages arising from the beams openings justify their application.

1 INTRODUCTION

In order to allow the passage of large diameter pipes and ducts under steel beams or due to architectural demands, large beam heights are normally required. A often used solution is the use beams with webs containing one or more openings with various geometries to accommodate the passage of pipes and other purposes. One of the commonly adopted web openings are the cellular (circular) and castellated (hexagonal) – with the last being the focus of the present paper.

Castellated beams are characterized by their multiple polygonal openings symmetrically distributed along the beam length. The present investigation aimed to develop an elasto-plastic numeric model including geometric nonlinearities, calibrated with experimental results [7], to evaluate the structural behaviour of castellated beams focused on their collapse mechanisms. This study had also the objective to assess, quantify and determine the influence of geometric characteristics differences of castellated beams when compared to solid in relation to the solid beams with the same disproportions for various span lengths. The methodology was based on a parametric analysis with the finite element method [1].

2 DESIGN STANDARDS

Nowadays there are several structural design standards and design procedures for steel beams that considers the possibility of using web openings. However, in general, these are limited to the restriction of parameters and scenarios where the gaps may, or may not, be adopted depending on the geometrical configurations of the structural element in question. Considering the European standard Eurocode 3 [5] as a reference to the design theoretical values of the elastic critical moments were evaluated, using two design alternatives: For beams with double symmetry sections, like the castellated beams profiles studied in this work, the

general design method is depicted by equation (1) for the critical moments calculation.

$$M_{cr} = A\left[\sqrt{B+C+D} - E\right] \quad (1)$$

where

$$A = C_1 \times \pi^2 \times E \times I_Z / (k_z \times L)^2 \quad (2)$$

$$B = (k_z / k_W)^2 \times C_W / I_Z \quad (3)$$

$$C = [(k_z \times L)^2 \times G \times I_T] / \pi^2 \times E \times I_Z \quad (4)$$

$$D = (C_2 \times z_g)^2 \quad (5)$$

$$E = C_2 \times z_g \quad (6)$$

with where: C_1 and C_2 are coefficients that depend on the type of loading and boundary conditions and special constraints; k_z is the end sections rotations restriction in the minor inertia axis; k_w is the warping restriction, also at the end sections; L is the beam lateral bracing length; E is the material longitudinal elasticity modulus; G is the material transverse elasticity modulus; I_z is the minor axis moment of inertia; C_w is the warping constant; I_T is the SaintVenant torsion constant; z_g is the distance measures from the load application point to the shear centre in relation to the section gravity centre. In the second particular method, considering the applicable boundary conditions the following equation was used:

$$M_{cr} = \alpha_m \times M_{cr}^E \times \left(\sqrt{1 + \left(\frac{0{,}4\alpha_m y_Q}{M_{cr}^E / N_{cr,z}} \right)^2} + \frac{0{,}4\alpha_m y_Q}{M_{cr}^E / N_{cr,z}} \right) \quad (7)$$

where: α_m is the factor that considers loading conditions, being equal to 1.35 for the studied beams; y_Q is the distance between the load application point to the section centre of gravity (in this case coincides with the shear centre); N_{cr}, z is the column Euler load evaluated on I_z axis that corresponds to the section lowest inertia and with a length L corresponding to distance between laterally braced sections; M_{cr}^E is the critical moment of a solid web beams subject to pure bending moment. According to Eurocode 3 (2005), the LTB (Lateral Torsional Buckling) resistance of the analysed members is performed with
while the beam plastic
moment capacity can be calculated with equation (9).

$$M_{b,Rd} = \chi_{LT} \times \frac{W_y \times f_y}{\gamma_{M1}} \quad (8)$$

$$M_{pl,Rd} = \frac{(W_y \times f_y)}{\gamma_{M0}} \quad (9)$$

where: W_y is the section elastic static moment; f_y is the material yield stress; γ_{M1} is the safety factor; χ_{LT} is the reduction coefficient due to lateral buckling.

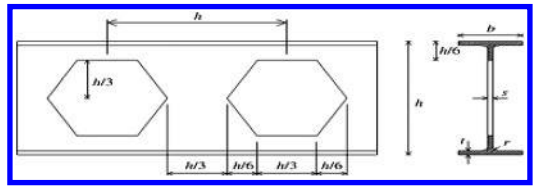


Figure 1. Cross-section and opening geometry (Zirakian & Showkati, 2006).

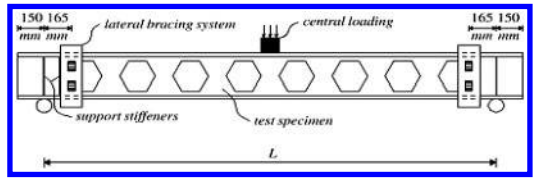


Figure 2. Adopted boundary conditions geometry (Zirakian & Showkati, 2006).

3 NUMERICAL MODELS

The numerical model calibration was carried out with the Zirakian & Showkati (2006) experiments [7], for a castellated beam (C180-3600) with the following dimensions (in mm): nominal height (h = 180) and measured (h = 176); flange width (b_f = 64); flange thickness (t_f = 6.3); web thickness (t_w or s = 4.4); curvature radius (r = 7) and length (L = 3600). The studied castellated beam openings were made with hexagonal non-regular polygons so that the maximum width and height of the opening are equal, as well as the side lengths (horizontal) and the smallest distance between them occur between its ends, Figure 1.

The experimental tests were performed on simply supported beams with two stiffeners near of the supports to prevent the web local buckling at these points due to the concentration of high shear stresses, Figure 2. The material mechanical properties that were used in experimental and numerical model of C180-3600 beam were: a 206010 MPa elasticity modulus, and yield stresses of 279.31 MPa (flange) and 233.93 MPa (web) and ultimate stresses of 894.35 MPa (flange) and 892.23 MPa (web).

The developed numerical model during the calibration phase had its geometry, loading and boundary conditions based on the experimental beam. Slender webs, as well as beams with large span lengths, in practice, are not perfectly straight. So it is essential to properly represent these imperfections in the finite element numerical model. The initially perfect beam (without any kind of imperfection), was evaluated as linear elastic. The elastic buckling load evaluation was performed based on eigenvalue analysis using the ANSYS (2009) program. The deformed configuration resulting from the beam first elastic buckling mode were introduced as the initial imperfection of the model.

Later, with these imperfections, the beam model was submitted to a non-linear elasto-plastic analysis, with the controlling displacement strategy, until the

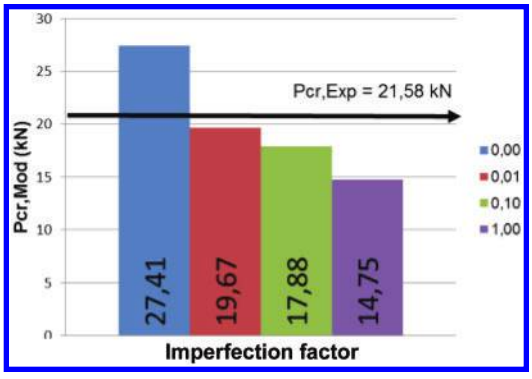


Figure 3. Influence of the adopted initial imperfection magnitude (C180-3600). Copying old text onto new file.

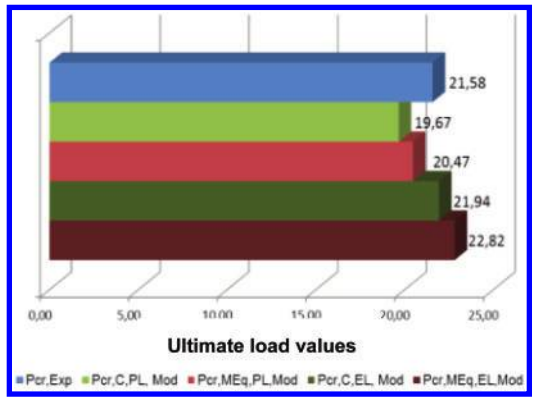


Figure 4. Ultimate load comparison (C180-3600).

lateral buckling LTB failure peak followed by the unloading phase. However, albeit within the limits allowed by the standard, the optimum magnitude of the initial imperfections are initially unknown and needed to be determined. A numerical model sensitivity analysis followed and its results are shown in Figure 3.

As has been seen, between the two extremes of the examined interval, the critical load nearly doubled, indicating the large model sensitivity to initial geometric imperfections variations. The imperfection factor optimal value however, was found to be close to the minimum imperfection values (Figure 3). These facts enabled the adoption of a 0.01 imperfection factor to be used in the nonlinear analysis. Additionally, in order to access the results robustness, solid beams, equivalent to the investigated castellated beams, were also analysed with the same initial imperfections.

Figures 4 and 5 depicts the above mentioned results where $_{Pcr,Exp}$ is the castellated beam critical load obtained in a plastic analysis in the experimental model; $P_{cr,c,EL,Mod}$ is the castellated beam critical load obtained in an elastic analysis on the numerical model; $P_{cr,C,PL,Mod}$ is the castellated beam critical load obtained in a plastic analysis on the numerical model; $P_{cr,MEq,El,Mod}$ is the equivalent solid beam critical load obtained in a elastic analysis on the numerical model; $P_{cr,MEq,PL,Mod}$ is the equivalent solid beam critical load obtained in a plastic analysis on the numerical model.

As can be inferred from Figure 4, for the critical loads of beams C180-3600 the numerical models non-linear analysis loads were 8.85% lower than the experiments, while the elastic critical loads were found to be 11.5% higher than those obtained in the nonlinear analysis, ratifying the numerical model calibration.

Figure 5 presents the load vs. lateral displacement curves obtained in numerical model and experimental results, superimposed at the section height most critical region (compression flange) for the beam C180-3600. The numerical curves followed the trend and the direction of the observed in the experimental curves.

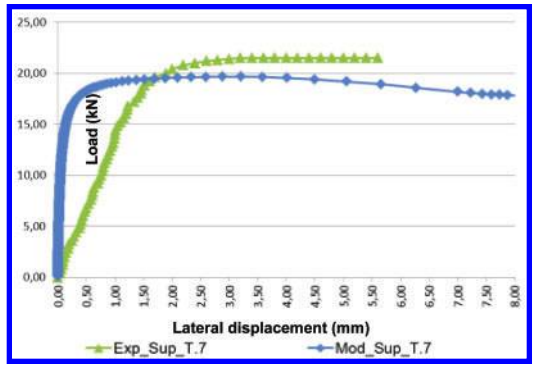


Figure 5. Load vs. lateral displacement curves (numerical & experiments) – top flange.

The above mentioned results enabled the adoption of the 0.01 initial imperfection factor in numerical models of this work since their ultimate loads were closer to the value obtained experimentally.

4 PARAMETRIC ANALYSIS AND RESULTS

A simplified verification of the LTB resistance is proposed in the Eurocode 3 (1998), which is nothing more than a calculation method similar to what is used in the solid beams, considering the reduction of the cross-section geometrical characteristics due to the openings. This motivated an evaluation of the elastic critical moment of these elements with the ANSYS (2009) program.

Once calibrated the numerical mode was used to all the investigated beam spans formed from by European IPEs steel profiles (200, 300, 400, 500 and 600), with the aim of covering from simple residential roofs and small frames (pipe racks, etc.) up to large structures such as bridges and viaducts. The Profiles have been chosen to embrace various design alternatives. Due to space limitation the present paper only highlights the

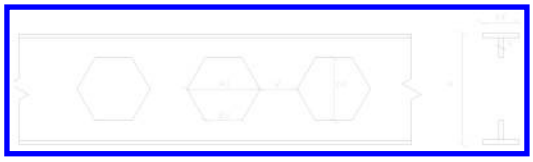


Figure 6. Castellated beams geometrical characteristics.

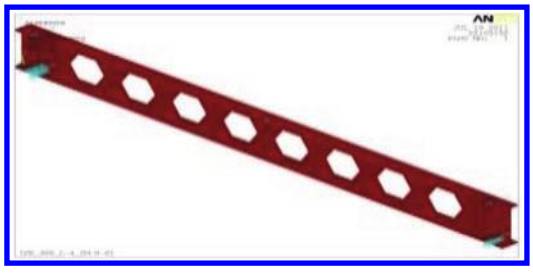


Figure 7. Adopted boundary conditions.

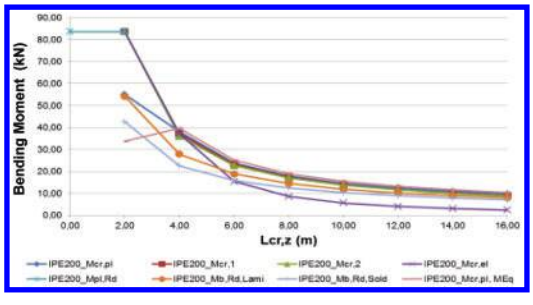


Figure 8. Moment rotation curves for the analysed IPE200 profile.

IPE 200 results. The studied castellated beams geometry are illustrated in Figure 6 where A0 and h0 are equal an all the openings had a hexagonal geometry.

In the case of the IPE 200 the geometric parameters were (in mm): height ($H_i = 200$); flange width ($b_f = 100$); thicknesses of the web (t_w or $s = 5.6$) and flanges ($t_f = 8.5$); curvature radius ($r = 12$); castellated beam height ($H_n = 300$); hole height ($H_0 = 200$); hole width ($A_0 = 200$); The hole base ($B_0 = 100$); area ($A = 2.164.8\ mm^2$). The material was modelled as a perfect elasto-plastic steel, bilinear and isotropic, but the properties and characteristics were changed to the material nominal values: modulus of elasticity ($E = 210\ GPa$); yield stress ($\sigma_y = 275\ MPa$).

The boundary conditions in general were maintained, the only modification was the location of the lateral braces that were positioned on the support, but acting on both ends of the beam at the top and bottom flanges. Figure 7 presents the new beams configuration where it should be noted that the warping is free in the support sections and the loading was applied as a prescribed displacement.

In this figure $M_{cr,1}$ is the standard elastic critical moment; $M_{cr,2}$ is the general elastic critical moment;

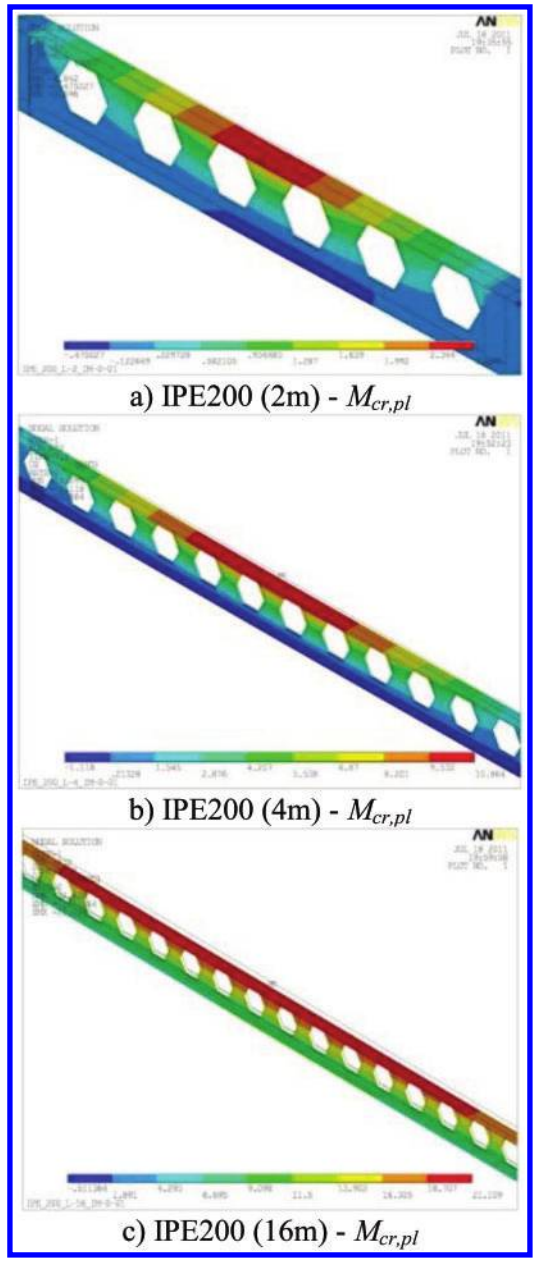


Figure 9. Lateral displacements UZ (in mm).

$M_{b,Rd,Lami}$ is the hot-rolled beam LTB critical moment; $M_{b,Rd,Sold}$ is the welded beam LTB critical moment; $M_{pl,Rd}$ is the hot-rolled beam plastic moment; $M_{cr,el}$ is the numerical model elastic critical moment; $M_{cr,pl}$ is the plastic critical moment from the nonlinear analysis; $M_{cr,pl,MEq}$ is the plastic critical moment from the nonlinear analysis for the equivalent solid beam; $M_{cr,1,Mor}$ is the elastic critical moment standard for the solid original beam; $M_{cr2,Mor}$ is the elastic critical moment for the general case of the solid original

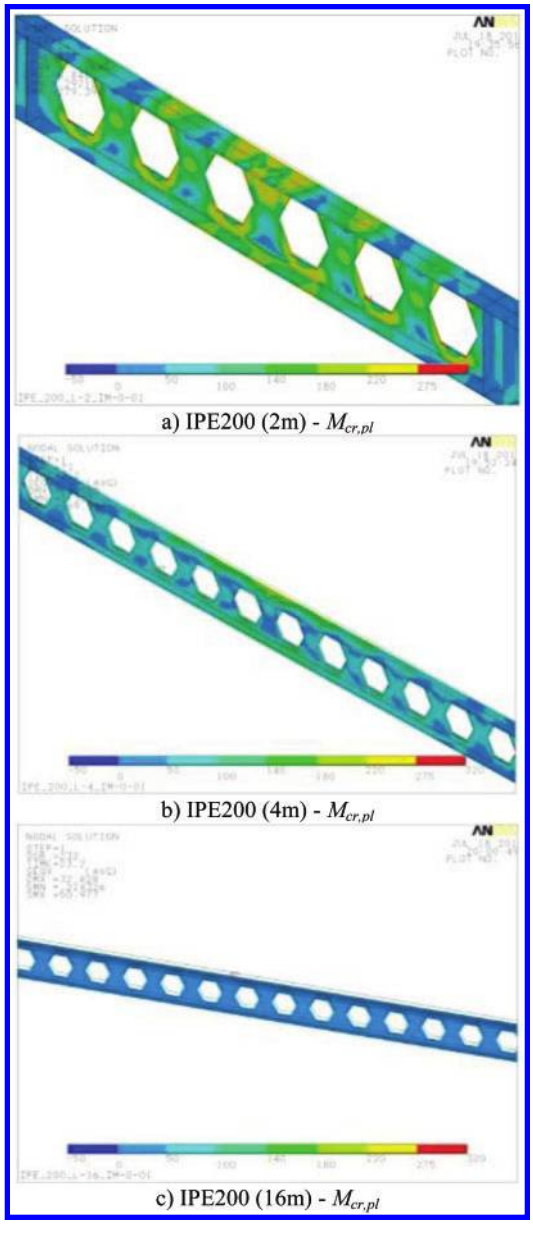


Figure 10. Von mises stress distributions (in MPa).

girder. The plastic moment capacity of the IPE 200 section ($M_{pl,Rd}$) was 83.57 kNm. Figure 8 below depicts the curves for the critical moments mentioned above.

To illustrate the obtained failure mechanisms: web local buckling (WLB) and the lateral torsional buckling (LTB) the spans present in Figures 9 and 10 were selected.

Notwithstanding the previous figures only refer to the IPE 200 figure 11 presents some data with the other analyzed profiles with the same spans since a similar behaviour has been observed on all the investigated beams regardless of the adopted profile.

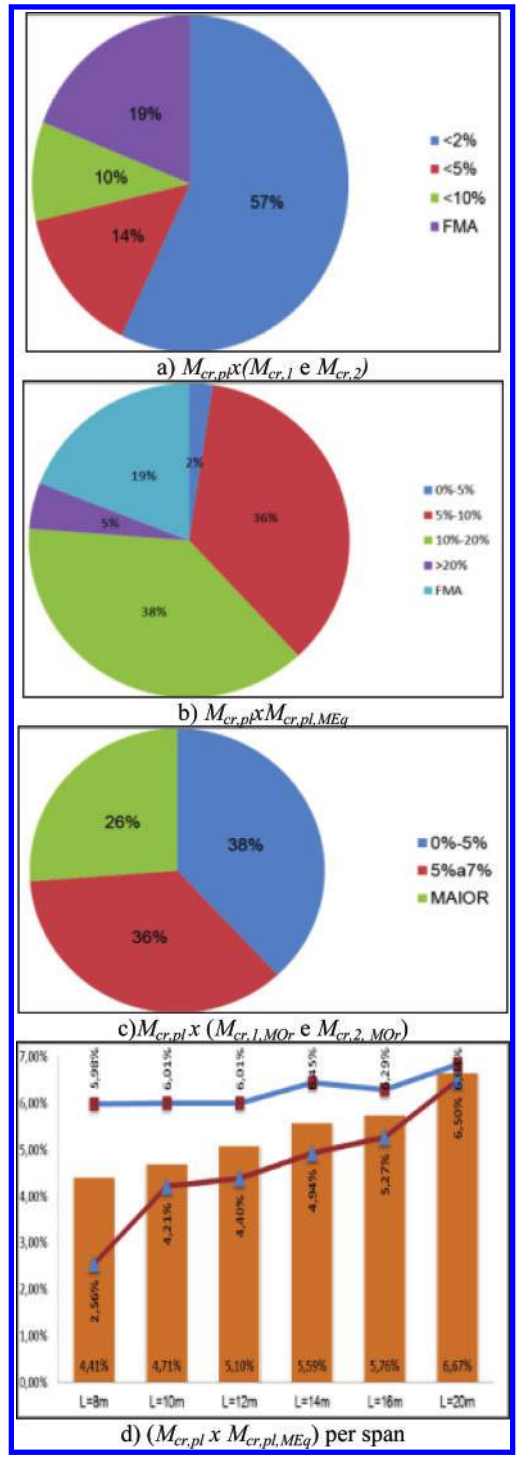


Figure 11. Results comparisons in terms of distribution of errors.

5 CONCLUSIONS

This paper presented some aspects of the structural behaviour of steel beams with web openings of

hexagonal geometry and castellated beams. From the results it was possible to observe that the vast majority of the differences between the moments ($M_{cr,pl}$ x ($M_{cr,1}$ and $M_{cr,2}$)) were less than 2% indicating that using the Eurocode 3 (1998) procedure for calculating of the elastic critical moment of beams castellated using the formulation applicable to solid beams, but considering the geometric differences between cross sections, can be used effectively for verification of this limit State. This can be done as long as the investigated beams did not present large initial imperfections.

The moment capacity results ($M_{b,Rd,Sold}$ and $M_{b,Rd,Lami}$) were consistent with the developed model, since the curves related to the rolled profiles LTB resistance ($M_{b,Rd,Lami}$) were closer to the curves obtained with the numerical nonlinear modelling ($M_{cr,pl}$).

For spans up to four meters in general, the failure mechanism that determines the structural capacity is the WLB (web local buckling), which occurs due to excessive longitudinal forces in the beam web, which in turn, as a function of castellated beams geometric conformation favours such occurrence. Increasing the beam span the lateral instability becomes more evident as the failure mechanism controller. As expected, due to the highest geometric properties values for the solid beams cross sections, when compared to the equivalent castellated beams, the critical moments values were about 9% and 6.5% higher for the solid section beams. However, these values have remained close those obtained experimentally and numerically.

As in practice the castellated beams are manufactured with profiles 33.3% smaller than the equivalent solid sections when gains inherent to the reduction of the structure weight are added it becomes evident the economy provided by the castellated structural solution. The same reasoning can be applied to solid profiles originating from the castellated beams, which referred to the small additional investments that arise from the castellated beams industrialization, offer gains of bending moment capacity ranging from 5% to 20% for the vast majority of the investigated beams (74%).

ACKNOWLEDGEMENTS

The authors would like to thank UERJ, CNPq and CAPES for financing the present investigation.

REFERENCES

ANSYS. version 12.0 (2009). Inc. Theory Reference.

CEN (1993) – EN 10034:1993 – "Structural steel I and H sections" – "Tolerances on shape and dimensions". *European Comittee for Standardization*. Brussels.

Estrada. H.. Jimenez. J.. and Aguíñiga. F. (2006). "Cost Analysis in the Design of Open-Web Castellated Beams. Building Integration Solutions". *Proceedings of the 2006 Architectural Engineering National Conference. ASCE* Conf. Proc. doi:10.1061/40798(190)53.

Eurocode 3 (1998). EN 1993-1-1. Design of steel structures: Part 1.1. General rules and rules for buildings. *Amendment A2 of Eurocode 3: Annex N*. "Openings in webs". British Standards Institution (1992).

Eurocode 3 (2005). EN 1993-1-1. Design of steel structures: Part 1.1. "General rules and rules for buildings".

Simões. R. A. D.. (2007). "Manual de Dimensionamento de Estruturas Metálicas". 2º Edição. CMM. *Associação Portuguesa de Construção Metálica e Mista*. (in portuguese)

Zirakian. T.. Showkati. S. (2006). "Distortional buckling of castellated beams". *Journal of Constructional Steel Research*. v. 62. p. 863–871.

Research and Applications in Structural Engineering, Mechanics and Computation – Zingoni (Ed.)
© 2013 Taylor & Francis Group, London, ISBN 978-1-138-00061-2

Buckling mode decomposition of thin-walled members with holes

M. Nedelcu, N. Chira, H.L. Cucu & A.G. Popa
Faculty of Civil Engineering, Technical University of Cluj-Napoca, Romania

ABSTRACT: Perforated cold-formed steel members are often used in civil engineering as structural elements for residential buildings and storage racks systems. The design capacity of any thin-walled member subjected to compressive stresses is usually governed by combinations of the fundamental buckling types (global, distortional and local). The paper presents an original method based on the Generalised Beam Theory (GBT) whereby the general buckling modes, provided by the Shell Finite Element Analysis (SFEA) of perforated thin-walled members, are decomposed in terms of the fundamental buckling types. The contribution of each fundamental buckling type can be calculated, allowing a better understanding of the member buckling behaviour and post-buckling strength reserve. The main feature of this method lies in using only the GBT cross-sectional deformation modes instead of member base mode shapes.

1 INTRODUCTION

Each fundamental buckling type (global, distortional or local) has its characteristic post-buckling behaviour; consequently, the derivation of the modal participation for a general buckling mode is a crucial step in assessing the real design resistance of the member. Nowadays there are a number of specialized methods capable to provide the modal decomposition, for example the constrained Finite Strip Method, or the Generalized Beam Theory (GBT), the only problem is that they are not able to perform this task for arbitrary cross-sections, boundary conditions, and loads. On the other hand, the shell Finite Element Analysis (SFEA), the most commonly used instrument to study the behaviour of thin-walled members, can easily handle complex geometries of perforated/unperforated members and arbitrary load and member end conditions, but it has no possibility of providing the modal decomposition.

To eliminate this drawback Nedelcu (2012) developed a method for unperforated thin-walled members, able to quantify the modal participation of the fundamental deformation types for any eigenvalue FEM buckling mode provided by SFEA. The method is based on GBT originally created by Schardt (1989) and extensively developed by Camotim, Silvestre et al. (2002). A conventional GBT analysis involves two steps: (i) *a cross-sectional analysis* leading to the GBT *cross-sectional deformation modes* and corresponding modal stiffness components and (ii) *a member stability analysis* to obtain the critical loading factors and the associated mode shapes (given by *the amplitude functions*). The method presented here performs only the GBT 1st step and uses the special orthogonality properties of the cross-sectional deformation modes, to extract from any general FEM buckling mode, the fundamental mode shapes and finally the modal participation. There is no need of the second step which is by far the largest part of a conventional GBT analysis. Following the GBT classical assumptions, the membrane shear strains and transverse extensions are neglected.

The main goal of this paper is to present the theoretical extension of the GBT-based modal decomposition method for the special case of isotropic thin-walled members with holes. In principle, the method uses the same technique as for the case of unperforated elements and it starts with a classic buckling SFEA. The GBT 1st step is used only to define the cross-sectional deformation modes, each one corresponding to a fundamental buckling type. Next, they are used to extract from buckling SFEA, discrete values of *the amplitude functions* of each fundamental buckling mode on a regular mesh of points along the member's axis. For the perforated regions, special assumptions and theoretical developments are introduced. Based on the obtained amplitude functions, the modal participation is computed. For validation, the displacement field provided by SFEA is compared with the one recreated using the extracted amplitude functions and the GBT cross-sectional deformation modes. This last step provides the approximation error of the entire procedure. Based on the versatility of SFEA there are no restrictions regarding the element cross-sectional shape, loading and boundary conditions (Nedelcu et al. 2012).

2 GENERALISED BEAM THEORY – SHORT PRESENTATION

Figure 1 presents an arbitrary thin-walled member with the local coordinate system *x-s-z* and the corresponding displacement field *u-v-w*. Classical

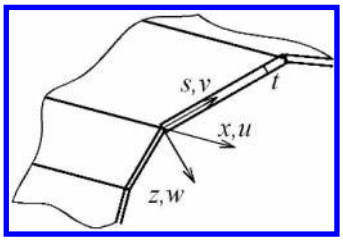


Figure 1. Thin-walled member: local axes/displacements.

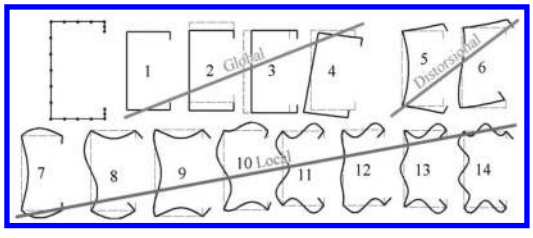


Figure 2. C-section: the cross-sectional deformation modes.

GBT assumes the classical Kirchhoff-Love hypotheses ($\varepsilon_{zz} = \gamma_{xz} = \gamma_{yz} = 0$) and also Vlasov's simplifying hypotheses (null membrane transverse extensions and membrane shear strains).

According to GBT, any displacement is considered as a linear combination of n orthogonal deformation modes, each one expressed as a product of two functions.

$$u(s,x) = \sum_{k=1}^{n} u_k(s)\phi_k'(x) \qquad v(s,x) = \sum_{k=1}^{n} v_k(s)\phi_k(x)$$
$$w(s,x) = \sum_{k=1}^{n} w_k(s)\phi_k(x) \tag{1}$$

where $u_k(s)$, $v_k(s)$, $w_k(s)$ are the components of the *cross-section deformation modes* and $\Phi_k(x)$ are the *amplitude functions* describing their variation along the member's length, and n depends on the cross-section type, the number of the fold-lines and the considered intermediate nodes. As an example, the cross-sectional deformation modes are given in Figure 2, by their in-plane shapes, for a lipped channel section.

For this particular discretisation of the cross-section, the number of fundamental modes $n = 21$, and one can see the 4 Global deformation modes (axial extension, major/minor axis bending and torsion), the 2 Distorsional modes (the cross-section exhibits edge displacements and also plate flexural deformations) and the first 8 Local modes (only plate flexural deformations).

Next, the member equilibrium equations are written based on Hamilton's variational principle, yielding the GBT system of differential equations in modal formulation. Considering only pre-buckling axial compression, the system is written (Bebiano et al. 2007):

$$C_{ik}\phi_k^{IV} - D_{ik}\phi_k'' + B_{ik}\phi_k = \lambda X_{ik}\left(N\phi_k'\right)' \tag{2}$$

where C, D, B and X are the cross-section linear and geometrical stiffness matrices provided by GBT 1st step, and N is the pre-buckling axial force. The GBT 2nd step (the *member stability* analysis) consists in solving the differential equations system, providing the critical load factors λ and the corresponding modal amplitude functions $\Phi_k(x)$, but this step is not used by the method described in this paper.

3 BUCKLING MODE DECOMPOSITION

3.1 *Unperforated thin-walled members*

A buckling SFEA of a thin-walled member is performed and the cross-sectional displacement field is extracted on a mesh of points along the member's axis ($0 \le x_1 < \ldots < x_g < \ldots \le L =$ the bar's length) and the GBT product formulation is considered according to Eq. 1:

$$u_{FE}(s,x_g) = \sum_{k=1}^{n} u_k(s)\phi_k'(x_g)$$
$$v_{FE}(s,x_g) = \sum_{k=1}^{n} v_k(s)\phi_k(x_g) \tag{3}$$
$$w_{FE}(s,x_g) = \sum_{k=1}^{n} w_k(s)\phi_k(x_g)$$

Next, the method uses two stiffness matrices, the *warping* stiffness matrix C and the *geometrical* stiffness matrix X. The first one has the following expression (involving Membrane and Bending components):

$$C_{ik} = C_{ik}^{M} + C_{ik}^{B} = E\int_s tu_i u_k ds + \int_s Kw_i w_k ds \tag{4}$$

where $K = Et^3/(12(1-\mu^2))$ is the plate bending stiffness. Matrix C is a diagonal matrix based on a simultaneous diagonalisation process of the warping and transverse bending stiffness matrices C and B (Schardt 1989).

The geometrical stiffness matrix X stands for the stiffness degradation due to pre-buckling axial force and has the expression:

$$X_{ik} = -\frac{1}{A}\int_s (v_i v_k + w_i w_k)tds \tag{5}$$

where A is the cross-sectional area.

Looking again at Equations 3 and 5, one can see the following relation

$$X_{FE,i} = -\frac{1}{A}\int_s (v_i v_{FE} + w_i w_{FE})tds = \ldots$$
$$= \sum_{k=1}^{n}\left(-\frac{1}{A}\int_s (v_i v_k + w_i w_k)tds\right)\phi_k(x_g) = \sum_{k=1}^{n} X_{ik}\phi_k(x_g) \tag{6}$$

which, written in matrix formulation, becomes

$$X\phi(x_g) = X_{FE} \tag{7}$$

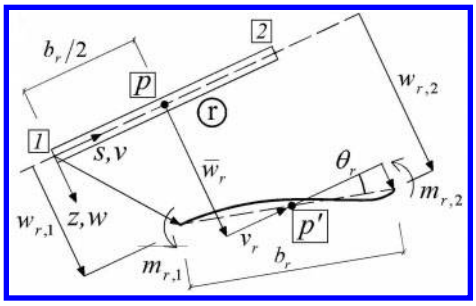


Figure 3. Discrete values of the deformation in the s-z plane.

Using the discrete values given in Figure 3 that approximate the element deformation, the expression X_{FE} becomes:

$$X_{FE,i} = -\frac{1}{A}\sum_{r=1}^{np} b_r t_r \left[v_{i,r} v_{FE,r} + \overline{w}_{i,r}\overline{w}_{FE,r} + \ldots + \theta_{i,r}\theta_{FE,r}\frac{b_r^2}{12} + \overline{m}_{i,r}\overline{w}_{FE,r}\frac{b_r^2}{12K} + \hat{m}_{i,r}\theta_{k,r}\frac{b_r^3}{360K} \right] \quad (8)$$

where np is the number of segments considered along the cross-section, delimitated by the fold-lines and the considered intermediate nodes, and having width and thickness b_r and t_r, respectively. For a segment r, $\overline{w}_r$ is the middle transversal displacement, θ_r is the plate absolute rotation, $\overline{m}_r$ and $\hat{m}_r$ are the semi-sum and the semi-difference, respectively, of the edge transversal moments m_r. The plate absolute rotations θ_r and the edge transversal moments m_r are provided by GBT 1st step for each cross-sectional deformation mode.

Next, the column vector Φ containing the discrete values of the amplitude functions for any specified point x_g ($0 \le x_g \le L$), is calculating by solving the system of linear equations given by Equation 7. By interpolation, the amplitude functions can be found on the entire domain.

Having the amplitudes functions, one can recreate the transversal displacements v and w using Equation 1b,c for the entire member. In order to recreate also the warping displacements u, one has to extract the derivatives of the amplitude functions $\Phi'_k(x)$. Of course, one could just make numerical derivation, but the process is very sensible of the mesh density along the bar's axis.

The procedure of extracting discrete values of Φ'_k is similar with the previously described; the difference stays in using stiffness matrix C instead of X. The bending components of the warping stiffness matrix given in Equation 4 are neglected in this paper. The membrane components are calculated using the nodal warping values (Fig. 4), considering linear warping along the cross-section.

$$C_{ik}^M = E\sum_{r=1}^{np} t_r b_r \left(\frac{u_{i,r1}u_{k,r1} + u_{i,r2}u_{k,r2}}{3} + \ldots + \frac{u_{i,r1}u_{k,r2} + u_{i,r2}u_{k,r1}}{6} \right) \quad (9)$$

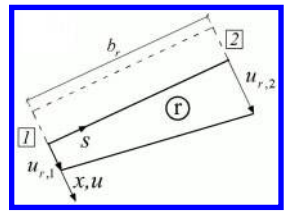


Figure 4. Discrete values of the warping displacements.

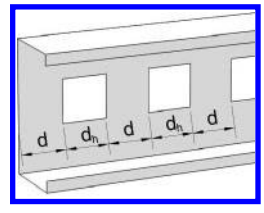


Figure 5. Thin-walled member with holes.

One recreates matrix C^M, by introducing the displacement field extracted from SFEA.

$$C_{FE,i}^M = E\int_s t u_i u_{FE} ds = \sum_{k=1}^{n} C_{ik}^M \phi_k(x_g) \quad (10)$$

and the final matrix equation yields:

$$C^M \phi' = C_{FE}^M \quad (11)$$

Having the amplitude functions and their derivatives, the entire displacement field (d_{GBT}) is recreated and compared with the initial one (d_{FE}), extracted from SFEA. An error vector is constructed $d_{err} = d_{FE} - d_{GBT}$ and the *approximation error* of the proposed method is measured as the norm of the error vector relative to the norm of the FE displacement vector.

$$error = \sqrt{d_{err}{}^T d_{err}} \Big/ \sqrt{d_{FE}{}^T d_{FE}} \quad (12)$$

Finally, the method provides the modal participation, the goal of the entire procedure, using the same procedure proposed by Silvestre et al. (2002), an easy and intuitive method based only on the amplitude functions. The modal participation factor (P_i) is introduced as follows:

$$P_i = \int_L |\phi_i(x)| dx \Big/ \sum_{k=1}^{n} \int_L |\phi_k(x)| dx \quad (13)$$

3.2 *Perforated thin-walled members*

The member is divided in two regions along its length as shown in Figure 5: continuous regions given by the intervals d, and regions with holes given by the intervals d_h.

These intervals don't have to be equal, there are no theoretical limitations concerning the shape, size and

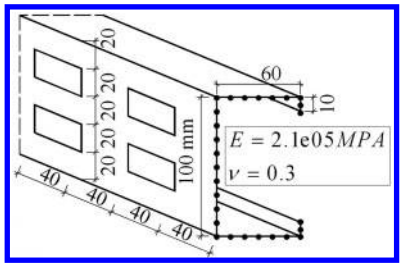


Figure 6. Lipped channel.

distribution of the holes. Of course a regular pattern will highly increase the speed of this procedure and it will ease its implementation in a computer application. Fortunately, in reality the vast majority of perforated thin-walled members have this property.

The buckling SFEA is performed. For any point $x_g (0 \le x_g \le L)$, situated inside and at the borders of the continuous regions, the method described in the previous section can be directly applied.

For the perforated regions, the method can be applied if a minor modification is performed, taking into account the missing segments along the cross-section. The cross-section deformation modes for the example given in Figure 2, remain the same, so the GBT 1st step is still applied for the continuous cross-section. The modification is introduced with respect the stiffness matrices. Basically, the components of these matrices are given by the virtual work produced by unit values of the amplitude functions, or their derivatives (Schardt 1989). So, for each missing segment, the virtual work is eliminated. Equations 8 and 9 are modified only by the number of segments *np*, which is now the initial number of segments minus the ones corresponding to the hole. The simplest example is of the warping matrix component $C_{11} = EA_h$, where A_h is now the area of the perforated cross-section. Next the procedure is applied for any point x_g $(0 \le x_g \le L)$ situated inside (and not at the borders) of the perforated regions.

4 ILLUSTRATIVE EXAMPLE

The parametric study is completed on a perforated symmetric steel lipped channel with boundary conditions of type clamped-free (cantilever member). Figure 5 presents the cross-sectional dimensions referred for the mid-line, the size and distribution of the holes, and the material properties (Young's modulus and Poisson's ratio). The thickness for all walls is $t = 2\,mm$ and the bar's length is $L = 1240\,mm$. The holes are rectangular, have equal size and they are placed in a regular pattern. The GBT cross-section discretisation is made with 5, 9 and 1 intermediate nodes between the corners, respectively in the flanges, web and flange lips. The GBT 1st step provides a number of 29 fundamental deformation modes; the first 14 can be seen on Figure 2.

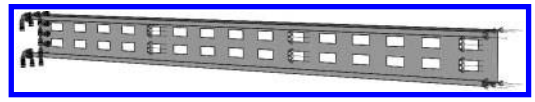


Figure 7. Loading and boundary conditions.

Table 1. Modal participation and approximation error for the first 10 buckling modes.

Buckling mode	G	D	L	error (%)
1	98.85	3.02	1.13	0.11
2	38.61	6.39	55.00	1.46
3	62.74	6.34	30.93	0.64
4	91.31	5.07	3.62	0.29
5	59.06	10.97	29.97	0.63
6	25.62	8.14	66.24	1.15
7	52.15	9.85	38.00	0.77
8	43.35	15.77	40.88	0.83
9	16.15	26.26	57.59	1.54
10	22.90	20.30	56.80	1.14

A buckling SFEA of a thin-walled member was performed using ABAQUS (Hibbit et al. 2002) for the first 50 eigenvalues. 2984 shell elements of type S4 were considered, in a highly regular square mesh (see Fig.7). The cross-section discretisation is constant along the member length and identical with the one used by the GBT 1st step. In longitudinal direction, all the elements have the same size of 10 *mm*. In order to implement the described method of buckling decomposition and to calculate the modal participation, a MATLAB (MathWorks 2005) application was written. It uses the FE displacement field of 125 cross-sections given by the shell elements sides normal to the member longitudinal axis. The member is axially compressed by edge uniform loads applied on the free end and also on one edge of the six holes indicated in Figure 6. For the free end, the loading magnitude is $q_1 = 4.1667\,N/mm$ and for the holes $q_2 = 12.5\,N/mm$.

The analysis provides the modal participation of the Global, Distorsional and Local deformation modes for the first 50 buckling modes and also the approximation error which had a maximum value of 5.89% for mode no. 38. A better approximation can be achieved by refining the GBT cross-sectional discretisation and also the member longitudinal mesh, but not significant changes were observed regarding the modal participation. Table 1 shows these results for the first 10 buckling modes. Figure 7 presents the deformated shapes of the first 5 buckling modes given by SFEA. Figure 8 presents the corresponding amplitude functions of the first 5 most significant fundamental modes, provided by the presented method and used to compute the modal participation by Equation 13.

It can be concluded that the first buckling mode is a Global mode of flexural-torsional type. Modes 2,3 exhibit a Global-Local behaviour, mode 4 is a global mode (flexural over the minor axis) and the rest are coupled instabilities of GDL type.



Figure 8. First 5 buckling modes provided by SFEA.

5 CONCLUSIONS

The paper presents a GBT-based method (originally developed by Nedelcu 2012) capable of identifying in a general buckling mode, the modal participation of the fundamental deformation modes of global, distorsional and local type. The buckling deformations to be decomposed can be determined by using FEM or any similar numerical method.

The main goal of the paper is to present the theoretical extensions and the applicability of the proposed method for the special case of perforated thin-walled members. There are no restrictions concerning the shape, size and distribution of the holes.

Only the GBT 1st step is used (the cross-section analysis) in order to have the modal cross-section deformation components, edge transverse moments, warping and geometrical stiffness matrices. Using the special orthogonality properties of the cross-section deformation modes, the GBT amplitude functions of the fundamental deformation modes, are extracted from the FEM deformations. Finally, the modal participation factors are computed based on the amplitude functions and also the approximation error of the entire procedure.

One numerical example is presented, in which the eigenvalue buckling modes are calculated by using SFEA. The small approximation errors and the comparison between the FEM mode shapes and the amplitude functions of the fundamental modes, prove the validity of the proposed method.

Regarding the method limitations, following the GBT classical hypotheses, the shear strains and membrane transverse extensions are neglected, together with the fundamental deformation modes which may

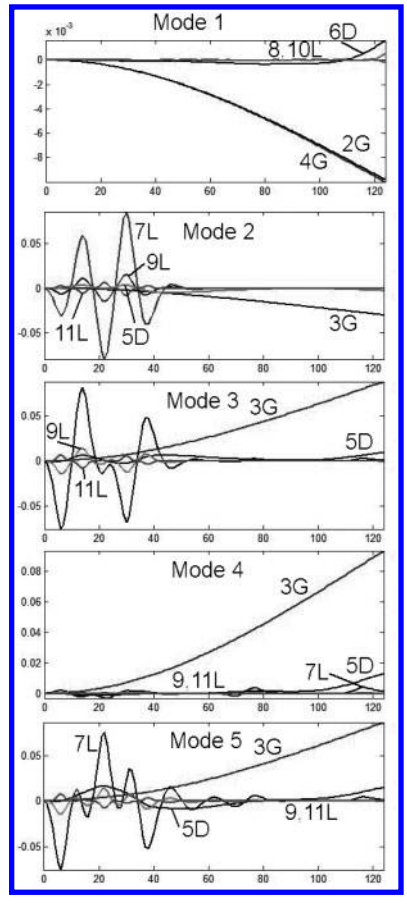


Figure 9. The amplitude functions $\Phi(x)$.

contain these deformations. At the present time, intensive research is dedicated to eliminate the Vlasov's hypotheses.

Regarding the method advantages, GBT is widely accepted as an elegant and fast method to analyse the behaviour of thin-walled members. The proposed method combines the best features of FEM and GBT, namely the FEM versatility with the GBT capability of providing the modal decomposition. As a consequence there are no restrictions regarding the cross-section shape, loading and boundary conditions. Its high speed must also be mentioned, and depends almost entirely of the time required by the SFEA. This is true because GBT 1st step involves an eigenvalue problem of small dimensions and there is no need for the GBT 2nd step (the member analysis) which is usually the most time-consuming in a GBT analysis (except for the use of analytical solutions, which are restricted to simply supported members).

Also, the derivation of the amplitude functions, modal participation and approximation error follow an analytical and simple procedure.

For all these reasons, the proposed method is elegant, extremely fast and a promising candidate to be combined with a general purpose finite element

code, providing in this way the buckling mode decomposition for arbitrary thin-walled members with and without holes.

REFERENCES

Nedelcu, M. 2012. GBT-based buckling mode decomposition from Finite Element Analysis of thin-walled members, *Journal of Thin-Walled Structures*; 54: 156–163.

Schardt, R. 1989. Verallgemeinerte Technische Biegetheorie. Springer Verlag Berlin.

Silvestre, N., Camotim, D. 2002. Second-order generalised beam theory for arbitrary orthotropic materials, *Journal of Thin-Walled Structures* 40: 791–820.

Nedelcu, M., Cucu, HL. 2012. Buckling modes identification from FEA of thin-walled members using only GBT cross-sectional deformation modes. *The 6th International Conference on Coupled Instabilities in Metal Structures*, *December 3–5,* Glasgow, Scotland, UK.

Bebiano, R., Silvestre, N. & Camotim D. 2007. GBT formulation to analyze the buckling behaviour of thin-walled members subjected to non-uniform bending. *International Journal of Structural Stability and Dynamics* 7(1): 23–54.

Hibbit, Karlsson, Sorensen Inc. 2002. ABAQUS Standard (Version 6.3).

Matlab Version 7.1.0246 Documentation, The Mathwork Inc., 2005. MathWorks – MATLAB and Simulink for Technical Computing

Research and Applications in Structural Engineering, Mechanics and Computation – Zingoni (Ed.)
© 2013 Taylor & Francis Group, London, ISBN 978-1-138-00061-2

Resistance assessment of the sinusoidal openings in cellular beams

S. Durif & A. Bouchaïr
Clermont Université, Université Blaise Pascal, Institut Pascal, Clermont-Ferrand
CNRS, Institut Pascal, Aubière, France

ABSTRACT: Experimental and numerical investigations have been conducted on cellular beams with sinusoidal openings. They showed new failure modes around the openings. Thus, a study is performed to develop a new analytical model adapted to the sinusoidal opening shape. Close numerical and experimental studies led on isolated opening parts pointed out the influence of the intermediate web-post on the stability of the opening panel and consequently on its ultimate failure load. The existing criteria of Eurocodes, initially developed for simple beams, is adapted to check the resistance of the tee sections along the sinusoidal opening considering more representative boundary conditions in the calculation of the local buckling critical stress.

1 INTRODUCTION

Castellated and cellular beams have a growing use in steel construction as long span system offering an efficient strength to weight ratio (Durif 2012, Tsavdaridis 2010). A new type of cellular beam has been developed by ArcelorMittal (Angelina™ beam) composed of regularly spaced sinusoidal openings (Fig. 1). In fact, changing the opening shape has an impact on the behavior of the beam and mainly its failure modes. Thus, experimental tests have been conducted on three full scale cellular beams with sinusoidal openings at Blaise Pascal University (Clermont-Ferrand) in order to evaluate and understand their complex behavior at ultimate limit state.

They showed the specific failure modes of sinusoidal openings that depend on the opening geometry (Durif et al. 2013). Thus, in the most stressed opening, it has been observed either the formation of plastic hinges at the four opening corners (Fig. 2) or the local buckling in the compressed panels (Fig. 3). Both failure modes can be linked to the well-known Vierendeel mechanism due to the local bending induced by the shear transfer around the large opening, presented by Chung et al. (2001) for circular web openings.

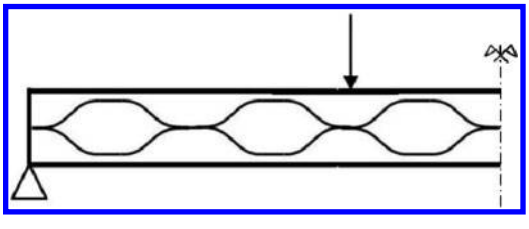


Figure 1. Cellular beam with sinusoidal opening.

A finite element model has been validated through the comparison with the tests results (Durif et al. 2013). The validated numerical model provided the evolution of the stress distribution around the opening allowing the understanding of the complex behaviour of those beams (Durif et al. 2013).

This analysis showed that, due to its length, the sinusoidal opening exhibits a mechanical behaviour similar to that of the rectangular or hexagonal openings mainly for the plastic failure mode as observed in Figure 2. It is characterized by the formation of four plastic hinges at the four opening corners.

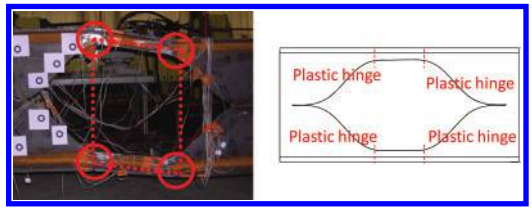


Figure 2. Failure by formation of plastic hinges.

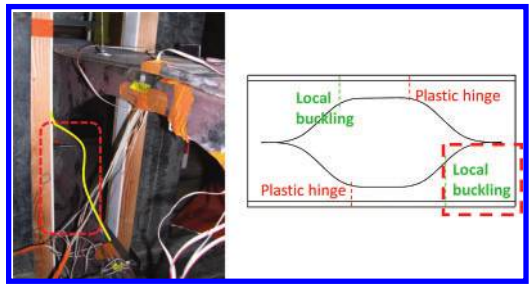


Figure 3. Failure by combination of local buckling and yielding of the opening quarters.

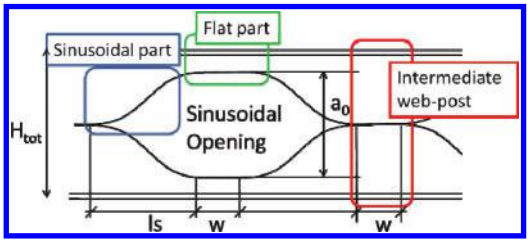


Figure 4. Terminology along a sinusoidal opening.

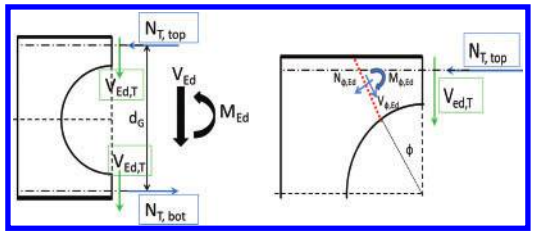


Figure 5. Distribution of forces around a circular opening.

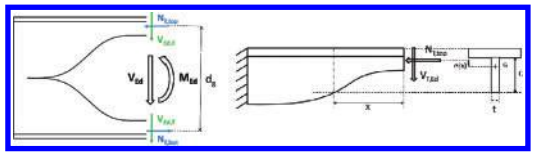


Figure 6. Distribution of forces around a sinusoidal opening.

However, due to the continuous variation of section along the sinusoidal part of the opening (Fig. 4), the position of the critical section to be checked (internal stress/resistance) is not known, especially with local buckling (Fig. 3). In the analytical models developed for circular opening, the position of the critical section is determined by small increments of angles of all the inclined sections around the opening.

In order to develop an analytical model predicting the resistance of the cellular beams with sinusoidal openings, the existing approaches used for circular openings are adapted to that specific opening shape. They are based on the evaluation of the internal forces and the resistances of the openings parts.

The adaptation of those methods to sinusoidal openings is presented. Then, this paper summarizes the principles of the analytical approach developed to predict the strength of the cellular beams with sinusoidal openings.

2 INTERNAL FORCES AND RESISTANCES AROUND OPENING

In general, the resistance of a cellular beam is checked considering the similarity with Vierendeel beam (Chung et al. 2001). Thus, the global moments and shear forces are transformed to local normal and shear forces around the opening (Fig. 5).

Then, the circular opening is checked considering each inclined tee section around the opening under the combined local axial force, shear force and local bending moment (Fig. 5). This method, initially proposed by Ward (1990), remains the common way to predict the resistance of the openings (Lawson et al. 2006). Each inclined tee section is considered with plastic or elastic strength regarding the class section criterion initially developed for rectangular openings and adapted to circular opening (Annex N of ENV 1993-1-1, 1995). This criterion gives a classification of opening that defines whether the section of the opening reaches their plastic of elastic resistance.

The Vierendeel beam equivalence is proposed for sinusoidal opening (Fig. 6). Due to the significant variation of section along the opening length, incremental verification of tee sections is considered.

Figure 6 presents an opening quarter submitted to the local forces $N_{T,top}$ and $V_{Ed,T}$. The authors made the choice to consider vertical tee sections in order to simplify the verification as the sinusoidal part can vary in function of the different opening parameters. This assumption has been validated through numerical simulations (Durif 2012). It has been concluded that the similarity between a cellular beam and a Vierendeel beam is independent of the opening shape, as much as the openings of a cellular beam remain enough deep and large.

However, no existing methods allow predicting the sinusoidal opening resistance. Indeed, the existing criterions for castellated and common cellular beams (Annex N ENV 1993-1-1, 1995) cannot be well adapted to the sinusoidal shape, especially because this opening shape implies a combination of different failure modes around the opening with either the yielding or the local buckling of the constituting opening quarters (Fig. 3) (Durif 2012). Thus an opening classification cannot be representative of the sinusoidal opening failure mode.

As a consequence, in this study, the resistance of each opening quarter is checked separately through incremental verification of each tee section along the opening length.

On the basis of the design rules for steel plates described in the Eurocodes (EC3-1-1 2003, EC3-1-5 2004), the authors propose to adapt the existing criterion for outstand flanges, to check the resistance of the tee sections along the opening length, considering the corresponding boundary conditions.

3 PROPOSITION FOR THE OPENING RESISTANCE

It has been chosen to develop the new analytical model on the basis of the principles of Eurocode 3. Those European rules define criterions based on the sections slenderness to assess the strain capacity of the compressed fibers before the ignition of local buckling.

The resistance of the tee sections can then be evaluated considering the classification of cross sections of

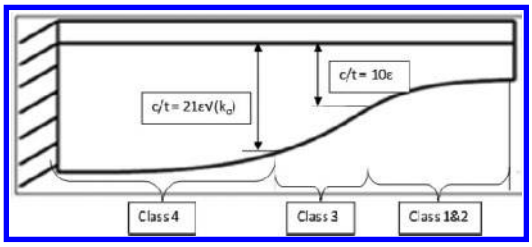


Figure 7. Example of classification of sections along a sinusoidal opening quarter.

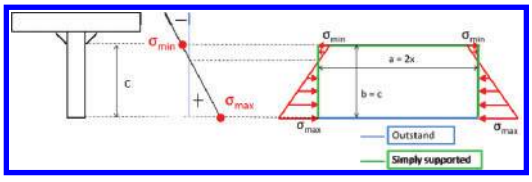


Figure 8. Tee section and its equivalent cantilever plate.

Eurocode 3 (EC3-1-1 2003, EC3-1-5 2004). However, those criterions have been developed for the design of beam flanges and webs and are not adapted to the verification of the tee sections in the opening quarters (Durif 2012).

Those criterions are function of the dimension (c) which is the tee web height. The transposition of those criterions to the vertical tee sections of a quarter of opening is presented in Figure 7.

As a consequence, this transposition considers that the sections the most expected to buckle (class 4 sections), are the sections of maximum vertical height. However, the authors have shown in previous works that this transposition of classification is too conservative. Indeed, the authors showed that the intermediate web-post (represented by hatchings in Fig. 7) supplies an out-of-plane support and should be considered in the calculation of the section resistance (Durif et al. (under review)).This out-of-plane support should be integrated in the formulas that define each section resistance.

The classifications of the Tee sections are based on the calculation of the critical stresses of equivalent cantilever plates (Johansson & Veljkovic 2001), submitted to axial stresses deduced from the corresponding forces (Fig. 8).

In the case of a tee section along an opening quarter (Fig. 6), the web of the tee section is submitted to linear varying axial stresses along its height, due to the axial and bending forces, as illustrated in Figure 8.

Figure 8 presents the equivalent cantilever plate considered to define the critical stress of the tee section web. The width of the plate "b" is taken equal to the tee web height "c".

Furthermore, in order to consider the stiffness supplied by the intermediate web-post to the adjacent tee sections, the authors propose to consider an equivalent plate of a defined length "a" taken equal to the double of the abscissa x of the studied tee section. This assumption remains conservative as it considers an equivalent plate simply supported on the three border lines without any rotational restraint (Durif 2012).

As a consequence, to calculate the critical stress of the tee sections along the opening quarter, the method consists of calculating the critical stress of the equivalent cantilever plates defined in Figure 8.

However, there is no existing formula defining the critical stress of such plates with a linear axial stress diagram. The authors propose a resolution with the energy method of this stability problem in order to get a formula of the critical stress coefficient k_σ which can directly be used in the design formulas of the Eurocodes (based on the work of Winter) in order to define the ultimate strength of steel plates (Johansson et al. 2007).

4 CRITICAL STRESS IN CANTILEVER PLATE

4.1 *Literature review*

Many works on the stability of steel plates show the efficiency of the energy method to solve the problem of plates buckling. For example, the paper of S.T. Smith, M.A. Bradford & D.J. Oehlers (1999) provides the values of buckling coefficients for different support conditions of a plate in pure shear. The method is similar to that developed by Timoshenko (1943), considering a virtual function of displacement "w" corresponding to the boundary conditions to calculate the strain energy of bending of the plate (U) and the external forces work (T). The critical value of the stresses is found when the strain energy of bending is equal to the external forces work (Timoshenko, 1943).

Klöppel and Sheer proposed abacuses that allow finding the critical stress value for different configurations of loading, boundary conditions and stiffeners properties. In the present study a value of the buckling coefficient is needed for a linear varying axial stress diagram. Thus, in order to get the value of the critical stress in function of the plate and loading parameters, it is necessary to go back to the resolution of the problem of stability or to use numerical tools (Yamashita & Kato 2001). Timoshenko (1943) and then, Bulson (1970), present a good description of the resolution of this kind of problems but do not give the solution for the case of the cantilever plate with linear varying load.

The paper of Kang & Leissa (2005) presents the resolution of the stability problem of a plate with various boundary conditions, with the problem of the cantilever plate. It gives the resolution method that is the same as Timoshenko, by integrating the equilibrium equation and by choosing a serial of Fourier for the function of displacement. The same results as the one obtained by Timoshenko and Bulson in the case of the fully compressed cantilever plate are observed. However, the paper does not give any useful formula that can be used in an analytical calculation.

Thus, no analytical formula is available in the literature for the cantilever plate, loaded by a linear diagram of axial stresses. Consequently, it has been chosen to propose a formula able to predict the critical stress of a cantilever plate submitted to a linear varying axial stress diagram. This formula has been developed using the energy method for both cases, whether the maximum compressive stress is on the out-stand fiber or on the simply supported fiber. In the present paper, just the first case is presented as the second one uses the same principles.

In order to use the energy method, the authors have chosen to use the deflected shape proposed by Bulson (1970) and described by the Equation 1.

$$w = A\frac{y}{b}sin\left(\frac{\pi x}{a}\right) \quad (1)$$

4.2 *Cantilever plate with maximum compression on the out-stand fiber*

The cantilever plate with linear distribution of normal stresses is analyzed. The results are summarized for the more sensitive case to local buckling mobilized by the maximum compressive stress on the out-stand fiber. The critical forces are obtained by comparing the internal energy U and the external work T obtained with a virtual displacement assumed to have the shape " w " defined by the Equation 1 (Bleich, 1952). The strain bending energy is given by the equation 2 (Timoshenko 1943).

$$U = \frac{D}{2}\int_{00}^{ab}\left\{\left(\frac{\partial^2 w}{\partial x^2}+\frac{\partial^2 w}{\partial y^2}\right)^2 - 2(1-\nu)\left[\frac{\partial^2 w}{\partial x^2}\frac{\partial^2 w}{\partial y^2}-\left(\frac{\partial^2 w}{\partial x \partial y}\right)^2\right]\right\}dxdy \quad (2)$$

The external forces work can be defined by the Equation 3 (Timoshenko 1943).

$$T = \frac{\sigma_{max}t}{2}\int_{00}^{ab}(\psi+(1-\psi)\frac{y}{b})(\frac{\partial w}{\partial x})^2 dxdy \quad (3)$$

The resolution of the energy method equations gives the critical stress defined by the Equation 4.

$$\sigma_{cr} = 4.D.\frac{(-6.a^2.\nu+6.a^2+\pi^2.b^2)}{t.b^2.a^2.(3+\psi)} \quad (4)$$

The value of the coefficient k_σ (Eq. 5) is obtained by comparison of this critical stress with the well-known Euler stress σ_E:

$$\sigma_{cr} = k_\sigma.\sigma_E$$

Where:

$$\sigma_E = \frac{\pi^2.E.(t/b)^2}{12.(1-\nu^2)}$$

$$k_\sigma = 4.\frac{(-6.\nu.a^2+6.a^2+\pi^2.b^2)}{a^2.(3+\psi).\pi^2} \quad (5)$$

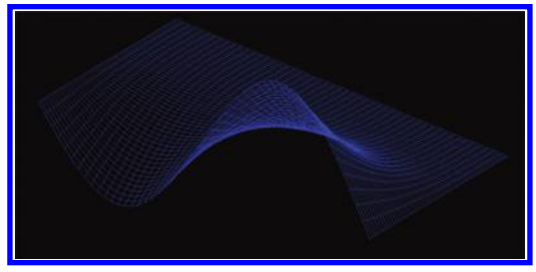


Figure 9. Buckling mode in two half waves for a plate with $\psi = -4$.

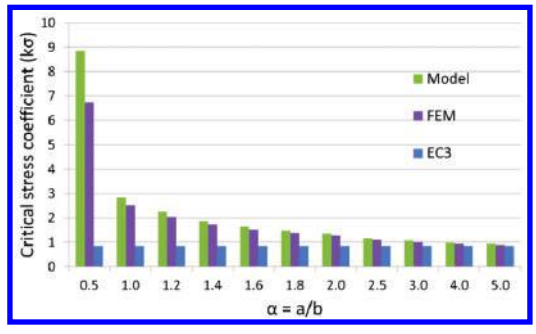


Figure 10. Comparison of k_σ values for the different methods with a stress ratio $\psi = -1$.

It can be noticed that the value of k_σ is not defined for a stress ratio $\psi = -3$. In this case, the authors chose to limit the value of k_σ considering a minimum stress ratio of -2.9. This limit value leads to conservative results of k_σ.

For cases with values of $\psi < -3$, the plates change of buckling shape. The buckling mode changes and leads to a buckling shape with several half waves (Fig. 9). Thus the shape function "w" assumed in the model of Equation 1 is no more representative.

Indeed, values of $\psi < -3$ correspond to an axial stress diagram with a maximum tensile stress three times higher than the compressive one. Thus, this configuration of plate is very stiff, which explain the buckling mode shape. However, those configurations do not have interest in the present study because those types of loading conditions generate a compressed part very small along the plate width, which should lead to the plate plastification before local buckling.

4.3 *Application of of the proposed model in pure bending ($\psi = -1$)*

The evaluation of the proposed model is done for the case with pure bending ($\psi = -1$). Figure 10 compares the critical stresses obtained with the analytical model, the Eurocode formulas (that are independent of the plate length " a ") and the numerical model (FEM).

The comparison is done for various values of aspect ratio (a/b) varying from 0.5 to 5. It can be observed in Figure 10 that the results of the analytical model are close to those of the numerical model. Furthermore,

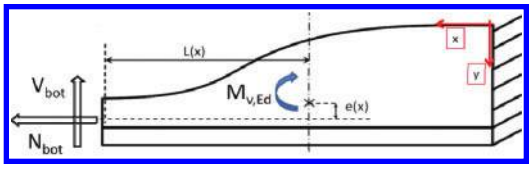


Figure 11. Bottom right opening quarter with corresponding forces.

the formulas of Eurocode, developed for infinitely long plates, are not well adapted for plates with an aspect ratio $\alpha < 3$.

Finally, the ultimate strength of each section is determined in function of the calculated critical stresses. To do so, the authors based the model on the design rules of EN1993-1-3 regarding the case of semi-compact plates.

5 SEMI-COMPACT PLATES

The work presented in the report (Greiner et al., 2009) proposes a formula in order to define the elasto-plastic strength of plates considered with class 3 in the Eurocodes. This formula considers a linear interaction between the plastic and the elastic moment resistance depending on the plate slenderness (Greiner et al., 2009). It has an equivalent formula in EN1993-1-3 (2006) presented hereafter.

– if the effective section modulus W_{eff} is less than the gross elastic section modulus W_{el} (EC3-1-3, 2006).

$$M_{c,Rd} = W_{eff} f_y / \gamma_{M0} \quad (6)$$

– if the effective section modulus W_{eff} is equal to the gross section modulus W_{el} (EC3-1-3, 2006).

$$M_{c,Rd} = f_y (W_{el} + (W_{pl} - W_{el}) 4 (1 - \lambda_p / \lambda_{el}) / \gamma_{M0} \quad (7)$$

In the case of cantilever plates:

$\lambda_p = \frac{(c/t)}{28{,}4\varepsilon\sqrt{k_\sigma}}$ and $\lambda_{el} = 0748$ (and not 0673 given in the Eurocode 3 part 1–3) (Johansson et al., 2007).

The new model proposed in this study to calculate k_σ can be incorporated in those formulas (Eq. 6) in order to take into account a more realistic stiffness of the sections close to the intermediate web-post.

As an example (Fig. 11), it is proposed to study the bottom right opening quarter of the opening of the tested beam presented in Figure 3.

This example aims at comparing two methods. First, the adaptation of the Eurocode design rules to the verification of the opening quarter is presented in Figure 12. Then the verification that considers the new calculation of critical stress proposed in the present paper is presented in Figure 13.

Both Figures, 12 and 13, show the diagrams of the plastic moment resistance (reduced by the axial force N_{bot}) $M_{pl,N}$, the elastic moment resistance $M_{el,N}$, the solicitant bending moment M_{Sd} and the resistant bending moment M_{Rd}.

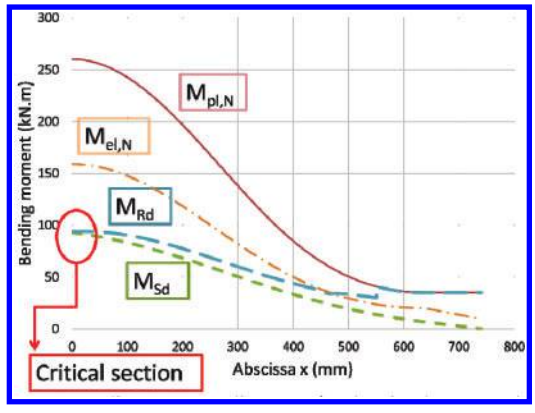


Figure 12. Bending moment diagrams for the simple approach along the opening quarter.

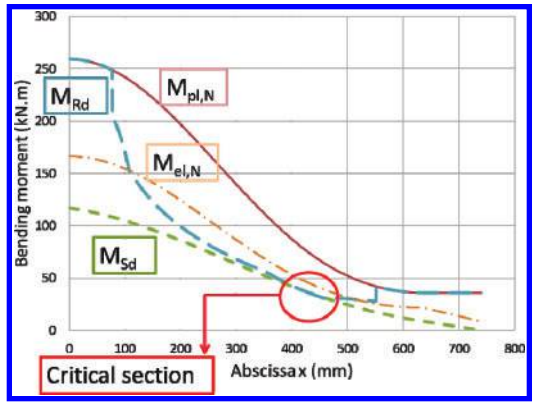


Figure 13. Bending moment diagrams for the proposed model approach along the opening quarter.

Figure 12 gives a bending resistance diagram M_{Rd} deduced from the direct adaptation of the Eurocode 3 part1-1 design rules. The critical section, where the failure is expected to arise analytically, is located at the junction of the sinusoidal panel and the intermediate web-post by local buckling.

Figure 13 gives another bending moment resistance diagram. It can be seen on this figure that the bending resistance of the sections close to the intermediate web-post reaches the plastic resistance. Thus, the failure occurs at a critical section which is deviated from the intermediate web-post and corresponds more to the corresponding failure mode observed experimentally and numerically (Fig. 3) by Durif et al. (2013).

It can be seen in Figure 14 that the bending resistance of the critical section remains under the elastic resistance. This resistance remains conservative in comparison to numerical results (Durif 2012). In order to better assess the opening resistance it should be necessary to consider the rotational restraint supplied by the flange and the intermediate web-post to the sinusoidal panel. Furthermore, so as to get the ultimate

load of the opening, the analytical model has to consider the opening failure mechanism of all the opening quarters (Durif 2012).

6 CONCLUSION

The work described in this paper proposes an original approach to define the opening quarter resistances. In order to predict the failure mode of the four opening quarters, a new analytical model has been developed. This model is based on the existing methods for standard cellular beams. However, a new calculation of critical stresses has been integrated in order to better represent the stiffness of the opening quarter panel. Thus, the new model allows taking into account the out-of-plane support supplied by the intermediate web-post. The formula proposed for the calculation of the critical stress has been compared and validated with numerical results. Finally, the proposed method appears representative of the behavior observed numerically or experimentally. Thus, this method can be used in order to assess each opening's quarter strength, which can define the partial failure of a sinusoidal opening which remains conservative in comparison to numerical ultimate failure loads.

In addition, so as to get a more accurate ultimate failure load, the authors proposed a cinematic approach which allows combining the different opening quarter strength. This analytical method can then be implemented in a cinematic approach in order to consider the opening failure mechanism (Durif 2012).

ACKNOWLEDGMENTS

This paper has been prepared as a result of a research carried out at University Blaise Pascal for the completeness of a PhDD degree. The authors would like to thank the Ministry of Research for the scholarship and ArcelorMittal group for the financial support and the supply of steel specimens for the experimental tests.

REFERENCES

Bleich F. 1952. Buckling Strength of Metal Structures. Mc Graw Hill Book Company.

Bulson P.S. 1970. The Stability of Flat Plates. Chatto&Windus.

Chung K.F., Liu TCH., Ko ACH. 2001. Investigation on Vierendeel Mechanism in steel beams with circular web openings. Journal of Constructional Steel Research, vol.5, pp. 467–490.

Durif S. 2012. Comportement mécanique des poutres cellulaires à ouvertures sinusoïdales –développement d'un modèle analytique adapté. PhD thesis, University Blaise Pascal.

Durif S., Bouchaïr A., Vassart O. 2013. Experimental tests and numerical modeling of cellular beams with sinusoidal openings. Journal of Constructional Steel Research, vol.82, pp. 72–87.

Durif S., Bouchaïr A., Bacconnet C. under review. Elastic rotational restraint of web-post in cellular beams with sinusoidal openings. Steel and Composite Structures.

ENV 1993-1-1. 1995. Eurocode 3 – Design of steel structures – Part 1–1: General rules and rules for buildings. Annex N.

EN 1993-1-1. 2003. Eurocode 3 – Design of steel structures – part1–1: General rules and rules for buildings.

EN 1993-1-5. 2004. Eurocode 3 – Design of steel structures – part1–5: Plated structural elements.

EN 1993-1-3. 2006. Eurocode 3 – Design of steel structures – part1–3: General rules – Supplementary rules for cold-formed members and sheeting.

Greiner R., Kettler M., Lechner A., Freytag B., Linder J., Jaspart J.-P., Boissonnade N., Borlotti E., Weynand K., Ziller C., Oerder R. 2009. SEMI-COMP : Plastic member capacity of semi-compact steel sections-a more economic design. Research fund for Coal and Steel, Final report.

Johansson B., Veljkovic M. Steel plated structures. Progress Structural Engineering, vol.3, pp.13–27, 2001.

Johansson B., Maquoi R., Sedlacek G., Müller C., Beg D. 2007. Commentary and worked examples to EN 1993-1-5 " plated structural elements ", JRC Scientific and Technical Reports.

Kang J.H., Leissa A. W. 2005. Exact solutions for the buckling of rectangular plates having varying in-plane loading on two opposite simply supported edges. International Journal of Solids and Structures, vol. 42, pp. 4220–4238.

Lawson R.M., Lim J., Hicks S.J., Simms W.I. 2006. Design of composite asymmetric cellular beams and beams with large web openings. Journal of Constructional Steel Research, vol. 62, pp. 614–629.

Smith S.T., Bradford M.A., Oehlers D.J. 1999. Elastic buckling of unilaterally constrained rectangular plates in pure shear, Engineering Structures, vol.21, pp.443–453.

Timoshenko S. 1943. Theory of elastic stability. Librairie Polytechnique Ch. Béranger.

Tsavdaridis KD. 2010. Structural performance of perforated steel beams with novel web openings and with partial concrete encasement. PhD thesis, School of Engineering and Mathematical Sciences City University London.

Ward J.K. 1990. Design of Composite and Non-Composite Cellular Beams. SCI Publication 100.

Yamashita T., Kato S. 2001. Elastic buckling characteristics of two-way grid shells of single layer and its application to evaluate the non-linear behavior and ultimate strength, Journal of constructional steel research, vol. 57, pp. 1289–1308.

Research and Applications in Structural Engineering, Mechanics and Computation – Zingoni (Ed.)
© 2013 Taylor & Francis Group, London, ISBN 978-1-138-00061-2

GBT buckling analysis of I-section steel girders under concentrated loads

P. Natário, N. Silvestre & D. Camotim
Department of Civil Engineering, ICIST/IST, TU Lisbon, Lisboa, Portugal

ABSTRACT: This paper illustrates the application of a Generalised Beam Theory (GBT) formulation to analyze the elastic localized web buckling of I-section steel girders under concentrated loads. The studied cases regard welded steel I-section beams with patch loading configurations: Patch Loading Test (PLT) and Opposite Patch Loading Test (OPLT). It is found that both pre-buckling longitudinal normal (σ_{ss}^0) and shear (σ_{xx}^0) stresses have to be included in the buckling analyses of I-section steel girders with PLT configuration. Furthermore, the pre-buckling transverse normal (τ_{xs}^0) stresses have to be included in the buckling analysis of I-section steel girders with OPLT configuration. In girders with PLT configurations, the GBT pre-buckling analysis should consider global and shear modes while the GBT buckling analysis may only consider local modes. In girders with OPLT configurations, the GBT pre-buckling analysis should consider transverse extension modes while the GBT buckling analysis may only consider local modes. The two illustrative examples (PLT and OPLT) are validated by comparison with Shell Finite Element (SFE) results.

1 INTRODUCTION

Due to the reduced width-to-thickness ratio of steel plates, the structural behaviour of I-section steel girders is strongly affected by the occurrence of several types of collapse with intrinsically nonlinear nature. The collapse of such thin-walled members is always associated with buckling phenomena, which arises due to action of (i) compressive normal stresses in the longitudinal direction, (ii) shear stresses and (iii) compressive normal stresses in the transverse direction, or due to a combination of these types. The buckling phenomenon arising from the action of compressive longitudinal normal stresses is, by far, the most well known and may be classified into one of three categories: global (flexural, torsional, flexural-torsional), lateral-distortional and local buckling. In I-section steel girders, the shear buckling phenomenon is also relevant in practical applications and its consideration is often needed in design safety checking procedures. However, the localized buckling phenomenon arising from compressive normal stresses acting in the member transverse direction is less well understood. This particular occurrence is due to concentrated loads applied transversally to the member axis or due to the simultaneous action of applied concentrated loads and the corresponding support reactions. The compressive normal stresses acting in the transverse direction also cause substantial material degradation due to gradual yielding and spread of plasticity. The failure of I-section steel girders under concentrated loads is mostly known as "patch loading collapse". This failure is due to the simultaneous occurrence of localized buckling (instability) and yield line mechanism (plasticity) in the web of the beam.

Due to the intrinsic tri-dimensional character of the phenomena, involving three stress components and their interaction in elastic buckling as well as the ensuing spread of plasticity, the success of theoretically grounded design procedures have not been reached. For more than 60 years, researchers used experimental test results of patch loading failure of welded steel beams (Granholm 1960, Tryland et al. 1999) to calibrate analytical expressions. These design procedures avoided the complexity of theoretical background inherent to localized web buckling but rendered their scope of application much narrower, i.e. specific for the case they were calibrated. Now that computational tools are widely available, accurate analysis of localised web buckling can be achieved using reliable numerical methods. Until now, this can only be achieved by using the shell finite element (SFE) method (Tryland et al. 1999). One very promising alternative to SFE method is the Generalised Beam Theory (GBT), a beam theory that incorporates genuine folded-plate concepts. GBT has been extensively applied to study the global, distortional and local buckling behaviour of members under longitudinal normal stresses. Most of all GBT formulations neglected the effect of transverse normal stresses. A first attempt to use GBT for localized web buckling analysis was done by Silva et al. (2008). Very recently, Natário et al (2012) developed a GBT formulation to study, systematically, the localized web buckling of thin-walled beams under concentrated loads. In this paper, GBT is applied to investigate the localized web buckling of a welded I-section girder.

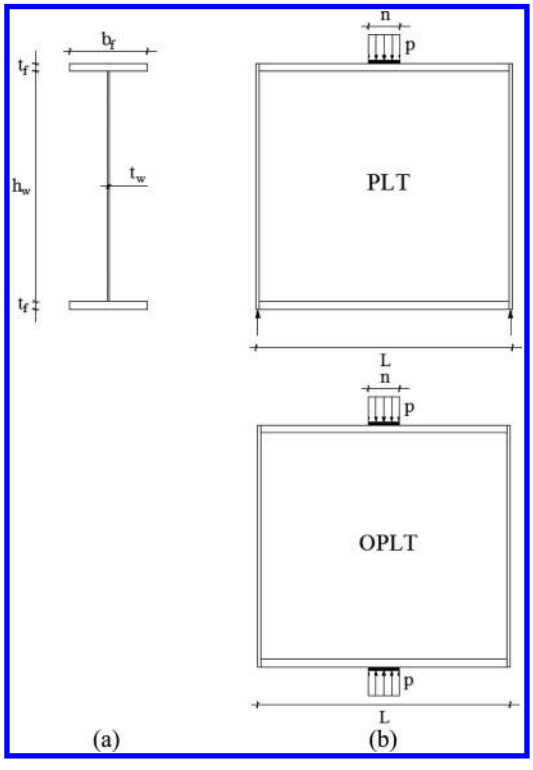


Figure 1. (a) Welded I-section dimensions and (b) patch loading configurations (PLT and OPLT).

2 ILLUSTRATIVE EXAMPLE

Consider now the welded steel ($E = 204000\,\mathrm{N/mm^2}$ and $\nu = 0.3$) I-section beam shown in Figure 1(a), which was tested and analysed by Tryland et al. (1999) for patch loading failure. The I-section dimensions are $h_w = 359.6\,\mathrm{mm}$ and $t_w = 3.8\,\mathrm{mm}$ (web), $b_f = 120.5\,\mathrm{mm}$ and $t_f = 11.9\,\mathrm{mm}$ (flanges). In GBT analysis, the I-section mid-line dimensions were used – the web height is $h_w + t_f$, as seen in Figure 1(a).

The cross-section discretization considers $n = 23$ nodes and 22 elements: each flange has 6 elements and the web has 10 elements. Thus, $4n = 92$ unit shape functions were imposed and 92 deformation modes were obtained from the GBT cross-section analysis, corresponding to 4 global modes (G), 44 local modes (L), 22 shear modes (S) and 22 transverse extension modes (TE). Figures 2 and 3 show some of the most relevant modes yielded by the cross-section analysis.

Mode 2-G, corresponding to major axis bending (see Figure 2), is the only global mode that is relevant for the analysis. The most relevant local modes (5-L, 6-L, 7-L and 8-L) are mainly characterized by web deformation (see Figure 2): the web bends transversally in single curvature for modes 5-L and 7-L while it bends in double curvature for modes 6-L and 8-L. It is also clear that the web-flange nodes exhibit significant rotation in modes 5-L and 6-L

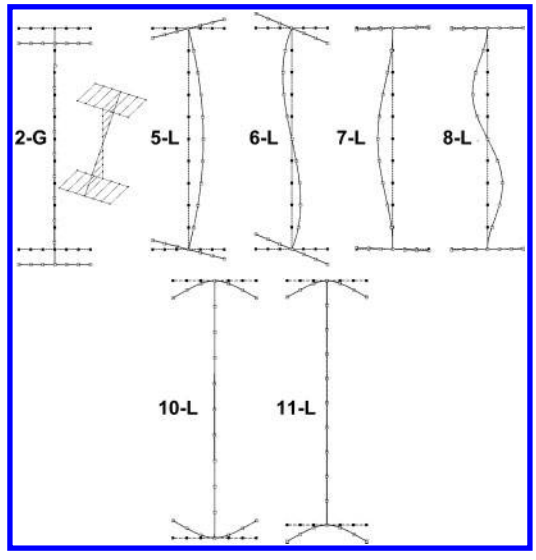


Figure 2. Most relevant global (G) and local (L) deformation modes for patch loading.

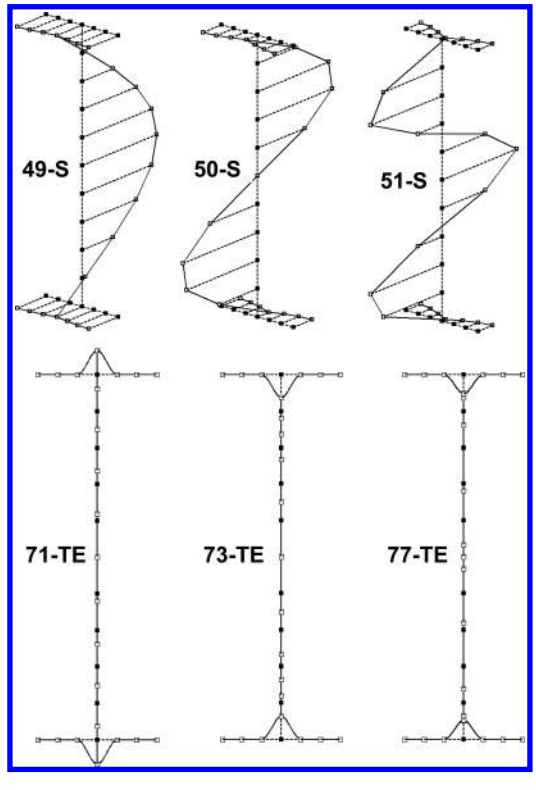


Figure 3. Most relevant shear (S) and transverse extension (TE) deformation modes for patch loading.

(web almost "simply supported") while their rotation is highly restrained in modes 7-L and 8-L (web almost "clamped"). In terms of shear deformation, the most relevant modes (49-S, 50-S and 51-S) are

depicted in Figure 3. They present negligible in-plane displacements but meaningful warping displacements. The number of warping displacement waves in the web increases from one (mode 49-S) to three (mode 51-S). Since the in-plane displacements are null ($v_k(s)=0$), it should be mentioned that the membrane shear strain varies with respect to the 1st derivative of the warping displacement ($\gamma_{xs}^M = u_(k,s)(s)$). Figure 3 also shows that flange shear lag effects increase from mode 49-S (almost uniform $u_k(s)$) to mode 51-S (slightly linear $u_k(s)$). Finally, the transverse extension modes deemed relevant (71-TE, 73-TE and 77-TE) involve solely the web deformation, as it is seen in Figure 3. In particular, the variation of the in-plane displacement $v_k(s)$ along the web height is shown in the left side of the modes in smaller scale. In all these modes, the web mid-point doesn't move ($v_k(s)=0$) and the non linearity of $v_k(s)$ increases from the mode 71-TE to the mode 77-TE. Figure 3 shows the in-plane deformed shapes of 71-TE, 73-TE and 77-TE modes. Since the transverse extension varies with respect to the 1st derivative of the in-plane displacement ($\varepsilon_{ss}^M \sim v_{(k,s)}(s)$, it is seen that the web is (i) stretched along its overall height (mode 71-TE), (ii) stretched in the bottom and top 1/3 part of the web and shortened in the middle 1/3 part (mode 73-TE), and (iii) stretched in the bottom, middle and top 1/5 part of the web and shortened in the remaining two 1/5 parts (mode 77-TE).

Following Tryland et al. (1999), the PLT (Patch Loading Test) and OPLT (Opposite Patch Loading Test) configurations are adopted herein (see Figure 1(b)). Load and support conditions were adapted according to the report by the aforementioned authors. The cross-section geometry defined before was considered for both PLT and OPLT configurations. Next, each test case is described in terms of the GBT modeling. The PLT case consists of a beam with length $L = 1315\,mm$. The top flange of the mid-span section is subjected to a load distributed along $n = 40\,mm$ (bearing length), as seen in Figure 1(b). In order to maximize the similarity between Tryland's and GBT models, the latter considers an imposition of the equal vertical displacement in every node contained in the load bearing region. As for the supports, all the displacements were restrained in the beam supports in order to simulate the rigid end-plates attached in the Tryland's experiments. The OPLT case considers a beam with $L = 1523\,mm$. Both top and bottom flanges of mid-span section are subjected to loads distributed along $n = 40\,mm$ (bearing length) and oriented in opposite directions (Figure 1(b)). Once again, the GBT model considers (i) an imposition of equal vertical displacement in every node contained in the load bearing region and (ii) null displacements at the beam supports. In order to maintain full symmetry of OPLT, the vertical and longitudinal displacements of the web midpoint at mid span section were set null. In both PLT and OPLT cases, the beam longitudinal discretization considers 20 beam finite elements.

First, we present the results of first-order GBT analysis, which are essential to characterize the pre-buckling behaviour of the beam in patch loading tests. Figures 4(a) and 4(b) show the variation of mode amplitude functions $phi_k(x)$ along the beam axis for PLT and OPLT, respectively.

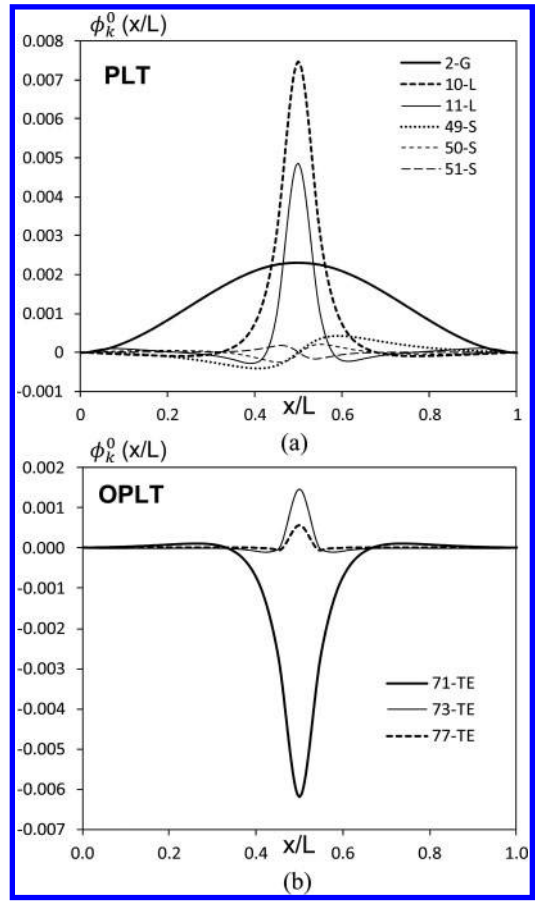


Figure 4. Pre-buckling mode functions $\phi_k^0(x/L)$ determined from 1st order analysis for (a) PLT and (b) OPLT.

The PLT (Figure 4(a)) is mostly influenced by modes 2-G, 10-L, 11-L, 49-S, 50-S and 51-S. It is seen that the amplitude of major-axis bending mode 2-G increases smoothly from the supports to the mid-span section while that of local modes 10-L and 11-L is null in a large portion of the beam length and increases hugely near the mid-span, thus exhibiting very pronounced local peak in the mid-span section. Since both amplitudes are positive at mid-span, the combination of these local modes (see Figure 4) leads a local deformation of the top flange (mode contributions add) where the load is applied but implies no deformation of the bottom flange (mode contributions cancel). Finally, the shear modes 49-S, 50-S and 51-S also have minor participations in the pre-buckling deformed shape of the beam. Since the local modes do not exhibit membrane stresses σ_{ss}^0 but only flexural ones, it is expected that pre-buckling longitudinal normal stress σ_{xx}^0 associated with major axis bending

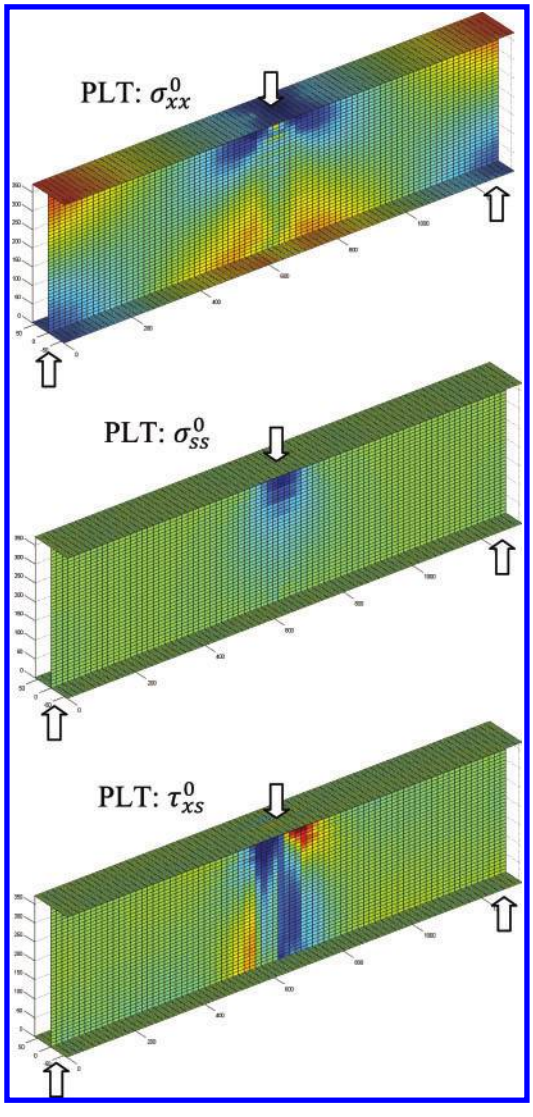


Figure 5. Pre-buckling stress (σ^0_{xx}, σ^0_{ss} and τ^0_{xs}) distributions obtained from GBT analysis for PLT.

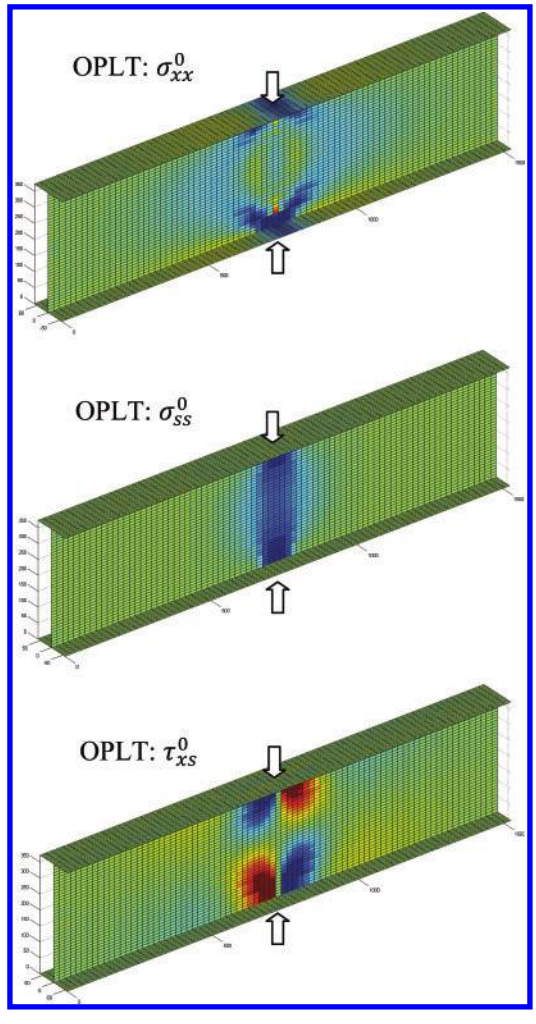


Figure 6. Pre-buckling stress (σ^0_{xx}, σ^0_{ss} and τ^0_{xs}) distributions obtained from GBT analysis for OPLT.

mode (2-G) and shear stress τ^0_{xs} associated with shear modes (49-S, 50-S and 51-S) will be the most relevant ones in the PLT case.

The OPLT (Figure 4(b)) is only affected by modes 71-TE, 73- TE and 77- TE. As expected, the participation of these modes occurs mainly in the mid-span region, where the loads are applied in opposite direction, leading to a local peak of $\phi_k(x)$ curves. Thus, modes 71-TE, 73-TE and 77-TE contribute to the web shortening in the mid-span region. Notice that mode 71-TE has higher contribution than the others since its $v_k(s)$ linear variation (see Figure 3) is more relevant that the non-linear variation of $v_k(s)$ of modes 73-TE and 77-TE. Since the web stretches in mode 71-TE (see Figure 3), its amplitude function depicted in Figure 4(b) is negative ($\phi_{71}(x) < 0$), giving a real (expected) web shortening ($v = v_{71}(s)\phi_{71}(x)$) due to opposite loads. Thus, if only these three modes are included in the GBT pre-buckling analysis, we certainly get the exact results. It is expected that pre-buckling transverse normal stress σ^0_{ss} associated with transverse extension modes (71-TE, 73-TE and 77-TE) will be the most relevant component in the OPLT case. Figure 5 presents tri-dimensional plots of the pre-buckling stress distributions (σ^0_{xx} – longitudinal normal stress, σ^0_{ss} – transverse normal stress, τ^0_{xs} – shear stress) for PLT – note that these plots are not obtained from a SFE analysis, but solely from the GBT first-order analysis. Figure 6 presents similar plots for the OPLT case.

First, it is obvious that PLT and OPLT stress distributions are clearly distinct (blue and red mean negative and positive values). One may observe that the longitudinal normal stress σ^0_{xx} is the most relevant component in the PLT case, whereas in the OPLT case we observe

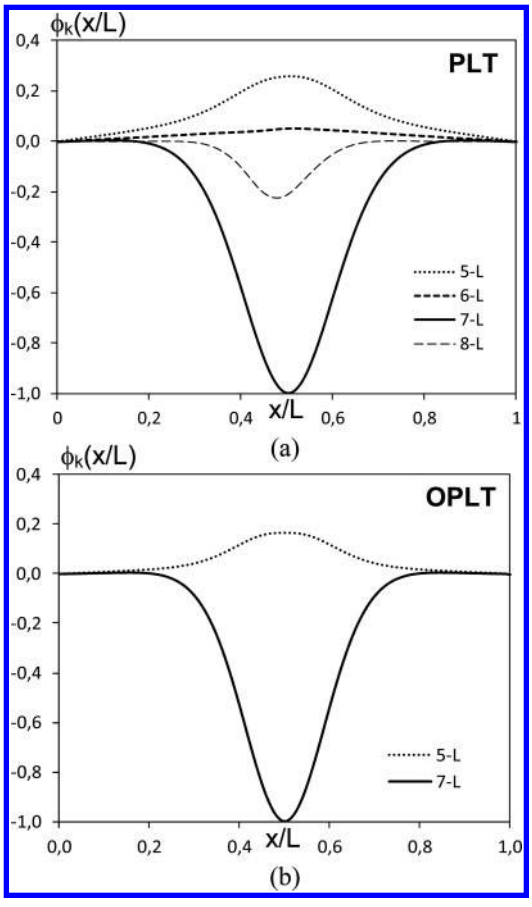


Figure 7. Buckling mode functions $\phi_k(x/L)$ for (a) PLT and (b) OPLT.

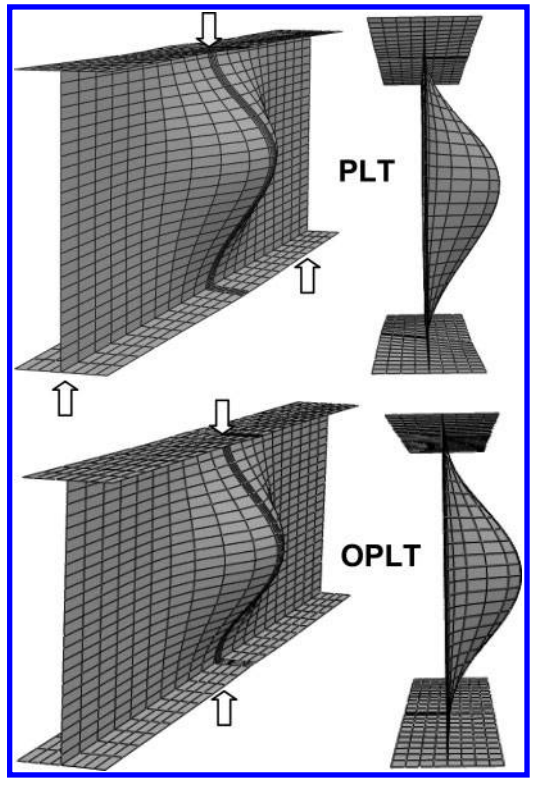


Figure 8. Buckling mode shapes obtained from SFE analysis.

that this stress component only displays high values very close to the load bearing plates. Concerning the transverse normal σ^0_{ss} component, it is clear that the roles are inverted, as it is possible to observe the high compressive (negative) stress level at the mid-span region due to load transfer between the top and bottom flange in the OPLT case. In terms of the shear stress τ^0_{xs}, both PLT and OPLT cases are characterized by relevant stresses in the mid span region.

After introducing the pre-buckling results (σ^0_{xx}, σ^0_{ss} and τ^0_{xs}) into the geometric stiffness matrices and solving the equilibrium equations, the results of buckling analysis are obtained. Figure 7 shows the variation of mode amplitude functions $\phi_k^{\$\$}(x)$ along the beam length determined from GBT buckling analysis for PLT (Figure 7(a)) and OPLT (Figure 7 (b)). In parallel, SFE analyses were performed and the beam buckling modes in PLT (Figure 8(a)) and OPLT (Figure 8(b)) are also shown. From a qualitative comparison between these results and those obtained in the web crippling tests by Tryland *et al.* (1999), it is possible to conclude that the local modes (5-L, 6-L, 7-L and 8-L) govern the beam deformed shape in patch loading tests. Since the flange rotation is restrained in the supports and load bearing region, it is observed that the local mode 7-L becomes the most important one in both PLT and OPLT, as it presents negligible flange rotation. To a much lesser extent, mode 5-L also contributes to the buckling mode deformed shape and introduces a slight flange rotation. Be aware of the fact that both 5-L and 7-L modes are symmetric as the web bends in single curvature.

From the comparison between Figures 7(a) and 7(b), it is seen that the individual contribution of local modes 5-L and 7-L is very similar in PLT and PLT cases. The main difference between PLT and OPLT resides in the contribution of local modes 6-L and 8-L, which are present in PLT but absent in OPLT. Since these modes are anti-symmetric (the web bends in double curvature), their "addition" to modes 5-L and 7-L in PLT case (see Figure 7(a)) leads to a buckling mode shape that is not totally symmetric with respect to the cross-section major axis. This evidence is confirmed by the SFE deformed shape shown in Figure 8(a), where it is seen that the maximum displacement occurs slightly above the web mid-point.

Due to the modal nature of GBT, if we include only (i) 4 local modes (5-L, 6-L, 7-L and 8-L) in the buckling analysis of PLT and (ii) 2 local modes (5-L and 7-L) in the buckling analysis of OPLT, surely we obtain the same results of all-mode analysis. The GBT and SFE buckling analysis presented the following elastic

critical load values: (i) 194 kN and 198 kN for PLT and (ii) 113 kN and 118 kN for OPLT. The results show a good agreement since the differences found were 1.8% for PLT and 3.8% for OPLT.

3 CONCLUSION

This paper illustrated a GBT formulation to analyse the elastic localized web buckling of thin-walled steel beams under concentrated loads. Details on the GBT formulation to analyse the localized web buckling of thin-walled steel beams under concentrated loads can be found in Natário et al (2012). The cases of welded steel I-section beams with PLT and OPLT configurations were considered for illustration purposes. It was found that:

- Few global and shear modes play a key role in the pre-buckling (1st order) behaviour of beams with PLT configurations. Transverse extension modes have a residual participation in the beam pre-buckling displacements. These facts imply that pre-buckling longitudinal normal (σ^0_{xx}) and shear (τ^0_{xs}) stresses associated with global and shear modes have to be included in the buckling analyses of beams with PLT configurations.
- Few transverse extension modes are needed to characterize the pre-buckling (1st order) behaviour of beams with OPLT configurations. Global and shear modes exhibit a negligible contribution to the beam pre-buckling displacements. These facts show that pre-buckling transverse normal (σ^0_{ss}) stresses associated with transverse extension modes must be considered in the buckling analyses of beams with OPLT configurations.
- The local modes also participate in the pre-buckling displacements of the beam, either in PLT or OPLT configurations. However, the membrane pre-buckling stresses (σ^0_{xx}, τ^0_{xs}, σ^0_{ss}) are not influenced by them and they can be disregarded in the pre-buckling analysis.
- In all cases, a stress concentration phenomenon exists and it leads to high non uniformity of pre-buckling stress distributions. The modal nature of GBT helps understanding the origin of this stress concentration, as well as the factors (i.e., deformation modes) that most affect the accuracy of the pre-buckling solution.
- As a consequence of this pre-buckling stress concentration, the results of buckling analyses show a strong localization of deformation. Thus, and conversely to pre-buckling analysis, the local modes are essential to correctly characterize the buckling behaviour of beams, either in PLT or OPLT configurations. Global modes may have residual participation in the beam buckling mode shape whereas the shear and transverse extension modes have null contribution.

From these remarks, the following conclusions are appropriate:

- Beams with PLT configurations: Pre-buckling analysis should consider global and shear modes while buckling analysis should consider local modes.
- Beams with OPLT configurations: Pre-buckling analysis should consider transverse extension modes while buckling analysis should consider local modes.

In conclusion, there are many parameters affecting the localized web buckling of thin-walled members under concentrated loads, such as (i) the type of concentrated loading, (ii) the geometric configuration of the web, (iii) the restraining effect provided by the flanges and (iv) the non uniformity of pre-buckling stress distributions. Only the consideration of a complete set of stresses (transverse normal stress, shear stress and longitudinal normal stress) ensuing exact distribution can lead to accurate solutions for localized web buckling of thin-walled members under concentrated loads. The GBT formulation presented in this paper has proven to be an efficient but rigorous way of dealing with this problem.

REFERENCES

Granholm CA (1960). Provning av balkar med extremt tunt liv. (Tests on girders with extremely thin web plates) in Swedish, Report 202, Inst. f. Byggnadsteknik, Goteborg, pp. 1–30.

Tryland T, Hopperstad OS, Langseth M (1999). Steel girders subjected to concentrated loading: validation of numerical simulations, Journal of Constructional Steel Research, 50(2), pp. 199–216.

Tryland T, Hopperstad OS, Langseth M. (2001). Finite-element modeling of beams under concentrated loading, Journal of Structural Engineering ASCE, 127(2), pp. 176–185.

Silva NF, Camotim D, Silvestre N. (2008). Generalized Beam Theory formulation able to capture load application and localized web buckling effects, In: Proceedings of 19th International Specialty Conference on Cold-Formed Steel Structures, R. LaBoube, W.-W. Yu (eds.), St. Louis, p. 33–59.

Natário P, Silvestre N, Camotim D. (2012). Localized web buckling analysis of beams subjected to concentrated loads using GBT, *Thin-Walled Structures*, Vol. 61, pp. 27–41.

Research and Applications in Structural Engineering, Mechanics and Computation – Zingoni (Ed.)
© 2013 Taylor & Francis Group, London, ISBN 978-1-138-00061-2

Design by inelastic analysis – 2010 AISC specification

R.D. Ziemian
Bucknell University, Lewisburg, PA, USA

ABSTRACT: In the latest edition of the American Institute of Steel Construction's *Specification for Structural Steel Buildings*, the design provisions for employing inelastic analysis have been fully revised. This paper provides an overview of the Specification's Appendix 1- *Design by Inelastic Analysis* and describes the new opportunities it presents to engineers who want to take better advantage of nonlinear material behavior, especially the redistribution of member forces as a result of yielding. Of particular interest to the design profession is that certain levels of inelastic analysis may now be used in place of the Specification's design equations in confirming the adequacy of components and/or the structural system. With this in mind, the associated requirements on this approach will be presented. The paper concludes by identifying topics in research that will need to be addressed in order to further expand current opportunities for design by inelastic analysis.

1 INTRODUCTION

Appendix 1 – *Design by Inelastic Analysis* of the 14th Edition of the American Institute of Steel Construction's *Specification for Structural Steel Buildings* (AISC 2010a) has been fully revised to permit engineers to take better advantage of advanced methods of inelastic analysis. The appendix allows for the use of a wide range of inelastic analysis methods, which vary from the traditional plastic design approaches to the more advanced nonlinear finite element analysis methods, to design continuous beams, moment frames, braced frames and combined systems. Presented as an extension of the Specification's primary design approach, termed the direct analysis method, a noteworthy feature of Appendix 1 is that for the first-time in an AISC Specification, engineers are permitted to evaluate strength limit states through the use of sophisticated methods of analysis in place of the Specification's design equations. Of course, the application of such an approach requires the designer to have a complete understanding of the particular method of inelastic analysis employed, the provisions of Appendix 1, and the Specification design equations being superseded.

2 GOALS OF APPENDIX 1

Strength limit states of structural steel systems almost always include significant amounts of yielding accompanied by large deformations. As a result of these destabilizing influences, significant redistribution of member and connections forces often occurs. The general objective of inelastic analysis and design (historically called *plastic design*) is to gain increases in economy through a better understanding and prediction of a structure's ultimate strength (Wong 2008). Such increases can come in the form of simply being able to use smaller member sizes by accounting for potential force redistribution or more broadly by providing structural systems with increased ductility through more informed design decisions.

There were four basic goals in preparing Appendix 1, including (1) recognizing the wide range of inelastic analysis available to today's engineer; (2) aligning the basic philosophy of inelastic analysis and design to the Specification's primary approach of the direct analysis method; (3) attempting to move in the direction of future design standards that are rooted in performance based engineering; and (4) being transparent and self-contained. Each of these goals will be covered in more detail below.

2.1 *Wide range of inelastic analysis methods*

In general, inelastic analysis covers a wide range of approaches based on concentrated plasticity models to the much more refined methods based on distributed plasticity procedures (McGuire et al. 2000). In addition, such methods may be classified as first- or second-order depending on whether or not equilibrium is formulated on the geometry of the deformed structure.

The concentrated plasticity or plastic hinge methods are typically based on comparing internal member forces and/or moments (stress resultants) to yield criteria and thus, lend themselves to the efficient analysis of systems such as continuous beams and two- or three-dimensional frames. Such methods may be modified

to indirectly include the effects of partial yielding that may be accentuated by the presence of thermal residual stresses due to nonuniform cooling during the manufacturing process. By doing so and also including second-order effects, these methods can provide the engineer with an analysis that is much more sophisticated than a program based on detecting plastic mechanisms.

In contrast, distributed plasticity algorithms are often stress-based and hence, can account for gradual yielding through the depth and along the length of structural members. These methods rely on at least discretizing the cross-section into fiber elements or, at the extreme, representing members and/or connections by a two- or three-dimensional mesh of continuum elements. When these methods include geometric nonlinear effects and explicitly model residual stresses by defining initial states of stress within the elements, they are often consider the most comprehensive or "exact." Such methods of analysis are available in commercial programs such as ABAQUS, ANSYS, and ADINA.

In all previous editions to the AISC Specifications, inelastic analysis was simply assumed to be the least rigorous of the plastic hinge methods, and although inelastic force redistribution was permitted, all member strength checks were based on satisfying the same Specification design equations that are defined for force distributions calculated from an elastic analysis. Given that most of these design equations were previously developed using the more refined (but now generally available) inelastic analysis methods, and further given that such sophisticated methods of analysis can model complex forms of nonlinear behavior and detect member and/or frame instabilities well before the formation of a plastic mechanism, one of the primary goals in developing Appendix 1 was to provide certain liberties to engineers who were willing to employ more rigorous and accurate methods of analysis. These liberties may include, for example, waiving the use of Specification design equations in lieu of the analysis being able to accurately model the strength limit state being considered. On the other hand, such liberties would be more restricted or eliminated if the inelastic analysis is too simplistic. Of course, in all cases it is the engineer's responsibility to fully comprehend the structural behavior being simulated and just as importantly, understand the theory, abilities, and limitations of the software being employed.

2.2 *Align with the direct analysis method*

In the 13th edition of AISC Specification for Structural Steel Buildings (AISC 2005), an alternative method for addressing structural stability was provided in its Appendix 7. This approach, termed the direct analysis method (Ziemian 2010), was well received and upgraded to Chapter C in the most recent 14th edition of the AISC Specification. The direct analysis method consists of calculating strength demands following fairly detailed analysis requirements and then comparing these required strengths with available strengths or capacities that are determined in accordance with design equations provided in the remaining chapters of the Specification. One of the key advantages of providing analysis requirements is that they can be defined such that assessment of stability of the system and members could be achieved without the need to rely on effective length K-factors. In other words, the direct analysis method provides an acceptable alternative to the effective length (KL) method, which had been the staple of the U.S. steel design profession for the past 50 years. This thereby allows engineers to simply use the unbraced length (L, with $K = 1$) of compression members in all related Specification design equations.

In breaking new ground in an AISC Specification by defining analysis requirements, the general philosophy of the direct analysis method could be easily extended beyond its original intent for elastic analysis and be equally employed in design based on inelastic analysis. Of course, the key is to define a set of analysis requirements that could apply to the wide range of inelastic methods described above.

2.3 *Move towards performance based engineering*

Performance-based engineering is a design philosophy that is receiving serious consideration by many standards organizations worldwide, including AISC, as they plan for the future. In general, functional objectives are defined and quantified such that the economies of improved performance can include life-cycle considerations that are well beyond initial construction costs. One of the keys to quantifying performance is an accurate prediction of structural behavior under a wide range of environmental effects.

Although Appendix 1 does not provide all of the elements of a performance-based engineering philosophy, it does include the general concept of applying more advanced methods of analysis to better predict structural response. That is, it provides for making more informed cost-benefit analyses when attempting to provide better performance.

2.4 *Transparent and self-contained*

One of the primary objectives in preparing all sections of the 13th and 14th editions to the AISC Specification was to provide provisions intended to be transparent (AISC 2005, AISC, 2010a). Design clauses and equations are now given in a format that allows the engineer to better understand which limit state behavior is being targeted by specific terms and mathematical expressions appearing in the Specification.

In addition to providing this same level of improved clarity, it was also desired that Appendix 1 should have its own self-contained provisions for assessing limit state behavior. Fortunately, this goal could be met with minimal repetition of information found in other parts of the Specification.

3 OVERVIEW AND GENERAL REQUIREMENTS

In meeting the above goals, Appendix 1 is presented in two basic tiers. The first provides general requirements that apply to all levels of inelastic analysis, varying from the traditional plastic mechanism methods to the much more sophisticated finite element procedures. The second tier provides the basis for an AISC-approved design method that is specific to second-order inelastic frame analysis. As such, this method can be used to assess the required strength of most structural members and systems. On the other hand, the first tier would provide the basis for employing a nonlinear finite element analysis using shell or brick elements to design more a complex component, such as a connection. In all cases, design by inelastic analysis is only permitted in accordance with the Specification's principles of load and resistance factor design, LRFD (the Specification also includes allowable strength design provisions).

3.1 *Essential 5*

Given that inelastic analysis permits the redistribution of forces and moments within structural systems or stresses within a connection, it is essential that the analysis provide an accurate representation of the effects of load on the system or component being designed. Factors that typically influence the stability of a structural system or component include deformations and reductions in stiffness due to yielding as well as variations in the design loads and anticipated strengths. With this in mind, Appendix 1 requires that the inelastic analysis shall take into account:

- Flexural, shear and axial member deformations, and all other component and connection deformations that contribute to the displacements of the structure
- Second-order effects (including P-Δ and P-δ effects)
- Geometric imperfections
- Stiffness reductions due to inelasticity, including the effect of residual stresses and partial yielding of the cross section
- Uncertainty in system, member, and connection strength and stiffness

It is important to note that these five requirements also appear in Chapter C where stability requirements for elastic analysis are provided. There is, however, one important distinction; in Chapter C it states that the requirements shall be considered, in contrast to the stronger language of shall take into account in Appendix 1. The committee felt that the firmer language of Appendix 1 was needed because engineering judgment of the importance of these factors is often much more difficult to exercise when employing a design procedure based on inelastic analysis.

Also in contrast to Chapter C, no further details are provided in this section regarding geometric imperfections or stiffness reductions, including predefined residual stress patterns. In this regard, such definitions vary greatly depending in the structural system or component being investigated. In general, it is expected that the engineer would define for example initial imperfections based on tolerances defined by the contract documents or include residual stress patterns that are specific to the profiles being analyzed.

Beyond requiring that uncertainty in strength and stiffness be included, the engineer is provided with the opportunity to define system and component reliabilities based on available theories that apply to the specifics of the design problem at hand (Buonopane & Schafer 2006, Nowak & Collins 2000, Thoft-Christensen & Murotsu 1986). In all cases, it is expected that a comparable or higher level of reliability forming the basis of the Specification will be provided.

3.2 *Assessing strength*

One of the primary objectives in developing Appendix 1 was to provide engineers the opportunity to better use advanced methods of inelastic analysis to confirm the adequacy of structural members, connections, and systems. All strength limit states assessed by the Specification must be considered, although the analysis could be used in place of the Specification design equations to demonstrate adequacy.

Consider, for example, assessing the strength of a compression member without slender elements. Section E3 of the Specification provides the pertinent design equation that accounts for several destabilizing factors including partial yielding accentuated by the presence of thermal residual stresses, initial member out-of-straightness, and second-order (P-δ) effects. If a level of inelastic analysis is employed that directly incorporates all of these factors, that is the analysis would be able to detect the limit state of inelastic/elastic flexural buckling, and a comparable or higher level of reliability can be assured, then that specific design equation need not be evaluated.

On the other hand, if the analysis does not accurately model flexural-torsional buckling or lateral-torsional buckling, then Specification equations given for these strength limit states would govern. In general, strength limit states not accurately modeled by the analysis would need to be assessed by the corresponding provisions of the Specification's Chapters D-tension, E-compression, F-flexure, G-shear, H-combined forces and torsion, I-composite, J-connections, and K-HSS and box sections.

3.3 *Ductility*

As a structural system reaches a strength limit state, significant force redistribution may take place as a result of yielding within members and connections. If a design procedure relies on this redistribution occurring, then all structural components subject to

yielding must be able to maintain their strength by accommodating the inelastic deformation demands.

There are two general methods for assuring this. The first, and more common approach, is to limit material properties, cross-section slenderness, and member unbraced length. The second is to make a direct comparison of inelastic deformation or strain demands with the component's deformation capacity. Examples of the first approach are provided below and examples of the second are provided in the literature (Galambos 1968, Gioncu & Petcu 1997, Kemp 1996, FEMA 2000, Ziemian 2010). Appendix 1 permits the use of either method to assure that adequate ductility is provided. In no case is force redistribution due to tensile rupture of an element of cross-section or connection permitted.

3.4 *Serviceability*

Beyond the general requirements for structural behavior at service loads provided in the body of the Specification, no provisions specific to design by inelastic analysis are included in Appendix 1. This should be expected given that (1) permanent deformations due to yielding at service loads should almost always be avoided, and (2) the benefits of inelastic analysis are only realized when assessing strength limit states.

3.5 *Seismic*

One of the more frustrating outcomes in preparing Appendix 1 was that its provisions had to be limited to non-seismic design applications, despite the fact that inelastic analysis has great potential in earthquake engineering. Two basic points complicated this matter, including (1) the equivalent static loads often used to represent seismic effects within factored load combinations assume a particular level of yielding and force redistribution has occurred, and as such it would be unconservative to use these loads within a design procedure based on inelastic analysis; and (2) all of the ductility requirements defined within Appendix 1 are unique to non-seismic effects and more stringent requirements would be needed for seismic design. Provisions for employing inelastic analysis in seismic design, however, are provided in *Seismic Provisions for Structural Steel Buildings* (AISC 2010b), *Minimum Design Loads for Buildings and Other Structures* (ASCE 2010) and *Seismic Rehabilitation of Existing Buildings* (ASCE 2006).

4 SPECIFIC PROVISIONS FOR FRAME DESIGN

As mentioned above, Appendix 1 is presented in two tiers, one universal and the other specific to frame design. With regard to the latter, detailed ductility and analysis provisions are given that collectively satisfy the above general requirements defined above. As such, these provisions define an AISC-approved procedure for using inelastic analysis to design structural systems, including frames and trusses, which are comprised of beams, columns, braces, and connections. An overview of these provisions is provided below.

4.1 *Ductility requirements*

To assure that structural components subject to yielding have adequate ductility, several design requirements are provided. The first is that the yield strength of the steel is not to exceed 450 MPa (65 ksi). This value was selected because extensive research into the use of such grades of steel in plastic design has been completed over the past 50 years. It is important to note that the use of higher strength steels is permitted per the general requirements presented in the first tier of Appendix 1, but not in association with the specific requirements given for frame design.

In assessing ductility, adequate inelastic deformation capacity can be confirmed by decoupling inelastic local buckling from inelastic lateral-torsional buckling, although in reality they often occur simultaneously. In both of these forms of buckling, requirements on the elements of the cross-section and on the unbraced length have been defined to provide adequate an rotation capacity at a plastic hinge of approximately $R_{cap} = 3$. Due to the complexity in inelastic behavior of members composed of singly- or non-symmetric cross-sections and their often-insufficient ability to provide adequate levels of ductility, this tier of Appendix 1 was purposely limited to doubly symmetric sections.

To prevent premature inelastic local buckling, guidelines are provided that limit the width-to-thickness ratios of cross-section components such as flanges and webs in the area of plastic hinges. Collectively, these slenderness requirements define "compact" sections, which are sections that have been shown experimentally and/or analytically to provide the desired inelastic rotation of capacity of $R_{cap} = 3$.

Inelastic lateral-torsional buckling can also significantly reduce the ductility of structural members with plastic hinges. In this regard, more closely spaced bracing in the vicinity of a plastic hinge will reduce the unbraced length of the member and thereby provide adequate rotation capacity. Appendix 1 provides unbraced-length requirements that are a function of the moment gradient for wide-flange and rectangular shapes bent about the major axis.

Finally, the axial force in a compression member is limited to 80% of the design yield load. This provision reflects a dearth of research that has been completed to ensure adequate inelastic rotation capacity in members subject to high levels of compressive axial force.

4.2 *Analysis requirements*

Per the requirements given above, a second-order analysis must be employed. The one exception to this rule would be for the design of continuous beams that are not subject to axial force.

Although there are several ways for including uncertainty in design based on inelastic analysis, Appendix 1 permits the simple strategy of reducing the system, member, and connection strength and stiffness by the AISC resistance factor of 0.9. In practice, this would typically be accomplished by using material yield strengths and stiffnesses of $0.9F_y$ and 0.9E, respectively. For a system of little-to-no redundancy, this factor will provide the same level of reliability as for design by elastic analysis. For more redundant systems, it can be shown that this approach is conservative.

Given that yielding in most frame design is the consequence of normal stresses acting in a direction parallel to the length axis of the members, Appendix 1 requires that these normal stresses include contributions by major- and minor-axis bending as well as axial force. In all cases, strain hardening is prohibited, thereby limiting the strength of a member to the plastic strength of its cross-section.

Initial imperfections, which include both member out-of-straightness and frame out-of-plumbness, must be included in the analysis. Although its impact depends on the amount of axial force in the member, its slenderness, and whether or not the member is subject to single- or reverse-curvature bending, a reasonable initial out-of-straightness might be of parabolic or sinusoidal shape with amplitude of L/1000, where L is the member length.

With regard to initial out-of-plumbness, the same provisions in Chapter C associated with the direct analysis method are to be used. Specifically, this would include incorporating a story sway out-of-plumbness of h/500, where h is the story height, or the use of an equivalent notional load at each level equal to the product of 0.002 and the factored gravity load on that particular level. In all cases, the initial imperfections should be modeled to produce the maximum destabilizing effect.

Finally, frame design by second-order inelastic analysis must include the effects of partial yielding, which can be accentuated by the presence of thermal residual stresses. Partial yielding may be included in the analysis either directly through the use of a distributed plasticity model or by a modified concentrated plasticity model (Ziemian and McGuire, 2002). It should be noted that no specific residual stress pattern is provided because the committee felt that it was not possible to provide a single idealized pattern for all potential cross sections and manufacturing processes. Instead, it is expected that the designer would reference the literature to obtain residual stress patterns that are appropriate to the given cross-sections employed.

5 FUTURE DIRECTIONS AND RESEARCH NEEDS

In preparing Appendix 1, several of the below limitations on the general application of design by inelastic analysis became apparent. Almost all of these limitations are the result of insufficient research. The committee is hopeful that such research will be completed in the near future and forthcoming editions of Appendix 1 will see increased opportunities in the following directions.

5.1 *Seismic design*

For the reasons indicated above, Appendix 1 does not permit buildings to be designed for seismic effects using inelastic analysis. Current thinking is that either Appendix 1 can be modified to include seismic design, or better yet, engineers will simply transition to other more applicable codes such as *Seismic Provisions for Structural Steel Buildings* (AISC 2010b) or *Minimum Design Loads for Buildings and Other Structures* (ASCE 2010).

5.2 *Singly-symmetric and non-symmetric shapes*

With additional research into the plastic rotation of capacity of singly-symmetric and non-symmetric shapes, the frame design tier for Appendix 1 can be expanded beyond permitting only doubly-symmetric shapes. Such research will need to address both slenderness requirements of cross-section elements and unbraced length requirements.

5.3 *Ductility requirements for high axial forces*

In providing guidance for frame design, Appendix1 limits the axial force to 80% of a shape's design yield load. With more research, this limitation could be relaxed or perhaps removed.

5.4 *High-strength steels*

A careful assessment of completed and future research of high-strength steels could provide their associated ductility requirements. In this regard, the benefits of steels with yield strengths in excess of 450 MPa (65 ksi) could be realized in frames designed by inelastic analysis.

6 SUMMARY

This paper presents an overview of Appendix 1 – *Design by Inelastic Analysis* that appears in the most recent 14th edition of AISC's *Specification for Structural Steel Buildings*. The appendix has been fully revised to permit the use of a wide range of inelastic analysis methods, in which significant advantages are provided for more sophisticated levels of analysis. In this regard, computational analysis (e.g., nonlinear finite element analysis) may be used in place of design equations to evaluate the strength limit states covered in the Specification. Of course, superseding Specification equations requires a thorough understanding of both the associated strength limit states and the

completeness and accuracy of the analysis software being employed to do so.

The appendix is presented in two tiers; one that is intended to cover all levels of inelastic analysis and a second that provides specific details that define a basis for an AISC-approved second-order inelastic frame analysis and design method. In both tiers, strength, ductility, and analysis requirements are provided. This paper concludes by suggesting future research that could provide more opportunities to design by inelastic analysis.

ACKNOWLEDGEMENTS

The author had the honor of chairing the AISC Appendix 1 sub-committee, whose members included:

W.F. Baker, Skidmore, Owings & Merrill
G.G. Deierlein, Stanford University
S.C. Goel, University of Michigan
R.A. Henige, LeMessurier Consultants
R. Kaehler, Computerized Structural Design
B. Leu, American Institute of Steel Construction
W. McGuire, Cornell University
C.-M. Uang, University of California, San Diego
D.W. White, Georgia Institute of Technology
R.D. Ziemian – Bucknell University

REFERENCES

ABAQUS® (Release 6.12) [Software]. (2013). Available from http://www.3ds.com/

ADINA® (Release 8.9) [Software]. (2013). Available from http://www.adina.com/

AISC 2005. *Specification for structural steel buildings.* Chicago.

AISC 2010a. *Specification for structural steel buildings*. Chicago.

AISC 2010b. *Seismic provisions for structural steel buildings*. Chicago.

ANSYS® (Release 14.5) [Software]. (2013). Available from http://www.ansys.com/

ASCE 2010. *Minimum design loads for buildings and other structures* (7–10). Reston: ASCE.

ASCE 2006. *Seismic rehabilitation of existing buildings* (41-06). Reston: ASCE.

Buonopane, S.G. & Schafer, B.W. Reliability of steel frames designed with advanced analysis. *Journal of Structural Engineering*. 132(2): 267–276.

FEMA, FEMA-350 2000. *Recommended seismic design criteria for new steel moment-frame buildings.* SAC Joint Venture for FEMA, Washington, DC: FEMA.

Galambos, T.V. 1968. *Deformation and energy absorption capacity of steel structures in the inelastic range*. Steel Research for Construction Bulletin No. 8. AISI.

Gioncu, V., & Petcu, D. 1997. Available rotation capacity of wide-flange beams and beam-columns. Part 1. Theoretical approaches, and Part 2. Experimental and numerical tests. *Journal of Constructional Steel Research*. 43-1-3:161–244.

Kemp, A.R. 1996. Inelastic local and lateral buckling in design codes. *Journal of Structural Engineering.* 122-4: 374–382.

McGuire, W., Gallagher, R.H., & Ziemian, R.D. 2000. *Matrix structural analysis*. 2nd ed. Hoboken: John Wiley & Sons.

Nowak, A.S. & Collins, K.R. *Reliability of structures*. New York: McGraw-Hill.

Thoft-Christensen, P. and Murotsu, Y. 1986. *Application of structural system reliability theory*. Berlin: Springer Verlag.

Wong, M.B. 2008. *Plastic analysis and design of steel structures*. Burlington: Butterworth-Heinemann.

Ziemian, R.D. (ed.) 2010. *Stability design criteria for metal structures*. Hoboken: John Wiley & Sons.

Ziemian, R.D. & McGuire, W. 2002. The modified tangent modulus approach, a contribution to plastic hinge analysis. *Journal of Structural Engineering*. 128-10: 1301–1307.

Research and Applications in Structural Engineering, Mechanics and Computation – Zingoni (Ed.)
© 2013 Taylor & Francis Group, London, ISBN 978-1-138-00061-2

Three-dimensional joist member design using equivalent beam theory

S.J. Kilber & A.E. Surovek
South Dakota School of Mines and Technology, Rapid City, South Dakota, USA

ABSTRACT: When selecting steel joists for a structure, design engineers have traditionally relied on standard load tables, but this is limiting when commercial software is used. Current structural design software packages lack the necessary capacities to estimate joist member weights and section properties accurately. Using custom tables for joist members with the application of Equivalent Beam Theory (EBT) allows joist member limit states to be analyzed by strength checks built into the design software. The custom tables for joist members are developed to represent approximate prismatic members based on the properties of typical chord sizes readily used in industry. This study presents the validation of custom tables for joist members. A case study illustrates the application of joist and joist girder tables in the design of a three-dimensional building.

1 INTRODUCTION

1.1 *Background*

Most current design software packages are limited to selecting simply-supported joists from standard load tables. These tables do not provide the design engineer with member section properties. They do provide member weights but only for specific joists types under uniform load conditions. The standard load tables are limited in that they are not equipped to support automated design of joists with non-uniform loads, such as drifted snow, pattern loading or point loads. Considering that joists and joists girders are custom designed by different manufacturers using proprietary combinations of chord and web components, the possibility of developing an all-inclusive list of the properties of available joists is infeasible. A more practical approach is to develop tables of approximate joist and joist girder weights and section properties based on the typical chord configurations used by joist manufacturers; these tables be then used with current software design packages. This method was originally validated for use with joist girder moment frames (Knodel et al. 2013).

1.2 *Equivalent beam theory (EBT)*

EBT is a simple modeling approach in which the properties of a flexural system (such as a steel joist) are approximated as those of a homogeneous, prismatic beam. The application of EBT has been shown to adequately capture the behavior of complex flexural systems in a single beam element. Giltner & Kassimali (2000) applied equivalent beam principles to modeling full truss systems. They evaluated two different equivalent beam methods:

1. The equivalent beam's stiffness was calculated from the deflection of the load truss.
2. Parallel axis-theorem was used to develop the equivalent beam moment of inertia based on the truss cross-sectional area. The vertical and diagonal web members were not considered in the calculation of the equivalent moment of inertia.

In their studies, Giltner & Kassimali compared and evaluated displacement and reaction values taken from a real three-dimensional model and those from equivalent models. They found that both equivalent methods provided acceptable results and two primary advantages. Equivalent beam theory greatly reduces the computational time needed for structural design software to analyze the given member. It also significantly reduces the overall time to model the structural (Knodel et al 2013).

Using EBT in the form of a Virtual Joist (VJ) table allows the multi-element flexural system to be modeled as a single beam element. This simplified element has approximate beam properties equivalent to those of the more complex system. In addition, the application of EBT allows both the design engineer and the joist designers to address common non-uniform loading conditions on their design members. If the section properties of the EBT accurately capture the properties of the joist within a reasonable variance, use of EBT allows the designers to move past the restrictions of simply-supported load tables when selecting an appropriate member. Panel-point loads, drifted snow loads, non-continuous uniform loads, etc. can be handled directly when selecting an appropriately sized member.

1.3 *Virtual joist and joist girder property tables*

The two joist properties that the design engineer must communicate to the joist designer are the moment of inertia (I_z) and the weight; both properties are based on chord sizes and are related to the combined chord areas

(A_x). The member weight is calculated from the cross-sectional areas of both the top and bottom chords; however, this calculation does not consider the web members due to the large variability in web member selection. To account for the web member weight, the density of joist and joist girder material is increased by 18%. This density increase provides a simple means to approximately account for web member weight in the virtual joist girder (VJG) and virtual joist (VJ) tables without affecting calculated values of axial capacity.

Because the tables represent complex geometry of a truss with a single beam member, they do not adequately capture out-of-plane joist behavior, nor can they capture local buckling of the joist member components. SJI developed these VJG and VJ tables based on industry bracing standards that eliminate out-of-plane limit states as member failure modes. For these studies, the joist members were considered to have continuous lateral bracing.

2 TABLE VALIDATION STUDIES

2.1 *Virtual joist girder table validation study*

The objective of the validation study, as detailed in Knodel et al. (2013), was to determine if the VJG moment of inertia and weight, as selected by the commercial design software, are within an acceptable variance from the moment of inertia and weight designed by the proprietary joist design software. First, simply-supported joist girder members were analyzed to eliminate the effect of support conditions. Second, fixed-end joist girder members were considered to account for end moment. Finally, portal frames were developed to establish proof of concept and to examine if the variation between VJG stiffness and the actual joist-girder stiffness has any impact on column or system design. These frame studies accounted for the influences of adjoining beam-columns on the member design.

Parameters for the single joist girder studies were selected to represent a practical range of design requirements. The parameter ranges for the single member studies are summarized in Table 1 (Knodel et al. 2013). The joist girder depth was not an independent parameter. The span-to-depth ratios were limited in the tests to a practical ratio of 12 to 24. For the single joist girder studies, the maximum chord depth was set to 15.2 cm. STAAD.Pro V8i (Bentley 2012b) was the design software used in all of the parametric studies.

Results of a single test were deemed "acceptable" if the value of Equation 1 was within a designated variance

$$\frac{\text{Design}_{\text{value}}\text{-P.Software}_{\text{value}}}{\text{P.Software}_{\text{value}}} \times 100 \qquad (1)$$

where:

$\text{Design}_{\text{value}}$ = member moment of inertia or weight selected by the design software; and

Table 1. Parameters for single joist girder studies.

Parameter	Range	Interval
Span (m)	6.10–24.38	3.05
Panel Point Loads (kN)	44.48–400.3	88.96
Panel Point Spacing (m)	1.22, 1.52, 1.83, 2.44	N/A

Table 2. Simply-supported virtual joist girders.

	Acceptable Variance (+/−)		
	10%	15%	20%
# Considered	78	78	78
I Acceptable	97%	99%	99%
Weight Acceptable	72%	86%	97%
Both Acceptable	72%	86%	97%

Table 3. Fixed-end joist girder studies.

	Acceptable Variance (+/−)		
	10%	15%	20%
# Considered	82	82	82
I Acceptable	91%	100%	100%
Weight Acceptable	71%	91%	99%
Both Acceptable	70%	91%	99%

$\text{P.Software}_{\text{value}}$ = member moment of inertia or weight designed by the proprietary joist software.

2.1.1 *Simply-supported joist girder studies*

With the parameters given, 78 simply-supported cases were designed. Table 2 summarizes the results.

As can be seen in Table 2, within the +/−10% variance, the moment of inertia approximation is close to complete acceptability and the weight approximation is at 72% of acceptability. When the variance is increased to +/−20% the weight approximation is also close to complete acceptability.

2.1.2 *Fixed-end joist girder studies*

Based on the single beam study parameters, 82 fixed-end joist girders were designed. Table 3 summarizes the results.

2.1.3 *Moment frame study*

To account for the effects of adjoining members on the design with the virtual joist girder table, a series of frames were analyzed in a similar manner as the single member studies (Knodel et al. 2013). The parameters and design loads for the frames studies are listed in Tables 4 and 5, respectively. Figure 1 gives a general frame layout.

From the moment frame studies, 72 joist girder designs were analyzed. The moment of inertia and weight variances of the moment frames studies are shown in Table 6.

Table 4. Parameters for frame studies.

Parameter [Symbol]	Increments
Length [L] (m)	12.2, 15.2
Height [H] (m)	6.10, 10.7
Load Amplifier [α]	0, 2, 6

Table 5. Design loads and for frame studies.

Load Type [Symbol]	Load kPa
Snow [S]	0.96, 1.92
Dead [D]	0.96
Wind [W]	1.2

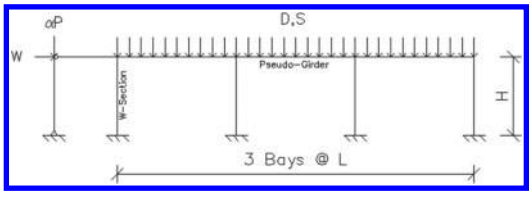


Figure 1. General frame layout.

Table 6. Moment frame joist girder results.

	Acceptable Variance (+/−)		
	10%	12.5%	15%
# Considered	72	72	72
I Acceptable	88%	96%	100%
Weight Acceptable	90%	100%	100%

Similar to the single joist girder studies, the moment frame cases demonstrated a high level of acceptability for both the moment of inertia and weight approximations within the +/−10% variance. With the variance was increased to +/−15%, both the moment of inertia and weight approximations were at compete acceptability.

2.2 *Virtual joist table validation study*

The VJ table validation was carried out in a similar manner as the VJG table validation. Simply-supported members were analyzed, and then followed by fixed-end member cases. Tables 7 and 8 show the single joist members used in both the simply-supported and fixed-end cases. The results were acceptable as defined by Equation 1.

2.2.1 *Simply-supported joist studies*

A total of 20 K-Series and 42 LH-Series joists were tested in the simply-supported condition to ensure that the VJ table functioned well in the simplest design case. Tables 9 and 10 show the results for the K-Series and LH-Series studies, respectively.

From Table 9, both the moment of inertia and weight approximations for the K-Series joists are at complete acceptability within the +/−15% variance. From

Table 7. K-Series joist testing schedule.

Depth cm	Span 1 m	ASD Total Load Span 1 kN/m	Span 2 m	ASD Total Load Span 2 kN/m
30.5	5.5	5.47	7.3	2.92
35.6	6.4	5.47	8.5	2.92
40.6	7.3	5.47	9.8	2.92
45.7	8.2	8.03	11.0	5.84
50.8	9.1	8.03	12.2	5.84
55.9	10.1	8.03	13.4	5.84
61.0	11.0	8.03	14.6	5.84
66.0	11.9	8.03	15.8	5.84
71.1	12.8	8.03	17.1	5.84
76.2	13.7	8.03	18.3	5.84

Table 8. LH-Series joist testing schedule.

Depth cm	Span 1 m	ASD Total Load Span 1 kN/m	Span 2 m	ASD Total Load Span 2 kN/m
45.7	8.2	8.76	11.0	5.84
50.8	9.1	8.76	12.2	5.84
61.0	11.0	8.76	14.6	5.84
71.1	12.8	8.76	17.1	5.84
81.3	14.6	8.76	19.5	5.84
91.4	16.5	8.76	21.9	5.84
101.6	18.3	8.76	24.4	5.84
111.8	20.1	8.76	26.8	5.84
121.9	21.9	8.76	29.3	5.84
132.1	23.8	8.76	31.7	5.84
142.2	25.6	8.76	34.1	5.84
152.4	27.4	8.76	36.6	5.84
162.6	29.3	8.76	39.0	5.84
172.7	31.1	8.76	41.5	5.84
182.9	32.9	8.76	43.9	5.84
203.2	36.6	8.76	48.8	5.84
223.5	40.2	8.76	53.6	5.84
243.8	43.9	8.76	58.5	5.84
264.2	47.5	8.76	63.4	5.84
284.5	51.2	8.76	68.3	5.84
304.8	54.9	8.76	73.2	5.84

Table 9. Simply-supported K-Series results.

	Acceptable Variance (+/−)		
	10%	15%	20%
# Considered	20	20	20
I Acceptable	100%	100%	100%
Weight Acceptable	90%	100%	100%
Both Acceptable	90%	100%	100%

Table 10. Simply-supported LH-Series results.

	Acceptable Variance (+/−)		
	10%	15%	20%
# Considered	42	42	42
I Acceptable	86%	98%	100%
Weight Acceptable	90%	100%	100%
Both Acceptable	79%	98%	100%

Table 11. Fixed-end K-Series results.

	Acceptable Variance (+/−)		
	10%	15%	20%
# Considered	20	20	20
I Acceptable	100%	100%	100%
Weight Acceptable	95%	100%	100%
Both Acceptable	95%	100%	100%

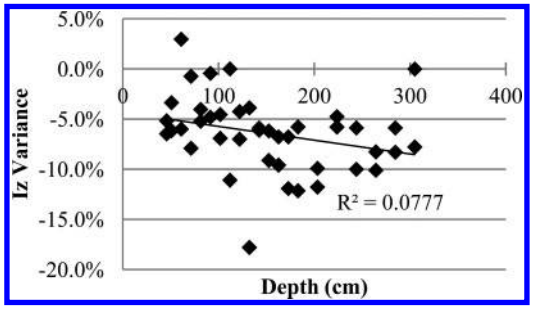


Figure 2. Moment of inertia variance vs. depth for simply-supported LH-Series tests.

Table 10 for the LH-series joists, the moment of inertia approximation is close to complete acceptability and weight approximation is at complete acceptability within the +/−15% variance.

Figure 2 shows the relationship between the moment of inertia variance and the member depth for the LH-series joists.

Figure 2 shows a downward trend, but insignificant correlation, in the moment of inertia variance as the joist depth increases. The design software selected virtual joist members with smaller moments of inertia than what the proprietary joist software calculated in a majority of the LH-Series tests. Further investigation into this difference yielded that the LH-Series joists have high interaction check values for the top chord in the end panels. Therefore, even in the simply-supported case, the top chord experiences combined axial and bending forces that need to be accounted for in the design software. This interaction is not captured by the equivalent beam.

2.2.2 *Fixed-end joist studies*

Similar to the simply-supported cases, 20 K-Series joists were tested with fixed-end conditions. Table 11 summarizes the results.

Table 11 shows that both the moment of inertia and weight approximations are at complete acceptability within the +/−15% variance.

3 THREE DIMENSIONAL BUILDING CASE STUDY

In order to demonstrate the effectiveness of both the VJ and VJG tables in a more realistic design situation,

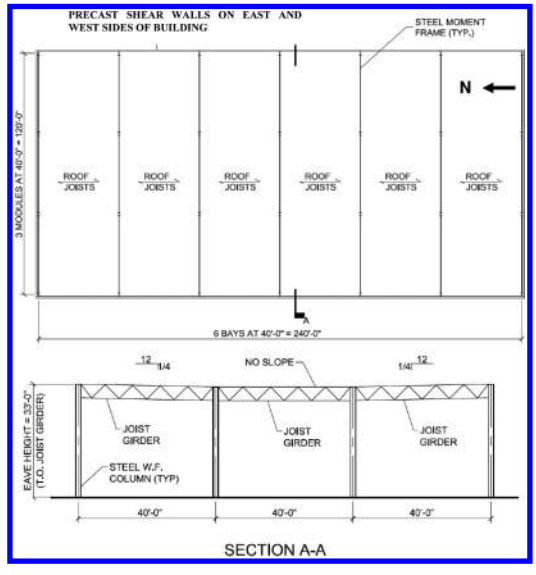


Figure 3. Building model dimensions and layout.

Table 12. Gravity design loads.

Load Type	Load kPa
Dead Load	0.96
Balanced Snow Load	1.53
Drifted Snow Load*	3.83

*Acts over 5.2 m in the north bays.

a three dimensional building model was developed. There were two primary goals for this case study: One was to adjust the table layouts to make them functional with RAM Structural System (Bentley 2012a) and the other was to determine the VJ table functionality with non-uniform member loads. In this instance, triangular drifted snow loads were applied on selected joists. The building geometry is shown in Figure 3 (Fisher et al. 2007). The bay dimensions in each direction are 12.2 m with overall building dimensions of 36.6 m by 73.2 m. Table 12 shows the gravity design loads. The wind loads were developed according to Structural Engineering Institute 7-05 (2006) requirements and were only applied in the E-W direction. Shear Walls are provided to withstand wind-load in the N-S direction.

Table 13. Exterior joist design results.

	Exterior Drift		Exterior	
Joist Type	Design	Proprietary	Design	Proprietary
Designation	VJ26-3	26K130/80	VJ24-2	24K130/80
W (kN)	0.89	1.11	0.87	0.974
I (mm^4)	7.2E+07	7.4E+07	6.0E+07	5.5E+07
W Variance	−19.4%		−10.7%	
I Variance	−2.0%		9.4%	

Table 14. Interior joist design results.

	Interior Drift		Exterior	
Joist Type	Design	Proprietary	Design	Proprietary
Designation	J30-13	30K260/160	J30-5	30K260/160
W (kN)	1.66	1.70	1.28	1.36
I (mm^4)	1.7E+08	1.6E+08	1.4E+08	1.3E+08
W Variance	−2.4%		−6.0%	
I Variance	5.1%		8.9%	

3.1 *Case study results – joist selection*

There are four different types of joists that needed to be designed in this case study: Perimeter Drift Joists, Interior Drift Joists, Perimeter Drift Joists, and Interior Joists. In the design, all of these members were considered to be pinned-pinned and have continuous bracing of the top flange. The results of the joist selection are shown in Tables 13 and 14.

Table 14 shows that for the two types of interior joists, both the moment of inertia and weight approximations fell within the +/−10% variance. Table 13 shows that for the exterior joists, the moment of inertia approximation fell within the +/−10% variance and the weight variance fell within the +/−20% variance. These results demonstrate the VJ table functionality with both drifted snow and uniform loading conditions.

3.2 *Case study results – joist girder selection*

For the design of the joist girders, the first-order analysis method as defined Appendix 7 of the American Institute of Steel Institute (AISC) Specification for Structural Steel Buildings, 14th Edition (2011) was applied. This approach is similar to notional load approaches currently used in various international design specifications (Galambos & Surovek 2008).

With joist girder moment frames (JGMF's) carrying the lateral loads in the east-west direction, there were four different types of joist girders that were designed: North Frame Drift Girders, Frame Drift Girders, Frame Girders, and South Frame Girders. For each of these frames, the first-order analysis member reactions were entered into the proprietary software, which designed the required member sizes. Then the equivalent virtual joist girder section was entered in RAM Structural System and analyzed using AISC 360-05 ASD design requirements. The results are summarized in Tables 15–18.

Table 15. North frame drift girder results.

	North Frame Drift	
Girder Type	Design	Proprietary
Designation	VJG36-40	36G8N8.1K/6.1
W (kN)	6.00	6.18
I (mm^4)	8.8E+08	8.8E+08
W Variance	−3.0%	
I Variance	0.0%	

Table 16. Frame drift girder results.

	Frame Drift	
Girder Type	Design	Proprietary
Designation	VJG36-52	36G8N10.9K/6.9
W (kN)	8.44	8.28
I (mm^4)	1.2E+09	1.2E+09
W Variance	1.9%	
I Variance	2.4%	

Table 17. Frame girder results.

	Frame	
Girder Type	Design	Proprietary
Designation	VJG36-48	36G8N10.4K/6.4
W (kN)	7.49	7.70
I (mm^4)	1.1E+09	1.1E+09
W Variance	−2.7%	
I Variance	0.8%	

Table 18. South frame girder results.

	South Frame	
Girder Type	Design	Proprietary
Designation	VJG36-19	36G8N5.2K/3.2
W (kN)	3.59	4.01
I (mm^4)	5.3E+08	5.6E+08
W Variance	−10.4%	
I Variance	−5.4%	

From Tables 15–17, the moment of inertia and weight approximations for three girder types fell within a +/−5% variance. In Table 18, the moment of inertia approximation fell within a +/−10% variance and the weight approximation fell just outside this variance. These results illustrate the functionality of VJG tables in RAM Structural System. Since the individual studies and the building design were both

able to produce acceptable results, the two studies validate the application of the tables and their adaptability to different commercial software packages.

3.3 *Case study results – overall member weight*

The total member weights from RAM Structural System and the proprietary joist design software were compared. The total member weight required by RAM was 340 kN; whereas, the proprietary joist design software required 356 kN of material. Thus, RAM was only 4.4% lower than the actual member weight required by the proprietary design software. In light of the total material needed, this is a minimal variance that would provide a design engineer a good initial material estimate. It should be noted that RAM Structural System does not allow for the creation of new design materials; thus, the member weights were adjusted after the analysis to account for the required joist density discussed in Section 1.3.

4 CONCLUSIONS AND FUTURE WORK

These studies show that the application of EBT to joist and joist girder design provides a reasonable approximation for the design engineer when estimating required stiffness and member weights. The case study provided a preliminary proof-of-concept and illustrates the use of the virtual joist and virtual joist girder tables in a more practical problem.

Further study is necessary to validate the use of EBT on joists, however. As stated earlier, equivalent beam theory allows complex models to be simplified and modeled as a single element. However, by simplifying a complex model, certain failure mechanisms, such as localized interaction of flexure and axial forces and local buckling, are not addressed in the simplified element. This was illustrated in the LH-Series studies. By using the VJ Table and EBT, the design software picked LH-Series joists with smaller moments of inertia than the same joists designed by the proprietary joist software. The design analysis failed to address the combined flexure and axial forces that these large joists experience when uniformly loaded. Thus, the selected members had smaller top chords; this results in lower moments of inertia and member weights. The next portion of this research will address methods to account for joist component interaction that cannot be captured by the EBT.

ACKNOWLEDGEMENTS

This research project was sponsored by the Steel Joist Institute. Bentley Systems, Inc. provided the STAAD.Pro and RAM Structural System software used in the research, and Habco Erectors, Inc. provided the proprietary joist design software.

The authors wish to acknowledge the input and assistance offered by the SJI Research Committee especially Dave Samuelson of Nucor Research and Development for Downstream Products and Walter Worthley with Valley Joist, Inc. In addition, the authors want to acknowledge Joe Pote with New Millennium Building Systems for both for developing the virtual joist and virtual joist girder tables and for his input on the project, as well as Jim Fisher of Computerized Structural Design for providing the building example. Findings, conclusions and recommendations are those of the authors and do not necessarily reflect those of the sponsoring organizations.

REFERENCES

American Institute of Steel Construction. 2011. *Specification for structural steel buildings*. Chicago, Illinios.

Fisher, J. M., Green, P. S., & Pote, J. J. 2007. *Design of lateral load resisting frames using steel joists and joist girders*. Myrtle Beach, South Carolina.

Galambos, T. V. & Surovek, A. E. 2008. *Structural stability of steel concepts and applications for structural engineers*. Hoboken, New Jersey.

Giltner, B. & Kassimali, A. 2000. Equivalent beam method for trusses. *Practice Periodical on Structural Design and Construction*, 5, 70–77.

Knodel, P. A., Surovek, A. E. & Pote, J. J. 2013. Accepted for Publication. A simplified approach for joist girder moment frame design using equivalent beam theory. *Engineering Journal*.

Structural Engineering Institute. 2006. *Minimum design loads for buildings and other structures*. Reston, VA.

Bentely. 2012a. *RAM Structural System Version 14.04.* Bentley Systems, Inc. Exton, Pennsylvania.

Bentely. 2012b. *STAAD.Pro V8i.* Bentley Systems, Inc. Exton, Pennsylvania.

Research and Applications in Structural Engineering, Mechanics and Computation – Zingoni (Ed.)
© 2013 Taylor & Francis Group, London, ISBN 978-1-138-00061-2

Behaviour of I-section columns experiencing local–global mode interaction: Analytical and finite element modelling

M. Ahmer Wadee & Li Bai
Department of Civil & Environmental Engineering, Imperial College London, London, UK

Dinar Camotim
Civil Engineering Department, ICIST, Instituto Superior Técnico, Technical University of Lisbon, Portugal

Cilmar Basaglia
Structural Engineering Department, São Carlos School of Engineering, University of São Paulo, Brazil

ABSTRACT: An extension of recent work on the local–global buckling mode interaction in thin-walled I-section columns is presented. The results obtained from an analytical model based on variational principles, which describes the column nonlinear buckling behaviour, are compared with those yielded by finite element analyses from the commercial software ANSYS. The comparisons are good and this provides encouragement to advance the understanding of the complex instability phenomena associated with nonlinear modal interactions.

1 INTRODUCTION

The buckling of struts and columns represents the most common type of structural instability problem. In the current work, the classic problem of a linear elastic column under axial compression with an open and doubly-symmetric cross-section – an "I-section" – is studied. Under this type of loading, long members are primarily susceptible to a global (or overall) mode of instability namely Euler buckling, where flexure about the weak axis occurs once the Euler buckling load is reached. However, when the individual plate elements of the column cross-section are relatively thin or slender, elastic local buckling of these may also occur. The interactive buckling behaviour of the aforementioned buckling modes is usually far more unstable than when the modes are triggered individually (Thompson & Hunt, 1973). Relevant recent work on interactive buckling include studies on stainless steel columns (Becque & Rasmussen, 2009a; Becque & Rasmussen, 2009b) with studies on thin-walled beams under uniform bending (Wadee & Gardner, 2012), sandwich struts (Hunt & Wadee, 1998) and corrugated plates (Pignataro *et al.*, 2000). Advances have been made recently on column behaviour where the junction of the web and the flange is assumed to be pinned (Wadee & Bai, 2012); cellular buckling (Hunt *et al.*, 2000) is thus triggered and a sequence of snap-backs is observed during the interactive buckling process.

The current work focuses on the scenario where the flanges and web have a rigid connection. In analytical terms, the boundary condition was currently switched from pinned to rigid and so the original model has been modified. It is found that this smoothes the post-buckling behaviour, the number of snap-backs is reduced and the response becomes more amenable to finite element (FE) simulation; the latter is performed in the commercial package ANSYS (2009). Comparisons between the analytical and FE model are found to be good and this offers encouragement to extend the study later using Generalized Beam Theory (GBT), where a semi-analytical approach may allow structural analysis to be performed for more generic cases (Basaglia *et al.*, 2011).

2 ANALYTICAL MODELLING

Figures 1(a) and (b) show the elevation and cross-section of the column with the coordinate system. The section geometries are chosen such that the local critical buckling load P_l^{C} is sufficiently close to the global buckling load P_o^{C}.

The investigation begins with defining appropriate descriptions for both the global and the local modes. The "sway" and "tilt" components from the previous work – see Figure 1(c) (Hunt & Wadee, 1998) – are combined to construct the global buckling mode such that shear deformations are allowed; this has been shown to be key in successfully modelling interactive buckling in an analytical framework. The lateral deflection W and the rotation of the plane sections θ are given by the following expressions:

$$W(z) = q_s L \sin\frac{\pi z}{L}, \quad \theta(z) = q_t \pi \cos\frac{\pi z}{L}, \tag{1}$$

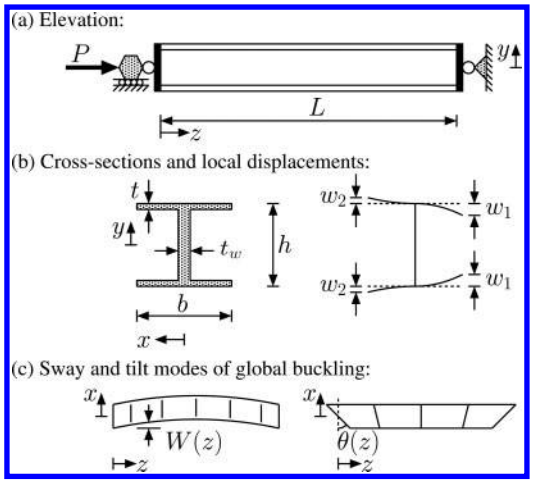


Figure 1. (a) Column elevation. (b) Cross-section dimensions and lateral flange displacements defining the local buckling mode. (c) Sway and tilt components of the minor axis global buckling mode.

where L is the column length with q_s and q_t being defined as generalized coordinates for the sway and tilt modes respectively. The shear strain γ_{xz} for the global mode is therefore given by the following expression:

$$\gamma_{xz,\text{global}} = \frac{\mathrm{d}W}{\mathrm{d}z} - \theta. \tag{2}$$

This is in essence a Timoshenko beam formulation (Wadee *et al.*, 2010).

An additional set of functions, w_i and u_i, where $i = \{1, 2\}$ representing the local lateral and in-plane displacements of the flange outstands respectively, is introduced (Wadee & Bai, 2012):

$$\begin{aligned} w_i(z,x) &= (-1)^i \left[\left(1 - \cos\frac{\pi x}{b}\right)\right] w_i(z), \\ u_i(z,x) &= (-1)^i \left(\frac{2x}{b}\right) u_i(z), \end{aligned} \tag{3}$$

where x is the transverse coordinate as shown in Figure 1(b), which also shows the cross-section lateral displacements w_i. Figure 2 shows the corresponding in-plane displacements u_i. For w_i, a sinusoidal distribution of displacement in the transverse direction is taken such that the flange–web connection is assumed to be rigid. For u_i the distribution is taken to be linear which is in accord with the Timoshenko beam assumption.

2.1 *Energy formulation*

The formulation of the total potential energy V is now presented. The component of the strain energy due to bending from global buckling U_B is given by:

$$U_B = \frac{1}{2} E I_w \int_0^L \left(\frac{\mathrm{d}^2 W}{\mathrm{d}z^2}\right)^2 \mathrm{d}z, \tag{4}$$

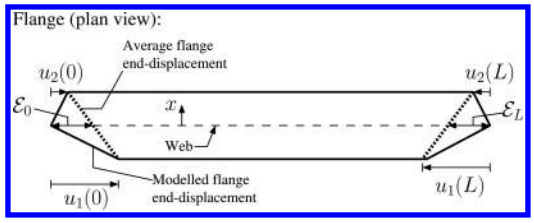


Figure 2. In-plane flange displacements u_1 and u_2 defining the local buckling mode. End shortening expressions $\mathcal{E}_0$ and $\mathcal{E}_L$ are $[u_1(0) + u_2(0)]/2$ and $[u_1(L) + u_2(L)]/2$ respectively.

where E is the Young's modulus and I_w is the second moment of area of the web about the global weak axis of the column cross-section and is given by $(h - 2t)t_w^3/12$. The local bending energy, accounting for both flanges buckling, is thus:

$$\begin{aligned} U_b = D \int_{-b/2}^{b/2} \int_0^L \Bigg\{ &\left(\frac{\partial^2 w_i}{\partial x^2} + \frac{\partial^2 w_i}{\partial z^2}\right)^2 \\ &- 2(1-\nu)\left[\frac{\partial^2 w_i}{\partial x^2}\frac{\partial^2 w_i}{\partial z^2} - \left(\frac{\partial^2 w_i}{\partial x \partial z}\right)^2\right]\Bigg\} \mathrm{d}z\,\mathrm{d}x, \end{aligned} \tag{5}$$

where $D = Et^3/[12(1-\nu^2)]$ is the flange plate flexural rigidity and ν is the Poisson's ratio. The integration with respect to x needs to be split; the integration is performed from $x = [-b/2, 0]$ with $i = 1$ and between $x = [0, b/2]$ with $i = 2$. The expression for the membrane strain energy U_m is given next and includes the contribution of the bending of the flanges from global buckling. The expression for U_m in fact neglects the transverse component ε_x, since it has been shown that it does not contribute significantly to the post-buckling stiffness of a rectangular plate with one free long edge and one rigid long edge (Koiter & Pig-nataro,1976). The longitudinal strain ε_z has to be modelled separately for the more and the less compressed flanges. The membrane energy is given by:

$$U_m = \frac{1}{2} E t \int_{-b/2}^{b/2} \int_0^L \varepsilon_z^2 \,\mathrm{d}z\,\mathrm{d}x, \tag{6}$$

where ε_z is given by the expression from von Kármán plate theory:

$$\varepsilon_z = x\frac{\mathrm{d}\theta}{\mathrm{d}z} + \frac{\partial u_i}{\partial z} + \frac{1}{2}\left(\frac{\partial w_i}{\partial z}\right)^2 - \Delta, \tag{7}$$

where Δ is defined as a purely compressive displacement to allow for elastic deformation before buckling. The integration with respect to x is split in precisely the same as for U_b. The shear strain γ_{xz} is also modelled separately for the more and less compressed sides of the flanges, and the shear strain energy is thus:

$$U_s = \frac{1}{2} G t \int_{-b/2}^{b/2} \int_0^L \gamma_{xz}^2 \,\mathrm{d}z\,\mathrm{d}x, \tag{8}$$

where G is the material shear modulus and γ_{xz} is given by the expression from von Kármán plate theory:

$$\gamma_{xz} = \gamma_{xz,\text{global}} + \frac{\partial u_i}{\partial x} + \frac{\partial w_i}{\partial x}\frac{\partial w_i}{\partial z}, \tag{9}$$

and the integration with respect to x is again split in precisely the same as for U_b. The work done by the axial load P is given by:

$$P\mathcal{E} = \frac{P}{2}\int_0^L \left[\left(\frac{\mathrm{d}W}{\mathrm{d}z}\right)^2 - \frac{\mathrm{d}}{\mathrm{d}z}(u_1+u_2) + 2\Delta\right]\mathrm{d}z, \tag{10}$$

where $\mathcal{E}$ is the total end-displacement of the roller support. The total potential energy V can then be obtained by the sum:

$$V = U_B + U_b + U_m + U_s - P\mathcal{E}. \tag{11}$$

2.2 *Governing equations*

The governing equilibrium equations are obtained by performing the calculus of variations on the total potential energy V. A system of nonlinear ordinary differential equations (ODEs) are derived. They comprise two fourth order ODEs for w_i and two second order ODEs for u_i. Equilibrium also requires the minimization of the total potential energy with respect to the generalized coordinates q_s, q_t and Δ – this essentially provides three additional integral equations. Finally, simply-supported boundary conditions for w_i and end strain conditions for u_i are derived from the first variation of V.

Linear eigenvalue analysis is carried out to determine the global buckling critical load, P_o^{C}:

$$P_o^{\mathrm{C}} = \frac{\pi^2 E I_w}{L^2} + \frac{2}{1/Gtb + 12L^2/Etb^3\pi^2}. \tag{12}$$

The critical stress σ_l^{C} for local plate buckling is determined using the well-known expression:

$$\sigma_l^{\mathrm{C}} = \frac{kD\pi^2}{b^2 t}, \tag{13}$$

where k is the plate buckling coefficient that depends on the edge conditions. The value of $k = 1.25$ represents the specific boundary conditions of the problem (Bulson,1970) and gives a slight upper bound on the actual computed solution. The local critical buckling load $P_l^{\mathrm{C}} = A\sigma_l^{\mathrm{C}}$ can then be determined, where A is the total area of the cross-section. For comparison purposes, it was possible for global (W_0) and local (w_0) imperfections to be included in the analytical model. These were introduced by assuming that the strain energy was zero in the initially deformed state.

Table 1. Buckling loads and eigenmodes from FE analysis.

L (mm)	P_o^{C} (kN)	P_l^{C} (kN)	Critical mode
2250	71.75	67.14	Local
2350	65.45	67.15	Interactive (approx.)
2450	60.61	67.13	Global

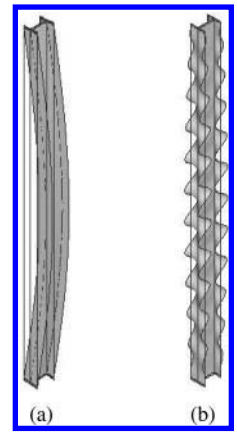


Figure 3. Buckling modes obtained by the FE model. (a) Global. (b) Local.

3 FINITE ELEMENT MODELLING

To validate the analytical model, an FE model within the commercial software ANSYS (2009) was created using a fine mesh of the "Shell181" element, which is an isoparametric 4-noded shell element; the "full integration" option was also employed. Buckling analysis was performed to obtain the local and global modes of instability. These were then substituted into the model as initial imperfections to conduct the nonlinear analysis for determining the post-buckling behaviour.

4 NUMERICAL RESULTS AND DISCUSSION

The system of nonlinear equations based on the analytical model was solved using the continuation and bifurcation software AUTO-07P (Doedel & Oldeman, 2009), which can capture bifurcation points and compute the post-buckling paths. To perform the numerical runs, the following isotropic material and cross-section properties were chosen: $E = 210000\,\mathrm{N/mm^2}$, $\nu = 0.3$, $b = 96$ mm, $t = 1.2$ mm, $t_w = 2.4$ mm and $h = 120$ mm. In this study, three separate lengths L were considered: global buckling being critical ($L = 2.45$ metre); local buckling being critical ($L = 2.25$ metre) and where the loads approximately coincide ($L = 2.35$ metre). The buckling loads from the FE model are given in Table 1.

Figure 3 shows the buckling modes that are obtained from the ANSYS analysis. As stated above, these are used as imperfections of small amplitudes to trigger the initial instability. For the global imperfection,

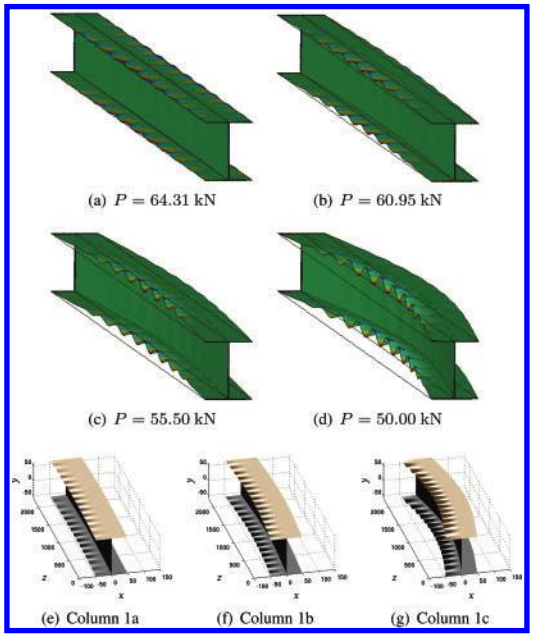


Figure 4. Numerical results for $L = 2.25$ metre. (a–d) Post-buckling results from ANSYS. (e-g) Post-buckling results from the analytical model; all dimensions are in millimetres.

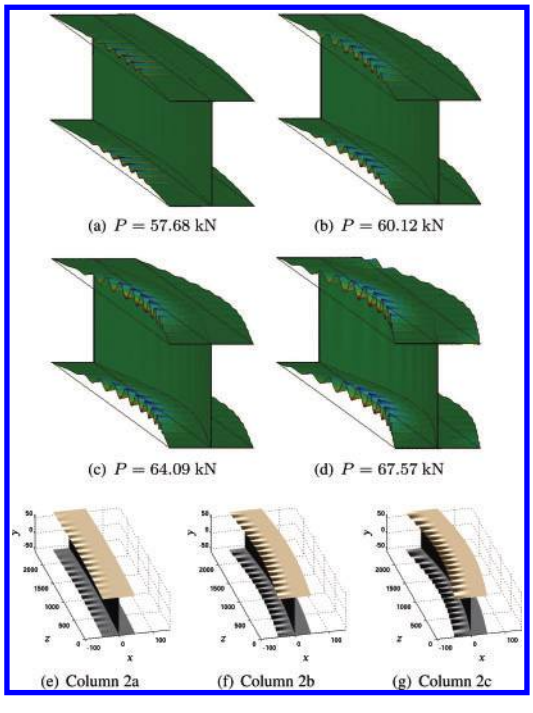


Figure 5. Numerical results for $L = 2.35$ metre. (a–d) Post-buckling results from ANSYS. (e-g) Post-buckling results from the analytical model; all dimensions are in millimetres.

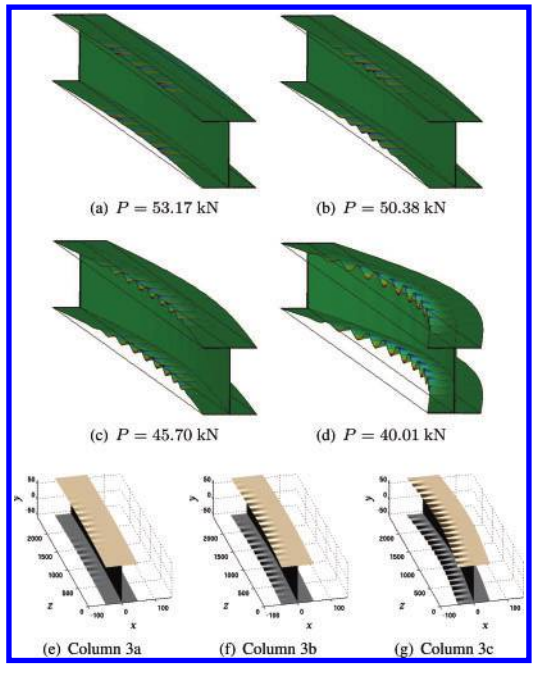


Figure 6. Numerical results for $L = 2.45$ metre. (a–d) Post-buckling results from ANSYS. (e-g) Post-buckling results from the analytical model; all dimensions are in millimetres.

Table 2. Load, global and local mode combinations for the strut images shown in Figures 4–6(e–g) derived from the analytical model.

Length (m)	Column	P (kN)	q_s	$w_{1,\max}/t$
2.25	1a	57.59	0.0020	0.546
	1b	57.23	0.0049	0.992
	1c	56.29	0.0148	1.63
2.35	2a	54.27	0.0022	0.524
	2b	52.85	0.0075	1.15
	2c	52.38	0.0118	1.44
2.45	3a	51.19	0.0014	0.220
	3b	50.44	0.0026	0.577
	3c	48.47	0.0076	1.13

an out-of-straightness of $L/5000$ was used. For the local imperfection the flange was assumed to be initially deflected out of the plane by an amount $t/1000$. For the analytical results, only a global imperfection of the same size was introduced to facilitate model comparisons.

For each case studied, four snapshots of the column modelled by FE and three snapshots of the column from the analytical model are presented in Figures 4–6. Table 2 show the loads, the relative magnitudes of the global and the local mode in the images shown in (e–g) of Figures 4–6. Figures 7–9 show comparisons of the equilibrium diagrams for all three cases, where $w_{\max}$ is the amplitude of w_1, and the plots in Figure 10 show comparisons of the local buckling mode.

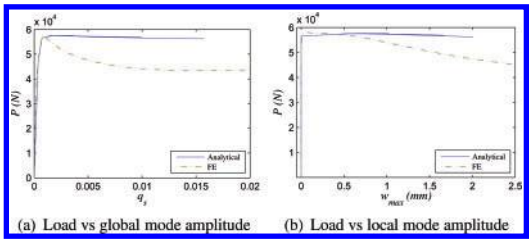


Figure 7. Comparisons between FE and analytical equilibrium paths for $L = 2.25$ metre.

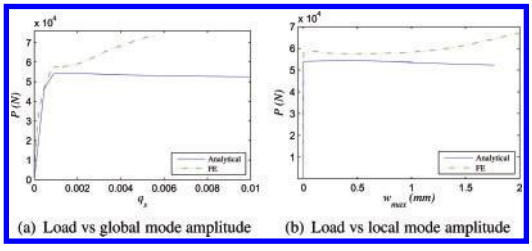


Figure 8. Comparisons between FE and analytical equilibrium paths for $L = 2.35$ metre.

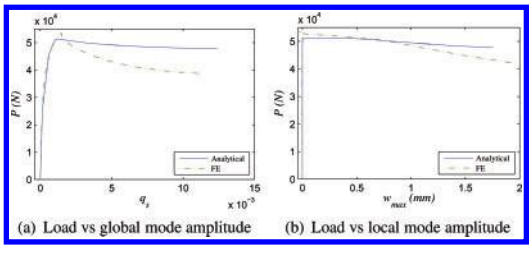


Figure 9. Comparisons between FE and analytical equilibrium paths for $L = 2.45$ metre.

These all demonstrate good correlation between the FE and analytical models. In particular, the buckling wavelength and the loads for the initial post-buckling compare very well, although there is some divergence as the post-buckling advances. Table 3 shows numerical comparisons of the lowest critical loads calculated by FE and those computed by the analytical model. The analytical model shows local buckling critical loads that are slightly below those calculated through Equation (13). All of the errors are seen to be well below 7%, which is most encouraging.

The comparisons of the analytical and FE models are quite interesting. As mentioned above, the load at the initial instability from the FE compares very well with the peak load from the analytical model. However, it is seen for the local and global buckling cases that the post-buckling response from the FE model is more unstable than the flatter results from the analytical model. If the FE results are taken as the benchmark, it suggests that the analytical model is too stiff and perhaps suggests that an extra degree-of-freedom is missing. It is worth emphasizing that the web is modelled not to buckle locally in the

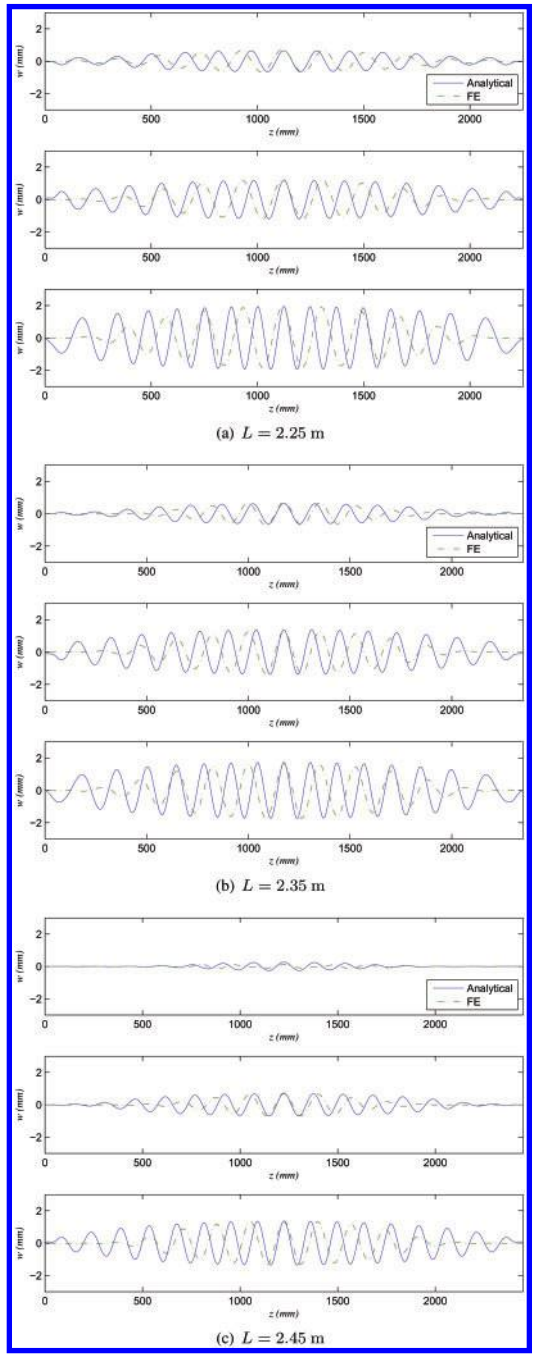


Figure 10. Comparisons between FE and analytical results of the local modes $w \equiv w_{1,\max}$ at different amplitudes for the different lengths as the column response advances in the post-buckling range.

analytical model currently, which could be important; allowing this would destiffen the column and may be sufficient to match the negative stiffness of the post-buckling better. Finally, the case where the buckling loads approximately coincide show a stable

Table 3. Key load comparisons.

Length (m)	Model	P^C (kN)	P_{peak} (kN)
2.25	Analytical	70.12	57.61
	FE	67.14	57.99
	Error	4.4%	0.7%
2.35	Analytical	66.23	54.49
	FE	65.45	58.44
	Error	1.2%	6.8%
2.45	Analytical	60.95	51.20
	FE	60.61	53.53
	Error	0.6%	4.3%

form of post-buckling in the FE model, which is a rather surprising result. The analytical model, however, shows a consistent pattern as the length changes which implies that there may be a possible discrepancy that requires further investigation. During the interactive post-buckling response, the convex side of the flanges continues to buckle locally in the FE model. This was not to be expected and perhaps is the source of the increased post-buckling stability exhibited. In the analytical model, local buckling on the convex side rapidly diminishes as the post-buckling advances, which perhaps is a more expected response.

5 CONCLUDING REMARKS

An analytical and a finite element model have been formulated to simulate interactive buckling in an I-section column with a rigid connection between the flange and the web. Generally, very good agreement has been found between the models for the critical and earlier post-buckling stages. Although certain modelling shortcomings have been identified, the results are very encouraging and the aim is to advance the study by using Generalized Beam Theory in future modelling. This is because it has been shown to be highly efficient and able to capture complex instability phenomena at times more reliably than the conventional finite element approach and is readily applicable to more generic loading cases and more complex geometries.

Work is also advancing on the analytical modelling front with the possible inclusion of the effect of lipped cross-sections; this would allow the modelling of global–distortional buckling mode interaction for which there has been little in the way of analytical studies in the literature, although semi-analytical models have been successful (Hancock, 1978; Schafer, 2002) in capturing the individual modes.

REFERENCES

ANSYS. 2009. *Reference manual*. v12 edn. Swanson Analysis Systems (SAS), USA.

Basaglia, C., Camotim, D., & Silvestre, N. 2011. Non-linear GBT formulation for open-section thin-walled members with arbitrary support conditions. *Comput. Struct.*, **89**(21–22), 1906–1919.

Becque, J., & Rasmussen, K. J. R. 2009a. Experimental investigation of the interaction of local and overall buckling of stainless steel I-columns. *ASCE J. Struct. Eng*, **135**(11), 1340–1348.

Becque, J., & Rasmussen, K. J. R. 2009b. Numerical investigation of the interaction of local and overall buckling of stainless steel I-columns. *ASCE J. Struct. Eng*, **135**(11), 1349–1356.

Bulson, P. S. 1970. *The stability of flat plates*. London, UK: Chatto & Windus.

Doedel, E. J., & Oldeman, B. E. 2009. AUTO-07P*: Continuation and bifurcation software for ordinary differential equations*. Tech. rept. Department of Computer Science, Concordia University, Montreal, Canada. Available from `http://indy.cs.concordia.ca/auto/`.

Hancock, G. J. 1978. Local, distortional and lateral buckling of I-beams. *ASCE J. Struct. Eng*, **104**(11), 1787–1798.

Hunt, G. W., & Wadee, M. A. 1998. Localization and mode interaction in sandwich structures. *Proc. R. Soc. A*, **454**(1972), 1197–1216.

Hunt, G. W., Peletier, M. A., Champneys, A. R., Woods, P. D., Wadee, M. A., Budd, C. J., & Lord, G. J. 2000. Cellular buckling in long structures. *Nonlinear Dyn*, **21**(1), 3–29.

Koiter, W. T., & Pignataro, M. 1976. *A general theory for the interaction between local and overall buckling of stiffened panels*. Tech. rept. WTHD 83. Delft University of Technology, Delft, The Netherlands.

Pignataro, M., Pasca, M., & Franchin, P. 2000. Post-buckling analysis of corrugated panels in the presence of multiple interacting modes. *Thin-Walled Struct.*, **36**(1), 47–66.

Schafer, B. W. 2002. Local, distortional, and Euler buckling of thin-walled columns. *ASCE J. Struct. Eng*, **128**(3), 289–299.

Thompson, J. M. T., & Hunt, G. W. 1973. *A general theory of elastic stability*. London: Wiley.

Wadee, M. A., & Bai, L. 2012. Cellular buckling from mode interaction in thin-walled I-section columns. *Pages 327–334 of:* Loughlan, J., Nash, D. H., & Rhodes, J. (eds), *Proceedings of the 6th international conference on coupled instabilities in metal structures*.

Wadee, M. A., & Gardner, L. 2012. Cellular buckling from mode interaction in I-beams under uniform bending. *Proc. R. Soc. A*, **468**, 245–268.

Wadee, M. A., Yiatros, S., & Theofanous, M. 2010. Comparative studies of localized buckling in sandwich struts with different core bending models. *Int. J. Non-Linear Mech.*, **45**(2), 111–120.

Research and Applications in Structural Engineering, Mechanics and Computation – Zingoni (Ed.)
© 2013 Taylor & Francis Group, London, ISBN 978-1-138-00061-2

Influence of the cross section slenderness on the buckling behaviour of steel welded tapered beam-column

I.M. Cristutiu & D.L. Nunes
"Politehnica" University of Timisoara, Timisoara, Romania

ABSTRACT: Pitched roof portal frames are often made of welded plate elements with tapered web classified as class 3 (semi-compact) and 4 (elastic) according to EN 1993-1-1. Moreover the class of flange, with constant variation along the element, can range from class 2 (compact) to class 3(semi-compact), function of their width to thickness ratio. Under gravitational load, that is the dominant case in design practice, these elements are mainly subjected to combined action of bending moment and axial compression force. Hence the tapering of the elements is made in accordance with internal force distribution under gravitational loads. Due to their cross section class type, the failure in buckling can be of different types. When class 2 and 3 sections, are restrained against lateral and/or torsional buckling, the coupling between sectional plastic buckling and overall in plane buckling of the members in compression and/or in bending is possible. When class 4 (slender) sections are used, which generally is the case of the rafter at the maximum height of the tapered web, the sectional buckling (e.g. local buckling of walls or distortion) may occur in the elastic domain. If no lateral restrains, or when they are not effective enough, the lateral torsional mode could characterize the global behaviour of the frame members, or interaction with sectional buckling modes may occur as well. The paper presents the results obtained experimentally, along with FEM analyses and a parametric study results. The failure mechanism, and hence the ultimate capacity is mainly influenced by the cross sectional and/or overall slenderness as well as the applied lateral restraints.

1 INTRODUCTION

Steel structures with pitched roof portal frames are widely used for low raised industrial and/or commercial buildings due to several advantages. Among them we can mention adaptability for long span (obtaining wide range of covered area without supplementary column), flexibility for further extension, accurate design solutions, easy assembling, cost efficiency and the last but not the least easy relocation. In most of the cases the main frame is designed accounting for gravitational load combinations, with significant values for dead, technological and snow load, which lead to important bending moment in the component elements. Besides bending moment, important compression forces develop within the column and rafter due to its pitch roof angle. Tapering of the component elements is made in accordance with the stress distribution. The variable section of the elements can be obtained in two different distinct ways: first one consist in hunching a prismatic European I profile in the requested zone (important values of bending moments), the second one consist in building the section with tapered web from welded steel plates, case which also makes the subject of the present study.

Due to web variation along the elements, the cross section is likely to vary as well, according to the provisions of EN1993-1-1. It can start from class 1 or 2 at the bottom of the column and can reach class 3 or even 4, function of the web thickness and cross section height. Although the flange class may fall into class 1 or 2, the final class of the cross section is dominated by the weakest class value, in our particular case the web class. These will lead the structural engineers to check the elements within the elastic range.

According to current European standard EN 1993-1-1 buckling verification only covers regular geometrical shapes, simple load cases and classical supports (rigid or pinned) and does not cover every case met regularly in design practice. However, advanced numerical computer aided analyses can be performed nowadays which allow the investigation of complex structures by using European provisions.

Structures made of slender elements with variable welded sections were previously studied by the authors, Cristutiu&Nunes, in 2012. The study was made on steel single story frames with pitch angle, different type of lateral restraints (rigid/actual), and initial imperfections. These studies revealed the importance of the lateral restraints on the capacity and structural behavior of frames made of elements with variable cross sections. For all the cases out-of-plane buckling of the frame elements was noticed to be independent of the applied lateral restraints. There were cases for which the global lateral- torsional buckling of the frames was coupled with local buckling of the web.

This was mainly observed when the restraints applied on the frame element are more effective against overall buckling. It was noticed that the considered imperfections has a low to significant influence on the final capacity of the frame, function of the applied lateral restraints.

Even though many papers regarding the behavior of steel elements subjected to bending moment and compression can be found in the literature (Taras 2008, Szalai 2009), the information regarding the ultimate capacity and behavior of the individual elements with variable cross section is still limited.

The ultimate capacity was determined by Shanmugam 2007 for tapered steel plate girders subjected to shear and by Salem 2009 for axially loaded thin-walled tapered columns with doubly symmetric sections. Shanmugam 2007 experimentally determined the ultimate behavior of tapered steel plate girders and concluded that the shear capacity of the girder is 5% less than the case of prismatic one, if the inclined flange is tensioned. Whilst the inclined flange is subjected to compression, the ultimate load of the tapered girder becomes higher than that of straight girders by more than 5%. In 2012 Marques et all developed a consistent buckling procedure for evaluating the ultimate capacity of tapered members subjected to compression. This procedure is rather difficult to apply in the actual design as it implies advanced numerical analysis. Behaviour under horizontal forces (earthquake) was studied analytically by Cristutiu&Nunes 2012 and experimentally by Hong&Uang 2012. Both studies concluded that the main failure mode is out of plane buckling and, consequently the seismic behavior could be improved by proper lateral restraints.

The aim of this paper is to analyze the behavior of tapered elements subjected to bending moment and axial compressive force when different type of lateral restraints are applied. For this purpose the results of an experimental program carried out at the "Politehnica" University of Timisoara, Romania, in the Laboratory of Steel Structures will be presented, along with a three dimensional FEM analysis results.

2 EXPERIMENTAL PROGRAM

2.1 *Specimens*

For the purpose of defining realistic specimen configurations a pitched-roof portal frame of 12 m span, 6 m bay, 4 m height and a pitch roof angle $\alpha = 8°$ was designed at first. The following load cases were considered: characteristic dead load of roof cladding $g_k = 0.7\,kN/m^2$; characteristic snow load $s_k = 2.0\,kN/m^2$. Both gravitational (dead, snow) and sidewise (wind and seismic) loads as well as corresponding load combinations were considered in the design. The steel frame was analyzed and designed according to the current EN 1993-1-1 provisions. The frames were considered pinned at the foundation level, while the rafter-to-column connection was considered fully rigid. The cross section dimensions of the two types of specimens and their codification are presented in Table 1.

Table 1. Main dimensions of the tested specimens.

Specimen	L [mm]	h_1 [mm]	h_2 [mm]	b [mm]	t_f [mm]	t_w [mm]
C3_8	3376	250	600	160	10	8
C4_6	3376	250	600	160	10	6
C5_8	3376	250	600	180	10	8
C6_6	3376	250	600	180	10	6

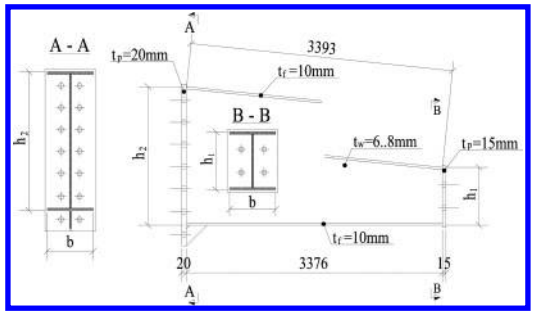


Figure 1. Specimen typology (dimensions are in mm).

The column specimens were extracted from the resulting frame and their global geometrical dimensions are presented in Figure 1. In order to analyse the influence of the web thickness (t_w) on the column behavior, two different values (i.e. 6 and 8 mm) were considered.

Each specimen was tested in its horizontal position. The bottom flange of the column was kept horizontally, whilst the opposite one was inclined following the shape of the tapered web. The connection at the left hand side (top in case of frames) of the specimen was assumed to be rigid and therefore an extended end plate with 8 bolt rows was provided. The opposite side of the specimen was considered pinned with a 15 mm end plate and 2 bolt row. The web cross section classes for the two specimens, ranging from 1(plastic) to 4(elastic), were evaluated and are plot in Table 2 along with its slenderness ratio (c/t). The flanges are of Class 2 and 3 (compact and semi-compact). The non-dimensional slenderness for the lateral torsional buckling, λ_{LT}, (that is the predominant way of failure) of the elements is presented in Table 2 as well.

Tensile tests were performed on coupons extracted from the same plate as the one used for the fabrication of the tests specimen. Three coupons were tested for each thickness. The tensile test was carried out using a UTS RSA 250kN-universal test machine. The obtained results confirmed that S355 steel was used for the fabrication of the tested specimens.

Three specimens of each configuration were tested, finally resulting in a number of twelve experimental tests (Table 2). The difference between the tests,

Table 2. Plate slenderness/section slenderness.

			Slenderness ($^c/_{ct}$)		Class		
		λ_{LT}	flange	web	flange	web	Elem.
C3-8	NR	0.533	7.6	28.8 . . . 72.5	2	1 . . . 3	3
	LR	0.505					
	TR	0.500					
C4-6	NR	0.625	7.7	38.3 . . . 96.7	2	3 . . . 4	4
	LR	0.625					
	TR	0.624					
C5-8	NR	0.515	8.6	28.8 . . . 72.5	3	1 . . . 3	3
	LR	0.515					
	TR	0.514					
C6-6	NR	0.632	8.7	38.3 . . . 96.7	3	3 . . . 4	4
	LR	0.632					
	TR	0.632					

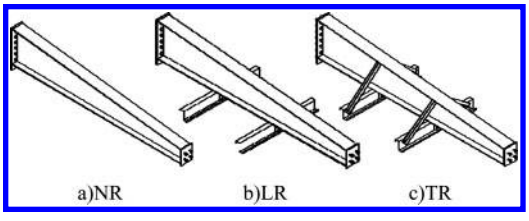


Figure 2. Lateral restraints typology.

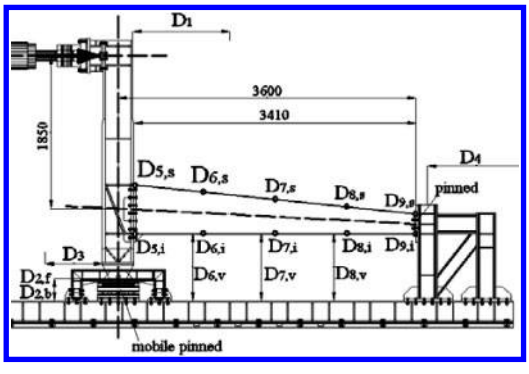


Figure 3. Testing se-up and instrumentation-schematic view.

for each specimen, was the provided type of lateral restraints. Six of the specimens had 8 mm tapered web (C3-8 and C5-8) and the other six were designed with 6 mm tapered web (C4-6 and C6-6).

The types of lateral restraints considered for each specimen configuration were (Fig. 3): (NR) – no restraints, (LR) – lateral restraints; and (TR) – torsional restraints respectively. Lateral restraints (LR) were provided by thin walled cold formed "Zed" purlins (Z150/1.5 mm), while in the case of torsional restraints (TR) supplementary L50x50x5 fly braces were provided at the compressed flange.



Figure 4. Testing set-up.

2.2 *Test set up*

The specimens were tested in horizontal position. The applied static scheme is a simple one, i.e. pinned connection at the right end of the column, and a roller at the bottom of the vertical element. The latter was designed stiff enough, so as not to suffer major deformations during testing as a horizontal force was being applied at the end of the vertical element.

The applied load and boundary conditions were designed in such a way as to load the specimen with a combination of axial compressive load and bending moment (Fig. 3 & Fig. 4). Apart from allowing a free horizontal displacement, the simple support also prevented the appearance of a horizontal reaction force that would lead to the change of the bending moment diagram in the tested specimen.

3 RESULTS OF EXPERIMENTAL TEST VS FEM ANALYSIS

A finite element model was built following the exact nominal geometrical dimensions and material properties of the tested specimens. Both geometrical and

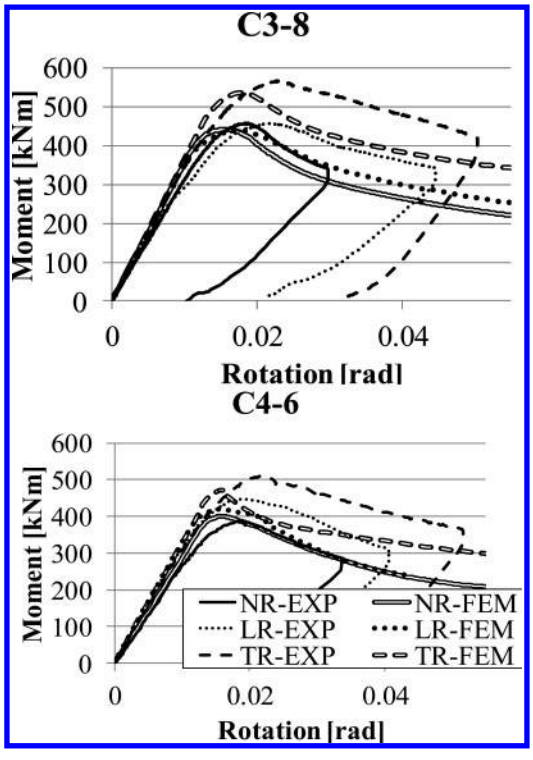


Figure 5. Moment rotation curve experimental/FEM.

material nonlinear behavior were considered, together with the equivalent global bow geometric imperfection, to determine elastic-plastic resistance in ULS, using GMNIA according to EN1993-1-5. Imperfections were applied according to EN1993-1-1 provisions, i.e. out of plane initial bow imperfection with the amplitude of L/150 from the length of the tested specimen, corresponding to a plastic analysis of a welded I-section element (buckling curve c about minor axis z-z). The material behaviour was generated with an elastic-plastic and linear strain hardening model according to the real experimental measured material parameters.

The experimental results recorded during the tests were initially in terms of forces (F) and displacements (d). These results were converted thereafter in terms of bending moment (M) and rotation (Φ) and finally the M-Φ curve was built. The moment rotation curve, plotted in Figure 5 for specimen C3-8 and C4-6, shows the behavior from the elastic point to the ultimate capacity of the tapered columns, laterally restrained or not.

Evaluation of the bending moment capacity was made according to the ECCS recommendations. The method of evaluation is presented in Fig. 6, where the bending moment capacity represents the intersection between two lines. First one corresponds to the initial rigidity while the second one represents the tangent to the capacity curve with a slope of 10% of the initial rigidity. An example is illustrated in Figure 6 for the C5-8-TR specimen.

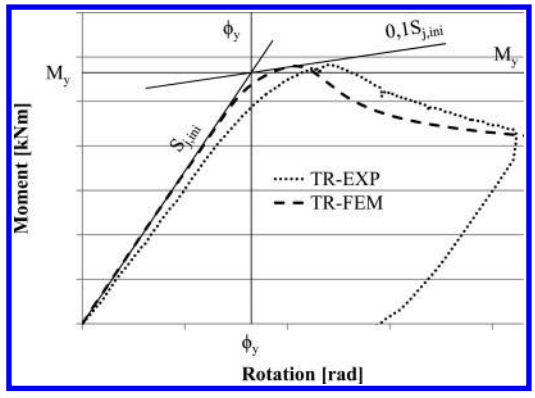


Figure 6. ECCS procedure for the evaluation of M_y.

Table 3. Experimental and FEM results.

		$M_{u,EXP}$ kNm	$M_{y,EXP}$ kNm	$M_{y,FEM}$ kNm	$M_{y,EXP}$ $M_{y,FEM}$
C3-8	NR	456.1	430.64	420.81	1.02
	LR	456.9	443.28	430.15	1.03
	TR	566.3	537.39	522.44	1.03
C4-6	NR	387.7	376.44	394.32	0.95
	LR	446.4	431.50	409.54	1.05
	TR	509.8	492.18	465.65	1.06
C5-8	NR	528.5	501.80	482.41	1.04
	LR	541.5	521.98	498.45	1.05
	TR	582.3	565.96	564.94	1.00
C6-6	NR	438.9	419.52	431.87	0.97
	LR	485.1	465.76	452.24	1.03
	TR	527.3	511.36	504.06	1.01

The experimental bending moment ($M_{y,EXP}$) within the specimen and the corresponding values obtained from the finite element ($M_{y,FEM}$) analysis are summarized in Table 3. In the same table $M_{u,EXP}$ represents the peak moment extracted from the capacity curve.

As it can be seen, for the case of 8 mm web series, the failure mode and capacity is influenced by the type of the lateral restraints. The specimens of 6 mm web thickness behaved in the similar manner (Tabel 3).

The failure modes of the 8 mm series of tests were the following: 8_NR – at first, overall lateral-torsional buckling of the column, followed by distortion of the compressed flange and finally the specimen failed by sectional plastic buckling; 8_LR – at first overall lateral-torsional buckling of the column, followed by distortion of the compressed flange an finally the specimen failing by sectional plastic buckling; 8_TR – started with distortion of the compressed flange and was followed by a slight overall torsional buckling ending in sectional plastic buckling.

In conclusion, the main failure mode is distortion of the compressed flange coupled with lateral torsional buckling, in function of the type of the lateral restraint. Lateral torsional buckling prevails in the case of 8_NR

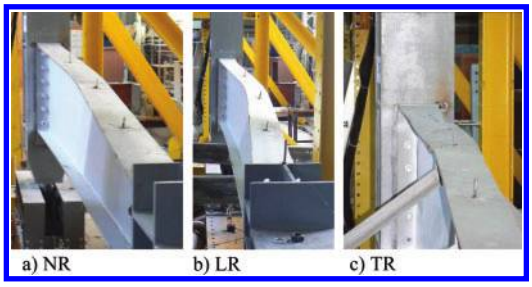


Figure 7. Failure of the 8 mm web specimen typology.

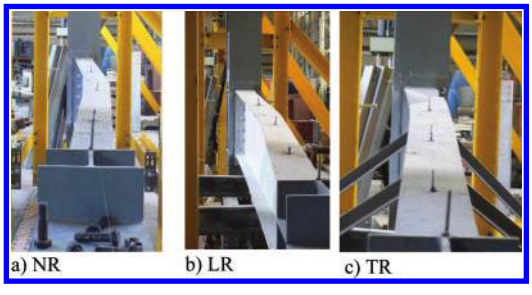


Figure 8. Failure of the 6 mm web specimen typology.

and 8_LR, while sectional plastic buckling with distortion of the compressed flange prevails in case 8_TR. In what concerns their ultimate capacity, this is slightly improved for the case with TR restraints.

Similar behavior was obtained from FEM analyses (Fig. 7). It was noticed that the flange slenderness did not influence the failure mode of the specimen.

The failure modes of the C2-6 series of tests were the following: C2_6_NR – started with distortion of the compressed flange, followed by isolated sectional buckling and slight overall lateral-torsional buckling of the column; C2_6_LR – started with distortion of the compressed flange, followed by isolated sectional buckling and slight overall lateral-torsional buckling of the column; C2_6_TR started with distortion of the compressed flange, followed by isolated sectional buckling and slight overall lateral-torsional buckling of the column.

The isolated sectional buckling for this series of tests prevailed over the global out of plane buckling. For this type of specimen series, the failure was almost the same regardless of the type of lateral restraints.

As it was described at the beginning of the present chapter, advanced FEM analyses were performed for all tested cases. The capacity curves were recorded as well as the failure mode. It was noticed that the failure mode is influenced by the type of lateral restraints as in the case of the experimental tests.

Due to lack of space herein only the failure mode of the 6 and 8 mm web thickness with 160 mm flange width are presented (Fig. 8&9). Although the 6 mm web thickness is more slender no difference was noticed in the behaviour for the same type of lateral restraint though.



Figure 9. FEM- Failure of the 6 mm web specimen typology.

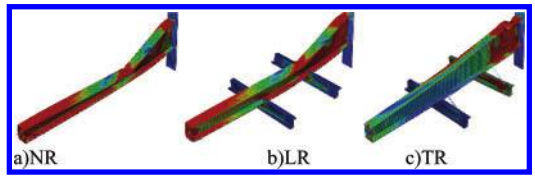


Figure 10. FEM- Failure of the 8 mm web specimen typology.

Table 4. Dimensions of the specimens for the parametric study

Specimen	L [mm]	h_1 [mm]	h_2 [mm]	b [mm]	t_f [mm]	t_w [mm]
60_8	3376	250	600	60	10	8
60_6	3376	250	600	60	10	6
80_8	3376	250	600	80	10	8
80_6	3376	250	600	80	10	6
100_8	3376	250	600	100	10	8
100_6	3376	250	600	100	10	6
120_8	3376	250	600	120	10	8
120_6	3376	250	600	120	10	6
140_8	3376	250	600	140	10	8
140_6	3376	250	600	140	10	6
160_8	**3376**	**250**	**600**	**160**	**10**	**8**
160_6	**3376**	**250**	**600**	**160**	**10**	**6**

4 PARAMETRIC STUDY ON TAPERED BEAM-COLUMNS

It is very well known that experimental test, especially when dealing with big specimens, are time and labor consuming. An alternative to experimental test are numerical simulations, where all the effects that might appear during test should be taken into consideration as well.

Further on numerical simulation were made using GMNIA in order to determine the behavior of beam-column elements with variable cross section, while different values of flange slenderness were applied. The analyses cases are descried in Table 4. The same length and height was kept for all the analyzed cases, while the flange varies between 60 to 180 mm, with an increment of 20 mm.

In Figure 10 is illustrated the behaviour of tapered beam columns with NR restraint (see Fig. 2). In Figure 10 an evolution from out of plane buckling (case of 60-8) to coupling of out of plane buckling and sectional plastic buckling (160-8) can be observed. The same evolution was observed in case of LR and TR

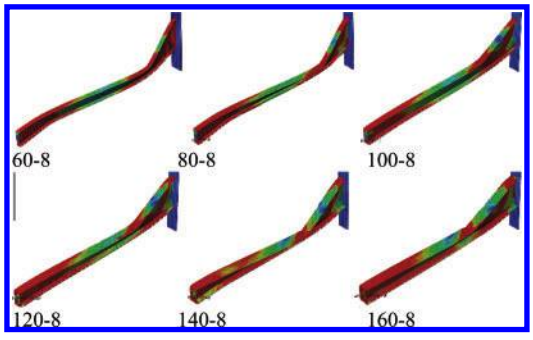


Figure 11. FEM- parametric – Failure of the 8 mm web specimen typology with NR.

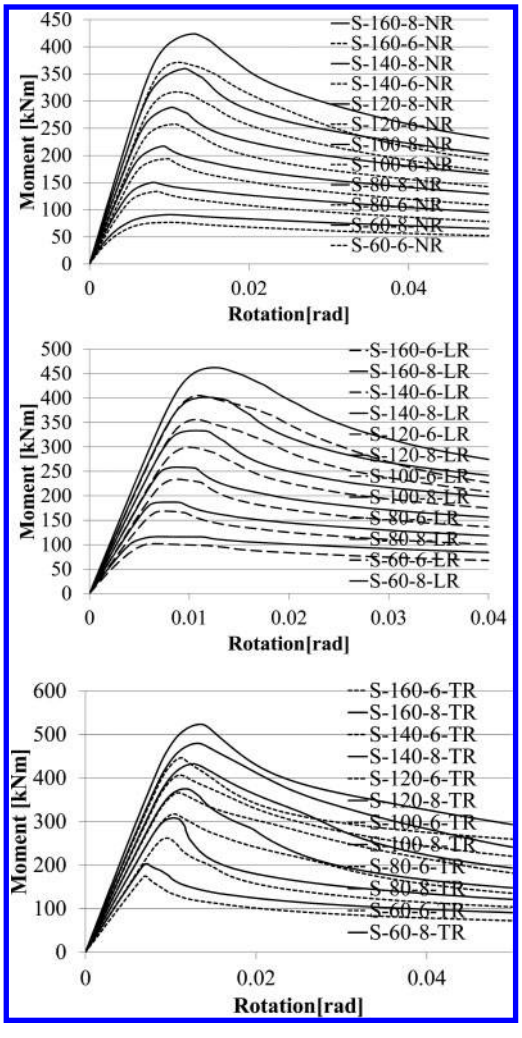


Figure 12. FEM- parametric – Capacity curves.

as well, except the position of the buckle changing correspondingly.

The corresponding capacity curves are plotted in Figure 11 for all the 3 type of lateral restraints.

5 CONCLUSIONS

Both the experimental and finite element study of the behaviour of tapered web beam-columns were depicted in the present work. A number of twelve specimens with different web thicknesses and lateral restraints were tested, while in the second part of the paper is presented a parametric study.

The failure mechanism for the selected specimen series varies in function of the cross section/overall slenderness and lateral restraints.

Although the initial rigidity increases from the slenderer case the less slender one, the post critical behaviour differs by the lateral restraints. The ductility decreases in case of less effective lateral restraints (NR, LR), while for the case of TR ductile behaviour is reversed.

ACKNOWLEDGEMENTS

The financial support given by "NURC —Romania" through the research grant PN-II-RU-TE-2010-1/38 is gratefully acknowledged.

REFERENCES

EN 1993-1-1 Eurocode 3: Design of steel structures Part 1.1: General rules and rules for bulidings, CEN – 2005.

Cristutiu, I.M. & Nunes D. 2012. Imperfection sensitivity analysis on the behaviour of single storey frames with tapered web members. *11-th International Conference on Computational Structures Technology.* Dubrovnik 4-7 september 2012.

Taras A. & Greiner R. 2008. Torsional and flexural torsional buckling — A study on laterally restrained I-sections, *Journal of constructional steel research*, 64 (2008) 7–8, S. 725–731.

Szalai J. & Papp F. 2009. On the probabilistic evaluation of the stability resistance of steel columns and beams. *Journal of Constructional Steel Research*, 65 (2009), 569–577.

Shanmugam, N.E & Min, H. 2007. Ultimate load behaviour of tapered steel plate girders. *Steel and Composite Structures*, 7(6), 469–486.

Salem, A.H et all. 2009. Ultimate capacity of axially loaded thin-walled tapered column with doubly symmetric sections. *Thin Walled Structures* 47(2009), 931–941.

Marques, L. et all. 2012. Development of a consistent buckling design procedure for tapered columns, *Journal of Constructional Steel Research*, 72 (2012) 61–74.

Cristutiu, I.M. & Nunes D. 2012. Influence of the initial imperfections on the seismic performance of pitched roof portal frames made of welded non-prismatic plated elements. *STESSA 2012 – Behaviour of Steel Structures in Seismic Areas.* Santiago de Chile 9-11 january 2012.

Hong, J.K. & Uang, C.M. 2012. Cyclic testing of a metal building moment frame system with web-tapered members. *Journal of Constructional Steel Research* 70 (2012), 248–255

EN 1993-1-5, "Eurocode 3 (2003) –Design of steel structures Part 1.5: Plated structural elements", CEN – Brussels, Belgium 2003.

Research and Applications in Structural Engineering, Mechanics and Computation – Zingoni (Ed.)
© 2013 Taylor & Francis Group, London, ISBN 978-1-138-00061-2

Analyzing portal frames using rotational springs

T.N. Haas, H.L. Albertyn & P.E. Dunaiski
Department of Civil Engineering, Stellenbosch University, South Africa

ABSTRACT: Portal frames are steel structures used in the construction of various types of industrial buildings. Very few portal frames are required to cover large areas. Portal frames predominantly consist of steel columns and rafters. Haunched connections are usually used to connect the columns to the rafters and rafters to each other. The base of the column is connected to the foundation through base plates. Design engineering professionals in South Africa consider the connections at the base as perfectly pinned, while all other connections are considered infinitely rigid (i.e. traditional analysis). This assumption is flawed and does not occur in reality, resulting in inaccurate displacement behaviour of the portal frame. This is especially more prominent when wind loads are applied to the side of the portal frame. An experimental and numerical study was conducted to determine the actual displacement response of the portal frame when subjected horizontal loading. When a horizontal point load was applied to the apex of the column, the traditional analysis yielded displacement responses that varied significantly from the experimental results. This led to obtaining a more accurate numerical solution. This was achieved by modelling the connections of the portal frame with rotational springs in a second order non-linear analysis. The rotational spring stiffness's were obtained from the moment-rotation behaviour of each connection. These were obtained from a detailed finite element analysis of each connection considering all members and their contact interaction properties. The displacement results of the advanced model yielded displacement responses which were comparable with the experimental results. However, the computational effort needed in obtaining the advanced model does not make it feasible to analyse the portal frame with rotational springs in structures which requires a limited number of portal frames.

1 INTRODUCTION

Portal frames are simple structures constructed of two columns and two rafters. The columns are connected to the rafters at its apex, while the rafters are connected to each other at the ridge. The column base is connected to the plinth/foundation through base plates. The connections between these members can either be considered infinitely rigid (fixed) or hinged (pinned). Haunches are introduced at connections to achieve a rigid connection. Figure 1 shows a two dimensional view of a portal frame consisting of a ridge connection without a haunch and eave connections with a haunch.

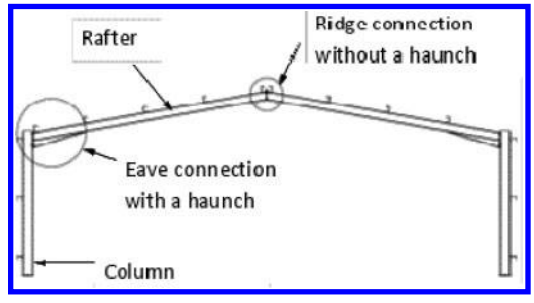


Figure 1. Two dimensional view of a portal frame.

In South Africa, design engineering professionals assume the column base connection as hinged, while all other connections are infinitely rigid. Based on SAISC (2001), this condition leads to a more economical design when compared to column bases which are considered infinitely rigid. Eave and ridge connections are always designed as infinitely rigid, i.e. a moment fixed connection which allows the transfer of bending moment between the respective members. Narayanan, (2003), showed that tension bolts within the height of the rafters are inadequate to develop sufficient bending moment capacity at the connections. For adequate bending moment to develop, haunches are introduced to the bottom flange of the rafters at these connections, Moore & Wald, 2003) and Narayanan, (2003). The design assumptions using infinitely rigid and perfectly hinged connections are flawed and leads to inaccurate displacement behaviour of the portal frame. This leads to uneconomical steel sections being used for construction, (Kruger et al., 1995).

Over the last few decades, higher grades of steel has been rolled in South Africa, which has led to higher yield strengths, SAISC Handbook (2008). The design of portal frames is governed by Serviceability Limit State requirements. The displacement of the structure is a function of the flexural stiffness and not the yield

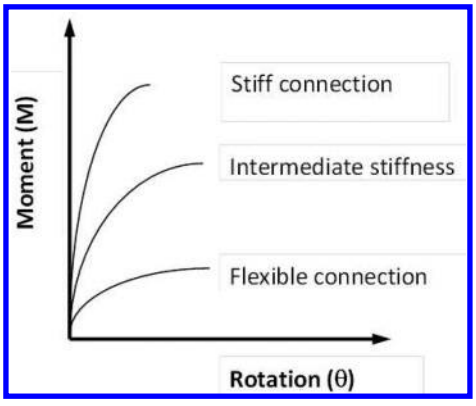


Figure 2. Moment-rotation behaviour of connections, Kruger *et al.*, (1995).

strength of the member. Therefore the use of higher grade of steel has no effect on the allowable informative codified guide presented in SANS 10162-1: 2004. This led to investigating the real behaviour of portal frames when modeled with rotational springs with the correct yield strength of the members.

2 MOMENT-ROTATION CONNECTION BEHAVIOUR

Kruger *et al.*, (1995), showed that deformations caused by axial and shear forces are negligible in comparison to in-plane rotational deformations caused by the bending moment at the connection. As a result only the in-plane rotational deformations will be considered in this study. From this, it can be established that the rotation of the connection is a function of the moment applied to it. Since no connection is infinitely rigid or perfectly pinned, the real behaviour of a connection lie somewhere between these theoretical conditions as shown in Figure 2, Kruger *et al.*, (1995).

The vertical axis (M) in Figure 2 represents a rigid connection, whereas the horizontal axis (θ) represents a hinged connection. The slope of the curve in the elastic region provides an indication of the stiffness of the connection, whereas the peak provides an indication of the ultimate moment capacity of the connection, Kruger *et al.*, (1995).

This suggests that modelling the real behaviour of the connection surely has an influence on the distribution of forces, the bending moment and also affects the displacement behaviour of the portal frame, Gerstle (1988). Therefore if the connection is modeled with incorrect stiffness, it will lead to some rotational deformation occurring before the bending moment is transferred. This will also lead to larger displacements occurring in the portal frame before the ultimate capacity of the connection is achieved. To overcome this problem the connections must be modeled using rotational spring with appropriate stiffness, Simitses *et al.*, (1984), Chan *et al.*, (2005).



Figure 3a. Pin (Hinged) column base support.

3 PORTAL FRAME CONFIGURATION

The investigation for this research was conducted on a 5 m portal frame with a column height of 1.5 m. The columns and rafters are composed of IPE AA 100 sections. The eave connections are supported by haunches 0.5 m in length, while the ridge connection consists of end plates. The experimental model was constructed in a manner that the column bases could be fitted with either hinged or grouted supports.

4 RESEARCH METHODOLOGY

The investigation was separated into an experimental and numerical study. For the experimental study, a horizontal load of 7.85 kN simulating the wind load was applied to the apex of the column in the direction of the span, when the model was fitted with hinged and grouted supports. A numerical model of the full scale experimental configuration was developed for both support conditions. In the numerical model, the hinged connections were easily modeled with pins. However, for grouted supports, rotational springs with appropriate stiffness were required. The rotational spring stiffness' was obtained from a detailed finite element (FE) analysis of each connection.

5 COLUMN SUPPORT CONDITIONS

As mentioned earlier, column bases in portal frames are usually analyzed using pin supports as shown in Figure 3a. The corresponding grouted support in practice is shown in Figure 3b. From Figure 3b it is clear that the grouted support provide some rotational restraint due to the base plate – concrete interaction. If this connection is modeled incorrectly in the numerical analysis it will result in inaccurate horizontal displacement behaviour of the portal frame.



Figure 3b. Actual (grouted) column base support.

6 NUMERICAL MODEL

Strand 7, a commercially available structural analysis software was used to develop a numerical model of the full scale experimental test configurations. After a displacement sensitivity analysis on a simple beam, the 1.5 m columns and the 2.54 m rafters were meshed with 0.1 m quadratic shear flexible (Timoshenko) beam elements. To obtain an accurate numerical model of the experimental configuration, a number of different types of connections were modeled, namely; hinged, rigid and rotational spring connections. The hinged and rigid connections were easily modeled using pin and fixed connections. The pin connections transfers axial and shear forces while the fixed connection transfers axial forces, shear forces and bending moments between the members. The rotational spring connection is however different from the fixed support as it allows a percentage of the bending moment to be transferred to the members depending on the rotational stiffness of the connection. Before the portal frame could be modeled with rotational spring connections, the rotational spring stiffness needed to be determined.

6.1 *Rotational spring stiffness*

Each connection of the portal frame is unique which results in different rotational spring stiffness's. The experimental rotational stiffness's are affected by various factors which include, but not limited to; the size of the steel profiles, the size of the haunch, the number and size of bolts, the position of the bolts, the torque of the bolts and the size of the connection end plate. However, the rotational spring stiffness's in a numerical analysis is also affected by; element type, element mesh density, contact formulation and material properties. The rotational spring stiffness's are obtained from the elastic region of the moment – rotation curve of each connection. The moment rotation curve of each connection was obtained by modelling a portion of the connection with all the necessary elements connected to it. This was accomplished in ABAQUS, a general FE analysis software. The moment rotation curves were obtained based on the guidelines presented by Prabha, (2007).

A previous experimental study conducted by Truter (1997), was used to determine the accuracy of the FE simulations based on the guidelines presented by Prabha. The FE simulation results within the elastic region yielded virtually an identical response compared to the experimental results. Based on the accuracy obtained, all other moment rotation curves were determined. The reader is referred to Albertyn (2010), for a complete review of all the moment – rotation curves as well as the spring rotational stiffness's of the connections. The displacement behaviour of the portal frame could now be determined using these rotational spring stiffness's.

Table 2. Description of the types of connections used in various models.

Model Name	Connection type at eaves and ridge	Connection type at column base
Exp hinged	Rigid	Hinged
Conv numer	Rigid	Hinged
Exp grouted	Rigid	Grouted
Rot spring	Rotational spring	Rotational spring

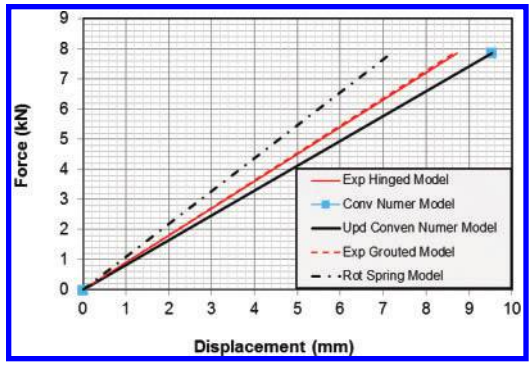


Figure 4a. Ridge's vertical displacement response when subjected to a horizontal point load at the apex of the column.

7 RESULTS AND DISCUSSIONS

Table 2 describes the different types of connections which were investigated for the hinged and grouted models.

Figure 4a presents the ridge's vertical displacement behaviour for the hinged and grouted models when a horizontal load is applied to the apex of the column. Figure 4b presents the column's apex displacement behaviour for the hinged and grouted models when a horizontal load is applied to the apex of the column.

From Figure 4a, it is observed that there is an insignificant difference of 0.08 mm or 0.9% which

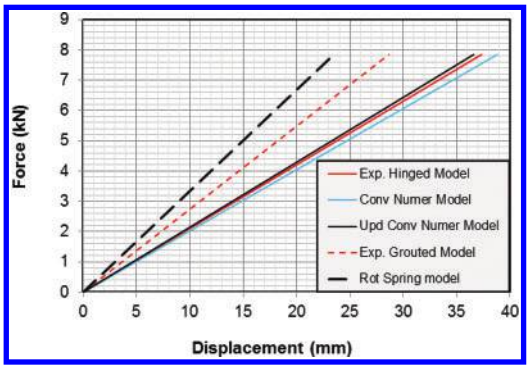


Figure 4b. The horizontal displacement response at the column apex when subjected to a horizontal point load at the apex of the column.

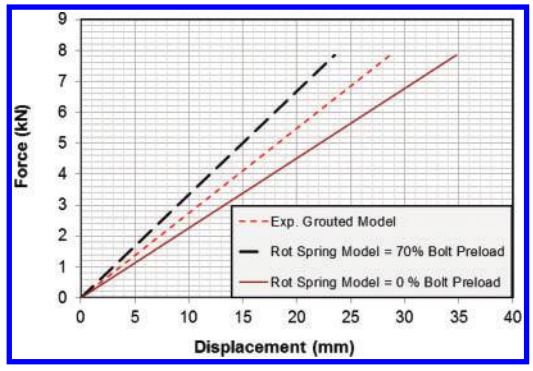


Figure 5. Horizontal column displacement.

exists between the experimental hinged and experimental grouted model's displacement behaviour. A difference of 2.4 mm or 24.6 % exist between the conventional numerical and the numerical model with rotational springs. A difference of 1.5 mm or 16.9 % exist between the experimental grouted and the numerical model with rotational springs.

When comparing Figures 4a and 4b, it is observed that the maximum horizontal displacement is 410% greater than the vertical displacement. From Figure 4b, it is observed that the maximum difference between the experimental hinged and grouted models' displacement is 8.7 mm or 23.3 %. This implies that the grout interface at the column base has a significant influence on the portal frame's displacement response. The maximum difference between the two numerical model's displacement is 15.3 mm or 39.4 %. The conventional numerical model over-estimates the experimental hinged model's displacement by 1.5 mm or 3.9%. The numerical model with rotational spring's under-estimates the experimental grouted model's displacement by 5.1 mm or 17.8%.

The true behaviour of the portal frame is expected to be the same as the experimental grouted model, due to the column base plate-foundation interaction. Therefore the only models of interest in this investigation now become the experimental grouted and the numerical model with rotational spring. A sensitivity analysis was conducted to quantify the effect of the column base plate-foundation interaction.

8 SENSITIVITY ANALYSIS

The results of the previous section probed an interest to determine what causes the discrepancies in the displacement responses of the experimental grouted and the numerical model with rotational springs. Since only the column base connection was changed, the sensitivity analysis focused on the preload of holding-down bolts.

8.1 *Effect of preload on the holding-down bolts*

Kulak et al., (2001), states that ordinary bolts in steel connections are tightened according to the "turn of the nut" method. Previous experimental studies found that the method results in a bolt preload of approximately 70% of the bolt proof stress. In the FE analysis a bolt preload of 70% was applied to all bolted connections to determine the moment rotation curves. Figure 5 shows the horizontal displacement responses of the 0% and 70% bolt preload superimposed with the experimental grouted support model's displacement response.

The displacement of the portal frame is affected by the stiffness of the column base connection. Therefore, the rotational spring stiffness of the column connection was adjusted until the same experimental displacement response was obtained. A numerical displacement of 28.8 mm was obtained when the linear rotational spring stiffness at the column base was adjusted to 52 kNm/rad. Based on the moment-rotation curves obtained from the FE analysis, a rotational spring stiffness of 219 and 290 kNm/rad was obtained for the 0 and 70% bolt preload. Since the experimental displacement response lie almost midway between these responses, a rotational spring stiffness of 250 kNm/rad was expected. The actual rotational spring stiffness was a quarter of what was expected. From this observation is could be concluded that the experimental model is less stiff than anticipated.

This led to careful inspection of the connection bases after the experimental tests were completed. When the base plate was removed, it was observed that the holding down bolts had insignificantly separated from the concrete. The authors felt that this could lead to excessive displacement of the portal frame. A simple calculation reveals that a slight rotation of the base plate can lead to large displacement of the portal frame. Table 3 presents the magnitude of the column displacement as a function of the rotation of the base plate.

From Table 3 we notice that a base plate rotation of 0.26^0 will lead to a horizontal column displacement of 6.8 mm. This implies that for an insignificant rotation of the base plate the portal frame's displacement will increase by 6.8 mm.

Table 3. Horizontal column displacement due to base plate rotation.

Vertical lift at end of base plate (mm)	Half base plate width (mm)	Base plate rotation (^{0})	Horizontal displacement of column (mm)
0.25	55	0.26	6.8
0.50	55	0.52	13.6
1.00	55	1.04	27.3

The numerical model with 0 and 70% bolt preload yield displacements of 34.8 and 23.5 mm, respectively. The experimental grouted model yields a displacement of 28.6 mm. This proves that the numerical model yields accurate results since the experimental results fall within these numerical displacements. If it is assumed that no slip of the holding down bolts occurs, an experimental displacement of 21.8 mm would be achieved.

9 CONCLUSION

This study shows that the numerical model with rotational springs yield accurate displacement responses of the portal frame, depending of the degree of fixity of the column base support.

The important question which now needs to be answered is whether the numerical model is an economically viable option. The rotational spring stiffness must first be determined before these stiffness's can be used in a non-linear 2nd order two dimensional numerical analysis. In order to obtain the rotational spring stiffness each connection was required to be modeled in ABAQUS. The computational time of each analysis was approximately 12 hours. This excludes the time the designer needs to become familiar with the software and to develop an accurate model of each connection. Based on this and considering that most industrial building are less than 50 m in length, it becomes uneconomical to model the portal frame with rotational springs, even though it yields more accurate results.

REFERENCES

Albertyn, H.L. 2011. *The effect of moment-rotation joint behaviour on the displacements of portal frames*. Master's thesis, Stellenbosch University

Gerstle, K.H. 1988. *Effect of connections on frames.* Journal of Constructional Steel Research, 10:241–267.

Kruger, T.S., van Rensburg, B.W.J., du Plessis, G.M. 1995. *Non-linear analysis of structural steel frames.* Journal of Constructional Steel Research, 34(2–3): 285–206

Kulak, G.L., .Fisher, John W., John HA Struik, and Geoffrey L.(r.) *Guide to design criteria for bolted and riveted joints*. Wiley, 1974.

Moore, D.B. & Wald, F. 2003. *Design of Structural Connections to Eurocode 3 – Frequently Asked Questions.* Watford: Building Research Establishment Ltd.

Narayanan, R., and V. Kalyanraman. "*The INSDAG guide for the structural use of steelwork in buildings*." *INSDAG, Kolkata, India* (2003).

Prabha P., Seetharaman S., Arul Jayachandran S., and Marimuthu V., *Mimicking expensive experiments using ABAQUS*, Third Abaqus User's India meet 2007, Bangalore, October 24th 2007

Simitses G.J., Swisshelm, J.D., Vlahinos, A.S. 1984. *Flexibly-jointed unbraced portal frames.* Journal of Constructional Steel Research, 4(1):27–44.

Southern African Institute for Steel Construction. 2008. *Southern African Steel Construction Handbook*. Johannesburg.

South African National Standard*: The structural use of steel Part1: Limit-state design of hot-rolled steelwork.* 2005. Standards South Africa. SANS 10162-1:2005.

Truter, A.N. 1997. *An experimental and theoretical investigation into the non-linear moment-rotation response of bolted endplate connections in single storey haunched steel portal frames*. Master's thesis, Stellenbosch University.

Research and Applications in Structural Engineering, Mechanics and Computation – Zingoni (Ed.)
© 2013 Taylor & Francis Group, London, ISBN 978-1-138-00061-2

Behaviour of pitched-roof portal frames with tapered web and flange members considering lateral restraints

I.M. Cristutiu & D.L. Nunes
"Politehnica" University of Timisoara, Timisoara, Romania

ABSTRACT: Pitched-roof portal steel frame, ranging from short to long free span, is the most commonly used type of structural system for single storey industrial buildings. Structural members are generally made of welded plate I sections with tapered web. The tapering is made according to the distribution of the bending moment along the major axis, resulting in a more economical use of the material. Besides web tapering, the flange can be tapered as well in order to obtain a more economical/structural efficient solution. Due to its non-prismatic shape, a slender web/flange section is likely to occur at the maximum cross section height. More than that being subjected to important compressive axial force, the length of the rafter is significant (function of the free span) and hence the problem of stability is much more complex than in the case of multi-storey buildings. They are partially restrained against out of plane buckling by side-rails and roof purlins cooperating with sheeting. If no lateral restraints, or when they are not effective enough, the lateral-torsional mode characterizes the global behaviour of frame members and interaction with sectional bucking modes may occur as well. The paper summarizes the outcome of a numerical study on a considerable number of such type of frames, performed by authors, considering different types of lateral restraints, (rigid and actual). A sophisticated nonlinear elastic-plastic FEM model and different types of initial imperfections were used to analyse the behaviour of the frames. Comparisons of FEM results with those obtained when applying the general method of EN1993-1-1 will also be provided. It was observed that the reduction of the flange by a certain slope, influences significantly the bearing capacity of the frame and their behaviour.

1 INTRODUCTION

Steel structural elements with variable cross section, made of welded plates, are largely used in the construction industry for both beams and columns in accordance with the stress and stiffness demand in the structure. Nonrectangular shape of the element might lead to thin/slender web section at its maximum height hence elastic to slender web results for the case of double T welded cross section. Due to their large relative slenderness about the minor axis, out of plane buckling usually governs their ultimate capacity. Nevertheless, the out of plane buckling strength of these structures is directly influenced by the lateral restraining, end support and initial imperfections.

The design, execution and erection of steel structures must take place under certain constraints. If in the design process, one must ensure strength, stability and rigidity to the structure, in the manufacturing and erection process certain admissible tolerance limits must be accounted for. EN 1090-2 is the European standard that establishes the values of admissible limit tolerances for the manufacturing and erection of steel structures. The European norm EN1993-1.1 contains provisions for several initial imperfections (vertical deviation and initial arc imperfections), which take values function of the considered buckling curve (a0, a, b, c, d) and buckling mode (minimum or maximum axis).

Nevertheless actual design codes do not cover the practical design of this kind of structure. The interaction formulas of EN1993-1-1 are provided only for uniform members, and it is rather difficult to be applied and many interpretations are necessary for non-uniform members. The General Method of EN1993-1-1 might be applied for these types of structures, but the constituent coefficients shall be obtained accounting for lateral restraints, end supports, initial imperfections. According to EN1993-1-1, different imperfection shapes shall be considered in the global analysis of steel frames. On this purpose a preliminary analysis shall be performed in order to emphasize the importance of imperfection shape to be considered in the analysis.

Previous studies made by Cristutiu&Nunes 2012, emphasized that the ultimate capacity and failure under gravitational loads of the whole frame is mainly influenced by lateral restraints. Although different types of initial imperfections were considered, their influence on the frame behaviour is rather small, unless the imperfections are applied all together (e.g. initial out-of-plane bow for elements and initial out of plane sway). Behaviour of pitched-roof frames with tapered members under horizontal loads were studied

in several papers. Cristutiu&Nunes 2012 analytically studied the behaviour under horizontal forces while experimental studies were performed by Hong&Uang 2012. Both studies concluded that the main failure mode is out of plane buckling and, consequently the seismic behaviour could be improved by proper lateral restraints.

Isolated members made of double T section with tapered web were investigated in several papers. The ultimate capacity was determined by Shanmugam 2007 for tapered steel plate girders subjected to shear and by Salem 2009 for axially loaded thin-walled tapered columns with double symmetric sections. Shanmugam 2007 experimentally determined the ultimate behaviour of tapered steel plate girders and concluded that the shear capacity of the girder is 5% less than the case of prismatic one, if the inclined flange is tensioned. Whilst the inclined flange is subjected to compression, the ultimate load of the tapered girder becomes higher than that of straight girders by more than 5%. In 2012 Marques et all developed a consistent buckling procedure for evaluation of the ultimate capacity of tapered members subjected to compression. This procedure is rather difficult to apply in the actual design as it implies advanced numerical analysis.

The objective of the present paper is to extend the previously obtained results by the authors to pitched roof portal frames made of variable web and flange simultaneously. Variation of the web along the element is made for both aesthetical and economic reasons. Variation of the flange shall be made according with the stress and stiffness distribution as well, allowing the use of a more efficient structural element. For the purpose of the work an advanced FEM model was built, different types of lateral restraints were applied and different values of the flange reduction slope. A series of frames of different spans and heights were analysed at first.

2 PARAMETRIC STUDY AND FEM MODEL

2.1 *Analysed frames*

A number of six pitched roof portal frames commonly used for the execution of single story buildings were analysed. They are of different spans and heights (see Fig. 1), to cover a wide range. The frames were designed to verify the ULS and SLS criteria under the gravitational loads. They have pinned column base, tapered columns, tapered rafters and a pitch roof angle of 8^0. Tapering ratio, h_{max}/h_{min}, is approximately equal to 2 for all the cases. The rafter is composes by both uniform and non-uniform regions, as can be seen from Figure 1. The length of the rafter haunch is 15% from the span in all the cases. The main sectional characteristics of frames are presented in Table 1. The chosen dimensions were selected as being quite common in practical applications

Four different slopes were analysed separately, i.e.: 0%, 0,5%, 1,0 % and 1,5% reduction of the maximum

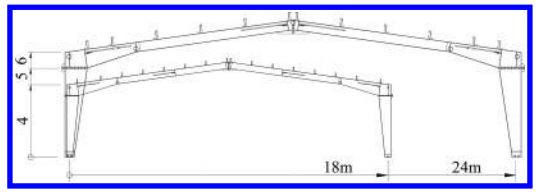


Figure 1. Geometry of the frames.

Table 1. Main dimensions of the analysed frame.

Frame	Dimensions h*b*t_f*t_w [mm]					
(Lxh)	Element	h_{min}	h_{max}	b	t_f	t_w
18 × 4	Tapered column	350	700	250	12	10
	Tapered rafter	360	700	200	12	10
	Rafter	360	–	200	10	8
18 × 5	Tapered column	350	700	250	14	10
	Tapered rafter	360	700	200	12	10
	Rafter	360	–	200	10	8
18 × 6	Tapered column	350	700	260	14	10
	Tapered rafter	360	700	200	12	10
	Rafter	360	–	200	10	8
24 × 4	Tapered column	350	850	270	14	10
	Tapered rafter	440	850	240	14	10
	Rafter	440	600	240	12	8
24 × 5	Tapered column	350	850	270	14	10
	Tapered rafter	440	850	240	14	10
	Rafter	440	600	240	12	8
24 × 6	Tapered column	350	850	300	14	10
	Tapered rafter	440	850	240	14	10
	Rafter	440	600	240	12	8

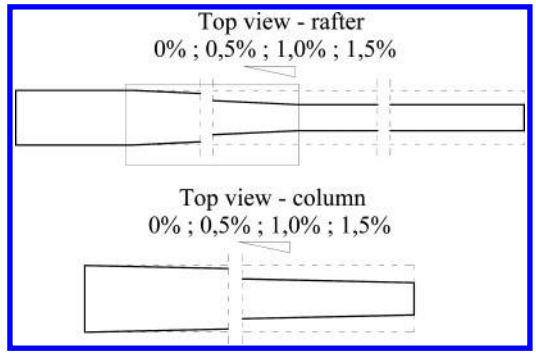


Figure 2. Reduction in size of the flange.

width of the tapered element, resulting thereafter a number of 24 analysed cases. The reduction in size of the flange is presented in Figure 2.

The same principle was applied both for column and rafter for the whole length of the tapered web. It has to be mentioned that the prismatic width of the rafter kept the minimum width of the tapered flange within its whole constant length.

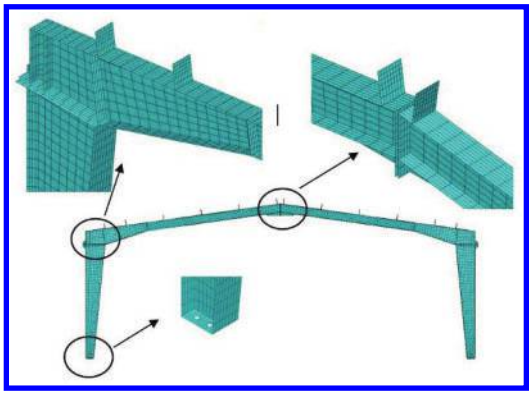


Figure 3. FEM modeling of the analysed frames.

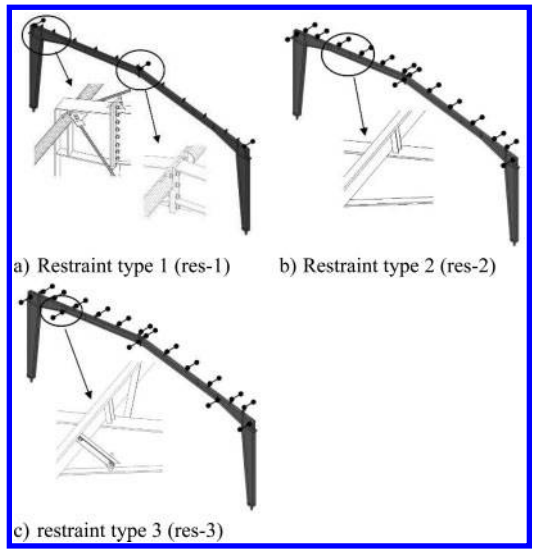


Figure 4. Types of lateral restrains.

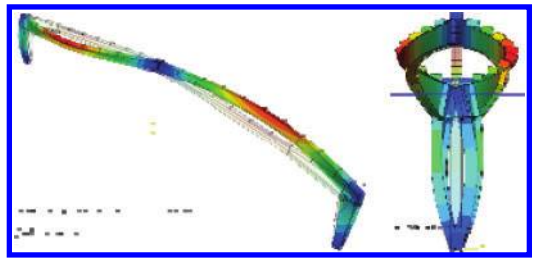


Figure 5. Manufacturing imperfections considered in the GMNIA analyses.

2.2 *FEM model*

For the analysis of the objects in study was developed a finite element model capable to overtake both geometrical and material nonlinearities. Both linear Eigen buckling (LEA) and nonlinear elastic-plastic considering geometric nonlinearities (GMNA and GMNIA) analyses, according to EN1993-1.5 have been applied using the finite element program ABAQUS. S4R-type elements were used (4-node shell elements with reduced integration) with 6 degrees of freedom on each node (translation and rotation in regard to the x, y and z-axis).

To determine the structural response of the nonlinear problem an implicit solution strategy was used. A load stepping routine was used in which the increment size follows from accuracy and convergence criteria. Within each increment, the equilibrium equations are solved by means of the Newton-Raphson iteration (through the arc-length method).

All plates were modeled in their mid-plane and the connections between beams and between beams and columns were defined as a surface-to-surface tie between both end-plates (Fig. 3). The material model was defined as elastic – perfectly plastic ($E = 210000$ N/mm2, $\upsilon = 0{,}3$, $f_y = 355$ N/mm2) and vertical loads from permanent and snow actions were introduced at the purlin location (e.g 1.2 m along the rafter). In all these cases, it was simulated the restraining effect induced by longitudinal beams located at eaves and ridges.

The lateral restraints applied are of 3 different types, as shown in Figure. 4, and were applied through a real model. Types 2 represent the purlin/sheeting effect, when the purlin is pinned when intersecting the rafter. Type 3 is similar with type 2 with an additional fly brace. Type 1, actually means no lateral restraints introduced by purlins. At first, to simplify the computational model, the lateral restrains had been considered axially rigid, in the analysis. The actual behaviour of the purlins (Z150/1.5) was considered later on. The three types of lateral restraints lead therefore to a number of 72 cases.

Manufacturing imperfections were considered in the analyses. The applied imperfections are presented in Figure 5 and consist of an initial out-of-plane bow imperfection of both rafter and column, with a magnitude of l/150. The magnitude of the imperfections was considered according to EN1993-1.1, curve c, for plastic analysis. For rafter a 60 mm initial bow was considered in the case of 18 m span, and 80 mm for 24 m span respectively. While for the column 3 values were considered, one for each corresponding height: 26.67 mm (4 m height), 33.33 mm (5 m height) and 40.00 mm (6 m height). Using shell elements, the imperfections are slightly different from those applied on bar elements, where perfect bending or perfect inclination might be applied. Herein twisting of the element was also recorded, this will lead to a more complex model and a more realistic imperfection shape.

3 RESULTS AND COMMENTS ON THE FEM ANALYSES

In order to identify the failure of the frames and their elastic buckling behaviour 3D GMNIA and 3D LEA

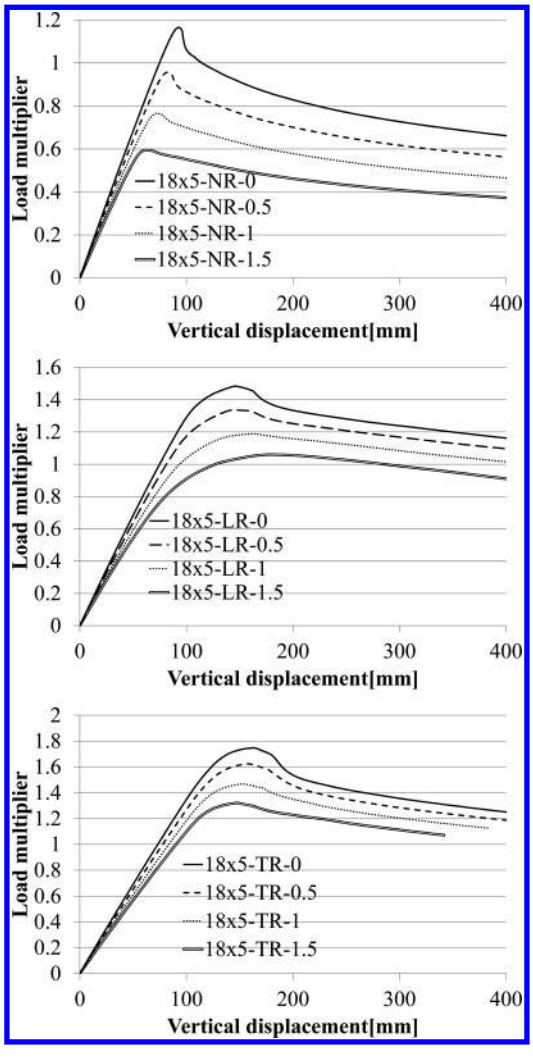


Figure 6. Capacity curves for 18 × 5 frame.

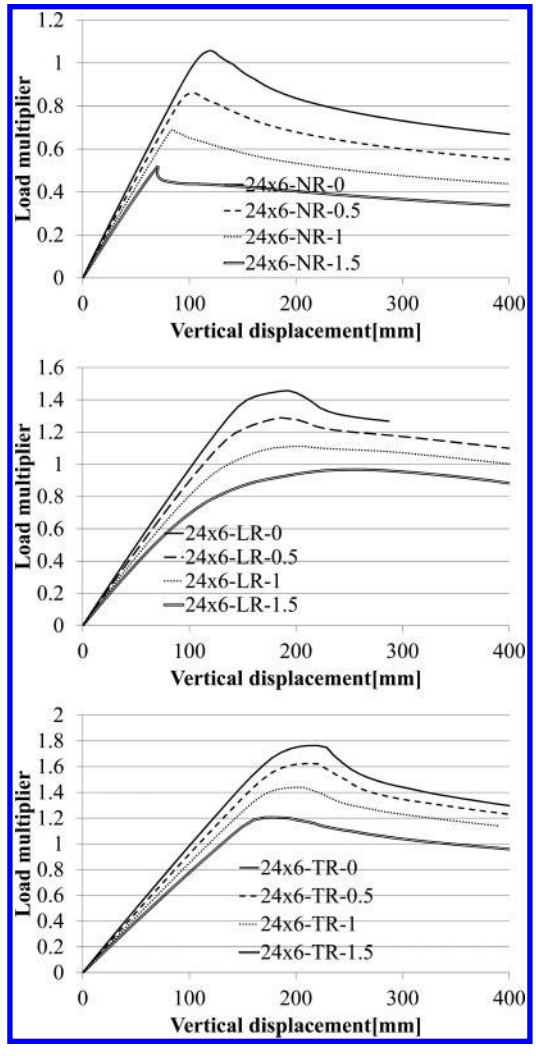


Figure 7. Capacity curves for 24 × 6 frame

analyses were performed. For the GMNIA analysis, initial out-of plane imperfections as the one presented in Figure 5 were considered. The capacity curve were recorder for each case of lateral restraints (NR, LR, TR, see Fig. 4) and slope of the flange (0%, 0,5%, 1,0 % and 1,5% see Fig. 2). The obtained results are presented in Figure 6&7. The critical load multipliers and ultimate load multipliers corresponding to the eigen-buckling shape and failure of the structure respectively were determined for all analysed frames. In the analysis, lateral restraints were taken into account, as actual elastic ones. Herein, due to lack of space only the case of 18 × 5 and 24 × 6 are presented in Figure 6&7.

Analysing Figure 6, one can conclude that the tapering ratio of the flange influences significantly the ultimate capacity of the frame. This influence is more consistent in the case of frames without lateral restraints. The lack of restraining leads to a greater non-dimensional slenderness according to EN1993-1.1, thus their buckling capacity is highly reduced. A reduction in the buckling strength was noticed in the case of laterally restrained frame (case of LR and TR see Fig. 3) as well. This reduction could be explained rather by the reduction in the elastic strength modulus, W_{el}, of the cross section, than by it's out of plane buckling strength.

The curves plotted in Figure 7, for the case of 24x6 frames, experience the same behaviour as those described in the previous paragraph. Namely the difference in the frame capacity is more pronounced for the case of less restrained frame (NR).

In Figure 8, the failure modes of GMNIA analysis are illustrated for the case 18 × 6 frames, with 3 types of lateral restraints (see Fig. 4) and two different values of the flange taper slope (i.e. 0% and 1.5%). The failure mode is influenced both by lateral restraints and

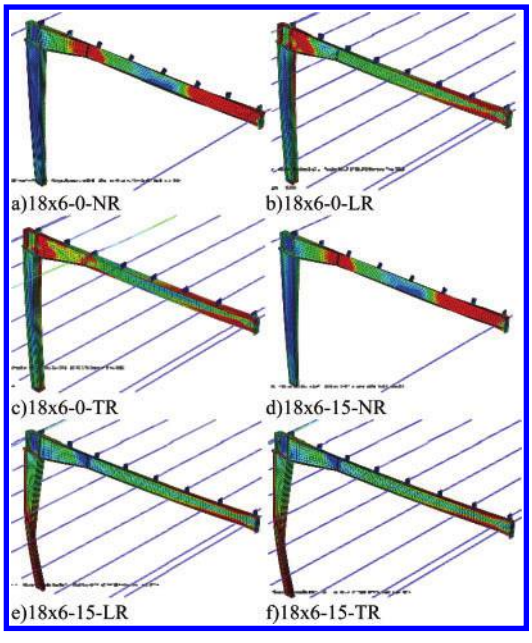


Figure 8. Failure modes – GMNIA analysis (Von Misses stress distribution scale factor 1).

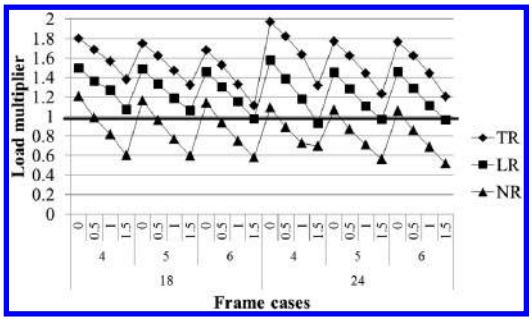


Figure 9. Ultimate load multiplier – GMNIA analysis.

flange taper slope. The latter one might influence the sequence of the element failure, i.e. rafter of column.

In Figure 9, the corresponding values of the ultimate load multiplier, resulting from GMNIA analysis, are illustrated. These values are significantly influenced by the slope reduction of the flange.

4 ANALYTICAL EVALUATION OF THE ULTIMATE CAPACITY

The European standard, EN 1993-1-1, describes three different procedures for verifying the stability of steel elements, including beam-columns (members under combined axial load and bending).

The first approach is the imperfection approach. This is achieved by incorporating in the second order structural analysis appropriate equivalent geometric imperfections to cover the possible effects of all type of imperfections. This approach is not widely used in current design practice, but it becomes useful when advanced finite element simulation is required. The second procedure deals with isolated members, and is the conventional engineering solution for buckling problems, but its application is limited to uniform members with simple support and loading conditions. This method makes two simplifications, one by considering the member isolated from the structure while applying boundary conditions (supports, restraints or loads). And the other by determining the buckling of the member separately for the pure buckling modes (i.e. flexural buckling for pure compression and lateral-torsional buckling for pure bending) and combined by applying interaction factors.

The method that might cover the particular case of frames in study is the "so-called" „general method". The method no longer isolates members nor separates the pure buckling modes. It considers the complex system of forces in the member and evaluates the appropriate compound buckling modes instead. One of the advantages of the general method is that it can examine irregular structural members such as tapered members, hunched members, and built-up members. Although in the current version of the EN1993-1-1 the general method is recommended only for lateral and lateral-torsional buckling of structural components, the basic approach may be extended to other cases as well. Many research projects are underway across Europe that intended to verify and widen its applicability.

According to the "general method" overall resistance to out-of-plane buckling can be verified assuring that:

$$\frac{\chi_{op} \cdot \alpha_{ult.k}}{\gamma_{M1}} \geq 1 \qquad (1)$$

where $\alpha_{ult.k}$ = is the minimum load amplifier of the design loads to reach the characteristic resistance of the most critical cross-section of the structural component, considering its in-plane behaviour without taking lateral or lateral-torsional buckling into account, however accounting for all effects due to in-plane geometrical imperfections, global and local, where relevant; and χ_{op} = is the reduction factor for non-dimensional slenderness to take account of lateral and lateral-torsional buckling.

The global non-dimensional slenderness, $\overline{\lambda}_{op}$, of the structural component should be deter-mined from:

$$\overline{\lambda}_{op} = \sqrt{\frac{\alpha_{ult.k}}{\alpha_{cr.op}}} \qquad (2)$$

where: $\alpha_{cr,op}$ = is the minimum load amplifier for the in-plane design loads to reach the elastic critical resistance of the structural component with regards to lateral or lateral torsional buckling without accounting for in plane flexural buckling.

This method was applied for the frames described in Table 1 and Figure 2. The minimum critical load

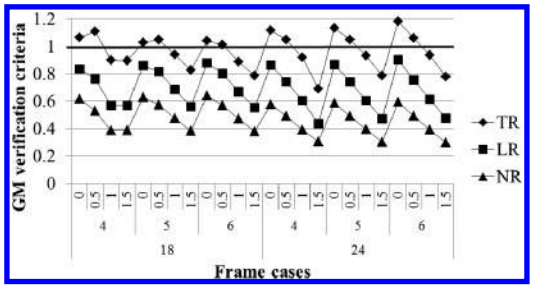


Figure 10. Verification criteria Eqn. (1) – general method.

multiplier was computed by means of linear eigen-buckling analysis using 3D FEM for different type of lateral restraints (see Fig. 4). The buckling reduction factor was evaluated for the case of lateral-torsional buckling according to EN1993-1-1 and γ_{M1} was set equal to 1,0. The minimum ultimate load amplifier, $\alpha_{ult,k}$, corresponding to the characteristic resistance of the most critical cross-section of the structural components was evaluated using a 3D FEM linear elastic analysis.

Comparison of the results obtained by applying the general method for all the analysed frames is illustrated in Fig. 8. The results are presented individually for each frame type, accounting for different lateral restraints.

The obtained results confirm once again the importance of the application of lateral restraints, when dealing with the buckling of tapered elements with respect to their minor axis. Restraints of type 1, provided by secondary structural elements (e.g. roof bracings and pinned longitudinal beams), are not enough in stability check of the structural elements, mainly when the span of the structure is significant. There are some cases in which restraints of type 2 satisfy Eq (1) but not for all the analysed frames. Type 3 provides enough lateral restraints against stability failure in all the cases. The bearing capacity of the frame is significantly influenced by the application of the flange reduction slope.

5 CONCLUSION

A parametric study was performed in order to analyse the sensitivity of different types of lateral restraints on pitched-roof portal frames made of elements with tapered web and flange as well with out-of-plane initial imperfections. For this purpose 72 cases were analysed and three different types of lateral restraints were considered. The magnitude of the imperfections was set equal with those prescribed in EN1993-1-1.

For all the cases out-of-plane buckling of the frame elements was observed to be the main failure mode indifferent of the applied lateral restraints, although there were cases in which the global lateral-torsional buckling of the frames was coupled with local buckling of the web. This was mainly observed when the restraints applied on the frame element are more effective against overall buckling (e.g. type 3 restraints).

It was noticed that the reduction of the flange by a certain slope influences significantly the behaviour of the frame and their ultimate capacity as well.

ACKNOWLEDGEMENTS

The authors gratefully acknowledge the financial support of "National University Research Council – NURC-CNCSIS-Romania" through the national research grant PN-II-RU-TE-2010-1/38.

REFERENCES

EN 1993-1-1 Eurocode 3: Design of steel structures Part 1.1: General rules and rules for bulidings, CEN – 2005.

Cristutiu, I.M. & Nunes D. 2012. Imperfection sensitivity analysis on the behaviour of single storey frames with tapered web members. *11-th International Conference on Computational Structures Technology.* Dubrovnik 4–7 september 2012.

Cristutiu, I.M. & Nunes D. 2012. Influence of the initial imperfections on the seismic performance of pitched roof portal frames made of welded non-prismatic plated elements. *STESSA 2012 – Behaviour of Steel Structures in Seismic Areas.* Santiago de Chile 9–11 january 2012.

Hong, J.K. & Uang, C.M. 2012. Cyclic testing of a metal building moment frame system with web-tapered members. *Journal of Constructional Steel Research* 70 (2012), 248–255

Shanmugam, N.E & Min, H. 2007. Ultimate load behaviour of tapered steel plate girders. *Steel and Composite Structures*, 7(6), 469–486.

Salem, A.H et all. 2009. Ultimate capacity of axially loaded thin-walled tapered column with doubly symmetric sections. *Thin Walled Structures* 47(2009), 931–941.

Marques, L. et all. 2012. Development of a consistent buckling design procedure for tapered columns, *Journal of Constructional Steel Research*, 72 (2012) 61–74

EN 1993-1-5, "Eurocode 3 (2003)—Design of steel structures Part 1.5: Plated structural elements", CEN – Brussels, Belgium 2003.

Research and Applications in Structural Engineering, Mechanics and Computation – Zingoni (Ed.)
© 2013 Taylor & Francis Group, London, ISBN 978-1-138-00061-2

Compressive resistance of circular hollow sections with squashed ends

M. Dundu & J. Tumkou
University of Johannesburg, Johannesburg, South Africa

ABSTRACT: Circular hollow steel sections are normal specified in truss and dome structures to take advantage of their efficiency in compression and the ease in which they can be curved to match the various radii of the different domes. However, it is not easy to connect these members together or to other members. In order to connect them together or to other members the ends are usually squashed or flattened. Although the process of flattening does not reduce area of the section, it does reduce the flexural stiffness the section. The aim of this paper is to study the behaviour of circular hollow members with flattened edges, in compression.

1 INTRODUCTION

Circular hollow sections (CHSs) are specified in many structural systems because of the inherent excellent geometric properties they have with respect to compression, torsion and bending and the ease in which they can be curved to match the various radii of different domes. A comparison of an open section with a CHS of the same size and area shows that a CHS will have a significantly higher compressive resistance because of the larger radius of gyration about the buckling axis (Kurobane et al., 2004). The manufacturing process of circular hollow sections also distributes residual stresses more effectively, which also results in a greater compressive resistance (Kurobane et al., 2004). In addition CHS do not contain sharp corners; this reduces the area to be protected and increases the corrosion protection life of a structure (Wardenier et al., 2008). However, connecting CHS together or to other members is cumbersome and difficult, and once they have been connected especially for complicated connections, accessing both sides for inspection and maintenance can be a challenge (Grundy, 1989).

One way of connecting CHS is to flatten the ends and then bolt the members together or to other members. Flattening the ends of the section does not reduce the area, but it does reduce the flexural stiffness (moment of inertia), since the squashed ends shape is no longer circular. This implies that the ends of the compression member may failure, which is not typical of member subjected to a compressive force. Most design codes do not provide guidance for the design of CHSs with reduced stiffness at the ends.

This paper seeks to establish the compressive strength of circular hollow sections (CHSs) with squashed/flattened ends, through laboratory tests. Variations in the tests include the diameter, thickness, material strength and bolt configuration of the CHS. Results from the tests are compared with the flexural compressive resistance in the South African code, SANS10162-1, with a view of determining a simple formula of designing such members. SANS10162-1 is based on the Canadian code, CAN/CSAS16.1-M01.

Table 1. Average material properties.

Series	CHS	f_y (MPa)	f_u (MPa)	E (GPa)
Series 1	60.0×3	450.51	463.36	208.35
	76.2×3	425.00	455.92	202.14
	101.6×3	409.73	460.68	205.39
Series 2	60.0×2	372.50	396.25	208.59
	76.2×2	272.50	318.75	201.39
	101.6×2	285.00	340.00	209.16

2 MATERIAL PROPERTIES

In order to determine the material properties of the CHSs, coupons were cut and machined into standard dimensions. The coupons were tested according to the requirements of the British Standard, BS 18. Before testing the width and the thickness of the coupon were measured in order to determine the cross sectional area. The tests were performed using an 1195 Instron, at a rate of 3 mm/min. An extensometer was placed on the reduced length of the specimen to measure strain. After testing, stress-strain graphs were plotted, from which the yield stress (f_y), ultimate stress (f_u) and the elastic modulus (E) were obtained. The average material properties from these tests are given in Table 1.

3 SECTION CLASS LIMITATION

Circular hollow sections of different diameters ($60 \leq d \leq 101.6$) and thicknesses ($2 \leq t \leq 3$) were chosen in this investigation so as to vary slenderness and

Table 2. Slenderness ratio and diameter-to-thickness.

Series	CHS	f_y (MPa)	r (mm)	KL/r	d/t	Limit (d/t)
Series 1	60.0 × 3	450.51	20.20	79.21	20.00	51.00
	76.2 × 3	425.00	25.80	62.12	25.40	54.12
	101.6 × 3	409.73	35.00	45.71	33.87	56.13
Series 2	60.0 × 2	372.50	20.50	78.05	30.00	61.75
	76.2 × 2	272.50	26.24	60.98	38.10	84.40
	101.6 × 2	285.00	35.22	45.43	50.80	80.70

diameter-to-thickness ratios. The slenderness ratios (*KL/r*) of the columns are given in Table 2, and ranges from 46 to 99. This range is significantly smaller that the slenderness limit of compression members of 200, prescribed by SANS10162-1. Parameters K, L, r, d, and t, in Table 2, represent the effective length factor, clear length (equivalent to 1600mm), radius of gyration, outside diameter, and thickness of the circular hollow steel sections, respectively. Since the stiffness of CHSs has been reduced significantly by flattening and huge rotations are expected at the end of the clear length, the effective length factor is taken as one Limitations are also prescribed by SANS10162-1 about the diameter-to-thickness ratio that must be used in circular hollow sections. SANS10162-1 requires that the maximum diameter-to-thickness ratio for circular hollow sections be $d/t \leq 23000/f_y$ to avoid local buckling. The actual values of the diameter-to-thickness ratios are given in Table 2. The diameter-to-thickness ratio, calculated using SANS 10162-1 suggests that all columns yields before failure.

4 TEST PROCEDURE

A total number of 24 specimens were tested; 18 specimens of these were flattened (squashed) at the ends and the remaining 6 CHS specimens were taken as control specimens. To ensure that the flattening process was done well an experienced company was hired to perform this function. The flattening process was performed mechanically by placing the ends of the circular hollow sections between dies, and then flattened. This deformed the member plastically in both the longitudinal and transversal directions. No cracks were observed after this process. As expected, flattening created a transition zone from a circular profile of the tube to a flattened section. The length of the transition zone (L) ranged from 1.2d to 1.5d, as recommended by Dutta (1998).

The clear length between the top and bottom connection of each specimen remained constant at 1600 mm length, however, the flattened length varied depending on the number of bolts of each specimen. Three different bolt configurations were investigated, namely; 1) with 2 bolts, 2) with 3 bolts and 3) with 4 bolts. As a result the 4 bolts CHS specimen had the longest squashed ends in comparison to the 2 bolts

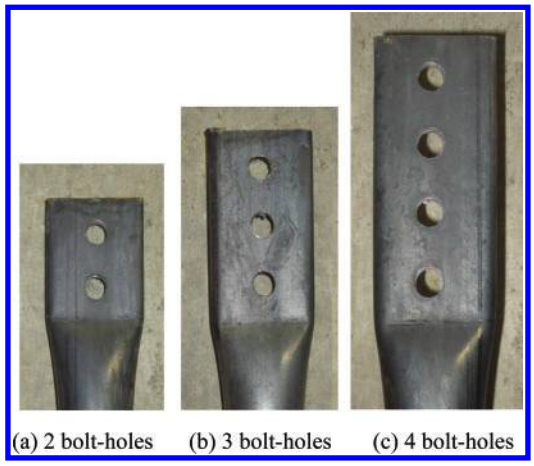


Figure 1. Bolt-hole configuration.

CHS specimen. A minimum of 2 bolts were used in each connection to reduce the amount of rotation at the end of the member. Figure 1 shows the squashed ends and the configuration of the bolt-holes of the CHSs. The lengths for the flat portions of the 2 bolt-hole, 3 bolt-hole and 4 bolt-hole configurations are 115 mm, 170 mm and 225 mm, respectively. The spacing of the bolt-holes was specified according to the requirements given in SANS 10162-1. The distance between the bolts is 55 mm and the end distance is 30 mm. SANS 10162-1 requires that the minimum end distance in a bolted connection with two or more bolts parallel to the direction of the load be at least 1.5 times the bolt diameter and the minimum distance between centres of bolt holes be 2.7 times the bolt diameter.

Figure 2(a) shows the test set-up of the CHSs. Details of the top and bottom connections of the set-up are given in Figures 2(b) and (c), respectively. Spacers were used to align the specimen vertical. M16, grade 8.8 bolts with ultimate tensile strength of 800MPa were selected in order to provide sufficient shear resistance for the double shear plane. Note that an M16 diameter bolt is the minimum structural bolt used in South Africa. The shear resistances for the 2, 3 and 4 bolts, in double shear, are 216kN, 324kN and 432, respectively.

No material tests were conducted on these bolts since the strength of the bolt was found to be less critical than the strength of the flattened portion. All bolts were fully threaded. An increasing compressive axial load was applied to the CHS, at a rate of 2 mm per minute in order to obtain a gradual displacement, until the specimen failed. The displacement and compressive load were recorded by a data acquisition system. Control specimens were tested with a steel ball between two plates at the top at the bottom-end of the member to simulate simply supported conditions.

5 FAILURE MODES

Two failure modes were observed in Series 1 tests. The first mode of failure observed was overall flexural



Figure 2. Test set-up and connection configuration.

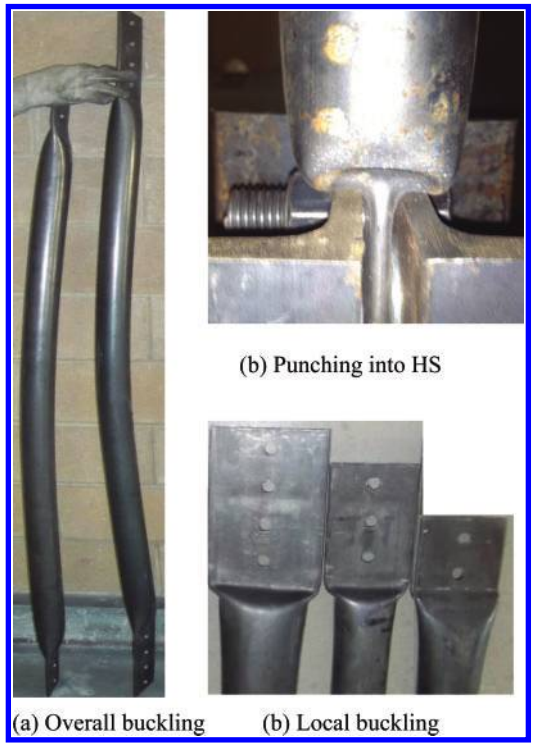


Figure 3. Failure modes.

buckling (F.B) of the member (Figure 3(a)). Overall flexural buckling was evident in the 60 × 3 mm CHSs. The second failure mode witnessed was local buckling (L.B), which formed at the beginning of the transition zone, from flat to circular section (Figures 3(b) and (c)). This mode of failure was common in larger diameter sections (typically the 76.2 × 3 mm and 101.6 × 101.6 × 3 mm), and was previously noted by Mistakidis and Tsiogas (2003). As shown in Figure 3(b), the specimens experienced extensive yielding or excessive plastic deformation in the transition zone. The deformation was caused by the punching effect of the flattened portion into the top of the circular region as it moved downwards, forcing the transition zone to bulge outwards. Both ends of the members (top and bottom) experienced this failure mode.

The modes of failure observed in Series 1 were governed by the diameter-to-thickness ratio (d/t) of CHSs. CHSs with larger diameter-to-thickness ratios failed by local buckling at the transition zone whilst those with lower diameter-to-thickness ratios failed by overall buckling. A significant number of specimens in Series 2 tests were expected to fail by overall flexural buckling because of the large slenderness ratios, however, this did not happen. Instead all sections failed by local buckling in the transition zone, near the flattened edge One possible cause of this local failure is the lower quality of steel exhibited by these sections. The second possible cause of this failure mode is the smaller thickness of the CHSs, which made it easier for the flat section to punch through circular hollow part of the member.

6 TEST RESULTS

Using the material properties in Table 1 and SANS10162-1, the axial compressive resistances (N_S) of CHSs in Table 3 were calculated. Table 3 also summarizes the test results obtained for the various specimens. In this table N_E is the maximum load applied to the tested flattened specimen and N_C is the compressive resistance of the control tests. Note that SANS10162-1 is based on the Canadian Code, CAN/CSAS16.1-M01. According to SANS10162-1, the unfactored compressive resistance of CHS for class 1, 2, or 3 sections is given by

$$C_r = Af_y(1+\lambda^{2n})^{-1/n} \quad (1)$$

where, A is the gross cross-sectional area and the parameter n reflect the difference in the patterns and levels of residual stresses and initial out-of-straightness. The value of n is equal to 1.34 for hot rolled, fabricated structural sections, and non-stress relieved hollow structural sections, and equal to 2.24 for doubly symmetric welded three-plate members with flange edges oxy-flame-cut and stress relieved

Table 3. Experimental and theoretical results.

Series	CHS (dxt)	Bolts	N_E (kN)	N_C (kN)	N_S (kN)	N_E/N_C	N_E/N_S	FM
S1	60 × 3	2	106.69	156.62	118.04	0.68	0.90	F.B
		3	119.92	156.62	118.04	0.77	1.02	F.B
		4	121.18	156.62	118.04	0.77	1.03	F.B
	76.2 × 3	2	134.90	211.50	189.47	0.64	0.71	L.B
		3	151.42	211.50	189.47	0.72	0.80	L.B
		4	153.01	211.50	189.47	0.72	0.81	L.B
	101.6 × 3	2	135.86	319.62	309.75	0.43	0.44	L.B
		3	174.57	319.62	309.75	0.55	0.56	L.B
		4	173.06	319.62	309.75	0.55	0.73	L.B
S2	60 × 3	2	58.00	94.00	78.00	0.62	0.74	L.B
		3	67.00	94.00	78.00	0.71	0.86	L.B
		4	55.00	94.00	78.00	0.59	0.71	L.B
	76.2 × 3	2	40.42	114.00	98.00	0.35	0.41	L.B
		3	55.00	114.00	98.00	0.48	0.56	L.B
		4	49.00	114.00	98.00	0.43	0.50	L.B
	101.6 × 3	2	54.00	167.00	157.00	0.32	0.34	L.B
		3	56.00	167.00	157.00	0.34	0.36	L.B
		4	54.00	167.00	157.00	0.32	0.34	L.B

hollow structural sections. Equation 1 was evaluated with the value of n=1.34. The non-dimensional parameter

$$\lambda = \frac{KL}{r}\sqrt{\frac{f_y}{\pi^2 E}} = \sqrt{\frac{f_y}{f_e}} \qquad (2)$$

where, r is the radius of gyration and E is the modulus of elasticity (200 000MPa). The effective length factor (K) is taken as 1 since the flattened end is considered as a flexible component. Whilst the first part of Equation 2 is more applicable to the common flexural buckling mode, the second part of Equation 2 is more general, since the elastic buckling stress (f_e) accounts for all possible forms of buckling.

With the exception of the 60 × 2 mm CHS, which has a significantly larger yield stress than the other sections in Series 2 (S2), the failure loads of larger diameter sections are generally higher than the smaller diameter sections (Table 3). A comparison of the test compressive strength of the flattened CHSs and the control compressive strengths in Table 3 shows the test strengths of the flattened CHSs to be significantly smaller than the control compressive strength. In Series 1 (S1), the flattened test strength range from an average of 75% of the control strength for the 60 × 3 mm specimens down to an average of 50% of the control strength for the 101.6 × 3 mm. This suggests that there is a 25% reduction in axial capacity for the 60 × 3 mm tubes, 30% reduction in axial capacity for the 76.2 × 3 tubes and 50% reduction in axial capacity for the 101.6 × 3 mm tubes, when the end is flattened. The flattened test strength range from a maximum of 71% to a minimum of 32% of the control strength for the 60 × 2 mm and 101.6 × 2 mm, respectively, for Series 2.

The axial capacity of the 60 × 2 mm, 76.2 × 2 mm, 101.6 × 2 mm tubes were reduced by an average percentage of 35%, 58%, and 67%, respectively, when the end is flattened. The section that experienced overall buckling (60 × 3 mm) was less affected by flattening. Local buckling in the transition zone resulted in a considerable loss of compressive strength when compared with standard circular hollow section of the same properties. This effect was felt more in sections with larger diameter-to-thickness ratios, lower yield strength of the material and smaller slenderness ratios than those with smaller diameter-to-thickness and high yield strength of the steel and larger slenderness ratio. CHSs with larger diameter-to-thickness ratio failed by local buckling at the transition zone whilst those with lower diameter-to-thickness ratio failed by overall buckling. From this analysis, it is clear that local buckling in the transition zone is more critical than overall flexural buckling of the member.

Although SANS10162-1 was able to predict the strength of the 60 × 3 mm section, which failed due to overall flexural buckling, the code could not predict all the sections that failed due to local buckling in the transition zone. The buckling strengths obtained using SANS10162-1 are larger than the test strengths for the specimens that experienced local buckling or excessive plastic deformation within the transition zone. As indicated above the effect is also more severe in sections with larger diameter-to-thickness ratios, lower yield strength of the material and smaller slenderness ratios than those with smaller diameter-to-thickness, high yield strength of the steel and larger slenderness ratio. These results compare well with the findings of Mistakidis and Tsiogas, who found the theoretical compressive strengths obtained from Eurocode 3 to be much larger than the experimentally strengths. Table 3 also shows that the number of bolts (2, 3 or 4 bolts) did not have any significant influence on the magnitude of the compressive resistance of the CHS specimens. The strengths obtained from bolt configurations were almost the same. The lower strength achieved by the larger flattened sections suggest that it might be uneconomic to use such sections as compression members.

7 PROPOSED DESIGN METHOD

Based on the analysis above the strength of flattened members has to be related either to the strength of the bolts or to the strength of the reduced cross sectional area of the flattened ends. The design method of the member, proposed in this paper, is an ultimate limit state approach and accounts for the two different failure methods observed in the tests. It is shown in Table 3 that the failure mode observed is governed by the diameter-to-thickness ratio of CHSs. CHSs with smaller diameter-to-thickness ratios (60 × 3 mm) failed by overall bucking and Equation 1 is able to model the results of these section. It is proposed to use this equation for CHSs with smaller diameter-to-thickness ($d/t \leq 20$).

Table 4. Design compressive resistance.

Diameter-to-thickness ratio	Design compressive resistance
$d/t \leq 20$	$C_r = \phi A f_y (1+\lambda^{2n})^{-1/n}$
$20 < d/t \leq 30$	$C_r = 0.75\phi A f_y (1+\lambda^{2n})^{-1/n}$
$30 < d/t \leq 38$	$C_r = 0.50\phi A f_y (1+\lambda^{2n})^{-1/n}$
$38 < d/t \leq 50$	$C_r = 0.35\phi A f_y (1+\lambda^{2n})^{-1/n}$

The second mode of failure observed is local buckling in the transition zone. This failure mode affected flattened tubes with larger slenderness ratios. The effect was felt more in tubes with larger diameters-to-thickness ratios ($d/t > 20$) and lower yield strength. Based on the analysis of the results in Table 3 it is proposed to reduce the strength of the tubes with $20 < d/t \leq 30$, $30 < d/t \leq 38$, $38 < d/t \leq 50$ by 25%, 50%, and 65%, respectively. The proposed expressions for designing such members are given in Table 4. In this table $\phi = 0.9$ is the resistance factor, to account for the variability of material properties, dimensions, workmanship, type of failure, and uncertainty in the prediction of member resistance.

Where flattened sections are used the effective length factor should be taken as 1 and the transition zone should be as short as possible to avoid a negative effect on the buckling behaviour.

8 CONCLUSION

This research shows that there are two possible failure modes of circular hollow sections with flattened ends, namely; overall flexural buckling of the member and local buckling in the transition zone. Local buckling was the dominant mode of failure and was associated with excessive plastification of the transition zone. Each mode of failure is directly connected to the ratio between the diameter and the thickness of the cross section. Smaller values of this ratio ($d/t \leq 20$) lead to the flexural buckling failure mode, while larger values ($d/t > 20$) promote the local buckling failure in the transition zone.

Local buckling in the transition zone was also promoted by CHSs of lower strength steel and lower slenderness ratio. This implies that CHSs of higher strength steel and larger slenderness ratio are more likely to favour overall flexural buckling. The investigation shows that the process of flattening CHSs reduces its compressive strength by big margin, and that all members that failed due to local buckling of the transition experienced a significantly lower ultimate compressive strength than those that failed due overall flexural buckling.

ACKNOWLEDGEMENTS

The author wishes to acknowledge University of Johannesburg Research Committee (URC) for sponsoring this research.

REFERENCES

BS 18. 1987. *British standard method for tensile testing of metals*. , London: British Standard Institution.

CAN/CSAS16.1-M01. 2001. *Limit States Design of Steel Structures*. Rexdale, Ontario, Canada: Canadian Standards Association.

Dutta, D., Wardenier, J., Yeomans, N., Sakae, K., Bucak, Ö. & Packer, J.A. 1998. *Design guide for fabrication, assembly and erection of hollow section structures*. TÜV-Verlag, Köln, Germany: CIDECT series No. 7.

Eurocode 3. 1996 *Design of Steel Structures, Part 1.3: General rules and rules for buildings*. London: British Standards Institution.

Grundy, P. *Squashed tubes in welded frames; Int. Symposium on Tubular Structures, Lappeenranta, November 1989*. Finland.

Kurobane, Y., Packer, J.A., Wardenier, J. & Yeomans, N. 2004. *Design Guide for Structural Hollow Section Column Connections*. Verlag TUV Rheinland, Cologne, Germany: CIDECT series No. 9.

Mistakidis, E. & Tsiogas, S. 2003. Failure Modes of Circular Hollow Members with Flattened Edges. *Journal of Construction Steel Research* 59: 1573–1592.

SANS 10162-1. 2005. *The structural use of steel, Part 1: Limit-state design of hot-rolled steelwork*. Pretoria, South Africa: South Africa National Standards.

Wardenier, J., Kurobane, Y., Packer, J.A., van der Vegte, G.J. & Zhao, X.-L. 2008. *Design Guide for Circular Hollow Section (CHS) Joints under Predominantly Static Loading*. 2nd Edition, CIDECT series.

Research and Applications in Structural Engineering, Mechanics and Computation – Zingoni (Ed.)
© 2013 Taylor & Francis Group, London, ISBN 978-1-138-00061-2

The influence of pallets on the behaviour and design of drive-in steel storage racks – Part I: Behaviour

B.P. Gilbert
Griffith School of Engineering, Griffith University, Australia

L.H. Teh
School of Civil, Mining and Environmental Engineering, University of Wollongong, Australia

R.X. Badet
Griffith School of Engineering, Griffith University, Australia

K.J.R. Rasmussen
School of Civil Engineering, The University of Sydney, Australia

ABSTRACT: Drive-in steel storage racks represent a popular alternative to the more common selective racks when available space is restricted or when storing the same good. In drive-in racks, the forklift truck drives into the rack and stores the pallets on beam rails on the "first-in last-out" principle. Recent experimental studies have shown that by acting as horizontal ties between uprights, pallets significantly influence the structural behaviour of the rack. However, due to the uncertainty in the degree of friction between the rail beams and the pallets, current industry design practice does not consider this effect. This paper quantifies the influence of the pallets on the bending moment distribution in the uprights using a 3D finite element model calibrated against experimental results on a full scale drive-in rack. Additionally, as 3D models may be computationally intensive when a large number of analyses are required, this paper presents an improved version of the 2D model of drive-in racks introduced by Godley. In the improved 2D model, all possible loading scenarios and the influence of pallets on the structural behaviour of the rack are considered. When compared to advanced 3D finite element analyses, the model is able to accurately reproduce the bending moment distribution in the upright, with and without the presence of pallets.

1 INTRODUCTION

Worldwide, steel storage racks are extensively used in the manufacturing, wholesale and retail industry to store goods. They are mostly freestanding structures and are often assembled from cold-formed steel profiles. Two main types of racks prevail, referred to as "selective racks" and "drive-in racks". In drive-in racks, pallets are stored on rail beams one after the other, and the forklift truck drives into the rack to store the pallets on the "first-in last-out" principle. The rail beams are offset from the centreline of the uprights so that the pallets apply both bending moments and axial compressive forces to the uprights. To allow the forklift truck passage, the rack is only braced horizontally at the top (plan bracing) and vertically at the back (spine bracing) in the down-aisle direction. Due to their floor space efficiency, drive-in racks are usually preferred to selective racks in storing the same goods with quick turnover, or in expensive storage spaces such as industrial freezers. Figure 1 shows an example of a drive-in rack.



Figure 1. Example of a drive-in rack.

Experimental tests performed by Gilbert and Rasmussen (2009a, 2012) have shown that pallets act as horizontal braces between adjacent uprights, significantly influence the structural behaviour of drive-in

racks and must be considered in order to accurately capture the 3D behaviour of drive-in racks. Similarly, earlier research by Salmon et al. (1973), who numerically investigated the buckling behaviour of symmetrically loaded drive-in racks by alternately considering and ignoring the pallet bracing restraints in the analysis, showed that pallet bracing restraints had significant influence on the non-sway buckling mode, although they had less influence on the sway buckling mode.

However, due to the uncertainty concerning the friction between the pallet bases and the rail beams, drive-in racks are currently designed without considering the bracing effects.

Hua and Rasmussen (2010) measured the friction coefficient between wood pallets and rail beams and found that the average static friction coefficient between the rail beams and the pallet bases to be as high as 0.576, with a recommended a design static friction coefficient of 0.439. This friction coefficient suggests that significant horizontal forces can develop between the pallets and the rail beams before sliding occurs, allowing the pallets to play a structural role in the behaviour of drive-in racks. It is noted, however, that this design static friction coefficient does not take into account grease or ice (in the case of industrial freezers) that may accumulate on rail beams.

The current paper evaluates the influence of the horizontal bracing effect of pallets on the bending moment distribution of the upright in the down-aisle direction only, as due to the upright frames, pallets are not believed to influence the behaviour of drive-in racks in the cross-aisle direction.

The 2D analysis model for drive-in racks proposed by Godley (2002) is improved herein by introducing the horizontal restraints provided by both the rail beams and the pallet bracing restraints. All possible loading scenarios are also able to be computed in the improved model. This model is checked against the 3D model developed by Gilbert and Rasmussen (2009b, 2012) that is calibrated against laboratory test results.

2 SINGLE UPRIGHT MODEL

2.1 *Single upright model proposed by Godley*

In order to reduce the computation time associated with large models, Godley (2002) developed a "single upright model" to analyse fully loaded drive-in racks in the down-aisle direction. The upright is restrained at its base by a spring support having a rotational stiffness K_c, and at its top by another having a rotational stiffness K_b and a translational stiffness K_t, as shown in Figure 2. K_c represents the restraint provided by the base plate to the floor connection, K_b the restraint provided by the portal beams in double curvature (sway mode) having semi-rigid connections to the upright, and K_t the combined restraint from the plan bracing (spanning the entire rack), spine bracing (spaning one bay) and upright frames. Pallet loads and out-of-plumb loads are applied to the upright as shown in Figure 2.

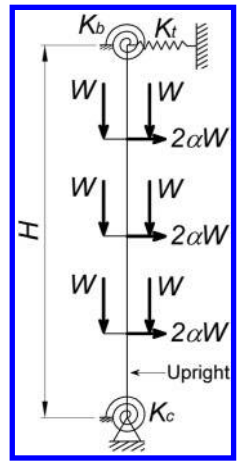


Figure 2. Drive-in rack single upright model from Godley (2002).

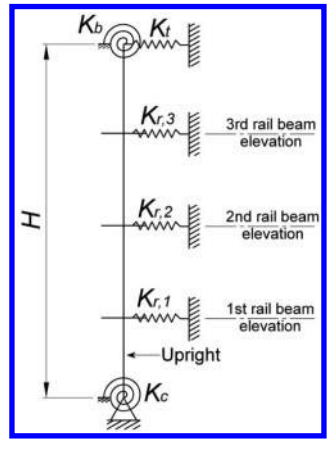


Figure 3. Single upright model with rail beam restraints for a 4 stories drive-in rack.

Detailed calculations for K_c, K_b and K_t, can be found in Godley (2002).

Despite its attractiveness, this model has limitations as it (i) ignores the restraint provided by the rail beams, (ii) does not take into account the horizontal bracing restraint provided by pallets, and (iii) does not consider all possible upright loading scenarios. The previous limitations are addressed in following sections.

2.2 *Improved single upright model*

2.2.1 *Rail beam restraints*

Typically, the out-of-plumb in drive-in racks is modelled by horizontal forces at the rail beam supports that are linearly proportional to the gravity loads of the pallets. For a fully loaded rail beam, the front and the back uprights are less loaded than the inner uprights, resulting in smaller out-of-plumb forces being applied to the front and back uprights. Therefore and since rail beams link the uprights together, they restrain the deflection of the inner uprights when subjected to the out-of-plumb forces.

Consequently, these restraints provided by the rail beams are introduced into the single upright model by adding a horizontal translational stiffness $K_{r,i}$ at each rail beam elevation i, as shown in Figure 3. While such an addition to the single upright model over-represents the restraints since it implies that there are no deflections of the front and back uprights, it has been found to lead to more accurate results than the neglect of same (Gilbert et al., 2013).

The stiffness $K_{r,i}$ is derived in Gilbert et al. (2013) for the critical upright (second from the front) of a drive-in rack with two upright frames and uniform spacing between uprights. For simplicity, the restraints provided by all rail beams to an upright are assumed to be independent of each other. $K_{r,i}$ is then expressed as,

$$K_{r,i} = \frac{11K_{uh,fb} - 4K_{uh,m}}{\frac{55L^3K_{uh,fb}}{6EI_r} + 15} \quad (1)$$

where $K_{uh,fb}$ and $K_{uh,m}$ are the down-aisle stiffness of the front and back uprights and inner uprights, respectively (Gilbert et al., 2013), L is the distance between two uprights in the cross-aisle direction, E is the Young's modulus of steel and I_r is twice the second moment of area of the rail beam, as two rail beams are typically connected to the uprights.

2.2.2 *Pallet bracing restraints*

The bracing effect provided by the pallets is now considered for any loading scenario of a studied single upright. Bays not directly in the vicinity of this upright are assumed to be fully loaded, as it would maximise the down-aisle displacement Δ of the rack and therefore the P-Δ effects in the upright. Specifically, two loading scenarios are considered for these bays, believed to represent the two design envelopes:

Bay loading scenario A: all bays not directly connected to the studied upright are fully loaded, as shown in Figure 4 (a).

Bay loading scenario B: the two bays on each side of the two bays directed connected to the studied upright are empty, while remaining bays are fully loaded, as shown in Figure 4 (b). This loading scenario aims to limit the influence of the pallets on the bending moment distribution in the studied upright, as contrary to the previous bay loading scenario A, the pallets only link the studied upright and its two neighbours.

2.2.2.1 Improved model for Bay loading scenario A

In a fully loaded rack, the influence of the pallets on the deformed shape of the uprights would be minimal, as all internal uprights in a row of uprights in the down-aisle direction would identically deform. Therefore, the overall deformation of the rack at the critical row of uprights can be found using the fully loaded improved single upright model introduced in Section 2.2.1, i.e. not considering pallets, as illustrated in Figure 5. Moreover, if the number of bays of the rack is large enough, as frequently encountered in drive-in racks (see Figure 1), removing pallets from each side

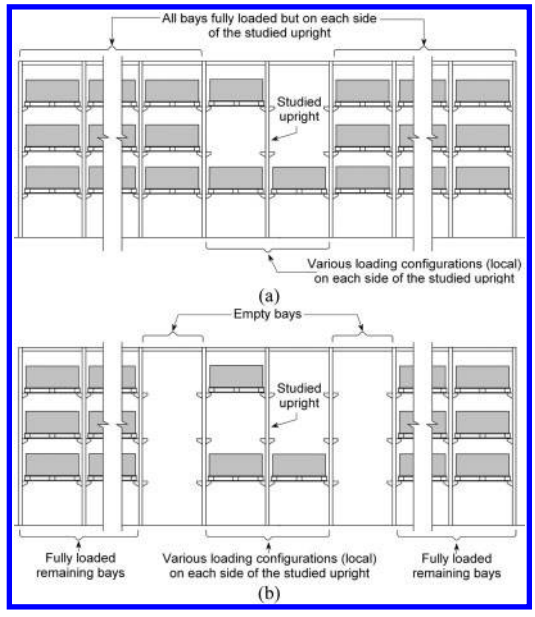


Figure 4. Studied upright for (a) Bay loading scenario A and (b) Bay loading scenario B.

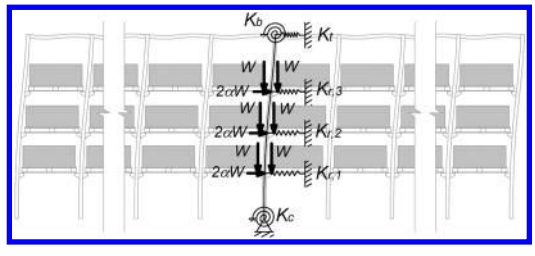


Figure 5. Deformed shape of the single upright model for a fully loaded rack.

of the studied upright would have negligible influence on the overall deformation of the rack, and the deformation of this upright would be a function of both its immediate loading configuration and the overall deformation of the rack imposed to the upright by the portal beams and the pallet bracing restraints.

Therefore, the bracing restraint provided by the pallets for a given loading scenario of the single upright is introduced into the model in the following manner, as illustrated in Figure 6:

Step 1: The overall down-aisle displacements of the rack at each rail beam elevation and at the top of the rack are determined using the fully loaded single upright model with out-of-plumb forces, as shown in Figure 5. The base plate to floor rotational stiffness K_c, and rail beam stiffness $K_{r,i}$ are calculated for the fully loaded configuration.

Step 2: The single upright model is loaded with its studied loading scenario, with the corresponding base plate to floor rotational stiffness K_c and rail beam stiffness $K_{r,i}$.

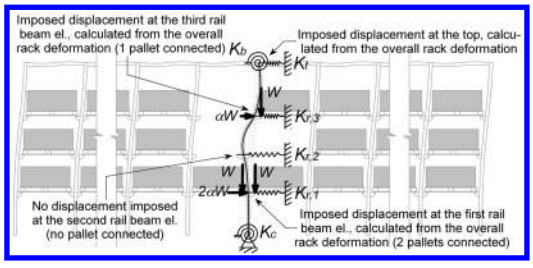


Figure 6. Improved single upright model for Bay loading scenario A.

Step 3: The overall down-aisle displacement at the top of the rack (portal beam elevation) found in Step 1 is imposed at the top of the single upright model created in Step 2.

Step 4: For each rail beam elevation of the model in Step 2, if there is at least one pallet at the elevation, then the overall down-aisle displacement at that elevation found in Step 1 is imposed on the upright.

2.2.2.2 Improved model for Bay loading scenario B As with previous Bay loading scenario A, the overall displacement imposed by the rack at the top of the critical upright in Figure 4 (b) and its two adjacent uprights can be determined from the fully loaded single upright model shown in Figure 5.

In order to determine the bending moment distribution in the studied upright for a given loading scenario of the upright, three single upright models are used and linked together by pinned rigid elements (ties) representing the pallet bracing restraints. The following steps are carried out as illustrated in Figure 7:

Step 1: The overall down-aisle displacement at the top of the rack is determined using the fully loaded single upright model with out-of-plumb forces, as shown in Figure 5. The base plate to floor rotational stiffness K_c, and rail beam stiffness $K_{r,i}$ are calculated for the fully loaded configuration.

Step 2: Three single upright models are created and loaded with the studied loading scenario, with the corresponding base plate to floor rotational stiffness K_c and rail beam stiffness $K_{r,i}$.

Step 3: The overall down-aisle displacement at the top of the rack (portal beam elevation) found in Step 1 is imposed at the top of the three uprights created in Step 2.

Step 4: Pallet bracing restraints are modelled using horizontal ties between rail beams, as shown in Figure 7.

3 INFLUENCE OF THE PALLET RESTRAINT ON THE BENDING MOMENT DISTRIBUTION AND VALIDATION OF THE SINGLE UPRIGHT MODEL

The 3D advanced Finite Element model for drive-in racks developed by Gilbert and Rasmussen Gilbert and

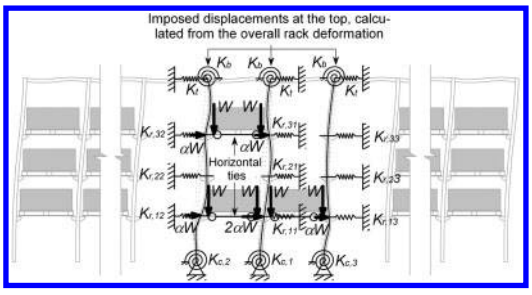


Figure 7. Improved single upright model for Bay loading scenario B.

Rasmussen (2009b, 2012) is used herein to (i) analyse the influence of the pallet restraint on the bending moment distribution in the upright and (ii) validate the improved single upright model introduced in Section 2.2. The 3D model has been calibrated against experimental test results and considers joint eccentricities, nonlinear portal beam-to-upright connections, nonlinear base-plate connections, and pallet bracing restraints, see Gilbert and Rasmussen (2009b, 2012) for more details. In the present 3D second-order analysis, the FE software Abaqus Abaqus (2010) is used, while the FE software Strand7 (2010) is used to run the 2D second-order analysis of the improved single upright model.

A rack with similar characteristics to the one tested by Gilbert and Rasmussen (2012) is used as a case study. Specifically, the rack is 12 bays wide, 4 pallets and 2 upright frames deep, and 4 stories high (i.e. featuring 3 rail beam levels). It has 3 spine bracing modules, each spanning one-bay, and 4 plan bracing modules, each spanning three bays. Each pallet is 2 tonnes. The rack is loaded as in Bay loading scenario A, described in Section 2.2.2. The shear stiffness of the pallets is taken as 7.2 N/mm, which is within the range experimentally found by Hua and Rasmussen (2010). The pallets are considered to be fastened to the rail beams as the static friction coefficient is assumed to be sufficiently high to prevent sliding. Two loading scenarios are studied, with a out-of-plumb of 0.0044 rad and other design parameters given in Gilbert et al. (2013). Further verification of the improved single upright model can be found in Gilbert et al. (2013).

3.1 *First loading scenario – Maximum combined axial compression and bending*

The load case involving the loading scenario shown in elevation in Figure 8 generally represents the governing load case for combined axial compression and bending of the adjacent upright to the unloaded compartment and to the aisle upright (critical upright) (FEM 10.2.07, 2010).

The down-aisle bending moment distribution of the critical upright from the 3D model accounting for pallet bracing restraints is plotted in Figure 9(a), and that obtained from the 3D model ignoring same in Figure 9(b). Figure 9 shows that the pallet bracing restraints significantly affect the bending moment distribution

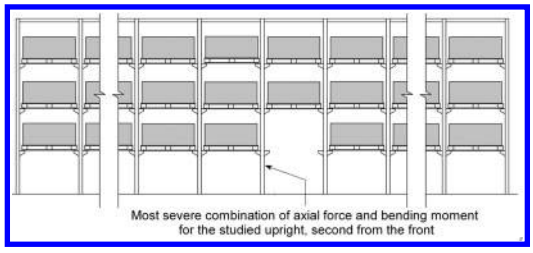


Figure 8. Loading scenario believed to generally govern the design.

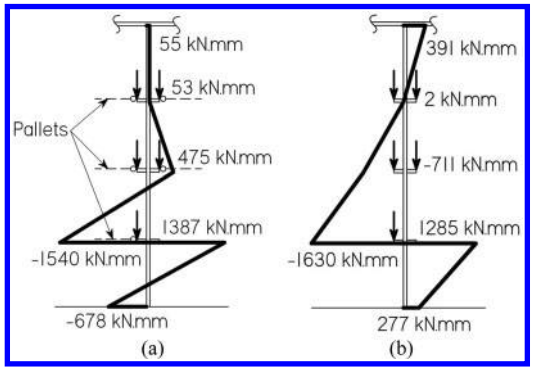


Figure 9. Bending moment distribution in the critical upright under vertical and out-of-plumb loads for the loading scenario shown in Figure 8 and 3D advanced analysis for (a) pallets considered and (b) pallets ignored.

of the critical upright, but have only a relatively minor impact on the design bending moment. This observation appears to be general for this type of loading scenario.

The down-aisle bending moment distribution of the critical obtained from the single upright model accounting for pallet bracing restraints described in Section 2.2.2.1 is plotted in Figure 10 (a), and that obtained from the single upright model ignoring same (i.e. ignoring Step 4 in Section 2.2.2.1) in Figure 10 (b). It can be seen from the comparison between Figure 9 and Figure 10 that the single model upright is able to accurately reproduce the bending moment distribution of the critical upright, with or without the pallet bracing restraints. The difference in the design bending moment between the 3D and the single upright models is less than 6%.

3.2 *Second loading scenario – Maximum bending*

The load case involving the loading scenario shown in Figure 11 typically incurs the largest design bending moment in the critical upright.

The down-aisle bending moment distribution of the critical upright under the second load case obtained from the 3D model accounting for pallet bracing restraints is plotted in Figure 12 (a), and that obtained

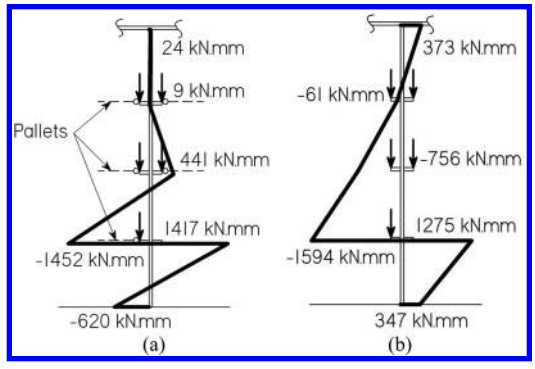


Figure 10. Bending moment distribution in the critical upright under vertical and out-of-plumb loads for the loading scenario shown in Figure 8 and 2D analyses for (a) pallets considered and (b) pallets ignored.

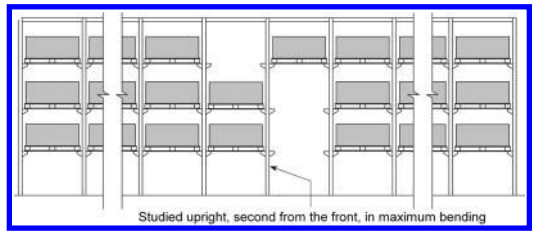


Figure 11. Loading scenario inducing maximum bending moment in a row of uprights.

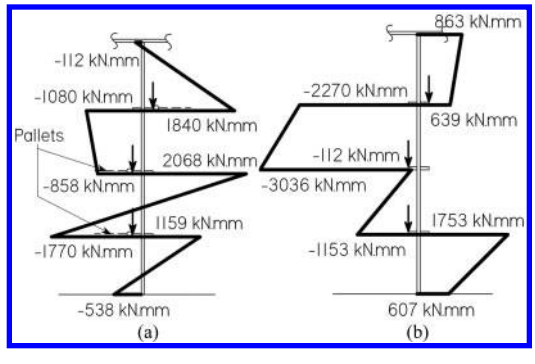


Figure 12. Bending moment distribution in the critical upright under vertical and out-of-plumb loads for the loading scenario shown in Figure 11 and 3D advanced analysis for (a) pallets considered and (b) pallets ignored.

from the 3D model ignoring same in Figure 12 (b). Figure 12 shows that not only the pallet bracing restraints significantly affect the bending moment distribution of the critical upright, but also reduces the design bending moment by almost one third under the second load case.

The down-aisle bending moment distribution of the critical upright obtained from the single upright model accounting for pallet bracing restraints is plotted in Figure 13 (a), and that obtained from the single upright model ignoring same in Figure 13 (b). Consistent with

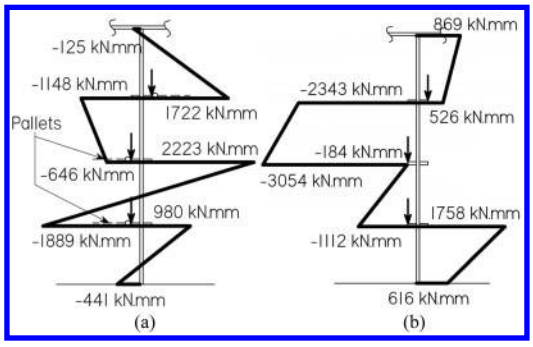


Figure 13. Bending moment distribution in the critical upright under vertical and out-of-plumb loads for the loading scenario shown in Figure 12 and 2D analyses for (a) pallets considered and (b) pallets ignored.

the results for the previous loading scenario, the comparison between Figure 12 and Figure 13 shows that the single model upright is able to accurately reproduce the bending moment distribution of the critical upright, with or without the pallet bracing restraints. The difference in the design bending moment between the 3D and the single upright models is less than 7%.

4 CONCLUSION

This paper analyses the influence of horizontal bracing restraints provided by the pallets on the behaviour of steel drive-in racks. The pallets are shown to significantly influence the bending moment distribution in the uprights. The single upright model presented by Godley is improved by including the restraints provided by the rail beams and the pallets. Comparison with advanced 3D Finite Element Analyses shows that the improved model is able to accurately reproduce the bending moment distribution in the upright in the down-aisle direction under gravity and out-of plumb loads and can be used to avoid large computational time associated with 3D models.

REFERENCES

ABAQUS 2010. *Abaqus ver. 6.10 – User manual,* Providence, U.S.A., ABAQUS, Inc.

FEM 10.2.07 2010. Version 0.12 – Draft – The Design of 'Drive-in' and 'Drive-through' pallet racking. Federation Europeenne de la Manutention, Brussels, Belgium.

GILBERT, B. P. & RASMUSSEN, K. J. R. 2009a. Stiffness tests, failure tests and load transfer in steel drive-in storage racks. Research Report R900. School of Civil Engineering, The University of Sydney, Australia.

GILBERT, B. P. & RASMUSSEN, K. J. R. 2009b. Finite Element modelling of steel drive-in rack structures. Research Report R901. School of Civil Engineering, The University of Sydney, Australia.

GILBERT, B. P. & RASMUSSEN, K. J. R. 2012. Drive-in steel storage racks I: Stiffness test and 3D load transfer mechanisms. *ASCE Journal of Structural Engineering,* 138**,** 135–147.

GILBERT, B. P., TEH, L. H., BADET, R. X. & RASMUSSEN, K. J. R. 2013. Determination of the influence of the pallets on the design of drive-in steel storage racks. Research Report CIEM/2013/R04. Centre for Infrastructure Engineering and Management, Griffith University, Australia.

GODLEY, M. H. R. The behaviour of drive-in storage structures. *In:* Laboule, R.A. & Yu, W.W., eds. 16th International Specialty Conference on Cold-Formed Steel Structures, October, 17–18 2002 Orlando, Florida, U.S.A., 340–352.

HUA, V. & RASMUSSEN, K. J. R. 2010. Static friction coefficient between pallets and beam rails and pallet shear stiffness tests. Research Report 914. School of Civil Engineering, The University of Sydney, Australia.

SALMON, M. A., WELCH, R. E. & LONGINOW, A. Analysis of drive-in and drive-thru storage racks. *In:* Yu, W.W., ed. 2nd Specialty Conference on Cold-Formed Steel Structures, October, 22–24 1973 St Louis, Missouri, U.S.A., 617–639.

STRAND7 2010. *Using Strand7 – User manual – Release 2.4.4,* Sydney, Australia, G+D Computing Pty Ltd.

Research and Applications in Structural Engineering, Mechanics and Computation – Zingoni (Ed.)
© 2013 Taylor & Francis Group, London, ISBN 978-1-138-00061-2

The influence of pallets on the behaviour and design of steel drive-in storage racks – Part II Design

B.P. Gilbert
Griffith School of Engineering, Griffith University, Australia

L.H. Teh
School of Civil, Mining and Environmental Engineering, University of Wollongong, Australia

R.X. Badet
Griffith School of Engineering, Griffith University, Australia

K.J.R. Rasmussen
School of Civil Engineering, The University of Sydney, Australia

ABSTRACT: This paper analyses the influence of the horizontal restraints provided by pallets on the ultimate capacity of drive-in racks. The paper is based on the assumption that one can accurately determine the coefficient of friction between the rail beams and the pallets or can design a device that restrains the pallets from sliding on the rail beams. Thirty-six drive-in racks representing the global sale of an Australian manufacturer over three years are analysed for all possible loading scenarios. For the sake of computational efficiency, the simple 2D model introduced in the companion paper is used for the study. The load case(s) governing the structural design is(are) also clarified and the friction coefficient or strength of a restraining device required to prevent the pallets from sliding is determined.

1 INTRODUCTION

This paper analyses the influence of the horizontal restraints provided by pallets on the ultimate capacity of drive-in racks. As introduced in the companion paper (Gilbert et al., 2013a), by acting as horizontal braces between adjacent uprights, pallets significantly influence the structural behaviour of drive-in racks and must be considered in order to accurately capture the 3D behaviour of this type of structure.

However, due to the uncertainty concerning the friction between the pallet bases and the rail beams, drive-in racks are currently designed without considering this bracing effects. If a device can prevent the pallets from sliding on the rail beams or if the coefficient of friction between the pallet bases and the rail beams can be reliably determined, the horizontal bracing effect provided by the pallets could be fully exploited in the design.

The current paper analyses the influence of the horizontal bracing effect of pallets on the design of steel drive-in racks in the down-aisle direction only. As mentioned in the companion paper (Gilbert et al., 2013a), due to the upright frames, pallets are not believed to influence the behaviour of the racks in the cross-aisle direction. It should also be noted that the friction between pallet bases and the rail beams would prevent the pallets from dropping through on account of the upright bowing deformations. As such, the serviceability check against upright bowing deformations is not considered in this paper.

Thirty six drive-in racks representing the global sale of an Australian manufacturer over three years are then analysed using the improved 2D single model introduced in the companion paper (Gilbert et al., 2013a) under all possible loading scenarios, alternately considering and ignoring the pallet bracing restraints. This paper evaluates the influence of pallet bracing restraints on the ultimate capacity of steel drive-in racks in the down-aisle direction, clarifies the loading scenario(s) governing the design and determines the friction coefficient or the strength of a restraining device required to prevent the pallets from sliding.

2 PARAMETRIC STUDIES

Thirty-six rack configurations, representing the global sale of an Australian manufacturer over three years and designed using industry practice (Dematic, 2006), are analysed using the improved single upright models introduced in the companion paper (Gilbert et al., 2013a). The racks are considered to be 4 pallets deep, with rail beams equally spaced apart along the rack height. The uprights are referred to as "SD" for standard uprights and "RF" for rear flanged uprights, their

Table 1. Rack configurations.

Rack n°	Height (mm)	Nb stories	Design pallet load (kg)	Upright		
				Type	Width (mm)	thk. (mm)
1	3775	2	950	SD	70	1.2
2		3	950	SD	90	1.5
3			1210	RF	90	1.2
4		4	690	RF	90	1.2
5	5025	2	950	SD	90	1.2
6			1210	SD	90	1.2
7		3	690	RF	90	1.2
8			950	RF	90	1.2
9			1210	RF	90	1.5
10		4	950	SD	110	1.5
11			1210	RF	110	1.5
12			1470	RF	125	1.5
13	6275	2	1470	RF	90	1.2
14		3	950	RF	90	1.5
15			1210	SD	110	1.5
16			1470	RF	110	1.5
17		4	430	SD	90	1.5
18			950	SD	110	1.2
19			1210	RF	110	1.9
20			1470	RF	125	1.5
21		5	950	RF	110	1.9
22		6	690	RF	110	1.5
23			950	RF	125	1.5
24	7525	3	1210	SD	110	1.5
25			1470	RF	110	1.5
26		4	430	RF	90	1.2
27			950	RF	110	1.9
28		5	950	SD	125	1.9
29	8775	3	1210	SD	125	1.5
30		4	430	RF	90	1.7
31			950	SD	125	1.9
32			1210	RF	125	1.9
33		5	950	SD	150	1.9
34			1210	RF	150	1.9
35			1470	RF	150	2.4
36		6	950	RF	150	1.9

widths range from 70 mm to 150 mm and their thicknesses from 1.2 mm to 2.4 mm. Table 1 summarises the rack configurations including the rack height, design pallet load, number of stories and upright type. More details can be found in (Gilbert, 2010, Gilbert et al., 2013b).

Specifically, three different single upright models are considered and their member action-to-capacity ratios are used as a measure to quantify the influence of the pallet restraints on the design of drive-in racks:

- Model A considers the pallet bracing restraints and represents the Bay loading scenario A. The model is described in the companion paper (Gilbert et al., 2013a) in its Section 2.2.2.1 and illustrated in its Figure 6.
- Model B considers the pallet bracing restraints and represents the Bay loading scenario B. The model is described in the companion paper (Gilbert et al., 2013a) in Section 2.2.2.2 and illustrated in its Figure 7.
- Model C is based on the current industry practice of neglecting the pallet bracing restraints. The model is similar to Model A at the exception of Step 4 in Section 2.2.2.1 of the companion paper (Gilbert et al., 2013a).

2.1 *Design parameters*

2.1.1 *Base plate to floor connection stiffness*

Base plates are generally bolted to the floor, and the strength and initial rotational stiffness of the base plate to floor connection depend on the axial load in the upright (Godley et al., 1998). Numerical investigations on the non-linear behaviour of a typical storage rack base plate assembly (Gilbert and Rasmussen, 2011) showed that (i) the connection strength is proportional to the upright width, (ii) in the presence of axial load in the upright, the initial rotational stiffness of the base plate to floor connection is proportional to the cube of the upright width and (iii) when no axial load is applied to the upright, the initial rotational stiffness is independent of the upright width.

The rules described above, combined with the test results in (Gilbert and Rasmussen, 2011) and applied to a 125 mm wide base plate assembly, are used in the following sections to determine the initial stiffness and strength of base plate to floor connections as functions of base plate widths. Detailed moment-rotation curves used in the present work are given in Gilbert et al. (2013b).

2.1.2 *Out-of-plumb*

The main international racking specifications (AS 4084, 2012, EN 15512, 2009, RMI, 2008) consider the initial looseness in the member connections as well as the initial out-of-plumb as frame imperfections, which are generally accounted for in the design by means of horizontal forces $F_{out\text{-}of\text{-}plumb}$ applied at each rail beam elevation as,

$$F_{out-of-plumb} = \alpha W \tag{1}$$

where α is the out-of-plumb angle and W is the vertical load applied to the upright by the pallets at the rail beam elevation. The out-of-plumb angle α is typically a function of the number of interconnected bays and the looseness in the portal beam to upright connections. A out-of-plumb angle of 0.0044 rad (about 1/250) is used in the present work. See Gilbert et al. (2013b) for more details.

2.1.3 *Other parameters*

Other design parameters used in the present work, which correspond to some drive-in rack configurations currently commercialised in Australia, are given in Gilbert et al. (2013b). The height of the rack$H$, the number of pallet levels N_s and the cross-sectional area of the upright A_u depend on the studied rack characteristics and are given in Table 1 and Gilbert et al. (2013b).

2.2 *Upright load cases*

According to the draft FEM specification for the design of drive-in racks (FEM 10.2.07, 2010), the load case involving the loading scenario depicted in Figure 5 in the companion paper (Gilbert et al., 2013a) and a fully loaded upright are usually "sufficient to consider the pattern load effects" for the Ultimate Limit State (ULS) design in the down-aisle direction. However, it is currently unclear if a different load case may govern the design. Moreover, in light of the horizontal bracing effect offered by the pallets, the load case involving the loading scenario depicted in in Figure 5 in the companion paper (Gilbert et al., 2013a) and a fully loaded upright may not always be sufficient for the ULS design of the upright.

Consequently, every possible load case is investigated in the present work for the 36 drive-in racks given in Table 1. Second-order geometric analyses are carried out using the general purpose FE software Strand7 (2010). The number of load cases analysed per rack is a function of the number rail beams and is equal to 4^{Ns}, where N_s is the number of rail beam elevations.

2.3 *Ultimate capacity*

For each of the three rack models and each upright load case, the Australasian cold-formed steel structures standard AS/NZS 4600 (2005) is used to calculate the member action-to-capacity ratios of the critical upright. When second order-geometric analyses are used, members subjected to combined axial compression and bending must satisfy the ULS design check in Eq. (2),

$$\frac{N^*}{\phi_c N_c}+\frac{M_x^*}{\phi_b M_{bx}}+\frac{M_y^*}{\phi_b M_{by}}\le 1 \tag{2}$$

where $N*$ is the design axial compression load, and M_x* and M_y* are the design bending moments about the x- (cross-aisle) and y- (down-aisle) axes, respectively, N_c is the nominal axial compression member capacity, M_{bx} and M_{by} are the nominal member bending moment capacities about the x- and y- axes, respectively, ϕ_c and ϕ_b are reduction capacity factors for members in compression and bending, taken as 0.85 and 0.90, respectively. As the present work is concerned with the design of drive-in racks in the down-aisle direction, the bending moment about the down-aisle axis is considered negligible and for the 2D single upright model, Eq. (2) becomes,

$$\frac{N^*}{\phi_c N_c}+\frac{M_x^*}{\phi_b M_{bx}}\le 1 \tag{3}$$

A load factor of 1.4 is used for the pallets to determine the design loads $N*$ and bending moments M_x*. The self-weight of the rack is ignored.

The Direct Strength Method (Schafer, 2006) in Section 7 of the AS/NZS 4600 (2005) is used in the present work to calculate the nominal capacities N_c and M_{bx} of the upright. Specifically, the axial capacity in compression N_c is defined as the lesser of the axial global, local and distortional nominal capacities N_{ce}, N_{cl} and N_{cd}, respectively, as,

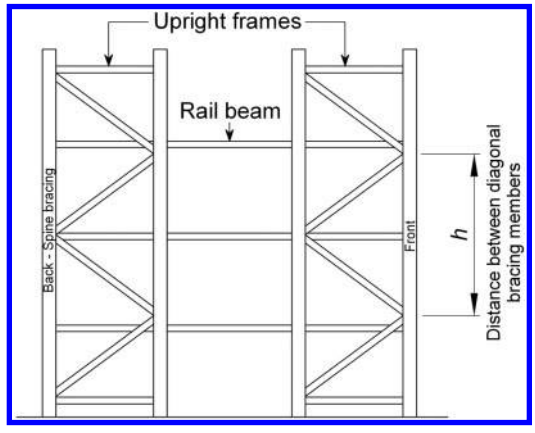


Figure 1. Frame bracing pitch h, unbraced segment.

$$N_c=\min\left(N_{ce},N_{cl},N_{cd}\right) \tag{4}$$

and the nominal bending moment capacityM_{bx} about the x-axis of bending is defined as the lesser of the global, local and distortional nominal moment capacities M_{bxe}, M_{bxl}, M_{bxd}, respectively, as,

$$M_{bx}=\min\left(M_{bxe},M_{bxl},M_{bxl}\right) \tag{5}$$

Specifically, the global nominal capacity M_{bxe} is a function of the bending moment distribution in the upright through the elastic buckling moment M_o,

$$M_o=C_b A_u r_{ol}\sqrt{f_{oy}f_{oz}} \tag{6}$$

where C_b is a coefficient depending on moment distribution in the unbraced segment of the upright,A_u is the gross cross-sectional area,r_{ol} is the polar radius of gyration about the shear centre and f_{oy} and f_{oz} are the elastic buckling stresses for flexural buckling about the y-axes (perpendicular to the symmetry axis) and torsional buckling, respectively.

Detailled rules to determine N_{ce}, N_{cl}, N_{cd}, M_{bxe}, M_{bxl}, M_{bxd} are given in AS/NZS 4600 (2005).

2.3.1 *Effective buckling lengths*

The Australian Standard AS 4084 (2012) recommends effective lengths l_{ey} and l_{ez} for buckling about the y- (down-aisle) and z- (torsional) axes equal to h and 0.7 times h, respectively, where h represents the upright frame bracing pitch, as shown in Figure 1. These values are adopted in the present work.

For each member of the simple upright model, the effective length l_{ex} for buckling about the x-axis (in

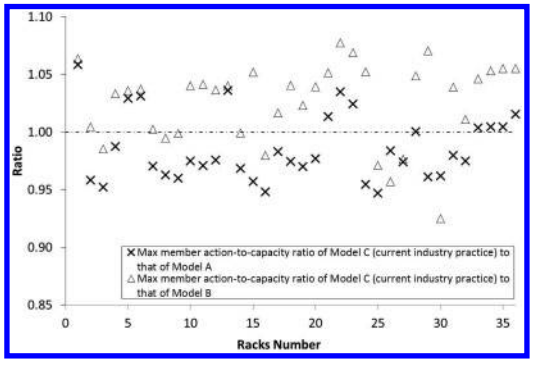


Figure 2. Influence of the horizontal pallet restraint on the action- to-capacity ratio for h = 1,500 mm.

the down-aisle plane) is calculated as (Teh and Gilbert, 2013),

$$l_{ex} = \pi \sqrt{\frac{EI_x}{N_{crb}}} \tag{7}$$

where I_x is the second moment of area about the x axis, and N_{crb} is the elastic buckling load of the upright determined from a rational frame buckling analysis (Teh and Gilbert, 2013).

3 RESULTS

3.1 *Effects of pallet restraint*

In this study, two values for the frame bracing pitch h, being 1,500 mm and 2,000 mm, are considered.

3.1.1 *Frame bracing pitch h = 1,500 mm*

Figure 2 plots the ratios of the maximum member action-to-capacity ratio of Model C (current industry practice) to that of Model A, and to that of Model B, for the 36 racks given in Table 1 having a frame bracing pitch h of 1500 mm. Detailed results can be found in Gilbert et al. (2013b). A ratio greater than 1.0 in Figure 2 indicates that the current industry practice results in uneconomical designs.

Figure 2 shows that for 12 racks out of 36, incorporating the horizontal restraining effect provided by the pallets would provide more economical designs than the current industry practice, with a decrease in the member action-to-capacity ratio of up to 6% (Rack 1). On average for the 12 racks, the decrease is 2%.

For the remaining 24 racks, ignoring the pallet restraints would lead to less conservative designs, with a increase in the member action-to-capacity ratio of up to 7% (Rack 30). On average for the 24 racks, ignoring the pallet restraints increases the design capacity by 3%. This counterintuitive result is mainly due to the effect of the pallet restraints on the design bending moment of the upright under the critical load case. Figure 3 shows the bending moment distribution in the upright for Models A and C, and the coefficient C_b

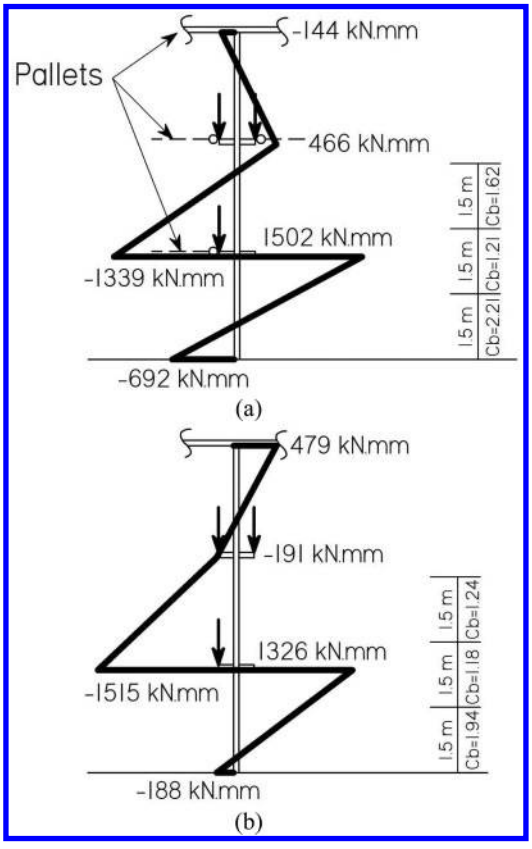


Figure 3. Bending moment distribution for the critical load case for rack 25 for (a) Model A and (b) Model C.

Table 2. Frame bracing pitch h, unbraced segment.

	Model C (current practice)/Model A		Model C (current practice)/Model B	
h (mm)	Average ratio	CoV	Average ratio	CoV
1,500 mm	0.99	0.029	1.03	0.034
2,000 mm	0.99	0.026	1.04	0.016

in Eq. (6), under the critical load case of Rack 25. It can be seen that ignoring the pallet restraints leads to a design bending moment that is 12% less than when considering same, but with similar C_b coefficient.

Table 2 summarises the average maximum member action-to-capacity ratios given in Figure 2.

3.1.2 *Frame bracing pitch h = 2,000 mm*

Figure 4 plots the ratios of the maximum member action-to-capacity ratio of Model C (current industry practice) to that of Model A, and to that of Model B, for the 36 racks given in Table 1 having a frame bracing pitch h of 2000 mm. Detailed results can be found in Gilbert et al. (2013b).

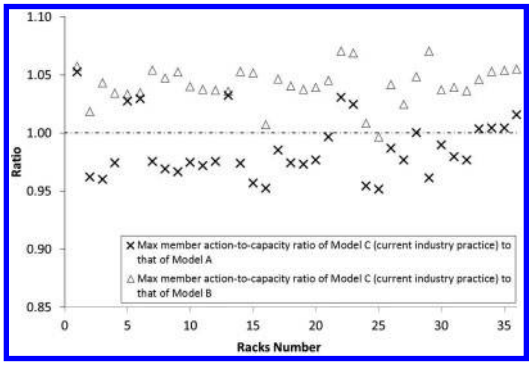


Figure 4. Influence of the horizontal pallet restraint on the action- to-capacity ratio for h = 2,000 mm.

Similar conclusions to those in Section 3.1.1 can be drawn. Results show that for 11 racks out of 36, considering the horizontal restraining effect provided by the pallets would provide more economical designs than the current industry practice, with a decrease in the member action-to- capacity ratio of up to 5% (Rack 1) and an average decrease of 2%. For the remaining 25 racks, ignoring the pallet restraints would lead to less conservative designs, with a maximum increase in the member action-to-capacity ratio of 5% (Rack 25) and an average increase of 3%. Table 2 summarises the average maximum member action-to-capacity ratios given in Figure 4.

3.1.3 *Critical load cases*

When the pallet restraints are considered in the analysis (Models A and B), the load case involving the loading scenario shown in Figure 5 in the companion paper (Gilbert et al., 2013a), which corresponds to a fully loaded rack except for one compartment at the first rail beam elevation, is found to govern the design in general. However, for the 4-storey drive-in racks number 26 and 30, the load case shown in Figure 5 (a) is found to provide an action-to-capacity ratio up to 13% higher than the load case involving the loading scenario shown in Figure 5 in the companion paper (Gilbert et al., 2013a). Despite a lower axial load incurred in the critical upright, the loading scenario induces a buckling length l_{ex} about twice that for the loading scenario shown in Figure 13, and therefore leads to a reduced axial capacity.

When the pallet restraints are ignored in the analysis, the load case involving the loading scenario shown in Figure 5 in the companion paper (Gilbert et al., 2013a) is also found to generally govern the design. However, the load cases shown in Figure 5 (b) for the 4-storey drive-in rack number 4, Figure 5 (c) for the 5-storey rack number 21 and Figure 5 (d) for the 6-storey drive-in racks number 21, 22 and 36 govern the design with an action-to-capacity ratio 2%, 3% and 4.5% higher that the loading scenario shown in Figure 5 in the companion paper (Gilbert et al., 2013a), respectively.

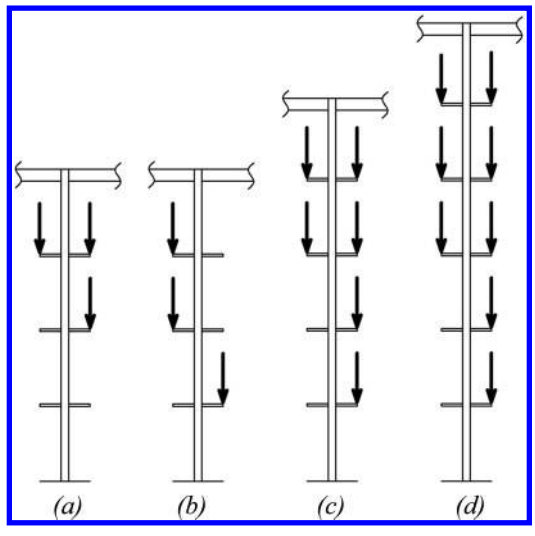


Figure 5. Specific load cases governing the design.

In view of the above results, for ULS design ignoring pallet bracing effects, limiting the analysis to the load case involving the loading scenario shown in Figure 5 in the companion paper (Gilbert et al., 2013a) and a fully loaded rack, would only induce a limited error in the action-to-capacity ratio and may be considered to be "sufficient for considering the pattern load effects".

3.2 *Friction coefficient analysis*

The minimum friction coefficient μ needed to prevent the pallets from sliding on the rail beams is investigated herein for Model A. The friction forces S_f developed between the pallets and the rail beams are extracted from the horizontal reactions at each loaded rail beam elevation of the single upright model. The friction coefficient μ is then calculated as,

$$\mu = \frac{S_f}{W} \tag{8}$$

where W is the axial load applied by the pallets to the upright at the rail beam elevation.

Figure 6 shows the minimum friction coefficient needed to prevent sliding of the pallets found for all loading cases and for the 36 drive-in racks in Table 1. All values in Figure 6 are less than the design static friction coefficient of 0.439 recommended by Hua and Rasmussen (2010) (see companion paper), indicating that, under normal operating conditions, sliding is unlikely to occur between the pallets and the rail beams, and that pallet bracing restraints could be considered in the design of drive-in racks. Moreover, the minimum friction coefficient μ is dependent on the number of stories (or rail beam elevations), as seen in Figure 6. The more the stories, the more likely the pallets are to slide. Results show that, for a given

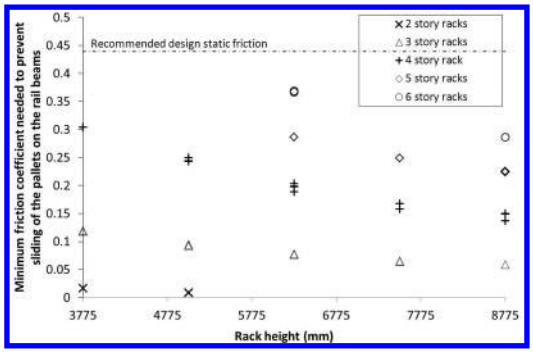


Figure 6. Minimum friction coefficient μ needed to prevent pallets from sliding.

number of stories, the minimum coefficient of friction required to avoid sliding of the pallets decreases somewhat linearly with the height of the rack.

4 CONCLUSIONS

This paper analyses the influence of horizontal bracing restraints provided by the pallets on the design of steel drive-in racks. Using the improved single upright model presented in the companion paper, analyses were run for 36 drive-in rack configurations. All possible loading cases were analysed. Results showed that ignoring the pallet bracing effects in design, as in the current industry practice, usually leads to a less conservative design with an action-to-capacity ratio for the critical upright being reduced in the order of 4%.

The load case involving a fully loaded rack except for one compartment at the first rail beam elevation was found to govern the Ultimate Limit State design of most racks. However, loading scenarios inducing the maximum bending moments were also found to govern the design of some drive-in racks having 4 to 6 storeys, with action-to-capacity ratios up to 5% greater than the previous load case when pallets are ignored.

Results show that under normal operating conditions, the friction coefficient between the pallets and the rail beams is sufficient to prevent sliding of the pallets, and therefore pallets could be considered in the design of drive-in racks.

REFERENCES

AS 4084 2012. Steel storage racking. Standards Australia, Sydney, Australia.

AS/NZS 4600 2005. Cold-formed steel structures. Standards Australia, Sydney, Australia.

DEMATIC 2006. *RAD – User manual,* Sydney, Australia, Dematic, Pty. Ltd.

EN 15512 2009. Steel static storage systems – Adjustable pallet racking systems – Principles for structural design. European Committee for Standardization (CEN), Brussels, Belgium.

FEM 10.2.07 2010. Version 0.12 – Draft – The Design of 'Drive-in' and 'Drive-through' pallet racking. Federation Europeenne de la Manutention, Brussels, Belgium.

GILBERT, B. P. 2010. *The behaviour of steel drive-in racks under static and forklift truck impact forces.* PhD PhD, School of Civil Engineering, The University of Sydney.

GILBERT, B. P. & RASMUSSEN, K. J. R. 2011. Determination of the base plate stiffness and strength of steel storage racks. *Journal of Constructional Steel Research,* 67, 1031–1041.

GILBERT, B. P., TEH, L. H., BADET, R. X. & RASMUSSEN, K. J. R. The influence of pallets on the behaviour and design of drive-in steel storage racks – Part I Behaviour. Fifth International Conference on Structural Engineering, Mechanics and Computation, 2013a Cape Town, South Africa.

GILBERT, B. P., TEH, L. H., BADET, R. X. & RASMUSSEN, K. J. R. 2013b. Determination of the influence of the pallets on the design of drive-in steel storage racks. Research Report CIEM/2013/R04. Centre for Infrastructure Engineering and Management, Griffith University, Australia.

GODLEY, M. H. R., BEALE, R. G. & FENG, X. Rotational stiffness of semi-rigid baseplates. *In:* Yu, W.W. & Laboule, R.A., eds. 14th International Specialty Conference on Cold-Formed Steel Structures, October, 15–16 1998 St Louis, Missouri, U.S.A., 323–335.

HUA, V. & RASMUSSEN, K. J. R. 2010. Static friction coefficient between pallets and beam rails and pallet shear stiffness tests. Research Report 914. School of Civil Engineering, The University of Sydney, Australia.

RMI 2008. Specification for the design, testing and utilization of industrial steel storage racks. Rack Manufacturers Institute, Charlotte, U.S.A.

SCHAFER, B. W. Designing cold-formed steel using the direct strength method. *In:* Laboule, R.A. & Yu, W.W., eds. 18th International Specialty Conference on Cold-Formed Steel Structures 29–27 October 2006 Orlando, Florida. 475–490.

STRAND7 2010. *Using Strand7 – User manual – Release 2.4.4,* Sydney, Australia, G+D Computing Pty Ltd.

TEH, L. H. & GILBERT, B. P. 2013. Second-order elastic analysis based design of drive-in racks. *ASCE Journal of Structural Engineering (in preparation).*

Research and Applications in Structural Engineering, Mechanics and Computation – Zingoni (Ed.)
© 2013 Taylor & Francis Group, London, ISBN 978-1-138-00061-2

Extension of the DSM to welded H profile cross-sections

B. Rossi & Li Y.
University of Liège, Belgium

ABSTRACT: The objective of the paper is to assess the accuracy of current Direct Strength Method (DSM) equations applied to steel structural welded H shapes in axial compression. Commercialised hot-rolled H sections covering IPE, HE, HD, HL, HP, W and UB profiles and made of three grades (235 MPa, 355 MPa and 460 MPa) were treated in (Li & Rossi 2012). This analysis focuses on welded sections made of the same three grades, including sections characterized by local buckling with a significant post-buckling reserve. The finite element model is described. Then, the results of a parametric analysis using the finite element model are reported. The codified resistances are also compared to the numerical results. For each cross-section, the recently developed analytical expressions provided in (Seif & Schafer 2010) for hot-rolled profiles are used to calculate the elastic cross-section local buckling stress. A comparison with CUFSM results is also reported. Then, the possibility to use the concept of DSM for the design of structural welded steel shapes is discussed.

1 INTRODUCTION

In most of the standards (CEN 2005a,b, NAS 2007a AISI 2005), the cross-section capacity of Class 4 sections is assessed using the Effective Width Method (EWM) to account for the effect of local buckling. The method proposes width-to-thickness b/tlimit ratios that each of the cross-section wall has to fulfill to be considered as non-affected by local buckling. The dimensions of the walls affected by local buckling are reduced to their effective parts.

Because of the complexity and limitations of this method – it has been shown that several values of the b/tlimit ratios in Eurocode 3 are frequently misleading and that the assumed support conditions of the plates composing the cross-section is not representative of the interaction between them (Semi- Comp 2007, Seif & Schafer 2009, Li et al. 2011) –, alternative methods have been developed, such as the Direct Strength Method (DSM) for cold-formed thin-walled profiles and the Continuous Strength Method (Schafer 2008, Gardner 2008). The DSM method is based on the assumption that the strength can be predicted using the yield strength to elastic critical load ratio in conjunction with a strength reduction curve. It has gained importance over recent years and the expressions of the strength reduction curves, validated against numerous experimental data for cold-formed thin-walled members, are now suggested in North American and Australian standards (NAS 2007b, SA 1996).

In Li & Rossi 2012, commercialized hot-rolled H sections covering IPE, HE, HD, HL, HP, W and UB profiles and made of three grades (235MPa, 355MPa and 460MPa) were studied. A finite element model was validated against tests results achieved in the frame of the Semi comp (2007) project and used to perform a parametric analysis. The resistance of the cross-sections under pure compression was dominantly governed by yielding. For slender sections, local buckling occurred in the web and involved rotation of the flange – in opposite directions by the same amount – about the line of the flange-web junction sometimes followed by post-buckling reserve. In this analysis, the elastic local buckling stress was calculated using the recently developed analytical expressions of Seif & Schafer (2010), which allow for cross-section slenderness evaluation. It was then possible to derive a DSM strength curve for this range of sections i.e. characterized by slenderness ranging from 0.7 to 1.3.

In Boissonnade et al. (2013), a series of tests results collected in the literature (Semi Comp 2007, Kettler 2008) together with some 400 FE results relative to semi-compact sections (HEA 280, HEAA 220 and HEAA 300) are used to assess the applicability of the design approach called Overall Interaction Concept in which, similarly, a generalized relative slenderness is used to calculate the strength of open and hollow sections via interaction curves.

Presently, welded sections are considered. A geometrically and materially nonlinear analysis using the FE method has been conducted to evaluate the resistance of axially compressed welded H profile cross-sections. The FE model was firstly verified against experimental data and then used to carry a parametric analysis. The combination of flange and web thickness and/or depth therefore led to various kind of interaction between the flange and the web. In the next sections, the FE model is detailed. The local buckling and post-local buckling behavior of short length welded H profiles is described. The numerical strengths are

compared to current Eurocode 3 and DSM predictions. The goal of the analysis is to discuss the opportunity of using the DSM concepts for calculating the resistance of non-compact and slender welded H profile cross-sections i.e. to check the generalization of the slenderness concept as the key parameter to rule the strength via a strength reduction curve.

2 EXPERIMENTAL INVESTIGATIONS

In the project Semi comp (2007), a testing program covering hot-rolled and welded HEAA sections as well as square hollow section (SHS) and rectangular hollow section (RHS) was carried out in the Laboratory for Structural Engineering at Graz University of Technology. Ten stub column tests were carried out between fixed end supports for all different cross-section types and materials i.e. hotrolled HEA260, S235; hot-rolled HEA260, S355; welded HEA260, S235; SHS 180/180/5, S355; RHS 200/120/4, S275. All specimens were welded to a thick steel plate (120mm thick) on both sides to facilitate a uniform loading condition. Both top and bottom compression plates of the testing machine were fully restrained in translation and rotation except the vertical translation of the top plate. The length of the specimens was 900 mm for H sections and 700 mm for tubular sections, based on the principle that the length is sufficiently small to prevent member buckling while long enough to avoid the influence of the boundary conditions. In practice, the length is chosen equal to approximately three times the largest cross-sectional dimension. Tensile coupons, cut from the webs and the flanges, were tested using a RKM testing machine to determine the material stress-strain behavior. The local geometrical imperfection was measured with linear variable displacement transducers for all the specimens while the residual stresses were measured only for one HEAA240 cross-section, in the frame of another experimental campaign carried out at the Materials and Structures Laboratory of the University of Liège. The axial load and vertical displacements were recorded during the stub column tests. For that purpose, four W200 inductive displacement gauges were used. Two welded sections were tested. The average measured crosssection dimensions $h \times b \times tw \times tf$ were 259.3 mm × 244.4 mm × 6 mm × 10 mm, where $h$is the web height, b is the flanges width and tf and tw are the flange and web thicknesses respectively. The ultimate loads for the two welded specimens are provided in Table 1.

Figure 1 shows the failure mode for the specimen A24-2.

3 FE MODEL

In the present work, a nonlinear FEM software FineLg (2012) has been used to model the aforementioned stub column tests. In this model, special attention was paid to the modeling of the initial geometric imperfection, residual stress distribution and interaction between flanges and web.

Table 1. Comparison of experimental and numerical results for stub column tests.

Specimen	FExp[kN]	FFEM[kN]	FFEM/FExp
A24-1	2135	2038	0.955
A24-2	2025	2038	1.006
		Mean	0.982
		CoV	0.026



Figure 1. Failure mode (yielding) for a loaded specimen.

3.1 *Geometry and boundary conditions*

The averaged measured geometrical dimensions were used in the FE model intended for calibration against the tests.

One way to simulate the boundary condition is to fix the bottom part of the specimen while the top is allowed for free translation along the stub column length direction. In the model, a thick rigid elastic plate is fixed to the specimen on both sides and the axial load is applied via the plates. The plates stiffness ensures that the movements of the nodes composing the profile cross-section occur simultaneously and allows even distribution of the concentrated load applied at the centroid of the plate. The plates prevent the cross-sectional deformation at both ends but allow the rotations. So, in the FE model, the boundary condition is a pinned-end condition.

3.2 *Cross-section discretisation*

Shell elements were employed to discretize the model. The QSCRA element, a general purpose shell element

with four nodes and reduced integration to form the element stiffness (S4R), was used to simulate the web and flanges.

Since a common node was used for the web and flange modelling, there exists an overlapped area of $tf \times tw/2$ mm2. Also, the area of the weld is neglected. The weld geometry is considered as being an isosceles triangle, the height of which is the minimum between $1,5\,t1$ and $1.2t2$ where $t1$ and $t2$ are the thicknesses of the thicker and the thinner plate respectively (Davids & Hancock1986, Welding Handbook 1976, GB50017 2003). In order to model this, an additional node is placed within the web height, at the exact vertical position of the centroid of the weld. It bears an addtional beam element, oriented in the longitutional direction, with an area that equals the welded area minus the overlapped area.

Another important aspect in the modeling of the H-shaped profiles concerns the development of local plate buckling. The zone at the intersection of the flange and the web remains unaffected by the extent of local buckling. Therefore, in the model, a truss system has been added in the web-flange junction zone meant to keep this zone rigid (Boissonnade & Somja 2012, Li & Rossi 2012).

3.3 *Local geometrical imperfections*

FE models generally include imperfections that correspond to the lowest buckling mode shape. Usually, the imperfections are introduced as eigenmodes that are scaled to a proper magnitude, Johannsson et al. (2007). This procedure may sometimes be lengthy to achieve if not implemented in the code. In this sense, it may be simpler to use the pre-knowledge of what are the possible instability modes and therefore to use a sinusoidal shape to represent the initial deformation, CEN (2005). Using this approach, the amplitude of the deformation for each plate element is chosen individually. The literature and measurements performed during the Semi Comp project indicates that, in welded sections, the geometric imperfection is a combination of overall twisting and plate ripple (Figure 2). This shape is due to shrinkage further to welding (Davids & Hancock 1986, Welding Handbook 1976, Kettler 2008). According to this, a half wavelength sine is used in the flanges and a sine is used in the web (as depicted in Figure 3). The amplitude is set to $h/200$as suggested in (CEN 2005b, Semi Comp 2007), where $h$is the clear width of the web or flange.

3.4 *Material stress-strain curve and residual stress*

The adopted material model is a perfectly elasticplastic model (CEN 2005b). The Young's modulus E and the yield strength fy are obtained from the tensile coupon tests perfromed during the Semi Comp project. Residual stresses are caused by the welding process. Based on recommendations (Boulton 1936, Weck, R. 1949, Tall & Rao 1961, Rao et al 1964, ECCS 1984a,b, Davids & Hancock 1986 and BSK 1999), a rectangular

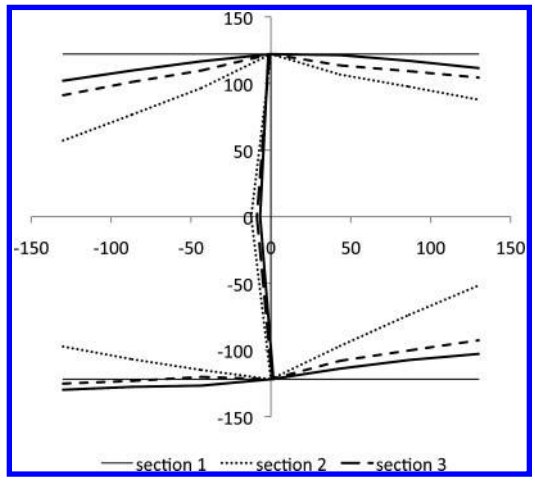


Figure 2. Measured geometrical imperfection (amplified by 20) for 3 sections (section 1: front, section 2: mid-length, section 3: back) along the profile length.

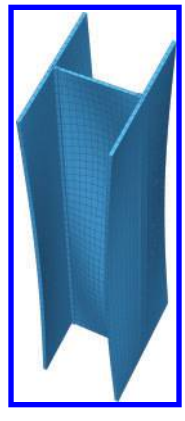


Figure 3. Local geometrical imperfection shape introduced in the FE model.

bloc distribution of the longitudinal residual stresses is considered in the FE model, as shown in Figure 4. The magnitude is assumed to be the yield strength at the junction of the flange and web, the rest of the distribution is calculated on the basis of the principle of autoequilibrium in the profile cross-sections.

3.5 *Comparison of numerical and experimental*

In Figure 5, the results of the linear elastic analysis, the Materially Nonlinear Analysis (MNA), and the Geometrically and Materially Nonlinear Analysis (GMNIA) with or without local geometrical imperfection and residual stresses respectively are provided together with the test results for the specimen A24-2.

It can be seen that the load-displacement curves coincide in the elastic range indicating that the FE model has the same stiffness as the tested specimen. This proves the effectiveness of the representation of the welded area.

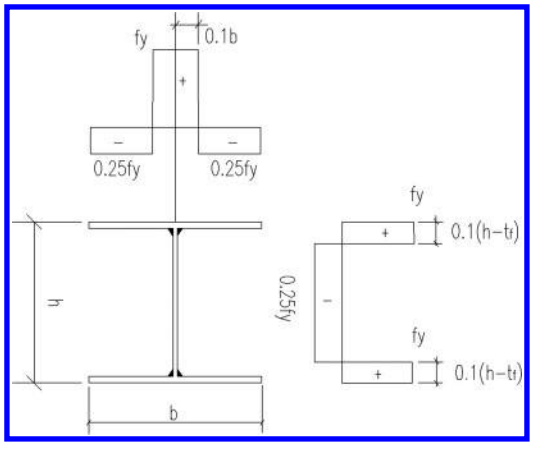


Figure 4. Assumed residual stress distribution and amplitude in the FE model.

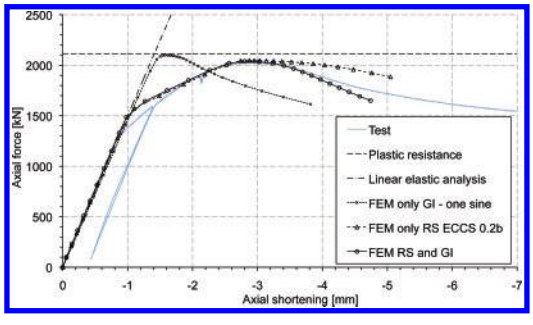


Figure 5. Finite element analysis of specimen A24-2.

Also, it can be noted that the residual stresses influence the axial stiffness by making the curve departs from linearity at an earlier point (the curve labeled with white triangle represents the model without local geometrical imperfection).

The plate geometric imperfections and residual welding stresses have a significant influence on the ultimate load. For the two tests, good agreement has been achieved between the numerical and experimental results (Table 1).

4 PARAMETRIC ANALYSIS

The parametric study firstly examines H profiles geometries taken from European, British and American catalogues. In total, 157 geometries covering IPE, HE, HD, HL, HP, W and UB profiles and made of three grades (235 MPa, 355 Pa and 460 MPa) have been considered resulting in 471 FE models. The FE model is similar to the one discussed in the previous paragraphs but with the following distinctions: (1) The cross-section dimensions are taken as the nominal ones (CEN 2005b); (2) The young's modulus E equals 210000 $N/mm2$and the yield strength $fy$is the nominal one. Second, the section geometries were changed by decreasing the thickness of the flange and web to

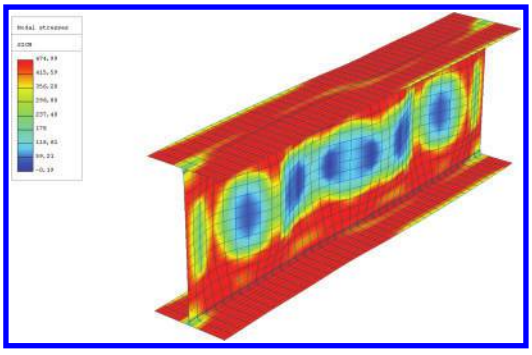


Figure 6. Failure mode: HE600A with a web thickness of 6 mm instead of 12 mm. The flanges remain straight and parallel to each other.

50% of their values in the catalogue resulting in a total additional number of simulations of 715. The range of cross-sections studied involves compact sections and slender sections (in the sense of Eurocode 3). It is extremely improbable that designers would select sections for which the web is thicker than the flange plates; a few of such sections are nevertheless included in the present analysis. This constitutes a first step into a more comprehensive parametric analysis to be performed in the future.

Looking at the results, it can be seen that different failure modes were tackled. Either the full plastic resistance was attained (yielding of the whole crosssection) or local buckling prevents the development of it. In this case, either the buckling mode involves rotation of the flange – in opposite directions by the same amount – about the line of the flange-web junction sometimes followed by post-buckling reserve, or, in sections with strong flanges, the local buckling develops in the web and the flanges remain parallel to each other (very little deformation). Loading in the post-buckling domain results in the attainment of the ultimate load with a significant post buckling reserve.

4.1 *Assessment of current design guidance*

The results of the simulations have been compared to the resistances predicted by the Eurocode 3 using the EWM. The usual plate slenderness limit ratios and approximation of critical stress assuming simple support conditions in Eurocode 3 provide reliable predictions: the codified-to-numerical predictions yield an average of 1.03 and coefficient of variation (CoV) of 0.06.

Nowadays, numerical advanced calculation of the elastic cross-section buckling stress is possible using software such as CUFSM or THIN-WALL for example. Herein, the expressions of $k$for hot-rolled H sections under pure compression suggested in Seif & Schafer (2010) was used to calculate the elastic local buckling stress and the cross-section slenderness for the geometries for which the normalized dimension $(h/tw) \times (2tf/b)$ ranges from 1.8 to 10.94 (the range for which the empirical expressions of the local plate

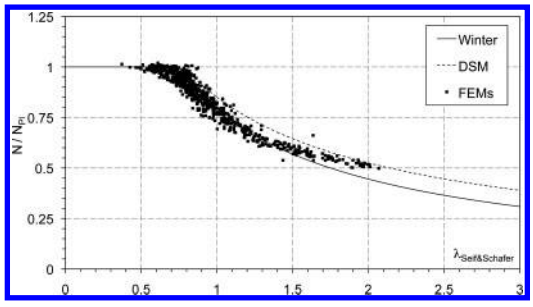


Figure 7. FEMs and DSM predictions versus Seif & Shafer (2010) slenderness.

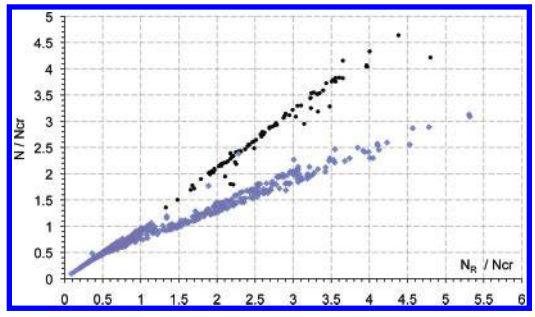


Figure 8. FEMs predictions versus predictions obtained using equations (1) (normalized by the critical load).

buckling coefficient k was developed). Even though it is not used as intended, the DSM equations NAS (2007b) were used to evaluate the strength using the (Schafer & Seif 2010) slenderness. It yields relatively good predictions as well, with an average of 1.05 and CoV of 0.06. For this range of geometries, the numerical failure loads normalized by the yield load Npl are depicted in Figure 7 together with the current DSM predictions. A comparison of the numerical loads with those computed using Winter's effective width formulas is also presented.

In this analysis, sections presenting very thick flanges are also included. When the web is much more slender than the flange, the DSM approach is overly conservative. For example, the following cross-section $460 \times 191 \times 4.95 \times 16$ with slender web and strong flanges is characterized by a normalized dimension $(h/tw) \times (2tf/b)$ of about 15 and has a strength equal to $0.87 \times$ NPl. Whereas, the section $450 \times 304 \times 7.6 \times 5.4$ (of approximately the same slenderness if calculated with Schafer & Seif expressions) has a strength equal to $0.52 \times$ NPl. For these geometries i.e. for which the normalized dimension ranges from 10.94 to 23.41, the elastic critical stress evaluated using Seif & Schafer (2010) expression is always underestimated. The elastic cross-section buckling stress was thus recalculated using the software CUFSM. In these cases, there exists a substantial post local buckling reserve after the web buckling leading to yielding in the flanges, with little flange deformation. As expected, the current DSM predictions are overly conservative (DSM-to-numerical predictions average = 0.75; CoV = 0.16).

In fact, for the whole range of sections corresponding to $(h/tw) \times (2tf/b)$ greater than 10.94, it is advised to evaluate the cross-section strength using:

$$N_R = 2bt_f f_y + h_{clear} t_w \sigma_{cr}, \quad (1)$$

where σ_{cr} is the elastic critical local buckling stress related to the web,

$$\sigma_{cr} = k \frac{\pi^2 E}{12\left(1-\nu^2\right)} \left(\frac{t_w}{h_{clear}}\right)^2, \quad (2)$$

and h_{clear} = the clear web height, E is Young's modulus of elasticity, ν is Poisson's ratio, and k is the local plate buckling coefficient, which accounts for the boundary conditions and loading (for this case, k is assumed to be equal to 4.0 i.e. simply supported compressed inner element). The numerical resistance versus the resistance obtained with equations (1) for this range of sections (strong flanges, bisector of the first quadrant angle, $(h/tw) \times (2tf/b) > 10.94$) together with the other group of sections ($1.8 < (h/tw) \times (2tf/b) < 10.94$) is depicted in Figure 8.

5 CONCLUSIONS

In this paper, a geometrically and materially nonlinear analysis using the FE method has been conducted to evaluate the resistance of axially compressed welded H profile cross-sections. The FE model was firstly verified against experimental data and then used to carry a first parametric analysis. Commercialized geometries covering IPE, HE, HD, HL, HP, W and UB profiles and made of three grades (235MPa, 355MPa and 460MPa) are considered. Then, the flange and web thicknesses are varied. The numerical results are then compared to Eurocode 3 predictions and predictions using the Direct Strength method established for cold-formed thin walled profiles. The application of the DSM equations in conjunction with Seif & Schafer (2010) expressions of the slenderness to predict the resistance is seen to be appropriate for sections with normalized dimension $(h/tw) \times (2tf/b)$ ranging from 1.8 to 10.94. For sections with strong flanges characterized by local buckling of the web (little deformation of the flanges) and yielding of the flanges in the post local domain, another approach seems to be required. In these cases, preliminary conclusions show that the strength can be predicted by adding the flange plastic resistance and the web critical elastic resistance, which is basically the concept underlying the Eurocode 3 EWM method.

ACKNOLEDGEMENT

The authors are very grateful for the financial support from ArcelorMittal. B. Rossi is supported by the

National Fund for Scientific Research in Belgium. Prof. Boissonade is acknowledged.

REFERENCES

AISC 2005. ANSI/ASIC 360-05:Specification for structural steel buildings. American Institute of Steel Construction, Chicago, USA.

Boulton N. and Lance M. 1936. *Residual stresses in arcwelded plates*, Proc. Inst. Mech. Eng. 61.133, London.

Boissonnade, N., Somja, H. 2012.Influence of Imperfections in FEM Modeling of Lateral Torsional Buckling. *Proceedings of the Annual Stability Conference*, Structural Stability Research Council, Grapevine, Texas.

BSK 1999, Swedish design rules for steel structures. Boverket. CEN2005a. Eurocode 3: Design of steel structures, Part 1-1: General rules and rules for buildings (EN 1993-1-1), CEN (Committee of European Normalization), Brussels.

CEN2005b. Eurocode 3: Design of steel structures, Part 1–5: Plated structural elements (EN 1993-1-5), CEN (Committee of European Normalization), Brussels.

Davids A. & Hancock G.J. 1986. Compression tests of short welded I-sections. *Journal of Structural Engineering.* 112:960-976.

ECCS1984a. European Convention for Constructional Steelwork ECCS (1984). *Ultimate limit state calculation of sway frames with rigid joints*. Technical Committee 8 – Structural Stability Technical Working Group 8.2 – System. Publication No. 33.

ECCS1984b. European Convention for Constructional Steelwork ECCS (1984). *Manual on Stability of Steel Structures*. Technical Committee 8 –Publication No. 22

FineLg2012. Non-linear finite element analysis program " FINELg", User's Manual, version 9.3, ArGEnCo Department, University of Liege, Greisch Info A.A., Liege, Begium.

Gardner L. 2008 The continuous strength method. Proc. Institution of Civil Engineers: Structures and Buildings, 161(3): 127–133.

GB 50017-2003. Code for design of steel structures. Beijing: China Architecture & Building Press (In Chinese).

Johannsson,J. Marquoi, R. Sedlacek,G. Mulller, C. & Beg, D. 2007. Commentary and Worked Examples to EN 1993-1-5 : Plated Structural Elements. JRC-ECSS Joint Report, Luxembourg.

Kettler, M.2008. Elastic- Plastic Cross-Sectional Resistance of Semi-Compact H and Hollow Sections. *PhD thesis*. Institute for Steel and Shell Structures. Graz University of Technology.

Li, Y., Rossi, B., & Jaspart, J.P. Extension of the direct strength method to hot-rolled profile cross-sections. In *Proceedings of the 6th European Conference on Steel and Composite Structures.* Budapest, august 31- September 2, 2011, pp. 1911–1916.

Li, Y. & Rossi, B. 2012. Finite element model for the extension of the direct strength method to hot-rolled profile crosssections", *Proceedings of the 12th Nordic Steel Construction Conference,* (Eds.: Laszlo D. etc.), Oslo, Norway, 1911–1916.

NAS2007a. North American specification for the design of cold-formed steel structures. *American Iron and Steel Institute*. Washington (DC).

NAS2007b. North American Specification. Appendix 1: Design of cold-formed steel structural members using the Direct Strength Method: supplement to the North American specification for the design of cold-formed steel structures. *American Iron and Steel Institute*, Washington (DC), 2007.

RFCS2007. Research Project *Semi-Comp: Plastic member capacity of semi-compact steel sections-a more economic design*, Final report, RFCS-Steel RTD (Contract RFSCR-04044).

Rao, N. Estuar, F. & Tall, L.1964. Residual stresses in welded shapes. The Welding Journal, Vol 43, July 1964, p. 295-s, Publication No. 241 (64-4)" .Fritz Laboratory Reports. Paper 64.

SAA1996. Standards Association of Australia. *SAA steel structures code. AS4100*, Sydney, Australia.

Schafer, B. 2008. Review: The Direct Strength Method of coldformed steel member design. *Journal of* Constructional Steel Research. 64(7–8): 766–778.

Seif, M. & Schafer, B.W. 2009. Finite element comparison of design methods for locally slender beams and columns. *SSRC Annual Stability Conference*.

Seif, M. & Schafer, B. W. 2010. Local buckling of structural steel shapes. *Journal of Constructional Steel* Research. 66(10): 1232–1247.

Tall, L. & Rao, N 1961. Residual stresses in welded plates, presented at *the Fall Meeting of the AWS in New York*, (April 1961). Published in *the Welding Journal*, (October 1961), Reprint No. 194 (61–20)" (1961). Fritz Laboratory Reports.

Weck, R. 1949. Residual stresses due to welding. *The Welding Journal*. 28(1) : 9-s.

AWS1976. Welding Handbook. Vol.1-Fundamental of Welding, 7th edition, American Welding Society, Miami, USA.

Research and Applications in Structural Engineering, Mechanics and Computation – Zingoni (Ed.)
© 2013 Taylor & Francis Group, London, ISBN 978-1-138-00061-2

On the strength of T-section columns

F. Sena Cardoso & K.J.R. Rasmussen
School of Civil Engineering, The University of Sydney, Sydney, Australia

ABSTRACT: The paper concerns hot-rolled T-section members and their failure behaviour under concentrically applied load. The paper first calibrates an accurate shell element Finite Element Model (FEM) against tests on steel T-section columns, and subsequently uses the model to determine the strength of several series of T-sections covering a wide range of cross-section geometries and column lengths. The paper then compares the numerical strengths obtained and test strengths with strength predictions by the Australian and European specifications for hot-rolled and fabricated steel structures, and suggests more accurate design approaches than those currently available.

1 INTRODUCTION

Despite the fact that T-sections are readily available commercially and can be easily obtained by cutting standard I-sections through the middle of the web, the failure behaviour of these members when subjected to a compressive force is still not fully understood as corroborated by the numerous different design approaches in various national specifications for steel structures.

Several features of T-sections contribute to a non-standard buckling and post-buckling behaviour and partly explain the non-existence of a uniform design methodology for T-section members.

T-sections feature negligible warping constants (I_w) derived only from secondary warping and small torsion constants (J), the combination of which leads to a weak resistance to torsion. Consequently, the failure mode commonly involves torsion.

On buckling behaviour, T-section columns are singly symmetric and hence, critical overall buckling modes are the flexural buckling mode in the plane of symmetry and the flexural-torsional buckling mode (coupled flexural about the symmetry axis and torsion about the shear centre).

Furthermore, when the flange and web elements are equal in width and thickness, the local buckling mode is essentially the same as the torsional buckling mode. Conversely, when the thickness of the flanges and web differ or for very slender component plates, the local buckling mode may involve plate flexure.

Because of the resemblance between the torsion and local buckling modes, care needs to be taken when designing T-section (or angles or cruciform section) columns in order to avoid taking into account the torsional/local buckling mode twice in strength predictions.

On the post-buckling behaviour, slender T-sections axially loaded are affected by the stress redistribution associated with local buckling, which leads to a shift of the effective centroid and induces bending when the column is loaded between pinned ends.

Both the buckling and post-buckling behaviour of a T-section column under compression are discussed in detail in (Sena Cardoso and Rasmussen, 2013).

2 FINITE ELEMENT MODEL (FEM) AND PARAMETRIC STUDY

2.1 *The model*

Because of the limited number of experimental tests available on T-section columns, a FEM was calibrated using available test data and subsequently used to perform a comprehensive parametric study of the strength of a wide range of T-section geometries. In all cases, the column was assumed to be pinned at the ends with respect to both principal axes and loaded through the geometric centroid.

The general purpose commercial finite element package ABAQUS was used for the finite element simulations. It is generally accepted that shell-element-based inelastic large displacement analysis can accurately predict the behaviour and ultimate capacity of structures undergoing local instability provided geometric imperfections and residual stresses are incorporated in the analysis (Bakker and Peköz, 2003, Sarawit et al., 2003). Thus, and considering the remarks made by Schafer (Schafer et al., 2010), T-section columns were modelled using S8R shell-elements. This type of element is available from the ABAQUS library and consists of an 8-node doubly curved thick shell with reduced integration. It employs quadratic shape functions and assigns six degrees of freedom per node. The default Simpson's rule was used considering five integration points through the thickness of the element and assuming a homogeneous cross-section. The mesh



Figure 1. Finite Element Model of a T-section column, a) undeformed shape and b) deformed shape of first buckling mode.

had no elements with width-to-thickness ratios greater than four.

To materialize the prescribed boundary conditions, two rigid plates were attached to each end of the T-section column and a reference point axially coincident with the geometric centroid of the T-section was assigned to each rigid plate. At one reference point, the three translational and the twisting degrees of freedom where fully restrained while at the other reference point, the two transverse translational and the twisting degrees of freedom were fully restrained.

Additionally, the described setup does not prevent secondary warping and thus the warping degree of freedom is deemed unrestrained at both ends. At the axially unrestrained end, a point load is applied at the reference point in order to simulate a concentric compression load. An example of the developed FEM is shown in Figure 1.

As for the hot-rolled steel material, the stress-strain curve was chosen as elastic-perfectly plastic being defined by Young's modulus (E) and yield stress (f_y). The following sections details how both residual stresses and geometric imperfections were incorporated in the FEM.

2.2 *Calibration*

The FEM was calibrated by comparing the results of (i) elastic buckling analyses to the global buckling loads and modes obtained from classical theory and (ii) ultimate strength analyses with the test strengths reported in (Kitipornchai and Lee, 1986).

Three cross-sections were tested by Kitipornchai and Lee. The sections were obtained by cutting three I-sections lengthwise through the centre of the web so as to produce two T-sections for each length of I-section, resulting in a total of six T-section specimens. The cross-section dimensions and column lengths are shown in (Kitipornchai and Lee, 1986). The measured values of Young's modulus and yield stress were 214 GPa and 300 MPa respectively.

Elastic buckling analyses were performed on the tested columns ignoring geometric imperfections and residual stresses. The first two buckling modes and loads obtained using ABAQUS were compared with the ones obtained from classical theory, showing that the FEM predicts the 1st and 2nd buckling loads to within 2.6% and 1.6% error, respectively. This degree of accuracy was deemed acceptable.

The residual stresses incorporated in the non-linear inelastic analyses were based on the ECCS I-section model (ECCS, 1976) where in this study the peak residual stress (σ_r) was taken as $0.3f_y$. When the I-section model is applied to a T-section, a non-zero moment results which causes bending in the plane of symmetry and a change in residual stress pattern, see (Sena Cardoso and Rasmussen, 2013) for details. These effects were included in the numerical model.

Imperfections were also included for deflections in the direction perpendicular to the web and twist rotations. These imperfections were incorporated by scaling the flexural-torsional buckling mode obtained from a linear buckling analysis by scaling factors of L/2000, L/1750 and L/1500. The resulting ultimate loads are compared with the experimental ultimate loads in (Sena Cardoso and Rasmussen, 2013).

Overall, it was concluded that the best agreement was obtained for a scale factor of L/2000. However, the ultimate loads are not strongly dependent on the magnitude of flexural-torsional imperfection and to comply with Bjorhovde's survey, which found that the mean minor axis geometric imperfection of rolled I-sections is L/1470 (Bjorhovde, 1972), the scale factor of L/1500 was chosen for generating imperfections in the shape of the flexural-torsional buckling mode in the parametric study. These were in addition to the residual stresses and associated imperfections in the plane of symmetry mentioned above.

2.3 *Parametric study – Methodology*

Two series of parametric studies were conducted, referred to as the N- and M-series. In the N-series, three generic cross-sections were selected to cover a wide range of geometries by changing the widths of the flange and web elements and assuming the same thickness for both flange and web, whereby $k_2 = T_w/T = 1$. Two cross-sections were chosen so that H/B=2 ($k_1 \cong 4$) and 1/4 ($k_1 \cong 0.5$), where B and H are the total flange width and the web width, respectively. The third section was chosen such that $I_x = I_y$, which implied equal flexural buckling stresses for buckling about the x- and y-axes. For each cross-section, four values of thickness were selected so as to obtain the values of the ratio N_Y/N_T ($I_w = 0$) of 0.5, 1.0, 1.5 and 2.0, where N_Y is the squash capacity ($A.f_y$) of the section and N_T ($I_w = 0$) is the torsional buckling load ignoring secondary warping.

For each cross-section, in order to determine the column strength curve, a minimum of five lengths were selected corresponding to normalised flexural slenderness values of $\lambda_e = 0.25$, 0.50, 1.00, 2.00 and 4.00, where the normalised flexural slenderness is given by:

$$\lambda_e = \max\left\{\sqrt{\frac{N_Y}{N_{Fx}}}, \sqrt{\frac{N_Y}{N_{Fy}}}\right\} \quad (1)$$

For some cross-sections, additional short lengths were chosen in order to determine the column strength

curve when plotted against the normalised global slenderness (λ_r) given by,

$$\lambda_r = \max\left\{\sqrt{\frac{N_Y}{N_{Fx}}}, \sqrt{\frac{N_Y}{N_{FT}}}\right\} \quad (2)$$

The M-series T-sections were chosen as one half of a selection of common Australian hot-rolled I-sections (OneSteel, 2011). Five cross-sections were chosen and modelled by ignoring the rounded transition between the web and flange elements. The column lengths for each cross-section were chosen in a similar manner as for the N-series T-sections. The cross-section geometry, column lengths, geometric properties, elastic buckling loads, column slenderness values and key ratios are shown in (Sena Cardoso and Rasmussen, 2013) for the Series N and M T-section columns.

For all Series N and M models, the assumed values of Young's modulus (E) and yield stress (f_y) were 210 GPa and 355 MPa respectively.

2.4 *Parametric study – Results*

Two separate numerical analyses were performed using ABAQUS for each of the aforementioned T-section columns, namely:

1 An elastic eigenvalue buckling analysis that provided the deformed shape of the flexural-torsional mode for implementing the geometric imperfection in this mode in the subsequent non-linear analysis.
2 A geometric and material non-linear failure analysis that used the modified Riks method including the effects of geometric imperfections and residual stresses. (The modified Riks method employs, in each step, proportional loading, solving simultaneously for both loads and displacements. ABAQUS uses the arc length along the static equilibrium path in the load-displacement space to measure the progress of the solution. (Simulia, 2011)).

The ultimate load (N_u) and the prominent mode of failure observed for each specimen are presented in (Sena Cardoso and Rasmussen, 2013).

3 DESIGN PROVISIONS

3.1 *General*

This section compares strength predictions obtained using the provisions of the Australian Standard AS4100 (AS4100, 1998) and Eurocode3 Part 1.1 (EN1993-1-1, 2005) with the ultimate strength data obtained from the parametric study described in Section 2.4 and experiments by Kitipornchai and Lee (Kitipornchai and Lee, 1986). The design approaches adapted in the two specifications are substantially different as will be highlighted in the following sections, which also propose improvements to existing provisions.

The two main difficulties encountered in formulating design provisions for T-sections are:

1 The cross-section deformations of the local and torsional buckling modes are similar, albeit the corresponding half-wavelengths may be different, as discussed in (Sena Cardoso and Rasmussen, 2013) and hence, strength predictions are conservative if both modes are accounted for through effective area and flexural-torsional buckling calculations.
2 When ignoring secondary warping ($I_w = 0$), as is customary in design, the critical buckling stress becomes the pure torsional buckling stress ($\sigma_{cr,T}$) in the limit $L \to 0$, implying a non-zero column slenderness of $\lambda_r = \sqrt{\sigma_y/\sigma_{cr,T}} \neq 0$. As a result, the design stress is less than the yield stress (σ_y) in the limit $L \to 0$. This is in contrast to designing for flexural buckling where $\sigma_{cr,Fx} \to \infty$ in the limit $L \to 0$, so that $\lambda_r = \sqrt{\sigma_y/\sigma_{cr,Fx}} \to 0$ and the design stress becomes the yield stress as required.

The abovementioned design specifications present different approaches to addressing these difficulties, or not.

3.2 *AS4100*

According to the Australian Specification for steel structures (AS4100, 1998), the strength of a concentrically loaded column is given by

$$N_c = \alpha_c \cdot A_e \cdot f_y \quad (3)$$

where α_c, A_e and f_y represent the geometric slenderness reduction factor, the effective area of the cross-section and the nominal yield stress, respectively.

The first variable (α_c) reflects the effect of flexural buckling on the member capacity as well as the distribution and magnitudes of the residual stresses for standard Australian sections. This parameter is function of the *flexural* geometric slenderness ratio (L/r), yield stress and section type. The second variable (A_e) is obtained by incorporating the effect of local buckling through the effective width methodology in determining the net area.

The ratios (N_u/N_c) between the experimental or numerical ultimate strengths and the AS4100 predictions are presented in (Sena Cardoso and Rasmussen, 2013), including the statistics of the same ratio. The mean value and CoV of the ratio are 1.12 and 0.170, respectively, while the minimum and maximum values of the ratio are 0.73 and 1.67, respectively. This implies a generally conservative design approach with a relative small scatter, except for a few particularly slender cross-sections with seriously low ultimate strengths. Sorted statistics for non-slender ($A_e/A = 1$) and slender ($A_e/A < 1$) sections were also presented in (Sena Cardoso and Rasmussen, 2013) from which followed that the AS4100 procedure is slightly more accurate for non-slender than slender sections. The fourth set of statistics exclude slenderness values (λ_e) less than 0.15. Since the mean and CoV are nearly unchanged from the statistics including all slenderness values,

1.08 and 0.153 respectively, it follows that the AS4100 procedure works equally well for columns of short and intermediate to long lengths.

Using the 4th set of statistics (excluding columns with $\lambda_e < 0.15$) and denoting the mean and CoV of the N_u/N_c-ratio by P_m and V_P, respectively, in conjunction with the LRFD framework for the dead and live load combination, the resistance factor is calculated as $\varphi = 0.88$ using,

$$\phi = 1.48\, M_m F_m P_m\, e^{-\beta_0 \sqrt{V_M^2 + V_F^2 + V_P^2 + V_G^2}} \tag{4}$$

where values of $M_m = 1.1$, $V_M = 0.1$, $F_m = 1.0$, $V_F = 0.05$, are assumed (Ellingwood et al., 1980). Equation (4) is derived on the basis of the load combination $G = \gamma_D D_n + \gamma_L L_n$ using $\gamma_D = 1.2$ and $\gamma_L = 1.6$ as per the ASCE-7 Standard (ASCE, 2010) and assuming a ratio (D_n/L_n) of nominal dead to nominal live load of 1/3. Using $V_D = 0.1$ and $V_L = 0.25$, the CoV of the load effect is obtained as $V_G = 0.19$. Consistent with the calibration of the AISC-360 Specification, the target reliability index is chosen as $\beta_0 = 2.6$.

The calculated value of resistance factor ($\varphi = 0.88$) is close to the value of 0.9 prescribed in AS4100.

3.3 *Eurocode 3*

According to Eurocode 3, Part 1.1 (EN1993-1-1, 2005), the nominal strength of a concentrically loaded column is given by,

$$N_{b,Rk} = \chi\, A_{eff}\, f_y \tag{5}$$

where χ, A_{eff} and f_y represent the geometric slenderness reduction factor, the effective area of the cross-section and the nominal yield stress, respectively. The reduction factor χ depends on the non-dimensional slenderness $\bar{\lambda}$ defined by,

$$\bar{\lambda} = \sqrt{\frac{A_{eff} \cdot f_y}{N_{cr}}} \tag{6}$$

where N_{cr} is the critical elastic buckling load, taken as the lower of the flexural (N_{Fx}) and flexural-torsional (N_{FT}) elastic buckling loads. In this study, the flexural-torsional buckling load (N_{FT}) has been determined using classical Timoshenko theory with I_w taken as zero. EN1993-1.1 specifies column curve 'c' for both the flexural and flexural-torsional buckling strength calculations of T-sections.

For slender cross-sections, EN1993-1.1 requires calculation of the effective centroid and the eccentricity between the effective and gross section centroids. In singly and non-symmetric cross-sections, the eccentricity causes overall bending in the plane of symmetry and accordingly, EN1993-1.1 requires the column to be designed as a beam-column. This approach is in contrast to AS4100, which does not require this effect to be considered. To enable a direct comparison between the column strength predictions of the various specifications, the effect of the shift of the effective centroid in slender T-sections is ignored in this paper.

The ratios ($N_u/N_{b,Rk}$) between the experimental or numerical strengths to the EN1993-1.1 strength predictions are again shown in (Sena Cardoso and Rasmussen, 2013). The mean and CoV of the ratio are 1.60 and 0.400, respectively, suggesting a very conservative design approach of poor accuracy. When considering only slender cross-sections, the mean and CoV change slightly to 1.62 and 0.403, respectively, suggesting that the design approach is conservative and of poor accuracy for both slender and stocky cross-sections.

The main reason for the conservative prediction of design strengths is that EN1993-1.1 accounts for both torsional buckling (in the calculation of N_{FT}) and local buckling (in the A_{eff} calculation), and as such, notwithstanding that the buckling half-wavelengths of the two modes may be different, accounts for the same mode twice. The conservatism is brought out by the fact that in calculating the flexural-torsional buckling strength, in the limit $L \to 0$, the buckling load equals the torsional buckling load ($N_T = GJ/(Ar_o^2)$) so that $\bar{\lambda}_{FT} \to \sqrt{A_{eff} f_y / N_T} \neq 0$ and consequently, $\chi_{FT} < 1$ rather than $\chi_{FT} = 1$ for $L \to 0$. When determining the column strength using equation 5, the section capacity $A_{eff} f_y$ is then unnecessarily further reduced by the factor $\chi_{FT} < 1$.

The conservatism of the Eurocode3 approach is particularly pronounced for short columns and the high $N_u/N_{b,Rk}$-ratios at short lengths contribute substantially to the high CoV. When excluding columns with slenderness $\lambda_e < 0.15$, the mean and CoV of the $N_u/N_{b,Rk}$-ratio reduce to 1.38 and 0.226 respectively. Based on these values for P_m and V_P, the resistance factor is calculated as $\varphi = 0.93$.

3.4 *Modified Eurocode 3 Approach ($N_{C,Rd} = A.f_y.\chi(\lambda_r)$)*

The main issue in improving the Eurocode design approach is to resolve the double consideration of the torsional/local buckling mode in the strength prediction, as discussed in Section 3.3. This may be achieved by ignoring flexural-torsional buckling in determining the member buckling load, as in the AS4100 approach, or by using the gross area rather than the effective area. Motivated by the plots of normalised strength (N_u/N_y) against slenderness shown in Figs 2a and 2b, the latter approach is here selected. As shown in Fig 2, when the normalised strength is plotted against the "global" slenderness (λ_r), which is defined by equation (2) and considers both flexural and flexural-torsional buckling, the strengths are grouped in a much narrower band than when plotted against the flexural slenderness (λ_e) defined by equation (1), suggesting that a more direct design approach may be achieved by employing the global slenderness. This implies the consideration of the flexural-torsional buckling load in determining the design strength, in which case the

area is taken as the gross area rather than the effective area, i.e.

$$N_{b,Rk} = \chi(\lambda_r)\, A\, f_y \tag{7}$$

Comparisons also show that a more accurate design procedure can be achieved using the b-curve rather than the c-curve as currently specified for T-sections in Eurocode3. The resulting strength predictions are shown in (Sena Cardoso and Rasmussen, 2013) for the cases where secondary warping is ignored ($I_w = 0$) and considered ($I_w > 0$), respectively. When secondary warping is ignored, the mean and CoV of the ratio between the experimental or numerical strength to the modified EN1993-1.1 strength prediction (N_u/N_{Rd}) are 1.36 and 0.353. These statistics compared to the mean and CoV of 1.60 and 0.400 obtained using the existing provisions. Excluding the results for short lengths ($\lambda_e < 0.15$), the mean and CoV improve to 1.20 and 0.205 respectively, leading to a resistance factor of $\varphi = 0.89$.

If secondary warping is taken account of, the mean and CoV of all columns are 1.15 and 0.132 respectively, indicating a relatively conservative procedure with a small scatter. The mean and CoV change slightly to 1.14 and 0.141 when the results for short lengths ($\lambda_e < 0.15$) are excluded, suggesting that the proposed procedure is consistent in terms of length. The resistance factor calculated on the basis of the latter statistics is $\varphi = 0.94$.

3.5 *Discussion*

As shown in (Sena Cardoso and Rasmussen, 2013), AS4100 is mainly optimistic for slender cross-sections in the short flexural slenderness range ($\lambda_e \in [0.25,0.5]$) where the design strength exceeds the ultimate strength by 20% or more. This result is attributed to the effect of bending induced by the shift of the effective centroid which is not considered in the design guidelines of the AS4100 Specification.

The provisions of AS4100 are generally satisfactory for T-section columns except when the web is slender and the column is pinned about the x-axis (the axis perpendicular to the plane of symmetry). It is suggested that such columns should be required to be designed as beam-columns when the A_e/A ratio is less than 0.8. This requirement is not necessary when the columns are fixed against rotations about the x-axis at the two ends, since local buckling does not induce overall bending in this case (Rasmussen and Hancock, 1994).

The statistics of the current and proposed modified design procedures of AS4100 and EN1993-1.1 are summarised in Table 1. The statistics exclude short columns (λ_e) and are based on design predictions that ignore secondary warping. It follows from the Table that comparable levels of accuracy and (P_m and V_P) and reliability (φ) are achieved using the current rules of AS4100 and the proposed modified rules

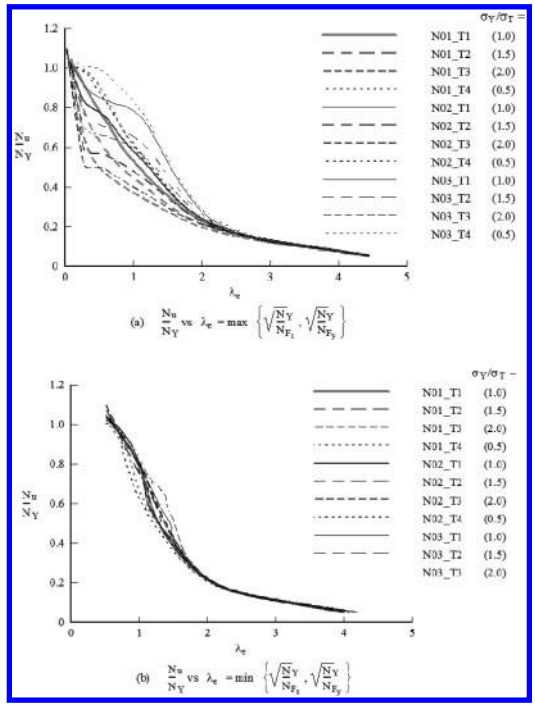


Figure 2. Relationship between the non-dimensional failure stress/yielding stress and: a) the normalised flexural slenderness (λ_e), b) the normalised global slenderness (λ_r). Note: In calculating λ_r, the flexural-torsional buckling load includes secondary warping rigidity by determining I_w.

Table 1. Statistics of current and modified versions of AS4100 (AS) and EN1993-1.1 (EC) specifications excluding short columns ($\lambda_e < 0.15$); P is the ratio of ultimate strength to design strength, P_m and V_P are the mean and CoV of the same ratio.

	Current procedure					Proposed modified procedure				
	P_m	V_P	φ	λ	A	P_m	V_P	φ	λ	A
AS	1.08	0.15	0.88	λ_e^*	A_e	–	–	–	–	–
EC	1.38	0.26	0.93	$\lambda_r^\#$	A_e	1.20	0.21	0.89	λ_r	A

* λ_e defined by equation (1), (flexure only)
\# λ_r defined by equation (2).

of the EN1993-1.1 Specification. The accuracy deteriorates considerably if short columns are included in the statistics and secondary warping is ignored. While the accuracy can be greatly improved for short columns by including secondary warping, it is considered appropriate to maintain $I_w = 0$ in the proposed modified design approaches for simplicity. A note could be added to the proposed modified design procedures to the effect that when designing short T-section columns, say $\lambda_e < 0.2$, the designer should consider to include secondary warping when determining the flexural-torsional buckling load.

4 CONCLUSIONS

A study of the strength of hot-rolled steel T-section columns has been presented. The study was motivated by the fact that the torsional and local buckling modes are similar for this cross-section, whereby design strength predictions may be conservative if accounting for both modes. The focus of the study is on columns compressed between pinned ends.

Numerically obtained ultimate strength data is compared with predictions obtained using the Australian and European specifications for hot-rolled steel structures. It is shown that the Australian Standard (AS4100) is reliable except for pin-ended columns with slender webs, for which the design strength may be seriously optimistic because of the effect of the shift of the effective centroid. It is proposed that pin-ended T-section columns shall be required to be designed as beam-columns when the A_e/A-ratio is less than 0.8, as determined using AS4100. However, this requirement is not necessary for fixed-ended columns.

The European (EN1993-1.1) code is shown to be excessively conservative because (i) it considers both flexural-torsional buckling and local buckling in the strength calculation, and (ii) the column slenderness for flexural-torsional buckling does not approach to zero for short lengths as in the design for flexural buckling. The paper proposes a modification to EN1993-1.1, allowing (i) the area to be taken as the full area (A) irrespective of cross-section slenderness and (ii) the b-curve to be used rather than the c-curve currently specified. It is shown that adequate reliability is achieved using this approach without considering bending arising from the shift of the effective centroid, which is required to be accounted for in the current version of the code.

The proposed rules for the European specification are shown to have comparable reliability to those of the current version of the Australian standard. This is remarkable seeing that the design approaches of the two specifications are completely different. The study shows that T-section columns with slender cross-sections are not required to be designed as beam-columns to account for the effect of the shift of the effective centroid, except for the Australian standard when the A_e/A-ratio is less than 0.8.

REFERENCES

AS4100 1998. Australian Standard – Steel structures. Standards Australia.

ASCE 2010. Minimum design loads for buildings and other structures: ASCE Standard 7–10, American Society of Civil Engineers.

BAKKER, M. C. M. & PEKÖZ, T. 2003. The finite element method for thin-walled members—basic principles. Thin-Walled Structures, 41, 179–189.

BJORHOVDE, R. 1972. Deterministic and probabilistic approaches to the strength of steel columns, Lehigh University, University Microfilms.

ECCS 1976. Manual on stability for steel structures. ECCS Publication, 22.

ELLINGWOOD, B. R., GALAMBOS, T. V., MACGREGOR, J. G. & CORNELL, C. A. 1980. Development of a probability based load criterion for American National Standard A58, Washington D. C.,, National Bureau of Standards.

EN1993-1-1 2005. Eurocode 3: Design of steel structures – Part 1-1: General rules and rules for buildings. CEN – European Committee for Standardization.

KITIPORNCHAI, S. & LEE, H. W. 1986. Inelastic experiments on angle and tee struts. Journal of Constructional Steel Research, 6, 219–236.

ONESTEEL 2011. Hot-rolled and structural steel products. In: LIMITED, O. M. P. (ed.) 5th ed.

RASMUSSEN, K. J. R. & HANCOCK, G. J. 1994. Design of thin-walled plain channel section columns against flexural buckling. Thin-Walled Structures, 20, 219–240.

SARAWIT, A. T., KIM, Y., BAKKER, M. C. M. & PEKÖZ, T. 2003. The finite element method for thin-walled members-applications. Thin-Walled Structures, 41, 191–206.

SCHAFER, B. W., LI, Z. & MOEN, C. D. 2010. Computational modeling of cold-formed steel. Thin-Walled Structures, 48, 752–762.

SENA CARDOSO, F. & RASMUSSEN, K. J. R. 2013. Research Report: The behaviour and design of concentrically loaded T-section steel columns. Sydney, Australia: School of Civil Engineering, The University of Sydney.

SIMULIA 2011. ABAQUS: User's manual.

Research and Applications in Structural Engineering, Mechanics and Computation – Zingoni (Ed.)
© 2013 Taylor & Francis Group, London, ISBN 978-1-138-00061-2

Stability, failure and design of I-section steel beams subjected to tension

J. Tomás
Instiuto Superior Técnico, Technical University of Lisbon, Lisbon, Portugal

J. Nseir
University of Applied Sciences of Western Switzerland, Fribourg, Switzerland

D. Camotim
Instiuto Superior Técnico, Technical University of Lisbon, Lisbon, Portugal

N. Boissonnade
University of Applied Sciences of Western Switzerland, Fribourg, Switzerland

ABSTRACT: This paper reports the results of an analytical, numerical and experimental investigation dealing with I-section steel members acted by a combination of major-axis bending and axial tension ("beams subjected to tension"), which is relatively rare in practice and, therefore, has received little attention in the literature. In particular, almost no guidelines for the design against buckling ultimate limit states may be found. As a consequence, the axial tension favorable effect on lateral-torsional failure is usually neglected, leading to over-conservative designs. In order to acquire scientific knowledge and to provide design guidance on this topic, the lateral-torsional stability, failure and design of hot-rolled steel I-beams with fork-type end supports and acted by in-plane transverse loadings combined with various axial tension values are addressed here. A modified analytical expression to calculate the critical bending moments of beams under uniform bending and axial tension is first presented. Then, two full-scale tests involving a narrow and a wide flange beam under eccentric tension are described and their results are used to develop finite element models, subsequently employed to perform a parametric study aimed at gathering a fairly extensive ultimate strength database. These reference results are used to assess the merits of a design approach which consists of slightly modifying the current procedure prescribed in Eurocode 3. It is shown to provide accurate predictions that correlate very well with the values obtained from the numerical simulations.

1 INTRODUCTION

Over the past decades, many research efforts have been devoted to "stability-related" topics within structural steel. As an example, Boissonnade et al. 2006 summarizes the most recent development on the behavior and design of steel beam-columns within Europe. However, quite surprisingly, virtually no information can currently be found concerning the structural response and design of I-section members subjected to major-axis bending and *tension* (i.e., beams under tension), namely on how the presence of tension affects (improves) the beam lateral-torsional buckling behavior.

Very little references indeed exist on this topic; the rather complete literature search carried out by the authors only resulted in one document, namely the Eurocode 3 "ENV" pre-normative design rules – yet not providing any background information on the proposed rules. Of course, part of the explanation for the "information void" on this problem is due to the fact that (i) beams under tension occur seldom in practice and (ii) neglecting the tension effects leads to conservative ultimate strength estimates regarding lateral-torsional failure modes, where the member is checked as a "pure beam".

The objective of this paper is precisely to contribute to such an investigation, by bridging the lack of scientific information and technical guidance concerning the lateral-torsional stability, behavior and design of beams under tension. It deals specifically with hot-rolled steel I-section beams exhibiting "fork-type" end supports and subjected to simple in-plane loading (e.g., applied end moments or uniformly distributed loads), and which are not affected by local buckling phenomena – beams with compact cross-sections that can reach their plastic resistance (class 1 "plastic" or 2 "slender" according to Eurocode 3 nomenclature).

Following section 2 first characterizes the lateral torsional stability and behavior of members under major-axis bending and tension. In particular, two full-scale experimental tests are described, as well as the development of shell FE models and their assessment against the experimental results. Section 2



Figure 1. Beam subjected to major-axis bending M_y and axial tension N_t.

also details consecutive numerical parametric studies where more than 2000 GMNIA reference results have been gathered.

Then, section 3 describes a new design approach for beams under tension and assesses its merits in comparison with the values obtained from the numerical simulations. The ability of the proposed rules to yield safe and accurate estimates of the carrying capacity of such members is clearly demonstrated, as well as the quite significant positive influence of tension on lateral torsional buckling – potentially leading to interesting material savings.

2 BEHAVIOR OF BEAMS SUBJECTED TO TENSION

2.1 *Lateral Torsional Stability*

This section addresses the influence of tension on the lateral-torsional stability behavior of simply supported ("fork-type" supports), doubly-symmetric I-section beams subjected to major-axis bending M_y and axial tension N_t (see Figure 1). The objective is to assess how the presence of an axial tension N_t increases the critical buckling moment M_{cr}. Obviously, it is assumed that N_t is such that the beam cross-section resistance is not reached prior to the occurrence of instability, *i.e.*, the beam collapse is not exclusively due to plasticity effects.

Following well-known analytical derivations presented in classical monographs (see for example Chen & Atsuta 1977 or Trahair 1993), adapted to ensure adjacent equilibrium for members subjected to constant major-axis bending and axial tension, it is possible to obtain the following expression:

$$M_{cr}(N_t) = \sqrt{\left(1+\frac{N_t}{P_{cr,z}}\right)\times\left(1+\frac{N_t}{P_{cr,f}}\right)}\times M_{cr}(0) \qquad (1)$$

which provides the critical buckling moment of a member subjected to bending and tension. In this expression, M_{cr} (0) denotes the critical buckling moment of the member under uniform bending only and $P_{cr.z}$ and$P_{cr.\phi}$ correspond to the minor-axis flexural and torsion buckling loads of the "pure column", respectively.

In order to assess the proposed expression, a series of corresponding ABAQUS beam finite element analyses (BFEA) have been conducted, which revealed a perfect agreement with analytical values (cf. Tomás 2013); further validation was contemplated through numerical investigations covering beams built from

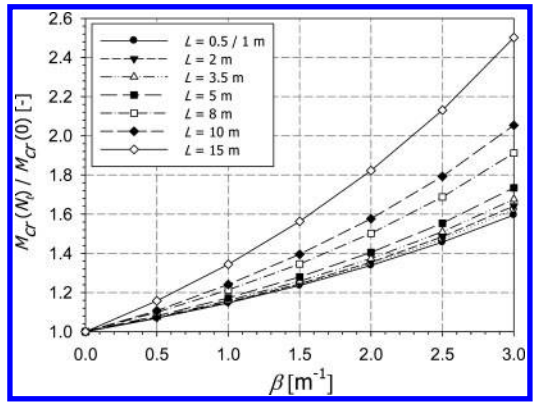


Figure 2. Evolution of M_{cr} $(N_t)/M_{cr}$ (0) with β for 0.5 m $\leq L \leq$ 15 m IPE300 beams, $\psi = 0$.

four hot-rolled profiles (IPE300, IPE500, HEB300, HEB500), with lengths comprised between 0.5 and 25 m, and subjected to various loading situations (linear bending moments characterized by end moment ratios $\psi = 1$; 0.5; 0; -0.5, -1 or a uniformly distributed load applied at the shear center level), and acted by N_t values such that $\beta = N_t/M_y = 0$; 0.5; 0.75; 1.0; 1.5; 2.0 (bending and axial load being applied proportionally).

Figure 2 shows a representative example of the obtained results, and the following comments may be made:

(i) Naturally, the critical moment increase always grows with β, *i.e.*, the amount of tension acting on the beam. Note that, eventually, the M_{cr} $(N_t)/M_{cr}$ (0) *vs.* β curves would tend to infinity as β approaches the "limit tension value" which is such that no section is acted by compressive stresses anymore;

(ii) Obviously, the importance of the tension effects grows with the beam length, as the beam becomes more prone to lateral-torsional instability;

(iii) Moreover, it possible to assess how the beneficial tension effects vary with the bending moment diagram shape. The key factor is the shape of the axial force diagram acting on the whole beam compression flange, combining the constant tensile value N_t with varying compressive values due to the bending moments. It is observed that this combination leads to tension effects that are highest for the $\psi = 0$ triangular diagram ("least compressed" compression flange) and lowest for the $\psi = 1$ uniform diagram ("most compressed" compressed flange).

2.2 *Ultimate Strength – Experimental Investigation*

This paragraph investigates the ultimate strength of beams under tension, and first describes two full-scale experimental tests performed to acquire in-depth knowledge about the problem under consideration and

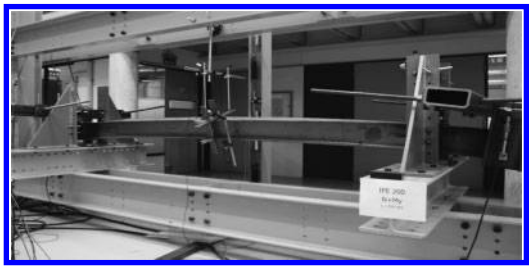


Figure 3. Overall view of the experimental set-up and deformed configuration at the brink of collapse for the IPE200.

to provide the means to develop and validate beam and shell finite element models.

Figure 3 provides an overall picture of the experimental set-up; it shows an $L = 4.00$ m beam submitted to eccentrically-applied tension at both ends, by means of rigid lever arms and 4 of hydraulic jacks. The (reduced) test program involved an IPE200 beam loaded with a 0.25 m N_t eccentricity, and a HEA160 beam loaded with a 0.5 m eccentricity.

Prior to the performance of each test, usual preliminary measurements have been carried out: tensile tests, residual stresses measurements and initial geometrical imperfections determination (both local and global). These were done with particular care, in order to use the measured information in shell FE models for validation purposes; detailed information can be found in Tomás 2013. Combinations of load or displacement-controlled increments have been set up to collapse, and suitable sets of LVDTs and inclinometers were used to record the behavior of the member at mid-span and at the end sections.

2.3 *Ultimate Strength – Numerical Investigations*

The experimental results were then employed to calibrate and validate a shell finite element model able to handle a realistic comparison with the experimental tests, including all measured properties (material, imperfections) and actual test configuration.

This was done using the non-linear finite FEM software FINELg; the experimental set-up was entirely modeled with fine meshes of 4-node shell elements (Kirchhoff's theory in bending), thus ensuring that the beam "real" end support conditions and "surroundings" were adequately simulated.

The results obtained during the performance of each test consisted of (i) experimental evidence concerning the occurrence of lateral-torsional buckling in beams acted by tension, (ii) equilibrium paths relating the applied load with various measured displacements and/or rotations and (iii) experimental failure loads: 269.2 kN (IPE200) and 150.0 kN (HEA160).

The numerical and experimental ultimate moments were found to correlate quite well: the numerical simulations either underestimate by 6% (IPE200 specimen) or overestimate by 2% (HEA160 specimen) the experimental values. Figure 4 also shows the IPE200 specimen deformed configuration at collapse, provided by

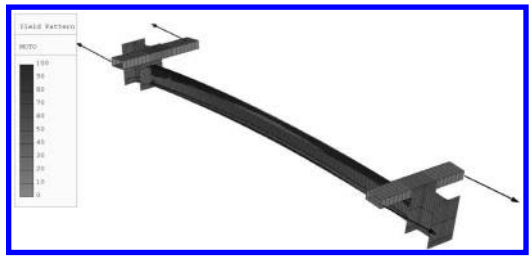


Figure 4. FE deformed shape and extent of yielding at peak load (IPE200 specimen).

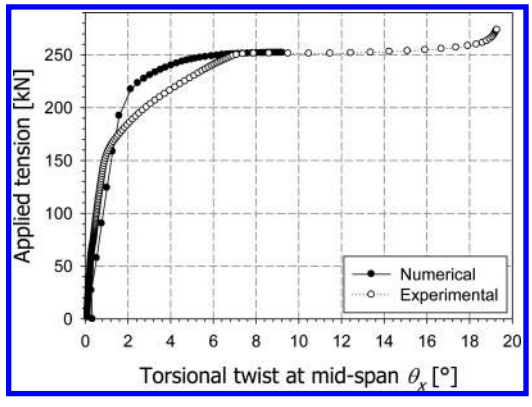


Figure 5. Test vs. FE model comparison (IPE200 specimen).

the FINELg analysis – note the qualitative and quantitative similarity with its experimental counterpart, shown in Figure 3.

Finally, Figure 5 compares the experimental equilibrium paths relating the applied load at the end section and mid-span torsional twist θ_x with the corresponding numerical simulations, where a visible perfect coincidence is observed in the elastic regime, beyond which the numerical model is a bit stiffer and, therefore, underestimates the θ_x values.

On the basis of the comparisons between the test results obtained and the corresponding numerical simulations, most of which were not presented here and can be found in Tomás 2013, it seems fair to conclude that the shell FE model developed provides reasonably accurate results and, thus, can be adequately used to validate the finite element model employed to perform the parametric study addressed in the next section.

2.4 *Parametric study*

The now-validated finite element model has been employed to perform about 2000 Geometrically and Materially Non-linear with Imperfections Analyses (GMNIA) of beams under tension. They comprised beams exhibiting several slenderness values, stemming from (i) 8 span lengths (between 0.5 and 25 m), (ii) two yield stresses ($f_y = 355$; 460 N/mm^2 – the steel material behavior modeled corresponds to the usual elastic-perfectly plastic constitutively with a marginal strain-hardening occurring for very large

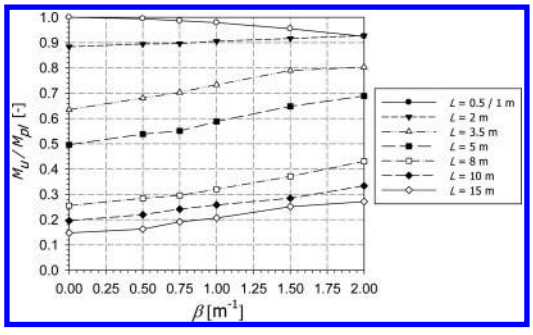


Figure 6. M_u/M_{pl} vs. β as a function of member length (S460 grade, IPE300 and $\psi = 1$).

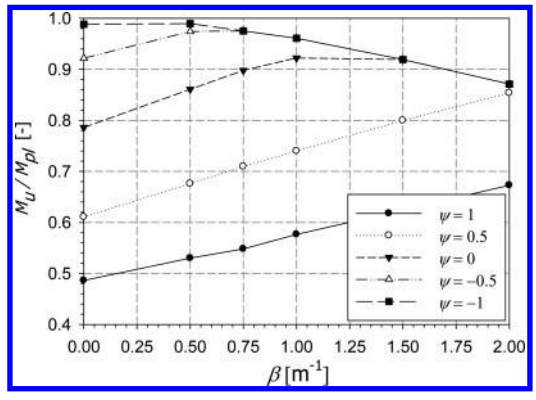


Figure 7. M_u/M_{pl} vs. β as a function of bending moment distribution (S355 grade, HEB300 and $L = 15$ m).

strains) and (iii) four cross-section shapes (IPE300, IPE500, HEB300, HEB500). The members were subjected to (i) five bending moment diagrams ($\psi = 1$; 0.5; 0; -0.5; -1) and (ii) six tension levels, corresponding to $\beta = N_t/M_y$ ratios equal to 0; 0.5; 0.75; 1.0; 1.5; 2.0. The non-linear analyses were performed with FINELg and the members were discretized into standard 3D beam finite elements based on Vlasov's theory for open-section thin-walled members. The numerical models also contained longitudinal normal residual stresses with a parabolic pattern as well as global sinusoidal initial geometrical imperfections that combine minor-axis flexure and torsion – shapes and values were adopted as proposed by Boissonnade & Somja 2012.

A detailed analysis of the results yields the following conclusions:

(i) First of all, as expected, the presence of axial tension is completely different in the stocky and slender beams, in the sense that their collapse is governed by either plasticity or instability effects, respectively. In the former, axial tension leads to an ultimate moment decrease, stemming exclusively from the drop in cross-section resistance; in the latter, axial tension leads to a ultimate moment increase, which grows with β and stems from the improved lateral-torsional buckling resistance;

(ii) The comparison between the M_u/M_{pl} vs. β curves (Figure 7) concerning the (ii$_1$) $L = 8$; 10; 15 m and (ii$_2$) $L = 3.5$; 5 m beams show different trends, even if all these curves have positive slopes throughout the whole β range considered. While in the former M_u/M_{pl} grows with β at an always increasing rate, which becomes percentage-wise more relevant as L increases, the latter exhibit points of inflexion at a given β value that seems to increase with L. These different trends reflect the contradicting influence of axial tension on the lateral-torsional buckling and cross-sectional resistances: the latter becomes progressively more relevant as β increases and L decreases. This assertion is fully confirmed by looking at the M_u / M_{pl} vs. β curve concerning the $L = 2$ m beam, which exhibits very little growth and ends up merging with their $L = 0.5$; 1.0 m beam counterparts for $\beta = 2.0$ – it would start decrease for larger β values, whenever collapse would start being governed by plasticity in the beam mid-span region;

(iii) Then, the influence of the bending moment diagram shape on the axial tension benefit, as shown in Figure 8 for the $L = 15$ m, S355 HEB300 beams, demonstrate that only the $\psi = 1$ and $\psi = 0.5$ curves (i.e., those leading to more relevant lateral-torsional buckling effects) are not limited by the descending curve associated to the mid-span cross-section full yielding up to $\beta = 2.0$. Indeed, the $\psi = 0$ and $\psi = -0.5$ curves merge into this curve at lower β values and following an "almost horizontal" segment. Finally the $\psi = -1$ curve decreases monotonically with ψ, meaning that the beam collapse is always governed by the mid-span cross-section resistance;

(iv) Quantitatively speaking, the highest M_u percentage increases due to the presence of axial tension occurs for the beams acted by the $\psi = 0.5$ bending moment diagram – they are slightly larger than their $\psi = 0$ and $\psi = 1$ diagram counterparts.

Finally, Figure 8 clearly shows the double influence of an increasing N_t, moving the M_u / M_{pl} vs. λ_{LT} plots (i) to the left (lateral-torsional slenderness decrease) and (ii) upwards (ultimate moment increase). Moreover, it can also be observed in this figure that the whole set of points, corresponding to various beams and β values (including $\beta = 0$), remain nicely "aligned" along a "design-like" curve. The design approach for beams subjected to tension that is proposed in the next section takes advantage of this feature.

3 PROPOSED DESIGN APPROACH

The current Eurocode 3 methodology stipulates that the ultimate moment of (compact) beams subjected to axial tension is the least of two values: (i) the cross-section reduced plastic moment and (ii) the beam bending resistance against a failure stemming from

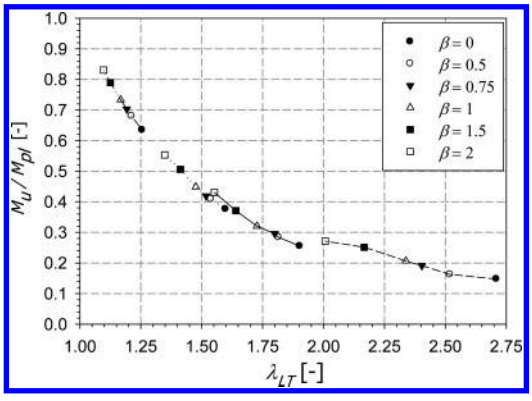


Figure 8. Variation of Mu / Mpl with the beam slenderness λ_{LT}.

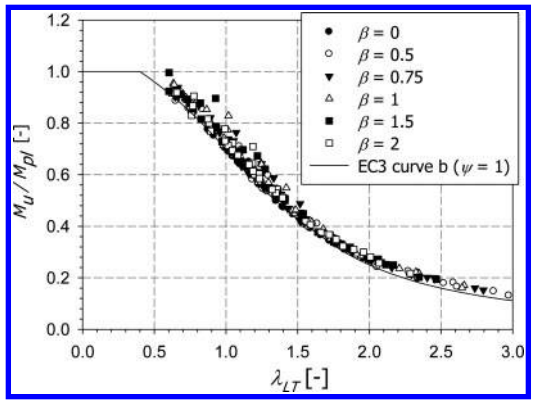


Figure 9. Comparison between the $M_{u,FE}$ / M_{pl} (points) and $M_{u,proposal}$ / M_{pl} (curve) for $\psi = 0$.

lateral-torsional buckling. While the former is determined through classical strength of materials concepts, the latter is obtained by means of a procedure based on the use of "beam strength curves". This procedure involves the following steps (Eurocode 3 nomenclature is adopted):

(i) Determine the beam lateral-torsional slenderness $\lambda_{LT} = (M_{pl}/M_{cr})^{0.5}$, where M_{pl} is the cross-section plastic moment (bending resistance) and M_{cr} is the beam critical buckling moment;
(ii) On the basis of λ_{LT}, use the appropriate buckling curve to obtain the reduction factor χ_{LT};
(iii) Further modify (increase) the reduction factor obtained in the previous step, by means of coefficient $\chi_{LT,mod} = \chi_{LT} / f$, where $f \leq 1.0$ is a parameter that aims at increasing the design resistance of the beam for non-constant bending moment diagrams, thanks to inelastic effects;
(iv) Evaluate the beam ultimate bending resistance against from lateral-torsional buckling failure $M_u = \chi_{LT,mod} \times M_{pl}$.

The proposed design approach consists of incorporating the axial tension beneficial effects into the critical buckling moment used to determine the beam slenderness, while keeping all the remaining steps unchanged – in particular, M_{pl} remains the cross-section pure bending resistance (i.e., does not account for the presence of axial tension). In other words, $M_{cr} \equiv M_{cr}$ (0) is replaced by M_{cr} (N_t), where N_t is the acting axial tension, which implies a λ_{LT} decrease and, therefore, larger $\chi_{LT,mod}$ and M_u values. It shall be noted that the calculation of M_{cr} (N_t) must be done by means of a numerical beam buckling analysis (e.g., using beam finite elements) – in the future, the authors plan to develop analytical expressions and/or other design aids that will render the performance of this task easier and more straightforward.

The assessment of the quality of the proposed design rules has been based on the results of the numerical simulations partially reported in Figure 9 – again, the full set of results can be found in Tomás 2013. It should be clarified here that the comparison between the proposed rules and the FE reference results that follows excludes members whose failure mode correspond to cross-sectional resistance, i.e., beams not collapsing in lateral-torsional modes, as the proposed design approach only concern the latter.

Table 1. Averages, standard deviations and maximum/minimum value of the ratio R_M.

	Aveg.	St.Dev.	Max.	Min.	Nb. results
$\beta = 0$	1.03	0.04	1.14	0.92	188
$\beta = 0.5$	1.04	0.03	1.13	0.93	172
$\beta = 0.75$	1.05	0.03	1.16	0.95	160
$\beta = 1$	1.06	0.03	1.20	0.97	149
$\beta = 1.5$	1.05	0.04	1.21	0.92	119
$\beta = 2$	1.05	0.03	1.21	0.98	91

Figure 9 concerns the various members analyzed under bending moment diagrams defined by $\psi = 1$ and compares the numerical ultimate moments with their predictions provided by the proposed design approach – use of Eurocode 3 buckling curve b with a lateral-torsional slenderness modified through the inclusion of the critical buckling dependence on N_t. Figure 9 appeals the following comments:

(i) It is impossible not to notice the remarkable agreement between $M_{u,FE}$ and $M_{u,proposal}$, both results being almost aligned;
(ii) Table 1 provides the detailed statistical values of the ratio $R_M = M_{u,FE}/M_{u,proposal}$ corresponding to Figure 9 results and for various N_t values. These indicators reflect the excellent quality of the ultimate moment estimates, the vast majority of them being safe and extremely accurate.

In order to better evidence the beneficial influence of axial tension on the beam ultimate strength, Table 2 provides the averages, standard deviations and maximum/minimum percentage values of the ultimate moment increase ΔM_u due to axial tension with respect to beam ultimate moments. It is observed that all the above generally increase with β, except for the

Table 2. Averages, standard deviations and maximum/minimum values of ΔM_u.

	Avg.	St. Dev.	Max.	Min.	Nb. FE
$\beta = 0.5$	14.7%	8.9%	43%	0.01%	172
$\beta = 0.75$	24.5%	14.3%	64%	0.01%	160
$\beta = 1$	34.0%	19.3%	91%	0.02%	149
$\beta = 1.5$	53.7%	30.4%	135%	0.01%	119
$\beta = 2$	79.9%	46.4%	202%	0.01%	91

minimum value that remains constant and very small, as it always corresponds to a slenderness located very close to the end of the design curve plateau.

4 CONCLUSIONS

This paper reported the results of an analytical, numerical and experimental investigation on the lateral-torsional stability, failure and design of hot-rolled steel I-section beams with fork-type end supports and acted by simple in-plane loadings and various axial tension values. Initially, the derivation and validation of an analytical expression providing critical buckling moments of uniformly bent beams subjected to tension was presented. Then, this analytical finding was followed by a numerical study on the beneficial influence of axial tension on beams under non-uniform bending, namely caused by unequal applied end moments or a uniformly distributed load – several beam finite element results were presented and discussed in detail.

Next, the paper addressed the performance of two experimental tests, carried out at the University of Applied Sciences of Western Switzerland – Fribourg and aimed at determining the behavior and ultimate strength of a narrow and a wide flange beam subjected to eccentric axial tension. These results were also used to validate FINELg beam and shell finite element models that were subsequently employed to perform an extensive parametric study that (i) involved more than 2000 numerical simulations, concerning beams with various cross-section shapes, lengths, yield stresses, acting bending moment diagrams and axial tension levels, and (ii) was aimed at gathering a fairly large ultimate strength/moment database.

These data were then used to assess the merits of a design approach proposed for beams subjected to tension and collapsing in lateral-torsional modes – this design approach consists of slightly modifying the current procedure prescribed in Eurocode 3 through the incorporation of the axial tension influence in a modified critical buckling moment.

The ultimate moment estimates provided by the proposed design approach were shown to correlate extremely well with the values obtained from the numerical simulations, thus making it a very promising candidate for inclusion in a future version of Eurocode 3. Last, the paper closed with a quick assessment of the beneficial influence of axial tension on the ultimate moment of beams failing in lateral-torsional modes; as expected, it was found that this influence can be quite significant and, thus, neglecting it (as is currently done in practically all steel structures codes) will certainly lead to over-conservative designs.

REFERENCES

Boissonnade, N., Greiner, R., Jaspart, J.P. & Lindner J. 2006. "Rules for Member Stability in EN 1993–1–1; Background documentation and design guidelines", *Eds. Mem Martins*, Portugal, E.C.C.S. – ISBN 92-9147-000-84, Vol. 119, 259 pages.

Boissonnade, N. & Somja, H. 2012. "Influence of imperfections in FEM modeling of lateral-torsional buckling". *USB Key Drive Proceedings of SSRC Annual Stability Conference*. (Grapevine. 17-21/4).

CEN (Comité Européen de Normalisation). 1992. "Eurocode 3: Design of Steel Structures – Part 1.1: General Rules and Rules for Buildings". ENV 1993-1-1. Brussels.

CEN (Comité Européen de Normalisation). 2005. "Eurocode 3: Design of Steel Structures – Part 1.1: General Rules and Rules for Buildings". EN 1993-1-1. Brussels.

Chen, W.-F. & Atsuta, T. 1977. "Theory of Beam-Columns – Space Behavior and Design" (vol. 2). *McGraw-Hill*. New York.

Non-linear finite element analysis program "FINELg". 2012. User's Manual, version 9.3, ArGEnCo Department, University of Liège, Greisch Info S.A., Liège, Belgium.

Simulia Inc. 2008. *Abaqus Standard* (vrs. 6.7-5).

Tomás, J. 2013. "I-Section Steel Beams under Tension: Lateral-Torsional Buckling. Ultimate Strength and Design". *M.Sc. Thesis in Civil Engineering (Structures)*. Instituto Superior Técnico. Technical University of Lisbon.

Tomás, J., Nseir, J., Camotim, D. & Boissonnade, N. 2013. "Stability, Failure and Design of I-Section Steel Beams Subjected to Tension". *Proceedings of the Annual Stability Conference*, Structural Stability Research Council, St. Louis, Missouri, April 16–20.

Trahair, N. 1993. "Flexural Torsional Buckling of Structures". E&FN Spon (Chapman & Hall). London.

17. Steel joints, steel connections

Research and Applications in Structural Engineering, Mechanics and Computation – Zingoni (Ed.)
© 2013 Taylor & Francis Group, London, ISBN 978-1-138-00061-2

Lateral torsional buckling behavior of members in steel structures with hanging-profile connections

Dasu Liu & Jörg Lange
Technical University Darmstadt, Darmstadt, Germany

ABSTRACT: The "hanging profile" is a commonly used type of joint in steel structures for horizontal bracing systems in large building projects, where huge compression forces are transferred. This kind of joint is characterized by the connection of a bracing beam to gusset plates only at the top flanges. This type of structures is usually simplified as a single-span beam with so-called fork bearings at ends. The present study using finite-element-methods to investigate structures with "hanging profiles" in 3d modeling showed partially unexpected but interesting results. According to this study this simplification is not generally valid because the individual shapes of the gusset plates as well as the distortional effects of beams and gusset plates at end supports are not taken into account.

1 INTRODUCTION

In large building projects, such as power plants (e.g. Medupi and Kusile in South Africa), the "hanging-profile" is very commonly used joint type for horizontal bracing systems. As illustrated in Figure 1 only top flanges of the bracing beam are connected to the gusset plates. This brings a significant advantage to the onsite assembly since the member is in vertical direction only restraint at only one height and the bolt hole clearance of 2 mm each side of the member should cover the possible erection imperfections.

Due to the eccentric load transfer a constant offset bending moment with an eccentricity of the half beam height is caused in addition to the axial force (see Figure 2 left). This type of structures is usually designed and verified as single-span member with so-called end fork bearings (see Figure 2 right), which strictly restraints the in plane cross section deformations.

Since the cross section deformation in connection areas and the twisting of the gusset plates are not taken into account under the fork bearing assumption, this assumption cannot reflect the reality correctly. Therefore the idealization of the support situation as fork bearing is incorrect and not justified. Due to the overestimation of the system stiffness in connection areas basic engineering with this conventional approach is considered generally not safe.

Being aware of this problem, however being lack of other satisfying approach the designers in practice have no choice but calculate conservatively to avoid high utilization. The reserve in the verification should hopefully compensate the unsafe assumption.

This study attempts to shed light on the calculation of this type of structures and develop a new and improved design method derived from Euro Code for lateral torsional buckling verification of here discussed cases.

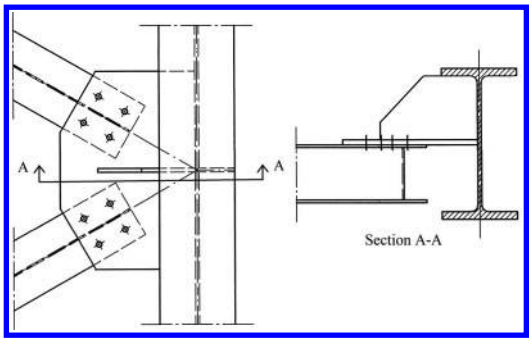


Figure 1. Joint of 2 bracing beams to a floor main beam via hanging profile connections; left: section view; right: top view.

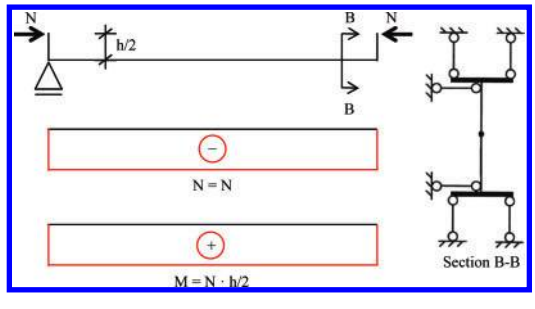


Figure 2. Internal forces of a beam with hanging-profile connections (left) and ideal fork bearing restraint (right).

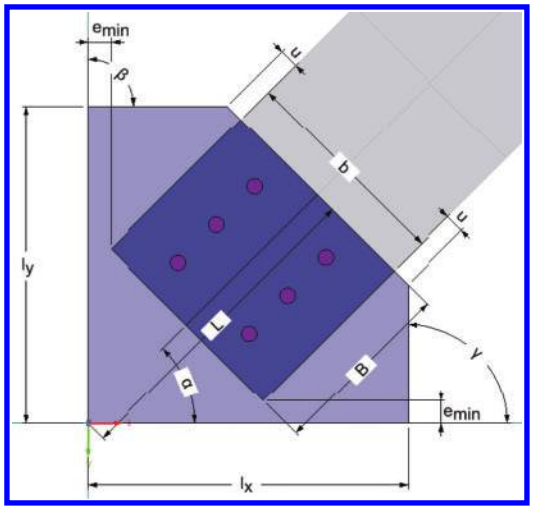


Figure 3. Geometrical parameters of gusset plates (top view).

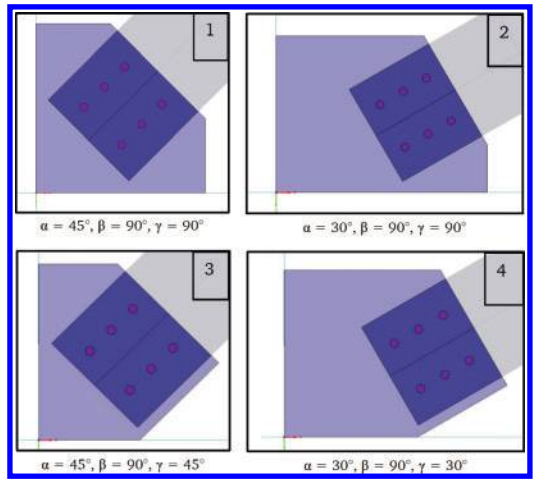


Figure 4. 4 general cases of gusset plate geometry with corresponding angle combinations (top view).

2 FINITE ELEMENT ANALYSIS

A geometrically und materially nonlinear analysis was conducted using FEM-program ANSYS Workbench to evaluate the resistance of structures with hanging profile connections. A 3-D large numeric model has been developed to represent the real properties of the aforementioned static system as close as possible. Special attention was paid to the correct representation of the interaction between the major joint components as well as the initial geometric imperfections and residual stresses. The details of this model are provided in the subsequent sections.

2.1 *Simplified gusset plate form and boundary conditions*

Depending on the geometric relation between bracing members and main beams as well as the load transfer situation, the form of the gusset plates can be very diversified and complex. To facilitate the parametric study the form of the gusset plates has been divided into 4 general cases, which are distinguished from each other by the angles α, β und γ (see Figure 3 and Figure 4).

The dimensions e_{min} and u were uniformly set to 3 cm and 2.5 cm for the whole parametric analysis. These are common dimensions for this kind of connections in Germen steel construction.

The gusset plates were assumed restraint in translation perpendicular to their plate plane at the boundary welded to the main beam web and at the boundary where the vertical stiffener (meant to prevent local plate buckling, see Figure 1) was placed. This is because the vertical stiffener has much higher in-plane bending stiffness compared to the out-of-plane bending stiffness of the gusset plate, so that the vertical displacement of the gusset plate along the stiffener can be ignored. These two boundaries were also restraint in their longitudinal translation directions. However the in-plane translation perpendicular to these boundaries was considered not restraint, since the support in this direction by the main beam web was due to its slenderness negligible.

2.2 *Model discretization*

In order to study the interaction between the major connection components, especially the load transfer through the bolts, volume elements were employed to discretize the model. The SOLID 186 element in ANSYS Workbench, a general purposed volume element with 20 notes and reduced integration to form the element stiffness, was used to simulate the beam, the gusset plates and the bolts.

Particular attention was paid to the web-to-flange curve area to correctly represent the cross-section torsional stiffness as well as the elastic fixing of web and flanges in this area. This was crucial to the simulation since the lateral torsional buckling was the typical failure type and the cross-section torsional stiffness had huge influence on the lateral torsional buckling behavior.

The bolts were simplified as three composited cylinder bodies with 2 mm hole clearance. Since the bolts were mainly subject to shear loads, it was essential to choose the correct diameter depending on if the shear plane passes through the threaded or the unthreaded portion of the bolt. In the conducted parametric analysis the shear planes always pass through the threaded portion of the bolt, so the tensile stress areas of the bolts were adopted in the modeling. 50% of the full preload was applied to the bolts, as this is standard in practical execution for not mainly tensile loaded bolts made of steel grade 10.9.

The interactions between all 3-D bodies, such as beam to gusset plate, bolt to beam, bolt to gusset plate and bolt shank to holes, were defined as surface-to-surface contact, where only compression forces can

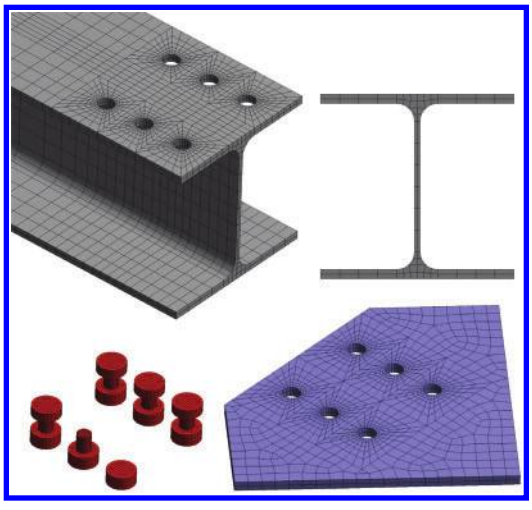


Figure 5. Model discretization: top left: beam; top right: cross-section; bottom left: bolts; bottom right: gusset plate.

be transferred. A friction coefficient of 0.2 was also adopted. This not only reflected the realistic steel to steel friction but also increased the numeric stability during the FE calculations.

2.3 *Geometric and structural imperfections*

The system imperfections were incorporated separately as geometric initial deformation and residual stress. As suggested in Annex C.5 in DIN EN 1993-1-5 (2010), the lowest buckling mode shape, which was in this case lateral torsional buckling (see Figure 6), was used for the geometric imperfection. This first buckling mode was scaled to a magnitude of 80% of the production tolerance (cf. DIN EN 10034 1993) also according to the aforementioned standard. For instance the scale for hot-rolled cross-section HEA260 was L/833, where L is the system length.

Structural imperfections are comprised of residual stresses and scatter of the yield limit over the cross-section. Since the distribution of yield limit is difficult to determine and there is no concrete general assumption, only residual stresses were adopted in the model.

As suggested by Wolf (2006), a linear distribution of the longitudinal residual stresses, which was adopted in ECCS-CECM-EKS (1984), was considered in the FE model. Compared to a parabolic distribution a linear distribution is more conservative, since there is no resultant tensile force built in each flange. A very important rule to the residual stresses is that the resultant force over the cross-section has to be zero, as the residual stresses are only internal stresses. However, the suggested distribution as shown in Figure 7 left is based the center lines of the profile. Because of the web-to-flange area this distribution has to be modified to avoid resultant tensile force over the cross-section. The modified distribution is depicted in Figure 7 right.

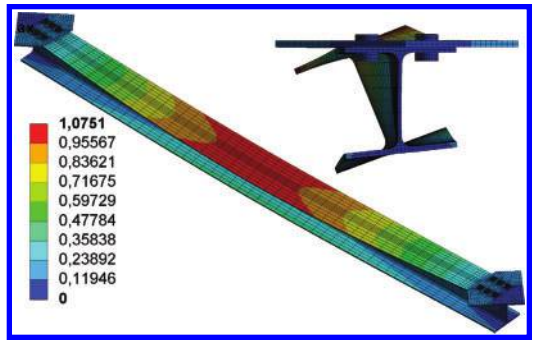


Figure 6. First system buckling mode: lateral torsional buckling (depicted only half of the model).

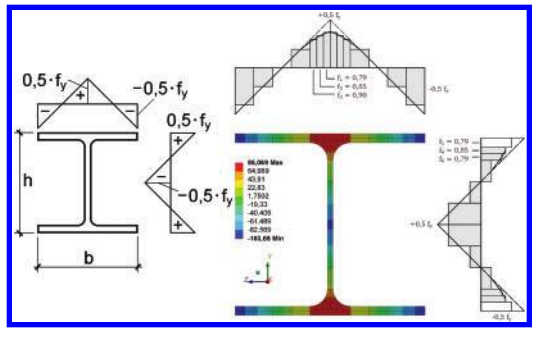


Figure 7. Residual stress distribution.

2.4 *Material properties and loading*

The adopted material model for the analyzed steel grade S235 was a perfectly elastic-plastic model without material hardening. Due to the possible large strain of the bolts true stress-strain curve instead of engineer stress-strain was adopted for the 10.9 grade bolts. The bolt material data were obtained from the tensile coupon tests by González (2011).

Systems with gusset plate angle combination $\alpha = 45°$, $\beta = 90°$ and $\gamma = 90°$ (see Figure 3) are symmetrical, while systems with other angle combinations are asymmetrical. To minimize the time consume of the FE calculations of symmetrical systems only half of the model was simulated and loaded with an imposed deformation at the plane of symmetry. The corresponding force was obtained from the bearing force at the support. For asymmetric systems however the loads were applied conventionally as external forces along the gusset plate boundaries.

2.5 *Parametric analysis*

A parametric analysis was conducted for hot-rolled HEA profile cross-sections with varied system lengths and different gusset plate forms. The results are presented in the subsequent sections.

The study aimed to analyze the stability behaviors of eccentrically compressed beam with hanging-profile connections, so it had to be assured that the connection

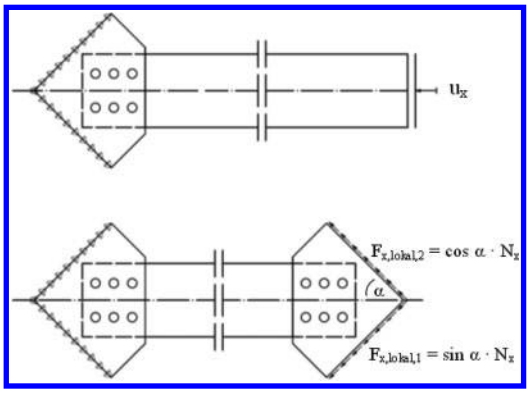


Figure 8. Loading for symmetric model as imposed deformation (top) and for asymmetric model as forces (bottom).

carrying capacities, such as shear- and bearing capacities of bolts, extended the member buckling load. In other words, the bolts and the gusset plates must over designed so that the system failed in form of lateral torsional buckling. The gusset plates were chosen at 5 mm steps and always thicker as the beam flange, which is also a common approach in practice.

The comparison models with endplates or full stiffeners at the beam ends were also analyzed to evaluate the influence of beam stiffening in connection areas on the system ultimate loads.

3 FE RESULTS

This section presents part of the results of the parametric analysis exemplarily on the hot-rolled HEA 260 profile cross-section with over designed 6 M24 bolts on each end of the beam as discussed in the previous paragraph. For each simulation the resistance was also calculated using the equivalent member method (further abbreviated as EMM) according to DIN EN 1993-1-1 (2010) bases on the assumption of single-span members with fork bearings. The partial safety factors were included in neither FE modeling nor calculation with EMM.

3.1 *Development of stress distribution and deformation on the critical cross-section*

The critical cross-section for the analyzed systems was located in the middle of the beam, where the cross-section lost its stiffness first with increasing external loads and so the system reached its labile status.

Figure 9 shows the development of equivalent stress (von Mises stress) and deformation on the critical cross-section with increasing load ranged from 428 kN to the ultimate load 741 kN on example of 5 m long HEA 260 profile with gusset plate geometry $\alpha = 45°$, $\beta = 90°$, $\gamma = 90°$ and thickness 20 mm (further abbreviated as 45° −90° −90° −20). It can be seen that the cross-section displacement grew proportionally to the cross-section area subjected to yield strength. After

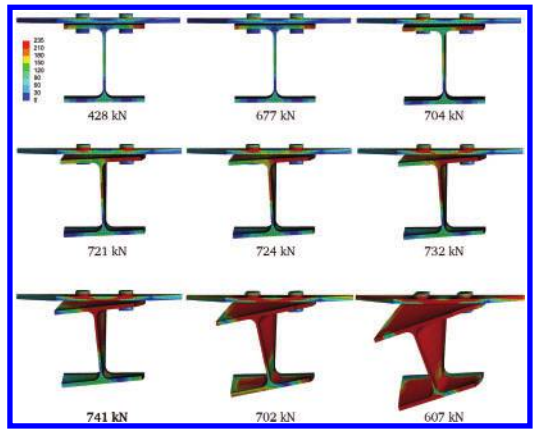


Figure 9. Development of equivalent stress distribution and deformation on critical cross-section.

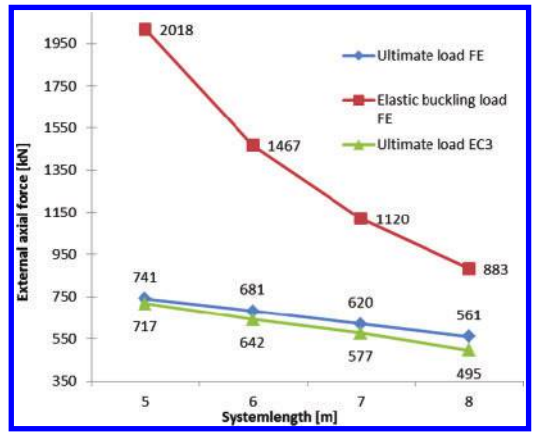


Figure 10. Ultimate loads comparison (HEA 260 S235 45° −90° −90° −20).

the system ultimate load was reached the cross-section continued to deform with further spread plastic area, while the external loads decreased.

3.2 *Length influence*

The numerical failure loads and elastic buckling loads compared with the results according to EMM are depicted in Figure 10. All three ultimate loads dropped with increased system length, which was plausible and expected. However, it was noticed that the FE ultimate loads were unexpectedly even higher than the failure loads according to EMM, despite of the fact that torsionally elastic boundary conditions are considered to be rigid (fork bearing) in EMM.

The higher ultimate loads of FE modeling are attributed to the fact that the beams are elastically fixed on the gusset plates through 3 lines of bolt each side and the gusset plates are also elastically fixed on the main beam and vertical stiffeners by the relatively long welds. These elastic fixings act favorably on the ultimate loads because a system with fixed end supports

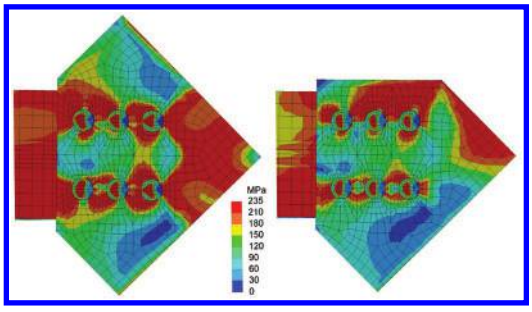


Figure 11. Geomery and equivalent stress distribution of gusset plates 45°–90° −90° (left) and 45° −90° −45° (right) (topview).

Table 1. Ultimate loads of systems with different gusset plate geometries (HEA 260 5 m S235).

Gusset plate geometry	Utimate load FE kN	Ultimate load EC3 kN
45° −90° −90°	741	717
45° −90° −45°	634	717

has a lower buckling length, which leads to a higher buckling load. This effect was so dominant that the incorrect assumed torsionally rigid end supports were fully compensated.

3.3 *Influence of gusset plate geometry*

It seems that in the cases presented in the last section the simplified design according to EMM suggested in EC3 is providing reliable predictions, since the system ultimate loads are underestimated. However, the results presented below will draw a different conclusion.

The result of a comparison simulation of the same HEA 260 profile and same bolts but with differ angle combination of gusset plate 45° −90° −45° −20 (see Figure 11) is shown in Table 1. Now the FE failure load is lower than the calculated ultimate load according to EMM and much lower compared with the FE result of gusset plate 45° −90° −90° . From the equivalent stress distribution (Figure 11) can be observed that due to the shorter boundary of gusset plate 45° −90° −45° the plastic stress spread over the entire short boundary, which cost highly percentual stiffness lost for the gusset plate. This led further to reduction of the system stiffness and consequently to lower ultimate load. On the contrary the yield area of gusset plate 45° −90° −90° concentrated mainly on the corner, thus the system stiffness were much less compromised.

3.4 *Beam stiffening*

Two alternatives were studied to evaluate the influence of beam stiffening on the system ultimate load.

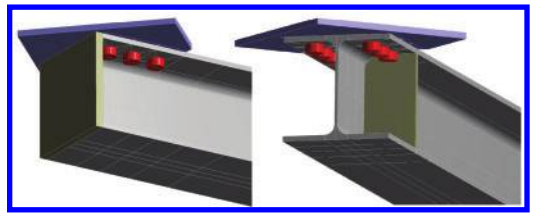


Figure 12. Beam stiffening with end plate (left) or full stiffener (right).

Table 2. Comparison between different stiffening alternatives.

Beam stiffening	Elastic buckling load FE kN	Ultimate load FE kN
End plate	2217	879
Full stiffener	2076	753
Without	2018	741

End plates and full stiffeners (see Figure 12) are common practical elements adopted in the steel construction for beam stiffening. These two kinds of stiffeners can be used to stiffen the cross-section in connection areas to prevent cross-section deformation.

Table 2 indicates that the end plates can increase the system ultimate load much more efficiently. This is due to the fact that end plates can not only prevent cross-section deformation but also act as a warp spring, which also increase the buckling load intensely.

4 CONCLUSIONS

This paper presented the results of the early stage of a research on the lateral torsional buckling behavior of members in steel structures with hanging-profile connections. A parametric study was conducted with nonlinear finite-element-models in ANSYS Workbench. The results of the analysis were compared with the Eurocode 3 predictions. It showed that the common design in practice based on the assumption single-span members with fork bearings was insufficient and not satisfying, since it provides sometimes overly conservative yet sometimes overestimated results. Therefore more detailed theoretical and experimental study is needed for this issue.

5 OUTLOOK

In the undergoing research the following points are being investigated. Firstly a test program will be carried out to verify the FE models. On the basis of the verified FE model, further parametric analysis will be performed to generate additional data covering a wider range of hot-rolled cross-section and more gusset plate geometries. In the meantime the formulized

elastic system buckling load considering the torsional stiffness of cross-section and gusset plate as well as the aforementioned elastic end fixing as springs is being studied. Ultimately a new and improved design method derived from Euro Code will be developed for lateral torsional buckling verification of here discussed cases.

REFERENCES

DIN EN 10034. 1993. *I- und H-Profile aus Baustahl; Grenzabmaße und Formtoleranzen.* Brüssel: CEN – Comité Europèen de Normalisation.

DIN EN 1993-1-5. 2010. *Eurocode 3: Bemessung und Konstruktion von Stahlbauten –Teil 1–5: Plattenförmige Bauteilen.* Brüssel: CEN – Comité Europèen de Normalisation.

ECCS-CECM-EKS. 1984. *Publication No. 33:Ultimate Limit State Calculation of Sway Frames with Rigid Joints.* Brüssel: s.n.

Gonzàlez Orta, Fernando. 2011. *Untersuchung zum Material- und Tragverhalten von Schrauben der Festigkeitsklasse 10.9 während und nach einem Brand.* Darmstadt: Dissertation am Fachbereich Bauingenieurwesen der TU Darmstadt.

Wolf, Christian. 2006. *Tragfähigkeit von Stäben aus Baustahl- Nichtlineares Tragverhalten, Stabilität, Nachweisverfahren.* Bochum: Dissertation an der Fakultät für Bauingenieurwesen der Ruhr-Universität Bochum.

Research and Applications in Structural Engineering, Mechanics and Computation – Zingoni (Ed.)
© 2013 Taylor & Francis Group, London, ISBN 978-1-138-00061-2

Design bearing stresses for injection bolts with short and long duration high loads

A.M. (Nol) Gresnigt
Delft University of Technology, The Netherlands

D. (Darko) Beg
University of Ljubljana, Faculty of Civil and Geodetic Engineering, Slovenia

ABSTRACT: The present design bearing stress for injection bolts is based on long duration creep tests. Recent research has shown that for short duration loads higher design bearing stresses can be allowed. This is especially important for structures where the main load consists of short duration loads e.g. wind load, such as the new glass roof in the Amsterdam Central Railway Station. A summary is given of the results of recent monotonic and cyclic short duration testing in the University of Ljubljana and Delft, as well as a recommendation and motivation to modify the present rules in Eurocode 3 and EN1090-2.

1 INTRODUCTION

The present recommended design bearing stresses for injection bolts are based on long duration creep tests. The criterion is that the displacement is not larger than 0.30 mm. This is the same criterion as for high strength friction grip bolts.

Injection bolts however, have the advantage that in case of overloading no sudden large displacements occur as may happen in connections with high strength friction grip bolts when they slip.

In the European Recommendations for Bolted Connections with Injection Bolts (ECCS, 1994) the design bearing stress as determined in long duration testing is used for the serviceability limit state verification. For the ultimate limit state a higher bearing stress is given (factor 1.2), motivated by the above mentioned advantage of injection bolts. The factor 1.2 was chosen by engineering judgment; virtually no test results were available. It was expected that the chosen values would be sufficient to avoid that the ultimate limit state would govern the design. The Eurocode 3 rules are formulated somewhat different, but are practically the same.

In recent applications of injection bolts, such as a new glass roof in Amsterdam Central Railway Station, it appeared that the short duration loads in the glass supporting steel structures due to wind may be much more than anticipated when the ECCS recommendations were drafted.

It was asked whether it would be possible to allow much higher bearing stresses for short duration loadings. To answer this question the results of research performed in the University of Ljubljana could gratefully be used. In addition to that, short duration tests were performed in the Stevin Laboratory of Delft University of Technology. The test results together with test results from the research in Ljubljana were sufficient to allow much higher bearing stresses for the glass roof in Amsterdam.

In this publication the main results are summarized and a recommendation is given for a modification to the present design rules in the Eurocode 3.

2 INJECTION BOLTS

Injection bolts are bolts in which the cavity produced by the clearance between the bolt and the wall of the hole is completely filled up with a two component resin. Filling of the clearance of an injection bolt is carried out through a small hole in the head of the bolt. After injection and full curing of the resin, the connection is slip resistant. Shear load is transferred through bearing and shear of the bolt.

Injection bolts can be manufactured from normal standard structural bolts. The bolts and washers are adapted to enable the injection of the resin. As compared to other mechanical fasteners, injection

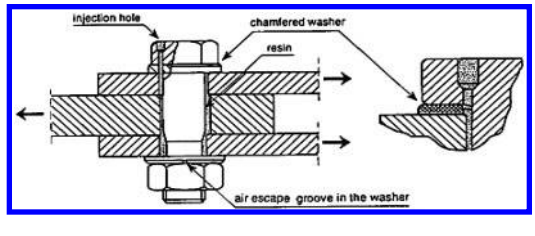


Figure 1. Injection bolt in a double lap joint.

bolts have several advantages. Injection bolts may be applied in new structures and in existing structures for repair and strengthening.

Design rules are given in the ECCS Recommendations (ECCS, 1994). These were the starting document for the sections on injection bolts in Eurocode 3 Part 1-8 (EN 1993-1-8, 2005). Rules for testing the resin and execution can be found in EN 1090-2 (EN 1090-2, 2008).

Resins are susceptible to creep deformation if the bearing stress is too high. In the Fourth International Workshop on Connections in Steel Structures in 2000 (Gresnigt et al., 2000), test results from long duration testing were presented on the two component epoxy resin Araldit SW 404 with HY2404 hardener, now available as RenGel SW 404 + Ren HY 2404.

The main conclusions are:

a. Injection bolts are an excellent alternative for replacing faulty rivets in (old) riveted structures.
b. Injection bolts can successfully be used for strengthening of (old) structures, especially where welding or HSFG bolting is difficult to apply.
c. Long duration creep tests were still going on at a bearing stress of 250 N/mm^2 without exceeding the allowable displacement.
d. A high temperature of 70°C as may occur in bridges has only a moderate influence on the deformations. The average creep for ambient temperature (20°C) is 0,19 mm and for 70°C 0,24 mm (at a bearing stress of 250 N/mm^2)
e. The allowable bearing stress may be raised from 130 N/mm^2 up to 175 or 200 N/mm^2.

3 UNIVERSITY OF LJUBLJANA

To promote the use of injection bolts in Slovenia and wider, a testing program on standard bolted lap connections was conducted at the University of Ljubljana. Altogether 22 tests were performed on three different types of connections:

a. Slip resistant connections
b. Connections with injection bolts
c. Connections with preloaded injection bolts.

For comparison, one test was performed on a standard connection with bolts in bearing. Monotonic long- and short duration tests were performed according to EN 1090-2. In addition, 4 cyclic tests were performed for a better insight into the behavior of injection bolts under cyclic loading.

3.1 *Description of the test program*

Monotonic tests: For all three types of connections monotonous tension tests followed strictly the procedure given in Annexes G and K of EN 1090-2.

With the results of the tests the slip factor μ and the bearing strength of the resin $f_{b.resin}$ were determined for the slip resistant connections (with pre-tensioned high strength bolts) and connections with injection bolts, respectively. The same procedure was also used to determine the resistance of connections with preloaded injection bolts, although this is explicitly not allowed for in EN 1090-2.

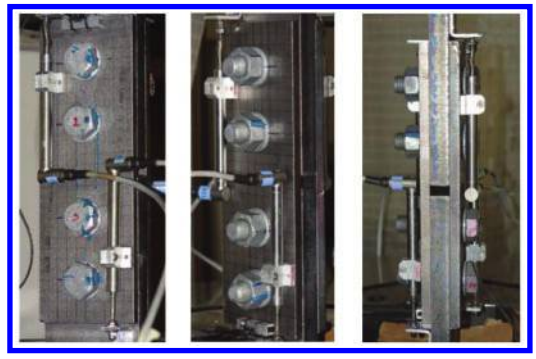


Figure 2. Instrumented test specimen.

The geometry of the standard test specimens with M20 bolts with instrumentation at the beginning of the test is shown in Figure 2. For each connection type 4 short-duration tests have to be done (10 min–15 min) where the resistance is determined at 0.15 mm slip. The fifth test is a long-duration creep test at constant load equal to 90% of the average resistances from the first four tests.

Because each specimen has two connections, there are actually eight results. The average slip in each of the four connections for the time period of 5 minutes – 3 hours after the full load is applied should not exceed 0.002 mm. If this is achieved, the specimen is tested to reach the slip of 0.15 mm and the characteristic resistance is determined based on the obtained results (mean – 2.05 × standard deviation).

If the creep test shows slip that exceeds 0.002 mm, the long-duration test should be extended until safe extrapolation of slip at 50 years is obtained; this slip should be smaller than 0.30 mm to guarantee appropriate long-term behavior of the connection.

It is worth mentioning that for connections with preloaded injection bolts EN 1993-1-8 allows summation of design slip resistance and design bearing resistance of the resin.

Cyclic tests: For connections with injection bolts cyclic tests are not standardized. Two tests at constant displacement amplitude of 0.135 mm (90% of allowable slip) and two tests at increasing the displacement amplitude were performed. The first of the constant amplitude tests was done at low frequency of 0.05 Hz for 120 cycles. The second test was performed at increasing frequency (0.5 Hz – 4 Hz) for 8000 cycles. The tests at increasing displacement amplitude were executed at low cyclic frequency 0.05 Hz.

Note: In the presentation of the test results the word slip is used for the measured displacements for both slip resistant connections with HSFG bolts and connections with injection bolts, although slip is not occurring with injection bolts.

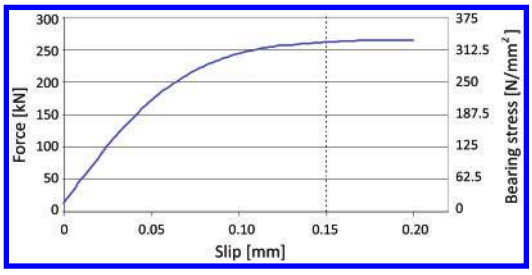


Figure 3. Slip resistant connection – Force-Slip diagram for average results from the first four short-duration tests.

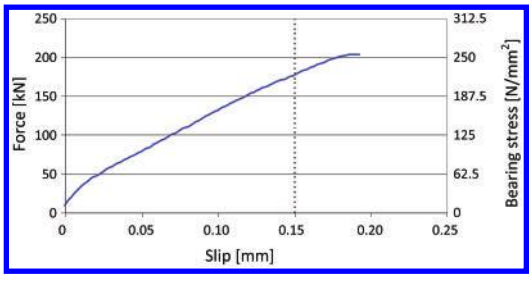


Figure 4. Connection with injection bolts – Force-Slip diagram for average results from the first four short-duration tests.

3.2 *Test results*

Monotonic tests: The results of the first four short-duration tests for all three types of connections are given in Figure 3 to Figure 6 in terms of the average force-displacement (slip) diagrams. Average values were determined for eight results (4 tests × 2 connections in each test specimen). For connections with injection bolts without preloading additional two "eccentric" tests were carried out (Figure 5), where the outer plates were shifted in relation to the inner plates as much as the hole clearance allowed. By this procedure the maximum thickness of the resin was 2 mm. This is the most unfavorable situation regarding the 0.15 mm slip criterion.

At 0.15 mm slip, the maximum value of the slip resistance is reached (Figure 3). The diagrams for injection bolts (Figure 4 and Figure 5) show a practically linear force-displacement relation and after the limit slip at 0.15 mm is exceeded, the force still increases.

The results for the most unfavorable eccentric test specimens give somewhat larger deformability that results in 14% smaller resistance, but from the diagram (Figure 5) it is evident that at slightly larger slip of 0.20 mm the same resistance as for "normal" test specimens can be obtained.

The results for preloaded injection bolts (Figure 6) show favorable summation of the contribution from the slip resistance and the bearing resistance without a force plateau at 0.15 mm slip.

In the three hour "long duration" creep tests according to EN 1090-2 at 90

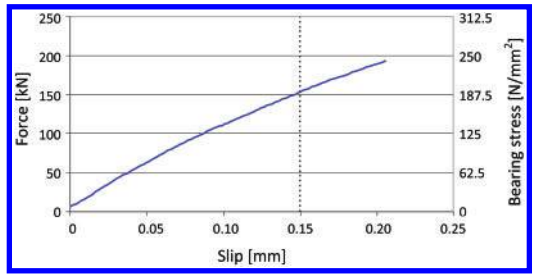


Figure 5. Eccentric connection with injection bolts – Force-Slip diagram for average results from the first four short-duration tests.

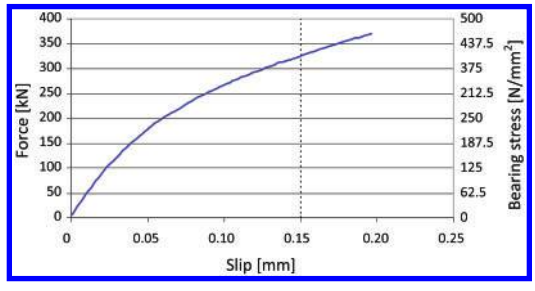


Figure 6. Connection with preloaded injection bolts – Force-Slip diagram for average results from the first four short-duration tests.

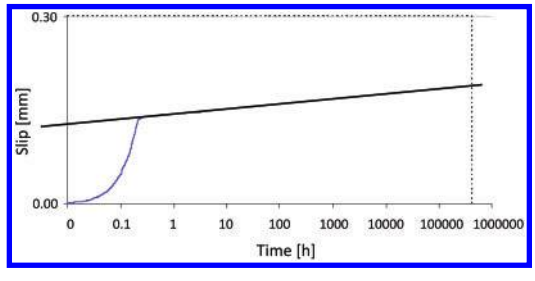


Figure 7. Connection with injection bolts – long-duration test and extrapolation of slip at 50 years.

% of average resistance from previous short-duration tests the additional creep limit of 0.002 mm was not exceeded. From tangent extrapolation to 50 years creep (Figure 7) it is evident that the final creep is less than 0.30 mm.

For the first two types of connections the characteristic values of the slip factor and of the bearing resistance of the resin can be determined from the characteristic resistances given in Table 1 and taking account of the corresponding resistance formulas from EN 1993-1-8:

$$\mu_k = 0.33$$
$$f_{b,resin} = 200 \text{ MPa}$$

Unfavorable eccentric location of bolts can reduce this bearing resistance up to 15%, if the same standard

Table 1. Test results of monotonous tests.

	Slip resistant F_{TEST}	Injection bolts F_{TEST}	Preloaded injection bolts F_{TEST}
Test 1	259.5	185.1	302.2
	251.2	166.3	320.2
Test 2	264.3	186.9	324.8
	255.5	182.0	303.5
Test 3	291.9	174.3	348.8
	286.1	188.5	337.9
Test 4	237	171.2	323.4
	244.3	177.7	331.3
Test 5	281.3	201.5	388.6
	285.8	197.4	407.9
$F_{TEST,AVER.}$	261.2	183.1	338.8
s	19.2	11.2	15.9
F_{RK}	221.8	160.1	306.2

deviation is assumed for eccentric specimens, as was obtained for normal specimens.

$$f_{b.resin}\ \min \approx 170\ \text{MPa}$$

In all test groups the spread of the results was small enough ($s/m \times 100 \leq 8\%$) that no additional tests (according to EN 1090-2) were necessary.

From Table 1 it appears that the connections with injection bolts have smaller resistance at the set deformation limit than the slip resistance connections. But it is remembered that for injection bolts the linearly increasing force-displacement diagram is more favorable (no sudden slip). Connections with preloaded injection bolts show good performance, but the obtained characteristic resistance $F_{RK}{}^{TEST} = 306.2$ kN is smaller than the sum of characteristic resistance of the slip resistant connection and the connection with injection bolts ($F_{RK}{}^{SUM} = 381.7$ kN).

It means that in this case the resistance obtained from EN 1993-1-8 (based on μ_K and $f_{b.resin,K}$ from the tests) is more than 20% higher than the test resistance of the connections with preloaded injection bolts. As stated above, this test resistance was determined with the same test procedure as for the basic two types of connections, although EN 1090-2 does not explicitly include this type of connections.

On the other hand it is evident that the Eurocode resistance is easy reachable at slip that is a bit larger than 0.15 mm (0.20 mm–0.25 mm).

Cyclic tests: Bridges under traffic loading and buildings under wind loading and in seismic events are subjected to cyclic loading. The basic idea is to examine the behavior of connections with injection bolts at cyclic loading that does not lead to exceeding of the bearing resistance of the resin. Namely, for larger actions such connection behaves as normal bearing connections with bolts in shear. For this reason only results of two cyclic tests at constant displacement amplitude of 0.135 mm are presented.

Force displacement diagrams for both tests are shown in Figure 8 and Figure 9. In both cases almost

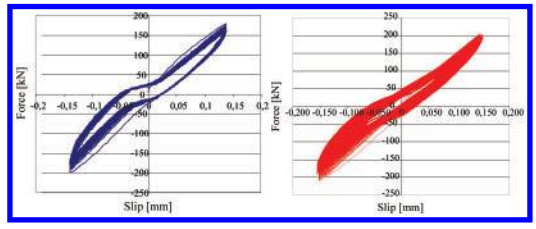


Figure 8. Force-slip diagrams for cyclic tests, a) test at 0.05 Hz, b) test at 0,5 Hz to 4 Hz.

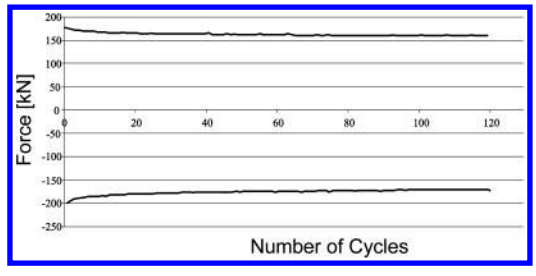


Figure 9. Force amplitudes for cyclic test at 0.05 Hz.

elastic behavior is observed with narrow hysteresis loops (Figure 8) and without visible influence on the loading frequency. In the first 10 or 20 cycles the force amplitude decreases by about 10%, but then it remains practically constant (Figure 9). This means that the behavior of connections with injection bolts at displacement amplitudes of 90% of the allowable slip is very good.

From the short duration cyclic tests it appeared that a much higher bearing stress could be applied without exceeding the deformation limits.

4 DELFT UNIVERSITY OF TECHNOLOGY

In Amsterdam an extension to the railway station is under construction (2011–2013) with a large glass roof (10). High demands were put on the stiffness of the glass supporting steel structure. Displacements in bolted connections had to be reduced to very low values. The main reason for that was the safety requirement in case of fire (bus station beneath). To avoid too much uneven heating of the glass a narrow supporting width of the glass panels was required.

The application of high strength friction grip bolts was problematic because of the need to remove locally the corrosion protection (paint system) and the risk of corrosion traces later on. Then it was decided to investigate the application of injection bolts M27.

The main load on the roof is wind load, which is short duration. It was asked whether it would be safe to allow higher bearing stresses for this load case than the bearing stresses based on long duration creep testing. Injection bolts would be applied in normal size and oversized holes.

To answer this question, the results of the tests in the University of Ljubljana were most helpful. The



Figure 10. Artist impression of the extension Railway Station Amsterdam and the glass roof under construction (April 2012, project IJSEI, see Google).

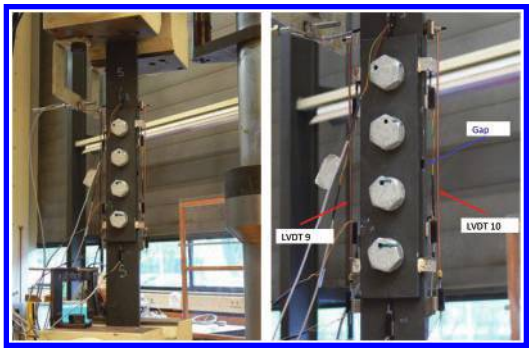


Figure 11. Test specimen with four short LVDT's and two long LVDT's.

authorities requested for extra testing focusing at the application in Amsterdam.

4.1 *Test program*

Six tests were performed on test specimens with M27 bolts as shown in Figure 11. The preparation of the test specimens was done by the contractor guided by the engineering office. The engineering office decided for at random position of bolts to simulate the situation in practice. This resulted in different distances of the main plates (position of bolts in the holes), giving different sizes of the gap.

The design bearing stress would be based on the allowed maximum displacement of 0.95 mm = 0.30 mm per bolt + 0.35 mm because of the elongation of the steel. Per test specimen 10 cycles were performed, with a loading speed of 2 kN/sec = 2 minutes till maximum load. Then waiting time was 5 sec followed by quick unloading, waiting 10 sec and start a new cycle.

4.2 *Test results*

Test main result of the first test is given in Figure 12. Other tests gave similar values.

The tests were displacement controlled. The maximum average displacement was 0.95 mm. The maximum bearing stress per cycle is given in Figure 13. The decline is the largest in the first cycles and then the average tends to stabilize at about 310 N/mm^2. It is noted that the last cycle had somewhat smaller displacement than 0.95 mm.

In test 5 and 6 the test was continued after the first 10 cycles with displacement 0.95 mm up to displacement

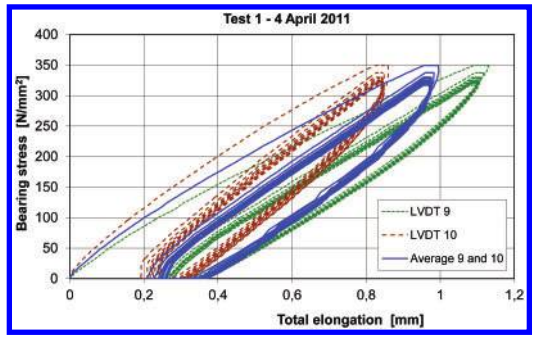


Figure 12. Main result of test 1: Bearing stress – Total elongation.

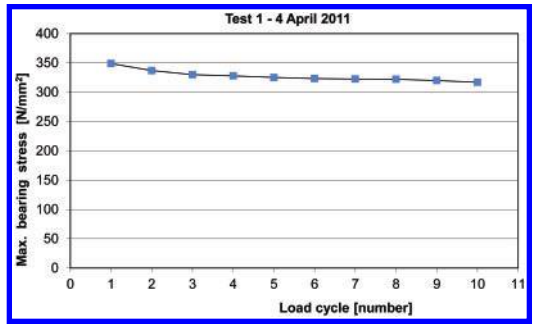


Figure 13. Maximum bearing stress per cycle in test 1.

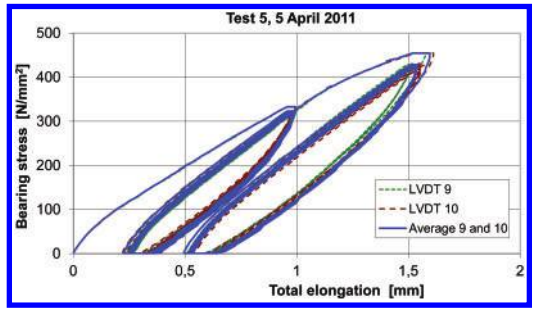


Figure 14. Main result of the fifth test: Bearing stress – Total elongation.

1.55 mm (Figure 14). Also at this larger displacement the decline in the bearing stress was very limited.

In Table 2 an overview of the main test results is given. Differences in the results probably must be mainly attributed to the differences in the position of the bolts in the holes as explained before.

For a 95% chance of exceeding the design value it was calculated that the allowable design bearing stress would be 284 N/mm^2. It was decided to adopt for the injection bolts in the glass roof the following values.

$$f_{b,resin,long\ duration} = 200\ N/mm^2$$

$$f_{b,resin,short\ duration} = 280\ N/mm^2$$

When short duration and long duration loads are considered in relation to creep it is noted that in the

Table 2. Overview of test main test results.

Test	F after 10th load cycle (kN)	$f_{b,resin}$ (N/mm^2)
1	257	317
2	233	287
3	242	298
4	262	323
5	250	309
6	242	299

Eurocode this is only applicable to structures where creep is relatively long duration (concrete, timber).

In injection bolts the creep process is quicker. Wind load is very short duration and will not lead to significant creep, but e.g. snow load and temperature load could be longer duration. In view of this it was decided to consider the following load combinations for the glass roof for the middle long term loads: and

$$1{,}2G+1{,}0Q_{snow}+0{,}5Q_{temp}$$

and

$$1{,}2G+1{,}0Q_{temp}$$

For the short term loads (wind) the standard load combinations were checked with $f_{b,resin,} = 280\ N/mm^2$.

5 CONCLUSIONS AND RECOMMENDATION

The main conclusions and recommendation from the research in the Universities of Ljubljana and Delft are:

a. The long duration bearing stress of the tested resin can be taken as $200\ N/mm^2$. It was proposed in the 2000 Roanoke paper on bases of the tests reported in that paper and conformed in the present testing.
b. The short duration bearing stress can be taken considerably higher than the long duration bearing stress.
c. It is recommended to modify Eurocode 3 part 1–8 and EN 1090-2 accordingly and make a distinction between long duration and short duration load combinations.

ACKNOWLEDGEMENT

The authors thank Hollandia (www.hollandia.biz), contractor for the steel structures of the extension of the Railway Station Amsterdam and engineering office Movares (www.movares.com) for their sponsoring and permission to publish the results.

REFERENCES

ECCS, (1994). European recommendations for bolted connections with injection bolts. ECCS publication No. 79, Brussels.

Gresnigt, A.M., Sedlacek, G., Paschen, M. (2000). *Injection bolts to repair old bridges*. Fourth International Workshop on Connections in Steel Structures, Roanoke, VA, USA.

EN 1993-1-8, (2005). Eurocode 3 Design of Steel Structures, Part 1–8: Design of joints.

EN 1090-2, (2008). Execution of steel structures and aluminium structures, Part 2: Technical requirements for steel structures.

Van Lint H.J., Van Wolfswinkel J.C., Gresnigt A.M., (2012) *Besparen op injectiebouten (Economic design with injection Bolts)*. Bouwen met Staal 226, April 2012 (in Dutch language; it contains several papers on the design and construction of the new glass roof in Amsterdam).

Research and Applications in Structural Engineering, Mechanics and Computation – Zingoni (Ed.)
© 2013 Taylor & Francis Group, London, ISBN 978-1-138-00061-2

On evaluation of a unified moment-rotation characteristic of steel and steel-concrete composite joints

M.A. Gizejowski & W. Barcewicz
Warsaw University of Technology, Warsaw, Poland

J. Uziak
University of Botswana, Gaborone, Botswana

A.A.K. Saleh
Warsaw University of Technology, Warsaw, Poland
Formerly Aljabl Al-Ggarbi University, Gharyan, Libya

ABSTRACT: The steel and steel-concrete composite joints moment-rotation characteristic postulated in present structural eurocodes is based on a piecewise relationship consisting of the linear part, in the quasi-elastic region (up to the limiting value of two third of the joint moment resistance), and – from that point – of the curvilinear part, valid for the inelastic region (up to the limiting value termed the joint moment resistance). This characteristic for end-plate joints is proposed to be of the same format for steel and composite joints, therefore its shape is not dependent upon the reinforcement ratio. Such an approach has an advantage of being simple but, on the other hand, leads to a discontinuous function describing the joint tangent stiffness. It is also not general enough to be able to account for the effect of joint post-limit hardening stiffness. In order to capture the effect of joint progressive stiffness degradation with the hardening effect taken into account, a unified three parametric continuous analytical model is developed. All the details of this model are presented together with the calibration procedure for basic model parameters. Experimental data obtained from laboratory tests carried out at the Warsaw University of Technology is used for the calibration of developed model. Its results are given together with the proposed values of calibrated model parameters for practical application. Finally, moment-rotation characteristics according to the developed model obtained with the use of calibrated model parameters are compared with the experimental results for different values of the joint reinforcement ratio. Conclusions with regard to engineering practice are drawn.

1 INTRODUCTION

In the design of frame systems in skeletal buildings technological and economical profits can obtained by using end-plate beam-to-column joints with a reduced number of stiffeners and supplementary plates, if any. Such joints are to be considered semi-rigid steel or steel-concrete composite joints for which the behavioral characteristic needs to be included in the design for analysis and verification procedure. The basic behavioral characteristic of beam-to-column joints used in frame systems of skeletal buildings, describing their actual behavior, is the moment-rotation relationship M-ϕ in which ϕ is the angle of relative rotation of the beam with reference to the column in the considered joint and M is the bending moment $M_{j,E}$ being the action effect to be transferred by the joint. The M-ϕ curves may be obtained from experimental tests or from analytical modeling.

The steel and steel-concrete composite joints moment-rotation characteristic postulated in present structural eurocodes (EN 1993-1-1, EN 1993-1-8 & EN 1994-1-1) are based on piecewise relationship consisting of the linear part in the quasi-elastic region (up to the limiting value of two third of the joint moment resistance) and from that point – of the curvilinear part valid for the inelastic region (up to the limiting value termed the joint moment resistance). This characteristic is postulated to be for end-plate joints of the same format for steel and composite joints, therefore its shape is not dependent upon the reinforcement ratio ρ. Such an approach has an advantage of being simple but on the other hand leads to a discontinuous function describing the joint tangent stiffness and is too simple to take into account the effect of joint post-limit hardening stiffness on the shape of the characteristic.

It has been proven in the experimental work carried out at the Warsaw University of Technology that the joint moment-rotation characteristic is a continuous function consisting of the quasi-elastic region, inelastic region and rotation hardening region, with a continuous function of its first derivative describing

the joint actual stiffness (Barcewicz 2010). Taking the approach used in the present design codes, a new analytical formulation was developed in which the joint moment-rotation characteristic is postulated to be dependent upon the reinforcement ratio (Barcewicz & Gizejowski 2011). Therefore the characteristic has the shape changing from that corresponding in the present eurocodes for steel joints ($\rho = 0$) to the one corresponding to composite joints with a certain limiting value of the joint reinforcement ratio ($\rho = \rho_0$). The limiting reinforcement ratio ρ_0 for a given joint corresponds to a situation when the resultant of its fully stressed tension zone is equal to the resultant of its fully stressed compression zone. For reinforcement ratios $\rho \geq \rho_0$ the shape of composite joint characteristic remains the same as for the case corresponding to $\rho = \rho_0$. This model is briefly summarized in this paper together with the former structural eurocode. The joint characteristics obtained in both ways are however conservative because they maintain to disregard the effect of post-limit hardening stiffness.

In order to capture the effect of joint progressive stiffness degradation with the hardening effect taken into account, the three parametric continuous model is adopted hereafter for the analytical formulation (see the models classified by Gizejowski et al. 1998). The Continuous Stiffness Degradation model (CSD model), first applied to describe the joint behavior by Gizejowski et al. (2012), has been chosen for adoption. The current paper is an extension of the previous work (Gizejowski et al. 2012) giving all the details of the developed model together with a calibration procedure for basic model parameters. Experimental data obtained from laboratory tests carried out at the Warsaw University of Technology for beam-to-column joints of different reinforcement ratio, namely $\rho = 0$ for steel joints and for composite joints $\rho = 0.0035$, $\rho = 0.0060$ and $\rho = 0.0135$ is used for calibration. The results of calibration exercise as well as the values of calibrated model parameters are given for practical application.

2 MODELING OF JOINT MOMENT-ROTATION CHARACTERISTIC

2.1 *Generalized eurocode's model*

According to eurocodes (EN 1994-1-1) to evaluate the M-ϕ characteristic of steel-concrete composite joints the same analytical model as for bare steel joints (EN 1993-1-8) should be used. Moment-rotation characteristics of composite joints are therefore independent from the reinforcement ratio. Mathematical description of the joint characteristic is represented by the following formulae:

– in the quasi-elastic region, i.e. $M_{j,E} \leq 2M_{j,R}/3$

$$M_{j,E} = S_{j,ini}\phi \tag{1}$$

– in the inelastic region, i.e. $2M_{j,R}/3 < M_{j,E} \leq M_{j,R}$

$$M_{j,E} = S_j\phi \tag{2}$$

– and finally in the plastic region

$$M_{j,E} = M_{j,R} \tag{3}$$

where $S_{j,ini}$ = joint initial stiffness for the joint linear response in the quasi-elastic region; S_j = joint secant stiffness for the joint nonlinear response in the inelastic region:

$$S_j = \frac{S_{j,ini}}{\mu} \tag{4}$$

and $M_{j,R}$ = joint moment resistance.

The joint secant stiffness factor μ is expressed as follows:

$$\mu = \left(\frac{M_{j,E}}{\alpha M_{j,R}}\right)^{\psi} \tag{5}$$

where $\alpha = 2/3$ is the constant describing the upper limit of joint linear response; ψ = constant describing the shape of curvilinear part of M-ϕ characteristic that for bolted end-plate steel and steel-concrete composite joints is equal to 2.7.

Experimental investigations conducted at the Warsaw University of Technology have shown that the shape of composite joints M-ϕ characteristic is strongly affected by the reinforcement ratio (Barcewicz 2010). Barcewicz & Gizejowski (2011) proposed a generalized eurocode's analytical model that includes the change of the model parameters α and ψ with regard to the reinforcement ratio of composite joints. This generalized approach adopts the reference value of reinforcement ratio ρ_0 and the linear interpolation formulae for model parameters α and ψ in relation to the reinforcement ratio:

$$\alpha = \frac{2}{3}\left(1 - \frac{\rho}{3\rho_0}\right) \geq \frac{4}{9} \tag{6}$$

$$\psi = 2.7 - \frac{\rho}{\rho_0} \geq 1.7 \tag{7}$$

The proposed approach has an advantage of being versatile because it describes the behavior of composite joints when $\rho > 0$ as well as it is valid for bare steel joints when $\rho = 0$. The boundaries of the developed analytical model are shown in Figure 1. For increased values of the reinforcement ratio the limit of the joint linear response decreases from 2/3 to 4/9 of the joint moment resistance while the shape factor of the curvilinear part of the joint moment-rotation characteristic decreases from 2.7 to 1.7. The change of basic model parameters results in decreasing of the secant stiffness corresponding to the joint moment resistance from one third to one fourth of the initial stiffness, and results also in shifting the limiting rotation φ_X, at the intersection of moment-rotation curvilinear part and the moment resistance, from $\varphi_{X,min}$, to the a larger value of $\varphi_{X,max}$.

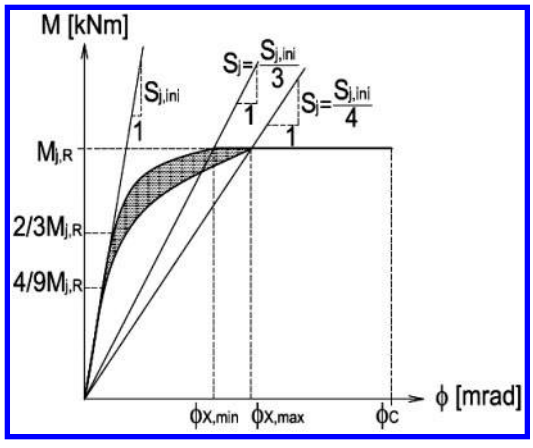


Figure 1. Envelope of reinforcement ratio dependent unified moment-rotation characteristics for steel and composite joints.

2.2 *Proposed CSD model*

As it has been mentioned before, present codification rules and their extensions for the evaluation of joint moment-rotation characteristic disregard the joint post-limit hardening stiffness (see Fig. 1). In order to capture the joint progressive stiffness degradation with hardening effect taken into account, the three parametric CSD model is adopted. It is based on a probabilistic considerations of independent linear mechanisms of initial response with the stiffness $S_{j,ini}$ and the post-limit response with the rotation hardening stiffness $S_{j,postlim} = \xi S_{j,ini}$ (Gizejowski et al. 1998). This relationship takes the following form:

$$M_{j,E} = \left[\left(\frac{1}{S_{j,ini}\phi} \right)^n + \left(\frac{1}{M_{j,R} + \xi S_{j,ini}\phi} \right)^n \right]^{-\frac{1}{n}} \tag{8}$$

where $\xi = S_{j,postlim}/S_{j,ini}$ is the factored hardening modulus; and $n =$ shape factor of the M-ϕ characteristic.

Note that for the evaluation of both factors, an optimization like procedure is needed with use of experimental data available from laboratory tests. As it has been mentioned earlier, results obtained from the tests conducted at the Warsaw University of Technology are considered throughout this paper.

3 CALIBRATION OF CSD MODEL PARAMETERS

3.1 *Error measures and approximation method*

Using any method for the best fit of developed theoretical model to experimental results, several error measures may be postulated. Referring to a single point, the routinely applied ones are the absolute (ABS) and relative (RE) errors:

$$ABS = M_{\exp,i} - M_{th,i} \tag{9}$$

$$RE = \frac{M_{\exp,i} - M_{th,i}}{M_{\exp,i}} \times 100\% \tag{10}$$

where, $\mathrm{Mexp}_{,i} =$ desired (known) value of the moment obtained from the experiment for the i^{th} recorded rotation φ_i; and $M_{th,i} =$ value of moment obtained from the developed CSD model for the same i^{th} value of rotation φ_i.

In case of assessment of the correlation of experimentally recorded joint multiple point moment-rotation characteristics, a number of error measures may be suggested to assess the accuracy of proposed analytical CSD model, among others:

– mean square error (MSE)

$$MSE = \frac{1}{m} \sum_{i=1}^{m} \left(M_{\exp,i} - M_{th,i} \right)^2 \tag{11}$$

– root mean square error (RMSE)

$$RMSE = \sqrt{\frac{1}{m} \sum_{i=1}^{m} \left(M_{\exp,i} - M_{th,i} \right)^2} \tag{12}$$

– maximal absolute error (MAE)

$$MAE = \max_{i=1,\ldots,m} \left| M_{\exp,i} - M_{th,i} \right| \tag{13}$$

– maximal relative error (MRE)

$$MRE = \max_{i=1,\ldots,m} \left| \frac{M_{\exp,i} - M_{th,i}}{M_{\exp,i}} \right| \times 100\% \tag{14}$$

– average relative error (ARE)

$$ARE = \frac{1}{m} \sum_{i=1}^{m} \left| \frac{M_{\exp,i} - M_{th,i}}{M_{\exp,i}} \right| \times 100\% \tag{15}$$

where, $m =$ number of recorded sets of $(M_{exp,i};\varphi_i)$ for an experimentally obtained moment-rotation characteristic of the tested joint.

In the least mean square approximation used hereafter for the best fit of moment-rotation characteristics of both steel and steel-concrete composite joints, the MSE measure is adopted.

3.2 *Experimental data used in calibration exercise*

The class of joints considered herein uses end-plates of the thickness ranging from 40 to 60% of the bolt diameter. The concrete slab of composite joints is cast on the deep-profiled sheeting and reinforced by the steel bars of the diameter ranging from 6 mm to 12 mm. The specimens are divided into four groups according to their reinforcement ratio in the hogging moment region. The summary of tested specimens and experimentally obtained joint properties of respective groups are presented in Table 1.

Table 1. Experimental data of considered joints.

Setting	Symbol	End-plate		Joint properties [kNm]	
		type*	t [mm]	$S_{j,ini}$	$M_{j,R}$
Group 0	ES1	F	10	22.63	55.52
($\rho = 0$)	ES2	E	10	44.44	92.40
	ES3	E	8	37.43	62.22
	ES4	F	12	27.85	64.60
Group 1	EZ1	F	10	46.91	123.61
($\rho = 0.0060$)	EZ2	E	10	66.89	157.28
	EZ3	E	8	53.38	139.94
	EZ4	F	12	48.28	133.10
Group 2	EZ5	F	10	56.29	178.79
($\rho = 0.0135$)	EZ6	E	10	78.19	201.18
	EZ7	E	8	64.71	183.95
	EZ8	F	12	60.51	187.88
Group 3	EZ9	F	10	36.07	90.01
($\rho = 0.0035$)	EZ10	E	10	50.56	126.11
	EZ11	E	8	48.50	95.00
	EZ12	F	12	37.90	107.77

* F- flush end-plate; E – extended end-plate.

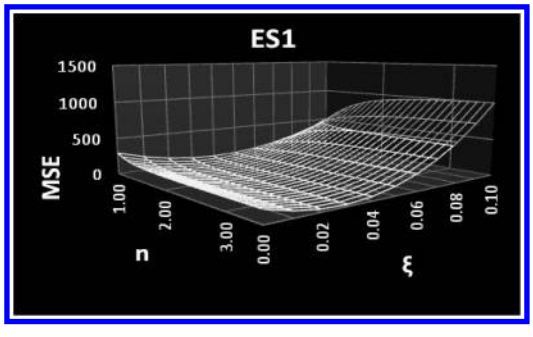


Figure 2. Surface of error measure MSE for specimen ES1.

3.3 *Results of calibration exercise*

For each tested specimen a set of experimentally obtained records ($M_{exp,i}$; φ_i) for $i = 1,2,\ldots,m$ and the number of records m were stored and used hereafter for the calibration exercise to find the best fit values of model parameters ξ and n. The ξ and n values are first established independently for experimentally obtained characteristics of each joint in Groups 0, 1 & 2. Figures 2 & 3 show typical MSE surfaces for specimens of Group 0 while Figures 4 & 5 for specimens of Group 1. The values of model parameter ξ and n leading to the best fit of these and other M-ϕ characteristics of Group 0, 1 & 2 joints are listed in Table 2.

From results obtained in the calibration exercise it is clear that: (a) some identified values of model parameters ξ and n are non-unique, (b) the applied approximation method leads to inaccurate results for specimens of Group 2 (shaded rows in Table 2). The non-uniqueness of the obtained solution is visible for example in Figure 3 where the MSE surface has a rather broad and flat valley meaning that there is a

Table 2. Calibrated model parameters.

Group	Specimens	Type F*		Type E*	
		ξ	n	ξ	n
0	1, 2	0.0275	2.20	0.0292	1.66
	4, 3	0.0278	1.70	0.0273	1.58
1	1, 2	0.0134	2.64	0.0198	1.51
	4, 3	0.0184	1.70	0.0192	1.54
2	5, 6	0.0270	1.34	0.0544	1.13
	8, 7	0.0409	1.17	0.0463	1.14

* Applicable to joints ES and EZ type.

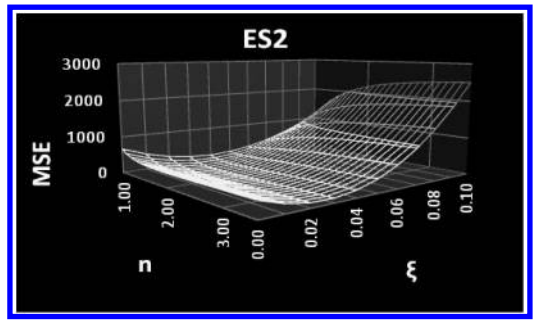


Figure 3. Surface of error measure MSE for specimen ES2.

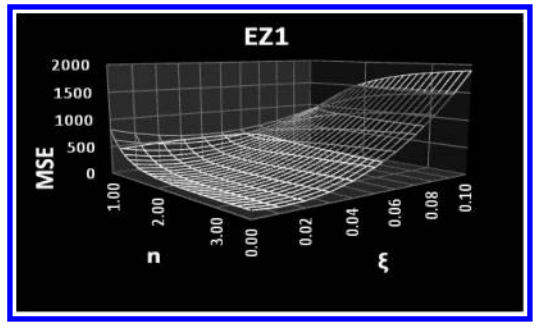


Figure 4. Surface of error measure MSE for specimen EZ1.

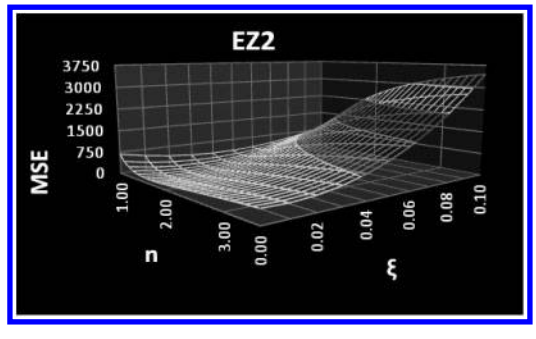


Figure 5. Surface of error measure MSE for specimen EZ2.

number of ξ and n pairs giving similar accuracy of the prediction of M-ϕ characteristic. The reason for inaccuracy is that the moment-rotation characteristics of specimens belonging to Group 2 end at the

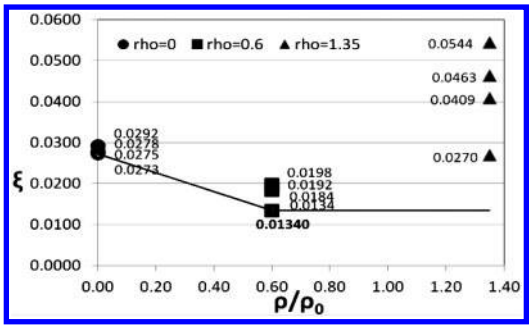


Figure 6. Proposed function of reinforcement ratio dependent model parameter ξ.

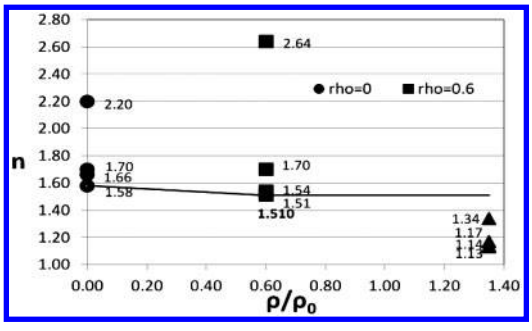


Figure 7. Proposed function of reinforcement ratio dependent model parameter n.

substantially smaller rotation if compared with the other two Groups 0 and 1, and therefore consist of substantially smaller number of records m. It is therefore postulated that at this stage of research, the model parameters ξ and n are approximated linearly at the lower bound values obtained for Groups 0 ($\rho = 0$) and 1 ($\rho = 0.006$), and for specimens with the reinforcement ratio $\rho > 0.006$ the values obtained for $\rho = 0.006$ are used.

3.4 *Proposed values of calibrated model parameters*

The specimens of Groups 0 and 1 are treated as belonging to two separate populations. The values of model parameters ξ and n are therefore evaluated at the lower bound level for each population. The value of ρ_0 ranges between 0.6% and 1.35% for the considered experimental investigations. For simplicity at this stage, an average value of $\rho_0 = 1.0\%$ is adopted.

Figures 6 & 7 present the proposed linear functions of lower bound approximation of model parameters ξ and n:

$$\xi = 0.0270 - 0.0227\frac{\rho}{\rho_0} \geq 0.0134 \tag{16}$$

$$n = 1.580 - 0.115\frac{\rho}{\rho_0} \geq 1.51 \tag{17}$$

The final values of calibrated parameters according to Eqns. (16) & (17) are used in the following section

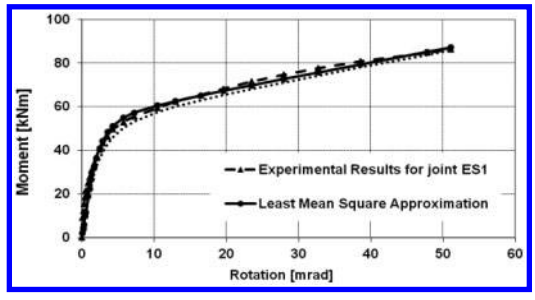


Figure 8. Comparison of moment-rotation curves for ES1.

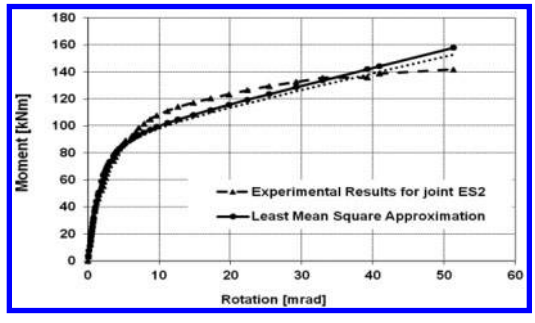


Figure 9. Comparison of moment-rotation curves for ES2.

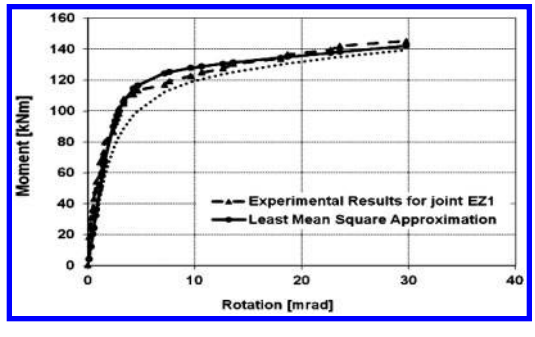


Figure 10. Comparison of moment-rotation curves for EZ1.

for the comparison of experimental characteristics and those evaluated according to Eqn. (8).

4 VERIFICATION OF DEVELOPED CSD MODEL

4.1 *Steel joints*

Verification of proposed unified moment-rotation characteristic is made for all tested joints of Group 0, with flush and extended end-plates. Exemplary results for the flush and extended end-plate steel joints are presented in Figures 8 & 9. The dotted line here and hereafter represents the results obtained with model parameter according to Eqns. (16) & (17).

4.2 *Composite steel-concrete joints*

The comparison is made also for all tested composite joints of Groups 1, 2 & 3. Figures 10 & 11 show typical results for the composite joints of Group 1 with

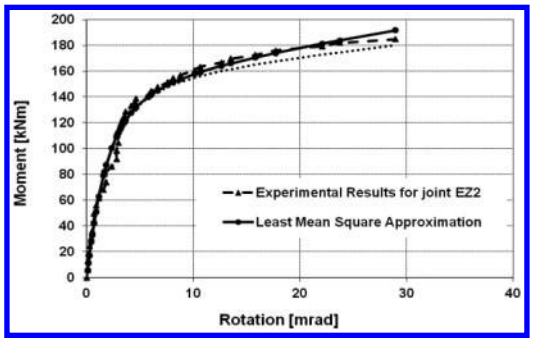


Figure 11. Comparison of moment-rotation curves for EZ2.

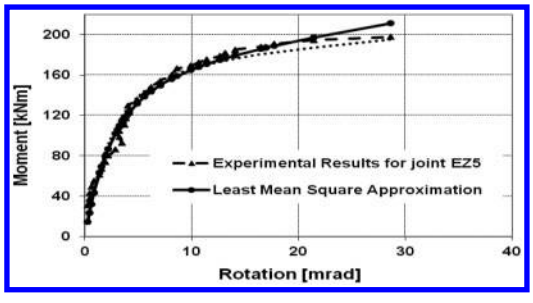


Figure 12. Comparison of moment-rotation curves for EZ5.

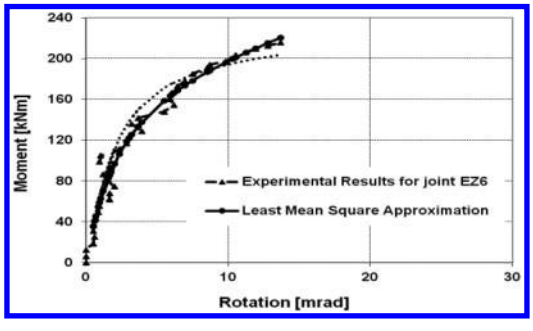


Figure 13. Comparison of moment-rotation curves for EZ6.

flush and extended end-plates. Similar comparison is made in Figures 12 & 13 for the composite flush and extended end-plate joints of Group 2.

4.3 *Joints under sagging moments*

Investigations presented herein deal with moment-rotation characteristics of joints subjected to hogging bending. Similar investigations are now underway for joints subjected to sagging bending (Saleh 2013).

5 CONCLUDING REMARKS

Semi-continuous frameworks composed of semi-rigid/partial-strength steel and/or steel-concrete composite joints are more frequently used in practical applications because of their technological and economical advantages. The most important factors affecting the performance of above mentioned joints are the moment-rotation characteristic and its property parameters, such as the initial stiffness, moment resistance, hardening stiffness and rotation capacity.

The paper investigates moment-rotation characteristic shape, also summarizing the eurocode's approach and its generalization to account for the effect of reinforcement ratio. A detailed study of Continuous Stiffness Degradation model (CSD model) parameters are presented using MSE approximation and experimental results obtained from tests conducted at the Warsaw University of Technology.

The proposed approximation method is proven to be a useful tool in the practical evaluation of model parameters in all the cases where there is a sufficient number m of records in the post-limit range of the experimental moment-rotation characteristic. The proposed best fit model parameters are therefore based only on the experimental results of joint Groups 0 ($\rho = 0$) and 1 ($\rho = 0.006$). The values of model parameters for the reinforcement ratio $\rho > 0.006$ are postulated to be the same as for $\rho = 0.006$.

Comparison of moment-rotation characteristics according to the developed model obtained with use of the calibrated model parameters with the experimentally obtained characteristics shows a good match. It supports the authors' confidence that the proposed unified approach to the evaluation of moment-rotation characteristics of both steel and steel-concrete composite joints adds the value to ongoing research on practical aspects of the behavior of semi-continuous structural systems.

REFERENCES

Barcewicz, W. 2010. *Stiffness, strength and rotation capacity of a certain class of joints in steel structures with composite slabs.* PhD Thesis, Warsaw University of Technology: Warsaw [in Polish].

Barcewicz, W. & Gizejowski, M.A. 2011. Evaluation of M-φ characteristic of composite joints. Influence of reinforcement ratio on the behavior of steel-concrete joints. In Dunai L., Ivanyi M., Jarmai K., Kovacs N., Vigh L.G (eds.), *Proc. 6th Eurosteel Conf., Budapest, 30 August – 2 September 2011*. Brussels: ECCS.

EN 1993-1-1 2005. *Eurocode 3: Design of Steel Structures, Part 1-1: General rules and rules for buildings.* Brussels: CEN.

EN 1993-1-8 2005. *Eurocode 3: Design of Steel Structures, Part 1-8: Design of joints*. Brussels: CEN.

EN 1994-1-1 2004. *Eurocode 4: Design of composite steel and concrete structures, Part 1: General rules and rules for buildings.* Brussels: CEN.

Gizejowski, M.A., Papangelis, J.P., Parameswar, H.C. 1998. Stability design of semi-continuous steel frame structures. *Journal of Constructional Steel Research* 46(1–3).

Gizejowski, M.A., Barcewicz, W., Uziak, J., Saleh, B. 2012. Composite steel-concrete joints for efficient applications in modern building structures. *Botswana Journal of Technology* 20(10): 12–24.

Saleh A.A.K. 2013. *Modelling of beam-to-column joints of steel-concrete composite frames subjected to standard and extreme load combinations*. PhD Thesis, Warsaw University of Technology: Warsaw (in prep.).

Research and Applications in Structural Engineering, Mechanics and Computation – Zingoni (Ed.)
© 2013 Taylor & Francis Group, London, ISBN 978-1-138-00061-2

The influence of the bolt grade on its behaviour under combined tension and shear

A. Renner & J. Lange
Institute for Steel Structures and Materials Mechanics, TU Darmstadt, Germany

ABSTRACT: Since the beginning of the use of bolts in steel construction structural engineers all around the world were used to limit the load bearing capacity of bolts that are loaded with both tension and shear against a quadratic interaction curve. When a few years ago new Europe wide valid standards – the so-called Eurocodes – where established, one was surprised to find a complete different and by far more conservative rule in this. Looking further into detail where this could come from, it occurs that both design rules go back on a very small number of test results, with sometimes questionable test methods and on arguable assumptions and statistical analyses. To ascertain how bolts under combined loads should be treated in future a new test series was conducted. The results are summarized in this paper.

1 BACKGROUND

1.1 *Interaction rules in standards*

A bolt can be loaded with a tension force parallel to its axis, or with a shear force normal to it. For both cases standards give a maximum resistance value to delimit the occurring force against it.

Then again, if a bolt gets a tension and a shear force at the same time the load bearing capacities will of course influence each other. An interaction of the forces has to be considered.

The long-time practised way to do so was by using a quadratic interaction rule (see i.e. German DIN (DIN 18800-1, 2008)):

$$\left(\frac{N}{N_{Rd}}\right)^2+\left(\frac{V}{V_{Rd}}\right)^2 \le 1{,}0 \qquad (1)$$

where N, V tensile/shear force in bolt
N_{Rd}, V_{Rd} loadbearing resistance of bolt under pure tension/shear

(some standards i.e. the British Standard (BS 5950-1, 2000) used a linearized version of this for the easier handling, but it basically describes the same borders).

Now, looking into the new established Eurocode 3 (EN 1993-1-8, 2010) one finds a different new interaction rule:

$$\frac{N}{1.4\cdot N_{Rd}}+\frac{V}{V_{Rd}} \le 1{,}0 \qquad (2)$$

In Figure 1 the functions of both interaction rules are pictured. It appears that for bolts with roundabout the same amount of tensile and shear force the new Eurocode rule is by far more conservative.

This gets even worse for bolts with the shank in the shear force: It would be sensible to look at that point of the bolt where the force interaction really happens, ergo in the shank. This was not a problem with earlier standards that gave a formula to determine the tension capacity of the shank as well (see i.e. DIN 18800-1, El. 809).

The Eurocode lacks a comparable method to determine the shank tension capacity. Following the Eurocode the bolt verification has to be done by mixing up the shear capacity of the shank with the

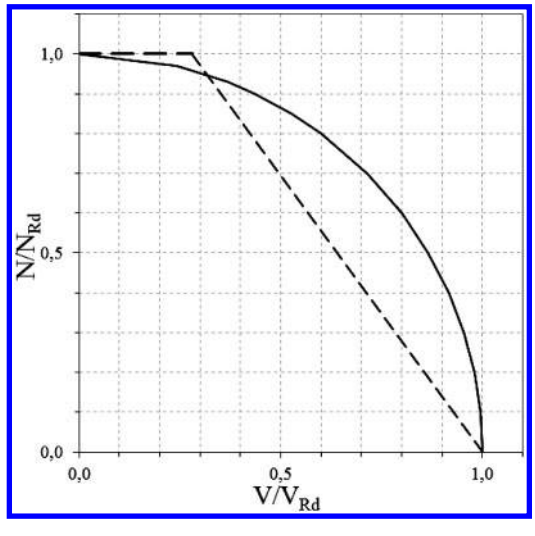


Figure 1. Comparison of interaction rules: Quadratic (i.e. German DIN (DIN 18800-1, 2008)) and linear (Eurocode 3 (EN 1993-1-8, 2010)).



Figure 2. High load connection in the main steel structure of a power plant.

tension capacity of the threaded part, which is not only inconsequent, but uneconomic.

In some adverse cases following the Eurocode this leads to up to 50 % more bolts that are needed.

1.2 *Background of the standard rules*

Of course, in most of the simple connections, which make a big part of steel construction, bolts are either loaded with tension or with shear (or at least were treated in design as if this was the case). So, the main focus in research was always on the load bearing behaviour under a pure load.

Nonetheless, when it comes to more spectacular buildings and the connections become larger and more ambitious and challenging, the occurring of tension and shear in a bolt occurs more often – and the necessity to tread it safe but efficient gets even higher.

Before in the 1980th the first interaction rules were included into the standards, designing engineers were left alone to find a way to handle interaction in bolts. The most common idea here was to superpose the load factors quadratically, as one would do in other interaction cases as well: The most common example is the equivalent stress for a combination of normal and shear stress:

$$\sigma_e = \sqrt{\sigma_x^2 + 3 \cdot \tau_{xy}^2} \tag{3}$$

where σ_e equivalent stress
σ_x normal stress
τ_{xy} shear stress

The transferability of the quadratic rule for the tension-shear-interaction in bolts was then derived from a rather small number of tests on the subject, which results showed indeed a roughly quadratic relation. Why the number of existing tests is so small and why the applicability of some of them could be questioned will be shown in Chapter 2.

For the Eurocode on the other hand in a first step the authors collected proposals for possible rules to include into the standard and then verified them via a statistical evaluation of existing test results. This

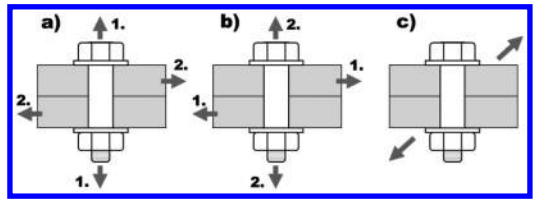


Figure 3. Ways to apply a combined load: a) apply tension force, then apply shear force until failure; b) first shear, then tension (hypothetical); c) diagonal force.)

worked rather well for most of the rules, but here again for tension-shear-interaction in bolts the number of tests on hand was rather small. Now, the statistical analysis showed that the quadratic interaction is not on the safe side for all of the test results, so the Eurocode authors decided to cut the interaction curve down to the now existing bi-linear function.

Sadly enough, the documentation on the utilised tests is quite poor (Snijder 1988 & Sedlacek 2004). It is possible to say that only a few of the tests missed the required safety level, but it is not possible to say which ones.

2 TENSION-SHEAR-INTERACTION TESTS

2.1 *Possible test methods*

To test a bold under a combined load one has to choose from three methods: First way would be to get the bolt onto a certain level of tension and then apply a shear force until the bolt fails (see Figure 3, a)). Second way would be to do so the other way around (first a shear force, then tension until failure, Figure 3, b)), but this way is rather theoretical for the shear force might bend the bolt that way that it will become impossible to apply a tension force afterwards. The third method would be to apply a diagonal force, which results in a corresponding tension and a shear force in the bolt (Figure 3, c)).

One major problem with interaction tests is to get the forces into the bolt. A bolt is a rather short, hard to grip item of a high strength material, there is not much space to grab the head and nut of it to apply tension and then apply shear via shear plates, as requested in the first way. Testers who followed this way helped themselves by not testing real bolts but round bars and threated rods (see chapter 2.2), which could be made much longer than a bolt and hence are easier to grab, but the negotiability of the results onto the behaviour of bolts is to be questioned.

To test a real bolt the test arrangement has to be rather large. For the load introduction stiff plates are needed. The force can be applied via a displacement of the plates, this would mean following the third way. It requests an appropriate construction for the load introduction – and therewith the number of different angles that can be tested is limited.

Additionally to the varying of the tested angles other factors to vary can be the bolt grade and the position of

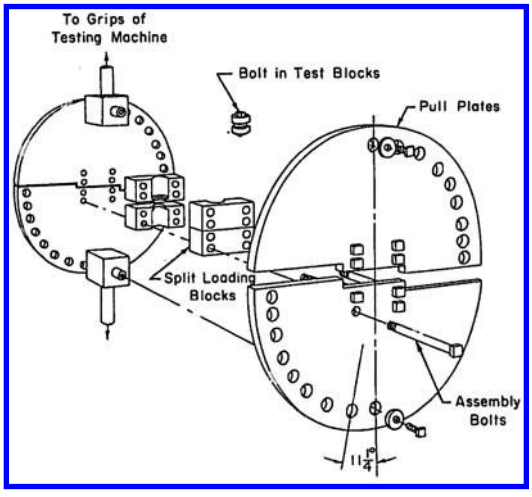


Figure 4. Test setup in Illinois, USA, 1965 (Chesso, 1965)

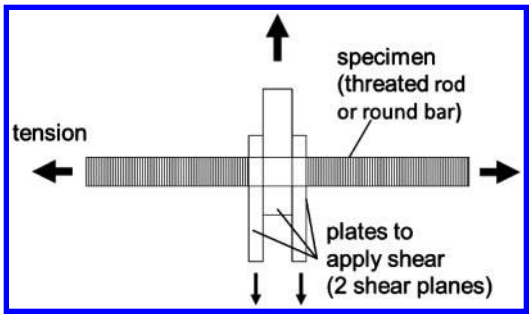


Figure 5. Schematic diagram of tests in Germany (Hassler 1973 & Knobloch 1987).

the shank, one could further think of varying the bolt diameter or even the clamping length. For the establishent of the Eurocode the results of 139 tested bolts were considered, considering the number of varieties this means for some combinations of bolt grade and tension-to-shear-ratio not more than 2 or 3 tests.

2.2 *Former test series*

The number of existing test series on bolts under combined load is limited. One of the earliest was conducted in Illinois, USA (Chesso, 1965), where an altered setup for tests on rivets was used (see Figure 4). The tests were done on real bolts that had fairly a material strength comparable to bolts today of a grade 8.8 or 10.9, but their properties can hardly be compared to them.

Two known tests series were conducted in Germany: The first one in Stuttgart in 1973 (Hassler 1973), the second, slightly bigger one in Essen in 1987 (Knobloch 1987). The later took a small part of a much bigger research project, in which mainly bolts under pure shear were tested.

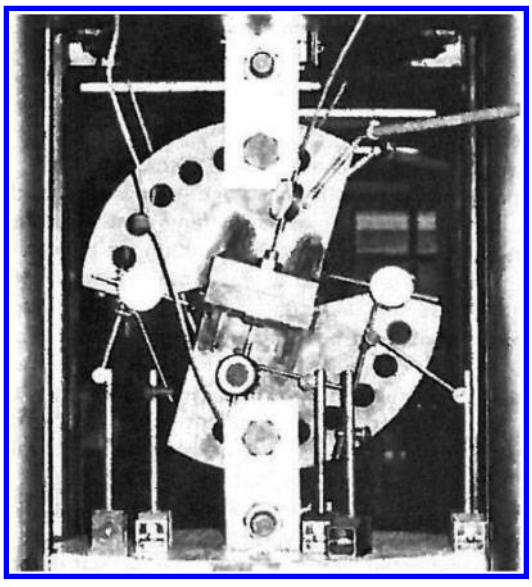


Figure 6. Test setup in Manchester, UK, 1979 (Shakir-Khalil 1979).

In both cases tests were not done on real bolts but on threaded rods and round steel bars instead. Figure 5 shows a schematic drawing of the test setup. First the rod is brought to e certain level of tension, then with a second machine a shear force is applied via the shear plates in the middle of the rod.

The use of rods made the handling a lot easier, but it stays to question whether the results are transferable for bolts, especially in a connection situation. Furthermore the shear force was applied using two shear planes – this keeps out an asymmetric bending in the rod, but it does not represent a possible situation in a connection.

Stuttgart only tested threated rods of grade 4.6 and a diameter of 24 mm. They conducted as a total 15 tests on three different tension levels.

The specimen in Essen were made from round bars with a diameter of 20 mm and the materials characteristics St 37-2, St 52-3, C 45 and 42 Cr Mo 4 that have comparable strength as the common bolt grades 4.6, 5.6, 8.8 and 10.9 (although not exactly the same). To represent bolts with the threat in the shear plane in Essen also threated rods with diameters of 16 mm and 24 mm were tested. It was planned to get materials that match the properties of a grade 5.6 and 10.9, but the available rods did slightly differ from that. They were tested anyway. All in all Essen conducted a total number of 68 tests, again on three different tension levels.

However, as with the Illinois tests before, the results indicated a basically quadratic relation between tension and shear capacity and, together with the theoretical assumptions described in 1.2, this sufficed to include the quadratic function into the standards.

Table 1. Tests for evaluating of Eurocode 3 rule.

	Bolt grade	thread in shear plane	shank in shear plane
Manchester	4.6	20	17
Delft	4.6, 8.8, 10.9	59	43

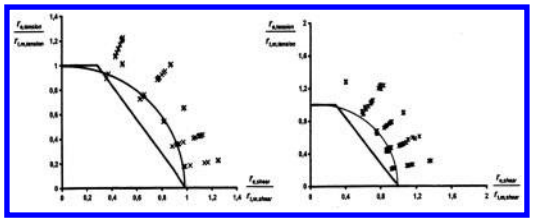


Figure 7. Test results evaluated for the Eurocode rule (Snijder 1988) with quadratic function laid over; left: thread in shear plane; right: shank in shear plane.

Two test series were analysed to evaluate the rule in the Eurocode, one from Manchester, UK conducted in 1979 (Shakir-Khalil 1979), and one from Delft, The Netherlands from 1971 (see Snijder 1988 & Sedlacek 2004).

Both test series were done on real bolts. Manchester used a T-stub-construction to induce the load, so in this case two bolts were tested in one go (setup see Figure 6). Delft used a test setup basically identical with the Illinois setup (Figure 4).

Manchester only tested bolts of a grade 4.6, Delft also tested grade 8.8 and 10.9. Both tested shank and thread in shear plane. The total numbers of tests conducted are shown in Table 1.

Both test series tested 6 different tension-to-shear-ratios plus pure tension and pure shear.

Unfortunately, the original report on the Delft test series is not available anymore. All information about the Delft tests is taken from the background report (Snijder 1988 & Sedlacek 2004) and it is not possible to separate the test results from each other. But by looking at the number of conducted tests and possibilities of variety one can easily tell that for some combinations (bolt grade, shear plane situation and tension-to-shear-level) there cannot be more than two or three evaluated tests results.

The background document shows all evaluated test results plotted into two graphs related to the basic material strength, see Figure 7. One cannot tell which point originates from which bolt grade test but it is obvious that indeed some tests lay below the quadratic function.

3 DARMSTADT TEST SERIES

To be able to judge, whether the bolt interaction rule was reasonably changed for the Eurocode or whether it would be appropriate to handle the subject more differentiated a series of new tests was conducted at the Technische Universität Darmstadt.

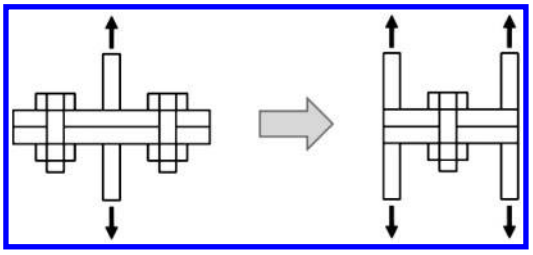


Figure 8. Principle of load introduction: U-Stub instead of T-stub to test only one bolt at a time.

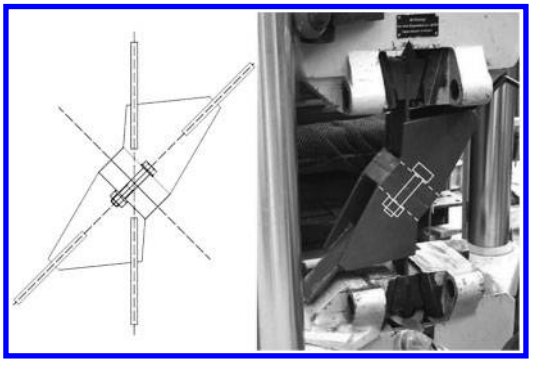


Figure 9. Test setup for tests under 45° and under pure tension (0°); schematic drawing and set up in tension machine (Renner 2012).

3.1 *Test setup*

A test setup was constructed that allows tests on real bolts in a realistic situation as would be found in a connection.

To be able to test only one bolt at a time the test arrangement was built as a U-stub, see Figure 8: The bolt is fixed between two head plates, which will be pulled apart at their sides.

To test a specific tension-to-shear-ratio the head plates are pulled under a certain angle by two plates that were fixed between the load introduction side plates, and which can be clamped into a tension machine, see Figure 9.

The prepared test setups could be used for two different angles each. It was chosen to test four different angles (15°, 30°, 45° and 67.5°) plus pure tension and pure shear. It was further decided to conduct an additional shear test with two shear planes.

Both bolts with thread and with shank in the shear plane were tested. From both types a low strength and a high strength bolt was chosen. For the high strength bolts with shank in the shear plane an additional test series was conducted with pre-loaded bolts to see whether this has any influence on the behaviour. All so far conducted tests are listed in Table 2. Table 3 lists all relevant test parameters.

Table 2. Conducted tests.

	Tension 0°	15°	30°	45°	68°	shear 90°	shrear 2 planes
Bolts with thread in shear plane:							
4.6	4	3	3	3	3	4	4
8.8	3	3	3	3	3	3	3
Bolts with shank in shear plane:							
4.6	4	3	3	3	3	3	3
10.9	4	3	3	3	3	3	3
Bolts with shank in shear plane, preloaded:							
10.9	1	1	1	1	1	1	1

Table 3. Tests parameters.

Bolt diameter:	20 mm
Clamping lenth:	88 mm
Load introduction:	displacement controlled
Testing rate:	2 to 5 mm/min
Test until failure	

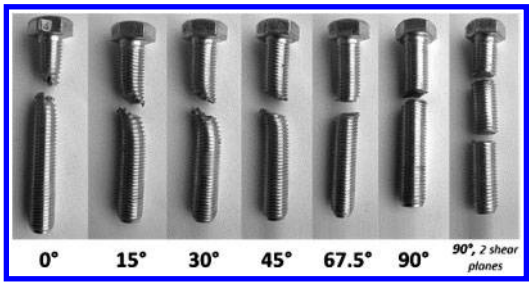


Figure 10. Grade 8.8 bolts with thread in shear plane after failure (Renner 2012).

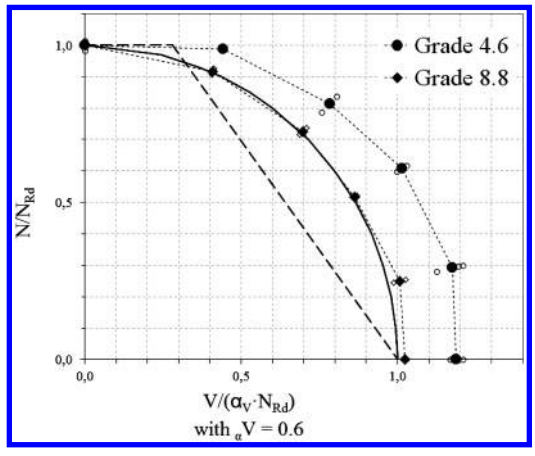


Figure 11. Test results for bolts with thread in the shear plane, related to pure tension and recalculated pure shear capacity.

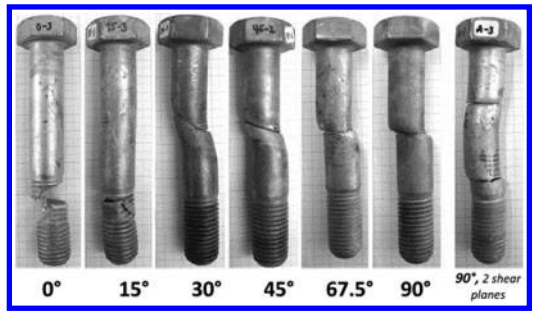


Figure 12. Grade 10.9 bolts with shank in shear plane after failure (Renner 2012).

3.2 *Test results*

All Bolts were loaded until failure. The resulting maximum load was divided into its tension and its shear part.

To plot the results into an interaction diagram the total values have to be related to the maximum pure tension and maximum pure shear load.

For threaded bolts the middle value of the maximum load from the pure tension tests can be used directly as reference value. It was further decided not to use the measured pure shear load for comparison, but to determine the reference value by multiplying the maximum tension load by the shear-to-tension reduction factor α_v given in the Eurocode, which is 0.6 for all tested bolts. This way the comparison to the standard rules is directly given.

Figure 11 shows the result for threaded bolts. In case of pure shear only the results of the two-shear-plane test are plotted here. A bolt tested under pure shear with only one shear plane gets higher load bearing results due to the inclination of the bolt under large deformations which makes the results useless for comparison.

For comparison there is also a quadratic and a bi-linear function as given in the Eurocode plotted into Figure 11. It is obvious that the test results of the bolts grade 8.8 matches the old quadratic function astonishing well. The test results for grade 4.6 are even on the safe side of it, which is due to the factor α_v which is on the safe side for low grade bolts. Apart from this, the resulting curve here is also perfectly quadratic.

For the bolts with a shank the pure tension capacity was recalculated to the capacity of the shank cross area. The results are plotted related to this value in Figure 13.

The bolts that were tested under pure tension and under an angle of 15° did not fail in the shank but in the thread, which has a cross section of 0.78 times the cross section of the shank. The interaction curves have to be limited at this value.

Figure 13 shows in grey a quadratic and bi-linear function for the interaction in the shank. As mentioned in 1.2 the Eurocode does not provide a possibility to consider the tension capacity of the shank, so

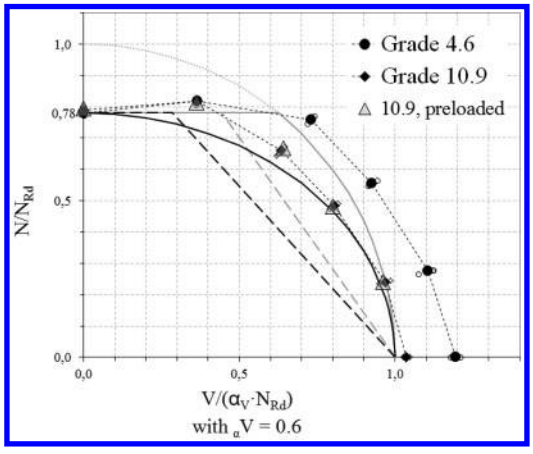


Figure 13. Test results for bolts with thread in the shear plane, related to pure tension and recalculated pure shear capacity of the shank.

the gray bi-linear function is just an adoption of the Eurocode rule. The two black comparison curves mark the non-existing case of interaction considering the shear capacity of the shank and the tension capacity of the thread.

The results in Figure 13 show that for both bolt grades 4.6 and 10.9 the Eurocode function (black bi-linear) lays by far on the safe side. The curve of the 4.6 bolts matches quite well with a quadratic function, here, again, it occurs that the α_v is lower than it could be for low strength bolts.

Nonetheless, the results of bolts with a grade 10.9 lay obviously below the quadratic function. It occurs that for high strength bolts the assumption of a full plastic utilisation of the bolt section is wrong. Due to the material being not as ductile as low strength steel the full plastic stage cannot be reached and the bolt loaded with a combined load fails before.

Figure 13 also shows the results of the tests on pre-loaded bolts. It shows that pre-loading has no influence at all on the load bearing behaviour.

The results of some of these tests can also be found in more detail in a previous paper, see Renner 2012.

4 CONCLUSION

A new test series helps to understand und judge the behaviour of bolts under a combined load of tension and shear. It shows that the long-time common assumption of a quadratic relation for the bolt interaction is not right for high strength bolts, which cannot reach a full plastic stage under a combined load. But for bolts of a lower grade the quadratic assumption fits perfectly well.

The approach of the Eurocode to change the interaction rule for bolts into a by far more conservative version is to a certain extent justified, but the rule that came out of this is too conservative even for the bolts concerned, let alone the bolts of a lower grade, for which a change of the rule was unnecessary. The new Eurocode rule does not allow a consideration of the tension capacity of the shank, if it lies in the shear plane, which makes it even more uneconomic. It stays to question whether it is wanted to stick with a simple one-fits-all rule that is in most of the cases inefficient, or to allow a more detailed treatment in future.

REFERENCES

EN 1993-1-8:2010-12. *Eurocode 3: Design of steel structures – Part 1-8: Design of joints.*

DIN 18800-1:2008-11. *Stahlbauten; Bemessung und Konstruktion (Steel structures; design and construction).*

BS 5950-1:2000. *Structural use of steelwork in building – Part 1: Code of practice for design – Rolled and welded sections.*

Chesso, E. JR., Fausino, N. L. Munse, W.H. 1965. High-Strength Bolts Subjected to Tension and Shear. *Journal of the Structural Division Proceedings of the American Society of Civil Engineers* ST 5: 155–180. Illinois, USA.

Hassler, M. 1973. Versuche mit Schrauben bei kombinierter Zug- und Scherbeanspruchung. *Bericht aus dem Institut für Stahlbau und Holzbau der Universität Stuttgart*. Stuttgart, Germany.

Knobloch, M., Schmidt, H. 1987. Tragfähigkeit und Tragverhalten stahlbauüblicher Schrauben unter reiner Scherbeanspruchung und unter kombinierter Scher- Zugbeanspruchung. *Forschungsberichte aus dem Fachbereich Bauwesen der Universität-Gesamthochschule-Essen* Heft 41. Essen, Germany.

Renner, A., Lange, J. 2012. Load-bearing behaviour of high-strength bolts in combined tension and shear. *Steel Construction Conference*. Oslo, Norway and *Steel Construction* Volume 5: 151–157.

Snijder, H.H., Ungermann, D. et al 1988. Evaluation of test results on bolted connections in order to obtain strength functions and suitable model factors – part A: Results. *Background report to Eurocode 3 "Common unified rules for steel structures"* TNO-report. Rijswijk, The Netherlands.

Sedlacek, G., Schneider, R. 2004. Evaluation of test results for design rules of tension members connected by bolts, *Background documentation to prEN 1993-1-8, Eurocode 3: Design of steel structures, Part 1.8: Design of joints* Third draft. Aachen, Germany.

Shakir-Khalil, H., Ho, C.M. 1979. Black Bolts under Combined Tension and Shear. *The Structural Engineer* Volume 57B/No. 4. UK.

Research and Applications in Structural Engineering, Mechanics and Computation – Zingoni (Ed.)
© 2013 Taylor & Francis Group, London, ISBN 978-1-138-00061-2

Finite element modeling of CHS T-joints strengthened using through bolts

M. A. Mohamed
Structural Engineering Department, Ain Shams University, Cairo, Egypt

A. A. Shaat
German University in Cairo – Assistant Professor (on leave), Ain Shams University, Egypt

E. Y. Sayed-Ahmed
American University in Cairo – Professor (on leave), Ain Shams University, Egypt

ABSTRACT: Increasing the joint capacity of tubular structures has always been a challenge for designers because of their closed nature. This paper investigates a new technique for strengthening the circular chord at the T-joint location against ovalization when subjected to brace member compression loads. The strengthening technique is based on bracing the chord member by radial through bolts with different arrangement patterns. A parametric numerical study based on the finite element method is carried-out. Effects of the chord diameter, brace diameter-to-chord diameter ratio (β), number of bolts, and spacing between them are numerically analyzed. The study revealed that high efficiency for the through bolts technique can be reached with small chord diameter and large β values. A maximum gain in strength of 41% is achieved for a T-joint strengthened with four bolts spaced at 50 mm. It is also found that for large spacing values, odd number of bolts with a central bolt is more efficient in strengthening the CHS T-joints.

1 INTRODUCTION

Various methods for strengthening hollow structural sections (HSS) were introduced over the past decades. The most known method is the "can" method, where the chord is partially thickened at the joints. The can must be accounted for in the design stage of the joint, similar to welding ring stiffeners, diaphragms, doubler plates, or concrete filling. Doubler plate is directly welded to the brace member through penetration weld and then welded to the chord using fillet weld. Another strengthening technique is the collar plates, which are fitted and welded to the chord around the fabricated joint forming the "collar" shape.

Choo et al. (2005) conducted a series of studies on uniplanar T-joints with different parameters such as type of loading (i.e. brace tension or compression), strengthening method (i.e. collar or doubler plates), and different brace diameter-to-chord diameter ratios (β). The study showed that using doubler or collar plates with $\beta = 0.54$ increased the brace compression by 39% and brace tension by 16%. Whereas, for $\beta = 0.28$ strength gain increased by 53% for brace compression and 28% for brace tension.

Banes (1983) and Bradfield et al. (1994) were among the first to use through bolts in rectangular hollow section (RHS) chord members. Holes were first drilled in the vertical walls and bolts were inserted through one end then anchored at the other wall to prevent the chord webs from buckling, which increased the static strength of RHS joints. This led to a maximum increase of 18% in the joint capacity. Zhao (1999) suggested that a wooden block to be inserted into the RHS in addition to the through bolt to also prevent the inward buckling.

Aguilera et al. (2012) investigated the effect of the number and pattern of bolts, as well as the web height-to-wall thickness ratio (h/t) of the chord. An experimental study was conducted for the above parameters. The percentage gain in strength using 15 bolts increased from 3.1% to 29% for h/t ratios ranging from 34 to 65. The study showed that the number and pattern of bolts did not have a major effect on the strength gain for the selected bolts.

Sharaf & Fam (2013) conducted a parametric study using numerical analyses to investigate the effect of chord depth-to-width ratio, brace breadth-to-chord depth ratio, chord span-to-depth ratio, welding the through bolts to chord's web, and the boundary conditions of the chord. The results showed that welding the through bolts affected the ductility of the joint significantly. The strength gain in the joint with welded bolts is 32%, while the strength gain with unwelded bolts is 25%. Aguilera & Fam (2013) also investigated the effect of chord preload on the strength gain. The results showed strength increase of joints by 38%,

46% and 38% when the axial compression loads in the chord were zero, 45% and 80% of its axial strength, respectively.

This paper numerically investigates the effect of through bolts in strengthening circular hollow sections (CHS) T-joints using finite element modeling.

2 NUMERICAL MODELING AND VERIFICATION

A finite element model is developed for the circular hollow sections (CHS) T-joints. Prior to adopting the model for the intended parametric study, three independent experimental studies are used to verify the results of the proposed numerical model. These experimental studies were performed by Zhao & Hancock (1991), Choo et al. (2005), and Aguilera et al. (2012). The finite element program ANSYS (14) is adopted for pre-processing, equation solution and post-processing of the model results. A brief description of the elements used, material modeling, and verification of the model is discussed in the following sections.

2.1 *Element types and material modeling*

Figure 1a shows the structural shell element (SHELL 181) used to model the chord and brace members. SHELL181 is a four-node element with six degrees of freedom at each node. This element is suitable for analyzing thin to moderately-thick shell structures and well-suited for linear, large rotation and large strain nonlinear applications. Shell thickness option is applied to account for the bending stiffness in the walls. Element size is chosen equal to 25 mm and is kept constant for the whole specimen. Figure 1b shows the 3D spar (LINK180) used to model the through bolts. The element is a uniaxial tension-compression element with three degrees of freedom at each node: translations in the nodal x, y, and z directions. Tension-only and compression-only options are supported. As in a pin-jointed structure, no bending of the element is considered. Plasticity, rotation, large deflection, and large strain capabilities are included. Since the chord's web is free to buckle inwards, tension only option is chosen.

The stress-strain curves of all specimens are modeled using a bilinear isotropic hardening plasticity model with a tangent modulus ($E_t = E/100$). In specimens tested by Aguilera et al. (2012) the tangent modulus (E_t) was taken equal to E/1000 with the exception of two specimens (T13 and T14), where a multi linear isotropic hardening plasticity model was adopted to accurately simulate the presented material properties. A bilinear isotropic hardening plasticity model was implemented to model the high-strength bolts with yield and ultimate strengths of 894 and 1034 MPa, respectively.

2.2 *Model Verification*

Due to symmetry only one half of the specimen is modeled. In order to account for the most critical buckling mode, an elastic Eigen buckling analysis is initiated, and the specimen geometry is then updated to simulate the geometric imperfections. A scale factor of 0.2 mm, which is equal to one thousands of the chord height (h/1000), is chosen for the imperfections simulation.

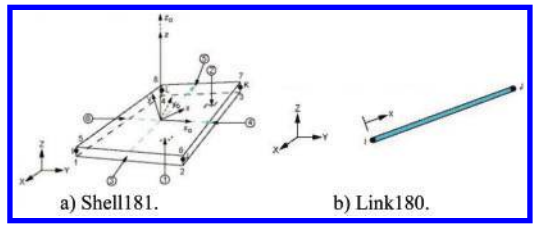


Figure 1. Elements used in the numerical analysis.

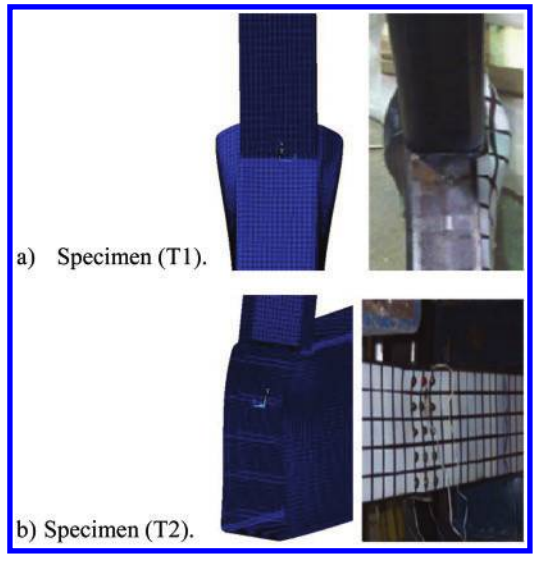


Figure 2. Comparison between failure modes of the FEM and experiments done by Aguilera et al. (2012).

Figure 2 shows the failure modes of specimens T1 & T2 resulting from the numerical model compared to those experimentally recorded by Aguilera et al. (2012). Figure 3 shows the failure modes and load-ovalization curves of specimens Ex-01 & Ex-10 resulting from the numerical model compared to those experimentally recorded by Choo et al. (2005).

A summary of the numerical model verification results in terms of the load at failure is presented in Table 1: it shows a minor discrepancy between the experimental and numerical results with an average of 1.00 and a standard deviation of 0.03.

As such, it can be concluded that the FE model provides realistic results and can capture the real behavior of the specimens. The model is considered suitable and dependable for the parametric study that follows.

3 PARAMETRIC STUDY

A parametric study is conducted using the verified numerical model. The study is performed on CHS

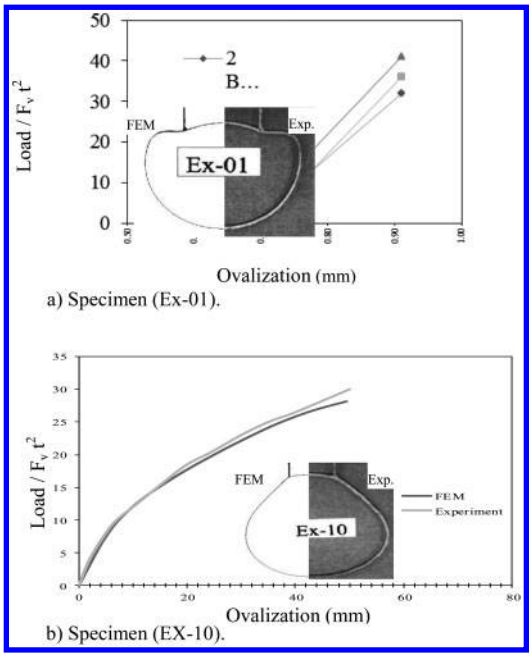


Figure 3. Comparison between failure modes of the FEM and experiments done by Choo et al. (2005).

T-joints strengthened using through bolts and subjected to brace compression force. The effects of the through bolts on the gain strength and reduction in chord ovalization are investigated. The chord ovalization is defined as the difference between the vertical deformations of points A & B, as shown in Figure 4.

Two sizes are selected for the chord members. The first size is of a diameter (d_{rmo}) equals to 356 mm and a thickness (t_o) equals to 6.35 mm, which gives diameter-to-thickness ratio (d_o/t_o) of 56.06. The second size is selected to provide almost the same (d_o/t_o) ratio of 54.80; it is of a diameter (d_o) equals to 610 mm and a thickness (t_o) equals to 11.13 mm. The chord length-to-chord radius ratio ($\alpha = 2L/d_o$) is taken equal to 8.99 (i.e. $L = 1600$ mm for $d_o = 356$ mm and $L = 2742$ mm for $d_o = 610$ mm). The radius-to-thickness ratio ($\gamma = d_o/2t_o$) is kept as constant as possible (i.e. $\gamma = 28.03$ for $d_o = 356$ mm and $\gamma = 27.40$ for $d_o = 610$ mm).

Six brace members are selected, three with each chord size. First group of brace members has diameters (d_1) of 219 mm, 273 mm and 324 mm and is used with chord diameter of 356 mm. These brace members provide different β ratios of 0.62, 0.77 and 0.91, respectively. The second group of brace members has diameters (d_1) of 406 mm, 508 mm and 559 mm and is used with chord diameter of 610 mm; they provide β ratios of 0.67, 0.83 and 0.92, respectively. The length of brace member is kept constant at 500 mm. All brace members are chosen with thick walls (11.13 mm) to avoid premature brace failure.

The load is applied as a point load on a thick plate at the top end of the brace member to ensure uniform

Table 1. Experimental results against FEM

Reference	Specimen ID	$P_{Exp.}$ (KN)	P_{FEM} (KN)	$P_{FEM}/P_{Exp.}$
Zhao & Hancock (1991)	S3B1C11A1	312.00	311.90	1.00
	S3B1C12A1	156.00	160.11	1.02
	S3B1C12A2	101.00	106.52	1.05
	S3B1C21A1	381.00	367.29	0.96
	S3B1C21A2	238.00	237.74	0.99
Choo et al. (2005)	Ex-01	305.10	312.28	1.02
	Ex-02	543.00	557.22	1.02
	Ex-10	407.80	395.14	0.97
Aguilera et al. (2012)	T1	131.00	142.59	1.09
	T2	169.00	168.32	0.99
	T3	164.00	159.17	0.97
	T4	162.00	164.70	1.02
	T5	164.00	162.87	0.99
	T6	165.00	153.94	0.93
	T8	281.00	281.80	1.00
	T11	294.00	295.76	1.00
	T13	448.00	436.80	0.98
	T14	462.00	459.35	0.99
			Average	1.00
			S.D.	0.03

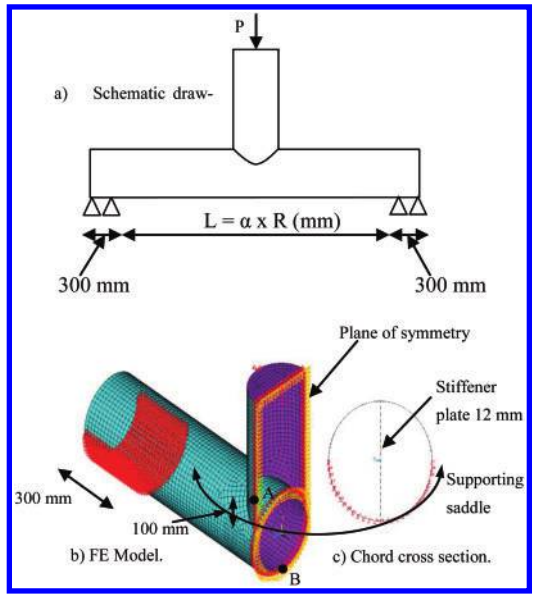


Figure 4. Geometry and finite element modeling of specimens

load distribution. The chord is rested on a half circle supporting saddle with an inner diameter equals to the outer diameter of the chord member. The saddle length is 300 mm; a vertical stiffener is fitted inside the chord member along the entire length of the saddle, as shown in Figure 4.

Due to symmetry, only one half of the specimen is modeled. The brace and the chord members are assumed to be welded using a full penetration weld

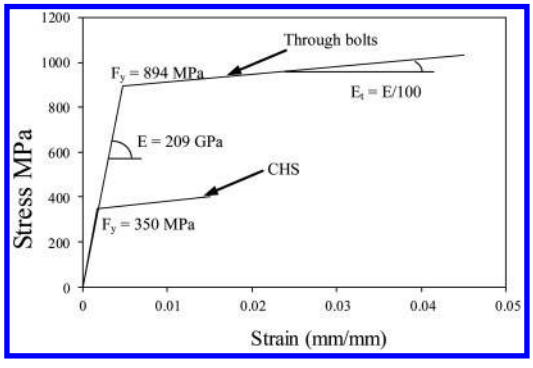


Figure 5. Stress-Strain curves for steel materials.

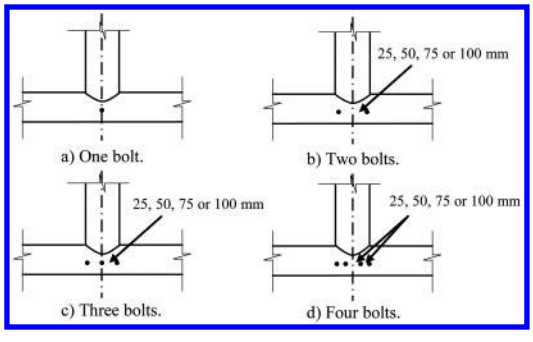


Figure 6. Number and configurations of bolts.

through the entire thickness of the member. Therefore, no additional elements are modeled to simulate the welding material. Yield strength is assumed to be 350 MPa and young's modulus of 209 GPa. Figure 5 shows the stress-strain curves for both the CHS and the through bolts.

A total of 84 specimens are considered in this parametric study: two groups each of 42 specimens. Each group consists of control specimen and 41 strengthened specimens.

The number of through bolts (n) studied is from one to four bolts. The arrangement of the bolts is always symmetric around the joint centerline. Different spacing values (s) between the through bolts along the centerline of the chord are considered (25 mm, 50 mm, 75 mm and 100 mm), as shown in Figure 6.

The following designation system (d_o-d_1-n-s) is considered in the parametric study. The first two numbers are for the diameter of the chord (d_o) and brace member (d_1) respectively, succeeded by the number of bolts (n) followed by the spacing between the bolts (s). For example, 356-219-3-075 designates a specimen with a chord diameter of 356 mm and a brace diameter of 219. The specimen has three bolts spaced at 75 mm. The specimens with zero number of bolts resemble the unstrengthened control specimens.

4 RESULTS

A summary of the results is given in Tables 2 and 3 for groups 1 and 2, respectively. Group 1 specimens are for chord diameter of 356 mm and thickness of 6.35 mm with brace members of 219 mm, 273 mm and 324 mm, while Group 2 specimens are for chord diameter of 610 mm and thickness of 11.13 mm with brace members of 406 mm, 508 mm and 559 mm.

Table 2. Summary of FE results of Group 1 specimens ($d_o/t_o = 56.06$, $\gamma = 28.03$, $\tau = 1.75$, $\alpha = 8.99$).

Specimen ID d_o-d_1-n-s	β	Ultimate Load (KN)	% gain
356-324-0-000	0.91	600.50	N/A
356-324-1-000	0.91	725.30	21
356-324-2-025	0.91	790.45	32
356-324-2-050	0.91	792.13	32
356-324-2-075	0.91	767.58	28
356-324-2-100	0.91	738.99	23
356-324-3-025	0.91	790.34	32
356-324-3-050	0.91	819.23	36
356-324-3-075	0.91	845.49	41
356-324-3-100	0.91	835.79	39
356-324-4-025	0.91	820.08	37
356-324-4-050	0.91	845.57	41
356-324-4-075	0.91	826.40	38
356-324-4-100	0.91	799.36	33
356-273-0-000	0.77	431.78	N/A
356-273-1-000	0.77	463.74	07
356-273-2-025	0.77	474.19	10
356-273-2-050	0.77	483.01	12
356-273-2-075	0.77	489.40	13
356-273-2-100	0.77	493.51	14
356-273-3-025	0.77	473.63	10
356-273-3-050	0.77	483.68	12
356-273-3-075	0.77	495.97	15
356-273-3-100	0.77	504.11	17
356-273-4-025	0.77	482.84	12
356-273-4-050	0.77	504.80	17
356-273-4-075	0.77	520.90	21
356-273-4-100	0.77	529.34	23
356-219-0-000	0.62	310.57	N/A
356-219-1-000	0.62	323.42	04
356-219-2-025	0.62	327.21	05
356-219-2-050	0.62	331.11	07
356-219-2-075	0.62	335.58	08
356-219-2-100	0.62	339.71	09
356-219-3-025	0.62	327.05	05
356-219-3-050	0.62	330.98	07
356-219-3-075	0.62	335.66	08
356-219-3-100	0.62	340.06	09
356-219-4-025	0.62	330.84	07
356-219-4-050	0.62	340.02	09
356-219-4-075	0.62	349.38	12
356-219-4-100	0.62	356.32	15

4.1 *Effect of number of through bolts*

Figure 7 shows the load versus ovalization curves for specimens 356-324-n-050 strengthened with one, two, three, and four bolts at spacing of 50 mm. The figure indicates that the gain in strength increases with increasing the number of through bolts. The results illustrated in Table 2 show that for spacing between

Table 3. Summary of FE results of Group 2 specimens ($d_o/t_o = 54.81$, $\gamma = 27.40$, $\tau = 1.00$, $\alpha = 8.99$).

Specimen ID d_o-d_1-n-s	β	Ultimate Load (KN)	% gain
610-559-0-000	0.92	1701.36	N/A
610-559-1-000	0.92	1813.22	07
610-559-2-025	0.92	1919.86	13
610-559-2-050	0.92	1917.30	13
610-559-2-075	0.92	1910.20	12
610-559-2-100	0.92	1900.12	12
610-559-3-025	0.92	2017.15	19
610-559-3-050	0.92	2016.46	19
610-559-3-075	0.92	2015.71	18
610-559-3-100	0.92	2009.30	18
610-559-4-025	0.92	2111.71	24
610-559-4-050	0.92	2099.14	23
610-559-4-075	0.92	2073.98	22
610-559-4-100	0.92	2043.41	20
610-508-0-000	0.83	1394.36	N/A
610-508-1-000	0.83	1459.02	05
610-508-2-025	0.83	1523.40	09
610-508-2-050	0.83	1522.82	09
610-508-2-075	0.83	1520.28	09
610-508-2-100	0.83	1516.34	09
610-508-3-025	0.83	1579.80	13
610-508-3-050	0.83	1584.46	14
610-508-3-075	0.83	1583.48	14
610-508-3-100	0.83	1579.36	13
610-508-4-025	0.83	1644.12	18
610-508-4-050	0.83	1642.20	18
610-508-4-075	0.83	1631.70	17
610-508-4-100	0.83	1618.32	16
610-406-0-000	0.67	938.27	N/A
610-406-1-000	0.67	969.47	03
610-406-2-025	0.67	1001.60	07
610-406-2-050	0.67	1001.37	07
610-406-2-075	0.67	1001.10	07
610-406-2-100	0.67	1000.86	07
610-406-3-025	0.67	1027.50	10
610-406-3-050	0.67	1030.31	10
610-406-3-075	0.67	1030.82	10
610-406-3-100	0.67	1030.67	10
610-406-4-025	0.67	1049.52	12
610-406-4-050	0.67	1030.74	10
610-406-4-075	0.67	1060.16	13
610-406-4-100	0.67	1060.01	13

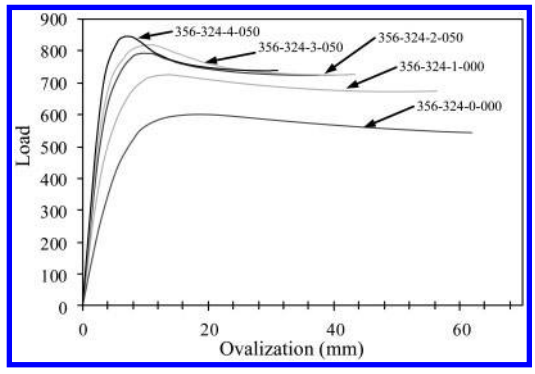


Figure 7. Load ovalization curves for specimens 356-324-n-s.

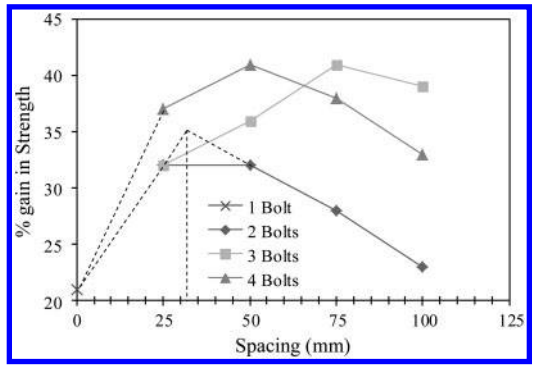


Figure 8. Percentage gain in strength versus spacing between bolts for specimens 356-324-n-s.

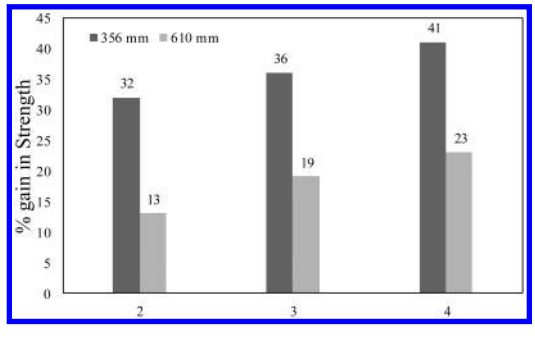


Figure 9. Percentage gain in strength versus number of bolts for two chord sizes 356 mm and 610 mm for 50 mm spacing (d_o-d_1-n-050).

bolts equals to 50 mm, the gain in joint strength is 21%, 32%, 36% and 41% for one, two, three, and four bolts, respectively.

4.2 *Effect of spacing between through bolts*

Figure 8 displays the percentage gain in strength versus the spacing between bolts for specimens 356-324-n-s strengthened with one, two, three, and four bolts. Figure 8 shows that a difference between the trends of the strength gain exists when using odd and even number of bolts. For small values of spacing (i.e. $s < 65$ mm), the trend in strength gain is consistent and in correlation with the number of bolts. For large values of spacing (i.e. $s \geq 65$ mm) the highest gain in strength cannot be achieved without a central bolt under the centerline of the brace member at the vicinity of the joint (i.e. odd number of bolts). The highest gain in strength may be estimated at spacing values of 30 mm, 50 mm, and 75 mm for specimens strengthened with 2, 4, and 3 bolts, respectively.

4.3 *Effect of chord diameter*

The results in Tables 2 and 3 reveal that increasing the diameter of the chord led to an increase in the joint

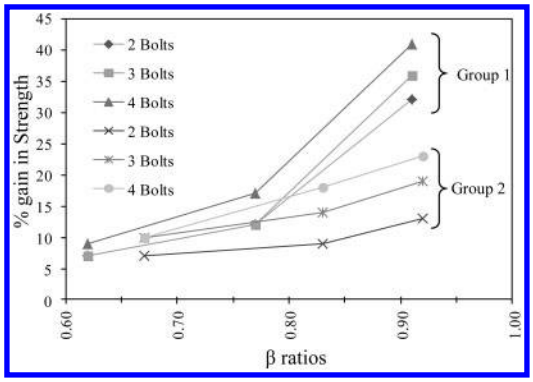


Figure 10. Percentage gain in strength versus different β ratios for 50 mm spacing for different bolts configuration (specimen d_o-d_1-n-050).

capacity. The diameter of the through bolts is kept constant; accordingly the bolts couldn't prevent the ovalization completely. However, increasing the number of bolts led to an increase in the strength gain. Figure 9 shows a comparison between the two sizes of chord (356 mm and 610 mm) for different number of bolts with the same spacing value of 50 mm.

4.4 *Effect of β ratio*

The results presented in Tables 2 and 3 show that β ratio has a significant effect on the gain in strength. Figure 10 shows the percentage gain in strength versus different β ratios for 50 mm spacing between bolts. In Group 1, the percentages gain in strength for specimens strengthened with four bolts are 9%, 17%, and 41% for β ratios of 0.62, 0.77 and 0.91, respectively. Similarly, in Group 2 the percentages gain in strength are 10%, 18%, and 23% for β ratios of 0.67, 0.83 and 0.92 for specimens 610-d_1-4-050, respectively.

5 CONCLUSIONS

This paper numerically investigates the effect of strengthening CHS using through bolts to prevent the ovalization of the chord under brace axial compression load. The study is carried out using ANSYS (14) program. The model is verified against independent experimental studies. The model accounts for geometric and material nonlinearities. It successfully provided realistic results. Accordingly, a parametric study is carried out to find the most suitable configuration for the through bolts, and the most suitable brace diameter-to-chord diameter ratio (β). The results are summarized as follows:

1) Increasing the number of through bolts has a significant effect on the percentage gain in strength. The maximum recorded gain in strength is 41% (specimen 356x324-4-050).
2) For large spacing values ($s \geq 65$ mm), a central bolt under the brace member centerline is very important to maximize the joint strength.
3) For the same configuration of through bolts, the smaller the chord diameter the more efficient the strengthening technique.
4) The larger the brace diameter-to-chord diameter (β) ratio, the more efficient the through bolts technique in strengthening CHS T-joints.

REFERENCES

Aguilera, J. & Shaat, A. & Fam, A. 2012. Strengthening T-joints of rectangular hollow steel sections against web buckling under brace axial compression using through-wall bolts. Thin-Walled Structures: 56: 71–78.

Aguilera, J. & Fam, A. 2013. Retrofitting tubular steel T-joints subjected to axial compression in chord and brace members u using bonded FRP plates or through-wall steel bolts. Engineering Structures. 48: 602–610.

ANSYS program. Release 14 user's manual, Swanson analysis system.

Bains, S. 1983. Investigating into the effects of through bolting on rectangular hollow steel beams in flexure. PhD thesis, UK, University of Sussex.

Bradfield, C. Morrel, P. Ibrahim, A. 1994. Improvements in the flexural capacity of rectangular hollow sections by through bolting. Tubular Structures. Rotterdam: Balkema: 109–114.

Choo, Y. S. & Vegte, G. J. & Zettlemoyer, Li, B. & Liew, J. 2005. Static Strength of T-Joints Reinforced with Doubler or Collar Plates. Journal of Structural Engineering, Vol. 131, No. 1, January 1, ASCE.

Sharaf, T. & Fam, A. 2013. Finite element analysis of beam-column T-joints of rectangular hollow steel sections strengthened using through-wall bolts. 64: 31–40.

Zhao, X. 1999. Partially stiffened RHS sections under transverse bearing force. Thin-Walled Structures: 35:193–204.

Zhao, X & Hancock, G. 1991. T-joints in rectangular hollow sections subjected to combined actions. Journal of Structural Engineering, (ASCE) Vol. 117, No. 8.

Research and Applications in Structural Engineering, Mechanics and Computation – Zingoni (Ed.)
© 2013 Taylor & Francis Group, London, ISBN 978-1-138-00061-2

In-plane shear flexibility evaluation of fastened steel flat plate by numerical simulation considering the interaction between connectors and thin plate

F. Bakhti & R. Tremblay
École Polytechnique de Montréal, Montréal, Canada

C.A. Rogers
McGill University, Montréal, Canada

ABSTRACT: This paper presents finite element analysis performed to examine the shear stiffness of steel roof deck diaphragms. The diaphragms are made from 914 mm wide corrugated steel deck panels with screwed side lap connectors and power actuated fasteners to the underlying frame. A flat sheet finite element model was first developed in which the response of the fasteners could be isolated from the influence of the warping deformations of the corrugated deck panels. A representative sub-panel configuration in terms of fastener spacing, fastener pattern and panel size was modeled and subjected to in-plane shear loading. The results show the presence of an interaction between the pure shear and the connectors' flexibilities, and the total in-plane flexibility of the connected panel, which can be defined as a function of three component flexibilities: shear strain of the plate, slip of the plate on support members at fastener locations and a corrected flexibility that accounts for the interaction between the panel and its connections.

1 INTRODUCTION

The in-plane shear stiffness of connected thin-walled metal structures, which are widely used for roof decking, cladding and shear walls, is of interest to the structural engineer. The analysis of these structures is one of the challenging problems in structural engineering. For example, the predication of the fundamental period of vibration of a typical low-rise steel framed building is directly dependent on an accurate determination of the shear stiffness of its cold-formed steel corrugated roof deck diaphragm (Tremblay et al., 2008).

The two commonly used diaphragm design standards, SDI (Luttrell, 2004) and ECCS (Davies, 2006), are semi-empirical in terms of shear flexibility calculations, which rely on an evaluation of the pure shear, fastener and warping deformations separately without accounting for any interaction. The total in-plane shear flexibility is given by a simple summation of these flexibilities. The fastener type, stiffness and pattern directly affect the response of the diaphragm. A noteworthy empirical method is also available (Tri-Services, 1982) which is still in use in the industry (CSSBI, 2006) for specific connection configurations. In this approach an interaction between the flexibility of the fasteners and the warping deformation is included. Dynamic testing of steel roof deck diaphragms has shown that the predicted in-plane shear stiffness G' using current design methods can be 1.5 higher than that measured in the laboratory (Massarelli et al., 2012).

To understand the behaviour of the connected roof deck panels under in-plane shear loading, the stiffness and the stress developed on them should be known. In the case of continuous fasteners, the analysis of the stiffness and stresses is feasible. However, if the connections are discrete, the prediction of the stiffness and stress becomes more challenging. In this paper, the shear flexibility calculation procedure for steel deck diaphragms revisit numerically considering specifically the connections and the pure shear deformations of the steel panels. The SDI method is referred to as background to the investigation. The presence of an interaction between the connection slip and pure shear flexibilities is investigated by means of finite element analyses.

2 NUMERICAL ANALYSIS

2.1 *Background*

The diaphragms studied are made of 0.91 mm thick, 914 mm wide corrugated panels with screwed side lap connectors and power actuated fasteners to the underlying frame. To eliminate warping deformations from the study, the corrugations were removed and only a flat panel was studied. Cantilever diaphragms composed of one deck panel connected to edge beams

with two fastener configurations were studied (Fig. 1). For the first configuration, the plate was continuously fixed along its perimeter, while for the second configuration a discrete number of connections with different fastener types, stiffness and patterns (Fig. 2) were investigated. The diaphragm length, L_v, corresponds to typical joist spacing.

According to the SDI method, the in-plane shear flexibility due to the pure shear deformations, F_s, and to the connectors, F_c, is expressed by:

$$F_{sc.SDI} = F_s + F_c = \frac{2(1+\nu)}{Et}\frac{w}{L_v} + \frac{2}{(2\alpha_1 + n_e)K_f} \quad (1)$$

The pure shear flexibility is obtained according to the SDI (Luttrell, 2004) and ECCS (1977) methods and corresponds to the theoretical value. The connection slip flexibility, F_c, is evaluated according to the SDI method assuming a rigid plate. In these equations:

- P Shear load (P = 1 kN)
- L_v Diaphragm depth in the direction of loading (L_v = 1525 mm o/c)
- w Panel width between fasteners (w = 912 mm)
- n_e Number of intermediate sheet-to-structure connections along depth at the diaphragm edge (excluding ends)
- n_v Number of frame fasteners at the ends (over w_{sh}, including ends)
- K_f Fastener shear stiffness, deck-to-structure
- α_1 End distribution factor with summation across a full width panel w_{sh} of the panel; is determined assuming linear distribution of the internal force (Table 1) according to the fastener patterns shown in Fig. 2.

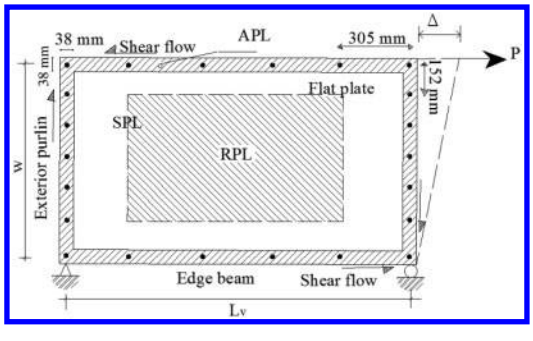


Figure 1. Typical cantilever diaphragm under monotonic shear load with connected flat plate.

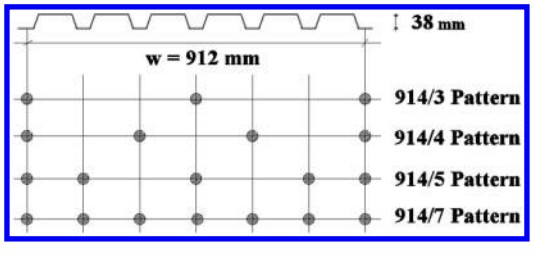


Figure 2. Frame fastener patterns, Canam panel P3606.

- E Young's Modulus (197 GPa)
- ν Poisson's ratio (for steel $\nu = 0.3$)
- t panel thickness (t = 0.91 mm)

The prediction of the overall response of the diaphragm is relevant to assess accurately the stiffness of the individual fastener, K_f, which influences the distribution of the internal forces (De Matheis, 1998). Semi-empirical formulations in North America and Europe are available to provide the equivalent elastic stiffness of connections for thin steel elements depending on the thickness. When the support thickness is greater than 1.21 mm (Sputo, 2010), the SDI (2004) equation for the stiffness K_f is expressed by:

$$K_f = 1000 c_f \sqrt{t} \quad (2)$$

where c_f is a coefficient that depends on the type of fastener.

2.2 *Finite element analyses*

2.2.1 *Numerical modelling*

Finite element analysis was carried out using the program Abaqus (2012). Diaphragms were subjected to applied in-plane shear loading lower than the critical buckling load such that out-of-plane deformations would not arise. Consequently, linear analyses were performed assuming linear material response and small displacements. The flat plate was discretized (Fig. 3) using four node shell elements (S4) having five degrees of freedom per node and five integration points, using Simpson's rule, over the thickness. The frame members which supported the panel were modelled using beam elements. The frame fasteners were modelled using zero length connectors with six degrees of freedom: two translational linear springs in the plane of the panel, one translational rigid spring out of plane of the deck and three rotational rigid springs. The deformations of the plate at the connection were not modeled in the connector, because the study was concerned with the relationship between the connector stiffness and the elastic stiffness K_o corresponding to the deformation of the plate at the connector vicinity due to the stress concentration.

2.2.2 *Finite element modelling assumptions*

The following assumptions were adopted for the finite element model:

– All edge framing was relatively stiff compared to the deck;

Table 1. α_1 factor modified values for each fastener pattern.

Fastener Pattern	α_1 (Modified)
914/3	1.000
914/4	1.111
914/5	1.444
914/7	1.555

– All edge framing connections were considered to be perfect pins to ensure complete shear transfer to the connected panel;
– The frame fasteners at the edge beams and purlins have unidirectional stiffness in the direction of loading (assuming that the direction of the corrugated panels is parallel to the direction of loading) according to the SDI method.

2.2.3 *Behaviour of mechanical fasteners*

The deformation of deck-to-frame connections under shear loading can be taken as the sum of the connector deformation and the localized deformations in the deck panel in the vicinity of the connection. Accordingly, the frame fastener stiffness K_f can be computed assuming two springs acting in series:

$$K_f = (K_0 + K_c)/K_0 K_c \quad (3)$$

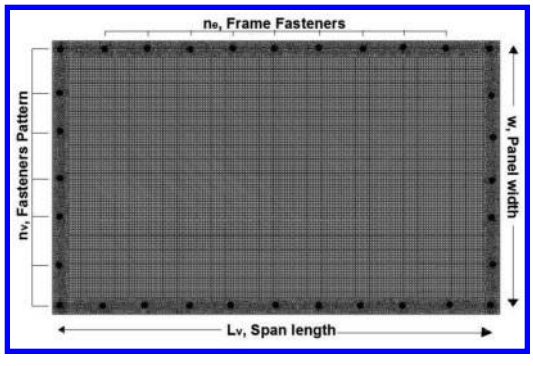


Figure 3. Discrete model of the connected flat plate.

where K_c is the connector stiffness and K_0 is the stiffness associated to plate deformations. Understanding this behaviour is essential when assessing diaphragm in-plane shear stiffness of the fasteners with finite element models such as the one used in this studied. In particular, the evaluation of the panel area affected by the connector, which affects the stiffness K_0, requires careful calibration.

The test setup (Rogers and Tremblay, 2003) used to determine the shear stiffness of frame connectors is shown in Fig. 4a. These tests were reproduced using finite element analysis to characterize the panel deformations (Bakhti et al., 2012). In these tests, the specimens had lateral stiffeners, had a width of 70 mm and the deformations were measured over a gauge length of 100 mm. As shown, non-uniform tension and compression stresses (Fig 4b) and shear stresses (Fig. 4c) develop on either side of the fastener. For 0.91 mm thick steel panel, the results indicate that the elastic stiffness K_o is approximately equal to 150 kN/mm. Calibration was also performed using data from similar tests carried out by De Matheis (1998) on un-stiffened 50 mm wide coupons having the same thickness and the same 100 mm gauge length. In that case, the elastic stiffness K_o was found to be 124 kN/mm, i.e., 17% less than the value determined from Rogers and Tremblay tests.

In Fig. 6, the non-linear load *vs.* displacement curve of a single connection, including deck deformations at the connector vicinity can be represented by Curve 2. The initial elastic stiffness of the connection corresponds to the stiffness K_f assessed by the SDI method. For a linear analysis, the curve follows that elastic stiffness. Knowing K_0, the connector stiffness K_c

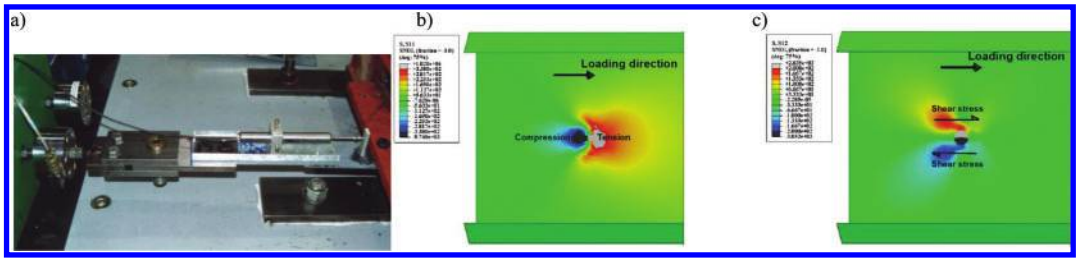


Figure 4. Frame fastener calibration: a) Test setup (Rogers and Tremblay, 2003), b) Tension and compression zone at the connection, c) Shear stress zone at the connection.

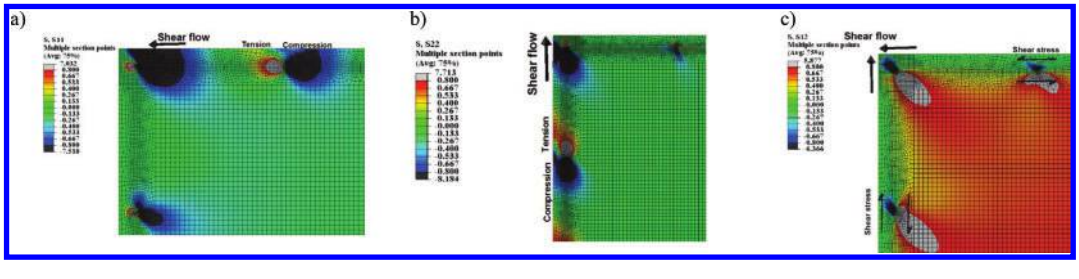


Figure 5. Behaviour at the connection of the connected flat plate (corner part of the diaphragm) [Stress: N/mm^2]: a) Tension (ts.) and compression (cp.) at the connection in the direction of loading, b) Ts. and cp. distribution at the connection in the perpendicular direction to the loading, c) Shear stress distribution at the connection.

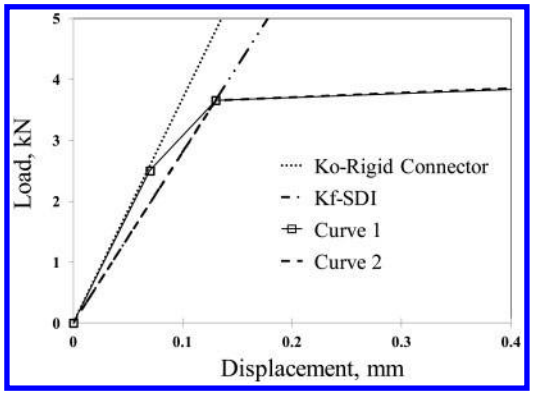


Figure 6. Typical curve for frame fastener calibration.

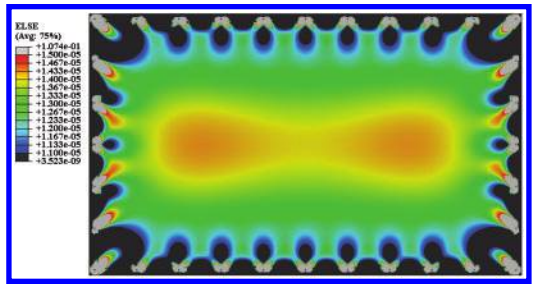


Figure 7. Elastic strain energy (N-mm) distribution on the connected thin flat plate.

can be back calculated using equation 3. The more realistic Curve 1, however, represents the non-linear behaviour of a single connection including the initial higher stiffness due to friction prior to connection slip (De Matheis, 1998). For diaphragms subjected to in-plane shear load with an internal force lower than the slip load, the connector deformation is assumed to be zero and the connection stiffness corresponds to K_0. Therefore, the discrete fixed flat plate is similar to the connected panel, due to the deformation of the plate at the fastener vicinity. For this reason, the stiffness of the connection K_f of the discrete fixed plate is equal to the elastic stiffness K_o of the deck.

For diaphragms with a fixed flat plate over the entire perimeter, the distribution of the shear stress is uniform everywhere on the plate. However, for diaphragms with discrete fasteners along the edges (Figs. 1 & 3), stress concentration occurs at the vicinity of the connectors and the distribution of the shear stress is not uniform (Fig. 5), which is significantly different from the first case. In the model, 5 mm diameter stiff regions representing the fastener shanks are used to represent more realistically this response. The behaviour at the connection during a numerical calibration of the fastener based on the test (Fig. 4) is very similar to the connection response in the connected flat plate (Fig. 5), except for the delimited area of the deformed plate at the connector vicinity, as discussed in Section 3.3.

3 ANALYSIS RESULTS

3.1 *Effect of the fastener configuration on the shear flexibility of the reduced plate*

This section explores plate areas potentially affected by the connector stiffness, pattern and spacing. The reduced plate (RPL) in Fig. 1 illustrates the zone not affected by the fastener stiffness, due to the distance from the connections. It is taken as the rectangular area having 40% of the area inside the fastener lines (912 × 1525 mm) of the entire plate EPL. In order to provide more information about the distribution of the shear in the plate, a parametric study was performed. In Fig. 7, non-uniform distribution of the element strain energy (ELSE) is shown, with the maximum values at the connections. The reduced plate RPL is located in the central zone for which the ELSE is approximately uniform.

For a shell element, the strain energy for elastic behaviour is defined as follows:

$$U_e = \frac{1}{2}\{\sigma\}^T\{\varepsilon\}tA_e \quad (4)$$

where $\{\sigma\}^T$ is the transpose stress vector, $\{\varepsilon\}$ deformation vector and A_e the area of the shell element. Therefore, the total strain energy of the reduced plate RPL is given by $U_{RPL} = \sum_{RPL} U_e$.

The elastic strain energy of a connector element is expressed as follows:

$$U_c = \frac{1}{2}K_c\delta_c^{\,2} \quad (1)$$

where δ_c is the slip connector. For the 912 × 1525 mm diaphragm with 0.91 mm deck thickness and 1 kN loading, the total elastic strain energy of the entire plate (EPLF) having continuous fixity to the edge members, U_{EPLF}, is equal to 4.34 N-mm. Therefore, the total elastic strain U_{RPL} of the reduced plate RPL with the 608 × 915 mm size depends only on the area ratio, i.e., $U_{RPL} = 40\%\ U_{EPLF}$.

Parametric studies on the connected plate under shear loading according to different connector stiffness K_c were performed. The fastener pattern and spacing was also varied. The ratio U_{RPL}/U_{EPLF} was first determined for the various fastener configurations. In Fig. 8, the U_{RPL} values for the discrete connected panels are always larger than 40% of U_{EPLF}. Larger elastic strain energy corresponds to larger shear deformations, indicating that the flexibility of the reduced plate region is higher than in the continuously fixed case. Examination of the results of the numerical simulations shows that at least 92% of the total strain energy of the reduced plate U_{RPL} is caused by shear stresses alone, meaning that the pure shear flexibility of the reduced plate far from the connectors is affected by the fastener configuration, even when the shear behaviour is nearly uniform. As expected, the

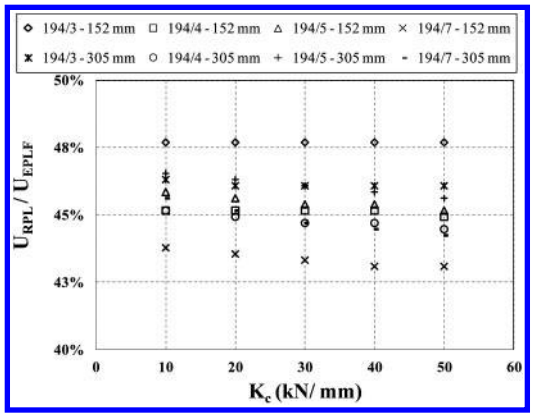


Figure 8. Connector stiffness impact on the shear deformation of the reduced plate.

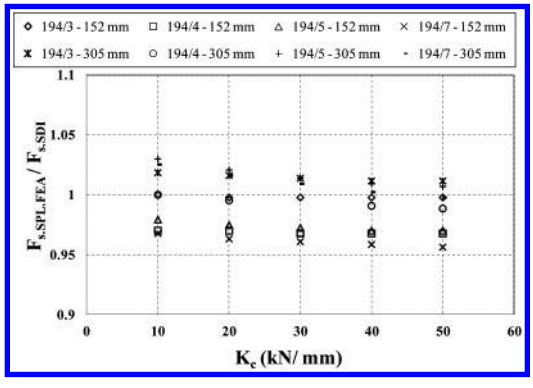


Figure 9. Connector stiffness impact on the shear flexibility.

U_{RPL}/U_{EPLF} ratios are not affected by K_c but they never reach the 40% value because of the discrete fastener arrangement.

3.2 *Effect of the fastener configuration on the shear flexibility*

This section presents the impact of the fasteners configuration with flexible connectors on the shear deformation. In order to avoid double counting the elastic stiffness, K_o, in both pure shear and connection flexibilities, and due to the uncertainty in defining the area at the connection, two trial zones were defined. In Fig. 1, the first is the affected plate zone (APL) containing all the connectors close to the edge of the entire plate. The APL may take into account all the deformed plate at the connector vicinity due to the stress concentrations. The second is the non-affected plate zone (SPL) that corresponds to entire plate area minus the APL zone. The SPL zone is 38 mm inset from the edge of the plate, i.e. 19 mm on either side of the fasteners, which resulted in an area 93% of the EPL area. This area was designed to take into account the shear deformation as the total strain energy dominated

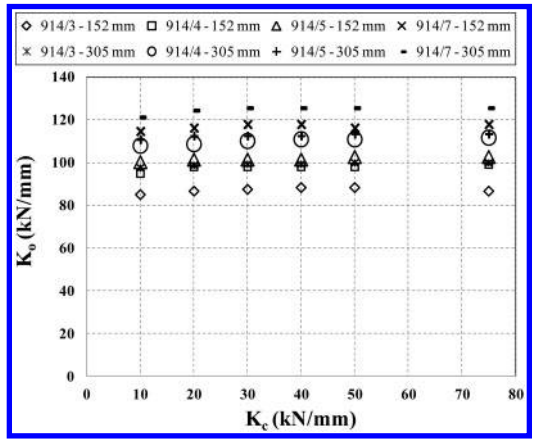


Figure 10. Impact of the connector spacing on the stiffness K_0.

by shear deformations. The corresponding shear flexibility for the SPL was computed using finite element analysis results using $F_{s.SPL.FEA} = 2U_{SPL}/P^2$. Figure 9 shows that $F_{s.SPL.FEA}$ is close to the shear flexibility from SDI, $F_{s.SDI}$, determined with equation 1. The ratio $F_{s.SPL.FEA}/F_{s.SDI}$ is generally not affected by K_c and varies only slightly with the fastener pattern and spacing.

3.3 *Effect of the fastener configuration on the slip flexibility*

The flexibility of the APL zone was obtained from $F_{s.APL.FEA} = 2U_{APL}/P^2$, where U_{APL} is the total strain energy from finite element analysis in APL. From this flexibility, the stiffness K_o was then deducted from equations 1 where K_f had been replaced by K_0. The results are shown in Fig. 10.

The stiffness K_o does not vary with K_c; however, it appears to be strongly affected by the connector spacing. The value of K_o varies between 80 and 120 kN/mm. A similar evaluation using an 60 mm wide affected plate zone (APL) revealed the same trend.

3.4 *Effect of the connector stiffness on the total flexibility*

In order to examine a possible interaction between shear and connection flexibilities, numerical simulations were performed to study the shear and the connector deformations together. The total flexibility, $F_{sc.FEA}$, from the analysis was compared with that calculated using the SDI method, $F_{sc.SDI}$. For the latter, the value of K_f was determined form equation 3 with the values of K_c assigned in the finite element analysis and $K_0 = 150$ kN/mm, reflecting the results of the numerical calibrations from individual connection tests. In Fig. 11, the flexibility assessed by the SDI method varies between approximately 92% and 100% of the values obtained numerically.

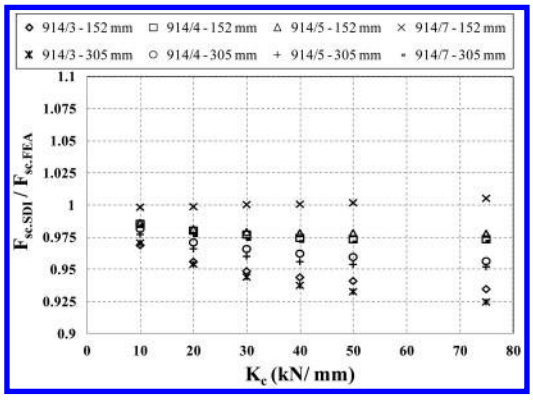


Figure 11. Impact of the connector stiffness on the total flexibility compared to the SDI method.

4 CONCLUSIONS

The main findings of this investigation can be summarized as follows:

1. The connection and the connector are two different concepts in term of shear behaviour. The connection includes the plates at the connector vicinity and the connector itself.
2. The determination of the delimited area of the deformed plate at the connection remains ambiguous. This area can be influenced by the connector spacing, which may affect the elastic stiffness K_o for elastic analysis.
3. The model studied was decomposed into three parts: the connectors, the affected plate zone and the non affected plate zone. The affected plate zone strongly interacts with the spacing and pattern of the fasteners. This gives evidence of a connections system being developed.
4. A non affected plate zone is defined to have a "pure" shear flexibility close to that assessed by the SDI method of the entire flat plate, regardless of the connectors spacing and stiffness. Hence, there is no interaction effect between the non affected plate zone and the connections.
5. The total in-plane shear flexibility of the connected plate based on the SDI method is between 92% and 100% of the values obtained from finite element analysis using K_o provided from the Rogers and Tremblay calibration tests, and is approximately 1% less than that obtained from the finite element analysis using De Matheis' calibration tests.
6. A good assessment of the total shear flexibility of the connected flat plate according to the SDI method is directly dependent on an accurate determination of the strain plate flexibility at the connector vicinity by individual fastener test calibration.

Further research is needed to obtain reliable information regarding the relationship between the interaction of shear and slip flexibilities considering the panel size and thickness.

ACKNOWLEDGEMENTS

Funding for this research was provided by the Natural Sciences and Engineering Research Council of Canada, the Vancouver Steel Deck Diaphragm Design Committee (VSDDC) and its many member companies, the Canadian Sheet Steel Building Institute, the Steel Deck Institute and Hilti Canada.

REFERENCES

Bakhti, F., Tremblay, R., & Rogers, C. A. 2012. Revisiting the SDI and ECCS methods for in-plane shear flexibility of metal roof deck diaphragms using non-linear finite element analysis. *Proc. 15th World Conference in Earthquake Engineering*, Lisbon, Portugal.

CSSBI 2006. *Design of Steel Deck Diaphragms, 3rd ed*., CSSBI B13-06, Canadian Sheet Steel Building Institute, Mississauga, Canada.

Dassault Systems Simulia, Corp. 2012. *Abaqus User's Manual* (Version 6.11). Providence, USA.

Davies, J.M. 2006. Developments in stressed skin design. *Thin-Walled Structures* 44(12): 1250–1260.

De Matteis, G. 1998. *The effect of cladding panels in steel buildings under seismic actions*. Italy: Univ. degli. Studi Napoli Federico II.

ECCS 1977. European Recommendation for the Stressed Skin Design of Steel Structures, *European Convention for Constructional Steelwork* ECCS-XVII-77-1E.

Luttrell, L. D. 2004. *Diaphragm design manual (3rd ed.)*. Steel Deck Institute. Fox River Grove, USA.

Massarelli, R., Franquet, J., Shrestha, K., Tremblay, R., and Rogers, C.A. 2012. Seismic testing and retrofit of steel deck roof diaphragms for building structures. Thin-Walled Structures, 61: 239–247.

Rogers, C. A., Tremblay, R. 2003. Inelastic seismic response of frame fasteners for steel roof deck diaphragms. ASCE *Journal of Structural Engineering* 129(12): 1647–1657.

Sputo, T. 2010. *Steel roof deck diaphragms on cold-formed steel framing*. Paper presented at the 20th International Specialty Conference on Cold-Formed Steel Structures.

Tremblay, R., Nedisan, C., Lamarche, C.-P., Rogers, C.A. 2008. Period of vibration of low-rise building with a flexible steel roof deck diaphragm. *5th International Conference on Thin-Walled Structures*, Brisbane, Australia.

Tri-Services Technical Manual 1982. *Seismic design for buildings,* Depts. of Army, Navy and Air Force, US Government Printing Office, Philadelphia, USA.

Research and Applications in Structural Engineering, Mechanics and Computation – Zingoni (Ed.)
© 2013 Taylor & Francis Group, London, ISBN 978-1-138-00061-2

New experimental method for determining the stiffness and strength of steel storage rack floor connections

F. Roure, M.M. Pastor, M.R. Somalo & M. Casafont
REMM (Research group in Structures and Mechanics of Materials) – Universitat Politècnica de Catalunya, Spain

ABSTRACT: To analyse the down-aisle global stability of a rack structure it is necessary to know the moment – rotation characteristic of the beam to upright connection and of the upright to floor connection. In EN 15512, the moment – rotation characteristic of the upright to floor connection is recommended to be obtained experimentally, according to Annex A.2.7. There a test method is suggested, using two lengths of upright connected to opposite sides of a concrete block; but it is also said that "alternative test set-ups may be used, provided they accurately reproduce the real structural condition". In this paper an alternative test set-up is presented, using only one length of upright, connected to a concrete block. The concept is presented and the data collection and the calculation of the moment – rotation curve of the floor connection are exposed. Then the practical implementation of the test set-up is explained. A series of experimental results obtained by the new method are presented, and compared to the results obtained with the two lengths method. Finally the conclusions about the new testing method are presented.

1 INTRODUCTION

The detail of a typical pallet racking system is shown in Fig. 1. The basic structural elements of the system are: the beams, the uprights and the diagonals. The beams support directly the load of the pallets, and transmit them to the uprights. The diagonals are bolted to the uprights and form the frames that guarantee the cross-aisle stability. Most of the systems are unbraced in the down-aisle direction; in this case the down-aisle stability relies on the beam to upright connection and the upright to floor connection. The present paper deals with the behaviour of the upright to floor connection. The upright to floor connection has a non linear semi rigid behavior, and the codes usually recommend determining it experimentally. The behavior is dependent of the value of the axial force acting on the upright, so a complete characterization of the behavior of this connection requires testing at different levels, covering the usual range of axial loads.

2 HISTORICAL REVIEW

In 1996 the preNorm FEM 10.2.02 has proposed in Ap. 5.8 an experimental way of determining the ultimate moment, the design moment and the stiffness of the upright-base plate-floor connection. In 2009, EN 15512 has reproduced in Ap. A.2.7 the same procedure. It consists in testing, simultaneously two uprights and base plates, subjected to axial compression, acting in opposite faces of a concrete block.



Figure 1. Detail of a rack pallet system.

Different authors have studied the behavior of the upright to floor connection and its influence on the stability of the uprights and the rack structures, experimentally and by FE simulation: Godley, Beale & Feng

(1998), Beale & Godley (2003), Del Coz, García, Betegón & Fernández (2006).

Gilbert & Rasmussen (2011) have suggested a way to improve the results of the test arrangement proposed in EN 155512.

3 EN 15512 TWO UPRIGHT TEST PROCEDURE

3.1 *Test procedure*

The test arrangement proposed in EN 15512 is shown in Figure 2 and 3. After applying an axial preload and setting the transducers to zero, the desired axial load is applied, and then the transversal load is increased progressively until failure of the connections. With the value of forces and displacements registered, the moment and rotation are calculated. with equation 1 for each of the two connections. It is supposed that the transversal force F_2 is absorbed

$$M = (F_2/2) \cdot L + F_1 \cdot (d_5 + d_6)/2 \qquad \theta = \frac{d_2 - d_3}{d_{23}} \qquad (1)$$

symmetrically bye the two lengths of uprights. The test is repeated for the different axial loads desired.

3.2 *The drawbacks of this procedure*

When applied in practice this procedure has several drawbacks:

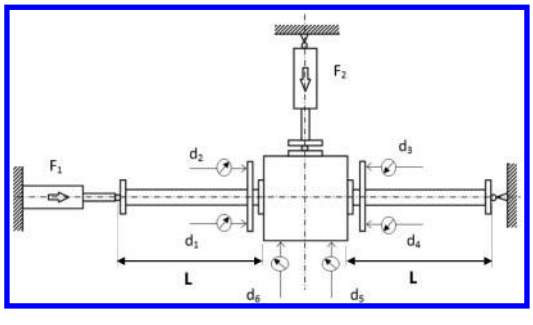


Figure 2. EN 15512 two uprights test arrangement.



Figure 3. EN 15512 two uprights test arrangement.

- it is very difficult to align correctly all the components.
- when the first uprights fails, the symmetry is loosen and there is no guarantee that the transversal force and the moment are still symmetrically distributed, and that equation [1] is still valid.

4 NEW PROPOSAL: SINGLE UPRIGHT TEST

4.1 *New test arrangement*

In A.2.7.2 of EN 15512 it is said that "alternatives may be used, provided they accurately model the real structure condition". Here an alternative method is proposed, that verifies these condition. Figures 4 and 5 show the test arrangement proposed. The concrete block is completely fixed. A single upright sample of 600 mm length with the base-plate is fixed to it (with or without anchorages, as the case may be), and at the head of the upright the axial and the transversal forces are applied.

The two force actuators, axial and transversal, are pinned at both ends. The head of the upright must be guided so that the axial and transversal displacements and the rotation around the vertical axis are free, and all the others degrees of freedom (vertical displacement and rotations around the axial and transversal axis) are restrained. The joint in the head of the upright has to guarantee that the rotations around the vertical axis of the axial force, of the transversal force and of the section of the upright are free and independent (see figure 6).

4.2 *Test procedure*

An axial pre-load is applied and the sense of the initial transversal displacement is noted. Load is released, transducers set to zero, and the desired level of axial load is applied. Then the transversal load is applied, in the same sense as the initial displacement, and is increased until failure of the connection.

Forces and displacements are continuously registered and moment and rotation are then calculated with the equations 2 and 3 (see Fig. 7):

$$M_b = (F_2 + F_1 \cdot \sin\beta) \cdot L + (F_1 \cdot \cos\beta) \cdot d_1 \qquad (2)$$

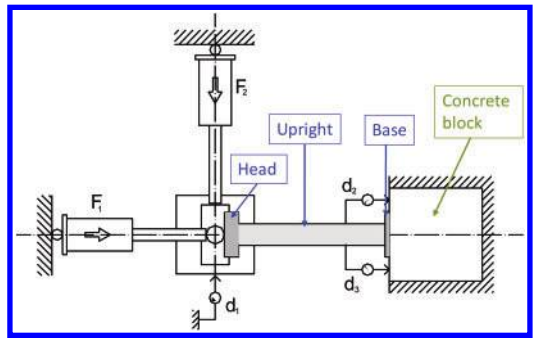


Figure 4. New proposal: single upright test arrangement.



Figure 5. Single uprights test arrangement.

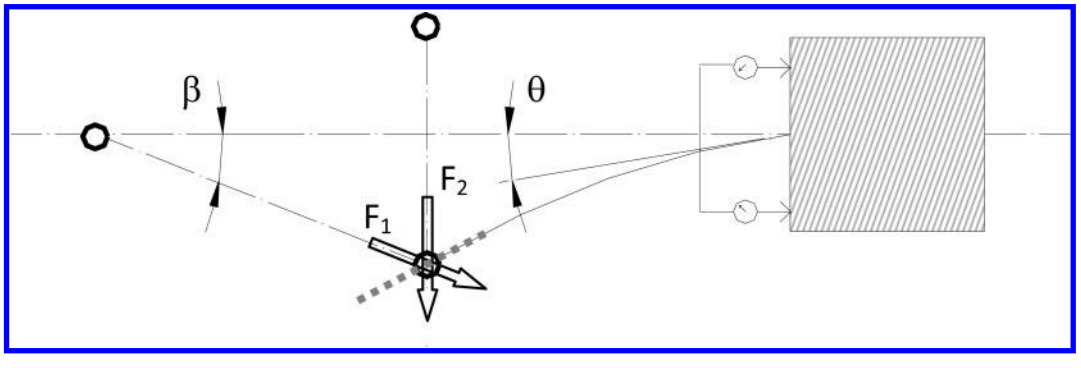


Figure 6. Free and independent rotations at the joint of the head of the upright.

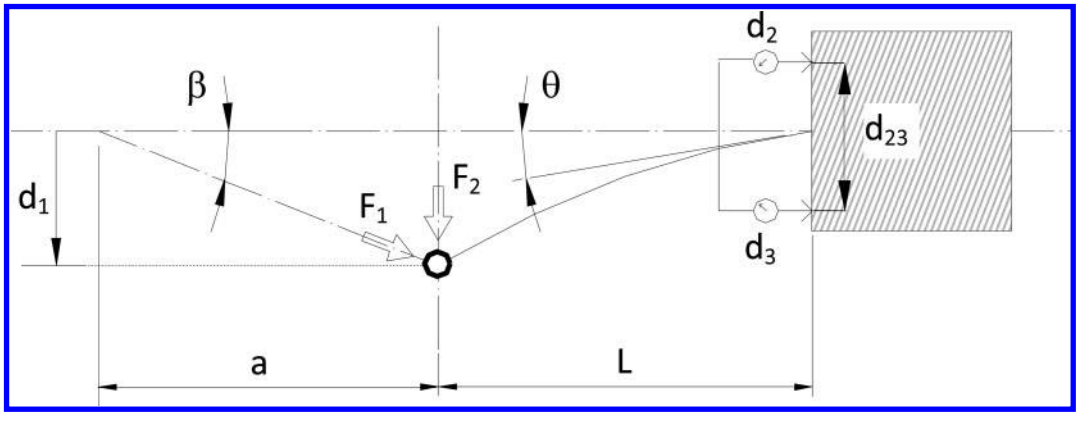


Figure 7. Single uprights test notation.

M_b: moment applied to the base plate.
F_1: axial load applied on the upright.
F_2: transversal load applied on the upright.
L: distance between the joint and the upright base.
d_1: transversal displacement sensor.
β: angle of axial load ($\beta = \text{atan}(d_1/a)$)
a: distance between pivot an joint.

$$\theta_b = \frac{d_2 - d_3}{d_{23}} \quad (3)$$

θ_b: rotation of the base plate.
d_2: displacement sensor 2.
d_3: displacement sensor 3.
d_{23}: distance between sensors 2 and 3.

4.3 *Advantages of the new test arrangement*

Compared to the arrangement proposed in EN 15512 the new test arrangement has several advantages:

- easier to implement (alignment of only one upright)
- it always allows full development of the failure
- gives consistent series of results
- needs only one sample per test

5 DISCUSSION OF RESULTS

5.1 *M – θ curves*

One type of medium load upright and its base plate have been tested with both methods, at different levels of axial load. One example of the M – θ curves obtained with the two upright and the single upright arrangement, for the same axial load level, are shown in Figures 7 and 8, respectively.

In the code it is recommended to do tests at least at 6 different axial load levels, and to do a minimum of 2 tests at each level. With these 12 results (M_{ti}) a suitable algebraic expression, by using a least square curve fitting process, is chosen to represent the ultimate moment M_b as a function of the axial load (see Fig. 10).

The M - θ curve, at each axial load level can be approximated by a bilinear curve. The two parameters that define it are the design moment M_{rd} and the stiffness K (see Fig. 10). To define the value of M_{rd} the process is.

- normalize the ultimate moments of each axial load level (M_{ti}/M_t)
- calculate the standard deviation s of all the normalized moments
- calculate the characteristic moment of each axial load level:

$$M_k = M_t\,(1 - k_s \cdot s) \quad (4)$$

where $k_s = 1{,}88$ for $n = 12$

- calculate the design moment of each axial load level:

$$M_{rd} = \eta \frac{M_k}{\gamma_M} \quad (5)$$

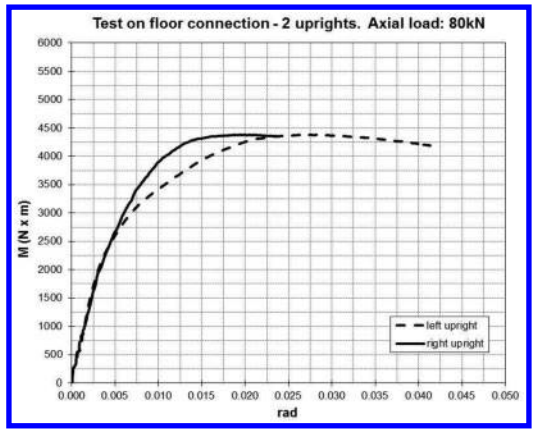


Figure 8. M – θ curve obtained with the two upright test arrangement.

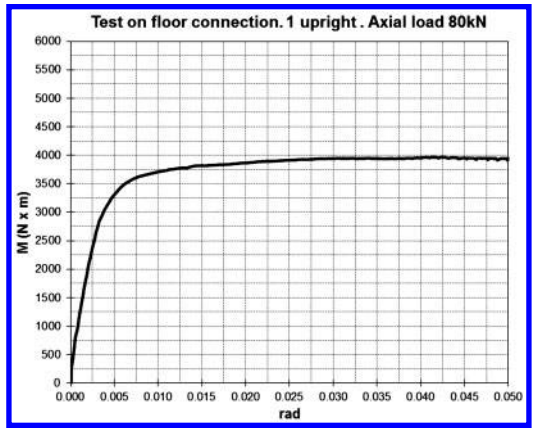


Figure 9. M – θ curve obtained with the single upright test arrangement.

where $\gamma_M = 1{,}1$ (according to 7.5 of EN15512)
$\eta \leq 1$ reduction factor to achieve a higher stiffness

In Fig. 10 two different bilinear approximations of the M – θ curve are shown, obtained with different values of η.

5.2 *M_b and K function of axial load*

In Figure 11 the ultimate moments of each test (M_{ti}) for the 6 axial load levels and the fitted curve (M_b), obtained with both test methods, are presented. The values obtained with both methods are very similar. The stiffness K at each axial load level has been calculated and is represented in Figure 12 as function of axial load. For both methods the same design moment M_{rd} has been used. The scatter of the single results obtained with the two uprights arrangement is clearly higher than with the single upright arrangement. The stiffness values obtained with the single upright arrangement are higher

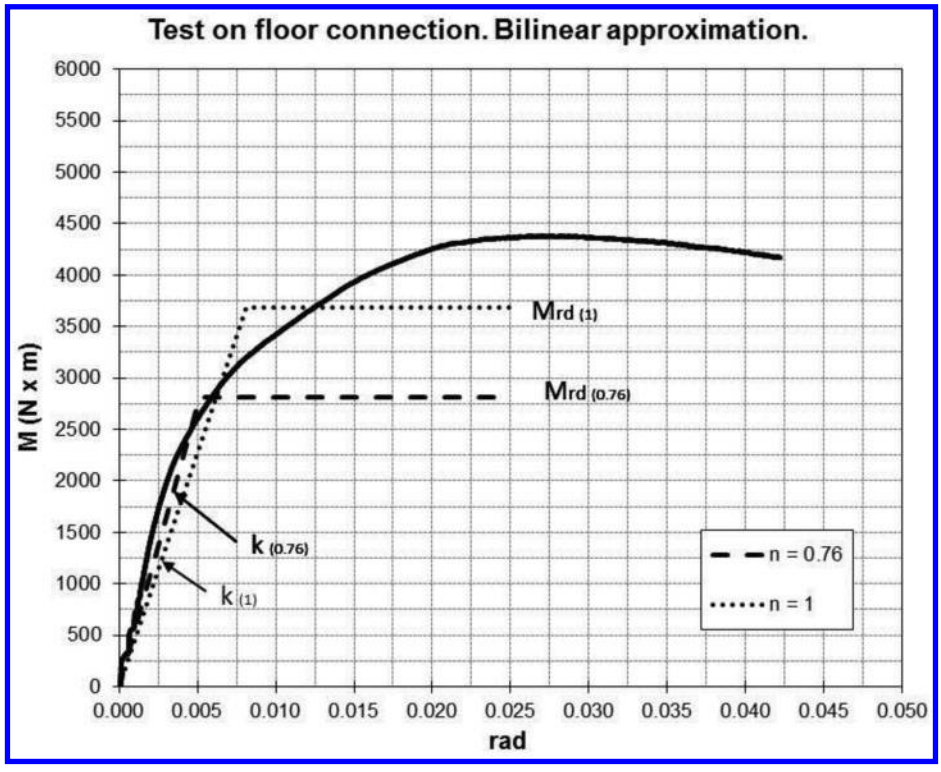


Figure 10. Bilinear approximation of the M – θ curve.

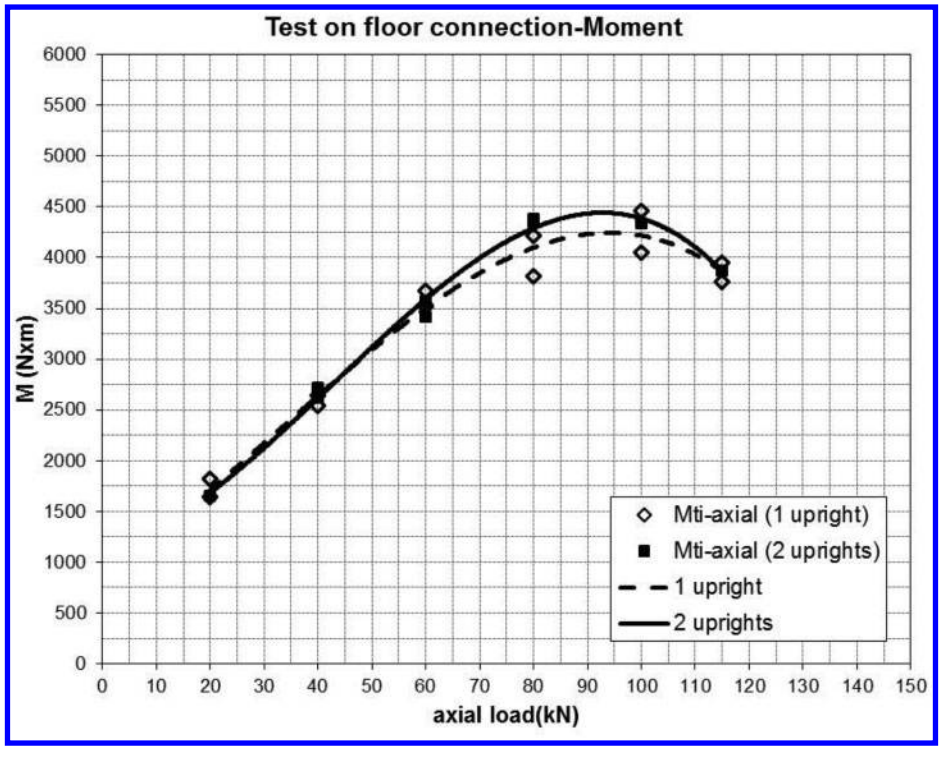


Figure 11. Ultimate moment as function of the axial load.

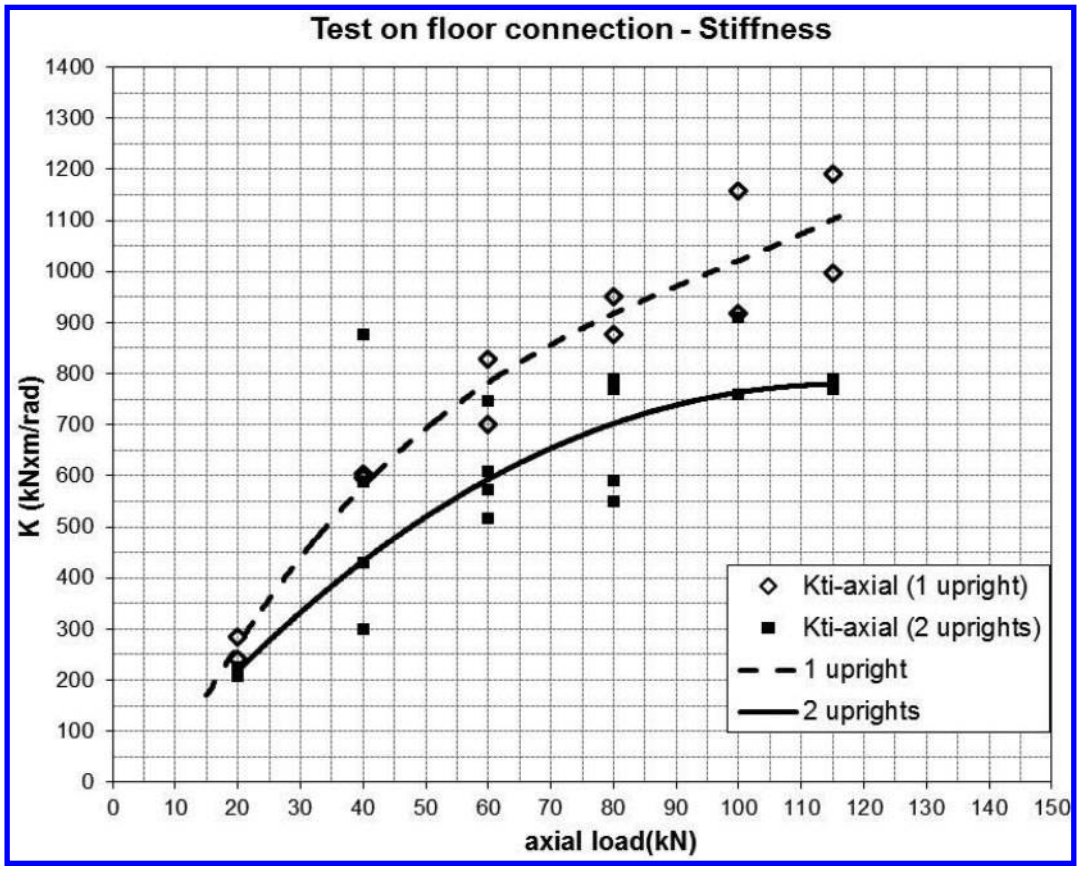


Figure 12. Stiffness as function of the axial load.

6 CONCLUSIONS

After using both test arrangements and comparing the results obtained, it can be concluded that:

- The new test arrangement is easier to implement (only one upright has to be aligned)
- It always allows full development of the failure
- The scatter in the results is lower
- Needs only one sample per test
- The values of the ultimate moments obtained with both methods are equal
- The values of the stiffness obtained with the single upright test are higher.

REFERENCES

FEM 10.2.02 The Design of Pallet Steel Pallet Racking. *Federation Europeenne de la Manutention* , 1996.

EN 15512 Steel Static storage systems- Adjustable pallet racking systems- Principles for structural design. *CEN European Committee for Standardization* , 2009.

Godley, M.H.R.; Beale, R.G.; Feng, X. 1998. Rotational stiffnesses of semi-rigid base-plates. 14th *International Specialty Conference on Cold-Formed Steel Structures*, St. Louis, Missouri, October 15–16.

Beale, R.G.; Godley, M.H.R. 2003. Sway buckling of down-aisle, spliced, unbraced pallet rack structures. *Steel and Composite Structures,* Vol. 3, No 5 (307–320)

Del Coz, J.J.; García, P.J.; Betegón, C.; Fernández, G. 2006. Non-linear analysis of unbolted base plates by the FEM and experimental validation. *Thin-Walled Structures* 44 (2006) 529–541.

Gilbert, B.P.; Rasmussen, K.J.R. 2011. Determination of the base plate stiffness and strength of steel storage racks. *Journal of Constructional Steel Research* 67 (2011) 1031–1041.

Research and Applications in Structural Engineering, Mechanics and Computation – Zingoni (Ed.)
© 2013 Taylor & Francis Group, London, ISBN 978-1-138-00061-2

Seismic behaviour of welded and bolted I-beam to box column connections

Qian-Yi Song, Amin Heidarpour & Xiao-Ling Zhao
Department of Civil Engineering, Monash University, Melbourne, Australia

ABSTRACT: The secondary disasters, as fire, colliding, explosion and so on, usually occur following an earthquake. The subsequent actions would be more destructive. In order to investigate structure behaviour after an earthquake, it's important to interpret seismic behaviour of structures and evaluate damage levers induced by various earthquake intensities. This paper presents a preliminary work on investigating behaviour of steel connections under seismic loading, focusing on test and analysis of popular used welded and bolted I-beam to hollow box column connections under cyclic loading. 4 connections, including 2 fully welded connections and 2 double-angle bolted connections were tested in the lab under cyclic loading. The load vs. deformation relationship, strength and dissipated energy were measured during the test, meanwhile deformation, fracture and final failure phenomena were observed. Ductility and earthquake induced damage based on test results are described and evaluated preliminarily. Test results could be useful for further investigation and analysis on pre-damaged connections under various possible post- earthquake actions.

1 GENERAL INSTRUCTIONS

The heavy ground motion in an earthquake often causes huge damages and loss of lives and properties. Moreover, the secondary disasters induced by the earthquake would cause more severe damages. Considering structures are subjected to earthquake induced secondary actions, researches on the behavior of structures under these extreme conditions are significantly necessary.

Damage evaluation after earthquake is basis as for above mentioned investigation. Several damage models can be found to define structure's damage degree after an earthquake. Castiglioni & Pucinotti (2009) summarised failure criteria and cumulative damage models for steel components under cyclc loading. So far, There are few published investigations on the residual capacity of steel components under various secondary actions after an earthquake.

Welded I-beam to hollow box column connection and bolted double-angle connection are the simplest configurations, usually used in low-rise and middle-rise buildings as framing connection. Although with limited seismic resisting ability, they are designed for the experimental investigation in this paper, which avoid complicated analysis with lots of parameters, while the load vs. resisting mechanism could be analysed clearly and generally.

There are several published research works on these two types of connections. Static tests were carried out by Sherman (1995) on the double-angle I-beam to box column bolted connections. The observed failure of double-angle connection was on the weld. It was proposed that the only limit state which should be considered for HSS column wall is the through-thickness shear rupture. The possible limit states for double angle I-beam to HSS connections were listed by Sherman (1996). Gong (2008) presented a static experimental study on double angle shear connections using small-size hollow section columns. Fully welded I-beam to box column connections can be considered as connections with two transverse plates conservatively, as mentioned in EC3-part8 (CEN, 2005). Shear strength of double angle connections is given in AISC steel construction manual (AISC-325, 2005).

This paper presents test results of I-beam to box-column connections under cyclic loading, which focuses on investigating damages induced by earthquakes. Main parameters as load vs. displacement relationship, energy dissipation and residual deformation after loading cycles were measured and analyzed. This research provides benchmark data for further investigation on connections behaviour under post-earthquake fire which is currently being developed at Monash University.

2 CONNECTION DETAILS AND TEST PLAN

2.1 *Connection specimens*

There are two types of connections investigated in the research work. One is fully welded tubular connection which assembled using an I-beam and a hollow box column through welding. Another type of connection is bolted double-angle tubular connection. The I-beam of bolted connection is bolted to two pieces of angle steel which are welded to column face, and

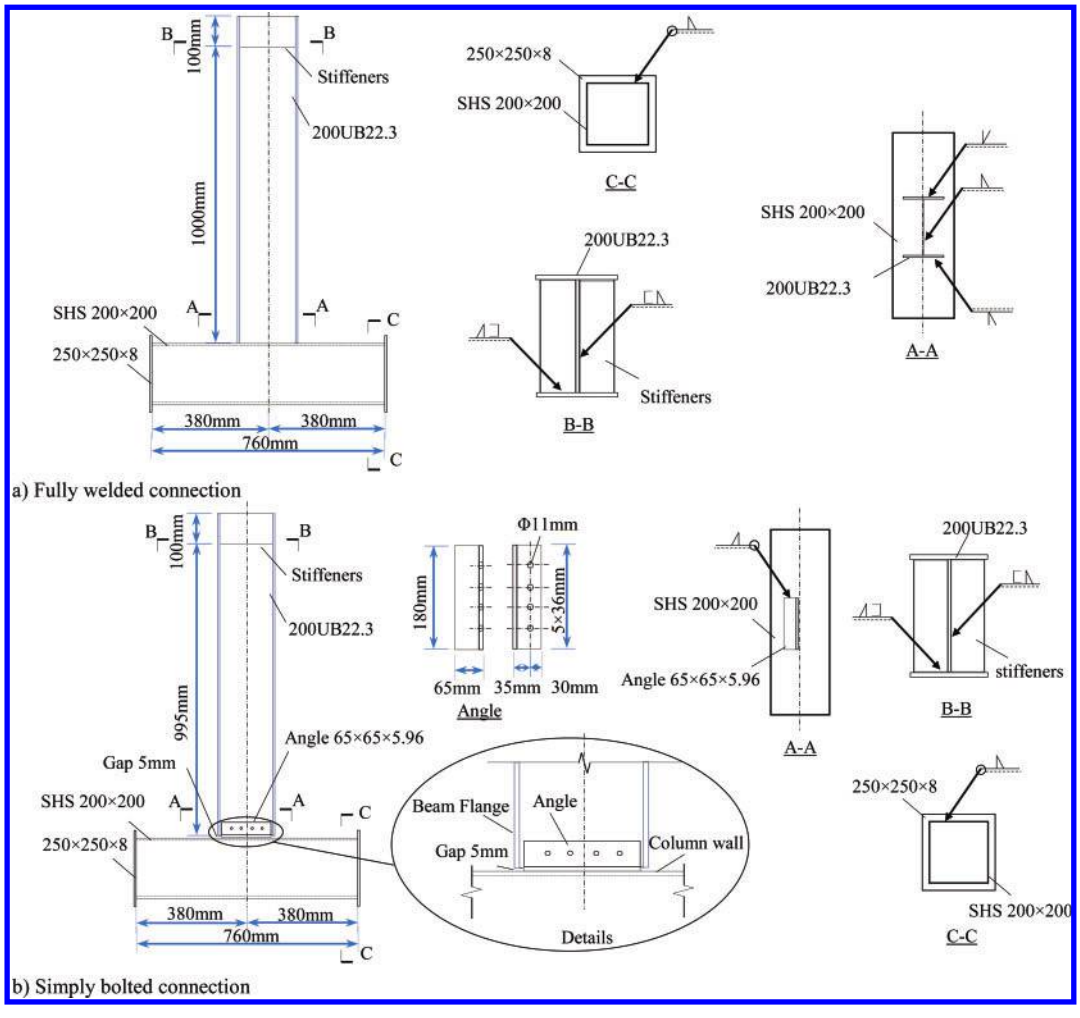


Figure 1. Component and configuration details of designed connections.

there is a small gap between I-beam with column face. The designed lengths of column and I-beam are the same, but columns with two different thicknesses, namely 4.76 mm and 8.75 mm, are used. All the I-beams used in the test are 200UB22.3 (Onesteel, 2003). The geometrical details of connections are listed in Table 1. All the bolts are G8.8M10, and angle section is 65 × 65 × 5.96 (unit: mm), with length of 180mm. Connection configuration details are shown in Figure 1a, b.

Table 1. Geometric properties of specimens.

	Column (mm)		Beam(mm)		
No.	B	t_c	Section	t_f	t_w
CWH1C	200 × 200	4.76	203.0 × 131.6	6.64	5.14
CWH2C		8.75			
CBH1C		4.76			
CBH2C		8.75			

Note: In the specimen number, the meaning of characters is as following: C-connection, W-welded, B-bolted, H-hollow section box column, the last C-cyclic loading.

2.2 *Boundary conditions and loading protocol*

The bottom end of column is fixed, while another side of the column is only axially movable and supported by a lateral triangular frame. A small constant axial load of 50kN is exerted on the column during the test. Cyclic loading is applied on the beam, 1 meter away from column face using displacement controlling. Test setups are shown in Figure 2. Compressing the beam towards ground is taken as positive loading direction. In the test, AISC-341 (AISC-341, 2005) cyclic loading protocol is adopted, shown in Figure 3. Cyclic test stops until the connection fails or the maximum travel displacement achieves.

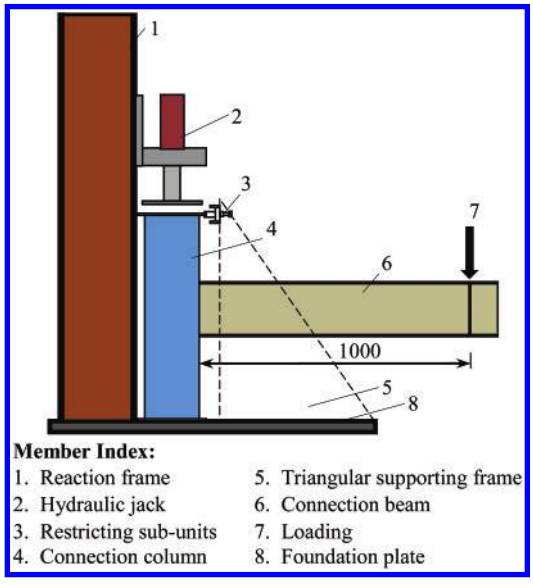


Figure 2. Loading setups.

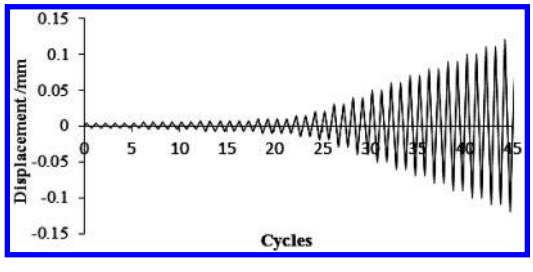


Figure 3. Cyclic Loading protocol (AISC-341, 2005).

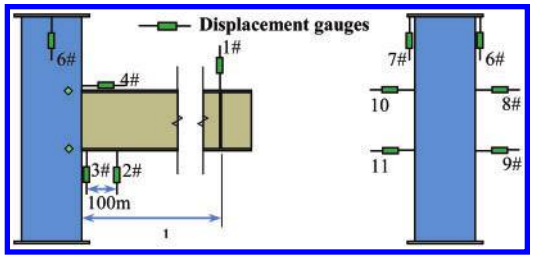


Figure 4. Arrangement of displacement gauges.

2.3 *Gauges and material properties*

The arrangement of displacement gauges are shown in Figure 4. Material properties as yielding strength f_y, ultimate strength f_u, initial elastic modulus E_s, yielding strain ε_y and the Poisson ratio ν_s, obtained from tensile coupon tests, are listed in Table 2.

3 EXPERIMENTAL RESULTS AND ANALYSIS

3.1 *Test results*

Figure 5 shows typical load vs. displacement relationships for tested welded and bolted connections.

Table 2. Material properties.

Properties	t (mm)	tf_y (MPa)	f_u (MPa)	E_s (MPa)	ε_y ($\mu\varepsilon$)
Column	4.76	359.32	448.82	181200	1983
Web	8.75	431.85	452.10	201267	2146
Beam	5.14	361.85	507.87	198250	1825
Flange	6.64	337.97	496.92	198750	1700
Angle	5.96	340.95	488.24	202900	1680
Bolt	–	1042.8	1164.1	235392	4430

Note: Poisson's ratio (ν_s) is 0.293.

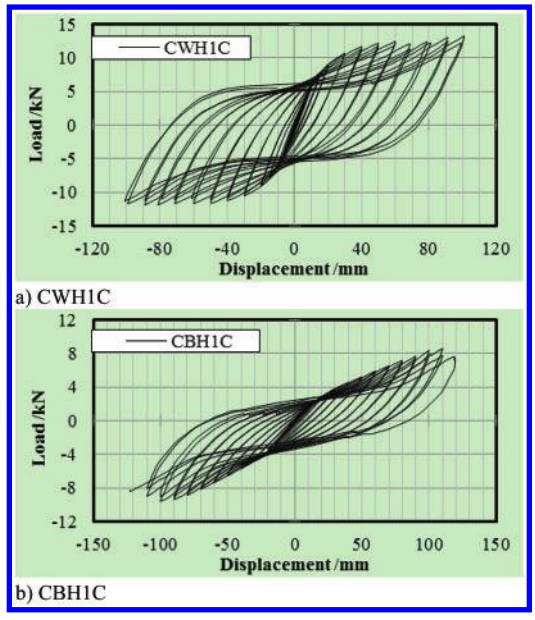


Figure 5. Load vs. displacement relationships.

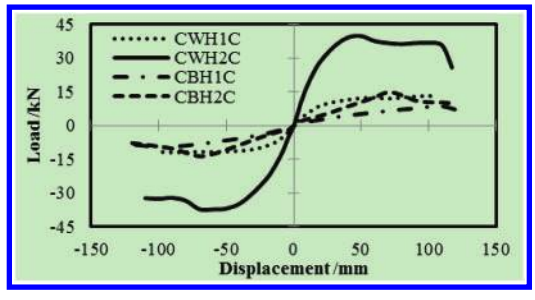


Figure 6. Skeleton curves of connections.

Skeleton curves are shown in Figure 6, which reflect the strength and ductility performance of connections under cyclic loading. As connections could be subjected to several cycles under the same displacement amplitude, the shown skeleton curve connects peak points of the first cycle. The determination of yielding strength F_y, ultimate strength F_u, the failure strength

F_f with associated displacements δ_y, δ_u, δ_f and the maximum displacement δ_{max} are given in Figure 7.

Main results of connections under cyclic loading tests are summarized in Tables 3 to 5. Table 3 shows the measured yielding strength F_y, ultimate strength F_u and related displacement δ_y, δ_u and the maximum loading deformation amplitude δ_{max} under both positive and negative directions. The total loading cycles, failure mode with the cycle number at which initial failure occurs are listed in Table 4. The failure displacement δ_f and displacement ductility coefficient $\mu(=\delta_f/\delta_y)$ in positive and negative direction and the average displacement ductility coefficient $\bar{\mu}$ are listed in Table 5. Due to loading travel capacity of equipment, the failure load F_f may be still higher than $0.85F_u$ at the end of the test, thus it is conservatively assumed that $\delta_f = \delta_{max}$ in calculating the ductility coefficient.

Dissipated energy during cyclic loading test can be calculated by the enclosed area of a single cycle from the load vs. displacement relationship, which of connections is shown in Figure 8.

3.1.1 *Fully welded connections*

The welded connection CWH1C was totally subjected to 42 cyclic loading cycles. Cracks at column face around tensile beam flange tips initially occurred after about 25 cycles with displacement amplitude of 20 mm. Then cracks were developed when the load increased. As both the top and bottom beam flanges were subjected to tensile load due to repeated loading, cracks at column face were symmetrical around all beam flange tips. The typical initial crack is shown in Figure 9a. It was developed through the column wall thickness quickly after several more cycles.

The test of CWH1C stopped when punching shear fracture extending towards the middle of column wall along the beam flange (Fig. 9a), when the maximum loading amplitude achieved 100mm. Due to setup arrangements, although fracture was still developing at the end of the test, there was no significant load drop. The maximum positive resisting strength

Table 5. Ductility characteristic.

Specimens	$\delta_{f,+}$ (mm)	$\delta_{f,-}$ (mm)	$\mu+$	$\mu-$	$\bar{\mu}$
CWH1C	101.07	−100.90	>4.60	>6.00	>5.30
CWH2C	111.28	−110.00	5.42	>3.93	>4.68
CBH1C	118.70	−119.37	2.76	>2.18	>2.47
CBH2C	83.41	−81.95	2.29	2.69	2.49

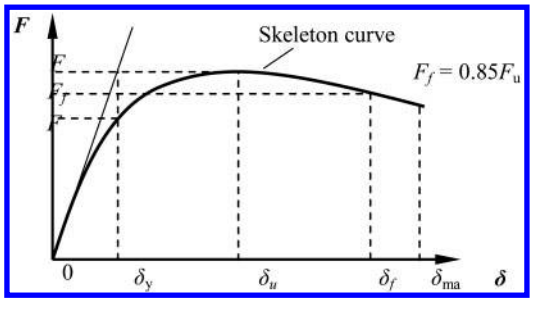


Figure 7. Determination of skeleton curve.

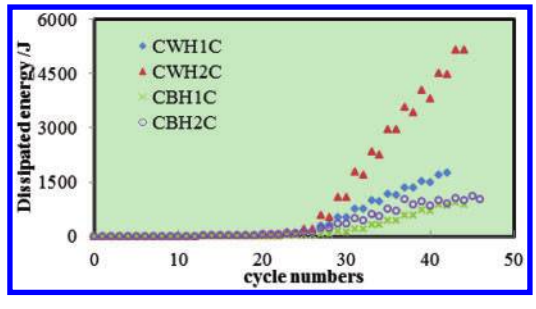


Figure 8. Energy dissipation during loading.

Table 3. Cyclic loading test results.

Specimens	$F_{y,+}$ (kN)	$\delta_{y,+}$ (mm)	$F_{y,-}$ (kN)	$\delta_{y,-}$ (mm)	$F_{u,+}$ (kN)	$\delta_{u,+}$ (mm)	$F_{u,-}$ (kN)	$\delta_{u,-}$ (mm)	δ_{max} (mm)	$\delta_{max,-}$ (mm)
CWH1C	9.22	21.96	−8.26	−16.81	13.21	100.8	−11.91	−88.8	101.1	−100.90
CWH2C	29.08	20.52	−28.53	−27.99	39.83	50.0	−37.28	−60.0	117.2	−110.00
CBH1C	4.72	43.04	−6.96	−54.70	8.60	110.0	−9.59	−99.9	122.7	−119.37
CBH2C	7.76	36.50	−6.46	−30.48	14.99	74.5	−13.76	−69.2	120.3	−119.81

Table 4. Observed failure characteristics.

Specimen	Total cycles	Failure phenomena	Cycle of initial failure
CWH1C	42	Column wall punching shear	25
CWH2C	44	Beam flange tearing with punching shear of middle column wall	26
CBH1C	45	Angle web tearing symmetrically at top and bottom corner	37
CBH2C	46	Angle welding tearing at top-side and angle web tearing at bottom-side	34

is 13.21 kN during the 41st loading cycle at displacement of 100.8 mm. The maximum negative resisting strength is −11.91 kN during the 39th loading cycle at displacement of −88.8 mm. Under the same displacement amplitude, strength of the second loading cycle is usually lower than the first cycle for damages caused in previous loading cycle.

Specimen CWH2C is stronger than CWH1C, and is the strongest connection among the 4 tested connections. Before the last loading cycle to the amplitude of 120 mm, it had been subjected to 44 loading cycles. The maximum positive resisting strength is 39.83 kN during the 31st loading cycle at the displacement of 50.0 mm. The maximum negative resisting strength is −37.28 kN during the 33rd loading cycle at displacement of −60.0 mm. The resisting strength of following cycles decreases a little. The test stopped with a load dropping of 15% at the 45th cycle. Because of asymmetrical tearing damages at the top and bottom beam flange tips, the positive half of loading cycles looks fuller than the negative part of cycles. The initial fracture occurred at about 26th cycle with the amplitude of 20 mm, which is at the tensile beam flange tips (Fig. 9a). The fracture then developed slantwise direct to column wall, and finally punching shear occurred at the middle of the column wall (Fig. 9a).

3.1.2 *Bolted connections*

Bolted connections are usually pin connections with negligible moment resisting capacity. It is obvious that the typical hysteretic curve shape of bolted connection is thinner compared with welded connections (Fig. 5). Moreover, the initial stiffness of bolted connections is much small as well.

CBH1C is a double-angle bolted connection with column wall thickness of 4.76 mm. It was subjected to 45 loading cycles totally during the test, which achieves 120 mm in the positive loading direction. The maximum positive resisting strength is 8.60 kN in the 43rd loading cycle at the displacement of 110.0 mm. The maximum negative resisting strength is −9.59 kN in the 41st loading cycle at displacement of −99.9 mm. The load amplitude of the last cycle dropped down obviously due to the tearing fracture of angle webs, which occurred initially at about the 37th cycle with loading amplitude of 80 mm symmetrically on the top and bottom. The typical failure phenomena are shown in Figure 9b.

CBH2C is another bolted connection with column wall thickness of 8.75 mm. It was totally subjected to 46 loading cycles. The maximum positive resisting strength is 14.99 kN during the 37th loading cycle at the displacement of 74.5 mm. The maximum negative resisting strength is −13.76 kN during the 37st loading cycle at displacement of −69.2 mm. The load dropped down obviously due to the tearing fracture of angle webs at bottom side and the fracture of welding lines at top side. Fracture damages occurred initially at about the 34th cycle with displacement amplitude of 60mm. The typical failure phenomena are shown in Figure 9b.

3.2 *Analysis*

Due to different configuration details, connections show various performances under cyclic loading test procedure. Fully welded connections are normally stronger than simple bolted connections, due to the fact that they can hold big enough moment while bolted connections are usually considered as shear connections with negligible moment resisting capacity. The positive displacement corresponding to ultimate load of CWH1C and CBH1C are 100.8 mm and 110.0 mm while CWH2C and CBH2C are only 50 mm and 74.5 mm respectively. The displacement corresponding to ultimate load in negative direction of CWH1C and CBH1C are bigger than those of CWH2C and CBH2C as well. This indicates that connections with thinner column wall thickness are of better flexible

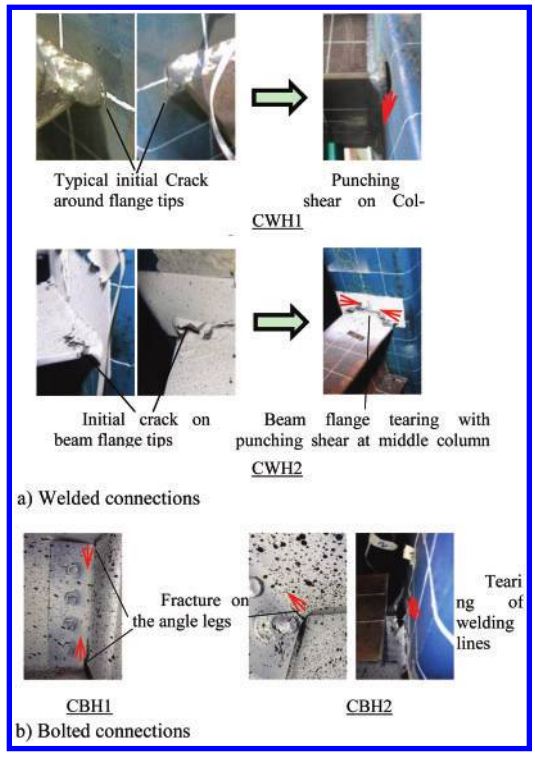


Figure 9. Failure phenomena of welded specimens.

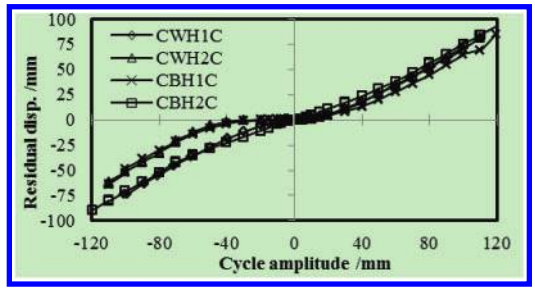


Figure 10. Residual displacement of connections.

capacities, although their bearing abilities are usually lower. The calculated average displacement ductility coefficient of CWH1C is at least 5.30, as shown in Table 4, while that of CWH2C, CBH1C and CBH2C are 4.68, 2.18 and 2.69, respectively. This indicates welded connections CWH1C and CWH2C are more ductile than bolted connections CBH1C and CBH2C.

From Figure 8, we can see that the energy dissipated by hysteretic loops increases with the increase of displacement amplitude. Cyclic Loading is carrying on by double cycles with the same displacement amplitude after 22 cycles, before which the dissipated energy of cycles is not apparent. From the 23th loading cycle, the energy dissipation keeps increasing obviously and that of the second cycle is usually lower than the previous one under the same amplitude. It indicates that before the 22nd loading cycle, all the connections are in elastic stage, after it due to inelastic behaviour caused by material plasticity, crack and column wall buckling, the plastic response becomes obvious. The energy dissipation capacity of CWH2C is the best, followed by CWH1C, CBH2C and CBH1C. Residual displacements also become bigger at the end of every loading cycle, compared with the original zero point. The measured residual deformation of each connection at the 0 load point is shown in Figure 10. The shown 0 load associated residual displacements of the 4 connections are very close after the same loading cycles.

As all the tested connections show obvious damage accumulation under cyclic loading, damage after different loading cycles can be assumed as damages induced by various earthquake intensities, which is concerned for the proposed investigation on connection behaviour under post-earthquake fire. The connection damage status after different loading cycles can be evaluated by several methods based on ductility and dissipated energy, as damage index (Newmark & Rosenblueth, 1974), cumulative plastic deformation index or cumulative ductility index (Krawinkler, 1987) and cumulative energy reduction index(Calado, et al., 2000). The evaluation and analysis work on these connections are currently under process at Monash University.

4 CONCLUSIONS AND FURTHER WORK

Totally 4 connections with different configurations including fully welded connection and double-angle bolted connection were tested under cyclic loading at ambient temperature. Load vs. deformation relationships and strength were measured during the test, together with observation on specimen deformations and the failure phenomena. Ductility and earthquake induced damage based on test results were analysed preliminarily.

The presented seismic test results form benchmark data for subsequent investigation work on connection behaviour under post-earthquake fire. Based on the theoretical classification and evaluation of the cyclic loading results, fire tests are currently performed using pre-damaged connections damaged by various cyclic loading cycles, which are used to simulate different earthquake intensity.

ACKNOWLEDGEMENT

The research work presented in this paper was supported by Australian Research Council through a Discovery Project (DP1096454) awarded to the second author. Moreover, I would like to express gratitude to the lab technicians Jeff Doddrell who made the specimens, Kevin Nievaart who made the laboratory equipment easily available and all others who worked for the project.

REFERENCES

AISC, A. 2005. AISC 325-05: *Steel Construction Manual, 13th edition, American Institute of Steel Construction*. Inc: Chicago, IL: American Institute of Steel Construction.

AISC, A. 2005. AISC 341-05: *Seismic Provisions for Structural Steel Buildings, American Institute of Steel Construction*. Inc: Chicago, IL: American Institute of Steel Construction.

Calado, L., Castiglioni, C. A. and Bernuzzi, C. 2000. Seismic behaviour of welded beam-to-column joints: Experimental and numerical analysis. In: *Proc. of the IV workshop on connections in steel structures. On CD*.

Castiglioni, C. A. and Pucinotti, R. 2009. Failure criteria and cumulative damage models for steel components under cyclic loading. *Journal of Constructional Steel Research*. 65(4): 751–765.

CEN. 2005. EN 1993-1-8: *Eurocode 3, Design of steel structures, part 1–8*: *Design of joints*. Brussels: European Committee for Standardization.

Gong, Y. 2008. Double-angle shear connections with small hollow structural section columns. *Journal of Constructional Steel Research*. 64(5): 539–549.

Krawinkler, H. 1987. Performance assessment of steel components. *Earthquake Spectra*. 3(1): 27–41.

Onesteel. 2003. *Structural steel in housing(Third enditio)*. Onesteel.

Sherman, D. R. 1995. Simple framing connections to HSS columns. In: *Proceedings of the National Steel Construction Conference*. 30.31–30.16.

Sherman, D. R. 1996. Designing with structural tubing. *Engineering Journal-American Institute of Steel Construction*. 33: 101–109.

Research and Applications in Structural Engineering, Mechanics and Computation – Zingoni (Ed.)
© 2013 Taylor & Francis Group, London, ISBN 978-1-138-00061-2

Analytical approach for the determination of the strength and stiffness of the T-Stub with four rows of bolts

N. Mehidi
University of Jijel, Department of Civil Engineering, Algeria

F.Z. Mimoune & M. Mimoune
University of Constantine, Department of Civil Engineering, Algeria

A. Bouchaïr
University of Blaise Pascal, Clermont Ferrand, France

ABSTRACT: This paper presents an analytical study on bolted in a T-Stub, subjected to static loading. These assemblies are tested for modeling the tensile part of an assembly of the type beam-column bolted with end plate extended. The originality of this work is the study of the influence of the second row of bolts, which is not treated in the literature. This configuration is commonly found in different countries of Europe and in particular Germany, where this configuration is standardized. The analogy between the tensile zone in an assembly and a T-Stub based on the Eurocode3 Part 1.8 has enabled to establish a simple mathematical formulation for the determination of the main characteristics, such as strength and stiffness, in order to put in evidence the influence of each parameter. In this study the thickness of the plate (flange of T-Stub) is the main parameter, as well as the number of bolts rows and the effect of the lever's force. The obtained results allow to proof the value of having another bolts rows and the role of the thickness of the plate, on the failure's modes that can occur during the application of the load to the state limit ultimate. A comparison is made between the experimental results, analytical results and results from the literature.

Keywords: Eurocode3, assembly, T-stub, bolt, stiffness, strength

NOMENCLATURE

L_{eff}: effective length
e_{pl}: plate thickness
fy: yield stress of steel
m: distance from the bolt axes to the weld edge
n_1: distance from the bolt axes to plate edge
n_2: distance between two bolts axes
d: diameter of the bolt
A: net area of the bolt
d_w: diameter of the washer
F_{Ri}: design strength of a T-stub equivalent to each failure mode
M_{pl}: plastic moment
N_{pl}: plastic resistance of the bolt
Fub_0: ultimate strength of bolt
K_{init}: initial stiffness of T-Stub
F_{el}: elastic load applied
F: load applied
Q, B: reactions

1 INTRODUCTION

Steel structures are usually made of columns and beams joined together by assemblage that have an influence on the overall behavior of the structure. Steel construction uses two main types of joints: the welded and bolted connections. However, the bolted assembly with end plate is widely used in steel structures. Generally, in practice the bolted end plate has various geometric configurations due to the variation in the number bolts per rows, the space between bolts axes, the dimensions of the end plate which may be flowing or not, the size of columns and beams (thickness of the flange and the web considered), the prestressed force in the bolts, the mechanical properties of the steel and the contact surfaces.

Bolted connections have recently attracted new research efforts after the unexpected failures of welded joints during earthquakes. Criteria and formulations to predict the stiffness and strength in static loading conditions, typologies of the most common joints were codified by the Eurocode3, which is based on the so-called components.

Eurocode3 retained the components method to characterize the behavior of beam-column assembly, considering that the assembly is a set of basic components.

In this study, we are interested in the analysis of the behavior of T-stub with two rows of bolts and

to confront the assembly of four rows of bolts vertically arranged, for which no recommendation appears in the current regulations (Eurocode3 , CCM97), and which are the principal components in the assembly. The behavior of the T-stub is more or less complex. The Simplification of the design formulas associated are then different. The effect of some parameters such as plate thickness, number of bolts, and the lever force play a very important role in determining the strength and stiffness of the beam-column assemblies.

2 COMPONENTS METHOD

In the spirit of Eurocode3, every assembly must be regarded as a set of elements, called "components", which all contribute in a manner more or less important to the strength and the stiffness of this assembly.

The "component" that immediately comes to mind in the case of a bolted assembly is obviously the bolt, or rather each of the bolt's assembly.

The method of components considers any assembly as a set of individual elementary components. The basic concept, upon which this method is based, has the following steps:

- Identification of all basic components of the assembly;
- Evaluation of characteristics (strength and stiffness) of these components;
- Association of components to obtain strength and rigidity of the entire assembly.

For an assembly with extended end plate and bolted, subjected to bending, several basic components can be identified, depending on the type of solicitations they are subjected to (Eurocode3, Aribert 1999)

Once the behavior of the main components of the assembly is determined, each one is modeled by a spring (Eurocode3). The assembly is effectively represented by a system of springs. The external forces are then applied to it and the response of the entire assembly is deduced from the study of the spring system, based on physical principles, such as equilibrium of forces, compatibility of displacements, respect of strength, ductility respect. . .

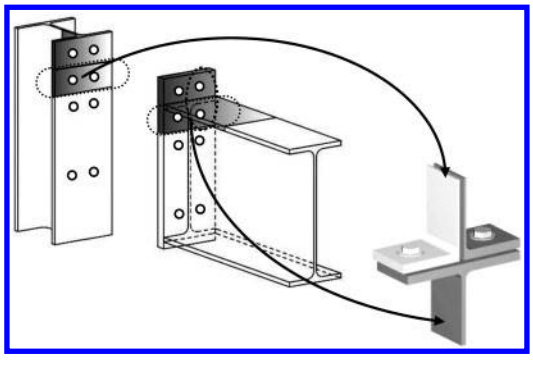


Figure 1. Theoretical model of a T-stub.

3 MODELLING OF TENSILE ZONE

The bolted connections beam to column with end plate can be classified according to their strength as, articulated, semi-rigid and rigid. In terms of bending's strength, they can be classified as rigid, partial strength and full strength.

The resistance of the T-stub (Fig. 1) is governed by the equivalent resistance of the plate (flange), bolts, web and the weld of web-flange (in the case of a welded T-stub).

4 CALCULATION OF T-STUB ASSEMBLY SUBJECTED TO TENSION

Eurocode3 adopts a modeling of the behavior of semi-rigid steel assemblies of the type beam-column bolted with end plate (Eurocode3, Aribert 1999). In our study, we only model the behavior of the column's flange and the end plate, by using a T-stub represented as a continuous beam, supported on ordinary bolts and taking into account the effect of lever due to longitudinal deformation of the plate (Aribert 1999).

4.1 *Modeling a T-stub with two bolts per row (Eurocode3, Aribert 1999, Mimoune 2003, 2008, Ana 2004, Al-Khatab 2007)*

According to Eurocode3, in order to calculate the initial stiffness of the T-stub for a single row of bolt vertical arranged, we cumulate the contribution of the column flange (first T-stub) and the end plate (second T-tub) and the bolts with their stiffness coefficients in series. An increase in thickness of the plate, does not allow the bending of the plate, and this was reflected by the increase of the effort applied right to the bolts due to the total load and the effect of lever force. A failure mode corresponds to the third category, which is the destruction of the bolts.

The theoretical model proposed by Aribert et al is the study of beam on four (04) supports subjected to a tensile force due to a gravity load type soliciting the beam (Fig. 2).

When the force F exceeds F_{el}, the deformation of the column flange (the plate) changes from domain elastic to domain elasto-plastic until failure obtained by the following three modes:

$$F_{R1} = \frac{4.M_{pl}}{m}\text{; mode1} \qquad (1)$$

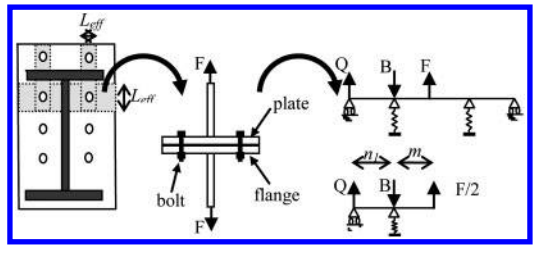


Figure 2. Model of the spring for T-sub (2 bolts per row).

with: $M_{pl} = 0.25 L_{eff} e_{pl}^2 f_y$

$$F_{R2} = \frac{2.(M_{pl} + n_1.N_{pl})}{n_1 + m}\text{; mode 2} \quad (2)$$

with: $N_{pl} = 0,675.fub_0 A$

$$F_{R3} = 2.N_{pl}\text{; mode 3} \quad (3)$$

When lever force may appear, it is convenient that the design strength of tension F_R of a T-stub, is taken equal to the smallest of the three possible failure modes according to Table 6-2 (Eurocode3).

The possible failure modes of the T-stub equivalent (Fig. 3) can be supposed to be similar to those provided in the Eurocode3. This classification is identified in Eurocode 3 and the literature (Aribert 1999, Mimoune 2003, 2008,. . .).

Tests were performed in the laboratory LMSS, Faculty of Engineering, University of Constantine, Algeria (Mimoune 2003, 2008). We can classify the failure modes observed in three categories:

- ruin of the end plate;
- ruin of the plate and destruction of the bolts;
- destruction of the bolts.

Regarding the first category, which corresponds to thin plates, the assembly continued to resist even with large deformation, the bolt failure is excluded. It was observed that the total ruin of the specimen comes with the breaking of the plate right next to the welded cords, which they have well resisted. Very important deformations were recorded at the holes also. The second category of failure mode, which corresponds to the plasticizing of the plate and the bolts destruction, was observed for assemblies of medium thickness. An important deviation right to the bolts is recorded at the beginning of loading; the destruction of assembly is reached after the deformation of the plate and the destruction of the bolts. Finally, the third mode is done by complete rupture of the bolt (Fig. 4).

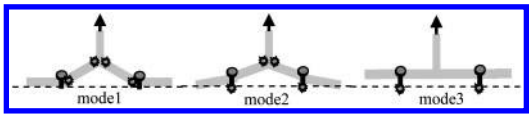


Figure 3. Failure modes observed for a T-sub with two bolts per row (Eurocode3).



Figure 4. T-stub tested (two bolts per row).

4.2 *Modeling a T-stub with four bolts per row:*

The analogy between the tensile zone of the beam-column assembly and the T-stub has enabled to establish simple mathematical formulations (Mehidi 2010, 2011) based the strength of materials methods, to determine the main characteristics such as strength and rigidity. These formulations easy to use in practice are not retained by the Eurocode3 or by CCM97.

We propose a new spring model of a T-stub relative to the end plate (column's flange) which is represented as a continuous beam rests on six supports in order to study the behavior of the end plate in the point of view strength, stiffness and the observed failure modes (Fig. 5).

Depending on the thickness of the end plate, the deviation between axes of the bolts, and when the tensile force F exceeds F_{el}, the plate is deformed in the domain of elasto-plastic until stage of ruin obtained (Fig. 6):

- by plasticization of the total plate (mode1);
- by plasticization the plate and ruin of intermediate bolts B2 (mode 2-1);
- by ruin of intermediate bolts B2 and plasticization total of the plate (Mode 2-2);
- either by formation of plastic hinges and bolts ruin (mode 2-3);
- either by breaking of all the bolts (mode 3).

Ultimate strength for each mode can be determined using the cinematic method which gives us:

$$F_{R1} = \frac{4.M_{pl}}{m}\text{; mode1} \quad (4)$$

$$F_{R2-1} = \frac{2(M_{pl} + N_{Pl}.n_2)}{m + n_2}\text{; mode2-1} \quad (5)$$

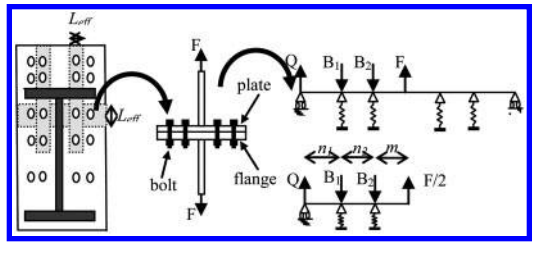


Figure 5. Spring Model proposed of the T-stub (four bolts per row).

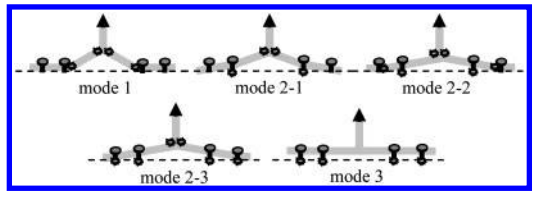


Figure 6. Failure modes observed for a T-stub with four bolts per row.

$$F_{R2-2} = \frac{4.M_{pl} + 2.N_{pl}.n_2}{m + n_2} \text{;mode2-2} \quad (6)$$

$$F_{R2-3} = \frac{2M_{pl} + N_{pl}.(4.n_1 + 2.n_2)}{m + n_2 + n_1} \text{;mode2-3} \quad (7)$$

$$F_{R3} = 4.N_{pl} \text{;mode3} \quad (8)$$

In the same context, tests have been made in the laboratory LMSS, Faculty of Engineering, University of Constantine, Algeria, allow the observed different failure modes mentioned above (Fig. 7).

When lever force may appear, it is convenient that the design strength of tension F_R of a T-stub is taken equal to the smallest of the five possible failure modes (Table 1). Eurocode3 proposed two formulas, the first simple (method 1) and the second alternative (table 6.2 .Eurocode3). For T-stub 2 bolts per row, $n_1 \leq 1.25\,m$, and for the T-stub with four bolts per row, $n1 + n2 \leq 1.25\,m$ (Demonceau 2011).

It should be noted that the effective length L_{eff} corresponding to each failure mode (Table 6.4 Eurocode3) is not taken into account in this study.



Figure 7. T-stub tested (four bolts per row).

5 PARAMETRIC ANALYSES

A parametric study has been initiated to study the sensitivity of different geometric parameters in order to determine the limits of applicability of the analytical formulas and evaluate the simplifications adopted. In this context, we analyze on the basis of analytical formulas (Eurocode3, Aribert 1999, Mehidi 2010, 2011) the evolution of the stiffness, the strength, and the lever force that acts upon the T-stub in function of the plate thickness (e_{pl}), curvature at the point of application of the load (displacement), and the position of the lever force resulting (n_1). The used values for either (e_{pl}) or (n_1) are more than those proposed by the Eurocode3 in a way to see its influence in a sufficient large domain.

In this analysis, we seek to confirm the new model mentioned above by comparing it with that given by Eurocode3 and the one in the literature (Demonceau 2011, Jiménez 2011). A computer program was carried out to study the role and influence of each component, in particular the effect of the fourth line of the bolts vertically disposed. The results obtained show that the simultaneous increase of the thickness of the end plate, diameter (d) and the number of bolts, have a considerable influence on the value of the strength, stiffness, and failure mode.

We show the main results of this analysis in the following paragraphs.

5.1 *Evolution of the initial stiffness in function (e_{pl}) and (n_1):*

Figure 8 shows the evolution of the initial stiffness in function of the thickness of the plate (e_{pl}) for both

Table 1. Summary of the strengths of T-stub.

Failure modes	T-stub with 2 bolts per row	T-stub with 4 bolts per row	
	Eurocode 3, méthode 1 , Table 6.2	Proposed model	(Demonceau 2011, Jiménez 2011) alternative Méthode
Mode 1	$F_{R1} = \frac{4.M_{pl}}{m}$	$F_{R1} = \frac{4.M_{pl}}{m}$	$F_{R1} = \frac{(8n_2 - 2d_w)M_{pl}}{2mn_2 - \frac{d_w}{2}(m + n_2)}$
Mode 2	$F_{R2} = \frac{2(M_{pl} + N_{Pl}.n_1)}{m + n_1}$	$F_{R2-1} = \frac{2(M_{pl} + N_{Pl}.n_2)}{m + n_2}$ $F_{R2-2} = \frac{4.M_{pl} + 2.N_{pl}.n_2}{m + n_2}$ $F_{R2-3} = \frac{2M_{pl} + N_{pl}.(4.n_1 + 2.n_2}{m + n_2 + n_1}$	$F_{R2} = \min(F_{R2,p}, F_{R2,np})$ $F_{R2,p} = \frac{2M_{pl} + 2N_{pl}(n_2{}^2 + 2n_1^2 + 2n_1n_2)}{(m + n_1 + n_2)}$ $F_{R2,np} = \frac{2M_{pl} + 2N_{pl}n_2}{(m + n_2)}$
Mode 3	$F_{R3} = 2.N_{pl}$	$F_{R3} = 4.N_{pl}$	$F_{R3} = 4N_{pl}$

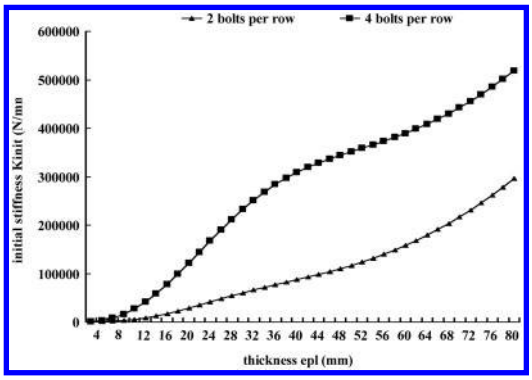


Figure 8. Variation of the initial stiffness depending on the thickness of the plate (e_{pl}).

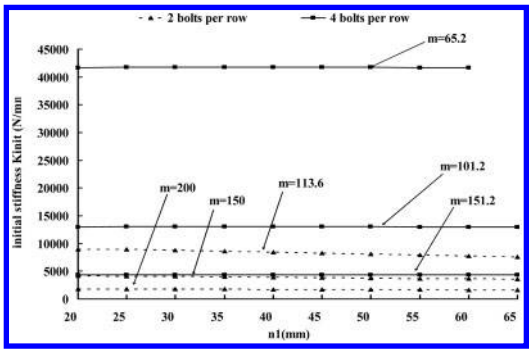


Figure 9. Variation of the initial stiffness based of (n_1) and (m) to thickness $e_{pl} = 14$ mm.

models 2 and 4 bolts per row, taking account of (m) between the bolt axis and the appearance of the first plastic hinge of the first model, is equal to the sum of (m) and (n_2) of the second model for a better taking into account the added row bolts. We observe that there is a slight difference for relatively thin plate, contrary the deviation is remarkable whenever the thickness increase. Generally, the model with 4 bolts per row gives initial stiffness always greater and becomes very significant compared to the first model with 2 bolts per row, which reflect the interest of the new model obtained and the appropriate business.

For the same values (n_1) given and (m) different, for example $n_1 = 20$ mm, the initial stiffness of the T-stub with two bolts per row, is less than the one with 4 bolts per row (Fig. 9). It is observed that the results of stiffness obtained, are very low due to the important value of (m), which causes a certain flexibility to the assembly; the T-stub with $m = 65.2$ mm, is stiffer than the one with $m = 101.2$ mm. The significance of the change of (n_1) is not shown by curves of figure 9, this is due to the values of the distance between the welding cord and the bolt axis which are important and that the T-stub has a flexibility, which at the same time reduces the transmission effect of the force applied to the position of the lever force.

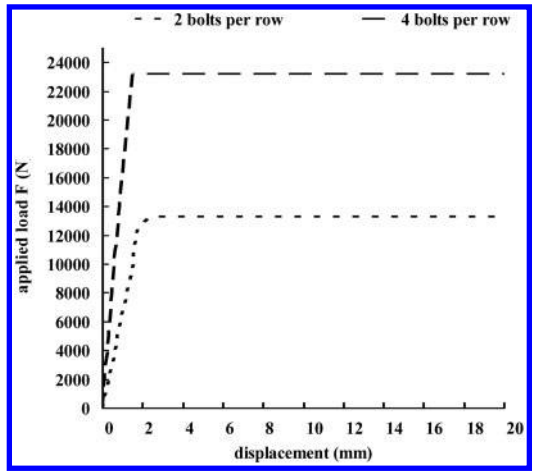


Figure 10. Variations of the load applied as a function of displacement of the plate- $e_{pl} = 10$ mm and $n_1 = 35$ mm.

5.2 *Evolution of strength versus (epl):*

Figures 10 show the variation of the applied load F versus displacement, right to the load application for plate $e_{pl} = 10$ mm. By varying the number of bolt rows; the distance between tow axis of the first row of the bolt and the welded web-flange decrease, we note that the strength will be almost doubled and the displacement (deviation) will decrease.

5.3 *Evolution of the force versus the lever (n1)*

Figure 11 shows a comparison between different T-stub reflecting the effect of thickness on the lever force, witch is not significant due to the simultaneous influence of several parameters such as, the number of bolts axis , the values of (m) and (n_2), and the force applied, giving by the end a very complex behavior of the assembly. For the first model, we notice that the contact between the plates done for thin and while we relatively thick ones. By contrary, the lever force decreases with the increase thickness for relatively thick plates, which reflects the deviation between the two plates without contacts. For the second model, is the opposite case of the first, with low values of lever force. We also attempt to know the evolution of the lever effort according to the external force applied by varying the position of the lever (n_1) (Fig. 12). Ratio of obtained values is 0.5 for T-stub with 2 bolts per row, this is due to large values of (m) compared to (n_1), which reflects the full transmission of the force applied at the lever force and which indicates that the spring model (Eurocode3, Al-Khatab 2007) has a large dilatation at the bolts level. This case will be resolved when we increases the diameter of the bolts (bolt becomes more rigid) or by adding another row of bolts that gives a ratio of about 0.06 which will be the case of a T-stub with four bolts per row.

After a plastic analysis of continuous beams on six supports, it reached the ruin in function of the number

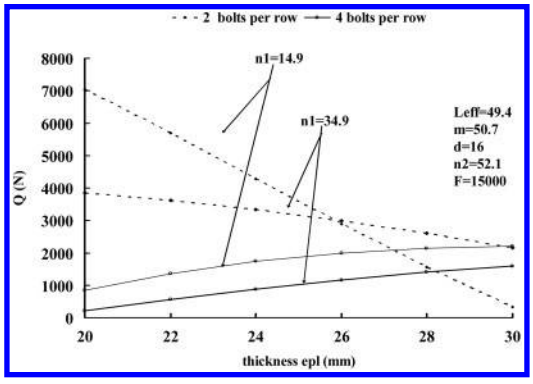


Figure 11. Variation in the lever force according to the thickness of the plate.

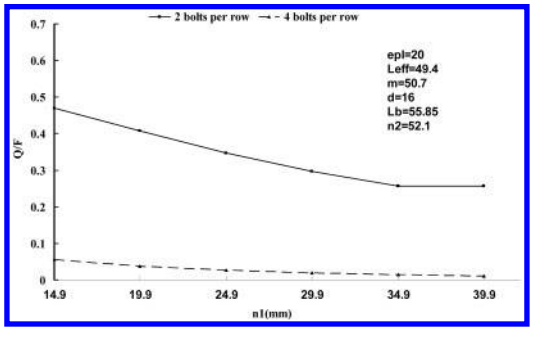


Figure 12. Variations in the ratio of lever force- applied load by the values of *nl*.

of hinges that appear, to say that a Mechanism. Therefore, the comparison can be made with (Demonceau 2011) is significant, except for failure mode 2, and contrary to the other (mode 1 and 3) have the same results.

6 CONCLUSIONS

In this article, we presented the principles of the component method adopted by the Eurocode3; to characterize the behavior of assemblies.

Then, we also analyzed the behavior of T-stub which conducted major components in the tensile zone assemblies, subjected to bending. In this context, we varied several geometrical parameters of the T-stub in order to see the sensitivity of the initial stiffness, the lever effort and strength depending on, thickness of the plate, the position of the resulting lever force and the number of the bolt per row (number of row arranged vertically).

At the end of this study, it can be argued the following conclusions:

– Increasing the thickness of the plate (flange) will increase stiffness for both models, but leads to a better decreasing of displacement and delay the appearance of the first plastic hinge for the new model with four rows of bolt;
– The addition of another row of bolt vertically arranged, has an influence on the value of the total force applied, compared with the same original T-stub.
– The geometrical dimensions as position of lever force, the distance between the bolt axis and welded cord, play an important role in determining the behavior of the plate (deformation) as well as the amplification of lever force.

The comparison of these results with those of the literature and experimental, we can confirm that the analysis of this new model offers the advantage of studying the tensile part of the bolted assembly beam-column with end plate. The behavior of assemblies with four or more lines arranged vertically (four bolts per row or more) and the obtained results are used to solve some problems in the design of steel frame nodes, as reducing the curvature of the plate (Demonceau 2011); the stiffness and strength in this case will be amplified in a non negligible manner.

REFERENCES

Al-Khatab, Z. & Bouchaïr, A. 2007. Analysis of a bolted T-stub strengthened by backing-plates with regard to Eurocode 3. In Journal of Constructional Steel Research 63: 1603–161.

Ana, M. et al. 2004. Experimental assessment of the behaviour of bolted T-stub connection made up of welded plates. In Journal of constructional steel Research 60 : 269–311.

Aribert, J.M. et al. 1999. Modélisation du comportement d'assemblages métallique semi-rigides de type poutre-poteau boulonnée par platine d'extrémité. In Steel construction 1 :25–46.

CCM97, 1997. Règles de conception et de calcul des structures métalliques .D.T.R-B.C. Ministère de l'habitat Algérie.

Demonceau, J.f. et al. 2011. Connections with four bolts per horizontal row.In Eurosteel, Budapest, August 31-September 2, 2011: Hungary.

Eurocode3. 2005. EN 1993-1-8. Design of steel structures-Part 1-8 :Design of joints. European committee for standardization. (May 2005).

Jiménez, J.J. et al. 2011. Stifness of T-Stub Component with four lines of bolts. In Eurosteel, Budapest, August 31-September 2, 2011: Hungary.

Mehidi, N. et al. 2010. Etude d'un assemblage porteau poutre par platine d'extrémité avec quatre files des boulons.In International Symposium on Aircraft Materials, MarraKech, 12–14 Mai 2010 : Morocco.

Mehidi, N. et al. 2011. Assemblages boulonnés par platine d'extrémité cas des assemblages par quatre files de boulons. In Algeria Equipment. 48 (January 2011):23–39.

Mimoune, M. & Mimoune, F.Z. 2003.Analyse du comportement des assemblages boulonnés par platine d'extrémité sollicités en traction. IN Canadian Journal of Civil Engineering. 30 (4) : 615–624.

Mimoune, M. et al. 2008. Etude des assemblages en T boulonnés par platine d'extrémité avec ou sans raidisseurs. In Algeria Equipment. 44 (May 2008):8–13.

Research and Applications in Structural Engineering, Mechanics and Computation – Zingoni (Ed.)
© 2013 Taylor & Francis Group, London, ISBN 978-1-138-00061-2

Axial capacity of transverse branch plate-to-CHS T-joints

A. A. Shaat
Lecturer, German University in Cairo – Assistant Professor (on leave), Ain Shams University, Egypt

ABSTRACT: The current international design guidelines estimate the axial capacity of transverse branch plate-to-CHS T-joints using a single formula for both tension and compression loads. In fact, the behavior of CHS under branch compressive loads is completely different from their behavior under tensile loads. A parametric numerical finite element study is undertaken to accurately assess the variation in joint capacity under both compression and tension loading cases. Various geometric and material properties are modeled and analyzed using commercially available software, ANSYS. An evaluation of the current CIDECT and AISC strength predictions concluded that general underestimation of the T-joint capacity exists specially when the branch plate is loaded in tension. New design strength functions associated with their valid ranges are proposed based on a nonlinear regression analysis of both the finite element results and previous research data.

1 INTRODUCTION

Steel hollow sections are extensively used in both offshore and onshore structures for their inherent strength and efficiency. In these structures, the hollow section chord members are either welded directly to the brace members or welded to a branch plate that is connected at its other end to the brace member, as shown in Figure 1. The branch plates could be welded at the longitudinal direction of the chord member or at its transverse direction. The behavior of these welded branch plates to either Rectangular Hollow Sections (RHS) or Circular Hollow Sections (CHS) has been studied in many research programs such as Cao et al. (1998), Kosteski et al. (2003), Wardenier et al. (2009), and Voth and Packer (2012a and 2012b). Design equations that predict the axial load capacity of these branch plates can be found in the Comité International pour le Développement et l'Etude de la Construction Tubulaire (CIDECT) Design Guide No. 1 (Wardenier et al., 2008a) and the American Institute of Steel Construction (AISC) Design Guide No. 24 (Packer et al. 2010).



Figure 1. Example of transverse plate-to-CHS joint.

Lu et al. (1994) proposed an ultimate deformation limit that can be used for hollow structural joints based on both experimental and numerical results. This deformation limit is estimated at 3% of the chord member breadth (b_0) in the case of RHS or the chord member diameter (d_0) in the case of CHS. The applicability of this limit was further validated by Zhao (2000). This deformation value is the most widely limit state used by both researchers and designers to determine the hollow section joint strength.

The following general format was established for calculating the axial capacity (N_1) of branch plate-to-CHS joint since its first development.

$$N_1 = Q_u \cdot Q_f \cdot f_{y0}\, t_0^2 \quad (1)$$

Where, Q_u = partial design strength function, Q_f = chord stress function, f_{y0} = yield strength of the chord member, and t_0 = thickness of the chord member.

The development of the partial design strength function (Q_u) for the transverse plate-to-CHS T-joint is briefly reported herein. First, Kurobane et al. (1976) developed the following formula;

$$Q_u = 6.43\,(1 + 4.60\,\beta^2) \quad (2)$$

Where, β = joint width ratio = b_1/d_0, and b_1 = transverse plate width.

Wardenier (1982) modified the coefficients of the previous equation to account for experimental results of subsequent research programs, as follows;

$$Q_u = 4.20\ (1 + 5.07\ \beta^2) \tag{3}$$

The 1st edition of CIDECT design guide No. 1 (Wardenier et al., 1991) implemented further simplified modifications to the previous design strength function as follows;

$$Q_u = 4.00\ (1 + 5.00\ \beta^2) \tag{4}$$

All the previous expressions have been originally derived based on the assumption of CHS-to-CHS T-joints. Subsequent modifications to the partial design strength function have been reported to account for the effect of the branch plate thickness (t_1) as well as the slenderness of the chord member (γ) (Wardenier et al., 2008b), as follows;

$$Q_u = 2.60\ (1 + 6.80\ \beta^2)\ \ (1 + 0.25\ \eta)\ \gamma^{0.2} \tag{5}$$

Where, γ = chord radius-to-thickness ratio = $d_0/2t_0$, and η = branch plate thickness-to-chord diameter ratio = t_1/d_0.

Based on reanalysis of existing numerical and experimental results for transverse branch plate-to-CHS joints, Wardenier et al. (2008b) adopted further modifications to Equation 5, as follows;

$$Q_u = 2.20\ (1 + 6.80\ \beta^2)\ \ (1 + 0.40\ \eta)\ \gamma^{0.2} \tag{6}$$

IIW sub-commission XV-E and the 2nd edition of CIDECT design guide No. 1 (Wardenier et al., 2008a) have assumed that the value of η is very small and close to zero for transverse branch plate T-joints. Therefore, further simplifications can be implemented to the partial design strength function as follows;

$$Q_u = 2.20\ (1 + 6.80\ \beta^2)\ \ \gamma^{0.2} \tag{7}$$

On the other hand, AISC steel design guide No. 24 (Packer et al., 2010) adopted one common equation for the strength function of both T- and X- types of joints, as follows;

$$Q_u = 5.50\ /\ (1 - 0.81\ \beta) \tag{8}$$

Exploring the development history of the axial capacity of the transverse branch plate-to-CHS joints (Equations 1 to 8) refers to one common approach that does not differentiate between the loading directions of the branch plate; whether tension or compression.

An experimental program consisting of 12 branch and through plate-to-CHS joints under both tension and compression loading was carried out by Voth and Packer (2012a). The experimental results revealed that the behavior of branch plate-to-CHS T-joints tested in tension and compression is significantly different. Using regression analysis that incorporates the results of both experimental and finite element model (FEM) analyses individual formula for each loading case is introduced by Voth and Packer (2012b), as follows;

$$\text{Compression} : Q_u = 2.90\ \zeta\ (1 + 3.0\ \beta^2)\ \gamma^{0.35} \tag{9}$$

$$\text{Tension} : Q_u = 2.60\ \zeta\ (1 + 2.5\ \beta^2)\ \gamma^{0.55} \tag{10}$$

Where, ζ is a reduction factor with a lower bound value of 0.85.

Two main factors were ignored while developing the design equations by Voth and Packer (2012b), which are;

1. The branch plates were assumed relatively thin (i.e. η = zero), while the large weld size (13.43 mm) in addition to the branch plate thickness (19.05 mm) used in their numerical analysis imply η ratio of 0.21. This large value of η will have a considerable impact on the regression analysis of the design equations.
2. The large values of β (i.e. $\beta > 0.85$) prevent the CHS chord member from reaching the predefined deformation limit of 3% of the chord member. This is mainly due to the stiffening effect of the wide transverse branch plate. Therefore, splitting each design equation into two equations with a limiting validation β ratio may provide more accurate strength predictions.

This paper introduces a FEM that captures the variation in strength of transverse plate-to-CHS joints under tension and compression loading. After verifying the model against the test results of Voth and Packer (2012a), a comprehensive parametric study was carried out to examine the validity of Equations 9 & 10 against a wider range of parameters. The following sections introduce the FEM details, verification against the test results, and the detailed parametric study. Finally, a regression analysis was carried out to propose new design equations that predict both compressive and tensile capacities of transverse branch plate-to-CHS joints.

2 FINITE ELEMENT MODELING

This section introduces the details of the FEM and methodology adopted for the branch plate-to-CHS T-joints, including element type, mesh density, boundary conditions, and material modeling. Commercially available finite element program ANSYS has been employed.

2.1 *Shell element and mesh size*

The symmetric geometry of the T-type specimens about two vertical planes allowed modeling only one quarter of the specimens, as shown in Figure 2.

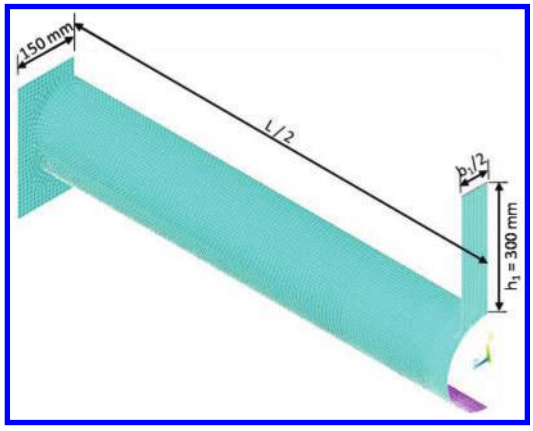


Figure 2. One quarter of the FEM.

Symmetric boundary conditions are applied at the specimen cut edges. Nominal center line dimensions are used to model the specimens. A 3-D SHELL181 element is used to model all components of the specimen including, the CHS chord, branch plate, chord end plates, and welding material between the branch plate and chord member. SHELL181 is suitable for analyzing thin to moderately thick shell structures. It is a 4-node element with six degrees of freedom at each node: three translations in the x, y, and z directions, and three rotations about the x, y, and z-axes. In the model, the element size is varied in such a way that relatively smaller elements with a size of 5 mm are used at the vicinity of the intersection between the branch plate and chord member where the stress gradient is more critical. The mesh density decreased towards the ends where size of elements reaches 10 mm.

2.2 *Material modeling*

Multi-linear isotropic hardening material model was used to model all components of the specimens. This model captures quite accurately the stress–strain curves obtained from coupons tests by Voth and Packer (2012a). The welds were assumed to have the same material properties as the base metal.

2.3 *Loading and boundary conditions*

Uniformly distributed pressure is applied at the top edge of the branch plate. End plate (20 mm thick) is modeled at the end of the chord member with complete fixity to the chord nodes. All nodes of the end plate are restrained in the x, y, and z translational degrees of freedom.

2.4 *Finite element model validation*

The finite element model is validated using the results of eight specimens tested by Voth and Packer (2012a). All specimens had the same chord size of (219 × 4.8) and yield strength of 389 MPa, which is outside the validity range for Equation 8. The design provisions of Eurocode 3 specify the limits for the diameter-to-thickness ratio (d/t) equal to ($11750/f_y$), ($16450/f_y$), and ($21150/f_y$) for classes 1, 2, and 3, respectively. Accordingly, specimens tested by Voth and Packer (2012a) are classified as class 3, which is outside the validity range of Equation 7. The tested parameters included different configurations such as the plate orientation (longitudinal or transverse), method of plate attachment (branch or through), and the type of loading (tension or compression). Table 1 lists a comparison between the experimental and FEM loads, where the load is measured at the 3% deformation of the chord diameter as a criterion for the joints capacities. Table 1 indicates an average value for the ratio between the FEM and experimental loads of 0.98 with a standard deviation of 0.06. The model is deemed suitable and reliable for the parametric study that follows.

Table 1. Comparison between experimental results and FEA results

Joint type	Branch plate orientation	Loading	$P_{Exp.}$ (kN.)	P_{FEM} (kN.)	$P_{FEM}/P_{Exp.}$
Branch	Transverse	Comp.	138	140	1.01
		Tens.	283	298	1.05
Through		Comp.	400	394	0.99
		Tens.	447	384	0.86
Branch	Longitudinal	Comp.	90	91	1.01
		Tens.	161	158	0.98
Through		Comp.	273	248	0.91
		Tens.	259	266	1.03
				Average	0.98
				S.D.	0.06

3 PARAMETRIC STUDY

The validated model is used to carry out an extensive parametric study to examine the validity of Equations 9 and 10 in predicting the tensile or compressive capacities of transverse branch plate-to-CHS T-joints. All specimens had the same chord diameter (219 x t_0). A chord effective length parameter (α) is taken equal to 20 as per the recommendations of van der Vegte and Makino (2006). The prescribed value of α resulted in a total length of chord member equal to 2200 mm. The branch plate thickness is taken equal to 20 mm and is kept constant throughout the parametric study.

A total of 64 specimens are examined in this research program to study the following parameters:

1. Chord sizes are 219 × 6.4, 8.0, 9.5, and 11, which are equivalent to chord thicknesses of 6.35 mm, 7.95 mm, 9.53 mm, and 11.13 mm, respectively.
2. Branch plate widths of 100 mm, 140 mm, 180 mm, and 200 mm, which are equivalent to β ratios of 0.49, 0.67, 0.84, and 0.94, respectively. It should be noted that the calculations of β ratios have accounted for the footprint of the branch plate including its weld sizes.

Table 2. Results of finite element analysis for joints under branch plate compression loading.

F_y MPa	d_0 mm	t_0 mm	b mm	γ	β	N_1 (Eq. 7) kN.	N_1 (Eq. 8) kN.	N_1 (Eq. 9) kN.	N_{FEM} kN.	N_{FEM}/N_1 (Eq. 7)	N_{FEM}/N_1 (Eq. 8)	N_{FEM}/N_1 (Eq. 9)
290	225.52	6.35	100	17.76	0.49	120	106	135	155	1.29	1.46	1.15
290	225.52	6.35	140	17.76	0.67	183	139	184	219	1.19	1.57	1.19
290	225.52	6.35	180	17.76	0.84	266	203	247	295	1.11	1.46	1.19
290	225.52	6.35	211	17.76	0.94	318	312	286	350*	1.10	1.12	1.22
290	227.12	7.95	100	14.28	0.48	178	166	195	225	1.26	1.36	1.15
290	227.12	7.95	140	14.28	0.66	272	217	265	308	1.13	1.42	1.16
290	227.12	7.95	180	14.28	0.84	395	313	355	399	1.01	1.28	1.12
290	227.12	7.95	211	14.28	0.93	471	476	411	465*	0.99	0.98	1.13
290	228.70	9.53	100	12.00	0.48	245	237	262	309	1.26	1.30	1.18
290	228.70	9.53	140	12.00	0.66	374	309	355	415	1.11	1.34	1.17
290	228.70	9.53	180	12.00	0.83	542	443	476	519	0.96	1.17	1.09
290	228.70	9.53	211	12.00	0.92	647	667	551	540*	0.84	0.81	0.98
290	230.30	11.13	100	10.35	0.48	322	322	338	395	1.23	1.23	1.17
290	230.30	11.13	140	10.35	0.65	490	418	456	510	1.04	1.22	1.12
290	230.30	11.13	180	10.35	0.83	710	596	610	627	0.88	1.05	1.03
290	230.30	11.13	211	10.35	0.92	846	887	706	755*	0.89	0.85	1.07
389	225.52	6.35	100	17.76	0.49	145	N/A	181	188	1.30	N/A	1.04
389	225.52	6.35	140	17.76	0.67	221	N/A	246	274	1.24	N/A	1.11
389	225.52	6.35	180	17.76	0.84	322	N/A	331	375	1.17	N/A	1.13
389	225.52	6.35	211	17.76	0.94	384	N/A	384	450*	1.17	N/A	1.17
389	227.12	7.95	100	14.28	0.48	215	N/A	262	270	1.26	N/A	1.03
389	227.12	7.95	140	14.28	0.66	329	N/A	355	384	1.17	N/A	1.08
389	227.12	7.95	180	14.28	0.84	477	N/A	476	514	1.08	N/A	1.08
389	227.12	7.95	211	14.28	0.93	569	N/A	552	588*	1.03	N/A	1.07
389	228.70	9.53	100	12.00	0.48	296	N/A	352	387	1.31	N/A	1.10
389	228.70	9.53	140	12.00	0.66	451	N/A	476	519	1.15	N/A	1.09
389	228.70	9.53	180	12.00	0.83	655	N/A	638	670	1.02	N/A	1.05
389	228.70	9.53	211	12.00	0.92	781	N/A	738	756	0.97	N/A	1.02
389	230.30	11.13	100	10.35	0.48	388	N/A	453	492	1.27	N/A	1.09
389	230.30	11.13	140	10.35	0.65	591	N/A	612	635	1.07	N/A	1.04
389	230.30	11.13	180	10.35	0.83	857	N/A	819	805	0.94	N/A	0.98
389	230.30	11.13	211	10.35	0.92	1021	N/A	947	902	0.88	N/A	0.95
									Average	1.10	1.23	1.10
									S.D.	0.14	0.22	0.07

*Specimens failed prior to reaching the 3%d_0.

3. Yield strength of the chord member equal to 290 MPa and 389 MPa.

4 RESULTS

Tables 2 and 3 list the results of the finite element analysis in terms of the joint compressive and tensile capacities (N_{FEM}), respectively. The tables also list the joints capacities (N_1) as calculated using the formulae given in Equations 1, and 7 to 10 as well as a comparison between these values and the FEM results.

The results show large discrepancy between the FEM results and the values given using Equations 7 to 10. Table 2 indicates that using Equation 7 (Wardenier et al., 2008a) and Equation 8 (Packer et al., 2010) to calculate the compressive strength of branch plate-to-CHS T-joints give conservative results with average differences of 10% and 23% lower than the FEM results. Equation 9 introduced by Voth and Packer (2012b) for the compressive strength of joints gives also conservative results with 10% lower than the FEM results. However, Equation 9 has a lower standard deviation of 7% compared with 14% and 22% for Equations 7 and 8, respectively.

Table 3 proves that using the same Equations 7 and 8 to calculate the tensile strength of the joints is way below their real capacities. Equations 7 and 8 underestimate the tensile strength of transverse branch plate-to-CHS T-joints by 47% and 63%, respectively. Equation 10 introduced by Voth and Packer (2012b) for the tensile strength of joints gives better results with an average of only 6% lower than the FEM results. Yet, Equations 7, 8, and 10 have large standard deviation values of 38%, 50%, and 15%, respectively.

5 NEW PROPOSED DESIGN EQUATIONS

A non-linear regression analysis is performed using the general format of partial design strength predictions (i.e. similar to Equations 5 and 6) that account for

Table 3. Results of finite element analysis for joints under branch plate tension loading.

F_y MPa	d_0 mm	t_0 mm	b mm	γ	β	N_1 (Eq. 7) kN.	N_1 (Eq. 8) kN.	N_1 (Eq. 9) kN.	N_{FEM} kN.	N_{FEM}/N_1 (Eq. 7)	N_{FEM}/N_1 (Eq. 8)	N_{FEM}/N_1 (Eq. 9)
290	225.52	6.35	100	17.76	0.49	120	106	201	255	2.13	2.40	1.27
290	225.52	6.35	140	17.76	0.67	183	139	265	333	1.82	2.39	1.26
290	225.52	6.35	180	17.76	0.84	266	203	349	404	1.52	1.99	1.16
290	225.52	6.35	211	17.76	0.94	318	312	401	422*	1.33	1.35	1.05
290	227.12	7.95	100	14.28	0.48	178	166	277	344	1.93	2.07	1.24
290	227.12	7.95	140	14.28	0.66	272	217	366	432	1.59	1.99	1.18
290	227.12	7.95	180	14.28	0.84	395	313	481	509	1.29	1.63	1.06
290	227.12	7.95	211	14.28	0.93	471	476	552	512*	1.09	1.08	0.93
290	228.70	9.53	100	12.00	0.48	245	237	360	453	1.85	1.91	1.26
290	228.70	9.53	140	12.00	0.66	374	309	474	548	1.47	1.77	1.16
290	228.70	9.53	180	12.00	0.83	542	443	622	620*	1.14	1.40	1.00
290	228.70	9.53	211	12.00	0.92	647	667	714	575*	0.89	0.86	0.81
290	230.30	11.13	100	10.35	0.48	322	322	451	546	1.70	1.69	1.21
290	230.30	11.13	140	10.35	0.65	490	418	591	645	1.32	1.54	1.09
290	230.30	11.13	180	10.35	0.83	710	596	775	724*	1.02	1.22	0.93
290	230.30	11.13	211	10.35	0.92	846	887	889	636*	0.75	0.72	0.72
389	225.52	6.35	100	17.76	0.49	145	N/A	269	306	2.12	N/A	1.14
389	225.52	6.35	140	17.76	0.67	221	N/A	355	423	1.91	N/A	1.19
389	225.52	6.35	180	17.76	0.84	322	N/A	468	540	1.68	N/A	1.15
389	225.52	6.35	211	17.76	0.94	384	N/A	538	511*	1.33	N/A	0.95
389	227.12	7.95	100	14.28	0.48	215	N/A	372	416	1.93	N/A	1.12
389	227.12	7.95	140	14.28	0.66	329	N/A	490	554	1.69	N/A	1.13
389	227.12	7.95	180	14.28	0.84	477	N/A	645	677	1.42	N/A	1.05
389	227.12	7.95	211	14.28	0.93	569	N/A	741	657*	1.15	N/A	0.89
389	228.70	9.53	100	12.00	0.48	296	N/A	483	566	1.91	N/A	1.17
389	228.70	9.53	140	12.00	0.66	451	N/A	636	695	1.54	N/A	1.09
389	228.70	9.53	180	12.00	0.83	655	N/A	835	828	1.26	N/A	0.99
389	228.70	9.53	211	12.00	0.92	781	N/A	958	734*	0.94	N/A	0.77
389	230.30	11.13	100	10.35	0.48	388	N/A	605	673	1.73	N/A	1.11
389	230.30	11.13	140	10.35	0.65	591	N/A	793	816	1.38	N/A	1.03
389	230.30	11.13	180	10.35	0.83	857	N/A	1040	965	1.13	N/A	0.93
389	230.30	11.13	211	10.35	0.92	1021	N/A	1193	993*	0.97	N/A	0.83
									Average	1.47	1.63	1.06
									S.D.	0.38	0.50	0.15

*Specimens failed prior to reaching the 3% d_0.

the effect of branch plate thickness. The finite element results of Voth (2010) are included in the regression analysis to have more reliable predictions. A limiting β ratio of 0.85 is adopted to exclude the specimens that failed prior to reaching the deformation limit of 3% d_0. It should be noted that two specimens out of the 16 specimens with β equal to 0.83 failed at a lower deformation limit. This small number of specimens was assumed insignificant to change the equations limit ($\beta = 0.85$). The proposed design equations are summarized as follows;

Compressive strength:

$$Q_u = 2.40\,(1 + 2.21\,\beta^2)\,(1 + 1.08\,\eta)\;\gamma^{0.40} \quad \text{for } \beta < 0.85 \tag{11}$$

$$Q_u = 10.81\,\beta^{3.34}\eta^{0.20}\,\gamma^{0.54} \quad \text{for } \beta \geq 0.85 \tag{12}$$

Tensile strength:

$$Q_u = 2.14\,(1 + 1.50\,\beta^2)\;\;(1 + 0.95\,\eta)\;\;\gamma^{0.64} \quad \text{for } \beta < 0.85 \tag{13}$$

$$Q_u = 26.90\,\beta^{3.13}\eta^{1.13}\,\gamma^{0.88} \quad \text{for } \beta \geq 0.85 \tag{14}$$

The strength ratio between the numerical results and the proposed equations' values ($N_{FEM}/N_{roposed}$) has average values of 0.99, 1.00, 0.99, and 1.02 for Equations 11 to 14, respectively. The previous strength Equations 11 to 14 have correlation coefficients of 0.996, 0.998, 0.991, and 0.987, respectively.

6 CONCLUSIONS

Evaluation of the current design guidelines, for transverse branch plate-to-CHS T-joints, has been undertaken using a numerical finite element parametric

study consisting of 64 specimens, under both tension and compression branch plate loading. The study has proved that the current international design guides (CIDECT Design Guide No. 1 and the AISC Design Guide No. 24) are generally conservative for transverse branch plate-to-CHS T-joints and under-utilize their capacities especially when the branches are loaded in tension. Based on regression analysis, of the FEM results as well as research data by Voth (2010), improved partial design strength functions are proposed to accurately predict the axial capacity of transverse branch plate-to-CHS joints.

REFERENCES

Cao, J. J., Packer, J. A., and Kosteski, N. 1998. Design guidelines for longitudinal plate to HSS connections. Journal of Structural Engineering. ASCE. 124(7): 784–791.

CEN, 2005: Eurocode 3: Design of steel structures: Pat 1-1: General rules and rules for buildings. BS EN 1993-1-1:2005, European committee for standardization, Brussels, Belgium.

IIW. 2008. Static design procedure for welded hollow section joints-recommendations. 3rd edition, International institute of welding, sub-commission XV-E, IIW Doc XV-1281-08.

Kurobane, Y., Makino, Y., and Mitsui, Y. 1976. Ultimate strength formulae for simple tubular joints. IIW Doc. XV-385-76, Kumamoto University, Kumamoto, Japan.

Kosteski, N., Packer, J. A., and Puthli, R. S. 2003. A finite element method based yield load determination procedure for hollow structural section connections. Journal of Constructional Steel Research. (59): 453–471.

Lu, L. H., de Winkel, G. D., Tu, Y., and Wardenier, J. 1994. Deformation limit for the ultimate strength of hollow section joints. Sixth International Symposium on Tubular Structures, Melbourne, Australia, A. A. Balkema: 341–347.

Packer, J. A., Sherman, D. R., and Lecce, M. 2010. Hollow structural section connections. Steel Design Guide No. 24, American Institute of Steel Construction (AISC), Chicago. USA.

Swanson analysis system. 2007. ANSYS program. Release 11 user's manual, Houston, USA.

van der Vegte G. J. and Makino, Y. 2006. Ultimate strength formulation for axially loaded CHS uniplanar T-joints. International Journal of Offshore and Polar Engineering. 16(4): 305–312.

Voth, A. P. 2010. Branch plate-to-circular hollow structural section connections. PhD Thesis. University of Toronto, Toronto, Ontario, Canada.

Voth, A. P. and Packer, J. A. 2012a. Branch plate-to-circular hollow structural section connections: I: Experimental investigation and finite-element modeling. Journal of Structural Engineering. ASCE. 138(8): 995–1006.

Voth, A. P. and Packer, J. A. 2012b. Numerical study and design of T-type branch plate-to-circular hollow section connections. Engineering Structures. (41): 477–489.

Wardenier, J. 1982. Hollow section joints. Delft University press, Delft, The Netherland.

Wardenier, J., Kurobane, Y., Packer, J. A., Dutta, D., and Yeomans, N. 1991. Design guide for circular hollow section (CHS) joints under predominantly static loading, 1st Ed., CIDECT and Verlag TUV Rheinland GmbH, Köln, Germany.

Wardenier, J., Kurobane, Y., Packer, J. A., van der Vegte, G. J., and Zhao, X.-L. 2008a. Design guide for circular hollow section (CHS) joints under predominantly static loading, 2nd Ed., CIDECT, Geneva, Switzerland.

Wardenier, J., van der Vegte, G. J., and Makino, Y. 2008b. Joints between plates or I sections and a circular hollow section chord. Proceedings of the Eighteenth International Offshore and Polar Engineering Conference, Vancouver, BC, Canada, 319–326.

Zhao, X. L. 2000. Deformation limit and ultimate strength of welded T-joints in cold-formed RHS sections. Journal of Constructional Steel Research. (53): 149–165.

18. Steel-concrete composite construction

Research and Applications in Structural Engineering, Mechanics and Computation – Zingoni (Ed.)
© 2013 Taylor & Francis Group, London, ISBN 978-1-138-00061-2

Sustainable composite beams with deconstructable bolted shear connectors

S.S.M. Lee & M.A. Bradford
Centre of Infrastructure Engineering and Safety, School of Civil and Environmental Engineering, The University of New South Wales, NSW Sydney, Australia

ABSTRACT: Composite structures using steel joists mechanically connected to concrete slabs serving as the flooring and decking systems are commonly used in buildings and bridges respectively. The use of the state-of-art sustainable geopolymer concrete and innovative deconstructable pretensioned bolts under service loads in composite beam design can reduce CO_2 emission by enhancing the sustainability of, and recyclability in, the construction industry by enabling deconstructability. Most previous research has been conducted on composite beams with welded shear studs with conventional concrete using ordinary Portland cement, with limited studies on beams with pretensioned bolted shear connectors being reported. This paper describes the results of five preliminary push tests that have been conducted to establish the strength and stiffness characteristics of pretensioned bolted shear connectors. The effects of the size of the clearance holes, the diameter of the bolts and the pretension force are also investigated. It is shown that the shear connectors can induce three types of shear interaction along a beam: viz. a region of "full interaction", a region of "zero interaction" and a region of "partial interaction", that are delineated by the shear flow force at the interface, by the coefficient of friction at the interface and bolt pretension, and by the size of the clearance hole relative to the diameter of the bolt. A mechanics-based model that can capture the beam behaviour based on the push test results is described.

1 INTRODUCTION

Composite structures using steel joists mechanically connected to concrete slabs are commonplace in buildings and bridges. Concrete is normally strong in compression but weak in tension, whilst steel in compression is prone to buckling effects, and so their symbiotic attributes in composite beams make the composite beam an efficient member. The mechanical shear connectors are designed to bring about composite action in these complementary materials to increase the strength, ductility and stiffness of composite beams above those of the individual materials themselves. Normally, the weakest component governs the strength of the composite structure.

Ordinary Portland cement (OPC) has been traditionally used as a paste to produce concrete for many years. It is widely-known that OPC is a major contributor to anthropogenic greenhouse gas production, with large CO_2 emissions being associated with the manufacture of OPC, with one tonne of OPC producing approximately one tonne of CO_2 (Davidovits 1994). The use of geopolymer concrete (GPC) as a replacement for OPC is seen as one means of mitigating the excessive CO_2 emissions associated with OPC, and is a topic of current research in cementitious materials science. Fly ash is a waste material from coal burning power stations around the world, and has been used and experimentally tested as a source of geopolymer for GPC that is reported to exhibit comparable if not better material properties to OPC-based concrete (Hardjito et al. 2004). The use of a waste material such as fly ash to replace OPC to produce high strength GPC is producing a new era of more sustainable concrete industry. However, GPC is not readily batched on-site by comparison to concrete based on OPC, and so its use in precast applications is an important research issue. The slab systems considered in this paper are precast GPC ones.

There are many types of mechanical shear connectors (Oehlers and Bradford 1995) as shown in Figure 1, but the most commonly used ones are the stud connectors normally welded to the top flanges of the steel joists before casting the concrete slabs (solid or profiled with steel sheeting) because they are economical and easy to install. Clearly the welding and casting of the concrete around headed stud connectors is highly problematic in formulating deconstructability and

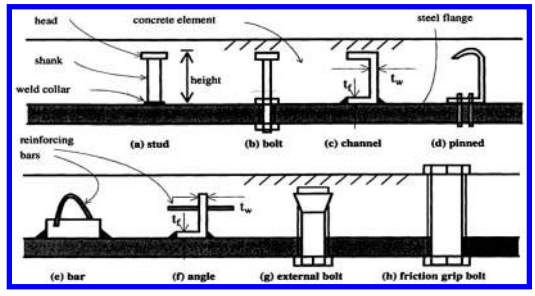


Figure 1. Mechanical shear connectors.

recycling technologies for composite beams. High-strength bolted steel shear connectors (Figure 1(h)) provide a viable alternative to headed connectors in terms of deconstructability. Despite this, and despite the potential for retrofitting composite bridge beams whose studs have failed under fatigue loading, surprisingly little has been reported in the open literature on high-strength bolts as shear connectors.

Most of the previous research of composite beams has been based on stud shear connectors for normal steel joists and with OPC slabs. Of the limited studies on bolted shear connectors in composite steel-concrete beams, Dallam (1968) and Dallam and Harpster (1968) reported push tests and beam tests undertaken with bolts embedded in the concrete, Marshall et al. (1971) undertook tests on embedded and post-installed bolts and recently Kwon et al. (2010) investigated the use of post-installed shear connectors under static and fatigue loading. However, none of those studies offered a complete understanding of the structural behaviour of these types of structures nor considered the issues of deconstructability and sustainability. Therefore, more detailed investigations of the structural behaviour of bolted shear connectors, bolted steel joists and precast GPC slabs, all of which can be recycled at the life end of a structure, is much-needed. The use of push tests and the potential of applying the push test data to predict the structural response of full-scale sustainable composite beams with deconstructable bolted shear connectors is the subject of this paper.

2 EXPERIMENTAL PROGRAM

Five push tests were conducted to obtain the load-slip characteristics of the pretensioned bolted shear connectors, with an aim to study the effects of the pretension, the size of the holes in the concrete panels, the diameter of the bolts and the number of bolts on the strength and stiffness of these types of shear connectors, and to provide data to model the response of composite beams theoretically. The key push test parameters are summarised in Table 1.

Two different sizes of high strength structural bolts were used, viz. M20 8.8 and M16 8.8 bolts pretensioned to their specified loads of 145 kN and 95 kN respectively. A smaller pretension of 80 kN was also applied in one of the push tests. Two sizes of holes were prepared for the push test specimens viz. 24.0 mm and 28.0 mm in diameters which gave clearances between the pretensioned bolt and the hole in the concrete panels of 2 mm and 4 mm all around respectively. Figure 2 outlines the precast slab dimensioning and the location of the holes.

The geopolymer concrete push test panels were prepared and cast by ZeoBond (E-crete) based in Melbourne, Australia. The details of the steel mesh reinforced concrete panels are shown in Figure 3. The precast concrete panels and 10 standard cylinders were cured with plastic cover at room temperature for 7, 14, 28 and 90 days and the strengths of the concrete at these ages were tested. Special bushes were made to align the centres of the holes in the steel flange and the concrete panels before drilling the holes through the steel flange. The bolts were then pretensioned using squirter (with orange colour squirts) washers which had been calibrated to give precise pretensions of 145 kN and 95 kN to the M20 8.8 and M16 8.8 bolts respectively

Table 1. Summary of test parameters and results.

Specimen	Bolt dia. (mm)	Hole dia. (mm)	No. of bolts	No. of panels	Pretension per bolt (kN)
001	20	24	4	2	145
002	20	28	4	2	80
003	16	24	4	2	95
004	20	24	4	2	145
005	20	28	8	4	145

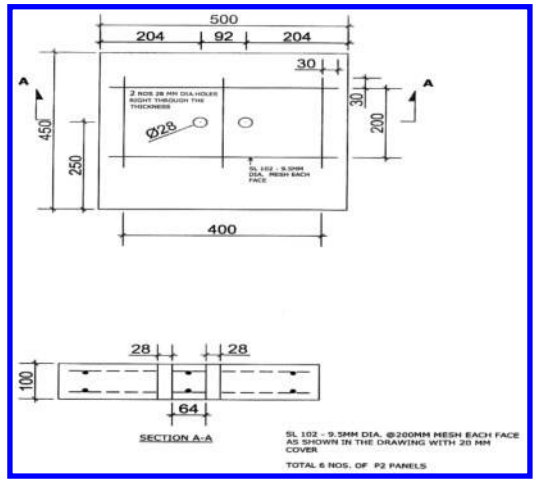


Figure 2. Details of mesh-reinforced GPC panels.



Figure 3. Push test preparation and test set-up process.

using an electric torque control wrench. The final positions of the pretensioned bolts were marked before loading in each push test. The push test specimens were then installed with two linearly varying displacement transducers (LVDT)s to measure the slips at the steel-concrete interface and a third LVDT was used to monitor the horizontal movements during the tests. Rollers were placed at one of the supports and the push test specimens were loaded using a displacement controlled Instron test rig in the Heavy Structures Research Laboratory at the University of New South Wales. During each push test, the test specimen was cycled 25 times between approximately 5% and 40% of the estimated failure load as per the EC4 push test procedure before loading it to failure.

3 RESULTS

The results of Push test 001 show that there are three distinctive stages of the load-slip curves, shown in Figure 4.

During the first stage of interaction, the friction created by the pretension of the bolts at the steel-concrete interface resisted slip at the interface giving rise to a very stiff or "near full" shear interaction. Towards the end of this stage, a loud "bang" was heard when the increasing applied vertical load finally overcame the friction at the interface. Once this friction was overcome at around 283 kN, slip started to occur during the second stage of interaction, and the shear connection became much more flexible under displacement control resulting in a "near zero shear interaction". The coefficient of friction was calculated to be 0.49 which is comparable to figures of 0.47 to 0.479 quoted in the work of Marshall et al. (1971) on push tests between their steel beam and precast slabs. It was possible that one of the bolts was slightly under pretensioned as indicated by the LVDT in the north-side, as not all orange coloured squirters came out after closer examination during the test. This explained why LVDT N showed an earlier slip than LVDT S, and so the coefficient of friction of 0.49 is an upper bound.

Under displacement control, the slipping continued to increase to a critical value which is consistent with the clearances between the pretensioned bolts and the circumferences of the holes in the precast concrete panels. In this case, it can be seen from Figure 4 that this value was very close to 4 mm, i.e. twice the hole clearance all around as would be expected as the bolts were located concentrically in the holes. Once this critical slip value (which depends on the clearance between the bolts and the circumference of the holes in the precast concrete panels) was exceeded, the bolts started to bear on the concrete producing a stiffer partial shear interaction response with increasing load until around 600 kN when there was indication of strain hardening with increased ductility during this third stage of shear interaction. The failure load was 866 kN (3.06 times the load at first slip; c.f. Marshall's equivalent value of 2.63) with all bolts fully

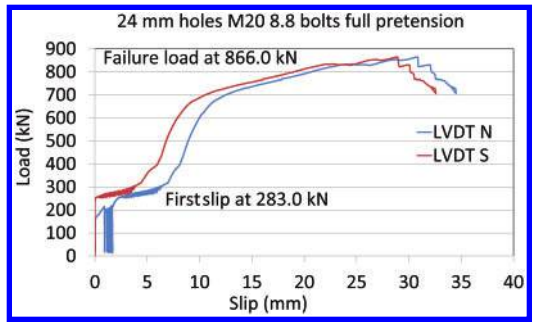


Figure 4. Load-slip evolution for specimen 001.

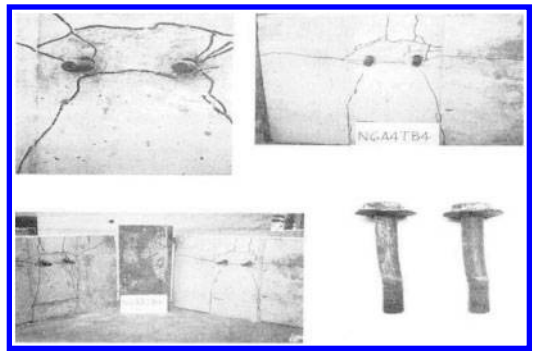


Figure 5. Dallam's push-test failure mechanism.

yielded and a block shear failure in the concrete resulting in a maximum slip of 30.8 mm and an ultimate shear stress of 689 N/mm^2 (c.f. Marshall's equivalent value of 607 N/mm^2). Closer examination of the failed test specimens shows evidence of friction with noticeable scuffing being overcome and the scale of scuffing which is broadly proportional to the applied pretension and also bearing on the concrete at the steel interface. This failure mechanism appears to be consistent with that in Dallam's push tests (Dallam 1968), as shown in Figure 5.

The second push test 002 was carried out at a 90 day concrete strength with an increase in the diameter of the holes from 24 mm to 28 mm and a smaller pretension of 80 kN (about half of that for specimen 001). The load-slip curves show a similar trend and failure mechanism as depicted in those of push test 001, as shown in Figure 6. A lower load of 80 kN at first slip was recorded as a result of smaller pretension of the bolts and the critical slip value was consistent with the size of the holes before bearing on the concrete occurred. A lower failure load of 808 kN, as a result of reduced the pretension (c.f. Marshall's similar observation) was measured with a maximum slip of 26 mm, indicating a high degree of ductility. The lower pretension gave rise to a lower coefficient of friction of 0.25 and this requires further investigation. The load-slip curve of a single 22 mm pretensioned shear connector from the push tests of Kwon et al. (2010) is very similar to that of Figure 6.

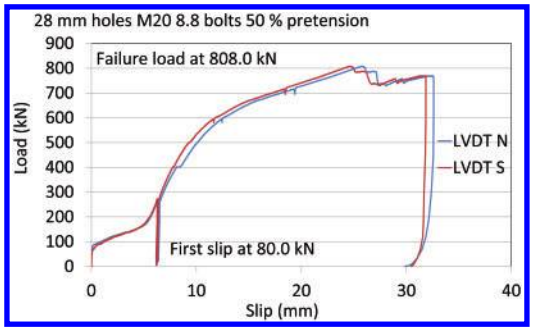


Figure 6. Load-slip evolution for specimen 002.

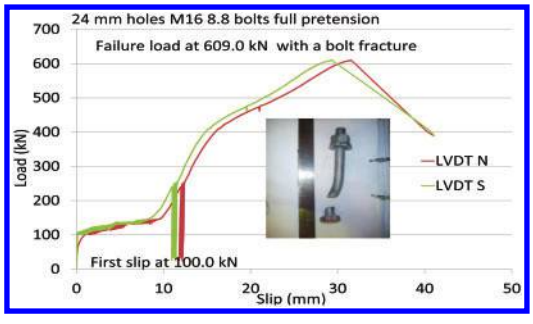


Figure 7. Load-slip evolution for specimen 003.

The third push test 003 involved the use of a smaller size of bolts, i.e. M16 8.8 pretensioned to 95 kN and the results are shown in Figure 7. Again, the load slip curves confirm the occurrence of three different stages of shear connector load-slip behaviour, i.e. changing stiffness as observed in two previous push tests. The lower pretension gave a similar load of 80.0 kN at first slip and the critical slip value recorded during the second stage of "near zero" shear interaction was consistent with the clearance between the pretensioned bolts and the holes in the precast concrete panels, i.e. 8.0 mm. The push test specimen failed at 609 kN with a maximum slip of 31.5 mm and with bolt fracture in addition to shear cracks in the concrete and three fully-yielded bolts.

The fourth push test was a repeated test of push test 001 and, as would be expected, the load slip curves show similar pattern to that of push test 001 as shown in Figure 9. The test specimen started to slip at a slightly lower value of 263.0 kN but failed by a bolt fracture in addition to shear cracks in concrete and three fully yielded bolts at a higher load of 890 kN with a maximum slip of 24.8 mm. During this test, the bolts were deconstructed at a service load between after the first slip and before the bolts started to bear on the concrete. The deconstructability of the bolts under service loads was confirmed. The bolts were then unloaded and then re-pretensioned and reloaded to failure. The test specimen failed at 890 kN with a maximum slip of 24.8 mm with a bolt fracture in addition to shear cracks in the concrete and three fully yielded bolts. One of the possible reasons that it failed at a higher load with a bolt

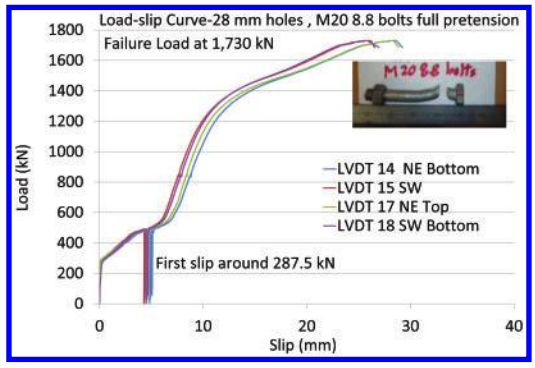


Figure 8. Load-slip evolution for specimen 005.

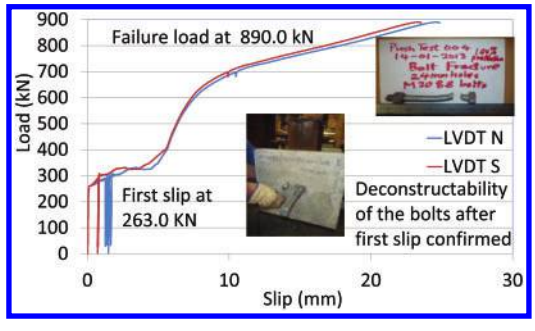


Figure 9. Load-slip evolution for specimen 004.

fracture could be due to the increased concrete strength to 48 MPa at 90 days rather than 43 MPa at 21 days.

The last of the push test series, push test 005, was a test in which the number of bolts and concrete panels was increased two-fold by stacking up two single panels on each side of the push test specimen, and the results are shown in Figure 8. This replicates more closely a full-scale test beam situation in which several precast panels are juxtaposed on the top flange of a steel joist.

The load slip curves and the failure mechanism are slightly different from the other four push tests, except push test 002. The second stage of the "near to zero interaction" appears to be replaced by some level of "semi-partial interaction" with a finite stiffness. There was evidence that some bolts slipped earlier than the others resulting in a situation where some bolts were still slipping while the others were already bearing on the concrete. This gave a combined overall "semi-partial" stiffness of the push test specimen. In the case of a simply supported beam under a distributed load, the varying shear flow along the span will cause the bolts to slip or bear on the concrete at different stages of the loading after the initial overcoming of the friction at the steel-concrete interface produced by the pretension. The failure load recorded was 1730 kN as predicted, being around twice of that in push test 004 single panel push test.

The key push test results are summarised in Table 2, while Figure 11 indicates some failure modes.

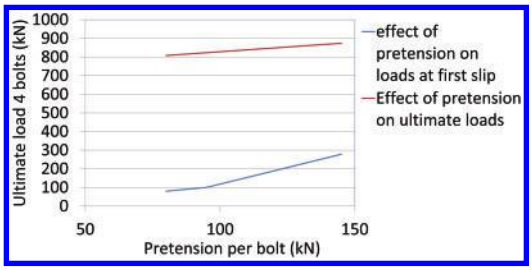


Figure 10. Effect of pretension on loads.

Table 2. Key push test results.

Test	P_{sp} (kN)	P_u (kN)	μ	s_b (mm)	s_u (mm)
001	283	866	0.49	4	30.8
002	80	808	0.25	6	25.8
003	100	609	0.26	8	31.5
004	263	890	0.45	4	24.8
005	288	1730	0.50	8	28.6

P_{sp} = load for first slip; P_u = ultimate load; μ = coefficient of friction; s_b = slip at first bearing; s_u = ultimate slip.



Figure 11. Failure modes.

The effect of the pretension on the loads at first slip and the ultimate loads is shown in Figure 10. It can be seen that, similar to the push tests of Marshall et al. (1971), pretension appears to have an increasing effect on the loads at first slip and the ultimate loads in specimens with pretensioned bolted shear connectors.

4 FRAMEWORK OF THEORETICAL MODEL

A theoretical model of the response of a beam with pretensioned bolted shear connectors at service loading can be developed, which uses the empirical results from the push testing (Rowe & Bradford 2013). This can be illustrated with reference to a simply-supported geometrically symmetrical beam of length L under a monotonically increasing uniformly distributed load

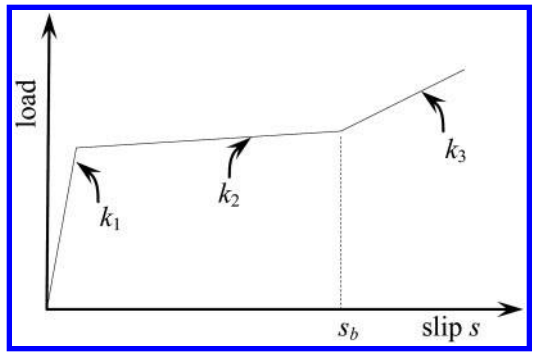


Figure 12. Idealised response in elastic range.

q, for which the shear flow force at the interface is $V = qx \cdot B/I$, where B is the first moment of area of the slab above the interface, I is the second moment of area of the composite beam with full shear interaction (both determined from transformed area principles) and x is the longitudinal coordinate measured from mid-span. The shear connection can be considered as continuous and distributed uniformly lengthwise.

Initially, the beam has full interaction because of the prestress provided by the bolts, which has a capacity of $p = \mu n P/L$, where P is the prestress in each of the n bolts and μ is the coefficient of friction. When the shear flow force at the ends of the beam $(1/2qLB/I)$ reach p, the bolts in that location start to slip, i.e. when $q = q_1 = 2pI/(LB)$. As q increases from q_1, the bolts slip in the region defined by $[-L/2, -a] \cup [a, L/2]$ where $a = (p/q) \cdot (I/B)$ until the slip at the ends of this region reach a limiting value s_b at $q = q_2$, where s_b is the slip at first bearing. The region then defined by $[-L/2, -b] \cup [b, L/2]$ experiences partial interaction, with the bolts bearing against the GPC slab. As q increases above q_2, the values of a and b decrease, and so the beam has five distinct regions of shear connection, viz. Γ_1: $[-a, a]$; Γ_2: $[-b, -a] \cup [a, b]$ and; Γ_3: $[-L/2, -b] \cup [b, L/2]$.

The regions of shear connection Γ_1, Γ_2 and Γ_3 are illustrated by the load-slip relationship shown in Figure 12, for which the slip moduli can be determined from the push test results. As an approximation from these, $k_1 \approx \infty$, $k_2 \approx 0$ and k_3 must be determined empirically. A beam-type finite element model (Ranzi et al. 2004) can be cast in an adaptive mode, with the element boundaries defined by a and b changing with an increase of q.

5 CONCLUSIONS AND ONGOING RESEARCH

This paper has described five push tests undertaken on precast GPC slabs connected to steel I-sections with high strength pretensioned bolts acting as shear connectors. The push test data confirmed one of the study's research hypotheses, in which three distinctive stages of the load-slip characteristics of the pretensioned

bolted shear connection at the steel-GPC interface occurred were observed. These are "near-to-full interaction" followed by "near-to-no interaction" and then finally "partial interaction", with some evidence of strain hardening resulting in the significant ductility of these types of deconstructable shear connectors. The potential of deconstructability of the bolts under service loads was explored and confirmed, with the bolts being removable. The push tests show that the pretension has an increasing effect on the loads to cause first slip and to some extent on the ultimate loads.

In a beam situation, it is likely that regions with these different stages of shear interaction will occur simultaneously, depending on the interface shear flow forces given other parameters being constant. The framework of a simply supported quasi-elastic bolted shear connection composite model under uniformly distributed loading has been described, which uses empirical results obtained from the push testing. Based on the push tests, further experimental work will be undertaken on full-scale beam specimens.

ACKNOWLEDGEMENTS

The work in this paper was supported by the Australian Research Council through an Australian Laureate Fellowship. Zeobond provided the GPC and Hobson Engineering Pty Ltd provided technical advice on the bolt installation. The support of the technical staff in the UNSW Heavy Structures Research Laboratory is acknowledged with thanks.

REFERENCES

Dallam, L.N. 1968. Pushout tests with high strength bolt shear connectors. Report for Missouri State Highway Department, Department of Civil Engineering, University of Missouri – Columbia.

Dallam, L.N. & Harpster, J.L. 1968. Composite beam tests with high-strength bolt shear connectors. Report for Missouri State Highway Department, Department of Civil Engineering, University of Missouri – Columbia.

Davidovits, J. 1994. High-alkali cements for 21st century concrete. In P. Kumar Metha (ed), *ACI SP 144*: 383–397. Detroit: American Concrete Institute.

Hardjito, D, Wallah, S.E., Sumajouw, D.M.J. & Rangan, B.V. 2004. On the development of fly ash-based geopolymer concrete. *ACI Materials Journal* 101(6): 467–472.

Kwon, G., Engelhardt, M.D. & Klinger, R.E. 2010. Behavior of post-installed shear connectors under static and fatigue loading. *Journal of Constructional Steel Research* 66: 532–541.

Marshall, W.T., Nelson, H.M. & Banerjee, H.K. 1971. An experimental study of the use of high-strength friction-grip bolts as shear connectors in composite beams. *The Structural Engineer* 49(4): 171–178.

Oehlers, D.J. & Bradford, M.A. 1995. *Steel and Concrete Composite Structural Members: Fundamental Behaviour*. Oxford: Pergamon.

Ranzi, G., Bradford, M.A. & Uy, B. 2004. A direct stiffness analysis of composite beams. *International Journal for Numerical Methods in Engineering* 61(5): 657–672.

Rowe, M., & Bradford, M.A. 2013. Partial shear interaction in deconstructable composite steel-concrete composite beams with bolted shear connectors. International Conference on Design, Fabrication and Economy of Welded Structures, Miskolc, Hungary.

Research and Applications in Structural Engineering, Mechanics and Computation – Zingoni (Ed.)
© 2013 Taylor & Francis Group, London, ISBN 978-1-138-00061-2

Numerical simulations of concrete-composite-slabs with perforated metal sheets

S. Pirringer & J. Kollegger
Vienna University of Technology, Vienna, Austria

ABSTRACT: A new approach for composite slabs, using perforated metal sheets as reinforcement, is currently under development at Vienna University of Technology. Compared to common composite slabs with profiled metal sheets, this new design allows a reduction of the slab thickness and two-way slab action. Thereby the transmission of the shear load across the interface between the steel sheet and the concrete is established by the concrete that fills the punched holes of the perforated metal sheet during the concreting process. This new approach of sustainable composite slabs can be used for small sized, structural elements, as for example covers for cable channels, deck slabs for pedestrian bridges and prefabricated parts for short spans. The aim of the research project is the investigation of the structural behavior of the slab and the bond between the concrete and the metal sheet by numerical simulations with ABAQUS and full-scale tests.

1 INTRODUCTION

There is a wide range of areas of application for small reinforced concrete slabs. Covers for cable channels, for example in tunnels and on bridges, is one of the common fields of application, and there-fore a matter of prefabricated, mass-produced articles.

For short spans both reinforced concrete slabs as well as composite slabs with profiled metal sheets show major disadvantages. On the one hand, reinforced concrete slabs need a concrete cover to activate the mild steel reinforcement and to reach the projected bearing capacity. In small concrete slabs this coverage can amount to 10 to 20% of the overall weight and material consumption. On the other hand, the minimum thickness of common one-way composite slabs is limited by the construction height of the profiled metal sheet.

With an approach that is currently under development at Vienna University of Technology the disadvantages mentioned above can be avoided. By using a perforated metal sheet (Fig. 1), it is possible not only to reduce thickness and weight and thus the CO_2 emissions during the manufacture and the costs of the slab, but also to offer a two-way slab action with a minimized effort and complexity of the formwork. The bond between the two basic materials of the metal-concrete-composite-slab (MCC slab) is established by the concrete filling the punched holes of the perforated metal sheet which is placed on the bottom side of the slab.

For a proper fabrication of the slabs, the metal sheet can simply be put on the bottom of the form-work. Another advantage of this system is the possibility of using commercially available metal sheets without any further treatment. Moreover, the costs of recycling are estimated to be low.

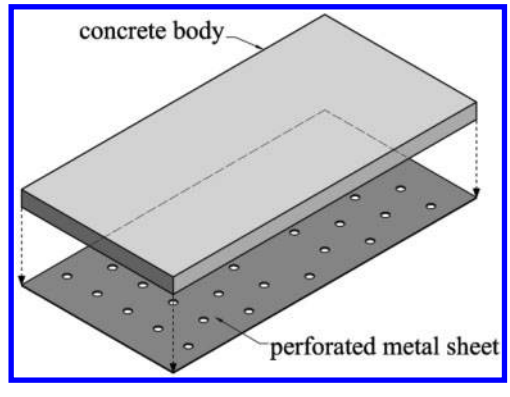


Figure 1. Schematic assembly of a MCC-slab.

2 TECHNICAL BACKGROUND

In contrast to common composite slabs, this approach means working without any of the usual mild steel reinforcement, and using only a perforated metal sheet instead. Since this method tends to be only used for small slabs with thicknesses down to 50 to 100 millimeters or even less, the end anchor-age poses the major problem. Due to the low construction height no end anchorage as known from common composite slabs, e.g. shear studs and/or dovetailed deformations of the profiled (trapezoidal) sheet at the bearing, can be used. Therefore, the whole anchorage has to be accomplished just by the load transfer through the shear

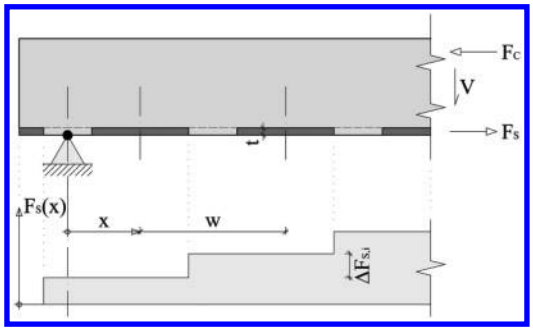


Figure 2. Schematically, longitudinal cut of a MCC-slab.

connectors (concrete dowels) placed in the perforation of the metal sheet (Fig. 2). Besides proving the resistance to bending and shear force, the structural stability of these concrete dowels plays a significant role. For a proper design of the composite slab their ultimate load needs to be known and predictable in advance.

On the one hand, the load bearing capacity of the concrete dowels P_{CD} was approximately calculated by formulas based upon the bearing pressure of holes (Berger 1994) assuming a sinus-shaped distribution of the contact pressure (Fig. 3). On the other hand, it was calculated by the bending stresses that result from the bending moment due to an offset $t/2$ of the dowel force $\Delta F_{s,i}$.

$$P_{CD,calc}(f_c) = \frac{f_c \pi \emptyset t}{4} \quad (1)$$

$$P_{CD,calc}(f_{ct}) = \frac{f_{ct} \pi \emptyset^3}{16t} \quad (2)$$

Where f_c = concrete (or mortar) compressive strength; f_{ct} = concrete (or mortar) tensile strength; $\emptyset$ = diameter of hole; and t = perforated metal sheet thickness.

Based on these approaches for the limit states of the concrete dowels, a threshold ratio $(\emptyset/t)_{lim}$, that considers the concrete compressive and tensile strength, can be derived by equating Equation 1 and 2.

$$P_{CD,calc}(f_c) = P_{CD,calc}(f_{ct}) \rightarrow \left(\frac{\emptyset}{t}\right)_{lim} = 2\sqrt{\frac{f_c}{f_{ct}}} \quad (3)$$

Thus, for known material properties and given parameters $\emptyset$ and t of the perforated metal sheet, this ratio theoretically serves as a parameter for the failure mode of the concrete dowel:

- $\emptyset/t > (\emptyset/t)_{lim} \rightarrow$ failure by exceeding the compressive strength of the dowel material
- $\emptyset/t < (\emptyset/t)_{lim} \rightarrow$ more brittle behavior expected and failure by exceeding the tensile strength of the dowel material

Taking these considerations into account, a $\emptyset/t$-ratio above the threshold ratio would be the best choice.

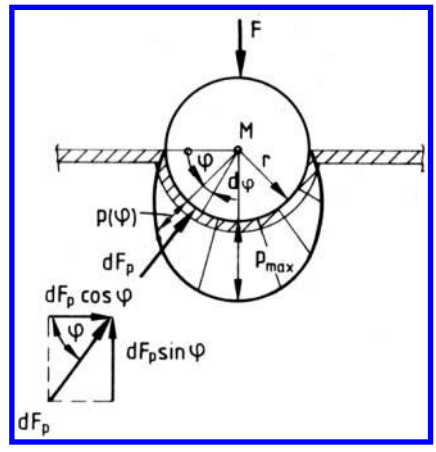


Figure 3. Bearing pressure of holes (Berger 1994).

3 LOAD TESTS ON MCC-SLABS AND THE BOND BEHAVIOR

3.1 *Load tests on MCC-slabs*

Up to now, a preliminary series of 5 specimens as well as 9 series (3 specimens per series) of 4-point bending tests on composite slabs by this approach were carried out. In all of those bending tests metal sheets with circular perforations, arranged in a constant, rectangular grid, have been combined with a concrete body made of self-compacting concrete.

The bending tests proved, that with the correct selection of size (diameter) and layout of the concrete dowels, in short the perforation of the metal sheet, the bond within the MCC-slab is strong enough to resist loads up to the bending load capacity according to Eurocode 2 and to cause a ductile behavior. Series that were designed to collapse due to exceedance of the shear resistance or the load capacity of the shear connectors collapsed at ultimate loads close to values calculated in advance.

3.2 *Load tests on the bond behavior*

For a validation of the calculated dowel capacity, separate tests on the bond behavior were carried out in addition to the 4-point bending tests (Pirringer & Kollegger 2012). Due to the geometry of the whole system and its concrete dowels, the standard shear test as described in Eurocode 4 (appendix B) could not be performed. A new test set-up, basically in accordance to EC 4, was developed for the investigation of the concrete dowel capacity.

Sendzimir galvanized, partly perforated metal sheets with an arrangement of cylindrical holes in a rectangular grid, and a concrete body in two different sizes ($100 \times 100 \times 50$ mm, $150 \times 100 \times 50$ mm) were used for all specimens (Fig. 4). In these experiments either self-compacting concrete (SCC) or grouting mortar was used for the concrete body of the specimens.

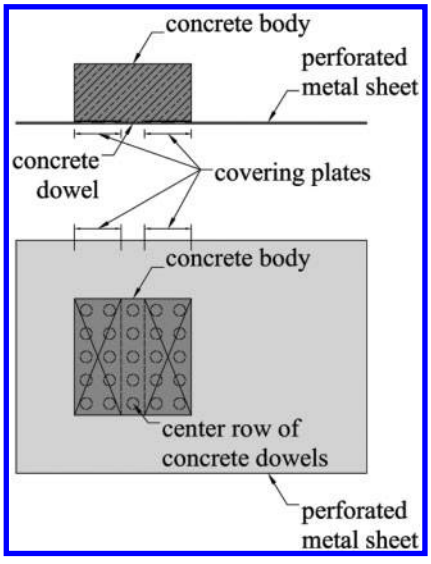


Figure 4. Specimen for shear tests.

3.2.1 *Test set-up*

The whole test set-up was designed in such a way that a shear force F_S as well as a lateral, normal force $F_L \geq 0$ can be applied by a hydraulic testing machine, to simulate the area of the composite slab close to the support (Fig. 5).

The displacement-controlled shear force F_S that was applied with a hydraulic jack, has been gauged with a load cell during the test. Simultaneously, the relative displacement in the direction of load be-tween the concrete body and the steel sheet (slip) has been measured with two displacement transducers on both sides of the concrete body.

Even for tests without a planned lateral loading, the hydraulic testing machine was put against the specimen with a low force of about 0,2–0,3 kN. Thus, a raising and detaching of the concrete body, caused by the resulting moment due to the offset between the applied shear force and the restraining force, should be prevented.

3.2.2 *Series of tests & test parameters*

So far 24 different sets of parameters – a total of 120 specimens, 5 specimens for each set of parameters – were investigated under static loading. A static, displacement-controlled test with a constant displacement-rate of 0,2 mm/min until failure of the concrete dowels was carried out for all specimens.

The resulting dowel capacity $P_{CD,test}$ had to be calculated from the measured shear force F_S. There-fore the friction in the composite joint between the covering plates as well as the concrete and the perforated metal sheet was taken into account.

Beside the material properties the following geometrical parameters of the perforated metal sheet have been of interest for the actual test series:

– Diameter of holes *Ø*
– Center-to-center distance of holes *w*

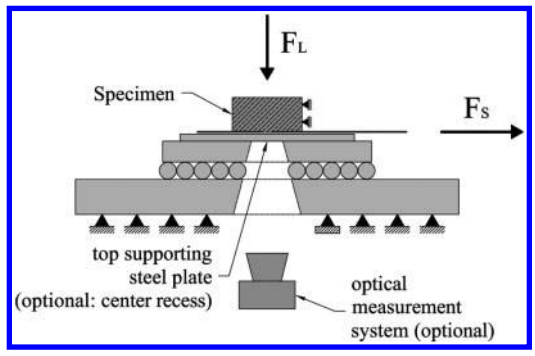


Figure 5. Schematic assembly of the test set-up for tests on the bond behavior with adjustable lateral loading ($F_L \geq 0$) and optional optical measuring.

– Metal sheet thickness *t*
– single or multiple rows of concrete dowels in the direction of the horizontal shear load F_S

For the tests on the concrete dowel capacity neither the tensile strength nor the modulus of elasticity of the metal sheet has been of relevance.

In several series also the influence of different lateral loadings F_L on the concrete dowel capacity was investigated, whereat the lateral load had to be limited to 45 kN because of structural reasons regarding the test set-up.

3.2.3 *Results and conclusion of the tests*

The resulting mean values of the concrete dowel capacities $P_{CD,test}$ were determined considering the overall number of concrete dowels from the ultimate shear force after deducing the calculated friction. The measured values were evaluated for the time of the maximum applied shear force F_S, equivalent to the ultimate dowel load, and were compared to the decisive value $P_{CD,calc}$ calculated according to Equation 1 and 2.

In general, the results of the tests showed a good correlation to the values calculated according to Equations 1 and 2, which are based upon simple mechanical aspects.

4 NUMERICAL SIMULATION OF THE BOND BEHAVIOR

As stated before, very useful information on the bearing capacity of the shear connectors, as well as the slip between the concrete body and the metal sheet, could be gained by the bending tests and the tests on the bond behavior. However, for finding a generally valid design method for this new approach of composite slabs, also detailed information on the distribution of strains and stresses within its individual components – especially the concrete dowel – will be needed.

Therefore, the Finite Element Method (FEM) offers a suitable tool for solving such highly nonlinear problems. For a validation of the tests on the bond behavior, the finite element program ABAQUS was used for calculations of the concrete dowel.

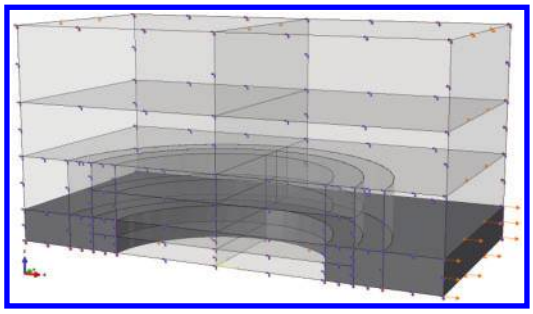


Figure 6. Model for numerical simulations in ABAQUS and zoning for mesh refinement (concrete body – light grey, transparent, steel sheet – dark grey). The arrows at the front side of the steel sheet symbolize the applied displacement-controlled shear load as a boundary condition.

4.1 *Modeling of the geometry*

For a first series of calculations, concrete dowels with the following dimensions were investigated:

- $\varnothing = 10$ mm
- $w = 20$ mm
- $t = 1.5$ mm

These settings were used in multiple test series and offer a good basis for comparisons.

For saving computational costs, only a single concrete dowel, by taking advantage of the concrete dowels symmetry, was modeled. Instead of the total height of the test specimens of 50 mm, also the model's height was reduced to 10 mm (including the perforated metal sheet thickness). By these simplifications, the total size of the model was downsized to 20 × 10 × 10 mm (Fig. 6).

For a practical mesh refinement of the whole model, the concrete part as well as the steel part of the model was separated into several, smaller parts. Parts of the same material were connected with *TieConstraints* among each other, and thus rebuilt the 2 major parts of the model – the concrete body and the perforated metal sheet. This partition was conducted in a manner that enabled the finest mesh at the changeover from the circular concrete dowel to the rest of the concrete body (Fig. 6).

4.2 *Material properties*

For both materials a nonlinear stress-strain relationship was chosen. Whereas a simple elastic-plastic model was chosen for the metal sheet, the self-compacting concrete was described by a *Concrete Damaged Plasticity* model with default values for the *Plasticity* parameters. The underlying material model for the compressive stresses, and all of its parameters, was adopted directly from Eurocode 2:

$$\frac{\sigma_c}{f_{cm}} = \frac{k\eta - \eta^2}{1 + (k-2)\eta} \tag{4}$$

Where σ_c = compressive stress; $\eta = \varepsilon_c / \varepsilon_{c1}$; ε_{c1} = compressive strain at highest compressive stress of concrete; $k = 1.05\, E_{cm} \cdot |\varepsilon_{c1}| / f_{cm}$

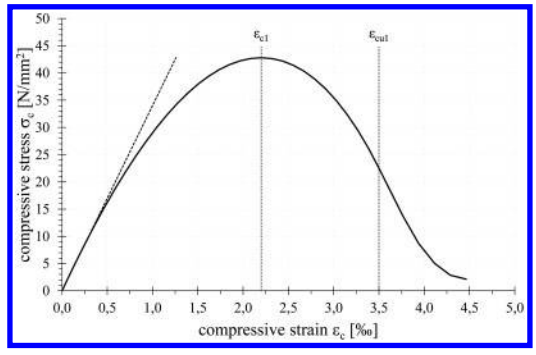


Figure 7. Concrete stress-strain relationship used for numerical simulation in ABAQUS.

Table 1. Material properties.

Material	f_{cm}/f_{ym} [N/mm²]	f_{ctm}/f_{ym} [N/mm²]	E_{cm}/E_{ym} [N/mm²]	ν [–]
Concrete	42.8	2.9	34,000	0.2
Steel	235.0	235.0	210,000	0.3

For strains exceeding the strain of failure ε_{c1u}, a linear decline of stresses with the gradient at failure strain was assumed. In separate calculations a better convergence of the calculation could be achieved with a rounded out stress-strain relationship for post-cracking stresses at the changeover to a stress-free state. A residual compressive stress of the post-cracking stresses also showed a beneficial convergence behavior of the calculation (Fig. 7).

The tensile behavior of the concrete after crack initiation was defined by an exponential stress-displacement relationship based upon the fracture energy G_F (Hordijk 1991):

$$\frac{\sigma_t}{f_{ctm}} = \left\{1 + \left(c_1 \frac{w}{w_c}\right)^3\right\} e^{-c_2 \frac{w}{w_c}} - \frac{w}{w_c}(1 + {c_1}^3) e^{-c_2} \tag{5}$$

Where σ_t = tensile stress; w = crack opening, $w_c = 5.14 G_F / f_{ctm}$ = the crack opening at the complete stress-free state; c1 = 3; c2 = 6.93.

The fracture energy G_F was calculated according to *fib* Model Code 2010:

$$G_F = 73 \cdot {f_{cm}}^{0,18} \tag{6}$$

The basic material properties are listed in Table 1.

4.3 *Mesh*

During the actual calculations different mesh densities have been tested and used for comparisons.

Models with a constant element size as well as models with different mesh densities with a fine mesh for the shear connector were investigated. The used mesh densities varied from very coarse meshes of 1 mm for regions of low stresses to fine meshes of 0.125 mm for regions around the concrete dowel. For models

with variable mesh densities the individual parts of the model were meshed with 4 different element sizes.

Quadratic elements often led to a poor convergence behavior wherefore mostly linear elements were used in the actual calculations (partly with reduced integration).

4.4 *Boundary conditions, constraints and loading*

The primary boundary condition to prevent displacements in vertical direction is defined in the bottom surface of the steel sheet which represents the top supporting steel plate of the test set-up in Figure 5. The top surface of the concrete body is fixed in vertical direction as well to prevent a rising of the concrete part as it is done by the hydraulic testing machine. In the actual simulations the bottom surface of the concrete dowel is not restrained in any degree of freedom to prevent nonexistent tensile stresses due to deformations of the dowel during the load step.

The shear load is applied as a displacement-controlled boundary condition at the front side of the steel sheet and is linearly increased during the load step. The front side of the concrete part acts as bearing for the applied shear load and is restrained in the same direction (Fig. 6).

In horizontal direction, perpendicular to the direction of the shear load, the whole model is fixed on both sides over its whole cross-section via boundary conditions for symmetry planes.

In simulations that have been carried out using *ABAQUS/Standard,* between all surfaces of the concrete and steel parts that may come into contact, a frictionless, *Hard-Contact*, *Contact Pair* Interaction was defined. Furthermore, in some models a *Contact Control* with a defined automatic stabilization and an adjustment to remove overclosures between parts in contact was added to obtain a better convergence behavior. In simulations that have been carried out using *ABAQUS/Explicit* a default *General Contact* was defined.

4.5 *Calculation method*

The numerical simulation of the shear connector was accomplished by different approaches. Thereby the load step was defined as one of the following step types:

- Static, General (SG)
- Dynamic, Implicit (DI)
- Dynamic, Explicit (DE)

In each case a step-duration of 1 second was chosen to apply the shear load. Mass scaling was used to accelerate the calculation in case of *Dynamic, Explicit* simulations.

The biggest problem during the calculations, independent of the chosen step type, was the convergence behavior in the post peak behavior of the concrete dowel.

5 RESULTS OF THE NUMERICAL SIMULATIONS

In the following, some of the carried out calculations will be presented and discussed. The investigated calculations and their varying model parameters are summed up and shown in Table 2.

Because of the used mass scaling, in series S9 to S14 the kinetic energy (*ALLKE*) as well as the internal energy (*ALLIE*) of the whole model was monitored and compared. In all cases the kinetic energy accounts for less than 1% of the internal energy, and therefore can be considered to be an appropriate choice.

In Figure 8 the several distributions of the reaction force F, measured at the front side of the concrete part, are shown as a function of the applied displacement in the steel sheet (simulation S1, S2 and S7 show an almost identical distribution).

In all suitable simulations, the reaction force of the whole dowel was underestimated in comparison to the decisive value calculated by Equation 1 and 2 (504 N) and the measured results of the load tests (609 N).

5.1 *Influence of the element size and type*

A comparison of simulation S1 and S6 as well as between S11 up to S14 shows that a mesh refinement has a major influence on the quantitative results of the simulation. Thereby, the qualitative progression of the distribution of the reaction force remains more or less unaffected.

In general, the maximum reaction force (F_{max}) decreases significantly due to a mesh refinement. In the actual calculations the effect was more pronounced in *DE*-steps:

- $F_{max,S6}/F_{max,S1} = 125.7\%$
- $F_{max,S11}/F_{max,S13} = 152.3\%$

The choice between linear elements with reduced and full integration showed a deviation of about 3% to 4% (S1/S3, S7/S8, S9/S13). In all cases the value of the maximum reaction force was higher when calculated with full integration.

5.2 *Influence of contact stabilization control*

As it can be seen in a direct comparison of S4 up to S6, the choice of the stabilization factor of the contact controls has a major influence on the simulation as well. A comparison between the energy dissipated by viscous damping (*ALLSD*) and the internal energy (*ALLIE*) can be used as an indicator, whether a reasonable value for the stabilization has been chosen. In case of S1 and S2 the ratio between those energies is on average below 1%, with the consequence that both distributions of the reaction force are almost identical. In case of S4 and S5 the ratio is bigger than 50% respectively 5% and thus the stabilization factor should be further reduced.

Table 2. Overview of the parameters used for the numerical simulations.

Simulation series	S1	S2	S3	S4	S5	S6	S7	S8	S9	S10	S11	S12	S13	S14
Step type	SG	SG	SG	SG	SG	SG	DI	DI	DE	DE	DE	DE	DE	DE
Element min.	0.25	0.25	0.25	0.75	0.75	0.75	0.25	0.25	0.25	0.25	0.75	0.5	0.25	0,125
size [mm] max.	1	1	1	const	const	const	1	1	1	1	const	const	1	1
Element type*	LR	LR	L-	LR	LR	LR	LR	L-	LR	LR	L-	L-	L-	L-
Contact: stabilization	10^{-2}	10^{-3}	10^{-2}	1.0	10^{-1}	10^{-2}	10^{-3}	10^{-2}	–	–	–	–	–	–
Mass scaling	–	–	–	–	–	–	–	–	10^{3}	10^{3}	10^{2}	10^{2}	10^{4}	10^{2}
Reaction force F_{max} [N]	181.1	179.9	188.3	348.9	234.9	227.7	180.0	184.5	172.7	174.0	273.2	217.0	179.4	165.6

*L−: linear elements (*C3D8*), LR: linear elements with reduced integration (*C3D8R*)

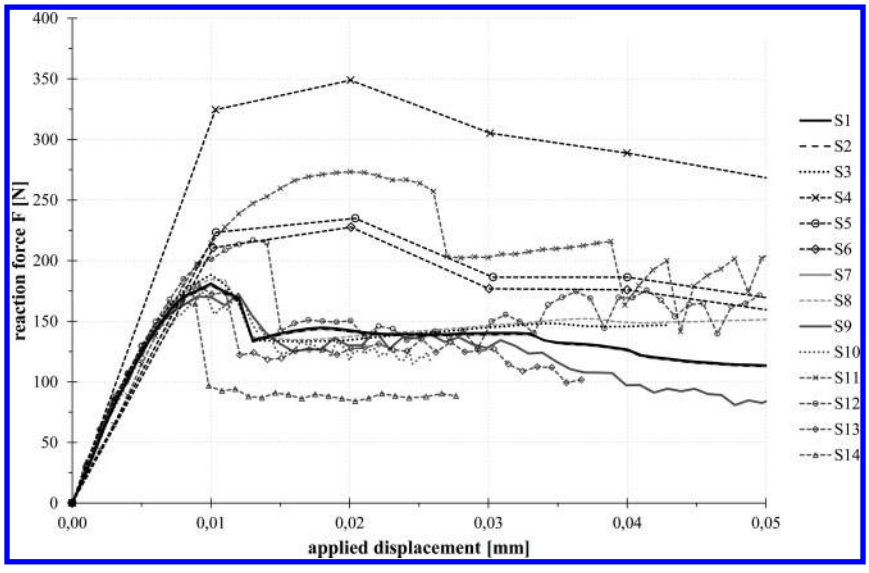


Figure 8. Results of the numerical simulations: distributions of the reaction force F as a function of the applied displacement.

6 CONCLUSION

At the present moment the calculations offer a basis for further investigations and calculations, but do not represent and describe the measured, quantitative results of the load tests realistically.

The convergence behavior still marks the major problem when using the *Concrete Damaged Plasticity* material model. Moreover, the contact behavior does not seem to cause computational problems as shown in accompanying simulations with purely, linear elastic material properties. Furthermore, the most computational costs seem to be a result of the used concrete material model, especially when reaching the post-cracked state.

Another problem to cause a poor convergence behavior might be exceeding deformations at the contact area during the loading process right at the changeover from the circular concrete dowel to the rest of the concrete body. In this area an addition of cohesive elements, element deletion and/or XFEM could lead to thoroughly stable simulations.

Apart from further load tests, the implementation of the above mentioned methods for improving the numerical simulations is one of the next objectives to be carried out in near future.

REFERENCES

Berger, J. 1994. *Technische Mechanik für Ingenieure. Band 2: Festigkeitslehre.* Braunschweig, Wiesbaden: Vieweg.

fib Bulletin 66. 2012. *Model code 2010, final draft, volume 2*. Lausanne: fédération internationale du béton (*fib*).

Hordijk, D.A. 1991. *Local approach to fatigue of concrete; doctoral thesis*. Delft: Delft University of Technology.

ÖNORM EN 1992-1-1. 2009. *Eurocode 2: Bemessung und Konstruktion von Stahlbeton und Spannbetontragkwerken, Teil 1-1: Allgemeine Bemessungsregeln und Regeln für den Hochbau.* Wien: Austrian Standards Institute.

Pirringer, S. & Kollegger, J. 2012. Bond behavior between concrete and perforated metal sheets for use in composite slabs. In J.W. Cairns, G. Metelli & G.A. Plizzari (eds), *Bond in Concrete: Bond, Anchorage, Detailing (Vol. 2); Proc. intern. symp., Brescia, 17–20 June 2012: 1093–1099.* Manerbio, Italy.

Research and Applications in Structural Engineering, Mechanics and Computation – Zingoni (Ed.)
© 2013 Taylor & Francis Group, London, ISBN 978-1-138-00061-2

A computer method for design and M-N-Φ analysis of composite steel-concrete cross-sections

C.G. Chiorean, A. Chira & M. Buru
Technical University of Cluj-Napoca, Faculty of Civil Engineering, Cluj-Napoca, Romania

ABSTRACT: This paper presents a general method for the rapid design, moment-curvature analysis and ultimate strength capacity evaluation of arbitrary-shaped composite steel-concrete cross-sections that are subjected to biaxial bending and axial force. The procedure may be used to assess the main features of elasto-plastic behaviour: multiple yielding points, flexural and axial rigidity, moment-curvature relationship, curvature ductility, and 3D interaction domains. The procedure allows cross-sections to be designed by solving directly for the reinforcement required to provide a cross-section with adequate strength. A computer program was developed, aimed at obtaining the ultimate strength capacity, moment-curvature relationships and reinforcement required by composite cross-sections subjected to combined biaxial bending and axial load. In order to illustrate the proposed method and its accuracy and efficiency, this program was used to study several representative examples, which have been studied previously by other researchers.

1 INTRODUCTION AND RESEARCH SIGNIFICANCE

The inelastic response of cross-sections can be represented by either moment-curvature diagrams for fixed values of axial force (M-N-Φ) or interaction diagrams that express, at failure, the interaction between the axial load and bending moments about major and minor principal axes of the cross-section. These analyses are based on assumption that all structural and reinforcement parameters are specified and, under given external loads either the cross section reach its failure (*ultimate strength analysis*) or inelastic behavior of cross-section is revealed (*moment-curvature analysis*). On the other hand, procedures for solving directly for the reinforcement required to provide a cross-section with adequate strength (*sectional design analysis*) are essential in practical design.

Some methods have been presented in literature for the ultimate strength analysis and design of various concrete and composite steel-concrete sections (Dundar & Sahin 1993; Rodrigues & Ochoa 1999; Chen et al. 2001; Rosati et al. 2008; Palares et al. 2009; Chiorean 2010). The method proposed herein, for design of cross-sections, consists of computing the required reinforcement area (A_{tot}) supposing that all structural parameters are specified and, under given external loads, the cross section reaches its failure either in tension or compression. The method proposed herein, for moment-curvature analysis, adopts Newton-Raphson procedure and the arc-length constraint equation to determine the moment-curvature diagrams for fixed values of axial force (M-N-ϕ) of an arbitrary composite steel-concrete cross-section. Residual stresses in structural steel component are due to uneven cooling of component parts during the rolling process. However, only a few works available in the literature have addressed this effect on the carrying capacity of composite steel-concrete cross-sections (Skrabek & Mirza 1990). For this reason, residual stresses were accounted for in encased steel sections used for the ultimate strength capacity evaluation of composite steel-concrete cross-sections and two types of residual stress patterns, EC2 and AISC-LRFD distribution, can be taken into account in the present formulation.

2 MATHEMATICAL FORMULATION

2.1 *Basic assumptions and constitutive material models*

Consider the cross-section subjected to the action of the external bending moments about both global axes and axial force as shown in Figure 1.

The cross-section may assume any shape with multiple polygonal or circular openings. It is assumed that plane section remains plane after deformation. Thus the resultant strain distribution corresponding to the curvatures about global axes $\mathbf{\Phi} = \{\phi_x, \phi_y\}$ and the axial compressive strain ε_0 can be expressed at a generic point, in concrete matrix, fiber of structural steel or ordinary reinforced bars, of coordinates (x, y) in a linear form as:

$$\varepsilon = \varepsilon_0 + \phi_x y + \phi_y x \tag{1}$$

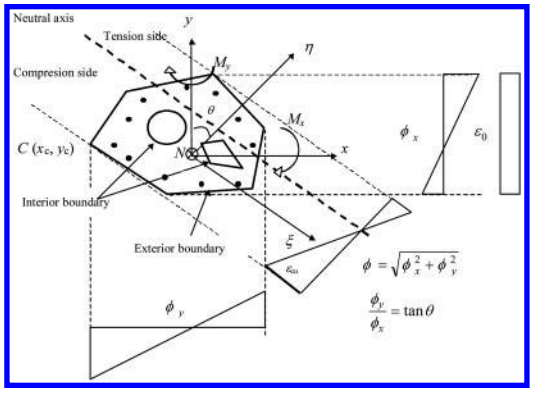


Figure 1. Model of arbitrary composite cross-section.

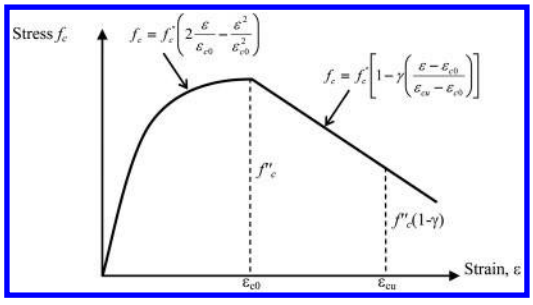


Figure 2. Stress-strain relationships for concrete in compression.

The constitutive relation to model the concrete under compression is represented by a combination of a second-degree parabola (for ascending part) and a straight line (for descending part), as depicted in Figure 2, where γ represents the degree of confinement in the concrete. Multi-linear elastic-plastic stress-strain relationships, both in tension and in compression, is assumed for the structural steel and the conventional reinforcing bars. Residual stresses may be incorporated in the analysis. The magnitude and distribution of residual stresses in hot-rolled members depend on the type of cross-section and manufacturing processes and different patterns are proposed. In the US, the residual stress is considered constant in the web although when the depth of a wide flange section is large, it varies more or less parabolically. Another possible residual stress pattern in the web is the one simplified by a linear variation as used in European calibration frames (Fig. 3).

Assuming that the residual strain can be linearized for individual zones in the steel section the total strain in a point can be computed as:

$$\varepsilon = \varepsilon_0 + \phi_x y + \phi_y x + \varepsilon_r \qquad (2)$$

where ε_r represents a linear residual strain field.

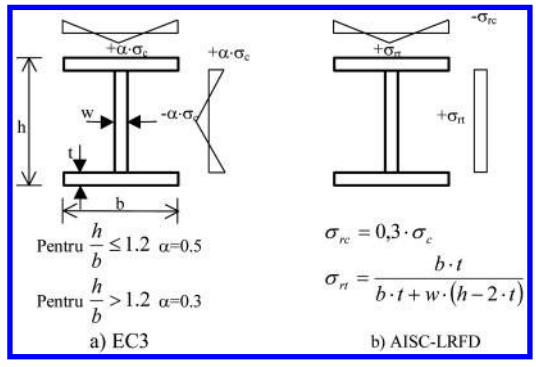


Figure 3. Residual stress patterns.

2.2 *Formulation of the proposed design procedure*

The method proposed herein consists of computing the required conventional reinforcement area (A_{tot}) supposing that all structural parameters are specified and, under given external loads (N, Mx, My), the cross section reach its failure either to maximum strains attained at the outer compressed point of the concrete section or to maximum strains attained in the most tensioned steel fibre. Consider an irregular composite section as shown in Figure 1 subjected to axial force and biaxial bending moments. The conventional reinforcement layout is given as percentage (α_i) of the total reinforcement steel area (A_{tot}) in each location. At ultimate strength capacity the equilibrium is satisfied when the external forces are equal to the internal ones and either in the most compressed or tensioned steel fibre the ultimate strain is attained. These conditions can be represented mathematically in terms of the following nonlinear system of equations as:

$$\begin{cases} \int_{A_{cs}} \sigma\left(\varepsilon\left(\varepsilon_0,\phi_x,\phi_y\right)\right)dA_{cs} + A_{tot}\sum_{i=1}^{N_{rs}} \sigma\left(\varepsilon_i\left(\varepsilon_0,\phi_x,\phi_y\right)\right)\alpha_i - N = 0 \\ \int_{A_{cs}} \sigma\left(\varepsilon\left(\varepsilon_0,\phi_x,\phi_y\right)\right)y dA_{cs} + A_{tot}\sum_{i=1}^{N_{rs}} \sigma\left(\varepsilon_i\left(\varepsilon_0,\phi_x,\phi_y\right)\right)y_i\alpha_i - M_x = 0 \\ \int_{A_{cs}} \sigma\left(\varepsilon\left(\varepsilon_0,\phi_x,\phi_y\right)\right)x dA_{cs} + A_{tot}\sum_{i=1}^{N_{rs}} \sigma\left(\varepsilon_i\left(\varepsilon_0,\phi_x,\phi_y\right)\right)x_i\alpha_i - M_y = 0 \\ \varepsilon_0 + \phi_x y_c\left(\phi_x,\phi_y\right) + \phi_y x_c\left(\phi_x,\phi_y\right) - \varepsilon_u = 0 \end{cases} \qquad (3)$$

in which A_{tot}, ε_0, ϕ_x, ϕ_y represent the unknowns, the surface integral is extended over concrete and structural steel areas (A_{cs}), N_{rs} represents the number of conventional steel reinforcement bars. In the above equations the first three relations represent the basic equations of equilibrium for the axial load N and the biaxial bending moments M_x, M_y respectively. The last equation represents the ultimate strength capacity condition, that is, in the most compressed or most tensioned point the ultimate strain is attained; in this equation $x_c(\phi_x, \phi_y)$ and $y_c(\phi_x, \phi_y)$ represent the

coordinates of the point in which this condition is imposed:

$$\varepsilon(\phi_x,\phi_y)=\varepsilon_u+\phi_x(y-y_c)+\phi_y(x-x_c) \tag{4}$$

In this way, substituting the strain distribution given by the Eq. (4) in the basic equations of equilibrium, the unknown $\varepsilon_0$together with the failure constraint equation can be eliminated from the nonlinear system (3). Thus, the nonlinear system of equations (3) is reduced to an only three basic equations of equilibrium in which the unknowns, total reinforcement steel area A_{tot}, and the ultimate sectional curvatures ϕ_x and ϕ_y, can be obtained iteratively following the procedure described in (Chiorean 2013).

2.3 *Moment-curvature (M-N-Φ) analysis procedure*

Consider an composite cross-section with arbitrary shape as shown in Figure 1 subjected to biaxial bending moments (M_{x0}, M_{y0}) and axial force (N_0). The equilibrium is satisfied when the external forces (N_0, M_{x0}, M_{y0}) are equal to the internal ones. These conditions can be represented mathematically in terms of the following nonlinear system of equations as:

$$\begin{cases}\int_{A_{cs}}\sigma(\varepsilon(\varepsilon_0,\phi_x,\phi_y))dA_{cs}+\sum_{i=1}^{N_{rs}}\sigma(\varepsilon_i(\varepsilon_0,\phi_x,\phi_y))A_{rsi}-N_0=0\\ \int_{A_{cs}}\sigma(\varepsilon(\varepsilon_0,\phi_x,\phi_y))ydA_{cs}+\sum_{i=1}^{N_{rs}}\sigma(\varepsilon_i(\varepsilon_0,\phi_x,\phi_y))y_iA_{rsi}-M_{x0}=0\\ \int_{A_{cs}}\sigma(\varepsilon(\varepsilon_0,\phi_x,\phi_y))xdA_{cs}+\sum_{i=1}^{N_{rs}}\sigma(\varepsilon_i(\varepsilon_0,\phi_x,\phi_y))x_iA_{rsi}-M_{y0}=0\end{cases} \tag{5}$$

where A_{rsi} $(i=1,N_{rs})$ denotes the area of conventional steel reinforcements, and in which $\varepsilon_0,\phi_x,\phi_y$ represent the unknowns. The above system can be solved numerically using, for instance, the load-controlled Newton method and taking into account the fact that the stresses are implicit functions of the axial compressive strain and curvatures through the resultant strain distribution given by the Eq. (1). Regarding the automatic drawing of the moment–curvature diagram, the strategy is as follows. Scaling the bending moments through the load factor λ and keeping the axial force constant $N=N_0$, the complete moment-curvature diagram can be obtained, under constant axial force by solving the system of equations (Eq. 6), where the axial compressive strain ε_0, the curvatures ϕ_x and ϕ_y and the load amplifier factor λ represent the unknowns.

$$\begin{cases}\int_{A_{cs}}\sigma(\varepsilon(\varepsilon_0,\phi_x,\phi_y))dA_{cs}+\sum_{i=1}^{N_{rs}}\sigma(\varepsilon_i(\varepsilon_0,\phi_x,\phi_y))A_{rsi}-N_0=0\\ \int_{A_{cs}}\sigma(\varepsilon(\varepsilon_0,\phi_x,\phi_y))ydA_{cs}+\sum_{i=1}^{N_{rs}}\sigma(\varepsilon_i(\varepsilon_0,\phi_x,\phi_y))y_iA_{rsi}-\lambda M_{x0}=0\\ \int_{A_{cs}}\sigma(\varepsilon(\varepsilon_0,\phi_x,\phi_y))xdA_{cs}+\sum_{i=1}^{N_{rs}}\sigma(\varepsilon_i(\varepsilon_0,\phi_x,\phi_y))x_iA_{rsi}-\lambda M_{y0}=0\end{cases} \tag{6}$$

This system can be rewritten in terms of non-linear system of equations in the following general form:

$$\mathbf{F}(\lambda,\mathbf{X})=\mathbf{f}^{\text{int}}-\mathbf{f}^{ext}=\mathbf{0} \tag{7}$$

where $\mathbf{X}=[\varepsilon_0\ \phi_x\ \phi_y]^T$ In this case, maintaining the axial force N_0 constant and scaling just the bending moments, we are in the situation of the non-proportionally applied loading, which involves two loading vectors, one that will be scaled and one fixed. The external loading can then be represented by:

$$\mathbf{f}^{ext}=\begin{bmatrix}N_0\\0\\0\end{bmatrix}+\lambda\begin{bmatrix}0\\M_{x0}\\M_{y0}\end{bmatrix}=\mathbf{f}^{ext}_{fixed}+\lambda\mathbf{f}^{ext}_{scaled} \tag{8}$$

so that the out of balance force vector becomes:

$$\mathbf{F}(\lambda,\mathbf{X})=\mathbf{f}^{\text{int}}-\mathbf{f}^{ext}_{fixed}-\lambda\mathbf{f}^{ext}_{scaled} \tag{9}$$

To obtain the equilibrium path, a proper parametrization is needed. A common setting of a continuation process is to augment the equilibrium equations (9) with a constraint (Crisfield 1991). In this procedure, commonly called arc-length method, these equations are solved in a series of steps or increments, usually starting from the unloaded state ($\lambda=0$). An indirect solution scheme for the constraint equation may be introduced. This procedure is iterated until convergence with respect to a suitable norm is attained. Assuming that a point (${}^{\tau}\mathbf{X}$, ${}^{\tau}\lambda$) of the equilibrium path has been reached, the next point (${}^{\tau+\Delta\tau}\mathbf{X}$, ${}^{\tau+\Delta\tau}\lambda$) of the equilibrium path is then computed updating the loading factor, axial compressive strain ε_0 and the curvatures ϕ_x and ϕ_y as:

$$\begin{aligned}{}^{\tau+\Delta\tau}\lambda&={}^{\tau}\lambda+\Delta\lambda_{k+1}\\ {}^{\tau+\Delta\tau}\mathbf{X}&={}^{\tau}\mathbf{X}+\Delta\mathbf{X}_{k+1}\end{aligned} \tag{10}$$

Adopting an automatic step length adaptation scheme (Crisfield 1991) for the loading factor, the entire moment-curvature interaction diagram of the cross section can be constructed for a given axial force.

2.4 *Evaluation of tangent stiffness and stress resultant*

Based on Green's theorem, the integration of the stress resultant and stiffness coefficients over the cross-section will be transformed into line integrals along the perimeter of the cross-section (Chiorean 2010). In order to perform the integral on a determined side of the contour (L_i), polygonal or circular, of the integration area, an adaptive interpolatory Gauss-Lobatto method is used (Chiorean 2010). The conventional steel reinforcements are assumed to be discrete points with effective area, co-ordinates and stresses. The effect of residual stresses may be included in the analysis providing that the residual stress can be linearized for individual zones in the steel section associated to variations of residual stresses throughout the height of cross-section (Chiorean 2013).

3 COMPUTATIONAL EXAMPLES

The accuracy and computational advantages of the numerical procedures developed here has been evaluated using several selected benchmark problems analysed previously by other researchers using different numerical methods. Furthermore new parametric studies and computational examples are given in order to demonstrate the effectiveness of the ultimate strength capacity evaluation procedure described in (Chiorean 2010).

3.1 *Composite steel-concrete cross-section with arbitrary shape*

The composite steel-concrete cross-section depicted in Figure 4, consists of the concrete matrix, fifteen reinforcement bars of diameter 18 mm, a structural steel element and a circular opening.

Characteristic strengths for concrete, structural steel and reinforcement bars are $f_c'' = 30$ Mpa, $f_{st} = 355$ Mpa and $f_s = 460$ Mpa, respectively. These characteristic strengths are reduced by dividing them with the corresponding safety factors $\gamma_c = 1.50$, $\gamma_{st} = 1.10$ and $\gamma_s = 1.15$. The crushing strain $\varepsilon_0 = 0.002$ and ultimate strain $\varepsilon_{cu} = 0.0035$ have been used. The Young modulus for all steel sections was 200 GPa. A bi-linear elasto-perfect plastic stress-strain relationship for the reinforcement bars and structural steel, both in tension and in compression, is assumed. This is an example proposed and analysed by Chen et al. (2001) and later studied by Rosati et al. (2008) and others.

The effects of confinement in the concrete were investigated for different values of degree of confinement γ. As it can be seen in Figure 5 by reducing the confinement in the concrete the interaction curves indicate lower capacities and the non-convexity of the diagrams is more pronounced. The bending moments are computed about the geometric centroidal axes for a compressive axial force $N = 10000$ kN. Figure 6 shows the bending moment-curvature diagrams of cross-section, considering uniaxial bending about X-axis with a compressive axial force $N = 8000$ kN and for different values of degree of confinement ($\gamma = 0;0.15;0.30;0.50$). As it can be seen, the strain softening effect exhibited by the concrete in compression ($\gamma > 0$) indicates lower bending capacity of cross section an also "snap-back" behaviour; this effect is more accentuated as degree in confinement is decreased.

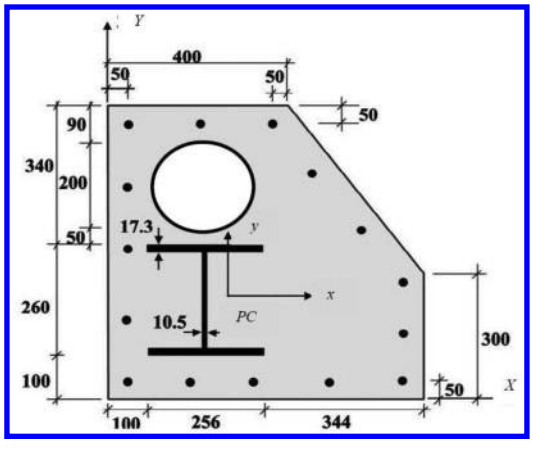


Figure 4. Composite steel-concrete cross-section.

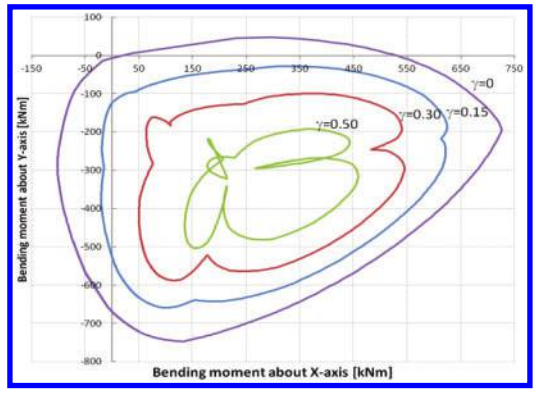


Figure 5. Moment capacity contours with compressive axial load $N = 10000$ kN: influence of degree of confinement.

Table 1. Influence of residual stresses over total reinforcement steel area ($M_x = 210.5$ kNm and $M_y = 863.5$ kNm).

N [kN]	A_{tot} [cm^2] (without residual stresses)	A_{tot} [cm^2] (EC3 distribution)	A_{tot} [cm^2] (AISC-LRFD distribution)
1000	58.82	58.28	57.69
3000	41.55	42.47	42.18
5000	31.19	41.85	36.64
6000	33.41	50.83	42.37
8000	61.01	86.60	71.25
9000	84.16	110.38	93.57
10000	110.43	136.37	118.83

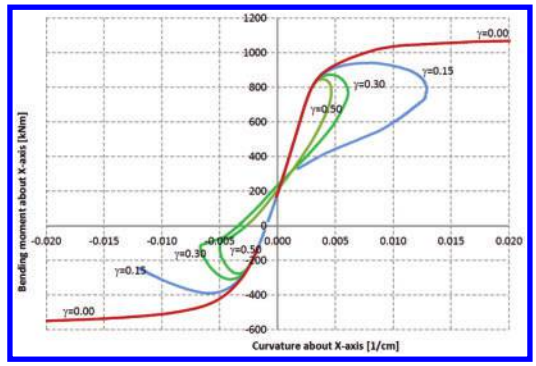


Figure 6. Moment curvature diagrams for different values of degree of confinement and compressive axial force $N = 8000$ kN

Let us consider this cross-section subjected to biaxial bending to carry the following design loads: $N = 4120$ kN, $M_x = 210.5$ kNm and $M_y = 863.5$ kNm. The distribution of the steel reinforcing bars are shown in Fig. 4, and we consider that all rebars have the same diameter. The iterative process of design was started with $\phi_x = 0$ and $\phi_y = 0$, and $A_{tot} = 0.005 A_g = 215$ cm^2. The equilibrium tolerance has been taken as $1E$-4. After only five iterations, the total area required of the rebars was found to be $A_{tot} = 34.347$ cm^2. Consequently, the required diameter of the selected rebar is $\Phi_{req} = 2\sqrt{\frac{A_{tot}}{N_b \pi}} = 1.71\ cm$ which compare very well with the required bar diameter reported by Chen *et al.* (2001), $\Phi_{req} = 1.78$ cm. In the above computational example, the axial force and bending moments are represented about the plastic centroidal axes of the cross-section. When the design loads are represented about the geometric centroid the total area required of the rebars was found to be $A_{tot} = 15.674$ cm^2. This result has been obtained after only six iterations. Table 1 presents the variations of total reinforcement area considering different values of compressive axial load and two types of residual stress patterns, EC3 and AISC-LRFD respectively, for structural steel element. As it can be seen the presence of residual stresses increases the total reinforcement steel area as axial compressive load is increased.

3.2 *Rectangular composite steel-concrete section. Influence of residual stresses*

In order to evaluate the effects of residual stresses over ultimate strength capacity, deformability and flexural rigidity of composite steel-concrete cross section, the moment-capacity contours and moment-curvature diagrams are determined for a very common composite cross- section under biaxial loading: rectangular cross-section with symmetrically placed structural steel. The cross-section consists of a concrete core and a symmetrically placed USA wide flange section W12 × 120 (Fig. 7). Characteristic strength for concrete in compression is $f_c'' = 20$ MPa and the stress-strain curve which consists of a parabolic and linear part was used in the calculation with crushing strain $\varepsilon_0 = 0.002$, ultimate strain $\varepsilon_{cu} = 0.0035$.

The strain softening of concrete is taken into account with $\gamma = 0.15$. The Young modulus for encased structural steel and reinforcements is 200 GPa. A bi-linear elasto-perfect plastic stress-strain relationship for the reinforcement bars and structural steel, both in tension and in compression, is assumed with the yield strength $f_y = 300$ MPa. Figures 8 and 9 shows the comparative bending moment-curvature diagrams of cross-section, considering uniaxial bending about X-axis (strong) and Y-axis (weak) respectively under several compressive axial loads and with and without residual stress effect. The effect of residual stresses is taken into account considering two types of residual stress patterns, EC3 and AISC-LRFD (Fig. 3), respectively, for structural steel element. The comparisons reveal that the influences of residual stresses play an important role on both carrying capacity and inelastic behaviour, during the loading process, on composite cross section and this effect becomes more effective with higher compressive axial load. Figure 10 presents

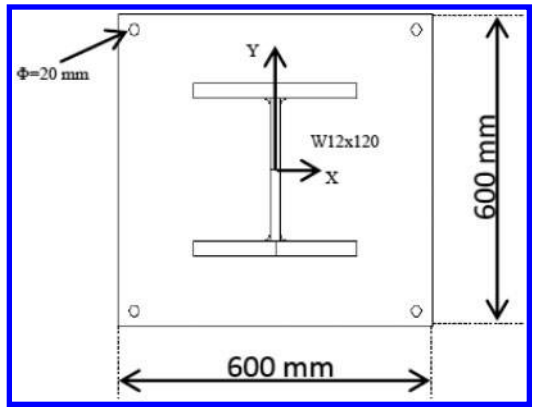


Figure 7. Rectangular composite steel-concrete cross-section.

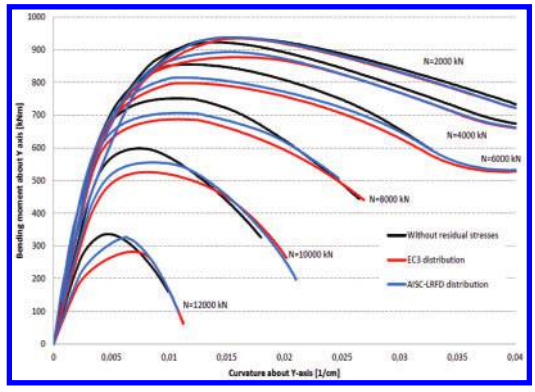


Figure 8. Moment-curvature analysis for different values of compressive axial loads: weak axis bending.

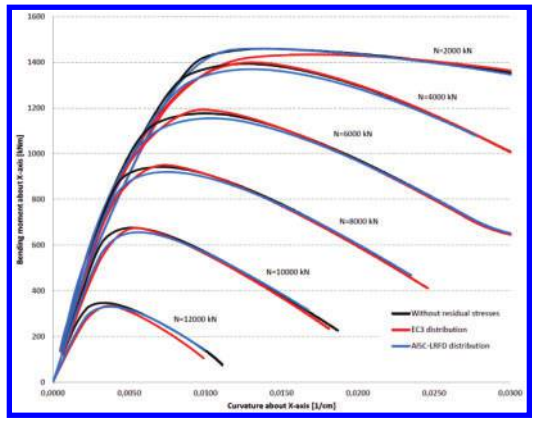


Figure 9. Moment-curvature analysis for different values of compressive axial loads: strong axis bending.

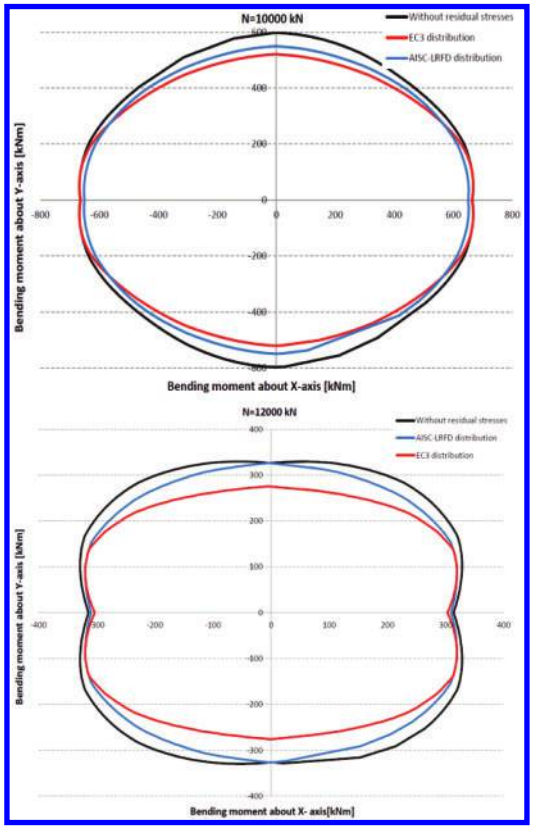


Figure 10. Moment capacity contours with different values of axial compressive load and different residual stress patterns for encased steel section.

the moment capacity contours for different values of axial compressive load with and without the presence of residual stresses. As it can be seen the residual stresses indicates lower capacity of cross section, and this effect is more pronounced as axial load increases especially in the case of EC3 distribution for residual stresses.

4 CONCLUSIONS

A new computer method has been developed for the rapid design, moment-curvature analysis and ultimate strength capacity evaluation of composite steel-concrete cross-sections subjected to axial force and biaxial bending. The iterative algorithm, proposed herein, to design the steel reinforcement of composite steel-concrete sections under biaxial bending and axial force, as compared to other iterative methods, is very stable and the convergence is very fast. The moment-curvature diagrams for fixed values of axial force are obtained by an incremental-iterative arc-length procedure, and the proposed approach has been found to be extremely powerful and efficient. Due to presence of residual stresses, for encased steel section, a reduction of capacity strength of composite steel-concrete cross-section was observed. The influence of residual stresses on the carrying capacity of cross- sections is most effective with higher axial load levels. From the numerical tests it may be concluded that the influence of the residual stress on the carrying capacity and inelastic behavior during the loading process is important and must be considered in the valuable advanced analysis of composite cross-sections. It can be concluded that the proposed numerical method proves to be reliable and accurate for practical applications in the design of composite steel-concrete beam-columns and can be implemented in the advanced analysis techniques of 3D composite frame structures.

ACKNOWLEDGEMENTS

The authors gratefully acknowledges the support from Romanian National Authority for Scientific Research (ANCS and CNCSIS- Grant PNII-IDEI No. 193/2008) for this study.

REFERENCES

Dundar, C., Sahin, B. 1993. Arbitrarily shaped reinforced concrete members subject to biaxial bending and axial load, *Computers and Structures*, 49:643–662.

Rodrigues, J.A. & Aristizabal-Ochoa, J.D. 1999. Biaxial interaction diagrams for short RC columns of any cross section, *Journal of Structural Engineering*, ASCE, 125:672–683.

Chen S.F., Teng J.G., Chan S.L. 2001. Design of biaxially loaded short composite columns of arbitrary section, *Journal of Structural Engineering*, ASCE, 127: 678–685.

Rosati, L., Marmo, F., Serpieri, R. 2008. Enhanced solution strategies for the ultimate strength analysis of composite steel-concrete sections subject to axial force and biaxial bending, *Computer methods in applied mechanics and engineering*, 197:1033–1055.

Pallares, L., Miguel, P.F., Prada, M.A.F. 2009. A numerical method to design reinforced concrete sections subjected to axial forces and biaxial bending based on ultimate strain limits, *Engineering Structures*, 31:3065–3071.

Chiorean, C.G. 2010. Computerised interaction diagrams and moment capacity contours for composite steel-concrete cross-sections, *Engineering Structures*, 32:3734–3757.

Chiorean, C.G. 2013. A computer method for rapid design of composite steel-concrete cross-sections, *Open Civil Engineering Journal*, 7:1–17.

Skrabek, B. W., and Mirza, S.A.1990. Strength reliability of short and slender composite steel-concrete columns. *Civil Engineering Report Senes. No. CE-90-1,* Lakehead University, Thunder Bay, Ontario: 323 p.

Crisfield, M.A. 1991. *Non linear finite element analysis of solids and structures*, Wiley:Chichester.

Research and Applications in Structural Engineering, Mechanics and Computation – Zingoni (Ed.)
© 2013 Taylor & Francis Group, London, ISBN 978-1-138-00061-2

Load-carrying capacity of steel and high-strength concrete composite columns

M. Karmazínová & J.J. Melcher
Brno University of Technology, Brno, Czech Republic

ABSTRACT: The paper deals with the problems of the buckling compression of steel-concrete composite columns. The paper presents some selected results of the more extensive research realized on the author's workplace and oriented to the utilization of high-strength steels and concretes in steel structural members and composite structural members composed of steel and concrete. This paper is directed towards one part of this research only that means theoretical analysis of the buckling resistance and experimental verification of the objective buckling resistance of columns in connection with the actual behaviour and corresponding relevant failure mechanism. Within the framework of the buckling resistance analysis two basic cross-section column types have been investigated: (i) steel HEA cross-sections of the dimensions in the range from HEA 140 up to HEA 200, encased by concrete between flanges, and (ii) steel circular tubes of the diameter in the range from 133 to 168 mm and thickness from 4 to 5 mm, filled by concrete; the buckling length of investigated columns was 3 m. Materials of investigated columns were as follows: steel grade in the range from S 235 to S 420 mostly, but in several cases even up to S 460 and S 700; concrete class in the range from C 20/25 to C 80/90. Within the experimental research, so far 56 specimens subjected to compression force have been tested in total, i.e. 29 HEA cross-section columns with concrete encasement and 27 tubes filled by concrete. Within the experimental investigation, also the material tests and their evaluation, as well as the measurement of actual geometrical imperfections, have been performed to verify the results obtained from theoretical studies. The attention has been mainly paid to the following significant problems: the efficiency of the usage of high-strength materials in steel-concrete composite columns; the effectiveness of concrete contribution to the buckling resistance of steel-concrete columns; the evaluation of the test results aimed to determine the design buckling resistance. This paper namely presents the results of the verification of the buckling resistance of HEA cross-sections with high-strength concrete, with accent to its contribution to the load-carrying capacity.

1 INTRODUCTION

The particular problem of the load-carrying capacity of composite columns composed of high-strength steels and concretes has been experimentally and theoretically investigated on the several groups of structural members simulating the typical building columns, from the viewpoint of their geometry and usual dimensions. According to this condition, the columns of 3 m length of two basic HEA cross-sections, HE 140A and HE 160A, have been chosen for the experimental and theoretical analysis. The attention was mainly paid to the influence of high-strength concrete on the buckling resistance. Steel and steel-concrete columns of the following material properties have been investigated: steel grades S 235 and S 355; concrete classes C 20/25 and C 80/95 for the first cross-section and C 50/60 and C 70/85 for the second one, in accordance with the overview of the investigated column types presented in Table 1.

Table 1. Overview of investigated column types

Cross-section	column group	steel grade	concrete class
HE 140A	TS 1	S 355	steel only
	TS 2	S 355	C 20/25
	TS 3	S 355	C 80/95
HE 160A	TS 4	S 235	steel only
	TS 5	S 235	C 50/60
	TS 6	S 235	C 70/85
HE 160A	TS 7	S 355	steel only
	TS 8	S 355	C 50/60
	TS 9	S 355	C 70/85

For investigation, the columns with such cross-section configurations and material combinations, for which the highest ratio of the buckling capacity to full-plastic capacity has been calculated. Table 1 shows the first two groups of specimens only, which have been

already tested; next test specimens have been produced and recently are preparing for testing.

2 CALCULATIONS OF BUCKLING LOAD-CARRYING CAPACITY

The buckling load-carrying capacity of the composite steel-concrete column, calculated using simplified methods given in EN 1993-1-1, EN 1994-1-1 (also Kuranovas, Liang, Yu) is usually written as

$$N_b = \chi N_{pl}, \tag{1}$$

where, for the column composed of open steel cross-section with concrete encasement, the full-plastic section load-carrying capacity (without buckling) N_{pl} is usually given in the form

$$N_{pl} = A_a \cdot f_y + 0.85 \cdot A_c \cdot f_c \tag{2}$$

with steel and concrete cross-section areas A_a, A_c, yield strength f_y and cylindrical concrete strength f_c. The reduction buckling factor χ depends on the non-dimensional slenderness $\bar{\lambda}$ known as

$$\bar{\lambda} = \sqrt{N_{pl} / N_{cr}}, \tag{3}$$

where the critical force N_{cr} is

$$N_{cr} = \pi^2 \cdot (EI)_{eff} / L_{cr}^2, \tag{4}$$

the effective flexural stiffness is

$$(EI)_{eff} = E_a I_a + 0.6 \cdot E_c I_c \tag{5}$$

with steel and concrete Young's modulus of elasticity E_a, E_c and corresponding second moments of area I_a, I_c. Then, the buckling reduction factor χ can be written as

$$\chi = \frac{1}{\phi + \sqrt{\phi^2 - \bar{\lambda}^2}}, \tag{6}$$

if the coefficient ϕ is

$$\phi = 0.5 \cdot \left[1 + \alpha_1 \cdot (\bar{\lambda} - 0.2) + \bar{\lambda}^2\right] \tag{7}$$

where the buckling curve (EN 1994-1-1) of "c" with the imperfection factor value of $\alpha_1 = 0.49$ is applied for I or H cross-sections encased between flanges.

Within the particular theoretical analysis, the expected buckling load-carrying capacities have been calculated for steel and steel-concrete columns with material specifications mentioned above, using formulas (1) to (7). The calculations have been performed with the characteristic values of concrete cylindrical strength and nominal values of steel yield strength, to obtain buckling load-carrying capacities corresponding with the predicted ultimate capacities. The capacity values have been determined for the buckling lengths, which are usually used for the columns of building constructions, i.e. in the range of about from $L_{cr} =$ 3 m up to $L_{cr} =$ 5 m, and also for the buckling length of $L_{cr} = 0$ m (pure compression), to compare the full-plastic load-carrying capacity N_{pl} and the buckling load-carrying capacity $N_b = \chi N_{pl}$ and to obtain the dependence of the capacity on the compression strength and Young's modulus of elasticity of concrete.

Table 2. Overview of test specimens: cross-section configuration and materials properties (mean values)

Column group	steel: yield strength $f_{y,m}$ [MPa]	steel: Young's modulus $E_{a,m}$ [GPa]	concrete: cylindrical strength $f_{c,m}$ [MPa]	concrete: Young's modulus $E_{c,m}$ [GPa]
TS 1		has not	–	–
TS 2	456	been	27.0	32.0
TS 3		measured	87.0	49.0
TS 4			–	–
TS 5	258	202	56.5	48.0
TS 6			71.1	42.0
TS 7			–	–
TS 8	439	216	56.5	48.0
TS 9*			71.1	42.0

3 test specimens in each column group.
* Specimens have not been tested so far.

3 EXPERIMENTAL VERIFICATION OF BUCKLING LOAD-CARRYING CAPACITY

To verify the actual behaviour of steel and steel-concrete columns and to evaluate the contribution of concrete to the buckling capacity, the test specimens of geometrical and material parameters corresponding with ones mentioned above have been experimentally verified. The overview of 77 specimen groups accordant to described column types is shown in Table 2, together with the mean values of measured physical-mechanical properties.

The illustrations of the test arrangement and test realization are depicted in Figs. 1 and 2. The photos show the testing equipment, the test specimen on the beginning loading process and failed test specimen.

The experimental verification has been realized in two basic phases. The first phase has been oriented to the comparison of the buckling load-carrying capacity of steel columns (column group TS 1) with the capacity of steel-concrete columns with normal-strength concrete (column group TS 2) and high-strength concrete (column group TS 3).

The European Standard rules are useable for steel grade up to S 460 and for concrete strength class up to C 60/75, but for higher strengths it cannot be used without other verification. In the first phase of this research

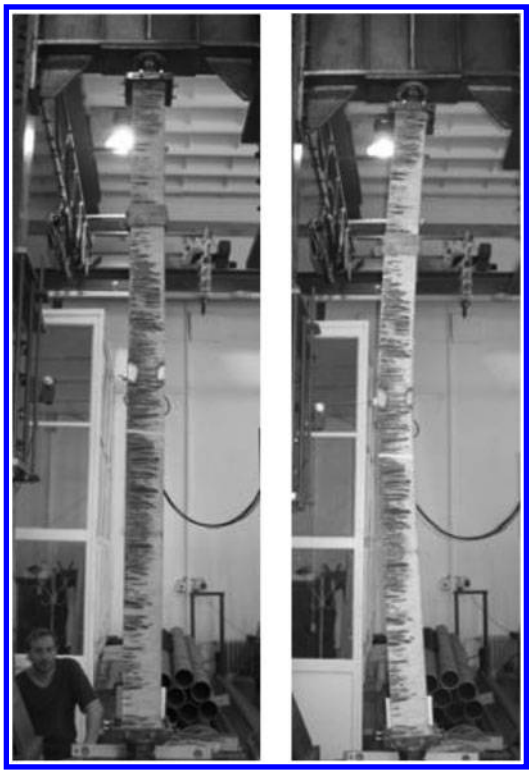


Figure 1. Illustration of test arrangement and test performance.



Figure 2. Strain gauges on test specimens and failed specimen.

it was verified, that the usage of high-strength concrete is effective because it gives increasing in load-carrying capacity, which corresponds with the assumed values calculated according to the standards. In both phases,

Table 3. Buckling compression load-carrying capacities: calculated values vs. test results

	buckling compression load-carrying capacity				
Column group	calculation N_{cal} [kN]	test results N_{test} [kN]			$\frac{N_{test}}{N_{cal}}$
TS 1	579	882	931	835	1.52
TS 2	858	1 240	1 322	1 079	1.41
TS 3	1 105	1 707	1 603	1 541	1.46
TS 4	627	901	955	864	1.45
TS 5	1 300	1 801	1 707	1 811	1.36
TS 6	1 352	1 803	1 570	1 866	1.29
TS 7	843	947	1 105	915	1.17
TS 8	1 562	1 958	1 830	1 698	1.17

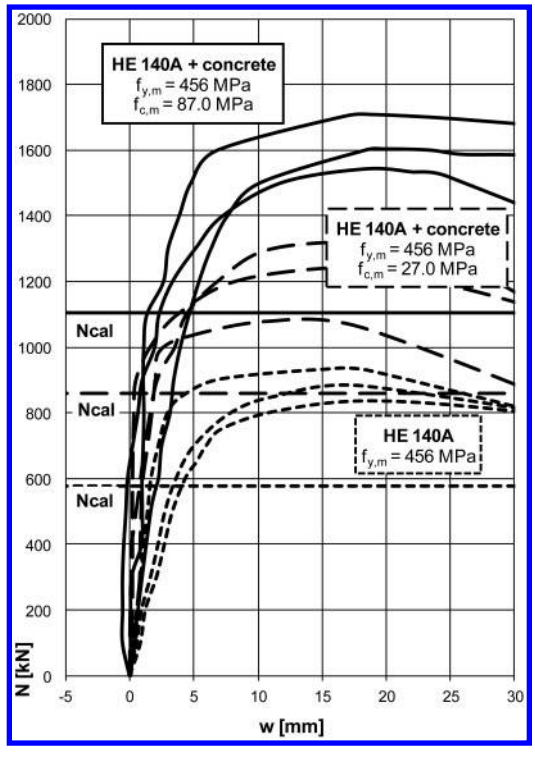


Figure 3. "*N*–*w*" diagrams: column groups TS 1, TS 2, TS 3 – HE 140A, steel grade S 355, concrete classes C20/25, C80/95.

the influence of particular concrete properties has been investigated in detail.

The buckling load-carrying capacities obtained from the loading tests in comparison with the expected capacities calculated, are listed in Table 3. The theoretical values have been calculated according to the procedure mentioned above, with the actual material properties.

Mechanical properties used for theoretical values calculation, have been measured helping the material test specimens cut from the failed specimens after

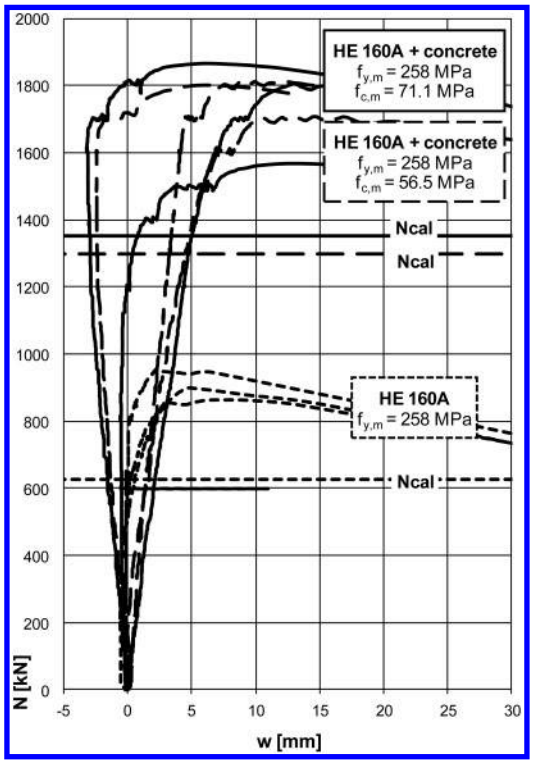


Figure 4. "*N*–*w*" diagrams: column groups TS 4, TS 5, TS 6 – HE 160A, steel grade S 235, concrete classes C50/60, C70/85.

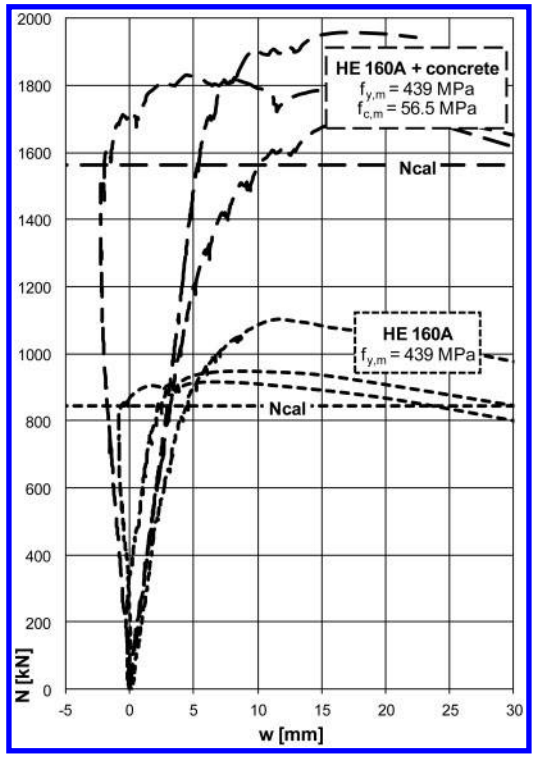


Figure 5. "*N*–*w*" diagrams: column types TS 7, TS 8 – HE 160A, steel grade S 355, concrete class C 50/60.

loading test finishing. For the comparison, the average ratio of the test capacity to the calculated values is added to Table 3, too.

In Figs. 3, 4 and 5 the basic relationships of the buckling capacity N_{test} and deflections w at the mid-length are drawn for steel columns (TS 1, TS 4, TS 7), for steel-concrete columns with normal-strength concrete (TS 2) and for steel-concrete column with two different qualities of high-strength concrete (TS 5, TS 6, TS 8). For the comparison, the calculated values of the buckling load-carrying capacity are added to the graphs in Figs. 3, 4, 5, too.

From Figs. 3, 4 and 5 it is seen in general encasement between flanges using concrete of mentioned material properties can increase the buckling compression load-carrying capacity even up to about two times in comparison with steel columns; the actual buckling capacity of steel-concrete columns obtained from the tests very good corresponds with the buckling capacity calculated by standard rules (see e.g. Karmazínová et al. 2009, 2010, 2011); they are higher approximately by 30 % (TS 5, TS 6) and by 17 %, respectively (TS 8); in this case, the buckling capacities of the members with concrete C 50/60 and C 70/85 are about the same (TS 5, TS 6), although the measured parameters of both concretes very good correspond with the assumed properties, but the Young's modulus of concrete C 50/60 measured has been obtained much more than normally assumed; the actual buckling load-carrying capacities of specimens TS 7, TS 8 are higher by 17 % only, because (probably) yield strength has been measured for very small number of material test specimens, so that the value can be influenced by that fact.

4 CONCLUSIONS

From particular results verified experimentally, for steel-concrete columns composed of H cross-section encased by high-strength concrete between flanges the following partial conclusions may be deducted:

- Buckling load-carrying capacity in compression can be calculated using the usual procedure given by European Standard rules, like as for the column with normal concrete.
- Actual values of buckling load-carrying capacity are approximately by 30 % higher than the values calculated with measured properties.
- As expected, from test results of column groups TS 5 and TS 6 it is seen, that the influence of Young's modulus is understandably more significant than the influence of concrete strength. One of the effective methods how to evaluate the importance of the influence of particular parameters, is sensitivity analysis (Kala et al. 2009, 2010, Melcher et al. 2009b), which

is continuously utilized in parallel with the loading tests realization and test results evaluation.
- For more correct evaluation the larger test number with specimens of different material and geometrical properties is needed. The research is continuing and new specimens prepared to test.

5 ACKNOWLEDGEMENT

The paper has been elaborated within the solution of the Research Centre Project of the Czech Ministry of Education, Youth and Sports MSM 0021630519 and the Czech Science Foundation grant projects Nos. 103/09/0597 and 103/09/H085.

REFERENCES

Kala, Z., Karmazínová, M., Melcher, J., Puklický, L. & Omishore, A. 2009. Sensitivity analysis of steel-concrete structural members, In *Proceedings of the 9th International Conference on Steel-Concrete Composite and Hybrid Structures „ASCCS 2009"* held in Leeds, Research Publishing Services: Singapore, 2009, pp. 305–310. ISBN 978-981-08-3068-7.

Kala, Z., Puklický, L., Omishore, A., Karmazínová, M. & Melcher, J. 2010. Stability problems of steel-concrete members composed of high-strength materials, *Journal of Civil Engineering and Management*, 2010, 16(3), pp. 352–362. doi: 10.3846/jcem.2010.40.

Karmazínová, M, Melcher, J. J. & Röder, V. 2009. Load-carrying capacity of steel-concrete compression members composed of high-strength materials, In *Proceedings of the 9th International Conference on Steel-Concrete Composite and Hybrid Structures „ASCCS 2009"*, Leeds, Research Publishing Services: Singapore, 2009, pp. 239–244. ISBN 978-981-08-3068-7.

Karmazínová, M. & Melcher, J. 2010a. Buckling of steel and steel-concrete compression members composed of high-strength materials", In *Proceedings of 10th International Conference "Modern Buildings Materials, Structures and Techniques"*, VGTU Vilnius, 2010, pp. 675–682. ISBN 978-9955-28-594-6.

Karmazínová, M. & Melcher, J. J. 2010b. Buckling resistance of steel-concrete columns composed of high-strength materials, In *Proceedings of the International Colloquium on Stability and Ductility of Steel Structures „SDSS'Rio 2010"*, Rio de Janeiro, 2010, pp. 895–902. ISBN 978-85-285-0137-7.

Karmazínová, M. & Melcher, J. J. 2011a. Design assisted by testing applied to the determination of the design resistance of steel-concrete composite columns, In *Proceedings of the 13th WSEAS International Conference on Mathematical and Computational Methods in Science and Engineering MACMESE '11*, WSEAS, Catania, 2011, pp. 420–425. ISBN 978-1-61804-046-6.

Karmazínová, M., Štrba, M. & Kvocák, V. 2011b. Steel-concrete composite members using high-strength materials in building constructions – structural design, actual behaviour, application, In *Proceedings of the 2nd European Conference on Civil Engineering "ECCIE'11"*, North Atlantic University Union, WSEAS: Puerto de la Cruz, Tenerife, 2011, pp. 47–52. ISBN 978-1-61804-057-2.

Karmazínová, M. 2012. Analysis of the actual behaviour, stress and moment capacity of composite beams composed of steel and glass-fibre-concrete, *International Journal of Mechanics*, Vol. 6, Issue 2, pp. 158–167. ISSN 1998-4448.

Kuranovas, A. & Kvedaras, A. K. 2007. Behaviour of hollow concrete-filled steel tubular composite elements, *Journal of Civil Engineering and Management*, Vol. 13, No. 2, 2007, pp. 131–141. doi: 10.3846/jcem.2010.40.

Melcher, J. Karmazínová, M. & Pozdíšek, J. 2009a. Experimental verification of behaviour of composite steel and glass-fibre-concrete beam, In *Proceedings of the 9th International Conference on Steel-Concrete Composite and Hybrid Structures „ASCCS 2009"* held in Leeds, Singapore: Research Publishing Services, 2009, pp. 390–395. ISBN 978-981-08-3068-7.

Melcher, J. Škaloud, M. Kala, Z. & Karmazínová, M. 2009b. Sensitivity and statistical analysis within the elaboration of steel plated girder resistance, *Advanced Steel Construction, an International Journal*, Vol. 5, No. 2, Hong Kong Institute of Steel Construction, June 2009, pp. 120–126. ISSN 1816-112X.

Liang, Q. Q. 2011. High-strength circular concrete-filled steel tubular slender beam-columns, Part II: Fundamental behaviour, *Journal of Constructional Steel Research*, Vol. 67, No. 2, 2011, pp. 172–180. ISSN 0143-974X.

Yu, Q. Tao, Z. & Wu, Y. X. 2008. Experimental behaviour of high-performance concrete-filled steel tubular columns, *Thin-Walled Structures*, Vol. 46, No. 4, 2008, pp. 362–370. ISSN 0263-8231.

EN 1993-1-1 *Design of Steel Structures – Part 1-1: General Rules and Rules for Buildings*, CEN Brussels, 2008.

EN 1994-1-1 *Design of Composite Steel and Concrete Structures – Part 1-1: General Rules and Rules for Buildings*, CEN Brussels, 2008.

Research and Applications in Structural Engineering, Mechanics and Computation – Zingoni (Ed.)
© 2013 Taylor & Francis Group, London, ISBN 978-1-138-00061-2

Behaviour of multi-span composite steel-concrete beams subjected to combined flexure and torsion

E.L. Tan
University of Western Sydney, Penrith, Australia

B. Uy
The University of New South Wales, Sydney, Australia

G. Hummam
University of Western Sydney, Penrith, Australia

ABSTRACT: This paper utilised experimental tests to provide further information and conclusions regarding composite steel-concrete beam specimens by examining the behaviour of multi-span composite steel-concrete beams which are subjected to combined actions of torsion and flexure for both full and partial shear connection and comparing the disparity in the varying degrees of shear connection. Generally, it was found that in the presence of torsion, there is no increase in the flexural capacity of a multi-span composite steel-concrete beam regardless of the degree of shear connection. Furthermore, there was no increase in the torsional capacity when flexure was present. In regards to shear connection, partial shear connection multi-span composite steel-concrete beam specimens attained nearly the same capacities in terms of both flexure and torsion as the full shear connection multi-span composite steel-concrete beam specimens. Additionally, it was discovered that the multi-span composite steel-concrete beam specimens achieved almost double the flexural capacities of similar single span composite steel-concrete beams. However, in terms of torsional capacity, there is a larger difference between multi-span composite steel-concrete beam specimens and single span composite steel-concrete beam specimens with multi-span composite steel-concrete beam specimens achieving more than three times the capacities of the single span specimens in certain cases.

1 INTRODUCTION

A great deal of research has been carried out in the field of composite steel-concrete beams. Yet, certain topics have been neglected or ignored in these researches. One of these issues is the behaviour of composite steel-concrete beams that are subjected to combined flexure and torsion. This topic has been researched by Ray and Mallick (1980), Nie et al. (2000), Thevendran et al. (2000) and Tan & Uy (2009a, b & 2011). However, the Australian Standard for composite members AS 2371.1 (Standards Australia, 2003) or other international standards on composite steel-concrete construction such as Euro-Code 4 (EN 1994-1-1, 2006), British Standard 5950 (BS 5950, 2000) or the American Institute of Steel Construction (AISC, 2006) does not cover this load combination.

Furthermore, much of the research and experiments on composite members has only considered full shear connection without looking at the effects of partial shear connection. This is a critical issue as partial shear connection composite beams have been shown to exhibit similar strength characteristics to full shear connection composite beams with increased ductility albeit at a reduced cost. Additional research into partial shear connections could produce further evidence that solidifies the fact that partial shear connection composite beams exhibit almost the same strength as full shear connection composite beams except at a fraction of the price.

Finally, more research needs to be performed on multi-span composite steel-concrete beams. The behaviour of multi-span composite beams is still largely unknown since the vast majority of research on composite steel-concrete beams has been carried out on single span members. Multi-span members are commonly used for bridges and highway interchanges and further knowledge on the behaviour of these members could vastly improve design techniques for these critical forms of infrastructure. Hence, multi-span composite steel-concrete beams will be examined for this paper.

The aim of this paper is to investigate the overall behaviour of multi-span composite steel-concrete beams subjected to combined flexure and torsion. This paper will aim to examine the characteristics and behaviours of multi-span composite steel-concrete beams, when the beams are subjected to varying

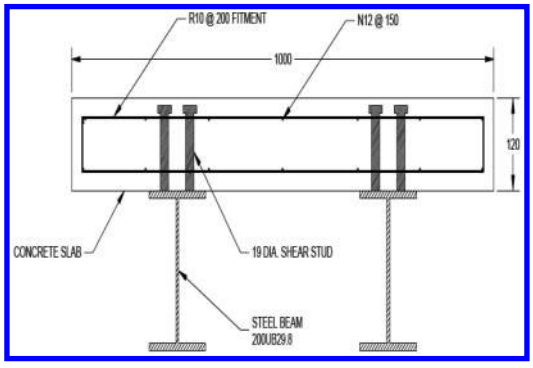


Figure 1. Typical Cross sectional view for multi-span composite steel-concrete beam.

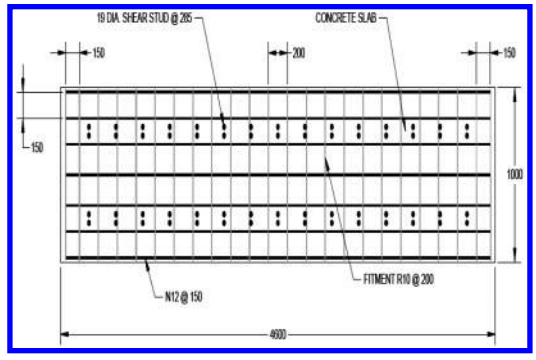


Figure 2. Typical plan view for multi-span composite steel-concrete beam.

degrees of flexure and torsion, by inspecting such traits as strength, torsional capacity, flexural capacity, deflection, interface slip, twist and failure modes. This paper will also investigate the main disparity between full shear and partial shear connection and their effects on multi-span composite steel-concrete beams and the difference between multi-span composite steel-concrete beams and single span composite steel-concrete beams. Finally, the interaction of torsion and flexure for multi-span composite steel-concrete composite beams will also be investigated.

2 EXPERIMENTAL PROGRAMME

2.1 *Details of test specimens*

A total of eight multi-span composite steel-concrete beam specimens were used in the experimental phase of this research. These included four beams with partial shear connection and four beams with full shear connection. All of the beams were 4600 mm in length with a simply supported span of 4000 mm. The beams were multi-span beams and consisted of two steel beams attached to one concrete slab for all the beams tested, for both full and partial shear connection.

The concrete slab for each composite beam was 1000 mm in width and 120 mm thick with a nominal compressive strength of 32 N/mm^2 for the concrete. As for the steel beam, a 200UB29.8 section was selected that encompasses a depth of 207 mm and a flange width of 134 mm. For each composite beam, 2 steel beams will be connected to the concrete slab as shown in Figure 1 and 2. Table 1 also highlights the details of all the multi-span composite beam specimens with their type of applied loading.

Table 1. Details of the test specimens.

Specimen	Shear connection (%)	Type of applied loading
MCBF1	100	Pure flexure
MCBF2		Low flexure & high torsion
MCBF3		Medium flexure & medium torsion
MCBF4		High flexure & low torsion
MCBP1	50	Pure flexure
MCBP2		Low flexure & high torsion
MCBP3		Medium flexure & medium torsion
MCBP4		High flexure & low torsion

2.2 *Experimental setup and procedure*

The test rig used for all of the experiments carried out on the multi-span composite steel-concrete beams was the INSTRON 1000 kN testing rig. The test rig has a maximum capacity of applying a total of 1000 kN. For different loading cases, the test rig was adjusted slightly to accommodate for the changes.

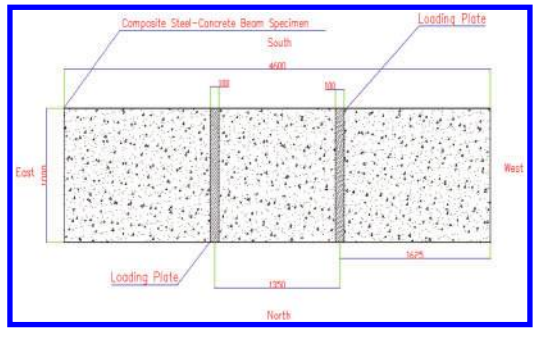


Figure 3. Loading setup for MCBF1 and MCBP1.

For each test, the beams were loading differently according to their type of applied loading. For MCBF1 and MCBP1, the loading plates were 100 mm wide and spanned the entire width of the concrete beam. Each loading plate was positioned 675 mm from the centre of the composite beam specimen which provided a loading span of 1350 mm as shown in Figure 3 and 4.

As for those beams such as MCBF2-4 and MCBP2-4 that required applied torque, the loading plate was positioned at a distance from the centre of the composite steel-concrete beam. An example for MCBF2 and MCBP2 which required low flexural and high torsional loading is showed in Figure 5 and 6.

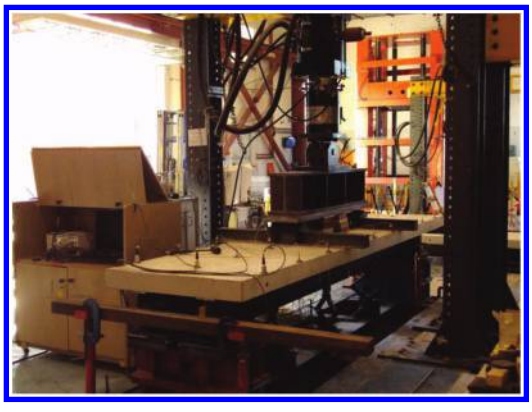


Figure 4. Test setup for MCBF1.

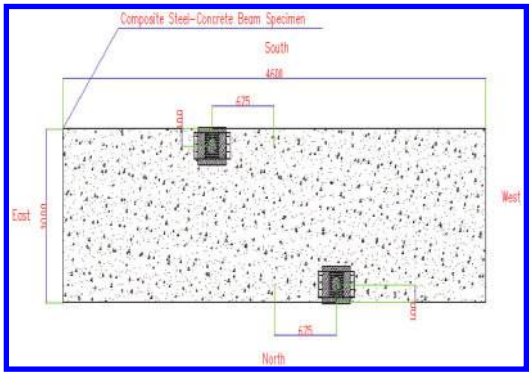


Figure 5. Loading setup for MCBF2 and MCBP3.

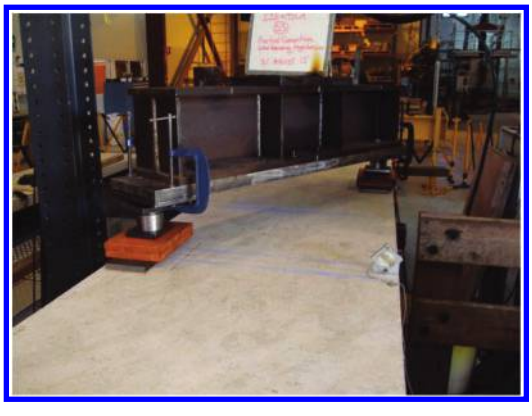


Figure 6. Test setup for MCBF2.

3 RESULTS AND DISCUSSION

3.1 *Flexural strength*

Table 2 shows the ultimate moment and the maximum mid-span deflection achieved by each composite beam specimen that was tested. As expected, the composite beam specimens that were subjected to higher degrees of flexure achieved a higher ultimate moment than the specimens that were subjected to higher degrees of torsion.

Table 2. Summary of ultimate moment and maximum mid-span deflection of all the beam specimens.

Specimen	Ultimate Load (kN)	Ultimate Moment (kNm)	Maximum mid-span deflection (mm)
MCBF1	646	428	114
MCBF2	415	275	20
MCBF3	522	346	45
MCBF4	597	395	60
MCBP1	591	392	150
MCBP2	372	247	17
MCBP3	512	339	71
MCBP4	577	382	94

Overall, the partial shear connection multi-span composite steel-concrete beam specimens achieved an average of 94% of the ultimate moment attained by the full shear connection multi-span composite steel-concrete beam specimens. The partial shear connection composite steel-concrete beam specimens demonstrated very high ultimate moments and applied loads when considering that they possess half the shear studs present in the full shear connection composite steel-concrete beam specimens. Especially when there was a combined action of flexure and torsion and the flexure induced was equal to or higher than the torque, the partial shear connection composite steel-concrete beam specimens attained almost the same strength as the full shear connection composite steel-concrete beam specimens albeit a difference of 2 or 3%.

Finally, by examining the results, it can be determined that in the presence of torsion, there is no increase in the flexural capacity of a multi-span composite steel-concrete beam. Furthermore, failure of the beam specimens arrives at an earlier stage when torsion is present since the beams fail in torsion in these cases and not by flexure. While, under higher levels of flexure, the beams failed by crushing of the concrete (flexural failure) and were able to achieve a higher applied load than the specimens that were loaded under higher levels of torsion.

3.2 *Torsional strength*

From Table 3, a total of six of the eight beams tested were subjected to some degree of torsion. After analysing the results, it is clear that the composite beam specimens that were subjected to higher degrees of torsion attained a higher torsional capacity than the composite beam specimens that were subjected to higher degrees of flexure. The only exception was beam MCBP3 which was subjected to medium torsion and medium flexure yet managed to attain a higher torsional strength than the partial shear connection composite beam specimen loaded under high torsion and low flexure, MCBP2. Additionally, regardless of

Table 3. Summary of ultimate torque and maximum twist of all the beam specimens.

Specimen	Ultimate Load (kN)	Ultimate Moment (kNm)	Maximum twist (mRad)
MCBF2	415	83	15
MCBF3	522	78	26
MCBF4	597	60	26
MCBP2	372	75	78
MCBP3	512	77	27
MCBP4	577	58	28

how high the amount of torque induced in the specimen was, the twist remained relatively low indicating that the beams only twisted slightly under the applied loads.

Overall, the partial shear connection multi-span composite steel-concrete beam specimens exhibited higher twist that the full shear connection multi-span composite steel-concrete beam specimens, except in the case of high torsion and low flexure. The beams loaded in this arrangement of high torsion and low flexure, MCBF2 and MCBP2, did not conform to this as the partial shear connection multi-span composite steel-concrete beam specimen, MCBP2, experienced a lower twist than the full shear connection multi-span composite steel-concrete beam specimen, MCBF2.

Furthermore, the presence of flexure did not cause any increase in the torsional strength. Overall, the partial shear connection composite steel-concrete beam specimens as well as the full shear connection composite steel-concrete beam specimens attained similar values of ultimate torque.

3.3 *Interface steel-concrete slip*

Overall, the interface slip between the concrete and the steel beams was greater for the partial shear connection multi-span composite steel-concrete beam specimens than for the full shear connection multi-span composite steel-concrete beam specimens as showed in Table 4. This was expected since the lower number of shear connector studs would obviously result in greater slip between the concrete-steel interface. Furthermore, the interface slip was greater in the specimens that were exposed to higher levels of flexure than the specimens that were exposed to higher levels of torsion. This leads to the conclusion that high flexure (or even pure flexure) will result in higher interface slip, while high torsion leads to lower values of interface slip.

3.4 *Crack patterns and failure modes*

The crack patterns and failure modes depended heavily on the type of loading the beam was subjected to rather than the degree of shear connection. The specimens subjected to pure flexure, MCBF1 and MCBP1, failed by flexure due to crushing of the concrete. This

Table 4. Summary of maximum interface slip of all the beam specimens.

Specimen	Maximum interface slip (mm)
MCBF1	1
MCBF2	4
MCBF3	0.7
MCBF4	0.8
MCBP1	1
MCBP2	3.1
MCBP3	1
MCBP4	1.7

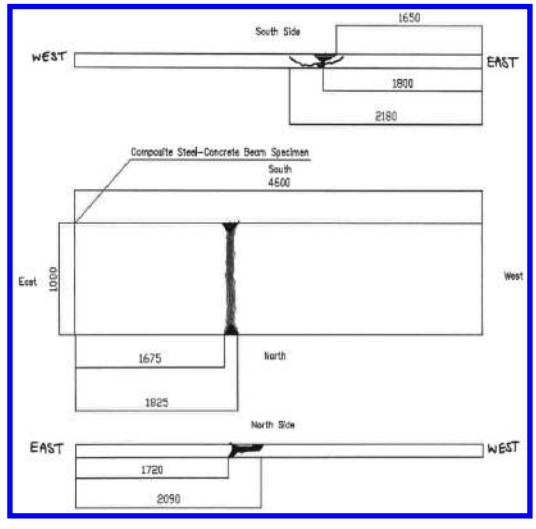


Figure 7. Crack patterns for MCBF1.

is evident in Figure 7 where it is visible that the cracking and crushing of the concrete occurred in the areas where the loading plates where located for MCBF1.

Beams MCBF2 and MCBP2, both loaded under medium torsion and medium flexure, failed in the same manner as beams MCBF3 and MCBP3 which was torsional failure. This can be clearly seen in Figure 8 as the cracks in MCBF3 developed all over the top surface of the concrete and numerous slightly horizontal cracks occurred on the North and South sides as well. Furthermore, beams MCBF3 and MCBP3 developed cracks on the bottom side of the concrete slab as well.

Finally, the beams loaded under high flexure and low torsion, MCBF4 and MCBP4, failed by crushing of concrete (flexural failure) similar to beams MCBF1 and MCBP1. The cracking of these two beams was localised in the area between where the two loading plates were located and consisted of deep cracks.

3.5 *Interaction flexure-torsion diagram*

Figure 9 illustrate the interaction diagram for the full and partial shear connection multi-span composite

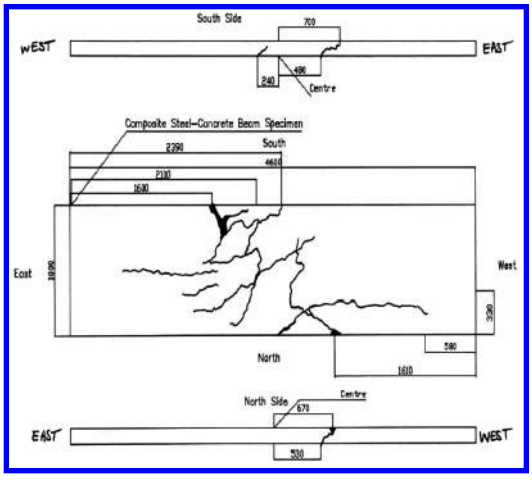


Figure 8. Crack patterns for MCBF3.

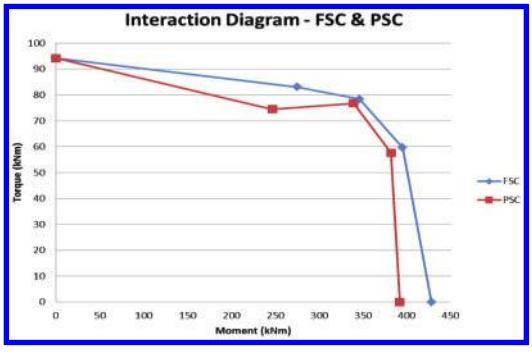


Figure 9. Interaction flexure-torsion diagram.

steel-concrete beam specimens. A point for each beam specimen is plotted on the graph (torque against moment). As one can deduce from Figure 9, the strength characteristics of the partial shear connection multi-span composite steel-concrete beam specimens is almost similar to the full shear connection multi-span composite steel-concrete beam specimens especially in the cases of medium flexure and medium torsion as well as high flexure and low torsion loading cases.

3.6 *Comparison with single span beams*

Similar to the research carried out for this paper, Tan & Uy (2009a) conducted experiments on straight composite steel-concrete beams subjected to combined flexure and torsion. The only distinction between this research and Tan & Uy (2009a) would have to be the size of the beam specimens and the number steel beams utilised.

From Figure 10, the ultimate moment attained by the multi-span composite steel-concrete beam specimens in this paper was larger than that of the single span composite steel-concrete beam. This was expected since the composite beam specimens tested

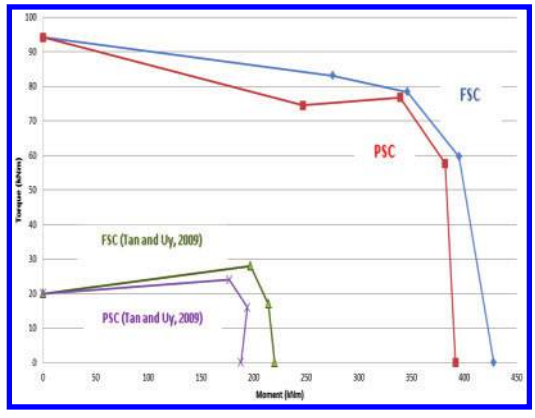


Figure 10. Comparison between the interaction flexure-torsion diagrams for multi and single span beams.

for this research were double the size of the specimens utilised in the experiments by Tan & Uy (2009a). For the specimens subjected to pure flexure, CBF-1 attained 51% of the flexural capacity of MCBF1, while CBP-1 attained 48% of the flexural capacity of MCBP1. This demonstrates that when loaded under pure flexure, the multi-span composite steel-concrete composite beams attain a flexural capacity roughly twice that of a single span composite steel-concrete beam. When considering the beams loaded under high flexure and low torsion, the same conlusion can be made since CBF-2 attained 54% of the flexural capacity of MCBF4 and CBP-1 attained 50% of the flexural capacity of MCBP4, the multi-span composite steel-concrete beam specimens achieve roughly double the flexural capacity of the single span beams for both full and partial shear connection.

However, when examining the specimens that were loaded under high torsion and low flexure, it is evident that CBF-3 achieved 72% of the flexural capacity of MCBF2 while CBP-3 achieved 72% of the flexural capacity of MCBP2. This demonstrates that the single span composite beam specimens obtained roughly 72 % of the flexural strength of the multi-span composite beam specimens.

4 CONCLUSIONS

In conclusion, in the presence of torsion, there is no increase in the flexural capacity of a multi-span composite steel-concrete beam, whilst in the presence of flexure did not cause any increase in the torsional capacity in the multi-span composite steel-concrete beam specimens.

In terms of failure modes, multi-span composite steel-concrete beams loaded under high flexure failed due to the crushing of the concrete while the multi-span composite steel-concrete beams loaded under higher levels of torsion failed due to shear torsional failure.

Multi-span composite steel-concrete beams subjected to higher degrees of torsion attained a higher torsional capacity than the specimens that were subjected to higher degrees of flexure.

Regardless of how high the amount of torsion was induced in the specimen, the twist remained relatively low indicating that the multi-span composite steel-concrete beams only twisted slightly under the applied loads. The twist of a multi-span composite beam specimen, when subjected to torsion, will be relatively similar regardless of the degree of shear connection.

The flexural capacity of partial shear connection multi-span composite steel-concrete beams is roughly similar to that of the full shear connection multi-span composite steel-concrete beams. This is especially true in the case of high flexure.

When a high degree of flexure was present, the multi-span composite steel-concrete beam specimens actually attained higher values of twist than the specimens that were exposed to high torsion. Overall, the partial shear connection multi-span composite steel-concrete beam specimens exhibited higher twist that the full shear connection multi-span composite steel-concrete beam specimens, except in the case of high torsion and low flexure loading.

The interface slip between the concrete and the steel was greater for the partial shear connection multi-span composite steel-concrete beam specimens than for the full shear connection multi-span composite steel-concrete beam specimens.

The disparity in flexural strength between full shear and partial shear specimens is lower in multi-span composite steel-concrete beams than in single span composite steel-concrete beams. Additionally, the degree of shear connection has a lower effect on flexural strength when considering multi-span composite steel-concrete beams than when considering single span composite steel-concrete beams.

REFERENCES

American Institute of Steel Construction. 2006. AISC steel construction manual. (13 ed.). *American Institute of Steel Construction*.

British Standards Institution. 2000. BS 5950-1-2000. Structural use of steelwork in building. Code of practice for design. Rolled and welded sections. *BSI Standards*.

EN 1994-1-1. 2006. Design of composite steel and concrete structures, Part1.1: General rules and rules for building. Brussels.

Nie, J., Luo, L. & Hu, S. 2000. Experimental study on composite steel-concrete beams under combined bending and torsion. *Composite and Hybrid Structures*, 2, 631–638.

Ray, M.B. & Mallick, S.K. 1980. Interaction of flexure and torsion in steel-concrete composite beams. *The Indian Concrete Journal*, 54, 80–83.

Standards Australia. 2003. Australian Standard AS 2327.1-2003 Composite structures, Part 1: Simply supported beams. Standards Australia International Ltd.

Tan, E.L. & Uy, B. 2009a. Experimental study on straight composite beams subjected to combined flexure and torsion. *Journal of Constructional Steel Research*, 65, 784–793.

Tan, E.L. & Uy, B. 2009b. Experimental study on curved composite beams subjected to combined flexure and torsion. *Journal of Constructional Steel Research*, 65, 1855–1863.

Tan, E.L. & Uy, B. 2011. Nonlinear analysis of composite beams subjected to combined flexure and torsion. *Journal of Constructional Steel Research*, 67, 790–799.

Thevendran, V., Chen S., Shanmugam, N.E. & Richard Liew, J.Y. 2000. Experimental study on steel-concrete composite beams curved in plan. *Engineering Structures*, 22, 877–889.

Research and Applications in Structural Engineering, Mechanics and Computation – Zingoni (Ed.)
© 2013 Taylor & Francis Group, London, ISBN 978-1-138-00061-2

Considerations on the long-term behaviour of composite steel-concrete bridges

G. Ranzi
School of Civil Engineering, The University of Sydney, Sydney, NSW, Australia

G. Leoni
School of Architecture and Design, University of Camerino, Ascoli Piceno, Italy

L. Dezi
Department of Architecture, Construction and Structures, Universita' Politecnica delle Marche, Ancona, Italy

R. Zandonini
Department of Civil, Environmental and Mechanical Engineering, University of Trento, Trento, Italy

ABSTRACT: This paper deals with the service behaviour of composite steel-concrete bridges, with particular attention devoted to how this is influenced by the time-dependent behaviour of the concrete, such as creep and shrinkage. The paper outlines some of the main aspects which need to be addressed in service design, which include the evaluation of the influence of creep and shrinkage on the stress state and deformations induced in the concrete slab and steel girder, and how these vary with time when the composite bridge is subjected to external static loads, geometrical actions and shrinkage effects. Considerations are also provided on how shear-lag effects, the shear deformability of the steel girder and different casting sequences specified during construction affect the deformations and stress distributions of a composite steel-concrete bridge over time.

1 INTRODUCTION

Composite steel-concrete construction represents a widely used form of construction for bridge applications thanks to its ability to well combine the advantages of both steel and concrete. In fact, composite members exhibit enhanced strength and stiffness when compared to the contribution of their components acting separately. The composite action is provided by means of shear connectors, welded to the top flange of the steel and embedded in the concrete during casting. The composite response at service condition is highly dependent on the deformability of the shear connectors, which enables relative movements to occur between the slab and the steel beam. This kinematic behaviour, in which slip can occur between the two components, is usually referred to as partial shear interaction.

This paper outlines some important considerations related to the service behaviour of composite bridges, with particular attention devoted to how this is influenced by the time-dependent behaviour of the concrete, such as creep and shrinkage. Extensive work has been carried out to date in this area. Despite this, it is beyond the scope of this paper to provide a review of the current state of the art in this area and, for this purpose, reference should be made to (Ranzi et al. 2013). In particular, this paper describes how time effects influence the deformations and internal stresses in composite bridges when subjected to external static loads, geometrical actions, shrinkage effects, and how the time-dependent composite response is affected by shear-lag effects, by the shear deformability of the steel girder and by different casting sequences specified during construction.

2 STATIC ACTIONS

Composite beams subjected to static actions exhibit an increase in deflections and deformations over time as well as a redistribution of stresses between steel beam and slab due to cross-section heterogeneity. This is illustrated in Figure 1 for a typical two-span continuous beam subjected to a uniformly distributed load. (Dezi & Tarantino 1993, Bradford & Gilbert 1992, Amadio & Fragiacomo 1993, Gilbert & Ranzi 2011)

Considering the applied external actions to remain constant with time, the resultant bending moment $M(z,t)$ (Figure 2b) does not undergo significant changes, as can also be highlighted in Figure 2d by the variation in time of the reaction at the inner support (R) is plotted. Theoretically, these differences

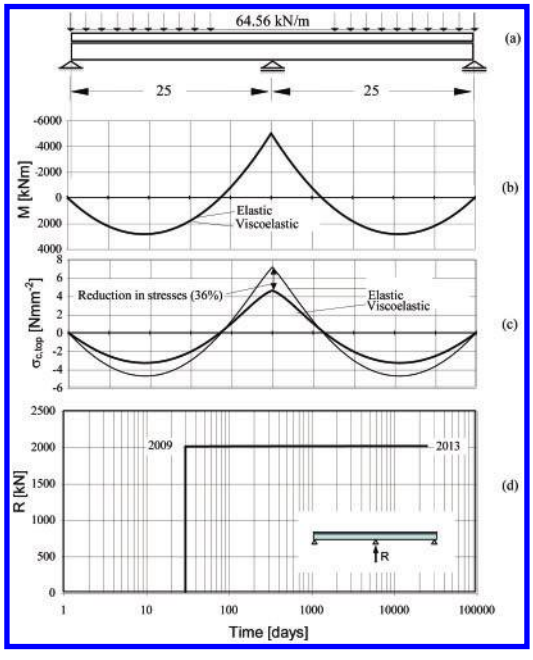


Figure 1. Effects of static actions on composite girders.

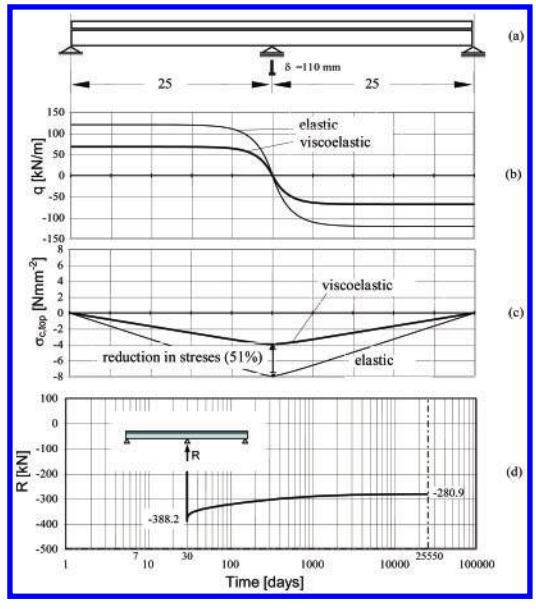


Figure 2. Effects of geometrical actions on composite girders.

become negligible for composite beams with stiff shear connections and where the only stress redistributions taking place are those between the concrete slab and the steel girder, with slab unloading over time and redistributing its stresses to the steel component. Under these ideal conditions, it could be possible to describe this time-dependent composite behaviour relying on the first theorem of linear visco-elasticity (CEB 1988, Dezi & Tarantino 1993) as follows: in composite steel-concrete prismatic beams with stiff connection and rigid restraints, subjected to static actions (also varying in time), the reactions and, consequently, the resultant bending-moment distribution coincide with those calculated with a purely elastic analysis. On the other hand, internal stresses, strains and displacements must be evaluated by summing the effects induced by creep to the corresponding elastic quantities.

For practical applications, negligible errors are made by evaluating the redundant restraint reactions under the assumption of stiff connection, while displacements should be calculated taking into account the flexibility of the shear connection.

3 GEOMETRICAL ACTIONS

Geometrical actions, such as support settlements, lead to a time-dependent response well represented by the classical relaxation behaviour, which produce a reduction in time of the self-equilibrated reaction forces and of the stress state in the concrete slab. Assuming the geometrical actions to remain constant in time, the displacements calculated in each cross-section of a bridge do not vary sensibly with time and, theoretically, vanish when specifying a stiff shear connection. It is possible to describe this trend following the second theorem of linear visco-elasticity as (CEB 1988, Dezi & Tarantino 1993): in composite steel-concrete prismatic beams with stiff shear connection and rigid restraints, and subjected to geometrical actions (also varying in time), the rotations and the displacements coincide with those calculated with a purely elastic analysis. On the other hand, internal strains, stresses and reactions must be evaluated combining the effects induced by creep to those obtained from the elastic response.

Suitable settlements are often imposed in order to control the tension of the slab in the hogging moment regions. An example related to a two-span composite beam is provided in Figure 2. For shear connection rigidities in the range of practical interest, the longitudinal normal stress (σ_c) is almost halved over time due to creep effects as shown in Figure 2c, therefore considerably reducing in time the benefits provided to the structure by this prestressing technique.

4 SHRINKAGE

Shrinkage is the result of the concrete volume reduction which takes place over time and is independent from applied loads. (CEB 1988, Gilbert & Ranzi 2011) In composite beams, the presence of the shear connection prevents the free shortening of the slab so that a distribution of shear forces takes place over time at the interface. In particular, the distribution of the shear force (q) is characterised by peaks at the beam ends, which are strongly influenced by the shear connection

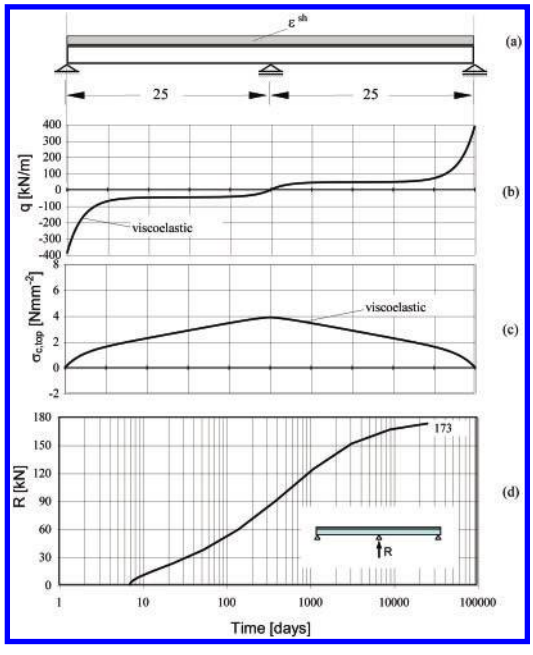


Figure 3. Effects of shrinkage on composite girders.

stiffness. This trend is outlined in Figure 3 for the case of a two-span composite beam. In statically indeterminate structures, a self-equilibrated system of reactions develops in time due to shrinkage effects, as depicted in Figure 3d considering the reaction of the internal support.

The distributions of internal actions, induced by concrete shrinkage and evaluated for different values of the shear connection stiffness, produce differences only at the ends of the spans. Under the assumption of stiff shear connection, it is possible to obtain acceptable results at locations away from the beam ends and from the internal supports. However, this approach does not allow for evaluation of the peak values exhibited for the shear force transmitted at the shear connection (Dezi 1994). Shrinkage also occurs and influences the time-dependent deflections and deformations of composite beams. Its effects are generally more pronounced than those observed in reinforced concrete structures due to the eccentricity of the concrete slab with respect to the overall cross-section.

5 SHEAR-LAG EFFECTS AND CONCRETE SLAB EFFECTIVE WIDTH

When a composite beam is subjected to external loads or deformations, the slab cross-section looses its planarity due to the concentrated forces induced by the shear connectors. This behaviour tends to produce higher longitudinal deformations within the slab in the vicinity of the connectors' line which decrease when moving away from the steel beam. This warping effect

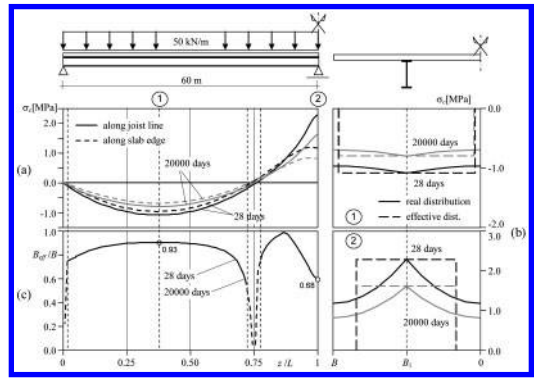


Figure 4. Uniformly distributed load: (a) stress distribution along the bridge axis; (b) stresses at the slab mid-height at two locations; (c) variation of the effective width along the bridge axis.

is usually referred to as shear-lag and its magnitude is dependent upon the type of applied action and support conditions.

From a design viewpoint, it is usually more convenient to remain within Bernoulli beam theory simplifying the analysis with the effective width method, in which plane sections remain plane after deformation and a constant stress is assumed over a modified effective slab width. This approach makes possible to obtain results 'equivalent' to those calculated with rigorous analyses reducing the width of the slab to the effective one. Work carried out to date on the influence of the time dependent response of concrete on the effective width values highlighted how the latter do not vary with time when considering static actions and geometric settlements. As a consequence, the effective width expressions adopted for the instantaneous cases can be applied also when accounting for time effects. In the case of prestressing, it was observed that there is a time-dependent decrease of the effective width and that areas in the vicinity of the prestressing anchorages are heavily affected by shear-lag, e.g. (Dezi et al. 2006a).

Typical results observed for two-span continuous composite bridges are depicted in Figures 4 and 5 for the cases of a uniformly distributed load applied at 28 days from concrete casting and of the settlement of the internal support. In both cases, stresses and effective width values calculated from the instantaneous (at 28 days) and time-dependent (at 20000 days) analyses are provided. To emphasise the occurrence of shear-lag effects, values plotted in the figures show variations along the slab edge and along the joist's line. For example, Figures 4a-b highlight how the edge stresses are typically smaller than those produced above the steel joist and these variations become more pronounced at the internal support (Gara et al. 2008). Considering the cross-sections of maximum positive and negative moments, i.e. located at about 0.375 L and L from the bridge end, respectively (where L is the length of one span), it can be observed that while the stress magnitudes vary with time, their actual trend

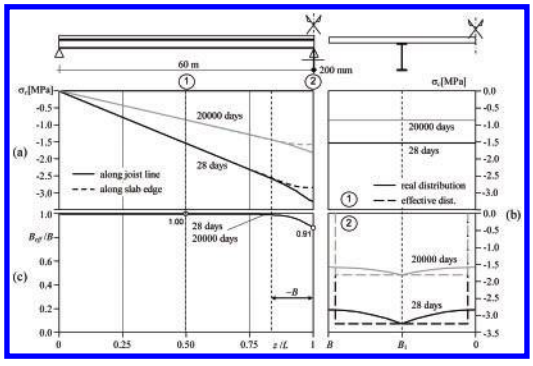


Figure 5. Support settlement: (a) stress distribution along the bridge axis; (b) stresses at the slab mid-height at two locations; (c) variation of the effective width along the bridge axis.

remains constant (Figure 4b). The consequence of this behaviour is that the effective width does not vary with time, as shown in Figure 4c. Considering the trend of the effective width, a linear variation is attained close to the internal support whereas, in sagging regions, it is almost constant. It is worth noting that for sections located in the regions where the bending moment is about zero, the calculated effective widths approach zero because of the low stresses in the vicinity of the contraflexure points: these values are not significant from a design viewpoint.

Similarly to the case of concentrated transverse forces, settlements of the supports produce shear force resultants varying stepwise at the location of the support. Under these loading conditions, the warping due to shear is constant along the member axis, except in the vicinity of the supports in accordance with Saint Venant's conditions. Even if the warping is non zero, the distribution of longitudinal stresses within the concrete slab is uniform and the effective width coincides with the geometric width. This trend is reflected by the results plotted in Figure 5.

6 SHEAR DEFORMABILITY OF THE STEEL GIRDER

The shear deformability of the steel girder significantly influences the magnitude of deformations and displacements exhibited by a composite bridge, especially when considering the relatively high plate element slenderness commonly specified in real applications.

The influence of the shear deformability of the steel girder on the structural response is outlined in Figure 6 based on the results of an extensive parametric study carried out on 200 realistic composite steel-concrete bridge arrangements designed with Australian guidelines (Rapattoni et al. 1998). These include both simply-supported and three-span continuous systems subjected to a uniformly distributed load (Ranzi & Zona 2007). For the shear connection rigidity, two limit cases have been considered with consist

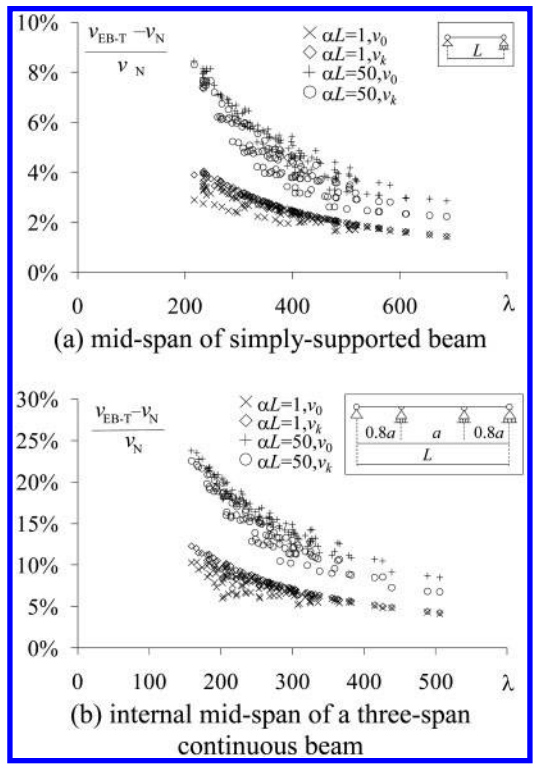


Figure 6. Differences between values calculated with the EB-T (v_{EB-T}) and Newmark (v_N) models.

of low ($\alpha L = 1$) and high ($\alpha L = 50$) shear connection stiffness, where αL is a dimensionless parameter commonly used in the literature.

The analytical model accounting for the shear deformability of the steel beam is derived coupling a Euler-Bernoulli beam model for the concrete slab with a Timoshenko beam model for the steel girder (referred to as EB-T model). Its results are compared with the classical Newmark model which considered two Euler-Bernoulli beams for the slab and steel beam. In this case, the analytical representations accounts for only the flexural deformations of the two components.

Based on these two models, the variations between the mid-span deflections calculated for the simply-supported bridges are outlined in Figure 6a, as a function of a dimensionless parameter λ which accounts for the flexural rigidity of the steel, its shear rigidity and bridge span. The shear connection stiffness significantly affects the discrepancy between these results. For low values of shear connection stiffness, the maximum difference between the two models remains within 4%, while this more than doubles for high shear connection rigidities, i.e. with maximum differences slightly greater than 8%. The concrete time-dependent behaviour tends to decrease these variations for high levels of shear connection stiffness while an opposite trend is noted with low stiffness. For clarity, t_0 and t have been introduced to denote the instant in time of

first loading and the one of interest in the time domain, respectively.

Similar trends can be observed for the three-span beam configurations (Figure 6b), even if the differences obtained for the indeterminate structure is significantly increased. Long-term effects tend to reduce these differences for high levels of shear connection stiffness while leading to an opposite result for low connection stiffness. This increase is justified by the consideration that shear deformations are not reduced by the continuity of a beam, as it occurs for flexural deformations.

7 EFFECTS OF EARLY AGE SHRINKAGE AND CONSTRUCTION PHASES

The behaviour of the early age concrete and the planning of the casting sequences have an important role in the concrete cracking phenomenon during construction of continuous steel-concrete composite bridge decks. In fact, in the case of long viaducts, the slab needs to be poured on unpropped steel beams fractionating the casting process. The weights of the concrete and of the travelling formworks may induce tensile stresses in the slab sections which have already hardened, e.g. (Ducret & Lebet 1999, Mari et al. 2003, Dezi et al. 2006b).

The behaviour of early age concrete characterised by significant shrinkage effects such as endogenous chemical shrinkage, thermal shrinkage due to cooling of the hardened concrete and drying shrinkage, is responsible for inducing further tensile stresses. The early cracking may affect not only the hogging regions but even the sagging regions which are usually considered uncracked. The phenomenon can be controlled by optimising the concrete pouring sequences by casting the slab sections first in the centre of each span and then over the interior supports. A basic role is played by the rheology of the early age concrete; in fact, tensile creep is involved in the incipient cracking mechanism and non linear phenomena are expected since tensile stresses are almost equal to the relevant strength.

The influence of different casting sequences is outlined considering case study of a 12 span continuous steel-concrete composite bridge with span lengths varying from a minimum of 55 m (for the external spans) to a maximum of 120 m (for the central span) for a total length of about 1 km. The slab is poured on precast-deck elements used as formworks. With reference to the longitudinal direction, a casting speed of 43 m/day is considered in the calculation. It is assumed that the concrete setting ends at 12 hours from pouring and that the curing duration is two days. Three casting schemes are considered: a continuous sequence from one end to the other end of the deck, referred to as scheme (a), and two fractionated sequences consisting in alternating the casting of a sagging segment to that of a hogging segment, denoted as schemes (b) and (c). Scheme (b) differs from scheme (c) for the length

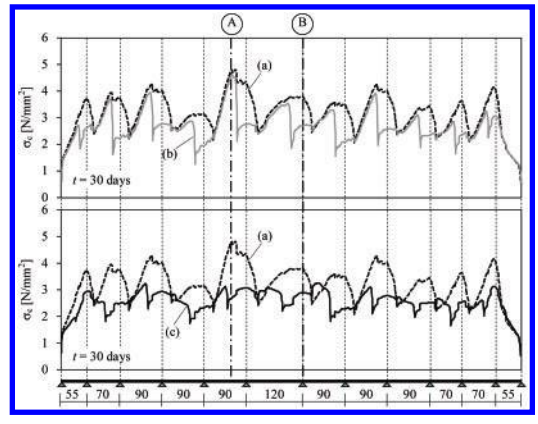


Figure 7. Concrete stresses at the end of constructive phases ($t = 30$ days).

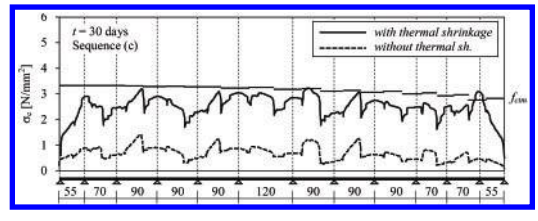


Figure 8. Influence of the thermal shrinkage on the tensile stress state.

of the various segments: in the first case sagging and hogging segments are chosen so as to be symmetric with respect to the axes of the relative spans (for sagging segments) and supports (for hogging segments); in the second case the sagging sections are reduced and the hogging section enlarged in a non-symmetric way.

Figure 7 shows the stresses, measured at the concrete slab mid-plane at the end of the slab construction, produced by the continuous and fractionated castings. All the slab segments are affected by tensile stresses for both cases of continuous and fractionated casting: in the case of continuous casting the maximum stresses are observed to occur in the hogging moment regions while in the fractionated castings these take place in the sagging moment regions. The differences between the two fractionated sequences can be summarised as follows: sequence (b) is not effective in limiting concrete tractions because the same stress levels of sequence (a) are achieved in the sagging moment regions despite the significant stress reduction produced in the hogging moment regions; on the contrary, sequence (c), obtained with non-symmetric sections, permits a sensible reduction of the stresses.

Figure 8 shows the importance of the thermal shrinkage and demonstrates that it is responsible for more than 50% of the tensile stresses at the end of casting (30 days). Structural analyses would be strongly not realistic and non conservative in predicting the bridge cracking tendency if thermal shrinkage was neglected.

8 CONCLUSIONS

This paper presented some of the main aspects to be considered in the design at service conditions of composite steel-concrete bridges. The main focus has been related to the influence of the time-dependent behaviour of the concrete on the stress state and deformations induced in the composite member. Particular considerations have been provided on how time effects influence the composite response when subjected to external static loads, geometrical actions and shrinkage effects, and how this is affected by shear-lag effects, by the shear deformability of the steel girder and by different casting sequences specified during construction affect the deformations and stress distributions of a composite steel-concrete bridge over time.

ACKNOWLEDGEMENTS

The work in this article was supported by the Australian Research Council through its Discovery Projects funding scheme (DP110103028).

REFERENCES

Amadio C, Fragiacomo M. A finite element model for the study of creep and shrinkage effects in composite beams with deformable shear connections. Construzioni Metalliche 1993; 4: 213–228.

Bradford MA, Gilbert RI. Composite beams with partial interaction under sustained loads. Journal of Structural Engineering ASCE 1992; 118(7): 1871–1883.

CEB. CEB design manual on structural effects of time dependent behavior of concrete" C.E.B. Bullettin d'information n.142/142 bis, Georgi Publ. Co., Saint-Saphorin, Switzerland 1988.

Dezi L, Gara F, Leoni G. Effective slab width in prestressed twin-girder composite decks. Journal of Structural Engineering ASCE 2006a; 132(9): 1358–1370.

Dezi L, Gara F, Leoni G. Construction sequence modelling of continuous steel-concrete composite bridge decks. Steel and Composite Structures 2006b; 6(2): 123–139

Dezi L, Tarantino AM. Creep in composite continuous beams. I: Theoretical treatment. Journal of Structural Engineering ASCE 1993; 119(7): 2095–2111.

Dezi L. Shrinkage effects in composite continuous beams with flexible connection. Journal of Constructional Steel Research 1994; 28(3): 295–320.

Ducret JM, Lebet JP. Behaviour of composite bridges during construction. Structural Engineering International 1999; 3: 212–218

Gara F, Ranzi G, Leoni G. Analysis of the shear lag effect in composite bridges with complex static schemes by means of a deck finite element. International Journal of Steel Structures 2008; 8: 249–260.

Gilbert RI, Ranzi G (2011) Time-dependent behaviour of concrete structures, Spon Press, London, UK.

Mari A, Mirambell E, Estrada I. Effects of construction process and slab prestressing on the serviceability behaviour of composite bridges. Journal of Constructional Steel Research 2003; 59: 135–163.

Ranzi G, Leoni G, Zandonini R. State of the art on the time-dependent behaviour of composite steel-concrete structures. Journal of Constructional Steel Research 2013; 80: 252–263.

Ranzi G, Zona A. A steel-concrete composite beam model with partial interaction including the shear deformability of the steel component. Engineering Structures 2007; 29(11): 3026–3041.

Rapattoni F, Eastwood D, Bennett M, Cheung H. Composite steel road bridges – concepts and design charts, 1998, BHP Integrated Steel.

Research and Applications in Structural Engineering, Mechanics and Computation – Zingoni (Ed.)
© 2013 Taylor & Francis Group, London, ISBN 978-1-138-00061-2

Nonlinear inelastic analysis of 3D composite steel-concrete frameworks

C.G. Chiorean, M. Buru, A. Chira & I. Marchis
Technical University of Cluj-Napoca, Faculty of Civil Engineering, Cluj-Napoca, Romania

ABSTRACT: This paper presents an efficient computer method for nonlinear inelastic analysis of three-dimensional composite steel-concrete frameworks. The proposed formulation is intended to model the geometrically nonlinear inelastic behaviour of composite frame elements using only one element per physical member. The behaviour model accounts for material inelasticity due to combined bi-axial bending and axial force, gradual yielding is described through basic equilibrium, compatibility and material nonlinear constitutive equations. Tangent flexural rigidity of cross-section is derived and then using the flexibility approach the elasto-plastic tangent stiffness matrix and equivalent nodal loads vector of 3-D beam-column element is developed. The proposed nonlinear analysis formulation has been implemented in a general nonlinear static purpose computer program. A computational example is given to validate the effectiveness of the proposed method and the reliability of the code.

1 INTRODUCTION AND RESEARCH SIGNIFICANCE

In recent years, have witnessed significant advances in nonlinear inelastic analysis methods for steel and composite steel-concrete framed structures and integrate them into the new and more rational advanced analysis and design procedures (Li & Li 2007). Reliable nonlinear analysis tools are, for instance, essential in performance-based earthquake engineering, and advanced analysis methodologies, that involves accurate predictions of inelastic limit states up or beyond to structural collapse. There currently exist several methods and computer programs concerning the nonlinear inelastic analysis that calculate strength limit states of steel and composite steel-concrete frame structures. At one extreme, two- and three dimensional finite elements enhanced with advanced material constitutive laws were used to investigate the nonlinear response of steel and composite steel-concrete frame members. Currently the available tools for such analysis are general purpose FE programs that require very fine-grained modelling that is often impractical to the structural engineer. At the other extreme, the line elements approach in conjunction with either distributed or concentrated plasticity models, have been devoted to the development of nonlinear analysis tools for frames that provide a desirable balance between accuracy and computational efficiency (Ngo-Huu & Kim, 2012; Iu et al. 2009; Izzudin et al. 2002, Chiorean 2009). In spite of the availability of such nonlinear inelastic algorithms and powerful computer programs, the nonlinear inelastic analysis of real large-scale frame structures still posses huge demands on the most powerful of available computers and still represents unpractical tasks to most designers.

The present work attempts to develop accurate yet computational efficient tools for the nonlinear inelastic analysis of real large-scale 3D composite steel-concrete frameworks fulfilling the practical and advanced analysis requirements. Essentially, nonlinear inelastic analysis employed herein uses the accuracy of the fiber elements approach for inelastic frame analysis and address its efficiency and modelling shortcomings both to element level, through the use of only one element to model each physical member of the frame, and to cross-sectional level through the use of path integral approach to numerical integration of the cross-sectional nonlinear characteristics.

2 MATHEMATICAL FORMULATION

2.1 *Basic assumptions and constitutive material models*

The following assumptions are adopted in the formulation of analytical model: (1) plane section remain plane after flexural deformation; no slip occurs at the steel-concrete interface, full composite action is considered (2) warping and cross-section distortion are not considered; (2) torsional buckling do not occur; (3) small strain but arbitrarily large displacements and rotations are considered. The proposed approach is based on the most refined type of second order inelastic analysis, distributed plasticity model, where elasto-plastic behaviour is modelled accounting for spread-of plasticity effect in sections and along the element and employs modelling of structures with only one line element per member, which reduces the number of degree of freedom involved and the computational time. Consider the cross-section subjected to the action of the

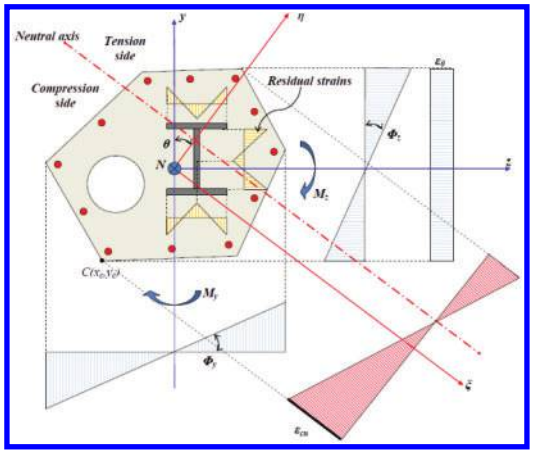


Figure 1. Model of arbitrary composite cross-section.

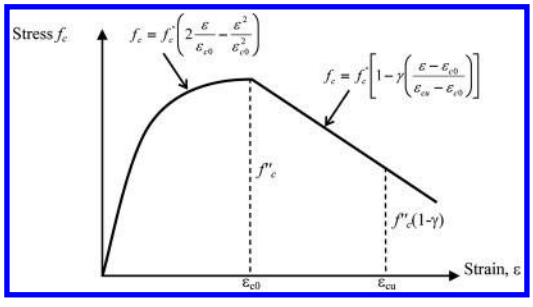


Figure 2. Stress-strain relationships for concrete in compression.

external bending moments about both global axes and axial force as shown in Figure 1.

The cross-section may assume any shape with multiple polygonal or circular openings. The constitutive relation to model the concrete under compression is represented by a combination of a second-degree parabola (for ascending part) and a straight line (for descending part), as depicted in Figure 2, where γ represents the degree of confinement in the concrete. Multi-linear elastic-plastic stress-strain relationships, both in tension and in compression, is assumed for the structural steel and the conventional reinforcing bars.

2.2 *Elasto-plastic flexural rigidity of cross-section*

Considering the cross-section subjected to the action of the external bending moments (M_y, M_z) about each global axes and axial force (N) as shown in Figure 1. The origin of the reference axis is usually considered in the geometric centroid of the cross-section. Under the above assumptions the resultant strain distribution corresponding to the curvatures about global axes $\mathbf{\Phi} = [\Phi_y \quad \Phi_z]$ and the axial strain ε_0 can be expressed in point $\mathbf{r} = [y \quad z]$ in a linear form as:

$$\varepsilon = \varepsilon_0 + \Phi_y z + \Phi_z y + \varepsilon_r = \varepsilon_0 + \mathbf{\Phi}\mathbf{r}^T + \varepsilon_r \qquad (1)$$

where ε_r represents the initial deformation produced by residual stresses, and is taken into account inabove equation only for the structural steel. The equilibrium is satisfied when the external forces (N, M_y, M_z) are equal to the internal ones. These conditions can be represented mathematically in terms of the following nonlinear system of equations as:

$$\begin{cases} \int_{A_{cs}} \sigma\left(\varepsilon\left(\varepsilon_0, \phi_y, \phi_z\right)\right) dA_{cs} - N = 0 \\ \int_{A_{cs}} \sigma\left(\varepsilon\left(\varepsilon_0, \phi_y, \phi_z\right)\right) z dA_{cs} - M_y = 0 \\ \int_{A_{cs}} \sigma\left(\varepsilon\left(\varepsilon_0, \phi_y, \phi_z\right)\right) y dA_{cs} - M_z = 0 \end{cases} \qquad (2)$$

in which $\varepsilon_0, \phi_y, \phi_z$ represent the unknowns and the surface integral is extended over concrete and structural steel areas (A_{cs}). The above system can be solved numerically using, for instance, the load-controlled Newton method and taking into account the fact that the stresses are implicit functions of the axial strain and curvatures through the resultant strain distribution given by the Equation (1). The tangent stiffness matrix for the cross section relates small changes in the deformations to small changes in the actions sustained. The incremental relationships between incremental efforts and incremental deformations can be expressed as:

$$\begin{bmatrix} k_{11} & k_{12} & k_{13} \\ k_{21} & k_{22} & k_{23} \\ k_{31} & k_{32} & k_{33} \end{bmatrix} \cdot \begin{bmatrix} \Delta\varepsilon_0 \\ \Delta\phi_y \\ \Delta\phi_z \end{bmatrix} = \begin{bmatrix} \Delta N \\ \Delta M_y \\ \Delta M_z \end{bmatrix} \qquad (3)$$

where the coefficients of the tangent stiffness matrix k_{ij} are evaluated considering the strains and stresses at equilibrium for given external actions. Tangent flexural rigidities for major and minor axis bending under conditions of constant axial load are evaluated by inverting the cross-section tangent stiffness matrix, imposing the condition of constant axial load to obtain a flexural flexibility matrix and inverting this to find the tangent flexural rigidities, about each principal axis, at constant axial load:

$$\begin{aligned} EI_{tz} &= \frac{k_{11}k_{22}k_{33} - k_{11}k_{23}^2 - k_{33}k_{12}^2 + 2k_{12}k_{13}k_{23} - k_{22}k_{13}^2}{k_{11}k_{33} - k_{13}^2} \\ EI_{ty} &= \frac{k_{11}k_{22}k_{33} - k_{11}k_{23}^2 - k_{33}k_{12}^2 + 2k_{12}k_{13}k_{23} - k_{22}k_{13}^2}{k_{11}k_{22} - k_{12}^2} \end{aligned} \qquad (4)$$

where stiffness coefficients k_{ij} ($k_{ij} = k_{ji}$) are given in Eqs. (4):

$$\begin{aligned} k_{11} &= \int_{A_{cs}} E_T dA_{cs}\,;\; k_{12} = \int_{A_{cs}} E_T z dA_{cs}\,;\; k_{13} = \int_{A_{cs}} E_T y dA_{cs}\,; \\ k_{22} &= \int_{A_{cs}} E_T z^2 dA_{cs}\,; k_{23} = \int_{A_{cs}} E_T yz dA_{cs}\,;\; k_{33} = \int_{A_{cs}} E_T y^2 dA_{cs} \end{aligned} \qquad (5)$$

and where the surface integral is extended over concrete and steel area (A_{cs}). The tangent axial rigidity

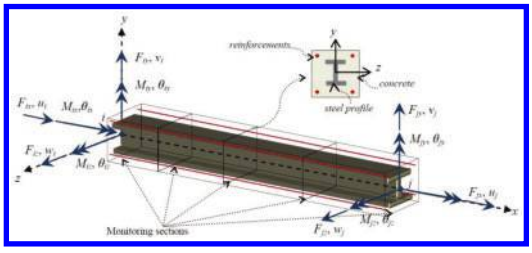


Figure 3. Beam column element with 12 DOF.

is computed as $EA_t = \int_{A_{cs}} E_T dA_{cs}$. Based on Green's integration formula according to which the domain integrals appearing in the evaluation of internal resultant efforts and tangent stiffness matrix coefficients of the section can be evaluated in terms of boundary integral. This approach is extremely rapid because stress integrals need only be evaluated at a small number of points on the section boundary and rapid convergence is assured by the inclusion of exactly determined tangent stiffnesses and, of great importance, it is assure convergence for any load case.

2.3 *Flexibility based derivation. Member analysis*

Flexibility-based method is used to formulate the distributed plasticity model of a 3D frame element (12 DOF) under the above assumptions. An element is represented by several cross sections (i.e. stations) that are located at the numerical integration scheme points (Fig. 3). The spread of inelastic zones within an element is captured considering the variable section flexural EI_y and EI_z and axial EA rigidity along the member length, depending on the bending moments and axial force level, cross-sectional shape and nonlinear constitutive relationships as already described. Figure 4 shows the deformed shape of a 3D beam-column element in local system attached to the initially straight center line, with the rigid body modes removed. Non-linear analysis by the stiffness method requires incremental loading, i.e. the inelastic behaviour is approximated by a series of elastic analysis. The element incremental flexibility matrix f_r which relates the end displacements to the actions $\Delta \mathbf{s}_r$ can be derived directly from energetic principles.

Assuming elastic behaviour within a load increment, and no coupling of axial and flexural responses at the section level, the increment of the strain energy ΔW can be written as follows, including the additional shear and torsional deformations:

$$\Delta W = \frac{L}{2}\int_0^1 \frac{N^2}{EA(\xi)}d\xi + \frac{L}{2}\int_0^1 \frac{M_z^2(\xi)}{EI_z(\xi)}d\xi + \frac{L}{2}\int_0^1 \frac{M_y^2(\xi)}{EI_y(\xi)}d\xi + \frac{L}{2}\int_0^1 \frac{M_x^2}{GI_t(\xi)}d\xi + \frac{L}{2}\int_0^1 \frac{T_y^2(\xi)}{GA_y(\xi)}d\xi + \frac{L}{2}\int_0^1 \frac{T_z^2(\xi)}{GA_z(\xi)} \quad (6)$$

in which the bending moments and shear forces are given by the following equations, supposing that the element is subjected to uniform distributed loads $q_{y(z)}$:

$$M_{y(z)}(\xi) = M_{iy(z)}(\xi - 1) + M_{jy(z)}\xi + \frac{q_{y(z)}L^2\xi(\xi-1)}{2}$$
$$T_{y(z)}(\xi) = \frac{dM_{y(z)}(\xi)}{d\xi} = \frac{M_{iy(z)} + M_{jy(z)}}{L} + \frac{q_{y(z)}L^2(2\xi-1)}{2} \quad (7)$$

Using the second theorem of Castigliano the relationship between incremental deformations and efforts can be readily calculated and partitioned as follows:

$$\begin{bmatrix} u \\ \theta_{iy} \\ \theta_{jy} \\ \theta_{iz} \\ \theta_{jz} \\ \theta_x \end{bmatrix} = \begin{bmatrix} \frac{\partial \Delta W}{\partial N} \\ \frac{\partial \Delta W}{\partial M_{iy}} \\ \frac{\partial \Delta W}{\partial M_{jy}} \\ \frac{\partial \Delta W}{\partial M_{iz}} \\ \frac{\partial \Delta W}{\partial M_{jz}} \\ \frac{\partial \Delta W}{\partial M_x} \end{bmatrix} = \begin{bmatrix} \mathbf{f}_{1(3x3)} & \mathbf{0}_{(3x3)} \\ \mathbf{0}_{(3x3)} & \mathbf{f}_{2(3x3)} \end{bmatrix} \cdot \begin{bmatrix} N \\ M_{iy} \\ M_{jy} \\ M_{iz} \\ M_{jz} \\ M_x \end{bmatrix} + \begin{bmatrix} 0 \\ \delta_{iy} \\ \delta_{jy} \\ \delta_{iz} \\ \delta_{jz} \\ 0 \end{bmatrix} \quad (8)$$

or in a condensed form:

$$\Delta \mathbf{u}_r = \mathbf{f}_r \cdot \Delta \mathbf{s}_r + \boldsymbol{\delta}_r \quad (9)$$

where $\mathbf{f}_r$ represents the incremental flexibility matrix of the beam-column element without rigid body modes, and $\boldsymbol{\delta}_r$ is a term resulting from loading actions (Chiorean 2009).

To produce the deformational-stiffness relation, the Equation (7) is inverted, resulting the following deformational-stiffness equation:

$$\Delta \mathbf{s}_r = \mathbf{k}_r \cdot \Delta \mathbf{u}_r - \mathbf{q}_r \quad (10)$$

where the vector $\mathbf{q}_r$ is the equivalent load vector, whereas k_r represents the instantaneous element stiffness matrix of the beam-column element without rigid body modes, determined by matrix inversion of the flexural matrix f_r:

$$\mathbf{k}_{r(6x6)} = \mathbf{f}_r^{-1} = \begin{bmatrix} \mathbf{f}_1^{-1} & \mathbf{0} \\ \mathbf{0} & \mathbf{f}_2^{-1} \end{bmatrix} = \begin{bmatrix} \mathbf{k}_{1(3x3)} & \mathbf{0}_{(3x3)} \\ \mathbf{0}_{(3x3)} & \mathbf{k}_{2(3x3)} \end{bmatrix} \quad (11)$$
$$\mathbf{q}_r = \mathbf{k}_r \boldsymbol{\delta}_r$$

The resulting element stiffness matrix is a 6×6 matrix. To include rigid body modes, the stiffness matrix is pre- and post multiplied by a transformation matrix to result in the required 12×12 matrix. The geometrical nonlinear effects for each element are taken into account in the present analysis, in a beam column approach, by the use of the inelastic stability stiffness functions and updating at each load increment the length, axial force and the flexural rigidity about of each principal axes of the element. This way minimizes modeling and solution time, generally only one or two elements are needed per member. The element force fields are described by the second order transfer matrix

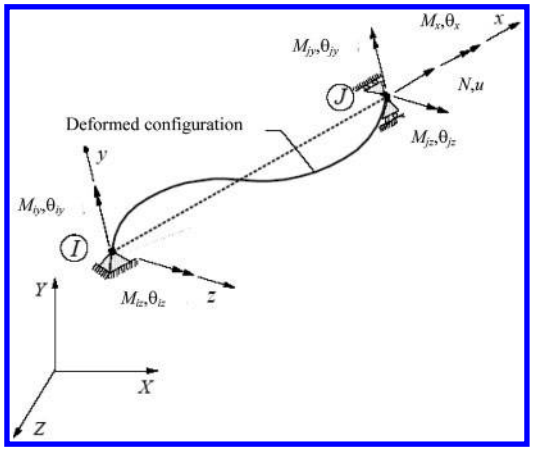


Figure 4. Beam column element with rigid body modes removed.

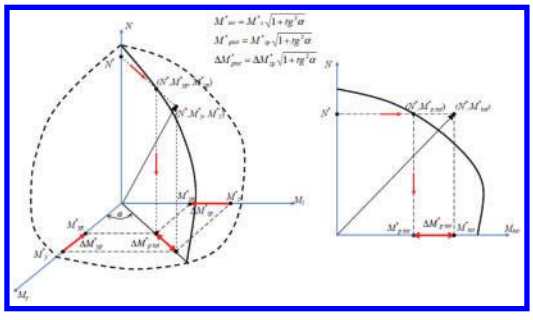


Figure 5. Interaction diagram for given bending moment's ratio. The plastic surface requirements.

as function of the nodal element forces (Chiorean 2009). If the state of forces at any cross-section along the beam column element equals or exceeds the plastic section capacity, the flexural stiffness at the respective location approaches zero. This effect is reflected in the tangent stiffness matrix coefficients given by the equations (9). Once the member forces get to the full plastic surface they are assumed to move on the plastic surface at the following loading step. Therefore, when the axial force of a member increases at the following loading step, the incremental force-displacement relationships at the element level has to be modified such that the loading result in motion along the interaction surfaces and the plastic strength surface requirement of the full plastified sections is always satisfied. Assuming that at the end of a loading step, at a cross-section, the forces violates the plastic surface, the bending moment is adjusted to be reduced, considering the member loaded by the correction bending moment ΔM_p, where ΔM_p is the change in the plastic moment capacity at the respective cross section as axial force changes (Fig. 5). The correction plastic bending moments are determined as follows. Let us consider that at the current loading step in a specified location the forces exceed the plastic surface, this means that for that loads the maximum strain in most compressed or tensioned fiber of the cross-section exceeds the assumed ultimate strain. For given value of axial force N^* the iterative procedure described in (Chiorean 2010) is applied in order to determine the ultimate bending moments (M_{yp}^*, M_{zp}^*) for a given bending moment ratio ($\tan\alpha = M_{zp}^*/M_{yp}^*$). Next the correction plastic bending moment is determined as:

$$\begin{aligned}\Delta M_{yp}^* &= M_y^* - M_{yp}^* \\ \Delta M_{zp}^* &= M_z^* - M_{zp}^*\end{aligned} \tag{12}$$

The additional incremental moments are applied as loadings on the element and are considered through equivalent nodal forces (Chiorean 2013). Since the force-point movement remains on the plastic strength surface of a member, the plastic strength surface requirement of a section is not violated by the change of member forces after the full plastic strength of cross-section is reached.

2.4 *Geometry updating and analysis algorithm*

In order to trace the equilibrium path, for proportionally and non-proportionally applied loads, the proposed model has been implemented in a simple incremental matrix structural-analysis program. In this approach the simple Euler stepping algorithm is used in conjunction with constant work-load increments. Using an updated Lagrangian formulation (UL) the nonlinear geometrical effects are considered updating the element forces and geometry configurations at each load increment. The natural deformation approach (NDA) in conjunction with the geometrical "rigid body qualified" stiffness matrix is adopted for the element force recovery and the web plane vector approach is effectively used to update the frame element coordinates (Chiorean 2009).

3 COMPUTATIONAL EXAMPLE

The Orbison's six story rigid space frame, studied previously by other researchers, has been modified and included in this verification study (Fig. 6). In order to demonstrate the effectiveness of the numerical procedure developed here, this example converts the pure steel frame to a composite frame (Iu et al. 2009). The steel beams in the frame rigidly support the concrete floor slab, and the steel columns are partially encased in the concrete (Fig. 6). The yield strength of all steel members is 250 MPa, Young's modulus is $E = 20700$ MPa and shear modulus $G = 79293$ MPa. The compressive yield stress of concrete is 16 MPa and the stress-strain curve which consists of a parabolic and linear part was used in the calculation, with crushing strain $\varepsilon_0 = 0.002$ and ultimate strain $\varepsilon_{cu} = 0.0035$. The strain softening of concrete is not taken into account ($\gamma = 0$). The frame is subjected to the combined action of gravity and lateral loads acting in

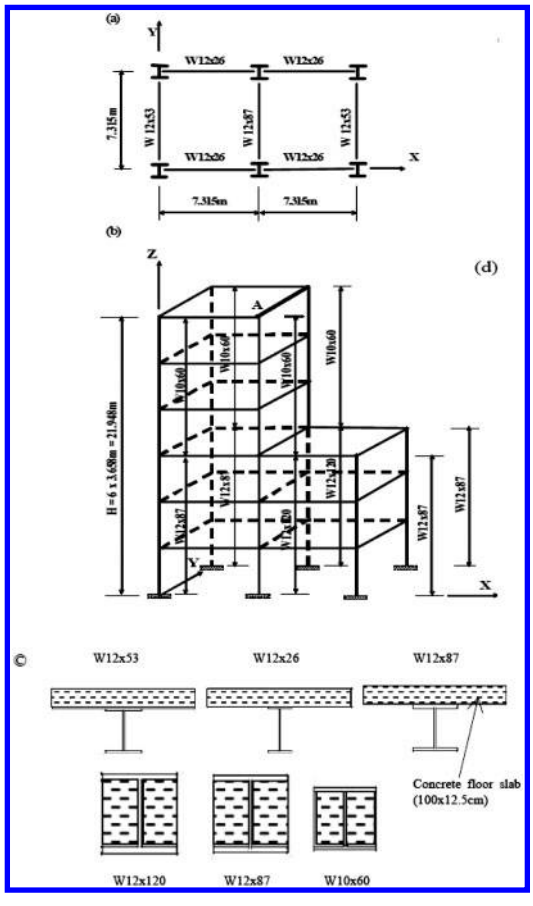


Figure 6. Orbison's six story rigid space frame.

the Y-direction. Uniform floor pressure is 9.6 kN/m^2 (simulated here as uniform distributed loads on each beam) and the wind loads are simulated by point loads of 53.376 kN in the Y direction at every beam-column joints. The inelastic behaviour represented by the load-deflections curves at node A in X and Y directions calculated by the proposed approach and those given in the literature is compared in the Figure 7. A refined plastic hinge model for composite elements was employed in (Iu et al. 2009), whereas a fiber finite element approach for pure steel elements was included in (Jiang et al 2002). Good correlation of the numerical results can be observed. However in the case of full composite frame (beams and columns) the proposed approach indicates the ultimate load factor 1.25 which is slightly higher than ultimate load factor obtained by Iu et al (1.17) (Iu et al. 2009) using a refined plastic hinge approach. Some differences can be observed also over the lateral stiffness of the frame. In the analysis of frame while considering the composite beams and columns the ultimate load factor is slightly higher than in the case of steel frame with composite beams only, in the last case the ultimate load factor resulting 1.19. As it can be seen the lateral stiffness of the frame slightly increases for full composite case (beams

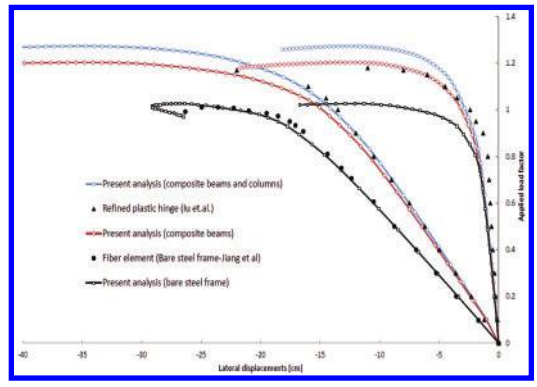


Figure 7. Load-deflection curves at node A in X and Y directions.

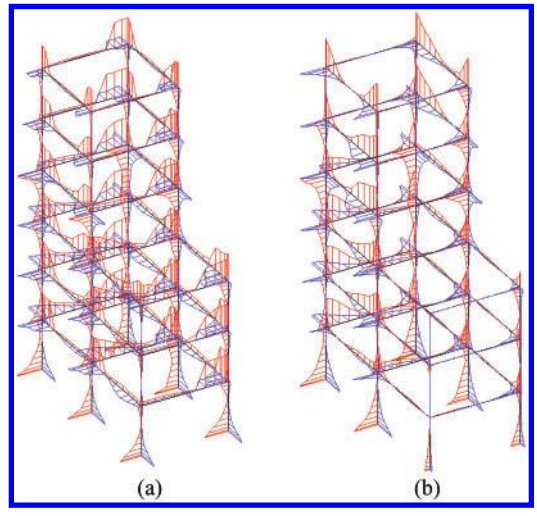


Figure 8. Tangent flexural rigidity distribution along the member's length at ultimate load factor: (a) Composite frame; (b) Pure steel frame.

and columns) as compared with the case in which the composite action is taken into account only for beams. Figure 8 shows the variation of flexural rigidities along the member lengths, at the ultimate load factor, for the pure steel frame and for the composite steel-concrete frame. It can be clearly observed the flexural stiffness degradation for beams and columns in these cases.

4 CONCLUSIONS

A reliable and robust nonlinear inelastic analysis method for composite steel-concrete space frames has been developed. The proposed model is based on the most refined type of second order inelastic analysis, the plastic zone analysis. Gradual yielding is described through basic equilibrium, compatibility and material nonlinear constitutive equations and path integral approach is applied to numerical integration of the cross-sectional nonlinear characteristics.

The proposed analysis can practically account for major factors influencing nonlinear composite steel-concrete space frame behaviour: gradual and distributed yielding associated with biaxial bending and axial force, stress-strain relationships for concrete in compression, residual stress distribution in encased steel elements, shear deformations, local and global second order effects with computational efficiency, and the necessary degree of accuracy, usually only one element per member is necessary to analyze. Lateral loads acting along the member length can be directly input into the analysis without the need to divide a member into several elements, leading to a consistency in the linear and nonlinear structural models.

The model has been implemented in a simple incremental matrix structural analysis program and allows proportionally and non-proportionally loading, and has been verified by comparing the predicted results with the established results available from the literature. The studies show that the proposed analysis compares very well to finite fibre element solution with much less computational effort. The proposed software is presented as an efficient, reliable tool ready to be implemented into design practice for advanced analysis and pushover analysis of spatial composite steel-concrete frame structures.

ACKNOWLEDGEMENTS

The authors gratefully acknowledges the support from Romanian National Authority for Scientific Research (ANCS and CNCSIS- Grant PNII-IDEI No. 193/2008) for this study.

REFERENCES

Li, G.Q., Li, J.J., Advanced analysis and design of steel frames, Wiley, 2007.

Ngo-Huu Cuong, Kim Seung-Eock 2012. Practical nonlinear analysis of steel-concrete composite frames using fiber-hinge method, *Journal of Constructional Steel Research*, 74: 90–97.

Iu C.K., Bradford M.A., Chen W.F. 2009. Second-order inelastic analysis of composite framed structures based on the refined plastic hinge method, *Engineering Structures*, 31: 799–813.

Izzudin, B.A., Siyam, AAFM, Lloyd Smith, D. 2002. An efficient beam-column formulation for 3D RC frames, *Computers & Structures*, 80.

Chiorean C.G. 2009. A computer method for nonlinear inelastic analysis of 3D semi-rigid steel frameworks, *Engineering Structures*, 2009, 31(12):3016–3033.

Chiorean C.G. 2010. Computerised interaction diagrams and moment capacity contours for composite steel-concrete cross-sections, *Engineering Structures*, 32(9): 3734–3757.

Chiorean C.G. 2013. A computer method for nonlinear inelastic analysis of 3D composite steel-concrete frame structures, *submitted for publication*.

Jiang, X.M., Chen, H., Liew, J.Y.R. 2002. Spread of plasticity analysis of three-dimensional steel frames, *Journal of Constructional Steel Research*, 58:193–212.

Research and Applications in Structural Engineering, Mechanics and Computation – Zingoni (Ed.)
© 2013 Taylor & Francis Group, London, ISBN 978-1-138-00061-2

Square concrete filled steel hollow columns

M. Dundu
University of Johannesburg, Johannesburg, South Africa

ABSTRACT: The behaviour of 12 square concrete-filled steel tubes (CFSTs) under concentric axial compression is investigated. The hollow steel sections are 102 × 102 × 3.0 mm, 120 × 120 × 3.5mm and 150 × 150 × 3.5mm and are filled with Grade 30 concrete. For each section size, the lengths tested are 1.0 m, 1.5 m, 2.0 m and 2.5 m. These lengths provide a range of columns, from relatively short to slender composite columns. The slenderness ratio (L/b) range from 6.67 to 24.61 and the depth-to-wall thickness (b/t) range from as 33.87 to 42.86. The compressive resistance of the composite columns are compared with the design strengths predicted by the South African standard (SANS 10162-1), as well as the European design standard (Eurocode 4). The test results of the slender members are found to be at variance with the codes.

1 INTRODUCTION

It is common knowledge in composite construction that the compressive resistance, ductility, and the energy absorption of square concrete filled steel tube CFST columns is lower than that of circular CFST columns. This is caused by the little concrete confinement exhibited by the square CFST columns. In spite of this huge disadvantage over its circular counterpart, square CFST are increasingly becoming more popular columns in the construction of high-rise buildings. This situation is necessitated by the cross-sectional shape of the member, which in most cases suits the plan of the buildings. The effect of this is that the beam–column joints are easy and less expensive to construct. The large moment of inertia of the square cross-section leads to higher capacity of resisting lateral load.

Although numerous publications of square CFST are available in literature, most of the investigations were performed on short columns, which failed in local buckling and crushing of the concrete only. This investigation is carried out to determine the behaviour of square composite columns, over a wider range of cross-sectional sizes and lengths. The experimental test strengths are compared to the strengths specified by SANS 10162-1 (2005) and Eurocode 4 (2004). Eurocode 4 (2004) is abbreviated as EC4 (2004) in this paper. Note that SANS10162-1 (2005) is based on the Canadian steel code (CAN/CSA-S160-01 (2001)).

2 TESTING PROGRAMMES

2.1 *Material properties*

Steel properties were established by carrying out tensile tests on steel coupons, cut from the square hollow sections (SHS) under consideration. All coupons were machined and tested according to the guidelines provided by the British Standard, BS 18 (1987). The yield strength (f_y), ultimate strength (f_u) and elastic modulus (E_s) of the steel tubes are given in Table 1. Grade 30 MPa concrete was specified for use in the composite columns. A total number of 6 concrete cubes, 100 mm × 100 mm × 100 mm, were cast from the same mix prepared for the composite columns. After 28 days the concrete cubes were tested according to SANS 5861-1 (2006), to give the concrete results in Table 1. In order to apply EC4 (2004), the cube strength of the concrete (f_{cu}) is converted into a cylinder strength (f'_{cu}), as required by the code.

Table 1. Average tensile coupon test results

	Steel tube			Concrete		
SHS size (mm)	f_y MPa	f_u MPa	E_s GPa	f_{cu} MPa	f'_u MPa	E GPa
102 × 102 × 3.0	483.9	552.7	204.7	31.2	25.0	28.3
120 × 120 × 3.5	401.0	456.5	205.8			
150 × 150 × 3.5	405.0	481.1	203.7			

2.2 *Specimen preparation*

A total number of 12 square composite columns were prepared for testing. These columns varied in lengths and cross-sectional areas. The column lengths chosen for this investigation are 1.0 m, 1.5 m, 2.0 m and 2.5 m and the size of the square tubes are 102 × 102 × 3.0 mm, 120 × 120 × 3.5 mm and 150 × 150 × 3.5 mm. All columns were filled with grade 30 concrete. A 5 mm thick end-plate was tack-welded to the bottom of each column to contain the

concrete during casting. The concrete was placed in 5 layers and compacted with a vibrator to remove air pockets. The top part of the specimens was covered with plastic sheeting to prevent moisture from evaporating for a period of 28 days. This was done to ensure that the concrete achieves its 28-day strength. After 28 days, the plastic sheeting was removed from each column and the top surfaces were levelled with an angle grinder to ensure uniform load distribution over the top surface.

2.3 *Test set-up and procedure*

The Moog machine, with a capacity of 2500k N, was used to test the composite columns. The specimens were loaded at a rate of 2 mm/min until failure to ensure that the behaviour was carefully observed. At the bottom of each specimen, pinned end conditions were simulated by placing a steel ball between two plates with grooves at the centre. Only one groove plate was used at the top of the specimens since the head of the machine had a socket. The columns were concentrically loaded to avoid end moments. Figure 1 shows the typical test set-up.

A linear variable displacement transducer (LVDT) was used to measure axial shortenings. The Moog machine is equipped with this LVDT, which automatically measures the axial deformation as the load is applied. Strain gauges were attached at mid-height, on two opposite sides of each column, to measure circumferential surface strains. Both strain gauge and LVDT readings were recorded on a computer connected to the machine.

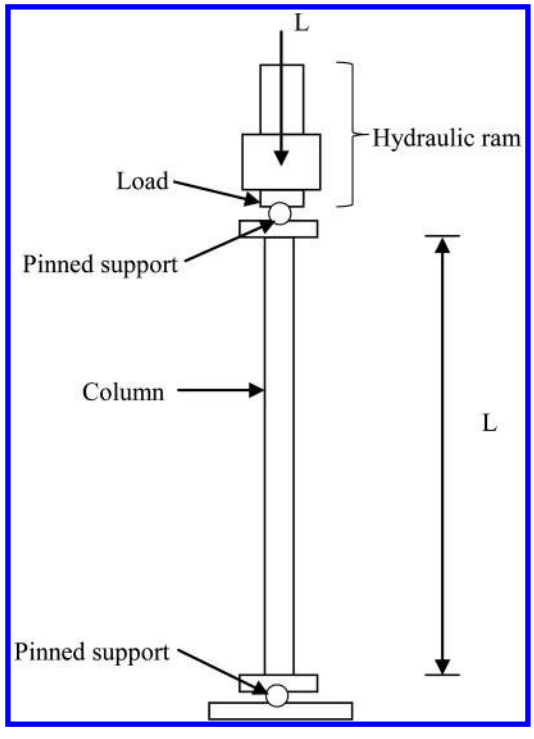


Figure 1. Schematic test setups.

3 FAILURE MODES

The general failure mode observed in the specimens was overall member buckling. All the 1.5 m to 2.5 m columns failed by overall buckling (Figure 2(b)). Overall instability was promoted by the large slenderness ratio. In addition to overall member buckling the shorter columns, typically 1 m of the larger sections ($150 \times 150 \times 3.5$), exhibited bulging (local buckling) behaviour at the centre and near the top end (Figure 2(a)). The other sections displayed local buckling away from the centre, at about a quarter of the column length from the top of the column. In both columns the concrete forced the steel tube to buckle outwards. Specimens with high b/t ratios had more local buckling or bulging compared to those with small b/t ratios. Bulging was characterised by plastic flow of concrete to fill up the sections where the steel buckled outwards.

4 ANALYSIS OF TEST RESULTS

SANS10162-1 (2005) and EC4 (2004) prescribes different limits about the compressive strength of concrete, steel yield strength and diameter-to-thickness ratio that must be used in composite columns. The limits are given in Table 2, where parameters b, L and t represent the outside width, length and thickness of the square hollow steel sections. SANS10162-1 (2005) requires the concrete strength to range from 25 MPa to 100 MPa for axially loaded CFST columns and limits the specified yield stress (f_y) of the steel to 700 MPa, to promote ductility. The characteristic concrete cylinder strength (f_{cu}) and the yield stress (f_y) of the steel ranges from 20 MPa to 50 MPa and 235 MPa to 360 MPa, respectively, in EC4 (2004). As shown in Table 1, concrete requirements satisfy both SANS10162-1 (2005) and EC4 (2004), however, the steel satisfies SANS10162-1 (2005) only, and not EC4 (2004). The slenderness ratio (L/b) of the composite column ranges from 6 to 25. This classifies the columns as intermediate to slender (Kuranovas et al (2009)), reflecting the lengths of that can be expected in practice.

The width-to-thickness ratio (b/t) of the columns ranges from 33.87 to 42.86. SANS 10162-1 (2005) and EC4 (2004) recommends that the outside width-to-thickness ratios of square hollow structural sections in compression be limited to $b/t \leq 1350/\sqrt{f_y}$ and $b/t \leq 52\sqrt{235/f_y}$, respectively (Table 2). These limits suggest that local buckling will not be the critical failure mode. A comparison of the provision from these codes shows that EC4 (2004) has more stringent requirements than SANS 10162-1 (2005).

Table 3 shows a comparison of the experimental results of square concrete-filled steel tube columns



Figure 2. Typical failure modes.

Table 2. Slenderness ratio and diameter-to-thickness

SHS size Mm	L M	f_y MPa	L/b	b/t	Limit (b/t) SANS	Limit (b/t) EC4
102 × 102 × 3.0	1.0	483.9	9.8	33.9	61.37	36.24
102 × 102 × 3.0	1.5	483.9	14.8	33.9	61.37	36.24
102 × 102 × 3.0	2.0	483.9	19.7	33.9	61.37	36.24
102 × 102 × 3.0	2.5	483.9	24.6	33.9	61.37	36.24
120 × 120 × 3.5	1.0	401.0	8.3	34.3	67.42	39.81
120 × 120 × 3.5	1.5	401.0	12.5	34.3	67.42	39.81
120 × 120 × 3.5	2.0	401.0	16.7	34.3	67.42	39.81
120 × 120 × 3.5	2.5	401.0	20.8	34.3	67.42	39.81
150 × 150 × 3.5	1.0	405.0	6.7	42.9	67.08	39.61
150 × 150 × 3.5	1.5	405.0	10.0	42.9	67.08	39.61
150 × 150 × 3.5	2.0	405.0	13.3	42.9	67.08	39.61
150 × 150 × 3.5	2.5	405.0	16.7	42.9	67.08	39.61

with the predicted compressive resistance calculated using SANS10162-1 (2005) and EC4 (2004). In this table N_{TEST} is the maximum applied load from the concrete filled SHS, N_{SANS} is the compressive resistance concrete filled SHS, calculated using SANS10162-1 (2005) and N_{EC4} is the compressive resistance of the concrete filled CFST, calculated using EC4 (2004). It should be noted that both codes do not consider confinement in determining the compressive resistance

Table 3. Test and predicted strengths columns

SHS size mm	L m	N_{TEST} (kN)	N_{SANS} (kN)	N_{EC4} (kN)	N_{TEST}/N_{SANS}	N_{TEST}/N_{EC4}
102 × 102 × 3.0	1.0	710.3	752.5	763.2	0.94	0.93
102 × 102 × 3.0	15	677.9	711.0	713.3	0.95	0.95
102 × 102 × 3.0	2.0	557.5	633.8	638.6	0.88	0.87
102 × 102 × 3.0	25	426.0	534.9	535.2	0.80	0.80
120 × 120 × 3.5	1.0	1163.2	917.7	947.3	1.27	1.23
120 × 120 × 3.5	1.5	986.4	894.7	907.0	1.10	1.09
120 × 120 × 3.5	2.0	870.7	846.2	854.1	1.03	1.02
120 × 120 × 3.5	2.5	729.1	770.9	780.4	0.95	0.93
150 × 150 × 3.5	1.0	1447.7	1259.9	1324.7	1.15	1.09
150 × 150 × 3.5	1.5	1323.3	1245.0	1283.8	1.06	1.03
150 × 150 × 3.5	2.0	1287.0	1211.7	1235.2	1.06	1.04
150 × 150 × 3.5	2.5	1183.9	1154.4	1173.6	1.03	1.01

of square CFSTs. As expected the compressive resistance of all columns decreases with increase in length of columns (Table 3).

It can be observed from the Table 3 that the strengths predicted by SANS 10162-1 (2005) are almost the same with those predicted by EC4 (2004). The result of this is that the ratios of the test strength to the code values are also the same. Both codes overestimate the strengths of 102 × 102 × 3 square composite columns. For the 102 × 102 × 3.0 section of 1 m length, both standards overestimate the test values by an average of 6.5%. This percentage increases to 20% for a 2.5 m length of the same cross-sectional size. On average, both codes overestimated the composite column capacity of this section by 11%. All the columns in this group are much slender than the other groups, and failed by overall flexural buckling. No evidence of confinement is observed in this group. The wall of the square tube resisted the concrete pressure by plate bending, instead of the membrane-type hoop stresses (Tomii et al. (1977)).

In the case of the 120 × 120 × 3.5 section the two codes overestimated the 1 m column by 23–25%. For the same length, the codes also overestimated the 150 × 150 × 3.5 section by 9–15%. This can be interpreted to imply that the stockier sections of larger b/t ratios possess some confinement. A previous study found the corner regions in square concrete filled tubes to generate some confinement, however, the confinement quickly diminished beyond the corners and vanished completely at the center of the side walls (Zhang (1989)). Thus the confining pressure is not sufficient to overcome the effect of concrete degradation. Although the codes could not predict the strength of the 1 m column accurately enough, they were able to predict the other lengths of the 120 × 120 × 3.5 and 150 × 150 × 3.5 sections. This seems to indicate that the codes are able to predict the strength of practical sized square composite columns reasonably well.

A clear trend is also shown in Table 3; the ratio of the test strength to the predicted decreases with increase in slenderness ratio. A probably cause of this is that the confinement effect is reduced with increasing length

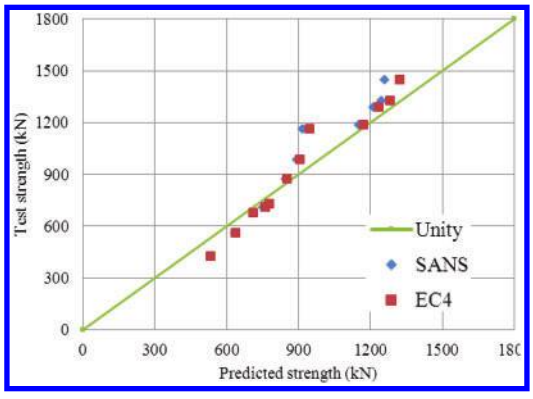


Figure 3. Test vs code predicted strength.

of the column, since the lateral deflection prior to failure increases the bending moment and reduces the mean compressive strain in the concrete. This trend means that both codes are not able to predict composite columns of different length or slenderness ratio at the same level of accuracy. Stockier test columns tend to have larger strength than slender sections.

A plot of the test strength as a function of code predicted loads is shown in Figure 3. In this figure, the points above the line are regarded as safe and those below the line are regarded as unsafe. As can be seen from the figure, all points for the $102 \times 102 \times 3.0$ are on the unsafe side. For the $120.0 \times 120.0 \times 3.5$, only the 2.5 length composite column data point is on the unsafe side. The figure also shows that the codes tend to underestimate the test strengths for the short columns.

5 LOAD-AXIAL SHORTENING

Figures 4 to 6 show the relationship between the axial load applied to the columns and the corresponding axial shortening. The graphs are linear-elastic, followed progressively by an inelastic portion, as the steel started yielding. From these graphs it can be seen that the shorter CFST columns has a higher stiffness and load carrying capacity than the longer columns. Generally, the stiffness decreases with increase in length of all columns. For constant compressive strength of the concrete, and constant thickness and yield stress of the circular hollow section, the stiffness increases with increase in the diameter of the CFST columns. As the length of the composite columns increases, the load carrying capacity decreases.

Composite columns with larger widths and steel thicknesses exhibited far much more inelasticity than the composite columns with smaller diameters and thicknesses. This is shown by a relatively flat graph at ultimate load, implying that local buckling occurred after achieving the yield strength (see Table 3 and Figure 6). The graphs also show that thicker tubes exhibited higher axial deformations just before local wall buckling. Smaller sized sections rapidly shaded

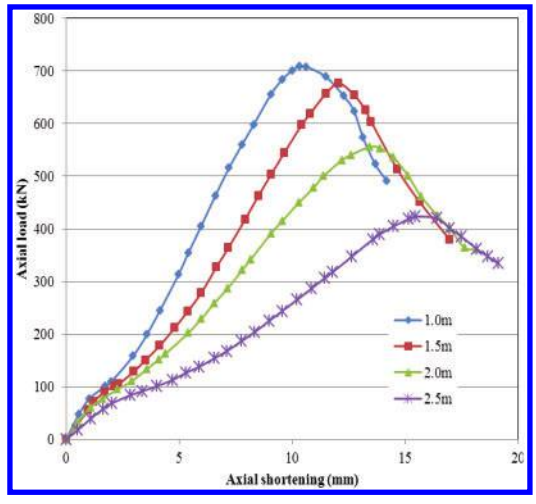


Figure 4. $102 \times 102 \times 3.0$ mm composite columns.

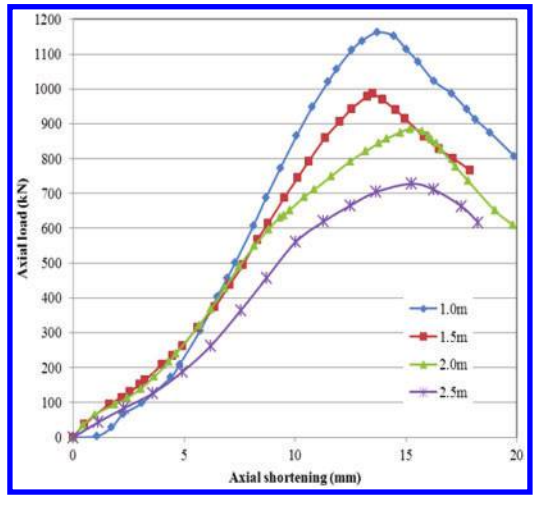


Figure 5. $120 \times 120 \times 3.5$ mm composite columns.

their load once the maximum load was attained (Figure 4 and 5). Once the composite column has reached the yield value the square tube walls fail to provide confinement of the concrete core. The load-displacement graph of the $150 \times 150 \times 3.5$ mm, 2.5 m long composite column was not included because of additional deformation of 30 mm thick end-plates initially used in the tests.

6 CONCLUSION

The failure mode observed in most specimens was overall member buckling. Overall buckling was observed in 1.5 m to 2.5 m length columns, whilst the shorter columns (typically 1 m of larger sections ($150 \times 150 \times 3.5$)) experienced both overall buckling of the member and local buckling at the centre and near the top end. Specimens with high b/t ratios had

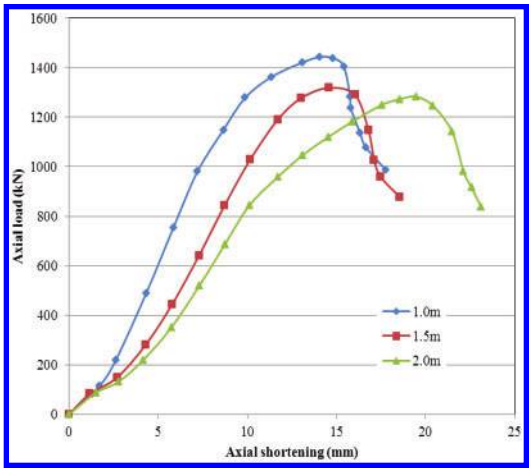


Figure 6. 150 × 150 × 3.5 mm composite columns.

more local buckling or bulging compared to those with small b/t ratios. All square concrete-filled tubes experienced a reduction in strength with an increase in slenderness ratio of the steel tube. The load-axial deflection curves showed that all specimens behaved in an inelastic manner; however, stockier sections were more inelastic than the slender sections.

Both codes overestimated the strengths of 102 × 102 × 3.0 square composite columns. On average, the codes overestimated the capacity of these composite columns by 11%. The two codes underestimated the stockier members of the 120 × 120 × 3.5 and 150 × 150 × 3.5 sections by 23–25% and 9–15%, respectively. These sections were found to possess some confinement; however, the confining pressure is not sufficient to overcome the effect of concrete degradation. The codes were able to predict the strength of 1.5 m–2.5 m of the 120 × 120 × 3.5 and 150 × 150 × 3.5 sections, implying that the codes are able to predict the strength of practical sized square composite columns reasonably well.

Transverse strains recorded at mid-heights of the specimens were very small. As a result, it was concluded that square concrete-filled steel tubes do not provide confinement of the concrete core.

ACKNOWLEDGEMENTS

The author wishes to acknowledge the University of Johannesburg Research Committee (URC) for sponsoring this research.

REFERENCES

BS 18. 1987. *British standard method for tensile testing of metals*. British Standard Institution.

CAN/CSA-S16-01. 2001. *Limit States Design of Steel Structures*. Rexdale, Ontario, Canada: Canadian Standards Association.

Eurocode 4. 2004. *Design of composite steel and concrete structures, Part 1–1: general rules and rules for buildings*. London: British Standards Institution.

Kuranovas, A. & Goode, D. & Kvedaras, A.K. & Zhong, S. 2009. Load-bearing capacity of concrete-filled steel columns. *J. Civil Eng. and Manag*. 15(1):21–33.

SANS 5861-1. 2006. *Concrete tests – Mixing fresh concrete in the laboratory*. Pretoria, South Africa: South Africa National Standards.

SANS 10162-1 (). 2005. *The structural use of steel, Part 1: Limit-state design of hot-rolled steelwork*. Pretoria, South Africa: South Africa National Standards.

Tomii, M. & Yoshimura, K. & Morishita, Y. 1977. Experimental studies on concrete filled steel tubular stub columns under concentric loading. Washington, D. C: International Colloquium on Stability of Structures under Static and Dynamic Loads 718–741.

Zhang, Z.G. 1989. Analysis of mechanism and load-bearing capacity of square concrete-filled steel under axial load. *China Ind Constr* 11:2–8.

Research and Applications in Structural Engineering, Mechanics and Computation – Zingoni (Ed.)
© 2013 Taylor & Francis Group, London, ISBN 978-1-138-00061-2

Study on the loading transferring efficiency of large dimension CFT column in joint zone with internal stiff ring

Y. Chen & X.Z. Zhao
State Key Laboratory for Disaster Reduction in Civil Engineering, Shanghai, China
Department of Structural Engineering, Tongji University, Shanghai, China

N.N. Yan & S.Y. Wu
Department of Structural Engineering, Tongji University, Shanghai, China

ABSTRACT: The vertical loading transfer mechanism of beam-column connection with internal stiff ring in large-dimension CFT column was studied. Two specimens which prototype was from a super-high rise building were tested. A finite element model was employed to simulate the behavior of the specimens and the result showed good agreement with experimental test. By both the test and FE analysis, it indicates that shear force on beam transfers to both steel tube and core concrete of CFT column, while for the latter the main path is through internal stiff rings and vertical ribs in the joint zone. The internal stiff ring is also key element to distribute vertical loads of above floors between steel tube and core concrete. The study shows that the ring with a width of 1/10 diameter of the steel tube could meet the requirement well, rather than the previously suggested size of 1/4 tube diameter by technical handbook, and adopting the new size can save quite a lot steel in super-high rise building structure.

1 INTRODUCTION

In concrete-filled tube (CFT) member, two materials, the concrete in-filled and steel tube outside, multiply the stiffness and strength of the CFT member: the concrete not only provides the strength, but also reduces the potential risk of the local buckling for steel tube, and the steel tube confines the concrete to efficiently resist compression, bending moment, and shear. Due to the composite action between steel and concrete, CFT member has large loading capacity and other good structural performances, such as high ductility and stable energy dissipation ability. Because of its excellent static and seismic performance, CFT has been generally used as columns in buildings, especially in super-high rise building where the CFT columns are usually with large dimensions due to the requirement for huge loading capacity.

There have been lots of researches conducted for investigation of the behavior of CFT column with common dimension under axial load alone or combined both axial load and moment.[Chol, Ge, Gupta] However, few studies have been carried out to investigate the behavior of those with large dimension. CFT columns offer advantages over either pure steel or concrete members, however, the structural benefits require stress transfer between the steel and the concrete. Although bond stress transfer is not well understood, it is considered as one of important measure to meet the requirement. Aim to improve the interaction, other measures has been used, including shear connectors on the inside of the tubes such as internal stiff ring.[Han, Kang, Zhang] However, in the background project of this research the structural engineers face new challenge. The project is a super-high rise building with 88 stories and the height of 438 meters above ground. The diameter of huge CFT columns is 3 meters. The designers consider the two issues. First, in the large diameter CFT column, which countermeasure is most efficient to transfer load from steel tube to core concrete? The studs densely arranged in the inner surface of steel tube, or the internal stiff ring with vertical rib which is designed in the beam-column connection location. Second, how to set the detailed sizes of the stiffeners rationally According to the previous constructional handbook, the recommended width of internal ring should be one fourth of the steel tubes. Considering the 88 stories and 3 meter diameter, the amount of steel for the internal ring shall be a big consumption.

The research conducted by the authors includes the following contents. An experiment was conducted through two specimens. Then a finite element model is established to simulate behavior of the experimental specimen. The model is then employed to investigate the distribution of stress and strain in steel tube and core concrete. Finally, the transfer mechanism of large-dimension CFT is analyzed combining the result of experiment and numerical simulating. The objectives of this study are: (1) investigating the path of the load transferring from steel beam to the core concrete; (2) studying the loading ratio share by steel tube and core

concrete; (3) checking the rational size of internal stiff ring which is smaller than the one recommended by the existed technical handbook.

2 EXPERIMENTAL PROGRAM

2.1 *Specimen Details*

Two specimens with connections consisted of internal stiff ring were designed and tested in this experimental program.

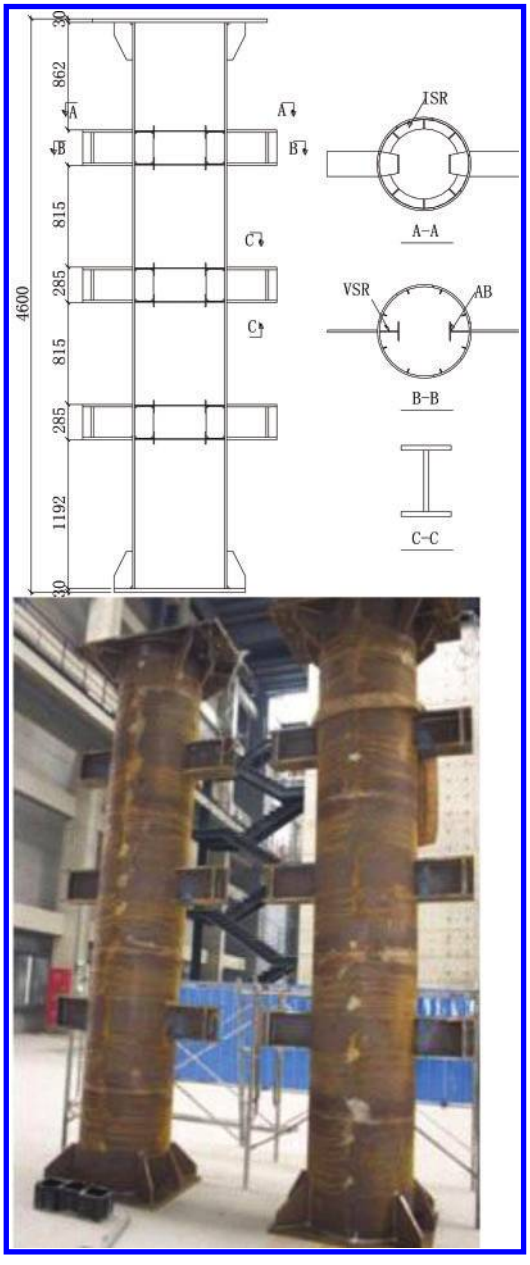


Figure 1. Overall dimension of specimen.

Due to the limit capacity of the testing rig and actuator, one-fourth scaled specimens were designed. The discreteness of the property of concrete was taken into account, so the two specimens were identical both in dimension and materials. The main body of the specimens was 4.6 meter long CFT column to which six 0.4 meter long steel I-beams were welded on both sides. Figure 1 and Table 1 show dimensions and details of the specimens. The beam-column connection of specimens consisted of internal stiff ring (ISR), vertical stiff rib (VSR) and anchorage board (AB). The width of the internal stiff ring was the main parameter, which was suggested as one-fourth of the diameter of the tube in Chinese technical handbook. However, by pre-analysis, it was found that one tenth of the tube diameter was enough for loading transferring and stiffening the joint zone. So in the test, the new size was adopted. The boards acted as an anchor to transfer horizontal force transferred from the flange of the beam.

For all specimens, steel components were fabricated first and the column was then filled and frequency vibrator was used to consolidate the concrete. The specimen was left to cure in the ambient temperature and humidity of the structures laboratory. The structural steel used in these specimens was Q345. Table 2 shows the mechanical properties of the steel in various part of the specimen. The strength of in-filled concrete was C70, and the actual strength was 68.7 N/mm^2.

2.2 *Test setup and specimen*

Figure 2 shows a photograph of the test setup with the specimen.

Table 1. Dimensions of specimen.

Item		Prototype (mm)	Specimen (mm)
Steel tube		3000×60	750×16
Joint Zone	Internal stiff ring	300×300×20	75×75×6
	Vertical stiff rib	1020×300×20	255×75×6
	Anchorage board	600×400×30	150×100×8
Steel Beam		H1100×600×18×40	H285×200×20×20
Stud		L = 120,φ19@ 300	L = 30, φ6@75
Reinforcement	Longitudinal bar	26φ20	16φ6
	Hoop	10@120	4@80

Table 2. Measured material properties.

	Yield strength (N/mm2)	Ultimate strength (N/mm2)	Elongation (%)
VSR	390	525	27.9
Steel tube	376	502	25.7
Steel beam	420	580	23.5

The bottom of the column was fixed in the shelf balanced reaction frame by eight M30 bolts. The column was subjected to a constant axial load on its top, which was provided by two 6000 kN jacks, representing the load received from above floors. Four beams were subjected to identical load by 1000 kN jack respectively, and another two beams were loaded by 1600 kN jacks. The beam loads were supposed to simulate the loads of corresponding floor in the building.



Figure 2. Test setup.

There were three loading modes programmed: (1) axial load on CFT column top alone, the column load was gradually applied until it reached the intended value; (2) only beam end loads; (3) both column and beam end loads, the column load was applied first until it reached the intended value and was kept constant during the rest of the test, then the beam loads were applied gradually until it reached the ultimate capacity of the jacks.

Figure 3 shows the layout of instruments to measure displacements and strains of the specimens. LVDT were employed at the top and bottom of the column

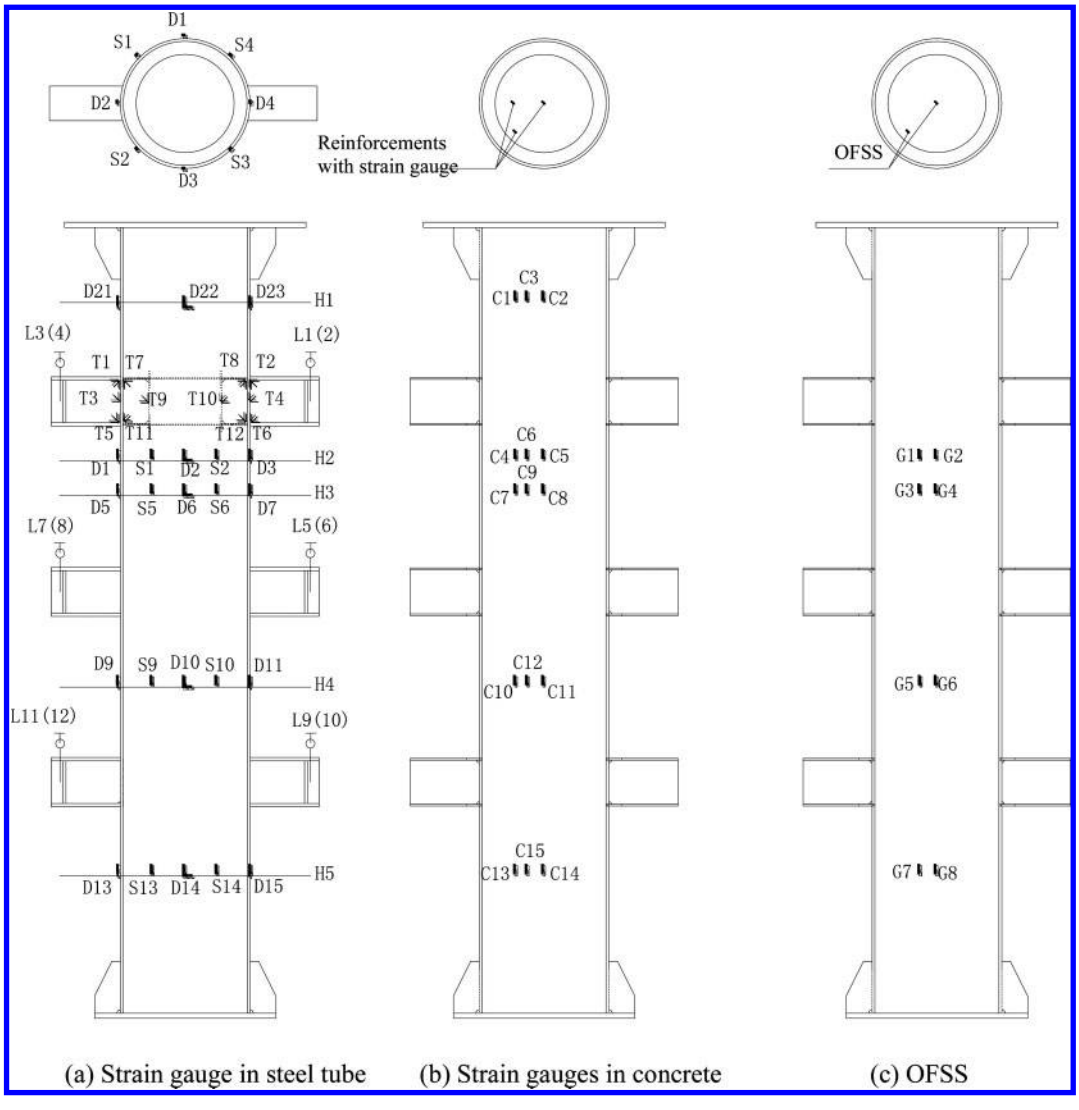


Figure 3. Location of strain gauges and displacement.

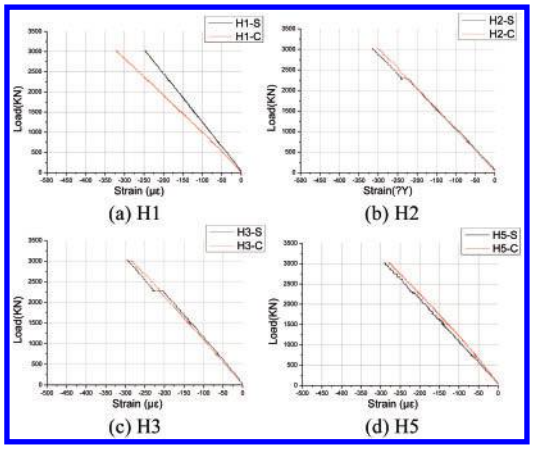


Figure 4. Load-strain curve under axial load.

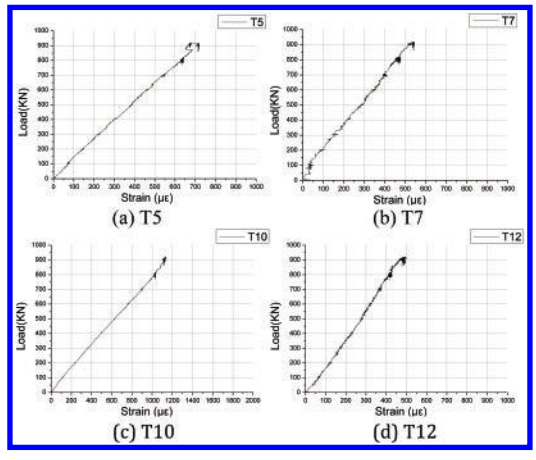


Figure 5. Load-strain curve of steel beam and rib in the case of beam load alone.

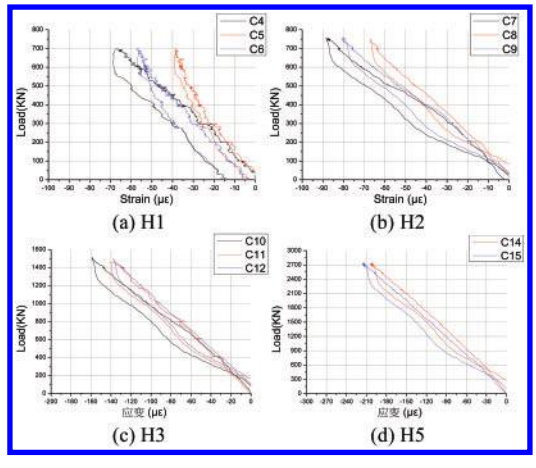


Figure 6. Load-strain curve of concrete in the case of beam load alone.

and ends of beams. Strain gauges were employed to measure the strain in the steel tube and beams. In the concrete, strain gauges were attached to steel reinforcement based on the hypothesis that the steel reinforcement and concrete have the same strain. Besides, nine optical fiber strain sensors (OFSS) were embedded into the core concrete to measure the compressive strain of concrete directly. In Figure 3, the symbol L denotes the LVDT, S, D and T denote the strain gauges with single, double and three directions respectively, C denotes the strain gauge in the concrete, and G denotes OFSS. Five sections corresponding to the location of strain gauge were denoted as H1 to H5.

2.3 *Specimen behavior*

Though there is unavoidable discreteness of concrete in-filled, no obvious difference of the specimen behavior was showed by test data and observation, so the data shown following are those from one specimen. The general behavior of the specimen is described in terms of load–displacement curve and load-strain curve.

Figure 4 shows the load-strain curves of the steel tube and the concrete in-filled in the case of axial load on column top alone. In the Figure, the strains are the average values of steel tube and concrete in the located section respectively. The linearity of the curves means that steel tube and concrete had not reached yielding strength. Except of the section H1, the curve of concrete strain almost overlaps with the one of steel strain, which implies that the existence of internal stiff ring and rib play important role in redistribution of axial load between steel tube and concrete, making the uniformity of the axial strain among the two materials. The other observation is the good agreement on strain value obtained from traditional strain gauges and OFSS.

Figure 5 shows the load-strain curves of tri-axial strain gauges arranged at the web of beam and vertical stiff rib in the case of beam load alone. The strain value is the result of the equivalent one. The value of strain in vertical stiff rib is grate larger than the one of stiff ring and near to the one of strain gauges at the corresponding position of beam web, these indicate that the beam load transfers from web of beam to steel tube then to VSR. Figure 6 shows the load-strain curve of the concrete in-filled in the same load case. It is found that the value of the strain gauge nearby ISR is generally larger than the one far away from ISR, which means the beam load sustained by concrete transfer from ISR to core concrete.

Table 3 shows the ratio of load sustained by steel tube under column top load and beam loads. The theoretical ratio is an ideal ratio based on the hypothesis that steel tube and concrete in-filled have identical strain. It seems that the steel tube shares the load a little larger than theoretical expectation in most sections expect H1. By comparing with the ratio by H1 and others in the case of column top load alone, we can see that the function of ISR in transferring axial load. Looking at the other ratios from H2 to H5, we can notice that the ratio has no big change. Thus we can deduce that the stud on the inner surface of tube contributes little to transfer the vertical load. Moving

Table 3. Ratio of load sustained by steel tube.

Section	Column Top Load	Beam Load	Theoretical Ratio
H1	31%	N/A	33%
H2	40%	40.37%	
H3	37%	34.33%	
H4	41%	30.99%	
H5	37%	38.42%	

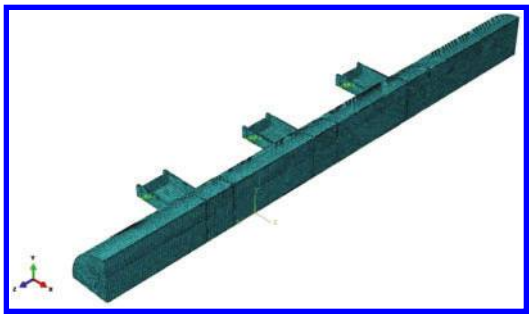


Figure 7. FEA model.

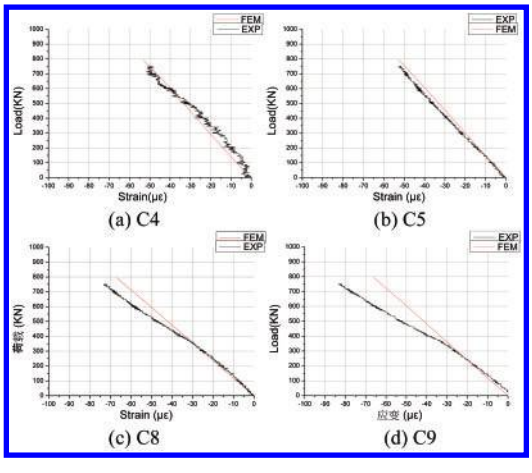


Figure 8. Comparison of strain of concrete between analysis and experiment.

to the data of beam load action, we found the identical fact.

3 NUMERICAL STUDY

3.1 *FEA model*

Numerical simulation has become an increasingly important measure to investigate the behavior of CFT column and connection. The commercial FEA package, ABAQUS, was employed in this numerical analysis. This study aimed to simulate the flexural behavior of the specimen and interaction of concrete and steel, and finally to find out the transfer mechanism of load

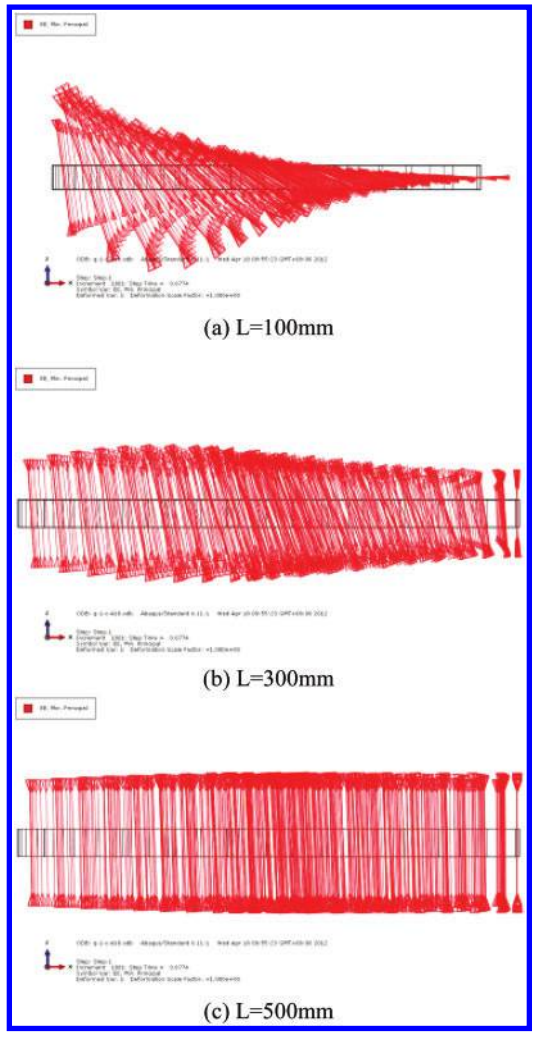


Figure 9. Distribution of strain of concrete.

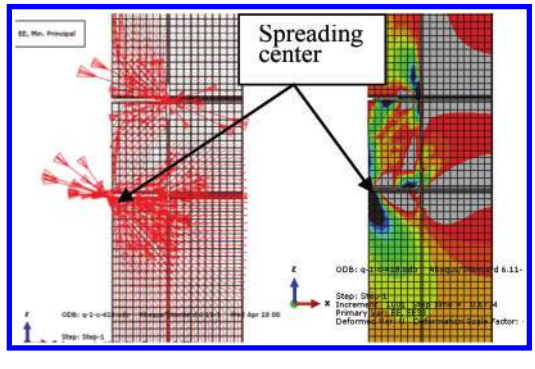


Figure 10. Spreading center.

in large-dimension CFT under column top load and beam load.

Owing to the symmetry of specimen and boundary conditions, only 1/4 of the specimen was taken

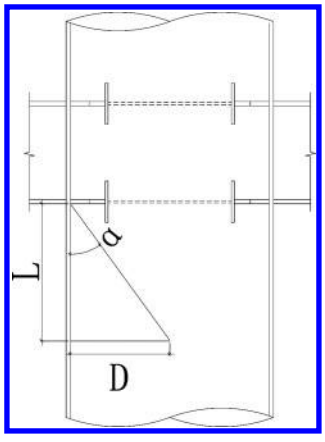


Figure 11. Diffusion angle.

with symmetric boundary conditions to establish a simulation model. The core concrete and steel tube were modeled by a reduced- integration 3D hexahedral solid element (C3D8R). The contact interaction model of ABAQUS was used to simulate the interaction of steel and concrete in CFT specimen. The model is capable of simulating the mechanical interaction of two parts at the interface. The mechanical property of the contact interaction was defined along normal and tangential respectively. The 'hard contact' relation was employed as normal mechanical property. The tangentia11 mechanical property of the contact interaction was simulated by an isotropic Coulomb friction model and the friction coefficient of 0.25 was assigned in the model. The FEA model is shown Figure 7.

3.2 *Numerical analysis results and comparison with tests*

Figure 8 shows the comparison of measured strain in core concrete and computed one. It indicates good agreement between the experimental and analytical results. Figure 9 displays the approximate distribution of axial strain of core concrete when the beam load is 1200 kN. The L represents the distance of strain section from the bottom of internal stiff ring. It is obvious that with increasing of the distance, the distribution of strain at section is more homogeneous. Strain of the section with distance of 500 mm has an almost uniform distribution. Comparing to the specimen in which transfer of load rely on bond purely, the existence of stiffeners is useful for transfer of stress.

According to Figure 10, the intersection point of ISR, VSR and steel tube is the point where the stress spreads distinguished, highlighted in the Figure 10. As is illustrated in the Figure 11, α is defined as spreading angle. D is the radius of tube and L represents the distance from bottom of ISR to uniform strain section. In the study case α is 51.3° $\alpha = \arctan(D/L)$ under the beam load.

4 CONCLUSION

The vertical load on beam mainly transfers from web of beam to steel tube, VSR and ISR and then to the concrete in-filled at last. During the transferring path from steel tube to core concrete, the main actor is the VSR and ISR, rather than studs. The existence of ISR and VSR also acts as main conductor transferring the above floor loads.

Almost uniform distribution of axial strain in core concrete can be obtained at the section with a certain distance from the bottom of ISR. In the studied case, we can set a stress spreading angle approximately equal to 51° corresponding to the vertical load transferring by beam.

The width of one tenth of ISR is enough to transfer vertical load on beam and above floors, from steel tube to core concrete. But it should be noticed that in this study, the conclusion relates to the existence of component VSR and AB. This conclusion was also withdrawn from a test where the beam end was mainly subjected moment.

REFERENCES

CHOI, S., LEE, S., HONG, S. & KIM, J. 2008. Structural capacities of tension side for CFT square column-to-beam connections with combined-cross diaphragm. *Advances in Structural Engineering,* 11, 209–227.

GE, H. & USAMI, T. 1996. Cyclic tests of concrete-filled steel box columns. *Journal of Structural Engineering-Asce,* 122, 1169–1177.

GUPTA, P. K., SARDA, S. M. & KUMAR, M. S. 2007. Experimental and computational study of concrete filled steel tubular columns under axial loads. *Journal of Constructional Steel Research,* 63, 182–193.

HAN, L.-H., LIU, W. & YANG, Y.-F. 2008. Behavior of thin walled steel tube confined concrete stub columns subjected to axial local compression. *Thin-Walled Structures*, 46, 155–164.

KANG, C. H., SHIN, K. J., OH, Y. S. & MOON, T. S. 2001. Hysteresis behavior of CFT column to H-beam connections with external T-stiffeners and penetrated elements. *Engineering Structures*, 23, 1194–1201.

ZHANG, D. X., GAO, S. B. & GONG, J. H. 2012. Seismic behaviour of steel beam to circular CFST column assemblies with external diaphragms. *Journal of Constructional Steel Research*, 76, 155–166.

Research and Applications in Structural Engineering, Mechanics and Computation – Zingoni (Ed.)
© 2013 Taylor & Francis Group, London, ISBN 978-1-138-00061-2

Connections by adherence – a numerical analysis of preliminary push-out tests

H.J.F. Diógenes, A.L.H.C. El Debs, & M.K. El Debs
University of Sao Paulo, Sao Carlos, Brazil

ABSTRACT: The process of building or retrofitting structures is affected by the speed of construction, not only in the cost, but also due to the potential of injury that it can produce (noise, pollution, traffic problems etc.). Thus, it is wanted a construction time as short as possible, especially in the case of bridges construction. The steel-concrete composite structures satisfy these requirements since steel and concrete members can be prefabricated, and only the structural assembly needs to be performed on site. Currently, however, the steel-concrete composite connections are not well adapted for using prefabricated slabs, which reduces the construction time and improves building durability. In this way, the development of new types of connections is clearly necessary. Looking for a practical, economical and fast solution for connections in steel-concrete composite structures, connections by adherence are themselves quite promising. This paper presents a numerical analysis performed with FEM based software Diana® simulating preliminary Push-Out tests of connections by adherence. To improve the performance of the steel-concrete interface, it is proposed a mechanical treatment on the involved interfaces, associated to the use of a high performance mortar connecting the elements. The numerical results demonstrated a high approach with experimental values, mainly in terms of load capacity prevision.

1 INTRODUCTION

1.1 *Generalities*

According to the fib Model Code (2010), the use of cast *in situ* concrete is, most of the times, the cheapest solution for conventional constructions. However, the prefabrication has the advantage of providing a rapid implementation and a better quality of structural elements, among others. Aiming industrialization of construction, the combination of precast concrete and composite structures can result in a system with good quality, executed with high speed and economy.

Composite structures made by steel and concrete are perfectly adaptable to the process of prefabrication, with a building system in which the whole structure or part of it can be made outside of the construction site. The main obstacle to the use of composite structures is to provide a full interaction among the structural elements.

In this way, connections are the most important part in the project of precast concrete and composite structures, affecting the whole production process. The most common connections, the pinned ones, lead to structures subjected to higher bending moments. On the other hand, connections that tend to reproduce the behavior of monolithic concrete structures reduce some of the advantages of prefabrication, mainly the speed of construction.

The process of building or retrofitting structures is affected by the speed of construction not only in the cost, but also due to the potential injury it can produce (noise, pollution, traffic problems etc.). Therefore, it is wanted a construction time as short as possible, especially in the case of bridges construction. The steel-concrete composite structures satisfy these requirements, since steel and concrete members can be prefabricated and only the structural assembly needs to be performed on site.

Currently, however, the steel-concrete composite connections are not completely adapted for using prefabricated slabs, which reduces the construction time and improves the building durability. In this way, the development of new types of connections is clearly necessary.

Looking for practical, economical and fast solutions for connections in steel-concrete composite structures, connections by adherence are themselves quite promising.

To improve the performance of steel-concrete interface, this paper proposes a mechanical treatment at the interfaces, associated to the utilization of a high performance grout connecting these materials.

1.2 *Brief review*

The study of connections by adherence, as well as the study of composite beams using this type of connection, can be divided into two fields. The first field concerns to the study of shear interfaces, and the second is related to the possible arrangements to be used

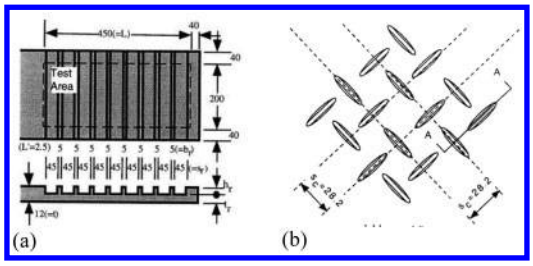


Figure 1. Grooves: (a) Parallel (ribbed plates), (b) Oblique (checkered plates).

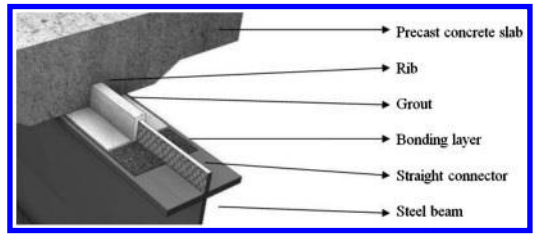


Figure 2. Connection by adherence (Thomann, 2005).

in the connection between steel beams and precast concrete slabs.

Numerous surveys have been carried out under the shear behavior of steel elements embedded in concrete, more significantly related to steel bars. Such studies are limited to a specific geometry (plain or ribbed bars) and concrete. However, some studies, although few, have sought to understand the interaction between a steel plate and cement-based materials, such as concrete and grout.

Studies related to the resistance of steel-concrete interface, when the steel surface has a roughness, are dated from the late '90s, although the idea of applying a certain roughness to the interfaces is even older. Kitoh & Sonoda (1996) studied the shear strength of the interface between concrete and a steel plate with grooves perpendicular to the direction of shear (ribbed plates – Figure 1 – (a)). Sonoda, Kitoh & Uenaka (2000) performed the same study, however for discontinuous oblique grooves, a type of surface called checkered plates (Figure 1 – (b)). Studies by Kitoh & Sonoda (1996) and Sonoda, Kitoh & Uenaka (2000) were strictly experimental, with no theoretical models being proposed for evaluating the steel-concrete interfaces proposed by the authors.

Few studies have considered the geometry of the interface as a parameter. Most researches have focused on specific geometry and materials. A more detailed understanding of shear behavior of interfaces, explicitly considering the geometry and materials (steel, concrete, mortar and a bonding layer), is therefore still quite scarce.

Thomann (2005), until then, represented the most extensive research on interface shear, considering the influence of geometry and materials. The purpose was to make a connection between steel beams and prefabricated concrete slabs to be used in steel-concrete composite bridges.

The second field is related to the development of new arrangements to connect precast concrete slabs and steel beams. Precast slabs provided with a longitudinal rib on the bottom were used to develop different connection systems. Among the most interesting researches using these systems, worth being mentioned those of Yamane et al. (1998), Shim, Lee e Chang (2001), Schmidt et al. (2004), Thomann (2005), Bouazoui et al. (2008), Hegger, Rauscher, and Gallwoszus (2010), Papastergiou (2012) and Diogenes, El Debs & El Debs (2012).

One advantage of using this type of connector is that straight connectors are characterized by the continuous transfer of forces along the interface, whereas connectors in the form of studs produce stress concentration. Straight connectors minimize stress concentration and also its consequences, such as cracking.

Since its inception, in the late 80's, the straight connectors were associated with composite connections using cast *in situ* concrete. Only from the last decade, composite connections with precast concrete have been used, producing what we now call **connections by adherence**.

This term refers to a connection based on the contact between interfaces, whose resistance is not associated to the compression of the concrete against a punctual connector. In this case, the connection is achieved through the shear between interfaces involving precast concrete slab and steel beam. The connection studied in this work was first proposed by Dauner & Antille (2002) and later studied by Thomann (2005) and Papastergiou (2012). Figure 2 shows a sketch of the mentioned connection.

By chemical or mechanical means, a certain roughening is introduced on the surface of the slab in contact with grout. After prestressing the precast slabs, grout is injected between the concrete slab and the steel beam.

Thomann (2005), as already outlined, did an extensive experimental research presenting data from push-out tests, direct shear, pull-out, and composite beams. He was able to demonstrate the viability of the new connection system, also proposing requirements for a specific geometry of grooves. It should be noted that the work of Thomann (2005) envisioned the use of this type of connection in composite bridges of concrete and steel structures, which are necessarily subject to fatigue.

Continuing the work of Thomann (2005), Papastergiou (2012) evaluated the same connection, now in terms of fatigue behavior, concluding that the connection by adherence also satisfies the limits set by the Swiss standard for fatigue behavior.

2 EXPERIMENTAL PROGRAM

This section describes the exploratory push-out samples tested by Diógenes, El Debs & El Debs (2012).

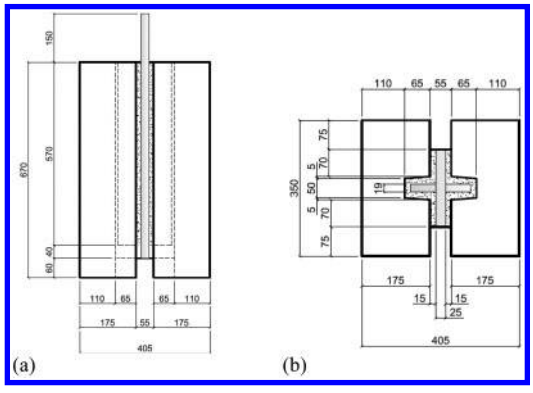


Figure 3. Dimensions of standard specimen: (a) View; (b) Cross section.

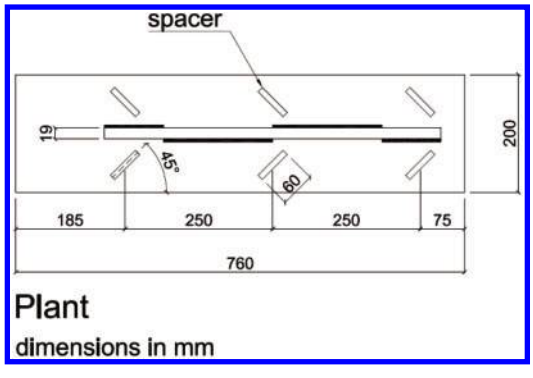


Figure 4. Standard dimensions of connectors.

2.1 *Samples description*

The tests were performed in pairs for each type of analyzed connector, totaling six specimens. At this stage of the work, only monotonic tests were performed. The trial data were the ultimate strength of the connection, the vertical displacement (slip) and the opening of the model (uplift).

The sample consisted of two blocks of plain concrete, subjected to a priming roughness of their surfaces and arranged to receive between the recesses a metallic element composed by a reaction plate and two opposing linear connectors welded in the faces. The merger between the elements was made with grouting. In all connectors, 12.5 mm bars were welded on the surface of the reaction plate, in order to serve as spacers and simulating the shear keys.

The differentiation among the connectors is a function of their surfaces. The L-type connector did not receive any type of mechanical treatment, as shown in Figure 6 – (a).

In contrast to the L connector, the R-type connector (Figure 6 – (b)) received a mechanical treatment (grooves to 45 degrees with 2 mm of depth and 10 mm of width) to improve the mechanism of transfer shear stresses.

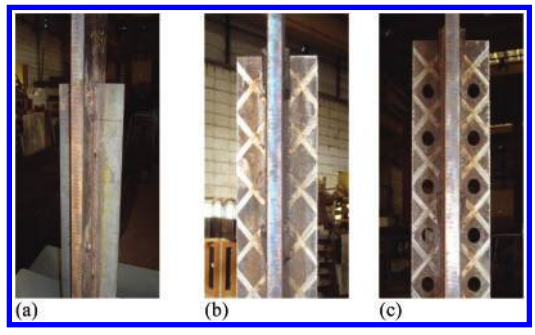


Figure 5. Connectors tested: (a) Connector L; (b) Connector R; (c) Connector RP.



Figure 6. Details of produced surface.

Besides, a variation of the R-type connector was also proposed. The RP-type connector (Figure 6 – (c)) is a composition of two others, the Perfobond proposed by Leonhardt et.al (1987) and the R connectors proposed by Thomann (2005). It is intended that the holes can generate a "dowel effect" and improve the adherence.

Once a mechanical treatment was performed on the steel surface, a roughness was designed in the concrete blocks in order to improve the transfer of forces between the interfaces, considering that, without "printing" the roughness on the concrete block, the connection failure should occur at the grout-concrete interface.

The collage of a rough blanket at the bottom of the formwork produced the printed roughness. Figure 7 shows the results produced by this procedure.

The option for a "printed" roughness was made in order to provide a greater uniformity of surface, once the use of retarders do not provide a homogeneous rough surface. The used blanket had a nominal depth of 1.2 mm.

2.2 *Materials properties*

Table 1 presents all data concerning the characterization of materials.

Table 1. Materials properties.

Model		P01	P02	P03	P04	P05	P06
Concrete	f_c	54.4	54.4	45.2	45.2	47.7	47.7
[N/mm^2]	f_{ct}	3.8	3.8	2.7	2.7	3.0	3.0
HPM	f_c	75.9	75.9	75.9	75.9	87.2	87.2
[N/mm^2]	f_{ct}	3.1	3.1	3.1	3.1	3.0	3.0
Connector		L	L	R	R	RP	RP
Steel		ASTM A-36					
[N/mm^2]		$f_y = 250$ N/mm^2 ; $f_t = 400$ N/mm^2					

The used grout admixtures were based on Vanderlei (2004), whose work was devoted to the study of Powder Reactive Concretes (PRC). PRC are basically composed of powders (quartz sand, cement common quartz powder and silica fume), small steel fibers, superplasticizer and water, where the solids are smaller than 2 mm. The PRC was manufactured under similar conditions of conventional concrete, but with very low water / cement ratio – around 0.15.

In order to obtain a mortar with compressive strength about 80 MPa, it was developed a mixture of PRC using fine quartz sand, Portland cement, superplasticizer, quartz powder and silica fume. This mortar was called high performance mortar (HPM), since the usual water/cement ratio (w/c = 0.5) was not compatible with the w/c ratio of a PRC. It is noteworthy that HPM must have sufficient fluidity and workability to permit its injection in openings about 15–20 mm wide.

3 NUMERICAL ANALYSIS

The numerical analysis reported in this work represents a preliminary numerical study of exploratory push-out tests performed by Diógenes, El Debs & El Debs (2012) and described at section 2. The analysis was performed using computational package Fx + DIANA v 9.4.4, based on finite element method.

3.1 *Finite elements adopted*

Solid elements were used to simulate steel and concrete, while surface elements modeled the steel-concrete interface.

The solid element adopted was the HX24L (Figure 8), which is an isoparametric finite element with 8-nodes and linear approximation for displacements.

Regarding the steel-concrete interface modeling, it was used the finite element Q24IF (Figure 9). This is an interface element between two planes in a three-dimensional configuration with linear interpolation.

3.2 *Hypothesis adopted*

To represent the experimental samples, it was developed a numerical model using symmetry with the presence of a single interface, which should be able to represent de structural behavior of the sample.

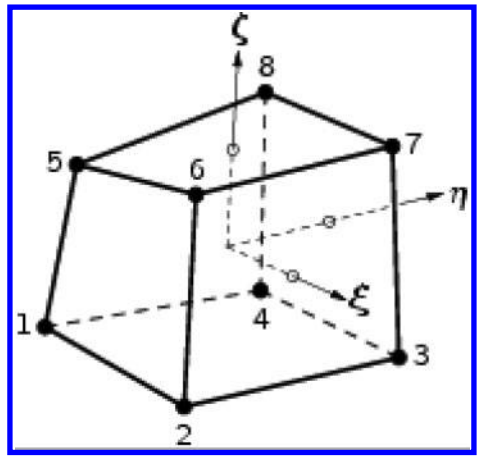


Figure 7. HX24L finite element (DIANA, 2012).

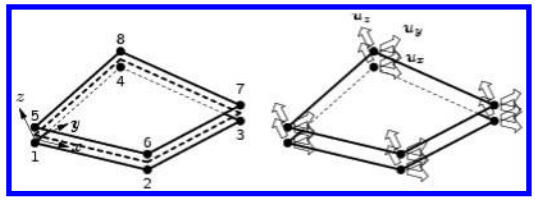


Figure 8. Q24IF finite element, typology and displacements (DIANA, 2012).

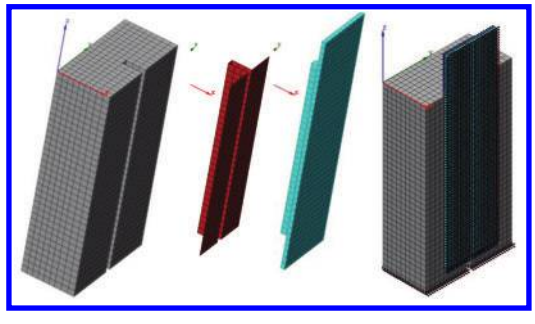


Figure 9. Numerical model overview.

So, the numerical model that represented the experimental sample did not show the region of HPM, i.e., the interface had zero thickness and the concrete block was placed directly over the connector. In Figure 10 are presented the elements of the numerical model individually.

Regarding the boundary conditions, the nodes at the bottom of the concrete block had its translation in Z restricted and the nodes of reaction plate restricted at X and Y translations in order to apply the symmetry condition.

3.3 *Materials models*

Concerning the interface behavior, a Bond-slip model was chosen. From the Bond-slip models available in DIANA, the Cubic Law was used. The Cubic law

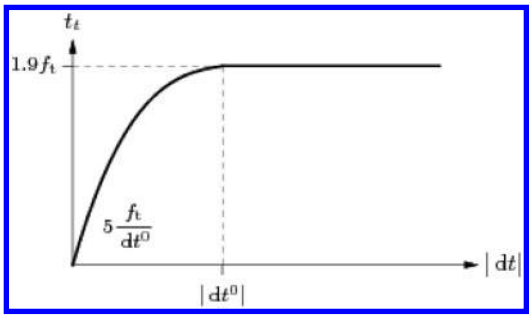


Figure 10. Bond-slip model for interface (DIANA, 2012).

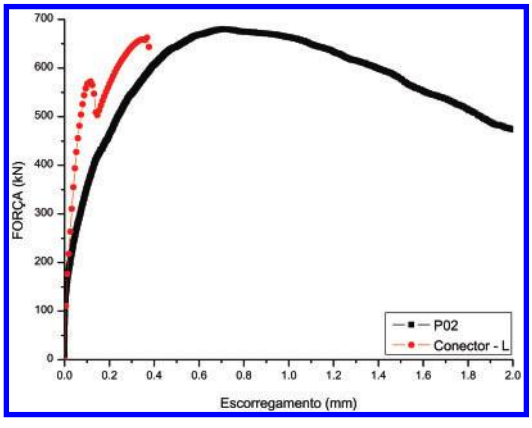


Figure 11. Numerical × Experimental result – L-type.

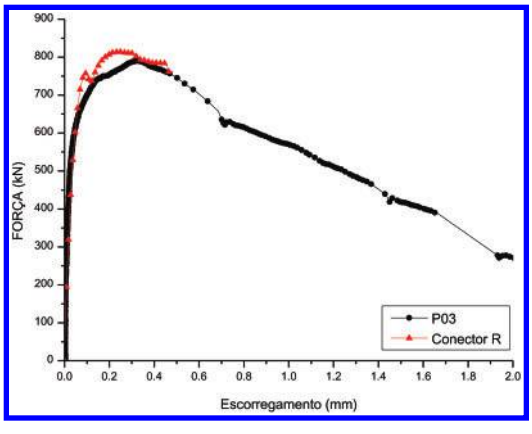


Figure 12. Numerical × Experimental result – R-type.

model represents a polynomial relation between shear traction and slip which shows a limit if the slip is larger than a certain value $\mathbf{d}_{to}$. This model requires that the tangential and normal stiffness to the interface be provided, beyond the parameters **C** and $\mathbf{d}_{to}$.

About the constitutive model for the concrete, a model based on total strain, also called 'Total Strain crack models' was used. These models describe the tensile and compressive behavior of a material with one stress-strain relationship. The tensile fracture energy was calculated according CEB Model Code 1990.

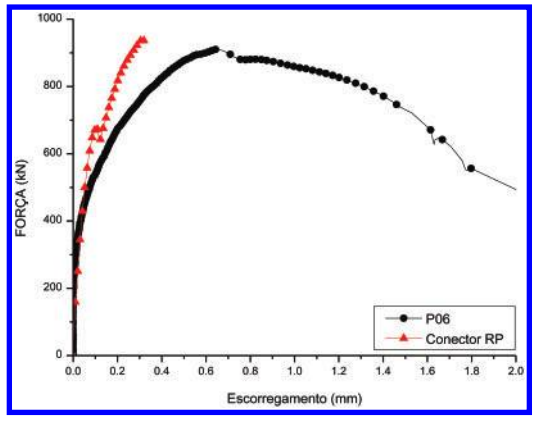


Figure 13. Numerical × Experimental result – RP-type.

Table 2. Strength – Experimental × Numerical.

	Ultimate strength		
Model	Experimental (kN)	Numerical (kN)	Difference (%)
L	680.14	658.81	+3.1
R	790.33	814.57	−3.1
RP	911.20	936.30	−2.8

Table 3. DIANA input parameters.

Parameter	**Value**
Concrete	
Total Strain model	FIXED
Tensile curve name	EXPONE
Compression curve name	PARABO
Tensile fracture energy (Gf)	CEB Model Code 1990
Compressive fracture energy	100 × Gf
Reduction due to lateral cracking	VC 1993
Shear retention function name	CONSTA
Shear retention	0.5
Interface	
Tangential Stiffness	*1 N/mm²/mm*
Normal Stiffness	10^{-4} *N/mm²/mm*
Parameters bond-slip model – **C**	0.95 (L-type); 1.1 (R-type); 1.25 (RP-type)
Parameters bond-slip model – $\mathbf{d}_{to}$	0.55 (L-type); 0.15 (R-type); 0.55 (RP-type)

To describe the steel behavior, Von Mises yield criterion was adopted.

4 RESULTS

Figures 12, 13 and 14 present de comparisons among de experimental and numerical curves obtained from the tests.

As it can be seen, the numerical model approximates the connection capacity relatively well, and in some cases also presents a reasonable approximation of slip (connector R-type). However, the numerical model is not able to reproduce the descending part of the experimental curve, which was expected, since the Bond-slip model is a failure criterion.

Table 2 presents the numerical values for the maximum strength obtained from the numerical simulation, compared to experimental values.

Finally, Table 3 shows the input values for the DIANA parameters which achieved those results.

5 CONCLUSION

The numerical model developed in this work demonstrated being adequate to describe the behavior of the connection, despite considering a single interface. However, the post peak behavior could not be obtained. It is believed that deviations of slip presented by numerical model response are due to the simplified option made.

Finally, it is worth noting that the numerical models were stiffer than the experimental prototypes, which might be corrected with the implementation of multi-linear models describing individually the various interfaces involved.

ACKNOWLEDGEMENTS

The authors would like to thank the research funding agencies FAPESP and CAPES for the financial support.

REFERENCES

Associação Brasileira de Normas Técnicas. *NBR 8800: 2008 – Projeto de estruturas de aço e de estruturas mistas de aço e concreto de edifícios*. Rio de Janeiro: ABNT.

BOUAZAOUI, L. et al. 2008. Static behaviour of a full-scale steel–concrete beam with epoxy-bonding connection. *Engineering Structures*, v. 30, n. 7, p. 1981–1990, jul.

CEB – Comité Euro-International Du Béton. **CEB MODEL CODE 1990**, 1990.

Dauner, H.-G., Antille, S. 2002. Ponts mixtes à construction rapide, *rapport OFROU 567*. Berne: Office fédéral des routes.

DIANA, T. DIANA Finite Element Analysis. *User's manual release 9.4.4*. Delft, Netherland, 2012.

Diógenes, H. J. F. ; El Debs, A. L. H. C.; El Debs. M. K. 2012. Push-out tests of straight shear connectors based on steel-concrete adherence. In: *6th International Conference on Bridge Maintenance, Safety and Management (IABMAS 2012),* Stresa, Lake Maggiore, Italy. Conference Handbook. London : Taylor & Francis Group.

Hegger, J. Rauscher, S. Gallwoszus, J. 2010. Modern hybrid structures made of UHPC and high strength steel. *3rd fib International Congress*. Washington, D.C.

Kitoh, H., Sonoda, K. 1996. Bond characteristics of embossed steel elements, In: *Composite Construction in Steel and Concrete III, Proceedings of an Engineering Foundation Conference*, *pp. 909–918*. New York: American Society of Civil Engineers.

Leonhardt, F. et al. 1987. Neues, vorteilhaftes Verbundmittel für Stahlverbund-Tragwerke mit hoher Dauerfestigkeit, *Beton und Stahlbetonbau, v. 12, pp. 325–331*. Berlim: Ernst & Sohn.

Papastergiou, D. 2012. *Connections by Adhesion, Interlocking and Friction for Steel-Concrete Composite Bridges under Static and Cyclic Loading*. PhD. Thèse, École Polytechnique Fédérale de Lausanne, Faculté Environnnement Naturel, Architectural et Construit. Lausanne.

Schmitt, V. et al. 2004. Verbundbrücke Pöcking – Innovative VFT-Träger mit Betondübeln. *Stahlbau*, v. 73, n. 6, p. 387–393, jun.

Shim, C.-S., Lee, P.-G., Chang, S.-P. 2001. Design of shear connection in composite steel and concrete bridges with precast decks. *Journal of Constructional Steel Research*, *Vol. 57, No 3, pp. 203–219*. Oxford: Elsevier Science Ltd.

Sonoda, K., Kitoh, H., Uenaka, K. 2000. Embossed steel plate-concrete composite member subjected to bending and shear. In: *Composite Construction in Steel and Concrete IV, Proceedings of an Engineering Foundation Conference*, pp. 355–367. New York: American Society of Civil Engineers.

Thomann, M. 2005. *Connexions par adherence pour les ponts mixtes acier-béton*. PhD. Thèse, École Polytechnique Fédérale de Lausanne, Faculté Environnnement Naturel, Architectural et Construit. Lausanne.

Vanderlei, R. D. 2004. *Análise Experimental do Concreto de Pós Reativos: Dosagem e Propriedades Mecânicas*. Tese (Doutorado), Escola de Engenharia de São Carlos – EESC/USP, São Carlos.

Yamane, T. et al. 1998. Full depth precast/ prestressed concrete bridge deck system, *PCI Journal, Vol. 43, No 3, pp. 50–58*. Chicago: Precast/Prestressed Concrete Institute.

19. Stainless steel structures

Research and Applications in Structural Engineering, Mechanics and Computation – Zingoni (Ed.)
© 2013 Taylor & Francis Group, London, ISBN 978-1-138-00061-2

Constitutive equations for stainless steels: experimental tests and new proposal

I. Arrayago, E. Real, & E. Mirambell
Department of Construction Engineering, Universitat Politècnica de Catalunya, UPC. Barcelona, Spain

ABSTRACT: During last decades some material models to reproduce the stainless steel behaviour have been developed. Recent studies have demonstrated that some current formulations to model stress-strain curves for stainless steel, such as the formulation presented in EN 1993-1-4, do not provide good estimations for ferritic alloys so new stress-strain relationships are required. A total of 14 tensile coupon tests on ferritic (1.4016), 14 on austenitic (1.4301) and 14 on duplex (1.4462) stainless steels have been conducted in order to obtain suitable parameters for different stainless steel grades. All coupons have come from the same steel producer and will have been tested in the same machine, in order to reduce the scattering of the experimental results (Young's modulus, 0.2% proof stress, 1.0% proof stress, ultimate stress and nonlinear parameters n and m). Therefore, new analytical expressions to determine these parameters are proposed for austenitic, ferritic and duplex stainless steels.

1 INTRODUCTION

The use of stainless steel elements has been increasing in last decades in structural applications, due to its corrosion resistance and material properties. It presents an important nonlinear stress-strain behaviour that makes it different from carbon steel. This behaviour can be analytically described by different material models available in the literature, which have derived from the expression originally proposed by Ramberg & Osgood (1943) and modified by Hill (1944).

Those material models use some parameters, obtained from experimental tests, which show a great variability between different stainless steel grades and are also different from the ones proposed in Standards. Hence, it is necessary to conduct some tensile tests and collect existing experimental data in order to correctly determine these parameters.

This paper presents the tensile tests conducted in annealed austenitic (1.4301), ferritic (1.4016) and duplex (1.4462) stainless steel coupons and the later result analysis. The expressions gathered in Standards and previous works, presented by Real et al. (2012), for the determination of the different parameters are checked herein and some new analytical expressions are also proposed.

2 MATERIAL MODELS

2.1 *Existing material models*

In last decades various material models reproducing stainless steel behaviour have been developed. All these models derived from the general expression shown in (1).

$$\varepsilon = \frac{\sigma}{E_0} + 0.002\left(\frac{\sigma}{\sigma_{0.2}}\right)^n \qquad (1)$$

whereE_0 is the initial Young's modulus, $\sigma_{0.2}$, conventionally considered as the yield stress, is the proof stress corresponding to a 0.2% plastic strain and $n$represents the nonlinear parameter. This expression is not accurate enough for stresses over the yield stress, so Mirambell & Real (2000) proposed a two stage model in order to describe stainless steel behaviour for higher stresses. The second stage is described by (2) for stresses over the 0.2% proof stress with a different nonlinear parameter m.

$$\varepsilon = \frac{\sigma-\sigma_{0.2}}{E_{0.2}} + \left(\varepsilon_u - \varepsilon_{0.2} - \frac{\sigma_u-\sigma_{0.2}}{E_{0.2}}\right)\left(\frac{\sigma-\sigma_{0.2}}{\sigma_u-\sigma_{0.2}}\right)^m + \varepsilon_{0.2} \qquad (2)$$

where $E_{0.2}$ is the elastic tangent modulus at 0.2% proof stress, σ_u and $\varepsilon_u$are the ultimate stress and strain respectively and $\varepsilon_{0.2}$is the total strain at the 0.2% proof stress.

This model was revised by Rasmussen (2003), assuming that the ultimate plastic strain is equal to the total ultimate strain and proposing some simplifications shown in (3) to (6) in order to reduce the number of parameters needed to define the material model. Afterwards, Gardner (2004) proposed some modifications to have a more consistent model for compression, ending the second stage at the 1% proof stress and providing excellent predictions for both tension and compression.

However, as advanced numerical modelling techniques require a better fit of the stress-strain curve up to high strains, some three stage models have been proposed by Quach (2008) and Hradil et al. (2012). Both models use three basic Ramberg-Osgood curves but with three different reference systems for different stress ranges. A more detailled description of the evolution of the material models in the literature can be found in Real et al. (2012).

$$\frac{\sigma_{0.2}}{\sigma_u} = \begin{cases} 0.2 + 185\frac{\sigma_{0.2}}{E_0} & \text{for austenitic and duplex} \quad (3a) \\ \frac{0.2 + 185\frac{\sigma_{0.2}}{E_0}}{1 - 0.0375(n-5)} & \text{for all stainless steel alloys} \quad (3b) \end{cases}$$

2.2 *EN 1993-1-4*

EN 1993-1-4, Annex C (2006) proposal for the description of the analytical curve of the stainless steel behaviour is based on the Rasmussen material model, using some of the expressions described in Rasmussen (2003) and presented in equations (4) to (6) for the determination of the material parameters. Values for $\sigma_{0.2}$, σ_u and E_0 are proposed in Table 2.1 and section 2.1.3 in EN 1993-1-4.

$$n = \frac{\ln(20)}{\ln\left(\frac{\sigma_{0.2}}{\sigma_{0.01}}\right)} \quad (4)$$

$$m = 1 + 3.5\frac{\sigma_{0.2}}{\sigma_u} \quad (5)$$

$$\varepsilon_u = 1 - \frac{\sigma_{0.2}}{\sigma_u} \quad (6)$$

2.3 *Modification proposal for EN 1993-1-4*

Some modification proposals for the expressions (3) to (5) were presented in Real et al. (2012) after analysing some gathered experimental stress-strain curves in ferritic and austenitic stainless steels. These modifications are summarized herein.

$$n = \frac{\ln(4)}{\ln\left(\frac{\sigma_{0.2}}{\sigma_{0.05}}\right)} \quad (7)$$

$$m = 1 + 2.3\frac{\sigma_{0.2}}{\sigma_u} \quad \text{for austenitic} \quad (8a)$$

$$m = 1 + \frac{\sigma_{0.2}}{\sigma_u} \quad \text{for ferritic} \quad (8b)$$

$$\frac{\sigma_{0.2}}{\sigma_u} = 0.46 + 145\frac{\sigma_{0.2}}{E_0} \quad \text{for ferritic} \quad (9)$$

The aim of the work presented in this paper is to validate the original expressions and the new proposals with the experimental data obtained from the conducted tensile tests and to study their applicability to duplex stainless steels.

3 TENSILE COUPON TESTS

Tensile coupon tests have been conducted in order to determine the material properties of the studied stainless steel grades. These coupons were cut and mechanized from an annealed sheet by the steel producer and were tested in the longitudinal direction. A total of 42 tensile tests were conducted, 14 in austenitic grade 1.4301, 14 in ferritic grade 1.4016 and 14 in duplex grade 1.4462 (see Fig. 1). Material properties including initial Young's modulus E_0, different proof stresses ($\sigma_{0.01}$, $\sigma_{0.05}$, $\sigma_{0.2}$ and σ_u) and ultimate strains were measured.



Figure 1. Austenitic stainless steel coupons before and after testing.



Figure 2. Coupon in the testing INSTRON machine.

Tested coupons were necked in accordance with ISO 6892-1 (2009) and were 12 mm wide with a gauge length of 50 mm. The coupons were tested in an INSTRON 8805 500 kN machine (see Fig. 2), driven by strain control. The strain rate was determined according to ISO 6892-1, and the adopted strain rates were 0.1 mm/min for the initial part of the stress-strain curves up to 1% strains and increased to 2.2 mm/min in the plastic range.

Longitudinal strain was measured by a two point contact MTS extensometer, with a gauge length of 50 mm, mounted directly onto the specimen. Additionally, two linear electrical resistance strain gauges were attached to the centre part of both faces of each coupon in order to accurately determine the initial Young's modulus and verify the accuracy of the data provided by the extensometer in the initial part of the stress-strain curves. Every specimen showed a necking effect at the mid-length as it is shown in Figure 1.

Tables 1 to 3 show the most important material parameter values obtained for the conducted tests. An example of a measured experimental stress-strain curve for each of the studied stainless steel grades can be seen in Figure 3.

Table 1. Experimental material properties for austenitics.

E_0 (MPa)	$\sigma_{0.01}$ (MPa)	$\sigma_{0.05}$ (MPa)	$\sigma_{0.2}$ (MPa)	σ_u (MPa)
200218	212	264	299	692
233841	209	265	296	674
198890	216	262	295	675
217104	210	266	297	665
219048	198	260	294	663
215123	211	262	294	663
207107	199	266	301	680
196514	206	260	296	676
201787	195	249	287	652
196345	199	249	284	655
193996	213	263	294	661
215307	205	264	297	667
204736	204	264	298	658
206301	215	268	299	667
Mean				
207594	207	261	295	668

Table 2. Experimental material properties for ferritics.

E_0 (MPa)	$\sigma_{0.01}$ (MPa)	$\sigma_{0.05}$ (MPa)	$\sigma_{0.2}$ (MPa)	σ_u (MPa)
182757	266	264	329	517
211874	257	258	332	527
209909	225	265	298	470
215090	244	262	329	512
205233	238	280	324	505
193768	245	266	296	466
232840	228	260	297	468
211421	245	262	333	516
237975	221	266	295	470
224922	233	260	327	514
233553	215	249	296	470
12779	233	249	328	521
215387	240	263	304	472
205301	244	264	334	524
Mean				
213772	238	285	316	502

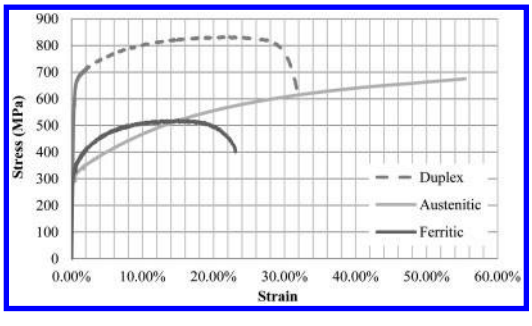


Figure 3. Measured experimental stress-strain curves for one of each of the studied stainless steel grades.

4 ANALYSIS OF RESULTS

The different expressions suggested in Real et al. (2012) and summarized in section 2.3 for the determination of some of the parameters needed for the analytical description of the stainless steel behaviour are checked herein, such as n, m, ε_u and σ_u. In addition, the applicability of those expressions to duplex stainless steels is also analysed.

Table 3. Experimental material properties for duplex.

E_0 (MPa)	$\sigma_{0.01}$ (MPa)	$\sigma_{0.05}$ (MPa)	$\sigma_{0.2}$ (MPa)	σ_u (MPa)
211375	385	532	636	826
193669	451	560	642	834
212097	388	537	642	830
211351	374	522	632	826
210781	367	519	626	820
217973	384	532	635	835
223323	381	526	631	831
220704	384	532	636	833
204949	412	543	638	830
212102	369	518	622	820
213851	378	528	630	835
209731	390	530	631	829
228098	360	530	640	834
220642	376	535	641	834
Mean				
213618	386	532	634	830

The calculation of the initial elastic modulus E_0 is performed by a linear regression on a set of representative points. The main material parameters and the optimum nonlinear parameters (n,m) for the different material models presented before are determined by using an interactive program. A more detailed description of the program can be found in Real et al. (2012).

The nonlinear parameters are optimized in order to provide the best curve fitting between the experimental curve and the analytical models from a least square adjustment by minimizing the error between both curves. The optimization range has been defined for strains up to 1%, an adequate range for structural purposes. An error expression involving both stress and strain terms has been defined for the optimization and different data density along different strain values due to changes in test rates has been considered including different weights.

In this work nonlinear parameters n and m obtained when fitting Rasmussen material model are considered. This model needs only 3 material parameters, the stress-strain equation is the same as the one proposed in EN 1993-1-4, Annex C and exhibits good agreement with experimental results for stresses up to 1% proof stress.

4.1 *Expressions for the nonlinear parameter n*

The classical expression (4) was originally proposed for alloys with a less rounded shape than the stainless steels analysed herein so a new expression (see eq. (7)) was suggested in Real et al. (2012). The accuracy of the classical expression and the new proposed one are

Table 4. Nonlinear parameter n analysis for austenitic coupons.

Optimized	Original (Eq. 4)		Proposal (Eq. 7)	
n	n	error (%)	n	error (%)
11.66	8.72	25.26	11.09	4.92
12.28	8.66	29.53	12.62	2.77
11.31	9.53	15.79	11.49	1.56
12.52	8.65	30.94	12.36	1.27
11.70	7.56	35.36	11.41	2.46
12.33	8.99	27.04	11.94	3.11
11.21	7.27	35.19	11.25	0.35
10.90	8.23	24.42	10.71	1.74
9.99	7.78	22.11	9.75	2.36
10.76	8.46	21.42	10.48	2.67
12.28	9.32	24.11	12.34	0.47
11.93	8.13	31.89	11.74	1.58
11.38	7.87	30.84	11.38	0.01
12.85	9.07	29.41	12.75	0.84
Mean				
11.65	8.44	27.38	11.52	1.87

Table 5. Nonlinear parameter n analysis for ferritic coupons.

Optimized	Original (Eq. 4)		Proposal (Eq. 7)	
n	n	error (%)	n	error (%)
9.43	14.1	50.10	12.1	27.89
13.36	11.8	11.81	13.7	2.36
16.40	10.7	34.98	14.6	10.98
12.00	10.0	16.67	11.9	0.93
11.35	9.8	13.97	11.3	0.28
16.37	15.9	2.73	16.5	1.11
16.22	11.4	29.71	18.9	16.73
11.60	9.7	16.05	12.1	4.59
17.76	10.4	41.24	16.9	5.00
10.78	8.9	17.81	10.9	0.71
17.31	9.4	45.87	16.6	4.16
10.95	8.8	19.90	11.5	5.32
17.47	12.5	28.27	17.2	1.42
11.04	9.5	13.76	11.4	2.85
Mean				
13.72	10.92	24.49	13.9	6.02

Table 6. Nonlinear parameter n analysis for duplex coupons.

Optimized	Original (Eq. 4)		Proposal (Eq. 7)	
n	n	error (%)	n	error (%)
8.24	6.0	27.54	7.8	5.05
7.27	8.5	16.20	10.2	39.68
8.14	6.0	26.78	7.7	5.01
7.97	5.7	28.13	7.3	8.43
7.75	5.6	27.44	7.4	4.40
8.09	5.9	26.47	7.8	3.25
7.81	5.9	24.11	7.6	2.53
8.06	5.9	26.40	7.8	3.59
8.90	6.9	22.96	8.6	3.10
7.71	5.7	25.54	7.6	1.33
8.07	5.9	27.34	7.9	2.05
8.09	6.2	23.04	8.0	1.72
7.59	5.2	31.46	7.3	3.36
7.87	5.6	28.57	7.6	2.89
Mean				
7.97	6.07	25.86	7.91	6.17

Table 7. Nonlinear parameter m analysis for austenitic coupons.

Optimized	Original (Eq. 5)		Proposal (Eq. 8a)	
m	m	error (%)	m	error (%)
1.94	2.56	31.63	2.02	4.14
1.86	2.58	38.74	2.04	9.60
2.06	2.57	24.66	2.03	1.45
1.89	2.61	37.80	2.06	8.66
1.98	2.59	31.15	2.05	3.51
1.91	2.55	33.52	2.02	5.67
1.92	2.58	34.81	2.04	6.49
1.92	2.56	33.59	2.03	5.64
1.93	2.57	33.60	2.03	5.59
1.97	2.55	29.59	2.02	2.55
1.99	2.59	30.65	2.05	3.12
1.89	2.59	36.85	2.05	8.03
1.90	2.62	38.17	2.07	8.87
1.93	2.60	34.90	2.05	6.41
Mean				
1.93	2.58	33.55	2.04	5.70

checked herein. Tables 4 to 6 compare the optimized nonlinear parameter n with the ones obtained with eq. (3) and eq. (6). A better agreement for the new proposal for the three stainless steel types is shown.

4.2 *Expressions for the nonlinear parameter m*

The applicability of the original expression for the calculation of the second nonlinear parameter m (5), proposed in EN 1993-1-4 Annex C, is checked herein and those results are compared with the ones derived from (8a) and (8b) proposals. As Tables 7 to 9 show, equation (4) provides inaccurate results for all the studied grades. However, the equation (8a) proposed in Real et al. (2012) for austenitics seems a good alternative for both austenitic and duplex stainless steels. Although equation (8b) seemed to correctly predict m values for the ferritic coupons studied in Real et al. (2012), Table 8 shows that the results obtained for this study are not accurate enough but expression (8a), originally proposed for austenitic grades, provides good results.

4.3 *Expressions for the ultimate stain ε_u*

The expression for the determination of the ultimate strain ε_u proposed in EN 1993-1-4 Annex C, (6), provides accurate results for the studied austenitic and

Table 8. Nonlinear parameter m analysis for ferritic coupons.

Optimized	Original (5)	Proposal (8b)	Proposal (8a)
m	error (%)	error (%)	error (%)
2.36	34.21	31.41	2.71
2.46	29.06	34.12	1.26
1.93	63.78	16.28	25.35
2.39	33.62	31.94	2.15
2.40	33.16	32.14	1.81
2.03	56.19	20.13	19.56
1.86	70.57	12.77	30.57
2.42	34.38	32.15	2.45
1.99	60.81	18.12	22.92
2.43	32.87	32.66	1.42
2.10	52.55	22.40	16.58
2.39	34.30	31.69	2.62
1.95	67.00	15.65	27.33
2.47	30.88	33.69	0.11
Mean			
2.23	45.24	26.08	11.20

Table 9. Nonlinear parameter m analysis for duplex coupons.

Optimized	Original (Eq. 5)	Proposal	(Eq. 8a)	
m	m	error (%)	m	error (%)
2.75	3.69	34.51	2.77	0.88
2.78	3.70	33.12	2.77	0.17
2.73	3.71	35.85	2.78	1.84
2.77	3.67	32.49	2.76	0.58
2.83	3.67	29.63	2.75	2.70
2.73	3.66	34.46	2.75	0.94
2.69	3.66	35.91	2.75	2.05
2.72	3.67	34.95	2.76	1.29
2.69	3.69	37.05	2.77	2.79
2.71	3.65	35.00	2.74	1.38
2.62	3.64	38.68	2.73	4.20
2.68	3.67	36.68	2.75	2.60
2.81	3.69	31.22	2.77	1.57
2.71	3.69	36.29	2.77	2.23
Mean				
2.73	3.68	34.70	2.76	1.80

duplex coupons, as it is shown in Table 10 for the austenitic specimens and in Table 12 for the duplex ones. However, this equation was not calibrated for ferritic stainless steels and as these show a stress-strain behaviour with a considerably lower ductility than austenitic and duplex grades, (6) provides inaccurate predictions of ε_u for ferritic stainless steels (see Table 11). Consequently, a new expression for the determination of the ultimate strain for ferritics, described by (10) and providing more accurate results, is suggested.

$$\varepsilon_u = 1 - 1.35\frac{\sigma_{0.2}}{\sigma_u} \qquad \textit{for ferritic} \qquad (10)$$

Table 10. ε_u and σ_u analysis for austenitic coupons.

ε_u		σ_u (MPa)
Experimental ε_u (%)	error (%) original (6)	error (%) original (3a)
56.74	2.20	9.31
57.13	4.03	1.11
56.35	2.14	7.87
56.68	4.71	1.38
57.24	4.91	1.15
55.63	0.00	1.97
54.60	0.37	5.58
54.96	0.61	8.56
56.38	2.40	5.00
56.11	0.89	7.30
55.99	2.77	7.33
56.42	3.37	2.27
55.39	3.09	3.38
56.21	3.61	4.27
Mean		
56.13	2.51	4.75

4.4 *Expressions for the ultimate strength σ_u*

Comparing the ultimate strength values obtained in the tensile tests with the ones predicted by the original expressions and the new proposals, different conclusions can be drawn. Table 10 shows that the original expression (3a) suggested in Rasmussen (2003) provides accurate ultimate strength predictions for austenitic stainless steels.

The original expressions for ferritic stainless steels (3b), and duplex (3a), do not correctly predict σ_u values so some new equations need to be proposed. A new proposal was suggested in Real et al. (2012), described by (9), for ferritic grades and this expression also provides good predictions for the coupons tested in this study, as it is shown in Table 11.

However, as duplex coupons were not studied in Real et al. (2012), no equation was given for these grades so a new proposal, described by (11), is suggested. Results obtained with this new equation can be seen in Table 12.

$$\frac{\sigma_{0.2}}{\sigma_u} = 0.76 + 0.0023\frac{\sigma_{0.2}}{E_0} \qquad \textit{for duplex} \qquad (11)$$

A summary of the expressions that more accurately predict the studied material parameters is presented in Table 13.

5 CONCLUSIONS

This paper presents and analyses the results of tensile tests conducted in annealed coupons on austenitic, ferritic and duplex stainless steels in order to more accurately characterize their main material parameters. The optimum nonlinear parameters n and m that better fit experimental data for Rasmussen material model, proposed in EN 1993-1-4, have been obtained.

Table 11. ε_u and σ_u analysis for ferritic coupons.

ε_u			σ_u (MPa)	
Experimental (%) ε_u	error (%) original (6)	error (%) proposal (10)	error (%) original (3b)	error (%) proposal (9)
13.65	178.46	19.94	3.04	14.03
15.25	147.61	5.19	12.76	9.43
16.30	133.41	0.78	23.31	6.95
13.95	167.44	10.60	4.27	8.04
13.76	171.86	13.14	3.09	9.15
17.57	117.04	5.84	26.40	9.19
16.00	138.44	3.60	17.85	4.13
12.91	174.77	0.31	1.20	6.28
17.83	108.82	13.99	23.77	1.88
14.17	155.96	0.95	6.35	5.03
19.15	93.462	1.28	21.95	2.20
15.06	145.93	0.00	0.81	7.87
17.87	98.84	27.03	25.61	3.04
14.78	144.82	5.76	1.53	8.34
Mean				
15.59	141.21	9.17	12.28	6.83

Table 12. ε_u and σ_u analysis for duplex coupons.

ε_u			σ_u (MPa)	
Experimental (%) ε_u	error (%) original (6)	error (%) proposal (10)	error (%) original (3b)	error (%) proposal (11)
22.11	4.29	41.81	0.67	
21.75	5.74	37.35	0.76	
20.35	11.20	41.21	1.23	
21.90	7.65	42.46	0.00	
20.76	14.40	42.88	0.22	
21.57	10.68	43.73	0.39	
21.77	10.38	45.08	0.60	
21.55	9.76	44.04	0.11	
21.86	5.63	40.31	0.64	
21.91	10.31	43.72	0.78	
22.78	8.03	43.87	1.36	
22.04	8.22	42.37	0.37	
21.29	9.10	44.79	0.45	
22.91	0.94	43.32	0.58	
Mean				
21.75	8.31	42.64	0.58	

Table 13. Summary of the expressions that more accurately predict material parameters.

	Austenitic	Ferritic	Duplex
n	eq. (7)	eq. (7)	eq. (7)
m	eq. (8a)	eq. (8a)	eq. (8a)
ε_u	eq. (6)	eq. (10)	eq. (6)
σ_u	eq. (3a)	eq. (9)	eq. (11)

The applicability and accuracy of some expressions proposed in EN 1993-1-4 for the determination of the material parameters and some modifications and new proposals have been checked herein. The accuracy of the most of the expressions has been confirmed with the conducted tensile tests and some new proposals have been suggested when needed.

These new proposals have been obtained from a limited number of test data, so further research needs to be done in order to adjust those proposals and extend their applicability to cold-formed stainless steel.

ACKNOWLEDGEMENTS

The research leading to these results has received funding from the Ministerio de Ciencia e Innovación (Spain) under the Project BIA 2012-36373. The first author also wants to knowledge the financial support given by UPC. The authors also want to thank Acerinox for providing the coupons and Francisco Gonzalez for his collaboration during the tests.

REFERENCES

EN ISO 6892-1. 2009. Metallic materials – Tensile testing – Part 1: Method of test at room temperature. Brussels: European Committee for Standardization (CEN); 2009.

European Committee for Standardization Eurocode 3. Design of steel structures. Part 1–4: General rules. Supplementary rules for stainless steels. Brussels, Belgium: 2006.

Gardner, L. & Ashraf, M. 2006. Structural design for non-linear metallic materials. Engineering Structures 2006; 28(6): 926–934.

Gardner, L. & Nethercot, D. 2004. Experiments on stainless steel hollow sections – Part 1: Material and cross-sectional behaviour Journal of Constructional Steel Research, no. 60, pp. 1291–1318, 2004.

Hill, HN. 1944. Determination of stress-strain relations from "offset" yield strength values, Technical Note No. 927; 1944.

Hradil, P., Talja, A., Real, E., Mirambell, E. & Rossi, B. 2013. Generalized multistage mechanical model for non-linear metallic materials. Thin-walled Structures Volume 63, February 2013, Pages 63–69.

Mirambell, E. & Real, E. 2000. On the calculation of deflections in structural stainless steel beams: an experimental and numerical investigation. Journal of Constructional Steel Research 2000; 54(4): 109–133.

Quach, W.M., Teng, J. G. & Chung, K. F. 2008. Three-Stage Full-Range Stress-Strain Model for Stainless Steels. Journal of Structural Engineering 2008; 134 (9): 1518–1527.

Ramberg, W. & Osgood, W. R. 1943. Description of stress-strain curves by three parameters. Technical Note No. 902. Washington, D.C., USA: National Advisory Committee for Aeronautics, 1943.

Rasmussen, KJR. 2003. Full-range stress–strain curves for stainless steel alloys. Journal of Constructional Steel Research 2003; 59(1): 47–61.

Real, E., Arrayago, I., Mirambell, E. & Westeel, R. 2012. Comparative study of analytical expressions for the modelling of stainless steel behaviour. Stainless steel in structures. Fourth International Experts Seminar. Ascot (U.K.), December 2012.

Research and Applications in Structural Engineering, Mechanics and Computation – Zingoni (Ed.)
© 2013 Taylor & Francis Group, London, ISBN 978-1-138-00061-2

Direct strength method and continuous strength method for cold-formed lean duplex stainless steel columns

Y. Huang & B. Young
Department of Civil Engineering, The University of Hong Kong, Hong Kong, China

ABSTRACT: The direct strength method and continuous strength method are gaining increasing acceptance in design of stainless steel columns. This study investigates the applicability of these design methods for cold-formed lean duplex stainless steel columns, which is a relatively new high strength material with low nickel content. Available data were collected and compared with design strengths calculated from the direct strength method for stainless steel and carbon steel columns as well as the continuous strength method. It is shown that these design methods are generally conservative to predict the column strengths. The direct strength method for stainless steel using tangent modulus approach to determine the column buckling strength provides accurate predictions, but this method involves iterative process in the calculation. Modified direct strength method for stainless steel using explicit strength method to determine the column buckling strength is proposed in this paper. It is shown that the modified direct strength method is capable of predicting the column strengths accurately with a relatively simple calculation procedure.

1 INTRODUCTION

Cold-formed stainless steel structures have been increasingly used, due to its structural and architectural advantages. However, the high cost of stainless steel material restricts its application in construction projects. In recent years, a relatively new type of lean duplex stainless steel of grade EN 1.4162 with high strength and low nickel content has been developed. The structural and economical advantages of lean duplex stainless steel offer great potential for the use of its material by structural engineers and architects. Previous researches on the design of column members mainly focused on austenitic stainless steel grades EN 1.4301 (AISI 304) and EN 1.4401 (AISI 316) as well as duplex stainless steel grade EN 1.4462. However, investigation on columns of lean duplex stainless steel is limited. A series of stub and pin-ended column tests as well as a wide range of parametric study using finite element analysis (FEA) on lean duplex stainless steel square hollow section (SHS) and rectangular hollow section (RHS) were conducted by Huang & Young (2012a,b, 2013). It was found that the existing design specifications are generally conservative for columns. Design rules for compression members in the Australian/New Zealand Standard (AS/NZS 2001) and European Code (EC3 2006) as well as direct strength method (DSM) for carbon steel were modified. It is shown that the modified design rules generally provide more accurate and less scatter predictions. In addition, Huang & Young (2013) also proposed a new design approach for lean duplex stainless steel columns using stub column properties and full cross-sectional area. Experimental and numerical investigations on stub columns and pin-ended columns of lean duplex stainless steel SHS and RHS columns were carried out by Theofanous & Gardner (2009). It is suggested that the class 3 limit ($c/t\varepsilon$) be relaxed from 30.7 to 37.0, and a new effective width equation has been proposed.

Generally, current design specifications require calculation of effective width, which is not easy to calculate for section with complicated shape. Therefore, the DSM and continuous strength method (CSM) that use full area instead of effective area are gaining increasing acceptance in design. The DSM for carbon steel columns has been developed by Schafer (2002) and included in the North American Specification and the Australian/New Zealand Standard. The DSM for stainless steel columns has been proposed by Becque et al. (2008). The CSM for stainless steel stub column strengths, which uses cross-section deformation capacity and utilizes the strain hardening in stainless steel has been developed by Afshan & Gardner (2012).

The objective of this study is to assess the suitability of DSM and CSM in predicting the cold-formed lean duplex stainless steel columns. A total of 259 available column strengths were compared with design strengths calculated by the DSM for stainless steel (Becque et al. 2008), DSM for carbon steel (AISI 2007) and CSM for stainless steel (Afshan & Gardner 2012). The suitability of each design rule is discussed, based on which modification of DSM for stainless steel columns is proposed. The available column strengths are compared with design strengths obtained by the modified

DSM. It is shown that the modified DSM is able to provide more accurate and less scattered predictions with relatively simple calculation procedure comparing to the other design rules, and thus is recommended to be used in designing lean duplex stainless steel columns.

2 EXISTING DESIGN RULES & COMPARISON WITH COLUMN STRENGTHS

2.1 *General*

The suitability of existing DSM and CSM to lean duplex stainless steel columns are assessed by comparing the available column strengths with the design values. A large data pool of 259 lean duplex stainless steel pin-ended and fixed-ended columns that obtained from previous researches is used. Table 1 summarises the available experimental and numerical data on lean duplex stainless steel column strengths. The pin-ended columns included short and long columns, whereas the fixed-ended columns only consisted of stub columns. Reliability analysis was performed on the existing design rules.

The unfactored design strengths (nominal strength) were calculated using various design rules described in this paper. It should be noted that the lean duplex stainless steel is not covered in the existing design specifications and the DSM. The comparison of the column strengths with the design strengths is shown in Tables 2–3. The reliability of the column design rules is evaluated using reliability analysis, as detailed in the Commentary of the ASCE Specifications (ASCE 2002). The design rules are considered to be reliable if the reliability index (β_0) is greater than 2.5. For the purpose of direct comparison, a constant resistant factor (ϕ_1) of 0.85 and a load combination of 1.2DL+1.6LL as specified in the American Specifications (ASCE 2002) were used to calculate the reliability index (β_1). The calculation procedure for the reliability index in this study is identical to that in Huang and Young (2012b). The mean value (P_m), coefficient of variation (COV) of tests and FEA to design predictions load ratio (V_P), resistance factors (ϕ_0 and ϕ_1) and reliability indices (β_0 and β_1) are shown in Tables 2–3.

Table 1. Summary of available lean duplex stainless steel column strengths.

# of column	End supports	References
26	Fixed-ended	Theofanous & Gardner (2009)
45	Pin-ended	Theofanous & Gardner (2009)
6	Fixed-ended	Huang & Young (2012a)
125	Pin-ended	Huang & Young (2012b)
25	Fixed-ended	Huang & Young (2012b)
32	Pin-ended	Huang & Young (2013)

2.2 *Direct strength method for stainless steel*

The direct strength method (DSM) for stainless steel (Becque et al. 2008) was used to calculate the design strengths of lean duplex stainless steel columns in this study. It should be noted that all of the available 259 data are consisted of RHS and SHS, where distortional buckling will not occur. Therefore, the determination of distortion buckling is not considered in this study. The critical column elastic local buckling stress (f_{ol}) of the cross-section was obtained from a rational elastic finite strip buckling analysis (Papangelis & Hancock 1995) with a 5 mm half-wave length interval.

There are three different approaches to calculate the column design strengths using DSM for stainless steel (Becque et al. 2008), where the overall buckling strength (N_{ce}) is determined from (i) the explicit strength method in AS/NZS (1st approach),

Table 2. Comparison of test and FEA column strengths with design strengths calculated by DSM using explicit strength method.

	$\frac{N_u}{N_{DSM,explicit}}$	$\frac{N_u}{N^*_{DSM,explicit}}$	$\frac{N_u}{N^{\wedge}_{DSM,explicit}}$	$\frac{N_u}{N^{\#}_{DSM,explicit}}$
Number of data	259	259	259	259
Mean (P_m)	1.19	1.13	1.13	1.09
COV (V_p)	0.107	0.105	0.095	0.090
Resistance factor (ϕ_0)	0.90	0.90	0.90	0.90
Reliability index (β_0)	2.86	2.67	2.71	2.58
Resistance factor (ϕ_1)	0.85	0.85	0.85	0.85
Reliability index (β_1)	3.27	3.08	3.13	3.00

* Equations (Rasmussen & Rondal1997) were used to calculate parameters (α, β, λ_0, λ_1).
^ Modified parameters (Huang & Young 2012b) were used.
# Proposed direct strength method using modified parameters (Huang & Young 2012b).

Table 3. Comparison of test and FEA column strengths with design strengths calculated by DSM and CSM.

	$\frac{N_u}{N_{DSM,tangent}}$	$\frac{N_u}{N_{DSM,EC3}}$	$\frac{N_u}{N_{DSM,AISI}}$	$\frac{N_u}{N_{CSM}}$
Number of data	259	259	259	29
Mean (P_m)	1.06	1.46	1.25	1.10
COV (V_p)	0.130	0.214	0.233	0.066
Resistance factor (ϕ_0)	0.90	0.91	0.85	0.91
Reliability index (β_0)	2.33	2.96	2.69	2.67
Resistance factor (ϕ_1)	0.85	0.85	0.85	0.85
Reliability index (β_1)	2.72	3.29	2.69	3.10

(ii) the tangent modulus approach (2nd approach) and (iii) European Code (3rd approach). In the DSM, the column design strengths were determined by the minimum of the overall buckling strength (N_{ce}) and local buckling strength (N_{cl}).

For the explicit strength method (1st approach), Eqs (1) – (3) proposed by Becque et al. (2008) were used to calculate the member capacity for local buckling (N_{cl}), which is the column design strength, where A is the full section area. Determination of parameters (α, β, λ_0, λ_1) is required in this approach. It should be noted that the lean duplex stainless steel is not covered in the current AS/NZS (2001). In calculating the column design strengths, three different ways were used to obtain the parameters (α, β, λ_0, λ_1), such as (i) the existing parameters for S31803 (duplex) in AS/NZS, (ii) equations proposed by Rasmussen & Rondal (1997) and (iii) modified parameters for lean duplex stainless steel proposed by Huang & Young (2012b). The column design strengths calculated by these three ways are represented by $N_{DSM,explicit}$, $N^{*}_{DSM,explicit}$ *and* $N^{\wedge}_{DSM,explicit}$, respectively, as show in Table 2. Comparison of the available column strengths with $N_{DSM,explicit}$ is shown in Table 2 and Fig. 1. The direct strength method for stainless steel using explicit strength method (1st approach) is conservative. The mean value of the column strengths (N_u) over the design strengths ($N_{DSM,explicit}$) ratio is equal to 1.19 with the COV equals to 0.107, and the reliability indices (β_o and β_1) equal to 2.86 and 3.27, which are higher than the target value of 2.5. However, the design rules, when the parameters (α, β, λ_0, λ_1) are determined from the equations proposed by Rasmussen & Rondal (1997) and using the modified parameters for lean duplex stainless steel (Huang & Young 2012b), are less conservative. The mean values of $N_u/N^{*}_{DSM,explicit}$ and $N_u/N^{\wedge}_{DSM,explicit}$ equal to 1.13 and 1.13, with COV of 0.105 and 0.095, and the reliability index (β_o) equal to 2.67 and 2.71, respectively.

$$N_{cl} = \begin{cases} N_{ce} & \text{for } \lambda_l \le 0.474 \\ \left(\dfrac{0.95}{\lambda_l^{0.8}} - \dfrac{0.22}{\lambda_l^{1.6}}\right) N_{ce} & \text{for } \lambda_l > 0.474 \end{cases} \quad (1)$$

where

$$\lambda_l = \sqrt{\frac{N_{ce}}{N_{ol}}} \quad (2)$$

$$N_{ol} = Af_{ol} \quad (3)$$

Eq. (4) proposed by Becque et al. (2008) was used when N_{ce} is determined from the tangent modulus approach (2nd approach), and design strength is represented by $N_{DSM,tangent}$ in this study, as shown in Table 3. Comparison of available column strengths with $N_{DSM,tangent}$ is shown in Table 3 and Fig. 2. The direct strength method for stainless steel using tangent modulus approach (2nd approach) provides a less conservative yet more scattered predictions comparing with the DSM for stainless steel using explicit strength method (1st approach). The mean value of the available column strengths (N_u) over the design strengths ($N_{DSM,tangent}$) ratio is equal to 1.06 with the COV equals

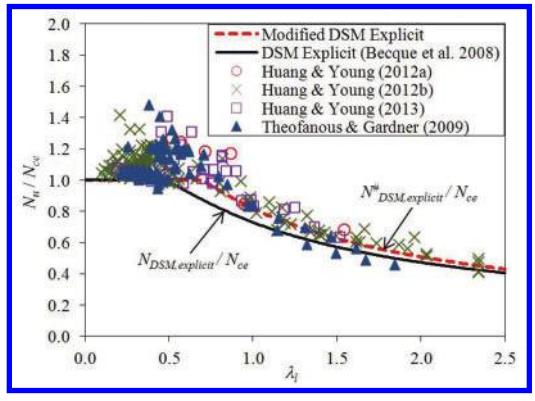


Figure 1. Comparison of column strengths with design strengths by existing and modified DSM using explicit strength method.

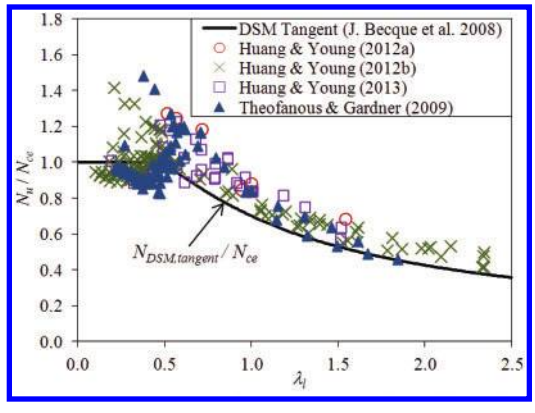


Figure 2. Comparison of column strengths with design strengths by DSM using tangent modulus approach.

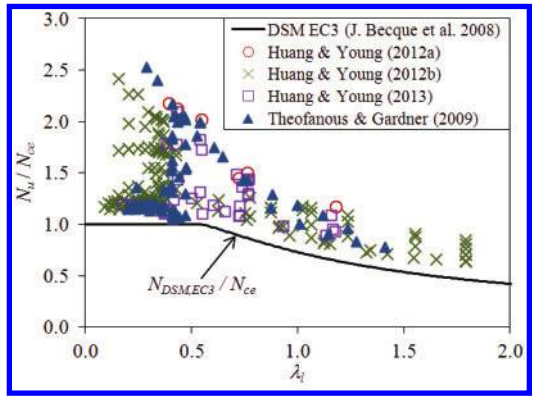


Figure 3. Comparison of column strengths with design strengths by DSM where the overall buckling strength was calculated in according to European Code.

to 0.130, as shown in Table 3. The reliability index (β_o) equal to 2.33, which is smaller than the target value 2.5. However, the method is considered reliable when the resistance factor (ϕ_1) of 0.85 is used, and the reliability index (β_1) is equal to 2.72.

$$N_{cl} = \begin{cases} N_{ce} & \text{for } \lambda_l \le 0.463 \\ \left(\frac{0.9}{\lambda_l^{0.9}} - \frac{0.2}{\lambda_l^{1.8}}\right) N_{ce} & \text{for } \lambda_l > 0.463 \end{cases} \quad (4)$$

Eq. (5) proposed by Becque et al. (2008) was used when N_{ce} is determined from European Code (3rd approach), and the design strength is represented by $N_{DSM,EC3}$, as shown in Table 3. Comparison of available column strengths with $N_{DSM,EC3}$ is shown in Table 3 and Fig. 3. The direct strength method for stainless steel using the European Code to determine the overall buckling strength (N_{ce}) provides quite conservative and scattered predictions comparing with the DSM for stainless steel using the other two approaches, especially for members with slenderness $\lambda_l \le 0.55$, as shown in Fig. 3. The mean value of the available column strengths (N_u) over the design strengths ($N_{DSM,EC3}$) ratio is equal to 1.46 with the COV equals to 0.214. The reliability indices (β_o and β_1) equal to 2.96 and 3.29, which are higher than the target value of 2.5.

$$N_{cl} = \begin{cases} N_{ce} & \text{for } \lambda_l \le 0.55 \\ \left(\frac{0.95}{\lambda_l} - \frac{0.22}{\lambda_l^2}\right) N_{ce} & \text{for } \lambda_l > 0.55 \end{cases} \quad (5)$$

2.3 *Direct strength method for carbon steel*

The direct strength method (DSM) for carbon steel was developed by Schafer (2002), and the DSM is shown in clause 1.2.1.1 of Appendix 1 in the AISI S100 Specification (AISI 2007) for the design of cold-formed carbon steel structural members. According to clause 1.2.1.1, the nominal member capacity in compression shall be the minimum of the nominal member capacity of a member in compression for flexural, torsional or flexural-torsional buckling (N_{ne}) and member in compression for local buckling (N_{nl}), as shown in Eqs. (6) and (7), respectively, where N_y is the nominal yield capacity of the member in compression, λ_c is the non-dimensional slenderness for N_{ne}, λ_l is the non-dimensional slenderness for N_{nl}, and N_{crl} is the critical column elastic local buckling load. Similar to the direct strength method for stainless steel, the determination of distortion buckling is not considered as distortional buckling will not occur for the RHS and SHS in this study. The design strength is represented by $N_{DSM,AISI}$, as shown in Table 3 and Fig. 4.

It is observed from Table 3 and Fig. 4 that the direct strength method for carbon steel provides conservative and scattered predictions for lean duplex stainless steel columns, especially for members with slenderness $\lambda_l \le 0.776$. The results are expected as the current direct strength method was developed based on cold-formed carbon steel members instead of stainless steel members. The mean value of $N_u/N_{DSM,AISI}$ equals to 1.25 with COV of 0.233. The current DSM for carbon steel is considered to be reliable, as the reliability indices (β_0 and β_1) of 2.69 are greater than the target value 2.5.

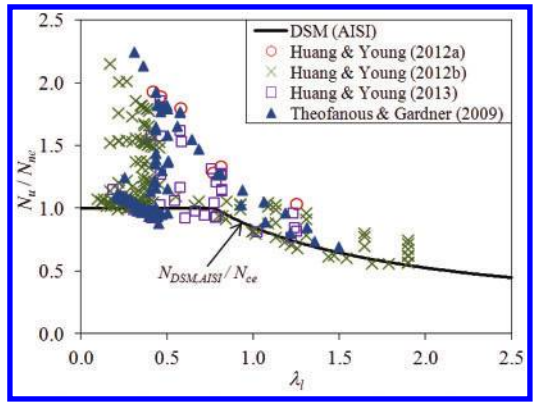


Figure 4. Comparison of column strengths with design strengths by DSM for carbon steel.

$$N_{ne} = \begin{cases} \left(0.658^{\lambda_c^2}\right) N_y & \text{for } \lambda_c \le 1.5 \\ \left(\frac{0.877}{\lambda_c^2}\right) N_y & \text{for } \lambda_c > 1.5 \end{cases} \quad (6)$$

$$N_{nl} = \begin{cases} N_{ne} & \text{for } \lambda_l \le 0.776 \\ \left[1 - 0.15\left(\frac{N_{crl}}{N_{ne}}\right)^{0.4}\right]\left(\frac{N_{crl}}{N_{ne}}\right)^{0.4} N_{ne} & \text{for } \lambda_l > 0.776 \end{cases} \quad (7)$$

2.4 *Continuous strength method for stainless steel*

The continuous strength method (CSM) (Afshan & Gardner 2012) that utilize the strain hardening of stainless steel is assessed by 39 available lean duplex stainless steel stub columns in this study. It should be noted that 10 specimens fall beyond the limit of applicability of the CSM (i.e. $\bar{\lambda}_p \le 0.68$), thus only 29 column strengths are compared with the design predictions, as shown in Table 3. The design strength is represented by N_{CSM} in this study, as shown in Table 3. The ultimate strength (f_u) and strain at ultimate strength (ε_u) are required in the calculation of design strengths.

The CSM for stainless steel is capable of predicting the stub column strengths of lean duplex stainless steel with the mean value of the available column strengths (N_u) over the design strengths (N_{CSM}) ratio equal to 1.10 and COV of 0.066. The design rule is considered to be reliable with the reliability indices (β_o and β_1) equal to 2.67 and 3.10, which are higher than the target value. Considering the relatively simple calculation procedure as well as accurate and reliable predictions, it is recommended that CSM be used for cold-formed lean duplex stainless steel sectional capacities.

3 MODIFIED DSM & COMPARISON WITH COLUMN STRENGTHS

Among various DSM discussed earlier, the DSM for stainless steel using tangent modulus approach ($N_{DSM,tangent}$) provides the most accurate predictions to lean duplex stainless steel columns, but the calculation is tedious due to the iterative process when compared to the other design rules. The DSM for stainless steel using explicit strength method (1st approach) with the existing parameters in AS/NZS ($N_{DSM,explicit}$), the DSM when N_{ce} is determined from European Code (3^{rd} approach), and the DSM for carbon steel base on AISI ($N_{DSM,AISI}$) provide quite conservative predictions. The DSM using explicit strength method with parameters obtained from equations proposed by Rasmussen & Rondal (1997) ($N^{*}_{DSM,explicit}$), and modified parameters for lean duplex stainless steel proposed by Huang & Young (2012b) ($N^{\wedge}_{DSM,explicit}$) are relatively less conservative than the aforementioned design rules.

The existing DSM are either conservative or tedious in the calculation process, therefore, modification to the DSM for stainless steel using explicit strength method (1^{st} approach) is proposed. It is suggested that the Eq. (1) to be modified to Eq. (8) as follows,

$$N_{cl} = \begin{cases} N_{ce} & \text{for } \lambda_l \le 0.7 \\ \left(\dfrac{0.96}{\lambda_l^{0.82}} - \dfrac{0.14}{\lambda_l^{2}}\right) N_{ce} & \text{for } \lambda_l > 0.7 \end{cases} \quad (8)$$

The N_{ce} is calculated using the explicit strength method and modified parameters for lean duplex stainless steel proposed by Huang & Young (2012b). The design strength determined from the modified DSM base on explicit strength method is represented by $N^{\#}_{DSM,explicit}$ in this study, as shown in Table 2.

The comparison results with the available column strengths are shown in Table 2 and Fig. 1. The mean value of $N_u/N^{\#}_{DSM,explicit}$ equals to 1.09 with COV of 0.090. It is shown that the modified DSM base on explicit strength method provides a more accurate and less scatter predictions than the existing DSM for stainless steel. For example, the mean value of $N_u/N_{DSM,explicit}$ equals to 1.19 with COV of 0.107. The modified DSM is reliable, where the reliability indices (β_o and β_1) equal to 2.58 and 3.00, which are greater than the target value of 2.5. The calculation procedure of the modified DSM for stainless steel is simple, since the iterative process and calculation of effective width are not required.

4 CONCLUSIONS

A total of 259 lean duplex stainless steel column strengths available in the literature were used to compare with the design strengths obtained from the direct strength method for stainless steel (Becque et al. 2008), direct strength method for carbon steel (AISI 2007) and continuous strength method (Afshan & Gardner 2012). It is shown that the design strengths calculated from the DSM for stainless steel using explicit strength method, the DSM for stainless steel when the overall buckling strength is determined from European Code, and the DSM for carbon steel are quite conservative in predicting the cold-formed lean duplex stainless steel column strengths. The DSM for stainless steel using tangent modulus approach is capable of providing accurate predictions, but the calculation is tedious due to the iterative process. The continuous strength method is able to provide good predictions to lean duplex stainless steel stub columns in this study, and the calculation procedure is relatively simple.

Modified DSM for stainless steel base on explicit strength method with modified parameters by Huang & Young (2012b) is proposed in this study. The modified DSM is proven to provide more accurate and less scatter predictions for cold-formed lean duplex stainless steel columns. Considering the accuracy, reliability and the simplicity of calculation, it is recommended that the modified DSM and the CSM be used in designing cold-formed lean duplex stainless steel members and sectional capacities, respectively. The modified DSM proposed in this study is capable of producing reliable limit state designs when calibrated with a resistance factor of 0.9.

ACKNOWLEDGEMENT

The research work described in this paper was supported by a grant from The University of Hong Kong under the seed funding program for basic research.

REFERENCES

Afshan, S. & Gardner, L. 2012. The continuous strength method for structural stainless steel design. *Proceeding of 4th International Structural Stainless Steel Experts Seminar.*

American Iron and Steel Institute (AISI). 2007. *North American Specification for the design of cold-formed steel structural members.* AISI S100-2007, Washington, D.C.

American Society of Civil Engineers (ASCE). 2002. *Specification for the design of cold-formed stainless steel structural members*. SEI/ASCE 8-02; Reston, VA.

Australian/New Zealand Standard (AS/NZS). 2001. *Cold-formed stainless steel structures*. AS/NZS 4673, Sydney, Australia.

Becque, J., Lecce, M. & Rasmussen, K.J.R. 2008. The direct strength method for stainless steel compression members. *Journal of Constructional Steel Research* 64: 1231–1238.

European Committee for Standardization (EC3). 2006. *Design of steel structures – Part 1.4: General rules – Supplementary rules for stainless steels.*, EN 1993-1-4, Brussels.

Huang, Y. & Young, B. 2012a. Material properties of cold-formed lean duplex stainless steel sections. *Thin-walled Structure* 54: 72-81.

Huang, Y. & Young, B. 2012b. Structural performance of cold-formed lean duplex stainless steel columns. *Proceeding of 4th International Structural Stainless Steel Experts Seminar.*

Huang, Y. & Young, B. 2013. Tests of pin-ended cold-formed lean duplex stainless steel columns. *Journal of Constructional Steel Research* 82: 203-215.

Papangelis, J.P. & Hancock, G.J. 1995. Computer Analysis of Thin-walled Structural Members. *Computers and Structures* 56(1):157–176.

Rasmussen, K.J.R. & Rondal, J. 1997. Strength curves for metal columns. *Journal of Structure Engineering ASCE* 123(6): 721-728.

Schafer, B.W. 2002. Local, distortional, and Euler buckling in thin-walled columns. *Journal of Structure Engineering ASCE* 128 (2): 289-299.

Theofanous, M. & Gardner, L. 2009. Testing and numerical modelling of lean duplex stainless steel hollow section columns. *Engineering Structures* 31(12): 3047-3058.

Research and Applications in Structural Engineering, Mechanics and Computation – Zingoni (Ed.)
© 2013 Taylor & Francis Group, London, ISBN 978-1-138-00061-2

Numerical study of lean duplex stainless steel plate girders with stocky flanges and slender unstiffened webs under bending

M.F. Hassanein
Department of Structural Engineering, Faculty of Engineering, Tanta University, Tanta, Egypt

N. Silvestre
Department of Civil Engineering, ICIST/IST, TU Lisbon, Lisboa, Portugal

ABSTRACT: The behaviour and ultimate strength of lean duplex stainless steel plate girders under bending are studied in this paper. Lean duplex stainless steel I-section plate girders (LDIPGs) with stocky flanges and slender unstiffened webs are prone to several buckling phenomena (local, lateral-torsional) and, in particular, to Lateral-Distortional buckling (LD). Firstly, shell Finite Element (FE) models are validated by means of comparison with experimental test results available in the literature. Secondly, these models are used to unveil the structural behavior and ultimate strength of LDIPGs subjected to uniform bending. After that, the LDIPGs are selected on the basis of three key parameters: the radius of gyration of the compression flange, the section modulus and the unbraced length. Finally, the numerical results are compared with predictions given by AS4100 and EC3. It is found that the EC3 provides conservative predictions for the LDIPGs under bending, with a relatively high margin of safety. In order to reduce this difference, the imperfection factor associated to buckling curve (c) is recommended to be used in the scope of the design method provided by EN 1993-1-4.

1 INTRODUCTION

The interest in metallic corrosion resistant materials for the structural application has significantly been increasing over recent decades. Most of these materials are stainless steel alloys, which combine high strength, durability, weldability and an aesthetically clean surface with high corrosion resistance. Lean duplex stainless steels with reduced nickel content are very competitive within the stainless steel grades due to the strong fluctuations in nickel price and better mechanical properties than those with austenitic alloys. The lean duplex grade EN 1.4162, for instance, contains a relatively low nickel content of about 1.5% of its alloy composition. Examples for the structural applications of lean duplex grade EN 1.4162 include the Likholefossen Bridge in Norway and Siena Footbridge in Italy. However, most design codes treat them in the same way as austenitic steels because most of the existing numerical and experimental results come from austenitic or duplex alloys. The behaviour of stainless steel material in fact differs from that of carbon steels (Gardner 2005, Baddoo 2008). Stainless steels have a rounded stress-strain curve with no yield plateau and low proportional limit stress compared to carbon steel ones. Nevertheless little information specifically dedicated to lean duplex grades is available in the literature whereas austenitic grades are much more covered. On the other hand, I-section plate girders (IPGs) are nowadays main elements in many industrial areas such as aerospace, shipbuilding, bridges, industrial buildings and offshore structures. They are regularly made of lightweight and/or high strength materials and are joined by modern welding techniques. Their behaviour depends on the structural response of the plate elements that are subjected mainly to in-plane loading. Steel design standards (e.g. AISC 2010) normally define the flexural resistance of IPGs based on the consideration of local buckling (L) and lateral-torsional buckling (LT) limit states. In general, local buckling of IPGs is defined as a mode involving deformations of their individual plates without the translation of the intersection lines of the adjacent plate elements. Accordingly, the local buckling depends on the slenderness ratios of flange and web elements as well as the applied compressive stress ratio (stress gradient). Conversely, the LT is characterized by a rigid-body lateral translation and twist of the cross-section and highly depends on the unbraced length. On the other hand, it is common fact (e.g Hancock et al. 1980) that IPGs with slender webs fail in a mode characterized by web distortion, which is commonly known as the lateral-distortional buckling (LD) mode. There has been much research work reported in the literature on the LD concentrating on the carbon steel beams. Hence, the flexural strength of lean duplex stainless steel I-section plate girders of Grade EN 1.4162 (LDIPGs) is presented in this paper. To the authors' knowledge, the LD of LDIPGs has never been studied.

2 FE MODEL AND VALIDATION

Before studying the behaviour of LDIPGs, it is essential to validate the numerical model. Since there are no experimental studies on LD and LT of LDIPGs, we consider the tests recently carried out by Saliba and Gardner (2013) on the local buckling (LB) of lean duplex stainless steel I-section beams. Regarding the geometry, four beams under three-point bending were analysed. The I-section dimensions are h_w (web depth), b_f (flange width), t_f (flange thickness) and t_w (web thickness). The I-sections have the following labeling (adopted from Saliba and Gardner 2013): $I-200\times140\times6\times6-1$, $I-200\times140\times8\times6-1$, $I-200\times140\times10\times8-1$ and $I-200\times140\times12\times8-1$ ($h_w\times b_f\times t_f\times t_w$). The length $L=2.8$ m is the same for the four beam specimens. The numerical model was used four-node isoparametric thin shell element with reduced integration S4R. A mesh size of 10 mm was found appropriate for the purpose of this validation task. In order to have physical reality, geometric imperfections were included in the FE model. The actual initial imperfection measured in Saliba and Gardner (2013), obtained herein from the first eigenmode of the beam, was added to the perfect geometry. This task requires the performance of a preliminary elastic buckling analysis to determine the buckling mode shape, and then, the consideration of its shape and amplitude as input to the non-linear analysis. The effect of the residual stresses on the behaviour of the beam was not taken into account because Saliba and Gardner (2013) found it was negligible. The boundary and loading conditions considered herein are similar to those adopted in the experimental tests (Saliba and Gardner 2013). Regarding the global rotations and in-plane displacements at the supports, simply supported boundary conditions were applied to end sections. Additionally, lateral restraints were provided at the load points and supports, typical to the experimental setup in Saliba and Gardner (2013), to prevent LTB. In order to avoid web crushing due to concentrated forces (load and reactions), three plates (transverse stiffeners) were considered, two at the supports and one at the mid-span section. Regarding the loading, each beam is acted by a vertical load at the mid-span section, above the top flange. Thus, the most stressed zone of the beams is the mid-span section. The stainless steel material relationship has been modelled as a Von Mises material with isotropic hardening. Therefore two-stage version of expressing the full-range stress-strain material behaviour of stainless steel was developed by Rasmussen (2003). In this respect, Rasmussen (2003) proposed the use of the expression:

$$\varepsilon=\begin{cases}\dfrac{\sigma}{E_0}+0.002\left(\dfrac{\sigma}{\sigma_{0.2}}\right)^{n} & \text{for } \sigma\le\sigma_{0.2}\\[2ex] \dfrac{\sigma-\sigma_{0.2}}{E_{0.2}}+\varepsilon_u\left(\dfrac{\sigma-\sigma_{0.2}}{\sigma_u-\sigma_{0.2}}\right)^{m}+\varepsilon_{0.2} & \text{for } \sigma>\sigma_{0.2}\end{cases} \quad (1)$$

Table 1. Average properties (Saliba and Gardner 2013).

t [mm]	E_0 [GPa]	$\sigma_{0.2}$ [MPa]	σ_u [MPa]	n
6	202	524	728	9.9
8	206	518	728	10.2
10	206	493	769	8.9
12	201	468	723	8.7

for the complete stress-strain curve for stainless steel alloys. where E_0 is the initial modulus of elasticity, $\sigma_{0.2}$ is the 0.2% proof stress, and n is the nonlinearity index. This index is a measure of the non-linearity of the stress-strain behaviour – note that lower n values imply higher non-linearity. The degree of non-linearity varies among different grades of stainless steel. As the value of n increases the material behaviour tends to converge to the elasto-plastic behaviour of carbon steel (elastic-perfectly plastic behaviour for $n=\infty$). In Eq. 1, $E_{0.2}$ is the tangent modulus of the stress-strain curve at the 0.2% proof stress, given by

$$E_{0.2}=\frac{E_0}{1+0.002n/e} \quad (2)$$

where $e=\sigma_{0.2}/E_0$ is the non-dimensional proof stress and $m=1+3.5(\sigma_{0.2}/\sigma_u)$. The expression (Eq. 1) involves the conventional Ramberg-Osgood parameters (n, $\sigma_{0.2}$, E_0) as well as the ultimate tensile strength (σ_u) and strain (ε_u). The expressions have been shown to produce stress-strain curves which are in good agreement with tests over the full range of strains up to the ultimate tensile strain. Therefore, Eq. 1 is used in the current investigation to generate the stress-strain curve of the lean duplex stainless steel material Grade EN 1.4162. The material behaviour provided by ABAQUS allows for a multi-linear stress-strain curve to be used. The first part of the multi-linear curve represents the elastic part up to the proportional limit stress with measured Young's modulus. In this validation study, we adopted the average measured properties obtained by Saliba and Gardner (2013) of those obtained from the six coupon tests for each material thickness (two longitudinal tensile, two longitudinal compressive and two transverse compressive coupons). Table 1 provides the measured material properties for different thicknesses (Poisson's ratio $\nu=0.3$ was considered).

The results shown here comprise (i) moment-rotation curves, (ii) failure modes and (iii) ultimate strength values. Figure 1 shows the moment-rotation curves obtained for the four beam specimens. In these curves, the white rectangles represent the experimental values while the black rectangles denote the numerical ones (note that the vertical axis is normalized against the plastic moment M_p while the horizontal axis is normalized against the cross-section flexural rotation at the onset of plastic failure). Generally speaking, the numerical curves agree well with those

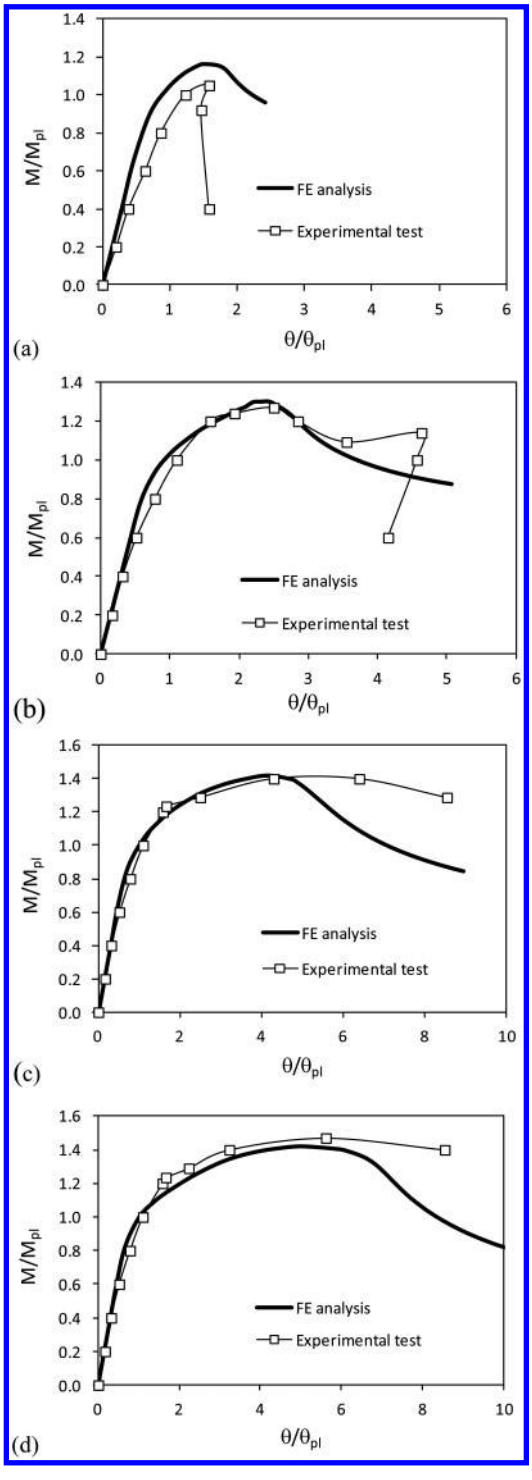


Figure 1. Moment-rotation curves of the lean duplex stainless steel I-section beams: (a) I – 200 × 140 × 6 × 6 – 1, (b) I – 200 × 140 × 8 × 6 – 1, (c) I – 200 × 140 × 10 × 8 – 1, (d) *I* – 200 × 140 × 12 × 8 – 1.

Table 2. Comparison between test and numerical results.

Beams	$M_{ul,Test}$ [kN.m]	$M_{ul,FE}$ [kN.m]	$\frac{M_{ul,FE}}{M_{ul,Test}}$
200 × 140 × 6 × 6 – 1	134	142	1.06
200 × 140 × 8 × 6 – 1	195	197	1.01
200 × 140 × 10 × 8 – 1	264	264	1.00
200 × 140 × 12 × 8 – 1	305	296	0.97

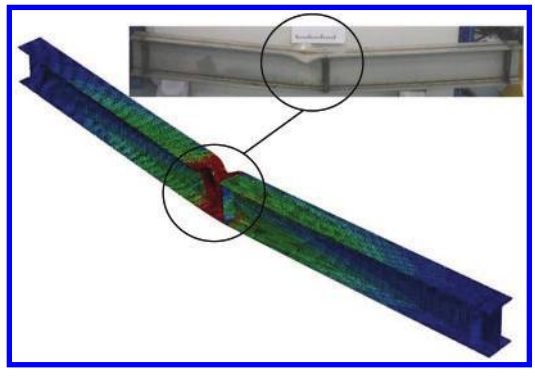


Figure 2. Failure modes of I – 200 × 140 × 6 × 6 – 1 beam under 3-point bending obtained from: (a) numerical analysis and (b) experimental test (courtesy of Saliba and Gardner 2013).

obtained experimentally, especially for the ascending branch of the curves. Regarding the beam strength, it is seen that the ultimate moments obtained numerically and experimentally compare fairly well (see Table 2). The percentage differences between the moments obtained experimentally ($M_{Test,ul}$) and numerically ($M_{FE,ul}$) are 6% (I – 200 × 140 × 6 × 6 – 1), 1% (I – 200 × 140 × 8 × 6 – 1), 0% (I – 200 × 140 × 10 × 8 – 1) and 3% (I – 200 × 140 × 12 × 8 – 1).

Finally, it is also interesting to note that the failure mode determined from the FE analysis compares very well with that obtained from experimental tests (Saliba and Gardner 2013). Figure 2 shows the failure mode of beam I – 200 × 140 × 6 × 6 – 1 determined from numerical analysis and experimental test. The formation of a plastic hinge at the left hand side of mid-span section is characterized by (i) local buckling of the top (compression) flange and (ii) yielding of the bottom (tensioned) flange.

3 PARAMETRIC STUDY

Since LDIPGs are frequently subjected to in-plane loading, it is important that design guidance takes into account several instability phenomena, such as local buckling and global buckling. The lean duplex stainless steel I-section beams previously studied failed by local buckling (L). However, it is probable that longer beams would fail either by lateral-distortional buckling (LD) or lateral-torsional buckling (LT). In order to

Table 3. LDIPGs geometrical properties and yield moments.

Group	b_f [mm]	t_f [mm]	t_w [mm]	h_w [mm]	r_T [mm]	S_{xc} [cm^3]	M_y [kN.m]
G1	250	30	10	1140	72.2	**10615**	5626
G2	300	30	10	1000	**86.6**	**10582**	5609
G3	350	30	10	890	101.0	**10595**	5615
G4	300	30	10	1250	**86.6**	13743	7284
G5	300	30	10	1500	**86.6**	17112	9070

analyze the flexural behaviour of LDIPGs of Grade EN 1.4162 and unveil their structural behaviour, numerical analyses on full-scale plate I-section girders are conducted next. The input data are shown in the next paragraphs.

The cross-sectional dimensions of the LDIPGs were selected assuming compact flanges and slender webs. The overall dimensions h_w, b_f, t_f and t_w remain, but their values for the LDIPGs are quite different from their I-section counterparts. Table 3 shows the dimensions considered in this study. The FE analysis program consists of five groups (G1, G2, G3, G4 and G5), as it is seen in Table 3. The parameters covered herein are based upon the AISC (2010) recommendations:

- the radius of gyration of the compression flange (r_T) assumes three values (72.2 mm, 86.6 mm and 101 mm), and
- the section modulus referred to compression (S_{xc}) assumes three values (10582 cm^3, 13743 cm^3 and 17112 cm^3).

Based upon the r_T, S_{xc} and L_b variables, the study considers sections with flange width-to-web depth ratio (b_f/h_w) that varies between 0.20 and 0.39. The flange-to-web thickness ratio defined by t_f/t_w was fixed to 3. The flange dimensions are assigned a b_f/t_f ratio that ranges from 8.33 to 11.67. Meanwhile, web plate slenderness is characterized by web height to web thickness (h_w/t_w) values that vary between 89 and 150. Since the unbraced length (L) assumes nine values (3, 5, 7, 9, 11, 13, 15, 17, 19 m), 45 LDIPGs are considered in this study. The LDIPGs are labelled herein such that the group number could be identified from the label followed by their unbraced lengths. For example, the label "G2-9" defines a girder of Group 2 with an unbraced length of 9m.

The structural behaviour of LDIPGs depends on the mechanical properties of the lean duplex stainless steel material. According to the EN 10088-4 (2009), the cold-formed lean duplex stainless steel Grade EN 1.4162 has a minimum 0.2% proof stress ($\sigma_{0.2}$) of 530 MPa and an ultimate tensile strength ranging from 700–900 MPa. The lower bound of the tensile strength (700 MPa) is considered in the present study. Furthermore, we considered the Young's modulus $E_0 = 200$ GPa, Poisson's ratio $\nu = 0.3$ and proportional limit $\sigma_{0.01} = 400$ MPa.

The numerical models adopted herein for the LDIPGs follow that previously validated for I-section

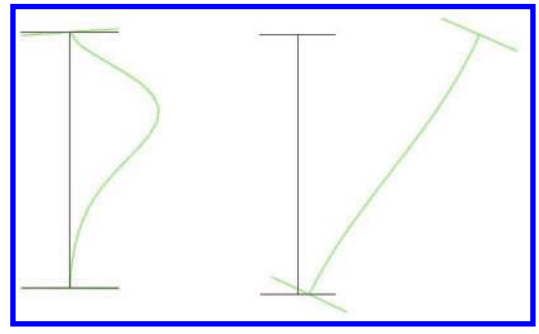


Figure 3. Local (L) and lateral-distortional (LD) buckling modes.

Table 4. Buckling/failure modes for the LDIPGs.

Group	3 m	5 m	7 m	9 m	11 m	13 m	15 m	17 m	19 m
G1	L	LD	LD	LD	LD	LD	LD	LT	LT
G2	L	LD	LD	LD	LD	LD	LD	LT	LT
G3	L	LD	LD	LD	LD	LD	LD	LT	LT
G4	L	LD	LD	LD	LD	LD	LD	LD	LD
G5	L	L	LD	LD	LD	LD	LD	LD	LD

beams. As previously stated, the aim of this paper is to show some representative flexural strength results for the LDIPGs considering the key parameters affecting them; namely the radius of gyration of the compression flange (r_T), neglecting the contribution of the web, and the section modulus referred to compression (S_{xc}). As can be seen in Table 3, Groups 1-3 have very similar S_{xc}, while Groups 2 and 4-5 possess a typical value $r_T = 86.6$ cm. Thus, we have a total of 45 girders analysed herein. The yield bending moment ($M_y = S_{xc}f_y$) of the sections are provided in Table 3.

Both elastic (bifurcation) buckling and nonlinear FE analyses of LDIPGs were conducted and the critical moment (M_{cr}) and ultimate moment (M_{ul}) were then obtained from these analyses, respectively. The deformed shapes at the ultimate moments (M_{ul}) of the LDIPGs with different spans are examined herein to thoroughly monitor the different failure modes. Three failure modes were noticed in the current program, arising from local buckling (L – Figure 3), lateral-distortional buckling (LD – Figure 3) and lateral-torsional buckling (LT – Figure 3). Table 4 shows the distribution of buckling/failure modes for the 5 groups and 9 lengths. Table 5 shows the numerical results (M_{ul}/M_y) obtained for G1, G2, G3, G4 and G5. It is clearly shown that the girder length as well as the radius of gyration of the compression flange and the section modulus might affect the girder buckling/failure mode.

4 COMPARISON WITH DESIGN RESULTS

The numerical results shown before are now used to investigate the suitability of current design rules when

Table 5. Ultimate-to-yield moment ratio M_{ul}/M_y values.

L_b [m]	G1	G2	G3	G4	G5
3	0.75	0.91	1.01	0.84	0.81
5	0.46	0.57	0.66	0.54	0.90
7	0.30	0.41	0.50	0.39	0.36
9	0.21	0.31	0.40	0.28	0.26
11	0.16	0.24	0.31	0.21	0.19
13	0.13	0.19	0.25	0.16	0.15
15	0.11	0.16	0.21	0.13	0.12
17	0.10	0.14	0.18	0.12	0.11
19	0.09	0.12	0.16	0.10	0.09

applied to estimate flexural strengths of the LDIPGs. The available design method of AS4100 (1998) and EN1993-1-4 (2006) do not account for web distortions in LDIPGs with stocky flanges and slender web. Accordingly, this section evaluates the lateral buckling predictions of both AS4100 (1998) andEN1993-1-4 (2006) for the use for the LDIPGs. It should be pointed out that the LT strength of IPGs in both elastic and inelastic ranges is defined in AS4100 (1998) and EN1993-1-4 (2006) by a single curve, not distinguishing elastic and inelastic strength. According to the AS4100 (1998), the strength of a laterally unrestrained girder subjected to major axis bending is estimated by the following formula:

$$M_{AS} = 0.6M_p\left[\sqrt{\bar{\lambda}_{LT}^{\,4}+3}-\bar{\lambda}_{LT}^{\,2}\right] \le M_p \qquad (3)$$

where $\lambda_{LT} = (M_y/M_{cr,LT})^{0.5}$ is the girder slenderness and M_p is the plastic moment of the section. According to the EN1993-1-4 (2006), the strength of a laterally unrestrained girder subjected to major axis bending is estimated by the following formula:

$$\chi_{LT} = \frac{1}{\Phi_{LT}+\sqrt{\Phi_{LT}^{\,2}-\bar{\lambda}_{LT}^{\,2}}} \le 1.0$$
$$\Phi_{LT} = 0.5\left[1+\alpha_{LT}\left(\bar{\lambda}_{LT}-0.4\right)+\bar{\lambda}_{LT}^{\,2}\right] \qquad (4)$$

where M_y is either (i) the yield bending moment of the effective cross-section ($M_{eff,y}$) if the cross-section is Class 4 or (ii) the yield bending moment of the gross cross-section ($M_{el,y}$) if the cross-section is Class 3. Additionally, χ_{LT} is the reduction factor for LT, α_{LT} is the imperfection factor (taken herein as 0.76 for welded open sections) and $\lambda_{LT} = (M_y/M_{cr,LT})^{0.5}$ is the girder slenderness. In the definition of the girder slenderness λ_{LT} for both AS4100 (1998) and EN1993-1-4 (2006), the elastic critical moment for LT ($M_{cr,LT}$) should be used. It is based upon the *gross* sectional properties and takes into account the loading conditions, the real moment distribution and the lateral restraint. The ultimate moments M_{ul} (or strengths) of the LDIPGs obtained from the FE nonlinear analyses, given indirectly in Table 5, are compared with the LT strengths predicted by the AS4100 (1998) and EN1993-1-4 (2006), shown in Tables 6 and 7. From Tables 6 and 7 it can be observed that the AS4100 (1998) predicts higher moments than numerical ones, while the EN1993-1-4 (2006) conservatively predicts such strengths. Pi and Trahair (2000) showed that the elastic LD moment ($M_{cr,LD}$) might be obtained from the Eq. 5. Their main idea suggests that a reduction in the warping stiffness due to web distortions should be taken into consideration in addition to a reduction in the torsional stiffness when calculating the LD moment of an I-beam with stocky flanges,

$$M_{cr,LD} = \frac{\pi}{kL}\sqrt{EI_y GJ_e\left(1+\frac{\pi^2}{(k_w L)^2}\frac{EC_{we}}{GJ_e}\right)}$$
$$GJ_e = \frac{(2GJ_f).(12D_w L^2/\pi^2 h_w)}{(2GJ_f)+(12D_w L^2/\pi^2 h_w)} \qquad D_w = \frac{Et_w^{\,3}}{12(1-\upsilon^2)} \qquad (5)$$
$$EC_{we} = \frac{EC_w}{1+r_{fw}^{\,3}.(h_w/12L_b).(1+b_f/h_w)}$$

where GJ_f is the torsional rigidity of the flange and r_{fw} is the smaller of t_f/t_w and 2. The elastic critical moment for LD ($M_{cr,LD}$) is now calculated using the *effective* torsional and warping rigidities (GJ_e and EC_{we}) proposed by Pi and Trahair (2000), and the ultimate strengths using $M_{cr,LD}$ are also shown in Tables 6 and 7. It can be seen from Tables 6 and 7 that the use of the *effective* torsional and warping rigidities in the context of AS4100 (1998) expression provides unconservative predictions for inelastic LD range, while it provides accurate results for the elastic LD range (long girders). However, utilizing such *effective* torsional and warping rigidities in the EN1993-1-4 (2006) equation provides higher conservative predictions of the LDIPG flexural strength than using the *gross* torsional and warping rigidities, for short unbraced lengths. Generally, it can be concluded that the design equation given by EN1993-1-4 (2006) (with *effective* torsional and warping rigidities) is suitable to be used in design.

Figure 4 shows the variation, with λ_{LT}, of the ratio between the ultimate moments obtained from numerical analyses (M_{ul}) and EC3 formulas (M_{EC3}). The current design approach is denoted by the black circles. It is seen that $M_{ul}/M_{EC3}>1.0$ and the mean value and standard deviation of M_{ul}/M_{EC3} are 1.24 and 0.04, respectively. This means that the EC3 design approach is too conservative and may cause economic losses. If we apply an imperfection factor α_{LT} of 0.49 rather than 0.76, which means that we use buckling curve (c) instead of curve (d), we get higher and less conservative M_{EC3} values. The results of the recommended design approach are denoted by the white circles in Figure 4.

It is seen that $M_{ul}/M_{EC3}>1.0$ but the mean value and standard deviation of M_{ul}/M_{EC3} are now 1.13 and 0.05, respectively – the mean error (13%) is now about one half of the mean error (24%) of the current EC3 approach.

Table 6. AS4100 and EN 1993-1-4 results for G1, G2 and G3.

	G1		G2		G3	
	M_{EC3}/M_y $[M_{AS}/M_y]$		M_{EC3}/M_y $[M_{AS}/M_y]$		M_{EC3}/M_y $[M_{AS}/M_y]$	
L_b [m]	LT	LD	LT	LD	LT	LD
3	0.66 [0.89]	0.62 [0.85]	0.78 [0.95]	0.75 [0.92]	0.88 [0.99]	0.85 [0.97]
5	0.39 [0.59]	0.37 [0.53]	0.52 [0.71]	0.49 [0.66]	0.62 [0.79]	0.60 [0.75]
7	0.25 [0.38]	0.24 [0.32]	0.35 [0.50]	0.34 [0.43]	0.44 [0.60]	0.43 [0.54]
9	0.18 [0.27]	0.17 [0.21]	0.25 [0.36]	0.24 [0.29]	0.32 [0.45]	0.32 [0.38]
11	0.14 [0.20]	0.13 [0.14]	0.19 [0.27]	0.19 [0.20]	0.25 [0.35]	0.25 [0.27]
13	0.11 [0.16]	0.11 [0.10]	0.15 [0.22]	0.15 [0.15]	0.20 [0.28]	0.20 [0.20]
15	0.09 [0.13]	0.09 [0.08]	0.13 [0.18]	0.13 [0.11]	0.17 [0.23]	0.17 [0.15]
17	0.08 [0.11]	0.08 [0.06]	0.11 [0.15]	0.11 [0.09]	0.15 [0.20]	0.15 [0.12]
19	0.07 [0.09]	0.07 [0.05]	0.10 [0.13]	0.10 [0.07]	0.13 [0.17]	0.13 [0.10]

Table 7. AS4100 and EN 1993-1-4 results for G1, G2 and G3.

	G1		G2		G3	
	M_{EC3}/M_y $[M_{AS}/M_y]$		M_{EC3}/M_y $[M_{AS}/M_y]$		M_{EC3}/M_y $[M_{AS}/M_y]$	
L_b [m]	LT	LD	LT	LD	LT	LD
3	0.78 [0.95]	0.75 [0.92]	0.75 [0.96]	0.72 [0.93]	0.72 [0.97]	0.68 [0.93]
5	0.52 [0.71]	0.49 [0.66]	0.49 [0.70]	0.46 [0.66]	0.47 [0.70]	0.43 [0.66]
7	0.35 [0.50]	0.34 [0.43]	0.32 [0.49]	0.31 [0.43]	0.30 [0.48]	0.29 [0.43]
9	0.25 [0.36]	0.24 [0.29]	0.23 [0.34]	0.22 [0.29]	0.21 [0.33]	0.20 [0.29]
11	0.19 [0.27]	0.19 [0.20]	0.17 [0.25]	0.17 [0.20]	0.16 [0.24]	0.15 [0.20]
13	0.15 [0.22]	0.15 [0.15]	0.14 [0.20]	0.13 [0.15]	0.12 [0.19]	0.12 [0.15]
15	0.13 [0.18]	0.13 [0.11]	0.11 [0.16]	0.11 [0.11]	0.10 [0.15]	0.10 [0.11]
17	0.11 [0.15]	0.11 [0.09]	0.09 [0.13]	0.9 [0.09]	0.08 [0.12]	0.08 [0.09]
19	0.10 [0.13]	0.10 [0.07]	0.08 [0.11]	0.08 [0.07]	0.07 [0.10]	0.07 [0.07]

5 CONCLUSION

The findings of a numerical investigation on the flexural behaviour of lean duplex stainless steel plate girders (LDIPGs) of Grade EN 1.4162 were presented. Firstly, the shell finite element model adopted in this study was validated by comparison with experimental results available in the literature. After that, the LDIPGs with compact flanges and slender unstiffened webs under the effect of uniform bending moments were considered. The obtained results were used to develop LD buckling design guidance for the LDIPGs. Several conclusions were drawn and described in the preceding section. For more details, the interested reader may refer to Hassanein and Silvestre (2013).

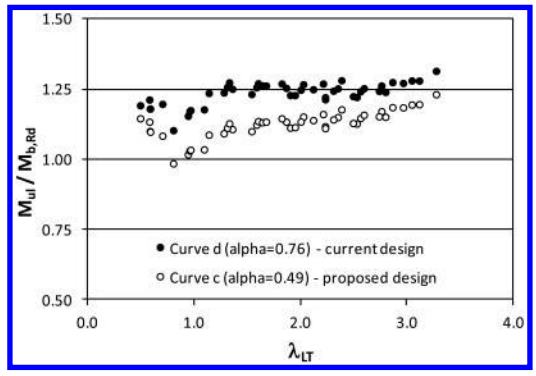


Figure 4. Numerical-to-predicted strength ratio vs. λ_{LT}.

REFERENCES

AISC (2010). Load and Resistance Factor Design Specification, for Structural Steel Buildings, American Institute of Steel Construction, Chicago.

AS 4100 (1998). Standards Association of Australia. AS 4100 steel structures. Sydney, Australia.

Baddoo NR (2008). Stainless Steel in Construction: A review of Research, Applications, Challenges and Opportunities, Journal of Constructional Steel Research, Vol. 64, pp. 1199–1206.

EN 10088-4. (2009). Stainless steels-Part 4: Technical delivery conditions for sheet/plate and strip of corrosion resisting steels for general purposes, CEN.

EN 1993-1-4 (2006). Eurocode 3: Design of steel structures – Part 1–4: General rules-Supplementary rules for stainless steel. CEN.

Gardner L (2005). The Use of Stainless Steel in Structures, Progress in Structural Engineering and Materials, Vol. 7(2), pp. 45–55.

Hancock GJ, Bradford MA, Trahair NS (1980). Web distortion and flexural-torsional buckling, Journal of the Structural Division (ASCE), Vol. 106(7), pp. 1557–1571.

Hassanein M, Silvestre N (2013). Behaviour of Lean Duplex Stainless Steel Plate Girders with Stocky Flanges and Slender Unstiffened Webs, JCSR, http://dx.doi.org/10.1016/j.jcsr.2013.02.003.

Pi YL, Trahair NS (2000). Distortion and Warping at Beam Supports. ASCE, Journal of Structural Engineering, Vol. 126, pp. 1279–1287.

Rasmussen KJR (2003). Full Range Stress-Strain Curves for Stainless Steel Alloys, Journal of Constructional Steel Research, Vol. 59, pp. 47–61.

Saliba N, Gardner L (2013). Cross-section Stability of Lean Duplex Stainless Steel Welded I-sections. Journal of Constructional Steel Research. Vol. 80, pp. 1–14.

Research and Applications in Structural Engineering, Mechanics and Computation – Zingoni (Ed.)
© 2013 Taylor & Francis Group, London, ISBN 978-1-138-00061-2

Structural response of stainless steel cross-sections under combined compression and biaxial bending

M. Theofanous & L. Gardner
Department of Civil and Environmental Engineering, Imperial College London, London, UK

E. Koltsakis
Department of Civil, Environmental and Natural Resources Engineering, Lulea University of Technology, Lulea, Sweden

ABSTRACT: The Continuous Strength Method (CSM) was developed and calibrated against experimental and numerical results as a design approach, which allows for a rational exploitation of the significant strain-hardening exhibited by stocky stainless steel cross-sections, thereby leading to more economic design. In order to extend its scope of application beyond the fundamental loading cases of concentric compression and uniaxial bending, a comprehensive numerical parametric study has been conducted and the obtained numerical results have been utilized to determine suitable interaction equations for cross-sections subjected to combined loading. This paper focuses on the ultimate response of I-sections under combined loading and complements a recent relevant study on RHS under combined loading. It is concluded that the current design guidance for stainless steel cross-sections under combined compression and biaxial bending is overly conservative and significant gains can be made if the effect of strain-hardening on ultimate capacity is taken into account.

1 INTRODUCTION

The material response of stainless steels deviates significantly from the elastic-perfectly plastic model assumed in EN 1993-1-4 (2006), due to the absence of a yield plateau and the significant strain-hardening exhibited at relatively low strains. Failure to account for the actual material response and the adoption of the 0.2% proof stress as a nominal yield stress, as is conventionally specified in design regulations, leads to significant underestimation of the ultimate capacity of stainless steel cross-sections of low to intermediate slenderness, which can sustain stresses far beyond their nominal yield stress. The conservatism embedded in EN 1993-1-4 (2006) has been highlighted by numerous researchers (Burgan et al. 2000, Gardner & Theofanous 2008).

Given the high material cost of stainless steels, the development of more advanced design approaches that allow for a rational exploitation of the special merits of stainless steels in design is warranted. To this end, the Continuous Strength Method (CSM) was developed by Gardner & Nethercot (2004a, 2004b) and calibrated against experimental and numerical results as a strain-based design approach which rationally takes into account the significant strain-hardening exhibited by stocky stainless steel cross-sections. The method has also been adapted to aluminum alloys (Gardner & Ashraf 2006) and carbon steel (Gardner 2008). Recently the CSM was modified to incorporate the effect of interaction of the constituent plate elements on the cross-sectional capacity (Theofanous & Gardner 2012) by employing the concept of cross-sectional slenderness, as defined within the framework of the Direct Strength Method (Schafer 2008) in place of the plate slenderness of the most slender constituent plate element, which is assumed to relate to a cross-section's deformation capacity. Additional advancements of the method include its extension to stainless steel members failing by distortional buckling (Theofanous & Gardner 2012), as well as to stainless steel continuous beams (Theofanous et al. 2012a). Moreover, significant simplifications in design arise by departing from the accurate Ramberg-Osgood based material model originated by Mirambell & Real (2000) and further developed by Rasmussen (2003), and adopting a bilinear elastic-linear hardening material model (Gardner et al. 2011). A full account of the CSM for stainless steel design is given by Afshan and Gardner (in press).

Initially the scope of the method was limited only to stainless steel cross-sections subjected either to compression or uniaxial bending. Clearly, more general loading cases have to be considered if CSM is to become a viable alternative to existing design procedures. However the relevant research on stainless-steel components under combined loading is scarce and focuses mainly on beam-column members rather than cross-sections (Talja & Salmi 1995, Burgan et al. 2000, Greiner & Kettler 2008). This is also reflected in the lack of design rules for stainless steel cross-sections under combined loading in EN

1993-1-4 (2006), which refers the designer to the relevant carbon steel design rules given in EN 1993-1-1 (2005). To address the lack of relevant experimental and numerical data, an extensive parametric study on stainless steel RHS stub columns under combined compression and biaxial bending has been conducted and interaction equations for stainless steel RHS have been proposed by Theofanous et al. (2012b). The present paper extends that research by investigating the ultimate capacity of stainless steel I-section stub columns under combined loading. Based on an extensive finite element parametric study of I-section stub columns under combined compression and biaxial bending covering a wide range of cross-section geometries and slendernesses, interaction expressions are derived, which allow the application of the CSM to stainless steel components under general loading conditions. The numerical results are compared with the codified ultimate capacity predictions and with the CSM predictions demonstrating the superiority of the CSM in terms of both economic design and consistency of the predictions, particularly in the low slenderness region.

2 NUMERICAL MODELLING

The general purpose FE software ABAQUS (2010) has been utilized to model 20 I-section geometries subjected to a large number of loading cases. A full account of the basic modeling assumptions adopted herein is given in Theofanous & Gardner (2012a). All modelled cross-sections had a flange width of 100 mm and a flange thickness varying from 6 mm to 10 mm in increments of 1 mm, whilst two section aspect ratios equal to 1 and 2 and two flange to web thickness ratios equal to 1 and 0.6 were investigated, thus resulting in 20 cross-section geometries. The mid-surface of the cross-sections was modelled with a relatively fine uniform mesh of linear reduced integration finite strain shell elements S4R (ABAQUS 2010). The length of the modelled stub columns was set equal to three times the largest cross-section dimension. This length was deemed short enough to exclude member instabilities yet sufficiently long for local buckling to develop with little effect from the end restraints. All modelled stub columns failed by local buckling and the obtained ultimate capacity was assumed to represent the cross-sectional capacity of the modelled component.

A two-stage Ramberg-Osgood material law (Mirambell & Real 2000, Rasmussen 2003, Gardner & Nethercot 2004a) was employed to represent the material response of the modelled components. The adopted material properties correspond to a typical austenitic stainless steel (Groth & Johansson 1990) and are given in Table 1, where E is the Young's modulus, $f_{0.2}$ (or f_y) and $f_{1.0}$ are the stresses corresponding to 0.2% and 1% plastic strain respectively and n and $n_{0.2,1.0}$ are strain-hardening exponents.

The initial geometric imperfections assumed the shape of the lowest elastic buckling mode shape as determined by means of an eigenvalue buckling analysis for each component and load case considered. The amplitude of the initial geometric imperfection was determined by means of a predictive model (Dawson & Walker 1972) modified for stainless steel (Gardner & Nethercot 2004c). No residual stresses were included in the analysis due to the inherent uncertainty regarding their magnitude and distribution and due to the fact that they were shown to have an insignificant effect for stub columns (Gardner & Nethercot 2004c). A typical elastic buckling mode shape and a typical failure mode are shown in Figure 1.

Table 1. Adopted material properties.

E	$f_{0.2}$ (N/mm^2)	$f_{1.0}/f_{0.2}$	n	$n_{0.2,1.0}$	f_u (N/mm^2)
200000	306.1	1.2	5.6	2.7	614.7

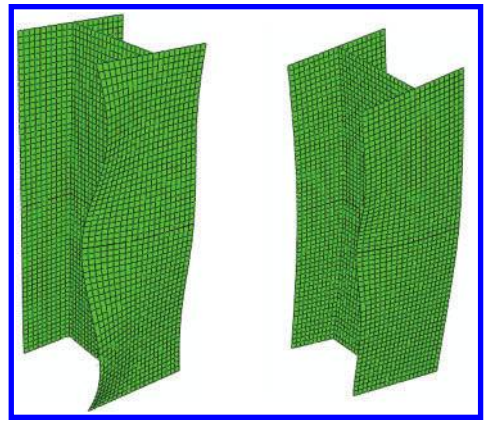


Figure 1. Lowest buckling mode shape and failure mode for a typical I-section subjected to compression and biaxial bending.

For each modelled component, 73 combinations of axial compression and biaxial bending about both principal axes were imposed, which contained the fundamental cases of pure compression and uniaxial bending about either axes. Moreover the interaction of axial force with uniaxial bending as well as the case of biaxial bending without a coexisting axial compression were also included as special cases. The loads were applied proportionally at the end cross-section of each component, which was constrained to displace and rotate as a rigid body, on which pin-ended boundary conditions were imposed.

Due to the large number of analyses performed, the computational cost was reduced by modelling half the length of each component and imposing appropriate symmetry boundary conditions. Scripting in Python was employed to utilize the parametric capabilities of ABAQUS (2010). Based on the obtained results, current design provisions are assessed in the following sections of the paper.

3 ASSESSMENT OF EN 1993-1-4

EN 1993-1-4 (2006) specifies special design provisions for stainless steel beam-column members, but refers to EN 1993-1-1 (2005) for cross-sectional checks, which allow for plasticity within a cross-section subjected to combined compression and biaxial bending, provided that the section is classified as Class 1 or 2. The codified interaction expressions of EN 1993-1-1 (2005) for a stocky (i.e. Class 1 or 2) I-section is given by Equation (1):

$$\left[\frac{M_{y,Ed}}{M_{N,y,Rd}}\right]^{2} + \left[\frac{M_{z,Ed}}{M_{N,z,Rd}}\right]^{5n} \leq 1 \qquad (1)$$

where $M_{y,Ed}$ and $M_{z,Ed}$ are the applied moments and $M_{N,y,Rd}$ and $M_{N,z,Rd}$ are the plastic moment resistances about the relevant axis, reduced due to the axial force N_{Ed} and $n = N_{Ed}/(Af_y)$. The design expressions for $M_{N,y,Rd}$ and $M_{N,z,Rd}$ are given in EN 1993-1-1 (2005). For Class 3 and Class 4 sections, the maximum longitudinal stress due to the applied loads should be limited to the yield stress f_y, which effectively results in a linear interaction equation.

For each modelled cross-section and load case, a triplet of axial force N_{Ed}, bending moment about the major axis $M_{Ed,y}$ and bending moment about the minor axis $M_{Ed,z}$ was obtained, thus enabling the determination of interaction surfaces in the (N_{Ed}, $M_{Ed,y}$, $M_{Ed,z}$) space and the assessment of current interaction equations.

In the following figures, $W_{pl,y}$, $W_{pl,z}$ are the section plastic moduli about the respective principal axes, A_{eff} is the effective cross-section area (gross area for Classes 1-3), $\beta_w = 1$ for Class 1 or 2 cross-sections, $\beta_w = W_{el}/W_{pl}$ for Class 3 cross-sections and $\beta_w = W_{eff}/W_{pl}$ and f_y is the nominal yield stress $f_{0.2}$. Figures 2-4 depict the comparison of numerical (normalized by codified resistance) and codified ultimate capacities for I-sections with an aspect ratio of 1 and a flange to web thickness ratio of unity for the special cases of compression and major axis bending (N-M_y), compression and minor axis bending (N-M_z) and biaxial bending respectively. All data points correspond to cross-sections classified either as Class 1 or 2 for which Equation 1 applies. As shown in Figures 2-4, the predictions of the Eurocode are overly conservative in all cases. The conservatism seems to increase with increasing slenderness, since the thicker cross-sections lie further away from the codified interaction curves. This suggests that the source of conservatism is the strain-hardening achieved by the stockier cross-sections which is not considered in the codified predictions.

Figures 5–7 depict the comparison of numerical and codified capacities for I-sections with an aspect ratio of 2 and a flange to web thickness ratio of 0.6. The classification of these cross-sections varies from Class 1 to Class 4 according to width to thickness ratio and applied loading, with all the cross-sections being Class 4 in pure compression, Class 1 or 2 for minor axis bending and Class 1 or 3 for major axis bending. It should be noted that this group of cross-sections is the most slender considered in this study, since the main focus of the paper is cross-sections of low to intermediate slenderness, for which the effect of strain-hardening is more pronounced.

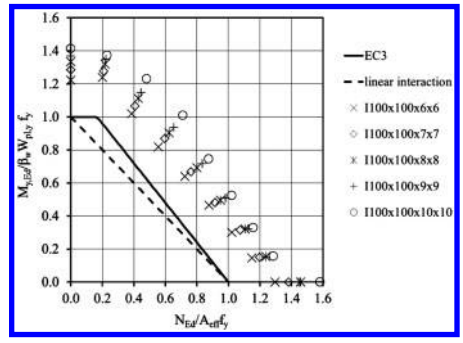


Figure 2. Interaction of axial compression and major axis bending (N_{Ed} + $M_{y,Ed}$, $M_{z,Ed} = 0$) for I-sections with aspect ratio 1.

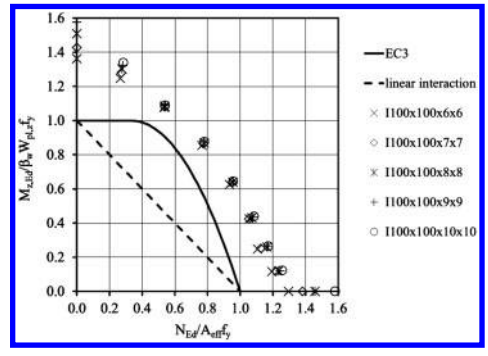


Figure 3. Interaction of axial compression and minor axis bending ($N_{Ed} + M_{z,Ed}$, $M_{y,Ed} = 0$) for I-sections with aspect ratio 1.

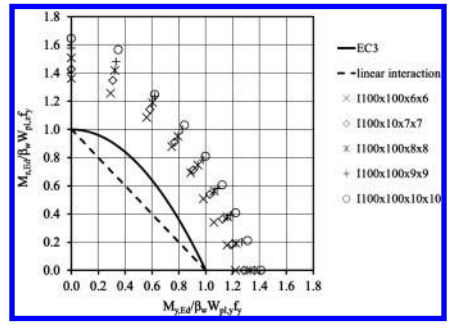


Figure 4. Interaction of minor axis and major axis bending ($N_{Ed} = 0$, $M_{y,Ed} + M_{z,Ed}$) for I-sections with aspect ratio 1.

Comparing Figures 5–7 to Figures 2–4 it can be observed that the level of conservatism of the codified predictions decreases with increased slenderness, due to the less pronounced effect of strain-hardening. However the codified predictions are still overly conservative. For the more general case of cross-sections subjected to compression and biaxial bending, similar

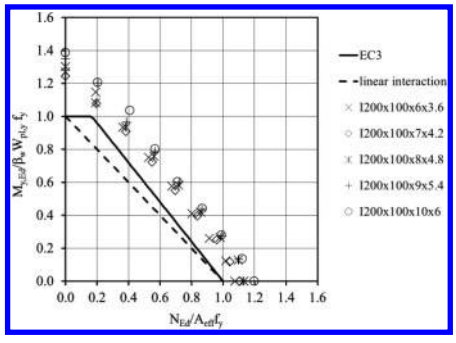


Figure 5. Interaction of axial compression and major axis bending ($N_{Ed} + M_{y,Ed}, M_{z,Ed} = 0$) for I-sections with aspect ratio 2.

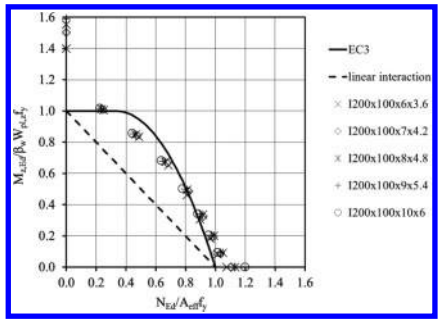


Figure 6. Interaction of axial compression and minor axis bending ($N_{Ed} + M_{z,Ed}, M_{y,Ed} = 0$) for I-sections with aspect ratio 2.

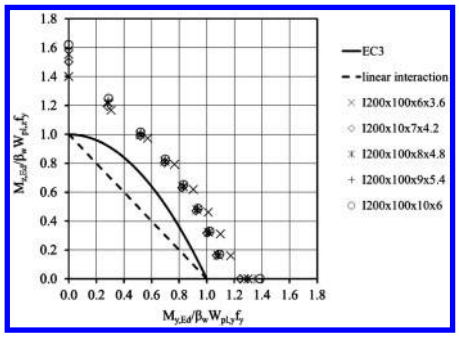


Figure 7. Interaction minor axis and major axis bending ($N_{Ed} = 0, M_{y,Ed} + M_{z,Ed}$) for I-sections with aspect ratio 2.

remarks on the conservatism and scatter of the predictions to the ones made for the more simplified loading cases previously hold. The numerically obtained interaction surfaces for $I100 \times 100 \times 10 \times 10$ and $I200 \times 100 \times 10 \times 6$ are shown in Figures 8 and 9. It can be observed the interaction surface of Figure 8 is more curved than the respective surface for Figure 9, due to the increased strain-hardening associated with the reduced slenderness.

A quantitative assessment of the accuracy of the predictions of EN 1993-1-4 (2006) and EN 1993-1-1 (2005) reveals that on average the Eurocode underestimates the numerically obtained capacities by 31%

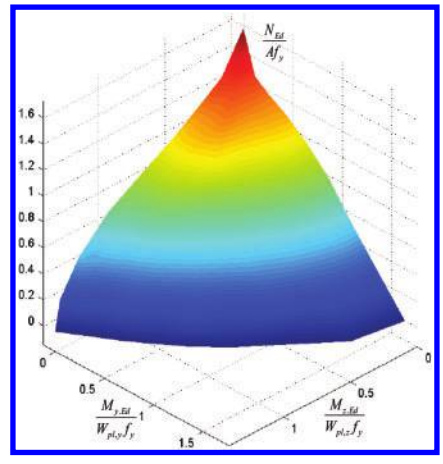


Figure 8. Interaction surface for $I100 \times 100 \times 10 \times 10$.

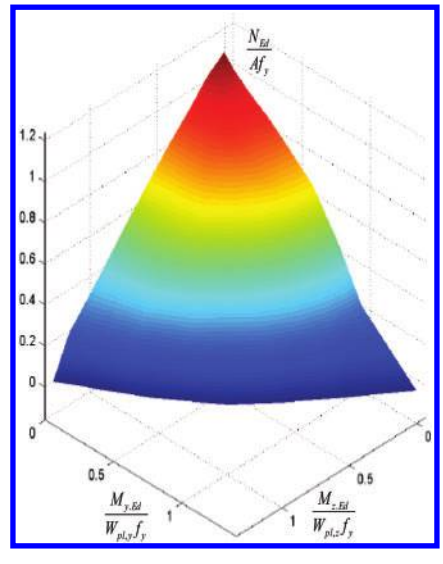


Figure 9. Interaction surface for $I200 \times 100 \times 10 \times 6$.

with a coefficient of variation (COV) of 0.158. The high COV is due to the different level of conservatism exhibited for cross-sections of different levels of slenderness; the embedded conservatism decreases with increasing slenderness. This is due to the effect of strain-hardening, which is more pronounced for stocky cross-sections and becomes insignificant with increasing slenderness.

4 THE CSM FOR COMBINED LOADING

The conservatism of the current design provisions highlighted in the previous section can be largely attributed to the inefficiency of current design provisions in determining the ultimate capacity for the fundamental loading cases acting in isolation for stocky cross-sections (i.e. the end points of the interaction surfaces). In this Section the numerically obtained

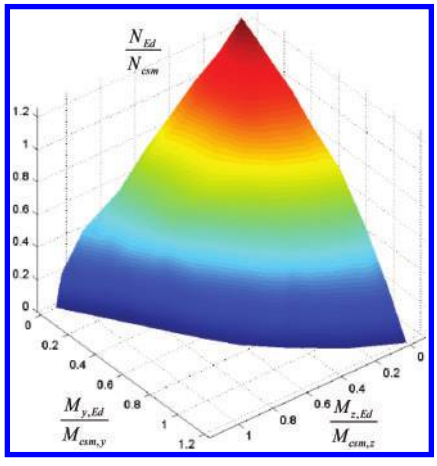


Figure 10. Interaction surface for I100 × 100 × 7 × 4.2.

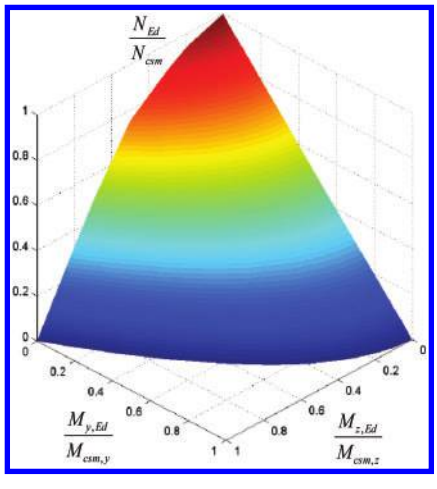


Figure 11. Interaction surface defined by Equation (4).

failure loads are normalized by the CSM predictions and an interaction equation which provides a best fit to the numerically obtained interaction surfaces is proposed, hence allowing the extension of the CSM to more general loading conditions.

A detailed account of the CSM is given in Afshan & Gardner (in press). In short, for each cross-section and load case considered, the corresponding elastic critical buckling stress f_{cr} is utilized to obtain the cross-sectional slenderness $\bar{\lambda}_p$ defined by Equation (2).

$$\bar{\lambda}_p = \sqrt{f_y / f_{cr}} \tag{2}$$

The maximum strain ε_{csm} that the section can attain (as limited by local buckling) is given by Equation (3):

$$\frac{\varepsilon_{csm}}{f_y/E} = \frac{0.25}{\bar{\lambda}_p^{3.6}} \le \min\left\{15; 0.1\frac{\varepsilon_u}{\varepsilon_y}\right\} \tag{3}$$

Having established the maximum strain that can be reached by the cross-section and assuming an elastic-linear hardening material model the axial and bending

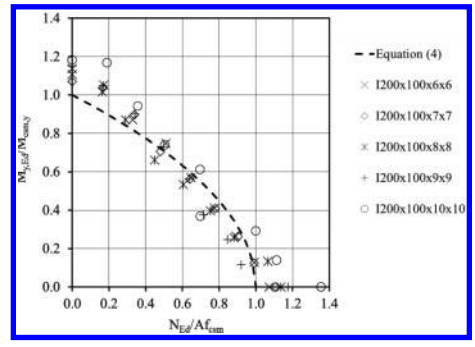


Figure 12. Interaction of axial compression and minor axis bending ($N_{Ed} + M_{y,Ed}$, $M_{z,Ed} = 0$) for I-sections with aspect ratio 2.

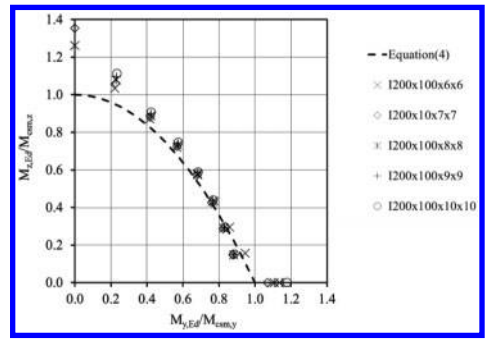


Figure 13. Interaction minor axis and major axis bending ($N_{Ed} = 0$, $M_{y,Ed} + M_{z,Ed}$) for I-sections with aspect ratio 2.

capacities according to CSM (i.e. N_{csm}, $M_{csm,y}$ and $M_{csm,z}$) can be obtained according to explicit equations (Gardner et al. 2011). The CSM allows for a rational exploitation of strain hardening up to strains 15 times larger than the elastic strain at f_y in accordance with codified ductility requirements (EN 1993-1-4 2006, EN 1993-1-1 2005). A further restriction pertaining to the CSM is the slenderness of the cross-sections at which it is applied, which is limited to $\bar{\lambda}_p \le 0.68$. From a total of 1460 obtained numerical results the CSM was not applicable only in 14 cases. For these cases the cross-sectional resistance was calculated according to the provisions of EN 1993-1-4 (2006).

Using the aforementioned procedure, the axial, minor axis bending and major axis bending capacities of all sections were determined. The numerical failure loads were normalized by the respective capacities and utilized to derive a suitable interaction curve that fits the data. A typical interaction surface is shown in Figure 10, whilst Equation (4) was shown to produce a slightly conservative but sufficiently accurate fit to the obtained results. Figure 11 depicts the interaction surface defined by Equation (4).

$$\frac{N_{Ed}}{N_{csm}} + \left(\frac{M_{y,Ed}}{M_{csm,y}}\right)^2 + \frac{M_{z,Ed}}{M_{csm,z}} \le 1 \tag{4}$$

The predictions of CSM in conjunction with Equation (4) are compared to the numerical results for the

Table 2. Assessment of codified and proposed design methods.

Design method	EN 1993-1-4		CSM and Equation (4)	
	Mean	COV	Mean	COV
All	0.690	0.158	0.904	0.108

special cases of axial compression and minor axis bending and biaxial in Figures 12 and 13 respectively for I-sections with an aspect ratio of 2 and a flange to web thickness ratio of 1. Generally, a good agreement between the proposed design approach and the numerical results can be observed. Finally, the accuracy of the proposed interaction equation is quantified in Table 2.

5 CONCLUSIONS

An extensive parametric study on stainless steel I-sections subjected to compression and biaxial bending has been reported and 1460 numerical results were extracted and utilized to assess the European design codes for stainless steel structures. As expected, the codified provisions are overly conservative since the strain-hardening exhibited by stocky I-sections is not allowed for. The CSM, which has been previously shown to offer improved ultimate capacity predictions for the fundamental load cases of axial compression and uniaxial bending in isolation, has been extended for I-sections under combined loading, by determining an appropriate interaction equation. Similarly to a recent study on RHS (Theofanous et al. 2012b), the CSM in conjunction with the proposed interaction equation, offers improved accuracy and design efficiency, particularly for stocky stainless steel cross-sections under general load cases likely to occur in practice.

REFERENCES

ABAQUS/Standard user's manual volumes I-III. Version 6.10. Hibbitt, Karlsson & Sorensen, Inc. 2010.

Afshan, S. & Gardner, L. (in press). The continuous strength method for structural stainless steel design. Thin-Walled Structures.

Ashraf, M., Gardner, L. & Nethercot, D.A. (2006). Finite element modelling of structural stainless steel cross-sections. Thin-Walled Structures 44(10): 1048–1062.

Burgan, B.A., Baddoo, N.R. & Gilsenan, K.A. 2000. Structural design of stainless steel members–comparison between Eurocode 3, Part 1.4 and test results. Journal of Constructional Steel Research. 54(1): 51–73.

Dawson, R.G. & Walker, A.C. (1972). Post-buckling of geometrically imperfect plates. Journal of the Structural Division, ASCE. 98:ST1, 75–94.

EN 1993-1-1. 2005. Eurocode 3. Design of Steel Structures: Part 1-1: General rules and rules for buildings. CEN.

EN 1993-1-4. 2006. Eurocode 3: Design of steel structures: Part 1.4: General rules – Supplementary rules for stainless steel. CEN.

Gardner, L. (2008). The Continuous Strength Method. Proceedings of the Institution of Civil Engineers – Structures and Buildings. 161(3), 127–133.

Gardner, L. & Ashraf, M. 2006. Structural design for non-linear metallic materials. Engineering Structures 28(6): 926–934.

Gardner, L. & Nethercot, D.A. 2004a. Experiments on stainless steel hollow sections – Part 1: Material and cross-sectional behaviour. Journal of Constructional Steel Research, 60(9), 1291–1318.

Gardner L. & Nethercot D.A. 2004b. Experiments on stainless steel hollow sections – Part 2: Member behaviour of columns and beams. Journal of Constructional Steel Research, 60(9), 1319–1332.

Gardner, L. & Nethercot D.A. 2004c. Numerical Modeling of Stainless Steel Structural Components-A Consistent Approach. Journal of Structural Engineering, ASCE 130(10): 1586–1601.

Gardner, L. & Theofanous, M. 2008. Discrete and continuous treatment of local buckling in stainless steel elements. Journal of Constructional Steel Research 64(11): 1207–1216.

Gardner, L., Wang, F. & Liew, A. (2011). Influence of strain hardening on the behavior and design of steel structures. International Journal of Structural Stability and Dynamics. 11(5), 855–875.

Greiner, R. & Kettler, M. 2008. Interaction of bending and axial compression of stainless steel members. Journal of Constructional Steel Research 64(11): 1217–1224.

Groth, H.L. & Johansson, R.E. 1990. Statistics of the mechanical strength of stainless steels. Proc. of the Nordic Symposium on Mechanical Properties of Stainless Steels SIMR, Sigtuna, Sweden October 1990: 17–31.

Mirambell, E. & Real, E. 2000. On the calculation of deflections in structural stainless steel beams: an experimental and numerical investigation. Journal of Constructional Steel Research 54(1): 109–133.

Rasmussen, K.J.R. 2003. Full-range stress-strain curves for stainless steel alloys. Journal of Constructional Steel Research 59(1): 47–61.

Schafer, B.W. 2008. Review: The Direct Strength Method of cold-formed steel member design. Journal of Constructional Steel Research 64(7–8): 766–778.

Talja, A. & Salmi, P. (1995). Design of stainless steel RHS beams, columns and beam-columns. Research Note 1619, VU Building Technology, Finland.

Theofanous, M. & Gardner, L. 2012a. Effect of element interaction and material nonlinearity on the ultimate capacity of stainless steel cross-sections. Steel and Composite Structures 12(1): 73–92.

Theofanous, M. & Gardner, L. 2012b. The continuous strength method for stainless steel sections failing by distortional buckling. In: Proceedings of the 6th International conference on coupled instabilities in metal structures, Glasgow, UK, p. 539–546.

Theofanous, M., Saliba, N., Zhao, O. and Gardner, L. 2012a. Tests on stainless steel continuous beams. In: Proceedings of the 4th International Stainless Steel Experts' Seminar.

Theofanous, M., Liew, A. & Gardner, L. 2012b. Ultimate capacity of stainless steel RHS subjected to combined compression and bending. In: Proceedings of the 14th International Symposium on Tubular Structures, London, UK, p. 423–430.

Research and Applications in Structural Engineering, Mechanics and Computation – Zingoni (Ed.)
© 2013 Taylor & Francis Group, London, ISBN 978-1-138-00061-2

Investigating the role of gradual yielding in stainless steel columns and beams by virtual testing

P. Hradil & A. Talja
VTT Technical Research Centre of Finland, Espoo, Finland

ABSTRACT: The metallic materials such as stainless steels are well known for the pronounced rounded shape of their stress-strain diagram. However, this material nonlinearity may change locally due to the fabrication, and therefore the load-displacement response of the structural member is not always the same as the stress-strain relation of the original material. The aim of this paper is to study the sensitivity of member resistance to the changes of gradual yielding rate in fabricated columns and beams. We used the automated finite element virtual experiments to demonstrate the effect of fabrication on the overall buckling of columns and beams.

1 INTRODUCTION

The buckling strength of members from metallic materials is, to some extent, governed by their nonlinear strain-hardening behavior (Rasmussen & Rondal 1997). Especially in the case of cold-formed stainless steels the large variety of stress-strain diagram shapes can be achieved by combining different material grades and fabrication methods. While the proper experimental investigation yields always credible results, it is long and expensive process. Numerical calculations can efficiently supplement the experimental program with additional data or completely replace it.

The nonlinear stress-strain relationship of stainless steels is usually described by formulas based on Ramberg-Osgood equation (Ramberg & Osgood 1943, Mirambell & Real 2000, Rasmussen 2003, Gardner & Ashraf 2006, Hradil et al. 2013). Such material models can vary in the complexity and number of required material parameters, however, only the basic nonlinear parameter n and the ratio of the ultimate and yield strength significantly affects the buckling behavior of columns and beams (Hradil & Talja 2012).

Fabrication of structural members introduces localized residual stresses and material changes that generally result in higher average strength and more rounded shape of load response diagram than expected (ECCS 1976). Even though the design codes offer the rules for the calculation of average section yield strength, the changes in nonlinear parameter n are not widely recognized.

2 SCOPE OF THE STUDY

The aim of our study is to investigate how significant is the gradual yielding in overall buckling of beams and columns, and how different fabrication methods affect the nonlinear factor n of the whole cross-section.

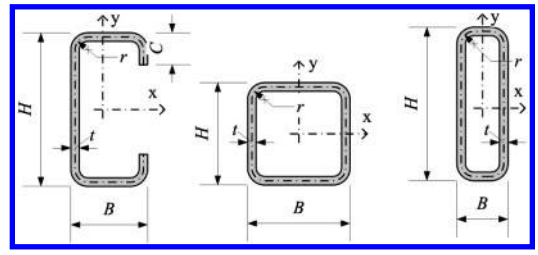


Figure 1. Studied cold-formed sections.

Table 1. Cold-formed sections, dimensions.

Section	*B* mm	*H* mm	*C* mm	*t* mm	*r* mm
C	36	72	15	4	6
SHS	48	48	–	4	6
RHS	24	72	–	4	6

2.1 *Cross-sections and tests*

Cold-formed open sections, hollow sections and welded open sections are the basic categories in Eurocode 3, Part 1–4. Therefore the study is based on cold-rolled RHS sections and press-braked C-sections (Fig. 1 and Table 1) where the effect of cold-forming may alter their nonlinear load response. Although the corner areas are not an issue in welded I-sections, we have included them in the study because of their membrane residual stresses due to fabrication (Fig. 2 and Table 2).

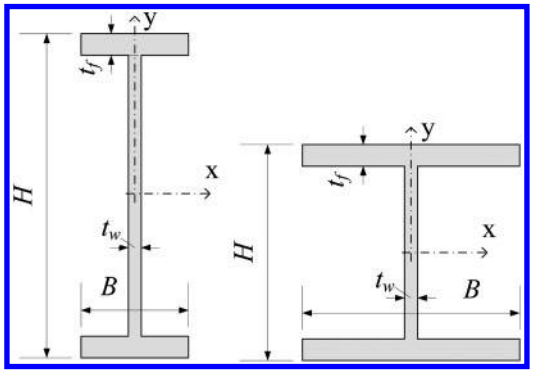


Figure 2. Studied welded sections.

Table 2. Welded sections, dimensions.

Section	B mm	H mm	t_f mm	t_w mm
I	50	150	10	5
H	100	100	10	5

The prediction of nonlinear factor degradation was validated by simulating full section tensile tests and the effect of this factor on member resistance was investigated in the cases of flexural buckling (FB), torsional-flexural buckling (TFB) and lateral-torsional buckling (LTB).

2.2 *Enhanced strength in corners*

The enhanced yield strength of press-braked open sections was applied in the corners according to Cruise & Gardner's model (2008). Assuming that the flat part strength of the channel section is 250 MPa, the predicted average strength results in 294 MPa with corner strengths 420 MPa (Fig. 3). Cold-rolled hollow sections have a larger area affected by the fabrication, which extends 2t from the corners to the flat parts. The current predictive models for the enhanced strength in corners and flat faces of hollow sections are based on the knowledge of virgin material yield strength. Moreover, the model proposed by Cruise & Gardner (2008) for hollow sections is limited to either low A/W or high f_u/f_y ratios, which was not acceptable in our study. Therefore we used Rossi's prediction (Rossi et al. 2009) with the virgin material yield strength 205 MPa that produced flat part strength of exactly 250 MPa and yield strength in the corners 290 MPa.

2.3 *Residual stresses*

Bending residual stresses of 36% of basic yield strength were inserted in corner areas and 15% of the basic strength in flats of press-braked open sections (Fig. 3), according to Gardner & Cruise (2009). In the case of hollow sections, the highest level of bending residual stresses in corners and flat parts was 37%

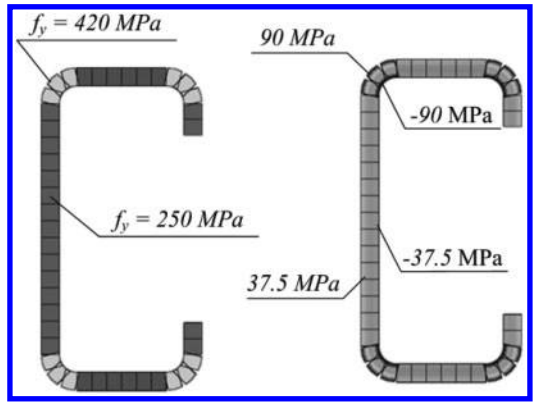


Figure 3. Example of finite element mesh with enhanced yield strength (left) and bending residual stresses (right) in the C-section.

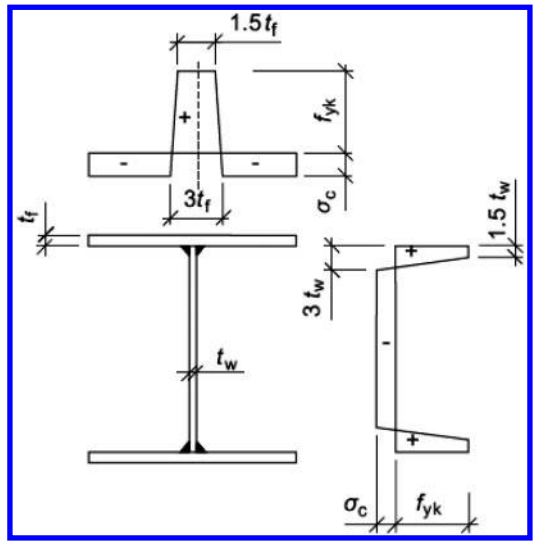


Figure 4. Distribution of membrane residual stresses according to BSK 99.

and 63% respectively. Membrane stresses are typically insignificant in such cross-sections, and therefore were neglected in our study.

The membrane stresses were, on the other hand, used in welded I-section models, where they play an important role. The model for carbon steels from the Swedish standard BSK 99, that was proposed by Gardner & Cruise (2009) for ferritic fabricated sections was used (Fig. 4). Then the compressive stress is calculated to maintain the equilibrium as described in the Equation 1.

$$\sigma_c = \frac{2.25(t_f + t_w)}{B + 0.5H - 2.25(t_f + t_w)} f_y \quad (1)$$

2.4 *Limitations*

The study is based on the current knowledge of material changes in the cold-formed cross sections and on

the existing predictive models for enhanced strength in corners. However, building complex numerical models with nonlinear material in corners requires the knowledge of all material parameters that define the shape of the stress-strain curve. In our study we assumed that parameters (excepting the material strength) remain unchanged if no suitable predictive model is available. The through-thickness distribution of bending residual stresses is fully plastic in our numerical calculations (Jandera et al. 2008) even though the latest studies showed that it is not always the most conservative case (Jandera & Macháček 2012).

3 METHODS

3.1 *Simple method for average material model prediction in cold-formed columns*

The prediction of n factor degradation was performed numerically with discrete strain increments. Simple Python script that iteratively calculates Ramberg-Osgood stress σ_{RO} for a given strain produced the average stress-strain diagram of the cross-section (Eqs. 2 to 5). Areas A_f and A_c are flats and corners sectional areas respectively.

$$\sigma = \frac{A_f\sigma_f + A_c\sigma_c}{A_f + A_c} \tag{2}$$

The total stress in flats σ_f or corner σ_c is composed of two parts with positive and negative residual components assuming that the residual stress has fully plastic through-thickness distribution (see Eq. 3). In the case of tensile residual stress, the unloading path is linear as described in Equation 5, where ε_R is the residual strain calculated by Ramberg-Osgood formula directly from the residual stress σ_R in flats and corners.

$$\sigma_{f(c)} = \frac{1}{2}\left(\sigma^{+}_{f(c)} + \sigma^{-}_{f(c)}\right) \tag{3}$$

$$\sigma^{+}_{f(c)} = \sigma_{RO(\varepsilon+\varepsilon_R)} \tag{4}$$

$$\sigma^{-}_{f(c)} = \begin{cases} E_0\varepsilon - \sigma_R & when\ \varepsilon < \sigma_R/E_0 \\ \sigma_{RO(\varepsilon-\sigma_R/E_0)} & else \end{cases} \tag{5}$$

The parameters of the overall cross-sectional material model were obtained by curve-fitting of Ramberg-Osgood equation to this diagram. The initial assumption was that both materials (in flats and corners) have the same n factor and initial modulus of elasticity E_0.

3.2 *Virtual experiments*

The finite element models were created and evaluated using the Abaqus plugin developed to simulate virtual testing of cold-formed steel members (Hradil et al. 2011). The plugin was designed to carry out the geometrically and materially nonlinear analysis with initial imperfections obtained from the linear eigenvalue analysis and scaled to the desired amplitude. The calculation usually stops after reaching the peak load or pre-defined deformation. The plugin was extended by the Python script that automatically executed series of models with variable member lengths, evaluated results and plotted buckling curves. With that level of automation a single buckling curve was calculated and plotted in less than hour on a common workstation with Intel core2 Duo CPU E8400 @ 3,00 GHz and 3.21 GB RAM. The same algorithm produced tensile test results of full cross sections. In that case no imperfections are needed and the eigenvalue analysis was turned off in the plugin settings.

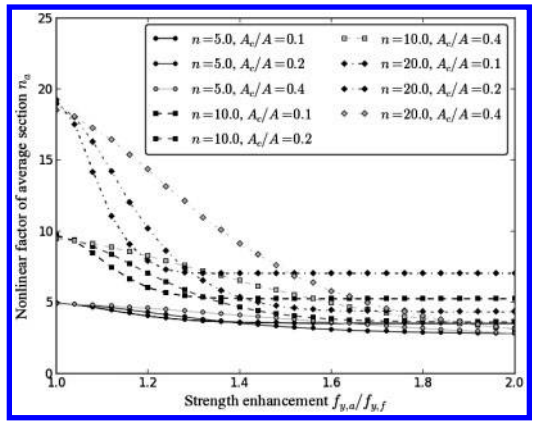


Figure 5. Nonlinear factor degradation due to enhanced corner properties in press-braked open sections.

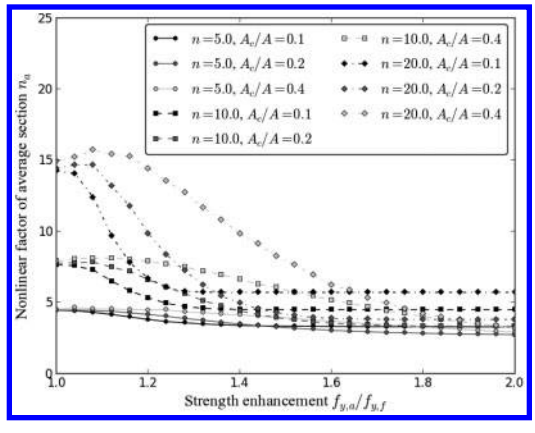


Figure 6. Nonlinear factor degradation due to enhanced corner properties in cold-rolled hollow sections.

4 RESULTS AND DISCUSSION

4.1 *Average material properties based on the simple method*

The predicted changes in nonlinear factor due to the strength enhancement and residual stresses are described in Figures 5–6. The degradation curves are

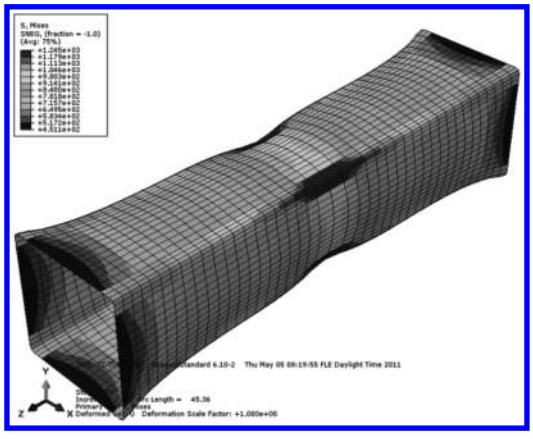


Figure 7. Square hollow section in tension.

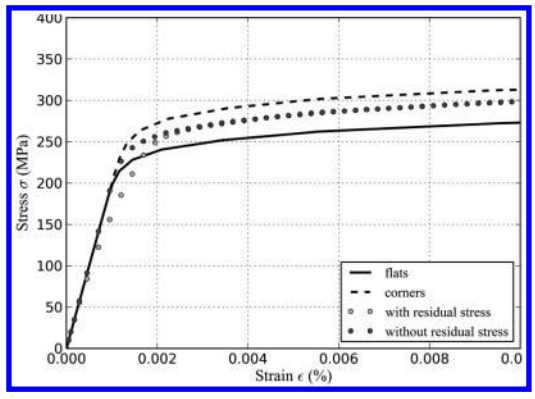


Figure 8. Example of stress-strain curve obtained from simulated tensile test of cold-rolled hollow section.

plotted for n factor 5, 10 and 20 and for the share of the corner area A_c/A equal to 10, 20 and 40%. The average yield strength and the flat parts yield strength are noted as $f_{y,a}$ and $f_{y,f}$ respectively.

The results show that the changes in nonlinearity are more significant with the increasing n of material. It can be also observed that increasing the average strength beyond a certain limit has no effect on the overall cross-section nonlinearity n_a. It stops decreasing at about $n_a = 5$, depending on the share of corner area A_c/A. Even if there is no strength enhancement ($f_{y,a}/f_{y,f} = 1.0$), the strong influence of residual stresses can be observed.

Table 3. Comparison of simply predicted n and the virtual tensile test results.

Section	A_c/A	$f_{y,a}/f_{y,f}$	n	n_a	$n_{a,TT}$
RHS	0.52	1.16	5	4.9	5.0
			10	8.2	7.6
			20	15.8	12.1
SHS	0.62	1.16	5	4.9	5.0
			10	8.3	7.5
			20	16.3	12.0
C	0.24	1.68	5	4.5	4.6
			10	7.9	8.0
			20	12.8	12.7

4.2 *Average material properties based on the virtual tensile tests*

Even though the method presented in the previous section is computationally very effective, it does not account for the interaction between corners and flats and gradual stress redistribution in the cross-section. To obtain more reliable results, the tensile load and displacement relation of the profiles was calculated by finite element models (Fig. 7). The load-displacement diagram of the profile served as the basis for stress-strain relation, as demonstrated in Figure 8. The material models of flats and corners were two-stage Ramberg-Osgood curves (Mirambell & Real 2000) with the second nonlinear factor m equal to 3 and the ultimate strain ε_u equal to 40%.

The regression analysis similar to the previous study was applied to the finite element results to produce nonlinear factor $n_{a,TT}$ of the cross-section. Results are compared to the predicted factors n_a in Table 3, which were produced by the simple method. This method was modified to take into account two-stage Mirambell and Real's material that was also used in finite element calculations.

It can be observed that the finite element analysis mostly resulted in lower n factor than the simple predictive method; however, both calculations showed the significant increase of nonlinearity in the full section loading response especially when the material n factor was high.

4.3 *Results of virtual buckling tests*

The cold-rolled hollow sections were studied in flexural buckling, press-braked open sections in flexural and torsional-flexural buckling, and welded open sections in flexural and lateral-torsional buckling. The dimensions of the cross sections are presented in Table 1. The main goal of this extensive study was to verify the current buckling curves in EN 1993-1-4 (Hradil & Talja 2012), and therefore only selected results are presented in this paper to demonstrate the effects of fabrication and material nonlinearity on the member buckling strength.

Figures 9–12 show the results of virtual buckling tests on various cross-sections, materials (parameter n) and overall buckling modes. In this comparison the ratio of ultimate and yield strength in flat parts (Equation 6) is 1.4.

$$\overline{\sigma} = f_u / f_y \tag{6}$$

Many experimental results are available for the flexural buckling of stainless steel hollow sections (Theofanous & Gardner 2009, Talja 2002, Ala-Outinen &

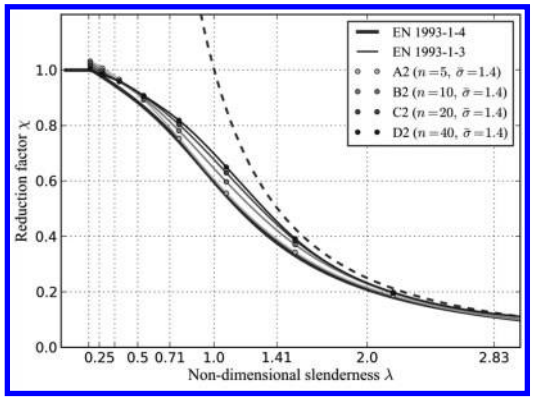


Figure 9. Calculated buckling curves of press-braked sections in torsional-flexural buckling.

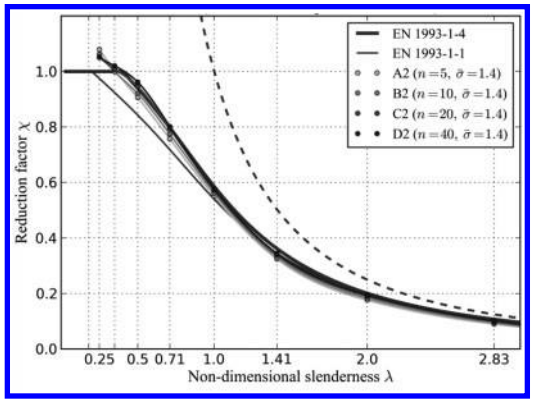


Figure 10. Calculated buckling curves of cold-rolled hollow sections in flexural buckling.

Oksanen 1997, Gardner & Nethercot 2004, Hyttinen 1994, Liu & Young 2003, Talja & Salmi 1995, Young & Liu 2003, Rasmussen & Hancock 1990, Ellobody & Young 2005). The example in Figure 13 shows collected results of major axis flexural buckling with n factor approximately 10 plotted against the predicted curve.

The interested reader may refer to the paper published in the proceedings of 4th International Experts Seminar (Hradil & Talja 2012) for more results of overall buckling.

5 SUMMARY

The computational tool was developed in VTT Technical Research Centre of Finland to simulate laboratory tests of cold-rolled, press-braked and welded members from metallic materials. Several predictive models for the effect of fabrication in form of enhanced material properties and residual stresses were included. The tool automatically generates finite element models for the geometrically and materially nonlinear analysis with initial imperfections (GMNIA), executes the calculation and evaluates the results provided by Abaqus solver. Therefore it is very suitable for parametric studies and optimization tasks.

We used this tool to predict buckling curves of cold-rolled hollow sections, press-braked lipped channels and welded I-sections in flexural, torsional-flexural

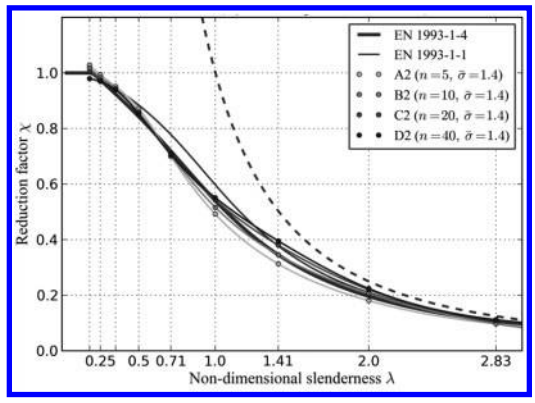


Figure 11. Calculated buckling curves of welded sections in flexural buckling.

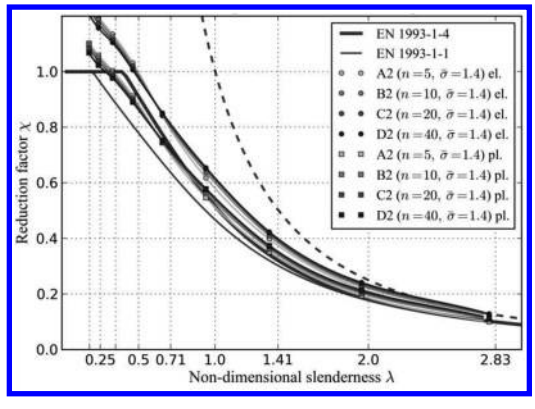


Figure 12. Calculated buckling curves of welded sections in lateral-torsional buckling (elastic and plastic design).

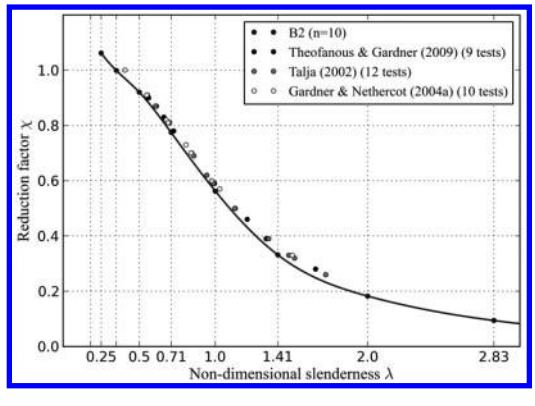


Figure 13. Experimental results of cold-rolled hollow sections in major axis flexural buckling and $n = 10$.

and lateral-torsional buckling. The curves generated by numerical calculations showed different levels of sensitivity to the variation of flat material's nonlinear factor *n*. The reasons for this behavior include the fabrication-related material changes in cold-formed corners and residual stresses from welding and forming. Currently, the finite element analysis is the only numerical method able to take this effect fully into account if the material changes and residual stress levels are correctly predicted.

The degradation curves of presented in this study can be a great source for the future development of predictive equations for the nonlinear factor *n* of the fabricated sections. Moreover, it was recognized that the material nonlinearity of sections that are not significantly affected by the fabrication can lead to different buckling curves for each *n*.

ACKNOWLEDGEMENTS

The research leading to these results has received funding from the European Community's Research Fund for Coal and Steel (RFCS) under Grant Agreement No. RFSR-CT-2010-00026, Structural Applications of Ferritic Stainless Steels.

REFERENCES

Ala-Outinen, T. & Oksanen, T. 1997, *Stainless steel compression members exposed to fire*, VTT Technical Research Centre of Finland, Espoo, Finland.

Cruise, R.B. & Gardner, L. 2008, "Strength enhancements induced during cold forming of stainless steel sections", *Journal of Constructional Steel Research,* vol. 64, no. 11, pp. 1310–1316.

Ellobody, E. & Young, B. 2005, "Structural performance of cold-formed high strength stainless steel columns", *Journal of Constructional Steel Research,* vol. 61, no. 12, pp. 1631–1649.

European Convention for Constructional Steelwork 1976, *Manual on Stability of Steel Structures, Second edition*, ECCS Committee 8 – Stability.

Gardner, L. & Ashraf, M. 2006, "Structural design for non-linear metallic materials", *Engineering Structures,* vol. 28, no. 6, pp. 926–934.

Gardner, L. & Cruise, R.B. 2009, "Modeling of Residual Stresses in Structural Stainless Steel Sections", *Journal of Structural Engineering,* vol. 135, no. 1, pp. 42–53.

Gardner, L. & Nethercot, D.A. 2004, "Numerical Modeling of Stainless Steel Structural Components—A Consistent Approach", *Journal of Structural Engineering,* vol. 130, no. 10, pp. 1586–1601.

Hradil, P., Fülöp, L. & Talja, A. 2011, "Virtual testing of cold-formed structural members", *Rakenteiden Mekaniikka (Journal of Structural Mechanics),* vol. 44, no. 3, pp. 206–217.

Hradil, P. & Talja, A. 2012, "Numerical verification of stainless steel overall buckling curves", *Stainless Steel in Structures, 4th International Experts Seminar*, 6.-7.12.2012.

Hradil, P., Talja, A., Real, E., Mirambell, E. & Rossi, B. 2013, "Generalized multistage mechanical model for nonlinear metallic materials", *Thin-Walled Structures,* vol. 63, no. 0, pp. 63–69.

Hyttinen, V. 1994, *Design of cold-formed stainless steel SHS beam-columns*, University of Oulu, Finland.

Jandera, M., Gardner, L. & Macháček, J. 2008, "Residual stresses in cold-rolled stainless steel hollow sections", *Journal of Constructional Steel Research,* vol. 64, no. 11, pp. 1255–1263.

Jandera, M. & Macháček, J. 2012, "Residual stress influence on material properties and column behaviour of stainless steel SHS", , 6.-7.12.2012.

Liu, Y. & Young, B. 2003, "Buckling of stainless steel square hollow section compression members", *Journal of Constructional Steel Research,* vol. 59, no. 2, pp. 165–177.

Mirambell, E. & Real, E. 2000, "On the calculation of deflections in structural stainless steel beams: an experimental and numerical investigation", *Journal of Constructional Steel Research,* vol. 54, no. 1, pp. 109–133.

Ramberg, W. & Osgood, W.R. 1943, *Description of stress-strain curves by three parameters*, National Advisory Committee for Aeronautics, Washington, D.C., USA.

Rasmussen, K.J.R. 2003, "Full-range stress–strain curves for stainless steel alloys", *Journal of Constructional Steel Research,* vol. 59, no. 1, pp. 47–61.

Rasmussen, K.J.R. & Hancock, G.J. 1990, "Stainless steel tubular columns tests and design", *Tenth International Specialty Conference on Cold-formed Steel Structures*, October 23–24,1990, pp. 471.

Rasmussen, K.J.R. & Rondal, J. 1997, "Strength curves for metal columns", *Journal of Structural Engineering,* vol. 123, no. 6, pp. 721.

Rossi, B., Degée, H. & Pascon, F. 2009, "Enhanced mechanical properties after cold process of fabrication of non-linear metallic profiles", *Thin-Walled Structures,* vol. 47, no. 12, pp. 1575–1589.

Talja, A. 2002, *Test results of RHS, tophat and sheeting profiles*, VTT Technical Research Centre of Finland, Espoo, Finland.

Talja, A. & Salmi, P. 1995, *Design of stainless steel RHS beams, columns and beam-columns*, VTT Technical Research Centre of Finland, Espoo, Finland.

Theofanous, M. & Gardner, L. 2009, "Testing and numerical modelling of lean duplex stainless steel hollow section columns", *Engineering Structures,* vol. 31, no. 12, pp. 3047–3058.

Young, B. & Liu, Y. 2003, "Experimental Investigation of Cold-Formed Stainless Steel Columns", *Journal of Structural Engineering,* vol. 129, no. 2, pp. 169–176.

Research and Applications in Structural Engineering, Mechanics and Computation – Zingoni (Ed.)
© 2013 Taylor & Francis Group, London, ISBN 978-1-138-00061-2

Experiments on ferritic stainless steel columns in fire

B. Rossi & J.M. Franssen
University of Liège, Belgium

N. Tondini
University of Trento, Italy

ABSTRACT: This paper presents the performance of ferritic stainless steel 1.4003 hollow section columns when exposed to fire loading. Three column tests were carried out in the framework of the RFCS project named Structural Applications of Ferritic Stainless Steels (SAFSS, RFSR-CT-2010-00026). Tubular thin-walled members were considered in this study because structural applications of ferritic stainless steels generally incorporate such profiles. Two cross-section geometries were selected: a square hollow sections (SHS) $80 \times 80 \times 3$ mm (the columns having nominal lengths of 3000 mm and 2500 mm, respectively); and a Rectangular Hollow Section (RHS) $120 \times 80 \times 3$ mm, (2500 mm long). Fire loading was applied under a constant concentrically compressive load. Identical columns tests at room temperature are also reported.

1 INTRODUCTION

The Steel Construction Institute (SCI) is currently coordinating a three-year European study into the structural applications of ferritic stainless steels (SAFSS, RFSR-CT-2010-00026) with the aim of increasing their use in load-bearing structures. The other partners are AcerInox (Spain), Aperam (France), Arup (UK), Institute of Metals and Technology (IMT) (Slovenia), Outokumpu Stainless Oy (Finland), Universitat Politechnica de Catalunya (UPC) (Spain) and VTT Technical Research Centre of Finland (Finland), as well as University of Liège as a subcontractor. The project includes material and member testing as well as analytical and numerical studies. Three target applications most suited to ferritic stainless steels have been identified: lattice roof trussed and space frame structures, exposed decking in composite floor systems and signage and security structures. The final aim of the project is to provide design guidance to practitioners for the specification of ferritic stainless steels in structures. The work packages include studies into: (*i*) Mechanical properties; (*ii*) Structural performance of light gauge members; (*iii*) Structural performance of steel decking in composite floor systems; (*iv*) Structural performance at high temperatures; (*v*) Structural performance of bolted and screwed connections; (*vi*) Structural performance of welded connections; (*vii*) Corrosion resistance; (viii) Design guidance and implementation into Eurocode 3. The study focuses on five grades with varying levels of corrosion resistance: 1.4003, 1.4016 (AISI 430), 1.4509 (AISI 441), 1.4521 (AISI 444) and 1.4621.

Work package (*iv*) seeks to obtain information on the performance of structural members when exposed to fire loading. Strength and stiffness retention factors have been derived from tensile tests carried out under isothermal and anisothermal conditions (for temperatures ranging from 25°C to 1000°C). The test data obtained will be employed to establish stress-strain relationships in accordance with the stainless steel model in EN 1993-1-2 Annex C (2005). In addition, a number of loaded member tests subject to fire loading have been carried out in order to calibrate a numerical model. Trusses and space frames made of tubular thin-walled members are typical structural typologies where ferritic stainless steel is employed. As a result, the tests focused on profiles used in these types of structures, which were tested under concentric compressive load. Three fire tests on SHS and RHS columns of varying global slenderness were carried out. In order to fully identify the effects of fire loading, identical columns were also tested at room temperature. In addition, mechanical properties at room temperature were established by means of tensile tests on material coupons extracted from members.

During this project, numerical simulations will also be performed to reproduce the test results, perform parametric analyses and assess the level of reliability of codified and new predictive models such as Ng & Gardner (2007), Uppfeldt et al. (2008), Lopes et al. (2010) and Lopes et al. (2012), in which the results of tests and numerical models are analyzed and used to derive new design models for stainless steel columns and beams-columns in fire.

2 SPECIMEN GEOMETRY

Two cross-section dimensions were selected: a square hollow sections (SHS) $80 \times 80 \times 3$ mm and a rectangular hollow section (RHS) $120 \times 80 \times 3$ mm. The cross-section areas were calculated on the basis

Table 1. Cross-section dimensions.

#	1	2	3
Section [mm]	80 × 80 × 3	80 × 80 × 3	120 × 80 × 3
Cross-section measured dimensions [mm]	$t_{av} = 2.87$ $B = 79.6$ $H = 79.2$	$t_{av} = 2.82$ $B = 79.2$ $H = 79.8$	$t_{av} = 2.97$ $B = 79.4$ $H = 119.5$
A [cm^2]	8.5	8.4	11.2
Massivity factor [m^{-1}]	338	342	329

Table 2. Mill certificate data (from Stalatube).

Section	80 × 80 × 3	120 × 80 × 3
$\sigma_{0.2}$ [MPa]	336.0	329.0
$\sigma_{1.0}$ [MPa]	360.5	350.0
σ_{ult}[MPa]	484.5	468.0
ε_{ult}[%]	42.5	37.0

of an average measured corner internal radius R_i of 4.0 mm for the 80 × 80 × 3 sections and 3.86 mm for the 120 × 80 × 3 section (Table 1); where t_{av} is the average of the thicknesses of the four faces.

The material was the ferritic 1.4003 stainless steel grade. At room temperature, this grade exhibits mechanical properties similar to those of traditional carbon steel. The main room-temperature mechanical characteristics of this grade, according to EN 10088-2 (2005), are: (i) 0.2% proof strength $\sigma_{0.2\%} \geq 280$ MPa, (ii) elongation after fracture $\varepsilon_{ult} \geq 20\%$ and (iii) ultimate tensile strength $\sigma_{ult} = 450$ to 650 MPa. The specimens were supplied by the steelwork company Stalatube. The mill certificate data are provided in Table 2.

3 TESTS AT ROOM TEMPERATURE

3.1 *Tensile coupon tests*

The material mechanical behavior was tested at room temperature by the steelwork company Aperam. For each section size, three tensile coupon tests were performed in accordance with EN 10002 (2004). The coupons were extracted from each of the three faces: namely 90°, 180° and 270°, as illustrated in Figure 1. The face that included welding was excluded. The average tensile coupon tests characteristics are provided in Table 3.

The sections considered herein are manufactured at ambient temperature and hence undergo plastic deformations, which result in an increase in yield stress and a reduction in ductility. Square and rectangular hollow sections are first formed into a circular section that is subsequently crushed into a square or a rectangular cross-section. Materials, such as stainless steel, with nonlinear stress-strain behavior and significant strain

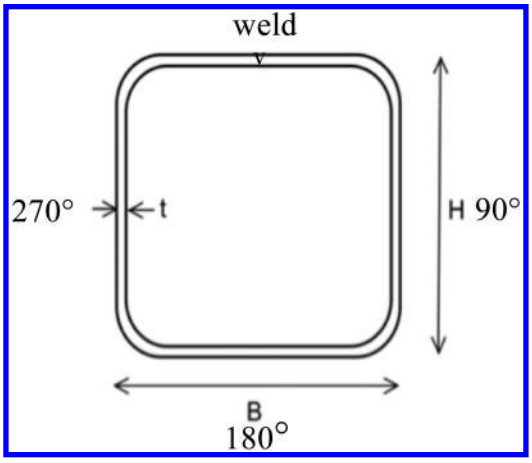


Figure 1. Notations for the cross-section dimensions.

Table 3. Average tensile coupon tests results.

Section	80 × 80 × 3	120 × 80 × 3
$\sigma_{0.2}$ [MPa]	458.7	437.2
$\sigma_{1.0}$ [MPa]	485.8	462.8
σ_{ult} [MPa]	505.4	490.1
ε_{ult} [%]	25.6	24.2
E_0 (MPa)	193	194

hardening show a more pronounced response to cold working, Rossi et al. (2013). Presently, compared to the mill certificate data, the tensile coupon tests indicate that the flats experienced significant strain hardening.

3.2 *Column tests*

Firstly, three column tests were performed at room temperature in order to obtain the compressive axial capacities and the failure modes. The out-of-straightness of the four faces was also measured and this was the only indication of the initial global imperfection. It is worth pointing out that the maximum amplitude of the out-of-straightness was less than 1 mm for the three columns that were tested at ambient temperature.

In order to be fully in contact with the end plates of the testing machine, the specimen ends were machine cut; the total length of each column resulted: $L_{\#1} = 2962.5$ mm, $L_{\#2} = 2473.5$ mm, $L_{\#3} = 2475$ mm, respectively. Each column was concentrically loaded using a Schenk hydropolus, the maximum capacity of which is 2500 kN. The machined ends of the columns allowed for a perfect contact with the loading device. Full-restrained boundary condition is achieved during the tests. The loading was controlled by displacement with a speed of 0.5 mm/min. Both axial and transversal displacements were measured. The global flexural transversal displacements in two perpendicular directions were measured using extensometers placed at

Table 4. Column tests results at ambient temperature.

#	1	2	3
Length [mm]	2962.5	2473.5	2475.0
Global imperfection amplitude at mid-length [mm]	<L/3000	<L/2500	<L/2500
Boundary conditions	Fixed	Fixed	Fixed
Ultimate axial capacity [kN]	314.7	343.6	417.9

mid-height of the column. These main features and the results of the tests are shown in Table 4. All the three columns failed in the same way, by combination of local buckling and global flexural buckling.

4 FIRE TESTS

4.1 *Elevated temperature material mechanical properties*

Elevated temperature material properties of stainless steel alloys are reported in the current provisions of EN 1993-1-2 (2005). A consistent review is also provided in Gardner et al. (2010): all available test data are analyzed and revised strength and stiffness reduction factors at elevated temperatures for a range of grades of stainless steel (including the ferritic grade 1.4003) have been proposed. In the frame of the aforementioned RFCS project, strength and stiffness retention factors will be derived from the results of tensile tests carried out under isothermal and anisothermal conditions. They will be made available in the final technical report of the project RFSR-CT-2010-00026.

4.2 *Specimen geometry, boundary conditions and loading protocol*

Three columns were selected and tested under fire in a vertical wall furnace (Figure 2): i) two square hollow sections (SHS) 80 × 80 × 3 mm having nominal lengths of 3000 mm and 2500 mm, respectively; and ii) a rectangular hollow section (RHS) 120 × 80 × 3 mm, 2500 mm long. This choice entailed the SHS to be classified as class 2 according to the EN1993-1-4 (2006) and the RHS as class 4.

From a behavior at elevated temperature viewpoint, the three columns have a massivity factor that is fairly the same and rather high (Table 1). The actual dimensions are reported in Table 1. For columns #1 and #2, the maximum out-of-straightness of the four faces was less than 1 mm. Only for column #3, a maximum amplitude of the out-of-straightness equaling 5.0 mm (i.e. about L/500) was detected at mid-height.

The specimens were welded to 20 mm thick end plates made of stainless steel grade 1.4307 and holes for bolts were allowed for to ensure a full degree of fixity at both column ends. The welding wire was made of

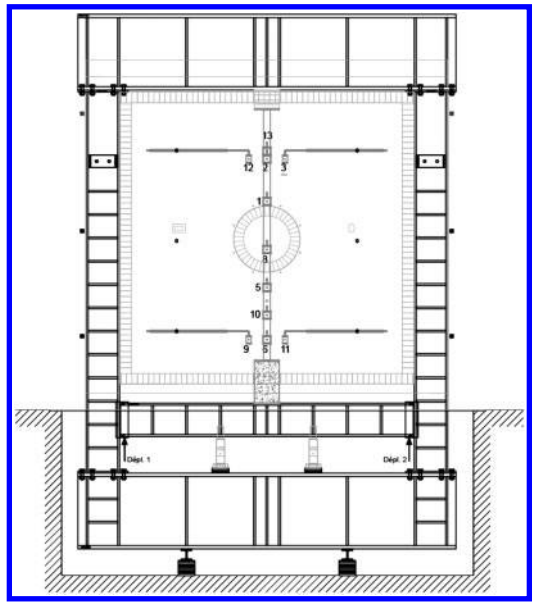


Figure 2. Schematic elevation of the vertical furnace.

1.4430 stainless steel grade. The depth of the welded lips was 5.0 mm thick. The interface between the plates and the concrete blocks on which the plates were bolted was filled with a fine grain temperature resistant plaster to guarantee an optimal contact with the plate. Full-restrained boundary conditions were imposed. The supports made of concrete were then covered with ceramic fiber. Therefore, the heated length reduced of approximately 50 mm (the fiber is 25 mm thick).

The distribution of the air temperature in the furnace was measured by using pyrometers (plate thermometers) located at 11 points around the column: 7 coming into the furnace through the closing wall and 4 located behind the column coming into the furnace through the brick wall where burners are located (Figure 2). They provided the air temperature at a distance of 100 mm from the steel surface. No thermocouples were installed on the specimens because it was reckoned that due to the small thicknesses, the temperature of steel at failure could be sensibly considered equal to that of air.

The load protocol followed the EN1363-1 provisions (2001), which entail to maintain the load constant at least during 15 minutes, time after which the ISO 834 heating curve was applied, with the load being maintained constant until failure.

In detail, the tests began by applying the static loading at ambient temperature until 30% of the design load $N_{b,Rd}$ calculated according to EN1993-1-4 (2006) (see Table 5).

In this table, the design load is calculated on the basis of a yield strength equal to 350MPa. After the static loading at ambient temperature was applied, the fire test began according to the ISO 834 fire curve. It is worth pointing out that, according to the EN1363-1 provisions (2001), *time zero* is taken as the time



Figure 3. Left to right – Seven pyrometers located at the front side of the column through the furnace closing device; four pyrometers located at the back side of the column.

Table 5. Applied static load at high temperature.

#	1	2	3
Calculated $N_{b,Rd}$ [kN]	239	260	336
Applied load [kN]	72	78	100

at which one pyrometer inside the furnace reaches 50°C. The failure time was defined from $t = 0$ to the time when the displacements increased with vertical asymptote.

It is important to mention that, as described before, a closing wall was necessary in order to seal the wall furnace during the tests (Figure 2). This means that a gradient of temperature may develop horizontally inside the furnace, causing the columns to get warmer on the side toward the hot bricks composing the furnace wall, the one in which the gas burners lay. This gradient may influence the direction of buckling and the overall behavior, Tondini et al. (2013).

4.3 *Main tests results*

In Figure 4, the main result in terms of Net vertical displacement versus time for column #1 is presented. It is possible to observe that the axial displacement was first positive owing to elastic shortening of the column at ambient temperature. Then, when the fire test began it became negative because of thermal expansion. The time of failure occurred at 12 min 9 s after *time zero* and at the air temperature of 709.4°C.

The failure mode involved the formation of a main plastic hinge at the column centre and, less developed, at about a quarter and at three quarters of the height. Thus, full *fixed-end* boundary conditions seemed to be achieved.

Similar considerations as those made for column #1 can be drawn for column #2 too. However, in this test the plastic hinge at the top of the column was

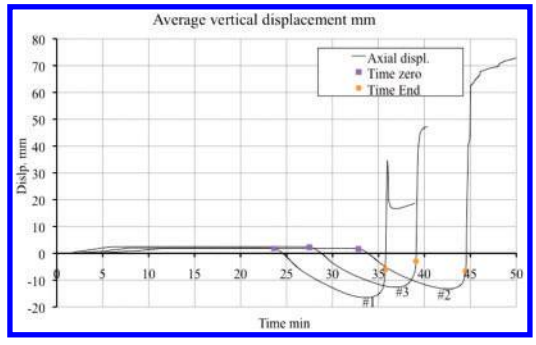


Figure 4. Average axial displacement versus time for column #1.



Figure 5. Failure mode for specimen #1 (3 m long).

more developed than in the previous test. The time of failure occurred at 12 min after *time zero* and at air temperature of 707.7°C.

For column #3 the time of failure occurred at 11 min 51 s after *time zero* and at the air temperature of 705°C. Thus, in terms of fire resistance it exhibited a similar behavior as the one experienced by column #1 and #2. As expected, it failed around its weak axis. The mode of failure was characterized by the formation of two clear plastic hinges (approximately at the top and at mid-height), as shown in Figure 6. The explanation of such a behavior is given in Section 4.4.

From the three tests it is possible to observe that the fire resistance was fairly the same, i.e. t_{tests}. This was expected since the massivity factors were very similar among the specimens (330–340 m^{-1}) as well as the applied load ratio ($0.3N_{b,Rd}$). Interesting to note that even though column #3 had the lowest massivity factor its fire resistance was the lowest. This is explicable because of a higher initial imperfection.

4.4 *Analysis of the effects of temperature gradients in the member and their influence on the failure mode*

In this experimental campaign, a *fixed-end* boundary conditions (no lateral displacements nor rotation



Figure 6. Failure mode for column #3.

Table 6. Column tests results at high temperature.

#	1	2	3
Length [mm]	3000.0	2499.5	2500.0
Global imperfection amplitude at mid-length [mm]	<L/3000	<L/2500	∼L/500
Boundary conditions	Fixed	Fixed	Fixed
θ_{tests} [°C)]	709.4	707.7	705.0
t_{tests} [min]	12 min 9 s	12 min	11 min 51 s
Min. axial displ. (under vert. load at ambient temp., [mm])	2.4	2.3	2.5
Max. axial displ. (dilatation, [mm])	−16.0	−12.7	−12.6

and warping) was achieved. Theoretically, in full-restrained conditions, failure would occur with an almost simultaneous formation of three plastic hinges located at the top section, at the mid-height section and at the bottom section of the column. However, in the tests it was observed the formation of two plastic hinges – at the top section and at the mid-height section – rather than three. This could be due to the fact that full-restrained conditions were not achieved, above all at the base section where in every test no clear plastic hinge formed.

In fact, the main reason of the observed failure modes lies elsewhere. By analyzing the data of the

Table 7. Axial resistance at three sections along the height in the last 30s for each test.

#	1	2	3
Top section	80.5	81.2	98.8
Mid-height section	83.3	83.5	101.1
Bottom section	97.9	97.1	121.4

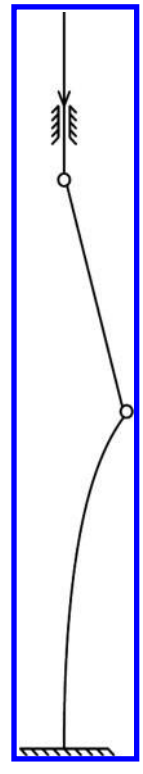


Figure 7. Failure mode of columns owing to a temperature gradient along the height of the column.

tests it was found that the temperature in the furnace was neither perfectly uniform along the height of the columns, nor in a horizontal plane, as already observed in Tondini et al. (2013).

In particular, the top of the column was, in all tests, warmer, whereas the bottom end was always colder with a temperature variation along the height of averagely 35°C–40°C in the last 30s of the test, i.e. close to failure.

In the horizontal plane, at the top, the face towards the brick wall was warmer of about 22°C–26°C than the face towards the closing wall; at mid-height basically no horizontal gradient appeared and; at the bottom, a difference of about 14°C–24°C between the brick wall side (hotter) and the closing wall side (colder) established.

On the basis of these measured temperatures, the reduction factors for yield strength of stainless steel according to EN1993-1-2 (2005) were computed at

the top, at mid-height and at the bottom sections of each column in the last 30s of each test for every faces composing the section. Each face was assumed at constant temperature based on the closest pyrometer. For the faces on the sides where no pyrometer was located the average temperature between the furnace wall face and closing wall face was taken. By doing this it was possible to estimate the axial resistance of the column at the three sections along its height by taking into account temperature gradients. The experimental yield strength was considered (see Table 3).

On the basis of these calculations, it was possible to observe that, owing to the colder temperature at the bottom end, the relative estimated average axial resistance in the last 30 s was significantly higher than the axial resistance at mid-height and even larger with respect to that at the top section, up to 23% higher for column #3. Moreover, the estimated axial resistances at the bottom end near failure were still well higher than the applied loads; whereas the axial resistances in the other sections were close to them. This means that the plastic hinge at base did not form and failure occurred due to the mechanism shown in Figure 7 owing to loss of resistance caused by elevated temperatures associated with second-order effects.

For column #1, the plastic hinge at the top did not clearly develop because the test was stopped soon after the first signs of instability whilst the others were pushed further.

5 CONCLUSIONS

Three fire tests on thin-walled columns made of ferritic stainless steel 1.4003 were performed. Two cross sections and two lengths were taken into account. All columns were loaded with a concentric axial compression up to 30% of the design $_{Nb.Rd}$ computed according to EN1993-1-4 (2006) and subsequently heated according to the ISO834 time-temperature curve. Full-restrained boundary conditions were imposed. Due to similar massivity factors and applied load ratios the fire resistance was fairly the same: about 12 minutes. The failure mode consisted of two plastic hinges and it was caused by the temperature gradient along the height developed inside the furnace

AKNOWLEDGEMENTS

The research leading to these results has received funding from the European Community's Research Fund for Coal and Steel (RFCS) under grant agreement no. RFSR-CT-2010-00026, Structural Applications of Ferritic Stainless Steels.

B. Rossi is supported by the Belgian National Fund for Scientific Research (F.R.S.-FNRS), which is gratefully acknowledged.

REFERENCES

EN 10002-1:2001 (2001) Tensile testing of metallic materials. Method of test at ambient temperature, CEN, Brussels.

EN10088-2:2005 (2005) Stainless steels. Technical delivery conditions for sheet/plate and strip of corrosion resisting steels for general purposes, CEN, Brussels.

EN1363-1 (2001) Fire resistance tests – Part 1: General requirement, CEN, Brussels.

EN 1993-1-2 (2005) Design of steel structures, Part 1–2: General rules–Structural fire design. CEN, Brussels.

EN 1993-1-4 (2006) Design of steel structures, Part 1–4 : General rules – Supplementary rules for stainless steels,CEN, Brussels.

Gardner L. and Baddoo N.R. (2006) Fire testing and design of stainless steel structures. *Journal of constructional steel researc*h, 62:6: 532–543.

Gardner L. and Ng K.T. (2006) Temperature development in structural stainless steel sections exposed to fire. *Fire safety journa*l, 41:185–203.

Gardner L., Insausti A., Ng K.T. and Ashraf M. (2010) Elevated temperature material properties of stainless steel alloys, *Journal of constructional steel research*, 66: 634–647.

Lopes N, Real P.V., da Silva L.S. and Franssen J.M. (2010) Axially loaded stainless steel columns in case of fire. *Journal of structural fire engineering,* 1:43–59.

Lopes N, Real P.V., da Silva L.S. and Franssen J.M. (2012) Numerical analysis of stainless steel beam-columns in case of fire. *Fire Safety Journal*, 50: 35–50

Rossi B., Afshan S., Gardner L., (2013) Strength enhancements in cold-formed structural sections – Part II: Predictive models. *Journal of constructional steel researc*h, In press.

Tondini N., Hoang V.L., Demonceau J.-F. and Franssen J.-M. (2013) Experimental and numerical investigation of high-strength steel circular columns subjected to fire loading. *Journal of constructional steel research*, 80: 57–81.

Uppfeldt B., Ala Outinen T. and Veljkovic M. (2008) A design model for stainless steel box columns in fire. *Journal of constructional steel research*, 64:1294–1301.

Research and Applications in Structural Engineering, Mechanics and Computation – Zingoni (Ed.)
© 2013 Taylor & Francis Group, London, ISBN 978-1-138-00061-2

Buckling response of ferritic stainless steel columns at elevated temperatures

S. Afshan & L. Gardner
Imperial College London, London, UK

N.R. Baddoo
The Steel Construction Institute, Ascot, UK

ABSTRACT: This paper presents a numerical study on the buckling behaviour of ferritic stainless steel columns in fire. Finite element models were developed and validated against existing test results to predict the elevated temperature non-linear response of ferritic stainless steel columns. A total of nine austenitic and three ferritic stainless steel column tests were replicated using the finite element analysis package ABAQUS. Parametric studies were performed to investigate the effects of variation of load level and global slenderness on the elevated temperature buckling response of ferritic stainless steel columns, and to extend the range of structural performance data. Both the experimental and numerical parametric study results were compared with the current design rules in EN 1993-1-2 (2005) and recent proposed modifications thereof by Ng and Gardner (2007), Uppfeldt et al. (2008) and Lopes et al. (2010).

1 INTRODUCTION

The characteristics of stainless steel, such as inherent durability, good mechanical properties and ease of maintenance, make it ideally suited for many civil engineering applications. Austenitic stainless steels, containing 17–18% chromium and 8–11% nickel, are the most widely used grades. However, the price of the alloying elements, in particular nickel, represents a major disincentive as far as material selection is concerned.

Hence, stainless steel grades with chemical compositions that offer similar benefits to the austenitics, but with lower nickel content, have been developed. Ferritic stainless steels, with little or no nickel content, have found applications in the automotive industry, road and rail transport, power generation, and mining. However, ferritic stainless steels have scarcely been used in structural applications. The aim of this study is to explore the fire resistance of ferritic stainless steel columns and assess the suitability of the current design provisions to this family of stainless steel.

2 REVIEW OF FIRE TESTS ON FERRITIC STAINLESS STEELS

The Steel Construction Institute is co-ordinating an ongoing RFCS project called Structural Applications of Ferritic Stainless Steels (RFSR-CT-2010-00026). This project includes an investigation into the performance of ferritic stainless steel members in fire. Experimental studies, focusing on the buckling response of columns made of grade EN 1.4003 ferritic stainless steel in fire were carried out at the University of Liège (Rossi, 2013). Elevated temperature material tests were also conducted and are reported in Manninen and Säynäjäkanas (2012). These results are utilized herein for the development and validation of the numerical models.

2.1 *Material properties*

Isothermal tensile coupon tests on material cut from EN 1.4003 cold-rolled sheets were performed in the temperature range of 20–1000°C (Manninen and Säynäjäkanas, 2012). Elevated temperature material properties are expressed as a portion of the corresponding room temperature properties. This leads to the use of strength and stiffness reduction factors for key parameters i.e. the elevated temperature 0.2% proof stress, ultimate tensile stress and Young's modulus. The stiffness retention factor $k_{E,\theta}$ is defined as the elevated temperature initial tangent modulus E_θ, normalized by the initial tangent modulus at room temperature E. The strength retention factors $k_{0.2,\theta}$ and $k_{u,\theta}$ are defined as the elevated temperature 0.2% proof stress and ultimate tensile stress normalized by their respective room temperature values. The $k_{2,\theta}$ factor is also used for determining the material strength at 2% total strain $\sigma_{t2,\theta}$, as defined in Annex C of EN 1993-1-2 (2005). Figures 1–2 show the measured reduction factors for the 0.2% proof stress and the ultimate tensile stress, respectively. The corresponding EN 1993-1-2 (2005) reduction factors for grade EN 1.4003 stainless steel and structural carbon steel are also depicted. EN 1993-1-2 (2005) provides a single set of stiffness

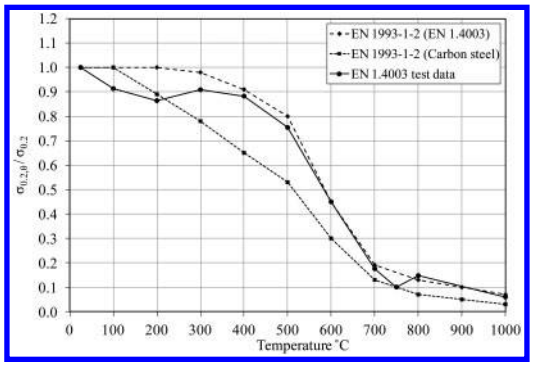


Figure 1. 0.2% proof stress reduction factor.

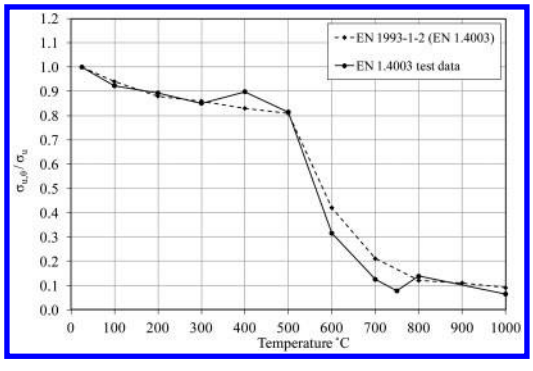


Figure 2. Ultimate tensile stress reduction factor.

reduction factors, common to all stainless steel grades. The test results obtained showed that in fact the elevated temperature stiffness of ferritic stainless steel (grade EN 1.4003) is somewhat in between that of the austenitics and structural carbon steel. The measured strength reduction factors are in good agreement with the EN 1.4003 codified values.

2.2 *Flexural buckling*

A total of three full scale fire tests on ferritic EN 1.4003 stainless steel tubular columns were conducted (Rossi, 2013). A summary of the test details, including nominal section size, specimen length, applied loads and critical furnace temperatures are provided in Tables 1. All columns were fixed at both ends. The manufacturing process of the tested columns involved cold-rolling into a circular tube followed by sizing into the final cross-section geometry. All fire tests were performed anisothermally, whereby the load – taken as approximately 30% of the specimen's codified room temperature buckling resistance – was applied at room temperature and maintained at a constant level while the temperature was increased, following the standard ISO-834 (2002) fire curve, until failure.

3 NUMERICAL MODELLING

The aim of this section is to develop and validate numerical models for predicting the resistance

Table 1. Summary of ferritic column fire tests.

Nominal section size	Length (mm)	Load (kN)	Critical furnace Temperature (°C)
SHS 80 × 80 × 3	3000	72	709.4
SHS 80 × 80 × 3	2500	78	707.7
RHS 120 × 80 × 3	3000	100	705.0

of stainless steel columns in fire. Fire test results from the literature on austenitic (EN 1.4301) stainless steel columns from Baddoo and Gardner (2000) and Ala-Outinen and Oksanen (1997) and ferritic stainless columns (Rossi, 2013) were gathered. These test results were used to validate the finite element models. The development of the numerical models leading into the results of parametric studies is described herein.

3.1 *Validation of numerical models*

3.1.1 *General*

The non-linear finite element analysis package ABAQUS, Version 6.10-1 (2010) was used to replicate the elevated temperature response of column tests from the literature. Shell elements were adopted to simulate the stainless steel tubular hollow section columns as is customary for modelling of thin-walled structures. The four-node doubly curved general-purpose shell element with reduced integration S4R, for the structural model, and D4S, for the thermal model, which has performed well in numerous similar applications (e.g. Ng & Gardner, 2007; To & Young, 2008) were used. A suitable mesh size, providing accurate results with practical computational times, with a minimum of ten elements across each plate was adopted.

The test boundary conditions were replicated by restraining suitable displacement and rotation degrees of freedom at the column ends. All boundary conditions were applied through reference points at the column ends. For the fixed column tests, all the six degrees of freedom of the lower reference point were restrained, while the upper reference point was allowed to move along the column axis and was fixed against all the other five degrees of freedom. To model the pinned end support condition, all degrees of freedom of the lower reference point, except rotation about the column minor axis, were fixed, while the upper reference point was free to displace along the column axis and rotate about the column minor axis. Measured geometric dimensions were used in each model to replicate the corresponding test behaviour.

3.1.2 *Elevated temperature material properties*

The performance of finite element models is highly sensitive to the prescribed material parameters, hence making an accurate representation of the material characteristics essential. In Baddoo and Gardner (2000), isothermal material tests at temperatures 20–1000°C were performed on the sheet material used to fabricate

the stainless steel sections. Ala-Outinen and Oksanen (1997) carried out anisothermal tensile tests on coupons cut from the flat faces of cold-rolled sections and the results were converted into stress-strain curves at temperatures 20–900°C. The measured material stress-strain curves at elevated temperatures were utilised in the development of the finite element models. For the ferritic column tests, the material model proposed by Gardner et al. (2010), along with the measured elevated temperature reduction factors, provided in Section 2, and the room room temperature material properties were used. ABAQUS requires that the material properties are specified in terms of true stress σ_{true} and log plastic strain ε^{p}_{ln}, which may be derived from the nominal engineering stress–strain curves as defined in Eqs. (1) and (2), respectively, where σ_{nom} and ε_{nom} are engineering stress and strain, respectively and E is the Young's modulus.

$$\sigma_{true} = \sigma_{nom}(1+\varepsilon_{nom}) \quad (1)$$

$$\varepsilon^{p}_{ln} = \ln(1+\varepsilon_{nom}) - \frac{\sigma_{true}}{E} \quad (2)$$

For austenitic stainless steel, the thermal properties from EN 1993-1-2 (2005) were incorporated in the models. The thermal properties of ferritic stainless steels are different from the austenitic stainless steels and are not covered in EN 1993-1-2 (2005). Thermal expansion data were sourced from EN 10088-1 (2005) and specific heat and thermal conductivity data were obtained from the StahlDat SX (2011) database.

3.1.3 *Corner material modelling*

Stainless steel exhibits a pronounced response to cold-work, resulting in the corner regions of cold-formed sections having significantly higher 0.2% proof strengths than the flat faces. For the ferritic column tests, corner material properties were measured at room temperature. For the austenitic stainless steel tests, where no corner material properties were reported, Cruise and Gardner's (2008) predictive equations for the strength enhancement in the corner regions of cold-rolled and press-braked stainless steel sections were used to determine the room temperature 0.2% proof strength of the corner regions.

The modified compound Ramberg-Osgood material model proposed by Gardner et al. (2010) was used to obtain a continuous prediction of the stress-strain response of the cold-worked corner regions at elevated temperatures. It has been shown that the beneficial effect of cold-work is lost at high temperatures of about 800°C and above (Ala-Outinen & Oksanen, 1997 and Chen & Young, 2006). Hence, in order to allow for this in the numerical models, the 0.2% proof strength reduction factors for temperatures of 800°C and above were reduced by 20% in relation to those used for the sheet material provided in EN 1993-1-2 (2005) as recommended by Gardner et al. (2010). The corner strength enhancement was confined to the corner region for the press-braked sections, while for the cold-rolled sections, a uniform strength enhancement for the corner region plus an extension of 2t, where t is the material thickness, beyond the corner radius into the flat faces of the section was used (Cruise & Gardner, 2008).

3.1.4 *Initial geometric imperfections*

Initial geometric imperfections are introduced into structural sections during production, fabrication and handling and can significantly influence structural behaviour. Imperfection shapes of the form of the lowest global and local buckling modes obtained from a linear elastic eigenvalue buckling analysis were utilized. A global imperfection amplitude of L/2000, where L is the column total length, was adopted for the austenitic stainless steel columns, while the test measured imperfection amplitudes were used for the ferritic stainless steel columns. The amplitude predicted by the Dawson and Walker model as adapted for stainless steel (Ashraf et al., 2006), given by Eq. (3) was used for the local imperfection amplitude w_0, where t is the plate thickness, $\sigma_{0.2}$ is the material 0.2% proof stress and σ_{cr} is the plate critical elastic buckling stress.

$$w_0 = 0.023t(\sigma_{0.2}/\sigma_{cr}) \quad (3)$$

3.1.5 *Analysis procedures*

Three types of numerical analyses were performed for each model – a linear elastic buckling analysis to determine the buckling mode shapes, and a heat transfer analysis to obtain the temperature development in the columns, were initially carried out. The results were subsequently incorporated into a geometrically and materially non-linear stress analysis. The non-linear stress analysis was performed in two steps to simulate the anisothermal loading condition of the column fire tests. In the first step, the load was applied to the top of the column, through its reference point, at room temperature. This load was maintained at a constant level during the second step while the evolution of the temperature with the fire exposure time was applied. For the case of the austenitic stainless steel columns, no heat transfer analysis were carried out, as the steel surface temperature was measured during the test and was directly imported into the models.

3.1.6 *Validation results*

A total of nine austenitic stainless steel columns and three ferritic stainless steel columns were modelled. The fire performance criteria set out in EN 1363-1 (1999) for vertically loaded members, stating that a column is deemed to have failed when both the vertical contraction and the rate of vertical contraction have exceeded L/100 mm and 3L/1000 mm/min, respectively, where L is initial column height in mm, were used to determine the critical failure temperature. A summary of the comparison between the test and FE results is provided in Table 2. For the austenitic stainless steel columns, the FE models give a mean FE/test critical temperature of 0.90 and a coefficient of variation of 0.03, and provide safe-side predictions of the fire resistance of the test column specimens.

Table 2. Comparison of critical temperatures between test and FE results.

Nominal section size	Classification	Critical temperature (°C) Test	FE	FE/Test
RHS 150 × 100 × 6	Class 1	801	757	0.91
RHS 150 × 75 × 6	Class 1	883	814	0.92
RHS 100 × 75 × 6	Class 1	806	744	0.92
SHS 40 × 40 × 4 (1)	Class 1	872	750	0.86
SHS 40 × 40 × 4 (2)	Class 1	579	502	0.87
SHS 40 × 40 × 4 (3)	Class 1	649	608	0.94
SHS 40 × 40 × 4 (4)	Class 1	710	646	0.91
SHS 40 × 40 × 4 (5)	Class 1	832	722	0.87
SHS 40 × 40 × 4 (7)	Class 1	766	681	0.89
SHS 80 × 80 × 3	Class 4	709	722	1.02
SHS 80 × 80 × 3	Class 4	708	713	1.01
RHS 120 × 80 × 3	Class 4	705	705	1.00

This under-prediction may be due to the application of uniform temperature through the thickness of the column section. In addition, all column tests were partially protected near the column ends to prevent the effect of sudden temperature variation at the start of the test, leaving a smaller exposed length than the full length used in the FE simulations. For the ferritic stainless steel columns, the FE and test results are in very good agreement with a mean FE/Test critical temperature of 1.01 and a coefficient of variation of 0.01. From the comparison of the test and FE results, it is concluded that the described FE models are capable of safely replicating the non-linear, large deflection response of the stainless steel columns in fire.

3.2 *Parametric studies*

Having validated the FE models, a series of parametric studies was performed to investigate the influence of variation of global slenderness and load level on the fire performance of ferritic stainless steel columns. Two section sizes, namely SHS 80 × 80 × 6 and RHS 120 × 80 × 6, were employed. The same modelling procedures as explained in the previous sections were employed. The global imperfection amplitude was taken as L/1000, where L is the column length, in accordance with the permitted out-of-straightness tolerance in EN 1090-2 (2008). The local imperfection amplitude was taken as that predicted by Eq. (3). All columns were pin-ended at both ends and were loaded anisothermally. Due to the symmetry in the geometry and the boundary conditions of the analyzed specimens, only half of the section, but over the full length, was modelled. The standard ISO-834 (2002) fire curve was applied to the specimens in the heat transfer model and the temperature development was simulated through the convection, conduction and radiation heat transfer mechanisms. The length of the column specimens was varied from 0.5 m to 3.0 m in order to cover a wide range of member slenderness values.

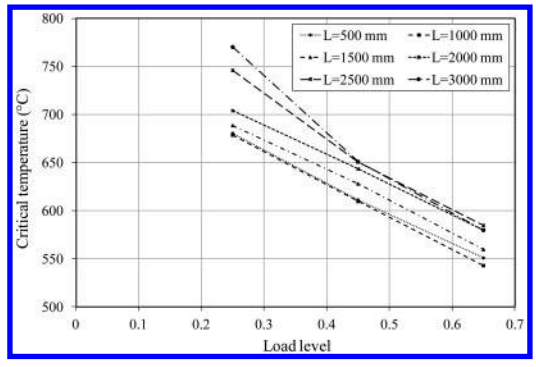


Figure 3. Effect of load level on the SHS 80 × 80 × 6 column critical temperature.

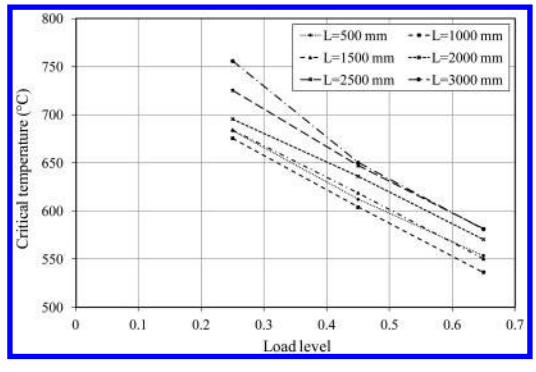


Figure 4. Effect of load level on the RHS 120 × 80 × 6 column critical temperature.

Three different load levels were applied to each column specimen: 25%, 45% and 65% of the room temperature minor axis buckling resistance, determined in accordance with EN 1993-1-4 (2006).

3.3 *Parametric results*

The effect of load level and member slenderness on the fire resistance of ferritic stainless steel columns, in terms of critical temperature, was studied, by fixing the cross-section size to SHS 80 × 80 × 6 and RHS 120 × 80 × 6. In order to focus on the member buckling behaviour, the thickness of the cross-sections was chosen such that both sections are Class 1. The column lengths of 0.5 m to 3.0 m provided a range of room temperature member slenderness $\bar{\lambda} = 0.25$–1.55. The obtained results are shown in Figures 3 and 4 for the SHS 80 × 80 × 6 and RHS 120 × 80 × 6 cross-sections, respectively. As anticipated, the column failure temperature reduces with increased load level. The variation of critical temperature with load level is also dependent on the member slenderness. This is expected as the member slenderness is dependent on the material strength and stiffness and its degradation with temperature.

4 ANALYSIS OF RESULTS AND DESIGN RECOMMENDATIONS

This section presents a comparison of the parametric study results with the existing design rules provided in EN 1993-1-2 (2005) and its modified versions proposed by Ng and Gardner (2007), Uppfeldt et al. (2008) and Lopes et al. (2010). Based on EN 1993-1-2, the design fire resistance of stainless steel structures, assuming a uniform temperature distribution, is based on the room temperature design resistance, supplied in EN 1993-1-4 (2006), modified to take account of the mechanical properties at elevated temperature and with a revised buckling curve. Since in fire situations higher strains than at room temperature are acceptable, EN 1993-1-2 uses the elevated temperature stress at 2% total stress, $\sigma_{t2.0,\theta}$ for the design of columns with Class 1, 2 and 3 cross-sections and the 0.2% proof stress $\sigma_{0.2,\theta}$ for Class 4 cross-sections. In classifying cross-sections, a reduced value for the strength parameter $\varepsilon = 0.85\ (235/f_y)^{0.5}$ is used to allow for variation of material strength with temperature. This definition is not consistent with its room temperature definition for stainless steel defined in EN 1993-1-4 (2006) as $\varepsilon = [(235/f_y)(E/210000)]^{0.5}$. Furthermore, it does not reflect the actual variation of strength and stiffness of stainless steel at elevated temperatures. EN 1993-1-2 (2005) also allows the effective section properties of Class 4 sections in fire to be based on room temperature design. Ng and Gardner (2007) recommended that the $\sigma_{0.2,\theta}$ strength should also be used for Class 3 sections as local buckling is expected to occur prior to reaching the 2% strain limit. In addition, it was proposed that the true variation of strength and stiffness should be employed in cross-section classification and in determination of the effective section properties, leading to the ε_θ definitions given by Eq. (4), where $k_{y,\theta}$ is taken as $k_{2,\theta}$ for Class 1 and 2 sections and $k_{0.2,\theta}$ for Class 3 and 4 sections.

$$\varepsilon_\theta = \left[\left(\frac{235}{f_y}\frac{E}{210000}\right)\left(\frac{k_{E,\theta}}{k_{y,\theta}}\right)\right]^{0.5} \quad (4)$$

The fire buckling curve in EN 1993-1-2 is of the same general form as the room temperature buckling curve with the exception of exhibiting no plateau (i.e. $= 0$), including a yield strength dependent imperfection factor ($\alpha = 0.65\ (235/f_y)^{0.5}$) and defining the elevated temperature member non-dimensional slenderness, . Ng and Gardner (2007) proposed a revised buckling curve with the plateau length $\bar{\lambda} = 0.2$ and the imperfection factor taken as $\alpha = 0.55$. Uppfeldt et al. (2008) adopted Ng and Gardner's (2007) recommendations for the cross-section classification and proposed to use the same buckling curve as room temperature, with $\bar{\lambda} = 0.4$ and $\alpha = 0.49$ (for hollow sections), for elevated temperature design, with the plateau length changing as a function of temperature, as given by Eq. (5).

$$\bar{\lambda}_{0,\theta} = \bar{\lambda}_0 \left[\frac{k_{0.2,\theta}}{k_{E,\theta}}\right]^{0.5} \quad (5)$$

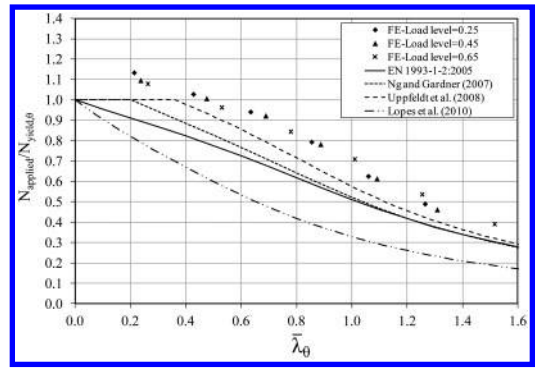


Figure 5. Comparison of SHS 80 × 80 × 6 FE results with the design models.

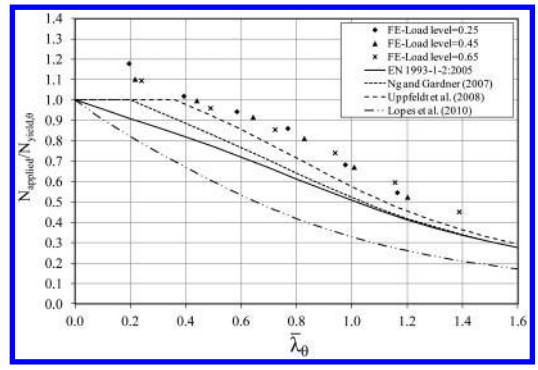


Figure 6. Comparison of RHS 120 × 80 × 6 FE results with the design models.

Based on their numerical study on welded I-section columns in fire, Lopes et al. (2010) modified the EN 1993-1-2 buckling curve such that it provides a good fit to the generated data. The imperfection factor α is defined as a function of temperature, resulting in different buckling curves for different temperatures. Figures 5 and 6 compare the above mentioned buckling curves with an average plateau length = 0.36 for the investigated specimens for the Uppfeldt et al. (2008) model, and an average failure temperature of 635°C for the Lopes et al. (2010) model with the parametric study results, where the applied load, normalized by the elevated temperature yield load based on $\sigma_{0.2,\theta}$ is plotted against the elevated temperature member slenderness.

A preliminary analysis of the results shows that the current EN 1993-1-2 (2005) buckling curve underpredicts the buckling load of ferritic stainless steel columns, while the proposals of Ng and Gardner (2007) and Uppfeldt et al. (2008) provide better predictions. The buckling curves proposed by Lopes et al. (2010) are considerably lower than other studies. This may be due to the section type analysed – welded I-sections which do not benefit from the corner strength enhancements found in cold formed sections and have higher residual stresses. The relative performance of different section types will be considered in future work.

5 CONCLUSIONS

A numerical study investigating the buckling response of ferritic stainless steel columns in fire was presented. A detailed description of the finite element models was provided, which were validated against test results. The results of the parametric study, investigating the effects of variation of load level and global slenderness were presented. Comparisons between the generated data and the existing buckling curves were made.

AKNOWLEDGEMENTS

The research leading to these results has received funding from the European Community's Research Fund for Coal and Steel (RFCS) under grant agreement no. RFSR-CT-2010-00026, Structural Applications of Ferritic Stainless Steels.

REFERENCES

ABAQUS (2010) ABAQUS, Version 6.10-1. Dassault Systèmes Simulia Corp., USA.

Ala-Outinen, T. & Oksanen, T. (1997) Stainless steel compression members exposed to fire. VTT research notes 1864. Espoo (Finland).

Ashraf, M., Gardner, L. & Nethercot, D. A. (2006) Finite element modelling of structural stainless steel cross-sections. *Thin-Walled Structures.* 44 (10), 1048–1062.

Baddoo, N. R. & Gardner, L. (2000) Member behaviour at elevated temperatures. ECSC project – Development of the use of stainless steel in construction, Contract No. 7210 SA/ 842. The Steel Construction Institute, UK, WP5.2.

Chen, J. & Young, B. (2006) Stress–strain curves for stainless steel at elevated temperatures. *Engineering Structures.* 28 (2), 229–239.

Cruise, R. B. & Gardner, L. (2008) Strength enhancements induced during cold forming of stainless steel sections. *Journal of Constructional Steel Research.* 64 (11), 1310–1316.

European Committee for standardization (CEN). (2005) *Eurocode 3: Design of steel structures – Part 1-2: General rules – Structural fire design, EN 1993-1-2*, Brussels, Belgium.

European Committee for standardization (CEN). (2002) *Eurocode 1: Actions on structures – Part 1–2: General actions – Actions on structures exposed to fire, EN 1991-1-2*, Brussels, Belgium.

European Committee for standardization (CEN). (2006) *Eurocode 3: Design of steel structures – Part 1–4: General rules –Supplementary rules for stainless steels, EN 1993-1-4*, Brussels, Belgium.

European Committee for standardization (CEN). (1999) *Fire resistance tests – Part 1: General requirements EN 1363-1*, Brussels, Belgium.

European Committee for standardization (CEN). (2005) *Stainless steels – Part 1: List of stainless steels. EN 10088-1.* Brussels, Belgium.

European Committee for standardization (CEN). (2008) *Execution of steel structures and aluminium structures – Part 2: Technical requirements for steel structures, EN 1090-2,* Brussels, Belgium.

Gardner, L., Insausti, A., Ng, K. T. & Ashraf, M. (2010) Elevated temperature material properties of stainless steel alloys. *Journal of Constructional Steel Research.* 66 (5), 634–647.

Gmbh, S. (2011) *Stahldat SX*. [online] Available at: http://www.stahldaten.de [Accessed: 12 November 2012].

Lopes, N., Vila Real, P., Silva, L. S., & Franssen, J. M. (2010) Flexural buckling of axially loaded ferritic stainless steel columns in case of fire. *Journal of Structural Fire Engineering*, 1(1), 43–59.

Manninen, T. & Säynäjäkanas, J. (2012) Mechanical properties of ferritic stainless steel at elevated temperature. Proceedings of the Fourth International Experts Seminar on Stainless Steel in Structures, December 2012, The Steel Construction Institute, Ascot, UK

Ng, K. T. & Gardner, L. (2007) Buckling of stainless steel columns and beams in fire. *Engineering Structures.* 29 (5), 717–730.

Rossi, B., Tondini, N. & Franssen, J. M. (2013) Experiments on ferritic stainless steel columns in fire, to be presented at SEMC 2013.

To, E. C. & Young, B. (2008) Performance of cold-formed stainless steel tubular columns at elevated temperatures. *Engineering Structures.* 30 (7), 2012–2021.

Uppfeldt, B., Ala Outinen, T. & Veljkovic, M. (2008) A design model for stainless steel box columns in fire. *Journal of Constructional Steel Research.* 64 (11), 1294–1301.

Research and Applications in Structural Engineering, Mechanics and Computation – Zingoni (Ed.)
© 2013 Taylor & Francis Group, London, ISBN 978-1-138-00061-2

Interaction effects of constituent plate elements on cold-formed high strength stainless steel cross-section behaviour in compression

F. Zhou & Y. Chen
Department of Building Engineering, Tongji University, Shanghai, China

B. Young
Department of Civil Engineering, The University of Hong Kong, Hong Kong, China

ABSTRACT: A numerical investigation of cold-formed high strength stainless steel square and rectangular hollow sections in compression has been presented in this paper. A non-linear finite element model that includes geometric and material non-linearities was developed and verified against experimental results. The model was then used for an extensive parametric study to investigate the interaction effects of constituent plate elements on Class 3 slenderness limit and section capacities of cold-formed high strength stainless steel square and rectangular hollow sections in compression. It is shown that the interaction effects of constituent plate elements on cross-section response are quite obvious particularly for slender sections. The design provisions on Class 3 slenderness limit in the EC3 Code and proposed by Gardner and Theofanous are suitable for square hollow sections, but not for rectangular hollow sections since they do not take into consideration of interaction effects of constituent plate element. Therefore, a new Class 3 slenderness limit is proposed in this study, which carefully considers the interaction effects of the constituent plate elements.

1 INTRODUCTION

The use of cold-formed stainless steel tubular members in construction is growing rapidly. Many researches have been carried out to study the structural behaviour of cold-formed stainless steel tubular members. Experimental and numerical investigations have been performed by Rasmussen & Hancock (1993), Young & Hartono (2002), Young & Liu (2003), Gardner & Nethercot (2004a), Young & Lui (2005), Ellobody & Young (2005), Gardner & Theofanous (2008), and Theofanous & Gardner (2009) on cold-formed stainless steel tubular columns. In most of these investigations, the applicability of the existing stainless steel design provisions on Class 3 slenderness limit and effective width formulae for internal elements in compression as well as the column buckling curve for hollow sections have been assessed.

Design rules for cold-formed stainless steel structural members are available including the ASCE Specification (2002) for the Design of Cold-Formed Stainless Steel Structural Members and the EC3 Code (2006) Design of Steel structures, Part 1.4: Supplementary Rules for Stainless Steels. The cross-section classification approach is used in the EC3 Code as a means of codified treatment for local buckling of cross-sections that are partly or fully in compression. However, the interaction of constituent plate elements is not taken into consideration. The EC3 Code treats the plate elements in the cross-section individually and classified according to their width-to-thickness ratios as compared to codified slenderness limits. The cross-section response is assumed to the behaviour of its most slender plate element in the cross-section. However, the interaction effects of constituent plate elements on cross-section response are obvious regarding the slenderness limits and the cross-section ultimate resistances for cold-formed stainless steel square and rectangular hollow sections subjected to compression (Theofanous & Gardner 2009) and also bending (Theofanous & Gardner 2010).

The purpose of this study is firstly to develop an accurate and efficient non-linear finite element model to simulate the cross-section response of cold-formed high strength stainless steel square and rectangular hollow sections in compression. The initial local imperfection and non-linear material properties of the flat and corner portions of the cross-section have been carefully incorporated into the finite element model (FEM). Secondly, a parametric study on a range of cross-section aspect ratios was performed based on the developed FEM. Thirdly, the interaction effects of constituent plate element on cross-section response of cold-formed high strength stainless steel square and rectangular hollow sections in compression are investigated. The design provisions on Class 3 slenderness limit specified in the current EC3 Code (2006), ASCE Specification (2002) and proposed by Gardner & Theofanous (2008) for internal elements in compression are assessed based on the results of the parametric

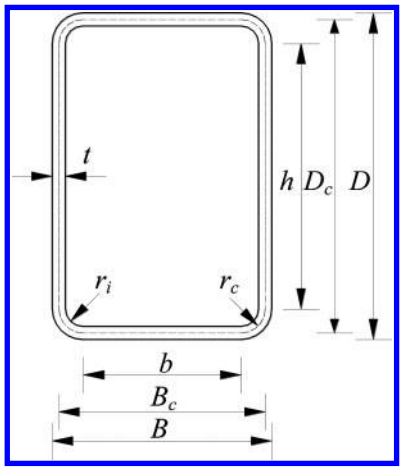


Figure 1. Definition of symbols.

Table 1. Summary of Test Specimens (Young & Lui 2005).

Section	D (mm)	B (mm)	t (mm)	r_i (mm)	L (mm)	$\sigma_{0.2}$ (MPa)	P_{Exp} (kN)
40 × 40 × 2	40.1	39.9	1.945	1.8	300	707	245.3
50 × 50 × 1.5	50.1	50.3	1.584	1.5	300	622	175.7
150 × 150 × 3	150.5	150.5	2.796	4.6	600	448	408.6
150 × 150 × 6	150.6	150.2	5.855	5.3	601	497	1927.4
140 × 80 × 3	140.0	78.8	3.075	7.0	600	486	558.2
160 × 80 × 3	160.1	80.8	2.869	6.3	600	536	537.3
200 × 110 × 4	196.2	108.5	4.010	9.1	600	503	9457.0

study. Lastly, a new Class 3 slenderness limit which carefully takes into account of the interaction effects of constituent plate elements is proposed in this study for cold-formed high strength stainless steel square and rectangular hollow sections in compression.

2 SUMMARY OF EXPERIMENTAL INVESTIGATION

The experimental investigation performed by Young & Lui (2005) reported the tests of cross-sections of cold-formed high strength stainless steel square and rectangular hollow sections in compression, which were used to verify the finite element model developed in this study. Table 1 summarizes the measured test specimen dimensions using the nomenclature defined in Figure 1. The material properties of the flat portions of the specimens for each section were determined by tensile coupon tests. Furthermore, the material properties of the corner portions of the specimen have also been determined by tensile coupon tests for section 160×80×3. The measured material properties of the flat and corner portions are detailed in Young & Lui (2005).

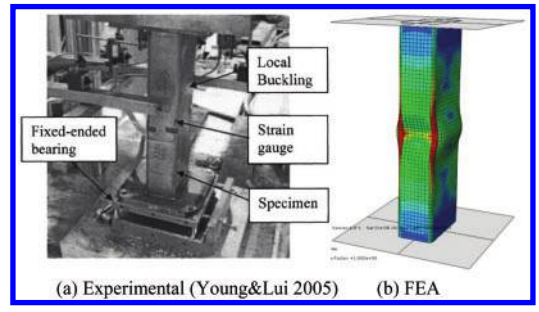


Figure 2. Comparison of experimental and finite element analysis failure mode for specimen RHS200 × 110 × 4.

The columns were compressed between fixed ends, as shown in Figure 2. A servo-controlled hydraulic testing machine was used to apply a concentrated compressive force to the test specimens. Displacement control was used to drive the hydraulic actuator at a constant speed of 0.5 mm/min for all test specimens. The experimental ultimate loads (P_{Exp}) of the specimens are also given in Table 1. The stub column tests are detailed in Young & Lui (2005).

3 NUMERICAL INVESTIGATION

3.1 *Finite element model*

The non-linear finite element program ABAQUS (2008) was used to simulate the cross-section response of cold-formed high strength stainless steel square and rectangular hollow sections in compression. Finite element analysis (FEA) for buckling requires two steps of analysis. The first step is linear perturbation analysis, which was performed on a "perfect" geometry to obtain probable elastic buckling modes of the cross-sections. The second step is non-linear analysis by incorporating both geometric and material non-linearities, which was performed to obtain the ultimate strengths and failure modes of the stub columns.

In the finite element model (FEM), the measured cross-section dimensions and material properties obtained from tensile coupon tests were used. The model was based on the centerline dimensions of the cross-sections. The corners of the cold-formed high strength stainless steel sections were carefully modeled. The S4R elements are used for all specimens. The finite element mesh used in the model was investigated by varying the size of the elements in the cross-section to provide both accurate results and less computational time. The finite element mesh sizes ranged from 2 × 2 mm (length by width) to 10 × 10 mm were used for the flat portions of the specimen depending on the cross-section size, whereas a finer mesh was used at the corners. The typical finite element mesh of a stub column is shown in Figure 2b.

The axial compressive force was applied by the load transfer plates. The load transfer plates were modeled using analytical rigid plates and the interfaces between

the load transfer plates and the specimen were modeled using the "tie constraint pair". The load transfer plates were the master elements, while the specimen was the salve element of the interface elements in the FEM model. The "tie constraint" ties two surfaces together, which ensure the translational and rotational degrees of freedom identical to the pair of surfaces.

Following the test procedure conducted by Young & Lui (2005), the load transfer plates were restrained against all degrees of freedom, except for the displacement at the top load transfer plate in the direction of the applied load. The loading method used in the FEM was identical to that used in the tests. The displacement control method was used for the analysis of the cold-formed high strength stainless steel square and rectangular hollow section stub columns. The load was applied to the specimen by specifying a displacement to the reference point of the analytical rigid plate that modeled the top load transfer plate.

The corner material properties of the rest of the sections were extrapolated from section 160 × 80 × 3 according to the measured initial Young's Modulus (E), the static 0.2% tensile proof stress ($\sigma_{0.2}$), the static tensile strength (σ_u) and the elongation after fracture (ε_f) based on a gauge length of 50 and 25 mm in the flat and corner portions, respectively. The measured and predicted stress-strain curves for flat and corner portions of each column were used in the analysis. Due to the absence of overall buckling for stub columns, only local geometric imperfection has been incorporated into the FEM in the form of the lowest buckling mode shape predicted in the linear perturbation analysis which is the first step of the finite element analysis as mentioned earlier. The local imperfection amplitude derived from the predictive model of Dawson & Walker (1972) as adapted by Gardner & Nethercot (2004b) for stainless steel was used in the finite element analysis. The local imperfection amplitude was defined in Eq. (1)

$$w_0 = 0.023\left(\frac{\sigma_{0.2}}{\sigma_{cr}}\right)t \tag{1}$$

where w_0 is the magnitude of the local imperfection, t is the plate thickness, $\sigma_{0.2}$ is the material 0.2% proof stress, and σ_{cr} is the elastic critical buckling stress of the plate that assuming simply supported boundary conditions.

3.2 *Verification of finite element model*

In the verification of the FEM, a total of 7 cold-formed high strength stainless steel square and rectangular hollow section stub columns were analyzed. A comparison between the experimental and FEA results was carried out. The main objective of this comparison is to verify and check the accuracy of the FEM. The comparison of the test results (P_{Exp}) with the ultimate loads (P_{FEA}) predicted from the FEA is shown in Table 2. It can be seen that a good agreement has been achieved between both results for all specimens. A maximum difference of 5% was observed between the experimental and numerical results for section 140 × 80 × 3. The mean value of the $P_{\text{Exp}}/P_{\text{FEA}}$ ratio is 1.03 with the small coefficient of variation (COV) of 0.020.

Table 2. Comparison of Experimental Results with Ultimate Loads Predicted from Finite Element Analysis.

Specimen	$h/t\varepsilon$	$b/t\varepsilon$	P_{Exp} (kN)	P_{FEA} (kN)	P_{Exp}/P_{FEA}
40 × 40 × 2	28.0	27.9	245.3	245.3	1.00
50 × 50 × 1.5	28.5	28.4	175.7	176.0	1.00
150 × 150 × 3	46.2	46.4	408.6	392.1	1.04
150 × 150 × 6	46.6	46.9	1927.4	1865.9	1.03
140 × 80 × 3	69.0	69.0	558.2	529.9	1.05
160 × 80 × 3	33.1	33.0	537.3	526.4	1.02
200 × 110 × 4	55.5	27.2	957.0	925.5	1.03
				Mean	1.03
				COV	0.020

The failure mode observed from the tests was also verified by the finite element model, as shown in Figure 2. It is shown that the FEM accurately predicted both the ultimate loads and the failure modes for cold-formed high strength stainless steel square and rectangular hollow section stub columns.

3.3 *Parametric study*

It was shown that the FEM accurately predicted the cross-section response of cold-formed high strength stainless steel square and rectangular hollow sections in compression. Hence, an extensive parametric study was carried out to investigate the effects of the cross-section aspect ratio ($\alpha = h/b \geq 1$), which directly related to the degree of interaction of constituent plate elements in square and rectangular hollow sections, on Class 3 slenderness limit and section capacities of cold-formed high strength stainless steel square and rectangular hollow sections in compression.

A total of 63 cold-formed high strength stainless steel square and rectangular hollow section stub columns with different cross-section aspect ratio were analyzed in the parametric study. The specimens consisted of 7 series with the cross-section aspect ratios α of 1.00, 1.13, 1.38, 1.80, 2.25, 3.00, and 6.00, respectively. For all the specimens, the web depth (D_c) between the midlines of the flanges was kept constant at 200 mm, the midline corner radius (r_c) was kept constant at 10 mm and the column length (L) was kept at 600 mm. The flange width (B_c) between the midlines of the webs ranged from 200 to 50 mm, such that the cross-section aspect ratios ranged from 1.00 to 6.00, were analyzed. The thickness (t) varied from 3.0 to 10.0 mm to cover from relatively compact sections to slender sections. The measured stress-strain curves of the flat and corner portions of the section 160 × 80 × 3 were used in the parametric study. The ultimate loads (P_{FEA}) predicted from FEA are summarized in Table 3.

Table 3. Ultimate Loads Predicted from the Finite Element Analysis of Parametric Study.

Specimen ($D_c \times B_c \times t$)	$P_{FEA}/\sigma_{0.2}A$						
	$B_c = 200$ $\alpha = 1.00$	$Bc = 180$ $\alpha = 1.13$	$Bc = 150$ $\alpha = 1.38$	$Bc = 120$ $\alpha = 1.80$	$Bc = 100$ $\alpha = 2.25$	$Bc = 80$ $\alpha = 3.00$	$Bc = 50$ $\alpha = 6.00$
$200 \times B_c \times 3.0$	0.48	0.50	0.54	0.59	0.62	0.66	0.66
$200 \times B_c \times 3.5$	0.53	0.55	0.60	0.65	0.69	0.72	0.71
$200 \times B_c \times 4.0$	0.59	0.61	0.66	0.72	0.75	0.77	0.76
$200 \times B_c \times 4.5$	0.66	0.69	0.75	0.79	0.81	0.82	0.81
$200 \times B_c \times 5.0$	0.75	0.79	0.84	0.87	0.89	0.90	0.90
$200 \times B_c \times 6.0$	0.89	0.89	0.94	0.95	1.00	1.01	1.02
$200 \times B_c \times 7.0$	1.02	1.03	1.08	1.10	1.13	1.14	1.15
$200 \times B_c \times 8.0$	1.11	1.12	1.15	1.17	1.20	1.20	1.22
$200 \times B_c \times 10.0$	1.20	1.22	1.23	1.25	1.28	1.28	1.29

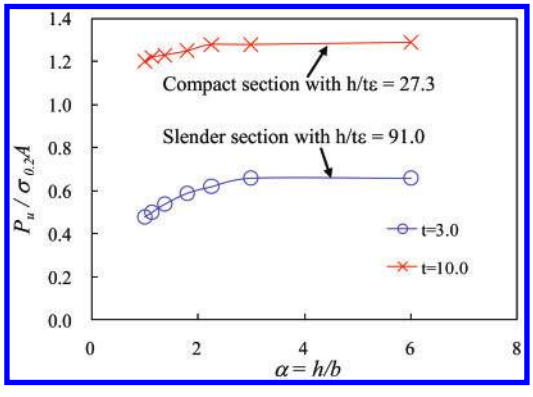


Figure 3. Effect of the interaction of constituent plate elements.

4 INTERACTION EFFECTS OF CONSTITUENT PLATE ELEMENTS

The cross-section response of the cold-formed high strength stainless steel square and rectangular hollow sections in compression is influenced by the interaction of constituent plate elements. The normalized section resistance ($P_u/\sigma_{0.2}A$) increases when the cross-section aspect ratio ($\alpha = h/b$) increases. This is attributed to the lower value of flange slenderness that provided a higher degree of restraint to the webs.

The effects of the cross-section aspect ratio (α) on the normalized section resistances for both the slender section with the normalized web slenderness ($h/t\varepsilon$) of 91.0 and the relatively compact section with the $h/t\varepsilon$ of 27.3 are shown in Figure 3. It is shown that the cross-section aspect ratio α has greater effect for the slender section than for the compact section. This is due to the fact that cross-section failed by either material yielding or inelastic local buckling in the case of stocky cross-section, and failed by local buckling below the yield stress for slender cross-section. The occurrence of local buckling will be delayed by the degree of restraint provided by the flanges to the webs. It is also shown that as the value of α increases the normalized section resistance also increases during the initial stage. Once α reached a value of approximately 3 ($\alpha = 3$) then the normalized section resistance hardly increase for both slender section having $h/t\varepsilon$ of 91.0 and the compact section having $h/t\varepsilon$ of 27.3, as shown in Figure 3.

5 ASSESSMENT OF CURRENT CLASS 3 SLENDERNESS LIMITS

The cross-section classification approach for stainless steel is similar to that adopted for carbon steel with the only difference lying in the adopted slenderness limits. The slenderness parameter $h/t\varepsilon$ specified in EC3 Code (2006) can be used to define the cross-section classification, where h is the flat width of the plate element considered, t is the plate thickness and ε is defined using Eq. (2).

$$\varepsilon = \sqrt{\frac{235}{\sigma_{0.2}} \frac{E}{210000}} \tag{2}$$

in which $\sigma_{0.2}$ is 0.2% proof stress and E is the Young's modulus. For square and rectangular hollow sections, the plate elements are simply supported and considered as internal elements where a buckling factor (k_σ) of 4 is used. Therefore, the relationship between slenderness parameter $h/t\varepsilon$ specified in EC3 Code (2006) and the slenderness parameter λ specified in the ASCE Specification (2002) is follows as in Eq. (3).

$$\frac{h}{t\varepsilon} = 56.83\lambda \tag{3}$$

For slender cross-sections (corresponding to Class 4 defined in EC3 Code) in compression, the section capacity is below the squash load as a result of local buckling. The numerical ultimate loads (P_{FEA}) obtained in this study together with the experimental results (P_{Exp}) reported by Young & Lui (2005) for the cold-formed high strength stainless steel square and rectangular hollow section stub columns were compared with the nominal section capacities ($\sigma_{0.2}A$) to assess the accuracy of the design provisions on Class

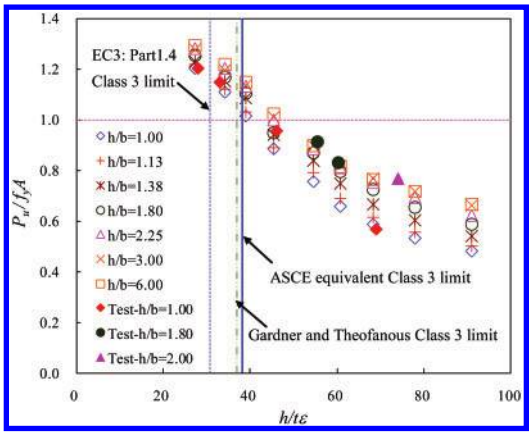


Figure 4. Current Class 3 slenderness limit for internal elements in compression.

3 slenderness limit. The cross-section ultimate loads (P_u) obtained from the tests and finite element analysis were normalized by the nominal section capacities ($\sigma_{0.2}A$) and plotted against the slenderness parameter $h/t\varepsilon$ of the web, which is the most slender plate element of the section in compression for all specimens, as shown in Figure 4. In ASCE Specification (2002), an equivalent Class 3 slenderness limit is defined in this study, when the reduction factor (ρ) for the calculation of effective width is less than 1.0, then the corresponding slenderness limit is defined as Class 3. The Class 3 slenderness limits for fully effective section specified in the current ASCE Specification (2002) and EC3 Code (2006) are 38.3ε and 30.7ε, respectively. The Class 3 slenderness limit of 37.0ε for fully effective section proposed by Gardner & Theofanous (2008) is also assessed using the cross-section ultimate loads obtained in this study. It is shown that the rectangular hollow sections ($\alpha > 1$) achieve the superior normalized section resistances to their square hollow sections ($\alpha = 1$) counterparts with the same web slenderness, particularly in the slender range of the graphs. It is also shown that the Class 3 slenderness limit for fully effective section proposed by Gardner & Theofanous is very close to that codified in ASCE Specification (2002), which is more suitable for square hollow sections instead of rectangular hollow sections. However, the Class 3 slenderness limit for fully effective section specified in the EC3 Code (2006) is quite conservative even for square hollow sections with the least normalized section resistances.

6 PROPOSED CLASS 3 SLENDERNESS LIMIT AND COMPARED WITH NUMERICAL RESULTS

In the current EC3 Code (2006) for stainless steel structures, the cross-section responses is considered to the behaviour of its most slender plate element, thereby neglecting the interaction of constituent plate

Table 4. Cross-section Dimensions and Ultimate Loads Predicted from the Finite Element Analysis for Proposing Class 3 Slenderness Limit.

Specimen ($D_c \times B_c \times t$)	$h/t\varepsilon$	$b/t\varepsilon$	α	P_{FEA} (kN)	$\sigma_{0.2}A$ (kN)	$P_{FEA}/\sigma_{0.2}A$
$200 \times 50 \times 5.9$	46.3	7.7	6.00	1534.2	1526.8	1.00
$200 \times 80 \times 6.0$	45.5	15.2	3.00	1764.5	1745.6	1.01
$200 \times 100 \times 6.1$	44.8	19.9	2.25	1938.9	1905.5	1.02
$200 \times 120 \times 6.2$	44.1	24.5	1.80	2112.6	2069.7	1.02
$200 \times 150 \times 6.4$	42.7	30.8	1.38	2372.9	2342.3	1.01
$200 \times 180 \times 6.7$	40.8	36.2	1.13	2698.6	2667.5	1.01
$200 \times 200 \times 7.0$	39.0	39.0	1.00	2984.1	2937.1	1.02

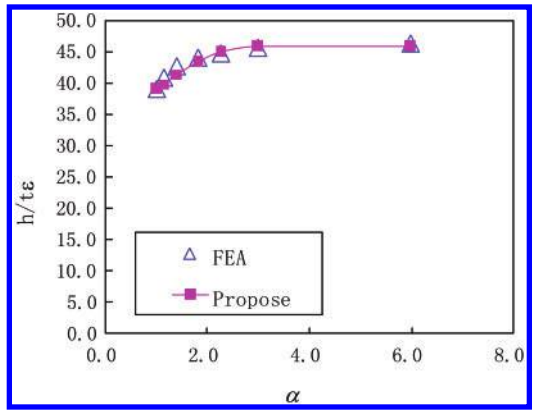


Figure 5. Proposed Class 3 slenderness limit for cold-formed high strength stainless steel square and rectangular hollow sections in compression.

elements, which are individually classified according to their width-to-thickness ratios, as compared with codified slenderness limits (Gardner & Theofanous 2008). However, it is shown that the effects of the interaction of constituent plate elements are quite obvious up to the cross-section aspect ratio (α) of 3. Therefore, a new Class 3 slenderness limit based on the whole cross-section response is proposed in this study for cold-formed high strength stainless steel square and rectangular hollow sections in compression, which takes into consideration of the interaction of constituent plate elements.

A total of 7 series square and rectangular hollow sections with the values of α equal to 1.00, 1.13, 1.38, 1.80, 2.25, 3.00, and 6.00, considered in the parametric study were re-analyzed using the finite element model developed in this study. For each series, the web depth between the midlines of the flanges (D_c), the flange width between the midlines of the webs (B_c) and the midline corner radius (r_c) are kept unchanged. The only change to the sections is the thicknesses (t). The aim of the investigation is to obtain the appropriate value for each series such that the normalized section resistances are close to 1.0 ($P_{FEA}/\sigma_{0.2}A = 1.0$). The cross-section dimensions and the ultimate loads

(P_{FEA}) predicted from FEA for the purpose of proposing a new Class 3 slenderness limit are summarized in Table 4. Based on this study, a new Class 3 slenderness limit, which is the function of the cross-section aspect ratio ($\alpha = h/b$), is proposed, as shown in Eq. (4).

$$\frac{h}{t\varepsilon} = \begin{cases} 30.5 + 10.2\alpha - 1.7\alpha^2 & 1 \le \alpha \le 3 \\ 45.8 & \alpha > 3 \end{cases} \quad (4)$$

where h and b are the flat widths of the web and flange elements, respectively, of the square and rectangular hollow sections ($h \ge b$); t is the plate thickness; ε is defined in Eq. (2) of this paper; α is the cross-section aspect ratio ($\alpha = h/b \ge 1$); and $\sigma_{0.2}$ is the 0.2% proof stress of the stainless steel. The limitations of the Eq. (4) are $1.0 \le \alpha \le 6.0$ and $448 \le \sigma_{0.2} \le 707$ MPa.

The slenderness parameters $h/t\varepsilon$ predicted using the proposed Class 3 slenderness limit as shown in Eq. (4) were plotted against the cross-section aspect ratio α in Figure 5. The $h/t\varepsilon$ data points shown in Table 4, where the normalized section resistance is close to 1 ($P_{FEA}/\sigma_{0.2}A = 1$) are used. It is shown that the proposed Class 3 slenderness limits agree well with the numerical results.

7 CONCLUSIONS

An accurate and efficient finite element model (FEM) was developed in this study for the analysis of cold-formed high strength stainless steel square and rectangular hollow section stub columns. The initial local imperfection and non-linear material properties of the flat and corner portions of the cross-section have been carefully incorporated in the FEM. It is shown that the FEM closely predicted the cross-section responses of the cold-formed high strength stainless steel square and rectangular hollow sections in compression. Hence, an extensive parametric study was carried out to study the interaction effects of constituent plate elements on cold-formed high strength stainless steel cross-section behaviour in compression.

It is shown that the interaction effects of constituent plate elements on the normalized section resistances are obvious, particularly for slender sections. It is also shown that as the value of cross-section aspect ratio (α) increases, the normalized section resistance also increases during the initial stage, and once α reached a value of approximately 3 then the normalized section resistance hardly increase for both slender section having $h/t\varepsilon$ of 91.0 and the compact section having $h/t\varepsilon$ of 27.3. The Class 3 slenderness limit in the EC3 Code, ASCE Specification and proposed by Gardner and Theofanous were also assessed using the results obtained from the parametric study. It is shown that the design provisions on Class 3 slenderness limit are more suitable for square hollow sections rather than rectangular hollow sections since they neglected the interaction of constituent plate elements.

Therefore, a new Class 3 slenderness limit is proposed in this study for cold-formed high strength stainless steel square and rectangular hollow sections in compression that takes into consideration of the interaction of constituent plate elements. It is shown that the proposed Class 3 slenderness limit agrees well with the numerical results for both square and rectangular hollow sections.

ACKNOWLEDGEMENT

The research work described in this paper was supported by the Fundamental Research Funds for the Central Universities of China.

REFERENCES

American Society of Civil Engineers (ASCE). 2002. *Specification for the design of cold-formed stainless steel structural members*. SEI/ASCE-8-02, Reston, Virginia.

Dawson, R.G. & Walker, A.C. 1972. Post-buckling of geometrically imperfect plates. *Journal of the Structural Division, ASCE* 98(ST1):75–94.

Ellobody, E. & Young, B. 2005. Structural performance of cold-formed high strength stainless steel columns. *Journal of Constructional Steel Research* 61(12):1631–1649.

European Committee for Standardization (EC3). 2006. *Eurocode 3: Design of steel structures – Part 1.4: General rules – Supplementary rules for stainless steels*. BS EN 1993-1-4, CEN, Brussels.

Gardner, L. & Nethercot, D.A. 2004a. Experiments on stainless steel hollow sections—Part 2: Member behaviour of columns and beams. *Journal of Constructional Steel Research* 60(9):1319–1332.

Gardner, L. & Nethercot, D.A. 2004b. Numerical modeling of stainless steel structural components – A consistent approach. *Journal of Structural Engineering, ASCE* 130(10): 1586–1601.

Gardner, L. & Theofanous, M. 2008. Discrete and continuous treatment of local buckling in stainless steel elements. *Journal of Constructional Steel Research* 64(11): 1207–1216.

Hibbitt, Karlsson and Sorensen, Inc. 2008. *ABAQUS standard user's manual, vols. 1–3, version 6.8*. USA.

Rasmussen, K.J.R. & Hancock, G.J. 1993. Design of cold-formed stainless steel tubular members. I: Columns. *Journal of Structural Engineering, ASCE* 119(8): 2349–67.

Theofanous, M. & Gardner, L. 2009. Testing and numerical modeling of lean duplex stainless steel hollow section columns. *Engineering Structures* 31(12):3047–3058.

Theofanous, M. & Gardner, L. 2010. Experimental and numerical studies of lean duplex stainless steel beams. *Journal of Constructional Steel Research* 66(6):816–825.

Young, B. & Hartono, W. 2002. Compression tests of stainless steel tubular members. *Journal of Structural Engineering, ASCE* 128(6):754–61.

Young, B. & Liu, Y. 2003. Experimental investigation of cold-formed stainless steel columns. *Journal of Structural Engineering, ASCE* 129(2):169–76.

Young, B. & Lui, W.M. 2005. Behavior of cold-formed high strength stainless steel sections. *Journal of Structural Engineering, ASCE* 131(11):1738–1745.

Research and Applications in Structural Engineering, Mechanics and Computation – Zingoni (Ed.)
© 2013 Taylor & Francis Group, London, ISBN 978-1-138-00061-2

Mechanical properties of austenitic stainless steel after exposed to fire

Xing-Qiang Wang
Institute for Infrastructure Engineering, University of Western Sydney, Penrith NSW, Australia
Department of Civil Engineering, Shandong Polytechnic, Jinan, Shandong Province, China

Zhong Tao & Tian-Yi Song
Institute for Infrastructure Engineering, University of Western Sydney, Penrith NSW, Australia

Lin-Hai Han
Department of Civil Engineering, Tsinghua University, Beijing, China

ABSTRACT: Experimental research was done to investigate the mechanical properties of austenitic stainless steel after exposed to fire. Three types of stainless steel coupons, including flat, curved and corner coupons, were tested after subjected to a designed heating and cooling fire, and the post-fire modulus of elasticity, yield strength, ultimate strength, ultimate strain and stress-strain curves of stainless steel corresponding to various historical maximum temperatures were measured and discussed. Finally, based on the experimental results of flat and curved coupons, a post-fire stainless steel stress-strain model was proposed, and the accuracy of the predicted results is acceptable.

1 INTRODUCTION

Stainless steel has been widely used in structural constructions due to its excellent performance, such as corrosion resistance, ease of maintenance and aesthetic appeal. Compared with carbon steel, stainless steel usually contains some special elements, such as chromium, nickel, molybdenum and titanium, which lead to the remarkable corrosion resistance and different mechanical properties of stainless steel. The shape of the stress-strain curve of stainless steel is a "round-house" type, and the pronounced yield plateau in mild steel stress-strain curve does not exist for stainless steel. Therefore, a systematic research on mechanical properties of stainless steel at ambient, elevated and after elevated temperatures is necessary.

To capture the stress versus strain relationship of stainless steel at ambient temperature, plenty of research has been done before. Ramberg & Osgood (1943) proposed a stress–strain relation equation, which can predict the stress–strain curve of stainless steel when stress is less than 0.2% proof stress. Mirambell & Real (2000), Rasmussen (2003) and Quach et al. (2008) extended Ramberg and Osgoods' model to perform an accurate prediction of stainless steel stress–strain curve when stress is higher than 0.2% proof stress. Van & Van (1992) and Cruise & Gardner (2008) investigated the corner mechanical properties of cold formed stainless steel.

For the research on mechanical properties of stainless steel at and after elevated temperatures, literature review indicates that limited work has been done, especially for the research regarding stress-strain models. Chen & Young (2006) proposed a stress-strain relation model for stainless steel at elevated temperatures. Felicetti et al. (2009) tested stainless steel bars (austenitic AISI 304L steel) after being heated up to 850°C, and the test results indicate that for hot-rolled stainless steel the yield strength degraded if the temperature was higher than 500°C, but the fire exposure had no apparent influence on the ultimate strength. Till now, no research has been done on the stress-strain model of stainless structural steel after fire exposure. Therefore, in this paper, tensile tests are conducted to investigate the post-fire properties of EN 1.4301 stainless structural steel, and a stress-strain relation model for austenitic stainless steel after exposed to high temperatures is proposed.

2 EXPERIMENTAL PROGRAM

2.1 *Test specimens*

Post-fire mechanical properties of austenitic stainless steel of grade 1.4301 (304) was investigated. Three types of test coupons, including flat, curved and corner coupons, were fabricated, in which, the flat coupons were cut from the middle of the flat surfaces of cold rolled square hollow section (SHS, $200 \times 200 \times 5.7$ mm) tubes, the curved coupons were cut from circular hollow section (CHS, 260×3 mm) tubes and the corner coupons were cut from the corners of the same cold rolled SHS tubes. The specimen configurations for tensile tests were adopted from

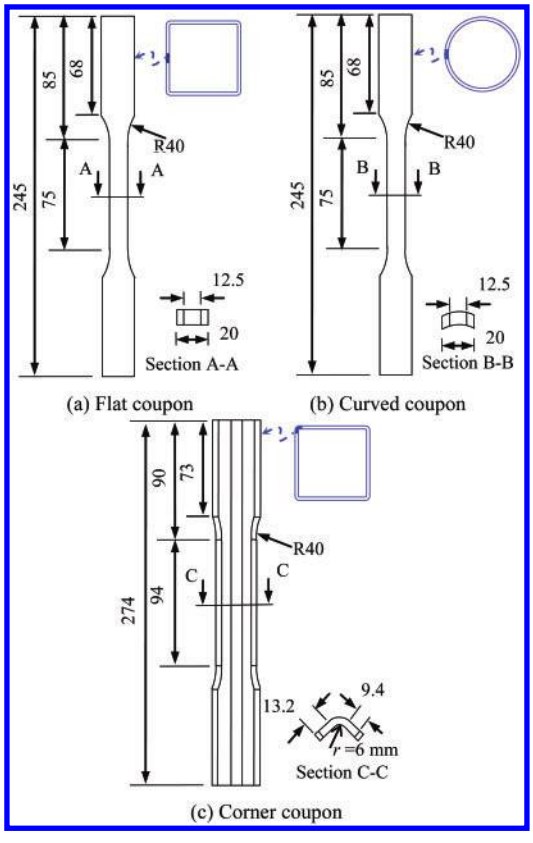


Figure 1. Dimensions of tensile coupons (Unit: mm)

AS 1391-2007 (2007). The specimen dimensions are shown in Figure 1.

2.2 *Test equipment and test procedure*

Heating was conducted in a temperature-controlled furnace. The coupons were heated from ambient temperature at a rate of 20°C/min to the historical maximum temperature (T), and then kept the maximum temperature stable until the expected heating time (t_h) was reached. Finally, the fire in the furnace was shut off to make the coupons cool down to ambient temperature with the furnace door closed. Figure 2 illustrates a typical temperature versus time relationship of coupons. The maximum temperature (T) and heating time (t_h) are listed in Table 1.

After cooled to ambient temperature, the coupons were taken out from the furnace and the tensile tests were conducted using a computer controlled test machine Instron 6027. Strain-controlled method was used and the coupons were loaded at a strain rate of 0.000 2/s. Two extensometers were placed on both sides of the coupon to measure the extension. The data, including post-fire full-range stress (σ)–strain (*varepsilon*) curves, modulus of elasticity (E_{0T}), 0.2% proof yield strength ($\sigma_{0.2T}$), 0.01% proof yield strength ($\sigma_{0.01T}$), ultimate strength (σ_{uT}), and ultimate strain

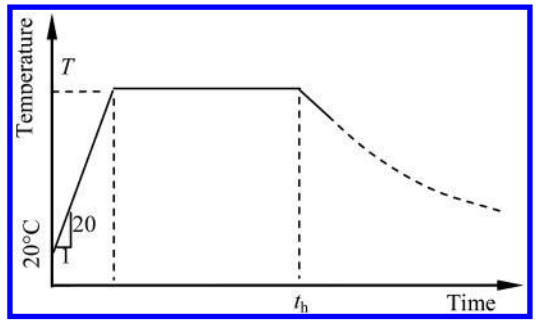


Figure 2. Typical coupon temperature versus time relationship.

Table 1. Summary of test program.

No.	T (°C)	t_h (min)	Coupon type
1	20	–	Flat
2	200	40	
3	300	45	
4	400	50	
5	500	55	
6	700	65	
7	800	40	
8	800	85	
9	800	130	
10	800	175	
11	1000	60	
12	20	–	Curved
13	300	45	
14	500	55	
15	700	65	
16	1000	60	
17	20	–	Corner
18	300	45	
19	500	55	
20	700	65	
21	1000	60	

(ε_{uT}) corresponding to σ_{uT}, were recorded. The strain hardening exponent (n_T) was calculated according to the equation suggested by Ramberg & Osgood (1943).

3 EXPERIMENTAL RESULTS AND DISCUSSION

3.1 *Experimental results*

Figure 3 illustrates the influence of fire exposure on the σ–ε curves. After fire exposure, the strength of the stainless steel undergoes deterioration, whilst the post-fire stress–strain curve maintains the same basic shape of the "rounded" type. The strength reduction in flat coupons and curved coupons is similar, but the corner coupon shows more significantly decrease in strength, as shown in Fig.3(c).

Furthermore, for corner coupons, the decreased ductility induced by cold-working seems to recover

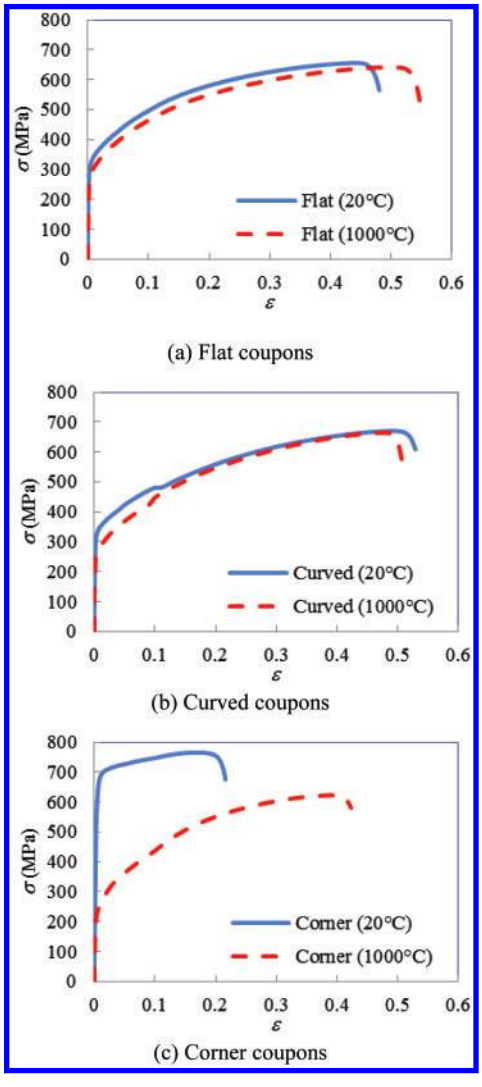


Figure 3. Post-fire full-range σ–ε curves

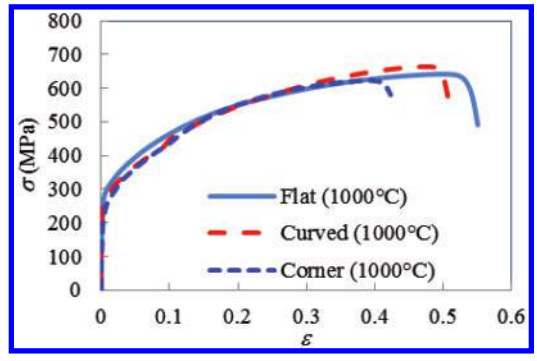


Figure 4. Influence of coupon types on σ–ε curves.

Table 2. Mechanical properties of stainless steel after exposure to elevated temperatures.

No.	E_{0T} (MPa)	$\sigma_{0.2T}$ (MPa)	σ_{uT} (MPa)	$\sigma_{0.01T}$ (MPa)	n_T	ε_{uT}	Coupon type
1	210190	305.5	655.5	219.1	9.02	0.440	Flat
2	202748	298.9	650.9	208.1	8.27	0.496	
3	177659	353.2	655.5	258.5	9.59	0.441	
4	203543	294.6	646.2	191.6	6.96	0.491	
5	184590	299.8	651.3	218.6	9.49	0.458	
6	197188	266.8	647.0	191.6	9.04	0.479	
7	196214	290.8	640.2	209.0	9.08	0.461	
8	224600	298.5	651.0	201.5	7.62	0.456	
9	210164	300.6	656.8	215.5	9.01	0.486	
10	218569	291.2	644.5	195.8	7.54	0.489	
11	173054	271.8	641.5	191.7	8.59	0.502	
12	200192	318.9	670.2	214.6	7.56	0.489	Curved
13	188840	316.6	676.6	221.6	8.40	0.505	
14	187480	305.8	666.6	220.1	9.11	0.471	
15	205389	263.6	662.3	195.3	9.99	0.467	
16	221041	250.4	664.1	176.3	8.54	0.476	
17	171120	622.9	765.2	404.4	6.93	0.176	Corner
18	174224	534.6	720.0	367.3	7.98	0.216	
19	184947	557.7	734.7	403.1	9.22	0.207	
20	194660	436.1	675.0	300.4	8.03	0.250	
21	–	226.4	622.2	147.8	7.03	0.391	

after fire exposure. Strength increase due to work-hardening at room temperature can be explained by the effects of corner region subjected to a high degree of plastic deformation. So the transformation of austenitic to martensitic phases can occur. The martensitic structure provides a greater strength than the former austenitic structure. If the material is exposed to extreme temperatures, however, the strength enhancing martensitic phase reverts to the lower strength austenitic phase. It can be found in Figure 4 that after being heated to 1000°C, the stress–strain curve of the corner coupon is close to those of flat and curved coupons.

From the post-fire full-range stress–strain curves of the coupons, modulus of elasticity (E_{0T}), 0.2% proof yield strength ($\sigma_{0.2T}$), 0.01% proof yield strength ($\sigma_{0.01T}$), ultimate strength (σ_{uT}), ultimate strain (ε_{uT}), and strain hardening exponent (n_T) are extracted and summarised in Table 2. To quantify the influence of high temperatures on the post-fire properties of stainless steel, the ratios of E_{0T}/E_0, $\sigma_{0.2T}/\sigma_{0.2}$, σ_{uT}/σ_u, $\varepsilon_{uT}/\varepsilon_u$, $\sigma_{0.01T}/\sigma_{0.01}$ and n_T/n are calculated, and the results are discussed in the following sections, where E_0, $\sigma_{0.2}$, σ_u, ε_u, $\sigma_{0.01}$ and n are the parameters corresponding to the unheated coupons.

3.2 *Influence of heating time*

To investigate the influence of heating time (t_h) on the post-fire mechanical properties of stainless steel, flat coupons were heated to 800 °C, and kept the temperature constant until the heating time reached 40 min, 85 min, 130 min and 175 min respectively. Ratios of E_{0T}/E_0, $\sigma_{0.2T}/\sigma_{0.2}$, σ_{uT}/σ_u and $\varepsilon_{uT}/\varepsilon_u$ corresponding to various t_h are illustrated in Figure 5. It can be found that all the ratios are close to 1.0, and the influence of t_h is

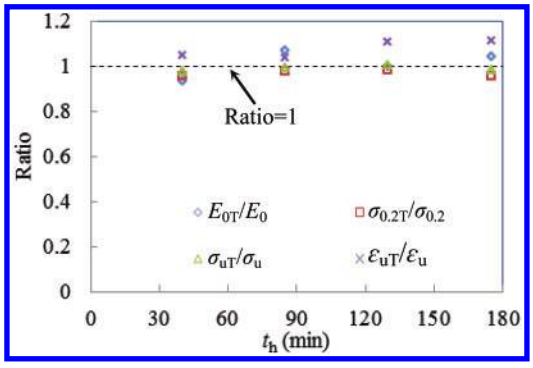


Figure 5. Influence of heating time (t_h) on E_{0T}/E_0, $\sigma_{0.2T}/\sigma_{0.2}$, σ_{uT}/σ_u, $\varepsilon_{uT}/\varepsilon_u$ of coupons with the same maximum temperature of 800 °C.

minor on the post-fire mechanical properties of stainless steel. It can be concluded that residual mechanical properties of stainless steel is not dependent on heating time if the heating time is long enough to achieve an even temperature inside the steel coupons.

3.3 *Influence of maximum temperature*

The influence of maximum temperature (T) on ratios of E_{0T}/E_0, $\sigma_{0.2T}/\sigma_{0.2}$, $\sigma_{0.01T}/\sigma_{0.01}$, n_T/n, σ_{uT}/σ_u and $\varepsilon_{uT}/\varepsilon_u$ are depicted in Figures 6(a-f), respectively.

It can be seen from Figure 6(a) that, when T ranges from 20°C to 700°C, E_{0T} shows a slight decline, and after T is higher than 700°C, E_{0T} remains almost the same as that of coupons at ambient temperature. In spite of the minor fluctuation, it is reasonable to assume that the change of E_{0T} can be ignored after exposure to high temperatures.

Figure 6(b) indicates the influence of T on $\sigma_{0.2T}/\sigma_{0.2}$, where the tested data from this paper and Felicetti et al. (2009) are included. It can be found that generally $\sigma_{0.2T}$ remains unchanged when T is lower than 500°C, and then an obvious decrease of $\sigma_{0.2T}$ can be observed when temperature is higher than 500°C. The same tendency as $\sigma_{0.2T}/\sigma_{0.2}$ can be observed for $\sigma_{0.01T}/\sigma_{0.01}$ as shown in Figure 6(c).

Generally, as shown in Figures 6(d-f), it can be found that the influence of T on n_T/n, σ_{uT}/σ_u and $\varepsilon_{uT}/\varepsilon_u$ is moderate, although significant variations in n_T and ε_{uT} are observed.

3.4 *Comparison between stainless and carbon steels*

Figure 7 depicts the typical measured σ–ε curves for stainless steel at ambient temperature and with a maximum temperature of 1000 °C. In Figure 7, the predicted σ–ε curves for carbon steel by Tao et al. (2013) are also shown. It can be found that, for the stainless steel, the reductions in yield strength and ultimate strength are 13.3% and 3.3%, respectively. The predicted reductions for the corresponding carbon steel are 21.3% and 9.8%, respectively. From the comparison, it can be concluded that stainless steel has superior post-fire performance than carbon steel.

4 POST-FIRE STRESS-STRAIN RELATION MODEL FOR STAINLESS STEEL

4.1 *Post-fire stress-strain model*

As mentioned before, for stainless steel after exposure to elevated temperatures, the tensile stress-strain curves remain the basic shape, as shown in Figure 3. Therefore it is reasonable to assume that the basic expression for ambient stainless steel can still be used for stainless steel after fire exposure. In this study the stress-strain relation equations for stainless steel at ambient phase proposed by Rasmussen (2003) is utilised to develop the post-fire stress-strain model. Five key parameters, including modulus of elasticity (E_0), 0.2% proof strength ($\sigma_{0.2}$), ultimate stress (σ_u), ultimate strain (ε_u) corresponding to σ_u and the strain hardening exponent (n), need to be decided to calibrate the stress-strain relation. As discussed before, among the five parameters, only $\sigma_{0.2}$decreases when the maximum temperature exceeds 500°C, whereas other parameters remain unchanged in general. Therefore the post-fire stress-strain model can be expressed by Equation (1) and depicted in Figure 8.

$$\varepsilon = \begin{cases} \dfrac{\sigma}{E_0} + 0.002\left(\dfrac{\sigma}{\sigma_{0.2T}}\right)^n & \sigma \le \sigma_{0.2T} \\ 0.002 + \dfrac{\sigma_{0.2T}}{E_0} + \dfrac{\sigma - \sigma_{0.2T}}{E_{0.2}} + \varepsilon_u\left(\dfrac{\sigma - \sigma_{0.2T}}{\sigma_u - \sigma_{0.2T}}\right)^m & \sigma > \sigma_{0.2T} \end{cases} \quad (1)$$

where,

$$n = \frac{\ln(20)}{\ln(\sigma_{0.2}/\sigma_{0.01})} \quad (2)$$

$$E_{0.2} = \frac{E_0}{1 + 0.002nE_0/\sigma_{0.2T}} \quad (3)$$

$$m = 1 + 3.5\frac{\sigma_{0.2T}}{\sigma_u} \quad (4)$$

The subscript T of the post-fire 0.2% proof yield strength ($\sigma_{0.2T}$) indicates that $\sigma_{0.2T}$ is the function of the maximum temperature (T). Because the 0.2% proof yield strength and the 0.01% proof yield strength decrease in the same pattern after fire exposure, as shown in Figures 6(b) and 6(c), $\sigma_{0.2T}/\sigma_{0.01T} \approx \sigma_{0.2}/\sigma_{0.01}$, therefore $\sigma_{0.2}/\sigma_{0.01}$ is used instead of $\sigma_{0.2T}/\sigma_{0.01T}$ in Equation 2.

In Equation 1, $\sigma_{0.2T}$ depends on the maximum temperature (T). Therefore, in this paper, $\sigma_{0.2T}$ is determined based on regression analysis to test data. The test results in this paper indicate that flat coupons cut from the centre part of the flat faces of the stainless SHS tubes and curved coupons cut from CHS tubes are much less work-hardened than the corner coupons, and the flat and curved coupons can be considered as one group without corner effect. Therefore,

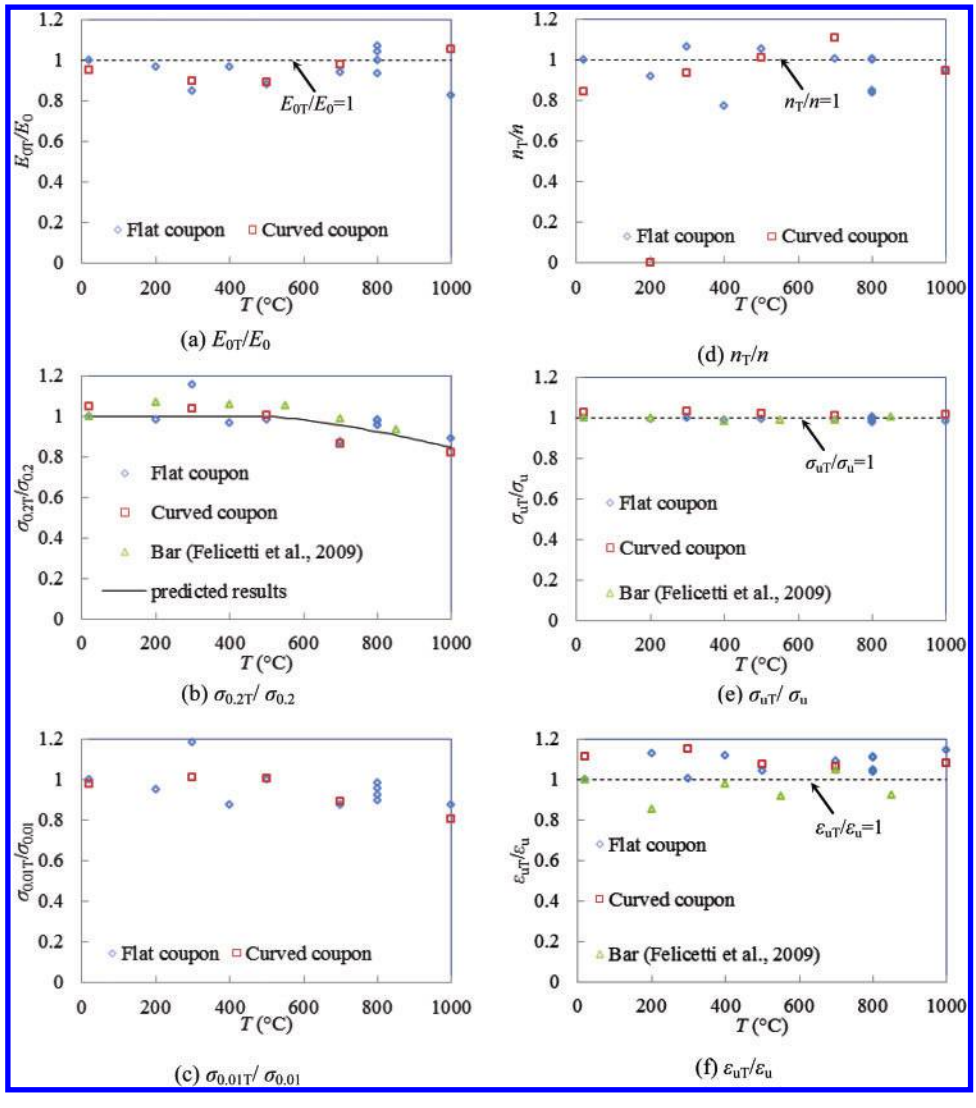


Figure 6. Influence of maximum temperature (T) on the post-fire mechanical properties of coupons.

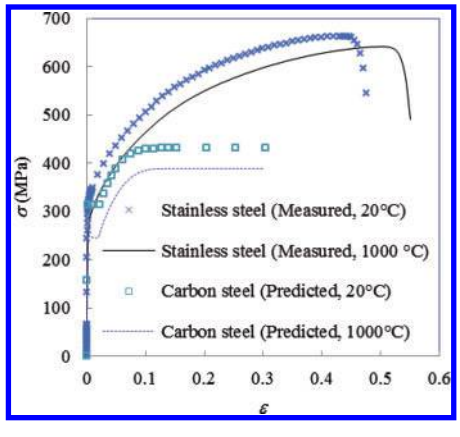


Figure 7. Typical σ–ε curves of stainless steel and carbon steel before and after exposed to fire.

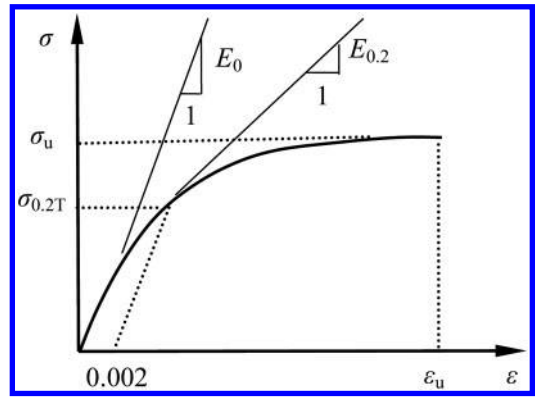


Figure 8. σ–ε model of stainless steel after exposed to elevated temperatures.

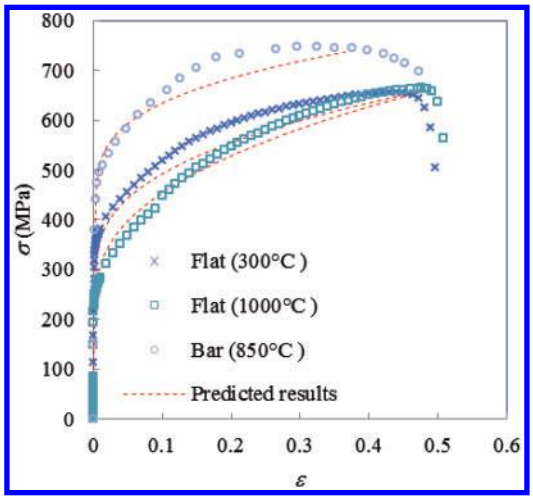


Figure 9. Comparison between tested and predicted σ–ε curves of stainless steel after exposed to elevated temperatures.

in this paper, to calibrate $\sigma_{0.2T}$ for stainless steel without considering corner effect, experimental data of flat coupon and curved coupon tests performed in this paper are adopted. Moreover, stainless bar test data reported by Felicetti et al. (2009) present the same variation tendency as flat and curved coupons. Due to the limited post-fire test data available, the test data of stainless bars are also adopted to calibrate $\sigma_{0.2T}$. Ratios of $\sigma_{0.2T}/\sigma_{0.2}$ corresponding to the three groups of test data are shown in Figure 6(b), and Equation (5) is proposed to predict the $\sigma_{0.2T}/\sigma_{0.2}$of stainless steel after exposure to elevated temperatures. It also can be found from Figure 6(b) that the predicted $\sigma_{0.2T}/\ \sigma_{0.2}$ curve is acceptable.

$$\frac{\sigma_{0.2T}}{\sigma_{0.2}}=\begin{cases}1 & T\le 500^{\circ}\mathrm{C}\\ 1-1.75\times10^{-4}(T-500)-2.71\times10^{-7}(T-500)^2 & T>500^{\circ}\mathrm{C}\end{cases} \quad (5)$$

4.2 *Verification of established model*

The experimental stress–strain curves of flat coupons, curved coupons and bar coupons are used to assess the accuracy of the proposed stress–strain model. For the stainless steel bar tests presented by Felicetti et al. (2009), the modulus of elasticity (E_0) and strain hardening exponent (n) are not reported, therefore, the proposed$E_0$and n according to Eurocode 3 (2006) are adopted, which are 200000 MPa and 6, respectively. Comparison between tested and predicted stress–strain curves is shown in Figure 9. In general, the proposed stress–strain model can predict the measured stress–strain curves of stainless steel very well.

5 CONCLUSIONS

Experimental study was carried out to investigate the mechanical properties of austenitic stainless steel after exposure to various temperatures, and the important post-fire mechanical property parameters, including stress–strain curve, modulus of elasticity, 0.2% proof yield strength, 0.01% proof yield strength, ultimate strength, ultimate strain and strain hardening exponent, were obtained. The comparison between stainless and carbon steel after exposed to fire demonstrates that stainless steel has superior post-fire performance than carbon steel. Based on the test results, a stress-strain model is proposed to obtain the full-range stress-strain curve for stainless steel without corner effect after exposure to elevated temperatures. The predicted stress-strain curves are generally in good agreement with test curves.

ACKNOWLEDGEMENTS

This work is supported by the Australian Research Council (ARC) under its Discovery Projects scheme (Project No: DP120100971). The financial support is gratefully acknowledged.

REFERENCES

Chen J. & Young B. 2006. Stress-strain curves for stainless steel at elevated temperatures. *Engineering Structures* 28(2): 229–239.

Cruise R.B. & Gardner L. 2008. Strength enhancements induced during cold forming of stainless steel sections. *Journal of Constructional Steel Research* 64(11): 1310–1316.

Eurocode 3: Design of steel structures, part 1-4: general rules-supplementary rules for stainless steel, *BS EN 1993-1-4: 2006*, London (UK): British Standards Institution.

Felicetti R., Gambarova P. G. & Meda A. 2009. Residual behavior of steel rebars and R/C sections after a Fire. *Construction and Building Materials* 23(12): 3546–3555.

Mirambell E. & Real E. 2000. On the calculation of deflections in structural stainless steel beams: an experimental and numerical investigation. *Journal of Constructional Steel Research* 54(1): 109–133.

Quach W.M., Teng J.G. & Chung K.F. 2008. Three-stage full-range stress-strain model for stainless steels. *Journal of Structural Engineering, ASCE* 134(9): 1518–1527.

Ramberg W. & Osgood W.R. 1943. Description of stress-strain curves by three parameters. Technical Note No. 902. *National Advisory Committee for Aeronautics*. Washington, DC.

Rasmussen K.J.R. 2003. Full range stress-strain curves for stainless steel alloys. *Journal of Constructional Steel Research* 59(1): 47–61.

Standards Australia. 2007. Methods for tensile testing of metals. *Australian Standard*, AS 1391–2007.

Tao Z., Wang X.Q. & Uy B. 2013. Stress-strain curves of structural steel and reinforcing steel after exposure to elevated temperatures, *Journal of Materials in Civil Engineering*. (In press)

Van den Berg G.J. & Van der Merwe P. 1992. Prediction of corner mechanical properties for stainless steels due to cold forming. In: *Proceedings of the eleventh international specialty conference on cold-formed steel structures*: 571–586.

Research and Applications in Structural Engineering, Mechanics and Computation – Zingoni (Ed.)
© 2013 Taylor & Francis Group, London, ISBN 978-1-138-00061-2

Study on ferritic stainless steel and its application on architecture structure

Ma Li & Wenbo Dong
Stainless Steel Technology Center, Baosteel Research Institute; Baoshan Iron & Steel Co.,Ltd., Shanghai, China

ABSTRACT: Ferritic Stainless Steels (FSS) are nickel-saving, corrosion-resistant, low cost steels. In this paper the feasibility of applying ferritic stainless steels on architecture structural fields is studied. Three typical ferritic stainless steels with 12%, 16% and 22% chromium content are chosen, and comparison of properties for these steels was made by performing physical testing, mechanical testing, corrosion resistance testing and welding experiment. The results show that FSS has not only excellent corrosion resistance but also good mechanical and physical properties. But following the increase of Cr, FSS exhibits a worse impact toughness in despite of a better corrosion resistance. Controlling a lower carbon, nitrogen and adding some stabilized elements titanium or niobium helps to improve the impact toughness, and other general properties are also developed to some extent. The impact toughness is also influenced by the thickness of the material, so the thickness should be limited to less than 4 mm for high chromium ferritic stainless steel on structural applications.

Keywords: Ferritic stainless steel; Structural; Impact toughness

1 INTRODUCTION

Stainless steels are being increasingly used as construction materials because of their attractive features such as excellent corrosion resistance, long service life span, low life cycle cost and unique aesthetic appeal. As a main type of stainless steels ferritic stainless steels(FSS) show lower cost, higher thermal conductivity, smaller linear expansion and better resistance to chloride stress corrosion cracking, atmospheric corrosion and oxidation compared to traditional austenitic stainless steels. FSS are essentially iron-chromium binary alloys containing about 12–30 percent of chromium, and According to the content of chromium they are divided into three series, the low-chromium, the medium- chromium and the high-chromium, and the corrosion resistance enhances with the increase of chromium content [1]. For engineers one of the important and practical aspects of materials selection in the design, development, and production of new components is the possibility of failure of the components under normal operation [2]. FSS are more easily to fracture in a brittle manner with little plastic deformation at low temperature, which may lead to sudden, unexpected, catastrophic failures [3−4]. Now FSS are only partially covered by European structural standards and used scarcely on structural applications because of the low temperature brittleness. Thus, in this paper the feasibility of applying FSS on architecture structural fields especially the impact toughness of FSS are studied.

2 EXPERIMENTAL

The experimental materials were cut from commercial hot bands, and the composition is shown in Table 1. Three series of commonly used ferritic stainless steels with 12%, 16% and 22% chromium content are chosen, and the effects of carbon content, nitrogen content and stabilization on the properties of these steels are studied. F1 and F2 are low chromium stainless steels with 12% chromium content and F2 has higher chromium and lower carbon and nitrogen than that of F1. F3 and F4 are typical medium chromium stainless steel with 16% chromium content and F4 has higher Cr content and lower carbon and nitrogen than that of F3, furthermore, in F4 Nb and Ti were also added to suppress the precipitation of chromium carbon nitride by forming stable carbide or nitride like Ti(C,N) and Nb(C,N) to avoid occurrence of intergranular corrosion. FSS5 is a high chromium stainless steel with lower C and N, more Ti and Nb, and a certain amount of Mo to get a better corrosion resistance. Comparative material 304 is a conventional austenitic stainless steel with 18% Cr and 8% nickel.

Comparisons of microstructure and properties for these steels were made by performing microstructure analysis, physical testing, mechanical testing and corrosion resistance testing. In order to obtain the influence of material thickness on the impact toughness, two section thickness of 4mm and 2.5mm samples were tested on the drop weight impact testing machine (INSTRON-9250) at temperature raging

Table 1. Composition of ferritic stainless steels /%.

Grade	C	Si	Mn	Cr	N	Nb	Ti	Mo	Ni
F1	0.028	0.3	0.3	12.3	0.027	–	–	–	–
F2	0.021	0.3	0.3	12.6	0.012	–	–	–	–
F3	0.044	0.3	0.3	16.1	0.037	–	–	–	–
F4	0.01	0.3	0.3	16.7	0.01	0.1	0.1	–	–
F5	0.01	0.2	0.3	22.5	0.015	0.2	0.2	1.5	–
304	0.05	0.6	1.0	18	0.07	–	–	–	8

Table 2. Physical properties of ferritic stainless steels.

Grade	Density, g/cm3	Electric Resistance, 10-6Ω*cm	Specific Heat, 25°,J/kg*°	Thermal Conductivity, 100°C,W/m*°	Thermal Expansion Coefficient, 20–100°C,10-6/°	Young's Modulus, Gpa
F1	7.75	57	460	24.2	11.0	200
F2	7.75	57	460	24.2	11.0	200
F3	7.7	60	460	26.1	10.4	200
F4	7.7	52	450	26.3	10.6	195
F5	7.67	62	470	20.4	10.1	211
SS400	7.87	13	460	57.7	12.6	206
304	7.93	72	502	16.2	17.3	193

from −60° to 2°, then the fracture surfaces after impact tests were observed by means of scanning electron microscopes (SEM). Mechanical properties were measured using a tensile test machine (INSTRON5985), and hardness tests were performed on Vickers hardness tester (Instron Wilson-Wolpert Turkon 2100B). At the same time corrosion resistance and physical performance index were obtained respectively with Princeton VMP3 type potentiostat, thermo dilatometer (DIL402C) and thermal conductivity meter, etc.

3 RESULTS AND DISCUSSION

3.1 *Physical properties*

The physical properties of five ferritic stainless steels are shown in Table 2 in comparison with those of typical carbon structural steel SS400 and conventional austenitic stainless steel 304. It is visible that these ferritic stainless steels show very similar physical properties and they have similar density, Specific Heat and Young's Modulus compared with those of SS400 and 304. Ferritic stainless steels also have smaller thermal expansion coefficient than that of SS400 and 304, which means that the thermal strain of FSS will be small due to the change of atmospheric temperature between day and night or during the welding process. In addition, the biggest different parameters among FSS, SS400 and 304 are Electric Resistance and Thermal Conductivity. Carbon steel SS400 shows best electrical and thermal conductivity and FSS takes the second place. The different physical properties of FSS, SS400 and 304 should attribute to the difference of the alloy component, the metallic crystal structure and the general arrangement of the atoms, and the electrical and thermal conductivity depend on the directional movement of free electrons and the vibrations of the metal's lattice of positive ions. Young's Modulus is an important parameter to determine the stiffness of structural members and metals with high Young's Modulus are relatively stiff and do not deflect easily. Young's Modulus is related to the bonding strength between the atoms in a metal or alloy and steels have similar high values

3.2 *Mechanical Properties*

The mechanical properties of ferritic stainless steels F1-F5, carbon structural steel SS400 and austenitic stainless steel 304 are shown in Table 3, where yield strength, tensile strength, elongation and hardness are measured. It can be seen that ferritic stainless steels show similar strength and elongation properties to those of carbon structural steel SS400, and they all show higher yield strength, lower tensile strength, lower elongation and lower work-hardening than austenitic stainless steel 304. The yield strength is a very important value for use in engineering structural design since it is the strength at which a metal or alloy shows significant plastic deformation, and the tensile strength is not used much in engineering design for ductile alloys since too much plastic deformation takes place before it is reached. During a plastic deformation the metal is deformed to such an extent and it can not fully recover its original dimensions, so it's more important for material having higher yield strength in the field of Structural Engineering Design. Above all it can be seen that ferritic stainless steels exhibit similar mechanical properties to those of carbon structural steel SS400, and can meet the requirement of architecture structural design.

Table 3. Mechanical properties of ferritic stainless steels.

Grade	Rp0.2, MPa	Rm MPa	A50 mm, %	Hardness, HV5
FSS1	300	480	29	142
FSS2	260	405	35	122
FSS3	285	465	31.5	133
FSS4	280	440	36	135
FSS5	330	515	34	170
SS400	300	450	33	-
304	265	650	52	154

3.3 *Corrosion Resistance*

Stainless steels are selected as engineering materials mainly because of their excellent corrosion resistance in many environments. The corrosion resistance of stainless steels is due to their high chromium contents, and the chromium forms a surface oxide film that protects the underlying matrix from corroding. The corrosion resistance in stainless steels is mainly dependent on the Pitting Resistance Equivalent (PRE = Cr% + 3.3Mo%), i.e., the chromium and molybdenum contents. But to increase the content of chromium even to 24% is not enough for complete prevention of rust, in some high chromium stainless the combination of chromium and molybdenum is necessary [5–6]. The PRE value and the pitting potential of FSS1-5 are shown in Fig1. It can be seen that the corrosion resistance of F1-5 improve with the increase of chromium content, and molybdenum added F5 shows a superior corrosion resistance to that of 304. At the same chromium content level, F2 with low carbon and nitrogen contents has a better corrosion resistance than that of F1 with higher carbon and nitrogen, and F4 with very low carbon and nitrogen, titanium and niobium stabilized has a better corrosion resistance than that of F3.

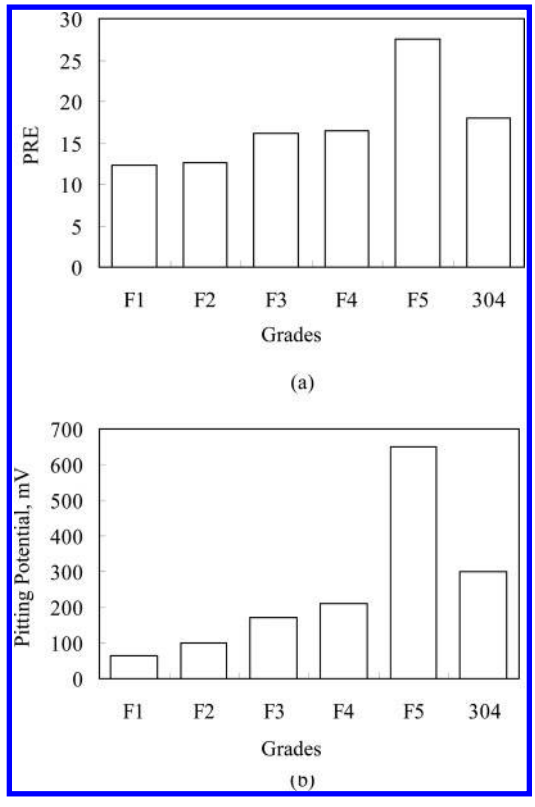


Figure 1. PRE and Pitting Potential of FSS: (a) PRE; (b) Pitting Potential.

3.4 *Impact Toughness*

FSS are more easily to fracture in a brittle manner with little plastic deformation at low temperature, which may lead to sudden, unexpected, catastrophic failures. Impact toughness is defined to measure the amount of energy that a material can absorb before fracturing. It becomes of engineering importance when the ability of a material to withstand an impact load without fracturing is considered. One of the simplest methods of measuring toughness is to use an impact testing apparatus. In this paper two section thicknesses of 4mm and 2.5mm samples were tested on the drop weight impact testing machine at temperature raging from −60° to 20°.

3.4.1 *Effect of Temperature*

Fig 2 shows the relative effect of temperature on the impact energy of F1-F5. The impact energy falls down with the decrease of temperature, and a distinct ductile to brittle transition temperature (DBTT) is observed. The DBTT of F1 to F5 is about −30°, 10°, −10°, −10°, and 10°. F1 shows best impact energy

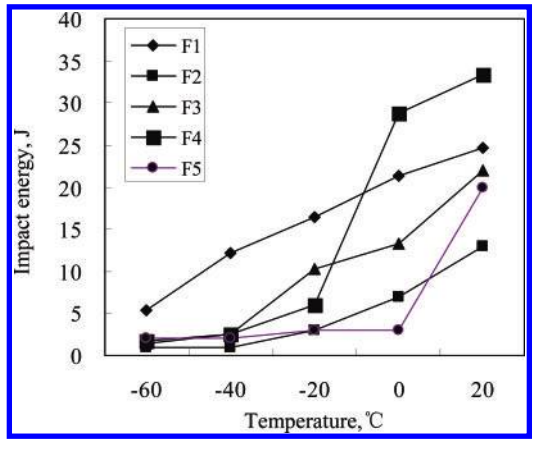


Figure 2. Charpy V-notch impact toughness of experimental material as a function of temperature (2.5 mm specimens)

because it is a semi-matensitic stainless steel with different microstructure from pure FFS. Then the fracture surfaces after impact tests were observed by means of scanning electron microscopes (SEM), and Fig 3 shows the different fracture manner of F4 steel in different temperature. When the impacted temperature is higher than the DBTT, ductile fracture occurs, otherwise brittle fracture happens. So FSS are strongly

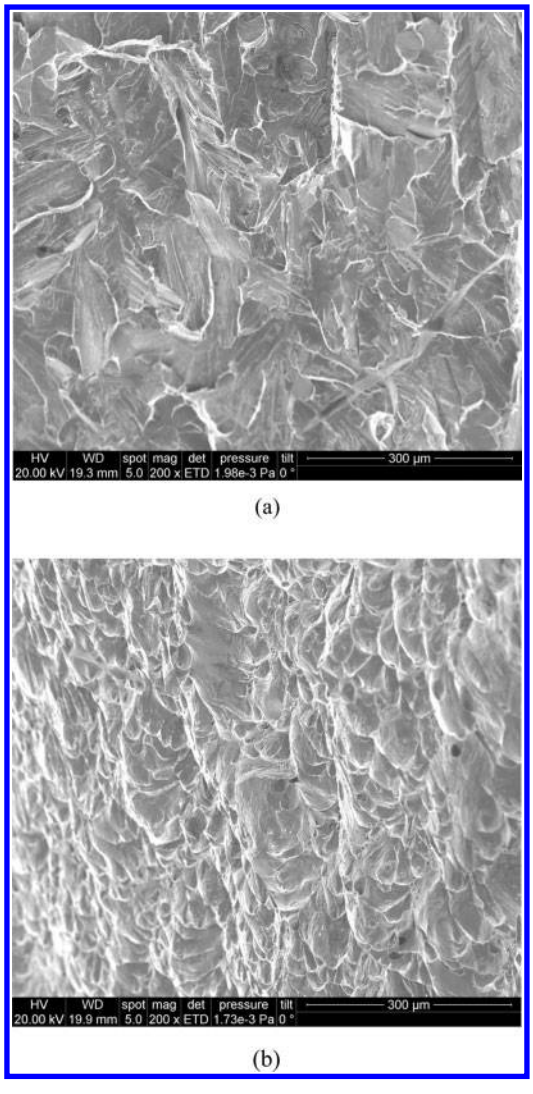


Figure 3. Scanning electron micrograph of specimen F4, ductile and brittle fractured: (a) −60°; (b) 20°.

recommended to be use in those environments where the service temperature is higher than the ductile to brittle transition temperature.

3.4.2 *Effects of alloy elements*

Fig 4 shows the relative effect of alloy elements on the impact energy of some FSS. Compared with F3, F4 has a lower C and N and adds some Ti and Nb as stabilization elements, which contributes to the improvement of impact toughness. The impact energy of F4 is distinct higher than that of F3 although the DBTT doesn't change.

3.4.3 *Effects of thickness*

Fig5 shows the effect of thickness on the impact energy of F4 steel. The 4mm specimen shows lower impact energy and a higher DBTT. This expressed that as the thickness of FSS increased, the steels become more

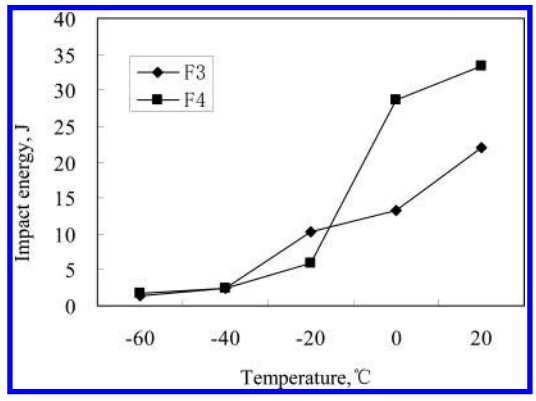


Figure 4. Charpy V-notch impact toughness of different alloy composition (2.5 mm specimens)

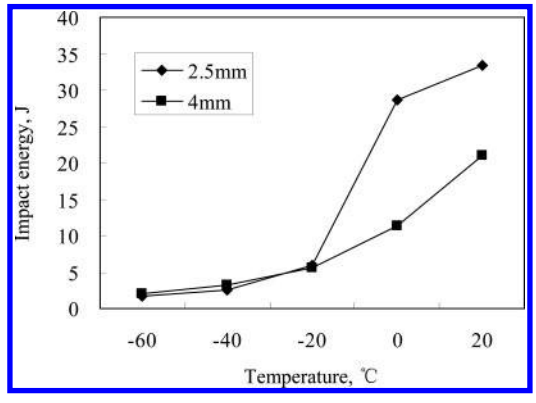


Figure 5. Charpy V-notch impact toughness of different thickness (F4).

brittle, and less energy is absorbed on impact during fracture.

3.4.4 *Effects of processing*

Fig6 shows the effect of processing on the impact energy of F5 high chromium stainless steel. F5 steels with same thickness of 2.5 mm are processed by different working methods. First materials are hot rolled to 2.5 mm and annealed directly, and the second materials are hot rolled to 5 mm, then annealed and cold rolled to 2.5 mm, finally annealed with same annealing technology. The cold rolled steel performs quite superior impact energy to that of hat rolled steel.

These results indicate that FSS has not only excellent corrosion resistance but also good mechanical and physical properties. Because FSS have body-centered cubic crystal structure, they are more easily to fracture in a brittle manner with little plastic deformation at low temperature.

Besides the crystal structure, the alloy composition, the thickness, and the processing are also factors influenced the impact toughness of FSS. Controlling a lower carbon, nitrogen and adding some stabilized elements titanium or niobium helps to improve the impact toughness. The thickness should be limited to

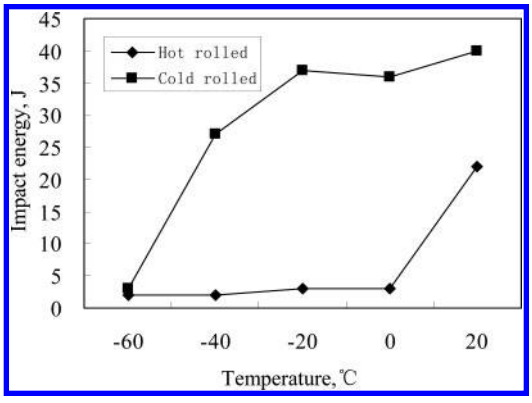


Figure 6. Charpy V-notch impact toughness of different processing (F5, 2.5 mm specimens)

less than 4 mm for high chromium ferritic stainless steel on structural applications. Adopting cold rolled steels to replace hot rolled steels is also a good choice for structural design.

4 CONCLUSIONS

Ferritic stainless steels show very similar physical properties and mechanical properties to those of carbon structural steel SS400, and can meet the requirement of architecture structural design.

With excellent corrosion resistance Ferritic stainless steels can be used in many environments, and some high chromium FSS show a superior corrosion resistance to that of austenitic stainless.

Although having the weakness of low temperature brittleness, FSS are also recommended to be use if the alloy composition, the thickness, and the processing methods are matched good with the environment.

REFERENCES

Lu shiying. 1995. Stainless Steel. Beijing: Atomic Energy Press: 479–488.

William F. Smith, Javad Hashemi. 2005. Foundation of Materials and Engineering. Beijing: China Machine Press: 271–281.

M. Vardavoulias, G. Papadimitriou. 1996. Effect of Ni addition on the fracture behaviour of a cast ferritic stainless steel. Materials Letters 27: 349–353.

A. Belyakov, R. Kaibyshev. 1995. Structural changes of ferritic stainless steel during severe plastic deformation. Nanostructured Materials. Vol. 6: 893–896

Yusuke Tsutsumi, Atsushi Nishikata and Tooru Tsuru. Pitting corrosion mechanism of type 304 stainless steel under a droplet of chloride solutions[J]. Corrosion Science, 2007, 49:1394–1407.

Yoshihiro Yazawa, Keiichi Yoshika and Fusao Togashi. Effect of Cr, Mo and Cu on the atmospheric corrosion resistance of ferritic stainless steels in a coastal environment[J]. Kawasaki Steel Technical Report, 1994,31:35–43.

Nancy Baddoo, Bassam Burgan. Architect's guild to stainless steel, SCI-P-179. The steel construction institute. Berkshire. England. 1997.

20. Concrete structures, concrete design

Research and Applications in Structural Engineering, Mechanics and Computation – Zingoni (Ed.)
© 2013 Taylor & Francis Group, London, ISBN 978-1-138-00061-2

Assessing the reliability of existing concrete bridges in terms of shear strength

D. Busse, L. Eckfeldt & M. Empelmann
Institut für Baustoffe, Massivbau und Brandschutz, Fachgebiet Massivbau, TU Braunschweig, Germany

ABSTRACT: In this paper, shear force design approaches referenced in literature are investigated on their potential to partially replace or to refine the shear design approaches provided by current codes. Using a comprehensive database providing experimental data, it is analysed how the different shear design approaches are able to adapt to experimental results. As a result, the advanced shear design approaches show calculated mean values almost equal to the experimental results, in combination with a very low variance. In addition, a probabilistic analysis verifies the required safety level demanded by the current standards. These results are confirmed by an example. As a consequence, it is noted that modern and advanced shear design approaches create the possibility to determine existing structural reserves.

1 INTRODUCTION

The German motorway network contains approximately 40,000 bridges with around 70% made of prestressed concrete and 20% of reinforced concrete. The majority of these bridges have been constructed in the decades after the Second World War and reached an average age between 40 to 60 years. Current investigations of existing concrete bridges reveal deficiencies in regard to material, construction, design and standard aspects.

Beneath the material degradation the main reasons for these deficiencies on the action side are the rapid growth of the traffic volumes on German motorways since the Second World War as well as the increase of the maximum permitted weight from 24 to in 1956 to 44 to today. In addition, a further rise of heavy good vehicles – numbers and maximum weights – is forecasted.

On the resistance side it has to be noted that the existing concrete bridges show in particular very low shear reinforcement ratios. Before 1966 e.g. no minimum shear reinforcement was required. In consequence, bridge structures with narrow cross-sections and high degrees of prestressing, but with hardly any shear reinforcement were designed and constructed. In the 1980s an increased load module, the SLW 60/30, was introduced into the load standards, as well as design specifications for imposed deformations (temperature constraint effects). As a result, bridges from the 1980's are much more able to handle today's traffic. Nevertheless, looking at the forecasted traffic growth in the near future their reserves are also nearly exhausted.

From today's point of view a way to deal with the existing bridges and their deficiencies must be found. First, it is possible to enhance their load carrying capacity by strengthening. However, a study of currently used strengthening methods shows that the strengthening in regard of shear is rather complex and usually requires interference with the existing structure as well as bridge closures (Empelmann et al. 2012). Alternatively, advanced and refined shear design approaches can be used to determine additional load carrying capacities allowing the further use of the existing bridges. In this paper the second idea is pursued.

2 BASICS

2.1 *Analysis of shear failure*

The design for a bending moment is based on the hypothesis of Bernoulli. However, this design approach is strictly valid only for non-cracked components that are also free of transverse forces. A general mechanical model for shear containing all different shear load-bearing mechanisms is desirable and currently being debated among experts.

In order to understand shear failure the consideration of experimental behaviour is mandatory. Figure 1 shows a test beam without shear reinforcement under transverse load. First, flexural cracks form at midspan. An increase of the load results in a parabolic shear crack. Simultaneously, there is a decrease in the rigidity followed up by a rearrangement of the load-bearing mechanisms. At first, the dowel effect of the longitudinal reinforcement and the load carrying capacity of the non-cracked concrete are activated. Altogether, a compression arch and tie-rod model is formed (Görtz 2004, Muttoni & Fernández Ruiz 2008).

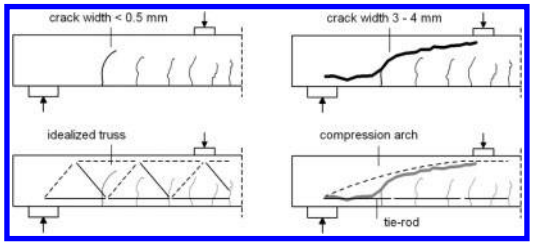


Figure 1. Cracking of a test beam under transverse load (up) and rearrangement into compression arch and tie-rod (down).

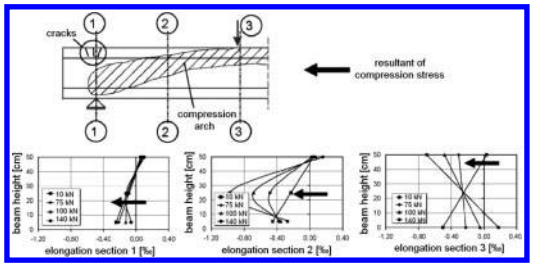


Figure 2. Definition of test beam sections and longitudinal strain in the defined sections (Hegger & Görtz 2006).

Shear reinforced members show a different behaviour. Not one single shear crack develops under transverse load but several parallel cracks. Figure 1 (left side) shows that the cracks are inclined at 35–45° to the members axis. The shear reinforcement is activated by the opening of these cracks. Depending on the amount of shear reinforcement the rearrangement into the arch and tie-rod model can be delayed due to the activation of a crack-bridging effect.

In addition, the analysis of tests shows a smooth transition between members without and with shear reinforcement. If the yield strength of the reinforcement is obtained, it comes to a sharp increase in the crack width and thus a failure of the crack friction, but not to a component failure. Figure 2 shows the longitudinal strain in three sections of a test beam. The locations of the resultants of the compressive stresses show the formation of the compression arch. In combination with the tie-rod in the longitudinal reinforcement, an increase beneath the yield strength of the reinforcement is provided. Failure of the beam occurs, analogous to the beam without shear reinforcement, through cracking into the compression zone.

2.2 *Current European Design Code – EC 2*

The verification of the shear resistance according to DIN EN 1992:2011 (EC 2) consists of three parts:

- resistance without shear reinforcement $V_{Rd,c}$,
- resistance of the shear reinforcement $V_{Rd,sy}$,
- resistance of the compression struts $V_{Rd,max}$.

Members without shear reinforcement are designed using the resistance $V_{Rd,c}$. The empirical formula is based on a comb model. The resistance is dominated by the crack friction and the dowel effect of the longitudinal reinforcement. The load bearing capacity of the concrete plays only a minor role. The relevant parameters of the empirical equation are the concrete strength f_{ck}, the longitudinal reinforcement ratio ρ_l and the geometric dimensions. The influence of a prestressing is included by a normal stress σ_{cp} in the members axis.

$$V_{Rd,c} = \left[0.10 \cdot k \cdot (100 \cdot \rho_l \cdot f_{ck})^{1/3} + 0.12 \cdot \sigma_{cp}\right] \cdot b_w \cdot d \quad (1)$$

To avoid a particularly strong deviation in the range of low shear slenderness, which is the distance between support and first single transverse load a in relation to the static height d, EC 2 provides an adaption factor β. Mechanically this adaption is justified by the formation of an additional load-bearing truss in the section near the support.

$$\beta = 2.0/(a/d) \text{ if } (a/d) < 2.0 \quad (2)$$

If the resistance $V_{Rd,c}$ is exceeded shear reinforcement is required, which then is determined on basis of a strut-and-tie-model analogy, i.e. with a completely different design model. The strut angle θ is modified based on the plasticity theory as a function of aggregate interlock. The influence of a prestressing is included by the normal stress σ_{cp}

$$1.0 \le \cot\theta \le \frac{1.2 - 1.4 \cdot \sigma_{cp}/f_{cd}}{1 - V_{Rd,cc}/V_{Ed}} \le 3.0 \quad (3)$$

For vertical shear reinforcement ($\alpha = 90°$) the load carrying capacity of the shear reinforcements $V_{Rd,sy}$ can be calculated using equation (4).

$$V_{Rd,sy} = a_{sw} \cdot z \cdot f_{ywd} \cdot \cot\theta \quad (4)$$

To prevent failure of the compression struts it has to be checked that the compressive strength of the concrete $V_{Rd,max}$ does not exceed. For bridge structures the strength of the compression strut is only decisive in a few cases, e. g. thin webs or large single loads. For vertical shear reinforcement ($\alpha = 90°$) the design formula is given in equation (5).

$$V_{Rd,max} = b_w \cdot z \cdot \nu_1 \cdot f_{cd}/(\cot\theta + \tan\theta) \quad (5)$$

It can be seen that the approach by EC 2 does not really reflect the experimental behaviour indicating a smooth transition between non-reinforced and shear reinforced members. Especially for existing bridges with low shear reinforcement ratios this inconsistent change of design models is problematic. In this case, advanced design approaches should be considered.

3 ADVANCED DESIGN APPROACHES

3.1 *Members without shear reinforcement*

Zink (Zink 2000) presents an advanced design approach for members without shear reinforcement.

Based on the experimental behaviour, his concept, in contrast to EC 2, contains three main components of the shear carrying capacity $V_{Rd,c}$.

$$V_{Rd,c} = V_0 \cdot k(a/d) \cdot k(l_{ch}/d) \tag{6}$$

Herein, the shear resistance is mainly determined by the resistance of the compression zone V_0. The most important parameter for the calculation of V_0 is the height of the non-cracked compression zone k_x, in which the influence of the longitudinal reinforcement ρ_l as well as the modulus of elasticity E_c is already implemented.

$$V_0 = \frac{2}{3} \cdot b_w \cdot k_x \cdot d \cdot f_{ct} \tag{7}$$

Especially in case of low static heights, two additional factors need to be considered. The tension-stiffening effect is, up to a limit value of the shear slenderness of $a/d < 4$, considered with the factor $k(a/d)$. The influence of crack friction, especially in the fracture process zone, is difficult to measure. The calculation of the factor $k(l_{ch}/d)$ and thus the stresses in the fracture process zone uses a tension block ($\alpha_v = 0.4$). Zink notes that the influence of the dowel effect is negligible and has already been considered by the factor $k(l_{ch}/d)$.

In addition, Zink directly determines a proportion of the shear carrying capacity V_λ in case of a prestressing force.

$$V_\lambda = P \cdot \lambda = P \cdot \frac{d}{a} \cdot \left(1 - \frac{k_x}{2}\right) \tag{8}$$

3.2 *Members with shear reinforcement*

The design approach of Görtz & Hegger (Görtz 2004, Hegger & Görtz 2006) is based on three separate load bearing components. In addition to the load bearing capacity of the shear reinforcement V_F, a concrete load bearing capacity V_C as well as a load bearing capacity in case of a prestressing V_P is added.

$$V_{Rd,c} = V_F + V_C + V_P \tag{9}$$

The capacity of the shear reinforcement V_F is based on an idealised strut-and-tiemodel. The strut angle θ corresponds to the inclination of the shear cracks β_r.

$$V_F = a_{sw} \cdot f_{ywd} \cdot z \cdot \cot \beta_r \tag{10}$$

$$\cot \beta_r = 1 + 0{,}15 \cdot \frac{\rho_w \cdot f_y}{f_{ctm}} - 0{,}18 \cdot \frac{\sigma_x}{f_{ctm}} \leq 2{,}15 \tag{11}$$

The basis for the determination of the concrete load capacity V_C is the approach by Zink (Eq. 6). Adaption of the results using the factor β is suggested by Görtz (Görtz 2004).

$$\beta = 3.0/(a/d) \text{ if } (a/d) < 3.0 \tag{12}$$

To guarantee a smooth and consistent transition between non-reinforced and shear reinforced members a factor κ is introduced to reduce the concrete load capacity in case of high shear reinforcement ratios.

$$V_C = \kappa \cdot V_{Rd,c} \tag{13}$$

$$0 \leq \kappa = 1 - \frac{\rho_w \cdot f_{ywd}}{3 \cdot f_{ct}} \leq 1 \tag{14}$$

Görtz & Hegger consider the influence of a prestressing force by the load capacity V_P Also here, a factor κ_p is established in order to reduce the additional load bearing capacity in case of high shear reinforcement ratios.

$$V_P = P \cdot \frac{d - k_x/2}{a} \tag{15}$$

$$0 \leq \kappa_p = 1 - \frac{\rho_w \cdot f_{ywd}}{f_{ct}} \leq 1 \tag{16}$$

4 COMPARISON OF SHEAR DESIGN APPROACHES AND TEST RESULTS

4.1 *Database*

The performance of the shear design approach of the EC 2, compared to the aforementioned advanced shear design approaches, is examined by evaluation of tests results. Therefore, a database of about 1000 results of shear tests by Görtz & Hegger (Kordina & Hegger 1987, Görtz 2004) was used, containing:

- 441 non-prestressed members without shear reinforcement,
- 195 prestressed members without shear reinforcement,
- 216 non-prestressed members with shear reinforcement,
- 151 prestressed members with shear reinforcement.

4.2 *Members without shear reinforcement*

The comparison of test results V_{exp} for reinforced members without shear reinforcement with the calculated values according to EC 2 $V_{EC\,2}$ (Eq. 1) and Zink V_{Zink} (Eq. 6) is shown in Figure 3 and Figure 4 in relation to the shear slenderness a/d. The calculations content the factor β (Eq. 2 and 12).

In summary, both approaches are able to map the experimental values relatively accurate for high shear slenderness. The shear design approach of Zink has advantages in case of low shear slenderness. As a consequence, the statistical evaluation of both design approaches shows for Zink a very low variance of 0.03 compared with the variance 0.31 for EC 2 (see Table 1).

Furthermore, the design approaches of EC 2 and Zink are compared for prestressed members without shear reinforcement. Table 2 shows the results of the statistical evaluation. The shear design approach of EC 2 shows more values on the safe side, i.e. above 1.0.

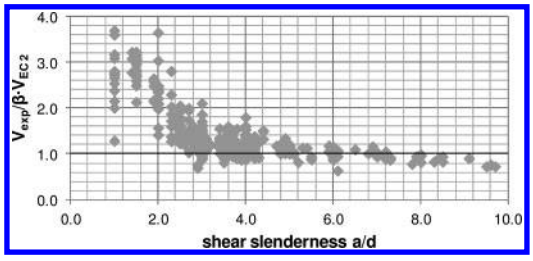


Figure 3. Comparison of test results without shear reinforcement with EC 2 design approach, adaption for low shear slenderness.

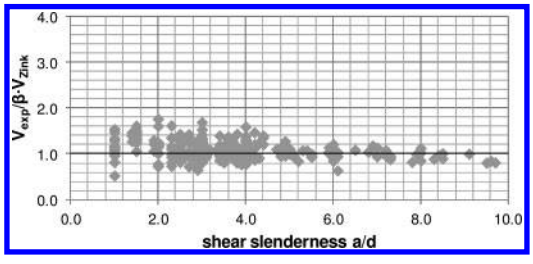


Figure 4. Comparison of test results without shear reinforcement with Zink design approach, adaption for low shear slenderness.

Table 1. Reinforced members without shear reinforcement.

	μ	Min	Max	σ	V
$\beta \cdot$ EC 2	1.39	0.63	3.70	0.56	0.31
$\beta \cdot$ Zink	1.08	0.53	1.77	0.17	0.03

Table 2. Prestressed members without shear reinforcement.

	μ	Min	Max	σ	V
EC 2	1.50	0.84	2.64	0.33	0.11
Zink	0.97	0.11	1.98	0.28	0.08

4.3 *Members with shear reinforcement*

Figure 5 shows the comparative values $V_{exp}/V_{EC\,2}$ plotted against the shear reinforcement ratio ρ_w, which is the cross-section of the shear reinforcement in relation to the concrete cross-section. In particular, in case of low shear reinforcement ratios differences between the experimental and theoretical values occur. This finding supports the statement that the shear capacity of reinforced components is not only generated by the shear reinforcement as indicated in the shear design approach of EC2.

The comparison of the same test results with the design approach by Görtz & Hegger in Figure 6, points out that using the additional load capacities V_C and V_P an excellent re-calculation of the test results is

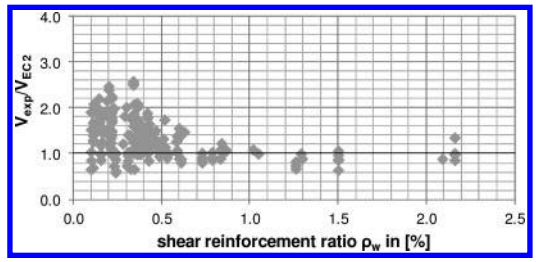


Figure 5. Comparison of test results with shear reinforcement with EC 2 design approach.

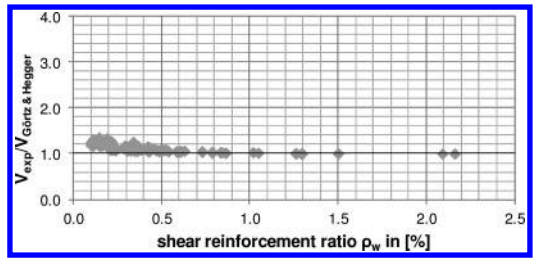


Figure 6. Comparison of test results with shear reinforcement with Görtz & Hegger design approach.

Table 3. Reinforced members with shear reinforcement.

	μ	Min	Max	σ	V
EC 2	1.35	0.59	2.58	0.42	0.17
Görtz & Hegger	1.12	1.00	1.36	0.08	0.01

Table 4. Prestressed members with shear reinforcement.

	μ	Min	Max	σ	V
EC 2	3.36	0.80	9.45	1.64	2.70
Görtz & Hegger	1.63	0.88	3.08	0.41	0.17

obtained. This statement is supported by the statistical evaluation shown in Table 3.

Table 4 sums up the results for prestressed test members with shear reinforcement. The shear design approach according to EC 2 provides a significantly high mean value and an excessive variance. This suggests that the influence of the prestressing has not been considered correctly. The approach by Görtz & Hegger shows better statistical values.

5 PROBABILISTIC ANALYSIS

5.1 *Basics*

The aim of the following probabilistic analysis is to show that the investigated shear design approaches achieve the currently required normative safety level.

Table 5. Basic variables for parameter study.

	mean	variance	distribution
1. load			
permanent load	g_k	10%	N
live load	q_k	25%	G
model uncertainty	1.0	5%	N
2. resistance			
dimensions	nom a	2%	N
concrete strength	$f_{ck}+8$	15%	LN
steel strength	f_y	5%	LN
steel area	a_{sl},a_{sw}	2%	N
3. prestressing			
prestressing force	P	5%	N

N: normal distr.; LN: log- normal distr.; G: Gumbel-distr.

Table 6. Results of probabilistic calculations.

Approach	μ_β	V
1. Members without shear reinforcement		
EC 2	3.79	0.004
Zink	3.93	0.115
2. Prestressed members without shear reinforcement		
EC 2	5.35	0.020
Zink	3.49	0.070
3. Members with shear reinforcement		
EC 2	3.28	0.000
Görtz & Hegger	3.49	0.004
4. Prestressed members with shear reinforcement		
EC 2	1.72	0.000
Görtz & Hegger	3.81	0.006

In the reliability considerations the safety index β is introduced as a key parameter. The DIN EN 1990:2010 requires a value of $\beta = 3.8$ in the ultimate limit state for a lifetime of 50 years. This corresponds to the probability of failure of $P_f = 10^{-4}$.

Each variable used in the investigated design approaches can be defined deterministically, by a fixed value, or probabilistically, with a statistical distribution. The challenge is to find generally accepted statistical distributions with their determining parameters. In literature a lot of different proposals can be found. In this paper the parameters provided by (Hansen 2004) and (JCSS 2006) are used (Table 5).

Especially the model uncertainty for shear is discussed controversial among experts (Song, J. et al. 2010; Sykora & Holicky 2011). In this paper, in order to capture the differences between the aforementioned shear design approaches, the model uncertainty is defined as the variance regained from the comparison with the test results of the database.

Finally, the equations of the introduced shear design approaches have to be transferred into limit state equations, which are examined by the program Comrel (RCP 2004).

Due to the large number of basic variables, which have an influence on the shear strength, and the large range of values, which have to be covered, it is useful to perform the probabilistic analysis as a parameter study. Different cross-sections (rectangles and t-members), different longitudinal and shear reinforcement ratios as well as different levels of concrete strength and prestressing were investigated.

5.2 *Results*

Table 6 sums up the results of the probabilistic calculations with the following conclusions:

For reinforced members without shear reinforcement both investigated shear design approaches achieve the required safety index of $\beta = 3.8$.

For prestressed members without shear reinforcement the shear design approach of EC 2 provides an average well above the required safety level. This confirms the finding that the shear design approach of EC 2 generates too many results below the experimental values ($\mu = 1.50$, Table 2). The approach by Zink has a slightly too low mean value of $\mu_\beta = 3.49$, which is also confirmed by the tendency to overestimate the influence of a prestressing.

Reinforced Members with shear reinforcement show little too low mean values for both investigated shear design approaches. Due to the low variance it can, however, be assumed that the design approaches work precisely.

Prestressed members with shear reinforcement present a low average safety index for the shear design approach of EC 2 ($\mu_\beta = 1.72 < 3.8$). This finding has to be put into perspective with the very high variance of the model uncertainty ($V = 2.70$, Table 4). The shear design approach according to Görtz & Hegger achieves a mean of $\mu_\beta = 3.81$ and only a very low variance of $V = 0.6\%$.

Figure 7 exemplarily shows the detailed results for prestressed members with shear reinforcement and the shear design approach by Görtz & Hegger.

Based on the results of Table 4 it is concluded, that the shear design approach by Görtz & Hegger provides more realistic values for prestressed and shear reinforced members. The values in Table 6 show that the required normative safety level is ensured. Because of these findings the exemplary calculation in the following chapter compares the shear strength of an existing bridge re-calculated using the shear design approaches of EC 2 and Görtz & Hegger.

6 EXAMPLARY BRIDGE STRUCTURE

As an exemplary calculation the superstructure of a four-lane prestressed concrete bridge is investigated. The bridge was built in 1968 with only a small amount of shear reinforcement. The structural system is a continuous beam of nine fields. The overall structure is 220 m long with span lengths of 20–26 m.

The re-calculation with EC 2 is performed in two steps. First, the shear resistance without shear reinforcement $V_{Rd,c}$ is determined. The second step

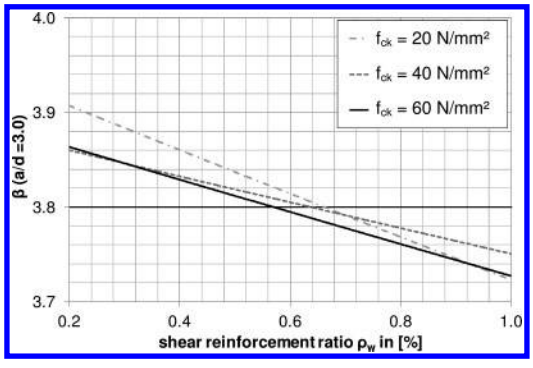


Figure 7. Safety index β for prestressed members with shear reinforcement – Shear design approach by Görtz & Hegger.

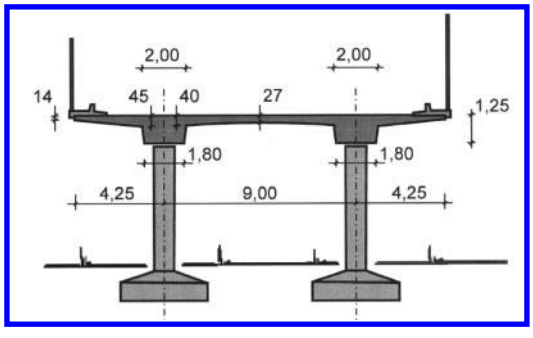


Figure 8. Bridge superstructure cross section.

contains the calculation of the shear reinforcements resistance $V_{Rd,sy}$.

$$V_{Rd,c} = 1{,}93\ MN \tag{17}$$

$$V_{Rd,sy} = 0{,}94\ MN \tag{18}$$

Based on the findings in chapters 4 and 5 of this paper the shear design approach by Görtz & Hegger was chosen for the alternative re-calculation. The three parts of the shear strength are determined to

$$V_F = 0{,}448\ MN \tag{19}$$

$$V_C = 0{,}849\ MN \tag{20}$$

$$V_p = 1{,}681\ MN \tag{21}$$

resulting into the total shear design strength of

$$V = 2{,}95\ MN \tag{22}$$

With the shear design approach according to EC 2 only shear design capacities of 0.94 and 1.93 MN can be determined. Whereas using the advanced shear design approach by Görtz & Hegger a load capacity of 2.95 MN (+53%) could be determined.

7 CONCLUSIONS

In this paper different shear design approaches are compared in regard to their load-bearing components as well as to their fitting with shear test results. It turns out that the shear design approach by EC2, which determines the shear capacity based on the capacity of the shear reinforcement only, is too conservative. Particularly, in case of low shear reinforcement ratios the load carrying capacity of the concrete is not to be underestimated, as well as in case of prestressing the load carrying capacity of the truss should be considered. This is demonstrated in the exemplary calculation of the shear strength of an existing bridge structure.

In consequence, it has to be noted that the assessment of the reliability and structural reserves of existing reinforced and prestressed concrete structures in terms of shear strength can be improved by using advanced shear design approaches.

REFERENCES

Empelmann, M. et al. 2012: Strengthening of box girders using adaptive "tube-in-tube" concepts. *IABMAS 2012*, Lake Maggiore, Italy.

Görtz, S. 2004. *Zum Schubrissverhalten von Stahlbeton- und Spannbetonbalken aus Normal- und Hochleistungsbeton*. Dissertation, RWTH Aachen (in German).

Hansen, M. 2004: *Zur Auswirkung von Überwachungsmaßnahmen auf die Zuverlässigkeit von Betonbauteilen*. Dissertation, University of Hannover (in German).

Hegger, J. & Görtz, S. 2006: Shear capacity of beams of normal concrete and high performance concrete. In Ernst & Sohn (ed.), *Beton- und Stahlbetonbau* 101, 695–705.

Joint Committee on Structural Safety (JCSS) 2006: Probabilistic Model Code. www.jcss.ethz.ch, 10.05.2010

Kordina, K. & Hegger, J. 1987: Systematische Auswertung von Schubversuchen an Stahlbetonbalken. In DAfStb, issue 381. Berlin: Beuth (in German).

Muttoni, A. & Fernández Ruiz, M. 2008: Shear strength of members without transverse reinforcement as function of critical shear crack width. In *ACI Structural Journal*, March-April 2008, 163–172.

RCP 2004: A Structural Reliability Analysis Program-System, Modul: COMREL, RCP GmbH, München.

Song, J. et al. 2010: Probabilistic shear strength models for reinforced concrete beams without shear reinforcement. In *Structural Engineering and Mechanics* 34, 15–38.

Sykora, M. & Holicky, M. 2011: Safety format for non-linear analysis in the model code – verification of reliability level. *fib Symposium PRAGUE 2011*, Prague, Czech Republic.

Zink, M. 2000: *Zum Biegeschubverhalten schlanker Bauteile aus Hochleistungsbeton mit und ohne Vorspannung*. Dissertation, University of Leipzig (in German).

Research and Applications in Structural Engineering, Mechanics and Computation – Zingoni (Ed.)
© 2013 Taylor & Francis Group, London, ISBN 978-1-138-00061-2

Dismantleable joints of load-bearing reinforced concrete units of prefabricated concrete building system with controlled stiffness

J. Witzany, T. Čejka & R. Zigler
Czech Technical University in Prague, Faculty of Civil Engineering, Prague, Czech Republic

ABSTRACT: An essential characteristic of dismantleable prefabricated reinforced concrete building system with controlled properties of joints is contact connection of load-bearing reinforced concrete units, which allows, due to compensation elements inserted into the joints capable of absorbing energy, the limitation of the intensity of dynamic effects to a level that will not cause the failure of a building and its parts. Another significant property of these joints is also the elimination of outside noise (traffic, building activity, industrial activity) below the absolute threshold of hearing and thus the enhancement of the quality of the internal environment, allowing development in areas with increased noise levels, traffic, etc. The system may analogically be applied in areas with poorer foundation conditions, with underground traffic, in undermined zones, etc.

1 INTRODUCTION

Monolithic reinforced concrete and prefabricated systems with "rigid" joints do not allow the regulation of the system's response to dynamic effects, active damping of vibrations and the elimination of their propagation through load-bearing parts of the system.

Systems with controlled joint properties allowing damping of vibrations may also find their applications in buildings with strict conditions and requirements such as special production plants, health care, research and development facilities, etc.

2 CHARACTERISTICS OF PREFABRICATED SYSTEMS

Prefabricated systems – with "rigid" joints (welded reinforcement projecting from joint sections of prefabricated units or anchored by steel elements embedded in prefabricated units with successive grouting of joints with concrete) – are characterised by such a deformation and failure mechanism in which the limit state of the structure as a whole is preceded by the joint failure, or in which the structure passes from linearly elastic behaviour to non-linear elastic to plastic state usually by exceeding the proportionality limit in its joints. Rigid joints tend to be the weakest point of a load-bearing system with insufficient capacity to absorb strain energy due to extreme short-term loading (exceptional effects, explosions, vehicle impacts, etc.).

In the plastic deformation state of mainly joints of load-bearing prefabricated units with energy dissipation, energy absorption occurs; is this phase of the bond action (plastic action phase) it is necessary that the respective static bond is not completely eliminated from the load-bearing system. This presumes that the plastic deformation mechanism should prevail at critical points of the load-bearing system during energy dissipation. In the case of prefabricated reinforced concrete wall systems, the joints of prefabricated wall units loaded predominantly by shear forces are, as a rule, the principal agent in this respect, while in the case of reinforced concrete pier systems the principal agents are the joints of piers and cross beams loaded predominantly by bending and twisting moments.

The "stiffness" of a floor slab binding together individual vertical elements into a 3D load-bearing system is essential for securing the stability of a prefabricated reinforced concrete system, and the fulfilment of this requirement primarily depends on the rigidity and strength of joints between the prefabricated floor units (slabs). In terms of energy dissipation, the implementation of the plastic deformation mechanism in these critical zones must avoid a substantial reduction in the so-called springy force and any potential instabilities. In this phase of the joint (connecting bond) action, the fulfilment of the condition δtotal. > δplast. is essential, i.e. with a drop in loading a joint (connecting bond) partially "returns" to the initial position before the respective i-th load cycle. In case of standard reinforced concrete systems with rigid joints the effective reinforcement of the prefabricated system in the part with joints is of utmost importance for energy dissipation through plastic deformation of joints of prefabricated units. The type, quality and amount of reinforcement are vital for reaching the necessary joint ductility. The full exploitation of joint ductility – in the range of non-linearly elastic and plastic deformations – in standard prefabricated systems is connected with a gradual development of cracks and joint rupture preceding the failure – collapse of joints (Fig. 1).

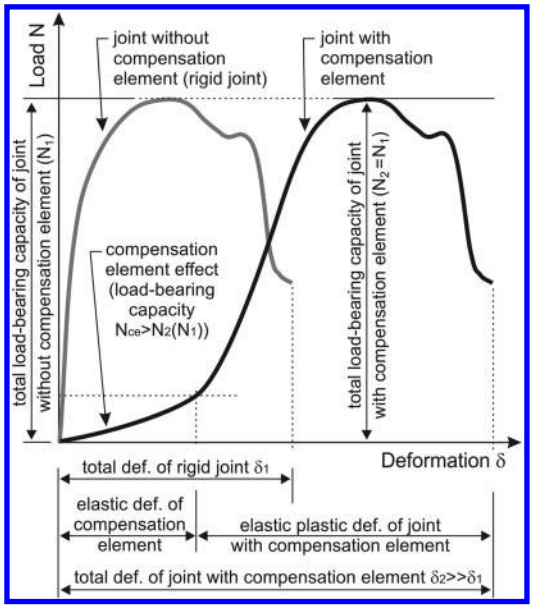


Figure 1. Load – deformation diagrams of rigid joints and joints with compensation (elastic) elements.

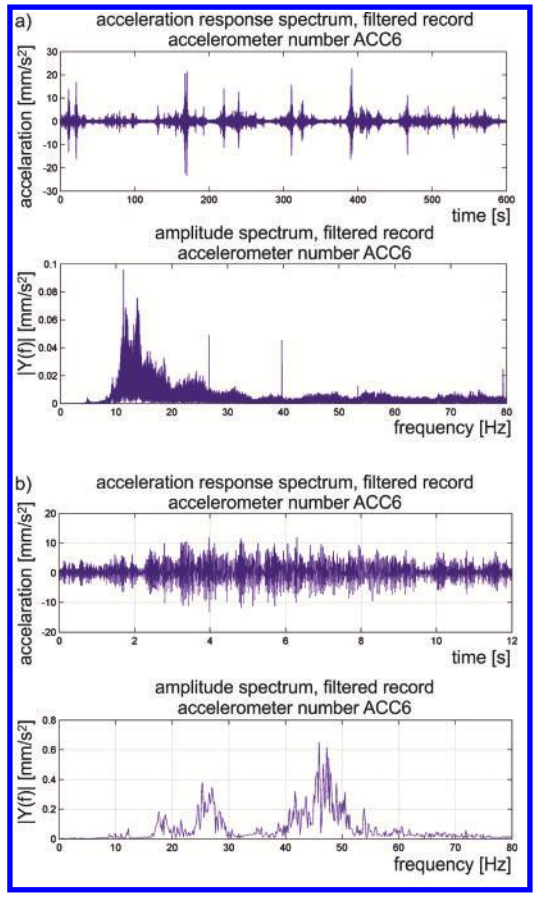


Figure 2. Records of vertical accelerations, a) passage of three cars, reinforced concrete skeleton, distance of 10 m from the source, b) metro, overground measurement, precast panel wall system, distance of 5 m from the source (Witzany & Makovička, in prep.).

The capacity of dissipative joints of prefabricated units which represent critical elements (zones) of a prefabricated load-bearing system in terms of its resistance to exceptional effects and impacts of seismic loads may be proved by means of a cyclic non-elastic test in which the so-called plastic deformation mechanism is verified under loading with repetitive shear force, or the bending or twisting moment (ČSN EN 1998 – Eurocode 8).

The results of numerous experimental studies (Witzany 1982) have proved that, depending on the method and amount of reinforcement, rigid (monolithised) joints of prefabricated reinforced concrete units are extremely sensitive to the effects of variable cyclic loads. Under cyclic (repetitive) loading amounting to 40 to 70% of the joint's limit load (i.e. around the limit of proportionality), the joint failure occurs by reaching the joint's deformation limit under the respective load – not under the limit load – which is called incremental failure. Time-variable, non-linear changes in the properties of joints – a drop in the joint rigidity due to the effect of loading with a dynamic component – in relation to the loading history and plastification, may be of crucial importance for the structural safety and service life of a load-bearing system in time (Makovička & Makovička 2011).

3 DYNAMIC LOADING OF PREFABRICATED STRUCTURES

Great emphasis is currently placed on the solution of issues of seismic loading and the response of structures to the effects of natural, technical and induced seismicity worldwide, these efforts are focused not only on buildings situated in zones of increased natural seismic activity, but also on buildings affected by growing volumes of overground as well as underground traffic and construction activity, and buildings exposed to the effects of technical and induced seismicity.

Technical seismicity due to traffic effects differs from natural seismicity particularly by higher frequencies which propagate into the surrounding environment and by frequent repetitions during which the fatigue limit of material may be exceeded. The frequencies of traffic shocks range between 10 to 200 cycles/sec being most frequently between 30 to 150 cycles/sec, while the amplitudes of shocks are small reaching no more than several tenths of a micrometre. Natural seismicity has approximately 100 times lower oscillation frequencies, while the amplitudes of shocks are, on the contrary, by several orders higher (Makovička & Makovička 2007). The acceleration of traffic shocks corresponds to values of catastrophic earthquakes of the 10th to 12th degrees on

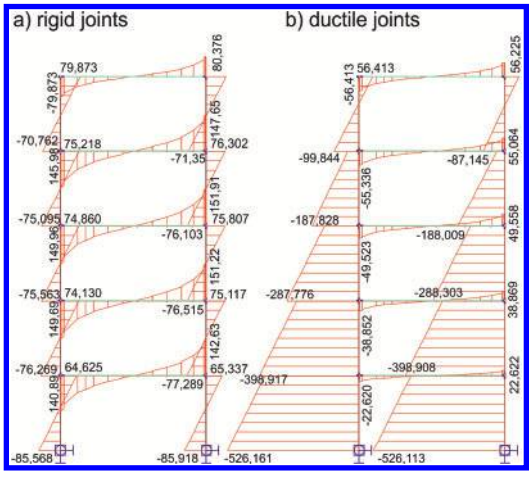


Figure 3. Comparison of the response of a reinforced concrete storey structure (frame) with rigid and ductile joints loaded by shearing force (100 kN) at the upper free end (bending moments [kNm]).

the Richter scale. Vibrations due to road traffic propagating through the environment into the surrounding buildings are usually in dominant frequencies ranging approximately from 5 to 25 Hz (Makovička & Makovička 2012). Vibrations due to overground railway traffic (trams, railway trains) have dominant vibrations roughly from 5 Hz to 50 Hz (Fig. 2)

High sensitivity of reinforced concrete prefabricated pillar or wall systems of particularly multi-storey buildings with "rigid" joints to the effects of induced deformations, strain and vibrations increases potential risks of the failure of the structural function of the load-bearing system exposed to long-term intensive vibrations and shocks, or seismic effects, and of a related loss of its static (dynamic) resistance (Witzany et al. 2009).

A simple example of a multi-storey frame on Figure 3 illustrates the effect of reduced rigidity on the static response of a structure.

4 DISMANTLEABLE JOINTS WITH CONTROLLED STIFFNESS

A characteristic feature of joints with controlled properties, i.e. an inserted compensation (elastic) element, is their ability of absorbing large amounts of strain energy exerted by the effect of exceptional loading, natural or technical seismicity, or long-term acting cyclic, variable loading effects (Fig. 4 and 5).

The required drop in rigidity and increased joint ductility of prefabricated units is achieved, in case of proposed solution of dismantleable joints of prefabricated reinforced concrete units, by inserting elastic components (compensation elements) in the area of the mutual contact of prefabricated units in the joint. The rigidity (ductility) of this elastic element must be

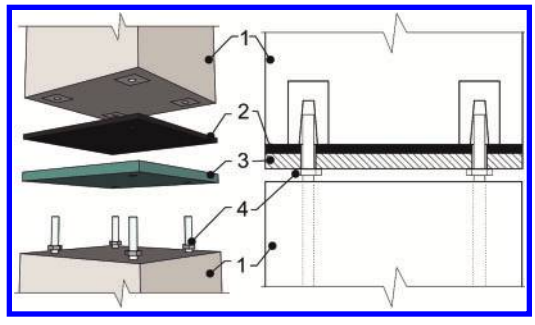


Figure 4. Design principle of dismantleable joint with a damping layer in the mutual contact zone (column – column joint). Legend: 1 – Column, 2 – Compensation (elastic) element, 3 – Spreading steel plate, 4 – Levelling nut.

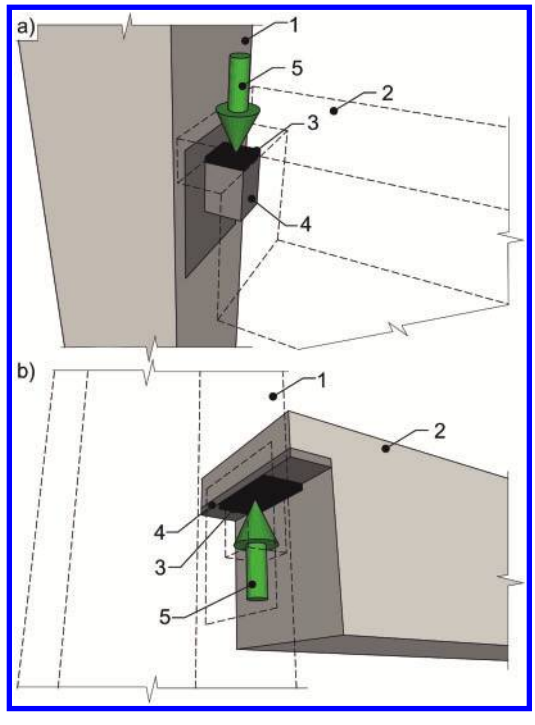


Figure 5. Design principle of dismantleable joints with a damping layer in the mutual contact zone (column – beam joint)
Legend: 1 – Column, 2 – Beam, 3 – Compensation (elastic) element, 4 – Spreading steel plate, 5 – Loading force.

determined with respect to structural demands resulting from loading and the effects transferred by jointed units and with respect to the requirement for the damping of vibrations and dynamic effects with specific characteristics.

The specific solution of dismantleable joints of prefabricated reinforced concrete system with controlled stiffness is currently the subject of patent procedure and therefore can not be publicly presented at the moment.

ACKNOWLEDGMENTS

The paper was written with support from research project TA02010837 “Multipurpose dismantleable prefabricated reinforced concrete building system with controlled joint properties and the possibility of repeated use”.

REFERENCES

Makovička, D., Makovička, D., Determination of Seismic Transport Effects on Buildings, In: Brebbia, C.A.: Earthquake Resistant Engineering Structures VI, WIT Press, Southampton, 2007, pp. 353–362.

Makovička, D., Makovička, D., Vibrobase insulation of a building excited by the technical seismicity effect of tube railway operation, In: Brebbia, C.A., Maugeri, M.: Earthquake Resistant Engineering Structures VIII, WIT Press, Southampton, 2011, pp. 79–88.

Makovička, D., Makovička, D., Analysis of vibro-based isolated building, 6th European Congress on Computational Methods in Applied Sciences and Engineering (ECCOMAS 2012), September 2012, Vienna, 9 pp.

Witzany, J., Working Diagrams of Joints under Repetitive Loading, In: *Pozemní stavby*, Vol. 25, No. 8, Prague, Czech republic, 1982

Witzany, J. et al, Prefabricated Planar Structure of a Multi-Storey Building Exposed to Cyclic Load and Engineering Seismicity. In *Proceedings of the Fifth International Structual Engineering and Construction Conference*, *Las Vegas, 21–27 September 2009*. Leiden: CRC Press/Balkema, 2009, p. 339–344

Witzany, J., Makovička, D., Response of buildings to the effects of traffic-induced technical seismicity, in preparation.

Research and Applications in Structural Engineering, Mechanics and Computation – Zingoni (Ed.)
© 2013 Taylor & Francis Group, London, ISBN 978-1-138-00061-2

Numerical investigations on the shear capacity of reinforced concrete slabs under concentrated loads

K. Reissen & J. Hegger
Institute of Structural Concrete, RWTH Aachen University, Aachen, Germany

ABSTRACT: The shear capacity of reinforced concrete slabs without shear reinforcement has been investigated at the Institute of Structural Concrete at RWTH Aachen University. To determine the effective width for shear under concentrated loads, 13 full-scale tests on single-span slabs with varying slab widths and shear-span-to-depth ratios were performed. Since full-scale tests are time consuming and expensive, nonlinear three-dimensional finite-element models were developed and calibrated based on the available test data. By means of parameter studies, further influences on the shear capacity were analyzed (e.g. concrete strength, longitudinal and transverse reinforcement ratio, reinforcement in the compression zone, slab dimensions, shear-span-to-depth ratio) and a modified approach for the effective width for shear is proposed.

1 INTRODUCTION

Rising traffic loads have increased the requirements for the load-carrying capacity of bridges significantly (Naumann 2010). Furthermore, German design code rules have changed during the last decades reducing the calculated shear capacity of reinforced concrete members without shear reinforcement (DIN 1045: 1988, DIN 1045-1:2001, DIN EN 1992-2:2005). Therefore, the calculated shear capacity of many existing bridge deck slabs without shear reinforcement is not sufficient according to the present design rules. Since shear failure and excessive crack formation have not been observed in existing bridges to date, the bridges are evidently able to carry the heavier traffic loads. Therefore, the shear capacity of reinforced concrete slabs without shear reinforcement has been investigated within a research project, which was funded by the Federal Highway Research Institute of Germany (BASt) and carried out at the Institute of Structural Concrete at RWTH Aachen University.

To investigate the effective width for shear, 13 full-scale tests on single-span slabs were performed (Reissen & Hegger 2011, 2012, 2013). Full-scale tests are time consuming and expensive, so that further influences were analysed by means of numerical simulations with the Finite-Element-Software Abaqus (2009). Firstly, nonlinear three-dimensional models were developed and calibrated based on the test data of six tests. Secondly, parameter studies with varying concrete strengths, longitudinal and transverse reinforcement ratios, reinforcement in the compression zone, slab dimensions and shear-span-to-depth ratios were carried out.

Most of the present design rules for the shear capacity of members without shear reinforcement were developed based on empirical evaluations of shear databases consisting of beam tests. So far, only few tests on the shear capacity of slabs under concentrated loads have been conducted. Hence, the investigation of slabs under concentrated loads reveals new aspects of the shear-bearing behaviour. For instance, the shear-span-to-depth ratio and the transverse reinforcement ratio affect the effective width for shear and thus the shear capacity.

2 EXPERIMENTAL INVESTIGATIONS

With tests on beams and slabs under concentrated loads with a constant height of 0.28 m, different widths of 0.5 m, 1.5 m, 2.5 m and 3.5 m (S5 to S35) and different shear-span-to-depth ratios of 2.91 (A), 4.16 (B) and 5.41 (C) (Fig. 1, Table 1, Reissen & Hegger 2012, 2013), the effective width contributing to the shear resistance in the cracked state was investigated. Each specimen was tested in a three-point shear test by means of a 0.4 m square load according to wheel loads in the European codes (DIN EN 1991-2, 2010). The varying widths cover the transition from beams to slabs exposed to concentrated loads.

All specimens featured a uniform reinforcement ratio of 0.98%. The tensile reinforcement was realized by high strength steel bars Ø15/7.5 ($f_{yk} = 900$ MPa). The further reinforcement layers consisted of normal strength steel bars ($f_{yk} = 500$ MPa), Ø10/15 in the compression zone and Ø12/10 in lateral direction in the tension and compression zone (Fig. 2). Concrete cover was 2 cm resulting in an effective depth of $d = 0.24$ m.

Normal strength concrete was used in all tests. The mean cylinder strengths $f_{c,cyl}$, uniaxial tension strengths f_{ctm} and modulus of elasticity E_{cm} were

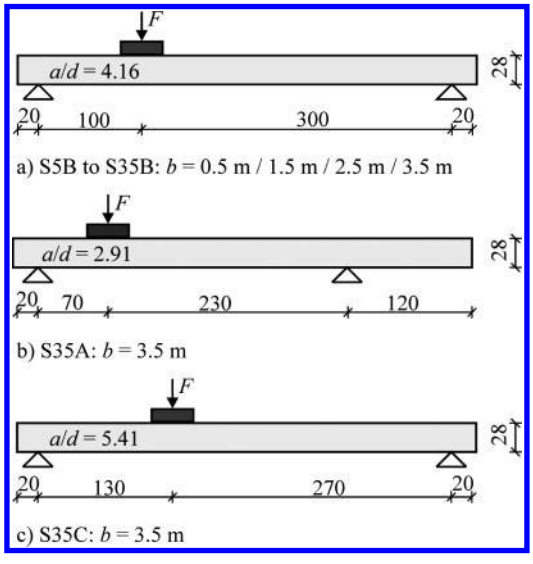


Figure 1. Static systems and dimensions (dimensions in cm).

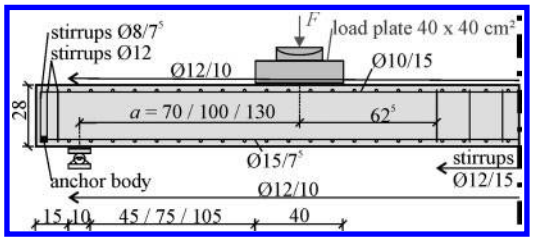


Figure 2. Load details and reinforcement layout (dimensions in cm).

Table 1. Test programme, concrete properties and test results.

test	b m	a/d –	$f_{c,cyl}$ MPa	f_{ctm} MPa	E_{cm} GPa	F_u kN	$V_{F,u}$ kN
S5B	0.5	4.16	39.2	3.0	26.2	183	137
S15B	1.5	4.16	37.7	2.8	27.3	543	407
S25B	2.5	4.16	27.9	2.5	22.4	664	498
S35B	3.5	4.16	35.9	2.8	28.2	985	739
S35C	3.5	5.41	39.6	2.4	27.2	1166	787
S35A	3.5	2.91	41.3	2.7	29.9	1143	876

measured at the day of testing and are listed in Table 1. Additionally, the test programme (specimen width b, shear-span-to-depth ratio a/d) and the test results (reached ultimate loads F_u and corresponding shear forces $V_{F,u}$) are given.

3 NUMERICAL INVESTIGATIONS

3.1 *Material Model*

The numerical investigations were performed with the FE-Software Abaqus (2009). The implemented

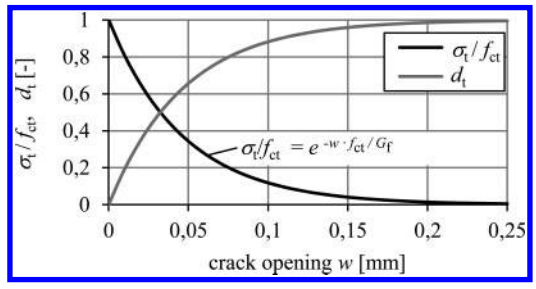


Figure 3. Stress-crack-opening relation in tension and corresponding tensile damage d_t.

plasticity theory based model Concrete Damaged Plasticity (CDP) was used consisting of the following three components to represent the inelastic behaviour of the concrete:

- The yield function determines whether the material responds elastically at a particular state of stress. It is defined by the uniaxial (f_c) and biaxial (f_b) concrete compressive strength, the uniaxial tensile strength f_{ct} and a parameter K_c describing the shape of the yield surface. The CDP model applies the yield function according to Lubliner et al. (1989) with modifications proposed by Lee & Fenves (1998) to account for different strength developments under tension and compression controlled by two damage variables for tensile and compressive damage, respectively.
- The hardening rule accounts for the modification of the yield function due to inelastic deformations.
- The flow rule defines the development of the inelastic deformations after leaving the elastic region. The Abaqus-Software applies a hyperbolic Drucker–Prager function, which depends on the dilation angle ψ of the concrete and the so-called eccentricity parameter ε.

Realistic modeling of the tensile behaviour is essential to investigate the typical shear-tension failure of plain concrete (Hegger et al. 2010). After the maximum tensile strength f_{ct} is reached under consideration of a linear stress–strain relation, the post-peak behaviour is defined by a stress-displacement relation according to Hillerborg's fictitious crack model (Hillerborg et al. 1976). The normalized transferred tensile stress σ_t/f_{ct} at a given crack width w is defined with the tensile strength f_{ct} and the fracture energy G_f by the exponential function according to Figure 3. The tensile damage variable d_t is defined as the inverted stress-crack-opening relation, where the tensile strength is normalized to the maximum tensile strength. Since d_t describes the stiffness degradation due to cracking, it will be used to illustrate the damage of the slabs in the following discussion.

3.2 *Model*

The concrete body of the slabs, the support and the load plate were modeled by 8-node volume elements

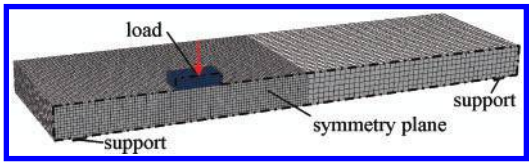


Figure 4. FE model of S25B.

(C3D8) considering the symmetry in transverse direction. Since the shear failure occurs between the load introduction and the nearest support, the corresponding region was meshed by a fine mesh with edge lengths of approximately 25 mm, while a coarser mesh with edge lengths of 50 mm was used in the remaining part to reduce the computing time (Fig. 4). The two parts were linked together by tying the nodal degrees of freedom in the plane between the dissimilar meshes with an applicable function in Abaqus named Tie Constraints. Comparative calculations using a continuously fine mesh revealed no significant influences on the load-bearing behaviour.

For modeling the reinforcement, two-node truss elements with elastic–plastic material behaviour were applied. The reinforcement bars were embedded in the surrounding concrete simulating a perfect bond by linking the nodal degrees of freedom.

All calculations were performed displacement controlled with an explicit solution technique for dynamic and highly nonlinear problems in Abaqus Version 6.9 (Abaqus 2009). The computing time corresponds to the critical increment size and for FE models with a great number of degrees of freedom, it is considerably shorter in comparison to the computing time under application of implicit solvers. In addition, convergence problems due to unstable crack propagation are avoided using the explicit solution technique. However, a linear load application would lead to too large acceleration changes between two increments. Therefore, the displacement was applied considering a so-called smooth-step function, where the first two derivatives at the beginning of the load application equal to zero.

The parameters of the material model were defined following reasonable values given in literature and by comparing the numerical results with test data concerning load–deflection behaviour, concrete and steel stresses, increase of slab thickness, ultimate load and failure mechanism:

- The tensile strength f_{ctm}, compressive strength $f_{c,cyl}$ and modulus of elasticity E_{cm} were derived from laboratory tests (Table 1). A reduction of f_{ct} to 70% of the mean test values considered a certain scatter of strength in the model.
- The tensile behaviour is strongly affected by the fracture energy G_f. While the shear capacities were considerably overestimated applying the fracture energy according to Model Code 2010 (CEB-FIP 2012), the numerical simulations are in good accordance with the experimental results, if the lower fracture energy according to Model Code 1990 (CEB-FIP 1993) is applied.
- To calibrate the parameters of the CDP model, parameter studies were performed based on reasonable values from literature. The variation of the parameters describing the yield function had no significant influence on the shear-bearing behaviour. Therefore, the relation of biaxial to uniaxial concrete compressive strength f_b/f_c was defined according to Grassl & Jirásek (2006) as $f_b/f_c = 1.16$ and the parameter K_c was chosen in accordance to Lubliner (1989) as $K_c = 0{,}66$. In contrast, the shear capacity was clearly affected by the variation of the parameters defining the flow rule. In the investigated range of variation of $\psi = 30°$ to $40°$, the shear capacity increased with increasing dilation angle due to increasing ductility. This increase was higher for the wider slabs, so that with a dilation angle of $\psi = 37°$ a good accordance between the numerical and experimental results could be achieved for nearly all tests. The eccentricity parameter ε was varied between 0.01 and 1.0 also resulting in an increase of shear capacity with increasing eccentricity parameter. The best results were achieved by the default value of $\varepsilon = 0.1$.

Furthermore, thorough parameter studies of further factors such as load introduction details, element type and mesh size indicated that reliable and reproducible results could be expected.

3.3 *Definition of shear-crack load*

As the numerical calculations with the explicit solution technique do not necessarily stop at failure, the numerical shear capacities had to be determined with the help of defined criterions. At first, the formation of a shear crack was detected with the help of the tensile damage variable d_t indicating a critical crack opening. The formation of the critical shear crack is accompanied by stiffness degradation in the load-deflection curve. A further possibility to verify the shear-crack load is given by the energy development. The ratio of external work to inner energy should equal 1.0 except for the beginning of the incremental load application. A further increase indicates energy conversion (e.g. in kinematic energy) due to instable crack propagation. With this, reliable shear-crack loads were defined as failure criterion, whereby possible redistributions of internal forces after shear cracking are not taken into account.

3.4 *Numerical results*

The experimental shear capacities and numerical shear-crack loads given in Table 2 reveal good accordance except for test S35C with a high shear-span-to-depth ratio of 5.41. In the following, comparisons between numerical results and test data are exemplarily shown for tests S35B and S35C explaining the greater deviation for S35C.

Table 2. Experimental ultimate loads and numerical shear-crack loads.

test	S5B	S15B	S25B	S35B	S35C	S35A
$F_{u,exp}$ [kN]	183	543	664	985	1166	1143
$F_{u,num}$ [kN]	167	510	702	983	901	1185
Δ [%]	−8.7	−6.1	+5.7	−0.2	−22.7	+3.7

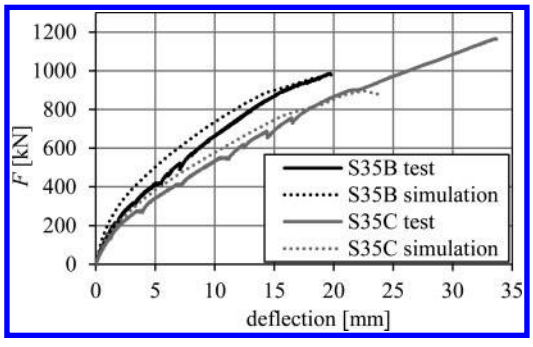


Figure 5. Experimental and numerical load-deflection curves for S35B and S35C.

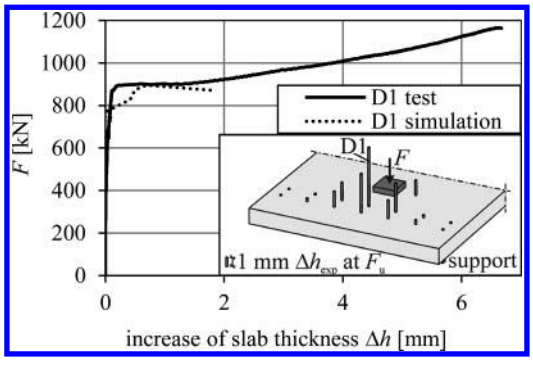


Figure 6. Experimental and numerical increase of slab thickness Δh for S35C at measuring point D1 and Δh_{exp} at ultimate load F_u.

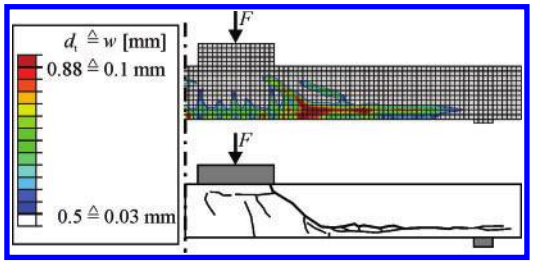


Figure 7. Crack pattern of S35C in symmetry axis in numerical simulation (above) and in test by saw cut (below).

In Figure 5, the experimental and numerical load-deflection curves for S35B and S35C are given. The initial stiffness in the linear-elastic range was slightly higher in the numerical simulations than in experimental tests leading to a parallel offset of the load-deflection curves. The experimental and numerical maximum shear capacities and deflections at maximum load are in good agreement for S35B (black curves). For S35C, the numerical maximum load coincides with stiffness degradation at approximately 900 kN in the test indicating the formation of a shear crack.

During the tests, the development of shear cracks within the slabs was detected by measuring the slab thickness. Figure 6 shows the experimental and numerical development of slab thickness increase Δh for S35C at measuring point D1 in front of the load plate depending on the applied load F and the experimental increases of slab thicknesses Δh_{exp} at ultimate load F_u for all measuring points. At approximately 800 and 900 kN, respectively, the measuring point D1 indicates the opening of a shear crack in the numerical simulation and in the test, respectively. In the test, the load could be further increased leading to a crack opening of several millimeters in front of the load plate at ultimate load, while the outer regions without shear crack were activated to carry the load. Obviously, this load redistribution could not be numerically reproduced. Except from that, the load-bearing behaviour, the shear-tension failure and the shear-crack formation are described appropriately. Figure 7 shows the crack pattern of S35C in the symmetry axis for the numerical simulation by the tension damage parameter d_t and in the test by a saw cut. Both the location and the inclination of the critical shear crack are in good agreement.

3.5 *Parameter study*

The described models served as basis to investigate further influences on the shear capacity of slabs without shear reinforcement under concentrated loads within a parameter study. The concrete strength, longitudinal and transverse reinforcement ratio, reinforcement in the compression zone, shear-span-to-depth ratio, slab height, width and span were varied based on the dimensions and reinforcement ratios of S35B considering concrete properties corresponding to strength class C30/37.

By comparison of the mean shear capacities $v_{Rm,c}$ according to DIN EN 1992-2 (2005) and the numerical shear capacities consisting of the shear forces due to the shear-crack load $V_{Fu,num}$ and the dead weight of the slab v_g, the effective widths b_{eff} were determined:

$$V_{\mathrm{Fu,num}} + v_{\mathrm{g}} \cdot b_{\mathrm{eff}} = v_{\mathrm{Rm,c}} \cdot b_{\mathrm{eff}} \Rightarrow b_{\mathrm{eff}} = \frac{V_{\mathrm{Fu,num}}}{v_{\mathrm{Rm,c}} - v_{\mathrm{g}}} \quad (1)$$

$$v_{\mathrm{Rm,c}} = [c_{\mathrm{m}} \cdot \kappa \cdot (100 \cdot \rho_l \cdot f_{\mathrm{ck}})^{1/3} - 0{,}12 \cdot \sigma_{\mathrm{cd}}] \cdot d \quad (2)$$

The shear capacity $v_{Rm,c}$ depends on the height of the uncracked compression zone (which is proportional to $(100 \cdot \rho_l)^{1/3}$, where ρ_l means the longitudinal reinforcement ratio), the tensile strength of the concrete (which is proportional to $f_{ck}^{1/3}$), the size-effect κ, the

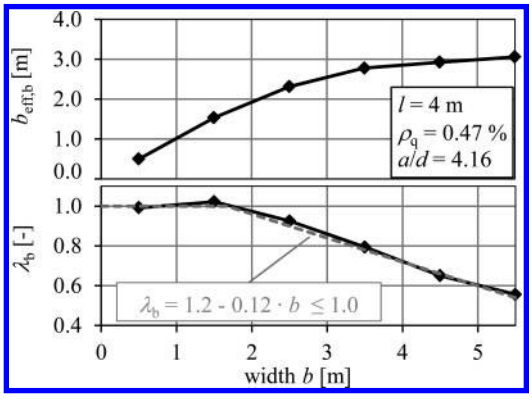


Figure 8. Effective width b_{eff} and factor λ_b depending on the slab width b.

influence of axial longitudinal stresses σ_{cd} and the effective depth d. The empirical factor $c_m = 0.18$ is based on an international shear database consisting of shear tests on beams.

By dividing these effective widths by the full slab width and a reference width, respectively, several factors λ_i could be derived representing the influences on the effective width of the various parameters. The effective width is than calculated as product of the slab width and the various factors as $b_{eff} = b \cdot \prod \lambda_i$.

It could be proved, that the influences of the concrete strength f_{ck}, the longitudinal reinforcement ratio ρ_l and the effective depth d, as they are described by equation (2), are also valid for simply supported slabs under concentrated loads. Furthermore, no influence of the reinforcement in the compression zone was detected. Hence, the results of the shear tests on beams without shear reinforcement (which normally do not have reinforcement in the compression zone) may be transferred to bridge deck slabs, which have reinforcement in the compression zone by default.

The effective width increases with increasing slab width (Fig. 8, above). However, this increase gets progressively smaller. For slab widths equal or smaller than 1.5 m, the full slab width is activated to carry the load indicating a beam bearing behaviour and resulting in a linear increase of the effective width with increasing slab width. In contrast, the effective widths of the models with a width of $b \geq 2.5$ m is smaller than the actual slab width indicating that not the full width of the specimens has been activated. These numerical results confirm the conclusions drawn from the experimental investigations (Reissen & Hegger 2011, 2012, 2013). Since the effective width b_{eff} is calculated by multiplying the factors λ with the full slab width b, the factor λ_b decreases with increasing slab width although the effective width increases (Fig. 8).

The shear-crack load and thus the effective widths and the factors λ_i also increase with increasing span (Fig. 9) and transverse reinforcement ratio in the tension zone (Fig. 10) due to higher potential for load distribution. Transverse reinforcement is essential to ensure lateral load distribution and to carry transverse

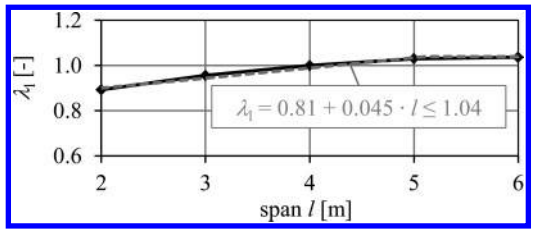


Figure 9. Factor λ_l depending on the span l.

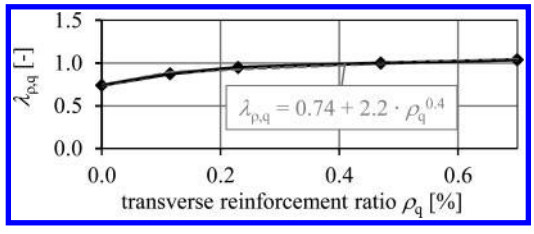


Figure 10. Factor $\lambda_{\rho,q}$ depending on the transverse reinforcement ratio ρ_q.

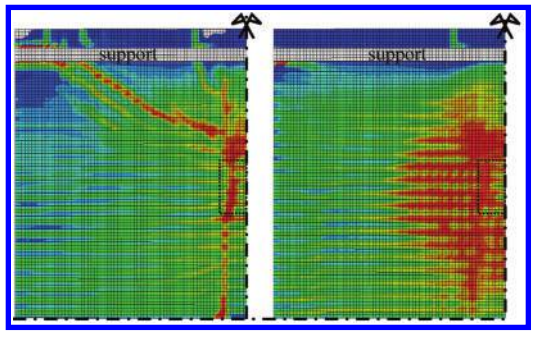


Figure 11. Crack pattern at soffit for different transverse reinforcement ratios of $\rho_q = 0\%$ (left) and $\rho_q = 0.47\%$ (right).

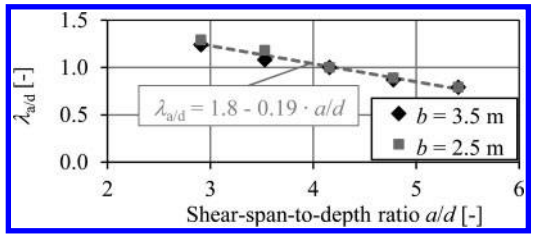


Figure 12. Factor $\lambda_{a/d}$ depending on the shear-span-to-depth ratio a/d.

stresses. While the formation of deep cracks in slabs without transverse reinforcement as shown in Figure 11 (left) leads to stiffness degradation and loss of shear capacity, sufficient transverse reinforcement ensures a fine crack distribution resulting in optimal load distribution as demonstrated in Figure 11 (right, $\rho_q = 0.47\%$).

The influence of the shear-span-to-depth ratio a/d has been investigated on numerical models with a width of 2.5 m and 3.5 m, respectively. Due to the

decreasing influence of the direct compression strut, the shear-crack load and thus the factor $\lambda_{a/d}$ decrease nearly linearly with increasing a/d (Fig. 12). Since shear-crack loads were used for the evaluation, possible redistributions of internal forces after shear cracking are not captured by this approach. Hence, with regard to structural design in the ultimate limit state, the following approach accounting for the identified influences of the slab width b, the transverse reinforcement ratio ρ_Q, the span l and the shear-span-to-depth ratio a/d provides slightly conservative results.

$$b_{\text{eff}} = b \cdot \lambda_{\text{b}} \cdot \lambda_{\text{pq}} \cdot \lambda_{\text{l}} \cdot \lambda_{\text{a/d}} \tag{3}$$

$$\lambda_{\text{b}} = 1.2 - 0.12 \cdot b \leq 1.0 \quad \text{for } b \leq 5.5 \text{ m} \tag{4}$$

$$\lambda_{\text{pq}} = 0.74 + 2.2 \cdot \rho_{\text{q}}^{0,4} \quad \text{for } 0 \leq \rho_{\text{q}} \leq 0.7\ \% \tag{5}$$

$$\lambda_{\text{l}} = 0.81 + 0.045 \cdot l \leq 1.04 \quad \text{for } l \geq 2 \text{ m} \tag{6}$$

$$\lambda_{\text{a/d}} = 1.8 - 0.19 \cdot {}^{a}\!/_{d} \quad \text{for } 2.91 \leq {}^{a}\!/_{d} \leq 5.41 \tag{7}$$

4 SUMMARY AND CONCLUSIONS

Nonlinear three-dimensional finite element models of single-span slabs under concentrated loads were developed and calibrated based on available test data using the software Abaqus. The applied plasticity theory based material model was able to reproduce the observed shear-tension failure of slabs without shear reinforcement appropriately. By means of parameter studies, further influences on the shear capacity were analyzed. Based on comparisons of the numerical shear-crack loads and the calculated shear capacities $v_{Rm,c}$ according to DIN EN 1992-2 (2005), a modified approach for the effective width for shear $b_{eff} = b \cdot \prod \lambda_i$ is proposed, where the factors λ_i account for the various influences. It could be proved, that the influences of the concrete strength f_{ck}, the longitudinal reinforcement ratio ρ_l and the effective depth d, as they are described by the shear capacity $v_{Rm,c}$, are also valid for simply supported slabs under concentrated loads. Furthermore, no influence of the reinforcement in the compression zone was detected. The shear-crack load and thus the effective width increases with increasing slab width, span and transverse reinforcement ratio due to higher potential for load distribution. Because of the decreasing influence of the direct compression strut, the shear-crack load decreases with increasing shear-span-to-depth ratio. Since the data bases to verify new approaches are limited, additional research is required to extend and further validate the proposed approach.

ACKNOWLEDGEMENTS

This report is based on parts of the research carried out at the request of the Federal Federal Ministry of Transport, Building and Urban Development, represented by the Federal Highway Research Institute, under research project No. 84.0110/2009. The authors are solely responsible for the content. We acknowledge the funding and the discussions with the project committee.

Furthermore, we would like to thank Mr. Paul Golus for his contribution to the presented numerical investigations.

REFERENCES

Abaqus 6.9 2009. *Abaqus Online Documentation*. Providence: Dassault Systèmes Simulia Corp.

CEB-FIP (Comité Euro-international du Béton-Fédération Internationale de la Précontrainte) 1993. *CEB-FIP Model Code 1990*. Lausanne: CEB.

CEB-FIP 2012. *Model Code 2010*. Lausanne: CEB.

DIN 1045:1988. *German Design Code 1045: Concrete and Reinforced Concrete, Design and Construction.* Berlin: Beuth.

DIN 1045-1:2001. *German Design Code 1045-1: Design and Construction of Concrete, Reinforced Concrete and Prestressed Concrete*. Berlin: Beuth.

DIN EN 1991-2:2010. *Eurocode 1: Actions on structures – Part 2: Traffic loads on bridges; German version EN 1991-2:2003 + AC:2010.* Berlin: Beuth.

DIN EN 1992-2:2005. *Eurocode 2: Design of concrete structures – Part 2: Concrete bridges – Design and detailing rules; German version EN 1992-2:2005 + AC:2008*. with DIN EN 1992-2/NA:2012. *National Annex*, draft april 2012. Berlin: Beuth.

Grassl, P. & Jirásek, M. 2006. Damage-plastic model for concrete failure. *International Journal of Solids and Structures* 43: 7166–7196

Hegger, J., Roggendorf, T. & Teworte, F. 2010. FE analysis of shear-loaded hollow-core slabs on different supports. Magazine of Concrete Research 62(8): 531–541.

Hillerborg, A., Modéer, M. & Peterson, P.-E.1976. Analysis of crack formation and growth in concrete by means of fracture mechanics and finite elements. Cement and Concrete Research 6: 773–781.

Lee, J. & Fenves, G.L. 1998. Plastic-damage model for cyclic loading of concrete structures. *Journal of Engineering Mechanics* 124(8): 892–900.

Lubliner, J., Oliver, J., Oller, S. & Onate, E. 1989. A plastic-damage model for concrete. *International Journal of Solids and Structures* 25(3): 299–326.

Naumann, J. 2010. Bridges and Heavy Goods Traffic – an Inventory. *Bauingenieur* 85(1): 1–9.

Reissen, K. & Hegger, J. 2011. Experimental Study on the Shear Capacity of Concrete Slabs. *IABSE-IASS Symposium Taller, Longer Lighter; Symposium Report, London, 2011.* London: Hemming Group.

Reissen, K. & Hegger, J. 2012. Shear Capacity of Reinforced Concrete Slabs under Concentrated Loads. *18th Congress of IABSE; Congress Report, Seoul, 2012.* Zürich: IABSE.

Reissen, K. & Hegger, J. 2013. Experimental investigations on the effective width for shear of single span bridge deck slabs. *Beton- und Stahlbetonbau* 108(2): 96–103.

Research and Applications in Structural Engineering, Mechanics and Computation – Zingoni (Ed.)
© 2013 Taylor & Francis Group, London, ISBN 978-1-138-00061-2

Analysis of the structural behaviour of shear-critical prestressed and reinforced concrete beams using digital image correlation

K. De Wilder, G. De Roeck & L. Vandewalle
KU Leuven, Department of Civil Engineering, Leuven, Belgium

P. Lava, D. Debruyne & Y. Wang
Catholic University College Ghent, Association KU Leuven, Department of Mechanical Engineering, Gent, Belgium

ABSTRACT: The reported study presents results of two full-scale I-shaped shear-critical prestressed and reinforced concrete beams subjected to a four-point bending test with monotonically increasing load. Full-field three-dimensional displacements and deformations are measured with two stereo vision digital image correlation (DIC) systems over both zones where a shear force occurs. In this paper, a numerically generated optimized speckle pattern was applied on both beams in a controlled manner using a stencil printing technique. The experimentally observed displacement and deformation data are used to validate numerical finite element models. A satisfying correlation was found between experimental and numerical results concerning failure load and mode, displacements and deformations. From the numerical models, it was found that a significant portion of the applied shear force is carried in the area of both flanges of both specimens.

1 INTRODUCTION

After more than a century of research, shear remains an area within the scientific community where disagreement remains amongst researchers. From the early days of concrete construction, engineers have sought for models that accurately determine the shear resistance of a structural concrete member. In the earliest contributions, Ritter (Ritter, 1899) idealized the flow of forces within a structural concrete member by means of a truss model, as shown in Figure 1. The top and bottom cord resist the applied bending moment whereas the combination of concrete compressive struts and steel tension ties take up the applied shear force. Important progress has been made in the last fifty years when, under the influence of the theory of plasticity, the truss model was extended and systematized. This model is easy to understand and is still the basis for current international codes of practice.

From the last thirty years onwards, research has shifted from (semi-)empirical design approaches towards more rational theoretical (Vecchio and Collins, 1986, Ruiz and Muttoni, 2009, Sigrist, 2011) based on the mechanical behaviour of structural concrete members loaded in shear. Some of these models are mature enough to be incorporated into current international codes of practice. Despite the large research effort, shear remains an open problem and our understanding is clearly incomplete (fib, 2010).

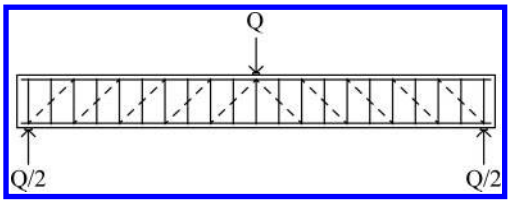


Figure 1. Truss model concept (compressive struts in dashed lines; vertical tension ties in full lines).

This paper aims to make a contribution to a better understanding of shear in prestressed and reinforced concrete structural elements by reporting the results of two preliminary tests of an extensive experimental program. In the first part of this paper, the specimen properties and experimental setup are summarized. Special attention is devoted to the use of the digital image correlation technique as a full-field measurement technique for measuring displacements and deformations. In the second part of this paper, the experimental data are used to validate numerical predictions obtained from nonlinear finite element models (FEM). A good correlation was found between the experimentally observed data and numerical predictions concerning failure load and mode, displacements and deformations. Finally, an investigation of the shear carrying mechanisms is performed based on the FEM output.

2 EXPERIMENTAL WORK

Two I-shaped girders, referred to as B105 and B111 and part of an extensive experimental program, were tested until failure occurred. Both beams are 7000 mm

Table 1. Concrete mixture properties.

Specimen	f_{cm} [MPa] (#*)	$f_{cm,cube}$ [MPa] (#,s**)	E_{cm} [GPa] (#)	$f_{ctm,fl}$ [MPa] (#)
B105	90.3 (2)	87.3 (3, 10.9)	39,9 (2)	5.3 (2)
B111	87.4 (2)	92.9 (3, 2.8)	36.5 (2)	6.1 (2)

*number of tested specimens; **standard deviation

Table 2. Reinforcement properties.

Type	d_p^*, d_s [mm]	E_s [GPa]	f_{ym} [MPa]	f_{tm} [MPa]	ε_u [%]
Top prestressing reinforcement					
7-wire	9.3	198	1737	1930	5.20
Bottom prestressing reinforcement					
7-wire	12.5	198	1737	1930	5.20
Conventional longitudinal reinforcement					
Hot rolled	25	209	530	635	12.90
Splitting reinforcement					
Cold worked	8	203	542	603	5.97
Shear reinforcement					
Cold worked	6	203	608	635	2.73

*nominal diameter of prestressing (subscript p) or conventional (subscript s) reinforcement

long, 630 mm high and have a flange width of 240 mm. The web of both beams is 70 mm wide. Specimen B105 is prestressed at the prestressing yard of a local precast manufacturer by means of 8 straight 7-wire strands with a nominal diameter of 12.5 mm at the bottom and two 7-wire strands with a nominal diameter of 9.3 mm at the top. An initial strain of 3.76 10^{-3} (744 MPa) was given to each strand. At the day of testing, after immediate and time-dependent prestress losses, a mean strain value of 3.31 10^{-3} (655 MPa) was found using demountable mechanical strain gauge points glued onto the concrete surface. Specimen B111 is conventionally reinforced with two hot-rolled bars with a nominal diameter of 25 mm. Specimen B105 has an effective depth d equal to 511 mm whereas the effective depth of specimen B111 equals 580 mm. Single legged stirrups were provided with a nominal diameter of 6 mm and a center-to-center distance of 150 mm. The geometry of both specimens is shown in Figures 2(a)–(b).

2.1 *Materials*

Together with each specimen, concrete cubes (sides 150 mm), cylinders (height 300 mm; diameter 150 mm) and prisms (length 600 mm; sides 150 mm) were cast to determine the mean compressive strength f_{cm} based on cylinders, the mean compressive strength $f_{cm,cube}$ based on cubes, the mean secant modulus of elasticity E_{cm} and the flexural tensile strength $f_{ctm,fl}$. A summary of the results per specimen is shown in Table 1. Tensile tests were performed on the conventional longitudinal reinforcement as well as on the shear and splitting reinforcement to determine the modulus of elasticity E_s, the yield and ultimate stress f_{ym} respectively f_{tm} and the strain at failure ε_u. The same characteristics of the prestressing strands were taken from the manufacturer. The results are summarized in Table 2.

2.2 *Experimental setup*

Both specimens are subjected to a four point bending test, as shown in Figure 3. The tests are carried out in load-control using a hydraulic press (Instron, maximum capacity of 2.5 MN). The force from the hydraulic press is converted to two point loads by means of a steel construction profile (HEB 400) lying on two steel bearing cylinders. The total load is monotonically increased at 0.250 kN/s (i.e. applied shear force rate: 0.125 kN/s) until failure occurs. The distance between the support points is equal to 5000 mm. The distance outside the support is therefore equal to 1000 mm at each end. This setup firstly enables the authors to study shear outside the length needed for the prestressing force to gradually develop over the member's height and secondly to prevent failure due to debonding of the longitudinal reinforcement. Two linear variable differential transformers (LVDTs) were provided at 1200 mm from the support point at the bottom of the beam.

2.3 *Digital image correlation (DIC)*

As an optical full-field measurement method, digital image correlation (DIC) has proven to be an ideal tool for a wide range of applications, including the identification of the mechanical material behaviour through inverse modeling, structural health monitoring and the study of the deformation characteristics of a wide range of materials. The basic principle behind the technique is to calculate the displacements on the surface of an object by taking images of a black and white speckle pattern in the undeformed and deformed state. There are three main steps in the DIC method: (1) capture images, (2) correlation process and (3) post-processing phase.

In the reported study, both zones where a shear force occurs were investigated by using two stereo-vision DIC systems. Each zone under investigation measures approximately 1500 mm by 630 mm. Each system consists of two CCD 8-bit cameras (AVT Stingray F-201 B; 1628 pixels by 1236 pixels resolution) with lenses having a focal length equal to 12 mm mounted on a tripod. The cameras are located at a perpendicular distance of approximately 2700 mm from the web of the test specimen, refer to Figures 3(b)–(c). To ensure good lighting conditions and small exposure times, two 500 W quartz iodine lamps are provided per investigated zone as shown in Figures 3(b)–(c). The image acquisition rate of each camera is equal to 2 Hz with an

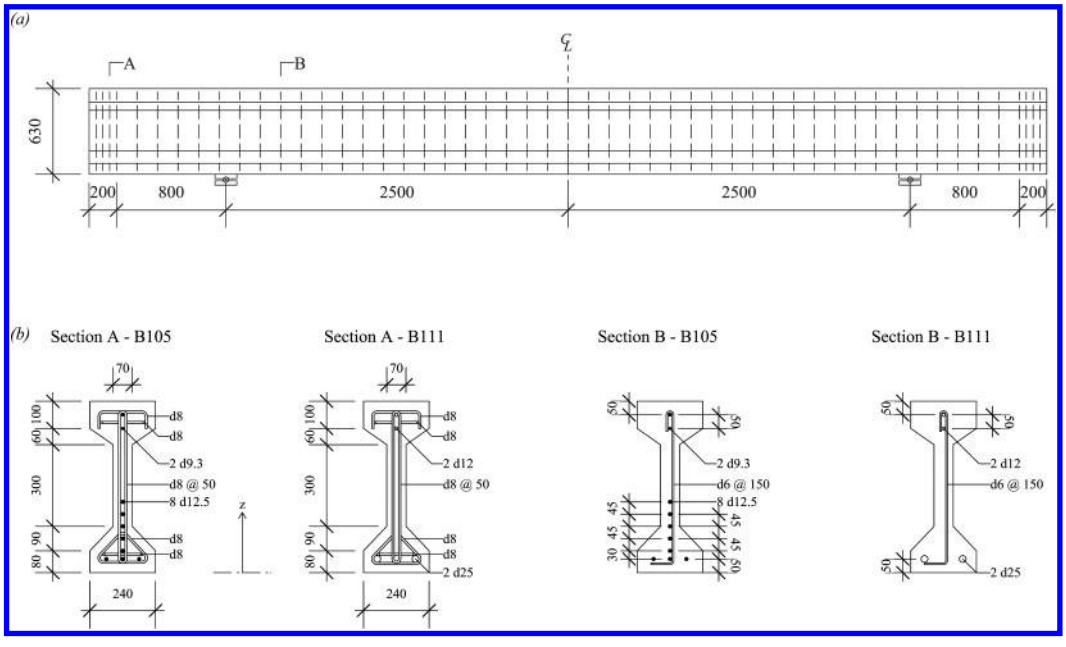


Figure 2. Geometry, prestress and reinforcement layout of specimens B105 and B111: (a) longitudinal view (units in millimeter); (b) cross sections of specimens and reinforcement details.

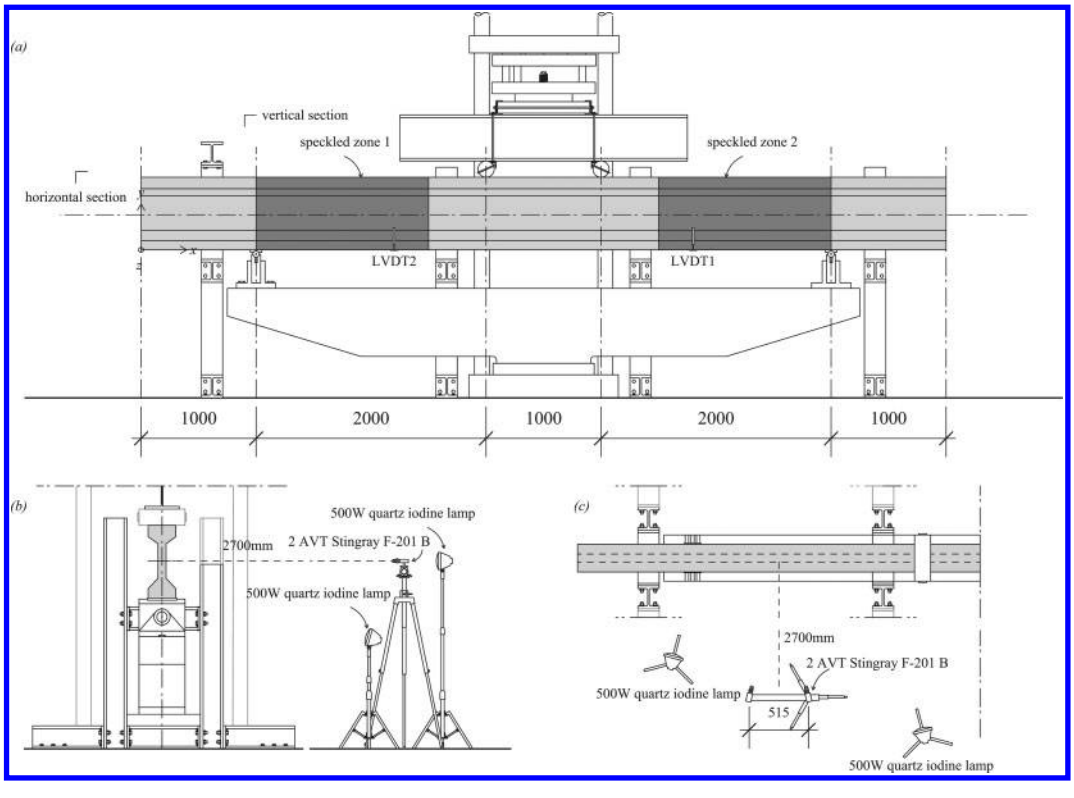


Figure 3. Experimental setup: (a) front view of experimental setup with indication of speckled zones (units in millimeter); (b) vertical section (units in millimeter); and (c) horizontal section of experimental setup (units in millimeter).

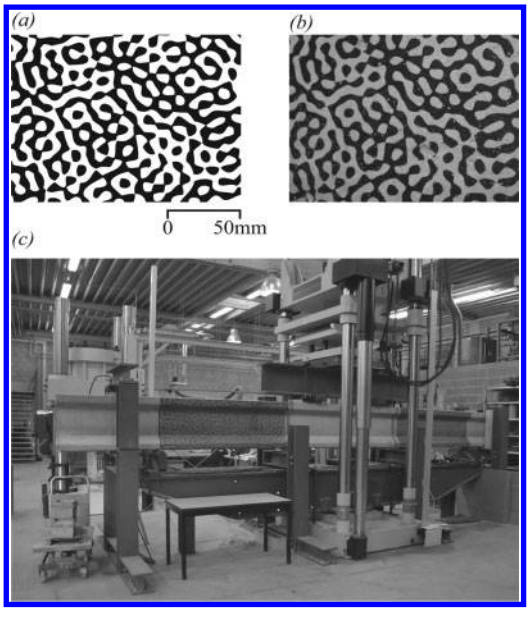


Figure 4. (a) detail of numerically generated speckle pattern; (b) part of applied speckle pattern onto specimen B105; (c) experimental setup of B105 indicating both speckled zones.

exposure time of 20 ms. All images of the four cameras are transferred to a desktop computer over FireWire and synchronized with the analog data (applied force and corresponding stroke) of the hydraulic press.

In this contribution, a subset-based method is applied to correlate two speckle patterns. This method considers a pixel and its neighborhood in the undeformed image f and searches the same subset in the deformed image g by adopting a maximization routine for a similarity function. The formalism is clearly explained in (Lava et al., 2009). In this study, maximization of the similarity function is obtained by adopting the zero-normalized sum of squared differences (ZNSSD) routine. The size of the subset can be chosen as desired prior to the evaluation. In this work, the dimensions of each subset were 27 by 27 pixels where each pixel has the physical dimension of approximately 1 mm.

Two specific problems are to be addressed when using DIC for the aforementioned experiments: (1) due to the large zone under investigation, a relatively large speckle size is required; and (2) reproducibility of the speckle pattern on a 3D surface needs to be accounted for to gain acceptance as a reliable measurement method. Here, a numerical technique is used to generate optimized speckle patterns for DIC, as proposed by (Bossuyt, 2012). This allows the authors to generate a pattern tailored to the experiments so that the speckle size and spatial distribution of the speckles are controlled. The generated pattern is applied onto each specimen by using a stencil printing technique. Figure 4(a) depicts a detail of the numerically generated speckle pattern whereas Figure 4(b) shows the same part of the speckle pattern applied onto specimen B105. Figure 4(c) shows the speckled zones in the experimental setup.

The correlation process and the post-processing of the data are done by using MatchID 3D (Lava et al., 2009). During the post-processing phase, strains are calculated by smoothing the displacement data over a certain zone to damp out the effect of noise and local uncertainties. This is a commonly adopted method (Lava et al., 2010). In the reported study, strains are averaged over 51 by 51 displacement data points. Taking into account the step size of 3 pixels and the physical dimension of one pixel, this means that strains are averaged over approximately 150 by 150 mm. This relatively large base length is justified when dealing with heterogeneous materials that exhibit a profound cracking behaviour such as concrete.

Relatively small displacements (order of magnitude 10^1 mm) and deformations (order of magnitude 10^3 μS) are expected during the experiments in view of the field of view and the spatial resolution involved. Therefore it is of the utmost importance to quantify the resolution of the measuring technique, i.e. the smallest signal above the noise level. Quantification of this noise level can be done by correlating two different images in undeformed state and assessing the predicted displacements and deformations. The noise on the displacement and strain data can be considered approximately normally distributed and can therefore be best expressed by the standard deviation of the considered displacement or strain component. For this setup, the standard deviation s of the in-plane horizontal U (x-axis) and vertical V (y-axis) displacement, refer to Figure 3(a), is found to be 21 μm and 11 μm respectively. The standard deviation of the out-of-plane displacement W (z-axis) is an order of magnitude higher, equal to 155 μm, but also less important for the reported experiments since primarily in-plane displacements and deformations will occur. The standard deviation of the horizontal ε_{xx}, vertical ε_{yy} and shear strain ε_{xy} is found to be equal to 112 μS, 241 μS and 140 μS respectively.

2.4 *Failure mode and load*

Both specimens failed due to diagonal tension due to rupture of the shear reinforcement in the web. The shear force applied at failure is 251.2 kN for specimen B105 and 141.5 kN for specimen B111. Using the shear strength provisions found in Eurocode 2 (CEN, 2004), based on the aforementioned truss analogy, the failure load can be estimated. According to Eurocode 2, the failure load of specimen B105 is equal to 131.8 kN (ratio of experimental to predicted failure load = 1.91) whereas the predicted failure load of specimen B111 is equal to 59.8 kN (ratio of experimental to predicted failure load = 2.37). These predicted failure loads were obtained by using average material strength properties and no partial safety factors.

Table 3. Comparison between experimentally observed and numerically predicted failure load and mode.

Specimen	Experiment		FEM		
	$V_{u,test}$ [kN]	mode [–]	$V_{u,pred}$ [kN]	mode [–]	$V_{u,test}/V_{u,pred}$ [–]
B105	251.2	DT*	247.9	DT	0.99
B111	141.5	DT	139.5	DT	1.01

*DT = diagonal tension due to rupture of the shear reinforcement.

3 FINITE ELEMENT MODEL (FEM) VALIDATION

A three-dimensional nonlinear finite element model was constructed using the commercially available software package ANSYS (v14). Due to double symmetry of the geometry and loading conditions, this model is reduced to a quarter of each specimen, minimizing the required computational time. The concrete matrix is modeled using eight-node hexahedron elements with linear shape functions. Each node has three translational degrees of freedom. Both longitudinal and shear reinforcement types are discretely modeled using truss elements. Experimentally determined material characteristics, as reported in Table 1 and Table 2, were used to define the material models for both concrete and reinforcement. To account for the influence of a multi-axial stress state on the overall structural behaviour of concrete, the three-dimensional failure surface, proposed by (Willam and Warnke, 1975), is adopted. Similar to the experiments, the simulations are carried out in load-control.

The ability of the FEM to reconstruct the experiment is validated by firstly assessing the numerically predicted failure load and mode. The results are summarized in Table 3. From Table 3, it can be seen that a good correlation between the experimental and numerical failure load and mode is obtained. Figures 5(a)–(b) show the experimentally observed cracking pattern at failure and the location of the shear reinforcement for specimens B105 and B111 respectively. The grey value of each shear reinforcement element represents the numerically predicted axial stress. These stress levels correspond well with the location and angle of the cracking pattern.

The load-displacement response curves, determined at 1200 mm from the support point at the bottom of each specimen, obtained with DIC and FEM, are shown in Figures 6(a)–(b). From Figures 6(a)–(b), it can be seen that the numerical model is capable of reconstructing the nonlinear behaviour due to cracking of the concrete matrix and subsequent yielding of the reinforcement.

Finally, a comparison is made between the experimentally and numerically computed horizontal strains. Therefore, the horizontal strain values as a function of

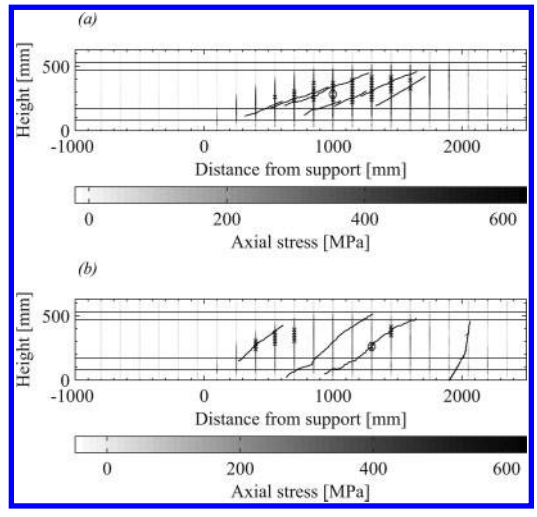


Figure 5. Experimentally observed cracking pattern at failure and numerically predicted axial stress in shear reinforcement elements. Location of rupture stress indicated with 'o'; location where the yield stress is exceeded indicated with 'x'; (a) specimen B105; (b) specimen B111.

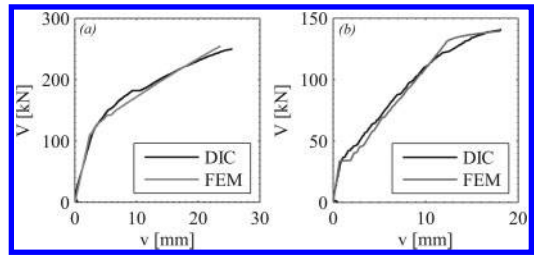


Figure 6. Load-displacement response curve obtained with DIC and FEM for specimen B105 (a) and B111 (b).

the member's height are calculated at three different load levels (50%, 80% and 95% of the experimentally observed failure load). The results for specimen B105 are depicted in Figures 7(a)–(i). Similar results were found for specimen B111. A satisfying correlation is found at the top and the web of the specimen. At the bottom however, a discrepancy between the experimental and numerical values is observable.

4 FINITE ELEMENT MODEL ANALYSIS

In this section, the various shear force contributions of each specimen during the experiment are identified and quantified based on the output of the numerical model. The numerically predicted shear stresses τ_{xy} will, if integrated over the element surface on which they act, resist the applied shear force. The contributions of the top (refer to Figure 2(b), area ranging from $z = 630$ mm to $z = 470$ mm) and bottom flange (area ranging from $z = 0$ mm to $z = 170$ mm) and the web (area ranging from $z = 170$ mm to $z = 470$ mm) can thus be determined as a function of the applied load

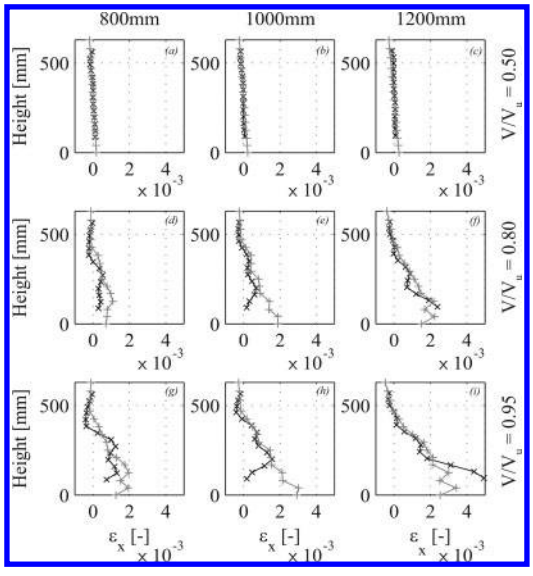


Figure 7. Experimentally (x) and numerically (+) computed horizontal strain values as a function of the height for specimen B105 at 800 mm (a, d, g), 1000 mm (b, e, h) and 1200 mm (c, f, g) from the support point for 50% (a, b, c), 80% (d, e, f) and 95% (g, h, i) of the experimentally observed failure load.

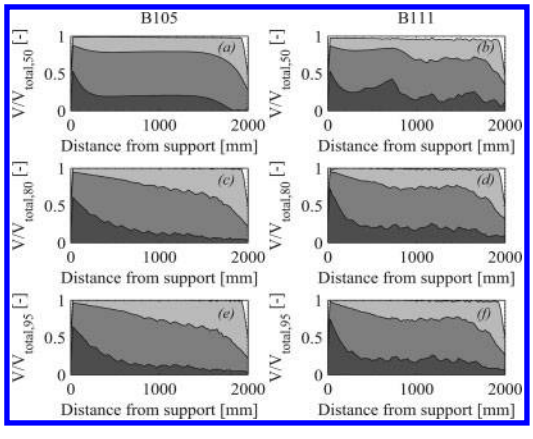


Figure 8. Numerically predicted shear force contributions of top (light grey) and bottom flanges (dark grey) and web (grey) of specimen B105 (a, c, e) and B111 (b, d, f) at various load levels.

and distance from the support point. Figures 8(a)–(e) depict the individual contribution of both flanges and the web of specimens B105 and B111 relative to the applied shear force at various load levels and as a function of the distance from the support point. From Figures 8(a)–(e) it can be noted that a relative large portion of the applied shear force is carried also in the area of both flanges of both specimens. However, this effect is usually neglected in codes of practice and could explain the poor failure load predictions as stated in Section 2.4.

5 CONCLUSIONS

This paper presents the results of two prestressed and reinforced concrete beams subjected to a four-point bending test until failure. During both tests, two stereo-vision digital image correlations (DIC) systems were used to continuously measure full-field displacements and deformations. The experimental data were used to validate nonlinear finite element models (FEM). A good correlation was found between the experimental observations and numerical predictions. Based on the numerical output, an investigation of the shear force contributions of top and bottom flanges and the web of each specimen was made. It was found that a significant portion of the applied shear force is carried in the area of both flanges of the specimens. This effect however, is usually neglected in current codes of practice.

REFERENCES

Bossuyt, S. Optimized patterns for digital image correlation. SEM International Conference & Exposition on Experimental and Applied Mechanics, 11–12 June 2012 Costa Mesa, California USA. Society for Experimental Mechanics.

CEN 2004. Eurocode 2: Design of concrete structures – Part 1-1: General rules and rules for buildings. Brussels: NBN.

FIB 2010. Shear and punching shear in RC and FRC elements: Workshop 15–16 October 2010, Salò (Italy). *In:* Sigrist, V. M., F.; Plizzari, G.; Foster, S. (ed.) *fib Technical Report.* Lausanne: fib.

Lava, P., Cooreman, S., Coppieters, S., De Strycker, M. & Debruyne, D. 2009. Assessment of measuring errors in DIC using deformation fields generated by plastic FEA. *Optics and Lasers in Engineering*, 47, 747–753.

Lava, P., Cooreman, S. & Debruyne, D. 2010. Study of systematic errors in strain fields obtained via DIC using heterogeneous deformation generated by plastic FEA. *Optics and Lasers in Engineering*, 48, 457–468.

Ritter, W. 1899. Die Bauweise Hennebique. *Schweizerische Bauzeitung*, 33, 41–61.

Ruiz, M. F. & Muttoni, A. 2009. Applications of Critical Shear Crack Theory to Punching of Reinforced Concrete Slabs with Transverse Reinforcement. *Aci Structural Journal*, 106, 485–494.

Sigrist, V. 2011. Generalized Stress Field Approach for Analysis of Beams in Shear. *Aci Structural Journal*, 108, 479–487.

Vecchio, F. J. & Collins, M. P. 1986. The Modified Compression-Field Theory for Reinforced-Concrete Elements Subjected to Shear. *Journal of the American Concrete Institute*, 83, 219–231.

Willam, K. & Warnke, E. 1975. Constitutive model for the triaxial behavior of concrete. *International Association for Bridge and Structural Engineering.* Bergamo, Italy: ISMES.

Research and Applications in Structural Engineering, Mechanics and Computation – Zingoni (Ed.)
© 2013 Taylor & Francis Group, London, ISBN 978-1-138-00061-2

The effect of steel fibres on the compressive ductility in lightweight aggregate concrete structures

J.A. Øverli
Department of Structural Engineering, Norwegian University of Science and Technology, Trondheim, Norway

T.M. Jensen
SINTEF Building and Infrastructure, Trondheim, Norway

ABSTRACT: The well-known brittleness in compression of lightweight aggregate concrete (LWAC) compared to normal density concrete can explain the limited use of the material for practical purposes. To study the ductility an experimental program was set up consisting of eight over-reinforced concrete beams subjected to four-point bending. The LWAC had a mass density around 1800 kg/m^3. Four different configurations of the beams were investigated, only LWAC in the compression zone, closed links with spacing 100 mm, 1% of steel fibre reinforcement, and a combination of closed links and steel fibres. The pre-peak behaviour was approximately the same for all configurations. As expected, the beams with only LWAC had a very brittle response after peak load. The others beams had different post-peak response, but all were able to carry load with quite large deflections after maximum loading. Especially the combination with both fibres and links experienced very ductile behaviour.

1 INTRODUCTION

The main objective for using lightweight aggregate concrete (LWAC) is normally to reduce cost by reducing the dead load of structures. E.g. with low weight the dimensions of the foundations in buildings can be reduced in areas with low bearing capacities, the inertia actions are reduced in seismic regions and it enables easier handling and transportation of precast elements. Even with the major advantage of reduced weight and the high strength-to-weight ratio of the material compared to conventional concrete, the use of LWAC is still limited as a mainstream construction material in the building industry.

The major disadvantage of LWAC is the brittleness in compression at the material level compared to normal density concrete. In overload situations adequate ductility is essential to ensure safety. Floating offshore structures and LNG-terminals are often post-tensioned. Thus the compressive ductility is of great importance. It is well known that confinement in the compression zone increases the ductility of concrete. Numerous researchers have investigated both experimental and theoretical, the effect of ordinary transverse steel reinforcement and the effect of adding fibres have on the confinement in normal density concrete (Attard & Setunge 1996, Cheong & Zeng 2002, Mander et al. 1988b, Sheikh & Toklucu 1993, Mander et al. 1988a). For lightweight aggregate concrete similar effects is reported (Balaguru & Foden 1996, Balendran et al. 2002, Campione & La Mendola 2004). The effect of confinement is also taken into account in design codes for concrete structures (Standard Norge 2008a). However, most studies on confinement focus on columns and cylinders subjected only to uniaxial loading (Kim & Harmon 2006, Kosaka et al. 1985, Mangat & Motamedi Azari 1985). Flexural behaviour of LWAC beams with focus on ductility has been reported, but only on under-reinforced beams (Sin et al. 2011, Ahmad & Barker 1991, Ahmad & Batts 1991, Altun & Aktaş 2013, Carmo et al. 2013). For heavily reinforced structures in bending or subjected to a combination of axial forces and bending moments, very little information is found in the literature.

The main objective in this study is to investigate the effect closed links and steel fibres have on the ductility in bending of LWAC structures. An experimental program was set up consisting of eight concrete beams, which were tested in flexure under a four-point loading system.

2 EXPERIMENTAL PROGRAM

The test program was designed to study the ductility enhancement in heavily over-reinforced lightweight aggregate concrete beams provided by steel fibres and steel confining transverse reinforcement. The main focus was on the ductility in the compression zone. Thus, the beams were heavily reinforced to ensure spalling in the compression zone of the cross section before yielding of the tensile reinforcement. The experimental setup and cross-sectional details is given

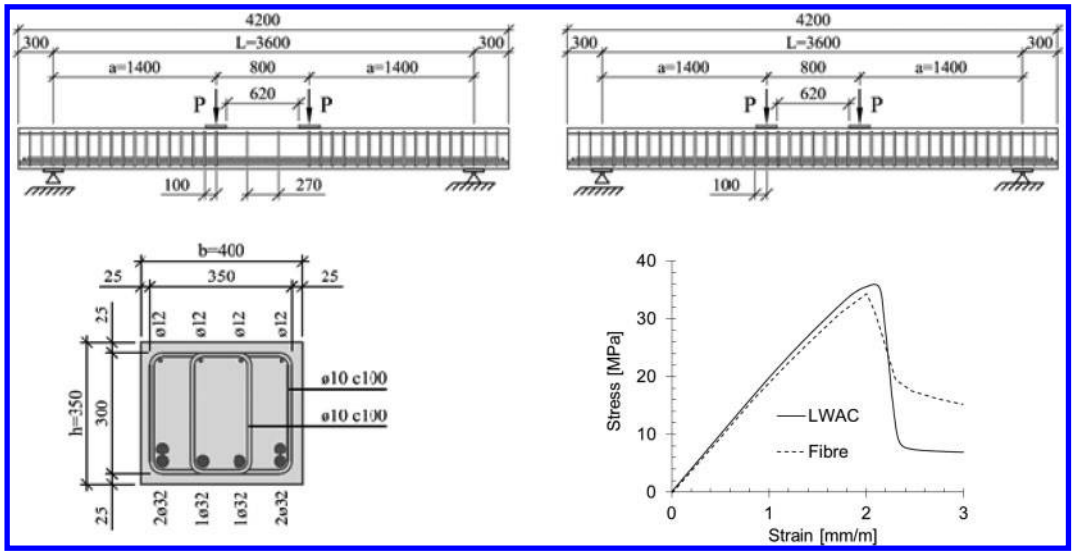


Figure 1. Experimental setup, and typical stress strain relationships for concrete.

in Figure 1. The experimental program consisted of eight simply supported concrete beams, which were tested in flexure under a four-point loading system. Hence, the central part of the beam is in pure bending which is the main focus in this work. The free span between the supports was 3.6 m. The two concentrated loads were applied symmetrical with a distance of 0.8 m. Four different configurations of the LWAC beams were investigated to study the response. Two beams only with LWAC (Beam 1) were considered beams for reference. Two beams each had closed links (Beam 2) and steel fibres (Beam 3) respectively. The final two beams had a combination of closed links and fibres (Beam 4).

To produce the concrete, lightweight expanded clay aggregate, commercially known as LECA, was used to achieve a density of the LWAC around 1800 kg/m^3. For beams with steel fibres, Dramix 65/60 was used, which is a cold drawn wire fibre of bright steel with hooked ends and a length of 60 mm. The fibre content was 78 kg/m^3, which corresponds to an amount of fibres of 1% by volume of concrete. After casting the beams were stored in the formwork under polyethylene sheets to prevent moisture loss. One day later demoulding took place and the beams were again covered with wet burlap sacks and polyethylene sheets to prevent rapid moisture loss.

To achieve an over-reinforced beam in bending, 6 deformed bars with diameter 32 mm were required. The transverse reinforcement consisted of 10 mm diameter deformed bars bent into closed stirrups with spacing 100 mm, see Figure 1. Typical obtained compressive stress strain relationship from cylinders for LWAC with and without fibres are also given in Figure 1.

The beams were suitable instrumented to measure displacements and strains. Deflections of the beams were measured at midspan and at the load transfer points by means of three vertical linear variable differential transformers (LVDT). To capture the concrete strains four LVDTs were placed horizontally at the top and bottom level at both sides of the cross-section, measuring over a distance of 0.5 m. Six strain gauges were used to measure steel strains both on the compressive and the tensile reinforcement.

The load was applied by a 1000 kN servo controlled hydraulic actuator, and distributed to the LWAC beam by a steel beam with two rolled supports. Up to a total load level of 200 kN the loading was applied in intervals of 33.3 kN. Above 200 kN the intervals was doubled to 66.6 kN. At each load level there was a 5 min break to study the formation of cracks. After reaching the peak load, the beams were continuously loaded until complete failure.

3 RESULTS

Table 1 gives the main results from the testing of the eight beams. In production of the beams one batch of concrete was required per beam. The achieved compressive strengths, f_c, for each batch are given in the table. The capacities, P_{calc}, are calculated according to the requirement for LWAC in Eurocode 2(Standard Norge 2008a) and compared to the load at spalling, P_{spall}. The spalling load is identified as the peak load when horizontal cracking in the compression zone occurs, followed by spalling of the concrete cover. For beams without steel fibres the spalling is much more severe than beams with fibres, where the cross-section remains much more intact. This is confirmed in Figure 2 where pictures of the failure zones in beams with and without fibres are shown. The failure zone without fibres is much more local and concentrated than with fibres where the zone is wider and deeper. A centre of rotation is formed close to the centre

Table 1. Experimental results.

Beam: Configuration	f_c (MPa)	E_c (GPa)	P_{spall} (kN)	P_{peak} (kN)	P_{calc} (kN)	P_{peak}/P_{spall}	P_{spall}/P_{calc}	Δ_{spall} (mm)	Δ_{peak} (mm)	$\Delta_{0.9,spall}$ (mm)	$\Delta_{0.9,spall}/\Delta_{spall}$
1A: Only LWAC	36.9	–	280.9	–	295	–	0.95	24.8	–	–	–
1B: Only LWAC	39.7	19.0	291.2	–	311	–	0.94	25.9	–	–	–
2A: Shear links	34.5	–	289.2	293.5	282	1.01	1.03	24.5	26.0	36.3	1.48
2B: Shear links	33.5	18.3	279.0	278.4	276	1.00	1.01	23.9	28.8	39.5	1.66
3A: Steel fibre	34.9	–	281.1	282.9	284	1.01	0.99	23.9	30.5	37.2	1.55
3B: Steel fibre	39.6	20.0	279.0	284.9	311	1.02	0.90	23.1	29.5	52.1	2.25
4A: Shear links + steel fibre	27.7	–	253.1	280.5	241	1.11	1.05	22.0	34.2	100.7	4.57
4B: Shear links + steel fibre	40.4	18.0	271.5	298.3	315	1.10	0.86	22.6	31.4	79.9	3.54



Figure 2. Failure zones in beams. a) LWAC only, Beam 1A; b) Confinement with shear reinforcement and fibres, Beam 4A.

of the longitudinal tensile reinforcement. The accordance between calculated and spalling loads from the tests is satisfactory. Due to a deformation controlled testing system, the peak loads in Table 1, P_{peak}, represents a second obtained maximum load level after the spalling load. The combination of shear links and fibres obtained an increase of approximately 10% from the spalling load.

The main goal in this study was to study the effect on the post-peak behaviour of adding fibres and using confinement reinforcement. Ductility is defined as the ability to sustain significant inelastic deformations after peak load without a significant loss in the capacity. It can be measured at various levels in a structure, on material, sectional, element or global level. A common way of quantifying ductility is to employ a ductility index, which on a local sectional level often is defined as the ratio of curvature at crushing of concrete to that of yielding of reinforcement, e.g. in seismic design where formation of yield hinges is important(Standard Norge 2008b). In this study the beams are over-reinforced meaning yielding of reinforcement cannot be used to find a ductility index. Thus, a displacement ductility index is found in order to assess the ductility. The index, μ_i, is calculated as the ratio between the centre point deflection when the spalling load level has been reduced to 90% after peak load, $\Delta_{0.9,spall}$, and the deflection at spalling load, Δ_{spall}. From Table 1 it can be seen that ductility ratio is at the same level for beams with either shear links or fibre. For the combination of links and fibre the ratio is approximately doubled. Thus, the effect of confinement reinforcement and fibres is an additive effect with respect to ductility in this test series.

Figure 3 shows the load displacement graph for the centre point of the beams. As expected the beams with only LWAC and no confinement experience very brittle behaviour after reaching load at spalling, i.e. no post-peak deformability. The responses for the beams demonstrate the strong influence of the different confinement configurations on the behaviour. In the beams with fibres transverse reinforcement or a combination of those two, the responses of the beams are very ductile. Especially the combination of fibres and shear links shows a continuous response and is able to maintain a high load level after peak load. The two beams with only steel fibres have the largest post-peak deviation. This is typical for fibre reinforced concrete. The variation is large due to the influence of casting process and workability of the concrete on the fibre distribution and orientation. Beams with shear reinforcement but no fibres, 2A and 2B, show a very clear unloading after the first peak load, associated with spalling of the concrete cover in the compression zone. However, the shear links are able to maintain a cross-section and after some redistribution of stresses a second peak point can be identified. This can clearly be seen in Figure 3b where loads and displacements for each beam are normalized with respect to the spalling load and the corresponding spalling displacement.

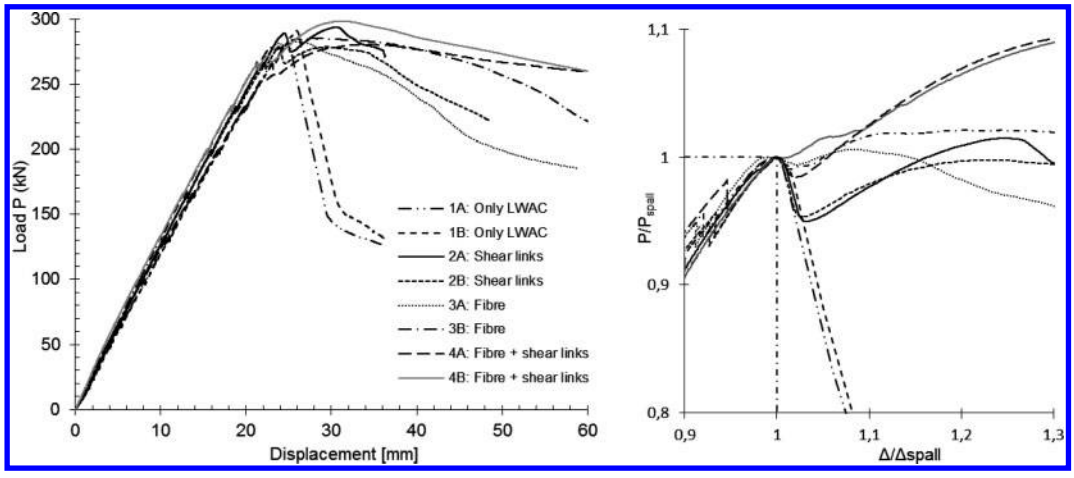


Figure 3. a) Load-displacement plots for all beams at mid span; b) Normalized load-displacement plot.

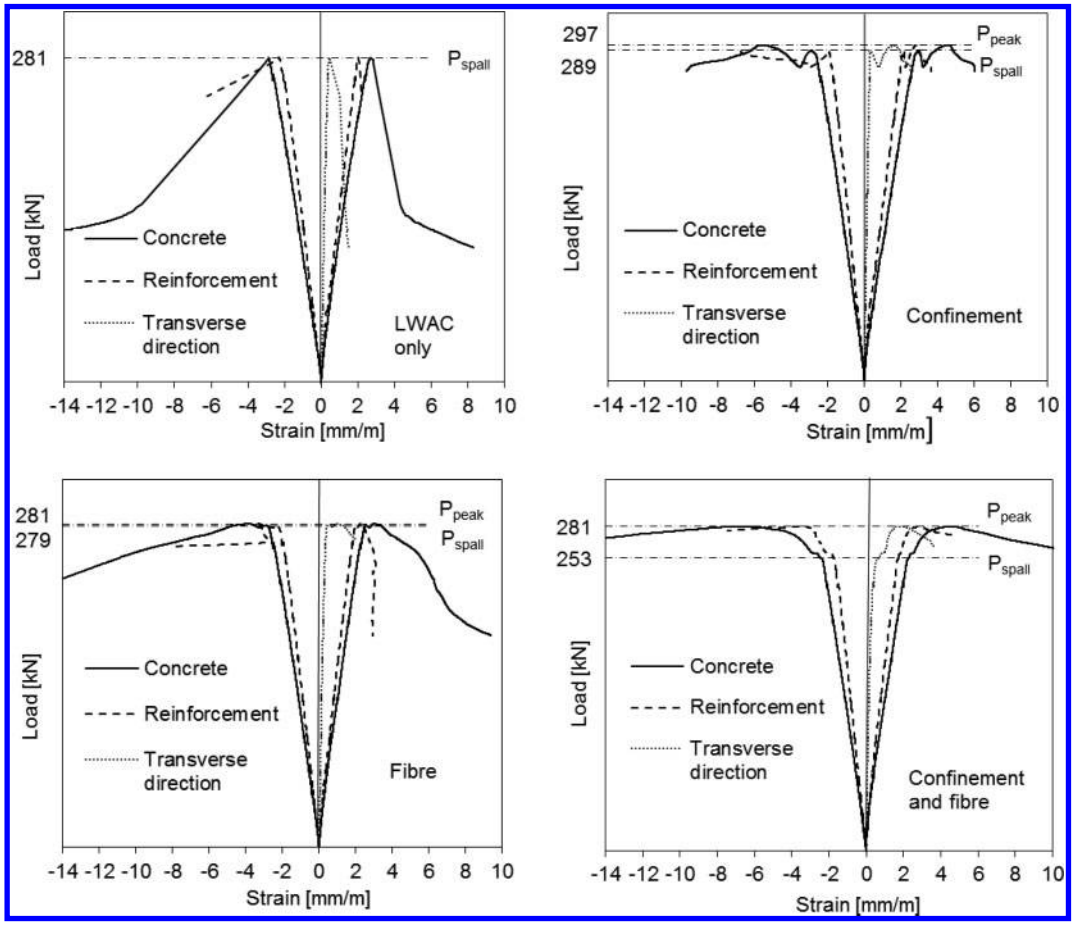


Figure 4. Strain development for the four different configurations of beams.

The strain development during loading is shown in Figure 4 with tensile strains having positive values. Only the results from the first beam (A-beam) in each of the four configurations in the test series are presented. Similar responses were obtained for the second beams. In the figure concrete strains are in longitudinal direction of the beam at top and bottom surface, reinforcement strains are in the top and bottom

reinforcement, and the transverse strains are in the horizontal part of the shear reinforcement close to the top surface. The strains in the reinforcement are measured locally with gauges while the concrete strains are average strains over a distance of 0.5 m. Hence, the reinforcement strains are more influenced by the location of cracks and the following spalling. The strain developments confirm the global load-displacement relationships. Up to the spalling load the strains are not significantly influenced by the introduction of fibre and shear reinforcement. The beam with only LWAC has a very brittle response after spalling, while the beam with both fibres and shear links experiences an increase in bending capacity with large strains in the compressive zone. This increase of ductility can be explained by the effect of confinement. The fibres and shear reinforcement are able to prevent some of the lateral expansion due to the large compressive strains. This introduces small lateral compressive stresses which increase the compressive ductility. From the strains in Figure 4 it is possible to estimate the lateral expansion coefficient, defined as the relationship between the lateral and the longitudinal strain. At load levels below the spalling load the coefficient is approximately 0.15, which is a typical value for lightweight concrete.

To be able to evaluate the design assumptions and the strains calculations, the deformed bar with diameters 10 and 32 mm were tested to characterize the properties(Standard Norge 2010). The bar with diameter 10 mm has an almost perfect linear-ideal plastic behavior with a yield strain of 0.0027. The bars with diameter 32 mm shows a more non-linear behavior where the yielding starts at a strain of 0.0027 before reaching perfect plastic at a strain of 0.0037. From Figure 4 it can be seen that before spalling of the compressive zone the reinforcement is elastic. Hence, the beams are over-reinforced as assumed in the design. However, with increasing load and ductility the tensile reinforcement yields before the ultimate failure.

4 CONCLUSIONS

This work is focusing on improvement of the compressive ductility of lightweight aggregate concrete. Testing of over-reinforced beams in this study shows a considerably increased flexural ductility of the beams when applying steel fibres and/or confinement reinforcement. Especially the combination of fibre and confinement reinforcement experienced a continuous response and the beams were able to maintain a high load level after reaching the maximum load. This study is only considered a first step to increase ductility in heavily reinforced and post-tensioned lightweight aggregate concrete structures by improving the confinement by employing fibres. The effect is confirmed in this work, but further studies are necessary to quantify the confinement effect of fibres and confinement reinforcement in LWAC.

ACKNOWLEDGEMENT

The authors would like to acknowledge the financial support from COIN, the Concrete Innovation Centre, which is a centre for research based innovation with funding from the Norwegian Research Council and industrial partners, and the assistance of L. Bakken, F. Lang, K. Sagosen and Ø. Rønningen for carrying out the experimental work as part of their master thesis(Bakken & Sagosen 2012), (Lang & Rønningen 2012).

REFERENCES

Ahmad, S. H. & Barker, R. 1991. Flexural behavior of reinforced high-strength lightweight concrete beams. *ACI Structural Journal*, 88, 69–77.

Ahmad, S. H. & Batts, J. 1991. Flexural behavior of doubly reinforced high-strength lightweight concrete beams with web reinforcement. *ACI Structural Journal*, 88, 351–358.

Altun, F. & Aktaş, B. 2013. Investigation of reinforced concrete beams behavior of steel fiber added lightweight concrete. *Construction and Building Materials*, 38, 575–581.

Attard, M. M. & Setunge, S. 1996. Stress-strain relationship of confined and unconfined concrete. *ACI Materials Journal*, 93, 432–442.

Bakken, L. & Sagosen, K. B. 2012. *Ductility of lightweight aggregate concrete*, Department of Structural Engineering, Norwegian University of Science and Technology.

Balaguru, P. & Foden, A. 1996. Properties of fiber reinforced structural lightweight concrete. *ACI Structural Journal*, 93, 62–78.

Balendran, R. V., Zhou, F. P., Nadeem, A. & Leung, A. Y. T. 2002. Influence of steel fibres on strength and ductility of normal and lightweight high strength concrete. *Building and Environment*, 37, 1361–1367.

Campione, G. & La Mendola, L. 2004. Behavior in compression of lightweight fiber reinforced concrete confined with transverse steel reinforcement. *Cement and Concrete Composites*, 26, 645–656.

Carmo, R. N. F., Costa, H., Simões, T., Lourenço, C. & Andrade, D. 2013. Influence of both concrete strength and transverse confinement on bending behavior of reinforced LWAC beams. *Engineering Structures*, 48, 329–341.

Cheong, H. K. & Zeng, H. 2002. Stress-strain relationship for concrete confined by lateral steel reinforcement. *ACI Materials Journal*, 99, 250–255.

Kim, Y.-J. & Harmon, T. G. 2006. Analytical model for confined lightweight aggregate concrete. *ACI Structural Journal*, 103, 263–270.

Kosaka, Y., Tanigawa, Y. & Hatanaka, S. 1985. Lateral confining stresses due to steel fibres in concrete under compression. *International Journal of Cement Composites and Lightweight Concrete*, 7, 81–92.

Lang, F. T. & Rønningen, Ø. 2012. *Ductility of lightweight aggregate concrete*, Department of Structural Engineering, Norwegian University of Science and Technology.

Mander, J., Priestley, M. & Park, R. 1988a. Theoretical Stress-Strain Model for Confined Concrete. *Journal of Structural Engineering*, 114, 1804–1826.

Mander, J. B., Priestley, M. J. N. & Park, R. 1988b. Observed stress-strain behavior of confined concrete. *Journal of Structural Engineering*, 114, 1827–1849.

Mangat, P. S. & Motamedi Azari, M. 1985. Influence of steel fibre and stirrup reinforcement on the properties of concrete in compression members. *International Journal*

of Cement Composites and Lightweight Concrete, 7, 183–192.

Sheikh, S. A. & Toklucu, M. T. 1993. Reinforced concrete columns confined by circular spirals and hoops. *ACI Structural Journal*, 90, 542–553.

Sin, L. H., Huan, W. T., Islam, M. R. & Mansur, M. A. 2011. Reinforced lightweight concrete beams in flexure. *ACI Structural Journal*, 108, 3–12.

Standard Norge 2008a. *NS-EN 1992-1-1:2004+NA:2008. Eurocode 2: Design of concrete structures – General rules and rules for buildings*, Norway, Standard Norge.

Standard Norge 2008b. *NS-EN 1998-1:2004+NA:2008. Eurocode 8: Design of structures for earthquake resistance. Part 1: General rules, seismic actions and rules for buildings*, Norway, Standard Norge.

Standard Norge 2010. *NS-EN ISO 15630-1. Steel for the reinforcement and prestressing of concrete – Test methods – Part 1: Reinforcing bars, wire rod and wire*, Norway, Standard Norge.

Research and Applications in Structural Engineering, Mechanics and Computation – Zingoni (Ed.)
© 2013 Taylor & Francis Group, London, ISBN 978-1-138-00061-2

Full-range behavior of FRP-to-concrete bonded joints with trilinear bond-slip law

H. Yuan & L. Wu
MOE Key Lab of Disaster and Control in Engineering, Institute of Applied Mechanics, Jinan University, Guangzhou, China

ABSTRACT: This paper presents a close-form analytical solution of both interfacial shear stress distribution and load-displacement response, which is capable of predicting the entire debonding propagation process including elastic, elastic-flow, elastic-flow-softening, elastic-flow-softening-debonding, flow-softening-debonding, and softening-debonding stages. Based on experimental result of high Young's modulus type of CFRP plate-to-concrete bonded joints, a nonlinear fracture mechanics method, in which the tri-linear local bond slip law is employed, is used to understand the stress transfer mechanism, interfacial crack propagation and ductility behavior in adhesive bonded joint. It is also shown how experimental load-displacement response of bonded joints can be used to identify interfacial properties, including the interfacial fracture energy and parameters of the local bond-slip relationship. The concept of serviceability limit state and ultimate limit state is considered.

1 INTRODUCTION

In the field of reinforced concrete structures, the use of FRP plates as an additional reinforcement appears to be a very promising technique, especially if such structures are in need of repair. However, a better understanding of the mechanical behavior of FRP plates is needed for the field use of this repair. The motivations of this research were that the assumption of perfect bond between the concrete and reinforcement may not apply to externally bonded FRP plates, and that strengthening and stiffening analysis of repaired members with high Young's modulus type of CFRP plate-to-concrete bonded joints requires a new model of local bond shear stress-slip relations. The objectives of this study are as follows

1. Develop a new model describing elastic, flow, softening and debonding along FRP-to-concrete interface.
2. Investigate the load-carrying capacity, effective bond length and full-range load-displacement relations.
3. Indicate how to identify the interfacial fracture energy and local shear stress-slip relation by comparing the analytical model with experimental results.
4. Study the effect of bond length and FRP plate stiffness per unit width on load-displacement response and effective bond length.

The most important and complicated failure mode for the FRP-strengthened structures is the delamination due to the unstable propagation of interfacial debonding initiating from the flexural and/or shear crack of concrete. In interfacial debonding failures, the stress state of the interface is similar to that in a shear test specimen in which a plate is bonded to a concrete prism and is subject to tension (Fig. 1). As a result, the adhesive bonded joint may be thought as a simple and typical model of FRP-strengthened structures to understand the stress transfer and debonding behavior. A large number of studies, both experimental and theoretical, have been carried out on bonded joints. Ueda et al. (1999) and Yoshizawa et al. (2000) conducted an experimental study on bonding behavior of FRP-concrete interface by using both types of single-lap and double-lap shear specimens. The test results show

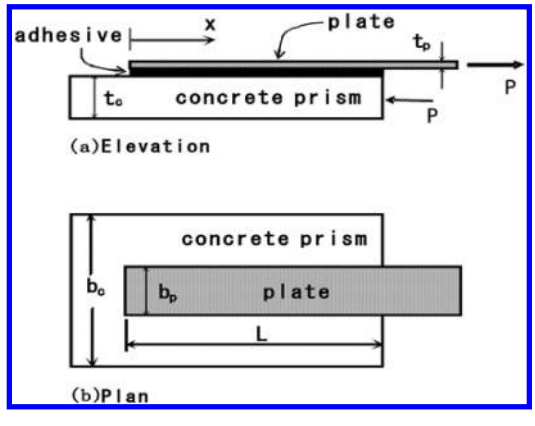


Figure 1. Pull-push shear test of a single-lap plate-to-concrete bonded joint.

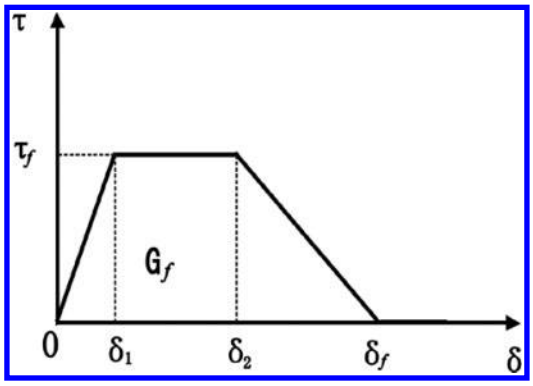


Figure 2. Local bond – slip model.

that the shear stress-slip relationship with a softening behavior can be used to represent well the initiation and propagation of interfacial cracks. However, the test results also shows that for the high Young's modulus type of CFRP plate-to-concrete bonded joints, the tri-linear model shown in Figure 2 which features a linear ascending branch followed by a linear platform, then followed by a linear descending branch provides a better approximation (Yoshizawa et al. 2000).

Of the available closed-form analytical studies, Täljsten (1996) analytically obtained the expression for the ultimate load using a linear ascending bond-slip model. Yuan et al (2000) and Wu et al. (2001, 2002) developed equations for the ultimate load, the interfacial shear stress distribution at the first attainment of the ultimate load and the effective bond length for various interfacial bond-slip models. Chen & Teng (2001) presented a review of most of the studies prior to theirs, assessed available models by comparison with experimental data gathered from the literature, and proposed accurate expressions for the ultimate load and the effective bond length. Yuan et al. (2004) presented an analytical solution for the prediction of the entire debonding propagation process in FRP-to-concrete bonded joints with bilinear local bond slip law. Recently, Yuan et al. (2012) studied the FRP-concrete interface with hardening and softening bond slip law. However, no analytical solution has been presented which is capable of predicting the entire debonding propagation process of tri-linear model with linear flow platform.

This paper presents a close-form analytical solution of both interfacial shear stress distribution and load-displacement response, which is capable of predicting the entire debonding propagation process including elastic, flow, softening, elastic-flow, flow-softening, elastic-flow-softening, elastic-flow-softening-debonding, flow-softening-debonding, and softening-debonding stages. Based on experimental result of high Young's modulus type of CFRP-to-concrete bonded joints, a nonlinear fracture mechanics method, in which the tri-linear local bond slip law with linear flow platform is employed, is used to understand the stress transfer mechanism, interfacial crack propagation and ductility behavior in adhesive bonded joint. It is also shown how experimental load-displacement response of bonded joints can be used to identify interfacial properties, including the interfacial fracture energy and parameters of the local bond-slip relationship. The concept of serviceability limit state and ultimate limit state is considered.

2 LOCAL BOND-SLIP MODEL AND EQUILIBRIUM EQUATIONS

2.1 *Fundamental assumptions*

Figure 1 shows a single-lap pull-push test of a plate-to-concrete bonded joint, in which the width and thickness of each of the three components (plate, adhesive layer and concrete prism) are constant along the length. The width and thickness of the plate are denoted by b_p and t_p respectively, those of the concrete prism by b_c and t_c respectively, and the bonded length of the plate (i.e. bond length) is denoted by L. The Young's modulus of the plate and concrete are E_p and E_c respectively.

In such a joint, the adhesive layer is mainly subjected to shear deformations, so mode II interfacial fracture is the expected failure mode. A simple mechanical model for this joint can be thus established by making the following assumptions for simplicity of problems:

- The two adherents (the plate and the concrete prism) are homogeneous and linear elastic;
- The adhesive is only subject to shear forces which are constant across the thickness of the adhesive layer;
- Bending effects are neglected;
- The normal stresses in both adherents are uniformly distributed over the cross-section; and
- The thickness and width of the adherents are constant throughout the bond line.

2.2 *Elastic-flow-softening-fracture model (Trilinear bond-slip model)*

The tri-linear model shown in Figure 2 provides a close approximation for high Young's modulus type of CFRP plate-to-concrete bonded joints. According to this model, the bond shear stress increases linearly with the interfacial slip until it reaches the peak stress τ_f at which the value of the slip is denoted by δ_1. Interfacial flow then starts with the shear stress being the constant peak stress τ_f (plateau) and interfacial slip increasing from δ_1 to δ_2. After interfacial slip attains δ_2, interfacial softening begins with the shear stress reducing linearly with the interfacial slip. The shear stress reduces to zero when the slip exceeds δ_f, signifying the shear fracture (or debonding) of a local bond element. The absence of any residual shear strength after debonding implies that friction and aggregate interlock over the debonded length of the joint is ignored. This

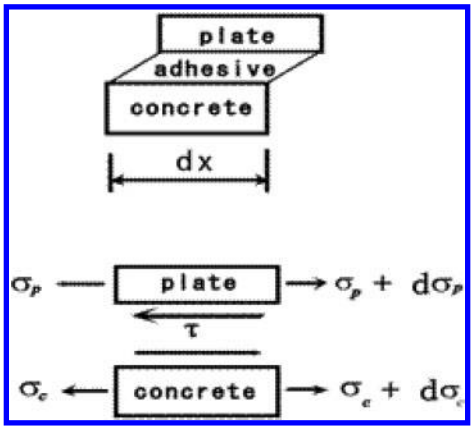


Figure 3. Deformation and equilibrium in a bonded joint.

bond-slip model shown in Figure 2 is mathematically described by the following

$$f(\delta)=\begin{cases}\dfrac{\tau_f}{\delta_1}\delta & when\ \ 0\le\delta\le\delta_1\\ \tau_f & when\ \ \delta_1<\delta\le\delta_2\\ \dfrac{\tau_f}{\delta_f-\delta_2}(\delta_f-\delta) & when\ \ \delta_2<\delta\le\delta_f\\ 0 & when\ \ \delta>\delta_f\end{cases} \quad (1)$$

2.3 *Equilibrium equations*

Considering the element shown in Figure 3, the equations of equilibrium for adherents can be written as

$$\frac{\mathrm{d}\sigma_p}{\mathrm{d}x}-\frac{\tau}{t_p}=0 \quad (2)$$

$$\sigma_p t_p b_p+\sigma_c t_c b_c=0 \quad (3)$$

where τ is the shear stress in the adhesive layer, σ_p is the axial stress in the plate and σ_c is the axial stress in the concrete prism. The constitutive equations for the adhesive layer and the two adherents are expressed as

$$\tau=f(\delta) \quad (4)$$

$$\sigma_p=E_p\frac{\mathrm{d}u_p}{\mathrm{d}x} \quad (5)$$

$$\sigma_c=E_c\frac{\mathrm{d}u_c}{\mathrm{d}x} \quad (6)$$

The interfacial slip δ is defined as the relative displacement between the two adherends, that is

$$\delta=u_p-u_c \quad (7)$$

After substituting Equations (3)–(7) into Equation (2) and introducing the parameters of local bond

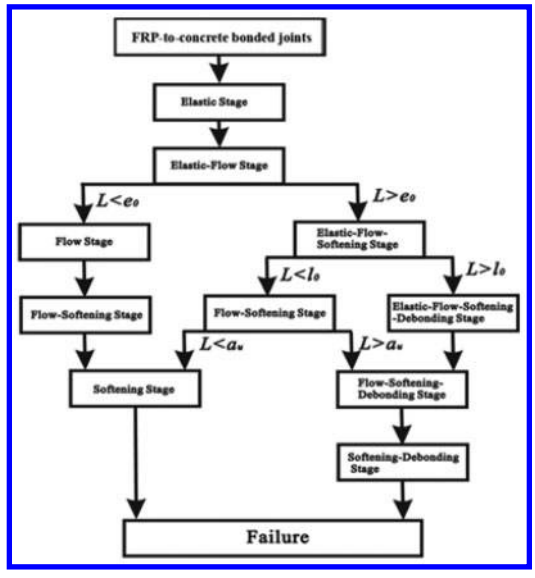


Figure 4. The flow chart with different bond lengths.

strength τ_f and interfacial fracture energy G_f yield the following

$$\frac{\mathrm{d}^2\delta}{\mathrm{d}x^2}-\frac{2G_f}{\tau_f^{\,2}}\lambda^2 f(\delta)=0 \quad (8)$$

and

$$\sigma_p=\frac{\tau_f^{\,2}}{2G_f t_p\lambda^2}\frac{\mathrm{d}\delta}{\mathrm{d}x} \quad (9)$$

where

$$\lambda^2=\frac{\tau_f^{\,2}}{2G_f}\left(\frac{1}{E_p t_p}+\frac{b_p}{b_c E_c t_c}\right) \quad (10)$$

Equation (8) is the governing differential equation of the bonded joint shown in Figure 1 and can be solved if the local bond-slip model relating the local interfacial shear stress to the local shear slip as represented by $f(\delta)$ in Equation (1) is introduced. The interfacial fracture energy, which is simply the area under the local bond-slip curve, is introduced because once it is known it can be used regardless of the exact shape of the local bond-slip curve where a particular quantity (e.g. the ultimate load) depends on the interfacial fracture energy but not on the shape of the bond-slip curve.

With the bond-slip model defined above, the governing equation (Eq. (8)) can be solved to find the shear stress distribution along the interface and the load-displacement response of the bonded joint. However, FRP-concrete interface with different bond length will lead to the difference of its failure process. Figure 4 gives the flow chart of failure process for different bond lengths. A detailed discussion will be given later.

3 THEORETICAL DERIVATIONS

The following values of critical length will be used to identify the different failure process

$$a_u = \frac{\pi}{2\lambda_2} \tag{11}$$

$$e_0 = \frac{1}{\lambda_1}\sqrt{\frac{2(\delta_2 - \delta_1)}{\delta_1}} \tag{12}$$

$$\tan(\lambda_2 a_0) = \frac{\lambda_1}{\lambda_2}\sqrt{\frac{\delta_1}{2(\delta_2 - \delta_1)}} \tag{13}$$

$$l_0 = e_0 + a_0 \tag{14}$$

where

$$\lambda_1^{\,2} = \frac{\tau_f}{\delta_1}\left(\frac{1}{E_p t_p} + \frac{b_p}{b_c E_c t_c}\right)$$

$$\lambda_2^{\,2} = \frac{\tau_f}{\delta_f - \delta_2}\left(\frac{1}{E_p t_p} + \frac{b_p}{b_c E_c t_c}\right)$$

Detail deduction of above equations will not be given here for length restriction of 6 pages.

3.1 *FRP-concrete interfacial bond length $L > l_0$*

The following stages of the debonding process will appear step by step only for a bond length which is longer than l_0. Equation (8) for each stage can be solved with appropriate boundary and continuous conditions. The debonding process includes elastic, elastic-flow, elastic-flow-softening, elastic-flow-softening-debonding, flow-softening-debonding, and softening-debonding stages.

3.2 *FRP-concrete interfacial bond length $L < l_0$*

The failure process of FRP-to-concrete bonded joints is discussed in the previous section for a bond length which is longer than l_0. However, FRP-concrete interface with shorter bond length will experience different failure process, which should be divided into three cases for clarity: (1) $L < e_0$; (2) $e_0 < L < a_u$, (3) $a_u < L < l_0$.

When the slip at the unloaded end reaches δ_1, the slip at loaded end doesn't reach δ_2 yet if the bond length is shorter than e_0. Its failure process will only experience elastic stage, elastic-flow stage, flow stage, flow-softening stage, softening stage.

If the bond length is larger than e_0 and shorter than a_u, its failure process will experience elastic stage, elastic-flow stage, elastic-flow-softening stage, flow-softening stage, softening stage.

If the bond length is larger than a_u and shorter than l_0, its failure process will experience elastic stage, elastic-flow stage, elastic-flow-softening stage, flow-softening stage, flow-softening-debonding stage, softening-debonding stage.

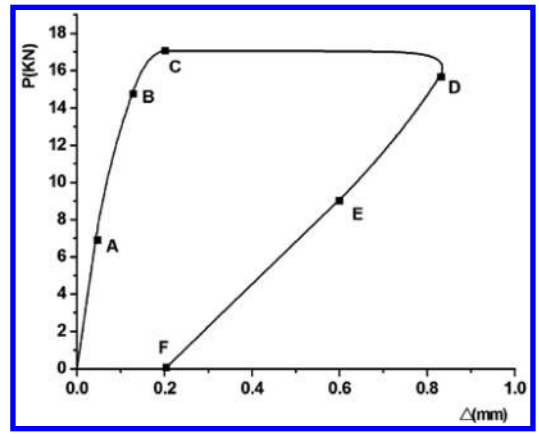


Figure 5. Theoretical load-displacement curve ($L > l_0$ and L = 150 mm).

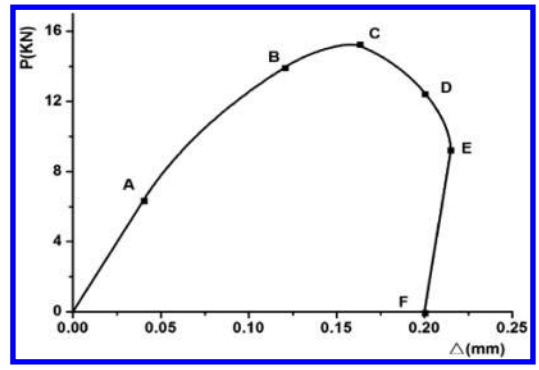


Figure 6. Theoretical load-displacement curve ($a_u < L < l_0$ and L = 40 mm).

4 NUMERICAL SIMULATIONS

To gain a clear understanding of the load-displacement response, interfacial shear stress distribution and crack propagation along the FRP-concrete interface, numerical simulations are conducted to simulate the loading condition depicted in Figure 1. The material and geometric properties are as follows: $t_p = 0.167$ mm (nominal thickness), $b_p = 40$ mm, $t_c = 60$ mm, $b_c = 300$ mm, $E_p = 390,000$ MPa and $E_c = 32,000$ MPa. The interfacial parameters were chosen as: $\delta_f = 0.2$ mm, $\delta_1 = 0.04$ mm, $\delta_2 = 0.12$ mm, $\tau_f = 10$ MPa, and $G_f = 1.4$ N/mm. Using above parameters yields that $e_0 = 32.2085$ mm, $a_u = 35.7747$ mm, $l_0 = 46.2260$ mm.

Figures 5–8 shows the theoretical load-displacement curves for different bond length($L > l_0$, $a_u < L < l_0$, $e_0 < L < a_u$, $L < e_0$). It shows that different bond length will result in different propagation process of

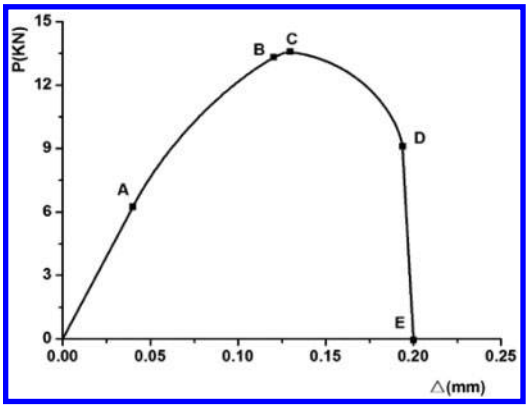


Figure 7. Theoretical load-displacement curve ($e_0 < L < a_u$ and L = 34 mm).

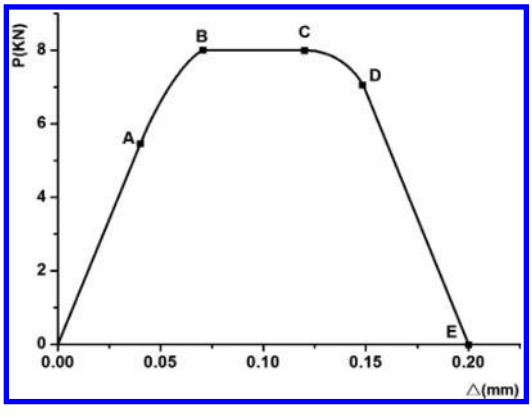


Figure 8. Theoretical load-displacement curve ($L < e_0$ and L = 20 mm).

debonding, and different bond length will also result in different load-displacement response. Generally, the bond length is larger than l_0. Therefore, the case of bond length $L > l_0$ will be discussed in the following. Other cases of bond length can be discussed similarly.

Figure 9 shows the shear stress distribution and debonding propagation along interface when the bond length is larger than l_0. All stages of the debonding process are given step by step. Figure 5 shows the full-range theoretical load-displacement curve when the bond length is larger than l_0. The elastic stage is represented by segment OA in Figure 5, elastic-flow stage represented by AB, elastic-flow-softening stage represented by BC, elastic-flow-softening-debonding stage represented by CD, flow-softening-debonding stage represented by DE, and softening-debonding stage represented by EF. Of particular importance are point A at the serviceability limit load, Point B at the initiation of softening and point C at the initiation of debonding. These three points can be obtained without difficulty from an experimental load-displacement curve. As the loading continues, the debonding length

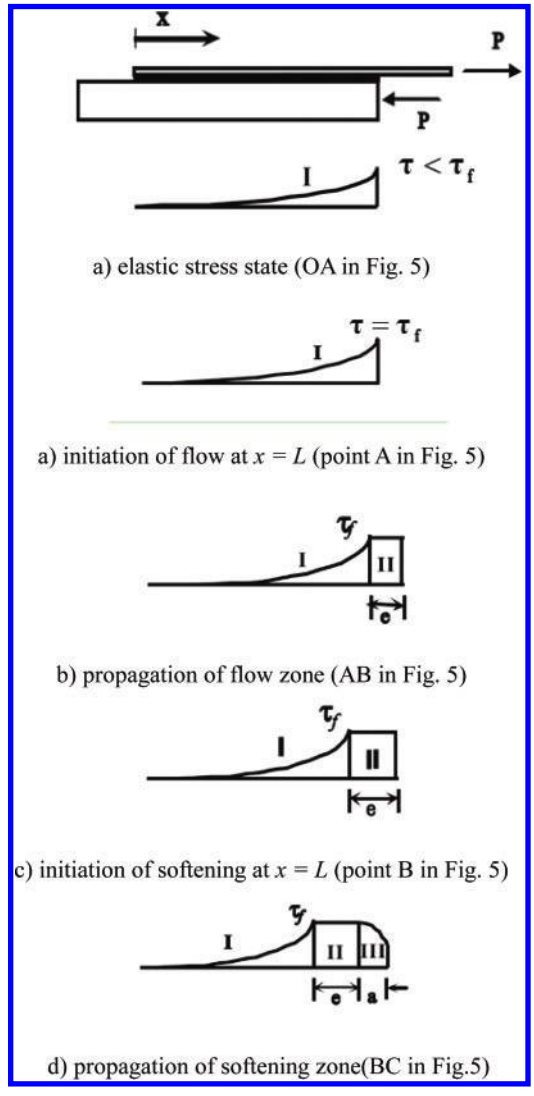


Figure 9. Interfacial shear stress distribution and propagation of debonding (bond length $L > l_0$).

is too long that the shear stress in elastic zone has begun to become incomplete, and the load P begins to decrease. Point D when the peak shear stress first reaches the unloaded end, point E when the flow zone just disappear and point F at complete debonding failure are generally not easy to obtain from experiment. The detail discussion may be made as follows.

As shown in Figure 9, section I is called the elastic stress zone, and there is no interfacial crack or micro-crack (flow and softening zone) along FRP-to-concrete interface. Section II and III are called the flow and the softening zone respectively, and the interface is micro-cracked but still able to transfer shear stress. In section IV an interfacial crack (debonding) without stress transfer occurs.

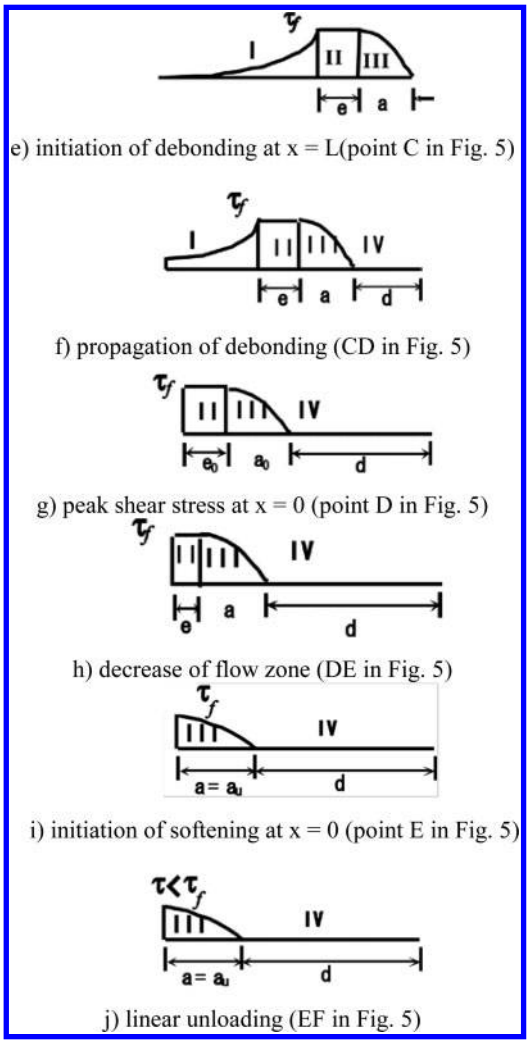


Figure 9. Continued.

5 CONCLUSIONS

In this paper, a nonlinear fracture mechanics approach has been introduced to derive theoretical solutions on interfacial stress transfer of the adhesive bonded joint. The analytical formulas indicate that the trilinear bond-slip model can be used to predict load-carrying capacity, and the model can predict the fracturing procedure such as initiation of micro-cracking and cracking (debonding), cracking propagation, load-displacement relation, shear stress distribution along FRP-to-concrete interface. The following conclusions can be made.

(1) The trilinear bond-slip model can better simulate the interfacial bond and debonding behavior.
(2) It is shown how measurement of the load-displacement relationship can be used for identifying the interface properties, including interfacial fracture energy and the local shear stress-slip relationship.
(3) The concept of serviceability limit state and ultimate limit state can be considered for the trilinear bond-slip model, which can be used to conduct serviceability state design and ultimate state design. Crack propagation stage and location on load-displacement curve are corresponded each other. Effect of bond length and FRP stiffness on load-displacement behavior, load-carrying capacity and effective bond length are studied in detail.
(4) The failure process with different bond length is given. The critical lengths for various failure process are obtained. Load-displacement curves and interfacial shear stress distribution for small bond length are also obtained.
(5) Bilinear bond-slip model is a particular case of the paper by letting $\delta_1 = \delta_2$, ie $e_0 = 0$.

ACKNOWLEDGEMENTS

The authors gratefully acknowledge the financial support provided by the Science and Technology Scheme of the Guangdong Province (2012A030200003) and the Natural Science Foundation of China (National Key Project No.11032005).

REFERENCES

Chen, J.F., Teng, J.G. 2001. Anchorage strength models for FRP and steel plates bonded to concrete. *Journal of Structural Engineering*, ASCE 127(1): 784–791.

Täljsten, B. 1996. Strengthening of concrete prisms using the plate-bonding technique. *International Journal of Fracture* 82: 253–266.

Ueda, T., Sato, Y., Asano, Y. 1999. Experimental study on bond strength of continuous carbon fiber sheet. *4th International Symposium on Fiber Reinforced Polymer for Reinforced Concrete Structures, SP-188, ACI International*, Michigan, USA, 407–416.

Wu, Z.S., Yuan, H., Niu, H. 2002. Stress transfer and fracture propagation in different kinds of adhesive joints. *Journal of Engineering Mechanics, ASCE* 128(5): 562–573.

Wu, Z. S., Yuan, H., Yoshizawa, H., Kanakubo, T. 2001. Experimental/Analytical study on interfacial fracture energy and fracture propagation along FRP-concrete interface, *in Fracture Mechanics for Concrete Materials: Testing and Applications, SP-201, ACI International*, Farmington Hills, Michigan, USA, 133–152.

Yoshizawa, H., Wu, Z. S., Yuan, H. 2000. Study on FRP-concrete interface bond performance. *Journal of Materials, Concrete Structures and Pavements, JSCE* 49(662): 105–119 (In Japanese).

Yuan, H., Lu X.S., Hui D., Feo L. 2012. Studies on FRP-concrete interface with hardening and softening bond-slip law. *Composites Structure* 94(12): 3781–3792.

Yuan, H, Teng, J.G., Seracino, R., Wu, Z.S., Yao, J. 2004. Full-range behavior of FRP-to-concrete bonded joints. *Engineering Structures* 26(5): 553–565.

Yuan, H., Wu, Z.S., Yoshizawa, H. 2000. Theoretical solutions on interfacial stress transfer of externally bonded steel/composite laminates. *Journal of Structural Mechanics and Earthquake Engineering, JSCE* 18(1): 27–39.

Research and Applications in Structural Engineering, Mechanics and Computation – Zingoni (Ed.)
© 2013 Taylor & Francis Group, London, ISBN 978-1-138-00061-2

A comparison of the variable strut inclination and alternative stirrup design methods

K.K. Mensah, C. Barnardo-Viljoen & J.V. Retief
University of Stellenbosch, Stellenbosch, Western Cape, South Africa

ABSTRACT: South Africa's adoption of EN 1992-1-1 *Eurocode 2: Design of concrete structures – Part 1-1: General rules and rules for buildings* will introduce the Variable Strut Inclination Method (VSIM) as an alternative analogy for stirrup design. The unbiased stirrup contribution of the EN 1992-1-1 VSIM has been shown to yield unsafe capacity predictions for relatively heavily shear-reinforced concretebeams. Conversely, the same model is excessively conservative for lightly reinforced beams. This contribution compares the performance of the EN 1992-1-1 VSIM to (1) the classical Ritter-Mörsch stirrup design analogy employed in the currently operational local design standard SANS 10100-1*The structural use of concrete*, and (2) the *fib* Model Code 2010 Modified Compression Field Theory (MCFT)-based design analogies (Levels of Approximation I & III). The VSIM seems to be in general agreement with the other design methods, but tends to offer higher capacity predictions at stirrup amounts in excess of 1 MPa.

1 BACKGROUND

South Africa (SA) is on the advent of adopting the European Standard EN 1992-1-1 *Eurocode 2: Design of concrete structures – Part 1-1: General rules and rules for buildings* as the equivalent standard for local use. Amidst a number of other changes, the adoption of EN 1992-1-1 as a local design standard will introduce the Variable Strut Inclination Method (VSIM) as an alternative analogy for stirrup design. The provision of stirrups or vertical reinforcement in design signifies an important and highly routine design situation that frequently occurs in practice to prevent sudden brittle failures in common reinforced concrete members. The assessment of the general performance of the VSIM as presented by EN 1992-1-1 therefore becomes one of the essential activities of the adoption process.

Investigations by Cladera & Mari (2007), later confirmed by Mensah (2012), have shown the unbiased stirrup contribution of the VSIM to be sensitive to the amount of stirrups provided in design. Figure 1 illustrates the trend of the ratio of the failure load from a laboratory test beam (V_{test}) to a corresponding unbiased VSIM prediction (V_{pred}) versus the nominal quantity of stirrups provided in design ($\rho_w f_{yw}$). The stirrup reinforcement ratio ρ_w is equivalent to the ratio of the area of the 2-legs of a stirrup (A_{sw}) over the product of the beam width (b_w) and stirrup spacing (s). f_{yw} represents the yield strength of the stirrups. The unbiased stirrup contribution of the VSIM seems to generally give excessively conservative capacity predictions when small amounts of stirrups are provided in design. Conversely, the model progresses to marginally conservative and eventually becomes unconservative as $\rho_w f_{yw}$ increases.

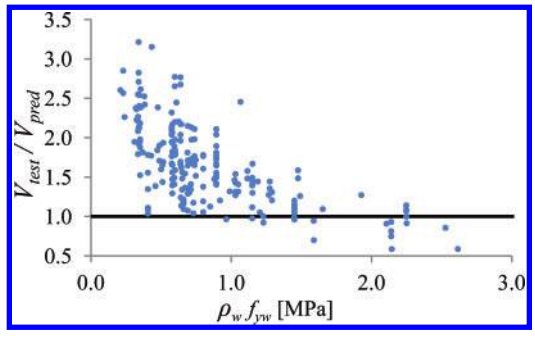


Figure 1. Relationship between V_{test}/V_{pred} and $\rho_w f_{yw}$.

Parametric correlation and regression analyses of the V_{test}/V_{pred} ratio against common variables affecting shear indicate that the VSIM is not significantly correlated to parameters such as concrete strength (f_c), beam width (b_w), shear span (a)-to-depth (d) ratio etc. It should be noted that the performance of the VSIM is to a large extent dependent on the limits governing the concrete compressive strut angle (θ). The limits for θ suggested by EN 1992-1-1 and used in this investigation are presented in Section 3.1

2 PROCEDURES FOR STIRRUP DESIGN

For member requiring stirrups, classical Ritter-Mörsch truss model idealisations have traditionally been used as conceptual basis for design. Historical approaches based on this analogy describe the post-cracking stirrup contribution to shear resistance ($V_{Rd,s}$) by a 45°

concrete strut angle (θ) truss with an empirically determined pre-cracking concrete contribution term ($V_{Rd,c}$). This is the approach followed by SA's currently operational concrete design standard SANS 10100-1 *The structural use of concrete – Part 1: Design*. The VSIM employed in EN 1992-1-1 is fundamentally a truss model that allows for a variable angle of the concrete compressive struts as derived based on the theory of plasticity (Bræstrup et al. 1976; Jensen & Lapko 2009). This model does not consider any direct contribution of the concrete to shear resistance. In EN 1992-1-1, the concrete compressive strut angle (θ) is assumed to vary between the confines of 21.8° and 45°.

The Modified Compression Field Theory (MCFT) is a rigorous procedure that can be used to predict the load-deformation response of a reinforced concrete element subjected to biaxial stressesThe MCFT, unlike the conventional constant angle and plasticity-based truss model approaches, accounts directly for the components of shear failure such as aggregate interlock and friction, dowel action and longitudinal steel, and shear carried across the uncracked concrete (ACI-ASCE Committee 445 Report 2009)The full procedure of the MCFT is described by Vecchio and Collins (1986), with applications in design standards described by Bentz & Collins (2006) and Kuchma et al. (2008) amongst a plethora of other publications.

The emerging *fib* Model Code 2010 (abbreviated MC 2010) (*fib* 2011) describes the four Levels of Approximation (LoA) that could be used to determine the shear resistance of a reinforced concrete member. Both the accuracy and computational effort required to make a prediction increase as the LoA increases. The first Level of Approximation (LoA I) is based on a simplified form of the LoA III approach and both are based on the MCFT (Bentz 2010). LoA II is based on the principles of plasticity modified with a strain term based on the MCFT to better model the behaviour of heavily reinforced concrete beams

LoA IV shear resistance predictions could be fulfilled by either LoA III or, if possible, higher order approximations proven to be of supreme accuracy. Response 2000 (Bentz, 2000) – hereafter referred to as R2k – is an MCFT-based sectional analysis program that can predict the load deformation response of concrete sections and members subjected to a combination of shear, flexure and axial load. R2k has proved to provide a more accurate and reliable prediction of the shear capacity of flexural members than any other method (Kuchma et al.2008). R2k cannot be used as a design method, but its accurate predictions could rather serve as the equivalent of physical test predictions.

2.1 *Comparison of stirrup design methods*

The 45° constant angle strut analogy that neglects the contribution of concrete to shear resistance has been proven to be over-conservative. It is for this reason that standards like SANS 10100-1 include an empirically determined concrete contribution term. Design procedures established in such a manner usually exhibit adequate performance within the range from which it has been derived. However, due to a lack of sound conceptual and scientific basis, the results of empirically derived design cannot be generalised and apply strictly within clearly defined boundaries. The VSIM and MCFT prediction models have evolved as the more economic and rational approaches to shear analysis, prediction and design.

Modern trends in structural design tend to prescribea variety of plasticity-based approaches for routine and conventional design situations, owing to their ease of use and quick execution times. The more computationally involving MCFT-based predictions usually suffice when more refined analyses are required or when they could yield significant economic benefits (usually for complex structures e.g. nuclear reactors, offshore structures, high-rise buildings). The approach taken by the *fib* MC 2010 for stirrup design offers a refreshing approach to the application of MCFT-based design procedures, specifically the simpler LoA I.

2.2 *Objectives of the investigation*

The inconsistentbehaviour of the VSIM at varied amounts of $\rho_w f_{yw}$ was highlighted in Section 1. To mitigate uncertainties and promote its economic use in SA, an extensive reliability investigation has been commissioned to calibrate the VSIM to suit local conditions and practice. The main outcomes of the process will be a set of rationally determined partial factors and design limits to support the optimal application of the VSIM in SA. As part of the general assessment of the performance of the VSIM, this contribution compares EN 1992-1-1 mean and design value predictions to those from, (1) the semi-empirical Ritter-Mörsch-based stirrup design analogy employed in the currently operational local design standard SANS 10100-1, and (2) the *fib* MC 2010 MCFT-based LoA I and LoA III design analogies.

The mean (unbiased) (V_{Rm}) and design (V_{Rd}) shear capacity predictions of the aforementioned procedures were compared for a beam of known cross-sectional and longitudinal geometry. Motivated by the systematic sensitivity of the VSIM portrayed in Figure 1, the design values of the different design methods were compared at parametric variations of $\rho_w f_{yw}$ for the chosen Test Case Furthermore, the performance of the V_{Rm} trend with $\rho_w f_{yw}$ for the various design approaches were compared to equivalent R2k predictions; with the R2k predictions serving as LoA IV or representative best estimate results across the parametric range considered. The objectives of this investigation are thus to;

1. Assess the trend of EN 1992-1-1 V_{Rm} predictions to the other approaches over the parametric range considered, and
2. Assess the trend of EN 1992-1-1 V_{Rd} predictions compared to the different approaches at varied amounts of $\rho_w f_{yw}$ in comparison to bullet 1. This analysis showcases the effect of the bias incorporated by partial factors and characteristic values for the different design methods across the parametric range considered.

Table 1. Design functions for determining shear resistance according to EN 1992-1-1, SANS 10100-1 and *fib* LoA I & LoA III.

No.	Approach	$V_{Rd,s}$	$V_{Rd,c}$	$V_{Rd,max}$	Strut angle (θ)
1	EN 1992	$\frac{A_{sw}}{s} z \frac{f_{ywk}}{\gamma_S} \cot\theta$	0	$\frac{b_w z \nu_1 (f_{ck}/\gamma_C)}{\cot\theta + \tan\theta}$	$21.8° \le \theta \le 45°$
2	SANS 10100-1	$\frac{A_{sw} f_{ywk}}{\gamma_S \cdot s} d$	$\frac{0.75}{\gamma_C}\left(\frac{f_{cu}^{*}}{25}\right)^{\frac{1}{3}}\left(\frac{100A_s}{b_w d}\right)^{\frac{1}{3}}\left(\frac{400}{d}\right)^{\frac{1}{4}} b_w d$	Lesser of $0.75\sqrt{f_{cu}}$ or $4.75\ MPa$	45°
3	*fib* MC LoA I & III	$\frac{A_{sw}}{s} z \frac{f_{ywk}}{\gamma_S} \cot\theta$	$k_v^{**} \frac{\sqrt{f_{ck}}}{\gamma_C} z$	$k_c^{**} \frac{f_{ck}}{\gamma_C} \frac{b_w z}{2}$	$= 36°$ (LoA I) $= 29° + 7000\varepsilon_x$ (LoA III)

*f_{cu} is the characteristic 28-day concrete cube strength / ** different values of k_v and k_c for LoA I & III

3 DESIGN AND MEAN VALUE FUNCTIONS FOR THE VARIOUS APPROACHES

For capacity predictions, the shear resistance V_{Rd} of the web of reinforced concrete member may be generally described by:

$$V_{Rd} = V_{Rd,c} + V_{Rd,s} \le V_{Rd,max} \quad (1)$$

where $V_{Rd,max}$ is an upper limit to shear resistance aimed at avoiding premature web-crushing failures of the concrete compressive struts. The $V_{Rd,c}$, $V_{Rd,s}$ and $V_{Rd,max}$ components of Equation 1 for the different design approaches are reported in Table 1. The strut angle (θ) specified by each design approach is also presented in Table 1. It should be noted that Table 1 presents simplifications of the general design equations that are applicable to stirrup design. Salient features regarding the application of the various design procedures are discussed in the following Sections.

3.1 *EN 1992-1-1*

For resistance capacity predictions, θ for non-prestressed reinforced concrete members can be determined by (European Concrete Platform 2008):

$$\theta = \sin^{-1}\left[\left(A_{sw}\left(\frac{f_{ywk}}{\gamma_S}\right)/b_w s \nu_1 \left(\frac{\alpha_{cc} f_{ck}}{\gamma_C}\right)\right)^{1/2}\right] \quad (2)$$

where f_{ck} and f_{ywk} are, respectively, the characteristic compressive cylinder strength of concrete and the characteristic stirrup yield strength; γ_C and γ_S are the partial material safety factors for concrete and steel. EN 1992-1-1 recommends the vales of $\gamma_C = 1.5$ and $\gamma_S = 1.15$. Figure 2 shows, for different concrete strengths, the variation of θ across the parametric range of $\rho_w f_{yw}$ considered in this investigation. The detailed parameters of the investigation are given in Section 3.6. α_{cc} is a coefficient accounting for the scale effects of concrete and can be taken conservatively as 0.85. ν_1 is a compressive strength reduction factor recommended in EN 1992-1-1 as $0.6(1\text{-}f_{ck}/250)$. The maximum spacing of stirrups should not exceed $0.75d$ where d is the effective member depth. The minimum stirrup ratio is defined by:

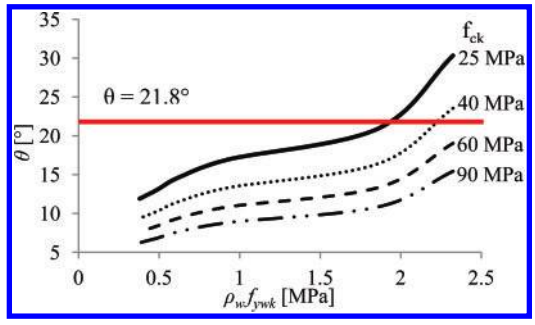


Figure 2. Variation of θ with $\rho_w f_{ywm}$ and f_{ck}.

$$\rho_{w,min} = 0.08\frac{\sqrt{f_{ck}}}{f_{yk}} \quad (3)$$

3.2 *SANS 10100-1*

SANS 10100-1 stipulates the same maximum spacing requirement as EN 1992-1-1, but suggests $\rho_{w,min}$ as 0.0012 when mild strength stirrups are used. $\rho_{w,min}$ assumes a larger value of 0.002 when high strength stirrups are used. The characteristic yield strength of SA's commercially available mild and high strength steel is 250 and 450 MPa, respectively. γ_C for shear is recommended as 1.4, whereas the same value of γ_S recommended in EN 1992-1-1 applies.

3.3 *fib MC 2010 LoA I*

Although the design function for the LoA I and LoA III design approaches is fundamentally the same, different values of k_v and k_c are applicable to either of the

methods. k_v indicates the ability of the web to resist aggregate interlock stresses which provide the concrete contribution to shear strength. For LoA I, k_v can be taken as 0.15 when the stirrups provided exceed $\rho_{w,min}$ as defined in Equation 3. k_c is a term that shall be taken as:

$$k_c = 0.5\left(\frac{30}{f_{ck}}\right)^{\frac{1}{3}} \quad (4)$$

where f_{ck} is expressed in MPa. The maximum spacing of stirrups should be taken as the lesser of $0.54d$ or 500 mm. The $\rho_{w,min}$ limit described by Equation 3 provides the minimum threshold ratio to which the *fib* LoA design functions apply to members with stirrups. However, for the design of new members MC 2010 requires that the 0.08 term from Equation 3 be replaced by 0.12. Both LoA I and LoA III apply the same values of γ_C and γ_S suggested for use by EN 1992-1-1.

3.4 *fib MC 2010 LoA III*

For LoA III, both k_v and θ are dependent on the calculated longitudinal strain ε_x at the mid-depth of the member. θ is defined in Table 1 and k_v is defined by:

$$k_v = 0.4/(1 + 1500\varepsilon_x) \quad (5)$$

provided the amount of stirrups exceeds $\rho_{w,min}$ from Equation 3. The expression for k_c for LoA III is similar to that given by Equation 4, save for the difference that 0.5 is replaced by 0.55. ε_x for non-prestressed members without axial forces is evaluated from:

$$\varepsilon_x = \frac{M_{Ed}/z + V_{Ed}}{2E_S A_S} \quad (6)$$

where M_{Ed} and V_{Ed} are the factored design forces for moment and shear, respectively. z is the inner lever arm and all design approaches commonly recommend its value as $0.9d$. E_s is the elastic modulus for steel and A_s represents the area of sufficiently anchored longitudinal tension reinforcement.

3.5 *Unbiased mean value predictions*

Characteristic values (f_{ck}, f_{ywk}) and partial factors (γ_C, γ_S) are introduced into design equations to incorporate some safety bias into the design process. For material and resistance models, the safety bias reduces the unbiased or best estimate resistance prediction of the analytical (or conceptual) function under investigation. Equations 1 through 6, as well as those presented in Table 1, can all be represented at their unbiased values by, where applicable, (1) expressing f_{ck} and f_{ywk} their mean values f_{cm} and f_{ywm}, respectively, and (2) not applying the partial factors γ_C and γ_S. The safety bias for the all other basic variables (A_{sw}, b_w, s etc.) is conventionally assumed as 1.0. For concrete strength, both EN 1992-1-1 and *fib* MC 2010 recommend the relationship:

$$f_{cm} = f_{ck} + 8\ MPa \quad (7)$$

For steel strength, Holický (2009) reports the following relationship:

$$f_{ywm} = f_{ywk} + 2\sigma_{f_{yw}} \ \ \& \ \ \sigma_{f_{yw}} = 0.1 f_{ywm} \quad (8)$$

where σ_{fyw} is the standard deviation of steel yield strength as observed from standard European steel production practice.

Table 2. Basic parameters of the Test Case.

Parameter*:	A_{sw} [mm^2]	b_w [mm]	d [mm]	f_{ck} [MPa]	f_{ywk} [MPa]	A_s [mm^2]
Quantity:	157.1	350	412	25	250	1885**

*spacing, s, varies / **6 Y20 bars – 2 layers of 3 bars each

Table 3. Additional information required by R2k.

Parameter:	a/d [mm]	f_{yl} [MPa]	C [mm]	h [mm]
Quantity:	2.5	450	30	500

3.6 *Parameters for the test case*

V_{Rm} and V_{Rd} predictions were compared at parametric variations of $\rho_w f_{yw}$. The parametric variation of $\rho_w f_{yw}$ was achieved by varying the stirrup spacing, s, whilst keeping fixed the values of all other parameters. Since other design parameters do not show any systematic trends in comparing VSIM to experimental results, a typical section geometry should provide representative indication of the performance of the shear design method. The parameters of the beam cross-section required to make a prediction according to either of prediction methods presented in Table 1, are reported in Table 2. It should be noted that f_{ck} was converted to the equivalent characteristic cube strength f_{cu} to enable a SANS 10100-1 prediction.

LoA III additionally required the shear span (a)-to-depth ratio (a/d), specified in Table 3, to enable a resistance prediction. The traditional beam setup with a single central point load on simple supports was assumed for longitudinal geometry. R2k was also implemented for a best estimate analysis of the beam. R2k, however, provides a complete implementation of the MCFT for flexural members, and consequently required the specification of additional information to enable a resistance prediction. Some of the additionally required parameters are given in Table 3. f_{yl} represents the yield strength of the longitudinal tension reinforcement, C the clear concrete cover from

beam soffit to outermost seal of the stirrups, and h represents the beam height.

According to O'Brien et al. (2012), shear-flexure cracks that propagate towards the load (splitting the member in the process) become frequent above a value of a/d of 2.5. For lower values of a/d, direct strut action or compression forces are prevalent and such situations are best analysed by strut-and-tie approaches for efficient design. The approaches discussed here would be overly-conservative Beyond a value of a/d of 2.5, the influence of flexure becomes more pronounced in the moment-shear interaction and flexural failures gradually become of primary concern. The value of a/d of 2.5 therefore represents a regime where shear stresses are prominent and shear strength is critical. It is for this reason that the value of a/d of 2.5 was selected for the LoA III and R2k analyses.

4 RESULTS OF THE MEAN AND DESIGN VALUE ANALYSIS

4.1 *Mean values*

The mean predictions of shear capacity (V_{Rm}) provided by the different design approaches are shown in Figure 3. By treating R2k observations as test results or the best possible prediction, the unbiased predictions offered by the different design approaches all tend to become unconservative at increased amounts of $\rho_w f_{ywm}$. This trend of results, particularly for the EN 1992-1-1 model, agrees with the observation reported in Figure 1. The EN 1992-1-1 VSIM is the first to exceed the R2k predictions and become unconservative at a value of $\rho_w f_{ywm}$ of approximately 1.2 MPa. The LoA III predictions provide the best approximation of the R2k predictions. Consequently, the LoA III predictions exceed those of R2k at the highest value of $\rho_w f_{ywm}$ of about 2 MPa. The SANS 10100-1 model, although semi-empirical, provides a closer match to the more accurate LoA III and R2k predictions than both EN 199-1-1 and LoA I. This is an indication that the SANS model has been appropriately calibrated (empirically) for the parametric range considered in this investigation. The early rise in EN 1992-1-1 predictions, making it the foremost model to become unconservative as $\rho_w f_{ywm}$ increases, should be of concern as South Africa adopts EN 1992-1-1, and should ideally be appropriately calibrated to suit local adoption.

4.2 *Design values*

Figure 4 shows the design value shear strength predictions yielded by the different design approaches for the characteristic range of $\rho_w f_{ywk}$, since design values and safety bias are now of concern. The EN 1992-1-1 design function is initially conservative and comparable with the other design methods below a value of $\rho_w f_{ywk}$ of 1 MPa. The model however rapidly progresses to become the least conservative design method by providing the highest capacity predictions at $\rho_w f_{ywk}$ in excess of 1.2 MPa. On the other hand, the

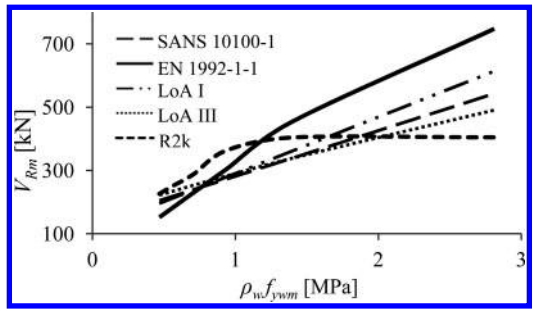


Figure 3. V_{Rm} for the various approaches and R2k *vs.* $\rho_w f_{ywm}$.

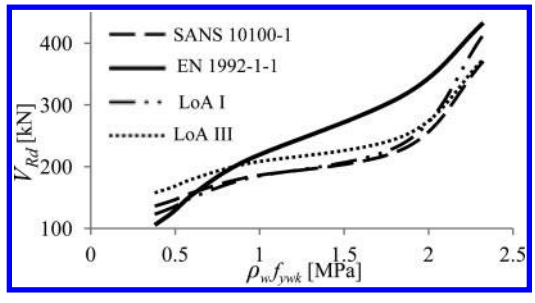


Figure 4. V_{Rd} for the various approaches *vs.* $\rho_w f_{ywk}$.

SANS 10100-1, LoA I and LoA III design approaches provided very similar capacity predictions over the parametric range, although the LoA III design values are slightly less conservative.

4.3 *General observations and comments*

The scatter of the different curves shown particularly by Figure 3, and to some degree for Figure 4 as well, indicate the wide-spread uncertainty and problems of the accurate prediction of shear resistance in structural design. Not only do the capacity predictions of the different methods vary from one another, they also vary from the actual value of resistance in a physical structure. Given these uncertainties, the issue of calibration of appropriate partial factors and characteristic values for shear design models becomes critical to ensure their safe and economic application in practice.

Although all the models deviate from the LoA IV R2k predictions in Figure 3, the EN 1992-1-1 VSIM portrays behaviour that is not only somewhat distinct from the others, but has the potential to become unsafe at lower quantities of $\rho_w f_{yw}$ than the other models. Proper calibration of the VSIM is thus essential for SA to adopt and apply EN 1992-1-1 reliably in practice. Mensah (2012)explores the prospects of calibration the VSIM as presented in EN 1992-1-1 to local SA conditions and practice.

5 CONCLUSIONS

The EN 1992-1-1 VSIM for the design of stirrups has been compared in this contribution to the

(1) semi-empirical Ritter-Mörsch based SANS 10100-1 approach, and (2) the fib MCFT-based LoA I and LoA III approaches. The investigation was motivated by two facts. The first is that South Africa intends to adopt EN 1992-1-1 as the local standard for the design of concrete structures. Following from the first, the second concern pertains to the economic and safety performance of the unbiased VSIM at parametric variations of the amount of shear reinforcement $\rho_w f_{yw}$. It was thus commissioned to compare the EN 1992-1-1 mean (V_{Rm}) and design (V_{Rd}) shear strength prediction trends at parametric variations of $\rho_w f_{yw}$ to those yielded by the previously established design approaches. A representative Test Case of selected cross-section and longitudinal geometry was used to for the investigation.

The EN 1992-1-1 VSIM is found to be in general agreement with the other design methods, but tends to offer higher capacity predictions at stirrup amounts in excess of 1 MPa. The practical implication is that the EN 1992-1-1 VSIM offers economic performance stirrup amount above 1 MPa as compared to SA's currently operational concrete design standard SANS 10100-1. The comparison to the *fib* LoA I & III approaches was included as part of the investigation to gain some insight of the relative performance of internationally available alternatives for stirrup design. The different prediction methods are not only conceptually different, but also offer different V_{Rm} and V_{Rd} trends as $\rho_w f_{yw}$ varies. This is a reflection of the existing contention in the fraternity on how to approach shear analysis, prediction and design.

Whatever the motivations for applying any given design approach, the method should be calibrated to incorporate sufficient conservative bias into the procedure. This would mitigate the various uncertainties associated with any given approach and support its safe and economic application in practice. The use of the EN 1992-1-1 VSIM is thus warranted for use in SA, but it should be calibrated to local conditions and practice to optimise its performance for designed structures.

REFERENCES

ACI-ASCE Committee 445 on Shear and Torsion. 2009 reapproved. Recent Approaches to Shear Design of Structural Concrete. *ACI Structural Journal* 124: 1375–1416.

Bentz, E.C. 2000. *Sectional Analysis of Reinforced Concrete Members*. PhD thesis, Dept. of Civil Eng., Univ. of Toronto, Canada, 210 pp. Retrieved May 27, 2011, from http://www.ecf.utoronto.ca/~bentz

Bentz, E.C. & Collins, M.P. 2006. Development of the 2004 Canadian Standards Association (CSA) A23.3 shear provisions for reinforced concrete. *Canadian J. Civ. Eng* 33: 521–534.

Bræstrup, M.W., Nielsen, M.P. & Bach, F. 1976. *Rational Analysis and Design of Stirrups in Reinforced Concrete Beams*. Report no. R79, Structural Research Laboratory, Technical University of Denmark.

Cladera, A.& Mari, A.R. 2007. Shear strength in the new Eurocode 2: A step forward? *Structural concrete* 8(2): 57–66.

EN 1992-1-1. 2004. *Eurocode 2: Design of concrete structures – Part 1-1: General rules and rules for buildings*. Brussels: European Committee for Standardisation (CEN).

European Concrete Platform. 2008.*Eurocode 2 Commentary*. Retrieved Dec 2008, from: http://www.ding.unisannio.it/ricerca/gruppi/ingciv/ceroni/commentario_EC2_2004.pdf

fédération internationale du béton (*fib*). 2010 *fib bulletin 55, Model Code 2010 – First complete Draft, Volume 1* Lausanne, Switzerland: *fib*.

fédération internationale du béton (*fib*). 2010 *fib bulletin 56, Model Code 2010 – First complete Draft, Volume 2* Lausanne, Switzerland: *fib*.

Holický, M. 2009. *Reliability analysis for structural design* ISBN 978-1-920338-11-4, SUN MeDIA, Stellenbosch, South Africa.

Jensen, B.C. & Lapko, A. 2009. On Shear Reinforcement Design of Structural Concrete Beams on the Basis of the Theory of Plasticity. *Journal of Civil Engineering and Management* 15(4): 395–403.

Kuchma, D.A., Hawkins, N.M., Sang-Ho, K., Shaoyun, S. & Kang, S.K. 2008. Simplified shear provisions of the AASHTO LRFD Bridge Design specifications. *PCI Journal*.

Mensah, K.K. 2012. *Reliability Assessment of Structural Concrete with Special Reference to Shear Resistance*. Masters thesis submitted to Dept. of Civil Eng, Univ. of Stellenbosch, Stellenbosch, South Africa.

O'Brien, E.J., Dixon, A.S. & Sheils, E. 2012 *Reinforced and Prestressed Concrete Design: The Complete Process (2nd ed.)*. Oxon, UK: Spon Press.

SANS 10100-1. 2000). *The structural use of concrete – Part 1: Design.* Pretoria: South African Bureau of Standards, Pretoria.

Vecchio, F.J. & Collins, M.P. 1986. The Modified Compression-Field Theory for Reinforced Concrete Elements Subjected to Shear. *ACI Journal* 83(22): 219–231.

Research and Applications in Structural Engineering, Mechanics and Computation – Zingoni (Ed.)
© 2013 Taylor & Francis Group, London, ISBN 978-1-138-00061-2

Shear strength of reinforced concrete plastic hinges subjected to seismic action

R.V. Mehrabani & V. Sigrist
Institute of Concrete Structures, TUHH-Hamburg University of Technology, Hamburg, Germany

ABSTRACT: The shear strength of reinforced concrete beams is reduced by axial elongation of the plastic hinge regions during cyclic loading. In members with shear reinforcement this elongation may also affect the path of the shear cracks and the inclination of the compressive stress field. Thus, the effective concrete compressive strength decreases and/or the contribution of the concrete to the shear strength is reduced.

This paper presents a model to predict the longitudinal strain (axial elongation) in plastic hinge regions under seismic loading at the shear failure stage. The background for this is the Cracked Membrane Model and the shear design provisions of fib Model Code 2010, respectively. The calculation procedures are based on compatibility considerations and take the longitudinal strain at mid-depth of the beam cross sections into account. The theoretical results are compared to experimental data taken from literature and in general, good correlation is found.

1 INTRODUCTION

There are well established approaches for predicting the shear strength of reinforced concrete members in monotonic loading but there still is scientific discussion in that field. The behavior under load reversals is even more complex. Until now, most of the effort towards models for the shear strength of RC beams subjected to seismic (reversed-cyclic) loads has been spent on extending the classical 45-degree truss analogy and to provide a degradation function for the concrete contribution V_c or for both, the contributions of the concrete V_c and of the transverse steel V_s. For considering the degradation of the shear strength of RC members subjected to cyclic loading, ACI 318-08 (2008), the New Zealand Concrete Code (1982) and CSA A23.3-04 (2006) neglect the concrete contribution V_c in the earthquake design of ductile frame structures. The ATC seismic design guideline (1996), from a more analytical and conceptual perspective, proposes a shear capacity curve that comprises different ductility levels. AIJ (1990) code combines the shear contribution of the steel reinforcement in a truss mechanism with a concrete contribution from an arch mechanism based on a lower-bound solution of the theory of plasticity. In addition, this code imposes a reduction of the effective concrete compressive strength for the cracked concrete and limits the inclination of the concrete struts in the truss model; this leads to an overestimate of the shear strength degradation in the plastic hinge region (Choi & Park 2010, Lee & Watanabe 2003a).

Priestley et al. (1994) present a shear capacity curve for columns which is applicable to both low and high ductility levels. Sezen & Moehle (2004) improved a semi-theoretical shear strength model on the base of a diagonal tension failure mechanism. Choi & Park (2010) developed an analytical method to predict the inelastic deformation capacity of RC beams subjected to cyclic or monotonic loading. Biskinis et al. (2004) developed a model for the degradation of the shear resistance relative to the cyclic displacement ductility demand on the basis of the contribution of the web reinforcement V_s from the classical 45-degree truss analogy. However, most of the existing shear models which describe the degradation of the shear capacity due to inelastic flexural deformations are empirically developed without sound theoretical background. Therefore, a more rigorous prediction model that includes the most important parameters and reflects the actual failure mechanisms is required.

Recently, the Generalized Stress Field Approach (GSFA) (Sigrist 2011) was introduced for the design and analysis of beams in monotonic shear; this approach combines limit analysis methods and the concept of the Cracked Membrane Model (Kaufmann 1998) and improves the present situation in view of structural assessment. The basic ideas have been incorporated in fib Model Code 2010.

Evan if there are attempts to introduce models for the degradation of the shear resistance within the framework of the present Eurocode (a variable strut inclination model, neglecting V_c) it is quite clear that such models are not suitable for the design for cyclic loading (Biskinis et al. 2004). On the contrary, the GSFA that considers the strain state in determining the effective concrete compressive strength has the potential for improvements. Therefore, in this paper

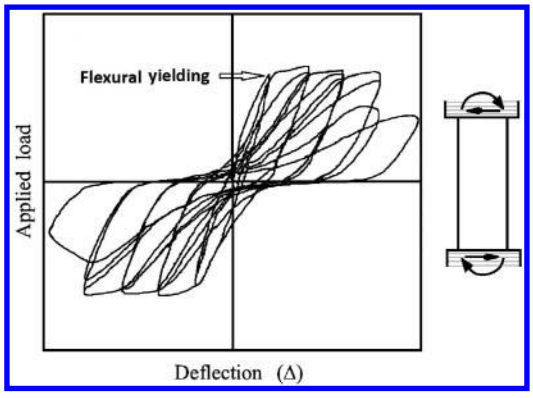


Figure 1. Load-deflection curve of a RC beam failing in shear after flexural yielding (Lee & Watanabe 2003a).

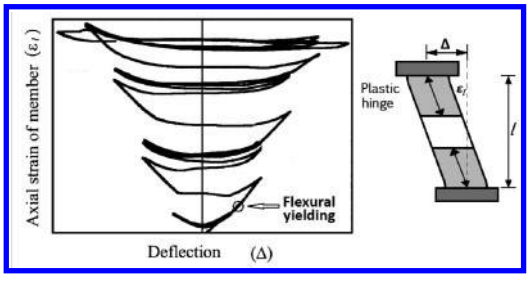


Figure 2. Axial strains versus deflections of a RC beam failing in shear after flexural yielding (Lee & Watanabe 2003a).

an (first) effort is made to extend the GSFA for plastic hinges of RC beams in reversed-cyclic shear.

2 SHAER DEGRADATION OF FLEXURAL PLASTIC HINGES

The results of previous studies show that the concrete shear resistance of RC members decreases with increasing displacement ductility demand μ (Priestley et al. 1994). Figure 1 shows the load-versus-deflection curve of a typical plastic hinge of a reinforced concrete beam with short span-depth ratio; the shear forces dominate the behavior. After the onset of yielding of the flexural reinforcement, plastic hinges were formed at both ends of the beam. Figure 2 shows the longitudinal axial strain at mid-depth of the beam versus the deflections of the beam. In the plastic hinges the longitudinal axial strain at mid depth of the section ε_l abruptly increases after the onset of flexural yielding and the residual strain of the longitudinal bars increases with each cycle. This increase of the axial strain widens the diagonal cracks and leads to an increase of the principal tensile strain ε_1 which results in a reduction of the effective concrete compressive strength $\eta_c f_c'$ until a shear failure occurs.

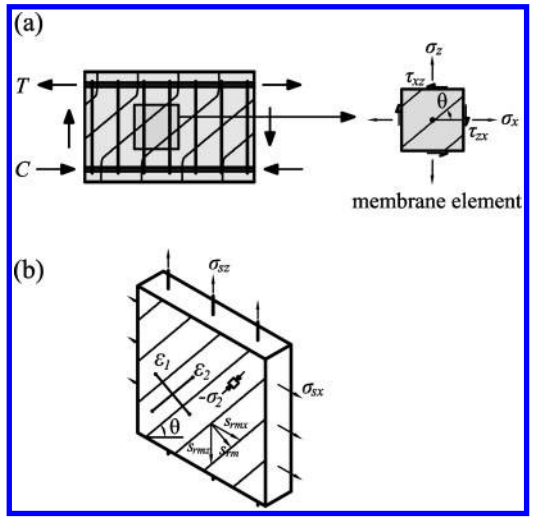


Figure 3. (a) Diagonally cracked RC beam segment and membrane element; (b) stresses in concrete and steel in a cracked membrane.

3 CRACKED MEMBRANE & STRESS FIELD ANALYSIS

3.1 *Cracked membrane*

Figure 3 shows a RC beam with flexural compression and tension forces and a diagonally cracked web. The web consists of a compound of orthogonally reinforced membrane elements subjected to the in-plane stresses σ_x, σ_z and τ_{zx}.

During the loading process cracks occur and subsequently, the applied stresses are resisted by the steel bars and the inclined concrete struts. From equilibrium for pure shear the shear stress τ_{zx} can be derived from nominal stress $\sigma_{sz}\rho_z$ or the principal concrete stress σ_2:

$$\tau_{xz} = \sigma_{sz}\rho_z \cot\theta \tag{1a}$$

$$\tau_{zx} = -\sigma_2 \sin\theta\cos\theta \tag{1b}$$

In Eq. (1) ρ denotes the reinforcement ratio of the stirrups $A_{sw}/b_w s$ The kinematic condition can be deduced from Mohr's circle of strains:

$$\tan^2\theta = \frac{\varepsilon_x - \varepsilon_2}{\varepsilon_z - \varepsilon_2} \tag{2}$$

ε_x, ε_z and ε_2 denote the average (smeared) strains in the respective directions. By adopting a bilinear stress-strain characteristic for the reinforcement, a stepped rigid-perfectly plastic bond shear stress-slip relationship to compute the deformations of the ties (Sigrist 1995) and an idealized quadratic parabola for the stress-strain response of concrete

$$\frac{\sigma_c}{f_{ce}} = 1 - (1 + \frac{\varepsilon_c}{\varepsilon_{c0}})^2 \tag{3}$$

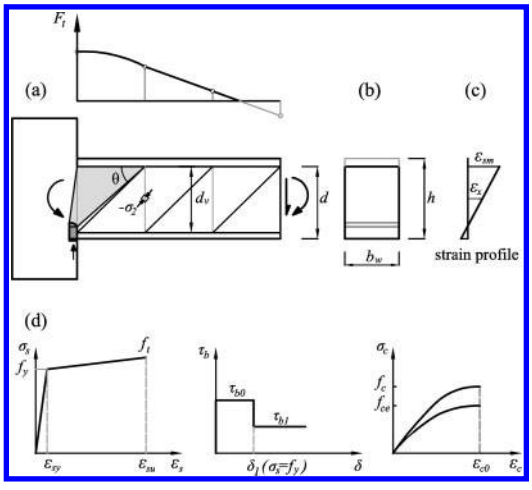


Figure 4. Discontinuous stress field and Generalized Stress Field Approach: (a) fan region and parallel stress bands of a RC fixed-end beam and variation of top chord force; (b) cross-section; (c) longitudinal strain at mid-depth of the beam; (d) constitutive laws for steel, bond shear stress-slip and concrete (Sigrist 1995).

the shear strength τ_R and the corresponding angle θ can be determined numerically; f_{ce} is the effective concrete compressive strength and defined as:

$$f_{ce} = \eta_c f_c' \left(\frac{30}{f_c'}\right)^{1/3} \leq \eta_c f_c' \tag{4}$$

where f_c' denotes the concrete cylinder strength and η_c the reduction factor accounting for strain influences which, based on investigations by Kaufmann 1998) and proposed by Sigrist (2011), can be taken to:

$$\eta_c = \frac{1}{1.2 + 55\varepsilon_1} \tag{5}$$

The principal tensile strain ε_1 perpendicular to the crack direction can be calculated with $\varepsilon_1 = \varepsilon_x + (\varepsilon_x - \varepsilon_2)\cot^2\theta$.

3.2 *Generalized stress field approach*

Figure 4(a) shows a discontinuous stress field for the RC fixed-end beam. The top chord force, F_t, changes hyperbolically within the fan region near the fixed end and linearly within band stress field outside of the fan region (Sigrist et al. 1995). F_t is defined as

$$F_t = -\frac{M}{d_v} + \frac{V}{2}\cot\theta \tag{6}$$

Stress fields are used for describing the stress state within a structure at ultimate. The Generalized Stress Field Approach combines limit analysis methods and the concept of the Cracked Membrane Model and

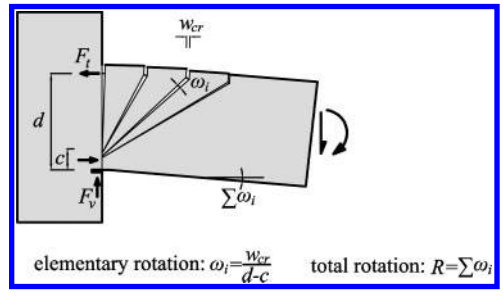


Figure 5. Determination of element rotation.

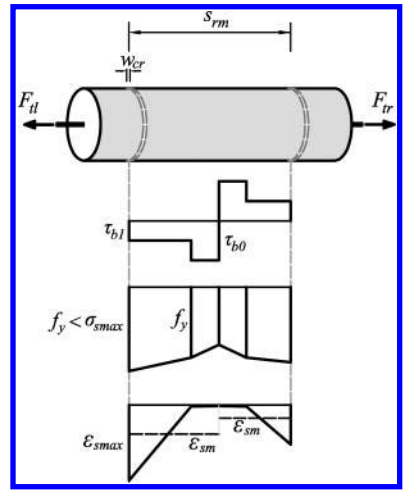


Figure 6. Tension Chord Model.

improves the present situation in view of structural assessment. GSFA comprises specific limits for the inclination angle θ, an upper limit for web crushing without yielding of the stirrups and a lower limit for rupture of stirrups; θ-values in between correspond to the so-called web crushing criterion. Longitudinal strains of webs are assumed to vary linearly over the depth and for reasons of applicability, the longitudinal strain at mid-depth of the web ε_x (Fig. 4) is taken as representative. With these determinations the shear strength τ_R of RC beams in the case of monotonic loading can be predicted.

4 PLASTIC HINGE REGION AND ELEMENT ROTATION

Rotations of plastic hinges are primarily due to the elongation of the tension chord. Accordingly, plastic rotations can be determined by calculating crack widths (Bachmann 1967). As shown in Figure 5, from the crack width w_{cr} elementary rotations $\omega_i = w_{cr}/(d - c)$ can be calculated. The sum of elementary rotations leads to the total rotation $R = \sum \omega_i$. Crack width can be calculated by the help of Tension Chord Model (Marti et al. 1998). By considering a tension chord element with unequal forces ($F_{tl} > F_{tr}$) and an

average crack spacing s_{rm} as shown in Figure 6, using the constitutive laws for steel and bond shear stress-slip of Figure 4(d) in which $\tau_{b0} = 0.6 f_c^{2/3}$ for the pre-yield range and $\tau_{b1} = 0.3 f_c^{2/3}$ for the post yield range may be used, crack width can be calculated. As a result, average steel strains ε_{sm} are found by dividing the crack width for each load stage by related values s_{rm}.

5 LONGITUDINAL AXIAL STRAIN OF REVERSED-CYCLIC PLASTIC HINGE

As mentioned above, longitudinal strains vary linearly over the member's depth and hence, axial strains at mid-depth of the beam can be calculated easily with help of the Tension Chord Model (Fig. 4(c)). In the case of reversed cyclic loading the determination of axial strains in plastic hinges is more complex. This is mainly because of the presence of residual axial strains due to previous cycles and also the effect of closing and opening of cracks during load reversal. Several researchers have studied the axial strain and elongation of reverse-cyclic plastic hinges (Lee & Watanabe 2003a,b, Peng et al. 2007, Eom & Park 2010). In most of these studies the efforts are focused on predicting the total elongation and axial strain in the plastic hinge or member. Alternatively, the axial strain is predicted directly by relations that are developed from deflections (or rotations) and the elongation or axial strain at mid-depth of the member without considering the interdependence of the chord elongation and the rotation.

In this contribution, the axial strain of the chord is predicted with help of the Tension Chord Model and, a simplified method for calculating the axial strain at mid-depth of the reversed-cyclic plastic hinge is proposed. As shown in Figure 2 only the elastic part of the axial strain recovers whereas the plastic part remains as a residual strain; hence, this portion adds to the axial strain of the next cycle. According to Lee & Watanabe (2003a,b) the decreasing rate of the axial strain in unloading is approximately the same as the increasing rate in elastic stage. Therefore, the recovered axial strain can be estimated to $2(\mu - 1)\varepsilon_{x,yield}$ where μ is the displacement ductility (Δ/Δ_y) and $\varepsilon_{x,yield}$ is the axial strain at flexural yielding at mid-depth of beam. This proposed simplified method neglects the effect of the load cycles that are imposed at the same deflection (rotation) magnitude. However, further work is needed to more precisely assess the axial strains; this research is continued by the authors.

The longitudinal elongation (axial strain) of plastic hinges at fixed beam ends is attributed mainly to 1) the plastic deformation of the flexural tensile reinforcement and 2) the fixed-end rotation due to pull out of the longitudinal reinforcement from the support. For the investigation of the shear capacity of RC beams on the basis of stress field approaches, the axial strain excluding the fixed-end rotation should be used; with help of the proposed method this separation is easily possible.

6 CALCULATION PROCEDURE

The reversed-cyclic shear response of RC beams is a complex issue. One of the complexities is the formation of cracks and, even more important, the development and variation of the crack inclination during the loading process. Many of the codes assume a fixed crack inclination, e.g. $\theta = 45°$ for high ductility demands. However, such a θ-value is for design at ultimate. Actually, the value of θ is very sensitive to load history and changes in the presence of imposed displacements. Therefore, for evaluating the shear degradation and the member's ductility a rigorous prediction of θ is required.

Previous studies have shown that after the onset of yielding of the longitudinal reinforcement in the plastic hinge, the crack inclination tends to be rather steep (Elmenshawi et al. 2009). If the main crack inclination is formed prior to first flexural yielding, principal concrete stresses and stress angles would vary to achieve equilibrium. The proposed model supposes the main cracks to be formed during the initial monotonic loading and crack inclination at first flexural yielding is close to the crack inclination at failure. This assumption may not be completely correct but it leads to a conservative prediction of the ductility capacity of a shear dominated plastic hinge of a RC beam in cyclic loading. The first step of the proposed method is, with help of the Cracked Membrane Model and the GSFA, to determine the crack inclination θ, related to the shear stress at the onset of first flexural yielding τ_y, numerically.

The average crack spacing in a fully cracked membrane is defined by

$$s_{rm} = s_{rmx} \sin\theta = s_{rmz} \cos\theta \tag{7}$$

and the distances in x-and z-directions are given by

$$s_{rmx} = \lambda_x s_{rmx0} \quad \text{and} \quad s_{rmz} = \lambda_z s_{rmz0} \tag{8}$$

The maximum crack spacing in either direction is calculated as

$$s_{rm0} = \frac{f_{ct} \varnothing (1-\rho)}{2\tau_{b0}\rho} \tag{9}$$

Finally, the crack spacing s_{rm} can be approximated on the basis of

$$\frac{f_{ct}}{2}(\lambda_x + \lambda_z) - \frac{\tau_{xz}}{2}(\cot\theta + \tan\theta) + \sqrt{\left[\frac{\tau_{xz}}{2}(\cot\theta - \tan\theta) - \frac{f_{ct}}{2}(\lambda_x - \lambda_z)\right]^2 + \tau_{xz}^2} \le f_{ct} \tag{10}$$

where the parameters λ_x and λ_z are limited by the conditions $0.5 \le \lambda_x \le 1$ and $0.5 \le \lambda_z \le 1$. Equation (10) was derived by Kaufmann (1998). Taking Equations (1) to (10) into account, the crack inclination θ related to the shear stress $\tau_{zx} = \tau_y$ can be calculated iteratively.

For this calculation procedure the constitutive laws of Fig. 4(d) are used. To achieve the smallest crack inclination θ, the lowest possible value for λ_z has to be considered.

As found in plastic hinge tests, the shear stress at first flexural yielding τ_y is about the maximum that the beam will experience in the next cycles; peak shear stresses of the cycles do not change much as the crack inclination θ related to first flexural yielding is the smallest inclination that can be predicted. Note that the smallest θ-value leads to the minimum required axial strain ε_x at failure.

The shear strength τ_R of a plastic hinge degrades due to longitudinal elongation. For a given value τ_R the computation of the principal tensile strain ε_1 is straight forward with help of $f_{ce} = \tau_R/(\sin\theta\cos\theta)$ and $-\varepsilon_2 = \varepsilon_{c0}$ as well as by adopting Equation (5). Axial strain ε_x at mid-depth of the beam at failure is found as

$$\varepsilon_x = \frac{\varepsilon_1 \tan^2\theta + \varepsilon_2}{1+\tan^2\theta} \tag{11}$$

7 VERIFICATION AND DISCUSSION

For verification, the proposed model is applied to the three RC fixed-ended beam tests BA2, BA4 and BA10 reported by Lee & Watanabe (2003a,b); these were tested at Kyoto University and subjected to reversed cyclic bending and shear. Shear span-to-depth ratio is $L_s/d = 2.3$. The test parameters are listed in Table 1. According to test report, shear forces dominated the behavior of the beams because of the short shear span and after the onset of yielding of the flexural reinforcement, plastic hinges were formed at both beam ends.

For these beams a crack spacing in the tension chords of $s_{rm} = 111$ mm is determined from the tensile reinforcement ratio and other parameters; furthermore, average axial strains at mid depth of the beams are calculated. The results are given in Figure 7. The horizontal axis of the diagrams shows the distance from the fixed end of the beam and the vertical the strain values. Three series of strains are plotted. The lowest values are the average axial strains at mid-depth, the highest values are the required axial strains at shear failure according to Eq. (11) and the values in between are the total (sum of the) average axial strains from the fixed end to the related points (Sigrist and Hackbarth 2010). For the required axial strains, the horizontal lines depict the calculated crack inclination θ of the parallel stress bands and the minimum points correspond to the crack inclination θ_y at first flexural yielding and the start of the fan region (Table 1); the branches of the curves on the left refer to crack inclinations θ bigger than θ_y. By comparing the required axial strains for shear failure and the total average strains it can be concluded that the average axial strains of the fan regions are very close to the predictions of the proposed model. This is an import outcome that illustrates the potential of the proposed model for evaluating the shear strength in reversed-cyclic (seismic) plastic hinges.

It is noteworthy that the predictions of the axial strains of RC beams that fail in shear after flexural yielding largely depend on the effective concrete compressive strength f_{ce}. Equation (5) that is used for determining f_{ce} is highly influenced by the principal

Table 1. Test properties and proposed inclinations.

Ref.	Specimen	f_c' (MPa)	f_{yl} (MPa)	f_{yz} (MPa)	ρ_l (%)	ρ_z (%)	θ_f (deg)	θ_b (deg)
Lee & Watanabe (2003a,b)	BA2	29.3	399	696	1.45	0.27	32	35
	BA4	29.3	399	692	1.45	0.80	40	42
	BA10	43.4	399	696	1.45	0.60	39	41

f_c' = concrete compressive strength; f_{yl} = yield limit of longitudinal reinforcement; f_{yz} = yield limit of shear reinforcement; ρ_l = tensile longitudinal reinforcement ratio; ρ_z = shear reinforcement ratio; θ_f = predicted inclination of fan; θ_b = predicted crack inclination of parallel stress bands.

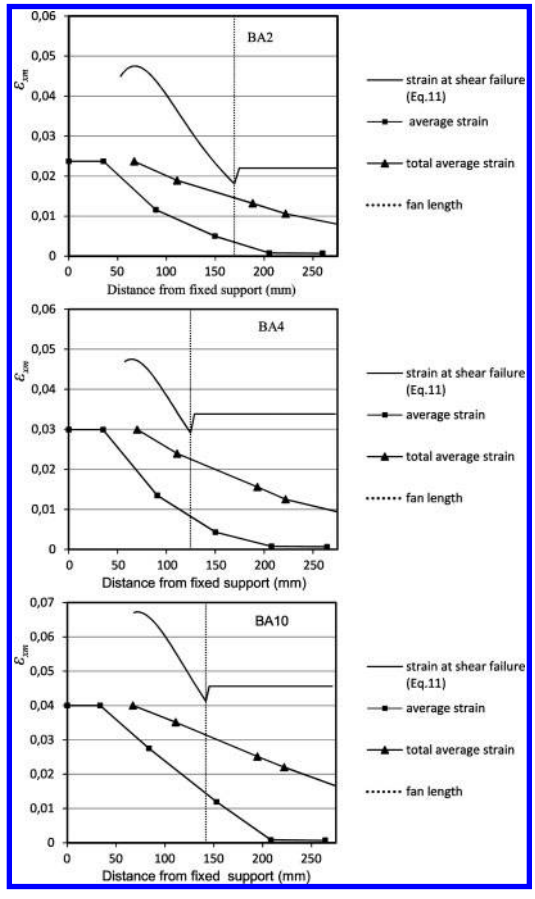


Figure 7. Predicted axial strains at mid-depth of the beams in plastic hinge regions.

tensile strain ε_1 perpendicular to the crack direction. This equation is based on test results of RC beams under monotonic loads with rather small values of ε_1 (Sigrist 2011); the ε_1-values in reversed-cyclic plastic hinges may be much bigger. Thus, additional work is needed to investigate strength reduction for reversed-cyclic plastic hinges of RC beams failing in shear at flexural yielding.

8 CONCLUSION

The research reported in this contribution presents a model that evaluates the longitudinal axial strain at the failure stage of plastic hinges in RC beams subjected to reversed-cyclic (seismic) loading. To predict the required axial strain of the beam for shear failure, this study is focused on the degradation of diagonally compressed concrete with help of a compatibility-based stress field model that takes the axial strain at mid-depth of the beam's cross section into account. The proposed model uses the crack inclination at first flexural yielding and predicts the longitudinal elongation capacity of the plastic hinge up to shear failure by extending the Cracked Membrane Model and the GSFA. From the comparison of the calculations with test results it can be concluded that the model has good potential to predict the required axial strain at shear failure and hence, to evaluate the shear capacity of reversed-cyclic (seismic) plastic hinges.

This contribution aims at giving an overview on these developments and at demonstrating that the model – even if originally developed for the design and analysis of members in static loading – forms a sound basis for the seismic assessment of structures. However, additional work is needed to investigate the concrete strength reduction for reversed-cyclic plastic hinges of RC beams failing in shear at flexural yielding.

REFERENCES

ACI 318-08 2008. American Concrete Institute (ACI), Building Code Requirements for Structural Concrete and Commentary.

Applied Technology Council (ATC 32) 1996. Improved Seismic Design Criteria for California Bridges: Provisional Recommendations.

Architectural Institute of Japan (AIJ) 1990. Design Guidelines for Earthquake Resistant Reinforced Concrete Buildings Based on Ultimate Strength Concept, 201 pp.

Bachmann, H. 1967. Zur plastizitätstheoretischen Berechnung statisch unbestimmter Stahlbetonbalken (on the Plastic Analysis of Statically Indeterminate Concrete Beams). Institute of Structural Engineering, ETH Zurich, report No. 13, Juris Druck und Verlag, July, 1967.

Biskinis, D. E., Roupakias, G. K. & Fardis, M. N. 2004. Degradation of Shear Strength of Reinforced Concrete Members with Inelastic Cyclic Displacements. ACI Structural Journal 101(6): 773–783.

Choi, K. K. & Park, H. G. 2010. Evaluation of Inelastic Deformation Capacity of Beams Subjected to Cyclic loading. ACI Structural Journal 107(5): 507–515.

CSA. 2006. Concrete design handbook. CSA standard A23.3-04. Canadian Standards Association. Ottawa, Ont.

Elmenshawi, A., Brown, T. & Loov, R. 2009. Behaviour of flexural plastic hinges under high seismic shear with consideration of concrete strength. Canadian Journal of Civil Engineering 36: 1711–1721.

Eom, T. S. & Park, H. G. 2010. Elongation of reinforced concrete members subjected to cyclic loading. Journal of Structural Engineering 136(9): 1044–1054.

Fédération Internationale du Béton (***fib***), Model Code 2010 – final draft, Vol. 1, Bulletin 65, and Vol. 2, Bulletin 66, Lausanne, Switzerland, 2012

Kaufman, W. 1998. Strength and Deformations of Structural Concrete Subjected to In-Plane Shear and Normal Forces. Report 234, Institute of Structural Engineering, ETH Zürich, 147 pp.

Lee, J. & Watanabe, F. 2003a. Shear deterioration of reinforced concrete beams subjected to reversed cyclic loading. ACI Structural Journal 100(4): 480–489.

Lee, J. & Watanabe, F. 2003b. Predicting the longitudinal axial strain in the plastic hinge regions of reinforced concrete beams subjected to reversed cyclic loading. Engineering Structures 25(7): 927–939.

Marti, P., Alvarez, M., Kaufmann, W. & Sigrist, V. 1998. Tension Chord Model for Structural Concrete. Structural Engineering International 8(4).

Peng, B.H.H., Dhakal, R.P., Fenwick, R.C., Carr, A.J. & Bull, D.K. 2007. Flexural, axial load and elongation response of plastic hinges in reinforced concrete member. 8th Pacific Conference On Earthquake Engineering (8PCEE), 5–7 Dec 2007, Paper 30. Singapore.

Priestley, M. J. N., Verma, R. & Xiao, Y. 1994. Seismic Shear Strength of Reinforced Concrete Columns. Journal of Structural Engineering 120(8): 2310–2329.

Sezen, J. & Moehle, J. P. 2004. Shear Strength Model for Lightly Reinforced Concrete Columns. Journal of Structural Engineering, ASCE 130(11): 1692–1703.

Sigrist, V., Alvarez, M. & Kaufmann, W. 1995. Shear and flexure in structural concrete beams. Comite' Euro-International du Béton(CEB), Bulletin d'Information No. 223. Ultimate Limit state design models, A state-of-art report, June, 1995.

Sigrist, V. 1995. Zum Verformungsvermögen von Stahlbetonträgern (On the Deformation Capacity of Structural Concrete Girderes). Report 210, Institute of Structural Engineering, ETH, Zurich, Switzerland, 159 pp. (in German)

Sigrist, V., Hackbarth, B. 2010. Stress Field Analysis of Structural Concrete Beams. 3rd *fib* International Congress, Washington D.C., *Proceedings*, May 2010.

Sigrist, V. 2011. Generalized Stress Field Approach for Analysis of Beams in Shear. ACI Structural Journal 108(4): 479–487.

Standards Association of New Zealand, Code of practice for the Design of Concrete Structures 1982. NZS-3101, Wellington, New Zealand.

Research and Applications in Structural Engineering, Mechanics and Computation – Zingoni (Ed.)
© 2013 Taylor & Francis Group, London, ISBN 978-1-138-00061-2

Experimental and numerical investigations on the punching behavior of thick footings with and without shear reinforcement

D. Kueres, C. Siburg, K. Reissen & J. Hegger
Institute of Structural Concrete, RWTH Aachen University, Germany

ABSTRACT: Although punching of reinforced slabs has been investigated extensively in the last decades, there are only limited test data with realistic specimen sizes for punching of footings. Thus, a number of twelve reinforced concrete footings with and without shear reinforcement were tested to investigate the punching behavior. The thickness of most of the slabs was set to 0.45 m, whereas four specimens were tested with a higher slab thickness of 0.65 m to investigate the punching behavior of thick footings. Examining the influence of the shear slenderness, the edge lengths of the square slab were varied from 1.20 m to 2.70 m. The main test parameters investigated are the shear slenderness, size effects of the effective static depth, concrete compression strength, longitudinal reinforcement ratio and shear reinforcement.

1 INTRODUCTION

In the past, the punching behavior of reinforced concrete slabs was investigated mainly by means of small-sized specimens. As a result of these investigations, theoretical and empirical models were developed to describe the main influences on the punching behavior of flat slabs and footings (Andrä 1982, Brooms 2005, Muttoni 2008, Ricker 2009). However, tests showed that the punching behavior of footings differs significantly from the behavior of flat slabs (Dieterle & Rostásy 1987, Hallgren et al. 1998, Timm 2003).

Based on a research project funded by the German Research Foundation (DFG – Deutsche Forschungsgemeinschaft) that has been concluded already, a number of twelve reinforced concrete footings with and without shear reinforcement were tested at the Institute of Structural Concrete at RWTH Aachen University to examine these differences. The tests primarily investigated the influences resulting from shear slenderness, size effects of the effective static depth, concrete compression strength, longitudinal reinforcement ratio and shear reinforcement.

2 EXPERIMENTAL INVESTIGATIONS

The specified test program consisted of twelve punching tests on reinforced concrete footings with and without shear reinforcement. The edge lengths of the footings varied from 1.20 m to 2.70 m with effective static depths between 0.40 m and 0.60 m resulting in shear slendernesses of 1.25 to 2.00.

Based on a tested footing without shear reinforcement (Hegger et al. 2006a) with an effective static depth $d = 0.40$ m, a shear slenderness $a/d = 1.25$, a longitudinal reinforcement ratio $\rho_l = 0.85\%$ and a concrete compression strength $f_{c,cyl} = 20$ N/mm^2, the influencing parameters on the punching behavior of thick footings were investigated systematically.

The thickness of most of the footings was set to 0.45 m, whereas four specimens (DF26, DF28N, DF33 and DF35) were tested with a higher slab thickness of 0.65 m to investigate the punching behavior of thick footings. For two specimens (DF41 and DF42) the longitudinal reinforcement ratio was reduced to 0.30%. One footing (DF20N) was produced with a concrete compression strength $f_{c,cyl} = 35$ N/mm^2 and two other footings (DF38 and DF39) had a concrete compression strength $f_{c,cyl} = 50$ N/mm^2. Besides the punching behavior of footings without shear reinforcement it was examined how shear reinforcement affects the punching shear capacity of thick footings. Therefore, a number of five specimens (DF29, DF31, DF32, DF33 and DF35) were equipped with shear reinforcement and constructed structurally identical to the reference test series without shear reinforcement. Compared to the specimens DF33 and DF35, where the distance s_0 between the first vertical stirrup and the column was set to $0{,}3d$, three footings (DF29, DF31 and DF32) were tested with a smaller distance. Whereas the shear reinforcement ratio generally was high enough to reach the maximum punching shear capacity, specimen DF32 contained 25% less shear reinforcement than DF31 to investigate the influence of the amount of shear reinforcement.

2.1 *Test specimens*

Considering the results of a former DFG research project (Hegger et al. 2006a, 2006b, 2009, 2010) the twelve reinforced concrete footings were planned and

Table 1. Test parameters and failure loads.

Test	S	d [m]	c [m]	b [m]	a/d [–]	$f_{c,cyl}$ [MPa]	f_y [MPa]	$Ø_l$ [mm]	ρ_l [%]	A_{sw} [cm^2]	s_0 [mm]	V_{Flex} [kN]	V_{Test} [kN]	V_{FE} [kN]	V_{Test}/V_{FE}
DF20N		0.40	0.20	1.20	1.25	34.5	541	20	0.85	–	–	7434	2831	3114	0.91
DF26		0.59	0.30	1.80	1.27	21.9	587	25	0.83	–	–	16299	5333	–	–
DF28N		0.58	0.30	2.70	2.07	22.4	549	25	0.88	–	–	13819	3797	3994	0.95
DF29	X	0.40	0.20	1.20	1.25	18.4	541	20	0.85	81.4	40	7001	3600	3249	1.11
DF31	X	0.40	0.20	1.80	2.00	21.2	541	20	0.83	72.4	80	6009	3243	3302	0.98
DF32	X	0.40	0.20	1.80	2.00	19.3	541	20	0.83	54.3	80	5935	3103	3083	0.93
DF33	X	0.58	0.30	1.80	1.29	23.7	587	25	0.85	135.5	170	16288	7037	–	–
DF35	X	0.59	0.30	2.70	2.03	19.4	515	25	0.86	135.5	180	12650	5731	5666	1.01
DF38		0.40	0.20	1.20	1.25	51.7	541	20	0.85	–	–	8079	4148	3589	1.16
DF39		0.40	0.20	1.80	2.00	53.3	541	20	0.83	–	–	6380	2996	2982	1.00
DF41		0.41	0.20	1.20	1.23	19.6	627	12	0.30	–	–	3401	1833	1985	0.92
DF42		0.41	0.20	1.80	1.98	22.2	627	12	0.29	–	–	2697	1505	1694	0.89
														x_m	0.99
														V	0.08

SR: shear reinforcement; d: effective static depth; c: edge length of the column; b: edge length of the footing; a/d: shear slenderness; $f_{c,cyl}$: concrete compression strength; f_y: yield strength of the longitudinal reinforcement; $Ø_l$: diameter of the longitudinal reinforcement; ρ_l: longitudinal reinforcement ratio; A_{sw}: cross-sectional area of the shear reinforcement (up to $0.8d$); s_0: distance between the first vertical stirrup and the column; V_{Flex}: flexural limit according to Yield Line Theory (Gesund 1983); V_{Test}: experimental failure load; V_{FE}: numerical failure load; x_m: arimethic mean; V: coefficient of variation.

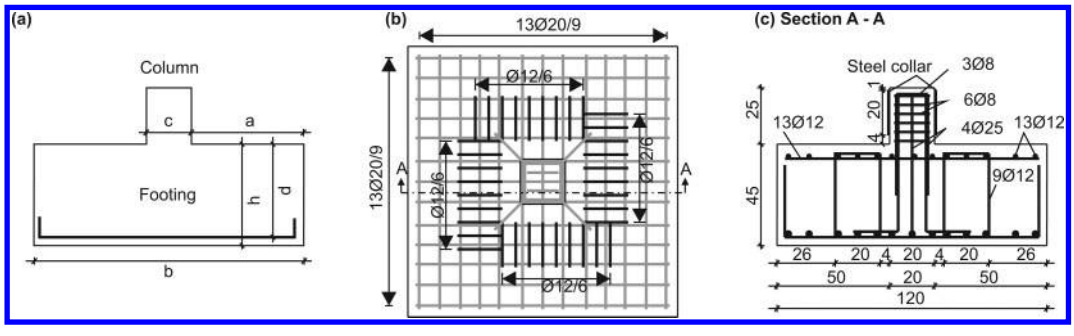


Figure 1. Notations and geometry of the specimens (a), horizontal projection of specimen DF29 (b), section A-A – reinforcement of specimen DF29 (c).

produced. In this context, Table 1 shows the varied test parameters as well as the failure loads for the investigated footings. The geometry and the reinforcement for a representative specimen are shown in Figure 1.

2.2 *Experimental setup*

To investigate size effects of the effective static depth particularly with regard to thick footings, it was necessary to test slabs with higher effective static depths. The experimental setup used in the former DFG research project was not designed for both the necessary geometry and the ultimate loads. Hence, a new experimental setup (Fig. 2) was developed.

The specimens were tested upside down with the base area up. A uniform pressure was created with 16 and 25 load points, respectively, depending on the footing dimensions. Twelve presses transferred their load through beams to two load points each. A further press with a piston area of half the size completed the load arrangement above the column. An equal distribution of the press forces was ensured since all presses were controlled by the same oil circuit. In order to avoid any formation of membrane forces in the test specimen, sliding and deformation bearings were placed between the footing and the cross beam.

2.3 *Test results*

2.3.1 *Bearing behavior and crack formation*

All tested specimens showed a punching failure located in the intersection of column and footing. The failure loads are given in Table 1. The comparison between the ultimate load V_{Test} and the load V_{Flex} according to Yield Line Theory (Gesund 1983) indicates that the flexural capacity was not reached which confirms the observations during the tests.

The crack patterns inside the footings were documented with the help of saw-cuts which are given in Figure 3. All specimens without shear reinforcement showed a discrete failure shear crack. The experimental investigations indicated that the angle of the crack is steeper in punching tests on compact footings than observed on more slender slabs (Fig. 3). While

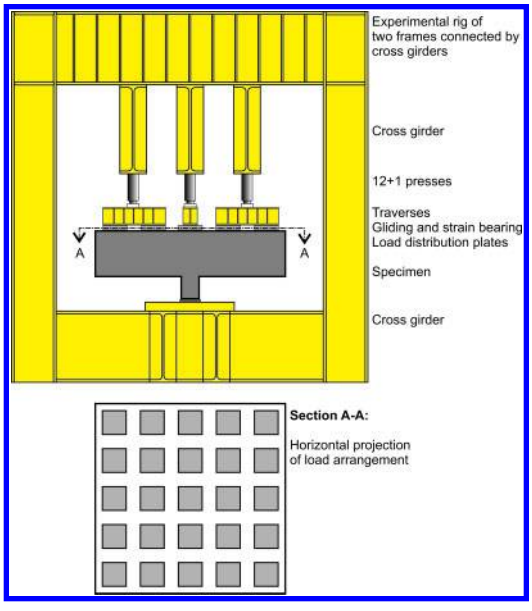


Figure 2. Experimental setup used for punching tests.

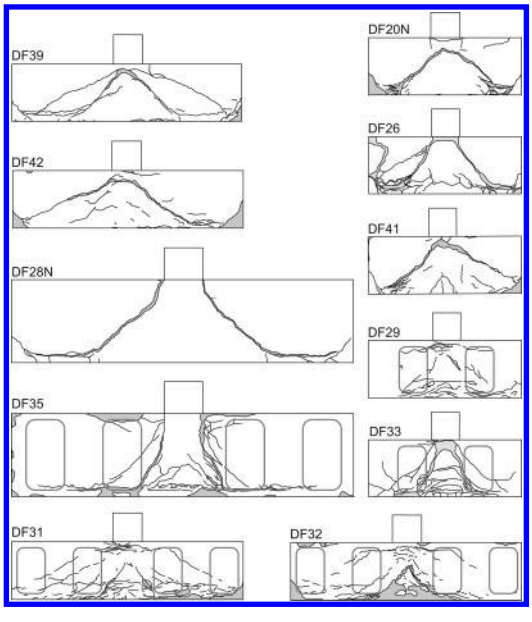


Figure 3. Saw-cuts of the specimen at edge of column.

footings without shear reinforcement showed a discrete crack, the crack patterns of footings with shear reinforcement were finely dispersed and seemed to be unattached by the shear slenderness.

2.3.2 *Influence of the shear slenderness*

Figure 4(a) shows the influence of the shear slenderness on the punching shear capacity of footings. The failure loads were normalized so that effects of the concrete compression strengths were eliminated. The shear slenderness significantly affects the punching shear capacity of slabs. Regardless of the longitudinal reinforcement ratio or concrete strength, the failure load decreases with increasing shear slenderness. Thus, the influence of the examined parameters was tested for different shear slendernesses.

2.3.3 *Influence of size effects of the effective static depth*

In Figure 4(b) the results of the experimental investigations to determine size effects of the effective static depth are presented. To visualize the relative reduction of the punching shear capacity of thick slabs, the failure test load was converted into a shear stress. The stress $v_{Ru,c}$ describes the shear stress along the decisive design location according to Eurocode 2 with German annex (DIN EN 1992-1-1 + NA 2011).

In the diagrams (Fig 4(b)), the dashed lines describe the factor k (DIN EN 1992-1-1 + NA 2011) which characterizes the size effect of the effective static depth as the result of punching tests on flat slabs. Whereas this factor is able to describe the relative reduction of the punching shear capacity of flat footings, current tests showed that the size effect of thicker slabs may be more distinct. This tendency can be observed for shear slenderness $a/d = 1.25$ and 2.00 as well as for specimens with and without shear reinforcement (Fig. 4(b)).

2.3.4 *Influence of longitudinal reinforcement ratio*

The punching shear capacity shows a dependency on the longitudinal reinforcement ratio. According to Eurocode 2 with German annex (DIN EN 1992-1-1 + NA 2011), this dependency can be described by a cubic root function which could be verified considering the current test data (Fig 4(c)).

2.3.5 *Influence of concrete compression strength*

Besides the longitudinal reinforcement ratio, the punching behavior of slabs shows a similar dependency on the concrete compression strength (DIN EN 1992-1-1 + NA 2011). In this context, Figure 4(d) presents the results of the experimental investigations. For footings with shear slendernesses $a/d \geq 1.50$ the normalized test load $V_{Test}/f_{ck}^{1/3}$ shows a slight rise for increasing concrete compression strengths. However, by use of habitual concrete strengths $f_{c,cyl} \leq 30$ MPa this normalization seems to be sufficiently precise.

2.3.6 *Influence of shear reinforcement*

For footings with vertical stirrups as shear reinforcement, higher loads than for comparable footings without shear reinforcement can be obtained. In this regard, Figure 4(e) shows the ratio of failure loads of specimens with and without shear reinforcement $V_{Test}/V_{c,Test}$. As can be seen, this load-increase up to the maximum punching resistance is hardly influenced by the shear slenderness and increases for slender slabs. Hence, shear reinforcement seems to be more effectively for higher shear slendernesses.

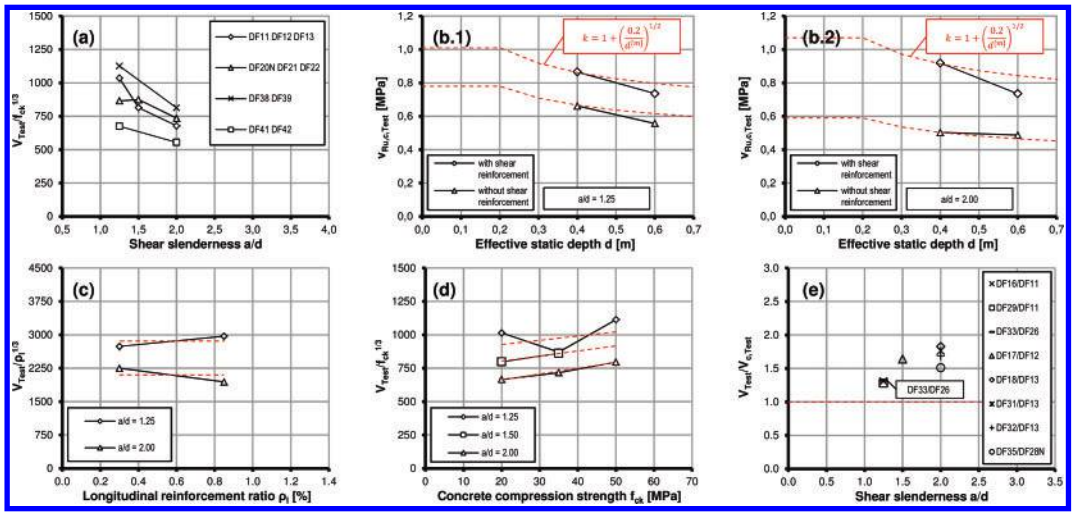


Figure 4. Influence of the shear slenderness (a), effective static depth (b), longitudinal reinforcement ratio (c), concrete compression strength (d) and shear reinforcement (e) on punching shear capacity of footings according to experimental investigations.

3 NUMERICAL INVESTIGATIONS

In addition to experimental investigations, nonlinear finite element analyses were carried out. The numerical investigations were performed by use of the FEM program ABAQUS/CAE 6.11.

3.1 *Computational model*

The tested specimens consist of concrete and steel reinforcement. To model the nonlinear behavior of these materials, physically nonlinear material models were used. In this context, the concrete was modeled by means of the CONCRETE DAMAGED PLASTICITY MODEL (Lubliner et al. 1989, Lee & Fenves 1998). To discretize the concrete, 8-noded, linear continuum elements with full integration were used. The nonlinear behavior of both, the longitudinal and shear reinforcement was considered by using the material law according to VON-MISES. The reinforcement bars were modeled with linear truss elements. The finite element model used for the numerical analysis for a representative specimen is shown in Figure 5.

For symmetry reasons it was practical to model only a quarter of the specimens. The load was applied incrementally so that the iterative NEWTON-RAPHSON method could be utilized. To evaluate the numerical results, the ultimate load at the time of abortion of the computations was used. Other abort criteria were not defined.

3.2 *Validation of the computational model*

To verify the computational model, the numerical results were compared with the experimental results. Hence, different criteria – such as failure loads, load-deflection curves, measured concrete and steel strains as well as crack patterns – were defined to evaluate the quality of the model.

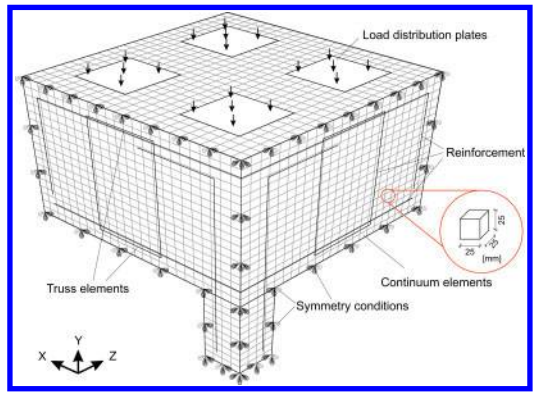


Figure 5. Finite element model used in analysis for specimen DF29.

The comparison between the actual failure loads and the calculated failure loads V_{Test}/V_{FE} is given in Table 1. Considering all analyzed footings, the arimethic mean was $x_m = 0.99$ with a coefficient of variation $V = 0.08$ which indicates that the results do not vary widely. Figure 6 presents the comparison of the measured and simulated load-deflection curves and concrete respectively steel strains for two representative specimens. As can be seen, the actual measured load-deflection curves and the simulated curves match well. Furthermore, the model has the ability to reproduce concrete strains (Fig 6(b)) as well as steel strains of the longitudinal reinforcement (Fig 6(c)) in radial and tangential direction in a sufficient way. In most cases steel strains of the shear reinforcement – especially in the first vertical stirrup – could not be simulated realistically (Fig 6(d)). In particular, if the stirrup is located in a shear crack, the load-strain curve shows a sharp bend. Since the CONCRETE DAMAGED PLASTICITY MODEL is

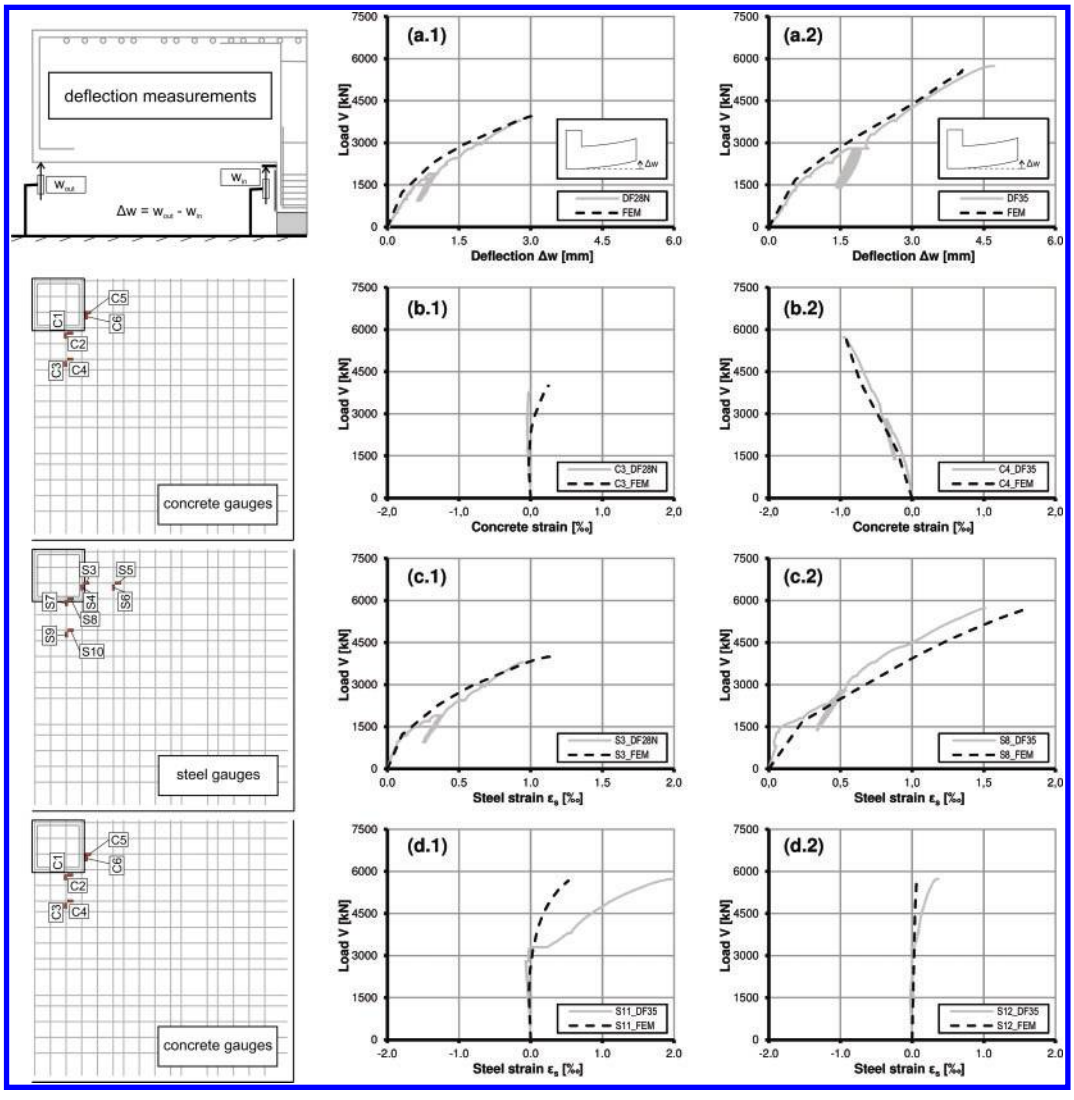


Figure 6. Representative load-deflection curves (a), concrete strains (b), strains of longitudinal reinforcement (c) and strains of vertical stirrups (d) of finite element model and test results for specimens DF28N and DF35.

not able to simulate discrete cracks, this bend cannot be reproduced.

3.3 *Parameter studies*

The validation of the computational model shows, that the punching behavior of thick footings can be simulated appropriately with the applies material models. Thus, the validated model can be used for further investigations.

In a first step, the influences of size effects of the effective static depth, concrete compression strength and shear reinforcement were examined. Further investigations considering the longitudinal reinforcement ratio as well as the shear reinforcement arrangement, amount and diameter have not been completed yet.

3.3.1 *Influence of size effects of the effective static depth*

Figure 7(a) presents the results of a parameter study regarding size effects of the effective static depth. The failure load was converted into a shear stress along the critical circular cut according to Eurocode 2 with German annex (DIN EN 1992-1-1 + NA 2011). Considering all examined shear slendernesses ($a/d = 1,25 - 3,25$) the punching shear capacity decreases with increasing thickness of the specimens. The factor k (DIN EN 1992-1-1 + NA 2011) seems to slightly underestimate this size effect which confirms the results of the experimental investigations.

3.3.2 *Influence of concrete compression strength*

The influence of the concrete compression strength on the punching behavior of footings was investigated by

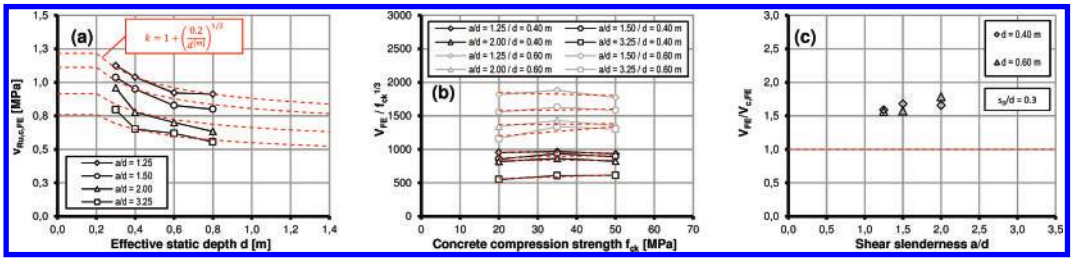


Figure 7. Influence of the effective static depth (a), concrete compression strength (b) and shear reinforcement (c) on punching shear capacity of footings according to numerical investigations.

further numerical calculations. For two effective static depths ($d = 0.40$ m and 0.60 m) concrete compression strengths between 20 and 50 MPa were examined. The results are given in Figure 7(b). As determined in the experimental investigations, the normalized test load $V_{\mathrm{Test}}/f_{\mathrm{ck}}^{1/3}$ shows a slight rise for increasing concrete compression strengths which seems to be negligible for habitual concrete strengths.

3.3.3 *Influence of shear reinforcement*

In analogy to the results of experimental investigations (Fig. 4(e)), Figure 7(c) shows the ratio of failure loads of specimens with and without shear reinforcement $V_{\mathrm{FE}}/V_{\mathrm{c,FE}}$ for different shear slendernesses. The distance s_0 between the first vertical stirrup and the column was set to $0{,}3d$. As already observed during the experimental investigations, shear reinforcement seems to be more effective with increasing slenderness.

4 CONCLUSIONS

Based on the experimental and numerical investigations the following findings can be summarized:

- The punching shear capacity is hardly influenced by the shear slenderness. Regardless of the longitudinal reinforcement ratio or concrete strength, the failure load decreases with increasing shear slenderness.
- For footings with different concrete compression strengths or longitudinal reinforcement ratios the observed effects are approximately equal to punching behavior of flat slabs.
- The influence of size effects of the effective static depth seems to be underestimated (according to DIN EN 1992-1-1 + NA 2011). This assumption should be verified through further investigations, especially with tests on thicker footings.
- The load-increase of footings with shear reinforcement is hardly influenced by the shear slenderness and increases for slender slabs.

ACKNOWLEDGEMENT

The tests and investigations presented were funded by the DFG (DFG-GZ HE 2637/11-2) to whom we express our sincere thanks.

REFERENCES

Andrä, H.-P. 1982. Zum Tragverhalten des Auflagerbereichs von Flachdecken. Dissertation Universität Stuttgart, Fakultät Bauingenieur- und Vermessungswesen. Stuttgart.

Brooms, C.E. 2005. Concrete flat slabs and footings – Design method for punching and detailing for ductility. Royal Institut of Technology. Stockholm.

Dieterle, H. & Rostásy, F.S. 1987. Tragverhalten quadratischer Einzelfundamente aus Stahlbeton. *Schriftenreihe des DAfStb* Heft 387: 5-91. Berlin.

DIN EN 1992-1-1 2011 + NA. Eurocode 2 + Nationaler Anhang: Bemessung und Konstruktion von Stahlbeton- und Spannbetonbauwerken – Teil 1-1: Allgemeine Bemessungsregeln für den Hochbau. Deutsche Fassung DIN EN 1992-1-1:2004 + AC:2010.

Gesund, H. 1983. Flexural Limit Analysis of Concentrically Loaded Column Footings. *ACI Journal* Proceedings 80 Nr. 3: 223–228.

Hallgren, M.; Kinnunen, S. & Nylander, B. 1998. Punching Shear Tests on Column Footings. *Nordic Concrete Research* 21 Nr. 3: 1–22.

Hegger, J.; Ricker, M.; Ulke, B. & Ziegler, M. 2006a. Untersuchungen zum Durchstanzverhalten von Stahlbetonfundamenten. *Beton- und Stahlbetonbau* 101 Heft 4: 223–243.

Hegger, J.; Sherif, A.G. & Ricker, M. 2006b. Experimental Investigations on Punching Behavior of Reinforced Concrete Footings. *ACI Structural Journal* 103: 604–613.

Hegger, J.; Ricker, M. & Sherif, A.G. 2009. Punching Strength of Reinforced Concrete Footings. *ACI Structural Journal* 106: 706–716.

Hegger, J.; Ziegler, M.; Ricker, M. & Kürten, S. 2010. Experimentelle Untersuchungen zum Durchstanzen von gedrungenen Fundamenten unter Berücksichtigung der Boden-Bauwerk-Interaktion. *Bauingenieur* 85 Heft 2: 87–96.

Lee, J. & Fenves, G.L. 1998. Plastic-Damage Model for Cyclic Loading of Concrete Structures. *Journal of Engineering Mechanics* 124 Nr. 8: 892–900.

Lubliner, J.; Oliver, J.; Oller S. & Oñate, E. 1989. A Plastic-Damage Model for Concrete. *International Journal of Solids and Structures* 25 Nr. 3: 229–326.

Muttoni, A. 2008. Punching shear strength of reinforced concrete slabs without transverse reinforcement. *ACI Structural Journal* 105: 440–450.

Ricker, M. 2009. Zur Zuverlässigkeit der Bemessung gegen Durchstanzen bei Einzelfundamenten. Dissertation RWTH Aachen, Institut für Massivbau. Aachen.

Timm, M. 2003. Durchstanzen von Bodenplatten unter rotationssymmetrischer Belastung. Dissertation Technische Universität Carolo-Wilhelmina, Fachbereich Bauingenieurwesen. Braunschweig.

Research and Applications in Structural Engineering, Mechanics and Computation – Zingoni (Ed.)
© 2013 Taylor & Francis Group, London, ISBN 978-1-138-00061-2

Reliability of EN1992 crack model applied to South African water retaining structures

C.H. Mc Leod
University of KwaZulu-Natal, Durban, South Africa

J.V. Retief & J.A. Wium
University of Stellenbosch, Stellenbosch, South Africa

ABSTRACT: Development of a design code of practice for concrete water retaining structures (WRS) in South Africa is currently underway, along with the revision of the code of practice for reinforced concrete structures (SANS 10100). This paper discusses part of the research undertaken in the development of the proposed South African design code for WRS, namely, the subject of model uncertainty. Cracking due to loads and/or restrained deformations (such as shrinkage) under serviceability limit state (SLS) is usually the limiting condition for the design of water retaining structures. The basic crack model considered is that utilized by Eurocode EN1992-1-1 (2004) and EN1992-3 (2006). A reliability model for load-induced cracking to EN1992 is formulated using the First Order Reliability method and applied to typical South African WRS. The modelling and influence of model uncertainty applied to the EN1992 crack model for load-induced cracking is investigated and discussed. It is found that model uncertainty has a significant effect on the reliability model for cracking.

1 INTRODUCTION

The South African civil engineering industry currently uses the British code of practice, BS8007 (1989) in the design and construction of reinforced concrete water retaining structures (WRS). With the introduction of the Eurocodes and subsequent withdrawal of the British design codes, there is a need for a design code of practice relevant to South African reinforced concrete WRS (which will be the proposed SANS10100-3). In updating the related South African design code for reinforced concrete buildings, there is a move towards adopting the corresponding Eurocode. With regard to WRS, the relevant Eurocode is EN1992-3 (2004) which is read in conjunction with EN1992-1-1 (2004). Serviceability limit state cracking tends to be the limiting state in the design of WRS, rather than ultimate limit state loading. A reliability analysis was thus performed to assess the reliability of the EN1992 crack model applied to South African conditions. The study focused on load-induced cracking due to direct tension and pure bending. Indirect evidence suggested that model uncertainty was influential in concrete cracking. The reliability analysis was used to determine if this indeed was the case and thus warranting further investigation.

2 RELIABILITY MODEL

The reliability analysis of the EN1992 crack model was performed using the First Order Reliability Method (FORM). The FORM algorithm is well documented as given in, for example, Ang & Tang(1990), so is not repeated here. The analyses included a sensitivity analysis from which the influence of the model variables could be assessed. Theoretical partial safety factors for the model variables were also determined. A reliability calibration exercise was then performed using known combinations of partial safety factors and reliability level, and constituted the first step in ultimately identifying a set of factors that would ensure sufficient reliability across the range of concrete cracking applications. The analyses were performed using Microsoft EXCEL.

2.1 *EN1992 crack model*

Serviceability cracking is deemed to be controlled by meeting a specified crack width limit for a given structural configuration and reinforcement. The EN1992 crack model is based on the compatibility relationship (as given in Narayan *et al* (2005)):

$$w = S_r \,.\, \varepsilon_m \tag{1}$$

where w is the crack width, S_r is the crack spacing and ε_m is the mean strain. The crack spacing is determined from:

$$S_r = 2c + 0.25\, k_1 k_2 \varphi \,/\rho_{p,eff} \tag{2}$$

where c is the concrete cover, φ is bar diameter and $\rho_{p,eff}$ is the effective reinforcement ratio. The coefficients k_1 and k_2 take into account the bond properties

of the reinforcement and distribution of strain, respectively. The values of these coefficients are:

k_1 0.8 (high tensile reinforcement)
k_2 0.5 (bending stress) or 1.0 (tension stress)

The effective reinforcement ratio is the ratio between the area of reinforcement, A_s and the effective area of the concrete zone in tension, $A_{c,eff}$. The concrete tension zone is calculated using $b.h_{c,eff}$ where b is the section width and $h_{c,eff}$ is the effective depth of the concrete tension zone. The latter is the lesser of *h/2, 2.5(h − d)* or *(h − x)/3* where h is the section thickness, d is the effective depth of section and x is the depth of the neutral axis, c is concrete cover. The equation *2.5(h − d)* may be expressed as *2.5(c + φ/2)* where φ is bar diameter.

The mean strain is determined using:

$$\varepsilon_{sm} - \varepsilon_{cm} = \left[\sigma_s - k_t \frac{f_{ct,eff}}{\rho_{p,eff}} \left(1 - \alpha_e \rho_{p,eff}\right)\right] / E_s \qquad (3)$$

where σ_s is the steel strain, k_t is a coefficient dependent on the duration of load, $f_{ct,eff}$ is the effective concrete tensile strength, α_e is the modular ratio and E_s is the steel modulus. The coefficient k_t has a value of 0.4 for long-term loading.

2.2 *Representative structural configuration of WRS*

Possible worst cases of cracking due to tension and flexural loading were investigated to determine the associated structural configuration. The following load cases were established:

2.2.1 *Flexural load case*

Consider a 1 m length ofa 5 m high wall in a rectangular reservoir subject to a liquid load only, deemed to be a permanent load as defined by SANS10160 (2011). The wall acts as a vertical cantilever and will therefore be subject to flexure about a horizontal axis. The liquid load, L, is γ_w. H where γ_w is the density of water and H is the depth of water taken as equal to the height of the wall. The maximum bending moment, M, occurs at the base of the wall, such that $M = L.H^2/6$.

2.2.2 *Tension load case*

Consider the wal lwith a sliding base in a circular reservoir of diameter (D) 28 m, subject to a liquid load only such that the wall is subject to hoop stress in the horizontal plane only. The resulting tensile force, T, on the wall is L D/2.

2.3 *Performance functions*

The performance function, g(X), of the sensitivity FORM analysis using the EN1992 crack model may be written as:

$$g(X) = w_{lim} - \theta\, w \qquad (4)$$

where w_{lim} is the limiting crack width, θ is model uncertainty and w is the calculated crack width using equation (1), which in turn is expressed in terms of the model basic variables (discussed in Section 2.5). Model uncertainty is modelled as a random variable and is discussed further in Sections 2.5 and 2.7.

The performance function for the reliability calibration exercise may be defined as follows:

$$g(X) = \theta.w(X) - w_d(X_k, \gamma_x) \qquad (5)$$

where $w(X)$ is the random crack width and $w_d(X_k, \gamma_x)$ is the design crack width. The theoretical partial safety factors, γ_i, applied design values of the model basic variables, X_k, are calculated using [define x*]:

$$\gamma_x = \frac{x^*}{\mu_x} \qquad (6)$$

where x* is the theoretical design value of the variable and μ_x is its mean value. Both the random and the design crack widths are determined using the compatibility relationship expressed in equation (1).

2.4 *Level of reliability*

The level of reliability for serviceability has generally not been well-researched, as emphasis is normally placed on the ultimate limit state as this is usually the limiting state in the design of buildings. However, in WRS serviceability is dominant. SANS2394 (2004) gives some guidance on an appropriate level of reliability, recommending a reliability index, β, of 1.5 for irreversible serviceability limit states such as cracking and 0 for reversible serviceability limit states, for a reference period of 50 years. Therefore, in this research, a reference level of 1.5 is used for β. Given the importance of serviceability cracking in WRS, analyses were performed using β of 0.5 and 2.0 (as a reasonable upper limit for SLS), enabling the effect of reliability on the model to be assessed.

2.5 *Parameters of model*

Once the performance function was defined, statistical data for the model parameters was gathered. Sources such as the JCSS (2001) and Holicky (2001) were consulted. A summary of the data for the model basic variables is given in Table 1.

Referring to Table 1, the basic variables of the reliability crack model were found to be concrete cover

Table 1. Crack model basic variables.

Variable	Unit	pdf	Nominal Value	Mean	Std Dev.
Concrete tensile strength	MPa	LN	2.00	2.89	0.55
Liquid load	kN/m^2	N	49.05	49.05	2.45
Concrete cover	mm	LN	40	40	6
Section thickness	mm	N	450	450	4.5
			250	250	2.5
Model uncertainty	–	LN	1	1	0.2

Note: LN = log-normal pdf, N = normal pdf.

(c), section thickness (h), liquid load (L), effective concrete strength ($f_{ct,eff}$) and model uncertainty (θ).

All other parameters in the model were considered as deterministic. Analyses were performed using a reinforcement bar diameter of 20 mm over a range of reinforcement areas. A steel modulus of 200 GPa and an effective concrete modulus (long term) of 13.7 GPa were used. All values were chosen assuming good construction and management practice.

2.6 *Limiting crack width*

The limited crack width specified by EN1992 depends on the tightness class of section defined by the acceptable amount of leakage through a section. For a Tightness class 2, with cracks going through the section, a general crack width limit of 0.2 mm is recommended. This limit decreases to 0.05 mm depending on the hydraulic ratio, h_D/h where h_D is the depth of water and h is the section thickness. At a 0.2 mm crack width limit, h_D/h is 5,increasing to 35 at a crack width limit of 0.05 mm. Reliability analyses were performed for crack widths of 0.2 mm, 0.1 mm and 0.05 mm.

2.7 *Model uncertainty*

Model uncertainty in the reliability crack model needed to be quantified as much as possible. First, the sources of uncertainty in the model needed to be defined. In general terms, two main types of uncertainty can be defined, namely, inherent random variability and uncertainty due to incomplete knowledge including statistical uncertainty, as defined in literature, for example, Ang & Tang (1990) and the Joint Committee on Structural Safety (JCSS) (2001).

Uncertainty due to random variability is generally dealt with by means of the coefficients of variation of the random variables of the reliability model. Uncertainty also exists due to mathematical simplifications of physical and probabilistic models. In the case of the EN1992 crack model, simplications due to the formulation of the physical crack model from experimental research, such as in using fixed-value coefficients to allow for the effects of reinforcement bond, duration of loading and type of stress distribution. Uncertainty exists in the stochastic model on normalizing non-normal distributions and in the first order approximation of using FORM for the mathematical solution of the failure probability integral.

For the reliability crack model, model uncertainty is allowed for by treating it as a random variable, as is commonly accepted, having a log-normal distribution. On reviewing literature on model uncertainty relating to concrete cracking, it was found that there is a lack of data in this regard. However, Holicky & Retief (2009) presented a reliability model of tension cracking using the EN1992 crack model. Model uncertainty was treated as a random variable with a log-normal distribution having a mean of 1 and coefficient of variation of 0.1. Quan & Gengwei (2002) also treated model uncertainty as a random variable with a log-normal distribution having a mean of 1.05 and coefficient of variation of 0.3.

In this study, model uncertainty was treated as a random variable having a log-normal distribution with a mean of 1. Given that the model uncertainty is not really known in this case, values of 0.1 to 0.3 were chosen as upper and lower limits for the coefficient of variation, with the value of 0.2 to represent a best estimate value. In this way, the effect of model uncertainty on the reliability crack model could be investigated.

3 RESULTS

Results concerning the influence of model uncertainty on the crack model are presented for both tension and flexural cracking.

It was found that in the tension cracking model, the limiting equation for the effective depth of the concrete tension zone, $h_{c,eff}$, was determined by the section geometry chosen, specifically, bar diameter, concrete cover and section thickness. The equation $2.5(c + \varphi/2)$ tends to be limiting. However, particularly for smaller section thicknesses, either both $2.5(c + \varphi/2)$ and h/2 apply (giving the same numerical answer for the physical model), or h/2 only is limiting. Therefore two reliability models were set up for the tension cracking case.

The reverse-FORM analysis was performed over a range of 0.1 to 0.3 for the model uncertainty variation, V_θ. Crack widths of 0.2, 0.1 and 0.05 mm were chosen. Analyses were done for reliability indexes, β, of 0.5, 1.5 and 2.0.

3.1 *Sensitivity analysis*

A reverse-Form analysis was done such that the sensitivity factors, α_i, of the model basic variables were determined for a given level of reliability. The sensitivity factors give an indication of the relative influence of a particular variable on the reliability model. Results are discussed for each of the three reliability models as follows:

Flexural cracking

Table 2 is a summary of the results of the sensitivity factors obtained for model uncertainty in the case of flexural cracking.

The sensitivity factors for model uncertainty, α_θ, indicated that the influence of this variable depended mainly on the variation chosen and on the limiting crack width. In the case of flexural cracking, the influence of model uncertainty increases as V_θ increases and as the crack width limit decreases. The sensitivity factors indicate that model uncertainty has a small influence at a V_θ of 0.1. Model uncertainty becomes more influential at a V_θ of 0.3. The influence of model uncertainty was found to increase as reliability was increased.

Comparing model uncertainty to the remaining flexural model basic variables, liquid load was found to dominate with sensitivity factors of nearly -1.0.

Table 2. Flexural cracking – sensitivity factors for model uncertainty, α_θ.

		Sensitivity factor, α_θ		
		Crack width limit, w_{lim}(mm)		
β	V_θ	0.2	0.1	0.05
0.5	0.1	−0.085	−0.114	−0.151
	0.2	−0.167	−0.223	−0.292
	0.3	−0.248	−0.324	−0.416
1.5	0.1	−0.095	−0.127	−0.170
	0.2	−0.188	−0.251	−0.321
	0.3	−0.280	−0.370	−0.474
2.0	0.1	−0.099	−0.134	−0.180
	0.2	−0.199	−0.267	−0.352
	0.3	−0.298	−0.396	−0.505

Table 3. Tension cracking – $h_{c,eff} = 2.5(c + \varphi/2)$: Sensitivity factors for model uncertainty α_θ.

		Sensitivity factor, α_θ		
		Crack width limit, w_{lim}(mm)		
β	V_θ	0.2	0.1	0.05
0.5	0.1	−0.318	−0.298	−0.270
	0.2	−0.555	−0.528	−0.486
	0.3	−0.706	−0.679	−0.638
1.5	0.1	−0.324	−0.308	−0.284
	0.2	−0.561	−0.537	−0.501
	0.3	−0.708	−0.683	−0.645
2.0	0.1	−0.326	−0.311	−0.289
	0.2	−0.563	−0.540	−0.506
	0.3	−0.708	−0.683	−0.646

Section thickness was found to have a neglible influence with sensitivity factors approaching 0. Concrete cover has a neglible to small influence with factors from about −0.04 to −0.16, as the model uncertainty variation and β increased, and the limiting crack width decreased. The effective concrete tensile strength has similar values to concrete cover, namely, about 0.06 to 0.13, but is a positive influence on the model.

Tension cracking – $h_{c,eff} = 2.5(c + \varphi/2)$

A summary of the model uncertainty sensitivity factors for tension cracking with $hc,eff = 2.5(c + \varphi/2)$ is given in Table 3. The influence of model uncertainty in the case of tension cracking with $h_{c,eff} = 2.5(c + \varphi/2)$ increases by a factor of about 2.2 as V_θ increases. There is a small decrease in the sensitivity factors as the crack width limit decreases. Model uncertainty was not found to be sensitive to a changing level of reliability, as there was only a marginal increase in the sensitivity factors as β increased.

Comparing model uncertainty to the remaining basic variables of this tension model, the dominant variable depends on the value of V_θ. At the lower value of 0.1, the effective concrete tensile strength and concrete cover are the dominant variables with sensitivity factors of about 0.6 and 0.7, respectively.

As V_θ increases to 0.3, model uncertainty is dominant with sensitivity factors of about −0.6. The effective concrete tensile strength and concrete cover sensitivity factors are about | 0.5 |. Liquid load has a small influence,having sensitivity factors of about −0.23 to −0.30. Section thickness obviously has no influence as it does not appear in the crack width equation for this tension cracking model.

Table 4. Tension cracking – $hc,eff = h/2$: Sensitivity factors for model uncertainty, α_θ.

		Sensitivity factor, α_θ		
		Crack width limit, w_{lim}(mm)		
β	V_θ	0.2	0.1	0.05
0.5	0.1	−0.470	−0.427	−0.370
	0.2	−0.719	−0.676	−0.613
	0.3	−0.834	−0.802	−0.691
1.5	0.1	−0.539	−0.496	−0.437
	0.2	−0.762	−0.723	−0.666
	0.3	−0.855	−0.825	−0.777
2.0	0.1	−0.566	−0.522	−0.463
	0.2	−0.777	−0.739	−0.684
	0.3	−0.862	−0.832	−0.785

Tension cracking – $h_{c,eff} = h/2$

Table 4 summarises the sensitivity factors obtained for tension cracking with $h_{c,eff} = h/2$.

The sensitivity factors indicate that model uncertainty is more influential in tension cracking with $h_{c,eff}$ of h/2 limiting, particularly at lower V_θ. This influence increases as V_θ increases. The crack width limit is a lesser influence on model uncertainty.

Comparing model uncertainty to the remaining basic variables, section thickness has a neglible influence and concrete cover has a very small influence with sensitivity factors of about −0.14. Liquid load has a small influence (sensitivity factors of about −0.33). Sensitivity factors for the effective concrete tensile strength are in the order of 0.54. Model uncertainty is the most influential variable for this case of tension cracking.

3.2 *Theoretical partial safety factors*

The theoretical partial safety factors, γ_i, as determined using Equation (6) were determined for the basic variables of the flexural and tension cracking models. Results at β of 1.5 are discussed for each of the three reliability models as follows:

Flexural cracking

Table 5 gives the γ_i determined for flexural cracking and shows that although the sensitivity factors indicated that load was the dominant variable, model

Table 5. Flexural cracking – partial safety factors.

Theoretical partial safety factors						
Crack width limit (mm)	V_θ	γ_c	γ_h	γ_L	γ_{ft}	γ_θ
0.05	0.1	1.02	1.00	1.07	0.95	1.02
0.05	0.2	1.02	1.00	1.07	0.95	1.08
0.05	0.3	1.02	1.00	1.07	0.95	1.18
0.20	0.1	1.00	1.00	1.07	0.97	1.01
0.20	0.2	1.00	1.00	1.07	0.97	1.04
0.20	0.3	1.00	1.00	1.07	0.97	1.08

Table 6. Tension cracking – partial safety factors.

Theoretical partial safety factors						
Crack width limit (mm)	V_θ	γ_c	γ_h	γ_L	γ_{ft}	γ_θ
Tension cracking – hc,eff = 2.5(c + φ/2)						
0.05	0.1	1.15	–	1.02	0.82	1.04
0.05	0.2	1.14	–	1.02	0.84	1.14
0.05	0.3	1.11	–	1.02	0.85	1.28
0.20	0.1	1.16	–	1.02	0.84	1.05
0.20	0.2	1.14	–	1.02	0.86	1.16
0.20	0.3	1.11	–	1.02	0.87	1.32
Tension cracking – hc,eff = h/2						
0.05	0.1	1.05	1.00	1.03	0.79	1.06
0.05	0.2	1.04	1.00	1.02	0.82	1.20
0.05	0.3	1.03	1.00	1.02	0.84	1.34
0.20	0.1	1.03	1.00	1.03	0.81	1.08
0.20	0.2	1.02	1.00	1.02	0.84	1.23
0.20	0.3	1.01	1.00	1.02	0.87	1.41

uncertainty requires the higher partial factor, particularly as the model uncertainty variation increases. The partial safety factors for model uncertainty also increase as the limiting crack width decreases.

Tension cracking

Table 6 is a summary of the γ_i determined for tension cracking using both formulation for $h_{c,eff}$. Model uncertainty factors (γ_θ) were found to depend on the model uncertainty variation, increasing as the variation increases as would be expected. The limiting crack width does not appear to significantly influence γ_θ. Concrete cover has varying influence depending on the limiting equation for $h_{c,eff}$. Section thickness and liquid load have partial safety factors of about 1.0 therefore can be modelled as deterministic.

3.3 *Reliability calibration*

Several sets of partial safety factors were chosen from the theoretical factors derived from the reverse-FORM analysis and a reliability calibration exercise was performed, such that γ_θ was calculated using fixed values

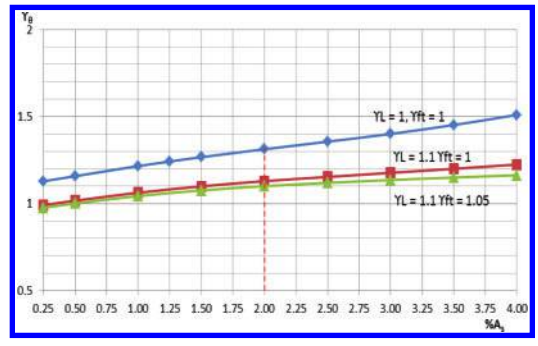


Figure 1. Variation of γ_θ with %A_s for β 1.5 and V_θ 0.2 for flexural cracking.

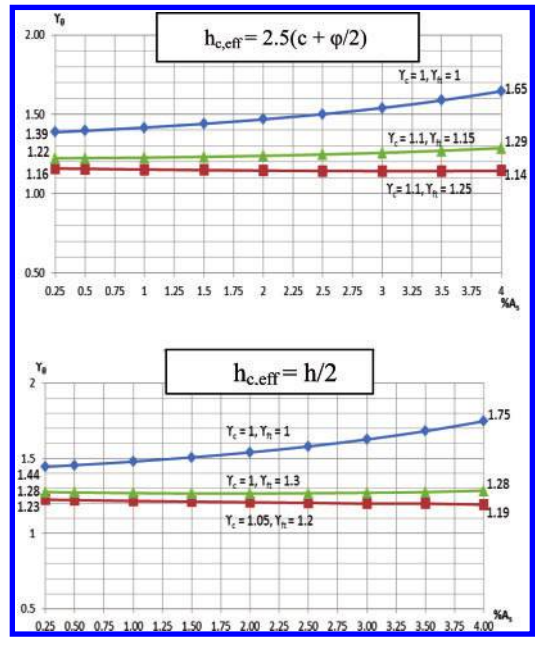


Figure 2. Variation of γ_θ with reinforcement area as %A_s for β 1.5 and V_θ0.2 for tension cracking.

for the other variable partial safety factors and different V_θ. Results are summarised as follows:

Flexural cracking

Referring to Figure 1, a reasonable value for model uncertainty γ_θ is about 1.2 using partial safety factors of 1.1 and 1.0 for load and the effective concrete tensile strength.

All other variables have partial safety factors of 1.0. If factors of 1.0 are used for all safety factors, then γ_θ is dependent on the reinforcement area (as %A_s). Values for γ_θ are also higher in this instance for a given %A_s.

Tension cracking

From Figure 2, for tension cracking with $h_{c,eff} = 2.5$ $(c + \varphi/2)$, γ_θ is independent of the reinforcement area and has a value of about 1.16, if factors of 1.1 and

1.25 are used for concrete cover and effective concrete tensile strength, respectively.

For $h_{c,eff} = h/2$ limiting, γ_θ is independent of the reinforcement area and has a value of about 1.28 if factors of 1.0 and 1.3 are used for concrete cover and effective concrete tensile strength, respectively. If values of 1.0 are used in both tension models, then as with flexural cracking, γ_θ values are significantly higher.

Comparing the three crack models, difficulty arises in choosing a single realistic design scheme that could be applied to all load cases without introducing undue conservatism into the design model, In addition, each model has different variables which have partial safety factors potentially greater than 1.0. If all variables except γ_θ are 1.0, then at a 4% A_s, partial safety factors of 1.51, 1.65 and 1.75 are obtained for γ_θ for flexural cracking and tension cracking with $h_{c,eff} = 2.5(c + \varphi/2)$ and h/2, respectively, using V_θ of 0.2. Further research is required if a reasonable design scheme is to be developed.

4 SUMMARY

The parametric range of model factors used in this analysis is based on indirect considerations to cover the range of validated probabilistic representations. The reliability analysis confirms that model uncertainty has a significant influence on the EN1992 crack model when applied to South African conditions for loading-induced cracking. Further research is therefore justified.

Model uncertainty is more influential in tension cracking. Its influence increases as V_θ increases and w_{lim} decreases.

REFERENCES

Ang AH-S, Tang WT (1990). *Probability concepts in engineering planning and design. Volume II – Decision, risk and reliability*. John Wiley & Sons.

BS EN 1992-1: *Eurocode 2: Design of concrete structures – Part 1: General requirements*. BSI 2004.

BS EN 1992-3: *Eurocode 2: Design of Concrete Structures – Part 3: Liquid Retaining and Containment Structures*, BSI 2006.

BS8007: *British Standards Code of Practice for the Design of Concrete Structures for Retaining Aqueous Liquids*, BSI 1987.

Holický M, Retief JV (2005). *Reliability assessment of alternative Eurocode and South African load combination schemes for structural design*. Journal of the South African Institute of Civil Engineering. Vol 47 No. 1, 2005, pgs 15–20.

Joint Committee on Structural Safety (2001).*Probabilistic model code.*JCSS, Zurich 2001. http://www.jcss.ethz.ch/.

Joint Committee on Structural Safety (2008).*Interpretation of Uncertainties and Probabilities in Civil Engineering Decision Analysis.*Background documents on risk assessment in engineering. Document No. 2. JCSS, Zurich 2008. http://www.jcss.ethz.ch/.

Narayanan RS, Beeby AW (2005).*Designer's guide to EN1992-1-1 and EN1992-1-2: Design of concrete structures. General rules and rules for buildings and structural fire design*. Thomas Telford.

Quan Q, Gengwei Z (2002). *Calibration of reliability index of RC beams for serviceability limit state of maximum crack width*. Journal of Reliability Engineering and System Safety. No. 75 (2002), pages 359–366.

SANS 10100 -1: 2000.*The structural use of concrete: Part 1: Design.* South African Bureau of Standards, Pretoria, South Africa.

SANS 10100 Part 3 (Draft) – *Design of concrete water retaining structures.* WRC Project group with the Institute of Structural Engineering. 2010.

SANS 10160: 2011.*Basis of structural design and actions for buildings and industrial structures*. South African Bureau of Standards, Pretoria, South Africa.

SANS 2394: 2004 Edition 1 (ISO 2394: 1998 Edition 2): *General principles on reliability for structures.* South African Bureau of Standards, Pretoria, South Africa.

Research and Applications in Structural Engineering, Mechanics and Computation – Zingoni (Ed.)
© 2013 Taylor & Francis Group, London, ISBN 978-1-138-00061-2

New design approach for crack width calculation in reinforced concrete structures

Hamdy A. Elgohary
Structural Engineering Department-Faculty of Engineering, Mansoura University – Mansoura, Egypt

Majid M. Assas
Civil Engineering Department-College of Engineering & Islamic Architecture, Umm al Qura University Makkah, KSA

ABSTRACT: Present paper provides a developed approach to improve the calculations of crack width in reinforced concrete cracking. A new relationships account for the effect of several important factors has been obtained. The considered factors are the strain in steel reinforcement at the cracked section, bond stress between steel and concrete, geometry of the cross section and properties of concrete and reinforcement, actual strain distribution in concrete along the axis of steel reinforcement, and, where appropriate, the effect of shear force. The results obtained using the recommended approach show good agreement with the experimental results.

1 INTROUDUCTION

At the present time, reinforced concrete is considered as the primary material in construction. Therefore the development of theory and methods for improving the calculation of reinforced concrete structures is one of the most important tasks of structural engineering science.

Reinforced concrete is a material in which cracks are developed by resistance of force and deformation. The process of crack formation and development is quite complex. Consequently, the accurate determination of the crack width is not a simple process.

Assessing the accumulated results of experimental studies on the crack width, it should be noted that, to date, little empirical data for the crack width and crack spacing calculation when checking multilevel process of their formation and the length of the crack as the load increases in the variation of reinforcement and concrete class.

The lack of theoretical justification and analysis of experimental data led in time to give preference to empirical methods of calculation, including the width of cracks, which requires a continuous time-consuming and costly experimentation.

It follows that research on the detailed study of the crack width of reinforced concrete structures subject to incompatibility strains of concrete and reinforcement material discontinuity is a topical problem.

2 CURRENT METHODS

Study of crack formation in reinforced concrete structures is devoted in a large number of researches and studies. Most of the known proposals for the calculation of the crack spacing and crack width can be divided into groups depending on the approach used to obtain the recommended relationships.

The first group includes all recommended empirical and semi-empirical formulas obtained on the basis of extensive experimental studies and taking into account the influence of various factors on the process of cracking. The experimental investigations showed that cracking is generally proportional to the tensile stress in steel and bar diameter and inversely proportional to reinforcement percentage. The fundamental equation for this group was developed by Gergely and Lutz. In their study they included 612 observations for bottom cracks and 355 observations for side cracks. The obtained formula has the form:

$$w_{cr} = [(11 \times 10^{-6})\beta f_{st}) \sqrt[3]{d_c(\frac{A_e}{n})} \quad (1)$$

where
d_c – thickness of concrete cover measured from the extreme tension fiber to the centre of the nearest bar
A_e – effective area of concrete in tension surrounding the main tension reinforcement,
n – number of bars in tension
f_{st} – stress in tension steel at its centroid
β – ratio of the distances to the neutral axis from the extreme tension fiber and from the centroid of reinforcement.

In equation (1) other important parameters were not considered. As it has been found in the experimental investigations these parameters are also important.

These parameters are: concrete quality, thickness of concrete cover, member thickness, bond strength and concrete tensile strength. Equation (1) was used in ACI up to 1995 and then replaced by a modified condition. The crack width calculation in Saudi Building Code follows the same provisions of ACI.

The second group is based on the premise of Murashov's theory. This theory states that the crack width is determined based on the condition: elongation in concrete tension zone along the axis of steel reinforcement plus crack width should be equal to the elongation of steel reinforcement in the segment between cracks. The basic equation of this group is used in EC-2 and ECC with the form:

$$w_{cr} = (\varepsilon_{sm} - \varepsilon_{ctm}).S_{cr} \quad (2)$$

The third group includes studies in which the crack width is considered as the accumulation of relative movement between reinforcement and concrete along the axis of the steel reinforcement in the segment between two consequent the cracks (Berg 1962). The crack width has the form:

$$w_{cr} = 2\int_0^{0.5S_r} \varepsilon_r(x).d(x) \quad (3)$$

Where
$\varepsilon_r(x)$ – relative strain between reinforcement and concrete along the axis of the steel reinforcement at x,
S_{cr} – spacing between the cracks.

Equation (3) has been assumed based on the assumption that the ε_r curve has a continuous parabolic profile.

3 PROPOSED METHOD

In the present paper the main idea of the third group will be used taking into consideration the relative strain distribution obtained experimentally. The basic assumptions are:

1. Relationship between bond stress and relative strain will have the form:
   $\tau(x) = G\varepsilon_r(x)$ (4)
   Where $G = 0.3E_c$
2. The strain distribution in concrete and steel reinforcement along the distance between two adjacent cracks will be used as shown in Fig. 1 (Bondarenko 2004).
3. Stress in the steel reinforcement at the cracked section is determined from the equilibrium conditions of the moments about the point of application of the resultant compressed concrete for the segment shown in Fig. 2

From Figure 1 the relative strain can be determined from the relationship

$$\varepsilon_r(x) = \varepsilon_s(x) - \varepsilon_{ct}(x) \quad (5)$$

Where $\varepsilon_s(x)$ and $\varepsilon_{ct}(x)$ – strain in steel reinforcement and concrete at distance x, respectively.

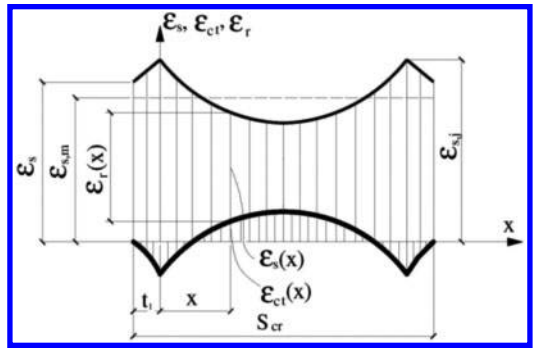


Figure 1. Experimental Strain Distribution in Steel and Concrete along segment between cracks.

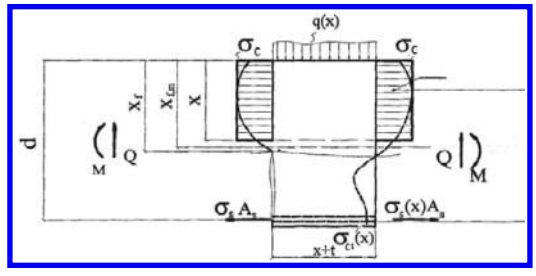


Figure 2. Stress Distribution at cracked Section and Section between cracks.

Steel strain at distance $t_1 + x$ from the crack will have the form

$$\varepsilon_s(x) = \varepsilon_s + \frac{\Delta T}{E_s A_s} + \frac{S_s}{E_s A_s}\int_0^x \tau(x)dx \quad (6)$$

Where $\tau(x)$ – the conventional shear stress

Concrete strain $\varepsilon_{ct}(x)$ can be determined from the equilibrium conditions of the segment of length $(t_1 + x)$ located between the cracked and uncracked sections shown in Figure 2.

$$\varepsilon_{ct}(x) = \delta\,\frac{\varepsilon_s E_s A_s Z_s - \varepsilon_s(x) E_s A_s Z_s(x) - Q(t_1+x)}{0.5A_{ct}(x).E_c Z_{ct}(x)} \quad (7)$$

Where $\delta = \frac{d-x}{h-x}$

Differentiating equation (5):

$$\frac{d\varepsilon_r(x)}{dx} + B\varepsilon_r(x) = \frac{\delta}{t}Q \quad (8)$$

Where $t = 0.5A_{ct}(x).E_c Z_{ct}(x)$ and B-parameter of bond between steel and concrete, depending on the perimeter of reinforcing bars, bond modulus, parameter K and the area of steel and the elastic modulus reinforcing steel and has the form

$$B = \frac{S_S.G}{K.A_S.E_S} \quad (9)$$

Where
S_s – perimeter of tension steel
A_s – tension steel area
E_s – modulus of elasticity of steel

$$K = \frac{1}{1+\beta} \quad \text{and} \quad \beta = \frac{\delta.\mu.\frac{E_s}{E_c}.Z.d}{0.32(h-X).(h+.03X)}$$

The solution of the nonhomogeneous first order differential equation (8) is:

$$\varepsilon_r(x) = C.e^{-Bx} + \frac{\delta.Q}{t.B} \tag{10}$$

The integration constant C can be found from the boundary conditions at $x = 0$, $\varepsilon_{ct}(x) = \frac{\partial_{ct}}{\nu_c E_c}$

$$C = \varepsilon_s + \frac{\Delta T}{A_s E_s} - \frac{б_{ct}}{\nu_c E_c} - \frac{\delta.Q}{t.B} \tag{11}$$

$t_1 = 1.5$ bar diameter (d), $\Delta T = 0.5.(\pi.d.t_c.f_c), t_c = 2d$

Using the condition the strain in concrete at the midpoint between two adjacent cracks will equal the ultimate value thus $\varepsilon_{ct}(0.5x - t_1) = \varepsilon_{ctu}$ and integrating for $\varepsilon_{ct}(x)$, the following relation for strain distribution in concrete along the reinforcement axis can be obtained:

$$\varepsilon_{ct}(x) = (1-K)\left\{C(1-e^{-Bx}) + \frac{\delta Q}{t}\right\} - \frac{б_{ct}}{\nu_c E_c} - \frac{\delta Q}{t}x \tag{12}$$

Or

$$-e^{-B(0.5S_{cr}-t_1)} = 1 + \frac{\varepsilon_{ctu}}{C.(K-1)} + \frac{б_{ct}}{C.\nu_c E_c.(K-1)} = C_1$$

On other hands

$$\ln C_1 = -B(0.5\,S_{cr} - t_1)$$

The crack width then will have the form

$$S_{cr} = \frac{2(B.t_1 - \ln C_1)}{B} \tag{13}$$

Crack spacing is the most important parameter required for crack width determination in concrete structures. Depending on loading level, several levels of cracking development up to failure will take place in concrete members under bending. Accordingly, the development of a new level of cracking corresponds to the load, satisfying the following condition

$$S_{cr,i} \le 0.5\,S_{cr,i-1} \tag{14}$$

Integration relative strain in both concrete and reinforcement leads to the following form for the crack width:

$$w_{cr} = 2\left\{\int_0^{t_1} \varepsilon_r(x)dx + \int_{t_1}^{0.5S_{cr}-t_1} \varepsilon_r(x)dx\right\}$$

After integration, we get:

$$w_{cr} = -\frac{2\Delta T}{G} + \frac{2C}{B}\left(1 - e^{-B(0.5S_{cr}-t_1)}\right) + 2\frac{\delta Q}{t.B}(0.5S_{cr} - t_1) \tag{15}$$

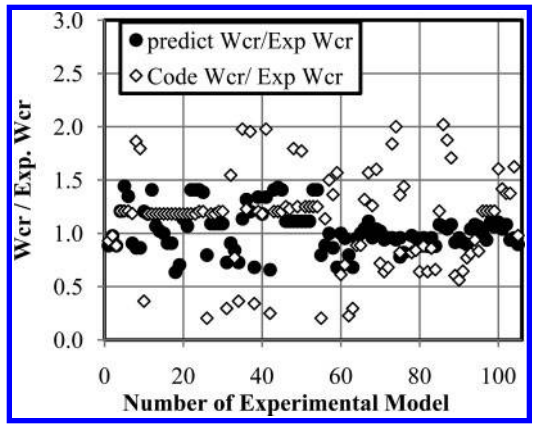


Figure 3. Comparison of Proposed Method Formula, EC-2 Equation and Experimental Results.

The obtained equations (13) and (15) account for the effect of several important factors, such as deformation of reinforcement in the section with a crack in the valve coupling parameters with concrete, and the geometric characteristics of the cross-section properties of concrete and reinforcement, deformation effects (occurring in concrete elements after violation continuity), the relative conditional focused mutual displacements of concrete and reinforcement, and, where appropriate, the effect of shear force Q.

4 VERIFICATION OF RESULTS

The recommended approach for determining the crack width is verified against experimental results to judge how the recommended approach can be applied for design practice. The test results obtained by (Ghattas 1994), (Korytnyuk 1974), (Maureen 1974) and (Shavykin 2009) we considered with total number of test samples 105. The crack width for all samples has been calculated using the recommended approach and by equation (15) and by EC equation. The relative crack width (predicted/experimental) calculated by the proposed equation and by EC-2 equations is shown in Figure 3. The results obtained by the proposed approach give average value of the relative crack width of 1.03, while EC-2 results give 1.13. This proofs that, unlike basic equation for all codes, the proposed method gives results with good agreement with the test results.

REFERENCES

[1] ACI Committee 318, (2008) "Building Code Requirements for Structural Concrete (ACI 318-08) and Commentary (ACI 318R-08)," American Concrete Institute, Farmington Hills, Mich.

[2] Baraishkov AJ, & Kolchunov V. I, (1995) Calculation of crack opening width of reinforced concrete elements based on new physical models of resistance / / Reconstruction – St. Petersburg-2005: Proceedings

of the International Symposium 3, St. Petersburg, May 16–20, Part 4 – St. Petersburg, – S. 87–96.
[3] Berg O. Y. (1962), Physical basis of the theory of strength of concrete and reinforced concrete – M. Gosstroyizdat.
[4] Bondarenko, V. M, Kolchunoe, V. I. (2004) Computational models of the power of resistance of reinforced concrete – Moscow: ASV Publishing House – 472 s
[5] Egyptian Code-203 for Design and Construction of Concrete Structures (2007), Housing and Building Research Centre, Cairo, Egypt.
[6] ENV 1992-1-1: Eurocode 2 (EC2) (1991) Design of ConcreteStructures, part 1: General Rules and Rules for Buildings, European Prestandard, December, 1991.
[7] Ghattas Antoine Fouad, Crack Resistance of Concrete Frame Elements, Abstract of Ph. D. thesis/ Kiev State Technical University of Construction and Architecture. – Kiev 1994.
[8] Gergely, P., & Lutz, L. A., "Maximum Crack Width in Reinforced Concrete Flexural Members, Causes, Mechanism, and Control of Cracking in Concrete," SP-20, American Concrete Institute, Farmington Hills, Mich., 1968, pp. 87–117.
[9] Gilbert, R. I, "Shrinkage, Cracking and Deflection-the Serviceability of Concrete Structures" Electronic Journal of Structural Engineering, Vol. 1 (2001).
[10] Fedorov, V. S., Shavykin, E. V. & Kolchunov, V. I. (2009) "Calculation Methodology for crack width in reinforced concrete eccentrically compressed considering the effect of discontinuity" Journal of Structural Mechanics and Design of Structures –
[11] Frosch, R. J., (1999) "Another Look at Cracking and Crack Control in Reinforced Concrete," ACI Structural Journal, May-June, pp. 437–442.
[12] Frosch, R. J., (2001) "Flexural Crack Control in Reinforced Concrete," Design and Construction Practices to Mitigate Cracking , SP 204, American Concrete Institute, Farmington Hills, Mich., pp. 135–154.
[13] Kolchunov, V.I., Yakovenko, I.A., Shavykin, E. V., (2009) "Experimental studies of crack width of eccentrically compressed concrete // Safety Building Fund of Russia. Problems and solutions." (Proceedings of the International Academic Readings on April 9–11, 2009). – Kursk: Kursk. State technical University NIIZhB,. – S. 99–103.
[14] Korytnyuk, Y., (1974) "Load Carrying Capacity of Eccentrically-Compressed Hollow Reinforced Concrete Elements with high grade concrete: Abstract of Ph. D. Kiev.
[15] Lee, W. K., Jansen D. C., Berlin K. B., and Cohen I. E., (2010) "Flexural Cracks in Fiber-Reinforced Concrete Beams with Fiber-Reinforced Polymer Reinforcing Bars", ACI Structural Journal, V. 107. No.3. May–June, pp 321–329.
[16] Maureen, A. L., Tkachuk, V. M., Korytnyuk Y. V. (1974) "Investigation of Eccentrically Compressed Reinforced Concrete Elements of high grade concrete" Journal of Concrete and Reinforced Concrete. No.1.
[17] Murashev, V. I., (1950) Crack resistance, stiffness and strength of concrete. Moscow, Mashstroyizdat, 268 p.
[18] Rosenboom, O, & Rizkalla, S. H, (2008) "Experimental Study of Intermediate Crack Debonding in Fiber-Reinforced Polymer Strengthened Beams" ACI Structural Journal, V. 105. No. I. January–February, pp 41–50.
[19] Saudi Building Code SBC-301 (2007) – Structural-Loading and Forces, Saudi Building Code National Committee.
[20] Shavykin, E. V, (2009) "Crack Width Calculation of Eccentrically Compressed Reinforced Concrete Elements Considering the Effect of Discontinuity", Ph. D. Thesis, Moscow State University of Railway Engineering, Moscow.
[21] Subramanian, N., (2005) "Controlling the crack width of flexural RC members", The Indian Concrete Journal, Nov.
[22] Thomas F.G. Cracking in reinforced concrete // "The structural Engineer" – Vol. XIV. – N . 7. – 1936. – P . 37–43.

21. Fibre-reinforced concrete, polymer-reinforced concrete, cement composites

Research and Applications in Structural Engineering, Mechanics and Computation – Zingoni (Ed.)
© 2013 Taylor & Francis Group, London, ISBN 978-1-138-00061-2

Multi-functional fiber reinforced concrete for sustainable structures

N. Banthia
University of British Columbia,Vancouver, British Columbia, Canada

ABSTRACT: Civil infrastructure around the world is in a state of utter disrepair and significant efforts are needed on the part of all stakeholders to render our failing infrastructure back to a serviceable and safe state. The root of the problem is at the apparent lack of durability in our construction materials, inability on part of the owners to provide timely maintenance, absence of advanced condition assessment tools and lack of long-lasting, cost effective repair materials and technologies. This paper will present data to support the argument that fiber reinforced concrete (FRC) is an ideal material for achieving these goals. The paper also discusses smart fiber reinforced concrete materials carrying carbon fibers and carbon nano-tubes that possess sensing abilities. These materials can help us develop intelligent infrastructure with elegantly integrated sensing and health monitoring abilities.

1 INTRODUCTION

Compared to other building materials such as metals and polymers, concrete is significantly more brittle and exhibits a poor tensile strength. Concrete carries flaws and micro-cracks both in the material and at the interfaces even before an external load is applied. These defects and micro-cracks emanate from excess water, bleeding, plastic settlement, thermal and shrinkage strains and stress concentrations imposed by external restraints. Under an applied load, distributed micro-cracks propagate, coalesce and align themselves to produce macro-cracks. When loads are further increased, conditions of critical crack growth are attained at the tips of the macro-cracks and unstable and catastrophic failure is precipitated. Under fatigue loads, concrete cracks easily, and cracks create easy access routes for deleterious agents leading to early saturation, freeze-thaw damage, scaling, discoloration and steel corrosion.

The micro and macro-fracturing processes described above can be favourably modified by adding short, randomly distributed fibers of various suitable materials. Fibers not only suppress the formation of cracks, but also abate their propagation and growth. The resulting material termed fiber reinforced concrete (FRC) is rapidly becoming a well-accepted mainstream construction material. Strain-softening characteristics that were typically obtained in these materials have now been replaced by strain-hardening capabilities in tension as demonstrated in Figure 1.

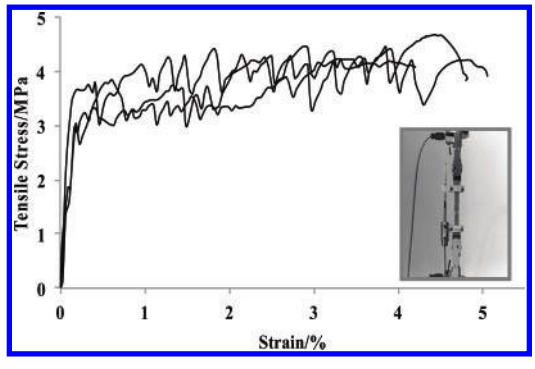


Figure 1. Strain Hardening Capabilities in High Performance FRC.

2 FIBER REINFORCED CONCRETE FOR DURABILITY

2.1 *Permeability under stress*

The decreasing life span of concrete structures is primarily due to corrosion of steel in reinforced concrete structures. Chloride penetration and carbonation are the primary reasons for such corrosion and any measures aimed at mitigating the ingress of chlorides or CO_2 into the body of concrete are expected to significantly enhance the durability of concrete structures. These deleterious agents enter the body of concrete through one of the three transport mechanisms: diffusion, capillary sorption and permeability—of

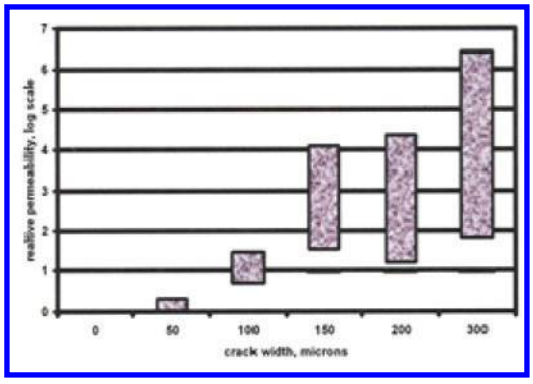


Figure 2. Effect of Crack Width on Permeability, Bentur [1].

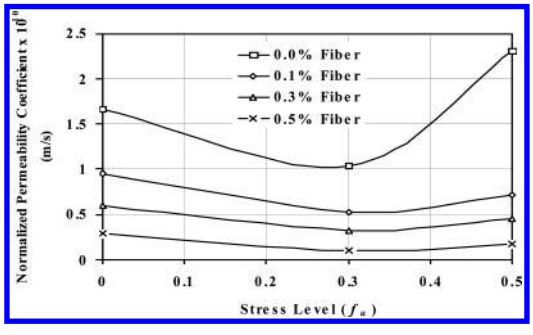


Figure 3. Normalized Permeability Coefficients [2,3].

these, the permeability is considered as the dominant mechanism. Any measures adopted to reduce permeability of concrete will therefore help in preserving durability. Results have indicated that permeability, in turn, is highly dependent upon cracking in concrete and an increase in the crack width will not only produce a highly permeable concrete (Figure 2) but also enhance the possibility of rebar corrosion Bentur [1].

Fiber reinforcement is the most effective way of controlling cracking and hence of permeability under stress. Indeed, tests conducted at the University of British Columbia [2] & [3] demonstrated such benefits. The results for cellulose fiber are shown in Figure 3. Notice that under conditions of no-stress, fibers reduce the permeability of concrete, and the reduction appears to be proportional to the fiber volume fraction. This is often explained on the basis of internal curing that occurs due to hydrophilic cellulose fiber. Data further indicate that stress has a significant influence on the permeability of concrete. When stress was first increased to $0.3f_u$, both plain and FRC showed a decrease in the permeability. However, when the stress was increased to 0.5fu, plain and FRC showed very different trends. At $0.5f_u$, the permeability of plain concrete increased substantially over that of the unstressed specimen, but for FRC, while there was an increase in the permeability over $0.3f_u$, the permeability still stayed below that of the unstressed specimen.

The above observations can be related to cracking. At $0.3f_u$, it is conceivable that in both plain and FRC, there is no discernible cracking that can affect the flow of water. However, at $0.5f_u$, the stress-strain response for both plain and FRC would become non-linear indicating the presence of cracking.

As given by the Poiseuille Law, Edvardsen [4], the flow of water through cracks is proportional to the cube of the crack width. In the case of FRC, one can expect the fibers to suppress cracking and hence maintain the rate of flow similar to an unstressed specimen. When combined with the phenomenon of 'pore compression', this implies that the permeability of FRC under stress can in fact be lower than that of an unstressed specimen.

2.2 *Diffusion control with fibers*

Chloride induced corrosion of reinforcing steel in concrete remains the most serious durability concern of our time. Need exists therefore to control transport mechanisms that allow an ingress of chlorides into concrete. Earlier studies have shown that fiber reinforcement of concrete reduces its permeability to water both with and without an applied stress. However, if fiber reinforcement also reduces diffusion of chlorides, is not known. Fiber reinforcement of concrete is known to reduce both environmentally-initiated and load-induced cracking and alter the transport properties, but a direct evidence of fibers mitigating rebar corrosion is lacking.

Sappakittipakorn and Banthia [5,6] performed Bulk Diffusion Tests as per ASTM C 1556 [7] and supplemented them by the Silver Nitrate Spray Tests on fiber reinforced concrete. By fitting the solution of Fick's second law to the results of the chloride profiles, the apparent and effective chloride diffusion coefficients were determined corresponding to the total and free chloride profiles, respectively. Their results are given in Figure 4.

Notice that the apparent diffusion coefficients are higher in the FRC samples possibly because of an increase of the volume of interfacial porosity at fiber-matrix interfaces that provided easier paths for chloride to transport. In the case of cellulose fibers, the hydrophilic nature of the fiber and the internal moisture entrapment most likely caused the upsurge. However, the effective diffusion coefficients are lower in the FRC as a consequence of the chloride binding effect. This ability of fibers to bind chlorides is an extremely useful property in combatting corrosion as was further demonstrated in tests described below.

2.3 *Corrosion control with fibers*

Sappakittipakorn and Banthia [5,6] designed tests to study the effect of fibers on the initiation of corrosion of reinforcing steel in concrete beams. Beams, 100 mm × 100 mm × 350 mm, were reinforced with three #10 carbon steel rebars similar to the specimen in ASTM G 109. One of the bars (working electrode)

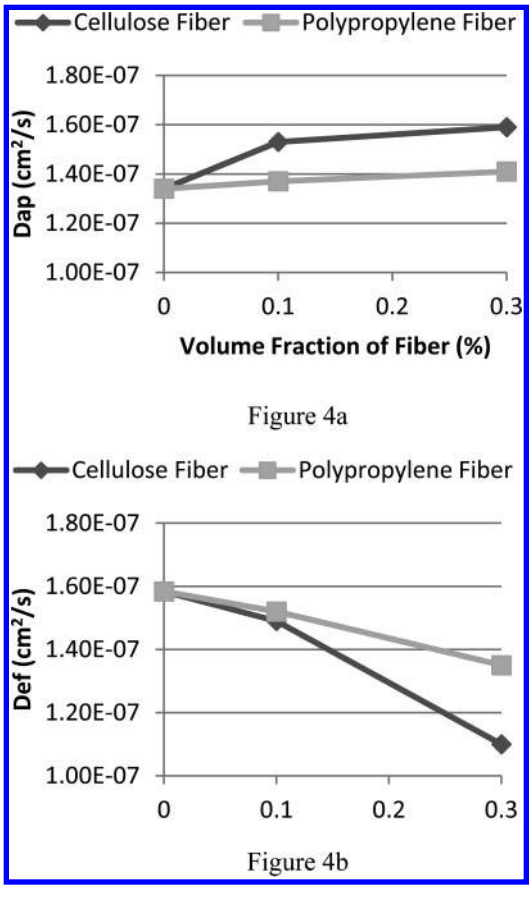


Figure 4. Apparent (a) and Effective (b) Coefficients of Chloride Diffusion for Various Volume Fractions of Fibers.

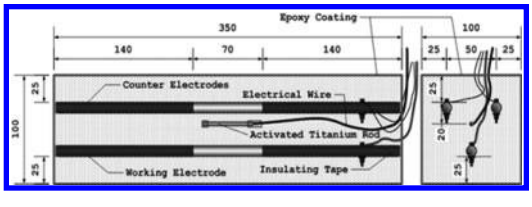


Figure 5. Schematic of a Specimen for Corrosion Control Tests; all dimensions are in millimeter.

was put in a tension zone and was corrosion monitored during the experiment. The other two were in a compression zone and were used as auxiliary electrodes. All of the bars were covered with a rubber paint at a distance of 140 mm from both ends so that the corrosion could take place only within the middle 70 mm of the bars. The concrete cover was uniform at 25 mm. The bars were electrically connected to wires for corrosion measurements. Each beam was coated with epoxy on all sides except for the side at the bottom, which was stressed in tension and exposed to chloride solution. A schematic of the beam specimens is shown in Figure 5.

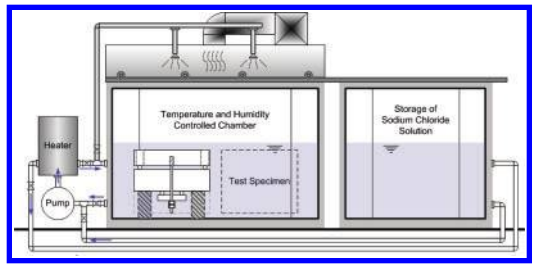


Figure 6. Chamber for Corrosion Tests.

Table 1. Time to Onset of Corrosion.

	Time to Corrosion Onset (weeks)		
Fiber	0% P_{ult}	25% P_{ult}	50% P_{ult}
0%	27	3	1
0.1% C	56	38	1
0.3% C	>56	51	1
0.1% P	41	8	1
0.3% P	47	13	1

C: Cellulose; P: Polypropylene

Two sets of beams were investigated: one with load and the other without. Across the middle of the tension surface, all the beams were pre-notched by the insertion of a thin steel sheet, 0.2-mm thick and 5-mm deep, prior to concrete casting. After a moist curing of 28 days, specimens designed for corrosion measurements were continuously loaded to two applied load levels of 15 and 30 kN; these are approximately 25% and 50% of the ultimate load (P_{ult}). To accelerate the corrosion, a conditioning tank (Figure 6) was used. Time to tidal zone marine environment was applied by using wet/dry cycles in 3.5% sodium chloride solution (4 days in dry and 3 days in wet conditions). In the wet cycle, the salt water in which the beams were submerged was circulated and controlled at 20–25°C. A steel frame was employed to maintain the loads on the beams, as shown in Figure 6. A torque was applied at the nuts on the threaded rods at both sides of the beam to control the flexural load.

To monitor the corrosion process, a potentiostat (Reference 600 from Gamry Instruments) was utilized to perform three electrochemical measurements, i.e., half-cell potential, galvanic current, and linear polarization resistance. The initiation of corrosion was assumed either when the electrical potential was below −350 mV (versus CSE) or when the galvanic current density and the corrosion current density were above 1 $\mu A/cm^2$ (6.45 $\mu A/in^2$). Based on these criteria, the times to onset of corrosion recorded with different monitoring methods were fairly consistent and are given in Table 1. As seen in Table 1, clearly, cracking induced in the concrete cover by loading accelerated the corrosion substantially. In the case of non-loaded specimens, there were no cracks involved, so that the corrosion developed very slowly. It was found that the

25% P_{ult} loaded samples responded in a manner similar to the non-loaded samples but the corrosion initiated sooner as a result of the crack. Because of the large crack in all samples subject to the 50% P_{ult} loading, the corrosion began sometime within the first week itself. The influence of the fiber was found in all samples if no extensive crack existed. The corrosion initiation was delayed at a rate proportion to the fiber dosage.

3 SMART FRCS FOR INTELLIGENT INFRASTRUCTURE

Fiber Reinforced Cement-based sensors, also described as smart (self-monitoring) structural materials, have recently been developed for use in structural health monitoring (SHM) systems. Cement-based sensors are designed to function based on the principle of piezoresistivity. Materials in which the electrical resistance changes in response to changes in the applied strain are referred to as piezoresistive materials. Piezoelectricity is referred to the coupling between internal dielectric polarization and strain and can be used for both sensing and actuation [8].

The most common fiber used as the conductive phase in cement-based sensors is carbon fiber (CF). Extensive research has been conducted to obtain the optimum volume fraction of carbon fibers, electrode type, effect of curing time, temperature, moisture and chloride on the performance of these sensors [9–16]. In a recent study [17], cement-based sensors were developed by incorporating carbon fibers either alone or in combination with multi-walled carbon nanotubes (MWCNT) in a cement paste matrix. Changes in the electrical resistivity of cement-based sensors under monotonic and cyclic compressive loading were monitored. Carbon fibers used in these studies were 6 mm long, 11 μm in diameter and had a volume resistivity of 2.3 × 10-6 Ω-m. The properties of the MWCNTs are shown in Table 2.

The experimental setup is displayed in Figure 6a. In order to evaluate the sensing ability of the developed sensors, load and strain values were compared against the Fractional Change in Resistivity (FCR).

$$FCR = \frac{\rho_t - \rho_0}{\rho_0} \tag{1}$$

where, ρ_t: Electrical resistivity at time t during the tests; ρ_0: Electrical resistivity at the beginning of the test (prior to loading)

And,

$$\text{Gauge Factor} = \frac{\Delta R / R_0}{\varepsilon} = \frac{\Delta\rho / \rho_0}{\varepsilon} = \frac{FCR}{\varepsilon} \tag{2}$$

where, ΔR (or $\Delta\rho$): Change in strain gauge resistance (or resistivity); R_0 (or ρ_0): Unstrained resistance (or resistivity) of strain gauge; FCR: Fractional Change in Resistivity; ε: Strain

Figure 7 (b) displays the response of the 15% CF sensors to cyclic loading at a rate of 0.002 cycles/s.

Table 2. Properties of Multi-Walled Carbon Nano-Tubes (MWCNT).

Outer Diameter (nm	10–2
Inside Diameter (nm)	3–
Purity	>95 wt%
Length (μm	10–3
Specific Surface Area ($m2/g$)	23
Specific Gravity	≈1.5
Electrical Conductivity (s/cm)	$>10^{-2}$

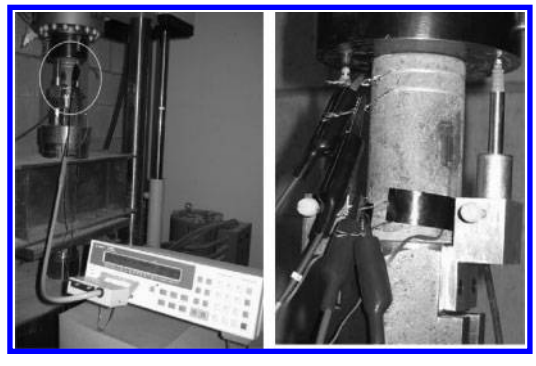


Figure 7(a). Experimental Setup Development of an FRC Sensor [17].

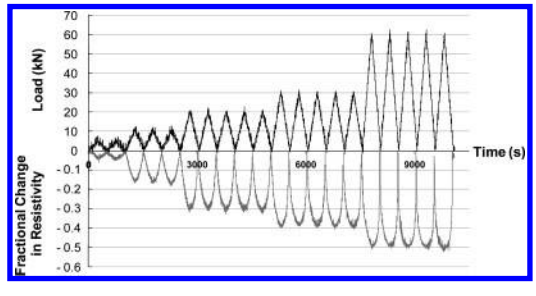


Figure 7(b). Response of 15% CF Sensor to Cyclic Compressive Loading.

Notice that the electrical resistivity of the sensors varied distinctly in response to the cyclic compressive loading: decreasing reversibly with the increasing branch of each compressive loading cycle and increasing reversibly with the decreasing or unloading branch of each cycle.

The averaged stress/strain and stress/FCR correlations for 15% CF and 15% CF + 1% MWCNT for five cycles of compressive loading are compared in Figure 8. The relationship between stress/FCR, although not as linear as that of the stress/strain, appears to have a sensible correspondence.

When gauge factors are computed, the 15% CF composites depicted gauge factors of 290 and 145 for strain values below and above 0.0007, respectively. The 15% CF + 1% MWCNT composites, on the other hand, demonstrated gauge factors of 410 and 110 for strain values below and above 0.0004, respectively. Notice that these gauge factors are well above those for

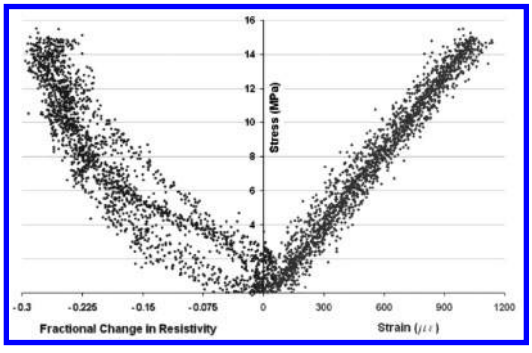


Figure 8(a). Stress/strain and stress/FCR relationships for 15% CF sensors.

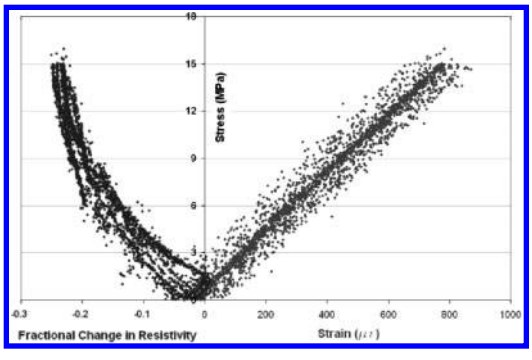


Figure 8(a). Stress/strain and stress/FCR relationships for 15% CF + 1% MWCNT Sensors (15% CF: $FCR = 185558\varepsilon^2 - 459.23\varepsilon + 0.118$ and for 15% CF + 1% MWCNT: $FCR = 331009\varepsilon^2 - 538.83\varepsilon - 0.0174$).

conventional strain gauges. Notice also a remarkable improvement in the gauge factor due to the addition of MWCNT.

4 CONCLUSIONS

With the current durability concerns for our concrete infrastructure, the use of sustainable fiber reinforced concrete for both new construction and repair appears highly promising. Fibers abate cracking and in turn reduce permeability under stress and delay corrosion. The paper also discusses smart fiber reinforced cementitious composites that are reinforced with conducting media such as carbon fibers and carbon nano-tubes and can inexpensive sensors, enabling effective structural health monitoring and active control.

REFERENCES

[1] Bentur, A., et al. ConMat05 Mindess Symposium Proc., University of British Columbia (Ed. Banthia, Bentur and Shah), 2005, 10 pp.

[2] Banthia, N. and Bhargava, A., ACI Materials Journal, 104(1), 2007, pp. 303–309.

[3] Bhargava, A. and Banthia, N. RILEM, Materials and Structures, 41, 2008, pp. 363–372.

[4] Edvardsen, C., 1999. ACI Materials Journal, 96(4): 448–454.

[5] Sappakittipakorn, M. and Banthia, N., ASTM, J of Testing and Evaluation, 40(**??**), 2012, pp. 127–136.

[6] Sappakittipakorn, M. and Banthia, N., The Indian Concrete Journal, 84(10) October 2010, pp. 7–20.

[7] American Society of Testing and Materials, "Standard Test Method for Determining the Apparent Chloride Diffusion Coefficient of Cementitious Mixtures by Bulk Diffusion," ASTM C 1556, 2004.

[8] Senturia SD. Microsystem Design. Boston: Kluwer Academic Publishers; 2001.

[9] McCarter WJ, Starrs G, Chrisp TM, Banfill PFG. Activation energy and conduction in carbon fibrereinforced cement matrices. J Mater Sci. 2007;42:2200-3.

[10] Xie P, Gu P, Beaudoin JJ. Electrical percolation phenomena in cement composites containing conductive fibres. J Mater Sci. 1996;31:4093-7.

[11] Chacko RM, Banthia N, Mufti AA. Carbon-fiber-reinforced cement-based sensors. Canadian Journal of Civil Engineering. 2007;34:284–290.

[12] Azhari F. Cement-Based Sensors for Structural Health Monitoring. MASc. Thesis. 2009; http://hdl.handle.net/2429/7324.

[13] Wen S, Chung DDL. Piezoresistivity-based strain sensing in carbon fiber-reinforced cement. ACI Mater J. 2007;104:171–179.

[14] Banthia N, Djeridane S, Pigeon M. Electrical resistivity of carbon and steel micro-fiber reinforced cements. CemConcr Res. 1992;22:804–814.

[15] Reza F, B B, Gordon, A Y, Jerry, S L, Jong. Volume electrical resistivity of carbon fiber cement composites. ACI Mater J. 2001;98:25–35.

[16] Reza F, Batson GB, Yamamuro JA, Lee JS. Resistance changes during compression of carbon fiber cement composites. J Mater Civ Eng. 2003;15:476–483.

[17] Azhari, F. and Banthia, N., Cement-Based Sensors with Carbon Fibers and Carbon Nanotubes for Piezoresistive Sensing, Cement & Concrete Composites 34 (7), August 2012, pp. 866–873.

Research and Applications in Structural Engineering, Mechanics and Computation – Zingoni (Ed.)
© 2013 Taylor & Francis Group, London, ISBN 978-1-138-00061-2

Comparison of strain measurement techniques for the characterization of brittle, cementitious matrix composites

D. Arboleda, S. Yuan, J. Giancaspro & A. Nanni
University of Miami, Coral Gables, Florida, USA

ABSTRACT: Five strain measurement methodologies are described and experimentally compared based on their performance to measure axial strain of brittle matrix composite materials under uniaxial tensile loading, and setup requirements. A clip-on extensometer, electrical strain gages, a laser extensometer, and two Digital Image Correlation (DIC) techniques (edge detection of a painted rectangle and speckle interferometry), are the focus of this investigation. The composite is a novel, fabric-reinforced cementitious matrix (FRCM) system intended for strengthening concrete structures. Instrumentation is not standardized for testing of FRCM materials, so this study is particularly relevant for this field. Results indicate that for this class of composite, both the laser and clip-on extensometers are well suited for strain measurement, while strain gage measurements are only valid prior to the onset of cracking. Poor results obtained using the DIC technologies are likely attributable to out-of-plane displacement due to specimen curvature and fiber straightening during testing.

1 INTRODUCTION

1.1 *Motivation*

A critical process in the introduction of new materials for structural applications is the evaluation of the mechanical material properties through experimental means. One of the essential tasks for this effort is the definition of test configurations that give meaningful measurements intended to achieve the desired accuracy and resolution used to derive the stress-strain behavior. Characterization of the basic material properties used for design, such as strain and strength allowables, elastic moduli, and any transition in mechanical behavior is, thus, highly dependent upon the techniques utilized for measuring strain. The motivation for this study is the evaluation of a new composite intended for structural rehabilitation, following the International Code Council Evaluation Service (ICC-ES) Acceptance Criteria 434 (AC434 2013), which is modeled after AC125 for fiber reinforced polymer (FRP) composites and RILEM Technical Committee 201 for textile reinforced concrete (TRC). This material is a fabric reinforced cementitious matrix (FRCM) composite described in the following sections. During preliminary uniaxial testing, a clip-on extensometer was used to measure axial strain. The inherent variability of the material's characteristic response, due in part to its lack of homogeneity, gave rise to a search for a better understanding of the material behavior and response through different available test measurement methods, specifically, strain measurement techniques.

1.2 *Background*

Various full-field and point measurement methods are available for measuring strain or deformation based on mechanical, optical, acoustical, pneumatic, and electrical phenomena. Direct tensile testing of continuous fiber reinforced brittle matrix specimens typically involves measuring the specimen strain response with strain gages (Silva *et al*2000), LVDT's, and clip-on extensometers (Naaman & Shah 1979, Contamine *et al* 2011, Qian & Zhang 2012). Published standards (ASTM C1275) and AC434 specify only the use of extensometers satisfying ASTM E83 class B-1 requirements, which are based upon the relative error of the gage length. Optical and digital image correlation (DIC) methods have been used for crack size measurements and crack distribution analysis (Mobasher 2012), but not extensively used for strain measurement in this class of composites.

One optical strain measurement apparatus is the laser extensometer, which reflects a laser beam from reflective targets placed at the endpoints of the gage length being investigated.

Digital image correlation is a non-contacting, optical strain measurement technique intended to measure surface deformation. By correlating the changes in a series of images before and after deformation, the displacement field of the surface can be quantified (Pan *et al* 2009). Compared to other strain measurement methods, DIC is advantageous due to its relatively low cost, simplicity in setup, and wide measurement range. However, the analytical and computational necessities can be much more complex and time-consuming.

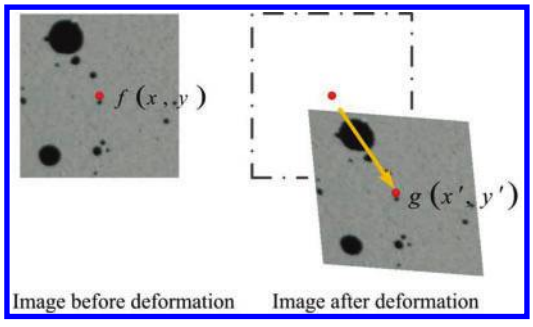


Figure 1. Correlation of pixel displacement by DIC (adapted from Pan *et al* 2009).

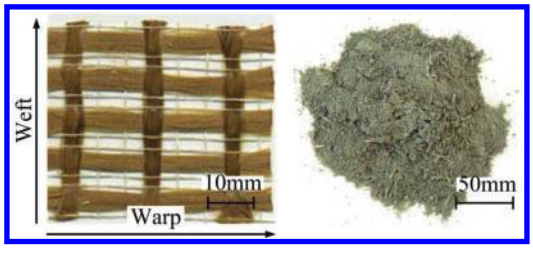


Figure 2. PBO-FRCM system: fabric (left), mortar matrix (right).

The basic principle of DIC is to analytically track the same point(s) through the deformation, as shown in Figure 1. For tracking the displacement, the specimen surface is painted with a grey background, followed by a random distribution of black spray-painted speckles. The arrangement of the specklesis separated into multiple subsets with a uniquely grey distribution that is identifiable, similar to a finger print. Using a correlation criterion to track the position change of each subset, the displacement map for the specimen is obtained.

A new approach developed by the authors is to paint a black rectangle on the specimen surface, then apply edge detection principles to measure the distance between the edges on the sub-pixel level. In this paper, both the speckle and rectangle-based approaches were used.

2 TEST SETUP

2.1 *Specimen description*

The FRCM system consists of two main elements, a cementitious matrix, which is typically a Portland cement-based grout system and a low dosage of dry polymers (less than 5% in weight), and a dry fiber network or fabric. For this study, a PBO-FRCM system was used, consisting of PBO fabric (polyparaphenylene benzobisoxazole) (Figure 2) and a stabilized inorganic matrix, intended for the strengthening of reinforced concrete structures(Arboleda *et al* 2012).

The PBO fabric is made of 10 mm and 20 mm spaced rovings in the warp and weft directions

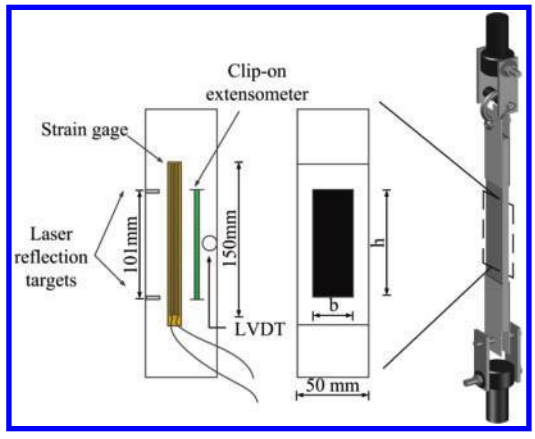


Figure 3. Specimen instrumentation set up.

respectively. The clear spacings are approximately 5 mm and 15 m min the warp and weft directions respectively, while the nominal thicknesses in the two fibers directions are 0.046 mm and 0.011 mm, respectively.

Tensile coupons measured 500 × 50 × 10 mm and were cut from larger panels. The larger panels were 410 × 563 mm, and were manufactured using a manual impregnation technique in a rectangular mold. In this process, a 5-mm thick layer of the cementitious matrix was placed, followed by a layer of the fabric, which was manually wetted with the wet cementitious material. The top layer of matrix was then applied to form the surface of the specimen. Panels were cured for 28 days at 20°C and 70% relative humidity before cutting. Individual coupons were cut using a diamond-tipped wet saw using a rigid fixture to ensure consistent specimen widths. 2 mm steel tabs were bonded with a polyurethane construction adhesive to each specimen 24 hours prior to testing.

2.2 *Experimental setup*

A49 kN test frame was used to apply the tensile load and recorded using a load cell with 9 kN capacity. A clevis grip set up was used to provide sufficient degrees of freedom in order to minimize secondary moment or torsion loading conditions at the supports due to specimen geometry. Test specimens were aligned at the grips and preloaded to 50 N.

To facilitate direct comparisons between the strain measurement approaches, the strain measuring devices were strategically arranged such that the laser extensometer, the clip-on extensometer, and the 150 mm long strain gage were arranged on one side of the specimen, whileone of the two DIC patterns (speckles or rectangle) were on the other side. This arrangement is shown in Figure 3.

The laser extensometer was mounted on a rigid frame (Figure 4) and directed at the test specimen at a target distance of 305 mm. The laser extensometer used a moving window of 256 scans averaged per reading. A mechanical, general-purpose, clip-on axial



Figure 4. Equipment set up.

Table 1. Instrumentation configuration for each specimen.

Specimen name	Laser gage length (mm)	Strain gage (mm)	Digital image pattern (mm)	Shutter speed (sec)	Focal ratio	LVDT
FRCM-1	102.2147	150	rectangle 101 × 35	1/10	f/3.2	Yes
FRCM-2	104.3457	N/A	rectangle 70 × 35	1/8	f/3.2	Yes
FRCM-3	106.0602	150	rectangle 52 × 35	1/6	f/3.2	Yes
FRCM-4	102.6998	150	speckle	1/40	f/3.2	Yes
FRCM-5	105.7580	N/A	speckle	1/40	f/3.2	No
FRCM-6	104.8385	N/A	rectangle 52 × 35	1/15	f/3.2	No
FRCM-7	101.1047	N/A	speckle	1/40	f/3.2	Yes

extensometer with an initial gage length of 100 mm was mounted directly on the test specimen using knife edges.

A 240-ohm strain gage with a 150-mm gage length was bonded along the axial direction on the specimen, and was connected to a quarter-bridge circuit.

Digital images were recorded by a charge coupled device (CCD) camera with a 40-mm micro lens and an image resolution of 3872 × 2592 pixels. The camera was mounted on a rigid frame (Figure 4), directed at the specimen, and calibrated by taking images of a checkerboard pattern of known dimensions at different angles (Zhang 1999). The camera shutter speed and focal ratio for each test are listed in Table 1. Shutter speed and aperture were manually selected based upon the lighting conditions which were controlled by using a lamp with a 35 Watt bulb supplying 1050 Lumens.

After executing the first two tests on specimens FRCM-5 and FRCM-6, and analyzing the data, it

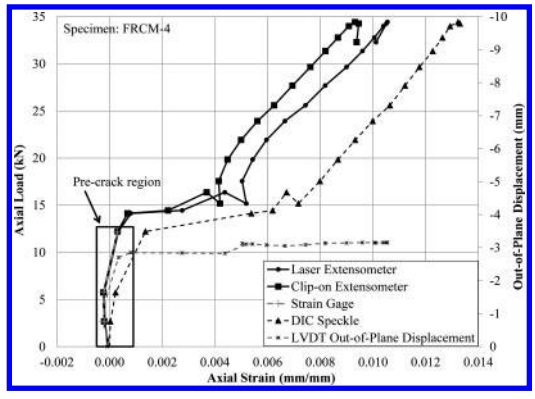


Figure 5. Comparison with speckle DIC.

became apparent that out-of-plane displacement due to specimen curvature and fabric straightening was occurring. This movement adversely affected the camera focus so the DIC data for those specimens was not usable. A new strategy was developed that included placing the camera on a bed of stainless steel ball bearings that attached to the specimen, allowing the camera to freely move with the out-of-plane movement of the specimen. In addition, two linear variable differential transformers (LVDT) were added at the specimen mid-section and top support to measure the out-of-planed eflection. A total of 7 specimens were tested with the instrumentation configurations shown in Table 1. All configurations included a 100 gage length clip-on extensometer.

The laser extensometer, clip-on extensometer, 150-mm strain gage, and load cell were connected to a data acquisition (DAQ) system, as were the two LVDTs. The test was programmed to run under displacement control at a rate of 0.25 mm/min with measurements recorded continuously at a rate of 1 Hz. To synchronize the digital images with the DAQ system, the test was paused every 0.25 mm of crosshead (stroke) displacement to take a series of images for subsequent DIC analysis.

3 RESULTS

3.1 *Summary*

Figure 5 shows a comparison between the speckle DIC and the other strain measuring methods in a dual axis graph with load vs. strain for each axial strain instrument on the left axis and out-of-plane vs. strain on the right axis.

Figure 6 shows the detail of the pre-cracked region which is the data collected before a crack occurs within the measurement gage. When a crack occurs outside the gage area, it is not recorded in the strain measurement.

Figure 7 shows a comparison between the rectangle DIC and the other strain measuring methods in a dual axis graph with load vs. strain for each axial strain

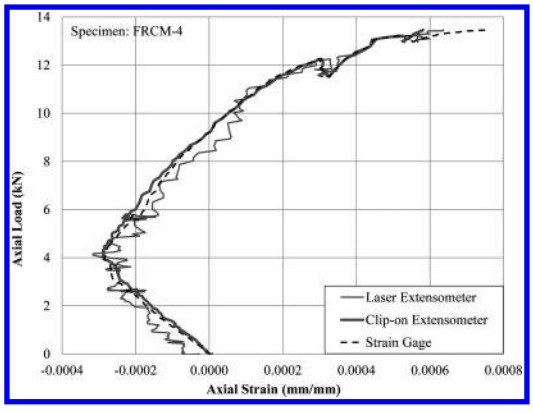


Figure 6. Detail of pre-cracked region of Figure 5.

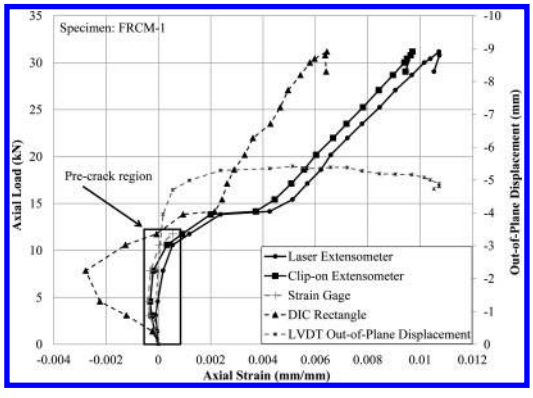


Figure 7. Comparison with rectangle DIC.

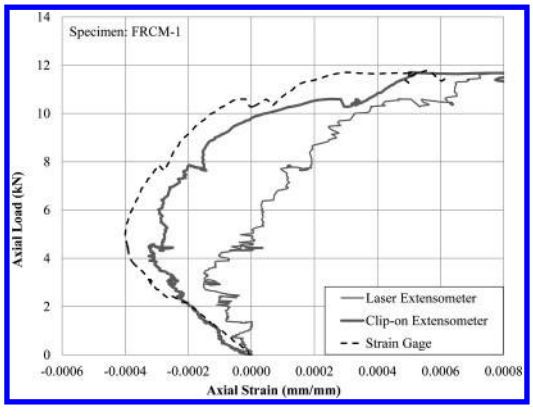


Figure 8. Detail of pre-cracked region of Figure 7.

instrument on the left axis and out-of-plane vs. strain on the right axis.

And finally, Figure 8 shows the detail of the pre-cracked region of the previous figure.

3.2 *Analysis*

Both Figure 5 and Figure 7 show that out-of-plane displacement occurred during the pre-cracking zone and then settled out as expected. It had the most significant effect in the DIC strain measurements.

The strain gage data is only useful until the initiation of a crack within the gage length. Before crack initiation, the correlation between the laser, clip-on, and strain gage is good. After the first crack occurs, the circuit is ruptured, rendering the strain gage inoperable. The laser and clip-on extensometers continue to provide consistent strain measurements with only a small offset between their strain readings. The width of each crack is not constant across the specimen and could explain this difference. Once the cracking zone of the matrix begins and the out-of-plane displacement stops, the slope of the remaining strain measuring devices are consistent with each other.

DIC methods to measure strain are based on the sub-pixel changes in the captured images. The length change indicated by the change in the number of sub-pixels is divided by the original length which is the original number of sub-pixels. The DIC methodology results show a relatively inconsistent strain result compared to the laser and clip-on extensometers. Since the DIC method is an optical method, maintaining a constant focal distance from the camera lens to the specimen is critical during the test. The LVDT data in Figure 5 and Figure 7 demonstrate that out-out-plane displacement occurred, thus, changing the distance from the camera lens to the specimen surface. A negative displacement implies the specimen surface is moving towards the camera. Any change in focal distance during loading(caused by out-out-plane specimen displacement) causes the camera to lose focus which leads to a blurred image. Moreover, that change in distance affects the perceived size of the image, which induces large errors in the subsequent strain computations.

For the DIC of the speckle pattern, a precise correlation was hard to achieve. Matlab code based on digital image correlation method was developed by Eberl et al. 2010. Matching is done by a normalized cross-correlation criterion. By detecting the extreme of the peak of C_{NCC}, the position of the deformed subset is found.

$$C_{NCC} = \frac{\sum f_i g_i}{\sqrt{\sum f_i^2 \sum g_i^2}} \quad (1)$$

Where, C_{NCC} is the coefficient of normalized cross-correlation, f_i is the gray intensity of the reference subset, and g_i is the gray intensity of the deformed subset. The Matlab code creates a list of images for analysis, and creates a grid of raster points. These raster points are considered as the center of each of the subsets. Then, during the point matching, the displacements of these raster points are detected. Finally, based on the displacement map, the full strain map is obtained.

For the DIC of the rectangle pattern, determining the change in length of the rectangle is based upon detecting the presence and location of edge pixels. Because the length change of the rectangle is smaller

than the resolution of one pixel, a sub-pixel precision edge detection algorithm was needed. In this analysis, a Gaussian curve fitting sub-pixel edge detection method was chosen (Shang *et al* 2010). The edge pixels of the image present a sharp change in grey value. The corresponding gradient curve of the edge pixels on the direction of gradient shows a gauss distribution. The Gaussian curve expression for one dimension is expressed as:

$$y = \frac{1}{\sqrt{2\pi}} e^{\frac{(x-\mu)^2}{2\sigma^2}} \quad (2)$$

Where y is the gradient value of the pixel, μ is the mean and σ is the standard deviation of the gradient value of the edge pixels.

A precise Gaussian curve is important for achieving sub-pixel accuracy. The least-squares method was applied to find the optimal Gaussian curve. Nine pixels near the edge (one pixel at the extreme gradient value and four on either side) were selected to determine a best-fit Gaussian curve. Based on the authors' judgment, the Gaussian curve was considered acceptable when the goodness of fit, R^2, was greater than or equal to 80%.Once the edge becomes blurry, the Gaussian algorithm is no longer applicable, and results in R^2 values near 0.

3.3 *Assessment of the techniques*

In addition to the analytical comparison presented earlier, other factors for comparison can be considered. These include requirements for specimen preparation, set up of equipment, and relative cost. This comparison is based upon the authors' experience as well as cost data acquired from the equipment manufacturers. In terms of specimen preparation requirements:

- Laser extensometer: to apply the reflective targets (tape),a smooth surface must be available at the gage length ends; the gage length surface should be free of any spurious reflections or covered to prevent laser beam interference.
- Clip-on extensometer: no specimen preparation is required.
- Strain gage: a smooth surface free of large discontinuities, voids, or elevations is necessary; surface preparation is extensive and includes removal of dust and other foreign debris particles, and neutralization of chemical residue on the surfaces of the specimen and strain gage; gage alignment, adhesive bonding, and wire soldering can be a time-consuming, delicate procedure requiring prior training and ample experience.
- DIC painted rectangle or speckle interferometry: a smooth surface free of voids and macrocracks is necessary; paint can be directly applied to the surface; for the rectangle DIC, a stencil or similar pattern should be utilized to achieve sharp external edges.
- LVDT: specimen preparation is not warranted, but requires the attachment of at least one contact point which can be cumbersome.

In terms of equipment set up requirements:

- Laser extensometer: the DAQ settings must be properly configured, and require adjustment depending on the brittle or ductile behavior of the specimen; a rigid base to support and align the laser to the specimen is needed.
- Clip-on extensometer: sufficient tension must be provided to prevent slippage of the knife edges or clip-on wireforms. DAQ input must be properly configured, though relatively simple.
- Strain gage: DAQ input must be properly configured, but the output signal conditioner can be complex and requires routine calibration with each strain gage.
- DIC rectangle or speckle interferometry: a rigid base and frame are needed to support the equipment and maintain alignment of the camera to the specimen; stringent lighting requirements, and software for image analysis is a necessity.
- LVDT: DAQ input can be properly configured in a simple manner.

For the cost analysis (based on having the test frame already equipped with DAQ and signal conditioning boards), the prices presented here have been normalized to the price of a strain gage (1sg) in order to show only a relative comparison since prices will vary from region to region and can be expressed in multiple currencies.

- Strain gage: 1sg per specimen and not reusable.
- Laser extensometer:750sg per device, and is reusable.
- Clip-on extensometer: 100sg per device, and is reusable.
- DIC painted rectangle or speckle interferometry: Camera with additional lens 50sg, plus Matlab license75sg (commercial or 5sg student version). This equipment is reusable.
- LVDT: 15sg and this equipment is reusable.

3.4 *Conclusions and recommendations*

The DIC method is difficult to apply for specimens which show bending or straightening behavior during the test. An improved strategy including fixtures and algorithms for minimizing the effects of out-of-plane displacement is needed for this method to work on this class of materials

Laser and clip-on extensometers are recommended as good and accurate strain measurement techniques with initial cost investment being the differential. These methodologies offer the most convenient set up ranging from little specimen preparation required to ease of equipment set up. Out-of-plane deformation should be addressed during specimen preparation if pre-cracked mechanical properties need to be studied.

LVDT's in the axial direction were not investigated in this study but are commonly used as noted in the literature. Attachment to the specimen can sometimes be cumbersome.

ACKNOWLEDGEMENTS

This material is based upon work supported by the National Science Foundation of the United States under Award No. CMMI-0922825.

REFERENCES

AC434 2013. Acceptance criteria for masonry and concrete strengthening using fiber-reinforced cementitious matrix (FRCM) composite systems. Whittier: ICC-Evaluation Service.

AC125 2010 Acceptance Criteria for Concrete and Reinforced and Unreinforced Masonry Strengthening Using Externally Bonded Fiber-Reinforced Polymer (FRP) Composite Systems. Whittier: ICC-Evaluation Service.

Arboleda, D., Loreto, G., De Luca, A., & Nanni, A. (2012). Material characterization of fiber reinforced cementitious matrix (FRCM) composite laminates. In H.W. Rivas, L.P. Seoane & I.G. Castro (eds), *10th International Symposium on Ferrocement and Thin Reinforced Cement Composite*: 29–37. Havana: FERRO 10.

ASTM Standard C1275 2010. Standard test method for monotonic tensile behavior of continuous fiber-reinforced advanced ceramics with solid rectangular cross-section test specimens at ambient temperature. *ASTM International*, West Conshohocken: ASTM.

Contamine, R., Si Larbi, A. & Hamelin, P. 2011. Contribution to direct tensile testing of textile reinforced concrete (TRC) composites.*Materials Science and Engineering*: A 528(29–30): 8589–8598.

Eberl, C., Gianola, D. & Bundschuh, S. 2010. Digital image correlation and tracking with Matlab [Online], Available: http://www.mathworks.com/matlabcentral/fileexchange/12413.

Mobasher, B. 2012. *Mechanics of fiber and textile reinforced cement composites*Boca Raton: CRC press.

Naaman, A. E. & Shah, S. P. 1979. Fracture and multiple cracking of cementitious composites. In S.W. Freiman (ed), *Fracture Mechanics Applied to Brittle Materials*: 183–201. Baltimore: American Society for Testing and Materials.

Pan, B., Qian, K., Xie, H., & Asundi, A. 2009. Two-dimensional digital image correlation for in-plane displacement and strain measurement: a review. *Measurement Science and Technology* 20: 1–17.

Qian, S.&Zhang, Z., 2012, Comparison of tensile properties of strain hardening cementitious composite cured in normal and accelerated conditions. *Journal of Testing and Evaluation*4(5): 1–6.

RILEM TC 201-TRC 2006. In Brameshuber, W. (ed), *Textile Reinforced Concrete State-of-the-art Report of RILEM TC 201-TRC*, Bagneux: RILEM.

Shang, Y.C., Chen, J. & Tian, J.W. 2010. The study of sub-pixel edge detection algorithm based on the function curve fitting, *2010 2nd International Conference on Information Engineering and Computer Science (ICIECS)*: 1–4.

Silva, F, Mobasher, B.,& Filho, R.D.T. 2000. Cracking mechanisms in durable sisal fiber reinforced cement composites. *Cement and Concrete Composites* 31(10): 721–730.

Zhang, Z. 1999. Flexible camera calibration by viewing a plane from unknown orientations, *Proceedings of the Seventh IEEE International Conference on Computer Vision* 1:666–673.

Research and Applications in Structural Engineering, Mechanics and Computation – Zingoni (Ed.)
© 2013 Taylor & Francis Group, London, ISBN 978-1-138-00061-2

Strut and tie models for disturbed regions: Steel fibre reinforced concrete dapped end beams

Jorun-Marie Hisdal
SINTEF Building and Infrastructure, Trondheim, Norway

Giedrius Zirgulis, Elena V. Sarmiento & Terje Kanstad
Department of Structural Engineering, the Norwegian University of Science and Technology (NTNU), Trondheim, Norway

ABSTRACT: Within a relatively large Norwegian research programme, denoted COIN (Concrete Innovation Centre) covering a broad range of concrete research topics, fibre reinforced dapped end beams (beams with corbel ends) have been tested to study the structural behaviour of fibre concrete in discontinuity regions (D-regions). Ordinary strength concrete with 1% (80kg/m^3) 60 mm long end hooked steel fibres has been used. The shear reinforcement and the splitting tensile reinforcement in the beam ends used in the traditional solution have been partially or fully removed. The typical strut and tie models commonly used in practical design of D-regions have been modified to include the effect of the fibres. A simplified reinforcement layout to be used together with steel fibres is proposed, and gives similar capacity and ductility as today's standard solution without fibres. Furthermore beams with fibres replacing all the transversal and splitting tensile bars, also give reasonable strength and ductility, and can therefore be recommended for structures with low load levels. In the current fibre project flowable concrete generally is preferred, and fibre distribution and orientation, and the influence of the casting process are major topics. Therefore fresh concrete testing has been carried out by the LCPC box and the 4C Rheometer, and sections are cut and the amounts of fibres recorded and compared to theoretical values. The research activity is continuing, and the results and conclusions are not final.

1 INTRODUCTION

Steel fibres may be used as replacement for shear, additional anchorage and splitting tensile bar reinforcement in the discontinuity regions (D-regions) of concrete structures, i.e. the regions where the beam theory (B-regions) does not hold. Only limited research is done with FRC for this type of problems, however the topic is important since design rules for FRC now are being to standardized for load carrying structures, see f.i. FIB Model Code (2011), and ongoing work for revision of Eurocode. One type D-region is the dapped ends (corbel ends) of prefabricated beams commonly used in precast concrete structures. Another problem considered within the same project is replacement of additional reinforcement around openings in beams, and replacement of these bars with fibres. The motivation for both topics are cost and work-hour savings, and potentially also better structural performance (i.e.less cracking).

These particular problems are not theoretically complicated problems; however, obtaining general design rules might be difficult due to the large number of important parameters involved: shear span to depth ratio, scale effect, concrete strength, fibre type, fibre content, fibre distribution and orientation, and finally amount of reinforcing bars. The work described in this paper must therefore be considered as a first attempt to establish a basis for the models, and one aim of the present paper is to compare test results with results from the proposed strut and tie model and illustrate the applicability of the theory on FRC structures.

In two experimental series, Backe-Hansen & Hamstad 2011 and Nordbrøden & Weydahl 2012, the shear reinforcement and the splitting tensile reinforcement in the dapped beam ends have been partially or fully removed to study the fibres effects on the structural behaviour. For simplicity reasons, only the second test series is presented in detail in this paper, however, the results from both series are included in the final evaluation of the proposed strut and tie model.

Due to well-known synergies between self-compacting concrete and fibres (Døssland 2008), the ambition in the on-going project is to use flowable concrete. Special attention is therefore being paid to the fresh concrete properties and the casting technique, and the fibre orientation and distribution in the critical sections have been studied on sawn parts of the structural elements.

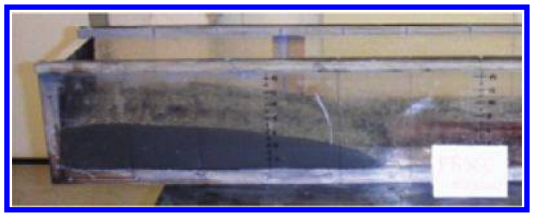


Figure 1. Flowable FRC (80 kg/m^3 steel fibres) in the LCPC box.

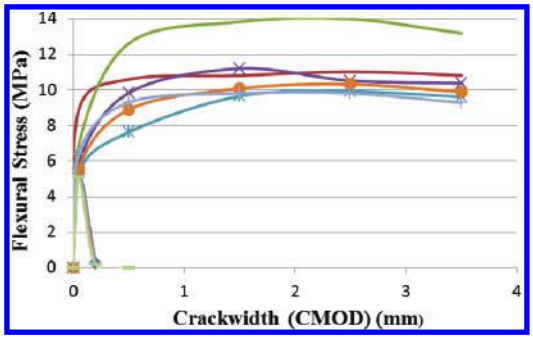


Figure 2. Stress-crackwidth (CMOD) relation for standard 3-point bending tests (EN14651).

2 MATERIALS AND TEST PROGRAM

The concrete qualities used in the two series are B70 and B40 in series 1 and 2, respectively. In both concretes 1 volume % (80kg/m^3) end hooked 60 mm long steel fibres were used.

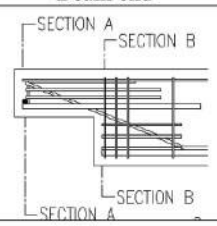
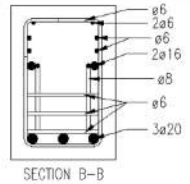
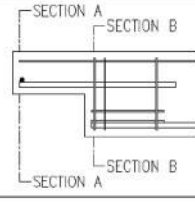
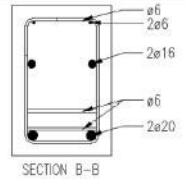
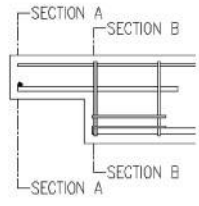
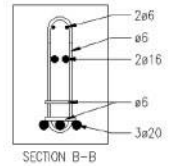
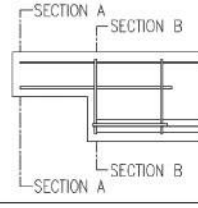
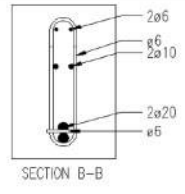
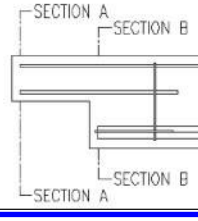
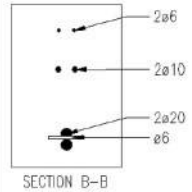
Fresh concrete testing was carried out, and the yield stresses measured from 4C-Rheometer (Thrane et.al. 2010) were 55 Pa for the plain concrete and 75 Pa for the fibre reinforced concrete, which are compatible with the values found from the LCPC box (Rousell 2007). The latter test is shown in Figure 1 below, and is also an illustration of the concrete's consistency and casting properties.

The residual tensile strengths were determined by three-point bending of notched standard beams according to EN14651 (150/150/550 mm), and the results for the six FRC-beams and 3 plain concrete beams for series 2 are presented in Figure 2. For this series the average strength values are: Residual bending strength at 2,5 mm crackwidth (CMOD): 10,9MPa, residual tensile strength at the same crackwidth: 4,0MPa, and finally the limit of proportionality in bending: 6,5MPa. The corresponding compressive cylinder strength is 52,3MPa.

The cross section and length of the beams were 200/300 mm and 2500 mm, and the vertical load was placed 2,5 times the effective height of the beam from the support. The load location was unsymmetrical so that each beam could be tested at both ends, i.e. two test results per beam.

The reinforcement layout of the beams in the second series is presented in Table 1 below. Beam A and B are the reference beams without fibres, while beam C, D and E are fibre reinforced beams with less reinforcing bars than A and B. As shown in the Table, the amount of transversal reinforcement is reduced with the beam names in alphabetic order. In the FRC beams the reinforcing bars are drawn towards the centre-line of the cross sections to improve the casting conditions, i.e. to prevent weak zones between the stirrups and the formwork walls, and to arrange for the wall effect which contributes towards favourable fibre orientation.

Table 1. Reinforcement layout of beam series II.

	Beam end	Section B-B
A		
B		
C		
D		
E		

3 STRUT AND TIE MODELS (STM) APPLIED TO DAPPED BEAM ENDS

The STM is a simplified method where the load carrying model consists of compressive struts, tensile ties and nodes where the concentrated loads act.

There are in general no unique models for the various design situations, but since the method is commonly used procedures and proposals are presented in many text books and research literature, see f.i. Schlaich et.al.1987. Following the right procedures, the method is a lower bound method related to the theory of plasticity, and gives in general results on the safe side.

Figure 3a below shows the typical load situation, and the principal stress fields for the considered D-region problem. For ordinary reinforced concrete the traditional solution is to locate the tensile reinforcement in accordance with the tensile stress lines as shown in Figure 3b, and thereafter define the tensile ties in the STM in accordance with the tensile bars as shown in Figure 3c and 3d. For the traditional solution with both vertical stirrups and diagonal bars the shear capacity can simply be expressed as:

$$V_{Rd} = V_{Rd,incl} + V_{Rd,vert}$$
$$V_{Rd,incl} = A_{s\alpha}\, f_{yk} \sin\alpha \text{ and } V_{Rd,vert} = A_{sv}\, f_{yk} \quad (1)$$

In which V_{Rd} is the total shear capacity, $V_{Rd,incl}$ and $V_{Rd,vert}$ are the shear capacities due to the diagonal and vertical bars, respectively, and $A_{s\alpha}$ and A_{sv} are the areas area of diagonal and vertical shear reinforcement.

For FRC it is impractical to include the diagonal bars, so in this case the capacity may be calculated by combining the contribution from vertical stirrups and a fictitious fibre concrete tie with geometry in accordance with the distribution of principal tensile stresses as illustrated in Figure 3e. Thus the capacity can be expressed as:

$$V_{Rd} = V_{Rd,vert} + V_{Rd,fibre}$$
$$V_{Rd,vert} = A_{sv}\, f_{yk} \text{ and } V_{Rd,fibre} = f_{res2,5}\, b_w\, t_f \quad \sin\alpha \quad (2)$$

The following symbols have been used: $V_{Rd,fibre}$ is the shear capacity due to the diagonal fibre concretetie, α is the angle between the system axis and the fibre tie, $f_{res2,5}$ is the residual tensile strength determined from EN14651 at CMOD = 2,5 mm, and b_w and t_f are the assumed dimensions of the fibre tie.

4 TEST RESULTS

Figure 4 presents measured load versus mid-point deflection curves for the tested beams. It can be seen that the simplified reinforcement layout proposed to be used together with steel fibres (beam C and D) gives about the same capacity and ductility as the traditional reinforcement solution (beam A). It is also shown that the solution with fibres only (beam E, with longitudinal bars, but no tranversal reinforcement) gives reasonable strength, and can be recommended for structures with relatively low load levels.

Furthermore Figure 5 does show typical crack patterns and measured crack deformations for beam types A (traditional reinforcement), and C (simplified reinforcement layout). Figure 6 shows corresponding results for beam E (no transversal reinforcement).

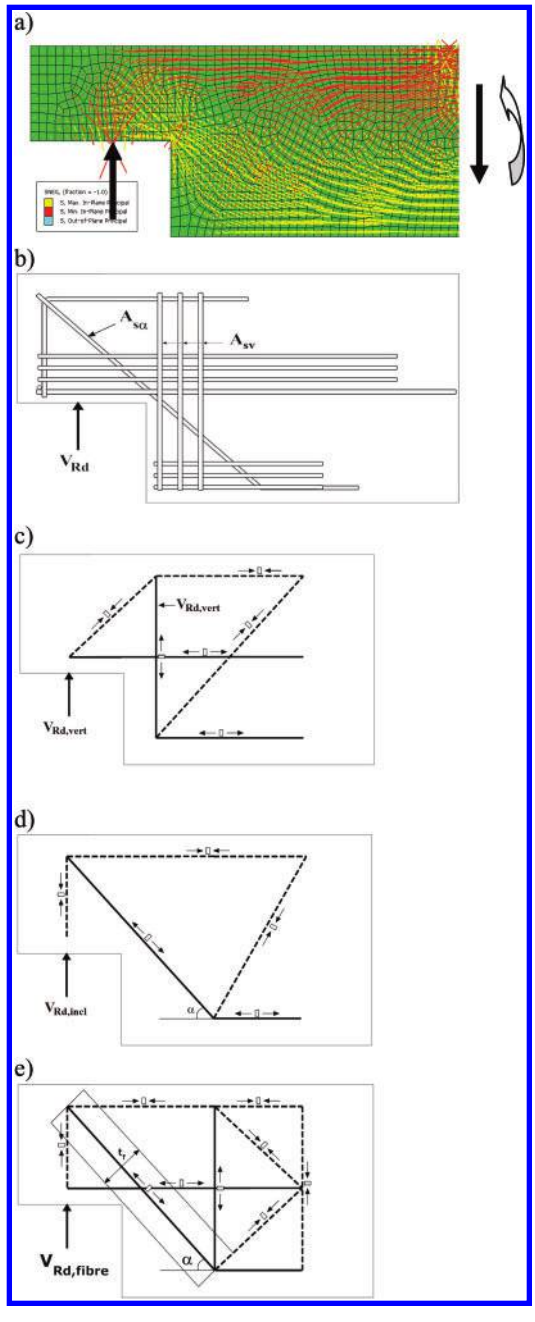


Figure 3. Strut and tie models. (a) Principal stresses from linear elastic FE analysis. (b) Traditional reinforcement layout, (c) Model for capacity contribution of vertical stirrups, (d) Model for capacity contribution from diagonal bars, (e) Model for the fibre contribution.

Comparing the crack patterns, it is seen that while the traditional solution contains several cracks distributed over a large area, only one or two cracks are present for the fibre reinforced beams. These experimental results are further evaluated by means of nonlinear

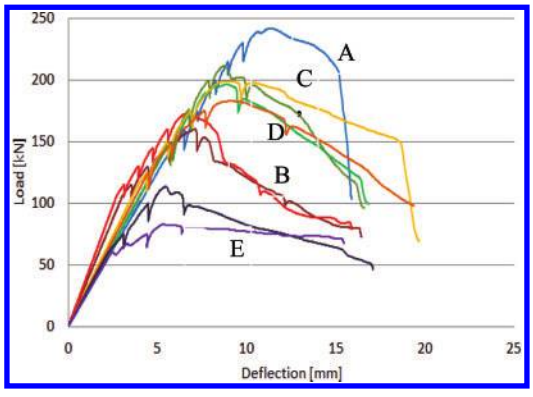


Figure 4. Load versus mid-point deflection for the tested beams in series 2.

FE analysis in an ongoing PhD work (Sarmiento to be published in 2015).

Finally, the overall agreement between the strut and tie model and the total amount of experimental results is presented in Figure 7 where it can be seen that the general agreement is satisfactory, and that the results generally are on the safe side.

As shown previously the fibre concrete's shear capacity contribution is described as:

$$V_{Rd,fibre} = f_{res2,5}\, b_w\, t_f\, \sin\alpha$$

Obviously there are uncertainties due to the involved parameters, but so far the parameters are based on Figure 3a with $\alpha = 35^o$.

The strength $f_{res2,5}$ is set to 0,37 times the residual bending strength at 2,5 mm CMOD although the fibre orientation is more favourable in the beam test of EN14651 than in the critical part of the dapped end beam as shown and discussed later in this paper.

5 FIBRE ORIENTATION

As previously stated, fibre distribution and orientation is a major topic within the current project, and therefore various sections have been cut and the amounts of fibres crossing the sections recorded and compared to theoretical values.

To relate the real fibre orientation to the corresponding theoretical values is an important part of the result evaluation, and therefore, the number of fibres crossing various sections of the tested specimens has been recorded by manual marking and image analysis. The orientation factor was calculated using the following expression:

$$\alpha = \frac{n_f \cdot A_f}{v_f} = \frac{N \cdot A_f}{A_c \cdot v_f}$$

where: n_f is the number of fibres per concrete unit surface; A_f is the cross-section of a fibre; v_f is the nominal fibre volume fraction; N_f is the number of fibres in the concrete cross-section with area A_c.

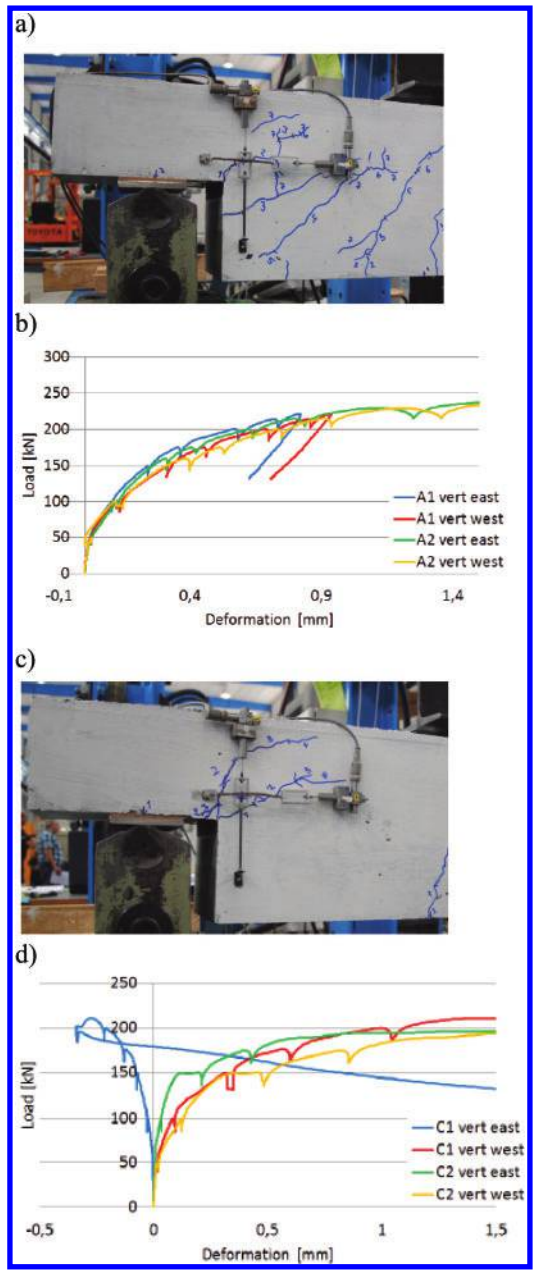


Figure 5. Crack pattern and measured vertical crack deformations for beam types A (a,b) (traditional reinforcement) and C (c,d) (simplified reinforcement layout and fibres)

Under isotropic conditions the orientation factor should be equal to 0,5, while it theoretically is 1,0 if all fibres are directed in one direction normal to the considered plane.

In beam series 1, 150 mm cylinders were drilled out in the critical zone as shown in Figure 8 below., Referring to the eight cylinder sectors the average orientation factors four of the tested beams were as follows: 1: 0,51, 2: 0,71, 3: 0,53, 4: 0,35, 5: 0,48, 6:

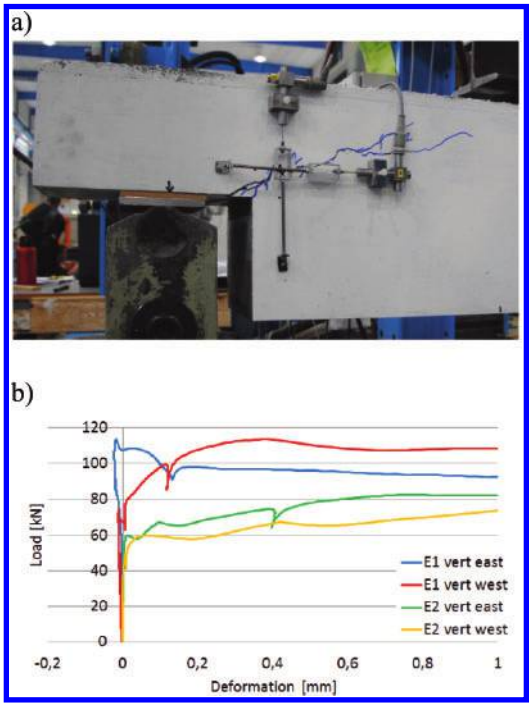


Figure 6. Crack pattern (a) and measured vertical crack deformations (b) for beam type E (no transversal reinforcement, only fibres)

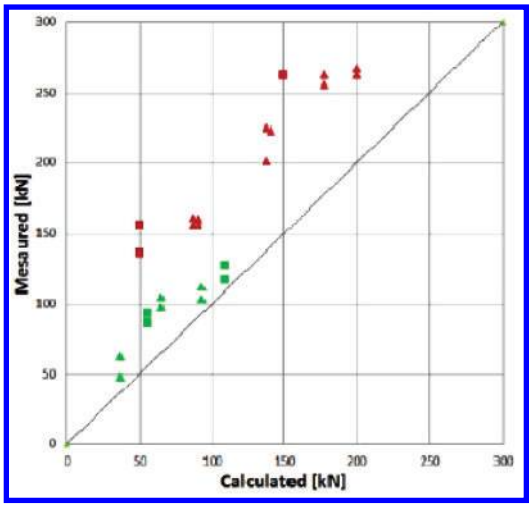


Figure 7. Experimental failure capacities versus strength calculated by the strut and tie models for all beams in both series.

0,56, 7: 0,55, 8: 0,51. The scatter is large, but as the overall average value is 0,51, the results indicate that the fibre distribution is isotropic.

For the second beam series the evaluation of the fibre distribution and orientation is not completed yet. However some interesting results can be referred. The standard beams (EN14651) used to determine the

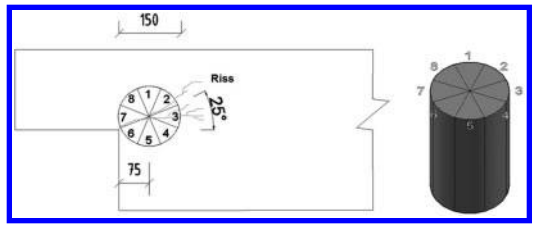


Figure 8. Drilled cylinders for fibre counting and determination of orientation factors.

residual tensile strength show a relatively favourable fibre orientation, in average $\alpha = 0{,}77$ for the longitudinal direction which is decisive for the residual strength. In general this is as expected based on previous experience with similar concretes even if the execution procedure of the standard is followed as closely as possible. Considering sections in the critical parts of the dapped end beams the orientation factor for the longitudinal direction is in average 0,43, for the beams with stirrups close to the height step, which corresponds reasonably well with the results on the cylinder shown previously in Figure 6. For beam E without stirrups, the fibre orientation is more pronounced in the longitudinal direction, $\alpha = 0{,}78$, which is more in agreement with the situation in the standard beams. Thus, it can be concluded that stirrups considerably influence the fibre orientation even if as in this case precautions are taken to reduce the problem by modifying the reinforcement layout. The strong fibre orientation in the longitudinal direction in beam E may also explain the direction of the cracks shown in Figure 6 which indicates that the horizontal plane is weaker than the vertical plane.

Currently these sawn sections are further evaluated by image analyses on several planes (directions) and CT scanning of sawn elements, and the data will be more thoroughly published later (Zirgulis to be published in 2014).

6 CONCLUSIONS AND PLANS FOR FURTHER WORK

Fibre reinforced dapped end beams have been tested to study the structural effect of fibres in D-regions, i.e. regions in structural elements where the beam theory doesn't hold. Ordinary strength concrete with 1% (80 kg/m^3) 60 mm long end hooked steel fibres have been used, and the shear reinforcement and the splitting tensile reinforcement in the beam ends used in the traditional solution have been partially or fully removed to study the effects of the fibres on the structural behaviour.

The proposed alternative simplified reinforcement layout to be used together with steel fibres gives similar capacity and ductility as today's standard solution without fibres. Furthermore does the solution with fibres only, also give reasonable strength, and can be recommended for structures with low load levels.

The typical strut and tie models commonly used in practical design of D-regions have been modified to include the effects of the fibres. In general the model is in good agreement with the experimental results, although a certain uncertainty is devoted to the input parameters in the model.

By recording the amount of fibres crossing sawn sections from the structural elements, it is shown that the fibre orientation in the standard beams (EN14651) is more favourable than in the critical zones of the dapped end beams. It is also shown that transversal reinforcement influences the fibre orientation considerably.

Three ongoing research activities continues the work described in this paper; (1)Nonlinear FE analysis of the tested elements, (2)More thorough registration of the fibre distribution and orientation, and finally (3) tests on beams with openings in the web.

ACKNOWLEDGEMENT

The paper is based on the work performed in COIN – Concrete Innovation Centre (www. coinweb.no) – which is a Centre for Research based innovation, initiated by the Research Council of Norway in 2006. The Centre is directed by SINTEF, with NTNU as research partner and with the present industrial partners: Kværner, Norcem, Norwegian Public Roads Administration, Rescon Mapei, Skanska, Unicon, Veidekke and Weber Saint Gobain.

REFERENCES

Backe-Hansen, T. & Hamstad B. 2011. Fibre reinforced concrete structures – Testing of prefabricated beams with dapped ends, MSc-thesis, Department of Structural Engineering, NTNU , Trondheim, Norway.

Døssland, Å.L. (2008),"Fibre Reinforcement in Load Carrying Concrete Structures". Doctoral Thesis. Department of Structural Engineering, NTNU 2008:50. Trondheim, Norway. ISBN 978-82-471-6910-0.

FIB Model Code (2011) . FIB Lausanne.

Kanstad, T., Sandbakk, S., Geiker, M.R. & Martius-Hammer, T.A. 2012. Flowable fibre reinforced concrete: materials development, fibre distribution and structural properties. Proceedings of the ERMCO conference, Verona, Italy.

Nordbrøden, H.H. & Weydahl, S.H. 2012. Testing of fibre reinforced concrete structures – Shear capacity of beams with corbel ends, MSc-thesis, Department of Structural Engineering, NTNU , Trondheim, Norway.

Roussel. N. 2007. The LCPC BOX: a cheap and simple technique for yield stress measurements of SCC. Materials and Structures (2007) Vol 40: pp 889–896.

Thrane, Lars N., Pade, Claus, Nielsen, Claus V. 2010. Determination of Rheology of Self-Consolidating Concrete Using the 4C-Rheometer and How to Make Use of the Results", Journal of ASTM International (JAI), Volume "7, Issue 1, 10 pages, January 2010.

Sandbakk, S. 2011. Fibre Reinforced Concrete Evaluation of test methods and material development, PhD thesis, Department of structural engineering, NTNU, Trondheim, Norway.

Sarmiento, E.V., Zirgulis, G., Sandbakk, S., Geiker, M.R. & Kanstad, T. 2012. Influence of concrete flow on fibre distribution, orientation and mechanical properties of fibre reinforced concrete, BEFIB 2012, The 8th International conference on fibre reinforced concrete, Guimaraes, Portugal.

Schlaich, J., Schafer, K. & Jennewein, M. 1987. Toward a Consistent Design of Structural Concrete. Journal of Prestressed Concrete Institute, V.32, No.3, May-June 1987, pp 74–150.

Research and Applications in Structural Engineering, Mechanics and Computation – Zingoni (Ed.)
© 2013 Taylor & Francis Group, London, ISBN 978-1-138-00061-2

Study of the properties of hybrid fibre reinforced concretes

T. Zych
Cracow University of Technology, Cracow, Poland

ABSTRACT: The results of research concerning the properties of fresh concrete (consistency and air content) and hardened concrete (water absorption, compressive strength, flexural strength, flexural toughness) of hybrid fibre-reinforced concretes are presented in this paper. Cases considered were as follows: five types of hybrid reinforcement;one combination of steel fibres: long (60 mm) hooked-end steel fibres and short (13 mm) straight steel fibres; three combinations of steel-polypropylene fibres: short (35 mm) hooked-end steel fibres (with single hooks), long (60 mm) hooked-end steel fibres (with single or double hooks) and (19 mm) fibrillated polypropylene fibres); one combination of polypropylene fibres: long (60 mm) bi-component macrofibres and (19 mm) fibrillated polypropylene fibres. These types of fibres are modern and popular. The results for concretes with hybrid fibres were compared with the obtained properties of concretes without fibres and with one type of fibre.

1 INTRODUCTION

Several types of fibres for cement composites, different in material and geometry (shape, dimensions) are produced. The most popular fibres are steel, polypropylene, glass. The addition of randomly distributed fibres into concrete improves its properties, mainly related to the behaviour under tension. Each type of fibres modifies concrete properties in different ways (Bentur& Mindess 1990, Hannant 2003). The effect of fibres, which are strong and stiff (having high tensile strength and modulus of elasticity), e.g. steel fibresdiffers from that observed in the case of fibres with low tensile strength and modulus of elasticity (flexible fibres), e.g. polypropylene fibres. Steel fibres can improve the mechanical properties (tensile strength, flexural strength, flexural toughness due to crack bridging, impact strength) whereas polypropylene fibres can prevent the cement matrix from shrinkage crack formation and propagation. Moreover, polypropylene fibres protect concrete against spalling under the impact of fire. As regards fibres different in geometry, short and long, their influence on the properties of concrete also varies (Markovic 2006). Short fibres can bridge microcracksmore efficiently than long fibres, because they are very thin and their number in concrete is much higher than that of the long thick fibres for the same fibre volume quantity. Taking into account that microcrack formation and crack bridging by fibres occurs in the first phases of tensile loading, short fibres can have a significant influence on the increase in tensile strength. However, long fibres can provide a stable post-peak response. When microcracks grow and join into larger macrocracks, long fibres become more and more active in crack bridging (Fig. 1). Ductility (toughness) can be

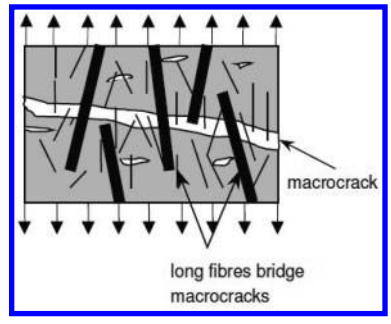


Figure 1. Short thin fibres and long thick fibres sewing cracks (Markovic 2006).

improved, and partly also tensile strength. During this time short fibres are less active, because they are pulled out.

To utilize the individual properties of each type of fibres, the combination of different types of fibres is applied. The benefits of combining fibres were recognized nearly 40 years ago (Walton & Majumdar 1975). However, experimental studies of the properties of concretes with hybrid fibres (combinations of different kinds of steel fibres, steel-polypropylene fibres, polymer fibres, etc.) have only been conducted by a number of research centersin the last few years.Because the hybrid reinforcementcan provide interesting application of fibre reinforced concretes, new researchis expected, but carried out by researchers using the same test method (to be able to compare the test results). The tests of flexural properties of hybrid fibre reinforced concretes, presented in the literature were conducted according to various standards (using notched or un-notched beams, with three-point or

four-point loading):American standard ASTM C1018 (1997), European standard EN 14651 (2007) (based on RILEM TC162-TDF), Italian standard UNI 11039 (2003),Japanese standard JCI-SF4 (1984), etc. (see References).

The paper presents the results of the investigations on the properties of fresh and hardened cement concretes withthe following types of hybrid reinforcement: steel-steel combination: long (60 mm) hooked-end steel fibres + short (13 mm) straight steel fibres,steel-polypropylene combinations: short (35 mm) hooked-end steel fibres (with single hooks) or long (60 mm) hooked-end steel fibres (with single or double hooks) + (19 mm) fibrillated polypropylene fibres, polypropylene-polypropylene combination: long (60 mm) bi-component macrofibres + (19 mm) fibrillated polypropylene fibres.

2 EXPERIMENTAL DETAILS AND TEST METHODS

2.1 *Materials*

Portland cement type I CEM I 42.5R (Gorazdze Cement SA), river sand 0–2 mm, crushed granite 2–8 mm and 8–16 mm, water and superplasticizer were used to make cement concrete – the matrix(M) of fibre reinforced concretes. The sand content was 33% of the aggregate content. Water-cement ratio was 0.45. The cementpaste content was 325 dm^3/m^3. The composition of concrete mixture is shown in Table 1.Different types of fibres were applied in the study – four types of steel fibres: 13 mm long, straight fibres (SF13), 35 mm or 60 mm long, hooked-end fibres with single hooks (SF35 or SF60), 60 mm long, hooked-end fibres with double hooks (SF60d) and two types of polypropylene fibres: 19 mm long, fibrillated fibres (PF19), 60 mm long, bi-component fibres (PF60). They are the most frequently used fibres in practice. The characterisics of applied fibres are shown in Tables 2-3 and Figures 2–3. Hooked-end steel fibres are glued in bundles. According to the producer fibrillated polypropylene fibres are two-side coated with a special substance that enlarges the surface of fibres and facilitates dispersion of fibres in the cement paste. Bi-component fibre consists of a core (high tensile strength, high E-modulus polymer) and a shell (Fig. 3). The structured and nano-modified shell (the embossed surface of the shell and surface activating additives) ensures excellent binding to the cement matrix.Fibres were applied as the mono-fibre reinforcement (SF35, SF60, SF60d, PF60) or hybrid reinforcement (SF60 + SF13, SF35 + P19, SF60 + P19, SF60d + P19, P60 + P19) of the concrete matrix (Table 4). The content of fibres was similar to that used in practice. Each type of steel fibres was added to the cement matrix in the amount of 30 kg/m^3 (0.38% by volume). The content of fibrillated polypropylene fibres was always 1 kg/m^3 (0.11% by volume). As regards bi-component polypropylene fibres, the content of fibres was 2 kg/m^3 (0.22% by volume) (minimum amount recommended by the manufacturer) in the case of mono-fibre reinforcement and 1 kg/m^3 in the case of hybrid reinforcement (the combination with 1 kg/m^3 of fibrillated polypropylene fibres).

Table 1. Composition of concrete mixture.

CEM I 42.5 R	421	kg/m^3
Sand 0-2 mm	590	kg/m^3
Crushed granite 2–8 mm	599	kg/m^3
Crushed granite 8–16 mm	599	kg/m^3
Water	189	kg/m^3
Superplasticizer Viscocrete 3088 M (0.7% m.c.)	2.9	kg/m^3
W/C	0.45	–
Cement paste content	325	dm^3/m^3

Table 2. Properties of steel, polypropylene fibres.

	Length l, mm	Diameter d, mm	Aspect ratio, l/d
SF13	13	0.2	65
SF35	35	0.55	65
SF60	60	0.75	80
SF60d	60	0.9	65
PF19	19	0.08	
PF60	60	0.5	

	Tensile strength, MPa	Modulus of elasticity, GPa	Quantity of fibres per kg	Name
SF13	2000	210	~314,000	OL 13/0.20
SF35	1345	210	~14,500	Dramix 3D 65/35 BG
SF60	1225	210	~4600	Dramix 3D 80/60 BG
SF60d	2300	210	~3200	Dramix 5D 65/60 BG
PF19	400	4.9	~2,500,000	High Grade 190
PF60	618	>10	~100,000	Concrix
Cement paste	3–6	10–30		

Table 3. Steel fibres (SF13, SF35, S60, S60d).

SF13	SF35	SF60	SF60d
Straight steel fibres, l = 13 mm	Hooked-end steel fibres, single hooks, l = 35 mm	Hooked-end steel fibres, single hooks, l = 60 mm	Hooked-end steel fibres, double hooks, l = 60 mm
—			

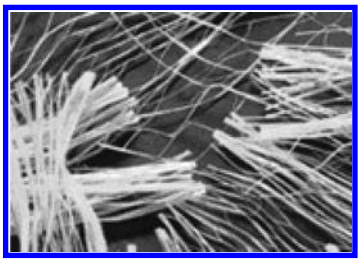


Figure 2. Fibrillated polypropylene fibres, l = 19 mm (PF19).

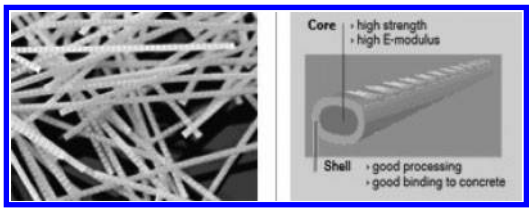


Figure 3. Bi-component polypropylene fibres, l = 60 mm (PF60).

Table 4. Content of fibres.

Name of concrete mixture	Steel fibres, kg/m^3	Polypropylene fibres, kg/m^3
M (without fibres)	–	–
M + SF35	30	–
M + SF60	30	–
M + SF60d	30	–
M + PF60	–	2
M + SF60 + SF13	30 + 30	–
M + SF35 + PF19	30	1
M + SF60 + PF19	30	1
M + SF60d + PF19	30	1
M + PF60 + PF19	–	1 + 1

2.2 *Preparation of specimens*

The research were conducted on fresh and hardened (28-day) cement concretes with and without fibres. All specimens were demoulded after 24 hours and cured in high humidity conditions RH > 90% and at the temperature of + 20°C until the age of 28 days.

2.3 *Test methods*

The following properties of fresh and hardened concretes, with and without fibres, were analysed: consistency, air content, water absorption after 28 days, 28-day compressive and flexural strength, load-deflection relation. Consistency was determined by the slump test (according to EN 12350-2). For measuring the air content in fresh concrete mixtures (after consolidation on the vibrating table)the pressure method (according to EN 12350-7) was used. Water absorption was tested according toPN-88/B-06250. Compressive strength test was conducted according to EN 12390-3. 100 mm and 150 mm cube specimens were used



Figure 4. Set-up for performing bending tests.

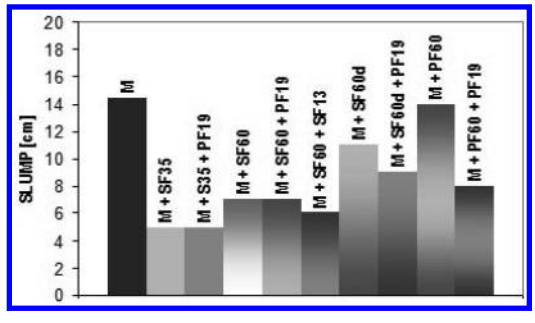


Figure 5. Slump (slump classes: S2- slump: 5-9 cm, S3- slump: 10-15 cm) of concrete mixtures with and without fibres.

to test water absorption and compressive strength, respectively. The behaviour of each concrete at bending was investigated using a 100 × 100 × 500 mm beam as a specimen. Three-point bending test (according to EN 12390-5) was used (Fig. 4). The distance between supports was 300 mm.The deflection rate was 1 mm/min. During the flexural strength examination, force-deflection relation was determined. The tests of mechanical properties of fibre reinforced cement concretes were carried out at Cracow University of Technology, Faculty of Civil Engineering; Zwick/Roell Z100 press was applied (Fig. 4). Water absorption for every type of concrete was tested on six specimens. Each mechanical property was assessed on three specimens.

3 RESULTS AND DISCUSSION

3.1 *Consistency*

The concrete mixtures tested characterize the classes of consistency of S2, S3 (Fig. 5). The influence of the presence of fibres on consistency depends on the type of fibres. As regards the mixtures with one type of fibre, the effect is more significant in the case of rigid steel fibres than polypropylene fibres. The dominant effect is noticeable for the mixture with steel fibres of

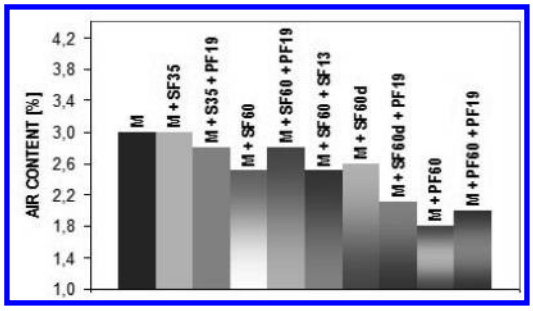


Figure 6. Air content of concrete mixtures with and without fibres.

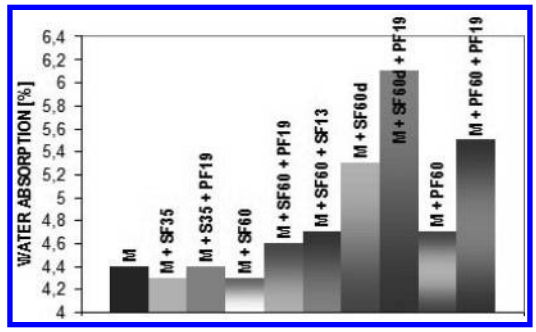


Figure 7. Water absorption of concrete with and without fibres.

the length of 35 mm (SF35) (the reduction of the slump from 14.5 cm to 5 cm for the fibre content of 30 kg/m^3). It can result from the large numberof fibres(about 14,500 fibres per kg), which is greaterthan 4600 and 3200 fibres per kgfor steel fibres of the length of 60 mm with single hooks (SF60) and double hooks (SF60d),respectively (Table 2). As regards the mixtures with hybrid fibres, polypropylene microfibres (fibrillated, 19 mm long) (PF19) (in the amount of 1 kg/m^3) have the insignificant influence when they are combined with SF35 or SF60 steel fibres. But polypropylene microfibres added together with SF60d steel fibres into the concrete matrix (M)reduce liquidity more than SF60d used as one type of fibres (the slump of 11cm for M + PF19 + SF60d and 9 cm for M+SF60d). Also in the case of the combination of short steel fibres of the length of 13 mm (SF13) with SF60 steel fibres, the mixture is less liquid than that with SF60 fibres (one type of fibres). The hugequantity of short fibres SF13 (about 314,000 fibres per kg) improves the compaction of the mixture. The influence of polypropylene fibres on consistency is negligible for macrofibres (bi-component fibres) (PF60) in the amount of 2 kg/m^3 and considerable for the combination of 1 kg/m^3 macrofibres and 1 kg/m^3 microfibres (PF60 + PF19). Although the amount of fibres – 2 kg per 1 m^3 is the same in both mixtures, consistency varies. The liquidity of the mixture with one type of fibres (macrofibres) and the mixture without fibres is hardly differ (the slump of 14 cm and 14.5 cm, respectively) whereas hybrid fibres reduce the slump from 14.5 cm to 8 cm. The greater effect of hybrid fibres than polypropylene macrofibres on liquidity can result from the huge quantity of microfibres (about 2,500,000 pieces of polypropylene microfibres as compared to about 100,000 pieces of polypropylene macrofibres, for the fibre content of 1 kg/m^3).

3.2 *Air content*

The values of air content are not larger than 2% for mixtures with polypropylene fibres (Fig. 6). The large number of fibres in the case of hybrid polypropylene reinforcement (PF60 + PF19) (see Section 3.1) and then the difficulty in the proper compaction of the mixturecan cause high air content (air content is larger than for mono-fibre polypropylene reinforcement (PF60)). The influence of rigid steel fibres on air content is noticeable. The higher the number of steel fibres (see Section 3.1), the higher the air content. The largest value of the air content (3%) is observed for the mixture with steel fibres of the length of 35 mm (SF35).

3.3 *Water absorption*

The slight decrease in water absorption of concretes with SF35 or SF60 steel fibres (Fig. 7) can result from the positive effect of fibres on the reduction of shrinkage strains and then crack formation. For other types of fibre reinforced concretes tested, water absorption is higher than for concrete without fibres. Since water absorption is highly dependent on workability of the concrete mixture, which considerably worsens after the addition of a large number of thin fibres (polypropylene fibres) or fibres long,complicated in their shape (e.g. steel fibres of the length of 60 mm with double hooks (SF60d)), the largest value of water absorption (6.1%) is observed in concrete with the combination of SF60d steel fibres and 19mm polypropylene fibrillated fibres (PF19).

3.4 *Compressive strength*

The influence of the addition of one type of steel fibres (SF35 or SF60 or SF60d) or hybrid steel fibres (SF60 + SF13) on 28-day compressive strength is insignificant (Fig. 8).

Polypropylene fibres decrease this property by about 10% in the case of the combination of polypropylene macrofibres (PF60) and microfibres (PF19), and by about 8% for polypropylene macrofibres. Also polypropylene microfibres (PF19) used with steel fibres of the length of 60 mm (SF60, SF60d) slightly reduce compressive strength.

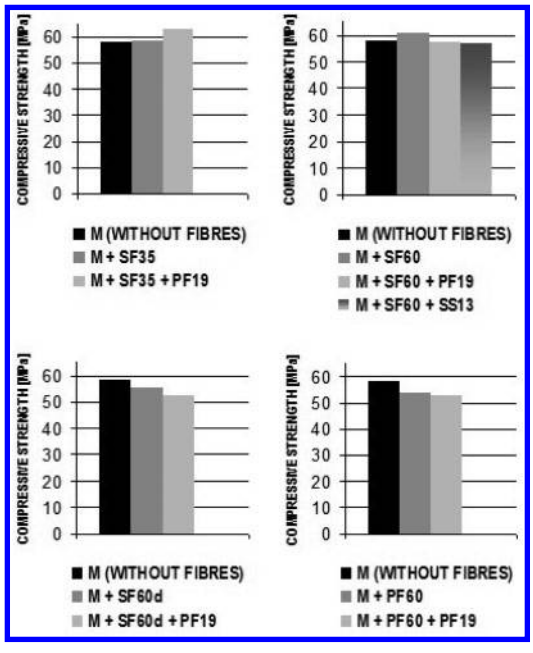


Figure 8. 28-day compressive strength of concretewith and without fibres.

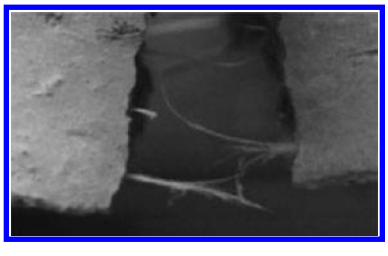


Figure 9. Bi-component polypropylene fibres, broken during the destruction of the beam.

3.5 *Flexural strength*

The behaviour at bending of 28-day concretes tested, recorded as the load-deflection curves is reported in Figure 10. The obtained curves show the synergistic effect of hybrid fibres. The deflection, accompanying the appearance of the first crack is greater for concrete containing the combination of SF35 steel fibres or SF60 steel fibres or PF60 polypropylene macrofibres with PF19 polypropylene microfibres than for concrete with the mono-fibre reinforcement and concrete without fibres. The positive influence of PF19 fibrillated polypropylene fibres, which reduce shrinkage strains and prevent the cement matrix from crack formation and propagation, is noticeable. The synergistic effect ofthree types of hybrid fibres,SF35 + PF19, SF60 + PF19, SF60 + SF13 is also observed in the behaviour of concrete after the peak load.The amount of energy, required for the deflection of 2 mm (the deflection, which is equal to the 1/150 beam span; $1/150 \times 300\,\text{mm} = 2\,\text{mm}$),

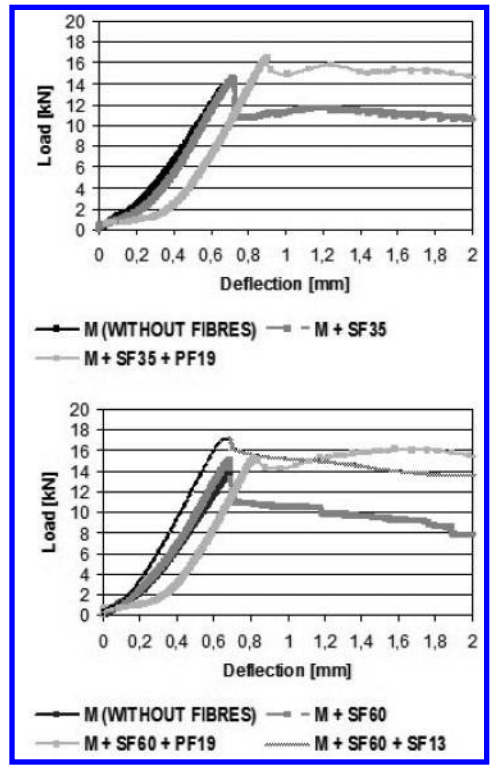


Figure 10. Load-deflection curves recorded for 28-day concretes with and without fibres.

calculated as the area under the load-deflection curve to the deflection of 2 mm, according to the Japanese standard JCI – SF4 (energy, which is used for the calculation of equivalent flexural strength)is higher for hybrid fibre reinforced concretes than for concretes with one type of steel fibres (SF35, SF60, respectively) (Table 5). The values of energy and equivalent flexural strength (calculated from the formula: $f_{eq} = T_b L/\delta_b bh^2$; where T_b = energy; L = beam span; L = 300 mm; δ_b = deflection; $\delta_b = 2$ mm, b = beam width; b = 100 mm; h = beam height; h = 100 mm) for concretes tested are given in Table 5. The analysis of calculated parameters has only comparative character because the dimensions of the tested specimens were not consistent with JCI – SF4.Steel fibres of length of 60 mm with double hooks (SF60d) are those which strongly enhance concrete after the peak load (Fig. 10). But SF60d steel fibres used together with polypropylene microfibres (PF19) as the hybrid reinforcement are not so effective (Fig.10).The values of flexural strength of tested concretes are illustrated in Figure 11. The largest flexural strength is observed for concrete with the combination of long (SF60) and short (SF13)steel fibres (with high quantity of fibres: 30 kg/m^3 of SF60 and 30 kg/m^3 of SF13).During the beam breaking, hooked steel fibres were pulled out from the cement matrix, but polypropylene fibres were broken (Figure 9).

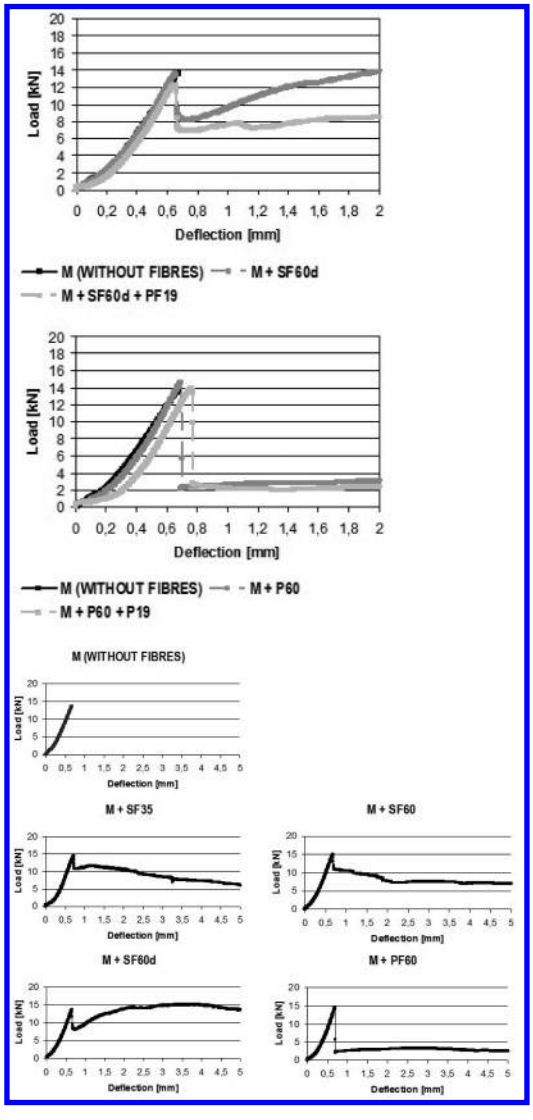


Figure 10. Continued.

Table 5. Toughness parameters for concretes with and without fibres (according to the Japanese standard JCI – SF4).

Name of concrete mixture	Energy required for the deflection of 2 mm, kNmm	Equivalent flexural strength, MPa
M (without fibres)	3.9	
M + SF35	18.3	0.6
M + SF60	17.1	2.8
M + SF60d	18.7	2.6
M + PF60	7.4	2.81
M + SF60 + SF13	28.0	4.2
M + SF35 + PF19	23.6	3.5
M + SF60 + PF19	24.6	3.7
M + SF60d + PF19	13.5	2.0
M + PF60 + PF19	6.4	1.0

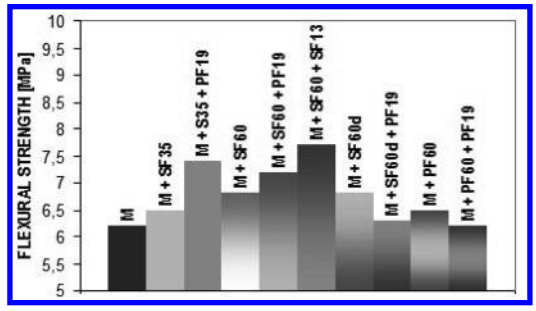


Figure 11. Flexural strength of 28-day concretes with and without fibres.

4 CONCLUSIONS

The presented research on cement concretes modified by hybrid fibres lead to the following general conclusions:

1. Hybrid fibres effect the physical properties. The huge quantity of fibresresults in lower liquidity and higher water absorption of hybrid fibre reinforced concretes compared to concretes with one type of fibres.
2. The influence of hybrid fibres on 28-day compressive strength is negligible. Polypropylene fibres in the mono-fibre and hybrid forms reduces this property by 10%.
3. The positive, synergistic effect of hybrid fibres on the flexural properties of concretes is noticeable in four of five types of hybrid fibres tested: SF60 + SF13, SF35 + PF19, SF60 + PF19, P60 + P19. The application of PF19 together with SF60d does not improve the properties of concrete with one type of fibres (SF60d).

REFERENCES

Banthia, N. & Gupta, R. 2004. Hybrid fiber reinforced concrete (HyFRC): Fiber synergy in high strength matrices. *Materials and Structures* 37: 707–716.

Banthia, N. & Nandakumar, N. 2003. Crack growth resistance of hybrid fiber reinforced cement composites. *Cement and Concrete Composites*25: 3–9.

Banthia, N. & Sappakittipakorn, M. 2007. Toughness enhancement in steel fiber reinforced concrete through fiber hybridization. *Cement and Concrete Research* 37: 1366–1372.

Banthia, N. & Soleimani, S.M. 2005. Flexural response of hybrid fiber-reinforced cementitiuos composites. *ACI Materials Journal* 102: 382–389.

Bentur, A. & Mindess, S. 1990. *Fibre reinforced cementitious composites*. London: Elsevier Applied Science.

Cominoli, L. et al. 2007. Steel and synthetic fibres for enhancing concrete toughness and shrinkage behaviour. In *Sustainable Construction Materials and Technologies*; *Proc. Intern. Conference, Coventry, UK, 11-13 June 2007*: 231–240.

Hannant, D.J. 2003. Fibre-reinforced concrete. In J. Newman & B.S. Choo (eds), *Advanced concrete technology. Processes*:6/1-6/17. Oxford: Butterworth-Heinemann.

Hsie, M. et al. 2008. Mechanical properties of polypropylene hybrid fiber-reinforced concrete. *Materials Science & Engineering A* 494: 153–157.
Lawler, J. et al. 2005. Microfiber and macrofiber hybrid fiber-reinforced concrete. *Journal of Materials in Civil Engineering* 17(5): 595–604.
Markovic, I. 2006. *High-performance hybrid-fibre concrete: development and utilisation.*Delft: Delft University Press.
Qian, C.X. & Stroeven, P. 2000. Development of hybrid polypropylene-steel fibre-reinforced concrete. *Cement and Concrete Research* 30: 63–69.
Singh, S.P. et al. 2010. Strength and flexural toughness of concrete reinforced with steel-polypropylene hybrid fibres. *Asian Journal of Civil Engineering (Building and Housing)*11(4): 495–507.
Sivakumar, A. 2011. Influence of hybrid fibres on the post crack performance of high strength concrete. Part I: Experimental investigations. *Journal of Civil Engineering and Construction Technology*2(7): 147–159.
Vandewalle, L. 2006. Hybrid fiber reinforced concrete. In Maria S. Konsta-Gdoutos (ed.), *Measuring, Monitoring and Modeling Concrete Properties*; *Proc. Intern. Symp. dedicated to Professor Surendra P. Shah*: 77–82. Springer.
Walton, P. & Majumdar, A. 1975. Cement-based composites with mixtures of different types of fibres. *Composites* 6(5): 209–216.
Yao, W. et al. 2003. Mechanical properties of hybrid fiber-reinforced concrete at low fiber volume fraction. *Cement and Concrete Research* 33: 27–30.
Yusof, M.A. et al. 2011. Mechanical properties of hybrid steel fibre reinforced concrete with different aspect ratio. *Australian Journal of Basic and Applied Sciences*5(7): 159–166.
ASTM C1018,1997. Standard test method for flexural toughness and first-crack strength of fiber-reinforced concrete (using beam with third-point loading). Withdrawn 2006.
EN 206-1 Concrete – Part 1: Specification, performance, production and conformity.
EN 12350-2 Testing fresh concrete. Slump-test.
EN 12350-7 Testing fresh concrete. Air content. Pressure methods.
EN 12390-3 Testing hardened concrete. Compressive strength of test specimens.
EN 12390-5 Testing hardened concrete. Flexural strength of test specimens.
EN 14651: 2007 Test method for metallic fibre concrete. Measuring the flexural tensile strength (limit of proportionality (LOP), residual).
EN 14889-1 Fibres for concrete. Steel fibres. Definitions, specifications and conformity.
EN 14889-2 Fibres for concrete. Polymer fibres. Definitions, specifications and conformity.
JCI-SF4, 1984. Method of test for flexural strength and flexural toughness of fiber reinforced concrete (Japan Concrete Institute).
PN-88/B-06250 Ordinary concrete.
RILEM TC162-TDF, 2003.Test and design methods for steel fibre reinforced concrete. *Materials and Structures* 36: 560–567.
UNI 11039-2, 2003. Steel fibre reinforced concrete. Part II: Test method for the determination of first crack strength and ductility indexes.
www.bosfa.com
www.bruggcontec.com
www.sika.com

Research and Applications in Structural Engineering, Mechanics and Computation – Zingoni (Ed.)
© 2013 Taylor & Francis Group, London, ISBN 978-1-138-00061-2

A review of the shear behaviour of reinforced steel fibre concrete

S. Zeranka & G.P.A.G. van Zijl
Stellenbosch University, Stellenbosch, Western Cape, South Africa

ABSTRACT: The shear behaviour of Reinforced Steel Fibre Concrete (RSFC) has undergone extensive research over the past 40 years. A comprehensive review of the literature is therefore essential in order to extend on the existing research. This paper will convey the origin, development and current status of the research topic and field, identifying the key issues and developments. In order to define the role and objectives of this research, this state-of-the-art will introduce a summary of the main findings from the primary research contributors and will present and evaluate to a limited extent the prominent research methodologies employed, both from an experimental design and modelling perspective. In conclusion, a research proposal will be established, based on the findings contained herein.

1 INTRODUCTION

1.1 *The shear transfer problem*

A shear failure originates as a tensile failure of the concrete, in the shear span of a reinforced concrete (RC) beam, when the principal tensile stresses exceed the tensile strength of concrete. Diagonal cracks develop and propagate in the beam web and due to the brittle nature of plain concrete in tension, collapse occurs suddenly, shortly after the formation of the first crack. Shear failure is therefore characterised by small deflections and a lack of ductility and is an undesirable mode of failure.

The shear behaviour of RC is a complex phenomenon which may lead to a variety of possible shear failure modes, which are dependent on a several interacting shear transfer mechanisms that are difficult to quantify. The shear transfer mechanisms themselves are also influenced by many factors related to the material properties and the structural configuration of the member.

1.2 *Research significance*

Over the past four decades, many authors have motivated the partial or complete replacement of conventional shear reinforcement with steel fibres. The shear performance of fibrous RC beams has been shown to be similar to beams reinforced with conventional stirrup reinforcement (Mansur et al. 1986) and in some instances exhibit improved behaviour (Narayanan & Darwish 1987).The structural use of steel fibre-reinforced concrete has not yet been fully achieved in the concrete industry. This is attributed to the current high cost of fibres and a lack of rational guidelines (with regard to standardised codes) for design and production (Slater et al. 2012, Noghabai 2000).

2 LITERATURE REVIEW

2.1 *Material and structural enhancement*

The increase in the first shear crack strength due to steel fibre-reinforcement can be significant, and is attributed to the crack-arresting mechanism of steel fibres (Roberts & Ho 1982). Steel fibre reinforcement can also substantially increase the ultimate shear capacity, especially for members without conventional shear reinforcement (Parra-Montesinos 2006). The rate of increase in ultimate shear strength is however dependent on several conditions, which will be discussed in the sections that follow.

A substantial post-cracking or residual strength is observed for RSFC beams after the formation of diagonal cracks (Sharma 1986). The structural stiffness can be enhanced both pre- and post-cracking (Furlan Jr. & de Hanai 1997). Increased structural ductility, energy absorption and toughness were observed for members containing steel fibres (Adebar et al. 1997). Fibre-reinforcement significantly reduces and possibly eliminates the occurrence of concrete spalling in the post-cracking stage and at final collapse (Lim & Oh 1999).This can protect reinforcement from corrosion in adverse environments, and hence improves structural durability (Li et al. 1992).

Fibre-reinforcement delays the formation and restrains the opening and propagation of cracks (Watanabe et al. 2010). In addition a more distributed cracking pattern develops, with more closely spaced cracks, which delays the localisation of a major shear-critical crack (Minelli & Plizzari 2008).

This is attributed to a more uniform distribution of stresses in FRC beams, compared to conventional beams (Narayanan & Darwish 1987). The cracks are also more diffused i.e. the crack width is reduced, which improves the transmission of shear load and the redistribution of stresses (Juárez et al. 2007). The cracking pattern of FRC beams has been observed to be similar to corresponding RC beams with conventional stirrup reinforcement (Narayanan & Darwish 1987). It is has also been postulated that in members without stirrup reinforcement, the effect of beam depth on shear strength is reduced with fibre-reinforcement (Dinh et al. 2011).

The effective control of cracking in FRC beams, results in a reduction of deflections as well as an increase in the deformation capacity and ultimate deflection (Kwak et al. 2002).

Fibre-reinforcement reduces the bar reinforcement strains, especially in the post-cracking range and thereby delays and reduces the stresses in the bar reinforcement (Cho & Kim 2003). This is an indication that the fibre-concrete is contributing to the shear strength (Furlan Jr. & de Hanai 1997).

The inclusion of steel fibres can change the mode of failure from a brittle shear failure to a ductile flexural failure, even in the absence of stirrups, allowing the RC member to reach its full flexural capacity (Swamy & Bahia 1985).

2.2 *The shear transfer mechanisms*

The efficiency of fibre-reinforcement depends on the governing load-carrying mechanisms, which may vary (Noghabai 2000). Fibre-reinforcement is known to enhance many of the shear transfer mechanisms.

The shear resistance increases as the longitudinal reinforcement ratio increases. The longitudinal reinforcement serves to increase the cracking strength, delaying the formation and propagation of flexural and inclined cracks and increasing the total dowel capacity (Li et al. 1992). The longitudinal reinforcement ratio also influences the size of the compression zone and the overall structural ductility (Dinh et al. 2010). Steel fibre-reinforcement improves the effectiveness of dowel resistance due to its ability to enhance the tensile strength (greater resistance to the propagation and widening of dowel cracks in the dowel zone along reinforcement) of concrete in the splitting plane along the longitudinal reinforcement (Li et al. 1992).

An increased concrete compressive strength does increase the shear capacity of both RC and RSFC beams (Mansur et al. 1986). The degree to which steel fibre-reinforcement influences concrete compressive strength varies from a significant increase in compressive strength (Lim & Oh 1999), to a marginal or insignificant increase (Tan et al. 1993), especially in low volume fractions (Dinh et al. 2011). Even a reduction in compressive strength may be observed, which is attributed to the reduced consolidation of concrete due to the presence of fibres (Adebar et al. 1997). The most significant enhancement of steel fibre-reinforcement to the compressive properties of concrete is the substantially higher compressive strain at peak stress compared to ordinary concrete. This is attributed to the confinement provided by the fibres (Tan et al. 1993). An increase in residual compressive strength is observed due to the reduced damage in tension (Minelli & Vecchio2004). This may be beneficial in deeper beams where arch action is prominent and compression forces are transmitted to the supports through compression struts. The key property influencing the effectiveness of fibre-reinforcement is the fibre-matrix interfacial bond (Li et al. 1992).

The shear behaviour of RC beams is affected by the shear span-to-depth ratio to a large extent. In general, for a span-to-depth ratio greater than 2.5, flexural effects predominate, whereas shear predominates for lower values of the span-to-depth ratio (Ashour et al. 1992). The cracking and ultimate shear strength decrease with increasing span-to-depth ratio. Arching and dowel action become less effective as the span-to-depth ratio increases (Kwak et al. 2002).There does appear to be some controversy with regard to when fibre-reinforcement is more effective i.e. for slender or deep beams. According to some authors the rate of increase in shear strength is higher at low values of the span-to-depth ratio and consequently arch action is believed to benefit more from fibre-reinforcement (Mansur et al. 1986, Narayanan & Darwish 1987, Ashour et al. 1992). This is attributed to the greater cohesion of fibre concrete and the improved tensile capacity of the concrete in the transverse direction. Contrary to these findings other authors state that the efficiency of fibres as shear reinforcement increases as the span-to-depth ratio increases. The reasoning is that improvements due to fibre-reinforcement are related directly to the pull-out performance of fibre concrete and the beam action failure mechanism has a greater capacity to utilise the improved material performance due to fibre-reinforcement (Li et al. 1992, Cucchiara et al. 2004).

In conventional design, the contribution of aggregate interlock or interface shear to the shear capacity is conservatively ignored. This is mainly because the aggregate interlock contribution diminishes with increasing crack width and is therefore not reliable. Aggregate interlock is believed to become more effective due to the crack width limitation provided by the fibres, however to the authors' knowledge this has not been investigated in detail. The fibres therefore have a function which is similar to conventional shear reinforcement, but unlike conventional reinforcement are uniformly distributed throughout the member volume (Sharma 1986, Wight & MacGregror 2009). The contribution of aggregate interlock in shear transfer is mainly influential during shear sliding of diagonal cracks in beams with a span-to-depth ratio greater than 2.5 (i.e. slender beams). The aggregate interlock contribution disappears for deeper beams which fail in arch action, where crack face shearing is negligible (Li et al. 1992).

In beams without conventional transverse reinforcement, size-effects significantly influence the shear behaviour and fibre-reinforcement is less effective in large-scale beams (Adebar et al. 1997). There is a general trend of decreasing shear strength with increasing beam size or depth and this is consistent with results of plain concrete beams as well as theoretical work (Li et al. 1992). Few tests have been conducted on large FRC beams. Steel fibres have been shown to beineffective in preventing catastrophic shear failures in full-scale beams (Williamson & Knab(1975) cited by Adebar et al. 1997).The contribution of fibres is therefore size dependent, whereas the contribution provided by stirrups is expected to be size independent. In larger beams, conventional shear reinforcement is more effective than steel fibres in terms of bearing capacity and ductility. The scale effects can be mostly eliminated using minimum transverse reinforcement (Minelli & Plizzari 2008). A reduction in crack spacing due to fibre reinforcement could at least in some instances potentially reduce or eliminate shear-size effects in beams without conventional transverse reinforcement (Dinh et al. 2010).

2.3 *Fibre properties*

The following composite properties related to the fibres, influence the shear behaviour of RSFC beams: fibre -content, -aspect ratio, -length, -shape (profile and end anchorage), -strength, -stiffness, and the fibre-matrix interfacial bond. At lower fibre volumes, the increase in shear strength is proportional to the quantity of fibre; however, the rate of increase is reduced at higher fibre volumes (Adebar et al. 1997). An optimum fibre dosage therefore exists for every composite type. In the practical range of typical steel fibres used (0.25–2.0% by volume), an optimum fibre dosage appears to lie between 1.0% and 1.5%. Volume fractions of fibres smaller than or equal to 0.5% did not produce shear resistance at failure substantially greater than the required minimum (Parra-Montesinos 2006).

High-strength fibres may produce an increased residual strength compared to normal-strength fibres, this attributed to a greater plastic strength of fibre hooks (Dinh et al. 2010). The beneficial effect of high-strength fibres is dependent on the properties of the composite, especially the fibre-matrix bond and matrix strength.

Longer fibres exhibit a more ductile response compared to shorter fibres (Adebar et al. 1997). The stress transfer capability of shorter fibres reduces faster than longer fibres, resulting in a faster rate of force transfer to the other shear-resisting mechanisms (Li et al. 1992). The fibre factor is a combined fibre parameter consisting of the fibre aspect ratio, the fibre volume and a bond efficiency factor which is dependent on the fibre type. The fibre factor has a greater influence on the shear strength than any individual fibre parameter and is used in most semi-empirical models (Slater et al. 2012). In a study by Li et al.(1992), polyethylene and steel fibres were found to be the most effective in increasing shear strength. Synthetic fibres are however not as effective as steel fibres in increasing the shear strength of concrete beams, due to its low modulus of elasticity (Furlan Jr. & de Hanai1997). Steel fibres are better able to redistribute the strains among cracks compared to non-metallic fibres (Noghabai 2000).

2.4 *The synergetic effect of fibre and stirrup reinforcement*

There are design instances where fibre-reinforced beams cannot achieve the same performance as beams containing conventional shear reinforcement. In these cases steel fibres alone are not effective in preventing catastrophic shear failures (Williamson & Knab (1975) and Lafraugh & Moustafa (1975) cited by Swamy & Bahia 1985). There is a limited amount of experimental data in the literature on the shear behaviour of beams where a combination of fibres and conventional transverse reinforcement is used (Cucchiara et al. 2004). Tests have shown that such a combination can form an effective system of shear reinforcement in a structural member (Craig (1984) cited by Sharma 1986). Fibres and stirrups in small quantities can be effective to enhance the shear strength, as well as the crack and deformation control, providing a ductile post-peak behaviour. Such a reinforcement combination can change the mode of failure and preserve the ductility and integrity of the structural member (Swamy & Bahia 1985, Meda et al. 2005). The amount of stirrups required can be reduced with the introduction of fibre-reinforcement (Lim & Oh 1999). A combined use of fibres and stirrups is believed to be more suitable, because the stirrups allow greater deformation capacity beyond the elastic limit (Cucchiara et al. 2004). The conventional shear reinforcement also reduces the scatter in the data and assists in crack width control and consequently assists the bridging of fibres along the diagonal crack, increasing the shear-resistance carried by the steel fibres. Stirrups effectively prevent the rapid opening and propagation of the diagonal crack, which increases the efficiency of the fibres. In conclusion, there exists a synergetic interaction between the shear resistance mechanisms (Watanabe et al. 2010). Other authors have also observed a positive composite effect and efficiency for a combination of stirrups and steel fibres, on the mechanical behaviour (including ultimate load, ductility, post-peak behaviour, toughness and failure pattern). The shear strength has been shown to be approximately proportional to the steel fibre content; however this is dependent on the conventional shear reinforcement ratio (Ding et al. 2011). Fibre-reinforcement is less effective at higher conventional shear reinforcement ratios i.e. the rate of improvement with increasing fibre content decreases with increased conventional shear reinforcement (Ding et al. 2012). This is attributed to a greater proportion of the load being carried by the stirrups and less by the fibres in the ultimate stages when cracks widen and fibre pull-out occurs (Swamy & Bahia 1985).

3 RESEARCH METHODOLOGIES

3.1 *Experimental design*

Experimental investigations to date have been predominantly shear tests of simply supported RC structural beam members subjected to flexural loading. The parameters related to the specimen geometry, loading configuration and conventional reinforcement are: the shear span-to-effective depth ratio, longitudinal reinforcement ratio, transverse reinforcement ratio and beam depth (size effect). Structural tests are usually accompanied with fracture mechanics tests such as flexural or splitting tests, where the residual post-cracking strength is of primary importance. This is used as input to reconcile material models with the structural response. The material parameters typically include: the concrete compressive strength, fibre content and the fibre properties (length, aspect ratio, strength, mechanical anchorage and profile).

The data typically recorded for these types of tests are the load vs. beam deflection response (at mid-span), crack widths, development and patterns, the load at first visible diagonal/shear cracking and ultimate load, failure modes, reinforcement and concrete strains, rotation at supports and specimen curvature.

Far less work has been done on the direct shear response of fibre reinforced concretes (Soetens &Matthys 2012, Lee & Foster 2006). These types of tests are performed to evaluate the direct/pure shear response in terms of the relative shear interfacial slip and shear capacity i.e. crack sliding or Mode II fracture. Two test methods are typically employed, the shear push-off (or Z-type specimens) (Lee & Foster 2006, Tan & Mansur 1990) and the shear push-through specimens (JSCE 1990) modified by (Mirsayah & Banthia 2002, Soetens & Matthys 2012, Boulekbache et al. 2012, Malatesta & Contreras 2009). Even fewer investigations, attempt to link the pull-out behaviour of single fibres to SFRC under mode II fracture i.e. the transverse pull-out of steel fibres (Lee & Foster 2006, Soetens & Matthys 2012).

3.2 *Modelling*

A rational and generic model for shear design with fibre-reinforcement requires an understanding of the governing load-carrying mechanisms. Experimentation alone is insufficient to expose the underlying mechanisms. Analytical formulations which implement the theory are required in order to explain the structural behaviour in mechanical terms and to correctly interpret the experimental results.

3.2.1 *Empirical and semi-empirical models*

The majority of predictive equations for the shear strength of FRC beams, including those found in most design codes, are empirical or semi-empirical (Cho & Kim 2003), fitted by test data, and therefore are not comprehensive (Kim et al. 2012). These types of models can only predict the ultimate shear capacity and in some instances also the cracking shear strength. Typically some form of an existing shear design model for conventional RC (such as those currently implemented in most design codes) is utilised as a framework which is modified to account for the contribution of fibres. Models are typically sourced from the ACI Building Code (ACI 318-08) or Eurocode 2 (2003)and in some instances the theory of concrete plasticity or limit analysis is also used. These models are sometimes used in conjunction with linear or nonlinear regression analysis. Empirical formulas usually only evaluate a limited set of parameters that typically only include the shear span-depth ratio, beam depth, compressive strength, reinforcement ratio and concrete flexural or tensile strength.

Semi-empirical models place greater emphasis on the fibre contribution. These models differ in their level of consideration. Some models will evaluate the fibre contribution at a single fibre level and include such parameters as the fibre distribution, mean fibre pull-out length, average fibre-matrix interfacial bond stress, fibre aspect ratio, fibre volume and bond efficiency factor (Narayanan & Darwish 1987, Al-Ta'an & Al-Feel 1990). Whereas other models consider the fibre contribution at a composite level, which typically includes a residual post-cracking strength parameter obtained from standard fracture mechanics tests, such as flexural and splitting tensile strength tests (Mansur et al. 1986, Minelli & Plizzari 2008, Dinh et al. 2011).

3.2.2 *Analytical models*

Analytical models are capable of simulating the stress-strain history and in some instances, the load-deflection response of a member. The model parameters typically include the stress-strain relations for FRC in tension and compression or alternatively the fibres are modelled explicitly as mentioned in the previous section (Kim et al. 2012). The earliest work was first performed by Tan & Mansur (1990) and then later again by Tan et al. (1993). The theoretical background of these models is based on the softened truss model (Hsu et al. 1987) and the modified compression field theory (MCFT) (Vecchio & Collins 1986), which is essentially a smeared, rotating crack model for cracked RC elements. These models have three basic requirements: equilibrium, compatibility and material constitutive equations. The MCFT has been used extensively as the theoretical framework for such models. Nonlinear truss or lattice models which incorporate geometric and mechanical modelling, have also been investigated (Noghabai 2000).

3.2.3 *Numerical/Finite element (FE) models*

Few numerical studies are published concerning FRC structures (Minelli & Vecchio 2004). In order to allow for a redistribution of stresses in the model, a FE method must be used. These models are capable of simulating the strength, stiffness, ductility, crack pattern development, and failure modes, essentially the complete member response. These types of models

allow for a more detailed investigation into the development of shear resistant mechanisms and an accurate evaluation of the fibre contribution to shear resistance is possible (Minelli & Vecchio 2006). The fibre contribution to concrete tension softening and the material nonlinearities are incorporated into the models. In addition these models include crack limits, arch action mechanisms and concrete residual strength in the presence of fibres. Once again models differ in their consideration of fibre-reinforced concrete, which may be on a composite level or single fibre level (Lee et al. 2012). The MCFT is once again used as the theoretical framework for the finite element analysis and is adapted for FRC in terms of the post-cracking behaviour and local conditions at cracks (Minelli & Vecchio 2004). An extension of the MCFT is the disturbed stress field model (DSFM) which is capable of simulating the crack shear-slip deformation (Minelli & Vecchio 2006).

Recent approaches, including the MCFT or plasticity theory are rational and have physical significance (Cho & Kim 2003). However, a model which is based on FRC performance in terms of the residual post-cracking strength (which is considered to be a significant index for structural design and is obtained through simple fracture mechanics tests), can easily be applied and transferred to practice (Minelli & Plizzari 2008).

4 DESIGN CODES AND RECOMMENDATIONS

There are very few standards or recommendations that allow for the quantification of shear strength and shear ductility enhancement provided by fibre-reinforcement (ACI 544 Committee 2008b, cited by Malatesta & Contreras 2009). A design procedure that considers the randomly distributed discrete fibre behaviour across cracks in a rational manner is still rare (Ding et al. 2012).

The design codes which provide shear design provisions for RSFC beams include the ACI Code (ACI 318-08), fib Model Code 2010 and the RILEM TC 162-TDF recommendations. These design provisions are similar in that they all incorporate and specify minimum post-cracking residual strength criteria which are evaluated through flexural test methods.

5 CONCLUSIONS

Based on the findings contained in this state-of-the-art, some omissions and areas of limited research have been identified. Limited research has been placed on examining the fibre pull-out/dowel and aggregate interlock (shear interface roughness)interaction at different loading stages or crack widths. Limited research has been performed on the composite effect of a fibre and conventional stirrup reinforcement combination. Extending the knowledge of the shear transfer mechanisms through carefully designed characteristic testing and the development of a refined analytical model is proposed and postulated to clarify the dominant shear mechanisms and structural resistance of RSFC beams.

REFERENCES

ACI Committee 318, 2008. *Building code requirements for structural concrete (ACI 318-08) and commentary (ACI-318R-08),* MI: Farmington Hills.

Adebar, P., Mindess, S., St.-Pierre, D. & Olund, B., 1997. Shear tests of fiber concrete beams without stirrups. *ACI Structural Journal,* January-February, 94(1), pp. 68–76.

Al-Ta'an, S. A. & Al-Feel, J. R., 1990. Evaluation of shear strength of fibre-reinforced concrete beams. *Cement & Concrete Composites,* Volume 12, pp. 87–94.

Ashour, S. A., Hasanain, G. S. & Wafa, F. F., 1992. Shear behavior of high-strength fiber reinforced concrete beams. *ACI Structural Journal,* March-April, 89(2), pp. 176–184.

Boulekbache, B., Hamrat, M., Chemrouk, M. & Amziane, S., 2012. Influence of yield stress and compressive strength on direct shear behaviour of steel fibre-reinforced concrete. *Construction and Building Materials,* Volume 27, pp. 6–14.

Cho, S. & Kim, Y., 2003. Effects of steel fibers on short beams loaded in shear. *ACI Structural Journal,* November-December, 100(6), pp. 765–774.

Cucchiara, C., Mendola, L. L. & Papia, M., 2004. Effectiveness of stirrups and steel fibres as shear reinforcement. *Cement & Concrete Composites,* Volume 26, pp. 777–786.

Ding, Y., You, Z. & Jalali, S., 2011. The composite effect of steel fibres and stirrups on the shear behaviour of beams using self-consolidating concrete. *Engineering Structures,* Volume 33, pp. 107–117.

Ding, Y., Zhang, F., Torgal, F. & Zhang, Y., 2012. Shear behaviour of steel fibre reinforced self-consolidating concrete beams based on the modified compression field theory. *Composite Structures,* Volume 94, pp. 2440–2449.

Dinh, H. H., Parra-Montesinos, G. J. & Wight, J. K., 2010. Shear behavior of steel fiber-reinforced concrete beams without stirrup reinforcement. *ACI Structural Journal,* September-October, 107(5), pp. 597–606.

Dinh, H. H., Parra-Montesinos, G. J. & Wight, J. K., 2011. Shear strength model for steel fiber reinforced concrete beams without stirrup reinforcement. *ASCE Journal of Structural Engineering,* October, 137(10), pp. 1039–1051.

Eurocode 2, 2003. *Design of concrete structures,* prEN 1992 Ver. December 2003.

FIB Model Code, 2010. Fibre reinforced concrete. Draft Ver.

Furlan Jr., S. & de Hanai, J. B., 1997. Shear behaviour of fiber reinforced concrete beams. *Cement and Concrete Composites ,* Volume 19, pp. 359–366.

Hsu, T. T. C., Mau, S. T. & Chen, B., 1987. Theory of shear transfer strength of reinforced concrete. *ACI Structural Journal,* 84(2), pp. 149–160.

JSCE-SF6, 1990. *Method of test for shear strength of steel fiber reinforced concrete (SFRC),* Tokyo: Japan Society of Civil Engineers.

Juárez, C., Valdez, P., Durán, A. & Sobolev, K., 2007. The diagonal tension behavior of fiber reinforced concrete beams. *Cement & Concrete Composites,* Volume 29, pp. 402–408.

Kim, K. S., Lee, D. H., Hwang, J. & Kuchma, D. A., 2012. Shear behavior model for steel fiber-reinforced concrete members without transverse reinforcements. *Composites: Part B,* Volume 43, pp. 2324–2334.

Kwak, Y., Eberhard, M. O., Kim, W. & Kim, J., 2002. Shear strength of steel fiber-reinforced concrete beams without stirrups. *ACI Structural Journal,* July-August, 99(4), pp. 530–538.

Lee, D. H. et al., 2012. Nonlinear finite element analysis of steel fiber-reinforced concrete members using direct tension force transfer model. *Finite Elements in Analysis and Design,* Volume 50, pp. 266–286.

Lee, G. G. & Foster, S. J., 2006. *Behaviour of steel fibre reinforced mortar in shear I: direct shear testing,* UNICIV Report R-444, Sydney.

Lim, D. H. & Oh, B. H., 1999. Experimental and theoretical investigation on the shear of steel fibre reinforced concrete beams. *Engineering Structures,* Volume 21, pp. 937–944.

Li, V. C., Ward, R. & Hamza, A. M., 1992. Steel and synthetic fibres as shear reinforcement. *ACI Materials Journal,* September-October, 89(5), pp. 499–508.

Malatesta, S. C. & Contreras, M. C., 2009. Shear behaviour of steel fiber reinforced concretes. *Revista Ingeniería de Construcción,* April, 24(1), pp. 79–94.

Mansur, M. A., Ong, K. C. G. & Paramasivam, P., 1986. Shear strength of fibrous concrete beams without stirrups. *ASCE Journal of Structural Engineering,* September, 112(9), pp. 2066–2079.

Meda, A., Minelli, F., Plizzari, G. A. & Riva, P., 2005. Shear behaviour of steel fibre reinforced concrete beams. *Materials and Structures,* April, Volume 38, pp. 343–351.

Minelli, F. & Plizzari, G. A., 2008. Shear design of FRC members with little or no conventional shear reinforcement. *Tailor Made Concrete Structures,* pp. 605–610.

Minelli, F. & Vecchio, F. J., 2004. Compression field modelling of fibre reinforced concrete: preliminary numerical study. *RILEM PRO 39,* September, pp. 885–894.

Minelli, F. & Vecchio, F. J., 2006. Compression field modeling of fiber-reinforced concrete members under shear loading. *ACI Structural Journal,* March-April, 103(2), pp. 244–252.

Mirsayah, A. & Banthia, N., 2002. Shear strength of steel fiber-reinforced concrete. *ACI Material Journal,* Volume 99, pp. 473–479.

Narayanan, R. & Darwish, I. Y. S., 1987. Use of steel fibers as shear reinforcement. *ACI Structural Journal,* May-June, 84(3), pp. 216–227.

Noghabai, K., 2000. Beams of fibrous concrete in shear and bending: experiment and model. *Journal of Structural Engineering ASCE,* February, 126(2), pp. 243–251.

Parra-Montesinos, G. J., 2006. Shear strength of beams with deformed steel fibers – Evaluating an alternative to minimum transverse reinforcement. *Concrete International,* November.pp. 57–66.

RILEM TC 162-TDF, 2002. Test and design methods for steel fibre reinforced concrete – sigma-w method (principles and applications). *Material and Structures,* Volume 35, pp. 262–278.

RILEM TC 162-TDF, 2003. Test and design methods for steel fibre reinforced concrete – sigma-epsilon design method (final recommendation). *Materials and Structures,* October, Volume 36, pp. 560–567.

Roberts, T. M. & Ho, N. L., 1982. Shear failure of deep fibre reinforced concrete beams. *The International Journal of Cement Composites and Lightweight Concrete,* August, 4(3), pp. 145–152.

Sharma, A. K., 1986. Shear strength of steel fiber reinforced concrete beams. *ACI Journal, Proceedings,* July-August, 83(4), pp. 624–628.

Slater, E., Moni, M. & Alam, M. S., 2012. Predicting the shear strength of steel fiber reinforced concrete beams. *Construction and Building Materials,* Volume 26, pp. 423–436.

Soetens, T. & Matthys, S., 2012. A semi-analytical model to simulate the direct shear pull-out behaviour of hooked-end steel fibres*. RILEM PRO88*, September, pp. 1–12.

Swamy, R. N. & Bahia, H. M., 1985. The effectiveness of steel fibers as shear reinforcement. *Concrete International,* March. pp. 35–40.

Tan, K. H. & Mansur, M. A., 1990. Shear transfer in reinforced fiber concrete. *Journal of Materials in Civil Engineering,* November, 2(4), pp. 202–214.

Tan, K. H., Murugappan, K. & Paramasivam, P., 1993. Shear behavior of steel fiber reinforced concrete beams. *ACI Structural Journal,* January-February, 90(1), pp. 3–11.

Vecchio, F. J. & Collins, M. P., 1986. Modified compression field theory for reinforced concrete elements subjected to shear. *ACI Journal Proceedings,* 83(2), pp. 219–231.

Watanabe, K., Kimura, T. & Niwa, J., 2010. Synergetic effect of steel fibers and shear-reinforcing bars on the shear-resistance mechanisms of RC linear members. *Construction and Building Materials,* Volume 24, pp. 2369–2375.

Wight, J. K. & MacGregor, J. G., 2009. *Reinforced concrete – mechanics & design.* 5th ed. New Jersey: Pearson Prentice Hall.

Research and Applications in Structural Engineering, Mechanics and Computation – Zingoni (Ed.)
© 2013 Taylor & Francis Group, London, ISBN 978-1-138-00061-2

Time-dependent behaviour of pre-cracked polypropylene fibre reinforced concrete (PFRC) under sustained loading

A.J. Babafemi & W.P. Boshoff
Department of Civil Engineering, Stellenbosch University, South Africa

ABSTRACT: This study investigated the delayed deformation behaviour of pre-cracked Polypropylene Fibre Reinforced Concrete (PFRC) under sustained loading. Post-peak residual strength, loading-unloading-reloading response, shrinkage and uniaxial tensile creep are reported. Specimens for the creep test were pre-cracked and subjected to 30% and 50% stress levels of the post-peak residual strength of PFRC. All tests were done using $100 \times 100 \times 500$ mm prism specimens in a controlled climate room. It is shown that the shrinkage deformation of unloaded specimens' exhibit increased reduction after 45 days of testing up to 4 months when compared to predicted behaviour of normal concrete. Specimens loaded at 50% post-peak residual strength showed increased creep when compared to those loaded at 30%. While specimens subjected to 30% sustained loading showed an almost stable response at 4 months, those loaded at 50% experienced creep fracture at same period.

1 INRODUCTION

The use of steel and synthetic fibres in concrete has become an interesting subject in the past few decades in the construction industry. Fibres have generally become known to improve the residual tensile capacity of concrete in the cracked state (toughness) by bridging the cracked surfaces (Buratti, et al. 2011). Hence, they are usually referred to as crack arresters. Depending on the fibre type, geometry and volume, the behaviour could be strain hardening or strain softening. Other benefits of using fibres in concrete as reported by numerous researches include impact resistance, fatigue resistance, reduction in early plastic shrinkage cracking, etc. (Zhang 2003, Mackay & Trottier 2004, and Zile & Zile 2013).

Many studies have been undertaken on the quasi static mechanical behaviour of fibre reinforced concrete (FRC). It should be noted that the fibres used in concrete becomes engaged only after the initiation of cracks (Arango et al. 2011). Hence, the European Code (EN 14651, 2005) made provision for the residual strength of concrete tested under three-point bending at different crack openings. However, there is still a dearth of information in literature on the time-dependent behaviour of FRC under sustained loading. It is required to understand the creep behaviour of FRC before this time-dependent behavior can be included in design guidelines. Hence, this pre-cracked samples need to be tested at different levels of sustained loading. Of concern is the increase of the crack opening of tensile and flexural samples.

Little work have been reported in literature on the long term behaviour of FRC under sustained loadings. Zerbino & Barragán (2012) reported on the flexural creep behaviour of beams reinforced with steel fibres (0.5% fibre volume) over a period of 21 months. The pre-cracked beams were said to display a significant load-bearing capacity with maximum residual stress as high as 60% above the first peak stress.

Beams subjected to flexural creep with a pre-cracked crack width of 0.2 mm at a constant stress of 100% of the residual post-crack stress were said to show stable responses after 18 months. With less than 50% of the post-crack stress, slight displacement that later stabilized to almost zero crack rate openings was also reported in the same study. However, for beams showing softening post-crack behaviour, Zerbino & Barragán (2012) reported that failure occurred when applied stresses were almost as much as the residual post-crack stress.

There are still little work reported in literature on the uniaxial tensile time-dependent behaviour of pre-cracked steel fibre reinforced concrete (SFRC). More researches have been reported on flexural creep of SFRC than on the uniaxial tensile creep (Tan et al. 1994, Mackay & Trottier 2004, Tan & Saha, 2005, and Zerbino & Barragán 2012). The positive results reported for SFRC can be attributed to the high stiffness of steel fibres unlike polypropylene fibre (PF) which has a low stiffness.

Recently, the use of PF to replace steel fibres (SF) in concrete is being advocated as it is cheaper, lighter and does not corrode in concrete (Richardson 2004). However, much remains unknown about the time-dependent behaviour of PFRC. In one study, beams reinforced with macro synthetic PF and subjected to 50% of the residual load in bending after pre-cracking have been reported to creep between 10-30 times more than those with steel fibres after 2 years (BEKAERT, 2008).



Figure 1. Polypropylene fibres.

Table 1. Properties of polypropylene fibre used.

Specific gravity	0.88–092
Modulus of elasticity	4.3 GPa
Colour	Translucent
Elongation at yield	15 to 25 %
Tensile strength	300 MPa
Melting point	150–170°C
Length (l_f)	40 mm
Nominal diameter (d_f)	0.8 mm
Aspect ratio (l_f/d_f)	50

Source: Fibsol, Technical data sheet.

2 RESEARCH SIGNIFICANCE

This study investigates the time-dependent behaviour of concrete prisms incorporating discrete monofilament macro synthetic fibres subjected to sustained loads over a period of 4 months. Specimens were loaded at 30% and 50% post-peak residual uniaxial tensile strength. The study provides an understanding of the delayed behaviour of concrete incorporating PF under varying levels of sustained loading.

3 EXPERIMENTAL PROGRAMME

The uniaxial tensile creep behaviour of cracked PFRC was investigated. All tests were performed using concrete prisms measuring $100 \times 100 \times 500$ mm. These tests included uniaxial tension, shrinkage and creep tests. All tests were done in a climate controlled room with a temperature of $23, \pm 1°C$ and an average relative humidity of 65 ± 5 %. Specimens were cast and demoulded after 24 hours and cured in water for a further 27 days before testing. Specimens for the creep and shrinkage tests were kept in the climate controlled room for about 12 hours before the test was started.

3.1 *Materials*

PF supplied by Fibsol (Fibre Reinforcing Solutions), South Africa, with a trade name Rocstay CXO 50/40 SS were used. Details of the fibres are shown in Figure 1 and Table 1.

The coarse aggregate (greywacke stone) used were those passing through the 6 mm sieve size while the fine aggregate was natural sand (Malmesbury) passing through 2.36 mm sieve with a fineness modulus (FM) of 2.34. CEM I 52.5 cement was used as the binder.

Table 2. Concrete mix design used.

Materials Type	kg/m^3
Cement	395
Stone	800
Sand	990
Water	190
Fibre	9.1
Super plasticizer (0.2%)	0.79

The requirement of the 6 mm stone size was justified by the relationship between maximum grain size and fibre volume in per cent given by Kobayashi & Cho in Markovic (2006). The maximum stone size can be calculated as follows

$$S = 5\sqrt{\frac{\pi}{0.002\,L/d + 0.4}}\frac{d}{\sqrt{V_f}} - d \qquad (1)$$

where S = maximum grain size in [mm]; L = fibre length in [mm]; d = diameter of fibre in [mm]; and V_f = volume ratio of fibre.

3.2 *Mix design*

A mix design was developed for the investigation as shown in Table 2.

Workability test was done using the slump test (SANS 5862-1:2006). Slump was measured before and after the additions of the fibres. The fibres were allowed to mix for 5 minutes after its addition to the concrete mix until a consistent mix was visible without any sign of segregation. Slump measurement was 160 mm and reduced to 100 mm after fibres were added. The average compressive strengths of the mix with and without PF were 40.19 MPa and 43.80 MPa respectively. Dynamon SP1 superplasticizer classified according to EN 934-2 (2009) and supplied by MAPEI South Africa was used.

3.3 *Preparation of test samples*

Uniaxial tensile strength, shrinkage and creep deformation tests were done using $100 \times 100 \times 500$ mm prisms. All specimens, except those for shrinkage test, were notched in the centre of the specimens on all four sides to a depth of 10 mm resulting in an effective area of 6400 mm^2. The notch thickness was 3 mm. The design of the sample preparation and test setup was based on the work of Mouton and Boshoff (2012). Specially designed steel hooks were used as anchors and embedded in the specimens during casting. The hooks protruded at both the ends of the beams and are shown in Figure 2(a). Hooks were welded to the ends of the anchors for the connections to the test setups. Apart from the prisms, cube samples of 100 mm were also cast to determine the compressive strength of the mixes with and without PF.

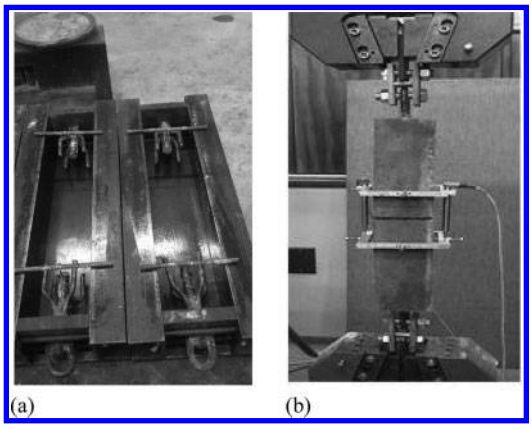


Figure 2. (a) Steel hooks positioned in moulds (b) Uniaxial tensile test.

3.4 *Uniaxial tensile test*

The benefit of FRC is only visible once the concrete is cracked. The uniaxial tensile tests were done in order to determine the ultimate and post-peak residual strength. Post-peak residual strength is required to determine the sustained load. The uniaxial tensile test was done in a Zwick Z250 Universal Testing Machine using the same setup as described by Babafemi and Boshoff (2013) and is shown in Figure 2(b). The tests were performed using a crack mouth opening rate of 0.8 mm/min and using two 10 mm linear variable displacement transducers (LVDT). The unloading specimens were unloaded at the same rate. The same setup was also used to pre-crack the tensile creep test specimens.

Three specimens were tested to study the post-peak uniaxial tensile response. Three other trial specimens were cracked and then unloaded at same rate to study their unloading response while one of the three specimens was reloaded again after unloading. The similarity in the post-peak strength after unloading was compared with the specimens that were tested to full post-peak strength without unloading.

3.5 *Shrinkage test*

Two specimens were used to study the shrinkage deformation of PFRC so as to distinguish it from the creep deformation of the unsealed specimens subjected to sustained loading. The specimens were unnotched and uncracked with a gauge length of 285 mm achieved by using an extender (Figure 3). The specimens were tested in an unrestrained condition by placing them on PVC rollers to minimise the restraint against shrinkage. The readings were measured electronically using a HBM Spider8 Electronic Measuring System.

3.6 *Creep of pre-cracked samples*

The frame used for the tensile creep test uses a lever arm system for load application. It is designed to

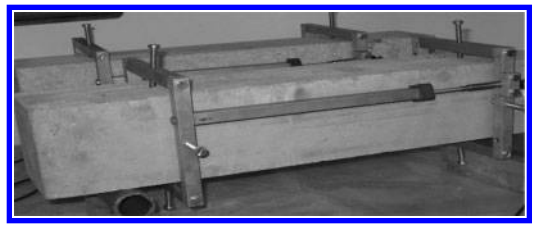


Figure 3. Shrinkage test.

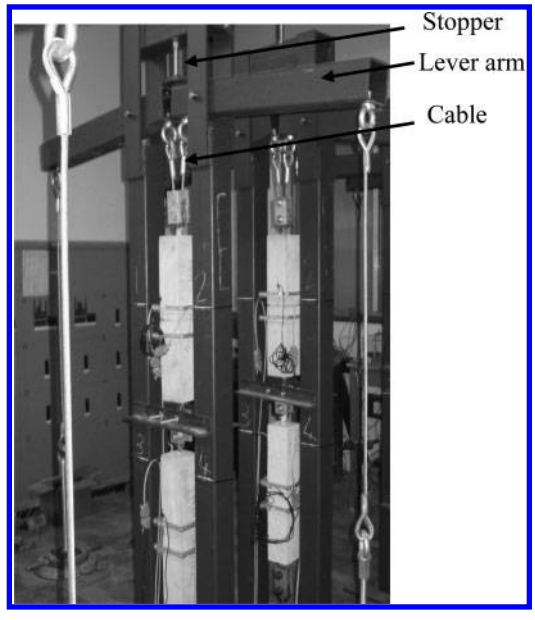


Figure 4. Creep frame with specimens under sustained loading.

accommodate two specimens in series, see Figure 4. A stopper was placed at the top of the specimens used to stabilise the setup should one of the specimens fails. The specimens were connected to the loading frame using cables fixed to the eyes welded on the anchors of the specimens. This ensures that no moments are induced in the specimens.

The deformation over the notched area was measured using two 10 mm LVDT fixed to the specimens using two aluminium frames. The gauge length between the aluminium frames was 70 mm. The measured creep consists of material creep and it also included the crack mouth opening displacement. As in the case of shrinkage reading, the displacement readings were acquired using the HBM Spider8 Electronic Measuring System. Data were saved at regular intervals for the full duration of the tests. The specimens were tested unsealed, therefore basic creep, drying creep, crack widening and drying shrinkage occurred at the same time. The drying shrinkage could be subtracted, but it was not possible to distinguish between the drying creep and basic creep.

The test frame was calibrated using a load cell in the specimen's position to find the relationship

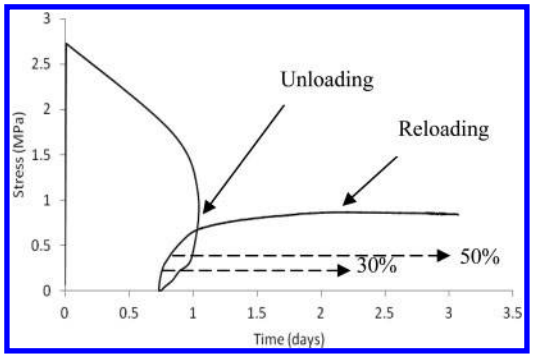


Figure 5. Pre-cracking, unloading and reloading of test specimens.

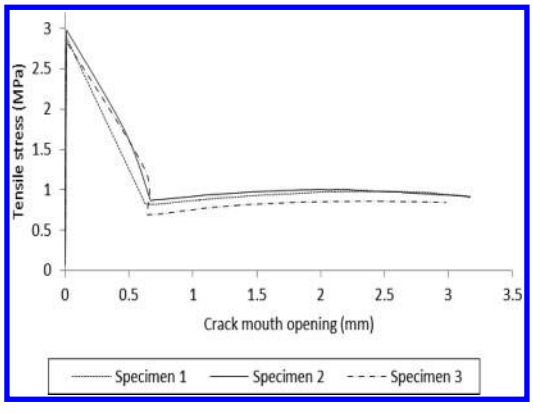


Figure 6. Ultimate and post-peak uniaxial tensile strength.

between the weights and the actual forced applied on the specimens. The load was applied on the set of specimens almost instantaneously while ensuring that no dynamic loading occurred. Two load levels were tested (30% and 50% of the post-peak residual strength) with four specimens each. Creep fracture was also observed for specimens loaded at 50% post-peak residual strength after 4 months under sustained loading. The two sustained load levels are shown in Figure 5.

4 EXPERIMENTAL RESULTS

4.1 *Uniaxial tensile strength results*

The results of the three specimens tested for uniaxial tensile strength are shown in Figure 6.

The main purpose of the test was to investigate the post-peak uniaxial tensile strength of the specimens.

Since the specimens to be tested for the time-dependent behaviour are to be subjected to sustained loads at fractions of the post-peak residual strength, this test was required in order to determine the post peak residual strength. Figure 6 shows an average post-peak residual strength of 0.78 MPa. When compared with the trial specimen shown in Figure 5 that

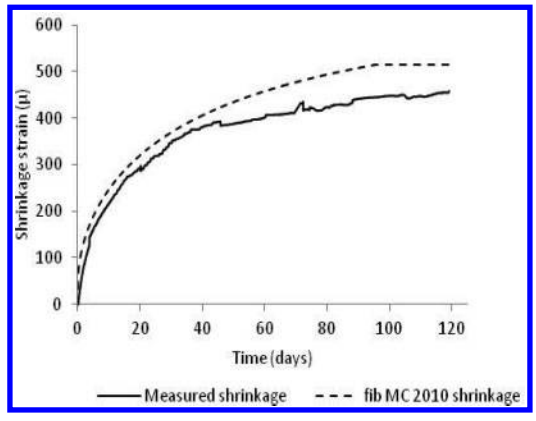


Figure 7. Shrinkage measured on unloaded, unsealed specimens.

was loaded, unloaded and reloaded again to maximum post-crack strength, the strain softening behaviour of both tests show the same pattern and specimens unloaded and reloaded attained the same stress with samples in the uniaxial tensile test.

4.2 *Shrinkage test results*

The average time-dependent shrinkage strain evolution of the two unloaded, unsealed specimens in the same climate controlled room where the creep specimens were also placed is shown in Figure 7.

The experimental shrinkage was compared with the predicted shrinkage using the final draft of the *fib* Model Code (2010). The experimental result showed close but slightly lower shrinkage when compared with the predicted shrinkage up to 45 days. This is in agreement with an earlier work by Babafemi and Boshoff (2013). Beyond this point, the experimental shrinkage became lower than the predicted. It should be noted that the *fib* Model Code prediction was for conventional concrete without fibres. The measured shrinkage strain as at 120 days is in the region of 482 μ while the predicted at same time is about 520 μ.

The reduction in the shrinkage of PFRC when compared to normal concrete is an indication that macro synthetic fibre such as polypropylene may not significantly reduced early age shrinkage, but with time, shrinkage is reduced when compared to normal concrete.

4.3 *Pre-cracked tensile creep results*

The time-dependent crack mouth opening from the time the specimens were loaded up to 120 days is shown in Figure 8. It should be noted that the average experimental time-dependent strain of the four specimens loaded in series (two apiece in the creep frame) and measured as crack mouth opening displacement (CMOD) is shown in Figure 8. An equivalent shrinkage strain had been deducted from the measured total creep strain.

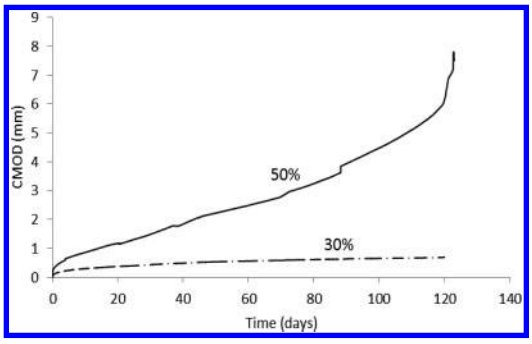


Figure 8. Average time-dependent strain for each loading level.

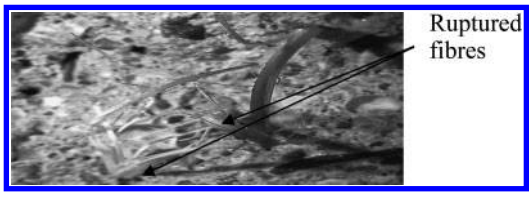


Figure 9. Damaged surface of PF after creep fracture.

Figure 8 shows significant creep for specimens loaded at 50% stress level when compared to those loaded at 30%. Specimens loaded at 50% stress level showed unstable response as the crack mouth continued to increase until creep fracture occurred. This behaviour showed a three-stage creep response of the specimens: primary, secondary and tertiary (Boshoff 2007). The specimens entered the third stage of creep failure after 80 days under sustained loading and eventually, creep fracture occurred after 4 months of testing. This is evident by the continued increase of the crack mouth until failure. However, specimens loaded at 30% stress level showed a decreasing rate of increase in creep at 4 months of testing with a CMOD of about 0.6 mm.

The time-dependent strain behaviour of specimens loaded at 50% stress level was alarmingly high and should be a cause of concern for potential users of synthetic fibre reinforced concrete when in the cracked state. The increased creep of the cracked PFRC may be attributed to the high creep rate of the macro synthetic fibres (BEKAERT, 2008). Figure 9 shows the deformed state of PF after the specimens tested at 50% stress level had failed.

It can be observed that one of the mechanisms that caused creep failure of the specimens was fibre rupture under sustained loading. However, it is intended that further studies will be done on single fibre pullout and fibre creep tests to understand the mechanism causing the time-dependent crack mouth opening of PFRC.

A comparison of the specific creep strain of specimens at both stress levels compared to the creep of normal concrete is shown in Figure 10.

The specific strain was obtained by subtracting the shrinkage strain from the total time-dependent strain,

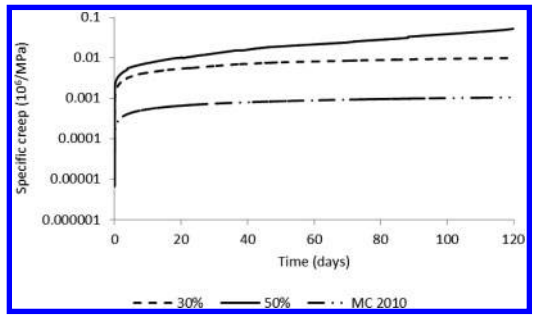


Figure 10. Specific creep of PFRC for each loading levels.

and normalizing by the creep stress levels. According to the *fib* Model Code 2010, the definition of stress-strain law for fibre reinforced concrete is based on the identification of the crack width and the corresponding structural characteristics length, l_{cs}, of the structural element when softening materials are considered. Hence, strain is assumed to be as below.

$\varepsilon = w/l_{cs}$, where w = crack mouth opening displacement and $l_{cs} = y$,where y = distance between the neutral axis and the tensile side of the cross section.

For sections without traditional reinforcement such FRC, the Code recommends that y = h be assumed. For a typical beam depth of 300 mm, $l_{cs} = 300$ mm. This was used to compute the specific creep of both specimens loaded at 30% and 50% stress level and a comparison made with the specific creep of a normal creep model using the Model Code. It is clear from Figure 10 that the cracked creep strain of specimens loaded at 30% and 50% were significantly more when compared to normal concrete. The specific creep was plotted on log scale because of the difference in specific creep value of cracked specimens when compared to normal concrete to an order of magnitude of two.

5 CONCLUSION

This study has investigated the time-dependent behaviour of PFRC under two different stress level; 30% and 50% of the post-peak residual uniaxial tensile strength. The tests performed were uniaxial tensile tests, shrinkage and creep test. The time-dependent tests were performed for 4 months in a climate controlled environment using concrete prisms measuring 100 × 100 × 500 mm. The investigation in this study indicted the following:

(a) Time-dependent deformation, i.e. shrinkage of unloaded PFRC specimens showed lower strain after the first 45 days when compared to the predicted deformation of conventional concrete as given in the Final Draft of the *fib* Model Code 2010. Measured shrinkage was 482 μ after 4 months as against the predicted 520 μ for conventional concrete at the same period.
(b) The creep response of pre-cracked PFRC was alarmingly high when subjected to 50% of the

post-peak residual uniaxial tensile strength. Creep fracture occurred after 4 months under sustained load. At 30% stress level, a decreasing rate of increase in the crack mouth opening was observed after 4 month.

(c) Fibre rupture is one of the mechanisms that caused the creep fracture of specimens subjected to sustained loading at 50% post-peak residual stress.

REFERENCES

Arango, S. E., Serna, P. & Marti-Vargas, J. R. 2011. A test method to characterize flexural creep be haviour of pre-cracked FRC specimens. *Experimental Mechanics,* doi 10.1007/s11340-011-9556-2. http://www.springerlink.com/content/5n20r01337ql5g68/.

Babafemi, A.J. & Boshoff, W.P. 2013. Preliminary creep behaviour of polypropylene fibre reinforced concrete under a high tensile stress. *Advances in Cement and Concrete Technology in Africa, 28–30 January 2013.* Johannesburg: South Africa.

BEKAERT. Creep test, 2008. Available online on http://www.bekaert.com/building.

Boshoff, W.P. 2007. Time-dependant behaviour of engineered cement-based composite. Doctoral Thesis, Stellenbosch University, South Africa.

BS EN 934-2:2009. Admixtures for concrete, mortar and grout. concrete admixtures. Definitions, Requirements, conformity, marking and labelling," BSI, London.

Burrati, N., Mazzoti, C. & Savoia, M. 2011. Post-cracking behaviour of steel and macro-synthetic fibre-reinforced concretes. *Construction and Building Materials*, 25: 2713–2722. doi:10.1016/j.conbuildmat.2010.12.22.

EN 14561: 2007. Test method for metallic fibre reinforced concrete – Measuring the flexural strength (limit of proportionality (LOP), residual).

fib Model Code 2010 First Complete Draft Volume 1. 1st (ed.) Lausanne, Switzerland: the International Federation for Structural Concrete, 2010.

Mackay, J. & Trottier, J. F. 2004. Post-crack creep behaviour of steel and synthetic FRC under flexural loading. In Shotcrete, *More engineering developments*, Taylor and Francis Group, London.

Markovic, I. 2006. High-performance hybrid-fibre concrete-development and utilisation. Doctoral Thesis, Delft University of Technology, DUP Science, Netherlands.

Mouton, C.J. & Boshoff, W.P. 2012. Initial Study on the tensile creep of cracked steel fibre reinforced concrete. *Proceedings of the 8th RILEM International Symposium on Fibre Reinforced Concrete: Challenges and Opportunities, 19–21 September*, Guimarães, Portugal.

Richardson, A.E. 2004. Electrical properties of Portland cement with the addition of polypropylene fibres: regarding durability, *Structural Survey*, 22(3): 156–163.

Rocstay – polypropylene fibres for concrete and mortar reinforcement: technical data sheet. A publication of Fibsol (Fibre reinforcing solution), South Africa.

SANS 5862 -1:2006 Concrete tests – consistence of freshly mixed concrete – Slump test. SABS Standards Division.

Tan, K.H., Paramasivan, P. & Tan, K.C. 1994. Instantaneous and long-term deflections of steel fibre reinforced beams under sustained loads. *ACI Structural Journal,* 91(4): 384–393.

Tan, K.H. & Saha, M.K. 2005. Ten-year study on the steel fibre reinforced concrete beams under sustained loads. *ACI Structural Journal,* 102(3): 472–480.

Zerbino, R.L. & Barragan, B.E. 2012. Long-term behaviour of cracked steel fibre-reinforced con crete beams under sustained loading, *ACI Materials Journals,* 109(2): 215–224.

Zhang, J. 20003. Modeling of the influence of fibres on creep of fibre reinforced cementitious compo site, *Composites science and technology,* 63, 1877–1884.

Zile, E. & Zile, O. 2013. Effect of the fibre geometry on the pullout response of mechanically de formed steel fibres, *Cement and concrete research,* 44, 18–24.

Research and Applications in Structural Engineering, Mechanics and Computation – Zingoni (Ed.)
© 2013 Taylor & Francis Group, London, ISBN 978-1-138-00061-2

Effect of temperature on the behaviour of polymer reinforced concrete façade

J.O. Akinyele
Department of Civil Engineering, Federal University of Agriculture, Abeokuta, Nigeria.

ABSTRACT: Polymer reinforced concrete is gradually becoming popular; due mainly to the damage caused to steel elements by corrosion. But the effect of temperature on polymer reinforced slabs has not been critically looked into.

This paper described the construction of concrete façade reinforced with polymer (polyethylene) rod and steel reinforcements. Ten number model sized elements of area 0.15 m^2 and a depth of 40 mm were considered, some models were exposed to an elevated temperature of 50°C for six hours (average temperature for a desert area), all samples were subjected to incremental load of 1 kN until failure. Thermal expansion, deflections and crack width were measured for each element.

Deflection in steel reinforced façade exposed to elevated temperature was 11.20 mm while that of polymer was 12.72 mm. The study concluded that the low thermal effect on polymer reinforced concrete is a result of low thermal conductivity of polymer.

1 INTRODUCTION

The construction sector is one of the world's largest consumers of polymer composites. Unreinforced polymer composite materials have been used by the construction industry for many years in non-load bearing applications such as trimmings, kitchenware, vanities and cladding. Recently efforts are being made to include reinforced polymer composites as load bearing materials in the construction industry. However, to date the number of primary structural applications of reinforced polymer composites in construction remains relatively low and there appears to be a number of issues contributing to their slow uptake by the construction industry, such as cost of production, lack of standard design codes, and poor understanding of the material properties.

Civil or building construction are commonly claimed to also place these materials at a disadvantage when considered against traditional construction materials. However, this paper proposes that as issues of sustainability become increasingly important to material choice, some fibre composite materials could be at an advantage over traditional materials in façade structure.

A polymer is a large molecule (macromolecule) composed of repeating structural units typically connected by covalent chemical bonds. Whereas the term *polymer* is sometimes taken to refer to plastics, it actually encompasses a large class of natural and synthetic materials with a wide variety of properties.

Natural polymeric materials such as shellac, amber, and natural rubber have been used for centuries. A variety of other natural polymers exist, such as cellulose, which is the main constituent of wood and paper. The list of synthetic polymers includes synthetic rubber, Bakelite, neoprene, nylon, PVC, polystyrene, polyethylene and many more (Wikipedia, 2011).

The problem of corrosion in reinforced concrete structures has made some of the elements like concrete façade to become less attractive to clients who would have love to have it. Though many solutions have been proposed, the use of non metallic materials readily comes to mind. Many works have gone into the use of Fibre Reinforced Polymer (FRP) by Sivagamasundari and Kumaran (2008). Also Hegger *et al* (2010) investigated the advantages of textile reinforced concrete applied to a pedestrian bridge in Germany, and the results concluded that it is possible to design slender and light weight concrete members by using technical textiles instead of steel as reinforcement. A small number of new loads bearing civil engineering structures have been made predominantly from FRP materials over the last three decades. These include compound curved roofs (Hollaway, 2002), pedestrian and vehicle bridges and bridge decks, energy absorbing roadside guardrails (Bank and Gentry, 2000), building systems, modular rooftop cooling towers (Barbero and GangaRao, 1991), access platforms for industrial, chemical and offshore (Hale, 1997), electricity transmission towers, power poles, power pole cross-arms and light poles and marine structures such as seawalls and fenders (Weaver, 1999).

The potential benefits offered by fibre composites include high specific strength and specific stiffness, tolerable durability, good fatigue performance and the potential to reduce long-term costs. However, in many cases these potential benefits are difficult to

Table 1. Properties of reinforcement.

Reinforcement	f (N/mm^2)	E_s (N/mm^2)	D_f (mm)	Strain, ε
Polyethylene	30	1,110	6	0.0270
Steel rod	250	200,000	6	0.0012

f = Tensile strength of reinforcement, E_s = Modulus of elasticity of Reinforcement, D_f = diameter of reinforcement, ε = Strain of reinforcement at ultimate load.

realize and are sometimes based on specious fact and irrelevant data. In addition to this, the lack of bona-fide applications has caused many constructors to be skeptical of the material's ability to provide a viable alternative to traditional materials. Many of the existing applications are experimental in nature and are aimed at demonstrating the ability of fibre composite materials to perform in certain applications. To this end they may be successful in terms of structural performance, but offer little by way of meaningful financial performance data.

The use of non metallic materials may not be popular yet because most of the design codes are silent about it. But some codes like the ACI code and CAN/CSA code allow the use of Glass Fibre Reinforced Polymer (GFRP) bars as main reinforcement for concrete structures such as bridge decks, floor slabs and wall type structures. (ACI committee, 1996, CAN/CSA-S6-02, 2002).

The aim of this paper is to determine the response of both polymer and steel reinforced concrete façades to increase in temperature under load.

1.1 *Mechanical properties of polymer*

The tensile strength of a material quantifies how much stress the material will endure before suffering permanent deformation (Ashby and David, 1996, Meyers and Chawla, 1999). This is very important in applications that rely upon a polymer's physical strength or durability. For example, a rubber band with a higher tensile strength will hold a greater weight before snapping. In general, tensile strength increases with polymer chain length and cross-linking of polymer chains. A High Density Polyethylene HDPE has strength between 25–30 MPa and a Low Density Polyethylene LDPE has strength of between 10–20 MPa (omnexus.com, 2011). The melting temperature for this material is 137°C.

Young's Modulus quantifies the elasticity of the polymer. It is defined, for small strains, as the ratio of rate of change of stress to strain. Like tensile strength, this is highly relevant in polymer applications involving the physical properties of polymers, such as rubber bands. The modulus is strongly dependent on temperature (Ashby and David, 1996, Meyers and Chawla, 1999). Table 1 showed the mechanical properties of polyethylene and steel rods.

2 MATERIALS AND METHOD

2.1 *Polyethylene Rod Production*

The polyethylene rods were made from sachets water packs. The packs were gathered in large amount, washed and spread to drain the water from it. After the water had been drained, they were taken to a polyethylene bag manufacturing company in Lagos Nigeria.

The sachets were introduced into intake of the extrusion machine after the temperature and the pressure for the melting had been set on the control panel of the extrusion machine. As the sachets were introduced into the intake, the sachets start melting and then came out from the mould at the mouth of the extrusion machine in rod form of 6mm diameter (Adjusted diameter).

As the rods came out, a water bath was provided where the rods were made to go through so as to cool off the temperature and make it harden. Also, a fan was provided to give additional cooling to the process.

2.2 *Specimen details*

The façade were designed based on the tensile strength of the reinforcing materials, mild steel rod with strength of 250 N/mm^2 and polyethylene rod of 30 N/mm^2 were used for the design of the slab prototypes. Both the steel and the polyethylene rods were arranged based on the design specifications which gave the diameter of the material and the spacing, for the polyethylene rod, 18 number 6 mm rod was used at a spacing of 25 mm while for steel rod 4 number 6 mm rod at 125 mm spacing was applied, the distribution reinforcement is based on the same spacing obtained for the short span for each type of slab. The reinforcing materials were then placed into the wooden mould (i.e. form work). These formworks are 500 mm by 300 mm by 30 mm. There were a total of ten (10) number concrete façade produced from the experiment, five number each for the Steel and polyethylene rods respectively. The concrete mix used was 1:2:4 i.e. the proportion of 1 part of cement to 2 parts of fine aggregate and to 4 parts of coarse aggregate while the water-cement ratio (the w/c ratio) was 0.5 i.e. 1 part of water to 2 parts of cement by weight.

The concrete was well mixed, the cement, fine and coarse aggregate were measured through the use of weighing balance i.e. batching was by weigh. Ordinary Portland cement was used and the fine aggregate was the sharp sand. The size of the coarse aggregate used was half an inch (12 mm).

The moulds were lubricated with oil before concrete was poured into it to allow easy removal of the slab specimens after it is set. After the preparation of thoroughly mixed concrete, it was then poured into the moulds and then compacted or vibrated manually by shaking the moulds. The slab specimens were removed from the mould after it has been allowed to set for 24hrs. The slabs were then cured to gain full strength by pouring water on it everyday. After 28 days, the slab specimens were put into test.

2.2.1 *Thermal and load test*

It is possible for stresses to be induced by temperature changes in composite members which are additional to those produced by applied loads. These stresses arise when the components of a composite member have different rate of thermal expansion: Hence the need to carryout the effect of temperature on the two different façade types.

Six of the specimen were placed in an oven that was regulated to 50°C, which is the average temperature of a dessert area in Africa, this samples were left in the oven for six hours, while the remaining four were left at an ambient temperature of 25°C. The specimens were placed in an axial load testing machine immediately after removal from the oven in such a manner that the point load was applied at the top surface of the slabs and supported on all four sides. The axis of the specimen was carefully aligned with the axis of loading device. The digital dial gauge attached to the retort stand was placed on the slab close to loading point to measure the deflection due to the applied load and the mechanical loading was monotonically increased by the adjusting knob and the corresponding deflection was recorded. The specimen was loaded until the ultimate load capacity of the slabs was achieved, the ultimate failure load was recorded and the crack width was measured at failure load.

Theoretical deflections of the slabs were computed using equation 1 while thermal expansions for each slab were obtained using equation 2.

$$\Delta_c = \frac{\alpha_c \Delta T l^2}{4h} \tag{1}$$

$$\delta = L_0 \Delta T \left(\frac{\alpha_c A_c E_c + \alpha_s A_s E_s}{A_c E_c + A_s E_s} \right) \tag{2}$$

where h is the slab thickness (30 mm), l is the slab span (500 mm), ΔT is the thermal gradient, and α_c is the coefficient of expansion, E is the young modulus of the material; A is the area of reinforcement.

3 RESULTS AND DISCUSSIONS

From the results showed in Table 2, polyethylene reinforced façade have higher experimental and theoretical deflections than the steel reinforced specimen, but the thermal expansion of steel reinforced specimen is marginally higher than that of polymer by 0.001 mm. At higher temperature of 50°C after six hours, the crack width for steel reinforced facades was 0.70 mm, the deflection was 11.20 mm while the slab failed at 5.30 kN load. Figure 1 showed the graph of load against deflections. For the polymer reinforced slab, crack width was 1.30 mm, deflection was 12.72 mm and failure load was 3.00 kN. The graph is showed in Figure 2. The above results showed that increasing the temperature of slabs has effect on its properties.

The increment in temperature led to increase in deflections and crack widths; these can be traced to the reinforcement used in both type of slabs. The wide difference in the deflection between the two steel elements (elevated and ambient) showed the effect of high temperature, while the very marginal difference in that of the two polymer elements showed that the effect of temperature on polymer façade is very minimal. The experimental deflection in steel façade at ambient temperature of 25°C was over 100% higher

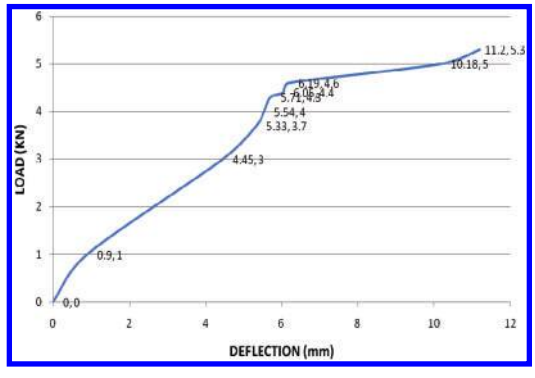


Figure 1. Deflection of Steel façade at 50°C.

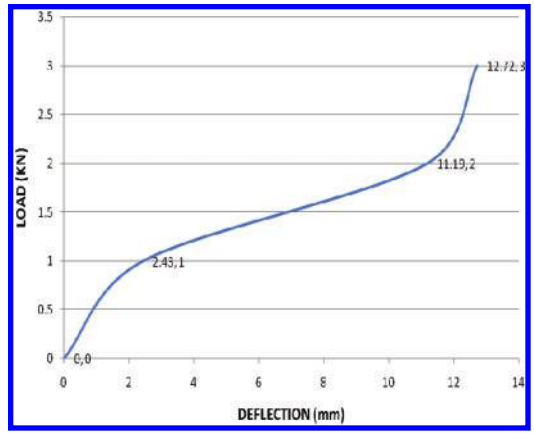


Figure 2. Deflection of Polymer rod façade at 50°C.

Table 2. Experimental and Theoretical Results.

Specimen	Experimental Δ_c(mm) 25°C	Experimental Δ_c (mm) 50°C	Theoretical Δ_c (mm) 25°C	Linear Expansion δ (mm)	Crack width (mm)
Steel	5.99	11.20	2.60	0.300	0.70
Polyethylene	12.25	12.72	12.50	0.299	1.30

than the theoretical results, the difference must have been due to many factors, since the theoretical results was based on ideal situations which may not be totally captured during the experiment. But for the polyethylene façade, the difference was about 5% which falls within an experimental error of ±10%, the consistency in the result of polymer reinforced façade deflections in the experimental and theoretical test and at both ambient and high temperature made the prediction for polyethylene deflection accurate, and this is a very good advantage when compared to the inconsistency observed in steel reinforced façade.

4 CONCLUSIONS

The present study have showed that steel is still the best reinforcing material, but it characteristics under certain conditions like temperature and corrosion which is not very consistent has prompt research in to looking for an alternative to it.

The use of polymer can be a good substitute especially with its low thermal conductivity which gave it advantage over steel reinforcement. Further research in nanotechnology can greatly improve the properties of polymer as alternative reinforcement materials in concrete in the nearest future.

REFERENCES

ACI Committee 440 R-96, (1996) *State-of-the-Art Report on Fibre Reinforced Plastic (FRP) Rein forcement for concrete structures*.

Ashby, Michael and Jones, David (1996). *Engineering Materials (2nd ed.)*. Butterworth-Heinemann

Bank, L.C. and T. R. Gentry, (2000), "Composite Materials for Roadside Safety Structures", *Proceedings of ACUN-II International Composites Conference*, University Of New South Wales, Australia

Barbero, E. and H.V.S.GangaRao, (1991), "Structural Applications of Composites in Infrastructure", *SAMPE Journal, Vol 27, No 6*, SAMPE, USA.

CAN/CSA-S6-02 (2002), "Design and Construction of building components with Fibre Reinforcement Polymers", *Canadian Standards Association*, Toronto, Ontario, Canada.

Hale, J. M., (1997), "Strength Reduction of GRP Composites Exposed to High Temperature Marine Environments", *Proceedings of ICCM11 International Conference* on Composite Materials, Australian Composites Structures Society, Australia

Hegger J., Kulas C., Goralski C. (2010)**.** "Advantages of textile reinforced concrete applied to a pedestrian bridge". *Advances and Trends in Structural Engineering, Mechanics and Computation,* Taylor and Francis Group, London. pp 215.

Hollaway, L., (2002), "The Development and the Future of Advanced Polymer Composites in the Civil Infrastructure", *Proceedings of the International Conference on Advanced Composites in Construction,* University of Southampton, Available November 2002.

Meyers, M. A. and K. K. Chawla (1999). *Mechanical Behavior of Materials*, Cambridge University Press.

Omnexus.com. Accessed (May 2011).

Sivagamasundari, R and Kumara, G. (2008)**.** "A comparative study on the flexural behaviour of one-way concrete slabs reinforced with GFRP reinforcements and conventional reinforcements when subjected to monotonic and repeated loading" *The open Civil Engineering Journal, Vol. 2.* pp. 24–34.

Weaver, A., (1999), "Composites: Worldwide Markets and Opportunities", *Materials Today.*

Wikipedia.com, Accessed (May, 2011)

Research and Applications in Structural Engineering, Mechanics and Computation – Zingoni (Ed.)
© 2013 Taylor & Francis Group, London, ISBN 978-1-138-00061-2

Flexural behaviour of normal and high strength concrete beams reinforced with GFRP rods

N.F.O. Evbuomwan
Accenture Inc, Irving, Texas, USA.

ABSTRACT: This paper reports on research done involving the use of Glass Fibre Reinforced Plastic (GFRP) rods as reinforcements in lieu of steel within concrete. The parameters investigated include types of concrete (Normal density and Lightweight), Reinforcement Ratios, Concrete Strengths (including very high strength concrete) and two beam lengths (1 m and 2 m long). Results of static flexural tests carried out on these beams are discussed in detail. The flexural and Load-Deflection behavior of the beams are greatly influenced by the reinforcement ratio and beam size. The cracking results (width, height and spacing) were found to be controlled principally by reinforcement ratio, beam dimensions and concrete type.

1 INTRODUCTION

For structural engineering applications, particularly in concrete structures, efforts are now being made to explore the potential of using FRPs as an alternative material to steel. FRPs do exhibit certain properties that particularly make them attractive to engineers, such as : low weight, high static and fatigue strengths, high tensile strengths, resistance to chemicals and corrosion, high damping capabilities, and so on (Deskovic 1995). Most of the research in the use of FRP with concrete, has involved (i) strengthening and rehabilitation of concrete members with CFRP and/or GFRP plates, (ii) the use of FRP rods as reinforcements in concrete beams and (iii) the use of FRP rods as prestressing tendons in concrete beams (Taerwe 1995). Currently, efforts are being made to generate adequate data on the behaviour of such composite members and there is need for the development of a sound technical basis and design guidelines that can be incorporated into future design codes (Clarke & Waldron 1996). Previous work in the use of non-prestressed GFRP in concrete is that of (Nawy et al 1971) and (Nawy and Neuwerth 1977). Their results showed that beams reinforced with steel had fewer cracks than the corresponding beams reinforced with fibreglass. They observed that failure of the GFRP reinforced beams occurred on the compression side due to the compression failure of the concrete rather than the tensile failure of the GFRP rods. They found that at ultimate loads, the deflections of the fibre glass reinforced beams were approximately three times greater than those of the corresponding steel reinforced beams. In an early work by (Nanni 1993), he posited that the working stress method was most suitable in design FRP reinforced concrete. This is due to FRP beams behaving linearly-elastic up to failure, exhibiting reduced rigidity compared to steel reinforced beams. More recently, many other researchers have investigated the use of GFRP rods with roughened surfaces (Benmokrane, B. et al 1995) as well as in hybrid form with steel (Nanni et al 1994). In their work, Benmokrane et al [6] reported that cracking of the beams in the flexural span consisted predominantly of vertical cracks perpendicular to the direction of maximum principal stress induced by pure moment. They observed that after cracking, the reduction in stiffness was greater in GFRP reinforced beams compared to steel reinforced beams. (Nanni et al 1994) in their paper observed that the beams reinforced with hybrid rods, had fewer cracks and a greater spacing between cracks than beams reinforced with steel. (Theriault & Benmokrane 1998) observed in their research inter-alia that concrete strength and reinforcement ratio had minimal effect on crack spacing and higher reinforcement ratio reduced crack width and height, for the same applied moment.

This paper reports on research done involving the use of Glass Fibre Reinforced Plastic (GFRP) rods as reinforcements in lieu of steel within concrete. It discusses results of static flexural tests carried out on both 1 m and 2 m beams reinforced with two GFRP reinforcement ratios. This involved load versus deflection readings as well as crack measurements (crack number, width, height and spacing). Experimental results of ultimate strength capacities are compared with theoretical calculations based on the code provisions in BS 8110 Part 1 (Rahmat 1997).

2 MATERIALS AND SPECIMEN PREPARATION

In this series of tests, the high strength normal density concrete beams (HN1-HN4) were prepared using Ordinary Portland Cement, 5 mm fine sand, 10 mm

Table 1. Reinforcement Details of Beams.

Specimen Number	Beam Length	Reinforcement Type	Reinforcement
HN1	1 m	GFRP	3 – 4 mmϕ
HN2	1 m	GFRP	2 – 6 mmϕ
HN3	2 m	GFRP	3 – 6 mmϕ
HN4	2 m	GFRP	2 + 4 – 6 mmϕ
SHN2	1 m	STEEL	2 – 6 mmϕ
HL1	1 m	GFRP	3 – 4 mmϕ
HL2	1 m	GFRP	2 – 6 mmϕ
HL3	2 m	GFRP	3 – 6 mmϕ
HL4	2 m	GFRP	2 + 4 – 6 mmϕ

HN1-HN4 – High Strength Normal Density Concrete
HL1-HL4 – High Strength Lightweight Concrete

coarse (gravel) aggregate, micro-silica and superplasticizer in the proportions of 1:1:3:0.1:0.02 with a water cement ratio of 0.4. For the high strength lightweight concrete beams (HL1-HL4), the mix ratio used was 1:0.58:1.21:0.1:0.02 representing the proportions of Ordinary Portland Cement, 5 mm fine sand, lightweight aggregate, micro-silica and superplasticizer with a water cement ratio of 0.3. Cubes were cast as control specimens along with the beams and were tested for compressive strength. Four beams (2 of 1 m length + 2 of 2 m length) were each prepared for the HN and HL series and reinforced using GFRP rods. The reinforcement details for these beams including the 1 m control beam are shown in Table 1 and Figures 1 and 2. The ultimate strength of the GFRP rods was taken as 700 N/mm^2.

The steel bars had a yield strength of 460 N/mm^2. For the 1m beams, T2.6Ø bars were provided as links at 50 mm c/c spacing, while in the case of the 2 m beams, T6.0Ø bars were provided as links at 100 mm c/c spacing. The 1 m and 2 m beams had a cross-section of 50 × 100 and 100 × 200 respectively. All the beams were cast in steel moulds and the mix was adequately vibrated with an electric vibrator to ensure full compaction. They were demoulded 24 hours after casting and then left to cure in water until tested. Each beam was then tested at the age of 42 days. The elevation and cross-sectional details of the beams, showing the loading and support conditions are shown in Figures 1 and 2.

3 TESTING PROCEDURES

The rectangular beams were loaded in bending using a four point loading arrangement, with two concentrated loads placed symmetrically about their mid-spans. The loads were applied via a load cell using a hydraulic jack. The applied load readings were read in percentages from a digital readout, and were converted afterwards into kilonewtons, with the maximum load cell capacity set to 100%. Each beam was loaded in gradual increments of percentage load (1–4%) until

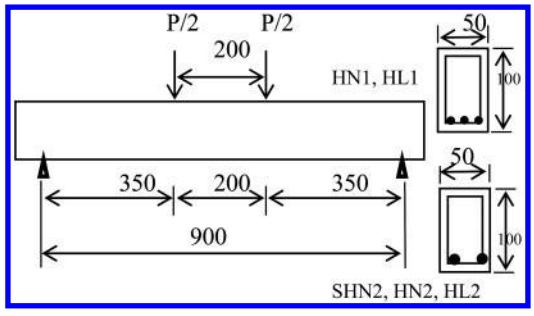


Figure 1. Loading Arrangement for 1 m Beams.

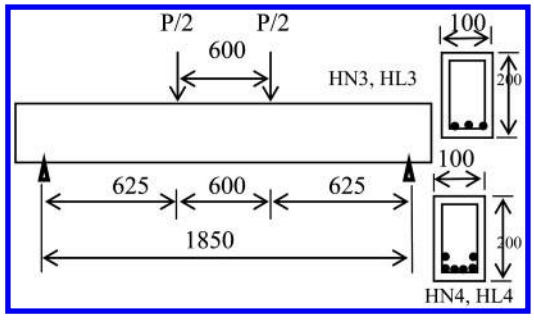


Figure 2. Loading Arrangement for 2 m Beams.

maximum (failure) load was reached. At each load increment, deflection readings were read from a dial gauge placed at the bottom of the mid-span position of the beam and strain readings were taken off demec discs placed on the 1 m and 2 m beams, using mechanical gauges of 100 mm and 200 mm gauge lengths respectively. During loading, when cracks occurred, readings of crack widths were taken using a crack microscope. In addition, crack number, heights and spacing were also recorded. Control cube specimens were tested after 42 days and the average compressive strengths are shown in Table 2.

4 RESULTS AND DISCUSSION

The Flexural and Cracking results of all the beams tested in this series are shown in Tables 2 to 6. It can be observed from Table 2 that Concrete strength had no major effect on cracking or ultimate failure loads for either the 1 m or 2 m beams. For both normal density and lightweight concrete 1 m beams, increase in reinforcement ratio generally resulted in slightly higher ultimate failure loads, but in the case of 2 m beams, this increase was much more significant.

Table 3 compares the theoretical moments and the experimental ultimate failure moments for all the beams. For the normal density beams with higher concrete strengths, the ratio of the experimental moments to the theoretical moments were generally about 60% irrespective of the reinforcement ratio or beam length. The lightweight concrete beams on the other hand showed closer correlation between the experimental

Table 2. Cracking and Ultimate Loads.

Beam ID	Beam Length	As/bd	Cube Strength Fcu (MPa)	Cracking Load (kN)	Ultimate Load (kN)
HN1	1 m	0.87	90	2.1	7.6
HN2	1 m	1.33	90	3.1	8.2
HN3	2 m	0.466	90	9.9	15.5
HN4	2 m	0.932	90	9.3	33.5
SHN2	1 m	1.33	90	8.2	24.84
HL1	1 m	0.87	52	2.2	8.6
HL2	1 m	1.33	52	3.2	9.7
HL3	2 m	0.466	52	8.3	24.1
HL4	2 m	0.932	52	2.3	35.3

SHN2 – As/bd Balanced = 3.3
HN1 – HN4 - As/bd Balanced = 1
HL1 – HL4 - As/bd Balanced = 0.644

Table 3. Experimental versus Theoretical Moments.

Beam ID	Theoretical Moment, M_T (kNm)	Experiment Moment, M_E (kNm)	Ratio M_E/M_T
HN1	1.82	1.36	0.75
HN2	2.42	1.43	0.59
HN3	9.06	5.16	0.57
HN4	17.46	10.47	0.60
SHN2	1.71	4.4	2.57
HL1	1.49	1.51	1.01
HL2	1.71	1.71	1.00
HL3	8.82	7.52	0.85
HL4	13.63	11.03	0.81

Table 4. Experimental versus Theoretical Deflections.

Beam ID	Deflection, d_T (mm)	Deflection d_E (mm)	Ratio d_E/d_T
HN1	10.94	22.73	2.08
HN2	8.33	24.9	2.99
HN3	18.2	32	1.76
HN4	19.31	36.23	1.88
SHN2	7.24	14.45	2.0
HL1	12.65	20.47	1.62
HL2	10.23	15.3	1.50
HL3	26.65	81.3	3.05
HL4	20.77	29.4	1.42

Table 5. Cracking Characteristics of Beams.

Beam ID	Max. Crack Width (mm)	Mean Crack Width (mm)	Max. Crack Height (mm)	Mean Crack Height (mm)	Max Crack Spacing (mm)	Mean Crack Spacing (mm)
HN1	0.80	0.74	90	86	160	137.5
HN2	1.88	1.51	94	86.3	175	160
HN3	1.86	1.33	189	182.3	414	308.5
HN4	1.94	1.24	185	120.9	200	105.9
SHN2	0.30	0.13	77	58.2	72	35.4
HL1	1.42	1.18	98	90.4	94	85.3
HL2	0.96	0.64	94	86.7	97	76.8
HL3	2.14	1.42	195	165.5	228	160.8
HL4	1.76	0.65	195	117.3	194	72.7

SHN2 - As/bd Balanced = 3.3
HN1 – HN4 - As/bd Balanced = 1
HL1 – HL4 - As/bd Balanced = 0.644

ultimate moments and theoretical values especially for the 1 m beams. These beams were more able to attain to the BS 8110 code predicted/expected moment capacity owing perhaps to higher extreme fibre compression strains in the HL series beams.In comparison however to the steel reinforced beam, the GFRP reinforced beams performed less effectively in attaining to ultimate moment capacity. The theoretical deflections and experimental deflections for all the beams are compared in Table 4. On the whole for all beams, the experimental deflections were significantly higher than their corresponding theoretical values irrespective of beam length, concrete strength or reinforcement ratio. With the exception of HL3, the HN series beams showed higher maximum deflection than the HL series. In Table 5, the cracking characteristics of the beams are shown for maximum and mean values of crack width, height and spacing. As expected the mean values were generally lower than the maximum values. For HN series, the maximum and mean crack widths with the exception of HN1, were generally similar in values did not seem to be affected by reinforcement ratio.

On the other hand for HL series, the maximum and mean crack widths generally decreased with increase in reinforcement ratios. The maximum and mean crack heights for both the HN and HL series showed very similar patterns. The maximum and mean crack heights in general, approximately doubled with increase in beam height from 100 mm to 200 mm. The exceptions were beams HN4 and HL4, where the mean crack heights were further affected and reduced by the increased number of cracks that occurred in both beams. In the case of maximum and mean crack spacing, the values observed for both the HN and HL series, approximately doubled when the beam lengths increased from 1 m to 2 m, with the exception of HN4 and HL4, where again the higher number of cracks played an additional factor in reducing the crack spacing.

It is interesting to observe the cracking behavior of beams HL2 and HL4 where HL4 had twice as many number of cracks (14) as HL2 (7) as shown in Table in 6. The maximum crack width, height and spacing of HL4 are about double those of HL2, whilst withthe exception of the mean crack height, the mean crack widths and spacing are approximately the same for both. The interplay here is both the height and length of the beams. This observed pattern shows that there is consistency in the bond between the GFRP rods and the

Table 6. Experimental vs Theoretical Crack Widths.

Beam ID	Total No. of Cracks	Experimental Max Crack Width, CW_E (mm)	Theoretical Max Crack Width, CW_T (mm)	Ratio CW_E/CW_T
HN1	3	0.80	0.78	1.03
HN2	3	1.88	0.57	3.30
HN3	3	1.86	0.77	2.42
HN4	10	1.94	0.83	2.34
SHN2	21	0.30	0.107	2.80
HL1	5	1.42	0.86	1.65
HL2	7	0.96	0.69	1.39
HL3	6	2.14	1.15	1.86
HL4	14	1.76	0.88	2.00

concrete irrespective of beam length and/or reinforcement ratio. In comparison with the GFRP reinforced 1 m beams, the steel reinforced beam showed much lower values for maximum and mean crack width, height and spacing.

Table 6 shows the comparison between the experimental maximum crack width for each beam and the theoretical values calculated based on BS 8110: Part 1, 1985. The total number of cracks observed for each beam is also shown. The number of cracks generally increased with increase in reinforcement ratio. All beams generally showed much higher maximum crack width than their theoretical counterparts and there is no significant observed pattern for concrete beam type/length, concrete strength or reinforcement ratio.

4.1 *Load Deflection Curves*

Figure 3 shows the applied load versus deflection curve for the HN series beams. It can be observed that up to about 2 kN, all the beams generally showed similar stiffness, but beyond there the 1 m GFRP reinforced beams showed much less stiffness and significantly increasing deflection with minimal increase in applied load up to failure.

The 2 m beams showed higher stiffness than the 1 m beams and slightly higher stiffness than the 1 m steel reinforced beam up to 10 kN beyond which they began to show increased deflection as applied load increased up to failure. For the 2 m beams, increasing the reinforcement ratio clearly showed improved ductility over the loading regime all the way to failure. Figure 4 shows the applied load versus deflection curve for the HL series beams.

The dominant observation is the improved stiffness for the 2 m beams with increased reinforcement ratio. The under-reinforced HL3 although showing a lower failure load compared to HL4 exhibited significantly higher ductility in comparison. In Figure 5, all the 1 m beams for both HN and HL series are compared. The GFRP reinforced beams all showed very similar deformational characteristics irrespective

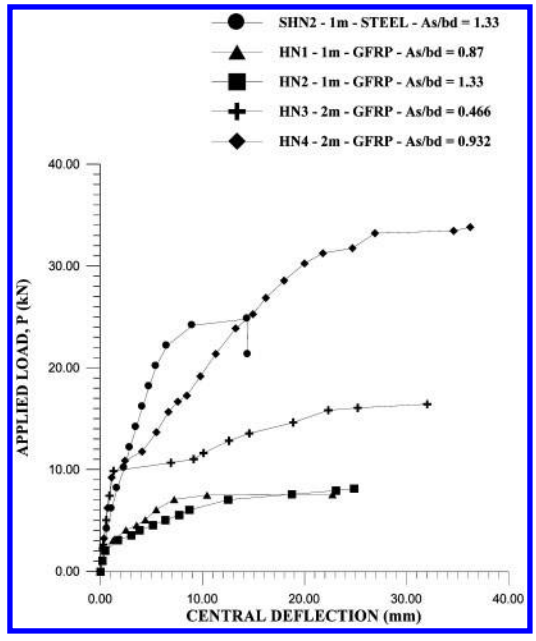


Figure 3. Applied Load vs Central Deflection for GFRP Reinforced High Strength Normal Density Beams.

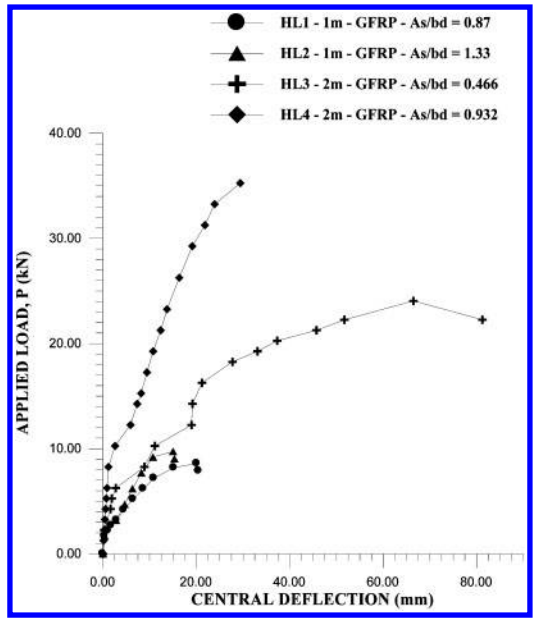


Figure 4. Applied Load vs Central Deflection for GFRP Reinforced High Strength Lightweight Beams.

of concrete strength and reinforcement ratio, but less stiffness compared to the steel reinforced beam. Similarly, the 2 m beams were compared in Figure 6. It can be seen that in this case, the beams with similar reinforcement ratio behaved similarly irrespective of the concrete type especially for HN4 and HL4 that showed very similar load-deflection behavior all the

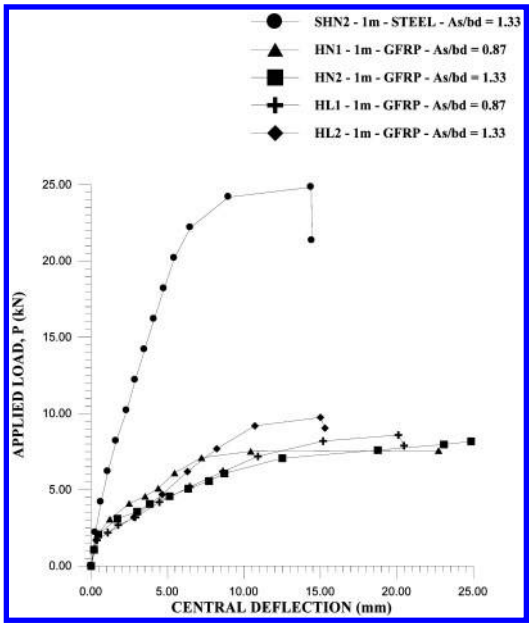


Figure 5. Applied Load vs Central Deflection for GFRP Reinforced 1 m Beams.

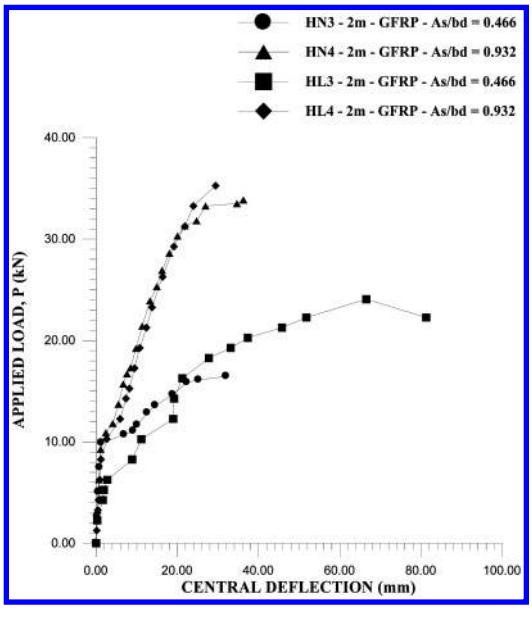


Figure 6. Applied Load vs Central Deflection for GFRP Reinforced 2 m Beams.

way to failure and much higher stiffness compared to HN3 and HL3 reinforced with half the reinforcement ratio.

4.2 *Cracking Behaviour*

In Tables 5 and 6, the cracking results of the beams were clearly elucidated. Figures 7 to 10 show in particular the Applied Load versus Maximum Crack Width

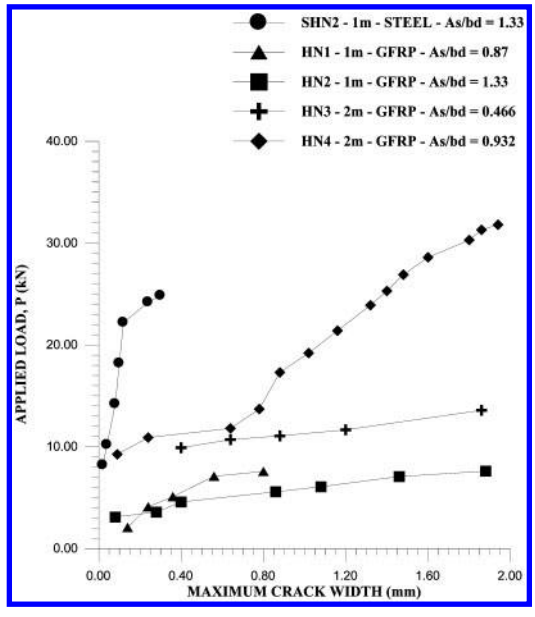


Figure 7. Applied Load vs Maximum Crack Width for GFRP Reinforced High Strength Normal Density Beams.

patterns throughout the loading regime of the beams. Figure 7 shows the results for the HN series, from which it can be observed that the GFRP reinforced beams showed higher maximum crack widths with slight increase in applied load compared to the steel reinforced beam.

This perhaps reflects poorer bonding performance of the GFRP beams compared to SHN2. Beam HN4 with higher reinforcement ratio showed higher applied load for the same crack width compared to the other beams.

The maximum crack width behaviour for the HL beams is shown in Figure 8. It can be observed that growth in crack width appear to be steadily increasing with increasing applied and that increasing the reinforcement ratio led to reduction in maximum crack width. This was more significant for the 2 m beams.

Figure 9 shows the maximum crack widths for all the 1 m beams irrespective of concrete strength and reinforcement ratio. It can be observed that the GFRP reinforced beams showed very similar patterns in their applied load versus maximum crack width curves, but higher values of maximum crack widths compared to the steel reinforced beam. Increase in reinforcement ratio resulted in moderate reduction in maximum crack widths.

In comparison the maximum crack width results for all the 2 m beams, we can observe in Figure 10 that increasing the reinforcement ratio resulted in significant reductions in crack width especially in the case of the lightweight concrete beams.

The lightweight beams HL3 and HL4 also showed reduced maximum crack widths compared to their normal density counterparts

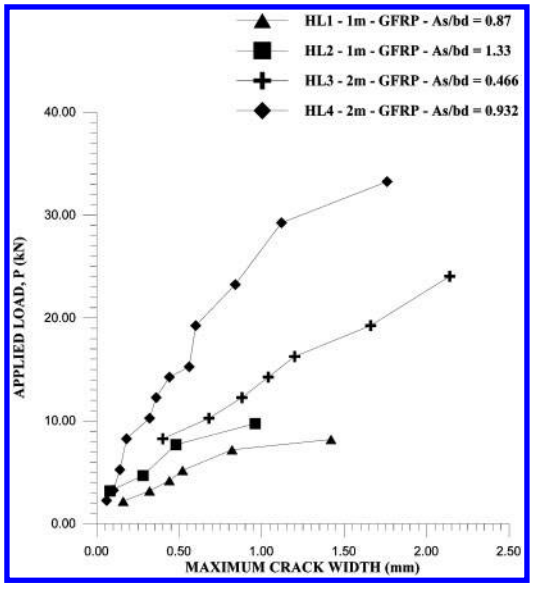


Figure 8. Applied Load vs Maximum Crack Width for GFRP Reinforced High Strength Lightweight Beams.

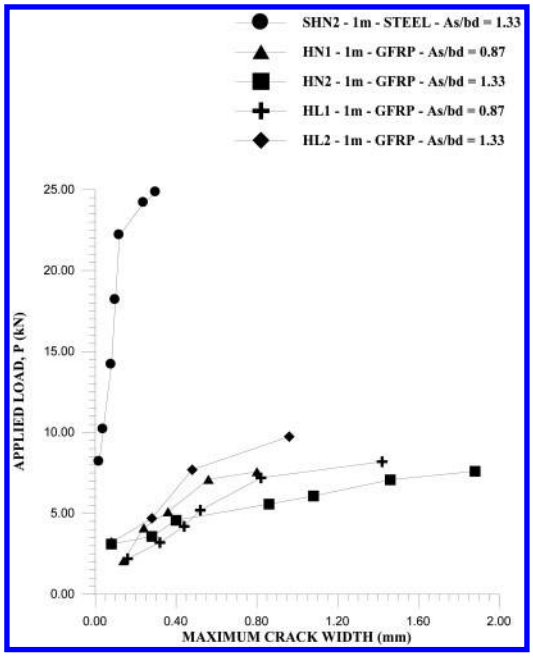


Figure 9. Applied Load vs Maximum Crack Width for GFRP Reinforced 1 m Beams.

5 CONCLUSIONS

Fundamental conclusions arrived at are as follows:

Reinforcement ratio, concrete type and compressive strength appear to have an effect on load deflection, stiffness and ductility of GFRP reinforced beams.

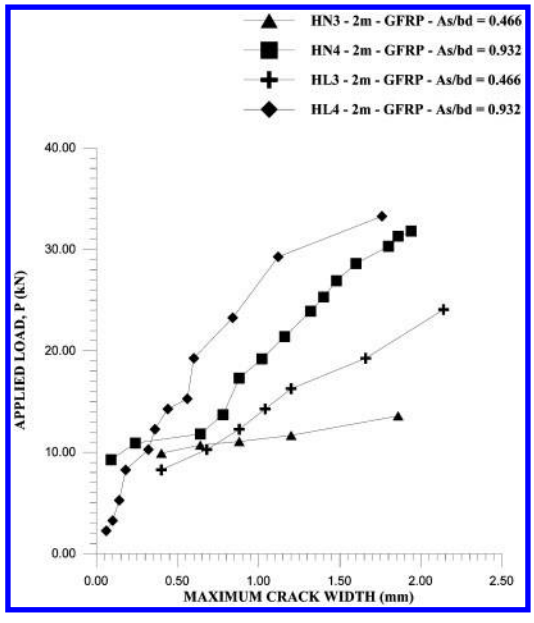


Figure 10. Applied Load vs Maximum Crack Width for GFRP Reinforced 2 m Beams.

Cracking characteristics are significantly influenced by reinforcement ratio and beam dimensions.

Using GFRP in High Strength concrete beams appear to show promise, but bond aspects as well as the challenge of the low modulus of the GFRP rods need to be addressed. Theoretical equations based on BS 8110 don't appear to be very suitable for estimating and/or predicting crack widths for GFRP beams and further research is needed to establish a more rational and suitable approach.

ACKNOWLEDGEMENTS

The Financial support given to the author while he was a Lecturer in Structural Engineering by the Department of Civil Engineering, University of Newcastle, UK, is gratefully acknowledged.

REFERENCES

Benmokrane, B. et al. 1995. Glass Fibre Reinforced Plastic (GFRP) Rebars for Concrete Structures. Construction and Building Materials. 9(6):353–364.

Clarke, J. L. and Waldron, P. 1996. The Reinforcement of Concrete Structures with Advanced Composites. The Structural Engineer. 74(17):283–288.

Deskovic, N et al. 1995.Innovative Design of FRP Combined with Concrete: Short-Term Behaviour. *Journal of Structural Engineering,* ASCE. **121(**7): 1069–78.

Nanni, A et al. 1994. Behaviour of Concrete Beams with Hybrid Reinforcement. Construction and Building Materials. 8(2):89–95.

Nanni, A. 1993. Flexural Behaviour and Design of RC Members Using FRP Reinforcement. Journal of Structural Engineering, ASCE. 119(11):3344–3359.

Nawy, E. G. et al. 1971. Behaviour of Fiber Glass Reinforced Concrete Beams. Journal of Structural Engineering, ASCE. 97(ST9):2203–2215.

Nawy, E. G. and Neuwerth, A. M. 1977. Fiberglass Reinforced Concrete Slabs and Beams. Journal of Structural Engineering, ASCE. 103(ST2): 421–440.

Nordin, H., & Taljsten, B. 2004. Testing of hybrid FRP composite beams in bending. Composites Part B: Engineering. 35:27–33.

Rahmat, F. 1997. Behaviour of High Strength Concrete Beams Reinforced with Composite Rods (GFRP). B.Eng Thesis, Department of Civil Engineering, University of Newcastle Upon Tyne, UK.

Taerwe L (ed). 1995. Non-Metallic (FRP) Reinforcement for Concrete Structures. Proceedings of the 2nd International RILEM Symposium, 23–25 August, 1995, Ghent, Belgium. E & FN Spon/Chapman & Hall, London.

Theriault, M & Benmokrane, B. 1998. Effects of FRP Reinforcement Ratio and Concrete Strength on Flexural Behaviour of Concrete Beams. Journal of Composites for Construction, ASCE. 2(1):7–16.

Research and Applications in Structural Engineering, Mechanics and Computation – Zingoni (Ed.)
© 2013 Taylor & Francis Group, London, ISBN 978-1-138-00061-2

Flexural behaviour of GFRP prismatic beams in composite action with concrete

N.F.O. Evbuomwan
Accenture Inc, Irving, Texas, USA

ABSTRACT: This paper reports on a major research done that involved the use of various forms of FRP in composite action with concrete. The paper elucidates succinctly results of experimental investigations performed on the structural behavior of FRP prismatic beams/sections bonded at the top to concrete slabs. These composite beams which were 1.18 m long, were investigated for varying parameters including normal and lightweight concrete, concrete slab dimensions, bonding systems and FRP section type (rectangular and I-sections). The effects and implications of these parameters on structural behavior of these beams, including failure patterns are discussed comprehensively. The paper concludes with highlights about the importance of developing a technical basis for the efficient use of Concrete/FRP composite beams as well as experimental and parametric data that can be employed in the development of design guidelines and codes of practice for Concrete/FRP composite structures and applications.

1 INTRODUCTION

In the early years the use of FRP in engineering applications was predominantly restricted to aerospace and automobile industries. The significant achievements and advancements in engineering application of FRP eventually resulted in its use within the Architectural, Engineering and Construction industry. Structural application and use of Fibre Reinforced Plastics (FRP) is increasingly becoming more evident in many buildings and Structures. The application of FRP in the construction industry, especially for structural engineering applications has been driven by the beneficial properties that make them attractive to engineers. Such properties include: resistance to chemical and corrosion, high stiffness and rigidity, low weight, superior static and fatigue strengths, high damping capabilities (Deskovic et al 1995a). Within the last few decades, besides other popular and emerging use of FRP in concrete structures, there has been significant interest in the use of FRP prismatic sections in composite action with concrete. The structural behavior of these hybrid FRP/Concrete beams has been the subject of a number of researchers over the years, with the general intent of understanding the structural behavior of such hybrid/composite beams (Taerwe 1995, Sims et al 1987, Maji et al 1997, Nagaraj & GangaRao 1997, Deskovic et al 1995b, Saiidi 1994). Such understanding can then be employed to further improve the design and application of FRP in real life structures. (Li 2006) studied hybrid beams of concrete and GFRP and observed that failure of the beams occurred predominantly by FRP web shear fracture and that the beams with thicker concrete showed more stiffness and rigidity. (Canning et al. 1999) in their investigation of the composite action of FRP/Concrete beams studied shear transfer at the interface between the two components for six methods of connection. They observed that using an adhesive compatible with freshly made concrete gave the most adequate level of composite action. (Khennane & Heslehurst 2009) in their study of a new design of hybrid FRP-Concrete beams involving both wrapped and unwrapped beams, observed that the wrapped beams exhibited 100% increase in load carrying capacity and significantly improved ductility compared to the unwrapped beams. A previous paper by (Evbuomwan 1998) involving various bonding parameters and combinations of FRP-Concrete for 500mm and 750mm long beams showed that in general, composite beams demonstrated much higher ultimate failure loads and lower deflections than the plain GFRP beams, particularly for the beams bonded with Epoxy alone. Various forms of failure mechanisms were observed for these beams similar to those reported by (Hulatt et al. 2004, Nordin & Taljsten 2004, Kavlicoglu 2001, Branco et al. 2003).

2 MATERIALS AND SPECIMEN PREPARATION

The objective of the experimental set up was to explore and investigate the composite behavior of rectangular and I-beam prismatic sections acting compositely with concrete under varying parameters and combinations. The plain rectangular GFRP sections were 50.6×101.62 mm with a flange thickness of 5.2 mm

and a web thickness of 3.48 mm. The plain GFRP I-sections were 49.52 × 100.94 mm with a flange thickness of 6.37 mm and a web thickness of 6.28 mm. The design of experiments was based on the use of 1180 mm long GFRP prismatic sections along with other parameters such as concrete type, width and thickness of the concrete slab and the bond type used in combining the two materials (Abeyasinghe 1997).

Nominal high strength concrete mixes were chosen for these series of tests for both the normal density and lightweight concrete beams. All the slab specimens were prepared using a mix proportion (by weight) of 1:1:3:0.28:0.2:0.02 (normal density) and 1:0.58:1.21:0.23:0.2:0.032 (lightweight), representing the ratio of Cement : Sand : Coarse Aggregate or lightweight aggregate: Water : Microsilica : Superplasticizer. Concrete cubes (100 mm square) were cast as control specimens for compressive strength tests. After mixing, the fresh concrete was poured into plastic moulds (for the slabs) and three cube moulds. The concrete in the moulds was then compacted using an electric vibrator and a tamper, and then left to cure for 24 hours before demoulding. On demoulding, after 24 hours, the concrete specimens were left to cure in water for 28 days, after which they were removed and then bonded to the GFRP and then left to cure in air for another 14 days.

Bond between the concrete slab and GFRP was achieved using two types of proprietary epoxy adhesives referred to here as Epoxy A and Epoxy B (Flexural strength at room temperature = 35 MPa) and/or mechanical shear connectors (bolts). The epoxy adhesives were two components types, that is, hardener and resin. Mixing was carried out as specified until a uniform colour was achieved. Prior to bonding, both the concrete slab and GFRP surfaces were roughened using a sand paper, followed by the application of acetone solvent. After mixing, the adhesives were applied onto both surfaces and then joined together. The thickness of the adhesive bond was estimated to be about 2 mm. When the bonding was completed, the specimens were left to cure in air for 14 days before being tested.

For specimens that required the use of mechanical connectors, Grade 8.8 bolts (25 mm long, and 6 mm diameter) and Grade 8 nuts in accordance with BS 3692 were used (Yield Stress = 628 MPa). Necessary analysis was carried out to estimate the total number of bolts required in the shear spans as well as their spacing. Bolts were also provided in the middle span to prevent the two materials separating as a result of bending. Each bolt was screwed through a tapped hole in the top flange of the GFRP and tightened with a nut from underneath the top GFRP flange. The length of the bolt left outside was embedded in the slab halfway along its thickness. The bonding of all the GFRP specimens with bolts was carried out when the concrete slab was cast. The concrete was poured into the plastic moulds and levelled to the appropriate thickness, while the GFRP-bolt surface was then pushed into the fresh concrete at the middle, until the surface was in contact with the concrete top layer. The beam was then supported in-place using pre-designed supports and C-clamps. When used in combination with bolts, the epoxy adhesive was applied on the GFRP-bolt surface before placing into the fresh concrete.

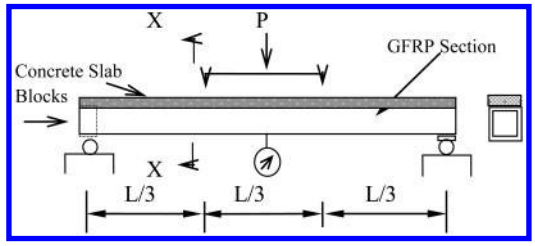


Figure 1. Details of the loading arrangement for a typical composite beam.

3 TESTING PROCEDURES

All the beam specimens were tested in Flexure 42 days after the concrete slabs were cast. Prior to testing, the GFRP box or I-sections were stiffened both from inside and outside the webs using wooden blocks and clamps. The beams were loaded in bending using a four point loading arrangement, with two concentrated loads placed symmetrically about their mid-span, as shown in Figure 1. The loads were applied via a load cell using a hydraulic jack. Readings of the applied load were taken from a digital meter, with each load increment applied gradually until maximum failure load was attained. Other necessary readings were taken at each load increment. These included deflection readings from a dial gauge placed at the bottom of the mid-span position of the beam, as well as strain readings taken off demec discs placed across the mid-span, using a mechanical gauge of 100 mm gauge length. After the test, cracks occurring in both the concrete and the GFRP, were identified. Control cube specimens were tested after 42 days and compressive strength values are shown in Table 1.

4 RESULTS AND DISCUSSION

The Flexural results of all the beams tested in this series are shown in Table 1.

It can be observed that for the composite beams involving the GFRP I-Sections, they generally exhibited higher failure loads than the plain GFRP I-Section by a factor of 37% (IB2) to 124% (IB3). For the composite beams involving the GFRP rectangular sections, only the beams with Normal density concrete exhibited much higher failure loads than the plain GFRP rectangular beam. The beams topped with Lightweight concrete exhibited lower failure loads than the plain GFRP beam. The type of bonding system used, concrete type and GFRP Section type had the most significant effect on maximum load attained as well

Table 1. Ultimate Load and Deflection Results.

Specimen No.	F_{cu} (MPa)	Slab width (mm)	Bond Type	Failure load P_{ult} (kN)	Mid-span deflection Δ_{ult} (mm)
IBP				21.85	9
IB1	76	200	Epoxy A	40.0	5.34
IB2	76	100	Epoxy A	30.0	4.56
IB3	72	200	Bolts	49.0	11.65
IB4	70	200	Epoxy A + Bolts	48.0	8.05
RBP				30.0	15.63
RB1	88	50	Epoxy A	53.0	13.66
RB2(LW)	59	200	Epoxy B	18.0	3.47
RB3	88	200	Epoxy A	42.0	11.00
RB4(LW)	59	200	Epoxy A	20.0	9.70

Table 2. Group Definitions.

Group name	Beam length	Member specimens	Differing parameter(s)
I-1	1180 mm	IB1, IB2, IBP	Slab Width
I-2	1180 mm	IB1, IB3, IB4, IBP,	Bond Type
R-1	1180 mm	RB2, RB4, RBP	Bond Type
R-2	1180 mm	RB1, RB3, RBP	Slab Width
R-3	1180 mm	RB3, RB4, RBP	Concrete Type
IR	1180 mm	IB1, RB3, IBP, RBP	GFRP Type

as resulting deflection. Table 2 shows the groupings of the beams that are compared based on the main varying parameter(s) as well as in relation to the behavior of plain GFRP control beams.

Group I-1 represents composite beams with GFRP I-Sections bonded with the same Epoxy A agent, but with different slab width. The beam with a 200 mm slab width (IB1) exhibited higher failure load, deflection ductility (Figure 2) than the one with 100 mm slab width. For Group I-2, the varying parameter compared is the Bond type.

The composite beams with concrete bonded either with steel bolts (IB3) or Epoxy A + bolts (IB4) showed higher failure loads than that bonded with Epoxy A (IB1) alone. Beams IB3 and IB4 also demonstrated much more ductility compared to beam IB1 as shown in Figure 2. Overall, we can observe that all the composite beams showed very similar stiffness up to a load of 20 kN, but significantly higher stiffness than the Plain GFRP I-Section throughout the loading regime and until failure load. The much higher stiffness demonstrated by these beams is corroborated by the lower compressive and tensile extreme fibre strain compared to the plain GFRP I-Section for the same applied moment as shown in Figure 3. The composite beams however at higher applied moments eventually demonstrated similar or higher tensile extreme fibre

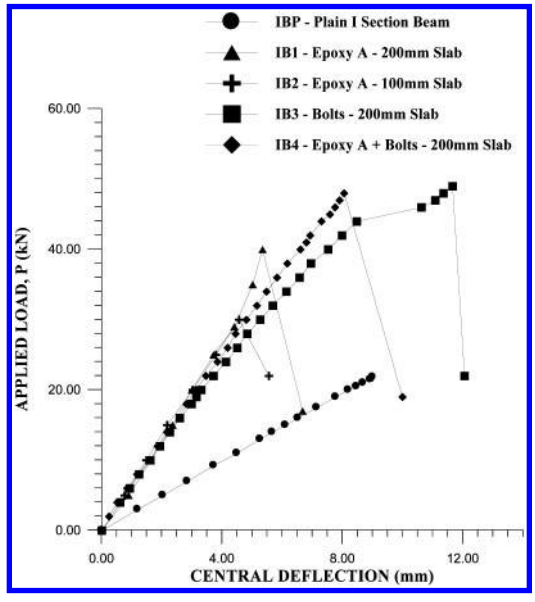


Figure 2. Applied Load vs Central Deflection for Composite GFRP I-Section Beams.

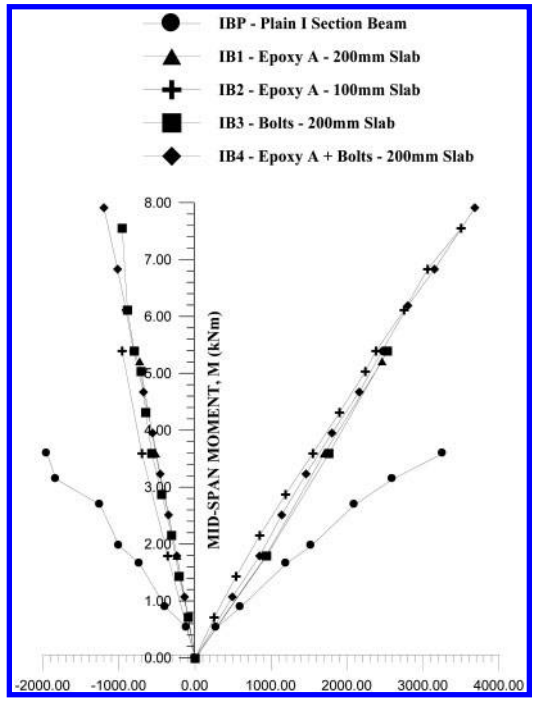


Figure 3. Mid-Span Moment vs Top & Bottom Extreme Fibre Strain of Composite I-Section Beams.

strain compared to the control beam. For the rectangular GFRP composite beams, their behaviour is discussed under the Groups R1, R2 and R3 representing the effect of Bond Type, Slab Width and Concrete Type (Table 2, Figures 4 & 5). The R1 group where the

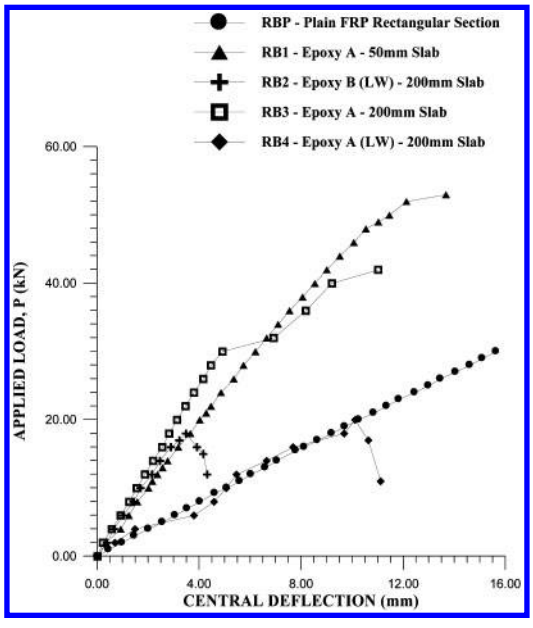


Figure 4. Applied Load vs Central Deflection for Composite GFRP R-Section Beams.

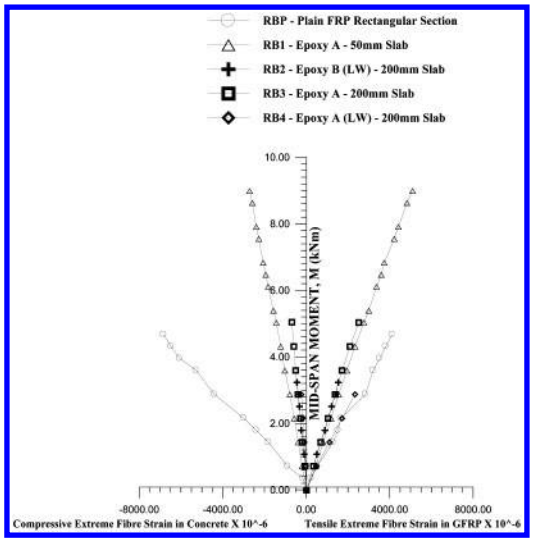


Figure 5. Mid-Span Moment vs Top & Bottom Extreme Fibre Strain of Composite R-Section Beams.

beams were topped with lightweight concrete showed no obvious difference in the ultimate failure load attained. The main differential is in the significantly higher deflection exhibited by beamRB4 bonded with Epoxy A compared with RB3 bonded with Epoxy B which showed much higher stiffness (Figure 4). For group R2, beam RB3 with 100 mm slab width showed higher stiffness in the early load regimes, but attained lower ultimate failure load than beam RB1 with 50 mm slab width.

Table 3. Failure Modes for the Composite Beams.

Specimen Number	Mode of Failure
Beam IBP	Fracture in top GFRP web-flange joint in symmetric mid-span region up to 200 mm long.
Beam IB1	Fracture/debonding of concrete + web shear fracture of GFRP in both midspan and shear span of the beam
Beam IB2	Fracture/debonding of concrete + web shear fracture of GFRP in both midspan and shear span of the beam
Beam IB3	Cracks in GFRP web-flange joint = concrete fracture along alignment of the bolts in one shear span
Beam IB4	Cracks in GFRP web-flange joint on both sides of beam
Beam RBP	Fracture in top GFRP web-flange joint near the point loads
Beam RB1	Fracture in top GFRP web-flange joint near the point loads followed by concrete crushing and buckling of webs in same region
Beam RB2	Concrete fracture followed by local bearing failure of bottom web
Beam RB3	Bearing failure and fracture of bottom web-flange joint.
Beam RB4	Concrete fracture followed by local bearing failure of bottom web

This is attributed to the fact that RB3 failed principally by bearing and the fracture of the GFRP web-flange compared to RB1 which was able to attain a higher failure load until it failed by crushing of the concrete in compression. For group R3 which for similar parameters compared effect of concrete type, beam RB3 topped with normal density concrete exhibited higher stiffness and ultimate failure loads than beam RB4 topped with lightweight concrete for about the same level of maximum deflection. In comparing the effect and significance of the GFRP type used, group IR (Table 2, Figures 6 & 7) is used.

We can observe that the plain GFRP I- section beam showed higher stiffness than the GFRP rectangular section beam, but attained lower ultimate failure load. The plain rectangular GFRP beamattained a much higher ultimate failure load, deflection and extreme fibre tensile strain. Both plain GFRP beams exhibited a linear elastic behaviour throughout the loading regime all the way until failure. The composite beams exhibited much higher stiffness than the plain beams all the way until failure, but similar.

Stiffness up to a load of about 30 kN, with RB3 showing more ductility beyond that until failure compared to IB1. Both composite beams however exhibited about the same ultimate failure load.

4.1 *Failure Modes*

Table 3 shows the various modes of failures for all the beams tested in this series. The plain beams were

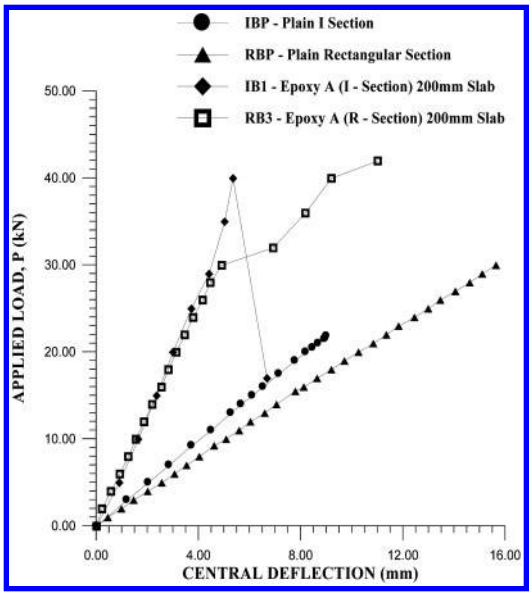


Figure 6. Applied Load vs Central Deflection for Composite GFRP I & R -Section Beams.

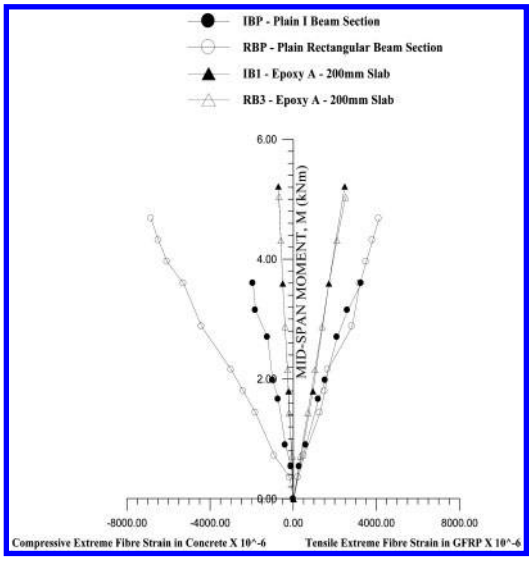


Figure 7. Mid-Span Moment vs Top & Bottom Extreme Fibre Strain of Composite I/R-Section Beams.

observed to fail by fracture of the top web-flange joint in symmetric mid-span region and close to the point loads. Virtually all the beams failed by fracture of either the top or bottom web-flange joint of the GFRP beam. For all the composite beams, with the

exception of IB4 and RB3, the GFRP failure occurred in combination with fracture/de-bonding and/or crushing of the concrete and in other cases some form of bearing failure of the GFRP at the supports. The Applied Load versus Central Deflection Curves shown in Figures 2, 4 and 6 were to some extent influenced by the modes of failure reported for all the beams. The kinks and departure from expected behavior in some cases, were undoubtedly due to how failures were initiated and up to ultimate failure of the beams.

5 CONCLUSIONS

In this paper, the results of tests performed on the behaviour of GFRP prismatic sections acting compositely with bonded concrete slabs have been reported. It was observed that in general, the use of epoxy adhesive and/or mechanical connectors (bolts) ensured adequate composite action. The composite beams exhibited much higher ultimate failure loads than the plain GFRP beams. The higher extreme fibre tensile strain exhibited by a number of the composite beams compared to the plain GFRP sections, clearly indicates that the use of concrete in composite action with GFRP can enable maximum utilization of FRP in tension and concrete in compression. Failure of the composite beams also appear to be governed principally by web shear and/or web-flange joint fracture in the GFRP, except in the beams bonded with bolts when re failure was initiated by longitudinal shear along the alignment of the bolts. Some of beams failed simultaneously with concrete fracture and web-flange fracture and in some cases in combination with bearing failure at the supports. In general, the use of FRP in composite action with concrete does show some promise that needs further investigation. To establish a more rational basis for the efficient use of concrete/FRP composites particularly with respect to the nature of the bond system/interface, controlling the mode of failure as well as numerical and analytical modeling, further work is needed.

ACKNOWLEDGEMENTS

The Financial support given by the Department of Civil Engineering, University of Newcastle, UK, is gratefully acknowledged. Mr Abeyasinghe as part of his M.Sc project work, carried out these experiments under the supervision of the author. The author is also grateful to Nufins Lid, Newcastle upon Tyne who supplied the Epoxy Adhesives.

REFERENCES

Abeyasinghe, M.C.L. 1997. Behaviour of GFRP Prismatic Sections in Composite Action with Concrete. M.Sc Thesis. Department of Civil Engineering. University of Newcastle Upon Tyne, UK.

Branco F.A. et al. 2003. The use of GRC and GFRP-concrete beams in bridge decks. Proceedings of FRP Composites in Bridge Design and Engineering, COBRAE Conference, Porto, Portugal.

Canning, L et al. 1999. An Investigation of the Composite Action of an FRP/Concrete Prismatic Beam. Construction and Building Materials. 13(8): 417–26.

Deskovic, N et al. 1995a.Innovative Design of FRP Combined with Concrete: Short-Term Behaviour.*Journal of Structural Engineering,* ASCE. **121(**7): 1069–78.

Deskovic, N et al. 1995b.Innovative Design of FRP Combined with Concrete: Long-Term Behaviour. *Journal of Structural Engineering,* ASCE. **121(**7): 1079–1089.

Evbuomwan, N. F. O. 1998. Behaviour of FRP prismatic sections in composite action with concrete. International conference on fibre reinforced composites No7, Newcastle upon Tyne, April 15, 1998. 53–62.

Hulatt J.A. et al. 2004. A novel advanced polymer composite/concrete structural element. Proceeding of the Institution of Civil Engineers Structures & Building. 157: 9–17.

Kavlicoglu, B.M. et al. 2001. Analysis and testing of graphite/epoxy concrete bridge girders under static loading. Proceedings of 9th International Conference on Structural Faults and Repairs, London, United Kingdom.

Khennane, A & Heslehurst, RB, 2009. A New Design Approach for a Hybrid FRP-Concrete Beam. Presented at Composites Australia Conference and Exhibition 2009, Gold Coast, 12–13 March 2009.

Li, T. 2006 Experimental Study On FRP-Concrete Hybrid Beams. Third International Conference on FRP Composites in Civil Engineering (CICE 2006), December 13–15 2006, Miami, Florida, USA.

Maji A. K. et al.1997. Evaluation of Pultruded FRP Composites for Structural Applications.*Journal of Materials in Civil Engineering,* ASCE.**9**(3): 154–158.

Nagaraj, V& GangaRao, H.V.S. 1997. Static Behaviour of Pultruded GFRP Beams.*Journal of Composites for Construction,* ASCE.**1(**3): 120–129.

Nordin, H., & Taljsten, B. 2004. Testing of hybrid FRP composite beams in bending. Composites Part B: Engineering. 35:27–33.

Saiidi, M. 1994. Behaviour of Graphite/Epoxy Concrete Composite Beams. *Journal of Structural Engineering*, ASCE. **120(**10): 2958–2976.

Sims G. D. et al. 1987. Mechanical and Structural Properties of a GRP Pultruded Section. *Composite Structures.* 8:173–187.

Taerwe L (ed). 1995. Non-Metallic (FRP) Reinforcement for Concrete Structures. Proceedings of the 2nd International RILEM Symposium, 23-25 August, 1995, Ghent, Belgium. E & FN Spon/Chapman & Hall, London.

22. High strength concrete, high performance concrete

Research and Applications in Structural Engineering, Mechanics and Computation – Zingoni (Ed.)
© 2013 Taylor & Francis Group, London, ISBN 978-1-138-00061-2

UHPC – a challenging material for innovative structures

Ekkehard Fehling
Institute of Structural Engineering, University Kassel, Germany

ABSTRACT: UHPC offers superior characteristics with regard to strength, durability, and – when reinforced by fibers – also ductility. Thus, it enables architects and designers new possibilities with regard to filigree and lightweight structures as well as for long spans and high rises. Since reliable knowledge about the material itself as well as a good understanding of structural behavior are essential, remarkable research efforts have been expended. The paper highlights a number of actual research results and shows some outstanding structures that have been built recently at different places in the world.

1 INTRODUCTION

The capability of Ultra High Performance Concrete is not represented by its high compressive strength only but as well by superior resistance against chemical attack and durability. Furthermore, by addition of fibres UHPC can become very ductile in compression and tension and a tensile capacity can be ensured which is much more reliable due to the fibers acting as micro-reinforcement than the plain concrete matrix. This enables the designer to build slender and filigree structures with UHPFRC and gives the architects degrees of freedom beyond actual possibilities when building with steel and concrete. With regard to the ecological footprint, UHPC gives new chances to reduce primary energy consumption and carbon dioxide emission.

UHPC further extends the potential of prestressed concrete. The extremely high compressive stress allows for much higher prestressing forces so that high tensile stressed can be compensated which makes lightweight and long span structures possible.

However, current design rules do not cover the range of extremely high concrete strength classes. In addition, the way of thinking during design of structures may be different for UHPC and, hence, special regard has to be paid to exploit the advantages of UHPC and specific research is required. During the last decade, for this reason a lot of research has been conducted throughout the world and an increasing number of buildings, bridges and other structures have been built using UHPC. This development has been triggered by French and Canadian colleagues (e.g. Aitcin & Richard 1996) who started in the 1990's to transfer the principles developed 1966 by Walz and Bache (1981) in Denmark to engineering structures.

This paper shall give a short overview of actual research results and developments in research and practice. With regard to research, mainly questions with regard to structural design shall be addressed here. Actual developments with respect to the material development and research and code provisions will be described in other contributions to this conference by Schmidt and Walraven.



Figure 1. Hybrid UHPC-Steel Bridge in Kassel across River Fulda (Gaertnerplatz – Bridge, Fehling et al. 2008).

2 RESEARCH

In Germany the Author has started to do research in the field of UHPC in 1998. The Deutsche Forschungs-Gemeinschaft DFG (German Research Council) has started a coordinated research program (SPP 1182) on sustainable building with UHPC in 2005. It deals with material related topics as well as structural design, both in the light of the aspect of sustainability.

2.1 *Material Aspects*

Regarding research into composition, optimization and behavior of the material, the following fields shall be mentioned:

- Optimization of mixture,
- Technology of (super)plasticizers,
- Ecological assessment and optimization,

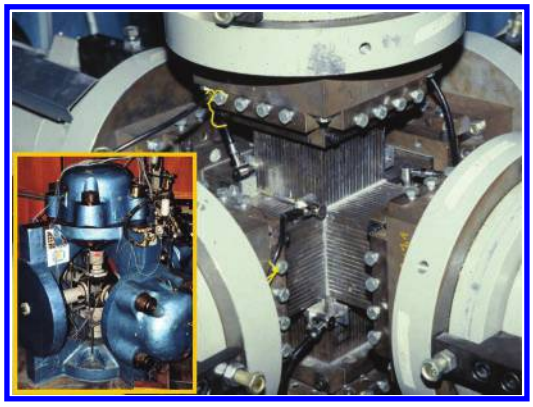


Figure 2. Experimental setup for triaxial tests at TU Dresden.

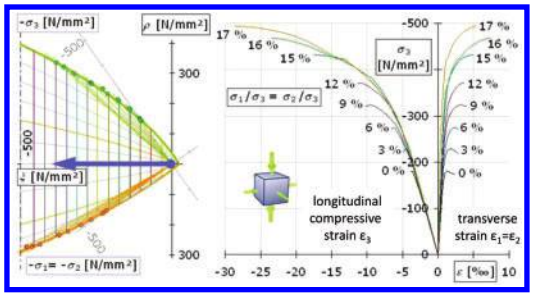


Figure 3. Strength curve in Rendulic-Plane and stress-strain relationshiip for compressive meridian.

- Nanotechnology for UHPC and "Smart Materials"
- Foam UHPC,
- Distribution and orientation of fibers in UHPFRC,
- Durability and resistance against chemical attack,
- Mechanical behavior of fresh concrete,
- Creep and shrinkage dependent behavior,
- Multiaxial strength and deformation behavior,
- Fatigue,
- Fire Resistance,
- Material testing for UHPC (destructive as well as nondestructive),
- Sustainable development using UHPC.

As examples, two topics shall be highlighted here.

2.1.1 *Multiaxial Strength of UHPC*

At the Technical University Dresden the two dimensional and three dimensional strength of HPC and UHPFRC has been investigated in a 3-axes testing setup, see e.g. Speck 2008. In order to minimize lateral restraint, metal brushes have been used to introduce the load into cubical specimens (see Fig. 2). For two dimensional compressive loading it could be shown that the strength increase is less pronounced than for normal strength concrete (NSC). As a consequence, the usual models and design equations cannot be transferred directly to UHPC.

For UHPC subject to triaxial compressive loading, the behavior changes from brittle to ductile starting at

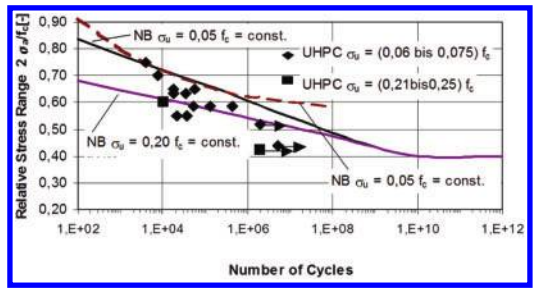


Figure 4. Fatigue in uniaxial compression.

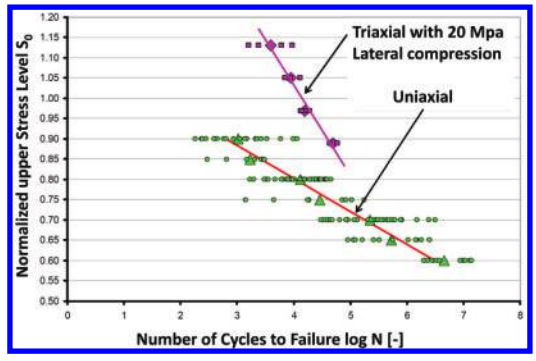


Figure 5. Uniaxial and triaxial fatigue loading.

6 to 9 % lateral compression stress. This can be seen in the right part of Fig. 2.

2.1.2 *Fatigue of UHPC*

First experimental investigations at the University of Kassel (Bunje 2002, see Fig. 4) have shown that fiber reinforced UHPC survived stress ranges of at least 0,4* fc for up to $5*10^6$ load cycles. Tests on UHPC without fibers showed a similar behavior, however with higher scatter. Within the DFG coordinated research program, investigations have been performed for uniaxial and multiaxial fatigue at different universities in Germany, see Fig. 5 from Grünberg & Ertel 2012.

2.2 *Structural Behavior*

With regard to design of structures, studies for many different topics may be mentioned:

- combination of fiber reinforcement with bar reinforcement,
- behavior and design for bending and normal force in SLS and ULS,
- design for shear, punching and torsion,
- application of strut and tie models,
- biaxial compressive/tensile strength of UHPC with fibres, rebars and combinations thereof,
- connection techniques and bond or rebars,
- use of UHPC for medium and long span bridges,
- Innovative connectors for composite structures using UHPC,
- modular construction techniques, implants for introduction of concentrated loads,

- columns using UHPC and high strength steel sections,
- prestressed/posttensioned UHPC girders with and without web openings,
- UHPC-coating and strengthening of reinforced concrete structural members,
- Structural gluing,
- behavior of UHPC for high strain rates and use of UHPC for impact resistance,
- fire safety of UHPC structures.

This listing can neither be complete nor is it possible to address all these projects in detail. However, some general remarks can be made.

2.2.1 *Preconditions for economic use of UHPC*

The cost for a cubic meter of UHPC is of course much higher than for ordinary normal strength concrete. In order to make the application of UHPC for structural applications interesting, it is important that specific advantages of UHPC such as superior durability or reduced overall volume, size, and weight of the structure can be exploited.

Due to the much higher durability of the very densely structured UHPC matrix there is a chance of a long life of the structure and low maintenance costs. Although that may be arguments for using UHPC, it is often necessary that further advantages, such e.g. regarding a simplified construction process come into play. This can be e.g. the elimination of scaffolding and/or formwork.

In many cases UHPC competes more with steel structures than with R/C or P/C structures. It can be stated, that the overall dimensions of UHPC elements do not differ so much from those of steel elements with the same bearing capacity, but the price and the weight can be significantly lower.

One possibility to reduce the cost is to minimize the use of expensive fibers, since normally the biggest cost factor is the addition of steel fibers. Following this observation, it becomes interesting to rely not only on fibers as reinforcement but to combine them with ordinary bar or mesh reinforcement or even prestressing This has been the starting point for several research projects (e.g. Leutbecher 2008) at the author's institute, where the interaction between fibers and bar reinforcement has been studied.

Another interesting line is structural gluing. Due to the dense structure of UHPC and the high surface tensile strength, it is much more promising to connect UHPC members by gluing than to do so with NSC members. In the consequence, gluing of large elements made of UHPC becomes interesting, especially when combined with prestressing across the joints, see contribution of Tue to this conference.

2.2.2 *Actual research projects*

Based on results of investigations for UHPC with combined fiber and bar reinforcement in Kassel, the behavior of structural UHPC members in bending has been studied experimentally and analytically. Different types or bar reinforcement (ordinary reinforcing steel and high strength reinforcing steel) as well as different amounts of fibers per volume have been investigated. Due to the fibers, very small crack widths are possible in SLS. Later on, however, a localization of deformation takes place and typically one crack may open extremely due to yielding of the bar reinforcement (ULS), see Figure 6.



Figure 6. Crack pattern of UHPC bending beam with combined bar and fiber reinforcement.

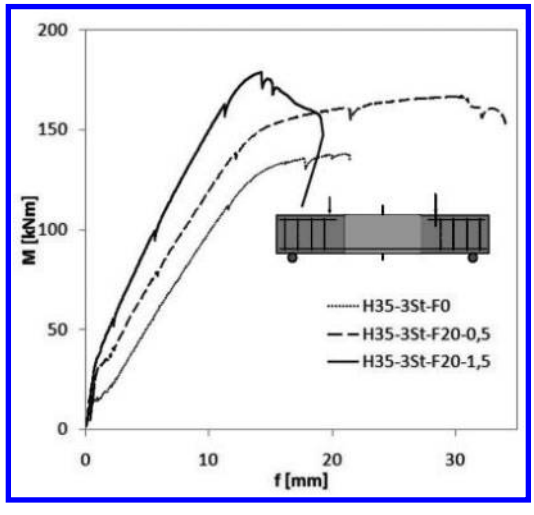


Figure 7. Force deflection relationships for UHPC beams with different amounts of fibers.

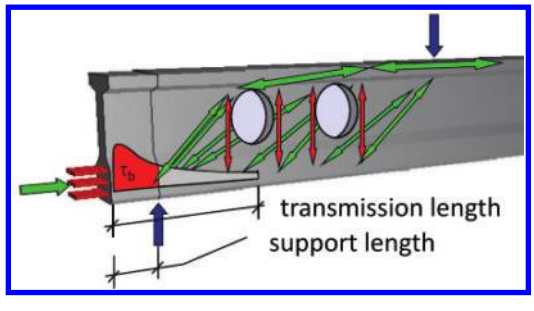


Figure 8. Investigations on end regions of prestressed UHPC girders.

At RWTH Aachen University, prestressed UHPC girders with openings have been investigated. Precast and prestressed girders are extremely important for hall structures both for industry and trade. UHPC with

fibers can help to eliminate stirrup type of reinforcement for shear forces as well against splitting tension, see Bertram & Hegger 2012.

To anchor prestressed strands in UHPC, it is possible to reduce the transmission length extremely due to the high possible bond stresses. This, in turn can lead to high local splitting tensile stresses, which has made research necessary to avoid problems in that respect. The investigations concerned different thickness of concrete cover as well as different prestressing degrees. A bond model for anchoring of prestressed reinforcement has been developed.

As a next step, 34 prestressed girders have been tested with regard to shear force capacity, influence of web openings and cyclic vs. static loading (see Fig. 6). Based on the results of the experimental tests as well as on nonlinear Finite-Element models, recommendations for design provisions have been deduced.

With regard to composite construction using thin UHPC slabs, innovative connectors have been proposed and investigated as alternative to usual shear connectors. Examples are the puzzle strip (see Fig. 9) or (plow-) shares (Schnell & Kurz, TU Kaiserslautern).

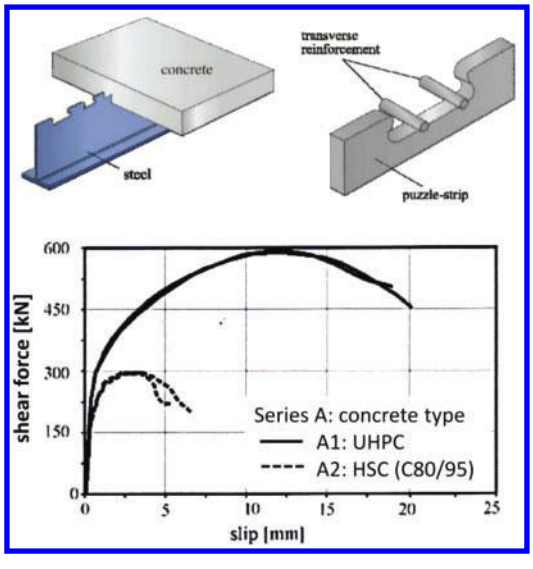


Figure 9. Puzzle strips and test results for UHPC and HSC.

The main advantages of the puzzle strip are its high initial stiffness and the high bearing capacity. Furthermore, two strips can be produced by one cutting process without loss of material. Fig. 9 depicts results of push out tests with puzzle strips. For UHPC with compressive strength of 180 MPa a much higher shear capacity and ductility has been achieved than for HSC with 90 MPa.

It should be noted, that in both cases transverse reinforcement (two bars with $d_s = 12$ mm diameter) were provided per puzzle opening.

3 PRACTICAL EXAMPLES

3.1 *Bridges*

As a high performance material, UHPC takes profit from well controlled fabrication conditions as can be found in precasting plants. Hence, most of the examples of built bridges were made from precast elements or segments. Some examples have been presented by the author at SEMC 2010.

A very elegant example is the Bridge of Peace in Seoul, Korea (Behloul et al. 2003), see Fig. 10. The structure consists of six precast segments, built using Ductal®. Each segment has a π-section with a transversely ribbed plate. In longitudinal direction the segments are posttensioned by 6 tendons, in transverse direction single strands are used in conjunction with small, specially produced anchors. Cross section and dimensions are depicted in Fig. 11.

Being also an arch bridge but suited for vehicle traffic, the WILD-Bridge in Austria near Völkermarkt shall be mentioned here (Sparowitz et al. 2012). It spans a romantic valley and leads to the production plant of the WILD company, a manufacturer of optical/mechatronical equipment.

The bridge has been built using the arch lowering method, for which the reduction of weight by the use of UHPC is a big advantage. Due to the small self weight forces, the hinges required at the abutments could became much cheaper. The construction principle is depicted in Figs. 12 to 14. The two arches consist of precast and externally posttensioned box segments. In order to facilitate the construction, flat dry joints have been used. In order to avoid stress concentrations due to unevenness, all contact surfaces have been milled with high precision using CNC-milling tech-



Figure 10. View of Seonyu footbridge in Seoul, Korea.

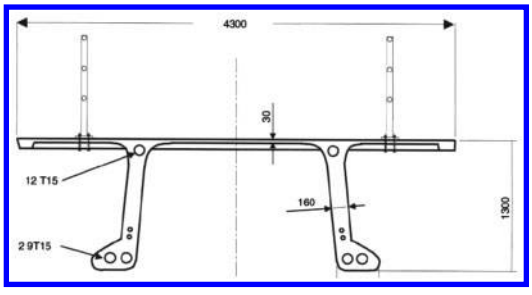


Figure 11. Cross section of footbridge in Seoul, Korea.



Figure 12. WILD-Bridge in Völkermarkt, Austria.

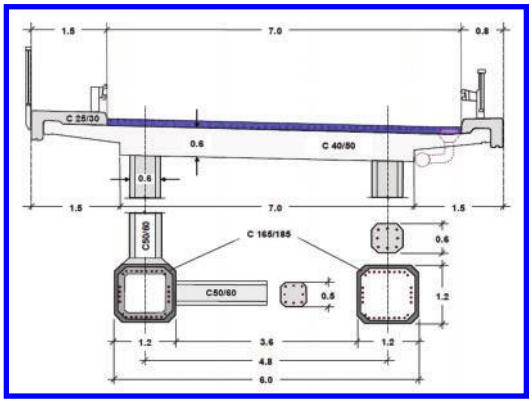


Figure 13. Cross section of Wild bridge.

nology. This technology has been developed by the Max Bögl company, Germany and was being used the first time for the production of slab tracks for railway lines.

Special knee elements have been inserted into the arch in order to accommodate the piers for carrying the superstructure which has been designed in a conventional way using C 40/50.

A comprehensive test program has been conducted in order to verify the design and to test the behavior of the posttensioned elements. Since the box segments are reinforced by fibers only, special attention has been paid to the distribution and orientation of the fibers as well as the optimization of the pouring process in that respect.

Another interesting Project is the GSE-Bridge at Tokyo Airport which connects the northern and southern airfields for the ground services (Watanabe et al. 2007), see Fig. 15. The client aimed at minimizing the volume of the ramp dam as well as ensuring the required clearance height below the bridge. Hence, the

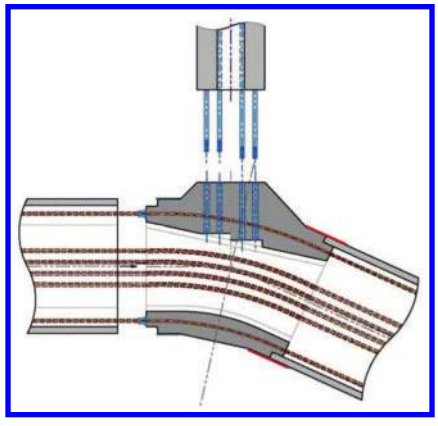


Figure 14. Knee Element of WILD-Bridge.



Figure 15. GSE-Bridge at Tokyo Airport.

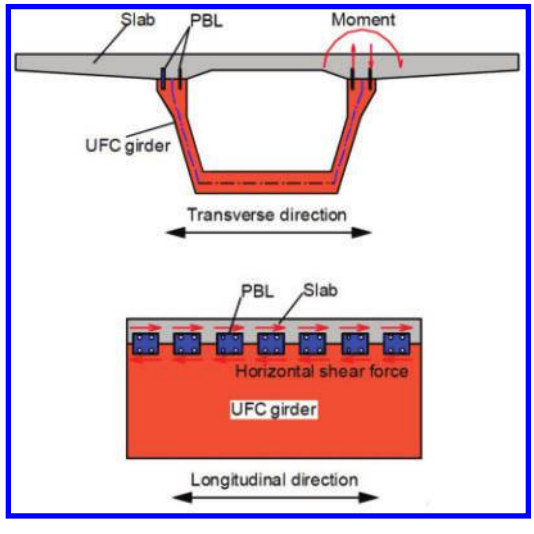


Figure 16. Position and load transfer by Perfobond shear connectors for GSE-Bridge at Tokyo Airport.

gradient should be positioned as low as possible and the construction height had to be minimized. These requirements could be fulfilled using UHPFRC for the bridge girders, in this case, UHPFRC with 2%



Figure 17. Museum MuCEM in Marseille: view to tree-type columns from inside. Insert: structure of facade element.



Figure 18. View / computer animation of MuCEM.

steel fibers (diameter 0,2 mm, length 15 mm). No conventional bar reinforcement has been necessary. The superstructure consists of three parallel segmental box girders with tendons inside the box girders. The shear connection between webs and the upper deck plate (made of conventional reinforced concrete) consists of Perfobond strips (PBL). These can also take tension forces arising due to the long cantilever deck plates.

3.2 *Buildings*

UHPC is also very interesting for building structures, as the following examples can show. In 2012/2013, the MuCEM museum in Marseille, France, is being built (Architect Rudy Ricciotti). It uses UHPC columns with tree-shaped columns and a very filigree UHPC façade (see Fig. 17). Further UHPC elements are the longitudinal edge girders carrying the slab and a slender UHPC bridge connecting the roof of the museum to the adjacent old Fort Saint Jean.

The columns are connected to the floor and to the foundation by tendons which increases the bending capacity of the columns significantly. Design checks have been performed with the aid of physically nonlinear Finite-Elements models and experimental investigations on three straight and one Y-shaped column configuration. Fig. 18 shows a 3-D computer view of the building.

REFERENCES

Aitcin, P. C. & Richard, P. 1996. The Pedestrian/Bikeway Bridge of Sherbrooke. In: Proceedings of the 4th International Symposium on Utilization of High-Strength/High-Performance Concrete, pp. 1399–1406, Paris.

Bache, H. H. 1981. Densified Cement Ultra/Fine Particle-Based Materials. In: Second International Conference on Superplasticizers in Concrete, Ottawa, Ontario, Canada.

Behloul, M. & Lee, K. C. 2003. Ductal® Seonyu footbridge. Structural Concrete , Vol. 4, pp. 195–201, Telford, London.

Bertram, G. & Hegger, J.2012. Shear Behavior of Pretensioned UHPC Beams – Tests and Design. In: Ultra High Performance Concrete and Nanotechnology in Construction (proceedings of HIPERMAT), Schriftenreihe Baustoffe und Massivbau, Vol. 19, pp. 493–500, kassel university press.

Bunje, K. & Fehling E. 2002. About the Fatigue Limit (Mechanical Durability) of Ultra High Performance Concrete. In: Proceedings of the 4th International Ph.D. Symposium in Civil Engineering, München, September 2002.

Fehling, E. & Bunje, K. & Schmidt, M. & Schreiber, W. 2008. The Gaertnerplatzbrücke, Design of the first hybrid UHPC-steel bridge across the River Fulda in Kassel, Germany. In: Schriftenreihe Baustoffe und Massivbau, Vol. 10, pp. 581–588, kassel university press, Kassel.

Leutbecher, T 2008. Rissbildung und Zugtragverhalten von mit Stabstahl und Fasern bewehrtem Ultrahochfesten Beton (UHPC). Dissertation, Schriftenreihe Baustoffe und Massivbau, Heft 9, kassel university press, Kassel.

Sparowitz, L. & Freytag, B. & Reichel, M. 2012. UHPFRC bridges built in Austria. In: Proceedings of the 5th International Conference on New Dimensions in Bridges, Flyovers, Overpasses & Elevated Structures, pp. 45–63, Wuyishan.

Speck, K. 2008. Beton unter mehraxialer Beanspruchung – Ein Materialgesetz für Hochleistungsbetone unter Kurzzeitbelastung. Dissertation, TU Dresden.

Watanabe, N. et al. 2007. Design and Performance tests for Bridge using Ultra High Strength Fiber Reinforced Concrete. In: 23th US - Japan Bridge Engineering Workshop, November 2007.

Research and Applications in Structural Engineering, Mechanics and Computation – Zingoni (Ed.)
© 2013 Taylor & Francis Group, London, ISBN 978-1-138-00061-2

Modular constructions made of UHPC

N.V. Tue
Graz University of Technology, Graz, Austria

M. Reichel
KHP Leipzig, Leipzig, Germany

ABSTRACT: UHPC (Ultra High Performance Concrete) is a high tech material with outstanding properties. Because of its need for special regard at production and casting an application in the precast industry is generally recommended. Furthermore, the costs of UHPC are nearly 10 times higher compared to ordinary concrete. For economic use of this new concrete material, new design philosophies in concrete construction have to be developed. Suitable construction types and building methods are filigree, flexible and modular constructions with precast elements. This effectively combines the high-performance material properties and the special features of this new material with the demands for sustainability, fast construction progress and wide application. This contribution presents general considerations on modular UHPC constructions by introducing four recent examples of UHPC application. Finally this illustrates the high potential of UHPC for sophisticated constructions in both aspects, architecture and structural engineering.

1 INTRODUCTION

UHPC with its inherent benefits of high compression strength and remarkable durability opens new possibilities in structural engineering. At the same time the increasing material and production costs of this innovative concrete material call for the development of suitable construction types and beneficial building methods.

Because of UHPC's high modulus of elasticity, compared with conventional concrete, very light and thin-walled cross sections with sufficient stiffness (light cross sections with high moments of inertia or arch and truss structures) are favorable. The modulus of elasticity-ratio between UHPC and structural steel of nearly a fourth indicates a classification of the construction concepts for UHPC structures between the construction concepts of conventional steel and concrete structures.

If such light cross sections were realized in conjunction with prefabricated segmental construction, external prestressing and dry joints, new or adapted erection methods, which speed up construction progress or allow erections in restricted areas, are imaginable.

Both, the material savings due to light cross sections and the benefits of fast and less environment effecting construction methods provide the way for an economic application of UHPC. Besides this, the remarkable durability of UHPC increases service life while costs for maintenance decrease. Finally this unburdens our public budgets for infrastructure.

The following four examples of recent UHPC projects, which are completed or in the last realization process, give an overview about efficient use of this innovative material and its economic application.

2 ROAD BRIDGE WILD

2.1 *Structure and construction sequence*

The first example is an arch road bridge in Austria (Reichel et al. 2010, Reichel et al. 2011). Due to the high stiffness of the arch structure a maximum utilization of the high compressive strength of UHPC was achieved. In contrast to this, beam structures for bridges with strict limits regarding deformation and vibration to achieve sufficient traffic safety never would reach such efficient utilization of compressive strength.

The road bridge, which consists of a main arch span with 69 m and two foreland bridges, has a total length of 157 m. At main span each of the two parallel arches is assembled of thin-walled (60 mm) precast hollow box UHPC-segments and seven connection segments, so called knee-segments. They are prestressed together by external tendons running inside the arches. Because of very low bending and shear force in the arches no further ordinary reinforcement was needed in all UHPC-segments. Only the tensile capacity provided by the steel fibres ensures a save load bearing behaviour. Furthermore, additional prestressing of the arch improves the stability. All further components of the bridge (columns, deck, foreland bridges) are made with cast in place normal strength concrete.



Figure 1. Road Bridge WILD - completed stage/summer 2010.

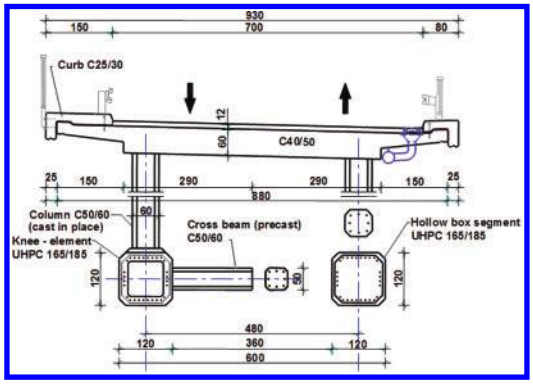


Figure 2. Standard cross section.

The road bridge, which consists of a main arch span with 69 m and two foreland bridges, has a total length of 157 m. At main span each of the two parallel arches is assembled of thin-walled (60 mm) precast hollow box UHPC-segments and seven connection segments, so called knee-segments. They are prestressed together by the use of external tendons running inside the arches. Because of very low bending and shear force in the arches no further ordinary reinforcement was needed in all UHPC-segments. Only the tensile capacity provided by the steel fibres ensures a save load bearing behaviour. Furthermore, additional prestressing of the arch improves the stability. All further components of the bridge (columns, deck, foreland bridges) are made with cast in place normal strength concrete.

Because the bridge is crossing a deep gorge, the most efficient construction method for the arch was to combine the swivel-in method of arch construction with the light precast UHPC-segments. After completion of the foreland bridges, the several arch-segments are assembled in a vertical position using external tendons. The effort for equipment is minimal: a mobile crane for the manipulation and temporary ties for fixing the arch's position. The very light arch halves can easily be swivelled in. The hinge for swivelling is a simple steel bolt with a diameter of merely 80 mm. The maximum tensile force in the temporary ties was about 2×450 kN and therefore 2×4 mono strands were sufficient. After joining the arch halves further tendons overlapping at the arch's crown were installed.

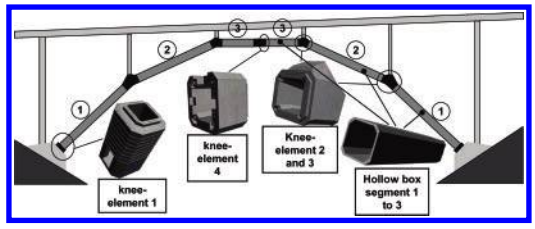


Figure 3. Assembly of the UHPC-precast segmental arch.

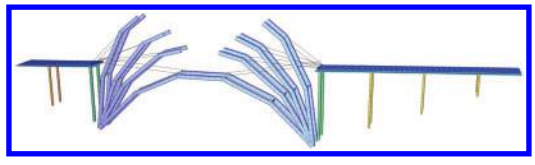


Figure 4. Principle of swivel-in method of arch construction.



Figure 5. Vertical assembling of the arch.

Due to pouring the space between the knee-segment 1 and the arch abutment, the arch gets a rigid restraint.

The connection of the segments is realized by dry joints without any shear keys due to the low shear force. The strict requirements on the evenness of those joint surfaces to reach the required final arch geometry and to transfer the high compressive stresses as well as due to durability reasons could only be met by milling with a CNC-machine.

Further investigation was needed to transfer the concentrated loads due to lifting devices or other anchorage elements during assembling into the thin walled UHPC-elements. Even the needed space for conventional lifting devices was often not available. Only the more massive knee-segments allowed a fixing of temporary lifting devices. Also special considerations regarding storage, transportation and handling during assembly were necessary in order to avoid damage or harmful cracking of the filigree thin walled segments. Specially developed lifting devices and a mobile crane with two independent winches provide simple and fast adjustment in all directions for a proper assembling.

2.2 *Design, Detailing and Tests*

In order to analyse and design the arch, the material laws, the associated partial safety factors for UHPC

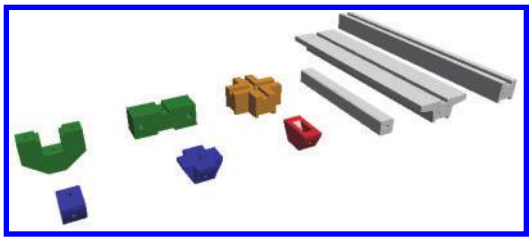


Figure 6. Elements of the truss structure.

and the design rules for ULS and SLS are gathered on the basis of (Schmidt et al. 2007, AFGC 2002, Reichel 2010). The buckling behavior of the segmental arch during the construction as well as in the final state was a special issue in the design and required the consideration of the stiffness change due to the gapping of the segmental joints. Therefore a special three-dimensional nonlinear calculation model based on beam elements was developed. This model was calibrated with the conducted full scale tests and other tests documented in literature.

The only steel fibre reinforced knee-segments with their complex shape at the bends of the segmental arch are sensitive discontinuity regions. Several actions such as anchoring and deviation of the prestressing tendons, bending moments induced by the columns as well as the shear and axial force in the compression zone of the segmental joint impact on those elements. Investigations by means of nonlinear and linear 3D-FE analysis delivered information about the expectable stress distribution.

Because present design codes and guidelines do not completely cover the use of UHPC in relation to the structure presented and the lack of experience, many experimental tests (including two full scale tests) gave answers to open questions for design and detailing (Freytag et al. 2009). The focus of the full-scale test was the load carrying behaviour in the region of the springing.

The used material models in the performed nonlinear 3D-FE analysis were calibrated and verified with the conducted tests. A recalculation of the full scale test confirmed the used material models.

3 MODULAR TRUSS CONSTRUCTION

3.1 *General description of the structure*

The second example is an UHPC truss construction according to Lego-system. Because of the prevention of monolithic nodes all components of the construction can be industrially produced in concrete plant.

The connection between node elements and other components of the construction is designed as dry joints. Precast elements and dry joints allow a high flexibility of the construction in span and in construction height. With the variation of the prestressing forces the bearing capacity can be adapted in any order. Due to strict requirements on surface evenness the



Figure 7. Elements of the truss structure.

grinding of the node elements with CNC machine is the precondition for the realisation with dry joints. External prestressing tendons satisfy the requirements of ULS and SLS. The construction weight is only about 20 % higher than comparable steel constructions and a non-destructive demounting of the construction is possible any time (Tue et al. 2010).

3.2 *Detailing, design and tests*

The most important detail of the construction is the node. In this element the transfer of compressive, tensile and shear forces is necessary. Due to the use of dry joints the friction coefficient between concrete surfaces is of high importance. Model tests considering different surface qualities are carried out in order to determinate the friction coefficient (Schoening et al. 2013) for the design of the shear bearing capacity. Additionally nonlinear calculations were conducted to analyse the stress state in the node element in ULS and SLS (Grube 2011). Furthermore, the influence of tolerances of the single components on the behavior of the whole construction was also analyzed in detail (Schwarz 2011).

4 UHPC FOOTBRIDGE MARKLEEBERG

4.1 *General description of the structure and of the construction process*

The third example is a hybrid construction for a pedestrian bridge in Markkleeberg near Leipzig to replace an about 10 years old wood arch bridge. An important design issue was to maintain the old arch shape, the clearance profile between bridge and river and the old abutments. Further demands on the design were aesthetic, a simple and fast erection, long service life and low effort for maintenance. These conditions can be perfectly matched by the proposed hybrid construction with UHPC.

The two parallel arches of the new bridge consist of conventional steel tubes and a flat UHPC-deck slab as a tie between the arch springing, which is suspended from the steel arch by inclined but non-intersecting hangers. The deck slab is assembled of 10 precast



Figure 8. Hybrid footbridge Markleeberg.

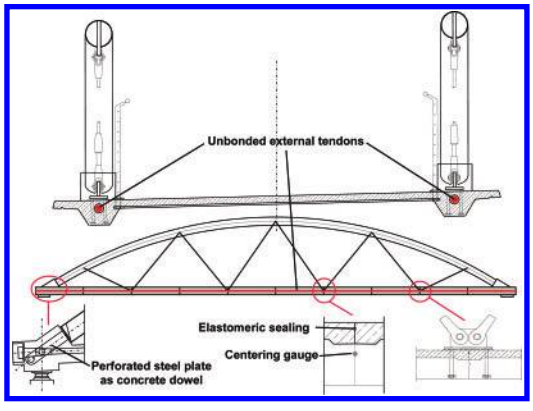


Figure 9. Standard cross section and details.

UHPC-segments and the tensile force is compensated at each arch by exchangeable external tendons, which are running inside of the deck slab. There is no waterproofing or other surface treatment for the deck slab due to the excellent durability properties of UHPC required.

The cross section has a width of 5.3 m. By a distance between the webs of 4.2 m the thickness of the slab is only 8 cm. In the line between the arch springing the slab is enlarged to so-called main girders which are 30 cm thick and inside of these main girders the tendons are positioned. Again, the joints between the precast segments are dry joints. A mechanical CNC-milling of the joint surface was not required, because the compressive stresses in longitudinal bridge direction are not so high. Therefore sufficient accuracy of the joint evenness could be reached be a highly precise steel formwork. To meet the durability requirement and a dense joint an additional elastomeric sealing between the precast segments was applied.

To reduce the construction time the new bridge will be assembled on one side of the river. After that the old bridge will be removed and the new bridge will be completely lifted into its final position by a mobile crane.

4.2 *Detailing, design and tests*

Because the load bearing behaviour of fibre reinforced structures depends on fibre orientation and distribution it is very difficult to guarantee the assumed



Figure 10. Full scale test in transverse direction.

design tensile strength in the produced segment. Furthermore the material costs increases significantly with increasing fibre content. Therefore in transverse direction a combination of fibres and ordinary reinforcement is used. Herewith a fiber content of only 1.0 Vol.-% is necessary for very small and not harmful crack widths, ensuring high durability adequate to the used UHPC. For bending design under ULS conditions only the ordinary reinforcement is sufficient and therefore the contribution of fibers negligible.

Because of the minor experience and missing codes for the design of UHPC structures, a full scale test in transverse direction was performed. A second issue of the test, was to investigate the deformation behaviour of the very slender deck slab at SLS, which was decisive for the design. This investigation was carried out under quasi permanent and rare loads and the development of the deformation was observed for 10 load cycles. After that the load was increased until load and finally failure. The load deformation behaviour in the test indicates a brittle failure due to localisation of the fracture process in one crack. However the ultimate bearing capacity is many times higher than required and the deformations at point of failure amounts more than 30 cm. According to this, the failure will be indicated due to large deformations and therefore sufficient ductility can be assumed.

Because of the less space in the thin-walled segments the dimensions of the load bearing plates of the prestressing anchors must be reduced comparing to the technical approval for ordinary concrete. Therefore additional tests according ETAG 013 for the span anchors with reduced dimensions were performed.

5 FLEXIBLE MODULAR TEMPORARY RAILWAY BRIDGE

5.1 *General description of the structure*

The fourth example is a modular temporary railway bridge made of UHPC (Reichel et al. 2009). Since a continuous ballast bed and ample working space under the structure are required, only a U-shaped cross section meets the preconditions by providing sufficient stiffness as well as low constructional depth. Due to assembling of single equal prefabricated segments

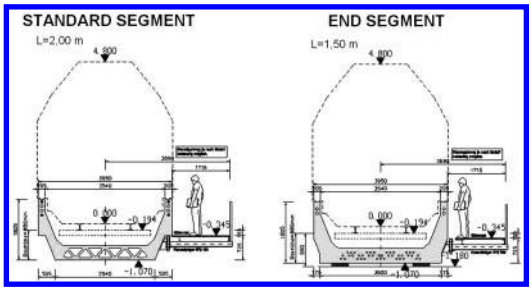


Figure 11. Cross sections with clearance diagrams.

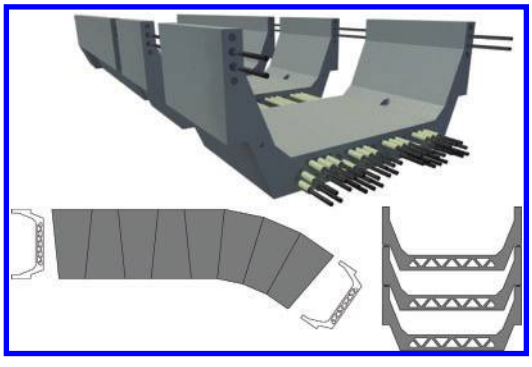


Figure 12. Basic principle and idea.

variable span lengths become possible and a trapezoidal shape of the segments in plan view enables a variable alignment of the rail. In addition assembling and dismantling is fast and simple by using re-usable Dywidag Steel Threadbars as external tendons. Further benefits of the U-shaped segments are the noise insulation, the segments ability to stack with minimum space for storage and the possibility to substitute single segments if they are damaged.

The width of the bridge is 3.95 m, the overall depth is 1.80 m and the possible span length ranges from 3 m to 26 m. Two different types of segments are used: 2 end-segments, which are 1.5 m long and more massive, to provide space for the elastomer bearings, the expansion joint and the anchorage for the prestressing bars. Further the end-segment supplies torsional resistance against lateral instability of the slender compression flange by activating a frame effect between the bottom plate and the webs. The more filigree standard segments, whose number depends on the aimed span length, have a hollow bottom plate which has a trussed framework in transverse direction to gain sufficient stiffness and load carrying capacity.

The prestressing bars running through the openings of the bottom plate are protected against deterioration by plastic ducts and by an additional spray coating. In transverse direction the upper and lower flange are pretensioned with strands and the diagonal ties are reinforced too. This results from high fatigue loadings as Austrian Railways demands a fatigue life of 50 years per segment. Furthermore the high railway loadings

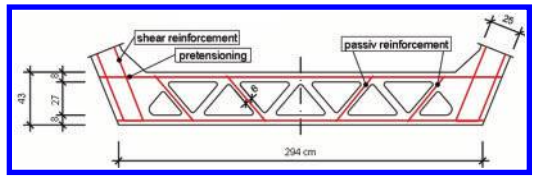


Figure 13. Cross section with reinforcement.



Figure 14. Full scale test in transverse direction.

and fatigue loadings require the arrangement of shear reinforcement in the webs. The segmental joints are dry joints and no additional shear keys were required because of the high amount of prestressing.

5.2 *Detailing, design and tests*

To achieve sufficient traffic safety at a maximum speed range of 200 km/h the deformation of the deck and the dynamic response due to train crossing were decisive for global design. The resistance of the steel fibres was disregarded because of too little experience and experimental results about the load carrying behaviour of fibres under cyclic loading in tension.

As Austrian Railways OBB demanded, one full scale test was performed in transverse direction and one test in longitudinal direction is currently under preparation with the maximum span length of 26 m. Furthermore tests according ETAG 013 for the smaller anchoring plates of the prestressing bars were already performed.

6 CONCLUSIONS AND OUTLOOK

The previously illustrated examples show, that an efficient and economical use of UHPC is possible. Especially the combination with filigree, flexible and modular segmental construction methods and the consequent involvement of all drawbacks and benefits regarding the special properties and features of this new building material offers a wide range of very promising solutions. Meanwhile a lot of experience could be gained with many completed pilot projects

all over the world, which showing the wide variety of new possibilities. But the next big step is to cast all the experience and the results from research in recommendations or codes to implement UHPC as a building material in practice and furthermore to enhance the acceptance of clients and authorities.

REFERENCES

AFGC, 2002. Association Française de Génie Civil (AFGC)/ Service d'études techniques des routes et autoroutes (SETRA): Bétons fibrés à ultra-hautes performances/ Ultra High Performance Fibre-Reinforced Concretes. Recommandations provisoires/Interim Recommendations. Janvier 2002.

Freytag, B. et al. 2009. Großversuch WILD-Brücke - Versuchsgestützte Bemessung einer UHPC-Bogenbrücke. Beton- und Stahlbetonbau 104 (3/2009): 134–144.

Grube, A 2011. Detailanalyse zum Tragverhalten von Trockenfugen in UHPC-Fachwerkträger. Master Thesis, TU Graz 2011.

Reichel, M. et al. 2009. UHPFRC-Prototype for a Flexible Modular Temporary High Speed Railway Bridge. *BFUP 2009/UHPFRC 2009 Actes/Proceedings, 2009*: Marseille.

Reichel, M. et al. 2010. Road Bridge "Wild" – Application of the UHPFRC precast segmental construction method for an arch structure. *3rd fib International Congress, 2010*: Washington.

Reichel, M. 2010. Forschungsbericht FFG-Projekt 819342. Endbericht Teil 1/6, Endbericht Teil 6/6. TU Graz, 2010.

Reichel, M. et al. 2011. Wildbrücke Völkermarkt – vorgespanntes Bogentragwerk aus UHFB-Segmentfertigteilen. Beton- und Stahlbetonbau 106 (11/2011): 760–769, 106 (12/2011): 827–835.

Schmidt, M. et al. 2007. Sachstandsbericht Ultrahochfester Beton. DAfStb Heft 561, Beuth, Berlin 2007.

Schoening, J. et al. 2013: Verbindungen von Fertigteilen aus UHPC. Bautechnik (90) 5/2013.

Schwarz, J. 2011. Statische Berechnungen zum modularen UHPC-Fachwerkträger, 2011. (unpublished).

Tue, N. et al. 2010. Innovative ultra-high performance concrete products in practice. Proceedings 54. Beton Tage, Ulm 2010.

Research and Applications in Structural Engineering, Mechanics and Computation – Zingoni (Ed.)
© 2013 Taylor & Francis Group, London, ISBN 978-1-138-00061-2

Development of ultra-high performance concrete and applications to bridges in Korea

C. Joh, S.Y. Park, K.T. Koh, S.W. Kim, Y.J. Kim & B.S. Kim
Korea Institute of Construction Technology, Goyang, Korea

ABSTRACT: This paper presents the features of K-UHPC, the ultra-high performance concrete that has been developed by the Korea Institute of Construction Technology since 2002 in terms of the total amount of shrinkage, improved tensile strength and toughness, and cost reduction compared to ordinary concrete. This presentation is followed by the description of the design guidelines of K-UHPC for the extensive exploitation of its tensile performance and deformed bars. Moreover, the future of K-UHPC cable-stayed bridge is forecast through the analysis of its economic efficiency and some examples of the application of the developed technologies to bridge structures.

1 INTRODUCTION

The application of ultra-high performance concrete (UHPC) featured by its ultra-high strength, high toughness and remarkable durability to structures will contribute to substantial weight reduction by realizing slender structures. Since a durable lifespan of 200 years will be secured, it can be forecast that the future concrete structures will evolve into cost efficient structures exhibiting innovative design by adopting UHPC. France, the first country to develop commercial UHPC products, Japan and Germany recognized the potential of UHPC since 1990s and initiated active R&Ds. Today, these countries have reached a stage aiming to apply UHPC to large civil structures from pedestrian bridges and construction materials to road and railway bridges (Schmidt 2012, Resplendino 2012). In Korea also, the Korea Institute of Construction Technology (KICT) started dedicated R&D in 2002 and developed its own UHPC called as to K-UHPC. KICT is now conducting research in various fields for further exploitation of K-UHPC in bridges like cable-stayed bridges (KICT 2012). This paper examines the features of K-UHPC and related design guidelines. The future of K-UHPC cable-stayed bridge is forecast through the analysis of its economic efficiency and some applications to bridge structures.

2 PERFORMANCE IMPROVEMENT OF UHPC: K-UHPC

Apart from its ultra-high strength and high durability K-UHPC developed by KICT presents three characteristics that distinguish it from other UHPCs (KICT 2012). Tables 1 and 2 arrange the mix proportions and mechanical properties of K-UHPC.

Table 1. Mix proportions of K-UHPC (in weight ratio, volume fraction for steel fiber).

W/B	Cement	Silica fume	Sand	Filling powder	Super-plasticizer	Steel fiber
0.2	1	0.25	1.1	0.3	0.016	$V_f = 2\%$

Table 2. Mechanical properties of K-UHPC*.

Design strength		Elastic	Poisson's	Total	Creep
Compr.	Tension	modulus	ratio	shrinkage	coefficient
180 MPa	9.5 MPa	45 GPa	0.2	600×10^{-6}	0.45

*Steel fiber: diameter 0.2 mm, 16 mm-length 1%, 20 mm-length 1%.

The first distinctive feature of K-UHPC is the total amount of shrinkage (autogeneous and drying), which with a value of about 600 με is comparable to that of ordinary concrete (Table 2). This enables to use deformed reinforcing bar as in ordinary concrete, which was difficult in UHPC due to the risk of cracking. The use of deformed bars in addition to the prestressing tendon usually applied in UHPC opens ways to achieve more efficient design for K-UHPC structures.

The second feature is the improved tensile strength and toughness developed by K-UHPC by using a combination of short and long steel fibers with a volume fraction of 2% similar to that adopted for previous UHPCs. Traditional UHPC developed a tensile strength of about 12 MPa by including 2% of steel

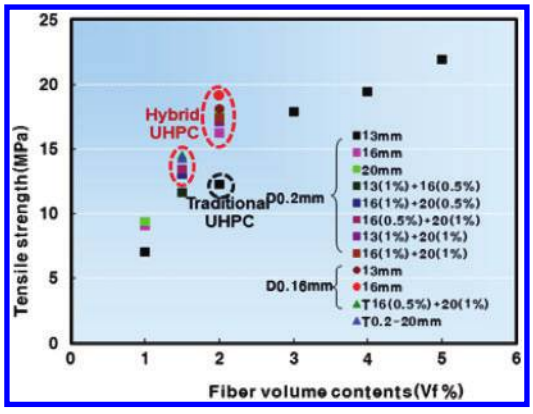


Figure 1. Comparison of the tensile strength of various UHPCs.

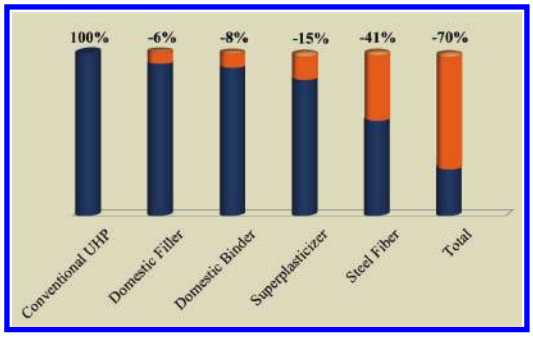


Figure 2. Cost reduction contribution per material of K-UHPC.

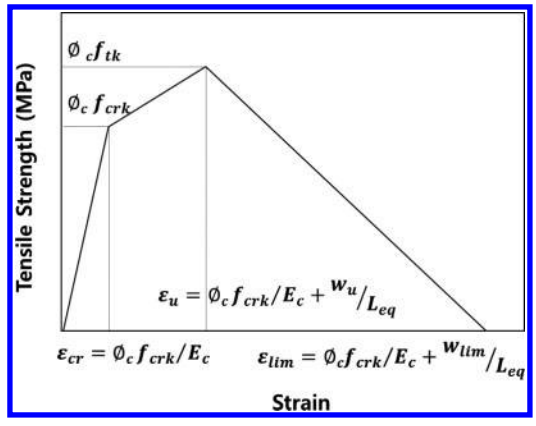


Figure 3. Tensile stress-strain diagram of K-UHPC.

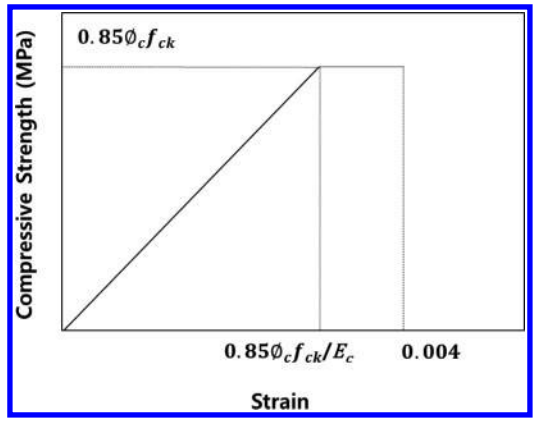


Figure 4. Compressive stress-strain diagram of K-UHPC.

fibers with diameter of 0.2 mm and length of 13 mm. Besides, K-UHPC develops a tensile strength of about 16 MPa by using steel fibers with diameter of 0.2 mm but lengths of 16 mm and 20 mm at respective volume fractions of 1% (Figure 1).

The third distinctive feature of K-UHPC is its fabrication cost, which is reduced by about 70% compared to previous products. This cost reduction was obtained by shifting the supply of the materials from import to regional areas and by replacing the costly water reducing agent and steel fibers by cheaper materials exhibiting equivalent performances (Figure 2).

3 DESIGN GUIDELINES OF K-UHPC

In 2012, KICT prepared design guidelines for K-UHPC (KCI 2012) by synthetizing the results of SUPER Bridge 200, a research project dedicated to K-UHPC (KICT 2012) and under the supervision of the Korea Concrete Institute. These guidelines deal with the material characteristics of K-UHPC and suggest structural design reflecting these characteristics. The latest research conducted in Korea and overseas like the French guidelines (SETRA-AFGC 2002), Japanese guidelines (JSCE 2004) and German research reports (DAfStb 2008) are reviewed and analyzed. The proposed guidelines are based on the results of more than 2500 material tests and 300 structural tests.

The guidelines present also material models enabling to exploit the improved performances of K-UHPC. Differently from the Japanese guidelines, the tensile stress-strain diagram selects a model with different values for the cracking strength (f_{crk}) and the tensile strength (f_{ck}) in order to consider the properties of K-UHPC exhibiting strain hardening and softening characteristics (Figure 3). For the compressive stress-strain diagram, the model is subdivided into the linearly elastic part and the perfect plastic part similarly to the Japanese guidelines. The difference is the ultimate compressive strain, which is set to 0.004 based upon test results (Figure 4). The strength reduction factor (ϕ) is used instead of the material factor (Figure 3 & 4). Apart from these contents, the guidelines specify also provisions relative to the elastic modulus, Poisson's ratio, shrinkage and creep, thermal properties, durability, water tightness and fatigue strength.



Figure 5. Torsional behavior of K-UHPC girder (no stirrups).

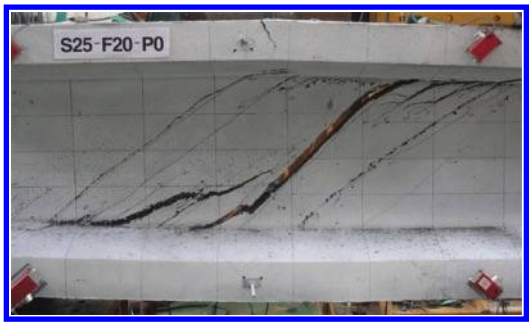


Figure 6. Shear behavior of K-UHPC girder (no stirrups).



Figure 7. Flexural test of K-UHPC girder prestressed with tendons.

In the provisions for the structural design, regulations related to torsion, prestress anchorage zone, connection of precast members, and deformed bars are proposed to allow the designer to exploit extensively the tensile behavior of K-UHPC and deformed bars considering the structural characteristics of UHPC structures that are mostly slender precast prestressed structures. Especially, for torsion, the guidelines adopt a novel design method taking into account the tensile behavior of K-UHPC. This is different from the French and Japanese guidelines referring to the specifications of ordinary concrete, which neglect the tensile force of concrete. For example, based on test results (Figure 5), the torsional rigidity (T_d) of the K-UHPC girder is assumed to be the sum of T_s provided by the transversal stirrups and T_{K-UHPC} provided by the tensile strength of K-UHPC (Joh et al. 2012). For the flexural, compressive and shear design, the guidelines propose provisions similar to those of the French and Japanese guidelines (Figures 6 and 7).

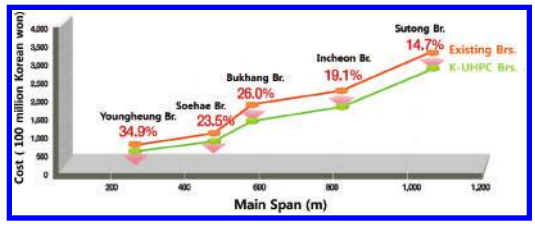


Figure 8. Cost analysis of cable stayed bridges.

4 ECONOMIC EFFICIENCY OF K-UHPC CABLE-STAYED BRIDGE

Detailed designs were carried out to compare the cost necessary for the erection of K-UHPC cable-stayed bridges to that of previously constructed cable-stayed bridges. The results revealed that the K-UHPC cable-stayed bridge offers economic efficiency for main spans ranging between 200 m and 1000 m (KICT 2012) (Figure 8). Especially, the cost analysis for Incheon Bridge, known to be the 5^{th} longest cable-stayed bridge in the world with its central span of 800 m, showed that the K-UHPC cable-stayed bridge of similar dimensions was cheaper by 19.1%. This significant cost-reduction is realized by the adoption of the K-UHPC girder which, despite of the slight increase of the weight of the superstructure, enables to diminish drastically the quantities of costly steel since steel composite or steel-box bridges are usually adopted for cable-stayed bridge longer than 400 m. Besides, in the case of cable-stayed bridges with main span ranging between 200 m and 400 m for which concrete bridges are known to be cost efficient, the replacement of the bulky and heavy concrete girder by the K-UHPC girder achieves significant lightening of the weight, which in turn enables to reduce the demand in cables and the size of the foundations, and thus contributes also to the cost efficiency.

5 DESIGN AND CONSTRUCTION OF K-UHPC BRIDGES

In 2009, KICT realized the design and erection of a K-UHPC pedestrian cable-stayed bridge for the first time in the world (KICT 2012) (Figure 9).

This bridge is composed of a single pylon with 3 planes of cables arranged in fan type. Four K-UHPC segments were fabricated with width of 2.5 m, length of 7.0 m, girder depth of 0.3 m and slab thickness of 70 mm. Then, two segments per span were assembled in the cast-in-place part of the pylon to realize a span length of 18 m. The design and erection of the bridge enabled to test and validate the core technologies necessary to the K-UHPC cable-stayed bridge.

In 2011, based on the cost analysis and research results related to the cable-stayed bridges using K-UHPC, the Korean construction company Daelim contracted technology transfer with KICT and bid for



Figure 9. View of the K-UHPC pedestrian cable-stayed bridge at KICT.



Figure 10. Rendering of Jobal Bridge.



Figure 11. Construction of K-UHPC road bridge (2012).

the turnkey of Jobal Bridge on National Road 77 linking Jobal Island and Dunbyung Island in the southern coast as the first tender of a K-UHPC cable-stayed road bridge in the world (KICT 2012) (Figure 10). This bridge is a 3-span cable-stayed bridge with main span of 200 m and pylon's height of 90 m. For a width of 15.4 m, the depth of the edge girder reaches only 1.2 m achieving a slender structure. Cost analysis showed that this proposal was cheaper by about 14% than the PSC cable-stayed bridge envisaged as an alternative.

In 2012, the first trial construction of a K-UHPC road bridge in Korea was conducted by exploiting the



Figure 12. Fabrication of ribbed K-UHPC deck.

fabrication and bridge design technologies developed by KICT (KICT 2012) (Figure 11). This structure is a single span bridge with span length of 11 m, width of 5 m and π-shape cross section of 0.6 m height. The weight is only 112 kN per segment. Even if the bridge is relatively small, its construction applied all the major technologies necessary for the construction of a K-UHPC bridge like the prestressed precast fabrication and connection technologies.

In late 2012, a bridge applying the ribbed K-UHPC deck developed by KICT was erected (KICT 2012) (Figure 12). This lightweight deck is lighter by 50% than the conventional precast concrete deck. The results of the cost analysis revealed that the construction cost of the superstructure can be reduced by about 10% only by replacing the deck of the traditional steel composite cable-stayed bridge.

6 CONCLUSIONS

KICT developed the K-UHPC, an ultra-high performance concrete exhibiting reduced amount of shrinkage, improved tensile behavior and substantial reduction of the fabrication cost. Corresponding design guidelines for K-UHPC were prepared to exploit its remarkable characteristics. Based on these results, cost analysis was conducted for the K-UHPC cable-stayed bridge and step-by-step field applications were realized. The analysis showed that the K-UHPC cable-stayed bridge could secure economic efficiency by 20% on the mean over the whole applicable portion of the cable-stayed bridge. It can be predicted that, based on its cost efficiency and innovative design, the K-UHPC cable-stayed bridge will take place as a strong alternative enabling to surmount the limitations faced by traditional bridges like concrete, steel composite and steel box cable-stayed bridges.

ACKNOWLEDGEMENTS

This research was supported by the grant from a Strategic Research Project (Super Bridge 200) funded by the Korea Institute of Construction Technology.

REFERENCES

DAfStb. 2008. *Sachstandsbericht Utrahochfester Beton*. Germany: DAfStb.

Joh C., Lee J., Yang I.H. & Kim, B.S. 2012. Torsional test of UHPC square members, *Proceedings of 3rd International Symposium on UHPC, Kassel, Germany*.

JSCE. 2004. *Recommendations for design and construction of ultra high-strength fiber-reinforced concrete structures-draft*, JSCE.

KICT. 2012. *SUPER Bridge 200/Development of Economic and Durable Hybrid Cable Stayed Bridges*, KICT 2012-075-1 Korea Institute of Construction Technology (KICT), Korea (in Korean).

KCI (Korea Concrete Institute). 2012. *Design Guidelines for K-UHPC*, Ministry of Land, Infrastructure and Transport (in Korean).

Resplendino, J. 2012. State of the art of design and construction of UHPFRC structures in France, *Proceedings of 3rd International Symposium on UHPC, Kassel, Germany*: 27–42.

Schmidt, M. 2012. Sustainable Building with UHPC - The Next Decade: From Research to General Application, *Proceedings of 3rd International Symposium on UHPC, Kassel, Germany*: 17–26.

SETRA-AFGC. 2002. *Ultra High Performance Fiber-reinforced Concretes Interim Recommendations*, BFUP Groups, France.

Research and Applications in Structural Engineering, Mechanics and Computation – Zingoni (Ed.)
© 2013 Taylor & Francis Group, London, ISBN 978-1-138-00061-2

Behaviour of hybrid PVA-steel fibre reinforced ultra high performance concrete at high temperature

S. Sanchayan & S.J. Foster
Centre for Infrastructure Engineering and Safety, School of Civil and Environmental Engineering, The University of New South Wales, Australia

ABSTRACT: Reactive powder concrete is an ultra-high performance concrete that exhibits superior strength, durability and ductility compared to normal concretes; this is due to its homogeneity, dense microstructure and the presence of steel fibres. To best utilize the benefits of this material in construction, it is essential to understand its behaviour under different loading conditions, with high temperature exposure being one of such conditions. Reactive powder concrete containing only steel fibres or no fibres has been found to perform poorly under extreme temperatures due to explosive spalling caused by a build-up of pore water pressure within its dense micro-structure; this may be alleviated with partial replacement of steel fibres with PVA fibres. This paper presents the behaviour of reactive powder concrete containing equal amounts of PVA and steel fibres, occupying a total volume fraction of 2% and tested at high temperatures. The behaviour is characterized by measuring the stiffness and axial deformation at various temperatures and at stress levels of 30 per cent of the cylinder compressive strength determined at room temperature. The elastic modulus at high temperature was found to decrease gradually with temperature. Transient creep was observed to develop between 200°C and 300°C, increasing gradually with temperature thereafter.

1 INTRODUCTION

Concrete technology is constantly evolving, pushing the limits of concrete compressive strengths. In these series of developments, reactive powder concrete (RPC) is a relatively recent innovation that can have compressive strengths up to 200 MPa, and greater (Richard and Cheyrezy 1995). Much of its improved mechanical properties are due to its dense micro structure, homogeneity and the presence of steel fibres. The dense micro-structure is achieved by optimizing the packing density of the mix by incorporating fine particles such as silica fume and/or silica flour. Such optimization requires the use of third generation superplasticisers that are effective in dispersing particles. Homogeneity is improved by eliminating coarse aggregates completely and improving the mechanical properties of the paste. The addition of steel fibres helps to improve both the strength and ductility.

For new materials, it is essential to understand their behaviour under different loading conditions before adopting into full scale applications. High temperature exposure is one of such loading condition. However, limited experiments have been reported on the behaviour of RPC under such conditions (Tai et al. 2011; Peng et al. 2012).

Concrete, in general, is perceived as a good material under high temperature environments as compared with steel and timber. However, some concretes show explosive spalling during heating to elevated temperatures that can lead to loss of cross section and, therefore, affect the structural performance of the member. Such spalling is caused mainly by the build-up of pore pressures and thermal stresses (Khoury 2000).

In a previous study by the authors, it was found that plain RPC and steel fibre reinforced RPC is susceptible for explosive spalling when heated to high temperatures (Sanchayan et al. 2012). This explosive spalling was reported to occur when the surface temperature of the RPC was between 350°C and 450°C. The standard practice of mitigating spalling risk in high-strength concrete structures is to add synthetic fibres with a melting point that is sufficiently low that the fibres melt and vaporize before the vapour pressures build to a level that cause stresses that cannot be sustained by the concrete. Once vaporised, mezzo-sized channels are left in the structure that provide passage of the vapour to the surface, reducing the build-up of pore pressures. It was found that adding 1% by volume of PVA fibres with a melting point of 220°C, with 1% by volume of steel fibres, improves the behaviour under high temperature and also to result in good mechanical properties at the ambient temperature.

This study investigates the behaviour of hybrid PVA-steel fibre RPC under high temperature. The deformation characteristics, as defined by the modulus of elasticity and transient creep, are found using a specially designed furnace in a universal testing machine for loading under high temperatures.

Table 1. Mix design data (mass ratios).

Component	Mass Ratio
Cement	1.0
Silica fume	0.25
Sydney sand	1.1
Superplasticizer	0.062
Steel fibres	0.087
PVA fibres	0.014
Water	0.17

The residual strengths of the hybrid RPC mix after exposure to high temperatures, and followed by a period of cooling, are also studied. The results are presented below.

2 EXPERIMENTAL PROGRAMME

2.1 *Materials and Mix design*

The materials used to make the RPC mix were Type 1 general purpose cement complying with AS3972, undensified silica fume manufactured by SIMCOA, Western Australia, Sydney sand with maximum particle size of 600 μ m and dried at 105°C and Glenium 51 superplasticizer. The mix contained equal volumes of 13 mm long by 0.2 mm diameter steel fibres and 12 mm long by 0.2 mm diameter PVA fibres. The fibres occupied a total volume fraction of 2%. The steel fibres were manufactured by Dramix, Belgium, and had a reported minimum strength of 1800 MPa and an elastic modulus of 200 GPa. The PVA fibres were manufactured by Kuraray, Japan, and had a reported minimum strength of 1000 MPa, an elastic modulus of 29 GPa and a melting point of 220°C. The detailed mix data is presented in Table 1 with the quantities expressed as mass ratios relative to the mass of cement.

2.2 *Mixing and fabrication*

The materials were batched using an electronic balance and mixed using a horizontal pan type mixer. The dry constituents were mixed for 10 minutes and then the water and superplasticizer were added together. Mixing was continued until the mix had an even plastic consistency. The fibres were then sprinkled into the mix and mixing was continued for another 5 minutes.

Cylinders of 100 mm diameter and 200 mm high were cast in steel moulds and were stored in a controlled environment room at 50% relative humidity (RH) and 26°C for a period of 24 hours. After 24 hours, the cylinders were de-moulded and cured for a further 72 hours at 85°C in a hot water bath. At the end of the curing period, the cylinders were removed from the hot water bath and stored in the controlled environment room at 50% RH and 26°C until the time of testing.

The mean compressive strength obtained for the batch was 158 MPa. The elastic modulus was 43 GPa.



Figure 1. Arrangement of the furnace with extensometer.

2.3 *Testing Apparatus*

Testing was carried out in a specially designed furnace loading frame arrangement which allows for simultaneous loading and heating of the specimen. The apparatus consisted of a vertical single zone split type furnace, and can be used to heat up to a maximum temperature of 1220°C, and a stiff 1 MN Instron servo-hydraulic controlled testing frame. The load was transferred from the frame to the specimens using Nickel Alloy 625 loading rods, which can tolerate high temperatures. There were also platens of the same material placed on top and bellow the cylinders. Ultra high strength concrete blocks were used between the loading rods and the frame to safeguard the frame from heat and the loading rods were also insulated using thermal blankets. A spherical seat was placed between the upper loading plate and the upper insulation block. A high temperature extensometer was used to measure the strain and the load and strain data were captured using a TMR 211 data logger. Figures 1 and 2 show, respectively, the testing frame and a schematic of the testing arrangement.

2.4 *Heating Procedure*

Two sets of experiments were conducted. In the first set four temperature points were selected, 150°C, 300°C, 450°C and 600°C and three specimens were tested for each temperature. To minimise the potential for explosive spalling at the higher temperatures, the cylinders to be tested at temperatures of 450°C and 600°C were first oven dried at 105°C. Explosive spalling had been

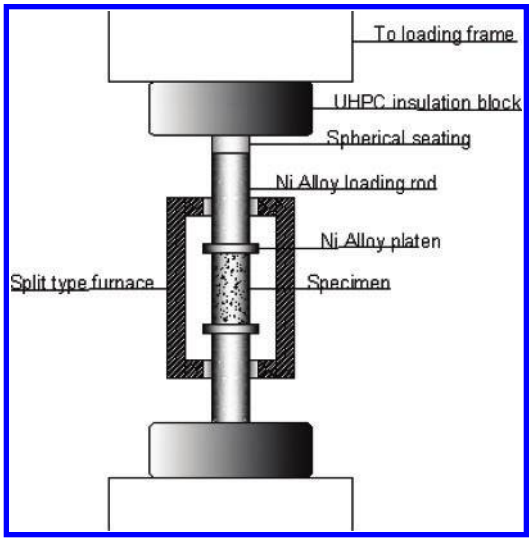


Figure 2. Schematic diagram of the furnace and the loading frame.

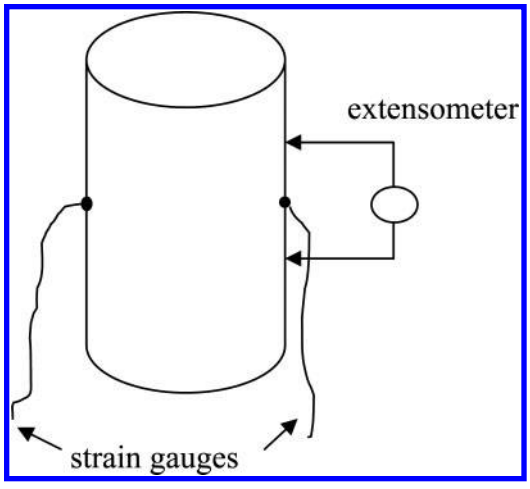


Figure 3. Position of strain gauges and the extensometer.

encountered during previous studies by the authors with significant potential for damage to the testing apparatus (Sanchayan et al. 2012).

Each specimen in the first series of tests was heated in the split type furnace frame arrangement at a rate of 5°C/min until the target temperature was reached. Thereafter, the specimen was maintained at the desired temperature for at least two hours to obtain a uniform temperature distribution through the specimen. The cylinder was then tested to obtain its modulus of elasticity in the hot state. Next, the specimen was allowed to naturally cool and was then again tested to determine its residual modulus of elasticity. Lastly, each specimen was tested to destruction to obtain its residual compressive strength in a different frame.

In the second set of experiments, a constant axial load was applied to the specimens and axial strains were measured as the heat was applied, up to temperatures of 600°C. The heat was applied at a rate of 2°C/min. The temperatures were measured using a thermocouple attached at the mid-height of the cylinder. The loading levels adopted in the tests were zero and 30% of the strength measured under ambient conditions. Two cylinders were used for each loading level. To eliminate shrinkage strains induced through drying at high temperatures, all cylinders used in this test series were pre dried at 105°C in an oven until a constant mass was attained. Thus, the resulting strains are due to heating and loading alone.

2.5 *Testing procedure*

Two strain gauges were attached at the mid-height of each cylinder in diametrically opposite positions. The cylinder was then placed in the loading frame and the extensometer was attached to the cylinder, aligned with one of the strain gauges. Figure 3 shows the position of strain gauges and extensometer. Next, the cylinder was loaded at the ambient temperature in 3 cycles to obtain a relationship between extensometer reading and average of the strain gauge readings. This data was used to obtain a calibration curve to correct the extensometer measurements taken under high temperature, which were taken from one side of the specimen only. This is required to adjust for the effect of small loading eccentricities on the cylinder induced from the ends not being perfectly square with the cylinder edges. The strain gauges were removed before heating of the specimen.

After the relationship between the average strain and the extensometers was obtained, the specimens were heated to the target temperature at the rate of 5°C/min; the target temperature was maintained for a period of 2 hours to stabilise the temperature through the specimen before testing for the elastic modulus. After the temperature stabilisation period, loading was applied to the cylinders to obtain their elastic modulus, with the strains measured using the extensometer and corrected using the previously obtained calibration curve for the given cylinder.

In the second series of tests for measurement of strain changes under constant axial load, the axial strains were measured using the extensometer only. In this case, loading eccentricity is not of concern as the load, and hence stress, is constant; any additional strain after the load is applied is due to the effect of heating alone. The load was applied, and maintained, while the temperature was increased from ambient (room) conditions to 600°C at a rate of 2°C/min.

3 RESULTS AND DISCUSSION

3.1 *Hot and Residual Elastic Modulus*

The change in the elastic modulus measured both at (i) the hot state and (ii) after cooling to room temperature is presented in Figure 4. The graph is plotted as a ratio of the elastic modulus resulting from high temperature

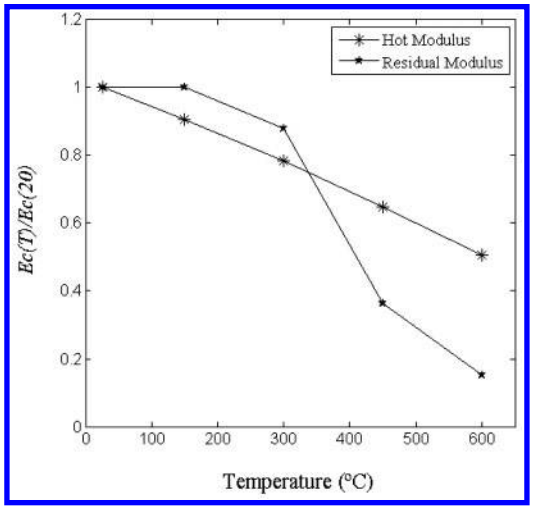


Figure 4. Hot and residual state elastic modulus.

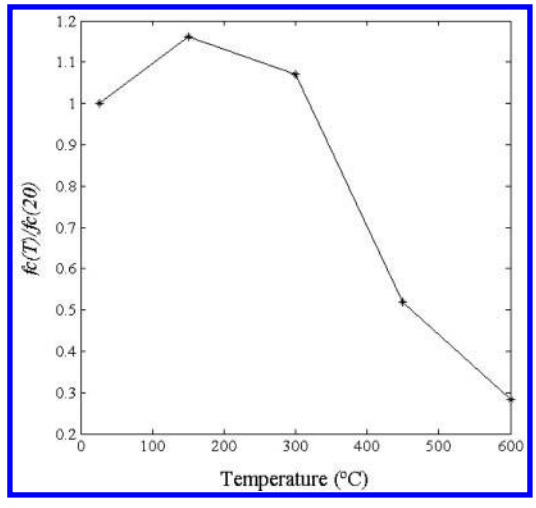


Figure 5. Residual compressive strength.

exposure, E_c(T), to that at the ambient temperature, E_c(20). The hot state elastic modulus shows a steady decrease with rising temperature. It reaches a value of 80% of that measured under ambient conditions between the temperature points of 200°C and 300°C, and 50% at 600°C.

The residual modulus of elasticity, which was measured after the specimens were cooled to the ambient temperature, shows a very different behaviour to that measured at the hot state. There is no appreciable change in the modulus up to the temperature of 300°C, thereafter it drops considerably reaching about 40% and 15% of the original modulus at temperatures of 400°C and 600°C, respectively.

It is interesting to note that there is an increase in the elastic modulus when cooled to room temperatures when the exposure temperature is lower than 300°C, while there is a significant drop in the elastic modulus for the temperatures greater than 300°C. Generally, the residual modulus is found to be higher than the hot state value reported in the literature for normal concretes (Bazant 1996). The hot state elastic modulus values produced in this study are in good agreement with that for steel fibre reinforced RPC containing Polypropylene fibres reported by Piementa et al. (2011). However, the residual elastic modulus produced by them was higher than the hot modulus, regardless of the temperature.

3.2 *Residual Compressive Strength*

Figure 5 presents the residual compressive strength as a ratio of compressive strength measured under heat, f_c(T), to the mean strength measured at ambient temperature, f_c(20). An increase in strength was observed up to the temperature of 300°C, reaching about 20% higher than the original strength. After 300°C, the residual strength drops significantly, reaching about 25% of the original strength at a temperature of 600°C. The initial increase in the strength is probably due to removal of adsorbed water, which leads to higher Van der Waal's forces.

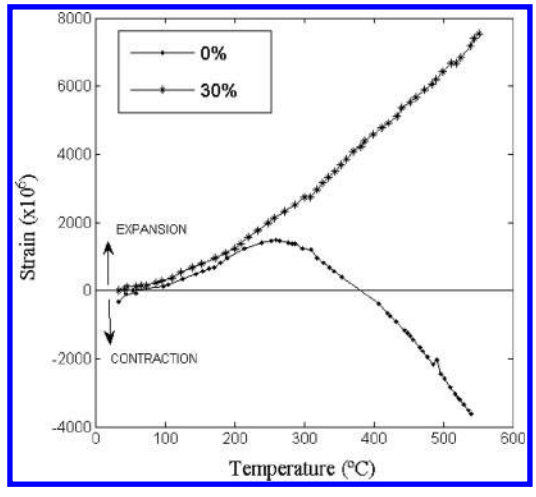


Figure 6. Thermal strains under heating with constant loading.

3.3 *Axial Thermal Strain Measurements*

Figure 6 shows the evolution of axial thermal strain of RPC cylinders when subjected to heating to 600°C under constant loading. The strains are presented as a function of the surface temperature of the cylinder. Positive strains indicate expansion; negative strains indicate contraction. Two constant loading levels were considered; 0% and 30% of the ambient mean average compressive strength. Under no loading, the specimen expands freely due to heat. When the specimen is heated under constant load, initially it undergoes free thermal expansion. Subsequently the matrix undergoes deterioration as result of dehydration that causes contraction in the specimen.

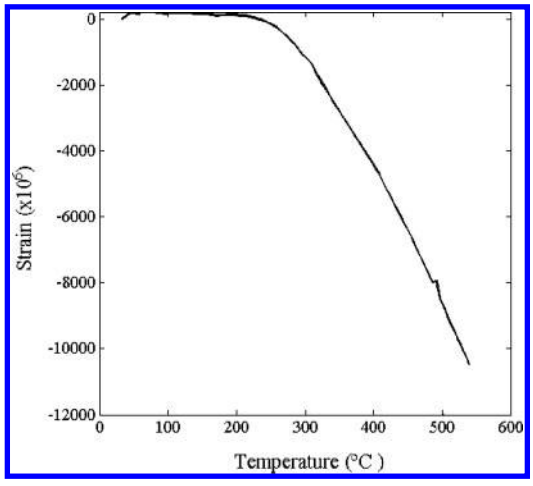


Figure 7. Load induced thermal strains for PVA-steel fibre reinforced RPC under load of 30% of the mean compressive strength at the ambient temperature.

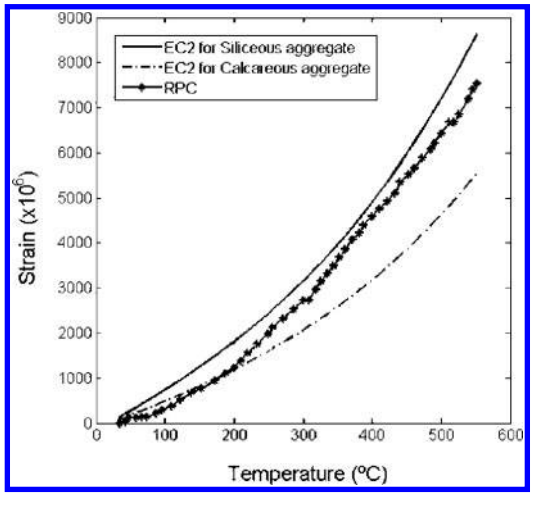


Figure 8. Comparison of thermal strains of hybrid fibre RPC with given values for siliceous and calcareous aggregate concretes in Eurocode 2(BS EN 1992-1-2:2004).

The contraction under load, i.e. difference in strain between 0% loading level and 30% loading level, is referred to as 'load induced thermal strains' (LITS) or transient creep, whereas the former is called 'free thermal strains' (FTS) (Khoury 1985). LITS depends on temperature and applied level of stress, whereas FTS depends only on temperature for a particular material. The LITS is calculated and presented in Figure 7. The transient creep for RPC used in this study is quite similar to that reported for other cementious materials. It becomes significant above temperatures of 250°C and continues to increase with increases in temperature. The co-efficient of thermal contraction due to transient creep is calculated as 40×10^{-6} per °C.

Figure 8 compares the thermal strain of RPC with the thermal strains for siliceous and calcareous aggregate concretes as given in the model in Eurocode 2 (BS EN 1992-1-2, 2004). From the figure it is observed that the behaviour of RPC is similar to that of the siliceous aggregated concrete.

4 CONCLUSIONS

This research studied the transient and steady state behaviour of PVA-steel fibre reinforced RPC subjected to high temperatures. In the first part of the study, variations in the elastic modulus were investigated for cylinders, while the temperature was held constant. The specimens were gradually heated to the target temperature, the temperature was then held constant for a period of two hours, after which the hot elastic modulus was determined. The specimens were then cooled to room temperature to find the residual elastic modulus and residual strength. Target temperatures from zero to 600°C were investigated.

In the second part of the study, transient creep and thermal strains were measured for RPC cylinders held under a constant load while the temperature was increased from zero to 600°C at the rate of 2°C/min.

The following observations are made and conclusions drawn:

1. The elastic modulus of hybrid fibre RPC drops gradually and approximately linearly with increasing temperature;
2. The residual elastic modulus shows no appreciable variation up to the temperature of 300°C. At higher temperatures, the residual modulus of elasticity reduces significantly;
3. The residual elastic modulus was found to be higher than the hot elastic modulus when the temperature was 300°C and lower;
4. An increase in residual compressive strength was observed when temperature was below 300°C. This increase is caused by removal adsorbed water, which increases the surface forces and, thus, strength;
5. At temperatures greater than 300°C, the residual compressive strength was significantly less than the compressive strength at room temperature;
6. Free thermal strains were found to be similar to that of a siliceous aggregate concrete; and
7. Load induced thermal strains (LITS), or transient creep, is significant when the temperature rises above 250°C.

REFERENCES

Bazant, Z., & Kaplan, M. F. 1996. Concrete at High Temperautre. Eds 1, Longman Group.

BS EN 1992 1-2; 2004, Design of Concrete Structures, Part 1-2 General Rules – Structural Fire Design.

Cheyrezy, M., Maret, V. & Laurent, F. 1995. Microstructural analysis of RPC (reactive powder concrete). *Cement and Concrete Research* 25(7).

Khoury, G. A. 1985. Strain of concrete during the first heating to 600°C under load. *Magazine of Concrete Research* 37(133).

Khoury, G. A. 2000. Effect of fire on concrete and concrete structures. *Progress in Structural Engineering and Materials* 2(4).

Peng, G.-F., Kang, Y.-R., Huang, Y.-Z., Liu, X.-P. & Chen, Q. 2012. Experimental Research on Fire Resistance of Reactive Powder Concrete. *Advances in Materials Science and Engineering* 2012(6).

P. Piementa, J-C., Mindeguia, Simon, A., Behloul, M. 2011. Behaviour of UHPFRC at high temperatures, *in: F. Toutlemonde, J. Resplendino (Eds.), Designing and building with UHPFRC State of the art and development,* Wiley Publication.

Richard, P. & Cheyrezy, M. 1995. Composition of reactive powder concretes. *Cement and Concrete Research* 25(7).

Sanchayan, S., Gowripalan, N., Foster, S.J., 2012. Mechanical properties of fibre reinforced reactive powder concrete after exposure to high temperatures, *Proceedings of the 22nd Australasian conference on the mechanics of structures and the materials,* Sydney 2012.

Tai, Y.-S., Pan, H.-H. & Kung, Y.-N. 2011. Mechanical properties of steel fiber reinforced reactive powder concrete following exposure to high temperature reaching 800°C. *Nuclear Engineering and Design* 241(7).

Research and Applications in Structural Engineering, Mechanics and Computation – Zingoni (Ed.)
© 2013 Taylor & Francis Group, London, ISBN 978-1-138-00061-2

Sustainable building with ultra-high performance concrete (UHPC) – coordinated research program in Germany

M. Schmidt
Institute of Structural Engineering, University of Kassel, Germany

ABSTRACT: In Germany, a 12 Mio. € Research Program on UHPC was performed since 2005, covering a wide range of topics related to UHPC. The program was funded by the German Research Foundation (DFG) and coordinated by the University of Kassel. More than 20 research institutes were involved. Its purpose was to elaborate the basic knowledge necessary to draft reliable technical standards covering materials, material-adequate design principles and innovative construction and fitting technologies to make UHPC a reliable, commonly available, economically favorable, regularly applied material. This paper describes the intention and the background of the program, and it gives an overview over the topics being dealt with and the results recently available. As one result material adequate limits for the composition of durable UHPC are presented.

1 INTRODUCTION

In Germany, a comprehensive 12 Mio. € Research Program on UHPC has recently reached its end. The program was funded by the German Research Foundation (DFG) and coordinated by the University of Kassel. More than 20 research institutes were involved, striving to elaborate the basic knowledge necessary to draft reliable technical standards covering both materials and design principles to make UHPC a reliable, commonly available, economically favorable, and regularly applied material. The fields of interest that the individual research projects concerned themselves with include the suitability and performance of raw materials including cements, inert or reactive mineral fillers, artificial nanoparticles, and improved plasticizers. Basic research on appropriate mix designs for different applications, the rheological specifics of the fresh concrete and its hydration are evaluated as well as the time dependent strength and deformation behavior of hardened UHPC with and without fibers. Also covered were material-adequate design and construction procedures including new appropriate technologies to build high performance light and slender and therefore sustainable structures.

2 OBJECTIVES AND TECHNICAL BACKGROUND

The most notable characteristic of Ultra-High Performance Concrete (UHPC) is its extremely dense microstructure, resulting in a steel-like compressive strength of about 180 to 250 MPa, combined with a significantly improved durability. The structural density is primarily due to the high packing density accomplished with an optimum grading curve comprising fine and ultra-fine particles $\leq 125\,\mu m$ in the cement matrix, and a comparatively low w/c-ratio of about just 0.20.

Undoubtedly, UHPC represents a milestone in concrete technology due to the new challenges for both civil engineering and architecture and the opportunity to develop material and energy conserving slim and slender concrete structures significantly reducing the energy and material related impact on the environment by up to 40% (Schmidt & Jerebic, 2008) Nevertheless apart from a small number of pilot projects, the application of UHPC has been restricted due to the fact that neither the material itself nor the material-specific design of the structures had already been sufficiently explored to draft technical standards as a basis for a common application.

To support the idea of promoting UHPC as a commonly available and standardized material based on individual regionally available raw materials, the German Research Foundation initiated an extensive research program in 2005. It would break the mold by far to report on all the theoretical and experimental research and the information that has already been gathered. A more extensive survey covering most of the findings already gathered is given in the Proceedings of the Second and the Third International Symposiums on UHPC, held in Kassel in 2008 and 2012, both available online (Fehling et al. 2008; Schmidt et al. 2012). Reports on all projects assorted in Table 1 will be presented in a comprehensive report to be finalized and published in 2013.

Table 1. Working groups inside the priority program and their individual research topics.

Working group	# of projects 2005–2013	Topics of the individual projects
Raw materials, rheology, processing, sustainability	4	– Influence of shape and texture of fine grains and of interparticle forces on packing density and rheology – Life cycle inventory on UHPC – UHPC with low-energy binders – Optimization of the mixing process
Hydration and microstructure	2	– Characterization of the microstructure – Micro- and nanostructure of UHPC with nanotubes and pyrogenous SiO_2
Time-dependent behavior (shrinkage, creep, cracking)	6	– Early age behavior of UHPC – Reduction of crack formation by internal curing – Shrinkage-reducing chemical admixtures – Time-dependent stress-strain behavior – Early age cracking and durability – Autogenous shrinkage and microstructure
Fiber efficiency and interaction with conventional reinforcement	3	– Load-bearing capacity of elements reinforced with fibers and bars under tension and bending – Ductility of UHPC with fibers and nanoparticles – Self-compacting UHPC with fiber meshes
Strength and deformation	2	– Fatigue under uni- or multiaxial loads – Modeling of multiaxial strength
Durability	4	– Resistance to freezing and deicing agents – Resistance to chemical attacks (acid, sulfates) – Fire safety of UHPC under load – Corrosion of steel fibers and influence on the microstructure
Design, construction, and application	11	– Prestressed beams – Performance of steel fitting elements for hybrid structures (UHPC/steel) – Loadbearing of extensively loaded columns – Fitting of elements by gluing – Thin fiber-reinforced UHPC layers on conventional concrete structures – UHPC under transverse (biaxial) forces – Anchorage and overlapping joints of reinforcing – UHPC/steel pipes for truss structures – Thin-walled pipes – Structural connection of precast elements – Miniaturized fitting devices for slender slabs
Testing	2	– Adjusted test procedures for rheology and strength – Fiber distribution and orientation

3 MICROSTRUCTURE

The most notable characteristic of Ultra-High Performance Concrete (UHPC) is its extremely dense microstructure of the matrix based on the high amount of fines with an optimum packing density and a low w/c-Ratio (Geisenhanslüke & Schmidt, 2004; Teichmann & Schmidt, 2004) Depending on the application and especially on the amount and the maximum grain size of the aggregates, UHPC contains between 450 and 1000 kg cement per m^3, between 50 and 250 kg/m^3 of microsilica and a significant amount of other mineral fillers (primarily fine ground quartz or basalt). Table 2 shows some quite different mixture compositions with different fresh concrete consistencies developed at the University of Kassel and already practically realized: Self compacting UHPC for precast elements and floor layers (M2Q, B5Q in Table 2), plastic consistency for concrete pavement layers to be placed by slipform pavers (UHPC-PV) or even no-slump consistency for sewer system pipes with an increased mechanical and chemical resistance (UHPC-NS) (Schmidt, 2012). The w/c-ratio ranges from 0.22 to 0.29, and the w/(c + m) ratio considering microsilica as part of the reactive binder is between 0.19 and 0.25. Independent of the w/c-ratio, the average 28-days compressive strength of all mixtures in table 1 was about 150–165 MPa when the concrete specimen were stored at 20°C under water. It was about 190 MPa when the concrete was heat treated at 90°C for app. 48 h.

The dense microstructure is the key factor that is determining the outstanding performance of UHPC. Electron microscopy investigations e.g. by Möser (Möser & Pfeiffer, 2008) using a NanoSEM microscope confirm that the hydrate phases in UHPC are significantly shorter as a result of the high packing density, the low w/c ratio of about 0.20 only Figure 1

(Fehling et al., 2005) shows a SEM micrograph of unhydrated microsilica particles surrounded by dense C-S-H phases in UHPC (left) compared to the long and instable phases and the rather porous structure of ordinary concrete.

The ability of concrete to withstand physical and chemical attacks is usually attributed to the amount of capillary pores in the cementitious matrix.

Capillary pores arise during the hardening period when excess water evaporates, which is the part of the total amount of water that is not chemically or physically bound in hydration phases or in the pores of the microstructure (gel pores). Thus, the amount of capillary pores is a quite reliable benchmark to classify the durability of a specific concrete. E.g., Figure 2 shows the characteristic pore size distributions of an ordinary concrete C45/55 with a w/c-ratio of about 0.48, a High Performance concrete C105 with a w/c-ration of 0.35, and UHPC M2Q acc. to Table 2 with a w/c-ratio of only 0.22 the latter being virtually free of capillary pores with diameters between 0.01 and 1 μ m. This accounts for its extremely high resistance to the ingress of harmful liquid or gaseous agents, e.g. chloride and alkaline ions or to frost attacks with and without deicing agents. As an example, Figure 3 shows the results of chloride diffusion tests on the three concretes already mentioned in Figure 2. When tested in an accelerated test, (Tang & Nilsson, 1992) both the depths of the chloride intrusion and the transmitted charge fairly correlated with the amount of capillary pores shown in Figure 2 and thus with the w/c-ratio of the concretes. The UHPC M2Q was practically impermeable to chloride ions.

Another indicator for the resistance of the microstructure is the relative absorption of water or other liquids in relation to the total pore volume.

Table 2. Application oriented UHPC compositions.

	UHPC fine M2Q (0/0,5)	UHPC coarse B5Q (0/8)	UHPC-PV Pavements	UHPC-NS Pipes
Water w	166	158	107	49
Cement c	832	650	404	186
Silica fume m	135	177	54	51
Superplastiziser [mass%]	1,1	1,2	0,6	1,2
Quartz powder 12000 m^2/g	207	325	–	93
Quartz powder 3600 m^2/g	–	131	32	38
Sand 0.125/0.5	975	354	541	101
Sand 0/2	–	–	–	616
Sand 0.6/2	–	–	283	–
Gravel 2/8	–	–	–	821
Gravel 8/16	–	–	–	616
Basalt 2/8	–	597	1123	–
w/c-ratio (w + 60%SP)	0.22	0.26	0.28	0.29
w/c + m	0.19	0.21	0.25	0.23
28d Compressive strength (150/300) Water 20°C	165	160	150	150
Heat 90°C, 48h	195	185	–	–

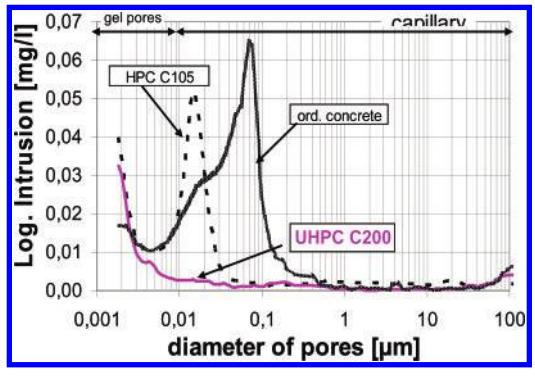


Figure 2. Typical pore size distributions of Ordinary Concrete C 45/55, High Performance Concrete and UHPC M2Q acc. to Table 2 (mercury intrusion) (Fehling et al., 2005).

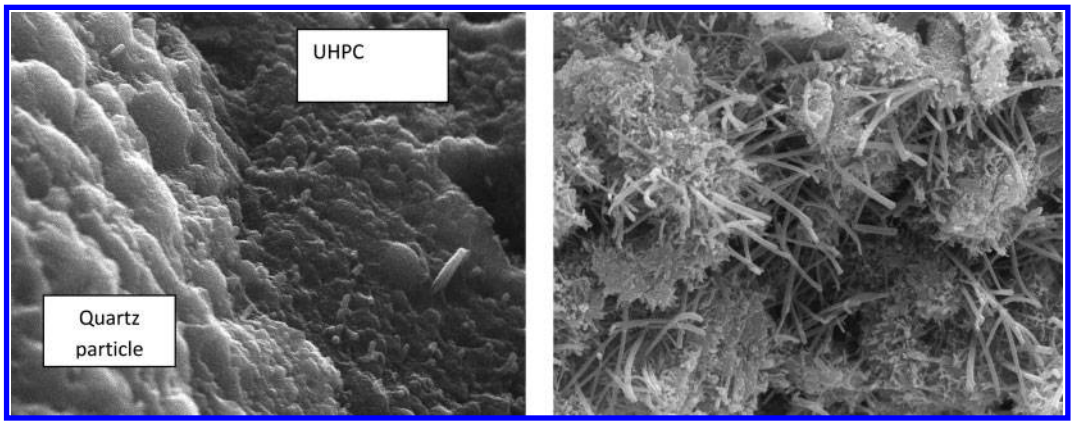


Figure 1. Matrix of UHPC, (left) compared to ordinary concrete (right).

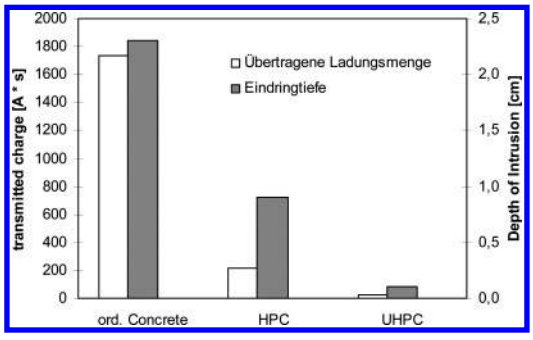


Figure 3. Resistance to chloride diffusion of heat treated UHPC M2Q (table 2), HPC C105 and OPC C45/55. Porosity as shown in Figure 2.

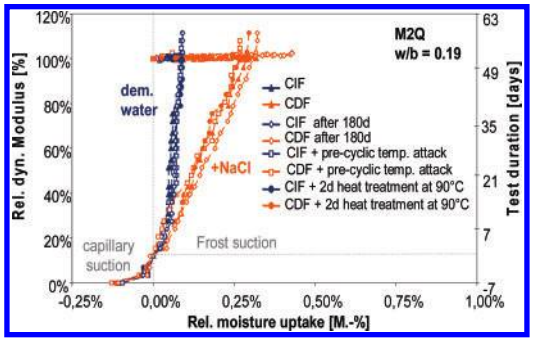


Figure 4. Absorption of water/NaCl-solution during freezing and sawing cycles. UHPC M2Q acc. to Table 2 (Setzer & Palecky, 2007).

Figure 4 shows the relative amount of water or of 3%-NaCl-solution respectively being absorbed by capillary suction and during freeze-thaw-cycles of UHPC when tested acc. to the CIF(water)- or the CDF (NaCl)-procedure respectively (Setzer & Palecky, 2007). The maximum uptake of water of about 0.25 % b.m. is significantly smaller than for ordinary concrete indicating an extremely high resistance to both frost attacks as well as to harmful liquids. Due to the low w/(c + m)-ratio of only 0.19 (w/c-ratio 0.22 acc. to table 2), the heat treatment seems to be of minor influence on the porosity of the matrix.

4 MATERIAL-ADEQUATE LIMITS WITH REGARD TO STRENGTH AND DURABILITY

Based on the strength classification system of the European Standard EN 206, the design strength of UHPC is commonly characterized by a minimum characteristic strength of 150 MPa after 28 days when tested on cylinders d/h = 150/300 mm. As can be seen from Table 2, this minimum strength can be achieved even at a w/c-ratio of up to 0.30. This is due to the increase in strength gained by the physical optimization of the packing density of the fine particles of the matrix.

But as for ordinary concrete, the compressive strength does not comprehensively describe the durability properties. A general boundary value for the appropriate w/c-ratio assuring an optimum impermeability of the microstructure can be derived from the shrinkage behavior of the two compositions M2Q and B5Q consistently used in all research projects given in Table 1. The amount of drying shrinkage fairly corresponds to the amount of free water evaporated during hydration and thus to the w/c-ratio. No drying shrinkage means that the water added to the fresh concrete is fully bound in the cement hydrates and/or in the gel pores. Figure 5a (left) shows the shrinkage-related contraction of the UHPC mixture M2Q with a w/c-ratio of 0.22 when stored at 20°C/65% r.h., measured in a shrinkage rim with and without waterproof plastic sealing (Scheidt & Müller, 2012). In both cases, the same contraction could be measured. This leads to the conclusion that the total deformation was caused by autogenous shrinkage only. As no free water evaporated, capillary pores were not formed as can be seen from the pore size distribution of the M2Q mixture presented in Figure 4. The w/c-ratio of the UHPC mix B5Q in Figure 5b (right) was 0.26. In this case, the unsealed specimen showed a small but significant amount of drying shrinkage due to evaporation of unbound water and thus capillary pores arose weakening the microstructure..

Based on these and also on further research results gained in other projects of the Coordinated Research Program dealing with the durability of UHPC (see table 1), a boundary value for a w/c-ratio assuring both high strength and a virtually negligible permeability and thus optimum durability is proposed to be 0.22 if the concrete hardens under ambient conditions and is not heat treated If one will consider the silica fume to be part of the rective binder content one must not forget that, primarily due to the low water content, without an intensive heat treatment only a small share of silica fume will react with the cement components to form additional C-S-H phases. (Heinz, 2012). In this case, silica fume primarily acts as a physical filler improving the packing density and thus partly contributing to the higher strength of UHPC. But it is not a reliable factor with regard to durability.

If the hydration is accelerated and improved by heating the young concrete e.g. for 24 to 48 h at 80 to 90°C a maximum value of 0.26 may be acceptable to assure a sufficient impermeability

5 CONCLUSIONS

In a comprehensive Coordinated Research Project performed in Germany a wide range of open scientific and technical questions of UHPC were clarified. The research results provide a safe foundation to develop technical regulations for UHPC based on regionally available raw material. One of the outcomes was that an appropriate compressive strength of at least 150 MPa can be achieved even at a w/c-ratio of up to 0.30 if the

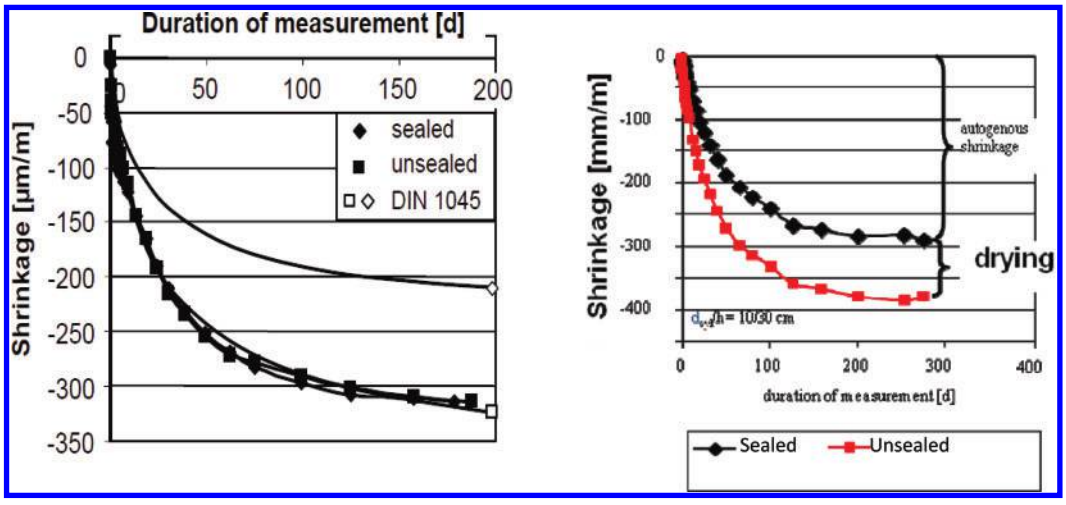


Figure 5. Shrinkage of UHPC with an w/c-ratio of 0.22 (left) and 0.26 (right) both tested at 20°C/65% r.h. sealed and unsealed respectively (Scheydt, Müller, 2012).

packing density of the matrix is sufficiently improved by means of calculated amounts of various micro-fine fillers of different fineness. This could be a sufficient definition for "Ultra-High Strength Concrete" aiming at a high design strength only. To make the microstructure of UHPC practically impermeable to harmful gases and liquids and thus to achieve its significantly improved resistance to concrete corrosion and its high ability to protect the steel reinforcement from corrosion as well UHPC must be practically free of capillary pores. Thus in addition to the optimized packing density the w/c ratio of UHPC hardening under ambient conditions shall be limited to no more than 0.22 if the kind of application calls for an improved durability ("Ultra-High Performance Concrete"). Without heat treatment, Silica fume should not be considered to be part of the binder. If the concrete is heat treated at temperatures of 80–90°C, a maximum w/c-ratio of 0.26 seems to be adequate.

REFERENCES

Burkart, I.; Müller, H. S.: Creep and shrinkage characteristics of ultra-high strength concrete (UHPC). In: Proc. of 8th International Conference on Creep, Shrinkage and Durability of Concrete and Concrete Structures (CONCREEP 8), Ise-Shima, Japan, 2008.

Fehling, E.; Schmidt, M.; Teichmann, T. et al.: Entwicklung, Dauerhaftigkeit und Berechnung ultrahochfester Betone (UHPC). Forschungsbericht DFG FE 497/1-1, Schriftenreihe Baustoffe und Massivbau, Heft 1, Kassel University Press, 2005.

Fehling, E., Schmidt, M. & Stürwald, S. (eds.) 2008. *Ultra-High Performance Concrete* – Proc. of the 2nd International Symposium on UHPC, Structural Materials and Engineering Series V. 10, Kassel: Kassel University Press.

Geisenhanslüke, C.;Schmidt, M. 2004: Methods for Modelling and Calculation of High Density Packing for Cement and Fillers in UHPC, *Proc. of the 1st International Symposium on UHPC* 303–312, Kassel: Kassel University Press.

Heinz, D.; Urbonas, L.; Gerlicher, T. 2012: Effect of Heat Treatment Method on the Properties of UHPC. In: Proc. of Hipermat 2012 – 3rd Int. Symp. on UHPC and Nanotechnology for High Performance Construction Materials (Hrsg.: Schmidt, M.; Fehling, E.; Glotzbach, C. et al.), Schriftenreihe Baustoffe und Massivbau, Heft 19, S. 283–290, Kassel University Press, Kassel.

Möser, B., Pfeiffer, C. 2008, "Microstructure and Durability of Ultra-High Performance Concrete", Proc. of the 2nd Internat. Symp. on UHPC, pp. 417–424.

Scheydt, J.; Müller, H. 2012: Microstructure of Ultra High Performance Concrete (UHPC) and its Impact on Durability. In: Proc. of Hipermat 2012 – 3rd Int. Symp. on UHPC and Nanotechnology for High Performance Construction Materials (eds. Schmidt, M.; Fehling, E.; Glotzbach, C. et al.), Schriftenreihe Baustoffe und Massivbau, vol. 19, 349–356, Kassel: Kassel University Press.

Setzer, M. J., Palecki, S.: Untersuchungen zum Frost/Frost-Taumittelwiderstand, dem autogenen Schwinden und der Gefügestruktur von UHPC. DFG Forschungsvorhaben Se 336/61-1 (SPP 1182). Bericht 20.4.2007, Universität Essen.

Schmidt, M.; Jerebic, D. 2008: Basis for Sustainable Structures – the Gaertnerplatz Bridge in Kassel. Second International Symposium on Ultra High Performance Concrete, Kassel, March 5–7, 619–625.

Schmidt, M. 2012. Sustainable Building with UHPC –The Next Decade: from Research to General Application. *Proc. of the 3rd International Symposium on UHPC*, Kassel: Kassel University Press.

Schmidt, M., Fehling, E. & Glotzbach, C. (eds.) 2012: *Proc. Of the 3rd International Symposium on UHPC*, Kassel: Kassel University Press.

Teichmann, T.,Schmidt, M. 2004. Influence of the packing density of fine particles on structure, strength and durability of UHPC, *Proc. of the 1st International Symposium on UHPC*, Kassel: Kassel University Press, 313–323.

Tang, L., Nilsson, C.O., 1992: Chloride Diffusivity in High Strength Concrete. Nordic Concrete research, vol. 11, 162–170.

Research and Applications in Structural Engineering, Mechanics and Computation – Zingoni (Ed.)
© 2013 Taylor & Francis Group, London, ISBN 978-1-138-00061-2

Composite structures of steel and filigree UHPC-elements – Experimental and numerical investigations

Thomas Lechner & Oliver Fischer
Chair of Concrete and Masonry Structures, Technische Universität München, Germany

Günter Seidl
SSF Ingenieure AG, Berlin, Germany

ABSTRACT: Composite structures of steel and filigree concrete elements can be realized utilizing the innovative material Ultra-High Performance Concrete (UHPC). This high-tech construction material allows the production of extreme thin but high-strength elements. Thus, using UHPC the dimensions and the dead weight of composite structures with a given load-bearing capacity can be minimized. Shear connectors with high shear strength and a ductile load-deformation behavior are necessary to connect the UHPC-member with the structural steel. Continuous shear connectors with a clothoidal shape, the so-called modified chlothoid strip (MCL-strip), were chosen for this research. These shear connectors are arranged parallel to the concrete surface and have only a minimum of concrete cover on each side. A series of push-out tests has been conducted to figure out the load bearing capacity and the failure mechanisms for this configuration. Furthermore, preliminary numerical simulations showed good results in comparison with the physical tests.

1 INTRODUCTION

The outstanding mechanical properties of Ultra-High Performance Concrete (UHPC) offer the opportunity to create filigree structures. In composite structures the steel carries the tensile forces and the concrete is arranged in the compression zone. This kind of task sharing led to structural elements made of normal or high strength concrete with conventional bar reinforcement and high load bearing capacities. If the normal or high strength concrete is replaced by UHPC for which the compressive strength and the durability are considerably better, a significant reduction of the outer dimensions and the dead-weight of the composite structures are possible. A modern type of continuous shear connector, the composite dowel, is investigated to connect thin UHPC-members with structural steel. The composite dowel consists of a steel-strip with a special cut, which is referred to as steel dowel in the following, and the concrete that fills the spaces between the steel dowel and which is called concrete dowel. From the existing different shapes of composite dowels the so-called modified chlothoid strip (MCL-strip) was chosen for this research. MCL-strips offer a high shear strength and a very ductile load-deformation behavior (Berthellemy et al. 2011) which is necessary to fully take advantage of the high concrete strength.

The load-bearing capacity and also the failure mechanism of shear connectors that are positioned parallel to the concrete surface (e.g. in thin concrete beams or wall panels) with only a few centimeters of concrete cover differ from the usual application in plates. Whereas the concrete failure in plates is mainly governed by concrete pry-out, the failure in panels or thin beams is mostly caused by splitting failure due to the small concrete cover and splitting tensile forces resulting from the concentrated load introduction of the steel dowel. Furthermore, concrete shearing or a combination of both might occur, if the thickness of the wall-panel is very small.

Experimental investigations with push-out tests have been designed to check the ductility behavior and steel failure loads for small MCL-strips in thin UHPC-elements with and without conventional bar reinforcement. Additionally, a main objective of this research was to determine the concrete failure mechanisms that can occur when such filigree UHPC-member are used. During these test series the influence of the yield strength and the thickness of the MCL-strip as well as the thickness of the UHPC-element were studied.

Numerical studies of the push-out tests accompanied the experimental investigations. Preliminary analyses show good results compared to the experimental tests and help to understand the different influence factors and also to examine the complex stress states in the steel and concrete.

2 ULTRA-HIGH PERFORMANCE CONCRETE

Ultra-High Performance Concrete is an extremely dense concrete with a compressive strength of more than 150 MPa. The composition of UHPC differs

Table 1. Composition of UHPC.

Raw materials	Amount in kg/m^3
CEM I 52,5 R HS-NA	650
Silica Fume	177
Quartz I	325
Quartz II	131
Sand 0,125/0.5	354
Basalt 2/8	597
Superplasticizer	30.4
Steel fibers	2.5 [vol. %]
Water	158
w/c-ratio	0.24 [–]

strongly from normal or high strength concrete since the matrix porosity is minimized with the help of a very low w/c-ratio and a very dense packing of fine particles due to the use of different mineral additions like silica fume and quartz.

For this research the mixture B5Q with a maximum grain size of 8 mm and a regular fiber volume content of 2.5 vol. % was used. It was developed during the priority program 1182 of the German Research Foundation. The chosen steel fibers had a length h of 9 mm and a diameter d of 0.15 mm which gives an h/d-ratio of 60. A certain amount of steel fibers assures a ductile behavior and enhances the tensile as well as the bending strength of UHPC.

3 CONTINUOUS SHEAR CONNECTORS

In composite constructions headed studs are the predominant shear connectors until today. The design follows DIN EN 1994-1-1 (EC 4, 2012) for concretes up to C60/75. Experiments on the behavior of headed studs in high strength concrete showed that the failure was becoming more brittle when the concrete strength was increased and the diameter of the headed studs decreased (Jähring 2008). Hence, an application of small studs in filigree elements of high strength concrete leads to a very low ductility even if steel failure occurs.

Composite dowels have been used in normal strength concrete since the development of the perfobond strip in 1985 (Andrä 1985). During the last two decades research mainly focused on the optimization of the geometry of this shear connector in order to achieve an economically advantageous connector, a higher shear-bearing capacity and a better behavior under cyclic loading. A few shapes of composite dowels that have been tested lately are displayed in Figure 1.

The puzzle-strip shear connector (PZ) offers the main advantage that the geometry is symmetrical and therefore with one cut two shear connector strips can be manufactured (Gallwoszus et al. 2012). An improvement of the CL-shape (clothoid-shape) in terms of fatigue behavior led to the modified CL-shape (MCL-shape) which is used for this research.

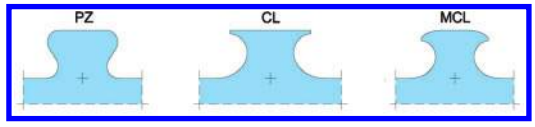


Figure 1. Shapes of composite dowels (Berthellemy et al. 2011).

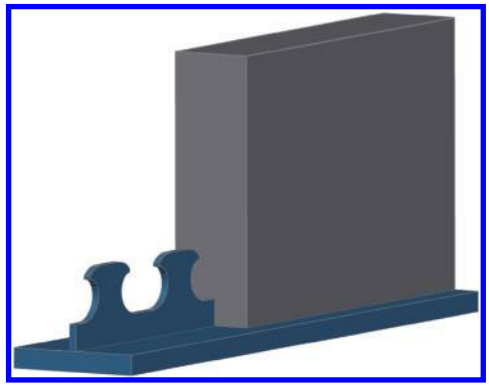


Figure 2. Application of MCL-strip in filigree UHPC-element.

Recent investigations with UHPC composite beams and puzzle-strips prove that composite dowels can carry high loads and show a good ductility in combination with UHPC (Gallwoszus et al. 2012). However, experiences concerning the structural behavior of MCL-strips in filigree UHPC-elements with a thickness of 4–6 cm, as displayed in Figure 2, are missing.

4 EXPERIMENTAL INVESTIGATIONS

4.1 *Test set-up*

To analyze the shear-carrying behavior of MCL-strips in thin UHPC a series of push-out tests (PO-tests) has been carried out. The geometries of the steel-element (left) and the push-out specimen (right) are shown in Figure 3. The right part of the UHPC-member is cut in the middle plane and because of this the steel-dowels and the screening made of polystyrene beneath the last dowel are visible.

The relatively small MCL-strips have a height of 40 mm and a longitudinal distance between the dowels of 100 mm. Deformation controlled loading allowed to measure the post-fracture behavior even if a brittle failure occurred. The slip δ between the shear connectors and UHPC-members was measured with two displacement transducers.

Testing of the specimen was usually after 28 days of concrete hardening. At this time the compression strength of the used UHPC was up to 183 MPa for a cube with 150 mm side length.

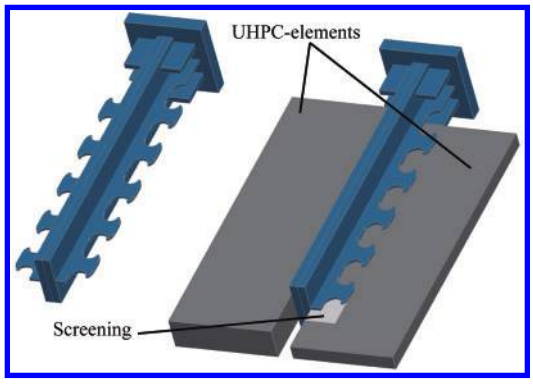


Figure 3. Steel-element (left) and push-out specimen with partly visible steel (right).

Table 2. Test program in extracts.

		Parameter			
Lable	No.	$f_{y,MCL}$ [MPa]	t_{MCL} [mm]	t_{UHPC} [mm]	stirrups/ bars
PO-1	2	438	5	60	w
PO-2	2	438	5	60	w/o
PO-3	2	438	5	50	w/o
PO-5	2	384	10	60	w
PO-6	2	384	10	60	w/o
PO-7	2	384	10	50	w/o
PO-8	2	384	10	40	w/o
PO-15	2	326	5	60	w/o

4.2 *Test program*

Especially parameters that influence the concrete failure mechanisms, e.g. splitting failure or shear failure, were investigated in the first test series, since these were expected to become the most critical for filigree UHPC-elements with only a few centimeters of concrete cover. Table 2 shows the test program in extracts and the most important research parameters.

Besides the yield strength of the MCL-strip ($f_{y,MCL}$), the thickness of the steel (t_{MCL}) and UHPC-Panel (t_{UHPC}) were studied. Furthermore, some specimens were equipped with stirrups (Ø 6 mm between each steel-dowel) and longitudinal bars (Ø 6 mm) and the others were plain fiber reinforced concrete without conventional bar reinforcement. For the specimens PO-1 to PO-8 the steel grade S355 was used, whereas the continuous shear connector of PO-15 was made of S235.

4.3 *Results*

Conclusions from the experimental push-out tests are that certain combinations of steel- and concrete-thickness guarantee a high load bearing capacity but a low ductility whereas with other combinations a good ductility with a reduced load-bearing capacity is reached.

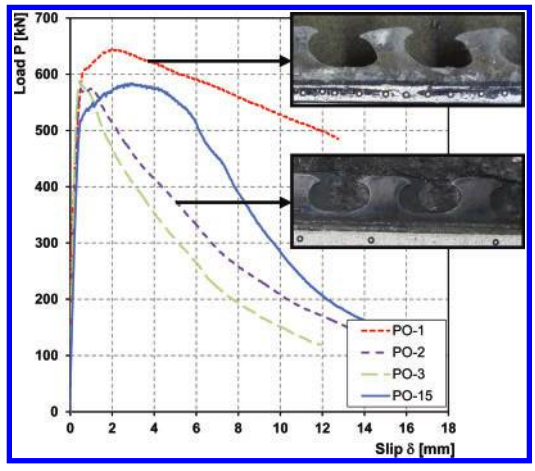


Figure 4. Load-slip diagram of push-out tests with $t_{MCL} = 5$ mm and exemplary deformation of steel after testing.

As the load-deformation behavior for the two specimens with the same test set-up is almost identical, it is possible to calculate mean load-slip-curves, which are presented in Figure 4.

The specimens with a 5 mm thick MCL-strip either showed a combined steel and concrete failure (PO-1 and PO-15) which was quite ductile or they failed more brittle by pure splitting (PO-2 and PO-3). A combined failure (first steel failure and later concrete-splitting) occurred for specimens with conventional bar reinforcement or if the steel grade S235 was used. In general, the thinner the UHPC-element and the higher the yield strength of the steel was, the more brittle was also the load-deformation behavior. The comparison between PO-1 and PO-2 shows that reinforcement can be used to increase the maximum load and ductility. However, it should be noted that reinforcement is not necessary to achieve a ductile behavior as can be found from PO-15. For this specimen the maximum load is only 10 % lower than for PO-1 and the reached ductility is nearly the same.

If steel failure occurs the steel-dowel deformation looks in principle as shown in the upper picture of Figure 4. It is obvious that the slip measured during the tests with a good ductility results at least partly from the steel deformation. In contrast the lower picture shows that the measured displacement for PO-2 results only from concrete failure since no steel deformation is visible.

Specimens with a steel thickness of 10 mm (see Fig. 5) reach a significant higher maximum load than specimens with only 5 mm MCL-strips. However, the main failure mechanism is a brittle splitting failure. Even the specimens PO-5 with reinforcement, for which a combined failure was observed, failed rather brittle in comparison to PO-1 because only small deformations of the steel dowel occurred before the concrete failed. Specimens without reinforcement (PO-6) behave clearly brittle. The difference

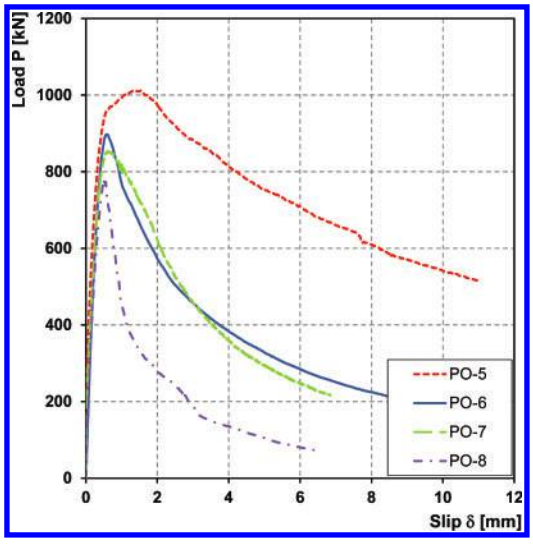


Figure 5. Load-slip diagram of PO-tests with $t_{MCL} = 10$ mm.

between UHPC with a thickness of 60 (PO-6) and 50 mm (PO-7) is small. For the push-out tests PO-8 with a UHPC-thickness of only 40 mm pure concrete shear failure occurred. This test resulted in the lowest ductility of all specimens.

In summary it was found that MCL-strips can be used as shear connectors in filigree UHPC-elements. Depending on the strength and thickness of the materials chosen it is possible to transfer very high shear forces up to 1250 kN/m (PO-5) or to achieve a composite element with a good load-deformation behavior and a load-bearing capacity of about 800 kN/m (PO-1).

5 NUMERICAL SIMULATIONS

5.1 *General overview*

A numerical model of the push-out test was developed using the finite element software ABAQUS and preliminary results are presented in the following paragraphs. Finite element calculations can be used as a tool to help understand the force flow and the three dimensional stress-state in the concrete dowel. Furthermore, it is possible to investigate the influence of different parameters that could not be tested in the lab if the results from the FE-program are verified by experimental data.

5.2 *Geometry and boundary conditions*

In all FE-models the twofold symmetry of the push-out test is taken into account so that only a quarter of the specimen has to be analyzed. Appropriate boundary conditions were applied at the symmetry planes for this reason. It was possible to reduce the number of elements and thus also the calculation time using a quarter-model as displayed in Figure 6.

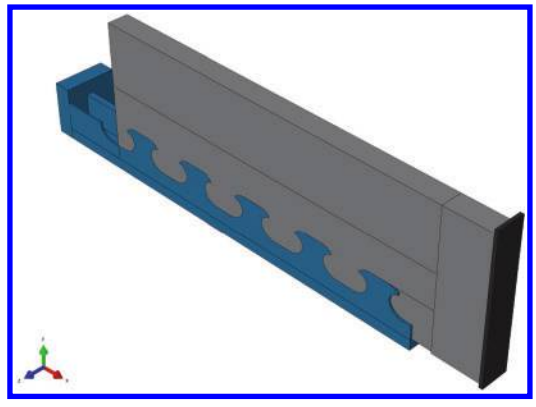


Figure 6. Geometry of quarter-model for numerical simulations.

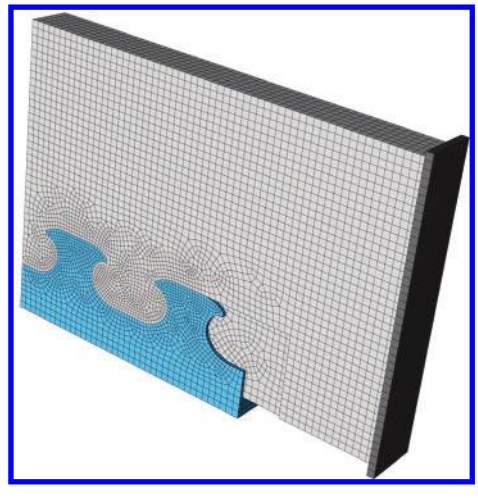


Figure 7. Geometry and mesh of OD-model with right dowel screened.

It seemed advantageous to further reduce the size of the FE-model since it is sufficient to know the behavior of one dowel for basic investigations. Thus, the quarter-model with four active steel dowels was reduced and simplified so that only one steel dowel transfers shear forces to the concrete. This model will be referred to as One-Dowel model (OD-model, see Fig. 7). In both models there is always one dowel which is screened so that there are five dowels visible in Figure 6 and two dowels in Figure 7. The connection between steel and concrete was established with the help of interactions for both models. Interaction properties were defined to allow compression and friction to be transferred between neighboring elements of steel and concrete whereas a separation occurs for tension.

5.3 *Materials*

All parts made of steel had the same material model. The stress-strain curve for the steel was found by direct tension tests. For the concrete the basic properties

such as compression and tension strength or Young's Modulus were taken from the material testing. FE-simulations were made with the assumption that the concrete behaves linear-elastic (e.g. for pure steel failure) and in addition simulations with consideration of nonlinear concrete behavior under tension and pressure (i.e. cracks and compression failure) were carried out. Material parameters that could not be determined in our lab were chosen as ABAQUS default values.

5.4 *Elements*

In general the steel and also the UHPC were modeled with continuum elements C3D8R. These are three-dimensional hexahedral (brick) elements with linear approximation of displacements, 8 nodes and reduced integration. The influence of mesh density was studied for the quarter-model and also for the OD-model and as a result a refined mesh was used along the steel dowel for all calculations. In Figure 7 the geometry and the mesh for a One-Dowel model is displayed.

5.5 *Solution procedures*

There are two methods for solving numerical problems with ABAQUS. The first one is an implicit method (ABAQUS/Standard) and the second one is an explicit method (ABAQUS/Explicit). Both techniques were tested and the results and efficiency of the calculations were compared. Finally, the explicit approach was chosen for the most simulations because this integration method very efficiently solves extremely discontinuous events, such as concrete cracking or contact. The explicit dynamic integration method is also known as the forward Euler or central difference algorithm. Especially advantageous is this solution technique because the elements use a lumped mass matrix which allows the program to calculate the nodal accelerations rather easily. However, since out-of-balance forces are propagated as stress waves between neighboring elements, oscillations may occur if the stability time limit of the central difference operator is not met. Therefore the time increments are calculated and chosen by ABAQUS to be sufficiently small. It is possible to identify if dynamic effects had impacts on the behavior of the model by checking the ratio between kinetic and internal energy.

5.6 *Results of the preliminary calculations*

The first calculations were designed to study the influence of some basic parameters such as the mesh density, the element formulation and interaction properties. Furthermore, the solution procedures of ABAQUS/Standard (imp) and ABAQUS/Explicit (exp) were compared to verify that the results are independent on the procedures used. All these parametric studies were done using the One-Dowel model. The results from the OD-model with different solution procedures are displayed exemplarily in Figure 8.

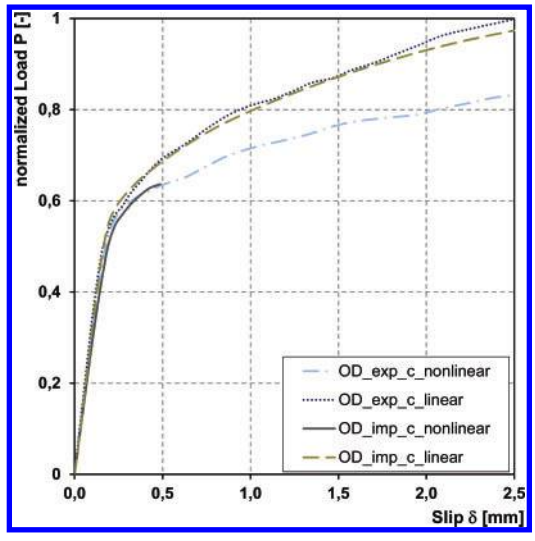


Figure 8. Normalized load-slip diagram of OD-results for different solution procedures.

In addition, for both solution procedures one FE-simulation was made with a linear-elastic concrete behavior (c_linear) and the other one with a nonlinear behavior under consideration of concrete failure effects (c_nonlinear). It could be confirmed that the load-slip curves for explicit and implicit procedures are quite similar if linear concrete behavior is assumed. However, the consideration of plasticity and damage effects for other concrete material model led to a premature termination of the ABAQUS/Standard calculation due to numerical problems. Still it is possible to see that the paths of both nonlinear curves are very close to each other. From these results it is possible to conclude that ABAQUS/Explicit can be used for static calculations if the kinetic energy is small compared to the internal energy, which was checked for all models.

In Figure 9 the first results of the numerical simulation with the quarter-model are compared to the load-slip curve of PO-15. The initial stiffness of the FE-model is quite close to the stiffness from the experiments. The small difference might be due to cohesion effects which were not considered in the numerical analyses. Nevertheless, the failure, which starts with yielding of the first dowel, appears at nearly the same load. After yielding of the first dowel a combined steel and concrete failure occurs in the quarter-model as well as in the real tests. The FE-curve is jagged because of sudden concrete failure. It might be possible to enhance this behavior with an even more refined mesh but an exact prediction or calculation of a combined failure is difficult since the concrete failure is strongly dependent on the distribution and orientation of steel fibers. Further numerical simulations have to verify these first results and it is intended to create models for sole concrete and sole steel failure.

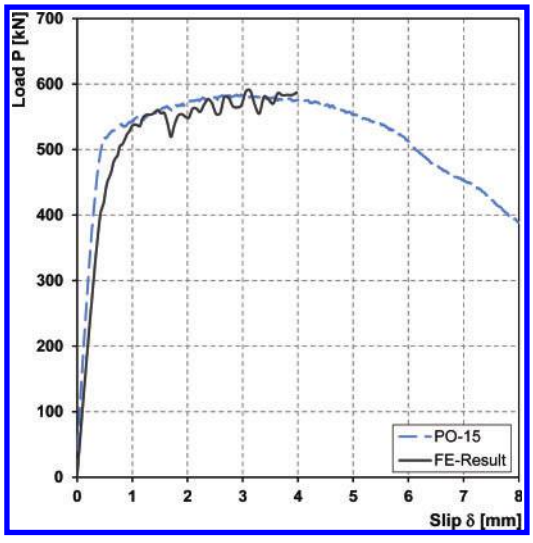


Figure 9. Comparison of real tests results with FE-simulation for quarter-model.

6 SUMMARY AND OUTLOOK

Steel and filigree Ultra-High Performance Concrete can be used to reduce the outer dimensions of composite structures because of the extraordinary load bearing capacity of UHPC under compression. A ductile behavior and a high bending strength of this innovative concrete are achieved by adding steel fibers. Push-out tests with miniaturized shear connectors and thin UHPC-members were conducted and it was found that a maximum shear force of 1250 kN/m could be transferred. However, the failure for PO-specimens with a 10 mm thick shear connector occurred rather brittle by concrete shearing or splitting. A ductile load-deformation behavior and shear forces up to 800 kN/m were achieved for specimens with a 5 mm thick MCL-strip. If the ratio of steel yield strength and tensile strength of the UHPC-panel is chosen well, there is no need for a conventional bar reinforcement since the ductility is sufficiently high.

Preliminary numerical simulations were realized to verify the parameters that influence such nonlinear Finite Element Analyses and to check how sensitive the results react if input parameters are changed. FE-analyses with the One-Dowel model were used to study the influence of different material models, mesh densities, interaction properties and solution procedures. The first simulations with the quartermodel showed that the load-slip curve fits well to the results from the experiments.

The conducted experimental and numerical researches confirm that continuous shear connectors offer an excellent method to transfer shear forces to filigree UHPC-elements. It is intended to carry out additional push-out tests and numerical simulations to verify the results obtained until now and to investigate the load-deformation behavior for specimens with changed parameters (e.g. fiber content, steel strength or thickness).

ACKNOWLEDGEMENT

The authors acknowledge the funding of the Federal Institute for Research on Building, Urban Affairs and Spatial Development (BBSR) within the research program Future Building.

REFERENCES

Andrä, H.-P. 1985. Neuartige Verbundmittel für den Anschluss von Ortbetonplatten an Stahlträger. *Beton- und Stahlbetonbau*. Vol. 80: 325–328.

Berthellemy, J.; Lorenc, W.; Mensinger, M.; Rauscher, S. & Seidl. G. 2011. Zum Tragverhalten von Verbunddübeln – Teil 1: Tragverhalten unter statischer Belastung. *Stahlbau*. Vol. 80: 172–184.

EC 4, DIN EN 1994. 2012. *Design of composite steel and concrete structures – Part 1-1: General rules and rules for buildings*. Berlin: Beuth publishing.

Gallwoszus, J.; Hegger, J. & Heinemeyer, S. 2012. Design Models for Composite Beams with Puzzle Strip Shear Connector and UHPC. In Proceedings of Hipermat 2012. Schmidt, M.; Fehling, E. (eds.).*3rd International Symposium on UHPC and Nanotechnology for High Performance Construction Materials*.

Jähring, A. 2008. *Zum Trag- und Verformungsverhalten von Kopfbolzendübeln in hochfestem Beton*. PhD thesis. Technische Universität München.

Research and Applications in Structural Engineering, Mechanics and Computation – Zingoni (Ed.)
© 2013 Taylor & Francis Group, London, ISBN 978-1-138-00061-2

Optimization process for thin-walled high performance concrete sandwich panels

K. Hodicky, T. Hulin, J.W. Schmidt & H. Stang
Danmarks Tekniske Universitet, Kongens Lyngby, Denmark

ABSTRACT: A Nearly zero energy buildings are to become a requirement as part of the European energy policy. There are many ways of designing nearly zero energy buildings, but there is a lack of knowledge on optimization processes in the sense of structurally and thermally efficient design with an optimal economical solution. The present paper aims to provide multi-objective optimisation procedure addressed to structural precast thin-walled High Performance Concrete Sandwich Panels (HPCSP). The research aim is concerned with developing a tool that considers the cost of HPCSP materials along with the specifications of the design constrains and variables. The tool integrates the processes of HPCSP design, quantity take-off and cost estimation into a single system that would provide different costs for different HPCSP designs. The proposed multi-objective optimisation scheme results into derivation of basic design recommendations, regarding the material's strength and HPCSP's geometrical parameters that fulfil the objective of minimum cost.

1 INTRODUCTION

According to EU (2010) residential and commercial buildings are responsible for about 40% of the total energy consumption and CO2 emissions in Europe. Therefore, ambitious targets for energy consumption of new buildings are being implemented, and by the year 2020 nearly zero energy buildings will become a requirement in the European Union. In consequence of this the building sector has faced a growing demand for development and manufacturing of modular, light and strong building elements having a high degree of insulation, a long life time, a low CO2 emission, a low consumption of raw material, and an attractive surface with minimum maintenance. Moreover, architects and engineers will face the challenge of designing these new buildings with only limited extra cost compared to new buildings today. Thus finding the balance between structural performances and economically optimal solution in building design is needed. The thin-walled High Performance Concrete Sandwich Panels (HPCSPs) are an interesting option for future low or plus energy building constructions.

The main objective of the research summarized in this paper is to present a general optimization procedure of HPCSPs in the sense of structurally and thermally efficient design with an optimal economical solution. A quick and accurate systematic optimization approach is based on material cost function in HPCSP design. The research aims at developing a tool that considers the cost of HPCSP materials along with the specifications of the design constrains and variables. The tool integrates the processes of HPCSP design, quantity take-off and cost estimation; thus a change of any parameter or design constrain in one process would have its effect on the other processes. The suggested optimization procedure could set the ground for further research in predicting optimal design dimensions, mixture proportions and structural designs and systems.

2 BACKGROUND AND DESCRIPTION OF THIN-WALLED HPCSP

The thin-walled HPCSPs are structurally, thermally and environmentally efficient elements for exterior walls in multi-stories residential, commercial and warehouse buildings. The HPCSPs have several beneficial features such as high quality, proven durability, fast erection, and attractive architectural appearance (Einea et al. 1994). A typical HPCSP consists of two precast High Performance Concrete (HPC) plates and layer of insulation separates the two HPC plates. The connectors penetrate the insulation layer and join the two HPC plates.

The HPCSPs may be designed as: non-composite, partially composite or fully composite (Rizkalla et al. 2009). The degree of composite action depends on the nature of the connection between two HPC plates. The connections between the plates have been traditionally made by using bent reinforcing bars or various specially-designed steel or non-metallic connectors (Frankl et al. 2008). Increasing degree of composite action between two HPC plates using any type of these connectors increases the structural capacity of the HPCSP making it more efficient. However, increasing degree of composite action leads to significant thermal efficiency reduction of the panel through thermal bridges (Wade et al. 1998). Recently,

the sandwich panel design concept has leaped forward by introducing fiber reinforced polymer, or FRP, shear reinforcement grids allowing for benefits that make the use of these panels even more desirable than ever before as they have a relatively low thermal conductivity compared to steel (Soriano & Rizkalla, unpubl.). Furthermore, undesirable thermal bowing may occur due to different temperatures between interior and exterior surfaces. The thermal deflections in long HPCSPs can be significant and may cause cracking due to southern exposure especially at building corners. Recent research and development work indicates that load-bearing thin-walled HPCSPs are prone to structural cracking due to the combined effect of shrinkage and high temperature load. The stiffness of the connectors is proportional to the thermal deflection and thus has significant role in the design of HPCSPs. The connector design represents tradeoff between development of fully composite action for resisting lateral loads, and reduction of composite action to limit thermal deflections. Two main categories of connectors exist: non-shear connectors and shear connectors. Non-shear connectors are used in non-composite HPCSPs to resist insignificant shear forces. These connectors primarily resist the tensile forces required to maintain integrity of the panel by keeping two HPC plates attached. Shear connectors must provide adequate stiffness and strength to create significant composite behaviour in the panel and resist the ultimate and service loads of the panel. Bond between the insulation and HPC plates provides some shear transfer, but this bond diminishes over time and will not provide full strength over the life time of the panel (Salmon et al. 1997). The insulation layer mainly provides thermal efficiency of the panel. This efficiency depends on the thickness of the insulation material, amount and type of penetrations through this layer. The insulation should have low absorption to minimize the loss of water from the fresh concrete during manufacturing the panel.

Several authors have attempted to optimize concrete sandwich elements. Their work focused mostly on standard thick walled concrete sandwich element where they attempted to reach full composite action and fulfil the requirements for thermal properties and material reduction. The literature review revealed that there is a lack of optimization studies in the design of HPCSPs. This fact is probably caused due to designers protect their optimization strategies as a result of competition among other producers. For thin plates, the work of Papanicolaou & Triantafillou (2002) should be mentioned. They performed the procedure on minimum cost design of concrete sandwich panels made of HPC faces and PAC core for the case of in-plane and out-plane loading.

3 OBJECTIVE FUNCTION

The objective of HPCSP development is to establish the elements with the best structural and thermal performances and minimum cost. The present paper includes the material costs and ignores others such a transportation and assembly costs. In the case of HPCSPs the cost of mold is not taken into consideration as the cost is included in fix production plant investment costs. The cost function can be described as the sum of material cost functions that already include other costs, such as labour cost per unit volume. The total cost of HPCSP, C per unit volume is shown beneath:

$$C = \frac{t_b}{t} C_{HPC} + \frac{t_f}{t} C_{HPC} + \frac{t_{ins}}{t} C_{ins} + \rho_s \rho_{sh} C_{sh} \qquad (1)$$

where t_b, t_f and t_{ins} are the thicknesses of the back, front plate and insulation layer, respectively; t is total thickness of the HPCSP. C_{HPC} and C_{ins} stand for the cost per unit volume of the HPC layer and insulation layer, respectively, C_{sh} is the cost of shear connectors/reinforcement per unit weight. ρ_{sh} is shear connectors/reinforcement ratio along HPCSP height and length; ρ_s stands for shear connectors/reinforcement density (density of steel/FRP).

4 CONSTRAINTS

The producers and designers can set certain constraints to the design of the HPCSPs, e.g. maximum wall thickness, composition of the wall, choice of materials etc. Above all, material strength constrains should be applied to resist flexural, shear and face local buckling behaviour problem (ULS). The SLS constrain in sense of maximum horizontal/vertical deformations should be prescribed by national codes and standards or by structural requirements for openings. Furthermore, thermal resistance requirement has to be set as design constrain. The HPCSPs can be used as load carrying members as well as fill-in non-bearing members. Hence, the composite/non-composite action of HPCSPs or particular degree of composite action has to be constrained prior to its optimization procedure. In the case of composite and partially composite load carrying HPCSPs the type of shear connectors/reinforcement ratio may be selected. Finally, the set of boundary conditions must be specified taking into account subgrade friction, temperature gradients over the thickness and connections between HPCSPs.

5 MATERIAL COST FUNCTION

Conduct a study of the HPCSP's cost for the past two years, and establish change indicator for these costs. This requires cost data collection from current and previous projects and HPCSP materials suppliers. The collected data will be developed in a database to be used for cost references. Although the economic data of raw materials vary across regions and countries and are influenced by local costs of energy, labour and material resources, attention should not be focused on single cost values. The present cost study is used in

order to draw useful conclusions on relative influences of design variables and variations on the HPCSPs cost and consequently to propose the optimum design solution.

5.1 *HPC plates*

Rougeron et al. (1994) and Ozbay et al. (2001) performed the studies on multi-objective mix proportioning optimization of HPC. Their studies may be implemented to find the optimum mix design for special performance characteristics. These characteristics should take into account structural requirements and production induced constraints, such as:

1. HPC mix must be designed to minimize autogenous shrinkage
2. Provide adequate strength to design load
3. High early age strength (time- related production cycles)
4. Durability (life time up to 100 years)
5. Improved crack control (avoiding damage risks during lifting, transport and assembly)

The total unit cost of HPC plates is equal to the sum of material and labour costs for all stages of production. The HPC cost is generally expressed as a non-linear function of its compressive strength for high-strength concretes (Papanicolaou & Triantafillou 2002).

5.2 *Insulation layer*

Bond between the insulation layer and HPC plates provides in the case of thin walled HPCSPs significant shear transfer, the shear stiffness depending on the insulation thickness. Hansen (2012) performed the optimization of the insulation thickness based on the energy performance requirement in European Union for 2020. The thickness was constrained to a maximum of 400 mm. Optimizing without this constrain would result in unrealistic insulation thickness. The cost function for insulation layers can be described by linear function with an increasing cost/thickness gradient.

5.3 *Shear connecting system/Reinforcement*

The number and position of shear connectors and degree of reinforcement is dependent on required structural systems. The steel provides relatively cheap solution but it can negatively influence thermal efficiency of HPCSPs. An interesting option is using different kind of FRP materials which do not affect thermal efficiency. However, the cost may be relatively high in comparison with steel solution. The choice of material should be chosen prior to optimization procedure. Hence, the cost function of shear connecting system/reinforcement is equal to individual costs of used materials.

6 OPTIMIZATION PROCEDURE

The design of full scale HPCSP usually requires a building block approach to testing and design. This approach involves increasing the testing complexity and size from small scale tests to full scale tests. The chemical and material tests in the first stages are generally well defined tests. As we move from the laminate level to sub-element component and sub-structure level the tests become more application dependent. Neither standard test methods nor databases exist for these large scale tests. Thus there is a need to reduce cost and increase the efficiency of structural design and structural failure prediction by a global local testing and analysis approach. The global local approach involves supporting the global tests and analyses used in traditional design approaches by critical local sub-element tests. These tests are intended to be in between a material and sub-structure test. They are cheaper to manufacture and test, and most importantly they are fully representative of structural configurations undergoing the same manufacturing processes and may even be cut from the real structure (Petras 1998). The testing procedure is used for verification and validation of numerical modelling performed in Abaqus FE software. The model has to take into account that improving some parameters can negatively influence other parameters. For instance significant thickness reduction of HPC plate may cause structural cracking. The numerical model with estimated geometrical proportions is a starting point for its design and optimization procedure. Multi-objective optimization is essential in the real design of HPCSP structures. The single objective simulated annealing was developed by Kirkpatrick et al. (1983). It is considered as the basis of the multi-objective optimization (Paya et al. 2008). The single objective optimization gives an optimum set of design variables with respect to single objective, while the same variables give an unacceptable design for other objectives. A reasonable design solution could be reached by using a combination of more than single objective by using multi-objective design optimization (Konak et al. 2006). The optimal set procedure is preferred in the multi-objective design optimization. In the movement from one solution to another solution, there is always an amount of loses in one objective to achieve some gain in the other objective.

The multi-objective optimization method gives a set of solutions and the best solution measured regarding to all objective functions. Engineers always like to get only one value from the set of solutions. Therefore, solving multi-objective optimization problems can be conducted by both searching and decision making (Awad et al. 2010).

Optimization process is closely related with environmental aspects, material reduction and cost reduction at the same time. Finding the optimum solution involves extended iterative calculations and, thus, need of powerful calculation tools. Optimization of all design parameters at the same time would lead to high

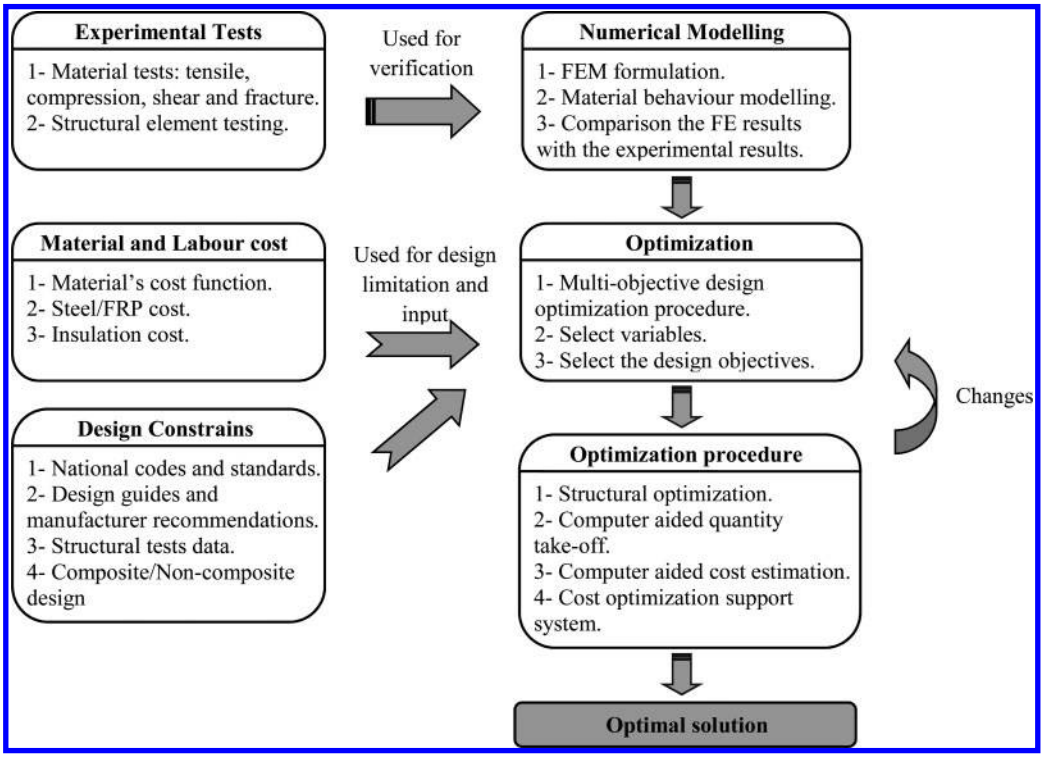


Figure 1. Proposed design optimization methodology of HPCSPs.

number of iteration and to very complicated ways to find the convergence in the sense of the best economically and structurally efficient solution. Therefore, all the design constrains should be carefully set before its optimization process. The proper selection of constrains leads to the faster convergence solution and significant reduction of computation time. Figure 1 shows the proposed design optimization methodology of HPCSPs.

Optimization procedure for which the cost is minimum and all bearing capacity values exceeded the respective design values is needed solution. Its optimization procedure is consists of the four phases as follows:

a) The structural FE software Abaqus is used to perform structural optimization. It automates the design process for accuracy and speed purposes.
b) The quantity take-off computer program. This program measures the total quantities of HPCSPs on basis of measured units trough given set of dimensions and number of elements.
c) Computer aided cost estimation. The program uses the cost data functions from material cost database and the quantity take off procedure to calculate total cost of materials.
d) Cost optimization support system. The three programs of HPCSP design, quantity take-off and cost estimating, are integrated into a single system that would provide different costs for different HPCSP designs.

The minimum cost is achieved when design performance demands exceed the panel's capacity. It is clear that thicknesses of the HPC plates have to be the lowest possible. The functionality of the cost optimization system requires additional testing in an iterative mode to ensure reliability prior to final implementation. As a result of successful testing, parametric cost studies are conducted to determine the relationship between the HPCSP's dimensions and its cost.

7 AUTHOR'S REMARKS

Two of the HPC layers of the HPCSP are made in the fabrication process and their performance is a result of how that process is carried out. Therefore, an assessment of the HPCSP concept must be closely linked to a clearly specified manufacturing process including the quality system in operation to control manufacturing and any inspection and checks to confirm quality. Qualification of the HPCSP technology would have to address these novel aspects carefully in relation to the intended use of the technology over the service life and foreseeable accident scenarios. Above all, the producers and designers attempting to develop and optimize novel thin-walled HPCSPs should keep in mind the subsequent steps:

1) HPC mix must be designed to minimize autogenous shrinkage and provide adequate strength to design load. (risk of cracking in HPCSPs)

2) The bond between layers of thermal insulation, HPC plates and insulation must be carefully evaluated.
3) Number and position of the shear connectors must be specified to eliminate the structural cracking of HPC plates.
4) Shear connectors must provide adequate strength and stiffness for optimum composite/non-composite action between the exterior HPC plates.
5) Shear connectors must be designed to eliminate thermal reduction of the panel through the thermal bridges.
6) No concrete penetrations through the insulation layer should exist.
7) The panels should be designed to withstand the applied loads.

8 CONCLUSION

The advantages of the HPCSPs make them attractive to be used in the building and construction industries recently. The challenge is to optimize the HPCSPs to achieve a high structural efficiency at minimum cost. Considering the limitations of the existing optimization methods, the authors proposed a design optimization procedure for HPCSPs. The multi-objective optimization method found to be the most suitable for HPCSPs allows considering different kind of variables and constraints. The method has several advantages but also some limitations. As costs of building materials vary across regions and countries and are influenced by local costs of energy, labour and material resources. The cost database requires regular updates and new inputs for different regions and countries. Nevertheless, further investigation is needed on the proposed methodology applied to different case studies to investigate its validity and limitations.

REFERENCES

Awad, Z.K., Aravinthan, T., Zhuge, Y. & Gonzalez, F. 2010. Multi-objective design optimization of an innovative fibre composite sandwich panel for civil engineering applications. *Incorporating Sustainable Practice in Mechanics and Structures of Materials*. Fragomeni, Venkatesan, Lam & Setunge (eds.).CRC Press 2010, ISBN: 978-0-415-61657-7, pp. 801–806.

Einea, A., Salmon, D.C., Tadros, M.K. & Culp, T. 1994. A new structurally and thermally efficient precast sandwich panel system. *PCI Journal*, Vol. 39, Issue No. 4, pp. 90–101.

EU. 2010. http://europa.eu/rapid/press-release_MEMO-08-699_en.htm.

Frankl, B., Lucier, G., Rizkalla, S., Blaszak, G. & Harmon, T. 2008. Structural Behavior of Insulated Prestressed Concrete Sandwich Panels Reinforced with FRP Grid; *Fourth International Conference on FRP Composites in Civil Engineering* (CICE2008), 22-24July 2008. Zurich, Switzerland.

Hansen, S. 2012. Economical optimization of building elements for use in design of nearly zero energy buildings, *Proceedings of the 5th IBPC*, Kyoto, Japan, May 28–31, 2012, pp. 749–755.

Kirkpatrick, S. & Gelatt, C. 1983. Optimization by simulated annealing. *Science* 220(4598), pp. 671–680.

Konak, A., Coit, D.W. & Smith, A.E. 2006. Multi-objective optimization using genetic algorithms: *A tutorial. Reliability Engineering & System Safety* 91(9), pp. 992–1007.

Ozbay, E., Gesoglu, M. & Guneyisi, E. 2011. Transport properties based multi-objective mix proportioning optimisation of high performance concretes, *Materials and Structures*, vol. 44, pp. 139–154.

Papanicolaou, C.G. & Triantafillou, T.C. 2002. Minimum cost design of concrete sandwich panels made of HPC faces and PAC core: the case of in-plane loading, *Journal: Structural Concrete*, vol. 3, no. 4, pp. 167–181.

Paya, I., Yepes, V., Gonzalez-Vidosa, F. & Hospitaler, A. 2008. Multiobjective optimization of concrete frames by simulated annealing. *Computer-Aided Civil and Infrastructure Engineering* 23(8):596–610.

Petras, A. 1998. Design of Sandwich Structures, *Ph.D. thesis*. Cambridge University Engineering Department.

Rizkalla, S.H., Hassan, T.K. & Lucier, G. 2009. FRP Shear Transfer Mechanism for Precast, Prestressed Concrete Sandwich Load-Bearing Panels, *Special Publication*, Vol. 265, pp. 603–625.

Rougeron, P. & Aïtcin, P.-C. 1994. Optimization of the composition of a high-performance concrete. *ASTM Journal of Cement, Concrete and Aggregates*, Vol. 16, No. 2, pp. 115–124.

Salmon, D.C., Einea, A., Tadros, M.K. & Culp T.D. 1997. Full scale testing of precast concrete sandwich panels, *ACI Structural Journal*, Vol. 94, No. 4, pp. 354–362.

Soriano, J. & Rizkalla, S. 2013. Use of FRP Grid for the Composite Action of Concrete Sandwich Panels, Submitted to *FRPRCS11 – 11th International Symposium on Fiber Reinforced Polymer for Reinforced Concrete Structures*, June 26–28, 2013, Guimarães.

Wade, T.G., Porter, M.L., & Jacobs, D.R. 1998. Glass-Fiber Composite Connectors for Insulated Concrete Sandwich Walls. *Report*, Engineering Research Institute, Iowa State University, Ames, IA.

Research and Applications in Structural Engineering, Mechanics and Computation – Zingoni (Ed.)
© 2013 Taylor & Francis Group, London, ISBN 978-1-138-00061-2

Quality control of UHPC by using non-destructive ultrasonic testing methods

Bernhard Middendorf
University Kassel, Department of Construction Materials and Building Chemistry, Germany

André Glaubitt
TU Dortmund University, Department of Building Materials, Germany

ABSTRACT: UHPC has a very dense micro structure, which possesses high compressive strength and deformation resistance. It has an excellent load capacity, as well as a high resistance to the penetration of liquids and gases. Such high performance building materials inevitably require efficient and reliable test and quality control procedures, because the high loaded cross sections are not suitable for destructive investigation. The non-destructive ultrasonic testing method is very well suited to the investigation of UHPC, because of its fine grained components and its homogeneous structure. Due to this, ultrasonic frequency ranges >1 MHz can be used. Using highly frequent probes results in a much higher resolution, and therefore a higher reliability of examinations and quality control of UHPC. On different UHPC samples it could be shown that the ultrasonic inspection can be used efficiently to detect structural changes within the framework of quality control or material research.

1 INTRODUCTION

The method of high-frequency ultrasonic testing of homogeneous materials such as steel or ceramics is nationally and internationally acknowledged and specified in various standards.

Meanwhile, ultrasonic testing has become standard in quality control of conventional concrete. However, testing frequencies (kHz-range) are by far lower than for example for steel or ceramics (MHz-range). Due to the small aggregate used for UHPC (1/5 to 1/20 of the grain diameter of normal concrete), it can be scanned with high frequencies in the MHz-range, this increases the resolution of the received signals which then causes a high reliability of the tests.

2 ULTRASONIC INSPECTION OF UHPC SAMPLES

In the following, results from measurements on UHPC samples-beams in bending, cylinders and laboratory prisms- are presented, in order to show the possibilities for a qualitative evaluation of UHPC by ultrasonic inspections which can be carried out quickly and non-destructively.

2.1 *Ultrasonic inspection for quality control of a UHPC beam in bending*

For these inspections, two differently composed and fabricated steel fiber reinforced UHPC beams in bending ($15 \times 15 \times 70\,cm^3$) were inspected with regards to their structural formation using non-destructive ultrasonic measurements. One of the beams in bending was made of a UHPC laboratory mixture (referred as LAB), the other was made of an industrially created mixture from a UHPC producing company, which will be referred as IND.

An ultrasonic procedure was used, in which transmitting and receiving probes are located at opposite positions of the scanned beam in bending. The beams in bending were fitted with a 2 cm spacing grid for the measurements and scanned with longitudinal wave probes (rated frequency 2.25 MHz). The measurement results were processed with the Hilbert transformation (Poularikas 1999) and generating the envelopes. The determination of the run time of the ultrasonic impulses is then done using the difference of the maximal peaks of the sending and receiving impulse under the consideration of the preliminary leadtimes of the probes. From the run time and the known thickness of the beams in bending, the longitudinal wave velocity was calculated and graphed (Fig. 1 and 2). Additionally, the beams in bending were scanned over their entire length (0.7 m) with the above mentioned probes. Based on the broad frequency bandwidth of the selected probes, receiving impulses up to 1 MHz with a significant onset could be detected on a measurement of this size.

A significantly lower longitudinal wave velocity v_p (by 4600 m/s) can be seen in the results from the LAB beam in bending in the margin than in the rest of the beam (4800–4900 m/s) (Fig. 1). These differences are

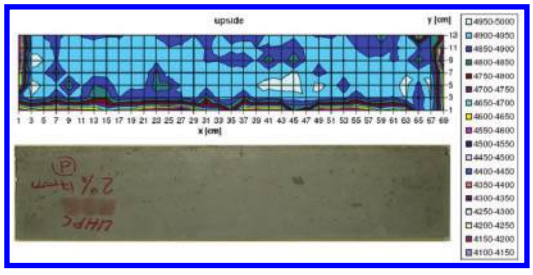


Figure 1. Longitudinal wave velocity v_p [m/s]; UHPC beam in bending LAB.

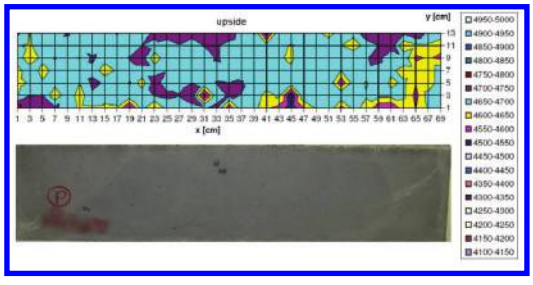


Figure 2. Longitudinal wave velocity v_p [m/s]; UHPC beam in bending IND.

Table 1. Wave velocity v_p and standard deviation of the inspected beams in bending LAB and IND.

Longitudinal wave velocity		LAB	IND
Median	m/s	4847	4668
Standard Deviation	m/s	130	42

a result of the structural inhomogeneities of UHPC, which can be traced back to non-uniform compaction of the beam in bending. Geometry effects, which sometimes can influence the measured ultrasonic signal, are not the cause of the deviations in the wave velocity in the margin, because then similar measurements would have to have been made on the IND beam in bending (Fig. 2).

The IND beam in bending showed a more homogenous structure than the LAB beam in bending with respect to the wave velocity (Fig. 2), though fluctuations of v_p were also present.

Looking at the obtained measurements (Table 1), one can clearly see based on the given standard deviation, that the LAB beam in bending shows a significantly higher structural inhomogeneity (see also Fig. 1 and Fig. 2).

Due to the high inhomogeneity of the LAB beam's UHPC, it was sawn at different positions, in order to inspect the apparent structure. Figures 3 and 4 show regions from the center of the beam (vertical section at $l = 35$ cm). The partial range in figure 3 shows the middle region with a comparably low porosity. In figure 4 a higher porosity can be detected, here the lower corner region of the beam is displayed at $l = 35$ cm.

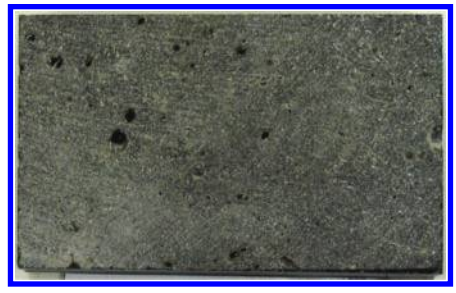


Figure 3. sample middle region (beam in bending LAB at $l = 35$ cm); picture width approx. 4 cm.

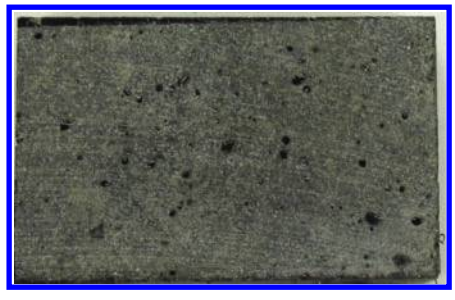


Figure 4. sample corner region (beam in bending LAB at $l = 35$ cm); picture width approx. 4 cm.

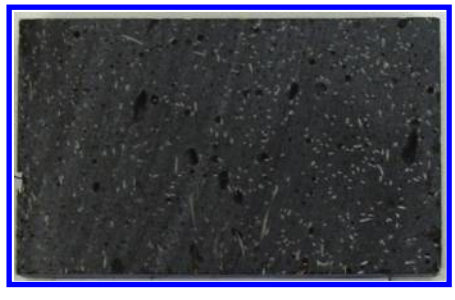


Figure 5. sample middle region (beam in bending LAB at $l = 0$ cm to 3 cm); picture width approx. 4 cm.

Observing the ultrasonic run time at this vertical section ($l = 35$ cm) in figure 1, it can be recognized that the deviation of the running time in the lower region is not as high as in the other boundary areas of the beam. Therefore, samples from the regions $l = 0$ to 3 cm and $l = 67$ to 70 cm were taken, which show significantly higher deviations in the ultrasonic run time. These samples are presented in figures 5 and 6 and hold a considerably higher amount of larger pores.

2.2 *Ultrasonic Inspection for Quality Control in Materials Research on Two Constricted Cylinders*

The ultrasonic run time measurement is well suited for, among other things, determining the dynamic elastic constants E_{dyn} and μ_{dyn} (see Eq. (1) and (2)). The elastic constants determined in this manner can be

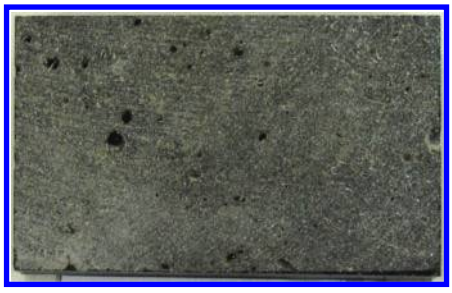


Figure 6. sample middle region (beam in bending LAB at l = 67 cm to 70 cm); picture width approx. 4 cm.

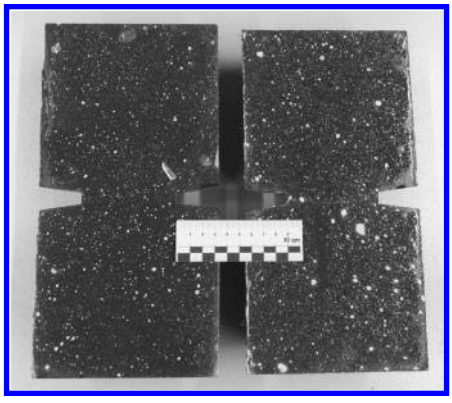


Figure 7. Photographic documentation of the structure of the inspected cylinders; left: without fibers, right: with fibers. The light specks in the UHPC are pores.

used both in quality assurance as well as in materials research and development, in order to, for example, show chronological (strength development) or local (workmanship) material changes (Facaoaru & Stamate 1968, Hennike & Leers 1965, Jones 1950, Kaplan 1959, Manns 1969, Morscichin 1969, Neisecke 1974, Rentsch & Krompholz 1963). By determining v_p, v_s and the bulk density, it is also possible to calculate the dynamic elastic constants E_{dyn} and μ_{dyn} for a material (Glaubitt et al. 2003, Lacouture et al. 2003). Therefore, not only the wave velocity, but also the physical properties of a material are taken into account for an evaluation (Beutel et al. 2008, Glaubitt et al. 2007).

Two constricted UHPC cylinders (Ø 15, 8, 15 cm, l approx. 30 cm, CYL1 und CYL2) were available for inspection (Fig. 7). Their recipes were identical, but one probe was additionally reinforced with 1.5 mass % steel fibers (lf/df = 9 mm / 0.15 mm). The cylinders were scanned with longitudinal wave probes (rated frequency 2.25 MHz) and transversal wave probe arrays (rated frequency 55 kHz) and the corresponding wave velocity v_p und v_s was calculated using the run times.

In the cylinder without steel fiber reinforcement (CYL1) $v_p = 4890$ m/s ($\sigma = 4$ m/s) and transversal wave velocity $v_s = 3183$ m/s ($\sigma = 2$ m/s) were measured. By adding steel fibers, the overall velocity of the longitudinal wave impulses in the cylinder with steel fibers should have increased, due to the higher wave velocity in steel ($v_p = 5900$ m/s, $v_s = 3230$ m/s) (Washer et al. 2003, Washer et al. 2004). However, this is not the case in the inspected cylinder (CYL2) ($v_p = 4870$ m/s ($\sigma = 26$ m/s) and $v_s = 3193$ m/s ($\sigma = 3$ m/s)). Because the median of v_p for the steel reinforced cylinder lies below the median of v_p for the non-reinforced cylinder, this indicates different material properties of the concrete used.

Table 2. Wave velocity and material figures, cylinder 1 without fibers and cylinder 2 with fibers.

Velocity and Material Figures		CYL1	CYL2
Longitudinal wave velocity	m/s	4890	4668
Transversal wave velocity	m/s	3183	3193
Bulk density	g/cm^3	2.26	2.31
Dyn. modulus of elasticity	N/mm^2	51,860	52,900
Dyn. Poisson's ratio	-	0.13	0.12

For the purpose of ocular assessment of the inspected UHPCs, the cylinders were sawed through along the ultrasonic measurement range (Fig. 7). The cylinder with steel fibers shows a significantly higher porosity – mostly air and compaction pores – than the non-reinforced cylinder. A direct comparison of the mechanical properties with respect to the influence of the steel fibers is not possible at this point, because the cylinders, despite having the same composition, could not be compared on the same terms.

$$v_s = \sqrt{\frac{E}{\rho} \cdot \frac{1}{2(1+\mu)}} \tag{1}$$

$$v_p = \sqrt{\frac{E}{\rho} \cdot \frac{(1-\mu)}{(1+\mu)(1-2\mu)}} \tag{2}$$

The material figures calculated in this manner for both cylinders are presented in Table 2.

The density of cylinder 2 is, due to the steel fibers (1.5 mass %) – despite a higher porosity (see Fig. 7) – larger than in cylinder 1. As expected, the dynamic modulus of elasticity of the steel fiber reinforced cylinder is higher than of the non-reinforced cylinder. Based on the porosity, CYL2 has a lower dynamic Poisson's ratio than CYL1. The dynamic elastic constants are in the range of statically determined values for UHPC ($E \approx 50{,}000$ N/mm^2, $\mu \approx 0.16$–0.24 (Fehling et al. 2005). Dynamically determined constants are larger than the statically determined constants (secant model) due to determining them in the purely elastic state of stress of the material (tangents in the coordinate origin). Therefore, E_{dyn} and μ_{dyn} of these two cylinders are rated as being low.

2.3 *Ultrasonic Inspection for Determination of Steel fiber Distribution*

Another possibility to use high frequency ultrasonic measurements on UHPC test samples, is



Figure 8. Photographic documentation of the inspected part of the steel fiber reinforced UHPC prism with scan areas for ultrasonic measurements.

an approximated determination of the fiber distribution in the UHPC matrix. For this, a part of a steel reinforced prism (see Fig. 8) with the dimensions $4.0 \times 4.0 \times 5.7\,cm^3$ was ultrasonically scanned laminary in different directions. This UHPC prism was reinforced with 1.5 mass % steel fibers (lf/df = 13.0 mm/0.19 mm). The same ultrasonic procedure as for the beams in bending was used. Therefore transmitting and receiving probes are located at opposite positions of the scanned part of the prism. The opposite sites (here areas of $4.0 \times 4.0\,cm^2$) were fitted with a 1 cm spacing grid for the measurements and scanned with longitudinal wave probes (rated frequency 2.25 MHz).

The measurements were taken in the longitudinal direction of the prism (l = 5.7 cm) and in lateral direction (l = 4.0 cm), from one side to another as well as from the bottom to the top side. The calculated longitudinal wave velocity was graphed (Fig. 9) and compared to a Microtomography (μ-CT) picture of the prism. In the μ-CT picture the cement matrix was removed by using image analyzing software so the only visible parts are the steel fibers. The here presented scan was taken of 2000 measurements with a voxel resolution of 32.4 μ m.

The first direction of the ultrasonic measurements was parallel to the direct-axis of the prism. In figure 9 it is obvious that the ultrasonic velocities determined correspond to the density of the steel fibers. In the boundary regions higher velocities than in the core of the prism were measured (see upper part of figure 9). This can be explained by the higher content of steel fibers in the boundary regions which can also be seen in the μ-CT picture.

Furthermore, the prism was scanned along the cross axis. Figure 10 graphically presents the ultrasonic scan from the formed side wall to the opposite formed side wall (cross axis 1). Here also, the higher ultrasonic

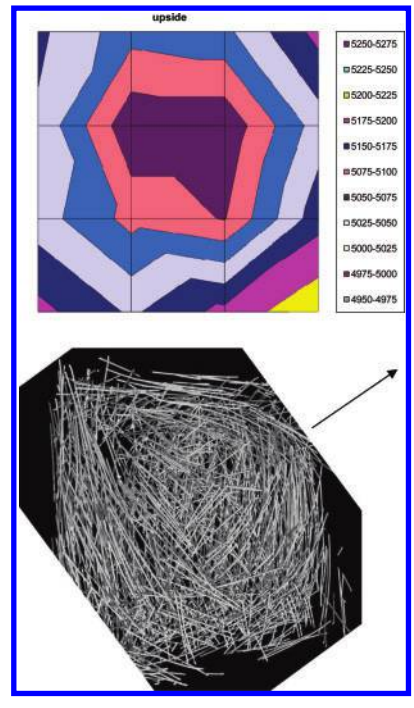


Figure 9. top: Longitudinal wave velocity v_p [m/s] of prism (direct-axis); bottom: μ-CT picture of the steel fibers of prism (arrow: measuring direction).

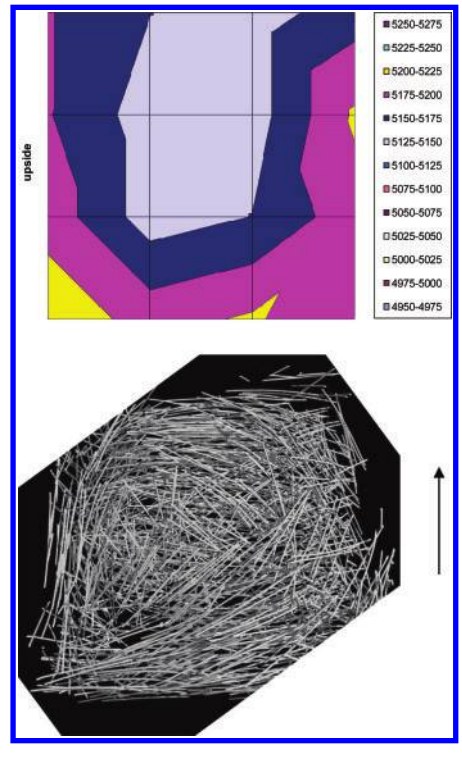


Figure 10. top: Longitudinal wave velocity v_p [m/s] of prism (cross axis 1); bottom: μ-CT picture of the steel fibers of prism (arrow: measuring direction).

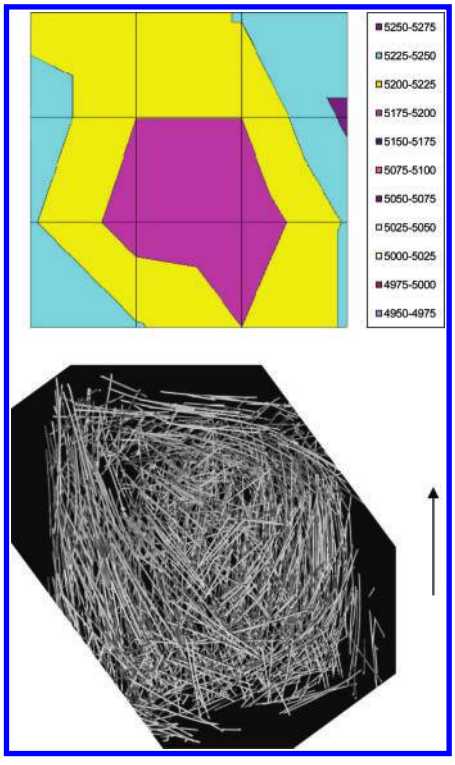


Figure 11. top: Longitudinal wave velocity v_p [m/s] of prism (cross axis 2); bottom: μ-CT picture of the steel fibers of prism (arrow: measuring direction).

velocities in the boundaries due to the higher content of steel fibers become significantly obvious.

A further ultrasonic scan was conducted along the axis from the formed bottom side to the top side (cross axis 2). These results can also be seen in figure 11. Again, the higher fiber content in the boundary regions reflects in higher sonic velocities. These are higher (Ø $v_p = 5217$ m/s) than those of the cross axis 1 scan (Ø $v_p = 5171$ m/s). This can be traced back to the alignment of the steel fibers, which increasingly adjust in the direction of the sound propagation (cf. figure 11 below, right and left area). This is being confirmed by the fact that the sonic velocities in the direction of the longitudinal axis are lower (Ø $v_p = 5135$ m/s), because there are less fibers existing parallel to the sound propagation.

In figure 12 a 2D scan taken by μ-CT is presented. It could be easily seen that the fibers are orientated parallel the sectional plane.

3 ASSESSING THE INSPECTIONS

The results presented here show, on the one hand, that the quality of UHPCs can be quantified using ultrasonic measurements. On the other hand, the results show the need for a qualitative assessment of UHPC samples using quickly executable, non-destructive

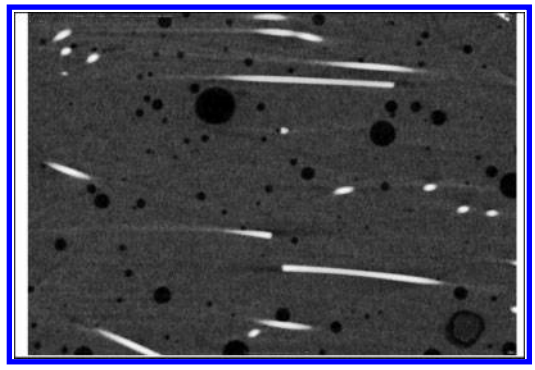


Figure 12. μ-CT picture of a part of prism (voxel resolution 55 μm), picture width approx. 15 mm.

ultrasonic measurements. It is apparent, that quality assurance of UHPC components is absolutely necessary. Both in material research of UHPC as well as in the later production of prefabricated UHPC parts, this quality assurance using ultrasonic inspection can be performed, but in its current state, it does not have the standard to be the only method of inspection for UHPC.

REFERENCES

Beutel, R. & Reinhardt, H.-W. & Grosse, C. U.& Glaubitt, A. & Krause, M. & Maierhofer, C. & Algernon, D. & Wiggenhauser, H. & Schickert, M. 2008. Comparative Performance Tests and Validation of NDT Methods for Concrete Testing. *Journal of Nondestructive Evaluation* 27 (1-3) : 59–65, Netherlands: Springer, ISSN 0195-9298 (Print) 1573-4862 (Online).

Facaoaru, I. & Stamate, G. 1968. On the Relation between some Static and Dynamic Constants of Concrete. In *Report for RILEM Working Group for NDT-Meeting*, Varna.

Fehling, E. & Schmidt, M. & Teichmann, T. & Bunje, K. & Bornemann, R. & Middendorf, B. 2005. Entwicklung, Dauerhaftigkeit und Berechnung Ultrahochfester Betone (UHPC) - Forschungsbericht DFG FE 497/1-1. Schriftenreihe edition *Baustoffe und Massivbau* 1. Kassel: Kassel university press GmbH.

Glaubitt, A. & Bussat, S. & Neisecke, J. 2003. Reference concrete for ultrasonic-testing and its creation by components with pre-analysed properties. *Proc. intern. symp., Non Destructive Testing in Civil Engineering (NDT-CE), Berlin, September 2003*, DGZfP, CD-ROM ISBN 3-931381-49-8.

Glaubitt, A. & Middendorf, B. & Neisecke, J. 2007. Ausbreitungsverhalten von Ultraschall in Referenzprobekörpern aus Beton. *Abschlusskolloquium DFG-Forschergruppe FOR 384, Moderne ZfP bei der Bauwerkserhaltung, Bergisch Gladbach, May 2007*.

Hennicke, H.W.& Leers, K.-J. 1965. Die Bestimmung elastischer Konstanten mit dynamischen Methoden. *Tonindustrie-Zeitung* 89 (23/24): 538–543.

Jones, R. 1950. The Elasticity and Rupture of Concrete and Stone at Constant Rates of Loading. *Nature* 165 (4184): 49

Kaplan, M.F. 1959. Ultrasonic Pulse Velocity, Dynamic Modulus of Elasticity, Poisson's Ratio and the Strength of

Concrete made with thirteen Different Coarse Aggregates. *RILEM-Bulletin* (1): 58–73.

Lacouture, J.-Ch. & Johnson, P. A. & Cohen-Tenoudji, F. 2003. Study of critical behavior in concrete during curing by application of dynamic linear and nonlinear means. *J. Acoust. Soc. Am*. 113 (3): 1325–1332.

Manns, W. 1969. *Über den Einfluss der elastischen Eigenschaften von Zementstein und Zuschlag auf die elastischen Eigenschaften von Beton.* Dissertation. RWTH Aachen.

Morscichin, W.N. 1969. Bestimmung des Elastizitätsmoduls von Beton mit der Schallimpulsmethode. *Zerstörungsfreie Prüf- und Meßtechnik für Beton und Stahlbeton*: Proc., Leipzig, 23-2 April1969: 45.

Neisecke, J. 1974. *Ein dreiparametriges, komplexes Ultraschall-Prüfverfahren für die zerstörungsfreie Materialprüfung im Bauwesen*. Dissertation. TU-Braunschweig.

Poularikas, A. D. 1999. The Hilbert Transform. In *The Handbook of Formulas and Tables for Signal Processing*. Boca Raton: CRC Press LLC Chapter 15.

Rentsch, W. & Krompholz, G. 1963. Die Bestimmung der Poisson'schen Zahl durch Schallgeschwindigkeitsmessungen. *Wissenschaftliche Zeitschrift der Hochschule für Bauwesen Leipzig* 9:177–181.

Washer, G. & Fuchs, P. & Graybeal, B. A. 2003. Elastic Properties of Reactive Powder Concrete. *Proc. intern. symp., Non Destructive Testing in Civil Engineering (NDT-CE), Berlin, September 2003*, DGZfP, CD-ROM ISBN 3-931381-49-8.

Washer, G. & Fuchs, P. & Graybeal, B. A. & Hartmann, J. L. 2004. Ultrasonic Testing of Reactive Powder Concrete. *IEEE Transactions on Ultrasonic, Ferroelectrics, and Frequency Control* 51 (2): 193–201.

Research and Applications in Structural Engineering, Mechanics and Computation – Zingoni (Ed.)
© 2013 Taylor & Francis Group, London, ISBN 978-1-138-00061-2

Statistical model for compressive strength prediction of high-performance concrete

A. Kapelko
Wrocĺaw University of Technology, Institute of Building Engineering, Wrocław, Poland

M. Kapelko
Wrocław University of Economics, Institute of Applied Mathematics, Department of Logistics, Wrocław, Poland

R. Kapelko
Wrocław University of Technology, Institute of Mathematics and Computer Science, Wrocław, Poland

ABSTRACT: Compressive strength is one of the most important mechanical properties of hardened concrete. In this paper we address the issue of compressive strength for high-performance concrete. High-performance concrete is a specially designed concrete with one or more characteristics, which are enhanced through the selection of component materials and mix proportions. This study proposes a statistical model to predict the compressive strength of high-performance concrete using the experimental data which control for the type of cement applied. The compressive strength of concrete is modelled as a function of water-to-cement ratio (W/C), compressive strength of cement, quantity of superplasticizer, grit basalt, silica fume and sand, and age of concrete. The coefficients of models are found with the use of Mathematica 5.0 program. The obtained explicit formulas are of great importance in building practice.

1 INTRODUCTION

High-performance concrete can be defined as a low water/cement concrete which receives an adequate water curing (Aïtcin, 2003). High-performance concrete was initially known as high-strength concrete to emphasize its high strength characteristic. Lately, however, it was coined as high-performance concrete because it was found to be much more than just stronger (Aïtcin, 2003, 2000). Compared to ordinary concrete, high-performance concrete has extraordinary rheological properties, especially its superworkability and flowability, which makes it superior to other concrete mixes (Zain et al., 1999). Other desirable properties of high performance concrete include: a high modulus of elasticity, high density, low permeability and resistance to some forms of attack (Neville & Aïtcin, 1998). The European Standard EN 206-1:2000 classifies the high-performance concrete as concrete with compressive strength greater than 60 MPa at 28 days. American Concrete Institute (ACI) defines the high-performance concrete as a specially designed concrete with one or more characteristics which are enhanced through the selection of component materials and mix proportions. These properties include high workability, very-high early compressive strength, high toughness and high durability to exposure conditions. High-performance concrete can be made with cement alone as a binder or any combination of cement and mineral components, such as blast furnace slag, fly ash, silica fume, metakaolin, rice husk ash, and fillers, such as limestone powder (Aïtcin, 2003).

High-performance concrete is nowadays more frequently applied in the building practice and it has become an active area of research. A number of studies analyzed its development, properties, compressive and tensile strength, durability and other characteristics. Despite the growing interest in high-performance concrete in research and practice, additional information is still needed in order to exploit in full its unique characteristics.

In particular, modelling the compressive strength of high-performance concrete is an important issue in the building practice as strength is a primary factor in selecting a concrete for a particular application. The compressive strength is regarded as one of the most important properties in concrete mixture design and quality control. In the case of high-performance concrete the development of compressive strength is especially complex in nature, which makes the prediction difficult to undertake. The compressive strength of high performance concrete has been modelled in some research papers. Some recent studies in the subject indicated that compressive strength of high-performance concrete is determined not only by the water-to-cement ratio (W/C), but is also influenced by the content of other concrete ingredients (Kapelko et al. 2010; Zain & Abd, 2009; Popovics & Ujhelyi, 2008). With many different factors used to explain

compressive strength of high performance concrete, however, no previous study has accounted for the impact of compressive strength of cement. In addition, most of attempts for compressive strength prediction are undertaken using neural networks.

Against this background, this paper extends previous research that was predicting the compressive strength of high performance concrete, in particular we extend the work of Kapelko et al. (2010). Our objective is to establish a statistical model for the prediction of compressive strength of high-performance concrete based on the experimental data. To attain this aim, the compressive strength of cement, W/C ratio, age and some variables which represent components' structure of concrete mixtures are included in the modified multiple lineal regressions. In order to disentangle the impact of type of cement used in concrete mixtures, our regressions control for this variable.

The rest of this paper is organized as follows. The factors explaining compressive strength of concrete are presented in the next section. This is followed by the description of experimental procedure. The next section summarizes and discusses the results of compressive strength tests and statistical modelling. Final section offers concluding comments and some potential future extension of present work.

2 FACTORS AFFECTING COMPRESSIVE STRENGTH OF HIGH PERFORMANCE CONCRETE

Abrams' exponential mathematical model is an equation relating compressive strength of concrete with water-to-cement ratio at a particular age of concrete testing (Abrams, 1918). The generally accepted rule is that an increase in the W/C decreases the concrete strength, whereas a decrease in the W/C ratio increases the strength. The implication, therefore, is that the compressive strengths of various concretes are identical as long as their W/C ratios remain the same, regardless of other variables.

In subsequent studies the Abrams' model was generalized for any age of concrete and applied for the prediction of concrete strength. In particular, De Tango (2000) confirms the validity of such models to high-performance concrete with silica fume. Popovics & Ujhelyi (2008) in the context of ordinary concrete propose to improve this formula with the second independent variable, such as the cement content or water content or paste content, etc. Following, the models were extended to include more variables, analyzed by multiple regression or neural networks (Kapelko et al. 2010; Peng et al., 2010; Zain & Abd, 2009; Öztas et al., 2006; Ni & Wang, 2000; Yeh, 1998).

The basic concept of model proposed in this paper is to produce a reliable relationship between compressive strength of high performance concrete, and compressive strength of cement, W/C ratio, age and some variables which define concrete's components. To differentiate from previous studies, we include compressive strength of cement as explanatory variable and we use a modified multiple lineal regression, where age is modelled as a natural logarithm. Some authors found that compressive strength of concrete versus time increases very slowly and it is well represented by a logarithmic function of time (Kapelko, 2004; Kearsley & Wainwright, 2001; Yeh, 1998). In particular, Kapelko (2004) analyzes the relationship between compressive strength and hardening time of high-performance concrete observed during a very long time (from 3 days until 5 years) and he founds that logarithmic curves are a good approximation of this relation (correlation coefficient ranging from 0.92 to 0.98).

The explanatory factors (independent variables) that we use in this study to predict the compressive strength of high performance concrete (dependent variable) are important from the point of view of technology and previous research. The variables which form a part of our model are following:

1. Water/Cement ratio (W/C)
2. Quantity of silica fume (SF)
3. Quantity of superplasticizer (PC)
4. Quantity of grit basalt 8–16 mm (CA_1)
5. Quantity of grit basalt 5–8 mm (CA_2)
6. Quantity of grit basalt 2–5 mm (CA_3)
7. Quantity of sand 0–2 mm (SA)
8. Age of concrete (t)
9. Compressive strength of cement (RC)

Therefore, the general formula for the model can be written as below:

$$f_c = [a \cdot \ln(t) + b] \cdot (c \cdot \frac{W}{C} + d \cdot PC + e \cdot SF + f \cdot CA_1 + g \cdot CA_2 + h \cdot CA_3 + i \cdot SA + j \cdot RC) \quad (1)$$

where: a, b, c, d, e, f, g, h, i and j are coefficients of explanatory variables.

3 EXPERIMENTAL PROCEDURE

3.1 *Materials and mixture proportions*

Following materials were applied in the experimental work: locally available coarse aggregate, sand, two types of cement: either CEM I 52.5R or CEM III/A 42.5N, silica fume, and polycarboxylate ether based superplasticizer. Tap water was used as mixing water. Superplasticizer was compatible with the cement utilized. Coarse aggregate and sand were experimentally combined in order to obtain an optimum aggregate composition, characterized by maximum compactness and minimum amount of water adsorbed by the aggregate (Kapelko & Kapelko, 2005). Twenty mixtures were cast from the aforementioned components: ten with cement CEM I 52.5R (indicated as concretes C1-C10) and ten with the application of cement CEM III/A 42.5N (concretes C11-C20). The consistency of concrete mixtures according to the slump test (Abrams' cone) was within the range of 30 and 220 mm.

Table 1. Content of concrete mixtures' components (per m^3).

Component	Content, in kg/m^3
CEM I 52.5R (C) or CEM III/A 42.5N (C)	450– 550
Tap water (W)	143–162
Coarse aggregate:	
Grit basalt 8–16 mm (CA_1)	535–570
Grit basalt 5–8 mm (CA_2)	468–652
Grit basalt 2–5 mm (CA_3)	201–659
Sand 0–2 mm (SA)	550–627
Silica fume (SF)	19.9–41.2
Superplasticizer (PC)	4.1–22.0

Table 2. Weight compositions of concrete mixtures.

Concrete mixture code	Cement (C)	Water (W)	Silica fume (SF)	Super-plasticizer (PC)
C1, C11	0.90	0.36	0.000	0.009
C2, C12	1.00	0.32	0.000	0.025
C3, C13	1.00	0.32	0.040	0.013
C4, C14	1.10	0.26	0.000	0.030
C5, C15	1.10	0.26	0.000	0.020
C6, C16	1.10	0.26	0.075	0.016
C7, C17	1.10	0.26	0.075	0.030
C8, C18	1.10	0.26	0.075	0.010
C9, C19	1.10	0.26	0.075	0.020
C10, C20	1.10	0.26	0.075	0.040
	Grit basalt 8–16 mm (CA_1)	Grit basalt 5–8 mm (CA_2)	Grit basalt 2–5 mm (CA_3)	Sand 0–2 mm (SA)
C1, C11	0.000	1.464	1.464	1.318
C2, C12	0.000	1.304	1.304	1.174
C3, C13	0.000	1.276	1.276	1.148
C4, C14	0.000	1.153	1.153	1.038
C5, C15	1.036	0.907	0.389	1.140
C6, C16	0.300	1.118	1.118	1.007
C7, C17	0.000	1.111	1.111	1.000
C8, C18	0.995	0.871	0.373	1.095
C9, C19	0.995	0.871	0.373	1.095
C10, C20	0.973	0.851	0.365	1.073

Table 1 shows the content of components per m^3 of concrete mixtures. Table 2 lists the weight proportions of concrete mixtures.

3.2 *Strength testing*

The compressive strength of cement was determined after 2, 7, 28, 56 and 365 days of curing following the European standard EN 196-1:2005.

The compressive strength of high-performance concrete was determined from 150 mm cube specimens

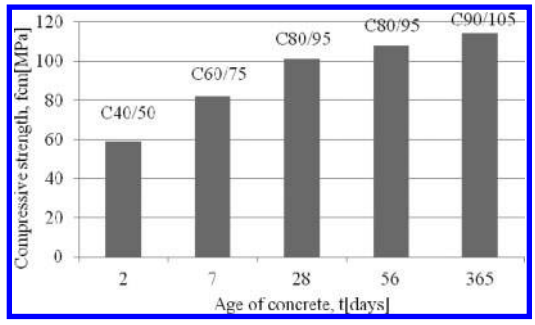


Figure 1. Compressive strength and classes of concrete C2.

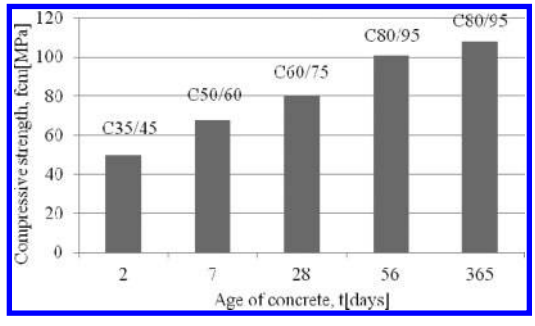


Figure 2. Compressive strength and classes of concrete C3.

and testing was performed after 2, 7, 28, 56 and 365 days of curing. For each of twenty concrete mixtures and time of testing, six specimens were made (hence, in total 600 specimens were prepared). They were cured in a climatic room at a constant temperature of 20° and a relative air humidity of 95% up to the due day of testing.

4 RESULTS AND DISCUSSION

The tests of compressive strength show seven different classes of compressive strength after 2 days of hardening according to the European Standard EN 206-1:2000: C25/30, C30/37, C35/45, C40/50, C45/55, C50/60 and C55/67 and six different classes of concretes after 28 days of hardening: C60/75, C70/85, C80/90, C8/95, C90/105 and C100/115.

The compressive strength results for some examples of concretes (C2, C3, C12 and C13) are illustrated on Figures 1–4.

The figures show that in the initial period of hardening of concretes the compressive strength is higher for concretes prepared with CEM I 52.5R (concretes C2 and C3) as compared to concretes with CEM III/A 42.5N (C12 and C13). On the contrary, for older age of concrete, compressive strength is higher for mixtures prepared with CEM III/A 42.5N. The explanation for this finding is directly connected with the differences in heat releases between these cements (heat release kinetics).

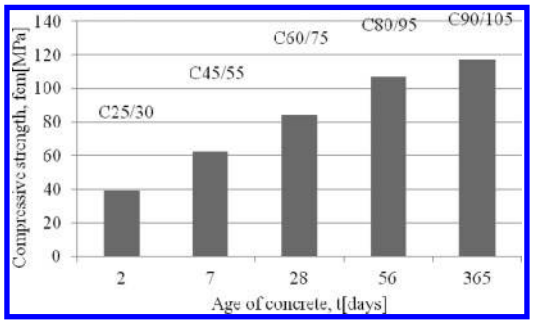


Figure 3. Compressive strength and classes of concrete C12.

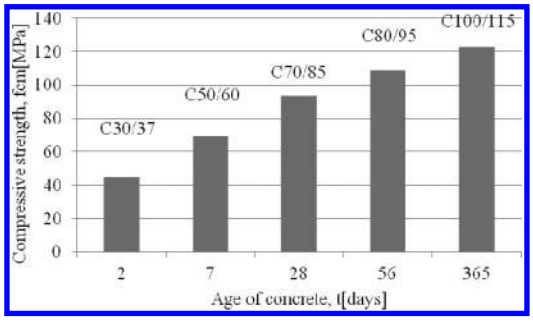


Figure 4. Compressive strength and classes of concrete C13.

Regression models of compressive strength on age, W/C, concrete mixtures' components and compressive strength of cement were developed from the results of tests. These analyses were conducted using the Mathematica 5.0 program. The equations below show the relationship between the compressive strength and all independent variables for the entire sample of concretes and separately for concretes casted with particular types of cements:

a) For all concretes:

$$f_c = [0.42 \cdot \ln(t) + 5.33] \cdot (-21.01 \cdot \frac{W}{C} - 0.18 \cdot PC + 0.05 \cdot SF - 0.80 \cdot CA_1 - 0.36 \cdot CA_2 - 0.80 \cdot CA_3 + 1.31 \cdot SA + 0.12 \cdot RC) \quad (2)$$

b) For concretes prepared with CEM I 52.5R:

$$f_c = [0.06 \cdot \ln(t) + 0.81] \cdot (-128.90 \cdot \frac{W}{C} - 0.89 \cdot PC + 0.35 \cdot SF - 1.59 \cdot CA_1 - 0.65 \cdot CA_2 - 1.60 \cdot CA_3 + 2.65 \cdot SA + 1.04 \cdot RC) \quad (3)$$

c) For concretes prepared with CEM III/A 42.5N:

$$f_c = [0.79 \cdot \ln(t) + 0.58] \cdot (-42.74 \cdot \frac{W}{C} - 0.28 \cdot PC + 0.13 \cdot SF - 2.04 \cdot CA_1 - 0.02 \cdot CA_2 - 2.39 \cdot CA_3 + 2.78 \cdot SA - 0.28 \cdot RC) \quad (4)$$

Table 3. Relationship between compressive strength (f_c) as the function of time (t) and compressive strength of cement (RC).

Concrete code	Equation
C1	$f_c = (0.08 \cdot \ln(t) + 2.34) \cdot (4.04 + 0.61 \cdot RC)$
C11	$f_c = (2.79 \cdot \ln(t) + 0.92) \cdot (14.96 - 0.1 \cdot RC)$
C8	$f_c = (0.31 \cdot \ln(t) + 3.22) \cdot (18.39 - 0.16 \cdot RC)$
C18	$f_c = (0.83 \cdot \ln(t) + 0.66) \cdot (51.68 - 0.32 \cdot RC)$

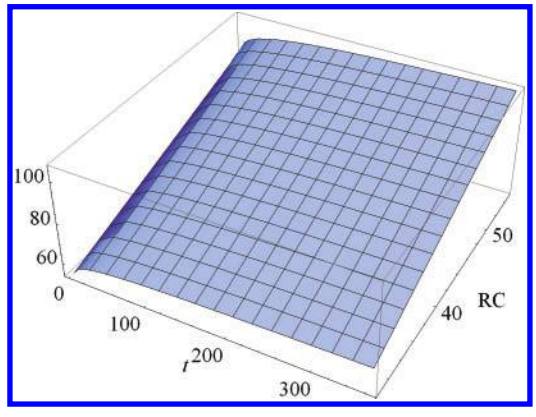


Figure 5. Relationship between compressive strength (f_c) as the function of time (t) and compressive strength of cement (RC) for concrete C1.

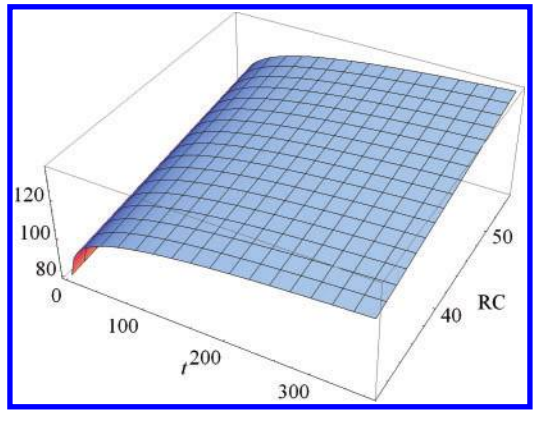


Figure 6. Relationship between compressive strength (f_c) as the function of time (t) and compressive strength of cement (RC) for concrete C11.

All equations confirm the Abrams' law that is the negative influence of W/C on the compressive strength of concrete. Also, W/C has the biggest impact as compared to other variables as shown by the coefficient that ranges between −128.90 and −21.01. Also, W/C has the biggest negative influence for concretes prepared with CEM I 52.5R. Interestingly, we find the differences in the impact of compressive strength of

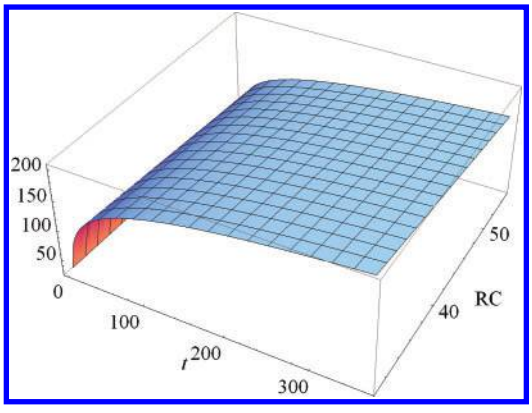


Figure 7. Relationship between compressive strength (f_c) as the function of time (t) and compressive strength of cement (RC) for concrete C8.

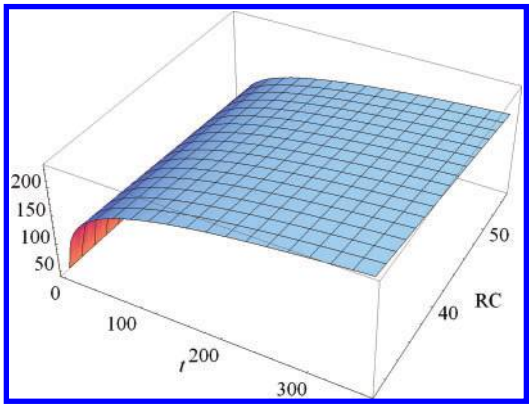


Figure 8. Relationship between compressive strength (f_c) as the function of time (t) and compressive strength of cement (RC) for concrete C18.

cement on compressive strength of concrete as positive association is found for concretes prepared with addition of CEM I 52.5R and negative, although not very substantial, for concretes with CEM III/A 42.5N.

For four exemplary concretes we obtained also the relationship between compressive strength as a function of time and compressive strength of cement (RC). The obtained formula is expressed in a form ($f_c = (\mathrm{A}\ln(t) + \mathrm{B}) \cdot (\mathrm{C} + \mathrm{D} \cdot RC)$), where: A, B, C and D are coefficients of explanatory variables (Table 3).

The figures below illustrate mathematical formulas relating compressive strength as the function of time with compressive strength of cement.

5 CONCLUSIONS

The objective of this study was to develop a statistical model to predict the compressive strength of high-performance concrete, based on the data obtained in experiments. Our model extended the Abram's law by including not only W/C ratio, but also other factors and components of concrete which influence compressive strength of concrete. To differentiate from previous research we applied a modified multiple lineal regression model, where the relationship between compressive strength and time is modelled as a natural logarithm. Also, we included the compressive strength of cement as an explanatory variable, while controlling for the type of cement used to cast concrete mixtures.

In this study we obtained several formulas which can explain the essence of strength models, linking compressive strength of concrete with compressive strength of cement, W/C ratio, age of concrete and several concrete's component characteristics. These explicit formulas are of great importance in building practice. The proposed models provide the practical opportunity to predict the compressive strength as the function of time under existing concrete's components conditions and compressive strength of cement. The models will be of value when one designs the high-performance concrete where specific compressive strength under technological demands must be achieved at certain ages.

As a future research we could consider other methods for compressive strength prediction of high performance concrete such as neural networks.

REFERENCES

Abrams, D.A. 1918. Design of concrete mixtures. Bulletin 1, Structural Materials Research Laboratory, Lewis Institute, Chicago.

Aïtcin, P.-C. 1998. *High performance concrete*. London: E & FN SPON.

Aïtcin, P.-C. 2000. Cements of yesterday and today. Concrete of tomorrow. *Cement and Concrete Research* 30: 1349–1359.

Aïtcin, P.-C. 2003. The durability characteristics of high-performance concrete: a review. *Cement and Concrete Research* 25: 409–420.

De Tango, C.E. 2000. Time-generalization of Abrams' model for high performance concrete and practical application examples. *Proceedings of the International Symposium on High Performance Concrete*. Hong Kong University of Science and Technology, Hong Kong, China, December 10–15.

EN 206-1:2000 Concrete – Part 1: Specification, performance, production and conformity. Brussels, 2000.

EN 196-1:2005 Methods of testing cement – Part 1: Determination of strength. Brussels, 2005.

Kapelko, A. 2004. The quality of high performance concretes as a function of their hardening time. *Engineering Transactions* 52(3): 153–174.

Kapelko, A. & Kapelko, R. 2005. Optimization of composite materials with cement-fly ash matrix. *Archives of Civil and Mechanical Engineering* V(2): 25–34.

Kapelko, A., Kapelko, M. & Kapelko, R. 2010. Modeling compressive strength of high-performance concrete with multiple regression, in Alphose Zingoni (ed.), *Advances and Trends in Structural Engineering, Mechanics and Computation*. London: Taylor & Francis Group.

Kearsley, E.P. & Wainwright, P.J. 2001. The effect of high fly ash content on the compressive strength of foamed concrete. *Cement and Concrete Research* 31: 105–112.

Neville, A. & Aïtcin, P.-C. 1998. High performance concrete – an overview. *Materials and Structures* 31: 111–117.

Ni, H.-G. & Wang, J.-Z. (2000). Prediction of compressive strength of concrete by neural networks. *Cement and Concrete Research* 30(8): 1245–1250.

Öztas, A., Pala, M., Özbay, E., Kanca, E., Caglar, N. & Bhatti, M.A. 2006. Predicting the compressive strength and slump of high strength concrete using neural network. *Construction and Building Materials* 20(9): 769–775.

Peng, Ch.-H., Yeh, I.-C. & Lien, L.-Ch. 2010. Building strength models for high-performance concrete at different ages using genetic operation trees, nonlinear regression, and neural networks. *Engineering with Computers* 26: 61–73.

Popovics, S. & Ujhelyi, J. 2008. Contribution to the concrete strength versus water-cement ratio relationship. *Journal of Materials in Civil Engineering* 20(7): 459–463.

Yeh, I.-C. 1998. Modelling of strength of high-performance concrete using artificial neural networks. *Cement and Concrete Research* 28(12): 1797–1808.

Zain, M.F.M. & Abd, S.M. 2009. Multiple regression model for compressive strength prediction of high performance concrete. *Journal of Applied Sciences* 9(1): 155–160.

Zain, M.F.M., Safiuddin, M. & Yusof, K.M. 1999. A study on the properties of freshly mixed high performance concrete. *Cement and Concrete Research* 29: 1427–1432.

Research and Applications in Structural Engineering, Mechanics and Computation – Zingoni (Ed.)
© 2013 Taylor & Francis Group, London, ISBN 978-1-138-00061-2

Experimental tests and analytical modeling of UHPC beams subjected to torsion

E. Fehling, M. Ismail & T. Leutbecher
Institute of Structural Engineering, University of Kassel, Germany

ABSTRACT: Twelve UHPC beams with different combinations of steel fibers, longitudinal and transverse reinforcement were investigated experimentally under pure torsion. Steel fibers having 17 mm length and 0.15 mm diameter with volumetric ratios of 0.5 % and 0.9 % were used. The average compressive strength of the reference UHPC standard cylinders was about 205 MPa. The UHPC beams with steel fibers only showed a ductile behavior. It was found that the addition of either longitudinal or transverse reinforcement to the steel-fiber UHPC beams added much to the ductility and very little to the ultimate capacity. The steel fibers having a volumetric ratio of 0.9 % together with the longitudinal or transverse reinforcement accomplished an effective load carrying mechanism after cracking. Only the case of both longitudinal and transverse reinforcement in addition to steel fibers provided a very high increase both in ultimate torsion capacity and ductility. An analytical model based on the well known ”thin-walled tube” analogy was developed. The comparison between the experimental and analytical results shows very good agreement.

1 INTRODUCTION

Torsion appears in structural elements when the line of action of the shearing force does not coincide with the shear center of the cross section. It appears, for example, in bridges, curved structural elements and spandrel beams in buildings.

Ultra High Performance Concrete (UHPC) is characterized by a very high compressive strength which may reach more than 200 MPa. The behavior of 0 plain UHPC under tension and compression has been established to be very brittle. Discontinuous fibers (normally steel fibers) are usually added to UHPC mix to introduce ductility. Little information is found in the literature about the behavior of this material under torsion.

2 EXPERIMENTAL PROGRAM

The test beam had a square cross section with extra enlarged reinforced ends in order to withstand the concentrated stresses due to load application at these areas and to gradually transfer the stresses to the main tested part of the specimen, see Figure 1.

The cross-sectional dimensions, the length of the test region and the reinforcement details for section A-A are shown in Table 1 for different beams. The parameters studied during the experimental program were: steel fiber volume, the capability of the steel fibers to replace the longitudinal or transverse reinforcement, the effect of combining both traditional

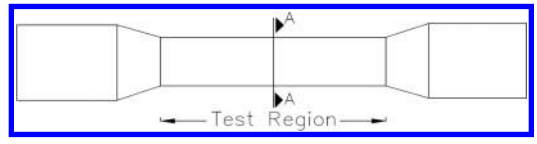


Figure 1. Shape of the test beam.

reinforcement and steel fibers and the wall thickness of the ”thin-walled tube”. The varied steel fiber volumetric ratios were 0.5 % and 0.9 %. The varied wall thickness were 45 and 90 mm. The test setup, the instrumentation and the test procedure can be found in details in (Fehling & Ismail 2012).

3 MATERIALS

A fine-grained (maximum grain size of 0.5 mm) UHPC mix (M3Q) was used. This mix was developed at the University of Kassel and was used as the reference mix in the priority program (Sustainable construction with UHPC, SPP 1182) of the German Research Foundation (Deutsche Forschungsgemeinschaft DFG). It is considered as a further development of the (M2Q) UHPC mix which is described in detail in (Fehling et al. 2005). For all the test beams, the average cylinder compressive strength was about 205 MPa and the average modulus of elasticity was about 49,000 MPa.

BSt 500 reinforcing steel with a yield strength of 550 MPa and an ultimate strength of 630 MPa was used. The steel fibers (F1) had a tensile strength of

Table 1. The Experimental Program.

Group	Cross section (cm)	Test region (cm)	Fiber volume %	Longitudinal reinforcement	Transverse reinforcement	Code	Cross section
1	18*18	170	0.5	–	–	UPF1(0.5)	
	18*18	170	0.9	–	–	UPF1(0.9)	
2	28*28	80	0.5	–	–	UPF1(0.5)28	
	28*28	80	0.9	–	–	UPF1(0.9)28	
3	18*18	170	0.5	4Ø16 mm, 2.48%	–	UL(2.48)F1(0.5)	
	18*18	170	0.9	4Ø16 mm, 2.48%	–	UL(2.48)F1(0.9)	
4	18*18	80	0.5	–	Ø8 mm@45 mm, 1.96%	UT(1.96)F1(0.5)	
	18*18	80	0.9	–	Ø8 mm@45 mm, 1.96%	UT(1.96)F1(0.9)	
5	18*18	95	0.5	4Ø12 mm, 1.4%	Ø8 mm@45 mm, 1.96%	UL(1.4)T(1.96)F1(0.5)	
	18*18	95	0.5	4Ø16 mm, 2.48%	Ø8 mm@45 mm, 1.96%	UL(2.48)T(1.96)F1(0.5)	
	18*18	95	0.5	4Ø16 mm, 2.48%	Ø8 mm@30 mm, 2.94%	UL(2.48)T(2.94)F1(0.5)	
6	18*18	80	0.5	4Ø12 mm, 1.4%	Ø8 mm@45 mm, 1.96%	UL(1.4)T(1.96)F1(0.5)H45	

Legend: U = UHPC, P = Plain concrete, L = Longitudinal reinforcement, T = Transverse reinforcement, F1 = Steel fibers, 28 = 28*28 cm cross section, H45 = 45 mm wall thickness, ( ) = Volumetric ratio.

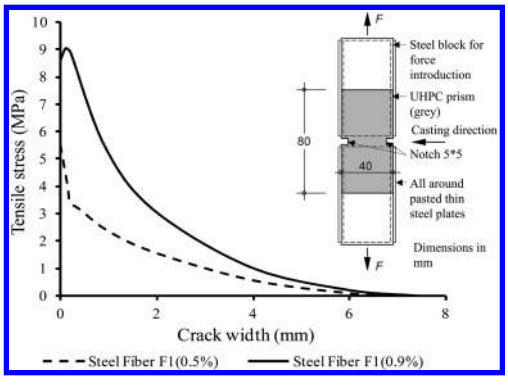


Figure 2. Average axial tensile tests of notched prisms.

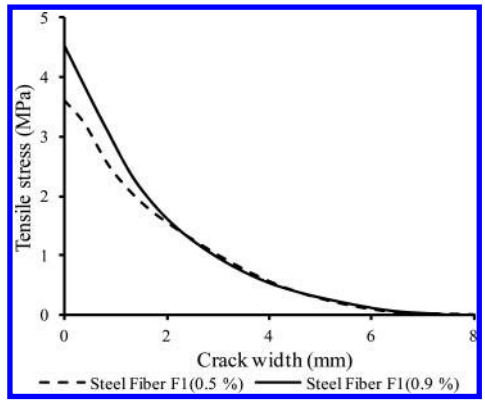


Figure 3. Average axial tensile tests after fiber analysis.

2500 MPa and dimensions of 17 mm in length and 0.15 mm in diameter. To study the behavior of the steel fibers in the hardened UHPC, axial tensile tests of notched UHPC prisms according to (Leutbecher 2008), having steel fiber volumetric ratios of 0.5 % and 0.9 % have been conducted. Figure 2 shows the average stress-crack width diagrams for these tests. However, the distribution and orientation of the steel fibers in the small size prisms may not agree with that in the actual test beams. In order to capture the actual distribution of the steel fibers in the test beams, an optical steel fiber analysis of the tested beams at the failure surfaces according to (Lange 2009) and also tensile tests on prisms cut from the test beams was conducted. According to this analysis, the UHPC with 0.5 % and 0.9 % steel fiber by volume show a softening behavior after cracking as shown (Fig. 3).

4 CASTING AND TREATMENT

The beams were cast in pairs together with the reference test specimens for the compression and tension tests. A mixer with 400 litres capacity was used, where the coarser materials were added first followed by the finer materials. Steel fibers were added to the mix through a sieve to insure that the fibers will not accumulate in bundles in the mix.

The beams were compacted using a vibrating table in order to keep the normal distribution of the fibers within the mix. After casting, the beams were left in the formwork for two days to harden. The forms were then removed and the specimens were heat treated under 90°C for two days.

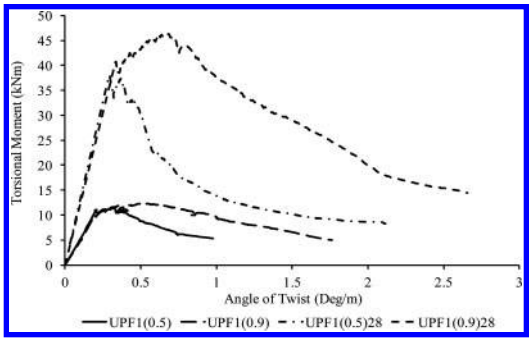


Figure 4. Torsion test results for UHPC beams with steel fibers only.

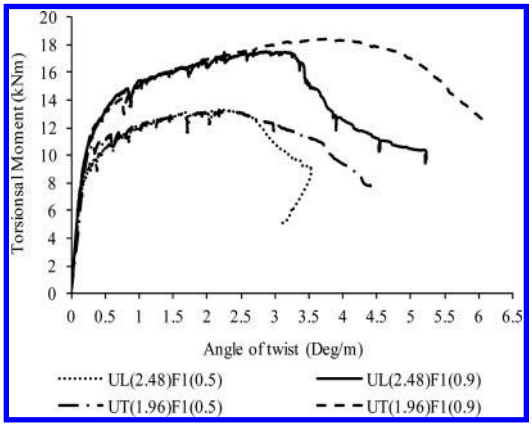


Figure 5. Torsion test results for UHPC beams with steel fibers and either longitudinal or transverse reinforcement.

5 TEST RESULTS

5.1 *UHPC with steel fibers only*

Figure 4 shows the load-deflection diagrams of these beams. After reaching the UHPC tensile strength, few cracks were developed before a localized failure at one crack occurred due to fiber pull-out from the UHPC matrix. As for all the tested beams, the cracks were initiated at the middle of the cross-sectional walls, then propagated inclined to the longitudinal axis of the beam to circulate around the beam walls. The initial cracks were very narrow in widths, where they begun at widths of about 0.03 to 0.05 mm.

Figure 4 shows also that the higher the steel fiber volumetric ratio in the mix, the higher the cracking torsion, the ultimate torsion, the stiffness after cracking and the ductility.

5.2 *UHPC beams with steel fibers and either longitudinal or transverse reinforcement*

This group of beams shows much more ductile behavior than the UHPC beams with steel fibers only (Fig. 5).

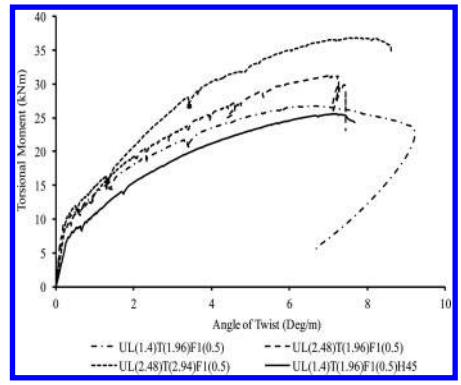


Figure 6. Torsion test results for UHPC beams with steel fibers and both longitudinal and transverse reinforcement.

These beams showed in general intensive cracking before failure. The number of cracks was directly proportional to the volumetric ratios of the steel fibers and the longitudinal reinforcement. The cracks were uniformly distributed along the length of the beams and closely spaced, while those of the UHPC beams with steel fibers only were non-uniformly distributed but rather congested in a cracking zone. This may be attributed to the different load resistance mechanisms of the two types of reinforcements: the pull-out of the steel fibers and the yielding of the reinforcement.

Failure of these beams was initiated by continuous widening of more than one crack, where the final failure was due to yielding of the reinforcement and pull-out of the steel fibers from the UHPC matrix at one crack location.

In comparison with the UHPC beams with steel fibers only, the combination of either longitudinal or transverse reinforcement with low steel fiber content (0.5%) added much to the torsional ductility and very little to the ultimate torsional capacity, however, the steel fiber content of (0.9%) increases the ultimate torsional capacity significantly.

Figure 5 shows also that the beams with the same fiber content but different type and a little bit different volumetric ratio of bar reinforcement have almost the same torsional capacity. Moreover, despite having a little bit less reinforcement ratio, the beams with steel fibers and transverse reinforcement show enhanced ductility in comparison with the other pair of beams. This reveals that the steel fibers have a better ability to perform as a longitudinal reinforcement than as a transverse reinforcement. It could also be argued that the transverse reinforcement in the test beams provides better confinement to the concrete core and hence better ductility. If this is the case, then the steel fibers have the same ability to perform as longitudinal or transverse reinforcement.

5.3 *UHPC beams with steel fibers and both longitudinal and transverse reinforcement*

The increase in the torsional capacity and ductility for the beams in this group was significant (Fig. 6). The



Figure 7. Deformation parallel to the crack direction.

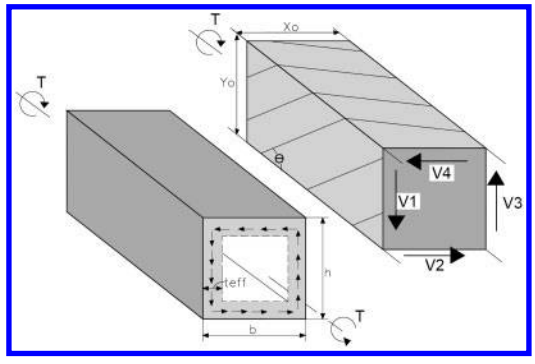


Figure 8. Thin walled tube (left) and Shear forces in the tube walls (right).

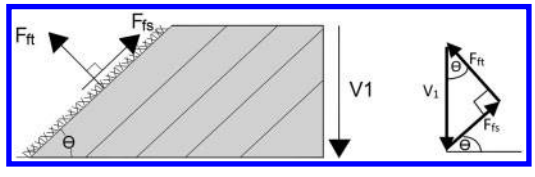


Figure 9. Resolution of the shear force V_1 (left) and Force equilibrium triangle (right).

failure occurred after very intensive cracking. Increasing the steel reinforcement ratio of any type, whether longitudinal or transverse, increases the ductility and post cracking stiffness, but the maximum increase of these factors happened when both the longitudinal and transverse reinforcement were increased.

The torsional capacity of the beam UL(1.4)T(1.96)F1(0.5)H45 is about 96% of that of the beam UL(1.4)T(1.96)F1(0.5), which reveals that the "thin-walled tube" thickness of the reinforced UHPC beams with steel fibers is a little bit larger than the cross sectional area divided by the circumference (in our case 45 mm).

6 ANALYTICAL MODELLING

An analytical model based on the well known thin-walled tube analogy is developed to estimate the torsional moment capacity of reinforced UHPC beams with steel fibers. This analogy considers that after cracking, the torsional resistance exists mainly at the outer shell of the cross section with a specific wall thickness (t_{eff}). Before describing the model and its resistance mechanism, an important aspect about the development of shear cracks will be reviewed.

At the onset of cracking, the shear cracks develop perpendicular to the principal tensile stress direction. Afterwards, the cracks generally do not open perpendicular to their direction (Fig. 7). This is because the reinforced concrete is considered as isotropic material before cracking as the reinforcement practically does not take part in torsion resistance before cracking. After cracking, the matter is different. The reinforced concrete is no longer isotropic and the influence of the reinforcement increases gradually which affects the load bearing behavior of the reinforced concrete. This induces shear stresses parallel to the crack direction. As a result the cracks can transmit shear forces parallel to their direction (Walraven 1980). In reinforced concrete, the resisting components are the dowel action and the aggregate interlock. In the fine aggregate UHPC with steel fibers only, the aggregate interlock can be assumed to be of minor influence, so that we are left with the shearing resistance of the steel fibers.

6.1 *The model resistance mechanism*

An UHPC beam with steel fibers only subjected to torsion is idealized as a thin-walled tube of dimensions b × h with a constant shear stress τ along the perimeter of the cross section (Fig. 8).

In Figure 8, the line of action of the shear flow encloses a gross area of A_k:

$$A_k = X_o \times Y_o = (b - t_{eff}) \times (h - t_{eff}) \quad (1)$$

where $X_o = b - t_{eff}$ and $Y_o = h - t_{eff}$

Figure 8 shows the shear forces V_1 to V_4 induced in the walls of the tube due to torsion. Once the beam has cracked in torsion, its torsional resistance is provided primarily by the tensile and shear stresses in the steel fibers along the cracked walls of the tube. Figure 9 shows the resolution of the shear force V_1 into tensile (F_{ft}) and shear (F_{fs}) forces perpendicular and parallel to the crack direction.

6.2 *Derivation of torsional strength formula*

According to Bredt's Theory, the torsional moment can be given as:

$$T = \frac{V_1}{Y_0} \times 2A_k \quad (2)$$

Table 2. Comparison between the model and the test results (steel fibers only).

Beam	σ_{cf0} (MPa)	Inclination of cracks θ (deg)	T_{ut} (test) (kNm)	T_{n1} (Eq5) (kNm)	T_{n2} (Eq6) (kNm)	T_{n1}/T_{ut}	T_{n2}/T_{ut}
UPF1(0.5)	3.60	47	11.36	11.84	10.42	1.04	0.92
UPF1(0.9)	4.60	47	12.24	15.13	13.32	1.24	1.09
UPF1(0.5)28	3.60	52	38.00	45.80	40.32	1.21	1.06
UPF1(0.9)28	4.60	47	46.32	55.64	48.97	1.20	1.06

From the force equilibrium diagram in Figure 9, V_1 can be given as:

$$V_1 = \frac{\sigma_{cf0} \times A_w}{\cos\theta} \tag{3}$$

where $F_{ft} = \sigma_{cf0} \times A_w$ is the tensile force corresponding to the fiber efficiency σ_{cf0}, σ_{cf0} is the value of the tensile strength of the test prisms after cracking according to Figure 3 and $A_w = t_{eff} \times (h - t_{eff})/\sin\theta$ is the inclined area to which both the tensile and shearing forces are acting.

Substituting Equation (3) into (2), the nominal torsional strength T_n can be written as:

$$T_n = \frac{\sigma_{cf0} \times A_w}{\cos\theta \times (h - t_{eff})} \times 2A_k \tag{4}$$

6.3 *UHPC with steel fibers only*

The Eurocode EC2 (2004) as well as the Model Code 90 (1991) define the "thin-walled tube" wall thickness for reinforced concrete beams as not less than twice the distance between the external face and the line joining the axes of the longitudinal reinforcement. As a first approximation, the two codes allow t_{eff} to be calculated as:

$$t_{eff} = \frac{A_{cp}}{P_{cp}} \tag{5}$$

For the calculation of the cracking torsion T_{cr}, the ACI Building Code (ACI 318-08) defines the effective wall thickness of the tube as:

$$t_{eff} = \frac{0.75 \times A_{cp}}{P_{cp}} \tag{6}$$

where A_{cp} and P_{cp} are the total area and perimeter of the cross section. A comparison between the estimations of the ultimate torsion of the steel fiber UHPC beams using Equations (5) and (6) and the test results is shown in Table 2. Using the definition of the wall thickness in equation (5) results in overestimation of the ultimate torsional capacity in all cases, whereas Equation (6) results in better agreement between the model and test results. It should be noted that the average angle of inclination of the cracks θ was taken from the test results found in (Fehling & Ismail 2012).

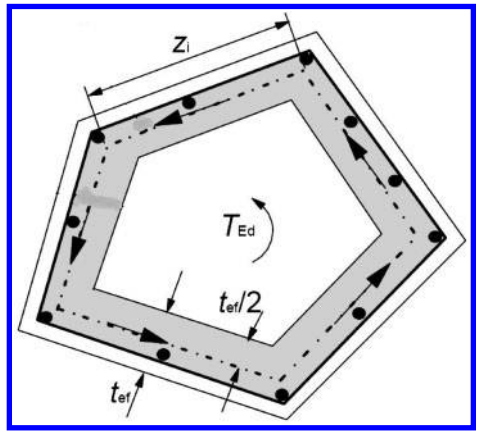


Figure 10. Definition of the centerline of the shear according to the Eurocode 2.

6.4 *UHPC beams with steel fibers and either longitudinal or transverse reinforcement*

To calculate the torsional capacity of UHPC beams with steel fibers and either longitudinal or transverse reinforcement, the only change that is made here is to use the definition of the Eurocode regarding the effective thickness of the tube wall t_{eff} for reinforced concrete elements (Fig. 10), where:

$$t_{eff} = 2\left(S_c + d_t + \frac{d_s}{2}\right) \tag{7}$$

where S_c = concrete cover, d_t = diameter of transverse reinforcement and d_s = diameter of longitudinal reinforcement.

It should be noted that for the beams with steel fibers and transverse reinforcement only, it was strictly adhered to the Eurocode 2 definition of the wall thickness (t_{eff}), such that only for the purpose of calculating t_{eff}, it was assumed as if at every corner of the cross section a longitudinal steel bar of 12 mm diameter exists. For this group of beams, the angle of inclination of the cracks θ was documented at three deformation stages (angles of twist) during the tests, but unfortunately not at failure.

The angle θ at failure was calculated assuming linear extrapolation between the last two documented angles. Table 3 shows good agreement between the model and the test results.

Table 3. Comparison between model and test results (steel fiber, in addition to either longitudinal or transverse reinforcement).

Beam	σ_{cf0} (MPa)	Inclination of cracks θ (deg)	T_{ut} (test) (kNm)	T_n (model) (kNm)	T_n/T_{ut}
UL(2.48)F1(0.5)	3.6	44	13.40	12.44	0.93
UL(2.48)F1(0.9)	4.6	41	17.40	16.04	0.92
UT(1.96)F1(0.5)	3.6	50	13.22	12.62	0.95
UT(1.96)F1(0.9)	4.6	53	18.44	16.16	0.88

Table 4. Comparison between the model and the test results (steel fiber, longitudinal and transverse reinforcement).

Beam	Inclination of cracks θ (deg)	T_f (kNm)	T_t (EC2) (kNm)	T_n (model) (kNm)	T_{ut} (test) (kNm)	T_n/T_{ut}
UL(1.4)T(1.96)F1(0.5)	46	10.42	15.73	26.15	26.72	0.98
UL(2.48)T(1.96)F1(0.5)	41	10.42	19.43	29.85	31.20	0.96
UL(2.48)T(2.94)F1(0.5)	47	10.42	24.85	35.27	32.00	1.10
UL(1.4)T(1.96)F1(0.5)H45	48	10.42	16.48	26.90	25.54	1.05

6.5 *UHPC Beams with steel fibers and both longitudinal and transverse reinforcement*

The assumption here is that the nominal torsional capacity of the beam is composed of two parts, the first is the contribution of the steel fiber (T_f) as calculated in paragraph 6.3 using the ACI code formula for t_{eff}, and the second is the contribution of the space truss model (T_t) as found in the Eurocode 2.

$$T_n = T_f + T_t \tag{8}$$

Table 4 shows very good agreement between the model and test results.

7 CONCLUSIONS

Addition of steel fibers to the plain UHPC beams increased both the cracking and ultimate torsional capacity and provided torsional ductility.

As the steel fiber volumetric ratio in the mix increases, the torsional capacity enhances and the number of cracks increases as well.

The addition of traditional reinforcement (whether longitudinal, transverse or both) to the steel-fiber UHPC results in almost uniformly distributed cracks along the beam, while the UHPC beams with steel fibers only show non-uniform distribution of cracks, such that the cracks were congested in a cracking zone.

The combination of either longitudinal or transverse reinforcement with low steel fiber volume enhanced very much the stiffness after cracking and the ductility but the resulted increase in the ultimate torsion was marginal. The most significant increase of these factors happens only when both the longitudinal and transverse reinforcement increased together.

The steel fibers show almost the same capability to behave as longitudinal or as transverse reinforcement.

The result of the traditionally reinforced hollow UHPC beam with steel fibers reveals that the thickness of the tube wall is a little bit larger than the cross sectional area divides by the circumference.

The developed analytical model shows very good agreement with the test results.

REFERENCES

ACI 318-08: *Building Code Requirements for structural concrete (ACI 318-08) and commentary (ACI 318R-08)*. 1st Printing 2008. American Concrete Institute, Michigan, USA: Farmington Hills.

CEB-FIP Model-Code 1991. *Design Code*. Comite Euro-International du Beton: Bulletin d'information No. 213/214, Lausanne.

Eurocode 2: *Design of concrete structures - Part 1-1: General rules and rules for buildings* (2004-2012). European Committee For Standardization, Brussels

Fehling, E.; Schmidt, M.; Teichmann, T.; Bunje, K.; Bornemann, R. & Middendorf, B. 2005. Entwicklung, Dauerhaftigkeit und Berechnung Ultra-Hochfester Beton (UHPC)", *Research report (DFG FE 497/1-1)*.

Fehling, E & Ismail, M. 2012. Experimental Investigation on UHPC Structural Elements Subject to Pure Torsion. *Proceeding: Third International Symposium on Ultra High Performance Concrete*, Kassel, Germany.

Lange, J. 2009. Mess- und Auswertungstechnik zur Riss- und Faserdetektion bei Betonbauteilen Von der Fakultät für Bauingenieurwesen. *Dissertation*. Technische Hochschule Aachen. Aachen, Germany

Leutbecher, T. 2008. Rissbildung und Zugtragverhalten von mit Fasern und Stabstahl bewehrtem Ultrahochfesten Beton (UHPC), *Structural Materials and Engineering Series No. 9*, kassel university press GmbH, Kassel. Germany.

Walraven, J.C. 1980. Aggregate interlock - A Theoretical and Experimental Analysis. *Doctoral Thesis*, Delft University of Technology. Netherland

Research and Applications in Structural Engineering, Mechanics and Computation – Zingoni (Ed.)
© 2013 Taylor & Francis Group, London, ISBN 978-1-138-00061-2

Compressive strength of high-performance concrete with absorption capacity of Super-Absorbing-Polymers (SAP)

B.J. Olawuyi & W.P. Boshoff
Department of Civil Engineering, Stellenbosch University, Stellenbosch, South Africa

ABSTRACT: This paper reports the absorption capacity of super-absorbent-polymer (SAP) in water and cement pore solution. This was considered for the free water requirement for high-performance concrete containing SAP. The rheology and compressive strength properties of this low water/binder (w/b) concrete are reported. A $2 \times 5 \times 4 \times 3$ factorial experimental arrangement was used for the study. Two sizes of SAP (03/08 μm and 06/12 μm) monomers acrylic acid were tested at different SAP contents (0%; 0.2%; 0,3%; 0.4%; and 0.6% by weight of cement) for concrete mix proportion of 0.25 w/b ratio ($F_{cu28} \geq 80$ MPa target strength).Specimens were also tested at different curing ages namely 3, 7, 21 and 28 days. The results are presented in this paper with a discussion on the influence of water absorbed by SAP at the mixing stage on the compressive strength of the high-performance concrete.

1 INTRODUCTION

1.1 *High performance concrete*

High performance concrete (HPC) is a generic term for all concrete exhibiting properties and constructability which exceeds that of normal strength concrete (Kosmatka et al., 2002). They are specially designed to meet combination of performance and requirements which specifically includes high workability, high strength, high early strength, durability and high modulus of elasticity amongst other properties (Kosmatka et al., 2002; Malhotra, 1994; Neville, 2006).

A recent definition by Mehta & Monterio (2012) presents HPC as concrete that has been designed to be more durable and if required, stronger than conventional concrete. The mixtures are essentially composed of the same materials as conventional concrete mixtures, but the proportions are designed or engineered to provide the strength and durability needed for structural and environmental requirements of the project. HPC application in building structure according to A_itcin (1998) was first recorded in the Water Tower Place, built in 1970 in Chicago, Illinois, USA (adopting 60 MPa concrete with lingosulfonate based water reducers). The use is now adopted extensively for the fabrication of precast pylons, piers and girders of many long span bridges in the world with variety of HPC classes available (Mehta & Monterio, 2012).

The growing trend in the utilisation of high-performance and ultra-high-performance concrete (HPC and UHPC) in the construction industry and the susceptibility of this concrete types to self-desiccation and autogenous shrinkagenecessitated research into materials for internal curing of concrete (IC-agents). The real site situation can hardly offer effective curing by complete immersion in water to prevent drying in concrete elements. An intensive study of the IC-agents being introduced in concrete is of essence. Any material for use as an IC-agent should be of appropriate type and optimum proportion while its addition should not result in any detrimental effect on the requisite properties of the concrete. This paper thereby presents a study of the influence of super-absorbent polymers (SAP) as IC-agent on the compressive strength of HPC of low w/b ratio (0.25) having 28 day cube strength specification of 90 MPa (C90/C105 strength class of the Eurode2 – BS EN 1992: 2008).

1.2 *Super Absorbent Polymers*

Super absorbent polymer (SAP) is defined by Siriwatwechakul et al.(2010) as a general term referring to polymers that are able to retain large amount of water. The two main categories mentioned are thermoplastic polymers (linear polymers) and thermoset polymers (cross-linked polymers). The thermoplastic polymers are noted to be of high molecular weight, having overlapping polymer chains with the junction acting as physical cross-links which form pseudo-three dimensional structures. The thermoset polymers on other hand are three dimensional polymer networks with chemical cross-links which hold polymer chains together, thus preventing it being dissolved when soaked in solvents (Siriwatwechakul et al., 2010). This study focuses on thermoset polymers specifically the covalently cross-linked polymers of acrylic acid and accrylamide, neutralised by alkali hydroxide, which according to Schrofl et al. (2012) have been proven efficient as internal curing agents in concrete.

This SAP types according to Siriwatwechakul et al. (2010) absorbs water when it comes in contact with water thereby causing water molecules to diffuse into the void space inside the polymer network to the hydrate polymer chain resulting in swollen polymer gel. This process can be reversed by removing water and the SAP returned to the collapsed state. This water absorbing ability is called the swelling rate i.e. the ratio of the weight of swollen SAP (swollen state) to the dried SAP (collapsed state). This is adjudged to be about 500 g/g in distilled water but only about 12 g/g in cement pore solution as argued by Hasholt, et al. (2012) while Craeye, et al. (2011) used an assumed value of 45 g/g in his work. Schrofl, et al. (2012) however made a proposal that the SAP swelling rate should be determined with the "tea-bag method". The swelling ratio may vary for the variants of SAP. The effectiveness of internal curing of SAP according to Siramanont, et al. (2010) is influenced by the swelling rate of SAP and the inter-particle spacing of the SAP. This work thereby examines the effect of SAP addition on the compressive strength of HPC when the mixture has additional water equivalent to water absorbed by SAP based on the SAP absorption capacity in cement pore solution.

2 MATERIALS AND METHODS

2.1 *Super absorbent polymer (SAP)*

SAP is the admixture introduced in the HPC as IC-agent. Two sizes of SAP (03/08 μm and 06/12 μm) were used at different SAP contents (0%, 0.2%, 0.3%, 0.4% and 0.6% by weight of cement (b_{woc})).

2.2 *Absorption capacity of SAP*

Absorption capacity of the SAP in distilled water and cement pore solution was determined using the so-called "tea bag method" cited in Schrofl et al. (2012). The cement pore solution was obtained from the ordinary Portland cement type – CEM I 52.5 N (conforming to SANS 50197-1 and BS EN 197 – 1:2000) available in the Western Cape, South Africa.

The cement pore solution was made with a mixture of 5.2 water/cement (w/c) ratio. The measuring scale used in this study was however of two decimal digits in grams (g) based on availability as against the four digit analytical scale specified. The result of the "tea bag test" is presented in Table 1. The SAP absorption capacity of 10 mins was chosen as the basis of additional water for the concrete mixes.

2.3 *Mix composition and testing procedure*

A natural sand with minimum particle size 300 μm having physical property values (FM (2.79), Cu (2.43), Cc (1.02) and dust content (0.3%)) of medium sand classification (Shetty, 2004) as observed in the preliminary sieve analysis reported in Olawuyi & Boshoff, (2013) was used as fine aggregate. 13mm crushed greywacke stone serve as coarse aggregate. OPC CEM I 52.5 N was the binder with silica fume (5% b_{woc}) added as cement extender while Premia 310 at 2.75% b_{woc} was added as super-plasticiser.

A concrete mix design for HPC with water/binder (w/b) ratio of 0.25 and 28 day target strength of C90/C105 using British Method was adopted as reference (CM) with the other mixes having varied SAP contents (0.2%, 0.3%, 0.4% and 0.6%) for the two SAP sizes. The concrete was cast in 100 mm cube moulds and tested in the Contest material testing machine after curing in water for 3, 7, 21 and 28 days in accordance with BS EN standards (BS EN 12350-1 & 5, 2000; 12390-1 & 2, 2000; 12390-3, 2002) for compressive strength. Slump flow test was conducted immediately after mixing to assess the consistency of concrete while the density (demoulded and at 28 day) of the cube specimens was also determined.

Table 1. Absorption capacity of SAP.

Time (min)	SAP1(g/g) Water	CPS*	SAP2(g/g) Water	CPS*
0.5	72.34	20.11	65.80	26.61
2	170.29	20.84	180.63	31.49
5	216.17	22.59	233.95	32.02
10	228.44	24.30	258.22	33.93
15	242.00	31.64	284.49	35.80
30	253.02	35.18	292.95	36.76
60	257.07	38.14	297.54	41.85
180	260.76	41.80	298.22	48.24

*CPS = cement pore solution.

3 RESULTS AND DISCUSSION

3.1 *Absorption capacity of SAP*

The result of the tea-bag test shows that (Table 1) absorption capacity (also known as swelling rate) of SAP in both water and cement pore solution increases as the time of immersion increases. This however increased at a decreasing rate after the first 10 mins of immersion. The swelling rate was also observed to be higher for the SAP2 having larger grain sizes (06/12 μm) than the SAP1 (03/08 μm size). The value at the 10 mins time in cement pore solution was however noted to be 24.30 g/g and 33.93 g/g for SAP1 and SAP2 respectively which is about 10% of the swelling rate in water for both SAP sizes. The value at 10 mins time of immersion (taken as the time required for complete concrete mix and casting after water addition to mix constituents) was thereby taken as 25 g/g (SAP1) and 30 g/g (SAP2) for the HPC mixes with SAP adopted for this study. This was kept at this value to avoid wide variation between the swelling rates of the two SAP sizes as they were known to be made from same material and production process. The two SAP sizes were expected to have the same swelling rate on

Table 2. Mix constituents for HPC.

Constituents (kg/m^3)	SAP Content (%)				
	0.0	0.2	0.3	0.4	0.6
Water	130	130	130	130	130
Cement	510	510	510	510	510
Silica Fume	44	44	44	44	44
Coarse Aggregate	1050	1050	1050	1050	1050
Fine Aggregate	700	670	670	670	670
SAP	–	1.1	1.66	2.21	3.31
Super-plasticizer (2.75% b_{woc}*)	15.75	15.75	15.75	15.75	15.75
Additional Water					
SAP1- Mix (25g/g)	–	27.5	41.5	55.25	82.75
SAP2- Mix (30g/g)	–	33	49.8	66.3	99.3
Total w/b**					
SAP1- Mix	–	0.31	0.34	0.36	0.41
SAP2- Mix	–	0.32	0.35	0.38	0.44

*b_{woc} = by weight of cement.
**Total w/b = (initial water + water added for SAP absorption + super-plasticiser weight)/total binder weight.

basis of their supposed chemical composition but a small variation was found.

The swelling rate determine in this study is however below the value assumed by Craeye et al. (2011) in their study (45 g/g) but above the value used by Hasholt et al. (2012) as the swelling rate of SAP (12 g/g).

The observed swelling rate in the cement pore solution for the respective SAP sizes was thereby adopted for calculation of additional water required in the HPC mixes containing SAP in this study. This was done to make allowance for water to be absorbed by SAP in the concrete mixture before casting as shown in Table 2. The total w/b ratios for the SAP mixes are thereby determined as 0.31, 0.34, 0.36, 0.41 for HPC containing SAP1 (03/08 μm) and 0.32, 0.35, 0.38, 0.44 SAP2 (06/12 μm) HPC mixes. The preference mix(CM) however has a total w/b ratio of 0.25.

3.2 *Consistency and Density of HPC*

Table 3 presents the observed values of the slump flow (i.e. consistency) and densities (demoulded and at 28 days) of the HPC mixes. All the slump flow values were noted to be within the acceptable values for a good and workable HPC with low w/b ratio (450 mm–550 mm) as specified in literature (Kosmatka et al., 2002; Neville, 2006). The trend shows that the slump flow value decreased as the SAP contents increases with a deviation from this trend at 0.6% SAP content for both SAP sizes. The slump flow value at this SAP content was however still within the acceptable value of between 450 mm and 550 mm. A physical observation indicated that none of the HPC mixes experienced any segregation.

The densities (both demoulded and at 28 days) of the HPC also decreased as the content of SAP increased, hence the porosity as calculated increased. Beyond

Table 3. Workability and Density of HPC with SAP.

S/No*	Slump Flow (mm)	Demoulded		28 Days	
		β_1 (kg/m^3)	P_1 (%)	β_2 (kg/m^3)	P_2 (%)
CM	530	2463.19	0.00	2498.17	0.00
MS_1^A	510	2423.38	1.62	2451.74	1.86
MS_1^B	490	2404.05	2.40	2444.42	2.15
MS_1^C	460	2424.93	1.55	2424.59	2.95
MS_1^D	510	2338.17	5.08	2351.63	5.87
MS_2^A	540	2442.57	0.84	2442.76	2.22
MS_2^B	530	2414.90	1.96	2444.58	2.15
MS_2^C	450	2364.46	4.01	2398.27	4.00
MS_2^D	510	2328.36	5.47	2377.46	4.83

*S/No = Specimen numbers. The subscripts ($_1$ and $_2$) as shown on the specimen numbers represent the SAP size incorporated as admixture (i.e.03/08 μm as "$_1$" and 06/12 μm as "$_2$") in the mix while superscript (^{A}, ^{B}, ^{C} and ^{D}) shows the SAP content (0.2%, 0.3%, 0.4% and 0.6% respectively) as contained in the various mixes.

Table 4. Compressive Strength of HPC with SAP.

S/No	3 Days	7 Days	21 Days	28 Days
CM	77.49 (73.02)	89.53 (84.37)	102.03 (96.15)	106.12 (100.00)
MS_1^A	66.86 (63.00)	79.24 (74.67)	92.69 (87.34)	97.81 (92.17)
MS_1^B	64.55 (60.83)	76.76 (72.33)	93.33 (87.95)	93.41 (88.02)
MS_1^C	59.86 (56.41)	67.89 (63.97)	83.66 (78.84)	86.66 (81.66)
MS_1^D	40.94 (38.58)	49.38 (46.53)	62.54 (58.93)	66.73 (62.88)
MS_2^A	62.83 (59.21)	79.85 (75.25)	91.74 (86.45)	92.00 (86.69)
MS_2^B	61.79 (58.23)	71.68 (67.55)	84.42 (79.55)	84.65 (79.77)
MS_2^C	58.60 (55.22)	64.06 (60.37)	72.81 (68.61)	80.64 (75.99)
MS_2^D	42.79 (40.32)	51.79 (48.80)	63.44 (59.78)	65.74 (61.95)

*values in parentheses () shows percentage of the 28 day strength of the control mixture (CM).

0.2% SAP content for both sizes of SAP, the porosity value fell out of the acceptable value of 2% for HPC. The situation is worsefor the larger SAP size which is believed to require additional water based on its observed swelling rate.

3.3 *Compressive strength of HPC with SAP*

The 28 day compressive strength of the HPC with varying SAP content is shown in Table 4. Figure 1 shows that the compressive strength decreases as SAP contents increases at a linear rate up to 0.4% SAP content (i.e. strength loss $\leq$ 25%) but with a strong deviation from the trend occurring at 0.6% SAP content (strength loss of about 40%) for both SAP sizes. All the

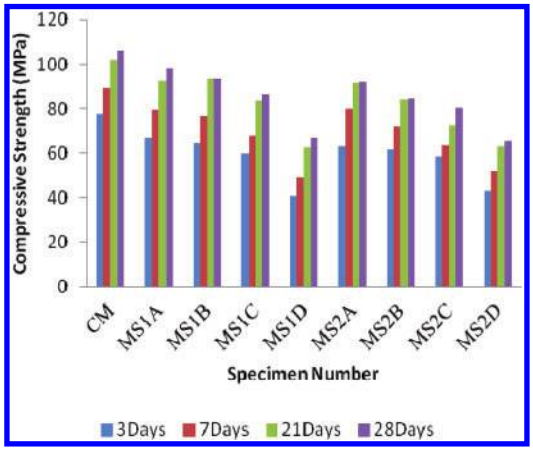


Figure 1. Compressive strength of HPC with SAP.

HPC specimens were observed to experience steady increase in strength development as the age of hydration increases. The 28 day cube strength (Fcu_{28}) of the mixes containing SAP1 at 0.2% (MS_1^A) and 0.3% (MS_1^B), 97.81 MPa and 93.41 MPa respectively both met the target 28 day cube strength of 90 MPa for the C90/C105 HPC classification. The Fcu_{28} for the 0.4% SAP content (MS_1^C) in this mix type is also close to the target strength with the possibility that it will develop a strength more than the target strength at later curing age since it contains silica fume (a pozzolanic material).

For the SAP2 HPC on the other hand only the mix with 0.2% SAP content (MS_2^A) with $Fcu_{28} = 92.00$ MPa met the target strength of 90 MPa. The 0.3% SAP content mix (MS_2^B) $Fcu_{28} = 84.65$ MPa has the possibility of achieving the design strength at later curing age. The excess water added to the mixes with SAP2 can be adjudged to be responsible for their low 28 day strength as the literatures affirms that the optimum actual water required for cement hydration is a total w/b ratio of 0.36. This is the point at which hydration stops ($\alpha_{max} = 1$) according to the Powers' model concept (Hasholt et al, 2012).

It can therefore be inferred that HPC with or without SAP having total w/b ratio below 0.36 (CM, MS_1^A, MS_1^B, MS_2^A) gave compressive strength values adequate for the design strength. The HPC mixes with SAP on the other hand with total w/b ratios around 0.36 (MS_1^C and MS_2^B) also has the possibility of achieving the design strength at later curing ages. The total w/b ratio of 0.36 should thereby be taken as the limit of SAP addition in HPC for no detrimental effect on the strength of the concrete.

4 CONCLUSION AND RECOMMENDATIONS

4.1 *Conclusion*

The following conclusions can be drawn from the results of this study.

The absorption capacity of SAP in both water and cement pore solution increases as the time of immersion increases. The swelling rate of SAP in cement pore solution is about 10% of the swelling rate in water. After 10 minutes of immersion, SAP1- 03/08 μm has a swelling rate of 25 g/g but 230 g/g in water while SAP2 – 06/12 μm has a value of 30 g/g in cement pore solution and 260 g/g in water. The "tea-bag" test involves dabbing the swollen SAP in your palm after been rolled in towel for removal of excess water. This might be the reason for the varied swelling rate of the two SAP sizes studied, both samples been from same chemical materials and production process should be of same nature and hence have the same swelling rate.

The higher the SAP contents in HPC, the lower the densities (both demoulded and at the hydrated stated) and hence the higher the porosity.

HPC of low w/b (0.25) with SAP as admixture gives compressive strengths that is commensurate to the expectations of the design mix up to the limits of SAP addition (0.3% for SAP1 and 0.2% for SAP2). This is the limit to which the total water addition is within the w/b value of 0.36 at which the optimum water required for complete hydration is provided. Beyond this limit the additional water provided in the mix to account for the requisite absorption by SAP in HPC with high SAP contents led to detrimental effect in the compressive strength. This work thereby concludes that the limit of SAP addition in HPC of low free w/b ratio (e.g. 0.25) is 0.3% by weight of cement based on the outcome of the tests in this study.

4.2 *Recommendations for further studies*

Towards advancement in the utilisation of SAP as IC-agent in HPC with low w/b ratio, attention thereby ought to be given to the followings in future studies.

Developing improved test method (i.e. modified tea-bag test) for determination of SAP absorption capacity. Effort should be geared towards elimination of inherent variations in measurement due to human error.

The size, structure, and intermolecular interaction of the material constituents of HPC containing SAP as IC-agent over a long hydration period should be studied.

REFERENCES

Aitcin, P. C. (1998). *High-performance concrete* Taylor & Francis.

British Standard Institution (2000) Cement – composition, specifications and conformity criteria for common cements, BS EN 197:Part 1, London, BSI.

British Standard Institution (2000) Testing of fresh concrete, BS EN 12350: Part 1, Sampling, London, BSI.

British Standard Institution (2000) Testing of fresh concrete, BS EN 12350: Part 5, Flow Table Test, London.

British Standard Institution (2000) Testing of hardened concrete, BS EN 12390: Part 1, shape, dimension and other requirement for specimens and mould, London, BSI.

British Standard Institution (2000) Testing of hardened concrete, BS EN 12390: Part 2, making and curing specimen for strength tests, BSI, London.

British Standard Institution (2002) Testing of hardened concrete, BS EN 12390: Part 3, compressive strength test specimens, BSI, London.

British Standard Institution (2004) Eurocode 2 – Design of concrete structures – Part 1-1: General rules and rules for buildings, BSI, London.

Craeye, B., Geirnaert, M., & Schutter, G. D. (2011). Super absorbing polymers as an internal curing agent for mitigation of early-age cracking of high-performance concrete bridge decks. *Construction and Building Materials, 25*(1), 1–13.

Hasholt, M. T., Jensen, O. M., Kovler, K., & Zhutovsky, S. (2012) Can superabsorent polymers mitigate autogenous shrinkage of internally cured concrete without compromising the strength?(report). *Construction and Building Materials, 31*(1), 226–230.

Kosmatka, S. H., Kerkhoff, B., & Panarese, W. C. (2002). Chapter 17: High performance concrete. *Design and control of concrete mixture: – engineering bulleting 001 (EB 001)* (Fourteenth ed., pp. 299–314). Illinois, USA: Portland Cement Association.

Malhotra, V. M. (1994). *High-performance concrete: Proceedings, ACI international conference, Singapore, 1994*. Detroit, Mich.: American Concrete Institute.

Mehta, P. K., & Monterio, P. J. M. (2012). High performance concrete. Retrieved August, 1st, 2012, from www.ce.berkeley.edu/∼paulmont/.../high_performance_concrete.pdf

Neville, A. M. (2006). Concrete with particular properties: High performance concrete. *Properties of concrete* (Fourth (Indian) ed., pp. 673-up to 688). New Delhi, India: Dorling Kindersley (India) Pvt. Ltd., licences of Pearson Education in South Asia.

Olawuyi, B. J., & Boshoff, W. P. (2013). Influence of particle size distribution on compressive strength and elastic modulus of high performance concrete. *International Conference on Advances in Cement and Concrete Technology in Africa,* Johannesburg, South Africa. 825–833.

Schrofl, C., Mechtcherine, V., & Gorges, M. (2012). Relation between the molecular structure and the efficiency of superabsorbent polymer (SAP) as concrete admixture to mitigate autogenous shrinkage. *Cement and Concrete Research, 42*, 865–873.

Shetty, M. S. (2004). *Concrete technology – theory and practice*. New Delhi, India: S. Chand and Company Limited.

Siramanont, J., Vichit-Vadaka, W., & Siriwatwechakul, W. (2010). The impact of SAP structure on the effectiveness of internal curing. *International RILEM Conference on use of Superabsorbent Polymers and Other Additives in Concrete,* Technical University Denmark, Lyngby, Denmark., *Proceeding Pro074* (15–18 August) 243–252.

Siriwatwechakul, W., Siramont, J., & Vichi-Vadakan, W. (2010). Superabsorbent polymer structures. *International RILEM Conference on use of Superabsorbent Polymers and Other New Additives in Concrete,* Technical University of Denmark, Lyngby, Denmark. *, Proceedings Pro074*(15-18 August) 253–262.

South African Bureau of Standards(2007) SANS 50197-1-Cement – Part 1: Composition, specifications and conformity criteria for common cements, Pretoria, SABS.

Research and Applications in Structural Engineering, Mechanics and Computation – Zingoni (Ed.)
© 2013 Taylor & Francis Group, London, ISBN 978-1-138-00061-2

A model for spalling of HPC thin plates exposed to fire

T. Hulin, K. Hodicky, J.W. Schmidt, J.H. Nielsen & H. Stang
Department of Civil Engineering, Technical University of Denmark, Kgs. Lyngby, Denmark

ABSTRACT: An experimental program was carried out to investigate the behaviour of high performance concrete (HPC) thin plates in fire for use in sandwich panels. To reveal the influence of moisture two initial moisture contents for wet and dry samples were examined. In addition, two thicknesses were used to disclose the temperature distributions during the test. A non-linear coupled model for time dependent heat and mass transfer in concrete thin plates was used for temperature and pore pressure computations. Results from modelling and tests are compared and discussed. Moisture content was found to be a critical parameter in the spalling process. The calculated pore pressure induced too low tensile stresses in the matrix to trigger failure, suggesting a major role played by thermal stresses.

1 INTRODUCTION

High performance concrete (HPC) allows making thin flanges (20 to 30 mm thick) suitable for structural purpose. Used in sandwich elements where the concrete layers frame a thick insulation material, they provide a construction system addressing some of the growing environmental challenges of the building industry.

The reduction of material use due to HPC makes the profiles lighter, which reduces production- and transportation-induced emissions. Furthermore the industrial manufacturing optimizes on-site building time. Those advantages coupled with a thick insulation result in an end-user friendly solution.

However, a major issue of this system lies in the explosive spalling tendency of HPC when exposed to fire (Hertz 2003, Majorana et al. 1998, Phan & Davis 2001), which has been seen in previous certification attempts within the scope of this research. The low permeability of HPC leads to high pore pressures when temperature rises, triggering a fracture process followed by explosion due to thermal stresses. This principle has been extensively studied analytically (Bažant & Thonguthai 1978, England & Khoylou 1995, Ahmed & Hurst 1997a,b, Tenchev et al. 2001) in the case of thick walls used in nuclear power plants, and is here addressed to thin HPC profiles.

This paper presents a preliminary study of spalling behaviour in HPC used for thin plates. Numerical modelling of temperature and pressure distributions as well as the hydrostatic stresses due to those pressures is investigated. The influence of thickness and moisture content on the spalling behaviour of those thin flanges have been investigated experimentally and compared to the analytical study.

2 METHODS

2.1 *Experimental work*

The experimental work presented in this paper intends to give preliminary test data on thin HPC plates exposed to fire. Only temperature was measured since the small thickness does not allow implementing pressure sensors that would significantly disturb the concrete behaviour.

The HPC mix used in those experiments has a compressive strength of 80 MPa and a tensile strength of 5 MPa. The precise composition is kept secret by the producer, only tested material characteristics are known.

The square profiles ($540 \times 540\,mm^2$) come in thicknesses of 20 mm and 30 mm and two different conditionings. The wet conditioning was achieved by keeping the samples in an ambient temperature water basin for the whole duration of hardening. The dry conditioning was achieved by keeping the samples in water for a week to develop a similar microstructure as the others, and placed in an oven at 35°C for the rest of the hardening period. Two samples of each configuration were tested for repeatability, the concrete coming from two different batches. The precise sample labelling is given in Table 1.

The samples are tested horizontally, exposed to fire on the bottom side and to the ambient air temperature on the other as shown in Figure 1. To record the temperature through the thickness, three sets of three thermocouples were embedded at 1/4th, 1/2nd and 3/4th of the thickness. An extra four thermocouples were glued on the outer surface of each plate. The plates are exposed to the environment on the sides but insulated from the furnace by mineral wool to avoid

Table 1. Sample labelling for fire test. W and D respectively stand for wet and dry conditioning. 1 and 2 stand for the two concrete batches.

Name	Thickness mm	Conditioning	Moisture sample
W20.1	20	wet	mW20.1
W20.2	20	wet	mW20.2
W30.1	30	wet	mW30.1
W30.2	30	wet	mW30.2
D20.1	20	dry	mD20.1
D20.2	20	dry	mD20.2
D30.1	30	dry	mD30.1
D30.2	30	dry	mD30.2

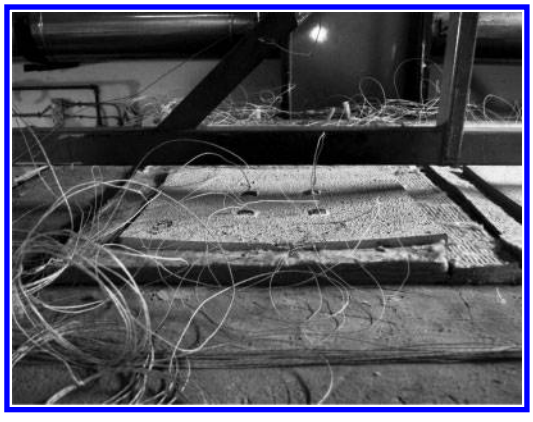


Figure 1. Sample laid on the top of the furnace. Thermocouples are visible on the cold surface exposed to the air, and going out of the sample sides.

heat conduction. The furnace provides only radiant and convective heating. Thermocouples are placed in the furnace to monitor the temperature which follows the ISO 834 (EN 1363-1) curve. The pressure in the furnace is kept at 20Pa. The specimens are heated up to 40 min or thermal equilibrium.

Along with each of those large plates a smaller plate ($300 \times 300\,mm^2$) was cast for moisture content measurement. Their central parts were crushed and placed in an oven, weighed at regular intervals until reaching equilibrium. The result is used as input data for the numerical model. Table 1 shows the moisture samples identification and link with the fire tested tiles.

2.2 *Numerical analysis*

The numerical analysis is carried out using a finite element program, as it enables modelling a coupled system of two non-linear differential equations for temperature and pressure. This is important since the temperature dependency of many material parameters used as coefficients in the coupled system makes the formulation highly non-linear.

The one-dimensional numerical model calculates temperature and pressure distributions over time through the thickness of the thin plates using Comsol Multiphysics. Both thicknesses (20 mm and 30 mm) are accounted for. To reproduce the experimental set-up, heating takes place on one side only, the other exchanges heat with the environment.

The equations for heat and mass transfer in porous bodies in general have been described by Luikov (1966) and extended specifically for concrete by various researchers (Bažant & Thonguthai 1979, Tenchev et al. 2001, Dwaikat & Kodur 2009). Under the assumption of local thermodynamic equilibrium of all phases of water between adjacent pores and considering concrete as a matrix of undistinguished mortar and aggregates including pores, a two-equation formulation for both heat and pressure describes accurately the problem (Bažant & Thonguthai 1978).

Fourier's law (Equation 1) governs temperature and Darcy's law (Equation 2) governs pressure.

$$q = -k\nabla T \quad ; \quad J = -\frac{a}{g}\nabla p \tag{1,2}$$

where $\boldsymbol{q}$ = heat flux; k = thermal conductivity; T = temperature of the sample; $\boldsymbol{J}$ = moisture flux in concrete; a = permeability; g = gravity acceleration; and p = pore pressure.

The cross-effects of Dufour and Soret fluxes are disregarded, found to be of negligible impact (Bažant & Thonguthai 1978). Additionally, Fick's law describes moisture diffusion but the high heating rate which follows the standard ISO 834 heating curve makes it unnecessary in the present model as Darcy's law predominates.

The balance equations are presented by Equation 3 and 4 for heat and pressure.

$$\left[\rho_S C_S - \left(C_a + \lambda_D\right)\frac{\partial w_d}{\partial T} - C_a\frac{\partial w}{\partial T}\right]\frac{\partial T}{\partial t} - \nabla.\left(q\right) = C_a\frac{\partial w}{\partial p}\frac{\partial p}{\partial t} \tag{3}$$

$$\frac{\partial w}{\partial p}\frac{\partial p}{\partial t} + \nabla.J = \left(\frac{\partial w_d}{\partial T} - \frac{\partial w}{\partial T}\right)\frac{\partial T}{\partial t} \tag{4}$$

where w = free water content; w_d = amount of chemically bound water released by heat increase ρ_s and C_s = density and isobaric heat capacity of the solid structure; C_a = heat of vaporisation of water; and λ_D = heat of dehydration of chemically bound water.

The temperature evolution of permeability is not easily described experimentally, thus curves from Bažant & Thonguthai (1978, 1979) are used. The sorption equations needed to characterise the free water content and the water released by dehydration have been described in Bažant & Thonguthai (1979) and Dwaikat & Kodur (2009). Those equations were implemented in Matlab to calculate the free water content and the water produced by dehydration and their derivatives according to temperature and pressure for various conditions of temperature and pressure. Other temperature-dependent material parameters were computed using Matlab. The result

of those computations was loaded in Comsol as interpolation functions, allowing reduced computation time.

The initial moisture content w_0 and initial permeability a_0 are of primary importance, governing the amount of free water in the concrete and its evolution through the pore system thereby affecting pressure. The former comes from the experimental work and the latter is estimated at $1{\cdot}10^{-13}$m/s regarding the compressive strength.

The boundary condition for heat takes into account both convection and radiation, as shown in Equation 5.

$$n.q = h\left(T_{amb} - T\right) + \varepsilon\sigma\left(T_{amb}^4 - T^4\right) \tag{5}$$

where h = heat transfer coefficient of concrete; ε = surface emissivity; σ = Stefan-Boltzmann constant; T = temperature just under the surface of concrete exposed to the environment; and T_{amb} = furnace temperature on the heated side and environment temperature on the other.

The boundary condition for pressure is set by ISO 834 to be 20 Pa inside the furnace for the duration of the test, and atmospheric pressure on the side of the sample exposed to the ambient air.

The time step for the simulations was chosen to be 1s, and the mesh contained 100 elements over the thickness.

From the computed pore pressure seen as hydrostatic stress in a spherical pore system, a preliminary tensile stress can be calculated to assess the spalling probability as described in a simple model by Ichikawa & England (2004). Considering the one-dimensional model as the heat and mass transfer through the thickness of a unit area plate, and the concrete as a new system of single-pore material surrounded by a solid matrix, allows calculating the pressure-induced tensile stress with the following Equation 6 (Ichikawa & England 2004)

$$\sigma_t = \frac{\left(1 + 2V_p\right)}{2\left(1 - V_p\right)} p \tag{6}$$

where σ_t = tensile stress; V_p = relative pore volume; and p = computed pore pressure.

The relative pore volume is calculated from the weight loss measurements on wet samples. Considered as initially fully saturated, they give a value of porosity of $V_p = 0.18$.

The values of pressure-induced tensile stress are computed and compared with the tensile strength found in wedge splitting test using inverse analysis performed within the scope of this research.

3 RESULTS

3.1 *Experimental results*

The results of the moisture content measurement in each tile are presented in Table 2.

Table 2. Moisture content of the fire tested tiles.

	Moisture content	
Tile ID	mass %	kg/m^3 of concrete
mW20.1	7,2	172
mW20.2	8,5	204
mW30.1	6,9	166
mW30.2	8,2	197
mD20.1	5,0	119
mD20.2	4,3	102
mD30.1	5,3	126
mD30.2	5,1	123

The two batches of the wet conditioning show different moisture content when the samples from the dry conditioning show consistent values.

The temperature distributions from the fire test are presented in Figure 2 where the plates are grouped by thickness. For each plate, the values from the three thermocouples embedded at the same depth are averaged. Thermocouples connection problems in the early phase of the recording of sample D30.1 caused measuring errors, making the results unreliable. The temperature distributions are very similar for both wet and dry conditioning, in the tendency of the curves as well as the values. A temperature plateau around 200°C is to be noticed on many curves, more pronounced for the samples with wet conditioning but still visible on some of the samples with dry conditioning. The temperature of this plateau occurred to be slightly lower for the 30 mm thick plates than for the 20 mm thick plates.

From the wet conditioning, the two plates with the highest moisture content (W20.2 in Figure 4b and W30.2) showed minor surface spalling (3 mm deep) between 7 and 10 min whereas the others did not spall as shown on Figure 4a. The spalling was distributed over the entire surface of the plates without specific location. W30.2 exhibited the most severe damage with respect to lost area when W20.2 showed slightly deeper cracks.

No plates stored according to the dry conditioning showed spalling.

3.2 *Numerical results*

Figure 3c shows numerical results when modelling sample W20.1. The other simulations are not shown but similar correlation between test and simulation is found in these.

The results from the temperature and pore pressure calculations are presented in Figure 3. The temperature curve (Figure 3a) shows a slope break at 200°C that corresponds to the release of chemically bound water. The temperature curves at given locations (Figure 3c) present this tendency as well, particularly closer to the outer surface. The pressure curves (Figure 3b) display a fast build up in the early time steps, reaching a maximum of 3.3 MPa at 1/2nd of the thickness at 13 min.

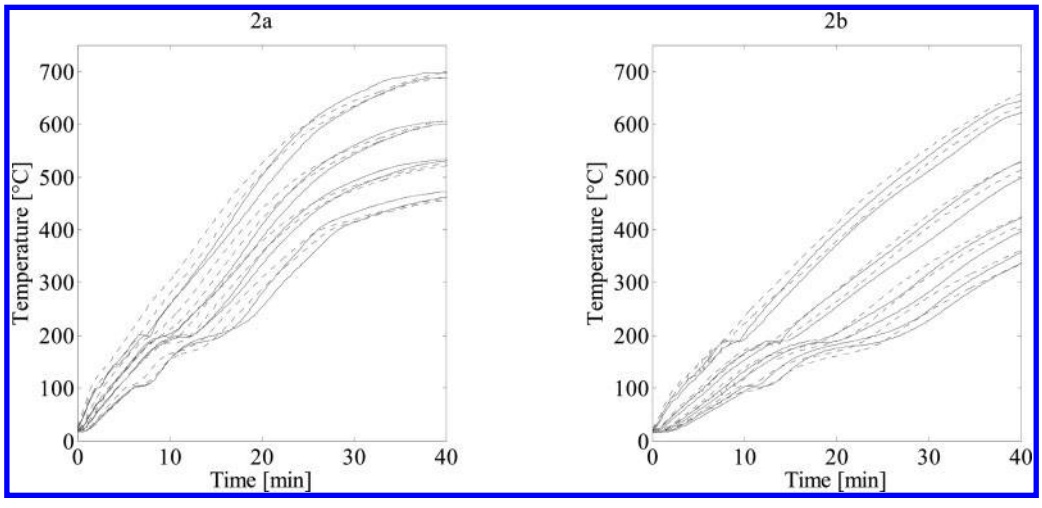


Figure 2. Temperature distributions from experiments for thickness 20 mm (1a) and 30 mm (1b) at 1/4th, 1/2nd, 3/4th of the thickness and on the surface (curves from top to bottom). Plain lines: wet conditioning. Dashed lines: dry conditioning.

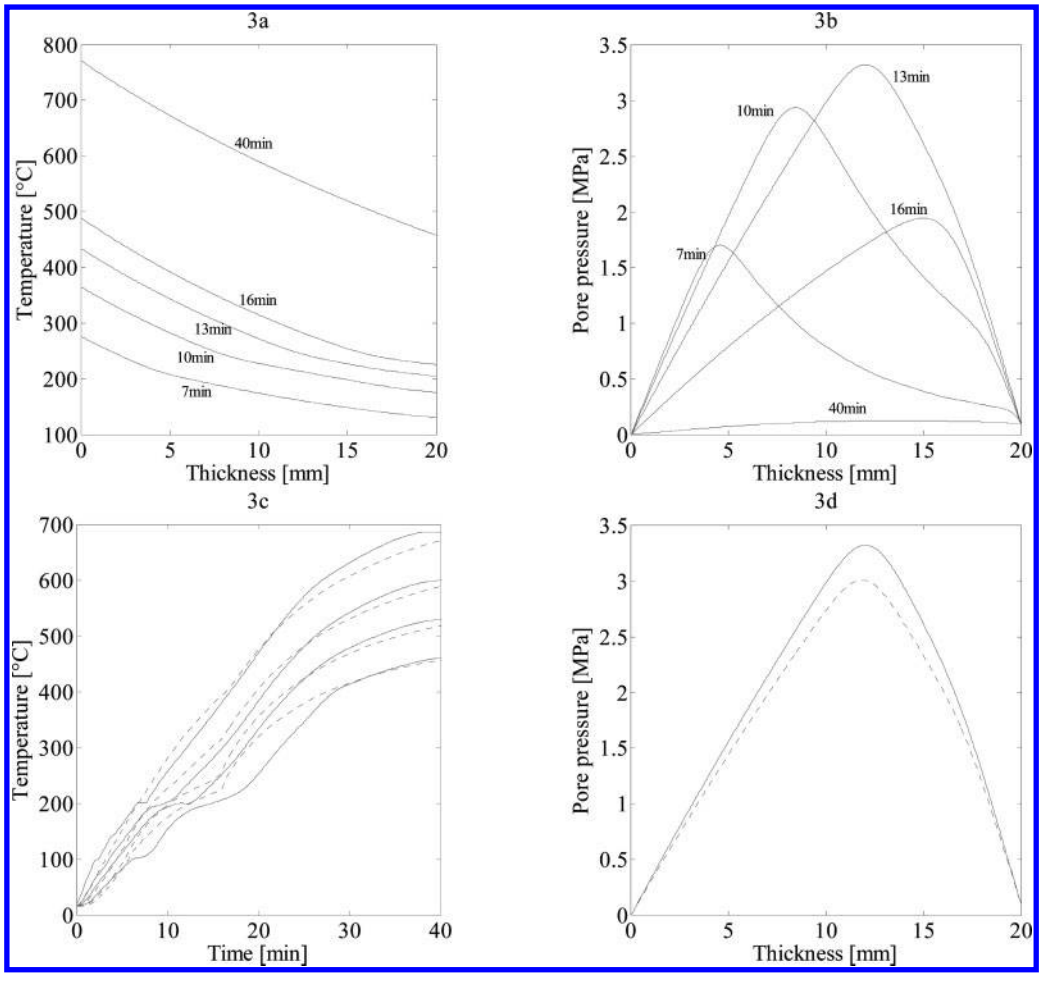


Figure 3. Numerical results for W20.1. Temperature over the thickness (3a).Pressure over the thickness (3b).Temperature over time (3c) with experimental results (plain lines) and numerical results (dashed lines). Max pressure for wet and dry sample W20.1 and D20.1 respectively plain and dashed line (3d).

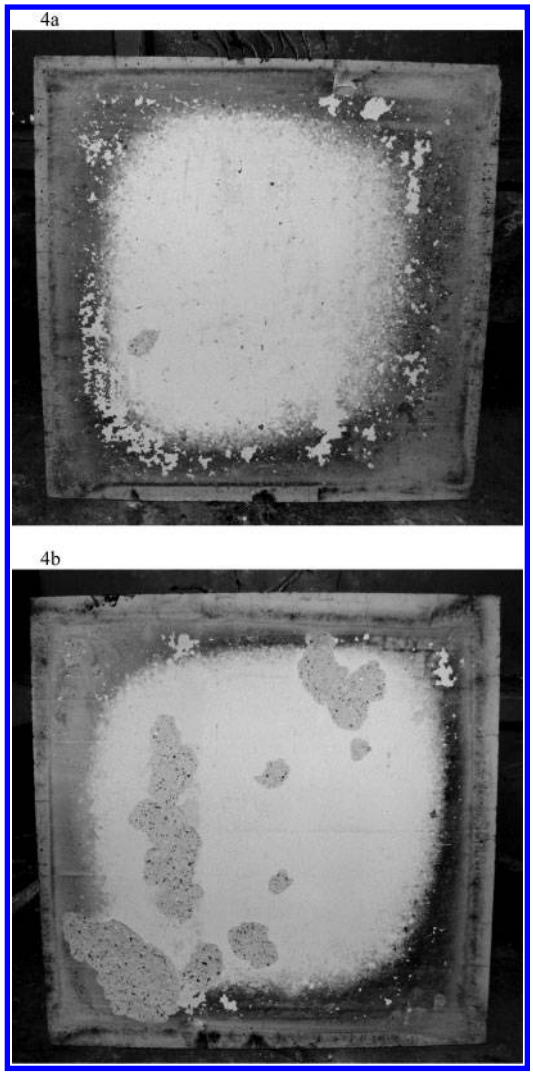


Figure 4. Results of the fire test on specimen W20.1 (4a) and W20.2 (4b)

A gradual decrease follows until pressure equilibrium at the end of the 40 minutes of testing.

Figure 2d presents a comparison of maximum pressures for W20.1 and D20.1. The dry sample experiences a lower maximum pressure at similar to the wet sample. The pressure difference remains small.

For the maximum pressure of 3.3 MPa and the pore volume calculated in Section 2.2, the pressure-induced tensile stress is found to be 2.7 MPa which remains below the allowable 5 MPa tensile strength.

4 DISCUSSION

The experimental data and behaviour of the test specimens tend to confirm that initial moisture content plays a critical role in the spalling phenomenon. The slight 30 kg (1.3%) difference in moisture content (Table 2) between the wet specimens and the fact that no dry specimens spalled suggest the existence of a moisture threshold for a given concrete type. Special care should be given to respect mix proportions during casting. No significant difference was noticed between the behaviours of 20 mm and 30 mm plates.

However, the output of the modelling work shows that pore pressure in this particular case does not suffice to trigger any cracks or spalling in the thin plates for any moisture content. According to the tendency of the pressure curves in Figure 3b, the sample dries out fast, explaining the pressure decay and moisture moves inwards to build a maximum pressure past half the thickness. Previous experiments carried out on thicker samples showed spalling at depths of 20 mm or more (Kalifa et al. 2000) which corresponds to the thickness of the plates considered here. In the case of thin plates, even for high initial water contents, the absolute amount of water is too low and cannot gather sufficiently to build up in high pressure. Hence the result of computed tensile stress from pore pressure of only 2.7 MPa. The time of spalling between 7 min and 10 min confirms this hypothesis since the maximum pressure is reached at 13 min. If this mechanism only were to lead to material failure, the pore pressure would have to be of 6 MPa which is reached in thicker profiles according to Ichikawa & England (2004).

Since the specimens spalled only on 3 mm, thermal stresses play a major role in the behaviour of the plates. It is then assumed that thermal stresses use a fair part of the tensile strength and a slight moisture content increase would create a sufficient pressure to induce total stresses comparable to the tensile resistance. Thermal stresses caused by thermal gradients have to be investigated further, considering that the geometry of the plate carrying the samples above the furnace might introduce large radiation differences on the edge of the specimens.

The pressure predictions of previously proposed models vary widely from 1 MPa up to 16 MPa (Tenchev et al. 2001) and few measurements were successfully performed. The pressures predicted by the present model enter this range and show likely tendency when compared to the output of early time steps in Tenchev et al. (2001).

To fit the test data, only the concrete thermal properties have been adapted since they were not recorded experimentally. The thermal conductivity equation from the standard prEN 1992-1-2 and a heat transfer coefficient of 40 W/(m^2.K) are used. With those parameters, the proposed model shows a good agreement with the temperature curves within concrete for wet and dry samples in both thicknesses as shown in Figure 3c. The temperature plateaus seen at 200°C correspond to the release of water by dehydration. At the interface with ambient air, experimental and numerical results differ largely (Figure 3c). The temperature plateaus at 100°C and 200°C on the experimental curves at the boundary (Figure 1a) describe the presence of large amounts of liquid water changing phase.

This water was not taken into account in the boundary conditions. Moreover, the glue fixing the thermocouples on the surface of the plates may influence the recording. Those two parameters explain the observed differences.

Despite the good agreement with test data, the model requires comparison with another kind of concrete with different composition, compactness, compressive strength and a known composition for final validation. The thermal properties of the concrete should be investigated as well. An experimental program in that sense is currently developed.

5 CONCLUSION

Preliminary test data from an experimental program on the fire resistance of HPC thin plates are presented, as a first step in the assessment of the possibility to use such profiles in sandwich elements. The influence of the initial water content on the spalling behaviour of HPC thin plates showed the existence of a threshold inviting to a careful respect of mix proportions when casting. Samples with thicknesses of 20 mm and 30 mm behaved similarly.

A coupled model for the time dependent distributions of temperature and pressure for HPC thin plates was presented and compared to the experimental data. The temperature profiles proved in good agreement and the predicted pressure within the range of published literature. The computed pressure was too low to be the only trigger to the spalling seen on some of the plates. Thermal stresses are assumed to use a significant amount of the tensile resistance which would not hold the extra pressure created by an increase in moisture content.

For further investigations concerning sandwich elements, the size effect should be considered with larger profiles. The delicate issue of loaded bearing structure should be carefully examined as external solicitations can significantly raise the inner stresses leading to complete material failure.

ACKNOWLEDGEMENTS

The authors are grateful for the support of Connovate, who provided the test specimens and the Dansk Brand ogsikringstekniskInstitue (DBI) for performing the fire tests.

REFERENCES

Ahmed, G.N. & Hurst, J.P. 1997a. An analytical approach for investigating the causes of spalling of high strength concrete at elevated temperatures. *International Workshop on Fire Performance of High-Strength Concrete, Gaithersburg, 13–14 February 1997*. Gaithersburg: NIST

Ahmed, G.N & Hurst, J.P. 1997b. Coupled heat and mass transport phenomena in siliceous aggregate concrete slabs subjected to fire. *Fire and Materials* 21: 161–168

Bažant, Z.P. & Thonguthai, W. 1978. Pore pressure and drying of concrete at high temperature. *Journal of the Engineering Mechanics Division*, ASCE

Bažant, Z.P. & Thonguthai, W. 1979. Pore pressure in heated concrete walls: theoretical prediction. *Magazine of Concrete Research* 31(107): 67–76

Dwaikat, M.B. & Kodur, V.K.R. 2009. Hydrothermal model for predicting fire-induced spalling in concrete structural systems. *Fire Safety Journal* 44: 425–434

England, G.L. & Khoylou, N. 1995. Moisture flow in concrete under steady-state non-uniform temperature states: experimental observations and theoretical modelling. *Nuclear Engineering and Design* 156: 83–107

Hertz, K. 2003. Limits of spalling of fire-exposed concrete. *Fire Safety Journal* 38: 103–116

Ichikawa, Y. & England, G.L. 2004. Prediction of moisture migration and pore pressure build-up in concrete at high temperatures. *Nuclear Engineering and Design* 228: 245–259

Kalifa, P., Menneteau, F.D. & Quenard, D. 2000. Spalling and pore pressure in HPC at high temperatures. *Cement and Concrete Research* 30: 1915–1927

Luikov, A.V. 1966. *Heat and mass transfer in capillary porous bodies*. Oxford: Pergamon Press

Majorana, C.E., Salomoni, V. & Schrefler, B.A. 1998. Hygrothermal and mechanical model of concrete at high temperature. *Materials and Structures* 31: 378–386

Phan, L.T., Lawson, J.R. & Davis, F.L. 2001. Effects of elevated temperature exposure on heating characteristics, spalling and residual properties of high performance concrete. *Materials and Structures* 34: 83–91

Tenchev, R.T., Li, L.Y. & Purkiss, J.A. 2001. Finite element analysis of coupled heat and moisture transfer in concrete subjected to fire. *Numerical Heat Transfer* 39: 685–710

Research and Applications in Structural Engineering, Mechanics and Computation – Zingoni (Ed.)
© 2013 Taylor & Francis Group, London, ISBN 978-1-138-00061-2

Micro structural optimization of high strength performance air hardened foam concrete

Bernhard Middendorf
University Kassel, Department of Construction Materials and Building Chemistry, Germany

Armin Just
EBZ Business School, University of Applied Science, Department of Building Technology, Bochum, Germany

ABSTRACT: In present-day constructions any building material fulfils its specific task. Concrete is mainly used for load transfer but it does not achieve thermal insulation properties. For heat insulation, highly porous materials with low density is necessary. Mixed constructions have energetic disadvantages because different composed building materials must be produced, assembled and also, finally, have to be recycled. An advantage of multifunctional building materials is that one building material can fulfil different tasks. A new type of foam concrete was developed by combination of chemical foaming with aluminium powder and air hardening. Compared to autoclaved aerated foam concretes the manufacturing of this new type of foam concrete consumes less energy and the production is not stationary. The new foam concrete combines high thermal insulating properties with high strength. The micro structural optimization of this foam matrix is based on the same approaches which were already developed for HPC and UHPC.

1 INTRODUCTION

Buildings require energy during any period of their life cycle. The energy consumption starts with the production of the building materials and the construction of the buildings. After that the use and operation of buildings need energy as well. Finally there is also energy required for the deconstruction of a building.

The paper deals with the benefits of multifunctional building materials. With present-day construction, any building material fulfils its specific task. Steel and concrete are used for load transfer but they do not achieve thermal insulation properties. For heat insulation, highly porous materials like foams are necessary. Such complex constructions have energetic disadvantages because different building materials and components must be produced, assembled and also, finally, have to be disposed of or recycled. One advantage of multifunctional building materials is that one component and of course one material can fulfil different tasks in a modern building.

High strength mineral bound foam is such a multifunctional building material. These fine grained foam concretes have a density ≤ 2.0 g/cm^3 and are classified as lightweight concretes. Some of them are applicable for load bearing constructions with thermal insulation properties at the same time. Thereby the use of this class of building materials requires less energy and supports the establishment of sustainable construction.

The process of forming air voids in the fresh foam concrete paste is significant. The methods of chemical expansion, as well as physical or mechanical foaming are well known and state of the art. Autoclaved aerated concrete can be based on a paste with finely grounded, quartzitic sand, cement and lime and water where a foaming agent, commonly aluminium powder, is added. The set material is cured after being removed from its mould in a saturated steam atmosphere in autoclaves at high pressure within a few hours and thereby receives its final properties (Homan, 2008).

Foam concretes are given their structure by using foam generators or stirring up the cement paste using foaming agents and fast rotating pug mill mixers. The paste consists of the binder, usually cement, finely grounded quartzitic sand, water and foam generating admixtures. After moulding the foam, the concrete hardens under normal atmospheric conditions. During the mechanical foaming procedure, a foam agent is added to the mortar. Numerous voids are mechanically introduced by high speed mixers. A relatively unstable foam develops with an irregular structure and undefined void structures. In practice, a more usual manufacturing method is physical foaming. A premanufactured foam consisting of water and chemical admixture is mixed with the additional components. Under these conditions, a more stable mortar with a fine pore structure can be created (Readymix 1978).

In addition to the two established representatives of mineral bound foams, the possibility to produce chemically expanded, air cured, mineral bound foams, with mechanical properties which allow their use as construction material has been established recently

Table 1. Basic materials used for the production of chemical expanded and air hardened foam concretes.

binder	
cement	CEM I 42.5 R
additives	
aluminium powder	I (average. Ø 60–70 µm)
	II (average. Ø 20–30 µm)
	III (average. Ø 15–20 µm)
	IV(average .Ø 15 µm)
plasticizer	PCE
admixtures	
microsilica	suspension

(Just, 2008, Just & Middendorf 2009, 2010, 2011). The physical mechanical properties of these air cured foams – like density, compressive strength and thermal conductivity – are partially superior to the conventional cellular concretes hardened in autoclaves. This type of foam concrete hardens without using an autoclave and therefore without the need of additional production energy. Thus it makes the further development of this innovative foam concrete ecologically worthwhile.

2 MATERIALS AND METHODS

The studies on chemical expanded and air hardened foam concretes were made by using a cement paste without aggregates. In part, admixtures and additives were added. In table 1 the used raw materials for the production of paste mixtures are listed.

CEM I 42.5 R according to EN 197-1 (2004) was used as binder. By using different grain sizes of the aluminum powder, the air void distribution in the hardened material was controllable, whereas the air void volume was adjusted by the total quantity of the aluminum powder.

The water/cement ratio (w/c) has a crucial influence on the increase of volume of the cement paste during expansion. In order to ensure an expansion in cement pastes with a low water volume, the introduction of superplasticizers on the basis of polycarboxylatether was necessary.

The structure of the hardened cement paste matrix was also optimized by using microsilica suspension.

The samples were examined by means of light microscopy with an associated digital image analysis, scanning electron microscopy as well as by mercury intrusion porosity.

For example figure 1 shows a chemical expanded air hardened foam concrete sample with a density of 0.85 kg/dm^3 and a compressive strength of approx. 10 MPa.

2.1 *Digital image analysis*

For structural examination of foam concrete digital image analysis were used for the investigation of air voids in cross sections. In the first step the sample were saturated with coloured epoxy resin. After hardening of the epoxy resin polished cross section were prepared. The digital image analysis detects air voids by means of differences of contrast between the cement paste matrix and the air voids which are filled with the coloured epoxy resin. The properties of the air voids are determined by analysing polished cross sections by means of light microscopy for each individual air void.



Figure 1. Chemical expanded and air hardened foam concrete sample.

For the investigations the digital image analysing software Omnimet by Buehler GmbH and a light microscope by Zeiss were used.

2.2 *Scanning electron microscopy (SEM)*

SEM images were acquired using a Philips XL30i scanning electron microscope. Imaging was performed in high vacuum with the application of a conductive coating based on carbon and/or gold.

2.3 *Mercury intrusion porosimetry (MIP)*

For the determination of the porosity and the pore size distribution a mercury intrusion porosimeter was used. Therefore the samples were first dried. After this the samples were put into a dilatometer which was afterwards filled with mercury up to a pressure of 200 MPa. Therewith pore radii to 4 nm could be determined. A mercury intrusion porosimeter type Pascal 140–240 by Porotec was used for the investigations.

3 RESULTS AND DISCUSSION

3.1 *Microstructure*

The structure of the hardened cement paste implies the spatial arrangement of the reaction products and the partly unfilled or filled areas with an aqueous solution: the pores. The pore area is composed in its entirety by the gel pores, the capillary pores and the air voids. The existing gel and capillary porosity are primarily responsible for the characteristics of the microstructure. Regarding the optimization of this structure of air hardened foam concretes, the same basic approaches maintain their validity for mineral bound foams, as they were already developed for high performance concrete (HPC) or even for ultra high performance

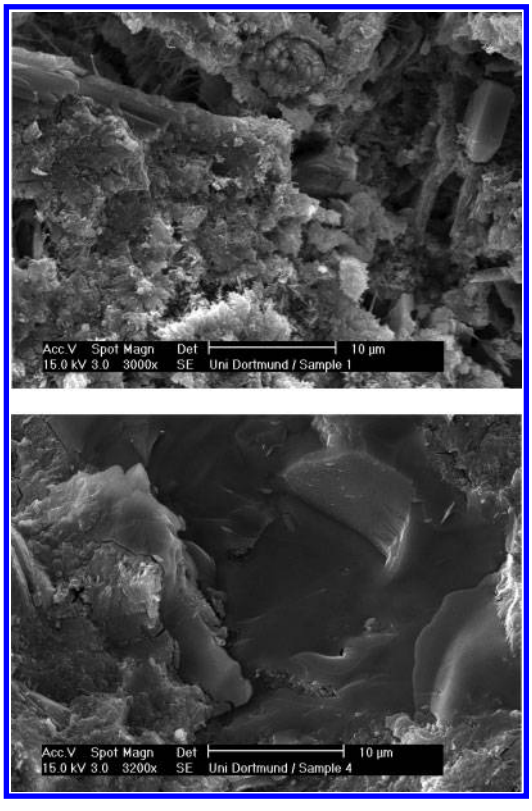


Figure 2. Microstructure of two foam concretes; top: w/c ratio = 0.60, without microsilica; down: w/c ratio = 0.35, 0.85 wt.% PCE, 10 wt.% microsilica.

concrete (UHPC) (Bornemann et al. 2001, de Larrad & Sedran 2002, de Larrad 1989, Richter 1999, Cwirzen et al. 2008).

The influence of the reduction of the w/c ratio and the simultaneous use of microsilica solidify and consolidate the microstructure of the hardened cement paste matrix. In figure 2a hardened cement paste is represented (top), which was manufactured without additives and admixtures and with a w/c ratio of 0.60. Figure 2 (down) illustrates a foam concrete, which is manufactured with a w/c ratio of 0.35 and the use of superplasticizers as well as microsilica. A clearly more consolidated and thus firmer structure is identifiable. This structure of the foam concretes' cement paste matrix is comparable with the dense structure of a HPC or UHPC. Usual for the production of UHPCs w/c ratios less than 0.20 are typical. This low w/c ratio is not applicable for mineral-bound foams. The approach taken by UHPC technology for improving the hardened cement paste structure often make the generation of an arranged air void area more difficult even by using superplasticizers. The lower limit for w/c ratio of chemically expanded, air hardened, mineral bound foams is 0.28 (Just 2008). Of course this sets limits to the properties of the structural optimized foams.

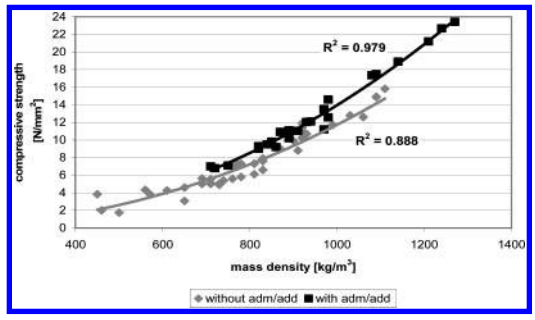


Figure 3. Compressive strengths as a function of the density with and without the usage of admixtures (adm) and additives (add).

Figure 3 clearly shows the influence of the selected structure optimizing methods by comparing more than 100 foam concretes which differ in their compositions. The trend line of the foam concretes, which were prepared by using additives and admixtures, is clearly above the trend line of the foam concrete mixtures which were produced only with cement, water and aluminum. The increase in compressive strength depends on the mass density which is illustrated in figure 3. The use of admixtures and additives increase the compressive strength by approximately 20%. The same methods for the improvement of the structure have a significantly larger influence on the properties of pure hardened cement pastes, which were manufactured without foaming agents.

3.2 *Structure of air voids*

The content and the distribution of air voids are responsible for the increase of compressive strength on air hardened foam concretes. By optimization of the microstructure a higher strength increase should be accessible.

Getting a detailed view of the structure of the porosity of the air voids, the results of three selected sample mixtures are examined and compared to each other. Sample A does solely consist of water, cement and aluminium powder. This three-substance-system is extended by a superplasticizer in sample B. In sample C the mineral-bound foam represents a five-substance-system consisting of water, cement, aluminium powder, superplasticizer and microsilica. Thereby the microstructure of the hardened cement paste of specimen C is comparable with the microstructure of HPC.

Although the composition of the single samples differentiate extremely, density and compressive strength are very similar. The compressive strength has values between 10.9 and 12.0 MPa with densities of 0.92 and 0.93 kg/dm^3. The compositions and the properties of the selected mixtures are shown in table 2.

The shape and the size distribution of the air voids are responsible for the properties of the hardened foam concrete. The structural differences within the air voids become clear when examining the roundness of the

Table 2. Recipes and properties of selected sample mixtures.

sample	w/c ratio	Al powder [wt.%]	micro-silica [wt.%]	super-plasticizer [wt.%]	density [kg/dm^3]	comp. strength [MPa]
A	0.60	0.05	0	0	0.92	11.9
B	0.40	0.08	0	0.04	0.92	10.9
C	0.40	0.10	10	0.85	0.93	12.0

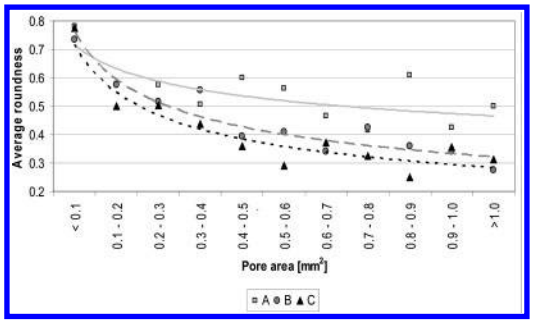


Figure 4. Average roundness of different air void classes of the three selected specimens.

pores. The roundness of all examined samples tends to decrease with rising pore sizes (Figure 4).

For all samples the roundness of the pores with a surface $<0.1\,mm^2$ is very similar. The roundness has values from 0.74 to 0.78 and has the least deviation from the cross section of all classes. Since these pores develop in all cases similarly, their influence on compressive strength must take place via the pores with an area larger than $1.0\,mm^2$. The roundness of the air voids of the class $>1.0\,mm^2$ ranges between 0.50 for sample A to 0.27 for sample B. These differences are justified in the consistency of the fresh paste. The high water content of the sample A permits the production of a foam with the dry bulk density of $0.92\,kg/dm^3$ when using an aluminium powder content of 0.05 wt.%. The remaining samples represented here reach this dry bulk density only with an accordingly higher aluminium ratio of 0.08 and 0.10 wt.%. This means that the roundness of the air voids decreases when the generation of gas bubbles is obstructed by stiffer fresh paste consistency. This change to the air voids finally results in a reduction of the compressive strength when comparing the samples A with B and C because the hardened cement paste matrix solidified due to the reduced w/c ratio and due to the use of admixtures and additives, as shown in (Just & Middendorf 2008).

The most important results can also be derived qualitatively from figure 5. With a high performance microstructure, that means with decreasing w/c ratios and simultaneous use of microsilica and superplasticizer, the average diameter of the air voids decreases and the number of inconsistently formed

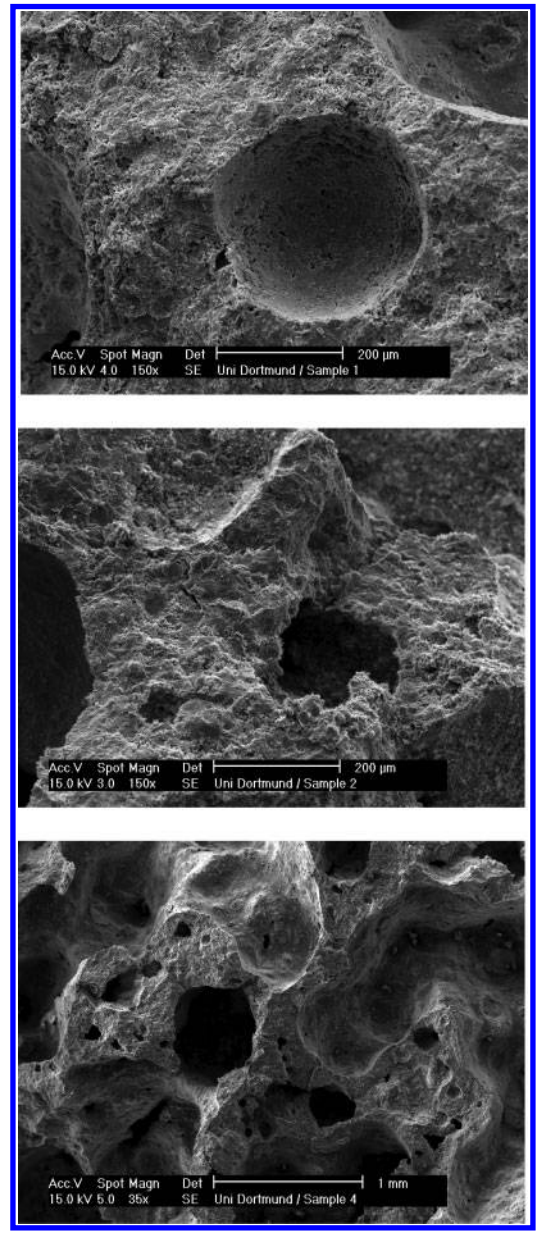


Figure 5. SEM pictures (different magnifications) of air voids in foam concretes: top: w/c ratio = 0.60, no microsilica, no superplasticizer; middle: w/c ratio = 0.40, no microsilica, 0.04 wt.% superplasticizer; down: w/c ratio = 0.40, 10 wt.% microsilica, 0.85 wt.% superplasticizer.

pores increases. This is because a stiffer fresh paste consistence requires a higher amount of aluminium for the same densities compared with less stiff consistences. Furthermore, the quantity of irregularly formed pores increases considerably. The smaller the diameter of the pores are, the more regularly they are formed. Regularly formed air voids, however, increase the compressive strength with comparable densities.

4 CONCLUSIONS

It is technically possible to manufacture chemically expanded, air cured, high performance mineral bound foams, which can be used for load bearing structures. These foams are sustainable and multifunctional because of the combination of high strength and high thermal insulating properties.

The properties of HPC and UHPC mineral bound foams can be improved by the specific use of microsilica as well as superplasticizer. The reduction of the w/c ratio and the simultaneous use of microsilica lead to a optimized cement paste matrix and a stiffer consistency. To get a processible consistency the use of a PCE superplasticizer is necessary. The microstructure of high performance foam concretes is largely comparable with the microstructure of HPCs or UHPCs. Furthermore the consistency of the stiff paste is influenced by the use of superplasticizer in such a way, that the growing of unequally shaped air voids, which occur during the chemical expansion, is encouraged. These unequally shaped air voids negatively affect the properties (e.g. compressive strength) of the hardened foam concrete, because the load transmission within the cement paste matrix is disturbed. The more superplasticizer is used the more irregularly formed air voids occur. It was observed that the size of the air voids plays a decisive role. The bigger the air voids the more irregularities occur.

It can be stated that optimized air hardened foam concretes, which should have increased compressive strengths, must be adjusted in such a way that they preferably possess as few air voids as possible, with a cross section area of $>1.0\,mm^2$. Independent of the paste composition, air voids with a cross section area $<0.1\,mm^2$ are consistently formed.

REFERENCES

Bornemann, R. & Schmidt, M. & Fehling, E. & Middendorf, B. 2001. Ultra-Hochleistungsbeton UHPC – Herstellung, Eigenschaften und Anwendungsmöglichkeiten, *Beton- und Stahlbetonbau*, 96 (7), 458–467.

Cwirzen, A. & Penttala, V.& Vornanen, C. 2008. Reactive powder based concretes: Mechanical properties, durability and hybrid use with OPC. *Cement and Concrete Research*, 38 (10), 1217–1226.

de Larrard, F. & Sedran, T. 2002. Mixture proportioning of high-performance concrete. *Cement and Concrete Research*, 32 (11), 1699–1704.

de Larrard, F. 1989. Ultrafine particles for the making of very high strength concrete. *Cement and Concrete Research*, 19 (2), 161–172.

EN 197-1, Cement – Part 1, 2004. Composition, specifications and conformity criteria for common cements.

Homann, M. 2008. Porenbeton Handbuch. 6. Auflage, Bauverlag.

Just, A. 2008. Untersuchungen zur Weiterentwicklung von chemisch aufgetriebenen, lufthärtenden, mineralisch gebundenen Schäumen. Shaker Verlag, ISBN 978-3-8322-6905-0.

Just, A. & Middendorf, B. 2009. Microstructure of High-Strength Foam Concrete. *Materials Characterization*, 07/2009, 741–748.

Just, A. & Middendorf, B. 2010. Influence of PCE on the Macro- and Microstructure of Air Hardened Foam Concrete. Proceedings 13th International Congress on Polymers in Concrete, 473–479, ISBN 972-99179-4-3.

Just, A. & Middendorf, B. & Klein, D. 2011. Structural Optimization of High Strength Air Hardened Foam Concrete, Proceedings fib Symposium 2011, 337–340, ISBN 978-80-87158-29-6.

Readymix. 1978. Sonderdruck 37, Fließfähiger Porenbeton. Transportbeton Beratungsgesellschaft.

Richter, T. 1999. Hochfester Beton – Hochleistungsbeton. Verlag Bau + Technik GmbH, Düsseldorf.

Research and Applications in Structural Engineering, Mechanics and Computation – Zingoni (Ed.)
© 2013 Taylor & Francis Group, London, ISBN 978-1-138-00061-2

The anchorage of rebars in UHPC

P. Lorenz & E. Fehling
University of Kassel, Kassel, Germany

ABSTRACT: Test-series were conducted to determine the influence of the main parameters for the bond-behavior of rebars in UHPC with small concrete covers and small bond lengths. To get basic information for the development of design rules for anchorage of rebars in UHPC, test results from specimens with parameter combinations of concrete cover and bond lengths were used which lead to splitting failure. By comparing test results and results from analytical back analysis as well as from back analysis using a non linear finite element model, bond stress-slip relations could be derived covering both ULS as well as SLS (slip s < 0.4 mm) situations.

1 INTRODUCTION

Ultra high performance concrete (UHPC) exhibits values of compressive strengths over or near to 200 MPa, which enables reducing cross sections and the use of less material and energy resources. In terms of reinforcement corrosion, the high packing density and the high resistance against ingress of fluids and gases allows markedly smaller concrete covers. At the same time, minimum concrete cover requirements must be observed in order to ensure adequate bond behavior and anchorage.

Therefore, systematic studies of the bond behavior of non-prestressed steel reinforcement in UHP(FR)C are necessary, regarding the relationship between anchorage length and concrete cover.

For normal strength and high strength concrete, the bond behavior of non-prestressed reinforcement is well described in fib (2000) or in fib (2012) regarding the different types of bond failure like splitting or pull-out. However, for ultra high performance concrete, there is currently no comparable publication. Considering this, different test series were carried out.

2 PULL-OUT TESTS

RILEM test specimens were used to study the pull out failure. Due to the high bond strength of UHPC, the ratio between bond length and rebar diameter was reduced to $l_b/d_s = 1.5$ (see Fig. 1). The bond strength was calculated by dividing the force through the bond length and perimeter of the rebar. The slip was measured at the unloaded side. After the test the specimens were split to check the bond length.

The results in Figure 1 show that the bond strength corresponds to a steel stress near to the yield strength. Due to the high concrete cover of 4.5 d_s all three tests had a pull out bonding failure. Splitting did not occur. These results cannot be applied universally to all anchorage types. The bond behavior, particularly the bond strength, depends on the confining action of the concrete surrounding the rebar. Hence, the failure mechanism is decisive.

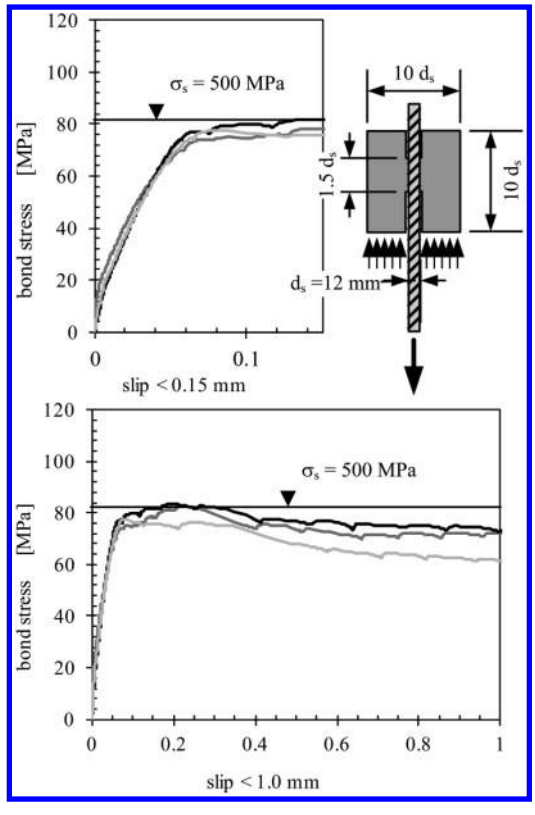


Figure 1. Pull out test results.

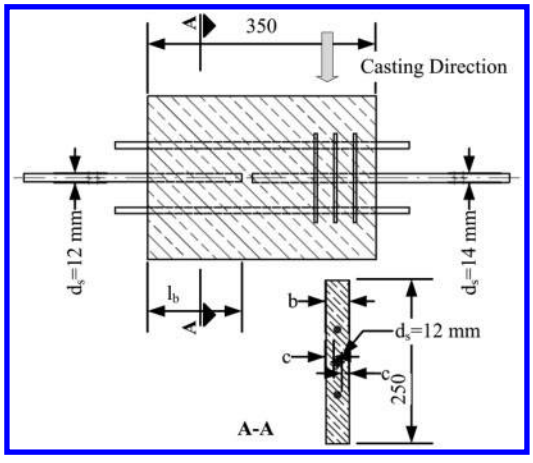


Figure 2. Test specimens regarding different bond length l_b and concrete cover c.

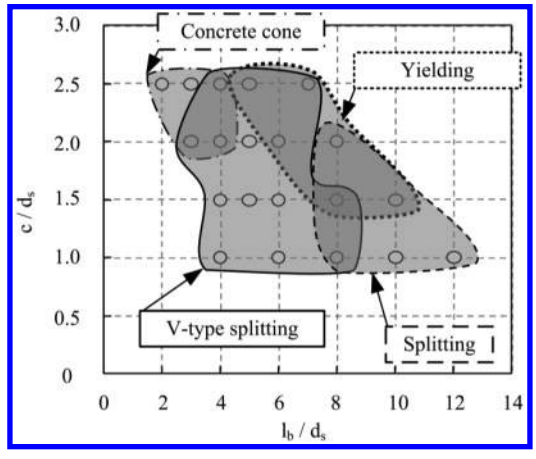


Figure 3. Examined parameters l_b and c with observed failure modes (for details see (Lorenz & Fehling 2012a)).

3 ANCHORAGE TESTS WITH SPLITTING

To consider different failure types, further test series were performed using a panel with constant length and width (see Fig. 2). Each panel contained a ribbed bar with $f_y = 500$ MPa, a diameter of $d_s = 12$ mm, an embedded length l_b, and a concrete cover c. Varying the concrete cover and bond length specimens were fabricated.

A steel fiber reinforced, fine grained UHPC M3Q from DFG (2013) with a fiber content of 1.5% by vol. ($l_f/d_f = 13$ mm/0.19 mm = 68.4) and a compressive strength of 170 MN/m^2 was used for all specimens. Details can be seen in (Lorenz & Fehling 2012a). Figure 3 shows the different observed failure modes for the examined combinations of c and l_b.

In cases of concrete cone failure (see Fig. 3) for the concrete cover $c = 2.5d_s$ and $c = 2.0d_s$ the maximum bond stress (see Fig. 5) shall be regarded with caution, since there was no bonding failure between the ribs of the rebar and the concrete. Instead, tensile failure occurred between the concrete cone and the remaining concrete.

In cases of v-type splitting, splitting and yielding, bond failure occurred, but it was strongly influenced by the degree of confinement by the surrounded concrete i.e. of the concrete cover and the post cracking behavior of UHPFRC.

4 ANALYTICAL BACK ANALYSIS

In (Lorenz & Fehling 2012b) an analytical model was described and a back analysis was presented. To verify the model, the test specimens were used which were presented in the section above. Only tests were considered where no plastic strains were measured and no concrete cone failure occurred. For the the local bond stress-slip law, a linear approach (see Fig. 6) was chosen. Using the known values of slip on both sides and of strain on the loaded side as well as the equilibrium

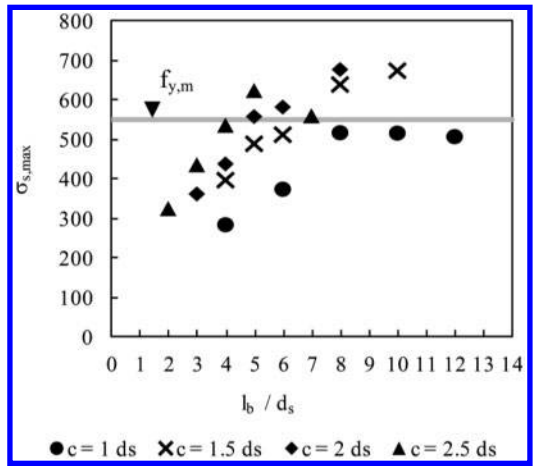


Figure 4. Maximum steel stresses ($\sigma_{s,max} = F_{max}/A_s$) in a relationship to concrete cover c and bond length l_b.

condition that stress and strain at the end of the bond length l_b should be zero, the unknown values $\tau_{u,BA}$ and $s_{u,BA}$ for the linear bond stress-slip law could be determined iteratively using data of all loading steps. This procedure was performed for all above mentioned tests, i.e. parameter combinations of c and l_b.

In Figure 7 the determined local bond stress-slip relations are shown for parameter combinations of $c \leq 1.5\ d_s$ and $l_b \leq 8\ d_s$.

For $c = 2.0d_s$ no bond slip relations were established due to the concrete cone failure mode. Here a large portion of the measured loaded end slip resulted from the crack opening behind the concrete cone.

These bond stress-slip laws are valid for large slips i.e. for slips much higher than 0.4 mm. For smaller values of slip, not only the bond stress-slip relation obtained by using the results from pull-out test (see Fig. 1) can be used. Additional considerations are necessary.

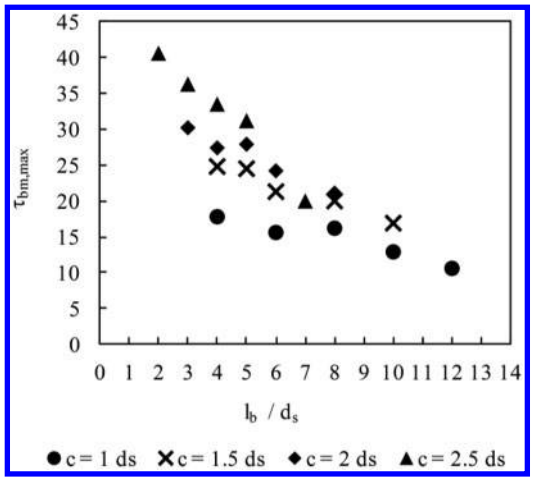


Figure 5. Maximum bond stresses ($\tau_{bm,max} = F_{max}/A_{lb}$) in a relationship to concrete cover c and bond length l_b ($A_{lb} = d_s \pi l_b$).

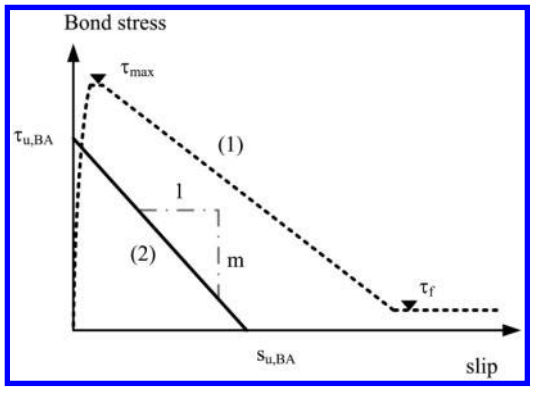


Figure 6. Linear approach (2) for the local bond stress slip-law in case of splitting failure and the approach for pull out failure (1) according to fib (2012).

5 BACK ANALYSIS USING NON LINEAR FINITE ELEMENT METHOD

Based on a non linear finite element model using ATENA 2D software, as described in (Červenka & Červenka 2012), it was possible to perform a back analysis based on the test results which were mentioned in the third section.

Due to symmetry, only a quarter of the specimen was modeled in ATENA 2D. For relevant combinations of concrete cover and bond length an FE-model was used for the calculations. The following mechanical values were used for the materials steel reinforcement and concrete.

5.1 *Iterative process to find a sufficient law*

The loading was applied in a displacement-controlled way. The slip was measured in the same way as during the real tests. For the back analysis, an iterative procedure was necessary. To start the iteration, an assumption for the bond relation was chosen based on the pull out tests in section 2 and the results as presented in section 4.

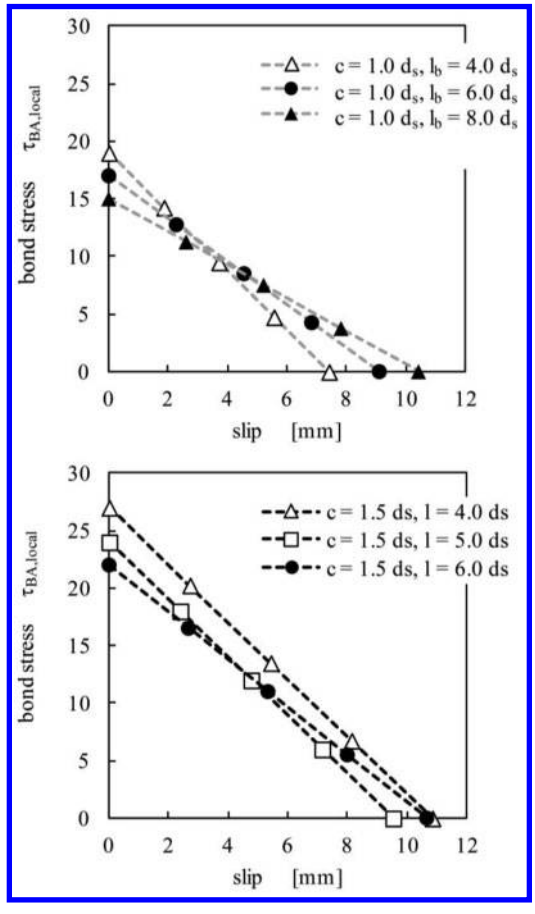


Figure 7. Determined linear bond stress slip laws for a rebar with $f_y = 500$ MPa and $d_s = 12$ mm embedded in UHPFRC M3Q from (DFG 2013) with 1.5% by vol. $l_f/d_f = 68.4$.

Table 1. Stress-strain law for the steel reinforcement material (measured at tested bar).

strain mm/m	tensile stress MPa
0.0	0
2.62	571
19.0	571
44.0	634
69.7	664
105.0	675

Table 2. Basic values for UHPFRC M3Q.

Elastic Modulus E_c	48,900 MPa
Tensile strength f_t	9.22 MPa
Compressive strength f_c	170 MPa

Table 3. Stress-strain post cracking tensile law for UHPFRC M3Q based on a characteristic size of 0.3 m.

strain mm/m	tensile stress –
0.0	1.0 f_t
0.178	1.12 f_t
21.7	0 f_t

Table 4. Stress-strain post crushing compressive law for UHPFRC M3Q based on a characteristic size of 0.3 m with no strain localization.

strain mm/m	compressive stress –
0.0	1.0 f_c
−0.178	0.0 f_c

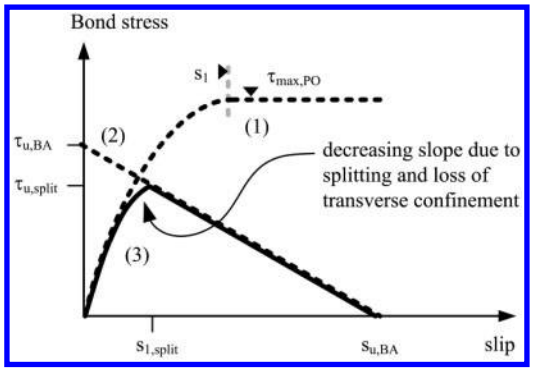


Figure 8. Proceeding in defining the bond stress-slip law for the finite element analysis. (1) represents the approximation for pull out test. (2) represents the analytical back analysis results and (3) represents the chosen bond stress-slip relation for the first iteration.

After a first calculation the output values i.e. the slip and the stress at the loaded side were compared to the values of the test results for different load steps. If there was no sufficient match, the assumed bond relation was changed. Then a new calculation was started and the results were compared again to decide if another change of the bond model was necessary. This procedure was repeated until there was a sufficient match between the FEM results and the test results (see Fig. 9).

For NSC and HSC in (fib 2000) it is shown that after the chemical adhesion is lost, a reduced slope in the ascending branch of the bond stress-slip relationship appears, depending on the presence of a transverse confinement (see Fig. 8). This transverse confinement can be the transverse reinforcement or the tensile UHPFRC ring which balances the compression struts around the rips of the rebar.

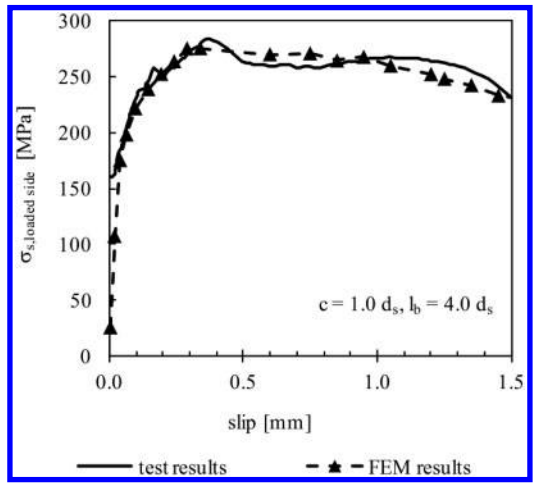


Figure 9. Sufficient match between test results and FEM results after iterative searching of the bond stress-slip law for a test specimen with $c = 1.0\ d_s$ and $l_b = 4.0\ d_s$.

This phenomenon could be confirmed with the FEM back analysis. During the process of the iterative solution, it was necessary to change the slope after loss of chemical adhesion. In Figs. 10 to 12, the results of the analytical back analysis are shown together with the approximation for the pull out tests results. In addition, the derived bond stress slip relationships are plotted.

One can see that for small bond stresses there is a very stiff bond behavior due to adhesion. After the chemical adhesion breaks down, the "bond – law" leaves the path of the approximation for the pull out tests. The gradient of the path goes down but the bond stress grows with growing slip until the path reaches the line of the analytical solution.

5.2 *Discussion of the results*

From the Figures 10 and 11 one can see that the chemical adhesion in the derived bond stress-slip relationships is between 3 MPa and 12 MPa. The slip $s_{1,split}$ where the path of the derived bond law reaches the line of the analytical solution is between 0.05 mm and 0.35 mm. To describe this path, an equation according to (fib 2012) may be used.

$$\tau_b = \tau_{u,split} \cdot \left(\frac{s}{s_{1,split}} \right)^{\alpha} \tag{1}$$

Here, $\tau_{u,split}$ is the maximum bond stress and $s_{1,split}$ the slip where the derived bond law path reaches the line of the analytical solution, i.e. where the maximum bond stress $\tau_{u,split}$ occurs (see also Fig. 8). For the exponential behavior in Eq. 1 a good approximation can be achieved with a value of $\alpha = 0.2$.

For larger slip values than $s_{1,split}$, the solution from the analytical back analysis remains valid. The slip at the end of the descending branch, i.e. where the bond stress becomes zero, can be seen in Figure 7. For

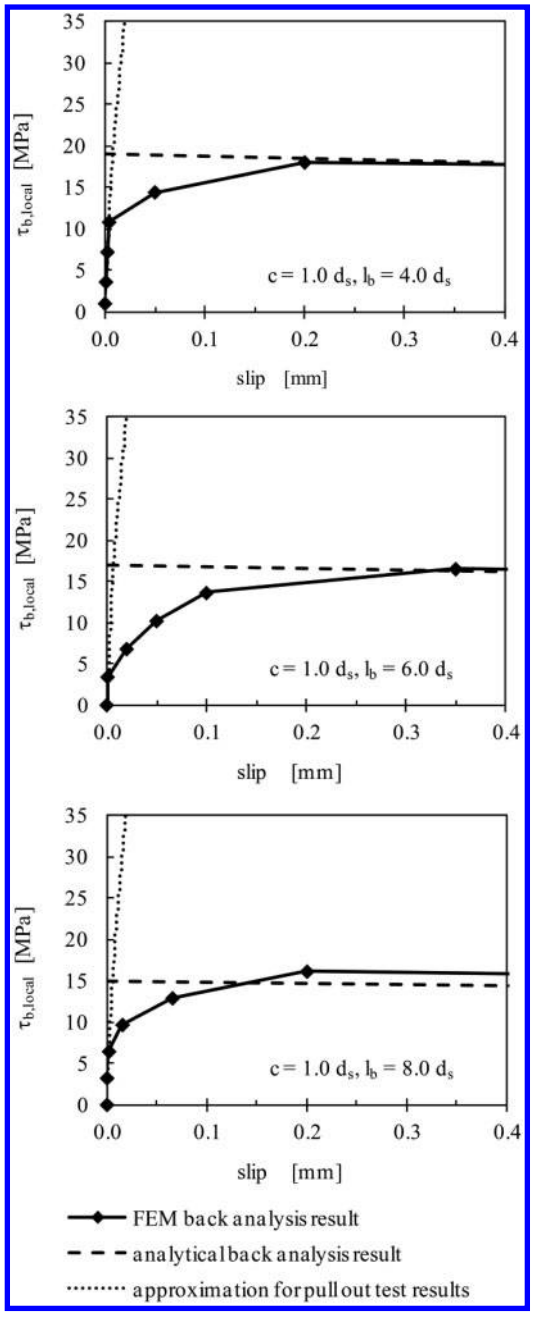


Figure 10. Derived bond stress slip-law for the test specimen with $c = 1.0\ d_s$ and $l_b = 4.0$, 6.0 and 8.0 d_s for $s \leq 0.4$ mm.

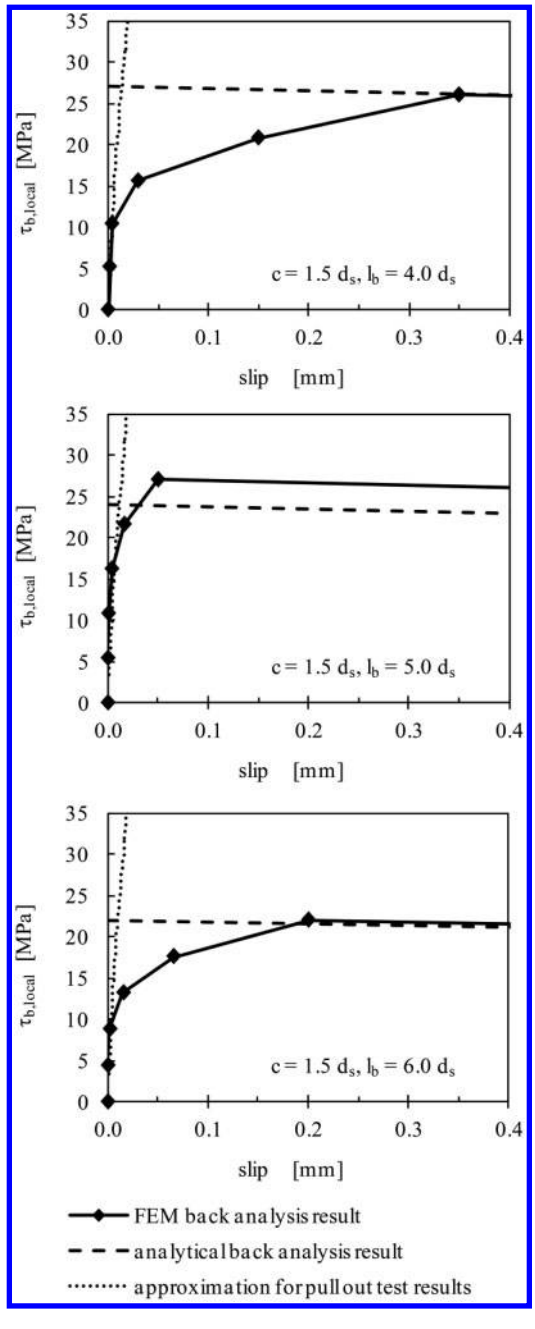


Figure 11. Derived bond stress slip-law for the test specimen with $c = 1.5\ d_s$ and $l_b = 4.0$, 5.0 and 6.0 d_s for $s \leq 0.4$ mm.

concrete cover $c \leq 1.5\ d_s$ the slip appeared between 8 mm and 11 mm.

6 CONCLUSIONS

The bond and anchorage behavior of rebars in UHPC has been studied experimentally. The combination of the described analytical and numerical back-analysis approaches enabled to derive bond stress-slip relationships.

It is well known that the bond behavior is affected by many parameters. Most important, however, it is to delineate between the different failure types.

Prior to pull out failure, the concrete around the ribs can resist high bond stresses. The pull out failure can

only be achieved, if due to transverse confinement the tensile ring which balances the struts around the ribs does not fail. If it fails and the splitting cracks propagate through the concrete over to the surface, the bond strength decreases linearly as described in fib (2012). If the splitting cracks do not propagate to concrete surface, the path of the bond-slip relation leaves the curve valid for pull out failure and approaches the curve valid for splitting failure.

In the consequence, the bond stress-slip law for concrete failure types v-type splitting and splitting and for concrete covers less than $c = 1.5\ d_s$ can be described by two parts. In the first part an exponential function (see Eq. 1) can be used for slip values $s \leq s_{1,slip}$. In the second part a linear decrease can be assumed for slips $s > s_{1,slip}$.

To find out the path of the second part, the first part may be ignored as has been done by using the analytical back analysis which was introduced in (Lorenz & Fehling 2012b).

To identify the path of the first part for small slip values, the back analysis using non linear finite element models can be used. The value $\tau_{u,split}$ can be calculated by dividing the maximum measured force through the rebar perimeter and the embedded length.

REFERENCES

Červenka, V. & Červenka, J. 2012. ATENA Program Documentation. User's Manual for ATENA 2D.

DFG 2013. German Research Foundation. final report. *in preparation.*

fib 2000. Bond of reinforcement in concrete. fib bulletin 10. State of the art report.

fib 2012. Model Code 2010. fib bulletin 66. Final draft – volume 2.

Leutbecher, T. 2008. Rissbildung und Zugtragverhalten von mit Stabstahl und Fasern bewehrtem Ultrahochfesten Beton (UHPC). *Baustoffe und Massivbau, Heft 9*. Kassel, 2008

Lorenz, P. & Fehling, E. 2012a. Experimental Investigations on Anchorage of Rebars in UHPC. *Proceedings of Hipermat 2012. 3rd International Symposium on UHPC and Nanotechnology for High Performance Construction Materials.* Kassel.

Lorenz, P. & Fehling, E. 2012b. Modellierung des Verbundes von Betonstahlbewehrung in UHPC. *Beiträge zum 53. Forschungskolloquium am 9. und 10. Oktober am Institut für konstruktiven Ingenieurbau der Universität Kassel.*

Research and Applications in Structural Engineering, Mechanics and Computation – Zingoni (Ed.)
© 2013 Taylor & Francis Group, London, ISBN 978-1-138-00061-2

Next generation nano based carbon concrete

P.S. Nagaraja
Associate Professor, UVCE, Bangalore University, Bangalore, India

Faraz Ahmed Khan, K.N. Narayana Gowda & Showkath Ali Khan Zai
Post Graduate Students, UVCE, Bangalore University, Bangalore, India

H.R. Srinivas
Doctoral Scholar, UVCE, Bangalore University, Bangalore, India

ABSTRACT: The focus of present research investigation was on exploring the use of nanotechnology-based nano-filament, such as carbon nanotubes (CNTs), the most promising nano material because of its unique physical and mechanical properties as excellent reinforcements in enhancing high ultra strength, stiffness, resilience and fracture toughness when integrated with conventional concrete. The main aim is to bridge the gap between Nano-technology and Construction industry. The present investigation is to study the behavior of CNT based carbon concrete in hardened state. The variables studied include dosage of CNTs with design Mix of M60 grade of concrete. CNTs specifically designed for use with concrete composites as admixture. Six different concentrations such as 0.025%, 0.050%, 0.075%, 0.1%, 0.125% and 0.15% of CNTs by weight of cement were used. Carbon Nanotubes were first dispersed in water and surfactant using an ultrasonic Mixer, then combined with concrete as per state-of-the-art techniques. The various mechanical properties like Compressive, Flexural and Split tensile strength can be improved with the addition of low concentrations of CNT in carbon concrete.

Keywords: carbon nanotubes, surfactant, SEM, carbon concrete

1 INTRODUCTION

Concrete is the second most used material on earth (after water), and is the most common and widely used construction material in the world. However, over the past several years, structural deterioration has become a critical issue the loss of structural capacity over time is caused mainly by the nucleation and growth of micro-cracks and their evolution into macro-cracks, which degrades the structural strength and stiffness of concrete structures. The control of concrete damage requires implementing inspection, maintenance, and rehabilitation programs, resulting in high costs. On the other hand, addition of nano-scale materials into concrete could improve its performance. Carbon nano-tubes (CNTs) have unique mechanical properties where their stiffness, strength, and resilience exceed any current material such that they offer tremendous opportunities for the development of fundamentally new material systems. The potential use of CNTs in concrete provides extraordinary specific stiffness and strength, which represents tremendous opportunity for its application in the 21st century.

1.1 *Carbon nanotubes*

Carbon nanotubes (CNTs) discovered in 1991, (Grigorij. 2006) are a unique form of carbon that has desirable mechanical, thermal and electronic properties. They can be easily visualized by considering a single graphene sheet, a lattice of carbon atoms distributed in a hexagonal pattern. A single walled CNT looks like a single sheet rolled up into a tube, while multi-walled CNT look like multiple sheets rolled into a series of tubes, one inside the other. A single walled CNT is typically 1–3 nm in diameter and a micrometer or more long. Multi-walled CNT typically range in diameter from 10 to 40 nm. Mechanically, CNT show elastic behaviour, with a Young's Modulus of approx, 1 TPa. Single walled CNT have measured yield stresses of between 20 and 60 GPa, with measured yield strains of up to 10%. Theoretical considerations suggest that the yield stress for single walled CNT may be as high as 100 GPa.

1.2 *Carbon nanotubes as reinforcing materials in cement composites*

CNTs are expected to have several distinct advantages as a reinforcing material for cements as compared to more traditional fibers. Firstly, they have significantly greater strengths than other fibres, which should improve overall mechanical behaviour. Secondly, CNT have much higher aspect ratios, requiring significantly higher energies for crack propagation around a tube as compared to across it than would be the case for a

lower aspect ratio fibre. Thirdly, the smaller diameters of CNT means both that they can be more widely distributed in the cement matrix with reduced fibre spacing and that their interaction with the matrix may be different from that of the larger fibres.

2 LITERATURE REVIEW

In the erstwhile high performance concrete is a concrete in which certain characteristics are developed for a particular application and environment, so that it will give excellent performance in the structure in which it will be placed, in the environment to which it will be exposed, and with the loads to which it will be subjected during its design life. The use of nanotechnology-based nano-filaments such as carbon nanotubes (CNTs) and nanofibers (CNFs) as reinforcement in improving the mechanical properties of cement paste as a construction material. This was achieved by testing (Jeongwoo Lee 2007, Perumalswamy Balaguru 2006) the integration of CNTs and CNFs in OPC paste through state-of-the-art techniques. Different Mixes in fixed proportions (e.g. water-to cement ratio, air content, admixtures) along with varying concentrations of CNTs or CNFs were prepared (Rashid K 2010). Small-scale specimens for mechanical testing in order to measure the modified mechanical properties as a function of nano-filaments concentration, type, and distribution. The results state that with 0.1%–0.4% CNTs (Roohallah 2011) showed by using nanofiber a new material which exhibits enhanced the ultimate strain capacity, flexural strength, fracture toughness, young's modulus and early age strain capacity can be improved with the addition of low concentrations of either CNTs or CNFs. Further Super plasticizer, which is a high range polycarboxylate-based water reducing admixture works well to disperse (Saez de Ibara Y. 2006) the CNTs without affecting the hydration of the cement paste, with use proper techniques involved in dispersing CNTs into an aqueous solution that would not adversely affect the cured cement such as use effective anionic surfactant, caused the cement paste to entrap 5 times more air than is typical in plain cement paste. But improper dispersion of CNTs will adversely affect the cementatious composites of carbon concrete.

Based on the existing literature, an attempt has been made in the present study to produce crack free carbon concrete made with nanofiber reinforcement with optimising the dispersion techniques and dosage of CNTs. Prior to their addition to cement matrix, the nanofiber were dispersed in water using a surfactant. The major drawback however, associated with the incorporation of CNTs in cement based materials is poor dispersion. Research conducted has shown that by applying ultrasonic energy and use of a surfactant, CNTs can be effectively dispersed in the cementatious matrix.

2.1 *Aim and scope of present investigation*

The objective of the research is to investigate the potential use of nano-filament such as CNTs as nano-reinforcement to improve the mechanical properties of High Performance Concrete. Due to their high surface area, they can act as excellent reinforcements in carrying internal stresses. To investigate the potential use of CNTs as nano-reinforcement in concrete, the main obstacle has to be overcome which lies in the difficulty of dispersing the nano-filaments.

The main tasks can be broken down into two major areas in following order:

i PRIMARY PHASE: Dispersion of nano-filaments in water.
ii SECONDARY PHASE: The compressive strength, tensile strength and flexural strength characteristics of Carbon concrete were evaluated.

Table 1. Properties of Materials used.

Parameter	Specification
Cement Specific Gravity	3.15
Fineness modulus of FA	2.64
Specific Gravity of FA	2.68
Fineness modulus of CA	6.1
Specific Gravity of CA	2.75
Specific Gravity of Silica Fume	2.26
Specific Gravity of GGBS	2.32
Nano Material	MWCNTs
Nano Material Colour	Black
Purity of MWCNTs	>92%
Specific Surface Area of MWCNTs	350 m^2/kg
Average diameter of MWCNTs	20 nm

3 MATERIALS AND TEST PROGRAMME

In the present work Ordinary Portland cement 53 grade, crushed granite with a maximum nominal size of 12.5 mm down size, fine aggregates satisfying the requirements of Zone II, Silica Fume, Ground Granulated Blast Slag (GGBS), MWCNTs having average diameter 25 nm with length of 30 to 60 μm, Glenium ACE 30 a High-range water reducing polycarboxylate-based admixture as super-plasticizer were used. Detailed mechanical properties of materials are shown in table 1.

3.1 *Dispersion of nano-filaments in water*

In Primary Phase, the entire dispersion of CNTs has been done, first the CNTs are dispersed in water as shown in figure 1. For carbon nano-filaments to be fully utilized within materials, they must first be properly dispersed.

The following chemicals are used for dispersion of CNTs

(a) ACETONE: Acetone is an organic compound with formula $(CH_3)_2CO$ is colourless, flammable liquid and is the simplest ketone. It is mainly used as a solvent and is a product of methyl methaacrylate and bisphenol A.

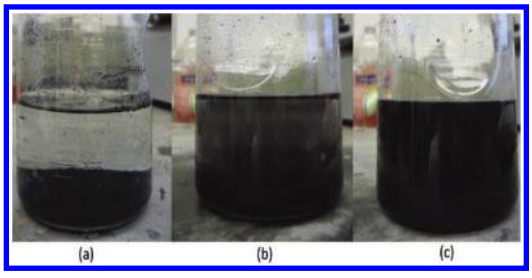


Figure 1. Effect of CNTs dispersion when mixed with water and Surfactant by (a) Hand Stirring (b) Hand Shaking (c) Ultrasonic Mixing.

(b) HDF (SODIUM DODCYL SULPHATE): HDF is an organic compound with formula $CH_3(CH_2)_{11}$ SO_4Na. This salt is an organo-sulfate consisting of 12-Carbon tail attached to a sulphate group giving the material the amphiphilic properties required of a detergent.
(c) TWEEN 20: This is a type of Polysorbate surfactant whose stability and relative non toxicity allows it to be used as a detergent and emulsifier in pharmacological applications.

To prepare each mixture, water, surfactant, and either CNTs are first measured, and then mixed with water and chemicals. In order to ensure a well-dispersed solution, an ultrasonic mixer is used, which can deliver up to 500 watts at 20 kHz. The energy in the shock waves is extremely high and significantly accelerates chemical reactions and breaks the lumps and agglomerations of particles. CNTs are mixed for 20 minutes.

3.2 *Test specimens*

In secondary Phase, weigh batching for materials was used for the experimental study. Cement, Silica fume, GGBS, Fine aggregate, coarse aggregate, water mixed with Super plasticizer and dispersed CNTs of known volume. Care should be taken when using CNTs. The dispersed solution of CNTs is added to the mix & the mixing is continued until the lump free homogeneous mix is obtained. A series of test specimens are chosen for the investigation and all are having a unique nominal sectional dimensions for cubes 150 mm, cylinders 150 mm dia. and 300 mm height and prisms 100 × 100 × 500 mm. The test programme consists of four different trail mixes of designed grade of M60 with varying percentage of silica fumes and GGBS as cementatious replacements. The four different trial mixes are.

Mix 1 M60 (Cement 79% + SF 06% + GGBS 15%)
Mix 2 M60 (Cement 71% + SF 09% + GGBS 20%)
Mix 3 M60 (Cement 63% + SF 12% + GGBS 25%)
Mix 4 M60 (Cement 55% + SF 15% + GGBS 30%)

From the above mentioned trail Mixes, Mix 2 M60 (Cement 71% + SF 9% + GGBS 20%) was found to satisfy sustainable point of view and optimized to obtain maximum compressive strength to which a Nano material i.e., carbon nanotubes (CNTs) are added. The integration of CNTs in Mix 2 M60 (Cement 71% + SF 9% + GGBS 20%) was added from 0.025% to 0.15% with regard to the cement content.

Table 2. Slump Values for M60 trial Mixes

Concrete Type	Slump mm
Mix 1 = M60 (SF6% + GGBS15%)	78
Mix 2 = M60 (SF9% + GGBS20%)	78
Mix 3 = M60 (SF12% + GGBS25%)	79
Mix 4 = M60 (SF15% + GGBS30%)	79

Table 3. Slump values for various Mix with CNTs.

Concrete Type	Slump (mm)
Mix 2 N1 = Mix 2 + 0.025% CNTs	76
Mix 2 N2 = Mix 2 + 0.050% CNTs	76
Mix 2 N3 = Mix 2 + 0.075% CNTs	74
Mix 2 N4 = Mix 2 + 0.100% CNTs	74
Mix 2 N5 = Mix 2 + 0.125% CNTs	75
Mix 2 N6 = Mix 2 + 0.150% CNTs	74

Mix N1 = Mix 2 + 0.025% CNTs
Mix N2 = Mix 2 + 0.050% CNTs
Mix N3 = Mix 2 + 0.075% CNTs
Mix N4 = Mix 2 + 0.100% CNTs
Mix N5 = Mix 2 + 0.125% CNTs
Mix N6 = Mix 2 + 0.150% CNTs

4 TESTS AND RESULTS

Most concrete structures designed under all assumption that the concrete develops compressive strength but not tensile stresses. The compressive strength is the main criteria for the purpose of structural design. The compression tests are relatively easy to carry out. The compressive strength is generally considered as most important property of concrete and gives overall picture of quality of concrete. The required slump values of various mixes with and without CNTs are shown in table 2 and 3. In the present study Compressive strength, Split tensile strength & Flexural strength are taken into account.

Figure 2–7 shows results obtained for compressive strength, split tensile strength and flexural strength for 3,7 and 28 days for the concrete matrix for the Mix 1 to Mix 4 and Mix N1toN5. It is seen that Mix2 N4 shows the significant increase in the load carrying capacity.

4.1 *SEM (scanning electronic microscope)*

SEM is an instrument used to investigate the structural morphology of any material to its nano scale level. Figure 8 and 9 shows the comparison between the Mix 2

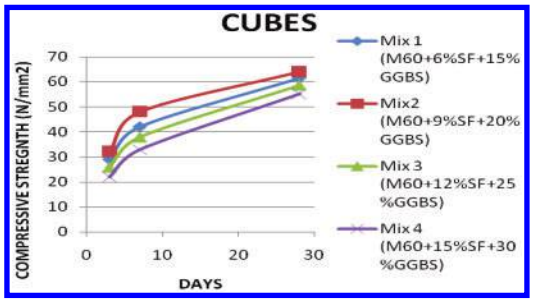


Figure 2. Compressive Strength of M60 trial Mixes.

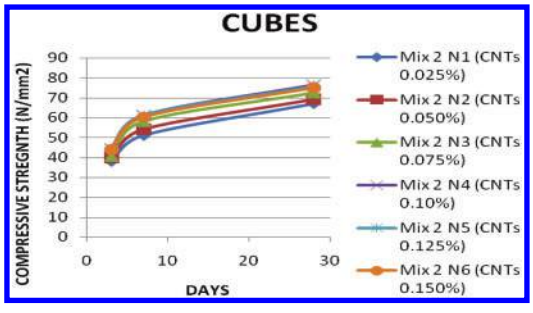


Figure 3. Compressive Strength of Mix 2 integrated with CNTs.

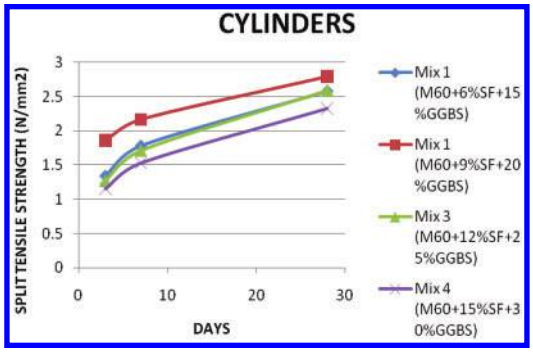


Figure 4. Split Tensile Strength of trial Mix.

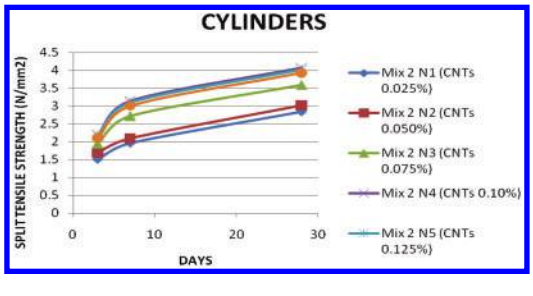


Figure 5. Split Tensile Strength of Mix 2 integrated with CNTs.

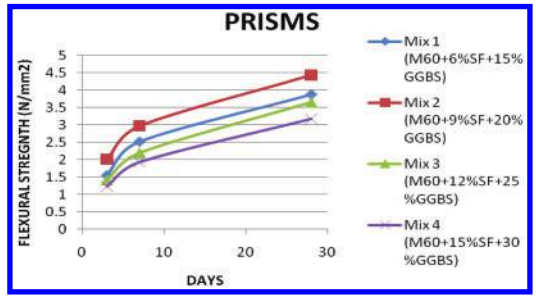


Figure 6. Flexural Strength of trial Mix.

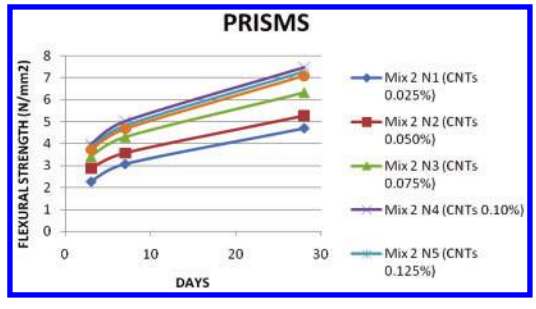


Figure 7. Flexural Strength of Mix2 integrated with CNTs.

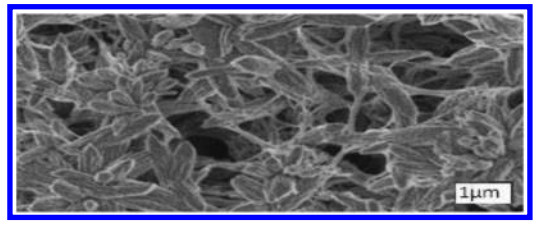


Figure 8. SEM image of fracture surface of hardened concrete Mix 2.

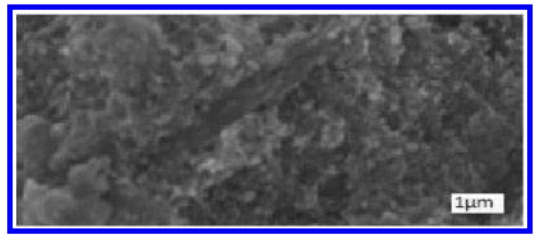


Figure 9. Fractured surface of hardened Concrete Mix 2 N4 reinforced with 0.1% of CNTs; The presence of CNTs shows filling of voids in the concrete matrix.

and the fracture surface of Mix 2 N4 having 0.10% CNT reinforced with concrete composites.

5 CONCLUSIONS

1. Among the four design Mixes of M60 grade with varying amount of cementatious materials such as Silica Fumes and GGBS viz. Mix 1; Mix 2; Mix 3

and Mix 4; compressive strength obtained at 28 days for Mix 2 was found to be increased by 106 % of the designed strength. The same has been optimised to add the Nano carbon to Mix N2.

2. The results showed that there is a significant improvement in the load carrying capacity of the CNTs composite material Nano concrete, when compared to the designed Mix without Nano carbon.
3. The Compressive strength results indicates that all six (Mix N1 to Mix N6) different percentage Mixes of CNTs with M60 grade showed an increased in strength of about 120% tested at 28 days. Carbon Nano tubes increase the compressive strength at early age in concrete.
4. The split tensile strength results of all six different percentage Mixes of CNTs with M60 grade exhibited an increased amount in strength of about 110% with respect to 28 days.
5. The flexural strength results indicate that all six different Mixes of CNTs with M60 grade exhibited an increase in strength of about 130% with respect to 28 days.
6. SEM observations of the fractured surface on the hardened concrete containing CNTs showed good dispersion within the cement matrix. Large areas observed under the SEM showed evidence of CNTs. A well dispersed aqueous Mixture with cement resulted in a relatively good dispersion and leading to production of dense concrete matrix with improved form of durability.

REFERENCES

Andrew W. Salamon, Patrick Courtney and Ian Shuttler, 2010, "Nanotechnology and Engineered Nanomaterials", PerkinElmer, Inc. 940 Winter Street Waltham, MA 02 451 USA.

Aref Sadeghi Nik, Ali Bahari and Behtash Amiri, 2011, "Nanostructural Properties of Cement – Matrix Composite", *Journal of Basic and Applied Scientific Research*, TextRoad Publication,

Baoguo Han, Xun Yu, and Jinping Ou, 2011, "Multifunctional and Smart Carbon Nanotube Reinforced Cement-Based Materials", *Nanotechnology in Civil Infrastructure*, Springer, Berlin Heidelberg, pp. 1–47.

Giuseppe Ferro, Jean-Marc Tulliani and Simone Musso, 2011, "Carbon nanotubes cement composites", Frattura ed Integrità Strutturale, pp. 34–44, Italy.

Grigorij Yakovlev, Jadvyga Keriene, Albinas Gailius, Ingrida Girniene 2006, "Cement Based Foam Concrete Reinforced by Carbon Nanotubes", *Materials Science*, Vol. 12, No. 2.

Jeongwoo Lee, Myunghun Kim, Chang Kook Ho and Sang Eun Shim, 2007, "Measurement of the dispersion stability of pristine and surface-modified multiwalled carbon nanotubes in various nonpolar and polar solvents" Meas. Sci. Technol. pp. 3707–3712.

Li GY, Wang PM, and Zhao X.2005, "Mechanical behavior and microstructure of cement composites incorporating surface-treated multi-walled carbon nanotubes Carbon", pp. 1– 43(6): 1239–45.

Perumalsamy Balaguru and Ken Chong, "Nanotechnology And Concrete: Research Opportunities", 2007, *Proceedings of ACI Session on "Nanotechnology of Concrete: Recent Developments and Future Perspectives*, Denver, USA.

Rashid K. Abu Al-Rub and Bryan M. Tyson,2010, "Assessment the Potential of Using Carbon Nanotubes Reinforcements for Improving the Tensile/Flexural Strength and Fracture Toughness of Portland Cement Paste for Damage Resistant Concrete Transportation Infrastructures", Texas Transportation Institute Zachry Department of Civil Engineering Texas A&M University, College Station, TX 77843–3136.

Roohollah Taherkhani, A. L. Saleh and Mohammad Ali Nekooie, 2011, "Potential of Nanotechnology in Construction Industry", *Proceeding of First Iranian Student Scientific Conference*, Malaysia, pp. 9-10

Saez de Ibrarra Y, Gaitero JJ, Erkizia E, and Campillo T. 2006, Aromic force microscopy and nano indentation of cement paste with nano tube dispersion. Physica Status Solidi A pp. 1076–81

Yazdanbakhsh A, Grasley Z, Tyson B, and Abu Al-Rub R, 2011 "Carbon nanofibers and nanotubes in cementitious materials: some issues on dispersion and interfacial bond". *ACI Special Publication*, Vol. SP 267: 21–34 200 Interface Science, Vol. 317(1): 346–49.

Research and Applications in Structural Engineering, Mechanics and Computation – Zingoni (Ed.)
© 2013 Taylor & Francis Group, London, ISBN 978-1-138-00061-2

Evaluation of behavior and ductility of polymer modified steel fiber reinforced high performance concrete beams

Sadath Ali Khan Zai
UVCE, Bangalore University, Bangalore, India

N. Munirudrappa
Dayananda Sagar College of Engineering, Bangalore, India

K. Muthumani
Advanced Seismic Testing and Research Laboratory, S.E.R.C., Chennai, India

R. Naveen & H.R. Srinivas
UVCE, Bangalore University, Bangalore, India

ABSTRACT: In the field of concrete technology the conventional ingredients were slowly and safely replaced by new and more efficient materials, which have opened a wide scope for research on their specific uses. Strength and ductility are the main important factors to be considered in the design of structures subjected to seismic and other dynamic forces. Hence many attempts have been made in the recent past to develop a new material which exhibits a higher strength and ductility than the conventional concrete so that they could be used in the case of structures subjected to seismic loading and impact or blast loading. The present study is aimed at the evaluation of behaviour of Polymer Modified Steel Fiber Reinforced High Performance Concrete at predefined plastic hinge location in beams for strengthening and improving seismic performance. A three point bending test is carried out on six concrete beams with dimension 150 mm × 230 mm and an effective length of 2000 mm to obtain load deflection response, as well as frequencies. The ultimate moment capacity, energy absorption, ductility index and toughness index have been evaluated. The results of the study indicates that modification at the central portion of the test beam specimens is replaced with a highly ductile composite such as Polymer Modified Steel Fiber Reinforced High Performance concrete ensures structural integrity with increase in natural frequency, resulting in enhancement of ductility and energy absorption capabilities.

Keywords: natural frequency, free vibration test, plastic hinge, SBR-Latex, ductility index, energy absorption, toughness index

1 INTRODUCTION

High Strength Concrete is a material often used in construction of high rise buildings, large span bridges where strength, durability and service behaviour are particularly important. Using high strength concrete it is possible to reduce size and weight of reinforced concrete structural members. But concrete with high strength can result in less ductility response of structural members under seismic loads. Use of admixtures such as Silica Fume, GGBS and Polymer (SBR-Latex) in a concrete matrix with inclusion of steel fibre in production of polymer modified high performance steel fibre reinforced concrete will increase the strain level corresponding to the value of peak stress. This enhances the resistance against deterioration as a result of high ductile, high fatigue, high impact strength and also reduces carbonation related shrinkage and controls the crack formation. Because of this property the member can absorb and dissipate large amount of energy compared to conventional concrete so that this could be used in structures subjected to seismic loads.

Ductility is important in the design of reinforced concrete structures subjected to seismic loads. The structural ductility and structural performance factor depends on both the structural form selected and the material used (M. Sudhakar 2009). Ductility of reinforced concrete structure is a desirable property where the resistance to brittle failure is required during flexure to ensure structural integrity. Ductile behavior in a structure can be achieved through the use of plastic hinges positioned at appropriate locations throughout the structural frame (J.M. Park 2009). In seismic design of reinforced concrete members it

is desirable to allow large ductility so that seismic energy is absorbed to avoid shear failure or significant flexural degradation of strength (S.M.R Lopes 2003). The design of ductile structures involves identifying a ductile failure mechanism for the structure and locating the position of associated plastic hinges (Monita Olivia 2005) these are referred as primary plastic hinges and are likely to develop in regions of maximum moment at the centre with shear free zone of the beam for a length which is twice the depth of the beam (Rajesh P 2008, Sreekala 2009) due to the design actions and these are the main source of inelastic response and the ductile behavior of a structure which is associated with energy dissipation. Hence beams should be required to have sufficient flexural ductility such that the potential plastic hinges in the beams are able to maintain their moment resisting capacities for seismic resistance (Young Jang 2008). For evaluation of stiffness due to low energy impact blow applied on reinforced and prestressed concrete beams natural frequency has been used (Muthumani et al. 1995, Zai 2008) thus variation in natural frequency is related to the stiffness characteristics and the ductile behaviour of system. In the present investigation ductile behavior of test beam specimens under three point bending involves formation of plastic hinges in the beam at the location where a modified concrete matrix with Polymer Modified Steel Fiber Reinforced High Performance Concrete has been incorporated only at the plastic hinge location where higher ductility is needed and also determination of natural frequencies to evaluate the ductile behaviour and energy absorption capacity.

2 EXPERIMENTAL INVESTIGATIONS

2.1 *Materials and mix proportions*

Ordinary Portland Cement (OPC) of 53 grade conforming to IS 12269:1987, locally available river sand and crushed stone coarse aggregate of 12.5mm passing, crimped round steel fibres having aspect ratio of 80, SBR-Latex, Ground Granulated Blast Furnace Slag (GGBS), Silica Fume and a high range water reducer (Glenium ACE 30) as admixtures were used. High yield strength deformed bars having characteristics strength of 415 N/mm^2 was used as longitudinal and transverse reinforcement in the entire test beam specimens. The mix ratio adopted is 1:1.03:2.03 with water binder ratio of 0.33, steel fibre 0.65% by volume, Glenium ACE 30 was added at the ratio of 0.8liter per 100 kg of binder, 9% of Silica Fume and 20% of GGBS were added as a cement replacement to the mix. The test beam specimens are Polymer modified steel fibre reinforced high performance concrete (SBR-Latex Polymer and steel fibres combined with design mix of M60 grade of concrete). Table 1 shows the hardened properties of concrete matrix of High Performance Concrete (HPC), polymer modified high performance concrete (PMHPC) and polymer modified steel fibre reinforced high performance concrete (PMSFRHPC). Figure 1 shows the reinforcement details adopted.

Table 1. Properties of Hardened Concrete.

Properties	Age	HPC	PMHPC	PMSFRHPC
Compressive strength (N/mm^2)	3 Days	32.00	26.66	32.33
	7 Days	48.00	45.33	42.00
	28 Days	64.01	55.11	66.00
Split tensile strength (N/mm^2)	3 Days	1.86	1.63	1.94
	7 Days	2.17	2.24	2.60
	28 Days	2.80	3.30	4.80
Flexural strength (N/mm^2)	3 Days	2.00	1.69	2.45
	7 Days	2.97	2.50	2.93
	28 Days	4.43	3.13	4.70

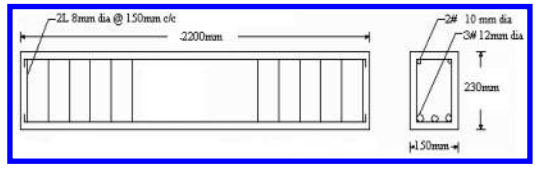


Figure 1. Reinforcement Details.



Figure 2. Concreting the Plastic hinge length.

3 PREPARATION OF TEST SPECIMENSS

The test beam specimens, for the condition of simply supported reinforced concrete under single point loading at the centre of span, the plastic hinge length was calculated as twice the depth of beam. The modified concrete matrix (PMHPC and PMSFRHPC) was first poured at plastic hinge at a length of 460 mm and remaining length on either side of beam high performance concrete (HPC) was poured as shown in figure 2.

4 TEST PROGRAMME

i. Flexural Behaviour of Test beam specimens.

The experimental programme consists of testing three series of test beam specimens under flexural loading. Loading arrangement and instrumentation are shown in figure 3. Test beam specimens consist of HPC, PMHPC and PMSFRHPC designated as A1, A2, B1, B2, C1, and C2 respectively.



Figure 3. Test Setup.

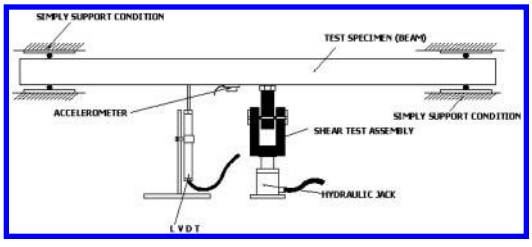


Figure 4. Free Vibration Test Setup.

ii Natural Frequency of test beam specimens.

A free vibration test is conducted to determine the natural frequencies as shown in figure 4. The test beam specimens were held rigidly between two supports depth wise and is given an initial lift within the elastic limit using loading jack so that the inertial effect will not come into picture. Then the test beam is let free with the failure of shear rods used to give the initial disturbance from the static equilibrium condition. The instruments used to record the natural frequencies are Linear Variable Differential Transducers (LVDT) and piezo electric accelerometers. The post processing of recorded data was carried out using data acquisition system which is equipped with MS Visual Basic 6.0 software. The natural frequencies were recorded during the free vibration test for three series of test beam specimens A1,B1 and C1 for un cracked condition respectively.

5 ANALYSIS OF TEST RESULTS

5.1 *Load-deflection curves*

Typical load-deflection curves for A1,A2, B1,B2 and C1,C2 test beam specimens are shown in figure 5. Major stages observed on load deflection curves are first cracking load (Pcr), Service Load (Psl), Yield point load (Pyl) and ultimate load (Pul).

5.1.1 *First crack load, yield load and ultimate load and deflection characteristics*

The first crack load P_{cr} in the entire test beam specimens was observed in the mid span of beam by visual inspection from the initial stages of loading. It is noted that B1,B2 cracked much before A1,A2 at lesser loads.

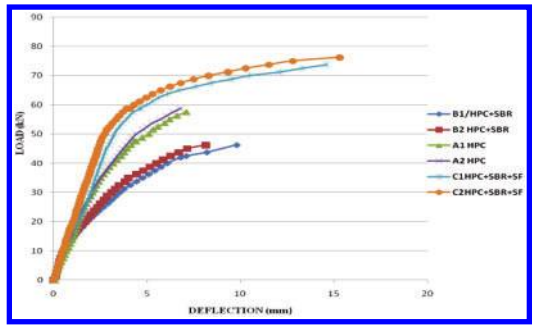


Figure 5. Load Deflection Curves.

Table 2. Load carried at various stages by the beams.

Beam	First Crack Load (P_{ct} kN)	Service Load (P_{sl} kN)	Yield Load (P_{yl} kN)	Ultimate Load (P_{ul} kN)
A1	10.00	39.12	45.00	58.75
A2	11.25	39.12	45.00	58.75
B1	8.75	30.84	35.00	46.25
B2	7.50	32.50	37.50	48.75
C1	12.50	49.12	55.00	73.75
C2	13.75	50.84	57.50	76.25

First crack in B1,B2 occurred at 24% lesser load. Similarly 18.7% decrease in service load, 19.5% decrease in yield load and 19.15% decrease in ultimate load was observed compared with A1,A2. The load-deflection pattern was similar to A1,A2 and C1,C2 but the beams sustained large deflection than A1,A2 but lesser than C1,C2. The large deflections at near maximum load of the B1,B2 beams exhibit high ductile behavior. On the other hand, A1,A2 carried higher loads than B1,B2 but did not undergo large deflection. This is mainly because of the brittle nature of beams. C1,C2 beams sustained higher loads than A1,A2 and B1,B2 beams. In C1,C2 the first crack was seen at 19% higher load, 21.8% increase in service load, 20% increase in yield load and 37% increase in Ultimate load capacities compared with A1,A2. This indicates that beams with steel fibres can carry higher loads and undergo large deformation. From table 2 and figure 5 shows a linear pattern for load-deflection values up to first crack then afterwards the rate of increase in deflection increases with load and this may be because of the cracking of concrete. After the yielding of steel C1, C2 beams continue to show ductility by undergoing higher deflections with non linearity without much increase in the ultimate load. This indicates that modification of HPC with polymer and steel fibre resulted in enhanced load carrying capacities.

5.1.2 *Prediction of cracking moment*

The cracking load depends on the tensile strength of the concrete and the geometry of the specimens. From

Table 3. Experimental and predicted cracking moment.

Test Beam	Experimental M_{CR} (kN-m)	Theoretical M_{CR} (kN-m)	Ratio of M_{CR} Exp./Theo.
A1	5.00	7.41	0.67
A2	5.63	7.41	0.76
B1	4.38	6.88	0.64
B2	3.75	6.88	0.55
C1	6.25	7.53	0.83
C2	6.88	7.53	0.92

Table 4. Experimental and predicted ultimate moment.

Test Beam	Experimental M_u (kN-m)	Theoretical M_u (kN-m)	Ratio of M_{CR} Exp./Theo.
A1	29.38	23.32	1.26
A2	29.38	23.32	1.26
B1	23.13	23.03	1.00
B2	24.40	23.03	1.06
C1	36.88	23.09	1.60
C2	38.13	23.09	1.65

the table 3 it can be observed that there is a significant increase in cracking moment when the HPC is modified with steel fibres. The experimental cracking moment (Mcr,exp) are compared with the corresponding moments calculated as per IS:456-2000.

5.1.3 *Prediction of ultimate moment*

The theoretical and experimental ultimate moments were calculated. The results show that the C1,C2 beams have higher moment capacities than A1,A2 and B1,B2 beams and the same has been tabulated in table 4.

5.2 *Natural frequency of test beam at virgin and cracked stage*

The natural frequencies are recorded during the free vibration test and are determined by evaluating the time taken for a given number of cycles. The natural frequency in Hz is obtained as n/T, where 'n' is the number of cycles and 'T' is the total time taken and is tabulated in table 5. Figures 6 to 8 show the variation displacement with respect to the time for virgin test beam specimens. It is observed that the frequencies increases in test beam specimens C1 as compared to A1 and B1.

5.3 *Evaluation of beam ductility*

The term ductility is defined as the ability of the material or member to sustain deformation beyond the elastic limit, while maintaining a reasonable load-carrying capacity before total collapse. Ductility is measured by the ratio called ductility index (μ). In this study, the member's ductility index was evaluated by

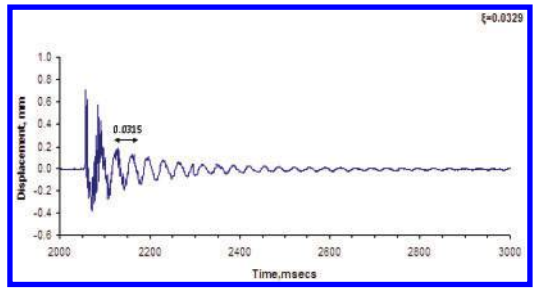


Figure 6. Variation of displacement with time for beam A1.

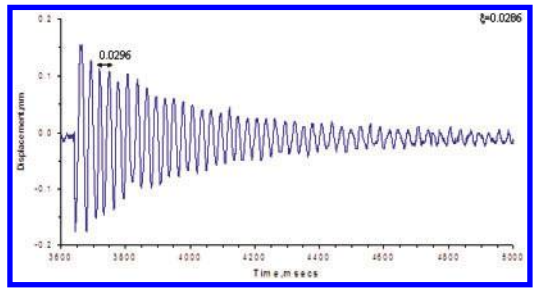


Figure 7. Variation of displacement with time for beam B1.

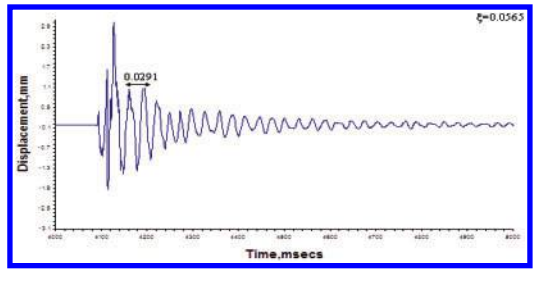


Figure 8. Variation of displacement with time for beam C1.

Table 5. Details of natural frequency.

Beam	Natural Frequency (Hz)
A1	31.74
B1	33.78
C1	34.36

displacement expressed by the ratio of the deflection at yield and the deflection at ultimate load. The specimen's ductility index is shown in table 6. The ductility for B1,B2 and C1,C2 beam type ranged between 2.05 to 2.40 and 3.77 and 4.14 respectively.

5.4 *Energy absorption capacity*

Energy absorption capacity of the entire test specimens was calculated as area under load deflection curve. Table 7 shows the results and it was found that C1,C2 have 43% increase in energy absorption capacity compared to A1,A2. This can be attributed to the effect

Table 6. Ductility Index.

Beam	δ_y,mm	δ_u,mm	$\delta_d = \delta_u/\delta_y$	Avg μ_d
A1	3.8	7.10	1.87	1.83
A2	3.8	6.80	1.80	
B1	4.77	9.80	2.05	2.23
B2	4.79	11.50	2.40	
C1	3.87	14.60	3.77	3.96
C2	3.70	15.30	4.14	

Table 7. Energy Absorption Capacity.

Beam	Energy absorption capacity (kN-mm)	Avg. Energy absorption capacity (kN-mm)
A1	136.23	133.40
A2	130.55	
B1	142.32	141.00
B2	139.46	
C1	236.93	232.50
C2	228.04	

Table 8. Toughness Index.

Beam	Toughness Index	Avg. Toughness Index
A1	41.42	42.54
A2	43.66	
B1	50.57	48.54
B2	46.52	
C1	74.62	72.31
C2	70.00	

of fibres and latex in bridging the crack and hence enhancement in energy absorption capacity. It is seen that the addition of both fibers and SBR does not have much influence on the behavior of a hardened concrete before peak load. However, a significant improvement in energy absorption is observed after peak load.

5.5 *Toughness index*

It is defined as the ratio of area under the curve up to ultimate load to area under the curve up to first crack load. The values of Toughness index for different concrete mix under investigation are given in table 8.

5.6 *Strain charactersitics*

The tensile and compressive strains of reinforcement and concrete respectively were measured at every 5 kN load increment as shown in table 9. The higher strains in C1,C2 beams may be attributed to higher deflection.

5.7 *Crack pattern and number of cracks*

The flexural cracks were the first to initiatein the plastic hinge length during the course of test as shown in figure 9. The number of cracks in A1,A2 beams was

Table 9. Strain Characteristics.

	Strain at ultimate load	
Beam	Compressive	Tensile
A1	1.35×10^{-3}	2.08×10^{-3}
A2	1.45×10^{-3}	2.40×10^{-3}
B1	1.85×10^{-3}	6.20×10^{-3}
B2	2.60×10^{-3}	6.35×10^{-3}
C1	3.43×10^{-3}	7.68×10^{-3}
C2	3.63×10^{-3}	7.89×10^{-3}

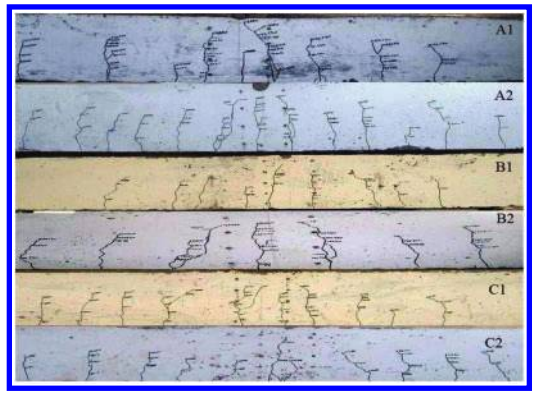


Figure 9. Crack Pattern and Number of Cracks.

more ranging about 10 to 13 with cracks propagating to the top surface of the beams. In case of B1,B2 cracks were ranging about 7 to10. C1 and C2 has about 9 cracks with the cracks not reaching up to the top this indicates the polymer modified steel fibre reinforced high performance concrete which is used in plastic hinge zone is more ductile and has significant energy absorption capacity.

6 CONCLUDING REMARKS

1. From the experimental investigation it is found that there is an increase in the natural frequency of modified concrete in test beams C1and C2. This has resulted in increase in the stiffness and thus corresponding increase in effective modulus of elasticity of modified test beams C1 and C2.
2. In general the longitudinal steel provides monotonic ductility at low reinforcement ratio and transverse steel are needed to maintain ductility through reverse cycles and at very high strain (plastic hinge development). Similarly, in the present experimental investigation the polymer modified steel fibre reinforced high performance concrete at the plastic hinge zone will enhance the ductility through reverse cycles at very high strain at these modified locations.

3. Further, from the load deflection curve it is observed that test beams C1 and C2 shows improvement in the maximum load carrying capacity as compared to test beams A1, A2, B1, and B2. Also it is evident from the experimental result that there is enhancement in ductility index, toughness index and energy absorption capacity of modified beams C1 and C2.

REFERENCES

R. Sreekala, N. Lakshmanan, K. Muthumani, A. Mehr Prasad and N. Gopalakrishnan, "Aseismic Design with pre defined Plastic hinges – A study", 2009, Asian *Journal of Civil Engineering (BUILDING and Housing)* Vol. 10, No. pp. 691–700.

M. Sudhakar , D.R Seshu and A. Kamasundara Rao,2009 "A Study of Confined SteeL Fiber Reinforced Concrete in the Plastic Hinging Regions of RC Beams" *Asian Journal of Civil Engineering (Building and Housing)* Vol. 10, No. 2, pp. 215–219

S.M.R Lopes and L.F.A Bernardo Materials and Structures, 2003, "Plastic Rotation Capacity of High Strength Concrete Beams", Materials and Structures, Vol. 36, Jan–Feb 2003, pp. 22–31.

D. Rajkumar and B. Vidivelli, 2010, "Performances of SBR Latex Modified Ferrocement for Repairing Reinforced Concrete Beams", *Australian. Journal of Basic & Applied Science.,* 4(3): 520–531.

J.M. Park , S.N. Hong , M.H. OH, T.W. Kim and S.K. Park, 2009, "Evaluation of Behavior and Ductility of Reinforced Concrete Beams Strengthened with AFRP", *Asia Pacific Conference on FRP Strucutres*, Seoul Korea.

Ru Wang, Pei-Ming Wang, Xin-Gui Li, 2004, "Physical and mechanical properties of styrene-butadiene rubber emulsion modified cement mortars", Cement and Concrete Research, pp. 900–906.

M.A. Islam, M.M. Rahman and M. Ahmed, 2011 "Polymer-modified Concrete: World Experience and Potential for Bangladesh", *The Indian Concrete Journal.*

Fahrizal Zulkarnain1, Mohd. Zailan Suleiman, 2008, Properties of latex ferrocement in Flexure, *2nd InternationaL Conference on Built Environment in Developing Countries.*

D. D. L. CHUNG, 2004, "Review Use of polymers for cement-based structural materials", *Journal OF MATERIALS SCIENCE.*

G. Barluengaa, F. Hernańdez-Olivaresb, 2004, "SBR latex modified mortar rheology and mechanical behaviour" *Cement and Concrete Research* pp. 527–535.

Payam Shafigh1, Mahmoud Hassanpour M., S. Vahid Razavi and Mohsen Kobraei, 2011, "An investigation of the flexural behaviour of reinforced lightweight concrete beams", *International Journal of the Physical Sciences*, Vol. 6(10), pp. 2414–2421.

U. Johnson Alengaram, Mohd Zamin Jumaat, Hilmi Mahmud, 2008, "Ductility Behaviour of Reinforced Palm Kernel Shell Concrete Beams" *European Journal of Scientific Research,* Vol.23 No.3 (2008), pp. 406–420.

Divya S Nair, Dr. Ruby Abraham, Dr.Lovely K M, "Shear Strength of High Strength Fibre Reinforced Concrete beams".

Mukesh Shukla, 2011, "Behavior of Reinforced Concrete Beams with Steel Fibres under Flexural Loading", *International Journal of Earth Sciences and Engineering*, Vol. 04, No. 06 SPL, pp. 843–846.

Ravindra Gettu, Zdenek P. Bazant and Martha E. Karr. 1990, *"ACI Material Journal"*Vol. 87, No.6.

Tamim a. Samman, Faisal F. Wafa and Talal A. Radain, 1999, "Mechanical Properties of Normal and High-strength Concrete with Steel Fibers", *JKAU*, Vol. 12, No.1.

F.B.A. Beshara, I.G. Shaaban and T.S. Mustafa, 2009, "Nominal Flexural Strength of High Strength Fiber Reinforced Concrete Beams", *11th Arab Structural Engineering Conference,* KFUPM, Dhahran, Saudi Arabia.

V. Bhikshma, K. Jagannadha Rao and Balaji, 2010, "An Experimetnal Study on Behaviour of Polymer Cement Concrete", *Asian Journal of Civil Engineering,* Vol. 11, No. 5, pp. 563–573.

Monita Olivia, Parthasarathi Mandal Jurnal Teknik Sipil, 2005, "Curvature Ductility of Reinforced Concrete Beam",Vol. 6 No. 1, pp. 1–13.

Rajesh P. Dhakal and Richard Fenwick, 2008, "Detailing of Plastic Hinges in Seismic Design of Concrete Structures", *ACI Strucutre Journal,* Vol. 105, No. 6.

Research and Applications in Structural Engineering, Mechanics and Computation – Zingoni (Ed.)
© 2013 Taylor & Francis Group, London, ISBN 978-1-138-00061-2

Structural behavior of high performance fiber-reinforced flowable concrete beams and plates

Samaan G. Ladkany & Abebe T. Berhe
Department of Civil and Environmental Engineering, University of Nevada, Las Vegas, USA

ABSTRACT: Some aspects concerning the characterization and potential applications of high strength (>10,000 psi) Steel Fiber Self Consolidating Concrete (SFRSCC) and flowable concrete, with fiber content ranging from 0%-to-2% in volume fraction, are presented. Research in the area of fiber concrete has been conducted at the University of Nevada, Las Vegas (UNLV) for several years with the latest emphasis placed on high strength and high steel fiber content. Such characteristics place this fiber-reinforced concrete amongst the new high performance materials. The high tensile and shear strength of this fiber concrete would allow its use in structures with little or no longitudinal reinforcement.

This paper discusses the behavior, under structural testing of beams 102 mm × 102 mm × 305 mm (4 in. × 4 in. × 12 in.) and very thin plates, 32 mm (1.25 in.) thick. The structural behavior and performance that were studied include: 3-point loading of beams, rectangular plates 305 mm (12 in.) wide by 1219 mm (48 in) long loaded in the transverse and longitudinal directions. The study encompasses the mechanical properties of the fiber-reinforced concrete, such as compressive and tensile strength, modulus of rupture and modulus of elasticity. Observation of the failure mode of the specimens will also be discussed.

Keywords: Flowable, High-Strength, Self Consolidating Concrete, SCC, Steel Fiber, beams, plates

1 INTRODUCTION

This research is the continuation of previous studies conducted at the Civil Engineering Department at University of Nevada, Las Vegas since 1997 (Ahmed 2001; Ahmed and Ladkany 2003, Ladkany and et al 2005). In this research 1% by volume fraction of one inch long steel-fiber and Styrene-Butadiene, rubber based polymer, were added to normal 27.6 MPa (4 ksi) concrete mixture to study the ductility behavior of steel-fiber and polymer concrete mixtures (Ahmed 2001). High strength steel-fiber mixtures, with 0.3% of steel by volume, were studied for compressive and tensile strength with different combinations of admixtures and cement substitutes (Doli 2007).

The desirability of high strength concrete is in the overall reduction in the weight of structures, the volume of concrete used in the construction, and the resulting beneficial environmental effects associated with reduction in weight and materials and to reduce the overall structural weight of the concrete especially in areas such as beam-column joint, two way slab-column joints and heavily loaded columns reinforcing steel are normally present triggered the launch of this particular research. Normal strength fiber SCC with 1% fiber volume fraction in Europe is being effectively used for slabs and flat plates with longitudinal reinforcement placed only between adjacent columns (Destree 2004). Other researchers have investigated SFSCC columns (Aoude 2009) and the shear behavior of beams (Greenough 2008). Longitudinal reinforcing steel can be reduced greatly and in some cases eliminated if steel-fiber reinforcements coupled with high concrete strength are used. Kearns (Kearns 1989), tested ultra thin straight and curved plates using normal 1% SFC, which prompted our research group to study the mechanical properties of HSSFSCC in thin plates and shells.

This paper discusses the behavior, under structural testing of beams 102 mm × 102 mm × 305 mm (4 in × 4 in × 12 in) and very thin plates, 32 mm (1.25 in.) thick. The structural behavior and performance that were studied include: 3-point loading of beams, rectangular plates 305 mm (12 in.) wide by 1219 mm (48 in.) long loaded in the transverse and longitudinal directions.

2 PURPOSE OF RESEARCH

The purpose of this phase of our research is to study the behavior of beams and very thin plates, 32 mm (1.25 in.) thick, under structural testing. The structural behavior and performance that were studied include: 3-point loading of beams, rectangular plates 305 mm (12 in.) wide by 1219 mm (48 in.) long line- loaded in the transverse and in the longitudinal directions. The next phase of this research, which will not be presented in this paper, will concentrate on the behavior of thin square, thick circular plates and thin pipes and shells.

The mechanical and fresh properties of the high strength SCC/flowable concrete were presented in previous publications by our research group for 0%, 1% and 2% steel fiber by volume fraction (Ladkany 2013, 2011 and 2005), however some of these properties will also be discussed in this paper.

3 STEEL FIBER CONCRETE PROPERTIES

3.1 *Raw material*

Coarse and fine aggregates were obtained from a local quarry in Las Vegas, Nevada. Since the application of the concrete mixtures were ultimately to be used for thin plates and shells (about 25.4 mm thick), the size of the coarse aggregate was limited to nominal sizes of 9.53 mm (3/8″) and #4. The oven-dry specific gravity and absorption of the coarse aggregate (ASTM C 128-07a) are 2.777 and 0.60%, respectively. Fine aggregate grading, with fineness modulus of 3.03, met the requirements of ASTM C33 grading limitations. The oven-dry specific gravity and absorption of the fine aggregate (ASTM C 128-07a) are 2.785 and 0.64%, respectively. Deleterious substances are substantially below the maximum allowable limits for both coarse and fine aggregates.

ASTM C 150 Type V Portland cement 404 kg/m^3 (25.2 lb/ft^3), which is widely used in the local area due to its resistance to sulfate and Class F fly ash, at 42.5% by weight of cement, meeting the requirements of ASTM C 618 were used. Silica fume, 7.5% by weight of cement, was also used.

The admixture used was High Range Water Reducers (HRWR).

ASTM 820-90 Type II Deformed cut sheet carbon steel fibers with equivalent diameter of 0.584 mm (0.023 in) and aspect ratio, l/D, of 47:1 were used. The steel fibers have rectangular cross section of 0.406 × 0.838 × 19.05 mm (0.016 × 0.033 × 3/4 in) and specific gravity of 7.85. The tensile strength of steel-fibers ranges between 379 to 763 MPa (55,000 to 111,000 psi).

The amount of water-to-cement ratio and coarse-to-fine aggregate ratio were adjusted to suite the concrete mixture under consideration. Optimum coarse-to-fine aggregate ratio for FRC was found to be 44% to 56% (724:920 kg/m^3), respectively. The water-to-cement ratio was set at about 0.435 to meet both self consolidating properties and high strength concrete requirements.

3.2 *Fresh properties of steel fiber reinforced SCC*

Concrete mixtures were subjected to the following fresh property SCC tests.

1. Slump flow Test (>482 mm (19 in.))
2. J-Ring Flow Test (≥50 mm (2 in.))
3. V-Funnel Test (flow time ≥5 sec)
4. U-Box Test (filling height ≥305 mm (12 in.))

Even though some of the V-Funnel and U-Box requirements for regular SCC were not fully met, the mixtures were highly flowable and the specimens were fully consolidated. The full results are shown in tabular format in SEI 2011 (Ladkany & Berhe 2011) and SCC Congress 2013 (Ladkany and Berhe to be published).

3.3 *Mechanical (hardened) properties SFRSCC*

From the current experimental study, it can be concluded that, with the increase of steel-fiber volume fraction the required HRWRA increases. Ultimately, VMA and water- to-cement ratio need to be adjusted to get the SCC properties for 1% and 2% steel fiber mixtures while maintaining the high strength concrete characteristics.

The test results show that mechanical characteristics, modulus of elasticity, compressive and tensile strength of high strength 69 MPa (10 ksi) concrete can be substantially enhanced by the addition of steel fibers in the neighborhood of 2%. The 7-Day compressive strength of HSSCC was in the range of 65% to 70% of the 28-Day strength, which may be favorable for construction methods that require high early strength concrete.

4 EXPERIMENTAL PROCEDURES

Two types of structural specimens were tested using concrete mixtures having 0%, 1% and 2% steel fiber by volume fraction. The structural specimens tested are Beams, rectangular plates loaded in transverse direction and longitudinal direction under line loads. The testing procures are described in section 4.1 through 4.3 below.

4.1 *Beams*

Beam specimens were prepared and tested per ASTM C78 standard for the computation of modulus of rupture and flexural capacity. The beam sizes were 102 mm (4 in.) wide × 102 mm (4 in.) deep × 356 mm (14 in.) long and supported at 305 mm (12 in.) on center. Line loads were applied at third points 102 mm (4 in.) apart from the support, as shown Figure 1. For beam experiments which were performed at the onset of this research, the amount of HRWR used in kg/m^3 (lb/ft^3) was: 6.279 (0.392), 6.023 (0.376) and 6.664 (0.416). Whereas, the amount of HRWR used for rectangular plates was constant for all steel fiber volume fractions as shown in section 4.2.

4.2 *Rectangular plates: Supported and line-loaded in the longitudinal direction*

Plate specimen sizes were 1219 mm (48 in.) long × 356 mm (14 in.) wide × 32 mm (1.25 in) deep. The plates were loaded in the longitudinal direction with a line load placed at the mid width of the plate. The supports were spaced at the 305 mm (12 in.) on center,



Figure 1. Beam under flexural load.

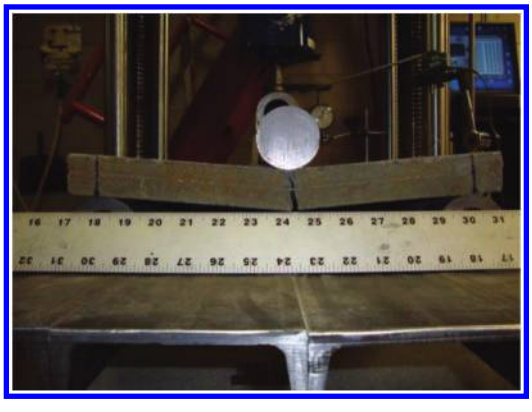


Figure 2. Rectangular plate under longitudinal load.

as shown in Figure 2. The HRWR used for both rectangular plates (section 4.2 and 4.3) were 6.279 kg/m^3 (0.392 lb/ft^3) for all steel fiber volume fractions.

4.3 *Rectangular plates: Supported and line-loaded in transverse direction*

Plate specimen sizes were 1270 mm (50 in.) long × 305 mm (12 in.) wide × 32 mm (1.25 in) deep. The plates were loaded in transverse direction with a line load placed at the mid length of the plate. The supports were spaced at the 1219 mm (48 in.) on center, as shown Figures 3 & 4.

5 RESULTS AND DISCUSSION

5.1 *Beams*

The average 28 day compressive (ASTM C 39) and splitting tensile strength (ASTM C 496) of four cylinders each for 0%, 1% and 2% steel fiber by volume fraction are given in Table 1.

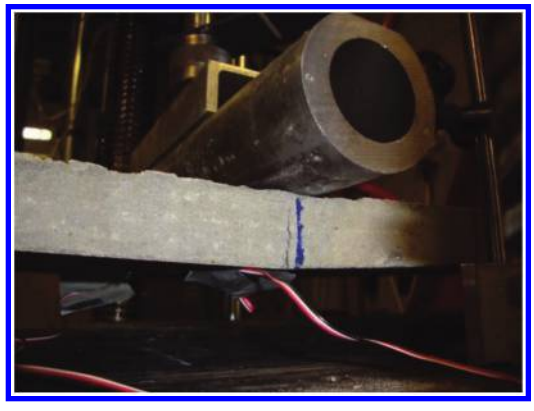


Figure 3. Rectangular plate under transverse load.

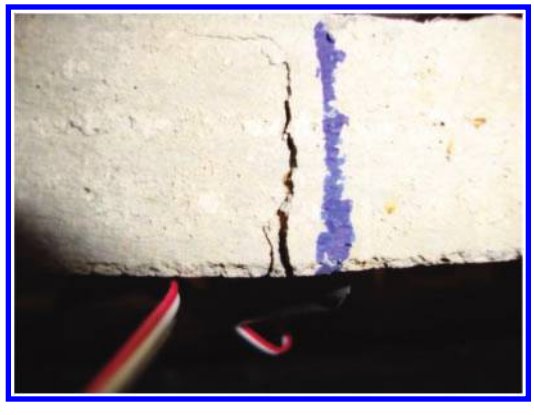


Figure 4. Rectangular plate under transverse load.

Table 1. 28 Day compressive and splitting tensile strength of cylinders used for beam tests and beam modulus of rupture.

Steel fiber	f'_c MPa/(ksi)	f_t MPa/(ksi)	f_r MPa/(ksi)
0%	68.0/(9.86)	6.69/(0.97)	9.7/(1.41)
1%	75.3/(10.9)	8.90/(1.29)	9.5/(1.38)
2%	80.7/(11.7)	10.35/(1.5)	11.5/(1.66)

As mentioned in section 4.1 the amount of HRWR used in the fresh mixture for the 1% SFRSCC was lower than the amount used for 0% and 2%, which affected the bonding between steel fiber and matrix. While the compressive and tensile strengths of the SFRSCC cylinders increased steadily with the increase of steel fibers, the short beam test for modulus of rupture, f_r for 1% fiber decreased slightly from the 0%. The cylinder tests were run at a load controlled rate, the beam tests were displacement controlled. Thus, it is difficult to make valid comparison. The short and stubby beams are too rigid and brittle to allow for any other study except for the modulus of rupture, shown in Table 1.

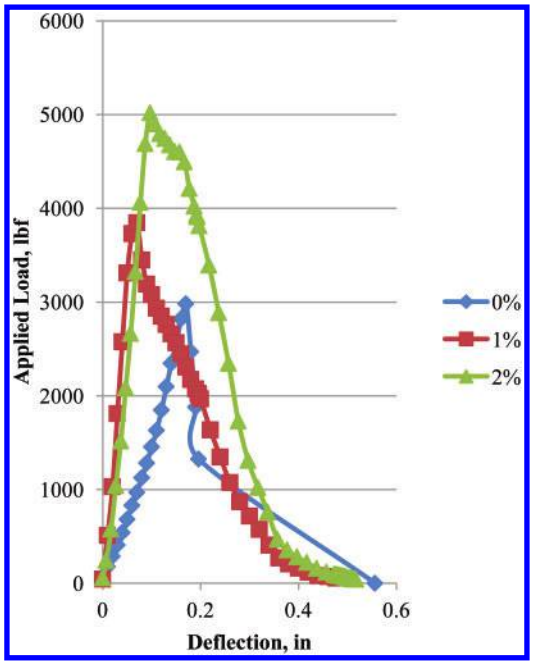


Figure 5. Applied load Vs deflection for 0%, 1% & 2% SFRSCC rectangular plates line-loaded in the longitudinal direction.

Table 2. 28 Day compressive and splitting tensile strength of cylinders used for rectangular plates.

Steel fiber	f'_c MPa/(ksi)	f_t MPa/(ksi)
0%	85.6/(12.4)	5.9/(0.85)
1%	84.2/(12.2)	7.5/(1.09)
2%	84.9/(12.3)	10.7/(1.56)

5.2 *Rectangular plates: Supported and line-loaded in the longitudinal direction*

Load-deflection curves for 0%, 1% and 2% steel fiber SFRSCC rectangular plates line-loaded and supported in the longitudinal direction are shown in Figure 5. While the compressive and splitting tensile strength of the cylinders associated with these plates tested are shown in Table 2.

The results taken from 6 cyliders for each test show a substatial increase, of 6.9, 8.9 and 12.6%, respectively in tensile to compressive strength ratios with increasing fiber percent. Similarily, the tensile strength increases by 28% and 184% for 1% and 2% over 0% respectively. The load- deflection curves for the plates shown in Figure 5, diplay similar behavior.

5.2.1 *Energy absorption*

The increase in ductility is impressive for steel fiber concrete compared to 0% high strength SCC.The load-deflection curves of longitudinally loaded SFRSCC are shown in Figure 5. The energy absorption of the plates within the elastic range were 223, 146 and 243 in-lb for 0%, 1% and 2%, respectivley. These results indicate that the energy absorption is not affected by the fiber content. The post-crack energy absorption were 59, 528 and 782 in-lb, showing substantial increase for the 1% and 2% SFRSCC over 0%.

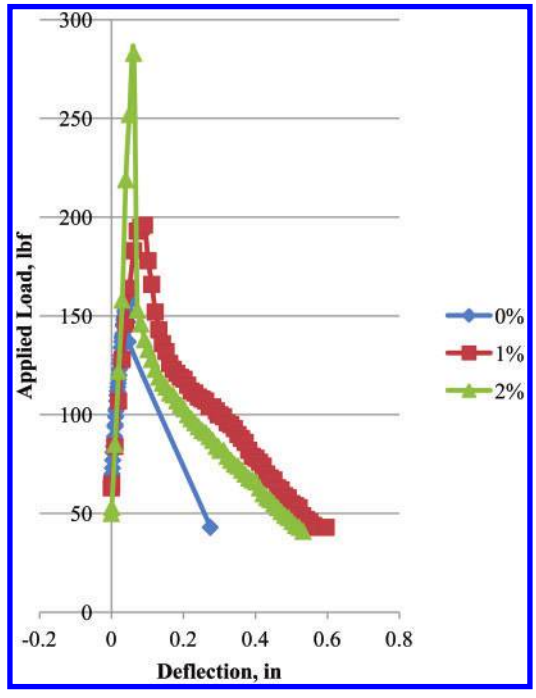


Figure 6. Applied load Vs deflection for 0%, 1% & 2% SFRSCC rectangular plates line-loaded in the transverse direction.

5.3 *Rectangular plates: Supported and line-loaded in the transverse direction*

The compressive and splitting tensile strengths of the cylinders associated with the plates tested, are shown in Table 2.

The load-deflection curves for the plates shown in Figure 6, diplay similar behavior to the plates loaded in the longitudinal direction shown in Figure 5.

5.3.1 *Energy absorption*

The increase in ductility is also impressive for steel fiber concrete compared to 0% high strength SCC for this case. The energy absorption of the plates within the elastic range were 5.1, 12.5 and 11.1 in-lb for 0%, 1% and 2%, respectivley. The post-crack energy absorption were 0.7, 47 and 41 in-lb, substantial over 0% as in the previous case.

6 CONCLUSION

Experiments with high strength 83 MPa (12 ksi) concrete with 1% and 2% steel fiber SCC indicate that

this material, due to its high compressive strength and ductile failure mode, is highly promising for use in a variety of engineering applications that require reduction in concrete volume, longitudinal and transverse steel reinforcement and labor cost. The thin plates tested show an impressive ductile failure mode and ability for energy absorption, which indicates much improved overall structural toughness over plain high strength concrete.

REFERENCES

Ahmed, A. 2001. Characterization of Steel Fiber and/or Polymer Concrete Mixes and Applications to Slender Rectangular and I-Beams. PhD Thesis, University of Nevada, Las Vegas.

Ahmed, A. and Ladkany, S. 2003. Effects of Adverse Hot Weather Curing Conditions on Plain and Polymer-Modified Concrete Mixes Used in Foundations and Basements. Proceedings of the 38th symposium of Engineering Geology and Geotecnical Engineering. University of Nevada, Reno. 197–201.

Aoude, H., Cook, W.D. and Mitchell, D. 2009. Behavior of columns constructed with fibers and self-consolidating concrete. ACI Structural Journal, 2009: Vol 106, Issue 3: 349–357.

ASTM C 39. 2001. Standard Test Method for Compressive Strength of Cylindrical Concrete Specimens American Society for Testing and

Materials. ASTM International, West Conshohocken, PA ASTM C 78. 2000. Standards Test Method for Flexural Strength of Concrete (Using Simple Beam with Third-Point Loading). ASTM Standards, West Conshohocken, PA.

ASTM C 496. 1996. Standard Test Method for Splitting Tensile Strength of Cylinderical Concrete Specimens. American Society for Testing and Materials. ASTM International, West Conshohocken, PA.

Destree, X. 2004. Structural application of steel fibre as only reinforcing in free suspended elevated slabs. Varenna, Italy: Symposium, 6th RILEM: 1073–1082.

Doli, V. 2007. *T*he Influence of Cementitious Materials and Steel Fiber Reinforcement on the Strength of Self-Consolidating Concrete. University of Nevada, Las Vegas.

Greenough, Tom, Nehdi & Moncef. 2008. Shear Behavior of Fiber-Reinforced Self-Consolidating Concrete Slender Beams. ACI Materials Journal, 2008.

Kearns, C.F. and McConnell, G.M. 1989. Structural behaviour of thin planar and curved microconcrete plates reinforced conventionally and with steel fibers. Materials and Structures, 1989: 357–363.

Ladkany, S.G. & Berhe, A.T. unpublished. Characterization and Applications of High Strength Steel Fiber SCC and Flowable Concrete; SCC Congress 2013, Chicago-Illonois.

Ladkany, S.G. & Berhe, A.T. 2011. Characterization of High Strength Steel Fiber Reinforced Concrete and Self-Consolidating Concrete Mixtures with Various Steel Volume Fractions for Infrastructures; SEI proceedings, Las Vegas, Nevada.

Ladkany S.G. et al. 2005. Mixing performance and strength of steel fiber-reinforced SCC with varing cementitious materials. SCC 2005 proceedings, Center for advanced cement-based materials. Chicago-Illinois, 387–391.

Research and Applications in Structural Engineering, Mechanics and Computation – Zingoni (Ed.)
© 2013 Taylor & Francis Group, London, ISBN 978-1-138-00061-2

Influence of fiber orientation on the properties of strain hardening ultra-high performance fiber reinforced concrete (UHPFRC) under direct tensile loading

C. Hollmann & K. Wille
University of Connecticut, USA

ABSTRACT: Research was conducted to investigate and analyze the uniaxial tensile behavior of strain hardening ultra-high performance fiber reinforced concrete (UHPFRC) in dependency of fiber orientation of the test specimen. Enhanced mix design, casting, and specimen preparation methods allow for an artificial alignment of fibers at different angles. Several research investigations have been carried out on the effect of single fiber pullout as well as the effect of fiber orientation on bending and tensile strength, however, the amount of research on UHPFRC tensile behavior in dependence on fiber orientation is still lacking. The paper will review a variety of casting methods and tensile test setups used by other researchers and will present a revised and tailored casting method and tensile setup herein. The experimental investigation will quantify, analyze, and link steel fiber orientation in UHPFRC to properties such as strain hardening and maximum strength. The results of the paper support the prediction of the tensile behavior of UHPFRC and should motivate carrying out further research of this composite material.

1 INRODUCTION

1.1 *Motivation and background*

Ultra-High Performance Fiber-Reinforced Concrete (UHPFRC) is shown to have a pronounced strain hardening effect depending on the mix proportions, fiber dosage, fiber distribution, fiber orientation, and casting methods used. The quantity of fibers bridging crack planes and the fiber orientation relative to the direction of applied tensile stresses can drastically influence mechanical properties under tensile loading. Casting method has a very influential effect on fiber orientation and therefore has the ability to negatively or positively affect the maximum strength and strain hardening properties after initial cracking. Casting methods can be designed to optimize fiber orientation longitudinally to the applied load direction which has been shown to produce the best results.

In this paper an optimized casting method is used to provide insight on how the angle of fiber orientation with respect to the direction of applied tensile load can affect the mechanical properties UHPFRC of a structural element. This is done by optimizing the casting method for a thin plate slab in order to align fibers in one direction as perfectly as possible. Tensile specimens were then cut out of the thin plate slab at angles of 0, 30, 45, 60, and 90 degrees with respect to initial direction and were subjected to uniaxial tension loading.

1.2 *Literature review*

Casting along the direction of applied load has a large effect on mechanical properties of UHPFRC. Wille et al. (2010) show that casting with a scoop in layers back and forth along the length of a dog-bone tensile specimen will lead to a preferable alignment of fibers in the direction of axis of the specimen and hence the direction of the applied load. The relatively constant flow and the casting motion have a pulling effect on the fibers which coaxes them to align along the casting direction. Kim & Kang (2011) poured tensile dog-bone specimens with a scoop along the direction of the applied load as well as across the direction of the applied load. The specimens poured across the direction of the applied load had an over 40 percent reduction in average maximum stress. In regards to flexural stress, Kang, Kim, Kim, & Lee (2010), found that flexural specimens cut longitudinally to the back and forth casting direction had a 61% greater flexural strength than those cut transverse to the pouring direction.

UHPFRC flow, such as channel flow or radial flow can also effect fiber alignment. Kang, Kim, Kwon, and Lee (2012) showed that when concrete is poured in the center of a plate and allowed to flow radially the fibers will increasingly orient more perpendicular to radial flow with increasing distance from the center of the flow. However, for a confined flow, the fibers orient parallel to the direction of the flow. Joh, Kim, & Yang (2011) cast one flexural beam

Table 1. Proportions for mix UHPFRC Mix.

Material	Proportions by weight	
	UHPC	UHPFRC
Cement	1.00	1.00
Silica fume	0.25	0.25
Powder	0.25	0.25
Water	0.24	0.24
HRWR	0.036	0.036
Steel fibers	0.00	0.25
F110 sand	0.3	0.3
F75 sand	0.70	0.70

specimen by pouring from the center of the beam and cast another beam specimen by pouring from the end of the beam. The beam poured from the end behaved better because the fibers aligned with the flow so that in the middle of the beam, where stresses were highest, the fibers were oriented longitudinally to the applied tensile stresses. Matinie & Roussel (2011) analyze simple channel flow. Along the length of the channel the shear effect of flow is highest near the faces of the mold and the fibers are very well aligned within 10 degrees in these areas. The shear flow orientation effect happens within a matter of seconds after flow begins. The walls do play a small role in forcing fibers to align through a mechanism known as the wall effect. This wall effect might be greater for smaller channel widths and smaller fibers. The experimental method of casting in this research paper utilizes shear flow, wall effect, and the pulling effect.

Fiber pullout tests have also been done with regard to fiber orientation angle. Kang, Kim, and Lee (2010) observed the largest peak fiber pullout load at an angle of 30 to 45 degrees due to the combined effect of snubbing and matrix spalling. However, research also suggests that inclined orientation in UHPFRC tension specimens does not lead to better strain hardening performance compared to longitudinal orientations due to the fiber group effect.

In regards to tensile test setup, many research uses dog-bone shapes, however this is impractical for specimens cut from a structural element. Bruehwiler et al. (2009) cut rectangular prism tensile specimens from a slab and placed aluminum plates on the tops and bottoms of the specimens. A regular servo-hydraulic machine was used with hydraulic clamping jaws to test the specimens. The aluminum plates prevented failure cracks from happening in the clamps and allowed for better LVDT readings within the zone not covered by the aluminum plates. Their method of specimen preparation and test method is a model for the preparation and experimental method used within this research paper.

2 MATERIALS AND CASTING

2.1 *Pouring device*

A pouring device was constructed from chemical resistant type-1 PVC U-channels that glued together along

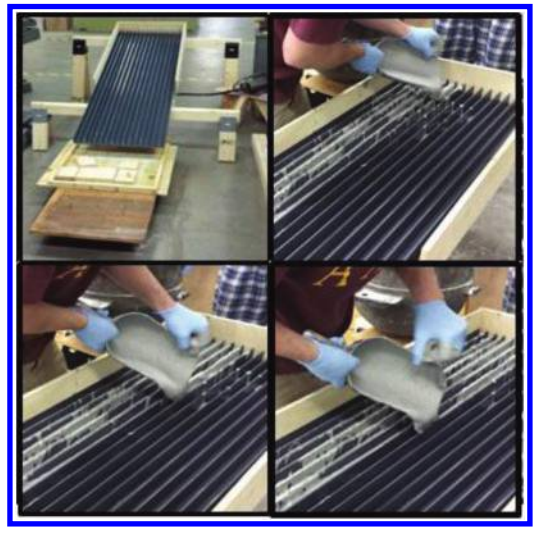


Figure 1. UHPFRC pouring device (top left). Placing UHPFRC into the pouring device (top right to bottom right).

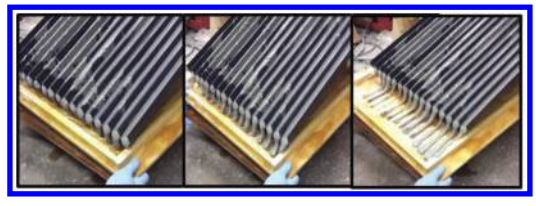


Figure 2. The beginning of the pouring device casting process.

their length (Figures 1, 2 & 3). A total of 16 channels were used, each with dimensions of $5' \times 1.14''$ base $\times$ $1.650''$ leg height $\times$ $0.080''$ wall thickness. Plywood backing and sides were added to increase structural stability. Two saw horses were made so that the pouring device can rest on them at a pouring angle of 20 degrees. On the back of the pouring device a concrete vibrator is latched using metal brackets. It is wrapped in cloth to dampen its force and is used to aid the UHPFRC to flow. Directly below the pouring device is a skateboard on which the final formwork will lie. The skateboard is fashioned out of two skateboard axles mounted onto a $5' \times 2'$ sheet of plywood.

2.2 *Mixture design*

Smooth brass coated high strength steel fibers of $0.5''$ length and of 2.5% volume fraction were used. Three $3'' \times 6''$ cylinder compression specimens were cast with this UHPFRC mix design and the average maximum compressive stress for the specimens is 32.9 ksi. A spread test was performed with both UHPC and UHPFRC in accordance with ASTM C 230/ C 230M. The UHPFRC had a spread of 250 mm whereas the UHPC had a spread of 265 mm.



Figure 3. Midway through the pouring device casting process.

2.3 *Mixing procedure*

The mixing procedure is modeled after that proposed by Wille et al. (2011). The process is designed to ensure that any agglomerations of UHPC particles are broken up properly and that everything is homogenously dispersed. In order to achieve homogeneity, materials are first mixed dry according to the mix proportions previously given. The mixer used is a 3/4 horsepower floor mounted rotary mixer.

At a low speed the full amount of sand was mixed with the silica fume for 8 minutes. The silica powder and cement were then added to the same bowl to mix for an additional 8 minutes at a low speed. A third of the HRWR was added to the water. Still on low speed, the HRWR and water mix was added to the mix within one minute of first pouring it. The remaining two thirds of the HRWR were added within the next minute. The mixing speed was turned from low to medium once all the liquids were added. The mix became fluid in about 3 to 8 minutes and immediately after this the mixing speed was put on high for 1 minute. The mixing speed was put on low and the fibers were added within 1 minute. Mixing at low speed continued for another minute so that the fibers could mix homogenously.

2.4 *Casting*

2.4.1 *Oriented using pouring device*

The pouring device is initially set in a horizontal position. The skateboard is set underneath the pouring device on top of which sets a plywood formwork roughly $18.5'' \times 24'' \times 1''$ height. The formwork is coated in mineral oil. Plastic shrink-wrap is used to line the formwork and the mineral oil helps it adhere to the plywood. This is done because previous trials without shrink-wrap resulted in shrinkage cracking along the fiber alignment due to the high surface area, high plastic shrinkage and the lack of crack bridging fibers.

After the mixing procedure is done the mixing bowl full of concrete is brought to the pouring device. The concrete vibrator is flipped on. A large scoop is filled with UHPFRC and its entire content distributed uniformly along one 5' length U-channel section at a time in one sweeping motion with the scoop (Figure 1). This helps jumpstart the fiber alignment process but most importantly it spreads out the material for an even flow during the casting process. The remaining 16 U-channels were filled in this fashion. Immediately the trough is lowered into its 20 degree position and the concrete begins to flow. Previous trials showed that due to the high surface area the UHPFRC can begin to set in the channels, if the filling procedure takes too long. This can create clumping and can negatively affect fiber orientation and the uniformity of the matrix.



Figure 4. Randomly oriented casting using a scoop.

Once the device is in the 20 degree position the UHPFRC is given 10-20 seconds to flow out of the device in order for the flow to reach a constant rate such as the flow shown in Figures 2 & 3. This flow is contained outside the formwork and is not used for the specimen. After the constant flow is reached, the roller supported slab specimen is pushed forward at a rate of about 0.2ft/s so that the formwork comes in contact with the flow from the pouring device. When the formwork reaches the end then the specimen direction is reversed and the process is repeated so as to cast in lifts. The flow from the pouring device is never broken which allows the UHPFRC to be dragged by the movement of the specimen. This dragging movement helps align the fibers. This process is repeated until the majority of the UHPFRC is in the mold and the flow from the pouring device becomes too weak to continue. A total of 5 separate slabs were poured with this method.

2.4.2 *Random oriented*

The same plywood formwork lined with plastic shrink-wrap is used for this method. However, instead of using the pouring device to orient the fibers, a large scoop is filled with UHPFRC and poured into the mold as randomly as possibly (Figure 4). Only one slab was poured with this method.

2.4.3 *Oriented in tensile mold with scoop*

This procedure is done much like the procedure of laying the UHPFRC into the U-channels (Figure 1). However, instead of filling U-channels, tensile molds are filled. The tensile molds are $16'' \times 1'' \times 2''$ height (not shown in figure) and are poured with the $2''$ side vertical and the $16 \times 1''$ sides horizontal. This size is roughly the same size as the specimens that will be cut at different angles from the plywood molds. Before starting, the tensile molds were coated with mineral oil as a release agent. This process was also repeated using a UHPC mix with the same proportions as the UHPFRC except without the fibers. In both cases the

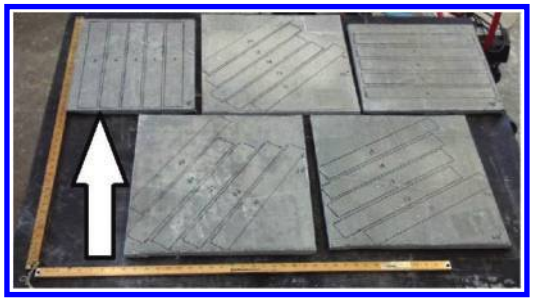


Figure 5. Proposed saw cut lines for 0, 45, 90, 30, 60 degree angles are drawn into the slabs (top left to bottom right respectively). The white arrow shows pouring direction.

Table 2. Description of test specimens.

Specimen #	Casting method	Series name
1–5	slab w/pouring device	0
6–10	slab w/pouring device	90
11–15	slab w/pouring device	60
16–20	slab w/pouring device	45
21–25	slab w/pouring device	30
26–30	slab w/scoop	random
31–35	tensile mold w/scoop	0 (scoop)
36–40	tensile mold w/UHPC	UHPC

molds were placed on a vibration table on the lowest possible setting so as not to induce fiber settling. Five specimens were cast with the UHPFRC and five specimens were cast with the UHPC.

2.5 *Preparation*

All specimens were covered with a plastic sheet immediately after casting. Special care was taken not to let the sheets touch the top of the slabs. All specimens were left covered and in their formwork for 36 hours. After 36 hours the specimens were de-molded and placed in a steam curer at a temperature of 90 Celsius degrees for 48 hours.

The proposed cut lines were drawn, using a permanent marker and a yardstick, on the slabs taken from the plywood formworks (Figure 5). A protractor was used to find angles of 0, 30, 45, 60, and 90 degrees. Five specimens were taken from each slab with dimensions of $2'' \times 16''$. A wet saw was used to cut the slabs along the lines drawn onto the slabs.

All of the tension specimens were lightly ground to help reduce the impact of irregularities such as surface air bubbles. $5'' \times 2'' \times 0.32''$ thick aluminum plates were adhered to the specimens using a two part epoxy. All of the specimens were labeled 1 through 40 and their exact dimensions were measured and recorded. The description to match the numbering of each specimen is shown in Table 2.

3 TESTING PROCEDURE

The $2'' \times 1'' \times 16''$ length specimens were placed in the wedge grips of a 60 kip serve-hydraulic testing machine. Tests were conducted in displacement controlled mode at a rate of .17 mm/min. The central part of the specimen, about $6''$ to $6.5''$ in length, was instrumented with two LVDTs to measure the displacement.

Table 3. Stress and strain comparisons.

Series	$\sigma\, m_{avg}$	εm_{avg}	$\%\sigma m_0$	$\%\varepsilon m_0$
0	1.8	.23	100	100
30	1.28	.059	71	26
45	1.03	.068	57	30
60	0.56	.12	31	51
90	0.41	.10	23	44
random	1.22	.15	68	67
0 (scoop)	2.15	.47	120	164
UHPC	0.41	.006	23	3

σm_{avg} average maximum stress (ksi)
εm_{av} average strain at max stress (in/in)
$\%\sigma m_0$ relation to the angle 0 value of σm_{avg} (%)
$\%\varepsilon m_0$ relation to the angle 0 value of εm_{av} (%)

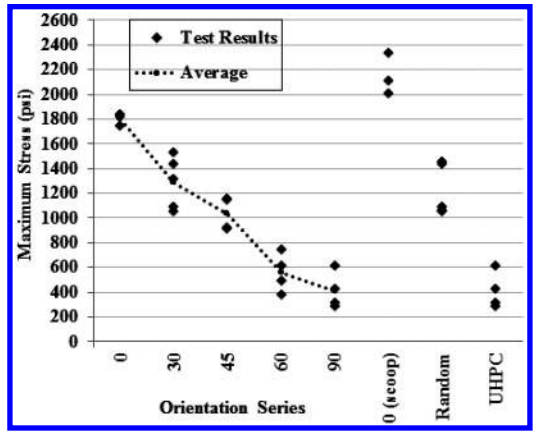


Figure 6. Maximum stress experimental results for specimens 1–25. A line connects the average of each angle group.

4 RESULTS

Specimen #'s 3 & 5 (0 series), 15 (60 series), 19 (45 series), 35 (0 scoop series), & 38 (UHPC series) were disregarded from analysis due to not representative stress strain curves. Several reasons for this include improper handling during saw cutting and preparation, improper assembly in the tensile grips system, LVDT alignment difficulties, specimen slip within the tensile grips during tests. All other specimens are included in analysis. The complete softening effects are not shown in every stress strain curve because failure crack opening were not always limited to within the zone of the LVDTs which leads to invalid strain results after maximum stress is reached.

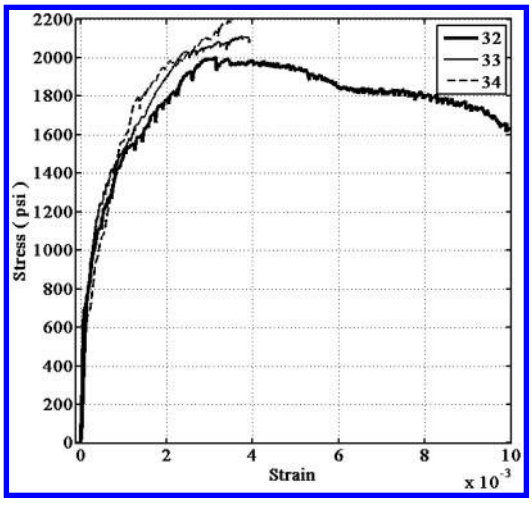


Figure 7. Stress strain curve for 0 degree (scoop) series.

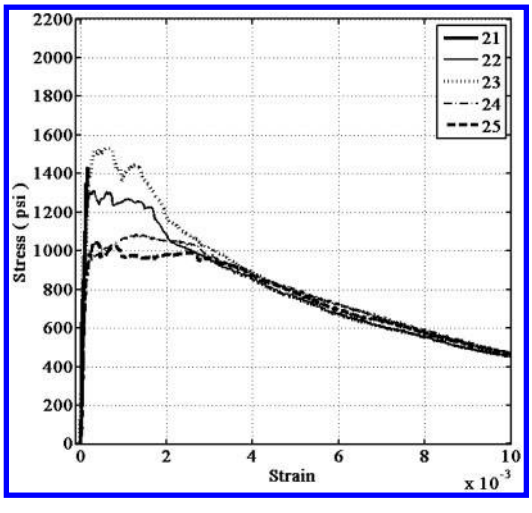


Figure 8. Stress strain curve for 30 degree series.

Figure 6 and Table 3 summarizes the test results of tensile strength and strain at maximum stress, whereas Figure 7 to 11 show the stress versus strain curves in dependency of fiber orientation and casting method. The UHPFRC specimens casted with a scoop directly in the prism shape mold achieved the highest values in average strength of 2.15 ksi and in strain at maximum stress of 0.47%. The higher values in comparison to the cut out slab specimens are attributed to the following effects: The shrink-wrap lining of the plywood molds resulted in wrinkle indents into these specimens. The slabs had roughly twice as much surface area subjected air bubble concentrations than that of the tensile mold specimens. The saw cut specimens were subject to fibers and matrix ripping out during the preparation process and the distribution of fiber quantity throughout the thickness of the tensile mold specimens was more uniform than the specimens cut from the slabs

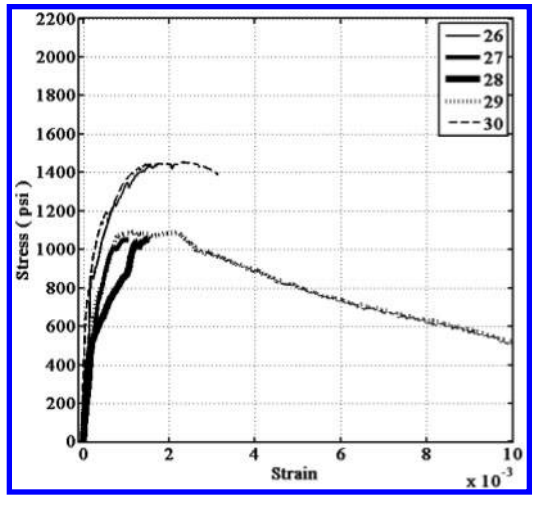


Figure 9. Stress strain curve for random degree series.

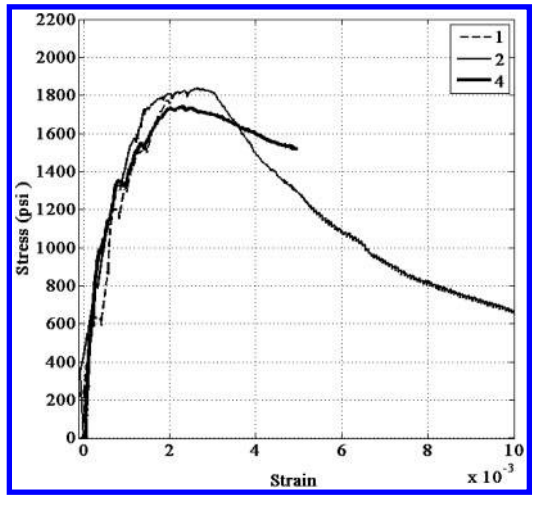


Figure 10. Stress strain curve for 0 degree series.

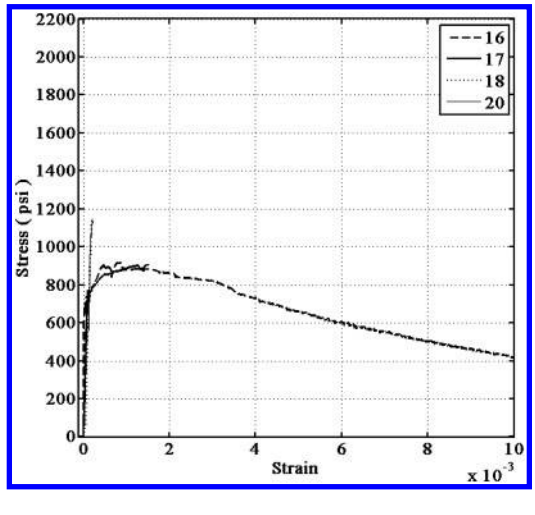


Figure 11. Stress strain curve for 45 degree series.

where the fibers tended to settle towards the middle and bottom the plywood mold.

The randomly poured slab specimens are comparable to the specimens with fiber alignment of 30 degrees to the applied load. The more the fibers were aligned perpendicular to the load direction the less strength and the more brittle behavior was achieved. It is worth noticing that the failure crack changed from a horizontal crack to an inclined crack along the fiber orientation the more the fibers were aligned perpendicular to the applied load. This was observed for some specimens of 45 and 60 degree fiber orientation. If the failure crack forms along the fiber orientation, which was the case for some specimens of 45 degrees, most of 60 degrees and all of 90 degrees fiber orientation, a sudden and brittle failure is observed, comparable to plain matrix (UHPC). This is in contradiction with single fiber pull out test results, in which the fiber pull out load at 45 or 60 degrees still provides significant strength and energy dissipation through fiber pull out. This mechanism and energy dissipation is not valid, if the crack in the composite is formed with an incline to the applied load along the fiber orientation. This crack formation is based on the path of least amount of energy.

5 CONCLUSIONS

The casting method used in this research was able to provide a uniform and repeatable way of casting fibers in one direction so that specimens could be cut out at angles and then uniaxial tension tested.

The results of this experiment support that fiber orientation has a significant impact on strain hardening effects of UHPFRC. The influence of the fiber group effect as well as the influence of failure crack development could be experimentally taken into account. The results do stress that in order to accurately predict the design strength of UHPFRC fiber orientation needs to be accounted for. Existing research shows that analytical models have promise in being able to predict UHPFRC behavior in tension when fiber distribution and orientation are known. However all models consider crack development perpendicular to the applied load. Alignment of fibers could change the failure crack development based on least amount of global energy dissipation. This can be of concern of the applied load acts at and larger 45 degrees to the aligned fiber orientation.

Future research will include validating of the research results, analyzing of the fiber group effect and extending the test matrix by including different types and lengths of fibers.

REFERENCES

Barnett S.J., Lataste J., Millard, S.G., Parry, T., Soutsos, M.N. 2009. Assessment of fibre orientation in ultra high performance fibre reinforced concrete and its effect on flexural strength. *Materials and Structures*. 43:1009–1023.

Bruehwiler, E., Denarie, E. Oesterlee, C. 2009. Strength and deformability distribution in UHPFRC panels. *Processing Sequence in the Production of Engineered Cementitious Composites*. 1:390–397

Custer, R., Stahli, P., van Mier, J.G.M. 2007. On flow properties, fibre distribution, fibre orientation, and flexural behavior of FRC. *Materials and Structures*. 41:189–196.

Hassan, A.M.T, Jones, S.W., Mahmud, G.H. 2012. Experimental test methods to determine the uniaxial tensile and compressive behavior of ultra high performance fubre reinforced concrete (UHPFRC). *Construction and Building Materials*. 37:874–882.

Joh, C., Kim, B., Yang, I. 2010. Structural behavior of ultra high performance concrete beams subjected to bending. *Engineering Structures*. 32:3478–3487.

Wille,K., Kim,D.J., Naaman, A.E.,. 2010. Strain-hardening UHP-FRC with low fiber contents. *Materials and Structures.* 44:583–598.

Kang, S., Kim, J.K.. 2011 The relation between fiber orientation and tensile behavior in an Ultra High Performance Fiber Reinforced Cementitious Composites (UHPFRCC). *Cement and Concrete Research*. 41:1001–1014.

Kang, S.T., Kim, J.K., Kim, Y., Lee, B.Y. 2011. The effect of fibre disrtribution characterisitscs on the flexural strength of steel fibre-reinforced ultra high strength fiber reinforced concrete. *Construction and Building Materials*. 25:2450–2457.

Kang, S. Kim, J.K., Kwon, S.H, Lee, B.Y. 2012. The variation of flow-dependent tensile behavior in radial flow dominant placing of Ultra High Performance Fiber Reinforced Cementitious Composites (UHPFRCC). *Construction and Building Materials*. 33:109–121.

Kang, S., Kim, J., Lee, Y. 2010. Pullout behavior of inclined steel fiber in an ultra-high strength cementitious matrix. *Construction and Building Materials*. 24:2030–2041.

Wille,K. Naaman, A.E., Parra-Montesinos, G.J., 2011. Ultra-High Performance Concrete with Compressive Strength Exceeding 150 MPa (22ksi): A Simpler Way. *ACI Materials Journal.*

Martinie, L., Roussel, N. 2011. Simple tools for fiber orientation prediction in industrial practice. *Cement and Concrete Research*. 41:993–1000.

23. Durability, creep, shrinkage, transport processes in concrete

Research and Applications in Structural Engineering, Mechanics and Computation – Zingoni (Ed.)
© 2013 Taylor & Francis Group, London, ISBN 978-1-138-00061-2

The origin of plastic settlement cracking and the effect of re-vibration

R. Combrinck & W.P. Boshoff
Department of Civil Engineering, Stellenbosch University, South Africa

ABSTRACT: Plastic settlement cracking is one of the earliest forms of cracking in concrete structures as it occurs within the first few hours after the concrete has been cast. The mechanism responsible for plastic settlement cracking is differential settlement of the concrete due to rigid inclusions in the concrete element. Although the mechanism and general location of these cracks are known, not enough attention has been given to the basic behaviour and origin of pure plastic settlement cracks. This is mainly due to the difficulty of observing purely plastic settlement cracks without observing some influence of plastic shrinkage cracking caused by evaporation. This study experimentally showed that the origin or start location of pure plastic settlement cracks are from the bottom upwards and not from the surface downward as would be expected. This indicates that plastic settlement cracks may be present in concrete elements even if the cracks are not visible on the surface. This observation was confirmed through a numerical analysis of the plastic settlement cracking using a visco-elastic approach combined with a total strain smeared crack model. The experiments also showed that these cracks can form even if curing is applied. Finally, since these cracks can form below the concrete surface, workers and engineers may not be aware of their presence. Robust mitigation methods are therefore of utmost importance to ensure concrete durability and prolong the service-life of the structure. Experiments were performed to determine if one such mitigation method, the re-vibration of concrete, adversely affects the concrete strength. The results showed that if re-vibration is to be used as mitigation method for plastic settlement cracking, it should preferable be completed well before the final setting time of the concrete is reached.

1 INTRODUCTION

The phenomena of plastic settlement cracking has been well documented in literature for the past 50 years (Powers 1968, Weyers et al. 1982 & Kwak et al. 2010). It is arguably the earliest form of cracking in concrete structures as it occurs within the first few hours after the concrete has been cast. The mechanism responsible for plastic settlement cracking is differential settlement of the concrete due to rigid inclusions in the concrete element, for example: reinforcing steel or a non-uniform concrete depth (Weyers et al. 1982). T-beam type elements and reinforced ground floors or decks are examples of structural elements prone to differential settlement and therefore plastic settlement cracking.

Although the mechanism and general location of these cracks are known, not enough attention has been given to the basic behaviour and origin of pure plastic settlement cracks. This is mainly due to the difficulty of observing pure plastic settlement cracks without observing some influence of plastic shrinkage cracking which is caused by evaporation (Kwak et al. 2010 & Combrinck et al. 2012).

The most common method to mitigate these cracks is through the re-vibration of the concrete while it is still in the plastic state (Owens 2009). The initial setting time of concrete serves as a good indication of the end of the plastic state as well as the point in time where the potential for plastic settlement cracking stops since settlement also typically ceases at this time. Re-vibration of the concrete before or at the initial setting time effectively removes all plastic settlement cracks and increases the concrete compaction and therefore also strength (Owens 2009 & Rao et al. 2008). In practise, re-vibration is seldom applied at the correct time and the question remains whether poor timing can negatively influence the concrete. Furthermore, if these cracks are not mitigated they act as potential weak spots where prospective crack widening due to plastic-, thermal- and drying shrinkage will originate. Cracks acts as access for aggressive and corrosive agents to penetrate the concrete surface. This accelerates concrete degradation and decreases the overall durability and the corresponding service life of the structure (Weyers et al. 1982 & Qi 2003).

With all of this in mind, this paper aims to determine the origin or start location of pure plastic settlement cracks. This is believed to be vital information if plastic settlement cracking is to be understood and prevented. In addition, the location of the cracks is also verified with a numerical analysis of the settlement and the cracking by combining a visco-elastic material approach with total strain smeared cracking behaviour. Finally, concrete was subjected to re-vibration at both the initial and final setting times to determine if

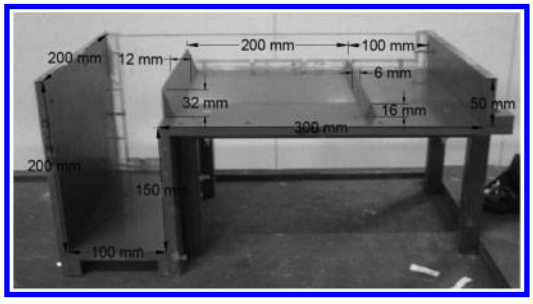


Figure 1. L-Shaped mould with transparent sides used to observe plastic settlement cracks in concrete.

re-vibration can be applied confidently as a robust mitigation method for plastic settlement cracking without adversely affecting the concrete.

2 PLASTIC SETTLEMENT CRACKING

The pattern of plastic settlement cracks generally coincide with the reinforcing steel layout or positions with significant changes in section height. In practice these cracks are only visible at the concrete surface and may in several cases be widened by plastic shrinkage. Plastic shrinkage is caused by the evaporation of concrete water which causes capillary pressure buildup within the concrete. This capillary pressure causes the concrete body to contract horizontally which causes cracking (Wittmann 1976 & Uno 1998). Although plastic shrinkage cracking normally occurs just after plastic settlement cracking, they may interact under conditions with high evaporation rates (Combrinck et al. 2012). This makes it difficult to distinguish between the two cracking types. The following experiment was conducted to determine pure plastic settlement cracking behaviour and origin. This is also confirmed with a numerical analysis.

2.1 *Experimental setup*

The aim of the experiment was to observe the formation of a pure plastic settlement crack without the influence of evaporation and therefore plastic shrinkage cracking. Two L-shaped moulds as shown in Figure 1 were used to ensure cracking. The mould has a deep and a swallow section that give pronounced differential settlement and therefore cracking at the boundary between the sections. The left triangular insert creates a clear boundary between the sections, while the right triangular insert plays no role in these experiments and can be ignored. The mould has transparent sides which allow cracks to be observed below the concrete surface.

The proportions and constituents of the mixture used are shown in Table 1. A 13 mm stone was chosen as the maximum size appropriate for use in a mould which is 50 mm deep. A coarse natural sand was used to give adequate bleeding/settlement to ensure cracking.

Table 1. Mix proportions and material constituents.

Content	(kg/m^3)
Water	215
CEM I 52.5 N	538
Greywacke stone (13 mm)	1050
Coarse natural sand	572

Bleeding and settlement is nearly identical if chemical shrinkage is negligible (Kwak et al. 2010). The mix showed good workability with no segregation and achieved a 28 day compression strength of more than 40 MPa.

The experiments were carried out in a controlled environmental room with a temperature of 23°C and relative humidity of 65%. The surface of the mould was continuously kept wet to ensure no capillary pressure buildup in the concrete due to the evaporation of concrete water. This ensured that no plastic shrinkage cracking could occur and that only the pure plastic settlement cracking is observed. During the experiments the moulds were continuously checked for cracks at the sides and on the surface.

2.2 *Experimental results*

Both L-shaped concrete specimens showed hairline cracks at the tip of the triangle at the boundary between the deep and swallow sections of the mould. One of the specimens also showed a clear crack just below the surface of the concrete. This crack was not visible at the surface of the concrete, but only from the side. All the cracks appeared around 80 minutes after the concrete was cast, which is long before the initial setting time was reached at 330 minutes. The crack widths were between 30 and 90 μm.

Figure 2 shows images of the specimen that had a crack just below the surface and at the tip of the triangle. The photo in Figure 2a was taken through the transparent side panel just after its first appearance. This photo also shows the water layer present on the concrete surface to prevent evaporation. The photo in Figure 2b was taken after 360 minutes with the transparent side panel removed.

Both images show that the dominate crack start forming from within the concrete at the triangle tip, while the top crack only occurred for one of the specimens and was not visible on the concrete surface. Plastic settlement cracks therefore form from the bottom upwards and not from the surface down as would be expected. This behaviour of plastic settlement cracks has important practical implications. It indicates that plastic settlement cracks may be present in concrete elements even if the cracks are not visible at the surface. In addition, these cracks may be present even if all evaporation was prevented through curing practices. These cracks may also be further widened due to drying shrinkage or structural loading and possibly expose reinforcing steel to the environment.

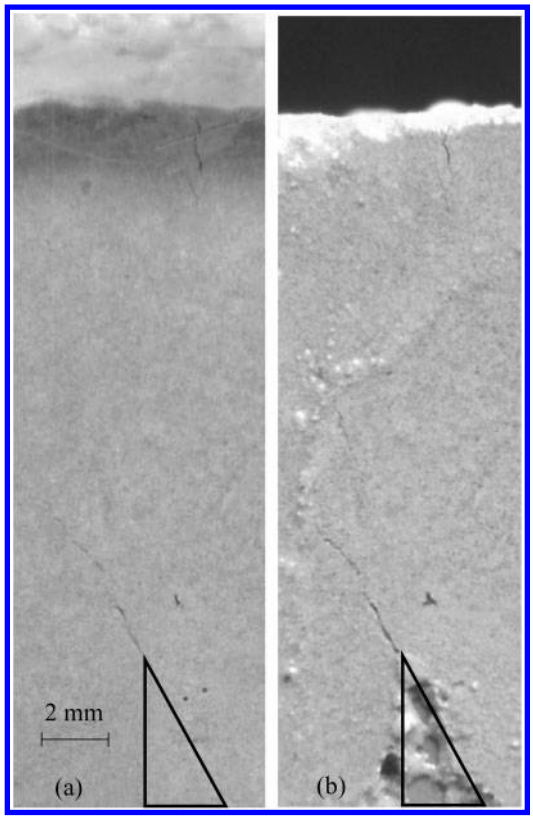


Figure 2. Observed cracks for the L-shaped specimen at the tip of the triangular insert as well as just below the concrete surface. Both images are of the same specimen but taken at different times. (a) Taken 80 minutes after casting through the transparent side panel. (b) Taken 330 minutes after casting with the transparent side panel removed.

2.3 *Visco-elastic approach to settlement*

The settlement of concrete is best described by the process of self-weight consolidation (Josserand et al. 2006 & Kwak et al. 2010). This analogy uses the concept of effective stress which is often used in soil mechanics. It means that if a load is applied to a saturated soil, the load is initially resisted by the solid soil skeleton as well as the pressure in the water (pore pressure). As time elapses the pore pressure dissipates and the full load is gradually transferred to the soil skeleton. This is similar to the settlement or bleeding of concrete and for both systems the soil/concrete skeleton can be seen as a spring element while the pore pressure can be seen as a dashpot. This makes it possible to model concrete settlement using time dependent visco-elastic material behaviour. Visco-elastic materials are commonly used to describe materials that exhibits behaviour that is part liquid and part solid such as fresh concrete. For settlement, a constant stress is applied through the self weight which gradually increases the cumulative settlement. The Kelvin chain visco-elastic model is best suited to represent constant stress and cumulative strain increase or simply creep (Illston et al. 2001). The

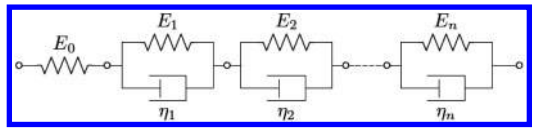


Figure 3. Kelvin chain visco-elastic model (DIANA 9.4.3, User's Manual 2010).

basic Kelvin chain model with springs and dashpots is shown in Figure 3.

In order to assign values to all the springs and dashpots of the entire Kelvin chain model, it is first necessary to consider only one chain element which consists of one spring and one dashpot in parallel. The viscosity η of the dashpot can be calculated by multiplying the relaxation time λ with the spring stiffness E as follows:

$$\eta = \lambda E \tag{1}$$

The stress in the spring (s) and the dashpot (d) can be calculated with the following equations respectively.

$$\sigma_S = E\varepsilon_S \tag{2}$$

$$\sigma_D = \lambda E\dot{\varepsilon}_D \tag{3}$$

where σ_S = stress in spring; ε_S = strain in spring; σ_D = stress in dashpot and $\dot{\varepsilon}_D$ = strain rate of the dashpot. The sum of the stress in the spring and the dashpot gives the stress in the chain element and can be expressed as follows:

$$\sigma = E(\varepsilon_0 + d\varepsilon) + \lambda E\frac{d\varepsilon}{dt} \tag{4}$$

where ε_O = strain at the beginning of the time step; d ε = change in strain during the time step and dt = duration of the time step. Rearranging Equation 4 and integrating over time and strain leads to the following equation which expresses the change in strain $\delta\varepsilon$ for each time step $\delta t = t - t_o$:

$$\delta\varepsilon = \varepsilon - \varepsilon_0 = \frac{\sigma - E\varepsilon_o}{\frac{\lambda E}{(t - t_o)} + E} \tag{5}$$

Now consider the entire Kelvin chain model as shown in Figure 3, where the stress in each chain element is constant and the total stain is equal to the sum of the strains in each chain element. Given this, the total strain in the Kelvin chain model at any time can be calculated as follows:

$$\varepsilon_{tot,m} = \varepsilon_{tot,m-1} + \delta\varepsilon_{0,m} + \delta\varepsilon_{1,m} + \ldots + \delta\varepsilon_{n,m} \tag{6}$$

where $\varepsilon_{tot,m}$ = total strain at time m; $\varepsilon_{tot,m-1}$ = total strain at time m less one time step and finally $\delta\varepsilon_{n,m}$ = change in strain for each Kelvin chain element

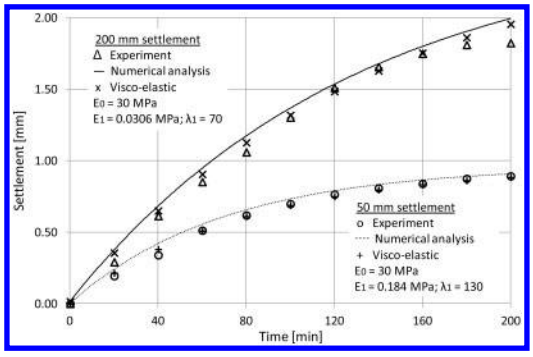


Figure 4. Experimental, Kelvin chain visco-elastic material approach and numerical results of concrete settlement with 50 mm and 200 mm depth.

n (from element 0 to n) over time step δt. $\delta\varepsilon_{n,m}$ can be calculated as follows:

$$\delta\varepsilon_{n,m} = \frac{\sigma - E_n \varepsilon_{2,m-1}}{\lambda_n E_n / \delta t + E_n} \quad (7)$$

Using Equations 6 and 7 any settlement behaviour can be represented by the equivalent visco-elastic Kelvin model though curve fitting using the method of least squares. This method minimizes the error between the experimental results and the equivalent visco-elastic material. The experimental results for the settlement were determined by measuring the bleeding of a 50 mm and 200 mm deep concrete specimen. The bleeding was considered to be equal to the settlement (Kwak et al. 2010). A more detailed description of the measuring procedure can be found elsewhere (Josserand et al. 2004). A time step of 20 minutes was chosen as this conforms to the experimentally measured time intervals. Figure 4 compares the measured settlement with the estimated settlement using a visco-elastic approach. The figure also shows the results of a numerical analysis which will be discussed in the next section.

Two Kelvin chain elements were found to adequately represent the measured settlement and Figure 4 also indicates the calculated visco-elastic parameters. The parameters were determined by choosing the spring stiffness of the first chain element and the relaxation time of the second chain element while the spring stiffness of the second chain element was iteratively solved to satisfy the least square method. This also simplified the numerical analysis described later in this paper. Figure 4 shows favourable agreement between the experimental results and the equivalent visco-elastic material behaviour. A visco-elastic approach using the Kelvin chain model can therefore be used to represent concrete settlement.

2.4 *Numerical analysis of settlement*

Figure 4 also shows the results of the numerical analysis which used the visco-elastic material parameters as input values. A two dimensional numerical analysis was performed with the commercially available finite element analysis program DIANA 9.4.3 (DIANA 9.4.3, User's Manual 2010). Both the 50 mm and 200 mm bleeding moulds were modeled separately using four-node quadrilateral isoparametric plane stress elements. The element size was 5x5 mm. Only self weight was applied where after the time dependent visco-elastic material behaviour influenced the settlement. A time step of 0.5 minutes was chosen. The specimens were fixed at the base against vertical translation. The results in Figure 4 show that the numerical analysis results, obtained using the calculated visco-elastic parameters, give an acceptable representation of the measured settlement.

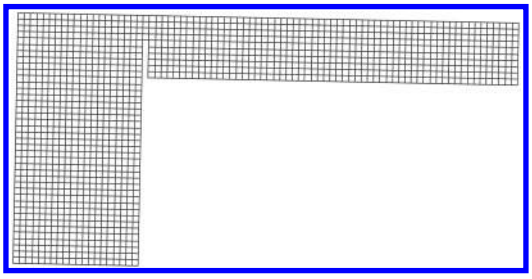


Figure 5. Model geometry and mesh.

2.5 *Numerical analysis of plastic settlement cracking*

A numerical analysis of the concrete settlement and possible concrete cracking in the plastic settlement mould was also performed. The same element types, applied loads and visco-elastic material behaviour were used as in the previous sections. Figure 5 shows the model geometry and mesh. The boundary conditions were as follows: all the base edges were fixed against vertical translation, while all vertical edges were fixed against horizontal translation. Figure 5 also shows that the triangular insert was modeled by removing a column of elements equal to the height of the triangle.

Cracking is taken into account by using a total strain smeared crack model which can be combined with direct input for Kelvin chain visco-elasticity (DIANA 9.4.3, User's Manual 2010). The analysis also requires the tensile behaviour of the fresh concrete. The experimental determination of the tensile behaviour of fresh concrete has proven to be troublesome, especially at very early ages (Hannant et al. 1978 & Doa et al. 2009). The post cracking behaviour is also unknown and as with the tensile strength will vary with time. The goal of this analysis is only to verify the experimental crack locations as observed in Figure 2 and therefore it is deemed sufficient to assume the post peak behaviour. The simple linear tension softening curve was chosen to represent the tensile behaviour. The tensile strength was chosen as 3000 Pa and the ultimate strain as 0.00011 as shown in Figure 6. This is

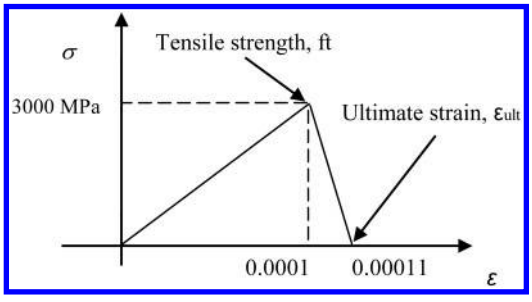


Figure 6. Predefined linear tension softening curve for total strain crack model (DIANA 9.4.3, User's Manual 2010).

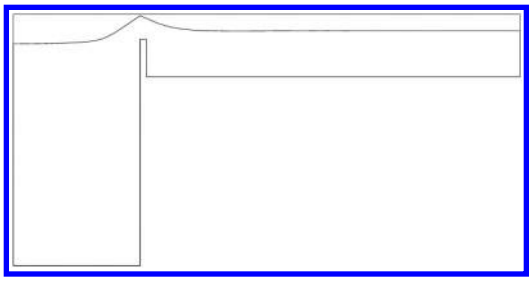


Figure 7. Deformed shape obtained from numerical analysis of concrete in the plastic settlement mould after 80 minutes.



Figure 8. Cracking as function of maximum principal strain as obtained from the numerical analysis of concrete in the plastic settlement mould after 80 minutes.

qausi-brittle crack behaviour since the ultimate strain is only 10% more than the strain at the tensile strength.

It is acknowledged that the chosen behaviour might not be correct. However, it is believed that it can still be used to verify the cracking positions. Furthermore, the characterization of the tensile behaviour of fresh concrete requires more investigation and is currently part of an ongoing project at Stellenbosch University.

The results of the analysis at 80 minutes are shown in Figures 7 and 8. Figure 7 shows the deformed shape and Figure 8 shows the maximum principal strain. Figure 7 clearly shows the difference in settlement between the deep and shallow sections as well as the influence of the triangular restraint.

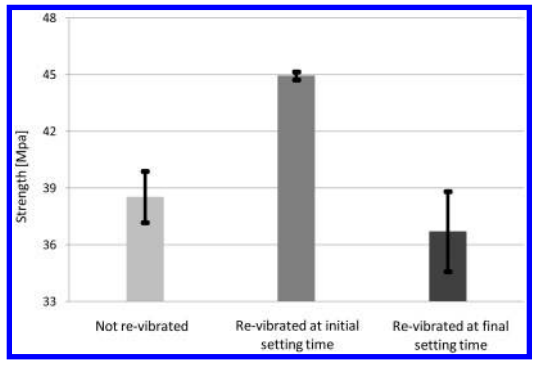


Figure 9. Compression strength results at 7 days of the re-vibration tests.

3 EFFECT OF RE-VIBRATION

The previous section discussed the behaviour of pure plastic settlement cracking. It showed that these cracks can be present below the concrete surface even if curing was applied successfully. Workers and engineers may therefore not be aware of the presence of these cracks. This observation highlights the importance of applying mitigations methods for plastic settlement cracks even when no cracks are visible on the concrete surface. The re-vibration of concrete just before it loses it plasticity is the most common mitigation method that has been shown to close plastic settlement cracks (Roa et al. 2008 & Owens 2009).

However, if this method is to serve as a practical solution, it should not adversely affect the concrete if applied at the wrong time. The aim of the following experiments is to determine whether the re-vibration of concrete at both the initial and final setting times respectively negatively influences the concrete's strength.

3.1 *Experimental setup*

The mixture given in Table 1 was also used for these experiments. After mixing the concrete, 100x100x100 mm specimens were filled and compacted. A number of the specimens were left undisturbed while the rest were either re-vibrated at the initial setting time or at the final setting time. The setting times were determined with the Vicat needle apparatus (Combrinck et al. 2012). The re-vibration lasted for 3 minutes on a standard vibrating table. Finally, the specimens were water cured and tested at 7 days.

3.2 *Results and discussion*

Figure 9 shows the 7 day compression strength results of the re-vibration tests. The figure indicates a noticeable increase in strength if re-vibrated at the initial setting time. One possible reason for this result was observed during the experiment where a significant amount of extra bleeding water was transferred to the concrete surface due to the re-vibration. This lowered

the water-cement ratio and is believed to be the reason for the increase in strength.

Figure 9 also shows that the re-vibration of the concrete at the final setting time reduced the strength. The reasons for this are possibly due to the disturbance of the initially formed hydration products as well as observation that no additional bleeding water was transferred to the surface when re-vibrated at the final setting time.

Although this requires further investigation, it can be concluded that if re-vibration is to be used as mitigation method for plastic settlement cracking, it should preferable be completed well before the final setting time to avoid a possible decrease in concrete strength.

4 CONCLUSIONS

In this study the origin of pure plastic settlement cracking was investigated experimentally. A numerical analysis of plastic settlement and plastic settlement cracking were also performed. Lastly, the effect of re-vibration on concrete strength was investigated. The following significant conclusion can be drawn:

- The most likely starting location or origin of plastic settlement cracking is from the bottom upward and not from the surface downwards.
- Due to its origin, plastic settlement cracks may be present in concrete elements even if not visible on the surface and even if curing prevented all possible plastic shrinkage cracking.
- The Kelvin chain visco-elastic approach can be used to represent the settlement of concrete.
- Kelvin chain visco-elastic material behaviour can be combined with a total strain smeared cracking model to predict the location of cracks.
- If re-vibration is to be used as mitigation method for plastic settlement cracking, it should preferable be completed well before the final setting time to avoid a possible decrease in concrete strength.

REFERENCES

Combrinck, R. & Boshoff, W.P. 2012. Influence of restraint on the early age cracking of concrete with and without fibres, 8*th RILEM International Symposium (BEFIB),* Guimarães, Portugal.

Dao, V.T.N., Dux, P.F. & Morris P.H. 2009. Tensile Properties of Early-Age Concrete. *ACI Materials Journal* vol. 106 no.6: pp. 483–492.

DIANA 9.4.3; User's manual. 2010. TNO Building Construction, Delft, The Netherlands.

Josserand, L., Coussy, O. & De Larrard, F. 2006. Bleeding of concrete as an ageing consolidation process. *Cement and Concrete Research*. vol 36: pp. 1603–1608.

Josserand, L. & De Larrard, F. 2004. A method for concrete bleeding measurement. *Materials and Structures* vol. 37: pp. 666–670.

Hannant, D. J., Branch, J. & Mulheron, M. 1999. *Equipment for tensile testing of fresh concrete.* Magazine of Concrete Research vol. 51 no. 4: pp. 263–267.

Illstone, J.M., Domone, P.L.J., Bonner, D.G., Dinwoodie OBE, J.M., Hannant, D.J., Hollaway, L., McColl, I.R., Moon, J.R., & De Vekey, R.C. 2001. *Construction Materials,* Oxon:Spon press.

Kwak, H.-G., Ha, S. & Weiss, W.J. 2010. Experimental and Numerical Quantification of Plastic Settlement in Fresh Cementitious Systems. *Journal of Materials in Civil Engineering vol.* 22 no. 10: pp. 951–966.

Owens, G. (ed). 2009. *Fulton's Concrete Technlogy*. Midrand, South Africa: Cement and Concrete Institute.

Powers, T.C. 1968. *The Properties of Fresh Concrete.* United States of America: John Wiley & Sons, Inc.

Qi, C. 2003. *Quantitative assessment of plastic Shrinkage cracking and its effect on the corrosion of steel reinforcement*. PhD thesis. Indiana, United States of America: Purdue University.

Rao, M. K., Kumar, P. R. & Bhaskar, N. B. 2008. Effect of re-vibration on compression strenght. *Asian journal of civil enigineering (building and housing) vol.* 9 no.3: pp. 291–301.

Uno, P.J. 1998. Plastic Shrinkage Cracking and Evaporation Formulas. *ACI Materials Journal* vol. 95 no.4: pp 365–375.

Weyers, R.E., Conway, J.C. & Cady, P.D. 1982. Photoelastic analysis of rigid inclusions in fresh concrete. *Cement and Concrete Research.* vol. 12: pp. 475–484.

Wittmann, F.H. 1976. On the Action of Capillary Pressure in Fresh Concrete. *Cement and Concrete Research* vol. 6 no. 1: pp. 49–56.

Research and Applications in Structural Engineering, Mechanics and Computation – Zingoni (Ed.)
© 2013 Taylor & Francis Group, London, ISBN 978-1-138-00061-2

Composite material under influence of moisture

Jan Skramlik, Miloslav Novotny & Karel Suhajda
Brno University of Technology, Faculty of Civil Engneering, Czech Republic

ABSTRACT: One of the properties of porous composite materials, which may be decisive for their utilization in a building structure, is their ability to absorb and release water. It is a case of moisture that flows through a material, saturates it, or drains it. The moisture content varies both in space and in time. Many properties of a material (insulating value, strength, etc.) depend on its moisture content and therefore material moisture must be taken into account.

Water penetrates a porous material from the environment and the equilibrium between the material moisture and the ambient air moisture is reached under steady temperature and moisture conditions. If the partial pressure of water vapor in a building material is lower than that in the ambient air, then the material absorbs water vapor from the air. Conversely, the material releases water vapor. Equilibrium moisture is characterized by zero increment of weight and temperature in time. An impact of moisture on coefficients of thermal conductivity varies according to the concrete temperature and moisture content of a material.

The research deals with the application of nondestructive measurement of moisture parameters of composite materials being developed for application in practice, using the experimentally assembled measuring apparatus on the principle of using electromagnetic microwave radiation.

Keywords: capillary conductivity, continuity equation, electromagnetic microwave radiation

1 INTRODUCTION

The publication introduces the results of experimental measurements carried out for the transport of humidity in porous steady masses in non-stationary conditions to express the moisture distribution by the help of measuring apparatus working on the non-destructive principle of electromagnetic microwave radiation. The aim is verify the mentioned method of measurement for the description of moisture parameters of the composite materials.

2 TESTING MATERIALS SAMPLES

We deal with the samples of materials, produced based on the waste products usage. The used samples are marked "R" concrete samples. See the Fig. 1. The development of these building materials is based on the recycling of waste materials.

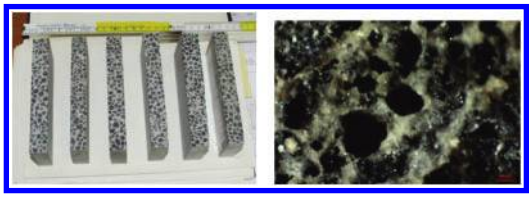


Figure 1. Material samples developed at Department of Building Materials at Brno University of Technology.

Material characteristic is porous structure as well as inert homogenous material. The homogenous material includes gradation in range 0 up to 8 mm or in range 4 up to 8 mm when used porous gravel. The composite material represents isolation with filling of light components. The usage of the mentioned materials in building activities is based on the material characteristics. These items are subject for the following examinations. The experimental measurement of the moisture parameters is based on the observation of the moisture transport. It allows describe distribution of moisture, needed for the calculation of the capillary conductivity coefficient using the nondestructive method.

The test results were acquired from the basic samples, see the following graphs.

Primary aim was to observe the transport of the moisture in order to find out the capillary conductivity coefficient. We used microwave method based on the set methodology and by the help the measuring instrument which was developed at the Department of Building Structures at the University of Technology by Brno.

3 MOISTURE BEHAVIOR

We tested time of intake of water through the material. The sample dimension was $60 \times 20 \times 200$ mm. The process was done by the close contact of lower sample surface with the liquid area. This behavior was

Table 1. Basic parameters of material sample labeled “R” concrete.

„R“ concrete material

Sample no.	Weight [g]	Size [mm]	Bulk [m^3]	Bulk weight [$kg.m^3$]
01	356	190x58x149	0,0001642	2168
02	353,2	190x58x149	0,0001642	2151
03	413,9	220x59x149	0,0001934	2140
04	355,7	190x59x149	0,0001670	2129
05	361,9	190x59x149	0,0001670	2167
06	358,7	190x59x149	0,0001670	2147
Average	366,56	195x59x14	0,0001714	2150

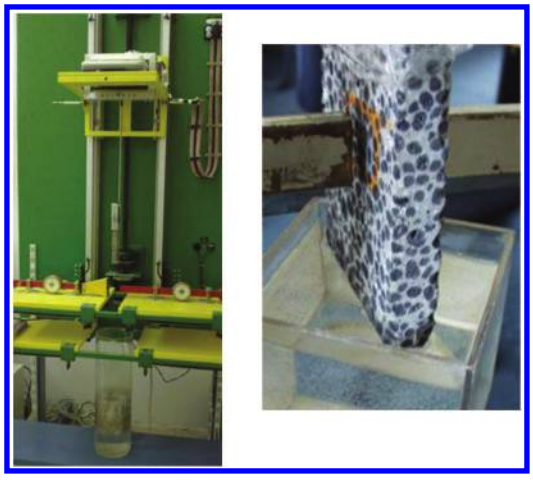


Figure 2. Position of the “R” concrete materials samples during moisture behavior measurement.

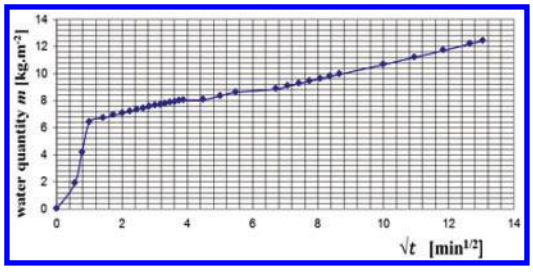


Figure 3. Process of dampness in time t.

tested in the time line (see the Fig. 2). For the measurement was used objective sample of the new developed material on the basis using of composites, marked as “R” concrete.

Graphical expression of the time line for the moisture can find on the Fig. 3. This is base to set right time period to calculate profile of the moisture front coordinates.

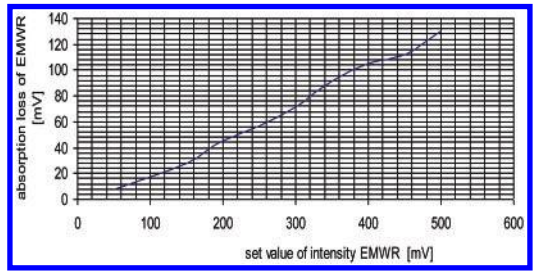


Figure 4. Dependency of the intensity change detection according the level of electromagnetic MW radiation (dry state material).

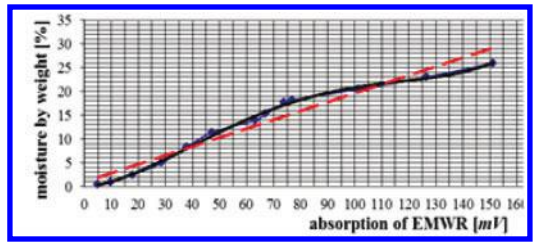


Figure 5. Dependence of change of the intensity of electromagnetic radiation on the moisture by weight of sample “R” concrete.

4 DEPENDENCY OF EMWZ PERMEABILITY BASED ON THE SET INTENSITY

Dependency of intensity changes of material permeability on electromagnetic MW radiation and its graphical expression is base to set intensity of the radiation. Dependency intensity of microwave radiation changes according to the specific moisture as well for detect of the moisture profile. Fig. 4 includes results of the measurement of the MW radiation.

Functional dependency of the tested sample materials has linear course. This confirms presumption for calculation of the capillary conductivity coefficient.

5 FUNCTION OF INTENSITY CHANGES DEPENDENCY EMWR ACCORDING TO THE MOISTURE BY WEIGHT

Using gravimetric method there were measured level of the radiation based on the moisture by weight of the samples’. The aim of the experiment was determination the function dependency of intensity changes on electromagnetic MW radiation on the moisture by weight (Fig. 5).

6 MOISTURE DISTRIBUTION IN SAMPLE

Fig. 6 shows a sample of the material in the apparatus during the measurement.

At the Fig. 7 is the output measurement of moisture distribution during wetting of the sample of the material in 3D.



Figure 6. "R" concrete and "H" material samples during recording of the moisture front profile position.

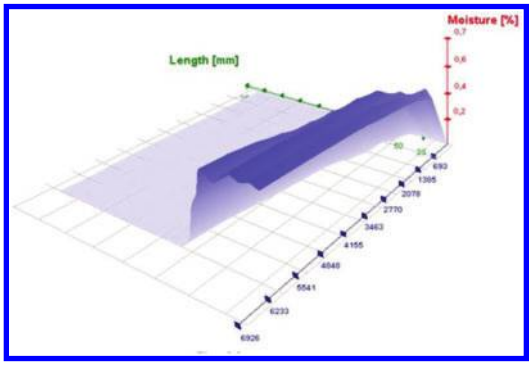


Figure 7. Distributions of moisture in the reference sample material.

Fig. 8 shows the change of EMWR intensity depending on the moisture by weight in the length of measured sample at time intervals in the course of its moistening and consequently determines functional dependence on moisture for calculation of capillary conductivity coefficient.

The values of coordinates determining location of the wetting front profile are obtained from measurements using the microwave measuring apparatus. Detection of moisture quantity diffusing in the material is carried out at certain time intervals from the start of moistening of sample material.

7 CAPILLARY CONDUCTIVITY COEFFICIENT

By using of mathematical method is possible to continue processing the results of measurement for expressing of capillary conductivity coefficient depending on the moisture by weight for expression the thermal insulation properties of materials depending on the moisture.

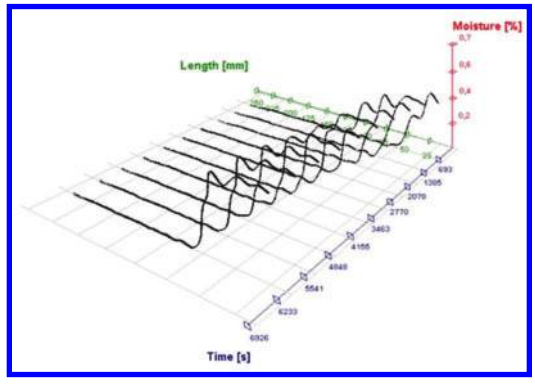


Figure 8. Graphical output - "R" concrete samples during non-stationary state for recording of the moisture front profile position.

The result of the derivation and application of boundary and the initial conditions is the basic equation:

$$\kappa(u(x,t)) = -\frac{1}{2.t.\frac{\partial u}{\partial x}} . \int_{x}^{\infty} x . \frac{\partial u}{\partial x} . dx \qquad (1)$$

where:
$\kappa(u(x))$ coefficient of capillary conductivity $[m^2.s^{-1}]$
t time interval $[s]$
ς substitution of the distance measured $[-]$
η Boltzmann transformation $[m.s^{-1/2}]$
x coordinate in the length of sample $[m]$
u_1 maximal value of humidity by weight $[-]$
u_2 humidity by weight of material $[-]$

Relationship between weight and the amount of moisture microwave radiation that passes through the sample can be approximated by a polynomial by a polynomial using least squares.:

$$y = \sum_{j=0}^{3} k_j . x^j \qquad (2)$$

Calculation of capillary conductivity coefficient can be solved numerically for each percent of moisture (eg from 15 to 80 percent) and gradually applied in equation (1). This yields a specific capillary conductivity coefficient values depending on the weight of moisture. The result can again be approximated to obtain a mathematical formula for this dependence:

$$\kappa(u) = f(u) \qquad (3)$$

$$\kappa(u) = \sum_{j=0}^{n} k_j . u^j \qquad (4)$$

Individual curve can be approximated using appropriate mathematical methods

$$^{1}u_m(\tau) = \frac{m(\tau) - m_s}{m_s} \qquad (5)$$

$^1u_m(\tau)$ moisture by weigh from measurements [%]
τ time [s]
$m(\tau)$ weight of sample in time τ [kg]
m_s– weight of sample in dry state [kg]

Moisture by weight of sample over time τ can also be expressed by integrating of the curve (see figure 8) according to the spatial coordinates x:

$$^2u_m(\tau) = \int_0^\infty v_m(\tau, x).dx \tag{6}$$

$^1u_m(\tau)$ moisture by weight by integrating [%]
τ time [s]
$v_m(\tau,x)$ wetting curve in time τ [m^{-1}]
x– dimensional coordinate [m]

Coefficient to expressing the relative systematic error:

$$k = \frac{^1u_m(\tau)}{^2u_m(\tau)} \tag{7}$$

After substitung (3) in (4):

$$k = \frac{m(\tau) - m_s}{m_s . \int_0^\infty v_m(\tau, x).dx} \tag{8}$$

The results of moisturizing curve corrected in time τ will be in the form:

$$v_{m,k}(\tau, x) = k.v_m(\tau, x) \tag{9}$$

Based on the above mentioned measurements, it is possible to express moisture curves (according to the methodology) as a base to calculate capillary conductivity coefficient.

8 CONCLUSION

Capillary conductivity of liquid moisture in the porous structure of the building materials for the needs of construction practice is still insufficiently explored. The standards on this issue mention only and refers to the experimental measurement using magnetic resonance imaging In fact there does not exist practically usable methodology for the integration of its impact on the thermal-technical characteristics of building materials. Experimentally prepared apparatus and proposed methodology allows continuing in the mathematical processing of the obtained data to calculate the capillary conductivity κ and to determine the functional dependence on moisture. It is the incorporation of the impact of liquid moisture in building materials in assessing the thermal insulation properties.

On samples of composite material has been tested the possibility of obtaining the description of distribution of moisture using non-destructive method by help of microwaves for verification of the mathematical solution for the outputs of the moisture measurement during non-stationary state and for the utilization of the integral method is considered in the current time. The integral method allows giving precision for the figures measured through the EMWR.

ACKNOWLEDGEMENTS

This article was supported by GACR P104/10/P388 “Experimental analysis of the effect of microwave radiation for destruction of biological agents causing corrosion of building materials” and by GACR P104/10/1390 “The analysis of influence of MW drying while application of chemical grouting into moist brickwork” at the Brno University of Technology, Faculty of Civil Engineering, Department of Building Construction.

REFERENCES

K. Kiessl, *Kapillarer und dampfförmiger Feuchtetransport in Bauteilen*. Essen 1983
European Standard EN ISO 15026 *Assessment of moisture transfer by numerical simulation*, 2007.
K. Gertis and K. Kiessl, *Feuchte Transport in Baustoffen*, 1980
M. Kutilek, *Dampness porous material*, CZ, Prague SNTL, 1992
K. Krischer, *Die Wisenschaftliche Grundlagen der Trocknugstechnik*, Springer Verlag 1978
J. Skramlik and M. Novotny, *Moisture transfer in building material,* PROHITECH 09, Italy 2009, ISBN 978-0-415-55803-7

Research and Applications in Structural Engineering, Mechanics and Computation – Zingoni (Ed.)
© 2013 Taylor & Francis Group, London, ISBN 978-1-138-00061-2

Chimney cracked reinforced concrete walls as a problem of durability exploitation

M. Kaminski, M. Maj & A. Ubysz
Institute of Building Engineering, Technical University of Wrocław, Poland

ABSTRACT: Some reasons of appearance of horizontal and vertical cracks as temperature, influence of construction joints, thermal insulation etc. are presented in this paper. There are presented some problems connected with reinforced concrete chimney operation in the aggressive environment. Chimney exhaust fumes have big influence on durability and longevity of chimney wall. Specially there are big difficulties in the case when it is impossible to disconnect chimney from constant work. The repair works are not effective and very expensive.

1 INTRODUCTION

In designing chimney walls there are no place for cracks. Horizontal and vertical cracks can caused corrosion of concrete and steel bars. Cracks decreases stiffness of reinforced concrete chimney shell construction. Local and global mperfactions of chimney walls are increasing according to greater number of cracks. Taking into account these facts, cracks reduce the service life of chimneys. Horizontal and vertical cracks allow condensate water infiltrates into wall. It causes corrosion and dank of concrete wall and during winter time cracks become bigger because if glaciations water in cracks.

Problems with a large number of cracks on chimneys walls occurred in last years in Poland. It was connected with changing chimney codes and in particularly introduction requirement of double reinforcement of concrete walls. Until the end of XX centaury reinforcement bars were located in one row, near the external surface. After receiving in Poland European Standards two rows of reinforcement are demanded. It caused several difficulties in building chimneys because of little space of reinforcement bars.

Additional problem of increasing number and widths of cracks is chimney insulation. Badly placed insulation results in an increase bending moments and on the creaks are wider.

2 ERRORS IN CONSTRUCTING CHIMNEYS WALLS

There are many mistakes which were made during building chimneys:

- too small distance between vertical and horizontal steel bars in concrete wall
- insufficient concrete care during building
- too rapid drying wall

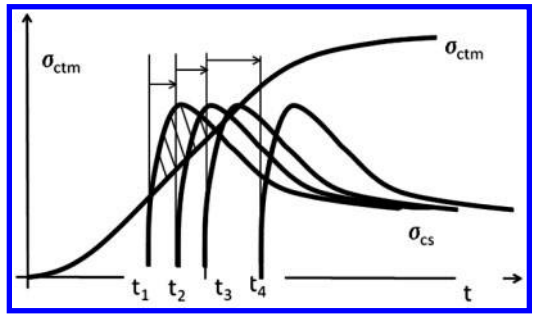


Figure 1. Increasing strength concrete σ_{ctm} versus stresses of shrinkage in concrete σ_{cs}.

- using adjustable formwork in building chimneys
- using joints in chimneys during building
- non proper joint design
- too long pause between subsequent concrete filling
- using vibrators inappropriate for steel bars diameter and for distances between them
- touching by vibrator steel bars (PN-63 B-06251)
- too small or destroyed thermal insulation
- destroyed moisture protecting coating
- too much condensate inside chimney
- too few steel bars calculated shrinkage for chimneys wall
- adding loads on chimney as satellite dishes

Figure 1 shows increasing strength concrete σ_{ctm} versus stresses of shrinkage in concrete σ_{cs} in the beginning of concrete bonding (Flaga 2002). Time t_i can be delayed from t_1 to t_4 through maintenance moisture in concrete wall or by using special plasticizers. Between time t_1 and time t_3 stresses caused by shrinkage are bigger than strength of concrete and cracks can occur in the time of strengthening concrete itself. In this case, when shrinkage stresses are bigger than concrete strength, special reinforcement steel bars should



Figure 2. Horizontal cracks in the place of joints.



Figure 3. Horizontal joints with condensate flowing from internal chimney space.



Figure 4. New chimney without any faults.

be used. But after this initiation time shrinkage stresses decrease.

Vertical and horizontal cracks on chimneys walls are shown on Figure 2 to Figure 10.

3 THE REASONS FOR APPEARANCE OF CRACKS IN THE PLACE OF JOINTS

After changes of chimney codes and particularly after acceptance condition of reinforcement in two rows near outside and inside surface of wall appeared many cracked in joint places. There were made many samples cut form chimney wall. On one of them it is shown that cracks were caused by vibration reinforcement bars (Figure 9 and 10). Joint as a place is between rather mature concrete and fresh concrete. Vibrated bars move on a their considerable length. Vibration of bars can initiate craks in place of high stresses which are in the joint places. High stresses are caused by process of shrinkage as is shown on Figure 7 to 8.

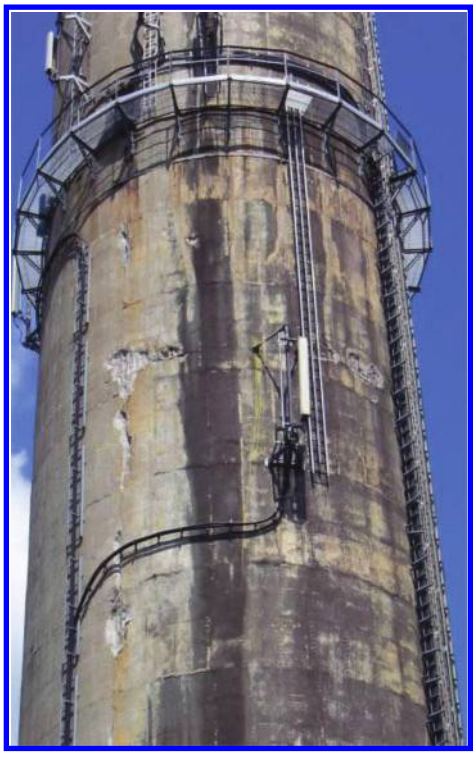


Figure 5. Chimney after many years of exploitation with many horizontal and vertical cracks and many surface defects.



Figure 6. Vertical and horizontal cracks on chimney wall with condensate flowing form horizontal cracked joints.

Figure 8 shows different consistency of concrete above and below joint.

4 THE THERMAL CHIMNEYS PROTECTION

Thermal insulation protects chimney wall against high temperature and high temperature gradient resulting in an increase of the tension force and of the bending moment. Additional non uniform distribution of temperature on chimney wall causes increasing of



Figure 7. Place of joint where the sample was picked up.



Figure 8. The sample with different consistencies of concrete above and below the joint.



Figure 9. The sample picked up from the place with joint.



Figure 10. The sample picked up from the place with joint.



Figure 11. The condensate flowing form horizontal cracked joints.



Figure 12. Chimney with demaged thermal protection.

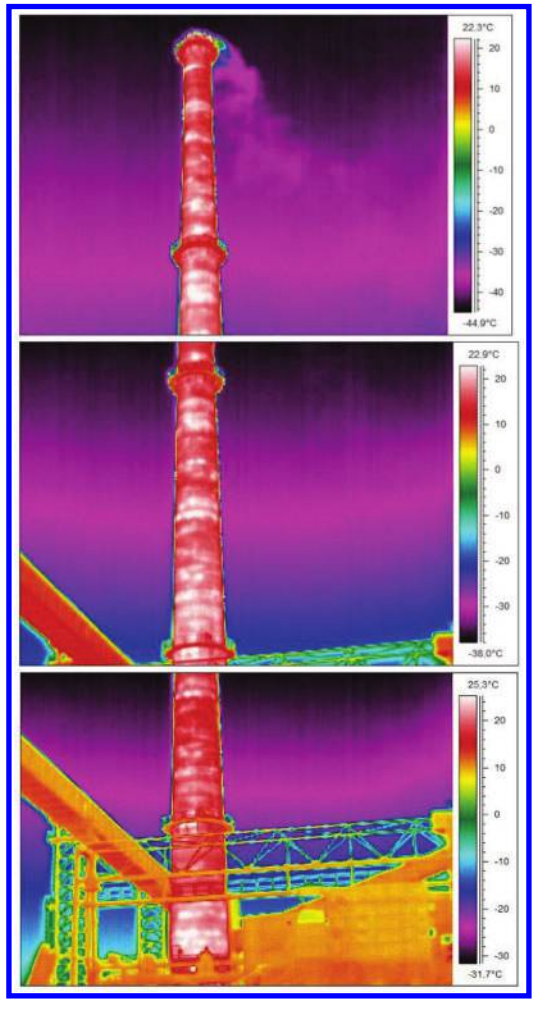


Figure 13. Destroyed thermal protection seen in the thermographic camera.

deflection of chimney and increasing vertical inner forces. This is the reason that vertical and horizontal cracks appear additionally.

Thermal insulation can be destroyed or may fall down because of excessive number of condensate penetrate to surface of chimney wall. Thermographic photographs were made (Maj&Ubysz 2012) on new built chimney (Figure 12). It is shown on Figure 13 where bright fields are places of high temperature i.e. spaces without insulation or with insulation weakened.

5 METHODS OF REPAIR CRACKED CHIMNEY WALLS

Methodology of repair of chimney wall can be presented in the following points:

a. Checking the current strength of concrete and reinforcement steel bars,

b. remove the cause of fracture design if possible i.e. repair of thermal insulation, repair of internal and external moisture insulation coatings,
c. cleaning and drying of damaged sites if it is possible,
d. filling under pressure the vertical and horizontal cracks using specialized mortar,
e. the annual chimney check the technical condition

6 CONCLUSIONS

During designing chimney constriction it is very important to provide a method of building, type of vibration of concrete, appropriate reinforcement spacing, choose the good technology of joints.

Suggests the use of sliding formwork which ensures no joints. During building chimney wall vibrators can not touch any reinforcement and any formwork. With a heavy an accuracy and under constant control building inspectors should be put thermal insulation.

REFERENCES

Kazimierz Flaga, Zbrojenie przeciwskurczowe, obliczenia, zalecenia *XVII Ogólnopolska Konferencja Warsztat Pracy Projektanta Konstrukcji Ustroń*, Luty 2002.

PN-63 B-06251 Roboty betonowe i żelbetowe.

Maj M. Ubysz A., W sprawie zarysowania żelbetowych ścian kominów obciążonych skurczem, termiką i innymi obciążeniami eksploatacyjnymi, *Konferencja Politechniki Wrocławskiej, Karpacz* 2012.

Research and Applications in Structural Engineering, Mechanics and Computation – Zingoni (Ed.)
© 2013 Taylor & Francis Group, London, ISBN 978-1-138-00061-2

Water transport in surface layer of fair-face concrete

Pavel Reiterman, Filip Vogel, Ondřej Holčapek, Karel Kolář & Petr Konvalinka
Experimental Centre, Faculty of Civil Engineering, Czech Technical University in Prague Technical University, Prague, Czech Republic

Martin Keppert, Monika Čáchová & Eva Vejmelková
Department of Material Engineering and Chemistry, Faculty of Civil Engineering, Czech Technical University, Prague, Czech Republic

ABSTRACT: In the production of fair-face elements is very popular, but aesthetic quality needs to withstand its lifespan. In the case of non-protected concrete surface, any failure is much more pronounced. An important parameter determining the durability of concrete is the quality of the surface layer, as it is directly exposed to the environment. In terms of durability properties, it is worth to monitor the parameters of the surface layers, particularly the transport processes. The paper presents the selected experimental methods for evaluation the quality of the surface layer of concrete aimed at monitoring the permeability of concrete, since concrete permeability is a property uniquely affecting durability of concrete. These methods are complemented by experimental results and other traditional tests. These findings will serve to further optimization of the structure being created, thus ensuring its better aesthetic and functional characteristics.

1 INTRODUCTION

The origin and character of the concrete surface layer is given by the technology of production of concrete elements; during vibration compaction is going on initiation and rising of air bubbles upward. This eliminates air content in concrete, but also the concentration of fine particles takes place close the walls of the formwork. Coarse aggregate – due to its geometry – cannot get its entire plane to formwork or to the corners (Reiterman). Hence the concrete surface exhibits completely different properties compared to bulk – it is called wall effect. The characteristic properties of the surface layer are low content of coarse aggregates and an increased amount of cement stone which consists of fine fractions of aggregate and cement hydration products. A very important feature is especially high content of pores in comparison with the inner layer (Reiterman). Such a surface layer having a thickness of 20–50 mm has highly very different, usually worse properties than the surrounding material. Therefore attention is drawn to quality of concrete surface layer. Each void and crack decreases a steel covering concrete layer and thus accelerates the process of its corrosion which is associated with visual degradation of the building (Kolář). Degradation processes are closely related to the quality of the surface layer and the pore system of concrete (Konvalinka).

2 EXPERIMENTAL PROGRAM

Permeability of porous materials is one of the principal parameter influencing their transport properties and durability. The intrinsic permeability of material K [m^2] is defined in terms of Darcy's law describing flow of a liquid through a porous material saturated by the liquid under the action of pressure gradient across the material. It is material property and thus does not depend on the kind of permeating liquid. One of possible definitions of K is given by equation (1) (Ěerný).

$$j = -K \cdot \frac{\rho_l}{\eta} \cdot \frac{\partial p}{\partial x} \tag{1}$$

There j is mass flux [$kg\,m^{-2}\,s^{-1}$], ρ_l is density of the liquid [$kg\,m^{-3}$], η is dynamic viscosity of the liquid [Pa s] and driving force is pressure gradient through the material. Intrinsic permeability is extremely dependent on properties of porous system of hardened concrete. That is one of the reasons of very different result of published experimental works.

Permeability was measured by means of high pressure permeameter made by CNE Technology. The design is based on work (Green). The method is based on definition equation (1). This method is not standardized in Europe, but there is an American standard (RILEM). Altogether were measured four concrete mixtures (tab. 1).

Experiment based on Darcy's law provides coefficient of permeability K valid for saturated state of material. The dependence of K upon volumetric moisture content w can be derived by help of pore size distribution of the material. Mualem [8] proposed equation (2) which uses experimentally determined pore size distribution function f(r); other input parameters are

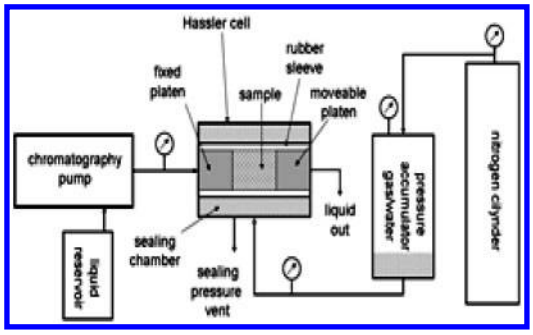


Figure 1. High pressure permeameter scheme.

Table 1. Composition of used concrete mixtures.

Mixture Components	I [kg/m^3]	II [kg/m^3]	III [kg/m^3]	IV [kg/m^3]
Cement CEM I 42,5 R	350	350	400	400
Aggregate: sand 0–4 mm	785	830	930	930
crushed 4–8 mm	350	350	315	315
crushed 8–16 mm	650	580	600	600
Plastisizer (Sika 1035)	0	0	3	2
Water	186	208	180	180
Water-cement ratio	0.53	0.59	0.46	0.46

saturated moisture content w_{sat} and parameter n. For computing was used software HydraPor developed at Department of Material Engineering and Chemistry Czech Technical University in Prague. Final composition and properties of the studied mixtures are at (tab.1 and tab. 2).

$$K(w) = K\left(\frac{w}{w_{sat}}\right)^n \cdot \left(\frac{\int_{R_{min}}^{R} r\,f(r)dr}{\int_{R_{min}}^{R_{max}} r\,f(r)dr}\right)^2 \quad (2)$$

Pore size distribution was determined by means of mercury intrusion porosimetry (MIP). The method is based on intrusion of mercury – non wetting liquid – to pores of studied sample. The penetrated pore's diameter is inversely proportional to applied pressure (Washburn equation). The applied pressure is gradually increasing during the experiment and thus mercury penetrates narrower pores. The result of experiment is dependence of pore volume (it corresponds to measurable volume of intruded mercury) upon pore diameter (corresponds to applied pressure). The experiment was carried out by means of Pascal 140 and 440 devices (Thermo).

The water vacuum saturation method was used for the measurements of bulk density, matrix density and open porosity (Vejmelková). Each sample was dried in a drier to remove majority of the physically bound water. After that the samples were placed into the desiccator with deaired water. During three hours air was evacuated with vacuum pump from the desiccator. The specimen was then kept under water not less than 24 hours.

Table 2. Properties of concrete mixtures.

Mixture	I	II	III	IV
Bulk density [kg/m^3]	2325	2330	2310	2320
ρ_{mat} [kg/m^3]	2614	2612	2598	2600
ψ_0 [−]	11.97	12.68	10.18	11.48
Compressive strength [MPa]	46.7	43.8	67.8	60.5
Hydraulic conductivity [m/s]	$0.8 \cdot 10^{-11}$	$1.2 \cdot 10^{-11}$	$1.2 \cdot 10^{-11}$	$1.2 \cdot 10^{-11}$
Depth of pressure [mm] water penetration	100	80	38	48
Equilibrium volume moisture [−]	4.8	4.0	6.2	5.8

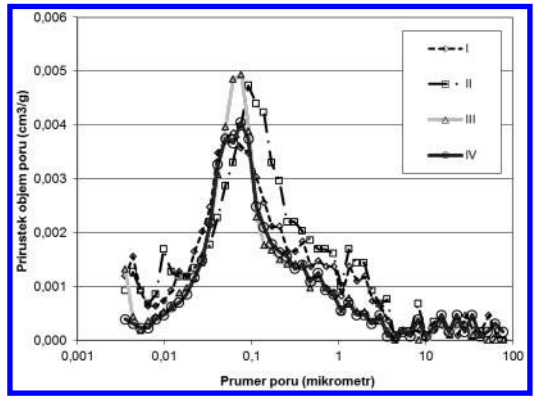


Figure 2. Pore distribution.

From the mass of the dry sample m_d, the mass of water saturated sample m_w, and the mass of the immersed water saturated sample m_a, the volume V of the sample was determined from the equation (3), (Vejmelková).

$$V = \frac{m_w - m_d}{\rho_w} \quad (3)$$

Where ρ_w is the density of water. The open porosity ψ_0, the bulk density ρ and the matrix density ρ_{mat} were calculated according to the equations (4), (5), (6).

$$\psi_0 = \frac{m_w - m_d}{\rho_w} \quad (4)$$

$$\rho = \frac{m_d}{V} \quad (5)$$

$$\rho_{mat} = \frac{m_d}{V(1-\psi_0)} \quad (6)$$

Sufficient concrete surface resistance depends not only on the quality of the surface layer, but also on the character of the pore system. It directly affects the

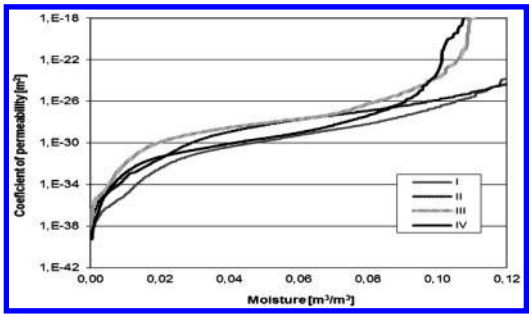


Figure 3. Coefficient of permeability as function of moisture content.

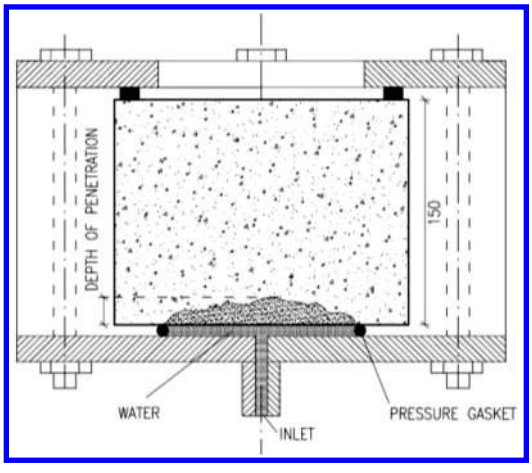


Figure 4. Water penetration test scheme.

rate of penetration of aggressive substances from the external environment to the internal structure of the concrete and thus the degradation rate of the material. It is very important therefore to reduce transport of liquid water solutions and water vapor as a primary protection against corrosion of reinforcement. Determination of depth of penetration was performed according standard ČSN EN 12390-8; water has a pressure of 0.5 MPa for 72 hours.

3 CONCLUSION

Durability of concrete depends not only on the quality of the surface layer, but also on the nature of the pore system that is truly defining parameter because it affects the rate at which aggressive substances, gaseous or liquid, penetrate from the external environment into the internal structure of concrete, and thus the rate of degradation of the material and its durability. Very important is the limitation of water and moisture transport of having a role in reinforcement protecting against corrosion. Results of these tests will become the basis for a correlation dependence permeability of concrete and concrete methodologies for evaluation in terms of its durability. At this point it should be noted that the in construction practice and research, the term of permeability is used quite freely (for different tests), it is always necessary to present the results along with the method and conditions of the experiment. It is obvious that a material will have a dramatically (ASTM C 1202-97) different permeability for air, for water or "permeability" of the chloride ions, reported in the Coulombs.

In connection with the introduction of the new standard system came into issues of concrete durability on importance. Action of aggressive media concentrated in the external environment is to develop a wide range of corrosion mechanisms (CRD C 163-92), (RILEM). Most buildings are protected from the effects of adverse conditions by other types of structures. In case of the fair-face concrete, however, this protective layer is formed by the material itself. Due to the fact that concrete degradation processes are going on a long-term, and aggressive substances act at low concentrations, it is very difficult to describe such effects and to quantify the resulting degradation phenomenon under test in the laboratory. In the case of porous building materials is intrinsic permeability one of the parameters that affect their behavior in structures; depend on it water resistance and indirectly resistance to action of frost, salts and other degradation processes, that is durability.

ACKNOWLEDGEMENT

This research was supported by MSM 6840770031 which is gratefully acknowledged.

REFERENCES

ASTM C 1202-97: Standard Test Method for Electrical Indication of Concrete's Ability to Resist Chloride Ion Penetration, American Society for Testing and Materials, 1997.

CRD C 163-92: Test method for water permeability of concrete using triaxial cell, U.S. Army Corps of Engineers Standards, 1992.

Černý, R., Rovnaníková, P.: Transport processes in concrete. London: Spon press, 2002.

ČSN EN 12390-8. Testing of hardened concrete – Part 8. Water penetration test. Czech Standardization Institute, 2007.

Doležel, T., Konvalinka, P., Jandeková, D.*: Vliv cyklù zmrazování-rozmrazování na materiálově charakteristiky betonu,* In: Stavební obzor. 2004, roč. 13, č. 5, s. 143–147. ISSN 1210–4027.

Green, K. M., Hoff, W. D., Carter, M. A., Wilson, M. A., Hyatt, J. P.: A high pressure permeameter for the measurement of liquid conductivity of porous construction materials. Review of Scientific Instruments, 1999, Vol. 70, pp. 3397–3401.

Kolář, K., Reiterman, P., Klečka, T., Dudíková, M., Huňka, P. *Surface Layer Study of Concrete Containing Metakaolin* In: Concrete under Severe Conditions – Environment and Loading. Leiden: CRC Press/Balkema, 2010, p. 675–692. ISBN 978-0-415-59318-2.

Konvalinka, P., Litoš, J., Jandeková, D.*: Volume Changes of Cement Pastes Using Metakaolin,* In: Proceedings of the 50th Annual Conference on Experimental Stress Analysis. Praha: Czech Technical University in Prague, 2012, p. 211–216. ISBN 978-80-01-05060-6.

Mualem, Y. A new model for predicting the hydraulic conductivity of unsaturated soils. Water Resources Research, Vol. 12, 1976, pp. 513–522.

Reiterman, P., Keppert, M., Holčapek, O., Kadlecová, Z., Kolář, K. *Permeability of Concrete Surface Layer* In: Proceedings of the 50th Annual Conference on Experimental Stress Analysis. Praha: Czech Technical University in Prague, 2012, p. 361–368. ISBN 978-80-01-05060-6.

Reiterman, P., Kostelecká, M., Kolář, K., Konvalinka, P. *Influence of Covercrete Morphology on Durability Properties* In: Journal of Civil Engineering and Architecture. 2012, vol. 6, no. 7, p. 928–932. ISSN 1934-7359.

RILEM TC 116-PCD: Permeability of concrete as a criterion of its durability. Materials and Structures, 1999, Vol. 32, pp. 174–179.

RILEM Report 12: Performance criteria for concrete durability. Ed. by J. Kropp and H. K. Hilsdorf, E. and F.N. Spon, 1995.

Vejmelková, E., Keppert, M., Rovnaníková, P., Ondráček, M., Keršner, Z., et al.*Properties of high performance concrete containing fine-ground ceramics as supplementary cementitious material* In: Cement and Concrete Composites. 2012, vol. 34, no. 1, p. 55–61. ISSN 0958-9465.

Vejmelková, E., Keppert, M., Rovnaníková, P., Keršner, Z., Černý, R. *Properties of lime composites containing a new type of pozzolana for the improvement of strength and durability* In: Composites Part B: Engineering. 2012, vol. 43, no. 8, p. 3534–3540. ISSN 1359-8368.

Research and Applications in Structural Engineering, Mechanics and Computation – Zingoni (Ed.)
© 2013 Taylor & Francis Group, London, ISBN 978-1-138-00061-2

Creep influence on concrete slabs, pre-stressed in both directions

G. Sossou
Kwame Nkrumah University of Science and Technology, Kumasi, Ghana

ABSTRACT: This report relates to pre-stressed concrete slabs, subjected to static long-term service loads.

For structural predictions, the well-known finite elements and multi-scale/multi-grid methods have been used to estimate (a) transient bi-directional forces and strains due to the concrete creep and shrinkage, (b) the resulting bi-directional stress redistribution, as well as (c) bi-directional displacement variations and (d) bi-directional pre-stressing losses in the pre-stressed high yield tendons.

A series of laboratory experiments with once evaluated strength parameters are planned to be used to provide encouraging support for the numerical evaluations said at above points (a) – (d) in addition to (e) calibrating the parameters likely to enable the estimations of the pre-stressing losses, (f) predicting the slabs sections' stiffness and strength by determining their long-term flexural and nonlinear creep capacity and hence, (g) devising a definition for structural durability and reliability, with regards to the concrete stress-strain relationship under prolonged service loads.

Keywords: concrete matrix creep, shrinkage, concrete slabs, strength, reliability, durability, pre-stressing tendons, pre-stressing losses

1 INTRODUCTION

During these last two decades many theoretical and experimental studies have shown that the use of pre-stressed concrete for precast concrete members, especially for slabs pre-stressed in both directions is effective comparable to our conventional monolithic in-situ cast slabs.

But many negative factors like ageing, time-dependent increased loads, exposure to aggressive environmental factors have resulted in the progressive deterioration of many potentially functional building structures like higher flat apartment house buildings, industrial buildings, office buildings, post-harvest structures, …, etc. This paper describes the present ongoing numerical and experimental analysis model used to evaluate the structural long duration flexural characteristics of reinforced concrete slabs, pre-stressed in both directions. This present study has been based on nonlinear differential equations of the concrete matrix creep theory which reflects the correlation between the matrix stress and strain by its modulus of elasticity and on the well-known geometrical preconditions of the theory of elasticity concerning thin plates with small flexural deformations.

Many Authors carried out a lot of research experiments to improve the strength of the structural material, predicting the eventual cracking characteristics of the structural members. Design formulas for stress-strain limit states of the structures have been previously proposed based on the well-known concepts. However this present ongoing study is of higher importance, as it is recognized that little information is available on the time dependent factors like the concrete matrix creep, shrinkage and loss of pre-stresses, in relation to bi-directional pre-stressing of reinforced concrete slabs, with high yield tendons, subjected to long-term service loads.

It may be of grate importance to allow for factors influencing on the structural performance characteristics of the slabs by averaging maximum, and minimum estimated effects, and provided that this is done and there are a number of calculation methods available which will give reasonable results. The methods adopted developed by the Code of Practice are comprehensive, and are based on calculation of curvatures of the slabs sections subjected to the appropriate forces and moments, with allowances for concrete creep and shrinkage effects.

2 THEORETICAL ANALYSIS – MAIN CONCEPTUAL DESIGN PARAMETERS

The numerical part of this study is based on the well-known concepts by Yasinskiy, Timoshenko, Barashikov, Yatsenko, Baykov, Vlasov, Drozdov, Juravskiy, … etc and many other Authors, on the problem of quality, stiffness, strength, reliability, durability, fatigue, life safety and stability of the precast concrete slabs, pre-stressed in both directions.

The main conceptual design of the slabs has been based also on the orthotropic plate theory with grillage analogy in a suitable finite element model. The

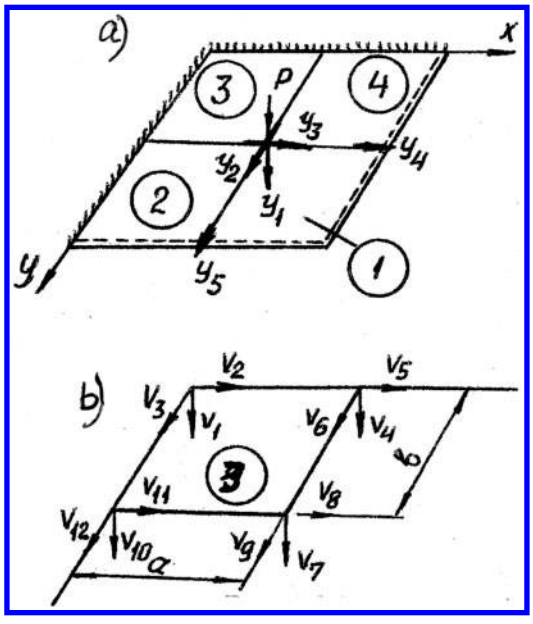


Figure 1. The concrete slab's design model.

Table 1. Each finite element's subscripts.

y_k 0	y_1	y_2	y_3	y_4	y_5
1	1	2	3	5	12
2	4	5	6	0	9
3	7	8	9	0	0
4	10	11	12	8	0

slab's model as shown in Figure 1- a) includes 4 finite elements having 5 nodal displacements y_1, y_2, y_3, y_4, and y_5. The finite elements are of the same dimensions a×b as shown in Figure 1- b) and each of them has 12 nodal displacement parameters: v_1, v_2, v_3, ..., v_{12}. Thus, the finite element method based on the displacement matrix formulations has been successfully used to solve the systems of matrix equations. Force equilibrium and deformation compatibility protocols have been observed at all stages of calculations.

Then the finite element's stiffness matrix has 12 columns and 12 rows, and its elements C_{ik} have subscripts i – the column's number and k – the row's number.

Now let us fill below the subscripts' table in which columns designate the finite element's number, and rows – the parameter's number y_k:

To fill the first column's subscripts, we need to bring the element from Figure 1 – b) to the place of element 1 in Figure 1 – a) and find out which parameters v_ℓ coincide with parameters y_k. Subscripts of coinciding parameters should be placed into corresponding boxes of first column.

For example, v_{12} coincides with y_5; consequently under y_5 we should place subscript 12. Similarly we need to fill the second column, bringing finite element from Figure 1 – b) to the place of element 2 in Figure 1 – a). For example, parameter v_9 coincides with parametery_5, consequently under y_5 we should place subscript 9. With parameter y_4 no coincidence, that is why under y_4 we should place zero. The procedure is similar for other columns.

Table 2. Stiffness matrix subscripts.

y_1	y_2	y_3	y_4	y_5	
r_{11}	r_{12}	r_{13}	r_{14}	r_{15}	y_1
	r_{22}	r_{23}	r_{24}	r_{25}	y_2
		r_{33}	r_{34}	r_{35}	y_3
			r_{44}	r_{45}	y_4
	Sym.			r_{55}	y_5

Now the complete subscripts' table could give us the opportunity for the stiffness matrix of the whole slab's model to choose from the original stiffness matrix those of its elements which coincide with a given node. For the slab's model shown in Figure 1 – a), the stiffness matrix is discussed using the subscripts' table.

More, this very subscripts' table gives us the opportunity to bring the global displacements y_k into the local Cartesian coordinate system according to the formula $\vec{v}_\ell = a_\ell \vec{y}$, where a_ℓ is coordinates transformation matrix.

$$
\begin{aligned}
&r_{11} = c_{11} + c_{44} + c_{77} + c_{10,10};\\
&r_{12} = c_{12} + c_{45} + c_{78} + c_{10,11};\\
&r_{13} = c_{13} + c_{46} + c_{79} + c_{10,12};\\
&r_{14} = c_{15} + c_{8,10};\ r_{15} = c_{1,12} + c_{49};\\
&r_{22} = c_{22} + c_{55} + c_{88} + c_{11,11};\\
&r_{23} = c_{23} + c_{56} + c_{89} + c_{11,12};\\
&r_{24} = c_{25} + c_{8,11};\ r_{25} = c_{2,12} + c_{59};\\
&r_{33} = c_{33} + c_{66} + c_{99} + c_{12,12};\ r_{34} = c_{35} + c_{8,12};\\
&r_{35} = c_{3,12} + c_{69};\ r_{44} = c_{55} + c_{88};\ r_{45} = c_{5,12};\\
&r_{55} = c_{12,12} + c_{99}.
\end{aligned}
$$

For example, concerning elements 1, 2, 3, 4 in Fig.1- a we have (according to the subscripts' table)

$$
\begin{aligned}
&v_1 = \{y_1\ \ y_2\ \ y_3\ \ 0\ \ y_4\ \ 0\ \ 0\ \ 0\ \ 0\ \ 0\ \ y_5\}^T;\\
&v_2 = \{0\ \ 0\ \ 0\ \ y_1\ \ y_2\ \ y_3\ \ 0\ \ 0\ \ y_4\ \ 0\ \ 0\ \ 0\ \}^T\\
&v_3 = \{0\ \ 0\ \ 0\ \ 0\ \ 0\ \ 0\ \ y_1\ \ y_2\ \ y_3\ \ 0\ \ 0\ \ 0\}^T\\
&v_4 = \{0\ \ 0\ \ 0\ \ 0\ \ 0\ \ 0\ \ 0\ \ y_1\ \ y_2\ \ y_3\ \ 0\ \ 0\}^T
\end{aligned}
$$

Now the slab's rectangular finite element shown in Fig. 1-b with dimensions a×b has 12 nodal displacement parameters v_j (j = 1, 2, …, 12) and corresponding 12 nodal reactions ς_j (j = 1, 2, …, 12). If the directions of these displacements coincide with the directions

of local coordinate axes x and y, then these displacements together with their corresponding reactions will be positive.

According to the number of the finite element's nodal displacements the function of its vertical displacements is defined in form of poly-nom with 12 coefficients, that is: $w(x,y) = W(x,y)\,\vec{\alpha}$, where $\vec{\alpha}$ is the 12 coefficients vector, and W(x, y) – the linear displacements' functional matrix having this following form:

$$W(x,y) = \{\, 1 \;\; x \;\; y \;\; x^2 \;\; y^2 \;\; xy \;\; x^2y \;\; xy^2 \;\; x^3 \;\; y^3 \;\; x^3y \;\; xy^3 \,\} \qquad (1)$$

Let us analyze the correlations between the components of the bending moments' units $M_x(x,y)$, $M_y(x,y)$, $mboxM_{x,y}(x,y)$ and their co-responding strains' components representing their flexural curvatures $\Re_x(x,y), \Re_y(x,y), \Re_{x,y}(x,y)$:

$$M_x = D(\Re_x + \mu\,\Re_y);\; M_y = D(\Re_y + \mu\,\Re_x);\; M_{x,y} = 2D(1-\mu)\Re_{xy}, \qquad (2)$$

where subscripts 'x' and 'y' indicate the directions of forces and strains, parallel to their corresponding Cartesian coordinates axes x and y;

μ – Poisson's coefficient; D – cylindrical stiffness:

$$D = \frac{E\,h^3}{12(1-\mu^2)}, \qquad (3)$$

with h – the thickness of the finite element.

Let us denote

$$\vec{M}(x,y) = \begin{Bmatrix} M_x(x,y) \\ M_y(x,y) \\ M_{xy}(x,y) \end{Bmatrix};\; \vec{\Re}(x,y) = \begin{Bmatrix} \Re_x(x,y) \\ \Re_y(x,y) \\ \Re_{xy}(x,y) \end{Bmatrix};\; \Im = \begin{Bmatrix} 1 & \mu & 0 \\ \mu & 1 & 0 \\ 0 & 0 & 2(1-\mu) \end{Bmatrix}.$$

Now Equations (2) should be re-written into single matrix equation as follows:

$$\vec{M}(x,y) = \Im\,\vec{\Re}(x,y). \qquad (4)$$

From the theory of elasticity concerning thin concrete matrix membranes with small flexural deformations these next Equations are true:

$$\Re_x(x,y) = -\frac{\partial^2 w(x,y)}{\partial x^2};\;\; \Re_y(x,y) = -\frac{\partial^2 w(x,y)}{\partial y^2};\;\; \Re_{xy}(x,y) = -\frac{\partial^2 w(x,y)}{\partial x \partial y}.$$

Now taking into consideration Equation (1) we obtain the stiffness matrix:

$$C = D\begin{Bmatrix}
c_{11} & c_{12} & c_{13} & c_{14} & c_{15} & c_{16} & c_{17} & c_{18} & c_{19} & c_{1,10} & c_{1,11} & c_{1,12} \\
 & c_{22} & c_{23} & c_{24} & c_{25} & c_{26} & c_{27} & c_{28} & c_{29} & c_{2,10} & c_{2,11} & c_{2,12} \\
 & & c_{33} & c_{34} & c_{35} & c_{36} & c_{37} & c_{38} & c_{39} & c_{3,10} & c_{3,11} & c_{3,12} \\
 & & & c_{44} & c_{45} & c_{46} & c_{47} & c_{48} & c_{49} & c_{4,10} & c_{4,11} & c_{4,12} \\
 & & & & c_{55} & c_{56} & c_{57} & c_{58} & c_{59} & c_{5,10} & c_{5,11} & c_{5,12} \\
 & & & & & c_{66} & c_{67} & c_{68} & c_{69} & c_{6,10} & c_{6,11} & c_{6,12} \\
 & & & & & & c_{77} & c_{78} & c_{79} & c_{7,10} & c_{7,11} & c_{7,12} \\
 & & & & & & & c_{88} & c_{89} & c_{8,10} & c_{8,11} & c_{8,12} \\
 & & & & & & & & c_{99} & c_{9,10} & c_{9,11} & c_{9,12} \\
 & & & & & & & & & c_{10,10} & c_{10,11} & c_{10,12} \\
 & & \text{Symmetry} & & & & & & & & c_{11,11} & c_{11,12} \\
 & & & & & & & & & & & c_{12,12}
\end{Bmatrix}$$

where with $k = \frac{b}{a}$

$$c_{11} = c_{44} = c_{77} = c_{10,10} = [4k + \frac{4}{k^3} + \frac{14-4\mu}{5k}]/a^2;$$

$$c_{22} = c_{55} = c_{88} = c_{11,11} = \frac{4k}{3} + \frac{4(1-\mu)}{15k};$$

$$c_{33} = c_{66} = c_{99} = c_{12,12} = \frac{4}{3k} + \frac{4k(1-\mu)}{15};$$

$$c_{12} = c_{10,11} = -c_{45} = -c_{78} = [2k + \frac{(1+4\mu)}{5k}]/a;$$

$$c_{13} = c_{46} = -c_{78} = -c_{10,12} = [2/k^2 + \frac{(1+4\mu)}{5}]/a;$$

$$c_{23} = -c_{56} = c_{89} = -c_{11,12} = \mu;$$

$$c_{14} = c_{7,10} = [-4k + 2/k^3 - \frac{14-4\mu}{15k}]/a^2;$$

$$c_{1,10} = c_{47} = [-\frac{4}{k^3} + 2k - \frac{14-4\mu}{5k}]/a^2;$$

$$c_{15} = -c_{24} = -c_{7,11} = c_{8,10} = [2k + \frac{(1-\mu)}{5k}]/a;$$

$$c_{25} = c_{8,11} = 2k/3 - \frac{(1-\mu)}{15k};$$

$$c_{36} = c_{9,12} = 2/3k - 4k\frac{(1-\mu)}{15};$$

$$c_{16} = c_{34} = -c_{7,12} = -c_{9,10} = [1/k^2 - \frac{(1+4\mu)}{5}]/a;$$

$$c_{1,11} = c_{2,10} = -c_{48} = -c_{57} = [k - \frac{(1+4\mu)}{5k}]/a;$$

$$c_{1,12} = -c_{3,10} = c_{49} = -c_{6,7} = [2/k^2 + \frac{(1-\mu)}{5}]/a;$$

$$c_{17} = c_{4,10} = [-2k - \frac{2}{k^3} + \frac{14-4\mu}{5k}]/a^2;$$

$$c_{18} = c_{5,10} = -c_{27} = -c_{4,11} = [k - \frac{(1-\mu)}{5k}]/a;$$

$$c_{19} = -c_{37} = c_{4,12} = -c_{6,10} = [1/k^2 - \frac{(1-\mu)}{5}]/a;$$

$$c_{2,11} = c_{58} = 2k/3 - 4\frac{(1-\mu)}{15k};\; c_{28} = c_{5,11} = k/3 + \frac{(1-\mu)}{15k};$$

$$c_{39} = c_{6,12} = \frac{1}{3k} + k\frac{(1-\mu)}{15};\; c_{3,12} = c_{69} = \frac{2}{3k} - k\frac{(1-\mu)}{15};$$

$$c_{26} = c_{29} = c_{2,12} = c_{35} = c_{38} = c_{3,11} = c_{59} = c_{5,12} = c_{68} = c_{6,11} = c_{8,12} = c_{9,11} = 0.$$

From past theoretical results, before the transfer of the pre-stressing forces P to the slab, in the eth steel reinforcement tendons' row were acting the initial controlled stresses $\sigma_{e,contr.}$, without first losses, independently on properties of the concrete. At the moment of the transfer, taken like the beginning of

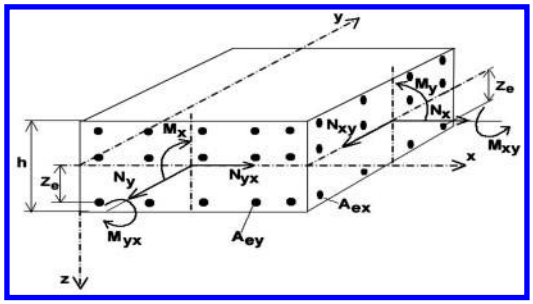


Figure 2. Slab element with acting forces and moments.

time-dependent counting out, in the steel tendons and in the concrete matrix were actively acting elasto-instantaneous increases of stresses respectively σ_{e0} and $\sigma_0(y_e)$, where $y_e = z_e$ is the distance from the slab's neutral axis to the axis of the eth tendons' row (Figure 2). At a certain maturity of concrete matrix t these above said elasto-instantaneous increases of stresses were changing and their values became equal to $\sigma_e(t)$ and $\sigma\ (y_e,t)$ respectively, with the fact that stresses in steel tendons were increasing, but in concrete matrix stresses were reducing. After the transfer the above said initial controlled stresses $\sigma_{e,contr.}$ have become equal to $\sigma_{e,contr.} - \sigma_e(t)$.

According to the Codes of Reinforced Concrete Structures, stress losses due to concrete matrix creep and shrinkage in a certain eth steel tendons' row have been calculated, taking into consideration that part of stresses, which cannot comply with the action of the initial pre-stressing forces P, applied with an eccentricity e_{0P} can nullify the stresses formed in the concrete matrix $\sigma\ (y_e, t)$ at the level of the same steel tendons' row. In that way, the stresses $\sigma\ (y_e, t)$ have been provoked by the pre-stressing forces P in the tendons, by the concrete matrix creep and shrinkage, by the slab's self weight and by the intensity and duration of the long-term service loads acting on the slab.

At the loading duration τ, as the long-term service loads were acting on the slab, the long duration of these actual loads can contribute to the fact that, stresses in the steel reinforcement tendons have been increased, but in the concrete matrix theses stresses have been reduced, and just this positive effect can contribute to the efficiency of the slabs. By applying to the slab the initial pre-stressing force P with an eccentricity e_{0P} at a certain concrete maturity t for the purpose to reduce the developed stresses $\sigma\ (y_e,\tau)$ to zero, we have changed the stresses in steel tendons to their actual value $\alpha_e(\tau)$ $\sigma\ (y_e,\tau)$, where $\alpha_e(\tau) = E_e/E(\tau)$ – elasticity modulus ratio of the eth steel tendons' row and the concrete matrix, at the concrete maturity t. In that way, proper stresses in steel tendons will become equal to:

$$\sigma_{eP} = \sigma_{e,\ contr.} - \sigma_e(t) + \alpha_e(\tau)\ \sigma(y_e,\tau). \tag{5}$$

These same stresses can be presented in the following way:

$$\sigma_{eP} = \sigma_{e,\ contr.} - \sigma_{loss2e}(t) \tag{6}$$

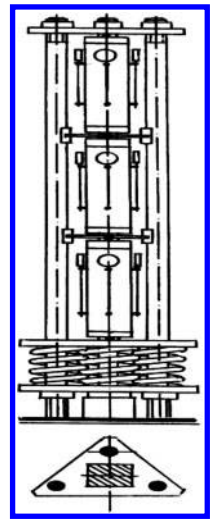


Figure 3. Loading frame for creep test.

where $\sigma_{loss2e}(t)$ – pre-stressing losses in the eth steel tendons' row at the application moment of the force P. By equating expressions (5) and (6) we have obtained the formula for the evaluation of the generalized losses, in the eth steel tendons' row:

$$\sigma_{loss2e}(t) = \sigma_e(t) - \alpha_e(\tau)\ \sigma(y_e,\tau) \tag{7}$$

Thus, for the determination of pre-stressing losses in any eth steel tendons' row of the slab, it is necessary just to know the current initial stresses in the tendons' row and in the adjacent concrete matrix at the level of the same row, provoked by all of the long-term influences on the slabs. These said current initial stresses can be evaluated by creep computation of the slabs. The pre-stressing forces P which can generalize the effect of proper stresses and the eccentricity of its application e_{0P} can be evaluated by following formulas:

$$\begin{aligned} P &= \sum_{e=1}^{s} (\sigma_{e,contr} - \sigma_{loss2e})A_e\ ; \\ e_{0P} &= [\sum_{e=1}^{s} (\sigma_{e,contr} - \sigma_{loss2e})A_e y_e]/P, \end{aligned} \tag{8}$$

where A_e is the cross-sectional area of eth steel tendons' row.

The displacements in the slab Δ have been determined on the basis of

$$\Delta = \sum_{i=1}^{n} \int_0^{\ell_i} (M_1 \Re + N_1\ \varepsilon)_i\ dx, \tag{9}$$

where $i = 1, 2,..., n$ – quantity of homogeneous elements with a length wise of λ_i;

M_1 and N_1 – forces from generalized force unity, applied in the place and to the direction of the unknown displacements;

$\Re$ and ε – components of deformations in the slab.

3 EXPERIMENTAL PROGRAM AND SOME TEST RESULTS

The experimental program consisted of casting twelve $180 \times 180 \times 5$ cm pre-tensioned concrete slabs with material properties of 40 MPa for the concrete matrix and $E_{SP} = 195$ GPa for the high-yield steel tendons with nominal diameter of 10 mm which will be contained in frames made of 6 mm bent mild steel mesh with $E_S = 200$ GPa. At the concrete age of 9 days with natural curing, all of the slabs, after the transfer of stresses from the steel tendons to the concrete matrix, will be compressed out by the initial pre-stressing forces and then will be taken away from the pre-stressing beds together with their deflection indicators, after cutting the steel tendons. Two of the slabs, marked S-1, will be maintained in the laboratory without loads. From them will be calibrated the variations of the deformations in the steel tendons and in the concrete matrix, due to pre-stressing forces and due to the shrinkage of the concrete matrix. Further, at the concrete matrix age of 36 days, 10 other slabs will be tested under long-term uniformly distributed static loads, with different force intensities. For the evaluation of concrete matrix physical-mechanical properties, specific subgroups of $300 \times 150\text{Ø}$ mm cylinders and 150 mm cubes will be tested periodically, using British Standards through Euro Codes. The variations in lateral deflections influenced by concrete matrix creep and shrinkage will be monitored continuously. At the concrete matrix age of 300 days, all of the members will be tested quasi-statically and after, under cyclic quasi-dynamic vertical loads up to their failure state.

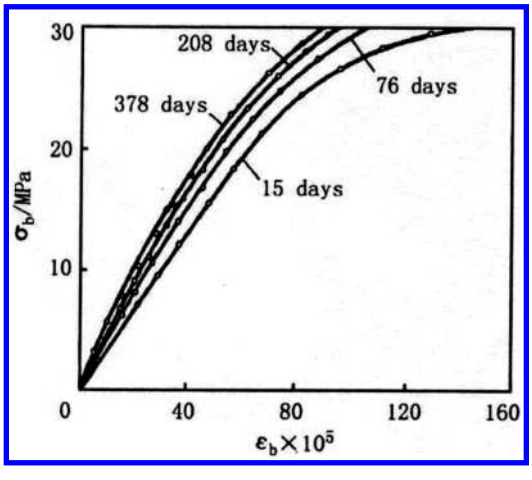


Figure 4. Compression diagrams of concrete prisms tested with static loads.

Parallel to all of these tests, as above said, will be also tested at specific different following concrete matrix ages of 9, 12, 15, 28, 36, 76, 118, 136, 200 and 300 days, concrete matrix cylinders and cubes (3 cylinders and 3 cubes at each concrete matrix age) for the determination of the concrete matrix physical and mechanical properties, and for the evaluation of the creep and shrinkage characteristics of the concrete matrix. During these creep tests, the cylinders will be mounted on the loading frame (Figure 3) which consisted of a hydraulic jack, a load cell, and a system of coil springs held in compression by a set of roads and plates.

Similarly to these experiments, for the determination of concrete physical-mechanical properties (Figure 4) and for the evaluation of creep and shrinkage behavior of the concrete (Figure 5), have been tested at different concrete ages of 9, 12, 15, 24, 36, 76, 118, 192, 208 and 378 days, concrete prisms and concrete cubes (3 prisms and 3 cubes at each above concrete age).

The concrete matrix prisms tested for creep were marked $P_{12}^{7,5}$; $P_{36}^{7,5}$; $P_{76}^{7,5}$ and P_{76}^{15}; where the superscripts of the prisms' series show the static stresses' values in MPa, and their subscripts show the different concrete ages.

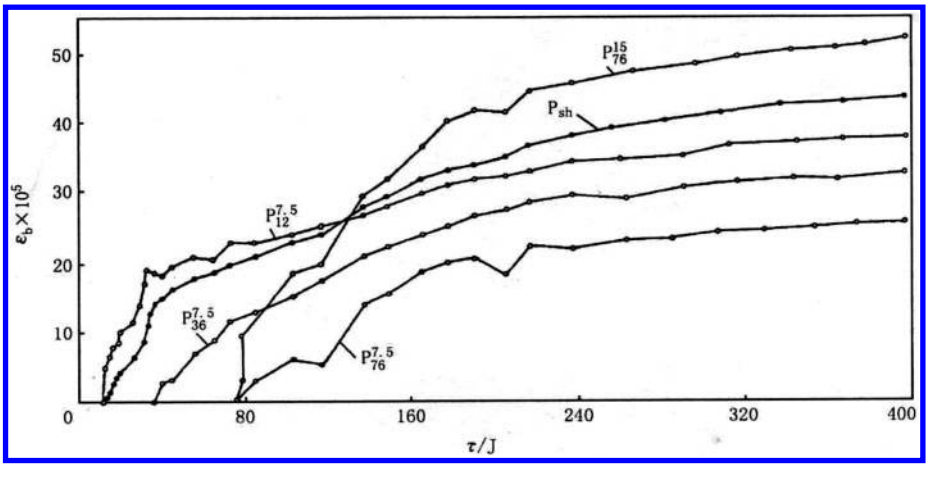


Figure 5. Experimental graphics of time-dependent strains due to shrinkage (index "sh") and to the creep of the concrete, obtained by the tests of concrete matrix prisms: $1 - P_{sh}$; $2\text{-}P_{12}^{7,5}$; $3 - P_{36}^{7,5}$; $4 - P_{36}^{7.5}$; and $5 - P_{76}^{15}$.

4 CONCLUSIONS

1. It is hoped to confirm at the end of the study that nonlinear concrete creep is capable to contribute to the redistribution of stresses between the concrete and the steel tendons with long-term loading influences on the slabs. This said redistribution is capable to provoke the accumulation of natural initial stresses in the steel tendons and in the concrete, which are equivalent to the artificial initial stresses due to the pre-stressing forces in the steel tendons, and this fact could reduce losses and, consequently, capable to increase the durability, the reliability and the exponents of the slabs' limit states.
2. The proposed slabs will help widely and reliably reveal the positive effects and generalize them to more complicated type of structural elements. These positive effects could be capable to predict the quality, the reliability, the durability, the life safety and the stability of the slabs and could be able to contribute for steel tendons' economies up to 15%.

REFERENCES

Backhouse J. K., Houldsworth S.P.T., Cooper B E. D., Horril P.J.F. 1992 *PureMathematics, Book 2*, Third Edition, Longman Group Limited.

Bolshakov V.I., Yatsenko E.A., Sossou G., Lemaire M., Reynouard J.M., Kestens J., Warzee G., Cormeau I. *The Bases of the Finite Element Method*, Pridnieprovskaya State Academy of Civil Engineering and Architecture, 'GAUDE-AMUS PUBLISHERS', Dniepropetrovsk 2000 – Ukraine, 254 pp.

Edwin H. Gaylord, Jr, Charles N. Gaylord and James E. Stallmeyer 1997, *Structural Engineering Handbook*, Fourth Edition, McGraw-Hill.

Sossou G. Ongoing Numerical and Experimental Analysis of Structural Characteristics of Reinforced Concrete Slabs, Prestressed in Both Directions and Subjected to Long-term Service Loads. EURO MAT 2000, *European Conference on Advances in Mechanical Behaviour, Plasticity and Damage,* November 7–9, 2000, Tours, France, pp. 547–552.

Research and Applications in Structural Engineering, Mechanics and Computation – Zingoni (Ed.)
© 2013 Taylor & Francis Group, London, ISBN 978-1-138-00061-2

Frost resistance property of concrete doped with scrap rubber powder

B.M. Wang, Y. Han & S. Liu
School of Civil Engineering, Dalian University of Technology, Dalian, China

ABSTRACT: The quick frost method was used to measure the mass loss rate and relative dynamic elastic modulus of rubberized concrete and ordinary concrete. The frost resistance property of the rubberized concrete in seawater environment was studied by comparing the difference of mass loss rate and relative dynamic elastic modulus between rubberized concrete and ordinary concrete. Results show that, the frost resistance property of rubberized concrete is superior to ordinary concrete in seawater environment, when the water-cement ratio was 0.40 the rubberized concrete could undertake 150 times freeze-thaw cycles, which is 2 times higher than ordinary concrete. The enhancement on frost resistance property is obvious by adding rubber power into concrete under the effect of freeze-thaw cycle and media corrosion, and this enhancement decreases with the water-cement ratio increasing.

1 INTRODUCTION

Concrete is the most widely used construction material in modern engineering structure[1]. Compared with other common building materials, its energy consumption is low, the sources of the raw materials are wide and the craft is simple. So it has some advantages such as low production cost, strong adaptability and easy application, etc. [2,3]. But concrete is one kind of brittle materials. Nearly years the strength of the concrete has been constantly improved, and the increasingly prominent contradiction between its high strength and brittleness has limited the development and application of concrete [4]. How to alleviate the contradictions through the concrete material modification gradually become people's research focus [5]. Rubberized concrete which through scrap tire rubber powder blending into the concrete can effectively improve the concrete brittleness [6–8]. It's a new type of "elastic concrete" and it gradually gets more and more attention of scholars both around the world [9]. The research shows that adding rubber powder to concrete can effectively improve the concrete toughness and impact resistance. In addition, its resistance to contraction and damping performance is also better, and the durable performance is improved [10–12].

The number of waste tyre is huge in our world, The powder can be used as a new type of material blended into concrete, and the application prospect of rubberized concrete is well. Through the rubber concrete characteristics, we can expect it can be widely used in road, square, high seismic area, basic engineering and railway station for vibration damping high places, retaining wall of highway and bunkers for impact resistance and blast resistance place, It also can be used in building decoration materials and self-leveling packing [13].

As a new type of concrete, rubberized concrete has owned widely attention in the industry. The existing researches mainly focus on the mechanical properties, anti-permeability, shrinkage, etc., there is no study on its anti-freezing endurance performance based on the sea water erosion medium.

2 EXPERIMENTAL

2.1 *Materials*

(1) Cement: This test used PO 42.5 R type cement produced by Dalian Onoda cement co., LTD. Table 1 and 2 show the concrete index.
(2) Fine aggregate: river sand. Its fineness modulus is 2.73. It's II area velvet. Apparent density is 2520 kg/m^3 and bulk density is 1540 kg/m^3.

Table 1. Cement component and physical parameters.

Chemical composition (%)		Specific Ignition loss (%)	surface area	Setting time (min)		Stability
MgO	SO_3	3.14	330	Initial set	Final set	Boiling
1.88	2.53			196	248	qualified

Table 2. Properties of cement.

Compressive strength (MPa)		Breaking strength (MPa)	
3days	28days	3days	28days
29.5	54.9	5.8	9.1

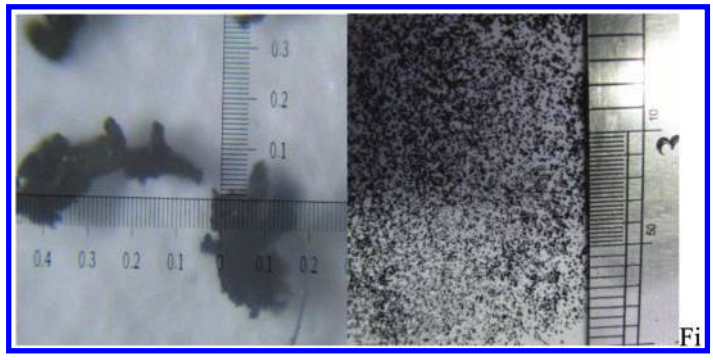


Figure 1. Rubber powder.

Table 3. Qualification of 120 mesh rubber power.

Project variety	Appearance	Mean grain size um	Screen specifications/ mesh	sieving rate %≦	moisture % ≦	Ash content % ≦	acetone extract % ≦	Fibre content % ≦	metal content % ≦
rubber powder	Black Powder	120	120	95	1.0	10	15	0.5	0.08

(3) Coarse aggregate: size for 5 ~ 25 mm uniform gradation. Apparent density is 2800 kg/m^3 and bulk density is 1590 kg/m^3.Faller gill degree is 4%. Crushing value is 2.65%.
(4) Mixing water: ordinary tap water.
(5) Admixture: SW – 4 type high efficiency water reducing agent, Dalian Shenwei building materials co., LTD., production.
(6) Rubber powder: Sichuan lvyuan technology co., LTD., production. It's 120 mesh waste tire rubber powder. Density is 1.116 g/cm^3. Mean grain size is 119 μm. Bulk density is 284 kg/m^3. The shape is shown in figure 1 and the specific technical data is shown in table 3.

2.2 *Mix proportion*

2.3 *Specimen preparation*

Because the rubber powder particle size is small, it's easy to occur reunion phenomenon when they are mixed in concrete. In order to make the rubber powder in cement mortar scattered as uniformly as possible, we adopt the method which put water reducing agent, rubber powder into cement mixing uniform in advance. In mixing concrete, put sand, stones into a blender firstly, dry mixing 60 s, then add in the mixture consist of cement powder and additive to mix 30 s, and then add water to mix 120 s.

Put the new concrete into the mold, vibrate dense on vibrostand immediately. Then take apart a die and numbers after 24 hours. Put the test-piece in 20 ± 2°, relative humidity 95% standard curing chamber, maintain to the standard required age, then test the performance [14].

Table 4. Mix ratio design.

Number	Water-cement ratio (%)	W (kg)	C (kg)	S (kg)	G (kg)	sand ratio	water reducing agent (%)	Rubber Powder (kg/m^3)
A-3-R	0.4	195	487.5	629	1118	36%	1.4	30
A-3-C	0.4	195	487.5	629	1118	36%	1.4	
B-3-R	0.45	195	433	656	1116	37%	1.3	30
B-3-C	0.45	195	433	656	1116	37%	1.3	
C-3-R	0.50	195	390	663	1082	38%	1.3	30
C-3-C	0.50	195	390	663	1082	38%	1.3	
D-3-R	0.55	195	354.5	686	1074	39%	1.3	30
D-3-C	0.55	195	354.5	686	1074	39%	1.3	

*List the letters from the ABCD representative water cement ratio are 0.40, 0.45, 0.50, 0.55, number 1 says erosion medium seawater. R says rubber concrete, C says ordinary concrete.

Table 5. Composition of seawater (g/kg).

Cl^-	Na^+	SO_4^{2-}	M_g^{2+}	Ca^{2+}	K^+	Other trace elements
19.10	10.62	2.66	1.28	0.40	0.38	0.25

Table 6. The mass loss of rubber concrete in seawater.

Freeze-thaw times	The mass loss rate of rubber concrete in seawater (%)			
	A-3-R	B-3-R	C-3-R	D-3-R
0	0.00	0	0	0
25	−0.05	−0.1	−0.18	−0.27
50	0.28	0.37	0.49	0.54
75	0.33	0.49	0.61	0.89
100	0.42	0.69	0.87	1.28
125	0.96	1.52	1.81	2.39
150	2.01	3.05	3.43	
175	4.28			

Table 7. The relative dynamic elastic modulus of rubber concrete in seawater.

Freeze-thaw times	The relative dynamic elastic modulus of rubber concrete in seawater (%)			
	A-3-R	B-3-R	C-3-R	D-3-R
0	100	100	100	100
25	101.9	102.4	104.6	105.9
50	98.1	98.0	90.0	85.7
75	90.6	87.9	83.4	70.1
100	83.4	74.9	77.6	64.9
125	75.6	63.1	64.4	39.7
150	64.5	53.9	44.9	
175	41.7			

2.4 *Testing procedures*

Put the test-piece into seawater for four days after 24 days age, then take them out according to GB/T 50082-2009 method, and injection seawater into specimen bucket to conduct quick freezing and thawing test. The seawater should be changed once every 25 times freeze-thaw cycle. The test index are mass loss rate and dynamic elastic modulus. The seawater is taken from seaside of HeiShiJiao in Dalian. Its composition is shown in table 5 below.

3 RESULTS

The mass loss rate and the relative dynamic elastic modulus of rubberized concrete and the corresponding normal concrete in seawater freeze-thaw environment see below table 6–9.

The destroyed appearance of rubberized concrete and ordinary concrete in seawater is shown in figure 2 and 3.

Table 8. The mass loss of ordinary concrete in seawater.

Freeze-thaw times	The mass loss of ordinary concrete in seawater (%)			
	A-3-C	B-3-C	C-3-C	D-3-C
0	0	0	0	0
25	−0.1	−0.36	−0.49	−0.56
50	1.29	2.69	3.79	4.89
75	3.95			

Table 9. The relative dynamic elastic modulus of ordinary concrete in seawater

Freeze-thaw times	The relative dynamic elastic modulus of ordinary concrete in seawater (%)			
	A-3-C	B-3-C	C-3-C	D-3-C
0	100	100	100	100
25	100.8	101.5	102.6	103.3
50	68.8	58.4	52.2	46.9
75	50.6			

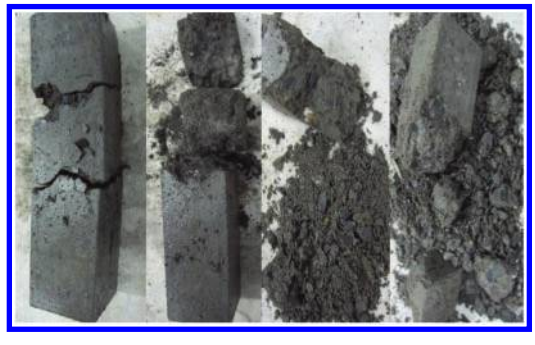


Figure 2. The destroyed appearance of ordinary concrete in seawater.

4 DISCUSSION

The mass loss of rubber concrete with the increasing of freeze-thaw cycle times in seawater are shown below.

From the test results and the figure above we can reach that:

1 At early stage of the freeze-thaw cycle, qualities of ordinary concrete and rubber concrete are slightly increased in seawater, rubber concrete increase slowly than ordinary concrete; Along with the

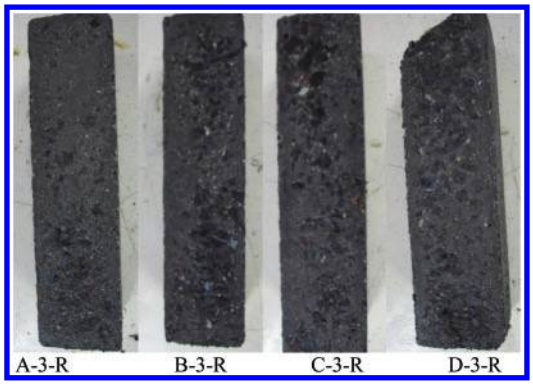


Figure 3. The destroyed appearance of rubberized concrete in seawater.

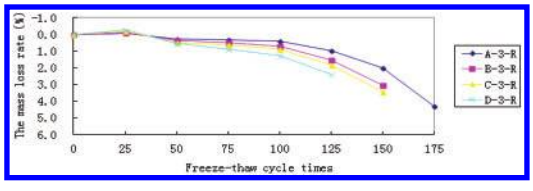


Figure 4. The mass loss rate of rubberized concrete with the increasing of freeze-thaw cycle times in seawater.

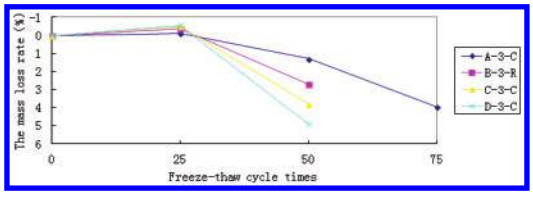


Figure 5. The mass loss of ordinary concrete with the increasing of freeze-thaw cycle times in seawater.

freezing and thawing cycle, mass loss rate ordinary concrete begin to increase sharply, rubber concrete is moderate relatively; Ordinary concrete of 0.40 water cement ratio failure in 75 times freezing and thawing cycles, rubber concrete of the same water cement ratio failure in 175 times cycles.

2 The failure characteristics caused by seawater: damage on the surface, the surface mortar peel seriously, aggregate exposure, failure at a very fast rate. From the final failure pattern we can see, the common concrete show collapse form with water cement ratio increasing, but rubberized concrete is only surface mortar peeling off and the coarse aggregate revealing.

The relative dynamic elastic modulus of rubberized concrete and common concrete with the increasing of freeze-thaw cycle times in seawater below figure 6 and 7.

From the test results and figure above we can reach that ordinary concrete and rubberized concrete in seawater are destroyed mainly in relative dynamic elastic modulus reducing to less than 60%. Rubber concrete

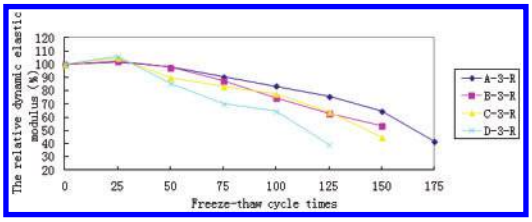


Figure 6. The relative dynamic elastic modulus of rubber concrete with the increasing of freeze-thaw cycle times in seawater.

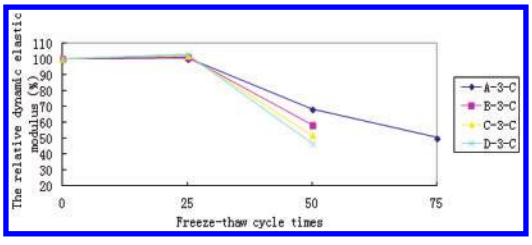


Figure 7. The relative dynamic elastic modulus of ordinary concrete with the increasing of freeze-thaw cycle times in seawater.

with water cement ratio 0.40, 0.45, 0.50, 0.55 reach freeze-thaw damage after 175, 175, 175, 150 times respectively, the relative dynamic elastic modulus are 64.5%, 53.9%, 44.9%, 39.7% when are destroyed; Common concrete with the same water cement ratio reach freeze-thaw damage after 75, 75, 75, 50 times respectively, the relative dynamic elastic modulus are 50.6%, 58.4%, 52.2%, 46.9% when are destroyed.

The anti-freeze mechanism analysis in the sea: the chlorine salt solution in seawater focus on the concrete surface pore firstly, so that the water saturation degree in the concrete surface pore increase. With the freezing and thawing, friction increases, unfrozen water in the surface pore flow to the interior, compared with unfrozen water internal, unfrozen water on surface is under more high hydrostatic pressure, the speed of producing and expanding micro-fracture is faster. The presence of salt causes that hole liquid produce concentration difference, the difference is bigger than that in the water, so that the freeze-thaw cycle times in seawater is less than that in fresh water [15]. In addition when concrete structure long-term exposure chlorine salt solution, NaCI can leach hydration products of cement paste [16], resulting in accelerated destruction of concrete structure.

5 CONCLUSIONS

In the seawater, freeze-thaw damage of rubberized concrete is mainly for obvious surface spalling, from the dropping speed of relative dynamic elastic modulus, the internal damage is more serious than external peeling, and ordinary concrete in seawater is more heavy damage, relative elastic modulus decline more rapidly, the whole test-piece is destroyed collapse form

block which water cement ratio is above 0.45. Ordinary concrete show the same failure trend as rubber concrete, but destroy faster than rubber concrete, and at the later stage of freezing and thawing damage, test-piece will fracture suddenly and then fail.

ACKNOWLEDGEMENTS

The author would like to express appreciation for the financial support by the National Natural Science Foundation of China (51278086), Liaoning Provincial Scientific Research Program of Higher Education (LS2010045), Supported by Program for New Century Excellent Talents in University (NCET-12-0084), and Construction safety and environmental state key laboratory open topics (201202).

REFERENCES

[1] Amos A, Roberts A D. Use of ground rubber tires in Portland cement concrete. Universitv of Dundee. UK. 1993. 379–390

[2] H A T. The use of rubber tire particles in concrete to replace mineral aggregates [J]. Cement and Concrete Composites. 1996, 18(2): 135–139

[3] Kew H Y, Cairns R, Kenny M. The use of recycled rubber tyres in concrete[C]. Proceedings of the International Conference on Sustainable Waste Management and Recycling. 2004

[4] Benazzouk A, Douzane O, Queneudec M. Transport of fluids in cement-rubber composites [J]. Cement and Concrete Research. 2004, 26(1): 21–26

[5] Segre N, Joekes L J. Use of tire rubber particles as addition to cement paste [J]. Cement and Concrete Research. 2000, 30(9): 1421–1425

[6] Segre N, Monteirop J, Gsurface S. Surface characterization of recycled tire rubber to be used in cement paste matrix. [J] Journal of Colloid and Interface Science. 2002(2):521–523

[7] Siddique R, Naik T R. Properties of concrete containing scrap-tire rubber-an overview [J]. Waste Management. 2004, 24(6): 563–569

[8] Barluenga F, M G B. Static and dynamic behavior of recycled tire rubber-filled concrete [J]. Cement and Concrete Research. 2002, 32(10): 1587–1596

[9] Guneyisi E, Gesoglu M, Ozturan T. Properties of rubberized concretes containing silica fume [J]. Cement and Concrete Research. 2004, 34(12): 2309–2312

[10] Benazzouk A, Mezreb K, Doyen G. Effect of rubber aggregates on the physico-mechanical behavior of cement-rubber composites-influence of the alveolar texture of rubber aggregates [J]. Cement and Concrete Research. 2003, 25(7): 711–720

[11] Benazzouk A, Queneude C. Durability of cement-rubber composites under freeze thaw cycles [C]. Proceedings of the International Conference on Sustainable Concrete Construction. University of Dundee, Scotland, UK. 2002

[12] Paine K A, Dhir R. Use of crumb rubber to achieve freeze thaw resisting concrete[C]. Proceedings of the International Conference on Concrete for Extreme Conditions. University of Dundee, Scotland, UK. 2002

[13] Kaloush Kamil E, Way G B Z H. Properties of crumb rubber concrete[J]. Transportation Research Record. 2005

[14] Jing Li. The Performance Research of Cement Concrete with Waste Tire Rubber [D]. Dalian University of Technology, 2010.

[15] Wencui Yang. Effect of Inorganic Salts on Pore Structure and Frost Resistance of Concrete [D]. Harbin Institute of Technology, 2009.

[16] Wencui Yang,Yong Ge,Chuanli Chang. Frost resistance of concrete in salt solution [J]. Low Temperature Architecture Technology, 2007, (1): 1-4.

24. Construction materials, construction technology, building performance

Research and Applications in Structural Engineering, Mechanics and Computation – Zingoni (Ed.)
© 2013 Taylor & Francis Group, London, ISBN 978-1-138-00061-2

Determination of the relation between the content of used reclaimed asphalt material and deformation characteristics of asphalt concretes

K. Milčèková, P. Mondschein & J. Valentin
Department of Road Structures, Faculty of Civil Engineering, Czech Technical University, Prague, Czech Republic

ABSTRACT: The objective of this paper is to summarize experimental findings of functionalities between the content of added reclaimed asphalt material (RAP) in asphalt mixtures of the AC (asphalt concrete) and HMAC (high modulus asphalt concrete) type, selected suitable bituminous binders (including the applicability of chemical additives) and performance characteristics describing the behavior of asphalt mixes in the range of high and low temperatures. The results of dynamic non-destructive stiffness measured in a temperature interval of 0–30°C, creep behavior at 40°C with the assessment of resistance to permanent deformation as well as the regular rutting test are presented here. Further, master curves for the complex dynamic modulus of the asphalt mixtures are determined and assessed. Finally, recommendations about acceptable contents of reclaimed asphalt material securing the minimum technical requirements of technical standards and sufficient asphalt mixture durability are formulated. The influence of combined use of reclaimed material and selected bituminous binders is described as well.

1 INTRODUCTION

Asphalt mixtures represent a kind of composite material which is traditionally based on natural aggregates and bituminous binders. With respect to the extent of infrastructural structures, the consumption of natural resources is enormous. In connection with the increasing necessity of gradual rehabilitation of the existing road infrastructure, the general trend is to reduce the material demand of pavement structures by the enforcement of maximized recyclability and re-use of existing structures and materials in use. By utilizing reclaimed asphalt material from existing pavements, efficient limitation in the consumption of natural aggregates is supported. The substitution of aggregates by reclaimed material can theoretically reach a level of up to 100%. It is, nevertheless, essential to assess and to consider the impact of reclaimed material on the performance behavior of the resulting asphalt mix and/or the pavement structural layer. The reasons are, in particular, degrading processes, which occur in the asphalt pavement during the road use and operation. The degradation usually leads to irreversible alterations of the functional characteristics of the asphalt mixture.

The issues of asphalt pavement recycling, taking, in particular, the form of cold asphalt mix technologies using asphalt emulsions, foamed bitumen or hydraulic binders, or combinations of the above binders have been the subject of growing interest in the last 5–10 years, both among numerous road construction companies and in applied research at technical universities. The main activity in the Europe-wide scale may be the European SCORE – Superior Cold Recycling (Potti, 2004) project which involved the performance of a series of laboratory tests of binders and mixes. In 2004–5, test sections were laid in France, Spain and the Czech Republic. The objective was to verify and further specify investigated key characteristics (both strength and performance-based ones). Laboratory tests within the SCORE project were done using the same methodology for both mixes with emulsions and cement and mixes with foamed bitumen.

In hot-in-place recycling, there is a common practice which, nevertheless, still limits the use of reclaimed asphalt material (RAP) in new asphalt mixes in the Czech Republic to only some types and only to amounts of max. 20%-wt. when used in existing mixing plants. This fact may be compared with the knowledge in some west European countries where technologies applying RAP in quantities exceeding 30%-wt. have been developed on a long-term basis because of a limited availability of natural resources or for the reason of active support for the principles of sustainable construction. In this context, the trends and experience from the Netherlands or from Germany are worth mentioning; in the latter case a comprehensive methodology, "Wieder-verwenden von Asphalt" (DAV 2009) must be pointed out, which delimits the links to the legislation on waste currently in force in Germany and, at the same time, describes in a relatively clear and detailed way how to handle RAP and what procedures to apply for it in the asphalt mix. Analogically, since 2007, these issues have been addressed by the LCPC French laboratories for roads and bridges with the aim of gaining a better understanding of the processes and

qualitative parameters in the application of more than 50%-wt. of RAP in asphalt mixes. In this context, the focus in France is both on the requirements for the production machinery and for the application of suitable additives which due to chemical reactions allow the application of RAP at higher rates observing the limit criteria for the quality of the new asphalt mix.

2 MIX DESIGN SPECIFICATION

Two types of asphalt mixes were selected for the experimental verification. In the first case, it was a mix with a high stiffness modulus (HMAC), which had originally been developed in France and is presently used in some countries mainly for constructions of highly loaded pavements. Its principle consists in a modified design of the aggregate matrix and a choice of harder or polymer modified bitumen thanks to which the reaching of higher stiffness of the mix is allowed, or its resistance to the permanent deformations is significantly improved. The mix should simultaneously allow reaching longer durability. HMAC mixes are used in binder and base courses; therefore, they are not immediately exposed to climatic effects. The second selected representative is the asphalt concrete mix for wearing courses (ACO). The key feature in this case is the compactness of the layer, which guarantees smooth and safe road traffic. The problems of the appearance of permanent deformations, however, play a minor role here as well, even though not so essential. Of greater significance is the durability of the asphalt mix expressed as a rule by the characteristic of the indirect tensile strength ratio (ITSR) considering the negative impacts of water.

The mixes designed for testing contained aggregates coming from the same locality characterized by a not quite perfect shape index in coarse fractions. As a standard for individual variants (except for the reference HMAC mix) the initial binder was chosen to be 50/70 as bitumen suitable for both applications. In contrast to the 30/45 binder applied in the reference HMAC mix which generally results in stiffer characteristics, the choice of the 50/70 binder is also supported by the fact that one half of the mixes designed use RAP where partly degraded binder of the original asphalt mix is already present and, therefore, the overall stiffness of the mix and, primarily, the increased brittleness of the binder from the reclaimed material must be limited and sufficiently regulated. Besides Storflux which is used as a rejuvenator based on special oils, another two additives were applied which are known mostly from the field of warm asphalt mix technologies, namely synthetic Fischer-Tropsch paraffin with the potential of lowering the manufacturing temperature of the mix preparation and paving by 15–20°C, and a surfactant based on tensides under the name IterLow T. For the ACO 11 mix, the Storbit additive was selected which combines the effect of a rejuvenator and an additive improving viscosity. The second additive is based on a different principle in comparison to FT paraffin; however, it allows reducing the working temperatures by a similar range. The content of Storflux and Storbit is related to the bitumen. The reason for the application of the additives is the possibility of reducing the necessary heating of the RAP while maintaining the workability needed, thus minimizing further degradation of the bituminous binder contained in the asphalt material.

Table 1. Experimentally assessed HMAC mixes.

A: HMAC with 4.5% 50/70 + 10% Storflux + RAP (0/11)
B: HMAC with 4.5% 50/70 + 0.5% Iterlow T + RAP (0/11)
C: HMAC with 4.5% 50/70 + RAP (0/11)
D: HMAC with 5.8% 50/70 + 0.5% Iterlow T
E: HMAC with 5.8% 50/70
F: HMAC with 5.8% 50/70 + 3% FTP
G: HMAC with 4.5% 50/70 + 3% FTP + RAP (0/11)
REF: HMAC with 5.8% 30/45

Table 2. Experimentally assessed ACO mixes.

I: ACO with 5,9% 50/70 + 10% Storflux + 40% RAP (0/11)
II: ACO with 59% 50/70 + 10% Storbit + 40% RAP (0/11)
III: ACO with 6.0% 50/70 + 10% Storflux + 20% RAP (0/11)
IV: ACO with 6.0% 50/70 + 10% Storbit + 20% RAP (0/11)

The effects of various bituminous binders and, particularly, the effect of applying 30%-wt. of RAP for HMAC 16 and 20%-wt. or 40%-wt. for the ACO 11 mix were examined. The design and optimisation of mixes as such were carried out based on the standard procedures applied for traditional asphalt concretes according to the ČSN EN 13108-1 standard. Test cylinders were usually compacted by 2 × 75 blows by the Marshall compactor for HMAC and 2 × 50 blows for the ACO mix.

In the case of HMAC mixes, RAP demonstrated a better aggregate shape index which led to improved compactability and satisfactory void contents. The average void content in mixes with no reclaimed material amounted to 5.3%-vol., while mixes with reclaimed material reached a lower void content of about 4.2%-vol. In both cases, the values correspond with the limits restricted by 6%-vol. for control testing (Tab. 3). The addition of RAP does not have a crucial negative effect on water susceptibility of the mix. In most cases, only a very small drop was identified. A similar situation is in the case of the water susceptibility test with one frost cycle (ITSR_frost cycle).

While analyzing ACO mixes with 40%-wt. or 20%-wt. of RAP material, then it is visible, that the Storbit additive leads to slightly lower bulk densities. With respect to the voids content, it was interesting to find out that better values are reached for mixes with higher RAP contents. A similar result can be obtained by comparing the ITS ratio. Generally, all mixes reached

Table 3. Fundamental empirical characteristics of ACO 11 asphalt mixes.

Characteristic/Mix	I	II	III	IV
Bulk density (g.cm^{-3})	2.407	2.396	2.419	2.373
Void content (%-vol.)	4.23	4.12	4.50	4.83
ITSR (−)	1.01	1.25	0.95	0.90
ITSR_frost cycle (−)	1.04	0.93	0.89	1.00
Elasticity modulus ratio (−)	0.77	1.07	0.76	0.80

Table 4. Fundamental empirical characteristics of HMAC 16 asphalt mixes .

Characteristic/Mix	A	B	C	D
Bulk density (g.cm^{-3})	2.388	2.398	2.407	2.416
Void content (%-vol.)	3.67	3.27	2.92	4.67
ITSR (−)	0.87	0.84	0.81	0.88
ITSR_frost cycle (−)	0.79	0.89	0.94	0.84
Elasticity modulus ratio (-)	0.82	0.68	0.60	0.88
Characteristic/Mix	E	F	G	REF
Bulk density (g.cm^{-3})	2.384	2.418	2.307	2.380
Void content (%-vol.)	5.92	4.58	6.94	6.08
ITSR (−)	0.85	0.93	0.84	1.01
ITSR_frost cycle (−)	0.74	0.82	0.72	0.78
Elasticity modulus ratio (-)	0.86	0.66	0.85	0.84

very high values but higher RAP contents lead to no changes in the indirect tensile strength performance.

3 EXPERIMENTAL ASSESSMENT OF DEFORMATION BEHAVIOR

3.1 *Stiffness modulus*

The stiffness modulus is generally identified as the absolute value of a complex modulus where it simultaneously holds true that its value equals the creep modulus for the loading time $t = \omega^{-1}$. This value is sometimes also denoted as a dynamic modulus.

The above-described fact stated by (Luxemburk, 1977) is of essential importance for the mutual comparison of the results of measurement obtained by static and dynamic tests. The definition of the stiffness modulus, at the same time, determines the conditions of its identification where for short-term loading it is expedient to identify the value of the modulus on the basis of tests in which a test specimen is loaded by a harmoniously variable force.

There are more potentially usable alternative methods suitable for the identification and analysis of the stiffness modulus characteristics; the EN 12697-26 standard does not strictly prescribe any specific device and its choice is at one's own discretion depending on traditional approaches used in a respective country. In any case, however, the prescribed test conditions must be observed. The procedure described in the relevant European standard is suitable for the classification of an asphalt mix based on its stiffness being also applicable for the specification of the pavement performance in terms of its bearing capacity.

For the purposes of comparisons in our study, a non-destructive test by repetitive indirect tensile stress under the EN 12697-26 standard (IT-CY method) was selected. The test principle is repetitive loading of a test specimen by force during which horizontal deformations in the range of 5-10 microns are exerted. To achieve this maximum required deformation 10 preparatory load impulses are applied before the test itself during which the experimental tester exerts the loading necessary for reaching the deformation.

Temperatures of 5°C, 15°C, 20°C and 30°C were selected for the stiffness measurement. The choice of these temperatures corresponds to the knowledge in mainly the temperature domain of 40°C where very low values are usually obtained and measurements at these elevated temperatures lose their credibility. The results reach a domain with very high measurement inaccuracies where deviations may dramatically distort the resultant values. To enhance the interpretation of the results, the minimum temperature selected for HMAC mixes was 5°C and the maximum temperature selected was 30°C. The value of 15°C is subsequently the essential one for gaining the characteristics which are considered in the pavement multilayer structure dimensioning. Additional calculation using linear regression, which best interprets the stiffness modulus to temperature relationship, was made for the temperature of 0°C as is displayed in Table 5. At the same time, the thermal susceptibility value which corresponds to the ratio of the stiffness modulus at the lowest and the highest test temperature was identified. The measurements were performed only for HMAC mix variants.

The results presented in Table 5 clearly manifest the following findings. The reference mix (REF) with a harder 30/45 bituminous binder manifested a very high stiffness modulus at 15°C, and complied with the requirement for its minimum value prescribed in TP 151. Comparing the reference mix with mix (E) the effect of the used binder was prominently manifested in this case. The mix with the 50/70 binder failed to reach the prescribed values. The result is not very surprising confirming the necessity of using harder binders or modified binders in HMAC mixes.

It may be stated that the use of RAP increases the stiffness modulus (C-E) thanks to the content of hard bitumen in the reclaimed asphalt. This result is not very surprising being in line with the experience of how binder gradation affects the mix behavior. The application of rejuvenators may lead to the reduction of the stiffness modulus below the minimum value required (C-A, C-B). The highest values of the stiffness modulus were achieved with the use of additives allowing the reduction of the manufacturing temperature in the whole production cycle of the mix and during its paving (F, G) where the measured values were higher even for the reference mix. This experience implies

Table 5. Results of stiffness modulus by IT-CY.

Mix	Temperature (°C)			
	5	15	20	30
A	8 100	4 500	2 800	1 100
B	17 200	9 079	6 300	2 000
C	16 650	11 450	6 900	2 450
D	16 500	9 350	6 250	2 300
E	12 250	7 400	5 200	2 400
F	18 550	14 750	9 400	4 250
G	18 950	14 400	8 750	3 350
REF	21 300	13 850	9 300	3 500

Mix	Calculated value at 0°C	Thermal susceptibility t_s
A	9 050	7.36
B	19 200	8.60
C	19 500	6.80
D	18 550	7.17
E	13 700	5.10
F	22 050	4.36
G	22 600	5.66
REF	24 550	6.09

that the application of RAP in the HMAC mix will not lead to the reduction in the stiffness modulus, but quite the contrary. The mix behavior at low temperatures, however, must be monitored; aged bitumen from the RAP might cause impaired mix qualities at low temperatures.

In terms of thermal susceptibility it is evident that the combination of bituminous binder with the Iter-Low T additive is the least suitable one in this respect, in this case both with RAP and without it. The variant containing only road asphalt or the variants with the Fischer-Tropsch paraffin (FTP) additive, on the contrary, lead to the most favorable results. It is even apparent that, apart from the significantly stiffening effect, FTP also has a favorable impact on a lower drop in stiffness at different temperatures of the stiffness modulus verification. This finding may be of importance for the operational behavior of mixes in the pavement structure where it will raise the mix resistance to temperature changes during the day and in different seasons.

3.2 *Stiffness with additional calculation of the master curve*

Another testing method suitable for the identification of the asphalt mix stiffness, including the possibility of a subsequent plotting of the so-called master curve is the procedure described in Annex F (CIT-CY method) to the EN 12697-26 standard. The principle of loading a cylindrical test specimen is based on its exposure to the effect of horizontal load which exerts compressive and tensile stresses on the vertical axis of the test specimens. The stiffness test is performed using the sinusoidal loading principle with the effect of indirect

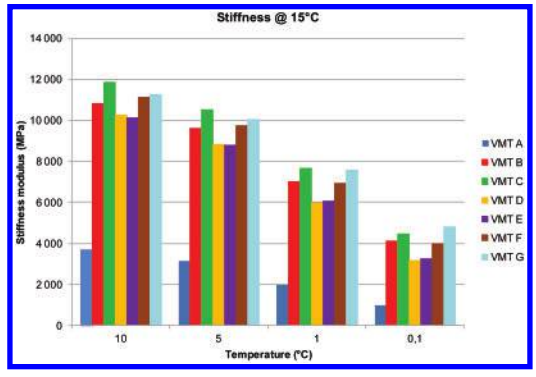


Figure 1. Stiffness modulus at 15°C for selected test frequencies.

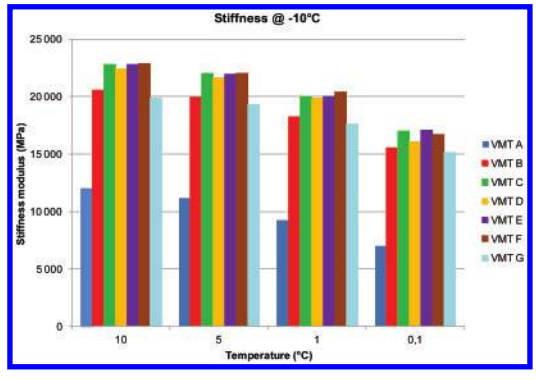


Figure 2. Stiffness modulus at −10°C for selected test frequencies

cyclic compressive loading. To assess the results the test must be performed at different temperatures to be able to assess the asphalt mix by means of the master curve whose main benefit is the option of the superposition of the results obtained at different temperatures and frequencies to one reference temperature. The test temperatures chosen for the analyses included values of −410, ±0, +15 and 25°C. Further the loading range of 50 kN with an accuracy of ±50 N is specified.

With respect to the selected mix designs and materials used, it is necessary to assess the effect of RAP for comparative purposes. The comparison always involved mixes with the application of RAP and without it for one selected additive. Assessing the effect of the used binder it may be seen in Figures 1 and 2 that a significant drop in the stiffness values may be registered in the mix with the Storflux rejuvenating additive.

In terms of the results achieved the following can be stated:

- The assessment of mixes without additives shows that the stiffness modulus master curve of the mix applying RAP is steeper at lower frequencies, which changes at a frequency around 10^4 Hz and starting from that point it is, on the contrary, more gentle. In the high frequency domain of around 10^5 Hz, the

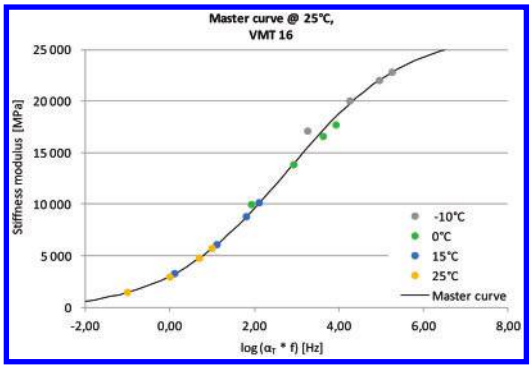


Figure 3. Typical stiffness modulus master curve, example for mix (E).

difference between the patterns of both curves is nearly constant.

- A trend similar to the master curve pattern for the mix without any additives is also manifested by the mix using the IterFlow additive. There is only one difference: the curve of the mix with RAP is steeper up to a frequency of 10^3 Hz, while its further growth is less steep for higher frequency.
- The last comparison by the effect of the used additive involves mixes with the addition of FTP. Here, the development trend differs from the comparisons above. In the low frequency domain, the stiffness master curve of the mix with RAP grows more slowly, which changes after reaching the frequency of 10^2 Hz; starting from that point, the curve is, on the contrary, steeper up to the high frequency domain (from 10^8 Hz) where another change occurs and their mutual difference gets smaller again.
- Another finding is the fact that, unlike the patterns of the other curves mixes (C), (F) and (G) show a difference from the very initial point. The results clearly show that at the initial low frequency they manifest higher stiffness (around 2 300 MPa). Comparing the values obtained by using stiffness master curves it was discovered that the highest values of the stiffness modulus had been reached by the mix (C) which simultaneously also has the steepest growth of the curve in the investigated medium frequency domain. The lowest values and the least steep growth in the curve, on the contrary, had been reached by the mix (A), which is most likely due to the very effect of the additive which plasticizes the bituminous binder.

3.3 *Resistance to permanent deformations*

The results of resistance to the formation of permanent deformations are presented in Table 6. The test was performed on a small testing device according to the European ÈSN EN 12697-22 standard currently in force. The testing has been dan at 50°C in a air bath. The measured values complied with the requirements for HMAC mixes as well as ACO mixes. The results are generally comparable. In the case of the HMAC mix,

Table 6. Results of rutting test in small test device.

Mix	Increment in rut depth WTS_{AIR} in mm	Relative rut depth PRD_{AIR} in%
A	0.023	1.9
B	0.026	1.6
C	0.043	2.9
D	0.032	2.7
E	0.024	1.6
F	0.012	1.5
G	0.016	1.6
I	0.046	5.0
II	0.042	3.9
III	0.072	3.0
IV	0.076	5.2

it was also manifested in this test that the application of 30%-wt. of RAP does not have a negative effect on the mix behavior. While comparing ACO mixes it even appears that in terms of the increment in the rut depth there is even an improvement in the value of this parameter. In the case of the PRD_{AIR} parameter, no straightforward conclusions may be drawn as the behavior of the mixes was quite opposite depending on the asphalt binder or the chemical additive used.

3.4 *Cyclic compression test*

European testing methods for asphalt mixes allow applying two testing methods to determine resistance to permanent deformations through dynamic creep. It is the test in an un-axial device and in a tri-axial device under EN 12697-25. The performed measurements focused on testing dynamic creep in an un-axial device. Its principle is based on the exposure of a cylindrical specimen to the effect of axial compression. At this point, it must be added that it is not a test which allows predicting the rut depth, but a test suitable for the assessment of a given mix.

The method is based on cyclic loading of cylindrical test specimens which are simultaneously exposed to elevated temperature whose standard value is 40°C. This test does not involve vertical loading. The output is the shift in the upper load plate measured always after a certain number of load cycles. Pursuant to the standard, deformation must always be measured after the following load cycles: 2, 4, 6, 8, 10, 20, 40, 60, 80, 100, 200, 300, etc. Permanent horizontal deformation is expressed as the function of the number of load cycles, i.e. as a creep curve. The test is terminated if the relative creep exceeds 4% or if the test reaches the final number of 10.000 load cycles; for this reason it is also necessary to record the number of load cycles at the moment of the test specimen failure.

The cyclic compression test may be assessed using several options of the expression of the relationships and characteristics. First, the relative strain relationship to the number of cycles reached in the inflexion point is expressed. The inflexion point denotes the moment during the test when a change in the creep

Table 7. Results of cyclic compression test for HMAC mixes.

Mix	No. of cycles [−]	Strain [‰]	Creep [‰*10^{-4}/n]	Creep modulus [MPa]
A	559	7.9	74.5	44.30
B	2.662	16.4	28.3	21.41
C	2.409	10.5	20.9	33.23
D	965	8.6	37.1	40.86
E	1.246	9.9	33.8	35.35
F	8.914	7.3	0.4	48.17
G	9,458	6.0	0.2	58.01

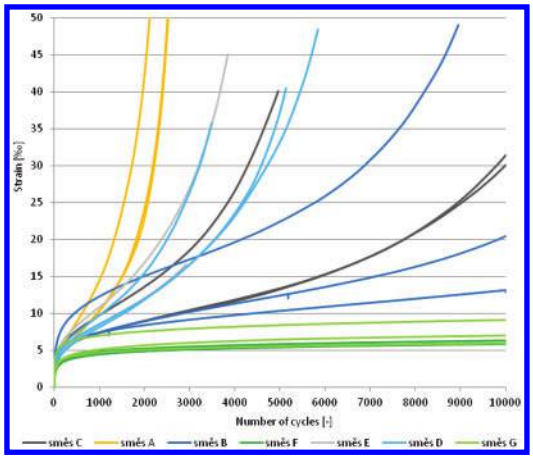


Figure 4. Creep curves of assessed HMAC mixes.

curve development occurs, it is usually situated at the end of the second phase, and then, due to deformation, a change in the structure of the specimen and thus also a change in its properties occurs lasting until the moment of its complete failure which may or need not occur during the test.

The trend of the inflexion point characteristics may be well derived from Figure 4 where it is evident that the lower the number of load cycles, the higher the relative deformations reached. On the contrary, in the case that a higher number of cycles has been reached, the lower the relative deformation of the specimen was. This figure allows us to draw a conclusion that the mixes reaching lower relative deformations in the inflexion point and simultaneously a relatively higher number of load impulses show better resistance to permanent deformations. At the same time, however, the total creep curve pattern is also important. Individual time patterns of the creep test for investigated mixes clearly show the scatter reached for individual mixes. The greatest deviations were reached for the mix (B), while much lower deviations were reached by mixes (C) and (F). Overall, it may be stated that by far the best results in terms of creep were reached by the mix variants where bitumen with FTP has been applied. In this very case, it was even mix with RAP that reached better results.

ACKNOWLEDGEMENT

This paper was prepared with the support of Alfa TACR project No. TA02030549.

REFERENCES

ČSN EN 12697-22+A1, 2005. Bituminous Mixtures – Test Methods for Hot Mix Asphalt – Part 22: Wheel Tracking

EN 12697-25, 2006. Bituminous Mixtures – Test Methods for Hot Mix Asphalt – Part 26: Cyclic compression test

EN 12697-26, 2012. Bituminous Mixtures – Test Methods for Hot Mix Asphalt – Part 26: Stiffness. Czech Office for Standards, Metrology and Testing

Luxemburk, F., et al. 1977. Use of Theory of Viscoelastic Material in Road Cosnturction. ÈVTS Praha (in Czech)

Neifar, M., Benedetto, di H., Dongmo, B. 2000: Permanent Deformation and Complex Modulus: Two Different Characteristics from a Unique Test. In: Performance Testing and Evaluation of Bituminous Materials, 6th International RILEM Symposium, Zürich, pp. 316–323

Potti J., et al. 2004. Superior Cold recycling: The SCORE Project. In: 3rd Eurasphalt & Eurobitume Congress Vienna, Book I, pp. 632–639.

Research and Applications in Structural Engineering, Mechanics and Computation – Zingoni (Ed.)
© 2013 Taylor & Francis Group, London, ISBN 978-1-138-00061-2

Feasibility of lightweight aggregate concrete for structural and non-structural works in Tanzania

A.L. Mrema
College of Engineering and Technology, University of Dar es Salaam, Tanzania

H.A. Mboya
Department of Civil Engineering, Mbeya University of Science and Technology, Tanzania

ABSTRACT: There has been serious land degradation in Tanzania due to extensive exploitation of granite aggregates even in areas where there is plenty of natural lightweight aggregates. Many Engineers have resorted to using normal weight aggregates in construction not only due to the feeling that lightweight aggregates (LWA) are too weak for structural purposes but also due to lack of knowledge of the design procedures for lightweight aggregate concrete (LWAC). Structures made of normal weight aggregates have higher dead loads which demand reduced span lengths, deeper structural members, more reinforcement and increased foundation area when compared to those made of LWAC. In Tanzania there are major deposits of LWA in areas of previous volcanic eruptions namely Kilimanjaro, Mbeya and Arusha and these remain largely un-exploited. Research was done to investigate the feasibility of using scoria and pumice aggregates in structural lightweight concrete. The aggregates were obtained from Kilimanjaro and Mbeya respectively. A mix design for grade 20 concrete was performed for both aggregates. It was found out that it was possible to use the scoria aggregates for structural concrete but not the pumice. Using pumice aggregates, the strengths obtained were less than 17 MPa which is the minimum strength acceptable for structural LWAC. It was concluded that the use of scoria aggregates for structural LWAC was feasible and that the pumice aggregates could be used for non-structural LWAC. Further research is required to characterize the lightweight aggregates present in Tanzania for better utilization in construction. Engineers in Tanzania are now in a position to design and use LWAC as the design procedures have now been elaborated. The use of light weight aggregates in areas where these deposits are present will reduce the costs of transport of normal weight aggregates from long distances and this will also protect the environment.

1 INTRODUCTION

Lightweight concrete (LWC) is defined as the concrete of substantially lower unit weight than that made of gravel or normal weight crushed aggregates. The dry densities are normally in the range of 800 to 2000 kg/m^3 (Schlaich & Zareef, 2008). In practice, designation of lightweight concrete is according to standardized strength and density classes (Chandra et al., 2002). Lightweight concretes having dry densities below 800 kg/m^3 are defined as Infra-lightweight concretes. Lightweight concrete is produced by either using lightweight aggregates or by formation of voids in concrete by omitting sand or by formation of voids in cement by addition of substances causing foam. There are three categories of LWC, namely structural LWC, low density LWC and moderate strength LWC (Neville & Brooke, 2005). According to NRMCA (2003), structural LWC has an in place density of between 1440 kg/m^3 and 1840 kg/m^3. Clarke (2005) defines structural LWC as having densities in the range of 1200 kg/m^3 to 2000 kg/m^3. Normal density concretes range from 2200 kg/m^3 to 2600 kg/m^3 depending on the type of aggregates used (Neville & Brooke, 2005). According to the above literature, structural LWC should have a minimum compressive strength of 17 MPa. LWC is manufactured by combination of fine and course lightweight aggregates or course lightweight aggregates with normal weight fine aggregates. Complete replacement of normal weight aggregates with lightweight aggregates reduces the air dry density to about a half that of normal weight concrete (Clarke, 2005 & NRMCA, 2003). Neville & Brooke (2005) defines three classes of LWC which can be made available according to their method of production: (i) No fines concrete obtained by omitting the finer fraction of normal weight or lightweight aggregates to create air filled voids, (ii) Aerated concrete produced by inclusion of air bubbles in cement paste or cement mortar matrix to form a cellular structure. This contains 30 – 50 % voids and (iii) Lightweight aggregate concrete obtained by replacing either wholly or



Figure 1. Scoria (L) and Pumice (R) aggregates used.

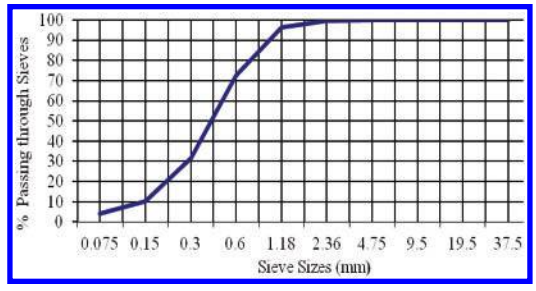


Figure 2. Sieve analysis of natural sand.

partially normal weight aggregates in a concrete mix with lightweight aggregates of low apparent specific gravity (porous aggregates containing large proportion of voids). This last type is the subject of the present investigation where all course aggregates were replaced with lightweight aggregates of pumice or scoria to obtain what we refer to as light weight aggregate concrete (LWAC). LWC does not provide only lighter structures but also structures with better insulation against heat and sound and such structures are more resistant to earthquakes.

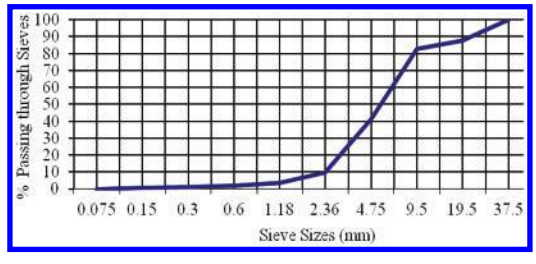


Figure 3. Volumetric analysis of scoria aggregates.

2 OBJECTIVES OF THE INVESTIGATIONS

The objective of the investigations was to find out whether pumice and scoria aggregates found in vast quantities in SW (Mbeya) and NE (Kilimanjaro) of Tanzania respectively were suitable for producing structural light weight concrete. Engineers in Tanzania prescribe the use of normal weight aggregates in these areas despite the fact that normal weight aggregates are very expensive as they have to be hauled from very long distances. One of the reasons why many engineers do not use these LWC aggregates is due to lack of knowledge of the mix design procedures for LWAC.

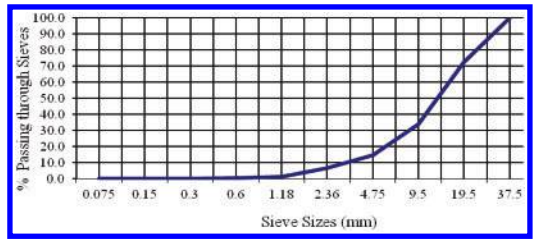


Figure 4. Volumetric analysis of pumice aggregates.

3 MATERIALS AND METHODS

Pumice and scoria aggregates were sampled from Mbeya and Kilimanjaro respectively (Fig. 1).

The cement used was Portland limestone cement CEM II/A-L/32.5R and was tested to conform to BS EN 197-1-2000. Natural sand was tested for its gradation (Figure 2) according to BS 812-103.1:1985. Volumetric sieve analysis according to TxDOT (2008) was performed on the scoria and pumice aggregates (Figures 3 and 4). The results show that about 60% and 70% of the scoria and pumice aggregates respectively lie between 4.75 mm and 37.5 mm.

The ten percent fines value test was done for scoria and pumice aggregates according to BS 812 part 111:1990 and the values obtained were 89 kN and 52 kN respectively. Table 1 shows the properties of the aggregates used.

Table 1. Properties of LWA used.

Aggregate type	Units	Scoria	Pumice	Sand
Bulk density	kg/m^3	882	411	1422
SSD Density	kg/m^3	1826	1087	–
Oven-dry Density	kg/m^3	1592	537	–
Specific Gravity	kg/m^3	1.754	0.886	2.625
Particle Density	kg/m^3	1754	886	2625
Agg. Crushing Value	(%)	47	–	–
10% Fines Value	(kN)	89	52	–

4 MIX DESIGN PROCEDURE FOR LIGHT WEIGHT AGGREGATE CONCRETE (LWAC)

The main emphasis in the design of LWAC is that the density and the strength of the LWA are related to the density and strength of the concrete.

4.1 *Determination of the mean compressive strength of concrete*

The compressive strength should satisfy the following conditions:

$$f_m = f_{cu} + \lambda S_n \tag{1}$$

where f_m = mean compressive strength; f_{cu} = specified characteristic strength; λ = statistical factor dependent of the acceptable probability of failure; and S_n = standard deviation of the distribution. The coefficient of variation is approximately 5 – 10% for the strength and 3 – 5% for the density (Chandra & Brooke, 2002)

4.2 *The strength of the LWA particles*

The recommendation is to design the concrete mortar with a compressive strength double that of the strength of the lightweight aggregate. The mean compressive strength of the lightweight aggregate is calculated using the formula:

$$f_{la} = a \cdot 10^{b\rho/1000} \tag{2}$$

where a and b are coefficients according to Table 2 and ρ is the particle density in kg/m^3. For all types of LWA, natural or factory produced, there are different relationships between the strength of the LWA and the particle density. There are special methods to measure the particle strength of the aggregate. Because the particles interact with the surrounding matrix, the cement paste or mortar, the method is based on estimating the strength of the concrete. The results are then used to evaluate coefficients a and b in equation (2).

The relationships among the strength of mortar, the strength of the LWA, the strength of the concrete, and the volume of the mortar or volume of the LWA are calculated using:

$$\log f_{con} = v_{la} \cdot \log f_{la} + v_M \cdot \log f_M \tag{3a}$$

or

$$\log f_M = \frac{\log f_{con} - v_{la} \cdot \log f_{la}}{1 - v_{la}} \tag{3b}$$

where f_{con} = strength of concrete; f_M = strength of mortar; f_{la} = strength of LWA; v_{la} = volume of the LWA particles; and v_M = volume of mortar.

4.3 *The compressive strength of mortar*

The compressive strength of mortar can be calculated from equation (4). Here natural sand and ordinary Portland cement are assumed to be used, and the specimens for mortar testing are the same type and size as used for the testing of concrete.

$$f_M = A \cdot 10^{-B(W/C)} \tag{4}$$

Table 2. Coefficients a and b in Equation (2) (Chandra & Leif, 2002).

Aggregate No.	a	b
1	1.52	1.14 (1.08, 1.03)
2	1.12	1.22 (1.16, 1.11)
3	1.00	1.25 (1.15, 1.14)
4	0.89	1.28 (1.22, 1.17)

In parenthesis the value of b is for 5 and 10% water content in the aggregate. The value of b is not or is marginally influenced by the water content. Aggregate no. 3 is for the bulk density of 300 kg/m^3. The LWA is some type of high quality sintered clay. Other LWA may have other values and shall be provided after the test.

where A and B are experimentally evaluated coefficients. With A = 140 and B = 0.87 (ordinary Portland cement after 28 days and W/C or W/binder > 0.30), the compressive strength is:

$$f_M = 140 \cdot 10^{-0.87(W/C)} \quad \text{or}$$

$$W/C = \log\left(\frac{140}{f_M}\right) / 0.87 \tag{5a}$$

When $W/C > 0.20$ and <0.25, the following formula is is used:

$$f_M = 160 \cdot 10^{-0.87(W/C)} \tag{5b}$$

When W/C is between 0.25 and 0.30, A is to be interpolated. According to accepted definition, the water/cement ratio is: $W/C = W \cdot 10^3/C$ where W is the water content in m^3/m^3 and C is the cement content in kg/m^3. The formulae are valid for natural sand, not lightweight sand, and for water/cement ratio less than 0.8. (Chandra & Leif, 2002).

4.4 *The volume of cement paste*

The volume of cement paste or binder in concrete should adhere to the principle of a constant paste-aggregate volume and should be about 30% of the volume of concrete. The volume of cement paste depends on many factors, for example, the type and shape of aggregate, consistency, stability of the concrete mixture, the strength of the mortar or concrete and water absorption of the LWA. According to experience even from normal weight concretes, the volume of the cement paste or binder may be in the range of 30 ± 2%. (Chandra & Leif, 2002).

4.5 *Cement content*

The cement content is calculated using the formula:

$$C = \frac{1000 \times v_p}{0.31 + W/C} \text{ kg/m}^3 \tag{6}$$

where v_p = volume of cement paste in concrete.

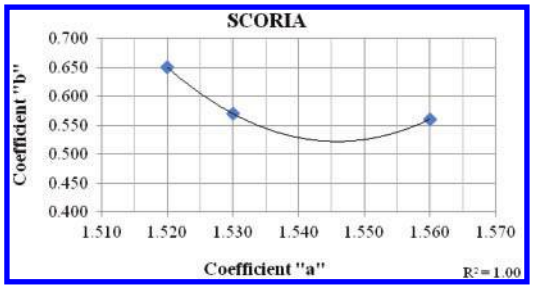


Figure 5. Strength coefficients for scoria aggregates.

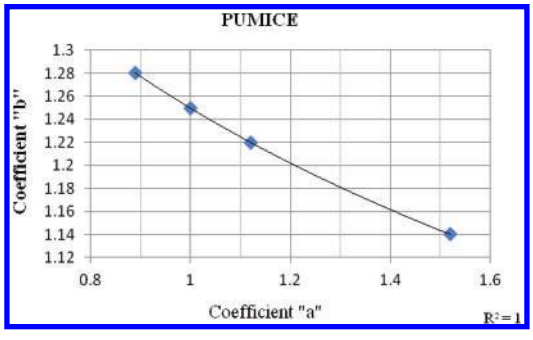


Figure 6. Strength coefficients for pumice aggregates.

4.6 *Volume of sand*

The volume of sand is calculated from the formula

$$v_s = 1 - \left(v_p + v_{la} + v_{air}\right) \tag{7}$$

where v_{la} = volume of LWA; and v_{air} = volume of air in the concrete. Normally, the air volume is 1.5–2% of the volume of concrete.

4.7 *The bulk density of the concrete*

The density of the concrete can be obtained by adding all the amounts of the ingredients in 1 m^3 of compacted concrete.

5 MIX DESIGN CALCULATIONS

The mix proportioning of the LWAC using the scoria and pumice aggregates was based on estimating first the coefficients a and b in equation (2) by interpolating the values shown on Table 2. The coefficients were then recalculated from trial mix design strength test results using Equation (3a). The re-calculated coefficients are plotted on Figures 5 and 6. Three trial mixes (Trial 1, Trial 2 & Trial 3) were then prepared each with the pumice and the scoria aggregates. Table 3 & Table 4 show the design parameters and the calculations respectively.

Confidence factor, $\lambda = 1.64$. Standard deviation, $S_n = 8.5$. Characteristic strength, $f_{cu} = 20$ MPa.

Mean Compressive strength, $f_m = f_{cu} + \lambda S_n =$ 33.94 MPa.

Table 3. Mix Design Parameters.

		Scoria	Pumice	Sand	Cement
Bulk density (kg/m^3)		882	411.0	1422	1670
Particle density (kg/m^3)		1760	869	2620	3150
Water Absorption (60 min.) (%)		0.8	5.0		
Coefficient "a"	Trial 1	1.520	1.0000		
	Trial 2	1.530	1.0500		
	Trial 3	1.560	1.0000		
Coefficient "b"	Trial 1	0.650	1.2490		
	Trial 2	0.57	1.2363		
	Trial 3	0.56	1.2242		

Table 4. Calculations.

Mean strength f_m		33.93 MPa	
Strength of LWA (MPa)			
		Scoria	Pumice
$f_{la} = a \cdot 10^{b\rho/1000}$	Trial 1	21.18	12.17
	Trial 2	15.41	12.46
	Trial 3	15.09	12.74
Strength of mortar (MPa)			
Equation 3(b)	Trial 1	43.75	58.95
	Trial 2	51.92	58.22
	Trial 3	52.51	57.52
Water cement ratio for OPC			
Equation 5(a)	Trial 1	0.58	0.43
	Trial 2	0.50	0.44
	Trial 3	0.49	0.44
Volume of cement paste=0.35			
Cement content (kg/m^3)			
Equation 6	Trial 1	393.00	471.86
	Trial 2	434.68	467.89
	Trial 3	437.76	464.17

6 TEST RESULTS

6.1 *Tests on fresh concrete*

The workability and density of the LWAC were measured according to BS 206-1:2000 and the air content was according to BE 96-3942/R4 (1999). The results are shown on Table 5.

6.2 *Tests on hardened concrete*

The test results on densities and compressive strength of the hardened concrete is shown on Table 6. Figure 7 shows the failure modes of the concrete cubes after the compressive strength tests and they clearly show that failure was initiated by failure of the aggregates which were weaker than the mortar. The development of strength of the concretes with age is shown on Figure 8.

Table 4. Calculations (continued)

		Scoria	Pumice
Water Content (kg/m^3)			
W = C x (W/C)	Trial 1	228.17	203.72
	Trial 2	215.25	204.95
	Trial 3	214.29	206.11
Slump between 25mm to 100mm O.K. Air Content 2.00%			
Effective Water (kg/m^3)			
		Scoria	Pumice
	Trial 1	208.17	183.72
	Trial 2	195.25	184.95
	Trial 3	194.29	186.11
Volume of natural sand (m^3)			
Equation 7	Trial 1	0.28	0.28
	Trial 2	0.28	0.28
	Trial 3	0.28	0.28
Weight of natural sand (kg/m^3)		733.6	733.6
Bulk volume of natural sand (m^3)		0.52	0.52
Weight of LWA (kg) : $W_{la} = V_{la} \times \rho_g$		616.00	304.15
Bulk volume of LWA: $V_{la} = V_{la} \times \rho_g/\rho_b$		0.70	0.74
Water absorption $W_{abs}=W_{la} \times w_{abs}$		4.93	15.21
Water to be added (kg)			
	Trial 1	213.10	198.93
	Trial 2	200.18	200.16
	Trial 3	199.22	201.31

Ingredients per cubic meter

Scoria	Trial Mix S1		Trial Mix S2		Trial Mix S3	
	kg	m^3	kg	m^3	kg	m^3
LWA	616	0.352	616	0.352	616	0.352
Natural sand	734	0.282	734	0.282	734	0.282
Portland cement	393	0.125	435	0.138	438	0.139
Water	213	0.213	200	0.200	199	0.199
Air		0.020		0.020		0.020
Density of fresh LWC	1956 (kg/m^3)		1984(kg/m^3)		1989(kg/m^3)	

Pumice	Trial Mix P1		Trial Mix P2		Trial Mix P3	
	kg	m^3	kg	m^3	kg	m^3
LWA	304	0.343	304	0.343	304	0.043
Natural sand	734	0.282	734	0.282	734	0.282
Portland cement	472	0.150	468	0.150	464	0.150
Water	199	0.199	200	0.200	201	0.201
Air		0.020		0.02		0.020
Density of fresh LWC	1709(kg/m^3)		1706(kg/m^3)		1703(kg/m^3)	

Table 5. Tests on fresh concrete.

Aggregate type	Scoria			Pumice		
Mix ID Number	S1	S2	S3	P1	P2	P3
Slump (mm)	30.0	30.0	32.0	30.0	37.0	35.0
Air Content (%)	4.8	4.2	4.0	7.8	7.6	7.0
Density (kg/m^3)	1833	1828	1816	1475	1480	1466

Table 6. Tests on hardened concrete.

Mix No.	Cement content (kg/m^3)	Density at 28 days (kg/m^3)	Strength (N/mm^2)			Coefficient of strength of LWA	
			3d	7d	28d		b
S1	393	1990	12.4	14.4	24.3	1.52	0.65
S2	435	2020	15.8	17.9	25.0	1.53	0.57
S3	438	2020	14.0	16.5	25.4	1.56	0.56
Ave.	422.3		14.1	16.3	24.9		
P1	472	1838	9.4	12.4	16.7	1.00	1.25
P2	468	1813	9.0	10.5	15.2	1.05	1.24
P3	464	1830	8.6	10.1	14.9	1.10	1.22
Ave.	468		9.0	11.0	15.6		



Figure 7. Modes of failure of the scoria (left) and pumice (right) concrete cubes.

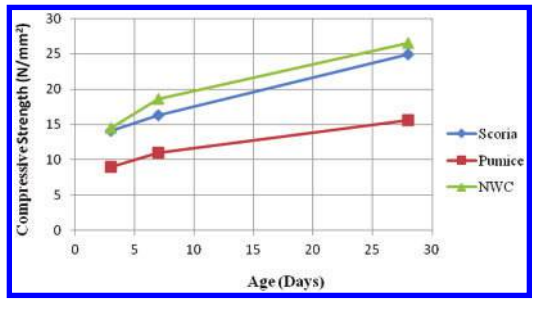


Figure 8. Relationship between compressive strength and age.

7 DISCUSSION OF RESULTS

The tests on fresh concrete for both the scoria and pumice concretes gave slump values between 25 mm and 100 mm as expected indicating medium workability. The air content was, however, higher than the 2% assumed in the design. The densities of the fresh concretes were also a bit lower than the design values (Tables 4 & 5). This might have partly been due to insufficient compaction of the concrete but it has to be mentioned here that some of the formulae used in the design are empirical in nature and these variations are not unexpected. Tests on the hardened

concrete (Table 6) showed that the dry densities of the LWAC produced were actually in the range of 1200 to 2000kg/m^3 as defined by Clarke (2005). The design characteristic strength of 20 MPa at 28days was reached with the scoria aggregates but not with the pumice. The average strength reached with pumice aggregates was 15.6 MPa which was lower than the 17 MPa recommended for structural LWC. Developing a concrete of grade 20 with pumice went beyond the capability of the pumice aggregate which was weaker than the scoria. This was actually observed in the modes of failure of the tested concrete cubes (Fig. 7) where it was found out that in both cases it was the aggregates that actually failed first in tension. The mortar was designed to be of strength greater than that of the lightweight aggregate as recommended (Table 4). Table 6 shows that using LWAC the demand for cement/m^3 is higher than with normal concrete using normal aggregates. This additional cost is offset by the additional costs which would be incurred by transporting normal aggregates from longer distances to these locations.

8 CONCLUSIONS AND RECOMMENDATIONS

It can be concluded from these investigations that the scoria aggregates are suitable for structural concrete and the pumice aggregates for non-structural purposes. Non-structural concrete is employed in the construction of non-load bearing elements, roof, floor and wall insulation and production of self curing concrete. In a separate study by Mboya et al, (2011), it was established that the pumice used in this study could also be used in the production of suitable concrete building blocks. It was noted from literature survey that mineral additives and chemical admixtures such as silica fume, ground blast furnace slag, fly ash, superplasticizers etc. are used in LWA concrete mixes to improve LWC strengths. This can also be applied with these aggregates to get better concrete strengths. There is a need of characterization of the lightweight aggregates that are present in vast amounts in Tanzania so that they can be better utilized. There is also a need to disseminate the knowledge of the use of lightweight aggregate concrete to engineers in Tanzania so that they can start utilizing this material in construction.

REFERENCES

BE 96-3942/R23. 2000. *Mechanical properties of lightweight aggregate concrete. Economic Design and Construction with Light Weight Aggregate Concrete*, European Union – Brite EuRam III.

BS 206: 1: 2010. *Concrete specification performance, production and conformity.*

BS 812 part 111:1990. *Testing aggregates. Methods for determination of ten percent fines value (TFV).*

BS 812-103, 1:1985. *Methods for determination of particle size distribution.*

BS EN 197-2000. *Cement Part 1: Composition, specifications and conformity criteria for common cements.*

Chandra, S. & Leif B. 2002. Lightweight Aggregate Concrete *(Science, Technology and Applications)* Chalmers University of Technology, Noyes Publications/William Andrew Publishing Norwich, New York, USA.

Clarke, J. L 2005, *Structural Lightweight Aggregate Concrete,* Second Edition, Taylor and Francis E-Library.

Mboya H.A. Makunza J. K. & Mwishwa Y.H. 2011. Assessment of Pumice Blocks on Comparison to Sand Blocks and Burnt Blocks – The case of Mbeya – Tanzania. *Journal of Civil Engineering Research and Practice*, Vol.8 No.1, April 2011: 43–55.

Neville A.M. & Brooke J.J. 2005. *Properties of concrete,* 4th Edition, Pearson.

NRMCA (National Ready Mixed Concrete Association) (2003). Concrete in Practice, *CIP 36 Structural Lightweight Concrete*, Silver Spring, Maryland USA.

Schlaich, M. & Zareef, M. E. 2008. *Infra-lightweight concrete.* Taylor & Francis Group, London, ISBN 978-0-415-47535-8.

TxDOT. 2008. *Test Procedure for Sieve Analysis of Fine and Course Aggregates,* Tex-200-F Texas Department of Transportation.

Research and Applications in Structural Engineering, Mechanics and Computation – Zingoni (Ed.)
© 2013 Taylor & Francis Group, London, ISBN 978-1-138-00061-2

Mechanical properties of aluminous cement paste at high temperature

O. Holčapek, P. Reiterman, F. Vogel & P. Konvalinka
Experimental Centre, Faculty of Civil Engineering, Czech Technical University, Prague, Czech Republic

E. Vejmelková
Department of Material Engineering and Chemistry, Faculty of Civil Engineering, Czech Technical University, Prague, Czech Republic

ABSTRACT: The hydrated Portland cement doesn't resist to high temperature very well. In the course of heating Portland cement loses its strength and also chemical changes take place in its mineral composition. For these reason we use composites based on aluminous cement at high temperature applications which shows much better characteristics. Experimental studies were conducted to examine mechanical properties of cement paste made from aluminous cement and reinforced by various types of fibers. During the experimental program was measured compressive strength and three-point bending strength. Specimen size of 160 × 40 × 40 mm were made from aluminous cement and used in experimental program. One series of specimen was deposited in laboratory condition and the second one was exposed to high temperature and all mechanical properties were compared. The effect of amount of water was also investigated, because the values of water ration has an influence to mechanical and also rheological properties of final product.

1 INTRODUCTION

Significant advances in the field of building materials leads to increasingly frequent enforcement these high performance materials in real constructions. Efforts to maximize the efficient use of non-renewable resources and especially energy-intensive materials lead to efforts to maximum efficiency and usability. For this reason new buildings design started gradually using high quality entrance raw materials to create super-construction while reducing the overall emission of carbon dioxide. The increasing the cost of input materials will significantly reduce the total volume and weight of structures. This leads to cost reduction of other part of construction.

However, a common problem of new types of structures, made from high performance materials, is their inferior properties in some very specific areas of their proposal. Typical example of these properties is a lack of fire resistance, especially in case of very subtle structures. The behaviour of concrete surface layer of High-performance concrete with special consideration to spalling was described in (Sicáková). This deficiency is necessary to be solved by other additional measures in the form of fire tiling or other kind of measures. Development of fire barriers, which are based on aluminous cement, has become an integral part of building industry, especially with regard to the current global political and security situation. Compared to traditional Portland cement the aluminous has excellent characteristics in relation to the high temperatures. There were many research focused on studying behaviour of concrete or high-performance concrete after exposure to temperatures up to 1000°C. There were researches on Young's modulus in his experimental investigations (Huo). Research of dynamic behaviour of concrete after exposure to high temperatures was also investigated (Bahr). All these researches and other one show the negative influence temperature to mechanical properties.

2 EXPERIMENTAL PROGRAM

The experimental program was focused on studying mechanical properties like tensile strength in bending and compressive strength of composite made from aluminous cement, various type and amount of basalt fibers, plasticizer and water. All these properties were examined on specimens with dimension 160 × 40 × 40 mm.

2.1 *Aluminous cement*

The original aluminous cement was developed as a mixture of limestone and bauxite in French company Lafarge. However there is still a place for application of aluminous cement especially in the form of composite materials for high temperature applications.

For the purposes of the experimental program was used aluminous cement manufactured by the French company Lafarge Aluminates SECAR ®71. The main component of the hydraulic binder is aluminium oxide in this case monocalcium-aluminate $CaO{\cdot}Al_2O_3$

Table 1. Chemical composition of aluminous cement.

Al_2O_3	CaO	Sio_2	Fe_2O_3	MgO	Na_2O	K_2O
70.8%	27.5%	0.58%	0.42%	0.21%	0.27%	0.06%

Table 2. Composition of used composite mixtures.

Mixture	Water kg·m^3	Cement kg·m^3	Fibers kg·m^3	Plasticizer kg·m^3
CI-a (1)	506.77	1447.90	7.24	–
CII-a (2)	506.77	1447.90	14.48	–
CIII-a (3)	506.77	1447.90	21.72	–
CI-b (4)	506.77	1447.90	7.24	–
CII-b (5)	506.77	1447.90	14.48	–
CIII-b (6)	506.77	1447.90	21.72	–
CI-c (7)	426.05	1704.20	8.52	3.30
CII-c (8)	426.05	1704.20	17.04	3.30
CIII-c (9)	426.05	1704.20	25.56	3.30

(Collepardi). This cement isn't made from natural sources of bauxite but from chemical clean artificial aluminium oxide. The manufacture of the aluminous cement takes place in electric arc furnace. The chemical composition of aluminous cement SECAR®71 is shown at (tab. 1).

2.2 *Basalt fibers*

Historical use of the asbestos fibers for high-temperature applications concrete composites is already overcome due to the health risk, especially laugh cancer. Fortunately the asbestos is not the only usable material with the required properties. We can use basalt fibers because they resist with success the temperatures up to 1000°C. In experimental program were used basalt fibers of two lengths. There were used fiber with length 6,35 mm (1/4″) and diameter 13 μm and length 12.7 mm (1/2″) with the same diameter. The density of used fibers is 2900 kg·m^{-3} and it's tension strength is 2000 MPa (Artemenko). Using two kinds of fibers with different amount leads to investigation their influence to the final properties.

2.3 *Treatment and manufacture*

All used mixtures and their designation are presented at (tab. 2). The first experiences with aluminous cement paste show that due to high hydration heat there were many cracks on the fresh samples which were kept in laboratory condition. This negative phenomenon was eliminate by leaving the fresh cement composite in forms in a humid environment with relive humidity over 90% while avoiding the water evaporation from the surface (Behnood). The specimens in steel forms were after 72 hours removed from steel forms and till its age 28 days were left in the humidity environment. After 28 days all samples were dried at 105°C for

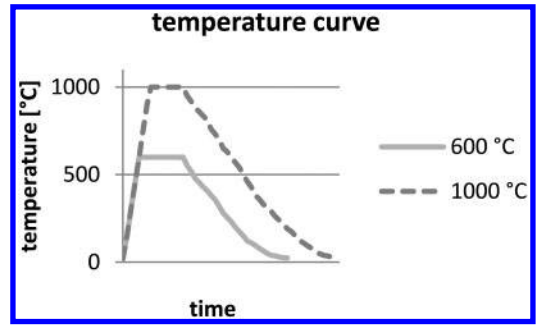


Figure 1. Temperature profile during loading.

Table 3. Compressive strength of composite.

	Compressive strength		
	f_c [MPa]	f_c [MPa] 600°C	f_c [MPa] 1000°C
CI-a (1)	65.99	35.55	23.13
CII-a (2)	49.11	26.72	16.33
CIII-a (3)	62.87	31.42	16.59
CI-b (4)	73.96	34.10	19.84
CII-b (5)	86.49	42.40	21.57
CIII-b (6)	83.47	40.07	21.04
CI-c (7)	75.51	61.28	27.35
CII-c (8)	101.20	61.84	41.29
CIII-c (9)	88.48	52.73	27.66

24 hours and then the influence of high temperature started being examining. The group of three samples was examined after dried at 105°C, second group of three samples was examined after exposure to 600°C and the last on group of three samples was examined after exposure to temperature 1000°C. The time process of temperature is show at (fig. 1).

3 RESULTS

There were designed nine mixtures of composites of aluminous cement, water, different length of basalt fibers and plasticizer. The amount of each components and the water-cement ration is shown at (tab. 1). From each mixture were made nine samples, three reference three for temperature load 600°C and the last three for temperature 1000°C. The water-cement ration was designed according to suitable workability, therefore it's lower while using plasticizer. Using the same values of water-cement ratio for mixtures with and without plasticizer leads to segregation of water during compaction because of high efficiency of plasticizer. The fibers were added in amount of 0.5; 1.0 and 1.5 of weight percent. Using of two different lengths of fibers was chosen to investigate their influence to the mechanical properties especially tensile strength in bending.

The results of tests of mechanical properties are presented at (tab. 3 and tab. 4). Tensile bending strength

Table 4. Tensile strength of composite.

	Tensile strength in bending		
	f_t [MPa]	f_t [MPa] 600°C	f_t [MPa] 1000°C
CI-a (1)	6.80	1.38	0.74
CII-a (2)	8.52	2.34	1.08
CIII-a (3)	12.02	4.14	1.36
CI-b (4)	11.73	1.88	0.89
CII-b (5)	13.41	2.44	1.10
CIII-b (6)	15.62	4.36	1.35
CI-c (7)	14.80	8.22	4.50
CII-c (8)	14.81	8.25	4.62
CIII-c (9)	14.49	8.51	4.59

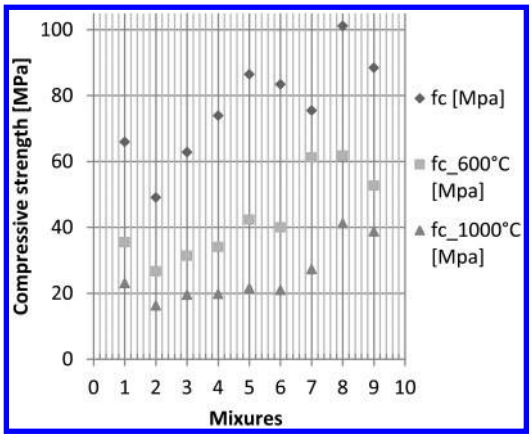


Figure 2. Compressive strength of composite.

and compression strength were measured on all specimens. The mechanical properties are very important parameter for fire resistance materials. For design is necessary to know changes of these properties caused by high temperature.

4 CONCLUSIONS

The exposure to high temperatures for silicate composites based on Portland cement has completely destructive consequences especially on hydrated cement paste. The primary phenomenon at high temperature load is the evaporation of free water, following losing of the gel water and crystalline water at 150°C. The disruption of cement binder's inner structure is indicated at 500°C, when the Portlandit is starting disintegrating. The complete disintegration of the cement binder takes place at temperatures higher than 800°C. By the temperature over 600°C the α-silica is converted to β-silica, which is accompanied by the volume expansion and increasing the tension in inner structure (Venkatesh).

Using aluminous cement appropriately supplemented by fibers and plasticizer leads to the creation

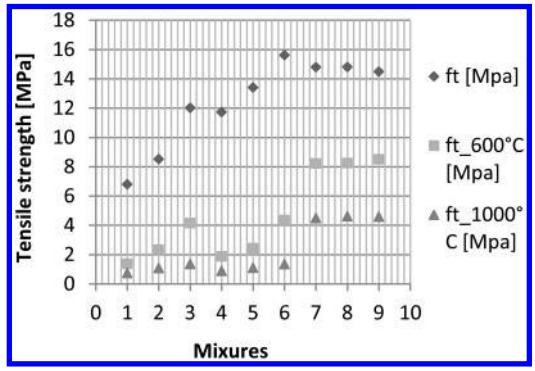


Figure 3. Tensile strength of composite.

of composite that resists the effect of high temperatures without volume changes and disintegration of inner structure. This is very important for design fire-resistance facing or other materials for high temperatures applications. The volume stability of presented composite prevents unwanted consequences like explosive spalling. The strength of aluminate cement also decreases by the influence of high temperature, but the residual strength still ensures cohesiveness and sufficient mechanical properties. The relationship between compressive strength of each mixture is determined at (fig. 2) and between tensile strength at (fig. 3). The tensile strength was very positively influenced by the value of water-cement ration and the amount of basalt fibers. Using of plasticizer while reducing the water-cement ration leads to an increase of compressive and tensile strength of the cement matrix, that results in higher properties. The length of basalt fibers was also investigated in this research. It showed the positive effect of length of fibers on tensile strength in bending, when the specimens with fibers 12.7 mm long (mixtures CI-b, CII-b, CIII-B) had higher values of tensile strength. With the growing amount of fibers in the total volume of the mixture decreases the workability and the mixing of all components. This negative effect leads to the formation of clusters of fibers. In these weaknesses starts the beginning of the development of cracks during testing mechanical properties. From this reason we can find lower values of tensile strength in bending in mixtures with the highest content of basalt fibers.

ACKNOWLEDGEMENT

This research was supported by GAČR P104/12/0791 which is gratefully acknowledged.

REFERENCES

Artemenko, S.W., *Polymer composite materials made from carbon, basalt and glass fibers. Structure and properties,* Fibre chemistry, Vol. 35, 226–229, 200

Behnood, A., Ziari H.: *Effects of silica fume addition and water to cement ratio on the properties of high-strength*

concrete after exposure to high temperatures, Cement & Concrete Composites 30 (2008)

O. Bahr, P. Schaumann, B. Bollen, J. Bracke, *Young's modulus and Poisson's ratio of concrete at high temperatures: Experimental Investigations*, Materials and Design, 2013

Collepardi, M.: *Modern Concrete*, ISBN 987-80-87093-75-7, Information centre CKAIT, Prague 2009

J. S. Huo, Y. M. He, L. P. Xiao, B. S. Chen, *Experimental study on dynamic behaviours of concrete after exposure to high temperatures up to 700° C*, Materials and Structures, 2012

Sicáková A. a kol, *New generation cement concretes – Ideas, Design, Technology and Applications*, Košice, 2008, ISBN 987-80-553-0040-5

Venkatesh, K., Kodur, M.: *High-Temperature Properties of Concrete for Fire Resistance Modeling of Structures*, ACI Materials Journal/September–October 2008

Research and Applications in Structural Engineering, Mechanics and Computation – Zingoni (Ed.)
© 2013 Taylor & Francis Group, London, ISBN 978-1-138-00061-2

The influence of percentage replacement from coarse recycled concrete aggregate

D.W. Immelman & W. de Villiers
University of Stellenbosch, Stellenbosch, South Africa

ABSTRACT: The aim of this study was to investigate the potential use of coarse recycled concrete aggregate (RCA) as a material in structural concrete. The lack of knowledge and specifications surrounding RCA in South Africa were the main reasons for this research. The reduction of accumulating construction and demolition (C&D) waste at landfills and mining of depleting virgin materials are subsequent aims from this investigation. By increasing the database of research of RCA in South Africa the possibility of specifications for this alternative building material can be initiated. The implications of such specifications would lead to RCA acceptance in concrete design. The objectives that were achieved through this research project are; what is the percentage replacement of RCA to a concrete mixture that will produce a material that achieves similar or the same results as a concrete mixture containing natural aggregates and what aggregate properties and limits should be defined in the specification of RCA for it to be accepted as material in a concrete mixture. The objectives were assessed through examining the physical, mechanical and chemical properties of the aggregate as a material and the fresh and hardened concrete properties of RCA as a constituent in structural concrete.

1 INTRODUCTION

Concrete is the most widely used construction material globally and is contributing to the extraction of natural resources and energy usage, thus responsible for large quantities of CO_2 emissions (Lui & Chern, 2008). The construction and civil works industries account for 60% of worldwide consumption of raw natural resources (Bribian et al, 2011). The amount of C&D waste generated each year is estimated by different sources to be in the region of 1-3 billion tonnes (Lui & Chern, 2008, Mohammend, 2007 and Van Zijl, 2010). This C&D waste is mainly sent to landfill sites or reused in low grade applications such as backfill and unbound road base.

The use of processed C&D waste or recycled concrete aggregate (RCA) in high grade applications has been limited due to the hesitance to utilise a secondary material in structural concrete because of uncertain characteristics. Countries such as Germany, Switzerland, Netherlands, Denmark, Great Britain, USA and Russia all have established standards or specifications for the use of RCA in concrete (Dehn, 2007), therefore providing the relevant stakeholders with the assurance that the material conforms to the necessary specifications.

Currently, South Africa does not have similar standards or specifications. The South African Bureau of Standards (SABS) is currently revising the standards and test methods related to aggregates in concrete to coincide with the European standards (Perrie, 2011). There are South African companies such as Cape Brick which produce concrete masonry products from recycled C&D waste using percentages of RCA. There is a perception that products such as these cannot meet the standards that natural aggregate (NA) can deliver.

2 METHODOLOGY

The research conducted consisted of an extensive literature review of both local and international research related to RCA. Included in this review was overview of the current South African standard for aggregates in concrete, SANS 1083:2006, as well as the international standards and specifications listed below:

- BS EN 12620:2008 Aggregates for concrete
- RILEM TC 121 – DRG 1994 Specifications for concrete with recycled aggregates
- JIS A 5021 Class H Recycled aggregate for concrete-class H
- BS 8500-2:2006 Complementary British Standard to BS EN 206-1 Part 2: Specification for constituent materials and concrete
- ACI 555R – 01 Removal and Reuse of Hardened Concrete
- ACI E1 – 07 Aggregates for Concrete

The shortcomings of the South African standard were identified and investigated through an experimental programme and recommendations were made based on the outcomes of the experimental research.

2.1 *Materials*

Greywacke stone (19 mm), which is commonly found in the Western Cape region of South Africa, was

used. The aggregate is also well known for demonstrating alkali-silica reactivity (ASR). For consistency the same coarse NA from a single batch was utilised throughout the experimental programme. Sand known as "Malmesbury" sand was utilised. Three different Malmesbury sand batches were used in this study. A single batch of CEM I 52.5 N Ordinary Portland cement (OPC) and ground granulated Corex® slag (GGCS) was used as binder.

The coarse RCA was obtained from Cape Brick. C&D waste is primary crushed by a mobile crusher. This material is pre-screened to remove large contaminant items such as steel, bricks and other foreign materials. Topsoil and clay are removed, while light weight material is removed by air-sifting. Magnets are placed over conveyor belts to remove ferrous metals. The secondary crushing process includes a jaw crusher and a gyro-crusher after which the material is about 15 mm in size. A vertical impact crusher concludes the crushing process with material below 9 mm in size. Potable water is sprayed throughout the factory to control dust and is localized over certain conveyor belts. The recycled material was collected from a point in the production process before the vertical impact crusher.

The collected material was relatively dirty, damp and not graded, hence it was decided that the material should be further processed. This would allow for consistency between the different batches of RCA and could still be considered a practical recycling method. This would result in a superior secondary material compared to an unwashed material. The material was cleaned by hosing batches of the material for 30 seconds under water. Once dry, the material was sieved so that the individual stone sizes could be obtained and later combined to produce a nominal size of 19 mm. SANS 1083:2006 specifies the limits for the combination of stone sizes for a nominally graded coarse aggregate (Table 1).

A total of three batches were collected from Cape Brick at 6–8 week intervals. The preparation process described above was employed to prepare each of the experimental batches of RCA. However, due to an error, the percentages for the March sample were incorrectly batched. The 9.5 mm stone amounted to 6.25 kg per 50 kg batch instead of the intended 5 kg.

Table 1. Grading of RCA according to SANS 1083:2006.

Sieve size (mm)	% passing*	% passing**	% retained	Mass/50 kg (kg)
26.5	100	100	0	3.75
19	100–85	92.5	7.5	33.75
13.2	0–50	25	67.5	7.5
9.5	0–25	10	15	5
6.7	0–5	0	10	0

*According to SANS 1083:2006
**Intended grading in this investigation

Table 2. Aggregate properties investigated.

Property	Standard/Method
Required	
Grading	SANS 201:2008
Dust content	SANS 201:2008
ACV	SANS 5841:2008
Flakiness Index	SANS 5847:2008
Additional	
Shape and surface texture	Visual
Compacted and loose bulk density	SANS 5845:2006
Relative Density	SANS 5844:2006
Fineness Modulus	SANS 201:2008
Water absorption	SANS 5843:2008
Constituents of coarse RCA	BS EN 933-11:2009
Water soluble cations and anions	CAF Method
Chemical mineralogy	XRF Analysis

Table 3. Hardened concrete tests and standards.

Property	Standard/Method
Mechanical	
Density	SANS 6251:2006
Compressive Strength	SANS 5863:2006
Tensile Strength	SANS 6253:2006
Durability	
Oxygen Permeability	Alexander et al. (2009)
Water Sorptivity	Alexander et al. (2009)
Chloride Conductivity	Alexander et al. (2009)
Dimensional stability	
Modulus of Elasticity	ASTM C469-10
Shrinkage	ASTM C157-08
Creep	ASTM C512-10

2.2 *Tests*

SANS 1083:2006 requires that certain properties are required for verification, but to correctly assess RCA additional tests are necessary to further define the sample material's properties (Table 2). The aggregate properties were examined for the percentage replacements: 0, 15, 30, 50 and 100%. Mass was taken as the measure of the percentage replacement for the aggregates tests. The aggregate properties are categorised according to the geometrical, physical and chemical properties. The chemical analyses for this study were done by the Central Analytical Facilities (CAF) at the University of Stellenbosch.

The fresh concrete was tested for workability and consistency through various tests which include: slump, slump loss with time, air content, and fresh concrete density. The hardened concrete was tested according to the properties of: mechanical, durability and dimensional stability (Table 3). The durability tests were conducted at the University of Cape Town.

2.3 *Mix design*

South Africa makes use of the C&CI method for guidelines to designing concrete mixtures. Most researchers pre-saturate the RCA to a surface saturated dry (SSD)

Table 4. Mix design examples.

Constituents	kg/m^3	RD	litres
MarR50C			
Water	175	1	175
Cement	292	3.14	93
Cement Extender	0	2.9	0
Natural Stone	503	2.74	184
Recycled Stone	486	2.65	184
Sand (CHOICE)	960	2.63	365
Total Stone	989		1000
MarN100S			
Water	175	1	175
Cement	146	3.14	46
Cement Extender	146	2.9	50
Natural Stone	995	2.74	363
Recycled Stone	0	2.65	0
Sand (CHOICE)	960	2.63	365
Total Stone	995		1000

condition to reduce the effects that the material may have on the concrete properties. The practical implications of following this method were not viable, not only for this investigation, but even more so in concrete production industry. Consequently, all the materials used were kept in an air dry condition. The concrete for this study was assumed to be a general structural concrete of 30 to 40 MPa for a coastal region and a W:C of 0.6 was chosen.

The percentage replacement was based on the volume and the sand amount was initially chosen and kept constant. Eight mixtures were prepared for comparison in the experimental programme. These mixtures are labeled according to the month the RCA concrete batch was produced (Mar, Jun or Aug), the percentage replacement (0–100%) and whether cement and/or cement extender (C or S) was used (Table 4).

Prior to mixing, items "X" and "FL" (Table 5) were removed. The inclusion of these contaminants may lead to results which are not representative of the larger sample of RCA due to the test specimen size. The screening process involved using a strong magnet to remove magnetic items and visual inspection to remove other items. All concrete specimens were mixed and compacted/vibrated in a similar manner for consistency.

3 RESULTS

3.1 *Aggregate properties*

The aggregate properties are summarised in Table 5. The increase in RCA percentage resulted in an improved continuous grading with higher proportions of smaller particles. The improved grading would result in a better packing ability. The dust content increased with increasing percentage replacement and although the dust content was higher in the RCA, it was still within the limits defined by SANS 1083:2006, RILEM TC 121 and JIS A 5021.

The RCA particles had an irregular, sub-angular and cubical shape with a lower Flakiness Index (FI). The NA was angular, elongated and flaky with a high FI value. The NA particles were rough in texture, while the RCA particles had a rough and porous surface texture associated to the adhered mortar and masonry particles. A higher FI value would improve the tensile strength by restricting the formation of continuous cracks through the concrete.

The RCA composition typically had a higher percentage of stone/mortar combination particles. The constituent composition is dependent on the source of the original material and the recycling process. A larger sample of RCA should be assessed to accurately determine the amount of foreign items found within an RCA batch. The floating items consisting generally of wood and plastics were below the 2 cm^3/kg limit defined in BS EN 12620. The amount of foreign items, especially larger items, should be limited to avoid localised corrosion and spalling.

The relative density (RD) decreased with increasing replacement percentage due to the higher presence of lower density materials such as brick and adhered mortar. The lowest RD measured was 2.59. RD could be used to reject a RCA batch due to the higher water absorption associated with a lower RD. The LBD and CBD increased with increasing RCA percentage due to the improving packing capacity. The LBD and CBD were lower when RCA with a lower relative density was assessed.

The water absorption increased with increasing RCA replacement. The highest water absorption was due to the presence of clay masonry items and adhered mortar particles. The water absorption percentage was below the 3.5% limit defined by JIS A 5021 and 3% in the RILEM recommendation for recycled aggregates.

The ACV was similar for all RCA combinations, except marginally higher for RCA with higher percentages of lower ensity particles. The lower density particles are fragile and crush at a lower force compared to the stone particles. The highest ACV was lower than the 30% limit defined in the SANS 1083:2006.

The water-soluble cations and anions analysis showed that the RCA combinations increased the amounts of the six ions analysed. The individual amounts from the various ions were not significantly high, with the highest total combination of all six ions amounting to 150 mg/l. The RCA samples which originated from C&D waste from a demolition project in the Cape Town harbour had higher amounts of chloride ions, but not considerably high with the highest amount of 9 mg/l.

The mineralogical composition of the RCA samples was similar to that of the reference material. The difference between the mineral oxides percentages for the various RCA combinations was not significant (below 5%). The CaO mineral increased with increasing RCA replacement, indicating the increasing presence of cement paste. The LOI also increased with increasing RCA percentage signifying the presence of water bound substances in materials such as brick and

Table 5. Summarised aggregate property results for the three batches of RCA collected from Cape Brick after processing.

Aggregate property	Control	RCA sample batch (month)								
		March			June			August		
Percentage replacement (%)	Reference 0	30	50	100	30	50	100	30	50	100
Grading (% passing)	*Geometrical properties*									
26.5	100.00	100.00	100.00	100.00	100.00	100.00	100.00	100.00	100.00	100.00
19.00	88.28	93.92	89.81	90.08	89.68	92.16	93.61	87.71	92.12	88.95
13.20	18.63	28.66	29.23	33.74	19.54	22.75	25.32	16.33	18.46	21.90
9.50	0.55	6.36	10.47	16.29	3.86	6.01	9.80	2.10	4.41	9.46
6.70	0.02	0.12	0.19	0.30	0.25	0.04	0.06	0.05	0.07	0.07
4.75	0.01	0.03	0.02	0.07	0.07	0.02	0.04	0.03	0.01	0.03
Dust content (%)	0.24	0.31	0.30	0.13	0.40	0.44	0.55	0.46	0.50	0.61
Fine modulus	3.93	3.71	3.70	3.60	3.87	3.79	3.71	3.94	3.85	3.80
Flakiness Index	24.8	20.1	14.8	7.3	19.7	16.1	7.4	20.0	18.0	7.0
Constituents of RCA	*Physical properties*									
Rc (concrete, mortar) (%)	0.0			55.87			54.36			74.35
Ru (unbound aggregate) (%)	100.0			41.68			42.67			17.95
Rb (clay masonry units) (%)	0.0			1.56			1.08			6.38
Ra (bitumious material) (%)	0.0			0.08			1.29			0.11
Rg (glass) (%)	0.0			0.00			0.00			0.03
X (foreign items) (%)	0.0			0.09			0.07			0.27
FL (floating items) (cm^3/kg)	0.0			0.21			0.90			0.50
Relative density	2.73	2.70	2.68	2.65	2.71	2.69	2.66	2.7	2.68	2.59
Loose density (kg/m^3)	1405	1428	1440	1462	1417	1432	1452	1402	1402	1401
Compact density (kg/m^3)	1557	1588	1597	1605	1575	1584	1600	1559	1555	1541
Water absorption (%)	0.52	0.8	1.13	1.67	0.82	1.01	1.44	1.15	1.71	2.59
ACV strength (%)	11	12.5	10.8	11.3	11.7	11.4	11.7	12.4	13.1	15.2
Water soluble ions	*Chemical properties*									
Ca (mg/l)	1.9	11.1	8.1	12	10.1	86.4	18.3	6.7	15.7	38.5
Mg (mg/l)	2.3	0.1	0.1	0.1	0.1	0.1	0.1	0.1	0.1	0.1
Na (mg/l)	6.1	16.1	12.9	26.1	9.4	15.1	17.9	11.7	15.7	17
K (mg/l)	18.3	36.5	36.3	53.4	33.6	34.1	32.8	40.4	39.5	28
Cl (mg/l)	2.7	4.3	6.1	9	3	8.9	8.3	2.8	3.4	3.7
SO_4 (mg/l)	8.2	29.5	31.4	9.9	23.1	6	49.5	22.7	11.5	10
XRF analysis	*Chemical properties*									
Al_2O_3 (%)	14.08	13.36	11.83	12.16	13.24	13.1	11.36	11.87	13.57	10.61
CaO (%)	1.15	2.58	2.95	4.03	2.42	3.37	4.14	3.47	3.38	5.15
Cr_2O_3 (%)	0	0	0	0	0	0	0	0	0	0
Fe_2O_3 (%)	5.89	5.28	4.65	4.78	5.5	5.33	4.92	4.93	5.59	4.29
K_2O (%)	3.21	2.79	2.54	2.69	2.89	3.1	2.42	2.64	2.91	2.22
MgO (%)	2.85	2.53	2.27	2.19	2.75	2.55	2.11	2.26	2.66	1.86
MnO (%)	0.09	0.09	0.1	0.08	0.11	0.08	0.07	0.07	0.08	0.07
Na_2O (%)	2.05	2.2	2.01	2.14	2.22	2.39	2.15	2.01	1.91	1.73
P_2O_5 (%)	0	0	0	0	0	0	0	0	0	0
SiO_2 (%)	68.36	68.65	71.48	68.39	68.89	67.13	69.33	69.54	66.79	69.41
TiO_2 (%)	0.76	0.69	0.65	0.69	0.69	0.73	0.66	0.69	0.71	0.7
LOI (%)	1.71	1.86	2.18	2.72	2.05	2.57	3.04	2.88	3.13	3.79

cement paste. The mineralogical analysis also showed that although the RCA batches originated from different C&D waste sources, the compositions were similar. Assessing the RCA batches for potential ASR showed that the samples had compositions almost identical to that of greywacke, granite and grandoirite which are aggregates which have displayed ASR potential when used in concrete.

3.2 *Fresh concrete properties*

The influence of percentage replacement on the initial slump value was negligible (Table 6). The slag mixtures displayed more workability (i.e. higher slump) than the OPC mixtures. The influence which the fine aggregate has on the fresh concrete workability was evident in this investigation. The one batch of concrete was produced with sand which was coarser (higher FM) than the other sand used in the concrete mixtures. The sand thus required less mixing water to produce the target slump and in this case the concrete was highly workable (slump > 150 mm) and less cohesive.

Although the RCA had higher water absorption than the NA, the RCA grading which was more continuous improved the loss of workability. The surface texture

Table 6. Fresh concrete property results.

Batch	March		June		August	
Mixture	Slump (minutes)					
Time	0	60	0	60	0	60
N100C	90	45	70	45	200	160
R30C	105	70	80	35	160	150
R50C	100	70	70	45	155	155
R100C	100	50	90	50	150	85
N100S	120	70	100	65	140	120
R30S	145	80	80	65	160	110
R100S	125	65	85	45	100	65
Mixture	Air Content (%)					
N100C	4.5		4.1		5.8	
R30C	4.9		4.2		5.7	
R50C	4.9		4.9		7.8	
R100C	5.5		5.9		7.4	
N100S	3.7		3.8		3.7	
R30S	3.6		3.9		5	
R100S	4		4.6		5.2	

and particle shape also contributed to the slump loss rate.

The increase in RCA replacement percentage resulted in an increase in air content (Table 6). The slag mixtures had the lowest air content. The lower air content in the slag mixtures can be attributed to the "fine-filler effect" of cement extender particles. Aggregates with a better grading should have lower air content due to improved packing ability. The higher air content in the RCA mixtures was attributed to the porous particles which entrapped air during mixing. The effect of less cohesive mixtures resulted in a higher air content than in mixtures which were cohesive. The higher percentages of RCA negatively influenced the fresh concrete properties, although not significantly.

3.3 *Hardened concrete properties*

The compressive strength displayed no clear trend with increasing percentage replacement of RCA (Table 7). The mixtures containing RCA produced strengths similar to and better than the control mixtures for both binder contents and curing periods. The slag mixtures produced low early age strength, but resulted in the highest overall strength with the mixtures containing 100% RCA. The water absorption and packing ability of the RCA were the reasons for the improved compressive strength results. The compressive strength tests also showed that mixture consistency is important in a fresh state. The RCA mixtures which had excess mixing water absorbed this water to produce higher strengths due to the W:C ratio being adjusted.

The RCA generally reduced the tensile splitting strength of hardened concrete due to the lower FI value with RCA (Immelman, 2013). The more angular and flaky the aggregate particles resulted in a better aggregate interlocking. The tensile strength was between 10

Table 7. Hardened concrete property results.

Batch	March		June		August	
Curing	7 days	28 days	7 days	28 days	7 days	28 days
Mixture	Compressive Strength					
N100C	29.3	35.7	26.5	33.5	20.2	26.6
R30C	26.4	32.9	27.1	33.2	21.9	27.8
R50C	24.8	36	25.3	34.5	22.2	27.5
R100C	25.5	35.4	26.7	34.9	24.5	30.2
N100S	21.9	35.7	23.3	34.7	22.4	33.2
R30S	22.4	35.7	23.9	35.9	21.8	32.9
R100S	24.9	38.6	25.9	39.6	25.7	34.3
Mixture	Oxygen Permeability					
N100C	10.02	9.96	9.60	9.74	9.82	10.16
R30C	10.06	10.06	9.87	9.82	10.08	9.89
R50C	10.28	10.28	9.68	10.00	10.05	9.96
R100C	10.13	10.20	9.68	9.64	9.94	10.15
N100S	9.75	9.68	9.28	9.44	8.94	9.00
R30S	9.86	10.01	9.43	9.40	9.03	9.74
R100S	10.04	9.90	9.38	9.79	9.78	9.85
Mixture	Water Sorptivity					
N100C	6.86	6.67	9.14	7.59	6.19	5.46
R30C	6.32	5.61	9.26	7.20	5.54	5.51
R50C	6.80	6.34	8.97	7.19	6.24	5.10
R100C	6.71	5.99	8.96	6.99	6.98	5.84
N100S	7.09	6.91	9.27	7.28	5.16	4.95
R30S	7.11	6.65	8.51	8.20	5.21	5.24
R100S	5.42	5.88	8.73	7.26	5.70	5.80
Mixture	Chloride Conductivity					
N100C	1.62	1.11	1.76	1.55	1.29	1.37
R30C	1.53	1.13	1.86	1.49	1.22	1.43
R50C	1.68	1.06	1.87	1.51	1.43	1.42
R100C	1.65	1.03	1.92	1.51	1.49	1.42
N100S	0.99	0.47	1.07	0.6	0.57	0.68
R30S	0.95	0.51	0.97	0.77	0.52	0.6
R100S	0.88	0.39	0.96	0.59	0.71	0.71

Table 8. Modulus of elasticity results for 28 days curing.

Month	March	June	August
Sample	Emodulus (GPa)	Emodulus (GPa)	Emodulus (GPa)
N100C	34.3	37.7	27.7
R30C	36.7	36.7	30.1
R50C	35.7	37.5	31.8
R100C	37.2	35.1	28.6
N100S	38.9	35.6	32.5
R30S	33.6	35.3	32.8
R100S	40.7	34.5	30.6

to 11% of the compressive strength. The weaker aggregate particles such as brick and old mortar had failure planes which passed through these particles.

The modulus of elasticity results were varied for the different mixtures (Table 8). There was no clear difference in RCA percentage replacement or binder content. The concrete mixtures generally had elastic moduli which were similar.

The durability of the concrete containing RCA was not significantly affected (Table 7). The durability

Table 9. Performance indexes durability index tests (Alexander et al, 1999).

Durability class	OPI (log scale)	Sorptivity (mm/$\sqrt{h}$)	Conductivity (mS/cm)
Excellent	>10	<6	<0.75
Good	9.5–10	6 – 10	0.75–1.5
Poor	9.0–9.5	10 – 15	1.5–2.5
Very Poor	<9.0	>15	>2.5

was assessed according to the performance indices in Table 9. The possible hydration of old cement in the adhered mortar could be the reason for the better performance in the RCA mixtures (Immelman, 2013). The difference between the results for the June concrete mixtures is due to the fact that the 7 and 28 day mixtures were cast from two separate concrete batches.

The hardened concrete properties were not significantly affected by the inclusion of RCA. The results from most of the hardened concrete tests produced no clear trend with the increase of percentage replacement (Immelman, 2013). Replacing NA with 100% RCA is possible based on the data presented in this investigation. This is based on concrete which utilises RCA with similar or better properties established in this investigation.

4 RECOMMENDATIONS

The incoming material should be visually inspected for any indications of large scale contamination. To assess the amount of foreign items or contaminants, a constituent composition analysis should be completed. The amount of constituents prescribed by the BS EN 12620:2008 and BS 8500-2:2006 should be used as limiting factors.

The material should meet the requirements for coarse natural aggregate as specified by SANS 1083:2006. The material should be graded in such a way that higher percentages of smaller particles are included in the material to improve packing capacity. Reducing the amount of foreign or weaker materials such as mortar or brick will improve the overall aggregate strength. It is recommended that RCA should be washed and graded. The RD will give a good indication of the amount of lower density materials in a sample of RCA. The RD according to this investigation should be limited to 2.6, but standards have allowed for lower RD values. The water absorption according to RILEM TC 121-DRG (1994) and JIS A 5021 Class H for high strength concrete should be limited to 3%. It is recommended that this limit be specified, as RCA with higher water absorption will possibly reduce the properties of fresh concrete and hardened concrete.

Finally, based on the current standard for aggregates in concrete for South Africa, RCA cannot be correctly specified. It is therefore recommended that the international standards and specifications should be consulted to accurately designate a particular RCA batch for the intended concrete class. According to the aggregate and concrete properties examined in this investigation, the full replacement of NA in structural concrete is possible and will improve the sustainable development of the construction industry.

REFERENCES

Alexander, M.G., Ballim, Y. & Mackechnie, J.R. (2009) *Durability index testing procedure manual. Version 1.0. 25 Feb 2009*. University of Cape Town.

Alexander, M.G., Mackechnie, J.R. & Ballim, Y. (1999) *Research Monograph No.2 Guide to the use of durability indexes for achieving durability in concrete structures*. University of Cape Town

Bribián, I.G., Capilla, A.V. & Usón, A.A. (2011) Life cycle assessment of building materials: Comparative analysis of energy and environmental impacts and evaluation of the eco-efficiency improvement potential. *Building and Environment*. 46 (2011). 1133–1140.

Dehn, F. (2007) Recycled aggregates for concrete: standards, guidelines and recommendations. *Concrete Technology*. 3 (2007). 36–41.

Immelman, D.W. (2013) *The influence of percentage replacement on the aggregate and concrete properties from commercially produced coarse recycled concrete aggregate*. MScEng thesis. University of Stellenbosch, South Africa.

Lui, T.C. & Chern, J.C. (2008) *Sustainable concrete technology for the 21st century. Sustainable Concrete Technology and Structures in Local Climate and Environment conditions: The 3rd ACF International Conference*. Vietnam, 11–13 November, 2008. 1168–1174.

Mohammed, T.U. (2007) *Sustainable development of concrete technology*. CBM-CI International workshop. Karachi, Pakistan.

Perrie, B.D. (2011) *Design Standards for Concrete: Aggregate Specifications*. Cement and Concrete Institute (C&CI) presentation.

Van Zijl, G.P.A.G. (2010) *Towards sustainability by efficient use of cement-based materials*. Proceedings of the National Symposium on concrete for a Sustainable Environment. Pretoria, South Africa, 3–4 August, 2010. 122–133.

Research and Applications in Structural Engineering, Mechanics and Computation – Zingoni (Ed.)
© 2013 Taylor & Francis Group, London, ISBN 978-1-138-00061-2

Full-scale model of road structure

M. Varaus, P. Hyzl & D. Stehlik
Brno University of Technology, Institute of Road Structures, Czech Republic

ABSTRACT: The objective of the paper is to make the road technology specialists familiar with the programme and goals of the research project "Advanced reliable and durable civil engineering structures" that is solved by the Institute of Road Structures – Brno University of Technology in parallel with other departments of the Faculty of Civil Engineering. The programme is oriented on the development of full-scale model of flexible pavement structures. The full-scale model is constructed for the accelerated evaluation of the bearing capacity of road structures and the life time of the materials used for them. It can be used also for the testing of railway structures. The described model should help to shorten both the development and testing of new and recycled materials used for the above mentioned structures, and prove their long-term behaviour.

1 INTRODUCTION

The test equipment, also simply called the "stand", is being built on the premises of the Road Laboratory of the Institute of Road Structures – Brno University of Technology. It is intended for accelerated assessment of the bearing capacity and life of new materials and courses in the road structure or railway substructure. There is an assumption of shortened cycle of research and development of these materials in laboratory conditions, including assessment of their long-term behaviour in the structure of the road, possibly proving the benefits of the tested courses. At the first stage, the stand will be used primarily as a test mould for modelling and testing assemblies of non-rigid pavements, including simulations of different humidity levels in subgrades occurring under pavements in reality. As part of the prepared project of the Czech Technology Agency – CESTI Competence Centre, the test stand will be used primarily to determine the deformation characteristics of:

- Recycled bitumen without and with binders, both hydraulic and asphalt binders, including combinations of both binders;
- Recycled materials from pavements;
- Recycled building materials;
- Other secondary raw materials such as foundry sands and waste materials from quarries, etc.;
- Waste rubber materials.

The aim is to use the results to create a real database of design characteristics of materials for road building to be used in the design method.

2 SEQUENCE OF PREVIOUS WORKS

The works were divided into several partial stages outlined below:

2.1 *Preparing the study with test stand calculations and sizing, including the design*

This first stage involved the search for a suitable shape and optimum dimensions of the test stand in collaboration with the Institute of Structural Mechanics of Brno University of Technology using the ANSYS computer program. Following entering input parameters such as estimated load parameters (max. traffic load, dynamic traffic load action, estimated number of passes etc.) or properties of building materials to be used for construction, the above-mentioned computer program designed a stand from steel elements forming a cube with an edge length of 1.5 m and a damping lining around the vertical walls 15 mm thick.

2.2 *Preparing the project documentation*

The project documentation was prepared in collaboration with the Institute of Metal and Timber Structures, and the documentation was also used to prepare quotations for the tender.

First thoughts assumed embedding the test equipment under the ground floor level, but this plan was abandoned due to the high density of utility lines. It was decided in following discussion that the ultimate full-scale test equipment prototype would consist of two independent, separate stands (with shape described above). At the first stage, the test stands were

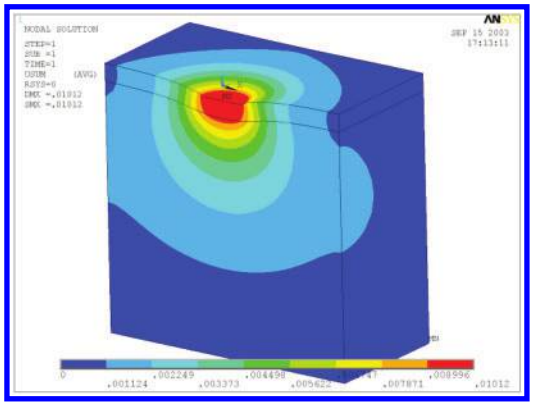


Figure 1. Computer simulation of the full-scale road model in the ANSYS environment.

supposed to be placed on the concrete floor 130 mm thick with aggregate bedding. Following computing the required loads with a maximum estimated load of up to 6000 kg, this method of foundation was abandoned, and a rigid steel damping grate was designed for the foundation of the dynamic full-scale test equipment. A stainless steel basin will always be located between the grate and the stand to simulate humidity modes in the model subgrade.

2.3 *Load unit acquisition*

In parallel with the manufacture of the test stand, a hydraulic dynamic load unit was purchased from the University Development Fund Project 2503/2008 in 2008. The load unit had the following configuration:

Linear drive AH 120-100
Control electronics EU 2000D-1
Hydraulic supply HU 40

2.4 *Manufacture of the stand*

Figure 2 below shows the 3D model of one assembled load stand (without lateral stepping grates) before surface treatment by hot-dip galvanizing.

2.5 *Transport and assembly*

A small 3-ton travelling crane and other handling equipment were used to handle the test samples and fixtures.

2.6 *Transport of soil for the subgrade*

Soil classified according to ČSN 73 6133 as clay with medium plasticity (F6 CI) was chosen for the subgrade of the pavement model being built. According to ČSN 73 6133, this soil is conditionally suitable for embankments and unsuitable for pavement subgrades. Large quantities of this soil can be taken from the Únanov u Znojma borrow pit. A total of 4 tons of soil were brought. The classification tests were performed in 2010. The test results are shown in Table 1.

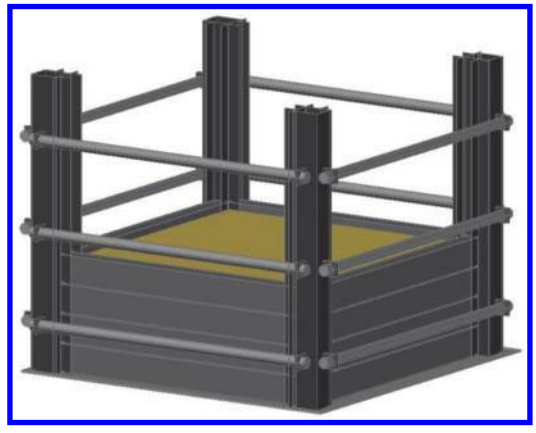


Figure 2. Computer 3D model of one load stand (without surface treatment).

Table 1. Classification tests of soil used for the subgrade under the test stand.

Grain size as per ČSN CEN ISO/TS 17892/4	
f (fine-grained particles)	82.4%
s (sand component)	17.2%
g (aggregate component)	0.4%

a) Plasticity as per ČSN CEN ISO/TS 17892/12: $w_L = 36\%$, $w_P = 20\%$, $I_P = 16$.
b) Compaction (standard Proctor test) as per ČSN EN 13286-2: $\rho_{d,max} = 1816\ kg/m^3$, $w_{opt} = 15\%$.
c) Immediate Bearing Index IBI as per ČSN EN 13286-47: 16%.
d) California Bearing Ratio CBR as per ČSN EN 13286-47: 10%.

Each compacted process layer of soil had 80 mm, and 2.0 kW, 60 kg Lumag vibrating plate was used for compaction. Compaction of the process layers compacted in the stand was tested by the direct method – by comparing the volume mass determined using cutting rings and a diaphragm stereometer and the maximum volume mass determined by the standard Proctor compaction test according to CSN EN 13286-2.

2.7 *Testing the performance and calibration of humidity sensors*

VIRRIB sensors are used to measure soil moisture by volume at any depth. The measuring sensor system is connected to the automatic measuring system capable of monitoring humidity with an accuracy of 0.1% at specific depth levels and specific intervals of time.

3 CONCLUSION

The pavement subgrade described in the paper is finished now, including the installation of measuring

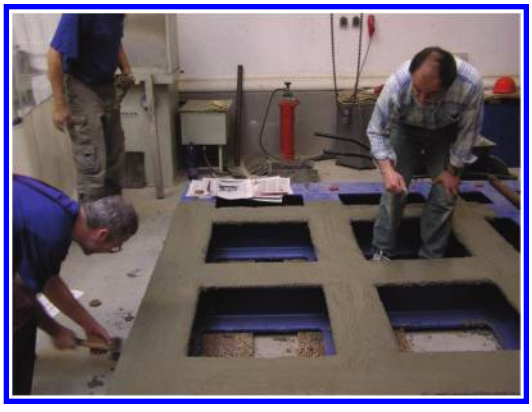


Figure 3. Preparatory work before placing the stainless steel basin on the grate.



Figure 4. Placing the stainless basin.



Figure 5. The layout after the first process layer compaction.



Figure 6. VIRRIB humidity sensors and their calibration.

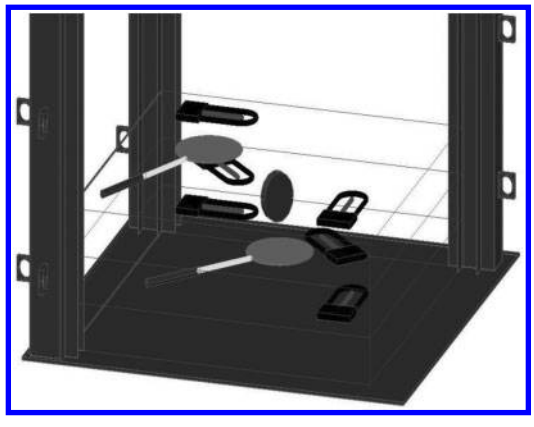


Figure 7. Model of arrangement of sensors in the soil.



Figure 8. Real location in the third process layer.

sensors. The building material for the pavement structure is being prepared. Also the design of layers for the test stand follows the system of pavement structures most frequently designed in the CR. Crushed-run rock ($ŠD_B$) of 0/31.5 fraction, 150 mm thick will be used

for the bottom base course. During measurements, this layer will be regularly replaced with unbound recycled concrete layer of the same thickness. The upper base course is designed to be from mechanically bound aggregate (MZK) 150 mm thick. The following materials were designed for the upper courses:

a) Asphalt concrete AC 16; and
b) Wearing course will probably contain SMA 11 with Crumb Rubber-modified Bitumen (CRmB).

The first real measurement on the finished full-scale model of the designed pavement is expected to take place in 2013. The series of verification measurements of the road structure will be followed by the design and assessment of pavements with bound and unbound recycled materials.

ACKNOWLEDGEMENTS

This paper has been prepared with the support of Research Projects MSM 0021630519 "Progressive reliable and durable load bearing structures", TA02030639 "Durable acoustic asphalt pavement courses with utilization of bituminous binders modified by rubber microfiller including innovative technology of rubber milling" and TA02030549 "The most effective utilization of reclaimed asphalt pavement layers for production of new asphalt mixes".

REFERENCE

ČSN 73 6133 Road earthwork – Design and execution, 2010

Research and Applications in Structural Engineering, Mechanics and Computation – Zingoni (Ed.)
© 2013 Taylor & Francis Group, London, ISBN 978-1-138-00061-2

Monitoring of experimental sections with recycled waste materials

D. Stehlik, M. Varaus & P. Hyzl
Brno University of Technology, Faculty of Civil Engineering, Institute of Roads Structures, Czech Republic

ABSTRACT: The full-scale test polygon is constructed as a classical road structure with the length of 225 m. There are seven test subsections with different road structures. The base courses are constructed from hydraulically bound recycled construction materials. The test polygon will be loaded by approximately 100–200 heavy lorries in 24 hours. The bearing capacity of the test sections is periodically controlled by the falling weight deflectometer. The values of the moduli of deformation are compared in one year period. This full-scale testing is the main part of the research project for intensive use of the recycled construction materials for road structures.

1 INTRODUCTION

Base courses are an important part of the road structure, and their design and construction should not be underestimated. Correct functioning of the bound layer depends primarily on the adequate design of type and quantity of hydraulic binder as well as compliance with the technological process during placing, compaction and treating these courses. In terms of placement technology, it is very important to perform a sort of fragmenting the bound layer using vibrating rollers in the transition period between setting and hardening of the compacted bound mixtures (1 to 3 days after placement) in order to eliminate contracting forces that occur during hydration. In terms of the mixture design, also materials that do not have standard grain size of normal unbound mixtures can be used in these mixture types for base courses. Such mixtures can be produced from materials, the non-processed form of which can be classified as soil with a significant content of aggregate or sand particles. These properties are typical of recycled waste prepared from demolition waste or old road material. The current trend of monitoring recycled construction material properties while reducing input investments in construction engineering shows that the use of recycled waste in bound mixtures for base courses is one option of application in semi-rigid and rigid pavement construction. Of course, properties of these bound mixtures with recycled waste have to be verified. A major part of preliminary tests of these mixtures were done in the first year of the Czech Technology Agency's research project titled TA 01020333 Recyklované stavební materiály v konstrukcích dopravních staveb (Recycled Waste Building Materials in Road Construction). An experimental section of road with different bound base course types is currently under real traffic load. This applied research included the design of 7 road structures for the test polygon constructed as an access road to the recycling line of DUFONEV, R.C., a.s.

2 DESIGNS OF MIXTURES BOUND WITH HYDRAULIC BINDER USING RECYCLED WASTE

The design of bound mixtures using recycled waste was based on the assumption that the most frequently used components will be used to make the use of satisfactory mixtures in practice as simple as possible. All of the 6 designed bound mixtures are based on 0/31.5 fraction. This maximum grain size was chosen as it is most frequently used for base courses. Recycled waste type is another input parameter. Following preliminary laboratory tests and based on foreign experience, recycled concrete was chosen for this mixture type. Some bound mixtures are an experiment, for which a mix of recycled waste from pavements and demolition waste is considered due to the local lack of recycled waste from bitumen pavements. In this research task, this is tested on one experimental subsection with bound mixture of recycled concrete and recycled bitumen in the ratio of 3:1.

The performance test of modulus of elasticity Er as described in ČSN EN 13286-7 was performed on each designed mixture in addition to regular preliminary grading test, compaction test, simple compressive strength test, splitting tensile strength test, freeze-thaw test and wet-dry test (see Table 1 and 2). This European standard is not intended for regular testing of bound mixtures. Among other things, this is due to the "bouncing" of the dynamically loaded thrust during deformation testing and measurement, in particular for bound mixtures with design strengths over 10 MPa, which results in about 15% bias of cyclic deformation readings. This fact forces to average the measured



Figure 1. Compressive strength test (R_c), test specimen sets in the moist chamber during curing; splitting tensile strength test (R_{it}).

Table 1. Preliminary and performance tests of designed bound mixtures with recycled waste – description.

No.	Description of mixture	Grading about ČSN EN 933-2	Proctor modified w_{opt}; $\rho_{d,max}$ ČSN EN 13286-2
1	SC 0/32 $C_{5/6}$		14.0%
	7% CEM II/R 32,5		1945 kg/m^3
2	SC 0/32 $C_{3/4}$		13.1%
	5% Doroport TB25	$G_A f = 16.7\%$	1926 kg/m^3
3	SC 0/32 $C_{3/4}$		12.5%
	5% CEM II/R 32,5		1955 kg/m^3
4	SC 0/32 $C_{1,5/2}$		11.4%
	3% CEM II/R 32,5		1959 kg/m^3
5	SC 0/32 $C_{1,5/2}$		12.5%
	5% CEM II/R 32,5		1955 kg/m^3
6	SC 0/32 $C_{1,5/2}$		11.5%
	4% CEM II/R 32,5		1957 kg/m^3

Note: SC …cement bound mixture; $C_{x/y}$ min. compressive strength, x – cylinder in ratio 1:2, y – cylinder in ratio 1:1 or cubic specimens; CEM II/R 32,5 is cement binder, class II, R …rapid-setting cement with compressive strength 32.5 MPa; f is content of fine parts.

Table 2. Preliminary and performance tests of designed bound mixtures with recycled waste – results.

No	IBI	R_c	R_{it}	R_{cf}	Er
1	min. 135%	6.7 MPa	1.3 MPa	6.0 MPa	1080 MPa
2		5.3 MPa	1.1 MPa	3.1 MPa	700 MPa
3		5.8 MPa	1.2 MPa	5.1 MPa	950 MPa
4		4.7 MPa	1.0 MPa	3.8 MPa	750 MPa
5		5.7 MPa	1.1 MPa	4.9 MPa	930 MPa
6		5.8 MPa	1.1 MPa	5.1 MPa	950 MPa

Note: IBI …immediately bearing index about CSN EN 13286-47; Rc …compressive strength about CSN EN 13286-41; Rit …indirect tensile strength about CSN EN 13286-42; Rcf …compressive strength after frost cycles (10 cycles with temperature −15°C about CSN EN 14227-1 NA (curing 28 days); Er …experimental moduli of elasticity about CSN EN 13286-7, average values by cell pressure 70 kPa.

moduli of elasticity of bound mixtures from measured intervals. The modulus of elasticity was subsequently compared with Er of natural aggregate-based mixtures to see which of the designed mixtures presents an optimum solution.

Table 3. Road structures designed for the test polygon

TS 1 0.000– 0.020 km	TS 2 0.020– 0.040 km	TS 3 0.040– 0.060 km	TS 4 0.110– 0.130 km
ACO 11 40 mm	ACO 11 40 mm	ACO 11 40 mm	ACO 11 40 mm
ACP 16 40 mm	ACP 16 40 mm	ACP 16 40 mm	ACP 16 40 mm
ŠD-R 0/32 150 mm	SC 0/32 $C_{5/6}$ 7% cem.; 150 mm	SC 0/32 $C_{3/4}$ 5% dor.; 150 mm*	Ra 0/16; 50 mm
			SC 0/32 $C_{3/4}$ 5% cem.; 150 mm
ŠD 0/32 150 mm (ROSA)	$ŠD_A$ Rc 0/32 150 mm	$ŠD_B$ Rc 0/32 150 mm	SC 0/32; $C_{1,5/2}$ 3% CEM; 150 mm

Table 4. Road structures designed for the test polygon-continuation.

TS 5 0.130–0.150 km	TS 6 0.150–0.170 km	TS 7 0.170–0.190 km
ACO 11 40 mm	ACO 11 40 mm	ACO 11 40 mm
ACP 16 40 mm	ACP 16 40 mm	ACP 16 40 mm
Ra 0/16 + Rc 0/32 (30:70); 150 mm	Ra 0/16; 150 mm	Ra 0/16 100 mm
SC 0/32 $C_{1,5/2}$ 5% cem.; 150 mm	SC 0/32 $C_{1,5/2}$ 4% cem.; 150 mm	ŠCM 32/63 200 mm

3 DESIGNS OF ROAD STRUCTURES USING RECYCLED WASTE

Seven road structures were designed for the test polygon based on preliminary tests of bound mixtures with recycled waste. These structures were designed using the LAYEPS computer design program. The main objective of the design involved specific applications of the designed and proven structures in practical use. That is why hydraulically bound structural base courses were designed for some subsections; one base course comprised grouted cement macadam and the other base courses were unbound. Table 3 shows an overview of road structures designed for the Cernovice test polygon. The same bituminous concrete pavement placed in two layers was used for the entire test polygon road section.

4 BUILDING THE TEST POLYGON

The old unpaved access road, the subgrade of which consists of different recycled waste types,

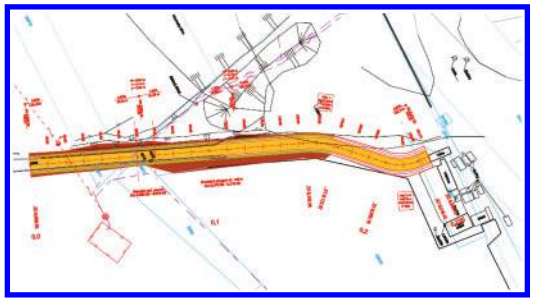


Figure 2. Layout of the test polygon with pavement using recycled waste for bound base courses.



Figure 3. Roadbed preparation before base course placement.



Figure 4. On-site preparation of bound mixtures with recycled material placement .

paradoxically had to be ripped due to its high bearing capacity, and mixed recycled material had to be added to reach a resulting compaction rate under $E_{def,2} = 100$ MPa as determined indirectly by static loading test.

5 MONITORING THE TEST POLYGON

Continuous monitoring of the bearing capacity is part of the test polygon construction where recycled waste is used for unbound base courses of the road. The monitoring benefits from the accurately known quantity



Figure 5. Compaction of bound mixtures with recycled material placement using vibratory rollers.



Figure 6. Subsequently two bituminous concrete layers were placed.

and structure of traffic load by heavy goods vehicles (HGVs) going on the test profile directly to the recycling line scales taking an accurate record of each vehicle's load and character. A daily average of 130 HGVs goes on the monitored road at present with up to 200 HGVs at peak hours and in high season. Bearing capacity will be measured continually by FWD impact test twice a year in the same climatic conditions. The first measurement was made in mid October 2012 and further measurements will be at six-month intervals.

5.1 *Road bearing capacity measurement*

Pavement load bearing capacity is the ability of a road's structure and subgrade to transfer traffic load. Each structural layer's bearing capacity can be measured using static or dynamic test equipment. Falling Weight Deflectometers (FWDs) are regularly used for load bearing capacity testing at present.

The principle of the non-destructive method consists in measuring and evaluating the response (deflection) of the pavement to the impact of a weight with a known mass on a round plate through a damping system from such height that the dynamic impact corresponds approximately to the effect of a crossing of a design HGV wheel axle. This dynamic impact is recorded by a force sensor and a set of deflection



Figure 7. The first load bearing capacity measurement on Brno-Cernovice experimental polygon sections.

sensors located at specific distances from the load centre on the pavement surface. The response of the pavement to the load is expressed by the measured deflection line determined as a pavement surface sag (deflection values) under the defined load depending on physical and mechanical properties of the environment, impulse magnitude and distance from the test point (load centre). The measurement is made using precision geophones (deflection acceleration sensors). Measurement evaluation is based on deflection line calculation along the laminated linear elastic half-space. The comparison of the computed and measured deflection line is used to determine the moduli of elasticity of each pavement layer by reverse calculation at each test point to compute bearing capacity, residual life and/or required pavement reinforcement. The impact load test using the FWD (Figure 7) was performed by PavEx Consulting, s. r. o. on the wearing course consisting of bituminous concrete (ACO 11).

The measurement was performed in the middle of each lane, in each of the seven sections in four measurements. Air temperature and pavement surface temperature were recorded during the research. The test was performed at a standard load of 50 kN and a load of 80 kN. The selected load was transmitted to the 300-mm diameter load plate through a damping system. Contact pressure was 0.707 MPa. Deflection sensors Y1 to Y9 were placed in recommended standard positions for non-rigid pavement testing as stated in Czech standard CSN 73 6192.

Distances of the sensors from the centre of the load plate were 0, 200, 300, 600, 900, 1200, 1500, 1800 to 2100 mm.

5.2 *Results of the first bearing capacity measurement using the FWD method*

Given the climatic conditions, the first measurement was made in autumn, when pavements and pavement subgrades in particular are subject to marked changes such as changes of bearing capacity. There is no risk of big changes to the pavement subgrade's water content and temperature in the test polygon. Therefore, the monitoring using the described FWD method focuses primarily on the test polygon pavement courses. The diagram in Figure 8 shows how the computed moduli of elasticity change depending on the spacing on each experimental subsection of the test polygon.

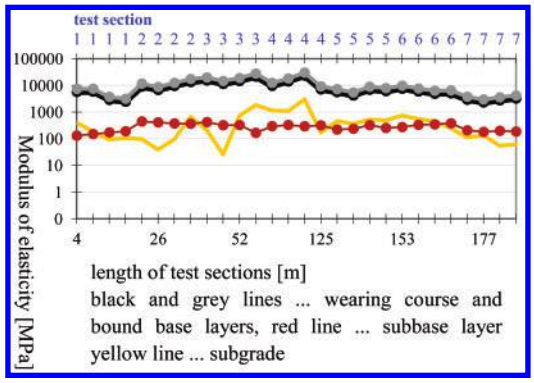


Figure 8. The result of the FWD dynamic impact test is the calculation of moduli of elasticity from measured deflection lines.

Following the evaluation of measured and computed deflections and moduli of elasticity determined by the FWD, the condition of each experimental subsection of the polygon pavement at the beginning of life was assessed (Table 4). There is a comparison of initial results of the non-destructive dynamic impact FWD test (Table 4) with design moduli of elasticity specified in technical conditions for the design of TP 170 road structures (Table 5).

Statistical evaluation of the monitored development of the modulus of elasticity of each structural course of the polygon is important to assess the designed road structures using recycled waste. As mentioned above, regular monitoring will be performed at six-month intervals, in spring and autumn.

Test cores will be made in 2013 to monitor additional properties of each compacted pavement course in the test subsections of the polygon. The time lag for the test cores was approved by all project investigators at one team meeting to discuss the project work progress in 2012.

Individual course segments will be separated from these cores. Properties characterizing materials used for the compacted bound mixtures will be consequently found by empirical and performance tests according to the plan for Project Stage 003 subgoal.

5.3 *Results of the first bearing capacity measurement using the FWD method*

Given the climatic conditions, the first measurement was made in autumn, when pavements and pavement subgrades in particular are subject to marked changes such as changes of bearing capacity. There is no risk of big changes to the pavement subgrade's water content and temperature in the test polygon. Therefore, the monitoring using the described FWD method focuses primarily on the test polygon pavement courses. The diagram in Figure 11 shows how the computed moduli of elasticity change depending on the spacing on each experimental subsection of the test polygon. Following the evaluation of measured and computed deflections and moduli of elasticity determined by the FWD, the

Table 5. Guidance values of moduli of elasticity [MPa] determined by the FWD impact test.

Test section No.	1.	2.	3.
Layers of pavement	ACO 11; 40 ACP 16; 40 SD-R; 150 SD-R; 150	ACO 11; 40 ACP 16; 40 SC $C_{5/6}$; 7%C SD-R; 150	ACO 11; 40 ACP 16; 40 SC $C_{3/4}$; 5%D SD-R; 150
ACO 11 ACP 16 base subbase subgrade	5700 5300 280 200 150	5500 4900 330 220 100	8400 12400 200 200
4.	5.	6.	7.
ACO 11; 40 ACP 16; 40 Ra 0/16; 50 SC $C_{3/4}$; 5%C SC $C_{1/2}$; 3%C	ACO 11; 40 ACP 16; 40 Ra:Rc ;30:70 SC $C_{1/2}$; 5%C	ACO 11; 40 ACP 16; 40 Ra 0/16; 150 SC $C_{1/2}$; 4%C	ACO 11; 40 ACP 16; 40 Ra 0/16; 100 SCM 32/63; 200 mm
13600 20000 900 300	5500 4900 330 220 100	8400 12400 200 200	7800 7450 500 300

Note:
ACO is asphalt concrete for surface, wearing course
ACP is asphalt concrete in base course
SD-R is crushed aggregate with recycled buidings material
SC is bound base layer with hydraulic binder (e.g. 5%C – cement or 5%D- Doroport TB25 by weigth)
$C_{3/4}$ is compressive strength with min. value 4 MPa for cubic or cylinder specimens (ratio between the diameter and height is 1:1) about EN 14227-1
Ra0/16 is recycled asphalt (max. grain size 16 mm)
Rc is recycled concrete material
Ra:Rc is ratio between recycled asphalt and concrete
SCM is crushed materiál 32/63 spilled cement mortar

condition of each experimental subsection of the polygon pavement at the beginning of life was assessed (Table 4).

There is a comparison of initial results of the non-destructive dynamic impact FWD test (Table 4) with design moduli of elasticity specified in technical conditions for the design of TP 170 road structures (Table 5). Statistical evaluation of the monitored development of the modulus of elasticity of each structural course of the polygon is important to assess the designed road structures using recycled waste. As mentioned above, regular monitoring will be performed at six-month intervals, in spring and autumn.

Table 6. Design moduli of elasticity of used pavement courses.

Type of layer	Min. value of design modulus of elasticity [MPa]	Standard	Notes
ACO, ACP	5500	TP 170[1)], CSN EN 12697-26	about CSN EN 12697-26. It's average value.
SC $C_{8/10}$	2500	TP 170	–
SC $C_{5/6}$	2000	TP 170	–
SC $C_{3/4}$	1200	TP 170	–
SC $C_{1,5/2}$	1000	TP 170	–
ŠCM	600	TP 170	–
ŠD	400	TP 170,	about CSN EN 13286-7. It's average value.

1) Technical condition no.170 is design of flexible pavement for Czech Republic
Note: Values shown in Table 5 apply to mixtures of natural aggregate and materials

Test cores will be made in 2013 to monitor additional properties of each compacted pavement course in the test subsections of the polygon. The time lag for the test cores was approved by all project investigators at one team meeting to discuss the project work progress in 2012.

Individual course segments will be separated from these cores. Properties characterizing materials used for the compacted bound mixtures will be consequently found by empirical and performance tests according to the plan for Project Stage 003 subgoal.

6 CONCLUSION

In the Czech Republic, a small country in the middle of Europe, regular and effective use of recycled waste for road pavement structures is very difficult to enforce. The quality of manufactured recycled materials has seen a marked improvement over the last 5 years, especially in established and known recycling lines. However, a more extensive use of recycled concrete in particular still faces legislative issues dictated by the state-owned investor of road construction. The aim of this paper was to present the potential of recycled waste used for bound course technologies, including the long awaited experimental section of pavement where these mixtures are used for base courses. The use of recycled waste in bound mixtures for base courses in the CR appears to be very advantageous in terms of required parameters of the final designed mixture of recycled material and binder. Properties of the final bound mixture are assessed according to EN standards applicable in the CR, which greatly facilitates the use of recycled materials, which have, in some cases, problems with grain size homogeneity and absorption capacity.

There is considerable potential for the use of recycled materials in the CR, particularly in the following areas:

- Homogeneous recycled aggregate production, primarily from recycled concrete;
- Use of bound mixture technology, primarily for road structures or other traffic areas with stationary traffic load or slow traffic;
- Use of dumps of old waste products for recycled material production;
- More specifically, setting realistic criteria of frost resistance for bound mixtures from recycled concrete.

ACKNOWLEDGEMENTS

This paper has been prepared with the help of results of the research project TA 01020333, Recyklované stavební materiály v konstrukcích dopravních staveb (Recycled Waste Building Materials in Road Construction).

REFERENCES

[1] Stehlík, D., Pecha, K., Pácha, P. Recycled Waste Building Materials to Bound Mixtures of the Pavements, Proceedings 2nd International Conference ISAP 2012, Fortalezza, Brazil

[2] Lažek, D., Recyklované stavební materiály konstrukcních dopravních staveb (Recycled Waste Building Materials in Road Construction), interim report on project TA01020333, Brno, 2011

[3] Pácha, P., Recyklované stavební materiály konstrukcních dopravních staveb (Recycled Waste Building Materials in Road Construction), No. TA01020333, level of documentation for building permit, Brno, 2012

Research and Applications in Structural Engineering, Mechanics and Computation – Zingoni (Ed.)
© 2013 Taylor & Francis Group, London, ISBN 978-1-138-00061-2

Experience with experimental designs and performance assessment of cold asphalt mixtures – New type of pavement structure in the Czech Republic

J. Suda, J. Valentin, J. Žák, J. Šedina & K. Miláčková
Czech Technical University in Prague, Faculty of Civil Engineering, Department of Road Structures

ABSTRACT: Presently there is a definite focus in road construction on technologies, which allow reducing energy demand during manufacturing and realization of pavement structures and equally minimizing cost severity of new structures within the development of road infrastructure. Stated presumptions try to make provision for techniques of cold asphalt mixtures based on bituminous emulsion applications. Generally cold asphalt mix is a composite material containing crushed natural aggregates and sand with corresponding grading and slow-setting cationic emulsion, which is produced and can be applied in normal atmospheric temperature. In comparison with traditional hot mix asphalts there is no requirement for heating some of the mix components. In the Czech Republic the technology of cold asphalt mixes laid by normal pavers is not presently used, therefore insufficient laboratory and practical experience and data are available. As a starting point experience and vast sets of data about cold recycling mixes can be used. Because of the absence of valid technical specifications and so far not approved preliminary specification prepared within the tasks of Ministry of Transportation French experience, valid standards and validated procedures have been used. Within the experimental activity done at the Czech Technical University selected physical and mechanical properties as well as performance-based characteristics (stiffness, resistance against permanent deformations or fatigue) are presented. At the same time the most suitable compaction method for test specimen preparation was assessed as well. So far gained results and experience are presented in this paper. The objective is to extend and specify more precisely technical parameters and their requirements in the national technical specifications.

1 INTRODUCTION

There is currently no "generally accepted" design method for cold asphalt mixes. Findings of the American approach formulated in the so-called Cold Mix Design Manual or national technical regulations used in France can be used. Besides, with respect to the lack of unified laboratory methods and assessment thereof, particularly in the early curing stage, it is difficult to find reliable correlations between the results of experiments described in the sources by various specialists and expert teams. This paper focuses on defining the composition of a cold asphalt mix produced under laboratory conditions and on the relationships between physical and mechanical properties, workability and functional characteristics of experimental design mixes and test specimens prepared in the laboratory.

2 MATERIALS USED

The preparation of CMAC 11 (Cold Mix Asphalt Concrete) used aggregate from the Libodrice quarry. This is a basic rock (amphibolite) which was formed by metamorphosis of igneous rocks, primarily basalt and andesite. The main elements are amphiboles and plagioclase. The most appropriate use is primarily in road construction; the site is a traditional quarry producing good-quality crushed aggregate with the characteristics as indicated below (Table 1). Cationactive, medium-setting bituminous emulsion, Katebit C60B6, which is used in cold recycling mixes as a standard, was used as the bituminous binder. The reason behind the choice of this emulsion was the fact that in CR, it is currently impossible to prepare a suitable bituminous emulsion adjusted to this type of mixes flexibly for laboratory purposes. The same type of bituminous emulsion prepared in France using a suitable emulsifier (0.7% wt. Indulin GE7) and bituminous binder AZALT 70/100 were used. Hydraulic binder used in cold asphalt mixes is Portland slag cement CEM II/B – S 32.5R and an active micro-filler know as Dastit®. Dastit is a mechanically activated fluid ash characterized by pozzolan properties which is modified by high-speed grinding in a disintegrator; the grinding increases the specific surface and significantly increases reactiveness of the material (Valentin 2012).

Table 1. Characteristics of the Amfibolit aggregate- 0/11.

Quarry/grading	[%]	Density [g/cm^3]	Absorptivity [%]	Shape index [−]	Voids content cast/shaked [%]
Libodřice 0/4	45	3.034	0.86	–	58.3/38.4
Libodřice 4/8	24	3.036	0.47	14.1	51.2/41.1
Libodřice 8/11	26	3.051	0.32	11.5	50.0/40.7
Filler Brant	5	2.43	–	–	–/–

3 COLD ASPHALT MIX – LAB DESIGN

In connection to the current non-existence of technical specifications for the design, implementation and control of cold asphalt mixes the mix design per se was carried out based on the French experience and methods with a modification of applying the existing national technical regulations for hot asphalt mixes as much as possible. At the same time, repetitive consultations with the MeadWestVaco European research centre took place.

The design of a suitable aggregate skeleton was made according to the methodology for asphalt concrete (ČSN EN 13108-1) which corresponds with the French methodology indicated in the technical national standard (NF P98-139). Using another grading curve does not achieve optimum results; the mixes primarily demonstrate higher void contents. The density of the aggregate and absorbing capacity for individual fractions are given in Table 1. However, it must be pointed out that not every aggregate is suitable for cold mixes; primarily the shape index and grading of the finer fractions must be watched since in this type of mixes, these are rather critical parameters. The proposed mix grading curve is given below (Figure 1). The aforementioned grain sizes are intentionally more stringent, the grading curve may vary from the aforementioned grading limits.

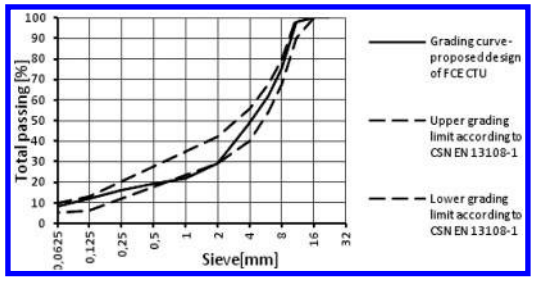


Figure 1. Grading curve of the proposed aggregate.

Table 2. Developed cold asphalt mix design.

Mix	Saturation coefficient K [−]	Emulsion content [%]	Residual bitumen content [kg/100 kg]	Cement [%]	Dastit [%]
1. E_{CZ} a/b	3.4	8.51	5.08	–	–
2. E_{CZ}	3.67	9.46	5.47	–	–
3. E_{Fr}	3.67	9.46	5.47	–	–
4. E_{CZ} DAS	3.67	9.46	5.47	–	5.0
5. E_{CZ} CEM	3.67	9.46	5.47	2.0	–

The theoretical optimal quantity of bituminous emulsion was determined using the calculation methodology according to the saturation coefficient which is applied in the French regulations, too (NF P 98-139). Hot asphalt mixes for wearing courses apply the saturation coefficient of 3.4 while other layers use the coefficient of 3.1. In the case of cold mixes, the calculation of the theoretical quantity of bituminous emulsion increases to a value exceeding 3.6 (for all layers). The saturation coefficient corresponds with the results according to (Suda 2012); however, contradictory trends affecting the optimum quantity of residual bitumen in the mix must be mentioned, particularly from the point of view of permanent deformation and thermal susceptibility against strength and deformation parameters along with the water susceptibility of cold asphalt mixes; the parameters must be in balance.

The ability of the emulsion to coat aggregate usually depends on the moisture of the aggregate during coating. Inappropriate (low) moisture causes the bitumen emulsion and fine aggregate particles to start forming clumps and the aggregate fraction is not coated sufficiently. In general, the minimum coating of the aggregate surface by the binder is stated at 50%. However, the value should be raised to 90% surface coating, particularly due to the susceptibility of the mix to water (Suda 2012). From the point of view of suitable moisture of a cold asphalt mix, two methods can be applied: determination of optimum moisture by the modified Proctor standard test according to (ČSN EN 13286-2). This method should be chosen if the emulsion and aggregate are not significantly affected by changes in the moisture. If the aggregate coating by bituminous emulsion is affected by moisture, the method of determining binder adhesion to the aggregate, the so-called "coating test" will be used. Within the framework of verifying the properties of cold asphalt mixes, five cold asphalt mixes have been designed with the compositions as indicated below (Table 2).

The individual experimentally designed mixes differ by the quantity and origins of the bituminous emulsion used. The effect of cement and mechanically

Table 3. Volumetric properties of cold asphalt mixes.

	Required void content	1a. E_{CZ}	2. E_{CZ}	3. E_{Fr}	4. E_{CZ}DAS	5. E_{CZ} CEM
Revolutions/600 kPa	[%]					
60	5–12	9.8	8.9	9.1	12.3	8.5
10	≥12	15.3	13.6	14.2	–	–
200	–	7.6	5.7	5.6	–	–
Bulk density [g/cm^3] after 60 revolutions		2.44	2.49	2.48	2.406	2.508
Moisture content [%]		5.56	5.89	5.97	6.19	5.39

activated fluid ash, considering the full or partial filler substitution, on the cold asphalt mix properties constitute another option of extending the use of cold mixes in road construction practice.

4 EXPERIMENTAL VERIFICATION OF COLD ASPHALT MIXES

Different compaction method can be used. Some reports mention use of impact compactor (Thanaya 2009) or a hydraulic press. However, according to (Suda 2012) these methods cannot meet the requirements for cold mix void content as listed below. With respect to the lacking uniformity of the design and test methods the compaction was performed by a gyrator (SUPERPAVE Gyratory Compactor Troxler 4140), which, according to the French methods, better simulates the compaction achieved during paving. The method is preferred despite the fact that there is only one such apparatus available in CR at present. From the methods used in France, the void content reached during paving corresponds with the compaction reached by the gyrator under 60 revolutions and 600 kPa pressure. The French methodology also prescribes the number of revolutions of the gyrator depending on layer thickness and mix type regardless of the traffic load. The 60 revolutions applied on the gyrator correspond with the layer thickness of 5–10 cm (Burán 2007). Within the framework of laboratory design of cold asphalt mixes, void content under 60 revolutions on the gyrator must range within 5–12 %-vol. and, at the same time, under 10 revolutions the void content must be >12% in accordance with the requirements of the French standard (XP P98-121); the value represents the qualitative parameter of compactability during paving. Compacting by gyrator using 200 revolutions and axial pressure of 600 kPa corresponds with the value of maximum compaction of a cold asphalt mix for layers under traffic operation. It is generally assumed that a cold mix reaches full consolidation in 2–24 months from paving (Thanaya 2009). The void contents of individual mixes are indicated below in Table 3.

The determination of the basic strength parameters of a mix involves the indirect tensile strength test (ITS test) depending on different conditions (air-water) and curing time, 7, 14, 28 days (Table 4). The curing itself could range from 2 to 24 months depending on the weather conditions (Thanaya 2007). The specimens examined cured under 18°C and under 30°C in the laboratory conditions. This paper examines cold asphalt mixes primarily at the early stages of curing.

Table 4. Determination of the ITS and water susceptibility.

	Indirect tensile strength @ 15°C – curing under 18°C/30°C					
	7 air	14 air	7 air + 7w.	28 air	ITSR	Decrease of ITS
Mix	[MPa]				[–]	[–]
1. a/b E_{CZ}	0.61	1.00	0.52	1.18 / 2.34	51.5	85.2
2. E_{CZ}	0.72	1.09	0.67	1.43	61.5	93.1
3. E_{Fr}	0.75	1.07	0.62	1.23	57.9	82.7
4. E_{CZ} DAS	0.92	1.11	0.78	1.32	70.3	84.8
5. E_{CZ} CEM	0.87	0.96	0.54	1.04	56.3	62.1

Table 5. Basic deformation parameters of the mix.

	Stiffness modulus @ 15°C (MPa) – curing under 18°C/30°C					
Mix	7 air [MPa]	14 air [MPa]	7 air + 7 water [MPa]	28 air [MPa]	Decrease of stiffness (ITMR) [–]	Thermal susceptibility [–]
1a/b. E_{CZ}	2100/ 3800	3200/ 5700	1400	3100/ 7800	44.3	13.1/8.3
2. E_{CZ}	1900	3200	2500	4300	78.1	7.5
3. E_{Fr}	2000	3200	2700	4100	84.3	8.1
4. E_{CZ} DAS	5500	7100	6700	8700	94.4	2.6
5. E_{CZ} CEM	4100	4400	3400	4200	77.4	5.1

The basic deformation parameters (Table 5) are characterized by the stiffness modulus which was defined depending on the different conditions and curing times. Also the indicators of modulus decrease after immersion in water and thermal susceptibility were determined. The stiffness moduli were determined for cylindrical specimens by cyclic tensile stress (IT-CY) according to (EN 12697-26) applying the method of controlled deformation of 3 μm and load impact of 125 ms under 5, 15, 27°C.

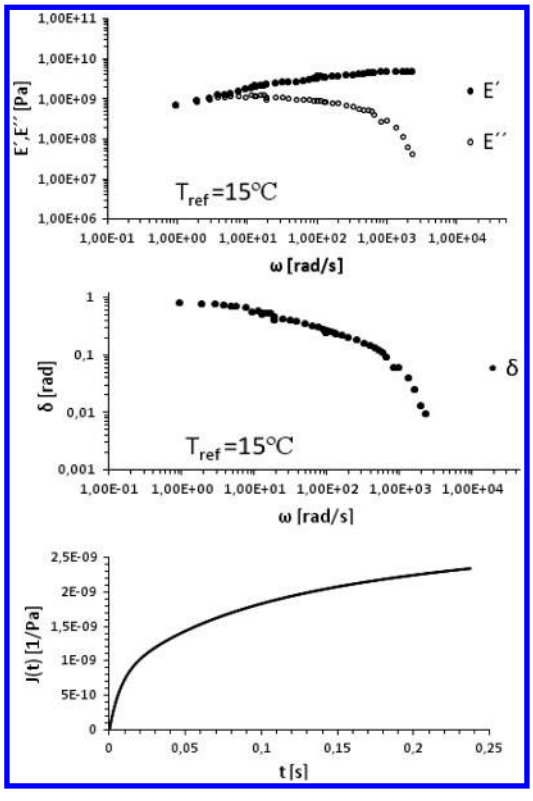


Figure 2. Linear viscoelastic parameters of the cold asphalt mix 2.ECZ examined.

As can be concluded from the results above, the difference between mixes with different bituminous emulsions is not too obvious. A higher quantity of residual bitumen in the mix improves the strength and deformation parameters of the mixes researched. Also from the point of view of using loose binders in cold mixes, the strength and deformation parameters improved in all regards, particularly in the case of Dastit. Another important property with respect to the viability of cold mixes in the wearing course of a pavement is water resistance which is determined by three methods, or ITS ratio under (TP 208), modified method under (ČSN EN 12697-12) and the stiffness modulus decrease coefficient respectively. In cold asphalt mixes, the thermal sensitivity is a rather essential quality parameter which is affected by the type of emulsion and bitumen used.

Cold asphalt mixes are a multi-stage system with many components some of which have a complicated inner structure with a high thermal sensitivity. They are basically components of irregular aggregate grains with a slightly higher binder content and small proportion of volume taken by air voids. Despite the complex structure, the material behaviour can be described by applying the viscoelasticity theory (Collop 1995; Ferry 1980; Tschoegl 1989; Underwood 2011; Zou 2010). One of the linear viscoelastic parameters is the complex modulus. Dynamic complex moduli were

Table 6. Permanent deformation parameters.

Mix	1a. E_{CZ}	2. E_{CZ}	3. E_{Fr}
WTS $_{AIR}$ [mm]	0.53	Ndef	Ndef
PRD $_{AIR}$ [%]	21.2	Ndef	Ndef

measured by the 4PB-PR method according to (ČSN EN 12697-26) within the temperature range of −20 to +27°C and frequency of 0.1 to 40 Hz. Master curves were generated by means of the time and temperature superposition method by a shift in both the horizontal and vertical plane to obtain the thermal dependencies of rheological behaviour of the material and extend the time frequency scope under the relevant temperature. The Wiliams-Landel-Ferry equation with parameters $C_1 = 100.00$, $C_2 = 2156.44$ K was used to describe the shift in the horizontal plane; a polynomial with parameters $a_0 = 1.524$, $a_1 = 1.302$E-01, $a_2 = 2.928$E-03 was used to describe the shift in the vertical plane (Ferry 1980; Dealy and Wissbrun 1999).

If we look at the master curves from right to left it is obvious that under the lowest temperatures and highest frequencies tested, the material tends to behave as almost elastic. The conversion from viscoelastic to elastic behaviour is visible in the last six values measured on the decreasing imaginary part of the master curve. With the increasing frequency the real part of the master curve grows gradually; its derivation gradually falls and the last values almost reach 0. The phenomenon correlates with the conversion of the material properties to the elastic part and with reaching the module equilibrium. (Ferry 1980; Kim 2008). The phase angle increases very fast and reaches temperatures from 0.5°C to 45°C within three values measured. Therefore, the phase angle change shows that cold asphalt mixes are highly thermally and mechanically sensitive materials (Tschoegl 1989) in comparison to hot asphalt mixes. The malleability function shown (Figure 2) is calculated by non-linear regression of the master curves with a Maxwell model of four elements (Žák 2012; Baumgaertel 1989). With respect to the reference temperature of 15°C and the narrow range of temperatures measured, it is only represented up to 0.25 s.

From the point of view of permanent deformations, the test of wheel tracking on a small test device at 50°C in air bath under (ČSN EN 2697-22 + A1) was taken. The test specimen was loaded by 10,000 wheel cycles with the frequency of 0.44 Hz. Test boards using different quantities and types of bituminous emulsion were used. The results achieved are not too reproducible (Table 6), because there were significant deformations and damage to the test specimens. The next stage should be a discussion on whether the test conditions reflect the actual conditions of use within the life of the pavement construction if cold asphalt mixes are applied, or whether there is any other factor at play. This fact is not restrict the use of such mixes in road

construction as, according to the findings from France where e.g. testing for mix resistance to permanent deformation which usually yielded poor laboratory results never corresponded with the reality in the road. Cold mixes have always behaved better in-situ during the entire life.

5 CONCLUSION

This paper deals with experimental design and examination of selected parameters of cold asphalt mixes. Cold asphalt mixes (coated under the temperature of the ambient environment, at least 10°C though) are mixes of wet fractions of aggregate and bituminous emulsion which demonstrate changes in their properties during bituminous emulsion breakdown (Choudhary 2011). Based on the results achieved, we can conclude that under the assumption of correct mix design and subsequent processing, albeit with respect to their negative properties, cold asphalt mixes are appropriate primarily for roads with lower level of traffic or pedestrian/cyclist tracks. Negative properties are understood as considerable thermal susceptibility which might result in higher risk of defects in the pavement; however, it must be mentioned that the monitoring of defects in roads in France verify the sufficient performance quality and low rate of defects in the roads monitored after the application of the technology. In the mix design stage, attention should be paid to the choice of materials. The aggregate must meet the requirements of grading and durability. The right choice of bituminous emulsion type is determining for the life of the entire layer. Another important factor in processing is the moisture of the aggregate which allows good-quality coating of the individual grains by bituminous binder and the necessary compaction. The properties of cold asphalt mixes can be further adjusted by adding appropriate additives like cement or mechanically activated fluid ash.

ACKNOWLEDGEMENT

This paper was compiled within the framework of project SGS12/039/OHK1/1T/11.

REFERENCES

Baumgaertel M., H. H. Winter. 1989. “Determination of Discrete Relaxation and Retardation Time Spectra from Dynamic Mechanical Data.” Rheologica Acta 28 (6): 511–519. doi:10.1007/BF01332922.

Burán F. 2007 In: Diplomová práce – Využití gyrátoru pri návrhu smesí recyklace za studena, Ceské Vysoké Ucení Technické v Praze,

Choudhary R.: Use of Cold Mixes for Rural Road Construction, In: International Conference on Emerging Frontiers in Technology for Rural Are, 2012, s. 20–24.

Collop, A. C., D. Cebon, and M. S. A. Hardy. 1995. “Viscoelastic Approach to Rutting in Flexible Pavements.” Journal of Transportation Engineering 121 (1) (January): 82–93. doi:10.1061/(ASCE)0733-947X(1995)121:1(82).

ČSN EN 12697-22 + A1, Asfaltové směsi – Zkušební metody pro asfaltové směsi za horka – Část 22: Zkouška pojíždění kolem, 2005

ČSN EN 13108-1, Asfaltové smesi – Specifikace pro materiály – Část 1: Asfaltový beton, 2008

ČSN EN 12697-12, Asfaltové smesi – Zkušební metody pro asfaltové smesi za horka – Část 12: Stanovení odolnosti zkušebního telesa vuci vode, 2009

ČSN EN 13286-2, Nestmelené smesi a smesi stmelené hydraulickými pojivy – Část 2: Zkušební metody pro stanovení laboratorní srovnávací objemové hmotnosti a vlhkosti – Proctorova zkouška, 2011

ČSN EN 12697-26, “Bituminous Mixtures – Test Methods for Hot Mix Asphalt – Part 26: Stiffness”. Czech Office for Standards, Metrology and Testing, 2012

Dealy, J. M., and K. F. Wissbrun. 1999. Melt Rheology and Its Role in Plastics Processing: Theory and Applications. Springer.

Ferry, John D. 1980. Viscoelastic Properties of Polymers. 3rd ed. Wiley.

Gaudefroy V., Wendling L., Odie L., Fabre J. C.2008. In: Laboratory characterization of cold mix treated with bitumen emulsion, In: Proceedings of the 4th Eurasphalt and Eurobitume congress, s. 1–11.

Kim, Y. 2008. MODELING OF ASPHALT CONCRETE. 1st ed. McGraw Hill Professional.

NF P 98-139, Enrobés hydrocarbonés, Couches de roulement: bétons bitumineux á froid, ISSN 0335-3931, 1994

Suda J., Valentin J., ,Šedina J., Milácková K. 2012. In: Poznatky s experimentálními návrhy a testováním studených asfaltových smesí, In: XVII. seminár Ivana Poliacka, Bratislava

Thanaya N. A. 2007, In: Rewiew and Recommendation of Cold Asphalt Emulsion Mixtures Design, In: Civil Engineering Dimension, s. 49–56.

Thanaya I. N. A., Zoorob S. E. 2009, In: A Laboratory Study on Cold-Mix, Cold-lay Emulsion Mixtures, In: Proceedings of the Institution of Civil Engineers, s. 47–55.

TP 208: Recyklace konstrukcních vrstev netuhých vozovek za studena, MD – OSI, 2009

Tschoegl, Nicholas W. 1989. The Phenomenological Theory of Linear Viscoelastic Behavior: An Introduction. Springer-Verlag.

Underwood, B. Shane, Taeyoung Yun, and Y. Richard Kim. 2011. “Experimental Investigations of the Viscoelastic and Damage Behaviors of Hot-Mix Asphalt in Compression.” Journal of Materials in Civil Engineering 23 (4) (April): 459–466. doi:10.1061/(ASCE)MT.1943-5533.0000197.

Valentin J., Suda J., Faltus M.2012, In: Use of alternative binders induced from the treatment of fluidized fly-ashes in cold-recycled pavement mixtures, In: Waste Forum

XP P98-121, Assises de chaussées, Graves.émuIsion, ISSN 0335-39312005, 2005

Žák, Josef. 2012. “IRIS Rheo-Hub, program description”. CVUT, FSv, Department of Road Structures.

Zou, G., X. Zhang, J. Xu, and F. Chi. 2010. “Morphology of Asphalt Mixture Rheological Master Curves.” Journal of Materials in Civil Engineering 22 (8): 806–810. doi:10.1061/(ASCE)MT.1943-5533.0000024.

Research and Applications in Structural Engineering, Mechanics and Computation – Zingoni (Ed.)
© 2013 Taylor & Francis Group, London, ISBN 978-1-138-00061-2

Knowledge sharing and constructability in structural design

V. Kuo & J. Wium
Stellenbosch University, Stellenbosch, South Africa

ABSTRACT: It is well known that close collaboration between structural designers and contractors may lead to more effective construction processes, economic structural solutions and improved safety. However, traditional procurement standards, do not allow sufficient collaboration between these parties at early stages of design. For these reasons it is imperative that the structural designer has sufficient experience and knowledge of construction processes to produce suitably constructible designs. This paper aims to address the topic of constructability in structural design and demonstrates how structural knowledge sharing between contractors and designers is a pertinent approach to reducing constructability problems. The principle conclusions are that designers do not always understand what constitutes a constructible design. Furthermore, although there is a vast field of knowledge required, some guiding principles can be formulated. In addition, considering the unique characteristics of each project, these guiding principles should be supported by initiatives to facilitate structured forums of knowledge sharing between different parties to develop and transfer constructability knowledge that would also assist to accelerate the process towards becoming an accomplished designer.

1 INTRODUCTION

In the 1980s, the term "constructability" evolved in the USA. The proponents of this concept believe that constructability, which embraces both design and management functions, is comprehensive in facilitating construction operations and solving problems on site. In particular, the Construction Industry Institute (CII) was instrumental in providing guidelines for implementing constructability at various project stages (CII, 1986; 1987a, b; 1993). Constructability can be defined by "the optimum use of construction knowledge and experience in planning, design, procurement, and field operations to achieve overall project objectives" (CII, 1986), or simply "the extent to which the design of a building facilitates ease of construction", as is intuitively interpreted.

Constructability problems cause dire repercussions in the construction industry, and mainly arise due to poor embodiment of construction know-how in the design of the project. Gambatese et al. (2007) described the barriers to addressing constructability as the lack of construction experience in the design team and the absence of tools to assist designers in addressing constructability. The prevalent procurement methods of building construction projects, such as design-bid-build, hinder the application of constructability concepts in design. This is problematic mainly during early project phases, in which constructability application is particularly desirable (Pocock et al., 2006; Song et al., 2009).

The scope of this research is within the South African building industry, as most civil engineering organizations would have had substantial experience in building projects, where constructability issues are prevalent. Needless to say, constructability expertise and knowledge is primarily retained by contractors with substantial experience in the project execution phase. However, this know-how remains in a tacit, non-codified form within the minds of the professionals. The extraction of constructability expertise and related problems from the minds of the industry thus forms the basis of this study. The primary methodology employed is a combination of questionnaire surveys and personal correspondences.

To address the constructability issues, while accepting the conventional procurement standards, this paper investigates the nature of constructability knowledge (in both tacit and explicit forms) and how it can be captured and shared, especially between design and construction disciplines. The way knowledge is shared in the industry forms the basis by which constructability expertise can be disseminated, which is investigated in detail in this study. Furthermore, examples of real constructability problems in the industry are obtained and analyzed to reach accurate and realistic principal deductions.

2 BACKGROUND

2.1 *Constructability knowledge*

Despite various definitions and classifications of knowledge, work by Polanyi (1958), Nonaka and Takeuchi (1995) divided knowledge into tacit and explicit. Tacit knowledge represents knowledge based on the experience of individuals, expressed in human actions in the form of evaluation, attitudes, points of

view, commitments and motivation (Nonaka et al., 2000). Explicit knowledge, in contrast, is codified knowledge inherent in non-human storehouses including organizational manuals, documents and databases.

Naturally, the greater part of constructability knowledge exists in a non-codified, tacit form, as opposed to deterministic design knowledge, which is arguably much easier to articulate and document, hence enabling the compilation of numerous design codes and guidelines. Yet, there is no comprehensive code, as design aid for consultants, to ensure good constructability.

Explicit constructability knowledge may exist in project archives, where constructability related problems would have been extracted during and after the project. Project archiving is a common method to capture project lessons learnt and thus pertinent for the capturing of constructability knowledge. Whether or not project archives offer serviceable constructability knowledge is investigated in detail in this study. This would indicate if enough usable knowledge from existing project archives can be used to derive constructability guidelines.

2.2 *Knowledge sharing*

Foy (1999) defines the concept as "facilitating learning, through sharing, into usable ideas, products and processes." This definition implies that there is a specific purpose behind knowledge sharing, and "learning" is an artifact from the knowledge sharing process. According to Hickins (2000) knowledge sharing is about capturing the tacit knowledge locked in people's heads.

McDermott and O'Dell (2001) find that organizational culture is more important to knowledge sharing than the approach or commitment to knowledge management. They highlight the importance of using tools and structures for knowledge sharing that are consistent with the overall style of the organization, and building reward and recognition systems that support knowledge sharing.

Irrespective of whether or not constructability knowledge can be codified, sharing of the knowledge still remains a great challenge not only due to the technical, but also the social aspects of organizational culture. Constructability knowledge, be it in tacit or explicit form, needs to be shared to yield some perceivable positive effect.

To find a knowledge sharing approach fit for improving constructability, it is important to understand the extent and modes of knowledge sharing in consulting and contracting companies. The sharing of not only explicit knowledge, but also the sharing of tacit knowledge is investigated in this paper.

3 METHODOLOGY

3.1 *Questionnaire surveys and investigations*

For this research, the questionnaire survey was primarily used to extract tacit knowledge on constructability from experienced South African industry practitioners. The investigations were done in three parts, which are discussed in detail in the following sections: 1) Explicit constructability knowledge; 2) Knowledge sharing; and 3) Tacit constructability issues in practice. The rationale, results and analyses for each part is presented accordingly.

It is worthy to note that the interpretation of all the results, arising from qualitative and quantitative analyses in the investigations, was done with reasonable degree of tolerance. It is appreciated that the groups of respondents involved in the study may or may not be representative of the industry at large. The research takes care to consider all the limitations implicit in the research principles and questionnaire processes. Furthermore, it has not been the intention to focus particularly on a large scale statistical or quantitative analysis of survey results. Rather, it was of greater significance to reach insightful practitioners to provide relevant and meaningful responses; hence the seemingly small number of respondents that participated. However, the opinions of the practitioners offer valuable experience, the credibility of which should not be ignored.

4 PART I SURVEY: EXPLICIT CONSTRUCTABILITY KNOWLEDGE

This *preliminary investigation* was done to establish the extent that documentable, explicit information in typical project archives can be used to derive constructability guidelines. Survey respondents of this investigation consist of 11 South African industry professionals with an average of 15 years of experience. They hold positions as: project manager, engineer, site agent and director; in the buildings, bridges, roads and civil disciplines. The investigation on project archives is generic and is not limited to a specific discipline. Thus, respondents from a few disciplines are involved here, not exclusive to Buildings. The main questions posed in the Part I Survey are:

- What are the typical contents/documentations of a project archive?
- Are project archive contents seen to be insufficient or lacking in some way?
- If so, what are current project archives lacking?

4.1 *Contents of project archives*

The respondents were first asked to provide a list of currently available items in their project archives at his/her organization. All the responses were combined and rudimentarily categorized, to compile a list of typical items of project archives as shown in Table 1. The items shown are not analyzed in terms of frequency of occurrence between all the respondents, as it would not be sensible to make such deductions from the small group of respondents. However, a good idea of the constituents of a project archive – or what information

Table 1. Categories and items of project archives.

Categories	Items in project archives
Project Information	Construction start date, end date Extensions of time Contractor and consultant details Project Programs Project close out reports Lessons learnt reports
Technical Details	Design drawings and specifications As-built drawings and specifications Construction specifications Material test results Design reports Quality control reports Current condition of infrastructure
Contractual Details	Contract documentation Tender documentation Completion certificates
Financial and Procurement	Budgets and cash flow Procurement documentation for contractors and consultants Payment files Purchase orders Costs and payment certificates for all vendors Retentions and amounts outstanding Subcontractor final payments
Site Records	Site instructions Health and safety records Accident records Training records
Correspondences	Contractual information flow Letters and emails Minutes of meetings Variation orders All project related correspondences between key project participants

a good project archive should include – is generated here.

4.2 *Need for additional items to be captured*

The respondents were then asked whether the capturing of more items, additional to what is currently available, is desirable and why. Out of 11 respondents, 9 desired additional items to be captured. Due to the small number of respondents, this number is not of particular importance; rather, the reasons/motivations provided are worthy of note.

Some conclusions can be made from the motivations given. There is an evident need for the capture of items in addition to what is currently available in the archives. The responses show a problem with the knowledge capturing itself. Moreover, the incentive for personnel to access the knowledge also poses a challenge. Lack of motivation by user to extract knowledge is attributed to the fact that the documented material is not properly organized into sensible packages to be stored. This results in excessive effort and time required by the user, to obtain the relevant applicable knowledge. Information available is regarded more as raw "historical data" rather than synthesized knowledge or lessons. Furthermore, lots of information gets lost before it gets captured. This indicates that information waste is still common and that there is no adequate system to record usable, accessible project lessons or knowledge efficiently.

4.3 *Additional items to capture*

Respondents who wanted additional items to be captured were asked to list these items and explain what benefits they can pose to the organization or future projects. All the responses were combined and briefly categorized to compile a list of additional items to capture. Due to the excessive number of items obtained, the list will not be presented here. Only the broader categories are shown, which gives an idea of the type of desirable items that are currently lacking in project archives.

- Risk related information and reports
- Planned vs. actual information
- Change related information and reports
- Lessons learnt information

The additional items listed are not mere data, but are rather meaningful project lessons, which require some synthesis to obtain. Processes must thus be introduced to promote the capturing and synthesis of such knowledge/lessons, which can be structurally stored and thus accessed/shared efficiently in future.

5 PART II SURVEY: KNOWLEDGE SHARING

The respondents for the *Part II Survey* consist of 11 consultants and 17 contractors, with an average of 22 years of experience and expertise in: civil structures, project management, buildings, precast structures, earthworks, mining, and roads. Respondents hold senior positions in technical and/or managerial functions, as directors, engineers and managers in South Africa.

For the survey, a list of knowledge sharing modes was identified and respondents were asked to qualify each of them in terms of "popularity of use", to share knowledge within their organizations. Popularity is rated on the following scale: 0.00 – never used; 1.00 – unpopular; 2.00 – neutral; 3.00 – popular; and 4.00 – very popular. The results can be roughly divided into three groups and listed in increasing popularity as shown in Table 2. These results offer strategic direction regarding how constructability knowledge may best be disseminated.

Results show the prevalence of human interaction and tacit knowledge sharing for both consultants and contractors. Knowledge sharing modes employed are mostly people-orientated methods requiring socialization, such as informal chatting and storytelling,

Table 2. Popularity of Knowledge Sharing Modes.

	Knowledge sharing modes and their respective popularity ratings* in brackets	
	Consultant	Contractors
Unpopular	(0.82) Knowledge sharing boards (1.18) Internal newsletters and circulars (1.18) Newsgroup and web-based discussions (1.6) Memoranda and letters	(1.06) Newsgroup and web based discussions
Neutral	(1.64) Phone calls (2.27) Internal databases (2.27) Emails	(1.65) Knowledge sharing boards (1.94) Internal databases (2.06) Memoranda and letters (2.12) Talks and seminars (2.18) Internal newsletters and circulars
Popular	(2.55) Training and mentorship program (2.91) Talks and seminars (2.91) Informal chatting and storytelling (3.00) Project briefing and review sessions (3.36) Meetings	(2.53) Phone calls (2.65) Project briefing and review sessions (2.76) Training and mentorship program (2.82) Meetings (3.12) Emails (3.24) Informal chatting and storytelling

*Popularity rating is done according to the scale described in Section 5

meetings, project briefing and review sessions, and mentorship and training programs. Social knowledge sharing is much more popular than modes that contain written, explicit knowledge, such as databases, memoranda, internal newsletters and circulars etc. This suggests that if a new knowledge management initiative is to be introduced and implemented, it is likely to gain the most effect if it embodies a human-orientated nature.

6 PART III: TACIT CONSTRUCTABILITY ISSUES IN PRACTICE

Respondents for the *Part III Survey* are the same as that of Part II. To gain further insight to constructability issues and the nature of constructability knowledge in practice, respondents were asked to provide descriptions of specific constructability issues or problems from their past experience. The synthesis of these constructability cases in practice gives deeper insight to the relationship between consultant and contractor during a real project.

6.1 *Preventability by "better design"*

A total of 61 constructability issues with descriptions were obtained from the contractors. Out of the 61 constructability issues, 58 of them were indicated to be preventable by "better design". On the other hand, 41 constructability issues were obtained from consultants, of which only 15 were indicated to be preventable by "better design". Irrespective of which side is correct, this shows a contrast or misalignment in opinions regarding the nature and causes of constructability issues mentioned. Much fewer consultants believe that a better design can improve/solve constructability problems. Discussions between consultants and contractors on specific issues are thus necessary, to reach understanding.

6.2 *Categories of constructability cases*

Since it is accepted that contractors embody more knowledge regarding the execution phase and the practical details of the construction environment, the cases provided by contractors were primarily regarded and analyzed. The cases were condensed and analyzed individually; similar cases were consolidated together, and can be roughly categorized into the following areas:

1) Design problem; 2) Timing of design issuance; 3) Alternative construction from contractors' input; 4) Simplicity and standardization; 5) Site related issues; 6) Aesthetics

Note that these categories are not mutually exclusive. Many constructability issues may well be associated with a few different categories. Irrespective, these myriad cases hold many valuable lessons to be learnt concerning the nature of specific constructability problems. Only a condensed summary is set out in the sections below, under each of the categories mentioned above.

6.2.1 *Design problem*

– Inherent incompetence of the design results in problems such as: excessive deflections during construction, structural failures due to poor design, lack of provision for certain components (e.g. services, water/electricity reticulation, ceiling voids etc.) and neglect of inherent distortion of building materials during the fabrication or construction (e.g. distortion of flat plate galvanized box gutters).

6.2.2 *Timing of design issuance*

- Drawings are issued late or just in time, stifling the motivation for change/optimizing of design.
- Designers often wait for vendors or clients themselves for information, who are late in issuing.

6.2.3 *Alternative construction methods by contractors' input*

- Contractors' input often involves changes to the design that lead to a better project solution. e.g. re-sequencing of work, changing configurations of building components.
- Changes that lead to alternative (better) construction are often instrumental for the completion of the project on time.
- Alternatives are often simply not considered – resulting in a much more expensive and difficult construction process.
- If contractors propose alternative designs or construction details, they must often also supply guarantees for the life of the proposed structure; contractors are thus discouraged to do so.
- The pressures involved in the project schedule are a great barrier to the adoption of alternative design and construction. Many potentially beneficial alternatives are not pursued further due to time constraints.
- Self compacting concrete saves time as no vibration is needed; however, it is more expensive and need stronger shuttering.
- In situ slabs with down-stand beams are best avoided; precast alternative or permanent formwork is preferable in most cases. Back propping of in situ slabs also cause delays.
- Mass and density of structural steel implies the assembly process – e.g. put together in position or first assembled aside and then lift into position with a crane. This must be discussed between consultant and contractor to clarify the circumstantial preference.
- Very slender columns are difficult to construct. Together with dense rebar specifications, causes limitations to the construction procedure and delays. It would be better to make the column thicker with less dense rebar details.
- The in situ ring beam is unsuitable for fast-track projects; rather box-steel beam or precast beam.
- Precast beams are used for better finish, consistent colouration and standard dimensions of moulds.
- Chasing of masonry walls causes numerous potential problems, such as compromising the stability of the wall, material waste, dust and health & safety issues. Less chasing is better in principle.
- Excessively dense rebar cages or long rebar are difficult to lift with the crane and difficult to handle on site.

6.2.4 *Simplicity and standardization*

- Formwork standardization is typically not considered in most projects, but makes a great difference for improving construction processes.
- Specification of products that are new to the market or not within familiarity of the contractor causes delays and inherent uncertainty risks, and may also require additional training of personnel carrying out installation or construction.
- It is better to use a simple concrete wall over a brick skin wall with concrete cavity, which makes construction more difficult.
- Coordination of services is typically problematic. Clashes in components and procedures occur often, causing delays and additional costs.

6.2.5 *Site related issues*

- Safety issues of working at high altitudes need to be considered during the design.
- Access to site may be a problem if in situ material is poor, which makes the supply of equipment very difficult. The material is also more vulnerable to rain, resulting in much rework and delays.
- Site congestion may prevent the use of the mobile cranes if there is not enough space to allow access for mobile cranes.
- Excavations must be provided with proper drainage to prevent flooding.

6.2.6 *Aesthetics*

- Aesthetics requirements are sometimes absolute, and take priority over practicality, resulting in poor constructability. Contractors are often in a position to suggest alternative/better construction approaches, while still maintaining the aesthetic requirements. This should be made possible.

7 CONCLUSIONS AND RECOMMENDATIONS

This study sets out to determine the nature of constructability and related problems, and how better collaboration between consultant and contractor can be a holistic way to address such issues.

Firstly, this study investigates project archives – a primary source of explicit constructability knowledge from projects. It is revealed that existing archives and documentation are inadequate in providing constructability lessons. The problem is not only the capturing activity per se, but also the lack of willingness from employees to use such a system – which may have been cause by the inadequacy of the system in the first place. This indicates that there is insufficient explicit constructability knowledge, as well as a lack of accessibility within organizations, let alone on an inter-disciplinary level.

Constructability knowledge is predominantly in tacit form – in the minds of expert professionals in the field. Tacit knowledge sharing thus proves significant in disseminating constructability knowledge, amongst consultants and contractors, themselves and/or each other. Indeed, this study shows that current popular knowledge sharing modes are informal and involves social, people-orientated methods. This seems apt for the dissemination of constructability knowledge.

However these modes also suggest that knowledge sharing is unstructured and ad hoc; and thus poses additional challenges for documenting and managing constructability knowledge.

To gain accurate insight into the problem, this study obtained and analyzed numerous constructability cases from the field, then categorized into 6 basic areas. However, one should bear in mind that one constructability issue is seldom mutually exclusive to another. This emphasizes the uniqueness and complex nature of constructability cases. Nevertheless, this simple exercise demonstrates that substantial amounts of constructability experience can be extracted and explicated for sharing. It is thus pertinent for such activities to take place on a larger and more systematic scale within organizations.

From this study some broad constructability guidelines may be inferred – such as: consideration for precast methods; allow more contractor input; promote standardization and/or simplicity etc. However, due to the variety of circumstances and uniqueness of these issues, the holistic approach is rather to promote collaboration and more knowledge sharing, where issues can be addressed in the context of the project, by the participants involved.

In principal, constructability problems arise from a "poor design" due to inadequate constructability knowledge. As this study shows, it is rather attributed to a misalignment between perceptions of consultants and contractors, regarding what constitutes good vs. poor constructability. These misaligned perceptions often has anecdotal reasons, and can thus only be properly addressed through open channel of communication, where the most relevant knowledge can be shared consistently, to achieve a more integrated project delivery process. The recommendations arising from this study are as follows:

- Improve project archives so that more useful knowledge can be captured, organized and stored to be easily accessible by future personnel.
- Promote more structured implementation of existing, human-orientated knowledge sharing modes (be it meetings, seminars, word-of-mouth etc.)
- Increase research to further explicate constructability, especially industries involving substantial repetition (such as housing, precast fabrication), where standardization is common, and thus construction processes easily expressed explicitly.
- The 6 categories of constructability issues produced in this study may well be used as a reference or checklist for constructability discussions between consultant and contractors.
- Closer collaboration and better knowledge sharing may be achieved through a variety of knowledge management initiatives (e.g. lessons learnt programs and discussion forums).
- Social knowledge sharing should be integrated with IT systems (such as Building Information Models) to harness full operational potential.

REFERENCES

Construction Industry Institute (CII). 1986. *Constructability: A Primer*. Texas, Austin, University of Texas.

Construction Industry Institute (CII). 1987a. *Constructability Concept File*. Texas, Austin.

Construction Industry Institute (CII). 1987b. *Guidelines for Implementing a Constructability Program*. Texas, Austin.

Construction Industry Institute (CII). 1993. *Preview of Constructability Implementation*. Texas, Austin.

Foy, P. S. 1999. Knowledge management in industry. *Knowledge management handbook*. New York: CRC Press.

Gambatese, J. A., Dunston, P.S., & Pocock J. B. 2007. "Introduction" of *Constructability concepts and practice*. ASCE. Virginia, Reston.

Hickins, M. 2000. Xerox shares its knowledge. *The knowledge management yearbook 2000–2001*. UK, Woburn: Butterworth-Heinemann.

McDermott, R. & O'Dell, C. 2001. Overcoming cultural barriers to sharing knowledge. *Journal of Knowledge Management*, 5(1): 76–85.

Nonaka, I. & Takeuchi, H. 1995. *The Knowledge-creating Company*. New York: Oxford University Press.

Nonaka, I., Konno, N. & Toyama, R. 2000. *Emergence of 'Ba'*. Oxford: Oxford University Press.

Pocock, J.B., Kuennen, S.T., Gambatese, J., & Rauschkolb, J. 2006. Constructability State of Practice Report. *Journal of Construction Engineering and Management*, 132(4): 373–383.

Polanyi, M. 1958. *Personal Knowledge: Towards a Post-critical Philosophy*. London: Routledge & Kegan Paul Ltd.

Song, L., Mohamed, Y., & AbouRizk, S. M. 2009. Early contractor involvement in design and its impact on construction schedule performance. *Journal of Management in Engineering*, 25(1): 12–20.

Research and Applications in Structural Engineering, Mechanics and Computation – Zingoni (Ed.)
© 2013 Taylor & Francis Group, London, ISBN 978-1-138-00061-2

Processes of ID-based linking of structural relevant construction phase data to planning phase data using auto-ID techniques

L. Laußat, A. Kelm, A. Meins-Becker & M. Helmus
Bergische Universität Wuppertal, Civil Engineering Faculty, Chair of Construction Management & Economics, Wuppertal, Germany

ABSTRACT: Today, architects' planning and modeling should be done object orientated. A unique ID number can be given to every object planned in the architects' model as the first step in the building information modeling (BIM) process. When in the next steps of this BIM process structural engineers are doing their work of detailing, e.g. for reinforcement, it is possible to link the ID of every part planned in detail to the ID of the architects' model – even if the work of detailing is done using traditional, but digital 2D methods, e.g. such resulting in lists of reinforcement. But a lot of questions dealing with the level of detail and data requirements have to be solved. In logistic processes a set of ID of single items can be aggregated to one delivery ID. If parts or sets are marked with automatic readable labels or tags (e.g. barcode or RFID), once the ITC environment is integrated, they can easily be tracked. Each part can be linked during logistic and construction processes to the BIM databases. The qualified staff on the construction site can be identified, e.g. using an identity card with barcode, RFID or biometric data, perhaps on an anonymous basis. The database entries for different processes on construction sites could then link material ID, personal ID, location ID and type of process ID to the virtual object ID. This would result in new status for the objects linked to the 'xD multi model data' usable for the BIM processes of the different participants. This new way of data generation, enabled by object orientated, digital planning and modern forms of ITC technology could be used as a basic step in processes of controlling and monitoring structural work. In the paper the authors give some impressions for the interdependence of BIM based data structures, auto-ID usage and process design requirements and possibilities reflecting their ongoing research.

1 INTRODUCTION

In past research projects the authors showed how auto-identification (ID) techniques could be used to support construction logistic processes (see e.g. Helmus et al. 2009 and 2011). They raise expectations, that real life ID Numbers (ID) used in the construction phase, such as product serial numbers or personal numbers, can be linked automatically to the object ID which are generated and used in building integrated modeling (BIM) processes in the planning phase using modern ITC technologies. They proposed e.g. using systems like article catalogs and classification systems for the building components and standardized ID for the real world processes (e.g. GS1/EPCglobal concepts). The detailed analysis of the multiplicity of processes needed to link the real life ID and the corresponding data to the virtual ID in the BIM database structure has not been focus in their past research.

This paper wants to describe the task of finding processes allowing these linking using two examples. These examples are able to illustrate the relevance of these issues for control and documentation of structural relevant construction work. The first example should be prefabricated reinforcement, the second example ready-mix concrete, both for a structural relevant concrete column.

2 IDENTIFYING AND DETAILING PLANNING PHASE DATA USING BIM METHODS

2.1 *BIM methods: The way for object based planning and building*

The BIM based, that means object orientated method of doing construction planning and work, usually is traced back to Eastman et al. 1974. Today due to software developments it has become very popular issue in different fields of research. The method allows the combination of geometrical data of objects with additional data in the objects' attributes and parametrical data bringing the objects in relations to each other. It is the logical enhancement of computer aided design (CAD) and engineering (CAE) systems.

Parts of the method will be described in the following sections looking at the above mentioned examples and a usual constellation of project participants. Here the authors make the assumption, that every participant uses his own model in a compatible multi

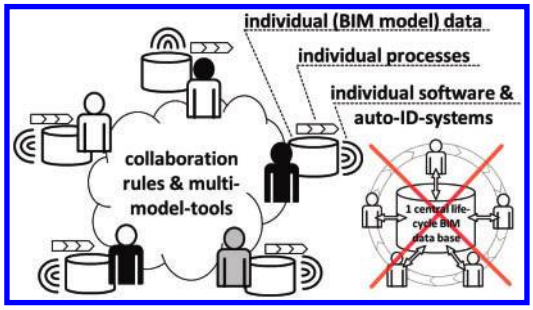


Figure 1. Auto-ID usage in decentralized (multi model) data structure: Collaboration rules for data interchange processes.

model landscape with data interchange possibilities. The early assumption that can be found in the literature, that all data of all participants should be put in one single central model respectively data base, is not part of the authors' concept. They want to reflect real world aspects such as decentralized database structures combined with collaboration rules for getting results relevant for the practice. The concept is drafted in figure 1.

One possibility of a multi model approach, that means a link-model-approach with several domain models, is shown e.g. in the reports to a German research project called Mefisto (see e.g. Mefisto 2013). This seems to be a good base for further developments.

2.2 *State of the art in using BIM methods in architectural planning*

Using an architectural BIM software, the architect today will begin his design work for a concrete column by defining the object as a simple geometrical volume that is parametrically integrated in the building structure. By doing this, the first virtual object ID for a part of the building is given to the column.

The object of the column will be further defined by the architect using attributes. E.g. he will attribute this object as a structural relevant, reinforced concrete column build as exposed architectural concrete class 'xy' with different other defined properties.

At this point the level of detail (LoD) of the planning phase model data is not very high. For further detailing the architect will submit his model to e.g. the structural engineer.

2.3 *State of the art in using BIM methods for structural detailing*

The structural engineer will import the architecture's BIM in his structural orientated BIM software linking the virtual ID of the column in the architect's model to the virtual object ID in his own structural model. (The processes of iteration between architect and structural engineer e.g. relating the column dimensions should be neglected at this point.)

Now the structural engineer will do his work of detailing, that means he will add structural relevant attributes such like e.g. specified concrete and exposition classes and he will plan or model the reinforcement. Using BIM methods or not, every single item of the reinforcement will get a position number, which is shown in the paper based position plans, the structural analysis and which is used for the lists of steel requirement. In the world of object orientated modeling every item could be modeled and made part of the structural model as a single object. In this case it can get its own virtual single item object ID which could be linked to the virtual column object ID of the structural model and so indirectly to the virtual column object ID of the architectural model.

So a new LoD of the structural model reflects the work of detailing by structural engineers in form of new attributes (e.g. ready-mix concrete quality requirements) and in form of assigned and linked single item (sub-)object ID (e.g. for the reinforcement).

2.4 *State of the art in using BIM methods during contracting*

Based on information at this LoD usually the contracting phase will start. In the world of using BIM methods the architect can use the data of both, the architectural as well as the structural model, for defining a work breakdown structure (WBS) and for getting quantity take offs (QTO) when working out the tender documents. For doing this, today special software is already available.

Using this software will change the LoD and generate a WBS with transparent QTO and directly linked properties (attributes and their values) of the building parts. This information is directly usable for contractors for defining construction processes and doing their calculation work. In their offers the contractors can also make their specification remarks (e.g. about the concrete supplier and recipe or about formwork systems incl. in the offer), which are automatically linked to the relevant virtual object ID.

2.5 *State of the art in using BIM methods for construction work scheduling*

When contractors are calculating their offers, they usually will make decisions about the chosen construction methods and therefore they will predesign construction processes and link them with resource requirements for answering resource leveling and allocation aspects resulting in scheduling assumptions.

In a BIM based world contractors can define their construction processes linking the object ID of BIM models to new process ID and adding construction relevant data to these processes, e.g. data about resource requirements. So virtual object ID and attributes as well as assigned virtual single item object ID will be linked to process ID and more, to resource requirements. When calculating the offer the LoD of process and resource linking will usually be very low. But

after getting the contract this will be the starting point of doing the resource and scheduling detailing work. This will be part of detailed examination about resource based scheduling in an ongoing research project mentioned in Laußat 2013.

2.6 *State of the art in using BIM methods for construction site logistics*

As shown in many research projects (see e.g. Günthner & Borrmann 2011 and Mefisto 2013 2013), using BIM methods can be very helpful also for planning the temporary construction site layout and for construction logistic and safety aspects. In a multi model approach temporary construction site models give information e.g. about crane availability, storage areas, working or safety place requirements etc. Also form- and framework as well as scaffold could be modeled in detail. These models and their data can be used and combined with the other models for different purposes. Hereby new virtual objects with own virtual object ID are designed which can be used e.g. for linking data of different systems. One example is a virtual location ID for a temporary storage area as a virtual zone in the 3D structure.

2.7 *State of the art in using BIM methods for manufacturing building products*

If the BIM-based planning is done in a suitable LoD and the relevant aspects are considered, BIM-data can be imported by computer aided production systems of the industry, which will produce and deliver the construction products or elements. E.g. computer aided production of reinforcement could be done using the detailed data of the structural BIM for every single reinforcement object. This can be seen as a logical enhancement of computer numerical control (CNC) machine tools' use of CAD data.

Using BIM methods in construction planning this way can open the door for the ongoing industrial revolution (in Germany called *"Industrie 4.0",* the 4th industrial revolution) for the construction sector, in which the gap between real and virtual reality will be closed allowing individualized production.

After getting the contract another possible process could be, as it is e.g. not unusual in the German construction industry, that the contractor changes the construction method and so switches from cast-in-place to precast columns. Then he or his precast element supplier can use the detailed data of the existing BIM models for making his own, new structural model. In this case, special additional processes of linking relevant data are required, e.g. for dividing one big cast in place concrete wall and its referenced reinforcement in several precast elements including reinforcement and connectors.

When prefabricated components shall be used production planning has to be done and the data from the production planning could be linked to the former planning phase data in the different models. So the produced element and its production data now can be virtually linked to all relevant planning phase data. To conserve this possibility of data linking outgoing from an object, it is necessary to make the real life objects identifiable.

3 CONCRETE CONTROL, MONITORING AND INSPECTION REQUIREMENTS

3.1 *German rules for building with concrete*

In Germany different rules have to be considered when building with concrete. Depending on concrete and building classes there can be inspection and documentation requirements by the suppliers, contractors and additional extern inspecting institutions (see e.g. BetonMarketing 2011). At different points of the construction phase the accordance of produced objects and chosen processes with the requirements set in the planning phase have to be inspected and documented. So the concrete, reinforcement and formwork have to be inspected as well from an object as from a process perspective. Thereby process-durations and whether conditions as well as confirmation paperwork and testing procedures, e.g. taking of test cubes, have to be checked and documented. Not at least the qualification of the staff as well as the machinery has to be reviewed and documented.

Next to these structural relevant inspections there are also inspecting requirements from an architectural point of view as e.g. the quality of formwork surfaces regarding exposed concrete quality aspects.

In a BIM based data environment it should be possible to use digital data from model databases when inspecting and testing as well as to document the results linked to this databases. Auto-ID techniques could be able to make these linking based or link producing procedures more efficient.

4 USING AUTO-ID TECHNIQUES FOR REAL LIFE CONSTRUCTION PHASE DATA

4.1 *Auto-ID techniques*

Today a lot of processes in different businesses are supported by the use of auto-ID techniques such as barcode, biometrics or radio frequency identification (RFID). Barcode techniques and biometric systems should be well known. Detailed information about RFID techniques could be found e.g. in Finkenzeller 2008. These techniques allow generating and processing data belonging to identifiable objects in real time, because no manual identification is necessary.

4.2 *AutoID techniques in context of construction*

The use of RFID techniques in construction context was first mentioned by Jaselskis 1995. It has been one focus of the authors' research in the last seven years (for results see e.g. Helmus et al. 2009

and 2011). Today already some RFID based systems supporting construction logistic processes exist (see e.g. AdNovum 2011 for planning and tracking transports in the ready-mix concrete industry).

In ongoing projects (see www.RFIDimBau.de & www.baubetrieb.de), the authors will focus on the combination of BIM methods and auto-ID usage. Figure 1 visualizes the authors' approach of decentralized systems usage when combining usage of auto-ID technique with BIM data structures.

A lot of interesting papers handling with the issue of RFID usage in BIM data structures already exists but cannot be reviewed at this point (e.g. Chin et al. 2008, Hajian & Becerik-Gerber 2009, Cho et al. 2009, Motamedi & Hammad 2009, Xie et al. 2010, Cheng & Chang 2011, Shiau et al. 2011). First systems using the new possibilities are already prospected by ICT companies (see e.g. Vela Systems 2008a, b).

4.3 *Using ID for construction resources*

One possibility of auto-ID usage, especially when looking at construction logistic tasks, is making resources identifiable and using this new possibility in new designed logistic, construction and control processes. So not only material, but also machinery and temporary frame- and formwork or scaffold as well as staff or locations etc. could be handled in a new way on construction sites, when the single objects are identifiable and when they as well as building model objects have virtual representations in the multi model context data bases.

5 LINKING REAL LIFE CONSTRUCTION TO BIM BASED PLANNING PHASE DATA USING AUTO-ID TECHNIQUES

5.1 *The challenge: Linking of real world resources' ID to virtual objects' ID in model data bases*

As shown e.g. in Helmus et al. 2009 and 2011 or Günthner & Borrmann 2011, in different research projects methods are searched for linking real life product and process data to BIM based, object orientated data structures. While some of these linking processes are possible today with existing software, for others linking processes concepts are still missing. This can be shown by using case examples.

A simple and trivial case example is to link an ID of a BIM object which is representing a prefabricated building element, e.g. a precast concrete column, to the real world product ID during production.

A more complicated, not trivial case example is to link the production phase data of a charge of ready-mix concrete to the different columns for which the concrete of one truck delivery was used and parallel to add more relevant process information (e.g. about the staff involved in the construction process, reinforcement control data consisting e.g. of the single item object ID of the mounted reinforcement, object ID of concrete test cubes, testing results, whether conditions, construction time).

Up to today, detailed descriptions of most processes in which construction phase data (real life object ID and corresponding data) is linked to planning phase data (virtual object ID of the BIM data-structure and corresponding data) are missing. Only a few basic approaches for some examples could be found in the literature mentioned above.

5.2 *Ongoing research: Requirements for the extension of the object orientated multi model data structure due to auto-ID technique usage*

In their ongoing research, the authors will define processes in which under the use of auto-ID techniques the linking of real life construction phase data to BIM multi model world , that means planning phase data structures will be essential. Therefore the usage of data generated from BIM models as well as the extension or reorganization of this data in processes of logistic, production, construction and control will be the focus of their ongoing research. The possibility to use the resulting data base for the rest of the building's life cycle will be a great add-on. The data requirements in the different processes will be used to overthink attributing systems for virtual objects as well as to overthink the requirement of new virtual object types. This will lead to the answer of the question: How must the BIM multi model data structures be designed for efficient usage in the processes of construction logistic, production of building elements, on-site construction work and control as well as process documentation when the use of auto-ID techniques should be possible? That means which model and which object types are needed and what has to be part of their attributes, when data using and adding through auto-ID systems should be possible?

Standardization of these data organization, data using and data generating processes will probably lead to new LoD and attribute requirements in the different models of a multi model approach. Perhaps new special model types or new virtual object types are needed for special tasks. These new attributes, model or object types shall on the one hand allow for new process designs not only for the whole construction phase, but also for the preconstruction phase and for the rest of the building's life cycle. On the other hand they will result from these new process designs.

5.3 *The context: Restrictions resulting from real life collaboration and software structures*

To answer these questions, the construction context has to be taken in account. This means, that the functions of the different software in use have to be considered when changing the data and software structures – at least when the development of new data-structures should be successful. For a better understanding some of the concerned systems should be named using examples: the individual BIM-software (e.g. Autodesk

Revit or Tekla Structures), the affordable multi model tools (e.g. model checker for collision control), the collaborative communication software systems (e.g. Groupwise), the computer aided production systems of the delivering industry (e.g. CNC software), the project management and scheduling software (e.g. Oracle Primavera or Asta Power Project), the calculation and contracting software (e.g. RIB iTwo), the enterprise resource planning (ERP) systems (e.g. SAP) and a lot more.

5.4 *Examples of linking or link using processes*

At the end of the planning phase (see lit. 2.2 to 2.7) there will be detailed planning phase data for the concrete column's reinforcement and attributes.

The architect now has added all his own special requirements in form of attributes. He exactly knows about the requirements of the structural engineer. The reinforcement is modeled and all items of the column's reinforcement are linked to the virtual column ID. The contractor's additional data has been made part of the contractor's planning phase data.

Looking at the start of the realization phase, the contractor now designs e.g. one or more separate processes with own process ID for the construction of the regarded column (cast-in-place method). He specifies the resource requirements and does his scheduling. Then he plans his processes of making the resources available at the right point of time. Due to flexibility reasons he will do this on a lower LoD. The processes of making resources available will get their own logistic process ID.

The logistic processes are now pre-planned on a low LoD, but the structure reflecting the chosen construction method and participants is fixed. Linkages between virtual object ID, construction process ID and logistic process ID now exist.

But yet no linking of the real life resource's object ID has been made. These linking procedures will be the focus of the authors' ongoing research. They will be done in the steps of detailing the construction work and logistic planning by the contractor and the production planning by the suppliers. Thereby new kinds of virtual objects like identifiable deliveries (delivery ID) or identifiable personal missions (mission ID) can be used.

The following resources will be needed for the cast-in-place concrete column: information, own staff for doing formwork and casting, sub-contractor's staff for reinforcing incl. their tools and material (e.g. tie wire), formwork (several elements, perhaps reused after finishing other cast-in-place columns at the same construction site), reinforcement (a set of several parts), tools and material from magazine container (e.g. vibration units for concrete compaction or formwork oil), crane capacity (for formwork, reinforcement and perhaps concrete hoppers), concrete-pump or concrete hopper, ready-mix concrete (part of one truck load, that means one delivery), sample taking equipment for concrete, electricity, water, gasoil etc. Every resource must fulfill different criteria like qualification of the personal, quality of the formwork surfaces, maximum age of the ready-mix concrete etc. Some of these criteria have to be proofed during the construction processes. Therefore control and monitoring processes are combined with the construction processes which probably could be supported by quick data delivering possibilities enabled by modern ITC technology combined with auto-ID techniques.

Some information about resource-requirement and allocation as well as about resource properties usually can be found explicit in the calculation software linked with resource planning data in project management and ERP software. Other information usually is taken into account implicitly when planning the construction work and during scheduling. But for high construction productivity it is necessary, to plan all resource requirements on a high LoD. The real life object ID for identifiable resources usually can be found in the companies' ERP and production software systems (e.g. personal ID, inventory ID of machines, serial numbers of produced material).

With a model based planning it should be possible to link the individual, identifiable real life resources to the different construction process ID and then to link the information belonging to logistic processes of making resources available after they are planned on a higher LoD. So all relevant data would be linked to the multi model ID. The detailed description of these backgrounds and the resource based linking from construction to logistic processes is part of an ongoing project (see Laußat 2013).

6 FUTURE PROSPECTS

The paper shows aspects of the authors' actual research focus. The task is to bring data structures of the planning and the construction phase to a level that allows linking virtual object ID from the planning phase to real life object ID of the construction phase by using defined processes during planning, preconstruction, fabrication, logistics, construction, monitoring, control and documentation. These process based data linking procedures could not be seen as solved from a scientific point of view, when real life constellations of participants and their rolls and challenges as well as their software structures and e.g. ERP environments are seen as restrictions that have to be considered in the system and process design.

The authors believe that combining BIM methods with process efficiency resulting from auto-ID usage can lead to a new quality in construction project execution coming along with cost reduction and shorter construction phases. Their general approach is visualized figure 1.

For the special point of controlling structural relevant work during the monitoring, control and acceptance procedures, e.g. before beginning the casting processes, a new quality of data transparence will be available. Process, product and resource property

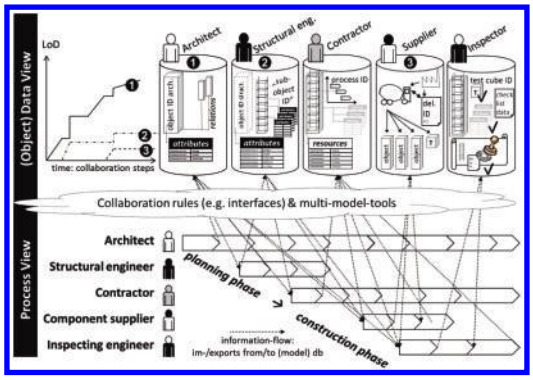


Figure 2. Principle of information flow resulting in a data set for usage in the inspection procedure of a concrete column.

information can be directly linked to virtual objects in the multi model data bases. They can be browsed by using virtual ID and links in one of the models or by using the real life ID fixed to the real life objects. Figure 2 shows an example visualizing the principal of information flow through collaboration rules.

This data can be held available over the lifespan of a building easily by using conventional methods of data aggregation, storage and backup. Usually in Germany it is the architect's challenge to aggregate a part of the decentralized and fragmented data generated during the planning and construction phase for giving it to the owner (HOAI Lph. 8-9). Once BIM methods are in use, this work package should be realized in a much more efficient way than today. Some of the auto-ID generated data which will be part of this data aggregation will lead to a much higher LoD of information also about structural relevant building parts.

REFERENCES

AdNovum (ed.) 2011: Holcim: Online-Logistik. In: AdNovum (ed.), *Solutio, No. 2, April*. www.adnovum.ch.

BetonMarketing Deutschland GmbH (ed.) 2011: Überwachen von Beton auf Baustellen. In *Zement-Merkblatt Betontechnik B5-1.2011*. www.beton.org.

Chin, S., Yoon, S., Choi, C. & Cho, C. 2008: RFID+4D CAD for progress management of structural steel works. *Computing in Civil Engineering* 22(2): 74–89.

Cheng, M.-Y. & Chang, N.-W. 2011: Radio frequency identification (RFID) integrated with building information model (BIM). In *Proc. 28th ISARC, Seoul, 29 June–2 July*: 367–371.

Cho, S., Sorensen, K.B., Fischer, M. & Dickey, A. 2009: ERP application of real-time VDC-enabled last planner system for planning reliability improvement. In *Proc. ASCE, Austin, 24–27 June 2009:*156–165.

Cong, Z., Yin, H., Manzoor, F., Cahill, B. & Menzel, K. 2010: Integration of radio frequency identification and building information modeling for decentralized information management. In Tizani, W. (ed.),*Proc. ICCCBE, Nottingham, 30 June–2 July*.

Eastman, C.M., Fisher, D. et al. 1974: *An Outline of the Building Description System.* Pittsburgh: Research Report No. 50 Carnegie-Mellon University

Finkenzeller, K. 2008: *RFID-Handbuch*. München: Hanser.

Günthner, W.A. & Borrmann, A. (eds.) 2011: *Digitale Baustelle.* Berlin Heidelberg: Springer.

Hajian, H. & Becerik-Gerber, B. 2009: A research outlook for real-time project information management by integrating advanced field data acquisition systems and building information modeling. In *Proc. ASCE Int. Workshop on Computing in Civil Engineering, Austin, 24–27 June*: 83–94.

Helmus, M., Kelm, A., Laußat, L. & Meins-Becker, A. 2009: *RFID in der Baulogistik.* Wiesbaden: Vieweg & Teubner.

Helmus, M., Kelm, A., Laußat, L. & Meins-Becker, A. 2011: *RFID-Baulogistikleitstand.* Wiesbaden: Vieweg & Teubner.

Jaselskis, E., Anderson, M., Jahren, C., Rodriguez, Y. & Njos, S. 1995: Radio frequency identification applications in construction industry, *Construction Engineering and Management*, June: 189–196.

Laußat, L. & Helmus, M. 2013: Uncertain and real-time construction logistic data for proactive-reactive simulation-based scheduling. In Yazdani, S. & Singh, A. (eds.), *New developments in structural engineering and construction, Proc. 7th ISEC, Honolulu, 18–23 June* (accepted paper).

Mefisto 2013: *'Das Buch über die Entwicklungen des Mefisto-Projekts' [place holder]* (Springer-publishing, for publication announcement see www.mefisto-bau.de)

Motamedi, A. & Hammad, A. 2007: Framework for lifecycle status tracking and visualization of constructed facility components. In *Proc. 7th CONVR, Pennsylvania, 22–23 Oct.:* 224–232.

Motamedi, A. & Hammad, A. 2009: Lifecycle management of facilities components using radio frequency identification and building information modeling. *Information Technology in Construction* 14: 238–262.

Shiau, Y.C., Wang, M.T., Lin, C.H. & Guo, Z.Y. 2011: Use BIM to construct electronic resume system for building project. In *Proc. 28th ISARC, Seoul, 29 June–2 July*: 367–371.

Vela Systems (ed.) 2008a: *Case study: Skanska uses field BIM solutions to save $1 Million on the new Meadowlands Stadium.* www.velasystems.com.

Vela Systems (ed.) 2008b: *Real-time BIM/RFID-enabled production management.* www.velasystems.com.

Xie, H., Shi, W. & Issa, R. 2010: *Integration of BIM and RFID in steel construction.* Saarbrücken: LAP Lambert.

Research and Applications in Structural Engineering, Mechanics and Computation – Zingoni (Ed.)
© 2013 Taylor & Francis Group, London, ISBN 978-1-138-00061-2

Verification of MZELWE module in ESP-r programme with experimental confrontation

M. Čekon & M. Kalousek
Institute of Building Structures, Brno University of Technology, Faculty of Civil Engineering, Brno, Czech Republic
J. Hraška
Department of Building Structures, Slovak University of Technology, Faculty of Civil Engineering, Bratislava, Slovakia

ABSTRACT: The paper deals with the verification of the simulation module MZELWE using Esp-r programme and its confrontation with experimental measurements. This module focuses upon the calculation of longwave radiation heat exchange between non-transparent external surfaces of a building and its environment. Basic mathematical operations are defined by default sky radiation models. This study analyzes the precision of thermodynamic methods applied by the given simulating module in ESP-r with the aim to highlight the weak points of the sky radiation model that play an important role in the radiation heat exchange during night-time. The experimental measurements in dynamic outdoor conditions were used for this study. The Clarke model appears to be the most convenient among them, having well interpreted the measured course under all circumstances.

1 INTRODUCTION

Computer simulation is a modern tool of the present day design and planning of structural engineering and building construction. It is broadly applied in all sorts of scientific disciplines as well as in practical technology. In various fields of science it supports the implementation of findings ensuing from the solved case studies. This approach of design and planning is ever more current in all stages of project preparation, of the actual implementation of building constructions and during the whole life time of structures. The energies within the buildings and the creation of the indoor environment offer considerable opportunities for simulation. This area tends to depend upon very complex and dynamic links due to the interactions between the indoor and outdoor environment, the design itself, the technology in question and the users of the building. However, the outcome of simulations may show problems when confronted with the reality (Hopfe, 2009). Such problems can be handled by various assessment mechanisms combining empirical and analytical verification methods. They can often help to solve complex tasks that have not been scientifically monitored and experimentally confirmed, either. Yet also further uncertainties due to the involvement of the human factor are often reflected in the final result. All sorts of scientific symposia are regularly organized for discussing problems in connection with the utilization of these new methods in science and technology.

The basic problems related to simulations of energy flow and the indoor environment within the buildings can be addressed by way of thermodynamic simulations that are well suited for the analysis of both the energetic and the mass flow in the interior of the buildings. The well known ones (especially in the scientific sphere) include the calculation oriented simulation programme ESP-r (2010) that has been gradually developed and complemented, and also various modules have been added within the scope of scientific and research activities all over the world. It has been expanded by numerous innovations, but new options can be discovered by further exploration and improvements. Being outside the group of commercially distributed software, its development practically depends upon the present need in the field of research.

Although the ESP-r programme serves mainly to support research purposes, it finds ever more frequent applications for addressing practical tasks. Its setups offer options requiring very thorough studying before the user can apply them, but there are also some "prefab" models which, in turn, need not always comply with the given situation and place.

2 SIMULATION MODULE MZELWE AND THE SKY MODELS IN THE ESP-R SYSTEM

In general the basic theory of the thermal sky radiation suggests two relatively approximate methods for the determination of the volume of atmospheric radiation. The first is the assumption that the atmospheric

radiation equals that of a black body ($\varepsilon_{sky} = 1$) with variable effective temperature of the sky (T_{sky}).

$$q_{0\downarrow} = \sigma . T_{sky}^4 \qquad [\mathrm{W/m^2}] \qquad (1)$$

The next is the assumption that the sky radiates as a grey body having the same temperature as the ambient air close to the Earth surface (T_{ae}) and variable effective emissivity of the atmosphere ($\varepsilon_{sky} < 1$).

$$q_{0\downarrow} = \varepsilon_{sky} . \sigma . T_{ae}^4 \qquad [\mathrm{W/m^2}] \qquad (2)$$

$$\varepsilon_{sky} = q_{0\downarrow} / (\sigma . T_{ae}^4) \qquad [-] \qquad (3)$$

This generalizing approach may be sufficient for fundamental balance analyses, however, uncertainties appear in the respective calculation methods, in particular relating to the subjective determination of some marginal conditions, such as the degree of cloudiness of the atmosphere. In addition to that these models have been specified for sites with certain concrete climatic and weather conditions, and the latter tend to be used in a general way. This approach, accordingly, bears predominantly informative character for the reflection of the dynamics of the outdoor environment. There are analogies also in the application of calculation models like MODTRAN, LOWTRAN and others in the calculation system SBDART (Ricchiazzi et al.). These are approximate and simplified methods, frequently banning the reflection of a specific site, which is a required and indispensable issue for the investigation of real values of atmospheric radiation. They are both generalized and simplified for certain regions, such as the North-Atlantic Continent, for deserts and semi-deserts or some European regions, however, depending upon various subjectively defined parameters of the environment as well as generalized models of the climate.

The MZELWE programme module is intended for the calculation of the balance of longwave radiation between an external non-transparent surface and its environment. MZELWE operates predominantly with pre-defined sky models. The basic algorithm calculates the radiant exchange between the surface and the environment taking up the semi hemisphere above its plane.

$$q_{\downarrow\uparrow} = A_s . \varepsilon . \sigma . \left(\theta_e^4 - \theta_s^4\right) \qquad [\mathrm{W/m^2}] \qquad (4)$$

where q = balance of radiant flow [W/m^2]; A_s = surface area [m^2]; θ_e = equivalent temperature in function of the temperature of the sky, the terrain and the surrounding structures [K]; θ_s = surface temperature [K].

The calculation formula is entered by the un-known equivalent temperature of the environment allowing to express the net balance of longwave radiation. The unknown equivalent temperature is corrected by weight factors depending upon the position and place of the surface. In a standard situation it consists of a part of the sky, of the terrain and the ambient structures. Actually, the programme offers both a specific and a standard setup of weight factors (Table 1).

Table 1. Standard setup of weight factors.

Location:	f_s	f_g	f_u
City centers: surrounding structures of same height, vertical planes	0.36	0.36	0.28
City centers: higher surrounding structures, vertical planes	0.15	0.33	0.52
Urban parts: vertical planes	0.41	0.41	0.18
Agglomerations and villages: vertical planes	0.45	0.45	0.10
City centers: skew roofs	0.50	0.20	0.30
Urban parts: skew roofs	0.50	0.30	0.20
Agglomerations and villages: detached houses	0.50	0.50	0.00

$$\theta_e^4 = f_s . \theta_{sky}^4 + f_g . \theta_{grd}^4 + f_u . \theta_{sur}^4 \qquad [\mathrm{K}] \qquad (5)$$

From the viewpoint of calculation the decisive value is the sky temperature. The simulation module makes use of the assumption that the atmosphere radiates like a black body ($\varepsilon_{sky} = 1$) with variableeffective sky temperature (T_{sky}). As based upon the climatic conditions, the first step of the algorithm is the evaluation of the cloudiness that is applied separately according to the possibilities of each model. The simulation module with its setups and algorithms disposes of six physical models for the purpose of the unknown sky temperature expression (Table 2). When calculating the sky emissivity, the pre-set model Berdhal a Martin (1984) takes into account also the situation of cloudiness and atmospheric pressure conditions. Further models use, as a rule, the basic clear sky model of Swinbank (1963). Whereas the Swinbank models leave out the effect of cloudiness, using a uniform formulation, Clarke (2001), Cole (1976) and Czeplak Kasten (1980) follow in the footsteps of Swinbank, while expanding the applicability of his models. They consider the effect of cloudiness in their computation of the resulting sky temperature. Swinbank, however, differentiates between the input values of outdoor air temperature in his models, using the so-called dry or wet thermometer. In spite of that Stanzel (1994) recommends his basic model for the northern regions of Europe.

3 DESIGN, ASSEMBLY, DESCRIPTION AND TESTING OF THE MODEL

Based upon the actual dimensions and concepts of casing structures a double-zone model called Twin-box was developed for the purpose of simulation at the Faculty of Civil Engineering in Bratislava (Čekon, 2011; Čekon, 2012b). The separate zones are the measuring part (box_zone) and the adjacent zone (hc_zone)

Table 2. Physical models list and their basic formulas in ESP-r simulation module.

author - model:	abbreviation / setup in programme		Basic formulas
Berdhal a Martin (1984)	berdh&mar	0	$T_{sky,bam} = \left(q_{sky,bam} / \sigma\right)^{0,25}$ $q_{sky,bam} = \varepsilon_{sky} . \sigma . T_{ae}^{4}$ $\varepsilon_{sky} = 0,711 + 0,56 . \left(T_{dp}/100\right) + 0,73 . \left(T_{dp}/100\right)^{2} + 0,013 . \cos\left(\frac{2\pi t}{24}\right)$
Clarke (2001)	clarke	1	$T_{sky,clarke} = \left(9,36.10^{-6} . (1 - CC) . T_{ae}^{6} + T_{ae}^{4} . CC . \varepsilon_{cloud}\right)^{0,25}$ $\varepsilon_{cloud} = \left(1 - 0,84 . CC\right) . \left(0,527 + 0,161 . e^{[8,45.(1-273/T_{ae})]} + 0,84 . CC\right)$
Cole (1976)	cole	2	$T_{sky,cole} = \left((1 - CC) . T_{sky,swinbank}^{4} + CC . \varepsilon_{cloud} . T_{cloud}^{4}\right)^{0,25}$ $\varepsilon_{cloud} = 0,16 . \varepsilon_{air} + 0,84$ $\varepsilon_{air} = 0,527 + 0,161 . e^{[8,45.(1-273/T_{ae})]}$, $T_{cloud} = T_{ae} + 273$
Czeplak a Kasten (1980)	cz&kasten	3	$\varepsilon_{sky,zenith} = 9,36.10^{-6} . T_{ae}^{2}$ $q_{sky,wolke} = \varepsilon_{sky,cz} + \left(1 - \varepsilon_{sky,cz}\right) . \left(0,9 - 0,065 . C_{hh}\right) . \sigma . \left(T_{ae} + 273\right)^{4}$ $q_{sky,klar} = \left(1,174 . \varepsilon_{sky,cz} . \left(T_{ae} + 273\right)^{4}\right) - 33,0$ $q_{sky,cz} = \left(1 - CC\right) . q_{sky,klar} + CC . q_{sky,wolke}$ $T_{sky,cz} = \left(q_{sky,cz} / \sigma\right)^{0,25}$
Swinbank clear (1963)	swcl	4	$T_{sky,swinbank} = 0,05532 . T_{ae}^{1,5}$ dry air temperature
Swinbank bld	swbld	5	$T_{sky,swinbank} = 0,05532 . T_{ae}^{1,5}$ wet air temperature

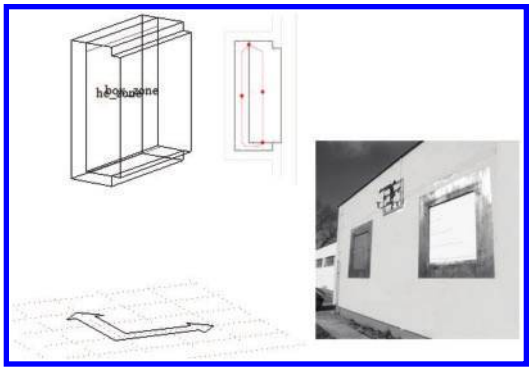


Figure 1. 3D model of Twin-box, zone model of air flow, external view on measured samples.

ensuring the preparation of heat and chilling down (Fig. 1). Thefigure shows a diagram of a network model of air streaming into the measuring part of the box. The model was derived from the existing dimensions and layout of casing structures. All surfaces were defined as non-transparent ones.

The box being surrounded from all sides by a compensation room ensuring air temperature at the level of air within the box, the external surfaces were chosen as adiabatic ones. As to the lateral sides of the box that are well insulated and contact the envelope of the compensation room, a certain simplification of the adiabatic condition has been considered. Physically the model was controlled so as to achieve constant temperature of air without any influence of internal temperature gain. The advantage consists in that the simulation serves to verify a simple model without large and changing numbers of variables, which allows concentrating exclusively upon the submitted objective.

The total of five measurements performed in three periods of time was subject to the verification. At the same time the effects of standard as well as low-emission surfaces were monitored in the field of thermodynamic behaviour of the simulation programme. Basic parameters of the tested models are represented in a table (Table 3). Radiative properties from different sources were applied to the internal and the external side of the simulated specimens (Chmúrny, 2003; Hagentoft, 2001; Halahyja et al., 1998) as well as calibrated with spectral measurements (Čekon, 2012a). The testing of each model was repeated with alternatives differing only as to the choice of the sky radiation computing model. The auxiliary database of the simulation comprised all climatic data registered by experimental measurements: outdoor temperature and humidity of air, velocity and speed of wind, horizontal, global and diffuse radiation and total solar radiation. Also the utilization of the measured ambient temperature was considered for the purpose of confrontation with the equivalent value of ambient temperature of the programme. The auxiliary database of measured data offers such option, but the present day setup of the algorithms did not support it. However, the 2-minute-step of the simulation was well in line with the interval of recording the measured values. The weight factors of model irradiation were set in the ratio 0.5 (f_s) : 0.5 (f_g) : 0.0 (f_u). We did not handle the calculation models of terrain temperature, having adopted the standard calculation used by the simulator with view to the combined effect of sun radiation and outdoor air temperature. The standard Perez model (Perez et al., 1990) was used in the model setup of solar radiation for all tested variants. Also the air flow models offered by the programme in broad scope play an important role for this verification.

Table 3. Basic parameters of the tested models.

Test/sim:	Measured period	composition:	interior		exterior	
			ε	α	ε	α
I.	12. 3. – 17. 3. 11	Zinc coated sheet 2 mm + Standard paint	0,23	0,35	0,90	0,25
II.	12. 3. – 17. 3. 11	Zinc coated sheet 2 mm + Low-emission paint	0,23	0,35	0,40	0,30
III.	20. 3. – 25. 3. 11	Zinc coated sheet 2 mm + standard paint	0,23	0,35	0,90	0,25
IV.	25. 3. – 1. 4. 11	Facade polystyrene 30 mm + Standard paint	0,90	0,70	0,90	0,25
V.	25. 3. – 1. 4. 11	Facade polystyrene 30 mm + Low-emission paint	0,90	0,70	0,45	0,35

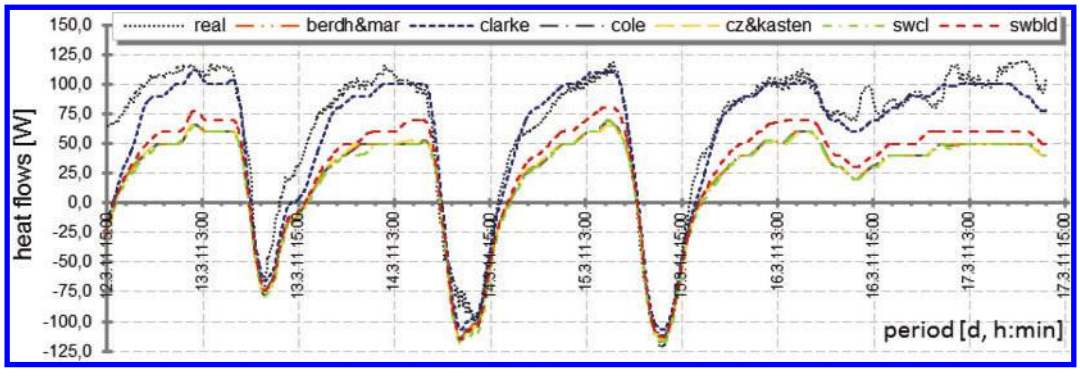


Figure 2. Simlulated heat flowsprogesses, "real" – measured heat flow; simulated heat flows form pre-defined models (Table 3).

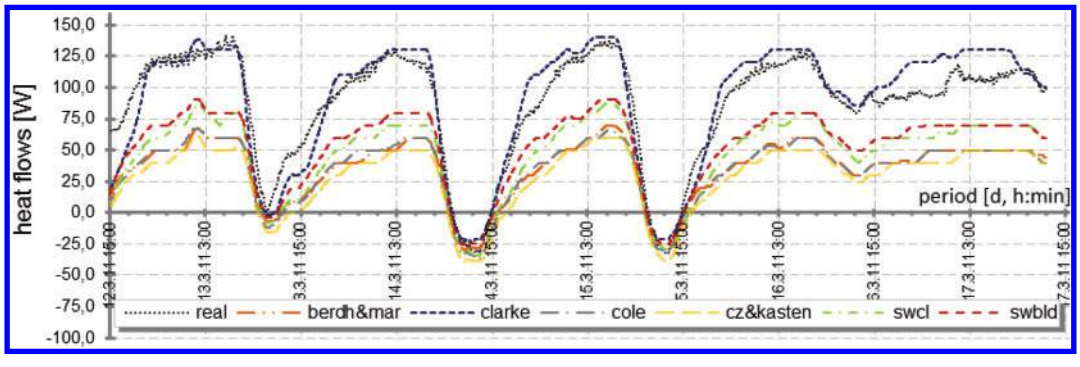


Figure 3. Simlulated heat flows progesses, "real" – measured heat flow; simulated heat flows form pre-defined models (Table 3).

4 ANALYSIS AND PROCESSING OF THE RESULTS

The simulation results are interpreted by way of diagrams showing the referential measured wave-forms of heat flow during the whole registered period as well as simulated ones. Simulations (Figs. 2–4) analyze compositions with close to zero thermal resistance where the essential part of the resulting heat flow is represented by the radiant flow and the transition phenomenon between the external surface of the composition and its environment. In this respect the sky models and temperature calculations play key roles. The compositions analyzed in further simulations (Figs. 5–6) were characterized by better thermal insulation capacity where, on the one hand, the effects of the sky radiation models compensate one another, and on the other hand their influence upon the resulting heat flows has been optically reduced. The mechanism of heat propagation by conduction takes over the decisive role. This enables the statement that along with the increasing influence of the thermal insulation properties of a structure the effect of the choice of model in the sky temperature calculation is seen to drop.

Yet another objective consisted in studying the effect of emissivity upon the non-stationary course of heat flow in the simulation programme under consideration. Since the simulator in its basic algorithm works in a clearly defined relation (4), reflecting the emissivity

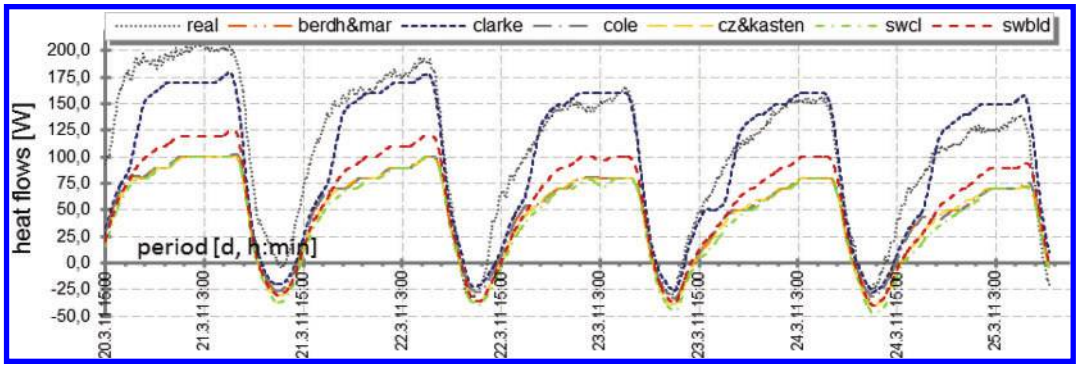


Figure 4. Simlulated heat flows progesses, "real" – measured heat flow; simulated heat flows form pre-defined models (Table 3).

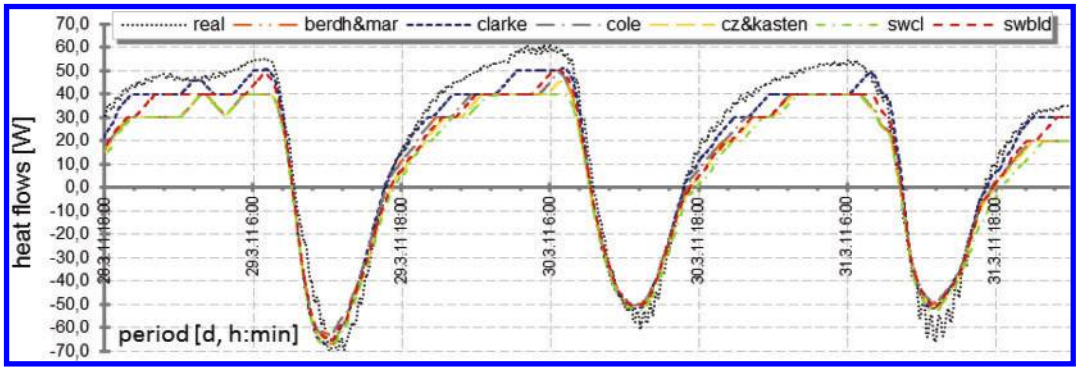


Figure 5. Simlulated heat flows progesses, "real" – measured heat flow; simulated heat flows form pre-defined models (Table 3).

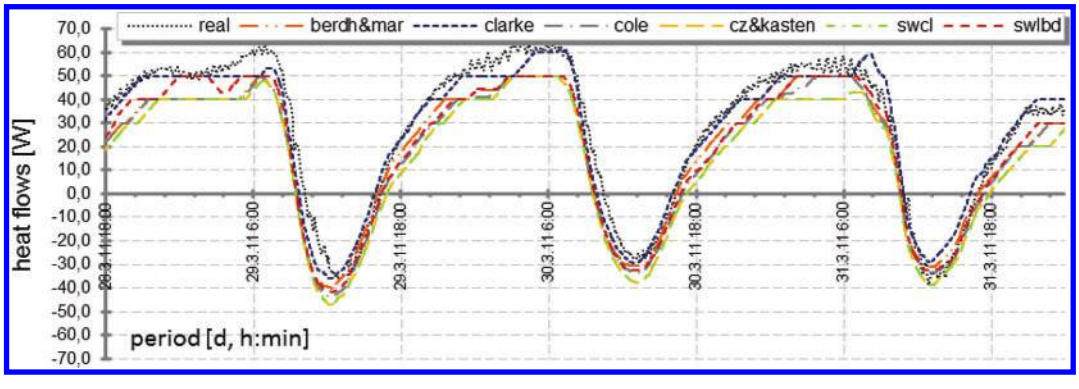


Figure 6. Simlulated heat flows progesses, "real" – measured heat flow; simulated heat flows form pre-defined models (Table 3).

of the external surface, the effects of different emissivity upon the results appear in this sense to have been proven.

5 CONCLUSION

The paper presents results of a study analyzing the programme module MZELWE in the ESP-r system, pointing to certain deficiencies of available sky radiation models that are of key importance for the radiation heat exchange during night-time conditions. The Clarke model appears to be the most convenient among them, having well interpreted the measured course under all circumstances. Detailed observations lead to the finding that Clarke operates with considerably lower sky temperature, which results in favourable heat flow. The other models operate with sky temperature calculations that do not comply with the actually measured heat flow course. This can be due to the

fact that these generalized models have been developed for certain specific circumstances of climate and need not reflect the conditions of some areas. It is also interesting that all of them show almost identical effects, doubtlessly in connection with the application of almost identical mathematical formulae. The mentioned analyses, accordingly, allow to recommend the Clarke model for the regions of central Europe (Slovakia and the Czech Republic) for the given task, i.e. for the calculation of radiation heat exchange between the external surface and the ambient environment, applying the MZELVE module in the ESP-r programme.

ACKNOWLEDGEMENT

This research was supported by the project CZ.1.07/2.3.00/30.0039 of Brno University of Technology and VEGA No. 1/0320/12 research project of Slovak University of Technology.

REFERENCES

Berdhal, P. & Fromberg, R. 1984. Emissivity of clear skies. In *Solar Energy*. 1984, 32(5), s. 663–664.

Berdhal, P. & MARTIN, M. 1982. The termal radiance of clear skies. In *Solar Energy*. 1982, 29, s. 299–314.

Clark, G. 1984. Passive Hybrid Comfort by Thermal Radiation. In *Passive Cooling: American Section of the International Solar Energy Society*. Miami Beach, 1981.

Clark, G.& Allen, CP. 1978. The estimation of atmospheric radiation for clear and cloudy skies. In *Proceedings of the second national passive solar conference*. Phil., Part 2, 1978, s. 676.

Clarke, J. A. 2001. *Energy simulation in building design*. Butterworth-Heinemann.Oxford, 2nd edition 2001. 362 s. ISBN 0 7506 5082 6

Cole, R. J 1976. The Longwave Radiation Incident upon the external Surface of Buildings. In *Building Services Engineer*. Vol 44, 1976, s. 195–206.

Čekon, M. 2011. Twin-boxes: Measurement methodology of building components in real climate conditions (Twin-boxy: Metodika meraniastavebných komponentov v reálnych klimatických podmienkach). In Juniorstav 2011: 13.Odborná konference doktorského studia. Brno, VUT, 4.2.2011. Brno: Vysokéučení technické v Brnč – Fakultasta vební, 2011, ISBN 978-80-214-4232-0. (in Slovak).

Čekon, M. 2012a.Spectral Emissivity Properties of Reflective Coatings. Slovak Journal of Civil Engineering Vol. 20, 2012, No. 2. p. 1–7.ISSN 1210-3896.

Čekon, M. 2012b. Twin-boxes: testing phase and initial experimental measurements. In Buildings and Environment – enviBUILD 2012 (Budovy a prostředí 2012): Proceeding of International Conference, Brno, Czech rep., 25.-26.10.2012. Brno: Vysoké učení technické v Brně, 2012, p. 308–313. ISBN 978-80-214-4600-7.

ESP-r 2010 [online]. ESP-rwindows v 11.8 GCC3: EnergySystemsResearchUnit, UniversityofStrathclyde, Glasgow Scotland, 2001, [cit 2010-11-28]. Available: <http://www.esru.strath.ac.uk/Downloads/downloads.htm#ESP-r>.

Hagentoft, C-E. 2001. *Introduction to Building Physics*: *Studentlitteratur.* Lung Sweden, 2001, s. 422. ISBN 91-44-01896-7

Halahyja, M. et al. 1970. Building thermal technique, lighting and acoustic (Stavebná tepelná technika, osvetlenia akustika), Alfa Bratislava, 1970. (in Slovak)

Hopfe, CH. J. 2009. *Uncertainty and sensitivity analysis in building performance simulation for decision support and design optimization dissertation thesis*. Eindhoven: Eindhoven University of Technology, 2009. 229 s. ISBN: 978-90-6814-617-2. Available: <http://www.bwk.tue.nl/bps/hensen/team/past/Hopfe.pdf>.

Chmúrny, I. 2003. Thermal Performance of Buildings (*Tepelná ochranabudov)*. Jaga group Bratislava, 2003, p. 216. ISBN 80-88905-27-3. (in Slovak)

Kasten, F. & Czeplak, G. 1980. Solar and terrestrial radiation dependent on the amount and type of cloud. In *Solar Energy*, 1980, vol. 24, s. 177–189.

Perez, R. et al. 1990. Modeling Daylight Availability and Irradiance Components from Direct and Global Irradiance. In *Solar Energy*, 44(5), s. 271–289.

Stanzel, B. 1994. External Longwave radiation. In *Chapter 5 in Final Report*, PASSYS Model Validation Subgroup EUR 15115 EN

Subsys. F 2011[online]. In: *Zdrojový kód* ESP-r: University of Strathclyde, Glasgow Scotland, 2001, [cit 2011-05-10]. Avaialable: <http://www.esru.strath.ac.uk/Programs/ESP- r_CodeDoc/esrubld/subsys.F.html>.

Swinbank, W. C. 1963. Long-wave radiation from clear skies. Quart. J. R. Meteorol. Soc. 1963, s. 339–348.

Research and Applications in Structural Engineering, Mechanics and Computation – Zingoni (Ed.)
© 2013 Taylor & Francis Group, London, ISBN 978-1-138-00061-2

Thermal comfort of the rooms in the designing of commercial buildings

K. Nowak, K. Nowak-Dzieszko & M. Rojewska-Warchal
Cracow University of Technology, Division of Building and Building Physics, Cracow, Poland

ABSTRACT: The paper presents the results of the annual computational simulations in the designing of commercial buildings. The calculations were carried out in the Design Builder program which allows preparing the simulation of the building envelope as well as building interior. The simulations conducted for the polish climatic conditions allowed the assessment of the thermal comfort of the entire building and of the particular rooms. Based on those simulations authors determined the influence of different materials, structural solutions, glazing, sunshades on the thermal comfort of the separate rooms. The article emphasizes the individual attitude to the designing of different rooms taking into account the orientation, location, and room usage.

1 INTRODUCTION

It is very rare in the design process to take into consideration the requirements connected with the overheating effect. This issue is closely related to the thermal comfort of the building, especially during the summer months. The microclimate of the interior space is the combined effect of the design process, erection and the utilization of particular rooms. Thermal comfort is affected by human activity, clothing insulation and the environmental parameters such as air temperature, average radiation temperature, air flow speed and relative humidity. The evaluation of thermal comfort is based on the PMV (Predicted Mean Vote) and PPD (Predicted Percentage of Dissatisfied) indexes.

Based on the simulations, the authors determined the influence of different materials, structural solutions, glazing, and sunshades on the thermal comfort of separate rooms during the summer season. The article emphasizes the need to consider thermal comfort in the design process of individual rooms taking into account the orientation, location, and room usage as well as different materials, structural solutions, glazing, and sunshades.

2 MICROCLIMATE OF THE ROOMS

The national regulations regarding building design process draw attention to the expected energy consumption, heat losses and heat gains. In order to increase the solar gains and reduce the heating need, large window areas are located in the southern rooms. The thermal conditions in those specific rooms often become critical due to focusing only on energy needs. In order to avoid those critical conditions the thermal comfort in such south facing rooms should be analyzed to determine the risk of overheating.

Both designing and thermal modernization of the buildings are very interdisciplinary issues. From the building physics point of view those are requirements regarding energy savings, thermal comfort and acoustic insulation of the constructions.

The requirements regarding energy savings become the most significant while the thermal comfort issues are often omitted.

According to the newest Polish regulations from 2009, the building should be designed to avoid risk of overheating during the summer months. This aspect is especially important in the designing of commercial buildings with the significant glazing areas. In those buildings usually the air-conditioning systems are used to ensure the thermal comfort of the users.

3 THERMAL COMFORT

Thermal comfort by ASHRAE 55 is “the condition of mind in which satisfaction is expressed with the thermal environment”.

It is related to the thermal balance of the body which is affected by different parameters: personal (activity level or metabolic rate, thermal resistance of clothing) and environmental (air temperature, mean radiant temperature, relative air velocity, relative humidity).

There are several different methods used for estimation of thermal comfort. International standard PN-EN ISO 7730 „Ergonomics of the thermal environment. Analytical determination and interpretation of thermal comfort using calculation of the PMV and PPD indices and local thermal comfort criteria” and ASHRAE 55 use Fanger’s method.

The PMV (Predicted Mean Vote) method combines the following environmental features: air temperature, air velocity, mean radiant temperature and relative humidity and two personal variables: clothing insulation and activity level into the index that can be used to predict the average thermal sensation of a large group of people. The ASHRAE thermal sensation 7

level scale with values between -3 and 3 describes the thermal sensation between "hot" and "cold".

The PPD (Predicted Percentage of Dissatisfied) index establishes a quantitative prediction of the percentage of thermally dissatisfied people who feel too cold or too warm.

The most well known two-node thermal model is Pierce's model based on two energy balance equations, one for core node and one for skin node. It takes into account the effects of heat accumulation, physical work done, conductive and convective heat transfer by blood, flow between the core and shell, heat loss caused by respiration, metabolic heat generated during physical activities and the heat exchange processes between the skin and its surroundings by means of convection, radiation and evaporation of moisture.

The KSU (Kansas State University) two-node model is based on the changes that occur in the thermal conductance between the core and the skin temperature in cold environments, and in warm environments, it is based on changes in the skin wettedness. In this model, metabolic heat production is generated in the core which exchanges energy with the environment by respiration and the skin exchanges energy by convection and radiation. In addition, body heat is dissipated through evaporation of sweat and/or water vapor diffusion through the skin.

The control signals, based on set point temperatures in the skin and core, are introduced into passive system equations and these equations are integrated numerically for small time increments or small increments in core and skin temperature. The control signals modulate the thermoregulatory mechanism and regulate the peripheral blood flow, the sweat rate, and the increase of metabolic heat by active muscle shivering. The development of the controlling functions of skin conductance, sweat rate, and shivering is based on their correlation with the deviations in skin and core temperatures from their set points.

4 BUILDING SIMULATION

The aim of the building simulations was to assess the importance of different factors influencing the thermal comfort of the entire building, of separate rooms and possible overheating during summer months.

The numerical building simulations were conducted for the academic building, plan area 72.9 m × 21.7 m; 10.5 m high with three levels.

In the chosen building there are many south facing windows. Visualization of the south building elevation is presented in Figure 1.

Percentage share of glazing areas at the elevations is as follows:

N – 69%
S – 44%
E – 46%
W – 46%

Exterior walls made of solid brick, 20 cm of insulation with plaster at both sides: $U = 0.18$ [W/m^{2}K] (the value meets the polish standard requirements for external walls in this kind of building which should not exceed $U = 0.3$ [W/m^{2}K]), concrete flat roof, insulated with 5 cm of styrofoam: $U = 0.59$ [W/m^{2}K], slab on ground insulated with 5 cm of styrofoam: $U = 0.50$ [W/m^{2}K], double glazing windows: $U = 1.7$ [W/m^{2}K].



Figure 1. Model view of the building, south elevation.

Building with the natural ventilation, gas heating system with convection heaters.

Communication area located in the center part of each building story, office rooms located at the south side of building (similar at each level). The area of office rooms is relatively small but the ratio of the window area to the single room area is significant.

Lecture classes located on the south, north-east and north-west sides of the building.

The calculations were carried out in the Design Builder v.3 program which provides a simulation of the building envelope and the Energy Plus program for simulations of building interiors. The simulations conducted for the Polish climatic conditions (building located in Cracow) allowed the evaluation of the thermal comfort of the entire building and of the particular rooms.

The main aim of simulations was to determine the temperature of the building interior space and of the particular rooms during summer months.

In the first phase of simulations the building was modelled in the service conditions.

The assumptions for the first phase of simulations (base case):

1. Heating system on from September to March (22°C), 7 days per week, 24 hours a day.
2. Occupancy density:
   – Office rooms – 0.1 person per m^2
   – Lecture classes – 0.85 person per m^2
3. Operating Schedule:
   – Office rooms – July thru August 8:00 – 16:00, 5 days a week; September thru June 8:00 – 21:00, 7 days a week
   – Lecture classes – September thru June 7:30 – 21:00, 7 days a week, July thru August 7:30 – 21:00, 5 days a week
4. Metabolic activity: factor 0.9, winter clothing – clo = 1.0, summer clothing clo = 0.5.
5. Ventilation
   – Office rooms – one ac per hour
   – Lecture classes – five ac per hour

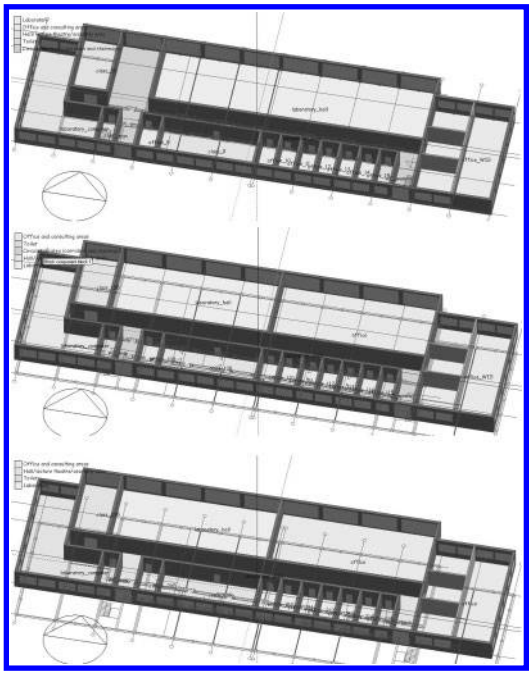


Figure 2. Building zones visualization – ground floor, first floor, second floor.

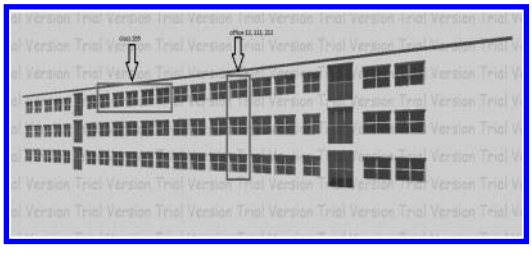


Figure 3. Visualization of south building elevation. Windows in rooms 13, 113, 213.

5 TESTS RESULTS

The thermal comfort of the entire building as well as microclimate conditions of three different office rooms, 13 at ground level, 113 at the first floor and 213 at the second floor, were separately analyzed, Figure 4.

The thermal comfort conditions of the entire building were not met. The simulation results, Figure 4, have shown that on a few days between 15th of May and 15th of September the average interior air temperatures of the different rooms exceed 30°C and the PMV factor is higher than 1.5. Those microclimate building conditions exceed the optimal internal summer temperature of 25°C and recommended value $-0.5 < \mathrm{PMV} < +0.5$.

In the lecture class located at the south building side, on the second floor, the operative temperature for most of time is significantly higher than 25°C. The daily maximum interior temperature is 34,41°C and

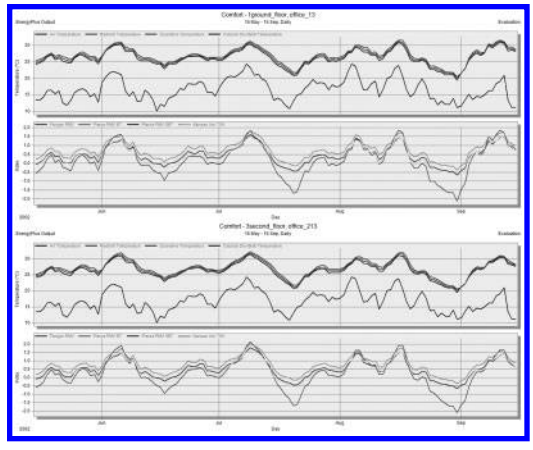


Figure 4. Simulation results for office rooms: 13,113 and 213. a – temperature – air temperature inside, radiant temperature, operative temperature, outside dry bulb temperature; b – PMV comfort factor (Fanger, Pierce, TSV Model).

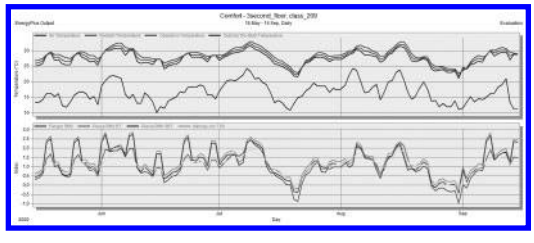


Figure 5. Simulation for lecture class 209. a – temperature – air temperature inside, radiant temperature, operative temperature, outside dry bulb temperature; b – PMV comfort factor (Fanger, Pierce, TSV Model).

the PMV value is above 2, Figure 5. The number of discomfort hours in the assumed period of time is 1127. Those negative room conditions continue almost for the entire day and do not change significantly during the night. Due to the safety conditions rooms cannot be cooled during the night through the open windows.

The primary factor affecting thermal comfort is the percentage share of glazing at the south elevation in those particular rooms.

The significant internal gains are affected by the high occupancy density especially in the lecture classes – 0.85 person per m^2. In practice the number of students in the lecture class (209) is usually smaller than assumed in the analysis.

The second phase of the modelling focused around the impact of internal shadings on the thermal comfort. To lessen the unfavorable influence of glazing during summer months with the same occupancy density, the internal gains were reduced by internal solar shadings (blinds with medium reflexivity slats).

Comparing Figure 4 with the findings shown in Figure 6 (for the same rooms) reduction of hours with the high operative temperature can be observed. The usage of internal shadings eliminated the temperature higher than 30^{o}C.

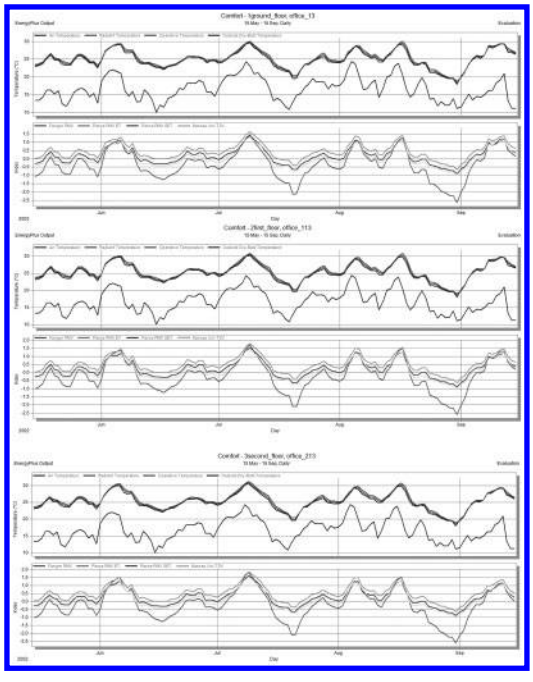


Figure 6. Simulation results for office rooms: 13,113 and 213 with the internal shadings. a – temperature – air temperature inside, radiant temperature, operative temperature, outside dry bulb temperature; b – PMV comfort factor (Fanger, Pierce, TSV Model).

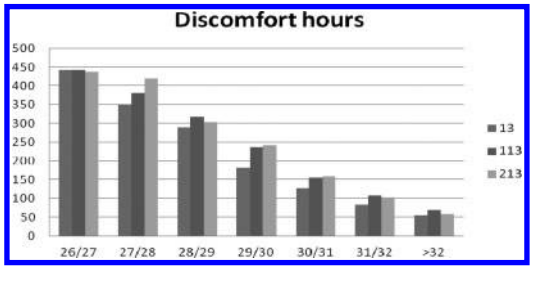


Figure 7. Number of overheating (discomfort) degree hours for separate office rooms (13, 113, 213) with the internal shadings.

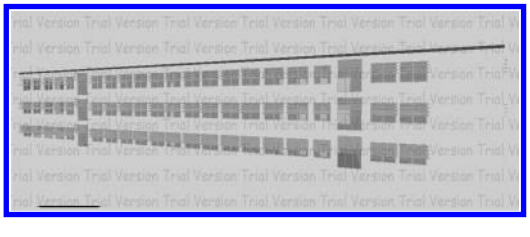


Figure 8. Visualization of the external louvers.

Much more significant results could be observed after applying the internal shadings together with the external shading panels. Four panels (louvers blade), were assumed, Figure 8.

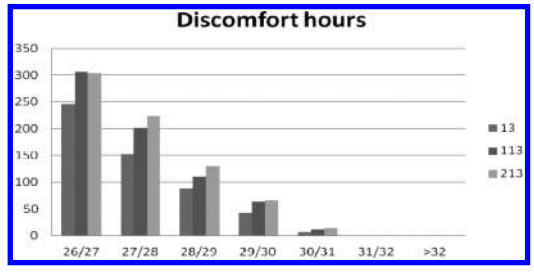


Figure 9. Number of overheating (discomfort) degree hours for separate office rooms (13, 113, 213) with the internal shadings and external louvers.

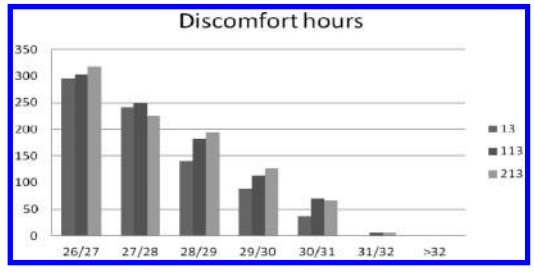


Figure 10. Number of overheating (discomfort) degree hours for separate office rooms (13, 113, 213) with the internal shadings and reduced window areas.

Both in the lecture class and office rooms with the extensive windows area at south elevation the combination of internal shadings and external louvers improved the thermal comfort significantly.

The number of discomfort hours during the summer months in the analyzed rooms was significantly lessened up to 65%. The usage of external shadings almost entirely eliminated the operative temperatures above 30^{o}C. It can be noticed that the number of discomfort hours is connected with the location of rooms at different levels.

The surface of the glazing at the south elevation of the building is 44%. In the single office room the window area is 4.72 m^2 which is the 23% of the floor area. Due to the lighting requirements the window area cannot be smaller than 2.5 m^2.

Such reduction of the window area should reduce solar gains in the summer months and reduce the heat need during winter months. The results of such simulations are presented in Figure 10 and Figure 11.

Comparing Figure 10 with the findings shown in Figure 7 (for the same rooms), for the external shadings combined with the reduced area of windows, the significant reduction of hours with the high operative temperature can be observed.

As it is the existing building structure, from the economical point of view, the more advantageous solution is the one presented in Figure 9 (glazing area 4.72 m^2, together with the combined external and internal shadings).

Another factor affecting the thermal conditions inside the building are the external shading objects

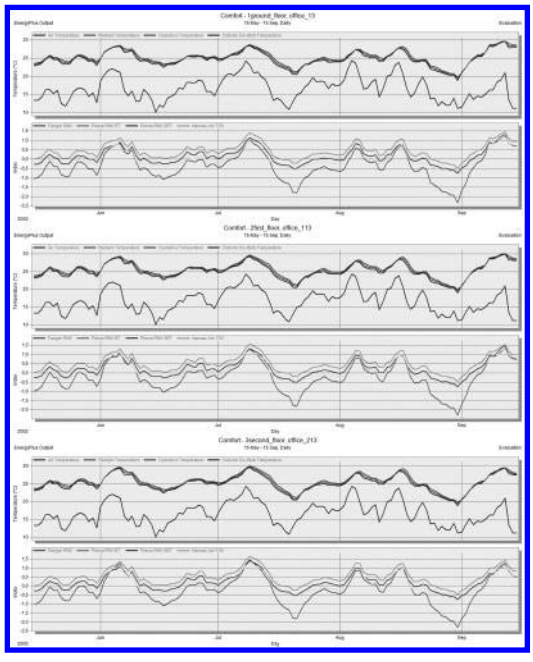


Figure 11. Simulation results for office rooms: 13,113 and 213 with the internal shadings and reduced window areas. a – temperature – air temperature inside, radiant temperature, operative temperature, outside dry bulb temperature; b – PMV comfort factor (Fanger, Pierce, TSV Model).

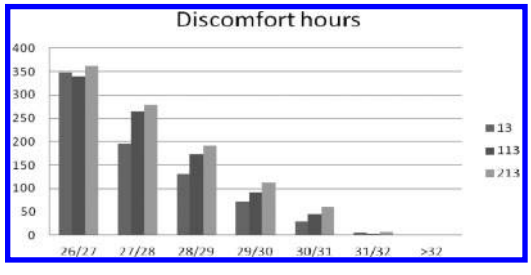


Figure 12. Number of overheating (discomfort) degree hours for separate office rooms (13, 113, 213) with the internal shadings including tree growing at the front of the building.

next to the building, such as different building structures or trees.

As the next modelling stage, a set of simulation runs was conducted for the actual window areas and including the tree growing in front of the south elevation of the building, opposite the windows in rooms 13, 113 and 213. Assumed diameter of trunk is 50 cm and branches 3.0 m.

The simulation results, Figure 12, are much better than for the ones for the same window area but without external shading object, Figure 7. The number of discomfort hours in the analyzed rooms was significantly lessened from 42% up to 48,8%. The significant reduction of the temperatures above 30°C may be observed. The tree does not allowed for the rooms overheating.

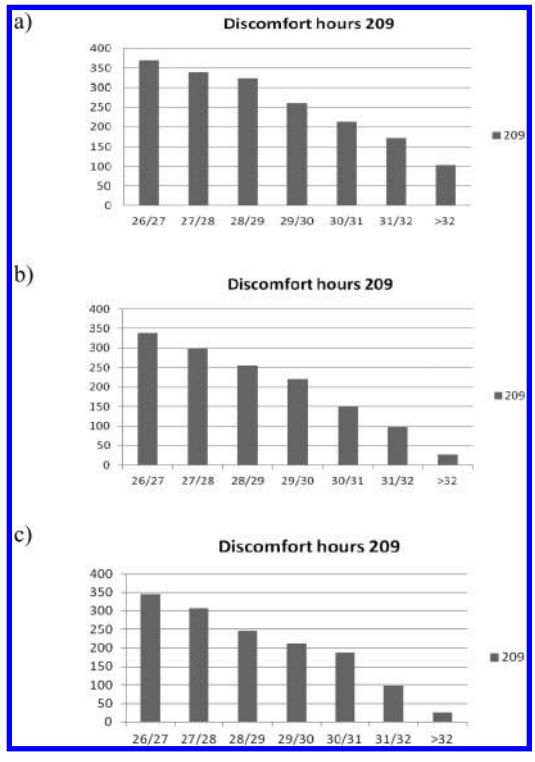


Figure 13. a) Number of overheating hours for lecture class 209; b) Number of overheating hours for room 209 with the internal and external shadings; c) Number of overheating hours for room 209 with the internal and external shadings combined with the reduced window areas.

For the lecture class 209, with the surface area of 93,51m^2, the proposed solutions do not improve the thermal conditions as significantly as in case of office rooms. The base simulation results for lecture class shown in Figure 5, for office rooms in Figure 13.

Such lecture class with 45 percentage of glazing and high occupancy density requires applying of air-conditioning systems in order to obtain the thermal comfort of users.

The significant influence of the external temperature drops on the lowering of PMV factors may be observed in Figures 4, 5, 6 and 11.

The users way of dressing is affected by the atmospheric conditions. If in the analyzed spring and summer periods the external temperat333ure drops below 15°C, than the higher clothing factor clo should be assumed. In the all conducted simulation the clo value was constant, equal to clo = 0.5. That explains the periodic drop of PMV factor below −0.5.

6 CONCLUSIONS

Most of the new office and commercial buildings are designed with extensive south facing window sections, which in most cases are poorly shaded from solar radiation. Glazing is the source of the excessive heat gains

and may result in the overheating of the entire building but specifically of separate rooms located at the south side of the building. The work conditions in those specific rooms appear to be very uncomfortable.

When using glass facades in building construction it is necessary to consider, at the designing stage, the thermal comfort conditions both for the entire building and for separate rooms.

The conducted simulations result in the following conclusions:

1. Modernization of the building should be preceded by the extensive analysis of how the changes influence thermal comfort of the rooms.
2. In the rooms with a significant glazing ratio the level of solar protection, shadings and window area appear to have the greatest influence on the thermal comfort.
3. Cooling of the rooms must be applied if none of the external or/and interior shading systems are used to avoid overheating.
4. The building surroundings, buildings and trees may affect the thermal comfort of individual rooms.

REFERENCES

ASHRAE 2001. *Thermal comfort conditions for human occupancy, Standart 55–81*. Atlanta.

PN-EN ISO 7730 *"Ergonomics of the thermal environment. Analytical determination and interpretation of thermal comfort using calculation of the PMV and PPD indices and local thermal comfort criteria"*

Nouidui, T. S., K. Phalak, W. Zuo, and M. Wetter 2012. Validation and Application of the Room Model of the Modelica Buildings Library. LBNL Report Number LBNL-5932E

Holopainen R. (ed.) 2012. *A human thermal model for improved thermal comfort*. Espoo: VTT Technical Research Centre of Finland.

Orme M., Palme J.r, Irving S., Control of Overheating in Well-Insulated Housing, CIBSE http://www.cibse.org/pdfs/7borme.pdf

Nowak K., 2011. Modernizacja budynków a comfort cieplny pomieszczen. *Energia i Budynek*, ISSN 1897-5879, 29–33

25. Timber structures

Research and Applications in Structural Engineering, Mechanics and Computation – Zingoni (Ed.)
© 2013 Taylor & Francis Group, London, ISBN 978-1-138-00061-2

Behaviour of steel to timber connections in fire and normal conditions

A. Bouchaïr & P. Racher
Clermont Université, Université Blaise Pascal, Institut Pascal, Clermont-Ferrand, France
CNRS, Institut Pascal, Aubière, France

D. Dhima
CSTB, Marne-la-Vallée Cedex 2, France

ABSTRACT: Experimental and numerical modelling program was performed in France. It concerned tests on steel-to-timber connections with various mechanical loadings, in normal and fire conditions. The experimental results show the failure modes of the connections including the brittle or ductile character. They are used to calibrate the developed numerical models simulating the mechanical and the thermo-mechanical behaviour of the tested connections. The accuracy of the mechanical model is evaluated on the basis of the global behaviour of the connections until failure. The thermo-mechanical model is evaluated comparing the calculated and the measured values of temperatures and fire duration resistances. The nonlinear behaviour of materials is considered in normal and fire conditions. In this study, the experimental and the numerical results are summarized for normal and fire conditions. The results show the failure mechanisms in steel-to-timber connections and illustrate the accuracy of the numerical approaches used in the modelling of the real behaviour of steel-to-timber connections in normal and fire conditions.

1 INTRODUCTION

In fire situation as well as in normal condition, the connections govern the bearing capacity and the mechanical behaviour of timber structures. Regarding the actual architectural trends and high strength requirements, connections with slotted-in steel plates are commonly used to improve the mechanical resistance in normal and fire conditions. The complex mechanical behaviour of timber connections is influenced by connection geometry, plastic moment of the fastener and the embedding properties of wood. As the stress distribution along the dowels is not uniform, 3D-FEM model is proposed to investigate the mechanical performance of timber connections (Xu et al 2009a, Xu et al 2009b).

Numerical studies using the 3D-FEM model with Hill yield criterion for orthotropic material showed that the mechanical behaviour of timber connections with multiple dowel-type fasteners is stiffer than the experimental ones (Racher et al 2010). However; the numerical models taking into account the progressive failure of timber using the Hoffman and Tsai-Wu criteria showed a good prediction of the real behaviour of timber connections (Xu et al 2009a).

For dowel-type connections with ductile failure mode, the behaviour is characterized by the bending of the fastener and/or the embedment of the fastener into the wood.

Although experimental and numerical studies exist in the literature (Buchanan 2000, Racher et al 2010) and the progress given by EN1995-1-2 (EN1995 2004) to the design of timber connections, large limitations still exist due to the lack of data (Audebert et al 2010, Audebert et al 2012). As for normal conditions, numerical models are proposed to study the behaviour of timber joints in fire conditions. Thus, a numerical modeling approach is initiated at Blaise Pascal University and CSTB to simulate the thermo-mechanical behaviour of dowelled timber connections in fire with mechanical loading.

The model represents well the thermal and thermo-mechanical behaviour of the connections in fire situation mainly the discontinuities at the interface between steel and timber. Some results are presented for the steel-to-timber connections loaded in tension parallel or perpendicular to grain in fire situation. The fire exposure of the connections considered in the tests and the models is based on the nominal fire given by the ISO 834 curve (EN1991-1-2 2003).

In this paper, the Hoffman failure criterion associated with the Hill criterion to control the plastic yielding is used. A non-linear 3D-FEM model predicts well the behaviour of steel-to-timber joints loaded in tension parallel or perpendicular to grain (Xu et al 2009a, Xu et al 2009b, Audebert et al 2011, Audebert et al 2012). This approach, validated by comparison with experimental results, is used in normal conditions

and fire. The thermal and the mechanical modeling are done using the finite element software MSC-Marc (Msc.Marc 2005).

2 CONNECTIONS IN NORMAL CONDITION

2.1 *Test setup*

The tests concern double shear steel-to-timber connections with 2*4 fasteners (6 dowels and 2 bolts) for the specimen in tension parallel to grains and 2*2 dowels for the specimen in tension perpendicular to grain (Figure 1). The bolts are generally used to prevent the separation between the connected members. Two or Three diameters of fasteners are considered (12, 16 and 20 mm) to cover the main range of diameters used in practice.

The experimental results of the steel-to-timber connections loaded in tension parallel or perpendicular to grain are used to validate the mechanical 3D-FEM model. The tests performed in normal condition provided the load-displacement curves and the failure modes.

The dimensions of the tested connections are chosen according to the requirements of spacing and size of EN1995-1-2. In addition to these minimum requirements, the end and edge distances towards the fasteners have been increased by a value a_{fi}. This additional thickness is used to take into account the charring rate of wood. The thickness t_1 is chosen considering the usual glulam dimensions and the thickness to dowel diameter ratio.

The tension load is applied on the steel plate with a fixed timber parts (Figure 1). Two or three replications were realized for each connection configuration. During tests, the relative displacement is measured between the steel plate and the wood members.

2.2 *Failure loads in normal conditions*

Figure 4 shows the load-slip curves of cold tests. Different failure modes are observed, depending on the ratio between the member thickness t_1 and the fastener diameter. In the connections loaded in the direction parallel to grain and the diameters of 16 mm, the ultimate failure arises mainly by wood block shear or splitting but with significant yielding of the fastener combined with wood embedment. With diameters of 20 mm, the connections exhibit generally a brittle failure in block shear or splitting of wood. In the direction perpendicular to grain, the failure arises mainly in splitting on one line of the fasteners (Figure 5) with yielding of the dowels.

2.3 *Finite element model*

3D-FEM model is developed where timber and steel materials with contact were modelled. Considering the symmetry, only one quarter of the connection geometry was modelled. The loads are introduced by increasing controlled displacements applied on all nodes in the top of timber member (Figure 2).

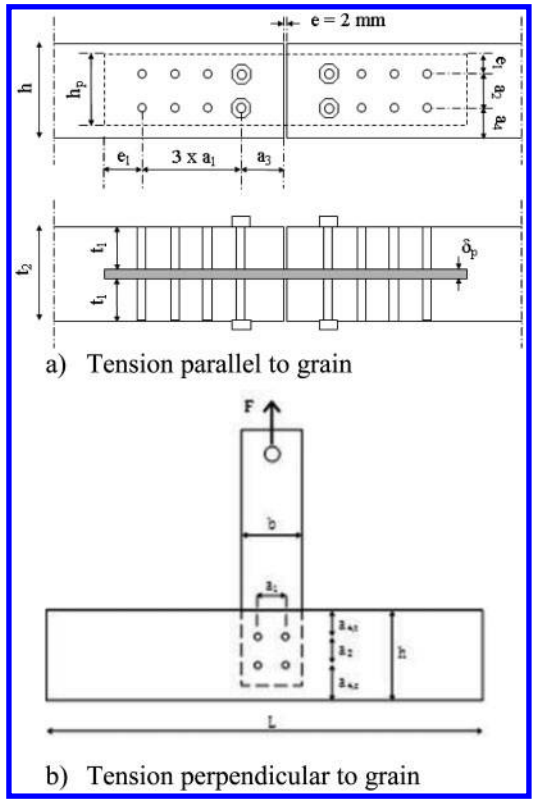


Figure 1. Tested steel-to-timber connections.

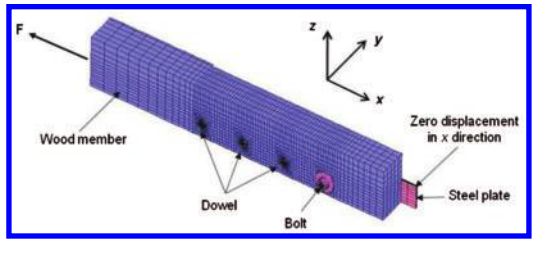


Figure 2. Meshing of a tested timber connection.

Steel is considered isotropic with elastic-plastic behaviour and its yielding is managed using Von Mises criterion. Timber is considered as orthotropic with elastic-plastic behaviour. The Hoffman failure criterion is used to control the damage evolution of timber during the load. It is an adaptation of the Hill criterion to allow unequal stresses in tension and compression.

$$\left[\begin{array}{l} C_1(\sigma_y-\sigma_z)^2+C_2(\sigma_z-\sigma_x)^2+C_3(\sigma_x-\sigma_y)^2+ \\ C_4\sigma_x+C_5\sigma_y+C_6\sigma_z+C_7\tau_{yz}^2+C_8\tau_{xz}^2+C_9\tau_{xy}^2 \end{array}\right] / F$$

$$\text{With}: C_1=\frac{1}{f_{t,90}f_{c,90}}-\frac{1}{2f_{t,0}f_{c,0}}; C_2=C_3=\frac{1}{2f_{t,0}f_{c,0}};$$

$$C_4=\frac{1}{f_{t,0}}-\frac{1}{f_{c,0}}; C_5=C_6=\frac{1}{f_{t,90}}-\frac{1}{f_{c,90}}; C_{7,8,9}=\frac{1}{f_v^2}.$$



Figure 3. Failure mode in tension parallel to grain (test and model).

The damage evolution is simulated through a reduction of the elastic modulus at the integration point where the criterion is reached (Xu et al 2009a). In order to control the plastic yielding with the damage evolution of timber, the Hoffman failure criterion, combined to the Hill yield criterion, is used in the finite element model. The contact at the interfaces between the components of the connection is managed using the deformable contact elements and the direct constraint method in MSC.Marc.

The 3D-FEM model is validated on the basis of the load-slip curves of timber connection and the failure modes.

Figure 3 shows the failure mode and figure 4 illustrates the comparison between the load-slip curves given by the 3D-FEM model and those from experiments using two models. In model 1, timber is elasto-plastic orthotropic with Hill yield criterion. In model 2, the Hoffman failure criterion is associated with the Hill criterion to control the plastic yielding combined with the damage evolution of timber. The failure load is determined when the load starts to decrease with the increase of the controlled displacement. The comparison between tests and models shows that the numerical load-slip curve of model 1 is stiffer than the experimental one. However, the model 2 predicts well the resistance of the connections. It shows a relative error less than 5% in comparison with the experimental values. Thus, this 3D-FEM model with Hoffman failure criterion is an appropriate tool to represent the nonlinear behaviour until failure of timber connections.

3 FIRE RESISTANCE OF THE CONNECTIONS

Based on the connections analyzed in normal condition, similar specimens are tested in fire conditions. The failure loads obtained in normal conditions are used to define the load to be applied on the connections during fire test using the chosen load ratio η_{fi}. Several thermocouples are introduced at different locations inside the connection members to measure the temperatures during fire tests. The thermal and the thermo-mechanical 3D-FEM models are validated on the basis of measured temperatures and the time to failure of connections.

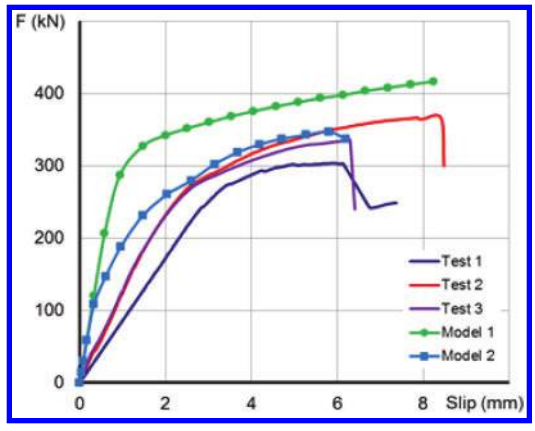


Figure 4. Comparison of experimental and numerical load-slip curves.

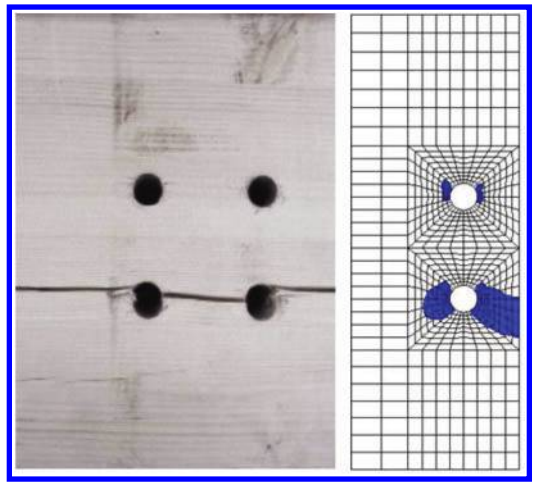


Figure 5. Failure mode in tension perpendicular to grain (test and model).

The thermo-mechanical behaviour of timber connections in fire is very complex because of the difficulty to analyze the mass transfer of water inside the wood members and the degradation of materials in fire (Audebert et al 2011, Audebert et al 2012). In the study, the evolutions of the physical and mechanical characteristics depending on the temperature are considered. Thus, the thermo-physical parameters, mainly the thermal conductivity, considered are called effective because they combine the coupled heat and mass transfers. In the approach, the thermo-mechanical problem is analyzed in two phases (König 2005). The thermal analysis is performed to obtain the temperature field inside the connection components. Then, the thermo-mechanical model is built with constant applied external load considering the evolution of the mechanical characteristics of the materials depending on the temperature.

During the fire tests, the temperature in the furnace and in various parts of the connection and the displacement between the connected members are measured.



Figure 6. Failure along the fasteners rows in tension parallel to grain.

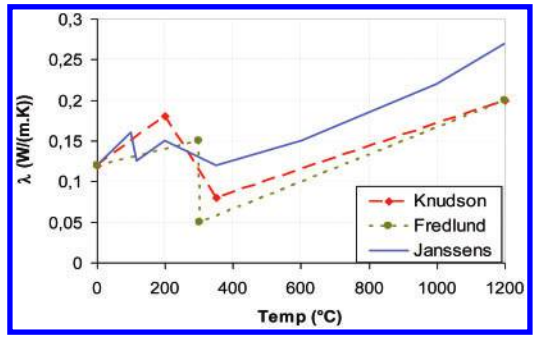


Figure 7. Thermal conductivity of wood.

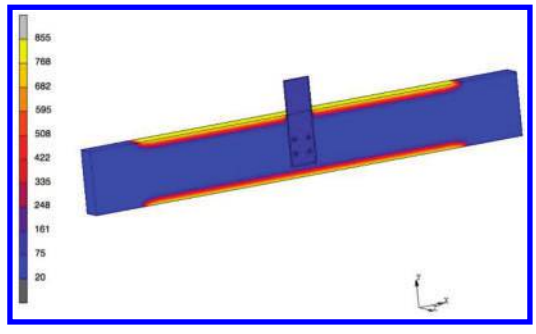


Figure 8. Temperature fields (direction perpendicular to grain, t = 30 min).

The time to failure of the connection corresponds to the acceleration of the displacement during fire exposure. The thermo-mechanical model is validated comparing its failure time with that from tests. In fire tests, the protocol for mechanical loading is defined with a pre-loading up to 40% and unloading to 10% of $F_{u,test}$, where $F_{u,test}$ is the failure load given by tests in normal conditions, the specimen is reloaded to a load ratio η_{fi} equal to 10%, 20% or 30% of $F_{u,test}$. Then, the fire exposure according to the curve ISO 834 starts. The load ratio is kept constant throughout the exposure to fire until the failure of the connection. The supports of the tested specimen are located out of the furnace where the fire action is considered homogeneous.

The obtained results show that, for all the considered loading ratios, the fire resistance is always greater than 30 minutes (Audebert et al 2011). The final failure mode observed for all the tests, in tension parallel to grain, is the shear in the wood members along the fasteners rows (Figure 6). However, the dowels showed a significant plastic deformation in bending mainly for the dowels of 12 and 16 mm.

3.1 *Thermo-physical properties of materials*

The heat transfer within the connection is modeled considering the evolutions of the apparent thermo-physical properties of wood such as the thermal conductivity and the specific heat (for example see figure 7). The well known thermo-physical properties of steel are given by Eurocode 3 (EN1993-1-2 2005). However, the evolutions of the thermo-physical properties of timber depending on temperature are taken from the bibliography. As wood is a complex material, many differences are shown in the available characteristics, particularly the thermal conductivity.

Under thermal and pressure gradient actions, a part of water vapor migrates outside the specimen and another part migrates toward the coldest parts inside the connection. This internal migration of water vapor is condensed back on a certain thickness of wood in contact with the steel plate, then, evaporates with heating. Thus, the apparent values of conductivity represent well the evolution of temperature inside wood only in the zones far from the steel plate. Some adaptations of the apparent values of thermophysical parameters are made to take account of the near the steel plate inside the connection (Audebert et al 2011, Audebert et al 2012).

A sensitivity analysis was performed to find the most appropriate thermo-physical characteristics to be used in the modeled connections. It shows that for wood components the best combination of thermal conductivity and specific heat, giving the best numerical results is obtained using the thermal conductivity values proposed by Janssens and the specific heat values proposed by Fredlund/Janssens.

An adaptation of specific heat is done to take account of the physical effects of the evaporation peak at 100°C near to steel plate playing the role of barrier. Thus a peak of specific heat to 100 kJ/(kg.°K) is taken into account in the model, for a layer of wood with a thickness of 3 mm, near the interface between the wood and the metal plate.

3.2 *Thermal model*

For the thermal calculation, it is assumed that all interfaces wood-steel plate, steel plate-fasteners and wood-fasteners are in perfect contact with continuous meshing. The faces in contact with the hot gases are subjected to thermal actions. The heat transfer modeling gives the distribution of the temperature field on the nodes of the elements constituting the connection components for each step of time or gas temperature (for example, see figure 8).

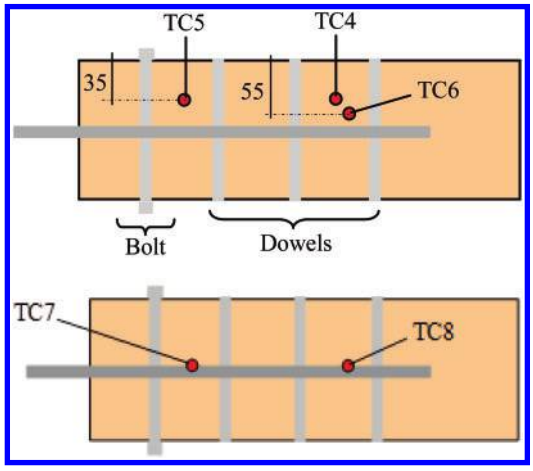


Figure 9. Thermocouple locations in wood member and metal plate.

The temperature values given by the numerical model are compared with those measured by the thermocouples in some locations in the connection along the fasteners, inside the wood members and on the steel plate. Figure 10 shows the evolution of the temperature versus time of fire exposure in the points of measurement given on figure 9.

The comparison between the temperature-time curves given by the numerical model (FEM) and the experimental results (Test) show the good accuracy of the numerical model. In wood members, the thermocouples TC4 and TC5 are located at 40 mm from the metal plate area and the thermocouple TC6 is placed at 20 mm from the interface wood-metal plate.

Differences between simulated and measured temperatures in the wood member appear beyond 300°C (Figure 10). The model does not represent accurately the temperatures in burned area. However, these differences have no influence on the thermo-mechanical behaviour of connections because the wood has no strength beyond 300°C. The measured temperatures at the metal plate area show a quasi-constant temperature between 80 and 100°C on a significant period of time confirming the barrier effect of the steel plate (Figure 10). The results obtained by the numerical model, using a local high value of the specific heat for wood, are in good agreement with the experimental values.

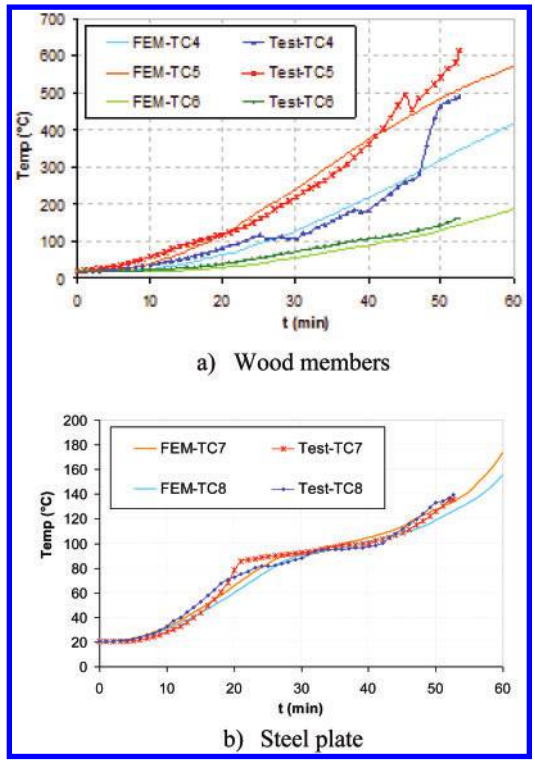


Figure 10. Numerical and experimental temperatures.

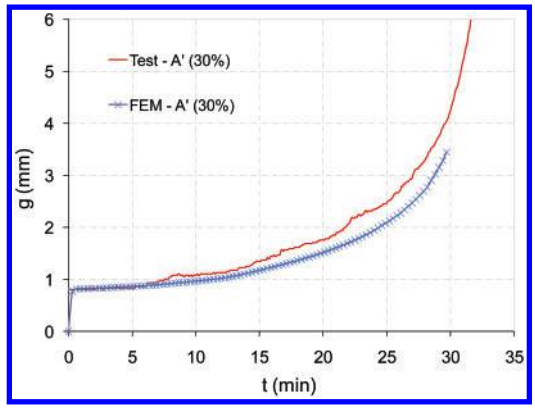


Figure 11. Time-slip comparison (FEM/test) with a load ratio of 30% (direction parallel to grain).

4 THERMO-MECHANICAL MODEL

The thermo-mechanical analysis of the connections takes into account the evolution of mechanical properties of materials depending on temperatures. This evolution is considered using reduction coefficients of the mechanical properties depending on the temperature at each point of integration in the finite elements of the mechanical model. The reduction factors used are those provided by the Eurocodes EN1993-1-2 (EN1993-1-2 2005) for steel and EN1995-1-2 (EN1995-1-2 2004) for timber.

The comparison of the fire resistance obtained by numerical model and tests is based on the evolution of the connection slip depending on the time of exposure to fire. The increment of time used in the model is constant and the duration of fire resistance is defined as the time from which there is a high increase of the slip (displacement between the connected components of the connection). These curves show comparable tendency where the numerical model represents well the linear and the nonlinear phases of the experimental slip-time curves. The model is used to predict the time

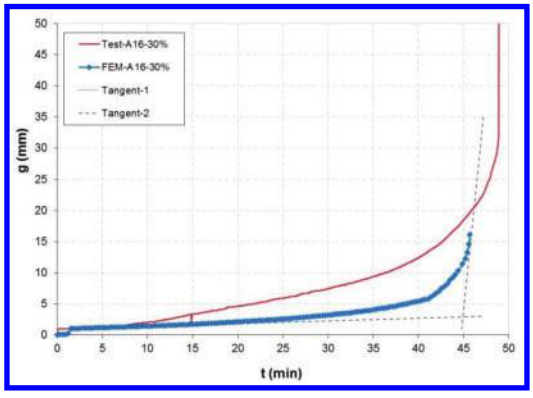


Figure 12. Time-slip comparison (Fem/test) with a load ratio of 30% (direction perpendicular to grain).

of failure of the connection exposed to fire. Figures 11 and 12 show the comparison for connections loaded in the direction parallel and perpendicular to grain.

5 CONCLUSIONS

3D-FEM model for steel-to-timber connections loaded in the direction parallel or perpendicular to grain is developed. Hoffman failure criterion associated with the Hill criterion is proposed to control the plastic yielding combined with the damage evolution of timber. The material model considers not only the asymmetric mechanical behaviour of timber in tension and compression, but also the elasto-plastic compression and the stiffness degradation governed by failure criterion with stress interactions. The proposed FEM model shows the capacity to describe the behaviour of timber connections made with dowel type fasteners. This is confirmed by the comparison of experimental and numerical load-slip curves.

The numerical model is extended to simulate the thermo-mechanical behaviour of the connections. The methodology developed for the thermo-mechanical analysis of the connection makes a distinction between the thermal and the mechanical models and use different meshes for each model. It is thus possible to create a continuous mesh for the thermal study, to guarantee the thermal continuity between the various components of the connection, and a discontinuous mesh for the mechanical calculation to take account of the contact between the different components of the connection.

The thermal model is validated by the comparison of the calculated and the measured temperatures during fire tests. The numerical model, with the chosen values of thermal characteristics, represents accurately the heat transfer in the connection components (timber, fasteners and metal plate). It should be noted that the hypotheses considered in this model, mainly the evolutions of the physical and the mechanical properties versus the temperature, have been validated for the connections considered in the study.

This 3D-FEM model is a practical tool to investigate timber connections with multiple dowel-type fasteners. It allows saving the experimental time and cost and also predicts well the stiffness and ultimate load of timber connections. Besides, there are only few 3D-FEM models for timber connections available in literature, which makes the proposed model as important contribution.

ACKNOWLEDGEMENT

The authors wish to thank the WoodWisdom-Net ERA-NET Project (FireInTimber, 2007–2010), the French Ministry of Agriculture (MAP), European wood industry through BWW Building With Wood, CSTB and Blaise Pascal University for the support provided to the study.

REFERENCES

Audebert M, Dhima D, Taazount M, Bouchaïr A. 2011. Numerical and experimental investigations on the thermo-mechanical behaviour of steel-to-timber joints exposed to fire. *Engineering Structures*, 33: 3257–3268.

Audebert M, Dhima D, Taazount M, Bouchaïr A., 2012. Behaviour of dowelled and bolted steel-to-timber connections exposed to fire. *Engineering Structures* 39: 116–125.

Buchanan AH. 2000. Fire performance of timber construction. *Progress in structural engineering and materials,* 2(2):278–289.

EN 1995-1-2: 2004, Eurocode 5. Design of timber structures. Part 1–2: General rules – Structural fire design. CEN TC 250-SC5, 2004.

EN 1991-1-2: 2003, Eurocode 1. Actions on structures. Part 1-2: General actions – Actions on structures exposed to fire. 2003, Brussels.

EN 1993-1-2: 2005, Eurocode 3. Design of steel structures. Part 1–2: General rules – Structural fire design. 2005, Brussels.

König J. 2005. Effective thermal actions and thermal properties of timber members in natural fires. *Fire and Materials,* 30:51–63.

MSC.MARC. 2005. User's Manual.Vol. A: theory and user information. MSC.Software Corporation.

Racher P, Laplanche K, Dhima D, Bouchaïr A. 2010. Thermo-mechanical analysis of the fire performance of dowelled timber connection; *Engineering Structures*, 32(4): 1148–1157.

Xu BH, Bouchaïr A, Taazount M, Vega EJ. 2009a. Numerical and experimental analyses of multiple-dowel steel-to-timber joints in tension perpendicular to grain. *Engineering Structures* 31:2357–2367.

Xu B.H., Taazount M., Bouchaïr A., Racher P. 2009b. Numerical 3D finite element modelling and experimental tests for dowel-type timber joins. *Journal of Construction and Building Materials*, 23(9): 3043–3052.

Research and Applications in Structural Engineering, Mechanics and Computation – Zingoni (Ed.)
© 2013 Taylor & Francis Group, London, ISBN 978-1-138-00061-2

Shaking table tests on a large scale moment resistant timber frame with post-tensioning and energy dissipating system

F.C. Ponzo, A. Di Cesare, M. Simonetti & D. Nigro
School of Engineering, University of Basilicata, Potenza, Italy

T. Smith & S. Pampanin
Department of Civil and Natural Resources Engineering, University of Canterbury, Christchurch, New Zealand

ABSTRACT: Post-tensioned timber is a new form of seismic resisting timber construction which already has real building applications in New Zealand. The innovative high seismic performance system combines the use of precast concrete PRESSS technology and engineered wood products combining post-tensioning rods with large timber members. These two elements provide elastic recentering to the structure when subjected to horizontal seismic excitation. Additional steel dissipation devices are often also placed in order to provide additional strength and dissipative capacity. The following paper describes the dynamic testing to be performed in the structural laboratory of the University of Basilicata, Potenza, Italy on a 3-storey post-tensioned timber structure. The specimen is 2/3rd scale and made up of frames in both directions. Testing will be performed both with and without the addition of dissipative steel angles. This paper describes the testing set-up, the details of the frame, the steel angle devices and the shaking table testing program.

1 INTRODUCTION

This paper presents the design and planned test set-up for the experimental investigation into the seismic performance of a 2/3rd scale three-storey post-tensioned timber frame building in the structural laboratory of the University of Basilicata in Potenza, Italy. This work is part of a collaborative experimental campaign between the University of Basilicata (UNIBAS), and the University of Canterbury, in Christchurch, New Zealand. An extensive dynamic experimental testing programme is scheduled to be performed. The aim of the project is to further evaluate the seismic performance of the system and improve understanding of its dynamic performance in its use for multi-storey timber construction.

The post-tensioned timber concept (under the name PRES LAM) has been developed at the University of Canterbury and extensively tested (beam-column, wall/column-foundation, 3d frame and wall structure) in the structural laboratory of the university (Newcombe et al. 2010; Palermo et al. 2005; Smith et al. 2007). This testing has however solely used Laminated Veneer Lumber (LVL) a product widely available in New Zealand but not globally.

In stage one of this current collaborative project a full-scale beam-column joint was designed, fabricated, constructed and tested in the structural laboratory of UNIBAS. This beam-column joint was the first to use glue laminated timber (glulam) in post-tensioned timber construction. The experimental programme was completed midway through 2011 providing excellent results and began to answer key questions regarding system performance. During testing the application of the post-tensioned timber concept to glulam timber was confirmed. Testing was performed both with and without dissipative elements and the system displayed the same excellent performance under static and seismic loading as when the system was employed with laminated veneer lumber (LVL).

The dissipative devices used were based on yielding steel angles which activate at low drift levels, both increasing the moment capacity of the system and adding energy dissipation (reducing seismic demand through damping) without inducing plastic deformations in other elements. A new method of vertical load transfer was also designed and tested, using a hidden steel pipe to resist shear loading without hindering the rocking movement of the beam-column joint. Modelling and design procedures were also implemented and verified (Smith et al. 2012).

In stage two of the project a 3-dimensional, 3-storey timber structure made up of frames in both directions composed of post-tensioned timber is to be dynamically tested at UNIBAS laboratory considering 7 natural earthquake inputs. This paper will describe the detailing and testing set-up of the experimental model.

2 THE FACTOR β

The key to this type of system is made up of the ratio β, between the moment resistance provided by the

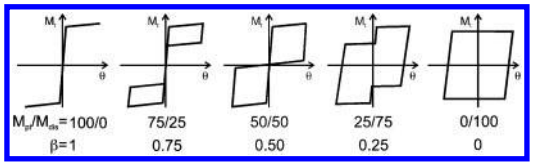


Figure 1. Influence of the factor β on moment response.

post-tensioning (M_{pt}) and the moment resistance provided by the dissipation (M_{dis}). Although a simple concept, this ratio provides the cornerstone in the understanding of system performance (Figure 1). Clearly, during design this choice affects both damping and moment capacity of the system and therefore changing this value will have a direct effect on both capacity and demand.

This experimental campaign will focus on how changes in the factor β relate to overall structural performance.

In order to do this an extensive Non-linear Time History Analysis (NTHA) in order to verify building performance under design seismic loading has been performed defining the selected test cases described in this paper. From the conception of the post-tensioned jointed ductile concept it has been clear that the nature of the controlled rocking mechanism lent itself well to the use of a lumped plasticity approach in modelling. This approach combines the use of elastic elements with springs which represent plastic rotations in the system. Description of these investigations, along with a comparison between SAP2000 (2004) and Ruaumoko (2006) structural calculation softwares is described in the companion paper by Di Cesere et al. (2013), which can be found in the conference proceedings.

3 EXPERIMENTAL TESTS

3.1 *Experimental model*

The prototype structure is three stories in height and has a single bay in both directions. All design has been performed in accordance with the current version of the Italian design codes (NTC 2008). The interstorey height of the building is 3 m and the frame footprint is 6 m by 4.5 m. The building has been designed to represent an office structure (live loading Q = 3 kPa) with the final floor being a rooftop garden. The flooring of the building is made from solid glulam panels. The lateral resistance of the building is governed by seismic loading. The test frame (Figure 2) is made from glulam grade GL32h (EN 1995-1-1 2004). A scale factor of 2/3 has been applied to the prototype structure resulting in the test specimen having an interstorey height of 2 m and a building footprint of 4 m × 3 m.

Seismic loading during testing will be monodirectional applied along the north-south axis of the building. Many of the design details developed for stage one of testing have been used in the design of the frame. The section sizes to be used in the frame

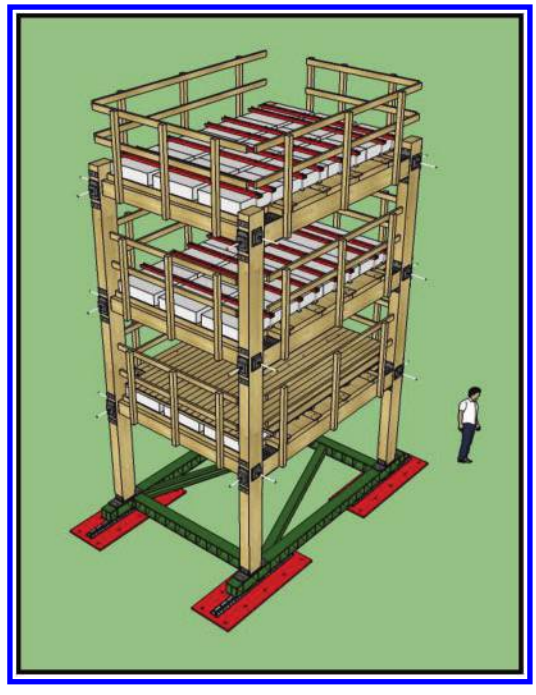


Figure 2. Rendering of test specimen.

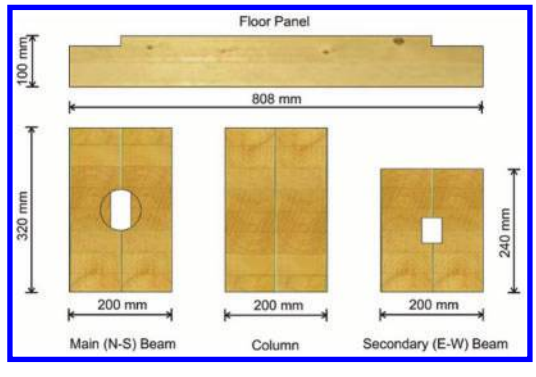


Figure 3. Section size used in PRESLAM dynamic testing.

are shown in Figure 3 with post-tensioning passing through the beams in both directions.

The flooring transfers load directly to the beams in the principle direction, therefore secondary beams are only required to provide torsional stability. The design of this type of structure can be complicated due to the rocking motion which occurs at the interface of the beam-column members during seismic loading. Rocking creates a concentrated displacement which must be accounted for in design and should not create damage to secondary members, flooring or non-structural elements.

The beam-column connection in the principle direction (Figure 4a) is based on the connection type which was tested successfully during stage one. Passing through the centre of the beam is a single 26.5 mm diameter bar which will be tensioned to varying

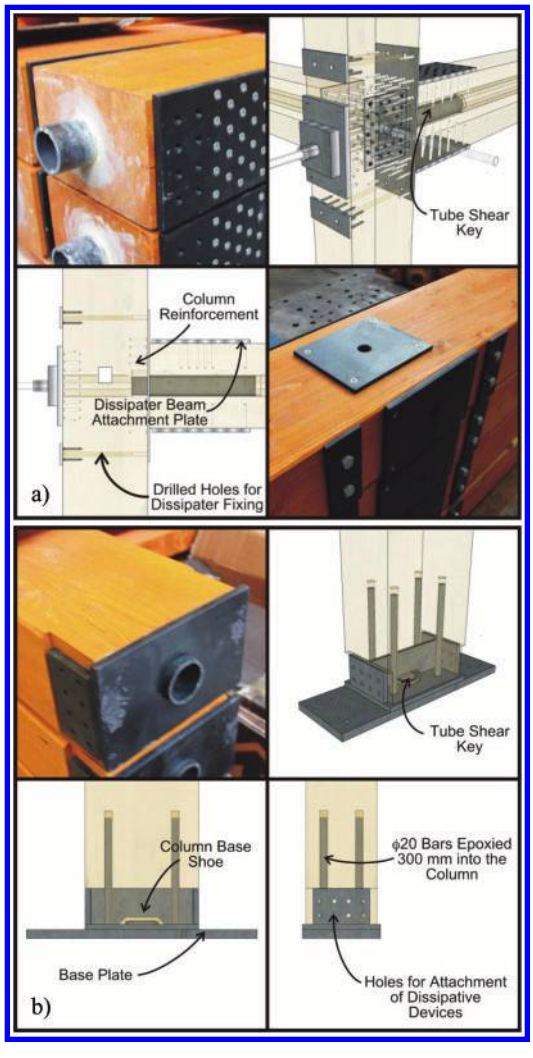


Figure 4. Details of a) beam-column, b) column-foundation joint.

values of initial loading throughout the test programme. This is a high strength steel bar with a yield strength $f_y = 1050\,N/mm^2$ and a Young's modulus of $170\,kN/mm^2$. Dissipation in the form of a yielding steel angle will be used (further described in Section 3.3). Screws have been used both to protect the column face and to connect each dissipater attachment plate. Vertical loading will be transferred through a ϕ 76.1 mm steel tube which extends 66 mm from the beam and sits inside the column. The beam-column connection in the secondary direction is similar to that in the principle direction however does not allow for dissipation attachement.

The base of the column (Figure 4b) is fitted with a steel shoe which is epoxied into the base of the column and left free to rock on a base plate (which will be used to represent the building foundations). Shear transfer is achieved using a ϕ 76.1 mm steel tube which extends

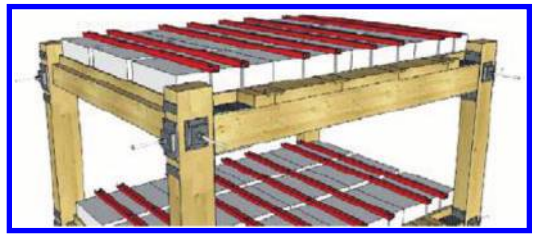


Figure 5. Additional mass arrangement for glulam test frame using concrete blocks and steel hold downs.

15 mm from the steel shoe and slots into a cavity in the base plate. Holes have been drilled and tapped in the steel shoe in order to facilitate the attachment of energy dissipation devices. In order to keep the base of the column as aesthetically pleasing as possible the steel shoe has been recessed into the column.

The floor is made from a series of deep glulam beams oriented flat-wise in order to make flooring panels running between the principal (N-S) beams. Each 808 mm wide panel is connected to the next using a 20 mm thick strip of plywood which is screwed (ϕ 6 mm, 80 mm length) at 150 mm centres. Attachment to the perimeter beams will be through the use of 16 pairs of skewed fully threaded screws ϕ 7 mm, 220 mm in length the N-S direction and 15 pairs of skewed partially threaded screws ϕ 6 mm, 240 mm in length in the E-W direction. During design the decision was made to skew these screws due to the significant increase in both stiffness and strength when a screw is placed on an angle.

Skewing of the screws in the direction of loading was also performed in order to mitigate the tearing of the flooring panel under tension during loading. As gap opening occurs the flooring panel near the gap opening is placed in tension as it is attached both to the principle and secondary beams. A section of the floor will be cut out in order to allow the attachment of dissipating devices and it is possible that stress concentrations will occur in the corner of the cut section. By significantly increasing the stiffness of the screw group in the loaded (N-S) direction when compared to those of the secondary (E-W) direction which are skewed in the opposite direction to loading, a fuse is created which will allow the flooring panel to slide over the top of the secondary beam. In order to further reduce stresses in the removed area the screw groups in both directions will begin at least 500 mm from the column.

In order to calculate the required amount of mass to be added to the test frame the masses of the prototype building must be multiplied by the scale factor of 2/3rd. Due to the fact that the frame is 2/3rd scale, mass similitude must be maintained. This is related to the use of Cauchy-Froude similitude laws which are to be used in testing. This means that additional mass must be added which will also represent the presence of a factored live load. The additional mass required is made up of a combination of concrete blocks and

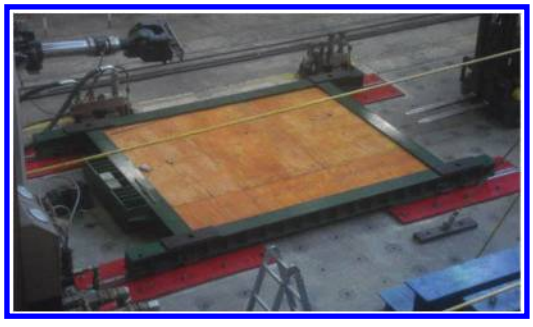


Figure 6. UNIBAS uni-axial shaking table.

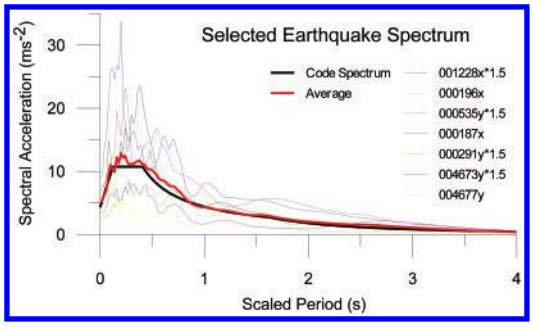


Figure 7. Selected Earthquake Input for Shaking Table Testing.

steel hold downs: 12 blocks are spread out across the flooring (Figure 5).

3.2 *Shaking table apparatus and seismic inputs*

Testing will be performed under dynamic loading in real time. This will be done using a shaking foundation testing rig. The testing apparatus consists of a shaking foundation present in the laboratory of the University of Basilicata (Figure 6). The foundation has a single degree of freedom in the N-S direction and consists of a steel frame made up of HEM300 sections. The foundation is driven by an MTS 244.41 dynamic actuator which has a capacity of ±500 kN and a stroke of ±250 mm. The actuator is fixed to a hinge at the base of the foundation and pushes against a 6 m thick strong wall. Pressure for the actuator is provided by 3 MTS SilentfloTM 505-180 hydraulic pumps. The foundation is situated upon 4 SKF frictionless sliders (Model LLR HC 65 LA T1) with one each situated under the four columns. These sliders sit upon a series of levelling plates which are adjustable to ensure that a system with a coefficient of friction of less than 1% is obtained.

The testing input will be a set of 7 spectra compatible earthquakes selected from the European strong-motion database (Figure 7). The characteristics of these are shown in Table 1. The code spectrum which was used when selecting the records was defined in accordance with the current Eurocode for seismic design (EN 1998-1:2003 2003) having a PGA of

Table 1. Earthquake characteristics.

ID Code	Location	Date	M_W	PGA (g)
001228x	Izmit, Turkey	17/08/99	7.6	0.357
000196x	Montenegro, Serbia	15/04/79	6.9	0.454
000535y	Erzican, Turkey	13/03/92	6.6	0.769
000187x	Tabas, Iran	16/09/78	7.3	0.926
000291y	Campano Lucano, It	23/11/80	6.9	0.264
004673y	South Iceland	17/06/00	6.5	0.716
004677y	South Iceland	17/06/00	6.5	0.227

Table 2. Dissipating devices.

Name	$F_{pt,i}$	β	ID angle – beam to column joint
Hybrid Cases (with the addition of steel elements)			
PT50_0.80	50 kN	0.8	ID10_2A/B
PT100_0.70	100 kN	0.7	ID5A/B

$a_g = 0.35$ and a soil factor of $S = 1.25$ (Soil class B – medium soil) giving a PGA for the design spectrum of 0.4375.

3.3 *Dissipative steel angles*

During testing passive energy dissipation devices will be added to the structure in order to add strength and reduce displacements without the increase of accelerations or base shears. 'Yielding steel angle' passive hysteretic energy dissipation devices are to be added to the frame (Di Cesare et al. 2013b) as shown in Figure 8c. The steel angle devices were applied with great success during stage one of the project, yielding at low levels of design drift and supplying high levels (up to 15% equivalent viscous damping at the joint, 10% when applied as part of a full frame) of stable hysteretic damping (Smith et al. 2011).

Two different types of steel angle have been considered (Table 2). The first of these, shown in Figure 8a, involves the milling down of a certain section of a steel equal angle in order to provide a zone of concentrated yielding. The second option, shown in Figure 8b, involves the removal of two holes in order to provide a concentrated yielding zone. The second steel device is taken from a section of square hollow section.

Throughout the testing programme several characteristic of the post-tensioned timber concept will be investigated. During the experimental campaign the size of the structural members, building layout and mass will not be altered, however different values of post-tensioning and steel moment capacity contributions (thus variations in the value β) will be investigated with the four cases shown in Table 3 being selected.

The above options are based around the standard case of PT100_1.00 which has an ultimate connection moment capacity of $M_t = 27$ kN. Adding steel without reducing the post-tension moment contribution (PT100_0.70) has the effect of both increasing capacity and decreasing demand. Adding steel in

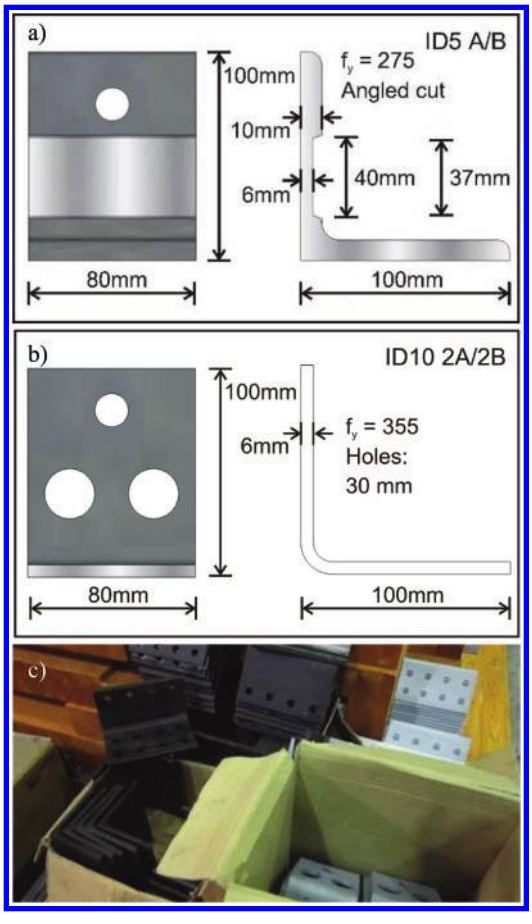


Figure 8. Steel angles considered for beam to column joint, c) Yielding Steel Angle Dissipation Devices.

Table 3. Experimental Cases.

			Moment Capacity at 2% connection rotation		
Name	$F_{pt,i}$	β	M_{pt}	M_s	M_t
Post-tension Only Case					
PT50_1.00	50 kN	1.00	22.5	0.0	22.5
PT100_1.00	100 kN	1.00	27.2	0.0	27.2
Hybrid Cases (with the addition of steel elements)					
PT50_0.80	50 kN	0.80	22.5	6.0	28.51
PT100_0.70	100 kN	0.70	27.1	13.1	40.1

combination with a decrease in post-tensioning force (PT50_0.80) decreases demand but retains equal capacity of elements.

3.4 *Fabrication of experimental model*

The fabrication of the frame (Figure 9a and 9b) was performed by Holzbau Sud SpA in Calitri, Italy. Although the beam and column were of the same



Figure 9. a) Beams pressed together, b) secondary beams fabricated, c) Timber elements with plates in UNIBAS laboratory.

dimension slightly different methods of fabrication were used. Due to the presence of the space inside the beam section to accommodate the post-tensioning tendon two separate sections were glued together after a hollow was made in each part using a computer numerical controlled (CNC) woodworking machine. The column was made of a single piece of glulam in which a hole was made for the tendon to be placed.

Timber elements have been fabricated off-site and arrived with all plates attached (Figure 9c) rendering the building truly modular.

4 CONCLUSIONS

An extensive dynamic experimental testing programme on a multi-storey timber frame building is scheduled to be performed in the structural laboratory of the University of Basilicata in Potenza, Italy. The aim of the project, in collaboration with the University of Canterbury in Christchurch, New Zealand is to develop the innovative post-tensioned timber concept (under the name PRES LAM) by extending its application to glulam timber and steel angle devices. In addition important knowledge regarding the systems dynamic behaviour will be obtained through dynamic testing.

Mono-directional shaking table testing will be performed on a 3-storey single bay frame scaled to 2/3rd. The dynamic testing input will be a set of 7 spectra compatible earthquakes selected from the European strong-motion database. In this paper the design and

detailing of the 2/3rd scale post-tensioned frame has been presented along with the details of the testing set-up. Testing results under dynamic conditions will provide additional information for the design of this innovative method of timber construction.

ACKNOWLEDGEMENT

The authors would like to acknowledge funding from the Structural Timber Innovation Company (STIC) and FederLegno Arredo (FLA).

REFERENCES

Carr, A. (2006). "RUAUMOKO." A. Carr, Christchurch, New Zealand, Inelastic Dynamic Analysis Software.

Computers and stuctures Inc. (2004). "SAP2000: Static and Dynamic Finite Analysis of Structures." Berkeley, CA, USA.

Di Cesare, A., Ponzo, F.C., Simonetti M., Smith, T., Pampanin, S., (2013a). "Numrical modelling of a post-tensioned timber framed building with hysteretic energy dissipation". 5th International Conference on Structural Engineering, Mechanics and Computation Cape Town, South Africa.

Di Cesare, A., Ponzo, F.C., Nigro, D., Simonetti M., Smith, T., Pampanin, S., (2013b). "Experimental testing and numerical analysis of steel angles as hysteretic energy dissipating systems". XV Convegno di Ingegneria Sismica, Associazione Nazionale di Ingegneria Sismica, Padova, Italy.

European Committee for Standardization. (2003). "Design of structures for earthquake resistance – Part 1: General rules, seismic actions and rules for buildings." Secondary Design of structures for earthquake resistance – Part 1: General rules, seismic actions and rules for buildings, Secondary Standardization, E. C. f., ed., European Committee for Standardization, Belgium.

European Committee for Standardization. (2004). "Design of Timber Structures Part 1-1: General – Common Rules and Rules for Buildings." Secondary Design of Timber Structures Part 1-1: General – Common Rules and Rules for Buildings, Secondary Standardization, E. C. f., ed., European Committee for Standardization, Belgium.

Il Ministro delle Infrastrutture. (2008). "Norme Tecniche per le Costruzioni." Secondary Norme Tecniche per le Costruzioni, Secondary Infrastrutture, I. M. d., ed., Il Ministro delle Infrastrutture, Italia.

Newcombe, M. P., Pampanin, S., and Buchanan, A. H. (2010). "Numerical Modelling and Analysis of a Two-Storey Post-Tensioned Timber Frame with Floor Diaphragms." 14th European Conference on Earthquake Engineering, Ohrid, Republic of Macedonia.

Palermo, A., Pampanin, S., Buchanan, A., and Newcombe, M. (2005). "Seismic Design of Multi-Storey Buildings using Laminated Veneer Lumber (LVL)." 2005 New Zealand Society for Earthquake Engineering Conference, Wairakei Resort, Taupo, New Zealand.

Smith, T., Ludwig, F., Pampanin, S., Fragiacomo, M., Buchanan, A., Deam, B., and Palermo, A. (2007). "Seismic Response of Hybrid-LVL Coupled Walls Under Quasi-Static and Pseudo-Dynamic Testing." 2007 New Zealand Society for Earthquake Engineering Conference, Palmerston North, New Zealand, 8.

Smith, T., Pampanin, S., Carradine, D., Buchanan, A., Ponzo, F., Cesare, A. D., and Nigro, D. (2011). "Experimental Investigations into Post-Tensioned Timber Frames with Advanced Damping Systems." Il XIV Convegno di Ingegneria Sismica, Associazione Nazionale di Ingegneria Sismica, Bari, Italy.

Smith, T., Ponzo, F. C., Cesare, A. D., Auletta, G., Pampanin, S., Carradine, D., Palermo, A., and Nigro, D. (2012). "Testing of a Post-Tensioned Glue Laminated Beam to Column Joint: Experimental and Numerical Results." 12th World Conference on Timber Engineering, Auckland, New Zealand.

Research and Applications in Structural Engineering, Mechanics and Computation – Zingoni (Ed.)
© 2013 Taylor & Francis Group, London, ISBN 978-1-138-00061-2

Fracture process under moisture content variation in timber structures

R. Moutou Pitti
Clermont Université, Université Blaise Pascal, Institut Pascal, Clermont-Ferrand, France
CNRS, UMR 6602, Institut Pascal, Aubiere, France
Cenarest, IRT, Libreville, Gabon

F. Dubois
University of Limoges, Heterogeneous GEMH, Egletons, France

E. Fournely
Clermont Université, Université Blaise Pascal, Institut Pascal, Clermont-Ferrand, France
CNRS, UMR 6602, Institut Pascal, Aubiere, France

B. Mbangagoye
USTM, Ecole Polytechniques de Masuku, Franceville, Gabon

ABSTRACT: Fracture processes due to the natural drying of green wood slices are investigated by experimental, analytical and numerical methods. The shrinkage of Douglas fir slices is observed in a test room where the environmental conditions are constant. In order to take into account stress relaxation coupled with hygrothermal effects, an ageing elastic behavior, including shrinkage–swelling effects with inhomogeneous properties in the radial and transversal directions, is considered. Results obtained from the experimental approach are compared with numerical modeling to predict crack growth initiation in a cylindrically and orthotropic material tree disk. The efficiency of the proposed model in the prediction of drying and fracture processes in wood material is proved.

1 INTRODUCTION

Among several building materials, the wood brings many responses in the regulation of environmental effects. Then, the use of the wood materials in engineering development or in timber structures appears very important. However, the wood material is difficult to understand due to its many complex behaviors (Saifouni et al. 2013). In addition, these behaviors are improved when the material is submitted to moisture content variation. In fact, the natural or artificial shrinkage due to drying is commonly responsible of strains and crack appears in wood peaces (Omarsson et al. 1998). Moreover, the initial crack presence after drying process can decrease the timber structure lifetime by inducing stress concentrations and the crack propagation.

The literature's background shows that the strain and the evolution of drying-induced stresses in wood are studied in terms of analytical (Cave, 1972; Husson et al. 2010), experimental (Kowalski and Smoczkiewicz, 2007; Moutou Pitti, 2012) aspects. Among them, Kowalski et al. (2004) have presented a model of drying that permits evaluation of moisture content distribution in dried wood during the drying rate periods with the acoustic emission method (AE). In numerical approaches, Dubois et al. (2012) have proposed a numerical model taking into account mecano-sorptif and cracks effects during relaxation loading. In the present work, the image analysis technique (Peuchot, 1993), is applied in order to measure the mechanical fields in a drying wood slice. A numerical model is developed for evaluating strain distributions according to transverse orthotropic and a mechano-sorptive approach inducing strain blockings during drying phase. This model then extrapolates stress distributions until the crack appear.

The first part presents the protocol and the experimental device. The green wood slice is directly placed on an electronically balance providing the weight measure versus time. In parallel, the mark tracking method composed of an acquisition system data, records the displacement of target posted on the sample surface during the drying phase. The second section deals with the analytical approach about the strains calculations. The method is based on a mathematical model coming from cylindrical strain calculations. The finite element routine and the incremental approach have shown in the last part. The model is based on a mechano-sorptive concept in which a hygro-lock

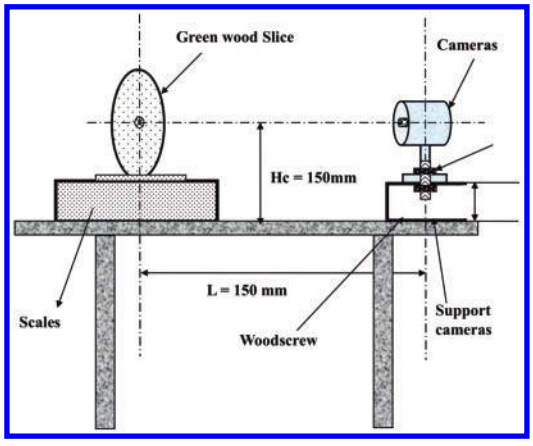


Figure 1. Experimental device (Moutou Pitti et al. 2013).

model is activated. Then, the experimental and numerical tangential strains are compared. Simultaneously, the identification of crack initiation is justified.

2 MATERIALS AND METHOD

2.1 *Description of materials and methods*

A green wood slice, debited on a peace log with an electric saw is placed on a sensitive scale, Figure 1. The sample is initially conditioned in water in order to assure its saturation. A flat of 40 millimeters is machined on the basis of the slice in order to assure stability on the side of the scale. Hence, the specimen is positioned on the experimental table, taking care to ensure its horizontality. The height between the table and axis of the camera and the slice center is hc = 150 mm. Also, the camera was immediately placed on a slidable support fixed on the table in order to reduce any disturbances due to external shocks. This ensures that the axis of the camera is absolutely horizontal and the distance between the between the actual text and figure (including caption). Seat of it and the specimen on the side of the scale is 100 mm (± 20 mm). Note that the distance between the axis of the slice and the axis of the support camera is L = 150 mm.

2.2 *Experimental protocol*

The experimental protocol is based on a green wood slice in Douglas fir with a thickness of 30 mm just peeled, Figure 2(a). In this picture, the left side of the slice corresponding to the hardwood region, and the right side represents the normal wood. The preparation of the specimen consists on draw black marks according to a polar reference centered at the sample heart. A marking tracking protocol is implemented in order to record displacements of these marks using the videometric technology (Peuchot, 1993), figure 2(b). Note that 23 images are recorded per second, with an automatic record of five seconds every 2 hours in order to reduce storage requirements of images during the

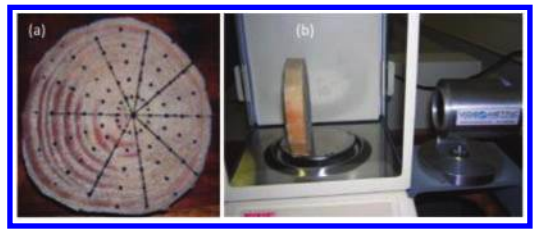


Figure 2. (a) Green wood slice and black marks. (b) Experimental device (Moutou Pitti et al. 2013).

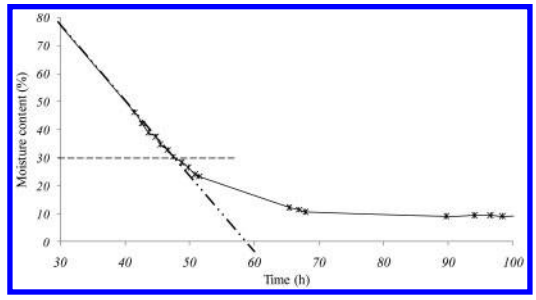


Figure 3. Fibre saturation point (FSP) localisation.

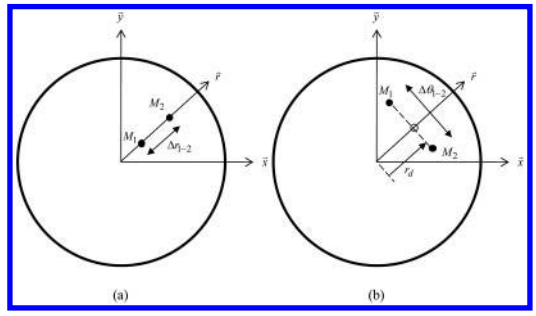


Figure 4. Referential radial (a) and tangential (b) representation.

test. The specimen is placed on a precision balance in order to measure the masse evolution during the drying process.

2.3 *Fibre saturation point*

Assuming that the fibre saturation point gives a non-linearity on the time – moisture content curve, an estimation for the specific moisture content value of 30% (figure 3) corresponding to the fibre saturation point limit is obtained.

2.4 *Analytical approach*

2.4.1 *Referential cylindrical coordinate*

In order to identify each black mark, Figure 4 proposes a notification by the intersection between radiuses and rings.

The radial strain is show by figure 4(a), where Δ^r_{1-2} is the length between M_1 and M_2. The tangential strain is defined by figure 4(b), where $\Delta\theta^r_{1-2}$ is the distance

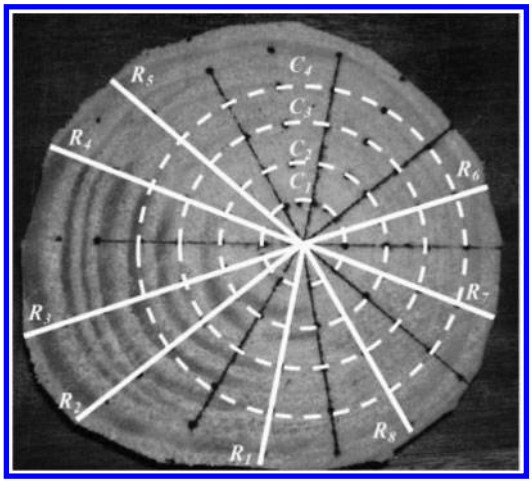


Figure 5. Radius and rings.

between M_1 and M_2 that $\vec{r}$ is their symmetric axis. r_d is the distance between the referential origin and the projection of the two points on $\vec{r}$.

For example, the mark M_i^j traduce the point at the intersection between the radius R_i and the ring C_j. Let us note that radial and tangential strains are defined at the middle point comprised between M_1 and M_2. With this consideration, the radial strain is calculated at the point M_2^{1-2} corresponding to a point placed in the radius n°2 and between rings 1 and 2, figure 4 (a) and 5. With the same way, the tangential strain is calculated at the point M_2^{2-3} placed in the ring n°2 and between radiuses 2 and 3, see figure 4(b) and 5.

2.4.2 *Strain analytical computation*

The mark tracking method calculating the displacement field in a Cartesian's referential (U_x, U_y), it's necessary to project this field in the polar system. In order to identify the crack initiation, only the tangential strains have been considered in this work. In this condition, we note the following transition formula

$$U_\theta = U_x \cdot \sin\theta - U_y \cdot \cos\theta \tag{1}$$

U_θ is the tangential displacement components, respectively. The tangential component of the strain tensor called $\varepsilon_{\theta\theta}$ is defined by

$$\varepsilon_{\theta\theta} = \frac{1}{r} \cdot \left(\frac{\partial U_\theta}{\partial \theta} + U_r \right) \tag{2}$$

According to figure 4(b), the tangential component can be evaluated as follow

$$\varepsilon_{\theta\theta} = \frac{1}{r_d} \left(\frac{U_\theta(M_1) - U_\theta(M_2)}{\Delta\theta_{1-2}} \right) + \left(\frac{U_r(M_1) + U_r(M_2)}{2} \right) \tag{3}$$

Figure 6 shows tangential strain evolution between the intermediary radius R_1 and R_2. The tangential strains are on the whole in compression, which increases during the drying process. Heterogeneity can be observed around the crack initiation vicinity

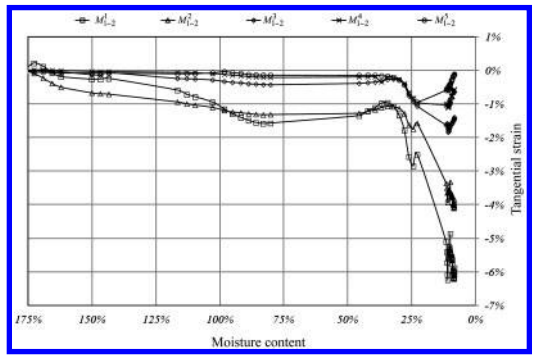


Figure 6. Tangential strains between radiuses R_1 and R_2.

(R_1, R_2). At around 18% moisture content, we can observe a jump in tangential strain near radius R_1 near the sample edge, which can be explained by crack growth initiation.

3 FINITE ELEMENT APPROACH

3.1 *Drying model and incremental law*

The coupling between moisture content variations and mechanical behavior is based on the addition of shrinkage-swelling response and mechano-sorptive behaviour. During drying process, Husson et al. (2010) have shown one hygro-lock effect affecting elastic and viscoelastic responses. In this study, let us limit our investigation for elastic properties with a time decreasing of elastic modulus with an uncoupling between elastic behavior and shrinkage process represented by the elastic and shrinkage deformations ε_e and ε_w. In this case, the mechanical model can be assimilated at a Bazant's (Bazan and Carol, 1993) model according to a hardening behavior during drying phases. The mechanical behavior representing the drying model written in terms of strain rate ε_w as follow:

$$\dot{\underline{\underline{\varepsilon}}}(t) = \mathrm{C}(t) \cdot \dot{\underline{\underline{\sigma}}}(t) + \underline{\underline{\alpha}} \cdot \dot{w}(t) \tag{4}$$

The total stress rate tensor is called $\underline{\underline{\sigma}}$. $C(t)$ is the four order compliance tensor adapted for a cylindrical orthotropic properties. In a 2D representation, C can be defined according to elastic moduli such as:

$$\mathbf{C}(w) = \begin{bmatrix} \frac{1}{E_R(w)} & -\frac{\nu_{RT}}{E_R(w)} & 0 \\ -\frac{\nu_{RT}}{E_R(w)} & \frac{1}{E_T(w)} & 0 \\ 0 & 0 & \frac{1}{G_{RT}(w)} \end{bmatrix} \tag{5}$$

$E_R(w)$, $E_T(w)$ and $G_{RT}(w)$ are the radial, tangential and shear modulus, respectively. $\upsilon_{RT}(w)$ is the Poisson's ratio.

$\underline{\underline{\alpha}}$ is the shrinkage-swelling expanse tensor. In the orthotropic referential, this tensor is diagonal. In this study, we assume a constant tensor in the hygroscopic domain. $\dot{w}(t)$ is the moisture content rate.

The implementation of the behavior law, expressions (4), requests its moisture content integration in the global RT base. By analogy with Randriabololona's developments (Dubois and Randriabololona 1997), the equation (4) can be solved using the following finite derivation method solving according to Ghazlan approach (Ghazlan et al. 1995)

$$\Delta\underline{\underline{\varepsilon}}(t_n)=\left[\frac{1}{2}\cdot\Delta C(t_n)+C(t_{n+1})\right]\cdot\Delta\underline{\underline{\sigma}}(t_n) +\underline{\underline{\alpha}}\cdot\Delta w(t_n) \quad (6)$$

where $\Delta\sigma$ and $\Delta\varepsilon$ are the stress and the strain increment, respectively.

In order to solve equation (6), the following finite element formulation, proposed by Ghazlan, is applied:

$$K_T\cdot\{\Delta u\}(t_n)=\{\Delta F^{\sigma}_{ext}\}(t_n)+\{\Delta F^{w}\}(t_n) \quad (7)$$

where K_T is the tangent matrix defined by using the Jacobian matrix B connecting displacements and strains and the equivalent compliance tensor present in expression (5) such as:

$$K_T=\int_{\Omega}B^T\cdot\left[\frac{1}{2}\Delta C(t_n)+C(t_{n-1})\right]^{-1}\cdot B d\Omega \quad (8)$$

$\{\Delta F^{\alpha}_{ext}\}(t_n)$ is the increment of nodal force vector induced by the external increment loading and incremental stresses $\Delta\sigma(t_n)$. $\Delta\underline{\underline{\sigma}}(t_n)$ designates the supplementary moisture content load vector representing the effect of moisture content variations in the time step.

3.2 *Finite element routine*

In order to implement the incremental law (4) in finite element software Castem, the following subroutine is applied.

Firstly, the referential state corresponding to the fiber saturation point is fixed. If we ignore growth constraints and relaxation effects after the tree felling, we can impose $\underline{\underline{\varepsilon}}(t)=\underline{\underline{0}}$ and $\underline{\underline{\sigma}}(t)=\underline{\underline{0}}$. In the same time, we admit an initial moisture content homogeneity w_{ini} in the disk surface and in this thickness. For each algorithm step, we consider, firstly, that mechanical state is known at time t_n and t_{n+1}, in the other hand, that moisture content variation is measured by weighing for the time t_i.

The compliance tensor C is updated according to the moisture content w. All terms of the equilibrium equation (6) are defined. The tangent matrix (8) is calculated and the balance equation (7) is solved by the finite element process. Mechanical state is updated in terms of displacements, strain and stress tensors. The crack growth initiation is detected by comparing the transverse component of the stress tensor and its critical value.

Table 1. Elastic properties.

E (MPa)	E (MPa)	G (MPa)	ν
1300	900	125	0.39

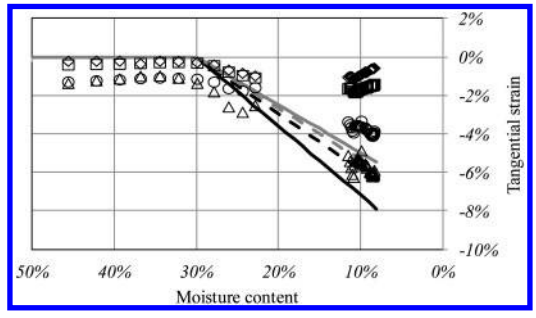


Figure 7. Experimental and numerical tangential strains.

4 TANGENTIAL STRAINS AND FRACTURE ANALYSIS

4.1 *Finite element mesh*

The finite element mesh is obtained according to an overall positioning system centred on the specimen heart, enabling the definition of the centre of the cylindrical orthotropic reference. The contact surface between specimen and balance is operated by blocking its vertical displacements. A reference point is also blocked vertically in order to eliminate a rigid body displacement. Specific lines (radius and crowns) have been integrated into mesh in order to have a concordance with the experimental black mark displacements, figure 5.

In the numerical process, the Poisson's ratio is assumed to be constant. The elastic properties of Douglas fir at w = 12% are given by the Table 1.

Elastic properties must be corrected by taking into account a linear formulation versus moisture content such that

$$E_{\alpha}=E^{0}_{\alpha}\cdot\left(1-0.03\cdot(w-12)\right) \quad (9)$$

Also, the shrinkage–swelling coefficients values are given by Guitard (1987): $\alpha_R=0.08\%$ and $\alpha_T=0.35\%$.

4.2 *Tangential strains*

According to the finite element routine detailed before, the green wood slice, presented in figure 5, is implemented in finite element software

Figure 7 shows the comparison between experimental and numerical results of tangential strains along the radius R_1. We note that the maximum strain is around 8% traducing the coming crack due to the drying process.

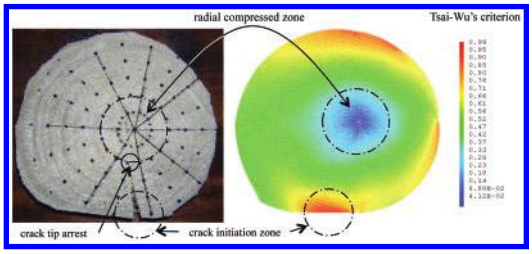


Figure 8. Crack initiation zone.

4.3 *Crack process*

4.3.1 *Crack growth initiation*

The crack growth initiation phase can be studied using an elasticity limit criterion, like Tsai or Hill (Tsai and Wu, 1971) have done, based on the combination of stress tensor components. In a plane stress configuration, the criterion can take the form of the following function f such that

$$f = \frac{<\sigma_{RR}>^{+}}{\sigma_{RR}^{c}} + \frac{<\sigma_{TT}>^{+}}{\sigma_{TT}^{c}} + \frac{|\sigma_{RT}|}{\sigma_{RT}^{c}} \quad (10)$$

σ_{RR}^{C}, σ_{TT}^{C} and σ_{RT}^{C} are critical values for radial, tangential and shear stresses, respectively, corresponding to the uniaxial elastic limit and fracture initiation assuming a brittle fracture process. The notation $< >$ designates the positive part of fields corresponding to tension parts. The criterion inducing crack initiation can be written as follows:

$$f < 1: \text{ no crack; } f = 1: \text{ crack propagation } f < 1 \quad (11)$$

The combination of tangential and shear stresses illustrates that crack growth initiation is based on a coupling between tangential tensions and shear state, depending on a mixed mode configuration.

In fact, by considering the Tsai-Wu's criterion, equation (10), figure 8 shows a stress concentration in the crack growth zone vicinity given by a finite element computation.

The radial compression state can explain a local mechanical containment that hinders the process zone development in front of the crack tip. This fact can explain the crack tip arrest at the limit between the tension and compression zones.

5 CONCLUSIONS

The strain evolutions and the crack growth initiation have investigated during the drying process in this work. The changes of tangential or circumferential strains versus the distance to the slice centre for different moisture have been studied. These strains are computed by defining a local orthotropic referential. During the evolution of moisture content between the FSP level and its critical value inducing the crack initiation (w = 11.48%) the numerical and experimental results illustrate a very good agreement. In the same time, the finite element model allows the localization of the crack initiation during drying process. In the coming work, the fracture analysis will apply and coupling with the viscoelastic model and the drying model in order to study the behavior of wood material under environmental variations crack growth processes.

REFERENCES

Bazant, ZP., Carol, I. 1993. Viscoelasticity with aging caused by solidifying of nonaging constituent. *Journal Engineering Mechanics* 119:2252–2269.

Bekhta, P., Ozarkiv I, Alavi S, Hiziroglu S. 2006. A theoretical expression for drying time of thin lumber. *Bioresource Technol*ogy 97:1572–1577.

Cave, I.D. 1972 A theory of the shrinkage of wood. *Wood Science and Technology* 6:284–292.

Dubois, F. Randriamolololona, H., Petit, C. 2005. Creep in wood under variable climate conditions: numerical modelling and experimental validation. *Mechanics of Time-dependent Materia ls* 9:173–202.

Dubois, F., Moutou Pitti, R., Destrebecq, J.F. 2012. Prediction of the crack initiation during drying process of green wood: experimental and modelling approaches. *Cost Action FP 0904, Thermo-Hydro-Mechanical Wood Behaviour and Processing*, Nancy, March 26–28.

Ghazlan, G., Caperaa, S., Petit, C. 1995. An incremental formulation for the linear analysis of thin viscoelastic structures. *International Journal of Numerical. Method Engineering* 38:3315–3333.

Guitard, D. 1987. Mécanique du matériau bois et composites, France, Cepadues – Edition.

Husson, JM., Dubois, F., Sauvat N. 2010. Elastic response in wood under moisture content variations: analytic development. *Mechanics of Time-Dependent Materials* 14: 203–217.

Kowalski, S.J., Smoczkiewicz, A. 2007. Stresses in dried wood, modelling and experimentation. *Transp. Porous Med* 66:145–158.

Kowalski, SJ., Molinski, W., Musielak, G. 2004. The identification of fracture in dried wood based on theoretical modeling and acoustic emission. *Wood Science and Technology* 38:35–52.

Moutou Pitti, R., Dubois, F., Fournely, E., 2013. Experimental results of green wood slice under natural drying. *Springer* 34:371-371.DOI 10.1007/978-1-4614-4226-4_42.

Moutou Pitti, R. 2012. Mesure des deplacements par analyse d'images: deformations lors du séchage d'une rondelle de bois vert, *EUE*. ISBN: 978-3-8417-9719-3

Saifouni, O., Moutou Pitti, R., Destrebecq, J.F. 2013. Determination of stresses in drying wood by means of a viscoelastic relaxation model. *Springer* 37:29-36. DOI 10.1007/978-1-4614-4241-7_5

Ormarsson, S., Dahlblom, O., Petersson, H. 1998. A numerical study of the shape of Sawn timber subjected to moisture variation, Part 1: Theory. *Wood Science and Technology* 32:325–334.

Tsai, SW., Wu, EM. 1971. A general theory of strength for anisotropic materials. *Journal of Computer Material* 5:58–80.

Peuchot, B. 1993. Camera virtual equivalent model 0.01 pixel detector. *Comput Medical Imaging Graphics*, 17: 289–294.

Research and Applications in Structural Engineering, Mechanics and Computation – Zingoni (Ed.)
© 2013 Taylor & Francis Group, London, ISBN 978-1-138-00061-2

The resilience of timber buildings

George Faller
Ove Arup and Partners SAU, Madrid, Spain

ABSTRACT: The issue of resilience of buildings is becoming an important consideration in the design of the built environment. The drive for more sustainable design has awaked a new interest in timber as a structural material due to its low or negative carbon emissions. A large body of work has been going into research into the performance of timber to get a better understanding of the robustness, structural stability, reaction to extreme natural conditions such as flooding, fire and seismic activities. The low weight-to-strength ratio of timber is being utilsed by developing industrialized off-site fabrication and quick construction techniques. A good case for timber for a resilient alternative is being made. More work however needs to be done to fully understand its capabilities, and also to explore its capacity to address a further characteristic of resilience; the ability for quick repair and re-use of the building.

1 INTRODUCTION

1.1 *The built environment*

As engineers for the built environment when looking at the building stock for the future we would want to see buildings with the following characteristics; buildings that are:

- Sustainable in construction and use
- Robust and structurally sound
- Resilient to occasional extreme natural events
- Safe for occupants and emergency services in fire
- Durable and with flexibility of use
- Easily restored to full use after an extreme event

When we consider what building materials are used for our buildings today we can observe that timber is one of the most traditional building materials, and yet it has only a 5–10% share of the construction market. The nineteenth and twentieth centuries saw the rise and dominance of steel and concrete as structural materials; this paper explores the case for a return to timber as one of the prime construction materials for the twenty first century.

The question of how timber measures up as a structural construction material and how it meets the multiple performance characteristics and usability requirements is discussed below.

2 TIMBER CONSTRUCTION

The intention of this paper is not to promote timber as a construction material that is better than other more traditional materials per se, but rather to explore where timber may provide a better solution on its own or in combination with other materials. It has tended to be ignored in evaluating alternative solutions by many structural engineers at concept design stage for a large range of typical building types. As new drivers begin to shape decision making as to which structural materials to recommend for a project, the relative advantages of using timber are changing.

2.1 *Sustainable construction and use*

A significant percentage of the total energy consumption during the typical lifetime of a building is related to the embodied energy of the structure and building fabric (typically 15–25%). The carbon emissions due to the production of the timber components for construction are usually small compared to other building materials, and represent net negative emissions in a 'cradle to gate' scenario (i.e. more CO_2 fixed in the new building than given off in the production process). This assumes use of timber from sustainable (renewable) sources of course. In addition to that timber is a 100% renewable material, reducing its carbon footprint further. Even in the 'cradle to grave' scenario, allowing for disposal of the timber at end-of-life, timber typically performs better than other construction materials regarding net emissions.

Another consideration to take into account is the ease of transport to site due to the relative lightness of the material. The main components of timber buildings are typically manufactured off site and the components transported to site for quick erection. The advantages of this type of construction are many; it results in savings and reductions in accidents on site due to easier handling, faster erection times and minimization of wet trades, and minimizes the requirement for storage of combustible materials on site.

Therefore when considering the use of timber from a sustainability point of view, little more needs to be said.

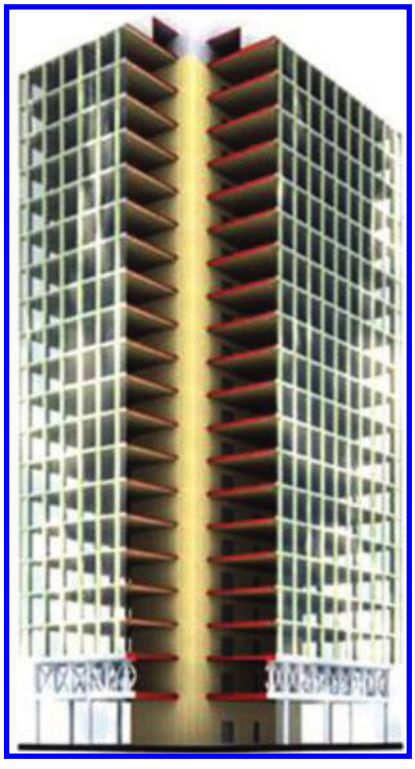


Figure 1. The Life Cycle Tower structure.

2.2 *Robust and structurally sound*

Over the past few centuries timber became seen as a 2nd rate structural material, a material more associated with low-rise buildings of little importance. The limited use of timber was largely related to the code limitations on maximum height, which arose out of fire safety considerations. Timber was seen as a combustible material, and as such not capable of providing the robustness demanded of larger and more valuable buildings that would stand the test of time.

As a result timber was largely ignored during the period in the 18th and 19th centuries when great technical advances were being made in understanding the material properties of construction materials and developing a better understanding the structural behaviour of structures under different loading conditions. With the recognition of the potential contribution of timber to sustainable design, this has changed and a number of research projects have been initiated to investigate the potential of timber as a structural material.

One of such projects is the Life Cycle Tower (LCT) project in which Arup participated, together with developer Rhomburg, the University of Gräz, timber contractor Wiehag and architect Hermann Kaufmann. The objective of the project was to demonstrate the feasibility of a commercial timber high-rise construction of 20 storeys in a densely populated urban context at detail design level (Figure 1). It sought also to demonstrate that this type of building could be built of timber without compromising on performance when compared to a steel or concrete building.

The main structural components of this prototype building with plan dimensions of 27 m wide × 43 m long were:

- Nucleus of solid load bearing glulam panels, 16 to 30 cm thick, providing structural stability and enclosures for lifts, stairs and service risers
- Solid timber glulam perimeter columns on a 2.7 m grid
- Composite concrete timber flooring system, the introduction of a light concrete topping was primarily to address acoustic issues.

This project demonstrated the structural feasibility of timber structures for high-rise buildings, and indicated a large unrealized potential for the use of timber in buildings.

Numerous other timber structural systems have been developed in parallel to the glulam component solution, such as cross laminated panel (CLT) system, which further demonstrate the versatility of timber as a structural material.

3 RESILIENCE OF TIMBER BUILDINGS

When talking about resilience in a more general sense there are many definitions of what it is, but what most have in common is that central to defining resilience is:

"the ability to withstand a severe/extreme event (shock) and recover".

Incremental change or disturbance including trends and seasonality however may also be the cause of stresses that occur over a longer period than shocks (Department for International Development, UK, 1999).

In the context of buildings resilience could be seen as an ability to withstand the effects of earthquakes, extreme winds, flooding and fire, and their ability to be quickly returned to normal use after such an event. Resilience of buildings to these events is increasingly being seen as an important design objective for all types of buildings.

3.1 *Extreme winds and seismic events*

Timber systems, due to their ability to deform while maintaining load carrying capacity, behaves well under seismic loading, but until recently not much work had been done to study the seismic behavior of medium- to high-rise timber structures. Over the past few years work has been done by the University of Canterbury (Buchanan, Palermo, Carradine & Pampanin 2011), to develop structural systems for timber using post tensioned self-centering vertical LVL wall panels to counter seismic loading, and Arup has collaborated on parts of this research. These systems make use of mild steel connections between the post-tensioned elements that act as energy dissipaters under extreme loading conditions, such as those resulting from seismic effects.

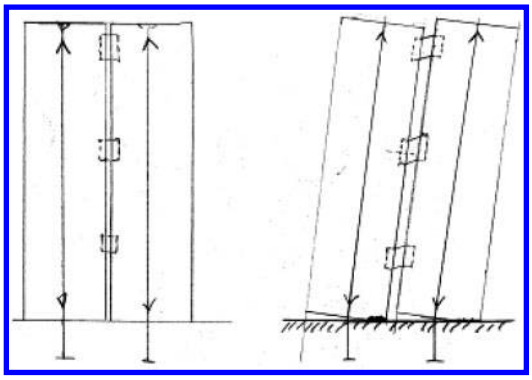


Figure 2. Self-centering post tensioned shear wall panels.



Figure 3. Shear walls with energy dissipaters linking panels.

Others such as the University of Columbia and CNR-IVALSA in Italy are investigating the use of load dissipating shear wall connectors without post-tensioning as alternative systems to address seismic and extreme wind loading.

3.2 *Flooding*

One of the drawbacks to timber as a structural material is the possibility of fungal decay of the material, which can occur under high moisture conditions in the timber. Any design solution for timber must take measures to prevent this, which normally takes the form of a plinth structure of moisture resistant material (e.g. concrete) and a weather tight exterior façade enclosure. Detailing must also be such that excessive internal water vapour or the possibility standing water in unseen cavities is eliminated.

Extreme weather conditions could result in flooding that result in the structure being exposed to water above the plinth designed to keep the timber above the moisture line. This occasional flooding should not be detrimental to the timber structure provided that adequate detailing is provided to drain the excess water after the incident without leaving any standing water in concealed spaces.

3.3 *Fire resistance*

Fire safety code limitations on the maximum height of buildings in the past, which limited the use of timber as a structural material for buildings over a certain height, have also resulted in a lack of research and development into timber structural solutions. These restrictions came about as a response to incidents in the past, without much differentiation between types of timber construction and the design application.

For timber particularly the fire safety measures governing its use have been based on gut feel reaction, without much scientific work to back them up. Prescriptive code requirements that govern the use of timber in many countries have not evolved in the same way as for other materials due to minimal demand for its use in many types of structure.

The introduction of a performance based approach to fire safety design in many countries towards the end of the 20th century has removed the legal height restriction. In this new legal environment, if it can be shown that the structure can meet all the stipulated performance requirements in the fire condition, including fire spread considerations and structural stability when subject to all plausible fire scenarios, then it can be considered as an acceptable solution. In other words, instead of applying a recipe of fire safety measures that may or may not be appropriate for the given case, a more rational engineering approach has been recognized as a valid alternative.

The shift towards a performance based environment has led to a spate of pioneering work in the field of fire safety design for timber structures over the past few decades, which has shown that timber buildings can be designed to be safe in fire.

For the 20-storey LCT building referred to above, the research project focused on numerous structural issues, but also on structural fire safety issues. In this programme there were three principal areas that were investigated that were of particular interest to fire engineers:

i The char rate of the solid load bearing glulam panels and solid timber columns
ii The performance of the solid glulam timber columns in fire
iii The performance of the composite lightweight concrete-timber slab panels

The behavior of the solid timber elements is well understood and the traditional way of ensuring continued structural stability after a certain period of fire, is to provide a sacrificial char layer which is assumed to provide no load carrying capacity. With the solid glulam panels in the LCT project it was found to be more economical to provide a plasterboard lining to the glulam load bearing panels than to provide additional thickness to the panels in order to achieve the 90-minute fire rating required for the core structure. The plasterboard lining also helped to address some acoustic issues, so this was felt to give the optimum solution.



Figure 4. Composite concrete-timber slab panel after 90-minute standard fire test.

The solid glulam columns on the other hand were provided with sufficient thickness of sacrificial char layer to resist the design fire duration. However the designers wanted also to address the issue of combustibility of the timber and the possibility of late fire brigade intervention, so a fiberglass 'interlayer' fabric was devised that could be inserted between the residual column section and the sacrificial layer in the build-up of the glulam column. This was intended to prevent the fire from progressing beyond the sacrificial layer even if the fire was not put out by the fire fighters.

The effectiveness of this measure has been tested theoretically, but further large scale testing is required to confirm that it can achieve the objective of halting the fire penetration into the core material.

A composite concrete-timber floor was developed for this project and was tested for acoustic and fire performance. The main function of the concrete topping was to address the acoustic issues, to which timber flooring systems are prone. It was also subject to full scale fire testing to determine its performance subject to a 90-minute standard fire.

The timber beams were mechanically connected to provide some shear connection but the shear resistance was provided principally by a glued interface, with the timber beam glued to the underside of the concrete topping. It was feared that due to the different rates of thermal expansion, a banana effect could develop that would cause the timber to peel away from the concrete topping or that the glue connection to fail. This did not happen and the tests demonstrated adequate performance in the fire condition.

The research and testing behind the development of the design for this 20-storey prototype building demonstrated that the fire safety requirements for structural timber even if applied to high-rise buildings can be met.

4 FLEXIBILITY OF USE

A sustainable and resilient building should be capable of being used for many different uses over its lifetime. One of the drawbacks of the timber panelized solutions is that a large number of structural walls can be needed for vertical load transfer and lateral stability. This limits the flexibility of use as the internal layout is fixed by the structural solution. Furthermore the panelized solution does not provide simple vertical load paths down to the foundations which can be problematic when considering lateral loading such as that due to wind on the building. It is not ideal either for design against seismic effects, for which the simpler the vertical load path, the easier it is to deal with the large horizontal forces induced in a seismic event.

Work has been done at the University of Canterbury to address this issue with the use of open post-tensioned timber moment frames (Buchanan, Palermo, Carradine & Pampanin 2011).

Unbonded post tensioned cables inserted in timber box beams are also capable of increased spans that allow more free space within the building. The beams can be used spanning continuously over columns to create moment resisting timber framed structures that can provide large free interior spaces. This allows the interior space to be divided up by non-structural partitions to suit the intended use, and it can then be easily modified for later alternative uses.

5 REDUNDANCY AND RE-USE

Another consideration for a resilient building is to consider how easily the building can be restored for use after an extreme event or other type of shock loading.

In the development of structural solutions for timber buildings a lot of effort has gone into developing designs that use an industrial process and systems approach. Using this approach the timber building components are manufactured in factories off-site and then transported to site and crane lifted into place and secured using quick fastening connection details. The relative lightness of the timber components lends itself to this approach, it avoids the need for storage space on site and it saves a lot of time in the construction process.

Panelized buildings however raise the question of progressive collapse, and the designer would normally be obliged to consider the redundancy of the structure by considering the failure of any one structural component and ensuring continued stability under these conditions. The designer would assume that damaged panels offer no further structural resistance and would have to show that stability is maintained under these conditions.

To take into account the ease of re-use this type of study needs to be extended to a study for the removal and replacement of the damaged component, particularly for timber wall panels spanning vertically and picking up loads from multiple floors.

According to the definition of resilience outlined above, a resilient building should also be capable of being returned to full use as soon as possible after an event that partially damages the structure, be it

due to a natural extreme event, a blast event or other unexpected impact.

Many countries would lack the expensive presses necessary to sandwich, glue and cure the wood into glulam or CLT panels. That means that often, particularly if large timber panels are used, the damaged components would need to be ordered from a distant source country. In these cases it would be preferable to develop alternative local manufacturing technologies to produce the components used in the design of the structure and in that way ensure much quicker reinstatement times.

Cutting out damaged pieces and glueing infill pieces into the damaged areas may provide a solution. The glue connections that have been tested to date have provided promising results, but the effectiveness of face glueing pieces in solid timber panels to restore continuity has still to be researched and validated.

More work therefore needs to be done into the area of repair and/or replacement of the structural components of timber buildings to address all the issues related to how timber buildings measure up to the resilience test.

6 CONCLUSIONS

Timber as a structural material has largely been ignored over the last few centuries; the period in which structural analysis techniques and systems for steel and concrete were developed. With the drive for more sustainable design of buildings, timber has come to the fore as the ideal structural material when it comes to minimizing the embodied energy in the built environment.

This paper considers the issues related to the resilience of buildings and discusses the issue in relation to timber as a structural material. There has been a lot of good work done over the past few decades investigating all aspects of design using timber as the structural material. The case for sustainable design has been well established, and systems for large and robust buildings, capable of good performance when exposed to extreme natural conditions, fire and explosion have been have been developed.

An industrial processes and systems approach has been developed to promote quick and safe construction methods, and redundancy of the designs has been considered. However one aspect associated with resilient design seems to have received less attention; that related to the repair and re-instatement of damaged components after a shock event, and this applies to all construction materials, not just timber.

More work needs to be done in this area to address all the issues related to how good a material timber is when measured against all factors that define the resilience of a building.

REFERENCES

Buchanan, A. Palermo, A. Carradine, D & Pampanin, S. Post tensioned timber framed buildings., *The Structural Engineer 89 (17) 6 September 2011.*

Department For International Development, United Kingdom, *Sustainable Livelihoods Guidance Sheets,* (1999).

Würm, J. Gockel, T Unger, M., *The Life Cycle Tower: a high-rise in timber construction,* Arup Research Review 2010.

Techniker. *Tall Timber Buildings The Stadthaus, Hoxton, London, Applications of solid timber construction in multi-storey buildings.*

Research and Applications in Structural Engineering, Mechanics and Computation – Zingoni (Ed.)
© 2013 Taylor & Francis Group, London, ISBN 978-1-138-00061-2

Numerical modeling of a post-tensioned timber frame building with hysteretic energy dissipation

A. Di Cesare, F.C. Ponzo & M. Simonetti
School of Engineering, University of Basilicata, Potenza, Italy

T. Smith & S. Pampanin
Department of Civil and Natural Resources Engineering, University of Canterbury, Christchurch, New Zealand

ABSTRACT: The following paper describes the numerical modelling used to predict the dynamic behaviour of a post-tensioned timber building with the addition of a hysteretic energy dissipation system. This modeling is in support of a shaking table test programme about to commence on a 2/3rd scale, 3-dimensional, 3-storey post-tensioned timber structure made from post-tensioned timber frames in both directions in the structural laboratory of the University of Basilicata in Potenza, Italy. This research is part of a joint collaboration with the University of Canterbury in Christchurch, New Zealand. The test frame has been modeled combining the use of elastic elements with a series of rotational springs which represent the moment rotation behaviour of the beam-column joints. These springs were calibrated against the moment rotation design procedure used for post-tensioned timber connections. Modeling was done by considering two non-linear finite element codes, SAP2000 and RUAUMOKO. This paper compares numerical results obtained from the model with and without additional dissipative elements in order to better understand the dynamic behaviour of post-tensioned timber structures.

1 INTRODUCTION

This paper presents the numerical modeling of a 2/3rd scale three-storey post-tensioned timber frame building to be tested in the structural laboratory of the University of Basilicata (UNIBAS) in Potenza, Italy. This work is part of a collaborative experimental campaign between UNIBAS and the University of Canterbury, in Christchurch, New Zealand. The complete study will evaluate the feasibility of applying jointed ductile post-tensioning technology, originally conceived for use in concrete structures (Priestley et al. 1999), to glue laminated timber (glulam). The aim of this phase of the project is to evaluate the dynamic seismic performance of the system and further develop the system for use in multi-storey timber buildings.

The post-tensioned timber concept (under the name PRES LAM) has been developed at the University of Canterbury and extensively tested in the structural laboratories of the university. In stage one of this current project a full-scale beam-column joint was designed, fabricated, constructed and tested at the structural laboratory of UNIBAS providing excellent results and beginning to answer key questions regarding system performance. During testing the application of the post-tensioned timber concept to glulam timber was confirmed. Testing was performed both with and without dissipative elements and the system displayed the same excellent performance under static and seismic loading as when the system was employed with laminated veneer lumber (LVL) (Smith et al. 2011). The dissipative devices used were based on yielding steel angles which activate at low drift levels, both increasing the moment capacity of the system and adding energy dissipation (thus reducing seismic load through damping) without inducing plastic deformations in other elements.

During this stage modeling and design procedures were also implemented and verified (Smith et al. 2012) using the quasi-static test results.

An extensive dynamic experimental testing programme is scheduled to be performed in the Structural Laboratory of the University of Basilicata (Ponzo et al. 2013). This paper will build on the techniques to be used during dynamic testing campaign, employing them as part of a time-history modeling investigation.

2 EXPERIMENTAL TEST MODEL

The prototype structure is three stories in height and has a single bay in both directions (Ponzo et al. 2013). All design has been performed in accordance with the current version of the Italian design codes (NTC 2008). The interstorey height of the building is 3 m and the frame footprint is 6 m by 4.5 m. The building has been designed to represent an office structure (live loading

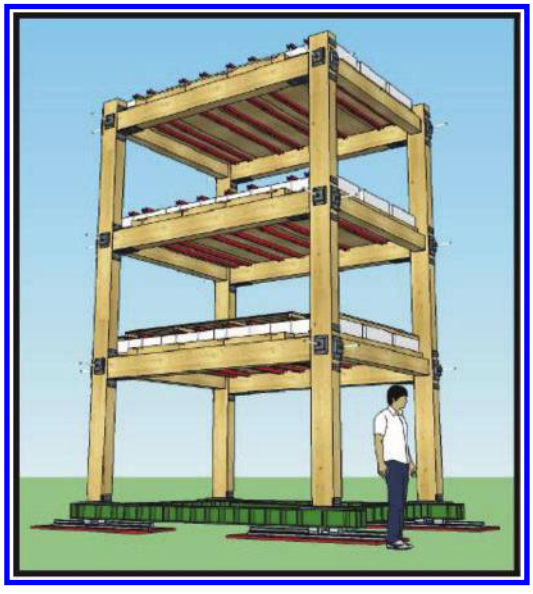


Figure 1. Rendering of test specimen.

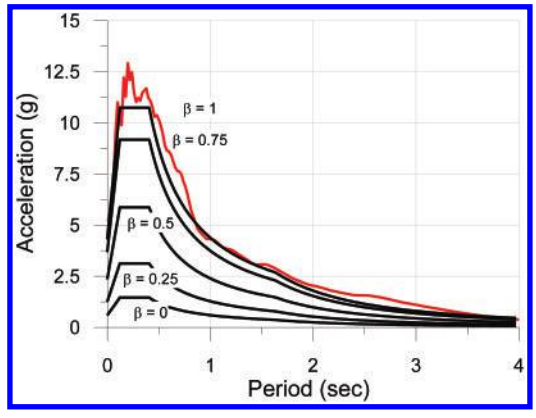


Figure 2. Effect of the parameter β on seismic structural demand.

Q = 3 kPa) with the final floor being a rooftop garden. The flooring of the building is made from solid glulam panels. The lateral resistance of the building is governed by seismic loading.

The test frame (Fig. 1) is made from glulam grade GL32h (EN 1995-1-1 2004). A scale factor of 2/3 has been applied to the prototype structure resulting in an interstorey height of 2 m and a building footprint of 4 m × 3 m.

The beam-column connection in the principle direction is based on the connection type which was tested during stage one. Passing through the centre of the beam is a single 26.5 mm diameter bar which will be tensioned to varying values of initial loading throughout the test programme. This is a high strength steel bar with a yield strength $f_y = 1050$ N/mm^2 and a Young's modulus of 170 kN/mm^2. Dissipation in the form of a yielding steel angle will be used. Screws have been used to protect the column face and also connect each dissipater attachment plate. Vertical loading will be transferred through a ϕ76.1 mm steel tube with extends 66 mm from the beam and sits inside the column. The beam-column connection in the secondary direction is similar to that in the principle direction.

The base of the column is fitted with a steel shoe which is epoxied into the base of the column and left free to rock on a base plate (which will be used to represent the building foundations in the case of the test building). Shear transfer is achieved using a ϕ76.1 mm steel tube which extends 15 mm from the steel shoe and slots into a cavity in the base plate. Holes have been drilled and tapped in the steel shoe in order to facilitate the attachment of energy dissipation devices. During testing passive energy dissipation devices will be added to the structure in order to add strength and reduce displacements without increasing accelerations or base shears. The passive hysteretic energy dissipation devices to be added are the 'yielding steel angle' (Di Cesare et al. 2013).

The testing input will be a set of 7 spectrum compatible earthquakes selected from the European strong-motion database with the characteristics shown in (Ponzo et al. 2013). The code spectrum which was used when selecting the records was defined in accordance with the current Eurocode for seismic design (EN 1998-1:2003 2003) having $a_g = 0.35$ g and a soil factor of S = 1.25 (Soil class B – medium soil) giving a PGA for the design spectrum of 0.44 g.

During testing several characteristic of the post-tensioned timber concept will be investigated. The key to this type of system is made up of the ratio β, the ratio between the moment resistance provided by the post-tensioning and the moment resistance provided by the dissipation. Clearly, during design this choice affects both damping and moment capacity of the system and therefore changing this value will have a direct effect on both capacity and demand.

The effect of the parameter β on demand is displayed in the acceleration spectra shown in Figure 2. With a decrease in the factor damping is introduced and therefore demand is decreased.

During the experimental campaign the size of the structural members, building layout and mass will not be altered, however different values of post-tensioning and steel moment capacity contributions (thus variations in the value β) will be investigated with the cases shown in Ponzo et al 2013 being selected for testing.

These options are based around the standard case of PT100_1.00 which has an ultimate connection moment capacity of $M_t = 27$ kN. Adding steel without reducing the post-tension moment contribution (PT100_0.70) has the effect of both increasing capacity and decreasing demand. Adding steel in combination with a decrease in post-tensioning force (PT50_0.80) decreases demand but retains equal capacity.



Figure 3. Dissipative elements: Experimental Testing and Modeling of ABAQUS.

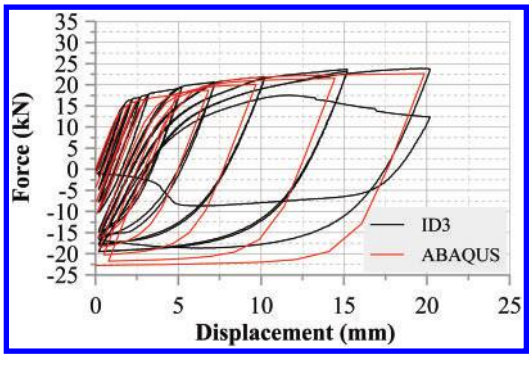


Figure 4. Comparison between testing results and ABAQUS model for ID3.

For further information regarding the testing details and set-up please refer to the companion paper of Ponzo et al. (2013).

3 NUMERICAL MODELLING

3.1 *Local modeling*

The ABAQUS finite element programme (ABAQUS Inc. 2011) was used to model the behaviour of each of the dissipative angles to be applied to the frame. A 3D deformable solid made up of 2 mm tetrahedral mesh elements was used. The steel material was modelled using a plastic yield model with (combined) cyclic hardening. The boundary conditions of the angle were set in order to mimic as closely as possible the loading of the steel angle however displacements were calibrated in order to represent the rotations of the top connection seen throughout testing and taken as being inherent to the systems design. The experimental test and the numerical model for the dissipative angle are shown in Figure 3.

Figure 4 shows a comparison between a selection of testing results and the ABAQUS model. Fatigue was not accounted for in the model. As shown the model provides a sufficiently accurate representation of the angles performance with close prediction of the key parameters of stiffness, both pre and post yield, yield and ultimate strength/displacement.

The model does however over-predict hysteretic dissipative capacity during larger cycles. This is likely due to the material degrading from low-cycle fatigue which is not accounted for in the model. More details are reported in Di Cesare et al. (2013).

3.2 *Global modeling*

Increasingly in the design of structures, engineers rely on the use of Non-linear Time History Analysis (NTHA) in order to verify building performance under design seismic loading. In the use of these models several trade-offs are made between complexity, accuracy, programming time, and processing time. In design it is crucial that simple models exist which provide sufficiently accurate building response without requiring a large amount of time in processing or programming.

From the conception of the post-tensioned jointed ductile concept it has been clear that the nature of the controlled rocking mechanism lent itself well to the use of a lumped plasticity approach in modelling. This approach combines the use of elastic elements with springs which represent plastic rotations in the system.

During the course of the post-tensioned timber project several authors have used finite element modeling in order to successfully replicate testing results. This was done using the RUAUMOKO (Carr, 2006) program. As mentioned previously, during stage one of this project these methods were further verified against quasi-static testing, this was performed using the widely spread SAP Non-linear (SAP2000, 2004) structural calculation program.

Two essentially identical numerical models have been set up in both RUAUMOKO and SAP 2000. These models combine elastic elements with rotational springs which have been calibrated against current design methods. Although the two models are essentially identical the length of the rotational spring differs between the two models. In the RUAUMOKO analysis the standard practice of setting the spring length to 1 mm was employed however this proved unstable when applied to the SAP model and a 10 mm spring length was used. The parameters of the rotational springs were set to match the predicted rotational response; Figure 5 shows representations of each springs moment-rotation characteristics.

Post-tensioning was represented using tri-linear elastic elements for both models with bounded Ramberg-Osgood and Buoc-Wen rotational spring models used to represent the steel elements in the RUAUMOKO and SAP2000 model respectively. A summary of both models is presented in Figure 6a and 6b.

As mentioned previously the base connection of the frame is also a rocking connection. With a column-foundation connection however moment capacity is provided by the axial load in the column in addition to the steel devices, if present. Under horizontal loading the axial load in the column changes and therefore a simple rotational spring was not adequate in modelling response. Work is ongoing in order to understand the most adequate way in which this base connection can be modelling and therefore two models have been

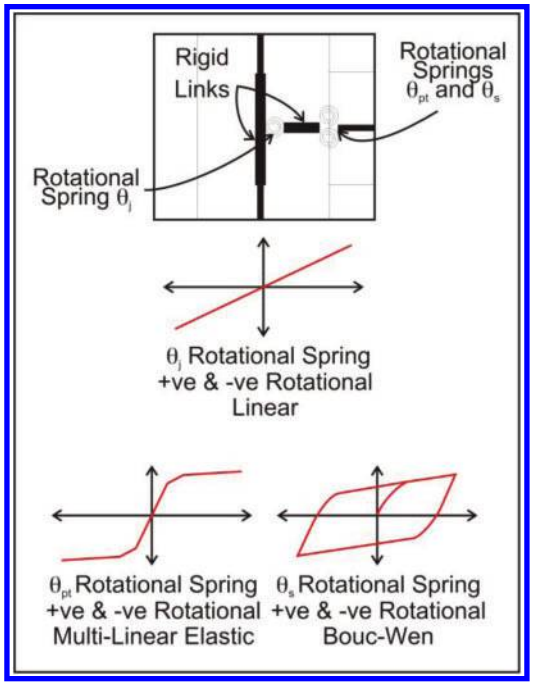


Figure 5. Local Modelling of beam to column joint.

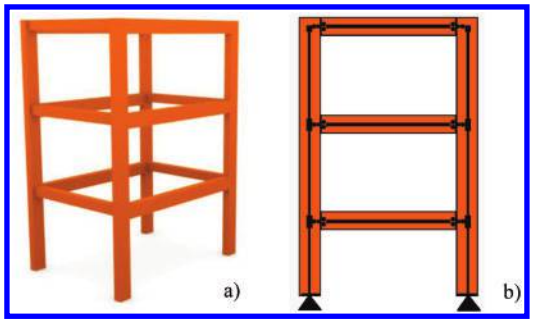


Figure 6. Global Modelling a) 3-dimensional numerical model for predictions, b) post-tensioned timber frame-pinned base model.

developed; one with a pinned based and one with a fixed base.

Recent studies have also recognised the importance of modelling and accounting for the elastic joint rotation in the calculation of the connection rotation. In order to model this, a rotational spring is added in the joint panel region. This linear elastic spring was given a rotational stiffness based on the moment-rotation relationship of the joint panel using formulas presented in Newcombe et al. (2010).

4 RESULTS OF NUMERICAL STUDY

In order to define the differences between the RUAUMOKO and SAP2000 model NTHA have been carried out for each testing configuration. Figure 7

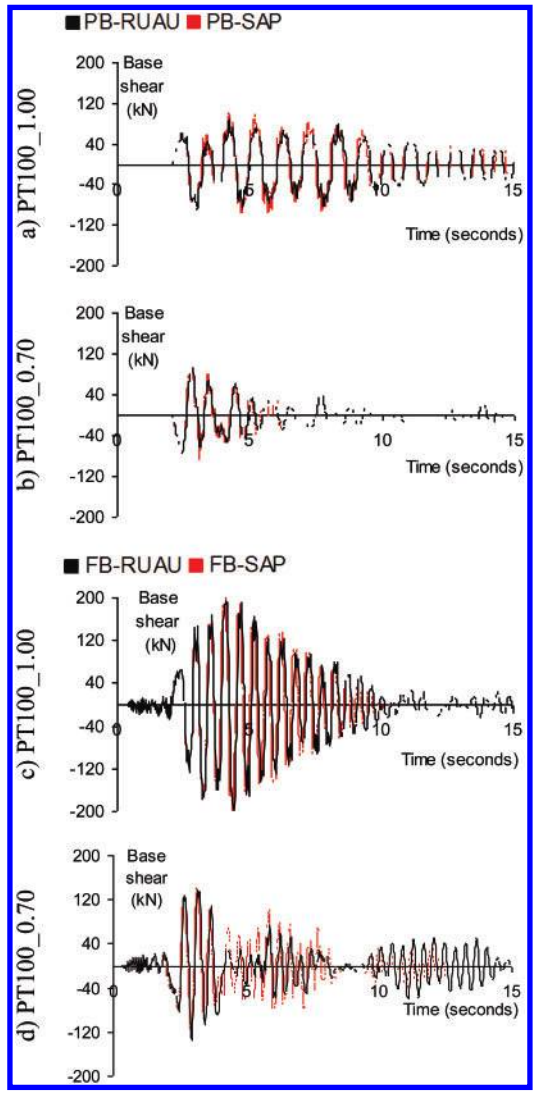


Figure 7. Time history base shear subjected to earthquake 535ya of Pinned Base model a) PT100_1.00 and b) PT100_0.70 and Fixed Base model c) PT100_1.00 and d) PT100_0.70.

compares the base shear response of the experimental model for the reference configuration (post-tension only case, PT100_1.00) and one of the hybrid cases with the addition of steel elements (PT100_0.70). The figure shows the time history results of base shear of the model with pinned based and with fixed base boundary conditions subjected to earthquake 535ya.

Figure 8 shows the RUAUMOKO and SAP2000 results in terms of i) maximum interstorey drift MID, ii) maximum accelerations MA at each floor and iii) maximum base shear MBS averaged across 3 input accelerograms (000196xa, 000535ya and 001228) for a) PT100_1.00 and b) PT100_0.70 configurations

As can be seen in Figure 7, the base shear of the structure reduces in amplitude when additional steel

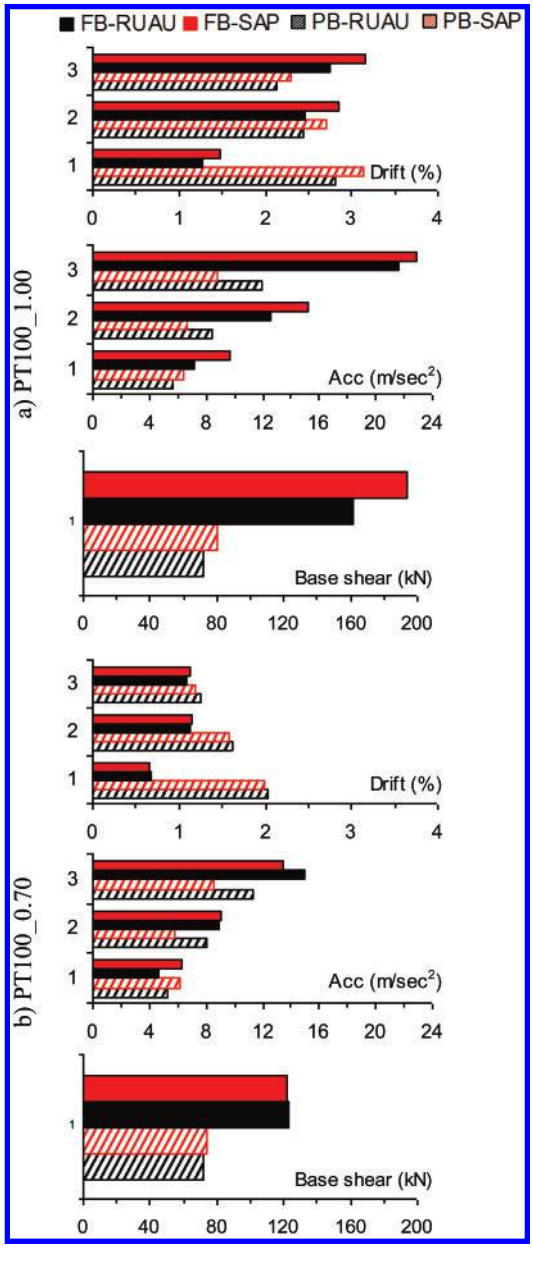


Figure 8. Comparisons SAP-RUAUMOKO results in terms of i) maximum acceleration MA, ii) maximum interstorey drift MID and iii) maximum base shear MBS averaged across 3 input ground motions for a) PT100_1.00 and b) PT100_0.70 cases.

devices are introduced (decreased demand). Comparisons between RUAUMOKO and SAP2000 non-linear time history analysis show that the results have the same trend in time with a small difference in maximum values (less than 10%) both for PT100_1.00 and PT100_0.70 configurations.

The comparison shown in Figure 8 clearly shows the difference that the base assumption makes in the

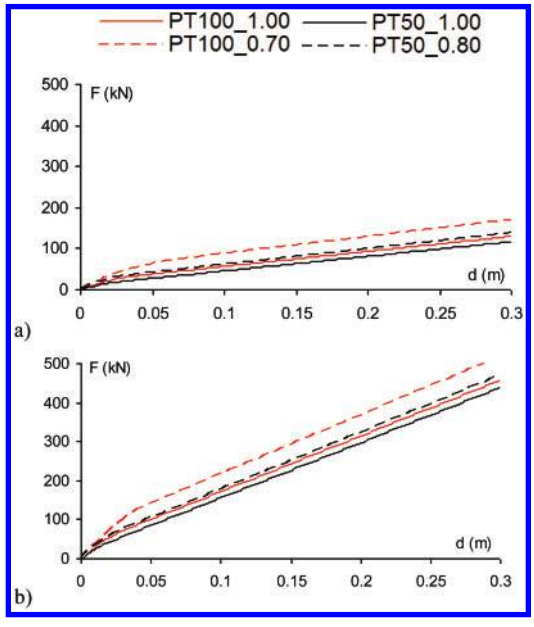


Figure 9. SAP Pushover comparisons between configurations to be tested with a) Pinned Base, b) Fixed Base.

response of the model and therefore in its ability to predict likely behaviour. Clearly the introduction of a pinned base in modelling reduces accelerations and base shears but leads to large levels of drift which can govern design of a flexible system such as post-tensioned timber. It is clear however that this discrepancy decreases with the addition of additional damping to the structure which also has a significant effect in reducing the values of all of the key performance parameters studied

In Figure 9 the numerical results of the pushover analysis considering pinned base and fixed base configuration are compared. These studies were performed with only SAP2000 in order to predict the variation in stiffness of the case studies. As can be seen in the figure, PT100_1.00 and PT50_0.80 display the same force-displacement behaviour however significant differences are present with relation to their base connection assumptions. The choice of pinned based of fixed base also therefore impacts on seismic demand (through change in period).

5 CONCLUSIONS

Non-linear analyses have been performed in order to define and better understand the test cases which will be used during the dynamic experimental tests on a 2/3rd scale, 3-dimensional, 3-storey, post-tensioned timber structure that will be performed in the structural laboratory of UNIBAS, Italy, in collaboration with the University of Canterbury, New Zealand. Time history analyses were performed in order to define total system behaviour of the considered configurations.

The numerical model has been considered with and without the addition of dissipative steel angles which are designed to yield at a certain level drifts with constant PT and varying PT.

As part of this testing programme a series of investigative tests have been performed in order to characterise the performance of the steel angles. In all different angle specimens the stress and strain distributions have been studied by means of local modelling.

Considering that the base of the column will also be left to rock against the foundation two assumptions have been made regarding the fixity of the base of the column. This displayed the significant impact that the boundary conditions of the column have on the total response of the structure and lead the authors to conclude that further attention and recommendations should be made regarding this point in day to day design.

NTHA results proved the effectiveness of dissipative steel devices in reducing seismic effects when compared to a PT only case. The configurations which will be used during the dynamic experimental tests have been identified.

These numerical results will now be compared against testing outcomes in order to provide useful guidelines for the non-linear dynamic modelling of post-tensioned timber structures.

ACKNOWLEDGEMENTS

The authors would like to acknowledge funding from the Structural Timber Innovation Company (STIC) and FederLegno Arredo (FLA).

REFERENCES

ABAQUS Inc. (2011). "Abaqus FEA." ABAQUS Inc., Providence, Rhode Island, United States, Finite element analysis software.

Carr A. (2006). "RUAUMOKO." A. Carr, Christchurch, New Zealand, Inelastic Dynamic Analysis Software.

Di Cesare, A., Ponzo, F.C., Nigro, D., Simonetti M., Smith, T., Pampanin, S., (2013). " Experimental testing and numerical analysis of steel angles as hysteretic energy dissipating systems". XV Convegno di Ingegneria Sismica, Associazione Nazionale di Ingegneria Sismica, Padova, Italy.

European Committee for Standardization. (2003). "Design of structures for earthquake resistance – Part 1: General rules, seismic actions and rules for buildings." Secondary Design of structures for earthquake resistance – Part 1: General rules, seismic actions and rules for buildings, Secondary Standardization, E. C. f., ed., European Committee for Standardization, Belgium.

European Committee for Standardization. (2004). "Design of Timber Structures Part 1-1: General – Common Rules and Rules for Buildings." Secondary Design of Timber Structures Part 1-1: General – Common Rules and Rules for Buildings, Secondary Standardization, E. C. f., ed., European Committee for Standardization, Belgium.

Ministrero delle Infrastrutture. (2008). "Norme Tecniche per le Costruzioni." Italy.

Newcombe, M. P., Pampanin, S., and Buchanan, A. H. (2010). "Numerical Modelling and Analysis of a Two-Storey Post-Tensioned Timber Frame with Floor Diaphragms." 14th European Conference on Earthquake Engineering, Ohrid, Republic of Macedonia.

Ponzo, F.C., Di Cesare, A., Nigro, D., Simonetti M., Smith, T., Pampanin, S. (2013). " Shaking table tests on a large scale moment resistant timber frame with post-tensioning and energy dissipating system". 5th International Conference on Structural Engineering, Mechanics and Computation, Cape Town, South Africa.

Priestley, N., Sritharan, S., Conley, J., and Pampanin, S. (1999). "Preliminary Results and Conclusions From the PRESSS Five-Story Precast Concrete Test Building." PCI Journal (November–December 1999), 42–67.

SAP2000 (2004). Static and Dynamic Finite Analysis of Structures. Berkeley, CA, USA.

Smith, T., Pampanin, S., Carradine, D., Buchanan, A., Ponzo, F., Cesare, A. D., and Nigro, D. (2011). "Experimental Investigations into Post-Tensioned Timber Frames with Advanced Damping Systems." Il XIV Convegno di Ingegneria Sismica, Associazione Nazionale di Ingegneria Sismica, Bari, Italy.

Smith, T., Ponzo, F. C., Cesare, A. D., Auletta, G., Pampanin, S., Carradine, D., Palermo, A., and Nigro, D. (2012). "Testing of a Post-Tensioned Glue Laminated Beam to Column Joint: Experimental and Numerical Results." 12th World Conference on Timber Engineering, Auckland, New Zealand.

26. Masonry structures

Research and Applications in Structural Engineering, Mechanics and Computation – Zingoni (Ed.)
© 2013 Taylor & Francis Group, London, ISBN 978-1-138-00061-2

In situ full-scale tests for old masonry elements: The out-of-plane response

A. Borri
D.I.C.A. Department, University of Perugia, Italy

M. Candela
P.A.U. Department, University of Reggio Calabria, Italy

R. Fonti
D.I.S.T. Department, University of Naples "Federico II", Italy

ABSTRACT: Regarding to old masonry response under seismic actions, destructive testing campaign was planned. It was directed to rubble masonry, with particularly reference to L'Aquila old masonry type. The 6th April 2009 Earthquake, strongly damaged L'Aquila historical centre; in the hearth of the so-called "red zone", a corner palace permanent damaged was chosen. The main masonry features are: no ordinary setting, small size of the stones, regular flattens made in bricks, no transversal links and stones contact; these marks are representative of the Italian smallest historical centres and European one.

Consolidation approach detection is obviously hard; therefore, in order to research and obtain an effective strategy of intervention, strictly connected to the above masonry type, seven panels were selected. Five strengthening approaches were pointed out; starting from the common injections until more advanced methods like "the reticolatus", without overlook the tradition techniques. This paper will be focused on the out-of-plane answer; in relation to consider the first collapse mode the primary cause of building break-down, during earthquake.

1 L'AQUILA CITY AFTER EARTHQUAKE

1.1 *The site*

The destructive in situ testing campaign was performed involving one old Palace permanently damaged by L'Aquila earthquake in L'Aquila city. It is placed in Saint Peter' Square, in the heart of the historical center (Figure 1).

L'Aquila is one of the Italian cities listed into UNESCO sites; it is the administrative centre of the Abruzzi region, (see Figure 2). During the 2009 seismic activity a great part of its historical centre was damaged; in order to research and obtain an effective strategy of intervention, strictly connected to the old masonry local features, the above testing campaign for full-scale specimens were carried out.

Seven panels were chosen as structural elements suitable as specimens. They were placed at the building first floor and tested in order to identify mechanical properties and in-plane and out-of-plane response.

1.2 *L'Aquila old masonry: the main features*

Before explain both testing campaign program and strengthening measures, it is really important point out L'Aquila old masonry features. L'Aquila built setting show several masonry typologies all closed into



Figure 1. Chosen building photo after the 6th April 2009 Earthquake.

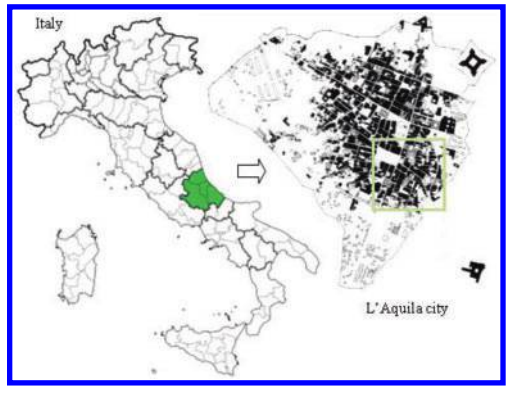


Figure 2. Italian Peninsula, Abruzzi region (in green), L'Aquila city (historical centre map).



Figure 3. Masonry typologies detection in relation to stonework failure.

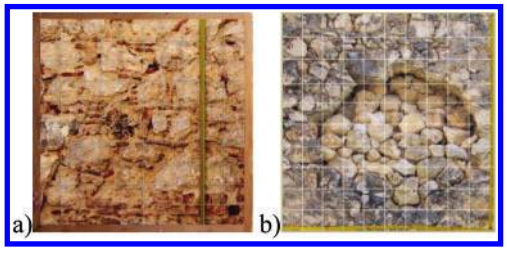


Figure 4. Masonry sampling (1 m × 1 m); a) type one, L'Aquila historical centre; b) type two, L'Aquila surrounding area.

rubble masonry category (see Figure 3); but it follows that two of them are most representatives, respectively widespread in L'Aquila city and in the neighborhood (Formisano et al. 2012).

The first type constructive scheme takes into account no ordinary stones setting, with no regular shape and small size. As a direct consequence of it, total absence of headers is noticed and lacks among the stones or thickness mortar joints can be pointed out. However some regular courses made by bricks and stones irregularity filled up by wedges elements can be identified. Therefore, regular flatten made in bricks and stretcher elements are present (see Figure 4a) (Ceradini 2004) (Candela and Fonti, 2010).

Instead, the second typology show a masonry setting lacking in many mechanical features: stone size smallest, no transversal section links, no stretcher elements, no bricks layers, no contact between the bigger stones, no vertical and horizontal interlock (see Figure 4b.). All that makes hard strengthening approach detection.

The building chosen for the full-scale tests match the first masonry typology; therefore, the followings strategies were focused on this specific masonry type. Regarding this first step two principal lacks were carried out: *absence of headers* and *no contact among stones*; they were all over posted like starting dates for strengthening approaches detection.

2 THE TESTING CAMPING

2.1 *The testing program*

Two façade involved:

Only first floor masonry elements – The panels selected are physically separated by a regular progression of windows, therefore, each masonry part closed to the openings was identified like a singular rigid block. Panel dimensions: wide 60 cm, high 400 cm, large – variable

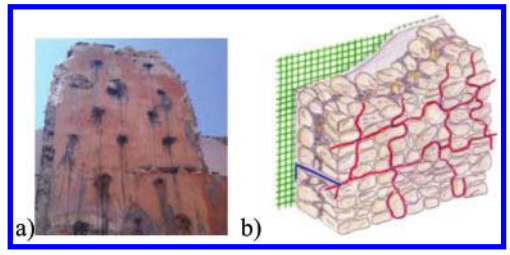


Figure 5. Specimen n.4; a) Masonry reinforcing with anchors; b)Specimen n.1 – reinforcement approach: Reticolatus (external surface) and GFRP reinforced plaster (internal surface).

Seven panels were tested:

Two panels were posted useful for masonry mechanical parameters characterization and behavior identification under horizontal actions (in plane and out-of plane tests in static conditions). Moreover, test with no destructive methods were applied.

Five panels were strengthened with different approaches and finally tested out-of-plane in static conditions.

University involved:

- *Sergio Lagomarsino working group, University of Genoa, Italy*
- *Antonio Borri, University of Perugia, Italy*
- *Michele Candela, University of Reggio Calabria,*
- *University of Naples "Federico II", Italy*

2.2 *The strengthening methods*

In order to provide different strengthening levels, the five reinforcement strategies take into account basic approach like injections or more advanced methods as artificial headers addition, without overlook tradition techniques. Starting from the no reinforced panel response, for out-of-plane mechanisms, the final goal is obviously improve panels resistance against horizontal actions in order to obtain the maximum possible resistance related to panel geometrical dimensions. The panels are considered rigid blocks.

Following panel strategies of intervention overview show – according to fault adjustment improving (Borri et al. 2012) (Fonti, 2013).

2.2.1 *Panel n.4*

Fault corrected: none;
Strengthening method: Injections (See Figure 5a);
Executive phases:

1) Panel drilling (n.17); 2) Anchors setting in the holes, pitch 60 cm; 3) Masonry cleaning; 4) The injection. Grouting (lightweight mortar) was injected with light pressure near 2 bar.

2.2.2 *Panel n.1*

Fault corrected: no transversal section links;
Strengthening method: "Reticolatus";
Strategy of intervention description:

The reinforcement approach applied use two different solutions for both internal and external surfaces. The last one surface was strengthened by the

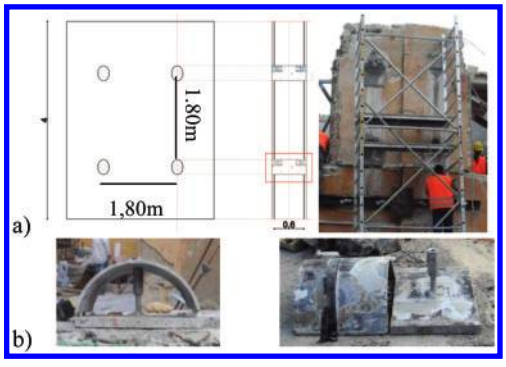


Figure 6. Specimen n.2 – a) technique applied design; b) photo of pushing metallic elements; b) final result.

"Reticolatus" technique related to restoration criteria for no plastered masonry. Instead, second one use GFRP reinforced plaster, like show in Figure 5b.

The transversal connections between the two differ solutions applied was realized by some little bars. A particular cable (Dyneema rope) was rolled around these tie elements; the rope setting follow the stones as a mesh. Therefore, bars connect the two meshes, one in GFRP and another in rope.

2.2.3 *Panel n.2*

Fault corrected: no transversal interlock;
Strengthening method: Traditional technique with original "headers";
Strategy of intervention description:

The strengthening idea starts from the traditional reinforcement technique of "headers" addition to achieve a new one, in order to guarantee good transversal connection and re-establish regular stresses conditions. The headers regarding their bigger dimensions can tie panel from side to side.

The innovative "header" is made of lighten concrete with a T shape modeled in order to fill the empty areas by pushing metallic elements. (See Figure 10).

Executive phases: (Figure 6)

1) Panel drilling; the horizontal boreholes were placed full in wideness, four in numbers; 2) The header's built up; elements dimensions 30 cm × 20 cm made about lighten concrete; 3) Setting of the T headers; 4) Setting of the pushing metallic elements.

2.2.4 *Panel n.3*

Fault corrected: no transversal section links;
Strengthening method: original "header" with Bossong system technology – injection anchors with sock;
Strategy of intervention description:

The strengthening idea begins from the improvement of drilling techniques, which allow the embedding of reinforcement steel anchors inside masonry walls with a minimum impact. This system patented by the Bossong Spa it's well-know namely "injection anchors with sock". It the special sock wraps the metal bar and guarantees the total control of injection and to

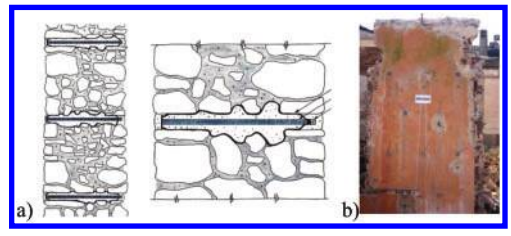


Figure 7. Specimen n.3; a)Injection anchors with sock-as headers; b) Panel final result.

create a strong mechanical interlock a long all over the section. The steel bars enclosed in a mesh fabric sleeve into which a specially developed grout is injected under low-pressure. Therefore, the injection anchors with sock arrange artificial headers perfectly bonded to masonry inner surfaces (Figure 7a).

Executive phases:

1) Panel drilling. The horizontal boreholes were placed full in wideness with variable length from 560 to 800 mm and diameter 60 mm;

2) Bars setting. bars, type GBOS, diameter 60 mm and 500 mm placement. The sock mesh is a porous membrane designed in order to contain the aggregates that constitute the mixture, and allow cement flow into the sock. chemical bond with the substrate is guarantee.

3) Very smallest nylon tube was used in order to give the injection. The injection devices are designed according to anchors size and features, in this case the diameter is about 8 mm.

At the end, thirteen headers were added into the panel with a pitch of 65 cm in the horizontal direction and 70 cm in vertical one. (See Figure 7b).

2.2.5 *Panel n.5*

Fault corrected: no transversal section links and no contact among stones
Strengthening method: Traditional technique – headers setting and mortar joints replacement.
Strategy of intervention description:

The strengthening idea (Fonti, 2013) start from Abruzzi' local structural engineering features for old masonry constructions. The Abruzzi built widespread employ wooden elements for masonry connections and building safety against horizontal actions. Therefore, some wooden headers were placed in order to obtain the mechanical interlocks (in transversal section); instead, little bricks elements were placed in order to increase compression resistance for vertical loads and avoid the modification of the hinge position during panel overturning under horizontal loads.

Executive phases: (See Figure 8)

1) Panel drilling. The horizontal boreholes were placed full in wideness with 4 holes diameter 200 mm; 2) Replacement of the mortar joints with little bricks elements; 3) Setting of the wooden headers and wooden wedge-elements in order to reestablish regular stress condition.

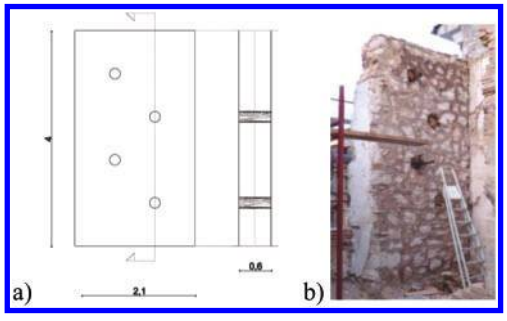


Figure 8. Specimen n.5. a) Schematic plan for wooden headers setting; b) Panel final result.

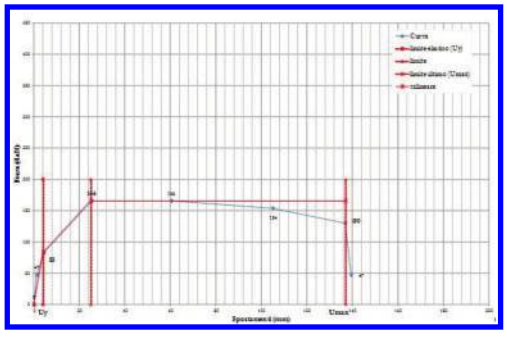


Figure 9. Specimen n.6. force-displacement constitutive curve.

3 THE OUT-OF-PLANE TESTS

3.1 *The pull-out tests*

According to the panels placement possibility, the specimens were tested by monotonous "force-control" or cyclic tests. No axial load has been applied.

Regarding the monotonous tests, the setup adopted use metallic anchor and cable positioned in the geometrical panel dimensions centre, in order to apply horizontal force.

The main marks obtained are the following (Borri et al. 2012): (from the no-reinforced to the best) Specimen n.6 – no reinforcement

3.1.1 *Specimen n.6*

The comparison between the no reinforced global panel force-displacement constitutive curve and the theoretical one show no codified response for L'Aquila masonry: three-linear curve trend with no frail behavior it's generally noticed. Gradual development of relevant horizontal displacements after the maximum strength is recognized.

From 0 to 4 mm pseudo-elastic behavior is identified with corresponding strengths values respectively equal to 47 daN and 83 daN(Uy).

Nonlinear response is noticed after the elastic limit with significant horizontal displacements increasing without strength one until the maximum displacement equal to 250 mm and the corresponding force value equal to 166 daN. (See Figure 9)

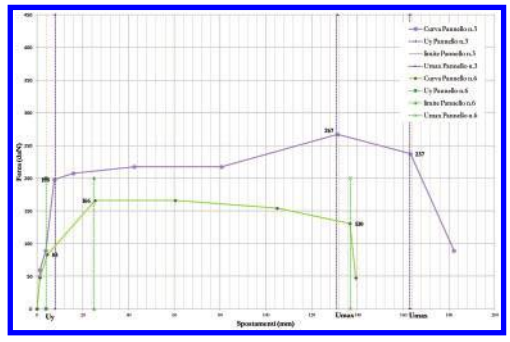


Figure 10. Specimen n.4 and 6 force-displacement constitutive curve comparison.

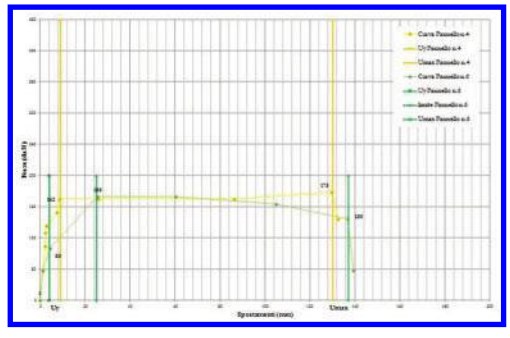


Figure 11. Specimen n.3 and 6 force-displacement constitutive curve comparison.

3.1.2 *Specimen n.4: Injection*

The comparison between the two experimental curves for specimens n.4 and 6 shows very similar response. (See Figure 10)

The force-displacement constitutive curve recognized for panel n.4 take into account a starting linear trend from 0 to 9 mm that show a pseudo-elastic behavior with corresponding strengths values respectively equal to 47 daN and 162 daN (Uy).

Nonlinear response is noticed after the elastic limit with significant horizontal displacements increasing without strength one until the maximum displacement of 130 mm.

3.1.3 *Specimen n.3*

The comparison between the experimental response of the panels n.3 and 6 shows a very similar trend curve with different resistance values (Figure 11).

In fact, from 0 to 8 mm a pseudo-elastic behavior is noticed with corresponding strengths values respectively equal to 49 daN and 198 daN (Uy). This last is more than double, in front of the specimen n.6. After the elastic limit nonlinear response is noticed, two different line segments could be distinguished: growing and plateau with significant horizontal displacements increasing until the maximum displacement of 163 mm. the maximum strength recognized is equal to 267 daN.

Therefore, in global panel response the artificial headers gave a little improvement contribution. This



Figure 12. Specimen n.3 experimental work – out-of-plane test, photo.

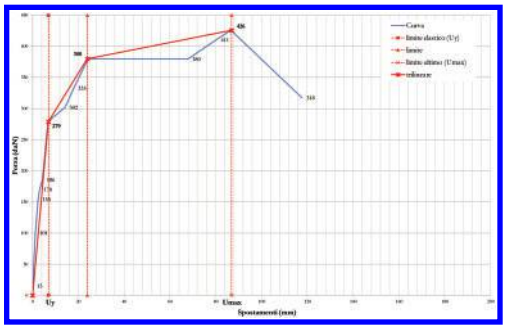


Figure 13. Specimen n.2 – force-displacement curve.

is mainly due to excess in number of them; in fact during the panel overturning they could be recognize as weak points. (See Figure 12)

3.1.4 *Specimen n.2*

The force-displacement constitutive curve recognized for panel n.3 is ever-grooving; it take into account a starting linear trend from 0 to 7 mm that show a pseudo-elastic behavior with corresponding strengths values respectively equal to 105 daN and 279 daN (Uy).

Nonlinear response is noticed after the elastic limit with both significant increasing of horizontal displacements and strength values until the maximum displacement 87 mm and relative strength value equal to 426 daN (See Figure 13).

It is obviously evident that the addition of artificial headers, good in number, could realize very well interlock in the transversal section avoiding partially hinge position modification during panel overturning under horizontal force (See Figure 14).

Therefore, a perfect rigid-block behavior was experimental noticed (See Figure 20); however, it was no taken in advance of all panel weight force against horizontal loads.

Note: In order to make a comparison all values listed were prorated to masonry specimens reduced in largeness to 1m.

3.1.5 *Specimen n.1*

The force-displacement constitutive curve recognized for panel n.1 is ever-grooving. It take into account a starting linear trend from 0 to 5 mm with corresponding strengths values respectively equal to 115 daN and 299 daN (Uy) (See Figure 15).

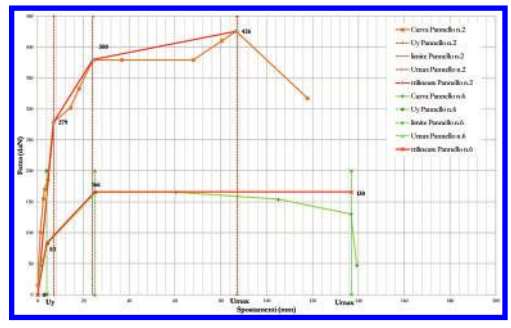


Figure 14. Specimen n.2 and 6 force-displacement constitutive curve comparison.

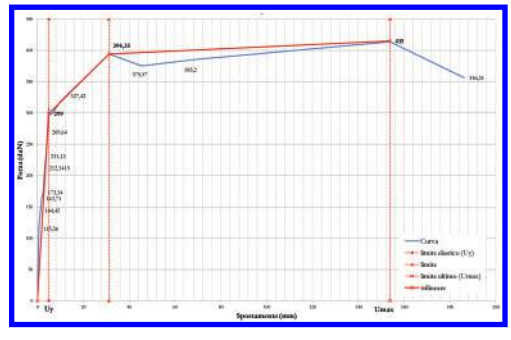


Figure 15. Specimen n.1 – force-displacement constitutive curve.

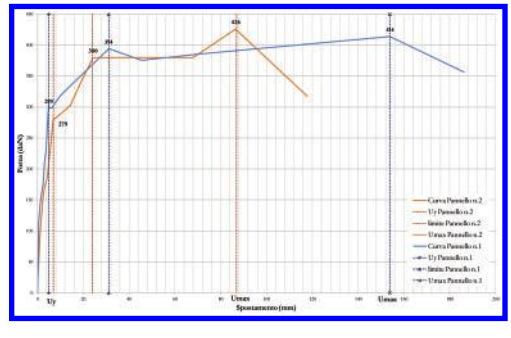


Figure 16. Specimen n.1 – force-displacement constitutive curve.

Nonlinear response is noticed after the elastic limit with both significant increasing of horizontal displacements and strength values until the maximum displacement 154 mm and relative strength value equal to 415 daN.

By comparing panel n.1 and 2 analogue responses were noticed (See Figure n.16).

3.2 *Cyclic test: the panel n.5*

The specimen n.5 was test by applying alternate horizontal action with loading and unloading cycles. The "force-control" tests was carry out with no axial load applied. The setup adopted use an horizontal actuator of 500 kN, in order to apply the alternated loading

Table 1. Specimen n.5 test.

cycles number	Maximum strength (daN)		Displacement (mm)	
Tot n: 5	Positive Phase	Negative Phase	Positive Phase	Negative Phase
I	1.101	1.014	30	−30
II	1.235	1.241	60	−60
III	1.422	1.276	91	−92
IV	1.448	1.380	124	−120
V	1.469	1.453	157	−161
Overturning	1.183		180	

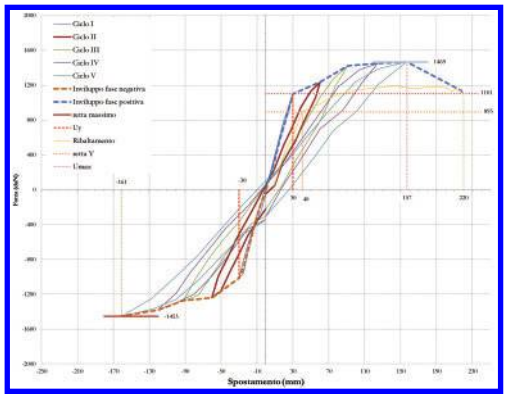


Figure 17. Specimen n.5-Cyclic test.

conditions to the panel which is free to roll on the top. The actuator was anchored by a steel beam placed in the geometrical panel dimensions centre. The mark obtained is the following:

The cycles were five in numbers with growing step 3 cm by 3 cm. latest overturning phase was performed.

The trend curve that interpolates the experimental maximum values filled in Table n.1 is described by a three-linear force-displacement constitutive curve.

It take into account a starting linear trend from 0 to 25 mm with corresponding strengths values respectively equal to 24 daN and 590 daN (Uy). The panel shows a starting rigidity very similar to the no reinforced one; this occurrence is mainly due to the reinforcement method aims. It was developed according to old masonry traditional techniques in order to guarantee seismic improvement with no constitutive curve trend changing. In fact, the resistance values and relative displacements result increased until the top strength of 787 daN with a corresponding displacement of 140 mm.

Therefore, after the elastic limit strong nonlinear response is noticed with significant increasing of both horizontal displacements and strength values until the maximum displacement of 240 mm recognized during the turning phase. (See Figure 17).

The response shows a symmetrical answer with asymptotic trend.

By comparing the specimen's n.6, 2 and 5 it is possible notice that mortar joints replacement gave a strong contribute during first collapse mode mechanism activation in order to obtain the maximum efficiency of the panel against seismic failure.

4 FINAL REMARKS

The final result of the experimental work consisting in two main outcomes: (i) identification of mechanical properties of individual stone elements inside the panel and (ii) derivation of force-displacement constitutive curves for global panels.

Therefore, the following experimental evidences pointed out (Fonti, 2013):

- different response for out-of-plane test were noticed, according to both masonry setting panel deviation from the rule of art and specific strengthening measures adopted; the above observations are referred to masonry resistance value checked during panel overturning under static horizontal loads;
- the check of header elements contribution in the out-of-plane collapse mechanisms and the importance of mortar joints replacement by small stone elements, in order to increase the compression resistance and to avoid the modification of the hinge position during panel overturning under horizontal loads;
- no possibility to consider masonry perfectly unilateral and infinitely resistant to the compression.
- The introduction of an additional parameter "the shape interlock" is proposed.

As a final remark: the comparison with the available technical literature reference about masonry mechanical models showed a significant gap between the experimental force-displacement constitutive curve and the theoretical ones.

REFERENCES

Borri, A., Candela, M., Fonti, R. (2012). Old masonry structures in L'Aquila historical centre: retrofitting strategies and full scale tests. The assessments, *Proc. of 15th World Conference on Earthquake Enginnering*, Lisbon, 24–28 September 2012.

Candela M., Fonti R. (2010). *The Solid Springer rule – behavior under dynamic stress*. In: Proc. of COST ACTION C26 Final Conference, Urban Habitat Constructions under Catastrophic Events. Naples, vol. 1, p. 331–334.

Ceradini, V. (2004) *Codice di pratica per la sicurezza e la conservazione degli insediamenti storici dell'Area Grecanica*. Gangemi: Roma.

Formisano, A Fonti, R. Mazzolani, F.M. (2012) The historical centre of Poggio Picenze after L'Aquila earthquake: behavior and strengthening of masonry aggregate-walls In the Proc. of *8th SAHC* 2012. Wroclaw, 15–17 October 2012.

Fonti, R. (2013) *La Statica delle Murature in pietra grezza*. PhD Thesis in Construction Enginnering, Naples.

Research and Applications in Structural Engineering, Mechanics and Computation – Zingoni (Ed.)
© 2013 Taylor & Francis Group, London, ISBN 978-1-138-00061-2

Seismic behavior of masonry walls with soft-layer wall bearings

N. Mojsilović, B. Stojadinović, A. Barandun & C. Vögeli
Institute of Structural Engineering, ETH Zurich, Zurich, Switzerland

ABSTRACT: A research project at ETH Zurich on the seismic behavior of masonry wallettes with two different soft-layer membranes (extruded elastomer and rubber granulate) placed in the bed joints is underway. The main goals of the research project are to investigate the influence of the soft layer on masonry behavior under static-cyclic shear, to assess the shear mechanical properties of different bearing layers, and to establish if and how it modifies the lateral load resistance mechanism of the wall. The preliminary analysis of the results of tests on seven wallettes show that, due to prevalently sliding failure, especially with built-in rubber granulate layer considerable energy dissipation and quasi ductile behavior, i.e. a large deformation capacity could be expected in actual masonry structures with soft layer placed in the bed joints. Such behavior would be desirable for enhanced seismic performance.

1 INTRODUCTION

A research project at ETH Zurich on the seismic behavior of masonry wallettes with soft-layer membrane placed in the bed joints is underway. The main goals of the research project are to investigate the influence of the soft layer on masonry behavior under static-cyclic shear, to assess the shear mechanical properties of different bearing layers, and to establish if and how it modifies the lateral load resistance mechanism of the wall.

This paper presents some preliminary results and discusses their significance in relation to current design practice. A number of conclusions as well as recommendations for future research are given.

In previous investigations, a series of static, static-cyclic and dynamic tests on masonry specimens with different types of soft layer, i.e. damp-proof courses (DPC), was performed. The results indicated that shear load can be transmitted through a joint containing a DPC. Griffith & Page (1998) performed monotonic, static-cyclic and dynamic shear tests on small masonry elements (triplets) with different types of DPC membranes (bitumen coated aluminum; polythene/ bitumen coated aluminum and embossed polythene) and reported the corresponding friction coefficients. The DPC membranes were placed in both mortar joints of the brick triplet; in one series the middle brick was made of concrete in order to simulate the concrete floor slab. Test specimens were initially subjected to a given level of pre-compression, which was kept constant during the test. The shear load was applied in the out-of-plane direction. The masonry materials used in these tests were typical extruded clay bricks with standard mortar. Similar results were reported by Zhuge & Mills (1998) and Simundic et al. (2000). Recently, static-cyclic tests were performed on masonry wallettes subjected to static-cyclic shear loading with embossed polythene DPC incorporated either in a mortar joint or at the masonry-concrete slab interface, see Mojsilović et al. (2010). Results from this investigation also confirmed good performance of the DPC subjected to cyclic loading. Finally, within the framework of the recently completed research project at ETH Zurich on the shear behavior of masonry elements (triplets) with DPC membrane placed in the bed joints, load tests on ten series of masonry triplets with three different DPC membranes (elastomer-, bitumen- and polythene-based membranes) have been done, see Mojsilović (2012). The shear behavior of the specimens was highly influenced by the applied pre-compression level, while influence of the location of the DPC membrane was much smaller. A considerable energy dissipation and large deformation capacity, compared to conventional masonry, can be expected in masonry structures with a soft layer incorporated in the bed joints.

2 TEST PROGRAM AND MATERIALS

Static-cyclic load tests on a series of masonry wallettes with incorporated soft layer have been performed at the Institute of Structural Engineering of ETH Zurich. Test series consisted of seven clay block masonry wallettes that were nominally 1200 mm wide and 1200 mm high (four units long and six courses high). The thickness of the wallettes was 150 mm. The wallettes were built in running bond using standard cement mortar, which had mean compressive strength of 21.5 MPa. Both the bed and the head joints were 10 mm thick and fully filled. Typical Swiss perforated clay blocks with



Figure 1. Typical Swiss clay block, extruded elastomer (E) and rubber granulate (G) soft layers.

Table 1. Test program and specimen designation.

Specimen	t_{sl} [mm]	layer material
W0	–	none
WE3	3	extruded elastomer
WE5	5	extruded elastomer
WE10	10	extruded elastomer
WG3	3	rubber granulate
WG5	5	rubber granulate
WG10	10	rubber granulate

nominal dimensions 290 × 190 × 150 mm and void area of 45% were used to build the specimens, see Figure 1. Block compressive strength was 25.5 MPa. Two types of soft-layer membrane have been used: extruded elastomer (E) and rubber granulate (G), see Figure 1. Three different thicknesses, t_{sl}, of each soft layer were tested, namely 3, 5 and 10 mm. During the wallette construction the soft layer strip was placed directly on the first block course. The bed joint mortar was then placed on top of the membrane and the blocks of the next course were laid on that mortar bed. Note that for the wallettes with 3 and 5 mm thick soft layers the total bed joint thickness was 10 mm. The total bed joint thickness was 15 mm in the two cases with 10 mm thick soft layers.

In addition to the specimens with built-in soft layer, a control specimen with the same dimensions and without soft layer was built. A summary of the test program is given in Table 1.

All specimens were built by a professional mason and were air cured at the testing site. After preparation and prescribed curing time (at least 28 days) the wallettes are first subjected to a gravity load pre-compression of 0.6 MPa (10% of the masonry compressive strength), which was kept constant during the test, and subsequently subjected to the cyclic shear load which was applied in an incrementally increasing displacement-controlled sequence. Prior to testing, the specimens were painted white in order to follow the crack development during the test.

3 WALLETTE TESTING PROCEDURE AND MEASUREMENTS

Figure 2 shows the test set-up. The axial load, i.e. pre-compression was applied by means of the hydraulic jacks (2) placed between the support frame (1) and the upper spreader beam (3). A roller support (5) was

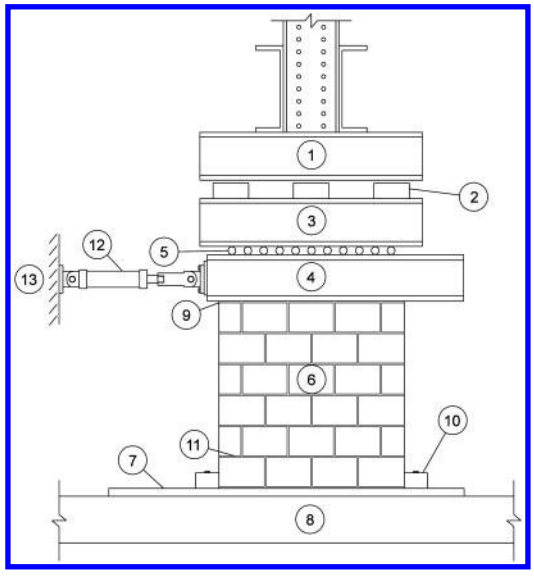


Figure 2. Test set-up.

installed between the upper (3) and the lower spreader beam (4). The test specimen (6) was placed between the lower spreader beam (4) and a thick steel plate (7), which lay directly on and was fixed to the laboratory strong floor (8). A mortar layer (9) was applied between the specimen (6) and lower spreader beam (4) in order to ensure a uniform vertical load distribution. Steel elements (10), which were fixed to the steel plate (7), ensured that the first wallette course remains static, i.e. that possible sliding takes place in the bed joint with the soft layer (11). After applying the vertical pre-compression the specimens were subjected to cyclic shear loading by means of the hydraulic actuator (12) which was fixed to the reaction wall (13).

The cyclic shear load was applied in computer-controlled displacement steps. Each step was repeated twice in a form of a sinusoidal wave. At the beginning of the test, i.e. for small displacements, the loading speed was only 1 mm/min. For the larger displacement steps the loading speed was gradually increased up to 20 mm/min for the maximum applied displacement of 40 mm, see also Table 2. This Table also gives information on the duration of each load stage. Using this procedure, test duration varied from 74 to 130 minutes.

Apart from the applied vertical and horizontal load and displacement (jack travel), measurements included vertical, horizontal and diagonal deformations of the specimen, see Figure 3. Horizontal and vertical deformations were measured by means of two potentiometers each, POT4 and POT5 and POT6 and POT7, respectively. Diagonal deformations were measured by means of another two potentiometers, POT8 and POT9. Slip of the specimen over the joint with soft layer (POT 10 and POT11) as well as the uplift of the wallette toes (POT16 and POT17) was measured

Table 2. Loading history.

Target displ. [mm]	Loading speed [mm/min]	Duration [min]
0.2	1	1.6
0.5	1	4.0
1.0	1	8.0
1.5	1	12.0
2.0	3	5.3
5.0	3	13.3
10.0	3	26.7
15.0	10	12.0
20.0	10	16.0
30.0	10	24.0
40.0	20	16.0

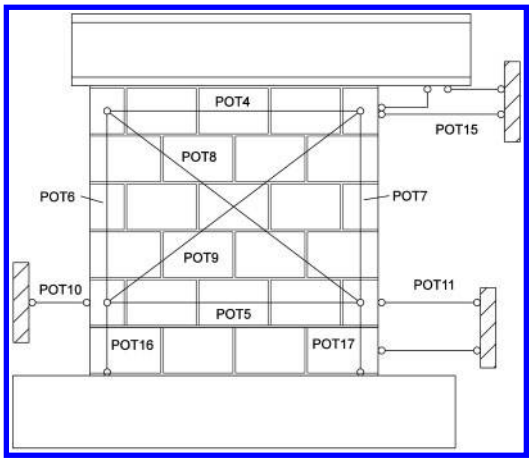


Figure 3. Potentiometer positions in the test set-up.

in relation to the strong floor. The horizontal displacement of the top of the specimen was captured by means of the potentiometer POT15. All measuring devices were connected to a computer, which processed the data in real time. The potentiometer measurements were zeroed after the vertical pre-compression was applied. During the test, the nature and extent of the cracking was continuously observed.

4 TEST RESULTS

Table 3 shows the values of the extreme (maximum and minimum) horizontal forces, H, recorded during the testing as well as maximum and minimum horizontal displacement (jack travel), v. For all tests, the jack initially extended to push the wallette (negative displacement and shear force). From Table 3 it is clear that the wallettes with extruded elastomer developed higher shear strength than those with rubber granulate. However, comparing the control specimen, a decrease of shear strength for the wallettes with built-in soft layers is obvious (except for Specimen WE3). On the other hand, wallettes with soft layers developed larger

Table 3. Test results.

Specimen	H_{max} [kN]	H_{min} [kN]	v_{max} [mm]	v_{min} [mm]
W0	94.0	−87.1	15	−15
WE3	60.0	−89.1	20	−20
WE5	70.0	−80.5	20	−30
WE10	54.0	−57.2	20	−20
WG3	46.1	−46.7	30	−30
WG5	46.3	−49.9	30	−30
WG10	50.4	−43.4	40	−35

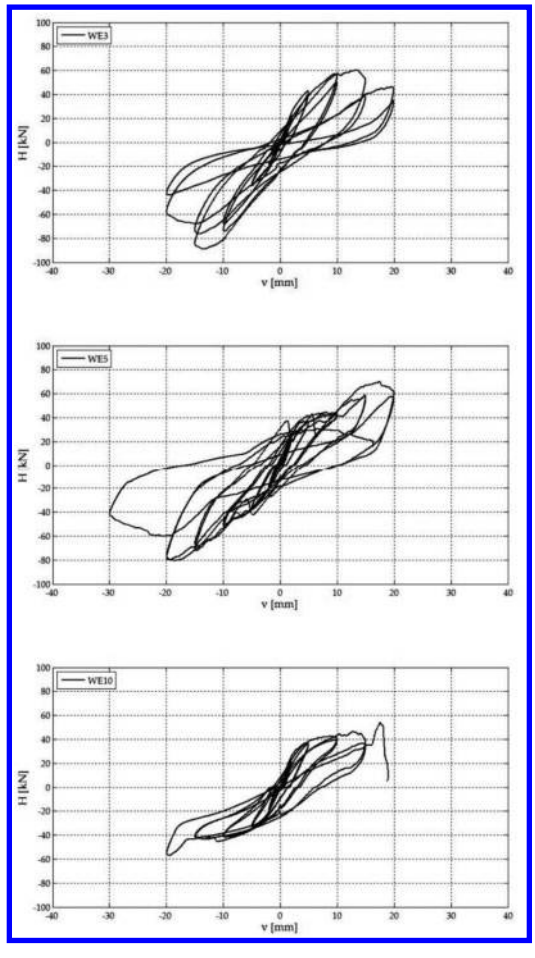


Figure 4. Hysteresis for specimens with extruded elastomer soft layer WE3, WE5 and WE10.

horizontal displacements prior to failure. It should be noted that there were problems in keeping the vertical force constant during the tests on Specimens W0, WE3 and WE5: vertical force increased with increasing horizontal displacement.

Figure 4 shows the shear force-deformation characteristics of specimens with built-in extruded elastomer soft layer subjected to cyclic loading. The deformation value shown in the diagram is the jack travel, v. The

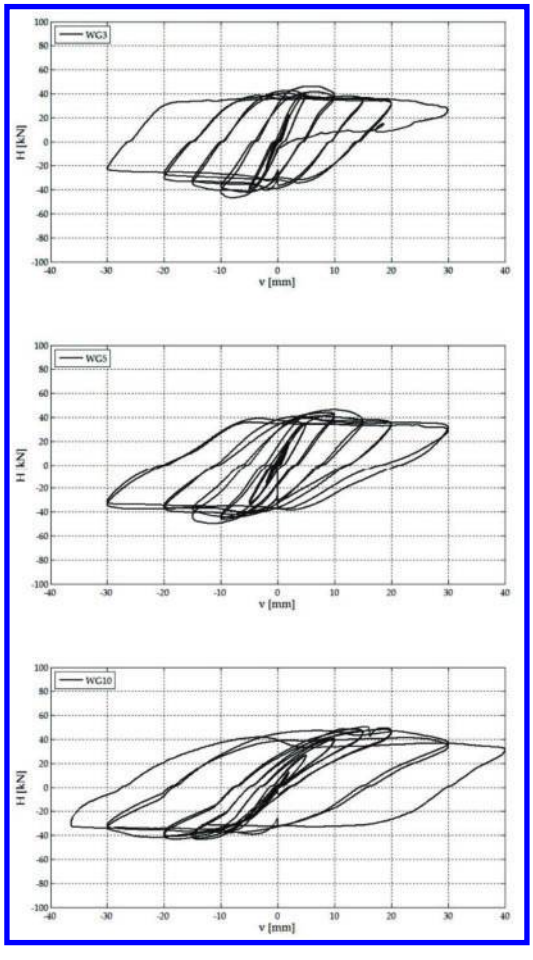


Figure 5. Hysteresis for specimens with rubber granulate soft layer WG3, WG5 and WG10.

cyclic force-deformation response (hysteresis) curves for all three soft-layer thicknesses are fairly typical: the response is initially linear-elastic, but becomes significantly non-linear when displacements exceed 2 mm. All specimens exhibited moderate energy dissipation (area under the hysteresis envelope) and behaved in a quasi-ductile manner.

From Figure 5 it can be seen that the specimens with rubber granulate soft layers, especially Specimens WG3 and WG5, were essentially linear-elastically up to the maximum value of shear resistance. Thereafter, with increasing deformation the response evolved into an ideal-plastic horizontal branch (plateau). All specimens exhibited considerable energy dissipation and behaved in a quasi-ductile manner.

A staircase-wise cracking of the specimens was observed during the tests, see Figure 6. Larger number of cracks as well as larger openings of the vertical cracks (along head joints) was observed for specimens with extruded elastomer soft layer than for those with the rubber granulate soft layer (at the same applied horizontal deformation). A similar outcome



Figure 6. Typical crack pattern (Specimens WE3 and WG3).



Figure 7. Sliding along the bed joint with soft layer (Specimens WG3 and WE10).



Figure 8. Failure of Specimens WE5 and WG5.

was observed for the thinner soft layers, independently of the layer material. A slip in the bed joint with soft layer was observed. Figure 7 shows, typically, shear deformation (sliding over the soft layer) in Specimens WG3 and WE10. The sliding planes formed between the layer membrane and adjoined block course. This means that, during the cycling, the soft layer moves together with the upper part of the wallette along the first block course.

The failure patterns observed during the tests were characteristic for masonry failing in sliding. Failures of the specimens with rubber granulate soft layer occurred due to exceeding the (very low) tensile strength of the blocks in the first course. These failures were induced by cycling movement of the upper part of the wallette over the first course, see, e.g. the failure pattern of Specimen WG5, shown in Figure 8. For the specimens with extruded elastomer soft layer a combined sliding and compression failure occurred, exemplified by crushing of the blocks in the first course, shown on Specimen WE5 in Figure 8. Prior to failure, the extruded elastomer specimens developed additional inclined, compression induced, cracks in the lower part of the wall. Simultaneously, uplift of the wallette corners was observed during the cycling.

5 DISCUSSION

Test data on the strength, deformation capacity, energy dissipation and overall behavior of the masonry wallettes with built-in soft layers subjected to static-cyclic loading has been obtained. In the following, the test results are discussed in respect to sliding in the soft-layer bed joint and the influence of different materials and thicknesses of the soft layer on the response mechanism. Soft layer degradation during the cycling is also briefly addressed.

5.1 *Sliding failure and friction coefficient in the bed joint with a soft layer*

Sliding observed in the soft-layer bed joint can be described by the classical Coulomb's failure criterion $\tau = c + \sigma \tan \varphi$, where c denotes the cohesion and φ is the angle of internal friction, i.e. $\tan \varphi$ is a friction coefficient. Taking into consideration the results of wallette tests with rubber granulate, which failed by sliding, cf. Table 3, a friction coefficient in the bed joint can be estimated from the levels of compression and shear in the joint once sliding has occurred. Since the soft layer was placed directly on the block course the cohesion can be set to zero. Thus, an average friction coefficient, calculated from WG3, WG5 and WG10 tests of $47.1/108.0 = 0.44$ was determined. As mentioned before, the wallettes with extruded elastomer soft layer exhibited a mixed sliding-compression failure, thus not allowing for an estimate of the friction coefficient.

5.2 *Influence of the soft layer material and its thickness*

Analyzing the influence of the type of soft layer it could be concluded, as seen from Figure 9, that the specimens with different types of soft-layer material behaved somewhat differently. All specimens with rubber granulate soft layer exhibited nearly the same values of shear resistance and dissipated a considerable amount of energy (exhibited large area under the hysteresis). The wallettes with built-in extruded elastomer exhibited smaller energy dissipation, for the same layer thickness. However, these specimens attained higher shear resistance. From Figure 9 it can also be seen that all specimens had a similar initial stiffness. As expected, the mechanical characteristics of the wallettes progressively degraded with an increasing number of cycles.

The observed energy dissipation obtained by soft-layer sliding, high compared to conventional masonry, is most desirable as it can provide additional damping to typically stiff masonry structures and thus reduce their seismic demand. It is clear from the obtained hysteresis, that considerable energy dissipation could be expected in practical applications, especially when the rubber granulate soft layer is incorporated in the shear wall.

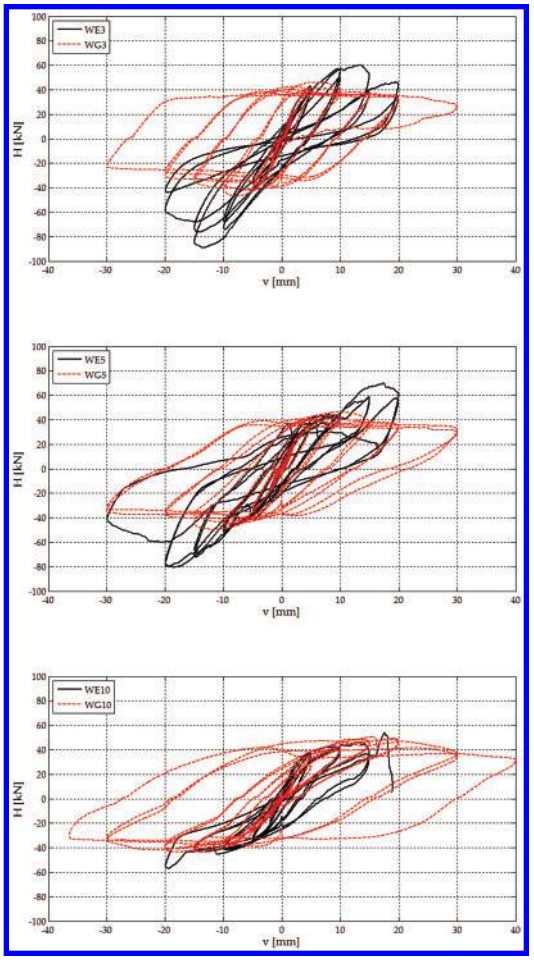


Figure 9. Hysteresis comparison for different soft-layer materials.

The influence of the layer thickness on the specimen response can be seen from the graphs in Figure 10. Specimens with extruded elastomer had the same initial stiffness, but the wallettes with thinner layers were stronger. It seems that the layer thickness had no influence on the shear resistance of the wallettes with built-in rubber granulate layers, but it affected their initial stiffness, see Figure 10, with thicker layers making for a softer initial response.

5.3 *Soft layer degradation*

With decreasing layer thickness, the degradation of the soft layer increased. Figures 11 and 12 show the extruded elastomer and rubber granulate soft layers after the tests, respectively. Degradation was greatest for Specimens WG3 and WG5, where rupture and crumbling of the layer was observed. For extruded elastomer layers, however, such pronounced degradation was not observed. This fact should be taken

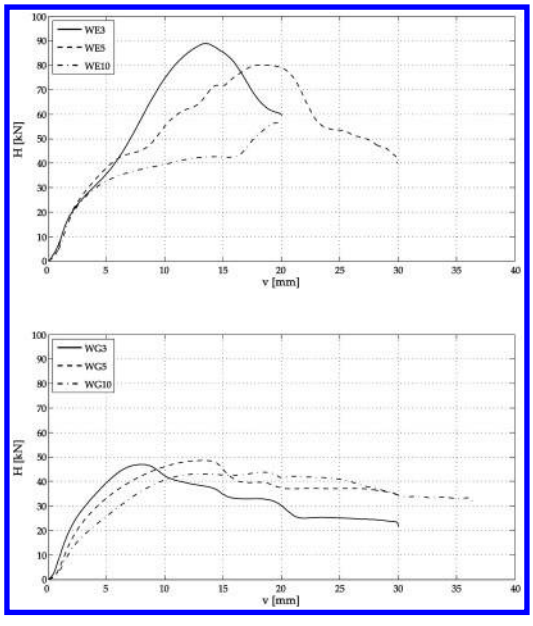


Figure 10. First-cycle force-displacement hysteresis envelopes.

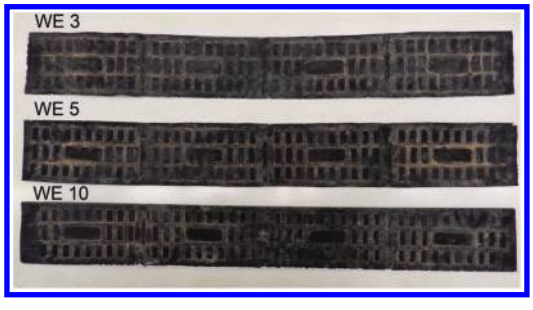


Figure 11. Soft layer damage after cycling: extruded elastomer.



Figure 12. Soft layer damage after cycling: rubber granulate.

into account in the case of cyclic (seismic) loading of masonry with soft layer built into the bed joint.

6 CONCLUSIONS

The presented analysis and discussion of the preliminary results of tests on the series of masonry wallettes with two different types of soft layer allow following conclusions to be drawn:

- Shear strength of the specimens was influenced by the type of the soft layer: the specimens with extruded elastomer layer were stronger. Further, the shear strength of the specimens with rubber granulate was independent on the layer thickness.
- A Coulomb failure criterion with zero cohesion can be applied to predict the horizontal shear capacity for wallettes with rubber granulate soft layer.
- Considerable energy dissipation and quasi ductile behavior, i.e. a large deformation capacity, compared to that of conventional masonry, could be expected in actual masonry structures with soft layer placed in the bed joints. Such behavior is desirable for enhanced seismic performance.

The extension of the presented research will include a new series of tests on the wallettes with the soft layer placed between the masonry wall and concrete base slab. The main parameter will be the pre-compression level and the soft-layer thickness. Further, due to the above-mentioned problems with the control of the applied pre-compression tests W0, WE3 and WE5 will be repeated.

REFERENCES

Griffith, M.C. & Page, A.W. 1998. On the seismic capacity of typical DPC and slip joints in unreinforced masonry buildings. *Australian Journal of Structural Engineering*, 1(2): 133–140.

Mojsilović, N. 2012. Masonry elements with damp-proof course membrane: Assessment of shear strength parameters. *Construction and Building Materials*, 35: 1002–1012.

Mojsilović, N., Simundic, G. & Page, A.W. 2010. Masonry wallettes with damp-proof course membrane subjected to cyclic shear: An experimental study. *Construction and Building Materials*, 24(11): 2135–2144.

Simundic, G., Page, A.W. & Chen, Q. 2000. The cyclic and long term behavior of slip joints in load-bearing masonry construction. *Proceedings of the 12th International Brick/Block Masonry Conference, Madrid*, pp. 1409–1420.

Zhuge, Y. & Mills, J. 1998. The behavior of masonry walls containing a damp proof course under cyclic loads. *Proceedings of the 2nd Australasian Structural Engineering Conference, Auckland*, pp. 655–661.

Research and Applications in Structural Engineering, Mechanics and Computation – Zingoni (Ed.)
© 2013 Taylor & Francis Group, London, ISBN 978-1-138-00061-2

Application of sequentially linear analysis to the seismic assessment of slender masonry towers

V. Mariani
Department of Architecture, University of Florence, Italy

A.T. Slobbe
Department of Structural Engineering, Delft University of Technology, Netherlands

M.A.N. Hendriks
Department of Structural Engineering, Delft University of Technology, Netherlands
Department of Structural Engineering, Norwegian University of science and technology, Norway

J.G. Rots
Department of Structural Engineering, Delft University of Technology, Netherlands

ABSTRACT: Brittle failure behavior is an intrinsic characteristic of slender masonry towers that behave as cantilever beams. The application of the classical nonlinear finite element analysis (NLFEA) methods for the seismic assessment of such structures often involves difficulties in the definition of post-peak behavior, which can be characterized by a sudden decay. In order to investigate the post-peak behavior of such structures the Sequentially Linear Analysis (SLA) method has been used as possible alternative tool to the usual nonlinear static analysis methods. Both NLFEA and SLA have been applied to a historical Italian masonry tower. A 2D plane stress and a 3D solid finite element model of the tower have been set up. The nonlinear behavior of the masonry material, both in tension and compression, has been taken into account. The different modeling approaches and the different analysis methods allowed for the comparison of the results. NLFEA showed a very brittle collapse, with convergence problems after the attainment of the peak load. The application of SLA confirmed the results of NLFEA in terms of base shear-top displacement curves and in terms of damage patterns at the peak load. In addition SLA allowed for the investigation of the post-peak behavior and confirmed the very brittle nature of collapse of the tower, since equilibrium has no longer been found after the peak. In conclusion, the application of SLA to the case study demonstrated the potential of the SLA method as alternative and very robust tool for seismic assessment of masonry towers.

1 INTRODUCTION

1.1 *Seismic vulnerability of masonry towers*

In the last decades, the interest of scientific community for the preservation of historical and architectural heritage has grown significantly. A lot of these historical structures are constructed with masonry, some of them being located in earthquake prone sites.

Towers represent a relevant part of this architectural heritage in many countries around the world, especially in Europe. Generally they have been erected before the last century and made of stone or brick masonry. The particular vulnerability of these structures is evidenced by the collapse of some towers under the effect of static loads only. For very high massive towers, the axial stress arising from the gravity loads can be similar to the compressive strength of historical masonry. Therefore these structures become rather vulnerable to low-intensity earthquakes. This phenomenon has been widely evidenced by a recent earthquake that occurred in Italy on May 20th 2012. The earthquake caused extensive damage of many historical masonry towers and for some of them even a collapse (Fig. 1). The presented scenario about possible damage and collapse of ancient masonry towers highlights the need to safeguard this important segment of our architectural heritage.

1.2 *Drawbacks of classical nonlinear analysis methods*

The protection for potential seismic actions requires an effective seismic assessment of the structures, which can be achieved through suitable finite element models and advanced nonlinear finite element analyses (NLFEA).

However, dealing with nonlinear analysis of masonry structures often leads to convergence problems and numerical instabilities. Several factors contribute to such computational issues. Firstly, both



Figure 1. Damaged and collapsed masonry towers after Emilia's earthquake: (a) Poggio Renatico Bell Tower; (b) Finale Emilia Tower.

the softening laws in tension and compression that describe the behavior of masonry after the attainment of the resistance imply the introduction of negative stiffness contributions. This will often lead to an ill-conditioned stiffness matrix and so to divergence of the numerical solution. Secondly, in case of slender towers, the limited ductility of the masonry combined with their slenderness generally provides an even more brittle behavior.

Moreover, such slender structures can be treated as vertical cantilever beams fixed at the base. This isostatic scheme is inherently brittle, which makes these structures particularly vulnerable to seismic actions. Finally, for large-scale structures the localization of damage involves a very narrow zone with respect to the dimension of the whole structure. As a consequence, the curves that express the global behavior of the structures (e.g. in terms of base shear-top displacement) often presents snap-backs and/or snap-through points.

Due to the above mentioned reasons, classical incremental-iterative methods are not always successful in solving this type of nonlinear problems, even when combined with complex computational strategies as arch-length methods or indirect displacement control.

1.3 *Philosophy of Sequentially Linear Analysis*

Within this context, a new analysis procedure, namely the Sequentially Linear Analysis (SLA) method, has been developed (Rots & Invernizzi 2004) to overcome these numerical difficulties with the incremental-iterative procedures. This robust approach can be an efficient alternative tool to the standard NLFEA for seismic assessment of masonry structures.

The SLA method involves the running of a series of subsequent linear analyses, in which strength and stiffness are locally reduced in each step. These strength and stiffness reductions can be applied by approximating the softening curve that describes the material behavior in tension and/or compression with a so-called saw-tooth diagram.

Due to the absence of an iteration process in the SLA method, convergence difficulties are avoided. The approach generally enables to capture the overall behavior of brittle structures, including their post-peak responses. Consequently, the effective ductility of existing structures can be assessed, which is of significant importance in the modern performance-based design/assessment methods.

In the present paper SLA has been applied to a historical Italian masonry tower, called the Civic Tower of Soncino (Fig. 2). Comparison of the results from pushover analyses using standard NLFEA and SLA confirmed the extremely brittle failure mode of the tower subjected to lateral loads.



Figure 2. Civic Tower of Soncino (Cremona, Italy).

2 THE CIVIC TOWER OF SONCINO: VALIDATION WITH STANDARD NONLINEAR ANALYSIS

The medieval Civic Tower of Soncino (Cremona, Italy) is a historical masonry structure that characterizes the landscape of the small town located in the northern Italy (Fig. 2). The tower of 41.8 m height was erected in the 12th century and presents a square plan with 6 m by 6 m sides. It is characterized by brick masonry walls with thickness varying from 1.55 m at the base to 0.98 m at the top.

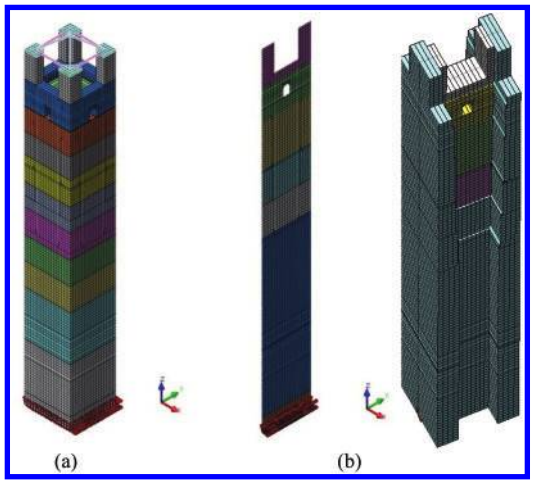


Figure 3. (a) 3D FEM; (b) 2D FEM and extruded view.

Previous studies have been carried out on a 3D finite element model of the tower (Fig. 3a), consisting of standard nonlinear pushover analyses and nonlinear dynamic analyses (D'Ambrisi et al. 2012). With the aim of performing analyses with SLA, a 2D plane stress model of the tower has been set up (Fig. 3b). The model is made of eight-node quadrilateral plane stress elements with 0.3 m by 0.3 m average dimensions. The self-weight and a system of lateral loads has been assigned to the tower, consistent with those assigned in the 3D model of the previous studies.

The 2D model has been preliminarily validated through NLFEA by comparing results of a pushover analysis with the results obtained from the 3D model. Comparisons are made between analyses that only consider nonlinear tensile behavior of the masonry and with analyses that include nonlinearities both in tension and compression.

2.1 *Comparison 3D-2D: nonlinear tensile behavior*

In the first validation of the 2D model the nonlinear behavior of the masonry material in tension is modeled by a Total Strain Fixed Crack Model (Feenstra et al. 1998). The behavior in compression is assumed as linear elastic. A tensile strength of 0.1 MPa and linear softening with an ultimate cracking strain of 1‰ have been adopted, consistent with D'Ambrisi et al. (2012). A reduction of the shear modulus based on the damage due to cracking is also assumed.

The comparison of the results obtained with the two different finite element models has been done by considering the global behavior (pushover curves) and damage patterns at the peak. Figure 4 shows the pushover curves by plotting the shear force at the base against the lateral displacements at the top of the tower models. The two dashed lines are in reasonably agreement. The 2D model shows an overestimation of about 12% and 6% in terms of top displacement and base shear respectively, compared to the 3D model. All the

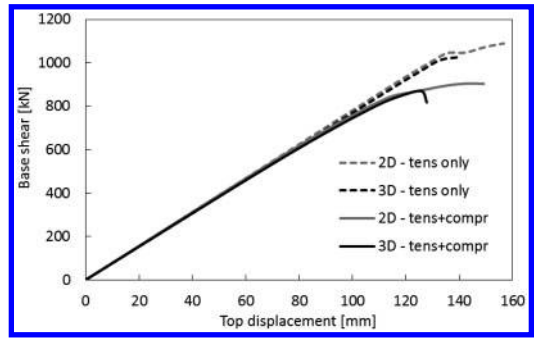


Figure 4. Comparison of the pushover curves obtained with the 3D model and the 2D plane stress model for nonlinear behavior in tension only (dashed lines) and for nonlinear behavior both in tension and compression (solid lines).

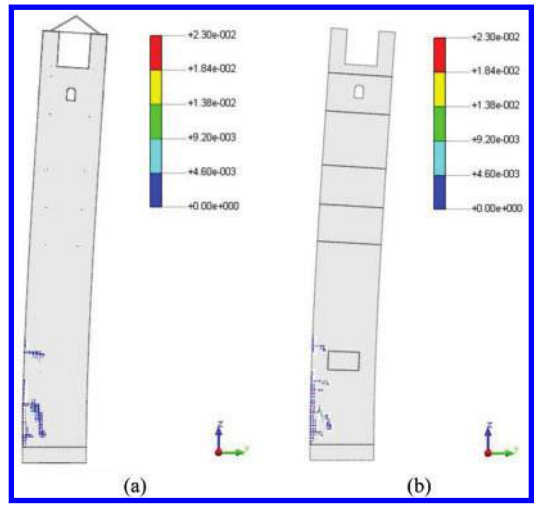


Figure 5. Crack strain contours at the collapse load step of the pushover analysis performed on a (a) 3D and (b) 2D model for nonlinear tensile behavior only.

performed analyses have shown a very brittle collapse, with no substantial softening branch and no convergence of the standard nonlinear analysis procedure after the attainment of the peak load.

Figure 5 shows the crack patterns of both analyses in the deformed shapes of the models. Again reasonable agreement is visible. The observed collapse mechanism involves the formation of a cracked area at the base, accompanied by the development of a severe diagonal macro-crack on the left tensile side.

2.2 *Comparison 3D-2D: nonlinear tensile and compressive behavior*

Subsequently, the nonlinear compressive behavior of the masonry has been considered in the 2D model and 3D model, by assuming elastic-plastic behavior with a compressive strength of 1.1 MPa and a maximum compressive strain of 3.5‰, consistent with D'Ambrisi et al. (2012). Again the pushover curves

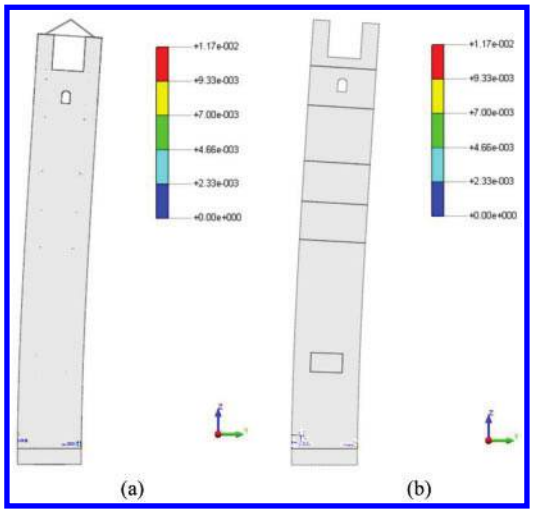


Figure 6. Crack strain contour at the collapse load step of the pushover analysis performed on the (a) 3D and (b) 2D model for nonlinear tensile and compressive behavior.

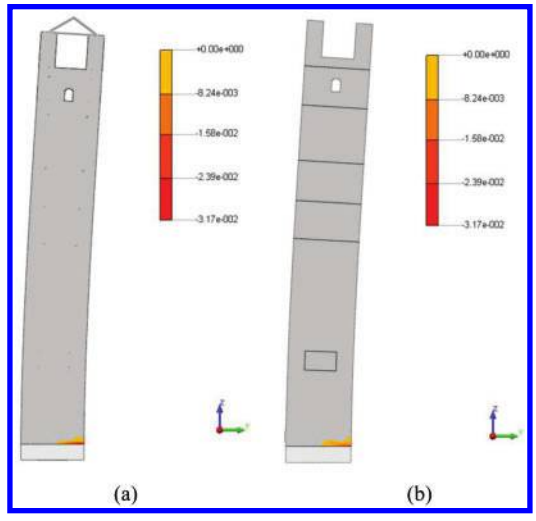


Figure 7. Principal plastic strain contour at the collapse load step of the pushover analysis performed on the (a) 3D and (b) 2D model for nonlinear tensile and compressive behavior.

(solid lines) are plotted in Figure 4. As in Section 2.1, the 2D model provides higher values of maximum top displacement and base shear with an overestimation of 15% and 4% respectively.

Concerning the damage patterns, a good agreement of results has been found, in terms of both cracked and crushed areas, as evidenced in Figures 6 and 7.

3 SLA APPLIED TO SEISMIC ASSESSMENT OF THE TOWER

3.1 *Review of the Sequentially Linear Analysis approach*

The SLA method (Rots & Invernizzi 2004, Rots et al. 2008) captures physically nonlinear behavior by performing a series of linear analyses. After each analysis the applied non-constant load is scaled, so that only in one integration point of the model a critical stress state occurs. Such a "critical event" can happen either in the tensile regime or in the compression regime. Subsequently, the strength and stiffness properties are reduced in the critical point. To apply this damage increment the used softening curves needs to be discretized, resulting in a so-called saw-tooth curve (see Section 3.2).

The nonlinear response of a structure is extracted by linking consecutively the results of each cycle. Especially its robustness and relatively simplicity make this damage controlled procedure attractive to analyze brittle failure behaviors.

The identification of the load scale factor in cases with only non-constant loads is relatively easy. When a constant load is involved the procedure becomes more complicated.

Suppose the structure carries an existing constant load F_A and the task is to sequentially add a new load F_B. The aim is to keep load multiplier λ_{const} for load A at 1, while searching for the critical load multiplier λ_{sca} for the scalable load B by comparing for all points their total principal tensile stress $(1\sigma_A + \lambda_{sca}\sigma_B)_1$ with the current saw-tooth strength. This leads to sets of quadratic equations in λ_{sca} and a unique solution not always exists.

Different points may lead to conflicting constraints for λ_{sca}. Physically, the new cracking for load B leads to redistribution of the constant load A in the system, which in turn may violate the stress criterion for other points and inner cascade cracking may result.

A solution to deal with above mentioned situation is the double-load multiplier method (Graaf, van de 2013). If required the last present total load $(F_A + \lambda_{sca,previous}\ F_B)$ on the system is temporarily scaled via λ_{temp}, allowing for redistribution cracking until all points recover, i.e. all stresses are below their current saw-tooth strength. Thereafter, $\lambda_{temp} = 1$ and the scaling for just load B via λ_{sca} proceeds.

3.2 *Definition of a decoupled saw-tooth material law*

Generally, the analyses with SLA in literature adopted discretized stress-strain curves for nonlinear material behavior only in tension or only in compression. For the present study a saw-tooth material law has been developed to define nonlinear behavior in both tension and compression simultaneously. Figure 8 shows a representation of the saw-tooth material law that has been used in this study.

For simplification it is assumed that for a fixed direction no switch will occur in an integration point from the tensile to the compression regime and vice versa. Within the adopted fixed crack model this means that an integration point can experience only

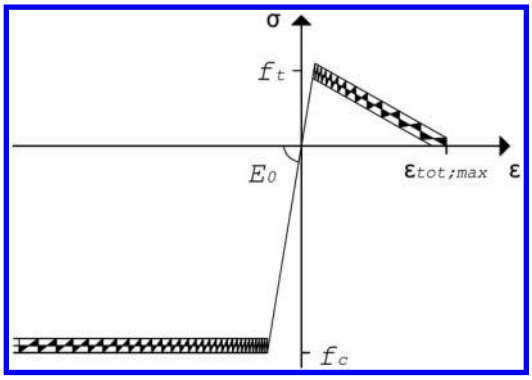


Figure 8. Generalized saw-tooth diagram with linear softening behavior in tension and elastic-plastic behavior in compression.

crushing or cracking in one of the orthogonal crack axes directions. If an integration point is cracked in one direction, it can only be crushed in the other orthogonal direction, and vice versa. Such restrictions were deemed acceptable within the application of a monotonic load, as in the present case. Note that cyclic loading cannot be captured properly with this model.

3.3 *Application of SLA to pushover analyses.*

After the validation of the 2D model for classical nonlinear pushover analyses in Section 2, the SLA method has also been applied on this model for the seismic assessment of the tower. The same material properties have been adopted, and again two load cases were considered. The "constant load" is the self-weight of the tower that will be associated to the λ_{const} multiplier, while the "scaled load" is the lateral load system reproducing the seismic action. Latter will be gradually increased through the λ_{sca} multiplier.

Firstly, the SLA has been applied in the case of nonlinear tensile behavior only in order to verify the reliability of previous results. In Figure 9a the top displacement-base shear trend has been plotted and compared with the pushover curve from the corresponding standard NLFEA in Section 2. The two curves show good agreement in terms of maximum base shear and maximum top displacement. Moreover, SLA confirms the very brittle nature of the collapse, since after the attainment of the peak load a sharp snap-back behavior is visible. However it should be noticed that, at the attainment of the peak load, SLA is no longer able to find equilibrium with the fully applied self-weight of the tower. Therefore the total load is scaled (see Section 3.1), as shown in Figure 9b by the downward trend of λ_{temp} with increasing step number. The convergence problems observed from the standard NLFEA, together with the results of this robust SLA method, indicate that an extremely brittle and large failure of the tower occurs after the peak load.

Secondly, a SLA is performed using the decoupled material law, as described in Section 3.2. The used saw-tooth constitutive relation is shown in Figure 8.

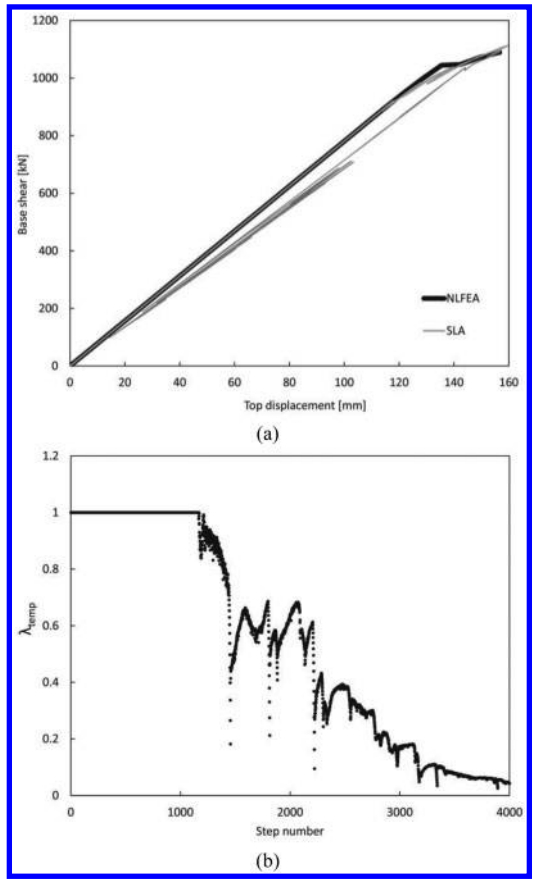


Figure 9. (a) Comparison of pushover curves from SLA and standard nonlinear approach for nonlinear behavior in tension only. (b) Values of λ_{temp} with increasing step number for SLA.

Figure 10a shows the resulting base shear-top displacement trend (light line). Again, comparison is made with the corresponding NLFEA pushover curve from Section 2 (dark line). Good agreement is observed regarding the predicted ultimate capacity of the structure. Differences of 6% with respect to the maximum base shear and 7% with respect to the maximum top displacement has been found. Once again, the SLA detected a snap-back behavior after the attainment of the peak load, confirming the very brittle nature of collapse due to loss of stability of the structure. Again after the attainment of the peak load, the SLA procedure has no longer been able to find equilibrium and consequently the total load has been scaled through the decrease of λ_{temp}, as shown in Figure 10b. This evidence implies that no reasonable solution can be found after the peak load and a very brittle collapse is observed.

Figure 11 shows the overall damage patterns at the peak load of SLA performed in the case of nonlinear tensile behavior only (Fig. 12a) and in the case of decoupled material law (Fig. 12b). While in the first case several macro-cracks develop at the tension side, in the second case the damage is more localized

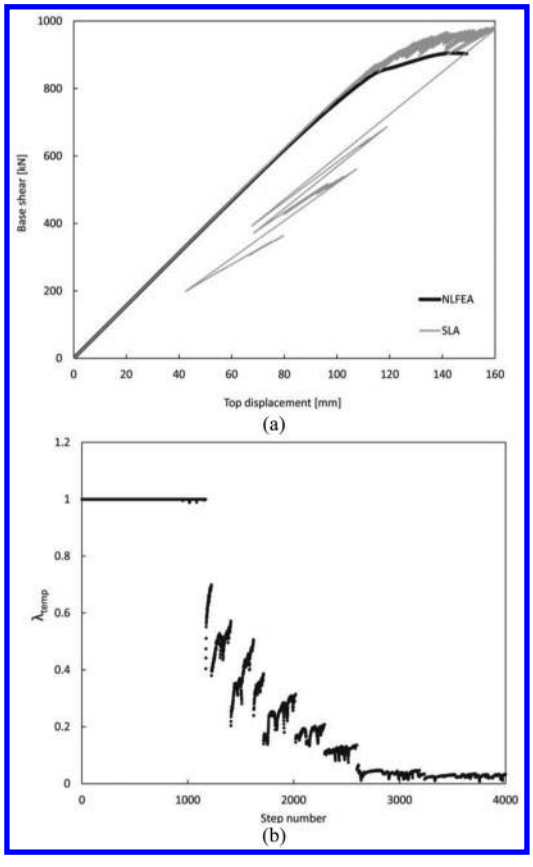


Figure 10. (a) Comparison of pushover curves from SLA and standard NLFEA for nonlinear tensile and compressive behavior. (b) Values of λ_{temp} with increasing step number for SLA.

at the base, where the formation of a wide hinge is observed. Reasonable agreement with the corresponding NLFEA damage patterns (Fig. 5a and Figs. 6b, 7c respectively) has been observed.

4 CONCLUSIONS

The Sequentially Linear Analysis method has been applied for the seismic assessment of the Civic Tower of Soncino. A 2D model of the structure has been set up and preliminarily validated through NLFEA by comparing the results of a pushover analysis with the results obtained from the 3D model developed in previous studies. Afterwards, the SLA procedure has been applied to the 2D model; firstly, considering nonlinear behavior in tension only and then defining a saw-tooth decoupled material law, with nonlinear behavior in both tension and compression simultaneously. Comparison of SLA and standard NLFEA results shows reasonable agreement in terms of pushover curves and crack/damage patterns. The standard NLFEA failed to overcome the peak load due to the occurrence of convergence problems.

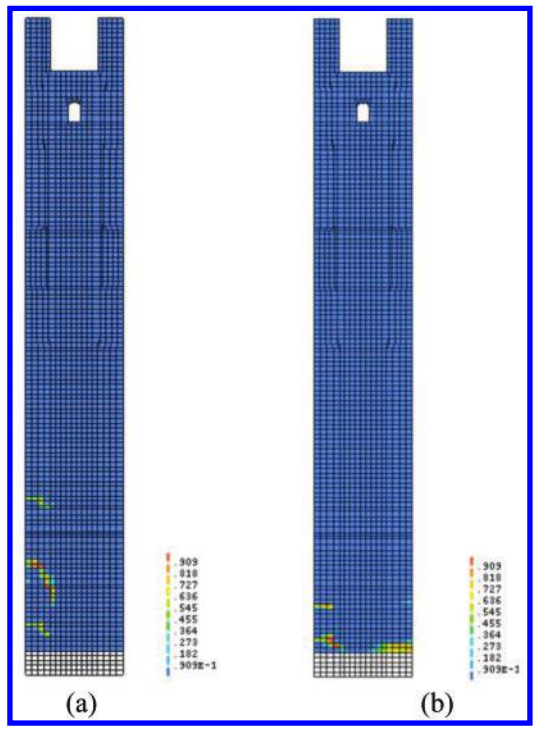


Figure 11. Contour of damage indicators at the collapse load step of the SLA for (a) nonlinear tensile behavior only and (b) nonlinear behavior in tension and compression.

From the results of the SLA method it can be observed that after the attainment of the peak load equilibrium can no longer be found with fully applied self-weight of the tower, meaning that the collapse occurs for the development of a very brittle mechanism.

In conclusion the application of the SLA procedure to the case study has shown its potential as possible robust alternative to the classical nonlinear analysis methods for the seismic assessment of masonry towers.

REFERENCES

D'Ambrisi, A. Mariani, V. & Mezzi, M. Seismic Assessment of a Historical Masonry Tower with Nonlinear Static and Dynamic Analyses Tuned on Ambient Vibration Tests. *Eng Struct* 2012; 36: 210–219.

Feenstra, P.H. Rots, J.G. Arnesen, A. Teigen, J.G. & Hoiseth, K.V. A 3D constitutive model for concrete based on a co-rotational concept. In*: Computational modelling of concrete structures*. Proc. EURO-C 1998, Eds. R. de Borst et al., pp. 13–22, Balkema, Rotterdam, 1998.

Graaf, van de, A.V., Sequentially Linear Analysis for simulating brittle fracture, Phd, TU-Delft, 2013.

Rots, J.G. Belletti, B. & Invernizzi, S. Robust modeling of RC structures with an "event-by-event" strategy. *Eng Fract Mech* 2008; 75: 590–614.

Rots, J.G. & Invernizzi, S. Regularized sequentially linear saw-tooth softening model. *Int J Numer Anal Methods Geomech* 2004; 28: 821–856.

Research and Applications in Structural Engineering, Mechanics and Computation – Zingoni (Ed.)
© 2013 Taylor & Francis Group, London, ISBN 978-1-138-00061-2

Experimental evaluation of the response of ferrocement strengthened lightweight masonry walls to impact loads

Mohamed A.N. Abdel-Mooty
Structural Engineering Department, Faculty of Engineering, Cairo University

ABSTRACT: Lightweight Autoclaved Aerated Concrete (AAC) blocks are used in external building's façade due to their favorable heat insulation characteristics that result in energy saving. However, such nonstructural unreinforced lightweight masonry walls have weak or no resistance to blast loads. They shatter under shock loads resulting in flying debris that increase the possibility of casualties and injury. Retrofitting and upgrading external masonry walls in existing buildings in high explosion-risk areas can provide the needed life protection for the users of those buildings. The use of ferrocement technology in strengthening of existing unreinforced nonstructural lightweight masonry wall to enhance their resistance to blast and short duration impact loads is proposed in this research. Two layers of ferrocement are applied to the external and internal face of the wall creating a sandwich structure with lightweight infill. The composite action of the strengthened wall is enhanced using shear connectors between the AAC masonry and the ferrocement. In this research program, the necessary laboratory tests to evaluate the dynamic response of ferrocement strengthened AAC masonry walls to short duration impact load simulating blast effect are carried out. The test programs included testing 7 full scale wall panels under impact. Different ferrocement reinforcement layouts are tested in this research. Three different types of shear connectors are used and their effect on the impact response of the wall is evaluated experimentally. The impact test apparatus developed in this research program is versatile enough to test a large variety of specimens modeling façade units.

1 INTRODUCTION

Blast resistant measures can be taken into consideration during the design stage of new structures ranging from choosing the building layout, the safe stand-off distance, appropriate construction materials and structural systems, and suitable details to resist a blast effect. However, existing structures do not have that advantage. Yet, existing buildings may be located in high risk area while they are not equipped to provide the needed protection to their occupants. In recent years, a significant amount of research work has been carried out to assess the resistance of structures under shock and impact loads and in particular blast loads (Abdel-Mooty *et al* 2010a and 2012a, Schenker *et al* 2008, Baylot *et al* 2005, and Jones 1989).

The primary causes of injuries and death in vehicle-bomb attacks against buildings are glass fragmentation, the impact of other debris from façade shattering, and building collapse. Resistance to these vulnerabilities is generally provided by passive features such as additional reinforcement and the use of composite fiber wraps and other coatings to prevent shattering of columns, slab and walls (Schenker *et al* 2005).

The use of ferrocement technology for strengthening existing lightweight masonry walls against impact and blast loads is proposed in this research. Lightweight autoclaved aerated concrete (AAC) blocks are used in external building's façade due to their favorable heat insulation characteristics that result in energy saving. However, such nonstructural unreinforced lightweight masonry walls have weak or no resistance to blast loads. They shatter under shock loads resulting in flying debris that increase the possibility of casualties and injury. Properly retrofitted façade elements should remain integrated to minimize the devastating effects of flying debris on occupants. A building façade should also minimize the blast load effect transmitted to the main structural frame to prevent building progressive collapse under such extreme loads.

Ferrocement is a type of reinforced mortar commonly constructed of hydraulic cement mortar reinforced with closely spaced layers of relatively small diameter wire mesh (IFC-Committee 2001). The ferrocement mortar matrix is a homogeneous mix composed primarily of Portland cement, well graded fine aggregate (sand), and water. It may contain chemical admixtures such as super-plasticizers and mineral admixtures like fly ash or silica fume to improve its properties. Intensive researches were conducted on ferrocement material to study the structural behavior of ferrocement sandwich load bearing wall panels (Swamy *et al* 1988, Fahmy *et al* 2006, and Abdel-Mooty *et al* 2010b and 2012b).

In this research an experimental program is developed to evaluate the dynamic response of wall panels to short duration impact loads. Two layers of ferrocement

are applied to the external and internal face of the wall creating a sandwich structure with lightweight infill. The composite action of the strengthened wall is enhanced using shear connectors between the AAC masonry and the ferrocement. The test programs included testing 6 full scale wall panels under impact in addition to one specimen tested under static load.

2 TEST PROGRAM AND SETUP

The impact test apparatus developed and used in this research is capable of testing different types of specimens with different supporting conditions. It is basically a pendulum mass that is released to fall freely from a specified height and hits the specimen at the lowest height of the pendulum (Figure 1). The apparatus is firmly attached to a concrete foundation to ensure its stability. The pendulum of the apparatus could be adjusted to have masses between 68.52 kg and 433.97 kg and a drop height between 100 and 300 mm. The impact mass is made of a steel plate with rigid impact head hung horizontally using four cables attached to the top of the pendulum support frame. The impact mass can be adjusted by securely attaching additional steel plates to the impact mass plate. Attached to the impact head is a fatigue rated impact load cell to measure the input impact load on the specimen. The impact load cell is of mass 2.68 kg and has maximum capacity of 200 kN impact. Four other load cells of the same type are attached to the specimen support frame between the back face of the specimen and the vertical columns of the support frame to measure the reactions forces transmitted to the support frame during impact (Figure 2).

The overall nominal dimensions of the tested specimens are 1800 mm wide, 1400 mm high and 250 mm thick as shown in Figure 2. The specimens are built using lightweight Autoclaved Aerated Concrete (AAC) blocks of dimensions 600×200×200 mm with a 25 mm thick mortar layer placed on each face. The normal mortar layers are replaced with ferrocement layers of the same thickness for strengthened specimens. Each specimen is placed vertically in the impact test frame, resting on a short bracket fixed to the steel columns. The specimen is horizontally supported on the vertical columns of the test frame where the reaction load cells are attached. The horizontal span between the load cell support points is 1280 mm, while the vertical span is 1000 mm. The applied impact force is measured by the load cell attached to the impact head that hits the specimen at the center point of the front face, while the reactions are measured by the four load cells at the supports on the back face of the specimen. A high speed data acquisition system is used in this study to measure the dynamic response parameters in terms of the applied load history, and reactions at supports.

Plaster layer of normal strength mortar 25 mm thick is applied on the two faces of the wall specimens. For ferrocement reinforced walls, high strength mortar reinforced with steel welded wire mesh is used in place of the normal plaster. Different types of connectors are used in the wall testing (Fig. 3). The first type is 50 mm steel nails placed in the fresh mortar joints during specimen preparation every 200 mm in both directions. The embedded part of the nail is 35 mm while the projected part is 15 mm which is connected



Figure 1. Impact test apparatus.

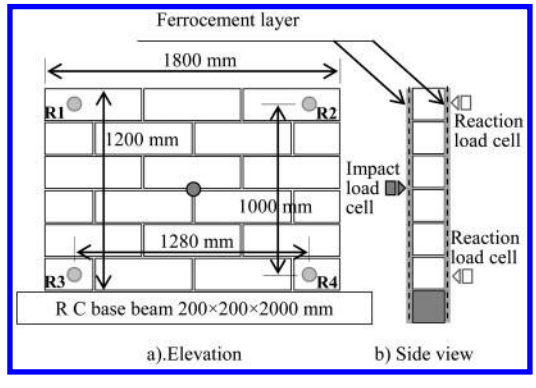


Figure 2. Specimen and instrumentation layout.

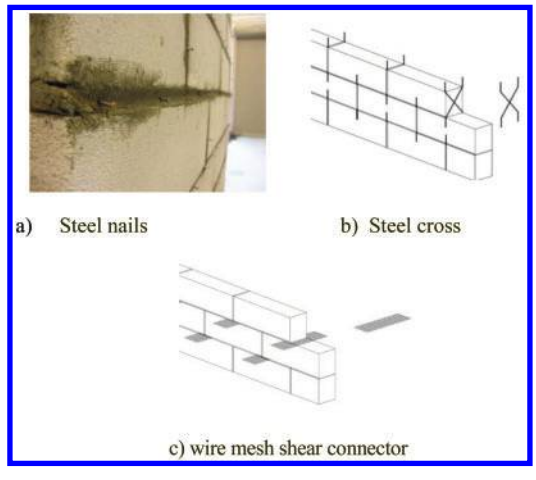


Figure 3. Different types of shear connectors.

to the welded wire mesh reinforcement. The other type of the connectors is welded wire mesh strip layed in the mortar bed joint during construction with 100 mm projected strip to be bent vertically and overlapped with the ferrocement reinforcement mesh. A third type of shear connector is made of steel cross bracing of 3 mm diameter steel bars placed in the vertical joints of the wall. The ferrocement mortar was applied using a standard plastering process. First mortar layer of thickness approximately 10 mm is placed then the welded wire mesh is placed on the mortar and attached to the shear connectors; then the rest of the mortar layer is applied to a total thickness of 25 mm. The test programs included testing 6 full scale wall panels under impact in addition to one specimen tested under static load as shown in Table 1.

The physical and mechanical properties of the component of the ferrocement reinforced AAC masonry wall specimens are experimentally measured. Compressive strength tests are conducted on cube specimens of 100 mm edge length tested in an air dried condition. The average compressive strength of the tested cubes is 3.13 MPa. The average dry density of the AAC blocks measures 597 kg/m^3 while the average moisture content measures 10.2% of weight.

The mortar used in this research consists of two different types. The first type of mortar is normal strength mortar used in joints of the wall specimens and in normal plastering on both faces of the control wall. According to common practice, the cement to sand ratio is 1 to 2.5 with cement content 350 kg/m^3 of mortar and water/Cement ratio 0.5 resulting in average compressive strength of 21.03 MPa. The second type of mortar is used in applying the ferrocement layer on the walls. To provide the needed strength and protection to the reinforcing wire mesh the ferrocement mortar matrix should be workable, high strength, and well compacted mortar. The cement to sand ratio is 1 to 2 with cement content 665 kg/m^3 of mortar and water/Cement ratio 0.3. Superplasticizer was used in the mix at 2.5% of the cement weight, to provide the mortar mix with high workability. Silica fume was used in the mix 12% of the cement weight to attain high strength. Standard cubes 50 × 50 × 50 mm cured for 28 days yields average compressive strength of 60.84 MPa.

Table 1. Test program for full scale ferrocement strengthened AAC masonry walls.

Specimen	Wall strengthening	Shear Connectors
Impact Load Test:		
Wall-1	Control (no ferrocement)	N/A
Wall-2	Ferrocement strengthened	Steel nails
Wall-3	Ferrocement strengthened	Steel nails
Wall-4	Ferrocement strengthened	Cross bars
Wall-5	Ferrocement strengthened	wire mesh strip
Wall-6	Ferrocement with RC Vertical ties on the sides	Steel nails
Static Load Test:		
Wall-7	Ferrocement strengthened	Steel nails

Galvanized steel welded wire mesh of diameter 1 mm at spacing 15 mm is used as reinforcement of the ferrocement layers. Samples of the steel wire mesh were tested to determine the yield and ultimate stress according to ASTM A 370. The average tensile strength of the tested wire meshes is 400 MPa.

3 TEST PROCEDURE AND RESULTS

The impact mass of 240 kg and drop height of 200 mm were kept constant for all tested specimens. The impact load and the reactions at the four supporting points are recorded with time for each hit. The specimen was visually inspected after each hit and cracks and damage are recorded. The impact test is repeated from the same height until failure of the specimen. The crack patterns and mode of failure are recorded for each specimen. The number of hits that a specimen can sustain before failure presents a quantitative measure of the ability of the specimen to resist impact load and maintains its integrity. The control specimen without ferrocement reinforcement failed at first hit where the wall broke into three large pieces as shown in Fig. 4, at a relatively low impact load of 7.59 kN. All other tested walls sustained several impacts before failure. Furthermore, the failure of all ferrocement reinforced specimens was ductile where the wall remained integrated. Typically, a vertical crack initiated in the back side of the specimen at the center. With successive hits, the crack propagates and widens then bifurcates to the corners of the RC beam. Finally a mechanism of failure formed and the specimen loses its strength. The mechanism of failure for Wall-6 with two columns on the sides was slightly different. It started with a crack that propagated vertically, followed by punching failure (Fig. 8).

The time history of the impact and the reactions at the four supports are recorded for all tests. Figure 4 shows the time history record for impact and reactions for the control specimen Wall-1. The initial (highest) impact record for specimen Wall-3 with steel nails connectors is shown in Fig. 5. It is clear from the figure that Wall-3 sustained much higher impact



Figure 4. Failure of control specimen Wall-1 at the first hit.



Figure 5. Failure of Wall-2 with nails connectors.



Figure 6. Failure of Wall-4 with cross connectors.

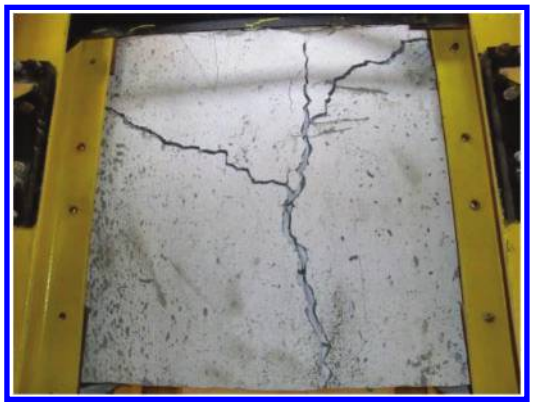


Figure 7. Failure of Wall-5 with mess connectors.

load than Wall-1 (control) with only hair crack and no failure. Wall-3 sustained 6 impact hits before its failure. Of course, with successive hits and increased propagation of cracks, the stiffness of the specimen decreases and the value of recorded impact decreases. It was also observed that the reactions at the support recorded exceed the impact force. This is expected due to the dynamic nature of the problem and the associated inertia force of the wall.

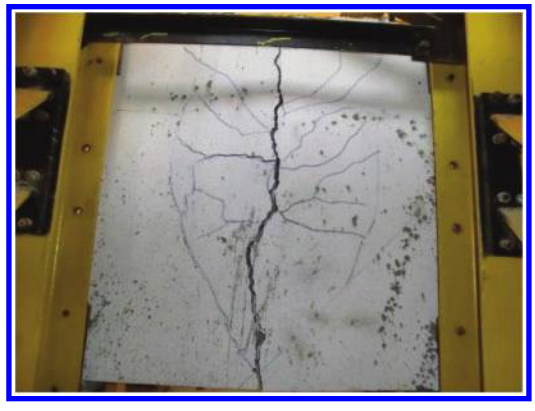


Figure 8. Failure of Wall-6 with two columns on the sides.

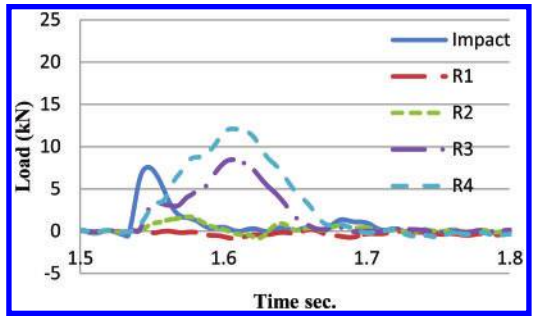


Figure 9. Impact record for control specimen Wall-1.

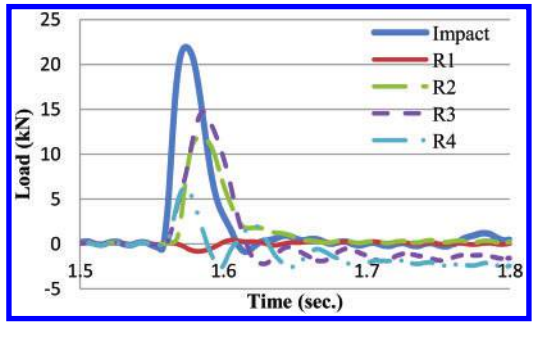


Figure 10. First impact record for Wall-3.

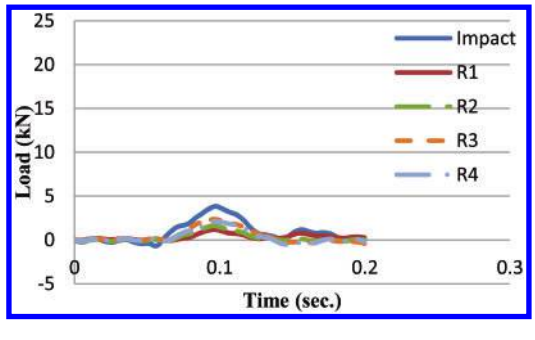


Figure 11. Sixth (final) impact record for Wall-3.

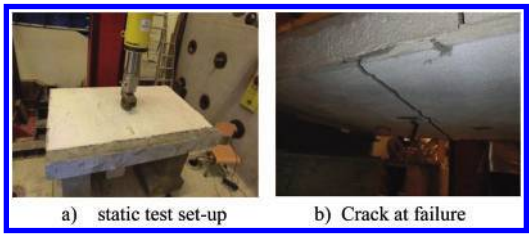


Figure 12. Failure of Wall-7 under increasing static load.

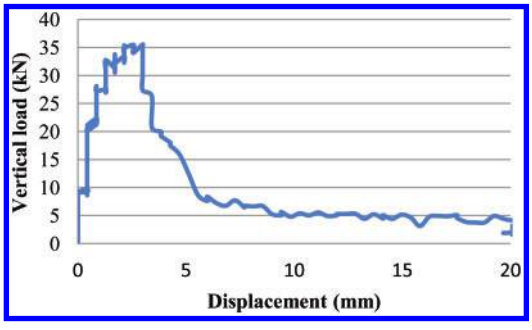


Figure 13. Static load-deformation relationship for Wall-7.

Table 2. Summary of impact test results.

Specimen	No. of impact hits to failure	Initial/high impact (kN)	Final/Failure impact (kN)
Wall-1	1	7.587	–
Wall-2	6	19.282	6.882
Wall-3	6	21.941	3.847
Wall-4	6	23.391	7.137
Wall-5	11	21.417	6.425
Wall-6	19	26.124	6.982

Wall-7 was tested under monotonically increasing vertical load up to failure. The test setup and cracks at failure are shown in Fig.12. Failure occurred suddenly at load 35 kN at which a longitudinal crack developed at the center of the specimen under loading point (Fig. 12b). Sudden decrease in load capacity occurs at failure as shown in Fig. 13.

4 ANALYSIS OF TEST RESULTS

The test results in terms of number of impact hits sustained by each specimen up to failure, the initial/maximum impact load and the final/failure impact are displayed in Table 2. Figure 14 shows the maximum initial impact for the tested wall. It is clear that the ferrocement reinforcement of the AAC masonry wall increases the initial strength almost three-fold. Furthermore, the toughness of the wall, represented by the number of impact hits that the specimen could sustain up to its failure, is significantly increased due to the addition of ferrocement as indicated in Table 2.

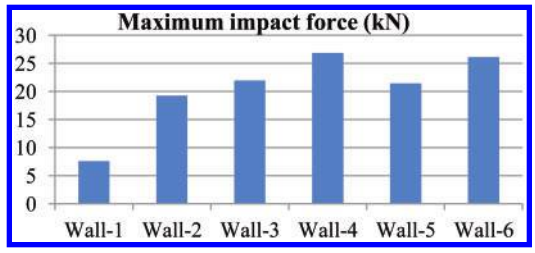


Figure 14. Initial maximum impact load for tested specimens.

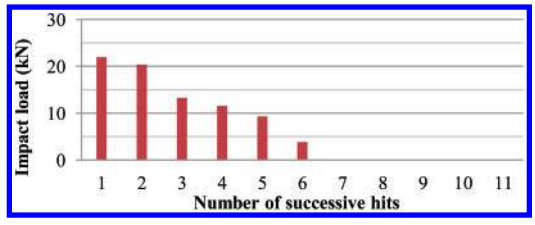


Figure 15. Variation in impact load for successive hits on Wall-3.

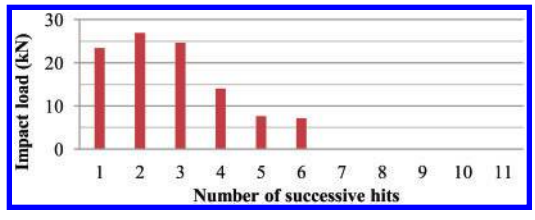


Figure 16. Variation in impact load for successive hits on Wall-4.

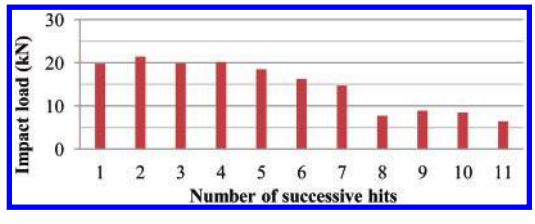


Figure 17. Variation in impact load for successive hits on Wall-5.

It is observed in all strengthened specimens that the recorded impact load gradually decreases with each successive hit up to failure. This is due to the initiation and propagation of cracks and the associated loss in stiffness of the specimen. Figures 15-18 show the variation in impact load with successive hits up to failure for Wall-3, Wall-4, Wall-5 and Wall-6.

The reactions at the four supporting points were measured and recorded for all tests. It is observed that the total reaction in general exceeds the applied impact for all tests. The difference between the applied impact and the reactions at support increases with the successive hits for all specimens. Initially, for sound specimens before damage, the measured reaction was approximately 150% of the applied impact. As the

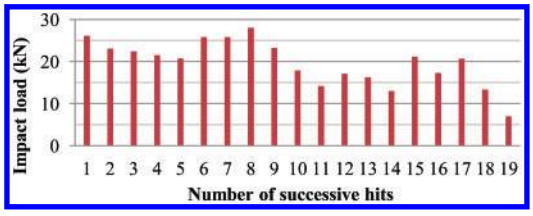


Figure 18. Variation in impact load for successive hits on Wall-6.

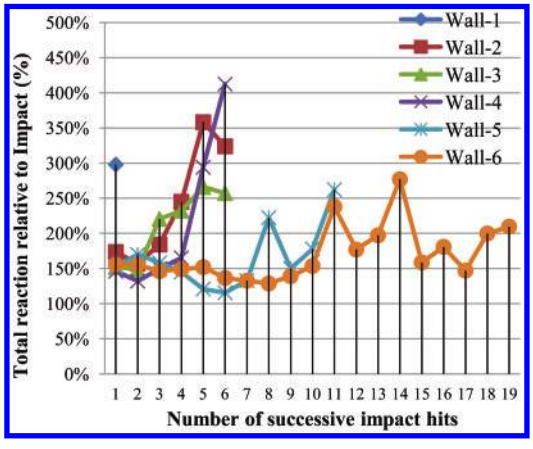


Figure 19. Variation in total reaction for successive hits.

cracking and damage in the specimen increase and propagate, the reactions increase by 2 or 3-fold near failure. This is due to the reduced stiffness of the specimen and increased period.

5 SUMMARY AND CONCLUSIONS

The performance of ferrocement reinforced AAC masonry walls under impact load is evaluated in this paper. The normal plastering on each face is replaced by a 25 mm thick ferrocement layer. Seven wall specimens were tested in this research, six under impact load and one under static loading to failure. Each specimen was subjected to several impacts up to its failure. The impact mass and the drop height were kept constant for all tests.

It is found that the ferrocement reinforcement improves significantly the impact performance of the specimens. While the unreinforced specimen failed at the first hit and disintegrated into pieces, all reinforced specimens survived several hits and remain integrated even after failure. This would result in better protection to the building and its occupants from the damaging effect of flying debris during the impact event. Ferrocement reinforced specimens sustained higher impact forces up to three folds of the unreinforced walls. With repeated impact hits, the strength of the specimen decreases which is represented by reduced impact load.

The total reactions measured at the support generally exceed the applied impact. This effect becomes more pronounced as the cracking and damage of the specimen increases with successive impact.

Several types of shear connectors were tested in this research, namely steel nails, cross bars, and wire mesh strips. It is found that the wire mesh connector provide better performance of the wall under impact. Furthermore, the addition of vertical RC ties at the edge of the wall significantly adds to the strength of the specimen and improves its impact response.

REFERENCES

Abdel-Mooty, M & Shaabaan M. 2010a. Numerical Modeling and Calibration of Impact Testing of Reinforced Concrete Panels, Proceedings of International conference on Computational Structural Technology CST 2010, Civil-Comp, 14–17 September 2010, Valencia, Spain.

Abdel-Mooty, M.N., Fahmy, E., Abu-Zeid, M., Saleh, M., & Haroun M. 2010b, Seismic Strengthening of Lightweight Masonry Wall Panels using Ferrocement Layers, 13th International Conference STRUCTURAL FAULTS + REPAIR 2010, 15–17 June 2010, Edinburgh, Scotland.

Abdel-Mooty, M. & Shaaban, S. 2012a. Nonlinear Dynamic Response of RC Building Façade Panels to Impact Loads. 12th International Conference on Structures Under Shock and Impact, 4–6 September 2012, Kos, Greece. WIT Transactions on the Built Environment, Vol. 126, Structures Under Shock and Impact XII, pp. 281–291.

Abdel-Mooty, M., Hendam, A., Fahmy, E., Abou Zeid, M., & Haroun, M. 2012b. Experimental Evaluation of Lightweight AAC Masonry Wall Prisms with Ferrocement Layers in Compression and Flexure, *Journal of Applied Mechanics and Materials*, Vols 166–169 Progress in Structures (2012), pp 1730–1735, (2012) Trans Publications, Switzerlans, doi: 10.4028/ www.scientific.net/ AMM.166-169.1730

Baylot J.T., Bullock, B., Slawson, T.R. & Woodson, S.C. 2005. Blast Response of Lightly Attached Concrete Masonry Unit Walls. *Journal of Structural Engineering*, ASCE, 131 (8), pp. 1186–1193.

Fahmy, E.H., Shaheen, Y.B.I., Abou Zeid, M.N. & Gaafar, H.M. 2006. Ferrocement Sandwich and Hollow Core Panels for Wall Construction. *Journal of Ferrocement*, Vol. 36, No. 3.

IFC-Committee 10-2001. 2001. Ferrocement Model Code; Building Code Recommendations for Ferrocement (IFS-Committee 10-2001), International Ferrocement Society, Asian Institute of Technology, Thailand.

Jones, N. 1989. Structural Impact. Cambridge University Press, Cambridge.

Schenker, A., Anteby, I., Nizri, E., Ostriach, B., Kivity, Y., Sadot, O., Haham, O., Michaelis, R., Gal, E. & Ben-Dor, G. 2005. Foam-Protected Reinforced Concrete Structures under Impact: Experimental and Numerical Studies. *Journal of Structural Engineering*, ASCE, 131(8), 1233–1242.

Schenker, A., Anteby, I., Gal, E., Kivity, Y., Nizri, E., Sadot, O., Michaelis, R., Levinant, O., & Ben-Dor, G. 2008. Full-Scale Tests of Concrete Slabs Subjected to Blast Loads. *International Journal of Impact Engineering*, 35, Issue 3, pp. 184–198.

Starr, C. M. & Krauthammer, T. 2005. Cladding-Structure Interaction under Impact Loads. *Journal of Structural Engineering*, ASCE, 128(1), 87–92.

Swamy, R.N. & Abboud, M.I. 1988. Application of Ferrocement Concept to Low Cost Lightweight Concrete Sandwich Panels. *Journal of ferrocement*, Vol. 18, No. 3.

Research and Applications in Structural Engineering, Mechanics and Computation – Zingoni (Ed.)
© 2013 Taylor & Francis Group, London, ISBN 978-1-138-00061-2

Externally applied retrofit system for existing masonry buildings subject to progressive collapse

A. Kousgaard & E. Erdogmus
University of Nebraska-Lincoln, Nebraska, USA

ABSTRACT: This study proposes the design of a cost effective retrofit method for progressive collapse that can be externally applied to existing masonry structures. An existing load-bearing masonry wall structure was investigated for progressive collapse resistance considering various wall-opening scenarios. Using commercially available finite element programs and the guidelines set forth by UFC 04-023-03, progressive collapse analysis was carried out on the macro model of the existing structure (i.e. entire building). Based on the deficiencies found, an externally applied retrofit system was then investigated using micro models of a deficient isolated wall with the appropriate boundary conditions. The analysis and design of retrofit carried out followed the relevant codes in United States.

1 INTRODUCTION

1.1 *Background*

Modern-era disasters have implemented standards for design against progressive collapse. After the explosion and subsequent progressive collapse at the Ronan Apartment towers in 1968, revisions of design criteria were adopted in England and the United States (Pearson & Delatte 2005). In 1995, after the bombing of the Alfred P. Murrah Building, the United States government adopted interim guidelines for design against progressive collapse (Marchand et al. 2006). Finally, after the collapse of the World Trade Center Towers in 2001, the United States Department of Defense developed and adopted the Unified Facilities Criteria (UFC) 04-023-03: Design of Buildings to Resist Progressive Collapse (Stevens et al. 2011).

Under the current codes and standards, in the case of an adaptive reuse, masonry wall buildings may require the evaluation of their resistance against progressive collapse. Due to the brittle material characteristics and otherwise complex behavior of masonry wall buildings, the progressive collapse analysis and the necessary retrofits for such existing buildings are challenging and costly to implement.

1.2 *Goals*

The goals of this study are to develop a parametric study of a load-bearing masonry wall structure using various opening scenarios and to design a cost effective retrofit for a deficient isolated wall from the parametric study.

1.3 *Scope and assumptions*

The studied building is based on an actual building in the United States. However, it is revised and idealized both for project confidentiality and parametric study purposes; and studied as a hypothetical three-story structure. The building is assumed to have a capacity of 250 people and to have a structural system composed of fully grouted load-bearing 20.3 cm CMU walls with a 9.2 cm architectural brick veneer. The interior is a reinforced concrete frame and slab. For the purpose of this study, the interior frame and slab were not investigated. The exterior load-bearing walls are continuous with the slab framed into each floor. This study also does not include seismic or blast effects on the structure, soil structure interaction and overturning, plastic deformations, and lateral loading. For this study, the following assumptions were also made:

- The building is a non-essential, government facility.
- Lower bound strength values are based on guide lines and values from UFC 04-023-03 (2009), ASCE 41 (2006), and MSJC (2008).
- The load-bearing exterior masonry walls have force-controlled modes of failure.
- The failure occurs before plastic deformations.
- The framing plans for each floor are the same.
- The floor system is a one-way rigid diaphragm.

2 METHODOLOGY

2.1 *Parameters*

The parameters that remained constant in this study can be seen in Table 1.

The variable parameters in this study included:

- Flexural lower-bound strengths used to determine structural adequacy
- Window scenarios/layout
- Reinforcement [unreinforced (URM) or reinforced (RM)]

Table 1. Constant parameters.

Parameter	Description
Building use	3 story office building
Occupancy category	II
Load bearing wall	20.3 cm* fully grouted hollow CMU
1st story height	4.06 m
2nd story height	3.91 m
3rd story height	3.91 m
Reinforcement	2# 4 in lintels

*The standard U.S. size of 8" CMU

Table 2. ASCE 41-06 masonry default properties.

Property	Masonry condition	
	Good	Fair
Compressive strength (f 'm)	6205 (kPa)	4137 (kPa)
Elastic modulus (E)	3411 (MPa)	2274 (MPa)
Modulus of rupture (f_r)	138 (kPa)	69 (kPa)

*Source: ASCE 41-06

Table 3. MSJC-08 material properties.

Property	Value
Compressive strength (f'_m)	10335 kPa
Elastic modulus (E)	9302 MPa
Modulus of rupture (f_r)	1034 kPa

*Source: MSJC-08

– Compressive strength (f'_m)
– Elastic modulus (E)
– Modulus of rupture (f_r)

Material properties that were used to model the masonry building in SAP2000 were taken from ASCE 41-06 and MSJC-08. The ASCE 41-06 properties can be seen in Table 2. These material properties are based on the deterioration and condition of the masonry. As the mode of failure investigated in this study is flexural tension, good and fair conditions of masonry were investigated; poor condition was not considered because it is assumed to have no tensile capacity. The material properties from MSJC-08 can be seen in Table 3. These material properties are representative of new masonry or masonry that has not yet deteriorated.

Lower-bound strengths for reinforced masonry were taken as the calculated strength of the masonry lintel (ΦM_n). Lower-bound strengths for unreinforced masonry were taken as the modulus of rupture (f_r) multiplied by phi (Φf_r). The respective lower-bound strengths based on ASCE 41-06 and MSJC-08 material properties can be seen in Table 4 and Table 5, respectively.

The openings are treated as a variable parameter to test the increased vulnerability of a masonry wall

Table 4. ASCE 41-06 flexural tension lower-bound strengths.

Property	Masonry condition			
	RM		URM	
	Good	Fair	Good	Fair
$\Phi Q_{CL} = \Phi f_r$ (kPa)	N/A	N/A	83**	41**
$\Phi Q_{CL} = \Phi Mn$ (kNm)	82.8*	82.5*	N/A	N/A

*$\Phi = 0.9$
**$\Phi = 0.6$

Table 5. MSJC-08 flexural tension lower-bound strengths.

Property	Masonry condition	
	RM	URM
$\Phi Q_{CL} = \Phi f_r$(kPa)	N/A	620**
$\Phi Q_{CL} = \Phi Mn$ (kNm)	82.9*	N/A

* $\Phi = 0.9$
** $\Phi = 0.6$

Table 6. Window scenarios.

Code or standard	Masonry type	Windows
MSJC-08	RM	No windows
		1.83 m × 1.22 m
		2.44 m × 1.83 m
		3.05 m × 1.83 m
ASCE 41-06	RM	No windows
	URM	No windows

with change in the amount and size of window/door openings. The tested "window" scenarios can be seen in Table 6. Each of the window scenarios was analyzed with each of the three removal cases presented in section 2.2.

2.2 *Removal cases*

Removal cases are based on UFC 04-023-03 (2009). Removals along the east wall, the south wall, and at the corner of the building were made. Each removal is made one at a time, followed by a linear static analysis to determine if failure has occurred. For load-bearing masonry walls, the length of the wall removed is twice the length of the story height (2H). For corner removals, each side of the corner has a length of the story height removed (H). The removal cases can be seen in Figure 1. All removals were done on the first story of the building.

UFC 04-023-03 specifies that removals along the wall should be made in the middle of the wall. For the south wall, this was done. However, based on judgment, the engineer can shift the wall removals by length H. For this study, the east side removal was shifted due to a door opening in the wall; this shift created a more vulnerable structure.

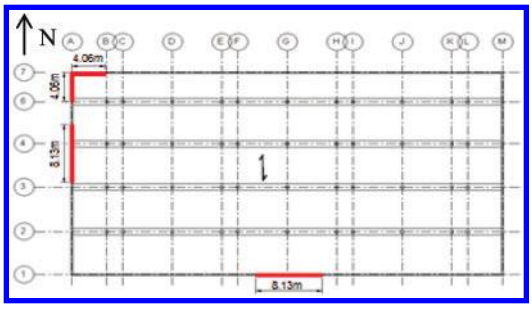


Figure 1. Removal locations.

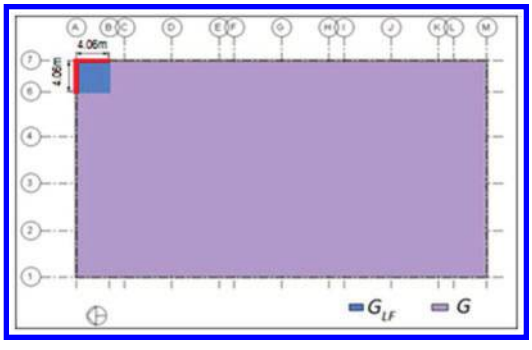


Figure 2. Gravity loading distribution.

2.3 *Loading*

Loading is determined by UFC 04-023-03. Increased gravity loading is required adjacent to the removed wall or element. The different gravity loadings used are defined by the floor areas away from the removed wall and adjacent to the removed wall in Equation 1 and Equation 2, respectively. The different loading areas can be seen in Figure 2.

$$G = [(0.9 \text{ or } 1.2)\, D + (0.5\, L \text{ or } 0.2\, S)] \quad (1)$$

$$G_{LF} = \Omega_{LF}\, G \quad (2)$$

where LF indicates force-controlled linear static analysis; Ω_{LF} = load increase factor; D = dead load; L = live load; and S = snow load.

The load increase factor is defined in UFC 04-023-03 and in this study was taken as 2.0.

For this study, no lateral loading was considered. The 2009 UFC 04-023-03 specifies the only lateral loads to be considered as notional loads. After preliminary results, notional loads were determined to not control the mode of failure of the building. Therefore, lateral loads and their effects are not discussed here.

2.4 *Analysis*

Modeling and analysis for this study was done using SAP2000 finite element analysis software. Because the masonry was fully grouted, it was modeled using the "concrete" elements but with modified material properties. A linear static analysis was used for the parametric study because it was assumed failure occurred before reaching plastic deformation. In order to consider material nonlinearities and geometric nonlinearities in the studied isolated wall, a nonlinear static analysis was used for the retrofit investigation.

Each removal case was modeled with the corresponding material properties and window scenarios presented in Table 2, Table 3, and Table 6, respectively. In total, there were 24 different models that were analyzed for progressive collapse. In order to account for the reinforcement tensile strength in the reinforced masonry, if the moment from the SAP2000 results was greater than ΦM_n from the respective Table 4 or Table 5, the building was considered inadequate for progressive collapse resistance. If the resulting tensile stress for unreinforced masonry was greater than the respective lower-bound strength in Table 4 or Table 5, the building was considered inadequate for progressive collapse resistance.

Table 7. Failure from the corner removal for reinforced masonry.

Criteria	Tensile failure	
	yes	no
MSJC 08 Criteria		
No windows		X
6′ × 4′ windows		X
8′ × 6′ windows		X
10′ × 6′ windows		X
ASCE 41 Default Properties		
Good – no windows	X	
Fair – no windows	X	

Table 8. Failure from the corner removal for unreinforced masonry.

Criteria	Tensile failure	
	yes	no
ASCE 41-06 Default Properties		
Good – no windows	X	
Fair – no windows	X	

3 ANALYSIS RESULTS

3.1 *Corner removal*

The results for the corner removal analysis for reinforced masonry and unreinforced masonry can be seen in Table 7 and Table 8, respectively.

3.2 *East wall removal*

The results for the east wall removal analysis for reinforced masonry and unreinforced masonry can be seen in Table 9 and Table 10, respectively.

Table 9. Failure from the east removal for reinforced masonry.

Criteria	Tensile failure	
	yes	no
MSJC-08 Criteria		
No windows		X
1.83 m × 1.22 m windows		X
2.44 m × 1.83 m windows	X	
3.05 m × 1.83 m windows	X	
ASCE 41-06 Default Properties		
Good – no windows	X	
Fair – no windows	X	

Table 10. Failure from the east removal for unreinforced masonry.

Criteria	Tensile failure	
	yes	no
ASCE 41-06 Default Properties		
Good – no windows	X	
Fair – no windows	X	

Table 11. Failure from the south removal for reinforced masonry.

Criteria	Tensile failure	
	yes	no
MSJC-08 Criteria		
No windows		X
1.83 m × 1.22 m windows	X	
2.44 m × 1.83 m windows	X	
3.05 m × 1.83 m windows	X	
ASCE 41-06 Default Properties		
Good – no windows		X
Fair – no windows	X	

Table 12. Failure from the south removal for unreinforced masonry.

Criteria	Tensile failure	
	yes	no
ASCE 41-06 Default Properties		
Good – no windows	X	
Fair – no windows	X	

3.3 *South wall removal*

The results for the south removal analysis for reinforced masonry and unreinforced masonry can be seen in Table 11 and Table 12, respectively.

It is worth noting that because of the window layout for the south side removal, the removal is larger than twice the height of the story. At a removal length of 2H, the removed area intersects with windows; this would leave unsupported masonry in the location of the windows. The unsupported masonry would not provide additional strength to resisting progressive collapse, therefore it was removed and the final removal length was 12.6 m. With respect to the removal length and the resulting tensile stress, this was the worst case scenario in the parametric study, thus it is selected for the retrofit design.

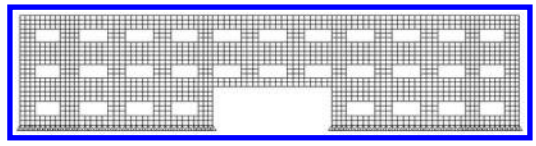


Figure 3. Elevation of south wall with removal.

3.4 *Observations*

The results from the parametric study showed that openings in a masonry wall create vulnerability to failure from flexural tension. Failure occurred around openings or removals due to in-plane gravity loading.

4 RETROFIT DESIGN

4.1 *Deficient isolated wall*

The worst case scenario and the selected wall to be investigated was the reinforced south wall with 3.05 m × 1.83 m windows and MSJC-08 properties seen in Table 4. Based on the results presented in section 3, the south wall was deemed vulnerable to failure. An elevation view of the south wall with the removal can be seen in Figure 3.

4.2 *Proposed Retrofit Scenarios*

A common technique used to increase the tensile strength of masonry is to apply fiber reinforced polymer (FRP) to the tension face of the masonry. However, the cost for FRP can be high. In 2011, Radik, Erdogmus, and Schafer showed that fiber reinforced cement (FRC), when used as an externally applied retrofit layer similar to FRP, has a comparable increase in tensile capacity to glass-fiber-reinforced polymer (GFRP) but could be as much as 215% less expensive.

In this study, FRC was investigated as a retrofit to the south wall with the removed area. The FRC was modeled after the properties found in the study done by Radik, Erdogmus, and Schafer. Type N PCL mortar was used with a 1% volume ratio. The fibers used were polypropylene synthetic fibers. The properties found and used in this study can be seen in Table 13.

Three types of retrofit scenarios were studied. The first retrofit (R-1) was a 2.5 cm layer of FRC applied to the backside of the entire wall, as it would be with typical out-of-plane failure. This was studied based on the hypothesis that increasing the wall thickness would decrease the flexural stresses due to in-plane gravity loads because of the increased moment of inertia.

Table 13. Properties of FRC.

Property	Value
f'_c	8.07 MPa
$f't$	0.11 MPa
E	10,204 MPa
γ	1922 kg/m^3

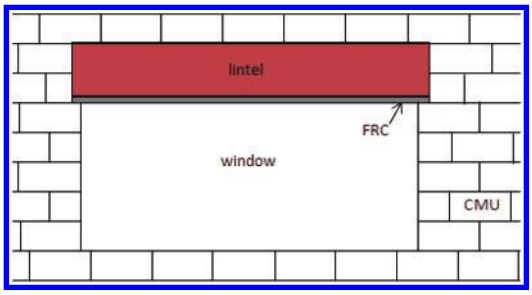


Figure 4. FRC layer under CMU lintel*Not to scale.

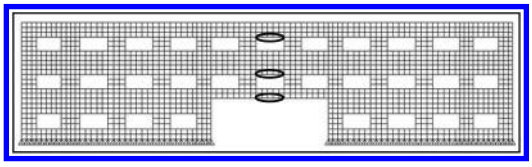


Figure 5. Investigated areas for failure.

The second retrofit (R-2) applied a 2.5 cm layer of FRC underneath the CMU lintel. The 2.5 cm layer was chosen based on the study done by Radik, Erdogmus, and Schafer. In that study, the 2.5 cm layer provided the highest tensile capacity gain and provided the largest cost difference (215%) compared to the GFRP retrofit. An example image of the 2.5 cm layer of FRC retrofit can be seen in Figure 4.

The third retrofit (R-3) applied a 20.3 cm layer of FRC underneath the lintel. The 20.3 cm layer of FRC reflects the size of a standard CMU in the U.S. (8 inches). As such, this 20.3 cm layer could be easily modeled as an additional course of masonry with the FRC material properties. As an externally applied retrofit, the 20.3 cm layer decreases the window size and the architectural alterations may need to be considered in a real life application.

4.3 *Results*

Before and after the application of the retrofits, tension stresses were investigated at the mid-span of: a) the removal area, and b) at the two window openings above the removed area. The areas investigated for failure are circled in Figure 5. Negative values within the following tables indicate compression stress.

The tensile stresses with retrofit R-1 can be seen in in Table 14.

The tension stresses with retrofit R-2 can be seen in in Table 15.

Table 14. Stresses before and after 2.5 cm FRC layer over entire wall per SAP2000 (R-1).

Opening	initial f_u (kPa)	f_u with R-1 retrofit (kPa)	pass/fail with R-1
Top window	−1070	−9.37	pass
Middle window	1210	1250	fail
Removal	1920	1710	fail

Table 15. Stresses before and after 2.5 cm FRC layer over openings per SAP2000 (R-2).

Opening	initial f_u (kPa)	f_u with R-2 retrofit (kPa)	pass/fail with R-2
Top window	−1070	−6.75	pass
Middle window	1210	8.20	pass
Removal	1920	1720	fail

Table 16. Stresses before and after 20.3 cm FRC layer over openings per SAP2000 (R-3).

Opening	initial f_u (kPa)	f_u with R-3 retrofit (kPa)	pass/fail with R-3
Top window	−1070	−7.17	pass
Middle window	1210	13.6	pass
Removal	1920	2010	fail

The tension stresses with retrofit R-3 can be seen in in Table 16.

5 CONCLUDING REMARKS

Higher stresses were seen in the wall where there were larger openings and openings that were near the removed area. Higher stresses were also observed at the corners of the openings. This is because the reinforcement was designed to be just longer than the lintel per appropriate development and embedment length provisions of older masonry structures. Modern lintel design horizontal reinforcement is continuous throughout the masonry. This development length provides added resistance to tensile forces. When the lintel is designed to have a development length of just longer than the lintel, there are areas of unreinforced masonry that are vulnerable to tensile stress. This stress often resulted in failure of the masonry.

The retrofit of the entire wall being layered with FRC does not decrease the stress above the removed area and the opening enough to adequately resist progressive collapse.

The retrofits using layers of FRC above the openings reduces the stress above the openings. However, the stress over the removal was not decreased enough to be adequate to avoid progressive collapse. It would be worth investigating a retrofit that involves placing FRC at floor level in order to strengthen the entire wall.

Another way to strengthen the entire wall may be to replace a portion of mortar joints with FRC. Because of the decreased tensile stress in the 2.5 cm layer of FRC above the openings, it would be worth investigating replacing this retrofit. This type of retrofit would require modeling the wall with differentiated CMU and mortar instead of modeling the wall as modified concrete.

Finally, because CMU and FRC have different material properties, the cohesion and bond between the FRC and CMU needs to be investigated further. If the joint between the FRC and CMU fails, the retrofit may become inadequate because the FRC would disengage from the CMU; the wall would return to the original state before a retrofit was applied.

REFERENCES

American Society of Civil Engineers (ASCE). 2007. *ASCE 41-06: Seismic Rehabilitation of Existing Buildings*. Reston: ASCE.

Department of Defense (DoD). 2009. *Unified Facilities Criteria (UFC) 04-023-03: Design of Buildings to Resist Progressive Collapse*. Washington, D.C.: DoD.

Marchand, K.A., Stevens, D.J., Crowder, B., and Campbell, T. 2006. UFC 4-023-03: Design of Buildings to Resist Progressive Collapse – A Review and Update on the Department of Defense Progressive Collapse Guidance." *Structure Magazine.* April 34–37.

Masonry Standards Joint Committee (MSJC). 2008. Building Code Requirements and Specifications for Masonry Structures. Boulder: MSJC.

Pearson, C. and Delatte, N. 2005. Ronan Point Apartment Tower Collapse and its Effect on Building Codes. *Journal of Performance of Constructed Facilities* 19 (2): 172–177.

Radik, M.J., Erdogmus, E., and Schafer, T. 2011. Strengthening Two-Way Reinforced Concrete Floor Slabs Using Polypropylene Fiber Reinforcement. *Journal of Materials in Civil Engineering.* 23 (5): 562–571.

Stevens, D., Crowder, B., Sunshine, D., Marchand, K., Smilowitz, R., Williamson, E., and Waggoner, M. 2011. DoD Research and Criteria for the Design of Buildings to Resist Progressive Collapse. *Journal of Structural Engineering-ASCE* 137 (9).

Research and Applications in Structural Engineering, Mechanics and Computation – Zingoni (Ed.)
© 2013 Taylor & Francis Group, London, ISBN 978-1-138-00061-2

Non-linear static analysis of masonry-infilled RC frames

A. Koçak & B. Doran
Yıldız Technical University, Istanbul, Turkey.

A. Kalyoncuoglu & B. Zengin
Istanbul Gelisim University, Istanbul, Turkey

ABSTRACT: A common type of construction is low-rise and mid-rise reinforced concrete buildings with unreinforced masonry walls which are usually referred to as infill walls filling the spaces bounded by their structural frames. The effect of these walls may be ignored if the frame is to be designed against gravity. However, ignoring the effect of infill walls against seismic loads may lead to a highly vulnerable situation under earthquake motions. Therefore, in non-linear analysis, this effect should be taken into account in numerical model using equivalent diagonal strut approaches for accurate solution. This study aims to explore the effect of masonry-infilled frame on the non-linear static analysis. In this context, non-linear static analysis (pushover) has been performed based on FEMA 356 for these approaches separately. Besides, the effect of thickness of the wall on the lateral response is also studied. Results show that frames with unreinforced masonry walls infills generally enhance lateral capacity and energy dissipation.

1 INTRODUCTION

Masonry-infilled walls as architectural elements of a typical frame structure can be found as interior and exterior walls in reinforced concrete and steel-framed structures. They are mostly considered as non-structural elements, and their presence is often ignored by structural engineers. Infill walls are often neglected in the analysis of building structures (Bare RC frame) because of their complex nature and also the absence of a realistic analytical model. Ignoring the effect of the infill in stiffening and strengthening the surrounding frame is not always a conservative approach, especially in seismic design. Different analytical models had been used considering experimental results to simulate the behavior of infill walls.

Infilled frames were first studied by Palyakov (1956). The infill walls placed in reinforced concrete frames did increase the rigidity of the building; and thus, it was suggested that infill walls should be modeled like diagonally crossing rods (Bounopane and White, 1999). Mehrabi et al. (1996) conducted experiments on bricks with and without hollow spaces and concluded that when vertical loads on the infill walls are increased, then the total horizontal bearing capacity of the composite frame also increases by 25%. Dolšek & Fajfar (2008) found that masonry infill highly increases the stiffness and strength of a structure as long as the seismic demand does not exceed the deformation capacity of the infills. On the other hand, Amanat & Hoqueb (2006) observed that, the beam and column stiffness have negligible effect on the period. This study also shows that randomness in the distribution of infill does not have a significant effect on the period; instead, it is the total amount of infill that is important. In their study regarding reinforced concrete frames with and without infill walls, Altın et al. (1992) reported an increase of 6 to 28% of the initial rigidity if a whole connection between the infill wall and the frames are considered. Puglisi et al. (2008) proposed a model for the behavior of infill panels in framed structures which is based on the equivalent strut model, the plastic concentrator concept, and damage mechanics. Hong et al. (2002) and Asteris (2003) observed the effects of reinforced concrete framed infill walls at earthquake conditions and the effects of infill walls with or without the door and window openings. They concluded that frames with door and window openings are less rigid and have higher periods than those without any openings. Dowrick (1987) concluded that infill walls did increase the structural strength and rigidity; Aytun (1972) and Bayulke (1998), on the other hand, stated that infill walls decreased the building periods while also increasing the rigidity of the system. Sivri et al. (2006) carried out a time history analysis utilizing the records of the Düzce and Erzincan earthquakes to a building which was also analyzed experimentally by Negro and Colomba. The structure was analyzed under three different conditions

for infill walls: no infill walls, with infill walls, and with infill walls above the ground floor. They concluded that infill walls had a significant effect on the building period and ignoring their effects negatively influences the safety of the building. Govindan et al. (1986) subjected cyclic loads to two different seven-storey buildings with infill walls and bare frames. They calculated and compared the horizontal rigidity, ductility and energy dissipation capacities of infill walls and frames. Govindan et al. found twice as high bearing capacity of infilled walls, five times higher rigidity and 2.6 times smaller displacement ratio at the top of the frame. Güler et al. (2008), performed a numerical analysis of data collected from an experimentally vibrated building, in which infill walls were defined as diagonal compression struts. Korkmaz et al. (2007) performed pushover analysis on a 3-story R/C frame structure with different amount of masonry infill walls using diagonal strut approach. Pushover curves were obtained for the structures using nonlinear analyses option of commercial software SAP2000. The effects of irregularities were determined in the structural behavior under earthquake. Hossein Mostafaei & Toshimi Kabeyasawa (2004) achieved three dimensional non-linear time history analyses for both bare frame and infilled frame in order to obtain an analytical answer for the performance of an existing building and an approach was developed to model masonry infill walls with or without opening. Kappos, A.J & Panagiotopoulos, CG. (2003) performed extensive analysis of typical R/C building including brick masonry infill walls arranged either regularly or irregularly. A nonlinear constitutive law was used for describing the contribution of infills with a diagonal strut model. Pereira et al. (2009) conducted a parametric study of pushover analyses of a RC frame of an office building to represent the influence of the masonry infill panels using three commercial software packages (SAP 2000, SeismoStruck and MIDAS/CIVIL). Due to length and location of the plastic hinges forming near the end of the structural elements and different loading patterns, the structural behavior and non-linear capacity curves of the RC frame were also studied.

In this study, the effect of infills on seismic performance has been investigated employing the nonlinear static analysis using commercial SAP 2000 package.

2 THE INFLUENCE OF DIFFERENCE EQUIVALENT STRUT MODELS ON THE LATERAL LOAD BEARING CAPACITY

Experimental and theoretical remarks have showed that a diagonal strut with appropriate geometrical and mechanical characteristics could simulate the behavior of infill walls. Polyakov (1960) first suggested the possibility of considering the effect of the infilling in each wall as equivalent to diagonal bracing. Holmes (1961) replaced the infill by an equivalent pin-jointed

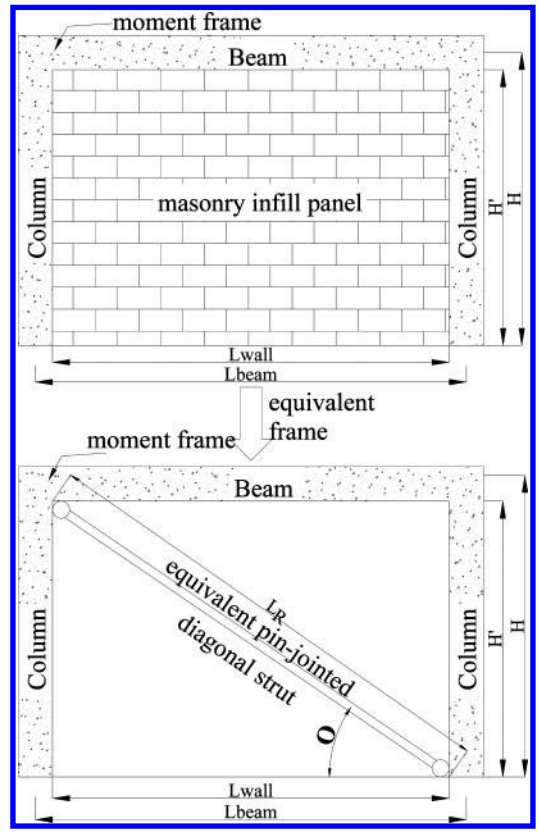


Figure 1. Equivalent strut model for masonry infill walls.

diagonal strut made of the same material and having the same thickness as the infill wall and a width equal to one third of the infill diagonal length (L_R) (Figure 1).

Stafford Smith (1966) and Stafford Smith & Carter (1969) suggested two pin- connected equivalent diagonal struts related the width of the equivalent diagonal strut to the infill/frame contact lengths using an analytical equation. Proposed model based on the elastic theory and frame/infill contact length has been related the effective width of the diagonal strut with a dimensionless relative stiffness parameter, λ:

$$\lambda_h = \sqrt[4]{\frac{E_{wall} \times t \times \sin(2\theta)}{4 \times E_{concrete} \times I_{column} \times H}} \quad (1)$$

where, E_{wall} is the modulus of infill, t is the thickness of infill, θ is the angle between diagonal and horizontal of infill, H is the height of infill (Fig.1). Based on the frame/infill contact length, alternative proposals for the estimation of the equivalent strut width are given in Table 1.

In this study, Eqs.(2–8) are used to simulate the mechanical behavior of infill walls considering compression failure mode. Geometrical properties together with the contact detail of sample 2D

Table 1. Effective width of an equivalent strut.

Holmes (1961)	$Weq = \frac{L_R}{3}$	(2)
Smith &Carter (1969)	$Weq = 0.58 \times \left(\frac{1}{H'}\right)^{-0.445} \times \left(\lambda_h H\right)^{0.335 \times L_R \times \left(\frac{1}{H'}\right)^{0.064}}$	(3)
Mainstone (1971)	$Weq = 0.175 \times L_R \times \left(\lambda_h H\right)^{-0.4}$	(4)
Liaw &Kwan (1984)	$Weq = \frac{0.95 \times H' \times \cos\theta}{\sqrt{\lambda_h \times H}}$	(5)
Decanini &Fantin (1986)	$Weq = \left(\frac{0.748}{\lambda_h} + 0.085\right) \times L_R$	(6)
Paulay &Priestley (1992)	$Weq = \frac{L_R}{4}$	(7)
Durrani &Luo (1994)	$Weq = \gamma \times L_R \times \sin 2\theta$ $\gamma = 0.32 \times \sqrt{\sin 2\theta} \times \left[\frac{(H')^4 \times E_{wall} \times t}{m \times E_{concrete} \times I_{column} \times H}\right]^{-0.1}$ $m = 6 \times \left[1 + \frac{6 \times E_{concrete} \times I_{beam} \times H'}{\pi \times E_{concrete} \times I_{column} \times L'}\right]$	(8)

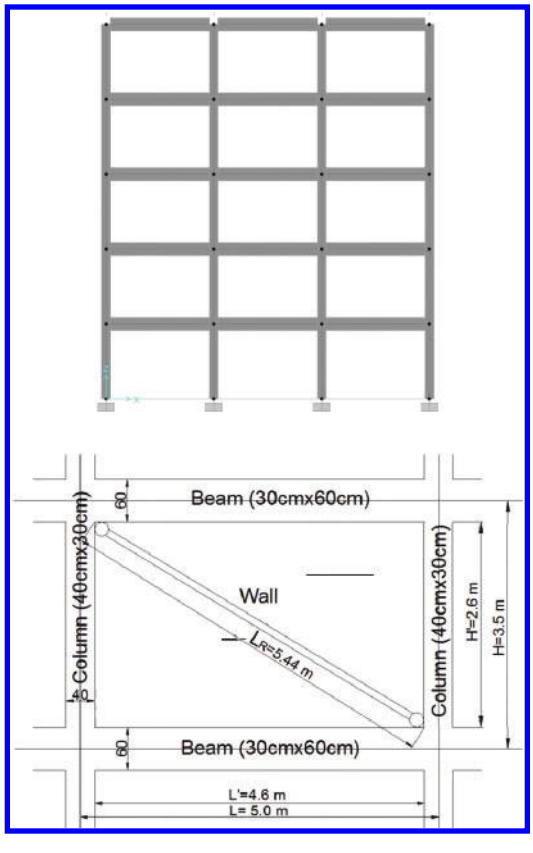


Figure 2. Sample 2D frame.

Table 2. Mechanical properties.

	Compressive strengths (MPa)	Modulus of Elasticity (MPa)
Frame	25 MPa	30250 MPa
Wall	2.5 MPa	6000 MPa

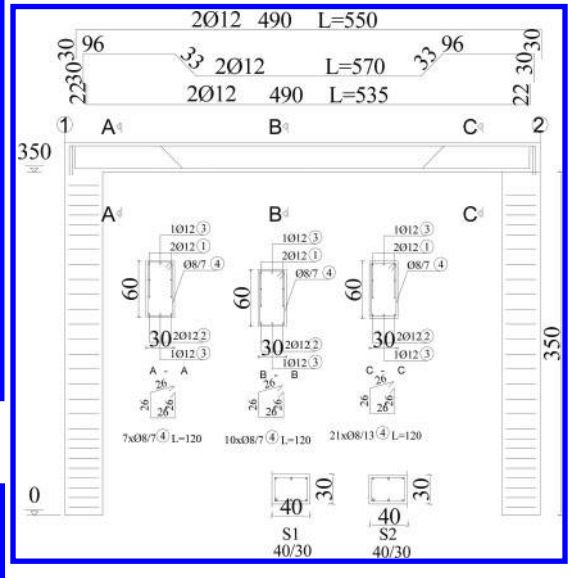


Figure 3. Reinforcement detail.

infilled frame are depicted in Figure 2 and mechanical properties are given in Table 2.

Furthermore, considering unreinforced wall with the effective width according to different researchers (Table 1), sample 2D frame system is modeled and nonlinear load-deformation characteristics of individual elements of the structure is formed. All frames were designed in accordance with Turkish Seismic Code (TEC 2008) for peak ground acceleration equal to 0.40 g, a medium soil and a high ductility class. Reinforcement details are depicted in Figure 3.

The pushover analyses were then performed with the following assumptions. The vertical distribution of the horizontal forces was always assumed according to an inverted triangle shape. Beams and columns were simulated with Takeda-type non-linear elements. All infills were simulated using equivalent diagonal struts with force-displacement curves (Fig. 4). The initial periods of vibration obtained for the different numerical models with different effective width predictions (Eqs.2–8) are reported in Figure 5. Finally, pushover curves are depicted in Figure 6 for comparison.

Furthermore, the change in wall thickness is also investigated throughout of this study. In this context, struts are modeled using Mainstone (1971) approach

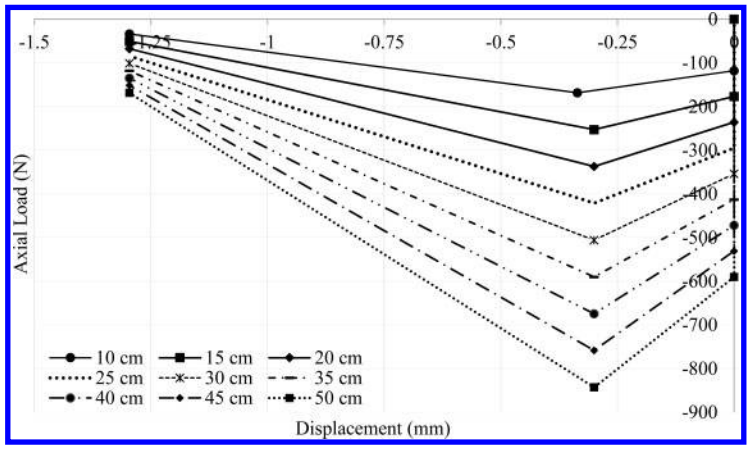


Figure 4. Force-displacement curves of infill (Ersin, 1997, Karasu, 2011).

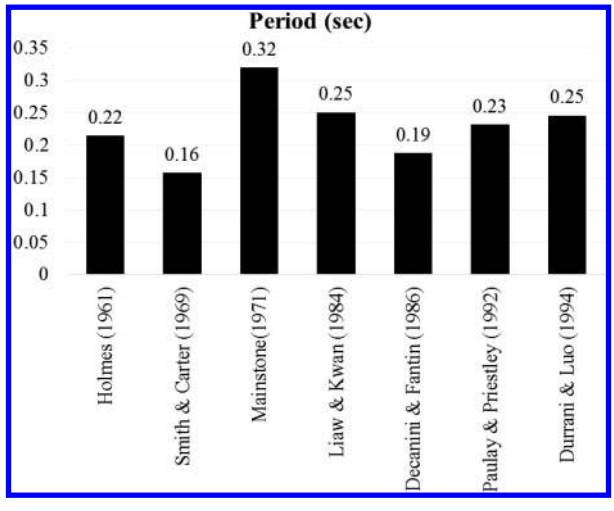


Figure 5. Natural periods of vibration.

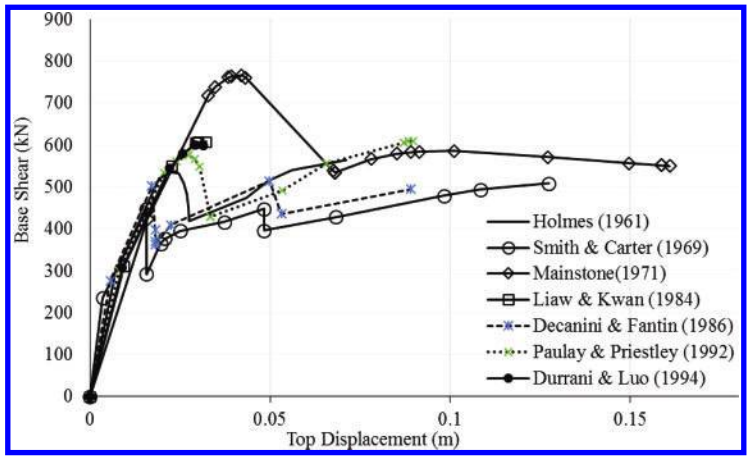


Figure 6. Pushover curves.

Table 3. Variation in the wall thickness.

Thickness (m)	0.00	0.10	0.15	0.20	0.25	0.30	0.35	0.40	0.45	0.50
Effective widths (m)	–	0.55	0.52	0.51	0.50	0.49	0.48	0.48	0.47	0.47
Period (s)	0.61	0.36	0.34	0.33	0.32	0.32	0.31	0.31	0.31	0.31

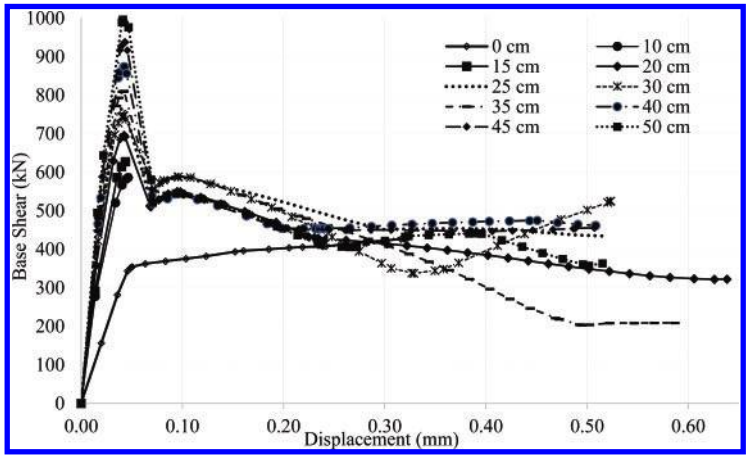


Figure 7. Pushover curves for different wall thickness.

proved to be the most popular over the years because of the ease with which it can be implemented practically into FE models. Considered applicable thicknesses, calculated effective widths and natural periods are given in Table 3. Pushover curves are than depicted in Figure 7 for comparison purposes.

3 CONCLUSIONS

The parametric analyses in this study aims to establish the influence of the modeling concepts of masonry infill mechanism on the performance of the structure to gather with the changes in wall thickness. It has therefore been shown that the establishment of masonry infill is always beneficial in terms of the energy dissipation (Figs.6,7), but depends on the choice of the mechanical modeling approaches which led to simulate the wall behavior accurately. In Figure 6, except Smith and Carter (1969), all curves look similar; when the first crack occurs in walls, a brief descending arises in total base shear of the structure. This is the expected effect for the infill mechanism on the lateral load bearing capacity of the whole structure. Same behavior can also be seen in Figure 7, for the case of increment in wall thickness.

REFERENCES

Altın, S., Ersoy, U., & Tankut, T. 1992. Hysteretic Response of Reinforced Concrete Infilled Frames, *Journal of Structural Engineering*, Vol. 118, No. 8, pp. 2133–2150.

Amanat, K.M. & Hoqueb, E. 2006. A rationale for determining the natural period of RC building frames having infill, *Engineering Structures*, Vol. 28, No. 4, pp. 495–502.

Asteris, P.G. 2003. Lateral Stiffness of Brick Masonry Infilled Plane Frames, *Journal of Structural Engineering, ASCE*, Vol. 129, No. 8, pp. 1071–1079.

Aytun, A. 1972. The Experimental Measurement of Structures' Natural Vibration Periods, *Türkiye' de Deprem Sorunu ve Deprem Mühendisliði Sempozyumu*, Ankara (in Turkish).

Bayülke, N. 1998. What is Period of a Structure? Which period of structure should be used during the design phase" *Turkish Chambers of Civil Engineers*, *Ankara Şubesi Bülteni*, Ankara (in Turkish).

Bounopane, S.G. & White, R.N. 1999. Pseudodynamic Testing of Masonry Infilled Reinforced Concrete Frame, *Journal of Structural Engineering*, Vol. 126, No. 6, pp. 578–589.

Decanini, L.D. & Fantin, G.E. 1986. Modelos simplificados de la mamposteria incluida en porticos. Caracteristicas de rigidez y resistencia lateral en estado limite. *Jornadas Argentinas de Ingenieria Estructural*, Argentina, Vol. 2, 817–836.

Dolšek, M. & Fajfar, P. 2008. The effect of masonry infills on the seismic response of a four-storey reinforced concrete frame a deterministic assessment, *Engineering Structures*, Vol. 30, No. 7, pp. 1991–2001.

Dowrick, D.J. 1987. Earthquake Resistant Design for Engineers and Architects, *John Wiley & Sons*, New York.

Durrani, A.J. & Luo, Y.H. 1994. Seismic Retrofit of Flat-slab Buildings with Masonry Infills. *NCEER workshop on seismic response in Masonry Infills*, Tech. Report NCEER-94-0004, 2004.

Ersin, U.D. 1997. Küçük Titreşim Ölçümleri ve Dolgu Duvarlarının Mekanik Modele Yansıtılması, *Yüksek Lisans Tezi*, *ITÜ Fen Bilimleri Enstitüsü*, Istanbul.

Govindan, P., Lakshmipathy, M., & Santhakumar, A.R. 1986. Ductility of Infilled Frames, *Journal of American Concrete Institute*, July–August, pp. 567–576.

Güler, K., Yüksel, E., & Koçak, A. 2008. Estimation of the Fundamental Vibration Period of Existing RC Buildings in Turkey Utilizing Ambient Vibration Records, *Journal of Earthquake Engineering*, Vol. 12, No. S2, pp. 140–150.

Holmes, M. 1961. Steel frames with brickwork and concrete infilling", *Proc., Instn. Civ. Engrs*., London, 2(19), 473–478.

Hong, H., Guo-Wei, M., & Yong, L. 2002. Damage Assessment of Masonry Infilled RC Frames Subjected to Blasting Induced Ground Excitations, *Engineering Structures*, Vol. 24, No. 6, pp. 799–809.

Kadir, M.R.A. 1974. The structural behavior of masonry infill panels in framed structures, *PhD thesis*, University of Edinburgh.

Kappos, A.J. & Panagiotopoulos, C. 2003. Inelastic static analysis of infilled R/C buildings", *ICCES'03 (Corfu, Greece, July 2003)*, CD ROM Proceedings.

Karasu, T.O. 2011. Performance based analysis of RC building which have soft story irregularities according to TSC2007, *M.D. thesis*, Celal Bayar University.

Korkmaz, K.A., Demir, F., & Sivri, M. 2007. Earthquake Assessment of RC Structures with Masonry Infill Walls, *International Journal of Science & Technology*, (2), 155–164.

Liaw, T.C. & Kwan, K.H. 1984. Nonlinear behavior of non-integral infilled frames. *Comput. Struct.*, 18, 551–560.

Mehrabi, A., Shing, P.B., Schuller, M.P., & Noland, J.L. 1996. Experimental Evaluation of Masonry Infilled RC Frames, *Journal of Structural Engineering*, 122(3), pp. 228–237.

Mainstone, R.J. 1971. On the stiffnesses and strengths of infilled frames, *Proc., Instn. Civ. Engrs*., Supp. (iv): 57–90.

Mostafaei, H. & Kabeyasawa, T. 2004. Effect of Infill Masonry Walls on the Seismic Response of Reinforced Concrete Buildings Subjected to the 2003 Bam Earthquake Strong Motion : A Case Study of Bam Telephone Center Bull. *Earthq. Res. Inst.Univ. Tokyo*, 79, 133–156.

Palyakov, S.V. 1956. On the Interactions between masonry filler walls and enclosing frame when loaded in *the plane on the wall", Translations* in Earthquake Engineering, Research Institute, Moscow.

Paulay, T. & Priestley, M.J.N. 1992. Seismic Design of Reinforced Concrete and Masonry Buildings, *John Wiley & Sons*, New York.

Pereira, V.G., Barros, R.C., & César, M.T. 2009. A parametric study of a r/c frame Based on "pushover" analysis" 3rd International Conference on Integrity, Reliability and Failure, Porto/Portugal, 20–24 July 2009.

Polyakov, S.V. 1960. On the interaction between masonry filler walls and enclosing frame when loading in the plane of the wall, *Translation in earthquake engineering, Earthquake Engineering Research Insitute*, 36–42.

Puglisi, M., Uzcategui, M., & Flórez-López, J. 2009. Modeling of masonry of infilled frames, Part II: Cracking and damage, Engineering Structures, Vol. 31(1), pp. 119–124.

SAP2000 User's Manual, (2005) Structural Analysis Program Advanced Version 10.0.1, Computers and Structures Inc.

Smith, B.S. 1966. Behavior of square infilled frames, *J. Struct. Div., ASCE*, ST1, 381–403.

Smith, B.S. & Carter, C. 1969. A method of analysis for infilled frames", Proc., *Instn. Civ. Engrs*., 44, 31–48.

Sivri, M., Demir, F., & Kuyucular, A. 2006. The effects of Infill Walls, Frame Structures on the Earthquake Behavior and Failure Mechanism, *S.D.Ü Fen Bilimleri Enstitüsü Dergisi*, pp. 109–115.

Research and Applications in Structural Engineering, Mechanics and Computation – Zingoni (Ed.)
© 2013 Taylor & Francis Group, London, ISBN 978-1-138-00061-2

Sisal reinforced cement-based masonry units

G. Coetzee & W.P. Boshoff
Department of Civil Engineering, Stellenbosch University, South Africa

R.D. Toledo Filho
Department of Civil Engineering, Universidade Federal do Rio de Janeiro, Brazil

ABSTRACT: Sisal Fibre Reinforced Concrete (SFRC) blocks has been proposed as a construction material that has the potential to address the economic and environmental issues typically associated with the low cost housing sectors of developing nations. Sisal, a natural fibre, is widely available in Brazil and East Africa. A high-alkalinity environment and the presence of Ca^{2+} causes rapid degradation of the durability properties of sisal fibre. This work addresses the strength and volumetric properties of SFRC blocks. Sisal fibres of length 10 mm were used to reinforce 290 × 140 × 90 mm concrete blocks. Two concrete matrices were developed. One matrix contained cement and fly-ash. To ensure durability, the second matrix had 10% of its cement content substituted by Condensed Silica Fume (CSF). Each matrix was reinforced with 0, 0.5 and 1% fibre by volume. The results showed a decrease in strength with an increase in fibre content. An increase in strength was also observed in blocks containing fibres and 10% CSF. Drying shrinkage tests revealed an increase in shrinkage strain with an increase in fibre content and CSF. Samples were also subjected to four cycles of wetting and drying to establish the effect on dimensional stability. The addition of fibres and CSF was found to improve dimensional stability significantly.

1 INTRODUCTION

A lack of adequate housing is not a problem restricted to Africa, nor to developing countries. Worldwide, there are a reported one billion people living in slums (United Nations, 2007). In South Africa, where 12 million people (or 23% of the population) live in slums (Statistics South Africa, 2012), the low cost housing (LCH) sector has been plagued by problems such as inadequate structural performance, poor policies and management and a lack of acceptance by beneficiaries. The need has arisen for a sustainable, economically viable building material that uses the existing construction methods and political structures.

Natural fibres have been used as reinforcing material, in some way or another, since man started building shelters. In more recent years, since the popularization of plastics and other synthetic materials, natural fibres have come to be considered a traditional building material. With mounting pressure worldwide to develop economically viable, sustainable construction materials, there has been growing interest in the development of new materials that enhance the optimal usage of natural resources, particularly renewable resources.

Sisal fibre, extracted from the leaves of the *Agave sisalana* plant, has been identified as a natural fibre with the potential to be used as reinforcement in cementitious matrices. The plant is widely cultived in Brazil, Tanzania, Kenya and China and smaller plantations exist in Mozambique and the northwest of South Africa (FAO, 2009).

The chemical composition and structure of a natural fibre is quite complicated. Rong et al. (2001) have stated that a fibre cell is essentially a composite in which cellulose microfibrils are embedded in a hemicellulose and lignin matrix. Microfibrils are helically wound around the fibre axis. The microfibular angle and lignin content essentially determine the amount of energy needed to uncoil a fibril, thus determining its strength. A single fibre can consist of many cells that are linked together through the middle lamella, which consists of hemicellulose and lignin. According to Bentur & Mindess (2007) both lignin and hemicellulose can easily be broken down in an alkaline environment, such as found in the pore water of concrete.

Sisal fibre bundles tend to have lengths of between 600 and 1000 mm and widths of between 50 and 400 μm (Müssig, 2010). The tensile strength of sisal ranges between 280 and 750 MPa while the modulus of elasticity is in the range of 9.4-26 GPa. Sisal fibre has a moisture absorption of between 60 and 110% by mass (Bentur & Mindess, 2007; Müssig, 2010). These properties can vary greatly by region of cultivation, extraction practices and age of leaves being harvested.

Natural fibre reinforced concrete (NFRC) tends to undergo an ageing process in which it loses strength

and toughness, especially in humid environments (Silva et al., 2010). The ageing process is mainly due to fibre mineralisation, caused by the migration of hydration products such as $Ca(OH)_2$, to the fibre structure. As mineralisation increases, the failure mechanisms of NFRC tends to shift from fibre fracture to fibre pull-out.

Efforts to improve the durability of NFRC have shown promising results (Tolêdo Filho et al., 2002; Mohr et al., 2005; Gram, 1988). To ensure durability, various matrices have been developed that are free of calcium hydroxide, through the partial substitution of cement content with pozollanic materials such as condensed silica fume (CSF) and metakaolin by as much as 50% by mass.

To address the environmental, structural and economical issues typically associated with low cost housing in South Africa, it was proposed to investigate the mechanical and dimensional properties of sisal fibre reinforced concrete blocks. Blocks of size $290 \times 140 \times 90$ mm, as is often used for LCH applications in inland regions of South Africa, were produced and subjected to compression and drying shrinkage tests as well and dimensional stability tests during cycles of wetting and drying.

2 EXPERIMENTAL PROGRAM AND SETUP

2.1 *Materials and processing*

2.1.1 *Matrix*

The matrix was designed using Mauá CPV-ARI cement, manufactured by Lafarge Brazil. It is fast reacting cement that reaches a relatively high strength in the first days of application. The clinker used is more or less the same as that used for conventional cement, although it stays in the mill for longer. CPV-ARI typically contains very little or no pozzolanic additives (Cimento.org, n.d.). It is comparable to the CEM I type found in South Africa. The ARI designation refers to a minimum 7 day compression strength of 34 MPa.

For the present work two different matrices were developed: one containing CSF to improve durability and one reference matrix. Both matrices were further reinforced with 0, 0.5 and 1% sisal fibre by volume, respectively (see Table 1). The fibre length used was 10 mm. Both matrix types contained a partial substitution of 30% of cement with fly-ash, in order to lower the matrix cost. The fly-ash used for this research was Pozofly, provided by Comércia de Conzas Lima Ltda.

Table 1. Mix proportions

Mix	Content [%]			
	Cement*	Fly-ash*	CSF*	Fibre**
M1	70	30	0	0
M2	60	30	10	0
M3	70	30	0	0.5
M4	60	30	10	0.5
M5	70	30	0	1
M6	60	30	10	1

*% by mass of total cementitious content
**% by volume of concrete

By replacing 10% of the cement content of a matrix with CSF, a matrix with a lowered calcium hydroxide content was developed. Silmix Sílica Ativa condensed silica fumes (CSF), provided by Indústria Brasileira, was used for this research.

The sand used had a relative density of 2.64 and a fineness modulus (FM) of 2.68. A nominal stone size of 9.5 mm was used with a relative density of 2.68 and a FM of 5.7.

The mix proportions were based on various literature sources and trial mixes (Holcim, 2004; Hydraform, 2006; Government of India Development Institute, 2011). All sources specified a low cement content leading to a very dry mix, which is acceptable for producing reasonable strength blocks cheaply. M1, M3 and M5 were all essentially the same (no CSF content), with the only difference being the fibre content. They all had a cementious material content ratio by weight of 7:3 (cement:fly-ash). Similarly, M2, M4 and M6 had the same mix (10% CSF content), with the fibre content being the varying factor. They had a cementitious content ratio of 6:3:1 (cement:fly-ash:CSF). All mortar matrices had a design mix ratio of 1:4.2:2.8:0.62(cementitious material:sand:stone: water by mass).

2.1.2 *Sisal fibre*

The fibres used in this research were obtained from the Municipality of Valente situated in the state of Bahia in the northwest of Brazil. The fibres were provided by the Association for Sustainable Development and Solidarity of the Sisal Region.

The leaves of the sisal plant are smooth with a length and width of about 150 and 10 cm, respectively. To obtain fibres, the leaves were cut and decorticated, after which they were beaten to remove excess decortication waste and left to dry. Lastly the fibres were made into bales.

The fibre bundles used had a length of between 90 and 100 cm. The surface of the fibres showed signs of waste from the extraction process, such as sugar and mucilage. To prepare the sisal fibre for use in concrete reinforcement it was washed in hot water (80–100°C) for two hours followed by a 56 hour drying period in a room held at a constant temperature of 40°C.

After drying, the fibres were brushed with a nail brush to align and separate fibres, after which they were cut to length of 10 mm with a paper guillotine. It should be noted that the brushing process resulted in a fibre loss of around 30% by mass. The fibre used had an average relative density of 1.1.

2.1.3 *Block production*

All matrices were mixed using a pan mixer. Batches of 18 to 24l were mixed at a time, producing 5 to 8 blocks. The aggregate was dry mixed for one minute, after which all cementitious material was added and

allowed to mix for another 30 seconds. For the mixes containing fibres, the fibres were loosened by hand and added to the drum in small volumes to prevent fibre balling. The mixture was allowed to mix for a further 30 seconds. The water was slowly added to the rotating drum and the final mix was allowed to mix for a further 2 minutes.

All test specimens were prepared with dimensions of 290×140×90 mm. Wet concrete was added to steel moulds in four thin layers and hand compacted with a small trowel following each new layer. Using a thick steel plate and an Amsler compression testing machine, each block was compressed to 500 kPa while still wet. Shrinkage test samples were produced similarly, using moulds of 280 × 70 × 70 mm. Blocks were allowed to cure for 12 hours in the moulds at 100% relative humidity (RH), after which they were removed and stored in a curing chamber at 100% RH and 23 ± 1°C.

2.2 *Test methods*

2.2.1 *Compression test*

A Shimadzu UF-F 1000 kN machine was used to determine the compression strength of blocks at 28 day age. The tests were performed under displacement control at a crosshead displacement rate of 3 mm/min. Five specimens of each mix type (M1-M6) were tested. Before testing, blocks were capped using capping mortar and a suitable table. Blocks were tested within 5 minutes of removal from the curing chamber. They were orientated so that the 290×140 mm faces lay horizontal.

2.2.2 *Drying shrinkage test*

Four specimens of each matrix type was tested, starting at an age of 28 days. Drying shrinkage tests were performed over a two month period for all samples. The environment where storing and testing was done was held at a temperature of 23 ± 1°C and relative humidity of 60±5%. During production all samples were embedded with 25 mm steel pins in the middle of the two 70 × 70 mm faces that protruded the faces by approximately 5 mm.

Shortly after removal from the curing chamber each sample was wiped with a damp cloth and weighed. A shrinkage testing rig was set up and the measuring device was zeroed using a metal calibration rod with a length of 295 mm. Each sample was measured pin to pin and the results were tabulated. The samples were stored on a rack, resting on two thin metal wires to allow for free drying shrinkage with minimum friction. For the first two days, measuring was done each hour within office hours. In the following 5 days samples were measured three times a day. In the next two weeks measuring was done once a day and over the remaining weeks, once every three days. In total the test was run for two months.

2.2.3 *Dimensional stability*

Three samples of each matrix type was tested for dimensional stability. Each block was cut to a length of 270 mm (from 290 mm). Three days prior to reaching an age of 28 days, the blocks were allowed to dry in an oven at 60°C for 48 hours. After drying, blocks were moved to a storage room at 34°C and allowed to cool down for 24 hours after which they were weighed.

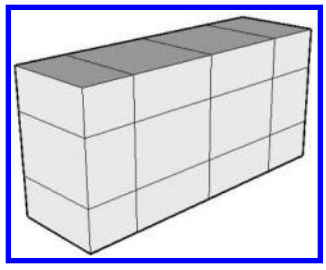


Figure 1. Block segments used for measuring dimensional stability.

Using a marker each block was subdivided into 12 segments as shown in Figure 1. A Vernier calliper was used to measure the lengths, widths and heights of the segments along the edges of the block where possible. Where impossible, linear interpolation was used to estimate values.

The blocks were then soaked in water for 48 hours at 34°C. This was deemed sufficient time to completely saturate the blocks. After removal, the blocks were wiped with a damp cloth so as to remove any excess surface moisture. The dimensions and mass of the blocks were once again measured.

After measurements, the blocks were dried in a wind tunnel at 34°C for 48 hours. This was deemed sufficient to properly dry out the blocks. The dimensions and weight of the blocks were measured once again and the whole process was repeated three more times. In total there were four wet and four dry values for each sample.

The Qhull algorithm (Qhull.org, 2012), used for calculating the volume of a convex hull, was used to determine the volume of each of the 12 segments. The volume of the block after each wet or dry cycle was taken as the sum of the volume of the segments.

3 RESULTS

3.1 *Compression test*

Typical force-displacement curves for the different matrix types obtained from the compression tests are shown in Figure 2.

The average compressive strength for each matrix type are shown in Figure 3. The dotted lines surrounding the curves represent the standard deviation band (distance between standard deviation above and below average). Also, the standard deviation (σ) and coefficient of variation (CoV) are displayed on graph.

3.2 *Drying shrinkage test*

The shrinkage strain was calculated by dividing the change in length at each time interval by the original

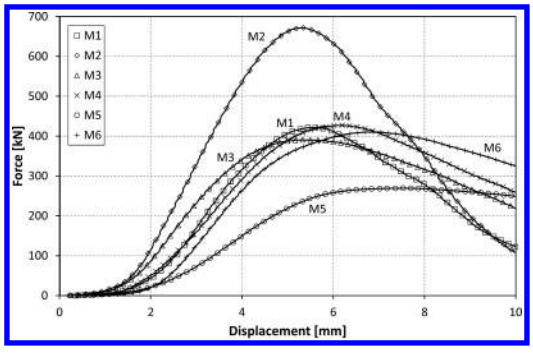


Figure 2. Force-displacement curves for all matrices.

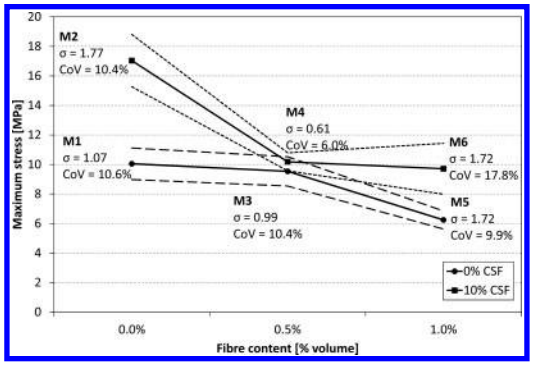


Figure 3. Average maximum compressive stress.

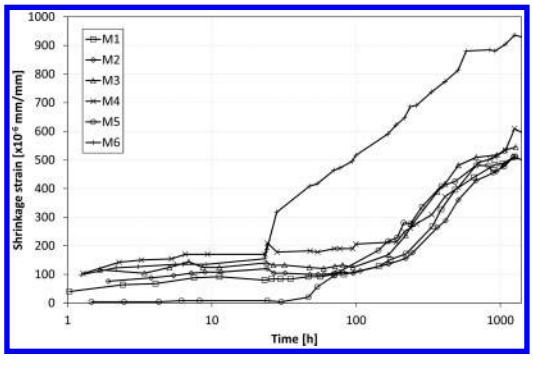


Figure 4. Shrinkage strain-time curves for all matrices.

length between the two metal pins. Typical shrinkage-time curves for each matrix type are presented on a logarithmic scale in Figure 4.

Figure 5 shows the average maximum shrinkage for all six matrices after two months.

3.3 *Dimensional stability*

The volume for each block during each cycle was calculated and the results are represented as a percentage of change in volume relative to the original dry volume (D1). The average change in volume for each matrix type was determined and the results are depicted in Figures 6 and 7.

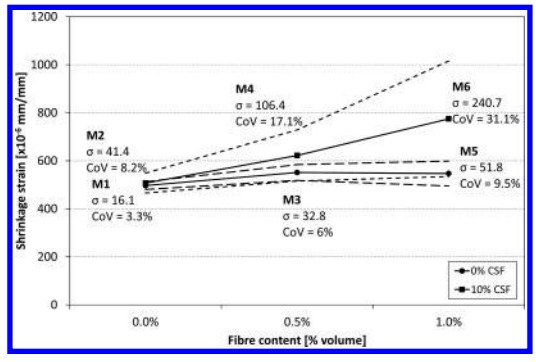


Figure 5. Average maximum drying shrinkage after two months.

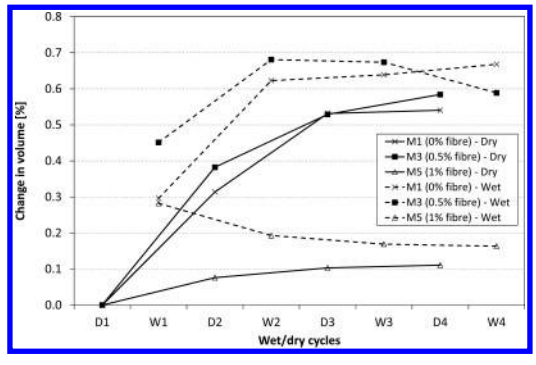


Figure 6. Average change in volume during wet/dry cycles (mixes with 0% CSF).

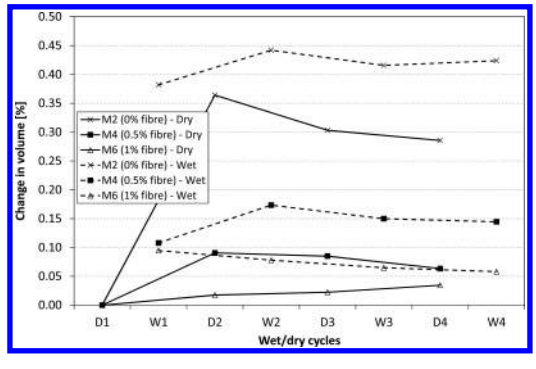


Figure 7. Average change in volume during wet/dry cycles (mixes with 10% CSF).

4 DISCUSSION

4.1 *Compression test*

Considering Figures 2 and 3 it is clear that there is a strong correlation between the compressive strength and fibre content. As fibre content increased, strength decreased as well. From Figure 2 it can be seen that for mixes containing CSF, the stiffnesses during loading (linear part of curve before reaching maximum) reduced with an increase in fibre content (see curves

M2, M4 and M6). The same is true for mixes without CSF (see curves M1, M3 and M5). Also, mixes containing CSF tended to have a higher strength and stiffness than similar fibre volume mixes without CSF. Blocks with higher fibre contents did exhibit higher ductility. The ductility was however not quantified.

Figure 3 shows that, as fibre content increases, the extra strength provided by the addition of CSF decreased from about 70% (0% fibre) to 7% (0.5% fibre) and then increased again to 56% as fibre content is increased to 1%. For 0% CSF mixes, the addition of 0.5% and 1% fibre reduced the stress by about 5 and 38%, respectively. Similarly, the reduction in stress of 10% CSF mixes was about 40 and 43%, respectively. The variation of all mixes was in the region of 10%, with the exception of the M6 results (CoV of 17.8%).

The loss in strength and stiffness with an increase in fibre content could be attributed to the fibre's tendency to increase the air void content and therefore the porosity of the concrete. This results in a lower the strength and stiffness. All strengths are however within the typical required specification for masonry units.

4.2 *Drying shrinkage test*

All matrices displayed a fairly constant shrinkage slope (rate at which shrinkage happens) for the first 50–160 hours (Figure 4). This rate increased significantly up to a time of 500–1000 hours, where after the slopes decreased slightly. It can be concluded that the addition in fibre increased the initial rate of shrinkage. After the first rate change, the effect of added fibres diminished and there seemed to be no significant difference between shrinkage rates. Similarly, the addition of CSF only significantly increased the initial rate of shrinkage, but after the first rate changes the effect became substantially less. The shrinkage result of M6 is seen as an outlier.

Figure 5 shows that in blocks without CSF, the addition of 0.5% fibres led to an increase of 11% in drying shrinkage after two months. Increasing the fibre content to 1% had no significant effect on the total drying shrinkage. For the blocks containing CSF, an addition of 0.5% fibre led to an increase in drying shrinkage of 22%. Similarly, increasing the fibre content to 1% led to a further increase in shrinkage of 24%. Furthermore, the blocks containing CSF showed a considerably higher variation in total shrinkage than the blocks without CSF.

Silva et al. (2010) have stated that the drying shrinkage of a cement matrix is related to the magnitude of its porosity and to the size, shape and continuity of the capillary system in the hydrated cement paste. The porous nature of the fibres creates more paths through which moisture can escape. The addition of sisal fibres therefore increases the porosity of the matrix which leads to higher shrinkages.

Siddique & Khan (2011) mentioned that the substitution of up to 15% of cement (by mass) for CSF in a cement matrix does not have a significant effect on drying shrinkage. This corresponds to the results for matrices without fibres, where the difference in shrinkage between M1 and M2 was less than 2%. However, with the addition of fibres the difference between matrices with and without fibres becomes larger. At 0.5% fibre content the shrinkage was 13% more for the samples containing CSF and the difference increased to 41% at 1% fibre content.

4.3 *Dimensional stability*

Figure 6 shows that the average curves for mixes M1 and M3 have a similar shape for both wet and dry cycles, although the initial change in volume of M3 after the first wetting cycle was about 52% higher than that of M1. Both dry and wet cycle volume changes increased rapidly during the first couple of cycles, but stabilised soon after.

The results of M5 (1% fibre) showed a very different trend. The initial increase in volume change was slower for dry cycles and for wetting there was a decrease in volume change. After a couple of cycles the volume change stabilised. After four cycles there was a difference in change in volume between wet and dry cycles of about 0.05%.

The final average wet change in volume of M5 was 0.163%. For M3, this value was 0.589% (3.6 times more) while the value for M1 was 0.668% (4.1 times higher).

For the average dry volume changes the final value for M5 was 0.111%, for M3 it was 0.584% (5.3 times higher) and for M1 it was 0.541% (4.9 times higher).

Figure 7 shows the average change in volume of mixes with 10% CSF. The blocks containing CSF showed a trend where there was an initial increase in volume during wet cycles, but a decrease as cycles continued. There is a clear decrease in change in volume as the fibre content of the blocks increases. The final average wet change in volume of M6 was 0.058%. For M4, this value was 0.144% (2.5 times more) while the value for M2 was 0.423% (7.3 times higher).

For the average dry volume changes the final value for M6 was 0.034%, for M4 it was 0.063% (1.8 times higher) and for M2 it was 0.285% (8.3 times higher).

For both matrix types (0 and 10% CSF content) there was a decrease in change of volume between wet and dry cycles with an increase in fibre content. Also, the initial change in volume decreased with an addition of fibre content.

Figures 6 and 7 show that at all fibre contents blocks with CSF displayed a smaller initial volume change, as well as a smaller difference between wet and dry blocks. The blocks without CSF and fibres had a 1.9 times higher change in volume for dry cycles than the blocks containing CSF. The final change in volume was about 1.6 times higher for wet cycles.

Similarly, at 0.5% fibre content the blocks without CSF had a 9.2 times higher change in volume for dry cycles and 4.1 times higher change for wet cycles. For blocks containing 1% fibre, the changes were 3.2 and 2.8 times higher, respectively.

It can be concluded that both an addition of fibre and CSF has a significant effect on the change in volumes during wet/dry cycles. Both additions tended to decrease the initial change in volume as well as the difference between wet and dry volumes, indicating that they improved dimensional stability.

5 CONCLUSION

The addition of short sisal fibres to a cementitious masonry unit does lead to a decrease in compressive strength and an increase in ductility. The addition of CSF to matrices did increase compressive strength, but the extent of the effect was lowered as fibre content increased.

Regarding the volumetric properties of blocks, mixed results were achieved. The addition of fibres led to an increase in total and rate of drying shrinkage, while the dimensional stability of blocks, after repeated wet-dry cycles, was significantly improved. The addition of CSF to matrices reduced pore sizes, leading to a significant increase in drying shrinkage and dimensional stability. Sisal fibre does seem to have a use as a means of dimensional stabilisation.

It was also shown that the use of sisal fibre as a cement content reducing material cannot be recommended. The study investigated blocks with fibre contents of 0.5 and 1% by volume and it was found that even at these low volumes the adverse effect on strength was significant. With respects to the results obtained in this research, the positive effects of volume that is added to concrete through the addition of fibre is diminished through the negative effect the fibre has on strength.

REFERENCES

Bentur, A. & Mindess, S., eds, 2007. Fibre reinforced cementitious composites. 2 edn. Oxon: Taylor & Francis.

Cimento.org, n.d. CP V-ARI – Cimento Portland de alta resistência inicial [Homepage of Cimento.org]. [Online] Avaible: http://www.cimento.org/index.php?option=com_content&view=article&id=109&Itemid=154 [Accessed 16 April 2012].

Development Institute: Government Of India, 2011. Project profile on cement concrete hollow blocks. Chennai: Ministry of MSME.

Food And Agriculture Organization, 2009. Jute, kenaf, sisal, abaca, coir and allied fibre- Statistics. Food and Agriculture Organization of the United Nations.

Gram, H.E., 1988. Durability of natural fiber in concrete. In: R.N. SWAMY, ed, Natural Fiber Reinforced Cement and Concrete. Glasgow and London: Blackie, pp. 143–172.

Holcim, 2004. The manufacture of concrete masonry units. Masonry Book. Holcim, pp. 80–91.

Hydraform, 2006. Vibraform Manual. Hydraform.

Mohr, B.J., Nanko, H. & Kurtis, K.E., 2005. Durability of kraft pulp fiber-cement composites to wet/dry cycling. Cement & Concrete Composites, 27, pp. 435–448.

Müssig, J., ed, 2010. Industrial Application of Natural Fibres – Structure, Properties and Technical Applications. 1 edn. West Sussex: Wiley.

Qhull.org, n.d. Qhull. 18 February, 2012. [Online] Available: http://www.qhull.org/ [Accessed 1 December 2012].

Rong, M.Z., Zhang, M.Q., Liu, Y., Yang, G.C. & Zeng, H.M., 2001. The effect of fiber treatment on the mechanical properties of unidirectional sisal-reinforced epoxy composites. Composites Science and Technology, 61, pp. 1438–1447.

Siddique, R. & Khan, M.I., 2011. Supplementary Cementing Materials. 1 edn. Heidelberg: Springer.

Silva, F., Tolêdo Filho, R.D., Melo Filho, J.A. & Fairbairn, E.M.R., 2010. Physical and mechanical properties of durable sisal fiber-cement composites. Construction and Building Materials, 24, pp. 777–785.

Statistics South Africa. 2012. Census 2011 – Fact sheet. Pretoria: Statistics South Africa.

Tolêdo Filho, R.D., Ghavami, K., England, G.L. & Scrinever, K., 2002. Development of vegetable fibre-mortar composites of improved durability. Cement & Concrete Composites, 25, pp. 185–196.

United Nations. 2007. The Millennium Development Goals Report. New York: United Nations.

Research and Applications in Structural Engineering, Mechanics and Computation – Zingoni (Ed.)
© 2013 Taylor & Francis Group, London, ISBN 978-1-138-00061-2

Structural design for earth buildings

A.C. Heath & P.J. Walker
BRE Centre for Innovative Construction Materials, Department of Architecture and Civil Engineering, University of Bath, Bath, UK

ABSTRACT: Earth (unfired clay) is used in construction around the world. Buildings can be constructed using compressed earth blocks, mud brick (adobe) or modern extruded earth masonry blocks. The alternative to masonry blocks is to construct as a monolithic structure as used for rammed earth and cob. Higher strength earth masonry systems can give advantages over lower strength alternatives as there is scope to utilise the flexural capacity and bond strength to provide similar structural capacity to fired masonry or concrete block alternatives while having lower embodied energy. Stabilisation of earth masonry can increase both strength and durability but this needs to be balanced with potentially greater environmental impact.

1 INTRODUCTION

Earth is one of the oldest building construction materials and is still in widespread use today, particularly in developing countries. While there are examples of earth building in wetter regions, such as the UK, areas with drier climates tend to have more vernacular earth buildings as earth is susceptible to water damage unless appropriately detailed or otherwise protected.

In 1994 it was estimated that nearly a third of the world's population still lived in a home built of earth (Houben and Guillaud, 1994). The majority of these earth dwellings were in developing countries and with the rapid urbanisation and population growth that has subsequently occurred, this proportion may have decreased, but is still a significant proportion of the world housing stock.

All masonry walls are required to support load, whether just the self-weight of the wall or applied permanent or variable actions. Earth masonry has many benefits over fired clay or concrete block masonry, including environmental sustainability, occupant health, building quality and cultural continuity (Morton, 2008, Minke, 2006) but can suffer from strength reduction with increasing moisture content (Heath et al., 2009, Jaquin et al., 2009). In order to design with these innovative materials, it is necessary to provide sufficient strength and durability while considering the environmental impact.

2 STRUCTURAL DESIGN

Some forms of earth construction (e.g. mud brick (adobe) or compressed earth blocks (CEB)) are similar to more conventional masonry structures where there are bricks/blocks and mortar, but with other forms such as cob and rammed earth, the wall is constructed monolithically resulting in different behaviour to walls with mortar joints.

The structural capacity of earth wall construction can be separated into its ability to carry vertical (compressive) loads or lateral (out of plane flexural or in plane racking) loads. As with other forms of masonry construction, the compressive strength is high compared with the tensile strength, leading to increased efficiency in compressive applications (such as walls, domes and arches) than in purely bending applications (such as beams or other spanning structures).

The analysis of earth buildings could be according to standard procedures such as Eurocode 6 (EN 1996) used in Europe, but the properties (strengths, etc.) will be very different and standard values for other masonry types should not be used. The standard test methods are also not necessarily appropriate and an increased material partial factor can be used to account for increased variability in properties and variations in moisture content.

All structural properties of earth are affected by the moisture content, as shown for a particular modern earth masonry system in Figure 1.

For this particular masonry system there is a sodium silicate based mortar which is stronger than the masonry units (Lawrence et al., 2010). As a result, the flexural strength of the masonry is similar to the flexural strength of the masonry units (blocks). The compressive strength of the masonry is lower than the units because of the increased height to width (aspect) ratio of the masonry.

2.1 *Compressive strength*

The compressive strength for earth masonry should always be presented as "standardised" values where the strength is corrected for the dimensions of the samples and correction factors are presented in masonry test standards. While the change in strength and stiffness

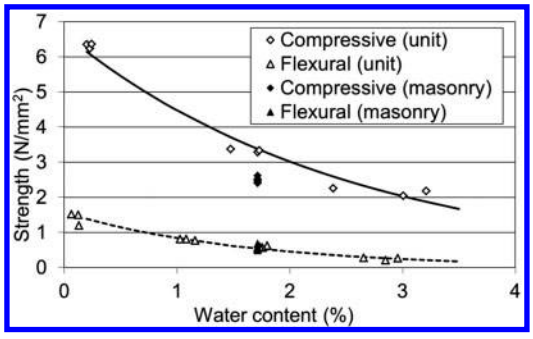


Figure 1. Decrease in strength with water content.

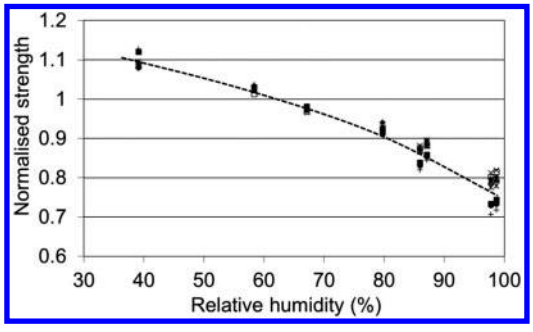


Figure 2. Effect of relative humidity changes on compressive strength of unstabilised earth blocks.

with changes in moisture content is important, it should also be viewed in the context of likely moisture contents to be experienced in a wall. Moisture may be added to a wall by an increase in the relative humidity, through wet trades during construction (mortar/render) or by accidental wetting (e.g. failure of a water pipe). While it is possible to predict the first two, it is not possible to predict the moisture content from accidental wetting, but detailing can help to minimise the risk of this occurring.

The effect of changes in relative humidity on earth masonry unit strength, for ten different commercially produced unstabilised earth masonry blocks, is illustrated in Figure 2. The information is presented with the compressive strength normalised to 65% relative humidity for each particular block type.

As shown, even at a very high relative humidity which is maintained for an extended period, the strength will not reduce to close to zero, showing that the walls are unlikely to collapse from being exposed to high relative humidity. For all of the 10 different block types, there is less than 30% strength reduction as the relative humidity increases from 65% to 97.5%.

A more onerous testing condition (such as immersion in water before testing) is inappropriate for unstabilised earth masonry as these materials should not be used in a situation where full saturation could occur. Immersion before testing can, however, be used for stabilised earth materials.

The Eurocode methodology uses material partial factors to quantify the reduction in strength as a

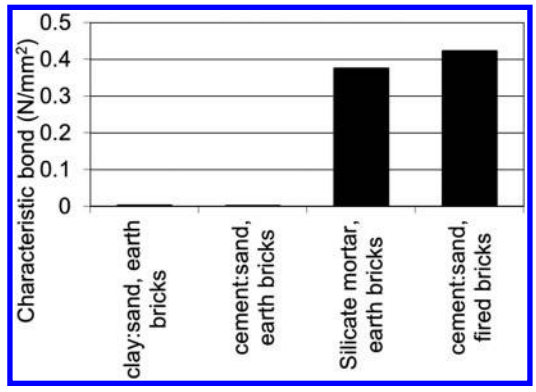


Figure 3. Bond strength of different mortars and unstabilised earth bricks.

result of variability in materials and construction, and of uncertainty in behaviour. Eurocode 6 specifies a minimum partial factor, γ_m, of 2.0 for Category II masonry (higher if perforated). While earth masonry is not included in Eurocode 6, it is recommended that γ_m is increased to at least 2.85 for unstabilised commercially produced earth masonry (very high quality control and low variability) to include the effect of a potential 30% strength reduction with increasing humidity shown in Figure 2.

For a more variable material such as rammed earth, Walker et al. (2005) recommend a minimum γ_m of 3.0 for experienced contractors with good quality control, increasing to 6.0 for contractors with limited experience with the material. In all cases these should always be applied while considering accidental wetting, and the resistance to erosion.

For materials produced under well controlled conditions and tested in a saturated state (such as cement stabilized CEB), the lower partial factors from Eurocode 6 for concrete blocks may be considered.

2.2 *Flexural strength*

Many traditional earth buildings have thick (300 mm or greater) walls and a large portion of their bending resistance comes from the self-weight of the walls. These walls often have sand/clay mortars which provide very little bond strength, as shown in Figure 3.

Included in Figure 3 is the characteristic bond strength for a cement mortar with earth bricks and fired clay bricks. The silicate mortar comprises a clay:sand mix with 8% by mass sodium silicate power with a molar ratio of 2.0 ($Na_2O{\cdot}2SiO_2$).

The thick walls of traditional earth construction can reduce available space and require additional material, thereby increasing costs and environmental impact. The structural requirements for flexural capacity are illustrated in Figure 4, showing how increased thickness results in a lower bond strength (flexural strength along bed joints) to provide the same lateral resistance.

As shown, with the wall thickness decreasing from 300 mm in traditional construction to 100 mm commonly used for concrete block and fired clay

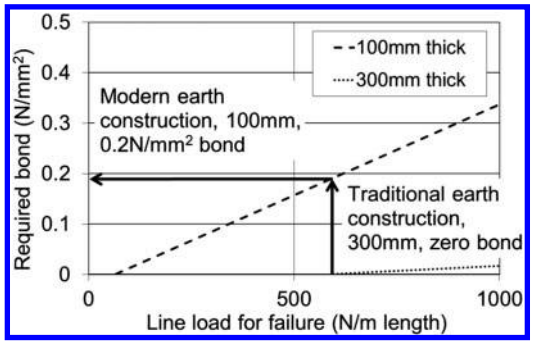


Figure 4. Required flexural strength to resist lateral loading for different thickness walls (no additional vertical loads applied).

masonry construction, the required bond strength increases from zero (typical design value for rammed earth or earth blocks with earth mortar) to approximately 0.2 N/mm^2 which is a typical characteristic value for 100 mm thick lightweight concrete blockwork in Eurocode 6.

As shown in Figure 3, the only mortar able to provide the required strength with 100 mm thick earth masonry is a sodium silicate based mortar. As sodium silicate is water soluble, when the wet mortar is applied to earth blocks, some silicate is transferred from the mortar to the dry block through initial absorption, leading to a strong bond across the interface between block and mortar. A higher percentage of sodium silicate can, however, inhibit mortar drying as the resulting gel structure can block pores leading to a decrease in vapour permeability.

These sodium silicate mortars are stronger than the earth blocks, leading to bond strengths which are similar to flexural strength both parallel and perpendicular to the mortar bed joints.

While achieving 0.2 N/mm^2 bond strength is possible with a 100 mm thick cement stabilized CEB and a cement based mortar, this is difficult with unstabilised earth blocks. At the time of writing, the only unstabilised earth block that has been shown to provide this is modern extruded earth masonry with very high density and excellent quality control of materials and end products. These were the type of blocks used for the testing shown in Figure 3 and examples available in Europe are shown in Figure 5. For other earth masonry forms such as CEB or mud bricks (adobe), it may not be possible to construct 100 mm thick walls without stabilization or a secondary structure (e.g. timber frame).

2.3 *Shear resistance*

In plane racking (or shear) behaviour of earth walls can be subdivided into two types:

- Walls where failure is along weak mortar joints (as with conventional masonry)
- Walls where the construction has no mortar joints or where the mortar joints are stronger than the masonry units.



Figure 5. Modern extruded earth masonry products available in Europe.



Figure 6. Racking failure of monolithic cob test wall.

Even walls of monolithic construction such as rammed earth or cob have joints which are normally weaker than the rest of the material, leading to reduced racking resistance and preferential along these planes, as illustrated for a cob test wall in Figure 6.

Where the earth wall is to be made of individual masonry units, a standard masonry triplet shear test can be used to determine both components of shear resistance: the initial shear strength (shear strength with zero normal load) and the coefficient of internal friction (representing an increase in shear capacity with increasing normal load).

While Eurocode 6 does provide typical design values for the initial shear stress and coefficient of internal friction for conventional masonry systems, earth masonry is not included. Unless a manufacturer provides information on the initial shear capacity of the masonry system (monolithic construction or brick/mortar system) these properties should be tested if the shear capacity is a concern for the particular construction.

There is not the body of evidence for earth masonry as there is for other forms of masonry construction, but testing on stabilized and unstabilised earth test walls have indicated the characteristic coefficient of

internal friction of 0.4 specified for masonry construction in Eurocode 6 appears appropriately conservative for earth masonry. The initial shear stress is more variable and testing is required to obtain this parameter.

3 STABILISATION

3.1 *Reasons for stabilisation*

Although some may consider densification (compaction/compression) of soil as stabilisation, it is assumed that all earth construction materials will include this, so this section is focussed on other materials added to the earth with a view to increasing performance. Stabilisation is usually performed for two reasons:

- To improve strength
- To improve durability (water resistance, abrasion, etc.)

If there is no requirement to improve strength or durability, there is no need to stabilise and the option of no stabilisation should always be considered. Any decision on stabilisation should be taken with great care as, although there are currently over 100 potential stabilisers available for use with earth, there has been no single stabiliser that has dramatically outperformed others.

The most commonly used modern stabilisers are cement and lime (with or without other pozzolanic materials). Various forms of bituminous, chemical and enzyme based stabilisers have also been used with the aim of improving strength and durability. Certain forms of earth construction (e.g. cob or adobe) will often have fibres such as straw added to the earth to limit tensile cracking and potentially increase flexural resistance, but these do little for durability and strength loss when wet.

The embodied energy in a stabiliser may result in a stabilised earth product with higher embodied energy than a more conventional counterpart such as a concrete block (see later). "Given similar local conditions, there may be no guarantee that a CEB will use less cement than a cement block." (Rigassi, 1995).

3.2 *Geopolymeric stabilisation*

There has been recent interest in the use of gepolymerisation of earth blocks, particularly using the Low Temperature Geopolymeric Setting (LTGS) methodology proposed by Davidovits (2011). Geopolymers are formed by activating an aluminosilicate powder (the precursor or clay minerals in this case) with an alkaline hydroxide and/or silicate solution (the activator). The term "geopolymer" was first used for alkali-activated calcined clay-based binders in the 1970s by French chemist Joseph Davidovits, but only since 2000 has there been concentrated research and in 2008, the world's first large scale geopolymer concrete manufacturer started production in Australia with fly ash and slag as precursors (Van Deventer et al., 2012). Most international research has focussed on geopolymers as an alternative to high environmental impact Portland Cement (PC) in concrete. The increasing move to geopolymers as an alternative to PC concrete is partly because of significantly lower Carbon Dioxide Equivalent (CO_{2e}) emissions and costs for large projects. Industrial by-products and slags are generally preferred to clay-based precursors in concreting applications as the water content required to achieve flow in clay based geopolymers is very high, leading to decreased strength (Provis et al., 2010).

Clay-based geopolymers can be based on either natural clays or clays which have been calcined (dehydroxylated by heating to 750–950 °C, depending on clay mineral). The goal for geopolymers from uncalcined (natural) clays is to achieve a solution molar ratio of 1:1 between silicon (Si) and aluminium (Al) once dissolved using the activator solution which is high in hydroxides (OH^-). This limits applications to clay minerals in the kaolinite group. For calcined clays such metakaolin, a molar ratio of 2:1 between Si and Al is preferred and higher strengths can be achieved but at a higher environmental impact. The 2:1 Si:Al ratio normally requires additional soluble silicate activators such as $Na_2O{\cdot}2SiO_2$.

Very little work has been done on uncalcined geopolymer earth blocks, although there are a number of research programmes around the world investigating this, including one at the University of Bath. To date, there are no published studies confirming saturated compressive strengths of 12 N/mm^2 for uncalcined clays mixed with 2% Sodium Hydroxide (NaOH) activator, and heated to 85 °C, as reported by Davidovits (2011). This strength is comparable to that for dense concrete blocks or earth blocks stabilized with 5% cement. Recent work at the University of Bath have shown that there is potential for this technology and that it is possible to develop materials with improved strength and durability than unstabilised earth. The mineralogy of the clay is, however, very important and small changes in mineral composition can have a large effect on final properties.

4 ENVIRONMENTAL IMPACT

While the environmental impact of construction materials covers a broad range of areas, the section is focused on Global Warming Potential (GWP) and figures refer to the 100 year CO_{2e} emissions based on a cradle to factory gate system boundary (extraction of materials to manufacture of products). Data is from the Ecoinvent database focused on western Europe with additional data from other sources if not in the Ecoinvent database. In order to provide consistency, data is provided per m^2 of wall, assuming a material density of 1800 kg/m^3 and also ignoring the effect of mortar.

Data for earth blocks is based on work by Morton (2006) which indicated approximately 86% of the

Table 1. GWP for different wall types.

Type	GWP per m^2 ($kgCO_{2e}$)
Fired clay brick, 100 mm	42.9
Dense concrete block, 100 mm	22.3
Unstabilised earth block, 100 mm	6.0
5% Cement stabilized earth block, 100 mm	12.4
2% NaOH geopolymer earth block, 100 mm	11.5*
Unstabilised earth block, 300 mm	18.0
Pneumatically rammed earth, 300 mm	26.1**

* includes 0.83 $kgCO_{2e}/m^2$ from heating by 60 °C
** all other walls should include mortar, disadvantaging rammed earth in this table

embodied CO_{2e} in fired brick comes from the firing process, and that this is eliminated for earth blocks. It is assumed no additional mixing will be required for stabilized earth as mixing to the required manufacture water content should be sufficient. The GWP value for rammed earth is from Lax (2010) but this could be considered artificially inflated in this analysis as it does not require mortar which would increase the GWP of all other wall types. The value for geopolymer stabilized earth includes heating by 60 °C (from 25 °C to 85 °C). It was assumed earth has a specific heat capacity of 1.0 kJ/kgK (Minke, 2006) and heating was using electricity at an 80% efficiency with no heat recovery, based on 6.4×10^{-5} $kgCO_{2e}/kJ$ for Europe (IEA, 2012). Data for the different wall types is summarized in Table 1.

The lowest GWP was for 100 mm thick earth walls and the lowest for the stabilized blocks was for the geopolymer stabilized earth block.

As shown in Table 1, as the wall thickness increases to 300 mm, the GWP of unstabilised earth walls can exceed that of 100 mm concrete block alternatives. There are other advantages to using thick earth walls including increased thermal mass leading to reduced energy consumption in use, but disadvantages include the increased use of materials.

In addition to increasing the embodied energy, stabilisation can have a negative impact on some of the beneficial properties of earth. This is a concern for the hygrothermal behaviour where stabilisers can limit the vapour permeability and can therefore limit the capacity to passively regulate humidity, but experimental studies have shown this effect may not be as significant as many believe with both cement and geopolymer stabilization having a limited effect (Mcgregor et al., 2012).

5 CONCLUSIONS

Earth masonry has the potential to provide reduced embodied energy and improved building performance if it is used as a replacement for concrete block masonry, but the structural behaviour needs to be quantified before it is used with confidence.

Modern earth masonry with unstabilised blocks and sodium silicate based mortars can provide similar structural capacity to light-weight concrete masonry, provided the risks of moisture susceptibility of the material can be successfully mitigated. This could be either through detailing (for example, a plinth of moisture resistant material), design (for example, the use of a timber frame as a secondary structure) or through modifying material properties to limit moisture susceptibility (through addition of a stabiliser).

Any decision on stabilisation should be taken with caution as stabilisation can increase the embodied energy, reduce the passive environmental control provided by the earth masonry and can actually decrease the material strength.

Geopolymer stabilisation may be able to provide good strength and durability at a lower environmental impact than cement stabilized earth blocks, or conventional fired clay or concrete block alternatives, but this aspect requires further investigation.

REFERENCES

Davidovits, J. 2011. *Geopolymer chemistry and applications*, Saint-Quentin, Institut Geopolymere.

Heath, A., Walker, P., Fourie, C. & Lawrence, M. 2009. Compressive strength of extruded unfired clay masonry units. *Proceedings of the ICE – Construction Materials*, 162, 105–112.

Houben, H. & Guillaud, H. 1994. *Earth construction: a comprehensive guide*, London, Intermediate Technology Publications.

IEA 2012. CO_2 emissions from fuel combustion: Highlights. Paris, France: International Energy Agency.

Jaquin, P.A., Augarde, C.E., Gallipoli, D. & Toll, D.G. 2009. The strength of unstabilised rammed earth materials. *Géotechnique*, 59, 487–490.

Lawrence, M., Heath, A. & Walker, P. 2010. Development of a novel binder for mortar for unfired clay bricks. *2nd International Conference on Sustainable Construction Materials and Technologies.*

Lax, C. 2010. *Life Cycle Assessment of Rammed Earth.* MEng, University of Bath.

Mcgregor, F., Heath, A., Ayre, G., Fodde, E. & Walker, P. 2012. The effect of stabilisation on humidity buffering of earth walls. *LEHM 2012: 6th International Conference on Building with Earth.* Weimar, Germany.

Minke, G. 2006. *Building with earth: design and technology of a sustainable architecture*, Basel; Boston, Birkhauser-Publishers for Architecture.

Morton, T. 2006. Feat of clay. *Materials World*.

Morton, T. 2008. *Earth masonry: design and construction guidelines*, Bracknell, IHS BRE Press.

Provis, J.L., Duxson, P. & Van Deventer, J.S.J. 2010. The role of particle technology in developing sustainable construction materials. *Advanced Powder Technology*, 21, 2–7.

Rigassi, V. 1995. *Compressed earth blocks*, Braunschweig, Vieweg.

Van Deventer, J.S.J., Provis, J.L. & Duxson, P. 2012. Technical and commercial progress in the adoption of geopolymer cement. *Minerals Engineering*, 29, 89–104.

Walker, P., Keable, R., Martin, J. & Maniatidis, V. 2005. *Rammed earth: design and construction guidelines*, Watford, BRE Bookshop.

Research and Applications in Structural Engineering, Mechanics and Computation – Zingoni (Ed.)
© 2013 Taylor & Francis Group, London, ISBN 978-1-138-00061-2

Affordable, sustainable, and resilient tornado shelter design using compressed stabilized earth block construction

Benjamin Wagner, Ece Erdogmus & Avery Schwer
University of Nebraska-Lincoln, Nebraska, USA

ABSTRACT: Non-engineered earthen construction is critiqued for being fit only for dry climates and performing poorly against extreme loads. The authors, as part of a National Science Foundation funded collaborative research project, are studying the performance of engineered earthen masonry against tornado-level wind pressures. This paper introduces an affordable, sustainable, and resilient construction system for residential units in high-wind regions utilizing compressed stabilized earth blocks (CSEBs). Interdisciplinary (architectural, structural, construction related) design criteria are considered for the determination of the required strength levels both for the entire residential units and dedicated tornado shelters to be tornado-resistant. The structural capacity required for high wind pressures is calculated using available analytical methods and current codes after the interdisciplinary criteria are optimally negotiated. A preliminary experimental program is then carried out to determine the resistance capacity of lime and cement stabilized CSEB construction. Parameters considered in the experimental work include, but are not limited to: soil characteristics, water to binder ratio, volume fraction of the stabilizer, stabilization type (lime and cement) and mortar composition. A preliminary testing program for CSEB prisms with and without a proposed externally applied strengthening method is also conducted. This paper presents the current findings of this on-going study.

1 INTRODUCTION

While the performance of CSEB subjected to compressive vertical loads has been examined in previous research, the performance of CSEB subjected to lateral wind loads requires further investigation (Heathecote 1991). Both tornados and hurricanes pose significant threats to structures including high wind speeds and thrown debris. Tornados annually cause an average of $1.1 billion of damage throughout the United States, $13.75 million of damage locally in Nebraska and $10.9 million of damage locally.in Florida. Hurricanes result in additional billions in damage throughout the United States annually, Florida alone experiences on average 2 hurricane events per year, and averages $9.6 billion in damage (Malmstadt, Schietlin, & Elsner 2009). Adequate design of structures to resist the mentioned climatic events can help to reduce such levels of damage.

CSEB is a sustainable building material that is composed of indigenous soils and a mineral stabilizer, commonly lime or cement. The compressive strength and resistance to moisture penetration of these CSEB units are derived from the proportional composition of the indigenous soil and the mineral stabilizer (Heathcote 1991). CSEB can be classified as a sustainable material as less energy is required in their production as compared to fired clay bricks. Unlike fired clay bricks, CSEB do not require kiln-firing and simply cure after molding much like concrete. By using local soils as an aggregate, CSEB eliminate energy used in shipping from a production facility to the job site.

The primary motivation is to develop a sustainable structural system of CSEB that can resist the considered high-wind loads. A solution for the demand for affordable and sustainable housing can be achieved by designing a system capable of resisting structural damage and promoting energy and material efficiency. For the purposes of this project, only threats from high wind speeds and associated pressures acting on the considered structure resulting from tornados and hurricanes were considered. The design of three structures focused on the specifications of the masonry walls. It was assumed that the foundations would be designed to continuously support the Main Wind Force Resisting System (MWFRS) exterior walls, and that the horizontal diaphragms within the three structures behaved rigidly.

2 DESIGN OF STRUCTURES

The proposed structures presented were developed to offer multiple design solutions for residential structures constructed of CSEB. Each structure was designed for wind events considered in two regions in the United States: 1) Eastern Nebraska and 2) Southern Florida Coast. Three two-story structures are designed by the authors and labeled as Structures 1, 2, and 3 (Figures 1–6).

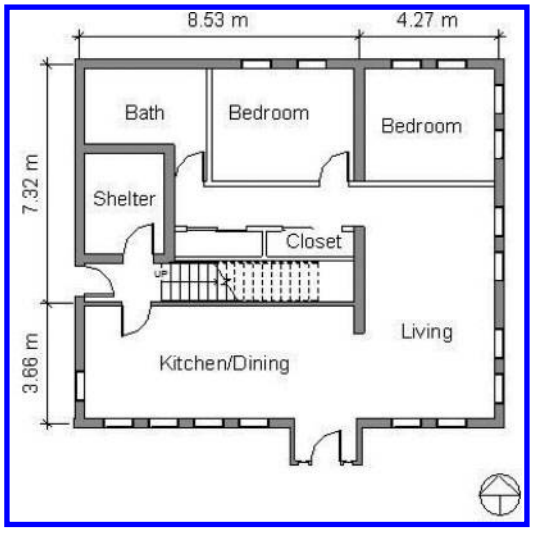


Figure 1. Structure 1 first floor plan.

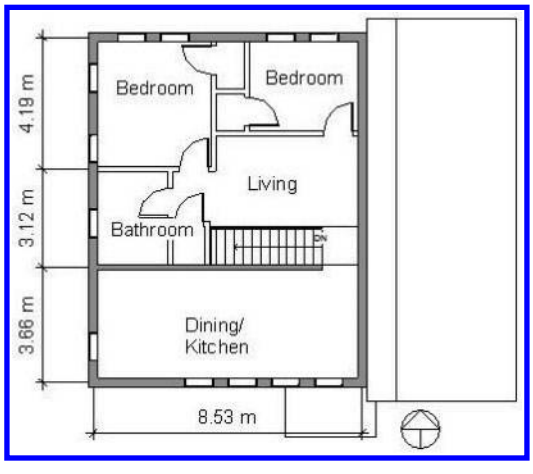


Figure 2. Structure 1 second floor plan.

Structure 1 was designed as a two-story, four-bedroom residence, to represent a larger single-family dwelling. ***Structure 2***, is a redesign of Structure 1 that accommodates three smaller single-family units instead of a larger single family unit. To accommodate the architecture for the new family units, the structural element configuration of Structure 2 is also different. The external wall openings of structure 2 were realigned to create continuous shear walls from roof to foundation. ***Structure 3*** presents a larger multi-family residential complex formed of 3 two-bedroom and 1 one-bedroom units between two floors. The floor plans of the units are nearly identical, allowing wall openings to coincide from floor level to floor level.

The intent of the study with 3 different architectural designs and structural configurations is to present a variety of affordable options for dwellings that may be used for ranges of tenant incomes and lifestyles, and to present multiple structural layouts to investigate the change in the distribution of lateral loads due to plan torsion.

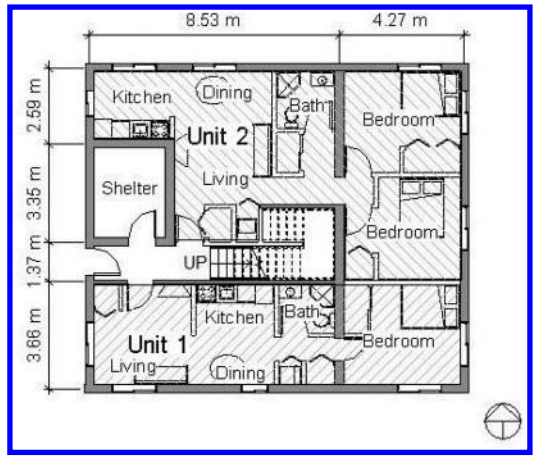


Figure 3. Structure 2 first floor plan.

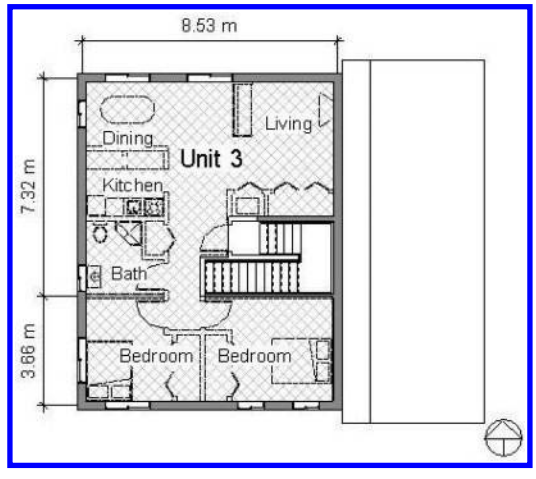


Figure 4. Structure 2 second floor plan.

2.1 *Design parameters*

Table 1 presents the general design parameters of each structure and considered wall thickness. The plans of the structures are presented in Figures 1–6. The floors will be considered simple, rigid diaphragms for the analysis of the walls. The interior walls were designed to reinforce the exterior MWFRS walls against shear, and considered to be of the same thickness and construction as the exterior MWFRS walls.

2.2 *Applied loads*

The wind speeds considered were 145 km/h, 241 km/h, 321 km/h, and 402 km/h. The 145 km/h and 241 km/h wind speeds were established by the minimum design wind loads as detailed in ASCE 7-05: Minimum Design Loads for Buildings and Other Structures

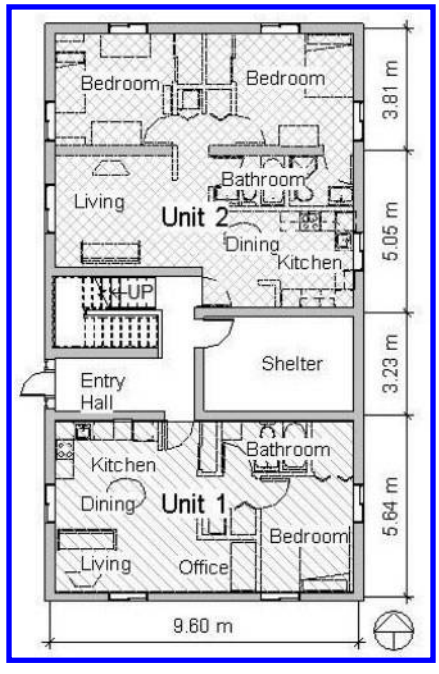


Figure 5. Structure 3 first floor plan.

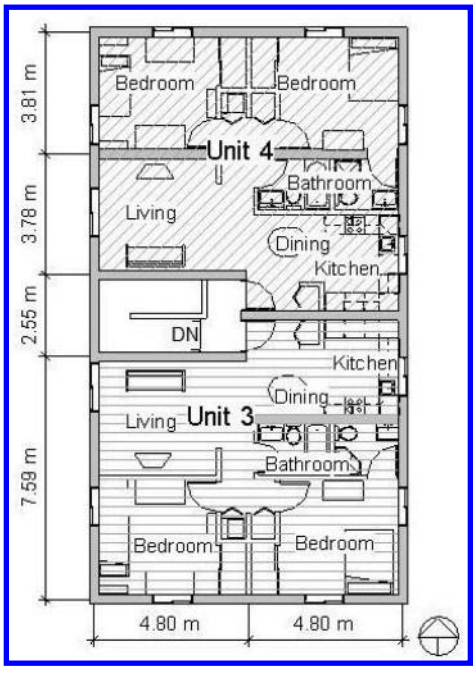


Figure 6. Structure 3 second floor plan.

for Nebraska and Florida, respectively. The 321 km/h wind and 402 km/h speeds were established by the FEMA 361: Design and Construction Guidance for Community Shelters, 2nd edition for Nebraska and Florida, respectively. The proposed structures were classified as Occupant Category II with an Importance

Table 1. General design parameters.

	Foot Print	Usable Area
Structure 1	12.8 m × 10.97 m	182.8 m^2
Structure 2	12.8 m × 10.97 m	182.8 m^2
Structure 3	17.67 m × 9.60 m	340.5 m^2

Ceiling Height	2.74 m
Floor–to–Floor Height	3.05 m
Roof Rise	9.84 cm rise for 30.5 cm run
Roof Overhang	45.7 cm

MWFRS Wall Parameters		
Thickness	Construction	Supports
30.5 cm	Double-Wythe	Pinned
45.7 cm	Triple-Wythe	Pinned
61.0 cm	Quadruple-Wythe	Pinned

Table 2. Applied gravity loads.

Load Type	Dead Loads (MPa)	Live Loads (MPa)
M/E/P	4.79×10^{-4}	
Roof		24.0×10^{-4}
Upper		19.2×10^{-4}
Lower		19.2×10^{-4}

Factor of 1.0, located in an Exposure C environment, and considered as enclosed and rigid by ASCE 7 – 05. Table 2 presents the considered gravity loads for all structures, in addition to the self weight of materials.

2.3 *Material and geometric parameters*

The modulus of elasticity, E, of the CSEB was considered to be $E = 700f'm$, in accordance with Masonry Standards Joint Committee Code, Specifications and Commentaries 2008 for clay masonry units.

The following properties of the walls in each structure were calculated for each wind load orientation: the bearing eccentricity of the floor and roof loads acting upon the supporting masonry wall segments, e, the moment arm between the internal tensile and compressive stresses, c, the cross-sectional area per foot of length, A, the cross-sectional moment of inertia per foot of length, I, the cross-sectional radius of gyration, r, and the slenderness ratio, k.

3 STRUCTURAL ANALYSIS AND RESULTS

Analyses of the structures were completed using the strength method as established by the MSJC 2008. The loads used in the analysis of the structures were determined in accordance with ASCE 7 – 05. The walls of the structures were assumed to be initially unreinforced barrier walls of solid cross-section. If the initial unreinforced design was found to be

inadequate, the minimum reinforcement with steel and fiber reinforced concrete (FRC) was determined for each wall segment in each structure for each wind case where the initial design failed.

3.1 *Unreinforced CSEB wall design*

The minimum modulus of rupture, f_r, and ultimate compressive strength, f'_m, required was calculated for each wall segment in each structure for each wall thickness and wind load condition. Table 3 presents the results of this analysis for the wall segments experiencing the greatest stresses in each considered load case.

The required material strengths of unreinforced CSEB for an entire structure exceed the MSJC 2008 code maximum compressive strength, $f'_m = 41.4$ MPa. None of the structures meet this requirement with a wall thickness of 30.5 cm. The required flexural strength required by each structure also exceeds the maximum flexural strength of the mortar joints. Reinforcement strategies must be considered.

3.2 *Steel reinforced CSEB design*

After each wall segment was designed as an unreinforced assembly, the wall segments exhibiting the greatest flexural and compressive stresses were redesigned with traditional steel reinforcement. The minimum area of steel reinforcement, A_s, required to resist the flexural and compressive stresses was determined by the equation below (MSJC 2008):

$$\Phi M_n = \Phi A_s f_y d\left(1 - \frac{0.63 A_s f_y}{b d f'_m}\right) \geq M_u \qquad (1)$$

Solving equation 4.24 for A_s:

$$A_s \geq \frac{-\Phi f_y d \pm \sqrt{(\Phi f_y d)^2 - 4\left(\frac{0.63\Phi {f_y}^2}{b f'_m}\right) M_u}}{2\left(\frac{0.63\Phi {f_y}^2}{b f'_m}\right)} \qquad (2)$$

Where: M_n = nominal moment capacity of the wall segment (N-cm/m), b = effective reinforcement width (cm), d = depth of steel reinforcement (cm), f'_m = specified ultimate compressive strength of CSEB (N-cm/m), ρ = reinforcement ratio, A_s = area of steel reinforcement (cm^2), f_y = yield strength of steel (MPa), M_u = factored ultimate moment due to wind and eccentricity of axial loads at the mid-height of wall per foot of wall length (N-cm/m), and Φ = reduction factor = 0.9.

The minimum required area of steel reinforcement is the smaller of the two solutions produced by the above quadratic. The minimum area of reinforcing steel, A_s, of the wall segments is present in Table 4. This minimum value is associated with a minimum specified f'_m, also presented in Table 4.

The CSEB blocks can allow up to a single reinforcing #25 metric bar per cell, or 5.09 cm^2 per cell, or 33.44 cm^2 per meter of wall length. With this limitation in consideration, only Structures 1 and 3 can be adequately reinforced at a wall thickness of 61 cm. While steel reinforcement may be achieved, a more practical solution is to consider only a part of the structure to resist the high-wind loads.

3.3 *FRC reinforced CSEB design*

Fiber Reinforced Concrete (FRC) is produced by adding fiber reinforcement to the composition of traditional concrete. This FRC is then applied to the extremities of slabs or wall segment experiencing tensile loads to provide additional flexural strength. The specific modulus of rupture of the FRC required for reinforcement of the three structures was determined in this project, and presented in Table 5.

The nominal moment capacity of a FRC strengthened CSEB wall can be determined similarly to a

Table 3. Minimum strength requirements of unreinforced CSEB wall segments.

Wall Segment		Wall Thickness 30.5 cm	45.7 cm	61 cm	Wind Case (km/h)
Structure 1	f'_m	63.4 MPa	28.2 MPa	15.9 MPa	402 NS
Wall 2.2C	f_r	50.5 MPa	22.4 MPa	12.6 MPa	
Structure 2	f'_m	76.3 MPa	34.0 MPa	19.2 MPa	402 WE
Wall 1.5B	f_r	60.7 MPa	26.9 MPa	15.1 MPa	
Structure 3	f'_m	59.2 MPa	26.4 MPa	14.9 MPa	402 WE
Wall 2.7	f_r	47.2 MPa	20.9 MPa	11.8 MPa	

Table 4. Minimum strength requirements of steel reinforced CSEB wall segments.

Wall Segment		Wall Thickness 30.5 cm	45.7 cm	61 cm	Wind Case (km/h)
Structure 1	f'_m	27.6 MPa	10.3 MPa	10.3 MPa	402 NS
Wall 2.2C	A_s	29.3 cm^2	20.4 cm^2	9.53 cm^2	
Structure 2	f'_m	34.5 MPa	13.8 MPa	10.3 MPa	402 WE
Wall 1.5B	A_s	41.2 cm^2	20.5 cm^2	12.0 cm^2	
Structure 3	f'_m	27.6 MPa	10.3 MPa	10.3 MPa	402 WE
Wall 2.7	A_s	29.2 cm^2	16.6 cm^2	8.79 cm^2	

Table 5. Minimum strength requirements of FRC reinforced CSEB wall segments.

Wall Segment		Wall Thickness 30.5 cm	45.7 cm	61 cm	Wind Case (km/h)
Structure 1	t_{frc}	15.24 cm	15.24 cm	15.24 cm	402 NS
Wall 2.2C	f_{frc}	79.1 MPa	42.7 MPa	33.8 MPa	
Structure 2	t_{frc}	15.24 cm	15.24 cm	12.7 cm	402 WE
Wall 1.5B	f_{frc}	90.1 MPa	49.6 MPa	34.5 MPa	
Structure 3	t_{frc}	15.24 cm	15.24 cm	10.16 cm	402 WE
Wall 2.7	f_{frc}	73.5 MPa	39.1 MPa	33.2 MPa	

FRC strengthened reinforced concrete panel (Radik, Erdogmus, & Schafer 2011). The equations presented by Radik, Erdogmus, and Shafer were adapted for use in the design of FRC reinforced CSEB. The equations for the nominal moment capacity of a FRC strengthened CSEB wall were determined to be:

$$M_n = bt_{frc}f_{frc}\left[h + \left(\frac{t_{frc}}{2}\right) - \left(\frac{a}{2}\right)\right] \quad (3)$$

Where:

$$a = \frac{t_{frc}f_{frc}}{0.6f'_m} \quad (4)$$

And: b = effective slab width (cm), t_{frc} = FRC thickness (cm), f_{frc} = compressive strength of FRC (MPa), h = slab thickness (cm), and f'_m = compressive strength of CSEB (MPa).

The required flexural strength of FRC, f_{frc}, that must be applied to the extreme fiber of the CSEB wall segment for a given thickness, t_{frc}, of a FRC strengthening layer was determined using the equation below:

$$f_{frc} = \frac{-\left(bht_{frc}+\frac{bt_{frc}^2}{2}\right) \pm \sqrt{\left(bht_{frc}+\frac{bt_{frc}^2}{2}\right)^2 - \left(\frac{bt_{frc}^2}{1.2f'_m}\right)M_n}}{\frac{2bt_{frc}^2}{1.2f'_m}} \quad (5)$$

Where: b = effective slab width (cm), t_{frc} = FRC thickness (cm), f_{frc} = flexural strength of FRC (MPa), h = slab thickness (cm), f'_m = compressive strength of CSEB (MPa), and M_n = nominal moment capacity (kNm).

The solution of this quadratic with the least value is the minimum required flexural strength of FRC, f_{frc}, for a given thickness of FRC, t_{frc}, for a considered CSEB wall segment. The thickness, t_{frc}, was considered to range between 1.27 cm and 15.24 cm. Table 5 presents the minimum thickness required of the FRC layer and the corresponding flexural strength for the considered wall segments.

The results of this analysis indicate that each structure would require an excessively thick FRC layer to adequately resist the considered wind loads. It is therefore recommended to consider the design of tornado shelters, instead of providing an entirely tornado-resistant building.

3.4 *Shelter design*

A room in each structure was selected to be designed as a tornado shelter. The laundry room of each structure was selected to fulfill this purpose. The locations of these shelters are presented in Figures 1–6. It should be noted that the shelter in Structures 1 and 2 are identical, and presented only once in the results tables.

Each shelter was designed in the same manner, using the same procedure and assumptions, as the entire structures. Table 6 presents the results of the analysis of each of the shelters.

Table 6. Minimum strength requirements of shelter CSEB wall segments.

Wall Segment		Wall Thickness 30.5 cm	45.7 cm	61 cm	Wind Case (km/h)
Shelter 1 and 2					
Unrein.	f'_m	25.1 MPa	11.2 MPa	6.33 MPa	402 NS
	f_r	19.9 MPa	8.83 MPa	4.95 MPa	
Steel Rein.	f'_m	13.7 MPa	10.3 MPa	10.3 MPa	402 NS
	A_s	10.5 cm^2	5.05 cm^2	3.39 cm^2	
FRC Rein.	t_{frc}	12.7 cm	7.62 cm	5.72 cm	250 NS
	f_{frc}	33.5 MPa	33.6 MPa	32.3 MPa	
Shelter 3					
Unrein.	f'_m	54.7 MPa	24.3 MPa	13.7 MPa	402 NS
	f_r	43.6 MPa	19.4 MPa	10.9 MPa	
Steel Rein.	f'_m	27.6 MPa	10.3 MPa	10.3 MPa	402 NS
	A_s	24.4 cm^2	14.1 cm^2	8.0 cm^2	
FRC Rein.	t_{frc}	15.24 cm	15.24 cm	11.43 cm	402 NS
	f_{frc}	67.2 MPa	35.4 MPa	33.0 MPa	

Based on the results presented above, it is not possible to use unreinforced CSEB for a tornado shelter. However, the shelters in Structures 1 and 2 can be adequately designed with a standard #25 metric bar (5.09 cm^2) every other cell of steel reinforcement for a wall thickness of 45.7 cm, and the shelter for structure 3 can be adequately designed with a standard #22 metric bar (3.87 cm^2) every cell of steel reinforcement for a wall thickness of 61 cm. It also possible to reinforce the shelters of Structures 1 and 2 with a 5.72 cm layer of FRC, or reinforce the shelter of Structure 3 with a 11.43 cm layer of FRC. All three shelters would require FRC with a modulus of rupture of 32.3 MPa or greater.

4 CSEB BLOCK AND PRISM TESTING

After the analytical work that determined the target strength levels for the system, a preliminary experimental work was carried out to understand the available compressive strength levels of various CSEB block compositions. CSEB with varying stabilizer type, weight fraction of stabilizer, and water-to-binder ratios were considered in this preliminary study. The blocks were cast and allowed to cure over a 28 day period. Table 7 summarizes the experimental program of the CSEB blocks.

The CSEB blocks were tested in compression in accordance with ASTM C67 – 09: Standard Test Methods for Sampling and Testing Brick and Structural Clay Tile. The blocks were loaded normal to bed joints, simulating gravity loads. Table 7 and Figure 7 present the results of the compressive testing.

CSEB block prisms were also assembled for testing the flexural capacity in out-of-plane bending. The

Table 7. CSEB block test results.

Mix #	% Stabilizer	Water-to-binder Ratio	Maximum Compressive Strength
X1	unstabilized	0.15	2.11 MPa
X2	unstabilized	0.20	1.72 MPa
X3	unstabilized	0.25	2.01 MPa
A1	5% port. cement	0.15	4.01 MPa
A2	5% port. cement	0.20	3.10 MPa
A3	5% port. cement	0.25	2.78 MPa
A4	5% NHL 5 lime	0.15	2.28 MPa
A5	5% NHL 5 lime	0.20	1.94 MPa
A6	5% NHL 5 lime	0.25	1.47 MPa
B1	8% port. cement	0.15	5.82 MPa
B2	8% port. cement	0.20	4.71 MPa
B3	8% port. cement	0.25	2.84 MPa
B4	8% NHL 5 lime	0.15	2.66 MPa
B5	8% NHL 5 lime	0.20	2.02 MPa
B6	8% NHL 5 lime	0.25	1.06 MPa
C1	10% port. cement	0.15	5.52 MPa
C2	10% port. cement	0.20	5.92 MPa
C3	10% port. cement	0.25	3.70 MPa
C4	10% NHL 5 lime	0.15	2.40 MPa
C5	10% NHL 5 lime	0.20	1.75 MPa
C6	10% NHL 5 lime	0.25	1.52 MPa
D1	15% port. cement	0.15	6.54 MPa
D2	15% port. cement	0.20	5.59 MPa
D3	15% port. cement	0.25	5.47 MPa
D4	15% NHL 5 lime	0.15	1.92 MPa
D5	15% NHL 5 lime	0.20	3.22 MPa
D6	15% NHL 5 lime	0.25	2.03 MPa

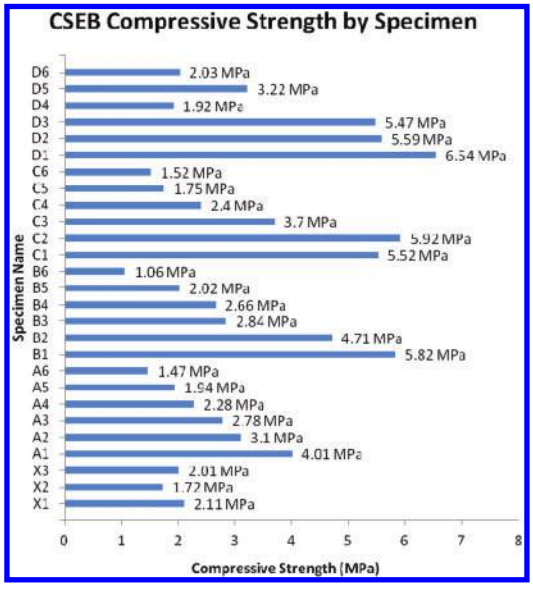


Figure 7. CSEB Compressive Strength.

prisms were constructed of five courses of CSEB with a 15% by weight Portland cement stabilizer and a 15% by weight water content. The blocks were bonded together using Type N PCL mortar. However, the CSEB and Type N mortar failed to bond, and the prisms were not suitable for flexural testing. Failure of the mortar joints occurred along the face of the CSEB and joint. The detailed causes of this failure, beyond apparent material incompatibility, are being investigated and an experimental program to optimize a more appropriate soil mortar mixture is ongoing.

5 CONCLUSIONS

From the design and analysis of the three structures, it can be concluded that shelter walls constructed of 45.7 cm thick, fully grouted CSEB, reinforced with 1 – #22 metric bar every other cell, can resist lateral loads from wind speeds up to 402 km/h.

It can also be concluded that shelter walls constructed of 61 cm thick, fully grouted CSEB, reinforced with a 5.72 cm layer of 33.09 MPa FRC can resist lateral loads from the highest wind speeds up to 402 km/h. As expected, tensile stresses due to out-of-plane bending will control the material failure of CSEB within the considered structures.

Based on the analysis of the considered structures and shelters, it is recommended that the structure 2 be selected to resist high wind loads. Structure 2 offers flexibility in occupancy of three residential units, and provides a shelter capable of resisting wind loads of up to 402 km/h with the reinforcement strategies described above. Based on the results of the compressive testing, it is recommended that CSEB comprise of a 15% by weight Portland Cement stabilizer and a 15% by weight water content, however, further experimental investigation into the flexural capacity of the CSEB is required.

REFERENCES

ASCE/SEI Standard 7-05. 2005. *Minimum Design Loads for Buildings and Other Structures*. Structural Engineering Institute of the American Society of Civil Engineers

ASTM C67 - 09. 2010. "Standard Test Methods for Sampling and Testing Brick and Structural Clay Tile". Vol. 4.5. West Conshohocken, PA: ASTM International.

FEMA 361, 2nd Ed. 2008. *Design and Construction Guidance for Community Safe Rooms.* Department of Homeland Security Federal Emergency Management Agency.

Heathcote, Kevan. 1991. "Compressive Strength of Cement Stabilized Pressed Earth Blocks". Building Research and Information. Volume 119.

Malmstadt, Jill, Schietlin, Kelsey, and Elsner, James. 2009. "Florida Hurricanes and Damage Costs". Florida State University. http://myweb.fsu.edu/jelsner/PDF/Research/MalmstadtEtAl2009.pdf.

MSJC Masonry Standards Joint Committee. 2008. *Building Code Requirements and Specification for Masonry Structures.* Masonry Standards Joint Committee (MSJC).

Radik, Matthew J., Erdogmus, Ece, and Schafer, Travis 2011. "Strengthening Two-Way Reinforced Concrete Floor Slabs Using Polypropylene Fiber Reinforcement". Journal of Materials in Civil Engineering, ASCE. May 2011.

27. Performance of structures in fire, design for fire resistance

Research and Applications in Structural Engineering, Mechanics and Computation – Zingoni (Ed.)
© 2013 Taylor & Francis Group, London, ISBN 978-1-138-00061-2

Global structural behavior in fire and consolidated testing of steel structures

M. Fontana, M. Knobloch & A. Frangi
ETH Zurich, Institute of Structural Engineering, Zurich, Switzerland

ABSTRACT: The fire behavior of steel structures in prescriptive design is commonly assessed by fire tests on single structural members under standard fire special testing furnaces; however the behavior of an entire steel structure is in most cases more complex due to a redistribution of loads (global behavior of the structure) as a result of large deformations in fire or even a change in the structural system. Favorable structural behavior of global structures was observed in full scale fire tests and in many real fires. However the huge costs of full scale fire tests on global structures prohibit their wide use. Therefore fire tests on global structures are usually replaced by numerical simulations. However numerical simulations have still difficulties to precisely model details like connections or cannot detect some failure modes if no test data is available (e.g. spalling, brittle failure modes, shear or anchorage failures, etc.). Consolidated testing merges testing and numerical simulations. Data measured in the test become input for the numerical calculation and results from calculation control the test. Consolidated testing is based on deformation and strain-based structural analysis and has a huge potential for fire safety and economy of structures and for the development of realistic structural modeling in fire. The paper first describes the basic principles of a deformation-based approach to global structural behavior and its study with consolidated testing technique. Then, it shows the benefits of considering global structural behavior in fire and its assessment by consolidated testing for fire safety and gives some applications and impacts.

1 INTRODUCTION

Today most structural engineers analytically verify the resistance of their structures based on ultimate limit states mostly using simplified rules given in codes. The verification usually concentrates on single structural members like columns or beams as well as their connections. The ultimate state of a member, however, may not be representative for the behavior of the global structure. It only represents one state of the relevant element and the influence of the member interaction is often either neglected or considered in a simplified way, e.g. critical buckling length of columns in frame structures.

Deformation-based design forms the basis of numerical methods like finite element analysis, which have become widely used during recent years thanks to the spread of specialized software and electronic tools. However the way of thinking and education in structural engineering is for most engineers still stress- and resistance-based. Global deformation-based methods and models are rarely applied, with the exception of plastic design methods (Thürliman 1979; Bruneau, Uang and Sabelli 2011), where deformation (e.g. rotation capacity of plastic hinges) capacity must explicitly be considered.

With the development of structural analysis and modeling, design based on constructional detailing and observation has become less important while rigorous structural analysis and the verification of structural elements according to codes is governing todays design practice to protect the engineer and the public against structural failures.

To make analysis feasible and economical often simplified rules based on strength and stresses are given in codes. They will lead to good results for standard structures, where a rich knowledge and experience exist. However they cannot cover novel types of structures and are an obstacle to innovation and will quickly become boring for well-educated engineers.

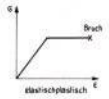
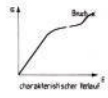
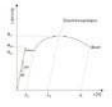
A performance-based approach (Hadjisophocleous et al. 1998; Meacham and Custer 1995) to structural design is based on basic principles and objectives as well as on functional requirements. It is therefore also applicable to novel types of structures and will foster innovation. The influence of deformation-based approach to structural analysis and its application to global structures and testing may lead to new knowledge and strongly future structural design.

2 STRUCTURAL ANALYSIS

Structural behavior can be studied on different levels (Tab. 1), mainly

- material
- cross-section
- structural element
- global structure.

Table 1. Interdependence of structural level of analysis and material-theory (cp. Fontana 2012).

Theory/ Level	Elastic	Plastic	Nonlinear
Material	linear-brittle 	rigid plastic linear elastic-perfectly plastic 	Nonlinear 
Cross-section 	Hook Bernoulli/ Navier elastic FEM/Eigenvalues local buckling 	Plastic hinges – Rotation capacity Post buckling behaviour Bernoulli/ Navier 	Nonlinear – strain-based nonlinear FEM Bernoulli/ Navier 
Member	Hook/Euler Elastic buckling, LT 	Redistribution of loads Mechanism Buckling curves	Nonlinear deformation-based alternative modells: Membranes-cables
Global structure	Hook/Euler Linear statics: (I. and II. Order Theory) Deformations Stresses Principle of work and energy Deformation method	Redistribution of loads Load transfer Bending -> Membrane action 	Redistribution of loads plastic springs – robustness Load transfer 

On the material level nonlinear material behavior is often simplified by linear behavior up to a limited stress level or by linear elastic, perfectly plastic behavior (Marti. 2013). Uniaxial behavior found by material test is mostly considered as basis for design.

The cross-sectional level applies the strain-stress curves found on the material level to the geometry of the two dimensional cross-section, additionally local buckling must be considered (Knobloch et al. 2012) Local buckling is generally strain dependent (Dubas & Gehri 1986). Therefore in an advanced design the available and required rotational capacity must be considered. However this is circumvented in many code designs by simplifications like e.g. cross-sectional classes (Fig. 1).

On the element level the third dimension is considered leading to additional influences caused e.g. by second order effects like global and lateral-torsional buckling or bearing conditions.

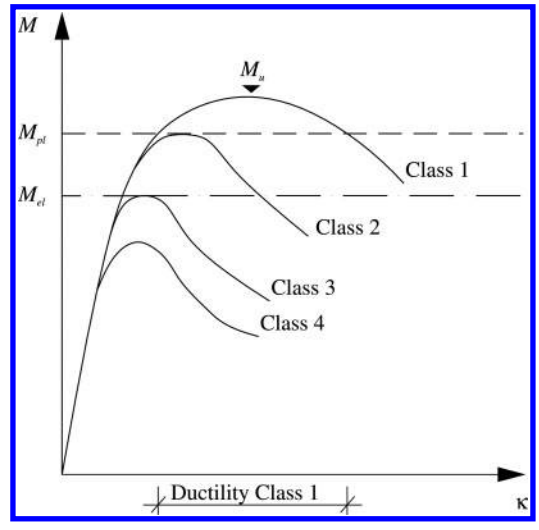


Figure 1. Cross-section classes depending on rotation capacity- according to EN 1993-1-1 (2005).

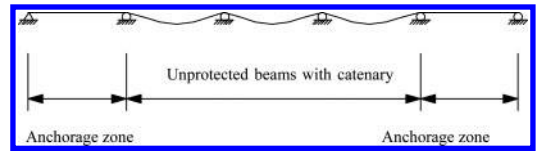


Figure 2. Change in structural system with large deformations e.g. from beam to catenary behavior.

On the global structural level elements are connected and their interaction may lead to reversible or irreversible deformations and load transfer and constraints. Deformation may even lead to changes in the structural system (Figs. 2, 3), reducing or increasing the resistance of the structure.

A realistic ultimate state analysis of a structure must not stop on the element level but should consider the global structure. This will need to consider strains and deformation not only ultimate strength of members and connections.

3 DEFORMATION-BASED ANALYSIS AND DESIGN

Nonlinear material behavior and the combination of elements with different nonlinear component and connection behavior, (e.g. glue and nails in timber) can only be assessed by a strain-based approach considering the whole stress – strain behavior of the component. A simple superposition of ultimate loads would lead to an overestimation of the total resistance cp. Figure 4.

However in general a deformation-based approach is very complex and time-consuming. Therefore simplifications are usually proposed for analytical

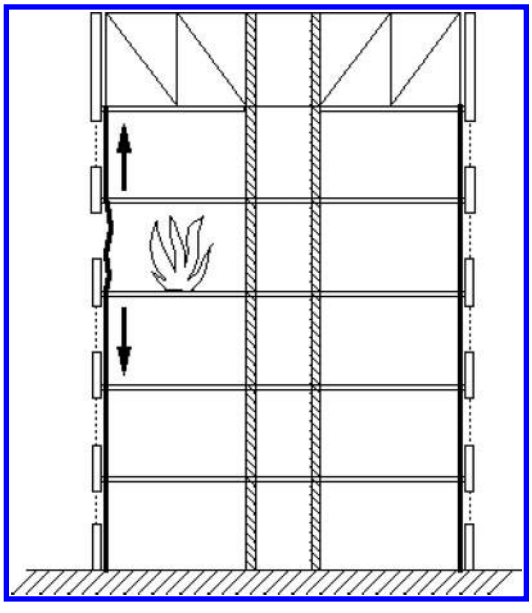
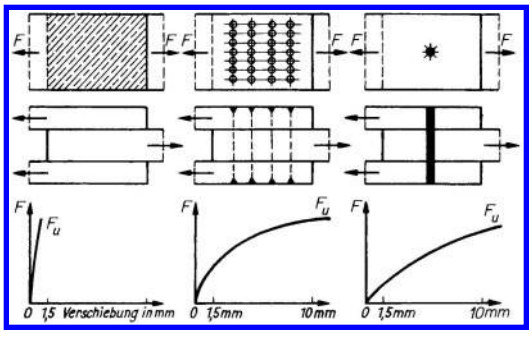


Figure 3. Load redistribution in a redundant structure in case of element failure.


F
F
F

regulations and codes and well-trained engineers as well as adequate review processes.

REFERENCES

Bailey Colin et al., The behaviour of multi-storey steel framed buildings in fire, BS, Swinden, Technology Centre, 1999.

Bruneau, M., Uang, C.-M., Sabelli, R. 2011. *Ductile Design of Steel Structures*. New York: Mc Graw Hill.

Dubas P., Gehri E. 1986. *Behaviour and design of steel plated structures.* Brussels: ECCS, TC 8, WG8.3.

EN 1993-1-1. 2005. Eurocode 3: Design of steel structures – Part 1-1: General rules and rules for buildings. Brussels: CEN.

Fontana, M. 2012. *Lecture notes Stahlbau III – Systemverhalten.* Zürich: ETH Zurich/Institute of Structural Engineering (in German).

Hadjisophocleous, G.V., Benichou, N., Tamim, A.S. 1998. Literature Review of Performance-Based Fire Codes and Design Environment. *Journal of Fire Protection Engineering* 9: 12–40.

Knobloch, M., Somaini, D., Pauli, J., Fontana, M. 2012. Numerical Analysis and Comparative Study of the Cross-Sectional Capacity of Structural Steel Members in Fire. *Journal of Structural Fire Engineering* 3(1): 19–35.

Marti, P. 2013. *Theory of Structures.* Berlin: Ernst & Sohn.

Meacham, B.J., Custer, R.L.P. 1995. Performance-Based Fire Safety Engineering: An Introduction of Basic Concepts. *Journal of Fire Protection Engineering* 7(2): 35–54.

Nakashima, M., Kato, H., Takaoka, E. 1992. Development of real-time pseudo dynamic testing. *Earthquake Engineering and Structural Dynamics* 21: 79–92.

Thürlimann, B. 1979. IABSE Conference Proceedings, Copenhagen

Research and Applications in Structural Engineering, Mechanics and Computation – Zingoni (Ed.)
© 2013 Taylor & Francis Group, London, ISBN 978-1-138-00061-2

Structures in fire or fires in structures? Assessing the true performance of structures in fire

J.L. Torero
School of Civil Engineering, The University of Queensland, Australia

ABSTRACT: When addressing the performance of structures in fire it is common to treat the fire as an imposed load. The analysis of the structural behaviour follows. The analysis of the structure can follow different levels of complexity and in some cases can lead to detailed finite element studies that incorporate complex models for the constitutive properties of the materials involved as well as detailed analysis of connection behaviour. When addressing the load, an attempt is made to establish a "worst case" condition together with statistically based error bars. This approach follows similar treatments used for dead loads, snow, wind, blast or earthquakes. While this approach seems to be useful, it poses two fundamental questions, first is "what is a worst case fire scenario when assessing the performance of structures in fire?" and second, "is it possible to separate structural behaviour from fire behaviour?" As opposed to other loads, fire behaviour can be drastically modified by the nature of the structure in as much as the structure can be affected by the fire. Thus, true optimization of structural design needs to address structural and fire behaviour in a coupled manner. A comprehensive analysis of fire and structure is the only means by which terms such as extreme events, failure and fire resistance can be defined. Furthermore, detailed structural analysis is only justified if an equally detailed fire analysis is conducted guaranteeing consistency. If the consistency of complexity is not respected the results are misleading in their pretence of precision and in the validity of the conclusions. Only if a coupled analysis with consistent complexity throughout the integrity of its components is conducted a true assessment of performance of the behaviour of a structure in fire can be achieved.

1 INTRODUCTION

The performance of a structure is a fundamental component of a fire strategy, thus its performance within the context of this strategy needs to be defined. Acceptable performance is therefore a relative term that will vary depending on the requirements posed by the strategy on the structure. Different strategies and buildings will require different acceptance criteria depending on what the structure is intended to deliver. In an industrial storage facility structural failure is an acceptable performance given that the structure has only secondary life safety functions. In contrast, in a tall building, stringent requirements of structural integrity are necessary because the structure has a fundamental role in life safety. Independent of the specific requirements to be met, a true assessment of performance for a structure needs to be established. Only then failure criteria can be stipulated to meet the needs of the fire strategy.

To be able to define the temporal and spatial evolution of a structure during the event of a fire, the following issues need to be resolved:

1. The temporal and spatial evolution of the fire needs to be specified in a manner that gas phase temperature, the velocity field and the concentration of different species (CO, CO2, H20, soot, etc. concentrations can be defined.
2. The evolution of the gas phase will enable to quantify the temporal and spatial evolution of the heat exchange between the structural elements and the gases. Thus a real thermal boundary condition can be stipulated.
3. With the boundary condition defined heat transfer through the structural elements needs to be resolved. For materials like steel the transient energy equation consists only of heat conduction and enthalpy terms with variable thermal properties but for other more complex materials such as concrete or plaster board, complex mass transfer equations need to be resolved to account for the vaporization enthalpy as well as moisture migration.
4. The spatial and temporal evolution of the temperature of the structural elements allows then to compute the solid mechanics equations to determine stresses and deformations within the structure.
5. The results of these calculations can then be used to establish quantitative failure thresholds.

The comprehensive formulation of the problem requires the coupling of gas and solid phase because the evolution of the structure can influence the evolution of the fire. Explicit finite element models coupled with transient CFD models become a necessity if the complete interaction is to be resolved. Despite many

attempts to do this, there is currently no combination of models that solve the coupled effects of fire and structure. Furthermore, there is currently no CFD model that comprehensively resolves the fire at the necessary scale and with full detail. Finite element models are more advanced but many of the mechanical and thermal properties that serve as inputs are still unavailable.

Numerous alternative approaches can be found in the literature, some of them are well argued simplifications that use the characteristics of the problem to either relax the coupling between gas and solid phase or to simplify certain terms of the equations. Among these simplifications are simplified connection models, constitutive property models, total heat transfer coefficients and spatial and temporal averaging of the gas phase. These simplifications take advantage of the very different time and length scales of the solid and gas phase problems to decouple and simplify many of the processes. When correctly argued these approaches are perfectly valid and provide a true assessment of the performance of the structure as well as quantified error bars linked to uncertainties and simplifications.

A second approach that is equally valid is that of establishing a series of constraints in the form of codes and standards. These constraints guarantee a simplified environment that can be quantified by means of a simple representation. The most common of these code based constraints are the requirements for compartmentalization. By reducing all buildings to a summation of standardized compartments, the evolution of the fire can be reduced to an energy balance and thus both gas and solid phase behavior can be deeply simplified. This particular approach still provides a true assessment of performance. The error bars, in this case, are linked to the simplifications of the physical models defining the gas and solids but also to the deviation of the real compartments from the standardized ones.

An approach that is acquiring popularity is that of using simplified models coupled with probabilistic estimations of error. These methods, based on theories of risk and reliability, are only valid if the representation of the physical phenomena incorporates in a correct manner all the necessary variables and couplings and the probabilistic distributions for all poorly defined properties are available. In this case a probabilistic distribution of true performance can be established.

A final method is the relative assessment of performance. This method creates a realistic scenario and assesses the performance of a system against it. The realistic scenario can be a standardized temperature vs. time curve, a parametric temperature vs. time curve to provide a relative performance of a structural component or system but also a standardized compartment to assess the relative severity of a fire given different fuels. While this approach can be used for the purpose of understanding or for classification, it will never provide true performance assessment.

This paper provides a brief analysis of some of these different methods, identifying potential areas where true performance assessment can be obtained and those where the methodology does not enable such assessment.

2 BACKGROUND

The history of explicit fire modeling is not very old with the first attempts done at the beginning of the 20th century but only formalized in the 1960's and 70's (Hottel (1984)). Probably the first descriptions of the fire are associated to fire resistance and attempts to guarantee adequate structural behavior. In the absence of most of the fundamental knowledge of combustion, heat and mass transfer, the fire was modeled by attempting to reproduce reality within a furnace (Ingberg (1928)). A combustion reaction was sustained within a realistic scale compartment in which the structural element was introduced. Heat transfer was bypassed by measuring directly the temperature of the structural element and the fire was generalized by attempting a "worst case" condition. The worst case condition was generated by reproducing the fastest possible temperature rise to the highest possible temperature. This "worst case" fire was formalized as the "standard fire" and the "standard fire" gave birth to the "structural temperature vs. time" concept. The "standard fire" could then be reproduced in a furnace according to a pre-defined "temperature vs. time" and structural systems tested within that furnace. No real fire could produce a faster temperature rise nor attain the temperatures obtained in the furnace. The exposure time was defined on the basis of attaining burn-out of the estimated fuel load, thus no real fire could last longer. The time required for burn-out was labeled the required structural fire resistance rating. While this "worst case" scenario allowed for confident extrapolation, it is clear that an important safety factor was embedded in this primitive form of fire modeling.

Understanding of structural behavior at high temperatures was limited to the characterization of the material properties as a function of temperature. Typical safety factors for structural design established how far the loss of mechanical properties could be tolerated. This loss of mechanical properties was then correlated with a temperature resulting in a failure temperature criterion. The time necessary for the structural element to attain this critical temperature in the furnace was then established as the failure time. If the failure time was greater than the required fire resistance rating then the structural element could be used without any thermal protection, if not, thermal protection should be added in quantities that enabled the time to attain the failure temperature to exceed the required fire resistance rating (Drysdale (1998), Buchanan (2002)).

An important concept associated to the extrapolation between thermal behavior in the furnace and real fire behavior was the compartment size. While there

was no clear understanding of the role of compartmentalization, it was inferred that extrapolation could only be robust if the conditions of burning were similar. Furthermore, accepting that single element behavior, based only on material properties, could be extrapolated to real scale structural behavior could only be tolerated heating was localized. If a zone of comparable size to the furnace was the only heated area, then the surrounding structure will remain cold and maintain its strength. Any stresses generated in the heated area could then be transferred (redistributed) to the rest of the building and will be of lesser magnitude than those tolerable by the cold structure. In modern terms this represents a requirement of mechanical restraint that is guaranteed by effective compartmentalization. As a consequence, very restrictive compartmentalization requirements were imposed by building codes of the time.

Combustion science progressed through the 20th century nevertheless these issues will not be revisited until the 1960's. Advancement in the understanding of fluid mechanics, heat transfer and combustion did not permeate into fire modeling because the complex problem of fire could not be effectively linked to fundamental knowledge in any of these areas. Modeling the fire from fundamental principles was not possible, the gain was not evident and the existing design methods seemed to provide satisfactory results. At the time excessive safety factors were not a matter of consideration.

The 1960's brought two fundamental changes to the construction industry, (1) the relaxation of compartmentalization and (2) the introduction of plastic materials. In the past, "worst case" fires were defined on the basis of burning wood and were limited to a compartment of a size and characteristics regulated by building codes. As buildings became more complex and features such as ventilation ducts and false ceilings were introduced, it became unclear how to maintain compartmentalization. Given that the link between compartmentalization and fire safety performance had not been established on the basis of fundamental principles, it was difficult to establish the implications of the changes associated to new forms of construction. The loss of some level of compartmentalization occurred unnoticed. The consequences of losing compartmentalization were made evident in several tragic fires (NFPA (2003)). In a similar manner, the migration towards plastics introduced novel failure modes induced by physical phenomena such as melting or dripping. These failure modes resulted in burning conditions that were different to those defined by the burning of cellulosic materials (e.g. wood). The need to better representation of the fire by incorporating these new features became the driver to a significant research effort that for the first time brought combustion knowledge into fire safety (NFPA (2003)).

In an attempt to describe the complexity of the fire in combustion terms, the problem was broken down into numerous components. The interaction between the compartment and the combustion reaction was named compartment/enclosure fire dynamics (Karlsson and Quintiere (2000)). The link between the fire and stoichiometry was established by quantifying buoyant flows that serve to supply oxygen to the pyrolyzing fuel (entrainment). The compartment itself was also linked to stoichiometry by quantifying heat transfer from the fire to the walls and from the walls to the fire (feedback). As the fire heats the walls, radiative feedback to the fuel increases leading to an increasing supply of gaseous fuel to the compartment. The global stoichiometry of the compartment then drifts from the lean to the rich and the transition results in the migration of the flames from the interior of the compartments towards the openings. Terminology such as flashover, oxygen limited and fuel limited fires were introduced to describe these phenomena (Drysdale (1998)).

In what concerns assessment of structural performance a better understanding of the burning behaviour lead to the better characterization of the compartment fire temperature distributions (Thomas and Nilsson (1973), Thomas (1967)) and the development of design "temperature vs time" curves that were meant to be realistic representation of the evolution of the temperature of a compartment. Notable is the study by Pettersson et al. (1976) that lead to the parametric curves. Nevertheless, all these work relies on the principle of compartmentalization and requires the dimensions of the compartment to be such that mixing dominates and results in a homogeneous compartment with very thick smoke (small extinction distance) that can be described with a single temperature that is spatially homogeneous and only a function of time. Thomas (1967) explores the limitations of homogeneity, but only Harmathy and Lie (1970) and Harmathy (1981) discuss the role of the compartment and its dimensions. Figure 1 presents the comparison between the standard fire and the parametric curve corresponding to a realistic fire (The Dalmarnock Fire Test – DFT (Rein et al. (2007)). The average temperature of the compartment is also presented. As it can be seen, the parametric curve brings some of the realistic features of the fire, nevertheless tends to be over-dimensioned.

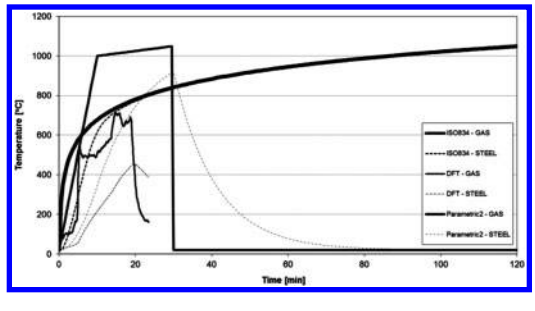


Figure 1. Temperature evolution of the gas phase of a compartment fire and a small cross section unprotected steel beam. Standard temperature time curve per ISO-834 (1999), DFT stands for Dalmarnock Fire Test as per Rein et al. (2007).

This is mostly due to the nature of the compartment used which had a very low thermal conductivity and thus retained the heat. For a similar reason the cooling curve was not introduced because it is defined by the walls, thus is not a representation of the gas phase. A very simple heat transfer calculation towards a beam was introduced only to show that the temperature evolution of the gas phase could potentially have drastic consequences on the structure. So, even without taking any heat transfer considerations or the limitations of the compartment, none of the design curves is a true representation of the fire.

It is clear that the capability of these procedures to lead to a true performance assessment is doubtful. No performance can be defined beyond establishing very simple failure criteria and methods to define if failure is attained.

3 TEMPERATURE VS. HEAT FLUX

When analyzing the heat transfer from the fire to a structural element the problem needs to be formulated in terms of heat fluxes. While temperatures result from the solution to the energy conservation equation, all quantities to be balanced are energies (Incropera and DeWitt (2002)).

Heat is transferred from gases to surfaces via radiation and convection resulting in a total heat flux, $\dot{q}''_{Tot}$, where

$$\dot{q}''_{Tot} = \dot{q}''_{rad} + \dot{q}''_{con} \quad (1)$$

and $\dot{q}''_{rad}$ is the heat transfer via radiation and $\dot{q}''_{con}$ is the heat transferred via convection. For simplicity the problem will be assumed as one dimensional, then the boundary condition for a solid element (structural element) becomes

$$\dot{q}''_{Tot} = -k_i \frac{\partial T}{\partial x} \quad (2)$$

where the thermal conductivity (k_i) is a property of the solid and the gradient of temperature is taken at the surface. In other words all the heat arriving is conducted into the solid. If there are multiple layers then at each interface the following boundary condition should apply:

$$-k_i \frac{\partial T}{\partial x} = -k_s \frac{\partial T}{\partial x} \quad (3)$$

where the gradients correspond to each side of the interface. Once the boundary conditions are defined, the energy equation can be solved for each material involved. Then the energy equations take the form

$$\rho_i Cp_i \frac{\partial T}{\partial t} = \frac{\partial}{\partial x}\left(k_i \frac{\partial T}{\partial x}\right) \quad (4)$$

$$\rho_s Cp_s \frac{\partial T}{\partial t} = \frac{\partial}{\partial x}\left(k_s \frac{\partial T}{\partial x}\right) \quad (5)$$

If the geometry is complex, then the problem needs to be resolved in all dimensions. If the properties vary with temperature then, as the temperature increases, these properties need to evolve with the local temperature. Variable properties thus require a numerical solution. If a simple analytical solution is to be obtained then adequate global properties need to be defined. It is important to note that whatever the solution methodology adopted, the temperature of the structure is the result of the resolution of equations (4) and (5) using potential boundary conditions such as those presented in equations (2) and (3).

To obtain the numerical solution it is necessary to input material properties for the insulation and the steel. The material properties required are all a function of temperature and are as follows:

ρ_i, Cp_i, k_i
ρ_s, Cp_s, k_s where the sub-index "i" stands for insulation and "s" for steel. For some materials such as steel the properties of are well known and thus very little difference can be found between the literature (EN (1993)). For other materials such as concrete, wood or different thermal insulations the scatter is much greater (Buchanan (2002), UL (1962)). The uncertainty is associated to the presence and migration of water but in the case of wood and insulation also to degradation. The wood and insulation that gets consumed (changes thickness) and retracts from the heating source increasing the overall thermal conductivity and density. Figure 2 shows an example for timber, a sample is heated (25 kW/m^2) and its temperature distribution monitored and presented in Figure 3. Figure 2 shows clearly the water front moving ahead of the degradation front and the degradation front close to the heat source. Figure 3 shows the experimental temperature 5 mm in depth on the exposed side of the sample.

As it can be seen, the temperature plateaus at approximately 400 K and then at 700 K. The first plateau corresponds to the evaporation of water, the second to the endothermic pyrolysis of the char. The

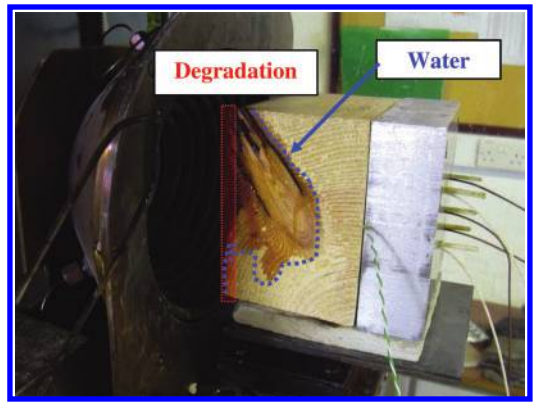


Figure 2. Timber sample heated at 25 kW/m^2 showing degradation and water fronts.

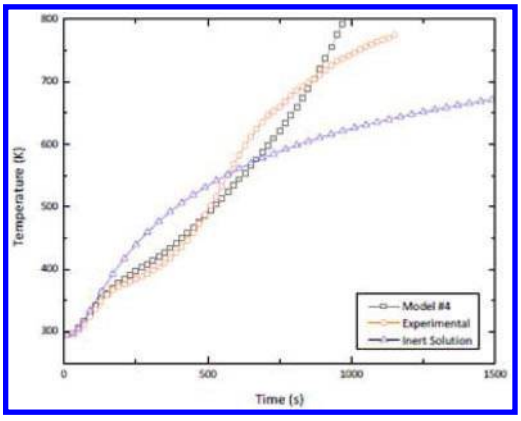


Figure 3. Evolution of the temperature of the temperature of a timber sample exposed to 25 kW/m^2 of heat. The values presented correspond to the temperature 5 mm below the exposed surface.

numerical models presented show the importance of including these processes. The data in red shows the experimental value while the models are presented in blue and black. The first model (blue) ignores the degradation and the water missing the water plateau (400 K) resulting in a faster initial heating but then reaching a plateau at 700 K. The second model (black) includes the water and the energy released by the char consumption nevertheless ignores the regression of the surface. The model captures well the water plateau but misses the final tampering of the temperature. While this example serves only to illustrate a point, it shows the importance of defining well the intricacies of the heat and mass transfer processes.

4 CONCLUSIONS

This paper has surveyed a number of different issues associated to the proper estimation of the fire input to the thermal evolution of a structure. It is essential that the thermal boundary condition is properly defined to be able to establish the performance of a structural system in a fire. While the analysis is not exhaustive and does not pretend to provide solutions to all these issues, it attempts to provide some clarification. The following main conclusions can be extracted:

- The evolution of the fire has to be established taking into consideration the specific geometry of the structure to be analyzed.
- When imposing constraints for simplification, the results cannot be extrapolated to spaces of different characteristics.
- The energy equation to be solved has to include all heat sources and sinks in particular those associated to water. It is also important to include in the properties and modeling domain processes such as surface regression and degradation.
- The thermal boundary condition associated to a fire has to be treated as a heat flux boundary condition and not a temperature boundary condition. Even in the case when this simplification is possible it is essential to formulate the problem in the correct way so that constants are evaluated correctly.
- Analysis of furnace results cannot avoid resolving the heat transfer between the furnace lining, the gas and the sample. Even if eventually the problem can eventually be formulated with a single gas phase temperature, this needs to be demonstrated by fully resolving heat exchange within the furnace. Furnaces are in many cases a more complex system to resolve.

REFERENCES

Buchanan, A.H. (2002) Structural Design for Fire Safety, Wiley.

EN 1993-1-2, Eurocode 3: Design of Steel Structures, Part 1-2 General Rules – Structural Fire Design, European Standard.

Drysdale, D.D., (1998) An Introduction to Fire Dynamics, 2nd Edition, Wiley.

Harmathy, T.Z. and Lie, T.T. (1970). "Fire Test Standard in the Light of Fire Research", ASTM Special Technical Publication 464, 85–97.

Harmathy, T.Z. (1981). "The fire resistance test and its relation to real-world fires", Fire and Materials, 5 (3), 112–122.

Hottel, H.C. (1984), "Stimulation of Fire Research in the United States After 1940 (A Historical Account)," Combustion Science and Technology, Volume 40, Issue 1–4, pp. 1–10.

Incropera, F.P. and DeWitt, D.P. (2002), Fundamentals of Heat and Mass Transfer, 5th Edition, Wiley.

Ingberg, S.H. (1928), "Tests of the Severity of Building Fires," National Fire Protection Association, 22, pp. 43–61.

ISO (1999). "ISO 834-1:1999: Fire Resistance Tests – Elements of Building Construction – Part 1: General Requirements". International Organization for Standardization, Geneva, Switzerland, 25pp.

Karlsson, B., Quintiere, J.G., "Enclosure Fire Dynamics," CRC Press LLC, Boca raton, FL, USA, 2000.

History of Fire Protection Engineering, J.K. Richardson, Editor, National Fire Protection Association, Quincey, USA, 2003.

Pettersson O., Magnusson S.E. and Thor J. (1976), "Fire engineering design of steel structures," Publication 50, Swedish Institute of Steel Construction, Stockholm.

The Dalmarnock Fire Tests: Experiments and Modelling (2007), Editors: G. Rein, C. Abecassis-Empis and R. Carvel, 221 pages, University of Edinburgh, ISBN 978-0955749704.

Thomas, P.H., Nilsson, L. (1973), "Fully-developed compartment fires: new correlations of burning rates," Fire Research Note 979, Fire Research Station, Borehamwood, England, UK.

Thomas P.H. (1967), "Fully-developed compartment fires – 2 kinds of behaviour," Fire Research Technical Paper N° 18, Ministry of Technology and Fire Offices Committee, Joint Fire Research Organization, Fire Research Station, London, England, UK.

UL 1962, File R4374-13, Underwriters Laboratories Inc., Northbrook, IL.

Research and Applications in Structural Engineering, Mechanics and Computation – Zingoni (Ed.)
© 2013 Taylor & Francis Group, London, ISBN 978-1-138-00061-2

Numerical simulation of thin RC structures exposed to fire

R. Harte
Department of Civil Engineering, University of Wuppertal, Germany
Krätzig & Partner Civil Engineering Consultants, Bochum, Germany

ABSTRACT: Building structures in general are designed with respect to the requirements of ultimate and serviceability limit states, considering ambient and operational temperatures. In addition, accidental design situations need to be investigated, like explosion, earthquake, impact or fire. In the past the fire case has been considered with different design philosophies, depending on the traditional practice in the different countries. Some have preferred active precautions to fight against fire, either by human facilities, like fire brigades and trained employees or porters, or by technical facilities, like automatic detectors, extinguishers and sprinkling systems. Other countries have favored passive fire protection measures, like defined fire walls and slabs to prevent fire from spreading across the whole building. In Europe, the introduction of Eurocode standards enables to internationally equalize the safety levels of fire design and proof. Following the Eurocode philosophy, the paper will present some numerical developments to analyze thin reinforced concrete structures in case of fire.

1 INTRODUCTION

In the past, the fire resistance of RC structures mainly has been determined by tabulated classes of structural elements, which were based on numerous fire tests. But those tests consume time and material and by this are very expensive. Thus the need for advanced and validated simulation models for the fire proof of RC structures is growing. Such an analysis is very complicated, because of the various factors which influence the structural behavior, mainly material properties, which are drastically reduced depending on high temperatures.

The Eurocode for RC structures (EN 1992-1-2:2004) offers three methods (Level 1–3) to prove the structural fire resistance:

The classical method Level 1 is based on tabulated limit values for the cross-section, concrete cover, grade of reinforcing steel, etc. of an individual structural element. This method is rather conservative and less economic and not valid for the overall bearing capacity of a structural system.

Level 2, called "simplified calculation methods", is more realistic by considering the time-dependant temperature profile across the structural element, by this quantifying a fire-reduced cross-section and the temperature-dependant reduction of the concrete compressive strength and of the reinforcement tensile and compressive strength.

The most realistic, but most expensive method Level 3, called "advance calculation models", is characterized by a holistic numerical simulation of the heat transfer in the "thermal response model" and structural behavior in the "mechanical response model"; it should be able to determine the structural behavior of the entire structure or of any part of it.

The present paper will touch the Level 2 methods for thin reinforced structures, but will mainly present numerical models on Level 3. For the fire proof of reinforced and composite beams a 3D-finite beam element has been developed, considering temperature-dependant material and geometrical nonlinearities. This element has been implemented in the software tool FS3D (Mihajlov 2009). For the holistic numerical simulation of RC plate and shell structures exposed to fire a coupled thermo-mechanical model has been developed and implemented in the finite element system FEMAS 2000 (Mannsfeld 2011).

2 RC BEAM STRUCTURES

2.1 *Simulation method*

In case of fire structural members heat up relatively quickly. This temperature change leads to material degradation which is characterized by rapid decrease of material strength and stiffness, changing the typical linear-elastic or perfectly-plastic material stress-strain relationship to nonlinearity. As a result, large structural deformations will appear which in case of compression might cause stability failure.

Numerical analyses of such complex problems need the application of finite element models considering material and geometrical nonlinearities. Such a numerical model is implemented in the program FS3D (Mihajlov 2009). This program is based on a 3D nonlinear beam finite element with arbitrary cross section. The calculation procedure is based on the formulations proposed by (Bathe 1982, Bathe 1996), but improved for analyses of steel, concrete and composite framed structures exposed to fire and high temperatures.

The cross section of the element is defined in segments (fibers), where each segment can obtain different materials, temperatures and mechanical properties. So-called "void" fibers allow the modeling of arbitrary cross section shapes. The beam element has 3 nodes, with 6 degrees of freedom in each node. Thermal expansion, cracking or crushing of concrete and changing of material properties of reinforcing steel are implemented regarding to the constitutive law defined in (EN 1992-1-2:2004). In addition the program involves modules which enable the calculation of the heat distribution in the cross sections which are exposed to an arbitrary heating/cooling action defined by specific time-temperature curves.

Calculation of the structural behavior in fire condition using the program FS3D is divided into two main steps. In the first step the program is evaluating the heat transfer and the resulting temperature profiles for all fire exposed elements which belong to the fire compartment. Regarding to the adopted integration time step, each heat distribution in the cross sections which appears in a certain time of the fire scenario is saved as separate thermal load case which later will be used in the static analysis. The second calculation step involves evaluation of the structural behavior during the fire process. The structural response under external loading at normal temperature is adopted as initial structural configuration. The solution strategy is to establish the new structural equilibrium under the previously calculated thermal load cases. The structural bearing capacity is defined with the first thermal load case which will not establish structural equilibrium. Beside this, the program enables analysis of post-fire structural behavior. This program option allows evaluation of the structural bearing capacity of the construction which already survived a certain fire scenario.

2.2 *Thermal response model*

In case of fire, the structure of a building is subjected to mechanical and thermal actions. The mechanical actions follow from the permanent loads like dead weight of the construction and the combination of existing live loads. The thermal actions follow from the increase of the gas temperature in the fire compartment. As a result, the thermal profile in the structure will lead to increased temperatures and to thermal elongation and curvature and to deterioration of the material properties of the structure. To determine this uneven thermal profile across the cross section, the following balance equation has to be solved.

$$(\rho_c c_c)\dot{\theta} = \mathrm{div}\left[\lambda \cdot \mathrm{grad}\,\dot{\theta}\right] + Q \qquad (1)$$

where ρ_c = density of dry concrete; c_c = specific heat capacity of concrete; λ = thermal conductivity matrix; θ = temperature; Q = heat source or sink; $(\dot{})$ = time derivative.

The temperature-dependency of these material parameters has to be considered. The differential equation (1), combined with initial and relevant boundary conditions, mainly convection and radiation, describes the initial value problem, which has to be converted into a finite element formulation. By this the thermal behavior in the structure can be determined.

Assumption for the uniform temperature distribution along the beam element length is adopted, which enables to simplify the 3D heat transfer problem into a 2D problem to be applied on the beam cross section. The program FS3D uses 4 and 8 nodes finite elements for calculating the heat distribution in the cross section. The implemented algorithm enables to solve the steady state and the unsteady state heat transfer problems. Using FEM for calculation of the heat distribution in the cross section enables to simulate heating and cooling of arbitrary shape composite cross sections, which can be exposed to any kind of fire load, defined by any time-temperature relationship. This approach allows consideration of nonlinear heat transfer effects like temperature dependent material thermal properties and radiation.

2.3 *Mechanical response model*

Material non-linear behavior caused by elevated temperatures is implemented in the numerical model by the temperature-dependant material properties. The program FS3D incorporates the material non-linear constitutive laws for steel and concrete according to (DIN EN 1992-1-2:2010). In general the concrete tensile strength is ignored for the proof and dimensioning the structural RC members. In order to achieve a realistic structural response by an advanced calculation model, the residual concrete tensile strength at elevated temperatures is employed in the program FS3D. The tension zone is described with the bilinear constitutive law according to Figure 1. The maximum tensile strength is a function of maximum compression strength of the concrete defined for a certain temperature level. After reaching maximum tensile strength,

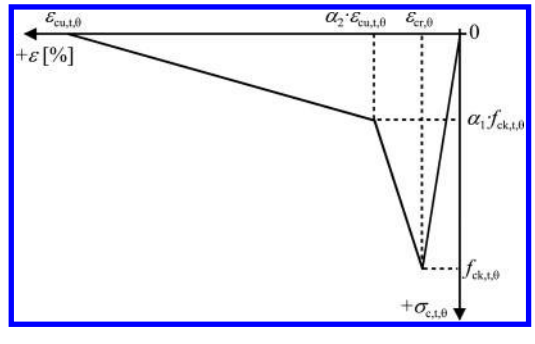


Figure 1. Schematic presentation of tension stress-strain relationship of concrete at elevated temperature θ; where $\sigma_{c,t,\theta}$ = tensile concrete stresses at θ; ε = tensile concrete strains; $\varepsilon_{cu,t,\theta}$ = ultimate tensile dilatation at θ; $\varepsilon_{cr,t,\theta}$ = concrete cracking tensile dilatation at θ; $\alpha_1 = 0.33$ (coefficient); $\alpha_2 = 0.22$ (coefficient); $f_{ck,t,\theta}$ = characteristic value of ultimate tensile concrete strength at θ.

a crack appears in the respective concrete fiber. For each cracked fiber, the constitutive matrix D involves zero values for the matrix members which are function of the concrete modulus of elasticity. All other members from the constitutive matrix D which are functions of the shear modulus have non-zero values as given in equation (2).

$$D = \begin{bmatrix} 0 & 0 & 0 \\ 0 & \mu G_c & 0 \\ 0 & 0 & \mu G_c \end{bmatrix} \tag{2}$$

The history of previous heating of the concrete fibers is also adopted into the material model. The concrete fibers which previously experienced higher temperature than the current one, are obeying constitutive law which is defined with the so-called residual concrete strength (ECCS TC3 2001). A short description of this concrete behavior is given in Figures 2 and 3. The solid line in Figure 3 represents the stress-strain relationship of the concrete when the fiber is heated up to temperature θ_1. After reaching the maximum temperature θ_{max} the process of cooling is starting (Figure 2). When the concrete fiber is cooled down to temperature $\theta_2 = \theta_1$ the material constitutive law (presented with the dashed line in Figure 3) is defined over residual concrete strength $f_{c,\theta 2}$, where $f_{c,\theta 2} < f_{c,\theta 1}$ even though the temperature $\theta_2 = \theta_1$.

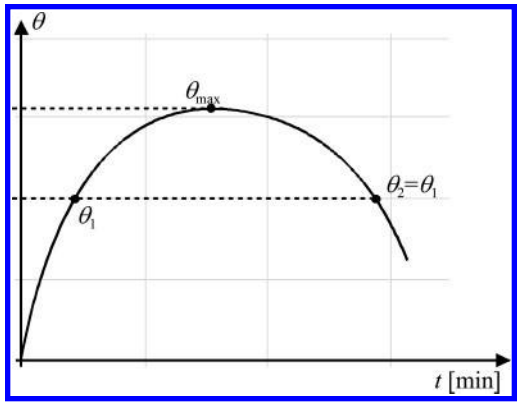


Figure 2. Time history of concrete heating, where θ = concrete temperature; t = time.

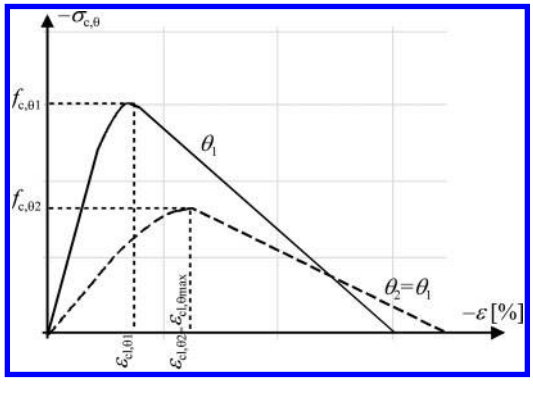


Figure 3. Stress-strain relationships for concrete with respect to heating history, where $-\sigma_{c,\theta}$ = compressive concrete stresses at elevated temperature θ; $-\varepsilon$ = compressive concrete strains; $\varepsilon_{c1,\theta}$ – strains at maximum compressive concrete strength at θ; $f_{c,\theta}$ = compressive concrete strength at θ.

This constitutive law for the concrete is implemented into the program FS3D. It enables the analysis of structural response during the cooling down process, finally simulating the post-fire load-bearing capacity.

2.4 *Non-linear 3D-finite beam element*

A general continuum mechanic equation for large displacements is used for deriving a non-linear stiffness matrix for a finite beam element employed in FS3D. The beam stiffness matrix is derived using the "equation of motion" (3) and is applied on the general body considering large displacements, large rotations and nonlinear constitutive response. The equilibrium of the body in motion for certain time configuration t can be obtained using the Total Lagrangian formulation.

$$\int_{0V} {}^{t+\Delta t}_{0}S_{ij}\ \delta\ {}^{t+\Delta t}_{0}\varepsilon_{ij}\ d^0V = \Re \quad i,j = 1,2,3 \tag{3}$$

where ${}^{t+\Delta t}_{0}S_{ij} = 2^{nd}$ Piola-Kirchhoff stress tensor at time configuration $t + \Delta t$; $\delta\ {}^{t+\Delta t}_{0}\varepsilon_{ij}$ = variation of Green-Lagrange strain tensor at time configuration $t + \Delta t$; ${}^{0}V$ = volume at time configuration 0; $\Re$ = components which describe external virtual work.

By using the Total Lagrangian incremental decomposition and employing the linearization procedure, a governing linearized form of the equation of motion is obtained.

$$\int_{0V} {}_0C_{ij}e_{rs}\delta e_{ij}d^0V + \int_{0V} {}^{t}_{0}S_{ij}\ \delta\eta_{ij}d^0V = \Re - \int_{0V} {}^{t}_{0}S_{ij}\delta e_{ij}d^0V$$

$$\text{with} \quad {}_0C_{ij} = \frac{\partial\, {}^{t}_{0}S_{ij}}{\partial\, {}^{t}_{0}\varepsilon_{rs}} \tag{4}$$

where ${}^{t}_{0}S = 2^{nd}$ Piola-Kirchhoff stress tensor in known time configuration t; ${}_0S$ = incremental 2^{nd} Piola-Kirchhoff stress tensor; ${}^{t}_{0}\varepsilon$ = Green-Lagrange strain tensor in known time configuration t; ${}_0\varepsilon$ = unknown incremental Green-Lagrange strain tensor; δe_{ij} = variation of linear part of the strain tensor; $\delta\eta_{ij}$ = variation of non-linear part of the strain tensor.

All terms in (4) are linear in the incremental displacements. The first integral from the left side of this equation defines the linear stiffness matrix of the beam, the second integral defines the nonlinear stiffness matrix and the integral on the right side represents the vector of unbalanced forces. This equation is implemented on a 3-nodes beam finite element shown in Figure 4.

Each node of the element has 6 degrees of freedom. The general definition of the beam cross section is

rectangular. Using the segmentation of the cross section and allowing some segments to be "void" (with zero mechanical and strength properties), modeling of arbitrary cross sections is possible. Further, the cross section can be offset from the beam reference line. The offset is defined by the distance Δt and Δs. The main assumption of the beam model can be summarized as follows:

- Plane section originally normal to the reference axis remains plane after the deformation, but not necessary normal to deformed axis. It is assumed that there is no slip between the fibers.
- Deformations and rotations can be arbitrarily large, but strains keep small. Thus the area remains unchanged after deformation.
- Each cross section fiber can obtain different temperature value but which is uniform along the element length.

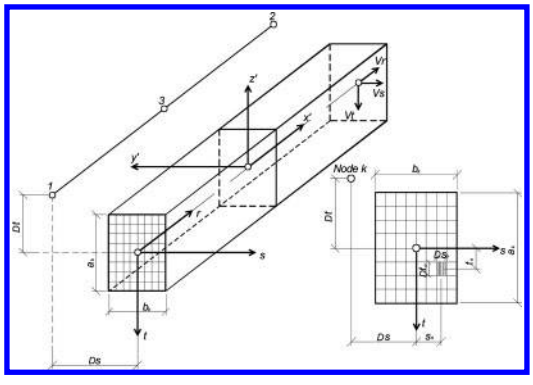


Figure 4. A non-linear beam column element (Mihajlov 2009).

- For each fiber within the cross section only the longitudinal stresses and two shear stresses are not zero.

Using the mentioned assumptions together with the beam shape function and employing in addition the second-order approximations (Argyris 1982), the linear and nonlinear beam-column stiffness matrix can be obtained. For more details see (Mihajlov 2009).

2.5 *Numerical example – RC cantilever column*

Figure 5 shows a RC cantilever column, which is exposed to fire from the left side only. The ultimate limit state of nonlinear load bearing is calculated to t = 64 min. duration of fire according to the numerical model of (Mihajlov 2009). The inner cold core of the cross section is totally cracked due to thermally induced tensile stresses, whereas the outer hot zones have to completely carry the compressive stresses. These zones are deteriorated due to the hot temperatures and the column is no longer stable and will collapse.

3 RC PLATE AND SHELL STRUCTURES

3.1 *Simulation method*

In case of fire, the slabs of buildings and the shells of curved structures like domes, tunnels and tanks, are subjected to mechanical and thermal actions, too.

Again the thermal behavior in the structure, in this case the thermal profile across the plate or shell thickness, needs to be determined.

For the mechanical calculations of reinforced concrete plate and shell structures exposed to fire, the

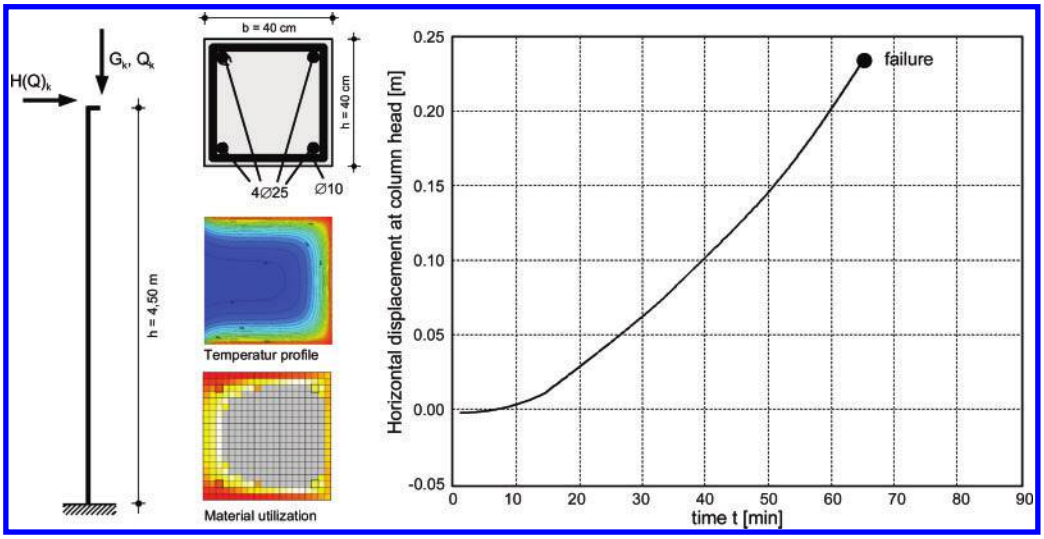


Figure 5. RC cantilever column – system data and results of numerical simulation; concrete C30/37 with concrete cover $c_{nom} = 3.0$ cm; steel BSt 500 S(A); actions at column head: permanent action $G_k = 725$ kN; variable action $Q_k = 125$ kN; $H(Q)_k = 5$ kN; eccentricity $e = 6$ cm (Harte et al. 2010).

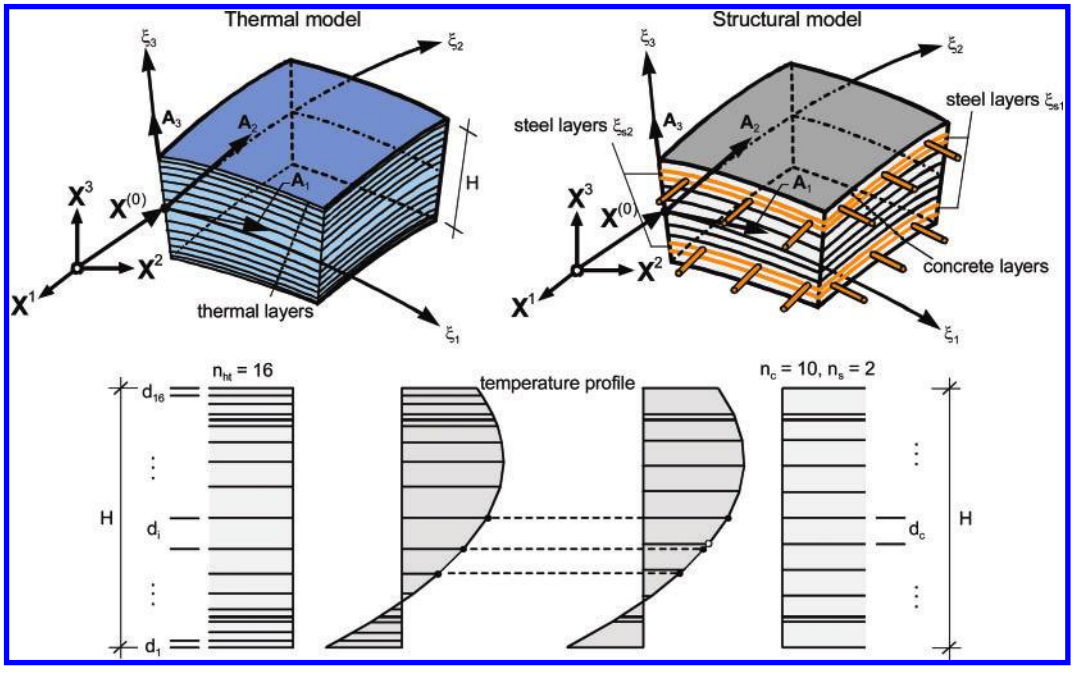


Figure 6. Multi-layered concept and interface element transformation between thermal model and structural model (Wörmann 2004).

existing Finite Element System FEMAS 2000 is used and extended by the component "fire or elevated temperature". The finite element, which is used, is a 4-node isoparametric Reissner-Mindlin-type finite shell element, where the shell theory is middle-surface orientated with rotational variables. By use of an interface element formulation (Wörmann 2004) combining the thermal simulation in thickness direction and the existing multi-layered concept (Krätzig 1997), it is possible to simulate the nonlinear behavior considering all temperature-dependant material data like strength, Young's modulus, etc. in each layer of the plate element. Both the thermal and the structural model with different number and spacing of layers and the respective transformation procedure is shown in Figure 6.



Figure 7. Fire test stand, slab and water drums to simulate the uniformly distributed load (Lim & Wade 2003).

3.2 *Numerical example – concrete slab*

The new developed model is verified by a comparison of experimental results and the results from the numerical simulations. Based on real fire tests in Cardington, England 1995/96, further fire tests of 6 two-way concrete slabs were realized by BRANZ Limited in 2002.

The selected reinforced concrete slab, called "661 flat slab" according to (Lim & Wade 2003), is 4.3 m wide, 3.3 m long and 10cm thick. The test stand is shown in Figure 7, and in Figure 8 you find the resulting deformation pattern after the fire test. Further information about the test program is given in (Lim & Wade 2003 and Mannsfeld 2011).

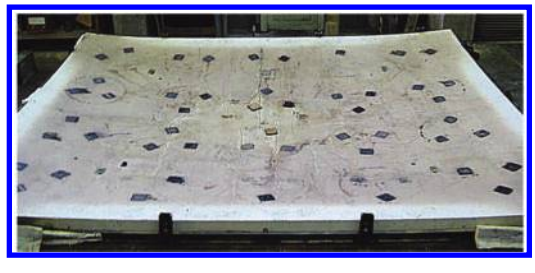


Figure 8. Top view of the slab after the fire test (Lim & Wade 2003).

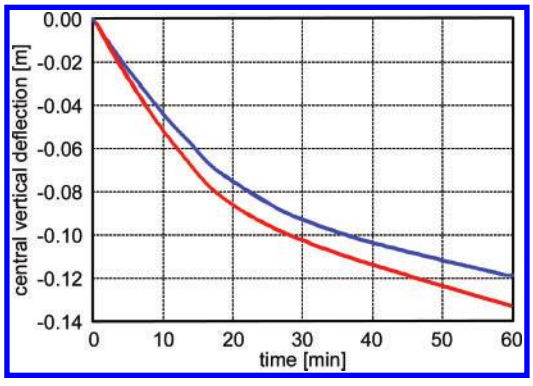


Figure 9. Numerical simulation with FEMAS 2000 – Central vertical deflection of the slab; upper line – experiment (Lim & Wade 2003); lower line – numerical simulation (Mannsfeld 2011).

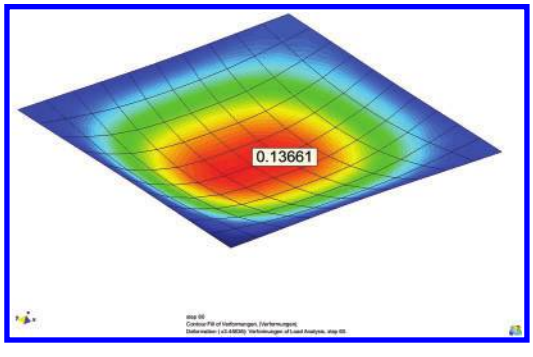


Figure 10. Deformation pattern after fire duration $t = 60$ min (Mannsfeld 2011).

To heat the slab the ISO 834 standard fire curve has been used both in the experiment and in the numerical simulation. The slab is modeled and calculated with FEMAS 2000 considering the coupled thermal and mechanical nonlinear simulation strategy according to (Mannsfeld 2011). Figure 9 and 10 show results at time-step $t = 60$ min. The central deflection according to the numerical simulation is slightly higher than the measured deformations, which is caused by the conservative assumptions for the material degradain case of elevated temperatures.

REFERENCES

Argyris, J. 1982. An excursion into large rotations. *Computer Methods in Applied Mechanics and Engineering* 32: 85–155.

Bathe, K.-J. 1982. *Finite element procedure in engineering analysis.* Prentice Hall Inc., New Jersey.

Bathe, K.-J. 1996. *Finite element procedure,* Prentice-Hall Inc., New Jersey.

ECCS TC3 2001. *Model code on fire engineering, 1st edition no. 111*. European Convention for Constructional Steelwork, ISBN 92-9147-000-65.

EN 1991-1-2:2002 (E). *Actions on structures – Part 1-2 general actions – actions on structures exposed to fire*. European Committee for Standardization.

EN 1992-1-2:2004 (E). *Design of concrete structures – Part 1-2: general rules – structural fire design*. European Committee for Standardization.

Harte, R., Ducke, M., Montag, U. 2010. Fire design in structural engineering (in German). Beucke, K., Mark, P. (eds.) *Innovations in structural engineering.* Proc. Jubilee Prof. Hirschfeld, Univ. Weimar and Univ. Bochum, 193–204.

Krätzig, W.B. 1997. Multi-level modeling techniques for elasto-plastic structural response. In D.R.J. Onate et al. (eds.) *Computational Plasticity, Part 1. Proc. 5th Int. Conf. CIMNE.* Barcelona: 457–468.

Lim, L., Wade, C. 2003. *Experimental fire tests of two-way concrete slabs.* Fire Engineering Research Report 02/12 University of Canterbury.

Mannsfeld, Th. 2011. *Structural behaviour of RC plates and shells considering temperature-depending nonlinearities in case of fire* (in German). Ph.D.-thesis, Bergische Universität Wuppertal, IKIB 18, ISBN 978-3-940795-17-5.

Mihajlov, V. 2009. *Numerical model for spatial steel and composite frame-structures exposed to fire and elevated temperatures*. Ph.D.-thesis, Bergische Universität Wuppertal, IKIB 14, ISBN 978-3-940795-13-7.

Wörmann, R. 2004. *On the simulation of hygrothermal influences on the nonlinear structural and deterioration behavior of RC plate and shell structures*. Ph.D.-thesis, Bergische Universität Wuppertal, IKIB 2.

Research and Applications in Structural Engineering, Mechanics and Computation – Zingoni (Ed.)
© 2013 Taylor & Francis Group, London, ISBN 978-1-138-00061-2

Shear capacity of steel plate girders with slender webs in fire

T. Ohtsuka
Meijo University, Nagoya, Japan

M. Knobloch & M. Fontana
ETH Zurich, Zurich, Switzerland

ABSTRACT: A simplified model for calculating the shear load-displacement relationship of steel plate girders with slender webs at high temperatures is proposed based on numerical results by FEM. This model uses the buckling degradation function which depends on the buckling parameter, and the post-buckling shear strength is given either by full plastic shear strength or full plastic moment using the buckling degradation function.

1 INTRODUCTION

The shear capacity of steel plate girders with slender webs can be calculated using Tension field theory proposed by Basler and other researchers (Galambos, 1998). Kimura et al. (2001) proposes the post-buckling shear strength of thin aluminum alloy plates by using the elastic limit width-to-thickness ratio and the plastic limit width-to-thickness ratio. Salminen and Heinisuo (2012) discuss the shear resistance of thin plate girder web panel at elevated temperatures and compare numerical results with results of an analytical model based on Eurocode.

This paper proposes a simplified analytical model for calculating the shear load-displacement curve of steel plate girders with slender webs at elevated temperatures. This model bases on the results of comprehensive numerical parametric study using the finite element approach.

2 NUMERICAL PARAMETRIC STUDY

The numerical parametric study considered three different finite element models. Model 1 (web plate model) just considered the web of the girder. The influence of the flanges was neglected. Model 2 (Plate girder model composed flange with beam element) considered the influence of flanges using beam elements. Thus, the influence of local flange buckling was neglected. Finally, model 3 (Plate girder model comprised of shell elements) considered both web buckling and local flange buckling using shell elements for the entire model.

The material coupon furnace test results for 500°C of Ave et al. (2011) are used in this study (Fig. 1). The following material properties were used: Young's modulus 156 [GPa], Yield stress 183.4 [MPa] and Tensile strength 241.7 [MPa]. This corresponds to reduction factors, given as the ratio of the material property at elevated temperature and corresponding property at ambient temperature, of $k_E = .0.74$, $k_y = 0.64$ and $k_u = 0.55$. In addition to the actual nonlinear stress-strain response (②)(Fig. 2) a linear elastic, perfectly plastic stress-strain relationship using Young's modulus and yield stress at 500°C(①) are used for comparison.

The finite element software SHIDEN (developed by Motoyui laboratory, Tokyo Institute of Technology) was used for all models of the numerical parametric study. The study considered three aspect ratios ($L/d = 1$, 2, 4, $d = 200$[mm]) and two width-to-thickness ratios ($d/t_w = 100$, 200, $t_w = 2$, 1 [mm]) for all models. The 1st and 2nd eigen mode were applied in all cases as the initial imperfections and it's maximum deflection was $t_w/100$.

2.1 *Web plate model*

The analytical model and its elastic buckling mode for an aspect ratio of $L/d = 2$ and a width-to-thickness ratio of $d/t_w = 100$ are shown in Fig. 3,4 as an example. All edges of the web plate model were simply supported, the boundary condition was simple shear (not pure shear) and the loading edge was allowed to move in the longitudinal direction but the rotation in plane was clamped.

Fig. 5 shows the load-displacement relationship. In Fig. 5, solid and dotted curve signify the results of material ② and ①, respectively. The shear force V is normalized by full plastic shear capacity ($V_p = dt_w\tau_Y$, τ_Y is shear yield stress) and displacement δ is

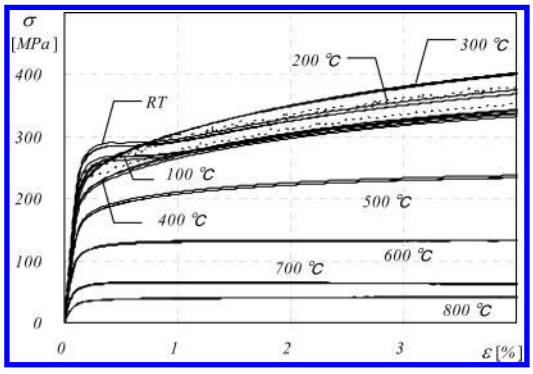


Figure 1. Stress-strain curve of coupon test.

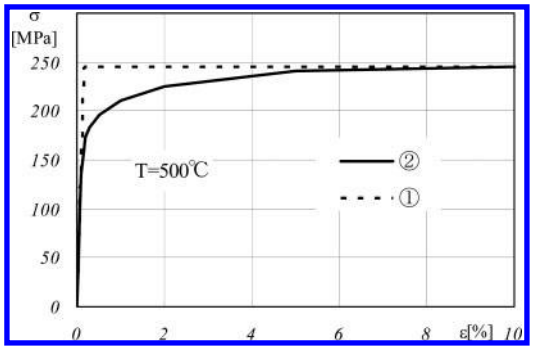


Figure 2. Stress-strain curve at 500°C in this paper.

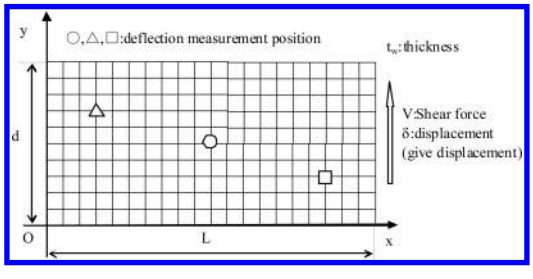


Figure 3. Analytical model (L/d = 2).

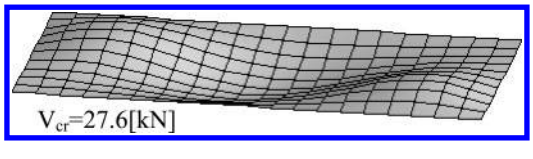


Figure 4. 1st eigen mode (L/d = 2,d/t_w = 100).

normalized by length L. In addition, Fig. 5 shows the elastic buckling shear force $V_{cr.}$(▲) The nonlinear stress-strain respond of material ② had a marked influence on the shear strength. Furthermore, V_{max}/V_p decreased for increasing aspect ratios.

Fig. 6 shows the out-of-plane deflection at locations given in Fig. 3. The displacement δ is normalized

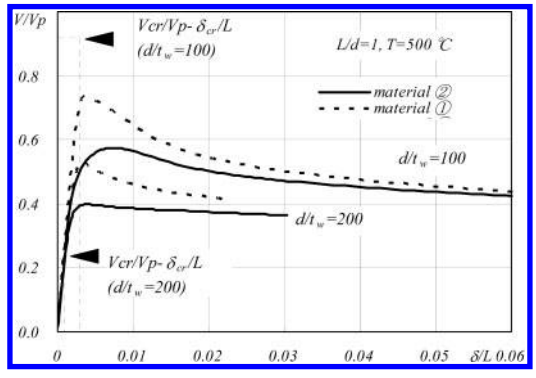


Figure 5(a). Load-displacement curve(L/d = 1).

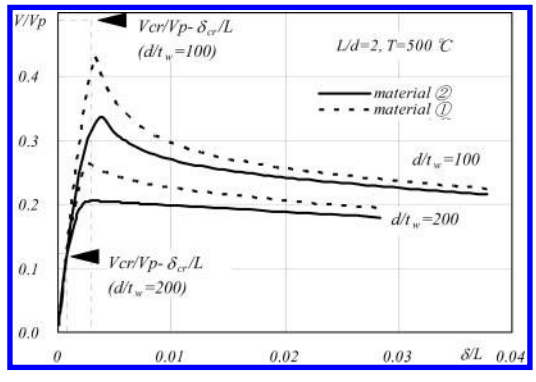


Figure 5(b). Load-displacement curve (L/d = 2).

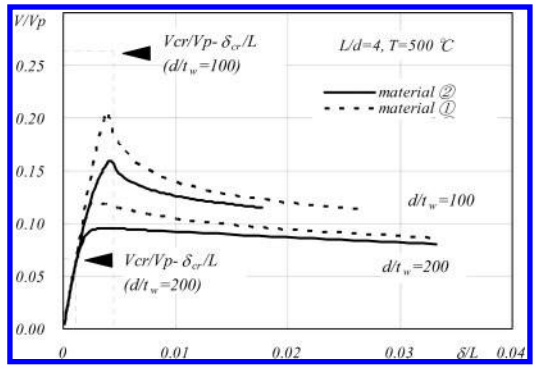


Figure 5(c). Load-displacement curve (L/d = 4).

by elastic buckling displacement δ_{cr} which is calculated by an eigenvalue analysis. Fig. 6 shows that the out-of-plane deflection strongly increased after the in-plane displacement exceeded the elastic buckling displacement.

Fig. 7 shows the bending moment at loading edge. The bending moment is normalized by full plastic bending moment capacity M_p and the in-plane displacement is again normalized by the elastic buckling displacement. In these models, the maximum load and post buckling behavior were limited by bending moment.

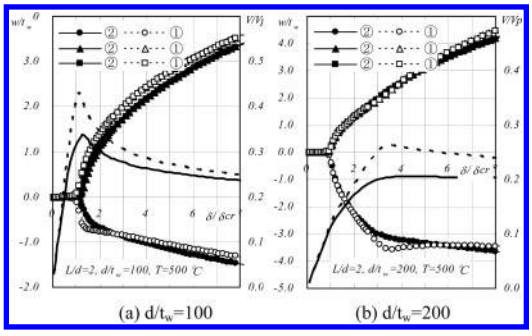


Figure 6. Deflection of out of plane (L/d = 2,T = 500°C).

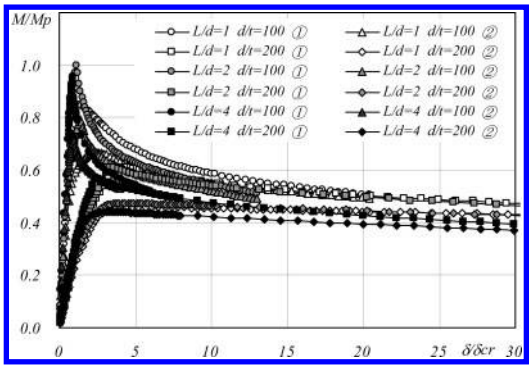


Figure 7. Bending moment-displacement relationship.

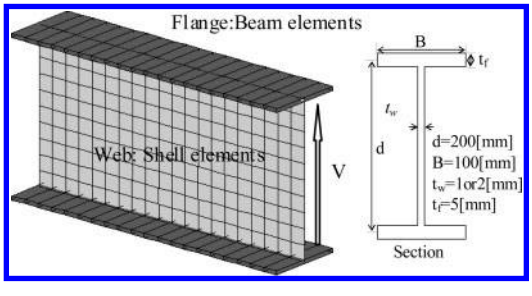


Figure 8. Analytical model (L/d = 2).

2.2 *Plate girder model composed flange with beam element*

Fig. 8 shows the numerical model. Beam elements were used to model the flanges of the girder, neglecting the influence of local flange buckling.

Fig. 9 show the elastic buckling mode calculated by an eigenvalue analysis. In comparison to the results of the web plate model, the elastic buckling load for aspect ratios L/d of 1 and 2 were bigger, but buckling modes were similar.

Fig. 10 shows the load-displacement relationship. The aspect ratio again markedly influenced the shear resistance V_{max} However, the shear resistance calculated with the plate girder model was significantly larger than the resistance calculated with the web plate model.

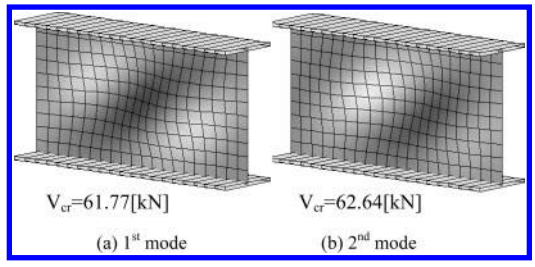


Figure 9. Eigen mode (L/d = 2, d/t$_w$ = 100).

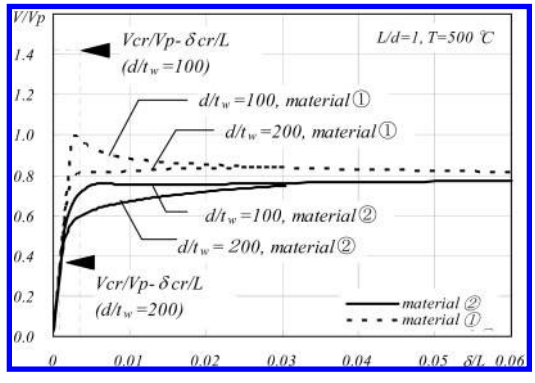


Figure 10(a). Load-displacement curve (L/d = 1).

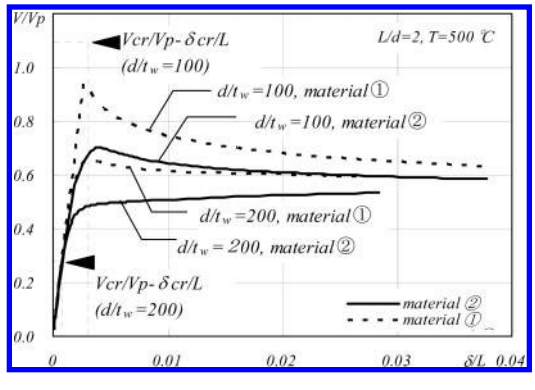


Figure 10(b). Load-displacement curve (L/d = 2).

2.3 *Plate girder model composed all of shell element*

Fig. 11 shows the model of the plate girder. The model consists of shell elements for the entire girder. In addition to a model without a stiffener, the study also analyzed the influence of a stiffener attached to the loading and supporting edge using a rigid beam for modeling.

Fig. 12 shows the elastic buckling mode. For an width-to-thickness ratio d/t$_w$ = 100, the flange was deformed by web buckling, but for d/t$_w$ = 200, the flange was not deformed.

Fig. 13 shows the load-displacement relationship of the model without a stiffener. Due to the rather

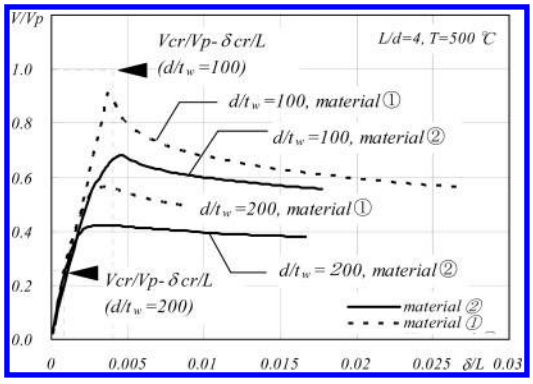


Figure 10(c). Load-displacement curve (L/d = 4).

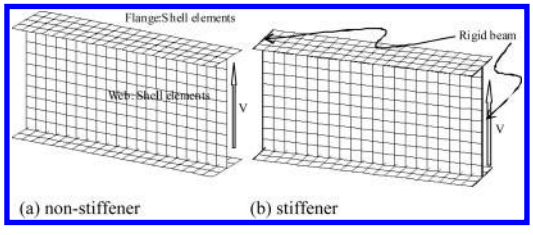


Figure 11. Analytical model (L/d = 2).

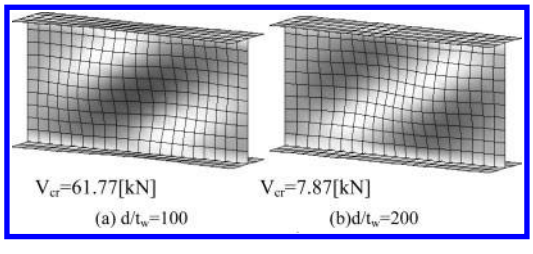


Figure 12. 1st eigen mode (L/d = 2, non-stiffener).

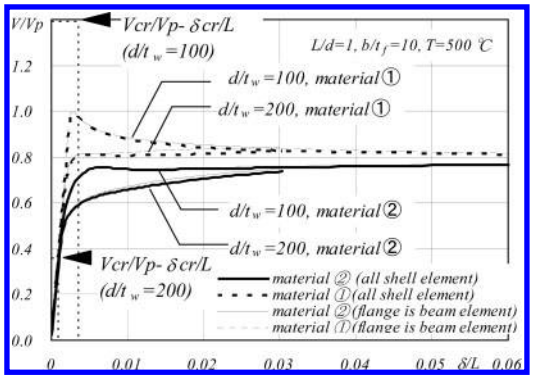


Figure 13(a). Load-displacement curve (L/d = 1).

low flange slenderness ratio the results of all shell element models were similar to the results of the model which used a beam element for flange modeling. For large in-plane displacements the relative shear loads V/V_p were 0.8 (L/d = 1), 0.6 (L/d = 2) and 0.4-0.5 (L/d = 4), respectively. The tension field might lead to the almost constant values for large displacements.

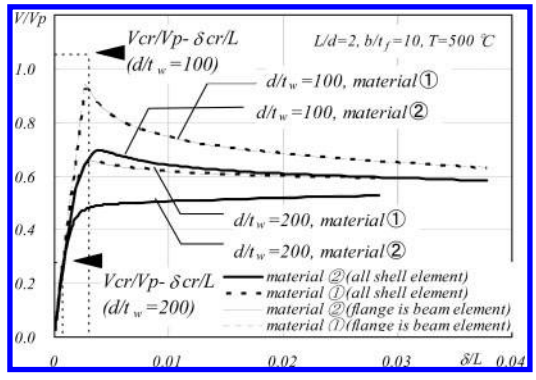


Figure 13(b). Load-displacement curve (L/d = 2).

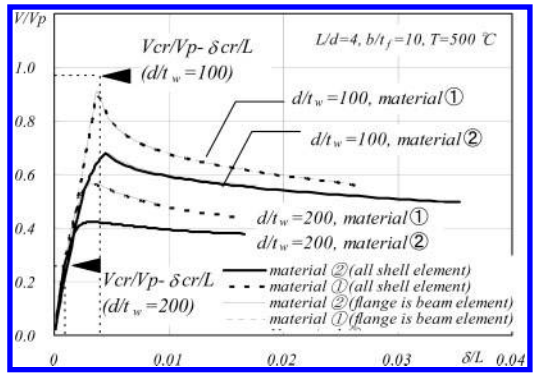


Figure 13(c). Load-displacement curve (L/d = 4).

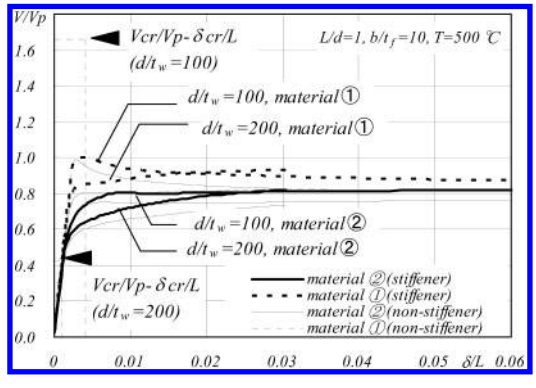


Figure 14(a). Load-displacement curve (L/d = 1).

Fig. 14 shows the load-displacement relationship of the models that considers stiffeners. The stiffener had almost no influence on the shear resistance and led to a small increase of the shear load for large displacements and small aspect ratios L/d. For small aspect ratios L/d the tension field might spread by attaching stiffeners.

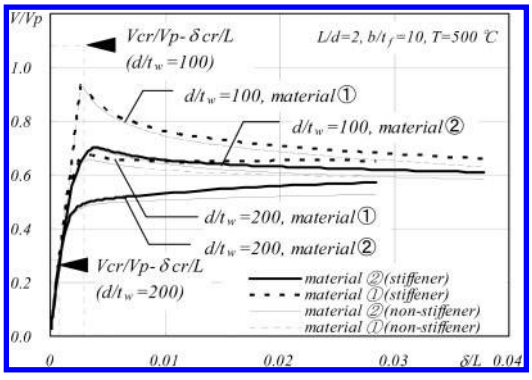


Figure 14(b). Load-displacement curve (L/d = 2).

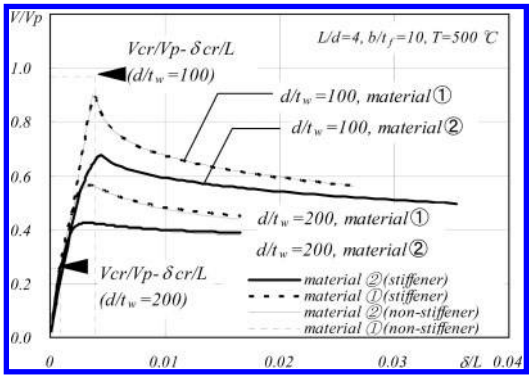


Figure 14(c). Load-displacement curve (L/d = 4).

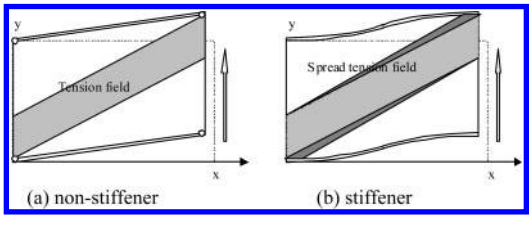


Figure 15. Deformation and tension field.

3 SIMPLIFIED MODEL FOR SHEAR LOAD-DISPLACEMENT BEHAVIOUR AT ELEVATED TEMPERATURES

3.1 *Proposed simplified model*

A simplified model for calculating the shear load-displacement relationship using a buckling degradation function $\bar{S}$ is proposed based on the results of the numerical study in this chapter.

The total displacement δ is divided into shear components δ_S and bending components δ_M.

$$\delta = \delta_S + \delta_M \tag{1}$$

Linear stiffness' given by Eq.(2) are used for calculating the shear load.

$$k_S = \frac{GA_w}{L},\quad k_M = \frac{12EI}{L^3} \tag{2}$$
$$V = k_S\delta_S,\quad V = k_M\delta_M$$

Three phases are considered.

1st phase: Elastic

The 1st phase is characterized by an elastic relationship between the shear load and the displacement (Eq. 3). The elastic buckling displacement can be calculated by either a numerical eigenvalue analysis or analytical models, e.g. Suzuki and Ikarashi, (2012).

$$\frac{V}{V_{cr}} = \frac{\delta}{\delta_{cr}} \tag{3}$$

2nd phase: Elastic shear buckling

After elastic buckling occurred the shear load can be calculated using Eq. (4)

$$\frac{V}{V_{cr}} = \bar{k}_{eb}\frac{\delta}{\delta_{cr}} \tag{4}$$

with $\bar{k}_{eb} = 0.7$

3rd phase: Plastic shear buckling

The 3rd phase constitutes plastic shear buckling. For this phase, the normal strain and shear strain can be calculated using Eq. (5). The yield normal stress σ_Y and yield shear stress τ_Y is then obtained by Eq. (6).

$$\varepsilon = \frac{6}{L^2}\frac{d}{2}\delta_M,\quad \gamma = \frac{1}{L}\delta_S \tag{5}$$

$$\delta_M = \frac{k_S}{k_S+k_M}\delta,\quad \delta_S = \frac{k_M}{k_S+k_M}\delta$$
$$\dot{\sigma} = \frac{E_{PT}E}{E+E_{PT}}\dot{\varepsilon},\quad \dot{\tau} = \frac{E_{PT}G}{3G+E_{PT}}\dot{\gamma} \tag{6}$$

with $\dot{\sigma} = sign(\sigma)E_{PT}\dot{\lambda}^p$, λ^p: plastic parameter.

The buckling degradation function $\bar{S}$ is given by Eq. (7). Using the buckling degradation function, the shear strength can be calculated with Eqs. (8) and (9), respectively, considering the full plastic bending moment and full plastic shear force.

$$\bar{S} = C_1 + (1-C_1)\{1-C_2(\Theta-\Theta_0)\}EXP\{C_3(\Theta-\Theta_0)\} \quad \{\Theta \ge \Theta_0\}$$
$$= 1.0 \quad \{\Theta < \Theta_0\} \tag{7}$$

where, buckling patameter $\Theta = \delta/\delta_{cr}$ and C_1, C_2, C_3 is softening coefficient for buckling.

$$\frac{V}{V_{cr}} = \frac{2Z_p\sigma_Y}{LV_{cr}}\bar{S},\qquad \frac{V}{V_{cr}} = \frac{A_w\tau_Y}{V_{cr}}\bar{S} \tag{8),(9)}$$

The shear strength is calculated as the minimum of Eqs. (3) or (4), (8) and (9).

$$\frac{V}{V_{cr}} = Min\{Eq.(3)or(4), Eq.(8), Eq.(9)\} \tag{10}$$

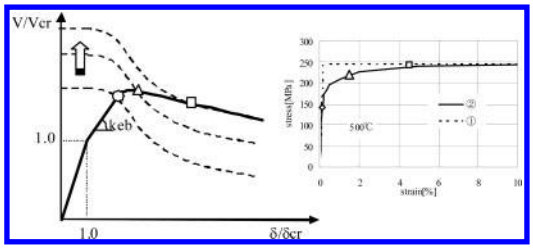


Figure 16. Illustrate the concept of proposed method.

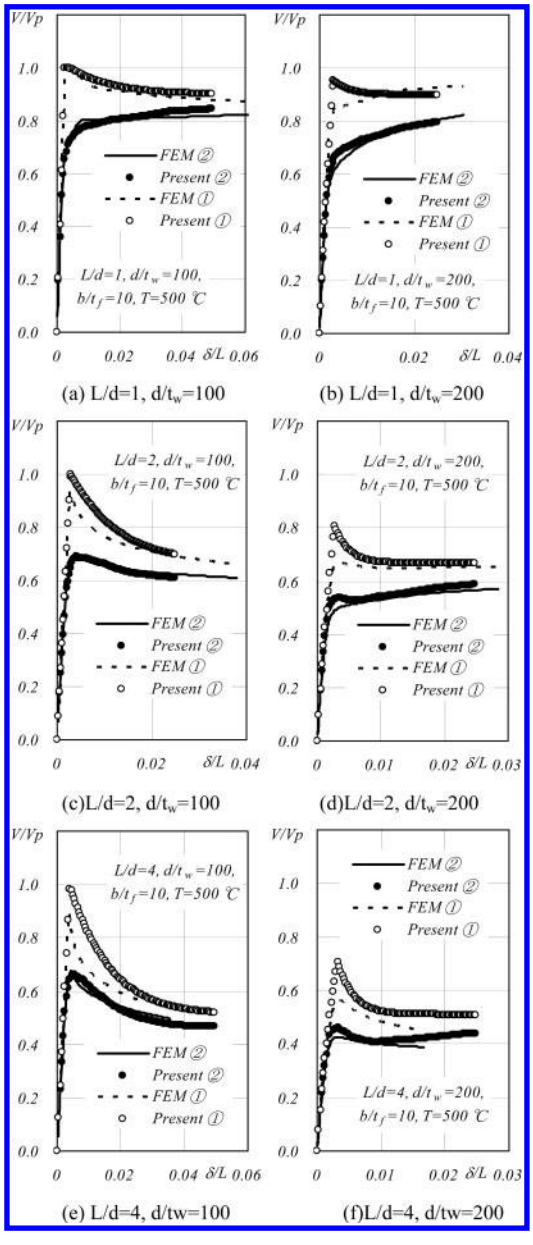


Figure 17. Comparison for stiffener models.

The concept of this simplified analytical model is illustrated in Fig. 16. For an elastic perfectly plastic material behavior, there is only one way of the plastic degradation curve. Considering strain hardening, the plastic degradation curve move according to the strain evolution.

Constant values are used for the softening coefficients C_2 and C_3 ($C_2 = -0.1$, $C_3 = -0.4$) The softening coefficient C_1 represents the shear load for large displacements. Thus, the aspect ratio affects C_1, and is calculated with Eq. (9) (girders with stiffeners) or Eq. (10) (girders without stiffeners).

$$C_1 = \begin{cases} 0.6\theta + \frac{1}{3} & \{\theta \le \theta_0\} \\ 1.0 & \{\theta > \theta_0\} \end{cases}, \quad \theta_0 = \frac{10}{9} \tag{11}$$

$$C_1 = \begin{cases} 0.72\theta + \frac{1}{3} & \{\theta \le \theta_0\} \\ 1.0 & \{\theta > \theta_0\} \end{cases}, \quad \theta_0 = \frac{100}{108} \tag{12}$$

with $\theta = \tan^{-1}(L/d)$[rad].

3.2 *Validation*

Figure 17 compares results according to the simplified analytical model (◯, ●) to numerical results. For all cases, the simplified model led to adequate results.

4 CONCLUSIONS

A simplified model for the shear load-displacement curve of steel plate girders with slender web in fire has been proposed. In this model, the buckling degradation function according to the buckling parameter Θ ($=\delta/\delta_{cr}$) is used. The shear strength is strongly influence by the shape of the stress-strain relationship. A distinct nonlinear stress-strain response decreases the shear strength. However, the shape of the material behavior has no influence on the shear load for large displacements.

REFERENCES

Ave, T., Ohtsuka, T., Shibata, S., Knobloch, M. & Fontana, M., Feb., 2011, Buckling Behavior of Cruciform Section Steel Stub Column at High Temperatures, *J. Struct., Constr., Eng.*, AIJ, Vol.76, No.660, pp.437–442. (in Japanese)

Galambos, T.V., 1998, Guide to Stability Design Criteria for Metal Structures Fifth Edition, John Wiley & Sons, Inc.

Kimura, M., Inoue, T., Taniguchi, H., Hashimura, T. & Komatsu, K., Jul., 2001, Post-buckling Strength of Thin-Plates, *J. Struct. Constr. Eng.*, AIJ, No.545, pp.135–140. (in Japanese)

Salminen, M. & Heinisuo, M., 2012, Shear Resistance of Thin Plate Girder Web Panel at Non-uniform Elevated Temperatures, *Nordic Steel Construction Conference*, pp.461–470.

Suzuki, T., Ikarashi, K., Mar., 2012, Stress separation concept for plate buckling strength under flexural-shear and axial force, *Journal of Constructional Steel Research*, No.70, pp.317–325.

Research and Applications in Structural Engineering, Mechanics and Computation – Zingoni (Ed.)
© 2013 Taylor & Francis Group, London, ISBN 978-1-138-00061-2

Modeling and assessment of the response of super-light elements to fire

K.D. Hertz
Civil Engineering Department, Technical University of Denmark, Lyngby, Denmark

B.M. Campeanu
COWI A/S, Lyngby, Denmark

M. Giraudo
Rambøll Danmark A/S, Esbjerg, Denmak

L. Giuliani
Civil Engineering Department, Technical University of Denmark, Lyngby, Denmark

ABSTRACT: Due to the significant weight of the elements, which raise the construction and transportation costs and the CO_2 production, concrete buildings may not meet the requirements for sustainable constructions. Furthermore, concrete is quite vulnerable to fire, as it undergoes a permanent degradation of its mechanical properties at temperatures commonly reached by structural elements during a fire in a building. As a consequence, several multi-story concrete buildings have collapsed or suffered major structural damages because of fire, and caused injuries and casualties among the occupants. Even in those cases, where a safe evacuation of the building is ensured, the high costs associated with the downtime and reparation of the building can be very high and not acceptable in the view of a safe and sustainable design of structures. In this respect, the newly patented building technology of superlight elements invented at DTU seems very promising in reducing the weight of the elements and improving their structural integrity in case of fire or other accidental actions. In particular, the behaviour under fire of a superlight floor slab element (SL-deck) is investigated in this paper. The implementation of a three-dimensional Finite Element Model (FEM) of the SL-deck is described and modelling aspects are discussed with particular reference to the sensitivity of the model to the thermal properties of the strong and light concrete. The results of the investigation are compared with the outcomes of a fire test performed on a prototype slab. The implementation of a FEM is useful in order to predict the structural behaviour of the slab under different fire and boundary conditions. However, the relevance of the study lies in particular in the presentation of a methodology for the investigation of the fire performances of complex concrete elements and in the focus on modelling issues related to the handling of the uncertainties.

1 INTRODUCTION

1.1 *Sustainability of concrete*

Concrete constructions are typically characterized by a significant weight of the elements. This has an impact on both the construction and transportation costs and on the increment of the CO_2 as well.

In the view of a more sustainable building process, the employment of light but resistant concrete elements, such as hollow core slabs (HCS) or high resistant concrete beams and columns, could favour the sustainability of buildings. Nevertheless, the behaviour of these elements under accidental actions such as a fire or an explosion can be critical, e.g. in case of spalling of the high resistant concrete (Hertz, 2003), loss of anchorage of the reinforcement (Hertz, 1982), and opening of the holes and consequent loss of insulation in a HCS (Jensen, 2005).

In particular, the integrity of slabs is essential in case of multi-storey building fires, where the failure of a concrete floor element may trigger a vertical propagation of both the damages and the fire, and potentially lead to a progressive collapse of the building, as happened in few recent building fires (Ikeda & Sekizawa, 2005), (Mecham, et al., 2010).

Even if quite rare, fire-induced collapses of buildings have very severe economical and societal consequences, as they imply high demolition costs and cause often several casualties or injuries among the occupants and the rescue personnel.

Also in those cases, where a major collapse is avoided and the safety of the occupants can be ensured by a rapid egress, fire-induced damages in concrete buildings have high economical repercussion in term of downtime and renovation costs. This is due to the fact that, contrarily to a common belief, concrete is quite vulnerable to fire. Unlike ordinary mild steel, which regains its initial strength and stiffness after cooling, concrete undergoes a permanent degradation of the mechanical properties when heated over 300°C

(Hertz, 2005). Despite the low conductivity of the concrete, this is a temperature that is easily overcome in the concrete cover of the reinforcement after the first 30 min of exposure and that can penetrate the inner part of a floor slab during the cooling phase a fire.

In addition to the weight of concrete elements, which affects the construction and transportation costs, sustainability issues should be therefore considered also in relation to the fire vulnerability of the elements, which significantly affects the reparation costs.

1.2 *Superlight elements*

The newly patented building technology that goes under the name of superlight structures (Hertz, 2010) seems able to combine sustainability issues related to both the weight and the vulnerability to fire of concrete elements (Hertz & Bagger, 2011).

The technology is based on encasing a core of strong concrete in a very light concrete aggregate. The light material stabilizes the core and protects it from accidental actions, such as fire, impacts, and explosions.

The result is a light, resistant, economic and robust structural element, which has proved to possess very good performances under ordinary loads and a very high resistance under fire in a test recently performed at DBI (Hertz, in publication).

In particular, super-light deck elements (Christensen & Hertz, 2012), referred in the following as SL-decks, are obtained by casting an ordinary concrete over an array of lightweight concrete blocks with pre-stressed wires acting in the longitudinal direction. The ordinary concrete contains the compression zone and surrounds the wires, while the light concrete, which contribute only very little to the overall resistance of the deck, is used in the remaining parts, in order to reduce the weight of the slab and consequently of the whole building.

Furthermore, the light concrete on the bottom of the deck works as a layer of insulating material for both the transmission of sound (Christensen, et al., 2012) and temperature. With respect to fire in particular, the high porosity and low conductivity of the light aggregate ensure low temperatures in the reinforcement and in the compression zone.

1.3 *Purpose of the study*

Being a new technology, the SL-deck requires the use of new methods for the assessment of the structural capacity in case of ordinary and accidental action. Analytical simplified methods for the calculation of load bearing capacity under ordinary actions have been developed in the framework of a M.Sc. project carried on at DTU (Halldórsson, 2012).

In the present study instead, an advanced numerical model has been used in order to investigate the fire behavior of a SL-deck. To this aim, a finite element model (FEM) of the slab has implemented and validated against data from the fire test.

Modelling aspects are presented, concerning the interaction of a high-resistant concrete and a light aggregate, the effect of pre-stressing and tension-stiffening of the concrete, the thermal degradation of the material. In particular, the sensitivity of the model to uncertainties, such as the thermal properties of the concrete aggregates, is investigated and discussed.

2 SL-DECK MODEL AND INVESTIGATION

2.1 *Geometry and properties of the slab*

The SL-deck here considered is made by casting a C50/60 concrete on three adjacent rows of Light Expanded Clay Aggregates (LECA™) concrete blocks.

The light blocks have a pyramidal shape with an outer box dimension of 500 × 400 × 185 mm and are covered with ordinary concrete. The concrete is cast up to a height of 30 mm from the highest point of the block, so that the height of the slab cross-section is 215 mm and the width is 1200 mm, as seen in Figure 2.

Two pre-stressing wires are placed in the ordinary concrete in between the light blocks at a depth of 75 mm from the bottom surface of the deck. One pre-stressing wire is placed on each side of the slab at a depth of 85 mm. The wires have a diameter of 12.5 mm made of S1860 steel.

In order to provide better anchorage to the pre-stressing wires, the last 100 mm at each deck end are made of solid ordinary concrete. A total length of 6.2 m has been considered for the slab.

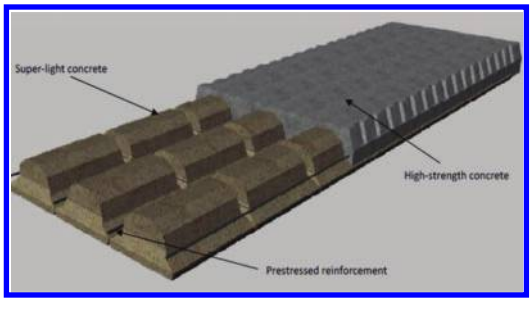


Figure 1. Sketch of a SL-deck element before and after the cast of ordinary concrete on the light blocks.

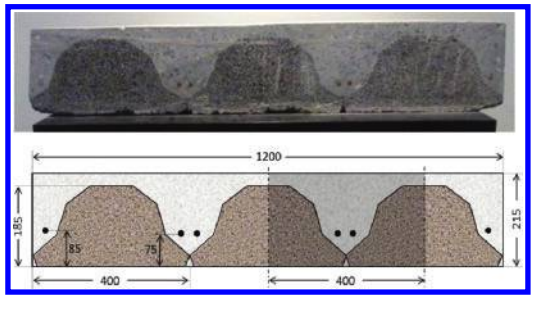


Figure 2. Cross section of a SL-deck. Top: picture of a deck slice; bottom: sketch of the section geometry.

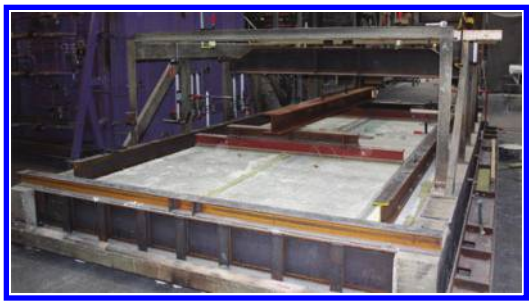


Figure 3. Setup for the fire test of the SL-deck at DBI.

2.2 *Fire test*

A fire test of the slab (Hertz, in publication) was performed in the laboratory of the Danish Institute of Fire and Security Technology (DBI).

In the test, two 1.2 m wide and 6.2 m long deck elements were placed side by side in a frame, which provided a support of 100 mm at each slab end, leaving a free span of 6 m. Mineral wool was placed along the deck junction and all around the slab sides, in order to avoid heat dispersion from the gaps without hindering the free expansion of the slab.

The frame was then placed above a large furnace and a load equivalent to a distributed load $p^{fi} = 2.5\,\mathrm{kN/m^2}$ was applied. This corresponds to the sum of service load $q_k = 1.5\,\mathrm{kN/m^2}$, as indicated by the Eurocodes for a domestic building (EN 1991-1-1, 2002), and a permanent load $g_k = 1.0\,\mathrm{kN/m^2}$ corresponding to the expected weight of the flooring and tributary separation walls. The load was applied by means of a hydraulic jack acting on a longitudinal steel beam, which transmitted the load to two transversal steel beams spacing 2 m from each side of the slab (Figure 3). An equivalent pointed load of 36 kN is found from the considered distributed load, by imposing the identity of the maximum moment corresponding to the two load distributions. By subtracting the weight of the three steel beams to this value the load to be applied by the hydraulic jack was found equal to 31.8 kN.

After having loaded the slab, the furnace was turned on and calibrated in order to reproduce a standard fire (ISO834-1, 1999) for 120 min. During this time, the load on the slab was kept constant by lowering the hydraulic jack, so that the vertical displacement of the slab could be followed. The temperatures in the slab were registered by means of thermocouples previously placed on the top and bottom surface of the slab and on the pre-stressing wires as well, before casting the concrete.

After 120 min, the vertical load on the deck was increased at a rate of ca. 18 kN/min. The intention was to reach the ultimate capacity of the slab, but the maximum force that the hydraulic jack could exert was reached before any slab failure occurred. The maximum force applied by the hydraulic jack plus the weight of the beams corresponded to 249 kN. The distributed load that would induce the same maximum moment at the mid-span can be calculated as $p_u^{120} = 17\,\mathrm{kN/m^2}$, whereas the load bearing capacity before fire had been assessed as $p_u = 23\,\mathrm{kN/m^2}$ in a previous test (Halldórsson, 2012).

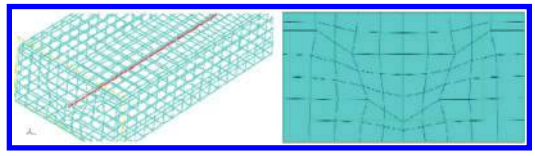


Figure 4. Structural (left) and thermal (right) model of the slab.

Table 1. Mechanical and thermal properties at of the materials at 20°C.

	Mechanical properties				Thermal properties		
Material	E GPa	f_k MPa	f_{tm} MPa	α K^{-1}	ρ kg/m^3	λ W/mK	c_p J/kgK
Steel	201	1860	–	–	–	–	–
C50/60	37	50	4.10	6E-6	2300	1.95	901
LECA	3	3	0.15	8E-6	600	0.3	840

3 FEM MODELING AND ANALYSES

3.1 *Structural and thermal model*

Two different models have been implemented in Abaqus™ (Simulia Corp., 2011): i) a thermal model, where the temperature distribution caused by the fire exposure has been computed along the slab section; and ii) a structural model, where the response to the mechanical and thermal load has been evaluated in terms of vertical displacement of the mid-span of the slab during the fire.

3.1.1 *Structural model*

A three-dimensional finite element model of a strip of the slab has been implemented. The strip is 400 mm wide and includes the wedge-shaped ordinary concrete with two wires on the bottom and half of the light blocks on each side (highlighted area at the bottom of Figure 2). This simplification is acceptable in consideration of the one-way action of the slab and allowed for a significant reduction of the computational onus.

The two types of concretes have been modelled with 8 node linear brick elements, while the two reinforcement wires pertinent to the slab strip have been modeled as one-dimensional rod elements embedded in the three-dimensional concrete elements. A mesh seed of 45 mm has been used, which corresponds to 9510 elements. The mesh size has been calibrated by means of a sensitivity study and on the basis of the minimum number of nodes required for a smooth variation of the thermal load.

The mechanical properties of the two concrete aggregates and of the steel wires are reported in Table 1 with respect to the values at 20°C. The degradation of these properties with the temperatures has been considered as specified in the Eurocodes for the steel

(EN 1993-1-2, 2005) and the ordinary concrete (EN 1992-1-2, 2004). With respect to the light concrete, no indication is given in the codes, but a model for the strength degradation can be found in literature (Hertz, 2005). However, the consideration of a refined model for the light concrete strength has been disregarded in this study and the same indications given for the ordinary concrete have been followed. Nevertheless, given the low contribution of the light concrete to the mechanical resistance of the element and the fact that compressive stresses are expected to develop only within the strong concrete, this simplification is not expected to affects the results significantly.

An elastic-plastic bilinear constitutive model has been assumed for the steel, while a damage plasticity model has been adopted for the ordinary and light concrete. The latter requires the definition of compressive hardening and tension-stiffening models. In order to overcome the problem of possible strain localization and mesh-dependent solutions (Bontempi & Malerba, 1997), the material law has been calibrated on the mesh chosen, so that the fracture energy at 20°C has been preserved (Feenstra & De Borst, 1995). It has to be noted that, since the fracture energy varies with the temperature, this calibration is not rigorously valid during fire. Nevertheless, in lack of experimental knowledge on the variation of the tensile fracture energy with temperature (Carstensen, et al., 2013), the temperature dependency of the tensile relation has been modelled by assuming the same stiffness of the compressive branch.

Due to the presence of geometric nonlinearities, the thermal expansion is expected to affect, even if in a limited way, the vertical displacement of the slab. In addition to the degradation of the mechanical properties of the materials, a temperature dependent expansion coefficient has therefore been considered in the structural models for the three materials, according to the Eurocodes specifications.

3.1.2 *Thermal model*

Since the section of the slab is constant and the whole length of the slab is considered to be exposed to the same temperature, the thermal model of the slab could be limited to a two-dimensional model of just one section of the slab strip. Nevertheless, due to the low computational onus of the thermal analysis and the convenience in importing the temperature history of the nodes into the structural model, the same three-dimensional geometry and mesh used for the structural model of the slab strip has been adopted for the thermal model too.

In this model 8-node brick heat-transfer elements have been used for the concretes, while the steel wires have not been represented. The reason is that, due to the small size of the wire and the high steel conductivity, the temperature in the wires can be assumed to be constant and equal to that one at the surface of the surrounding concrete.

In Table 1, the thermal properties assigned to the two concrete types are reported with respect to the values at 20°C. The degradation of the thermal properties of the ordinary concrete has been defined according to what specified in the Eurocodes (EN 1992-1-2, 2004), while for the light aggregate the thermal properties, defined in accordance to what specified in Hertz (2009), have been assumed to stay constant in a first stage of the study. This choice was motivated by past tests presented in literature (Pettersson & Ödeen, 1978), which showed that the conductivity of light aggregate concrete does not vary much with temperature.

However, in absence of a well-established modeling procedure of superlight elements, the presence of uncertainties should be taken in proper consideration. In particular, the uncertainties on the moisture content and on the composition of the light aggregate could influence the diffusivity of the light blocks and consequently the thermal and structural response of the slab under fire exposure. A validation of the steel temperatures against the test results has been therefore performed with the aim of improving the thermal model. In the following, results related to the original (a-priori) and the improved (a-posteriori) thermal model are compared.

3.2 *Boundary conditions and analysis steps*

The slab is considered to be simply supported. This is realized by restraining the displacements of the nodes lying on the horizontal axis of the outmost sections of the slab, in order to minimize the localization of stresses and favour the convergence.

The slab is pre-stressed to the 70% of the maximum wire strength, corresponding to a pre-stressing force of 128.25 kN. The effect of the pre-stressing force is accounted in the model by means of a negative temperature applied on the wires before the application of the distributed vertical load and of the thermal load due to fire. The negative temperature to be applied on the wires in order to simulate the compression of the pre-stress has been calculated as −540°C and applied to the wires in a fist load step. This temperature has been used to scale the degradation of all steel properties, in order to reproduce the correct loss of the pre-stressing effect and strength of the steel during the fire, so that the steel properties at 20°C corresponds to the properties at −540°C in the model. The slab is also considered to carry a distributed load at the time of fire assessed as $p^{fi} = 2.5\ \mathrm{kN/m^2}$, as specified in the previous section. This is accounted in a second load step, by means of a uniformly distributed load applied on the upper surface of the element. The slab is then considered to be exposed to a standard fire for 120 min. Since the thermal and mechanical problems are uncoupled, the thermal load history can be computed by means of a separated analysis on the thermal model of the slab.

In this analysis, the sides and the upper surface of the slab have been considered insulated and modelled as adiabatic surfaces. The bottom surface of the slab has been instead considered to be fire exposed and a standard temperature-time curve has

been applied to the nodes of the bottom surface of the slab model. In the analysis, a heat transfer coefficient $\dot{h} = 25\,\mathrm{W/(m^2K)}$ and a resultant emissivity $\varepsilon_r = 0.7$ (Purkiss, 2007) have been used. The temperature history obtained in each node was then imported in the structural model and applied in a third load step to the correspondent nodes of along all slab length.

Finally, a fourth load step was considered, where the temperature corresponding to 120 min of fire has been maintained constant and the vertical load has been incremented up to the crisis of the slab.

4 RESULTS OF THE INVESTIGATION

4.1 *Thermal analysis*

The results of the thermal analysis related to the original thermal model are reported in Figure 5. The temperature at the bottom surface is in good accordance with the temperature calculated with simplified analytical methods. As an example, a bottom surface temperature of 1033°C is given by the thermal analysis after 120 min, whereas the formulas of Hertz (1981) and Wickström (1986) gives temperatures of 980°C and 1015°C respectively, for the same time of exposure. For a more detailed comparison, reference is made to the M.Sc. project report this paper is based on (Campeanu & Giraudo, 2011)

The results reported in Figure 5 refer to a first thermal model, where the assumptions specified in the previous section have been taken with respect to the uncertainties present in the initial thermal properties of the concretes and in their variation with the temperature.

After the test has been performed, it has been possible to compare the results yielded by the thermal model with the outcomes from the test. The comparison proved the inaccuracy of the thermal model in predicting the temperature after the first 40 min of fire. In particular, the temperatures of the steel wires registered during the test were significantly lower than the ones predicted by the model, as shown in Figure 6.

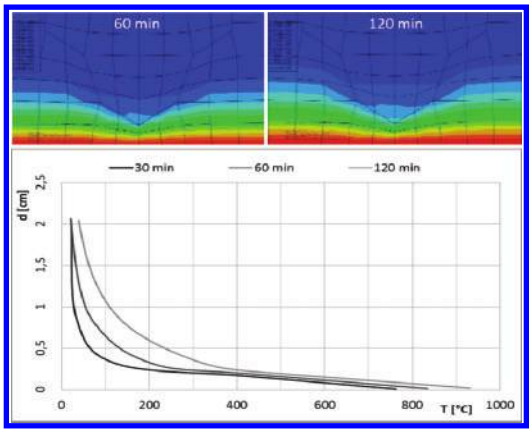


Figure 5. Thermal map (top) and temperature profile along the section central vertical axis at given times (bottom).

The thermal model has been therefore modified and calibrated in a way to better fit the results of the test. In particular, it has been seen that a very good fitting of the steel temperatures is yielded by accounting for the degradation of the conductivity of the light concrete and by assuming for the ordinary concrete the lowest conductivity curve indicated in the Eurocodes (corresponding to a value at 20°C of $\lambda_c = 1.36\,\mathrm{W/(m{\cdot}K)}$ and of the value $\lambda_c = 1.95\,\mathrm{W/(m{\cdot}K)}$ initially assumed).

4.2 *Structural analysis*

The results of the structural analyses performed with the temperatures obtained from the a-priori and a-posteriori thermal models are presented in the following. In Figure 7 the vertical displacements of the mid-span during fire is reported in both cases and compared with the data from the test.

It can be seen that the displacements related to the two thermal models are very similar in the first phase of the fire. However, after ca. 40 min of fire the displacement calculated with the a-priori model continues to increase almost linearly with the temperature, while the displacement-temperature curve obtained from the a-posteriori model assumes a convex form. This corresponds well to the test, where the increment of the vertical displacement was constant for the first 40 min of fire and then slowed down and stopped after ca. 90 min at the value of 2.5 cm, displacement that was kept constant until 120 min.

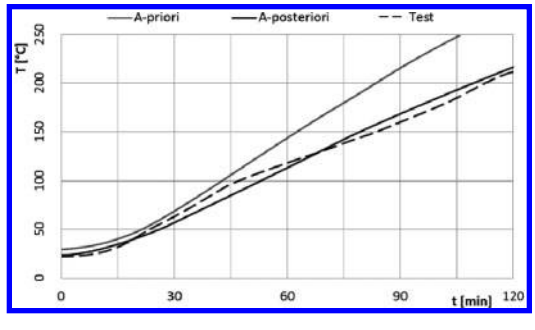


Figure 6. Temperature of the wire in the test and comparison with the a-priori and a-posteriori thermal model.

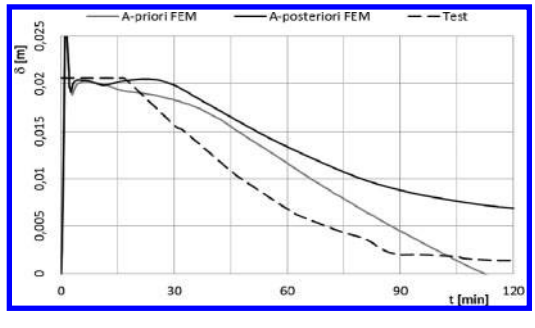


Figure 7. Mid-span displacement registered during the test and predicted by the a-priori and a-posteriori FEMs.

Even if there is a discrepancy between the displacement at 120 min registered in the test and the one of 1.3 cm predicted by the a-posteriori model, the difference between the two displacements stays almost constant between 40 and 120 min of fire. Therefore, the global behaviour of the slab can be said to be correctly predicted.

This is not the case for the a-priori model that predicts a final displacement of 2.7 cm (value, which is closer to the test than what predicted by the a-posteriori model), but doesn't catch the global trend of the displacement, which is underestimated up to 105 min of fire and overestimated afterwards.

5 CONCLUSIONS

In this paper, the behaviour under fire of a superlight floor slab element (SL-deck) has been described with respect to the results of a fire test performed on a prototype and the outcomes of numerical investigations performed on a three-dimensional thermal and structural FEM of the slab.

The implementation of the FEM is described and modelling aspects such as the sensitivity of the results to the thermal properties of the concrete are discussed. In particular, the validation of the model against test data showed a high sensitivity of the results to the conductivity of the concrete, which affects the accuracy of the temperature profile of the slab at a given temperature and also strongly influences the structural response. While very little information are given in the codes on the conductivity of the different type of concretes, the evaluation of this property and an accurate assessment of its variation with temperatures seem essential factors for a reliable structural fire design.

In particular, the methodology highlighted in this study for the implementation of a FEM of complex concrete elements such as the SL-deck seems relevant in the framework of a sustainable design of buildings, where the use of new technologies is envisaged in order to improve the fire response of structures and mitigate the consequences of accidental events.

REFERENCES

Bontempi, F. & Malerba, P., 1997. The role of softening in the numerical analysis of R.C. structures. Structural Engineering and Mechanichs, 5(6), pp. 785–801.

Campeanu, B. & Giraudo, M., 2011. Modeling the response of R.C. elements in fire, Lyngby, DK: Technical University of Denmark.

Carstensen, J., Jomaas, G. & Pankaj, P., 2013. Element Size and Other Restrictions in Finite Element Modeling of Reinforced Concrete at Elevated Temperatures. Journal of Engineering Mechanics, Volume in press.

Christensen, J. E. & Hertz, K. D., 2012. Super-Light Prefabricated Deck Element Integrated in Traditional Concrete Prefabricated Element Constructions. Seoul, Suoth Korea, ASS Annual Symposium.

Christensen, J., Hertz, K. & Brunskog, J., 2012. Simulation of flanking transmission in super-light structures for airborne and impact sound. New York City, USA, Inter Noise 2012 Conference.

EN 1991-1-1, 2002. Eurocode 1: Actions on structures – Part 1-1: General actions – Densities, self-weight, imposed loads for buildings. Brussels, Belgium: Comité Européen de Normalisation CEN.

EN 1992-1-2, 2004. Eurocode 2: Design of concrete structures, Part 1-2: General rules – Structural fire design. Brussels: Comité Européen de Normalization CEN.

EN 1993-1-2, 2005. Eurocode 3: Design of steel structures, Part 1-2: General rules – Structural fire design. Brussels: Comité Européen de Normalization CEN.

Feenstra, P. & De Borst, R., 1995. Constitutive Model for Reinforced Concrete. Journal of Engineering Mechanics, 121(1), pp. 587–595.

Gentil, F., Carstensen, J. & Giuliani, L., in preparation. Comparison of the performances of two concrete floor slabs in the case of fire.

Halldórsson, E., 2012. Load bearing capacity of superlight decks, Reykjavik, Iceland: Faculty of Civil and Environmental Engineering, University of Iceland.

Hertz, K., 1981. Simple temperature calculations of fire-exposed concrete construction, Lyngby, Denmark: Technical University of Denmark.

Hertz, K., 1982. The anchorage capacity of reinforcing bars at normal and high temperatures. Magazine of concrete Research, 34(121), p. 213–220.

Hertz, K., 2009. Super-light concrete with pearl-chains. Magazine of Concrete Research, 61(8), pp. 655–663.

Hertz, K., 2010. Light-weight load-bearing structures. EU, US, Patent No. PCT/EP2008/066013 Patent Cooperation Treaty.

Hertz, K. D., 2003. Limits of spalling of fire exposed concrete. Fire Safety Journal, 38(2), pp. 103–116.

Hertz, K. D., 2005. Concrete Strength for Fire Safety Design. Journal of Magazine of Concrete Research, 57(8), pp. 445–453.

Hertz, K. D. & Bagger, A., 2011. CO_2 emissions from Superlight Structures. London, UK, proc. of the International Association for Shell and Spatial Structures (IABSE-IASS) Symposium 2011 – "Taller, Longer, Lighter".

Hertz, K., in publication. Super-light deck structures.

Ikeda, K. & Sekizawa, A., 2005. collapse Mechanism of the Windsor Building by fire in Madrid and the Plan for its Demolition Process. Taipei, China, International Workshop on Emergency Response and Rescue.

ISO834-1, 1999. Fire resistance tests – Elements of building construction – Part 1: General requirements for fire resistance testing. Geneva, Switzerland: International Organization for Standardization (ISO).

Jensen, J., 2005. Huldæk og brand (Hollow core slabs and fire, in Danish). Brandposten, 32(1), pp. 34–35.

Mecham, B. et al., 2010. ire and Collapse, Faculty of Architecture Building, Delft University of Technology: Data Collection and Preliminary Analysis. Lund, Sweden, 8th nternational Conference on Performance-Based Codes and Fire Safety Design Methods.

Pettersson, O. & Ödeen, K., 1978. Brandteknisk dimensionering, principer, underlag, exempel (Fire safety design, principles, basis, exemples – in Swedish), Stockholm, Sweden: Förlag Vällingby.

Purkiss, J., 2007. Fire Safety Engineering – Design of Structures. 2nd a cura di Oxford, UK: Butterworth-Heinemann, Elsevier Ltd..

Simulia Corp., 2011. Abaqus v6.11 Documentation. RI, USA: Dassault Systèmes.

Wickström, U., 1986. A very simple method for estimating temperatures in fire exposed structures, London, UK: eds S.J. Grayson and D. A. Smith, Elsevier Applied Science.

Research and Applications in Structural Engineering, Mechanics and Computation – Zingoni (Ed.)
© 2013 Taylor & Francis Group, London, ISBN 978-1-138-00061-2

Composite floors with steel fibre reinforced concrete slabs exposed to fire

J. Bednář & F. Wald
Department of Steel and Timber Structures, Czech Technical University in Prague, Czech Republic

J. Vodička & A. Kohoutková
Department of Concrete and Masonry Structures, Czech Technical University in Prague, Czech Republic

ABSTRACT: The composite steel and concrete floor slabs reinforced with steel fibres were tested at ambient and at elevated temperature at Czech Technical University in Prague. During the tests at elevated temperatures the slabs and secondary beams were fire unprotected. The edge beams were protected only. The concrete slabs were reinforced by steel fibres only without added steel bars. The tests demonstrated the suitable properties of the steel fibre reinforced concrete in fire, which enable creating the membrane action. The material properties of the fibre-concrete allowed forming a beam, the plate and tensile membrane mechanisms, which increase the fire resistance of the floor slabs. For the fire resistance of the floor slabs was utilised the tensile strength and ductility of the steel fibre reinforced concrete. The material properties tests at ambient and at elevated temperature, summarised in this contribution, approved the required ductility and tensile strength of the steel fibre concrete reinforced by 70 kg per cubic meter.

1 INTRODUCTION

The design of concrete, composite steel and concrete and composite timber and concrete slabs for fire resistance is usually based on prescriptive ratings that specify the minimum slab thicknesses and the required concrete cover of the reinforcement. These ratings are generally based on standard fire resistance tests of particular elements using furnaces or simple design models of behaviour of slab as separated element. However, such approach does not represent a real structure as a whole as it does not account for overall floor behaviour, see (Bailey & Moore, 2000). Fire resistance ratings of properly designed full floor systems is higher than those of single elements because the compressive restraint in the edging of the slab allows in the central part of the slab for membrane action to develop increasing the time to failure of the elements compared to the standard tests. For design of floor slabs et elevated temperature based Eurocode rules, see (EN1994-1-4, 2005), may be applied advanced procedures by FEM analyses and simple procedures, see (Vassart & Zhao, 2011). The ductility of steel fibre reinforced concrete (SFRC) broadens the range of application of the reinforced concrete and composite steel-concrete structures. These materials are characterized by high resistance to cracking, corrosion, abrasion, impacts, fatigue and good resistance in exposition to the high temperatures, see (Lie & Kodur, 1996). Steel fibre reinforcement helps to maintain the strength, residual strength, ductility and fracture toughness after being heated, see (Rustin & Kodur, 2011).

In the last years, composite SFRC floor slabs at ambient and at elevated temperature have been tested at the Czech Technical University in Prague. Concrete slabs were reinforced by steel fibres only without added steel bars. The main aim of the tests was to demonstrate the sufficient properties of the SFRC slab in fire, the ductility and adequate tensile and shear strength to assure the fire resistance of the floor slab. These material properties of the SFRC should allow for the slab to create a appropriate load bearing mechanism, which increases its fire resistance.

2 FURNCE TESTS

Six slabs were tested with sizes of 4.5×3.0 m. The slabs of the thickness 40 mm were concrete to trapezoidal sheets TR40/160/0.75. The concrete was reinforced by 70 kg per cubic meter. Added steel fibres had the sizes of 0.75×50 mm and its strength was 1100 N/mm^2. Four slabs were tested at the ambient temperature and two at elevated temperature. The tests at ambient temperature were performed in Prague in UTAM and the tests at the elevated temperature in Veselí nad Lužnicí in PAVUS, see Figures 1 and 2. The first floor slab tested at elevated temperature reached the collapse in 195 min of the test. Integrity of the slab was maintained during 75 min and criterion of isolation was transgressed after 65 min. The second floor slab tested



Figure 1. Collapse of the composite slab during the first fire test in PAVUS laboratory.

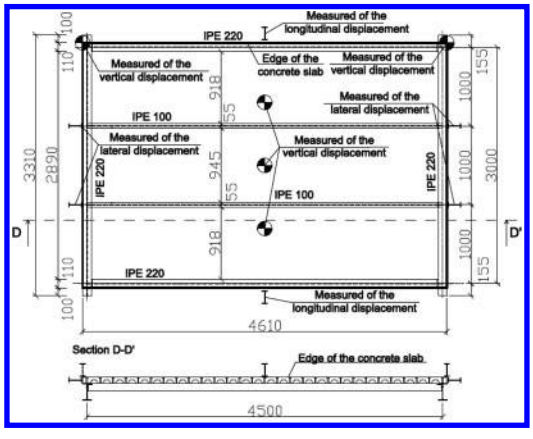


Figure 2. Sizes of the specimen and location of the deflectometers by the test.



Figure 3. Scantling H-1-20 after the test at ambient temperature.

at elevated temperature approved the resistance of R120.

3 MATERIAL TESTS

3.1 *Material properties at ambient temperature*

For the prediction model developed under the project were created tests of the materials properties. Concrete mixtures were two. In concreting plants, for each mixture there was made 9 cubes and 9 scantlings. Concreting plants were in the towns Jindřichův Hradec and Písnice. Sizes of the cubes were 150 × 150 × 150 mm and scantlings 150 × 150 × 700 mm. The cubes were tested in simple compression and scantlings by for point bending test to describe the tensile properties of concrete according (EN12390-5. 2009), see Figure 3. The scantlings were tested at 20°C, at 500°C and 600°C

The six cubes from concreting plant Písnice reached an average compression strength of 80.9 N/mm^2 and three cubes in lateral tension showed by the tests an average tensile strength of 7.4 N/mm^2. This concrete was used on the tests of the slabs at ambient temperature. The six cubes from concreting plant Jindřichův Hradec reached the average compression strength 68.3 N/mm^2 and three cubes in lateral tension showed by the tests an average tensile strength 7.1 N/mm^2. This concrete was used on the test of the slab at elevated temperature.

There were tested 2 × 3 scantlings at 21°C. The scantlings were tested by four-point bend, see Figure 3. There is shown a specimen after creation of the macro-crack. The fibre concrete achieved average tensile strength of 6.42 N/mm^2 and its average ductility was 1.1‰ (concrete plant Jindřichův Hradec). Second concrete mixture achieved average tensile strength of 7.22 N/mm^2 and average ductility was 0.92‰. This ductility was measured at the initiation macro-cracks. After creating the macro-cracks, stretch was increasing and load bearing capacity was decreasing.

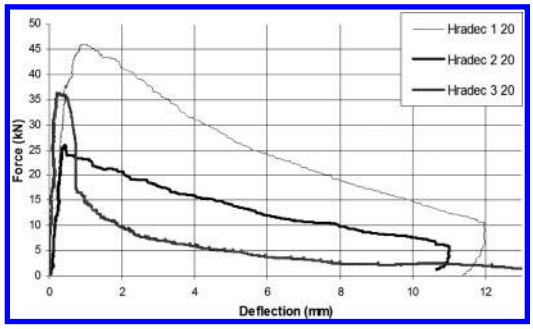


Figure 4. Force–deflection relation from four point bending test at 20°C.



Figure 5. The specimen during heating.

The force–deflection relation from four point bending test at 20°C is shown in Figure 4.

3.2 *Material properties at elevated temperature*

Materials property tests were performed on the specimens, which were heated up by five electrical heaters to the temperatures of 500°C and 600°C. The specimens were thermally protected and were heated up four hours so that the temperature in the scantling is uniformly distributed. The temperature was control by four thermocouples. The deflections were measured by two mechanical deflectometers, which were due to the temperature installed a before the loading of a specimen. The loading scheme was the same as by the test at ambient temperature. The heating was performed directly in the press, see Figure 4. Figure 5 shows the specimen during the heating and loading. Table 1 summarizes the measured values of tensile strengths at ambient and elevated temperature, Table 2 average values of tensile strengths at ambient and elevated temperature, and Table 3 related reduction coefficients calculated for selected relative deformations.

There were tested 2×3 scantlings at 500°C and 600°C by four-point bending. The ductility was calculated at the initiation macro-cracks. The fibre



Figure 6. The heated specimen during loading.

Table 1. Tensile strengths at ambient and elevated temperature with reduction coefficient.

Specimen	Max tensile strength (MPa)	Tensile strength $\varepsilon = 6‰$ (MPa)	Tensile strength $\varepsilon = 10‰$ (MPa)	Tensile strength $\varepsilon = 14‰$ (MPa)
H1-20	5.41	2.88	1.92	–
H2-20	5.84	3.56	2.40	–
H3-20	6.11	3.09	2.31	–
HA-20	5.78	3.15	2.20	–
H4-500	2.92	2.86	2.89	1.67
H5-500	4.50	4.31	2.95	2.18
H6-500	3.15	2.83	3.13	2.94
HA-500	3.38	3.34	3.09	1.98
H7-600	1.69	1.59	1.69	1.67
H8-600	1.34	1.29	1.34	1.32
H9-600	1.56	1.45	1.06	0.83
HA-600	1.47	1.45	1.46	1.37

Table 2. Average values of tensile strengths at ambient and elevated temperatures.

Temperature of specimen	Max tensile strength (N/mm^2)	Tensile strength $\varepsilon = 6‰$ (N/mm^2)	Tensile strength $\varepsilon = 10‰$ (N/mm^2)	Tensile strength $\varepsilon = 14‰$ (N/mm^2)
20°C	5.8	3.2	2.2	
500°C	3.5	3.3	3.0	2.2
600°C	1.5	1.4	1.4	1.3

concrete achieved at temperature 500°C was average tensile strength of 3.52 N/mm^2 and its average ductility 8.77‰. At 600°C it was 1.53 N/mm^2 and ductility

Table 3. Reduction coefficient at elevated temperature.

Temperature of specimen	k_{max}	$k_{6‰}$	$k_{10‰}$	$k_{14‰}$
20°C	1.00	0.55	0.38	–
500°C	0.59	0.58	0.53	0.34
600°C	0.26	0.25	0.25	0.24

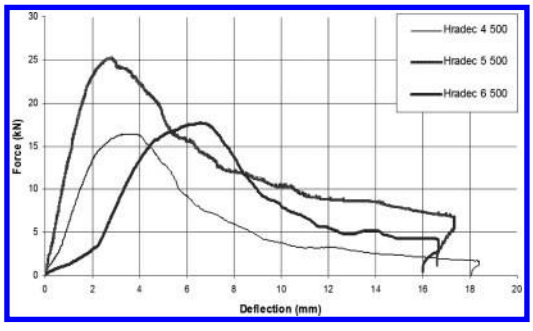


Figure 7. Force–deflection relation from four point bending test at 500°C.

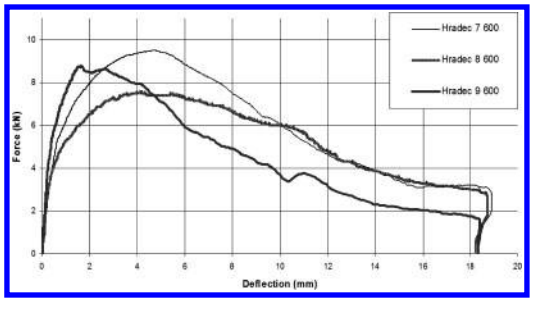


Figure 8. Force–deflection relation from four point bending test at 600°C.

was 6.99‰. Figures 7 and 8 show force – deflection relation at four point bending tests.

4 CONCLUSIONS

Homogeneity of the results of material tests of fibre concrete was good. The steel fibre reinforced concrete demonstrated appropriate ductile behaviour. Based on experiments the reduction coefficient of decrease strength of SFRC was prepared, see (Bednář et al, 2011 and 2012). The ductility of SFRC by 500°C was higher than by 20°C but also than by 600°C.

The evaluation of the material properties of SFRC and the tests with floor slabs allows the preparation of FEM model and analytical prediction model. The models are taking into account the contribution to the behaviour of the steel beam and SFRC slab in bending and the development of membrane behaviour at large deformation at elevated temperature.

ACKNOWLEDGEMENT

This outcome has been achieved with financial support of the Grant Agency of Czech Republic No. P105/10/2159.

REFERENCES

Bailey C.G. & Moore D.B., The structural behaviour of steel frames with composite floor slabs subjected to fire: Part 1: Theory, *The Structural Engineer*, Vol. 78 (11), pp. 19–27, 2000.

Bednář J., Wald, F., Vodička J. & Kohoutková A., *Membrane Action of Composite Fibre Concrete Slab in Fire*. Procedia Engineering, online, 2012, vol. 40, no. 40, p. 498–503, ISSN 1877-7058.

Bednář J., Wald F., Kohoutková A. & Vodička J.: *Properties of the fibre concrete in fire*. In 6th International Conference Fibre Concrete 2011 – Technology, Design, Application. Praha: vydavatelství ČVUT v Praze, 2011, p. 87–94. ISBN 978-80-01-04917-4.

EN1994-1-4, Eurocode 4: *Design of composite steel and concrete structures* – Part 1-2: General rules – *Structural fire design*, CEN, Brussels, 2005.

EN 12390-5, *Testing hardened concrete* – Part 5: *Flexural strength of test specimens*, CEN, Brussels, 2009.

Lie T.T., Kodur V.R., Thermal and mechanical properties of steel-fiber-reinforced concrete at elevated temperatures, Canadian *Journal of Civil Engineering*, Vol. 23(4), pp. 511–517, 1996.

Rustin F. & Kodur V.R., Enhancing the fire resistance of composite floor assemblies through the use of steel fibre reinforced concrete, *Engineering Structures*, pp. 2870–2878, 2011.

Vassart O., & Zhao B., *Fire Resistance Assessment of Partially Protected Composite Floors*, FRACOF+, 2011, http://fire.fsv.cvut.cz/fracof.

Research and Applications in Structural Engineering, Mechanics and Computation – Zingoni (Ed.)
© 2013 Taylor & Francis Group, London, ISBN 978-1-138-00061-2

Engineering solutions for structures in fire: Should concrete care?

L.A. Bisby
Arup Professor of Fire and Structures, School of Engineering, University of Edinburgh, UK

ABSTRACT: So-called 'fire engineered solutions' for designing and assessing the performance of structures in fire have advanced a great deal in recent decades. This been enabled by the emergence of performance based design codes in Europe and elsewhere, which rather than prescribing the specific means by which fire resistance is achieved, allow designers to take any approach provided that it can be *shown* that the solution will meet *acceptable*, *quantifiable* performance objectives. In structural fire engineering, this typically refers to collapse prevention during fire. Whilst the benefits of performance-based structural fire engineering design are available to all sectors of the construction industry, only the steel-framed building construction sector has truly embraced these approaches. The steel industry continues to promote performance based design for fire largely because this can justify removal of passive fire protection from large portions of steel structures, where it would otherwise be required by prescriptive guidance. This makes steel framed structures more economical, most notably in competition with concrete buildings. In the face of these advances the concrete industry has expressed concern about the evolution of Fire Safety Engineering methods, the shortcomings that might be observed, and the potential level of risk they could create. In general the concrete industry appears to be opposed to further regulatory advances. Whilst concrete structures generally perform well during fire, this paper discusses current opportunities and challenges resulting from performance based structural fire design of modern structures. An attempt is made to address the issue of how advanced, performance based structural fire engineering can positively influence the optimized design and construction of concrete buildings, particularly as compared with steel-framed buildings. The overarching objectives are: to provide a balanced and rational assessment of the challenges and opportunities for design and construction of concrete buildings with inherent structural fire safety; and to demonstrate that rather than being a threat to the concrete construction industry, performance based structural fire engineering may represent a considerable opportunity.

1 INTRODUCTION

Structural design for fire is concerned primarily with the provision of 'fire resistance' to protect against loss of life and spread of fire to adjacent buildings. Fire resistance has historically been defined as the time of exposure to the standard fire (ASTM 2012, ISO 1999) during which an isolated structural element (beam, column, slab, etc), typically tested in a standard fire testing furnace, can resist failure due to one of: (1) loss of load bearing capacity under service loads; (2) unacceptable temperature rise at the unexposed face; and (3) passage of flames or hot gas through the element.

The historical approach to fire resistance design based on furnace testing is unrealistic and irrational for reasons too numerous to discuss here (Bisby et al. 2013). During the 1990s, the emergence of performance-based fire codes (e.g. CEN 2004, 2005) enabled the use of more rational approaches to fire resistant design. With regard to structural fire resistance, the fire and the structural response can be rationally assessed and the performance of the structures quantified and compared against fundamental performance objectives. Designers can take any approach they choose to meet these performance objectives for the structure. In practice, in the absence of more rational and quantifiable performance objectives, this typically means that structures are engineered to perform 'at least as good' as structures which meet the available prescriptive guidance.

Beginning in the early 1990s, the steel industry has devoted considerable funding and effort to understanding the true response of steel structures in fire in an effort to be able to demonstrate (primarily through the development of validated computational modeling tools) the ability to performance engineer steel structures in fire. A range of large scale non standard fire tests of steel structures have are discussed by Bisby et al. (2013); these have led to the development of several bespoke structural fire design software (e.g. www.vulcan-solutions.com).

The most significant result of this dedicated research effort has been an ability to justify removal of large amounts of passive fire protection from steel structures, leading to market advantage in the building construction. The concrete industry appears to have made little effort to capitalize on performance based structural fire engineering, and has devoted comparatively little resource to research in this area. On the contrary the concrete industry has expressed

concern about the emergence of performance based codes, the shortcomings that might be observed, and the perceived risks they might create.

This paper attempts to provide an assessment of the challenges and opportunities for design and construction of concrete buildings with inherent structural fire safety, and to demonstrate that rather than being a threat to the concrete construction industry performance based structural fire engineering may represent an opportunity on various levels.

2 STATE-OF-THE-ART

The current state-of-the-art in performance based structural fire engineering, from a practical and regulatory perspective, is best represented by the Structural Eurocodes for fire design of concrete (CEN 2004) and steel (CEN 2005) structures. These codes provide simplified means by which engineers can approximate natural or 'parametric' design fires based on a compartment's geometry and lining materials, its fuel load, and its ventilation during fire. It is noteworthy that the parametric fires include a cooling phase; this is far more realistic than the perpetual heating of a standard fire. The Eurocodes also allow designers to take various approaches, of increasing complexity, to assess a structure's performance during exposure to a parametric fire. These range from adhering to simple tabulated requirements (e.g. limiting temperatures of steel or minimum concrete cover to internal reinforcement), through simplified analytical techniques, to advanced thermal-structural finite element models which rely on a detailed understanding of material and structural response to heating.

Details of all of the above approaches are not included here. Instead, this paper touches on various relevant issues in an attempt to present possible opportunities for concrete structures in a performance based structural design for fire environment.

3 OPPORTUNITIES

3.1 *More realistic fire exposures*

The most obvious benefit to concrete structures in a performance based design for fire environment is that, provided engineers rationally account for the challenges discussed in Section 4, concrete structures are likely to perform much better under realistic fire scenarios compared to standard fires. All that this requires is a regulatory recognition that real fires have a cooling phase as in the Eurocode parametric fires (e.g. ISO 1999, ASTM 2012).

This benefit can be demonstrated simply by considering the thermal criteria which are widely applied to steel and concrete structures in North America to define the fire resistance. For reinforced concrete flexural elements this means exceeding a steel reinforcement temperature of 593°C.

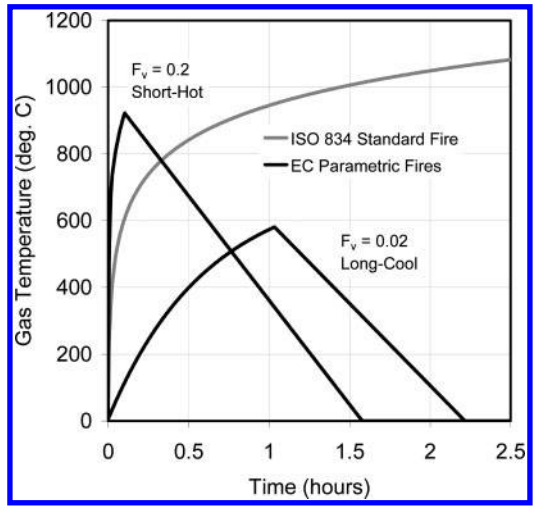


Figure 1. ISO 834 (ISO 1999) standard fire and Eurocode (CEN 2002) parametric fires similar to those applied by Lamont et al. (2004).

Figure 1 shows temperature versus time profiles for the standard (ISO 834) fire along with two possible Eurocode parametric fires. The details of the derivation of the parametric fires is not important to the current discussion; suffice it to say that these two curves are assumed to represent the possible extremes of permissible fire behaviour for a compartment within a reinforced concrete structure with a fuel load representing the 80th percentile value for an office occupancy in Europe (CEN 2002).

For illustrative purposes Figure 2(a) shows the predicted temperatures of steel reinforcement within a 150 mm thick carbonate aggregate concrete slab, with a moisture content of 5% by mass and 25 mm axis distance to the bottom steel; assuming fire from below. The predictions were made using a 1-dimensional finite difference heat transfer code written and validated by Bisby and Kodur (2005).

Figure 2(a) shows that with 25 mm of concrete cover the fire resistance of the concrete slab would be reached after about two hours of standard fire exposure, whereas it would 'never' be reached for either of the parametric fires (the fires would burn out due to full consumption of the available fuel).

By contrast, and again simply for the purposes of illustration, for a steel-framed building with unprotected secondary beams all three fires would result in secondary beam temperatures close to or exceeding 550°C in less than two hours. Whilst this may not correspond to structural failure, it would likely result in considerable permanent damage to the structure (and very large deflections, as shown in the following section).

It seems reasonably assured, however as yet unproven, that the concrete structure would perform better under a parametric fire provided that spalling an unexpected failure modes can be avoided.

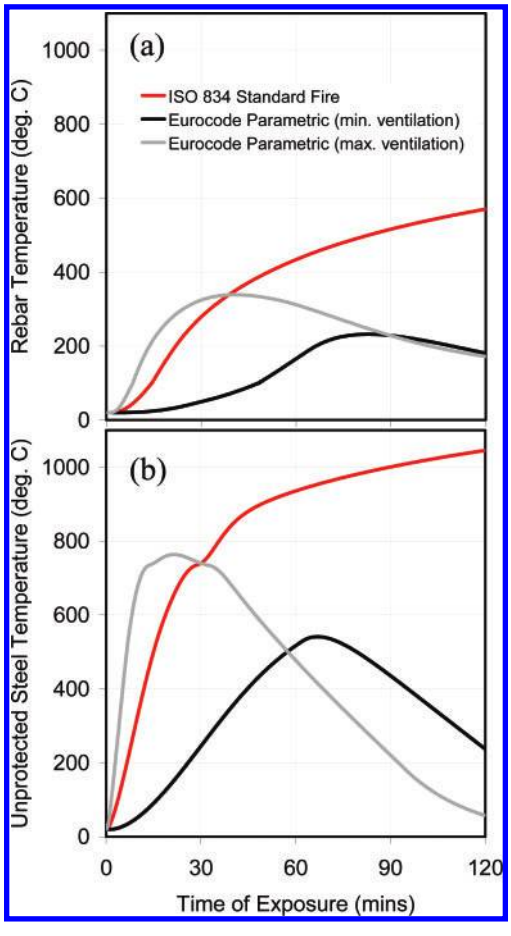


Figure 2. Predicted temperatures in (a) internal steel reinforcement in a concrete slab with 25 mm cover and (b) unprotected secondary steel beams in a steel frame with a steel-concrete composite deck slab, in both cases subjected to the three temperature versus time curves given in Figure 1.

3.2 *Shifting the design goal posts*

At present, the fundamental functional objectives which are used in performance based structural fire engineering design in most jurisdictions are firmly rooted in the available prescriptive guidance and are, in general, relatively poorly quantified. Structural fire designers are required to demonstrate protection of human life and adjacent properties by comparison with prescriptive 'deemed to satisfy' requirements.

There is currently little (if any) regulatory requirement to protect buildings themselves against fire. Thus, structural fire engineers operating in a performance based environment are typically required only to demonstrate that a building can resist collapse and prevent spread of fire from the compartment of origin for the required period; or for the full duration of a parametric fire (i.e. 'burnout'). Little consideration is given to the degree of damage that the building might suffer, to whether it is likely to be re-occupied, or to other considerations such as business continuity, economic loss, or sustainability.

For structural fire design and assessment of steel structures the use of advanced finite element software is now commonplace (e.g. Flint et al. 2013). This has become possible in large part to the seminal tests performed on a steel framed building at Cardington (Bailey et al. 1999), which allowed computational models for steel structures in fire to be extensively validated. A similar testing program has not yet been performed for concrete structures (notwithstanding the single concrete building test performed at Cardington by Bailey (2002).

For steel structures, detailed computational models are created and exposed to a number of credible design fire scenarios (most often defined using the Eurocode parametric fires for a range of possible ventilation conditions). The response of the structure is tracked to watch for 'problematic' behavior. Structural fire engineers use these models to evaluate trends in structural response including runaway deflections, large (plastic) strains in structural steelwork and in steel reinforcement of concrete, large tensile strains in concrete (with concrete cracking almost universally modeled using a 'smeared cracking' approach), connection forces (during heating *and* cooling) and lateral deflections and the resulting secondary moments in columns. This allows a relatively confident assessment of structural response during fire. Using this approach structural fire engineers can demonstrate in many cases that steel-framed structures with unprotected slabs and secondary beams will perform satisfactorily (i.e. will not collapse) under exposure to fire, however at comparatively large deflections, through tensile membrane action (see Bailey et al. (1999) and below).

It is noteworthy that the available models do not deal well with singularities arising from failure localization, discrete cracking, tensile rupture, shear failures, reinforcement anchorage, etc. Indeed, many of these are not explicitly modeled in most cases. For concrete structures use of such advanced techniques is currently limited, both because test data do not exist for credible model validation and, more importantly, because the practical benefits of the additional analysis effort are marginal within the context of current regulatory drivers.

In a life-safety only design environment, advanced structural fire analysis is unlikely to provide a competitive advantage for concrete. If the goal posts for design were to move, however, such that avoiding a given level of structural damage was the functional requirement, it is possible that conventional concrete structures might drastically outperform conventional steel framed structures.

To interrogate this issue one could perform structural fire analyses of comparable cast in place concrete and steel framed concrete composite deck structures under the same design fire. No such comparative analyses are available in the literature, although a number of relevant studies are available which do provide a useful initial comparison.

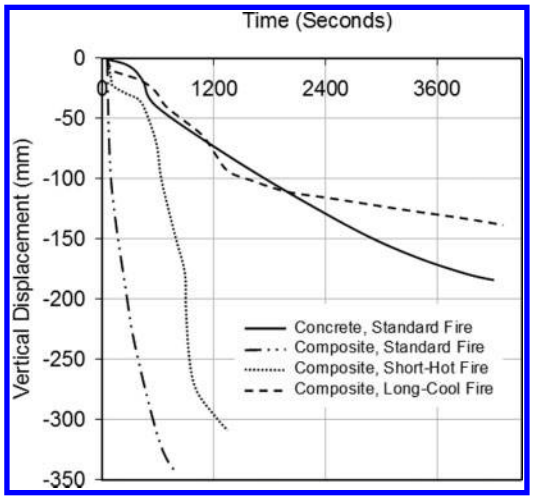


Figure 3. Approximate deflection versus time for typical cast in place concrete frame (Huang et al. 2006) or steel frame with steel-concrete composite concrete deck and unprotected secondary beams (Huang et al. 2004, Lamont et al. 2004).

As far as computational studies of steel structures in fire are concerned, Huang et al. (2004) present a detailed finite element study on a steel framed building with a steel-concrete composite slab on steel beams. Full details of the structure are not presented here; the overall bay size is 9 m × 9 m in plan, with two unprotected secondary beams in each bay. Data are presented on the vertical deflection of an interior bay with the temperature of the unprotected secondary beams, using temperature histories measured during the Cardington tests (Bailey et al. 1999). The deflection data can be approximately transposed into deflection versus time of standard fire exposure using the Eurocode 3 (2005) method for determining the temperature of unprotected steelwork in fire. This has been done and the resulting approximate mid-bay vertical displacement for this structure is shown versus time of exposure to the standard fire in Figure 3. Lamont et al. (2004) have also presented deflection versus time predictions for a steel framed composite deck structure with bays 6 m × 6 m in plan including a single unprotected secondary beam. In this case the structure was subjected to non-standard fires; a short-hot fire and a long-cool fire, both with cooling phases (similar to the two Eurocode parametric fires shown in Figure 1). The predicted mid-bay deflections are also given in Figure 3.

As far as computational studies of concrete structures are concerned, Huang et al. (2006) have presented an analysis of a typical cast in place reinforced concrete frame structure. In this case the structural bays were 7.5 m × 7.5 m in plan. The predicted mid-bay vertical deflection in this concrete structure (albeit with slightly smaller spans) is also shown in Figure 3.

Even accounting for the subtle but potentially important differences between the structures compared in Figure 3, it seems clear a steel framed composite slab structure with unprotected secondary beams is likely to deflect considerably more rapidly during fire than a comparable concrete frame structure with a cast in place concrete slab. While clearly not an exhaustive comparison, Figure 3 hints that concrete frame structures may perform 'better' during fire than steel frame structures with unprotected secondary beams. Of course, this assumes that total vertical deflection during fire is a useful damage index for these types of structures, and as already noted research is needed to determine whether this is the case. This also assumes that the challenges for concrete structures in fire, discussed in Section 4, are rationally addressed.

The potentially superior resistance to fire damage of concrete structures described above requires a change in the performance drivers for buildings in fire, with life-safety and protection of adjacent buildings no longer being the only goals, as well as a shift towards performance based design for fire.

3.3 *More realistic structural response assessment*

Another group of potential advantages for reinforced concrete structures in fire from performance based approaches might arise from moving away from the prescriptive approach of defining fire resistance on the basis of isolated structural elements tested in furnaces subjected to the standard fire. Standard fire testing is widely acknowledged as unrealistic on various thermal and physical bases (Bisby et al. 2013). Most notably the thermal and structural boundary conditions (e.g. restraint, redistribution, continuity) are not well accounted for in such tests.

The steel industry has openly acknowledged the shortcomings of standard furnace testing and this, combined with extensive research and computational modeling studies, has allowed the structural fire design community to develop fire resistance design procedures for steel-framed composite slab structures which explicitly rely on *tensile membrane action* to prevent collapse during fire. This is a drastic departure from the traditional approach to fire resistant structural design based on fire resistance testing; it explicitly uses structural actions which would never be observed during a standard furnace test.

With sufficient research, the concrete industry may be able to take similar advantage of structural actions which arise in real buildings but which are not observed during standard furnace tests. There are two main structural actions which may be beneficial and which are relevant to this discussion: continuity and membrane actions.

Continuous beams are statically indeterminate and continuous over multiple supports. Unlike simply-supported beams, which require only a single location of flexural failure for collapse to occur, continuous beams require multiple failure locations before a failure mechanism can form. Continuous beams are therefore redundant structures, and they can benefit from moment redistribution, both at ambient temperature

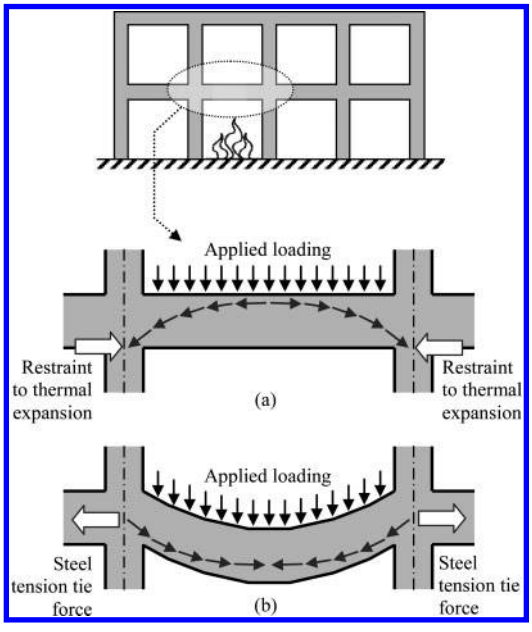


Figure 4. Schematic two-dimensional representations of (a) compressive membrane and (b) tensile membrane actions in concrete slabs in fire.

and during fire. Techniques to account for moment redistribution during fire are described in detail elsewhere (e.g. Buchanan 2001). This is a potential serious advantage for concrete structures in fire which is rarely considered, providing that structural damage during fire is acceptable.

An additional structural action which often plays an important role in the response of real structures during fire is membrane action. Membrane action, which can be either compressive or tensile, manifests itself in planar structures such as steel-concrete composite and reinforced concrete slabs. Figure 4 shows two-dimensional idealizations of both tensile and compressive membrane actions.

Compressive membrane action is particularly important in continuous reinforced concrete structures during fire, where restrained thermal expansion can lead to the development significant lateral restraint forces resulting in arching action during fire (provided of course that the thrust forces have a line of action below the neutral axis of bending of the slabs). This type of behaviour has been observed in large scale fire tests of real concrete structures (Bailey 2002).

Tensile membrane action is particularly important during the late stages of fires for structures with relatively thin concrete or steel-concrete composite slabs. In these cases tensile membrane action can prevent structural collapse (however under very large vertical deflections as already noted) for durations of fire exposure much greater than would be expected on the basis of a single element analysis. This may present advantages for highly optimized concrete structures with thin floorplates over large spans, for instance post tensioned concrete slabs (provided of course that sufficient bonded reinforcement is provided such that tensile membrane actions can be accommodated and anchored).

Membrane actions are discussed in detail in specialized references (e.g. Buchanan 2001, Wang et al. 2012), however typically with reference to steel-concrete composite slabs rather than cast in place reinforced or prestressed concrete slabs.

4 CHALLENGES

It is crucial to recognize that there are a number of potential challenges for modern concrete structures in fire; these have yet to be properly addressed through research but must be accounted for in order for the potential advantages for concrete structures noted above to be fully realized in practice. The most important of these are: concrete cover spalling and unexpected or unaccounted for failure modes.

4.1 *Explosive concrete cover spalling*

The majority of the potential advantages for concrete in fire noted previously can only be realized if the concrete cover to the reinforcement remains in place. Spalling refers to the sudden and explosive deterioration of the surface of a concrete element during heating, resulting in loss of concrete cover and thermal exposure of the internal steel reinforcement; thus decreasing the element's load carrying capacity and risking structural collapse. Propensity for spalling is exacerbated by many factors, including concrete age, strength, mix design, compressive stress, moisture content, aggregate type, and restraint to thermal expansion, as well as the specific fire exposure and resulting thermal gradients and restraint. A large body of research (e.g. Koenders and Dehn 2011) has shown that inclusion of polypropylene microfibers within the concrete mix can reduce spalling, but little is known regarding the mechanisms causing this and there is no ability to model the beneficial effects of the fibres nor to optimize concrete mixes and fibres to prevent spalling.

Furnace testing of large scale concrete elements for spalling is required in most real project applications when spalling represents a serious concern (e.g. in tunneling projects), and this is expensive and time consuming. Considerable additional research is needed before the concrete community can defensibly assume that spalling is guaranteed not to occur for a given concrete in a given structural application.

4.2 *Unexpected failure modes*

Over the years a number of problematic failure modes, which are generally not accounted for in structural fire design of concrete structures and which could, by definition, not be observed during standard furnace testing, have been observed in real concrete structures

during real fires. The factors leading to these failure modes need to be understood in order for rational performance based structural fire design of reinforced concrete structures to be performed with confidence. The most notable of these, which should be studied in more detail, are:

- explosive spalling of the concrete cover as discussed in the previous section;
- shear failure of perimeter columns (and generation of secondary column moments) due to lateral thermal expansion of the floorplate which is not considered during design;
- punching shear failure of concrete slabs (particularly in the cooling phase) (Bamonte et al. 2012);
- anchorage and shear failure of prestressed precast concrete elements (notably hollowcore slabs) (Fellinger et al. 2005); and
- tendon rupture in locally heated unbonded post-tensioned concrete slabs (Gales et al. 2011).

5 CONCLUSIONS

This paper has suggested that, rather than being a threat to the reinforced concrete construction community, performance based structural fire design of concrete buildings provides numerous possible advantages for the concrete industry. However, these advantages will only be achieved if:

- the concrete industry takes a positive approach to performance based design for fire; supporting research directed at addressing the challenges noted in the current paper and promoting, rather than opposing, regulatory advances in this area;
- the regulatory approach to provision of fire safety in buildings moves away from a 'life safety only' approach to one which also considers property protection, business continuity, sustainability, etc (i.e. the 'goal posts' are shifted);
- explosive concrete spalling is prevented with a high level of confidence; and
- all possible failure modes are understood and rationally accounted for during the design process.

ACKNOWLEDGEMENTS

I am grateful to Prof JL Torero and Dr TJ Stratford for useful discussion on the ideas presented. I would also like to thank my team of stellar PhD students (notably C Maluk and JA Gales) for digging up numerous references and ideas relevant to the paper.

REFERENCES

ASTM E119. 2012. *Standard Test Methods for Fire Tests of Building Construction and Materials*. American Society for Testing and Materials.

Bailey, C.G. 2002. Holistic behaviour of concrete buildings in fire. *Structures and Buildings* 152(3): 199–212.

Bailey, C.G., Lennon, T. & Moore, D.B. 1999. The behaviour of full-scale steel framed buildings subjected to compartment fires. *The Structural Engineer* 77(8):15–21.

Bamonte, P., Fernández Ruiz, M. & Muttoni, A. 2012. Punching shear strength of R/C slabs subjected to fire. In M. Fontana, A. Frangi, M. Knobloch (eds.), *Proc. 7th Int. Conf. on Structures in Fire*: 689–698. Zurich: ETH.

Bisby, L.A. & Kodur, V.K.R. 2007. Evaluating the fire endurance of concrete slabs reinforced with FRP bars: Considerations for a holistic approach. *Composites Part B* 38(5–6): 547–558.

Bisby, L.A., Gales, J.A. & Maluk, C. 2013. A Contemporary Review of Large Scale Non-Standard Structural Fire Testing. *Fire Science Reviews*. In press.

Buchanan, A. 2001. *Structural design for fire safety*. Wiley.

CEN. 2004. *Eurocode 2: Design of concrete structures – Part 1-2: General rules – Structural fire design*. Brussels: European Committee on Standardization.

CEN. 2005. *Eurocode 3: Design of steel structures – Part 1-2: General rules – Structural fire design*. Brussels: European Committee on Standardization.

CEN. 2002. *Eurocode 1: Actions on structures – Part 1-2: General actions – Actions on structures exposed to fire*. Brussels: European Committee on Standardization.

Fellinger, J., Stark, J. & Walraven, J. 2005. Shear and anchorage behaviour of fire exposed hollow core slabs. *HERON* 50(4).

Flint, G., Lamont, S., Lane, B., Sarrazin, H., Lim, L., Rini, D. & Roben, C. 2013. Recent Lessons Learned in Structural Fire Engineering for Composite Steel Structures. *Fire Technology*. In press.

Gales, J., Bisby, L.A. & Gillie, M. 2011. Unbonded Post Tensioned Concrete in Fire: A Review of Data from Furnace Tests and Real Fires, *Fire Safety Journal* 46(4): 151–163.

Huang, Z., Burgess, I.W. & Plank, R.J. 2006. Behaviour of Reinforced Concrete. In Vila Real, P., Franssen, J-M., Tan, T.H. (eds.), *Proc. 4th Int. Conf. on Structures in Fire*. Aveiro: University of Aveiro.

Huang Z., Burgess, I., Plank, R. & Bailey, C. 2004. Comparison of BRE simple design method for composite floor slabs in fire with non-linear FE modeling. *Fire & Materials* 28: 127–138.

ISO. 1999. *Fire-resistance tests – Elements of building construction – Part 1: General requirements*. Geneva: International Organisation for Standardisation.

Koenders E.A.B. & Dehn, F. 2011. *Proc. 2nd Int. Workshop on Concrete Spalling due to Fire Exposure*. France, Rilem.

Lamont, S., Usmani, A.S. & Gillie, M. 2004. Behaviour of a small composite steel frame structure in a "long-cool" and a "short-hot" fire. *Fire Safety Journal* 39: 327–357.

Wang, Y., Burgess, I., Wald, F. & Gillie, M. 2012. *Performance-Based Fire Engineering of Structures*. UK: Spon Press.

Research and Applications in Structural Engineering, Mechanics and Computation – Zingoni (Ed.)
© 2013 Taylor & Francis Group, London, ISBN 978-1-138-00061-2

The application of fire engineering methods for the design of open steel car parks

G. Woźniak
Building Research Institute, Warsaw, Poland

R. Obiała
Arcelor Mittal, Long Products R& D, Esch-sur-Alzette, Luxembourg

ABSTRACT: The paper aims to present a new method of the fire design of open steel car parks based on fire safety engineering approach (FSE). According to the fire safety regulations in many European countries, steel buildings have to be fire protected, sometimes without sufficient technical grounds. For economic reasons certain types of buildings, like multi-storey open car parks, practically can be built only as concrete structures. However, when applying performance based concept of fire safety, steel or composite structures turn out to be equally effective in meeting fire resistance requirements.

The paper presents theoretical background and experimental evidence supporting this attitude. The concept of natural fire in car parks is accompanied by the discussion of possible fire scenarios. The background engineering knowledge concerning thermo–mechanical behaviour of composite floors, as well as methodology of the fire design of car park structures is presented.

1 INTRODUCTION

This paper summarizes the development of the project "Open Steel Car Park Design for the Polish Market" (Project CAPP 2011). The project was completed in the years 2009–2011 as a result of co-operation between the following companies: ArcelorMittal R&D Esch, ArcelorMittal Construction Poland, Building Research Institute ITB, Warsaw and Poznan University of Technology.

The main aim of the project was to propose fire engineering approach to the open steel car park design. Based on the experimental results the appropriate fire scenarios were proposed and applied to car park structures. Fire actions were determined and the behaviour of structural elements in fire conditions was evaluated by numerical methods. As the result of the project conclusions were formulated and practical design methods were developed in relation to open steel car parks structures in Poland.

2 OPEN CAR PARKS CHARACTERISTICS

2.1 *Technical description*

According to Polish Building Regulations a car park is considered open if the total area of openings (at each level) is greater than 35% of overall wall area and the distance between walls with openings is less than 100 m.

These conditions ensure the natural ventilation which helps to avoid accumulation of smoke and additional increase of temperature in case of fire (see Figure 1).

Open car parks are typically multi-storey buildings. In Poland they are almost always erected as concrete structures. The basic technical problem which was dealt with during CAPP project, was whether it is possible to adhere to Building Regulation principles when constructing car parks with composite slabs and steel hot rolled beams.

According to Polish Regulations the following minimum dimensions have to be ensured for open car parks:

- Single parking space: 2.3 m × 5 m
- Height (between floor and ceiling): 2.2 m
- Height (between floor and installations under ceiling): 2.0 m
- Width of access road: 5.7 m.

All research and analyses were performed for structures with composite slab system (profiled steel decking with casted "in situ" concrete slab), steel hot rolled I beams, acting compositely with slabs, and steel columns.

The aim of the research was to investigate fire resistance of structural elements, assuming no fire protection of slabs and beams. Steel columns were assumed to be fire protected by traditional means (intumescent coatings, sprayed mortars or insulating boards) and were not the object of investigation.

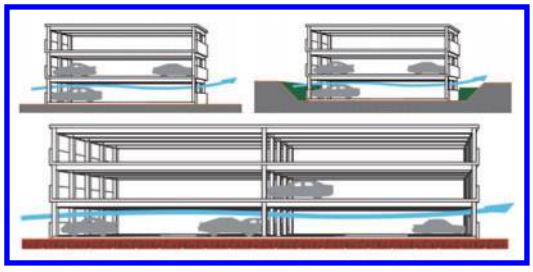


Figure 1. Natural ventilation in open car parks.

2.2 *National building regulations and current fire safety approach in Poland*

According to Polish Building Regulations, open car parks not higher than 25 m have to satisfy requirement of 30 minutes of fire resistance (R 30 class for beams and columns and REI 30 class for slabs). Technical bases are given in European classification standard (EN 13501-2 2007) and are associated with fire resistance of single elements under standard fire conditions. Current regulations do not allow for alternative approach based on fire safety engineering and analysis of fire performance of the whole structures and natural fire concept.

The performance based approach has been adopted for the design of car parks in many European countries e.g. France, Germany and United Kingdom. Fire safety engineering methods, when compared with traditional, prescriptive approach allow for different view of fire performance of building elements and especially of whole structural system. Individual fire scenarios (natural, parametric or localized fires) and realistic assessment of fire actions together with ventilation conditions can be applied. Furthermore, these methods allow to analyse interactions in structural system, redistribution of inner forces and additional effects which may appear in fire conditions.

Traditional fire safety concept may lead to unrealistic, conservative solutions. Open steel car parks, commonly used in many countries, as probably the best choice, cannot be constructed in other countries (e.g. Poland) because single steel elements, without additional fire protection, cannot meet requirement of 30 minutes standard fire resistance.

3 FIRE TESTS

In the fire engineering approach with application of the natural fire concept it is important to establish location of the fire and its power represented by rate of heat release (RHR). It is essential that fire scenario which is most critical for the structure is selected for the design. It should be most realistic, based on tests, research and numerical analysis.

In Table 1, results from fire tests in open car parks recorded in the last decades are given.

The results of fire tests, especially well documented tests from Vernon, 2002, were analysed by

Table 1. Results of fire tests in open car parks.

Test	Fire spread among cars	Temperature [°C]	
		Beam	Column
England 1968	No	275	360
Japan 1970	No	245	242
USA 1973	No	226	
Australia 1985	Yes	340	320
France 2002	Yes	700	640



Figure 2. The fire test of car park, France, 2002.

means of calculation methods and served as the basis for the development of advanced calculation models, including actions, fire scenarios and models of thermo-mechanical response of structures.

The simulations for real steel car parks, the development of which dates back to years 2001–2004, included the most dangerous, and yet realistic, fire scenarios. Those simulations were applied on the stage of designing open car parks with steel and composite structure, allowing for the conclusions to be drawn and assessments to be made regarding fire resistance of elements and stability of the entire structure in fire conditions.

4 FIRE SCENARIOS AND ACTIONS

The assessment of actions in fires in open car parks is based on the following factors:

a) Rate of heat release in a single car fire
b) Data related to spread of fire among cars
c) Fire statistics (the number of cars exposed to fire, their class)

In a fire scenario analysis usually 3rd class cars are used (i.e. Passat, Laguna, Mondeo). RHR curve for a single 3rd class car is shown in Figure 3. The highest RHR value recorded after 25 minutes of burning is 8.3 MW.

Figure 4 shows a RHR curve for three burning, neighbouring cars (curves are shown separately for each car). The ignition of the 2nd and 3rd cars occurs after 12 minutes of the first car being on fire.

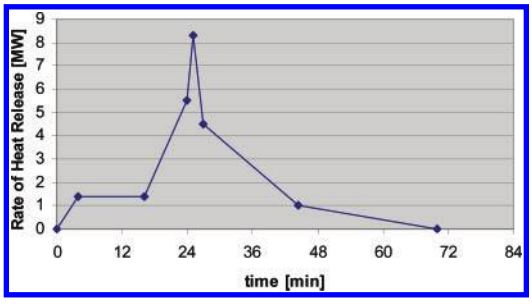


Figure 3. RHR curve for a single burning car.

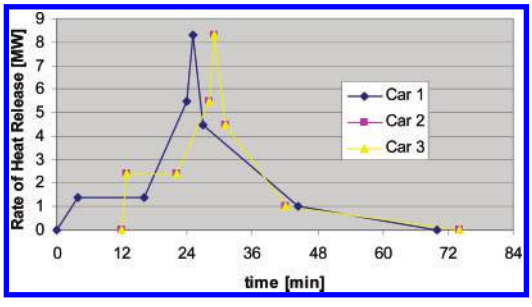


Figure 4. RHR curve for the fire of 3 cars (seperate curves for individual cars).

Based on the above characteristics of cars burning, it is possible to determine thermal actions on structural elements in open car parks exposed to fire.

Real fires statistics in open car parks indicate that the number of cars in fire practically never exceeds 3 vehicles and in 80% fire cases only one car gets burned.

5 STRUCTURAL PERFORMANCE OF CAR PARK STRUCTURE IN FIRE

5.1 *Design scenarios*

The car parks structural behaviour analysis was carried out by means of two basic fire scenarios:

- the fire involving 4 cars located around the central column,
- the fire involving 3 cars standing in one row beside the parking corner.

Scenario 1

The analysed configuration of cars along with the RHR curve are presented in Figure 5. The fire starts with the ignition of the car no. 1. After the time $\Delta t = 12$ minutes the cars no. 2 and 3 are ignited, and subsequently the fire spreads onto the car no. 4 after $\Delta t = 24$ minutes. The maximum total rate of heat release reaches RHR = 23 MW after 29 minutes of fire.

Scenario 2

The analysed configuration of cars along with the RHR curve are presented in Figure 6. The fire starts with the ignition of the car no. 1. After the time $\Delta t = 12$ minutes the cars no. 2 and 3 are ignited. The maximum rate of heat release reaches RHR max = 20.5 MW after 30 minutes of fire.

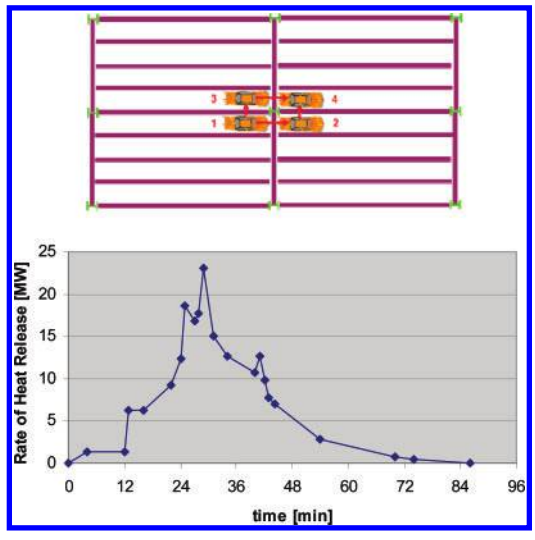


Figure 5. Scenario 1 for the fire involving 4 cars along with the total RHR curve.

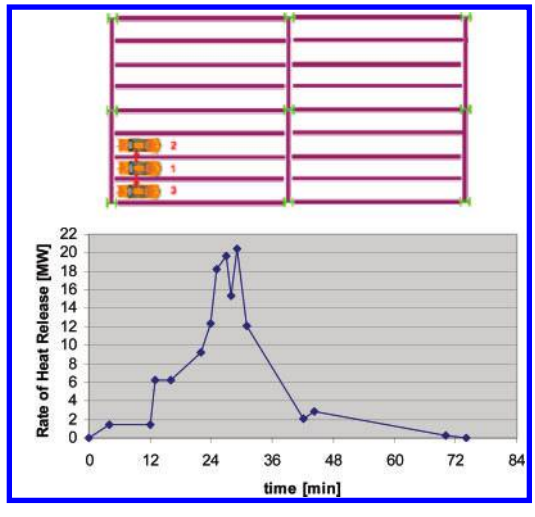


Figure 6. Scenario 2 for the fire involving 3 cars in the corner along with the total RHR curve.

5.2 *Thermal actions*

The model of localized fire has been applied to analyse thermal actions on a car park structure. The heat flux received by the elements is the function of their positioning with regard to vehicles in fire and time. Calculations were carried out in accordance with Eurocode 1 (EN 1991-1-2 2002). The following parameters indicated in Figure 7 were applied.

As a result of calculations, the net heat flux $\dot{h}_{net}$ [kW/m^2] is determined depending on RHR of burning cars and geometrical parameters of car park. The total

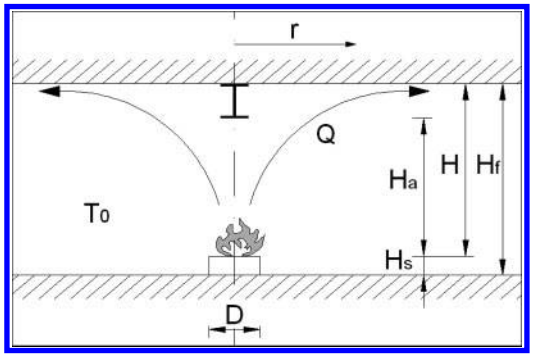


Figure 7. Parameters of the localised fire.
Q [W] – RHR of cars
Ha [m] – vertical distance from the beam lower flange to the floor,
Hs [m] – vertical distance from the fire source to the floor. For the fire coming from the cars it is taken Hs = 0.3 m (Schleich 1999),
D [m] – diameter of fire. For the car park calculations D = 3.9 m (Schleich 1999),
r [m] – distance between the fire axis and the point where the net heat flux is computed.

net heat flux (the sum of fluxes from single burning items) is limited to $\dot{h}_{net} = 100\,\mathrm{kW/m^2}$.

5.3 *Heat transfer*

From the thermal actions (see clause 5.2), time – dependant temperatures in structural members are determined. For a non-homogenous field of temperature in element (variable across the section), the calculation of the heat transfer must be performed by means of numerical methods, applying non-linear analysis system. In the CAPP project software SAFIR (Franssen 2005) was applied.

For homogenous temperature fields, the simplified model of calculations according to the Eurocode 3 (EN 1993-1-2 2005) was applied. From the total neat flux received by the structure, the net heat flux $\dot{h}_{net}$ received by the exposed unit surface on the level of the ceiling needs to be deducted.

The following formula applies:

$$\dot{h}_{net} = \dot{h} - \alpha_c\,(\Theta_m - 20) - \Phi\,\varepsilon_m\,\varepsilon_f\,\sigma\,[(\Theta_m + 273)^4 - (20 + 273)^4] \quad (1)$$

where:

α_c – the coefficient of heat transfer by convection of the material of the element,
Θ_m – surface temperature of the element [°C],
Φ – shape factor,
ε_m – emissivity of the surface of the element,
ε_f – emissivity of flames,
σ – Stephen Boltzmann's constant ($=5.67 \cdot 10^{-8}\,\mathrm{W/m^2K^4}$).

Increase of temperature during the time interval Δt, can be determined from:

$$\Delta\theta_{a,t} = k_{sh}\,\frac{A_m/V}{c_a\rho_a}\,\dot{h}_{net}\,\Delta t \quad (2)$$

where:

k_{sh} is correction factor for the shadow effect,
A_m/V is the section factor for unprotected steel member [1/m],
A_m is the surface area per unit length [m^2/m],
V is the volume of the member per unit length [m^3/m],
c_a is the specific heat of steel [J/kgK],
$\dot{h}_{net}$ is the design value of the net heat flux per unit area [W/m^2],
Δt is the time interval [sec],
ρ_a is the density of steel [kg/m^3].

5.4 *Mechanical actions*

Designing open car park structures under fire situation, accidental load combination compliant with Eurocode (EN 1990 2002) should be applied:

$$\sum_{i\geq 1} G_{k,i} + \Psi_{1,1}\,Q_{k,1} + \sum_{i\geq 1} \Psi_{2,i}\,Q_{k,i} \quad (3)$$

where:

$G_{k,i}$ is a characteristic value of permanent actions,
$Q_{k,1}$ is a characteristic leading variable action,
$Q_{k,i}$ is a characteristic value of accompanying variable action,
$\Psi_{1,1}$ is a factor for frequent value of variable action,
$\Psi_{2,i}$ is a factor for quasi-permanent values of variable actions.

Applying the recommended values of Ψ_1 and Ψ_2 given in table A 1.1 of Eurocode (EN 1990 2002) the accidental combination for fire situation in the car park is as follow:

$$1{,}0\,G + 0{,}7Q \quad (4)$$

For comparison, the basic combination of loads at strength design (STR) for normal conditions is:

$$1{,}35\sum_{i\geq 1} G_{k,i} + 1{,}5Q_{k,1} \quad (5)$$

The load reduction coefficient in fire situation for car parks design is $\eta_{\mathrm{fi}} = 0.6$–0.65. The same value is given in Eurocodes 3 (EN 1993-1-2 2005) and 4 (EN 1994-1-2 2005) for steel and composite structures.

6 NEW METHOD OF CAR PARKS DESIGN

6.1 *Construction of car parks*

The main purpose of CAPP project was to investigate possibilities of complying with Polish Building Regulations in steel open car parks (30 minutes of fire resistance) by application of fire safety engineering

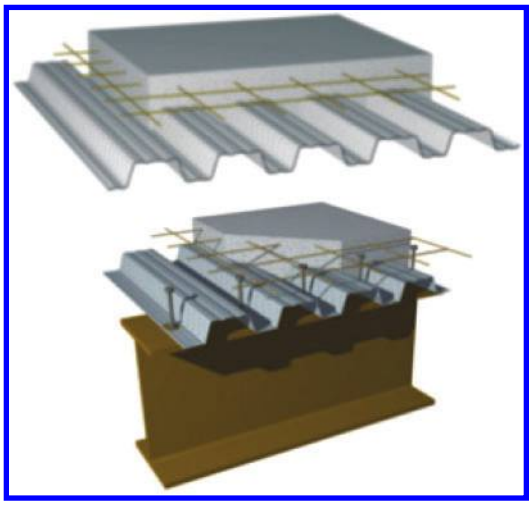


Figure 8. Composite slab and composite beam.

methods and developing design methodology for these structures in fire conditions.

Composite slabs comprise profiled steel decking as a permanent formwork to concrete slabs. Light mesh reinforcement is placed in the concrete mainly to act as "fire reinforcement" but also to reduce cracking from shrinkage.

The composite I beams form essentially T profile with wide upper flange. The concrete flange is in compression and the steel section is mainly in tension. Forces between two materials are transferred by shear connectors.

A composite slab and a composite beam are shown in Figure 8. Steel columns of car park structure were not analysed in the project. It was assumed that they are fire protected in traditional way and fulfil fire resistance requirements.

Steel and composite elements, when constructed with appropriate materials and connectors, may gain higher load bearing capacity in normal conditions and higher fire resistance than are expected in traditional approach. The improvement is due to the interaction of structural elements and additional beneficial effects, e.g. a membrane effect in composite slab.

Proper selection of structural materials is assured by:

- Steel grade S 235 or S 355 for beams
- Concrete class C30/37 for slabs
- Steel grade S 500 for reinforcement of slabs

Welded studs should be supplied between steel beams and a slab in order to provide lateral restraint of beams and their buckling resistance. Special type of beam to beam and beam to columns connections were designed. Additional reinforcement between outermost columns and slabs should be supplied.

6.2 *A membrane effect in composite slabs*

Under the influence of high temperatures steel elements lose their stiffness and strength. It is directly

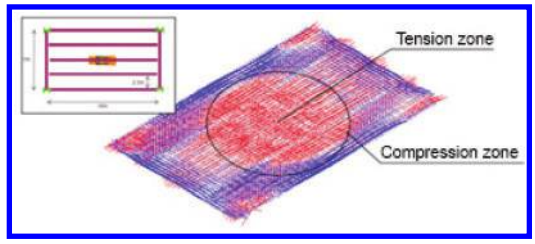


Figure 9. Membrane effect in the slab above a burning car.



Figure 10. Visible membrane effect in the slab.

affecting the performance of structure in fire conditions. In the discussed open car park structures made of steel frame and composite slab the membrane effect is observed when the structure is exposed to fire.

This effect is connected with the development of membrane forces in composite slabs with the simultaneous growth of the deflection, when beams lose their capacity and stiffness. The deflection may reach 30–40 cm for 10 m distance between columns. This effect is beneficial to the capacity of the structure because the arising membrane forces maintain the balance between compression in concrete and tension in reinforcement mesh inside the slab.

Figure 9 shows the deflections of slab under membrane effect. Tension zone is located in the centre of the slab and the compression ring runs along its edges. The same effect is shown in Figure 10.

6.3 *Numerical analysis and design calculations*

On two column grids of 16×10 m and 16×5 m five different types of open car parks were designed, following the method described above.

Composite slabs constructed on the profiled steel decking Cofraplus 60 reach 12 cm or 15 cm in thickness.

Analysis and calculations of the performance of the open car structures in fire conditions were carried out using the program of non-linear structural analysis system SAFIR. Finite elements method calculations were conducted in two stages: thermal analysis and mechanical analysis.

Calculations of the transient heat flow were conducted for a two-dimensional model consisting of a steel beam and a composite slab, exposed to a heat

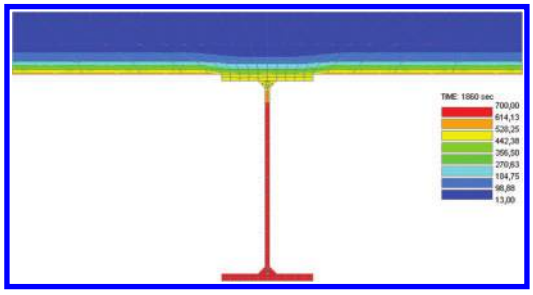


Figure 11. Calculated temperature field in the cross section.

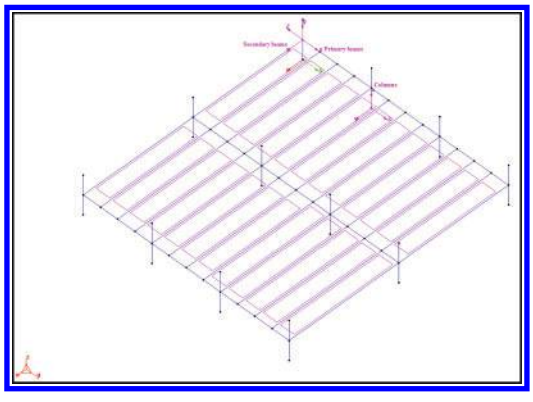


Figure 12. Mechanical calculation model of designed structure.

flux determined for the localized fire conditions. A sample temperature field is shown in Figure 11.

The calculation model used for the mechanical analysis of structure consisted of beam elements representing columns and beams and shell elements representing slabs. The model is shown in Figure 12. Design calculations were conducted for different varieties of geometrical and structural features of open car parks.

7 CONCLUSIONS

– Fire safety engineering approach presented in the paper made it possible to use fire scenarios and thermal actions on structure in accordance with the fire test results. Structural performance described by results of numerical calculations proved to be very similar to the performance observed in real fires. Thus, it can be said that this approach has been well documented and empirically verified.
– The results of tests and numerical analysis confirm that designing and building of open car parks as steel structures with composite steel and concrete slabs provides the satisfactory level of fire safety. Properly designed slabs, without additional fire protection, preserve their stability for not less than 30 minutes of fire caused by burning cars.
– FSE method applied during presented design process of open car parks is currently successfully applied in several European countries i.e. France, United Kingdom, the Netherlands, Switzerland. It can be expected that prescriptive rules currently given in national fire safety regulations in Poland and other counties will be soon replaced by fire safety engineering approach and the design method proposed in the paper will be applicable in engineering practice.

REFERENCES

EN 13501-2. Fire classification of construction products and building elements – Part 2: Classification using data from fire resistance tests, excluding ventilation services, 2007.
EN 1990. Eurocode. Basis of structural design, 2002.
EN 1991-1-2. Eurocode 1: Actions on structures – Part 1–2: General actions – Actions on structures exposed to fire, 2002.
EN 1993-1-2. Eurocode 3: Design of steel structures – Part 1–2: General rules – Structural fire design, 2005.
EN 1994-1-2. Eurocode 4 : Design of composite steel and concrete structures – Part 1–2: General rules – Structural fire design, 2005.
Franssen J.M. – "Users manual for SAFIR 2007 a computer program for analysis of structures subjected to fire", 2007
Project CAPP. "Open Steel Car Park Design for the Polish Market". ArcelorMittal R& D Esch, Building Research Institute Warsaw, ArcelorMittal Constructions, Poznan University of Technology, 2011.
Schleich J.B. et al – "Development of design rules for steel structures subjected to natural fires in closed car parks ", project ECSC, 1999.

Research and Applications in Structural Engineering, Mechanics and Computation – Zingoni (Ed.)
© 2013 Taylor & Francis Group, London, ISBN 978-1-138-00061-2

Numerical study on structural behaviour of cold-formed steel columns under fire conditions

S.J.C. Almeida & J.M. Neto
Engineering School of Sao Carlos, University of Sao Paulo, Sao Carlos, Brazil

J.P.C. Rodrigues
University of Coimbra, Coimbra, Portugal

ABSTRACT: This paper presents the results of numerical studies on the behaviour of cold-formed galvanized steel columns under fire conditions, based on results of experimental tests, previously conducted by the authors. This numerical study was performed by the finite element program ANSYS. First, it is presented the details of the finite element models used in this research and compared the finite element analysis results with those obtained in the experimental tests. Moreover, it is carried out a parametric study in order to investigate the influence of the axial restraining to the thermal elongation of the column, the axial preload ratio on the columns mechanical behaviour.

1 INTRODUCTION

The behaviour of cold-formed steel members at room temperature has been widely investigated and is somewhat well known. On the other hand, the fire performance of cold formed steel members is not well understood. The researches on cold-formed steel members in fire situation are recent and thus the knowledge about the behaviour of these members at elevated temperatures is still being built.

Concerning cold-formed steel columns it is known that is important evaluate the influence of the columns surrounding structure in order to investigate their behaviour at elevated temperatures in a consistently way, once the restraining to the thermal elongation has an important role on the mechanical behaviour of these members in fire situation.

However to date the number of information about the behaviour of cold-formed structural members at elevated temperatures based on test results is small. Consequently, there are few theoretical studies on compressed cold-formed steel members under high temperatures validated by experimental results.

Nevertheless, studies have been done to establish analytical formulations for determining the fire resistance of compressed steel members with axial restraining to the thermal elongation. These formulations beyond prescribe the fire resistance of these members can be useful to the simplified design methods available in design codes for steel structures in fire situation.

With regard to the steel columns, there are some analytical models proposed for determine the strength of steel columns with restraining to the thermal elongation (Cabrita Neves et al., 2002), (Cabrita Neves, 1995), (Valente & Cabrita Neves, 1999) and (Wang, 2002). However, these models were designed for hot rolled sections and the usefulness of these models to represent the behaviour of cold-formed steel columns needs further investigation.

In this context the numerical modeling becomes extremely important. Since that a numerical model performs satisfactorily the aspects of interest regarding the behaviour of cold-formed steel members at elevated temperatures, it may be used to support analytical formulations which subsequently can be implemented in simplified design methods.

In the present work was performed a numerical analysis on the behaviour of compressed cold-formed steel members at high temperatures considering the influence of the restraining to the thermal elongation. The numerical models were constructed based on the tests carry out in Almeida (2012).

2 NUMERICAL ANALYSES

The finite element analyses were performed using the computer code ANSYS. The analyses were conducted at ambient temperature and at high temperatures. The numerical analyses at high temperatures have been divided into two steps, namely thermal analysis and thermo-structural analysis.

The present study was performed using only one cross-section, a lipped channel, $150 \times 43 \times 15 \times 1.5$, (called here C section) with length of 3000 mm, chosen according the tests conducted in Almeida (2012). The columns were simulated with fixed-end and pin-ended supports conditions.

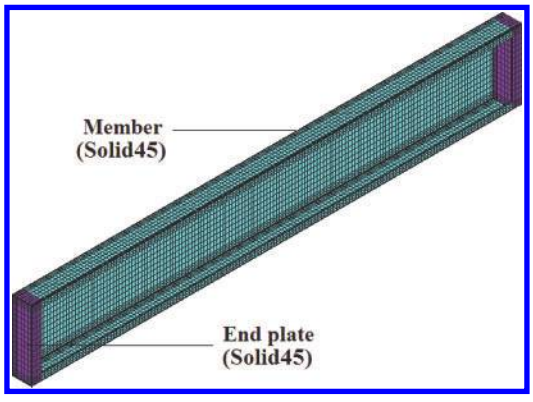


Figure 1. Three dimensional finite element model.

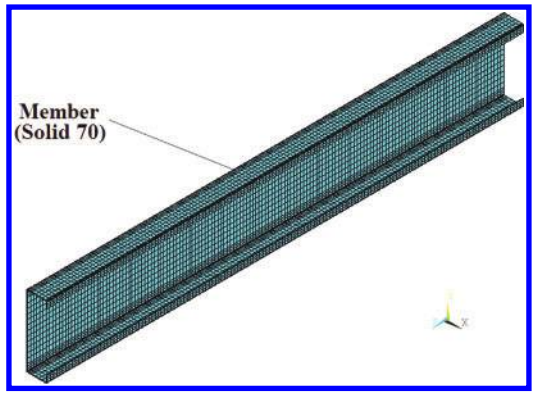


Figure 2. Thermal model: built with element type SOLID70.

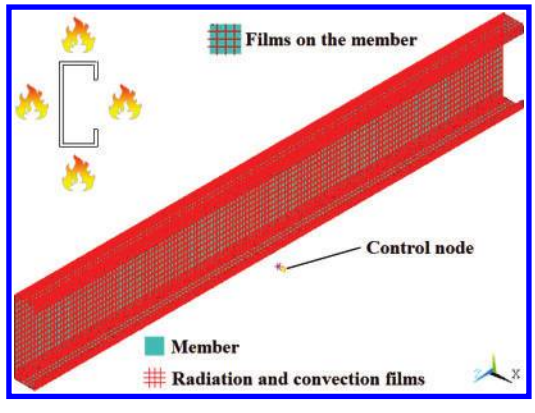


Figure 3. Thermal model: application of the convection and radiation films and the fire exposure condition.

The selected finite elements, the thermal and mechanical properties of steel at high temperatures and the strategy of modeling the axial restraining to the thermal elongation are given in the following items.

2.1 *Room temperature analyses*

The numerical analyses at room temperature were performed to assess compliance of numerical models before being used in the numerical analyses at elevated temperatures.

Moreover, the results of ultimate loads obtained numerically at room temperature were used to compare with those obtained by Eurocode 3 part 1.3 (2006), which were used for calculate the preloads applied to the numerical models of the thermo-structural analyses. The models built at room temperature were calibrated based on the results of ultimate loads obtained by the Eurocode 3 part 1.3 (2006) and ABNT NBR 14762 (2010) design methods, as shown in the item 3.1.

The geometric imperfection was generated through eigenvalue buckling analysis. The global flexural mode was adopted to represent the geometric imperfection. The out-of-straightness of L/500 was used for the amplitude of initial imperfection.

The stress–strain relationship at room temperature used in this study is based on the models in Eurocode 3 part 1.2 (2005) with material properties at 20 °C. Figure 1 shows the general outline of the model used in these analyzes, which were constructed with element type SOLID 45.

2.2 *Thermal analyses*

From the thermal analysis were obtained the temperature fields to be implemented in the thermo-structural analyses. The *temperature vs. time* relationships used in the thermal analyses were obtained based on the tests results presented in Almeida (2012). The numerical models for the thermal analyses were built with element type SOLID70. The thermal action and the effects of radiation and convection were simulated with the aid of element type SURF152.

The values adopted for thermal conductivity, specific heat and thermal elongation of the steel were those available in the Eurocode 3 part 1.2 (2005).

Regarding the parameters inherent to the mechanisms of heat transfer, the coefficient of heat transfer by convection used was equal to 25 W/m2 °C and the emissivity resulting, ε, was adopted equal to 0.5.

The temperature distribution along the height was modeled considering a non uniform distribution of temperature based on the distribution of temperature measured experimentally in Almeida (2012).

The Figure 2 shows the model used in the thermal analyses. The Figure 3 illustrates the application of the films of convection and radiation on the numerical models and the fire exposure condition used in the thermal analyses.

2.3 *Thermo-structural analyses*

The results obtained from the thermo-structural analyses were: (i) ultimate load, (ii) critical time and (iii) critical temperature.

The stress–strain relationship at elevated temperatures adopted for the steel is based on the models in

Eurocode 3 part 1.2 (2005) to temperatures ranging between 20 and 1100 °C.

The effects of the thermal action on structural analysis at high temperatures were considered by the reduction factors of the mechanical properties according EN 1993-1-2:2005 for the design of class 4 sections.

The numerical models used to perform structural analyses at elevated temperatures were built with element type SOLID45 which is compatible with the SOLID70 used in thermal analyses, allowing the transference of the thermal field obtained in the thermal analyses to the models of thermo-structural analyses.

The boundary conditions applied to the models at elevated temperatures present a difference in relation to those imposed at room temperature. In Almeida (2012), the columns were tested at elevated temperatures considering a surrounding structure. Thus, it was possible evaluate experimentally the influence of the restraining to the thermal elongation on the behavior of the columns.

Then, in the numerical models built to perform the thermo-structural analyses was considered the restraining to the thermal elongation through the strategy presented in Dorr (2010), which simulated a spring by means of a bar element (LINK 10) and the elastic properties of steel of the structural members.

In Dorr (2010), several studies were conducted to define the geometric properties of the element LINK10 used to modeling the restraining to the thermal elongation. According to the results of these studies was determined that a single element is sufficient to discretize the finite element LINK10 and the length of 0.1 m adopted for the LINK10 was adequate to represent the restraining to the thermal elongation.

The stiffness of the restraining to the thermal elongation was determined based on the axial stiffness (EA) of the members according to equation 1, where R is the elastic constant of the spring constraint (LINK10), k_r is the coefficient of proportion, E is the modulus of elasticity of the steel, A is the cross-sectional area, L is the member length and L_s is the length of the restraining to the thermal elongation. Figure 4 shows the scheme used to model the restraining to the thermal elongation.

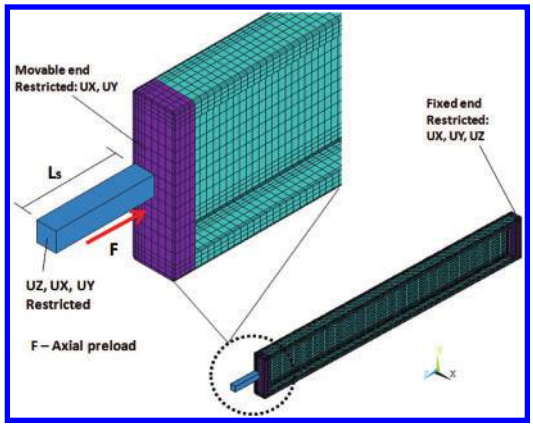


Figure 4. General scheme of the axial restraining to the thermal elongation.

$$R = k_r \frac{EA}{(L / L_s)} \quad (1)$$

The global flexural mode was adopted to represent the geometric imperfection. The out-of-straightness of L/500 was used as the amplitude of the imperfection. The mechanical action was performed using increments of load keeping agreement with the experimental procedures.

In summary, in the thermo-structural analysis first of all the geometric imperfection generated by eigenvalue analysis is introduced into the members. After that, it is applied the preload, which in this study was taken as a percentage of the ultimate load at room temperature determined according to Eurocode 3 Part 1.3 (2006). Finally the temperature field obtained from transient thermal analysis is incremented.

3 RESULTS

3.1 *Room temperature analyses*

Table 1 shows the comparative results between the ultimate load obtained numerically and those calculated by the design methods of the Eurocode 3 part 1.3 (2006) and ABNT NBR 14762:2010, where $F_L/500$ is the maximum compressive force obtained numerically for the global imperfection of L/500 and λ is the global slenderness. The labels C-F and C-P refer to the numerical models end support conditions, fixed-ended and pin-ended respectively.

According to the results shown in Table 1, the numerical models showed agreement with the results prescribed by the design codes confirming the compliance of the models. Moreover, these results attest the consistency of the preloads applied to models in the thermo-structural analyses.

3.2 *Thermo-structural analysis*

In the analyses conducted at elevated temperatures were evaluated (i) two values of preloads (30% and 50% of ultimate load determined according to EN1993-1-3:2006) and (ii) three values of restriction to thermal elongation ($k_r = 0.13$, 0.26 and 0.52), where k_r is the proportion coefficient according to

Table 1. Ultimate loads at room temperature.

Model		λ (L_{ef}/r)	EC3 P1.3 (kN)	NBR (kN)	$F_{L/500}$ (kN)	$\frac{F_{L/500}}{EC3}$	$\frac{F_{L/500}}{NBR}$
P01 P02	C-F	192	46.5	49.1	44.0	0.95	0.90
P07 P08	C-P	154	17.5	18.0	17.2	0.98	0.96

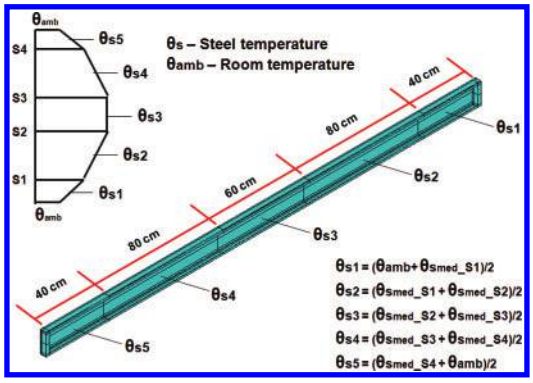


Figure 5. Non uniform temperature distribution along the height: simplified model.

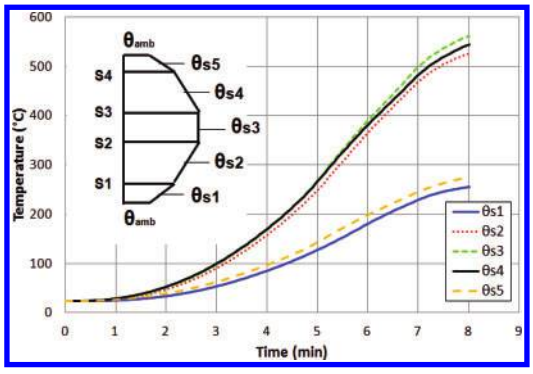


Figure 6. *Temperature* × *time* relation: Model C-F with non uniform temperature distribution along the height.

equation 1 and $k_r = 0.13$ is the value corresponding to the axial rigidity imposed experimentally to members. It follows the analysis and discussions of the results.

The fields of temperature was defined as shown in Figure 5, where θa1, θa2, θa3, θa4 θa5 are calculated as a function of average temperatures recorded in the sections S1, S2, S3 and S4 distributed along the height of the members as shown in the detail in Figure 5.

Figure 6 shows the heating curves used for the members with fixed ends. These curves were built based on the *temperature* × *time* curves recorded for column P02. For the members with pinned ends the heating curves were built based on the *temperature* × *time* recorded for the column P07.

Tables 2 and 3 show the summary of the results found for the C-F and C-P models respectively, where k_r is the proportion coefficient from the equation 1, F is the maximum numerical compression force, P is the maximum experimental compression force, θ_s is the critical temperature, t is the critical time and the preload is a percentage of the ultimate load determined with EN1993-1.3:2006.

According these tables, the numerical and experimental ultimate loads were close. On the other hand, the critical temperatures prescribed numerically showed a significant difference from the value found

Table 2. Numerical results: Model C-F.

		Numerical			Experimental		
Preload	k_r	F (kN)	θs (°C)	t (min)	P (kN)	*θs (°C)	t (min)
30%	0.13	33.25	246.55	5.9	33.7	383.48	5.94
	0.26	36.32	161.26	5.0	–	–	–
	0.52	38.26	110.55	4.3	–	–	–
50%	0.13	35.12	196	5.4	–	–	–
	0.26	37.47	129.7	4.6	–	–	–
	0.52	38.89	90.23	3.9	–	–	–

*θs – Measured at the section S2 of the column P02

Table 3. Numerical results: Model C-P.

		Numerical			Experimental		
Preload	k_r	F (kN)	θs (°C)	t (min)	P (kN)	*θs (°C)	t (min)
30%	0.13	16.06	226.03	6.0	–	–	–
	0.26	16.79	235	6.0	–	–	–
	0.52	17.15	235.12	6.0	–	–	–
56%	0.13	16.58	197.83	5.6	15.3	251.95	5.06
	0.26	17.10	180.72	5.5	–	–	–
	0.52	17.21	225.01	6.0	–	–	–

*θs – Measured at the section S2 of the column P07

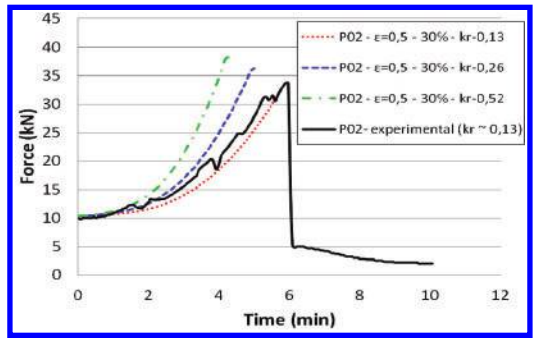


Figure 7. *Force* × *time* relation: numerical to experimental comparison: Model C-F with non uniform temperature distribution.

experimentally. Regarding the critical time, the numerical prescriptions were close the values recorded experimentally.

Figures 7 and 8 shows the comparisons between the experimental and numerical relationships, *force vs. time* and *force vs. temperature*, for the models with fixed-end supports. According to the Figure 7, the numerical model represents, satisfactorily the experimental *force vs. time* curve and as shown in Figure 8 the numerical model tends to simulate satisfactorily the experimental *force vs. temperature* curve.

Figures 9 and 10 shows the comparisons between the experimental and numerical relationships, *force vs. time* and *force vs. temperature*, for the models

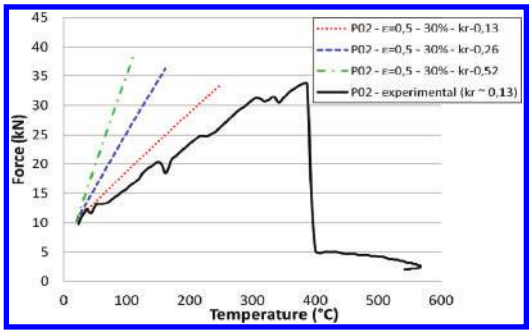


Figure 8. *Force* × *temperature* relation: numerical to experimental comparison: Model C-F with non uniform temperature distribution.

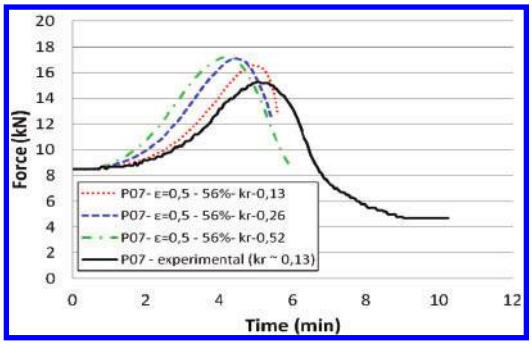


Figure 9. *Force* × *time* relation: numerical to experimental comparison: Model C-P with non uniform temperature distribution.

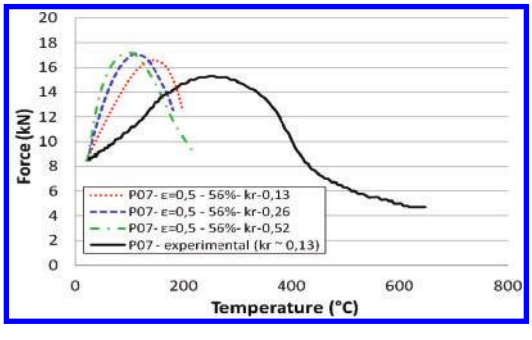


Figure 10. *Force* × *temperature* relation: numerical to experimental comparison: Model C-P with non uniform temperature distribution.

with pin-ended supports. According to Figure 9, the numerical model represents satisfactorily, the experimental curve *force vs. time*. On the other hand, the numerical model showed rigidity much greater than that registered experimentally, as shown in Figure 10.

Figures (11 and 12) and (13 and 14) show the *force vs. time* and *force vs. temperature* curves obtained numerically for different combinations of parameters, for the models with fixed-end and pin-ended respectively.

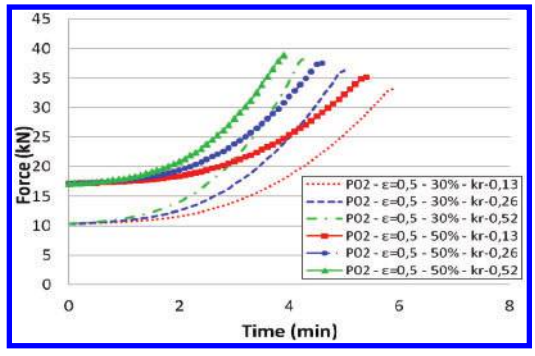


Figure 11. *Force* × *time* relation for different parameters combinations: Model C-F with non uniform temperature distribution.

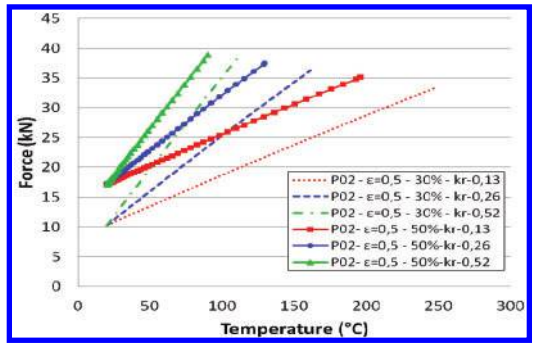


Figure 12. *Force* × *temperature* relation for different parameters combinations: Model C-F with non uniform temperature distribution.

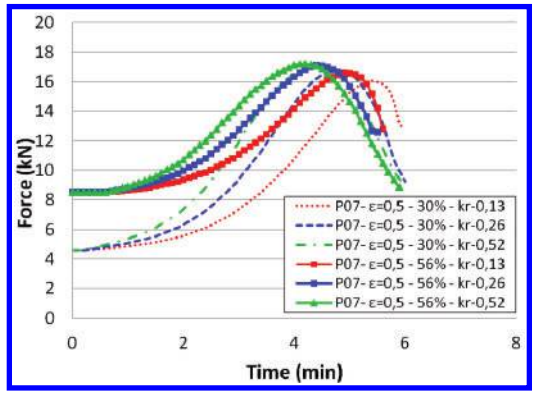


Figure 13. *Force* × *time* relation for different parameters combinations: Model C-P with non uniform temperature distribution.

According to Figures 11 and 12, for the models with fixed-end, the variation of the ultimate load with the preload was negligible. Similarly, the intensity of ultimate load practically not varied with the axial restraining to the thermal elongation imposed to the models.

From the Figures 13 and 14, similar to the models with fixed-end, the ultimate load practically not varied

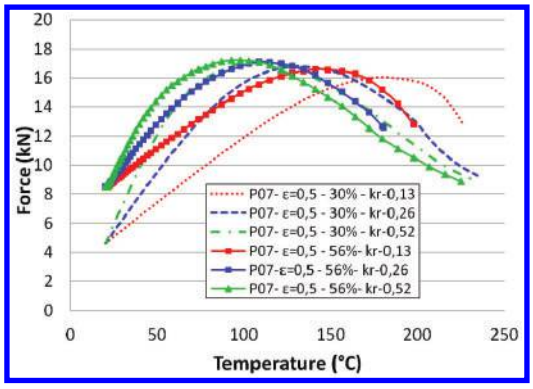


Figure 14. *Force* × *temperature* relation for different parameters combinations: Model C-P with non uniform temperature distribution.

with the preload nor with the axial restraining to the thermal elongation for models with pin-ended.

However, a particularity of the models with the pin-ended was the identification of the descending branch of the curve *force vs. time*. This behaviour was not observed in the models previously analyzed and until then had no knowledge of the capability of the numerical model built to capture this information.

With the results, it is proved the efficiency of the model to represent the descending branch of the curve *force vs. temperature*, which means that the model is able to represent the post-critical behaviour of the compressed steel member with restraining to the thermal elongation.

4 CONCLUSION

In the present work we carried out numerical analyses on the behaviour of cold-formed steel members at elevated temperature submitted to compression with restraining to the thermal elongation. The numerical models presented some limitations to reproduce satisfactorily the critical temperature. On the other hand, the modeling strategy was capable to prescribe the ultimate load and the critical time with reasonable error margin compared to test results obtained in Almeida (2012). Moreover, the models also reproduced satisfactorily the experimental curve *force vs. time*. The model has potential to represent satisfactorily the post-critical behavior of cold formed steel members submitted to compression with axial restraining to the thermal elongation. Using the simplified non-uniform temperature distribution the model could obtain the descending branch of the *force vs. time* curves and *force vs. temperature* observed in the experimental investigation of pinned end compressed cold formed steel members with restraining to the thermal elongation.

ACKNOWLEDGEMENTS

The authors gratefully acknowledge to the Portuguese Foundation for Science and Technology – FCT (www.fct.mctes.pt) and to the National Council for Scientific and Technological Development – CNPq (Brazil) for their support.

The first author also acknowledges FAPESP for his postdoctoral scholarship, 2012/02693-0.

REFERENCES

Almeida, S.J.C. Analysis on the behaviour of cold formed steel columns under fire conditions with restrained thermal elongation. 292 p. Thesis – Engineering School of Sao Carlos, University of Sao Paulo, Sao Carlos, Sao Paulo, Brazil. University of Coimbra, Coimbra, Portugal, 2012.

ANSYS. 2009. Reference manual. v12 edn. Swanson Analysis Systems (SAS), USA.

ASSOCIAÇÃO BRASILEIRA DE NORMAS TÉCNICAS (2010). NBR 14762: Dimensionamento de estruturas de aço constituídas por perfis formados a frio. Rio de Janeiro.

Cabrita Neves, I. The Critical Temperature of Steel Columns with Restrained Thermal Elongation, Fire Safety Journal, vol. 24 , n° 3, 1995, p. 211–227.

Cabrita Neves, I., Valente, J. C., Rodrigues, J.P.C. Thermal restraint and fire resistance of columns, Fire Safety Journal, vol. 37 , n° 8, 2002, p. 753–771.

Dorr, J. B. Numerical models of steel columns under fire condition considering the axial restraint. 2010. 210p. Dissertation (master) – Structural Engineering Department, Engineering School of São Carlos, University of Sao Paulo, Sao Carlos, Sao Paulo, Brazil.

EUROPEAN COMMITTEE FOR STANDARDIZATION (2005). EN 1993-1-2:2005 Eurocode 3 – Design of Steel Structures. Part 1-2: General rules – Structural Fire Design. Brussels.

EUROPEAN COMMITTEE FOR STANDARDIZATION (2006). EN 1993-1-3:2006 Eurocode 3 – Design of Steel Structures. Part 1-3: General rules – Supplementary rules for cold-formed members and sheeting. Brussels.

Valente, J. C., Cabrita Neves, I. Fire resistance of steel columns with elastically restrained axial elongation and bending, J Construct Steel Res, vol. 52 , n° 3, 1999, p. 319–331.

Wang, Y. C. Steel and Composite Structures – Behaviour and Design for Fire Safety. Spon Press, London, 2002, 352 p.

Research and Applications in Structural Engineering, Mechanics and Computation – Zingoni (Ed.)
© 2013 Taylor & Francis Group, London, ISBN 978-1-138-00061-2

An analytical method for determining the loading on connections in heating and cooling during a fire

David Lange & Joakim Albrektsson
SP Technical Research institute of Sweden

ABSTRACT: This paper presents a proposed analytical method for calculating the mechanical loading on a beam column connection in fire. The behavior of connections in fire has received considerable interest over the last decade since it is well known and demonstrated experimentally that composite steel concrete construction is able to adopt alternative load bearing mechanisms in fire as a result of large displacements. This global behavior is different from behavior which is studied in standard furnace testing and places additional loads on the supporting structure which must be able to support elements which are effectively 'hanging' in tension as opposed to supporting the load through shear and bending, as at ambient.

First, this paper explores the mechanisms which lead to time varying mechanical loading on a beam / column connection in fire. Then a simple method for calculating a loading envelope of the connection is proposed. The analytical method is derived from fundamental principles of structural behavior at high temperatures and is a development of previous work published by the authors elsewhere. New developments presented include a discussion of the mechanisms which govern the response of composite structures during cooling following a fire and inclusion of these in the analytical model. The analytical method is then compared with the results of finite element analyses and is shown to compare favorably.

1 INTRODUCTION

Design of connections in steel concrete composite frames for fire traditionally assumes that the connections do not lose as much of their strength at high temperatures as the structure as a result of their high massiveness. Work conducted has focused on evaluating the response of connections in fire – evaluating their capacity at elevated temperatures and when exposed to forces with large horizontal components arising from large thermally induced deflections in the structure (Wang et al. 2011), (Yu et al. 2008). Researchers at Sheffield University have also developed a component model for steel connections in fire (Block et al. 2013).

The focus of the work presented in this paper is the study of the forces which act on connections as a result of the mobilization of membrane or catenary action of a structure in fire. These large displacements in horizontal building elements are known to induce large horizontal loads on the supporting construction. This paper presents a simple analytical method for determining the loads on connections in fire which is based on other work by the main author and which is published elsewhere (Lange et al. 2012).

2 NUMERICAL ANALYSIS

The basis for the validation of the analytical model for determining the load on connections in fire is a simple finite element model comprising solely beam elements representing a composite floor system. All three of the slab, beam and reinforcement were considered in the finite element model and a range of section sizes were used in the study. A separate heat transfer analysis was conducted using simple analytical techniques and this was used as input to the finite element model and to the analytical model.

2.1 *Thermal model*

The thermal model was based on simple or codified solutions. Two fires were used in the analyses, an ISO fire of duration 2 hours and a parametric fire with floor area of 225 m^2, total area of 612 m^2, Ventilation opening of 46.6 m^2, c_p of the enclosure linings of 837 J/kgK, conductivity of the enclosure linings of 0.48 W/mK, density of the linings of 1442 kg/m^3 and a fuel load of 511 MJ/m^2. A medium fire growth rate was used. The two fires used in the analysis are shown in Figure 1.

Heat transfer to the steel beam was carried out using the simple methods described in Eurocode 3 Part 1–2, assuming lumped capacitance. The steel beam is assumed unprotected in this study.

Heat transfer to the concrete was carried out using a finite difference heat transfer algorithm, with material properties as defined in Eurocode 2.

Output from the heat transfer analysis was used both for the finite element calculation, with temperature at 7 points through the depth of the concrete slab being exported to abaqus as well as the temperature

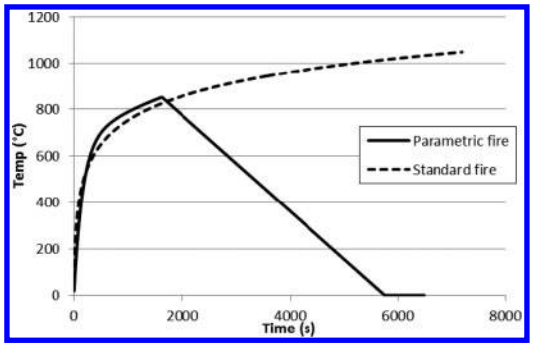


Figure 1. The standard fire and the parametric fire used in the analysis.

of the beam. In addition to this, a sectional analysis was carried out on the heated floor system taking account of the reduced modulus and modular ratios at different temperatures and different depths in both the concrete and the steel. Cooling was considered during the parametric fire exposure by not allowing the concrete to recover strength during cooling when carrying out the sectional analysis, while allowing the steel to recover all of its strength during cooling. From the sectional analysis an equivalent thermal gradient, T_z, and equivalent uniform temperature increase in the entire section, ΔT, were determined.

2.2 *Finite element model*

Finite element analysis of the response of the composite floor comprising 9 different beam section sizes and 4 different loading levels was carried out using the abaqus explicit finite element solver and were time scaled by a factor of 1000 (no rate dependent material properties were used in the models). The system was modeled using beam elements representing the steel beam, the concrete slab and the reinforcement within the slab. All parts were tied at the nodes to represent composite action between the slab and the beam and the concrete and the reinforcement. The beam was offset from the slab to account for the thickness of the slab and the depth of the beam. The beam was pinned at both ends, representing a non-continuous concrete construction, it should be noted however that this influenced primarily the deflected shape – with no restraining moment applied at the ends – and that the reinforcement was also subject to the support conditions through the constraint between the different parts in the model.

The slab was 100 mm thick, and the floor spanned 6 m in all cases, with a 6 m distance between the beams.

The steel beam acting in composite with the slab varied from an IPE 180 section to an IPE 450 section (including IPE 200, IPE 220, IPE 240, IPE 270, IPE 300, IPE 330, and IPE 400 sections). Reinforcing steel was provided in the form of an A142 anti cracking mesh, providing a total area of reinforcement of 852 mm^2. The steel reinforcement was located at the mid depth of the concrete slab.

The abaqus Concrete Damaged Plasticity model was used for the concrete material, with a maximum compressive load of 35 MPa at ambient and a maximum tensile strength of 2 MPa at ambient. The steel had a modulus of elasticity of 210 000 MPa, and an elastic limit of 355 MPa and yield modulus of 455 MPa at a strain of 0.045, and ultimate strain of 0.2. The steel for the anti-cracking mesh was the same as the steel for the structural beam.

Strength and stiffness reduction of both concrete and steel at high temperatures are taken from Eurocode 2 Part 1–2 and Eurocode 3 Part 1-2 respectively.

Uniform loading was applied to the model at magnitudes of 30, 45, 50 and 60 N/mm length of the floor. All models were run for both the standard fire for a period of two hours and the parametric fire shown. To include cooling during the parametric fire, a user subroutine was used within abaqus which maintained the temperature of concrete at the maximum temperature observed for determination of the temperature dependent material properties. The material properties of the steel beam and the reinforcement were allowed to return to their unreduced properties at ambient.

2.3 *Results and discussion*

For brevity, not all results are presented here. However an exemplar of the horizontal load at the supports and the mid span deflections is shown in Figure 2 for both the standard and the parametric fire; results are plotted against 1000's of seconds. Figure 2 a) shows the response of a floor comprising the IPE220 beam under a load of 30 N/mm length exposed to the standard fire and Figure 2 b) shows the response of a floor comprising an IPE 300 section under a load of 60 N/mm exposed to the parametric fire.

The overall behavior of the floors is similar in both the standard and the parametric fire. In both cases the floor experiences a short period where it 'pushes' against the support. Further heating results in the development of large deflections and the adoption of a catenary mechanism and a corresponding large horizontal load 'puling' on the connection. In figure 2 b) it can be seen that the catenary mechanism is actually mobilized in the floor exposed to a parametric fire after approximately 2000 seconds, corresponding with a sudden increase in the deflection and the reversal of the overall compressive force in the floor to a tensile force. It should be noted that some of the floors were unable to carry the load in either bending or a catenary. In these cases very large deflections resulted. These were the models of floors with a small beam section and the largest applied loads, typically those exposed to the long standard fire.

During the cooling phase and the post cooling phase of the parametric fire, there is little or no relaxation of the deflections beyond the peak deflection observed. In addition to this, the horizontal load shows little or no increase as the floor system cools. This is perhaps

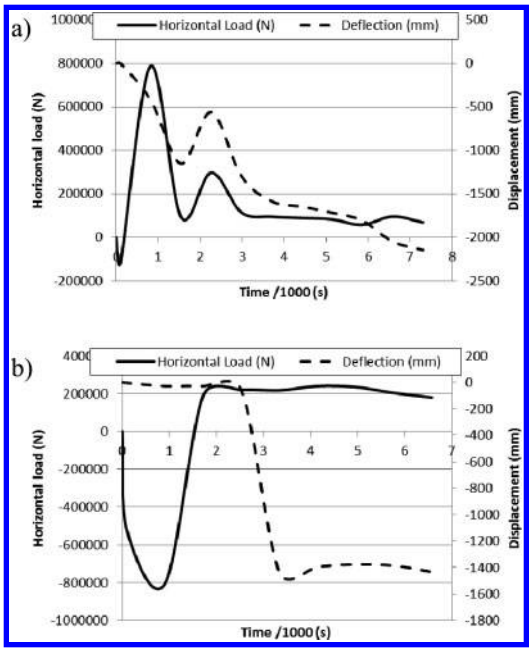


Figure 2. Example of horizontal load and displacement of floor system under a) a standard fire and b) a parametric fire (tension positive, compression negative).

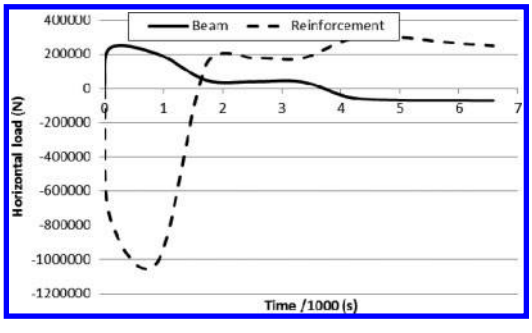


Figure 3. Reaction from the beam and the reinforcement of a floor comprising an IPE 300 section when exposed to the parametric fire described.

contrary to what may be expected as contraction of the steel beam upon cooling may intuitively be expected to result in a significant increase in the horizontal load on the connections, further; experience from a number of tests has shown that there is little to no reduction in the total deflection of a composite floor following a fire, which should serve to increase the tension in the steel beam. Figure 3 shows the contribution to the horizontal load at mid span from the beam and the reinforcement in the slab. It can be seen that in fact the horizontal force at mid span in the steel beam is in fact small and compressive rather than tensile following cooling.

The following explanation is proposed in order to explain why the horizontal load does not significantly increase as the steel beam cools and contracts.

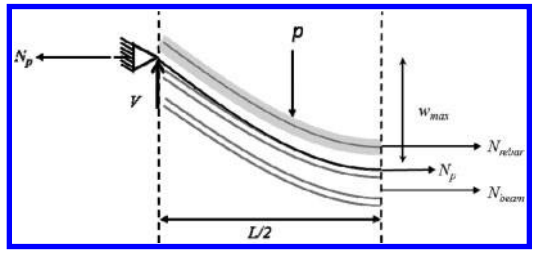


Figure 4. The contribution to horizontal load from both the reinforcement and the beam in a catenary is shown. The slab, reinforcement and steel beam are shown in grey. The load resultant is shown rather than the distributed load.

Figure 4 shows the contribution to the horizontal load from the reinforcement in the slab and the steel beam. At the peak of heating of an unprotected floor system the two components of the horizontal load, N_p, may be determined based on the sum of these two components, N_{rebar} and N_{beam}. N_{rebar} is based on mechanical strain and the temperature dependent modulus of elasticity in the floor for the reinforcement assuming that it is still in the elastic region of the stress strain curve, equation (1a). If the rebar is no longer in the elastic range then the force may be approximated by the product of the temperature dependent yield stress and area of the steel reinforcement, equation (1b). N_{beam} at high temperatures may always determined from the temperature dependent yield stress of the steel beam since at high temperatures associated with the peak of heating in a fire the yield stress of the steel beam will have been exceeded by the entire floor adopting the deflection required to support the load.

$$N_{rebar} = \varepsilon_s A_r E_r(T) \tag{1a}$$

$$N_{rebar} = A_r \sigma_{yr}(T) \tag{1b}$$

$$N_{beam} = A_b \sigma_{yb}(T) \tag{2}$$

At the end of a heating phase, the floor has adopted the deflection required to support the load in a catenary. Based on the relative magnitudes of equations 1 and 2 the majority of the tensile load is supported by the steel reinforcement in the floor rather than the beam. This is because the temperature dependent yield stress of the beam is considerably lower than either the yield stress or the modulus of elasticity of the much cooler reinforcement located within the slab.

Once heating stops and the temperature of the steel begins to reduce, thermal strain decreases. However the total deflection is still required by the floor system to sustain the load and therefore the majority of the thermal strains are 'locked in' to the steel beam as plastic deformations. As the temperature decreases, this effect will reduce however the additional tensile load on the floor boundaries will not be as high as were the beam able to contract without absorbing the expansion strains as plastic strains. With increasing section size, the beam will absorb less of the expansion

strain as plastic strain since the relative magnitude of the forces in the beam and the rebar are higher and the tensile load on the beam connections will be larger as a result, however they will not be as large as were the beam able to contract unhindered.

Finally, during cooling of the steel beam the slab in the model is subject to some reversal of the thermal moment which may result in some compressive load on the steel beam, an effect which is slower than cooling of the steel beam. This effect may however be unlikely in practice as a result of tensile cracking of the concrete.

3 ANALYTICAL METHOD

There are three stages in the calculation of the load on a beam-column connection in fire:

1. Calculate the thermal loading on the floor. This can typically be carried out via a 1D heat transfer analysis, or similar. It is assumed that the temperature distribution is 1 dimensional, i.e. varies only through the depth of the floor system. Regardless of the method employed, the ultimate goal is to obtain an equivalent temperature distribution consisting of an average temperature increase and a uniform thermal gradient.
2. Calculate the thermally induced deflection of the floor system, based upon the results of the heat transfer analysis.
3. Calculate the combined thermal and mechanical response of the floor system, and evaluate the total loading at the boundary from both the beam and the reinforcement before splitting this load into the component from the beam (supported by the connection) and the reinforcement (supported by overlap and continuity of the reinforcement

3.1 *Thermal deflection*

The thermal response of the floor system can be deduced by considering in turn the thermal expansion caused by the average temperature increase, ΔT, and the thermal bowing induced by the temperature gradient, T,z.

At interior columns, the in-plane restraint to expansion is large. In contrast, at exterior columns in-plane restraint to expansion is much smaller. However, where fire exists on only one floor, the translational stiffness of the column may be assumed to be large, and therefore the lateral translation of the connection is assumed to be fully restrained by this stiffness.

The thermal deflection, w_T in Figure 5, is given by the following equation:

$$w_t = \frac{2L}{\pi}\sqrt{\varepsilon_\phi + \varepsilon_T + \frac{(\varepsilon_\phi + \varepsilon_T)^2}{2}}, \qquad (3)$$

where $\varepsilon_\phi = 1 - \frac{\sin L\phi/2}{L\phi/2}$ and $\phi = \alpha T_{,z}$, $\varepsilon_T = \alpha \Delta T$, L is the length of the floor system, α is the coefficient of thermal expansion , ΔT is an equivalent temperature of the floor system, and $T_{,z}$ is the equivalent thermal gradient calculated for the whole floor system according to (Usmani 2000).

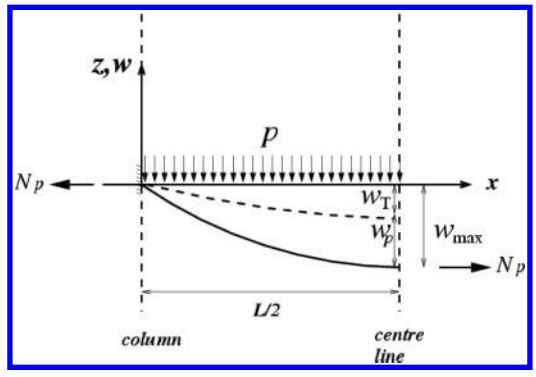


Figure 5. Deflected shape and forces acting on the floor system.

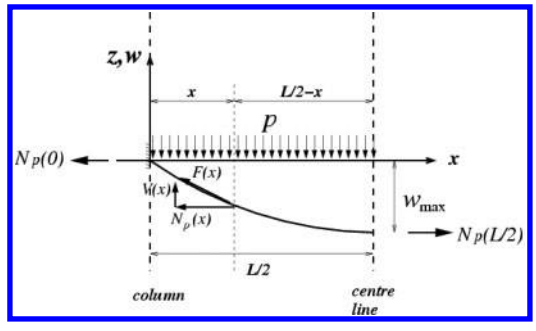


Figure 6. Tension in the floor is calculated as shown.

3.2 *Mechanical loading during heating*

The deflected shape and forces acting on the floor system, after a catenary mechanism has been adopted, are shown in Figure 5.

Considering the total tension in the floor system, N_p, at distance x along the span, Figure 6, and taking moments about the mid span of the floor then the horizontal reaction is given by:

$$N_p = \frac{pL^2}{8w_{\max}} \qquad (4)$$

Consistent with other work, at large displacements, the contribution from concrete to the floor system is ignored due to widespread tensile cracking of the concrete (Cameron & Usmani 2005). The maximum possible tension before failure, F_{max}, in the floor system may be determined from the yield stress of the available reinforcement and the steel.

$$F_{\max} = A_s\sigma_{ys}(T) + A_r\sigma_{yr}(T) \qquad (5)$$

This maximum tension occurs at the support, where the shear reaction is highest.

The shear reaction is given by:

$$V(x) = p\left(\frac{L}{2} - x\right) \tag{6}$$

The maximum possible horizontal reaction for the entire floor may therefore be calculated based on the resultant reactions of the floor system at $x = 0$:

$$N_{p\max} = \sqrt{F_{\max}{}^2 - p^2\left(\frac{L}{2}\right)^2} \tag{7}$$

This value of $N_{p\max}$ is an upper bound for the horizontal load which could by placed on the support of the composite floor adopting a catenary. It is also important to note that this load is the total load carried by both the reinforcement and the steel beam. In order to determine the load on the connection and the load which must be carried either by horizontal shear connection at the perimeter beams or through continuation of the steel reinforcement to adjacent bays the total force must be split into these two components.

However, inspection of equation (4) indicates that at high deflections the total horizontal load is reduced below the maximum possible tension in the floor system. Previous work by the main author of this paper has included a formulation for determining the increased length required to support a distributed load in a similar floor system (Lange et al. 2012). However this formulation assumes that the reinforcement in the floor remains elastic.

The simpler formulation proposed in this article therefore includes a simpler estimation of the total deflection based on the assumption that strain hardening of the steel reinforcement as it yields will lead to the yield strain being distributed along the length of the reinforcement before any increase in plastic strain occurs. As with the numerical models, initial strain hardening of the reinforcement is assumed to occur at a strain of $\varepsilon_{pl} = 0.0185$ and this is therefore taken as the strain in steel in the floor when determining the total deflection.

$$w_{\max} = \frac{2L}{\pi}\sqrt{\varepsilon_{pl} + \frac{\varepsilon_{pl}^2}{2}} + w_T \tag{8}$$

Substituting equation (8) into equation (4), the horizontal load on the connection at this increased deflection is given by:

$$N_{p\delta} = \frac{pL}{16\pi\sqrt{\varepsilon_{pl} + \frac{\varepsilon_{pl}^2}{2}} + w_T} \tag{9}$$

The horizontal load on the connection therefore lies between the maximum given by equation (7) at the transition between bending and catenary action and the value given by equation (9) at high deflections. During cooling, equation (9) may be used as a reasonable upper bound since it may be assumed that no reversal of the deflections which develop during heating occur.

The component which is taken by the connection between the steel beam and the column should first be determined from equation (2) since it is assumed that the steel beam has yielded as a result of the high temperatures and the tensile load which is placed on it as it is forced to follow the deflected shape of the concrete. The component which is taken by the steel reinforcement is then determined based on the difference between either $N_{p\delta}$ and $N_{p\max}$ as appropriate and N_{beam}.

4 VALIDATION AND CONCLUSIONS

Validation of the analytical method in comparison to the numerical results is presented in this section for the parametric fire for the maximum horizontal load on the connection during the heating phase and at the end of the. Comparison of the analytical method with the maximum horizontal load during a standard fire will be made elsewhere however it can be reasonably assumed that validation against the heating phase of a parametric fire may represent a good approximation to the results with the standard fire.

Figure 7 shows the maximum horizontal load which may be expected to occur during the heating phase of the parametric fire. The analytical results for each of the analysis are plotted against the numerical results for the same. The dashed line in the figure represents equivalency between the results and therefore everything below the dashed line shows conservatism over the numerical results. These results are given for a time of approximately 600 seconds, approximately one third of the way through the heating phase of the parametric fire, with the temperature dependent properties of the steel beam chosen accordingly.

It can be seen that the simple method compares favorably with the numerical results, with every example being on the conservative side.

Figure 8 shows the comparison between the simple solution presented here and the numerical results

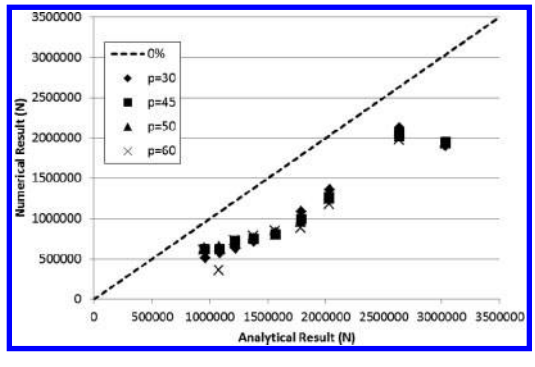


Figure 7. Maximum horizontal load during a parametric fire.

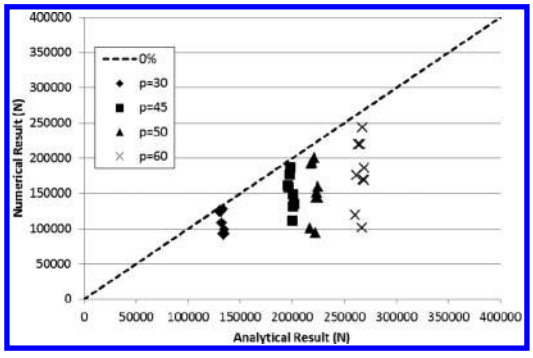


Figure 8. Minimum load during a parametric fire and load during cooling.

during the cooling phase of the fire, representative of the minimum bound of the horizontal load imposed on the connections during the parametric fire. The results are presented in the same way as the maximum results during the heating phase, with everything below the equivalency line being on the conservative side. Again, all of the results of the simple method presented are on the conservative side in comparison with the numerical results.

The horizontal loads presented may then be separated into the components carried by the beam and the reinforcement using equation (2) to determine the load on the beam and using equation (1) to determine the load on the reinforcement at the maximum horizontal load or based on the remainder of the load during the cooling phase.

REFERENCES

Block, F.M., Davison, J.B., Burgess, I.W., Plank, R.J. 2013. Principles of a Component-Based Connection Element for the Analysis of Steel Frames in Fire, *Engineering Structures*, 49 1059–1067

Cameron N, Usmani AS. 2005. A new design method to determine the membrane capacity of laterally restrained composite floor slabs in fire. Part 1: Theory and method. *The structural engineer* 83 28–33

Lange, D., Röben, C. and Usmani, A.S. 2012. Tall building collapse mechanisms initiated by fire: mechanisms and deisgn methodology. *Engineering Structures* 36 (2012) 90–103

Usmani AS. 2000. Application of fundamental structural mechanics principles in assessing the Cardington fire tests. *In Proceedings of the First International Workshop on Structures in Fire*.

Wang, Y.C., Dai, X.H., Bailey, C.G. 2011. An experimental study of relative structural fire behavior and robustness of different types of steel joint in restrained steel frames, *Journal of Constructional Steel Research,* 67 1149–1163

Yu, H., Burgess, I., Davison, J.B., Plank, R.J. 2008. Experimental investigation of the behavior of flush endplate connections in fire, in *Proceedings of the Fifth international conference on Structures in Fire*

Research and Applications in Structural Engineering, Mechanics and Computation – Zingoni (Ed.)
© 2013 Taylor & Francis Group, London, ISBN 978-1-138-00061-2

Fire protection of multi-storey straw bale buildings

J. Wachtling, D. Hosser & J. Zehfuß
Institute of Building Materials, Concrete Construction and Fire Protection (iBMB),
Technische Universität Braunschweig (Institute of Technology), Braunschweig, Germany

ABSTRACT: Straw bale buildings consist of load bearing timber frame elements with straw bales used as insulation. These constructions with special emphasis on sustainability can be found worldwide (FASBA 2013, Minke & Krick 2009, King 2007, Jones 20010). As a lighthouse project, a multi-storey building is planned in Germany with the iBMB in charge of the fire safety concept and supporting research. The Model Building Code of Germany (MBO 2008) allows buildings with timber frame structures for a height of 13 m (from ground level up to the floor of the highest occupied room) with noncombustible insulation, a classified fire protection coating and a fire resistance of 60 minutes (REI 60 $K_2$60). In case combustible insulations are used, researches showed that not only ignition but even thermal decomposition must be prevented. To reach this objective the outer surface of the straw bale walls will be protected by a lime coating and the inner surface by a clay coating. The fire protection properties of the coating materials with different aggregates and thickness have been investigated by small and intermediate scale tests (Kampmeier & Wachtling 2012). Also the thermal parameters of the coating materials, which are needed for numerical simulations using state-of-the-art FE-software, are determined in laboratory tests. Some results of the research are presented in this paper.

1 INTRODUCTION

Building with timber, straw and clay is one of the oldest building techniques. During the course of the time this technique was replaced by modern building materials and methodologies. But since sustainability is becoming more important there is a trend of ecological building design (Kampmeier & Wachtling 2012).

As a lighthouse project, a multi-storey building is planned in Germany with the iBMB in charge of the fire safety concept and supporting research. It is planned to establish such straw bale buildings up to five stories and a height of 13 m (Kampmeier & Wachtling 2012).

The research is supported by the German Federal Ministry of Economics and Technology. Some of the fire protection research results for multi-storey straw bale constructions are presented below.

2 STROW BALE CONSTRUCTIONS

Straw is a by-product of grain production, in which carbon dioxide (CO_2) is stored. In the form of bales it is suitable as insulating material due to its low thermal conductivity ($\lambda = 0.052\,W/(m \cdot K)$). The energy required for the production of straw bales is very low compared to other insulation materials such as polystyrene (about 1/30). Straw bales are also available locally, so the transport is highly favorable in the eco-balance compared to other building materials. The produced amount of straw bales in Germany would be sufficient to insulate about 350.000 single-family homes in this way every year. In fact, Germany has about 150 buildings in straw bale construction; an example is shown in figure 1. The oldest inhabited straw bale building was built about 100 years ago. At the end of the life-cycle the straw and timber can be biological decomposed (Minke & Krick 2009, Scharmer 2011, King 2007, Jones 2010).

To spread straw bale constructions in Germany the German national organization of straw bale building (FASBA) has obtained a general building approval for building straw bales. In this approval, building straw bales are classified with a normal flammability (B2). Figure 2 shows building straw after the fire test according to DIN 4102-1 (1998). In addition, "commercial" building straw bales have to be dry and the density must be between 85 kg/m^3 and 115 kg/m^3 (Kampmeier & Wachtling 2012).

In Germany straw bale constructions are approved only in combination with a load bearing timber construction. In the traditional way of building, the straw bales are plastered directly with clay which, like straw, has a very good eco-balance. There are straw bale houses with clay on the outer surface, but in general the use of more weatherproof lime plaster (figure 3) is recommended (Kampmeier & Wachtling 2012).

A great disadvantage of this design is the combustibility and smoldering of the straw bales. These problems must be solved by constructive solutions.



Figure 1. Straw bale house in Leiferde, Germany (Scharmer 2011).



Figure 2. Fire test according to DIN 4102-1 (Scharmer 2011).



Figure 3. Straw bale house plastered directly with lime in Bösel, Germany (Scharmer 2011).

3 BUILDING CODE AND RISK ASSESMENT

Prior to the amendment of the Model Building Code of Germany (MBO 2002) in the year 2002, timber constructions were limited to low buildings with a maximum height of 7 m. For an extension of the application range of buildings with a height up to 13 m researches had to demonstrate that the fire risk will not increase in comparison to solid construction with concrete or masonry. Evidence was provided in a research project completed in the year 2001. The additional fire risks resulting from the use of timber can be mainly offset by so-called "effective fire protection coating" as main structural compensation measure. The purpose of these coating materials is to protect the wooden components against ignition during the required fire resistance of 60 minutes. In addition, prevention of smoke propagation is often required. In standards harmonized at the European level, these structural components would be classified as "REI 60 $K_2$60" according to DIN EN 13501-2 (2010) (Kampmeier & Wachtling 2012).

In further studies (Hosser & Kampmeier 2007, Kampmeier 2007), it could be demonstrated that combustible insulation materials can also be used with additional constructive measures without lowering the safety level below the accepted level of fire protection. It must be considered that below the ignition temperature of flammable insulations combustible gases can be produced during thermal decomposition. This can be dangerous for the fire fighters, who must open the coating to extinguish the fire inside the construction. When oxygen is supplied at sudden, these gases can be ignited abruptly.

The objective of effective fire protection coating must be extended when using combustible insulation. In addition, there cannot be any weak spots in the form of sockets, switches and distribution boxes in the fire protection coating, which could cause a fire or allow a fire to enter the combustible insulation material. Likewise, no electrical wires are allowed as potential ignition sources in or on the renewable raw material without effective fire encapsulation (Kampmeier 2008).

Fire tests have to demonstrate that the previously described expanded protection objectives of the protective coating for straw bale insulation can be fulfilled. It has to be shown that the constructions behave the same way as components of fireproof materials would during the protection period of 60 minutes.

4 FIRE SAFETY ENGINEERING STUDIES

4.1 *Limit temperature of thermal decomposition of straw*

For the definition of the required performance of the fire protection coatings, the limit temperature of the thermal decomposition of straw had to be determined. In case of fire, not only ignition, but even the smallest

thermal change of the insulation material must be prevented during the entire protection period of 60 min. As part of a feasibility study (Niemann 2010) straw was examined in the cone calorimeter according to the method described in (Kampmeier 2008). Figure 4 shows the cone calorimeter according to ISO 5660 (2002).

By assessing the discoloration in figure 5 at different temperatures, a value of 200°C was determined as temperature limit for the thermal decomposition of straw bales (Niemann 2010).

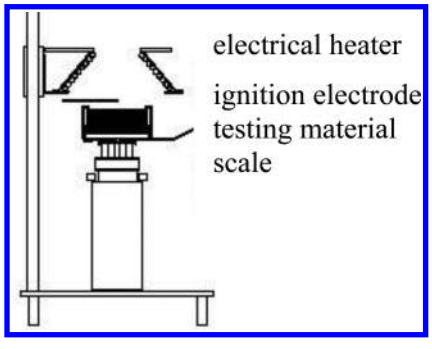


Figure 4. Cone calorimeter (Kampmeier & Wachtling 2012).



Figure 5. Determining the limit temperature of the thermal decomposition (Niemann 2010).

4.2 *Coating requirements*

On the outer surface of the straw bale walls a lime plaster is planned (Fig. 6). It must be demonstrated, that the fire protection coating protects the straw against temperatures greater 200°C during a full-scale fire exposure for 60 minutes (Kampmeier & Wachtling 2012).

On the inner surface of the exterior walls the coating is planned to be installed on 18 mm thick OSB panels (Fig. 6) to improve the building stiffness. This reduces the required fire protection properties of the clay coating for the protection of timber constructions according to DIN EN 13501-2 (2010): On the surface of the timber construction, temperature increase may not exceeded 270°C on average, and 290°C at the maximum ($K_2$60-coating). From a previous research project (Hosser & Kampmeier 2007, Kampmeier 2007) is known that even 8 mm thick timber panel in combination with a $K_2$60-classified coating reaches the protective requirements of the straw (Kampmeier & Wachtling 2012).

4.3 *Fire protection investigations of clay coatings*

To assess the performance of various clay coatings, comparative experiments were also performed in the cone calorimeter. Before it was decided to use a timber panel on the inner surface of the exterior walls to stiff the building, investigations concentrated on examining whether clay coatings can protect the straw against temperatures of greater than 200°C.

The heater of the cone calorimeter produces a nearly continuous heat flux. For these investigations, the heat flux was set to 40 kW/m^2; this is nearly equal to the heat flux of standard fire tests with uniform-temperature-time-curve (ISO-curve) according to ISO 834 (1999). Nevertheless, the results of the cone calorimeter tests are not directly transferable to standard fire tests. The cone calorimeter tests are for orientation and comparison of samples with one another, so that a reasonable

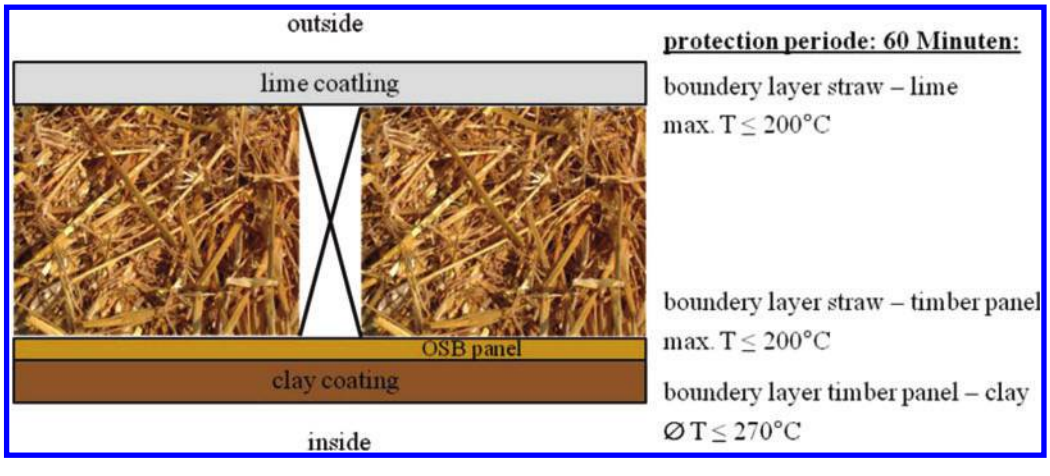


Figure 6. Coating-requirements (Kampmeier & Wachtling 2012).

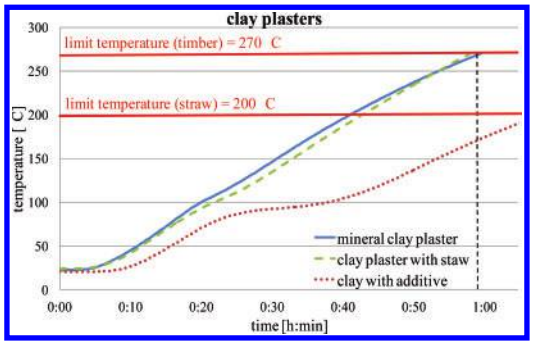


Figure 7. Clay plaster samples in the cone calorimeter.



Figure 8. Sample in furnace according to DIN 4102-8 (2003).

choice can be made for more expensive standard fire tests (Kampmeier & Wachtling 2012).

Straw clay plaster, mineral clay plaster and clay plaster with a fire protection additive were investigated at a 6 cm thickness. The results are shown in figure 7.

These initial test results showed that plastered clay layers ≥6 cm directly on straw bales would be necessary to meet the fire protection requirements. This is problematic for technical and economic reasons, so it was decided to replace part of the clay plaster layer by prefabricated clay boards. Therefore, clay boards were developed by the project partner Claytec with lightweight aggregates and a fire protection additive. These boards were investigated in various thicknesses in the cone calorimeter and a preliminary selection was made (Kampmeier & Wachtling 2012).

Pure board coatings would cause continuous joints, which could allow the passage of hot gases. Therefore, in addition, various plasters were examined in different thicknesses. The combination of a 45 mm thick clay board with a 10 mm thick mineral clay coating yielded promising results, so that an examination under standard fire conditions in a small scale test according to DIN 4102-8 (2003) was carried out. In this test, the specimen size is approximately 50 × 50 cm^2 (Fig. 8) (Kampmeier & Wachtling 2012).

The cost of testing at this scale is much lower than in the large-scale furnaces, so it is suitable for

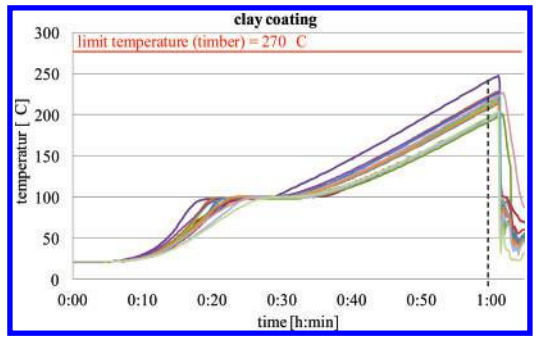


Figure 9. Temperature evolution in the boundary layer between the clay coating and the chipboard (Kampmeier & Wachtling 2012).

preliminary testing. Due to the positive results of this small-scale test, an intermediate scale test according to DIN EN 13501-2 (2010) and modeled after DIN EN 14135 (2004) in a ceiling fire chambers followed. This furnace chamber has a base area of 1.0 × 1.5 m^2 and a height of 1.5 m. The space is open at the top, which enables the installation of a ceiling element. Testing a ceiling element is the worst case scenario for the plaster, and thus envelopes the use as wall construction (Kampmeier & Wachtling 2012).

The samples were made of timber-frame construction with chipboard as an indicator to detect any discoloration. They were manufactured under practical conditions by the participating companies: The newly developed 34 × 60 cm^2 clay boards were attached on the chipboard. A newly developed thermal clay adhesive with a cellulose proportion of less than 1% was used to attach the full board surface to the chipboard. This adhesive was also used to complete the joints between the boards. Additionally, the boards were fixed with screws. The boards were then plastered with 10 mm mineral clay. Near the surface a flax tissue was plastered to avoid cracks during drying (Kampmeier & Wachtling 2012).

For determination of the temperature in the boundary layer between the clay coating and the chipboard 15 thermocouples were positioned. The temperature evolution is shown in figure 9. Throughout the fire resistance period of 60 minutes, the maximum temperature of 270°C was not reached. This also applies to the thermocouples arranged behind the joints of the clay boards.

After 60-minutes under standard fire conditions, the sample was removed from the fire chamber and it became visible that the plaster layer was intact and had no cracks. The sample was water-cooled immediately after the test and the clay was chopped off. No thermal damage in the form of discoloration or burning was found on the chipboard and near sunk screws. Under these conditions, the requirements were achieved for a fire protection coating in $K_2$60-quality. If the screws are not sunk and only flush with the board surface, discoloration can be localized at these areas. (See right half of the sample in figure 10) (Kampmeier & Wachtling 2012).



Figure 10. Chipboard behind the clay coating after 60-minutes under standard fire conditions (Kampmeier & Wachtling 2012).

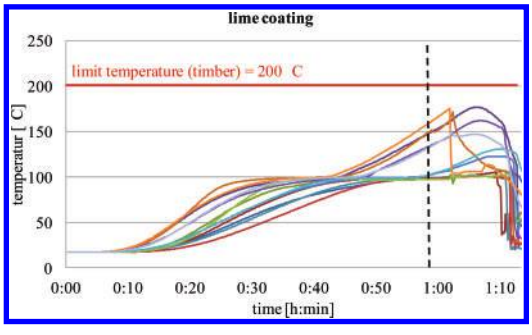


Figure 11. Temperature evolution in the boundary layer between the lime coating and the straw.

4.4 *Fire protection investigations for lime coatings*

For the outer surface the plaster is applied directly to the straw, the layer of mixed straw and lime is not counted when determining the plaster thickness. The straw should be flush with the timber, so that the plaster thickness can be defined from here.

For lime plasters from the participating company Endress, preliminary investigations with the cone calorimeter and small scale tests according to DIN 4102-8 (2003) were performed. They yielded promising results for a 6 mm thick lightweight lime plaster and a 5 mm lime plaster with fire protection additive. Yet, the intermediate scale tests (according to DIN EN 13501-2 (2010) and DIN EN 14135 (2004)) showed that only the 6 mm thick plaster could fulfill the requirements (Fig. 11).

The samples were manufactured under practical conditions by the participating companies like the clay sample. But in this application, the coating was applied directly to the straw, since the coating has to protect the straw against the limit temperature of 200°C. The temperatures in the boundary layer between straw and plaster are shown in figure 11. The limit temperature is not reached during 60-minute standard fire conditions (Kampmeier & Wachtling 2012).

During and after the test, no cracks or other damage of the plaster could be noticed. After the experiment, the sample was cooled with water, and the plaster was chopped off. This was followed by a visual test, in which no discolorations on straw were noticed (Fig. 12). Hence, it could be shown that the protection of straw bales with the directly applied 6 cm thick lightweight lime plaster can be ensured for 60 minutes fire exposure (Kampmeier & Wachtling 2012).



Figure 12. Plaster surface and coloration of straw behind the lime coating under standard fire conditions (Kampmeier & Wachtling 2012).

4.5 *Thermal properties of the coating materials*

As part of the research project, the thermal properties of the coating materials were determined. These are needed for numerical simulations of the material properties using state-of-the-art FE-software. These simulations could enable performance-based fire protection concepts with optimization of the newly developed coatings.

The experimental parameters from the standard fire tests were fed into a simple FE-software utilizing an isotropic formulation of the Fourier equation. It was found that this approach is not suitable for this application, because the temperature plateau (Figs. 9, 10) at about 100°C cannot be represented realistically. This plateau is an essential criterion for the fire protection ability, especially in case of plasters. For that reason, a suitable software has yet to be found or developed. It is considered to modify the software model DEPHIN (Nicolai & Grunewald 2006), which is currently used for the determination of detailed physical processes like convective transport processes in the porous media. This software is capable of reproducing diffusion processes. In addition, the required input parameters are already available, because the physical construction investigations also being part of the research project.

5 CONCLUSION

As described above, the additional fire risk of using straw bale insulation (instead of noncombustible insulation required for multi-storey timber frame constructions in Germany) can be compensated by constructive



Figure 13. Study of the planned multi-storey straw bale building in Germany (NZNB 2012).

measures. In addition, fire protection coatings of clay and lime were investigated and can now be classified as $K_2 60$ according to DIN EN 13501-2 (2010). They also show a better eco-balance than conventional products.

The fire protection coatings must fulfill additional requirements: Any thermal decomposition of the insulation material has to be prevented during the fire protection period of 60 minutes. Furthermore any weak spots like electrical installations must be avoided within the construction in general. Solutions for these and other details were developed in the research project.

From the fire protection research point of view there is no bar to the realization of the planned multi-storey straw bale building in Germany (Fig. 13). Further information on the fire safety concept is provided in (Kampmeier & Wachtling 2012). As a lighthouse project it can contribute to the spread of the multi-storey buildings with renewable raw materials.

REFERENCES

BMWi (200)

DIN 4102-1 (1998). Brandverhalten von Baustoffen und Bauteilen – Teil 1: Baustoffe; Begriffe, Anforderungen und Prüfungen

DIN 4102-8 (2003). Brandverhalten von Baustoffen und Bauteilen – Teil 8: Kleinprüfstand

DIN EN 13501-2 (2010). Klassifizierung von Bauprodukten und Bauarten zu ihrem Brandverhalten – Teil 2: Klassifizierung mit den Ergebnissen aus den Feuerwiderstandsprüfungen

DIN EN 14135 (2004). Brandschutzbekleidungen – Bestimmung der Brandschutzwirkung

FASBA (2012). Homepage of the German national organization of straw bale building: www.fasba.de

Hosser, D. & B. Kampmeier (2007). Untersuchungen zur Optimierung und Standardisierung von Dämmstoffen aus nachwachsenden Rohstoffen. Braunschweig, Germany. FKZ:22008905

ISO 5660 (2002). Prüfungen zum Brandverhalten von Baustoffen – Wärmefreisetzung , Rauchentwicklung und Masseverlustrate

Jones, B. (2010). Building with Straw Bales – A practical guide for UK and Ireland. ISBN 1903998131

Kampmeier, B. & J. Wachtling (2012). Norddeutsches Zentrum für nachhaltiges Bauen – Ein Pilotprojekt mit angewandter Forschung. Braunschweiger Brandschutz-Tage ‘12, Tagungsband. iBMB, TU Braunschweig, Heft 199. Braunschweig, Germany. ISBN 978-3-89288-203-9.

Kampmeier, B. (2008). Risikogerechte Brandschutzlösungen für den mehrgeschossigen Holzbau. Dissertation. iBMB, TU Braunschweig, Heft 206. Braunschweig, Germany. ISBN 978-3-89288-189-6.

Kampmeier, B. (2007). Verwendbarkeit von Dämmstoffen aus nachwachsenden Rohstoffen im Holztafelbau. Braunschweiger Brandschutz-Tage ‘07, Tagungsband. iBMB, TU Braunschweig, Heft 199, Braunschweig, Germany. ISBN 978-3-89288-181-0.

King, B. (2007). Design of Straw Bale Buildings. USA. ISBN: 0976491117. EAN: 9780976491118.

Minke & Krick (2009). Handbuch Strohballenbau. Germany. ISBN 978-3-936896-45-9

MBO (2002). Musterbauordnung (MBO). Fassung November 2002, zuletzt geändert im Oktober 2008

Nicolai & Grunewald (2006). Delphin 5 – User Manual and Program Reference. Institut für Bauklimatik; TU Dresden, Germany 2006. (http://bauklimatik-dresden.de)

Niemann, T. (2010). Brandschutztechnische Untersuchungen zum Nachweis der Verwendbarkeit von strohgedämmten Holzbauteilen als gleichwertig zur hochfeuerhemmenden Bauweise nach der Muster-Holzbaurichtlinie. Diplomarbeit, HTW Dresden, Germany

NZNB (2012). Homepage des Norddeutschen Zentrums für Nachhaltiges Bauen, www.nznb.de vom 24. August 2012

Scharmer, D. (2011). Fachgerechter Strohballenbau, Seminar im Ökodorf Sieben Linden vom 14.–16. Oktober 2011

Research and Applications in Structural Engineering, Mechanics and Computation – Zingoni (Ed.)
© 2013 Taylor & Francis Group, London, ISBN 978-1-138-00061-2

Structural analysis at the fire limit state: Practical applications

A. Jowsey & P. Scott
Structural Fire Design Department, International Paint, Felling, UK

ABSTRACT: Structural engineers consider a multitude of load cases in design, ranging from standard dead and imposed loading through to snow, wind and seismic loading. Recent years have seen a new load case take an ever important role in structural designs – that of fire. Structural codes and guidance documents present methodologies to take advantage of steelwork to demonstrate substantial savings in passive fire protection. These methodologies range from advanced numerical models to simplified structural checks. It is these simplified approaches combined with a fundamental understanding of structural assessments that can quickly and easily produce robust and quantified designs at elevated temperature.

This paper presents the analysis of a structural member in terms of cost of steel and fire protection combined with direct attention being given to structural fire engineering approaches. The analysis considers the development of a structural member from initial design by the structural engineer through to modifications by the steelwork fabricator with respect to weight optimisation. Consideration of the fire protection material in direct conjunction with the structural analysis clearly demonstrates that the lightest and most structurally-efficient design is not always the most economic.

1 INRODUCTION

Structural design standards including British Standards and the Eurocodes both cover the design of steel structures in fire. These provide designers with the opportunity to exploit the properties of structural steel to its maximum capacity in the fire limit state, termed Structural Fire Engineering. This allows passive fire protection to be integrated into structural design as part of the steelwork specification. If used effectively it can bring significant benefits to the project, including robust and safe designs, quantified structural performance and cost savings.

The reality is that many structural engineers are not familiar with the fire design of structures as this aspect of design may not fall within the remit of their work or it is taken as being the responsibility of the architect or an appointed fire engineer. In the absence of structural calculations at high temperature, the design of fire protection for the vast majority of jobs is assumed based on conservative assumptions.

2 OPTIMISATION

Structural engineers often design for the most efficient use of structural steelwork for the variety of structural load cases or load combinations that they are considering. Efficient in this context is taken as being the lightest steel member, while load combinations are likely to incorporate dead, super dead, imposed, wind, snow and potentially seismic loads (EN, 2002). Most structural engineers have a good grasp of the price of steelwork and can therefore come up with indicative steelwork costs for their designs. However, few structural engineers at present have sufficient understanding of passive fire protection and their associated costs to appreciate what impact fire protection has on the cost of their designs and the potential for optimisation.

Figure 1 illustrates a high-level cost comparison for a single steel member in terms of steel cost and fire protection cost. If the weight of a member is increased, for example an increase in the serial size with respect to its weight or an increase in the web or flange thickness, then it is obvious that the cost of the steel will increase. However, the increase in steel weight can generally have a large impact on the amount of fire protection required. A heavier (thicker) steel section will heat more slowly than a light (thin) steel section. As such, it will have an increased inherent fire resistance and therefore require a comparatively thinner thickness of applied fire protection to achieve the same level of required fire resistance. From Figure 1 it is intuitive that there is likely to be an optimum weight that results in the cheapest design by factoring steel and fire protection costs together.

When considering fire protection costs it is important that the overall volume of material for a project is not priced in isolation. The application costs of various fire protection options are important too.

A structure that has been subject to a structural fire assessment should ideally take a full cost benefit analysis into account to arrive at the optimum design. This should account for the combined cost of steel, fire protection and application costs as a minimum.

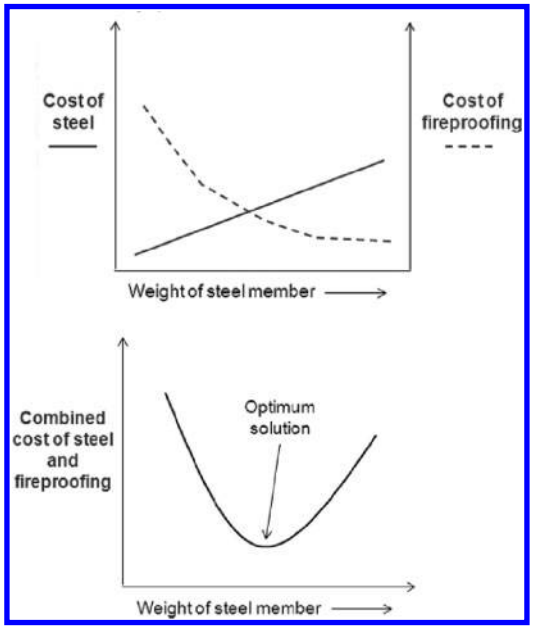


Figure 1. (Left) Illustration of the typical steel and fire proofing costs associated with an increase in the weight of a steel member, (right), combined cost of steel and fire proofing, showing optimum solution with respect to steel weight.

3 STRUCTURAL ANALYSIS AT ELEVATED TEMPERATURES

Many structural design codes and guidance documents include 'fire resistant' design. In the UK the relevant standard is BS 5950 Part 8:2003 (BS, 2003) and in Europe the relevant codes are EN 1993-1-2:2005 (EN, 2005) for steel and EN 1994-1-2:2005 (EN, 2005) for composite steel and concrete design.

In BS 5950-8 and the Eurocodes methods are given for determining the thermal and mechanical response of the structure and evaluating the fire protection required, if any, to achieve the required performance. An important feature of the standards is that they use the concept of a variable steel temperature, i.e. they allow the limiting steel temperature to be evaluated. The following sections provide examples of the application of these methods.

A common method of assessment is to assess the degree of utilisation of a structural member in the fire limit state through a single element analysis. This approach considers beams or columns in isolation with conservative boundary support conditions and effectively reproduces the load-bearing scenario of a standard fire test as close as possible by calculation. Depending on the member subject to the analysis, a number of checks at elevated temperature may need to be accounted for including:

- Tensile or buckling resistance for tension or compression members
- Moment resistance and shear capacity for beams
- Lateral torsional buckling resistance moment for beams

Manufacturers of passive fire protection subject their products to a fire test package that comprises unloaded and loaded beams and columns at minimum and maximum product thicknesses. In the UK and Europe (BS 476, EN 13381), the result of this test package is a dataset that defines the required protection thickness for structural sections over a range of limiting steel temperatures, typically 350°C to 700°C in 50°C intervals. Certified product listings (Certifire, LPCB, etc.) typically only show the thickness of material required to satisfy the accepted industry standard temperatures. In the interest of commercial sensitivity, manufacturers do not typically publish their product-specific multi-temperature assessment (MTA) thicknesses.

The following sections in this paper use the Eurocode approach to demonstrate the benefits of a single member analysis in the context of design for standard beams and columns, and long span beams with web openings.

3.1 *Typical beams and columns*

The majority of structural members in buildings including high rise are typical serial sections, including I-sections, H-sections, W-shape and tubular columns and beams. With these members there is potential to make big economic savings in the volume of fire protection using simplified structural assessments.

A sensitivity study was presented by (Jowsey & Scott, 2012) in which the failure temperatures and intumescent coating thicknesses for 203 × 203 × 52 UC section in compression were calculated using Eurocode calculations in accordance with the UK National Annex. The steel strength, column height and degree of loading were all varied and comparisons for all cases were made back to the corresponding thickness of fire protection for the UK adopted temperature of 550°C (in the absence of a calculated limiting steel temperature) for fire resistance periods of 90 and 120 minutes. It was shown that a simple structural check using conservative assumptions could reduce the amount of fire protection by approximately 28% with potential further reductions being possible with more accurate loading information.

Figure 2 depicts the compression member and also shows the calculated limiting steel temperature for a range of column heights and occupancy types assuming a fully loaded column and grade s355 steel. It is evident that the UK industry adopted temperature of 550°C for a column is generally conservative.

In order to appreciate the benefit of calculating the limiting steel temperature, the corresponding thickness of fire protection is used to quantify the saving in fire protection material volume. Figure 3 shows the potential saving for the 203 × 203 × 52 UC section at a height of 4.5 m at 90 and 120 minutes fire resistance in comparison to assuming a conservative limiting steel temperature of 550°C.

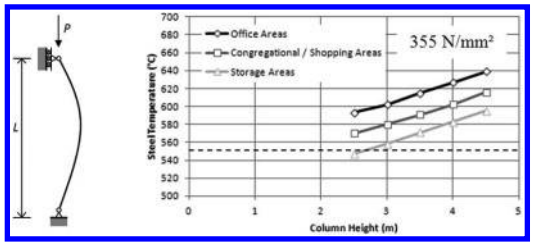


Figure 2. (Left) Column acting in compression. (Right) Limiting steel temperature variation for a fully loaded, Grade s355, 203 × 203 × 52 UC for a range of column heights and occupancy uses. The dashed black line represents the UK industry adopted temperature of 550°C (Jowsey & Scott, 2012).

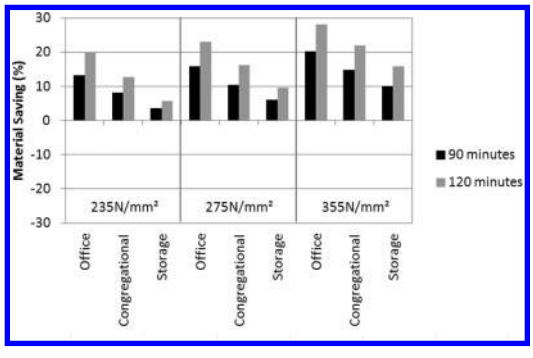


Figure 3. Fire protection material saving by calculating a limiting steel temperature for a fully loaded 4.5 m high 203 × 203 × 52 UC in comparison to an UK adopted temperature of 550°C (Jowsey & Scott, 2012).

3.2 *Beams with web openings*

Beams with web-openings are becoming more and more popular with tall building design as they are a relatively lightweight and efficient method to achieve long spans to facilitate open plan floor layouts. They permit services to be passed through the openings rather than below the steel beam and are therefore efficient in terms of increasing the number of floors in high-rise buildings. These beams are commonly referred to as cellular beams in the UK and Europe or smart beams in North America.

The behaviour of these beams in fire has been the subject of much research over recent years both in terms of structural response (SCI, 2011) and thermal behaviour (EN, 2012). The openings in the web create a complex distribution of temperature on the web, specifically at the areas between adjacent openings (web-posts). It is important that such a temperature distribution is taken into consideration as part of structural assessment. Indeed, there are no industry adopted temperatures for these types of beam and a limiting temperature must be calculated and given to a fire protection manufacturer to determine an appropriate thickness of fire protection (ASFP, 2010). The structural response of these beams is more complex than solid-web beams. The distribution of force around the

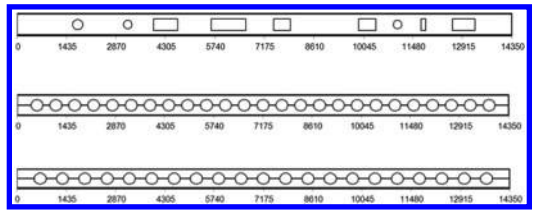


Figure 4. (Top) Initial beam design from the structural engineer, (middle) an alternate lightweight beam design from the steel fabricator, and (bottom) a lightweight design that is optimised for fire protection.

openings on the web means that in addition to bending and shear, the following failure modes are important to assess (SCI, 2011):

- Vertical shear check at openings
- Bending moment check at openings
- Vierendeel bending moment check at openings
- Web-post buckling
- Web-post bending
- Web-post horizontal shear

4 COST BENEFIT ANALYSIS

The following example considers three beam designs to span 14.35 m as shown in Figure 4. The initial plate girder beam design was proposed by the structural engineer. The steel fabricator produced an alternate lightweight beam design, based on stock serial sections that reduced the cost of the steelwork; however this proved to be an overall more expensive solution as the fire protection costs were not factored into the design. Following a value engineering exercise by the authors, a final revised design was created that was optimised for fire with respect to steel cost, fire protection cost and application cost.

Figure 5 shows the relative cost and weight savings of the alternate and revised beam designs with respect to the original beam design. The fabricator's alternate solution resulted in a 9% saving in the steel weight, with a corresponding 9% saving in the cost of steel. However this design now had closely spaced web-openings creating hotter web-posts in the event of a fire – the result being an increased thickness of intumescent coating to the extent that the application had gone from one coat of paint to two, with an associated increase in application cost. This has the effect of increasing the fire protection cost to 180% of the original beam. Following the value-engineering exercise with close attention paid to the fire protection, a revised structural design was proposed in which the openings were spaced further apart to create relatively cooler steel in the web-posts and the web thickness was increased to add 2 kg/m to the linear weight of the beam. This had the effect of providing enhanced structural capacity to combat the web-post buckling structural failure mode. The effect of these modifications was a beam that was 7% lighter and cheaper in terms of steelwork than the original design, but



Figure 5. Representation of the three beam designs in terms of cost saving of steel and fire protection, both with respect to weight saving of steel.

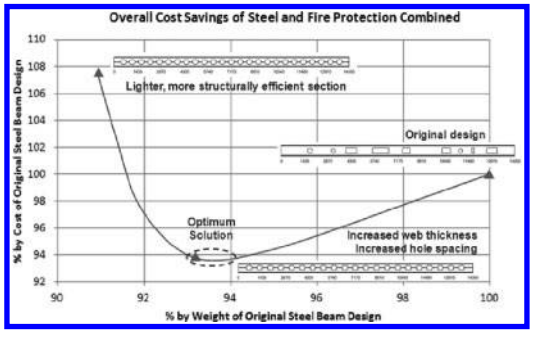


Figure 6. Overall cost savings of steel and fire protection combined for the three beam designs with respect to weight saving of steel.

also approximately the same cost in terms of fire protection, i.e. it remained a single coat application of intumescent paint.

Figure 6 shows the combined cost of the steel and fire protection saving with respect to the original design for the alternate and revised beam designs. It is seen that the alternate design, although being 9% lighter in terms of steel weight, is 108% of the cost of the original beam design due the cost of the additional fire protection. The revised solution with an increased web thickness and opening spacing was shown to be 7% lighter in terms of steel weight, however it was 6% cheaper overall than the original beam design.

This example demonstrates that an optimum cost structural solution based on cost of steel and fire protection is possible and importantly it shows that the lightest structural design is not necessarily the cheapest solution. Given that these long-span structural members are commonly used in tall building design, the economic savings of analysing beams in this manner can be significant.

5 CONCLUSIONS

The issue of structural fire resistance is one that has been developing with a fast past over recent years. Structural engineers are now starting to acknowledge and recognise that they can add significant value to their designs by considering fire as a load case in its own right. Structural design codes provide engineers with the opportunity to exploit the properties of structural steel to its maximum capacity in the fire limit state. If used effectively, benefits of structural fire engineering include significant cost and time savings on projects.

The following conclusions are noted:

- A structural fire engineering assessment leads to informed performance, rather than assumed performance in the event of a fire.
- In the absence of a structural fire engineering assessment to determine a member's limiting steel temperature, fire protection manufacturers will assume generally conservative temperatures for the purpose of defining volumes of fire protection for a project.
- Simple approaches are available in published codes and standards to permit structural engineers to determine limiting steel temperatures for individual members.
- A truly optimised structure for fire should take into account the combined cost of steel, fire protection and application costs as a minimum.

This paper has shown that through simple structural checks, a quantified performance of a member can be made at elevated temperatures through the definition of a limiting steel temperature. This can then be used to determine a volume of passive fire protection and compared to industry adopted approach to demonstrate a value-engineered solution. The worked examples included are for a single member in isolation, however the same approach can be adopted for all structural members within a building. This approach has the benefit of reducing passive fire protection requirements for an entire project.

Alternatively, structural steel sections may be deliberately oversized and then structural checks repeated to reduce passive fire protection requirements.

REFERENCES

Association of Specalist Fire Protection Engineers (ASFP). Fire Protection for Structural Steel in Buildings. 4th Edition. August 2010.

BS 5950-8:2003 Structural Use of Steelwork in Building – Part 8 Code of Practice for Fire Resistant Design

BS EN 1993-1-2:2005 Eurocode 3: Design of Steel Structures – Part 1-2: General Rules – Structural Fire Design

BS EN 1994-1-2:2005 Eurocode 4: Design of Composite Steel and Concrete Structures – Part 1-2: General Rules – Structural Fire Design

BS 476-21:1987 Fire Tests on Building Materials and Structures – Part 21: Methods for Determination of the Fire Resistance of Loadbearing Elements of Construction.

BS EN 1990:2002 Eurocode – Basis of Structural Design

European Country Specific Fire Safety Standards and Guidance Docuements

Product reference: Interchar 1190. Loadings – Details available in the Reb Book online at the BRE Global Loss Prevention Council Board website

Research and Applications in Structural Engineering, Mechanics and Computation – Zingoni (Ed.)
© 2013 Taylor & Francis Group, London, ISBN 978-1-138-00061-2

Fire design of wooden box floors

Dhionis Dhima
CSTB, Champs sur Marne, Marne-la-Vallée cedex 2, France

Renaud Blondeau-Patissier
METSÄ WOOD, Construction, Courbevoie Cedex, France

ABSTRACT: The design of the floors made up of prefabricated wood-based loadbearing box elements facilitates the construction of these floors and reduces significantly their cost. According to the fire requirements of different types of building, where this type of floor is used, different wooden box slab configurations are designed: unprotected, protected by plasterboard or other protections and with or without insulation inside the box. The behaviour in fire of these configurations are different. EN1995-1.2 proposes a simplified method for the design of the floor assemblies with cavities, but this method does not take into account correctly the reduction of strength and stiffness of wooden elements at elevated temperatures. Consequently, the design of wooden box slabs according to this method could lead to a very high risk concerning the fire stability of these floors.

The fire behaviour of box floors made up of Laminated Veneer Lumber (LVL) has been studied. The numerical modelling of heat transfer, by finite element program, allows investigation of the influence of each component of the floor over its fire resistance. The numerical results have been validated by experimental results of floors tested under ISO fire conditions. Different parameters are defined and a simplified procedure is proposed in order to design LVL box floor classified REI30 and REI60. The results of this study are inserted in the French technical approval in order to be used by the industrialists. Finally, the results of research will be used to improve the methods suggested by EN 1995-1.2 for the design of safety wooden floor assemblies in fire conditions.

1 CONTEXT

1.1 *Introduction*

Building context, particularly in France, but more generally in Europe, requires better understanding of each building component, considered separately, but also when it is integrated in the building (floor, partition wall, roof). Reliability of such co*m*ponents must be now guaranteed regarding thermal behaviour, acoustic properties, cold situation design and fire design.

Sticks built structures, the traditional way of building timber structures is now more and more often replaced by prefabricated ready-made components. These components integrate wooden structure, insulation (acoustic, thermal, fire), protection and finishing (plasterboards, wooden acoustic panels. . .) but also installations (electricity, ventilation, pipes..) when required. Wooden panels are then assembled on site, in a short time, with few technical workmen and provide high level quality of the building.

1.2 *Multifunctional prefabricated wooden elements*

Using prefabricated elements allows architects and builders to achieve higher performance and to reduce significantly cost deviations.

Separate elements assembled on site can lead to a large number of non-conformities compared to prescribed and design structures. Acoustic and fire weaknesses are recognized as main disorders for the final customer. Using 2D components (panels) reduces significantly non-conformities. Indeed these continuous structures are prefabricated in controlled mills and limit number of joints which have to be sealed on site. Management of quality in industrial prefabrication units, mandatory in Europe for building components (CE-marking with external controls), must guaranty performances of building components. And site controls can be improved and concentrated on limited number of elements.

In that context, wooden panels, in general, and wooden floors are now widely used as building components. The performances of such elements are now more and more studied on a multifunctional level (mechanic, acoustic, thermal. . .).

Despite good behaviour of wooden structure, the fire resistance remains the main criteria for most of wooden constructions to enter market and convince authorities.

Performance of wooden floors are following principles of EN 1995-1-2 “Design of Timber Structures – Structural fire design”, design instructions validated

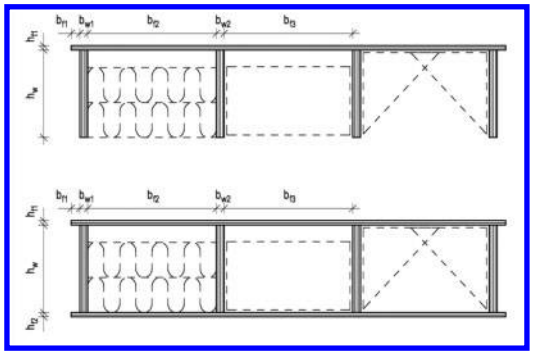


Figure 1. Cross section of ribbed or box Kerto-Ripa elements.

and further described with additional tests under ISO fire conditions.

1.3 *Kerto-LVL wooden box elements – Kerto-Ripa®*

MetsäWood Company (former Finnforest) has developed since the late 90's wooden structurally glued loadbearing panels. These "Kerto-Ripa®" elements are composite slabs made of Kerto, structural laminated veneer lumber (LVL). The adhesive is of type I (full exposure to the weather) as defined in (EN 301). Large horizontal panels (Kerto-Q panels, max. 2.5 m × max. 25 m) are structurally assembled with vertical ribs (Kerto-S beams, max. 0.6 m × max 25 m) using structural gluing to form hollow box elements. Kerto-Ripa elements may contain thermal or acoustic insulation inside the cavities and plasterboards in fire side in order to improve their fire resistance. These elements may or may not have wooden bottom slab (see figure 1).

The products are shaped according to the specification of the customer and design according to project requirements. The maximum size of the elements is 25 m × 2.5 m and the height varies from 150 to 1200 mm, for roofs and floors. Typical distances between supports are 4 m to 12 m for floor panels and 7 m to 18 m for roof panels (see also ETA 07/0029).

The panels are produced in dedicated production units and assembled on site to build horizontal diaphragms as roofs and floors (see figure 2).

The design of such elements is covered by Eurocode 5 (EN 1995-1-1) in cold situation, but in fire situations it is not completely covered by the standards (EN 1995-1-2) which may lead to insufficient reliability.

2 EXPERIMENTAL APPROACH

2.1 *Test setup*

Two floors made up of Kerto-Ripa box elements have been tested in fire conditions and analyzed. In this paper has been briefly described a floor composed with three Kerto-Ripa box elements exposed to ISO-fire (No RTE1057/04) in accordance with EN 1365-2

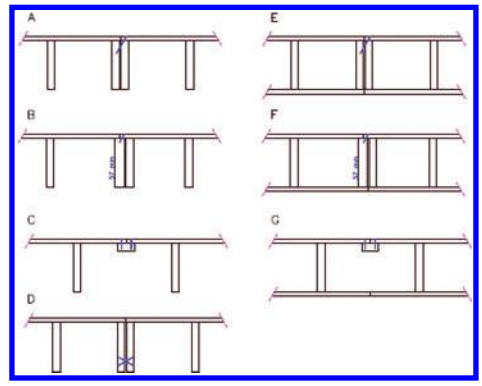


Figure 2. Typical connections between panels to create roof and floor surfaces.

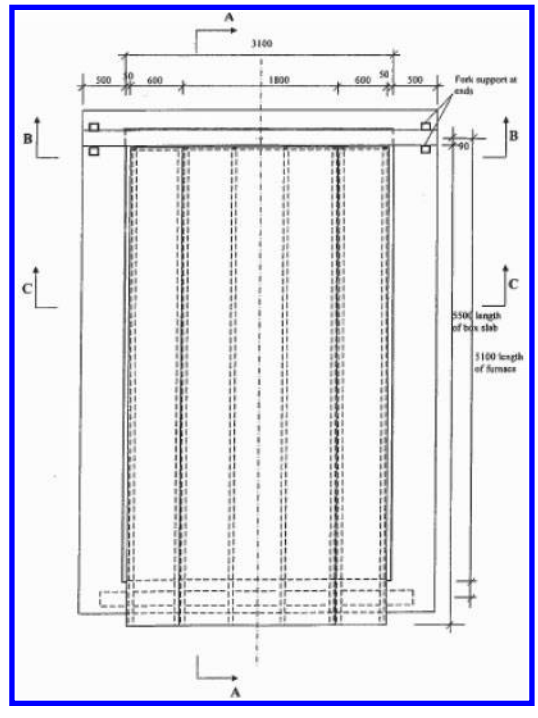


Figure 3. Horizontal view of tested floor.

"Fire resistance tests for loadbearing elements – Part 2: Floors and roofs" (see figures 3, 4 and 5). Only "boxed" panels are suitable for fire exposure without any additional protection (plasterboards ceiling).

The height of the tested floor elements was 337 mm. The bottom and the deck plate, with thickness respectively 37 mm and 26 mm, were composed by Kerto-Q, and joists (b × h = 50 mm × 274 mm) were composed by Kerto-S. Inside each box 100 mm stone wool were installed on the bottom slab. The dimensions of the tested floor were 3100 mm × 5500 mm. It was composed by three elements (see figures 3, 4 and 5). The tested floor was loaded by 32 concentrated loads and 4 hydraulic jacks. Finally the applied load was equal to 5.4 kN/m^2 distributed live load.

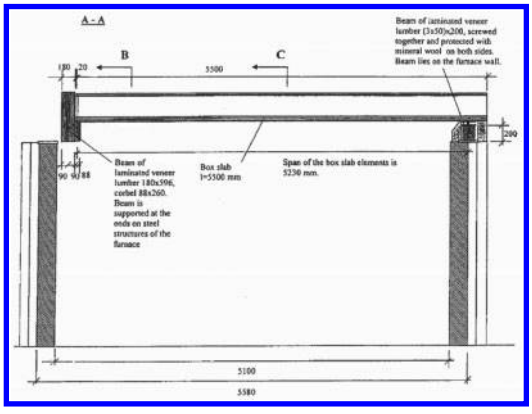


Figure 4. Vertical cut of tested floor in main span direction.

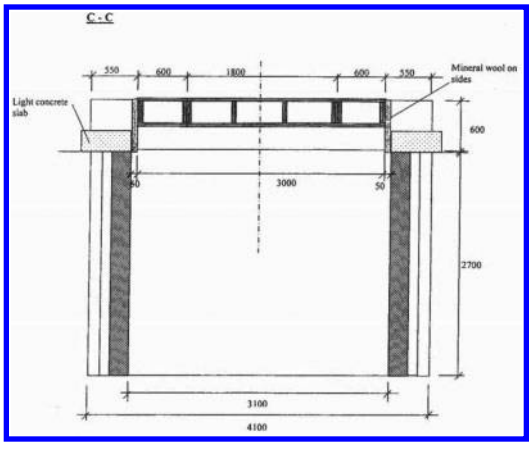


Figure 5. Vertical cut of tested floor in transversal direction.

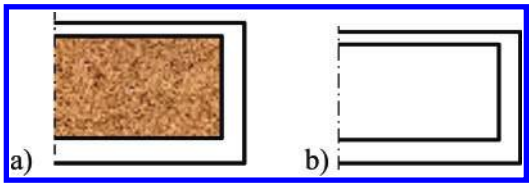


Figure 5. Modelled floor box: a) with insulation, b) without insulation.

45 different temperatures were monitored during the test in order to measure the evolution of the temperature on different points of the floor elements. These measurements allow to define the charring rate of timber elements. Observations inside the furnace and on the opposite side of the specimen have been recorded during the fire test (smokes, visible disorders...). Deflections have also been measured in six locations.

2.2 *Test results*

In order to avoid the collapse of tested specimen the fire test has been stopped after 70 minutes. The bottom plate burnt completely after 47 minutes. Consequently the mean charring rate defined by this test was 0.79 mm/min. The maximal vertical displacement measured in the mid-span of the floor was about 17 mm. The maximum temperature measured on the top of the floor, at the end of the test, was 80°C. Consequently the fire integrity and fire insulation were not affected during the fire test.

In fact the charred boards of the bottom plate remained fastened and supported the insulation until the 62nd minute.

Nearly the same results have been observed in a second fire test (No RTE344/04) realized with a floor of dimensions 1200 mm × 1400 mm, but having the same composition and thickness that the floor described here-above for the first fire test.

3 MODELLING AND DISCUSSION

3.1 *Modelling results*

The figure 6 represents the modelling section of the floor box. The boundary conditions take into account de symmetric thermal actions. Two modelling are realized. In the first one the cavity between the bottom and deck plate was filled with mineral wool and in the second one the cavity is empty. The objective of these two modelling was to study the influence of the insulation over the charring rate of the bottom plate.

Two steps were necessary for the modelling of floor box. The first one allows simulating the heat transfer of the tested floor, given by the figures 3 to 5, in order to find by calculation the same mean charring rate like the one defined by the test.

The second step has been used to simulate the heating of the floor box without insolation and to define the mean charring rate of bottom plate in this case.

The results showed that the charring rate of the bottom plate for the floor box without insulation in the cavity was about 0.72 mm/min. This value is lower that the charring rate of the bottom plate with insulation in cavity.

3.2 *Design of wooden box floors in fire conditions*

The simplified method proposed for the design of wooden box floor takes into account the difference charring rates of the different elements that compose these types of floors. The principle of different charring rates is given by EN 1995-1.2 in section 3.4.3 (see figure 6). It takes into account different charring rates in function of conditions that elements are exposed to fire.

In figure 6 for timber cladding protection or plaster boards type A, (t_{ch}) is equal to (t_f).

The charring rate values for each phase of the curve given by the figure 6 are defined in function of the tests and numerical results.

In the tables 1 and 2 are given the charring rates defined respectively for the design of wooden box floors with or without insulations in cavities.

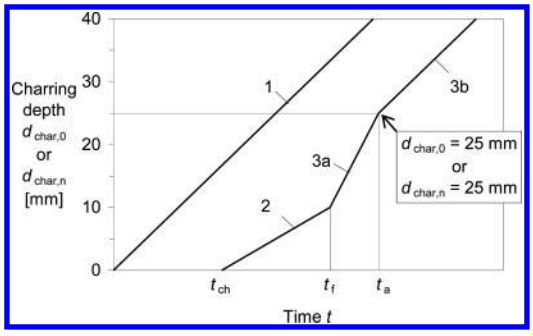


Figure 6. Charring depth vs. time when charring takes place behind the fire protection ($t_{ch} < t_f$).
Key:

1 Relationship for members unprotected throughout the time of fire exposure for charring rate β_n (or β_0).

2, 3a, 3b Relationship for initially protected members where charring starts before failure of the fire protection:

1 Charring starts at t_{ch} at a reduced rate when the fire protection is still in place

3a After the fire protection has fallen off, charring starts at increased rate

3b After the char depth exceeds 25 mm, the charring rate reduces to the rate for initially unprotected members.

Table 1. Data for design of Kerto-Ripa box floors without insulation in cavities.

Classification	Minimal thickness of the bottom plate of Kerto-Ripa wooden box (mm)	Bottom member	Design charring rates (mm/min)	
			For bottom member	For top member and webs
REI 30	21	without protection	0.7	1,4
REI 30	20	protected by one BA13 plasterboard layer, type A	0 : during 15 minutes, 1,3 : during minutes	1,4
REI60	42	without protection	0.7	1,4
REI60	39	protected by one BA13 plasterboard layer, type A	0 : during 15 minutes, 1,3 : during 15 minutes, 0,7 during 30 minutes	1,4
REI60	31	protected by one BA15 plasterboard layer, type F	0 : during 20 minutes, 0,35 : during 7 minutes, 1,3 during 15 minutes, 0,7 during 18 minutes	1,4

The load bearing capacity and the deformations of the elements composing a self-supporting box Kerto®-Ripe, subjected to fire, must be calculated in accordance with EN 1995-1-2, taking into account the charring rates and the assumptions given in tables 1 and 2.

Moreover, the load level of the wooden floor box in cold conditions (applied load/resistant capacity) will not have to exceed 40%.

In fire conditions the maximal vertical displacement (δ_{max}) should not exceed the value given by the following relation:

$$\delta_{max} = L^2/(4300 \cdot (h_1 + h_2 + h_3))$$

Table 2. Data for design of Kerto-Ripa box floors with insulation in cavities.

Classification	Minimal thickness of the bottom plate of Kerto-Ripa wooden box (mm)	Bottom member	Design charring rates (mm/min)	
			For bottom member	For top member and webs
REI 30	24	without protection	0,8	1,4
REI 30	20	protected by one BA13 plasterboard layer, type A	0 : during 15 minutes, 1,3 : during minutes	1,4
REI60	41	without protection	0,8	1,4
REI60	37	protected by one BA13 plasterboard layer, type A	0 : during 15 minutes, 1,3 : during 15 minutes, 0,8 during 30 minutes	1,4
REI60	27	protected by one BA15 plasterboard layer, type F	0 : during 20 minutes, 0,4 : during 7 minutes, 1,3 during 15 minutes, 0,8 during 18 minutes	1,4

where:

- L is the span of the floor,
- h_1, h_2, h_3, are respectively the height of bottom member, webs and upper member.

In order to improve the fire behaviour of wooden box floors protected by plasterboards, fixed directly in the bottom member, the maximum distance between two screws and the minimal length of the screws have been defined.

4 CONCLUSIONS

The fire behaviour of wooden box floors, Kerto-Ripa types, has been studied experimentally. The influence of the insulation in the cavities of box floor has also been studied by numerical simulations.

The analysis of experimental and numerical results made it possible to define the charring rates for the design of wooden Kerto-Ripa box floors in fire conditions.

Furthermore constructive recommendations such as: the maximal load level of box floors in cold conditions, the maximal vertical displacement of box floors in fire conditions and the maximal distances between screws that fix the plasterboards over the fire side of box floors are defined.

Concerning the panels type A, B, C and D (see figure 2), panels without bottom plate, their fire resistance depends completely on the fire resistance of the screens.

More details about the design of wooden box floors composed with Kerto Ripa elements are given by Dhima in the fire resistance report N° CO10.1821.

REFERENCES

Dhima D.: “Avis de résistance au feu pour avis technique concernant les éléments Kerto-Ripa”, rapport d’étude n° CO10.1821, 26 juillet 2010, CSTB, Champs sur Marne, France.

EN 1995-1-2: Eurocode 5: Design of timber structures – Part 1-2; General Structural fire design, September 2005 2004.
EN 301: Adhesives, phenolic and aminoplastic, for load-bearing timber structures. Classification and performance requirements, August 2006.
EN 1995-1-1: Eurocode 5: Design of timber structures – Part 1-1; General – Common rules and rules for buildings, November 2005.
European Technical Approval, ETA -07/0029, Kerto Ripa elements, MetsäWood – CSTB.
Kajastila R & Tenhunen: "Fire resistance test on a wooden floor contruction", Test report No RTE1057/04, VTT – Finnforest Oyj, 9 august 2004, Espoo, Finland.
Kajastila R & Tenhunen: "Fire resistance test on a wooden floor contruction", Test report No RTE344/04, VTT – Finnforest Oyj, 11 august 2004, Espoo, Finland.

Research and Applications in Structural Engineering, Mechanics and Computation – Zingoni (Ed.)
© 2013 Taylor & Francis Group, London, ISBN 978-1-138-00061-2

No-sway collapse of steel frames under fire conditions: A parametric investigation

A. Monti, T. Pariciani, F. Gentili & F. Petrini
School of Civil and Industrial Engineering, Sapienza University of Rome, Italy

ABSTRACT: Fire represents a significant danger for frame structures hosting industrial activities. In this context, the numerical investigation of fire effects and fire induced collapse mechanisms becomes of interest. According to many studies on the topic, two failure modes are identified for a steel frame in fire: an outward (or sway) collapse and an inward (or no-sway) collapse. Above others the failure mode is determined by the following parameters: i) the acting load combination; ii) the typology of the column base restrain and iii) the two interacting mechanical effects of the fire (thermal expansion of the structural elements and thermal degradation of the steel properties). In this paper, a set of nonlinear transient analyses, which take into account for thermo-plastic material behavior and geometrical nonlinearities, has been performed in order to understand the influence of different parameters on the collapse mode of the frame.

1 INTRODUCTION

Portal frame construction is the most common structural typology used in industrial single-storey buildings. A no-sway collapse is characterized by an implosion of the construction envelope consequently of the failure of structural elements. On the other side a sway collapse is characterized by an outward movement of elements. The sway collapse represents a not acceptable threat for single-storey industrial structures in terms of sustainability of constructions, because it can involve adjacent structures and endanger people who are not inside the building.

In this paper some parameters that influence the collapse mode of single-storey frames in fire are investigated. Starting from an initial geometry and fire condition, different schemes have been defined. By means of the commercial non-linear finite element software ABAQUS®, a model of the frame is defined through beam elements.

This study is aimed to understanding on how and why the collapse occurs, to assess the influence of local action and constructional details on the frame behavior under fire action.

2 BEHAVIOR OF SINGLE-STOREY PORTAL FRAMES IN FIRE

The analysis of the effects of internal fires in industrial buildings requires the definition of different scenarios (Gentili, 2011).

In a two dimensional analysis the number of possible scenarios is relatively low: in fact, the fire could affect only one of the columns, both columns or no one of them, but certainly the hot gases heat the rafter.

In an initial fire phase, the portal rafter begins to heat and expand (for the gathering of hot gasses under the ceiling), this causes an outward deflection of the eaves together with an upward deflection of the apex (Wong, 2000). As the fire continues to burn, the rafter temperature rise and the thermal expansion increase (Bong, 2005).

If the columns have an adequate stiffness to retain the thermal expansion of the rafter, plastic hinges are realized on the rafter which loses its resistance and droop into a catenary causing the columns to lean inwards, defining a no-sway collapse. General condition for this kind of behavior is a moment resistant base connection for the column and a ratio of the span to the height to eaves less than two (Newmann, 1990).

On the contrary, if the columns have not a stiffness that is sufficient to retain the beam deformation, large displacements can occur at the top of the columns, so the sway collapse is more probably. Usually, due to the common presence of pinned connections at the bases of the columns, large rotations are possible and the consequence is a sideways of the frame (Song, 2007).

Also the load combination and fire location have an important role for the whole behavior of the structure. Heated elements experiment a decay of their resistance, so are the firsts to reach plastic yielding, and the load define the mode of the collapse.

3 CASE STUDY

3.1 *Initial configuration*

Starting from an initial configuration for the portal frame, some parametric analyses have been carried out to assess the structural behavior under fire condition.

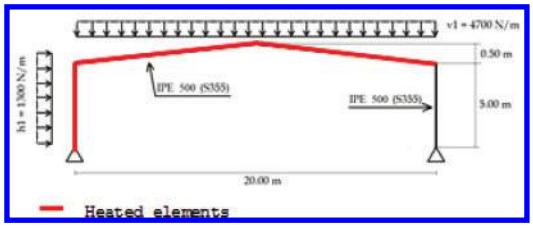


Figure 1. Starting portal frame geometry.

The initial configuration is shown in Figure 1. The IPE 500 standard profile is used for columns and beam, joined with moment and shear resisting connections. The restraints to the ground are assumed to be ideal, frictionless hinges. The constitutive law of steel (S355) used is the relationship defined in the ENV 1993-1-2: Section 3.2 for heating rates between 2 and 50 K/min. Vertical and horizontal loads are also considered as shown in Figure 1.

The considered fire scenario involves the left column and the rafter. This assumption is consistent with the case of a fire triggered in a corner of the structure, so that the most heated elements would be the column near the flame and the beam heated by the hot gasses, that gather under the roof.

The thermal action on the heated element is modeled with the nominal fire curve ISO 834 (European standard curve), shadow effect is not considered. The temperature in the heated elements is assumed uniform and equal to the temperature defined by the fire curve.

The structure is modeled by beam elements; no limits for the rotational capacity of the beam-column connections are considered; bi-dimensional, nonlinear transient analyses have been performed taking into account the effects of displacements on the overall behavior.

3.2 *Collapse mode definition*

With reference to general considerations of the collapse typology given in section 1.1, in the paper, for an asymmetric fire scenario, the following definitions are taken into account:

Inward (or no-sway) collapse is defined when a opposite direction shift of top of the columns is observed at the collapse.

Outward (or sway) collapse is defined when a same direction shift of top of the columns is observed. Sway collapse could be left side or right side direction.

Collapse is defined by the runaway of appropriate parameters.

3.3 *Analysis results*

Three response parameters have been assumed as representative of the structural behavior: the vertical displacement of the mid-point of the beam (dy_{P2}) and the horizontal displacements at the top of the columns (dx_{P1}, dx_{P3}) as shown in Figure 2.

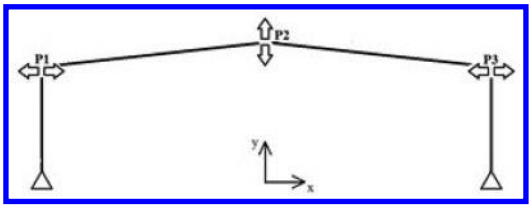


Figure 2. Monitored displacements.

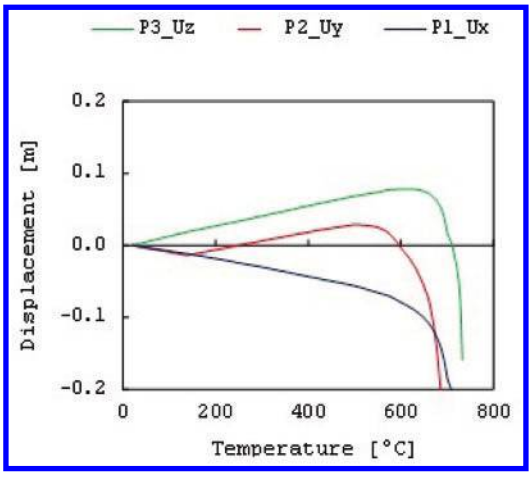


Figure 3. Analysis results.

The trend of these parameters versus the applied temperature for the initial configuration is shown in Figure 3. It is possible to define two different phases. In the first one, under 600°C, the elastic expansion of the rafter causes an outward deflection of the eaves. Then the decreasing of the stiffness of the frame, caused by the plastic hinge formation, lead to a rapid increasing of the displacements. Looking at the direction of the top of the columns displacements is possible to identify a sway collapse to the left side. The critical temperature is 732°C.

4 PARAMETRIC ANALYSIS

4.1 *Problem definition*

A parametric analysis has been carried out in order to understand the influence of the design parameters on the frame collapse modality.

The basic assumptions for the different models are always the same (defined in 3.1), if different specifications are not provided.

The influence of the following parameters on the collapse modality has been investigated: support conditions, load conditions, frame height, column and beam sections. The comparison of the different models is made for eight different column sections.

The outputs monitored are the displacements (defined in 3.3), for the definition of the collapse

mode, and the critical temperature (the temperature of collapse).

4.2 *Pinned vs fixed support conditions*

The first parameter analyzed is the support conditions. A pinned frame (an ideal, perfect, frictionless pinned support) is compared against a fixed frame (rigid, full strength support). The cross section (IPE 500) of the beam has been maintained, while the cross section of the column has been varied.

From the results of the analysis (shown in Table 1) is possible to understand that in case of a pinned support, large rotations are realized and the consequence is a sideways of the frame. In this condition the column's section parameter influences not only the temperature but also the direction of the sway collapse.

A fixed support is able to retain the thermal expansion of the rafter, and the column section variation influence only the temperature and not the mode of the collapse, which is always a no sway typology.

Table 1. Results for pinned vs fixed support.

Columns	pinned	fixed
section	Tcr [°C]	Tcr [°C]
IPE 400	**681**(l-sw)	735(no-sw)
IPE 450	**699**(l-sw)	740(no-sw)
IPE 500	**732**(l-sw)*	746(no-sw)
IPE 550	**726**(r-sw)	756(no-sw)
IPE 600	**723**(r-sw)	765(no-sw)
IPE O600	**723**(r-sw)	776(no-sw)
IPE 750 × 137	**723**(r-sw)	780(no-sw)
IPE 750 × 196	**723**(r-sw)	782(no-sw)

(l-sw) left sway collapse (r-sw) right sway collapse
(no-sw) no sway collapse * initial configuration

4.3 *Interpretation of results*

As a result of analysis performed three different collapse typologies have been founded: inward collapse, left side sway collapse and a right side sway collapse.

The only condition able to retain the expansion of the rafter and inducing an inward collapse is a moment resistant for the columns. This can be explained by looking at the evolution of the stress and plastic hinge formation on the structure. Referring to the schematic behavior defined in Figure 4: in the first phase (Figure 4.1.a) due to the thermal expansion of the beam in elastic range, a moment reaction at the base of the columns is induced. That moment increases with the temperature inducing a plastic hinge formation at the base of the heated column (Fig. 4.1.b). The resistance of the beam is reducing so the next plastic hinges are on the beam, due to the plastic expansion (Figs. 4.1.c, 4.1.d) and vertical load (Fig. 4.1.e). The formation of a plastic hinge at the mid-length of the beam creates inward force at the top of the column (due to vertical load), together with an inversion of the moment at the bases of the columns, which rises until reaching the maximum column moment strength.

As expected, increasing the dimension of the columns' section leads to an increasing of the collapse temperature.

Pinned columns' support is not able to retain the expansion of the rafter and inducing an outward collapse. In this case are noticeable two different direction of the sway collapse as defined in Figure 5. The parameter which influences the direction of the collapse is the resistance of beam to column stiffness ratio.

All the left sway collapses happen when the stiffness of the column is less than the beam's one (column's weaker section than the beam's one). As evidenced in Figure 5.1, in this case the first plastic hinge is formed on the top of heated column (Fig. 5.1.b). From this stage both the horizontal load and the force

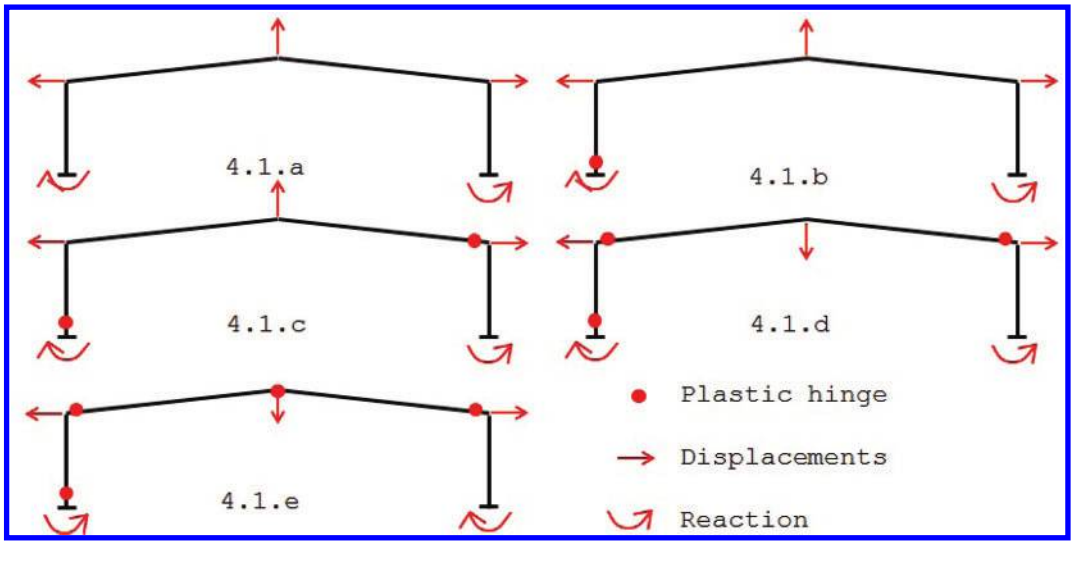


Figure 4. Fixed support collapse scheme.

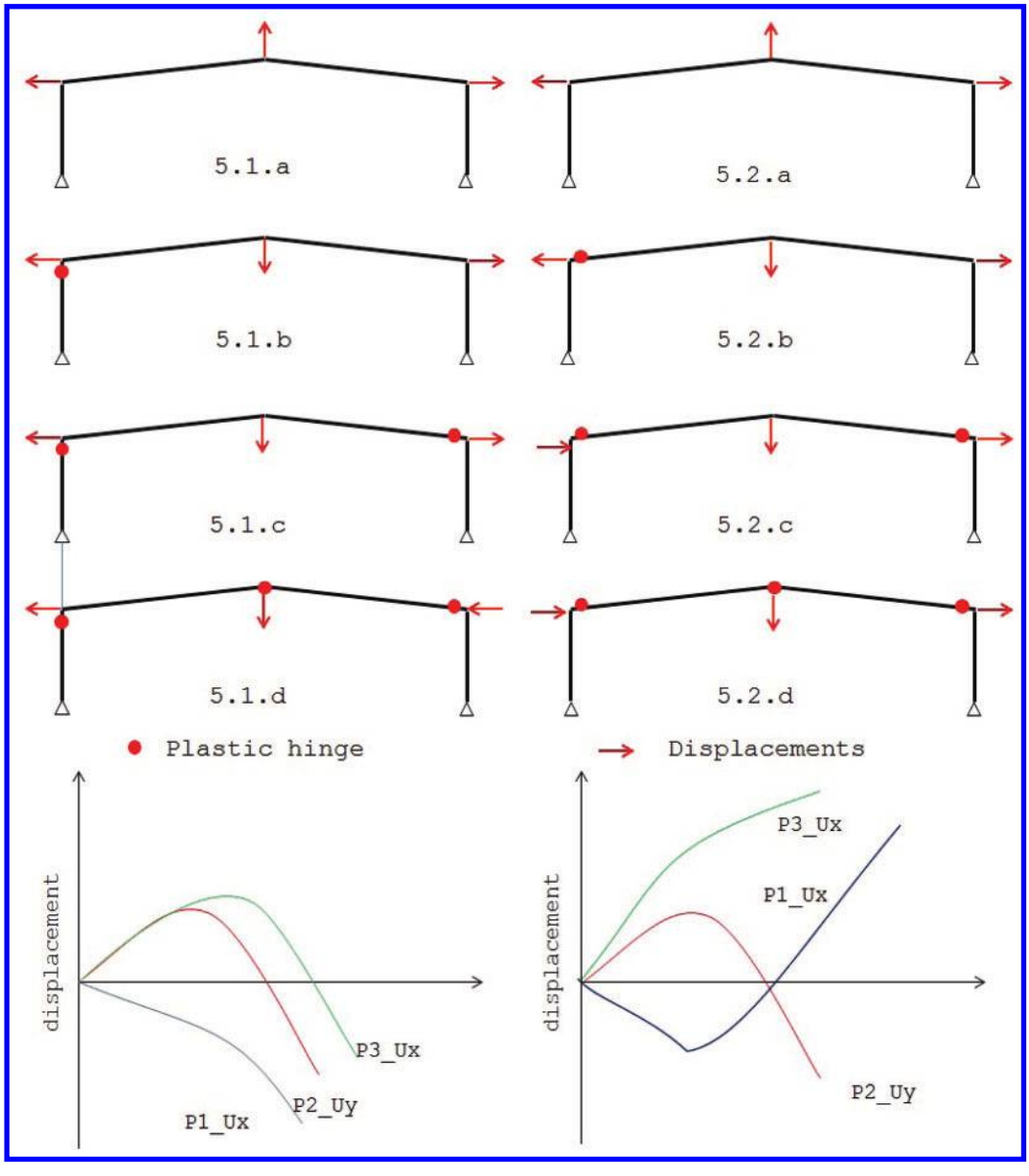


Figure 5. Pinned support collapse scheme. Left sway collapse (left); right sway collapse (right).

induced from the thermal expansion of the beam cause significant deformation of the heated column.

The subsequent loss of stiffness of the structure with the formation of the plastic hinge on the beam, due to the thermal expansion (Fig. 5.1.c) and vertical load (Fig. 5.1.d), determines the collapse towards the heated column, caused from the high plastic deformation on the column and the loss of vertical alignment of the structure. All the right sway collapses happen when the stiffness of the column is greater than the beam's one. As evidenced in the Figure 5.2, this case the first plastic hinge is formed on the beam in proximity of the heated column (Fig. 5.2.b). With the formation of the other plastic hinge on the beam, due to the thermal expansion (Fig. 5.2.c) and vertical load (Fig. 5.2.d) the beam lose its stiffness and the structure became instable for horizontal load, defining by its direction the side of the sway collapse. It is worth to highlight that the value of the collapse temperature increases as the dimension of the columns' cross section grows. This behavior occurs until the cross section of the column is weaker than the beam. While, when the section of the columns became stronger then the beams one (IPE 500) the critical temperature of the portal frame became steady (because the plastic hinge on the rafter happen always at the same temperature).

Is of interest to remark some points:

- when the collapse is induced by the plastic deformation of the beam the temperature of collapse is always equal to the temperature of 723°C due to the collapse of the beam;
- a slight increasing of the temperature of collapse is obtained for frames having the column and the beam with approximately the same stiffness. In these cases the zone of plastic deformation is greater than the previous, the elements are allowed to experiment significant deformations and the stress in the connection between the heated column and the beam are reduced;
- due to the chosen load combination, horizontal load acts in the opposite direction of the thermal expansion induced by the fire, it is possible to point out how, in this condition, the strength of the column in relation to the beam strength is the parameter that influence the direction of the sway collapse.

In conclusion is remarkable that a fixed support frame have a greater resistance to this load combination than the pinned support frame (approximately 3–8% in terms of temperature), this is due to the inversion of the sign of the flexural moment at the base of heated column which delays the collapse.

4.4 *Load conditions*

The second parameter that has been analyzed is the load combination. The section profile of the beam is still a IPE 500 and the columns have a pinned support. Three different load combinations are investigated: LOAD 0 (only vertical load); LOAD 1 (vertical plus horizontal load on the left column pushing to the right side); LOAD 2 (vertical plus horizontal load on the right column pushing to the left side). Results are listed in Table 2.

The results confirm that pinned support is unable to adequately retain the thermal expansion of the rafter and the consequence is a sideways of the frame.

It is important to remark how the LOAD 1 combination is defined from a horizontal load which pushes the frame in an opposite direction from the one of the thermal expansion due to the fire. This is the optimal load condition for the structure and the temperature of the collapse reaches the maximum value. The worst load combination is LOAD 2.

Except for the LOAD 1 case, all the other load combinations cause always a left sway collapse. The collapse explanation is not different from the previous, but when the structure became unstable for horizontal load, the collapse occurs in the direction of the maximum deformation (LOAD 0) or in the direction of horizontal load (LOAD 2).

4.5 *Columns height*

The third investigated parameter has been the columns height. Three different heights are defined, 4, 5 and 6 meters, the span length is always the same, 20 meter. The section profile of the beam is always an IPE 500 and the columns have pinned supports. Results are listed in Table 3. The load combination and the fire scenario considered is the one previously defined as LOAD 1. In this case is important to evidence as the variable parameter is the beam to column stiffness ratio.

The obtained results confirm the consideration given in 4.2.1. When the collapse is induced from the plastic hinge on the heated column, the maximum temperature is not influenced from height and stiffness of the columns. When the collapse is induced by the plastic hinge on the beam the stiffness of the columns has a small influence on the maximum reached temperature (the deformations of slender and longer, column allow greater deformation of the beam).

4.6 *Beam section*

The fourth investigated parameter has been the beam section. Four different beam sections are considered: IPE 450, IPE 500, IPE 550 and IPE 600. The columns have a pinned support and the height of the column is 5 meters while the span of the beam is equal to 20 meters. The load combination and the fire scenario is the one previously defined as LOAD 1. The results are listed in Table 4.1 and Table 4.2.

Table 2. Results for load conditions.

Columns	LOAD 0	LOAD 1	LOAD 2
section	Tcr [°C]	Tcr [°C]	Tcr [°C]
IPE 400	675(l-sw)	**681**(l-sw)	672(l-sw)
IPE 450	693(l-sw)	**699**(l-sw)	690(l-sw)
IPE 500	722(l-sw)	**732**(l-sw)*	713(l-sw)
IPE 550	732(l-sw)	**726**(r-sw)	720(l-sw)
IPE 600	732(l-sw)	**723**(r-sw)	722(l-sw)
IPE O600	734(l-sw)	**723**(r-sw)	722(l-sw)
IPE 750 × 137	734(l-sw)	**723**(r-sw)	722(l-sw)
IPE 750 × 196	734(l-sw)	**723**(r-sw)	722(l-sw)

(l-sw) left sway collapse (r-sw) right sway collapse
other no- sway collapse * initial configuration

Table 3. Results for columns height variation.

Columns	H = 4 m	H = 5 m	H = 6 m
section	Tcr [°C]	Tcr [°C]	Tcr [°C]
IPE 400	681(l-sw)	**681**(l-sw)	681(l-sw)
IPE 450	699(l-sw)	**699**(l-sw)	699(l-sw)
IPE 500	732(l-sw)	**732**(l-sw)*	734(l-sw)
IPE 550	729(r-sw)	**726**(r-sw)	719(r-sw)
IPE 600	728(r-sw)	**723**(r-sw)	717(r-sw)
IPE O600	728(r-sw)	**723**(r-sw)	717(r-sw)
IPE 750 × 137	728(r-sw)	**723**(r-sw)	717(r-sw)
IPE 750 × 196	726(r-sw)	**723**(r-sw)	716(r-sw)

(l-sw) left sway collapse (r-sw) right sway collapse
other non sway collapse * initial configuration

Table 4.1. Results for beam section variation.

Columns	IPE 450	IPE 500
section	Tcr [°C]	Tcr [°C]
IPE 400	670(l-sw)	**681**(l-sw)
IPE 450	690(l-sw)	**699**(l-sw)
IPE 500	687(r-sw)	**732**(l-sw)*
IPE 550	684(r-sw)	**726**(r-sw)
IPE 600	684(r-sw)	**723**(r-sw)
IPE O600	684(r-sw)	**723**(r-sw)
IPE 750 × 137	684(r-sw)	**723**(r-sw)
IPE 750 × 196	684(r-sw)	**723**(r-sw)

(l-sw) left sway collapse (r-sw) right sway collapse
other non sway collapse * starting model

Table 4.2. Results for beam section variation.

Columns	IPE 550	IPE 600
section	Tcr [°C]	Tcr [°C]
IPE 400	696(l-sw)	723(l-sw)
IPE 450	716(l-sw)	740(l-sw)
IPE 500	744(l-sw)	759(l-sw)
IPE 550	765(l-sw)	798(l-sw)
IPE 600	764(r-sw)	794(l-sw)
IPE O600	762(r-sw)	792(r-sw)
IPE 750 × 137	762(r-sw)	792(r-sw)
IPE 750 × 196	761(r-sw)	791(r-sw)

(l-sw) left sway collapse (r-sw) right sway collapse
other no- sway collapse * initial configuration

As previously concluded in the 4.2.1 the beam section is the most important parameter in the determination of the resistance of the frame in fire situation. Increasing the strength of the beam the maximum temperature reached from the frame increase. On the other side, is also confirmed how the relationship between the strength of the column and the beam, for asymmetrical fire scenario and opposite horizontal load, is the main factor in the determination of the direction of the sway collapse.

5 CONCLUSION

A wide parametric analysis of a bi-dimensional industrial steel portal frame has been performed in order to understand the fundamental mechanism determining sway or no-sway collapse.

The sway-collapse represents a not acceptable threat for single-storey industrial structures in terms of sustainability of constructions, because it can involve adjacent structures and endanger even people who are not in the building.

From the obtained result is clear how in pinned support columns, large rotations are allowed and a sway collapse always occur. For the sway collapse the beam to column section stiffness ratio and the load combination for asymmetrical fire scenario are the factors that determine the sway direction and the collapse temperature.

Concerning the frames having, In the examined cases, the adoption of moment resisting support for the columns is sufficient to avoid a sway collapse.

REFERENCES

Bong M.W. 2005, Structural fire performance of steel portal frame buildings, PhD Thesis.

EC3, 2002. Eurocode 3: Design of steel structures, ENV 1993: Part 1.2: General rules – Structural fire design, European Committee for Standardization, Brussels, Belgium.

Gentili F. 2011, Advanced numerical analyses for the assessment of steel structures under fire, International Journal of Lifecycle Performance Engineering, Special Issue of fire safety design and robustness consideration in steel structural engineering.

Newmann, E.G. 1990. Fire and steel construction: The Behaviour of Steel Portal Frames in Boundary Conditions, Second Edition, The Steel Contruction Istitute, UK.

Song Y., Huang Z., Burgess I.W., Plank R.J. 2007, The design of pitched-roof frames against fire, 5th international conference on advanced in steel structure (ICASS07), National University of Singapore.

Wong S.Y., Burgess I.W., Plank R.J. 2000, Simplified estimation of critical temperature of portal frame in fire, paper 09.03, Proc. International conference in steel structure of the 2000s, Istanbul

Research and Applications in Structural Engineering, Mechanics and Computation – Zingoni (Ed.)
© 2013 Taylor & Francis Group, London, ISBN 978-1-138-00061-2

Numerical studies of load bearing LSF walls under realistic design fire conditions

P. Keerthan, A. Ariyanayagam & M. Mahendran
Queensland University of Technology, Brisbane, Queensland, Australia

ABSTRACT: Fire safety of light gauge steel frame (LSF) stud walls is important in the design of buildings. Currently LSF walls are increasingly used in the building industry, and are usually made of cold-formed and thin-walled steel studs that are fire-protected by two layers of plasterboard on both sides. Many experimental and numerical studies have been undertaken to investigate the fire performance of load bearing LSF walls under standard fire conditions. However, the standard time-temperature curve does not represent the fire load present in typical residential and commercial buildings that include considerable amount of thermoplastic materials. Real building fires are unlikely to follow a standard time-temperature curve. However, only limited research has been undertaken to investigate the fire performance of load bearing LSF walls under realistic design fire conditions. Therefore in this research, finite element thermal models of the traditional LSF wall panels without cavity insulation and the new LSF composite wall panels were developed to simulate their fire performance under recently developed realistic design fire curves. Suitable thermal properties were proposed for plasterboards and insulations based on laboratory tests and literature review. The developed models were then validated by comparing their thermal performance results with available results from realistic design fire tests, and were later used in parametric studies. This paper presents the details of the developed finite element thermal models of load bearing LSF wall panels under realistic design fire time-temperature curves and the results. It shows that finite element thermal models can be used to predict the fire performance of load bearing LSF walls with varying configurations of insulations and plasterboards under realistic design fires. Failure times of load bearing LSF walls were also predicted based on the results from finite element thermal analyses.

1 INTRODUCTION

Gypsum plasterboard is used as fire resistance material in the building industry due to its ease of fabrication and workmanship, the widespread availability of the primary material for its production, and for the energy consuming (endothermic) dehydration process during fires. Currently, gypsum plasterboard based LSF wall and floor systems are increasingly used in low-rise and multi-storey buildings, but without a full understanding of their fire performance. LSF wall and floor systems are made of cold-formed thin-walled steel lipped channel sections and gypsum plasterboards. Under fire conditions, cold-formed thin-walled steel stud and joist sections heat up quickly resulting in fast reduction in their strength and stiffness. Therefore they are commonly used in structural wall and floor systems with plasterboard linings on both sides used as fire protection (see Figure 1). Gypsum plasterboard protects steel studs and joists during building fires by delaying the temperature rise.

Many experimental and numerical studies have been undertaken to investigate the fire performance of load bearing LSF walls under standard fire conditions. However, the standard time-temperature curve does not represent the modern accessories in typical residential and commercial buildings, where they incorporate both traditional wooden furniture and modern items such as cushion furniture, mattresses, fabric coated partitions and many other items that make use of thermoplastic materials. Therefore finite element analyses were performed to investigate the fire performance of LSF wall systems under recently developed realistic design fire curves (Ariyanayagam and Mahendran, 2012).

2 THERMAL PROPERTIES

In order to develop suitable finite element models of Australian gypsum plasterboard, thermal properties of gypsum plasterboard were summarized based on a series of experimental results (Keerthan and Mahendran, 2012) and past research (Thomas, 2010; Cooper, 1997). These proposed thermal properties were used in the finite element models developed using SAFIR (Franssen et al., 2004). Figure 2(a) shows the proposed thermal conductivity of gypsum plasterboard. In order to include the effect of ablation, the thermal conductivity of plasterboard was modified to 0.80 W/m/K at 1200°C.



Figure 1. LSF wall with gypsum plasterboard lining.

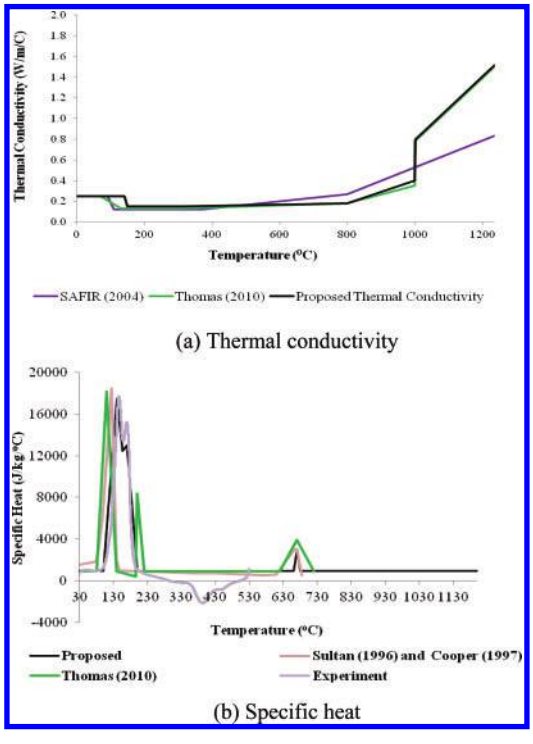


Figure 2. Proposed thermal properties of plasterboard.

Past research showed some discrepancy in relation to the second dehydration reaction. However, it is concluded that the first and second dehydrations occur at 100 to 150°C and 150 to 200°C, respectively, based on our experiments (Keerthan and Mahendran, 2012). Figure 2(b) also shows the proposed specific heat values as a function of temperature and compares them with test and other researchers' specific heat values (Thomas, 2010; Cooper, 1997). Further details of the proposed thermal properties of plasterboards are given in Keerthan and Mahendran (2012). The specific volumetric enthalpy of gypsum plasterboard is given by the area under the specific heat multiplied by the density versus temperature curve. The proposed specific volumetric enthalpy values were used as input to SAFIR in our thermal analyses.

When the proposed thermal properties were used as input to SAFIR, the time-temperature profiles agreed well with Ariyanayagam and Mahendran's (2012) fire test results.

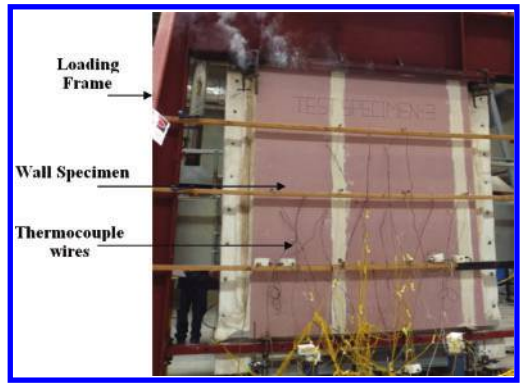
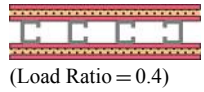


Figure 3. Experimental set-up (Ariyanayagam and Mahendran, 2012).

Table 1. Failure times of LSF walls.

LSF Configuration		Fire Curve	Failure Time
 (Load Ratio = 0.2)	Test 1 Test 2 Kolarkar (2010)	ECS 1 BFD 1 ISO Curve	No Failure 139 min 111 min
 (Load Ratio = 0.2)	Test 3 Test 4 Kolarkar (2010)	ECS 2 BFD 2 ISO Curve	28 min 39 min 53 min
 (Load Ratio = 0.4)	Test 5 Gunalan (2011)	BFD 1 ISO Curve	118 min 134 min

3 EXPERIMENTAL STUDIES

In order to investigate the thermal performance of load bearing LSF wall panels under realistic fire curves, five fire tests of full scale panels of dimensions 2400 mm × 2100 mm were conducted by Ariyanayagam and Mahendran (2012) as shown in Figure 3. The wall assemblies typically consisted of four commonly used cold-formed steel lipped channel section studs (90 × 40 × 15 × 1.15 mm) spaced at 600 mm. The studs were fabricated from galvanized steel sheets (G500) having a nominal base metal thickness of 1.15 mm and a minimum yield strength of 500 MPa. Test specimens were built by lining the test frames with one or two layers of gypsum plasterboards manufactured by Boral Plasterboard under the product name of Firestop. All the plasterboards used were 1200 mm in width and 2400 mm in height with a thickness of 16 mm. There were two groups of wall specimens made of (1) no insulation and (2) external insulation (composite panels). Rockwool was used in composite panels (see Table 1).

Tests were conducted using the recently developed realistic design fire curves (Ariyanayagam and Mahendran, 2012). Figure 4 shows the realistic design fire time-temperature curves used in fire tests while

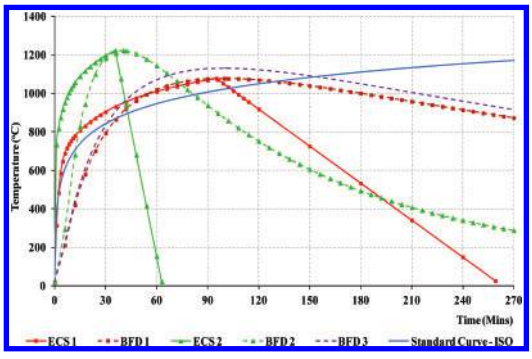


Figure 4. Realistic design fire time-temperature curves used in fire tests.

Table 2. Realistic design fire compartment characteristics used in developing fire test time-temperature curves.

Fire Curve	Opening Factor ($m^{1/2}$)	Compartment Thermal Inertia ($J/m^2S^{1/2}K$)	Fuel load (MJ/m^2)
ECS 1	0.03	702	1268
BFD 1	0.03	702	1268
ECS 2	0.08	715	1268
BFD 2	0.08	715	1268
BFD 3	0.03	585	1268

Table 2 shows the realistic design fire compartment characteristics used in developing fire test time-temperature curves. One face of the test specimens was exposed to heat in a propane-fired vertical gas furnace (Figure 3). Time-temperature profiles at various locations across the specimen thickness were measured during the tests using thermocouples. Table 1 shows the failure times of test specimens. Ariyanayagam and Mahendran (2012) provides a full description of these realistic design fire tests while this section provides their important details and some results.

Table 1 shows that some real building fires (Fire tests 3 to 5) can cause severe damage to LSF wall panels than the standard fire specified in various fire codes while other real building fires (Fire tests 1and 2) are not as severe as the standard fire.

4 NUMERICAL STUDIES

4.1 *General*

This section presents the details of the numerical studies into the thermal behaviour of the tested load bearing LSF wall panels under realistic fire curves and their results. Recently many numerical heat transfer models have been developed (SAFIR, 2004; Alfawakhiri, 2001). There are also many general finite element packages that can be used for thermal analyses. The finite element model employed in this study to predict the thermal behaviour of load bearing LSF wall

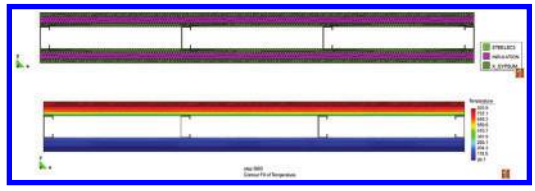


Figure 5. Finite element modelling of LSF wall panels.

panels was based on SAFIR (2004). SAFIR is a special purpose finite element program for the analysis of structures under ambient and elevated temperature conditions. In this research the GID software was used to create the input file for the models as well as analysing the model output results.

4.2 *Thermal boundary conditions and material properties*

The heat flux at the LSF wall boundary conditions can be calculated from the temperature of the fire curve T_g and the temperature on the surface T_s according to Equation (1).

$$q = h(T_g - T_s) + \sigma\varepsilon(T_g^4 - T_s^4) \quad (1)$$

where q is the total heat flux, ε is the relative emissivity, σ is the Stefan–Boltzmann constant (5.67E–08 $W/m^2/K^4$), T_g and T_s are the gas and surface temperatures, respectively. For fire exposure to the standard cellulosic curve, $T_g = 345\log(8t + 1) + 293$. Convective heat transfer coefficient (h) is approximately 25 W/m^2K on the fire exposed side, and it is 10 W/m^2K on the unexposed side. Emissivity of 0.9 was used for both exposed and unexposed surfaces. The proposed thermal properties in Section 2 were used in this research. To investigate the thermal performance of load bearing LSF walls under realistic fire curves, finite element models of Ariyanayagam and Mahendran's (2012) test wall panels were developed. Figure 5 shows the finite element models of LSF walls under realistic fire curves. The developed finite element models were validated using the fire test results of load bearing LSF walls under realistic fire curves (Ariyanayagam and Mahendran, 2012).

4.3 *Validation of finite element models of LSF walls*

To validate the developed finite element models for the thermal analyses of load bearing LSF walls under realistic fire curves, the stud time-temperature curves were compared with the corresponding fire test results from Ariyanayagam and Mahendran (2012). It is noted that load bearing LSF walls exposed to fires are affected by processes not described by heat transfer such as ablation of plasterboard and insulation, migration of moisture vapours and penetration of cool ambient air or hot furnace gases into the cavity. Effects of these processes were taken into account in the models through the use of suitable thermal conductivity values for plasterboards and insulations (Section 2).

Figures 6(a) to (e) show the finite element analysis (FEA) results in the form of temperature versus time curves compare them with corresponding test results. The average time-temperature curves of the studs were considered in this comparison of test and FEA results. These figures indicate that the developed finite element models predict the time-temperature curves of load bearing LSF walls under realistic fire curves with reasonable accuracy. Good agreement was obtained for Tests 1, 2 and 5, where pro-longed fire time-temperature curves are used and in Tests 3 and 4 when rapid fire curves are used FEA overestimated the temperatures. This could be due to the effect of higher rate of temperature increase and corresponding thermal properties. The heating rate of rapid fires is well above 50°C/min, which affected the dehydration reaction of gypsum plasterboard significantly. Also the likely cause for this is the negligence of the processes such as moisture flow and ablation of plasterboards caused by rapid fires in FEA.

In summary, the comparisons between FEA and fire test results confirmed the accuracy of the finite element models in simulating the thermal behaviour of load bearing LSF walls under realistic fire curves and the accuracy of the values used for relative emissivity, convective coefficient and other thermal properties. But for rapid fires FEA predicted temperatures were seen to be higher than the actual test results. In FEA the thermal properties at elevated temperatures used for the standard fire curves were used for both rapid and pro-longed fire curves. Hence a good agreement was obtained for pro-longed fires but not for rapid fire curves. Similar observations were made by Hopkin et al. (2012), Sergey et al. (2012) and Thomas (2010) in their thermal analysis and found that the thermal properties of gypsum plasterboard depends on the heating rate.

Hopkin et al. (2012) found that thermal properties of gypsum plasterboard depend on the heating rate and can result in inaccuracies when they were used in the simulation of temperature development under natural fire conditions. The likely cause of this is the

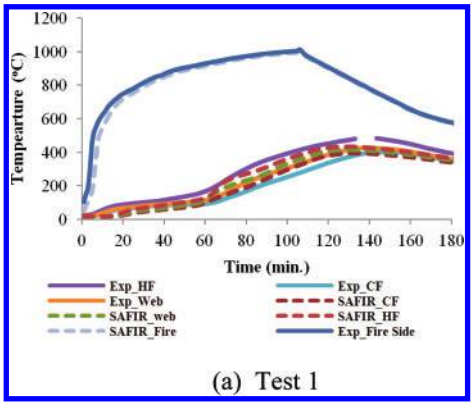


Figure 6. Time-temperature profiles of test specimens (Steel stud).

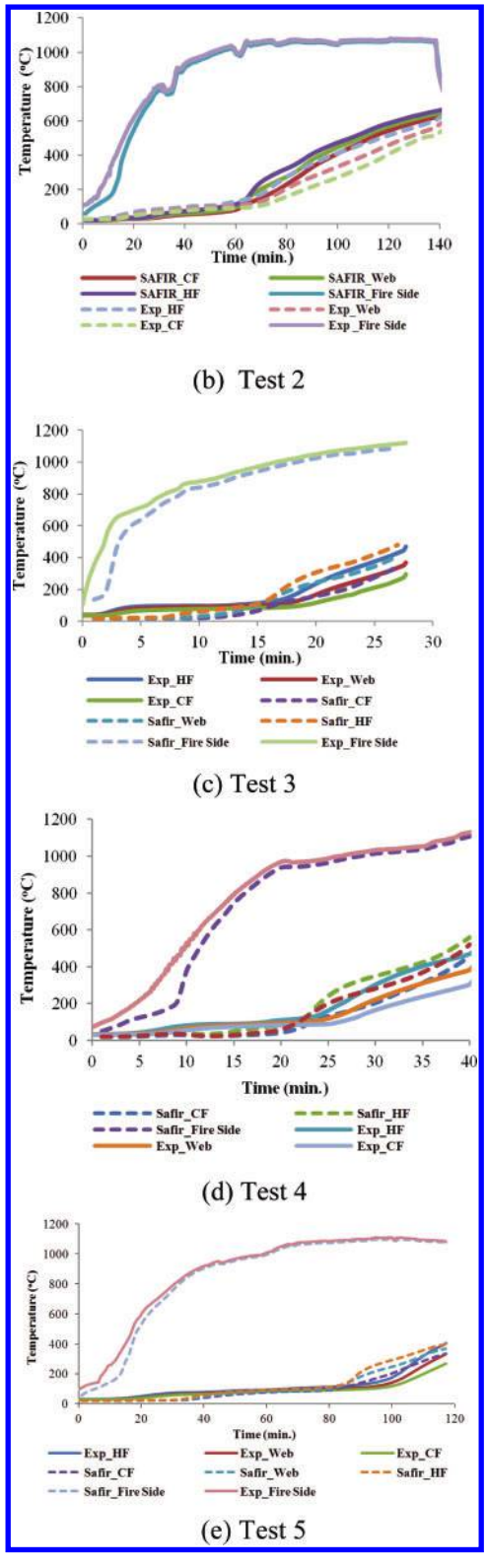


Figure 6. Time-temperature profiles of test specimens (Steel stud). Note: HF- hot flange, CF- cold flange.

relationship between heating rate and other behaviours such as moisture flow, ablation and cracking.

Sergey et al. (2012) developed a mathematical model to investigate the thermal performance of plasterboard panel exposed to hydrocarbon, external and standard fires. Their mathematical models predict the time-temperature profiles of plasterboard panels with good accuracy. However, some discrepancies observed in the early and late stages of the dehydration reaction are shown to be caused by the high local heating rate of the material during those stages. Sergey et al. (2012) found that the heating rate of plasterboard affects the course of dehydration reaction, and it should be accounted for when developing the models of plasterboards.

Thomas (2010) investigated the thermal performance of lined light timber frame walls (LTF) under standard fire, slow developing fire and rapid fire conditions using numerical studies. Numerical studies gave better overall results for slower developing fires than more rapidly growing fires. Their numerical model also overestimated the temperature profiles of LTF walls in the case of rapid fire (Thomas, 2010). Hence detailed experimental and numerical studies will be undertaken to investigate the effect of rapid real fires on the thermal performance of LSF wall panels.

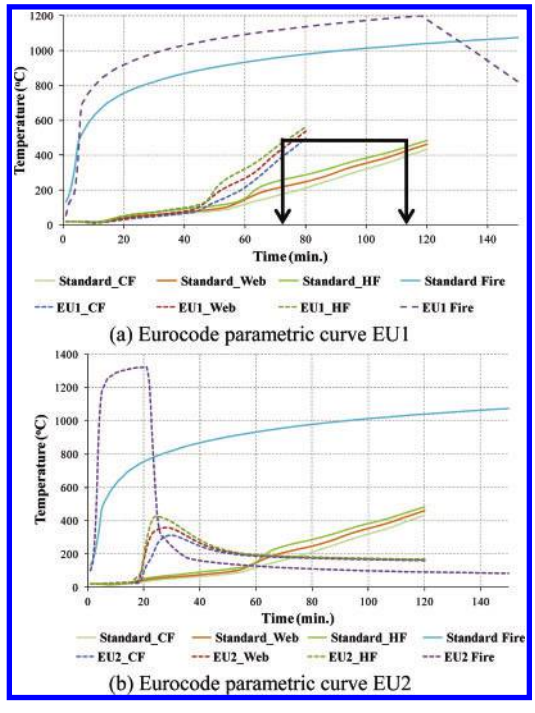


Figure 7. Time-temperature profiles of double plasterboard lined LSF wall under realistic design fire curves (EU1 & EU2).

5 PARAMETRIC STUDIES

A detailed parametric study was undertaken based on the validated finite element model to develop an extensive fire rating data of LSF walls and to investigate the thermal performance of load bearing LSF walls under realistic design fire curves.

Numerical analyses were performed to investigate the thermal performance of three different LSF wall configurations (single plasterboard, double plasterboard and composite panel) under 16 realistic design fire curves (total of 48 FEA). However, only the results for two Eurocode parametric curves (EU1 and EU2) are reported in this section. EU1 and EU2 curves represent the opening factors of 0.02 (EU1) and 0.12 (EU2) as they cover the entire range, and are conservative. Also EU1 (0.02) and EU2 (0.12) are the ideal time-temperature curves for this study on load bearing LSF walls for realistic building fires as they include a rapid (EU2) and a prolonged (EU1) fire curve falling between the two extremes. Figure 7 shows these two Eurocode parametric curves developed for dwellings based on a fuel load density of 1268 MJ/m^2 (ECS, 2002). Figures 7(a) and (b) show the finite element analysis results in the form of temperature versus time for a load bearing LSF wall panel (Double plasterboard) under these two realistic design fire curves (ECS, 2002) and compare them with those under standard fire conditions.

Figure 7(a) shows that the LSF steel stud temperatures under realistic design fires [hot (HF) & cold (CF) flanges, web] are considerably increased in comparison to LSF wall studs under standard fires. This means that the failure time (fire resistance rating) decreases from 111 to 73 minutes based on a limiting temperature of 500°C, ie. 35% reduction. Figure 7(a) shows that the time-temperature profiles of load bearing LSF wall panels under the realistic design fire curve – EU1 are much higher than those under the standard fire curve while Figure 7(b) shows that the time-temperature profiles of load bearing LSF wall panels under the realistic design fire curve – EU2 are lower than those under the standard fire curve. It is clear from Figure 7(a) that realistic design fires such as EU1 can cause severe damage to LSF wall panels protected by two plasterboards than standard fires. However, realistic design fires such as EU2 will not cause severe damage to these wall panels than standard fires (Figure 7(b)). Fire resistance rating is determined based on insulation, integrity and structural failure. This paper uses the limiting temperature of the stud, which is an indirect measure of the structural failure.

Table 3 shows the fire compartment characteristics used in developing Eurocode parametric curves. Figure 8 shows the Eurocode parametric fire curves (ECS, 2002) while Figure 9 shows the stud hot flange temperatures obtained from thermal finite element analyses. Failure times of LSF walls under realistic fire curves can be determined using this figure and the concept of limiting temperature.

Table 3. Fire compartment characteristics used in developing Eurocode parametric curves.

Eurocode Parametric Fire Curves (ECS, 2002)	Opening Factor ($m^{1/2}$)	Compartment Thermal Inertia ($J/m^2S^{1/2}K$)	Fuel Load (MJ/m^2)
Db – EU-a	0.06	715	1268
Db – EU-b	0.03	702	1268
Db – EU-c	0.06	715	780
Db – EU-d	0.03	702	780
Db – EU-e	0.06	423	1268
Db – EU-f	0.03	423	1268
Db – EU-g	0.06	423	780
Db – EU-h	0.03	423	780

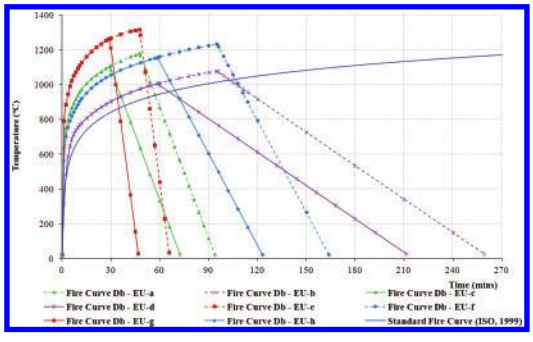


Figure 8. Eurocode parametric fire curves (ECS, 2002).

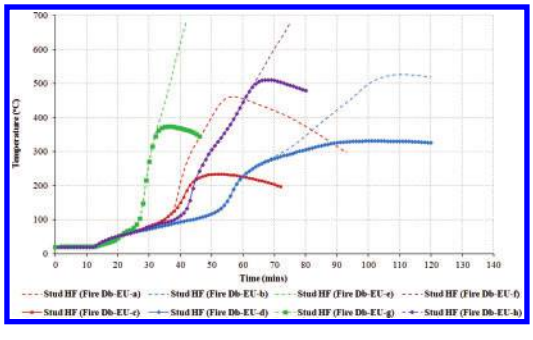


Figure 9. Stud hot flange temperatures obtained from finite element thermal analysis.

6 CONCLUSIONS

This paper has presented the details of a numerical study on the thermal performance of load bearing LSF wall panels under realistic fire time-temperature curves. It included the details of the developed finite element models of load bearing LSF wall panels, the thermal analysis results from SAFIR under realistic design fire curves and their comparisons with fire test results obtained by Ariyanayagam and Mahendran (2012). A reasonable agreement with fire test results showed that accurate finite element models can be developed and used to simulate the thermal behaviour of full scale load bearing LSF wall panels under realistic fire conditions. However, for rapid fires the developed numerical model overestimated the temperature values. This could be due to rapid heating rate and other behaviours such as moisture flow, ablation and cracking. Hence detailed experimental and numerical studies need to be undertaken to investigate the effect of rapid fires on the thermal properties LSF walls.

ACKNOWLEDGEMENTS

The authors would like to thank Australian Research Council for their financial support and Queensland University of Technology for providing the necessary facilities and support to conduct this research project.

REFERENCES

Alfawakhiri, F. 2001. Behaviour of cold-formed steel-frames walls and floors in standard fire resistance tests. PhD Thesis, Dept. of Civil and Environmental Eng., Carleton University, Canada.

Ariyanayagam, A. and Mahendran, M. 2012. Fire tests of load bearing steel stud walls exposed to real building fires. *Proceedings of the 7th International Conference on Structures in Fire*, ETH, Zurich, 105–114.

Cooper, L.Y. 1997. The Thermal response of gypsum-panel/steel stud wall systems exposed to fire environments – a simulation for the use in zone-type fire models. *NIST Report NISTIR 6027, Building and Fire Research Laboratory*, NIST, Gaithersburg, USA.

EN 1991-1-2, 2002. Eurocode 1: Actions on structures. Part1-2: General Actions–Actions on structures exposed to fire, Burssels: European Committe for Standardization, Belgium.

EN 1993-1-2, 1995. Eurocode 3: Design of steel structures – Part 1-2: General Rules – Structural Fire Design, European Committee for Standardization, Brussels.

Franssen, J.-M. 2005. SAFIR. A Thermal/structural program modelling structures under Fire. *Engineering Journal*, A.I.S.C., 42 (3), 143–158.

Gunalan, S. 2011. Structural behaviour and design of cold-formed steel wall systems under fire conditions. *PhD Thesis*, Queensland University of Technology, Brisbane, Australia.

Hopkin, D.J., Lennon, T., Rimawi, J.E., and Silberschmidt, V.V. 2012. Numerical study of gypsum plasterboard behaviour under standard and natural fire conditions. *Fire and Materials*, 36(2), 107–126.

Keerthan P. and Mahendran M. 2012. Numerical modelling of non-load bearing LSF walls under fire conditions. *Journal of Fire Sciences*, 30(5), 375–403.

Kolarkar, P.N. 2010. Structural and thermal performance of cold-formed steel stud wall systems under fire conditions. *PhD Thesis*, Queensland University of Technology, Brisbane, Australia.

Thomas G. 2010. Modelling thermal performance of gypsum plasterboard-lined light timber frame walls using SAFIR and TASEF. *Fire and Materials*, 34(8), 385–406.

Sergey, V. S., Wakili, K.G. and Hugi, E. 2012. Investigation of heat transfer in gypsum plasterboard exposed to fire for three nominal fire scenarios. *Journal of Fire Sciences*, In press.

Standards Australia (SA). 2005. Methods for fire tests on building materials, components and structures, Part 4: Fire-resistance tests of elements of building construction. AS 1530.4, Sydney, Australia.

Research and Applications in Structural Engineering, Mechanics and Computation – Zingoni (Ed.)
© 2013 Taylor & Francis Group, London, ISBN 978-1-138-00061-2

Numerical study of travelling fire in full-scale experimental building

K. Horová & F. Wald
Department of Steel and Timber Structures, Czech Technical University in Prague, Czech Republic

ABSTRACT: With the view to expand family of traditional design fire models travelling fire is investigated. The paper describes fire test in two-floor experimental building performed in September 2011 in Czech Republic. In upper floor scenario of travelling fire was prepared. As flames were spreading across the compartment considerable temperature gradients appeared. To study travelling fire, FDS 5 was used. Numerical results of gas and beam temperatures validated by experimental measurements were compared to temperatures induced by uniform temperature conditions of zone model and standard temperature-time curve to highlight the level of difference between both assumptions – travelling fire and traditional design fire models. The potential impact of the non-uniform gas temperature on structural behaviour is discussed. The fire test in middle large compartment proved that there were clear needs and benefits in using a travelling design fire as the basis for structural design.

1 INTRODUCTION

The traditional fire design methods used for structural fire analysis are based on assumption of uniform temperature conditions in the entire compartment. Regardless whether the standard temperature-time curve (ISO 834) or parametric temperature-time curve (EN 1991-1-2: 2002) is used, both analytical methods give one temperature distribution in all locations of an enclosure. Zone models as well as introduced analytical methods based on the uniform temperature assumption adopted the justification that there is a small gradient in vertical temperature distribution and even smaller in horizontal direction. However, according to (Stern-Gottfried 2011) the justification has not been evaluated any further. Due to lack of fire experiments in large compartments with real compartment conditions and due to limited number of measuring devices, the presence of horizontal temperature heterogeneity was not investigated and is rarely reported (Stern-Gottfried, 2011).

For the purpose of investigation non-uniform temperature conditions in real compartment (so called travelling fire), a full-scale fire test was executed in Czech Republic in 2011 (Wald et al. 2011). Since the scale of experimental enclosure was not large in comparison to the scale of real buildings, high degree of temperature non-uniformity appeared. Differences in temperature of the upper smoke layer of 400°C confirmed that the homogeneous temperature assumption did not hold well in compartment fires.

Observations of the gas and beam temperature from numerical calculation which were validated by experimental measurements showed that travelling fire had a significant impact on structural behaviour.

2 TRAVELLING FIRE TEST

2.1 *Experimental building*

A two floor composite steel-concrete experimental object of dimension of $10.4 \times 13.4 \times 9$ m was designed (Wald et al. 2011). Composite ceiling slab composed of simple trapezoidal sheets and steel wires reinforced concrete of height 60 mm was supported by IPE 270 and IPE 240 steel beams. Vertical bearing members of round tube columns filled with concrete and columns of sections HEB 200 were used. Ground plan scheme of bearing structure is shown in Figure 1.

2.2 *Fire load*

The fire load using wooden cribs of dimensions 50/50/1000 mm placed into 24 piles (8×3 wooden piles placed closely together) of area 24 m^2 was created. Each pile consisted of 42 cribs. Total volume of ligneous mass of 2.52 m^3 (9.9 kg/m^2) was used. The fire load corresponded to value of 173.5 MJ/m^2. A thin-walled channel filled by mineral wool and penetrated by paraffin placed on the south side of fire compartment served as outbreak of burning. The linear ignition source ensured spreading of fire from the south side of the compartment to the north side, see a scheme at Figure 1. The opening of size 2.0×5.0 m with parapet of 1.20 m ventilated the fire compartment.

2.3 *Measurements*

To measure the gas temperature in the fire compartment 20 jacketed thermocouples with diameter of

3 mm were located at the level of the lower beam flange and the upper beam flange, mainly in direction of fire spread. The temperature of steel beams was measured by 8 jacketed thermocouples located at upper side of lower flange. Besides jacketed thermocouples adiabatic surface temperature was measured by 7 plate thermocouples. In Figure 2 thermocouples to measure gas temperature are marked TG2-TG13. To measure steel beam temperature thermocouple TB2 is highlighted.

The fire spread from the linear ignition source to the opposite side of the compartment accompanied by high degree of non-uniform temperatures was observed. Maximum degree of gas heterogeneity was reached about 15 min between thermocouple TG2 and TG4. Whereas the distance between these thermocouples was only 6 m, temperature difference of 400°C was measured. The highest gas temperature of 979°C was measured on thermocouple TG3 close to the column B2 at 26 min. The maximal steel beam temperature reached 855°C.

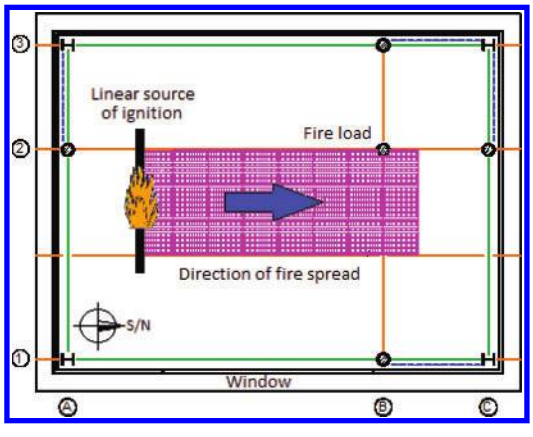


Figure 1. Scheme of fire load in upper floor of the experimental building.

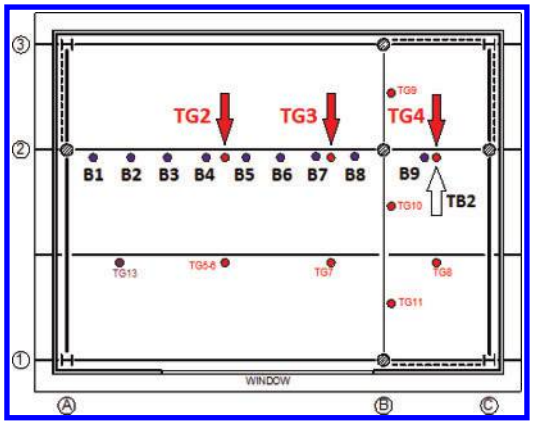


Figure 2. Scheme of gas and beam thermocouples during the experiment and sensor positions during numerical calculation – groundplan.

3 NUMERICAL SIMULATION

3.1 *Model description*

To study the travelling fire scenario numerically, a model corresponding to the size of the upper floor of the experimental building was created. The gas temperature and steel beam temperature were calculated by FDS 5 (McGrattan et al. 2010) to obtain data for evaluation with the fire test.

Four different materials including steel, concrete, mineral wool and wood were used in the model. Properties of wood came from cone calorimeter tests executed immediately after the fire experiment. Obstructions surface properties included steel column filled with concrete, steel beams, concrete walls, floor, ceiling and wooden piles. Burner block of dimensions $0.15 \times 3 \times 0.05\,m^3$ placed under wooden crib in the south edge of the fire load was used to simulate the fire outbreak. Ignition time of wood was ensured by using ramping function. The model was compiled from a total of 24 computational grids of two sizes of cells. Basic cell size was $10 \times 10 \times 10\,cm^3$, cell size around the fire load was $5 \times 5 \times 5\,cm^3$. The total number of computational grid cells reached almost 1 mil.

3.2 *Validation of numerical results*

To validate numerical results, the gas temperature and steel beam temperature measurements from the fire test were used. Figure 3 shows measured (with index *ex*) and calculated gas temperature at thermocouples TG2, TG3 and TG4, located in the direction of the fire spread. Positions of sensors are shown at Figure 2. During growing phase of the fire, slower increase of calculated temperatures compared to the measured values was observed. However the peak temperatures were reached about 25 min by both, calculated and measured values. Regarding maximum temperatures which were closed to 1000°C, tolerable agreement was obtained. In decay phase differences between measured and calculated results were observed. As the increase of calculated gas temperature was slower

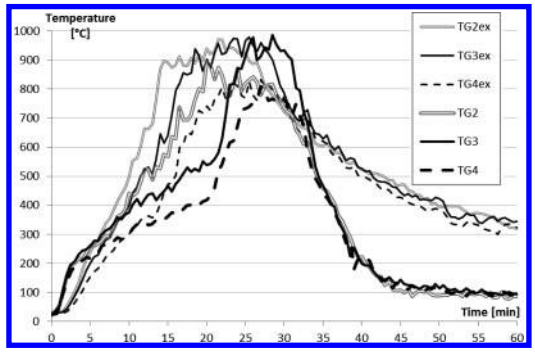


Figure 3. Comparison of measured (index *ex*) and calculated values of gas temperature in three locations in direction of the fire spread.

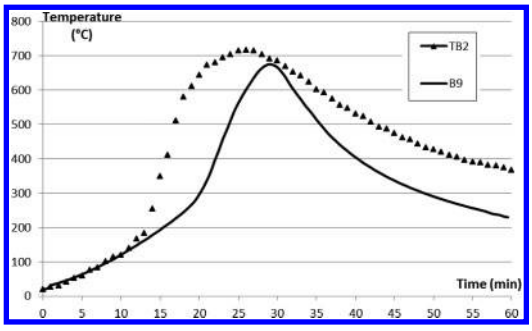


Figure 4. Comparison of measured (TB2) and calculated (B9) beam temperature development.

compared to measured gas temperature, the calculated beam temperature reached its peak temperature in 30 min, 5 min later compared to the measured beam temperature, see Figure 4. The calculated peak beam temperature was 40°C lower compared to the measured values.

However, calculated values of gas and beam temperature were slightly delayed in comparison with the measured values, the numerical model represented the tendency of the measured temperatures mainly in the heating phase, where the highest temperature differences appeared. Numerical calculation confirmed spreading fire phenomena. In order to investigate temperature heterogeneity and its impact on structural behaviour, numerical simulation was applicable.

4 STRUCTURAL RESPONSE TO NON-UNIFORM TEMPERATURES

4.1 *Steel beam temperature during travelling fire*

As the fire spread in the compartment gas temperature under the ceiling fluctuated significantly. In relation to gas temperature variation, structural members were affected. By numerical calculation non-uniform temperature of steel beam was confirmed. Eight sensors were located along the length of the beam 2 with spacing of 1 m from the south side of the enclosure, where the fire started to burn. Beam temperature sensors were placed in the middle of the web (cross-section IPE 270). Length of the beam was 9 m. For positions of sensors B1–B8 see Figure 2. As it is shown in Figure 5 the temperature distribution along the beam length was not uniform. It was highly affected by phenomena of the travelling fire which caused developing of fields with higher and lower temperature of gas. Although heat conductivity of steel was very high, the variance of gas temperature together with direct temperature of flames created temperature fields increasing in accordance to fire spread. In Figure 5, temperature difference between the first (B1) and the last sensor (B8) which reached 250°C is highlighted by lines connecting maximum and minimum values.

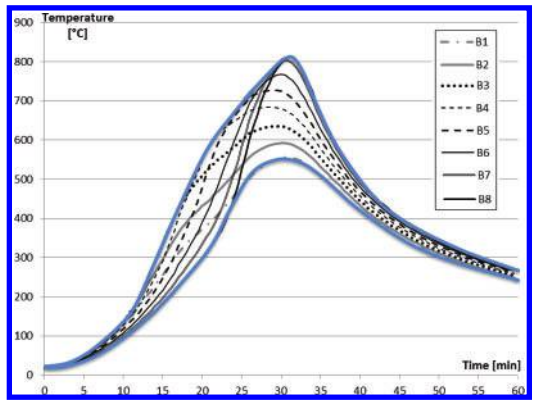


Figure 5. Numerical results of beam temperatures in eight locations with spacing of 1 m.

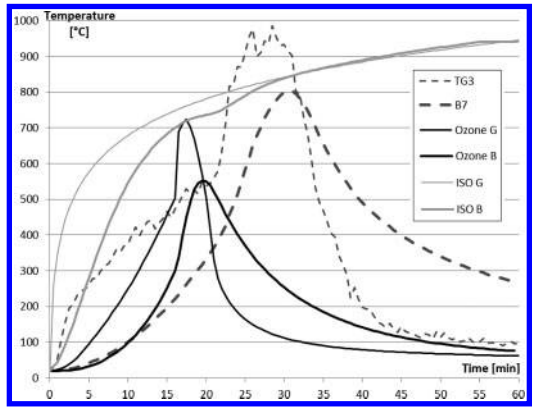


Figure 6. Comparison of gas and beam temperature calculated in FDS (marked TG3 and B7), Ozone (Ozone G and Ozone B) and standard temperature-time curve (ISO G and ISO B).

4.2 *Comparison to traditional design fire models*

In order to compare an impact of the travelling fire on structural behaviour with impact of uniform temperature distribution in the entire compartment, a calculation of the same case was completed in Ozone V2.2 (Cadorin & Franssen 2004). The standard temperature-time curve (EN 1991-1-2, 2002) and curve of uniform temperature distribution in the steel beam 2 calculated by the aid of step-by-step method (EN 1993-1-2, 2005) was introduced as a conservative comparison. The only difference between both assumptions – travelling fire and traditional design fire method was fire outbreak. By both, Ozone and ISO curve which are based on the assumption of uniform temperature across the floor area, it was assumed all wooden piles started to burn in one moment. However, a situation when a fire grew uniformly over an entire floor area could hardly occur. In Figure 6 gas and beam temperatures calculated by both methods were compared. The gas temperature at position TG3 coming from FDS calculation (assumption of travelling fire) induced higher beam

temperature (B7) compared to Ozone gas (Ozone G) and beam (Ozone B) temperature (uniform temperature assumption). The uniformly burning fire within the entire compartment (Ozone) generated high temperature in short time. However, the travelling fire created regions with high temperatures and areas with elevated temperatures with longer duration. In given case the duration of travelling fire was almost double. The travelling fire can therefore cause worse-case fire scenario and more onerous structural conditions. In this figure it can be observed that the highest beam temperature (ISO B) was induced by the standard temperature-time curve (ISO G).

5 CONCLUSIONS

Observations of the fire experiment executed in 2011 in Czech Republic confirmed that the homogeneous temperature assumption did not hold well in compartment fires. Since the scale of experimental enclosure was not large as the scale in real buildings, high degree of temperature non-uniformity appeared.

Numerical simulation of the travelling fire scenario validated by measurement carried out during the fire test verified temperature differences of the upper smoke layer of 400°C. In relation to gas temperature variation, the temperature distribution along the beam length was not uniform. Differences in steel beam temperature varied in 250°C, whereas the length of the beam was 9 m.

However, numerical simulations of large enclosures can have high demands on number of computational operations as well as on time. A compromise between the physical requirements and available potentialities of computer technology can be always found. Accurate prediction of fire growth and spread on the bases of the physical properties of the fire room and the combustibles is a promising approach how to stress the safety and design fire models economy. The method only needs more validation.

The comparison of the numerical simulation of the travelling fire and calculation of compartment fire with uniform temperature conditions finalized in Ozone highlighted different assumptions of temperature by each design fire method. Travelling fire scenario created regions with high temperatures and areas with elevated temperatures with longer duration. However the uniformly burning fire within the entire compartment (Ozone) generated high temperature in short time. In terms of structural temperature the travelling fire caused more onerous temperature conditions. It is therefore important to consider travelling fire scenario into traditional design methods to ensure that the worst-case scenario is considered.

ACKNOWLEDGMENT

Work on the research presented in this paper is supported by project grant LD11039 and SGS12/122/OHK1/2T/11.

REFERENCES

Cadorin, J.F. & Franssen, J.M. 2004. Ozone V2.2.5. University of Liege.

EN 1991-1-2 2002. Action on structures, Action on structures exposed to fire. Brussels: CEN.

EN 1993-1-2 2005. Design of steel structures, Part 1.2: General rules. Structural fire design. Brussels: CEN.

Horová, K. et al. 2012. Modelování požáru ve Veselí nad Lužnicí. *Konstrukce* 2012(1).

McGrattan, K. et al. 2010. Fire Dynamics Simulator (Version 5) User Guide. *NIST Special Publication 1019-5*. Baltimore.

Stern-Gottfried, J. 2011. Travelling Fires for Structural Design. *PhD thesis*. Edinburgh.

Wald, F. et al. 2011. Design of joints to composite columns for improved fire robustness to demonstration fire tests. CTU Publishing House. Prague.

Research and Applications in Structural Engineering, Mechanics and Computation – Zingoni (Ed.)
© 2013 Taylor & Francis Group, London, ISBN 978-1-138-00061-2

Numerical and experimental investigation of the toxicity and light extinction of fire smoke using experimental data from fire tests of polymers

A. Löhnert, N. Monreal & C. Knaust
BAM Federal Institute for Materials Research and Testing, Berlin, Germany

U. Krause
Otto-von-Guericke-University Magdeburg, Magdeburg, Germany

ABSTRACT: The Fractional Effective Dose model was used to predict the fire smoke toxicity numerically. In this context fire tests were carried out for three different building materials: polyurethane, flame retardant polyurethane and polyvinyl chloride. The fire tests were performed for flaming and smoldering combustion. The aim of the fire tests was to determine the light extinction, the smoke density and the combustion products at varying oxygen concentrations, different temperatures and different irradiance levels. The fire tests were performed in the German DIN-tube and also in the Cone Calorimeter. Stoichiometric coefficients at varying oxygen concentrations and temperatures were determined from measurements. With these stoichiometric coefficients reaction equations were defined and implemented in the Computational Fluid Dynamics (CFD) program, ANSYS CFX. The implemented reaction equations were used to account for different ventilation and temperature conditions in the simulation. The fire and smoke propagation was calculated numerically with CFD in the room corner test geometry. Equations to account for toxicity and light extinction were also implemented and were used to analyse the toxicity and the optical properties of fire smoke with CFD.

1 INTRODUCTION

Fire smoke contains a variety of highly toxic substances and can lead to unconsciousness within a few minutes and to death for critical concentrations. Currently the engineer's methods of fire safety include various procedures to calculate the fire propagation and smoke spread in buildings. However, up to now the evaluation and calculation of smoke concerning its optical properties and toxic potential on the basis of a detailed combustion is still a field of research. Since smoke composition is highly variable and not fully characterised it has to be examined whether and how the chemical composition and the optical properties of smoke are correlating.

A method has been developed that establishes the relation between the smoke components and smoke toxicity.

Increasingly, numerical methods like Computational Fluid Dynamics (CFD) are used to predict fire and smoke spread and for designing fire protection systems. For a given fire scenario (e.g. fire load, smoke exhaust systems, ventilation condition) not only safety parameters such as smoke layer height and visibility but also the influence of heat storage in the component layers of the structure can be predicted taking into account the temperature dependent material properties in the course of time by means of CFD. Several CFD codes with different radiation models, turbulence models and combustion models are available for the user. The temporal and local distributions of chemical components of smoke like CO, CO_2, HCN, HCl and soot can be calculated solving the corresponding balance equations numerically. Experimental and numerical investigations are the major prerequisites of this work.

However, smoke density and toxicity are not scalar quantities and hence a gap exists between the output of the models underlying the CFD simulations and the information needed for fire risk assessment. With respect to this, the development of a method for characterising smoke numerically is a part of a German research project. A smoke model can deliver information about the tenable risk and the rescue situation for people in fire scenarios. It also delivers information about the conditions for fire fighting or how to design smoke extraction systems to prevent fire scenarios. This paper is focused on the analysis of smoke toxicity and the determination of the optical properties of fire smoke from experimental investigations and their numerical calculation with the CFD code ANSYS CFX.

2 FIRE SMOKE, SMOKE TOXICITY AND LIGHT EXTINCTION

There are different ways to characterise fire smoke. Smoke can be divided into two parts. The first part is fire gases and the second part is aerosol properties.

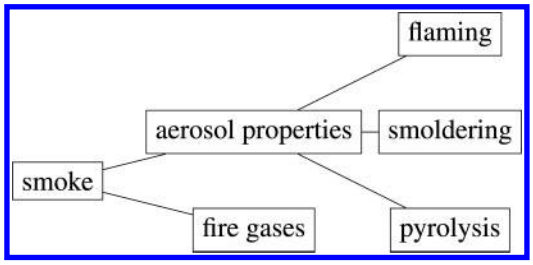


Figure 1. Definition of fire smoke.

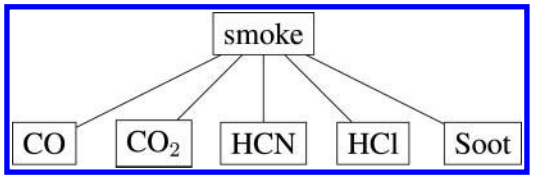


Figure 2. Harmful combustion products of fire smoke.

This is shown in figure 1. Fire gases can be further divided according to the combustion conditions under which smoke is produced (Mulholland 1995).

However, it makes sense to define fire smoke toxicity with those chemical components which affect the toxicity qualitatively and quantitatively. As a consequence a smoke definition was established which includes the relevant harmful products. The composition of the fire gases depends on the available oxygen concentration and temperature in the room and also on the material which is burned. The main harmful combustion products were considered in this investigation and are shown in figure 2.

The fire behaviour of building materials in the combustion process and the combustion products depend on the oxygen concentration and the temperature in the room (e.g. smoldering fire or well-ventilated fire). Therefore two different polyurethanes and a polyvinyl chloride were tested under various oxygen concentrations and temperatures to derive reaction equations for ranges of oxygen concentrations and temperatures.

The assessment of a dose is the first step of calculating fire smoke toxicity. The most important parameters for assessing a dose are the concentration of a toxic substance and the exposure time. The law of the chemist Fritz Haber (Haber's rule) describes the relationship between the concentration of a toxic gas and the duration of exposure until any toxic effect, e.g. incapacitation or death, occurs. The following equation describes the dose by the product of concentration and time, which causes any effect:

$$W = C * t, \tag{1}$$

where W-dose [g*s/l]; C-concentration [g/l]; t-time [s].

2.1 *The fractional effective dose model*

To predict the toxic hazards of fire smoke the concept of the Fractional Effective Dose (FED) is used (ISO13571 2012, ISO13344 2004). The general equation for FED describes a specific dose received at time to that dose, which causes incapacitation or death (Hartzell & Emmons 1988, Purser 1992). The general equation is given below:

$$FED = \frac{\text{dose received at time (Ct)}}{\text{effective Ct dose to cause death}}, \tag{2}$$

where C-concentration [g/l]; t-time [s].

The Fractional Effective Doses of the main components from the fire smoke (CO, CO_2, HCN etc.) are formed for every minute of the exposure interval and then summed up. If the sum of all doses over the exposure time reaches the value 1, incapacitation or death occurs ISO13571 2012.

For the interaction between the main toxic products in fire smoke a fraction of an incapacitating dose for all these narcotic gases is given in equation 3 (Purser 1995):

$$FED_{IN} = [(F_{CO} + F_{HCN}) * V_{CO_2} + F_{O_2}, F_{CO_2}] \tag{3}$$

where FED_{IN} – fraction of an incapacitating dose of all narcotic gases [1]; F_{CO} – fraction of an incapacitating dose of CO [1]; F_{HCN} – fraction of an incapacitating dose of HCN [1] ; V_{CO_2}-multiplication factor for CO_2-induced hyperventilation [1]; F_{O_2}-fraction of an incapacitating dose of low-oxygen hypoxia [1]; F_{CO_2}-fraction of an incapacitating dose of CO_2 [1].

The individual quotients are explained in more detail below.

Carbon monoxide is the result of an incomplete combustion and it is an odourless, colourless, flammable and toxic gas. Already a concentration of 0.15 vol % is critical and 1 vol % leads to death immediately. The fraction of an incapacitating dose for carbon monoxide is given in equation 4 (Purser 1995):

$$F_{CO} = \frac{8.2925 * 10^{-4} * c_{CO}^{1.036}}{30}, \tag{4}$$

where F_{CO}-fraction of an incapacitating dose of CO [1]; c_{CO}-concentration of CO [ppm].

The next toxic component, which has major influence on the smoke toxicity, is hydrogen cyanide (HCN). It is a colourless and a fast acting poison, which diffuses easily through cell membranes. If HCN is absorbed through the lungs oxygen cannot be activated. The lethal dose of HCN is about 0.027 vol %. The fraction of an incapacitating dose of HCN is given in 5 (Purser 1995):

$$F_{HCN} = \frac{1}{exp\,(5.396 - 0.023 * c_{HCN})}, \tag{5}$$

where F_{HCN}-fraction of an incapacitating dose of HCN [1]; c_{HCN}-concentration of HCN [ppm].

Carbon dioxide is a colourless, odourless gas with sour tasting. CO_2 is heavier than air. By no means is it allowed to classify CO_2 as a non-hazardous component

of fire smoke, because a concentration of 3 vol % to 5 vol % causes a low pH-value in the blood. About 12 vol % of CO_2 lead to death. The equation for an incapacitating dose of CO_2 and an equation for a CO_2-induced hyperventilation are given in equation 6 and equation 7 (Purser 1995):

$$F_{CO_2} = \frac{1}{exp\,(6.1623 - 0.5189 * c_{CO_2})}, \tag{6}$$

where F_{CO_2}-fraction of an incapacitating dose of CO_2 [1]; c_{CO_2}-concentration of HCN [ppm].

and

$$V_{CO_2} = \frac{exp\,(0.1903 * c_{CO_2} + 2.0004)}{7.1}, \tag{7}$$

where V_{CO_2}-multiplication factor for CO_2-induced hyperventilation.

Also hypoxia, caused by low oxygen, is integrated in the calculation of all narcotic gases. Hypoxia affects an under supply of adequate oxygen in the body. Dizziness, incapacitation and later death occur if the O_2-concentration decreases under 7 Vol%. The equation 8 is given here (Purser 1995):

$$F_O = \frac{1}{exp\,(8.13 - 0.54 * (20.9 - c_{O_2}))}, \tag{8}$$

where F_O- fraction of an incapacitating dose of low-oxygen hypoxia [1]; c_{O_2}-concentration of O_2 [$vol\%$].

If only the incapacitating dose of CO_2 should be considered then the equation 6 must be applied in equation 3 instead of equation 8.

In addition to the toxicity the light extinction of fire smoke was analysed. The light extinction through fire smoke is responsible for loss of visibility. Furthermore the light extinction is depending on the characteristics of fire smoke. The characteristic of fire smoke is influenced from the chemical components, the size of the particles, the burning behaviour of the material, the combustion conditions, the flow and the temperature field. For the description of the light extinction the transmittance T is used. The transmittance is described with the Beer-Lambert law shown in eq. 9:

$$T = \frac{I}{I_0} = e^{-\kappa * d}, \tag{9}$$

where T-transmittance [1]; I-intensity of the radiation coming out of the media [W/m^2]; I_0-intensity of the incident radiation [W/m^2]; d-path length [m]; κ-absorption coefficient [m^{-1}].

In the numerical simulation the absorption coefficients for the smoke components were specified from literature (Tien et al. 1995).

Both concepts FED_{IN} and the Beer-Lambert law were implemented in ANSYS CFX to predict the smoke toxicity and the light extinction of fire smoke numerically.

3 EXPERIMENTAL INVESTIGATIONS

The smoke production of materials were measured in the German DIN-tube, originally developed to assess smoke production of construction materials. The fire tests in the DIN-tube have been done for the polyurethanes and polyvinyl chloride under different smoldering conditions. Experiments were carried out with oxygen concentrations of 15 vol %, 18 vol % and 21 vol % and temperatures of 473 K, 673 K and 973 K (Loehnert et al. 2012). During the fire test a FT-IR spectrometer was analysing the fire gases. In addition to the FT-IR analysis, the temperature, the oxygen concentration, the flow and the smoke density were recorded during the test. The sample size for the DIN-tube measurements for polyurethane was $10 \times 10 \times 270\,mm^3$. The sample size of polyvinyl chloride is smaller $0.5 \times 0.5 \times 270\,mm^3$ than the sample size of polyurethane, while the masses of the polyurethane and of the polyvinyl chloride samples should be equal. To ensure the reproducibility of the measured values, all measurements were performed at least three times for each test configuration.

In addition to the DIN-tube fire tests further experimental studies were performed with the Cone Calorimeter. This test method is based on the principle of oxygen consumption. The net heat of the combustion is proportional to the amount of oxygen consumed in the combustion process. Approximately 13.1×10^3 kJ of heat is released per kilogram oxygen consumed (Babrauskas 1995). The polyurethanes and the polyvinyl chloride were tested under ambient conditions and with two levels of irradiance (35 kW/m^2 and 50 kW/m^2) (Loehnert et al. 2012).

The sample sizes of the three materials were $100 \times 100\,mm^2$. The thickness of both polyurethane samples was 30 mm and the sample thickness of polyvinyl chloride was 0.5 mm. A more detailed overview of the experiments, which were performed, and a description of the test facilities is available at (Loehnert et al. 2012).

The analysis of the evaluated data and the stoichiometric coefficients e.g. for polyurethane for the different test configurations in the DIN-tube and Cone Calorimeter is shown in figure 3. The x-axis shows the experimental set-up, temperature and oxygen concentration for the DIN-tube and irradiance and oxygen for the Cone Calorimeter. The vertical axis shows the value of the stoichiometric coefficients for every smoke product. Reaction equations for every studied material and test configuration were formed with the generated stoichiometric coefficients. It is assumed that 10% of the mass loss of the specimen goes into soot.

In figure 3 it is shown that the stoichiometric coefficients of CO from the DIN-tube measurements are much higher than from the Cone Calorimeter measurements. Within the DIN-tube measurements the CO-coefficient increases with temperature. It can also be seen that the CO_2-coefficients are much higher in the Cone Calorimeter than in the DIN-tube measurements.

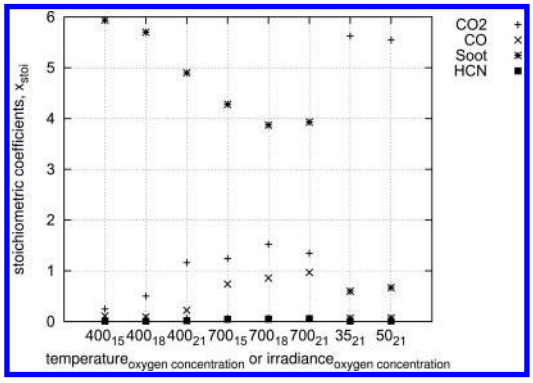


Figure 3. Stoichiometric coefficients x_{stoi} for the smoldering and flaming combustion of polyurethane from the DIN-tube measurements 400_{15}–700_{21} [°C$_{vol\%}$] and the Cone Calorimeter measurements 35_{21}–50_{21} [$\frac{kW}{m^2}{}_{vol\%}$].

By means of the experimental data from the measured concentrations, reaction equations were developed for every range of oxygen concentration, temperatures and irradiance levels. The reaction equations for polyurethane (equation 10) and polyvinyl chloride (equation 11) were formed with the general reaction equations below. The molecular formula for polyurethane is based on literature (Goottuk & Lattimer 2002) and for polyvinyl chloride on (Janssens 2002). Six reaction equations for polyurethane from the DIN-tube and two reaction equations from the Cone Calorimeter measurements can be formed with the values from figure 3:

$$C_{6,3}H_{7,1}NO2 + x_{stoi}O_2 \rightarrow \\ x_{stoi}CO_2 + x_{stoi}CO + x_{stoi}soot + x_{stoi}HCN, \quad (10)$$

where $C_{6,3}H_{7,1}NO_2$-molecular formula for polyurethane; x_{stoi}-stoichiometric coefficient for every smoke product.

In (Loehnert et al. 2012) the same was done for polyvinyl chloride:

$$C_2H_3Cl + x_{stoi}O_2 \rightarrow \\ x_{stoi}CO_2 + x_{stoi}CO + x_{stoi}soot + x_{stoi}HCl, \quad (11)$$

where C_2H_3Cl-molecular formula for polyvinyl chloride; x_{stoi}-stoichiometric coefficient for every smoke product.

4 NUMERICAL INVESTIGATIONS

4.1 *Fundamentals*

The numerical simulation of turbulent fluid flows as well as the heat and mass transfer and chemical reactions are based on physical models of fluid mechanics. The fundamental equations of numerical fluid computation are the continuity equation (conservation of mass), the Navier-Stokes equations (conservation of momentum), the energy equation (conservation of energy) and the turbulence equations. In the present study Reynolds averaging was used and the turbulence model selected was the shear stress turbulence model (SST). All conservation equations mentioned above can be written in a generalized form as transport equation for each mass related and transported quantity (e.g. velocity v, turbulent kinetic energy k), where describes the molecular diffusivity (Yeoh & Yuen 2009, Ferziger & Perié 2002). The generalized form is given in equation 12:

$$\underbrace{\frac{\partial}{\partial t}(\rho\phi)}_{\text{time alteration rate}} + \underbrace{V_j \frac{\partial}{\partial x_j}(\rho\phi)}_{\text{convective transport}} = \underbrace{\Gamma_\phi \frac{\partial^2 \phi}{\partial x^2{}_j}}_{\text{diffusive transport}} + \underbrace{S_\phi}_{\text{production}}, \quad (12)$$

where ρ-density $[kg/m^3]$; ϕ-general scalar quantity (variable); Γ_ϕ to ϕ belonging transport coefficient; S_ϕ-source term of the scalar quantity ϕ.

Radiation is considered by the discrete ordinates approximation model and the calculation of the turbulent flow with the SST turbulence model. The SST model is an eddy-viscosity model, which combines the $k-\omega$ (near-wall region) and the $k-\epsilon$ (in the outer part of the flow) models (ANSYS 2012). The combustion is modeled using the Eddy Dissipation model. The Eddy Dissipation model is an approach to consider the influence of the turbulence using detailed reaction kinetics. When reactants mix at the molecular level, they instantaneously form products (ANSYS 2012).

For the simulation the eddy dissipation combustion model was used. With the use of the eddy dissipation coefficient A it was possible to control the calculation of the different reaction equations. The stoichiometric model used for the combustion of polyurethane is given in equation 10 and the one used for polyvinyl chloride is given in equation 11.

4.2 *Model*

The combustion of polyurethane will be calculated numerically using the commercial CFD solver ANSYS CFX in room corner test geometry (ISO9705 1996) shown in figure 4. The room corner test geometry has the dimension $3.6 \times 2.4 \times 2.4\,\text{m}^3$ shown in figure 5. There is an inlet in the edge at the bottom and a door, defined as an opening. All the other parts are defined as a wall.

A structured mesh with 165.888 elements was generated. The simulation time was $300\,s$ and a time step of $0.01\,s$ was applied for the transient calculation. The convergence criteria were maximum residuals of $1.0 * e^{-3}$ and the conservation target was 1%. The pyrolysis flow rate of polyurethane was 0.015 kg/s for the inlet.

4.3 *Results*

For the numerical calculation of smoke migration and toxicity figure 5 shows the isovolume of a mass

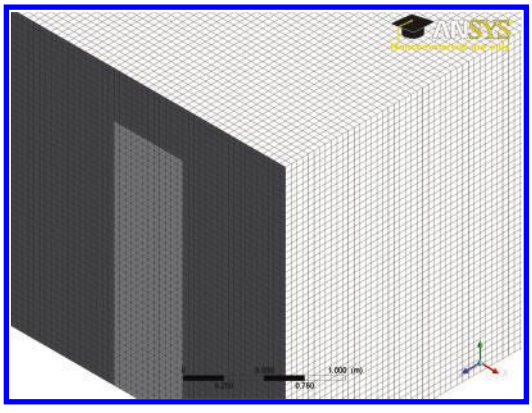


Figure 4. Model of the room corner test with a structured mesh.

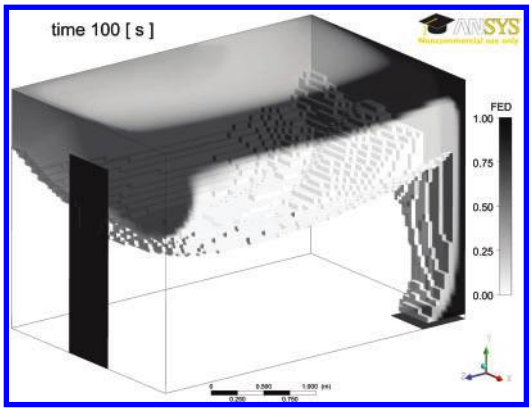


Figure 5. Result of the transient simulation of the FED_{IN} [1] at 100 s for the combustion of polyurethane in the room corner test.

weighted fraction of all fire gases higher than 1% for the combustion of polyurethane at a time step of 100 *s*. The Fractional Effective Dose FED_{IN} is indicated by the greyscale contour within the range of 0 and 1.0. The inhalation of the smoke gases leads to incapacitation or death that is what the FED_{IN} value of 1.0 (dark grey region) means. After 100 *s* the FED_{IN} reaches values from 0.25 to 1.0 for the upper layer in the room. In this case effects like incapacitation have to be expected. If FED_{IN} reaches values equal to 1.0 for nearly every section of the room occurrence of death is very likely. However FED_{IN} values of 0.3 (ISO13571 2012) can already be critical for certain groups of people (e.g. children, old people). Numerical studies of the same scenario without considering HCN lead to lower values for FED_{IN} at the same time. Therefore it is necessary to consider HCN in toxicity assessment for a polyurethane combustion process.

Figure 6 shows the isovolume of a mass weighted fraction of all fire gases higher than 1% for the combustion of polyurethane at a time step of 100 *s*. The isovolume shows the transmittance in greyscale colours.

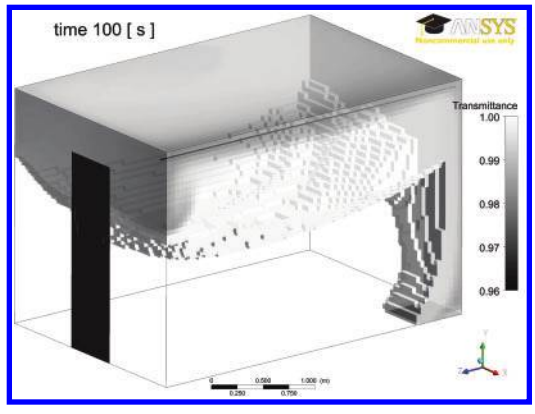


Figure 6. Result of the transient simulation of the value of the transmittance [1] in every cell at 100 s for the combustion of polyurethane in the room corner test.

The transmittance according to equation 9 was calculated for each cell numerically. The calculation of light extinction a long a path and the visibility will be part of the future work and will be shown in the next publication.

5 CONCLUSIONS

The aim to calculate fire smoke toxicity and light extinction with CFD was carried out successfully. The evaluated data from the fire tests in the DIN-tube and in the Cone Calorimeter were the basis to form reaction equations for every studied range of oxygen concentration and temperature/irradiance. At least six reaction equations for the DIN-tube measurements and two for the Cone Calorimeter measurements could be determined for every material. The numerical prediction of fire smoke toxicity and light extinction were realized by implementing the reaction equations from fire tests, the Fractional Effective Dose concept and the equations for calculating light extinction in the commercial CFD code ANSYS CFX. The numerical simulation of fire smoke toxicity respectively the FED value of the fire gases of the combustion of polyurethane could be demonstrated in the room corner test geometry in this paper. With the formed reaction equations from the fire tests and the switching between the reaction equations, it was possible to consider well-ventilated and under-ventilated conditions at the same time. From this follows that different concentrations of the smoldering and flaming combustion products could be consider for calculating the FED and the visibility numerically. The experimental data and the numerical model to calculate smoke toxicity and the optical properties of fire smoke were implemented. From the practical point of view this developed method to predict fire smoke toxicity and visibility could help to guarantee calculated results for fire risk assessment. Also safety parameters such smoke layer height,

temperature and influences of heat storage in a component of a structure can be holistically analysed with the presented method. The next step will be the validation of the model. This is part of recent and future studies. The results will be shown in a next publication.

REFERENCES

ANSYS (2012). *ANSYS 14.0 Theory Guide, 2.2.6 The Shear stress Transport and 9.3.1.5. Eddy Dissipation Model Coefficient A/B* (14 ed.).

Babrauskas, V. (1995). The cone calorimeter. In *SFPE Handbook of Fire Protection Engineering* (2 ed.), pp. 3–38. NFPA.

Ferziger, J. & M. Perié (2002). *Computational Methods for Fluid Dynamics*. Springer Verlag.

Goottuk, D. & B. Lattimer (2002). Effect of combustion products on species production. In *SFPE Handbook of Fire Protection Engineering* (3 ed.). NFPA.

Hartzell, G. & H. W. Emmons (1988). The fractional effective dose model for assessment of hazards due to smoke from materials. *J. Fire Sciences 6*, 356–362.

ISO13344 (2004). *Estimation of the lethal toxic potency of fire effluents*.

ISO13571 (2012). *Life–threatening components of fire Guidlines for the estimation of time to compromised tenabilty in fires*.

ISO9705 (1996). *Fire tests-Full scale room test for surface products*.

Janssens, M. (2002). Calorimetry. In *SFPE Handbook of Fire Protection Engineering* (3 ed.), Chapter 3, pp. 48. NFPA.

Loehnert, A., F. Rabe, C. Knaust, & U. Krause (2012). Numerical and experimental investigation of fire smoke toxicity. In *Fire Computer Modeling*.

Mulholland, G. (1995). Smoke production and properties. In *SFPE Handbook of Fire Protection Engineering* (2 ed.), pp. 2–217. NFPA.

Purser, D. (1992). The evolution of toxic effluents in fires and the assessment of toxic hazard. *Toxicology Letters*.

Purser, D. (1995). Toxicity assessment of combustion products. *SFPE Handbook of Fire Protection Engineering*, 2–85–146.

Tien, C., K. Lee, & A. Stretton (1995). Radiation heat transfer. In *SFPE Handbook of Fire Protection Engineering* (2 ed.), Chapter 4. NFPA.

Yeoh, G. & K. Yuen (2009). *Computational Fluid Dynamics in Fire Engineering*. Elsevier.

Research and Applications in Structural Engineering, Mechanics and Computation – Zingoni (Ed.)
© 2013 Taylor & Francis Group, London, ISBN 978-1-138-00061-2

Development of a simplified design method to predict the fire rating of LSF walls

S. Gunalan & M. Mahendran
Queensland University of Technology, Brisbane, Queensland, Australia

ABSTRACT: Recent fire research into the behaviour of light gauge steel frame (LSF) wall systems has developed fire design rules based on Australian and European cold-formed steel design standards, AS/NZS 4600 and Eurocode 3 Part 1.3. However, these design rules are complex since the LSF wall studs are subjected to non-uniform elevated temperature distributions when the walls are exposed to fire from one side. Therefore this paper proposes an alternative design method for routine predictions of fire resistance rating of LSF walls. In this method, suitable equations are recommended first to predict the idealised stud time-temperature profiles of eight different LSF wall configurations subject to standard fire conditions based on full scale fire test results. A new set of equations was then proposed to find the critical hot flange (failure) temperature for a given load ratio for the same LSF wall configurations with varying steel grades and thickness. These equations were developed based on detailed finite element analyses that predicted the axial compression capacities and failure times of LSF wall studs subject to non-uniform temperature distributions with varying steel grades and thicknesses. This paper proposes a simple design method in which the two sets of equations developed for time-temperature profiles and critical hot flange temperatures are used to find the failure times of LSF walls. The proposed method was verified by comparing its predictions with the results from full scale fire tests and finite element analyses. This paper presents the details of this study including the finite element models of LSF wall studs, the results from relevant fire tests and finite element analyses, and the proposed equations.

1 INTRODUCTION

Cold-formed steel sections are commonly used in various configurations to provide load-bearing Light gauge Steel Framed (LSF) wall systems in buildings. Under fire conditions, cold-formed steel stud sections heat up quickly as they are thin-walled, resulting in fast reduction to their strength and stiffness. Therefore these stud sections are commonly used in planar structural wall systems with plasterboard on both sides as fire protection. Plasterboards protect the steel studs by delaying the temperature rise in the studs during building fires. Since the LSF walls are often subjected to fire on one side, non-uniform temperature distributions will develop across the depth of LSF wall studs. This will induce additional bending moments on the studs due to thermal bowing, neutral axis shift and magnification effects. Hence the thin-walled steel studs will be subjected to combined actions of axial compression and bending moment during a fire event. This fire behaviour of LSF wall panels has been investigated by many researchers in the past and several fire design rules have been proposed. Klippstein (1980) and Gerlich et al. (1996) developed their fire design rules based on AISI design provisions (2007) while Alfawakhiri's (2001) study was based on Canadian cold-formed steel design rules. Ranby (1999), Kaitila (2002), Feng & Wang (2005) and Zhao et al. (2005) developed their fire design rules based on Eurocode 3 Part 1.3 (2006). These design rules are complex and time consuming and hence do not suit routine design purposes.

In order to overcome this problem related to the need for simplified design rules and to address the lack of research data on Australian LSF wall systems, a detailed investigation based on full scale fire tests and finite element analyses was conducted on both conventional Australian LSF walls with and without the use of cavity insulation and the new composite panel system developed recently at the Queensland University of Technology. Details of 10 full scale fire tests and their results including the temperature and deflection profiles measured during the tests are presented in Gunalan et al. (2013) along with the failure times and modes. A suitable finite element model of LSF wall studs subject to fire conditions was then developed using ABAQUS, and validated using the results of fire tests (Gunalan and Mahendran, 2013).

In this paper idealised time-temperature profiles were first proposed for LSF wall studs based on the results from the full scale fire tests. These idealised time-temperature profiles were then used with the validated finite element models to investigate the behaviour of LSF walls. A simple design method was then proposed based on the parametric study results to predict the fire resistance rating of LSF wall panels with varying wall configurations (single and double layers of plasterboards, cavity and externally

Table 1. LSF wall systems considered in fire tests.

Test	Configuration	Insulation type	Insulation location	Load ratio	Failure time (min.)
1		Glass Fibre	External	0.2	118
2		Glass Fibre	External	0.4	108
3		Rockwool	External	0.4	134
1*		None	–	0.2	111
2*		None	–	0.2	101
3*		Glass Fibre	Cavity	0.2	107
4*#		Rockwool	Cavity	0.2	136
5*		Cellulose Fibre	Cavity	0.2	111
6*		Rockwool	External	0.2	101
7*		Cellulose Fibre	External	0.2	107

(1–3) – Tests conducted by Gunalan (2011); (1*–7*) – Tests conducted by Kolarkar (2010); (#) – Earlier failure time due to lack of space for thermal expansion.

insulated) and structural parameters (steel grade and thickness) under varying load ratios.

2 EXPERIMENTAL STUDY

This section provides brief details of the series of full scale fire tests of LSF walls conducted first to evaluate the fire resistance rating (FRR) of load bearing LSF wall assemblies. One wall specimen was tested to failure under an axial compression load at room temperature while ten wall specimens subjected to a constant axial compression load were exposed to standard fire conditions on one side to evaluate their fire performance (Table 1). Conventional Australian LSF wall panels lined with single or double layers of plasterboard with or without cavity insulation were considered. A new LSF wall system based on a composite panel was also included in which external insulation was sandwiched between the two plasterboards (Gunalan et al., 2013).

All the steel frames used in the load bearing LSF wall panels were built to a height of 2400 mm and a width of 2400 mm. The studs and tracks used in the test frames were fabricated from G500 galvanized steel sheets with a nominal base metal thickness of 1.15 mm, a yield strength of 569 MPa and an elastic modulus of 213,520 MPa at ambient temperature. Test frames were lined on both sides by single or double layers of 16 mm gypsum plasterboards manufactured by Boral Plasterboard. Table 1 shows the details of the 10 LSF wall specimens used in this study with two load ratios.

The furnace was designed to deliver heat based on the standard fire curve given in AS 1530.4 (2005). The loading frame was designed (Fig. 1) to load the individual studs of LSF wall specimens in compression from the bottom side using hydraulic jacks.



Figure 1. Experimental Study.

The axial shortenings of the studs and the out-of-plane movements of the wall specimen were measured using linear variable displacement transducers. K type thermocouples were used to measure the temperature development across the wall specimens. The stud (hot flange, web and cold flange) temperatures were measured at three levels for interior studs, namely, at 0.25 H, 0.50 H and 0.75 H, and at mid-height for exterior studs.

In each fire test an axial compression load of 15 kN (for a load ratio of about 0.2) or 30 kN (for a load ratio of about 0.4) was applied to each stud (i.e. 0.2 or 0.4 times the ultimate capacity of each stud at room temperature as obtained by Kolarkar (2010)). The load was held constant at room temperature before the furnace was started and then maintained throughout the fire test. During the fire test, the furnace temperature was regulated to follow the standard time-temperature curve. The test was stopped after one or more of the wall studs failed, and the time to failure was recorded. Table 1 shows the failure times obtained from the experimental study. Further details are given in Gunalan et al. (2013).

3 IDEALISED TIME-TEMPERATURE PROFILES

Table 1 shows the LSF wall test configurations and insulations used in the experimental study. The new externally insulated wall panels with glass fibre and rockwool were tested under two load ratios of 0.2 and 0.4. Hence these 10 full scale fire tests were essentially conducted using eight different wall configurations (Table 2). Therefore idealised time-temperature profiles were developed for these eight wall configurations using the measured hot and cold flange temperature distributions along the wall stud. In the development of idealised time-temperature profiles of studs with externally insulated glass fibre and

Table 2. Idealised Time-Temperature values up to 100°C.

Index	W/C	Insulation	Time (min.)	HFT (°C)	Time (min.)	CFT (°C)
1 × 1		None	2 6 14	20 100 100	2 11 21	20 100 100
2 × 2		None	2 25 41	20 100 100	2 35 54	20 100 100
CI-GF		Glass fibre	6 20 52	20 100 100	6 50 65	20 100 100
CI-RW		Rockwool	6 25 52	20 100 100	6 50 65	20 100 100
CI-CF		Cellulose fibre	6 25 52	20 100 100	6 50 65	20 100 100
CP-GF		Glass fibre	6 40 42	20 100 100	6 55 60	20 100 100
CP-RW		Rockwool	6 55 70	20 100 100	6 60 80	20 100 100
CP-CF		Cellulose fibre	6 45 70	20 100 100	6 60 80	20 100 100

W/C – Wall Configuration; HFT – Hot Flange Temperature; CFT – Cold Flange Temperature.

rockwool, the average temperature values of the two fire tests were used (load ratios of 0.2 and 0.4 – Tests 1 & 2; Tests 3 & 6*). The critical stud in a LSF wall panel was the stud with the vertical plasterboard joint against it. The temperature values of this stud were high compared to other studs due to the opening of this vertical joint at higher temperatures. Therefore the average temperatures along this stud were considered in the development of all the idealised time-temperature profiles for LSF wall studs under standard fire conditions.

When the LSF wall was subject to standard fire conditions, the hot and cold flange temperatures of the stud were 20°C for the initial few minutes. They then increased gradually (linearly) to reach 100°C and remained at the same temperatures during the plasterboard dehydration process. After this the steel temperatures increased rapidly with time. Table 2 shows the time-temperature values of hot and cold flanges up to 100°C. Beyond 100°C, Equations 1 to 8 represent the idealised time-temperature profiles for the LSF wall panels with eight configurations shown in Table 2, where T_{HF} and T_{CF} are the average hot and cold flange temperatures in °C and t is the time in minutes.

1) LSF wall lined on both sides by a single layer of plasterboard (Test 1*).

$$T_{HF} = -0.1066t^2 + 20.17t - 165 \quad (15 \le t) \quad (1a)$$
$$T_{CF} = 10.29t - 125 \quad (22 \le t \le 50) \quad (1b)$$
$$T_{CF} = 29.35t - 1090 \quad (50 < t \le 60) \quad (1c)$$
$$T_{CF} = T_{HF} \quad (60 < t) \quad (1d)$$

2) LSF wall lined on both sides by two layers of plasterboard (Test 2*).

$$T_{HF} = 6.35t - 160 \quad (42 \le t \le 110) \quad (2a)$$
$$T_{HF} = 12.11t - 790 \quad (110 < t) \quad (2b)$$
$$T_{CF} = 6.07t - 230 \quad (55 \le t) \quad (2c)$$

3) LSF wall lined on both sides by two layers of plasterboard with glass fibre used as cavity insulation (Test 3*).

$$T_{HF} = 11.17t - 490 \quad (53 \le t) \quad (3a)$$
$$T_{CF} = 4.92t - 225 \quad (66 \le t \le 96) \quad (3b)$$
$$T_{CF} = 12.04t - 915 \quad (96 < t) \quad (3c)$$

4) LSF wall lined on both sides by two layers of plasterboard with rockwool used as cavity insulation (Test 4*).

$$T_{HF} = 10.2t - 435 \quad (53 \le t) \quad (4a)$$
$$T_{CF} = 4.06t - 165 \quad (66 \le t) \quad (4b)$$

5) LSF wall lined on both sides by two layers of plasterboard with cellulose fibre used as cavity insulation (Test 5*).

$$T_{HF} = 8.94t - 360 \quad (53 \le t \le 106) \quad (5a)$$
$$T_{HF} = 19.83t - 1530 \quad (106 < t) \quad (5b)$$
$$T_{CF} = 3.83t - 150 \quad (66 \le t \le 106) \quad (5c)$$
$$T_{CF} = 17t - 1550 \quad (106 < t) \quad (5d)$$

6) LSF wall lined on both sides by two layers of plasterboard with glass fibre used as external insulation (Tests 1 & 2).

$$T_{HF} = 0.001007t^3 - 0.1605t^2 + 12.15t - 205 \quad (43 \le t) \quad (6a)$$
$$T_{CF} = 0.0904t^2 - 9.56t + 350 \quad (61 \le t) \quad (6b)$$

7) LSF wall lined on both sides by two layers of plasterboard with rockwool used as external insulation (Tests 3 & 6*).

$$T_{HF} = -0.000212t^3 + 0.0931t^2 - 5.47t + 100 \quad (71 \le t) \quad (7a)$$
$$T_{CF} = 0.0586t^2 - 6.69t + 260 \quad (81 \le t) \quad (7b)$$

8) LSF wall lined on both sides by two layers of plasterboard with cellulose fibre used as external insulation (Test 7*).

$$T_{HF} = -0.000286t^3 + 0.1024t^2 - 2.92t - 100 \quad (71 \le t) \quad (8a)$$
$$T_{CF} = 0.0846t^2 - 9.5t + 320 \quad (81 \le t) \quad (8b)$$

4 FINITE ELEMENT MODELS

A finite element model of LSF wall studs (Fig. 2) was developed with appropriate thermal and structural boundary conditions to simulate the behaviour of LSF wall studs under standard fire conditions and to determine the FRR. Finite element analyses were conducted under steady state conditions. Here, the

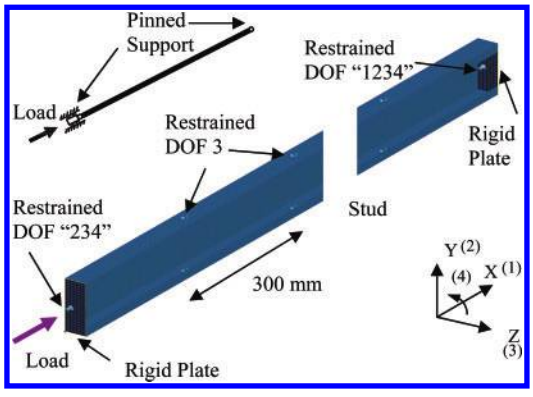


Figure 2. Loading and boundary conditions used in FEA.

non-uniform temperature distributions in the steel stud cross-section were raised to the target levels at any given time during the standard fire and then maintained. A load was then applied in increments until the failure of LSF wall stud.

Based on other numerical studies and the experimental behaviour of LSF wall studs, one of the two central studs that had the vertical plasterboard joint against it was considered in the analyses. Pinned support conditions were simulated for studs using rigid plates while an axial compressive load was applied at the section centroid at one end as shown in Figure 2. It was assumed that the plasterboards screw-fixed to both flanges provided sufficient lateral restraint until the failure of studs (Kaitila 2002, Feng et al. 2003 and Zhao et al. 2005).

S4R shell element type with a 4 mm × 4 mm mesh size was selected based on detailed convergence studies. Nominal mechanical properties and idealised time-temperature profiles using the predictive equations were used (Equations 1–8). The yield strength and elastic modulus reduction factors at elevated temperatures and the stress-strain curves were based on the predictive equations developed in Dolamune Kankanamge & Mahendran (2011). The strain hardening material model was used for steels with gradual yielding type stress-strain curve except for G250 steels at 20°C, 100°C and 200°C for which an elastic-perfect plastic material model was used (Dolamune Kankanamge & Mahendran 2011) as they had a well defined yield point. The coefficient of thermal expansion given in Eurocode 3 Part 1.2 (2005) was used.

The first eigen mode of the elastic buckling analyses was used to introduce the initial geometric imperfection with an amplitude of 0.006b. The residual stresses were not considered in the modelling of studs under fire conditions since they are insignificant at elevated temperatures.

Under fire conditions, many steady state analyses conducted in close time intervals led to a load ratio (ultimate load of stud in fire conditions / ambient temperature capacity) versus failure time (FRR) curve for the LSF wall systems. Figure 3 shows this curve for the

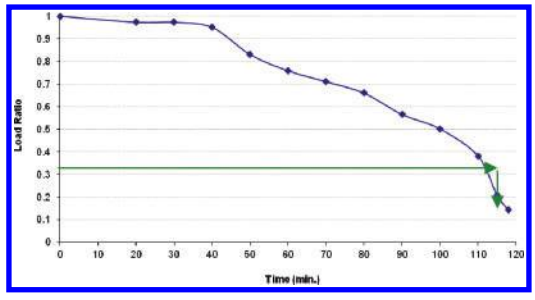


Figure 3. Variation of load ratio with time.

case of LSF wall with glass fibre external insulation. As shown in the figure, the failure time for Test 1 with a load ratio of 0.2 was obtained as 115 minutes. The main advantage of FEA with steady state conditions is that figures such as Figure 3 can now be used to obtain the fire resistance rating (failure time) for any given load ratio. Table 3 gives the failure times predicted by FEA under steady state conditions for all the tests. These comparisons show that the developed finite element model accurately predicts the ultimate capacities and failure times of LSF wall studs subjected to axial compression under standard fire conditions. Further details on the development and validation of the finite element model can be found in Gunalan and Mahendran (2013).

The results from finite strip analyses (CUFSM) and tests (Gunalan et al., 2013) were used to validate the results of finite element analyses (FEA). The validated finite element model was used in a detailed parametric study into the fire performance of LSF wall panels using a 90 × 40 × 15 stud section.

5 SIMPLIFIED DESIGN METHOD BASED ON THE CRITICAL HOT FLANGE TEMPERATURE

Lawson (1993) adopted the so-called limiting temperature method used for hot-rolled steel structures to cold-formed thin-walled steel structures. In this method the limiting temperature is defined as a function of the load ratio of the structural member. The load ratio is the ratio between the load on the member at the fire limit state and the load carrying capacity of that member under ambient conditions. Kolarkar (2010) proposed simple design rules to determine the failure times of LSF walls by combining the yield stress reduction factors and idealised time-temperature profiles. The critical temperature (ie. the maximum hot flange temperature at failure) corresponding to a load ratio (strength reduction factor) was used with idealised time-temperature profiles to obtain the approximate failure times of each type of wall specimen.

In this study FEA results of eight wall configurations (Table 2) were used to determine the critical temperature of LSF wall studs. Figure 4 shows the variation of load ratio with hot flange temperature at failure for LSF walls with glass fibre, rockwool and

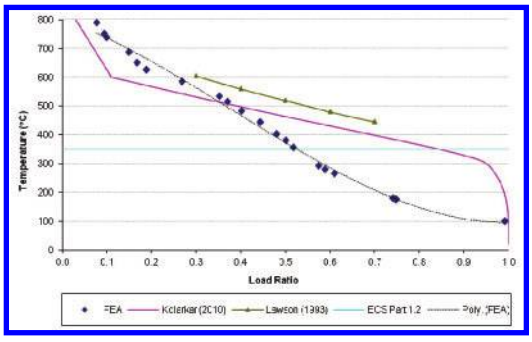


Figure 4. 1.15 mm G500 steel studs lined on both sides by two layers of plasterboards with cavity insulation.

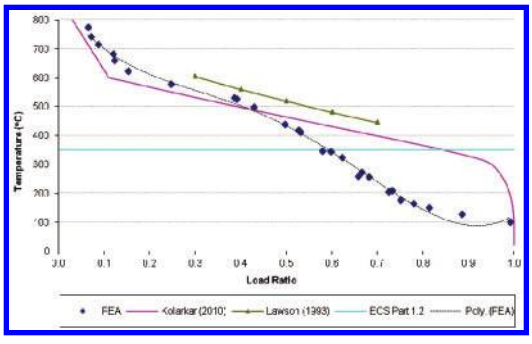


Figure 5. 1.15 mm G500 steel studs lined on both sides by two layers of plasterboards with external insulation.

cellulose fibre used as cavity insulations for 1.15 mm G500 steel studs. It is interesting to note the plots for different insulations merged together. This clearly indicates that the failure temperature of LSF wall studs does not depend on the type of insulation. In other words the effect of using different types of insulation is simply to delay the time to reach the same hot flange temperatures in the LSF wall studs. Similar behavior was observed in externally insulated wall panels as well (Fig. 5). The results of cavity and externally insulated wall panels did not merge when they were plotted together. This indicates that the arrangement of insulations and plasterboards influences the failure temperature although the type of insulation does not. Similar behavior was also observed for LSF wall studs made of G250 1.15 mm and 1.95 mm steels.

Eurocode 3 Part 1.2 (2005) recommends a limiting temperature value of 350°C irrespective of the load ratio as shown by a horizontal line in Figures 4 and 5. This did not agree with the FEA results. Kolarkar's (2010) and Lawson's (1993) design methods were also found to be unsuitable. Therefore it was decided to propose a new set of equations (Equations 9 to 20) to determine the critical hot flange temperatures at failure. These equations represent the temperature values ranging from 100°C to 800°C where T is the critical hot flange temperature in °C and LR is the load ratio. The load ratio was more than 0.90 when the hot flange temperature was below 100°C. Similarly the load ratio was less than 0.10 when the hot flange temperature was above 800°C. They were not included in the proposed equations.

1.15 mm G500 steel studs lined on both sides by A single layer of plasterboard

$$T = 1298LR^3 - 1894LR^2 - 14LR + 708 \quad (9)$$

Two layers of plasterboard

$$T = -527LR^3 + 895LR^2 - 1166LR + 825 \quad (10)$$

Two layers of plasterboard with cavity insulation

$$T = 196LR^3 + 428LR^2 - 1379LR + 854 \quad (11)$$

Two layers of plasterboard with external insulation

$$T = 870LR^3 - 1291LR^2 - 260LR + 768 \quad (12)$$

1.15 mm G250 steel studs lined on both sides by A single layer of plasterboard

$$T = -1300LR^3 + 2312LR^2 - 1927LR + 934 \quad (13)$$

Two layers of plasterboard

$$T = -1113LR^3 + 2583LR^2 - 2367LR + 968 \quad (14)$$

Two layers of plasterboard with cavity insulation

$$T = 863LR^3 - 990LR^2 - 581LR + 804 \quad (15)$$

Two layers of plasterboard with external insulation

$$T = 314LR^2 - 1136LR + 891 \quad (16)$$

1.95 mm G250 steel studs lined on both sides by A single layer of plasterboard

$$T = 866LR^2 - 1712LR + 938 \quad (17)$$

Two layers of plasterboard

$$T = 5455LR^4 - 10681LR^3 + 6727LR^2 - 2244LR + 868 \quad (18)$$

Two layers of plasterboard with cavity insulation

$$T = -1162LR^3 + 2085LR^2 - 1811LR + 920 \quad (19)$$

Two layers of plasterboard with external insulation

$$T = -708LR^3 + 1846LR^2 - 1995LR + 921 \quad (20)$$

In the simplified method proposed here to predict the fire resistance rating of LSF wall systems, Equations 9 to 20 predicting the limiting hot flange temperature of LSF wall studs are used with Equations 1 to 8 giving the idealised hot flange time-temperature

Table 3. Predicted Failure Times for 1.15 mm G500 Steel Studs Lined on Both Sides by Plasterboard.

	Failure time (min.)							
	LR = 0.2			LR = 0.4			LR = 0.7	
Index	Test	FEA	Eqn.	Test	FEA	Eqn.	FEA	Eqn.
1 × 1	53*	54	57	–	42	41	20	21
2 × 2	111*	117	121	–	106	106	61	65
CI-GF	101*	99	103	–	87	86	62	62
CI-RW	107*	106	107	–	90	89	63	63
CI-CF	110*	108	110	–	95	93	64	64
CP-GF	118	117	116	108	109	108	76	77
CP-RW	#136*	144	144	134	132	131	95	95
CP-CF	124*	128	129	–	119	117	86	88

(*) – Tests conducted by Kolarkar (2010); (#) – Earlier failure time due to lack of space for thermal expansion; LR – Load ratio; Eqn. – Proposed equations.

profiles. For one of the 24 LSF wall systems considered here (3 LSF wall stud cases with different steel grades and thicknesses X 8 wall configurations as shown in Table 2) with a given load ratio (LR), the limiting hot flange temperature can be found first by using Equations 9 to 20, which can then be used in Equations 1 to 8 to find the time required to reach the calculated limiting hot flange temperature. This is the fire resistance rating in minutes (stud failure time) for the selected wall system. Table 3 shows the fire resistance rating (failure times) of LSF walls predicted by the simplified method proposed in this section and the corresponding FEA and test results. This table shows that the results agree well.

6 CONCLUSIONS

This paper has presented the details of an investigation into the fire performance of LSF wall panels based on an extensive finite element analysis based parametric study and the results. The LSF wall panels with eight different plasterboard-insulation configurations were considered under standard fire conditions. This paper has developed two sets of equations to predict (1) the hot flange temperature as a function of time during a standard fire and (2) the critical (failure) hot flange temperature as a function of load ratio for LSF wall systems with varying plasterboard-insulation configurations. It then proposes a simplified design method to predict their fire resistance rating based on these two sets of equations.

ACKNOWLEDGEMENTS

The authors would like to thank Australian Research Council for their financial support and the Queensland University of Technology for providing the necessary facilities and support to conduct this research project.

REFERENCES

Alfawakhiri, F. 2001. Behaviour of Cold-formed steel framed walls and floors in standard fire resistance tests. *PhD Thesis*, Carleton University, Ottawa, Ontario, Canada.

American Iron and Steel Institute (AISI). 2007. Specifications for the cold-formed steel structural members. *Cold-formed Steel Design Manual*, Washington, USA.

Dolamune Kankanamge, N. and Mahendran, M. 2011. Mechanical properties of cold-formed steels at elevated temperatures. *Thin-Walled Structures*, 49: 26–44.

European Committee for Standardization (ECS). 2005. Eurocode 3: Design of steel structures. Part 1-2: General rules – Structural fire design. EN 1993-1-2, Brussels.

European Committee for Standardization (ECS). 2006. Eurocode 3: Design of steel structures. Part 1-3: General rules – Supplementary rules for cold-formed members and sheeting. EN 1993-1-3, Brussels.

Feng, M., Wang, Y.C. and Davies, J.M. 2003. Axial strength of cold-formed thin-walled steel channels under non-uniform temperatures in fire. *Fire Safety Journal*, 38: 679–707.

Feng, M. and Wang, Y.C. 2005. An analysis of the structural behaviour of axially loaded full-scale cold-formed thin-walled steel structural panels tested under fire conditions. *Thin-Walled Structures*, 43: 291–332.

Gerlich, J.T., Collier, P.C.R. and Buchanan, A.H. 1996. Design of steel-framed walls for fire resistance. *Fire and Materials*, 20(2): 79–96.

Gunalan, S. 2011. Structural behaviour and design of cold-formed steel wall systems under fire conditions. *PhD Thesis*, Queensland University of Technology, Brisbane, Australia.

Gunalan, S., Kolarkar, P.N. and Mahendran, M. 2013. Experimental study of load bearing cold-formed steel wall systems under fire conditions. *Thin-Walled Structures,* 65: 72–92.

Gunalan, S. and Mahendran, M. 2013 Finite element modelling of load bearing cold-formed steel wall systems under fire conditions. *Engineering Structures*, (in press).

Kaitila, O. 2002. Finite element modelling of cold-formed steel members at high temperatures. *Licentiate Thesis,* Helsinki University of Technology, Espoo, Finland.

Klippstein, K.H. 1980. Strength of cold-formed studs exposed to fire, American Iron and Steel Institute. Washington DC, USA.

Kolarkar, P.N. 2010. Structural and thermal performance of cold-formed steel stud wall systems under fire conditions. *PhD Thesis*, Queensland University of Technology, Brisbane, Australia.

Lawson, R.M. 1993. Building design using cold formed steel sections: fire protection. The Steel Construction Institute, *Publication P129*, London, UK.

Ranby, A. 1999. Structural fire design of thin walled steel sections. *Licentiate Thesis*, Department of Civil and Mining Engineering, Lulea University of Technology, Stockholm, Sweden.

Standards Australia (SA). 2005. Methods for fire tests on building materials, components and structures, Part 4: Fire-resistance tests of elements of building construction. AS 1530.4, Sydney, Australia.

Zhao, B., Kruppa, J., Renaud, C., O'Connor, M., Mecozzi, E., Apiazu,. W., Demarco, T., Karlstrom, P., Jumppanen, U., Kaitila, O., Oksanen, T. and Salmi, P. 2005. Calculation rules of lightweight steel sections in fire situations. *Technical Steel Research*, European Union, France.

Research and Applications in Structural Engineering, Mechanics and Computation – Zingoni (Ed.)
© 2013 Taylor & Francis Group, London, ISBN 978-1-138-00061-2

Fire resistance assessment of steel structure exposed to fire for differentiated safety requirements

M. Maślak
Cracow University of Technology, Cracow, Poland

ABSTRACT: An alternative evaluation technique, helpful in fire resistance assessment of steel structure exposed to fire is presented and discussed in detail. The proposed calculation methodology deals with the probability-based approach and it is connected with the identification of the most probable failure point. Furthermore, the influence of model uncertainty, describing the steel mechanical properties reduction ratio under fire, is taken into account in this analysis. Conclusively, the critical steel temperature is obtained as the reliable safety measure for which the failure probability may not be accepted. Various levels of the acceptable failure probability can be assumed in such study. In the presented paper they are specified by the adoption of the adequate value of required reliability index β. The design algorithm, proposed by the author, is illustrated by simple example of uniformly heated unrestrained steel beam.

1 INTRODUCTION

The classical safety condition, commonly specified in many standards to determine ultimate limit state for considered structural member, deals with the comparison between two conclusive design values. The first one is usually identified for the reliable action effect, whereas the second - for the member resistance associated with this effect. It is a general knowledge that such approach is only the simplification of more detailed fully probabilistic calculation technique and, as a consequence, it leads to the solutions being always safe but frequently overestimated. However, this reassuring conclusion does not have to be correct in relation to structural analysis made for the accidental fire situation, therefore it seems to be advisable to look for the new, better justified algorithm which could be suggested for application in structural safety analysis for members under fire conditions. The aim of this paper is to present an alternative probability-based design methodology helpful in the evaluation of critical temperature of steel members exposed to fire. This temperature is connected to the point-in-fire-time when the considered member, with constant level of external loading, reaches fire resistance limit state under monotonically increasing steel temperature. Let us notice that such limit state does not mean the immediate member collapse but only the fire moment when the member failure probability becomes too high to be acceptable. The additional advantage of the proposed methodology is the possibility to take into account differentiated safety requirements being specified by means of the adoption of various levels of acceptable failure probability. Such concept is realized by the acceptance of particular values of required reliability index β. The design algorithm discussed in the presented paper is illustrated in detail by simple example of uniformly heated unrestrained steel beam.

2 THE PROPOSED DESIGN METHODOLOGY

2.1 *Alternative failure definition*

Let the failure be the case, defined for random realization, when random value of the reliable action effect becomes at least equal (or higher) to suitable random member resistance, associated with such effect and reduced because of the influence of high material temperature Θ_a. It means that for fire conditions then occurs $E_{fi} \geq R_{fi,\Theta}$. Furthermore, let us assume that the value of the reliable action effect is constant during the whole of fire time because there are no constraints for potential thermal deformations and owing to that no additional internal forces and moments are generated. Such definition leads to the conclusion that even if the random value of the conclusive action effect E_{fi} is unsafely high but at the same time the random member resistance $R_{fi,\Theta}$, compared to this effect, still remains higher, then this situation should be treated as fully acceptable in context of the structural safety analysis and, as a consequence, no failures are identified in the considered structure. Analogously, the same interpretation can be made for member resistance not large enough if only the corresponding action effect remains sufficiently small. As a result, the failure probability $p_f = P(E_{fi} \geq R_{fi,\Theta}) < p_{f,ult}$ is estimated. Its value is limited by the probability $p_{f,ult}$, being the maximum acceptable and specified, for example, as dependents on the assumed reliability class RC (according to EN 1990).

2.2 *Specification of limit state condition*

In further analysis only the simple case is discussed when both the action effect E_{fi} and the member resistance $R_{fi,\Theta}$ are random variables described by normal probability distribution (Maślak 2013). To obtain the value of the reliability index β considered random variables must be transformed into the standardized space. It is sufficient to take:

$$u_E = \frac{E_{fi} - m_E}{\sigma_E} \quad \text{and} \quad u_R = \frac{R_{fi,\Theta} - m_R}{\sigma_R} \tag{1}$$

which means that:

$$E_{fi} = m_E + u_E \sigma_E \quad \text{and} \quad R_{fi,\Theta} = m_R + u_R \sigma_R \tag{2}$$

In those formulae m_E and m_R are the suitable mean values, specified for the action effect and for the member resistance, respectively, whereas σ_E and σ_R are the adequate Gaussian standard deviations. As a consequence of such specification, the limit state condition, identified for considered value of Θ_a, leads to the linear equation:

$$R_{fi,\Theta} - E_{fi} = 0 \rightarrow m_R - m_E + u_R \sigma_R - u_E \sigma_E = 0 \tag{3}$$

To standardize this formula the quantity $\Xi = \sqrt{\sigma_E^2 + \sigma_R^2}$ is previously defined. As a result of its application one obtains:

$$\begin{aligned} &(m_R - m_E)/\Xi + (\sigma_R/\Xi)u_R - (\sigma_E/\Xi)u_E = \\ &= \beta + \alpha_R u_R - \alpha_E u_E = 0 \end{aligned} \tag{4}$$

Let us notice that such formula contains not only the reliability index equal to $\beta = (m_R - m_E)/\Xi$ but also the coefficients $\alpha_E = \sigma_E/\Xi$ and $\alpha_R = \sigma_R/\Xi$ being the direction cosines of the strain line connecting the origin of the Cartesian coordinate system (u_E, u_R) with the most probable failure point (closest to the origin and localized on the limit state surface). The value of $\Theta_{a,cr}$ is understood as the lowest steel temperature for which the beam failure probability p_f may not be accepted. This means that in the ultimate limit state occurs $\beta = \beta_{req}$. The required value β_{req} is explicitly connected with the maximum acceptable probability $p_{f,ult}$. Values of such index can be adopted adequately for the assumed safety requirements. In the example presented below three of them are examined in detail: $\beta_{req} = 4.3$ for range, $\beta_{req} = 3.8$ for moderate (ordinary) and $\beta_{req} = 3.3$ for minor required safety level. They are taken directly from the standard EN 1990 as those determining particular reliability classes: RC1, RC2 and RC3, respectively.

3 NUMERICAL EXAMPLE

3.1 *Description of the analysed steel beam*

To make easier interpretation of the methodology recommended by the author the case of unrestrained and simply supported steel beam is analysed in detail (Maślak 2012a). It is assumed that the span length is set at $L = 6$ m. Furthermore, the beam is made of the S235 grade steel and the IPE300 cross-section (belonging to class 1 according to EN 1993-1-1), for which $W_{pl} = 628\,\text{cm}^3$, is adopted for the study. The permanent load g and only one variable load q, both uniformly distributed, are applied to the beam. Let us assume that all considered external loads are random variables with normal probability distribution. In the presented example one has: $\overline{g} = 5$ kN/m, $\sigma_G = 0{,}3$ kN/m, $\overline{q} = 12$ kN/m, $\sigma_Q = 1{,}5$ kN/m, $\psi_2 = 0{,}3$ (ψ_2 is the ratio reducing the characteristic value of variable action to its quasi-permanent equivalent). Member resistance is proportional to the steel yield point, being the random variable with log-normal probability distribution $LN(\breve{f}_y, \upsilon_f)$. Its median value $\breve{f}_y$ can be estimated assuming that $\upsilon_f = 0.08$ – in accordance with numerous statistical data:

$$\begin{aligned} &\breve{f}_y = f_{y,k}\, exp(2\upsilon_f) = 235\, exp(2 \cdot 0{,}08) = \\ &= 275.8\ \text{MPa} \end{aligned} \tag{5}$$

Steel yield point is reduced if the beam is subject to fire exposure (reduction factors $k_{y,\Theta}$ are assumed according to the standard EN 1993-1-2):

$$f_{y,k,\Theta} = k_{y,\Theta} f_{y,k} = k_{y,\Theta} \breve{f}_y\, exp(-2\upsilon_f) \tag{6}$$

In further analysis the hypothesis that υ_f does not depend on the steel temperature is accepted. Such statement leads to the conclusion that:

$$\breve{f}_{y,\Theta} = k_{y,\Theta} \breve{f}_y \tag{7}$$

Moreover, it is assumed that the steel temperature monotonically rises during fire; nevertheless, at each particular fire moment the member temperature distribution is always uniform both in considered cross-section and along the beam length. This model is adequate for fully developed fire conditions and in general it may be qualified as the conclusive in structural analysis. Such simplification allows to conclude that also the plastic bending modulus W_{pl} does not change under fire exposure. Consequently, the median value of beam resistance can be calculated as follows:

$$\begin{aligned} &\breve{R}_{fi,\Theta} = W_{pl} k_{y,\Theta} \breve{f}_y = 628 \cdot 10^{-6} \cdot k_{y,\Theta} \cdot 275.8 \cdot 10^3 = \\ &= 173.20 k_{y,\Theta}\ \text{kNm} \end{aligned} \tag{8}$$

As one can see, the bending modulus W_{pl} as well as the reduction factor $k_{y,\Theta}$ are treated as deterministic parameters; however, their variability is added to the global coefficient of variance υ_R calculated for the resistance. Let the symbol υ_f^2 denote the variance of steel yield point, υ_A^2 – the variance of beam geometrical dimensions, υ_k^2 – the variance resulting from the uncertainty of a model describing mechanical properties of

steel under fire conditions. In this example it is adopted that $\upsilon_f = 0.08$ and $\upsilon_A = 0.06$ which is also consistent with many statistical estimates, made also in Poland. Furthermore, let us assume that $\upsilon_k = 0.10$. According to the suggestion given by Holicky (Holicky 2005) it is statistically legitimate to use even $\upsilon_k = 0.10$–0.30. Consequently, for such accepted data one obtains:

$$\upsilon_R = \sqrt{\upsilon_f^2 + \upsilon_A^2 + \upsilon_k^2} = \\ = \sqrt{0.08^2 + 0.06^2 + 0.10^2} = 0.141 \quad (9)$$

Recalculation the log-normal resistance parameters into Gaussian characteristics gives:

$$m_R = \bar{R}_{fi,\Theta} = \tilde{R}_{fi,\Theta} \exp\left(\upsilon_R^2/2\right) = \\ = 173.20 k_{y,\Theta} \exp\left(0.141^2/2\right) = 174.93 k_{y,\Theta} \text{ kNm} \quad (10)$$

$$\sigma_R = \bar{R}_{fi,\Theta} \sqrt{\exp\left(\upsilon_R^2\right) - 1} = \\ 174.93 k_{y,\Theta} \sqrt{\exp\left(0.141^2\right) - 1} = 24.79 k_{y,\Theta} \text{ kNm} \quad (11)$$

Similarly, for the action effect one has:

$$m_E = \bar{E}_{fi} = \left(\bar{g} + \psi_2 \bar{q}\right) L^2/8 = \\ = (5 + 0.3 \cdot 12) 6^2/8 = 38.7 \text{ kNm} \quad (12)$$

$$\sigma_E = \sqrt{\sigma_G^2 + \psi_2^2 \sigma_Q^2}\, L^2/8 = \\ = \sqrt{0.3^2 + 0.3^2 \cdot 1.5^2}\, 6^2/8 = 2.43 \text{ kNm} \quad (13)$$

3.2 *Evaluation of critical temperature by the standard approach*

At the beginning of the analysis it is necessary to show that the considered beam safely carries all applied loads for the conditions of persistent design situation (without any fire influences). In fact, according to classical approach given in the standard EN 1990 one can obtain that:

$$g_k = \bar{g} + 1.64\sigma_G = 5 + 1.64 \cdot 0.3 = 5.49 \text{ kN/m} \quad (14)$$

$$q_k = \bar{q} + 1.64\sigma_Q = 12 + 1.64 \cdot 1.5 = 14.46 \text{ kN/m} \quad (15)$$

$$E_d = \left(\gamma_G g_k + \gamma_Q q_k\right) L^2/8 = \\ = (1.35 \cdot 5.49 + 1.5 \cdot 14.46) 6^2/8 = 130.96 \text{ kNm} \quad (16)$$

$$E_d < R_d = W_{pl} f_{y,k}/\gamma_M = \\ = 628 \cdot 10^{-6} \cdot 235 \cdot 10^3/1.0 = 147.58 \text{ kNm} \quad (17)$$

The design value of the action effect estimated for accidental fire situation is significantly lower:

$$E_{fi,d} = \left(g_k + \psi_2 q_k\right) L^2/8 = \\ = (5.49 + 0.3 \cdot 14.46) 6^2/8 = 44.23 kNm \quad (18)$$

Let us notice that, according to Eq. (17):

$$R_{fi,\Theta,d} = 147.58 k_{y,\Theta} \text{ kNm} \quad (19)$$

because $\gamma_{M,fi} = \gamma_M = 1.0$.

The ratio $\rho(\Theta_a) = E_{fi,d}/R_{fi,\Theta,d}$ can be adopted as a measure helpful in the evaluation of critical beam temperature $\Theta_{a,cr}$ for which $\rho(\Theta_{a,cr}) = 1,0$. The results of the analysis are shown in Table 1.

Finally, by linear interpolation, one obtains:

$$\Theta_{a,cr} = 600 + \frac{(700 - 600)(1.0 - 0.638)}{1.303 - 0.638} = \\ = 654.4\ ^{o}C \quad (20)$$

3.3 *Application of the probability-based approach proposed in the presented paper*

Substituting values taken from Eqs. (10 ÷ 13) to Eq. (3) yields in turn:

$$174.93 k_{y,\Theta} - 38{,}7 + 24.79 k_{y,\Theta} u_R - 2.43 u_E = 0 \quad (21)$$

$$\Xi = \sqrt{\sigma_E^2 + \sigma_R^2} = \sqrt{24.79^2 k_{y,\Theta}^2 + 2.43^2} = \\ = \sqrt{614.54 k_{y,\Theta}^2 + 5.90} \quad (22)$$

Let us assume that the safety requirements are ordinary and $\beta_{req} = 3.8$ (for the reliability class RC2 and for the reference period equal to 50 years – according to EN 1990). Detailed results obtained owing to the application of Eq. (4) are presented in Table 2.

Table 1. Evaluation of $\Theta_{a,cr}$ by the standard approach.

Θ_a [°C]	$k_{y,\Theta}$	$E_{fi,d}$ [kNm]	$R_{fi,\Theta,d}$ [kNm]	$\rho(\Theta_a)$
400	1.00	44.23	147.58	0.300
500	0.78	44.23	115.11	0.384
600	0.47	44.23	69.36	0.638
700	0.23	44.23	33.94	1.303

Table 2. Estimation of beam critical temperature by the probability-based approach if $\upsilon_k = 0.10$.

Θ_a [°C]	$k_{y,\Theta}$	Ξ [kNm]	β	α_E	α_R
400	1.00	24.91	5.47	0.098	0.995
500	0.78	19.49	5.02	0.125	0.992
563	0.58	14.58	4.30	0.167	0.986
590	0.50	12.63	3.86	0.193	0.981
593	0.49	12.39	3.79	0.196	0.980
600	0.47	11.90	3.66	0.204	0.979
618	0.43	10.93	3.34	0.222	0.975
620	0.42	10.69	3.25	0.227	0.974

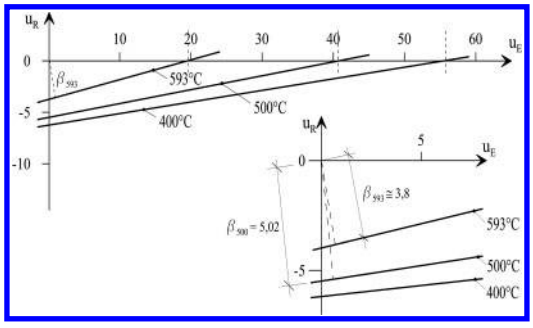


Figure 1. Graphical interpretation of the reliability index $\beta_{593} \cong 3.8$ leading to the evaluation $\Theta_{a,cr} \cong 593°C$ (see Table 2).

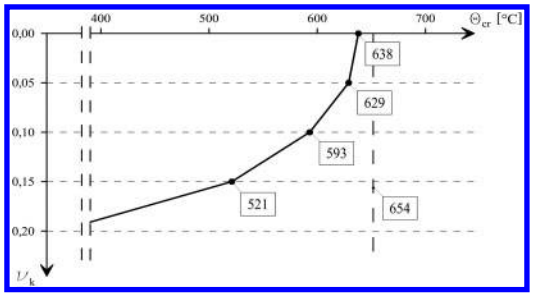


Figure 2. Resultant values of the temperature $\Theta_{a,cr}$ in relation to the adopted level of model uncertainty when the value $\beta_{req} = 3.8$ is assumed.

As one can see the value of $\Theta_{a,cr}$, estimated using proposed methodology, is equal to $\Theta_{a,cr} \cong 593\,°C$. The geometrical interpretation of such solution is given in Figure 1. It is noteworthy that the coefficients $\alpha_E = \sigma_E / \Xi$ and $\alpha_R = \sigma_R / \Xi$ change with the steel temperature growth and, as a result, inclination of the limit state line is also unstable.

3.4 *Assessment of beam critical temperature for differentiated safety requirements*

Basing on the data collected in Table 2 one can assess also the beam critical temperature specified for the other safety requirements, different than those accepted as the ordinary ones. Let us assume firstly that $\beta_{req} = 4.3$ which is an equivalent of the range required safety level. It is easy to see that the adequate critical temperature is then equal to $563°C$. Similarly, for the adoption of the minor required safety level and, in consequence, making the assumption that the index $\beta_{req} = 3.3$ one can obtain the searched temperature being much lower than previously indicated and equal to $619°C$. All obtained solutions, characteristic for particular assumed safety requirements, are shown in the diagram presented in Figure 2.

3.5 *Influence of model uncertainty*

The value of the temperature $\Theta_{a,cr} \cong 593\,°C$, obtained as a result of the application of alternative probability-based design procedure for ordinary safety requirements, is much more conservative in relation to the other, resulted from using the classical standard analysis. The main reason of such difference is the consideration of inevitable model uncertainty by joining to global variance of beam resistance an additional component $\upsilon_k = 0{,}10$. It seems to be informative to analyse more precisely the influence of various levels of model uncertainty on the resultant critical temperature assessment. To do this selected values of variability υ_k are adopted to detailed examination, particularly: 0.00; 0.05; 0.10; 0.15 and 0.20 (Maślak 2012b). As a consequence Eq. (8) is simplified to the form:

$$\upsilon_R = \sqrt{0.08^2 + 0.06^2 + \upsilon_k^2} = \sqrt{0.01 + \upsilon_k^2} \tag{23}$$

Let us notice that as a result of the correction of υ_R many other values connected to beam resistance simultaneously change, especially m_R, σ_R and even Ξ. On the other hand, no parameters dealing with the action effect are corrected in such approach. Consequently, formulae describing the limit state condition, adequate for the formula previously specified as Eq. (21), are now defined by the following equations:

- if $\upsilon_k = 0.00$:

$$174.07k_{y,\Theta} - 38.7 + 17.45k_{y,\Theta}u_R - 2.43u_E = 0 \tag{24}$$

- if $\upsilon_k = 0.05$:

$$174.29k_{y,\Theta} - 38.7 + 19.58k_{y,\Theta}u_R - 2.43u_E = 0 \tag{25}$$

- if $\upsilon_k = 0.10$:

$$174.93k_{y,\Theta} - 38.7 + 24.79k_{y,\Theta}u_R - 2.43u_E = 0 \tag{26}$$

- if $\upsilon_k = 0.15$:

$$176.03k_{y,\Theta} - 38.7 + 31.94k_{y,\Theta}u_R - 2.43u_E = 0 \tag{27}$$

- if $\upsilon_k = 0.20$:

$$177.60k_{y,\Theta} - 38.7 + 40.29k_{y,\Theta}u_R - 2.43u_E = 0 \tag{28}$$

It is easy to see, by interpretation of the solutions collected in succeeding tables (Tables 2–6), that for ordinary safety requirements occurs:

- if $\upsilon_k = 0.00$ than $\Theta_{a,cr} \cong 638°C$ (see Table 3),
- if $\upsilon_k = 0.05$ than $\Theta_{a,cr} \cong 629°C$ (see Table 4),
- if $\upsilon_k = 0.10$ than $\Theta_{a,cr} \cong 593°C$ (see Table 2),
- if $\upsilon_k = 0.15$ than $\Theta_{a,cr} \cong 521°C$ (see Table 5),
- if $\upsilon_k = 0.20$ than $\Theta_{a,cr} < 400°C$ (see Table 6).

As one can see, taking $\upsilon_k = 0.20$ leads to the inequality $\beta = 3.44 < \beta_{req} = 3.8$ which means that the safety condition can be unsatisfied even just before reaching the steel temperature equal to $\Theta_a = 400°C$. In this point-in-fire-time any reduction of steel yield point is

Table 3. Evaluation of critical temperature $\Theta_{a,cr}$ when the value $\upsilon_k = 0.00$ is assumed.

Θ_a [°C]	$k_{y,\Theta}$	Ξ [kNm]	β	α_E	α_R
400	1.00	17.62	7.72	0.138	0.990
500	0.78	13.83	7.02	0.176	0.984
600	0.47	8.55	5.04	0.284	0.959
626	0.41	7.56	4.32	0.321	0.946
630	0.40	7.39	4.19	0.329	0.945
637	0.38	7.06	3.89	0.344	0.939
640	0.37	6.90	3.73	0.352	0.936
650	0.35	6.57	3.38	0.370	0.930
653	0.34	6.41	3.20	0.379	0.926

Table 4. Evaluation of critical temperature $\Theta_{a,cr}$ when the value $\upsilon_k = 0.05$ is assumed.

Θ_a [°C]	$k_{y,\Theta}$	Ξ [kNm]	β	α_E	α_R
400	1.00	19.73	6.87	0.123	0.992
500	0.78	15.46	6.29	0.157	0.988
600	0.47	9.52	4.54	0.255	0.967
610	0.45	9.14	4.35	0.266	0.964
612	0.44	8.95	4.24	0.272	0.963
625	0.41	8.39	3.90	0.290	0.957
630	0.40	8.20	3.78	0.296	0.955
640	0.37	7.64	3.38	0.318	0.948
644	0.36	7.46	3.22	0.326	0.945

Table 5. Evaluation of critical temperature $\Theta_{a,cr}$ when the value $\upsilon_k = 0.15$ is assumed.

Θ_a [°C]	$k_{y,\Theta}$	Ξ [kNm]	β	α_E	α_R
400	1.00	32.03	4.29	0.076	0.997
500	0.78	25.03	3.94	0.097	0.995
520	0.72	23.12	3.81	0.105	0.995
525	0.70	22.49	3.76	0.108	0.994
570	0.56	18.05	3.32	0.135	0.991
574	0.55	17.73	3.28	0.137	0.991

Table 6. Evaluation of critical temperature $\Theta_{a,cr}$ when the value $\upsilon_k = 0.20$ is assumed.

Θ_a [°C]	$k_{y,\Theta}$	Ξ [kNm]	β	α_E	α_R
400	1.00	40.36	3.44	0.060	0.998
450	0.89	35.94	3.32	0.068	0.998
460	0.87	35.14	3.30	0.069	0.998

not yet performed ($k_{y,\Theta} = 1.0$) so, as a consequence, any decrease of beam cross-section resistance has not occurred.

Such result leads to the unexpected conclusion that the considered beam cannot carry all external loads applied just from the beginning of the fire, even if the accidental load combination rule is adopted to the study. Let us notice that quite a different conclusion was reached previously, regarding the behaviour of the same beam but dealing with persistent design situation – all loads applied to this beam were safely carried under such conditions. Comparison of both above conclusions leads to the formal inconsistency, indeed, and as a consequence allows to give the recommendation to adopt the level of model uncertainty with great thought, conservatively in general but never more than enough.

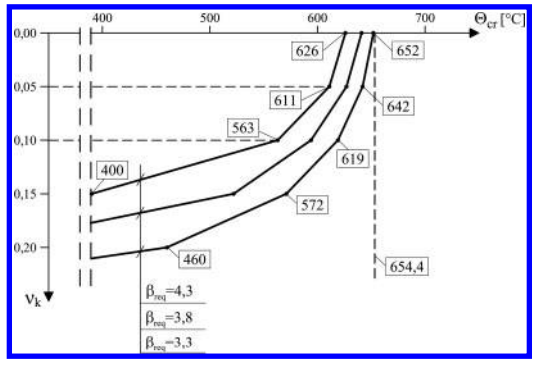


Figure 3. Resultant values of the temperature $\Theta_{a,cr}$ in relation to the adopted level of model uncertainty, obtained for diferrentiaded safety requirements.

Evaluations of beam critical temperature, completed in the considered example for the ordinary required safety level, are presented in detail in Figure 2. It is important that all those values are much more restrictive in relation to the solution obtained previously as an effect of the application of classical standard approach (marked in this diagram by the dashed line).

Moreover, in Figure 3 the similar presentation is made, but it is prepared taking into account the results obtained for differentiated safety requirements. As one can see, quantitative differences between the obtained solutions seem to be essential.

4 CONCLUDING REMARKS

The example presented in this paper shows that the alternative probability-based approach, recommended by the author for application in engineering practice, can be effectively used to assess the reliable value of critical temperature of steel structural members exposed to fire. Solutions obtained in this way seems to be better justified in relations to those resulted from the implementation of classical standard calculation technique because no representative values of considered random variables are established and calibrated. Moreover, the failure is defined more rationally. The fact that all evaluations of critical temperature $\Theta_{a,cr}$ being the results of practical use of proposed methodology are more restrictive in comparison to the adequate solutions obtained owing to the application of classical

standard design technique must be underlined. This means that such standard approach, commonly used in practice, gives in this field the safety assessments being in general too optimistic and, as a consequence, inaccurate.

ACKNOWLEDGEMENTS

This paper was prepared with the financial support of the project granted by Polish Ministry of Science and Higher Education (N N506 243938).

REFERENCES

Holicky M. 2006. Calibration of combination factors for fire design situations. In: G. Augusti, G.I. Schuëller, M. Ciampoli (eds.), *Proc. of the 9th Intern. Conf. ICOSSAR, Rome, Italy, 2005*. Rotterdam. Millpress.

Maślak M. 2012a. Simplified probability-based assessment of a safety level for unrestrained steel beam exposed to fire. In: S.L. Chan, G.P. Shu (eds.), *Proc. of the 7th Intern. Conf. on Advances in Steel Structures (ICASS 2012), Nanjing, China, April 14–16, 2012*, Nanjing. Southeast University Press.

Maślak M. 2012b. Model uncertainty in the evaluation of critical temperature of steel beam exposed to fire (in Polish). In: G. Sztarbała & W. Węgrzyński (eds.), *Proc. of the 7th Intern. Conf. "Fire Safety of Construction Works", Warsaw, November 6–8, 2012*. Warsaw. Building Research Institute.

Maślak M. 2013. Critical temperature evaluation for steel loadbearing structure exposed to fire by means of probability-based approach. In: K. Jármai & L. Kota (eds.), *Proc. of the 5th Intern. Conf. "Design, Fabrication and Economy of Metal Structures" (DFE 2013), Miskolc, Hungary, April 24–26, 2013*. Springer Verlag.

Research and Applications in Structural Engineering, Mechanics and Computation – Zingoni (Ed.)
© 2013 Taylor & Francis Group, London, ISBN 978-1-138-00061-2

Numerical experimental design approach to evaluate the fire resistance of timber connections

M. Audebert
Université de Lyon, Ecole Nationale d'Ingénieurs de Saint-Etienne (ENISE),
Laboratoire de Tribologie et de Dynamique des Systèmes (LTDS), Saint-Etienne Cedex 2, France

D. Dhima
CSTB, Marne-la-Vallée Cedex 2, France

A. Bouchaïr
Clermont Université, Université Blaise Pascal, Institut Pascal, Clermont-Ferrand CNRS,
Institut Pascal, Aubière, France

ABSTRACT: A large experimental and modeling program concerning fire tests on timber connections under various mechanical loadings was performed in France since 1999. Numerical models, simulating the thermo-mechanical behavior of these tested connections were developed and validated on the basis of experimental results. The developed model is sufficiently relevant to realize parametrical studies on timber connections. Then, considering the four main parameters influencing the fire resistance of the connections (type and diameter of fasteners, thickness of timber members and load ratio), the model is used to analyze the combined influence of these factors and to realize a complete numerical experimental design. The thicknesses of the timber beam elements commercially available and the fastener diameters commonly used in timber structures are considered. This numerical experimental design, taking into account a predominant loading case of timber connections in fire situation, allows obtaining a simplified analytical formula giving the possibility to predict easily the fire resistance of the connection configuration studied.

1 INTRODUCTION

The use of timber for buildings is actually encouraged by environmental concerns. However, as wood is a combustible material, fire safety represents a main area of investigation to support this development. Indeed, the knowledge of the thermo-mechanical behavior of timber structures remains insufficient. Timber is the structural material for which the studies relative to the properties and the tools of simulation under fire exposure are the least numerous.

In timber structures, the connections are the weakest zones among the various structural components. The analysis of the fire behavior of these connections is complex due to the influence of several parameters (geometry combining various materials, fasteners types, different thermo-physical and thermo-mechanical properties). The design procedure given in Eurocode 5 (EN 1995-1-2) for timber connections in fire situation is based on a limited number of experimental and numerical results. The calculation method proposed to estimate the fire resistance of the connections has a limited range of application (not more than 30 or 40 minutes according to the connection type) and does not allow obtaining precise or safe results (Audebert et al 2010a).

To improve the knowledge of the behavior of timber connections in fire, a large experimental and modeling program began in France in 1999 (Dhima 1999, Audebert 2010b). Complying with the actual architectural trends and high strength requirements, timber connections using dowel-type fasteners and slotted-in steel plates were mainly studied. This research concerned connections using bolts, dowels or a combination of both and subjected to various loading types (tension parallel-to-grain, tension with an angle to the grain and bending). The experimental results were used to validate a numerical model simulating the thermo-mechanical behavior of the tested connections. The validation is based on the comparison between the calculated and the measured values of temperatures and fire duration resistances. Considering the large number of connections tested and the comparisons with the numerical models, the model developed can be considered sufficiently relevant to be used as a basis for a numerical experimental design.

In the present study, the main parameters affecting the fire resistance of timber connections are defined and a numerical experimental design approach is adopted. In a first part, the experimental results of the tests on timber connections under fire exposure realized since 1999 are exposed. These results allow

determining the factors influencing the fire resistance of the connections and show the existence of a dominant loading case for fire situation. Then the numerical model used to realize the numerical experimental design is briefly presented and some numerical results are given to show the precision ad the accuracy of the simulation. Finally, a complete numerical experimental design is done for a steel-to-timber connection configuration. The results are commented and a simplified analytical formula is obtained, giving the possibility to predict easily the fire resistance of the connection configuration studied.

2 EXPERIMENTAL RESULTS

In this section, the geometrical configurations of timber connections tested in France since 1999 are presented and the experimental results of fire duration resistances are commented.

2.1 *Fire tests*

The fire tests were conducted following the evolution of the temperatures of a conventional fire ISO 834. For each specimen, the temperatures are measured by thermocouples situated along the fasteners, inside the timber members and on the slotted-in steel plates. The protocol for mechanical loading under fire exposure was defined by the standard NF-EN 26891. After a preloading up to 40% and unloading to 10% of N_u (N_u is the failure load given by tests in normal conditions), the specimen was reloaded to the value of $F = \eta_{fi} * N_u$, retained as the loads in fire situation. Then, the fire exposure was started and the load ratio η_{fi} kept constant throughout the exposure to fire until the failure of the connection. The end of the fire tests is defined when a significant acceleration of the measured displacements is observed.

All the tests were realized on connections made with glulam members of resistance class GL24h. The steel elements used in the connections are the fasteners and the plates.

2.1.1 *Timber connections in tension parallel-to-grain*

These tests concern double shear steel-to-timber connections with a variable number of fasteners (bolts or dowels) subjected to a parallel-to-grain tension. The choice of the tested connections aimed at covering the most used real applications and at comparing the various types of connections under fire exposure. The connections satisfy the requirements of spacing and size for dowelled and bolted timber connections of the EN 1995-1-2. The variable parameters studied were the thickness of the timber members (50, 60, 75 and 95 mm), the diameter of the fasteners (12, 16 and 20 mm), the load ratio in fire situation (10 to 90% of N_u). Two examples of the geometrical configurations tested are shown on figures 1 and 2. In Table 1 are given

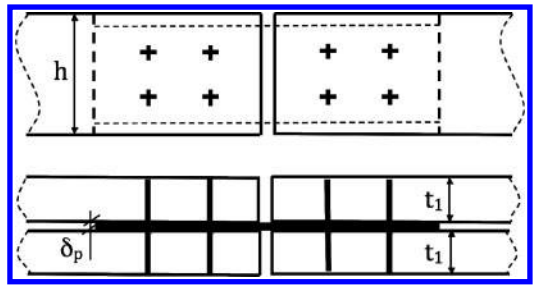


Figure 1. Geometry of a connection made with 4 dowels.

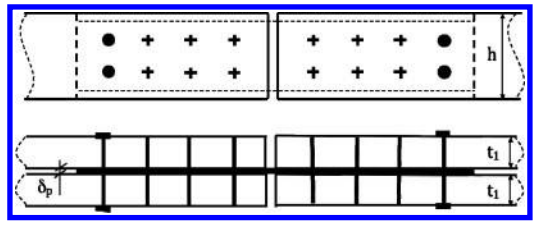


Figure 2. Geometry of a connection made with 6 dowels and 2 bolts.

Table 1. Experimental fire resistance of the connections (parallel-to-grain tension).

N°	Nb	d mm	t_1 mm	η_{fi} % N_u	$t_{fi,exp}$ min
1	2 × 4 bolts	12	50	46	17
				91	10
2	2 × 8 bolts	12	50	41	18
				83	11
3	2 × 16 bolts	12	50	40	18
				80	13
4	2 × 8 bolts	20	60	37	22
				75	15
5	2 × 16 bolts	20	60	37	23
				73	16
6	2 × 6 dowels + 2 × 2 bolts	12	75	10	54
				30	39
7	2 × 6 dowels + 2 × 2 bolts	16	75	10	55
				20	41
				30	36
8	2 × 6 dowels + 2 × 2 bolts	20	75	10	52
				30	37
9	2 × 6 dowels + 2 × 2 bolts	20	95	10	90
				30	45

the fire duration resistances of the tested connections and their geometrical characteristics.

These results show that timber connections can reach fire resistance upper than 30 minutes when load ratios lower than 30% of N_u are applied. Comparing the results for connections 7 and 8, it can be noted that increasing the fasteners diameter from 16 to 20 mm does not allow improving the fire resistance. For the connection 6, the use of fasteners with diameter 12 mm does not reduce the fire resistance of the connections. So, the thickness of the timber members seems

to be the predominant factor for the fire resistance of the timber connections. This comment has been confirmed by experimental results of timber-to-timber connections (Audebert et al. 2013). The fire resistance values obtained for tests 6 to 9 are higher than those obtained with tests 1 to 5. This is due to the values of load ratios and the increase of the thickness of timber members. Moreover bolt type fasteners play a negative role in the fire resistance of the connections (Audebert et al. 2012).

2.1.2 *Timber connections in tension with an angle to the grain*

These tests concern connections subjected to a perpendicular-to-grain tension or a tension with an angle of 45° to the grain. To compare the results of these tests to those of timber connections tested under a parallel-to-grain tension, the size of the connections were taken close to those retained in the design of connections 6 to 9. To avoid the negative effect played by the bolts on the fire resistance, only dowel type fasteners were used in the connections. Four dowels are used.

The geometrical configurations tested are illustrated on figures 3 and 4. Table 2 presents the experimental values of fire resistance $t_{fi,exp}$ depending on the load ratio η_{fi}.

Despite the low strength of wood material in perpendicular-to-grain direction, high values of fire resistance were obtained in this loading case. The results show also high values of fire resistance in tension with an angle to the grain of 45° (connections 13 and 14). The fire resistances of these connections are close to those of equivalent connections tested under a perpendicular-to-grain tension while being always lower.

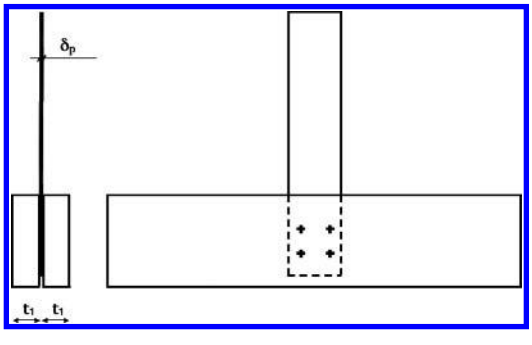


Figure 3. Steel-to-timber connections tested in tension perpendicular to the grain.

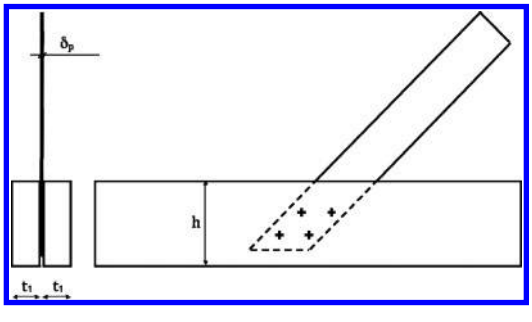


Figure 4. Steel-to-timber connections tested in tension with an angle of 45° to the grain.

2.1.3 *Timber connections in bending*

Two types of steel-to-timber connections were tested. These connections are constituted by two timber beams, connected by a slotted-in steel plate and 6 dowels of diameter 16 mm. Two dowel configurations were tested (figure 5). Table 3 summarizes the experimental results for these connections.

As for timber connections subjected to a transversal tension, high fire resistances, close to one hour, were obtained.

Table 2. Experimental fire resistance of the connections (tension with an angle to the grain).

N°	Load angle	d mm	t_1 mm	η_{fi} $\%N_u$	$t_{fi,exp}$ min
10	90°	16	75	10	71
				30	48
11	90°	20	105	30	69
				45	62
13	45°	16	75	10	69
				30	35
14	45°	20	105	10	92
				30	62

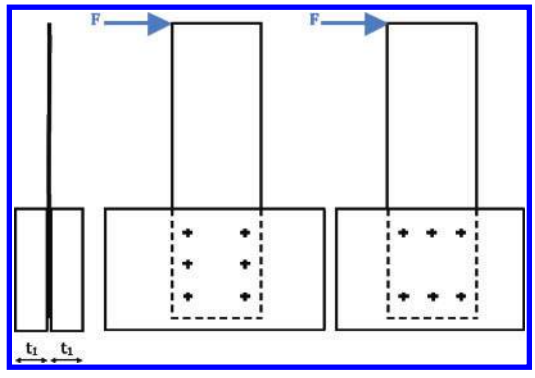


Figure 5. Steel-to-timber connections tested in bending.

Table 3. Experimental fire resistance of the connections (bending).

N°	Configuration	d mm	t_1 mm	η_{fi} $\%N_u$	$t_{fi,exp}$ min
15	Type A	16	75	12	88
				38	61
16	Type B	16	75	38	58
				45	50

2.2 *Conclusion on the experimental program*

This testing program allows concluding on the main parameters influencing the fire resistance of the connections. It appears that the timber members thicknesses and the load ratio applied are the two main factors influencing the fire resistance. Moreover, from the various experimental results presented, the load parallel to grain appears predominant in the design of the connections in fire situation. It would mean that, in term of fire resistance, a connection configuration designed with regard to the tension parallel-to-grain following the recommendations of EN 1995-1-1, would be, de facto, checked for all the loading types.

3 NUMERICAL MODELING

In this section, the main assumptions retained to develop the numerical modeling of the tested connections are presented. The model is developed in two steps using the MSC-MARC software.

3.1 *Heat transfer modeling*

The numerical simulations of heat transfer within the connections are performed considering the evolutions of the thermo-physical properties such as the thermal conductivity and the specific materials. The thermo-physical properties of steel are taken from EC 3 (EN 1993-1-2) and those of wood are chosen with a sensitivity analysis (Audebert et al. 2010a). For the thermal calculations, it is assumed that all the interfaces between the components are in perfect contact with continuous meshing.

The heat transfer model was validated for each tested connection by comparison of its calculated values with the measured charring rates and temperatures using thermocouples. The results obtained by the numerical model were in good agreement with the experimental values (Audebert et al. 2010a, Audebert 2010b).

3.2 *Thermo-mechanical modeling*

In the mechanical modeling, steel plates and dowels are considered with isotropic elastic-plastic behavior according to the von-Mises criterion. The mechanical behavior of wood was considered with transverse isotropy. The evolution of the plastic deformations was taken into account using the 3D Hill yield criterion, associated to the Tsaï-Wu failure criterion in the case of connections with transversal loadings, to take into account the dissymmetric behavior of the material in tension and compression. The evolution of the mechanical properties with temperature is considered using the reduction coefficients provided by the Eurocodes.

The mechanical model takes into account the material and geometrical nonlinearities, and the contact evolutions. The meshing is discontinuous and differs from that of the heat transfer. A procedure has been developed to make the transposition of the temperatures calculated with thermal meshing to the mechanical meshing. The thermo-mechanical model was validated by comparison with the experimental results. The comparison concerns the evolutions of the connection slip versus the time of exposure to fire (figure 6). From these evolutions, the fire resistance duration is determined. The fire resistance times obtained by the numerical model are always lower than those obtained from the experimental tests with a mean relative error of about 15%. Based on these results, the thermo-mechanical model is considered sufficiently accurate to represent safely the behavior of the connections exposed to fire.

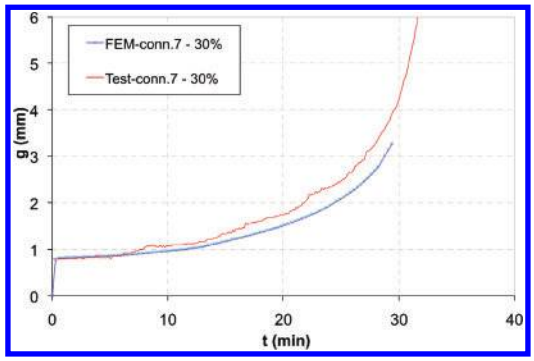


Figure 6. Comparison of numerical and experimental load-slip curves (connection $7 - \eta_{fi} = 30\%N_u$).

4 NUMERICAL DESIGN APPROACH

4.1 *Numerical experimental design*

The experimental results show that the fire resistance of the connections is influenced by three main parameters, which are the diameter of fasteners, the thickness of timber members and the load ratio. These three parameters represent the three factors of which the combined influence will be studied in the numerical design. Other influencing parameter is the type of fasteners used: dowel or bolt. In the practice, bolts are commonly used in association with dowels to connect timber elements. Their function is to prevent the separation of the connected members. The use of one bolt with three dowels (for four fasteners) is common and this distribution is mentioned in Eurocode 5 (EN 1995-1-1). The influence of this ratio bolts/dowels on the fire resistance of timber connections was studied (Audebert et al. 2012). It appears that the presence of one bolt for four fasteners reduces by about 15% the fire resistance comparing to a connection assembled only with dowels (figure 7).

Thus, the numerical experimental design is realized for dowelled steel-to-timber connections loaded in tension parallel to grain. This loading case is predominant in the design of the connection for fire situation. The geometrical configuration studied is identical to

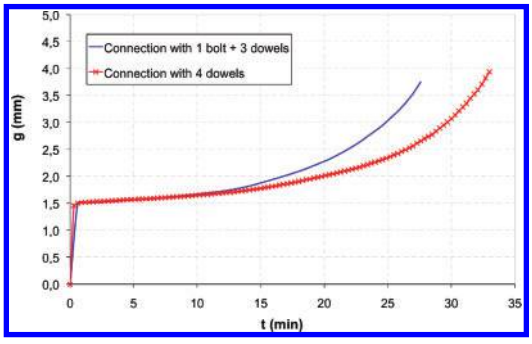


Figure 7. Influence of the presence of one bolt on the slip-time curves evolution of a timber connection.

the one presented in figure 2 but with dowels only. The number of fasteners is kept constant for all the studied configurations (2 × 8 dowels). The decrease of fire resistance generated by a bolt under fire exposure can be estimated by the introduction of a specific reduction coefficient.

Three different values are considered for the diameter of dowels (12, 16 and 20 mm) to cover the common fastener diameters used in timber structures. Six values of timber member thickness are retained to take into account the thicknesses commercially available. Two values are considered for the load ratio (10 and 30%). It is necessary to realize, at least, 36 simulations to obtain a complete factorial design considering the influence of each parameter. The interaction term between the three parameters (d-t_1-η) is neglected. Table 4 summarizes the numerical experiments and the corresponding calculated fire resistance durations ($t_{fi,sim}$).

From these numerical values of calculated fire resistance, a polynomial function is fitted according to the three selected parameters, using the least squares method on Matlab. The exponential relation between the load ratio and the fire resistance proposed by EN 1995-1-2 is kept. Indeed, this relation corresponds to the tendency observed with the experiments. Then, the polynomial function of Equation (1) is chosen:

$$\tilde{t}_{fi} = 31.92 - 1.79d + 1.03t_1 - 7.51\ln(\eta) + 0.003d \cdot t_1 + 0.49d \cdot \ln(\eta) - 0.24t_1 \cdot \ln(\eta) \quad (1)$$

Considering the fire resistance of the 36 calculated connections, the Equation (1) gives a mean relative error equal to 7.85% (Equation (2)).

$$\|\varepsilon\| = \frac{\left\| t_{fi,sim} - \tilde{t}_{fi} \right\|}{\left\| t_{fi,sim} \right\|} = 7.85\% \quad (2)$$

In Equation (1), the interaction term $d.t_1$ is weighted by a low coefficient. This interaction can be neglected. The final Equation (3) is then obtained:

$$\tilde{t}_{fi} = 27.32 - 1.51d + 1.07t_1 - 7.51\ln(\eta) + 0.49d \cdot \ln(\eta) - 0.24t_1 \cdot \ln(\eta) \quad (3)$$

Table 4. Numerical experimental design and simulated fire resistance durations.

N°	d mm	t_1 mm	η $\%N_u$	$t_{fi,sim}$ min
1	12	55	10	33.1
2		55	30	18.4
3		75	10	48.0
4		75	30	18.4
5		95	10	57.2
6		95	30	31.8
7		115	10	62.0
8		115	30	42.6
9		135	10	79.6
10		135	30	37.0
11		160	10	90.0
12		160	30	42.9
13	16	55	10	32.3
14		55	30	15.3
15		75	10	42.8
16		75	30	24.6
17		95	10	56.7
18		95	30	35.4
19		115	10	68.0
20		115	30	45.0
21		135	10	80.0
22		135	30	43.3
23		160	10	81.8
24		160	30	44.0
25	20	55	10	31.7
26		55	30	15.2
27		75	10	43.2
28		75	30	23.2
29		95	10	48.3
30		95	30	31.8
31		115	10	63.0
32		115	30	43.0
33		135	10	75.5
34		135	30	45.0
35		160	10	90.0
36		160	30	40.5

With the mean relative error:

$$\|\varepsilon\| = \frac{\left\| t_{fi,sim} - \tilde{t}_{fi} \right\|}{\left\| t_{fi,sim} \right\|} = 7.87\% \quad (4)$$

This formula is elaborated from the numerical models of dowelled connections. To take into account the reduction of fire resistance due to the use of one bolt for four fasteners, a reduction coefficient of 15% can be applied to the formula.

Using Equation (3), design abacuses can be drawn. The graphical representations are obtained for each given diameter. Figure 8 shows an example of these abacuses for a dowel diameter of 16 mm.

These abacuses give the possibility to obtain easily the duration of fire resistance of a connection knowing only the value of the three parameters retained.

The analytical formula presented in Equation (3) is used to estimate the fire resistance of the tested connections 6 to 9 (Table 1). As these connections are made with bolts and dowels, the reduction coefficient

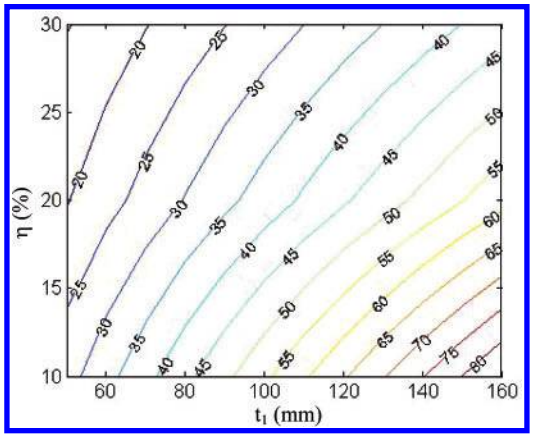


Figure 8. Abacus of the fire resistance of connections for fastener diameter d = 16 mm.

Table 5. Fire resistance of connections: calculated values (Eq. 3), experimental values and Eurocode 5 values.

N°	η_{fi} % N_u	$t_{fi,exp}$ min	$t_{fi,calc}$ min	ε_1 (%)	$t_{d,fi}$ min	ε_2 (%)
6	10	54	38.7	28	31.6	41
	30	39	20.0	49	18.4	53
7	10	55	37.4	32	31.6	43
	20	41	26.7	35	23.2	43
	30	36	20.3	44	18.4	49
8	10	52	36.1	31	31.6	39
	30	37	20.9	44	18.4	50
9	10	90	43.8	51	31.6	65
	30	45	24.7	45	18.4	59

of 15% to take into account the negative effect of the bolt is applied. The calculated fire resistances ($t_{fi,calc}$) are compared to the experimental ones ($t_{fi,exp}$) and to the values of the fire resistances $t_{d,fi}$ determined with the actual simplified calculation method, the "Reduced Load Method" provided by EN 1995-1-2 (Table 5).

Table 5 shows that Equation (3) allows obtaining fire resistance values of connections closer to the experimental values in comparison with the method provided by Eurocode 5 (relative errors of 39% and 49%). The error can be explained partly by the mechanical properties of the timber. Indeed, the experimental numerical design was made with normalized mechanical properties of timber corresponding to resistance class GL24h. These standardized mechanical properties underestimate significantly the real mechanical properties. For example, for connections 6 to 9, the standardized mechanical properties of timber underestimate the measured mechanical properties $f_{c,0}$ and f_v by 53% and 75% respectively.

The numerical experimental design approach presented in this study is being improved to take into account the resistance class of timber, the number of fasteners and the connection configurations exclusively made with bolts. This approach will be extended to various other geometrical configurations usually used in timber constructions.

5 CONCLUSIONS

The study presented a review of results of a large experimental program conducted in France on the fire resistance of timber connections. These results allowed to determine the main parameters influencing the fire resistance and allowed to identify a predominant loading case in fire situation. The results were used to elaborate a precise numerical model simulating the thermo-mechanical behavior of the connections. As this model is sufficiently accurate, it is used to realize parametrical studies on timber connections in fire situation. Thus, a numerical experimental design approach is performed on a common connection configuration. This numerical design allows obtaining a simplified analytical formula to calculate the fire resistance of the connections giving more precise results than the actual standards.

REFERENCES

Audebert M, Bouchaïr A, Dhima D, Taazount M. 2010a. Analysis and modelling of the thermo-mechanical behaviour of dowelled steel-to-timber joints. *4th Int. Conf. on Structural Engineering, Mechanics and Computation, Capetown, 6–8 September*. South Africa.

Audebert M. 2010b. Approche expérimentale et modélisation du comportement au feu d'assemblages bois sous différents types de sollicitations. *PhD Thesis*, Université Blaise Pascal Clermont-Ferrand et CSTB, France; 233p.

Audebert M, Dhima D, Taazount M, Bouchaïr A. 2012. Behavior of dowelled and bolted steel-to-timber connections exposed to fire. *Engineering Structures* 39:116–125.

Audebert M, Dhima D, Taazount M, Bouchaïr A. 2013. Thermo-mechanical behaviour of timber-to-timber connections exposed to fire. *Fire Safety Journal* 56:52–64.

Dhima, D. 1999. Vérification expérimentale de la résistance au feu des assemblages d'éléments en bois. Saint Remy les Chevreuses: CTICM; 1999, 61p.

EN 1995-1-2 (Eurocode 5). 2004. Design of timber structures, Part 1-2: General rules – structural fire design. CEN TC 250-SC5, Brussels.

Research and Applications in Structural Engineering, Mechanics and Computation – Zingoni (Ed.)
© 2013 Taylor & Francis Group, London, ISBN 978-1-138-00061-2

Performance of reinforced concrete structures in post-earthquake fire

B. Behnam & H. Ronagh
School of Civil Engineering, The University of Queensland, Brisbane, Australia

M. Ashraf
School of Engineering and IT, The University of New South Wales, Canberra, Australia

ABSTRACT: Post earthquake fire (PEF) can lead to the collapse of buildings that are partially damaged in a prior earthquake that occurred immediately before the fire. Most standards for the design of structures against earthquake ignore the possibility of post earthquake fire and hence buildings designed following these codes could be vulnerable under PEF. An investigation based on FEMA 356 is performed here on the performance based safety level of structures designed to the ACI code after they are subjected to an earthquake load with the PGA of 0.30 g. This is followed by a fire analysis of the weakened structure from which the time it takes for the weakened structure to collapse is calculated. The results show that the vulnerability of structures increases dramatically when a deformed structure is exposed to PEF. While the investigation is for a certain class of structures (intermediate reinforced concrete frame, 3 stories), the results confirm the need for the incorporation of post earthquake fire in the process of analysis and design.

1 INTRODUCTION

Earthquakes cause catastrophic damages to civilization but post-earthquake events resulting from the shock, such as fire, could potentially make things a lot worse. The effects of post-earthquake fire (PEF) on buildings are two-fold; one is the damage due to the burning of non-structural material, which possesses material value, and the other is the damage that can be caused due to excessive structural loads on the building Chen et al (2004). The structures are usually not designed for these additional loads and this could be significant when combined with the earthquake damage (even if moderate) leading to the collapse of buildings. On the other hand, structural elements are normally designed to satisfy a specific level of safety or performance. Fire is considered as one of the most problematic conditions and therefore, the provision of appropriate fire safety measures is essential. In general, fire resistance rating is defined as a period of time for which the integrity of a member subjected to fire is maintained to resist applied loads. This definition is correlated with various factors, one of which is the type of building that is being designed. The purpose of fire rating is not only to provide adequate time to evacuate trapped people under the fire, but to reduce the possibility of any conflagration Taylor (2003). Fire-resistance ratings are usually presented in national building codes such as NRCC (2005) and IBC (2006) but are not suitable for the post-earthquake fire. This is an important point because the vulnerability of earthquake-damaged structures exposed to post earthquake fire is much more than the fire itself. This is because earthquake excitation may produce residual lateral deformation as well as residual stresses on the members Mousavi et al (2008). Both active and passive fireproofing systems such as sprinklers and fire control systems may become seriously damaged during an earthquake and the fire resistance of the structure could reduce by a considerable margin. The fire resistance is defined as a time at which the element is unable to resist applied loads such as gravity loads Kodur and Dwaikat (2007). Evaluation of structural performance under PEF condition is an important issue that has to be scrutinized carefully. PEF resistance of a building is dependent on various factors including the deformed geometry and the degradation in stiffness resulted from earthquake Zaharia and Pintea (2009). In reinforced concrete structures, in addition to the aforementioned factors, the effects of level of damage including tensile cracking, removal of rebar cover and compressive crushing on PEF resistance should be considered as well. Assuming ductile behavior of RC elements, a typical moment-curvature relationship can be idealized to separate stages Kwak and Kim (2010). While it seems that tensile cracking, as the first stage of cracking, has no significant effect on the PEF resistance, major cracking as a result of removal of rebar cover or crushing of concrete in compression could drastically reduce the PEF resistance Ervine et al (2009).

Della Corte et al (2003) investigated unprotected steel moment-resistant frames and their response subjected to fire following an earthquake. Assuming

elastic perfectly plastic behavior for steel and considering P-Δ effect with P from gravity loads and Δ from the earthquake, the fire resistance was evaluated. It is worth noting that the degradation of stiffness was ignored in Della Corte et al.'s work. Further study on steel frames was carried out by Zaharia and Pintea (2009). They investigated two different steel frames, designed for two various return periods of ground-motion; 2475 years return period and 475 years. The seismic response of the structures was then evaluated by a pushover analysis. While the frame designed for the 2475 years return period remained elastic in the pushover analysis, the weaker frame designed for 475 years return period sustained notable inter storey drift. They then performed a fire analyses on both frames, which confirmed that the fire resistance of the structures considering their deformed state under earthquake is notably lower than the structures that do not have any history of deformation prior to the application of the fire. Mostafaei and Kabeyasawa (2010) investigated PEF resistance of reinforced concrete structure with shear wall. The model was first subjected to the Kobe 1995 earthquake on a shaking table. The damage sustained by the structure was quantified by the method of observation as well as using a developed method called Axial-Shear-Flexure Interaction (ASFI), as proposed by Kabeyasawa and Mostafaei (2007), followed by a numerical thermal analysis to find the temperature rise in and around both the seriously damaged and the intact sections subjected to fire. Fire loading was then applied to the damaged structure considering the effect of concrete degraded compressive strength. The results showed that the ability of the structure to sustain gravity loads in the damaged components is considerably lower in comparison to the intact components. In the same year, Faggiano and Mazzolani (2011) investigated steel structures exposed to post earthquake fire. They performed coupled analyses consisting of both earthquake and fire. Based on the FEMA356 procedure, Faggiano and Mazzolani (2011) developed a method for evaluating the performance of buildings subjected to earthquake, suggesting fire performance levels for various conditions of fire. In the coupled analyses, both residual deformation and degradation of mechanical characteristics were applied. However, the method can be more effective for steel structures, because as was previously mentioned, in reinforced concrete structures, seriously damaged sections play an important role on PEF resistance. Recently, Ervine et al (2012) conducted an experimental and a numerical study on a reinforced concrete element subjected to conventional loads followed by a fire load. Applying two concentrated vertical loads on the specimen and recording the subsequent deflection, the created cracks were observed through the member. The model was then subjected to fire load to find the effect of created cracks on the changes of thermal propagation inside the section. The results showed that minor tensile cracking would not considerably change the heat penetration inside the section. They concluded that fire resistance of the intact specimen and the minor damaged specimen are roughly identical. However, exposing the rebar directly to fire, i.e. in case of crushing of cover, considerably changes both the thermal and the structural behavior of the specimen. Another study on this issue was recently undertaken by Bhargava et al (2010) on the fire resistance of an earthquake damaged RC frame. A nearly full-scale portal frame was firstly loaded by the relevant gravity loads and then subjected to a cyclic lateral load based on the Indian standard in a quasi-static fashion. Moreover, load-controlled mode was considered to meet 2% drift corresponding to the Life Safety performance level as described in FEMA 356 code. The crack widths were then observed using optical tools, non-destructive tests and ultrasonic method. A computational analysis was also performed using the finite element package ABAQUS for making a comparison between the test and the analytical results. The results showed a good conformity with FEMA356 descriptive definition of damage levels at various performance levels as such Immediate Occupancy (IO) and Life Safety (LS). It was suggested that the results of quasi-static cyclic test can be used for the subsequent fire analysis.

More recently, Behnam and Ronagh (2012a, b) investigated the effects of prior damage on the PEF resistance of RC portal frames. The results showed that there was minor difference between the fire resistances of the fire alone situation and the situation where the frames are pushed to the IO level of performance under PEF. However, a significant difference was observed between the fire only situation and the situation where the frames are pushed to arrive at LS or CP levels of performance under PEF. The results also showed that fire resistance decreases more significantly when beams are exposed to fire in comparison to column exposure. In separate studies, they proposed different engineering solutions in order to improve the PEF resistance of existing structures and those to be constructed in future (Behnam and Ronagh 2012c, 2013).

Inspired by the aforementioned studies, the current research numerically investigates the PEF resistance of an RC frame designed for Life Safety performance level. The reported study includes a sequential analysis comprising both earthquake and the post-earthquake fire.

2 SEQUENTIAL ANALYSIS

A sequential analysis is used to appropriately analyze a structure under post-earthquake fire. Fig. 2 schematically shows the stages of a nonlinear sequential analysis. The first stage of loading is the application of gravity loads, which are assumed to be static, uniform and constant throughout the analysis. A pseudo earthquake load, in addition to the gravity loads, follows in a push over fashion reaching its maximum value and returning back to zero in a short time. The pattern chosen for the pseudo earthquake load is similar to pushover analysis with a difference that the structure

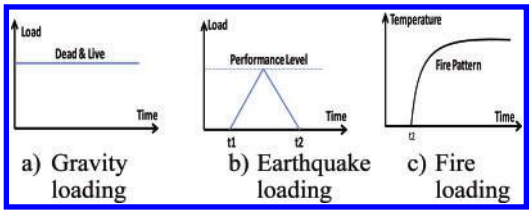


Figure 1. Stages of the sequential analysis.

is unloaded after reaching certain level of load. It is assumed that the maximum level of earthquake load corresponds to life safety level of FEMA356. This assumption is in line with the seismic design philosophy in which the performance level of structures shall not exceed life safety level when subjected to the "Design earthquake". Therefore, the structure is pushed to this life safety level and then is unloaded. It should be noted that no dynamic effects are considered in this study. Finally, as can be seen in Fig. 1, the fire load is applied to the structure after the lateral load is unloaded. Prior to fire loading, properties of structures are set to the reference temperature, but during fire, mechanical properties change with temperature.

In this research, incorporating the pattern shown in Fig. 1 and using SAP2000 for the pushover analysis and SAFIR (Franssen 2011) for the fire analysis, sequential seismic and fire analyses are performed.

3 PUSHOVER ANALYSIS

The static pushover analysis is one of the nonlinear static methods that are used for analyzing structures subjected to seismic loads. This method is becoming a popular tool for seismic performance evaluation of existing and new structures (Cardone et al 2009). In this method, using a specific load pattern, the structure is pushed to arrive at a displacement called the target displacement. The target displacement serves as an estimate of the global displacement that the structures is expected to experience in a design earthquake often represented by the roof displacement at the center of mass of the structure. In this study, a vertical distribution of loads proportional to the shape of the fundamental mode in the direction under consideration is used. Building performance is a combination of the performance of both structural and nonstructural components. According to FEMA356, the structural performance level is divided into four main categories: Operational (O), Immediate Occupancy (IO), Life Safety (LS) and Collapse Prevention (CP), which represent states of minor damage to notable damage.

4 FIRE FRONTIERS

Life Safety performance level is considered in the current study for the seismic analysis prior to fire loading. Structures experiencing plastic deformations do not return to their initial condition as residual deformation remains within the structure. Using the definition of lumped plasticity, the potential locations of high plasticity are introduced by plastic hinges in SAP2000 (2002).The moment-rotation behavior of each plastic hinge follows FEMA definition. These definition in a concrete cross section are required for the post-earthquake fire analysis, because variation of temperature across the section is highly dependent on the state of damage (Ervine et al, 2012). In FEMA356, it is stipulated that in the Life Safety performance level, extensive damage is observed in beams and columns, resulting in spalling of cover and mostly in the areas of created plastic hinges. The experimental tests conducted by Sharma et al. and Meada et al. also showed the good agreement between the FEMA prescriptive definition of damage state with the experiments (Behnam & Ronagh 2012c, 2013).

5 FIRE PATTERNS

Several methods have been proposed to determine the thermal actions produced by a fire within a compartment (Ramesh and Tan 2007 and Lundin 2005). These methods are established either using parametric fires called time-temperature curves such as those mentioned in ISO 834, and ASTM E119 (based on experiment and tests) or using natural fire which rely mainly on the volume of the produced gas by the combustible materials within a covered space such as those stated in SEI and ASCE. Both models, i.e. the time-temperature curve and the natural fire, are represented assuming a fully developed fire. The produced temperature resulted from burning combustible materials are lumped into one single parameter (Drysdale 2011).

A finite element method (FEM) based program SAFIR is used in the current study to calculate the fire resistance of the selected models. The program performs nonlinear analyses on one, two or three dimensional structures considering both geometrical and material nonlinearity. The analyses can be performed under ambient or elevated temperature. The stress-strain relationships for various materials as well as their thermal characteristics are embedded in the software according to Eurocodes. Meanwhile, accounting for thermal action in a structure, both 'time-temperature curves' and 'natural fire' can be used. Structures that are exposed to fire are analyzed in two stages – thermal analysis and structural analysis. In the thermal analysis, the temperature within a cross-section at every thermal step is stored to be used for the subsequent structural step. For the purpose of this study, the time-temperature curve according to ISO 834 without cooling phase is used as shown in Fig. 2.

6 CASE STUDIES

A reinforced concrete frame designed for PGA of 0.35 g is chosen for the current study, which is loaded and designed based on ACI 318-08 code; the properties of the designed frame are presented in Fig. 3.

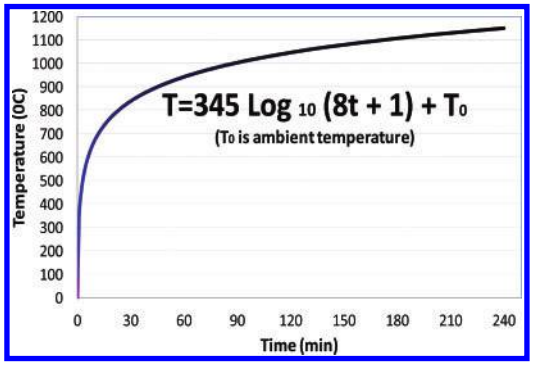


Figure 2. Fire pattern according to ISO834.

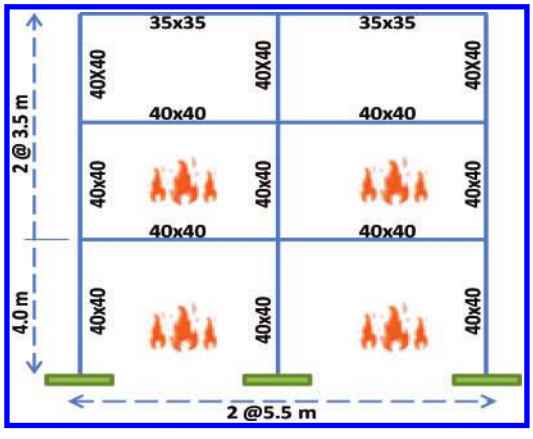


Figure 3. Geometric properties of selected case.

The structure is made of normal strength concrete with compressive strength of 25 MPa and longitudinal and transverse reinforcing bars with a yield stress of 400 MPa. The frame is dimensioned for the load combinations of 7.5 kPa dead load and 2.2 kPa live load. Combination of total dead load and 20% of live load is used to find the mass for calculating the earthquake load (ACI 318, 2008). The plastic hinge length (L_P) could be determined using a number of available methods; the formula proposed by Park and Paulay (1975) formula has been used due to its simplicity yet widely accepted accuracy. The plastic hinge length L_P is taken equal to $0.5H$ and H is the section height.

The model has been exposed to a standard fire (ISO834 curve) scenario for 4 hours. Concrete moisture content is assumed to be 2% for thermal analysis. The thermal expansion coefficients of rebar and that for concrete are taken as $12 \times 10^{-6}/°C$ and $10 \times 10^{-6}/°C$ respectively, whilst the Poisson's ratio of concrete is taken as 0.2. To achieve a clear understanding of the behavior, fire analysis was performed for the undamaged frame i.e. before occurrence the ground-motion. It must be noted that while exterior side of external columns is not exposed to fire, all sides of interior columns are subjected to high-temperature. Meanwhile, three sides of beams are exposed to fire as the top face is assumed to be protected by the concrete slab.

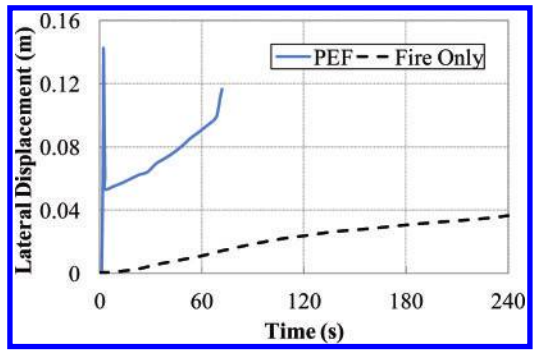


Figure 4. PEF resistance of the frame. Note: 2nd story lateral displacement plotted.

7 RESULTS

The sequential analysis comprises of three main stages that are gravity loading, followed by seismic pushover analysis, and finally post earthquake fire. In seismic analysis, the structure is subjected to a monotonically increasing lateral load to attain a certain level of drift. According to seismic codes philosophy, it is expected that ordinary structures like residential buildings remain at life safety level of performance. According to ASCE 7-10, the drift limit of 2% is used to control the lateral displacement of structures with the first period greater than 0.70 second. FEMA assumes that controlling this limit adequately provides for the life safety performance of a structure. The first modal period of the selected cases is greater than 0.70 seconds, thus, the selected structures are pushed to 0.02 drift. SAP2000 program is used for utilizing nonlinear pushover analysis with the hinges defined according to FEMA 356.

Fig. 4 plots displacement against time for the cases considered referring to the fire resistance of the frames for both scenarios (fire and PEF). The fire resistance is defined as the time at which the displacements, either globally (i.e. the drift of a certain point) or locally (i.e. the deformations at the middle of a beam), go beyond the chosen thresholds. The thresholds have been identified by the curve for displacements versus time step merging towards a vertical asymptote by 1% error. These thresholds implicitly represent the definition of fire resistance of a member as described earlier, where the member is not able to resist the initially applied gravity loads (Kodur and Dwaikat 2007).

It is obvious that the fire resistance of the damaged frame is much lower than the intact frame. While the fire resistance rating for the undamaged frame is around 4 hours, that for the PEF situation is only around 55 minutes. The collapse mechanism in fire alone scenario is local collapse, typically originating from the collapse of beams, whilst it fails in global fashion in PEF scenario causing a considerable lateral

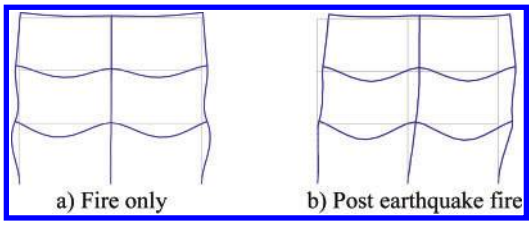


Figure 5. Collapse mechanism.

movement in the columns. Fig. 5 schematically shows two types of stated collapse failures.

8 CONCLUSION

Post-earthquake fire is one of the most problematic situations in seismic regions. The current paper presents a sequential nonlinear analysis for post earthquake fire. A three story RC frame was selected and designed for a PGA of 0.35 g, which was pushed to the maximum allowable inter-story drift and is assumed to satisfy the Life Safety performance level. Pushover curve was extracted for use in subsequent analysis. In addition, 1st and 2nd floor were subjected to fire. Sequential loading consisting of gravity and lateral loads followed by fire was a key aspect of the study conducted using FE package SAFIR. P-Δ effect and residual lateral deformations as well as degradation in stiffness were considered in SAFIR. Defining damaged sections – in terms of spalling of cover – in thermal analysis was another aspect considered in the fire analysis. The patterns of the damaged members were inspired from the descriptive definition of FEMA356 for building designed for the Life-Safety level of performance and the results of experimental tests. The following remarks can be made from the observations:

- While the fire resistance of the frame in the fire only situation was around 240 minutes, it considerably declined to around 55 minutes in post-earthquake fire. Thus it is obvious that structures suffering damage from earthquake loads could have significantly lower fire resistance than the undamaged structures. This could be the result of residual lateral displacements, the degradation in strength and stiffness, the direct heating of the steel reinforcement as a result of removal of cover that exacerbate the effects of fire.
- Two types of collapse mechanisms were observed during the fire analyses. While the global collapse occurred in the frames subjected to fire after an earthquake, the local collapse happened for the fire only case. The global collapse is mostly because of considerable lateral movement of the columns, whilst the local collapse occurs because of beam failure.
- The investigation performed herein represents a certain class of structures; further studies are required, either numerical or experimental, on different levels of performance and structures subjected to post-earthquake fire in order to develop a better understanding of this important issue.

REFERENCES

ABAQUS, 6.8, 2008, Dassault Systemes Simulia Corp: Providence.

ACI318, *Building code requirements for structural concrete (ACI 318-08) and commentary*, 2008, American Concrete Institute: America.

Behnam, B. and H.R. Ronagh, *Methodology for Investigating the Behavior of Reinforced Concrete Structures Subjected to Post Earthquake Fire.* Advances in Concrete Construction, An international Journal, 2012.

Behnam, B. and H.R. Ronagh, *A Post-Earthquake Fire Factor to Improve the Fire Resistance of Damaged Ordinary Reinforced Concrete Structures.* Accepted in Journal of Structural Fire Engineering, 2012a.

Behnam, B. and H.R. Ronagh, *Post-Earthquake Fire Resistance of CFRP strengthened Reinforced Concrete Structures.* Accepted in The Structural Design of Tall and Special Buildings 2013.

Bhargava, P., et al. *Fire testing of an earthquake damaged RC frame*. in *Sixth International Conference of Structures in Fire*. 2010. Pennsylvania, America.

Cardone, D., G. Palermo, and M. Dolce, *Direct Displacement-Based Design of Buildings with Different Seismic Isolation Systems.* Journal of Earthquake Engineering, 2009. **14**(2): p. 163–191.

Chen. S., Lee. George C., and Shinozuka.M. *Hazard mitigation for earthquake and subsequent fire*. in *Annual meeting: Networking of young earthquake engineering researchers and professionals*. 2004. Honolulu, Hawaii: Multidisciplinary Centre for Earthquake Engineering Research, Buffalo, N.Y.

Della Corte, G., R. Landolfo, and F.M. Mazzolani, *Post earthquake fire resistance of moment resisting steel frames.* Fire Safety Journal, 2003. **38**(7): p. 593–612.

Drysdale, D., *Introduction to Fire Dynamics (3rd Edition)*, 2011, John Wiley & Sons.

Ervine, A., et al., *Thermal propagation through tensile cracks in reinforced concrete.* Journal of Materials in Civil Engineering, 2012. **24**(5): p. 516–522.

Faggiano, B. and F.M. Mazzolani, *Fire after earthquake robustness evaluation and design: Application to steel structures.* Steel Construction, 2011. **4**(3): p. 183–187.

Franssen, J.M., *User's manual for SAFIR 2011 a computer program for analysis of structures subjected to fire*, 2011, University of Liege, Belgium.

International Building Code, *IBC*, in *Facilities 3. NFPA 101-100* 2006, National Fire Protection: America.

Kabeyasawa, T. and H. Mostafaei, *Axial-shear-flexure interaction approach for reinforced concrete columns.* ACI Structural Journal, 2007. **104**(2): p. 218–226.

Kodur, V.K.R. and M. Dwaikat, *Performance-based Fire Safety Design of Reinforced Concrete Beams.* Journal of Fire Protection Engineering, 2007. **17**: p. 293–320.

Kwak, H.-G. and S.-P. Kim, *Simplified monotonic moment–curvature relation considering fixed-end rotation and axial force effect.* Engineering Structures, 2010. **32**(1): p. 69–79.

Lundin, J., *On quantification of error and uncertainty in two-zone models used in fire safety design.* Journal of Fire Sciences, 2005. **23**(4): p. 329–354.

Mostafaei, H. and T. Kabeyasawa. *Performance of a six-story reinforced concrete structure in post-earthquake fire*. in *10th Canadian Conference on Earthquake Engineering*.

2010. Toronto, Ontario: Institute for Research in Construction.

Mousavi, S., V.K.R. Kodur, and A. Bagchi, *Review of post earthquake fire hazard to building structures.* Canadian Journal of Civil Engineering, 2008. **35**(7): p. 689–698.

National Research Council Canada, *National fire code in buildings* in 2005, National Research Council Canada: Ottawa, Canada.

Park, R. and Paulay, T. *Reinforced concrete structures*. 1975, New York: John Wiley & Sons. 769.

Remesh, K. and K.H. Tan, *Performance comparison of zone models with compartment fire tests.* Journal of fire sciences, 2007. **25**(4): p. 321–353.

Ronagh, H.R. and B. Behnam, *Investigating the effect of prior damage on the post-earthquake fire resistance of reinforced concrete portal frames.* International Journal of Concrete Structures and Materials 2012.

SAP2000-V14, *Integrated finite element analysis and design of structures basic analysis reference manual*, 2002, Berkeley, CA, USA.

Taylor, J., *Post earthquake fire in tall buildings and the New Zealand building code*, in *Civil Engineering* 2003, University of Canterbury: Christchurch, New Zealand. p. 160.

Zaharia, R. and D. Pintea, *Fire after earthquake analysis of steel moment resisting frames.* International Journal of Steel Structures, 2009. **9**(4): p. 275–284.

Research and Applications in Structural Engineering, Mechanics and Computation – Zingoni (Ed.)
© 2013 Taylor & Francis Group, London, ISBN 978-1-138-00061-2

Behaviour of structural steel subjected to post-earthquake fire

S. Sinaie, A. Heidarpour & X.L. Zhao
Department of Civil Engineering, Monash University, Melbourne, Australia

ABSTRACT: The mechanical response of a structural element not only depends on the inherent properties of the materials which constitute the element, but also on the history of any previously applied loads. An important instance is the response of steel structures subjected to post-earthquake fire, whereby the behaviour of steel at high temperatures is highly dependent on the existence and intensity of any prior cyclic load. While the individual effects of cyclic and thermal loadings on structural steel have been widely investigated in the literature, the effect of their sequential action is yet to be determined. This research aims to yield a fundamental understanding of the effect of a prior history of cyclic loads on the proceeding monotonic properties of grade 300PLUS steel at high temperatures. Results indicate that the effect of prior cyclic loads should be induced into fire resistant guidelines.

1 INTRODUCTION

Behaviour of structural steel not only depends on the innate properties of the material itself, but also on the history of loads it has already sustained. In other words, the responsive outcome of a certain type of load (e.g. monotonic) acting on a steel sample may differ if the sample had previously been subjected to another type of load. This is an example of what is further referred to as multi-phase loading history. In this work, multi-phase loading history is defined as the sequential action of different types of loads, whereby each type invokes a disparate behaviour of the material.

From a crystallographic point of view, the behavioural change in subsequent phases of an multi-phase loading history is due to the rearrangement of the dislocation structure during the previous phase (Kitayama et al., in press). On the other hand, from a modelling perspective, the memory of this history is preserved in the internal variables of the model, e.g. the hardening variables of a constitutive plasticity model (Lubliner 1990).

This work addresses the changes that cyclic loading induces on the subsequent response of steel under monotonic loads at high temperatures, or in other words, the post-cyclic thermal response of structural mild steel. While the individual effect, and the combined simultaneous effect of cyclic loading and thermal loading have been widely examined in the past (Kent & Park 1973, Outinen & Mekelainen 2002, Dusikia et al. 2007), research on their sequential effect in the form of a multi-phase loading history is scarce. An instance of such research is the work of Song et al. (2012).

Understanding post-cyclic thermal response at the material scale provides the means to the understanding of post-earthquake fire response at the structural scale. While design codes provide expressions for the mechanical properties of steel as a function of temperature for fire-resistant design, post-earthquake fire-resistant design of steel structures requires more knowledge about the multi-phase behaviour. The experimental work carried out in this research aims to address this phenomenon. The following sections briefly describe the test setup as well as the experimental results.

2 TEST PROGRAM

2.1 *Test setup*

All specimens used in this study were made from grade 300PLUS steel taken from the flange of 200UB22.3 hot rolled sections (BHP 1998). The preparation of the samples is consistent with the requirements of ASTM E606-92(1998). The specimen geometry is illustrated in Figure 1. Both faces of the specimens were grinded to give uniform thickness and a smooth finish across the entire surface. Specimens were restrained by means of two 12 mm high strength bolts at each end. the mechanical properties of the material at ambient state are given in Table 1.

In Table 1, E is the elastic modulus. σ_y and ε_y represent the yield stress and yield strain, respectively. σ_u and ε_u are the ultimate stress and ultimate strain, respectively. $H_{2.0}$ is the tangent modulus at $\varepsilon = 2.0\%$ where strain hardening initiates.

2.2 *Cyclic phase*

For the cyclic phase, a specifically built fixture was used to prevent the specimens from buckling about

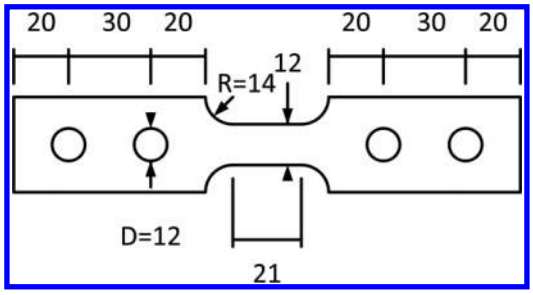


Figure 1. Sample geometry and dimensions in millimetres.

Table 1. Mechanical properties of test specimens.

E (GPa)	σ_y (MPa)	ε_y (%)	σ_u (MPa)	ε_u (%)	$H_{2.0}$ (GPa)
205	349	0.1807	518	19.55	4.465

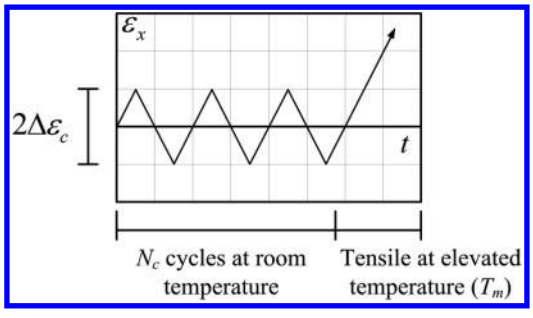


Figure 2. Multi-phase loading history including a cyclic phase at ambient state and a monotonic tensile phase at elevated temperature.

the weak axis. This fixture was comprised of two 12 mm plates with aligned holes in order to be fastened by appropriate bolts. The inner faces of these two plates which would be in contact with the specimen were polished and greased to yield minimum friction. Loads were applied by an Instron test machine (model 5892) with a 100 kN capacity. Axial force values were attained by the machine's built-in transducer, while strains were accumulated by a non-contact MTS laser extensometer (model LX1500). Tests were carried out in displacement control, however, the displacement rates were adjusted such that strain rates never exceeded 10^{-4} s^{-1}, which guarantees rate-independent behaviour. Figure 2 illustrates the loading history applied to the samples, where the number of cycles (N_c) and their amplitude ($\Delta\varepsilon_c$) are considered as variables for different test cases.

2.3 *Monotonic tensile phase at elevated temperature*

The anti-buckling fixture was removed prior to starting this phase of the test. The temperature was raised by means of an Instron thermal chamber (model 3119-408). The temperature of the sample was logged using

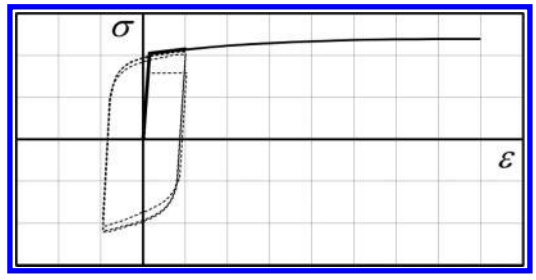


Figure 3. Multi-phase response of steel under strain-controlled cyclic load followed by a monotonic tensile load.

three thermocouples at three different heights of the sample's gage length. Loading was initiated after the temperature of these three points had stabilized with a gradient of less than 2%. Again, with the loading being in displacement control, the displacement rate was accordingly adjusted to limit the resulting strain rates to a rate-independent range. Strains were accumulated as before using the noncontact laser extensometer. Loading as well as data accumulation (at a frequency of 4 Hertz) was continued until failure. However, only the data attained up to the formation of necking will be presented.

3 TEST RESULTS

Five different combinations of $(\Delta\varepsilon_c, N_c)$ where used: that is $(0\%, 0)$, $(1\%, 3)$, $(1\%, 9)$, $(2\%, 3)$ and $(2\%, 9)$. The first combination represents a simple tensile test and is only expressed in this form for consistency. Hence, each sample's label will be expressed in the form AXCY, where A indicates amplitude and X is substituted with the value of amplitude ($\Delta\varepsilon_c$) in percentage strain and C indicates cycle and Y is substituted with N_c. For example, A1C9 represents a sample with a history of being subjected to 9 cycles of 1% strain amplitude. Each $(\Delta\varepsilon_c, N_c)$ combination is coupled with four different temperatures (T_m), namely Room temperature, 150°, 300° and 450° Celsius.

Figure 3 illustrates the typical behaviour of steel under the case of a cyclic-tensile multi-phase loading history. In this figure, the dashed line indicates the strain-controlled cyclic behaviour, whereby cyclic hardening is evident. While this figure shows only three cycles, it is worth noting that the cyclic hardening effect is observed to get stabilized around the sixth cycle, and by the ninth cycle a completely stabilized hysteresis loop is experienced. The solid line in this figure represents the response under the subsequent monotonic tensile phase of loading.

With the properties of the monotonic phase being of primary interest, Figure 4 is presented to indicate the selected properties. In this figure, $\sigma_{0.2}$ indicates the proof stress while $\varepsilon_{0.2}$ represents its corresponding strain. The ultimate stress and its corresponding strain are denoted by σ_u and ε_u, respectively and W represents the work per unit volume from the origin of the

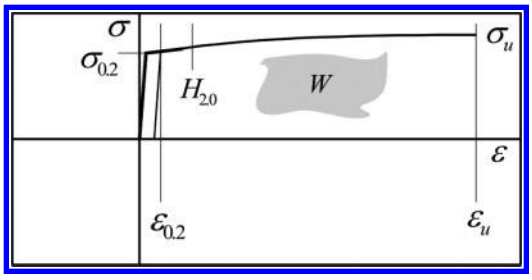


Figure 4. Mechanical properties of the post-cyclic tensile phase.

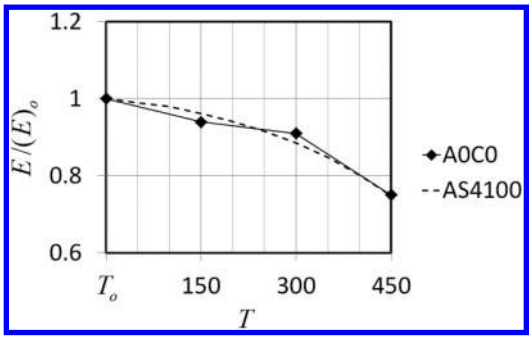


Figure 5. Variation of elastic modulus with temperature.

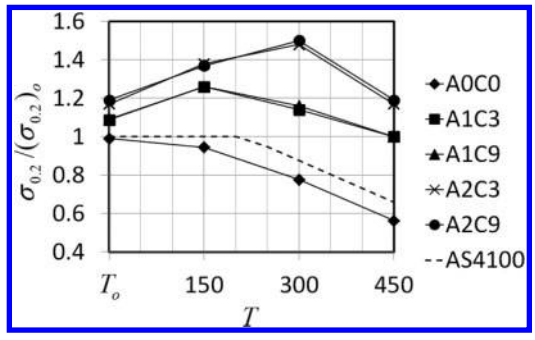


Figure 6. Variation of proof stress with temperature.

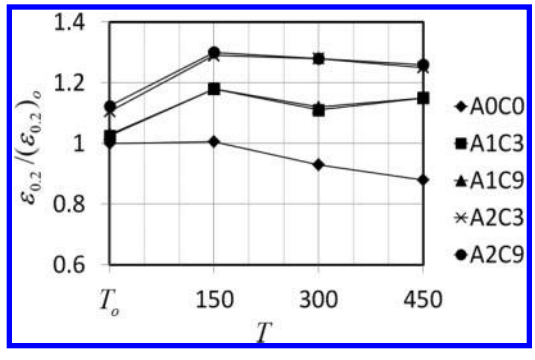


Figure 7. Variation of the strain corresponding to proof stress with temperature.

solid line up to the point of ultimate stress. In addition, with $\varepsilon = 2\%$ being the strain at which strain hardening initiates under a standard tensile test at ambient state, the tangent modulus $H_{2.0}$ at $\varepsilon = 2\%$ is also indicated as a variable of interest.

Before presenting the results, it is worth mentioning that given the common chemical composition of structural mild steel, this material gains hardened properties as the temperature rises up to about 150° C. However, the hardened properties tend to diminish as the temperature reaches 380° C, which afterwards, the material starts to soften. This behaviour was witnessed in the test program and is observed in the following results.

Figures 5–11 illustrate the variation of each of the aforementioned monotonic-phase variables as a function of temperature and cyclic-phase parameters, i.e. T_m, $\Delta\varepsilon_c$ and N_c. All values are normalized using their corresponding value for A0C0 at ambient temperature (denoted by the 'o' subscript).

Figure 5 shows the variation of the elastic modulus against temperature. The monotonic decrease of elastic modulus as the result of increasing temperature is the expected behaviour. The dashed line in this figure is the graph of the expression given by the Australian standard (AS4100 1998). It can be seen that the results obtained by experiment show good agreement with the design code expression.

The variation of the proof stress ($\sigma_{0.2}$) with temperature is presented in Figure 6. This figure shows that for the case with no previous cyclic history (i.e. A0C0), the proof stress monotonically decreases as temperature increases. However, for all other cases (which had previous cyclic histories), as the temperature increases, the value of $\sigma_{0.2}$ exhibits an initial increase followed by a decrease. Also shown in this figure, by the dashed line, is the graph of the expression given by AS4100 for the yield stress. The test results and design code expression are rather consistent, both in terms of value and variation pattern.

Figure 7 illustrates the variation of the strain corresponding to the proof stress, denoted by $\varepsilon_{0.2}$, with temperature. For the case with no cyclic history (A0C0), a monotonic decrease is observed. This is not the case for tests with previous cyclic histories and for these cases, the variation of $\varepsilon_{0.2}$ with temperature doesn't present a specific pattern. However, it is evident that the amplitude of the strain controlled cycles ($\Delta\varepsilon_c$) has a significant effect on $\varepsilon_{0.2}$. Moreover, what can be understood from Figures 6 and 7 is that the number of cycles does not affect the proof stress and the corresponding strain.

Illustrating the variation of the ultimate stress with temperature, Figure 8 can be considered as one of the most important results regarding post-cyclic thermal response. It has already been mentioned that this type of steel tends to attain hardened properties up to a temperature of 150° C. This is clearly evident in Figure 8. However, this figure demonstrates that a similar behavioural pattern also exists for samples which have a history of cyclic loading. Moreover, this figure shows a small increase of σ_u with the increase of cyclic loading parameters ($\Delta\varepsilon_c$ and N_c). While this increase in σ_u

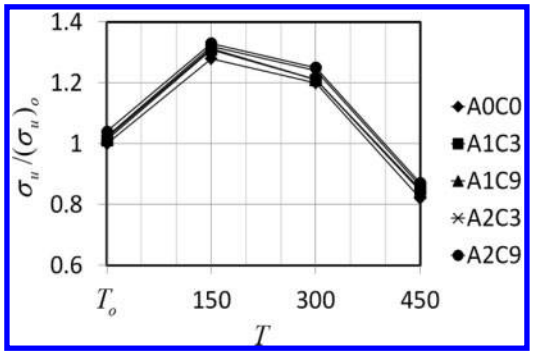


Figure 8. Variation of ultimate stress with temperature.

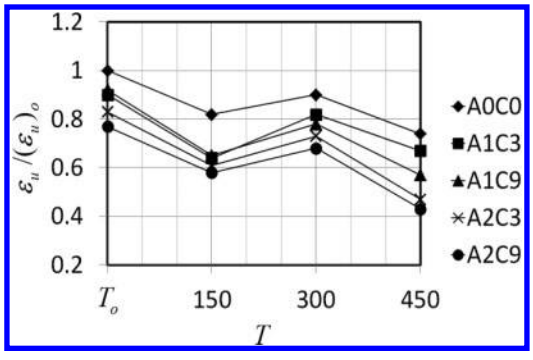


Figure 9. Variation of ultimate strain with temperature.

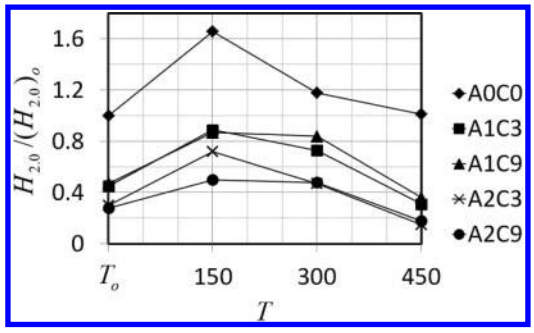


Figure 10. Variation of tangent modulus (at 2% strain) with temperature.

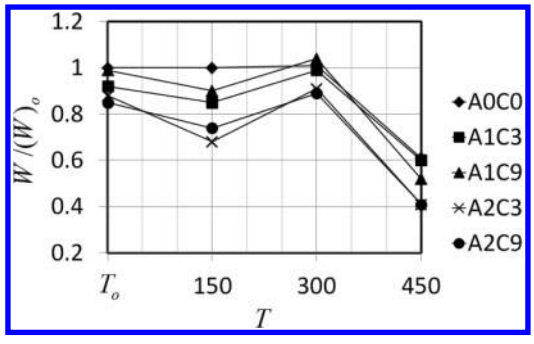


Figure 11. Variation of work per unit volume with temperature.

is small compared to the value of σ_u at temperatures up to 380° C, it becomes more prominent as the value of σ_u decreases with temperature. It appears that the value of σ_u for a post-cyclic thermal scenario can be obtained by adding the value of σ_u for a given temperature without a cyclic history (A0C0) to the increase that σ_u exhibits as the result of cyclic loads alone. This can be quite useful for design purposes, eliminating the need for exhaustive calculations.

As the counterpart for σ_u, the variation of ε_u with temperature is illustrated in Figure 9. This figure shows a fluctuation of the ultimate strain with rising temperature for A0C0 (no previous cyclic history). With the presence of a cyclic history, the same pattern is followed, however, with a significant drop in the value of ε_u as the cyclic-phase loading parameters are increased. It seems that further tests at higher temperatures must be carried out in order to gain a more definite understanding of these variations (These tests are currently being carried out at Monash University).

Figure 10 shows the variation of $H_{2.0}$ with temperature. This figure shows that for A0C0, the value of $H_{2.0}$ initially increases and then decreases with rising temperature. A nearly similar pattern is followed by other cases with a previous cyclic history, however, with lower values of $H_{2.0}$ as the cyclic-phase loading parameters ($\Delta\varepsilon_c$ and N_c) are increased.

Figure 11 illustrates the variation of work per unit volume against temperature. For A0C0, an almost constant value of W is observed for temperatures up to 300° C. However, W tends to decrease as the temperature passes 300° C. A different pattern is observed for cases with previous cyclic history. While these cases follow a similar pattern, they result in lower values of W, especially as $\Delta\varepsilon_c$ increases.

4 CONCLUSIONS

The aim of this research was to gain a fundamental understanding of the effect of a prior history of cyclic loads on the subsequent monotonic properties of a specific type of structural steel known as grade 300PLUS at elevated temperatures. For this purpose, steel specimens were initially subjected to a number of strain-controlled load cycles, and then monotonically loaded in tension at different temperatures until failure. With the number of cycles and strain amplitude serving as variables for the cyclic stage, and temperature being the variable for the monotonic stage, their combined influence on the mechanical properties of structural steel was examined.

The following conclusions can be drawn from the experimental results.

– Regarding the variations illustrated in Figures 8 and 9, the fact that the variations of σ_u and ε_u do not change pattern as a result of a previous cyclic history, but only shift in value, has great implications in view of developing design guidelines. This feature

allows the superposition of the individual effects of cyclic loads and thermal loads, in order to get the effect of their sequential combination.
- Whether ductility is viewed as the ratio of $\varepsilon_{0.2}/\varepsilon_u$, or work per unit volume (W), or simply by comparing combinations of $(\sigma_u, \varepsilon_u)$, it is evident that the existence of a previous cyclic phase decreases the ductility of the proceeding monotonic phase. This decrease is combined with the changes caused by elevated temperature. Therefore, it is reasonable to say that the sequential effect of cyclic load and temperature may lead to situations more severe than when the rise in temperature had not been preceded by a cyclic load. This indicates the fact that new formulations need to be developed for a post-earthquake fire-resistant design.
- Further tests should be conducted at higher temperatures in order to get a better understanding of the variations of $\varepsilon_{0.2}$ and ε_u. These test are currently being carried out at Monash University.

ACKNOWLEDGEMENT

The research work presented in this paper was supported by the Australian Research Council through a Discovery Project (DP1096454) awarded to the second author.

REFERENCES

ASTM E606-92(1998), Standard practice for strain-controlled fatigue testing. American Society of Testing and Materials. Annual book of ASTM standards, Philadelphia, PA.

Broken Hill Proprietary Limited. Hot rolled products. Melbourne: BHP; 1998.

Dusicka, P., Itani, A. M. & Buckle, I. G. 2007. Cyclic response of plate steels under large inelastic strains. *Journal of Constructional Steel Research*, 63(2), 156–164.

Kent, D. C. & Park, R. 1973. Cyclic load behaviour of reinforcing steel. Strain, 9(3), 98–103.

Kitayama, K., Tomé, C. N., Rauch, E. F., Gracio, J. J. & Barlat, F. 2012. A crystallographic dislocation model for describing hardening of polycrystals during strain path changes. Application to low carbon steels. International Journal of Plasticity, http://dx.doi.org/10.1016/j.ijplas.2012.09.004.

Lubliner, J. 1990. *Plasticity theory,* New York, Macmillan Publishing.

Outinen, J. & Mäkeläinen, P. 2002. Mechanical properties of structural steel at elevated temperatures. *Advances in Steel Structures (ICASS '02)*. Oxford: Elsevier.

Song, Q., Heidarpour, A., Zhao, X. L. & Han, L. H., 2012, Nonlinear finite element modelling of flexible I-beam to square hollow section column connections subjected to earthquake and subsequent fire, Tubular Structures XIV, 12 September 2012 to 14 September 2012, CRC Press – Taylor & Francis Group, London UK, pp. 591–598.

Standards Australia, AS4100-1998 Steel structures, Sydney; 1998.

28. Structural safety, structural reliability, risk assessment

Research and Applications in Structural Engineering, Mechanics and Computation – Zingoni (Ed.)
© 2013 Taylor & Francis Group, London, ISBN 978-1-138-00061-2

Target reliability for engineering structures

M. Holický
Klokner Institute, Czech Technical University, Prague, Czech Republic

ABSTRACT: The target reliability levels recommended in national and international documents vary within a broad range, while the reference to the cost of construction and failure consequences is mentioned only very vaguely. In some documents the target reliability index β is indicated for one or two reference periods (1 year and 50 years) without providing an appropriate link to the design working life. This contribution attempts to clarify the relationship between the target reliability levels, structural costs, failure consequences, reference period, the design working life and the discount rate. The theoretical study based on probabilistic optimization is supplemented by recommendations useful for code developers and practicing engineers. It appears that the optimal reliability level depends primarily on the construction costs, failure costs and relative cost for improving structural safety, and less significantly on the discount rate and the time to failure. In design based on the partial factor method, it is recommended that the characteristic values of the basic variables be defined independently of the design working life; to specify the design values on the bases of optimal reliability index; and to derive the partial factors from the specified design values and defined characteristic values.

1 INTRODUCTION

The target reliability levels recommended in various national and international documents for new structures are inconsistent in terms of the recommended values and criteria according to which the appropriate values are to be selected. Almost no recommendations are available for temporary structures. In general, optimum reliability levels can be obtained by considering both the cost of the structure and the expected cost of failure over the design working life.

The design working life is understood as an assumed period of time for which a structure is to be used for its intended purpose without any major repair work being necessary. Indicative values of design working life (10 to 100 years for different types of new structures) are given in EN 1990 (2002). Recommended values of reliability indexes are given for two reference periods, 1 year and 50 years (see Table 1), without any explicit link to the design working life that generally differs from the reference period, while no specific indicative values are available for temporary structures.

It should be emphasized that the reference period is understood as a chosen period of time used as a basis for statistically assessing time variable basic random variables and the corresponding probability of failure. The concept of reference period is therefore fundamentally different from the concept of design working life. Confusion is often caused when the difference between these two concepts is not recognized.

It should be recognized that the couple of β values (for 1 year and 50 years) given in Table 1 for each reliability class correspond to the same reliability level. Practical application of these values, however, depends on the time period considered in the verification, which may be linked to available probabilistic information concerning time variant basic variables (imposed load, wind, earthquake, etc.). It should be noted that the reference period of 50 years is also accepted as the design working life for common structures (see discussion by Diamantidis (2009)).

For example, considering a structure of reliability class 2 having a design working life of 50 years, the reliability index $\beta = 3.8$ should be used, provided that probabilistic models of basic variables are available for this period. The same reliability level is achieved when a reference period of 1 year and a target of $\beta = 4.7$ are applied using the theoretical models for a reference period of one year. Thus, when designing a structural member, similar dimensions (reinforcement area) would be obtained considering $\beta = 4.7$ and basic variables related to 1 year or $\beta = 3.8$ and basic variables related to 50 years.

A more detailed recommendation concerning the target reliability is provided by ISO 2394 (1998) where the target reliability indexes are indicated for the whole design working life without any restriction concerning its length, and are related not only to the consequences, but also to the relative costs of safety measures (see Table 2).

Similar recommendations are provided in the JCSS (2001) Probabilistic Model Code (Table 3). Recommended target reliability indexes are also related to both the consequences and to the relative costs of safety measures, though for a reference period of

Table 1. Reliability classification in accordance with EN 1990 (2002).

Reliability classes	Consequences of structural failure	Reliability index β for reference period		Examples of buildings and civil engineering works
		1 year	50 years	
RC3 – high	High	5.2	4.3	Bridges, public buildings
RC2 – normal	Medium	4.7	3.8	Residences and offices
RC1 – low	Low	4.2	3.3	Agricultural buildings

Table 2. Examples of life-time target reliability indexes β in accordance with ISO 2394 (1998).

Relative costs of safety measures	Consequences of failure			
	small	some	moderate	great
High	0	1.5	2.3	3.1
Moderate	1.3	2.3	3.1	3.8
Low	2.3	3.1	3.8	4.3

Table 3. Tentative target reliability indexes β (and associated target failure rates) related to one year reference period and ultimate limit states in accordance with JCSS (2001).

Relative costs of safety measures	Minor consequences of failure	Moderate consequences of failure	Large consequences of failure
Large	$\beta = 3.1$ ($p \approx 10^{-3}$)	$\beta = 3.3$ ($p \approx 5 \times 10^{-4}$)	$\beta = 3.7$ ($p \approx 10^{-4}$)
Normal	$\beta = 3.7$ ($p \approx 10^{-4}$)	$\beta = 4.2$ ($p \approx 10^{-5}$)	$\beta = 4.4$ ($p \approx 5 \times 10^{-6}$)
Small	$\beta = 4.2$ ($p \approx 10^{-5}$)	$\beta = 4.4$ ($p \approx 5 \times 10^{-6}$)	$\beta = 4.7$ ($p \approx 10^{-6}$)

1 year. The consequence classes in JCSS (2001) (similar to those in EN 1990, 2002) are linked to the ratio ρ defined as the ratio $(C_{str} + C_f)/C_{str}$ of the total cost induced by a failure (cost of construction C_{str} plus direct failure costs C_f) to the construction cost C_{str} as follows:

- Class 1 Minor Consequences: ρ is less than approximately 2; risk to life, given a failure, is small to negligible and the economic consequences are small or negligible (e.g. agricultural structures, silos, masts);
- Class 2 Moderate Consequences: ρ is between 2 and 5; risk to life, given a failure, is medium and the economic consequences are considerable (e.g. office buildings, industrial buildings, apartment buildings);
- Class 3 Large Consequences: ρ is between 5 and 10; risk to life, given a failure, is high, and the economic consequences are significant (e.g. main bridges, theaters, hospitals, high rise buildings).

However, it is not quite clear what is meant in JCSS (2001) by "the direct failure costs". This term indicates that there may be some other "indirect costs" that may affect the total expected cost. Here it is assumed that the failure costs C_f cover all additional direct and indirect costs (except the structural costs C_{str}) induced by the failure. The structural costs are considered separately and related to the costs needed for an improvement of safety (costs per unit of decision parameter C_1).

Both documents ISO 2394 (1998) and JCSS (2001) seem to recommend reliability indexes that are lower than those given in EN 1990 (2002) even for the "small relative costs" of safety measures. It should be noted that EN 1990 (2002) gives the reliability indexes for two reference periods (1 and 50 years) that may be accepted as the design working life for common structures (see also a discussion provided by Diamantidis (2009)). ISO 2394 (1998) recommends indexes for "life-time, examples", thus related to the design working life, without any restrictions, while Probabilistic Model Code by JCSS (2001) provides reliability indexes for the reference period of 1 year.

However, a clear link between the design working life and the target reliability level is not apparent from any of the above-mentioned documents. Thus, it is not clear which target reliability index should be used for a given design working life different from 50 years (say 10 years).

The basic aim of this contribution is to clarify the link between the design working life and the reliability index and to provide guidance for specification of the target reliability level for a given design working life. The submitted theoretical study based on probabilistic optimization is supplemented by practical recommendations. This contribution is an extension of the previous study by Holicky and Retief (2011).

2 GENERAL PRINCIPLES OF PROBABILISTIC OPTIMIZATION

Probabilistic optimization is based on a fundamental form of the objective function (not covering monitoring and maintenance) expressed as the present value of the total expected cost $C_{tot}(x, q, n)$

$$C_{tot}(x,q,n) = C_{str} \sum_1^n P_f(x,i) + C_f \sum_1^n P_f(x,i) Q(q,i) + \\ + C_0 + x\, C_1 \qquad (1)$$

Here x denotes the decision parameter of the optimization (a parameter of structural resistance), q is the annual discount rate (e.g. 0.03, an average long run value of the real annual discount rate in European countries), n is the number of years to the failure, which may differ from the design working life (specified usually as 50 or 100 years).

Further, $P_f(x, i)$ is the failure probability in year i, $Q(q, i)$ is the discount factor dependent on the annual

discount rate q and the year number i, C_0 is the initial cost independent of the decision parameter x and failure (a quantity not affecting the optimization), and C_1 is the cost per unit of the decision parameter x (a structural parameter quantity affecting the structural resistance and optimization).

Note that the design working life may generally differ from the time to failure denoted by the number of years n and considered here as an independent variable affecting the probability of failure. Maintenance and possible repair of the structure is not included in the objective function (1) and these aspects are to be considered in further studies.

Assuming independence failure events in subsequent years, the annual probability of failure $P_f(x, i)$ in year i may be approximated by the geometric sequence

$$P_f(x,i) = p(x)\,(1 - p(x))^{i-1} \tag{2}$$

The initial annual probability of failure $p(x)$ is dependent on the decision parameter x. Note that annual failure probabilities can be assumed to be independent when failure probabilities are chiefly influenced by time-variant loads (climatic actions, traffic loads, accidental loads). Then the failure probability $P_{fn}(x)$ during n years can be estimated by the sum of the sequence $P_f(x, i)$, that can be expressed as

$$P_{fn}(x,n) = 1 - (1 - p(x))^n \approx n\,p(x) \tag{3}$$

Note that the approximation indicated in equation (3) is fully acceptable for small annual probabilities $p(x) < 10^{-3}$.

The discount factor of the present value of the expected future costs in year i is considered in the usual form as

$$Q(q,i) = 1/(1+q)^i \tag{4}$$

Thus, the cost of malfunctioning C_f is discounted by the factor $Q(q, i)$ depending on the discount rate q and the point in time (year number defined as i) when the loss of structural utility occurs.

Considering equations (2) and (4) the total costs $C_{tot}(x, q, n)$ described by equation (1) this may be written in a simplified form as

$$C_{tot}(x,q,n) = C_{str}\,n\,p(x) + C_f\,p(x)\,PQ(x,q,n) + \\ + C_0 + x\,C_1 \tag{5}$$

Here the total sum of expected malfunction costs during the period of n years is dependent on the product of the present value of malfunction cost C_f, the annual probability $p(x)$ and a sum of the geometric sequence having the quotient $(1 - p(x))/(1 + q)$, denoted as the time factor $PQ(x, q, n)$:

$$PQ(x,q,n) = \frac{1 - \left[\frac{1-p(x)}{1+q}\right]^n}{1 - \left[\frac{1-p(x)}{1+q}\right]} \tag{6}$$

In general the total cost $C_{tot}(x, q, n)$ depends on the costs C_0, C_1, C_f, the annual probability of failure $p(x)$, the discount rate q and the design working life n. Note that for small probabilities of failure $p(x)$ (for appropriate structural parameter x) and very small (zero) discount rate q, the time factor $PQ(x, q, n) \approx n$.

The necessary condition for the minimum of the total cost follows from (1) as

$$\frac{\partial C_{tot}(x,q,n)}{\partial x} = C_{str} \sum_{i=1}^{n} \left[\frac{\partial P_f(x,i)}{\partial x}\right]_{x=x_{opt}} + \\ + C_f \sum_{i=1}^{n} Q(q,i) \left[\frac{\partial P_f(x,i)}{\partial x}\right]_{x=x_{opt}} + C_1 = 0 \tag{7}$$

Equation (8) represents a general form of the necessary condition for the minimum of total cost $C_{tot}(x, q, n)$, the optimum value x_{opt} of the parameter x and the optimum annual probability of failure $p_{opt} = p(x_{opt})$. The optimum probability for the total design working life $T_d = n$ years follows from equation (7) as

$$\sum_{i=1}^{n} Q(q,i) \left[\frac{\partial P_f(x,i)}{\partial x}\right]_{x=x_{opt}} + \\ + (\rho - 1) \sum_{i=1}^{n} Q(q,i) \left[\frac{\partial P_f(x,i)}{\partial x}\right]_{x=x_{opt}} = -\frac{C_1}{C_f} \tag{8}$$

Equation (8) represents a general form of the necessary condition for the minimum of total cost $C_{tot}(x, q, n)$, the optimum value x_{opt} of the parameter x and the optimum annual probability of failure $p_{opt} = p(x_{opt})$. The optimum probability for the total design working life $T_d = n$ years follows from equation (3) as

$$P_{fn,opt} = 1 - (1 - p_{opt})^n \approx n\,p_{opt} \tag{9}$$

The corresponding optimum reliability index $\beta_{opt} = -\Phi^{-1}(P_{fn,opt})$. These quantities are in general dependent on the cost ratio C_f/C_1, discount rate q and the design working life n.

3 FAILURE PROBABILITY OF A GENERIC STRUCTURAL MEMBER

Consider a generic structural member described by the limit state function $Z(x)$

$$Z(x) = x\,f - (G + Q) \tag{10}$$

Here x denotes a deterministic structural parameter (e.g. the cross-section area), f the strength of the material, G the load effect due to permanent load and Q the load effect due to variable load. Theoretical models of the random quantities f, G and Q considered in the following example are given in Table 4 (adopted from JCSS (2001) and Holicky (2009)).

Table 4. Theoretical models of the random variables f, G and Q (annual extremes).

Variables	Distribution	Mean	Standard deviation	Coef. of variation
f	Lognormal	100	10	0.10
G	Normal	35	3,5	0.10
Q	Gumbel	10	5	0.50

Considering the theoretical models given in Table 4, the reliability margin $Z(x)$ may be well approximated by the normal distribution $\Phi_{Z(x)}$ that provides sufficient accuracy. The annual failure probability $p(x)$ is then given as

$$p(x) = \Phi_{Z(x)}(Z(x) = 0) \tag{11}$$

In equation (11) the normal distribution is evaluated for $Z(x) = 0$; then for $x = 1$ and $n = 50$ the probability $P_{fn}(1, 50) \approx 6.7\ 10^{-5}$ and corresponding $\beta \approx 3.8$.

4 AN EXAMPLE

The following example illustrates the general principles, as well as a special case of probabilistic optimization. To simplify the analysis, the total costs $C_{tot}(x, q, n)$ given by equation (5) are transformed to the standardized form $\kappa_{tot}(x, q, n)$ given as

$$\kappa_{tot}(x,q,n) = \frac{C_{tot}(x,q,n) - C_0}{C_1} = \\ = p(x)C_{str}/C_1\left[n + (\rho - 1)PQ(x,q,n)\right] + x \tag{12}$$

Here ρ denotes the cost ratio $(C_{str} + C_f)/C_{str}$ of the sum of cost and failure costs $(C_{str} + C_f)$ to structural costs C_{str}.

The annual probability of failure $p(x)$ considered here for a general structural member is given by equation (11). However, the following procedure may be applied for any relevant dependence of the failure probability $p(x)$ expressed as a function of a suitable structural parameter x.

In the example, illustrated in Figure 1, it is assumed that the discount rate is $q = 0.03$ and the year number when the failure occurs is $n = 50$. Under these assumptions, Figure 1 shows the variation of the total standardized costs $\kappa_{tot}(x, q, n)$ (given by equation (12)), and the optimum reliability index β_{opt}, with structural parameter x. The optimal values $x_{opt}(q, n)$ of the structural parameter x, given by equation (8), are indicated by the dashed vertical lines. Indicated values of $\beta = 2.6$, 3.2, 3,5 correspond to annual rates 3,7, 4.2 and 4.4 recommended by JCSS (2001) (Table 3) for "normal relative costs of safety measures".

Note that the cost ratio $\rho = (C_{str} + C_f)/C_{str} = 1$ describes the extreme case when the failure costs C_f are negligible, $C_f \approx 0$, and the failure consequences

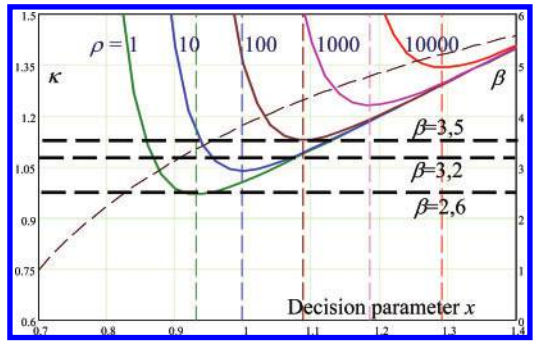


Figure 1. Variation of the total standardized cost $\kappa_{tot}(x, q, n)$ and the optimum reliability index β_{opt} with the decision parameter x for $q = 0.03$, $n = 50$, $C_{str}/C_1 = 100$ and selected cost ratios ρ.

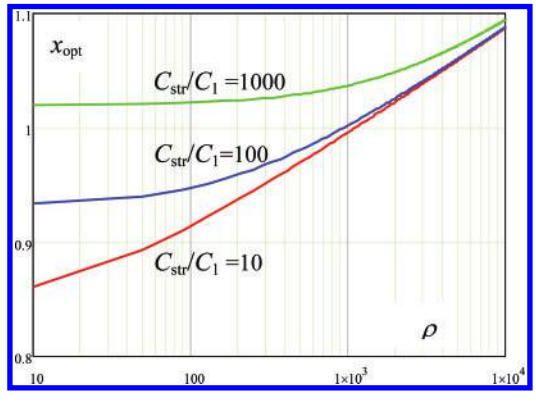


Figure 2. Variation of the index $\beta_{opt}(q, n, C_{str}/C_1, \rho)$ with the number of years n for the cost ratios $C_f/C_1 = \rho = 100$ and selected discount rates $q = 0.01, 0.03, 0.05$.

are confined to the structural costs C_{str}. Assuming the conditions considered in Figure 1 ($q = 0.03$, $n = 50$, $C_{str}/C_1 = 100$) the corresponding optimal reliability index $\beta_{opt} \approx 3.3$.

5 THE OPTIMAL RELIABILITY INDEX

The optimal decision parameter x_{opt} given by equation (8) is indicated in Figure 2.

The optimal reliability index $\beta_{opt}(q, n, C_{str}/C_1, \rho)$ depends in general on the discount rate q, the time to failure (number of years) n, and on the two cost ratios C_{str}/C_1 and $\rho = (C_{str} + C_f)/C_{str}$. Note that the failure C_f is discounted to the present price.

The dependence of $\beta_{opt}(q, n, C_{str}/C_1, \rho)$ on q and n seems to be insignificant. This is well illustrated by Figure 3.

Figure 3 shows the variation of the optimal reliability index β_{opt} with the time to failure (number of years) n for the cost ratios $C_f/C_1 = \rho = 100$ for selected discount rates $q = 0.01$, 0.03 and 0.05. The optimal reliability index β_{opt} is almost independent

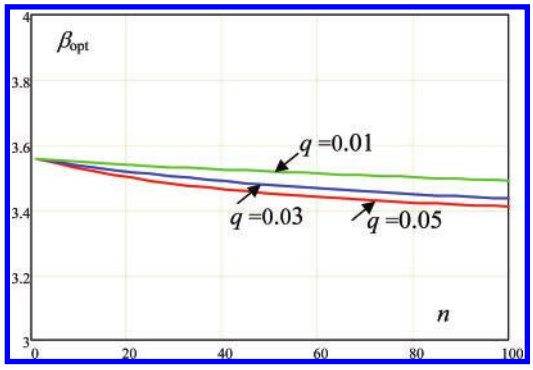


Figure 3. Variation of the index $\beta_{opt}(q, n, C_{str}/C_1, \rho)$ with the number of years n for the cost ratios $C_f/C_1 = \rho = 100$ and selected discount rates $q = 0.01, 0.03, 0.05$.

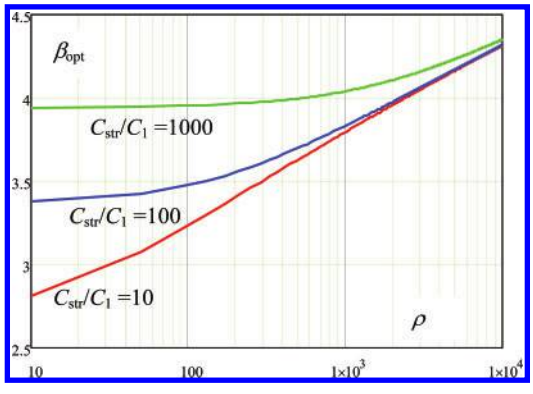


Figure 4. Variation of the index $\beta_{opt}(q, n, C_{str}/C_1, \rho)$ with the cost ratio $\rho = (C_{str} + C_f)/C_{str}$ for $q = 0.03$, $n = 50$, and selected ratios $C_{str}/C_1 = 10, 100, 1000$.

of q and n. Thus, as a conservative approximation, the target β can be determined considering a small discount rate q (for example 0,01) and a minimum number of years n (say 10).

The following Figure 4 shows variation of the index $\beta_{opt}(q, n, C_{str}/C_1, \rho)$ with the cost ratio ρ for $q = 0.03$, $n = 50$, and selected ratios $C_{str}/C_1 = 10, 100, 1000$.

Similarly, Figure 5 shows the variation of the index $\beta_{opt}(q, n, C_{str}/C_1, \rho)$ with the cost ratio C_{str}/C_1, for $q = 0.03$, $n = 50$, and selected ratios and for $\rho = 10, 100, 1000$.

The variation of the index $\beta_{opt}(q, n, C_{str}/C_1, \rho)$ with the cost ratio C_{str}/C_1, shown in Figure 5, slightly differs from the variation with the ratio ρ, indicated in Figure 1. This difference is due to the effect of the discounting of the failure consequences C_f. Nevertheless, the optimal reliability level depends also on the costs C_1 (in addition to the costs C_{str} and C_f). That is why the recommendation provided by ISO and JCSS consider also "the relative costs of safety measures". Nevertheless, the indicated values of the ratio $\rho = (C_{str} + C_f)/C_{str}$ within the interval from 2 to 10 seem to be rather low.

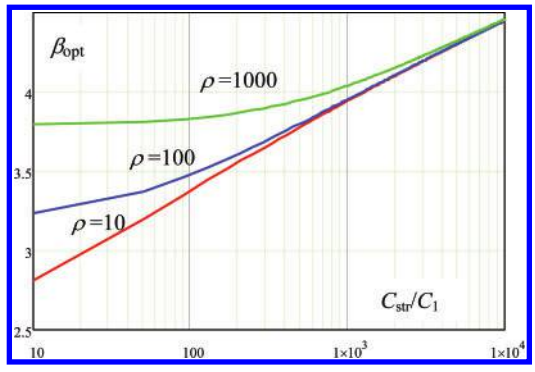


Figure 5. Variation of the index $\beta_{opt}(q, n, C_{str}/C_1, \rho)$ with the cost ratio C_{str}/C_1 for $q = 0.03$, $n = 50$, and selected ratios $\rho = (C_{str} + C_f)/C_{str} = 10, 100, 1000$.

The optimization results shown in Figures 2, 3 and 4 clearly indicate that the optimal reliability index β_{opt} depends primarily on both the cost ratios C_{str}/C_1, and $\rho = (C_{str} + C_f)/C_{str}$. For the cost ratios $C_f/C_1 = \rho = 100$ (a reasonable estimate) the optimal reliability index β_{opt} is about 3.5, and that corresponding to probability of failure is 2.3 10^{-4}.

However, when the cost ratios are small (say $C_f/C_1 = \rho = 10$), the optimal index β_{opt} is about 2.8, and that corresponding to probability of failure is 2.6 10^3, and is thus about ten times greater.

It is interesting to mention that the actual reliability level observed in common design using the partial factor method is quite conservative (Holicky and Schneider (2001)), and often corresponds to the reliability index β above 5.

6 CONCLUSIONS AND RECOMMENDATIONS

The available documents and codes for structural design do not provide a clear link between the design working life and the target reliability level, and no recommendations are offered to specify the target reliability index for temporary and long life structures.

It has been shown that the target reliability of structures can be derived from theoretical principles of probabilistic optimization considering the objective function as the total costs expressed as a sum of the initial costs C_0, the marginal costs x C_1 (where $x$denotes decision parameter and C_1 the incremental cost of decision parameter x), and the failure consequences consisting of the construction costs C_{str} and failure costs C_f (the loss of structural utility at the time of failure), these being taken into account by the cost ratio $\rho = (C_{str} + C_f)/C_{str}$. The failure cost C_f is discounted considering an annual discount rate q and the time to failure (number of years) n. In such a way the total cost is affected by the discount rate q and the number of years n.

An example of probabilistic optimization of a generic structural member clearly shows (see Figure 1, 4 and 5) that the optimal reliability level, reliability index β, depends primarily on:

- the structural costs C_{str},
- failure costs (malfunctioning costs) C_f,
- costs for improving structural safety C_1.

Less significant seem to be the discount rate q (about 0.03) and the time to failure n (figure 3).

It is recommended that the obtained results be considered in the development of design codes based on the partial factor method as follows:

- to specify the reliability level taking into account the optimal reliability index,
- to define the characteristic values of the basic variables as time independent quantities,
- to determine the design values on the basis of the specified reliability index design working life,
- to determine the partial factors considering the design and characteristic values.

It should be stated that further investigations are needed in order to include the costs of monitoring and the repair of structures, to improve assessment of failure consequences and to illustrate the application of general results in practical design.

ACKNOWLEDGEMENT

This study is an outcome of the research project GAČR P105/12/0589: "Probabilistic optimisation of the target structural reliability".

REFERENCES

Diamantidis D. (2009), "Reliability differentiation", In.: Holicky et al.: Guidebook 1, Load effects on Buildings, CTU in Prague, Klokner Institute, ISBN 978-80-01-04468-1, pp. 48–61.

Holicky M. and Schneider J. (2001), "Structural Design and Reliability Benchmark Study", In.: Safety, Risk and Reliability – Trends in Engineering c/o IABSE, ETH Zűrich, International Conference in Malta, ISBN 3-85748-102-4, pp. 929–938.

Holicky M. (2009), "Reliability analysis for structural design", SUN MeDIA Stellenbosch, ZA, ISBN 978-1-920338-11-4, 199 pages.

Holický, M. and Retief, J. (2011), Theoretical Basis of the Target Reliability. In: 9th International Probabilistic Workshop. Braunschweig: Technische Universität, pp. 91–101. ISBN 978-3-89288-201-5.

ISO 2394 (1998), General principles on reliability for structures, International Organization for Standardization, Geneva, Switzerland, 73 pages.

JCSS (2001), Joint Committee for Structural Safety, "Probabilistic Model Code", http://www.jcss.ethz.ch/.

Research and Applications in Structural Engineering, Mechanics and Computation – Zingoni (Ed.)
© 2013 Taylor & Francis Group, London, ISBN 978-1-138-00061-2

Reliability evaluation and design of steel frames with BRBs under severe earthquakes

Y.S. Liu, G.Q. Li & X.K. Guo
Tongji University, Shanghai, China

ABSTRACT: The steel Buckling-Restrained Braced Frame (BRBF) is a promising earthquake resisting structural system. However, the reliability assessment and design method of the structure still needs to be studied deeply for practical use. In this paper, inter-story and roof drift of the structure are chosen as the damage indexes to assess the reliability of the structural system. Firstly, the equivalent linearization method is introduced; then extensive time history analyses are conducted according to the seismic code of China. By combining the equivalent linearization method with the statistical characteristics of the elastoplastic displacement of the structure, the probability density function of the displacement can be determined, and the failure probability of the structure with different performance levels can be obtained. Finally, the proposed reliability evaluation method is illustrated by an example and the reliability design method of the structure under severe earthquake is given for the reference of engineering design.

1 INTRODUCTION

The buckling restrained brace (BRB) is generally composed of a ductile steel core that carries axial load and a constraining element that prevents the core from buckling under compression. The steel core is designed to yield in both tension and compression that can dissipate a significant sum of energy in earthquakes. After the Northridge (1994) and Kobe (1995) earthquakes, BRBs have been quickly accepted (Uang, 2004 and Xie, 2005) and the buckling restrained braced steel frames (BRBFs) also have become a very promising structural system to resist seismic load. Many researchers have conducted study on the design method of BRBFs. B. Asgarian and H.R. Shokrgozar (2009) used static pushover analysis and nonlinear incremental dynamic analysis to study BRBFs with various stories and different bracing configuration including diagonal. Over-strength, ductility and response modification factor *R* of BRBFs were evaluated. Choi and Kim, et al. (2006) developed the performance-based design method of BRBF based on the energy-balance concept. The errors associated with the energy-balance concept were identified and corrected by implementing proper correction factors. Also, they (Choi and Kim, et al., 2006) proposed an energy-based seismic design procedure for BRBFs using hysteretic energy spectra and accumulated ductility spectra. The procedure is based on the premise that the gravity load-resisting elements, such as beams and columns, are designed to remain elastic during earthquakes, and all the seismic input energy is dissipated by the buckling-restrained braces. However, the proposed design methods mentioned above are all deterministic schemes. The seismic reliabilities of the BRBFs are unknown. Lin, et al. (2010) evaluates the seismic reliability of eccentrically braced frame (EBF) and BRBF systems in comparison with that of moment-resisting frame (MRF) systems. The results show that the effectiveness of braced frames can vary significantly with ground motions and building rises. The added braced frames help to reduce story drifts, decreasing the probability of failure against ordinary ground motions. In China, seismic design of building is based on the frequent earthquake level, and collapse check is performed by nonlinear time-history analysis adopting several ground motions (GB 50011, 2010). The design concept cannot determine seismic reliability of structures under severe earthquakes.

For practical purpose, there is a pressing need to propose an easy way to assess the collapse probability and propose a design procedure of BRBFs considering the stochastic factors, such as ground motion, site category and structural arrangement. In this paper, inter-story and roof drift of the structure are chosen as the damage indexes to assess the reliability of the structural system. By combining the equivalent linearization method with the statistical characteristics of the elastoplastic displacement of the structure, a method to make reliability assessment and design of BRBF is presented.

2 DEFINITION OF LIMIT STATE

Performance-based seismic design (PBSD) is developed very fast in the recent decades, purpose of which is to ensure that the structure has different

Table 1. Performance levels in terms of roof drift θ_r.

Level	Performance	State	Limitation/%
1	Safe, immediate use	No damage	<0.2
2	Can be used after minor repair	Minor damage	<0.5
3	Structural damage, much repair needed	Medium damage	<1.5
4	Cannot be repaired	Severe damage	<2.5
5	Collapse	Collapse	>2.5

Table 2. Performance levels against inter-story drift θ_i.

Level	Severe earthquake
1	Almost no damage, $\theta_i > [\theta_e]$ a little
2	Minor damage, $\theta_i < 2[\theta_e]$
3	Obvious plastic, $\theta_i \approx 4[\theta_e]$
4	No serious damage, $\theta_i < 0.9[\theta_p]$

performance levels against different seismic hazard probabilities. However, definition of performance index varies among different researchers, such as story drift, energy dissipation capacity, damage and multi-parameter index. The most accepted and used is story drift, including inter-story and roof drift, with its convenience and directness for practical use. Displacement-based seismic design is the most important way to realize the PBSD methodology. In this paper, the limit state of BRBF at different performance levels is expressed as

$$G = D - [D] \le 0 \tag{1}$$

where D is the displacement of the story (inter-story and roof drift), $[D]$ is the displacement limitation according to performance levels. By comparing and summarizing the achievement of SEAOC (1995), ATC(1996) and FEMA(1996), Smith (2001) suggests that the performance of structures can be classified in terms of roof drift as shown in Table 1.

Performance-based seismic design is also developed in China, which is recently presented in the Seismic Design Code for Buildings (GB 50011, 2010) after Wenchuan earthquake in 2008. The performance of structure is divided into four levels according to the inter-story drift and seismic hazard, as shown in Table 2, where $[\theta_e]$ is the elastic inter-story drift limitation (1/250 for BRBFs), $[\theta_p]$ is the plastic inter-story drift limitation (1/50 for BRBFs).

3 SIMPLIFIED METHOD TO CALCULATE INELASTIC DISPLACEMENT OF BRBF

3.1 *Equivalent linear method*

Equivalent linear method is proposed to predict the peak elasto-plastic displacement response of structures in earthquakes. By using different principles of equivalence, the equivalent linear method consists of secant stiffness method (Rosenblueth, 1964), Hwang (1996) empirical coefficient method, average stiffness and energy method (Iwan, 1979), etc. The methodology is basically dependent on assuming that energy absorbed by the elasto-plastic structure equals to that dissipated by the damping of a corresponding elastic structure. Meanwhile, the fundamental period is modified to reflect stiffness decrease of the structure. The peak elasto-plastic displacement response can be easily estimated by linear analysis of the equivalent elastic structure with the modified design response spectrum. To compare with the nonlinear time history analysis, the calculating time is reduced dramatically. The equivalent linear method is adopted by FEMA273&274 and the Seismic Design Code for Buildings (GB 50011,2010) of China.

3.2 *Equivalent damping ratio and period*

According to the Seismic Design Code for Buildings of China (GB 50011, 2010), the equivalent damping ratio ζ_{eq} provided by the energy dissipation elements can be estimated as

$$\zeta_{eq} = W_p / (4\pi W_s) \tag{2}$$

where W_p is the hysteretic energy dissipated by structural elements in one cycle of the expected displacement; W_s is the total strain energy at the expected displacement.

The skeleton curve of BRBF is shown in Figure 1, which can be considered as combination of load-displacement curve for Frame and BRBs. W_p and W_s are illustrated in Figure 2, when the expected displacement U_m is achieved.

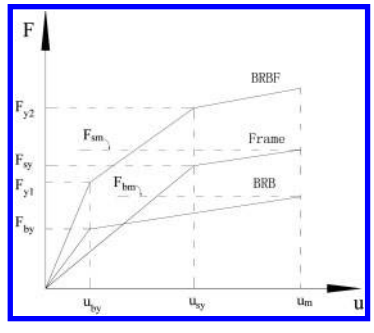


Figure 1. Skeleton curve.

where F_{by} is the story shear capacity provided by BRBs; u_{by} is the story displacement when BRB yields; F_{sy} is the yield capacity of frame; u_{sy} is the yield displacement of frame; U_m is the expected displacement of BRBF; F_{y1} is the story shear force of BRBF when the BRB yields; F_{y2} is the story shear force of the frame when the BRBF totally yields; F_{bm} is the story shear capacity provided by BRBs at U_m; F_{sm} is the story shear capacity provided by the frame at U_m.

The total damping ratio of the BRBF structure contains two parts, i.e., viscous damping ratio ζ_e and equivalent damping ratio ζ_{eq}, which is shown as

$$\zeta_P = \zeta_e + \zeta_{eq} \tag{3}$$

where ζ_e is 0.05 for analysis in severe earthquakes.

The frequency ω_r of structure with damping ratio ζ can be calculated as

$$\omega_r = \omega\sqrt{1-\zeta^2} \tag{4}$$

where ω is the fundamental frequency without damping ratio ζ.

So, the elasto-plastic period of structure T_p can be given by

$$T_p = T_e\sqrt{1-\zeta_e^2}/\sqrt{1-\zeta_p^2} \tag{5}$$

where T_e is the fundamental period of the elastic model without damping ratio ζ.

3.3 *Modified design response spectrum*

When the equivalent damping ratio and period are got, the elastic design response spectrum can be modified to consider the hysteretic energy dissipated by BRBs. The design response spectrum adopted by the Seismic Design Code for Buildings (GB 50011, 2010) is shown in Figure 3.

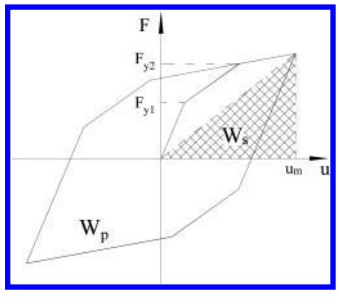


Figure 2. Hysteretic curve.

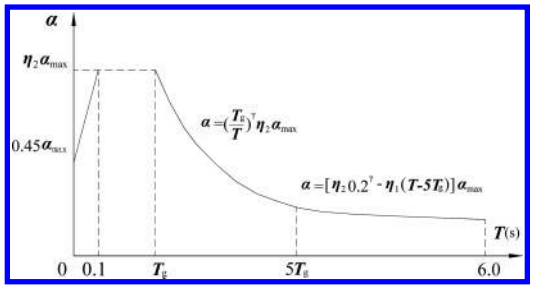


Figure 3. Design response spectrum in GB 50011.

where α is the horizontal earthquake influence factor, α_{max} is the maximum value of α, η_1, η_2 and γ is the modification parameters (GB 50011, 2010), T_g is characteristic period.

4 STATISTICAL CHARACTERISTICS OF ELASTO-PLASTIC DISPLACEMENT OF BRBF

4.1 *Sampling models*

Five sampling models are used to obtain the statistical characteristics elasto-plastic displacement of BRBFs. The stories are 1, 3, 6, 9 and 12 respectively, fundamental periods of which vary from 0.2 s to 1.8 s. First story height of the models is 4 m, while the other stories are 3.6 m high. The dead load is 5 kN/m^2, and the live load is 2 kN/m^2. The steel of frames is Q345B, while the BRBs' core is Q235B. Layout of the models is shown in Figure 4 and section properties are show in Table 3.

4.2 *Ground motions*

To reflect the randomness of ground motions, 120 earthquake records are collected and divided into 4 groups according to the characteristic period T_g, as the input ground motions to make nonlinear time history analysis of the sampling models. Response spectrum of the ground motions is shown in Figure 5, the damping ratio of which is 0.05 (take site type I for example).

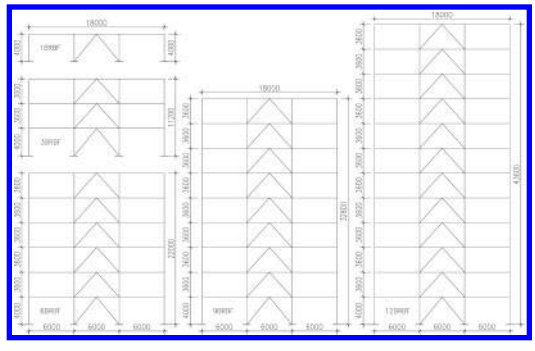


Figure 4. Layout of the sampling models.

Table 3. Section properties of sampling models.

Model	Beam (HN)	Middle Column(□)	Side Column(□)	BRB
1BRBF		250 × 250 × 16	200 × 200 × 16	200 × 10
3BRBF-1		250 × 250 × 16	200 × 200 × 16	200 × 20
3BRBF-2		250 × 250 × 16	200 × 200 × 16	150 × 10
3BRBF-3		250 × 250 × 16	200 × 200 × 16	100 × 10
6BRBF-1/2		300 × 300 × 16	250 × 250 × 16	300 × 20
6BRBF-3/4	300 × 175	300 × 300 × 16	250 × 250 × 16	200 × 20
6BRBF-5/6	× 8 × 11	300 × 300 × 16	250 × 250 × 16	100 × 20
9BRBF-1/3		300 × 300 × 25	300 × 300 × 20	150 × 20
9BRBF-4/6		300 × 300 × 25	300 × 300 × 20	100 × 20
9BRBF-7/9		300 × 300 × 25	300 × 300 × 20	100 × 20
12BRBF-1/4		300 × 300 × 25	300 × 300 × 20	150 × 20
12BRBF-5/8		300 × 300 × 25	300 × 300 × 20	150 × 20
12BRBF-9/10		300 × 300 × 25	300 × 300 × 20	100 × 20

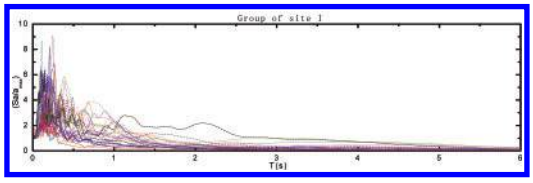


Figure 5. Response spectrum of the ground motions (site I).

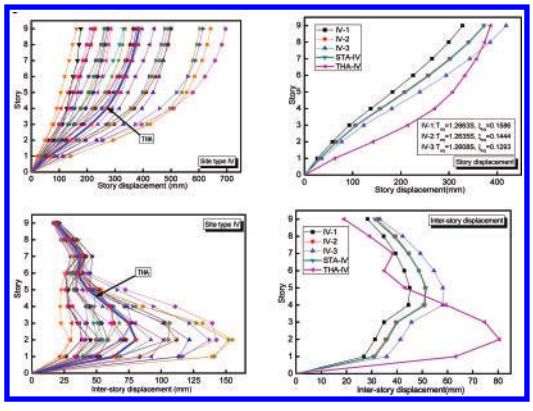


Figure 6. Displacement response of 9BRBF at site IV.

4.3 *Sampling results and statistical characteristics*

According to the Seismic Design Code for Buildings of China (GB 50011,2010), the peak ground acceleration (PGA) is adjusted to 620 gal for 9-level of seismic hazard in severe earthquake. By 600 times nonlinear time history analysis of the sampling models in total, the statistical characteristics of the BRBFs can be obtained and the accurateness of simplified method to calculate the inelastic displacement is also examined. To take the 9BRBF as an example, the displacement response (inter-story and roof) at site type IV is shown in Figure 6, where STA is static average value of the displacement, THA is time history average value of the displacement.

From the simulating results, it can be noticed that:

(1) The roof displacement obtained by simplified method is close to that of the average value from 30 times nonlinear history analysis.

(2) The position of maximum inter-story displacement predicted by simplified method is different from that of nonlinear time history analysis. Also, the maximum inter-story displacement by simplified method is smaller than the result from nonlinear time history analysis.

Statistical analysis is made for the roof and inter-story displacement of the BRBFs based on the sample points. The typical cumulative probability distribution curve and probability density curve of the BRBFs are shown in Figure 7. It can be seen that probability distribution model of elasto-plastic displacement of the BRBFs is most like the lognormal distribution model in severe earthquakes.

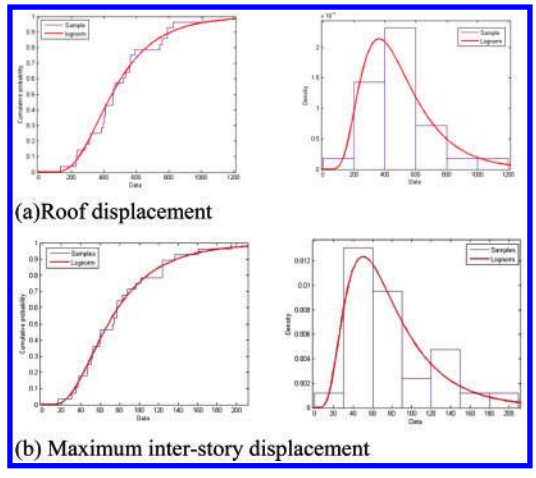


Figure 7. Displacement response probability distribution of 12 BRBF at site IV.

5 SEISMIC RELIABILITY ASSESSMENT METHOD OF BRBF

5.1 *Probability description of elasto-plastic displacement*

As mentioned above that the roof and maximum inter-story drift are lognormally distributed, so the random variation D (roof drift D_r and maximum inter-story drift D_i) can be determined by

$$D=\lambda\varphi D_d \tag{6}$$

where λ is a random factor, the mean value is 1.0 and the standard deviation is the variation of displacement response; φ is the uncertainty calculation factor, D_d is the displacement obtained by the simplified method, which is a deterministic value.

The probability density function of D is determined by

$$f(d)=\begin{cases}\dfrac{1}{\sqrt{2\pi}\sigma d}e^{\frac{(\ln d-\mu)^2}{2\sigma^2}}, & d>0\\ 0, & \text{other}\end{cases} \tag{7}$$

The cumulative distribution function of D is determined by

$$F(d)=\int_0^d f(x)dx=\Phi\left(\frac{\ln d-\mu}{\sigma}\right)/\sigma d \tag{8}$$

where σ is the standard deviation, $\sigma=\mu\delta$; μ is the mean value, calculated by equation (9); δ is the variation, got by equation (10).

$$\mu=\mu_\lambda\times\mu_\varphi\times\overline{D} \tag{9}$$

Where μ_λ is the mean value of λ, μ_φ is the mean value of φ.

$$\delta=\sqrt{\delta_\lambda^2+\delta_\varphi^2} \tag{10}$$

Table 4. Simulation samples of $\delta_{\lambda r}$.

Model	1BRBF	3BRBF	6BRBF	9BRBF	12BRBF	
T(s)	0.204	0.366	0.680	1.252	1.754	Average
Site I	0.314	0.309	0.403	0.460	0.557	0.409
Site II	0.244	0.198	0.424	0.759	0.630	0.451
Site III	0.275	0.270	0.320	0.590	0.691	0.429
Site IV	0.283	0.265	0.201	0.410	0.643	0.360
Average	0.279	0.261	0.337	0.555	0.630	0.412

Table 5. Simulation samples of $\delta_{\lambda i}$.

Model	1BRBF	3BRBF	6BRBF	9BRBF	12BRBF	
T(s)	0.204	0.366	0.680	1.252	1.754	Average
Site I	0.314	0.309	0.332	0.411	0.631	0.399
Site II	0.244	0.256	0.298	0.467	0.745	0.402
Site III	0.275	0.318	0.341	0.521	0.848	0.461
Site IV	0.283	0.279	0.286	0.462	0.478	0.358
Average	0.279	0.291	0.314	0.465	0.676	0.405

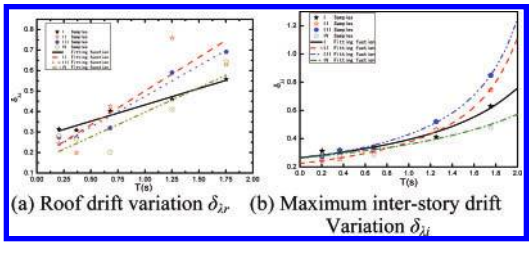


Figure 8. Fitting function of δ_λ.

Where δ_λ is the variation of λ, δ_φ is the variation of φ. δ_λ can be obtained by least square method to fit the samples from numerical simulations. The samples are shown in Table 4 and Table 5, and the fitting functions are shown in Figure 8.

5.2 *Uncertainty of the calculation model*

Difference between the displacements obtained from the two methods can be described by the uncertainty calculation factor φ, which is the ratio of THA to STA. Considering the two damage indices (roof drift and maximum inter-story drift), φ_r and φ_i are the uncertainty calculation factors for roof drift and maximum inter-story drift, respectively. Simulation samples are shown in Table 6 for φ_r and Table 7 for φ_i based on the 600 times nonlinear analysis. The statistical characteristics of φ_r and φ_i is shown in Figure 9.

5.3 *Seismic reliability assessment method*

When the probability density function of D is determined, the seismic reliability of BRBFs can be assessed by integration according to the limit state of performance levels as shown in Table 1 and Table 2. The seismic reliability assessment method is illustrated through a numerical example as below.

Table 6. Simulation samples of φ_r.

Model	1BRBF	3 BRBF	6 BRBF	9 BRBF	12BRBF	
T(s)	0.204	0.366	0.680	1.252	1.754	Average
Site I	1.323	1.021	0.971	0.779	0.564	0.932
Site II	1.207	1.418	1.281	1.035	0.917	1.172
Site III	1.277	1.461	1.220	0.980	0.957	1.179
Site IV	1.065	1.597	1.231	1.035	0.971	1.180
Average	1.218	1.374	1.176	0.957	0.852	1.116

Table 7. Simulation samples of φ_i.

Model	1BRBF	3 BRBF	6 BRBF	9 BRBF	12BRBF	
T(s)	0.204	0.366	0.680	1.252	1.754	Average
Site I	1.323	1.333	1.490	1.019	0.782	1.190
Site II	1.208	1.517	1.448	1.453	1.444	1.414
Site III	1.278	1.538	1.501	1.470	1.275	1.412
Site IV	1.066	1.452	1.410	1.443	1.214	1.317
Average	1.218	1.460	1.462	1.346	1.179	1.333

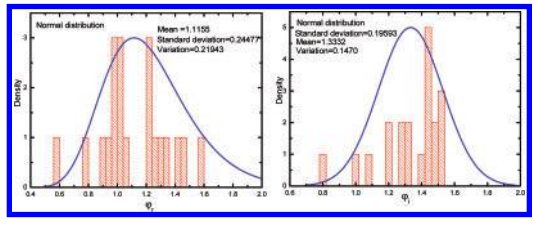


Figure 9. Probability density distribution of φ_r and φ_i.

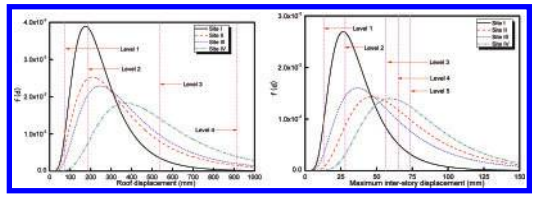


Figure 10. Probability density function of the displacement.

Table 8. Failure probability p_f based on roof drift.

Performance	Site I	Site II	Site III	Site IV
level 1	98.7%	98.9%	99.6%	99.9%
level 2	66.6%	80.2%	86.6%	97.1%
level 3	4.39%	17.8%	22.7%	40.5%
level 4	0.35%	4.03%	5.36%	10.9%

A 10-story BRBF is configured, with the same load conditions and materials as the sampling models in Chapter 4.1. To use the roof and maximum inter-story drift as the performance indies, seismic reliability of the structure can be obtained as shown in Figure 10, the failure probabilities of corresponding performance levels are shown in Table 8 and Table 9.

Table 9. Failure probability p_f based on maximum inter-story drift.

Performance	Site I	Site II	Site III	Site IV
level 1	95.9%	99.8%	98.6%	99.9%
level 2	63.0%	92.8%	83.9%	98.2%
level 3	14.1%	54.9%	41.6%	69.5%
level 4	9.37%	45.6%	33.8%	59.4%
level 5	6.31%	37.9%	27.5%	49.9%

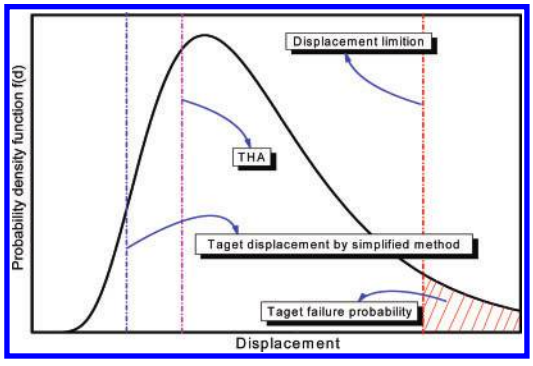


Figure 11. Seismic reliability design procedure of BRBFs.

6 SEISMIC RELIABILITY DESIGN METHOD OF BRBF

The seismic reliability design procedure of BRBFs is inverse against the reliability assessing process, which consists of the steps as follows (see Figure 11):

(1) to assess the seismic risk loss and determine the target reliability;
(2) to configure the BRBF and calculate the fundamental period T_1 of the structure;
(3) to determine the displacement probability density function;
(4) to obtain the target displacement meeting with the simplified method;
(5) to use the simplified method to estimate the displacement of BRBF;
(6) to compare the calculated displacement by step (5) with the target displacement by step (4);
(7) to adjust the structure till the calculated displacement meeting the target value.

7 CONCLUSIONS

In this paper, the seismic reliability assessment and design method of BRBFs is proposed by combining the equivalent linearization method with the statistical characteristics of the elastoplastic displacement of the structure. It can be found that:

(1) the equivalent linearization method to estimate the roof drift of BRBFs is better than that of the inter-story drift of BRBFs.
(2) the roof, inter-story, and maximum inter-story drift of BRBFs in severe earthquakes distribute likely lognormal.
(3) the variation of roof and inter-story drift increases with the fundamental period of BRBFs.
(4) BRBFs in site type IV has the highest failure risk among the four site types.
(5) the proposed method to assess seismic reliability of BRBFs is easy to be applied for practical use.

ACKNOWLEDGEMENTS

The authors wish to acknowledge the support from National Natural Science Foundation of China (Grant No. 51108340) for the work reported in this paper.

REFERENCES

Applied Technology Council(1996). Seismic evaluation and retrofit of existing concrete building. ATC-40. Redwood City (CA),

Asgarian B., Shokrgozar H.R.(2009). "BRBF Response Modification Factor." Journal of Constructional Steel Research, 65(2), pp.290–298.

Choi H., Kim J., Chung L.(2006) "Seismic Design of Buckling-Restrained Braced Frames Based on a Modified Energy Balance Concept." Canadian Journal of Civil Engineering, 33, pp.1251–1260.

Federal Emergency Management Agency(1996).NEHRP guidelines for the seismic rehabilitation of buildings. FEMA 273. FEMA 274. Commentary. Washington (DC).

GB 50011 (2010). Code for seismic design of buildings of China.

Hwang J S. (1996). "Evaluation of Equivalent Linear Analysis Methods of Bridge Isolation." Journal of Structural Engineering, ASCE, 122 (8), pp.872–976.

Iwan W D, Gates N C. (1979). "Estimating Earthquake Response of Simple Hysteretic Structures." Journal of the Engineering Mechanics Division, ASCE, 105(3), pp.391–405.

Lin Ker-Chun, Lin Chu-Chieh J., et al. (2010). "Seismic reliability of steel framed buildings." Structural Safety, 32(3), pp.3174–3182.

Rosenblueth E, Herrera I. (1964). "On a kind of hysteretic damping." Journal of Engineering Mechanics Division, ASCE, pp.37–48.

Smith K G. (2001). "Innovation in earthquake resistant concrete structure design philosophies: A century of progress since Hennebique's patent." Engineering Structures, 23(1), pp.72–81.

Structural Engineers Association of California (2000). SEAOC Version 2000. Performance based seismic engineering of buildings. Vols. I and II: Conceptual Framework.

Uang C.M., Nakashima M. and Tsai K.C. (2004). "Research and applications of buckling-restrained braced frames", Journal of Steel Structures, 4(4), pp. 301–313.

Xie Q. (2005). "State of the art of buckling restrained braces in Asia." Journal of Constructional Steel Research, 61 (6), pp. 727–748.

Research and Applications in Structural Engineering, Mechanics and Computation – Zingoni (Ed.)
© 2013 Taylor & Francis Group, London, ISBN 978-1-138-00061-2

Reliability analysis of corroding pipelines by enhanced Monte Carlo simulation

Bernt J. Leira
Department of Marine Technology, Norwegian University of Science and Technology, Trondheim, Norway

Arvid Naess
Centre for Ships and Ocean Structures & Department of Mathematical Sciences, Norwegian University of Science and Technology, Trondheim, Norway

Ole E. Brandrud Næss
Programme for Industrial Mathematics, Department of Mathematical Sciences, Norwegian University of Science and Technology, Trondheim, Norway

ABSTRACT: The present paper addresses reliability analysis of corroding pipelines also considering system reliability effects. The analysis is performed by utilization of enhanced Monte-Carlo simulation methods which have been found to be very efficient for quantification of system reliability in the case of multiple components with arbitrary correlation levels. The example studies in the paper comprise corrosion defects which are both independent and correlated.

1 INTRODUCTION

Corrosion of ageing pipelines is found to be a significant problem both onshore and within the subsea area. In order to determine the remaining time in service for such pipelines, it is required that deterministic capacity models are established as well as associated probability models for the key parameters. Having obtained these models, a proper reliability analysis and risk assessment can be performed.

The importance of this issue is reflected by the large number of associated publications in the existing literature. Some examples of probabilistic reliability analyses are found in the papers by Ahammed & Melchers (1996), Ahammed (1998), Caleyo et al. (2002), Lee et al. (2006), Santosh et al. (2006), Li et al. (2009a), Li et al. (2009b), Pandey (1998), Zhou (2011) and Hasan et al. (2012). Examples of relevant historic and more recent design guidelines are respectively ANSI/ASME B31G (1980) and DNV (2010).

As discussed in more detail below, there are significant differences between the applied probabilistic models which are employed in the various reliability analysis. This applies in particular to the statistical parameters which are employed for characterization of the internal pressure and the corrosion defects. Furthermore, in most cases a single corrosion defect is analysed. Only brief comments are usually given with respect to the system modeling that will be required in order to account for multiple defects.

In a few cases system analyses are performed by means of Ditlevsen bounds for estimation of failure probability for series systems. In the present paper, system modeling is focused upon both with respect to method of analysis and computational results.

2 METHOD FOR SYSTEM RELIABILITY ANALYSIS

2.1 *Basic formulation*

The enhanced Monte Carlo (MC) based method for estimation of system reliability which is applied for the present study is further described in Naess et al. (2009). The aim of this method is to reduce computational cost while maintaining the advantages of crude MC simulation. This applies in particular when dealing with complex systems. The key idea is to exploit the regularity of the tail probabilities. Based on results obtained from small Monte-Carlo samples for moderate levels of reliability this regularity enables prediction of far tail failure probabilities.

The motivation behind this approach is that systems with multiple and complex failure modes or limit states are often exceedingly difficult to analyze using traditional methods of structural reliability. On the other hand, even if direct MC does not suffer from this problem, it is computationally burdensome for small probabilities. This gives rise to the idea of sampling in a different less reliable range and performing a statistical tail extrapolation. A related idea is presented by Bucher (2009).

The fundamentals of the Naess et al. (2009) method are as follows. A safety margin $M = G(X_1, , X_n)$ expressed in terms of n basic variables, is extended

to a parameterized class of safety margins using a scaling parameter λ ($0 \le \lambda \le 1$):

$$M(\lambda) = M - E(M)(1-\lambda) \tag{1}$$

The failure probability is then assumed to behave as follows:

$$p_f(\lambda) = \text{Prob}\,(M(\lambda) \le 0) \underset{\lambda \to 1}{\approx} q(\lambda)\exp\{-a(\lambda-b)^c\} \tag{2}$$

where the function $q(\lambda)$ is slowly varying compared with the exponential function $\exp\{-a(\lambda-b)^c\}$. Clearly, the relevant failure probability $p_f = p_f(1)$ can be obtained from values of $p_f(\lambda)$ for $\lambda < 1$. It is now far easier to estimate the (larger) failure probabilities $p_f(\lambda)$ for $\lambda < 1$ accurately than the relevant value itself, since they require less simulations. Fitting the parametric form (2) for $p_f(\lambda)$ to the estimated values would then provide an estimate of the target value by extrapolation. The viability of this approach is demonstrated by both analytical and numerical examples e.g. in Naess et al. (2009) and Naess et al. (2010).

2.2 *System reliability analysis*

Using Monte Carlo methods for system reliability analysis has several attractive features, the most important being that the failure criterion is relatively easy to check almost irrespective of the complexity of the system. In order to limit the amount of computational effort that may be involved, it is hence useful to extend the above approach to systems.

Let $M_j(\lambda) = G_j(X_1, \ldots, X_n, \lambda), j = 1, \ldots, m$ be a set of m given safety margins expressed in terms of n basic variables and a single design parameter λ. The series system reliability expressed in terms of the failure probability can then be written as,

$$p_f(\lambda) = \text{Prob}\left(\cup_{j=1}^{m}\{M_j(\lambda) \le 0\}\right) \tag{3}$$

while for parallel systems,

$$p_f(\lambda) = \text{Prob}\left(\cap_{j=1}^{m}\{M_j(\lambda) \le 0\}\right) \tag{4}$$

In general, any system can be written as a series system of parallel subsystems. The failure probability would then be given as,

$$p_f(\lambda) = \text{Prob}\left(\cup_{j=1}^{l} \cap_{i \in C_j}\{M_i(\lambda) \le 0\}\right) \tag{5}$$

Here each C_j is a subset of $\{1, \ldots, m\}$, for $j = 1, \ldots, l$. The C_js denote the index sets defining the parallel subsystems. We then make the assumption that $p_f(\lambda)$ can also be represented as in Eq. (7) for the system reliability problems.

2.3 *Implementation*

The method to be described in this section is based on the assumption expressed by Eq. (2). For practical applications it is implemented in the following form:

$$p_f(\lambda) \approx q(\lambda)\cdot\exp\left\{-a(\lambda-b)^c\right\} \quad \text{for } \lambda_0 \le \lambda \le 1 \tag{6}$$

for a suitable value of λ_0. An important part of the method is therefore to identify a suitable range for λ so that the right hand side of Eq. (7) represents a good approximation of $p_f(\lambda)$ for $\lambda \in [\lambda_0, 1]$.

For a sample of size N of the vector of basic random variables $\boldsymbol{X} = (X_1, \ldots, X_n)$, let $N_f(\lambda)$ denote the number of samples in the failure domain of $M(\lambda)$. The estimate of the failure probability is then

$$\hat{p}_f(\lambda) = \frac{N_f(\lambda)}{N} \tag{7}$$

The coefficient of variation C_v of this estimator is

$$C_v\left(\hat{p}_f(\lambda)\right) = \sqrt{\frac{1-\hat{p}_f(\lambda)}{\hat{p}_f(\lambda)N}} \tag{8}$$

A fair approximation of the 95% confidence interval for the value $\hat{p}_f(\lambda)$ can be obtained as $\text{CI}_{0.95}(\lambda) = (C^-(\lambda), C^+(\lambda))$, where

$$C^{\pm}(\lambda) = \hat{p}_f(\lambda)\left(1 \pm 1.96 C_v(\hat{p}_f(\lambda))\right) \tag{9}$$

Assuming now that we have obtained empirical Monte Carlo estimates of the failure probability, the problem then becomes that of optimal use of the information available. By plotting $\log|\log \hat{p}_f(\lambda)/q(\lambda)|$ versus $\log(\lambda - b)$, it is expected that an almost perfectly linear tail behavior will be obtained according to Eq. (2). Recalling that the function $q(\lambda)$ was assumed to be slowly varying compared with the exponential function $\exp\{-a(\lambda-b)^c\}$ for relevant values of λ, it is now tentatively proposed to replace $q(\lambda)$ by a suitable constant value, q say, for tail values of λ, say $\lambda \ge \lambda_1 (\ge \lambda_0)$. Hence, we will investigate the viability of the following simpler version of Eq. (2):

$$p_f(\lambda) \approx q\exp\{-a(\lambda-b)^c\} \quad \text{for } \lambda_1 \le \lambda \le 1 \tag{10}$$

for a suitable choice of λ_1.

The problem of finding the optimal values of the parameters q, a, b, c is carried out by optimizing the fit on the log level by minimizing the following mean square error function with respect to all four arguments (Naess and Gaidai, 2009),

$$\text{F}(q,a,b,c) = \sum_{j=1}^{M} w_j\left(\log \hat{p}_f(\alpha_j) - \log q + a(\alpha_j - b)^c\right)^2 \tag{11}$$

where $\lambda_1 < \cdots < \lambda_M$ denotes the set of λ values where the failure probability is empirically estimated. w_j denotes a weight factor that puts more emphasis on the more reliable estimates.

A Levenberg–Marquardt least squares optimization method (Gill et al., 1981) is applied for the present minimization. Although this method generally works well, it may be simplified by exploiting the structure of F. It is realized by scrutinizing Eq. (16) that if b and c are fixed, the optimization problem reduces to a standard weighted linear regression problem. That is, with both b and c fixed, the optimal values of a and $\log q$ are found using closed form weighted linear regression formulas in terms of $w_j, y_j = \log \hat{p}_f(\lambda_j)$ and $x_j = (\lambda_j - b)^c$.

The optimal values of a and q are then given by the following relations,

$$a^*(b,c) = -\frac{\sum_{j=1}^{M} w_j (x_j - \bar{x})(y_j - \bar{y})}{\sum_{j=1}^{M} w_j (x_j - \bar{x})^2} \tag{12}$$

and

$$\log q^*(b,c) = \bar{y} + a^*(b,c)\bar{x} \tag{13}$$

where

$$\bar{x} = \sum_{j=1}^{M} w_j x_j \,/ \sum_{j=1}^{M} w_j, \quad \bar{y} = \sum_{j=1}^{M} w_j y_j \,/ \sum_{j=1}^{M} w_j.$$

The Levenberg–Marquardt method may now be used on the function $\tilde{F}(b,c) = F(q^*(b,c), a^*(b,c), b, c)$ to find the optimal values b^* and c^*, and then the corresponding a^* and q^* can be calculated from Eqs. (13) and (14).

3 EXAMPLES

3.1 *General*

An adequate reliability formulation for a corroding pipeline system requires that the time variation of both the internal pressure and the corrosion damage are taken into account. If the largest defect throughout the time period which is applied in combination with the highest pressure during the same period a conservative estimate of the failure probability for a single pipe cross-section will result. This model is frequently applied in the literature.

A convenient and quite accurate simplification is to apply the distribution of the annual maxima of the internal pressure (instead of the extreme pressure during the entire period). This distribution is then combined with the distribution of the corrosion damage during the same year (instead of the distribution of the largest defect during the period under consideration). This modeling can also be combined with the system reliability formulation to reflect the possibility that failure may occur at one out of a multiple of different defects.

In this approach, the probability distribution of the total population of corrosion defects is applied for each of the cross-sections (instead of that for the single largest defect at a given point in time). Hence, the possibility of failure at a number of "competing" cross-sections is properly represented through the series system model. This formulation is applied as the basis for the numerical studies in the present paper.

In many of the reliability studies found in the literature, the probability distribution of the instantaneous (normal) operation pressure is applied instead of the distribution for the extreme pressure during a specified time interval. The reason for this is a bit unclear and also it creates difficulties when trying to establish a reference time period for the calculated probability of failure (unless some characteristic short-term duration of the pressure is specified, i.e. of the order of minutes or hours).

In the present paper, the probability distribution of the annual extreme pressure is applied as discussed above. Representation of the annual maximum pressure then should than be based on the maximum instantaneous pressure (MAIP) which in general is higher than the maximum allowable operation pressure (MAOP). The mean value of the former pressure is typically given by means of a bias factor times the latter, typically 1.05 or 1.07.

The failure function which is presently applied for a pipeline cross-section where a corrosion defect is present is expressed as follows:

$$g(X) = \left\{ 2 \cdot m_f s_y \left(\frac{t}{D}\right) \frac{1 - \left(\frac{d}{t}\right)}{1 - \left(\frac{d}{tM}\right)} - p_a \right\} \tag{14}$$

Here, s_y is the yield stress of the steel material and m is a multiplying factor which converts yield stress into flow stress. This expression is based on a rectangular or nearly rectangular defect shape, with a defect depth of d and a defect length of L. The pipe wall thickness is designated by t and the pipe diameter by D. The quantity p_a is the internal overpressure that is acting at the relevant cross-section.

The quantity M is the Folias factor (also known as the bulging factor). The expressions which are applied for the Folias factor are as follows, Kiefner and Vieth (1990):

$$M = \left(1 + 0.6275\frac{L^2}{Dt} - 0.003375\frac{L^4}{D^2 t^2}\right)^{\frac{1}{2}} \quad \text{for } \frac{L^2}{Dt} \le 50$$

$$M = \left(0.032\frac{L^2}{Dt} + 3.3\right) \quad \text{for } \frac{L^2}{Dt} > 50 \tag{15}$$

For pipeline steels, the value of the conversion factor above, i.e. m, is usually taken to be between 1.10 and 1.15. This shows that there is also uncertainty in the value of m. In order to take this uncertainty into consideration, m, is represented as a random variable.

It is referred to Ahammed & Melchers (1996) as well as ANSI/ASME B31G (1984) and Kiefner & Vieth (1990) for further details associated with the present formulation. Clearly, it would be relevant to introduce an additional model uncertainty factor to reflect differences between observed versus calculated pressure levels at failure. However, this topic has not been pursued in the present study due the illustrative scope of the computed results.

A refined reliability analysis should distinguish between different types of failure modes with different consequences. This is discussed in more detail by Zhou (2011). Distinction is made between small leaks, large leaks and burst. Clearly, the latter will represent the failure mode with the worst consequence. In the present paper a more simplistic approach with only the single type of failure mode (which is defined by the failure function given above) is applied. Hence, the effect of a more refined sub-division will need to be studied as part of future investigations.

3.2 *Example 1: Single corrosion defect*

In order to illustrate the above concepts, a pipeline with known corrosion defects was analysed. This reflects the situation where defect dimensions are known from measurements by 'intelligent' tools. The random variables considered in this study are presented in Table 1 along with the typical statistical values and distribution functions for the variables. The distribution functions and statistical values were mainly based on those found in Ahammed and Melchers (1996). In the present paper, the intention is mainly to illustrate how the simulation procedure can be applied for the analysis of pipeline corrosion reliability. The distributions should hence be adopted to the available information for a specific application.

In the present study, the effect of applying different types of distributions for the internal pressure is investigated. The base case analysis corresponds to the pressure having a Gaussian distribution as indicated by the letter N in Table 1. In addition, results for a pressure distribution corresponding to the Gumbel distribution are also computed.

The case with a Gaussian pressure distribution and a single corrosion defect is first considered. A counting

Table 1. Random variables and statistical properties.

	Variable		Properties	
Symbol	Description	Dist*	Mean	C.o.V.
d	Defect depth	N	5 mm	0.10
D	Pipe diameter	N	610 mm	0.03
L	Defect length	N	305 mm	0.05
m	Multiplying factor	LN	1.1	0.05
p	Fluid pressure	N	5–8 MPa	0.05
sy	Material yield str.	LN	425 MPa	0.056
t	Pipe wall thickness	LN	12.5 mm	0.05

* N: Normal (Gaussian) LN: Lognormal

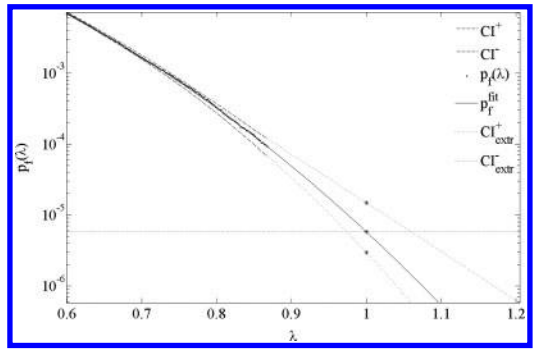


Figure 1. Extrapolation of failure probability from sampled values to relevant failure probability level. Mean value of internal pressure is 7 MPa.

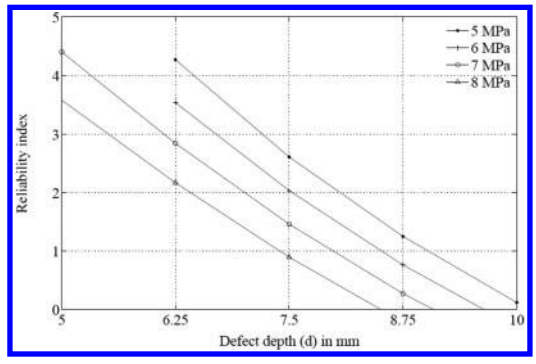


Figure 2. Failure probability as a function of mean values of internal pressure and defect depth. Pressure distribution is Gaussian.

of the observations with negative values of the failure function, N^- is performed for each value of the parameter lambda.

The simulated results for different values of lambda together with extrapolation to the relevant probability level are shown in Figure 1. It is seen that the failure probability which corresponds to $\lambda = 1$ is of the order of $3.0\ 10^{-5} +/- 0.4\ 10^{-5}$ with the best estimate being $2.0\ 10^{-5}$. It is noted that this probability is somewhat lower/higher than the value which was obtained based on performing a Taylor series expansion of the failure function around the mean point, see Ahammed & Melchers (1996).

3.3 *Parametric studies for a single defect*

The effect of varying the mean values of the pressure and the defect depth is also investigated. The results for a Gaussian pressure distribution as a function of the mean value of the pressure (from 5 MPa and upwards) and the mean value of the defect depth are shown in Figure 2. It is seen that the combination of low internal pressure and small defect depths give very high reliability levels, while a high internal pressure and large defects give very low reliability levels (with failure being almost a certain event).

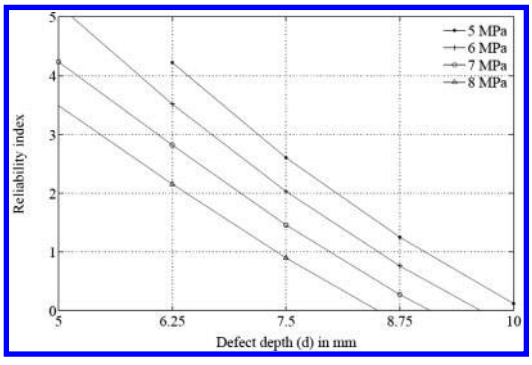


Figure 3. Failure probability as a function of mean values of internal pressure and defect depth. Pressure distribution is of the Gumbel type.

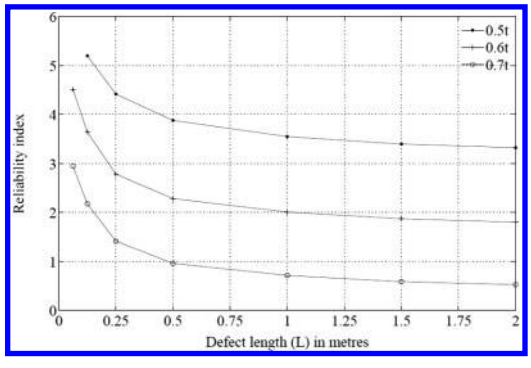


Figure 4. Failure probability as a function of mean values of defect depth and defect length. The former is normalized by wall thickness. Pressure distribution is of the Gumbel type.

Corresponding results for a pressure distribution of the Gumbel type are shown in Figure 3. Slightly lower reliability levels than for the Gaussian model are observed for the smallest defect depths. However, it should be noted that as the Gumbel model should refer to an annual extreme pressure as discussed above, the mean value should be significantly higher than for Gaussian distribution if the latter is intended to represent the normal operation pressure. This would result in much larger differences for the associated reliability levels.

The effect of varying the mean value of the defect length is illustrated by the results in Figure 4. It is seen that the reliability level decreases quite rapidly for the left part of the diagram but decreases very slowly for the right part of the diagram.

3.4 *Example 2: Multiple corrosion defects and effect of correlation*

The series system effect is illustrated by the curves in Figure 5. The lowermost (red) curve corresponds to results for a single defect, while the uppermost (green) curve corresponds to 100 defects. Since the coefficient of variation for the internal pressure is quite low

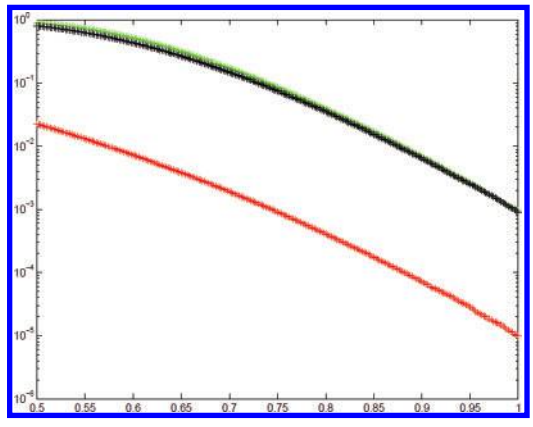


Figure 5. Failure probability of single defect (lowermost red curve) versus 100 defects (uppermost black curve). Application of independent versus fully correlated pressure at each cross-section is given by the upper green versus black lines.

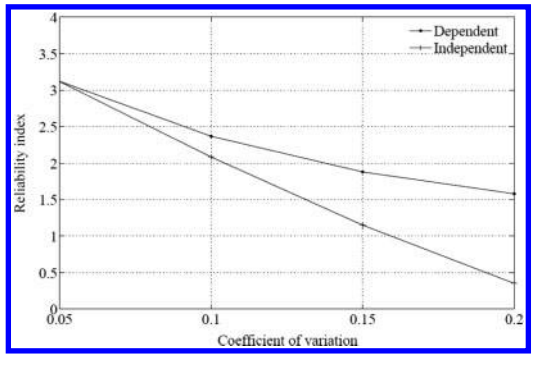


Figure 6. Failure probability of single (lowermost red curve) for system with 100 corrosion defects as function of C.o.V. for internal pressure. Independent (uppermost curve) versus dependent (lower curve) failure events. Correlation coefficient is equal to 0.04 for a C.o.V. of 0.05 and equal to 0.42 for a C.o.V of 0.2. (avg. pressure = 7 MPa).

(i.e. 0.05) the results for the case where the correlation between the failure events is taken into account are quite similar to the case with independent components. In fact, it is almost not possible to distinguish the upper blue (correlated events) versus the upper green (independent events) curves. However, this is not the case when the coefficient of variation for the internal pressure increases as shown by the results in the next section (see Figure 6).

The effect of correlation between the individual failure events is next investigated by increasing the coefficient of variation for the internal pressure. The results are shown in Figure 6 for a C.o.V. in the range from 0.05 to 0.2.

4 CONCLUSIONS

The present paper deals with application of an enhanced Monte Carlo simulation method to pipeline

systems with multiple corrosion defects. The presence of such multiple defects requires that a system analysis is performed. Furthermore, the effect of correlation between the failure events is highlighted. The failure probability decreases strongly as the degree of correlation increases as expected. However, the degree of correlation needs to be higher than around 0.2 before this effects starts to have any influence. For low values of the correlation coefficient the system failure probability can simply be obtained by multiplying the failure probability for a single defect (based on the ensemble probability distribution for the corrosion defect dimensions) with the total number of defects.

As mentioned, the present study is mainly intended as an illustration of how systems reliability analysis can be applied to corroded pipelines. There are multiple topics to be addressed in more detail as part of future work. Just a few examples are differentiation of failure modes and the effect of introducing model uncertainty factors as discussed above.

REFERENCES

ANSI/ASME (American National Standard Institute/ American Society of Mechanical Engineers). 1984. B31G Manual for Determining the Remaining Strength of Corroded Pipelines.

Ahammed, M. 1998. Probabilistic estimation of remaining life of a pipeline in the presence of active corrosion defects. *Int. J. Pressure Vessels and Piping 75*: 321–329.

Ahammed, M. & Melchers, R.E. 1996. Reliability estimation of pressurized pipelines subject to localized corrosion defects. *Int. J. Pressure Vessels and Piping 69*: 267–272.

Bucher, C. 2009. Asymptotic sampling for high-dimensional reliability analysis. *Probabilistic Engineering Mechanics 24*: 504–510.

Caleyo, F.; Gonzales, J.L. & Hallen, J.M. 2002. A study on the reliability assessment methodology for pipelines with active corrosion defects, *Int. J. Pressure Vessels and Piping 79*: 77–86.

Det Norske Veritas. 2010. *Recommended Practice DNV-RP-F101 Corroded Pipelines*. Høvik, Norway.

Hasan, S.; Khan, F. & Kenny, S. 21012. Probability assessment of burst limit state due to internal corrosion. *Int. J. Pressure Vessels and Piping 75*: 321–329.

Pandey, M.D. 1998. Probabilistic models for condition assessment of oil and gas pipelines, *NDT & E International 31(5)*: 349–358.

Kiefner, J.F. & Vieth, P.H.. 1990. New method corrects criterion for evaluating corroded pipe. *Oil Gas J. 6*: 56–59.

Lee, S-M; Chang, Y-S; Choi, J-B & Kim, Y-J. 21012. Probabilistic Integrity Assessment of Corroded Gas Pipelines, *J. Pressure Vessel Technology 128*: 547–555.

Li, S.-X; Yu, S-R; Zeng, H-L; Li, J-H & Liang, R. 2009a. Predicting corrosion remaining life of underground pipelines with a mechanically-based probabilistic model. *J. Of Petroleum Science and Engineering* 65: 162–166.

Li, S.-X; Zeng, H-L; Yu, S-R; Zhai, X.; Chen, S-P; Liang, R. & Yu, L., 2009b. A method for probabilistic analysis for steel pipeline with correlated corrosion defects. *Corrosion Science* 51: 3050–3056.

Naess, A. & Gaidai, O. 2009. Estimation of extreme values from sampled time series. *Structural Safety 31*: 325–334.

Naess, A.; Leira, B.J. & Batsevych, O. 2009. System reliability analysis by enhanced Monte Carlo simulation. *Structural Safety 31*: 349–355.

Naess, A.; Leira, B.J. & Batsevych, O. 2010. Efficient Reliability Analysis of Structural Systems with a high number of limit states. *Proc. 29th International Conference on Ocean, Offshore and Arctic Engineering.* Paper no. OMAE2010-21179, Shanghai, China.

Santosh, G.V; Shrivastava, O.P.; Saraf, R.K.; Ghosh, A.K. & Kushwaha, H.S. 2006. Reliability analysis of pipelines carrying H_2S for risk based inspection of heavy water plants. *Reliability Engineering and System Safety 91*: 163–170.

Zhou, W. 2011. Reliability Evaluation of Corroding Pipelines Considering Multiple Failure Modes and Time-Dependent Internal Pressure, *J. Infrastructure Systems 17(4)*: 216–224.

Research and Applications in Structural Engineering, Mechanics and Computation – Zingoni (Ed.)
© 2013 Taylor & Francis Group, London, ISBN 978-1-138-00061-2

Some practical aspects of statistics methods of estimation reliability computed for existing silo constructions

M. Kaminski & M. Maj
Institute of Building Engineering, Technical University of Wrocław, Poland

ABSTRACT: The authors of this paper who are members of the research team in the Institute of Building Engineering of the Technical University of Wroclaw, for more than 40 years have been carrying out researches on silos for bulk materials. They had big influence on preparing polish silo codes . These investigations were carried out on silo batteries, free-standing silos and silo models. The researches include the evaluation of value of pressure and temperature field on the silo wall as well as temperature gradient, registration of simultaneity of these loads The researches include either the evaluation of influences of the wall stiffness and wall inclination on pressure changes, parameters connected with silo strength and geometry etc. According to the data of the mentioned above parameters values the evaluation and estimation of density function of these random values and first, second order statistics were calculated based on Level-1, Level-2 reliability methods. These experimental data were subjected to statistical accounts. The data obtained from calculations can be used in designing similar silos and in preparing silo codes. The experimental results and theoretical considerations help to determine the degree of safety of silos construction. Some aspects of the estimation of safety factors and values of partial safety coefficients are presented in this paper.

1 THE BASIC EQUATION OF RELIABILITY

The basic equation of reliability of silo wall can by described in following equation

$$R \geq S \quad , \tag{1}$$

where R-construction resistance, S-loadings acting on construction. This equation is used by engineers in stresses quantities, or resultant forces. Forces are compressive or tensile or bending moments. Generally in Limit State Design R is regarded as a strength S as stresses. In Serviceability Limit State R is allowable deflection or a allowable scratch and S is static deflection or calculated scratch. R is not simply limits stresses and S is not simply loads of snow, winter, pressure etc. Equation (1) has not simple, i. e, the linear form. It involves many parameters appropriate for the loads and strength. Equation (1) can be written in the following formula

$$R - S \geq 0, \tag{2}$$

or knowing that right side of equation (2) is function we can define function of safety or reliability by:

$$f(R - S) \geq 0, \tag{3}$$

Function f(R − S) is depended of many variables, generally X variables which are random values. We can write it as sequence variables X_i:

$$X = (X_i) \tag{4}$$

X_i variables are associated one with another with formula of reliability (1). They form a set Ω of variables in the inequality (1). The reliability measure is the probability of survival P_B, calculated as

$$P_B = \int_{\Omega} f_X(X)dx \tag{5}$$

where $f_z(X)$, is the probability density function of the variables X_i, $X = (X_i) = (\Delta T, p_h, T, w, a_{ct} \ldots, h, t, a, f_{cd}, f_{yd},,a_{th}..)$, Ω is the safe set (Figure 1). There are the following X_i

a) parameters connected with acting loads "***S***" ΔT-temperature gradient across the silo wall, p_h-horizontal pressure caused by grain pressure, aeration and homogenisation, concentrated loads, T-temperature field on the silo wall caused by storage grain, insolation and daily temperature variation, w-displacement caused by for example shrinkage, wind, a_{ct}-other extreme loads, etc.,

b) parameters connected with silo wall strength "***R***" D-silo diameter, α-temperature coefficient, h-thickness of the silo wall, EJ-wall stiffness, s-distance between the horizontal bars, f_{yd}-strength of bars, f_{cd}-strength of concrete, a_1-concrete cover, ϕ-diameter of bars, A_{s1}-area of bars, e_{s1}-eccentricity, x_{eff}-height of compressed concrete area, quantity of reinforced horizontal and vertical bars, adhesion of bars to concrete, quality of lap splices, type and quality of wall strengthening, openings in the silo wall, imperfections, cracks, steel corrosion, technical condition of concrete, i.e. carbonisation, etc.

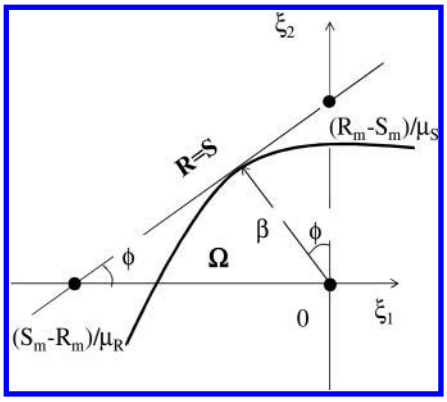


Figure 1. Index β as a minimum of distance between tangent to limit state surface and central point; area Ω is safety state of construktion computing methods.

Generally calculation of probability P_B employs probability of failure as a measure and require a knowledge of the joint distribution of all random value parameters. It is Level-3.

Probability of non failure can be written in terms of safety margin Δ:

$$f(R-S)=\Delta=R-S\geq 0, \tag{2}$$

is $P_B=P(\Delta>0)$. As an alternative to P_B, a reliability index is often defined as $\beta_B=\Phi^{-1}(P_B)=-\Phi^{-1}(P_F)$, where $P_F=1-P_B=\int_F f_X(x)dx$ is failure probability and F is the failure set. β is interpreted as minimum distance between central point and limit state surface (Figure 1). In general this integral cannot be computed analytically. Method solving this integral is rather difficult because of its complexity. There are many based on simplification and additional assumptions (Madsen,1986, Hasofer & Lind 1974, Faber, 2006,. Borges & Castanheta, 1971). Sometimes we can simplified problem to the basis variables which are jointly normally distributed and the failure surface is a hyperplane then the failure probability is simply $P_F=\Phi(-\beta_C)$ where β_C is second order moment reliability index for safety problem. We can use in the place of β_C another reliability indexes as for example general β_G or (Hasofer & Lind 1974) reliability index β_{HL}. In another words we can use methods of Level-2 or even Level-1 to evaluated index of reliability.

The limit condition $\Delta=0$ implicate reliability index

$$\beta\leq \tilde{\Delta_m}/\mu_d \tag{3}$$

and

$$\Delta_m=(R_m-S_m)/((\mu_R{}^2+\mu_S{}^2)^{1/2}) \tag{4}$$

where R and S with index m denotes mean value of R and S, μ denotes standard deviation. If are used standardized variables $\xi_i=(x_i-x_{im})/\mu_I$ then β is the shortest distance to limit surface (Figure 1)

$$\beta=(R_{mr}-S_m)/\sqrt{(\mu_R{}^2+\mu_S{}^2)} \tag{5}$$

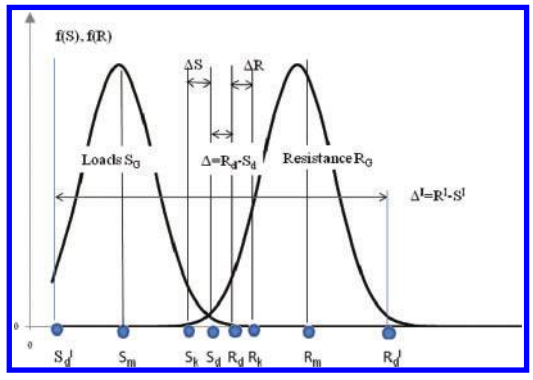


Figure 2. Safety for $\Delta=$R-S, Δ is minimum safety margin (certainty of safety) and Δ^I as certainty of construction destruction.

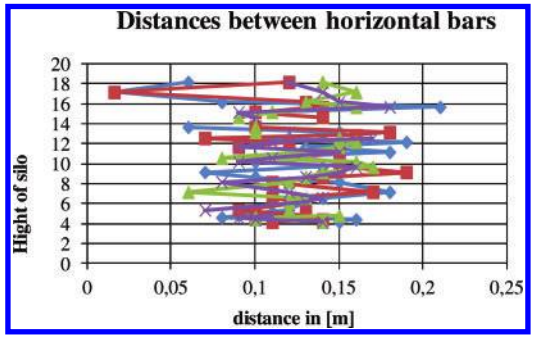


Figure 3. Random value of distances between horizontal bars.

When R and S are separated than index β in Level-2 is divided to two indexes for resistance and action consecutively

$$(S-S_m)/\mu_S\geq\beta_S,\ (R-R_m)/\mu_R\geq\beta_R \tag{6}$$

Simplifying safety phenomenon $\Delta=R-S$ to one dimension space margin of safety area Δ is shown on Figure 2 where $\Delta S=S_d-S_k$, $\Delta R=R_d-R_k$. For example certainty of construction destruction (e.g. during silo demolition) is Δ^I. From the equations, it is clear that it is very important to know the distribution of random variables.

2 RANDOM DATA OF SILO QUANTITIES

The problem gets complicated when we do not have full knowledge of the distributions of random variables. From our investigation we received distribution of basic variables which are shown on Figure 3–14 researches we get the frequency distributions of random variables presented on figures values of quantities as pressure and strength parameters were investigated on rape stored in full scale silo (Borcz & Maj & Trochanowski 1995) and (Kamiński & Maj 2000, 2006). Characteristics value of experimental data are

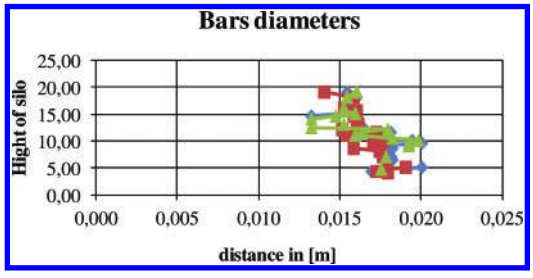


Figure 4. Random value of bars diameter.

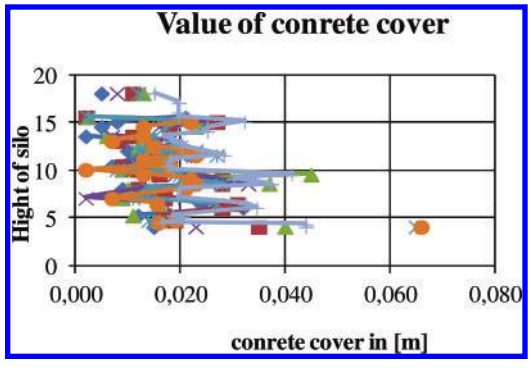


Figure 5. Random value of concrete cover.

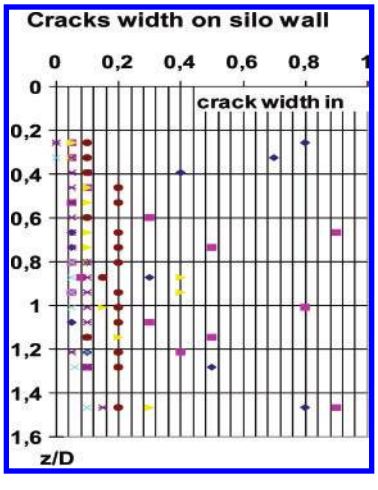


Figure 6. Distribution of random value of cracks width.

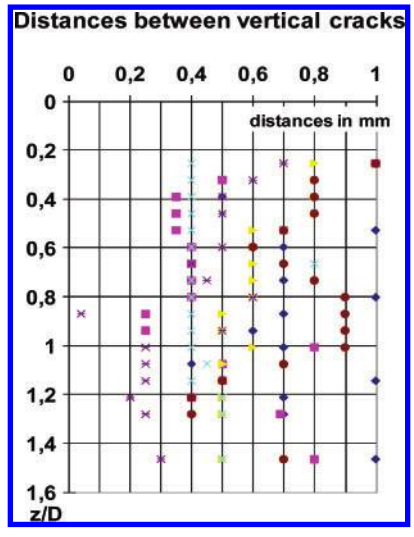


Figure 7. Distribution of random value of distances of vertical cracks.

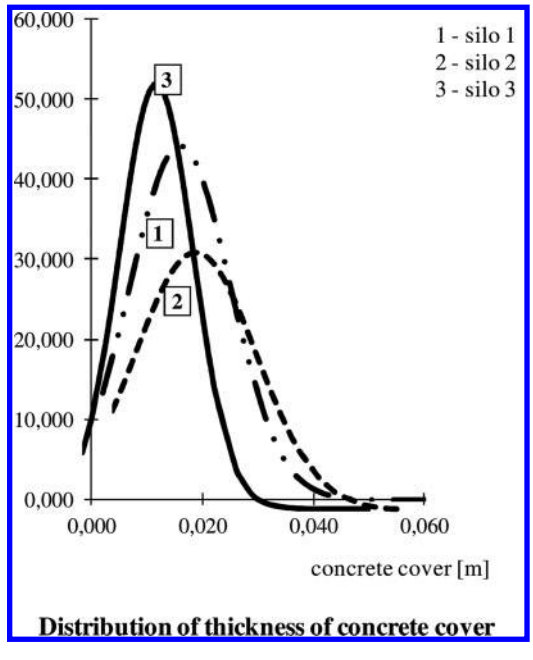


Figure 8. Density functions of thickness of concrete cover.

computed based on kind and richness of data collection. Same results obtained by Authors research team based on special constructed measurement sensors. Some of them were placed in for rape, investigated on full scale silo silo wall and bottom, some worked as sensors sounds (Borcz & Maj, 2002). Thereafter there are some mistakes of passing data's signals through interfaces in experimental devices (Leciejewski & Maj, 2013), and the range of mistakes is even 10–20%. So additional random value is the technical way of getting dates form experiment. Another problem of value of variation coefficient is selection of probability density function or distribution function (Gaussian, Gumbel, Rayleigh, empirical, extreme, etc.) to calculate mean, characteristic values of random data. Skewness of density function, double modal functions (Figure 9) etc can change the value of calculating statistics. The variation of value of measured pressure on rape silo (Borcz Maj, & Trochanowski, 1995) are shown on Figure 12, 13. Model of interaction between live loads and silo wall has influence of value of calculating pressure in concrete and steel bars. The very important is influence of cracks, changing

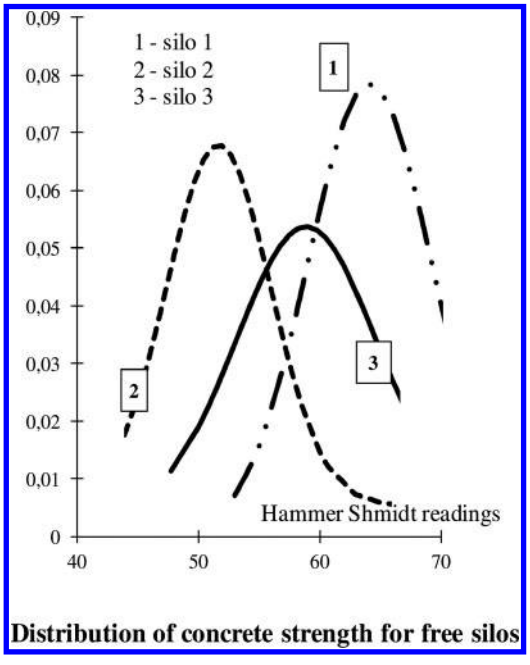


Figure 9. Concrete strength as a random value.

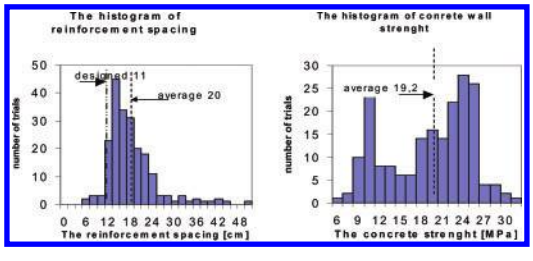


Figure 10. Histograms of strength parameter of cement.

width construction and its stiffness, no homogeneity of geometry etc. Variation of typical material strength parameters are shown on Figure 3–10. The presence of imperfection is shown on Figure 11. As follows limited values R_{di}, S_{di} (e.g. design values) and R_{ki}, S_{ki} (characteristic values) are usually calculated from linear formulas:

$$(S\text{-}S_m)/\mu_S \geq \beta_S, \tag{7}$$

$$(R\text{-}R_m)/\mu_R \geq \beta_R \tag{8}$$

with help of β_{Si}, β_{Ri} indexes (Madsen 1986). It implies separated load and material coefficients as γ_{fi}, γ_{mi} according as follows $\gamma_{fi} = S_{mi}/S_{ki}{}^*(1 + \beta_{Si}{}^*\nu_{Si})$; $\gamma_{fi} = (1 + \beta_{Si}{}^*\nu'_i)/(1 + t_S{}^*\nu_i)$; $\gamma_{mi} = (1 + \beta_{Ri}{}^*\nu'_i)/(1 + t_R{}^*\nu_i)$, where β_{Si}, β_{Si}-reliability indexes, ν_i-coefficient of variation, ν'_i-coefficient of variation is increased because of sensitivity on parameter changes μ_a, $\nu'_i = (\mu_i^2 + \mu_a^2)^{1/2}/(S_{mi})$, μ_a-standard deviation regarding to material fluctuation, t_S-calibration coefficient, e.g. probability quintile.

From this formula we see that the most important influence on safety index β and γ_{fi}, γ_{mi} has

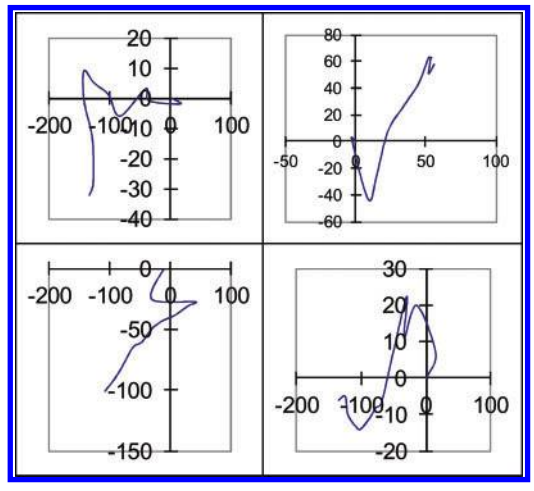


Figure 11. Imperfection of the geometric center of silo.

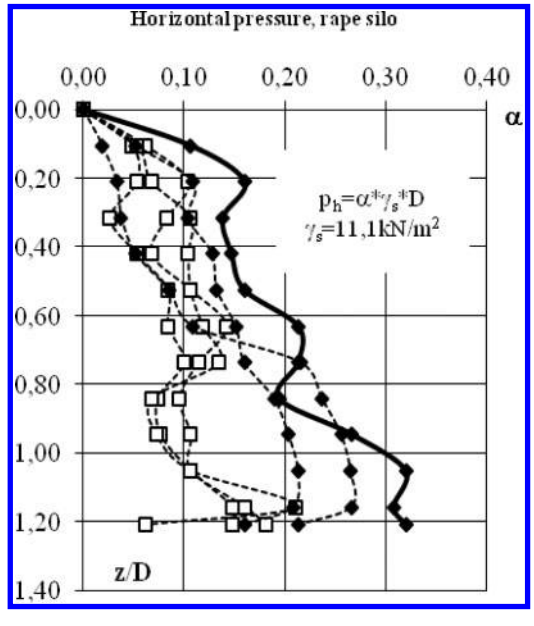


Figure 12. Distribution of random value of horizontal pressure.

coefficients of variation ν_i ν'_i. Some of loads and strength parameters are very susceptibility on changes and their value are variable. The variation exemplify values of standard coefficients k_i increasing or decreasing characteristic values. E.g. coefficients of: dead, live, extreme, dynamic loads $k_{QA} = 1{,}0\text{-}2$; loads simultaneous $k_{Acfi} = 0{,}6\text{-}1{,}0$; material: steel, concrete, cooperation $k_{mat} = 1{,}1\text{-}1{,}5$; construction dimension correction during its life $k_{ccs1} = 1{,}0\text{-}1{,}3$; consequence of destruction $k_{ccc} = 1{,}0\text{-}1{,}5$; performance factor $k_{wc} = 1{,}0\text{-}1{,}4$; material fatigue buckling $k_{mf} = 1{,}1\text{-}1{,}5$; construction validity, durability $k_{cim} = 1{,}0\text{-}1{,}3$; mode of constriction destruction $k_{cc} = 1{,}0\text{-}1{,}3$; periodic control $k_{ccon} = 1{,}0\text{-}1{,}3$; imperfections

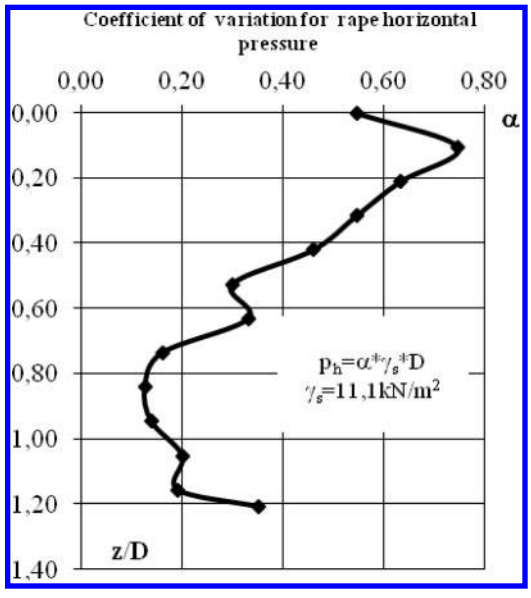


Figure 13. Coefficient of variation for pressure of in full scale rape silo.

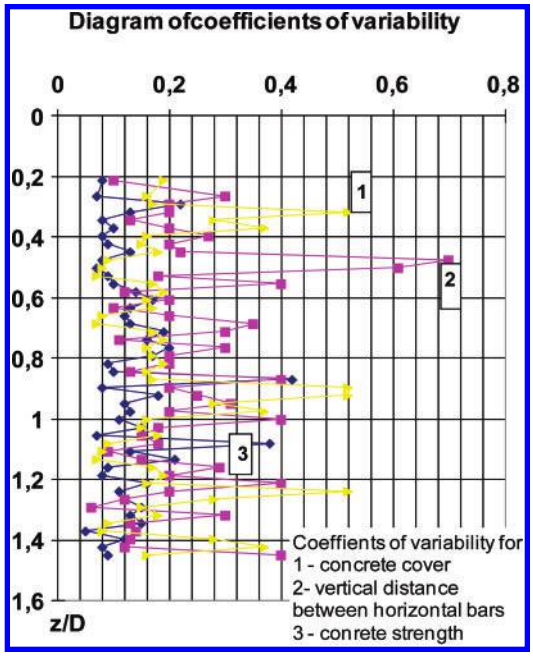


Figure 14. Distribution of coefficients of variably for concrete cover, concrete strength, vertical distances between bars.

$k_{cim} = 1,0\text{-}1,4$; adequacy of applied static models, calculating mistakes $k_{mis} = 1,0\text{-}1,5$. Another solution for $\Delta = R - S$ is evaluate global reliability index $\boldsymbol{\varpi}$: in equation

$$R^k \geq \boldsymbol{\varpi} S^k \tag{9}$$

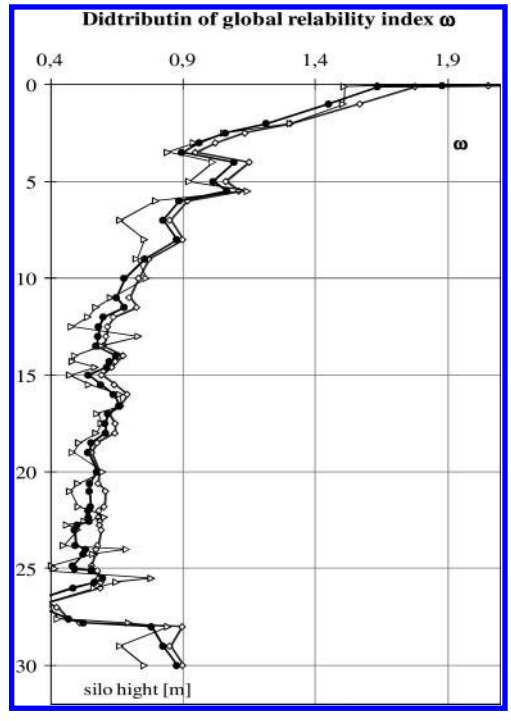


Figure 15. Distribution of global reliability index ω.

where S^k, R^k are characteristic value of S and R. It is simple method FORM with using calibration method in SORM. Results of calculation of this coefficient $\boldsymbol{\varpi}$ for repaired rape silo are presented in (Kaminski & Maj, 2000, 2006) and on Figure 15 Value of this index verify from 0,4 to 1,4. Another coefficient of construction safety is described by β, the reliability indices interval: $\beta = z_m/\sigma_z$ and reliability index of risk failure $p_f = \Phi(-\beta)$ where z_m i the mean value of function Δ, σ_Δ is standard deviation of Δ, $\Phi(-\beta)$ is Laplace function. For $\Delta_m \geq \beta^*\sigma_z$ construction work in safe area. Coefficient β is equal in European standards $3,7 \div 6,7$, $p_f = 10^{-3} \div 3 \cdot 10^{-8}$. Coefficient β can be separated to two β_R and β_S connected with strength and loads. According to (Pawlikowski, Jaskulski, Wiliński, 2004), there are three classes of safety coefficients RC1, RC2, RC3 but in we can use either RC0 class. In the last proposal, in case typical for silo loads, where live loads are greater than dead, and when $p(R \leq R_d;\ S \geq S_d) = \max$, R and S are independent (index d is design level) $\beta = 3,7$ ($p_f = 10\text{-}4$), $\beta_S = 2,59$ ($p_f = 0,005$), $\beta_R = 2,96$ ($p_f = 0,0015$).

3 CONCLUSIONS

The value of safety global factor $\boldsymbol{\omega}$ for the investigated and new designed silos is included within the range 0,9-7 which depends on the silo exploitation mode and "silo conditions", Kaminski & Maj 2006.

Reliability index β depends on kind of stored material, construction geometry etc should be individual calculated. It is useful to separate β to β_R and β_S.

REFERENCES

Madsen H. O., 1986 Methods of structural safety, Prenice Hall

Hasofer M., Lind N.C. 1974 Exact and Invariant Second-moment Code Format, Journal of the Engineering Mechanics Division, ASCE.

M.H. Faber, 2006 Risk and safety in civil, surveying and environmental engineering. Lecture Notes.

Ferry Borges, J. Castanheta. M. 1971 Structural Safety. Laboratorio Nacional de Engenharia Civil.

Borcz, A Maj, M. Trochanowski,A 1995 Guiding principles of silo designing, construction and operating, Prace Naukowe Instytutu Budownictwa Politechniki Wrocławskiej, Wrocław 1991.

Borcz, A Maj, M. 2002 Intern. Conf. "Reinforced and posttensioned concrete silos." Kraków, Poland

Kaminski, M. Maj, M 2006 Experimental and design loads of pressure of bulk materials against silo wall, Bulk Europe 2, Spain, Barcelona

Kaminski, M. Maj, M 2000 Reliability analysis of the global safety index design for conrete silo., The 3d Israeli Conference for Conveying and Handling of Particulate Solids, Dead Sea, Israel

Leciejewski S., Maj M., 2013 Komputery w badaniach doświadczalnych a metodologia badań eksperymentalnych, Konferencja Badania Konstrucji, PWr, Wroclaw

Pawlikowski J., Jaskulski R., Wiliński P., 2004, Oszacowanie Akceptowalnej Miary Zapasu Bezpieczeństwa istniejących Konstrukcji z Betonu, Konferencje ITB Wwa Cedyna

Research and Applications in Structural Engineering, Mechanics and Computation – Zingoni (Ed.)
© 2013 Taylor & Francis Group, London, ISBN 978-1-138-00061-2

Model uncertainties in reliability analysis of reinforced concrete structures

M. Holický & M. Sykora
Czech Technical University in Prague, Klokner Institute, Prague, Czech Republic

C. Barnardo-Viljoen, K.K. Mensah & J.V. Retief
University of Stellenbosch, Stellenbosch, South Africa

ABSTRACT: Resistances of civil engineering structures are primarily dependent on material properties, geometry and uncertainties associated to an applied resistance model. While materials and geometry can be relatively well described, the resistance model uncertainty is not yet well understood. The present contribution proposes a general concept of the model uncertainty. Factors affecting results obtained by tests and models and influences of actual structural conditions are overviewed. In a numerical study statistical characteristics of the uncertainties in resistance of reinforced concrete members are then provided. Simple engineering formulas are considered. To facilitate practical applications the partial factors for the model uncertainties are derived using a semi-probabilistic approach.

1 INTRODUCTION

Safety formats for the analysis of reinforced concrete structures were investigated in numerous previous studies; see e.g. Bertagnoli et al. (2004), Schlune et al. (2011), Sykora & Holicky (2011), Allaix et al. (2012) and Cervenka (2012). It was indicated that structural resistances can be predicted by appropriate modelling of material properties, geometry variables and uncertainties associated with a model under consideration. The effect of variability of materials and geometry is relatively well understood and was extensively addressed by the aforementioned studies. However, better description of model uncertainties is desired.

The submitted study is thus aimed at the model uncertainties. A general concept is proposed and selected influencing factors are illustrated by examples concerning resistance of reinforced concrete members. Statistical characteristics of the model uncertainties are summarized from available data considering simple engineering formulas (beam models, section-oriented approaches). To facilitate practical applications the partial factors for model uncertainties related to various types of the analysis are derived using a semi-probabilistic approach.

2 MODEL UNCERTAINTY

2.1 *General concept*

According to JCSS (2011) the model uncertainty is generally a random variable accounting for effects neglected in the models and simplifications in the mathematical relations. Model uncertainties can be related to:

- Resistance models (based on simplified relationships or complex numerical models),
- Models for action effects (assessment of load effects and their combinations).

The model uncertainty can be obtained from comparisons of physical tests and model results. Actual structural conditions not covered by tests should be taken into account if needed. Obviously the model uncertainty should be associated with a computational model under consideration. General concepts of model uncertainty applicable to both resistance and load effect models are indicated in Figure 1. The significance of factors affecting tests, model results and actual structural conditions depends substantially on an analysed structural member or load effect.

2.2 *Factors affecting the uncertainty related to resistance models*

Examples of factors affecting the uncertainty related to resistance models are given in Table 1. Similar list could be provided for load effect models. However, only resistance models are addressed hereafter.

In general the following aspects should be considered in the assessment of the model uncertainty:

- Test conditions should be correctly defined and test results properly evaluated.
- The uncertainty of a resistance model is dependent on the failure definition (maximum load, strain, deflection, crack width etc.). Here it is assumed that the maximum load is to be estimated by a model. Larger variability of the model uncertainty is anticipated for other failure criteria.

– It should always be assured that a specimen fails in an investigated failure mode; e.g. when the model uncertainty in shear is investigated beams failed in bending should not be considered.

2.3 *Assessment*

In this study the model uncertainty θ is considered to be a random variable. The multiplicative relationship for θ is assumed in accordance with JCSS (2011):

$$R = \theta \, \mathrm{R}_{\mathrm{model}}(\mathbf{X}) \tag{1}$$

where R = response of a structure – actual resistance estimated from test results and structural conditions; $\mathrm{R}_{\mathrm{model}}$ = model resistance – estimate of the resistance based on a model; and $\mathbf{X}^{\mathrm{T}} = (X_1, \ldots, X_m)$ is the vector of basic variables X_i.

Realistically assuming a lognormal distribution with the origin at zero (hereafter simply "lognormal distribution") for R and $\mathrm{R}_{\mathrm{model}}(\cdot)$, the model uncertainty is also lognormal. Its characteristics can be assessed using standard statistical techniques such as the Method of moments, Maximum likelihood method or Bayesian updating. An alternative procedure of the assessment of the model uncertainty is provided in Annex D of EN 1990 (2002). This method, based on the regression analysis and the Least Square Method, is focused on estimation of a regression coefficient rather than on the assessment of statistical characteristics of a random variable according to the JCSS definition. That is why the EN 1990 procedure is not considered hereafter.

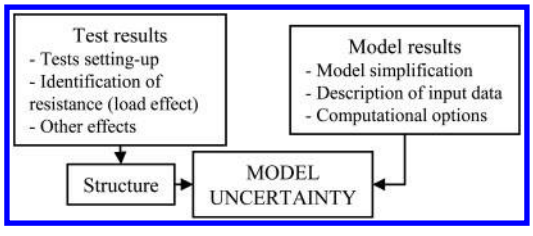


Figure 1. General concept of the model uncertainty.

Note that an additive relationship or combination of the multiplicative and additive formulas may be used to assess the model uncertainty, JCSS (2011). In more advanced analyses the model uncertainty may be represented by functions of several auxiliary random variables $\boldsymbol{\theta}$ and variables $\mathbf{X}$ as considered e.g. by Song et al. (2010).

The model uncertainty θ in general depends on basic variables $\mathbf{X}$. Influence of individual variables on θ can be assessed by a regression analysis as described e.g. by Ditlevsen & Madsen (1996). It is also indicated that the model describes well the essential dependency of R on $\mathbf{X}$ only if the model uncertainty:

– Has either a suitably small coefficient of variation (how small is the question of the practical importance of the accuracy of the model) or
– Is statistically independent of the basic variables.

It may also be important to define ranges of the input parameters $\mathbf{X}$ for which the accepted model uncertainty is valid. Such intervals should be established on the basis of:

Table 1. Examples of factors affecting the uncertainty related to resistance models.

Factors	Partial factors	Explanation	Examples
Test results	Tests setting-up	Differences between laboratory and in situ conditions	– accuracy of test method (accuracy of gauges, friction, assembly stiffness) – deviations of individual tests (variability of particular conditions) – boundary conditions (supports of specimens) – loading conditions (transfer, speed) – temperature, moisture conditions – size effect (scale of tests)
	Identification of resistance	Vagueness in failure indicator	– ultimate strength – strain, deflection – crack width
	Other effects	Effects not covered by tests	– time variant effects (time dependent material properties)
Structure	–	Actual structural conditions (may not always be known)	– boundary conditions (supports, continuous members) – loading conditions (transfer, combination of shear and bending moments) – temperature, moisture conditions - size effect (actual size)
Model results	Model simplification	Simplifications and approximations of model under consideration	– assumed stress distributions, constitutive laws – boundary conditions – bond between concrete and reinforcement – size effect
	Description of	Assumptions concerning input data actual values of variables not measured	– internal dimensions – tensile strength – fracture energy – plastic strain
	Computational options	Choices to be made by analysts in setting-up of model	– discretisation – type of finite elements – boundary conditions (simplifications made by analysts)

– Admissible ranges of **X** for the model (for instance limits on a reinforcement ratio) and
– Simplifications in modelling of θ (for instance when θ can be considered independent of the basic variable in a specified interval).

2.4 *Model uncertainty methodology*

The main properties of uncertainties in resistance models can be treated in the following steps, starting off from the resistance model and model uncertainty observations, ending up at a reliability function on which the design function is based:

1. The database of observations or test results, including all test parameters required for repeating of the tests and calculating the resistance by the model under investigation forms the basis of model uncertainty assessment.
2. The range of parameters for the dataset, such as material strength classes or geometry, defines the range of strict applicability of the derived model uncertainty.
3. Statistical treatment of model uncertainty observations includes proof of unbiased sampling and goodness of fit tests.
4. Deviations from such statistical treatment of model uncertainty observations introduce uncertainties which should be accounted for.
5. Additional uncertainties are introduced when the model uncertainty derived from experiment is applied to the design function as expressed in terms of the resistance model and related design rules.
6. Derivation of a generic model uncertainty for a given failure mode and design function includes provision for additional uncertainties resulting from the scope of application allowed by the procedure, such as structural and material classes, geometry including amount of steel and detailing rules.
7. The model uncertainty is furthermore dependent on the safety format of the design function across the scope of application, including the effects of predefined characteristic values and (material) partial factors.

Examples of this process were given by Huber (2005), Dithinde et al. (2011), Mensah (2012) and Sykora & Holicky (2012).

3 UNCERTAINTIES RELATED TO THE MODELS PROVIDED IN EN 1992-1-1

The numerical part of this contribution is focused on the uncertainties related to resistance models for reinforced concrete structures provided in EN 1992-1-1 (2004). It is assumed that the uncertainties of action effects can be treated separately. Model resistances of structural members exposed to compression, bending, and shear (members without and with special shear reinforcement distinguished) are given as follows:

$$R_{model}(\mathbf{X}) = b^2(\alpha_{cc} f_c + \rho_l f_y) \tag{2a}$$

$$R_{model}(\mathbf{X}) = \rho_l b\, d f_y [d - 0.5\rho_l\, d\, f_y / (\alpha_{cc} f_c)] \tag{2b}$$

$$R_{model}(\mathbf{X}) = \max[0.18k\,(100\rho_l f_c)^{1/3} b_w d;\quad 0.035k^{3/2} f_c^{1/2} b_w d] \tag{2c}$$

$$R_{model}(\mathbf{X}) = \max_{1 \le \cot\xi \le 2.5}\{\min[\rho_w b_w z f_{yw} \cot\xi,\ \alpha_{cw} b_w z \nu f_c / (\cot\xi + \tan\xi)]\} \tag{2d}$$

where b = width; $b_w = b$ is the minimum width between tension and compression chords; d = effective depth; f_c = concrete compressive strength; f_y and f_{yw} are yield strengths of reinforcement (longitudinal, shear); $k = \min[1 + \sqrt{(200\text{ mm} / d)};\ 2.0]$; $z \approx 0.9d$ is the inner lever arm; $\alpha_{cc} = 1$ is the coefficient accounting for long-term effects on concrete strength; $\alpha_{cw} = 1$ is the coefficient taking account of the state of the stress in the compression chord; $\nu = 0.6(1 - f_c / 250\text{ MPa})$ is the strength reduction factor for concrete cracked in shear; ξ = angle between concrete compression struts and the main tension chord; and ρ_l and ρ_w are the longitudinal/shear reinforcement ratios.

Note that the symbol ξ is introduced here instead of θ used in EN 1992-1-1 (2004) to avoid confusion with the symbol for model uncertainty. Neither the partial factor γ_C nor the characteristic value of f_c are applied in Equations (2). For shear without special shear reinforcement (such as stirrups or inclined bars, hereafter referred to as "shear reinforcement" to simplify the text), no axial compressive force is considered.

Statistical characteristics of the uncertainties related to the resistance models in Equations (2) obtained in several studies are provided in Table 2. The mean of the model uncertainty indicates a systematic deviation of the model from test results (bias). The following comments are made:

– Available experimental data are not supplemented by sufficient information on test conditions (see Figure 1 and Table 1) which are thus not appropriately accounted for; uncertainties due to description of input data may concern uncertain effective depth and material properties,
– Effects of actual structural conditions are unknown and not included,
– Computational options (Figure 1 and Table 1) seem to be irrelevant since simple structural members are considered.

Some of the studies are based on overlapping experimental results and thus are partly dependent. It follows from Table 2 that a broad agreement is mostly achieved for failure modes where several results are available.

The considered studies also provided a valuable insight into factors affecting the model uncertainties for bending and shear. As background information for the paper by Holicky et al. (2007) the analysis of experimental data revealed no significant statistical correlation between the model uncertainty and any of the basic variables influencing flexural resistance (including

Table 2. Statistical characteristics of θ related to the resistance models provided in EN 1992-1-1 (2004).

Failure type	μ_θ	V_θ	Sample size	Source
Axial compres.	1	0.05	[1]	[1]
Bending	1.08	0.09	$n = 109$	Holicky et al. (2007)
	1.07	0.08	$n = 10$	Prieto & Tanner (2008)
Shear	1.02	0.22	$n = 193$	Cladera & Marí (2004a)
without	0.94	0.13	$n = 184$	Unpublished study
shear rft.	1.00	0.13	$n = 174$	Sykora & Holicky (2012)
Shear	1.83	0.40	$n = 123$	Cladera & Marí (2004b)
with	1.7	0.37	$n = 160$	Hawkins et al. (2005)
shear rft.	1.64	0.32	$n = 122$	Cladera & Marí (2007)
	1.65	0.31	$n = 222$	Mensah (2012)
$\rho_w f_{yw} \leq 1$ MPa	1.80	0.26	$n = 147$	Sykora et al. (2013)
1 MPa $< \leq 2$ MPa	1.24	0.23	$n = 45$	Sykora et al. (2013)
2 MPa $< \rho_w f_{yw}$	0.76	0.19	$n = 8$	Sykora et al. (2013)

[1] Validated to comply with the model uncertainty factors in Eurocodes, draft of bulletin on semi-probabilistic methods for verifications of RC structures by *fib* SAG7.

reinforcement ratio $0.25\% < \rho_l < 3.5\%$ and concrete compressive strength 17 MPa $< f_c <$ 45 MPa).

For shear resistance of members without shear reinforcement a research team at the University of Stellenbosch concluded that the model uncertainty:

- Is significantly decreasing with the ratio of the shear span to the effective depth $a/d$and the effective depth d while
- It is not subject to trends with the other shear parameters.

The results were limited to the range of $2.9 < a/d$ as deep beam and shear bond failures are expected for lower values of a/d in accordance with O'Brien & Dixon (1995). For lower a/d the shear resistance is likely to be underestimated since the positive contribution of an arch action is neglected in the Eurocode model. Cladera & Marí (2004a) reported decrease of the model uncertainty with d and also with ρ_l which does not comply with the conclusions of the South African team confirmed later by Sykora & Holicky (2012). It is emphasised that the failure of members without shear reinforcement is sudden and brittle and adequate reliability should be assured.

For shear resistance of members with shear reinforcement Cladera & Marí (2007) and Mensah (2012) indicated that the model uncertainty significantly decreases with an increasing strength of shear reinforcement $\rho_w f_{yw}$. Influences of the other basic variables are much lower. In addition Cladera & Marí (2004b) noted that influence of the amount of shear reinforcement is not linearly proportional to the shear strength and the truss model in EN 1992-1-1 (2004) may be unconservative for highly reinforced concrete members ($\rho_w f_y > 2$ MPa). These conclusions are confirmed by a more recent study of the authors where a significant trend of μ_θ with $\rho_w f_{yw}$ is observed (Table 2). Figure 2 shows variation of θ with $\rho_w f_{yw}$

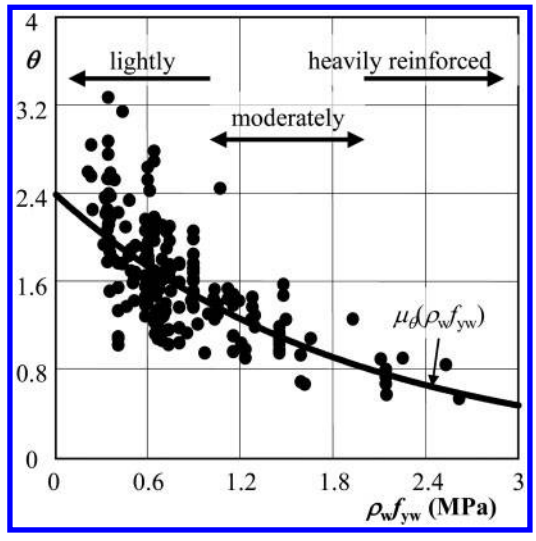


Figure 2. Variation of θ with $\rho_w f_{yw}$ and the trend of μ_θ.

and the trend of the mean value of θ based on an exponential regression. The influence of the strength of shear reinforcement on the coefficient of variation of the model uncertainty is less significant. A significant bias of the model uncertainty is primarily attributed to a limit for the angle ξ.

4 MODEL UNCERTAINTY FACTOR FOR DETERMINISTIC VERIFICATIONS

For deterministic reliability verifications EN 1990 (2002) introduces the partial factor γ_{Rd} to describe the uncertainty associated with the resistance model ("design value of the model uncertainty"). In accordance with fib SAG 9 (2010) the model uncertainty factor γ_{Rd} for reinforced concrete structures can be obtained as a product of:

$$\gamma_{Rd} = \gamma_{Rd1}\ \gamma_{Rd2} \tag{3}$$

where γ_{Rd1} = partial factor accounting for model uncertainty; and γ_{Rd2} = partial factor accounting for geometrical uncertainties.

EN 1992-1-1 (2004) provides no specific recommendations concerning model uncertainties. EN 1992-2 (2005) introduces the global safety format for a nonlinear analysis with the recommended model uncertainty factor of 1.06. However, Sykora & Holicky (2011) indicated that such a factor is low and should be increased in most cases depending on relevant failure mode (bending, shear, compression). In accordance with fib SAG 9 (2010) $\gamma_{Rd1} = 1.05$ for concrete strength and $\gamma_{Rd1} = 1.025$ for reinforcement may be assumed in common cases. However, larger model uncertainty needs to be considered for punching shear when concrete crushing is dominating.

A value of $\gamma_{Rd2} = 1.05$ may be assumed for geometrical uncertainties of the concrete section size or

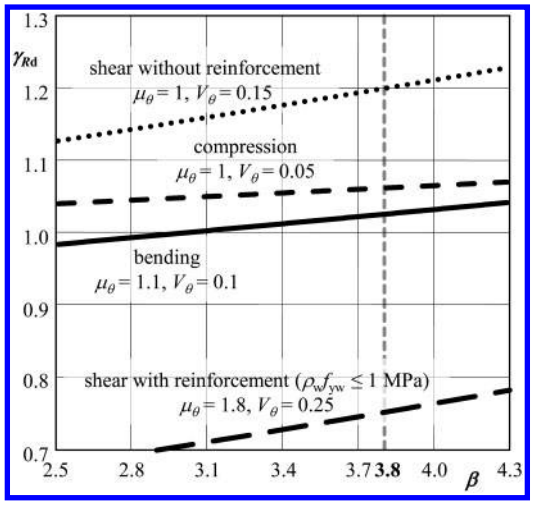


Figure 3. Variation of the partial factor γ_{Rd} with β for $\alpha_R = 0.32$.

reinforcement position. When measurements of an existing structure indicate insignificant variability of geometrical properties, $\gamma_{Rd2} = 1.0$ may be accepted.

Alternatively, the partial factor γ_{Rd} can be obtained from the following relationship based on a lognormal distribution:

$$\gamma_{Rd} = 1 / [\mu_\theta \exp(-\alpha_R \beta V_\theta)] \quad (4)$$

where α_R = FORM sensitivity factor; and β = target reliability index according to EN 1990 (2002). Assuming the probabilistic models for the model uncertainty given above (with rounded statistical characteristics), variation of the partial factor γ_{Rd} obtained from Equation (4) with the target reliability β and $\alpha_R = 0.32$ ("non-dominant resistance variable") is indicated in Figure 3.

It follows from Figure 3 that the model uncertainty factor γ_{Rd} is close to unity for the well-established models of flexural and axial compression resistances. The partial factor then drops below unity for the shear model for the members with shear reinforcement due to the high value of $\mu_\theta(\rho_w f_{yw} \leq 1\,\text{MPa})$. For $\beta = 3.8$ the model uncertainty factor of about 1.2 is obtained for the shear model for the members without shear reinforcement.

The selection of $\alpha_R = 0.32$ deserves additional comments. Leading and accompanying actions (with $\alpha_E = -0.7$ and $\alpha_E = -0.4 \times 0.7 = -0.28$) are distinguished in EN 1990 (2002) while $\alpha_R = 0.8$ is recommended for resistance variables. When the uncertainty factor γ_{Rd} and material factor γ_m are assessed separately for $\alpha_R = 0.8$, conservative designs may be obtained. Taerwe (1993) and ISO 2394 (1998) considered the model uncertainty as a non-dominant resistance variable and accepted the reduction $\alpha_R = 0.4 \times 0.8 = 0.32$. Note that the α_R-value significantly affects the partial factor γ_{Rd} (Sykora et al. (2013)).

5 DISCUSSION AND OUTLOOK OF FURTHER RESEARCH

This study indicates that the uncertainties related to the resistance models for reinforced concrete structures should be further investigated. Basically two classes of models should be distinguished:

- Engineering models with strictly defined assumptions (beam and sectional approaches),
- Complex models based on general principles of structural mechanics with much wider options and potentially higher uncertainties.

The following steps of research concerning the uncertainties in resistance models are foreseen:

1. *Data acquisition*. For structural members actual resistances will be obtained from available experimental tests. When experimental data is little or missing, test values are to be found by interpretation of test results in different conditions (simpler structural members), using different software tools and verification methods. Yet, this will introduce an additional uncertainty. The test results might be associated with weights reflecting types and frequencies of structures designed in practice.
2. *Uncertainties related to different test methods and actual structural conditions* will be assessed; use of expert judgements will often be inevitable.
3. *Uncertainties affecting model results*. Particularly for numerical models significance of the three partial factors affecting "model results" is to be assessed to provide background information for development of further guidelines.
4. *Differentiation of the model uncertainty* with respect to complexity of the task, failure mode, underlying structural models and level of control will be proposed. Appropriate probabilistic description will be suggested and the partial factors for model uncertainties derived.

For deteriorating structures the resistance model should inevitably incorporate degradation effects that may be a source of additional uncertainties and should be also quantified within the further research; Tanner et al. (2011) provided the first insight.

6 CONCLUDING REMARKS

Description of uncertainties related to resistance and load effect models can be a crucial problem of reliability analyses. The present paper focused on the uncertainties in resistance models of reinforced concrete structures reveals that:

1. The model uncertainty should be related to test uncertainties, to actual structural conditions and computational model under consideration.
2. In common cases actual resistance can be estimated as a product of the model uncertainty and resistance obtained by the model.
3. Uncertainties related to models provided in EN 1992-1-1 (2004) can be described by the following

statistical characteristics and partial factors (when combining different failure modes a less favourable model uncertainty may apply):

- Axial compression without effects of buckling: mean $\mu_\theta \approx 1$; coefficient of variation $V_\theta \approx 0.05$; model uncertainty factor $\gamma_{Rd} \approx 1.05$,
- Bending: $\mu_\theta \approx 1.1$; $V_\theta \approx 0.1$ and $\gamma_{Rd} \approx 1.05$,
- Shear of the members without special shear reinforcement: $\mu_\theta \approx 1$; $V_\theta \approx 0.15$ and $\gamma_{Rd} \approx 1.2$,
- Shear of the members with special shear reinforcement:
  - lightly reinforced beams ($\rho_w f_{yw} \leq 1$ MPa): $\mu_\theta \approx 1.8$; $V_\theta \approx 0.25$ and $\gamma_{Rd} \approx 0.75$,
  - moderately reinforced beams (1 MPa $< \rho_w f_{yw} \leq 2$ MPa): $\mu_\theta \approx 1.25$; $V_\theta \approx 0.25$ and $\gamma_{Rd} \approx 1.1$,
  - heavily reinforced beams (2 MPa $< \rho_w f_{yw}$): $\mu_\theta \approx 0.8$; $V_\theta \approx 0.2$ and $\gamma_{Rd} \approx 1.6$ (particularly these values are indicative since they are based on eight test results only).

ACKNOWLEDGEMENTS

This study is partly an outcome of the research project P105/12/2051, supported by the Czech Science Foundation.

REFERENCES

Allaix, D.L., Carbone, V.I. & Mancini, G. 2012. Global safety format for non-linear analysis of reinforced concrete structures. *Structural Concrete*. DOI: 10.1002/suco.201200017.

Bertagnoli, G., Giordano, L. & Mancini, G. 2004. Safety format for the nonlinear analysis of concrete structures. *Studi e ricerche – Politecnico di Milano. Scuola di specializzazione in costruzioni in cemento armato* 2004(25): 31–56.

Cervenka, V. 2012. Reliability-based Nonlinear Analysis According To MC 2010. *Structural Concrete*. DOI: 10.1002/suco.201200022.

Cladera, A. & Marí, A.R. 2004a. Shear design procedure for reinforced normal and high-strength concrete beams using artificial neural networks. Part I: beams without stirrups. *Engineering Structures* 26(7): 917–926. DOI: 10.1016/j.engstruct.2004.02.010.

Cladera, A. & Marí, A.R. 2004b. Shear design procedure for reinforced normal and high-strength concrete beams using artificial neural networks. Part II: beams with stirrups. *Engineering Structures* 26(7): 927–936. DOI: 10.1016/j.engstruct.2004.02.011.

Cladera, A. & Marí, A.R. 2007. Shear strength in the new Eurocode 2. A step forward? *Structural Concrete* 26(7): 917–66.

Dithinde, M., Phoon, K., De Wet, M. & Retief, J. 2011. Characterization of Model Uncertainty in the Static Pile Design Formula. *Journal of Geotechnical and Geoenvironmental Engineering* 137(1): 70–85. DOI: 10.1061/(ASCE)GT.1943-5606.0000401.

Ditlevsen, O. & Madsen, H.O. 1996. *Structural Reliability Methods.* Chichester (England): John Wiley & Sons.

EN 1990:2002. *Eurocode – Basis of structural design.*

EN 1992-1-1:2004. *Design of concrete structures – Part 1-1: General rules and rules for buildings.*

EN 1992-2:2005. *Eurocode 2 – Design of concrete structures – Part 2: Concrete bridges – Design and detailing rules.*

fib SAG 9 2010. *Revision of partial safety factors (report),* December 2010.

Hawkins, N.M., Kuchma, D.A., Mast, R.F., Marsh, M.L. & Reineck, K. 2005. *Simplified Shear Design of Structural Concrete Members,* NCHRP Report 549. Transportation Research Board.

Holicky, M., Retief, J.V. & Dunaiski, P.E. 2007. The reliability basis of design for structural resistance. In A. Zingoni (ed.), *Proc. SEMC 2007, University of Cape Town,* Rotterdam: Millpress.

Huber, U.A. 2005. *Reliability of Reinforced Concrete Shear Resistance (MSc thesis).* Stellenbosch: Department of Civil Engineering, University of Stellenbosch, Stellenbosch, South Africa.

ISO 2394:1998. *General principles on reliability for structures.*

JCSS 2011. *JCSS Probabilistic Model Code.* Zurich: Joint Committee on Structural Safety. <www.jcss.byg.dtu.dk>.

Mensah, K.K. 2012. *Reliability Assessment of Structural Concrete with Special Reference to Shear Resistance (MSc thesis).* Stellenbosch, South Africa: University of Stellenbosch.

O'Brien, E.J. & Dixon, A.S. 1995. *Reinforced and prestressed concrete design: the complete process.* Longman Scientific & Technical.

Prieto, M. & Tanner, P. 2008. Incertidumbres del modelo de resistencia a flexión para vigas con armaduras corroídas. *Comunicaciones del IV Congreso de ACHE en Valencia, Madrid, 24–27 noviembre 2008.*

Schlune, H., Plos, M. & Gylltoft, K. 2011. Safety formats for nonlinear analysis tested on concrete beams subjected to shear forces and bending moments. *Engineering Structures* 33(8): 2350–2356. DOI: 10.1016/j.engstruct.2011.04.008.

Song, J., Kang, W., Kim, K.S. & Jung, S. 2010. Probabilistic shear strength models for reinforced concrete beams without shear reinforcement. *Structural Engineering and Mechanics* 34(1): 15–38.

Sykora, M., Cervenka, V. & Holicky, M. 2013. Uncertainties of resistance models for reinforced concrete structures (accepted for publication). In D. Marian, I. Leviathan & A.N. Dancygier (eds.), *Proc. fib Symposium Tel Aviv 2013, Tel Aviv, 22–24 April 2013.*

Sykora, M. & Holicky, M. 2011. Safety format for non-linear analysis in the model code – verification of reliability level. In V. Sruma (ed.), *Proc. fib Symp. PRAGUE 2011 Concrete engineering for excellence and efficiency, Prague, 8–10 June 2011.* Prague: Czech Concrete Society.

Sykora, M. & Holicky, M. 2012. Assessment of the model uncertainty in shear resistance of reinforced concrete beams without shear reinforcement (to be published). *Transactions of the VSB – Technical University of Ostrava, Civil Engineering Series* XII(2): 10.

Sykora, M., Holicky, M. & Krejsa, J. 2013. Model uncertainty in shear resistance of reinforced concrete beams with shear reinforcement (to be submitted for publication). *Proc. Modelovaní v mechanice 2013, Ostrava, May 2013.* Ostrava: VŠB-Technical University of Ostrava, Faculty of Civil Engineering.

Taerwe, L. 1993. *Towards a consistent treatment of model uncertainties in reliability formats for concrete structures,* CEB Bulletin d'Information n° 219 'Safety and Performance Concepts'. Lausanne: CEB.

Tanner, P., Lara, C. & Prieto, M. 2011. Semi-probabilistic models for the assessment of existing concrete structures. In *Proc. ICASP11, ETH Zurich, 1-4 August 2011.* Leiden: CRC Press/Balkema.

Research and Applications in Structural Engineering, Mechanics and Computation – Zingoni (Ed.)
© 2013 Taylor & Francis Group, London, ISBN 978-1-138-00061-2

Safety in design for industrial and mining structures

Travis Langbecker
Senior Consultant, PDG – Structural Assets, HATCH, Brisbane, Australia

Sabaratnam Loganathan
Deputy Global Discipline Director, PDG – Structural, Director PDG – Structural Assets, HATCH, Brisbane, Australia

ABSTRACT: Safety in Design is an integral part of the design process for industrial and mining structures. Safety in design is a philosophy which integrates risk management into the design process to identify and address safety issues over the whole of life (by elimination or minimization) and to communicate hazards and residual risks to "downstream" users. Hazards and risks associated with both work practices and structural safety are required to be considered. Solutions to reduce safety risks may require higher level structural analysis and/or rigorous measurements to verify design assumptions, minimize uncertainties and/or ongoing monitoring during the construction and operation phases. Engineering challenges, opportunities and lessons learnt from a number of taxing projects are presented.

1 INTRODUCTION

"Safety in Design" is defined as the integration of hazard identification and risk assessment methods early in the design process to eliminate or minimize risks throughout the life cycle of the structure or plant being designed and communicating hazards and risks to "downstream" users [modified from Safe Work Australia, 2006]. Prevention through design, HSE in design, safety by design, safe design and designing for safety are alternative expressions/terminology for Safety in Design.

Various studies have shown that design plays a role in accidents and that designers can do more to prevent such accidents [Safe Work Australia, 2004], [Bennett, 2004].

There are many reasons for Safety in Design approaches to be adopted by structural engineers:

1. It is the right thing to do, from a general engineering ethics standpoint. HATCH, the employer of the authors, has the implementation of Safety in Design principles as one of the main components of the company HSEC policy, and "No Harm' philosophy.
2. Most large mining and resource companies have Safety in Design principles directly embedded into their safety policies/standards. These embedded elements may relate to compliance with legislative requirements, requirements to undertake risk assessments for new designs, consideration of the structure/plant life cycle, identification of critical components, documentation of operating limits and design data, and reviews of design for use, maintenance and construction. Requirements for dealing with fatal or catastrophic risks may also involve Safety in Design principles.
3. Various government bodies around the world are enforcing the implementation of Safety in Design practices through various legislative instruments. Some typical examples can be found in [Safe Work Australia, 2012], [Department of Mines and Petroleum, 2010].

Structures for the mining and resource industries operate in an aggressive environment. Many types of these structures are subjected to "abnormal" or unusual operational loads during their service life and these structures are generally required to survive these abnormal events without compromising safety. As such Safety in Design is warranted for mining and resource structures, and in particular in the design of service life extension/risk reduction strategies for existing structures.

This paper will present the engineering challenges and lessons learnt from a Safety in Design perspective for a number of challenging projects. A "broad" definition of "Safety in Design", and "designer" is adopted throughout this article.

2 HAZARD IDENTIFICATION AND RISK MANAGEMENT FOR SAFETY IN DESIGN

Identification of hazards and management of risks forms a central pillar of Safety in Design. Risk management principles are well established in the mining and resource industries with specific publications to supplement general risk management publications such as ISO 31000. Briefly, the context of the risk assessment is defined, hazards are identified, risks evaluated against a tolerance criteria, and additional controls implemented where necessary. This

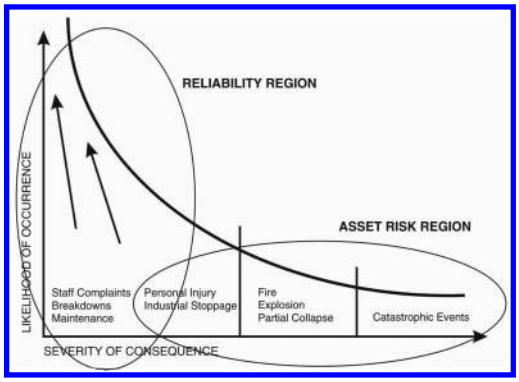


Figure 1. General distribution of probability vs consequence.

is generally undertaken by an experienced multi-discipline team with staged risk reviews and in parallel with client operability, maintainability and/or constructability reviews.

Although this process appears to be straight forward for structural engineering, it in fact requires structural engineers with appropriate experience, skills, knowledge, attitude and professionalism to carry out these tasks to achieve the correct outcomes.

The context for the hazard identification and risk management process is important. A general profile of all the hazards for a particular design will generally yield a distribution with the two extremes being low frequency, high consequence technical/process safety hazards, as opposed to high frequency, low consequence hazards generally slips, trips and falls. The source of these hazards can also range from the operation, maintenance and systems of work associated with the equipment/plant supported on the structure, adjacent items, through to the structure itself. Safety in Design generally requires that more than one hazard identification/risk management methodology is required to cover the full range of issues.

Several publications giving an overview of Safety in Design are available [Safework Australia 2012], [Workcover NSW, 2001] as a starting point.

These can be supplemented with recommendations from codes of practice and guidance material, which deal with good practice on issues as plant, steel or concrete construction, bridge beams, and bins/silos. Further information on hazards specific to the resources industry can be obtained from industry initiatives, safety alerts/bulletins from various government agencies or from reports relating to major or fatal accidents.

A major source of hazards often overlooked is the structure itself. Hazards relating to the construction of the structure or maintenance/operability of associated equipment may be well known, however the structure itself requires regular cleaning, maintenance, in particular maintenance of the protective coatings, and ongoing structural integrity inspections.

The ongoing structural integrity management of numerous types of structures for the resource

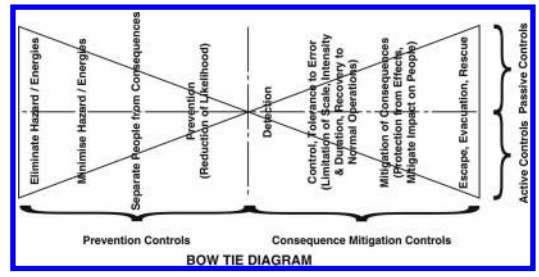


Figure 2. PFEEER mapped on a bow tie diagram.

industries are important. The selected structural configuration should consider potential failure modes, the ability to detect early signs of structural distress in critical elements, and acess requirements required for ongoing structural inspections.

2.1 *Hierarchy of controls and control philosophy*

Control measures are generally required to further reduce the level of risk, and the hierarchy of controls is used as a guide on the most suitable types of controls to use. ERIC (Eliminate, Reduce, Inform | Control) or the standard hierarchy of controls (Eliminate, Substitute, Isolate, Engineering, Administration PPE) are good starting points. The OMAT [EMERST, 2012] hierarchy of controls (Eliminate, Substitute/Minimize, Passive Engineering, Active Engineering, Alarms and Warning Systems, Procedural, Awareness/Competency) was derived for large earth moving equipment and is useful for items with mechanical equipment and interaction. The overall resilience of the controls for major hazards can be appreciated by mapping the type and functionality of the controls against the PFEEER [HSE, 1997] hierarchy (Elimination, Minimize hazards/energies, Separate people from consequences, Prevention – reduction of likelihood, Detection of event, Control – limitation of scale, intensity, duration & recovery to normal operations, Mitigation of consequences, Evacuation, escape and rescue). This presentation is best suited using a bow-tie assessment.

Care is required for structures where the structural integrity for particular design loads/scenarios is dependent on safety devices, even though "fail to safety" principles may be adopted. Good practice is generally to implement multiple, independent safety devices (preferably passive/without human action required) which do not have common failure modes. Critical safety devices should be identified during the design phase, their accuracy, effectiveness and consequences of failure understood, and communication to the user in place to ensure their continued safe operation through a traceable audit system.

There can be considerable differences between structural design standards relating to this issue. The Australian standards for bulk material handling machines (AS4324.1) and cranes (AS1418) require scenarios to be considered where the control system has been ineffective, or alternatively requires specific

requirements to mitigate and limit the effects of failure of critical components.

The bow-tie risk assessment methodology is a useful tool for these scenarios as it can enable the full spectrum of scenarios from a safety and enterprise viewpoint to be developed. In general, most of the systems used to limit the probability of an event occurring, or to limit the consequences of an event are dependent on humans for correct installation, maintenance, and in extreme conditions, not to remove or bypass the system.

2.2 *Risk tolerability*

The tolerability criteria for the risk management is critical, the criteria is often referenced as being ALARP – As Low As Reasonably Practicable. One of the key issues in practice is defining this criteria. Reviews of general risk management practices, which are applicable for engineering design, have identified issues with the application of the ALARP criteria such as not applying good practice, reverse ALARP, salami slicing, and inappropriate controls amongst others.

The legislative definition of the ALARP is also a challenge in terms of structural engineering in general and in particular Safety in Design. Various legislative guides generally define ALARP by weighing up several factors which involve: the likelihood of a hazard or risk occurring; the degree of harm that may result from the hazard or risk; what a person concerned knows or ought reasonably to know about the hazard or risk and the ways of eliminating the risk, including knowledge available at the time, understanding the impact of failure of risk controls measures, human error and interaction between multiple hazards; the availability and suitability of ways to eliminate or reduce the hazard or risk; and the cost of eliminating or reducing the risk and whether this cost is "grossly disproportionate" to the risk. This criteria is very difficult to apply to a design engineering perspective. UK's HSE and IStructE and Institutions of Civil Engineers have a discussion document on this issue [Institution of Civil Engineers, 2010] which highlights the further work required in this particular issue.

Extreme care needs to be taken using risk prioritizing matrices to determine if a risk is tolerable.

2.3 *Transfer of information*

A key requirement of Safety in Design is the transfer of information from the designer to other parties. Lessons from the UK, which are being adopted in parts of Australia, indicate that particular attention should be placed on exceptional/significant hazards. These hazards are defined [Department of Mines and Petroleum, 2010], [Safe Work Australia, 2010] as being (a) not likely to be obvious to a competent contractor or designer; (b) unusual in they occur in unusual circumstances or because of the nature of the site or (c) are difficult to manage. This method avoids extensive tick and flick sheets where these hazards are mixed with obvious hazards. The design basis for structures for mining and industry should be communicated as part of this to enable the structure to be operated within its design basis.

Ideally this information should be transferred in a suitable formation for other parties, such as drawing mark-ups or the creation of a health and safety file. These records are then maintained and used by downstream parties.

3 DISCUSSION OF ISSUES AND EXAMPLES

Safety in Design will be a key component in further reducing the accident and fatality rate in the mining and resource industries, however it is not without its challenges.

A balanced Safety in Design approach is required for structures in the mining and resources industries. Construction preferences to reduce working at heights and other construction risks (and perhaps even construction and initial project costs) may introduce vulnerabilities to the structural integrity of the structure over its life span. Management of this residual risk may require ongoing monitoring over the life of the structure. This may introduce additional hazards to inspection personnel, in addition to the structural integrity risks which depend on the effectiveness of the inspections to detect the presence of structural distress or other issues. One key element of Safety in Design involves assessing the relative risks during the initial construction of a facility vs the relative residual risks over the life of the facility. This is quite challenging where hazards relating to low probability, high consequence events are involved.

Challenges may be encountered on cost issues related to safety in design. Adopting Safety in Design principles will lead to reduced costs due to fewer incidents, longer life, reduced maintenance, higher maintenance etc. from a global, whole of life perspective. However, on an elemental level, initial capital costs may be higher, even though the total costs may be reduced and/or have a lower risk residual profile, more appropriate maintenance profile etc. A significant portion of these decisions are based on personal experience of decision makers, which can vary significantly.

Structural designs generally consider pre-service scenarios to an extent that the construction methodology and other pre-service actions are known. One key challenge is the interface at and the determination of the construction sequence for the works and other pre-service actions. It is not unusual for the pre-service scenarios to govern certain components and joints, particularly lifting of sub-assemblies at ground level fully fitted out. Further checks are generally required to validate the assumptions as part of standard construction practices.

The following examples discuss several projects where Safety in Design challenges were encountered and how the Safety in Design approach was adopted.



Figure 3. Large door for confined space entry into a tank.

3.1 *Design basis for a structure to load large trucks*

A new bin structure was being designed and constructed to load large trucks. A key issue was the interaction between the vehicles and the structure. Significant work was undertaken to minimize the probability of a collision between the vehicles and the structure with considerations for alignment, space, protection walls at local points in place to minimize the probability of a vehicle impacting the structure. The design basis for the support structure was determined in conjunction with the client and other stakeholders. The support structure was designed to withstand a collision load calculated from the Australian standard. However, the design basis for the support structure was required to go further and include the requirement that the structure not collapse should a support leg be ineffective as the result of a vehicular collision.

This example shows how there may be a considerable difference of opinion with the definition of ALARP and the tolerance of risk between various stakeholders. The explicit considerations for the post-vehicle collision integrity of the structure had significant implications on the fundamental nature of the framing system. These requirements were in additional to the various controls to reduce the probability and severity of a truck collision.

3.2 *Considerations for tanks*

Significant long term advantages can be achieved by adopting Safety in Design approaches with tanks, particularly relating to confined space entry. Requirements relating to confined space entry typically require entry into the confined space to be minimized, and then access into the tanks be of sufficient size to allow for evacuation of the confined space if necessary. The size of the openings into the tank should be as large as possible from a maintenance perspective. This may enable protected vehicles to enter the tank to minimize safety risks or to minimize down time of the tank.

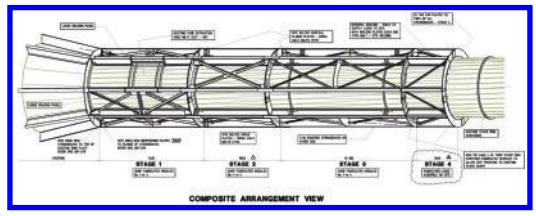


Figure 4. Module strengthening methodology for a stack.

These options however may increase the initial fabrication and erection cost of the tank. The optimum size of the entry points into the tank may be beyond the limits in simplified standards for tanks and higher order analysis such as FEA may be required to design the tank in these instances. These up-front increases in costs need to be balanced against increase in tank life and reduced down time of the tank and associated process equipment.

3.3 *Stack life extension and risk reduction works*

A modular strengthening arrangement was adopted for the temporary life extension of a stack. The stack at an industrial facility had undergone corrosion to the extent that its structural integrity was in doubt by the relevant stakeholders. From a constructability viewpoint, the use of an external modular skeleton structure minimized working at height issues and minimized the extent of work on site which could be influenced by process conditions at the construction area.

Safety in Design considerations were also considered for the demolition of the stack at the end of the life extension work and for the design of the new stack. Temporary structures to assist with the removal of the corroded stack were designed in collaboration with the contractors. The new stack was designed with splice connections to minimize the on-site work, construction materials were selected for superior corrosion resistance, the stack configuration incorporated aspects to enable further works, for process reasons, at a later stage with minimal down time.

3.4 *Duct life extension*

Safety was a key consideration in the design of life extension and risk reduction works for an existing large diameter duct. The duct had undergone an earlier process event which resulted in significant distortion. Risk reduction works were judged to be necessary based on the operational criticality of the duct, the findings of a condition assessment and other items.

A key Safety in Design criteria was the structural integrity of the duct and other structures during the erection of the new works. There were numerous structures placing constraints on the construction methodology, along with the preference for minimum disruption to operations. A staged approach was chosen to temporarily support the duct on new supports, install temporary works for positioning the new

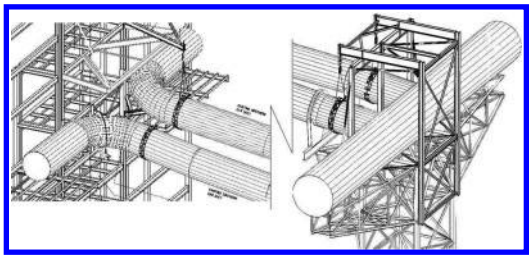


Figure 5. Temporary works for duct life extension.

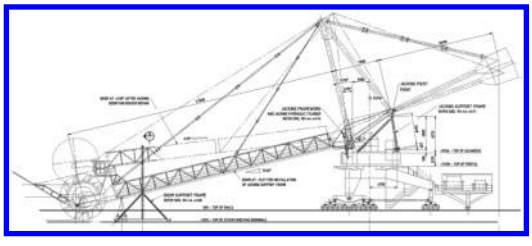


Figure 6. Temporary works for reclaimer remediation.

support truss, and then to lift in the new support truss in a very congested area. The new support truss was lifted onto the temporary steelwork, rolled under the ducts and other permanent steelwork and connections completed. One of the key lessons learnt from this project was that in this situation developing the most appropriate methodology for the works was the key to the project success, far more so than the analysis tools for the works.

3.5 *Reclaimer remediation works*

Stability considerations played key considerations for the return to service works for a bucket wheel reclaimer. Reclaimers are balanced machines and overturning of the machine about the rails or slew bearing failure has occurred previously. The machine balance and the stability of the machine was a significant hazard that needed to be proactively managed throughout the works from a Safety in Design perspective.

The balance and stability of the machine was a key criteria in the design of the work packages for the refurbishment works. The balance of the machine was baselined prior to the works commencing. Calculations on the balance were undertaken on almost a daily basis depending on the mass distribution on the reclaimer. Measurements of the mass of items removed from the reclaimer were undertaken as well as ongoing measurements of the luff cylinder pressures to determine the safety of the machine from a overturning stability and slew bearing loading perspective.

4 CONCLUDING COMMENTS

Safety in Design is an essential component of the continuing effort to reduce and eliminate fatalities and injuries in the mining and resources industries. Structures for these industries have inherent risks associated with the construction, operation, maintenance, disposal and ongoing management of their structural integrity. It is at the planning and design stages that these hazards are best identified, designed out where practicable or appropriate controls integrated into the works by knowledgeable and safety focused staff who are part of an overall team committed to safe, planned, predictable, professional project outcomes. This approach is essential for the development of long life, low operating cost, "Tier One" mining and resource industry facilities.

REFERENCES

Bennet, L. 2004, *Peer review of analysis of specialist group reports on causes of construction accidents*, HSE Research Report 218, HSE Books, London.

Department of Mines and Petroleum, 2010, *Safe design of buildings and structures – code of practice*, resources Safety, Department of Mines and Petroleum, Western Australia

EMERST, 2012, Section 4 EMERST Design OMAT Training Manual, 2012

Gadd, S. & Keeley D. & Balmforth H. 2003, Good practice and pitfalls in risk assessment, HSE Research Report 151, HSE Books, London.

HSE, 1997, Prevention of fire and explosion, and the emergency response on offshore installations, HSEBooks, London.

Institution of Civil Engineers. 2010, *A review of, and commentary on, the legal requirement to exercise a daty 'so far as is reasonably practicable' with specific regard to designers in the construction industry*, http://www.ice.org.uk/getattachment/7eb5b064-c3a9-4bca-8711-de4b243569e6/So-Far-As-Is-Reasonably-Practicable.aspx

Safe Work Australia (formerly ASCC] 2005, *The role of design issues in work-related injuries in Australia 1997–2002*, Office of the Australian Safety and Compensation Council, Canberra, Australian Government

Safe Work Australia (formerly Australian Safety and Compensation Council) 2006, *Guidance on the Principles of Safe Design for Work*, Canberra, Australian Government

Safe Work Australia, 2012 *Safe Design of Structures – Code of Practice*, Canberra, Australian Government

Workcover NSW, 2001, *CHAIR Safety in Design Tool*, Workcover New South Wales.

Research and Applications in Structural Engineering, Mechanics and Computation – Zingoni (Ed.)
© 2013 Taylor & Francis Group, London, ISBN 978-1-138-00061-2

Risk-based design in mining structures

M. Mmusi
Worley Parsons TWP (Department of Civil/Structural Engineering), Worley Parsons Group, South Africa

A. Masarira
Anglo American Technical Solutions (Structural Engineering), Anglo Operations Limited, South Africa

ABSTRACT: The structural infrastructure in mining is exposed to excessive and even extreme loading conditions due to the nature and environment of mining operations. The structures in most mining plants often support mechanical equipment for material processing and the loads applied to these structures are often dynamic in nature and could vary in magnitude and intensity. Most loading conditions in mining are unique especially underground mining. Therefore a clear understanding of these conditions is important. The critical aspect is ensuring that proper assumptions are made. It is therefore imperative that a risk based approach be adopted in dealing with these structures. The risk based approach would consider the fact that mining operations rarely follow processes that are easily predictable. During all the stages of the design the structural engineer needs to ask the following questions: what are the possible risks the structure will be exposed to, what are the possible unwanted events (accidental loading) that could occur during the life of the structure, what could go wrong during the life of the structure. This paper proposes a risk based design approach for mining structures. It considers the operating and environmental conditions to which mining structures are exposed to.

Keywords: Risk-based design, mining structures, extreme loading

1 INTRODUCTION

As the pressures of production continue to increase in the mining industry, the soundness and integrity of the associated structures is also continually tested. Failure investigation and analysis more than often reveals cases where only vendor supplied loads were applied and not much thought was put into other possible loading conditions. This is generally as a result of over-reliance on vendor supplied drawings (i.e not exploring other loading possibilities), and what are the risks of not exploring other loading possibilities, lack of understanding of the production conditions and project time constraints. As such risk based design is imperative.

Risk based design is centred on the risk needs of a specific structure. The probability of failure will allow certain uncertainties to be captured such as unknown loading conditions especially in dynamically loaded structures. The major benefits of this method is firstly safety as this is paramount in any mining activity, and secondly economical as the client would reduce costs over the long term through unnecessary and often expensive re-engineering, repair, strengthening and in the extreme cases replacement structures which results in disruption of production. The author proposes that the risk based design approach be applied only to "critical/complex" structures as per the agreement of the structural engineer and the client. This will save the client cost and time and focus on areas of necessity.

This paper will provide an overview of the basic concepts and benefits of risk-based design as applied to the mining and minerals industry. A framework will be proposed on how to apply risk-based design. A case study will also be presented on a complex mining structure on how specific aspects of risk-based design could have been applied.

2 RISK BASED DESIGN: PHILOSOPHY AND PRINCIPLES AS APPLIED IN MINING

Risk can be defined as the potential losses resulting from exposure to hazard. Ayyub et al. (1998) define risk as a method used to asses and evaluate uncertainties associated with an event. Therefore risk should be based on an identifiable failure scenario, its occurrence probability or likelihood, its consequences, consequence significance, and population at risk.

3 UNCERTAINTY

The analysis of a structural engineering problem frequently involves the development of a computational model. In some cases it is the model of the entire structure or a particular aspect of interest of the structure. Therefore the engineer decides which aspects of the structure to include and which to leave out.

Depending on the information about the structure and the background of the analyst, other characteristics of the system might end up unknown consequently increasing the overall uncertainty of the structure. Therefore, based on the level of accuracy of the model three categories surface; Abstracted, non-abstracted and unknown aspects of the structure. Some of these uncertainty types can be dealt with probabilistically (what is the likely hood of a particular loading type occurring), statistically (depending on past events there is a likely hood of a particular event/loading condition occurring) and reliability (based on experience a particular method is suitable in solving an event/loading condition). Reliability also takes into account the limitations of the codes of practice and experience has an important role to perform. For example at the preliminary stage of design it is well known that span/300 as per design codes is insufficient for sizing dynamically loaded structures and from experience span/80 works well as a thumb-suck value on what to expect. Uncertainty can be viewed as a subset of ignorance in the context of human knowledge.

The three main types of uncertainty in risk assessment that are commonly identified are (i) parameter uncertainty, (ii) model uncertainty, (iii) and completeness uncertainty. Parameter uncertainties are as a result of the estimation of parameters, contained in the model either through limited data or lack of experience. Model uncertainty fundamentally addresses the ability of the model to represent reality this will involve accuracies of applied boundary conditions. Completeness uncertainty addresses the uncertainty of the model in representing all possible risk scenarios. It is imperative that the differences of these uncertainties are understood, because a complete consideration of one type of uncertainty may still lead to insufficient understanding of the model. Parameter uncertainty can easily be addressed since a series of possible loading conditions can be established from experience and from the full knowledge of the operating conditions this allows the analyst to focus on critical loading conditions which are not only confined to vendor supplied information.

4 SAFETY

Safety can be defined as the judgement of risk acceptability for the structure (Ayyub et al 1998). Safety and safety requirements are relative since the decision of risk acceptance may vary depending on the individual making the judgement, the sensitivity of the industry towards risk, transportation of structural components to site which in turn is governed by the construction sequence. Safety standards also differ from client to client.

5 PERFORMANCE

The performance of a structure is its ability to meet functional requirements during the expected design life of the structure. The performance of a structure can be described by various elements such as reliability, capability, efficiency, and maintainability (Modarres 1993). Under operational conditions the performance of a structure is influenced and therefore lifecycle and structural health monitoring (SMH) of the structure is necessary to ensure continued performance at optimal levels.

6 HUMAN ERROR

The human contribution of risk can be estimated from an understanding of behavioural sciences. Hardware failure and human error should be addressed in the risk assessment since they both contribute to risk associated with the system. Therefore once human error probabilities are determined, human error/failures are treated in the same manner as hardware failures in performing risk assessment quantification.

Human reliability analysis is generally considered to be composed of three stages, namely (i) error identification, (ii) modelling and (iii) quantification. With use of FEA or any other tools one of the techniques that can be used to mitigate human risk is model verification. This simply allows the design engineer to verify that the applied loads are indeed as per design requirements (Mmusi, 2012).

7 RISK BASED DESIGN FRAMEWORK AND RISK MANAGEMENT

A framework has been developed which follows a step by step procedure which will assist the design engineer in mitigating risk. It would not be feasible to apply the proposed framework to each and every structure in a plant, as such risk based design would only be confined to critical structures. The initial step is to identify what a critical structure is. A critical structure can be defined as and to only confined to (i) a complex structure by nature of its design (ii) a structure supporting complex mechanical equipment that is in some instances on the critical path, (ii) a complex dynamical loaded structure with either one or more vibrating equipment. The above categories can be expanded as deemed satisfactory by the design engineer in agreement with the client.

The structure should firstly be designed as per the relevant design codes and in the case of supported mechanical equipment the loads should be applied as per vendor drawings, this will provide for all legal requirements and otherwise. It is the responsibility of the designer to identifying the potential failure modes, and to look beyond the scope vendor supplied loading. In the process of brainstorming possible loading and failure scenarios some structures will require unreasonable member sizes. The design engineer's judgement in consideration with cost restraints should be applied. It is fundamentally impossible to cover all possible risks however, a level of confidence should be

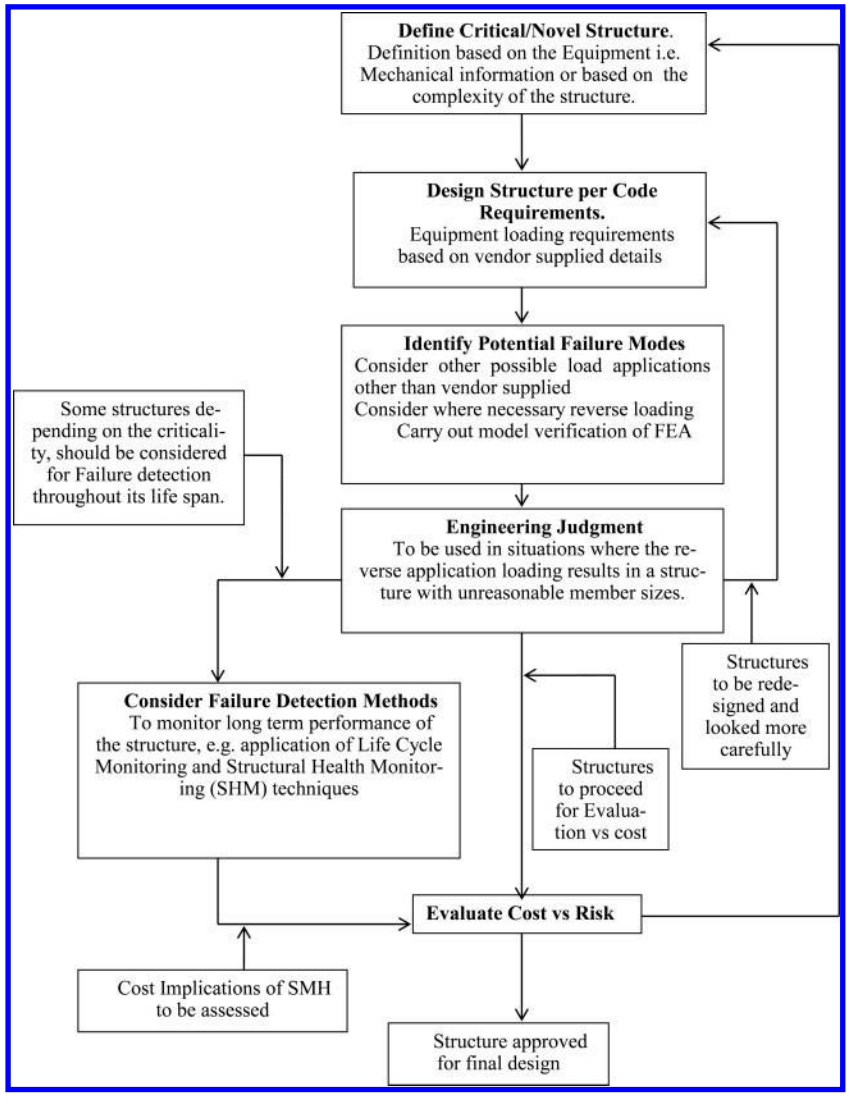


Figure 1. Risk Based Design Framework.

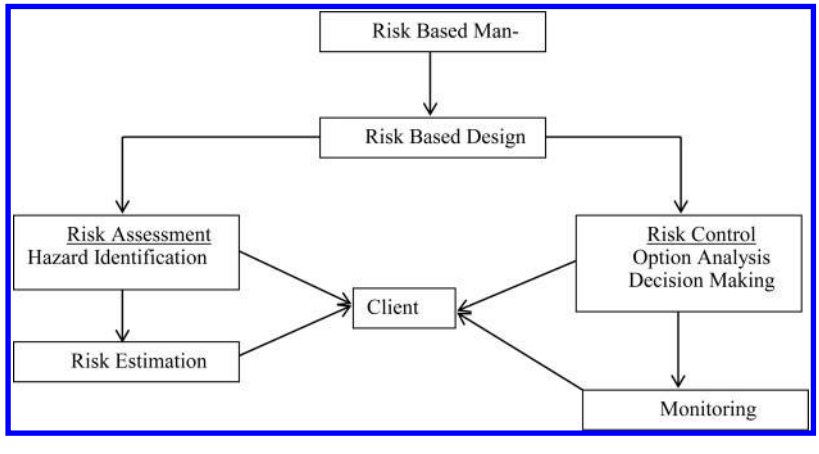


Figure 2. Risk Based Methodology/Management.

attained by the design engineer that sufficient work has been carried out and this will form part of the design calculations. The final stage is to ensure that the structure would last the intended design life. Various tools are available and the application of life cycle monitoring and structural health monitoring is essential. For dynamically loaded structures sensors and accelerometers can be used to monitor the performance of a structure over time. This stage will assist in detecting possible damage due to operational effects or loading conditions that could not have been established or were missed due to the complexity of structure.

8 RISK BASED METHODOLOGY AND MANAGEMENT

In order to close the loop on Risk based design, a methodology on management is required. The engineering consultants (for example Engineering Procurement and Contracting Management (EPCM)) are primarily responsible for identifying and implementing risk. However this should be communicated with client at all stages as this will have cost implications.

9 CONCLUSION

A systematic approach allows an engineer to evaluate expediently and easily complex engineering systems for safety and risk under different operational and extreme conditions. The ability to quantitatively evaluate these systems helps reduce cost. Risk based design can be used as a management tool that assists the structural engineer and project manager to foresee possible risk items, failure prevention, and consequence mitigation and finally risk communication with client.

REFERENCES

Ayyub, B. M. (1999). "Guidelines on expert-opinion elicitation of probabilities and consequences for corps facilities." Institute for Water Resources, USACE

Modarres, M. (1993). What every engineer should know about reliability and risk analysis. Mercel Deccer, Inc. New York

Mmusi, M (2012). Case Study: Design of a Mobile Steel Support Structure Using FEA and How to Avoid Pitfalls, Proceedings of Structures for Mining and Related Materials Handling Conference 2012

Sorensen, J.D., Kroon, I.B. and Faber, M.H. Optimal – based code caliberation. Structural Safety, Vol, 15, pp 197–208, 1994

Thoft-Christensen, P. and Baker, M.J. Structural Reliability and ita application. Springer Verlag, Berlin, 1992.

Base, Ha-Rok, Grandhi, Ramana V., "Uncertaintity Quantification of Structural Response using Evidence Based Theory.

Research and Applications in Structural Engineering, Mechanics and Computation – Zingoni (Ed.)
© 2013 Taylor & Francis Group, London, ISBN 978-1-138-00061-2

Simulated virtual portfolio for masonry buildings

A. Mühlhausen, U.E. Dorka & F. Obón Santacana
University of Kassel, Germany

A. Smolka & M. Stupazzini
Munich Re, Munich, Germany

ABSTRACT: Assessment of damage costs due to an earthquake currently lacks the level of detail that is required for realistic pricing of individual insurance risks. Sophisticated numerical tools, which are widely used to assess structural behavior in great detail (like FEM), have been developed to a level where they may be used with confidence in seismic risk assessment and as such, enable the insurance industry to perform more realistic assessments.

In order to produce a virtual damage database, the "Simulated Building Portfolio"-Tool (SBP-Tool) was developed at the University of Kassel in cooperation with Munich Re. For using this tool several input parameters are needed in order to simulate a whole portfolio consisting of 3-D Finite Element models.

Thus validated virtual portfolios can be created now in regions with similar masonry buildings in order to assess damage costs where no or little event data are available.

1 INTRODUCTION

The assessment of damage losses due to an earthquake is an important issue for the insurance and reinsurance industry, but currently lacks the level of detail that is required for realistic pricing of individual risks.

Once a again, recent earthquakes that stroke Chile (Maule, Mw 8.8, February 6, 2010), New Zealand (Darfield, Mw 7.0, September 3, 2010 and Lyttelton, Mw 6.1, February 21, 2011) and Japan (Honshu, Mw 9.0, March 11, 2011) in the last three years proved the strategic importance of this kind of industry and renewed the crucial question of how to develop a resilient concept for society.

Any further advancement in that respect is strictly related to the capabilities of creating reliable models to predict seismic risk. This process implies a better understanding of the hazard, of the vulnerability and of the exposure that is involved.

Even if important on-going projects, like the Global Earthquake Model (GEM), are aiming at sharing and improving our knowledge, the "state-of-the-art" of the empirical data-set regarding earthquake's economic losses presents a severe non-uniformity. The worldwide information available is extremely different from both the quality and the geographical points of view.

Since earthquakes are rare events, the situation will not likely change significantly in the foreseeable future. It is therefore necessary to further investigate the development of innovative concepts based on consolidated numerical simulation techniques.

2 A NEED FOR COMBINING SOPHISTICATED SEISMOLOGICAL AND STRUCTURAL MODELS IN RISK SIMULATION

Guidotti (2012) shows how to describe a spatial variability of strong-ground motions through large-scale 3D simulations of wave propagation in near-surface soils. He developed complex 3D FE-models for a region of 1 km × 1 km and a depth of 50 m. More than 1.000.000 Finite Elements are typically required to simulated the wave propagation in a particular soil system.

Using these complex soil models, Guidotti assessed the response of buildings due to the simulated wave propagation by modeling them as rigid bodies (Fig. 1). This neglects the dynamic characteristics and the nonlinear structural behavior of buildings despite being the controlling factors for the response of buildings under seismic actions. Furthermore, the seismic damage to a particular building cannot be estimated with such over-simplified models; a combination of such detailed wave propagation models with sophisticated structural models for the buildings in question is required if reliable data for seismic risk analysis is to be provided.

3 THE SBP-TOOL FOR GENERATING A VIRTURAL PORTFOLIO

To create this kind of building models, the so-called "Simulated Building Portfolio-Tool" (SBP-Tool) was

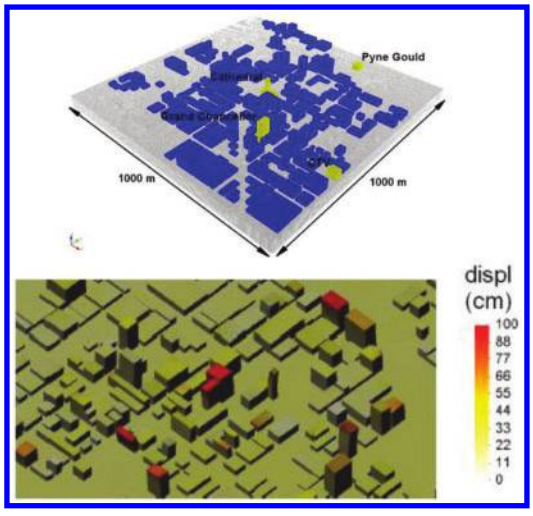


Figure 1. Top: Sophisticated 3D FE model of sub-soil with rigid blocks on top representing buildings in Christchurch. Down: A snapshot of the simulated displacement of the rigid block buildings. Guidotti (2012).

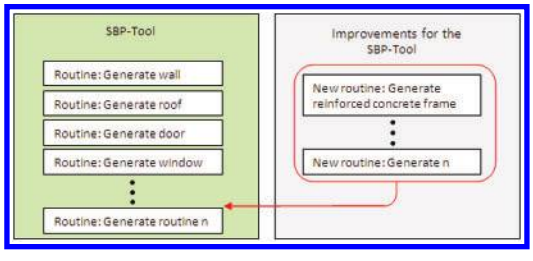


Figure 2. Import new routines to generic SBP-Tool, Mühlhausen (2012b).

developed at the University of Kassel in cooperation with the Munich Re, Mühlhausen (2010, 2011a, 2011b, 2012a). It provides a virtual portfolio of realistic buildings by using a set of global building criteria provided by the user in a configuration file. A statistical process automatically generates each individual building for the portfolio using the given range for each criterion.

The program is written in ISO C99 and features a modular design (Fig. 2). This allows for easy adaptation to different structures (steel frames, rc-frames with masonry infill, etc.) and inclusion of additional building features, like stairs or penthouses. Currently, the SBP-Tool is used to generate 3D linear FE-models of masonry buildings (Fig 3).

Using the configuration file, the SBP-Tool creates two ASCII files. The first contains the geometric and material data necessary for a FE-software to create a complex numerical model. It contains all the information regarding the nodes, elements, restraints and constraints, material properties for the roof, outer and inner walls, and the degrees of freedom (DOFs) subjected to loads. The second ASCII file contains the commands required for assembling the stiffness and mass matrices in the FE Software Slang (2004).

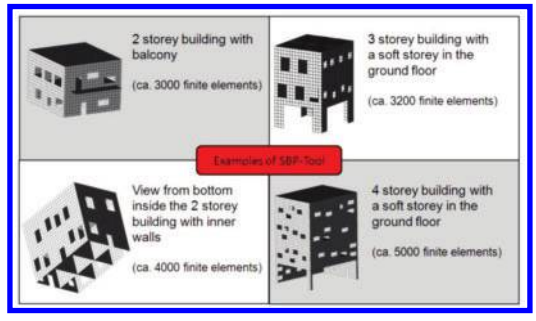


Figure 3. 3D linear FE-models for masonry buildings created by the SBP-Tool, Mühlhausen (2012b).



Figure 4. A regional portfolio of 3D FE-models for masonry buildings simulated with the SBP-Tool. This can be combined with any seismic input, e.g. wave propagation models, Mühlhausen (2012b).

Whereas the first file does not depend on any particular FE-software, the second one must be adapted to its specific commands. This allows the use of other FE-software (Ansys, Open Quake etc.) without interfering with the initial generation process of the buildings.

SLang imports the ASCII files and, by executing the commands, it creates the mass and stiffness matrices. They are exported as two additional output files. Furthermore, Slang creates a file with all the information associated with each DOF. Thus, a set of 4 files is created for each building generated containing all the necessary information to perform a dynamic in particular a time history analysis.

In general (e.g. non-linear structures) around 500 power spectra are required to determine the standard deviation of a local variable with an accuracy of greater than 99% according to the central limit theorem.

That means for a given portfolio like the one in figure 4 with 65 buildings and approximately 1.700.000 DOFs, 8.500.000 time histories analyses are required. To compute 8.500.000 time histories in a short period of time, the use of an efficient algorithm in combination with parallel computing (see chapter 4) is necessary.

In the case of linear structures, the use of power spectra provides an efficient way to calculate the required statistical values of local variables, which can be obtained by multiplying the transfer function of the local variable with the power spectrum of the input process (ground motion).

This transfer function describes the relationship between the output, a local variable (e.g. stresses),

and a normalized input, the loading (e.g. excitation at the foundation – earthquakes). They are a property of an individual structure, and they can be determined without the knowledge of the loading event. Only the location where the load is applied must be known. For linear models, these functions are constant over time and therefore, they only have to be computed once.

They can be obtained by evaluating a single time history.

4 THE PORTFOLIO SIMULATION

To perform the time history analysis with the required efficiency and speed a parallel implementation of Dorka's substructure algorithm Roik (1989), Dorka (1991, 1998, 2002), Bayer (2005) and Dorka (2006, 2007) is needed. This algorithm is a discrete formulation of the dynamic equilibrium equation (1):

$$M\frac{d^2u}{dt}+C\frac{du}{dt}+Ku=p(t)+f_r+f_s \qquad (1)$$

Its integration constants γ and β are variables. With $\gamma=0.5$ and $\beta=0.25$, it becomes the well-known Newmark scheme. It also accommodates experimental and non-linear numerical restoring forces f_r+f_s through a parallel sub-stepping process within each time step, thus avoiding time-consuming matrix inversions and iterations. Therefore, this algorithm can take advantage of multi-core and multi-processor computers using parallel libraries and other optimisations, resulting in solving 10000 DOFs in 43,94 ms per time step on a regular laptop computer Obón Santacana (2011a, 2011b, 2012). In other words: the simulation of one of the buildings in Figure 3 with 10000 to 12000 DOFs subjected to an earthquake of 40 seconds (4000 time steps) needs app. 3 minutes regardless of non-linearities, because the sub-stepping within each time step does not cause any significant reduction in performance due to its parallel implementation if the adequate number of cores or processors is available.

The time histories will be stored in a HDF5 format with all necessary information for the time parameters (date, duration, number of DOF, number of time steps and duration of time step) and for the time integration (acceleration, velocity, displacement and stresses) for further processing, e.g. Matlab.

Thus, several thousand realistic 3D FE building models are created and simulated under earthquake loading using only a few hours on a regular desktop. Figure 4 shows a small simulated portfolio of 65 buildings using around 500.000 finite elements (1.700.000 DOFs). Approximately 30% of the buildings have a balcony and 20% of the buildings have a soft storey.

5 DEFINING A VIRTUAL PORTFOLIO

The global building stock is highly heterogeneous in terms of design, construction practices and vulnerability to natural hazards.

GEM, the Global Earthquake Model Foundation, delivers in this respect powerful tool to get a better understanding of how to simulate a virtual portfolio in a particular region in the world. On one hand there is the open source Inventory Data Capture Tool (IDCT) and on the other hand the GEM Earthquake Consequences Database (GEMECD). Both applications deliver information regarding the earthquake event itself and a first idea of the building stock. The development of a third tool, and from the point of view of this paper the most interesting one, was launched in December 2010, namely "GEM Building Taxonomy". This tool intends to provide a classification of building characteristics in an ordered system.

The newest version of the GEM Building Taxonomy V2.0 should be available in March 2013 and will require 13 attributes to describe a building. These are: material of the lateral load-resisting system; types of lateral load-resisting system, roof and floors; height; date of construction; structural irregularity; occupancy; direction (to describe the orientation of the building with different lateral load-resisting systems in two principal horizontal directions); building position within a block, shape of building plan; exterior walls; and foundation, Brzev (2012).

The vision of the GEM Building Taxonomy team is to create a unique description (code) for a building or a building typology.

Although developed independently, both tools use similar or even the same attributes (Table 1) to identify a building or define a portfolio.

The SBP-Tool is written in a generic way that allows adding new attributes from the GEM Building Taxonomy or to modify the currently used SBP-Tool's parameters. This allows the direct use of the GEM Building taxonomy in the SBP-Tool. It also allows further development of the GEM taxonomy with respect to additional criteria needed for risk simulation.

6 INSURANCE LOSS ESTIMATION FOR VIRTUAL MASONRY BUILDINGS

Loss curves are an important tool for the insurance industry to estimate the potential risk and damage to a building (single risk) or portfolio and can be described by the relationship between renovation costs and return period.

The loss curves in figure 5 and 7 were determined with a sophisticated statistical process that has already been published in Mühlhausen (2010, 2011a and 2011b).

As a first approximation for a crack criterion for masonry, a threshold for the principal tension stress was chosen and also, a linear relationship between costs and damaged area was assumed. These assumptions allow estimating loss curves for a typical building (single risk), using the linear simulation method based on power spectra, as described in chapter 3.

By looking at four seemingly similar buildings (figure 6) from this study, it is apparent that, the simulated

Table 1. The 13 attributes of "GEM Building Taxonomy" and the required input parameters of the SBP-Tool.

Attribute or SBP-Input Parameter	GEM Building Taxonomy	SBP-Tool
Material of lateral		
Load- resisting system	x	x
Lateral load-resisting system	x	x
Roof *	x	x
Floor	x	x
Height*	x	x
Date of construction	x	x
Structural irregularity	x	x
Occupancy	x	x
Direction	x	x
Building position within a block	x	o
Shape of the building plan	x	x
Exterior walls	x	x
Foundation	x	o
Further SBP-Tool input parameter for describing a portfolio:		
Number of buildings		x
Number of storeys		x
Dimension of ground plan*		x
Dimension of rooms*		x
Dimension of windows and doors		x
Number of storeys*		x
Number and size of windows*		x
Storey height*		x
Balcony**		x
Soft storeys**		x
Thickness for outer walls		x
Thickness for inner walls		x
Thickness for the roofs		x
Stiffness for outer walls		x
Stiffness for inner walls		x
Stiffness for the roofs		x

x Attribute or Parameter is used
o Attribute or Parameter is not used
* A range (minimum and maximum) must be defined
** % of the whole portfolio has this input parameter

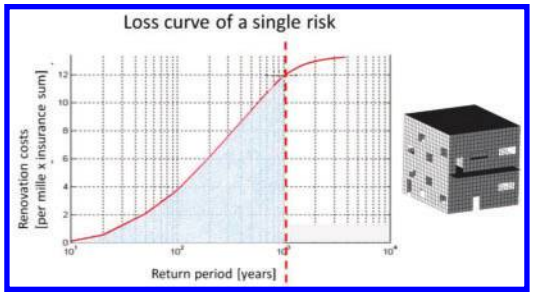


Figure 5. Typical loss curve for one building (right) with the expected linear threshold for masonry buildings, Mühlhausen (2012b).

loss curves (figure 7) may be grouped according to certain attributes.

In this case, there is a first indication, that the ratio of wall openings may be an important criterion.

Currently, studies are under way to clarify the role of such attributes in insurance loss estimation. Once clarified, such attributes should be made available through GEM's building taxonomy.

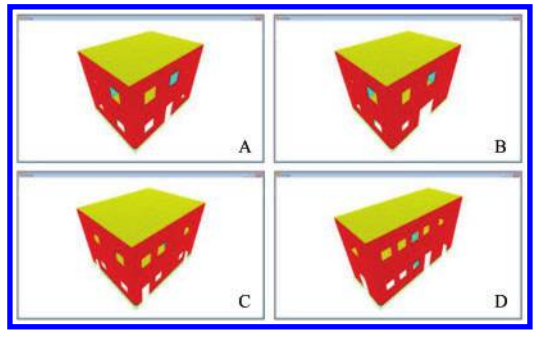


Figure 6. Typical masonry buildings (variant A to D) with sligthly different dimension and openings, Mühlhausen (2010).

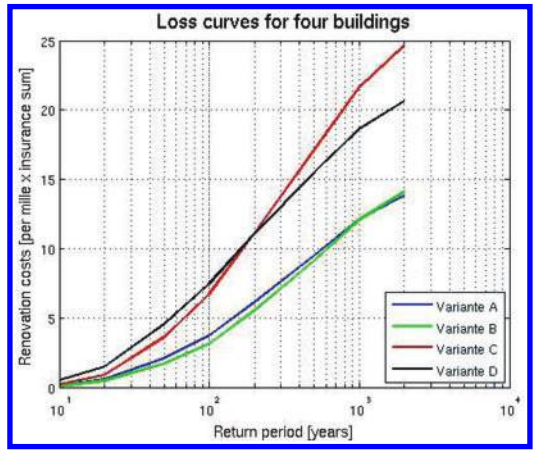


Figure 7. Loss curves for the four buildings from figure 6. Building A, B and C, D may be placed in different loss groups based on their ratio of wall openings, Mühlhausen (2010).

7 CONCLUSION AND OUTLOOK

Reliable seismic damage and loss simulation not only requires sophisticated seismological ground models, but foremost detailed structural models, since damage and repair needs depend on the dynamic characteristics and local non-linear structural behavior. Virtual building portfolio consisting thousands of FE models can now be generated with the SBP-Tool developed at the University of Kassel. Their seismic risk can be within a reasonable time frame by using an efficient algorithm in combination with parallel computing.

Although developed independently, GEM's building taxonomy and the SBP-Tool use similar or even the same attributes to identify a building or to define a portfolio. It allows further development of the GEM taxonomy with respect to additional criteria needed for risk simulation.

In this respect, the SBP-Tool can only generate masonry buildings but an extension for other building types (e.g. steel-concrete composite structures) is already under development.

ACKNOWLEDGEMENT

The first author was supported with a doctoral scholarship by the Munich Re. The author gratefully acknowledges this support.

REFERENCES

Bayer, V., Dorka, U. E., Füllekrug, U. and Gschwilm J. (2005). On real-time pseudo-dynamic substructure testing: algorithm, numerical and experimental results". *Aero. Sc. and Tech* (9): 223–232.

Brzev, S., Scawthorn. C., Charleson, A.W. and Jaiswal, K. (2012) Interim Overview of GEM Building Taxonomy V2.0, GEM Foundation

Dorka, U.E. and Heiland, D. (1991). Fast online earthquake simulation using a novel pc supported measurement and control concept", *Proc. 4th Int. Conf. Structural Dynamics*, Southhampton: 636–645.

Dorka, U.E., and Füllekrug, U. (1998). Algorithmen für realtime pseudo-dynamische Substrukturtests", Report of the DFG project "SubPSD-Algorithmen, project number Do 360/7, University of Kaiserlautern, Germany.

Dorka, U.E. (2002). Hybrid experimental – numerical simulation of vibrating structures", *Proceedings of the International Workshop WAVE 2002:* 183–191. Okayama, Japan.

Dorka, U.E., Queval, J.C., Nguyen V.T. and Maoult, A.L. (2006). Real-time sub-structure testing on distributed shaking tables in CEA Saclay. *Proceedings of 4th World Conference on Structural Control and Monitoring*, San Diego, USA.

Dorka, U.E., Queval, J.C., Nguyen V.T. and Maoult, A.L. (2007). Substructure testing on distributed shaking tables", *Proceeding of the 2nd International Conference on Advances in Experimental Structural Engineering (2AESE)*, Shanghai, China.

GEM, Web page \\http://www.globalquakemodel.org/, Accessed 27th of February 2013.

Guidotti, R., Castellani, R., Paolucci, R. and Stupazzini, M. (2012). Near-field earthquake ground motion rotations and relevance on civil engineering structures. Doctoral Thesis, Department of Structural Engineering, Politecnico di Milano.

HDF5, Web page \\http://www.hdfgroup.org/HDF5/, Accessed 27th of February 2013.

Mühlhausen, A., Dorka, U., Smolka, A. and Stupazzini, M. (2010), *Vorschlag eines Konzeptes für die Versicherungswirtschaft zur realistischen regionalen Abschätzung von Erdbebenschäden an Mauerwerksbauten auf der Grundlage numerischer Tragwerkssimulationen.* Masterthesis, Cooperation between Universität Kassel and Munich Re.

Mühlhausen, A., Dorka, U., Smolka, A. and Stupazzini, M. (2011a). Vorschlag eines Konzeptes für die Versicherungswirtschaft zur realistischen regionalen Abschätzung von Erdbebenschäden an Mauerwerksbauten auf der Grundlage numerischer Tragwerkssimulationen. *12. D-A-CH Tagung – Erdbeben und Baudynamik*, Hannover, Germany.

Mühlhausen, A., Dorka, U., Smolka, A. and Stupazzini, M. (2011b). Improving Seismic Risk Assessment for the Insurance industry by using 3-D Finite Element Modelling. *The 2011 World Congress on Advances in Structural Engineering and Mechanics*, Seoul, South Korea.

Mühlhausen, A., Dorka, U., Smolka, A. and Stupazzini, M. (2012a). Seismic Risk Assessment for Masonry Buildings based on Discriminant Analysis of a Virtual Database. *Proceeding of the* 15th *World Conference on Eartquake Engineering,* Lisbon, Portugal.

Mühlhausen, A., Dorka, U., Smolka, A. and Stupazzini, M. (2012b). Seismic Risk Assessment for Masonry Buildings based on Discriminant Analysis of a Virtual Database. *Presentation of the* 15th *World Conference on Eartquake Engineering,* Lisbon, Portugal.

Obón-Santacana, F. and Dorka, U.E. (2011a). Use of large numerical models and high performance computers in geographicall distributed seismic tests, In Fardis M. And Rakicevic, Z. (eds.), *Role of Research Infrastructures in Performance-based Earthquake Engineering (SERIES Workshop)*, Springer.

Obón-Santacana, F. and Dorka, U.E. (2011b). Large Numerical Models in Continuous Hybrid Simulation, *The 2011 International Conference on Earthquakes and Structures (ICEAS'11)*, Seoul, Korea, September 18–23.

Obón-Santacana, F. and Dorka, U.E. (2012). Effects of Large Numerical Models in Continuous Hybrid Simulation. *Proceeding of the the 15th World Conference on Earthquake Engineering*, September 12–17, 2012, Lisbon, Portugal.

Roik, K. and Dorka, U.E. (1989). Fast online earthquake simulation of friction damped systems. *SFB151 Report No. 15*, Ruhr-University Bochum, Germany.

SLang – The Sturctural Language (2004), Veit Bayer, Maik Brehm, Christian Bucher, et. Al. Documentation. Institute of Structural Mechanics – Bauhaus-University Weimar.

29. Structural optimisation, manufacturing processes

Research and Applications in Structural Engineering, Mechanics and Computation – Zingoni (Ed.)
© 2013 Taylor & Francis Group, London, ISBN 978-1-138-00061-2

Effective lightweight design of a rocket interstage ring through mixed-integer optimization

H. Köke, L. Weiß & C. Hühne
Institute of Composite Structures and Adaptive Systems,
DLR German Aerospace Center, Braunschweig Germany

ABSTRACT: The full lightweight potential of carbon fiber reinforced plastics in complex structures can only be exploited using an adequate combination of material and design. Potential combinations can be found, using an optimization routine integrated into the design process. This paper presents a detailed comparison of the optimization results for distinctive rocket interstage design concepts. The complex cylindrical grid structure has to withstand the mission loads while being as light as possible. For the efficient use of the superior material properties, carbon fiber reinforced plastics are combined with a foam core to form a sandwich configuration. To minimize the total mass, parametric finite element models are used within a constrained, mixed-integer optimization. The structure is modeled using a bottom up strategy. An optimization framework, incorporating the CAE software Ansys into the multi-purpose optimization package pyOpt, is presented. The augmented lagrangian particle swarm algorithm is used to find the configurations having minimal weight. As manufacturability is an important design requirement, a winding process is represented by constraints in the parameter set of the geometry. The stiffnesses of the structure, as well as strength criteria of the laminate are used as inequality constraints for the optimization. Further on, a lower bound of the first natural eigenfrequency using additional constraints, is investigated. Finally, the impact of the governing geometry, material parameters and hence their influences on the optimization problem are carefully reviewed. It is shown that appropriate design – material combinations can significantly reduce the structural mass.

1 INTRODUCTION

Within this paper, the interstage ring of a two stage rocket will be optimized (fig. 1). For the purpose of the start of engine number 2, the ring must be constructed in a way that the hot gases can leave, while still maintaining a target stiffness. Therefore a grid concept was established, consisting of axial bars wich are interconnected with wounded helix like sandwich structures. This concept provides enough open sectional area for the gas to exhaust.

In order to save weight, the interstage was designed to be constructed out of carbonfiber reinforced plastic (CFRP). The high specific stiffness and strength characteristics of uni-directional CFRP can be used to adjust the structure to achieve the required targets for stiffness, buckling constraints and different strength criteria for each loadcase.

The main configuration consists of axial CFRP bars and wounded sandwich helixes. Whereat the wounded helix structures consists of a foam core, which is interrupted by the axial bars, and two CFRP cover skins which are applied in a following manufacturing step. Thereby covering also the axial bars and acting like a further stiffener.

Thus, the needed parameters for setting up the finite element (FE) model are continuous and discret valued. Usually such problem would be simplified by relaxing the integer parameters to continuous ones and a concluding rounding to possible steps. In this case, it is not possible to relax the optimization problem by making the integer division of the axial and helix bars continuous. The manufacuring constraints for a wounded grid structure demand an equal distribution of knot points across the structure. Therefore the optimization model in combination with the optimization algorithm has to be chosen carefully.

In previous studies the augmented lagrangian particle swarm algorithm has proven reliable in finding an optimium under challenging contitions, as shown by Jansen and Perez (2011).

2 INTERSTAGE RING

The structural modelling of the interstage ring is done in Ansys Classic. The internal script language APDL is used for the pre- and post-processing and also for solving the different loadcases. This offers an easy way for enabling the optimization algorithm to retrieve the structural response of each probed parameter set.

The fundamental parameters of the model are shown in tab. 1. The height and the diameter of the interstage ring are not variable, as they are the assembly

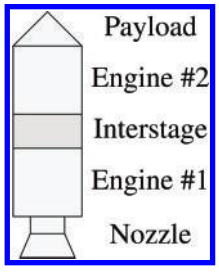


Figure 1. Generic rocket system.

Table 1. Model parameter.

Geometry			
H_{Ring}	Height	[m]	1
Ø D_{Ring}	Diameter	[m]	1.4
Loads			
LC 1	F_{axial}	[kN]	530
LC 2	$F_{horizontal}$	[kN]	46
LC 3	$M_{horizontal}$	[kNm]	350

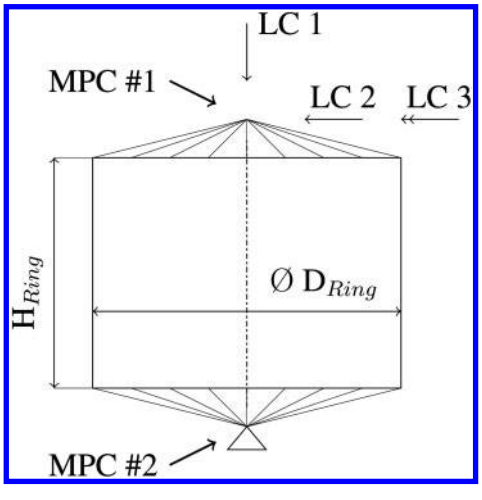


Figure 2. Model with Constraints.

constraints for integrating the ring in the rocket. The loads are generated in a preliminary, analytical process and are covering the main acting forces.

The optimization of the model is a step in the preliminary design, therfore 4-node shell elements are used, to keep calculation time as low as possible.

The constraints are modeled by two multi-point-constraints (MPC) as shown in fig. 2. MPC # 2 forms a displacement constraint on the lower end of the ring, with all degrees of freedom being zero. This overestimates the stiffness of the assembly point, as it would appear rigid.

This optimization is, as mentioned before, part of an early preliminary design, Therefore the stiffness can be adjusted in a following step. MPC # 1 transmits

Table 2. Optimization parameter.

x_i	Variable		Min	Max	Type
1	t_{core}	[mm]	0.2	20.0	c
2	w_{bars}	[mm]	10	60.0	c
3	w_{helix}/w_{bars}		1	1.2	c
4	t_{out}	[mm]	0.125	5.0	c
5	t_{in}	[mm]	0.125	5.0	c
6	n_{height}		2	6	i
7	$n_{cir} \cdot 2$		6	12	i
8	Foam material		1	4	i
9	CFRP material		1	2	i

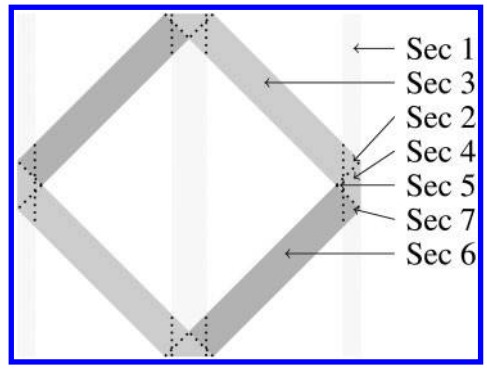


Figure 3. Model of the unit cell.

the loads in the ring. An overview of all considered loads is given in tab. 1. In addition, MPC # 1 constrains a radial widening of the structure. This, like MPC #2, acts like an infinitelly stiff adjacent component.

Every loadcase was calculated individually followed by a linear buckling and modal analysis. Each response for the load case specific stiffness, the linear buckling load and the first eigenfrequency was saved. The CFRP failure criteria for maximum strain in each bar was also calculated, using the given allowables in tab. 3.

To avoid an overestimation of the calculated failure criteria due to high element strain in the boundary areas, the only elements for failure criteria evaluation are between 30%–70% of the ring's height. But, as will be shown, the strength criterias are not the driving factor behind the optimization.

3 UNIT CELL

In order to keep the amount of optimization parameters to a minimum and to reduce the time for the pre-processing of the FE model, a unit cell approach is used to implement all necessary data. Thus, to build the whole model, copying the unit cell in a specific manor is sufficient. Fig. 3 shows the geometry of the unit cell and the used element sections. The optimization model builds upon this specific topology. This is the same in every model.

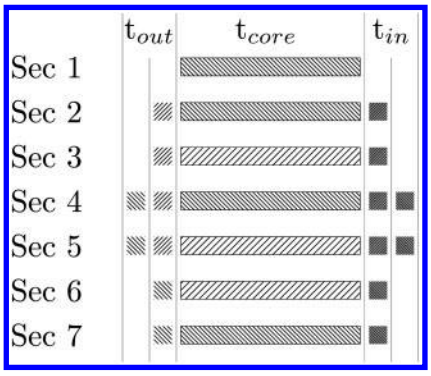


Figure 4. Composition of element sections.

The unit cell contains all used optimization parameters, tab. 2 gives an overview. As mentioned above, the parameter set includes continuous and integer parameters. As can be seen, parameter x_3 is a continuous factor for the width of the helix bars. This is required to maintain the topology of the unit cell constant.

In order to reduce the assemblage points at the boundaries, it was defined to begin and end the structure at the knot points. This requirement together with an integer amount of axial bars, defines the angle between the helixes and the axial bars. The helixes were then modeled in a cylindrical coordinate system, using the diameter of the interstage and the helix angles. As buckling is an important constraint for the optimization, the curved geometry of the helix is supposed to be a key factor for a correct calculation of the load factor.

Using boolean operations, the overlapping areas are sliced to build the specific topology and are then linked to the defined element sections. For each section a material composition representing the manufacturing process is imposed fig. 4. The model is build upon the thickness of the core (t_{core}) and width of the axial bars (w_{bars}), since they represent the stiffest part of the interstage. The thickness of the bars is coded in element section Sec 1. Together with the width of this specific area and the used CFRP material, as shown in tab. 3, the cross-section of the axial bar ist defined. Based on parameter t_{core}, the thickness of the foam core is set equal to this of the axial bar, otherwise there would be a gap in the winding process. This element section modelling approach was used for every other definition. The counterclockwise wound sandwich skin is always on top of the clockwise wound ones. Thus, making the whole structure an unsymmetric. But the overall impact is, as will be shown, negligible.

4 OPTIMIZATION PROCEDURE

The overall goal was to reduce the weight of the interstage ring. Therefore the optimization objective is to minimize the total mass of the interstage ring.

Table 3. Material Parameters.

CFRP			
#1 UMS3536/UMS45	E_1	[GPa]	246.0
	E_2	[GPa]	8.0
	G_{12}	[GPa]	4.5
	ν_{12}		0.3
	ϵ_1^{tens}		0.0097
	ϵ_1^{comp}		−0.004
	ϵ_2^{tens}		0.0061
	ϵ_2^{comp}		−0.02
#2 IMS5131/IMS60	E_1	[GPa]	167.0
	E_2	[GPa]	9.5
	G_{12}	[GPa]	4.5
	ν_{12}		0.32
	ϵ_1^{tens}		0.0133
	ϵ_1^{comp}		−0.007
	ϵ_2^{tens}		0.0068
	ϵ_2^{comp}		−0.022
Foam			
#1 Rohacell 110 IG	E	[MPa]	167.0
	ρ	[gcm^{-3}]	110.0
#2 Rohacell 71 IG	E	[MPa]	92.0
	ρ	[gcm^{-3}]	75.0
#3 Rohacell 51 IG	E	[MPa]	70.0
	ρ	[gcm^{-3}]	52.0
#4 Rohacell 31 IG	E	[MPa]	36.0
	ρ	[gcm^{-3}]	32.0
All Foams	ν		0.3

The framework for the optimization was programmed in Python. Ansys Classic is used for calculating all needed structural responses and saving them in text files. The optimization was carried out by pyOpt, Ruben E. Perez (2012). This optimization framework provides the implementation of the augmented lagrangian particle swarm algorithm (ALPSO).

The ALPSO algorithm is a heuristic and derivative-free global optimization method. It enforces the constraints by a Lagrangian formulation, while maintaining the Karush-Kuhn-Tucker conditions. None the less, the results must be carefully investigated, since the explicit constraint equations are not known.

The optimization constraints include material (max strain), stability (buckling of the bars), and stiffness (of the interstage concerning LC 1 and eigenfrequency re) specific values, see tab. 4. Regarding the structural requirements of the interstage, a minimum axial stiffness was demanded, to trim the eigenfrequency of the rocket. Also, buckling should not occur until 1.5 times the load of each load case.

5 OPTIMIZATION RESULTS

The displayed results of the optimization are only one sixth of all calculations. The optimization was done with 6 workers, using the mpi implementation in pyOpt. Only the results of worker 1 are shown.

Table 4. Optimization constraints.

Name		g_i	value
c_{LC1}	[MN/mm]	1	≥ 0.506
b_{LC1}		2	≥ 1.5
b_{LC2}		3	≥ 1.5
b_{LC3}		4	≥ 1.5
max $strain_{LC1}$		5	< 1.0
max $strain_{LC2}$		6	< 1.0
max $strain_{LC3}$		7	< 1.0
first eigenfrequency	[Hz]	8	> 8.0

Table 5. Optimization results.

Objective			Value
mass	[kg]		8.172
Name		x_i	Value
t_{core}	[mm]	1	16.72
w_{bars}	[mm]	2	14.7
w_{helix}/w_{bars}		3	1.107
t_{out}	[mm]	4	0.49
t_{in}	[mm]	5	0.65
n_{height}		6	4
$n_{cir} \cdot 2$		7	9
Foam		8	1
CFRP		9	1

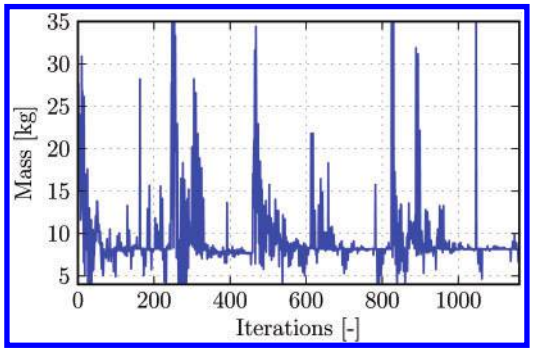


Figure 5. Convergence of total mass.

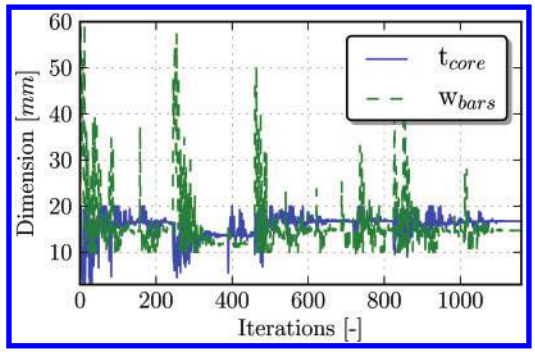


Figure 6. Width and height of the axial bars.

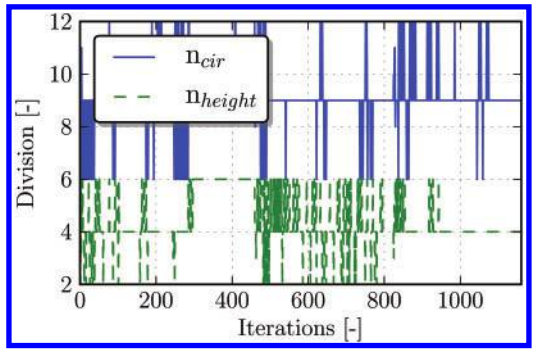


Figure 7. Divison of height and circumference.

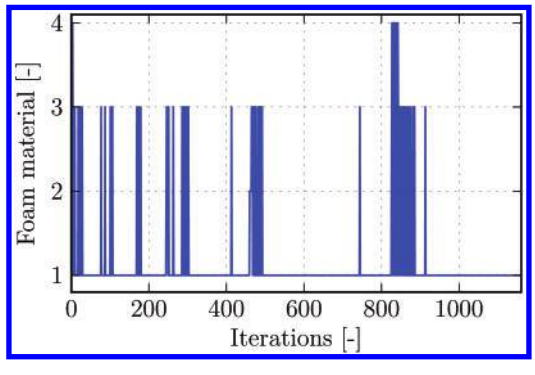


Figure 8. Foam material.

Fig. 5 shows the convergence history of the total mass of the interstage ring. The optimization algorithm is able to probe parameter sets within a total mass range from 4.5 kg to over 35. It can be seen that after 1000 iterations the total mass converges to around 8kg. It must be noted, that with 6 workers, the total amount of iterations must be multiplied with 6. Therefore, the total number of iterations is around 7500.

The driving factors of the total mass are n_{cir}, n_{height} and the cross section of the axial CFRP bars. Fig. 6 shows the convergence of the cross sectional parameters of the bars. The two parameters converge after 1050 iterations.

As described earlier, the integer parameters in this optimization are the division in axial and helix bars. The convergence history of this two parameters are shown in fig. 7. The division in height converges in under 980 iterations to a value of 4, while the algorithm still tries minor variations to optimize the total mass. Similarily, the division in circumference needs around 1100 iterations to achieve the final value of 9.

The used foam material ranges between 1 to 4, as can be seen in tab. 3. From 4 being the weakest but lightest to 1 being 4.6 times stiffer, but also 3.4 heavier. The optimization algorithm converges after 900 iteration to the Rohacell 110IG.

The convergence between the two CFRP materials can be seen in fig. 9. The buckling constraints are the most demanding, therefore the stiffer CFRP material is preferred by the optimization algorithm. Since failure

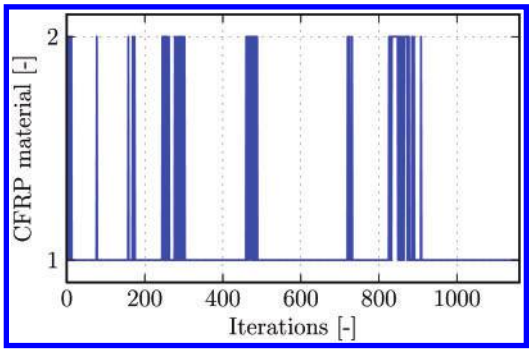


Figure 9. CFRP material.

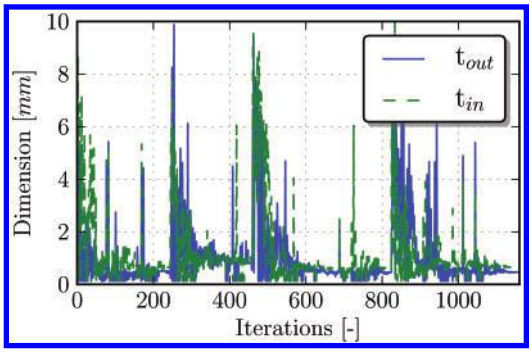


Figure 10. Thicknesses of the inside and outside CFRP plies.

is not the main driving constraint, the lower allowables of the UMS3536/UMS45 are acceptable.

The converged thicknesses of the wounded CFRP skins of the helix bars are shown in fig.10. The algorithm tends to make the inner plys thicker then the outside ones. This can be explained with the overall tendency of the wounded helixes to deform radial to the interstage, thus, making bending the dominating load. As the compression allowables of the CFRP materials are lower then the tensile ones, the laminate thickness must be greater on the compression side.

Fig. 11 shows the maximum strain failure index, for tension or compression, for each load case. As mentioned before, the evaluation of the maximum strain criteria takes place between 30%–70% of the interstage height. It can be shown that LC2 is the most demanding load case, although the one with the least force. The evaluation of the results indicates that at the knots, the helix bars are highly stressed due to an alternating orientation of the deformation.

Fig. 12 shows the maximum strain failure index for LC 1 of the optimized interstage ring. The achieved values are acceptable, since the failure constraints are not the driving parameter behind the optimization.

Another constraint is the axial stiffness of the interstage. Since there are accelerated masses during launch above the interstage, a required minimal stiffness must be achieved. The axial stiffness is directly linked to eigenmode of the whole rocket and must

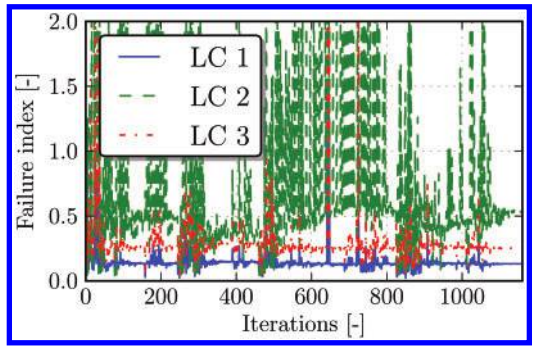


Figure 11. Convergence of load case specific maximum strain failure.

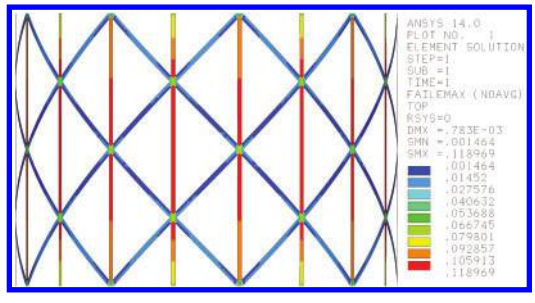


Figure 12. Maximum strain failure index for the best configuration with LC_1.

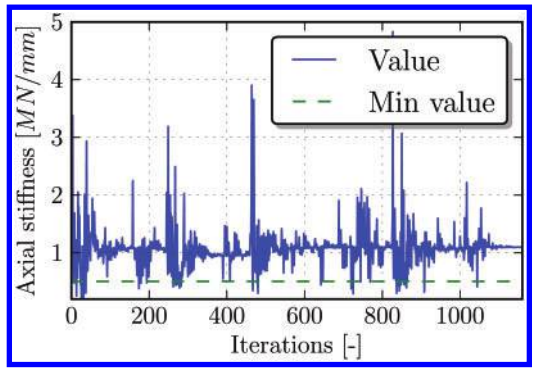


Figure 13. Convergence of the axial stiffness.

therefore be achieved. As shown in fig. 13 the required stiffness is over accomplished. To infer from that, the axial stiffness is not the restricting parameter in this optimization. Nearly every parameter set results in an axial stiffness over 1 MN/mm.

The convergence history of the load case specific buckling constraint is shown in fig. 14. They were extracted from the prestressed structural model and imply the multiple of the load before buckling might occur. The first buckling mode, along with the multiple load factor, was calculated using lanczos algorithm. Load case 3 is the most demanding. The applied moment compresses a small part of the interstage ring, containing just one or two axial bars. This immense

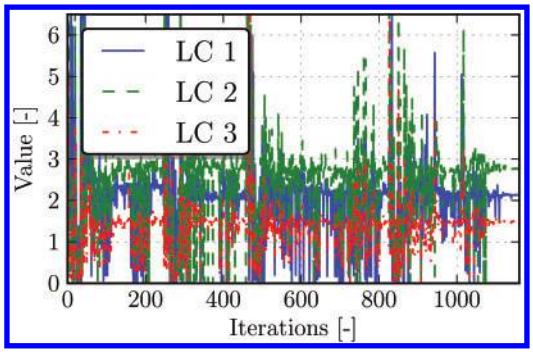


Figure 14. Load case specific buckling constraint.

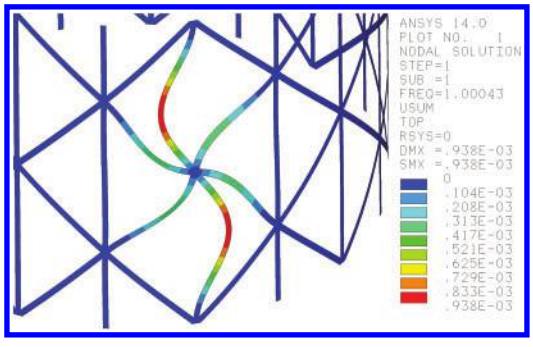


Figure 15. Exaggerated nodal displacement for critical buckling mode in LC 3.

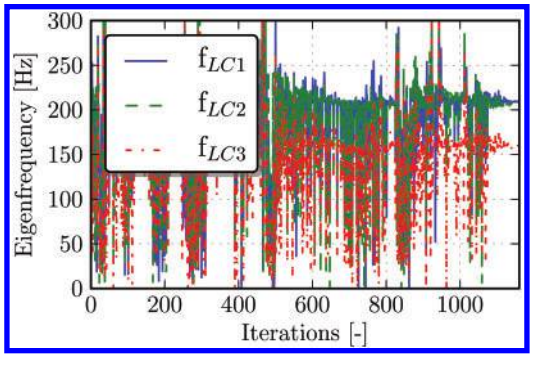


Figure 16. Eigenfrequency of the prestressed interstage.

load, results from the first eigenmode of the rocket and must be endured at all times, without stability failure. One can see that this is the only constraint nearby the specific boundary, hence the most driving parameter behind the optimization. In fig. 15 the buckling eigenform is shown. Since the thickness of the bar is greater then the width, an s-like mode lying in the tangential plane of the interstage ring occurs.

The convergence history for the first eigenfrequency for each load case specific pre-stressed model is shown in fig. 16. It can be seen that the majority of all probed parameter sets are above the required 8 Hz.

6 CONCLUSION

The presented optimization of a grid interstage structure, shows the capability of the used unit cell approach combined with the augmented lagrangian particle swarm algorithm to solve mixed-integer constrained optimization problems.

The investigation of the results gives insight to the system response. The optimization of the grid structure tends to be only constrained by stability. Local buckling of bars is the most critical factor. This constraint is governed by the acting bending moment. The buckling mode for this load can be in the tangential plane of the interstage, or normal to it. Depending on the chosen second area moment. The optimization algorithm tends to make the bars thicker then wider, maximizing the bending stiffness of the sandwich-helix bars. The originating mode depends therefore upon the usage of a sandwich helix.

In a continuative investigation, the stiffening effect of the sandwich should be investigated. It is most likely that a monolithic helix and their implementation in the unit cell would steer the stability criteria, because of the changing moment of inertia for the axial bars.

REFERENCES

Jansen, P. & R. Perez (2011). Constrained structural design optimization via a parallel augmented lagrangian particle swarm optimization approach. *Computers & Structures* *89*(1314), 1352–1366.

Ruben E. Perez, Peter W. Jansen, J.R.R.A.M. (2012). pyOpt: A Python-based object-oriented framework for nonlinear constrained optimization. *Structures and Multidisciplinary Optimization* *45*(1), 101–118.

Research and Applications in Structural Engineering, Mechanics and Computation – Zingoni (Ed.)
© 2013 Taylor & Francis Group, London, ISBN 978-1-138-00061-2

Topology optimization with local stress constraints in a simultaneous analysis and design setting

Dirk. P. Munro & Albert. A. Groenwold
Department of Mechanical and Mechatronic Engineering, University of Stellenbosch, South Africa

ABSTRACT: We present a simultaneous analysis and design (SAND) formulation for the topology optimization of continuum structures with local stress constraints. We argue that the SAND formulation significantly decreases the burden on computational resources, compared to the traditional nested analysis and design (NAND) approach, especially for very large scale problems. The topology optimization problem is solved in a sequential approximate optimization (SAO) setting in which the availability of the exact analytical form of the constraint equations allow for the inclusion of exact second-order information in the Hessian of the sub-problem. The combination of the SAND formulation and a new form of stress-constraint allow for a zero lower bound on the design variables. Results are presented for the two-bar truss topology optimization problem.

1 INTRODUCTION

Topology optimization of continuum structures is a branch of structural optimization that sets out the achieve the optimal distribution of material in a design space subject to a set of boundary conditions, applied loads and constraints. It is sought that minimal human creative input be required to arrive at an optimal design. The definition of optimality and the design constraints might take on a wide variety of forms depending on the requirements on the design. Bendsøe & Sigmund (2003) present an extensive review of the numerous problem formulations in topology optimization.

Topology optimization of continuum structures requires the union of structural analysis and numerical optimization. This is achieved, in part, via the material distribution method, which requires the discretization of the entire design domain; the spatial area where material may or may not be present. The discretization of the design domain give rise to a system of equations that describe the physical responses of the structure, also referred to as the equilibrium equations. The solution of which form the structural analysis component of the optimization procedure. Finding the solution of the set of equilibrium equations adds significantly to the storage requirements and computational effort required to solve the optimization problem. Especially as the size of the elements are reduced (and number of elements increased) to obtain more accurate solutions.

Traditionally, the union of structural analysis and numerical optimization is achieved via the nested analysis and design (NAND) approach. The NAND approach is an iterative procedure that requires alternate phases of structural analysis (finite element analysis being the most popular) and numerical optimization. The large system of equilibrium equations is solved exactly in each iteration to obtain the structural responses for a given design. In this paper we explore an alternative to the NAND approach, namely simultaneous analysis and design (SAND). See Arora & Wang (2005) for an extensive review of the NAND and SAND formulations. In the SAND approach the equilibrium equations enter the optimization problem as a set of equality constraints. Although the optimization problem increases in complexity, no computational effort is spent on solving the equilibrium equations in each iteration. What is more, the equilibrium equations need not be satisfied exactly in each iteration; only the final solution should be feasible.

The size of problem considered in the NAND formulation is limited by the computational storage requirements of the structural analysis phase as well as the information required by the optimization phase. Currently sequential approximate optimization (SAO) is the dominant solution methodology. It is considered more efficient to solve a series of approximations to the problem, especially as each evaluation of the constraint functions requires a structural analysis to be carried out. We argue the SAND formulation is even more suited to the efficient implementation of sequential approximate optimization due to the sparsity of the equilibrium equations and the availability of the exact analytical form, which reduce computational storage requirements substantially. This formulation, we believe, lends itself to the solution of very large scale problems in a reasonable amount of time.

In section 2 we review the general statement of the topology optimization problem. Section 3 is a brief overview of SAO. Section 4 is a description of the SAND problem formulation. Finally, in section 5,

results are presented for the optimization of the two-bar truss test problem. Please note at this stage the work presented should be considered as a work in progress. The solution procedure is a proof of concept and by no means optimal.

2 THE TOPOLOGY OPTIMIZATION PROBLEM

We consider the problem of determining the optimal distribution of an isotropic material subject to a set of boundary conditions and applied loads. Bendsøe & Sigmund (2003) present the material distribution method as the predominant approach to determining the optimal *lay-out* of material.

Let f_0 denote the structural objective, defined as a function to be minimized, and f_j the constraints on the design. The material distribution method sets out to identify the optimal distribution of material $x(s)$ in the known, pre-defined design domain Ω. The boundary conditions and applied loads are defined in terms of Ω. The general form of the problem, where $x(s)$ denotes the presence or absence of material at the spatial position s, is defined as:

$$\begin{aligned} \min_{x} \quad & f_0(x) \\ \text{subject to} \quad & f_j(x) \leq 0 \qquad j = 1,2,...,m, \\ \text{with} \quad & x(\boldsymbol{s}) \in [0,1] \quad \forall \ \boldsymbol{s} \in \Omega. \end{aligned} \tag{1}$$

where m is the number of constraints. However, the discrete programming problem is NP-complete. In the light of the this and the desire to implement efficient continuous non-linear programming algorithms the binary requirements on the material variables are relaxed to $0 \leq x(s) \leq 1$. Variables at intermediate values are then penalised to encourage purely binary or 'black-white' designs. The most popular being the 'simple isotropic material with penalization' (SIMP) approach, suggested, amongst others by Bendsøe (1989). Form here on we will refer to the material variables as the design variables of the problem.

The topology problem (1) is discretised using the finite element method. The most popular discretised model involves the parametrization of the elasticity matrix for element i as (with SIMP parameter p)

$$\boldsymbol{C}_i(x_i) = x_i^p \boldsymbol{C_0} \tag{2}$$

where C_0 is the elasticity matrix of the solid isotropic material. In the case where stress constraints are considered the material strength is also parametrized to ensure a realistic model (Duysinx & Bendsøe 1998). Although attempts have been made to provide physical interpretation of the design variables at intermediate densities in terms of specific types of composite structures (Bendsøe & Sigmund 1999), questions still exist around the general interpretation and comparison of designs with material at intermediate values. Therefore, we consider a simplified approach where the material thickness is parametrized. The thickness, h, is expressed as $h_i = x_i^p h_0 = x_i^p$ with h_0 defined with value 1. Hence, the optimization problem is viewed as a sizing problem. It is important to note that this distinction is only conceptual. Mathematically the two models are exactly equivalent. Both yield exactly the same discretised equilibrium and stress equations. The elemental stiffness matrices are expressed as

$$\boldsymbol{K}_i = x_i^p \int_{v_i} \boldsymbol{B}_i^T \boldsymbol{C}_0 \boldsymbol{B}_i dv_i \tag{3}$$

Then the general topology optimization problem is stated as

$$\begin{aligned} \min_{x} \quad & f_0(\boldsymbol{x}, \boldsymbol{q}) \\ \text{subject to} \quad & f_j(\boldsymbol{x}, \boldsymbol{q}) \leq 0 \qquad j = 1,2,...,m, \\ & \boldsymbol{K}(\boldsymbol{x})\boldsymbol{q} = \boldsymbol{w}, \\ & 0 \leq \boldsymbol{x}_i \leq 1 \qquad i = 1,2,...,n \end{aligned} \tag{4}$$

where $x \in \mathbb{R}^n$, q and $w \in \mathbb{R}^u$, $f_0 : \mathbb{R}^{n+u} \rightarrow \mathbb{R}$ and $f_j : \mathbb{R}^{n+u} \rightarrow \mathbb{R}, j = 1,2,...,m$. Respectively, m and n are the number of constraints and the number of finite elements in the mesh. The vector q denotes the vector of nodal displacements and w the vector of nodal forces (assumed to be design independent), the dimension of which, u, depend on the method of discretization. We restrict ourself to the use of Q8 elements.

3 SEQUENTIAL APPROXIMATE OPTIMIZATION

Sequential approximate optimization (SAO) is a branch of optimization algorithms in which successive approximate sub-problems are solved to arrive at a final solution. The sub-problems, which approximate the local behaviour of the actual problem, are deemed easier to solve in each successive iteration.

A sub-problem is constructed by approximating the objective and constraint functions around the current iteration point. Usually analytical functions, which are inexpensive to evaluate, are used as surrogate functions. An approximate sub-problem in iteration k has the form

$$\begin{aligned} \min \quad & \tilde{f}_0(\boldsymbol{x}^{\{k\}}) \\ \text{subject to} \quad & \tilde{f}_i(\boldsymbol{x}^{\{k\}}) \leq 0, \quad i = 1,2,...,m \end{aligned} \tag{5}$$

where the optimization variable in iteration k is $x^{\{k\}} \in \mathbb{R}^n$ and $\tilde{f}_i : \mathbb{R}^n \rightarrow \mathbb{R}, i = 0,1,2,...,m$ are approximated (analytical) constraint functions. The solution to the sub-problem in iteration k forms the starting point for the subsequent sub-problem, $x^{k+1} = x^{k*}$.

We consider sub-problems with quadratic objective functions and linear constraints. These approximations are based on second- and first-order Taylor-series expansions respectively. However, second-order information of the constraints are incorporated in the sub-problem by considering the Hessian of the Lagrangian

in the quadratic objective function. We consider the Lagrangian

$$L^k = \tilde{f}_0(\boldsymbol{x}^{\{k\}}) + \sum_{j=1}^{m} \lambda_j^{\{k-1\}} \tilde{f}_j(\boldsymbol{x}^{\{k\}}) \tag{6}$$

with, λ_j^{k-1}, the Lagrange multiplier of constraint j at the previous iteration. To limit storage requirements only the diagonal terms of the Hessian matrix are incorporated. Also, to ensure convex approximations, only the combination of positive second-order terms and Lagrange multipliers are added to the Hessian of the Lagrangian. Refer to Etman, Groenwold, & Rooda (2011) for an extensive view on sequential convex programming using approximate diagonal QP sub-problems.

For topology optimization in a SAND setting the analytical form of the constraint equations are readily available. This allows the exact second-order derivatives of the constraint functions to be included in the diagonal part of the Hessian of the Lagrangian.

4 SIMULTANEOUS ANALYSIS AND DESIGN

4.1 *Problem formulation*

The most popular approach to structural approximation has been one where a clear distinction exist between the structural analysis and numerical optimization phases. In this view only the the design variables are treated as optimization variables. All other response variables such as displacements, stresses and strains being implicit functions of the design variables. Hence the nodal displacements and design variables are not independent, but related by the equilibrium equations:

$$\boldsymbol{K}(\boldsymbol{x})\boldsymbol{q} = \boldsymbol{w} \tag{7}$$

Therefore the system of equilibrium equations need to be solved exactly in each iteration. An analysis code is used to calculate q given x in each iteration of the optimization procedure.

In gradient based optimization first order sensitivities of the objective and constraint functions are also required. Consider function $f(x, q)$, either denoting the objective function or a constraint function in (4). The first-derivative of which, to the design variables, is

$$\left.\frac{df(\boldsymbol{x},\boldsymbol{q}(\boldsymbol{x}))}{d\boldsymbol{x}}\right|_{n\times 1} = \left.\frac{\partial f(\boldsymbol{x},\boldsymbol{q}(\boldsymbol{x}))}{\partial \boldsymbol{x}}\right|_{n\times 1} + \left.\frac{d\boldsymbol{q}(\boldsymbol{x})}{d\boldsymbol{x}}\right|_{n\times u} \left.\frac{\partial f(\boldsymbol{x},\boldsymbol{q}(\boldsymbol{x}))}{\partial \boldsymbol{q}}\right|_{u\times 1} \tag{8}$$

The partial derivatives in (8) present no particular difficulty. However the calculation of dq/dx requires further analysis. Two methods to determine the sensitivity derivatives are the direct and adjoint methods, see Haftka & Gurdal (1992).

In contrast, the SAND formulation requires both the design variables and the nodal displacements to be treated as design variables in the optimization problem. In this distinction lies the main difference between SAND and NAND formulations. The variables x and q are now independent and no sensitivity derivatives need to be calculated. However the equilibrium equations are imposed on the optimization problem as a set of equality constraints relating x and q. Problem 4 is redefined as

$$\begin{aligned} \min_{x} \quad & f_0(\boldsymbol{x},\boldsymbol{q}) \\ \text{subject to} \quad & f_j(\boldsymbol{x},\boldsymbol{q}) \le 0, \\ & h_l(\boldsymbol{x},\boldsymbol{q}) = \boldsymbol{K}_l(\boldsymbol{x})\boldsymbol{q} - \boldsymbol{w} = 0, \\ & 0 \le \boldsymbol{x}_i \le 1 \end{aligned} \tag{9}$$

where $i = 1, 2, ..., n$, $j = 1, 2, ..., m$ and $l = 1, 2, ..., u$. The equality constraints (and/or inequality constraints), denoted by the vector $h(x, q) \in \mathbb{R}^u$, need not be satisfied in each iteration of the optimization procedure. Only at the final solution point should $h_l(x^*, q^*) = 0$.

Further, in the NAND formulation elements may not assume values of zero due to the ill-conditioning of the stiffness matrix, K. Zero lower bounds on the design variables pose no particular problem in a SAND setting. The system of equilibrium equations are defined as equality constraints and not solved *per se*. We speculate that this characteristic allow continuation strategies to be implemented on the SIMP parameter p to improve designs towards purely 'black-white' solutions.

4.2 *Sparsity and storage requirements*

Due to the decoupling of x and q in the SAND formulation the Jacobian and Hessian matrices of f_j and h_l are extremely sparse. For large problems sparsity in the order of 99% can be expected. This lends itself to an efficient sparse implementation in a SAO setting. Figure 1 depicts the number of non-zero elements in the constraint Jacobian and Hessian matrices for a given number of Q8 finite elements with local stress constraints. The number of elements is denoted by n_e and a arbitrary 3×1 proportioned design domain is considered. We consider the separable approximate sub-problem where only diagonal Hessian terms are stored. The storage requirements of which, as seen from figure 1, is negligible compared to the constraint Jacobian. Note that the storage requirements scale linearly relative problem size. In comparison the NAND formulation has less design variables than an equivalently sized SAND formulation. However, due to the calculation and storage of the sensitivity derivatives (dq/dx) in each iteration, the storage requirements do not scale linearly. Also, the solution of the equilibrium equations requires forward reduction and back substitution for n_e pseudo-load vectors to solve for the vector q and matrix dq/dx. This procedure becomes very

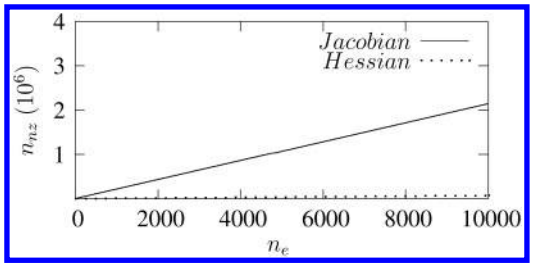


Figure 1. Storage requirements of the SAND formulation.

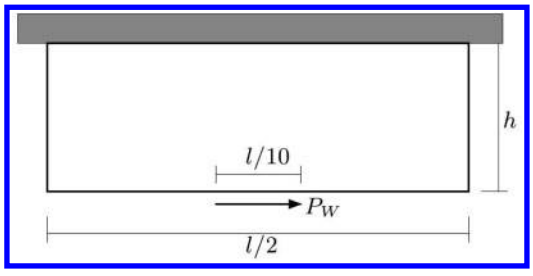


Figure 2. The two-bar truss ($P_W = 6N$, $l = 6$m, $h_0 = 1$m, $S_y = 20N/\text{m}^2$, $E = 1N/\text{m}^2$, $\nu = 0.3$)

expensive in terms of computation time as problem size grows.

5 WEIGHT MINIMIZATION OF THE TWO-BAR TRUSS WITH LOCAL STRESS CONSTRAINTS

5.1 *Problem description*

We here present some results obtained when applying a SAO procedure to a SAND formulation of the topology optimization of a continuum structure. The test problem is the well-known two-bar truss problem with ground structure as shown in figure 2. The structure is modelled under the assumption of plain stress, with P_W the load and S_y the yield stress of the material. E and ν denote the Young's modulus and Poisson ratio of the material respectively. The discretisation of the problem is denoted by mesh multiplier m_e; with the height and width of the ground structure divided into $5m_e$ and $15m_e$ elements respectively.

We consider the problem of weight minimization, defined by the objective function

$$f_0(\boldsymbol{x}) = \sum_{i=1}^{n} x_i \tag{10}$$

We assume values of unity for the density and volume of the material elements.

5.2 *Local stress constraints*

Stress constraints, which are by their nature local restrictions, place a limiting value on some stress-related failure measure anywhere in the structure. We consider the von Mises stress failure measure. Defined, for planar problems, as

$$\sqrt{\sigma_x^2 - \sigma_x\sigma_y + \sigma_y^2 + 3\tau_{xy}^2} \leq \bar{\sigma} \tag{11}$$

where the maximum stress value, $\bar{\sigma}$, is defined as the yield stress of the material. The stress components are calculated with equations derived with the finite element method.

Stress constraints may enter the optimization problem in a wide variety of forms to either ease the use approximations or to improve physical representation of the problem (See Bendsøe & Sigmund (2003, 83)). The well documented stress-singularity problem also plays a major role in the formulation of the stress constraints. Briefly, the stress-singularity problem is described as the degeneracy of the feasible design domain caused by the stress measure tending to infinity as the density or thickness of the material tends to zero. These degenerate domains protrude from the feasible domain as infinitely thin slivers into the infeasible region. The global optimum of the problem might be located in one of these degenerate domains which is virtually inaccessible by the optimizer. Refer to Cheng & Wang (2000) for a complete description of the stress-singularity problem. Currently, the dominant procedure is to make the feasible domain more accessible with so called ϵ-relaxation (Cheng & Guo 1997).

Note that the von Mises stress measure is only a function of the nodal displacements, q. However, as stated by Bendsøe & Sigmund (2003, 82),, the stress constraints should *only* be imposed if material is present. Therefore a dependency on x_i is enforced to facilitate a mechanism to remove stress constraints from the optimization problem as elements tend to zero thickness.

We depart with the form of stress constraints devised by Wood (2012, 180)

$$\frac{\sigma_i^m}{\bar{\sigma}}(1+\epsilon) - \frac{\epsilon}{x_i} - 1 \leq 0 \tag{12}$$

Where a continuation strategy is applied such that $\epsilon \to 0$. This formulation is preferred due to the more conservative limit imposed on the allowable stress of an element at intermediate thickness (Wood 2012, 180). Note that the function is concave in x_i. Therefore to improve the convexity of the constraint and to allow $x_i \to 0$ we consider the slightly altered form

$$f_j(\boldsymbol{x}, \boldsymbol{q}) = x_j \left[\frac{(\sigma_j^m)^2}{\bar{\sigma}^2}(1+\epsilon) - 1 \right] - \epsilon \leq 0 \tag{13}$$

Where the entire constraint is simply multiplied with x_i, note $x_i \geq 0$. The notion that the dependency on x_i effectively removes the constraint from the problem for elements at zero thickness is clear from this formulation. The von Mises stress and yield stress are both squared to simplify the analytical form of the equations and derivatives.

5.3 *Numerical considerations and standard settings*

A continuation strategy is employed whereby ϵ is reduced with $\epsilon/1.1$ whenever the maximum constraint violation is less than 1×10^{-6}. This is done until $\epsilon = 1 \times 10^{-4}$ at which point ϵ is set to zero[1]. This, along with $\check{x} = 0$ (see section 4.1), leads to the solution of a unrelaxed problem with zero lower bounds on the design variables.

Bendsøe & Sigmund (1999) argue that a SIMP parameter of value $p \geq 3$ is required to realistically interpret design variables at intermediate values in terms of certain configurations of composite structures. However since we view the thickness of each element as the design variables we are not confined to this requirement in a conceptual sense. We chose $p = 2$ such that the equilibrium equations are quadratic in x_i. Thus the second-order Taylor-series expansion approximates the separable part of the equilibrium equations exactly. It should be noted that the severity of intermediate design variable penalization is indeed sacrificed. Therefore we expect designs with more variables at intermediate thickness. That is more 'gray' areas. For now we accept this with a greater focus on the solution procedure as opposed to the interpretation of the final design.

The design variables, x, are initialised at 1 and the nodal displacements, q, at 0. Also, a filter is applied to the constraint Jacobian such that all terms with a magnitude of less than 1×10^{-6} are set to zero. This not only reduces computation time, as shown by Wood (2012, 193), but also prevents numerical difficulties in solving the sub-problems. The algorithm is deemed to have converged once ϵ acquires a value of zero and the infinity norm of all the design and displacement variables is less than 1×10^{-2}.

The optimization code used to determine the optimal topologies is SAOi (Groenwold, Etman & Tosserams 2009), a FORTRAN-based sequential approximate optimization algorithm developed by Groenwold and Etman[2] for the solution of large-scale non-linear constrained optimization problems. The IBM ILOG CPLEX optimizer is employed as sub-problem solver. All optimization runs were done on a machine with the following configuration:

Processor:	Intel(R) Xcon(TM) 8 core CPU 3.73GHz
Memory:	Total memory (RAM), 31.5 GiB
Operating System:	Linux 2.6.34-12-desktop x86-64, openSUSE 11.3 (x86-64)

[1] This departs slightly from the commonly accepted continuation strategy, proposed by Cheng & Guo (1997), whereby the lower bound of the design variables and ϵ are related by $\check{x} = \epsilon^2$. Also, ϵ and thus $\check{x}$ are only reduced to some, small, non-zero value.

[2] Freely available for academic use from the originator, Albert A. Groenwold, via e-mail.

Table 1. Results

m_e	n_e	f_v	$\phi_{B\&W}$	N_{iter}	T_{avg}
4	1200	0,228	0,807	502	1,46
6	2700	0,223	0,833	743	4,86
10	7500	0,221	0,865	831	13,14

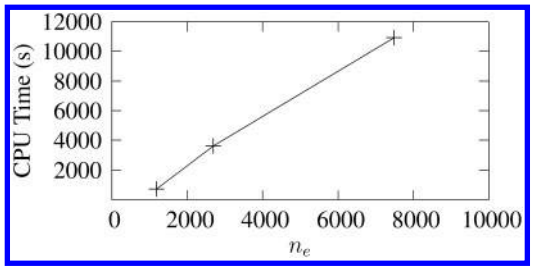


Figure 3. Computation Time.

5.4 *Results*

Table 1 is a summary of the results obtained for three mesh sizes. The volume fraction, f_v, is defined as the objection function value at final design normalised to the amount of elements, n_e, in the mesh. The 'black-white' fractions of the final designs are denoted by

$$\phi_{B\&W} = \frac{n_{e[0]} + n_{e[1]}}{n_e} \tag{14}$$

with $n_{e[0]}$ and $n_{e[1]}$ the number of elements on their lower bounds and upper bounds respectively. N_{iter} is the number of iterations required for convergence and T_{avg} the average time per iteration in seconds. Figure 3 depicts the overall computation time for the three problem sizes. From this we deduce, although only three data points are considered, that the computation time scales linearly relative to problem size. Figure 4 shows the representative optimal topologies for the three meshes considered. Note the design denoted by mesh multiplier $m_e = 6$ converges to some local minimum resulting in a different overall shape to the solution. This characteristic is related to the fact that the equilibrium equations are not solved exactly in each iteration. Highlighting one of the main challenges of the topology optimization problem in a SAND setting.

6 CONCLUSION

This paper reflects a work in progress. Topology optimization with local stress constraints is computationally extremely expensive and the size of problem that can currently be solved in a reasonable amount of time, with a reasonable amount of computational resources, is disappointingly small. In the light of this we pursue the SAND formulation in a SAO setting of

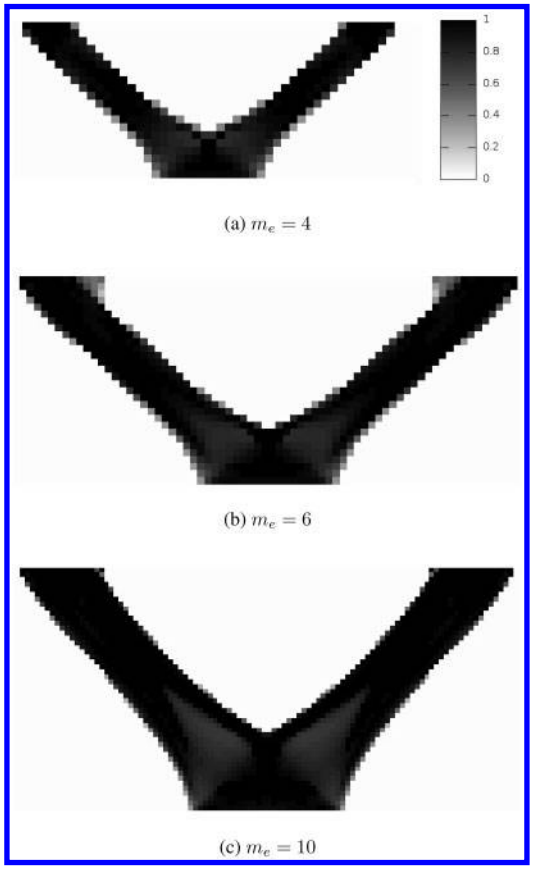


Figure 4. Optimum topologies generated by weight minimization of the two-bar truss structure.

the topology optimization problem with local stress constraints.

We show the storage and computation requirements of the SAND formulation scale linearly with problem size. Hence, although our solution procedure is not currently optimal, we suspect the SAND formulation can be exploited to drastically reduce time to solution, especially for very large problems.

The system of equilibrium equations, solved exactly in the NAND formulation, is incorporated in the optimization problem as a set of equality constraints. Thus the system of equations is not solved *per se*, allowing the design variables to obtain values of exactly zero, completely removing elements deemed to be void for an optimal design. This aspect is not only physically more representative, but also facilitates the removal of constraints that no longer influence the optimization problem, speeding up the solution procedure.

Future work will include the solving of the subproblems as a quadratically constrained quadratic problems (QCQP). Further, with the equilibrium equations formulated as equality constraints, continuation strategies on the SIMP parameter, p, become possible. Ill-conditioning of the stiffness matrix in the SAND formulation having no effect on the solution procedure. Such strategies may be used to improve 'black-white' fractions of final designs.

Finally, although we consider relaxed stress constraints, we speculate the SAND formulation may yield a different view of stress-relaxation altogether. The equilibrium equations, defined as equality constraints, need not be satisfied in each iteration. Hence iterations to final design are allowed to be infeasible, possibly making stress relaxation redundant.

REFERENCES

Arora, J. & Q. Wang (2005). Review of formulations forstructural and mechanical system optimization. *Structural and Multidisciplinary Optimization 30, 4*, 251–272.

Bendsøe, M. (1989). Optimal shape design as a material distribution problem. *Struct. Optim*. 1, 193–202.

Bendsøe, M. & O. Sigmund (1999). Material interpolation schemes into pology optimization. *Archive of applied mathematics 69*, 635–654.

Bendsøe, M. & O. Sigmund (2003). *Topology Optimization: Theory, Methods and Applications*. Berlin: Springer.

Cheng, G. & X. Guo (1997). – relaxed approach instructural topology optimization. *Struct. Optim*. 13, 258–266.

Cheng, G. & Y. Wang (2000). On simgular topologies and related optimization algorithm. *SeriesII: Mathematics, Physics and Chemistry 7*, 133–147.

Duysinx, P. & M. Bendsøe (1998). Topology optimization of continuum structures with local stress constraints. Int. J. Nu-mer. Meth. Enging. 43, 1453–1478.

Etman, L., A. Groenwold, & J. Rooda (2011). First-order sequential convex programming using approximate diagonal qp subproblems. *Struct Multi disc Optim 45*, 479–488.

Groenwold, A. A., L. F. P. Etman, & S. Tosserams (2009). Globally convergent optimization algorithm using conservative convex separable diagonal quadrati capproximations. *AIAAJ. 47*, 2649–2657.

Haftka, R. & Z. Gurdal (1992). *Elements of Structural Optimization: Third Revised and Expanded Edition*. Dordrecht, The Netherlands: Kluwer Academic Publishers.

Wood, D. W. (2012). *Dual Sequential Approximation Methods in Structural Optimization*. Ph. D. thesis, University of Stellenbosch, Stellenbosch, South-Africa.

Research and Applications in Structural Engineering, Mechanics and Computation – Zingoni (Ed.)
© 2013 Taylor & Francis Group, London, ISBN 978-1-138-00061-2

Reliability-based robust optimization using variance based methods

G. Karaki
Civil Engineering Department, Faculty of Engineering, Birzeit University, West Bank

ABSTRACT: Numerical models are built for structural systems to obtain response predictions. The system input parameters are uncertain due to the lack of information in one hand and to their inherent variability on the other hand. Thus, under uncertain conditions, the field of reliability-based optimization provides a realistic tool for structural optimization. This paper is concerned with exploring an approach based on variance methods of sensitivity analysis to ensure the robustness of the optimized design. The suggested procedure is performed on an engineering problem.

1 INTRODUCTION

The models of the engineering systems are not of deterministic nature as variability and uncertainty in the input parameters defining the model exist. Hence, in design tasks finding an optimum solution that cope with these uncertainties is a current goal for researchers in engineering practice. Therefore, researchers have proposed different methods for reliability analysis and reliability-based optimization algorithms where the input parameters are considered as random variables. Furthermore, the robustness of the optimum solution is of high importance. As a probabilistic analysis is performed, assumptions are made for the characteristics of the probability density functions of input parameters. However, there is uncertainty in these characteristics of the distribution functions; mean value, variance and distribution type. The influence of the uncertainty mentioned need to be checked and a procedure for this to be proposed.

A record of some of the recent work on reliability-based optimization methods can be found in numerous references, e.g (Frangopol, 1985, Tu et al., 1999 & Dubourgh et al., 2011). The different studies are concerned in deriving methods and algorithms for the optimization problem, deterministic- or reliability-based. The topic of robust design when using reliability-based optimization is often performed by simplifying the problem for which a weighted average of the sensitivity factors can be used as an objective function for the optimization problem (Wang et al., 2001 & Kim, 2010). This limits the application of such procedures to the possibility to formulate the relations, in other words, the gradients, of the responses of engineering problem to the input parameters studied. Furthermore, the interaction between the inputs and their effect on the responses studied are ignored. Thus, an exact statement regarding the robustness of the optimized design cannot be made.

This paper suggests a procedure to find the best design parameters of the engineering system using a global optimization algorithm. The randomness of the input parameters and the uncertainty in their definition using reliability and sensitivity analysis measures are used to check the reliability and robustness of the optimized design solution.

2 RELIABILITY OPTIMIZATION

2.1 *Reliability based design optimization*

In a deterministic design optimization, the designs are often driven to the limit of the design constraints, neglecting the uncertainties in the input parameters and the modeling process. These uncertainties in simulation based designs are to be considered in the design optimization process, as these uncertainties may lead to large variations in the performance of the designed system and lead to failures in that are not accounted for. Reliability based design aims to obtain optimal designs characterized by a low probability of failure when considering the different uncertainties of the system studied. The uncertain input parameters are considered as random variables following a probability distribution function with deterministic mean and standard variation. The probability of failure considering a design limit state is used a measure for the reliability of the designed system. Then an optimization algorithm is performed to find an optimum design by minimizing the probability of failure. A mathematical optimization problem has the form

Minimize $f_0(x)$
Subject to $f_i(x) \leq 0,\ i = 1 \ldots n$

Where x is the optimization (design) variables, f_0 is the objective function, and f_i are the constraints function with n is the number of constraints

2.2 *Optimization algorithm*

The particle swarm optimization (PSO) is a parallel evolutionary computation techniques developed by Kennedy and Eberhart (Kennedy & Eberhart, 1995). The optimization is based on the social behavior of bird flocks or fish schools. The core idea behind PSO is the fact that social information is shared among a population. Each particle is assigned with a random speed and is relatively moved through the problem space. It is attracted towards the location of the best fitness achieved by the particle itself and by the location of the best fitness achieved by the whole population. This search and movement makes this algorithm of a global nature

PSO is chosen for its global nature, direct and simple implementation, and its independence of gradient information of the objective function considered. PSO is an effective and robust optimization algorithm. However, these algorithms need the appropriate setting for their control parameters, which often are chosen depending on a form of trial-and-error for each particular optimization problem at hand (Eberhart & Shi, 1998).

The general steps of the algorithms as the following:

1. Initialization where the speed and position of all particles are randomly set to pre-defined ranges
2. Speed updating where at each iteration the speeds of all particles are updated according to

$$\vec{s}_i = w\vec{s}_i + b_1 R_1(\vec{x}_{i,best} - \vec{x}_i) + b_2 R_2(\vec{g}_{i,best} - \vec{x}_i)$$

   Where x_i and s_i are the position and speed of particle i, $x_{i,best}$ and $g_{i,best}$ are the position with the best objective value found by particle i and the entire population, w is a weighting parameter, R_1 and R_2 are random variables between [0,1], and b_1 and b_2 are controlling factors of the algorithm
3. Position updating by assuming a unit time interval between successive iterations, the location of all particles are updated according to

$$\vec{x} = \vec{x}_i + \vec{s}_i$$

4. Memory updating at which $x_{i,best}$ and $g_{i,best}$ are updated when the following condition is met

$$\begin{aligned} \vec{x}_{i,best} &= \vec{x}_i \quad if\ f(\vec{x}_i) > f(\vec{x}_{i,best}) \\ \vec{g}_{i,best} &= \vec{g}_i \quad if\ f(\vec{g}_i) > f(\vec{g}_{i,best}) \end{aligned}$$

   where $f(x)$ is the objective function
5. Termination criterion at which the algorithms repeat steps 2 through 4 until a certain termination conditions are met

3 ROBUST DESIGN

3.1 *Robustness*

Not only the reliability of the optimized design of importance, but also its robustness. Robust designs are the designs at which the variation in the objective function or optimized solution is minimal against the uncertainties in the inputs of the system. For this purpose, a sensitivity analysis is suggested to check the assumptions regarding the uncertainties of the system's inputs, e.g. mean value, standard deviation and distribution type.

3.2 *Variance based sensitivity indices*

Sensitivity analysis is the study of how uncertainties in the output of a model are apportioned to the uncertainties of the inputs. The use of sensitivity analysis in this study is to apportion the variance of the optimized solution to the assumed characteristics used in the reliability study. It is employed as a means of robustness for the design solution using reliability based optimization.

Variance-based methods have been chosen as they are independent from the engineering problem investigated and the interactions between input parameters. Moreover, such sensitivity analysis provides the importance ranking of the input parameters, and quantifies their contribution to the variance of optimization solution.

The main idea of variance-based methods is to estimate the amount of variance that would disappear if the true value of the input parameter X_i is known. This can be described by the conditional variance of an objective function $f(x)$ fixing at its true value $V(f|X_i)$, and is obtained by varying over all parameters, except X_i. Since the true value of X_i in complex engineering problems is unknown, the average of the conditional variance for all possible values of X_i is used, i.e. $E(V(f|X_i))$. Having the unconditional variance of the output $V(f)$ and the expectation of the conditional variance $E(V(f|X_i))$, the following relation holds:

$$V(f) = V\big(E(f|X_i)\big) + E(V(f|X_i))$$

The variance of the conditional expectation $V(E(f|X_i))$ is determined. This term is often referred to as the main effect, as it estimates the main effect contribution of the X_i to the variance of the objective function. Normalizing the main effect by the unconditional variance $V(f)$ results in the first order sensitivity index:

$$S_i = V\big(E(f|X_i)\big)/V(f)$$

Interaction between input parameters that affect the variance of the objective function can also be detected, which are known as higher order effects. The total effect index S_{Ti} is used to represent the total contribution of the input parameter X_i to the output, i.e. the first order effects, in addition to all higher order effects. A total effect index is defined as:

$$S_{Ti} = 1 - V\big(E(f|X_{\sim i})\big)/V(f)$$

Sampling based methods are used to evaluate the sensitivity indices (Saltelli et al., 2008).

3.3 *General procedure of robust reliability-based design*

1. The uncertainty in the inputs of the engineering system is considered using the probability theory
2. The probability of failure for a required design limit state using Monte Carlo simulation is determined

$$PF = 1/m \sum_{k=1}^{m} I_f(x^k)$$

   where m is the number of run samples of input parameter, $I_g(x^k)$ is an indicator function, where its value is 0 for a based sample output and 1 for a failed sample
3. The Optimization process is performed to obtain the design variables that minimize the probability of failure when considering the uncertainty of the systems input.
4. A variance based sensitivity analysis is run for the variability of the definition of the uncertainty of system's input
5. The sensitivity indices indicates which of the input parameters that need further study to ensure a higher robustness of the optimized design solution

The procedure is independent of the field of engineering problem or the type of its developed models. The optimization algorithm used is an effective and robust algorithm. Furthermore, the sensitivity analysis detect the first order and higher order effects which is of importance to complex engineering problems.

4 NUMERICAL EXAMPLE

A Test engineering problem is used for the illustration of the application of the suggested procedure. This engineering problem is concerned with the drift of a single story frame due to lateral loading applied at floor level. The force may represent the static equivalent lateral loading of a seismic action on a building, which is considered as a random variable described using a probability distribution function with specific characteristics. The design objective is to limit the drift of the upmost corner of the frame to an acceptable limit. The objective function for the optimization problem is the probability of failure which is related to the possibility that frame's drift exceeds a chosen design limit. However, the specific probabilistic characteristics that define the uncertainty of the lateral force, which is of main importance to the drift values, are themselves uncertain. Therefore, the sensitivity analysis is used to examine the performance of the output of the reliability-based optimization process against the uncertainty of the probabilistic characteristics of the input parameter (force). This is performed using variance based methods as mentioned before.

Table 1. Particle Swarm Optimization (PSO) characteristics.

Parameter			
No. of Particles	200	Control parameter (b1)	0.2
No. of iterations	100	Control parameter (b1)	0.2
Weight (w)	0.7		
LB Height	2.0 m	LB EI ($\times 10^6$)	0.5 kNm^2
UB Height	4.0 m	UB EI ($\times 10^6$)	2.0 kNm^2

Table 2. Input parameters used for the sensitivity analysis.

Parameter		
Distribution type	Uniform distribution	$0 \leq$ xdis$<1/3$ 'Normal' $1/3 \leq$xdis$\leq 2/3$ 'Lognormal' $2/3 <$ xdis < 1 'Gumbel'
Mean value	normal distribution	mean = 120 kN
COV		COV = 0.10
	lognormal distribution	mean = 0.25 COV = 0.10

A single span, single bay frame loaded with lateral loading is chosen as mentioned before. The failure condition is described as:

$$\mathcal{F} = \{(F, H, EI): \Delta > FH^3/(24EI)\} = \{(F, H, EI): 0 > FH^3/(24EI) - \Delta\}$$

where Δ is the limiting drift of the upper most corner of the frame. The optimization process is executed to find the height of the frame (H) and its flexural stiffness (EI). The objective of the optimization problem is to minimize the probability of failure (PF) conditioning on upper and lower bounds for the design variables. PF is estimated using Monte Carlo estimation where 1000 samples are used.

It is important to ensure that the optimized solution is only dependent on the variability of the considered inputs and not on the performance of the optimization process. A check is done on the PF of the frame for every optimized design parameters to ensure the negligible effect of PSO algorithm on the variability of the output. The following are the main characteristics of the optimization process obtained from trial-and-error-procedure.

The sensitivity analysis is used to apportion the variability of the optimized solution to the assumptions made regarding the force input description. For each sample, a type for the distribution is chosen randomly with a random assignment of a mean value and a standard deviation as presented in Table 2 is run using the reliability-based optimization algorithm. Figure 1 and 2 present the optimized design parameters histograms for 1000 samples.

The sensitivity analysis is performed for the input parameters presented in Table 2.

The sensitivity analysis is performed using sampling-based methods where 1000 samples are run

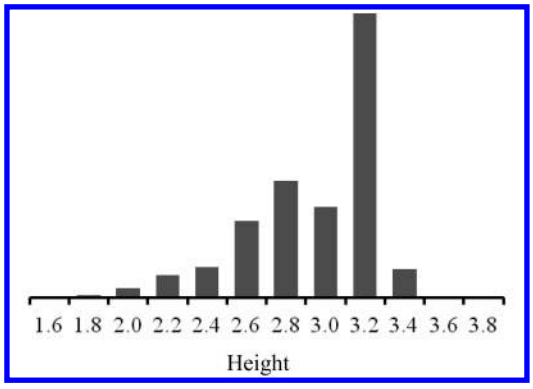


Figure 1. Histogram of optimized design variable of Height, mean value of 2.85 m. and standard deviation 0.31 m.

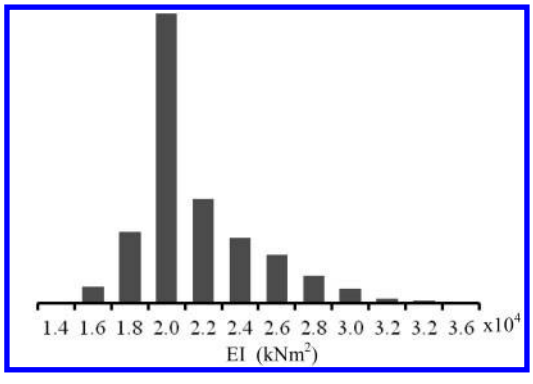


Figure 2. Histogram of optimized design variable of flexural stiffness, mean value of 2.07 m^4 and standard deviation 0.30 m^4.

Table 3. Sensitivity indices for characteristics of probabilistic definition.

Parameter	Opti. Height		Opti. EI	
	S_i(%)	S_{Ti}(%)	S_i(%)	S_{Ti}(%)
Mean Value	2	24	1	45
Standard Deviation	51	73	43	83
Distribution type	22	58	12	66

for every input parameter considered. The estimated sensitivity indices are presented in Table 3.

From Table 3, it can be seen that the main contributor to the variance of the optimized solution of the suggested problem is the assumed coefficient of variation followed by the assumed type of distribution. The higher the uncertainty in these assumptions, the lower is the robustness of the optimized solution. It can also be noticed that high interactions exist between the input parameters considered in the sensitivity analysis (S_{Ti}-S_i). This is expected as the inputs are inter-related in defining the probabilistic descriptions of a random variable. It also means that when controlling one of these inputs by increasing the degree of certainty in its value would significantly decrease the variability of the performance of the reliability based optimization and consequently increase the robustness of the procedure. This procedure of using variance based methods shed light on the variables where attention should be given to ensure the robustness of the reliability-based optimization design.

5 CONCLUSIONS

The design and analysis of engineering systems require creating numerical models that are exercised to obtain the desired outputs. However, these models are data dependent, e.g. geometric information or/and physical parameters. These data have uncertainties in their value and description. This paper is concerned with reliability-based optimization for which the uncertainty of the system inputs are considered in the design. Furthermore, the effect of the definition of this uncertainty is tested using variance based sensitivity analysis. This is performed to highlight the main sources of the variance for the optimized output in order to comment on the robustness of the reliability-based design. This procedure is applied and illustrated for a simple example; however the algorithm is generic and problem/model independent. It is to be applied to a large-scale engineering problem for which local meta-models are used to over-come the computational cost of such a procedure.

REFERENCES

Dubourgh, V.; Sudret, B.; Bourinet, J.M. 2011. Reliability-based design optimization using kriging surrogates and subset simulation, *Structural and Multi-discipline Optimization* 44(5): 573–690.

Eberhart, R.; Shi, Y. 1998. Comparison between genetic algorithms and particle swarm optimization. In *Evolutionary Programming VII*: 611–616.

Frangopol, D. 1985. Structural optimization using reliability concepts. *Journal of Structural Engineering* 111(11): 2288–2301.

Kennedy, J.; Eberhart, R. 1995. Particle swarm optimization. In *Neural Networks, 1995. Proceedings., IEEE International Conference on* 4: 1942–1948.

Kim, N. K.; Kim, D. H.; Kim, D. W.; Kim, H. G.; Lowther, D. A.; Sykulski, J. K. 2010. Robust optimization utilizing the second-order design sensitivity information. *Magnetics, IEEE Transactions on*, 46(8): 3117–3120.

Saltelli, A.; Ratto, M., Andres, T., Campolongo, F., Cariboni, J., Gatelli, D., Saisana, M. and Tarantola, S. 2008 Introduction to Sensitivity Analysis, in Global Sensitivity Analysis. The Primer, John Wiley & Sons, Ltd, Chichester, UK.

Tu, J.; Choi, K.; Park, E. 1999. A new study on reliability-based design optimization. *Journal of Mechanical Des* 121:557–564.

Wang, K. W.; Chung. C. Y.; Tse, C. T.; Tsang K. M. 2001. Probabilistic eigenvalue sensitivity indices for robust PSS site selection. In *Generation, Transmission and Distribution, IEE Proceedings-*, 148(6): 603–609.

Zeeb, C. N.; Burns, P. J. 1998. *A Comparison of Failure Probability Estimates by Monte Carlo Sampling and Latin Hypercube Sampling*. Tech. Rep., Sandia National Laboratories.

Research and Applications in Structural Engineering, Mechanics and Computation – Zingoni (Ed.)
© 2013 Taylor & Francis Group, London, ISBN 978-1-138-00061-2

Designing adaptive structures for whole life energy savings

Gennaro Senatore
Civil Environmental & Geomatic Engineering UCL – Expedition Engineering

Philippe Duffour
Civil Environmental & Geomatic Engineering, UCL

Sean Hanna
Bartlett School of Architecture, UCL

Pete Winslow
Expedition Engineering

Chris Wise
Civil Environmental & Geomatic Engineering, UCL – Expedition Engineering

ABSTRACT: Designing structures with minimal environmental impact is emerging as a serious concern in the construction sector. Conventional structural design practice involves designing first for strength, followed by secondary checks on deflections and other serviceability limits states. If these limits are exceeded, the conventional solution has been to add material to increase stiffness. When the design is governed by unpredictable events such as fluctuating loads, strong wind storms or earthquakes, the structure is effectively overdesigned for most of its working life. This paper presents a methodology to design adaptive structures that minimize the whole life energy consumption. The methodology is illustrated on plane pin-jointed trusses, both determinate and indeterminate. Strategically placing actuators allow the internal flow of forces to be homogenized and displacements to be controlled. The actuators only start working when the loads reach a certain threshold. Below this threshold, the structure resists loads mainly passively thereby limiting significantly the operational energy used. It was found that both indeterminate and determinate topologies bring substantial energy savings up to 70% of the total energy.

1 INTRODUCTION

1.1 *Background and conceptual framework*

Active control has been used in civil engineering structures for a variety of purposes. The most widespread application so far has been in vibration control (Soong, 1988). Shape morphing has also been studied (Ramrakhyani, et al., 2005). The potential of using adaption to save material has been investigated by a few (Teuffel, 2004) but whether the energy saved by using less material makes up the energy consumed through control and actuation is a question that has so far received little attention. The methodology presented in this paper aims to address this. A design process is proposed that produces an optimum adaptive structure that minimizes the total energy spent throughout the whole life of the structure (embodied in the materials + operational).

The process is illustrated diagrammatically in the conceptual graph shown in Fig. 1. This graph shows the total energy as a function of some notional degree of active control of the structure. The whole life energy is made of two components: operational energy and the embodied energy. For a completely passive design the embodied energy (mass of material) dominates the whole life energy: members are designed to bear 100% of the maximum expected load to meet strength and serviceability requirements. By contrast for a highly adaptive design, the embodied energy will be small but the operational energy necessary to control and actuate throughout the life of the structure will be high. The methodology proposed here seeks the minimum in whole life energy that lies between these two extremes.

In a conventional design, members are sized based on a worst case scenario i.e. the maximum expected load combination. If embodied energy is to be saved, clearly, member sizing should not be governed directly by this worst load combination but by some fraction of it. As the loads approach their worst values, conventional members will reach their capacity. Then strategically located active elements provide controlled output energy (actuators) in order to manipulate actively the internal flow of forces and stresses. In this way stresses can be homogenized and deflections kept

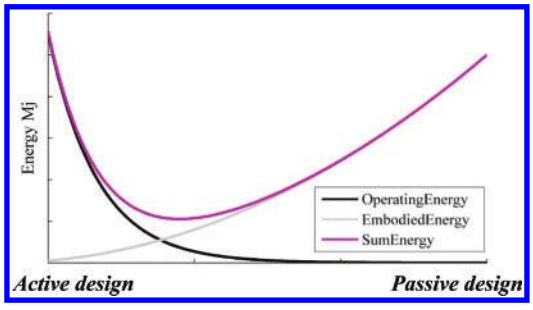


Figure 1. Whole-life energy vs. degree of adaptation.

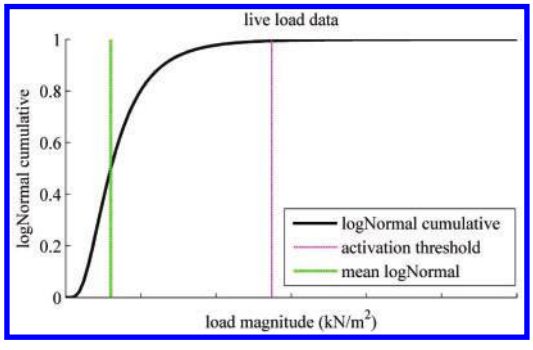


Figure 2. Load activation threshold.

within desired limits. The active elements (actuators) are only activated for compensation of the displacements and internal forces when the loads reach a certain threshold. Therefore operational energy is only used when necessary.

It is intuitively clear that this design process will be particularly beneficial when the design is governed by large loading events that have a small probability of occurrence (storms, earthquakes, unusual crowds but also transient rolling loads such as trains). To illustrate this, Fig. 2 shows the cumulative frequencies of occurrence for a generic stochastic load. The pink line represents the activation threshold which demarcates two zones in the load range. On the left hand side are the more probable low levels of load that the passive load-bearing capacity of the structure will be able to withstand without actuation. On the right are rarer loads with higher magnitude which the structure will only be able to withstand using both passive and active load-bearing capacity.

1.2 *Case study*

The design process is illustrated on a roof made of simple indeterminate cantilever planar trusses supporting 10 meters of cover each (out of plane). Fig. 3 shows the truss constrained at one end and subjected to both dead load and live load.

To test the effectiveness, the ratio of the cantilever's span to depth is deliberately set high at 25 (depth = 1.2 m). The dead load on the roof panels is set to 3 kN/mˆ2 which means each truss supports a

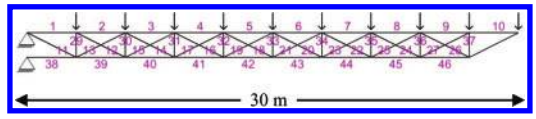


Figure 3. Cantilever pin-jointed truss.

uniformly distributed load (UDL) of 30kN/m. The live load is modeled as a log-normal distribution with 0.5 standard deviation and mean at 20% of the max expected load. The load distribution acts on the structures for the 10% of structure's life-cycle assumed to be 50 years. For the purpose of this case study, the type of distribution can be considered representative of the majority of loading scenarios such as earthquake, strong winds, snow, rolling loads or even occupancy patterns in building. In terms of magnitude the maximum expected live load is set equal to the dead load.

2 DESIGN METHODOLOGY

2.1 *Load path optimization*

The first stage of the design process consists in minimizing the set of member cross-section areas A_i and the bar forces F_{ik} subjected to satisfying equilibrium constraints as well as a set of inequality constraints expressing that the member' forces are limited by material yield in tension and buckling in compression. At this stage, geometric compatibility is not yet respected. This initial phase of the methodology is inspired from Teuffel (Teuffel, 2004) but unlike Teuffel, the self-weight and buckling constraints are introduced making the problem nonlinear. The problem was solved using a nonlinear sequential quadratic solver (SQP) (Nocedal & Wright, 2006). The problem can be formulated as follows:

$$\min\ V = \sum_{i=1}^{n} \mathrm{A}_i * l_i \tag{1}$$

s.t.:

$$\boldsymbol{B} \cdot \boldsymbol{F}_k - \boldsymbol{P}_k = 0 \tag{2}$$

$$a)\ \frac{F_{ik}}{A_i} \leq \sigma_T \cdot MUT; \quad b)\ -\frac{F_{ik}}{A_i} \leq \sigma_C \cdot MUT \tag{3}$$

$$\frac{F_{ik}}{A_i} \leq \sigma_{crit} \tag{4}$$

where V is the total volume, l_i is the length of the i^{th} element and $n$is the total number of elements. Eq.2 is a set of equality constraints which represents the equilibrium equations: **B** is the cosine direction matrix and k numbers the load cases. These constraints are nonlinear because the self-weight of the structure changes iteratively and so does the vector of external loads **P**. Ultimate limit states (ULS) are represented by the set of linear inequalities in eq. 3

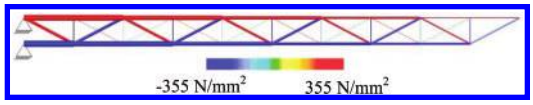


Figure 4. Optimal (non-compatible) forces distribution.

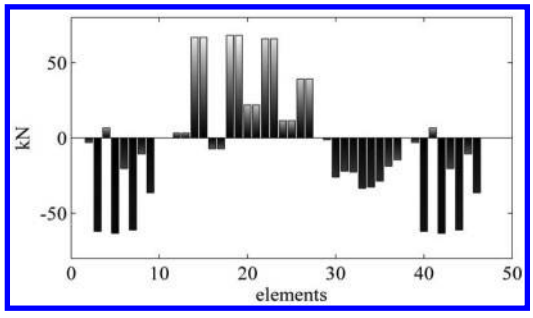


Figure 5. Difference between compatible and non-compatible axial force for each element.

where σ_T and σ_C are material yield stress in tension and compression respectively. Setting the material utilization factor (MUT) to 1, gives absolute minimum weight structures. The nonlinear stability constraints are represented in eq. 4 where critical loads (σ_{crit}) are computed iteratively using the Euler buckling formulation. Eq. 3b and eq. 4 are mutually exclusive for each element.

Fig. 4 shows the optimal (non-compatible) distribution of axial forces and cross sectional areas obtained for the cantilever case study.

The set of section areas is found by optimizing against the maximum expected load. Then a minimum set of bar forces must be found for any other instance of the load distribution. The problem can be formulated as:

$$\begin{cases} a)\ \min\left(norm\left(\boldsymbol{F}_{\boldsymbol{k}}^{\boldsymbol{eq}}\right)^2\right) \\ s.t. \\ b)\ \boldsymbol{C}^{\boldsymbol{ULS+buckling}} \cdot \boldsymbol{F}_{\boldsymbol{k}}^{\boldsymbol{eq}} - \boldsymbol{A}_{\boldsymbol{k}}^{\boldsymbol{optimal}} \leq 0 \\ c)\ \boldsymbol{B} \cdot \boldsymbol{F}_{\boldsymbol{k}}^{\boldsymbol{eq}} = P_{jk} \end{cases} \quad (5)$$

where F_k^{eq} is the optimal equilibrium pattern of forces for lower levels of loads than the maximum expected load; $C^{ULS+buckling}$ is the matrix of the constraints from eqs(3–4) and P_{jk} is j^{th} component of load case k. If a determinate topology had been chosen for the truss, the actuator length changes would have only affected the geometry but not the state of stress of the structure (small displacements), i.e. F_k^{eq} is obtained by eq.5(c) directly.

Fig.5 shows the difference $\Delta\mathbf{F}_k$ between the optimal (non-compatible) forces and the compatible axial forces of the structure without active control. The x-axis shows the element numbers as labeled in Fig. 3 while vertical axis shows the force difference in kN.

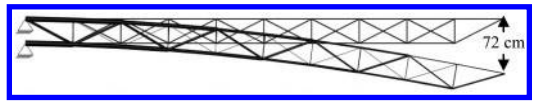


Figure 6. Compatible displacements without active control.

As can be seen from Fig. 6, the maximum displacement is well beyond serviceability limits (span/180 = 16 cm)

For these reasons, active work in the form of actuator length change is needed for both forces and displacements correction.

2.2 *Active element topology*

The next stage in the design process involves finding the best location for the actuators. The optimum actuator positioning is found by first choosing a set of nodes whose displacement must be controlled (CDofs). For the truss studied here, the vertical displacements of all the nodes of the top chord are selected and constrained so that the cantilever tip moves within span/180 (i.e. 16cm). The difference between compatible and optimal forces $\Delta\mathbf{F}_k$, and between the desired and compatible displacements $\Delta\mathbf{u}_k$, are the inputs to find the most efficient (minimum operational energy) topology for the actuators.

The minimum desirable number of actuators is equal to the indeterminacy of the system plus the number of controlled DOFs which in this case is $8 + 9 = 17$. This is the minimum number of actuators necessary to turn the structure into a controlled mechanism. The most efficient positions for the actuators are those where the active elements have the largest effect on both axial forces and controlled displacements. This problem can be formulated as a least square optimization routine starting with the computation of the sensitivity matrices S^U and S^N for displacements and axial forces. These matrices store the effect of a unit length change for each element on nodal displacements (SU) and axial forces (SF) on the other elements. Each element length is increased by one unit length at a time. The resulting axial forces and nodal displacements are obtained using a flexibility approach (Patnaik, et al., 1991).

It is then possible to find the active element length changes ΔL that satisfy the desired controlled DOFs (Δu) eq.6 and compatibility conditions eq.7:

$$\min\left\|\boldsymbol{S}^{\boldsymbol{U}} \cdot \Delta\boldsymbol{L}^{\boldsymbol{all}} - \Delta\boldsymbol{u}\right\|^2 \quad (6)$$

$$\boldsymbol{S}^{\boldsymbol{F}} \cdot \Delta\boldsymbol{L}^{\boldsymbol{all}} = \Delta\boldsymbol{F} \quad (7)$$

At this stage $\Delta\mathbf{L}_{\text{all}}$ is obtained considering all elements as active. In order to derive the set of most efficient elements the contribution towards the desired control displacement is evaluated as efficiency (8) of each member as:

$$eff_{ik} = \frac{\sum_i^{nCDofs} \frac{\boldsymbol{S}^{\boldsymbol{U}} \cdot \Delta\widetilde{\boldsymbol{L}_{ik}}}{\Delta\boldsymbol{u}_k}}{nCDofs} \quad (8)$$

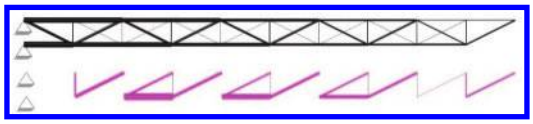


Figure 7. Optimal actuators topology.

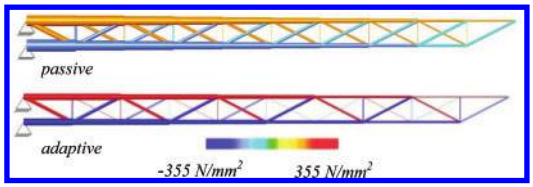


Figure 8. Optimal stress distribution passive vs. adaptive.

$$Eff_i = \frac{\sum_{k=1}^{nloadCases} \boldsymbol{eff}_k}{nloadCases} \quad (9)$$

where $\Delta\tilde{L}_{ik}$ is the vector composed of the length change of element i for the load case k having all the others components set to 0 and nCDofs is the number of controlled Dofs. The global efficiency Eff_i of each member is obtained from eq. (9). Fig. 7 shows the optimum positioning of the actuators for our cantilever truss structure, given a free choice of their number and location.

Once the position of the actuators is known, their required length changes is computed to bring the controlled nodes as close as possible to their required limits while enforcing the compatibility conditions eq.(11) as constraints:

$$\min \left\| \mathbf{S}_{\boldsymbol{red}}^{\boldsymbol{U}} \cdot \Delta\mathbf{L} - \Delta\mathbf{u}_{\boldsymbol{red}} \right\|^2 \quad (10)$$

$$\mathbf{S}_{\boldsymbol{red}}^{\boldsymbol{F}} \cdot \Delta\mathbf{L} = \Delta\mathbf{F} \quad (11)$$

$\mathbf{S}_{red}^{U}$ and $\mathbf{S}_{red}^{F}$ are reduced versions of $\mathbf{S}^{u}$ and $\mathbf{S}^{F}$ obtained by only keeping the columns corresponding to the chosen active elements. Finally, the length changes (ΔL_i for each actuator as initial deformation) are imposed together with external loads to check that the displacements of the controlled DOFs are within the desired limits. Fig. 8 shows the comparison between the adaptive truss and the corresponding passive optimized version.

2.3 *Embodied-operational energy optimization*

The work done by the actuators can be expressed as:

$$W_k = \sum_{actThr}^{size(P_k)} \sum_{i}^{na} \frac{\left(F_{ik}^{comp} + {}^1\!/_2 \cdot \Delta F_{ik}\right) \cdot \Delta L_{\,ik} \cdot fq \cdot t_k}{actMechEff} \quad (12)$$

In eq. (12) it is assumed that an actuator exerts a total force sum of F_{ik}^{comp}, the passive element contribution with no active control (compatible), and additional force contribution ΔF_{ik} performing a length change ΔL_{ik}. The operational frequency is kept constant for

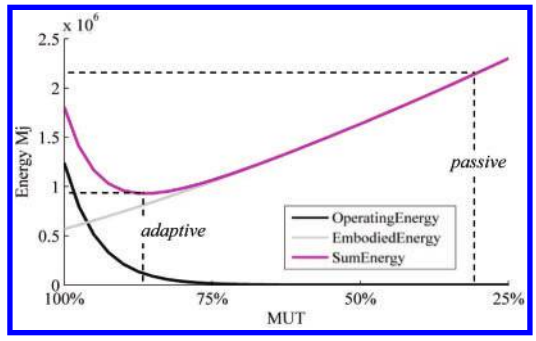


Figure 9. Embodied & operational energy curves.

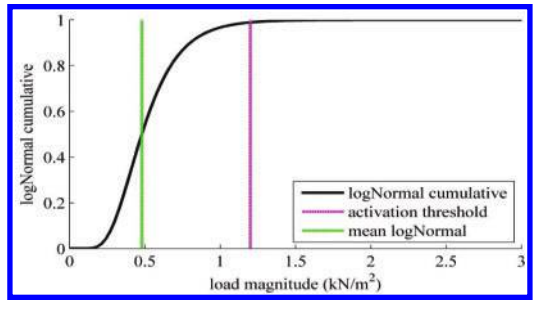


Figure 10. Load activation threshold (LAT).

any occurrence $time_k$ of each load case P_k (hours of occurrence). Working frequency and working efficiency of the actuators are set as 5 Hz and 50% respectively as conservative assumptions. The total operational energy is the sum of the energy needed for compensation of forces and displacements for all the loads above the activation threshold (actThre) and for all the actuators (na).

In order to take into account the minimization of the operational energy, the design process described in eqs.(1–10) is repeated iteratively within an outer loop. The main variable of the outer loop is the parameter MUT (material utilization factor). The active-passive system that corresponds to the minimum of the sum of embodied and operational energy is the optimum sought (fig.9).

Fig. 10 shows the activation threshold that corresponds to the optimal MUT value. Comparison between the adaptive and an analogous structure optimized using the same formulation of eqs.(1–4) with additional compatibility constraints $\mathbf{K} \cdot \mathbf{u}_k = \mathbf{P}$ shows that total energy savings remain substantial (55% in this case) even when considering the operational energy (fig. 11).

In both cases, embodied energy savings represent the major benefit when taken over the whole life of the structure, with other significant benefits in size reduction and construction transport and erection weight demands. The embodied energy is computed using the Bath Inventory of carbon and energy (Hammond & Jones, 2008).

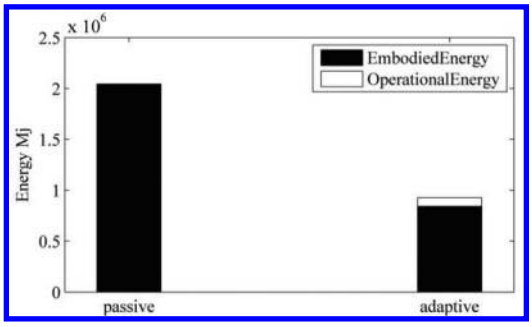


Figure 11. Energy savings comparison.

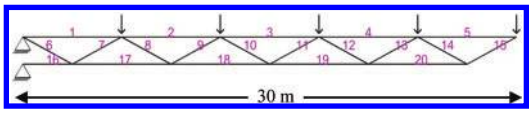


Figure 12. Determinate cantilever truss.

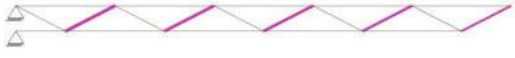


Figure 13. Optimal actuators topology determinate.

2.4 *Modifying the method for determinate cases*

This section studies the behavior of the determinate version of the cantilever truss described in the previous section (Fig. 12).

The only difference in the mathematical formulation is in the computation of the actuators topology. For the determinate case the actuators length change does not change the state of stress of the structure thus eq. (7) and eq. (11) are not necessary. The problems in eq. (6) and eq. (10) can be solved directly by computing the pseudo-inverse of the sensitivity matrix for displacements:

$$\Delta \boldsymbol{L} = \boldsymbol{S}^{U+} \cdot \Delta \boldsymbol{u} \tag{13}$$

which gives the actuators length change that compensate for displacements. Applying eqs.(8–11) gives the optimum actuator configuration for the displacements compensation. This is shown in Fig. 13.

Displacement correction can be dealt with in several ways. The simplest consists in setting the desired nodal displacement so as to stay within serviceability limits. A better way is to assign the desired displacement by taking into account the rate of change of the curvature between consecutive bays to avoid the formation of kinks in the deflection. Fig.14 shows the difference of the controlled shape with and without curvature constraints.

Comparison with an equivalent optimised passive truss gives energy savings of 60%. Optimal forces at maximum expected load for the adaptive and passive configuration are shown in Fig. 15.

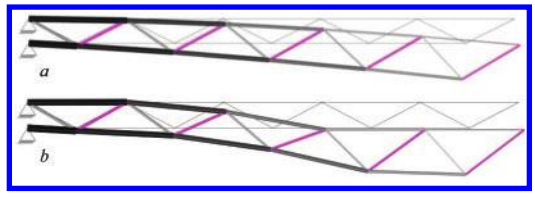


Figure 14. (a) curvature constr. (b) no curvature constr.

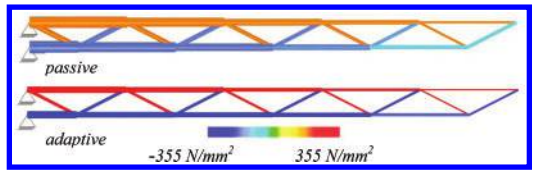


Figure 15. optimal stress distribution passive vs. adaptive.

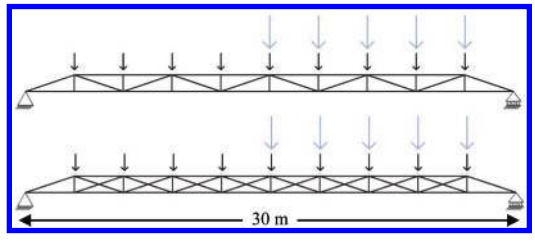


Figure 16. Determinate & indeterminate simply supported.

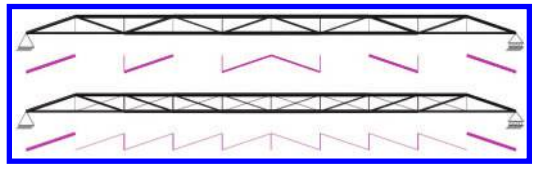


Figure 17. Adaptive trusses with actuators positions.

3 DETERMINATE VS INDETERMIANTE

In this section determinate and indeterminate trusses are compared in order to assess the effect of the load path redirection by the actuators for the control of internal forces and displacements. The next case study focuses on a simply supported truss beam supported by a pin at the bottom left corner and a roller at the bottom right node (Fig.16). The dead load is again 3 kN/m^2 supporting 10 m of roof out of plane. Two cases of live load are considered: in the first, a UDL is applied over the whole top cord whereas for the second only on the right half of the truss. The magnitude of the first UDL is set to dead load for the first load case and to twice the dead load for the second. The same load probability distribution as previously is taken for both the load cases.

The result of the optimization routine in terms of sections and actuators topology, only taking into account the first load case, are shown in Fig.17.

The optimal forces for both determinate and indeterminate adaptive/passive designs are shown in Fig. 18.

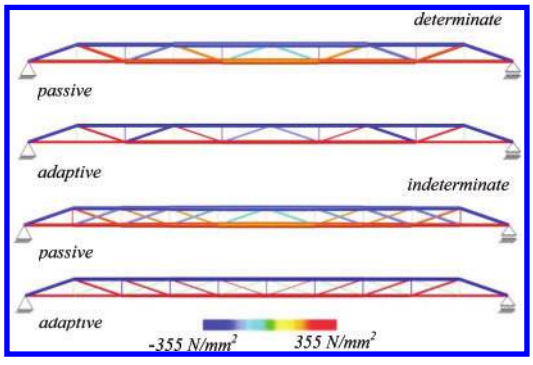


Figure 18. Comparison force distributions determinate vs. indeterminate case.

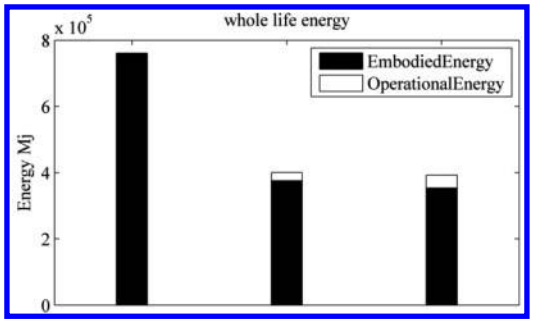


Figure 19. Comparison passive vs det. & indet. trusses.

For the determinate case the axial forces in the adaptive and passive structures are simply scaled version of each other. The material is more efficiently utilized and stresses tend to reach the maximum allowable values in the active structure.

By contrast, in the indeterminate case the axial forces in the passive and active truss are different. In the passive truss, the vertical elements work very little whereas the cross bracings are quite heavily used both in tension and in compression. The active indeterminate structure has all its vertical members in compression and in the cross bracing, the tension members have become dominant. Actuation has effectively turned the truss structure into a Pratt truss which is the best topology for the type of load acting on it.

In terms of total energy savings, both determinate and indeterminate designs achieve 50% with respect to the passive structures. Breaking down the total energy into embodied and operational shows that the adaptive indeterminate achieves 10% reduction for the former but a 40% increase for the latter compared to the adaptive determinate (Fig.19). The increase in operational energy is due to the load path redirection and the bigger number of actuators (Fig. 19).

Similar results are obtained when the two load cases are applied as combination case (fig. 20).

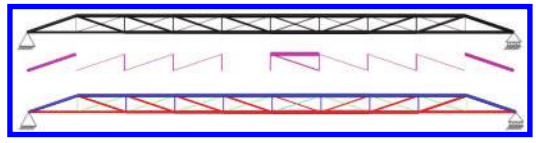


Figure 20. Force-sections distribution and actuators positions found for the load combination case.

4 CONCLUSIONS

A design procedure was presented that allows the design of structures that minimize whole life energy by introducing actuations at optimum placement in pin-jointed truss structures. Maximum energy savings are achieved by embedding the actuators with optimum placement and by finding the load threshold at which active control becomes necessary. Results from two planar structure case studies were presented. First for a determinate cantilever it was shown that the optimal active design allowed 50% of the total energy to be saved compared to an optimized passive design with the same topology. The second structure studied was a simply truss beam. Both a determinate and an indeterminate topology were tested. Similar savings around 50% were achieved for both. The indeterminate truss allows load path redirection. This in principle could allow a better homogenization of the stresses inside the truss. However, the whole life energy costing showed that the extra actuation needed in the indeterminate truss allows only minor further substantial energy savings with respect to the determinate case.

ACKNOWLEDGEMENTS

The authors would like to thanks the EPSRC and Expedition Engineering for funding this research project.

REFERENCES

Hammond, G. & Jones, C., 2008. *Embodied Energy & Carbon,* Bath: University of Bath.

Nocedal, J. & Wright, S. J., 2006. *Numerical Optimization.* s.l.:Springer Verlag.

Patnaik, S., Hopkins, D. & Halford, G., 1991. Integrated Force Method versus Displacement Method for Finite Element Analysis. *Computers and Structures,* 38(4), pp. 377–407.

Ramrakhyani, D. S., Lesieutre, G. A., Frecker, M. & & Bharti, S., 2005. Aircraft Structural Morphing Using Tendon-Actuated Compliant Cellular Trusses. *Journal of aircraft,* 42(6), pp. 1615–1621.

Senatore, G. et al., 2011. Large Scale Adaptive Structures for Whole Life Energy Savings. *International Association for Shell and Spatial Structures (IASS),* 52(No. 4 December n. 170).

Spillers, W. & MacBain, K., 2009. *Structural Optimization.* New York: Springer.

Teuffel, P., 2004. *Entwerfen adaptiver Strukturen.* http://elib.unistuttgart.de/opus/volltexte/2005/2172/pdf/Teuffel_Entwerfen_Adaptiver_Strukturen.pdf

Research and Applications in Structural Engineering, Mechanics and Computation – Zingoni (Ed.)
© 2013 Taylor & Francis Group, London, ISBN 978-1-138-00061-2

Softening some effects of the no free lunch (NFL) theorems in optimization via parallel computing

S. van Huyssteen & A. Groenwold
Department of Mechanical and Mechatronic Engineering, University of Stellenbosch, Matieland, South Africa

ABSTRACT: The no free lunch (NFL) theorems, aptly named by Wolpert and Macready, imply that no search or optimization (SO) algorithm will always outperform all other SO algorithms. Not only may an algorithm fare very different when applied to different classes of problems, but different implementations of a given algorithmic paradigm may result in the same. In this paper, parallel computing is used to soften this effect of the NFL theorem which is very well known in practice.

In this parallel paradigm different optimization solvers compete in parallel to solve a nonlinear optimization subproblem. The first successful iterate is then accepted. This approach allows us to solve SO problems far more efficiently than is possible with a single solver. Our numerical experiments show that the most suitable solver, usually selected a priori, may change as the iterations progress, contrary to intuition.

1 INTRODUCTION

In search and optimization the famous no free lunch (NFL) theorems of Wolpert and Macready (Wolpert & Macready 2005) imply that "any two algorithms are equivalent when their performance is averaged across all possible problems", although some authors have argued for an *(almost) no free lunch*[1] theorem. Nevertheless the theorems are still applicable in practice, see Droste (Droste, Jansen, & Wegener 2002). In an attempt to soften some of the implications of the NFL theorems we discuss a strategy in which we let different optimization solvers compete in parallel, to solve a nonlinear optimization subproblem. The first valid iterate obtained is accepted which lets the program follow the most efficient search path while ignoring the slow or erroneous subsolvers.

We are equipped with three solvers, one dual solver `l-BFGS-b` (Byrd, Lu, Nocedal, & Zhu 1995, Zhu, Byrd, Lu, & Nocedal 1994) and two QP solvers `E04NQF` (NAG Library Manual, Mark 22 2009) and `LSQP` (Gould, Orban, & Toint 2004). Two asynchronous parallel algorithms were developed in a sequential approximate optimization (SAO) framework. The first algorithm relies on thread cancellation by setting signal flags written with OpenMP, while the second algorithm forces cancellation of threads using POSIX libraries, also know as Pthreads.

We concentrate on the solution of inequality constrained nonlinear optimization problems. Since there exists many different methods for solving such problems we only give the general form of the problems here. Consider the inequality constrained nonlinear optimization problem $\mathcal{P}$ of the form

$$\begin{aligned} &\min_{\boldsymbol{x}} \; f_0(\boldsymbol{x}) \\ &\text{subject to} \;\; g_j(\boldsymbol{x}) \leq 0, \qquad j = 1,2,\ldots,m, \\ &\qquad\qquad \check{x}_i \leq x_i \leq \hat{x}_i, \qquad i = 1,2,\ldots,n, \end{aligned} \tag{1}$$

where $f_0(\boldsymbol{x})$ is the real valued scalar objective function, and the $g_j(\boldsymbol{x}), j = 1,2,\ldots,m$ are m inequality constraint functions. $f_0(\boldsymbol{x})$ and $g_j(\boldsymbol{x})$ depend on the n real (design) variables $\boldsymbol{x} = [x_1, x_2, \ldots, x_n]^T$. $\check{x}_i$ and $\hat{x}_i$ represent lower and upper bounds on the primal variable x_i respectively. Additionally, functions $f_0(\boldsymbol{x})$ and $g_j(\boldsymbol{x}), j = 1,2,\ldots,m$ are assumed to be (at least once) continuously differentiable.

To solve the general nonlinear optimization problem above most state of the art methods construct successive approximate subproblems $\tilde{\mathcal{P}}[k], k = 1,2,3,\ldots$ at successive approximations $x^{\{k\}}$ to the solution x^*. The solution of subproblem $\tilde{\mathcal{P}}[k]$ is $\boldsymbol{x}^{\{k*\}}$, which may be obtained by using any suitable continuous

[1] An *(almost) no free lunch* (ANFL) theorem shows that for any problem that can be optimized efficiently by a search heuristic/solver there can be constructed many related functions where the same heuristic is bad. As a consequence, search heuristics use some idea how to look for good points and can be successful only for functions when given the correct information.

programming method. Then $\boldsymbol{x}^{\{k+1\}} = \boldsymbol{x}^{\{k*\}}$ is the minimizer of subproblem $\tilde{\mathcal{P}}[k]$.

To solve the subproblem $\tilde{\mathcal{P}}[k]$ multiple optimization solvers are started in parallel. This results in a highly irregular parallel algorithm, because it contains subcomputations whose amount of work is not known in advance. Irregular parallel algorithms are complex from a parallel programming standpoint since the workload can only be distributed at runtime. Important subclasses of irregular algorithms include algorithms using *taskpools* and *speculative algorithms* (Guerraoui 2010). Our focus is on speculative algorithms[2]. Like any parallel algorithm, a speculative algorithm A is supposed to solve a problem P assuming a set of executions (or traces) M. By the characteristics of speculative algorithms the complexity of the path in A is supposed to be lower than its complexity in M, a serial component in A, Guerraoui (Guerraoui 2010). There are several possibilities to consider when writing a speculative algorithm of this kind of which we discuss only two.

Since the OpenMP 3.0 standard (OpenMP Architecture Review Board 2008) does not support forced thread cancellation, flagged thread cancellation is used in our first parallel algorithm, an approach proposed by Leopold (Süß & Leopold 2006). However, the lack of proper thread cancellation has a negative effect on the performance of the algorithm. Therefore we developed a second algorithm using Pthreads. Pthreads allows *forceful cancellation*, where a thread has the ability to cancel another thread from the outside. This type of cancellation runs the risk of memory leaks due to the fact that the canceled thread may not get the opportunity to clean up after itself. We will ignore this warning because there exists several ways to overcome this as will be elaborated on later.

This paper is arranged as follows. We depart with a description of thread parallelism and highlight the pitfalls of flagged and forced cancellation. The algorithms are then applied to a well-known design optimization problem; other problems were also considered, but are not provided in this paper. Finally the benefits that these methods have over existing sequential equivalents are summarized in the conclusion.

2 THREAD CANCELLATION ALGORITHMS

This section discusses the two parallel algorithms that are used in this paper. The first is the flagged thread cancellation algorithm and second is a forced thread cancellation algorithm.

2.1 *Thread cancellation using flags*

Tasks are called from within a parallel region, where the number of threads must be assigned before the start of the parallel region. This may be done anywhere in the serial code before the parallel region. In OpenMP parallel tasks are started using the SECTIONS directive. Each task nested within the SECTIONS directive is then executed once by each thread in the team.

Contained within each parallel task is an iterative check. Once any one of the solvers have completed, a flag is set with the appropriate task number. The iterative check will pick up that the value of the task number has changed and will immediately return from the task. If there has been no change in the flag value, the task continues until it itself returns. Since OpenMP does not include forceful thread cancellation, one must wait until all threads have attained the changed flag state and have exited successfully. This becomes a big problem when the size of each task iteration is highly irregular, as is often the case with different QP solvers.

Great care needs to be taken by the programmer to ensure that all flags are checked correctly. Human error could be encountered when using flags to indicate that the parallel region should be aborted. Problem-specific values that must be updated are flushed for each solver. However, this is important to ensure data conformity. If flags are not appropriately flushed, the program will most likely exhibit deadlock[3]. In OpenMP the sequence of barrier constructs must be the same for every thread in the team in order to exit correctly.

Since it is not possible to use language-level thread cancellation in OpenMP, flags are used to indicate when execution of a thread must halt. If flags are iteratively checked in competing threads and one of the competing threads is having difficulty during an iteration, the remaining set of threads must wait for a checkpoint to be reached in that thread. Even if all the other competing threads have completed, this thread may be detrimental to the overall performance of the algorithm. The information in this troublesome thread is not needed for further execution in our case, making forceful thread cancellation more effective.

2.2 *Forced thread cancellation*

POSIX is an acronym for Portable Operating System Interface. Although the acronym originated to refer to the original IEEE Standard 1003.1–1988, which was required after code portability became a concern for software developers. Thus, a standardized C language thread programming interface was specified for UNIX systems, namely the IEEE POSIX 1003.1c standard. Implementations that adhere to this standard are often also referred to as Pthreads. The POSIX standard has

[2] Speculation is the idea that the design of an algorithm follows an *if-then-else* control structure. The speculative path is the specific (expected) path of the algorithm which is executed. If the conditions are not met, a backup path is executed instead.

[3] A *deadlock* is a runtime situation that occurs when a thread is waiting for a resource that is never going to be available (Chapman, Jost, & Pas 2008. It is sometimes referred to as *software lock* or *soft lock*.

continued to evolve and undergo revisions. The latest version is known as IEEE Std 1003.1 (POSIX 2004).

Other than using on-node task communication via shared memory, such as MPI, the threads of a Pthreads process share the same address space, eliminating intermediate memory copy operations. Therefore, most memory operations are cache-to-CPU, or memory-to-CPU in the worst case scenario. This type of multithreading proves to be very effective when asynchronous requests need to be handled (Dongarra, Foster, Fox, Gropp, Kennedy, Torczon, & White 2003) on large server systems. For this reason Pthreads includes a thread cancellation library. However, Pthreads is highly platform dependent and is mostly aimed at codes written in C and C++, see (Barney 2008). We have therefore written wrapper functions for the needed C library functions in order to use them in our program which is written in FORTRAN.

Unfortunately, because we use wrapper functions for the use in our FORTRAN program, the cleanup functions that free the memory in canceled threads could not be implemented. These cleanup functions need to be called within the same lexical context (within the same brackets) as the parallel function and ensure memory conformity. This is an obvious problem for (official) modules. For our investigation we use these non-thread safe functions only to demonstrate the advantages. If the source codes were to be modified (rewritten in C) this would not be a problem.

In this implementation the competing processes are canceled, instead of setting flags, with a call to `thread_cancel(tid)` where supplying the appropriate thread-ID will cancel that thread no matter where the thread is in its execution process. This following section presents detailed results on solving a subproblem with both of the above mentioned methods.

3 RESULTS

The cam design problem (Dolan, More, & Munson 2004) is used to illustrate how solving the subproblems in parallel compares with solving the problems with the respective solvers in a serial application. The cam design problem has $3n+4$ constraints, where n is the number of design variables. Therefore, since the number of design variables and constraints are high, it is expected that the QP solvers will perform better for this problem.

Non-fatal errors are allowed for the subsolvers; for more information the reader is referred to the respective Warnings and Errors sections in the manuals. For the `l-BFGS-b` routine, only the error-(`msg`) value of 0 is allowed, for `E04NQF` `msg` $= 0, 5$ and for `LSQP` `msg` $= 0, -5$. The 5 and -5 errors are non-fatal, but indicate the presence of some numerical difficulties and 0 indicates that no errors were encountered. It is possible to restrict all warnings and errors, but for some problems this increases the execution time with little gain in accuracy. The capability to suppress errors is something that cannot be done during serial execution without aborting the routine.

3.1 *Cam design problem*

The cam design problem (Dolan, More, & Munson 2004) aims to maximize the area of a valve opening for one rotation of a convex cam, with constraints on the curvature and on the radius of the cam. Refer to Appendix A.1 for problem specific information and some tables showing the performance of the solvers in serial and the two parallel algorithms.

Below we show the iteration history of the cam design problem for one of the parallel algorithms, the problem size is $n = 2000$. Here we wish to illustrate the algorithm's ability to filter errors during execution. This can be seen in the last column of the iteration history where the first couple of iterations return with error state 5. Figure 1 shows the execution times for the respective solvers and parallel algorithms on a log-scale graph. Here we see that our parallel algorithm with forced thread cancellation executes faster than the slowest solvers, but never faster than the fastest solvers. This may be attributed to the overheads of spawning and cancelling new threads or waiting for flags to be set. We left the serial-`l-BFGS-b` solver out of the plot as it fails for problem sizes within the range where we are testing. The flagged thread cancellation algorithm does well but suffers from long wait times because flags cannot be checked.

Another desirable quality of using solvers in parallel is that the algorithms follow the shortest execution path. Please refer to tables 1 through 5. After inspecting k^* and l^* in the tables, which indicate the amount of outer and inner iterations respectively, one can clearly see the dominance of the parallel algorithms. The parallel algorithms tend to converge faster and with much less computational effort. The presence of inner iterations indicate that the solver is struggling to reach the required accuracy in the solution.

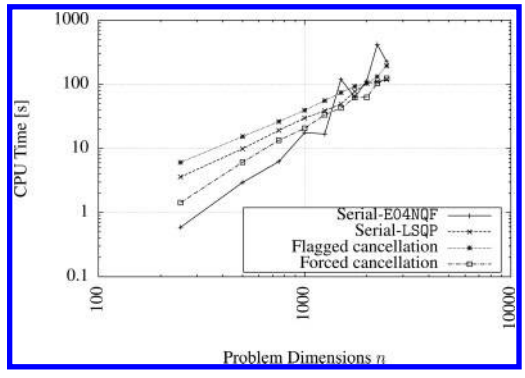


Figure 1. Maximization problem for the area of a valve opening for one rotation of a convex cam and solved using dual and QP solvers in both serial and parallel.

For some solvers the execution times vary abruptly when problem size is increased as the serial-E04NQF routine in Figure 1 depicts. This behaviour is not reflected in the parallel algorithms, when threads are forcefully canceled or when flags are checked in regular intervals.

Iteration history for cam design problem SAOi algorithm

Outer	...	ActHi	ActC	Message
0				
1	...	0	2140	5 E04NQF
2		0	2221	5 E04NQF
3		1	2000	5 E04NQF
4	...	4	2303	5 E04NQF
5		2	2476	5 E04NQF
6		37	2596	0 E04NQF
7		128	2596	0 LSQP
8	...	128	2596	0 LSQP
		n = 2000		

4 CONCLUSION

A parallel SAO method was created to show that it is beneficial to solve subproblems with multiple solvers in parallel. The source code for some of these solvers were not available, therefore, flags could not be checked regularly using the flagged thread cancellation routine. Without the ability of flagged thread cancellation to check the flags at sufficiently short intervals the algorithm waits unnecessarily for slow routines to check the required flags. To overcome this deficiency, a similar parallel algorithm was written to forcefully cancel these slow threads. This method is not thread safe, and is only used to show how the parallel algorithms would perform, if flags could be checked regularly.

These parallel algorithms present several desirable properties. The first is the ability of the parallel algorithms to filter out selected errors. If one solver does not return a good enough answer, it is likely that one of the others will. There is no way to do this with a serial program.

Secondly, the parallel algorithms follow the most efficient search path, resulting in the number of iterations needed by the parallel algorithms to complete being generally less than those of the serial algorithms. This property is very desirable in FEM and/or CFD programs, as many function evaluations are done between these iterations. Therefore, when the number of iteration steps is reduced, the performance of these FEM and CFD models will increase substantially.

Thirdly, the parallel algorithms tend to be almost as fast as the most effective serial routines for a greater range of problems, accounting for overheads and provided that flags are checked regularly. There is therefore no need for the user to tune a specific algorithm to his problem to get a result in as short a time as possible, which eliminates the re-running of programs.

Finally, parallel algorithms are more stable than serial algorithms because solvers that suffer from numerical errors are simply ignored. The results therefore tend to be more accurate than those of individual serial routines.

In conclusion, the proposed parallel methods are very promising alternatives when the problem types to be solved are not known in advance. Thus, by performing two (or more) evaluations in parallel and terminating the competing thread whenever a viable solution is returned, we ensured that the most effective solver is used for the solution of the subproblem at each approximation of an SO algorithm. This softens the implications of the classic NFL theorem by eliminating the need for user interaction in tuning or selecting the best solver for any problem.

4.1 *Future work*

These parallel algorithms present the opportunity for further investigation. The first would be to create stable thread-safe solvers which allow flags to be checked regularly, or the development of thread cancellation libraries for different programming languages.

Single precision solvers which are on average two times faster than double precision routines now become a viable method for solving nonlinear optimization subproblems. By adjusting the desired precision of the solution, single precision solvers may be used during the initial iterations and only updated to double precision during the final iterations. If any of the single precision routines fail to return a viable solution, the double precision routines take over.

The inclusion of single precision routines lend the ability to use single precision arithmetic on GPUs. This should show considerable speedups.

Finally, several different solvers may be added in parallel which might produce interesting results.

REFERENCES

Barney, B. (2008). POSIX Threads Programming.

Byrd, R., P. Lu, J. Nocedal, & C. Zhu (1995). A limited memory algorithm for bound constrained optimization. *SIAM Journal of Scientific Computing 16*, 1190–1208.

Chapman, B., G. Jost, & R. V. D. Pas (2008). *Using OpenMP: Portable Shared Memory Parallel Programming*. MIT Press.

Dolan, E. D., J. J. More, & T. S. Munson (2004, November). Benchmarking optimization software with COPS. Tech. Report ANL/MCS-246, Mathematics and Computer Science Division, Argonne National Laboratory, IL.

Dongarra, J., I. Foster, G. Fox, W. Gropp, K. Kennedy, L. Torczon, & A. White (2003). *Sourcebook of Parallel Computing*, Chapter Part III, pp. 852. Morgan Kaufmann Publishers.

Droste, S., T. Jansen, & I. Wegener (2002). Optimization with Randomized Search Heuristics – The (A)NFL Theorem,

Realistic Scenarios, and Difficult Functions. *Theoretical Computer Science 287*, 131–144.

Gould, N., D. Orban, & P. L. Toint (2004). GALAHAD, A library of thread-safe Fortran 90 packages for large-scale nonlinear optimization. *ACM Transactions on Mathematical Software (TOMS) 29*, 353–372.

Guerraoui, R. (2010). Foundations of speculative distributed computing. In *Workshop on Distributed Algorithms/International Symposium on Distributed Computing*, pp. 204–205.

NAG Library Manual, Mark 22 (2009). *E04NQF NAG Library Manual*. Oxford: The Numerical Algorithms Group Ltd.

OpenMP Architecture Review Board (2008). OpenMP Application Program Interface. Technical report, OpenMP Architecture Review Board.

POSIX (2004). *IEEE Standard for Information Technology: Portable Operating System Interface (POSIX) Base Definitions*. IEEE Computer Society Press. IEEE Standard.

Süß, M. & C. Leopold (2006). Implementing irregular parallel algorithms with OpenMP what's missing and how to solve it. Technical report, University of Kassel, Research Group Programming Languages / Methodologies, Wilhelmshöher Allee 73, D-34121 Kassel, Germany.

Wolpert, D. & W. Macready (2005). Coevolutionary Free Lunches. *IEEE Transactions on Evolutionary Computation 9*(6), 721–735.

Zhu, C., R. Byrd, P. Lu, & J. Nocedal (1994). L-BFGS-B: FORTRAN subroutines for large scale bound constrained optimization. Technical Report NAM-11, Northwestern University, EECS Department.

A PROBLEMS AND TABLES

A.1 *Cam design problem*

The cam design problem (Dolan, More, & Munson 2004) aims to maximize the area of a valve opening for one rotation of a convex cam, with constraints on the curvature and on the radius of the cam. The cam design problem has $3n + 4$ constraints, where n is the number of design variables. Since the optimal cam shape is symmetric, one considers only half of the design angle. The tables of results for this problem are listed below. The tables start with the serial solvers and end with the routines where the solvers are used in parallel.

In the tables, n indicates the number of design variables, m the number of constraints, k^* indicates the number of outer iterations, and l^* the number of inner iterations. The optimal function values are indicated with f^*, where h^* and r^* respectively indicate the maximum constraint violation and KKT-condition of the result. CPU is the real execution time.

Table 1. Serial execution of cam design problem–`l-BFGS-b`.

n	k^*	l^*	f^*	h^*	r^*	CPU
2	6	49	−4.785	1.37×10^{-05}	3.33×10^{-04}	0.05
4	6	31	−4.542	1.18×10^{-06}	1.56×10^{-04}	0.28
6	9	72	−4.451	5.45×10^{-05}	6.15×10^{-04}	2.91

Table 2. Serial execution of cam design problem–`E04NQF`.

n	k^*	l^*	f^*	h^*	r^*	CPU
250	9	0	−4.277	8.88×10^{-16}	3.04×10^{-08}	0.59
500	9	0	−4.275	1.51×10^{-14}	3.38×10^{-09}	2.96
750	9	0	−4.274	2.49×10^{-14}	3.74×10^{-09}	6.25
1000	11	5	−4.274	9.93×10^{-12}	3.28×10^{-02}	17.68
1250	9	0	−4.274	4.07×10^{-12}	2.85×10^{-02}	16.76
1500	23	28	−4.274	5.90×10^{-12}	3.08×10^{-02}	119.06
1750	13	5	−4.274	3.18×10^{-12}	2.68×10^{-02}	62.82
2000	22	4	−4.273	2.18×10^{-12}	2.19×10^{-02}	112.47
2250	38	42	−4.273	2.14×10^{-12}	2.64×10^{-02}	416.71
2500	20	13	−4.273	1.79×10^{-12}	3.21×10^{-02}	224.90

Table 3. Serial execution of cam design problem–`LSQP`.

n	k^*	l^*	f^*	h^*	r^*	CPU
250	13	0	−4.277	3.36×10^{-13}	2.07×10^{-08}	3.60
500	14	0	−4.275	1.91×10^{-14}	2.17×10^{-08}	9.92
750	15	0	−4.274	7.64×10^{-14}	5.87×10^{-08}	19.11
1000	15	0	−4.274	1.37×10^{-13}	3.00×10^{-07}	29.78
1250	15	0	−4.274	3.96×10^{-13}	6.42×10^{-08}	38.78
1500	15	0	−4.274	2.01×10^{-13}	1.14×10^{-06}	49.30
1750	16	1	−4.274	3.94×10^{-13}	1.50×10^{-07}	77.21
2000	16	0	−4.273	6.31×10^{-13}	7.18×10^{-08}	103.89
2250	16	0	−4.273	5.79×10^{-13}	3.46×10^{-07}	109.45
2500	16	0	−4.273	9.03×10^{-13}	2.27×10^{-07}	119.08

Table 4. Flagged thread cancellation for cam design problem.

n	k^*	l^*	f^*	h^*	r^*	CPU
250	9	0	−4.277	8.88×10^{-16}	3.04×10^{-08}	6.06
500	9	0	−4.275	1.91×10^{-14}	9.63×10^{-09}	15.33
750	9	0	−4.274	7.37×10^{-14}	5.74×10^{-08}	26.22
1000	9	0	−4.274	1.38×10^{-13}	3.00×10^{-07}	39.37
1250	9	0	−4.274	3.97×10^{-13}	2.25×10^{-08}	55.52
1500	9	0	−4.274	2.02×10^{-13}	2.73×10^{-07}	74.21
1750	9	0	−4.274	3.97×10^{-13}	7.22×10^{-08}	92.85
2000	8	0	−4.273	5.57×10^{-13}	8.53×10^{-07}	103.15
2250	9	0	−4.273	5.77×10^{-13}	6.85×10^{-08}	131.35
2500	10	0	−4.273	4.58×10^{-13}	5.03×10^{-07}	194.39

Table 5. Forced thread cancellation for cam design problem.

n	k^*	l^*	f^*	h^*	r^*	CPU
250	9	0	−4.277	8.88×10^{-16}	3.04×10^{-08}	1.43
500	9	0	−4.275	1.91×10^{-14}	9.63×10^{-09}	6.10
750	9	0	−4.274	7.37×10^{-14}	5.74×10^{-08}	13.41
1000	9	0	−4.274	1.38×10^{-13}	3.00×10^{-07}	20.58
1250	9	0	−4.274	3.97×10^{-13}	2.25×10^{-08}	33.50
1500	9	0	−4.274	2.01×10^{-13}	1.02×10^{-07}	42.72
1750	9	0	−4.274	3.97×10^{-13}	7.22×10^{-08}	62.16
2000	8	0	−4.273	5.57×10^{-13}	8.53×10^{-07}	62.41
2250	9	0	−4.273	5.78×10^{-13}	4.79×10^{-08}	103.21
2500	9	0	−4.273	4.58×10^{-13}	5.03×10^{-07}	124.08

Research and Applications in Structural Engineering, Mechanics and Computation – Zingoni (Ed.)
© 2013 Taylor & Francis Group, London, ISBN 978-1-138-00061-2

Exploring the domain of application of adaptive structures

Gennaro Senatore
Civil Environmental & Geomatic Engineering UCL, Expedition Engineering

Philippe Duffour
Civil Environmental & Geomatic Engineering, UCL

Pete Winslow
Expedition Engineering

Sean Hanna
Bartlett School of Architecture, UCL

Chris Wise
Civil Environmental & Geomatic Engineering, UCL – Expedition Engineering

ABSTRACT: A new design methodology for adaptive structures was presented in a companion paper. In it, it was shown that active control can lead to significant whole life energy savings when the design is governed by rare but strong loading events. In this paper a systematic exploration is presented of the domain in which adaptive two-dimensional pin-jointed cantilever and simply supported trusses are beneficial in terms of whole life energy savings and monetary costs. This exploration took three directions. First, the influence of the ratio of live load over dead load was investigated for various spans. Second the aspect ratio of the truss (span to depth) was varied. It is shown that that the biggest percentage energy savings remain substantial for the whole solution domain reaching maxima from small/medium span structures. However, considering the outcome of monetary cost analysis it reveals that adaptive structures only become cost effective for medium/high span structures. Third the results from both studies are combined and an optimal region where adaptive structures are both energy and cost effective is identified.

1 INTRODUCTION

1.1 *Understanding the domain of applications for adaptive structures*

The potential of active control for structures to be more energy efficient has received little attention (Korkmaz, 2011). Actuation itself consumes energy therefore any investigation into using active control to save material in structures must account for the total energy spent throughout the life of the structure: the embodied energy as well as the operational energy necessary for actuation. In a companion paper (Senatore, et al., 2013) a design methodology for adaptive structures was presented and it was shown how active control can be used to bring significant total energy savings in discrete structural assemblies (pin-jointed trusses). In this methodology, the structures were subjected to a dead as well as a randomly fluctuating live load.

The procedure consists of two nested optimization processes. The inner optimization starts by designing a minimum weight structure by first ignoring compatibility. Compatibility is then satisfied by strategically replacing some members by actuators whose length changes can manipulate actively the internal flow of internal forces and deflection. The hybrid passive-active structural system is designed so that in normal loading conditions it can take the load using its passive capacity and actuators locked into position. If a change in the loads causes a state of stress that violate an ultimate limit state (ULS) constraints, internal load path redirection is performed by the active system. Also in the event of very high level of loads above the activation threshold, it can rely on the full active load-bearing capacity to provide for displacement correction. In this way passive resistance (through material and form) is replaced with operational energy. By looping over different values of the material utilization factors, the load activation threshold can be adjusted. Figure 1 show how the total energy, made up of embodied and operational energy reaches a minimum as the MUT is changed from 100% (fully active) to 25% (passive design). This process allows a design that minimizes the total energy to be found. It is implemented as multi-objective optimization routine using non-linear programming and variational analysis. The methodology applied to simply supported and cantilever trusses

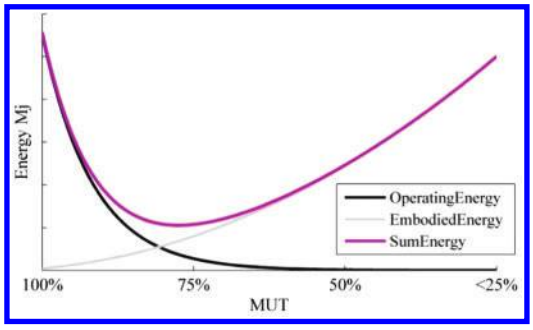


Figure 1. Whole-life energy vs. degree of adaptation.

achieves whole life energy savings (considering 50 years life time) of 55% and 70% respectively (Senatore et al., 2013). However those conclusions were reached by making a number of assumptions. The purpose of this paper is to find out how robust the energy savings achieved are as some of the assumptions made are examined critically and the input parameters used are varied systematically.

1.2 *Built-in assumptions and performance metrics*

First it is necessary to list those assumptions. It is assumed throughout that idealized linear motors are used with a mechanical efficiency set to a low level (50%). This is a conservative value as the mechanical efficiency of such motors is usually around 80% (Sclater et al., 2011). The maximal operational frequency is set at 5 Hz. This is the upper natural frequency that will dominate the response of most structures excited by wind, earthquakes or pedestrians. A higher frequency means higher operational energy so assuming a high value does not favors active technology.

The operational energy needed to power the sensors and control system is considered negligible compared to the work done by the active elements. Sensors generally need low power inputs (usually around 1 W) to operate (Culshaw, 1996) and many strain sensors do not need any power at all. This means that the whole control system can stay in "hibernate" mode consuming very little for most of the life of the structure. When the sensors detect higher internal stresses or strains then the control system is activated. Generally the occurrence of severe loads is expected to be less than the 5% of the life-cycle of a building (Culshaw, 1996). Assuming a value of 100 W for the power needed by the control system (similar to the power needed by a modern 4-core PC) in operational mode (5% of the total time), the energy consumption due to the control system would equal 200–300 kg of steel (conversion obtained using the Inventory of carbon and energy (Hammond & Jones, 2008)) over the design life of the structures (50 years). This additional penalty can be neglected for most cases except for very small structures (for instance span lower than 8 meters) where the absolute savings in terms of mass becomes comparable with the loss of energy due to power the control system.

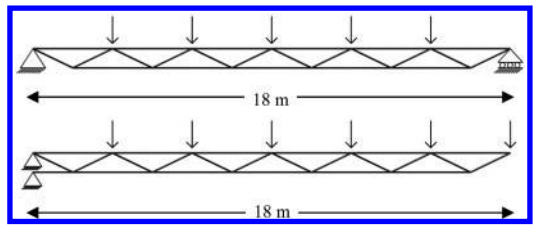


Figure 2. Sample for simply supported and cantilever case.

1.3 *Parametric exploration*

The parametric study presented in this paper will three main directions:

1. It studies the influence of the ratio of the live load over the dead load vs. the length of the span.
2. A simplified cost analysis will be carried out to check to which extent the energy saving made translate into monetary savings.
3. The main geometrical features such as span and span to depth ratio of the trusses are varied to study the importance of the shape of the structure.

Results from the three strands will be combined in order to identify an optimal region where adaptive structures are most effective in terms of both energy and monetary savings.

2 LIVE TO DEAD LOAD V. SPAN

2.1 *Settings*

In this section the performances of a cantilever and a simply supported pin-jointed determinate truss beam are studied when the ratio of live to dead load is varied from 0 to 2. The performances in terms of energy savings will in general depend on the particular type of topology chosen. However, in the companion paper it was shown that when two comparable trusses, one determinate and the other indeterminate are optimized through the proposed methodology, the total energy savings achieved through optimum actuation in both structures are in fact very similar. Therefore the sensitivity study to the live to dead load ratio is limited to determinate topologies.

The span of the trusses is varied from 18 m to 126 m for the simply supported truss and from 9 m to 63 m for the cantilever. The ratio between the span and the depth (height) of the trusses is kept constant at 30. The dead load is set to 3 kN/m^2 on the roof panel and each truss supports a 10 m wide span of roof resulting in a UDL of 30 kN/m for each truss. Fig. 2 shows one example from the range of structures tested for both the simply supported and cantilever case.

The live load is modeled using parameterized log normal distributions. Their mean is set to 10% percent of the maximum expected load. In this way, the higher

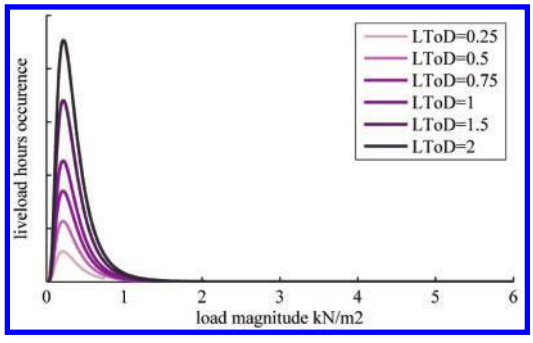


Figure 3. Live load distributions.

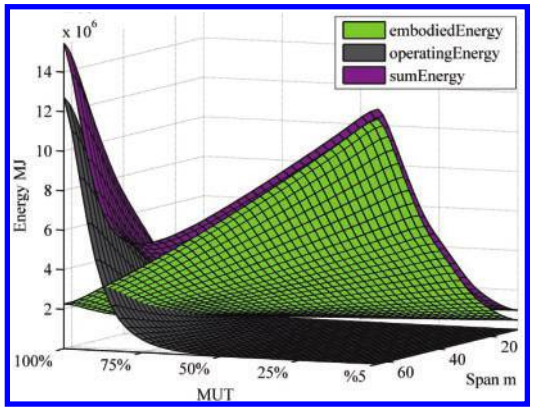


Figure 4. Embodied-Operational energy | liveToDead = 0.75.

the live to dead load ratio, the stronger and rarer the max expected load while the lower level of loads have higher occurrence. Fig. 3 shows the log-normal distribution for a live to dead ration ratio varying from 0.25 to 2.

All the adaptive trusses are compared with their passive version which is optimized using the non-linear technique described in the companion paper.

2.2 *Energy analysis*

The first set of simulations focuses on the simply supported case. Fig. 4 is a 3D plot showing the total energy (embodied + operational) against varying MUT (material utilization factor) and span. For the particular simulation shown here the live to dead load ratio was set to 0.75. For each span at different live to dead load ratios, a global optimum of the total energy can found. This plot is a straightforward three dimensional extension of the graph shown in Fig. 1.

For clarity, the same data is shown again in fig 5 as a colored contour map. The almost horizontal black line shows the locus of the optimal MUT for each span.

Generally, the performances of adaptive structures in terms of energy savings are at their highest when the passive design is stiffness-governed i.e. when the size of the members is controlled by deflection limits rather than strength. In fact, as the live to dead load increases

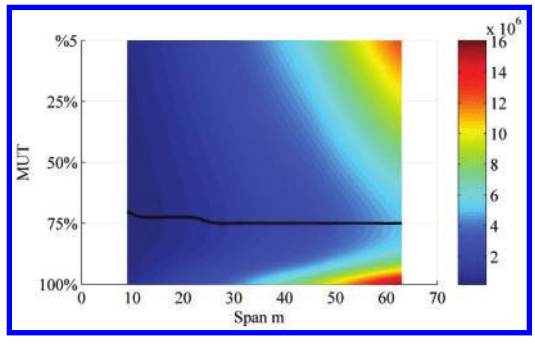


Figure 5. Total energy | live to dead ratio = 0.75.

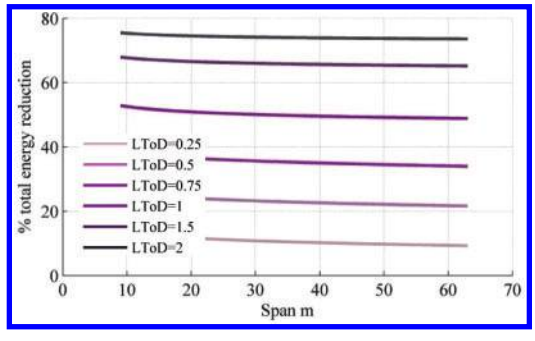


Figure 6. Percentage energy savings cantilever.

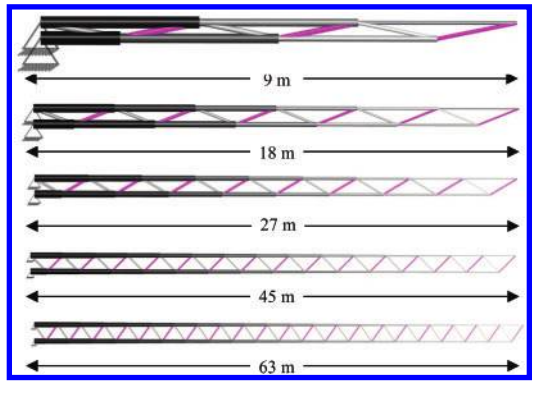


Figure 7.

so do the energy savings (Fig. 6). While the span and live to dead load ratio are varied, the ratio between span and depth is kept constant. For this reason the energy savings in percentage in terms are very similar for different spans which are at the same live to dead load ratio. However there is a slight decrease in energy saving as the span increases (Fig. 6).

This decrease is due to the fact that the width of each bay is kept constant at 3 m thus becoming deeper (more structurally efficient) as the span increases. There is therefore less to be saved from the passive structures as the span increases. Fig. 7 shows the optimized adaptive trusses at different spans at live to dead load ratio equals to 1.

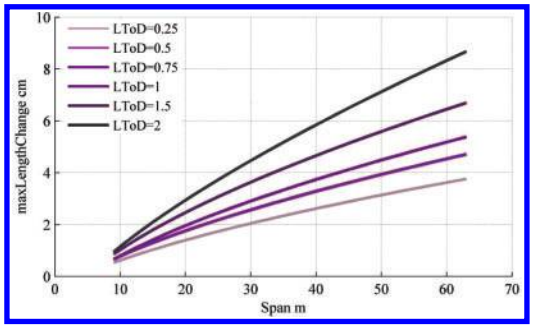


Figure 8. Max actuators' length change.

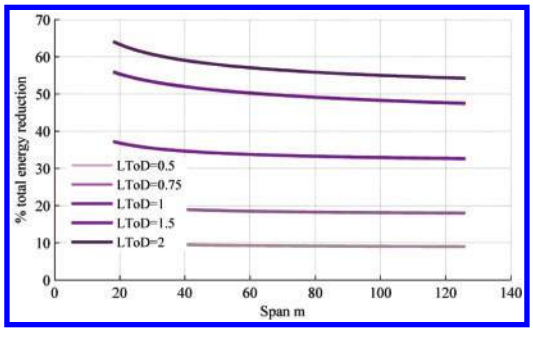


Figure 9. Energy percentage savings simply supported.

Fig. 8 shows that the actuator length changes remain small (always less than 10 cm) even for very long spans (up to 63 m) which experience large tip deflections and high live to dead load ratios.

This is possible as the coordinated small length changes of the actuators manage to achieve an effective control of the structures.

Fig. 9 shows the percentage energy savings for the simply supported case. Note that, although similar percentage energy savings are achieved, the span of the trusses has doubled.

2.3 *Monetary costs analysis*

An adaptive truss structure is made of sensors (strain gauges), structural steel, actuators and the control system. The cost of sensors (strain gauges) actuators and the control system are mainly dependent on the type of technology adopted. Electric linear motors and hydraulic are the most commonly used technologies for actuation. The most important characteristics affecting the cost of an actuator are the stroke length, the max static and dynamic force and the duty cycle. Strain gauges are cheap; their cost is therefore neglected from the model. The cost of construction material (structural steel for this case) depends on the type of building. The assumptions made in this study are:

- The actuator cost is set to £2000/unit. This is the average cost of a hydraulic cylinder with a push/pull load of 100 tons (Rexoth, 2013) (Hydrover, 2013).

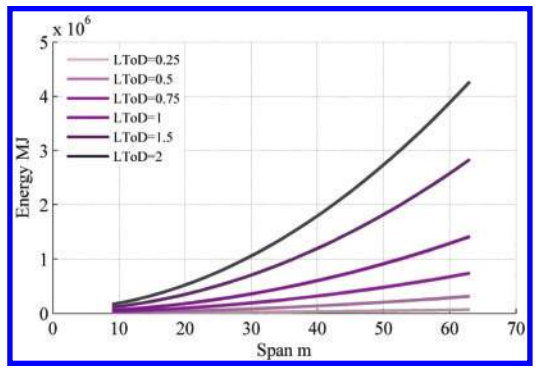


Figure 10. Embodied energy difference (passive-adaptive).

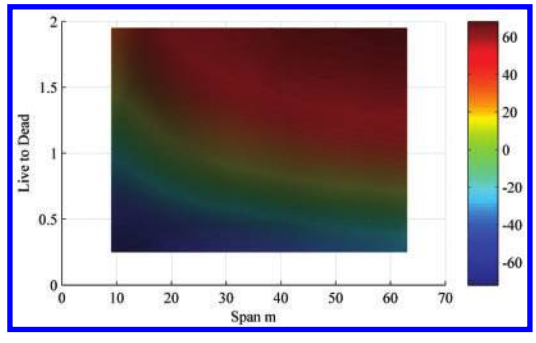


Figure 11. Cost savings adaptive vs. passive cantilever.

The latter is an average value for the internal forces considered for the both the cantilever and simply supported trusses;

- The cost of the control system mainly depends on the number of channels necessary to gather data from the sensors and input signals to the actuators. The average cost for both a single dual channel strain gauge amplifier and actuator control board is £200 respectively (Fylde, 2013); (RobotEq, 2013);
- the cost of steel per tonnage is set to £ 3000/tonnage (TATA Steel, 2012);
- The maintenance for the actuators is assumed to happen once per year involving a technician taking a full-day to inspect 5 actuators. The cost of one inspector is 500£ per day;

Unlike the percentage of energy savings (Fig. 6), the energy difference in absolute terms increases with the span. This means that the gap between the embodied energy (or mass) of the passive and the adaptive structure become very large for longer span (Fig. 10).

For long spans, the large difference in mass between the adaptive and the passive structure outweighs the additional expenditure for sensors, actuators and control systems as shown in fig 11 which compares the percentage monetary cost savings for the adaptive and the passive designs. Note that below a live to dead load ratio of 0.75, cost savings are negative even for long spans (from green to blue).

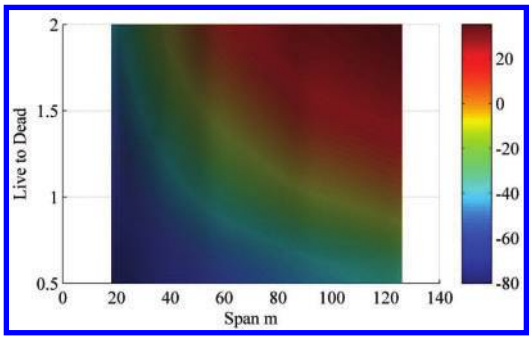


Figure 12. Percentage cost savings simply supported.

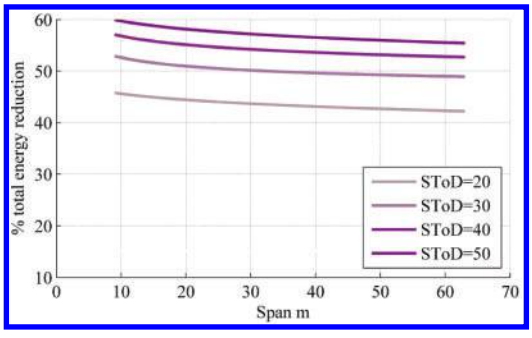


Figure 13. Energy percentage savings cantilever case.

Similar results are obtained for the simply supported case (fig. 12). However in that case the area where the adaptive trusses are cost effective compared to the passive ones is reduced (green to red area).

3 SPAN TO DEPTH VS. SPAN

3.1 *Energy analysis*

In the next set of simulations, the influence of the span to depth ratio on the performances of adaptive structures is investigated. The setting described in section 2 holds except that this time the live to dead load ratio is kept constant and equals to 1. The span to depth ratio is varied from 20 to 50 going from deep to very slender configurations.

The performances of the adaptive structures in terms of energy savings against span and span to depth ratio are plotted in fig. 13 for the cantilever case.

As observed in section 2, the percentage savings remain very similar along the span axis while the increase substantially as the span to depth ratio increases. Similar results are obtained for the simply supported case. Fig. 14 shows simply supported adaptive trusses with identical spans but different span to depth ratio.

Because the ratio of live to dead load is constant, in this case it is possible to show the variation of the activation threshold which goes from being very close to the maximum expected load for deep trusses to much lower value for slenderer configurations.

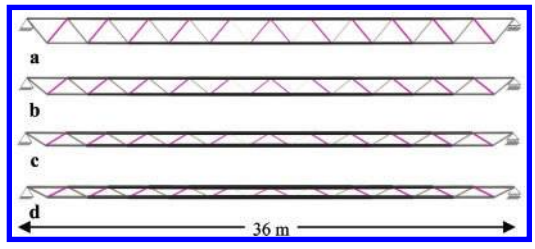


Figure 14. a) StoD = 20; b) StoD = 30; c) StoD = 40; d) StoD = 50.

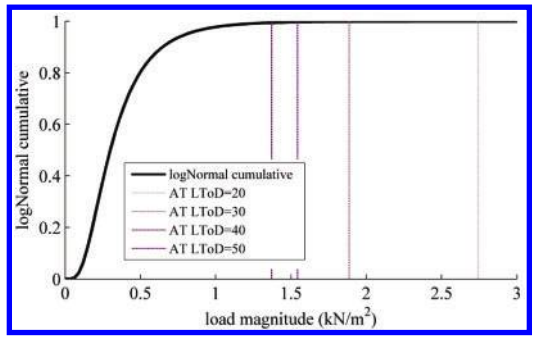


Figure 15. Load activation threshold variation for different span to depth ratios.

As seen previously, the maximum length change of the actuators does not exceed 20 cm even for very slender trusses (span to depth of 50).

3.2 *Monetary costs analysis*

A similar cost analysis to that done for live to dead load variation was carried out for the span to depth ratio variation. The conclusions are similar to both for the cantilever and simply supported beam.

4 CONCLUSIONS: OPTIMAL REGION OF THE SOLUTION DOMAIN

In order to determine the boundaries of the region where adaptive structures of the type studied here bring the most benefit, the results obtained so far must be combined. To do this, the percentage energy savings are first filtered through cost savings test. If the active design costs more than the passive one, the active design is assigned a score of 0 (i.e. no energy savings are considered). Then positive costs savings and energy savings are averaged thus forming a unique value for each span and live to dead load ratio for the cantilever (fig. 16) and simply supported case (fig. 17). In this way it is possible to identify an optimal region where adaptive structures are effective in terms of both energy and monetary cost savings.

The curves in the graphs show how the fronts of these optimal regions change for different span to depth ratio. The optimal region tends so to cover larger

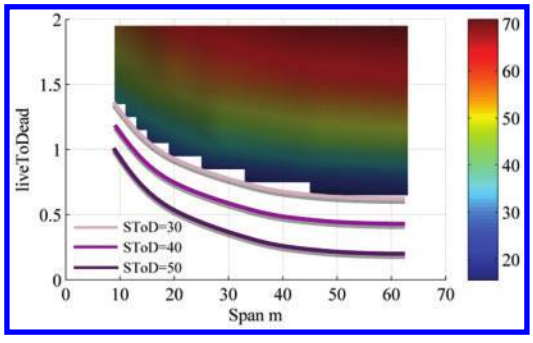


Figure 16. Optimal region cantilevers.

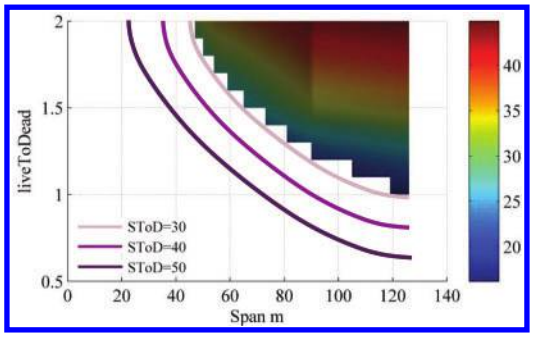


Figure 17. Optimal region simply supported.

area of the solution domain as the span to depth ratio increases.

Fig 16 and 17 are consistent. This means that for the two classes of structures studies in this paper, the conclusion is similar: adaptive structures are most beneficial both in energetic and monetary terms for long span structures where the live load is larger than the dead load. However, as the slenderness of the structure increases, adaptive structures become both energy and cost effective even at medium/small spans. This is broadly the type of structures that are stiffness governed.

ACKNOWLEDGEMENT

This work could not have been carried out without funding from the UK Engineering and Physical Sciences Research Council (EPSRC) as well as financial and technical support from Expedition Engineering. Their help is greatly appreciated.

BIBLIOGRAPHY

Fylde, 2013. *Fylde Modular Instrumentation*. [http://www.fylde.com/ [Accessed 3 March 2013].

Hammond, G. & Jones, C., 2008. *Embodied Energy & Carbon*, Bath: University of Bath.

Hydrover, H., 2013. *Position-Sensing Smart Hydraulic-Cylinders*. http://www.hycoglobal.com/Position-Sensing-Smart-Hydraulic-Cylinders.php [Accessed 3 March 2013].

Korkmaz, S., 2011. A review of active structural control: challenges for engineering informatics. *Computers and Structures*, Volume 89, pp. 2113–2132.

Rexoth, B., 2013. *Bosch Rexoth Industrial Hydraulics*. http://www.boschrexroth.co.uk/country_units/europe/united_kingdom/en/products_solutions/industrial_hydraulics/product_specials/downloads/rd17334_CDH_2.pdf

RobotEq, 2013. *NxtGen Brushed DC Motor Controllers*. [http://roboteq.com/brushed-dc-motor-controllers/nxtgen-controllers-selector [Accessed 3 March 2013].

Senatore, G. et al., 2013 . *Designing adaptive structures for whole life energy savings*. Cape Town, s.n.

TATA Steel, 2012. *Sections Publications*. http://www.tatasteeleurope.com/en/products_and_services/products/long/sections/sections_publications/ [Accessed 18 March 2013].

Hammond, G. & Jones, C., 2008. *Embodied Energy & Carbon*, Bath: University of Bath.

Research and Applications in Structural Engineering, Mechanics and Computation – Zingoni (Ed.)
© 2013 Taylor & Francis Group, London, ISBN 978-1-138-00061-2

Effect of serviceability limits on optimal design of steel portal frames

T.D. Phan & J.H. Lim
Department of Civil Engineering, Universiti Tunku Abdul Rahman, Petaling Jaya, Malaysia

J.B.P. Lim & W. Sha
SPACE, Queen's University Belfast, Belfast, UK

T.T. Tanyimboh
Department of Civil Engineering, University of Strathclyde, Glasgow, UK

M. Dundu
Department of Civil Engineering, University of Johannesburg, Johannesburg, South Africa

ABSTRACT: The design of hot-rolled steel portal frames can be sensitive to serviceability deflections. In such cases, in order to reduce frame deflections, practitioners can increase the size of the haunch and/or the sizes of the steel standard sections used for the column and rafter members of the frame. This paper investigates the effect of such serviceability deflection on the optimal design of steel portal frames, using evolutionary algorithms that optimizes frame weight, taking into account both ultimate as well as serviceability limit states. The results show that heuristic search methods, namely, real-coded and real-coded niching genetic algorithms are efficient and reliable. The niching strategy results in a 66.7% reduction in the computational time. It is shown that serviceability deflections, as recommended by the Steel Construction Institute, govern the design of a 30 m span portal frame, where material cost increases by 27% compared to an ultimate limit state design only.

1 INTRODUCTION

It is estimated that 50% of all constructional steelwork in the UK is used for the primary framework of single-storey buildings. Within this major market sector, the hot-rolled steel portal frame has become the most common structural form in pitched roof buildings (see Figure 1), because of its economy and versatility for a wide range of spans (Lim and Nethercot 2003, Salter *et al.* 2004, Phan *et al.* 2011, and Wrzesien *et al.* 2012).

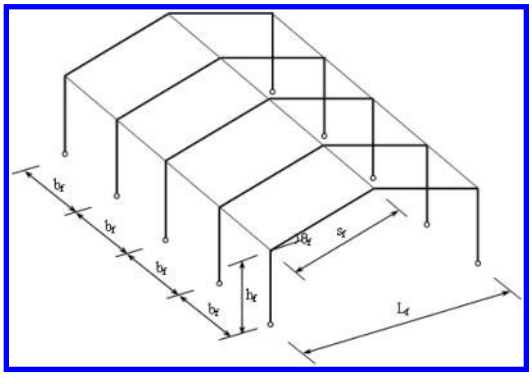


Figure 1. Parameters used to define portal framing system.

In this paper, the serviceability limit state requirements for steel portal frames, as recommended by the Steel Construction Institute (SCI), are used for the frame design; these limits are proposed in order to avoid problems of tearing in cladding fixings, due to differential deflections in between adjacent frames (SCI Advisory Desk AD-90 2010). In addition, less stringent deflection limits, as recommended by practitioners in industry, are also considered. These deflection limits are shown in Table 1. This paper investigates the effect of such deflection limits on the optimal design of hot-rolled steel portal frames using heuristic search techniques, namely, real-coded genetic algorithm (RC-GA) and real-coded niching genetic algorithm (RC-NGA).

Using the proposed optimal algorithms, the frame weight per unit area on plan of the building is minimized through selecting the most appropriate steel standard cross-section (i.e. Universal Beam Section) for the columns and rafters of frame, as well as the size of eaves haunch, by designing the frame to both ultimate and serviceability limit states (Phan *et al.* 2013a).

In this paper, the frame is designed to the ultimate limit state with two design procedures, either rigid-plastic or elastic design methods. It is shown that serviceability deflections, as recommended by the

Table 1. Deflection limit for steel portal frames

	SCI recommendations		Industry suggestions	
	Absolute deflection	Differential deflection	Absolute deflection	Differential deflection
Lateral deflection at eaves	$\leq \frac{h_f}{100}$	$\leq \frac{b_f}{200}$	$\leq \frac{h_f}{100}$	$\leq \frac{h_f}{150}$
Vertical deflection at apex	–	$\leq \frac{b_f}{100}$ and $\sqrt{b_f^2 + s_f^2}/125$	–	$\leq \frac{L_f}{200}$

Steel Construction Institute, govern the design of a 30 m span portal frame, with material cost increasing by 27% compared to an ultimate limit state design alone.

2 OPTIMIZATION PROBLEM FORMULATION

2.1 *Frame description*

Details of the frame used for the benchmark design example are shown in Figure 2; the geometry of the frame and section sizes for the column and rafter are taken from a worked example in an SCI guide on steel portal frame design (Salter *et al.* 2004).

As can be seen in Figure 2, Benchmark Frame has a span of 30 m, height-to-eaves of 7 m, and pitch of 6°; other parameter for the building topology is the distance between adjacent frames (b_f) of 6 m. In the design of the Benchmark Frame, it can be seen that the eaves haunch length is taken as 10% of the frame span and uses the same section size as the rafter section. It is assumed in this paper that side rails and purlins are placed close enough on the columns and rafters to prevent lateral torsional buckling.

2.2 *Frame loads*

The dead load (DL) and live load (LL) acting on the Benchmark Frame are 0.66 kN/m^2 and 0.6 kN/m^2, respectively. Under such loads, the frame should be checked under the following ultimate load and serviceability load combinations as follows:

$$\begin{aligned} &\text{ULC1} = 1.4\text{DL}+1.6\text{LL} \\ &\text{SLC1} = 1.0\text{DL}+1.0\text{LL} \\ &\text{SLC2} = 1.0\text{LL} \end{aligned} \tag{1}$$

It is worth noting that SLC1 is applied to determine the absolute deflection, whilst SLC2 is for differential deflections (see Table 1).

2.3 *Frame analysis and design*

In this paper, the Benchmark Frame is designed to the ultimate limit state using either rigid-plastic or elastic design methods. The internal forces, namely, axial forces, shear forces, and bending moments at the critical sections are determined in order to carry out the member checks. For instance, the columns, rafters and eaves haunches are checked for local capacity under shear, axial, or moment capacity, and combined

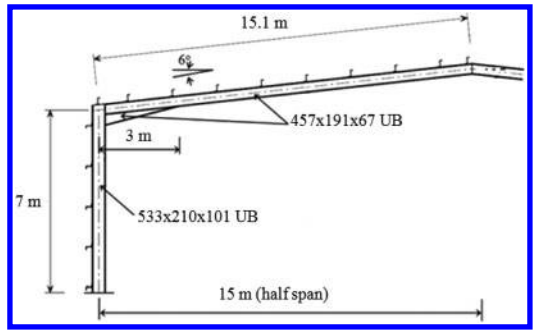


Figure 2. Details of Benchmark Frame (Salter *et al.* 2004).

moment and axial force. Frame deflections at the eaves and apex are determined from elastic frame analysis.

Comparing the two serviceability requirements to the Benchmark Frame, the vertical deflection at the apex of the SCI recommendations is 60% more stringent than that from industry suggestions.

2.4 *Weight function and design constraints*

The objective of the overall design optimization is to determine the portal frame having the minimum steel material weight, whilst satisfying the design requirements. The objective function can be expressed in terms of the weight of the primary members per square meter of the plan as follows:

$$\text{Minimize W} = \frac{1}{L_f b_f}\left(\sum_{i=1}^{m} w_i l_i + \sum_{j=1}^{n} w_{hj}\right) \tag{2}$$

where W = weight of frame; w_i = weight per unit length of standard steel section used for members; l_i = length of members; m = number of members; w_h = weight of a single haunch; and n = number of haunches.

The objective function (Eq. 2) is minimized, subjected to the following normalized constraints for plastic design, in accordance with BS 5950-1 (2000):

$$\begin{aligned} g_1 &= \frac{F_v}{0.6 p_y A_v} - 1 \leq 0 \\ g_2 &= \frac{F_c}{p_y A_g} - 1 \leq 0 \\ g_3 &= \frac{M_x}{M_{cx}} - 1 \leq 0 \\ g_{4P} &= \frac{M_x}{M_{rx}} - 1 \leq 0 \\ g_5 &= \frac{1}{\lambda_p} - 1 \leq 0 \\ g_6 &= \frac{\delta_e}{\delta_e^u} - 1 \leq 0 \\ g_7 &= \frac{\delta_a}{\delta_a^u} - 1 \leq 0 \end{aligned} \tag{3}$$

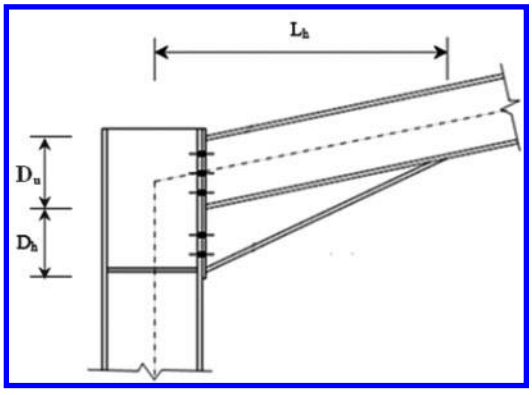


Figure 3. Details of eaves haunch.

For elastic design, the constraint g_5 is excluded and the design constraint g_{4P} is replaced by the constraint g_{4E} below:

$$g_{4E} = \frac{F_c}{A_g p_y} + \frac{M_x}{M_{cx}} - 1 \le 0 \qquad (3')$$

where g_1 = shear capacity; g_2 = axial capacity; g_3 = bending capacity; g_{4P} = reduced moment capacity for plastic design; g_{4E} = combined axial force and bending moment for elastic design; g_5 = constraint for plastic load factor; g_6 and g_7 = horizontal and vertical deflection limits, respectively (see Table 1); F_v = shear force; p_y = yield stress; A_v = shear area; F_c = axial force; A_g = gross area of cross-section; M_x = applied moment; M_{cx} = moment capacity of cross-section; M_{rx} = reduced moment capacity of cross-section; λ_P = collapse load factor for plastic design; δ_e and δ_a = deflections at eaves and apex, respectively; and superscript u indicates the maximum permissible deflection.

2.5 *Design variables*

The weight of frame is minimized by selecting the most appropriate cross-section for columns and rafters from the list of 72 Universal Beam cross-sections, S275 steel grade, along with optimizing the size of eaves haunch. It is assumed that the eaves haunch flange is the same as rafter flange and its web thickness is also the same as the web of rafter cross-section. The section properties of such haunches are calculated based on equations by Saka (2003).

In this paper, the haunch length (L_h) is varied in the range from [5%, 25%] of the frame span; haunch depth (D_h) varied from range of [$0.05D_u$, $4D_u$], with D_u being the depth of rafter cross-section inclined with the relevant pitch (see Figure 3). The cross-section of columns and rafters are processed as discrete variables, whilst the size of the eaves haunch, *i.e.*, haunch length and haunch depth is processed as continuous variables, using the optimal algorithms as described in the next section.

3 EVOLUTIONARY ALGORITHMS

3.1 *Real-coded genetic algorithm*

Real-coded genetic algorithm (RC-GA) is an evolutionary computation technique involving the principle of natural selection, such as survival of the fittest. The characteristic of RC-GA is that genetic operators are directly applied to the design variables without coding and decoding as with binary GAs. Solving optimization problems using RC-GA is therefore less cumbersome when compared to the binary-coded GAs (Deb 2001). The algorithm used in this paper randomly generates a set of solutions known as an initial population. From this population, the next generation of solutions is evolved by conducting three genetic operations: selection, crossover and mutation.

The steps for carrying out RC-GA are summarized as follows:

Step 1: Initial population of individual designs is constructed randomly. In the optimal design of the Benchmark Frame, the size of initial population (*Pop-size*) is selected, which is approximately larger than ten times the design variables. The probability for conducting crossover and mutation is set as 0.9 and 0.1, respectively (Deb and Gulati 2001, Phan et al. 2013b). The evolutionary process is terminated after 240 generations.

Step 2: Each candidate in the population is evaluated by calculating its fitness function that is applied to transform an optimization problem having design constraints to an unconstrained problem using penalty method. In this paper, penalty values are imposed empirically, in proportion to the severity of design constraint violation, which are checked through either plastic design or elastic design methods, as mentioned in Eq. 3.

Step 3: Elite strategy is applied to preserve the candidates having lowest/lightest fitness values for the next generation without being destroyed by random crossover and mutation operators. In this paper, two of best candidate is kept as offspring for the population in the next generation.

Step 4: Using the tournament selection randomly comparing the fitness values of two candidates, individuals are copied into the mating pool for crossing over and mutating, so that the better candidates may be created as in the natural selection. The SBX crossover and polynomial mutation is applied (Deb 2001). The individual that satisfies the design constraints and has the minimum weight is recorded.

Step 5: The initial population is replaced by the new population and steps 1–4 are repeated until a predefined number of generations is reached. This individual with the minimum weight of all generations is assumed to represent the fittest/best design.

3.2 *Real-coded niching genetic algorithm*

The real-coded niching genetic algorithm (RC-NGA) also uses five steps, as described in the RC-GA, to search for the optimum solution. However, the

difference with RC-GA is that two individuals are randomly selected and their fitness values compared if their distance is smaller than a critical one; this distance is empirically predefined, known as niching radius (Deb 2001). For the convenience of applying the niching strategy, the normalized distance, d_{ij}, between two individuals is calculated as follows:

$$d_{ij} = \sqrt{\frac{1}{n}\sum_{k=1}^{n}\left(\frac{x_k^{(i)} - x_k^{(j)}}{x_k^u - x_k^l}\right)^2} \quad ; \; 1 \le i, j \le Pop\text{-}size \qquad (4)$$

where n = number of design variables; $x_k^{(i)}$ and $x_k^{(j)}$ = corresponding kth decision variable in two vectors $x^{(i)}$ and $x^{(j)}$; x_k^u and x_k^l = respective upper and lower bounds of the kth decision variable.

If after a certain number of checks, no solution $x^{(j)}$ is found to satisfy the critical distance, $x^{(i)}$ is selected for the crossover operation. By this way, only solutions in same region (or niche) compete against each other for crossover. The application of niching strategy to crossover is referred to as mating restriction. The effect of niching technique is to maintain the diversity of the population by the preferential retention of candidate solutions from regions that are under-represented whilst simultaneously eliminating some of the candidate solutions from regions that are overcrowded based on the presumption that candidate solutions in the same neighborhood would tend to be similar.

4 DESIGN EXAMPLES

4.1 *Plastic design of Benchmark Frame*

In this section, the Benchmark Frame is designed plastically, using the plastic collapse mechanism (see Figure 4) under symmetric line load, w, obtained from the ultimate load combination (Davies and Brown 1996).

As can be seen in Figure 4, the frame collapses with the first plastic hinge forming at the underside of the haunch of the column, and the second plastic hinge forming along the rafter near to the apex; the sections between the hinges are assumed to remain rigid. It is worth noting that second-order effect is not considered in this paper since the frame geometry satisfies the sway check requirements (BS 5950-1 2000, and Lim *et al.* 2005).

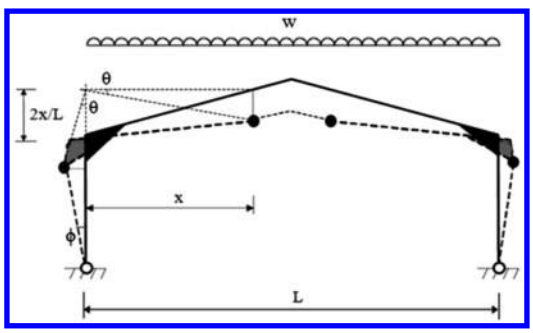


Figure 4. Plastic collapse mechanism under symmetric load.

The horizontal position of the second hinge (x), measured relative to the centerline of the left hand side column, can be determined from the following virtual work expression as follows (Davies and Brown 1996):

$$M_{cx_c}(\phi+\theta) + M_{cx_r}\theta = wx\frac{x\theta}{2} + w\left(\frac{L}{2} - x\right)x\theta \qquad (5)$$

where M_{cx_c} = moment capacity of column cross-section; and M_{cx_r} = moment capacity of rafter cross-section.

Based on such a collapse mechanism, the internal forces, namely, bending moment, shear and axial forces are determined for the ultimate limit state design, whilst elastic analysis is used to determine the deflections at the eaves and apex of the frame, under the serviceability load combinations. Industry deflection limits are used for serviceability limit state design (Phan *et al.* 2013a).

For the optimization of Benchmark Frame using RC-GA, three population sizes of 40, 80 and 120 are used to investigate its capacity of convergence to the optimum solution. RC-GA was run 10 times to check for the consistency of the result. Table 2 shows the best solution obtained after number of trials.

It can be seen from Table 2 that the best design obtained from the RC-GA is improved when the population size increases. The population size of 40 does not generate the design as good as the design obtained from these population sizes of 80 and 120. The RC-GA shows the best performance with the population size of 120.

The minimum unit weight obtained is 19.21 kg/m^2. It is also observed in Table 2 that the population in the last generation from the evolutionary process is dominated by the best solution, in which the diversity of population in later generations has been significantly reduced, as compared to the initial population.

Details of the best design obtained from the RC-GA are shown in Table 3.

As can be seen, the optimum haunch length accounts for 13% of frame span, which leads to a lighter cross-section assigned to the rafter, as compared to the frame design in SCI example. The design obtained from RC-GA is 5% lighter than the SCI frame design. It is observed that the ultimate design constraint governs the optimal design with plastic collapse load factor achieving the unity, *i.e.*, $g_5 = 0$, whilst the

Table 2. Effect of population size on RC-GA.

Pop-size	Minimum weight (kg/m^2)	Average weight (kg/m^2)	Maximum (kg/m^2)	Function evaluations
40	22.80	22.80	22.80	96000
80	19.21	19.21	19.21	32000
120	19.21	19.21	19.21	28800

constraints of such factor for the SCI frame is not active, *i.e.*, $g_5 = -0.04$.

For the optimization using RC-NGA, three population sizes of 40, 80 and 120 are also used to investigate its capacity of convergence to the optimum solution. The critical distance of niching radius is found 0.25 when the proposed algorithm shows the best performance. The results obtained after 10 trials from the optimization with each population are shown in Table 4.

As expected, RC-NGA generates the same minimum weight as the best design obtained from the RC-GA, with details of frame as shown in Table 3. It is interesting to see in Table 4 that the distribution of population in the last generation still shows the diversity of individuals and RC-NGA can effectively search for the optimum solution with small population size of 40 individuals. The computational time is therefore reduced by 66.7%.

4.2 *Elastic design of Benchmark Frame*

In this section, the Benchmark Frame is designed with elastic method for both ultimate and serviceability limit state. A first-order elastic analysis using the general purpose finite element package ANSYS (ANSYS Inc. 2009) is used to analyze the portal frame. The frame is optimized based on the steps as described in Section 3. For serviceability limit requirements, either industry or SCI deflection limits are applied to the optimization.

Based on the appropriate population size observed in the plastic design, the RC-GA with population size of 120 is used to optimize the Benchmark Frame. The consistency of optimal result is considered through 10 times of trials.

It is observed that RC-GA converges to the optimum solution within the predefined number of generations. The minimum weight of the Benchmark Frame with industry deflection limits is 21.12 kg/m^2 and that with the SCI deflection limits is 24.34 kg/m^2. As can be seen, the Benchmark Frame with using SCI deflection limits is 27% heavier than the same frame with plastic design using industry deflection limits. Details of the best design obtained after running 10 times of trials are shown in Table 5.

As can be seen in Table 5, the optimum haunch length of the Benchmark Frame using industry deflection limits accounts for 14% of frame span. With the stringent requirement of the SCI deflection limits, the haunch length accounted for 17% of frame span.

The ultimate design constraint governs the optimal design of Benchmark Frame with industry deflection limits; the critical constraint of strength at the shallow end of the eaves haunch nearly achieved the unity, *i.e.*, $g_{4E} = -0.01$. However, using the SCI deflection limits, it is observed that the constraint of vertical deflection at the apex of Benchmark Frame governs the optimal elastic design, *i.e.*, $g_7 = 0$.

For the optimization using RC-NGA, it is found that the population size of 40 candidates is suitable to search for the optimum solution. The critical niching distance is also 0.25. It was observed that 10 runs converged to the same optimum solution with same design as shown in Table 5, for either industry or SCI deflection limits.

Figure 5 shows the progress of RC-NGA converging to the optimum solution for the Benchmark Frame under industry serviceability requirements. As can be seen, RC-NGA converged to the best solution after 230 generations. The diversity of the population can be observed in Figure 5 through the distribution of minimum, mean, and maximum values, whilst these values become the same in the RC-GA after around 75 generations. This fact demonstrates the limit of RC-GA, as compared to RC-NGA.

The computational time for solving the optimization problem, with the population of 40, was 8.0 hours, for a laptop machine having a processor speed of 2.0 GHz and memory of 2.0 GB RAM.

Table 3. Plastic design of Benchmark Frame.

Frame design	Haunch sizes L_h/L_f	Haunch sizes D_h/D_u	Column section (UB)	Rafter section (UB)
SCI	0.10	1.0	510 × 210 × 101	457 × 191 × 67
RC-GA	0.13	0.96	610 × 229 × 101	457 × 152 × 60

Table 4. Effect of population size on RC-NGA.

Pop-size	Minimum weight (kg/m^2)	Average weight (kg/m^2)	Maximum weight (kg/m^2)	Function evaluations
40	19.21	26.33	60.02	9200
80	19.21	24.61	74.21	18400
120	19.21	24.54	65.39	27600

Table 5. Details of Benchmark Frame elastic design.

Deflection limits	Haunch sizes L_h/L_f	Haunch sizes D_h/D_u	Column section (UB)	Rafter section (UB)
Industry	0.14	1.05	610 × 229 × 125	457 × 152 × 60
SCI	0.17	1.32	686 × 254 × 125	457 × 191 × 74

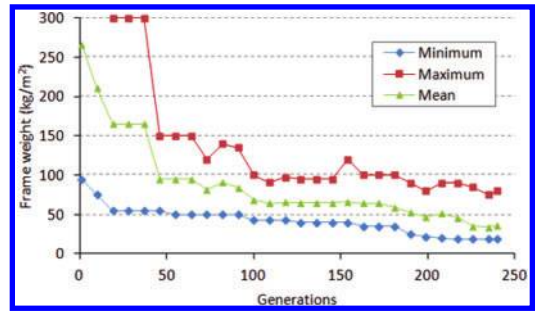


Figure 5. Convergence history of RC-NGA.

5 CONCLUSIONS

The effect of serviceability limit state on the optimal design of steel portal frame with haunch rafter is considered with a frame span of 30 m, under the action of gravity loads. When the cladding system does not require stringent deflection limits, industry suggestions for deflection limits can be used; the constraint for ultimate limit state governs the design. If the concern of cladding damage, owing to frame deflection, is considered, more stringent deflection limits from the SCI can be applied. The optimal design of the benchmark frame using SCI deflection limits is 27% heavier than optimal plastic design of such frames using industry deflection limits and 15% heavier than optimal elastic design of such frame, also using industry deflection limits.

The evolutionary algorithms, namely, RC-GA and RC-NGA have demonstrated the robustness and efficiency in searching for the best solution in design space. The mixture of design variables, *i.e.*, discrete and continuous variables is effectively processed by the proposed optimal algorithm using real parameters. The effect of niching method in maintaining the diversity of the population is also investigated and it is found that a small population size can be applied, as described in the RC-NGA. The computational time is therefore reduced by 66.7%, as compared against the RC-GA.

REFERENCES

ANSYS Inc, 2009. *Programmer's manual for mechanical APDL*, USA: SAS IP.

British Standard, 2000. *BS 5950: Structural use of steelworks in building. Part 1. Code of practice for design - Rolled and welded sections*, London: British Standards Institution.

Davies, J.M. & Brown, B.A. 1996. *Plastic design to 5950*, Great Britain: The Steel Construction Institute.

Deb, K. 2000. An efficient constraint handling method for genetic algorithms, *Computer Methods in Applied Mechanics and Engineering*, 186: 311–338.

Deb, K. 2001. *Multi-objective optimization using evolutionary algorithms*. Chichester: John Wiley and Sons, Inc.

Deb, K. & Gulati, S. 2001. Design of truss-structures for minimum weight using genetic algorithms, *Finite Element in Analysis and Design*, 37: 447–465.

Lim, J.B.P., and Nethercot, D.A 2003. Serviceability design of a cold-formed steel portal frame having semi-rigid joints. *Steel & Composite Structures*, 3(6), 451–474.

Lim, J.B.P., King, C.M., Rathbone, A.J., Davies, J.M., and Edmondson, V. 2005. Eurocode 3 and the in-plane stability of portal frames. *The Structural Engineer*, 99, 1–7.

Phan, D.T., Lim, J.B.P., Siew, C., Tanyimboh, T., Issa, H., and Sha, W. 2011. Optimization of cold-formed steel portal frame topography using real-coded genetic algorithm. *Procedia Engineering*, 14, 724–733.

Phan, D.T., Lim, J.B.P., Tanyimboh, T.T., Lawson, M. R., Xu, Y., Martin, S., & Sha, W. 2013a. Effect of serviceability limits on optimal design of steel portal frames, *Journal of Constructional Steel Research*, JCSR-D-12-00471, Accepted for publishing.

Phan, D.T., Lim, J.B.P., Sha, W., Siew, C.Y.M., Tanyimboh, T.T., Issa, H.K., & Mohammad, F.A. 2013b. Design optimization of cold-formed steel portal frames taking into account the effect of topography, *Engineering Optimization*, DOI:10.1080/0305215X.2012.678493.

Saka, M.P. 2003. Optimum design of pitched roof steel frames with haunched rafters by genetic algorithm, *Computers and Structures*, 81: 1967–1978.

Salter, P.R., Malik, A.S., & King, C.M. 2004. *Design of single-span steel portal frames to BS 5950-1: 2000*, SCI publication P252, Ascot: The Steel Construction Institute.

SCI Advisory Desk, 2010. *AD-090: Deflection limits for pitched roof portal frames (Amended)*, Ascot: The Steel Construction Institute.

Wrzesien, A., Lim, J.B.P., and Nethercot, D.A. 2012. Optimum joint detailed for a general cold-formed steel portal frame. *Advances in Structural Engineering*, 15(9), 1635–1651.

Research and Applications in Structural Engineering, Mechanics and Computation – Zingoni (Ed.)
© 2013 Taylor & Francis Group, London, ISBN 978-1-138-00061-2

Optimization of the injection molding processes using the Moldflow simulation program on the example of electrical connectors

M. Szostak & R. Staniek
Poznan University of Technology, Poznan, Poland

ABSTRACT: The paper presents the optimization process of two prototype injection molds for the production of electrical connectors. Simulation using the Moldflow2012 program shows the filling processes of injection molds in terms of manufactured products quality. The simulation showed only the minor hazards (during the filling and packing phases) that can occur during the manufacturing of these two parts. After finishing the computer simulation, on the selected injection molding machines the optimization of the production parameters were carried out for both molds. As a result of the optimization carried out, it was possible to shorten the cycle time for manufacture of the products, respectively: from 10.1 s to 9.1 s for the first product and from 9.5 s for 8.5 s for the second one. As a result of the work it was possible to increase the efficiency of the manufacturing process and reduce the manufacturing costs of those parts.

1 INTRODUCTION

The task of the work was to prepare the initial 3D models of injection molds selected for the production and carried out simulation studies of the filling process in terms of shortening the cycle time and reduce internal stress and improve the quality of chosen products. These include the analysis of the polymer filling of the molds, determining of the injection pressure value, the pressure drop during the process, temperature of the front of flowing material, the orientation of the surface and the average temperature of the products, the time to obtain a temperature which allowed to remove the products from injection mold, areas of rapid solidification, shrinkage of the products, air traps, weld lines, differences of products temperature and cooling time, distortions associated with the differentiation of molding cooling, shrinkage and orientation of the products. In this paper filling simulations of two selected prototype injection molds has been presenting, allowing determining the parameters such as the time of filling the mold material and the potential closure of the gas. The results of the analysis are used to design optimal cooling channels, optimal points for ejectors and venting points.

2 MOLDS AND MATERIALS

Two molds with number 7344 and 7405 has been selected for the analysis and it was assumes that in both cases the products are made from PA 6.6. type FRIANYL A63 RVO. The two products obtained on the chosen molds are shown at the figure 1 and 2.



Figure 1. The view of product no 7344.



Figure 2. The view of product no 7405.

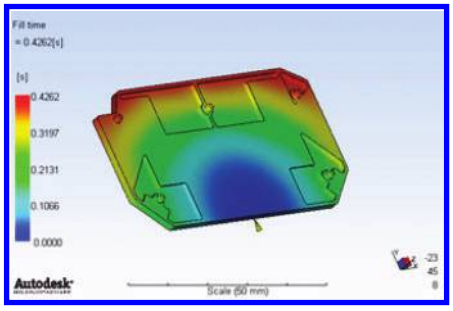


Figure 3. Study for the mold 7344: Fill time.

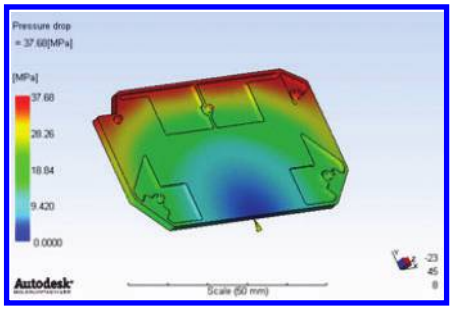


Figure 4. Study for the mold 7344: Pressure drop.

3 MOLDFLOW SIMULATION

3.1 *Results for the mold 7344*

On the figures 3–9 the results of a few selected analyzes made ??by the program are presented. Autodesk Moldflow is showing all phases of the process, and indicating the potential hazards of the process and its possible impact on the quality of the manufactured part. These include the analysis of the filling time of the mold, the injection pressure, the pressure drop during the process, the temperature of the front of flowing material, the orientation of the surface of the molding, the average temperature of the molding, the time to obtain a molding temperature allowing the product for removal from the injection mold cavity, areas of rapid solidification, shrinkage of molding, air traps, weld lines, locations of possible subsidence, differences in molding temperature, cooling time and its spread, distortions associated with the molding cooling temperature differences and molding contraction. On the drawings 3–9 selected seven important parameters describing the process of injection molding products has been shown.

Summarizing the simulation results for the mold 7344 it can be concluded that the Moldflow program pointed out that the main problem in the molding process is associated with scattering of the cooling time of individual areas of the molding which is caused by non-uniform wall thickness of the product. In addition, the program pointed out the possibility of quality problems of the molds associated with filling and holding pressure phases. Simulation showed no problems

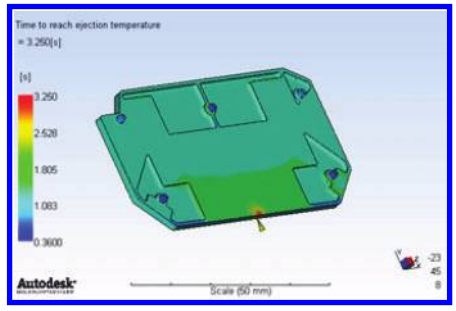


Figure 5. Study for the mold 7344: Time to reach ejection temperature.

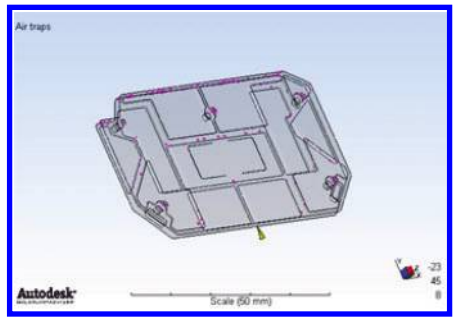


Figure 6. Study for the mold 7344: Air traps.

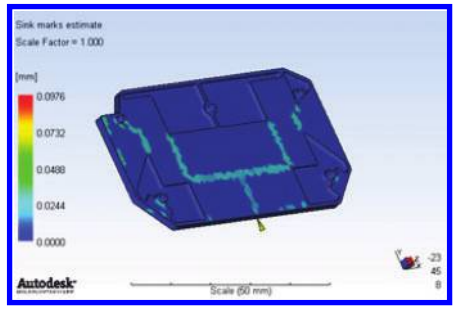


Figure 7. Study for the mold 7344: Sink marks.

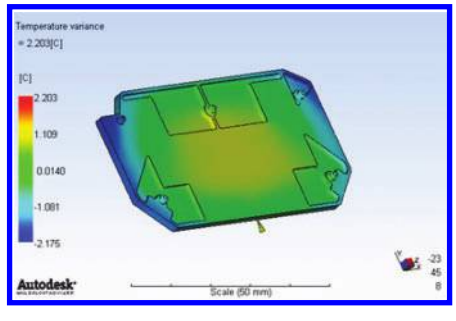


Figure 8. Study for the mold 7344: Temperature variance.

related to sink mark on the molding surface or its deformation. Calculated process times were: filling time 0.41 s, holding pressure time 1.5 s, cooling time 3.5 s, the time to open the mold 5.44 s and the total cycle time 10.85 s (see Figure 10).

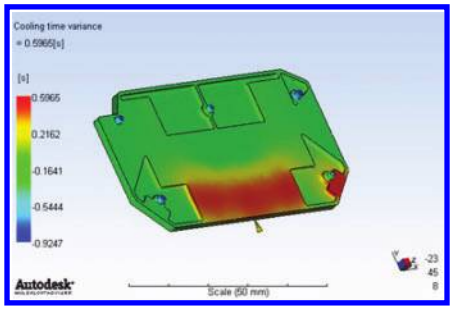


Figure 9. Study for the mold 7344: Cooling time variance.

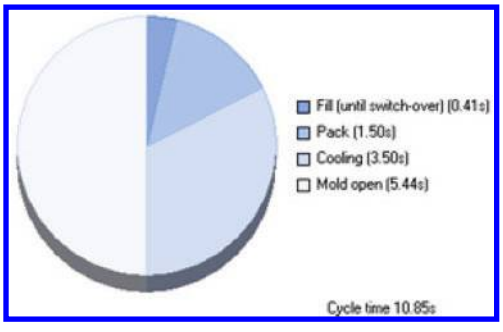


Figure 10. Graphic presentation of the total cycle time for the mold 7344.

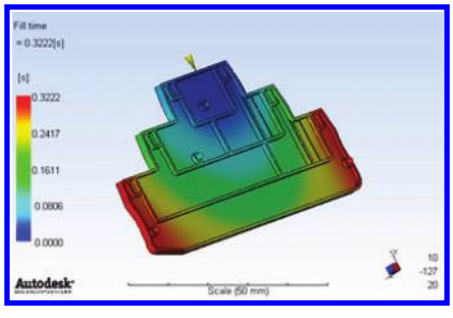


Figure 11. Study for the mold 7405: Fill time.

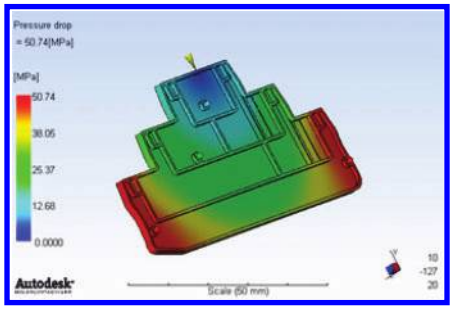


Figure 12. Study for the mold 7405: Pressure drop.

3.2 *Results for the mold 7405*

Below, similar like for the mold no.7344 on figures 11–18 has been shown the results of analysis performed by the Moldflow program showing all phases of the process and indicating the potential hazards of the process and its possible impact on the quality of the manufactured part.

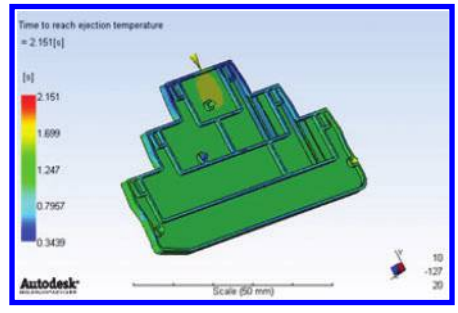


Figure 13. Study for the mold 7405: Time to reach ejection temperature.

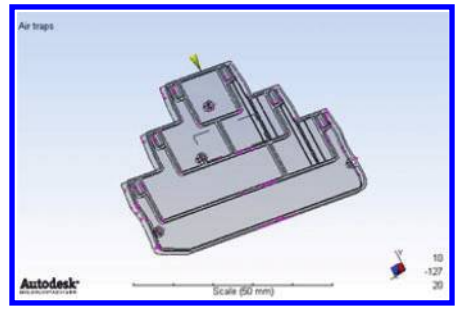


Figure 14. Study for the mold 7405: Air traps.

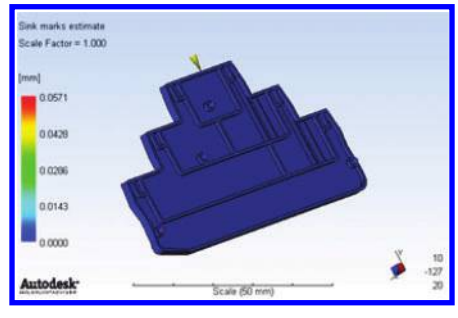


Figure 15. Study for the mold 7405: Sink marks.

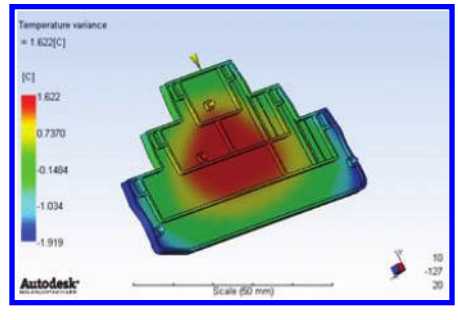


Figure 16. Study for the mold 7405: Temperature variance.

Summarizing the simulation results for the mold 7405 it can be concluded that the program Moldflow indicated a possibility of molding quality problems associated with filling and holding pressure phases. Simulation has not revealed any problems with the

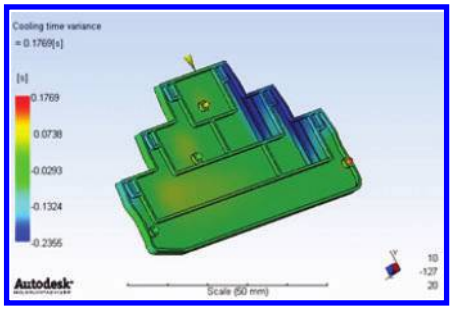


Figure 17. Study for the mold 7405: Cooling time variance.

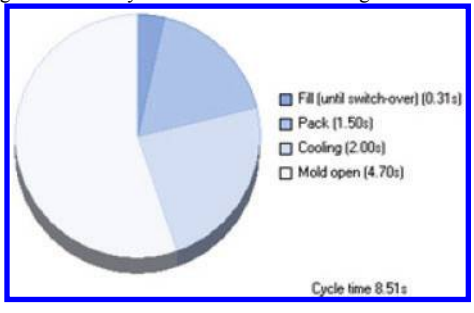


Figure 18. Graphic presentation of the total cycle time for the mold 7405.

molding and cooling. As in the previous mold any problems related to the sink mark on the molding surface or its deformation has been observed. Calculated process times were, respectively: filling time 0.31 s; holding pressure time 1.5 s; cooling time 2.0 s; the time to open the mold of 4.70 s and the total cycle time of 8.51 s (see Figure 18).

4 PROCESS OPTIMIZATION ON THE INJECTION MOLDING MACHINES

After testing the mold filling process of prototypes mold using the simulation software in terms of the quality of the molded parts, as well as the efficiency of the injection molding process, the optimization process of the injection parameters, for these two molds, on selected production machines has been carried out. For the optimization of the injection molding process the two DEMAG injection molding machines, D-50 for the 7344 mold and D-35 for the 7405 molds, has been chosen.

Three attempts were made to optimize the injection molding process for each of these molds (7344 and 7405). Within the framework of the optimization process mainly the following settings: temperatures in plasticizing cylinder, injection pressure, injection speed, dosing time, cooling time, holding pressure time, has been changed.

As a result of the optimization process, without degrading the mechanical properties and surface moldings quality, we have managed to reduce the cycle times by 10.5% for the mold 7405 and 12.4% for the 7344 mold. Visualization of reducing cycle times for all the forms are shown in figures 19 and 20.

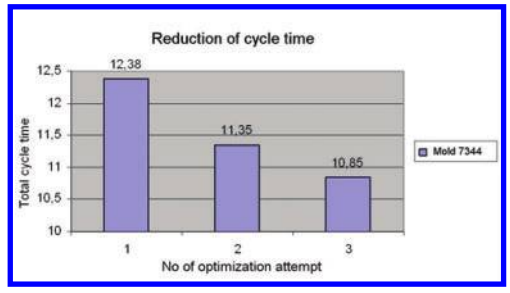


Figure 19. Cycle times after optimizing the injection molding process on the mold 7344.

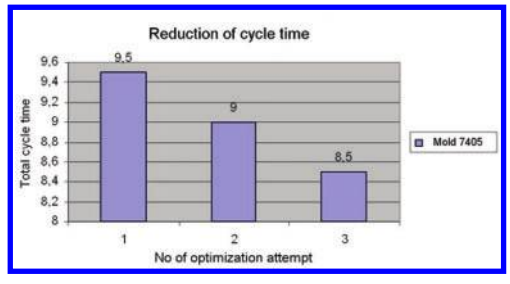


Figure 20. Cycle times after optimizing the injection molding process on the mold 7405.

Optimization of the production process for a 7344 mold enabled the cycle reduction of the 1.53 seconds which is about 12.4% of the total cycle time.

Optimization of the production process for a 7405 mold enabled the cycle reduction of the 1.0 seconds which is about 10.5% of the total cycle time.

5 CONCLUSIONS

Conducted simulations of the injection molding process for the two prototype injection molds showed only minor hazards that can occur during a production process.

Larger risks arising from the diversity of molding wall thickness can occur for the mold 7344.

The simulation for 7405 mold shows only a small possibility of molding quality problems associated with the filling and packing phases.

Practical tests on the injection molding machines made with use of the technological parameters identified in the simulation showed no technological problems and quality of products manufactured on that two molds.

The studies have shown that design of the molds is correct and guarantees a good quality product at a high injection efficiency of the described products.

REFERENCE

Staniek, R. Szostak, M. Twardowski, P. Bakowski, D. Golon, M. Tanona, D. 2012. Technical report from project no. 6 ZR7 2008/C 07025. *Implementation of new technologies in the production of improved injection molds for electrotechnical and electronic connectors.* 1–134. Poznan: Poznan University of Technology.

Research and Applications in Structural Engineering, Mechanics and Computation – Zingoni (Ed.)
© 2013 Taylor & Francis Group, London, ISBN 978-1-138-00061-2

Comparison of simulation results of injection molding process obtained by MoldFlow and Moldex3D programs

M. Szostak & R. Staniek
Poznan University of Technology, Poznan, Poland

ABSTRACT: The paper describes the problem of difference in computer simulation's results of injection molding process. In this paper the results from Autodesk Moldflow Insight and CoreTech Moldex3D are compared. In both programs obtained parts were free from quality defects, however their output properties were different. Analyzed simulation systems showed compliance in the calculation of cycle time and injection volume. The calculated clamping pressure was similar to that shown in the experimental test. For the calculation of air bubbles, the programs showed only the qualitatively similar results. Areas of occurrence of defects were similar, but their number varies. Proper preparation of the model and parameters of the simulation depends on the user and his knowledge of the injection molding process. This, how the simulation will be carried out, has an impact on the output results of the simulation, which in the face of a real process may sometimes mislead the users.

1 INTRODUCTION

The aim of the study is a comparative analysis of the results of computer simulations of the injection molding process made in Autodesk Moldflow and Moldex3D CoreTech programs on the example of molding used in the electrical industry. The study shows also the differences in the obtained results from simulations and an attempt to determine their origin.

For the purposes of the simulation the geometry of the connector used in the electrical industry, made of PA 6.6 has been prepared. Model details in both programs are presented in Figure 1 (MoldFlow) and Figure 2 (Molde3D). In the table 1 the actual parameters of the injection molding process used in the manufacturing plant for the production of this piece are shown.

Computer simulation of injection molding process must be preceded by the preparation of a model part. Depending on the type of software, the process is carried out in separate modules of the package or with the main program. In the case of the "Moldflow" program: import geometry, FEA mesh application, the choice of material, the definition of injection points, selection the type of simulation and the cooling system is possible without the use of additional modules. In the case of the "Moldex3D", the above processes except to choice of material and the type of simulation are defined in the subprogram "Moldex Designer".

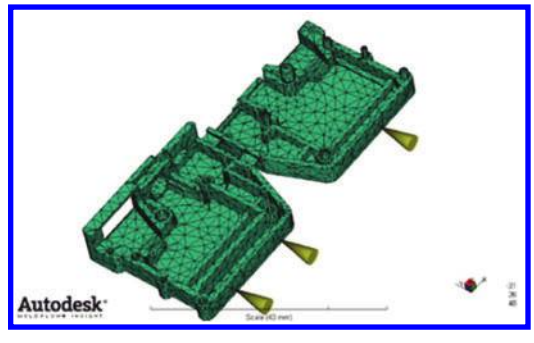


Figure 1. The geometry of the connector with FEA mesh and injection points in MoldFlow.

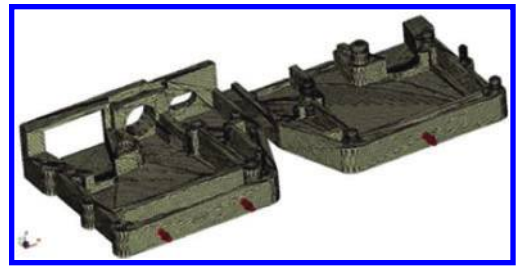


Figure 2. The geometry of the connector with FEA mesh and injection points in Moldex3D.

Table 1. Injection molding parameters set on the machine.

Parameter	Value
Temperature zone 1 [°C]	268
Temperature zone 2 [°C]	265
Temperature zone 3 [°C]	265
Nozzle temperature [°C]	270
Screw moving [ccm]	28
Switch point [ccm]	8
Residual pillow [ccm]	6.6
Decompression [ccm]	3
Backpressure [MPa]	7
Injection speed [ccm/s]	28
Injection pressure [MPa]	64
Holding pressure [MPa]	25
Clamping force [kN]	500
Injection time [s]	0.96
Holding time [s]	2.0
Dosing time [s]	1.38
Cooling time [s]	5.0
Cycle time [s]	13.0

Table 2. Processing parameters introduced to the "Moldflow" program .

Parameter	Value
Mold temperature [°C]	70
Injection temperature [°C]	270
Mold opening time [s]	5
Cycle time [s]	8
Polymer speed [ccm/s]	5
Switch point [s]	0.96

2 MOLDFLOW SIMULATION RESULTS

Based on the entered injection molding parameters (Table 2) the molded part without quality defect was obtained. Complete filling of the mold cavity will take place earlier than switching into holding pressure phase. This is related to the high speed of material flow set on 5 cm/s. If we will use a lower value, filling time would be longer, but there is risks that switch to the packing process will appear before the end of the injection phase. Simulation result did not show a significant numbers of voids. These sites are the result of retention of air or gas bubbles due to plastic flow fronts. They are present in the space between the two injection points and at the edges of the geometry. We can prevent to avoid them by changing the distribution of injection points and using the ejectors in the places their appear.

Analyzing the pressure distribution at the end of the injection phase, we will find a significant drop in pressure on the molding side with a single point of injection and the even distribution of pressure on the molding side with two injection points. The minimum pressure is visible in the farthest part of the molding on the side with a single point of injection. In this section,

Table 3. Processing parameters introduced to the "Moldex3D" program.

Parameter	Value
Mold temperature [°C]	80
Injection temperature [°C]	285
Mold opening time [s]	5
Injection time [s]	0.96
Polymer speed [ccm/s]	15
Switch point [%]	98
Holding pressure time [s]	2

the temperature at the front of plastic is also the lowest. This results in the greatest deformation in that part of the connector of nearly 0,5 mm.

3 MOLDEX3D SIMULATION RESULTS

With the assumed parameters of the injection molding process, the simulation shows the obtained molding without quality defects. Injection time was set at 0.96 sec and the pressure switch point at 98% of filling the cavity volume.

The simulation showed the possibility of appearing the number of air bubbles, especially in the areas of the pivots, and on the geometry surfaces. The largest number of voids is located on the inner side of the part.

In the case of pressure distribution at the end of the injection phase, it can be observed a significant decrease of pressure on the molding side with a single point of injection. The polymer in this part of the geometry flows more slowly, so the time to fill a cavity is longer, as is confirmed by the measurements of the injection time.

The temperature at the front of the flowing polymer is uniform and is about 285°C, being close to the set point of injection temperature. This is indicated by a uniform color throughout the entire volume of the mold. The characteristic distribution of the results allows obtaining similar properties in the cross-section geometry of the product. The only decrease of the temperature at the front of flowing polymer was recorded on the surface of the hinge connecting of the two parts of the product.

The thickness of the hinge is much lower than the wall thickness of the part. The analysis showed no overcooling or overheating points on the part. Distribution of volume contraction, which contributes to the deformation of the product, is also uniform. In the areas most distance from the injection points, is about 10%.

4 COMPARIZON OF THE SIMULATION RESULTS

In table 4 the results of the simulation are comapred with the data obtained in the experiments on the

Table 4. Comparison of the computer simulations results with machine parameters.

Processing parameters	Moldflow	Moldex 3D	Injection test
Injection time, [s]	0.54	0.96	0.96
Injection temperature, [°C]	270	285	270
Mold temperature, [°C]	70	80	70
Real injection pressure, [MPa]	97.6	28	64
Injection volume, [ccm]	2.42	2.43	
Holding time, [s]	2.0	2.0	2.0
Holding pressure, [MPa]	29.3	17.75	25
Switch point	0.96 s	98.00%	8 ccm
Mold opening time, [s]	5.0	5.0	5.0
Cycle time, [s]	13.00	12.96	13.00
Total weight, [g]	2.6001	2.485	2.6
Polymer flow speed [ccm/s]	5,0	2.53	5
Clamping force, [T]	2.2	11.87	50
Calculation time (for injection and holding phase)	1 h 26 min	2 h 24 min	–

injection molding machine. We can notice a difference in the definition of the switching point. For "Moldflow" program it is given in seconds – 0,96 s, for "Moldex3D" in percentage of the volume of the cavity – 98% and for real machine parameters in ccm – 8 ccm. The greatest difference in the results was observed for the injection pressure which was the result of different speed of the polymer flow.

5 CONCLUSIONS

Received results of injection molding process in Autodesk Moldflow Insight and CoreTech Moldex3D programs have shown that the obtained parts were free from quality defects, however their output properties were different. Analyzed simulation systems showed compliance in the calculation of cycle time and injection volume. The calculated clamping pressure was similar to that shown in the experimental test. For the calculation of air bubbles, the programs showed only the qualitatively similar results. Areas of occurrence of defects were similar, but their number varies. Due to the time-consuming process connected with preparation of model of the produced part, very important become the computation time. In the case of "Moldflow" program, this time was much shorter, the calculation last for 1 h 26 min, while for the "Moldex3D" – 2 h 24 min. Proper preparation of the model and define the parameters of the simulation depends on the user and his knowledge of the injection molding process. This, how the simulation will be carried out, has an impact on the output results of the simulation, which in the face of a real process may mislead the users. In the case of the purchase cost, it is significantly higher for the "Moldflow" program. However, the price is justified, because the program is obtained with a highly developed data base of polymer material, with a user-friendly interface and with relatively fast computational processes. Engineering support programs help users to reduce the number of experimental trials carried out. These decrease the start up time of the new product, as well as reduce the cost of its implementation. However, some knowledge of the injection process and training of the program user is required to obtain the intended benefit after purchasing the simulation program.

REFERENCES

Staniek, R. Szostak, M. Twardowski, P. Bakowski, D. Golon, M Tanona, D. 2012. Technical report from project no. 6 ZR7 2008/C 07025. *Implementation of new technologies in the production of improved injection molds for electrotechnical and electronic connectors.* 1–134. Poznan: Poznan University of Technology.

Research and Applications in Structural Engineering, Mechanics and Computation – Zingoni (Ed.)
© 2013 Taylor & Francis Group, London, ISBN 978-1-138-00061-2

The use of modified three axes forging to strengthen Nb for superconducting radio frequency cavities

P.N. Kalu
Mechanical Engineering Department, FAMU-FSU College of Engineering, Tallahassee, FL, USA

N. Bembridge
Formerly at FAMU-FSU College of Engineering, now at Medtronic Inc., MN, USA

I. Dagwa
Department of Mechanical Engineering, University of Abuja, Abuja, Nigeria

ABSTRACT: Severe Plastic Deformation (SPD) such as Equal Channel Angular Extrusion (ECAE) and three-Axis forging are now standard methods employed to strengthen structural metals. Here, we assess the viability of a modified three axes forging method (an SPD technique) for pre-processing of high purity Niobium, used for Superconducting Radio Frequency Cavities (SRFC) fabrication. Starting with a Nb of hardness and grain size of HVN 52.4 ± 2.5 and $139 \pm 118\,\mu$m, respectively the processing resulted in a significant increase in hardness to HVN 100.2 ± 5.2 ($D = 97.52 \pm 41.15$), and an average HAGB of 10%, after only one cycle of deformation. Although additional cycles of deformation produced modest increase in hardness, the microstructure underwent substantial refinement and homogenization to the extent that the grain size was about $1.41 \pm 0.46\,\mu$m (HAGB of 61%), after 16 cycles. Comprehensive analysis of the microstructure and hardness using Orientation Imaging Microscopy and Vickers microhardness techniques, respectively clearly indicated that two processing regimes existed during the use of modified three axis forging: at low strain ($\varepsilon \leq 2.6$), in which grains segment into deformation bands or cell blocks (or subgrains), the percentage of High angle boundaries is low (HAGB $\leq 10\%$). At high strain ($\varepsilon \geq 2.6$), orientation splitting occurs leading to significant grain refinement and increase in the HAB%. It can be concluded that the 3-axis forging of Nb using reshaping die resulted in the production of billet with microstructure and microtexture suitable for the manufacture of superconducting radio frequency cavities.

1 INTRODUCTION

1.1 *Superconducting radio frequency cavities*

Superconducting radio frequency (SRF) technology involves the application of electrical superconductors to radio frequency devices. The material of choice for Superconducting Radio Frequency Cavities (SRFC) is pure Niobium. The cavities are traditionally made of Niobium sheets, which are deep drawn or spun into half cells and then e-beam welded together to form multi-cell accelerator cavities as shown in Figures 1a&1b.

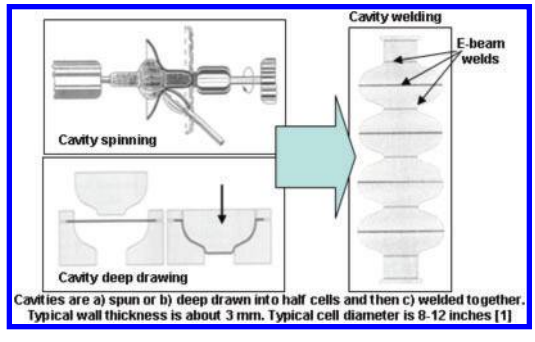


Figure 1. Schematic showing how superconducting radio frequency cavities are spun or deep drawn into their required geometry and e-beam welded together. Typical cell wall thickness is about 3 mm. (Padamsee, 2008).

Deep draw-ability of the sheets used for manufacturing SRFCs depends heavily on the microstructure and texture of the niobium sheet. Unsuitable microstructure or texture can lead to a variety of issues during cavity manufacturing. Of paramount importance is the electrical resistivity, which needs to be ultra-low in order to allow the Radio Frequency resonator to obtain an extremely high quality factor, Q. Production of bulk quantities of Nb with favorably refined microstructure and texture through the use of innovative severe plastic deformation methods is currently being explored to facilitate easier manufacture and improved function of SRFCs. This study examines the suitability of a modified three axes forging method as an SPD technique for producing the

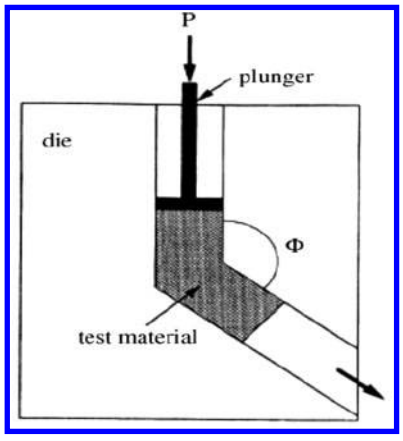


Figure 2. Schematic diagram showing equal channel angular pressing process (Cherukuri, 2005).

requisite microstructure and texture in Nb for the production of SRFCs. The requisite microstructure and texture for niobium for SRFC manufacture include: uniform, equiaxed (grain shape aspect ratio ≤ 2), fine grain ($\leq$50 μm) microstructure required to avoid tearing/surface roughness during deep drawing or spinning; sufficiently high percentage of high angle grain boundaries ($\geq$60%) for complete and continuous recrystallization during annealing.

1.2 *Severe plastic deformation (SPD)*

Severe plastic deformation process is any metal forming operation in which a very high level of plastic strain is imposed on a material (Azushima, 2008). Although there are different definitions of what is considered to be severe plastic strain, a convenient convention was laid out by Prangnell, 2007:

- low strains : $\varepsilon < 2$
- low medium strains $\varepsilon = 2 - 4$
- medium to high strains $\varepsilon = 4 - 6$
- ultra/very high strains $\varepsilon > 6$

Significant reduction in cross-sectional area results when conventional methods such as rolling, wire drawing or swaging are used to achieve severe plastic deformation. However, with Equal Channel Angular Extrusion (ECAE) method there is little or no reduction in the cross sectional area of the deformed piece. The technique of Equal Channel Angular Extrusion entails pressing a billet through a die made of two intersecting channels of equal cross section as shown in Figure 2 (Cherukuri, 2005).

Shearing deformation is imposed on the material at the bend region. Deformation is achieved through a combination of shear strain and redundant deformation (Prangnell, 2007). This results in the material being plastically strained while the cross sectional dimensions of the work piece are maintained

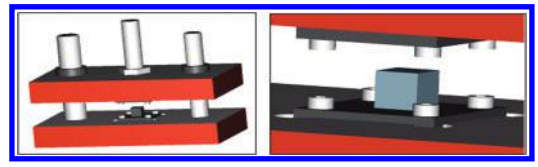


Figure 3. Three axis forging apparatus and the position of billet (the MTS hydraulic press not shown).

(Azushima, 2008). The work pieces must be either square bars or round rods. Recently, research has been undertaken to scale the method up for refining sufficiently large ingots of niobium for SRFC manufacture (Hartwig, 2007). ECAE processing is limited by the billet geometry. Therefore, there are efforts to use another form of severe plastic deformation process, known as the three-axis deformation method as an alternate method of processing the microstructure (see Fig. 3). In this case, the work piece, usually of cube dimension, is compressed in the 3-Orthogonal axis to complete a cycle. This method of processing has been shown to be capable to refine microstructure of copper (Belyakov, 2003) and other materials (Azushima, 2008).

Most severe plastic deformation methods have not yet been fully developed for industrial scale production of SPD material, and there is a great deal of continuing research into the development of SPD technology.

1.3 *Applications of severely plastically deformed materials*

There are a number of applications and potential applications that can capitalize on the ultra fine-grained materials resulting from severe plastic deformation. The applications range from military (lighter and more durable armor plates and more effective armor penetrators), medical (UFG titanium for joint implants), electronics (nano-scale grained sputtering targets), to aerospace (airframe weight reduction through the usage of lightweight UFG components). A comprehensive review of most of the applications of severe plastic deformation can be found in a 2008 study on SPD technology (Azushima, 2008), which illustrates the current state of SPD processes for engineering metals and alloys. It is noted that grain refinement through SPD can serve as an alternative to alloying as a means of material strengthening. This is forecasted to lead to greater simplicity, cost reduction and easier recycling of waste metals (Azushima, 2008) and (Han, 2008). In the study reported here, we assess the viability of a modified three axes forging method (an SPD technique) for pre-processing of high purity Niobium, used for Superconducting Radio Frequency Cavities (SRFC) fabrication. It is our believe that the manufacture of niobium RF cavities stands to benefit substantially from advances in SPD technology.

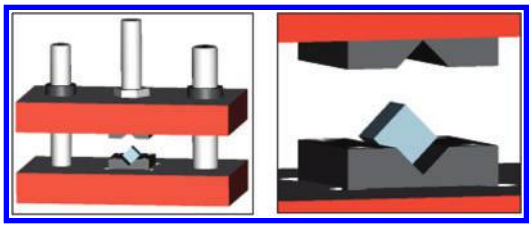


Figure 4. Re-shaping die and the position of the billet (MTS hydraulic machine not shown).

Table 1. A list of three axis forged niobium samples.

Three axial forging strain	# of Cycles	Mean strain per cycle
$\varepsilon = 0.65$	1	0.65
$\varepsilon = 1.33$	2	0.68
$\varepsilon = 2.60$	4	0.65
$\varepsilon = 5.20$	8	0.65
$\varepsilon = 10.0$	16	0.63

2 MATERIALS AND EXPERIMENTAL

2.1 *Material*

High purity grade of niobium (purity 99.99%) known as Residual Resistively Ratio grade was used in this study. The material was supplied by Ati-Wah Chang Allegheny Technologies. This type of niobium is used in the manufacture of superconducting radio frequency cavities for particle accelerators. Niobium purity is of importance as inclusion atoms can severely degrade cavity performance. In order to be of this grade, it was manufactured using the electron beam melting technique, which causes impurities to outgas prior to ingot solidification.

2.2 *Three axis forging*

The three axis forging apparatus used for this work comprised of a two post Danly die set fitted with hardened D2 tool steel forging surfaces which were set in and bolted to the die as shown in Figure 4. Die surfaces were finely ground using 3 μm diamond solution. The billets for forging were in the form of 15 mm cubes cut to size by electron discharge milling (EDM) and finely polished on all sides with P4000 silicon carbide paper. The tool steel forging platens were cleaned with alcohol and inspected for surface flaws or visible scratches. Damaged forging platens were removed and re-polished with a silicon carbide paper followed by 3 μm diamond solution. Platens then were lubricated with several coats of colloidal graphite lubricant prior to each forging. The strain per pass (i.e. 1 uniaxial compression) was approximately $\varepsilon = 0.2$ for a total of $\varepsilon = 0.6$ per cycle (i.e. 3 compressions). The imposed true strain for each compression pass was determined by the formula:

$$\varepsilon = \ln(h_0/h) \tag{2.1}$$

Where h_0 is the initial height and h is the height after the billet has been compressed. The total strain was the summation of the strain imparted during each compression pass. Dimensions of the billet were taken in between compression passes. The actuator on the hydraulic press was set to move at a standard compression rate of 0.015 mm/s for both forging and reshaping and for both materials, which provided an average strain rate of 0.001/s. The load cell was set to record stroke height and load data at a sampling rate of 1 Hz. A list of the samples and their forging strains are listed in Table 1.

2.3 *Re-shaping apparatus*

The reshaping dies (also made of hardened D2 tool steel) could also be fitted to the same die set (Figure 4) and used to undo undesired warping of the billet. The platens were a pair of thick plates with 90 degree grooves that combined together formed a square channel matching the exact geometry of the work piece. The reshaping dies were used as needed in between cycles to re-shape the billet, thereby returning it to its original cube shape before any subsequent three axis forging would be done.

2.4 *Vickers hardness testing*

Vickers hardness testing is a common and fairly simple non destructive test for mechanical properties. It is widely employed in studies on SPD of niobium and other materials (Mathaudhu 2006). The Vickers hardness testing machine imparts a specified load for a set amount of time to a surface using diamond indenter of a distinct geometry. It produces a Vickers Hardness Number, which is a measure of material hardness. The size of the indent was measured and used in conjunction with the load on the Vickers hardness equation to give a Vickers hardness number. By indenting the entire surface, it was possible to produce a hardness map, which can be used to assess the level of homogeneity of the hardness in a material following processing. In each case a matrix of indents (totaling 576 in the form of a 24×24 square array) was done over the sectioned face to generate a hardness map.

2.5 *Orientation imaging microscopy*

Orientation Imaging Microscopy (OIM) is a fully automated Electron Back-Scattered Diffraction (EBSD) technique. Electron Back Scatter Diffraction (EBSD) is a scanning electron microscopy (SEM) based technique widely employed as a material characterization technique used to determine localized crystallographic orientation and microtexture (or preferred crystallographic orientation). EBSD has been used to routinely determine grain boundary character distribution, grain

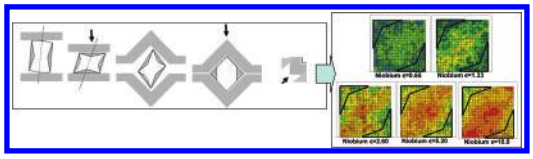


Figure 5. Diagrammatic representation of how reshaping leads to the formation of dead corners (indicated by gray cross hatchings) where there is less strain than the bulk material.

diameter, grain shape, microtexture in studies of niobium (Hartwig, 2007 and Mathaudhu 2006) and copper (Zhao, 2008), subjected to SPD. Investigation of microstructure and microtexture of the SPD materials is often carried out using automated EBSD.

3 RESULTS AND DISCUSSION

3.1 *Vickers hardness*

The Vickers hardness data is provided as a hardness map (a matrix of indents totaling 576 in the form of a 24×24 square array) over the entire sectioned face of the sample. With the exception of the increasing contour level with strain, the hardness profiles of all the samples were similar (see Figure 5). The variation and the shape of the hardness profile can be traced back to the use the reshaping die, which subjected the samples to additional compression along one diagonal in order to return it to cube shape. Because of the inhomogeneity in hardness, three main regions can be identified, and they are: dead corner, core region and compressed corner.

During uniaxial compression the areas of a deformed billet that are near to the forging surface are restricted by friction from free outward expansion. Within these areas, cone shaped regions called dead zones form, which experience less deformation (Figure 5) than the bulk material. Lubrication and polishing of forging surfaces can reduce the size of the dead zones however they are unavoidable. However, during reshaping, samples are subjected to an additional compression along one diagonal to return it to cube shape. This results in additional strain within the region aligned with compressed diagonal. The area that sees this additional straining consists of the core and deformed corners. Conversely, dead corner areas form in the off-diagonal billet corners where there is no additional strain during reshaping (Figure 5).

The Vickers hardness of the processed samples, ranging from cycle 1 to cycle 16 are presented in the form of contour plots, which are superimposed on the plot of hardness versus strain (number of cycles) in Figure 6. It is evident that Niobium strain-hardened very fast at the early stages ($\epsilon = 0.65$) of the processing. Strain hardening was gradual in the intermediate stage ($0.65 \leq \epsilon \leq 2.6$) and then taper off

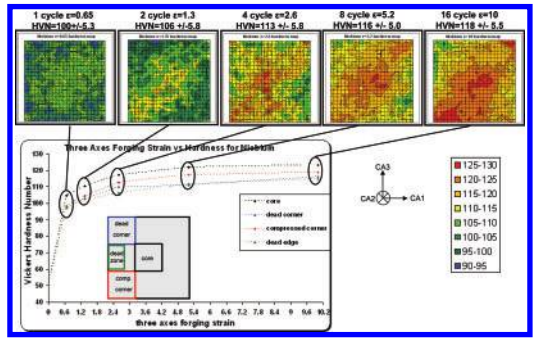


Figure 6. Plot of Vickers hardness as a function of strain for various regions of billets of three axes forged niobium.

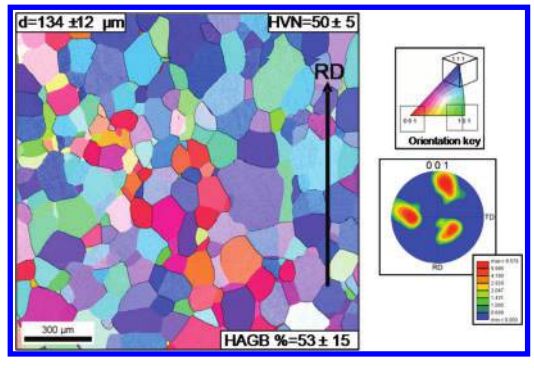


Figure 7. OIM Micrograph, inverse pole figure map and its corresponding pole figure along with a GBCD plot for the niobium in the as-received condition.

with increasing strain. One may argue that the material had not been fully hardened after 16 cycles and strain of $\epsilon = 10$.

The precipitous increase in hardness at the early stages of processing may be attributed to either the build up of dislocations or substantial refinement in grain size of the material or both. By applying a comprehensive OIM analysis, it will be possible to resolve which of these are responsible for the increase in hardness that was noticed at the early stages of processing.

3.2 *Evolution of microstructure with strain*

The OIM micrograph of the as-received microstructure is presented in Figure 7. The microstructure was characterized by equiaxed grain structure suggestive of a fully recrystallized material. This is more so, because individual grains maintained a near uniform coloration, indicating that there are no remnants of deformation or recovered regions within the grains. Analysis of the OIM data revealed that the grain size was large ($d = 134 \pm 12\,\mu m$) and a high percentage of high angle grain boundaries ($53 \pm 15\%$).

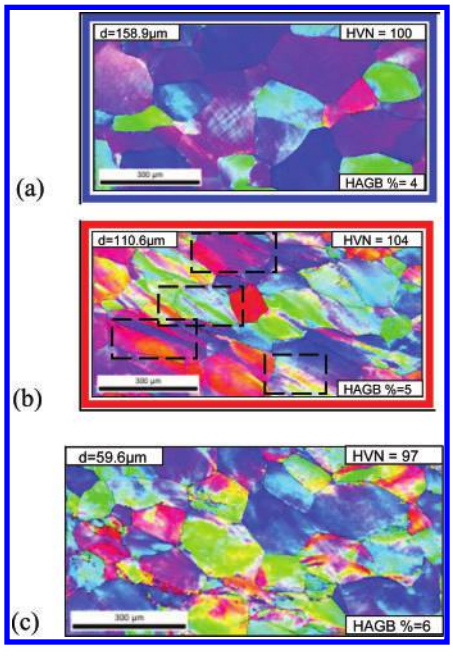


Figure 8. OIM maps for Nb subjected to 1 cycle ($\epsilon = 0.65$). The variation in colors within the grains is an indication of deformation.

The hardness profile of section 3.1 revealed that the hardness of the material upon processing was heterogeneous and led to the classification of three distinct regions, namely, the dead corner, core region and compressed/deformed corner. It is noteworthy that the OIM analysis of the processed material showed similar characteristics. Henceforth, the microstructure results for each strain will be presented for these three regions.

The OIM micrographs of the dead corner, core region and the compressed corner are presented in Figures 8a, b and c, respectively for material processed to 1 cycle ($\varepsilon = 0.65$). The grains in the dead corner region (Fig. 8a) are characterized by near uniform coloration, similar to the as-received material. This suggests that the dead region had seen little or no deformation. However, the microstructure of the deformed corner and the core region shown in Figs 8b and c, respectively displayed grains with varied colors. The diagonal nature of some of the deformed regions within the grains is indicative of shear banding. The percentage of high angle grain boundaries (HAGB) in the dead corner, deformed corner and core region was 4%, 5% and 6%, respectively. Additional processing of the material up to the strain, $\varepsilon \sim 1.33$, resulted in the intensification of the shear bands, which resulted in inhomogeneous microstructure. Even the dead corner started showing deformation bands. Furthermore, there was reduction in grain width, with little or no change in the percentage of HAGB. Processing of the material at strains, $\varepsilon \geq 2.66$ resulted in substantial refinement of the microstructure and an abrupt increase in the percentage of HAGB.

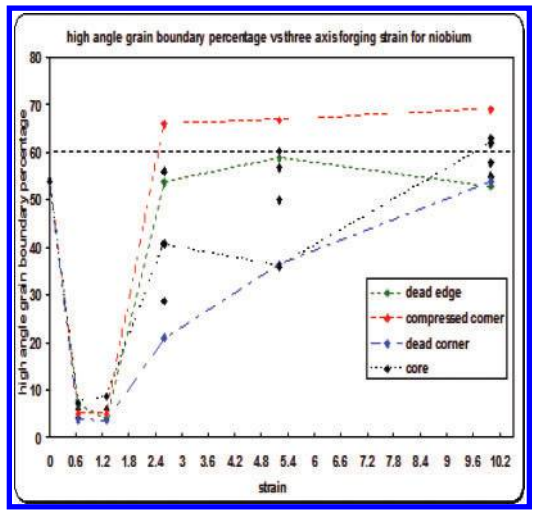


Figure 9. Plots of high angle grain boundary percentage as a function of the three axes forging strain.

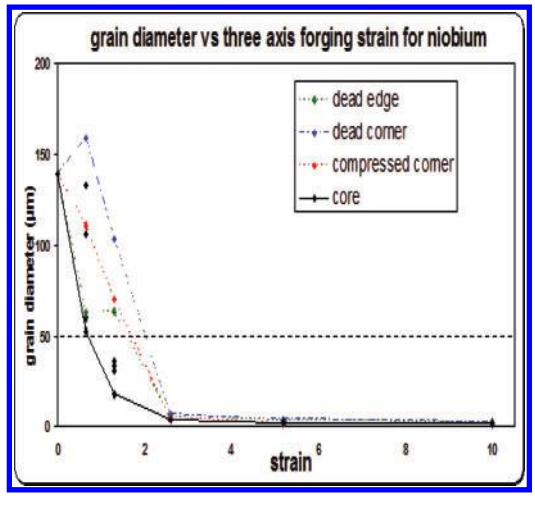


Figure 10. Plots of grain diameter as a function of the three axes forging strain.

Figures 9 and 10 present the evolution of HAGB as a function of strain and grain diameter as a function of strain, respectively for all the processing strains. The predominance of low angle boundaries (percentage of HAGB ~5%) in the microstructure at the early stages of processing indicates that the microstructure was characterized by subgrains and deformation bands. Therefore, the plot of Figure 10 is essentially of cell diameter refinement, which were subgrains at low strains ($\varepsilon \leq 2.66$) and grains at high strains. At strain, $\varepsilon = 10$, the microstructure of the deformed corner was very much similar to that of the core region as can be seen in Figure 11.

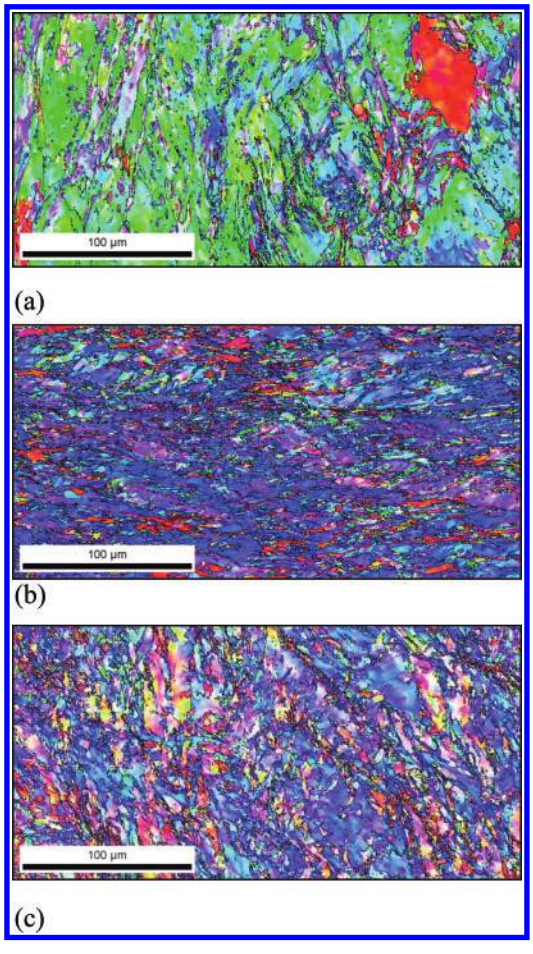


Figure 11. OIM maps for Nb subjected to 16 cycles ($\epsilon = 10$). There was little or no difference between the deformed corner (b) and core region (c) microstructure.

4 CONCLUSIONS

The microstructure produced via three axes forging with reshaping die can be characterized as non-homogeneous and consisting of three main regions, namely, the dead corner, core region and compressed/deformed corner. The core of the billet underwent more intense straining while the dead corner was the least heavily deformed. The most important result is that the forging procedure was able to produce microstructure suitable for the manufacture of SRFCs. The microstructure after a strain of $\epsilon = 10$ was characterized by equiaxed (GSAR ≤ 2) fine grain ($d = 1.4 \pm 0.5\,\mu m$), with sufficiently high percentage of HAB ($59 \pm 6\%$). These properties are necessary to promote formability and cavity wall strength in addition to ensuring continuous recrystallization during pre-production annealing.

REFERENCES

Azushima, A., Kopp, R., Korhonen, A., Yang, D.Y. , Micari, F., Groche, P., Yanagimoto, J., Tsuji, N., Rosochowski, A., Yanagida, A., (2008) Severe plastic deformation (SPD) processes for metals, CIRP Annals – Manufacturing Technology 57, Page 716–735.

Belyakov, A., Tsuzaki, K., Miura, H., Sakai, T., (2003), Effect of initial microstructures on grain refinement in a stainless steel by large strain deformation, Acta Materialia 51, Page 847–861.

Cherukuri, B., Nedkova, T. S., Srinivasan, R., (2005) A comparison of the properties of SPD-processed AA-6061 by equal-channel angular pressing, multi-axial compressions/forgings and accumulative roll bonding, Materials Science and Engineering A 410–411, Page 394–397.

Han, B., Xu, Z., (2008), Grain Refinement under multiaxial forging in Fe-32%Ni alloy, Journal of Alloys and Compounds 457, Page 279–285.

Hartwig, K. T., Wang, J., Baars, D. C., Bieler, T. R., Mathaudhu, S. N., and Barber, R. E., (2007) Microstructural Refinement of Niobium for Superconducting RF Cavities, IEEE Transactions on applied superconductivity, Vol.17, No. 2, Page 1305–1309.

Mathaudhu, S. N., Blum, S., Barber, R. E., Hartwig, K. T., (June 2005), Severe Plastic Deformation of Bulk Nb for Nb3Sn Superconductors, IEEE Transactions on Applied Superconductivity, Vol. 15, No.2, Page 3438–3441.

Padamsee, H., Knobloch, J., Hays, (1998) T., RF Superconductivity for Accelerators, New York, John Wiley and Sons.

Prangnell, P.B., Huang, Y., Berta, M. and Apps, P.J., Mechanisms of Formation of Submicron Grain Structures by Severe Deformation, (2007), Materials Science Forum, Vol 550, Page 159–168.

Zhao, Y. H., Bingert, J. F., Zhu, Y. T., Liao, X. Z., Valiev, R. Z., Horita, Z., Langdon, T. G., Zhou, Y. Z., and Lavernia, E. J., (2008), Tougher ultrafine grain Cu via high-angle grain boundaries and low dislocation density, APPLIED PHYSICS LETTERS 92, page 81–90.

Research and Applications in Structural Engineering, Mechanics and Computation – Zingoni (Ed.)
© 2013 Taylor & Francis Group, London, ISBN 978-1-138-00061-2

Biomass in materials processing: Using cassava leaves to case harden mild steel

R. Gordon
Department of Mechanical Engineering, FAMU-FSU College of Engineering, Tallahassee, USA

K.J Akinluwade
Materials Science and Engineering Department, Obafemi Awolowo University, Ile-Ife, Nigeria

A.R. Adetunji
Materials Science and Engineering Department, Obafemi Awolowo University, Ile-Ife, Nigeria,
National Agency for Science and Engineering Infrastructure, Abuja, Nigeria

P.N. Kalu
Department of Mechanical Engineering, FAMU-FSU College of Engineering, Tallahassee, USA

O.O. Adewoye
National Agency for Science and Engineering Infrastructure, Abuja, Nigeria

ABSTRACT: Steel is widely used in all types of structures, due to its relatively low cost, high strength to weight ratio and speed of construction. When used in most automobile applications, steel may require case-hardening processing. Conventional case-hardening of steel have major drawbacks in being very expensive and hazardous to perform. In this study, an alternative method, which involves the use of cassava leaves and peels is being explored. Cassava contains varying degrees of cyanogenic glucoside (15-1000 mg of HCN per kg of cassava). These cyanogenic glucosides, when hydrolyzed by enzymes, form Hydrogen Cyanide (HCN) in the form of triple bond of Carbon and Nitrogen, which is responsible for the case-hardening process. The actual processing involves pack-cyaniding of the cassava leaves with $BaCl_2$ as energizer. Because the process relies on diffusion, our study has focused on grain boundary diffusion and the effect of grain size on the case-hardening of mild steel. Grain refinement of the mild steel was carried out via a severe plastic deformation technique known as three-axis forging. The microstructure analysis results via Orientation Imaging Microscopy (OIM) were correlated with the hardness data for case-hardening using cassava leaves.

1 INTRODUCTION

Most developing countries have an acute shortage of spare parts and components for maintenance work, especially in the automobile industry. With the high local exchange rates, the importation of such spare parts in these countries has become virtually impossible (Adetunji et al, 2009).

Gear teeth, camshaft, and other automobile components, need considerable toughness to withstand impact and good surface hardness to resist wear or abrasion. These components are generally made from mild steel and can be produced by surface or case hardening. The result of Case Hardening is an outer case that is wear-resistant with a ductile inner core. A major drawback with conventional case hardening methods is that they are expensive and involve handling extremely poisonous and toxic substances in the form of gas or liquid.

This research utilizes a novel technique in which cassava leaves are pack-cyanided to case harden various types of steel (Ibironke, 2004).

1.1 *Case Hardening*

Case hardening utilizes the diffusion of Carbon (C) and/or Nitrogen (N) as interstitial atoms into the surface of a material. The result is an outer case that is wear resistant with an inner core that is ductile and able to absorb impact.

Case hardening can be done by at least four methods: carburizing, nitriding, cyaniding, or carbonitriding. With the cyaniding method in particular, a major drawback is that the process is expensive and involves the handling of extremely poisonous and toxic substances in the form of gas or liquid. Therefore, cassava leaf pack-cyaniding has been developed as an alternative method for case hardening.

1.2 *Cassava*

Cassava is an important source of carbohydrate for millions of people due to its large tuberous and starchy roots. It is grown in tropical and subtropical regions.

Cassava, as well as more than 2500 plant species, contains cyanogenic glucosides (Zagrobelny, 2003). Cyanogenic glucosides act as a defense mechanism against herbivore attack for plants. They are stored in plant vacuoles and when the tissue is disturbed (i.e. chewing), cyanogenic glucosides are brought into contact with lyases that hydrolyze the cyanogenic glucosides causing the release of toxic hydrogen cyanide (HCN).

This HCN can breakdown into Carbon (C) and Nitrogen (N) atoms, which can be made to diffuse interstitially into the surface of steel, thereby serving as case hardening source during the pack cyaniding. The HCN distribution in cassava is within the range of 15-1000 mg of HCN per kg of cassava. This level of toxicity in within the optimal range for pack cyaniding applications.

1.3 *Grain Size and Diffusion*

Pack-cyaniding utilizes C and N as diffusing agents into interstitial sites of the steel work piece. This is due to the fact that the difference in atomic diameters of C/N and Fe is greater than 15% as can be seen in Table 1. For interstitial diffusion, the activation energy is substantially lower than that of substitutional diffusion (Table 2).

Much research has established that the mean jump frequency of atoms at dislocations, grain boundaries, and surfaces is much higher than that of the same atom within the lattice (Shewman, 1989). This means that grain size can affect the rate of diffusion. Therefore, it is important to investigate the effect of starting grain size on pack cyaniding, especially since this may influence the final case and core microstructure. In this study, grain refinement was accomplished by 3-Axis Forging, a form of Severe Plastic Deformation (SPD).

Table 1. Atomic radii of C, N, and Fe.

Element	Atomic Radius **(nm)**
C	0.077
N	0.071
Fe (BCC)	0.124

Table 2. Diffusion coefficients and activation energies for substitutional (Fe in Fe) versus interstitial (C or N in Fe) atoms.

Diffusion Process	D_0**(10**$^{-4}$ m^2s^{-1}**)**	Q(kJmol^{-1})
Fe in Fe (α)	118	281
N in Fe (α)	0.005	76
C in Fe (α)	0.008	83
C in Fe (γ)	0.7	157

2 EXPERIMENTAL

2.1 *Materials*

Two types of steel, namely Low-Carbon Steel and Nitridable-Grade Steel were used for this investigation. The chemical components of these alloys are presented in Table 3.

It is expected that 1018 Steel will be involved in high temperature processing where C will be diffused into interstitial vacancies. However, there is limited solubility of C in Fe at low temperatures. In fact, maximum solubility is 0.022 wt% C in Ferrite. Therefore, C cannot be used as a diffusion element in case hardening at low temperatures. Steel containing Aluminum and Molybdenum (Nitralloy 135 M) are preferable for they can form Nitrides at low temperatures.

With the formation of both carbides and nitrides during pack cyaniding, varied results are expected for Steel with dependence on chemical composition and temperature.

2.2 *Three-Axis Forging*

Severe plastic deformation (SPD) via Three-Axis Forging is performed on cube-shaped billets of approximately 12mm, using both grades of steel, to achieve an ultra-fine microstructure. It is expected that steel with initial fine grains will need less processing to achieve a fine, hard case with a fine, ductile core.

Table 3. Chemical composition of low-carbon steel (1018) and nitridable steel (Nitralloy 135 M).

1018 Steel **Component**	**Wt %**
Carbon	0.15-0.20
Manganese	0.60-0.90
Silicon	0.15-0.30
Phosphorus	0-0.04
Sulfur	0-0.05
Nitralloy 135M	
Carbon	0.38-0.43
Chromium	1.6
Molybdenum	0.35
Aluminum	1.1

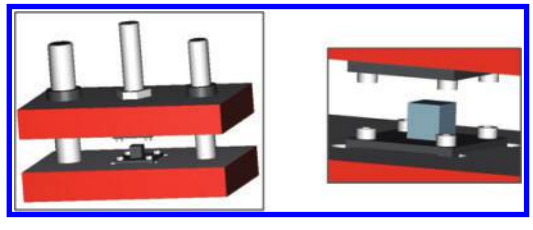


Figure 1. Three-axis forging apparatus. Forging die is actuated by a hydraulic press. A cube-shaped billet of 12 mm is compressed in an open die along 3 axes. The initial dimensions of the cube are retained.

2.3 *Experimental Procedure*

This work consists of two sub-tasks: (1) pre-processing of the steel and (2) pack-cyaniding processing. The effect of pre-processing on the cassava pack cyaniding method will be analyzed.

The pre-processing (1) consists of using Three-Axis Forging to refine the microstructure of Steel. Preliminary work in our laboratory has shown that Three-Axis Forging can substantially refine grain structure (Bembridge, 2011). The Three-Axis Forging technique was. adopted for grain refinement. It is expected that steel with initial fine grains will require less pack-cyaniding processing to achieve a fine, hard case with a fine, ductile core.

The pack-cyaniding processing stage (2) involves converting the cassava peels and leaves to the appropriate condition from which C and N are extracted from it. Different energizers, including $BaCO_3$ and $BaCl_2$, are then packed in pouch with the cassava leaves and mild steel. These were heated at various temperatures (400°C – 950°C) at a series of time periods (1hr-5hr). Average powder particle size ranged from 0.125–1.0 mm. All samples were then analyzed with Orientation Imaging Microscopy (OIM) and Vickers hardness testing.

3 RESULTS

3.1 *Initial Microstructure*

Scanning Electron Microscope (SEM) micrographs of 1018 Steel and the Nitralloy 135 M are presented in Fig. 2a and 2b, respectively. It is evident that the 1018 microstructure consists mainly of proeutectoid Ferrite (α) and Pearlite. On the contrary, the microstructure of Nitralloy consists of a mixture of Bainite and Martensite.

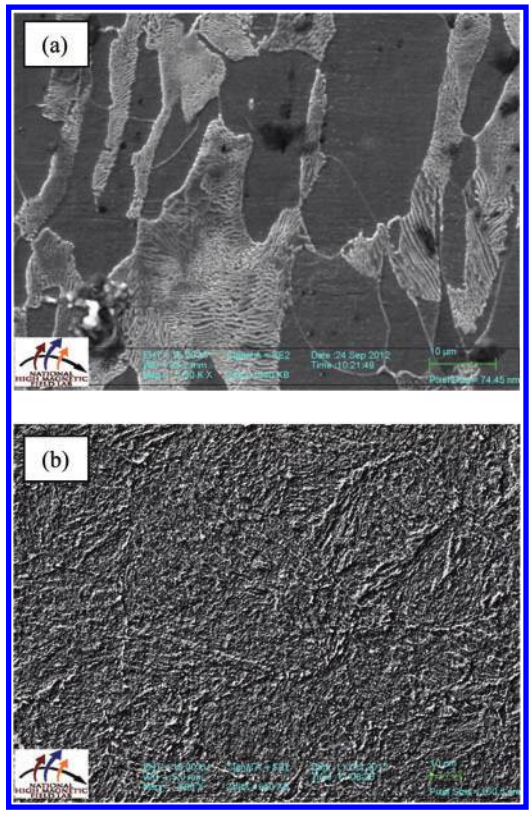


Figure 2. SEM micrographs of as received (a) 1018 Steel and (b) Nitralloy 135 M.

3.2 *Preliminary Results*

3.2.1 *Cassava Pack Cyaniding at 800°C*

Preliminary work was conducted to investigate the effect of cassava pack-cyaniding on the as-received 1018 Steel. Figure 3 presents the hardness profile of the material when processed at 800°C. It is evident that the hardness of the surface region (known as the case region) was about 35% higher than the core region. Furthermore, the case region extended to about 0.25 mm from the surface of the work piece.

Figures 4(a) and (b) are the Orientation Imaging Micrographs of the work pieces processed at 800°C for 1 hr and 3 hrs, respectively. In each case, the grain structures of the case regions were finer than that of the core regions. One hour processing time resulted in a smaller case region and larger core grain size when compared to the 3 hr processed material. The presence of very fine grain size in the case region can suggest that in addition to the diffusion of Carbon there was multiple nucleation of recrystallization in this region.

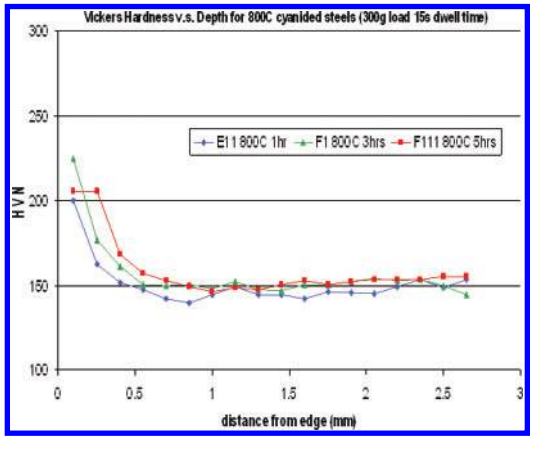


Figure 3. Vickers hardness profiles of Cyanided Steel at 800°C (from 1 hr to 5 hrs) plotted as a function of distance from outer edge (case).

3.2.2 *Grain Size Refinement in Niobium*

As stated in section 1.2, part of the study was directed at understanding the effect of grain size on diffusion rate. Therefore, there was need to refine the grain size of the work piece. Previous work in our laboratory has utilized Three-Axis Forging to refine the

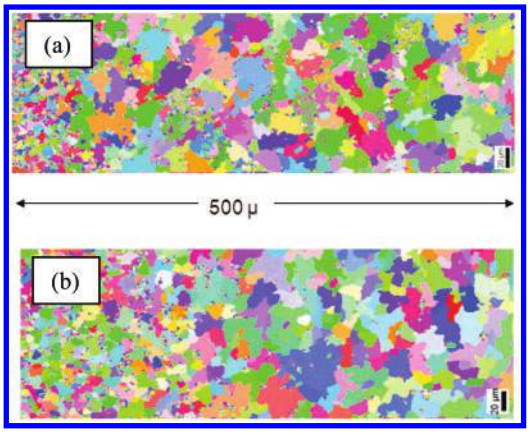


Figure 4. OIM micrographs of Mild Steel reveal variation from case to core (left to right) through the depth of Steel at 800°C for (a) 1 hr and (b) 3 hrs.

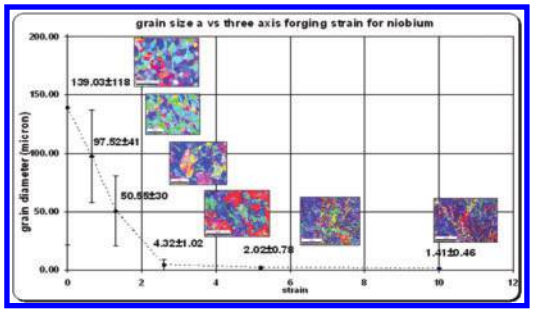


Figure 5. Average grain diameter as a function of true strain for Niobium that has undergone SPD via 3-Axis Forging.

grain size of Niobium at room temperature (Bembridge, 2011). Starting with an average grain diameter of $\sim 139\,\mu$m, this procedure was able to refine the grain size to $\sim 1.41\mu$m, as can be seen in Figure 5. Clearly, the average grain diameter decreased by one order of magnitude at the completion of processing.

Figure 6 shows Vickers microhardness testing data performed on Niobium as a function of strain, ranging from $\epsilon = 0$ up to $\epsilon = 10$. The data shows a noticeable strain hardening response at low strain ($\epsilon = 0.65$). The hardness continued to increase gradually up until $\epsilon = 2.6$, then very slowly beyond that point (Bembridge, 2011).

3.3 *Grain Size Refinement in Steel*

Using the Three-Axis Forging procedure, the 1018 steel was deformed to strains up to 3. Figures 7(a) to (d) present the OIM micrographs of the as-received, $\varepsilon = 1$, $\varepsilon = 2$ and $\varepsilon = 3$, respectively. The as-received microstructure (Fig. 7a) was characterized with large discernible grain structure. However, upon processing, the microstructure was fibrous in nature, showing that grain refinement had commenced in the material.

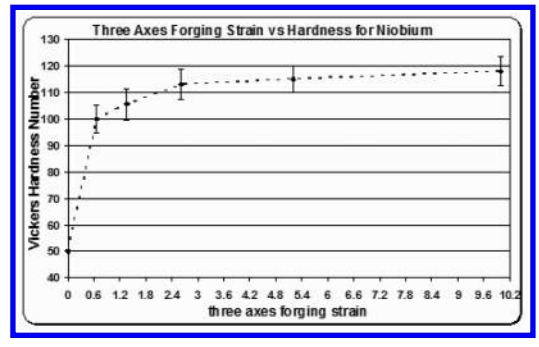


Figure 6. Plot of average Vickers hardness as a function of true strain for Niobium.

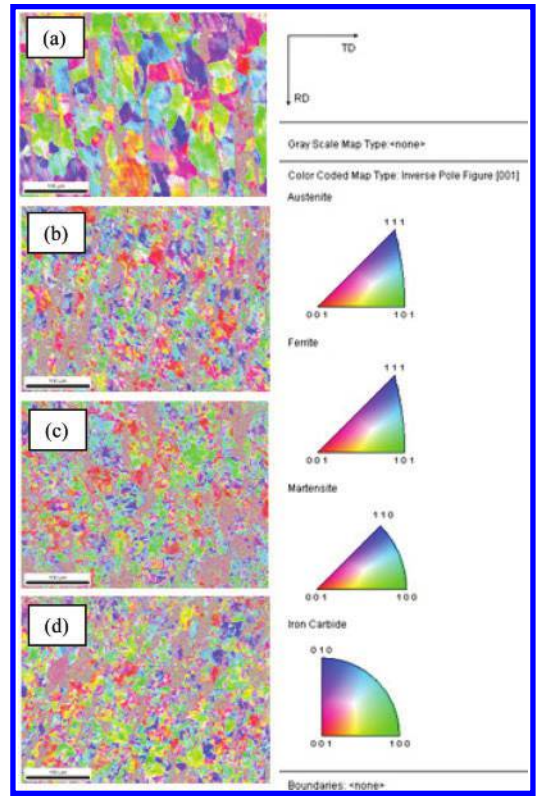


Figure 7. OIM micrographs of 1018 Steel at (a) $\epsilon = 0$, (b) $\epsilon = 1$, (c) $\epsilon = 2$, and (d) $\epsilon = 3$.

There are indications that the shear bands may have cut across several grains. Additional analysis will be carried out to determine the average misorientations in the material.

Automatic Vickers hardness testing was conducted on the samples for strains of $\epsilon = 0$ to 2. Average hardness was plotted as a function of the true strain (Fig. 8). The strain hardening response was very pronounced at low strain ($\epsilon = 1$). This is due to the buildup of deformation bands at low strains in Steel.

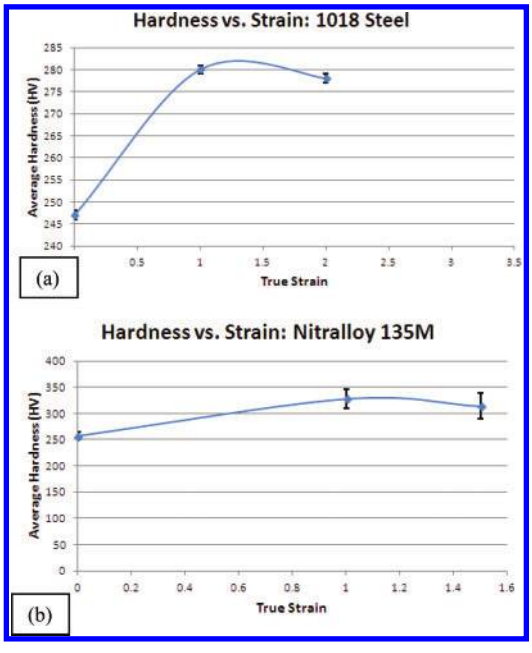


Figure 8. Average Vickers Hardness (HV) as a function of true strain for (a) 1018 Steel at $\epsilon = 0,1,2$ and (b) Nitralloy 135M at $\epsilon = 0,1,\ 1.5$.

4 CONCLUSIONS

An alternative case-hardening method utilizing cassava leaves as the source for pack-cyaniding was developed. Low-Carbon Steel and Nitridable-Grade Steel were subjected to severe plastic deformation by three-axis forging for the purpose of grain refinement. Because the pack-cyaniding process relies on diffusion, this work was conducted to analyze grain boundary diffusion and the effect of grain size on the case-hardening of mild steel.

1. Using cassava leaf pack-cyaniding, mild steel was processed at 800°C at 1 hr, 3 hrs, and 5 hrs. Vickers microhardness values for mild steel revealed an increase in hardness to a depth of approximately 0.25 mm within the case. The finer microstructure within the processed case region of mild steel is associated with the higher Vickers hardness values. This validates the cassava leaf pack-cyaniding produces case depths comparable to conventional cyaniding methods.
2. Three-axis forging of Steel at low strain ($\epsilon \leq 3$) resulted in grain refinement with microstructural features similar to deformation bands which cut across several grains.

REFERENCES

Adetunji, A. R.; Elero, S. A.; Akinluwade, K. J.; Adeoye, M. O., Kalu, P. N. and Adewoye, O. O. 2009. "Effect of Pulverized Cassava Leaves Particle Size on the Case Depth of Pack-Cyanided Mild Steel Components". AMRS: Lagos, Nigeria.

Bembridge, Nicholas. 2011. "Innovative Severe Plastic Deformation of Niobium with Application to Superconducting Radio Frequency Cavities".

Ibironke, O.J., Falaiye, A., et. al. 2004. *Materials and Manufacturing Processes*, Volume 19, No. 5, Pages 899–905.

Liangcheng Du, Mpoko Bokanga, et. al. 1995. *Phytochemistry*, Volume 39, Issue 2, Pages 323–326.

Raghavan, V. 2004. *Materials Science and Engineering*. New Delhi: Prentice Hall of India Private Limited.

Rybal'chenko, O.V. , Dobatkin, S.V., et al. 2004. *Materials Science and Engineering: A*, Volumes 387–389, Pages 244–248.

Shewman, Paul. 1989. *Diffusion in Solids*. Warrendale: The Minerals, Metals & Materials Society.

Zagrobelny, Bak, et al. 2003. *Phytochemistry*, Volume 65, Issue 3, Pages 293–306.

30. Structural health monitoring, damage detection, non-destructive evaluation

Research and Applications in Structural Engineering, Mechanics and Computation – Zingoni (Ed.)
© 2013 Taylor & Francis Group, London, ISBN 978-1-138-00061-2

Non-destructive evaluation (NDE) practice for concrete bridges in USA

A. Ghorbanpoor
University of Wisconsin-Milwaukee, Milwaukee, Wisconsin, USA

S. Boone
Federal Highway Administration, US DOT, McLean., USA

ABSTRACT: A large number of concrete bridges in the United States have reached or exceeded their initial design life. Over the last several years, frequent deterioration of these bridges has occurred. Also, some of the relatively new bridge structures have experienced pre-matured degradation due to poor construction practices or use of inferior materials. Bridge owners in the US are beginning to more frequently include non-destructive evaluation (NDE) techniques to assess the conditions of in-service and new bridge structures. This facilitates more informed and cost-effective decisions to be made on repair, rehabilitation, or replacement of such structures.

Over the last several years, the US Department of Transportation (US DOT), the Federal Highway Administration (FHWA), and other research agencies within the US, have supported research efforts of various investigators to develop state-of-the-art NDE capabilities to overcome the long existing problem of bridge condition assessment. As a result, numerous NDE capabilities have been developed that can address the needs of bridge owners for bridge condition assessment.

This paper will present a discussion on the state of concrete bridge condition in the US as well as the state-of-the-art NDE practice for condition assessment of these structures. Concrete bridges rely on conventional, prestressing, or post-tensioning steel reinforcement to resist all relevant applied tensile loads while they are in service. Unfortunately, many of these bridge structures experience exposure to harsh environments and loading conditions during their service lives. This has lead to various modes of concrete deterioration and most importantly to severe corrosion of reinforcing steel within concrete. While research and development related to NDE techniques and instrumentation have advanced over the last few decades, it has been recognized that more need to be accomplished in areas such as education, standardization, data integration and interpretation.

1 INTRODUCTION

According to the US National Bridge Inventory (NBI) data, there are just over 600,000 bridges in the United States. Among these structures, concrete bridges constitute more than 65 percent. While concrete bridge structures are inherently durable, many in the US are now more than 50 years old. Many of these bridges have shown signs of distress and deterioration due to age and exposure to aggressive environments. In most cases, concrete deterioration in bridges develops over time and the bridge owners have sufficient time to perform necessary repairs. Examples include spalling of concrete in bridge decks, thermal and creep cracks, minor corrosion of non-structural and structural steel, etc. However, under some circumstances, bridge deterioration can lead to structural collapse. Examples include major corrosion of prestressing or post-tensioning steel, and major chemical concrete degradation leading to material softening. To keep bridge structures in service, bridge owners have invested significantly to repair and maintain them. In the US, bridge owners include states, cities, counties and other municipalities. The US Department of Transportation (US DOT) and Federal Highway Administration (FHWA)provide guidelines and resources for bridge safety evaluation program throughout the US. The FHWA has established the National Bridge Inspection Standard (NBIS) that mandates a minimum of a biannual safety bridge inspections for all bridges in the United States. It has long been recognized that effective and economical repairs in bridges can be possible only when structural and material conditions are understood first. This understanding can be achieved through the use of practical and effective inspection techniques including visual and other non-destructive evaluation (NDE). Effective and successful bridge evaluation is required in order to meet one of the five strategic goals of the US DOT which is to maintain a "State of Good Repair." This is defined as ensuring the United States proactively maintains its critical transportation infrastructure in a state of good repair. To enhance the effectiveness and more successful application of various NDE techniques to bridge

structures, more research, validation, standardization and education will need to be done. Recent efforts from the FHWA has focused on identifying such NDE needs for application to bridge structures. In Fall 2012, the FHWA coordinated the work of experts from the United States during a workshop to identify critical NDE needs for the US infrastructure (Boone 2013). These critical needs, as listed below, are not unique only to the United States as many nations face similar needs.

i Provide NDE education and training/certification.
ii Develop a NDE validation center for material and real bridge level specimens.
iii Standardize NDE procedures and protocols.
iv Create bridge condition and reference baseline data for quality assurance.
v Overcome the limitations of existing NDE and identify methods to address these limitations.
vi Determine cost benefit analysis of NDE.
vii Develop decision making/risk-based analysis framework to help put NDE in the design, maintenance, inspection, and repair process (incentives for States).
viii Determine the probability of detection for different NDE techniques.
ix Incorporate maintenance and inspection into the design process.
x Create improved methods for data visualization and presentation.
xi Implement a data/technology repository.
xii Create improved methods for data fusion and combination of techniques.
xiii Identify mature technologies and develop an applicability and deployability matrix.
xiv Identify limitations of visual inspection and identify easier methods to determine when NDE is required.

Meeting the above stated needs can significantly enhance the use of NDE in highway bridge structures.

In spite of the expressed concerns for the successful use of NDE techniques for bridge applications, the use of certain NDE methods have proven to be valuable in condition assessment of bridges.

Concrete bridge deterioration primarily results from material degradation and corrosion of reinforcing or prestressing steel. Corrosion of steel in concrete causes cracking and eventual failure of the structure if it is not detected early and repaired in a timely fashion. The most common method of bridge evaluation in the US has been based on performing visual inspection. While visual inspection, if performed by a qualified inspector, is often informative and useful, it cannot produce all the necessary information regarding the condition of the structure due to its inherent limitations. Specifically, visual inspection cannot reveal information on defects and signs of deterioration that are internal or invisible to the inspector. Accordingly, bridge owners are relying more on the use of currently available conventional NDE tools as well as more advanced methods.

Bridge decks represent the largest volume of materials and structural members in bridges. Since bridge deck failures and steel corrosion in concrete bridges are the most common and significant deterioration types, they will be the primary focus of discussion in this paper.

2 BRIDGE DECK DEFECTS AND INSPECTION

Beside corrosion of steel inside concrete, bridge deck deterioration includes delamination, honeycombing due to poor construction practice, concrete cracking due to temperature and load, and material degradation. At the initial stages, most defects in bridge decks are small and below the deck surface. They gradually advance to become larger defects with time, thus adding exposure to aggressive environments and the service load to which they are subject. When bridge deck defects reach the deck surface, they are usually at a critical state of deterioration where major repair and retrofit will be required. Concrete deck defects at early stages are more difficult to detect since they are usually located under the deck surface. These defects are not visible and visual inspections cannot detect them. Special NDE techniques have been developed that can help detect such defects in bridge decks. There is no single NDE technique that can be used to detect all defects caused from various deterioration mechanisms. Accordingly, one will need to utilize one or more appropriate NDE techniques to detect defects caused by specific deterioration mechanisms. A comprehensive research study sponsored by the Wisconsin Department of Transportation and the FHWA has identified various deterioration mechanisms for bridge decks as well as relevant NDE techniques that have shown promise for bridge deck defect detection (Ghorbanpoor & Benish 2003). The research has also identified advantages and limitations for these techniques. The identified techniques include chain drag and hammer sounding, ultrasonic pulse velocity, ultrasonic pulse echo, spectral analysis of surface waves, infrared thermography, impulse response, radiography, impact-echo, ground penetrating radar, and petrographic analysis.

A more recent study supported by the Transportation Research Board, SHRP2 program, has determined the effectiveness of a series of relevant NDE techniques for bridge decks through performing a series of validation tests in both laboratory and field (Gucunski et al. 2013). The research examined the performance of the techniques based on five measures of accuracy, precision or repeatability, ease of use, speed of test and data interpretation, and cost. The study placed its focus on non-destructive test evaluations for four types of deterioration in bridge decks. They included delamination, corrosion, vertical cracking, and concrete degradation. These deterioration types were selected due to their frequency of occurrence and the level of priority bridge owners place on them routinely. The NDE methods that were evaluated

under this study included chain dragging and hammer sounding (CDHS), impact echo (IE), ultrasonic pulse echo (UPE), ultrasonic surface waves (USW), impulse response (IR), ground-penetrating radar (GPR), half-cell potential (HCP), galvanostatic pulse measurement (GVP), electrical resistivity (ER), and infrared thermography (IR). For detecting delamination, only four of the selected methods (IE, CDHS, GPR, and IR) showed fair to good ability, based on the five criteria of accuracy, precision, ease of use, speed and cost, for detection of delamination in bridge decks. Among the four methods, the impact echo was more effective with a score of 2.8 in a scale of 1 to 5, with 1 representing poor and 5 excellent. The IR and GPR methods were ranked next but with the limitations of sensitivity to the time of the test during the day and the amount of moisture on the surface, in the material, and in the void. The CDHS method was only effective when the defect size was relatively large and when it was close to the surface. With respect to corrosion of steel in bridge decks, no method included in the study has the capability for accurate and direct measurement of corrosion due to their inherent physical characteristics. However, three techniques (HCP, GVP, and ER) were identified as having fair to good ability to provide information regarding the characterization of the corrosive environment. Only one method, ultrasonic surface wave, was found to have a fair to good ability to detect vertical cracks with known crack depth and to provide quantitative assessment of concrete material degradation.

The study by Gucunski et al. (2013) concluded that there is no single method of NDE that is able to successfully detect all types of defects in bridge decks and that the ultimate choice for the method and equipment depends on the type of deterioration that is a primary concern. The results of this study confirmed the same finding by others, including Ghorbanpoor & Benish (2003).

3 CORROSION INSPECTION IN BRIDGES AND CABLES

According to an estimate by the Strategic Highway Research Program (SHRP) of the U.S. National Research Council, the total cost of corrosion damage in United State bridges is approximately $20 billion and it is increasing at $500 million per year (NACE International 2011). If corrosion damage plus prevention and mitigation are considered for the US bridges, the total direct annual cost is about $8.3 billion (Koch et al. 2002). The expressed staggering cost of corrosion damage and mitigation is primarily due to the aging of the US bridge structures (Ghorbanpoor 2000, Ciolko & Tabatabai 1999).

Corrosion in bridges occur in all members including those in the substructures and superstructures. Over the last several decades, various methods of NDE have been utilized to determine the extent of corrosion and mixed levels of success have been achieved. Many NDE methods that sometimes have been claimed to yield success for detection of corrosion in bridges do not have such capability due to their inherent physical characteristics. At best, some of these techniques can only be effective in assessing the corrosive condition of the environment under test. Several of the more advanced NDE methods have been studied by different researchers to determine their effectiveness for detection of steel section loss due to corrosion in bridge structures. They included ultrasonic, ground penetration radar, radiography, acoustic emission (Ciolko & Tabatabai 1999), magnetic flux leakage or MFL (Ghorbanpoor et al. 2000), and remnant magnetic field or RMF (Scheel & Hillemeier 1997, Scheel & Hillemeier 2003, Hillemeier & Scheel 1998). These studies have concluded that the magnetic-based NDE methods have the most potential for success in detection of steel section loss due to corrosion in bridges. A more recent corrosion detection study at Lehigh University included a validation program for various NDE methods to detect corrosion and steel section loss due to the corrosion as well as defects in prestressing steel for concrete box girder bridges as well as laboratory concrete slabs with known defects in their embedded reinforcing and prestressing steels (Jones et al. 2010, Naito & Jones 2010). The NDE methods that were included in the Lehigh study included ground penetrating radar, line scanning thermography, galvanostatic pulse corrosion, ultrasonic shear wave, magnetic flux leakage, remnant magnetic field, and electromagnetic corrosion detection. Non-destructive testing experts with expertise in the above stated methods participated in the "blind testing" study. The concrete box girder test samples were removed from a Pennsylvania bridge that was being replaced due to excessive corrosion in the prestressing strands within the lower flanges of its girders. After the conclusion of the validation test program, the concrete box girders were sectioned and the strands were exposed to measure and record the amount of section loss at various locations along the length of each strand. The laboratory concrete slabs included reinforcing and prestressing steel that were placed in different depths within the slabs. Each reinforcing bar or prestressing strand had one or more manufactured areas of section loss of varying amounts at different locations along its length. The information about the amounts and locations of the manufactured section loss were not made available to the participants before the testing program was concluded at Lehigh University and before the final test reports were submitted by all participants. The results of the study indicated that only the magnetic flux leakage and remnant magnetic field were able to detect, with good accuracy, section loss in prestressing and reinforcing steel due to corrosion and manufactured defects.

Other studies have shown that the MFL method is a field worthy nondestructive evaluation technique that offers a very good capability for detection of corrosion or section loss in the tendons of post-tensioned (P-T)

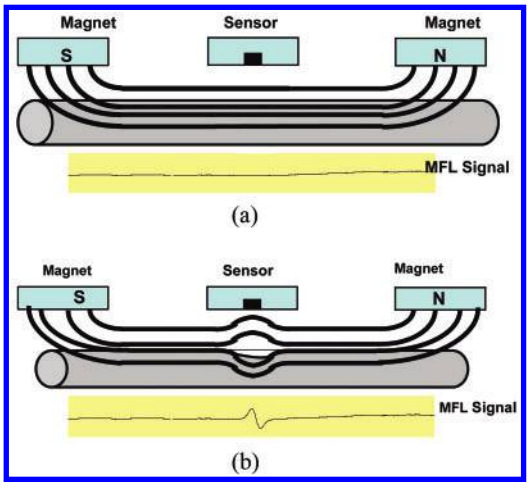


Figure 1. Concept of magnetic flux leakage (MFL). (a) MFL signal from a tendon without flaws, (b) MFL signal from a tendon with a flaw (Ghorbanpoor & Abdelsalam 2012).

concrete segmental box girder bridges (Ghorbanpoor 2000 & 2008, Christen et al. 2003, Ghorbanpoor & Abdelsalam 2012). The successful corrosion detection capability of the MFL technique in P-T tendons leads to the conclusion that there is a good potential for the method to be used effectively for corrosion detection also in cables of cable stay bridges. Corrosion of steel in external P-T tendons has been recognized by bridge owners and engineers as being a serious concern. The tendon corrosion has sometimes led to severe section loss that results in a major reduction of the load carrying capacity, or full fracture of such tendons. The problem arises from various design and construction shortcomings that lead to grouting voids and penetration of aggressive materials inside the tendons. Major degradation of prestressing steel may be avoided through the use of an effective NDE method, such as MFL, when tendon corrosion can be detected at an early stage of deterioration.

The basic operating principle of the magnetic flux leakage (MFL) is based on introducing a DC magnetic field to the reinforcement or P-T tendon and measuring the changes in the magnetic field caused by the presence of corrosion or loss of section. Any loss of section in the steel will result in the leakage of the magnetic flux to the neighboring areas where they can be detected by magnetic sensors. Figure 1 demonstrates a magnetic field change resulting in a MFL signal that is due to a loss of section in the bar as an assembly of a set of magnets and a sensing device are moved along the length of the bar.

Through laboratory tests and calibration exercises as well as mathematical modeling, specific data can be obtained to assist with the correlation of results in terms of flaw sizes and locations in steel bars and prestressing strands during MFL tests in real structures. The extent of the leakage of the magnetic field is proportioned to the level of loss of section in the steel from corrosion or fracture. It is also a function of the magnetic properties of the steel and surrounding media, and the distance between the sensing element and the location of the defect (Ghorbanpoor et al. 1991). Mathematical relations to determine the peak-to-peak variations, or the amplitude, of the magnetic flux leakage for subsurface flaws may be used for the purpose of calibrating the MFL test results (Brady & Stanley 1997). Equations 1 & 2 provide estimates of the MFL signal peak-to-peak values for cylindrical and spherical inclusions, respectively, in a steel structure.

$$\Delta H_y \approx 2.6 H_a \left(\frac{a}{d}\right)^2 \quad (1)$$

$$\Delta H_y = \frac{1.717(\mu-\mu_o)}{(2\mu+\mu_o)} H \left(\frac{a}{d}\right)^3 \quad (2)$$

In Equations 1 & 2, ΔH_y is the amplitude variation in the magnetic field in a direction vertical to the test surface, H is the magnetic field strength, μ and μ_0 are magnetic permeability for the medium and the flaw, respectively, a is the flaw radius, and d is the distance between the flaw and the position of interest or the location of the sensing element.

Several demonstrations of the successful application of the MFL method for detection of corrosion in bridge structures have been cited in this paper. Additional successful applications of the MFL technique for corrosion detection in concrete and cable stay bridges may be found in the available literature (Bertrand et al. 2012 & 2012).

4 CONCLUSION

Concrete bridges in the United States constitute a large portion of all bridges and they face deterioration problems due to aging, exposure to harsh environments, and loading. Efforts by the US Department of Transportation, Federal Highway Administration, State DOT offices and various researchers have led to the development of a series of NDE techniques and methods of testing to address early detection of defects and remediation for bridge structures. While several NDE techniques have already been developed and are being used in highway bridges, it has been found that no one method has the ability to detect all defect types that are encountered in various bridge members. For detection of bridge deck delamination, it has been found that IE and to some extent IR and GPR are effective. For measuring the corrosion activity in an environment, HCP, GVP, and ER may be used with the consideration of their inherent limitations. For detection of vertical cracks in concrete, USW may be used successfully. It has been found that the MFL technique is the most effective NDE technique for detection of steel section loss in prestressed and post-tensiond structures. Generally, it is more effective to use more than one suitable technique to make an assessment of the structural condition of bridge structures. It has also been concluded that more needs to be done in terms of

NDE related education, standardized procedures, overcoming current limitations, probabilistic and decision support approaches, data visualization, and data fusion and interpretation from multiple techniques.

REFERENCES

Bertrand, F., Titus, M.D., Nims, D.K., Ghorbanpoor, A. & Devabhaktuni, V.K. 2012. Practical Assessment of Magnetic Methods for Corrosion Detection in an Adjacent Precast, Prestressed Concrete Box-Beam Bridge. Journal of Nondestructive Testing. August.

Bertrand, F., Titus, M.D., Nims, D.K., Ghorbanpoor, A. & Devabhaktuni, V.K. 2012. Field Test of Magnetic Methods for Corrosion Detection in Prestressing Strands in Adjacent Box-Beam Bridges. ASCE Journal of Bridge Engineering, vol. 17:984–988, November.

Boone, S.D. 2013. Identification of Nondestructive Evaluation Needs for the United States Highway Infrastructure. Publication No.: FHWA-HRT-13-056.

Brady, D.E. & Stanley, R.K. 1997. Nondestructive Evaluation: A tool in design, manufacturing, and service. *CRC Pres,* New York.

Christen, R., Bergamini, A. & Motavalli, M. 2003. Three-Dimensional Localization of Defects in Stay Cables Using Magnetic Flux Leakage Methods. Jurnal of Nondestructive Evaluation, Vol. 22, No. 3. September.

Ciolko, A. T. & Tabatabai, H. 1999. Nondestructive Methods for Condition Evaluation of Prestressing Steel Strands in Concrete Bridges. Final Report: Phase I – Technology Review, National Cooperative Highway Research Program, Transportation Research Board, Washington, DC.

Ghorbanpoor, A., Steber, G.R. & Shew, T.E. 1991. Evaluation of steel in concrete bridges: The magnetic field disturbance (MFD) system. Final *Report No. FHWA-SA-91-026; Federal Highway Administration, US Department of Transportation.*

Ghorbanpoor, A. 2000. Condition Assessment of External P-T Tendons in the Mid-Bay Bridge. Final Report, Florida Department of Transportation, Tallahassee, FL.

Ghorbanpoor, A., Borchelt, R., Edwards, M. & AbdelSalam, E. (2000). Magnetic-Based NDE of Prestressed and Post-Tensioned Concrete Members – The MFL System. Final Report FHWA-RD-00-026, Federal Highway Administration, US Department of Transportation, McLean, VA.

Ghorbanpoor, A. & Benish, N. 2003. Non-Destructive Testing of Highway Bridges. Final Report # 0092-00-15, Wisconsin Department of Transportation.

Ghorbanpoor, A. 2008. MFL Inspection of External Post-Tensioned Tendons in the Varina-Enon Bridge, Final Report, Viginia Department of Transportation.

Ghorbanpoor, A. & Abdelsalam, E. 2012. Corrosion Detection in Tendons of Segmental Concrete Bridges. Proceedings of the 6th International Conference on Bridge Maintenance, Safety and Management, IABMAS 2012, Lake Maggiore, Italy, July 8–12.

Gucunski, N., Imani, A., Romero, F., Nazarian, S., Yuan, D., Wiggenhauser, H., Shokouhi, P., Taffe, A. & Kutrubes, D. 2013. Nondestructive Testing to Identify Concrete Bridge Deck Deterioration. SHRP2 Report No. S2-R06A-RR-1, Transportation Research Board.

Hillemeier, B. & Scheel, H. 1998. Magnetic Detection of Prestressing Steel Fractures in Prestressed Concrete. Materials and Corrosion, 49, 799–804.

Jones, L., Pessiki, S., Naito, C. & Hodgson, I. 2010. Inspection methods & techniques to determine non visible corrosion of prestressing strands in concrete bridge components, Task 2 – Assessment of candidate NDT methods. ATLSS Report No. 09-09, Lehigh University, Bethlehem, PA and Pennsylvania Department of Transportation, Harrisburg, PA.

Koch, G.H., Brongers, M.P.H., Thompson, N.G., Virmani, Y.P. & Payer, J.H. 2002. Corrosion Costs and Preventive Strategies in the United States. Publication N. FHWA-RD-01-156. Federal Highway Administration, US Department of Transportation.

NACE International. 2010. NACE International: Bridge Corrosion. White Papers: Bridge Corrosion, www.nace.org/content.cfm?parentid=1046&currentID=142.

Naito, C. & Jones, L. 2010. Nondestructive Inspection of Strand Corrosion in Prestressed Concrete Box Beam Members. NDE/NDT for Highways and Bridges: Structural Materials Technology Conference, ASNT, New York City, NY, 214–219.

Scheel, H. & Hillemeier, B. 1997. Capacity of the Remnant Magnetism Method to Detect Fractures of Steel in Tendons Embedded in Prestressed Concrete. NDT & E International, 30(4), 211–216.

Scheel, H. & Hillemeier, B. 2003. Location of Prestressing Steel Fractures in Concrete. Journal of Materials in Civil Engineering, ASCE, 15(3), 228–234.

Research and Applications in Structural Engineering, Mechanics and Computation – Zingoni (Ed.)
© 2013 Taylor & Francis Group, London, ISBN 978-1-138-00061-2

Rapid and economical condition assessment of concrete bridge decks through automation of NDE data collection, analysis and interpretation

N. Gucunski & A. Maher
Rutgers University, Piscataway, New Jersey, USA

H. Ghasemi & F.S. Ibrahim
Federal Highway Administration, McLean, Virginia, USA

ABSTRACT: Federal Highway Administration (FHWA) have invested into the development of an automated system for condition assessment of concrete bridge decks using nondestructive evaluation (NDE) technologies. The primary objective of the system development is to enable rapid and economical assessment and monitoring of a large number of bridges as a part of the Long Term Bridge Performance (LTBP) Program. The automated system is a robotic platform equipped with multiple NDE sensor and imaging technologies. In particular, the system carries ground penetrating radar (GPR) and acoustic arrays, four electrical resistivity (ER) probes, and three cameras for deck surface and panoramic bridge imaging. The NDE sensors and applied NDE methods enable assessment of corrosion, delamination and concrete quality. The data collected by multiple technologies are wirelessly transferred and analyzed in a "command van", and in most case presented in a near real time. The condition assessment of decks using a robotic system enables data collection at far higher rates than by the manual collection by a group of NDE technicians.

1 INTRODUCTION

Bridge decks, due to their high exposure to the environmental conditions and direct application of traffic loading, deteriorate faster than other bridge components. Providing bridge deck maintenance or rehabilitation of roughly 600,000 bridges in the United States is a formidable task. It is especially so considering the fact that their average age is 44 years. The Federal Highway Administration's (FHWA's) Long Term Bridge Performance (LTBP) Program research team interviewed a number of state Departments of Transportation (DOTs) regarding the expenditure levels for maintenance, rehabilitation, and replacement of bridge decks. The conclusion of the interviews was that bridge decks constitute between 50 and 80 percent of the overall expenditures for bridges.

Good bridge management requires periodical inspections and evaluations using the means that can provide objective information about the condition of the bridge and its components. The predominant practice of condition assessment of concrete bridge decks in the States is by visual inspection and the use of simple nondestructive evaluation (NDE) tools like chain drag and hammer sounding (Figure 1). While such approaches have its merits, they also have limitations in terms of the early problem detection and characterization of deterioration or defects with respect to their state of progression. More advanced NDE technologies have shown promise in condition assessment of concrete bridge decks and have been implemented in the FHWA's LTBP Program.

While many advanced NDE technologies can accurately detect and characterize problems in bridge decks and other structures, there is a need to improve their application in a number of ways. Firstly, the speed of data collection should be increased. Secondly, both the data collection and data analysis and interpretation need to be automated. Thirdly, the condition assessment should be as close as possible to real time. Finally, the presentation of the results of the evaluation needs to be more comprehensive and data presentation more intuitive. With all these goals in mind, the FHWA initiated development of a robotic system for condition assessment of concrete bridge decks. A strong argument for this investment was the need to evaluate and monitor performance of hundreds of bridge decks throughout the States in the next phase of the Program.

2 LTBPP BRIDGE DECK PERFORMANCE STUDY

Interviews with state DOTs and the LTBPP's expert task group indicated the performance of bridge decks as the key bridge performance issue. For that purpose the LTBPP initiated in 2009 a program of comprehensive condition assessment of concrete decks using multiple NDE technologies (Gucunski et al., 2012 and 2013). The assessment of bridge



Figure 1. Assessment of bridge deck delamination using chain drag.



Figure 2. Assessment of delamination using IE method.

decks within the LTBPP concentrates on the detection, characterization and progression monitoring of corrosion, delamination and concrete degradation. A multi-faceted program of performance evaluation was developed for that purpose, which relies on NDE, visual inspection and physical sampling and testing. Five NDE technologies are implemented for the characterization of the three deterioration types: ground penetrating radar (GPR), electrical resistivity (ER), half-cell potential (HCP), impact echo (IE), and ultrasonic surface waves (USW) method. The GPR is used to identify bridge deck areas with likely deterioration and highly corrosive environment, to map all metallic objects and to measure the concrete cover. The ER is used to assess the potential for corrosive environment, while the HCP is used to measure corrosion activity. The primary goal of IE is to detect and characterize delamination. A device called Stepper that carries three IE probes is used for that purpose (Figure 2). Finally, the USW method is deployed to obtain information about the concrete quality through a measurement of concrete elastic modulus.

As an illustration a typical result of the NDE based condition assessment, delamination maps from 2009 and 2011 surveys of a bridge in Virginia are presented in Figure 3. The condition maps demonstrate the ability of IE to detect and define the boundaries of delamination, to describe the severity of delamination, and to monitor delamination progression with time. In addition, the quantitative nature of the results of NDE surveys enable a quantitative description of deterioration and more objective assessment of condition rating. As it is illustrated in Table 1, percentages of the deck at various stages of delamination can be easily calculated, and the progression of delamination well monitored. Combined with bridge deck segmentation, percentages can be calculated also for different sections of the deck. This can be utilized to identify the areas of faster deterioration progression and or the ones that should have priority in maintenance or rehabilitation. Finally, condition indices are calculated using a weighted area approach. According to the formula used, on a scale 0 to 100, where 100 is the best condition, this bridge received a condition rating with respect to delamination of 70 in 2009, and 57.2 in 2011.

Table 1. Assessment of deck delamination of a bridge in Virginia for 2009 and 2011.

	Severe Delamination		Incipient Delamination	
	2009	2011	2009	2011
Shoulder	24%	33%	20%	26%
Slow Lane	12%	21%	32%	40%
Fast Lane	12%	23%	36%	40%
Entire Deck	15%	25%	30%	36%

The NDE data collection, analysis, interpretation and presentation for surveys using multiple technologies represents a significant effort. Typically, a team of five to six NDE experts and technicians are involved conduct evaluations using the described five NDE technologies. The condition assessment using a further described robotic system significantly reduces that effort and is also expected to significantly reduce costs of evaluation and monitoring.

3 AUTOMATED DATA COLLECTION AND ANALYSIS

3.1 *Description of the robotic platform*

The robotic system with its components is shown in Figures 4 and 6. The robot itself is approximately 1.25 m wide and 1.5 m long. It has four omnidirectional wheels, which enable the robot to move in any direction or turn in place. The robot carries multiple NDE sensors, digital cameras, positioning devices and devices for obstacle avoidance.

The front side of the robotic platform is shown in Figure 4. Two acoustic arrays and four electrical resistivity probes are attached. Each of the acoustic arrays has multiple sources (impactors) and receivers (Figure 5). Different combinations of those are utilized to conduct multiple IE and USW tests. As a result, both IE

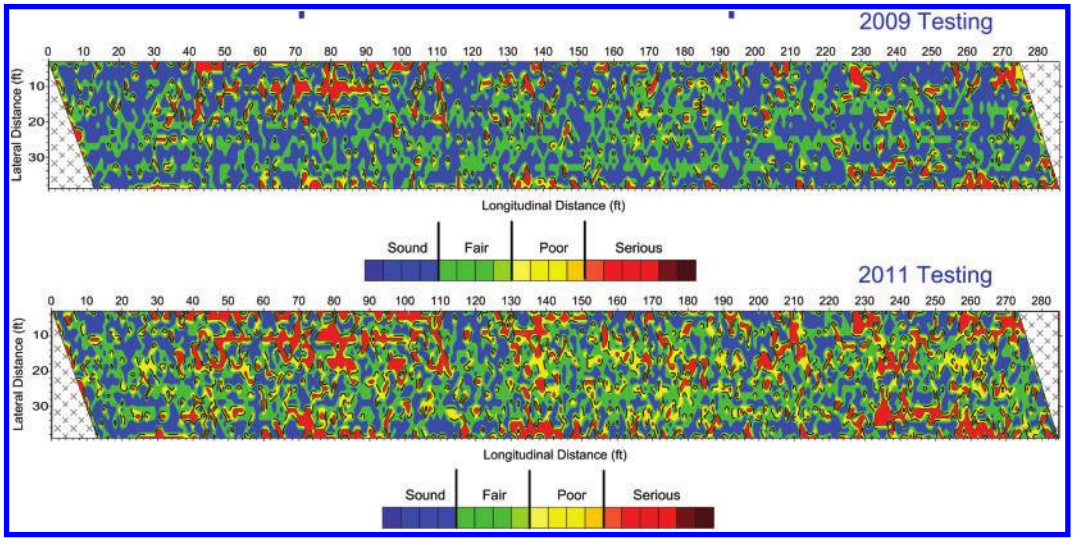


Figure 3. Delamination maps from impact echo testing for a bridge in Virginia.



Figure 4. The front view of the robotic platform and the attached components.

and USW data are collected at a resolution three to five times higher than typical data collection within the LTBPP, which is on a 0.6 m by 0.6 m grid. The two acoustic arrays are 1.8 m wide enabling surveys over a half of the width of a typical lane in a single robot run. The four resistivity probes are the Wenner probes (Figure 5) spaced 45 cm apart. There is a spraying system that keeps the probe electrodes moist at all times to ensure electrical coupling between the probes and concrete deck.

There are also two digital cameras positioned approximately 90 cm above ground that are used for imaging of the surface of the bridge deck. Each of the cameras covers approximately a 0.9 by 0.6 m deck area. The images collected are being automatically stitched into a single high resolution image of the deck surface. Also on the robot's front end is a laser scanner, which is used for obstacle avoidance. Two additional laser scanners on the sides (not visible in the figures) are used primarily for collision avoidance with curbs and barriers.

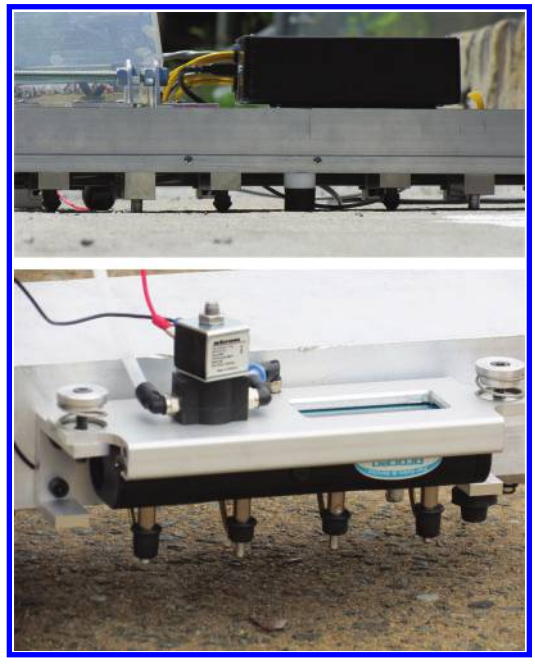


Figure 5. Impactors and sensors of the acoustic array (top) and a Wenner type electrical resistivity probe (bottom).

Two IDS Hi-Bright GPR arrays are mounted on the rear side of the robotic platform. Each of the arrays has sixteen antenna, or eight pairs of antennas of dual polarization. Similar to the acoustic arrays, the GPR arrays cover a strip of the deck 1.8 m wide. Finally, there is the third digital camera mounted on a mast in the middle of the robotic platform. The mast can lift pneumatically the camera to a 4.5 m height to take 360 degree panoramic images of the bridge deck.



Figure 6. The rear view of the robotic platform with GPR arrays.

The robot utilizes three systems for path planning and maneuvering. Those include a differential global positioning system (GPS), a wheel encoder and an inertial measurement unit (IMU). As shown in Figures 4 and 6, the robot carries two Novatel GPS antennas on the front and rear ends of the robot. The third GPS antenna, "the base station", can be placed at any point of the bridge deck. The data from the three positioning systems are fused using Kalman filter to secure the movement of the robotic system with the accuracy of several cm. It is necessary to take only three GPS coordinates on the bridge deck to fully define the robot's path. The robot moves fully autonomously, i.e. when the robot completes one survey strip it turns 180 degrees and slides laterally to a position for scanning of the next strip. The robot can also be operated manually using a joystick, Iphone or android type devices.

3.2 *Data analysis and presentation*

As stated in the introduction, the objectives of the robotic platform development included an automated and near real time data analysis, an improved data interpretation through a multi NDE complementary approach, and advanced and more intuitive data visualization. The data analysis, interpretation and visualization are conducted in the "command van" (Figure 7). The van is also used to transport the robot. The robot is unloaded and loaded using a pair of light ramps. During the transportation the sensor arrays are folded, as shown in the figure.

The data are wirelessly transmitted from the robot to the command van as they are collected. The data are analyzed as received. For example, the impact echo records are analyzed to create a delamination map, the deck surface images are stitched and analyzed to create a cracking map, etc. The robot operator can control and monitor data collection and analysis on four main monitors in the van. As an illustration, a screen describing the GPR data collection and analysis is shown in Figure 8. The top of the figure shows a GPR B-scan with the "picked" rebars (tips of hyperbolas). Below the scan are the diagrams of the amplitudes of reflections of the rebars, and the evaluated depth of the rebars



Figure 7. The command van with the robot in position for transportation.

(concrete cover). The information is used to map the reinforcement, plot the concrete cover map, describe the corrosive environment of the deck, and to identify zones of possible deterioration. In addition, condition indices are calculated and compared to the ones from the previous testing, if that one was conducted. A complete list of the functions that can be displayed on the four monitors is presented in Table 2. In addition, the operator has two additional monitors that allow monitoring of the robot movement and position on the deck. The monitoring of the movement is done by a camera on the roof of the van, as shown in Figure 7.

The results of all the evaluations listed in Table 2 can be reviewed using the condition maps, similar to the ones shown in Figure 2. In addition to the described data presentation, a 3D data visualization platform enables a very intuitive review of all the main deterioration types in the deck. In the 3D view, zones of low modulus, poor quality concrete are described as clouds of different levels of translucency and color. Similarly, delaminations are presented as predominantly horizontal surfaces, where the degree of translucency, and color type and intensity define the extent and severity of delamination. Finally, the corrosive environment is described through coloring of rebars, where hot colors indicate a highly corrosive environment. The 3D body of the deck can be overlaid by the image of the

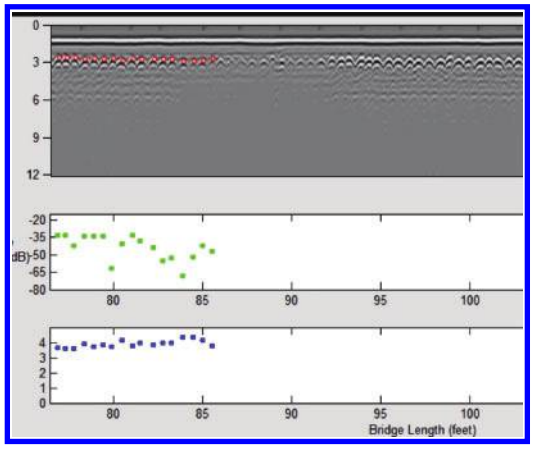


Figure 8. A screen with the GPR B-scan with identified rebars (top), the amplitudes of reflections form rebars (middle) and the depth of rebars (bottom).

Table 2. Data display options in the command van

GPR	Data collection (B-scan)
	Rebar picking
	Condition map
	Concrete cover map
USW	Data collection
	Concrete quality map
Impact Echo	Data collection
	Delamination map
Electrical Resistivity	Data collection
	Resistivity map
Imaging	Image collection
	Image stitching
	Crack mapping
	Panoramic view image
Other	Condition ratings
	Fused data
	Robot position

deck surface for a comparison of visible and internal damage.

4 CONCLUSIONS

The robotic system with integrated multiple NDE technologies enables condition monitoring of concrete bridge decks on a regular basis. The system overcomes deficiencies of the manual and single NDE technology data collection approaches in several ways: 1) the data collection is rapid and fully autonomous, 2) the application of the robotic system significantly reduces exposure of the bridge inspection crews to the passing traffic, 3) the complementary use of multiple NDE technologies enables detection of different deterioration type and enhances the certainty of detection, and 4) the associated platform for data visualization facilitates a more complete and more intuitive presentation of the deterioration and defects in the deck. While the initial objectives of the development were to address the needs of the LTBP Program, it is expected that the robotic platform will also in longer term be of benefit to state DOTs and other bridge owners. The benefits will stem from getting the information that will allow better planning, better selection of intervention procedures, and from reduced frequency and duration of traffic interruptions during inspections.

ACKNOWLEDGMENTS

This work was conducted under DTFH61-08-C-00005 contract from the U.S. Department of Transportation – Federal Highway Administration (USDOT-FHWA). A large number of individuals from Rutgers' School of Engineering working within the Center for Advanced Infrastructure and Transportation (CAIT) have contributed to various aspects of the robotic system development, construction and implementation. The authors gratefully acknowledge contributions of: Professors Basily Basily, Jingang Yi and Kristin Dana, Research Associates Drs. Hung La and Seong-Hoon Kee, Research Engineers Hooman Parvardeh, Ronny Lim and Francisco Romero, and graduate students Parneet Kaur and Prateek Prasanna.

REFERENCES

Gucunski, N., Romero, F., Imani, A. & F.A. Fetrat 2013. Non-destructive evaluation-based assessment of deterioration progression in concrete bridge decks. *Proc. 92nd Annual Transportation Board Meeting*, Washington, D.C., January 13–17, on CD.

Gucunski, N., Maher, A., Ghasemi, H. & F. Ibrahim 2012. Segmentation and condition rating of concrete bridge decks using NDE for more objective inspection and rehabilitation planning. *Proc. 6th Intl. Conf. on Bridge Maintenance, Safety and Management-IABMAS 2012*. Stresa, Lake Maggiore, Italy, July 8–12, on CD.

Research and Applications in Structural Engineering, Mechanics and Computation – Zingoni (Ed.)
© 2013 Taylor & Francis Group, London, ISBN 978-1-138-00061-2

Making sense of bridge monitoring: Vision for the future

Aleksandar Pavic
Professor of Vibration Engineering, College of Engineering, Mathematical and Physical Sciences, University of Exeter, Exeter, UK

James M.W. Brownjohn
Full Scale Dynamics Ltd, The Sheffield Bioincubator, Sheffield, UK

ABSTRACT: This paper presents a vision for the future monitoring systems which will become normal requirements for management of bridges as key objects of national infrastructure in the UK and elsewhere. Rather than being pushed by authorities and legislation, we expect that bridge managers will recognize the clear business cases for investing in well-designed targeted monitoring. To support this proposition, the paper presents two case studied where state-of-the-art bridge monitoring technology was used or potentially could be used to:

- Decide when to inspect and change bridge bearings, and
- Decide when to close various traffic lanes to reduce probability of overstressing bridge structural components.

1 INTRODUCTION

The UK Government's 2011 National Infrastructure Plan [1] signalled the need for investments of up to £250bn over 10 years to return UK infrastructure (transport, power, communications, water, and waste) to world class levels of performance. Only about a third of this can be provided from a public purse in the UK. The rest must come from private funding - most likely overseas sovereign investment funds. The key problem is clearly how to attract such funding and how to convince private finance that the investment in the UK infrastructure is sound. Having hard data about past and future physical performance of such infrastructure is a way forward to justify investment and attract private funding. In fact, it could well be the *only* way forward.

Focusing on bridges as key elements of any national infrastructure, the American Society of Civil Engineers (ASCE) reports a cost of $140bn to repair all deficient bridges in the United States [2]. Similar to the UK, whilst taxpayers in the USA can be expected to fund a small proportion of such enormous investment, as for the general infrastructure mentioned above, the remainder must come from private sources. The primary requirements for attracting both private and public investment in an infrastructure asset are managed risk and reliability of performance in continuous operation with ever increasing service and safety demands. Maximising return on investment requires minimisation of costs necessary to achieve that performance – put simply *getting more from less*. These requirements highlight the process of the whole-life performance management of civil infrastructure, a process involving decisions about design, construction, operation, maintenance, repair, decommissioning and demolition. Ensuring that such decisions are informed, correct and cost effective is the most important unsolved challenge in civil infrastructure management, attracting hundreds of researchers and multi-£M global research investment. These people and this investment are all trying to solve one of the most challenging problems in civil structural engineering nowadays: how to convert testing and monitoring data from objects of infrastructure, into knowledge and decision making when managing infrastructure as public assets? The problem is particularly acute for bridges, considering their importance, and is really about how to make sense of bridge testing and monitoring data. This research has yet to deliver significant benefits in the real world due to incoherent engagement with stakeholders, misdirected emphasis in the past focusing on hardware rather than data interpretation, tendency to view infrastructure assets in isolation and the lack of a systematic approach to link experiences between different structures. This is a recognised problem in the USA and Federal Highway Administration (FHWA) are still "working the problem" [4].

Focusing on bridges, the above stated problem is obviously not new. A paradigm shift is needed across the board and with all stakeholders in the way how bridges are managed from their conception to their decommissioning. Considerable cultural changes are needed and these will follow changes in the business models used for managing bridges including the legal

and economical framework within which public assets like bridges operate. This applies not only to the USA, but also to the UK, Europe and rest of the world. The prolonged crisis which has been shaking the foundations of the world economy for several years now may well become a badly needed catalyst for the required paradigm shift.

The continued drive for better and more enduring performance from bridges is crippled by the lack of technically sound, reliable, harmonised and economic means for monitoring asset condition. Hence, informed decision making by bridge managers is severely impaired. There is potential nowadays to transform monitoring into an *enabling technology* that will revolutionise the decision making process at all stages of an infrastructure's life-cycle: from design to demolition. This will yield extraordinary reduction of the currently very high direct and indirect cost of bridge performance management. The enabling technology will also foster growth of the infrastructure monitoring and decision support systems as a new technology sector which key role would be to resolve the £multi-trillion global challenge of managing deteriorating and failing infrastructure.

The aim of this invited paper is therefore to present a case and vision for this paradigm shift, making use of existing examples not only in civil engineering, but also in other engineering disciplines where such paradigm shifts happened and changed forever the ways how industries operated.

2 FUNDAMENTAL CAUSES OF PROBLEM

In essence, the problem lies in the nature of civil structural engineering design and disproportionately low level and certainty of information on which it is based relative to the huge importance of such structures. Because of this, in civil engineering the acceptable level of risk of structural failure or lack of its serviceability is at least an order of magnitude lower than for more technologically advanced structures employed in mechanical and aerospace engineering. There are three key reasons for this low risk approach:

1. Civil infrastructure, in particular major long-span bridges, underpin human society and supports not only traffic but the daily lives of hundreds of thousands of people and economies of linked regions.
2. Unlike aircraft, automobiles, trains and other mass produced machinery, which are extensively tested as prototypes during their design, objects of civil infrastructure including bridges are unique one-off designs with no opportunity for extensive prototype testing during design and before going into service. As such, they are designed with considerably reduced knowledge base and their structural performance is poorly understood making prediction of future behaviour difficult if not impossible.
3. The ambiguity and degree of uncertainty related to the actual operation of the structure, and potential increases in load and usage in the future, force the use of an extremely conservative design embedded in design guidelines which are used instead of prototype testing.

Notwithstanding the low-risk design methodology, critical infrastructure items such bridges deteriorate with time to such a point that, if no action is taken, they become unserviceable requiring closure and repairs, or may even collapse. To guard against this, operating authorities prescribe methods of routine, typically visual, inspection, which are slow, costly, and subjective, hence potentially quite unreliable.

The prime example of the dubious reliability of the current bridge inspection regime was generated in the UK during winter 2011/2012. A sudden and totally unexpected decision to completely close the Hammersmith flyover in London was made on 23 December 2011 after many nights of closure of the flyover for maintenance and visual inspection throughout 2011. This structure takes 90,000 vehicles per day on a strategically vital A4 route making it the prime gateway to London, not just for the West of the country, but also for one of the world's largest and busiest airports at Heathrow. This prime route remained completely closed until 13 January 2012, causing traffic chaos in West London for a period of three weeks, covering the Christmas and New Year holidays before partial reopening slightly reduced the chaos. This situation lasted for months. Apparently, an exceptional overloading event worsened the state of corroded tensioning cables of the 50-year old structure so that they started snapping at a rate fast enough for the authorities to close the flyover. This is speculation, since the structure had not been monitored over a long enough period of time. Hence, there is no information about 'normal loading' and no evidence that that the dramatic closure was actually necessary.

If anybody thought this was a chance the identification of a *new crack* on the already damaged Boston Manor viaduct forced a dramatic closure of the M4 between London and Heathrow airport – a key section along the Olympic Route Network. This lasted for five days in early July 2012. The new crack had been identified in a "sensitive location" following the final stages of the complex repairs to 15 mm long hairline cracks discovered *by chance* [5] in April in welds on the viaduct just west of junction 2 near Hounslow. A 7.5t weight restriction on the damaged stretch had been imposed immediately, diverting coaches and lorries onto busy local roads. The latest news is that Boston Manor viaduct is beyond further repairs and will be replaced.

How many similar cases and surprise total closures are lurking within the UK fleet of key bridges on the national transportation network?

3 THE WAY FORWARD

Interestingly, if a sudden event happened to a Roll Royce aero-engine high above the Pacific, such as a

lightning strike causing the engine to cough, monitoring sensors within the engine would automatically record all relevant responses. This data would be transmitted immediately from the aeroplane to the Rolls Royce 24/7 operations room in Derby, UK which continuously assesses on-line the performance of thousands of working jet engines around the world. Based on the instantaneous information from the aircraft and the expected performance, a decision would be made while the plane is still in the air if the engine requires additional inspection after landing, causing delays and financial losses. In the past and without the benefit of permanent monitoring and data streaming and analysis, this would almost certainly be the case as – similar to bridges – safety is paramount. However, it is not anymore due to this *service based* business model of manufacturing jet engines which is based on the on-line condition monitoring technology and instantaneous decision making process which Rolls Royce mastered and commercialised around the world. The data constantly collected from engines is invaluable to airlines as the information enables Rolls Royce to predict when engines are more likely to fail, letting the airlines schedule engine changes efficiently. Embracing such technology and innovation transformed Rolls Royce from a failing company in 1971 into a currently most successful manufacturer of jet engines in the world.

Why can't the same business model be employed in the management of bridges? Over many years in the UK there has been fragmentation of construction industry and infrastructure management characterised by significant shift towards the use of subcontracting, overly complex procurement approaches and uncertainty of future work on key infrastructure due to lack of vision and leadership. This has increased transaction costs, encouraged shortermism and deterred industry from a more strategic approach to investment in skills, technology and innovation [6]. There are, however, clear signs that this approach is changing offering great opportunities to the sector, one of them being use of permanent monitoring for effective decision making in managing key objects of infrastructure, including bridges.

4 MOTIVATION

Wenzel [7] noted that construction sector is conservative needing strong push to motivate it to implement new technologies, such as converting monitoring data into decision making. He outlined the following motivation drivers:

1. Responsibility-driven motivation, stemming from design standards, codes and guidelines which make mandatory requirements to instrument, monitor and interpret before deciding what to do with a particular structure, such as bridge in operation. This is particularly so when covering events such as emergencies or accidents whereby monitoring data before the event can describe what is 'normal' and data after the event can be used to establish if the structure still behaves as 'normal'. Conventional assessment in such situations tend to be overly conservative, usually to compensate for the lack of reliability.
2. Economy-driven motivation, stemming from, say, the need to reduce unnecessary maintenance costs, such as expensive and not particularly reliable regular inspections, or from the need to prioritise repairs within limited budgets which make use of more reliable information about the remaining life prediction of the structure. Another emerging motivation within this category is the need for an informed transfer of ownership from public to private hands, whereby hard data from the structure provides a more reliable information of the value and longevity of the structure which is an asset for the new owner, including their finance and insurance organisations.
3. Curiosity-driven motivation whereby forward-looking owners, operators and – in general – clients, understand limitations of the current civil engineering design practise and want to learn about the actual behaviour to help them plan future designs.

The following example will demonstrate usefulness of monitoring in decision making about their operation.

5 ASSESSMENT OF BRIDGE BEARINGS

The Humber Bridge was opened in 1981. Spanning 1410 m, it held the record of the world's longest single spans suspension bridge until 1997. The Bridge spans the Humber Estuary between Hessle (North) and Barton-on-Humber (South). The Hessle side span is 280m and the Barton side span is 530 m (Figure 9).

The aerodynamically shaped bridge box girder is discontinuous at the towers. At each end there is a pair of 'A-frames' which are approximately 3.8 m tall and 3.4 m wide (Figure 10). These bearings primarily accommodate axial movement of the span ends, but also permit rotation of the deck in the horizontal plane and in the vertical plane of bridge axis and towers as the bridge deforms under a combination of traffic, wind and temperature effects. In total there are 12 of these bearings, four on each span.



Figure 1. Humber Bridge instrumentation.

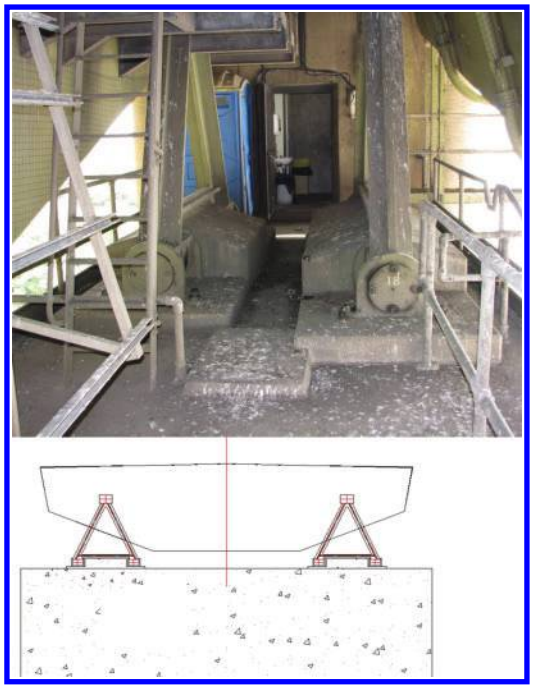


Figure 2. Top: Photo showing a pair of A-frames, one for the main and one for the side span. Bottom: The sketch shows a pair of A-frames connected to the main span box girder.

A pair of Hilti PD4 extensometers on each end of the main span was used to monitor the longitudinal deck movement at the positions of the two A-frames in Figure 10 (bottom). Hence, these two sets of data provided information to measure both longitudinal extension and horizontal plane rotation of the bridge at its end.

The end rotation is strongly dependent on wind speeds, as shown in Figure 11.

Ambient acceleration response of the deck is continuously recorded at midspan and used to estimate (in real time) the natural frequencies and damping ratios of the lowest frequency vibration modes. For the first (lateral) mode of vibration, Figure 12 shows the estimated natural frequencies as a function of the RMS of the corresponding block(s) of acceleration data. It can be seen that at about 0.2 m/s^2 RMS the frequency generally reduces and stabilises at about 0.054 Hz for higher levels of response. This indicates the likely non-linear 'stick-slip' behaviour somewhere in the structure, as confirmed by damping estimates whereby a similar 'unsticking' effect is observed roughly at the same RMS acceleration levels (Figure 13). The damping, however, is amplitude-dependent with lower damping corresponding to higher responses.

Figure 14 (top) shows diurnal variation of the four horizontal displacements measured extensiometers.

Figure 14 (bottom) cumulative quasi-static horizontal displacements of the four points on the two ends of the main span which indicate that their total travel is between 2 m and 3 m over the 10 day analysed. This means that each bearing travelled at least

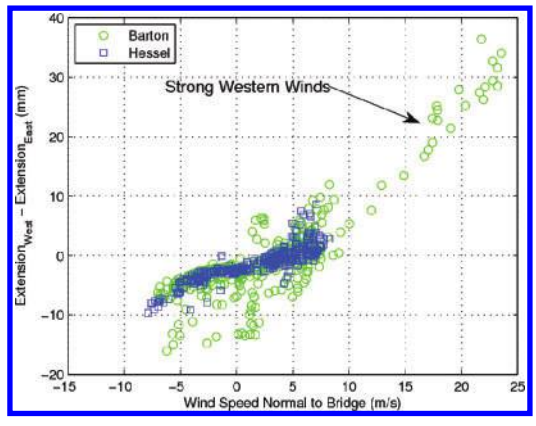


Figure 3. Hessle end rotates less than the Barton end under strong Western winds.

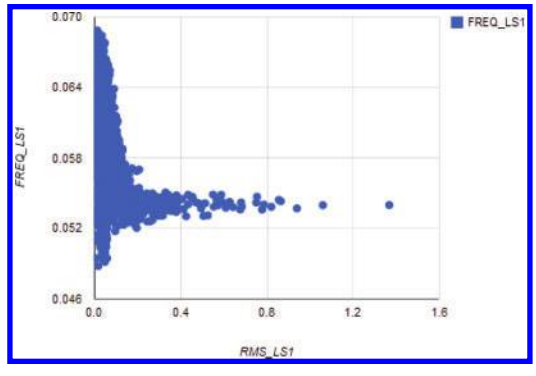


Figure 4. Amplitude-dependent natural frequency.

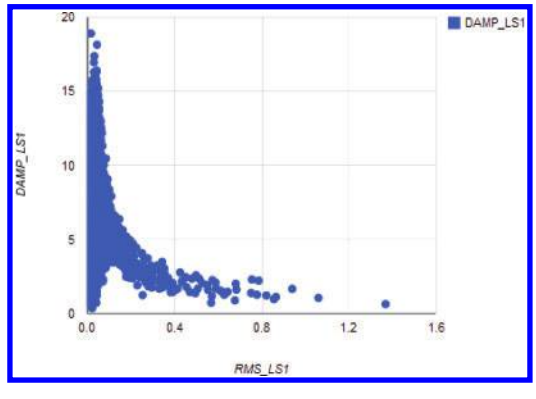


Figure 5. Amplitude-dependent damping.

3km since the opening in 1981. Not surprisingly, this has been linked with excessive wear at the A-frames and the likely stick-slip effect previously mentioned. Closer inspection indicated that one of the bearings visibly dropped and is resting on the concrete plinth underneath due to wear of the bottom of the pin-bush arrangement. Hence, in recent years the adequacy of capacity and performance of the main span A-frames

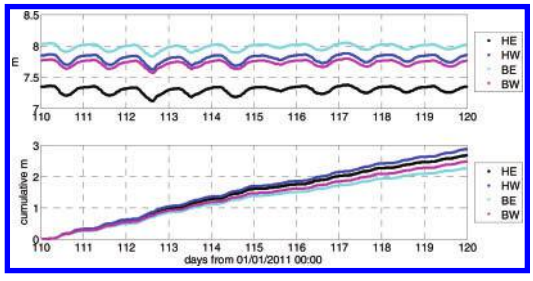


Figure 6. Diurnal variation of horizontal displacement at the bridge ends (top). Cumulative displacement of bridge decks over 10 days.



Figure 7.

has been questioned, based on the monitoring results which highlighted potential issue in the structure.

6 BRIDGE DAY-TO-DAY TRAFFIC MANAGEMENT

Modern bridge monitoring technology enables on-line access to continuous data streams, including video data, which can be used to see live performance of the bridge. Such systems may be used to control day-to-day bridge usage to avoid potential overstressing of structural elements.

Figure 15 shows a situation on a major partly loaded suspension bridge where one half of the bridge cross section is empty and the other is fully loaded due to a morning rush-hour accident.

As a consequence, the on-line monitoring system immediately registered that the stay cable tensions suddenly peaked whereas the natural frequency of the system dropped suddenly (Figure 16).

Figure 17 shows a major 6-lane road bridge in Continental Europe. The steel structural system with inclined supports acts as a 'shallow' frame with end columns rigidly connected to the structure that are 'sensitive' to temperature effects.

Figure 18 shows bending moment diagrams due to partial traffic load and temperature effects of +35°C. A potential problem for this bridge structure is that

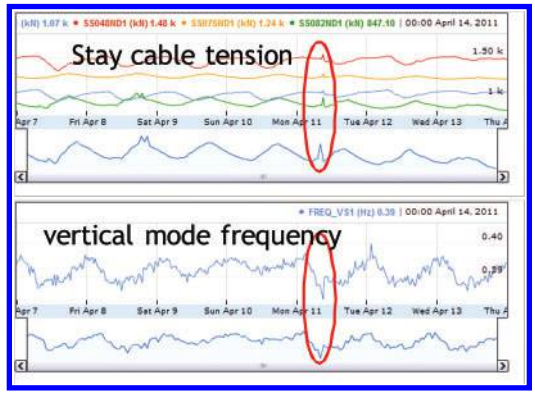


Figure 8. On line monitoring system picked up sudden tensions in stay cables and drop in the natural frequency of the bridge structure, which could be set up to trigger alert when managing traffic in cases of frequent bridge congestions.



Figure 9. Major road steel bridge.

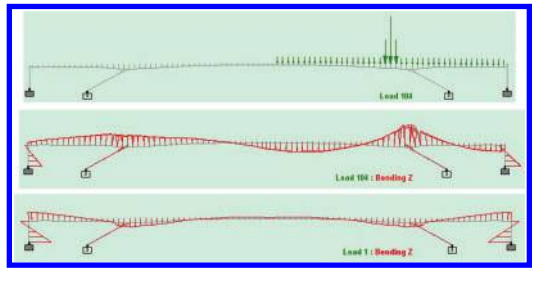


Figure 10. Critical load case – partial traffic loading combined with extreme temperature effects.

the combination of live load as shown in Figure 18 (top) with winter temperature of −35°C will make sure that the two bending moments arithmetically add at the bottom of the vertical end column which is fixed.

This is potentially unsafe situation which can be managed by a permanent monitoring system which would monitor temperature and strain/stresses at the bottoms of the end columns. In case of low temperatures and if the strain readings require, the traffic over this vital bridge can be reduced, reducing the

risk of a potentially unsafe situation that would otherwise require prevention by disruptive and expensive remedial work on the end columns.

7 CONCLUSIONS

This paper presents a vision for the future monitoring systems which will become normal requirements for management of bridges as key objects of national infrastructure in the UK and elsewhere. Rather than being pushed by authorities and legislation, we expect that bridge managers will recognize the clear business cases for investing in well-designed targeted monitoring.

To support this proposition, the paper presents three case studies where state-of-the-art bridge monitoring technology was used or potentially could be used to manage the following key aspects of bridge operation and maintenance:

- Deciding when to inspect and change bridge bearings, and
- Deciding when to close various traffic lanes to reduce probability of overstressing bridge structural components.

REFERENCES

[1] National Infrastructure Plan 2011, HM Treasury. http:/ /www . hm - treasury . gov . uk / national _ infrastructure_plan2011.htm

[2] http://www.infrastructurereportcard.org

[3] Moon FL, Aktan AE 2011, International guidelines for application of technology to bridges, for FHWA Long Term Bridge Program (draft), Also Aktan et al., 2000, ASCE EMD 126(7).

[4] http://www.fhwa.dot.gov/research/tfhrc/programs/infrastructure/structures/ltbp

[5] Wynne, A. Worsening cracking problem closes M4 betwteen London and Heathrow, NCE, 7 July 2012. http://www.nce.co.uk/news/structures/worsening-cracking-problem-closes-m4-between-london-and-heathrow/8632760.article

[6] HM Treasury & Infrastructure UK, 2010.

[7] Wenzel, H. The Character of SHM in Civil Engineering, Chapter 118, Encyclopedia of Structural Health Monitoring, John Wiley & Sons Ltd., 2009.

[8] Moyo, P., Brownjohn, J. M. W. and Omenzetter, P. Highway bridge live loading assessment and load carrying capacity estimation using health monitoring system. Structural Engineering and Mechanics, 18(5), 609–626, 2011.

[9] Das, P. C. Assessment loading criteria for bridge decks, piers and parapets, Structures and Buildings, ICE, 146(1), 411–421 2001.

Research and Applications in Structural Engineering, Mechanics and Computation – Zingoni (Ed.)
© 2013 Taylor & Francis Group, London, ISBN 978-1-138-00061-2

Structural model updating using combined global mode and local primary frequency

J.L. Hou
School of Civil Engineering, Dalian University of Technology, Dalian, China

J.P. Ou
School of Civil Engineering, Dalian University of Technology, Dalian, China
School of Civil Engineering, Harbin Institute of Technology, Dalian, China

Ł. Jankowski
Smart-Tech Centre, Institute of Fundamental Technological Research,
Polish Academy of Sciences, Warsaw, Poland

ABSTRACT: In Structural Health Monitoring (SHM), structural model updating plays an important role in maintaining integrity and safety of structures. This paper presents a model updating method using the measured global mode and local primary frequency. First the global test is experimented to obtain the low order modes which reflect the global information of the structure. Then the mass is added on the member of structure to increase the local dynamic characteristic and to make the member have local primary frequency. When a local excitation is applied on a member, if the caused vibration mainly consists of only one single modal which represents most of the local distortion, then the corresponding frequency is defined as the local primary frequency. Local primary frequency reflects more local information of the member and hence is more sensitivity to the local damage. Therefore, both low mode and local primary frequencies are combined and used for model updating. The effectiveness and accuracy of the proposed method is verified by the experiment.

1 INTRODUCTION

Structural health monitoring is a hot research in civil engineering, thereinto model updating is one of its important theoretical base, and provides reliable evidence for structural monitoring, forecasting and its safety assessment. However in civil engineering with the structures more and more huge and complexity, the accurate modal updating has becoming more and more difficult, which requires the proper dynamic measurements, as well as the efficient exploitation of the measurements.

Structural modal represents the structural basic dynamic information which is easy to be obtained or identified, and so modal-based damage identification or model updating methods are applied widely in civil engineering. In 2010 Zhao etc. identified the damage location and extents via the difference of the frequencies and mode shapes before and after damage occurred. In 2012, Shi etc. via the perturbation of the modes, damages of a bridge structure is identified considering variation of its boundary condition. However in practice, usually only a few low order modals can be identified, and are not sensitivity to local damages. Therefore it is hard to identify accurately all the parameters of the whole structure only via those data.

Recently substructure methods are popular on model updating of important local members via the local responses which avoid the difficulties of the whole structural model updating. Yang used continuous nonlinear least squares methods to estimate the substructure acceleration, velocity and displacement as well as parameters of its stiffness and damping etc.; meanwhile, the interface forces of the substructure are estimated. This method can effectively trace the variance of the structural damage. Xing and Mita identified structural damages of a shear model via ARMAX methods by staggered substructure, where degree freedom of each substructure is limited. Ou etc. proposed the Isolated Substructure Method which isolated the substructure virtually from the global structure into an virtual independent structure via local responses, and thus the classical methods aiming at the global structure can be used for substructure model updating. Substructure methods are usually used for identifying the local structure, and often required to monitor or identify the substructure boundary. The application becomes difficult on the substructures with complex boundary.

Above all, for the global structure test, it is not easy to capture the local modification, while local test can't accurately reflect the information of global

structure, especially structures like truss. Truss usually consists of hundreds of thousands of bars, and the change or damage of each bar has little influence on the global structure. In order to simultaneously update the global structure and local modification, this paper combines the global and local dynamic information, and performs a fine model updating of the truss structure.

2 MODAL UADATING

In structural model updating, the measured dynamic information is taken as known, and proper physical parameters are selected as optimization parameters, which are often optimized by minimizing the errors between the tested modal and the theoretical finite element model. The precision and the amount of the measured data are the key factors in structural model updating. Aiming at the characteristic of space truss, this paper respectively uses modal test on global structure and amounts of tests on local bars. The dynamic information which is sensitivity tothe local damage is digged for the updating.. The objective function is built via combing the information of both global structure and local structure, which is shown in Equation 1.

$$f(\mu)=\sum_i \alpha_{g,i}\left\|\frac{\omega_{g,i}(\mu)-\bar{\omega}_{g,i}}{\bar{\omega}_{g,i}}\right\|+\sum_j \alpha_{s,j}\left\|\frac{\omega_{s,j}(\mu)-\bar{\omega}_{s,j}}{\bar{\omega}_{s,j}}\right\| \quad (1)$$

where μ is the modification factor to be updated; $\bar{\omega}_{g,i}$ is the identified ith low order frequency of the global structure, while $\omega_{g,i}(\mu)$ is the corresponding frequency of the theoretical FEM model, $\alpha_{g,i}$ is the weight of error of the corresponding measured global information; $\bar{\omega}_{s,j}$ is the jth measured frequency which reflects the local information, while $\omega_{s,j}(\mu)$ is the corresponding frequency of the theoretical FEM model, $\alpha_{s,j}$ is the weight of error of the measured local information.

3 TRUSS EXPERIMENT

An experiment of a space truss model is performed here to introduce the proposed model updating method by combing the global and local information, and the efficiency of the method is verified.

3.1 *Truss model*

A supported steel 20-span space truss is shown in Figure 1, which is an experimental rail-cum-road bridge model. It is 8 m long with the height of 0.9 m, width of 0.56 m, and consists of 312 bars, with the nodes of 108. The young's modulus is 2.06 Gpa, and the density is 7850 Kg/m^3. The bars, steel tubes, are connected by bolted spherical joint (bottom right in Figure 1), of which the diameter is 80mm. The bars are classified into three types according to its radius, see Table 1.



Figure 1. A truss experimental model.

Table 1. Three types of bars in truss structure.

Types		Bar A	Bar B	Bar C
Number		80	198	34
Tubes	Outside diameter(mm)	30	20	14
	Thick(mm)	8	3	3
Bolt	Types	M20	M16	M10
	Length(mm)	100	90	60

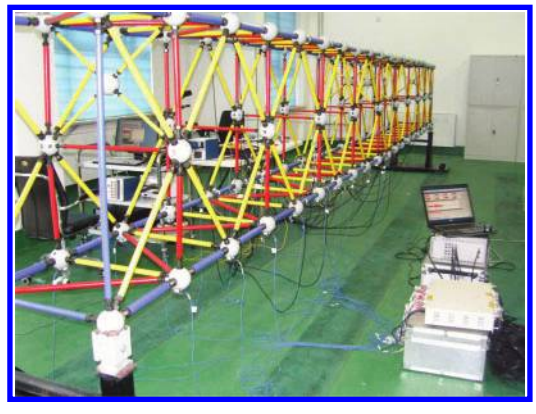


Figure 2. Accelerations placement.

3.2 *Model test of the global truss*

Accelerometers are located on the bottom nodes of the truss, shown in Figure 2. Ambient excitation is applied on the structure, and the modal shapes and frequencies are identified via the caused random responses, shown in Figure 3 and Table 2.

First the theoretical finite element model (FEM) is built, where each bar is defined as an element. The model has 312 elements with 108 nodes and 638 degree of freedoms. The element cross sections

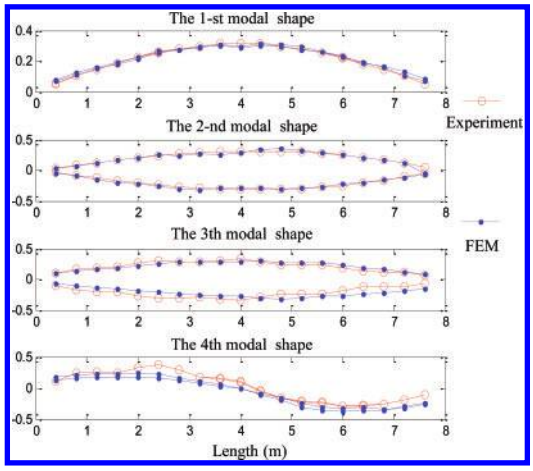


Figure 3. The comparison of modes of global structure.

Table 2. The errors of lower order natural frequencies of global structure.

Order	Experimental	Theoretical	Error
1	18.4	23.27	26.47%
2	27.6	34.41	24.67%
3	36.8	52.58	42.89%
4	53.3	76.97	44.41%

and initial moment are calculated from the geometric dimensioning. The nodes are rigid and set as mass points to consider the weight of the spherical joints and bolts. The mass is evaluated as 2.83kg. Figure 3 and Table 2 respectively compares the modal shapes and frequencies which are obtained from the experimental model and FEM model. It shows that the errors between them are rather obvious, around 30%, which tells that the built theoretical FEM model is very coarse.

3.3 *Local dynamic test*

The members of bar B in Table 1 are classified into four kinds according to their lengths and positions (Figure 4). Local dynamic tests are performed on the four kinds of bars. In order to increase the local dynamic characteristic, masses are added in the middle of the bars. Due to that the weight of one accelerometers and its connector is 340g, so in the experiment location of the accelerometer plays the role of the additional masses, and the value of added mass is adjusted by the number of the located sensors. For long bar, its local stiffness is relatively small, and one additional mass is enough, that is, one accelerometer is located. For short bar, its local stiffness is rather big, and more sensors are needed. The location of the sensors or additional masses is shown in Figure 5.

A straight bar in horizontal plane is taken as an example to illustrate and experimentally verify that

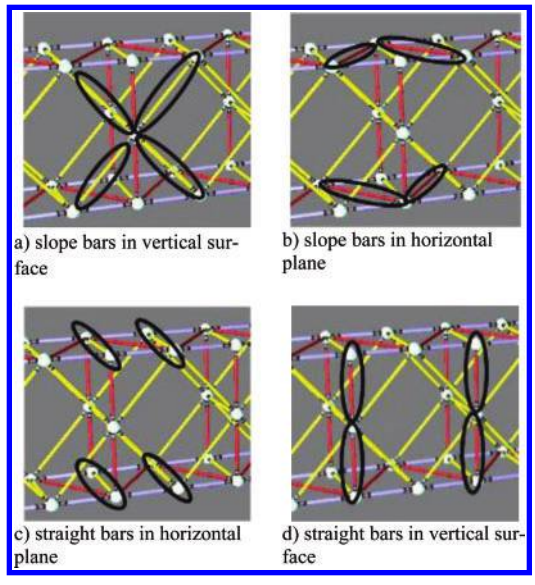


Figure 4. Four kinds of elements.

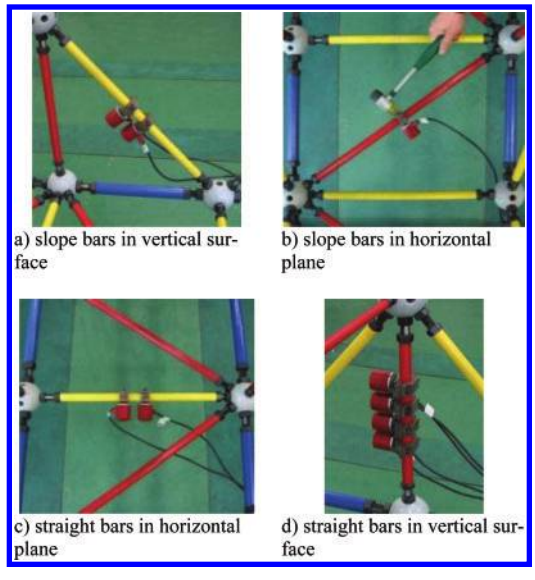


Figure 5. The placements of additional masses.

local characteristic can be increased via adding mass on the corresponding bar. Three cases are discussed, that is, two, three and four masses (sensors) are respectively added on the bar. In each case, a hammer excitation is applied on the middle of the bar, and the corresponding responses are measured, then the spectrum analysis is performed. The obtained power spectrums in the three cases are shown in Figure 6. Because the excitation is applied on the local bar, so the local model is certain to be excited. The bigger the additional mass value is, the more obvious the caused local characteristic will be. In the cases of two or three additional masses, the power spectrum

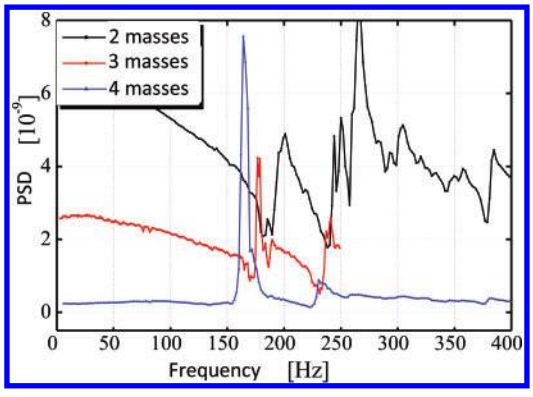


Figure 6. The power spectrum.

of the global structure has multiple peaks. It is hard to judge which frequency belongs to the local bar, and which frequencies reflect the model of the global structure, that is to say, the local characteristic is not obvious. While in the case of four additional masses, the power spectrum only has one peak, it shows that the action of the local excitation is mostly absorbed by the local bar itself and the additional masses. In this case, the caused vibration mainly is the distortion of the local bar, so the frequency corresponding to the peak in the power spectrum belongs to the local bar and is defined as the local primary frequency primary frequency. Certainly the local primary frequency is mainly determined by the stiffness of the bar. In order to compare the measured local primary frequency and that of the theoretical model, 58 bars are picked up to perform an test, which are respectively 14 bars from the slope bars in vertical surface, 16 bars from slope bars in horizontal plane, 20 bars from straight bars in horizontal plane and 8 bars from straight bars in vertical surface. Sensors(masses) are located on these bars respectively according to the way shown in Figure 5, and the hammer excitation is applied. The identified local primary frequencies are shown in Figure 7. Table 3 compares the measured local primary frequency and that of the theoretical model, where respectively one bar is chosen from each kind of bars. It shows that the identified value from the experiment has obvious difference from the theoretical value, which tells that the theoretical model has significant error compared to the actual model, and needs to be updated.

3.4 *The selection of updating parameters*

In practice, the actual Young's modulus of the steel, physical dimension and the density have little error from the theoretical values. Then the factor which causes the errors of FEM model is mainly due to the node model, and so node model is updated in the model updating.

First the fine model of the bolted spherical joint, bolt and the steel pipe are built considering their actual way of connection, shown in Figure 8. It considers the local reinforcement of the spherical joint($r = 4$ cm) to the

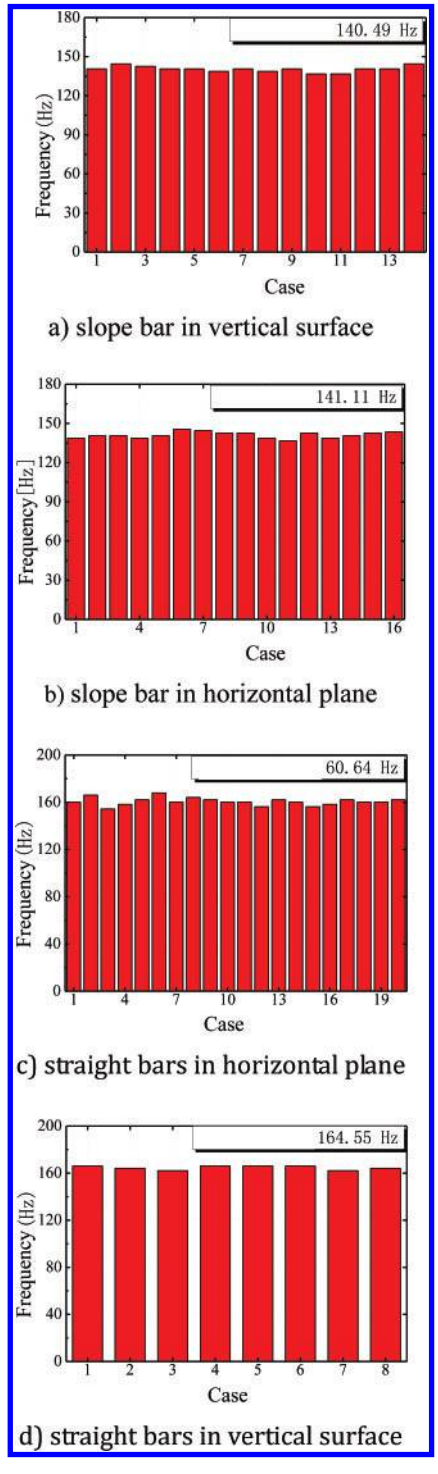


Figure 7. The identified local primary frequencies.

ends of the pipe by a reinforcement parameter k which is the ratio of the spherical joint stiffness to the pipe stiffness. The definite value of k needs to be optimized. In addition, it considers the local weakening caused by

Table 3. The errors of local primary frequencies of 4 kinds of elements

Types	Identified	Theoretical	Error
Slope bar in vertical surface	138.67	151.24	9.06%
Slope bar in horizontal plane	140.63	155.57	10.62%
Straight bars in horizontal plane	166.02	176.28	6.18%
Straight bars in vertical surface	164.06	186.52	13.69%

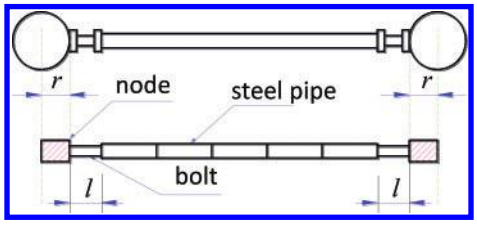


Figure 8. Fine modeling of the element.

bolt. Denote l the weakening length, which needs to be optimized. The stiffness in the weakening range takes the value of the bolt. Because there are holes in the spherical joint and it is connected with bolts and nuts, so it is hard to determine the joint weight, which needs to be updated. Above all, reinforcement parameter k, weakening length l and the joint weight m are taken as the model updating parameters.

According to the model in Figure 8, a bar is divided into 9 elements including 2 spherical joint elements, 2 bolt elements, and 5 pipe elements. Then the fine model will have 2606 nodes with 2918 bar and 15614 degree of freedoms(Dofs). Certainly the model is complicated and the computational work will be huge. Therefore, model reduction is considered.

For each bar, the fine model has 9 elements and 60 Dofs. Through Guyan reduction, the 60 Dofs are condensed into 12 Dofs on the two ends of the bar, and thus the dimension for the condensed substructure stiffness and mass matrix is 12. Then the condensed stiffness and mass matrix are used to assemble the parameter matrix of the whole structure model, except the bar with additional mass, i.e. the bar to be updated, of which its fine model with 60 Dofs is directly used without reduction. In this way, it balances the considerations on the computational work, the relative accurate connection and the accuracy of the local bar analysis.

3.5 *Model updating*

After building the fine FEM, the identified 4 models (Figure 3) and 58 local primary frequencies (Figure 7) are used to optimize the joint mass m, reinforcement parameter k_i, and weakening length l_i of the four kinds of bars via the objective function (Equation 1). The optimized joint mass m equals to 3.33kg, and the parameters k_i, l_i are shown in Table 4. Substitute the modified parameters into the FEM, the frequencies and modes of the model are estimate and compared with the values identified from the measurements, respectively shown in Table 5 and Figure 9. The comparison of the local primary frequencies here only lists some typical cases, shown in Table 6. In all the comparisons, the biggest error is 5.55%, which shows that the updated space truss model reflects the actual truss structure on both global dynamic behavior and local characteristic and the model is updated effectively and accurately.

Table 4. The model updating of the node parameters

Type	l(cm)	k
Straight bars in vertical surface	4.5	3.2
Slope bars in vertical surface	2.9	4
Straight bars in horizontal surface	6.7	1.6
Slope bars in horizontal surface	2.7	8

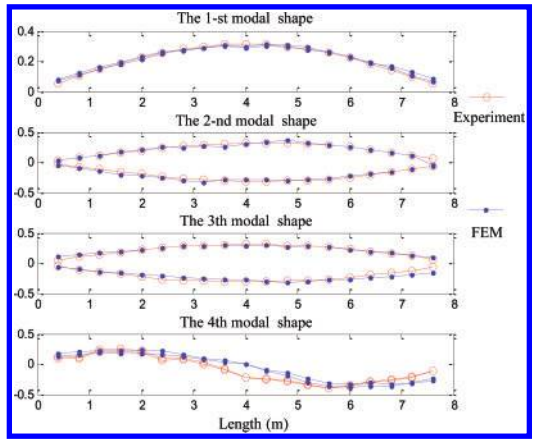


Figure 9. The comparison of modes of global structure.

Table 5. The errors of lower order natural frequencies of global structure

Order	Identified	Theoretical	Error
1	18.4	18.82	2.28%
2	27.6	27.25	−1.25%
3	36.8	38.63	4.97%
4	53.3	50.34	−5.55%

4 CONCLUSION

This paper effectively combines the dynamic information of the global structure and the local structure, and performs the model updating of a space truss structure

Table 6. The errors of local primary frequencies.

Types	Identified	Estimated	Error
Straight bars in vertical surface	166.02	162.81	−1.93%
Slope bars in vertical surface	140.63	138.99	−1.17%
Slope bars in horizontal surface	138.67	138.24	−0.31%
Straight bars in horizontal surface	164.06	167.55	2.13%

experimentally. The obtained main conclusions are as follows:

(1) According to the characteristic of the space truss, masses are added on the local bars to enlarge their local characteristic. In this way, under local excitation the vibrates mainly represented by the local bar.
(2) Local primary frequencies mainly reflect the characteristic of the local bar, while the easily identified low order models mainly reflect the global structural characteristic. So their combination can adequately use the measured data and effectively performs the structural model updating.
(3) Fine model of the local bar is built; meanwhile model reduction is used to reduce to the number of Dofs. This improves the optimization efficiency and on the other hand also assures the built FEM reflect the structural real information as much as possible.

ACKNOWLEDGMENTS

The authors gratefully acknowledge the support of the Major State Basic Research Development Program of China (973 Program) (2013CB036305), of the National Natural Science Foundation of China (NSFC) (51108057,51108066), of the Special Financial Grant from the China Postdoctoral Science Foundation (2012T50255), of the Project of National Key Technology R&D Program (China) (2011BAK02B01, 2011BAK02B03). Financial support through the FP7 EU project Smart-Nest (PIAPP-GA-2011-28499) and of Structural Funds in the Operational Programme–Innovative Economy (IE OP) financed from the European Regional Development Fund—Project "Modern material technologies in aerospace industry" (POIG.0101.02-00-015/08) is gratefully acknowledged.

REFERENCES

Zhao, J. & Zhang, L. & Xiang. B. etc. 2010. A method for structural damage identification based on incomplete measured data. *Chinese Journal of Applied Mechanics*. (04): 670–673.

Shi, Z. & Zhao, R. D. 2012. Damage detection of bridge structure accounting for boundary condition variation based on mode parameters. *Chinese Journal of Applied Mechanics.* 02 191–196.

Yang, J. & Huang, H. Substructure Damage Identification Using Sequential Nonlinear Lse Method, *Proc. 4th International Conference on Earthquake Engineering, Taipe 12–13 October, 2006.*

Xing, Z. & Mita, A. 2012. A substructure approach to local damage detection of shear structure. *Structural Control and Health Monitoring.* 19(2): 309–318.

Hou, J. & Jankowski, L. & Ou, J. 2012. Experimental study of the substructure isolation method for local health monitoring. *Structural Control and Health Monitoring*. 19(4): 491–510.

Sun, X.D. 2010. Optimal sensor placement and damage identification for Structural Health Monitoring. *PhD thesis, Harbin Institute of Technology*.

Research and Applications in Structural Engineering, Mechanics and Computation – Zingoni (Ed.)
© 2013 Taylor & Francis Group, London, ISBN 978-1-138-00061-2

On the application of artificial boundary condition frequencies in structural identification

Y. Lu & L. Mao
Institute for Infrastructure and Environment, School of Engineering, The University of Edinburgh, UK

Z.G. Tu
IKM Ocean Design As, Norway

ABSTRACT: The acquisition of pertinent modal data in good quality and sufficient quantity is fundamental to the success of a structural identification/damage detection process using a global dynamics based approach. A series of studies have been conducted recently to explore the potential use of the so-called artificial boundary condition (ABC) frequencies for structural identification. The ABC frequencies correspond to the natural frequencies of the structure as if additional pin supports (artificial boundary) were inserted at certain locations, but they are derived from the frequency response measurements on the original structure without the actual need of inserting the additional pins. This paper introduces and discusses the studies investigating into the effectiveness of using such frequencies in a FE modal updating procedure and the practicality of extracting such frequencies from a typical modal testing survey.

1 INTRODUCTION

Structural identification and damage detection have attracted considerable attention in the civil engineering research community over the last three decades. In the context of global structural assessment, a lot of researches have been devoted to develop techniques for evaluating the condition of an existing structure based on the assumption of availability of the required modal data, particularly natural frequencies and mode shapes. In real applications, however, measurement errors and environmental noises dictate that only a limited amount of such data as acquired from a physical test may be truly useful in a parameter identification or damage detection procedure.

It is well recognised that modal frequencies may be measured with generally much higher accuracy as compared to mode shapes. Typically the errors in the measured natural frequencies may be controlled within 1%, whereas the errors in elements of a measured mode shape vector could be as much as 20% (Mottershead & Friswell 1993). However, the limitation in relying on the frequency information is also obvious; the total number of such frequencies that may be measured from a structure is limited; and moreover, lower order natural frequencies are generally insensitive to local damages. In this respect, seeking additional modal frequency data becomes a subject of much research interest.

The use of the zeros (anti-resonances) in the frequency response function (FRF) curves for damage detection of structures has been explored by many researchers. Since the zeros occur generally at different frequencies for different measurement points, there exist many more zeros than resonances, and thus it provides a plentiful resource for the enlargement of the frequency dataset (Lallement & Cogen 1992). Studies on the use of anti-resonances for finite element model updating (e.g. Ambrogio & Fregolent 2000, Jones & Turcotte 2002) tend to suggest that the anti-resonances from the driving-point FRFs are more suitable for model updating. As a matter of fact, the anti-resonances in a driving-point FRF are effectively the natural frequencies of a modified system by adding a pin (restraint) to the respective DOF.

A more general approach to generating additional modal frequency would be altering the boundary condition so as to derive the perturbed natural frequencies of a structure (Li et al. 1995). However, such an idea can hardly be implemented in practice due to the obvious impracticality of physically changing the boundary condition of a real structure for a measurement purpose.

The possibility of obtaining a diverse range of "perturbed" natural frequencies without the need to actually impose the additional supports has been theoretically established through the introduction of the concept of artificial boundary condition (ABC) frequencies (Gordis 1996, 1999). Using this approach, the natural frequencies of a structure with "artificially" added pin supports at certain locations may be derived from the incomplete frequency response function (FRF) matrix measured from the original structure. The term of "artificial boundary condition"

reflects the fact that, although the frequencies thus derived are equivalent to the natural frequencies of the perturbed system, the perturbed boundary conditions need not be actually imposed. In the case of ABC frequencies with a single ABC pin, it degenerates to the driving-point anti-resonances.

With the incorporation of the ABC frequencies, the modal frequency dataset can potentially be expanded dramatically. Three key questions then naturally arise, namely,

a) how effective the ABC frequencies could be in a structural parameter identification or finite element (FE) model updating process,
b) given the large number of possible ABC configurations, even for a limited number of ABC pins, how should a selection be enforced so that the chosen ABC frequency information would only improve the general condition of the identification, and
c) how accurate the ABC frequencies may be extracted from physical measurements.

A series of investigations have thus been organised to comprehensively address the above questions (see for example Tu & Lu 2008, Lu et al. 2008, Mao & Lu, in prep.). In this paper, an overview of the above investigations will be provided, along with brief descriptions of the relevant techniques and discussion on some key measurement and data processing considerations.

2 BACKGROUND THEORY

The concept of the ABC frequencies is somewhat analogous to the driving point anti-resonances, in which case the singularities in the frequency response function (FRF) correspond to the natural frequencies of the structure as if a single artificial pin was added at the respective DOF. It is conceivable that if multiple pins could be involved, the resonant frequencies will generally become more sensitive to structural parameter changes. The way of deriving such ABC frequencies (with multiple pins) was first proposed in the works by Gordis (1996, 1999). For a linear system and considering the partition between the measured and unmeasured coordinate (DOF) sets, the steady-state equation of motion of the forced vibration at a forcing frequency (rad/s) may be written as:

$$\left(\begin{bmatrix} \mathbf{k}_{mm} & \mathbf{k}_{mo} \\ \mathbf{k}_{om} & \mathbf{k}_{oo} \end{bmatrix} - \omega^2 \begin{bmatrix} \mathbf{m}_{mm} & \mathbf{m}_{mo} \\ \mathbf{m}_{om} & \mathbf{m}_{oo} \end{bmatrix} \right) \begin{Bmatrix} \mathbf{x}_m \\ \mathbf{x}_o \end{Bmatrix} = \begin{Bmatrix} \mathbf{f}_m \\ \mathbf{f}_o \end{Bmatrix} \quad (1)$$

where $\mathbf{k}$ and $\mathbf{m}$ are stiffness and mass matrices, $\mathbf{x}$ and $\mathbf{f}$ are vectors of generalized response and excitation amplitudes, respectively. Subscript *'m'* and '*o*' represent the measured coordinates (or DOFs) and unmeasured DOFs ('omitted coordinate set' or OCS), respectively. The OCS is effectively a reduced system, in which all the measured DOFs are restrained or pinned to the ground. Introducing the impedance matrix, $\mathbf{Z} = \mathbf{k} - \omega^2\mathbf{m}$, Eq. (1) can be re-written as:

$$\begin{bmatrix} \mathbf{Z}_{mm} & \mathbf{Z}_{mo} \\ \mathbf{Z}_{om} & \mathbf{Z}_{oo} \end{bmatrix} \begin{Bmatrix} \mathbf{x}_m \\ \mathbf{x}_o \end{Bmatrix} = \begin{Bmatrix} \mathbf{f}_m \\ \mathbf{f}_o \end{Bmatrix} \quad (2)$$

Assuming no excitations are imposed on the omitted coordinates, i.e., $\mathbf{f}o = \mathbf{0}$, it follows:

$$(\mathbf{f}_m) = \left(\mathbf{Z}_{mm} - \mathbf{Z}_{mo}\mathbf{Z}_{oo}^{-1}\mathbf{Z}_{om}\right)(\mathbf{x}_m) \quad (3)$$

or

$$\frac{\mathbf{f}_m}{\mathbf{x}_m} = \mathbf{H}_{mm}^{-1} = \left(\mathbf{Z}_{mm} - \mathbf{Z}_{mo}\mathbf{Z}_{oo}^{-1}\mathbf{Z}_{om}\right) \quad (4)$$

where $\mathbf{H}_{mm} = \mathbf{x}_m/\mathbf{f}_m$ is the incomplete frequency response function (FRF) matrix measured from the structure.

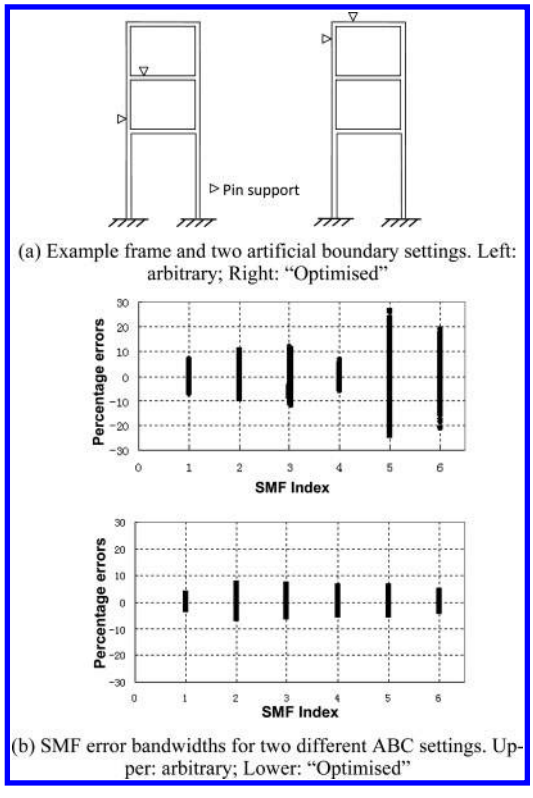
Eq. (4) expresses the inherent relationship between the inverse of $\mathbf{H}_{mm}$ and the dynamic characteristics of the OCS as represented by $\mathbf{Z}_{oo}$, such that at the natural frequencies of the OCS, $\mathbf{Z}_{oo}^{-1}$ is singular, so $\mathbf{H}_{mm}^{-1}$ is also singular, and vice versa. Consequently, by identifying the singularities (resonance frequencies) from the elements of $\mathbf{H}_{mm}^{-1}$, one can determine the natural frequencies of the OCS, i.e., the frequencies of the structure as if it was physically pinned at the measured DOFs. Thus, from a theoretical point of view the determination of the perturbed natural frequencies (called ABC frequencies herein) of the structure with additional pin constraints would become a matter of measuring and processing the relevant FRFs from the existing structure.

3 EFFECTIVENESS OF INCORPORATING ABC FREQUENCIES IN STRUCTURAL IDENTIFICATION

Prior to embarking on the investigation of the extraction of ABC frequencies from physical tests, it was considered necessary to establish a comprehensive understanding with regard to the potential effectiveness of incorporating ABC frequencies in a parameter identification process. For this purpose, a numerical simulation study has been conducted in a FE model updating framework. To assist in the selection of more effective ABC frequencies, a Genetic Algorithm (GA) based optimisation approach has also been developed (Tu and Lu 2008).

3.1 *General effectiveness of ABC frequencies in FE model updating*

A 3-storey 1-bay frame from a set of cases being studied is used here as an illustration, see Fig. 1(a). The frame is simplified to have 6 flexural rigidity parameters to be determined, one for each individual beam and



(a) Example frame and two artificial boundary settings. Left: arbitrary; Right: "Optimised"

(b) SMF error bandwidths for two different ABC settings. Upper: arbitrary; Lower: "Optimised"

Figure 1. Illustration of effect of incorporating ABC frequencies in FE model updating (Tu and Lu 2008).

one for all columns in an individual storey. A dimensionless stiffness modification factor (SMF), which is defined as the ratio between the actual flexural rigidity and that of the reference (intact) beam or column, is considered in the updating process.

For a comparison, three different sets of frequency information are used respectively, namely i) the first 6 natural frequencies, ii) the first six natural frequencies plus six ABC frequencies with two artificial pins at randomly selected locations (see Fig. 1(a)), and iii) similar combination as above but with the ABC frequencies selected via an optimization procedure, which will be described in 3.2.

Fig. 1(b) depicts the projected update results of the 6 SMFs in terms of the variation (error) range for a fixed level of 1% perturbation (uniformly distributed error) in the frequency data for the above mentioned dataset ii) and iii), respectively, from a sensitivity analysis. For dataset-i) the results are worse than case ii) and so they are not shown. It becomes clear that the incorporation of a reasonable number of ABC frequencies generally improves the model updating conditions. Furthermore, through a rigorous selection procedure the incorporation of the same number of ABC frequencies could yield considerably more accurate results; in the present illustrative example the maximum error in the updating result reduces from 30% to around 8%.

Similar analysis was also performed on different combinations of the two pin locations, as well as on other frame configurations, and the trends are generally consistent. Two general observations are thus established, namely, a) with the addition of a reasonable number of ABC frequencies, the condition of the parameter identification is generally improved; and b) the effectiveness of using a certain set of ABC frequencies, e.g., with two artificial pins, is dependent upon the locations of these pins. For this reason, a systematic selection of the ABC patterns is deemed to be necessary.

3.2 *A GA-based algorithm for optimisation of the ABC configurations*

For the optimal configuration of possible artificial boundaries, a novel method using binary GA has been developed (Tu and Lu 2008). The essential consideration in this approach is to code the ABC pin positions, normally being a sub-set of the DOFs where measurements are considered possible. This DOF library is then arranged in the form of a row vector, which consists of the numbers of the candidate DOFs in the search domain. The phenotype variables in GA are integer numbers which identify the DOFs in the DOF library, herein using a sequential number. In principle, all combinations of the ABC pins may be incorporated. For practicality and simplicity, a pre-defined fixed number (e.g. two) of ABC pins will usually suffice. Subsequently the optimisation reduces to determining the optimal locations of these pins.

In the proposed procedure, the integer variables identifying the DOFs are coded using binary bits in the GA chromosome. The single point crossover is used and mutation is implemented by bit flip (binary mutation). Once the evolution process is completed, the binary chromosomes are converted back to the corresponding DOFs, thus the "optimal" artificial boundary is obtained.

The fitness of a chromosome, which represents the adequacy of a particular ABC pin arrangement, may be evaluated in different ways. The present approach uses a sensitivity analysis concerning the variation in the updated parameters $\{\delta p\}$ for a given margin of variation in the measurements $\{\delta R\}$, i.e., $\{\delta R\} = \mathbf{S}\{\delta p\}$. In a numerical analysis, the sensitivity matrix $\mathbf{S}$ may be evaluated as the percentage changes of the response components due to one percent change of the structural parameters from a reference state. The sensitivity of the ABC frequencies is calculated by extending the sensitivity of the natural frequencies (Friswell and Mottershead, 1995), as:

$$\frac{\partial f_i}{\partial p_j} = \frac{\{\phi_i\}^T \left(\frac{\partial \mathbf{K}}{\partial p_j} - 4\pi^2 f_i^2 \frac{\partial \mathbf{M}}{\partial p_j} \right) \{\phi_i\}}{8\pi^2 f_i \{\phi_i\}^T \mathbf{M} \{\phi_i\}} \tag{5}$$

where f_i and $\{\phi_i\}$ here become the ith "natural frequency" and the associated mode shape of the ABC

system, and the matrices **K** and **M** represent the stiffness and mass matrix of a structural system incorporating the ABC as well. By an inversion procedure, the parameter change vector can be related through a gain matrix G to the response change vector as:

$$\{\delta p\} = \left(\mathbf{S}^T\mathbf{S}\right)^{-1}\mathbf{S}^T\delta\{R\} = \mathbf{G}\{\delta R\} \tag{6}$$

After obtaining the vector of $\{\delta p\}$ for a randomly sampled response dataset within a pre-defined perturbation (error) bound (1% herein), the overall variation of $\{\delta p\}$ is taken to represent the fitness of the chromosome using the following formula:

$$\text{Fitness} = -\left(\mu_{\text{SD}} + \sigma_{\text{SD}}/\mu_{\text{SD}}\right) \tag{7}$$

where μ_{SD} denotes the mean of the standard deviation (SD) in each element of $\{\delta p\}$, and σ_{SD} is the standard deviation of SD.

The example case given in 3.1 (Fig. 1(b)) is clearly illustrative of the effectiveness of the above GA-based ABC selection procedure.

4 EXTRACTING ABC FREQUENCIES FROM PHYSICAL TESTS

The next and even more crucial question is how practical and reliable the ABC frequencies may be extracted from real measured responses. From the experimental investigations conducted so far on a laboratory scale, the results are generally encouraging. A comprehensive coverage of the experimental study is reported elsewhere (Mao and Lu, in prep.). In this section a brief overview of representative experiments and the main observations are provided and discussed.

4.1 *Test programme and sampling requirement*

The test specimens included a steel model beam and an aluminum slab, with fixed end supports. Fig. 2 shows the basic set-up on the model slab. A measurement grid was arranged such that a variety of combinations of input-output locations could be accommodated. The beam was actually divided into 30 segments along its length, whilst the slab had a 10 × 5 measurement grid points, denoted as A1 through J5.

For this exploration, the excitation was generated by hammer impact. The responses were recorded with small-size modal testing accelerometers. Confining to one and two artificial pin supports, which already allows for the examination of a large number of ABC configurations, only two accelerometers were needed, one fixed at the impact point, and another being moved from point to point for different tests. After measurements from all tests were collected, FRFs were calculated.

As high quality FRF curves is key to the derivation of the ABC frequencies, an accurate record of the impact force becomes important, and this necessitates

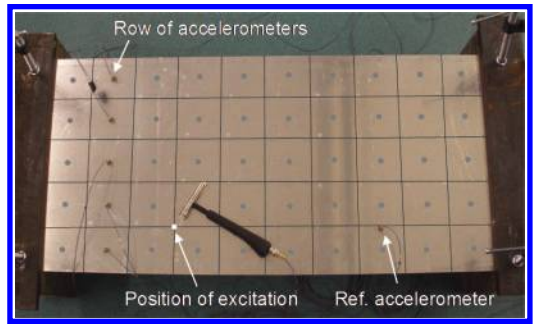


Figure 2. Test set-up for the model slab.

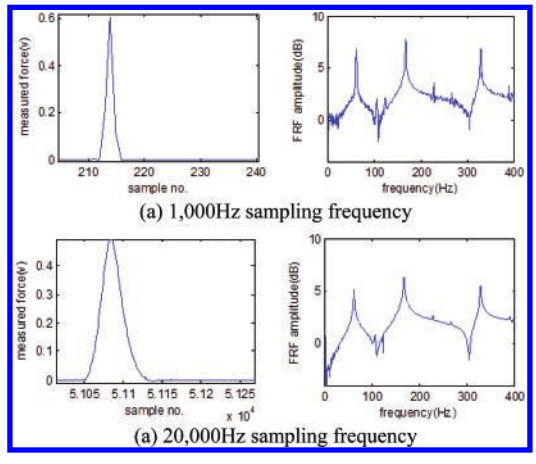


Figure 3. Measured impulse forces (left) and corresponding FRF curves (right) using different sampling frequencies.

a sampling rate which could be orders of magnitude higher than what may be appropriate for sampling the structural responses. Figure 3 gives a comparison of a FRF curve resulting from the tests where the impact force was sampled using a sampling rate of 1000 and 20000 per second, respectively. The improvement with the increased sampling rate is apparent. In different applications, a sufficient sampling rate for the impact force will depend on the pulse duration which in turn depends upon the type (hardness) of the impactor tip. A trial measurement would help determine an appropriate sampling rate satisfying both the recording accuracy and the efficiency in terms of processing and computational costs.

4.2 *Processing of FRFs for improved quality*

Standard signal processing techniques, such as windowing, averaging and filtering were implemented in the calculation of the FRFs.

A procedure based on the Single Value Decomposition (SVD) is also employed to further improve the quality of the measured FRFs. In the procedure adopted, the impulse response function (IRF) is firstly obtained from FRF data using inverse Fourier transform, and these IRF data are then used to form a Hankel

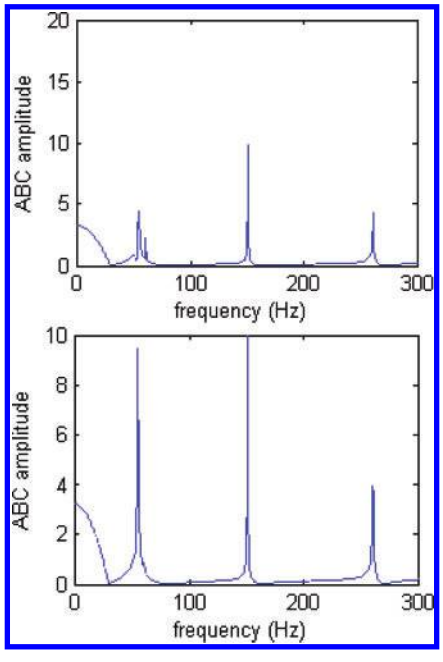


Figure 4. Typical one-pin ABC curves from the test beam. Upper: before applying SVD; Lower: after SVD.

Table 1. Beam's one-pin ABC frequencies: experimental vs. and FE predicted results.

Scenario	Frequencies (Hz): measured / FE		
(Pin location)	1st	2nd	3rd
"6"	39.9 / 38.8	105.2 / 104.8	210.3 / 206.4
"22"	54.2 / 53.7	152 / 150	261 / 262.7

matrix following the recommendation in Sanliturk and Cakar (2005). The rank of the Hankel matrix is then determined from the singular value distribution curve, and higher singular numbers are eliminated. Finally, the modified Hankel matrix is reinstated, and with an inverse Fourier transform a noise-removed FRF is obtained.

4.3 *Extraction of ABC frequencies*

Combining the impact and response measurement positions yields various ABC configurations. With the processing described above, the required FRFs are made available to compute the $\mathbf{H}_{mm}^{-1}$, from which the ABC frequencies for the respective ABC pin arrangements can be identified. For verification, the test beam and slab were also analysed using FE models to predict the respective modal properties.

Figure 4 illustrates some typical one-pin ABC curves for the test beam. The first few peaks can be firmly identified as the corresponding one-pin ABC frequencies, and this is confirmed by comparing to the FE predicted natural frequencies of the beam where

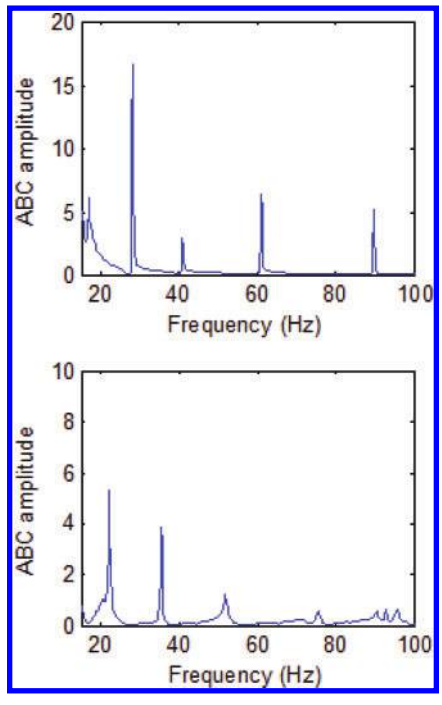


Figure 5. Typical one-pin ABC curves from the test slab (Pin at locations of A1 and D2, respectively).

a real pin is inserted at the respective location, see Table 1. From the results shown in Figure 5, it can also be observed that the ABC curves resulting from SVD-processed FRFs are smoother and the (ABC) frequencies are more clearly identifiable.

Figure 5 presents some typical one-pin ABC curves from the test slab. The extracted first three ABC frequencies also compare well with the FE predicted results (not shown).

For the two-pin ABC frequencies, there are a large number of permutations of possible two-pin configurations. For a general observation, two typical scenarios may be of interest, namely i) two pins at nearby locations, and ii) two pins at well-separated locations. Typical two-pin ABC curves obtained for cases falling into the above two scenarios, respectively, are given in Figure 6. Comparison of the extracted ABC frequencies with those predicted by the respective FE model shows a reasonable agreement.

Summarising the above results and observations, it may be concluded that effectively all one-pin and two-pin ABC frequencies may be extracted for a beam or slab having similar dynamic characteristics as the test specimens. The adopted data processing procedure pertaining to an impact testing approach appears to work well in improving the quality of the measured FRF functions, and subsequently improves the quality of extracted ABC frequencies. The extracted one-pin and two-pin ABC frequencies tend to exhibit similar accuracy as the natural frequencies, thus these data may be employed for the general structural identification purpose.

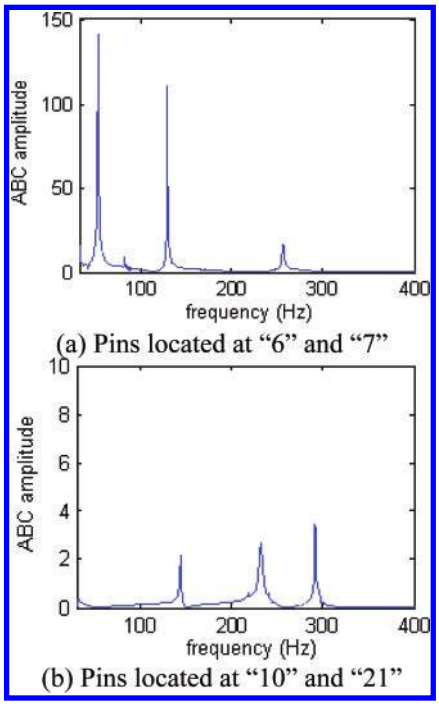


Figure 6. Typical two-pin ABC curves for different 2-pin configurations.

5 CONCLUSIONS

The availability of ABC frequencies provides a seemingly promising opportunity to expand the modal frequency dataset, and consequently enhance the overall sensitivity of the dataset to global as well as local structural changes. A series of studies have been conducted in an attempt to address several pertinent questions towards the potential use of such novel frequencies information in practice. Results so far tend to support the following conclusions:

1) the effectiveness of incorporating ABC frequencies in structural parameter identification; this has generally been established through a systematic numerical simulation study;
2) the scope for optimisation of the ABC configurations so as to assist in the selection of more effective ABC frequencies. A binary GA-based methodology has been developed and the approach proves to work out satisfactorily, and
3) obtaining the ABC frequencies in a real measurement environment; the results from the laboratory experiments are clearly encouraging.

The experimental investigations thus far have demonstrated that, with a careful implementation of testing, data acquisition and processing procedures as outlined in this paper, effectively all one-pin and two-pin ABC frequencies in the first few ABC modes can be obtained with quality and accuracy matching the comparable orders of natural frequencies. Considering the availability of abundant one- and two-pin ABC configurations, the scope for selecting the more effective ABC frequencies for a particular parameter identification task is promising.

Further investigations are ongoing to look into the workability of extracting the ABC frequencies in more realistic and ultimately real-life structures.

REFERENCES

Ambrogio, W.D. & Fregolent, A. 2000. The use of antiresonances for robust model updating. *Journal of Sound and Vibration*, 236(2): 227–243.

Friswell, M. I. & Mottershead, J. E. 1995. *Finite Element Model Updating in Structural Dynamics*, Kluwer, Dordrecht, The Netherlands.

Gordis, J.H. 1996. Omitted coordinate systems and artificial constraints in spatially incomplete identification. *Modal analysis*, 11: 83–95.

Gordis, J.H. 1999. Artificial boundary conditions for model updating and damage detection. *Mechanical systems and signal processing*, 13(3): 437–448.

Jones. K. & Turcotte. J. 2002. Finite element model updating using antiresonant frequencies. *Journal of Sound and Vibration*, 252(4): 717–727.

Lallement, G. & Cogan, S. 1992. Reconciliation between measured and calculated dynamic behaviours: enlargement of the knowledge space. *Proc. 10th IMAC*, 487–493.

Li, S., Shelley, S.J. & Brown, D.L. 1995. Perturbed boundary condition testing concepts, *Proc. 13th IMAC,* Feb. 13–16, 1995, Nashville, Tennessee.

Lu, Y., Mao, L. & Tu, Z.G. 2008. Practical considerations in FE model updating with artificial boundary condition frequencies. *Proc. 10th Int. Symposium on Structural Engineering for Young Experts*, Oct. 19–21, Changsha, China.

Mao, L. & Lu, Y. (in prep). Experimental study on extraction of artificial-boundary-condition frequencies for damage detection. *(to be submitted)*

Mottershead, J.E. & Friswell, M.I. 1993. Model updating in structural dynamics: a survey. *Journal of Sound and Vibration*, 167(2): 347–375.

Sanliturk, K. Y. & Cakar, O. 2005. Noise elimination from measured frequency response functions. *Mechanical Systems and Signal Processing*. 19: 615–631.

Tu, Z. & Lu, Y. (2008). FE Model Updating Using Artificial Boundary Conditions with Genetic Algorithms. *Computers and Structures*, 86: 714–727.

Research and Applications in Structural Engineering, Mechanics and Computation – Zingoni (Ed.)
© 2013 Taylor & Francis Group, London, ISBN 978-1-138-00061-2

A novel two-step method for localization and assessment of cracks in beams

G.R. Gillich & Z.I. Praisach
Universitatea "Eftimie Murgu" Resita, Resita, Romania

ABSTRACT: This paper proposes a new approach for damage assessment in beams, based on a relation contrived by the authors describing the frequency changes for bending vibration modes in respect to damage location and depth. It involves one term controlled by damage location, proportional with the mode shape curvature squares, and one influenced by damage depth alone. This permits decoupling the location issue with that of damage severity estimation. To find the damage location the relative frequency shift for several bending vibration modes are determined by measurements and compared with the corresponding mode shape curvature squares calculated for numerous locations; the location is found when the calculated series fit the measured one. The second step is to find the depth of damage placed on the identified location, producing the measured frequency change. The method is simple and reliable, is not affected by noise and is applicable to all types of beams.

1 INTRODUCTION

Regular inspection of engineering structures is crucial to detect damages in real time and assess their safety and reliability. Early damage identification permits properly programmed maintenance in order to extend the service life of structures, or the putting out of operation and replacement to avoid accidents. Dynamic nondestructive evaluation methods, due to their global perspective, are able to indicate the occurrence of damages even in large structures, locate the damaged area and estimate their severity. Intensive researches in this domain where performed last decades in order to develop reliable damage detection methods, focused on the use of various features identified from measured response time-histories or spectra of these time-histories.

A comprehensive review regarding damage identification in structures from changes in their vibration characteristics is provided by Doebling et al. (1998). Some authors use natural frequency shifts for damage detection (Cawley & Adams 1979, Salawu 1997). Due to low sensitivity of frequency shift to damage, precise models on one side and measurements on the other are required. Because discrete models are mainly used, the similitude between the real structure and the model is often inadequate, so that changes in frequency caused by damage can be smaller than those observed between the undamaged structure and the mathematical model. This makes almost impossible to discern between inadequate modeling and changes due to damage, consequently the use of models is difficult to be used (Friswell 2007). Other problems in using natural frequency shifts to detect damages reside in the fact that natural frequencies are sensitive to changes in temperature and loads applied on the structure.

Methods based on mode shape changes compare differences between the measured modal shapes before and after damage. A single-number measure of mode shape changes to assess damage in beams is proposed by West (1984), namely the Modal Assurance Criterion (MAC); it compares a mode shape in the undamaged and damaged state respectively. The Coordinate Modal Assurance Criterion (COMAC) combines information from different vibration modes and is able to indicate the probable location of damage (i.e. Maia et al. 1997, Heylen et al. 1997). Mode shape curvatures are more sensitive to damage and can also be used (Pandey et al. 1991). The decrease in modal strain energy caused by damage is used by Cornwell et al. (1999) to identify structural damage. In all cases the mode shape vectors must be one-to-one associated to the measurement points coordinates, difficult to achieve while a large number of measurement locations is required to accurately characterize mode shape vectors and to provide enough resolution for determining the damage location. Additionally, because the methods use discrete models with multiple degrees of freedom, the sensor locations must be carefully matched to the finite elements associated to these degrees of freedom.

Methods based on flexibility of the structure constitute another class of damage identification methods. They make use of dynamically measured flexibility matrix, written as a mode superposition, to estimate changes in the static behavior of a structure, in most cases completed with static measurements. Several variants of this method are known, like the change in flexibility method, the change in uniform flexibility

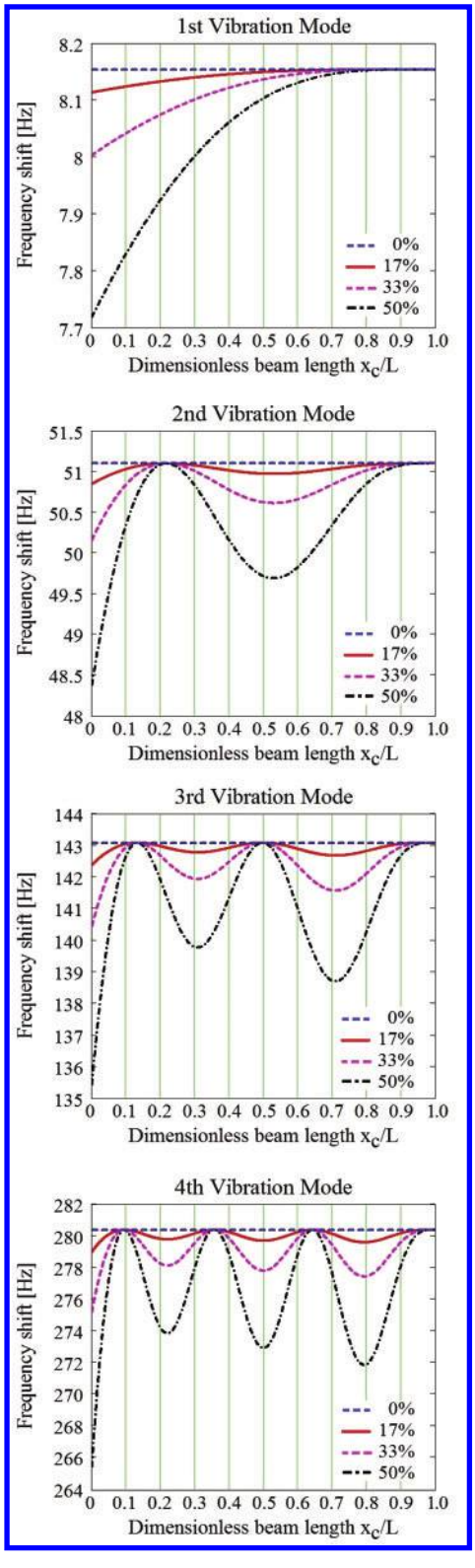


Figure 1. Frequency shift curves for the first four bending vibration modes of the cantilever beam.

curvature method and other similar methods, largely described by Pandey & Biswas (1994).

Even if Rytter (1993) present the damage location and quantification problems on different levels, suggesting the possibility to separate the two attempts, most methods presented in literature are focused on directly linking changes of modal parameters to a given damage, without decupling the localization and assessment problem (Gillich & Praisach 2012). Furthermore, no simple relation between damage location and depth on one side and frequency changes due to damage for bending beams on the other are presented in literature. Approaches like that presented by Chondros et al. (1998) offer solutions, but imply to solve an 8×8 matrix for all possible damage scenarios.

Previous researches performed by the authors, focused on natural frequency changes since they are the most easy to acquire data characterizing the beam dynamics. As result we have find a relation providing the exact solution for frequency changes of all bending vibration modes, for any damage scenario and irrespective of the beam support type. It allowed to trace, for damaged beams, frequency shift curves and to better understand the phenomenon occurring by the appearance of damage. This paper presents a simple, reliable method to detect, locate and evaluate damages in beam-like structures, developed basing on this relation.

2 FREQUENCY SHIFT CURVES

Detailed investigations using the finite element method were performed on a beam in four support type cases: fixed-free, fixed-fixed, fixed-pinned and pinned-pinned. While researches reported in literature present numerical and experimental analyses considering few vibration modes (mainly three or less) and a low number of damage scenarios, it is impossible to get a global picture about how a damage affect the dynamic behavior of beams. To overcome this, we analyzed the effect of damages in form of closed cracks in 200 locations along the beam, for 9 levels of depth. For all 1800 scenarios we found, by means of the finite element method (FEM), the first ten natural frequencies of the damaged beams. The results allow to accurate represent the frequency shift curves for all analyzed cases; Figure 1 shows these curves for the first four vibration modes of the cantilever beam.

One observes in Figure 1 that, for each vibration mode, there are particular locations in which damage does not affect the natural frequency. These locations are identical with the inflection points of the mode shape curvature; Figure 2 presents them for the fourth bending vibration mode of the cantilever beam. In these locations the beam dose not curve, maintaining its linearity, consequently no bending stress is present. Obviously, these locations, expressed in terms of dimensionless distance x_C/L, are different for the different vibration modes of a beam.

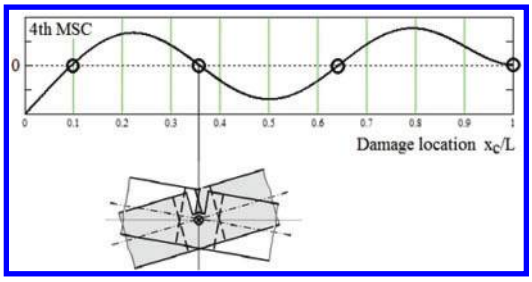


Figure 2. Fourth mode shape curvature with highlighted inflection points and slice behavior; one observe just rotation.

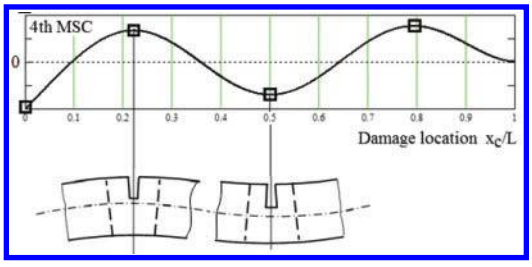


Figure 3. Fourth mode shape curvature with highlighted extreme points and slice behavior; one observe strong bending.

On the other hand, the locations x_C/L in which no frequency changes due to damage occurs in a given mode are similar for all beams identically supported.

On other particular locations natural frequency changes attend local maxima; these points fit the points of extreme of the respective mode shape curvatures (Fig. 3). In these locations the slices suffer the most important bending and consequently the slices placed on these locations store important strain energy. Thus, a damage placed here reduces dramatically the strain energy stored in the slice, and therefore the total stored energy in the beam, so that a significant effect upon the dynamic behavior of the beam in terms of natural frequency decrease takes place. These locations, expressed in terms of dimensionless distance x_C/L, are also different for the different vibration modes of a beam, but similar for a given mode for identically supported beams.

The location of these two classes of points is dependent of the mode shape $\phi_i(x)$ and its second derivative, the mode shape curvature, thus specific for different boundary conditions. The good concordance between particular points of the mode shape curvature and the frequency shifts is found analyzing the strain energy distribution along the beam. For a slice, the strain energy is expressed as:

$$\mathrm{d}U_i(x) = \frac{1}{2} EI\left(\phi_i''(x)\right)^2 \mathrm{d}x \tag{1}$$

where E = Young's modulus, I = moment of inertia of the transversal cross-section of the healthy beam and dx = slice length. For a slice affected by damage, e.g. with reduced moment of inertia I_D, the stored strain energy is:

$$\mathrm{d}U_{i-D}(x) = \frac{1}{2} EI_D\left(\phi_i''(x)\right)^2 \mathrm{d}x \tag{2}$$

and consequently the strain energy decrease

$$\begin{aligned}\Delta\mathrm{d}U_i(x) &= \mathrm{d}U_i(x) - \mathrm{d}U_{i-D}(x) \\ &= \frac{1}{2} EI\left(\phi_i''(x)\right)^2 \mathrm{d}x - \frac{1}{2} EI_D\left(\phi_i''(x)\right)^2 \mathrm{d}x \\ &= \frac{1}{2}(EI - EI_D)\left(\phi_i''(x)\right)^2 \mathrm{d}x\end{aligned} \tag{3}$$

Equation 3 reveals that the effect of a damage occurring on a slice reduces the total strain energy of the beam proportional with the decrease of the slice rigidity $\Delta EI = EI - EI_D$ and the value of the mode shape curvature square at that location. It can be assumed that the frequency decrease due to damage is proportional with the strain energy reduction in the beam caused by that damage.

This hypothesis is confirmed by results obtained by Chondros et al. (1998), who consider a rotational spring placed at the damage location, linking the two halve segments and reducing the transferred energy; the spring stiffness must be adjusted every time in concordance to its location. Opposite to their approach, we consider the effect of damage (i.e. stiffness reduction) at the location where the mode shape curvature square and implicit the bending moment attends the global maximum. Afterwards, we adjust it for different locations by the value of the mode shape curvature square at that location. A study comparing results obtained by the two methods lead to similar results (Gillich et al. 2012).

Based on this theory, we contrived a relation expressing the natural frequencies f_{i-D} for a beam with a transversal closed crack of depth a placed at distance x_C from the beam end, as:

$$f_{i-D}(x_C, a) = f_{i-U}\left[1 - \gamma(0,a)\cdot\left(\bar{\phi}_i''(x_C)\right)^2\right] \tag{4}$$

where $\gamma(0,a)$ = coefficient representing the stiffness reduction and f_{i-U} = frequency of the undamaged beam.

The undamaged beam's natural frequencies for the i-th bending vibration mode can be calculated using the well-known relation:

$$f_{i-U} = \frac{\lambda_i^2}{2\pi}\sqrt{\frac{EI}{\rho A L^4}} \tag{5}$$

where λ_i = mode number value, ρ = beam's mass density, A = cross-section area and L = beam length.

Normalizing the frequency of the damaged beam given in Equation 4 by the frequency of the undamaged beam, one obtains

$$\bar{f}_{i-D}(x_C, a) = 1 - \gamma(0,a)\cdot\left(\bar{\phi}_i''(x_C)\right)^2 \tag{6}$$

with the maximum 1 if no damage occur. This relation is important when qualitative analyses are performed.

One remark that in Equations 4, 6 the normalized mode shapes curvature square is used, taking values between 0 and 1. Its can be expressed as:

$$\bar{\phi}_i''(x_C) = \left| \frac{\phi_i''(x_C)}{\max(\phi_i''(x))} \right| \tag{7}$$

The coefficient $\gamma(0,a)$ has, for a given damage and beam geometry but irrespective to the support type, the same value for all bending vibration modes. It can be determined using the stress intensity factor from fracture mechanics, for mode I - opening crack. Functions for the stiffness reduction in respect to damage depth are reported by Liebowitz & Claus (1968), Ostachowicz & Krawczuk (1991), Chondros et al. (1998). Highlighting the stiffness decrease, Gillich et al. (2012) proposed a simpler relation to determine the value of $\gamma(0,a)$ as:

$$\gamma(0,a) = 1 - \sqrt{\frac{\delta_{U\max}}{\delta_{D\max}}} \tag{8}$$

where $\delta_{U\max}$ = maximum static deflection of the healthy beam under own load and $\delta_{D\max}$ = maximum deflection of the damaged beam when the discontinuity is placed in the location where the bending moment have the biggest value. These deflections are determined using the FEM for various damage depths, so that the function $\gamma(0,a)$ can be determined.

The relation providing the frequency value of the damaged beam, presented in Equation 4, permit plotting relative frequency shift curves, for beams with any support type, just using the adequate mode shape curvature. Results obtained analytically are in good concordance to them obtained by means of the finite element method.

Equation 4 is valid for open cracks too, but obviously the values of coefficient $\gamma(0,a)$ for the same damage depth a increase, consequently the natural frequency of beams with closed cracks are lower than that of identical beams with open cracks, if placed on the same location.

Attention should be paid to the fact that, for open cracks associated with mass loss, the natural frequency of the undamaged beam cannot be used as a base-line, while the frequency due to mass loss increase.

3 DAMAGE LOCATION COEFFICIENTS

The frequency shift curves presented in Figure 1 show that any location along the beam can be characterized by a series of n values representing the frequency change of n bending vibration modes. These series are unique for asymmetric structures, or characterize mirrored pairs of locations for symmetric structures. The natural frequency shifts for any damage location and vibration mode can be found from the modified form of Equation (4), as:

$$\begin{aligned} \Delta f_i(x_C,a) &= f_{i-U} - f_{i-D}(x_C,a) \\ &= f_{i-U}\left[\gamma(0,a)\cdot(\bar{\phi}_i''(x_C))^2\right] \end{aligned} \tag{9}$$

Dividing Equation 9 by f_{i-U} result the relative frequency shift as the product of two terms, of which the first is proportional to the severity and the second depends solely on the location of the damage:

$$\Delta f_i^*(x_C,a) = \gamma(0,a)\cdot(\bar{\phi}_i''(x_C))^2 \tag{10}$$

Normalizing the n values of the relative frequency shift for a location x_C by the biggest value of the series, the effect of damage depth is isolated, and a series defined by the location alone is obtained. We denoted the individual values

$$\frac{\Delta f_i^*(x_C,a)}{\max(\Delta f_{1\ldots n}^*(x_C,a))} = \Phi_i(x_C) = \frac{(\bar{\phi}_i''(x_C))^2}{\max((\bar{\phi}_{1\ldots n}''(x_C))^2)} \tag{11}$$

damage location coefficients (DLC), and the whole series, containing n coefficients

$$\Phi : \{\Phi_1(x_C), \ldots \Phi_i(x_C), \ldots \Phi_n(x_C)\} \tag{12}$$

damage location index (DLI).

Obviously, the biggest value of a DLC in a damage location index is the unit, all other DLC being smaller (possible also zero). In very particular cases two DLCs can have the unit value or can be very close to it. Figure 4 depict the normalized frequency shift curves for a cantilever beam, presenting the normalized frequency shifts for damages placed at $x_C/L = 0.15$, 0.3, 0.45 and 0.6 respectively. Figure 5 show the values of the corresponding damage location indexes for the analyzed cases, the DLCs being calculated using Equation 11.

One observes that sets of these values constitute patterns for all damage locations. While they are determined exclusively using data obtained from the undamaged beam, being used as reference values, the damage localization procedure is not based on models, so that modeling errors are avoided.

The damage localization procedure is therefore reduced to comparing measured data with a priori known patterns. Suppose that by starting monitoring a beam, the measured frequencies for n vibration modes are:

$$F_U^m : \{f_{1-U}^m, \ldots f_{i-U}^m, \ldots f_{n-U}^m\} \tag{13}$$

Afterwards, the frequencies are measured either continuously or periodic. Samples extracted from time in time provide new results:

$$F_D^m : \{f_{1-D}^m, \ldots f_{i-D}^m, \ldots f_{n-D}^m\} \tag{14}$$

If differences between the two series are observed, the appearance of a structural damage is presumed

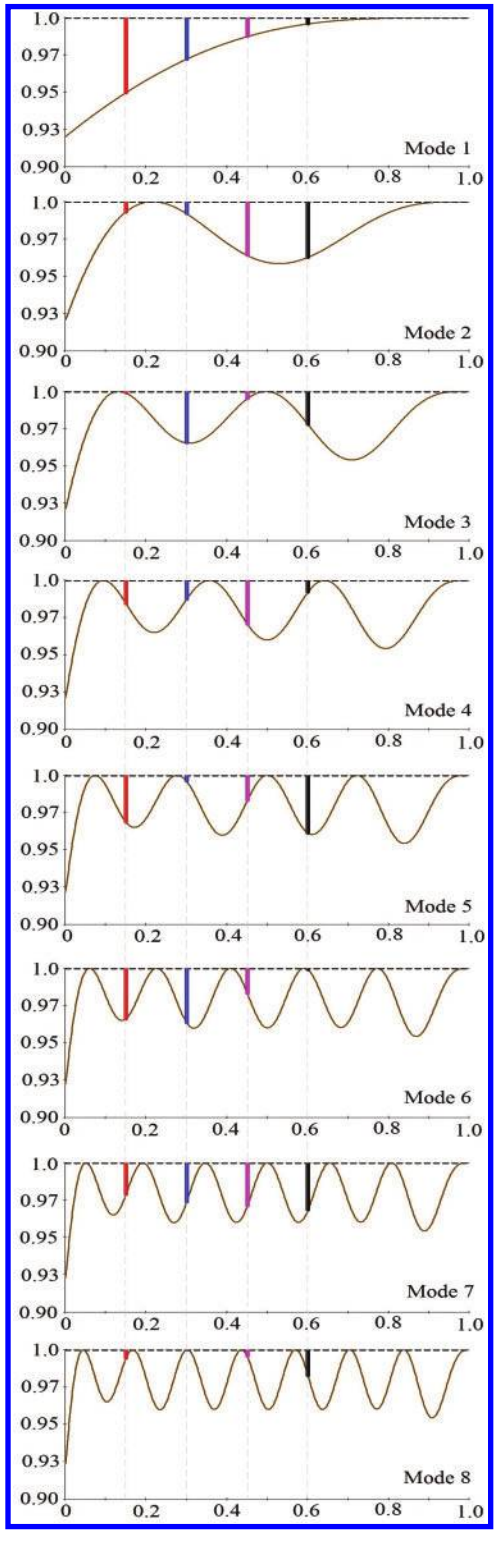


Figure 4. Normalized frequency shift curves for a cantilever with four damage scenarios: S1 ($x_C/L = 0.15$); S2 ($x_C/L = 0.3$); S3 ($x_C/L = 0.45$) and S4 ($x_C/L = 0.6$).

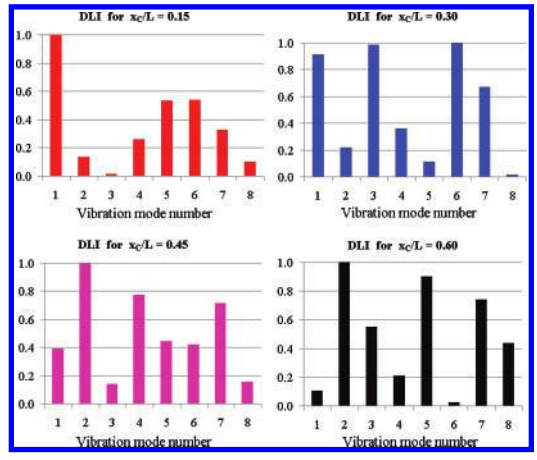


Figure 5. Damage location indexes for the four analyzed damage scenarios.

and the measured data is processed in order to find its location. First the frequency shifts are calculated inserting in Equation 10 the measured series presented in Equations 13 and 14. The relative frequency shift

$$F^{*m} : \{\Delta f_1^{*m}, ... \Delta f_i^{*m}, ... \Delta f_n^{*m}\} \tag{15}$$

for the n analyzed modes are obtained. These values are than normalized by dividing each of them to the biggest value of the series, how it is presented below:

$$\Psi_i = \frac{\Delta f_i^{*m}}{\max(\Delta f_{1...n}^{*m})} \tag{16}$$

obtaining the values:

$$\Psi : \{\Psi_1(x_C), ... \Psi_i(x_C), ... \Psi_n(x_C)\} \tag{17}$$

Comparing the series Ψ given by Equation (17) with series Φ obtained from Equation (11) for numerous locations x along the beam, one can find the location x_C where the terms of the two series match together; so the crack location is identified.

The recognition process, finalizing the first step in damage assessment, can be done by visual methods, where the values are replaced by segments, or it can make use of statistical methods. The authors have developed a program to automatically indicate crack location when frequencies of the healthy and damaged beam are known.

4 DAMAGE SEVERITY EVALUATION

Once the crack location identified, the normalized mode shape curvature' square of mode one for that location can be calculated from Equation 7. Knowing the relative frequency shift for mode one Δf_1^{*m} from measurements, the coefficient $\gamma(0,a)$ indicating

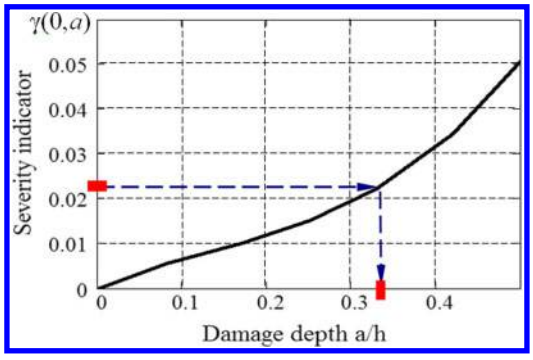


Figure 6. Damage severity vs. dimensionless damage depth.

damage severity can be computed using Equation 9. While the relation $\gamma(0,a)$ in respect to depth a is given by Equation 8, it can be graphically represented, like shown in Figure 6. For the determined value of $\gamma(0,a)$ the dimensionless damage depth a/h is identified.

This second step is simple and offers an image about damage depth, without being highly accurate. For precise geometrical damage characterization local methods are needed.

5 CONCLUSIONS

This paper presented a two-step damage detection method able to assess damages in beams from changes in their natural frequencies. For these kind of structures the rule how frequencies change due to damage in respect to their location and beam support type was establish for all bending vibration modes. The manner how these changes take place characterizes a location along the beam, consequently constitutes a pattern proper to be used for damage localization. In this paper patterns where derived from mode shape curvatures, as indicators of stored energy; for short beams the strain energy has to be directly involved. The method implies the use of a single accelerometer and is not affected by noise, while solely the frequency has to be identified. The method is applicable to all kind of beam-like structures with initial constant bending stiffness EI, or to structures with initially known damage.

ACKNOWLEDGEMENT

The research was co-funded by the Sectoral Operational Programme Human Resources Development 2007–2013 of the Romanian Ministry of Labour, Family and Social Protection through the Financial Agreement POSDRU/89/1.5/S/62557.

REFERENCES

Cawley, P. & Adams, R.D. 1979. The location of defects in structures from measurements of natural frequencies. *Journal of Strain Analysis* 14(2): 49–57.

Chondros, T.J., Dimarogonas, A.D. & Yao J. 1998. A continuous cracked beam vibration theory. *Journal of Sound and Vibration* 215(1): 17–34.

Cornwell, P., Doebling, S. & Farrar, C.R. 1999. Application of the strain energy damage detection method to plate-like structures. *Journal of Sound and Vibration* 224(2): 359–74.

Doebling, S.W., Farrar, C.R. & Prime, M.B. 1998. A summary review of vibration based damage identification methods. *Shock Vibration Digest* 30(2): 91–105

Friswell, M.I. 2007. Damage identification using inverse methods. *Phil. Trans. R. Soc. A 365*: 393–410

Gillich, G.R. & Praisach Z.I. 2012. Robust method to identify damages in beams based on frequency shift analysis. Proc. SPIE 8348, Health Monitoring of Structural and Biological Systems 2012, 83481D.

Gillich, G.R., Minda, P.F., Praisach, Z.I. & Minda, A.A. 2012. Natural frequencies of damaged beams – a new approach. *Romanian Journal of Acoustics and Vibration* 9(2): 101–108.

Heylen, W., Lammens S. & Sas, P. 1997. *Modal Analysis Theory and Testing*. Leuven: KUL Press.

Liebowitz, H. & Claus Jr. W.D.S. 1968. Failure of notched columns, *Engineering Fracture Mechanics* 1(1): 379–383.

Maia, N.M.M. & Silva, J.M.M. 1997. *Theoretical and Experimental Modal Analysis*. Taunton: Research Studies Press LTD.

Ostachowicz, W.M. & Krawczuk C. 1991. Analysis of the effect of cracks on the natural frequencies of a cantilever beam. *Journal of Sound and Vibration* 150(2): 191–201.

Pandey, A.K., Biswas, M. & Samman, M.M. 1991. Damage detection from changes in curvature mode shapes. *Journal of Sound and Vibration* 145(2): 321–332.

Pandey, A.K. & Biswas, M. 1994. Damage Detection in Structures Using Changes in Flexibility. *Journal of Sound and Vibration* 169(1): 3–17.

Rytter, A. 1993. *Vibration Based Inspection of Civil Engineering Structures*, Ph.D. Dissertation, Aalborg University, Denmark.

Salawu, O.S. 1997. Detection of structural damage through changes in frequency: a review. *Engineering Structures* 19(9): 18–723.

West, W.M. 1984. Illustration of the use of Model Assurance Criterion to detect structural changes in an orbit test specimen. Proc. of Air Force Conference on Aircraft Structural Integrity: 1–6.

Research and Applications in Structural Engineering, Mechanics and Computation – Zingoni (Ed.)
© 2013 Taylor & Francis Group, London, ISBN 978-1-138-00061-2

Model updating of strategic building structures under real earthquake loading

R. Ceravolo, A. De Stefano, E. Matta, A. Quattrone & L. Zanotti Fragonara
Department of Structural, Geotechnical and Building Engineering, Politecnico di Torino
Torino, Italy

ABSTRACT: Public buildings such as hospitals, schools, churches and city halls constitute an asset of strategic importance into the life of a community. The assessment of the safety conditions and the vulnerability to natural catastrophic events must be checked, also resorting to experimental techniques. The adoption of vibration monitoring procedures represents a particularly appealing perspective for existing structures. The growing use of permanent monitoring systems allows collecting data of the structural response during earthquakes. An invaluable tool for structural health monitoring and damage detection, parametric system identification through model-updating is an inverse problem, affected by several kinds of modelling assumptions and measurement errors. By minimizing the discrepancy between the measured data and the simulated response, traditional model-updating techniques identify one single optimal model that behaves similarly to the real structure.

1 INTRODUCTION

In the event of an earthquake, dynamic monitoring systems can supply precious information on the actual behaviour of existing buildings, allowing for the calibration of numerical models, which can be used for assessing the structural seismic safety as well as for designing possible rehabilitation interventions. In the latter connection, FE models are updated on an experimental basis from data supplied by the permanent monitoring system.

This concept has recently inspired the foundation, within the Italian Department of Civil Protection (DPC), of the Structures Seismic Observatory (OSS), a national-wide network for the permanent monitoring of the seismic response of more than one hundred strategic public buildings in Italy. This network allows a rapid evaluation of the damage induced by seismic actions on monitored structures and on neighbouring similar buildings, helping DPC in planning and managing emergency activities in the earthquake's aftermaths. The OSS network includes: (i) the primary sub-network, comprising 105 strategic public buildings (schools, hospitals and city halls), 10 bridges and a few dams, all intensely instrumented with a dynamic permanent monitoring system (16–32 accelerometers each), and (ii) the secondary sub-network, comprising 300 buildings, all equipped with a simplified monitoring system (7 accelerometers each).

Four of the buildings included in the main sub-network, monitored during the Lunigiana/Garfagnana event (January 27th, 2012), have been selected as case studies in the framework of the inter-university Italian DPC-ReLUIS 2010–2013 Project, and commended to the Department of Structural, Geotechnical and Building Engineering at Politecnico di Torino, as a partner Unit, to the aim of dynamic characterization. This paper briefly introduces these four case studies and exemplifies the modal identification and model-updating procedure on one of them, namely the city hall of San Romano in Garfagnana.

2 THE FOUR SELECTED CASE STUDIES

The four case studies are listed in Table 1 and depicted in Figure 1. They have all been monitored

Table 1. The four selected case-study buildings (buildings description provided in Figure 1).

	Building (a)	Building (b)	Building (c)	Building (d)
Structural typology	Masonry	RC frames	RC shear walls	Masonry
Year of construction	1930	1972	1972	1359 (rebuilt 1761)
Volume (m^3)	2990	1687	7726	1764
Height (m)	14.8	15.8	16.3	9.5 (bell tower 23)
Number of sensors	20	16	22	26
PGA X (g)	0.023	0.024	0.035	0.035
PGA Y (g)	0.018	0.031	0.020	0.053

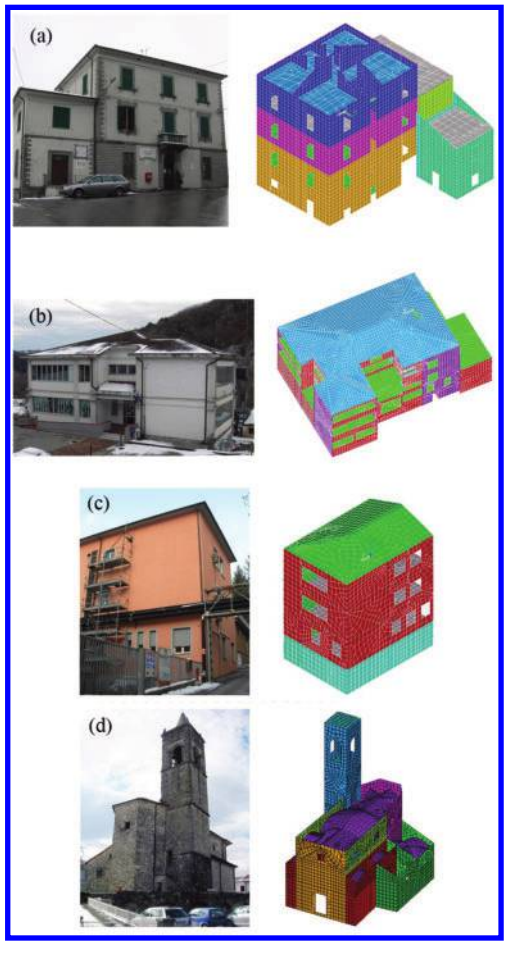


Figure 1. Four selected case-study buildings: (a) City hall of San Romano in Garfagnana; (b) City hall of Casola in Lunigiana; (c) Hospital of Castelnuovo di Garfagnana; (d) Church of S. Caterina a Collegnago.

Table 2. Synthetic parameters of the Lunigiana/ Garfagnana event (27 Jan. 2012).

Epicenter	UTC Time	Magnitude
Lat./long.: 44.483°/10.033°	27/01/2012	5.4
Depth: 60 km	14:53:14	

by DPC during the seismic event which has stroked the Lunigiana/Garfagnana area on the 27th of January, 2012, whose synthetic properties are summarized in Table 2. For each of the four buildings, a dynamic identification has been performed using the acceleration data recorded during the said seismic event and a finite element (FE) model has been accordingly constructed and updated. For the sake of brevity, the identification and calibration procedure is exemplified in what follows for the first building only, i.e. the city hall of San Romano in Garfagnana.

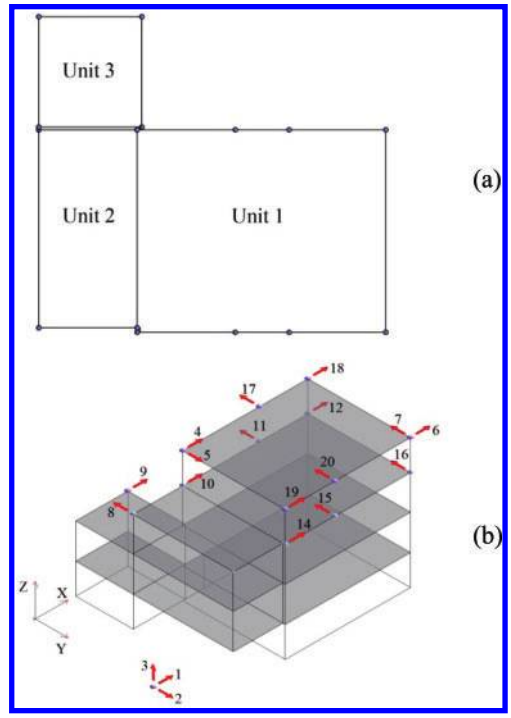


Figure 2. City Hall of San Romano in Garfagnana: (a) planar view; (b) sensors position and orientation.

3 THE CITY HALL OF SAN ROMANO IN GARFAGNANA

Particular attention will be given in this paper to the case study of the city hall of San Romano in Garfagnana whilst the principal results will be listed for all the four buildings.

3.1 *The building*

San Romano in Garfagnana is located in a medium-to-high seismicity area (seismic zone 2 according to the OPCM 3274 Seismic Code, 2003). The city hall consists of a main building and two adjacent smaller units constructed at a later time (Figure 2a). The main building is a 4-storey masonry structure built on reinforced concrete foundations, having a 19.2 × 11.4 m^2 rectangular plan and a 14.8 m height. Built in the '30s, it was seismically and statically retrofitted in 1998. Foundations were sandwiched between new r.c. curbs, in order to achieve a more uniform distribution of soil pressures. Main masonry walls were plated with reinforced cement mortar, in order to increase shear strength. The original masonry walls distribution was recovered through reconstructing those elements which had been removed through the years. Floors were stiffened and strengthened, and their connection with masonry improved. In order to enhance structural regularity, a structural joint was realized between units 2 and 3, while units 1 and 2 were connected through steel bars' reinforcements inserted in adjacent walls. A survey on

the mechanical properties of the constituent materials indicates a characteristic compressive strength of 115 MPa for the stone blocks and of 7.2 MPa for the masonry panels.

3.2 *The monitoring system*

OSS permanent monitoring system consists of 20 force-balance uniaxial accelerometers. 17 accelerometers are installed along the building height and the remaining 3 accelerometers, constituting the ground reference channels, are placed inside an underground inspection hole. The position and orientation of the sensors are shown in Figure 2b. Among the 17 accelerometers deployed along the elevation, 16 are installed in units 2 and 3 (attached to the floors at the first and second levels) and only one is deployed in unit 3 (along the X direction). The acquisition system incorporates an AD converter and is connected with a GPS receiver for synchronization with the international UTC time.

4 THE NUMERICAL MODEL

For each building analyzed, based on original archive documentation a preliminary model has been constructed in order to highlight possible critical issues in the structural dynamic response and help interpreting processed signals. The structural members have been modeled using mono and bi-dimensional finite elements and adopting linear, elastic and isotropic material properties.

In details, the model of the city hall of San Romano in Garfagnana model consists of bi-dimensional plate- and shell-type finite elements grouped in macro-elements. The wooden roof has been modeled only in terms of its inertial contribution, as a uniformly distributed mass on the beams which crown the masonry walls.

Masonry properties have been deduced partly from destructive and non-destructive tests and partly from typical values suggested by the literature and by current Italian codes, depending on the outcome of visual inspections. In order to simply account for soil-structure interaction, the structural nodes are clamped at the foundation level and the stiffness of the underground wall elements is initially increased.

The efficacy of the structural joint located between units 1 and 3 is highly uncertain because of the lack of documental information and because of the presence of only one sensor in unit 3. The joint is therefore modeled as a stripe of shell elements with reduced equivalent stiffness.

5 DATA ACQUISITION AND MODELLING

Dynamic identification from signals recorded during the seismic event requires that the input spectral components be distinguished from structural frequencies. In the assumption that the three ground reference signals reflect the input load into the dynamic system, the dominant earthquake components can be easily identified, helping with the estimated transfer functions and coherence functions.

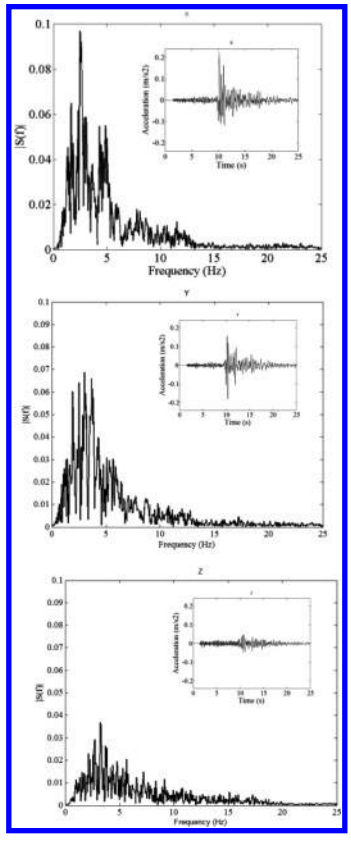


Figure 3. Acceleration spectra (and time-histories) of the three input components.

5.1 *Data acquisition and pre-processing*

The analyzed experimental data are represented by the 20 acceleration signals recorded during the Lunigiana/Garfagnana earthquake. Figure 3 reports the time history and the acceleration spectra of the three input components, as recorded by the three ground reference sensors, respectively along the X, Y and Z directions. The seismic energy content appears to be mostly concentrated in the 2–7 Hz frequency band. Dynamic identification from signals recorded during the seismic event requires that the input spectral components be distinguished from structural frequencies. In the assumption that the three ground reference signals reflect the input load into the dynamic system, the dominant earthquake components can be easily identified.

5.2 *Experimental modal analysis*

Structural modal identification has been conducted through applying an algorithm belonging to the family

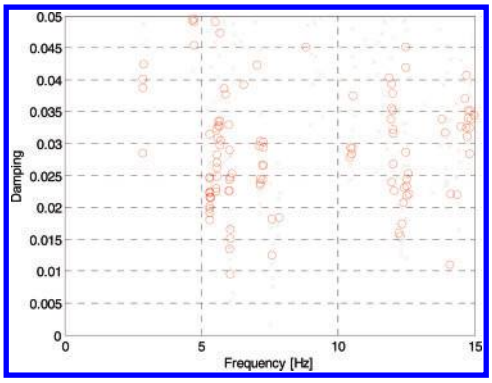


Figure 4. Example of Frequency-damping clustering diagram for the City Hall of San Romano.

Table 3. Modal frequencies and damping ratios identified through SSI for the four case studies.

Mode	f (Hz)	ζ (%)	Mode type
CITY HALL OF SAN ROMANO			
1	5.32	1.8	1st flexural along Y
2	6.08	1.8	1st flexural along X
3	7.17	2.9	1st torsional
4	11.98	3.6	Local mode
5	15.65	1.5	2nd torsional
CITY HALL OF CASOLA			
1	5.85	1.0	1st flexural along X
2	6.36	1.7	1st flexural along Y
3	7.90	2.2	1st torsional
HOSPITAL OF CASTELNUOVO DI GARFAGNANA			
1	3.53	1.0	1st flex. X, bell tower
2	6.52	1.7	1st flex. Y, bell tower
3	7.68	2.2	2nd flex. X, global
CHURCH OF S.CATERINA			
1	1.97	3.0	1st flex.X, bell tower
2	2.63	1.6	1st flex. Y, bell tower
3	3.41	3.0	2nd flex. X, global
4	4.20	4.0	1st torsional, bell tower
5	4.40	1.6	2nd flex. Y, global

of SSI (Stochastic Subspace Identification) (Peeters & DeRoeck, 1999; Larimore 1990), implemented in the SDIT3 code (Ceravolo & Abbiati, 2013).

5.3 *Dynamic identification procedure*

The identification algorithm has been applied to the output signals through progressively increasing the system order. In order to discriminate between real structural modes and spurious numerical modes the following stabilization criteria have been applied: (i) frequency variation <2%; (ii) damping variation <15%; (iii) damping ratio values comprised between 0% and 10%; (iv) MAC (Modal Assurance Criterion) >95% (Allemang 2002). Stabilization and frequency-damping clustering diagrams are reported in Figure 4. The seismic dominant frequency components, apparent in the stabilization diagram, have been subsequently identified and excluded from the model-updating procedure. The resulting identified frequencies and damping ratios for all the four buildings are reported in Table 3.

Identified mode-shapes 1 to 4 of the city hall of San Romano are represented in Figure 5. It is worth noting that unit 3 seems not significantly involved in

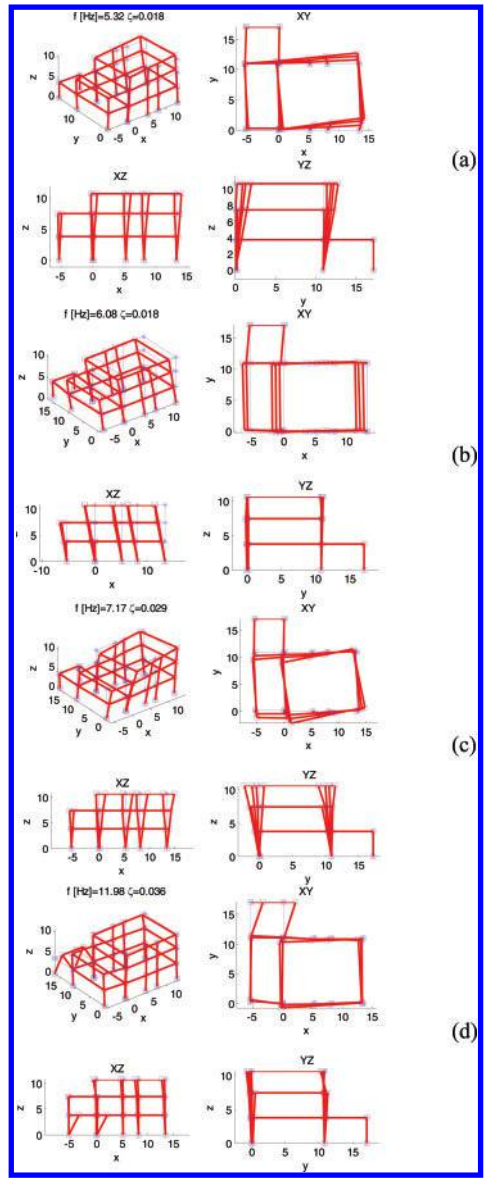


Figure 5. Identified mode-shapes: (a) mode 1 - 1st flexural along Y; (b) mode 2 - 1st flexural along X; (c) mode 3 - 1st torsional; (d) mode 4 - local mode.

the first global modes but provides the largest displacement component in the fourth mode, which is therefore labeled as a local mode. This suggests a very limited participation of this unit to the overall dynamics of the building, and consequently a substantial efficacy of the uncertain structural joint between units 1 and 3.

6 MODEL UPDATING

The updating procedure adopted consists in three main steps:

1. Discretization of the FE model in homogeneous zones, to reduce the numbers of updating variables;
2. Sensitivity analysis, to choose the most influencing parameters involved in the overall dynamic behavior;
3. Minimization of error function, updating the parameters so that the analytical modal model would match the experimental modal model.

6.1 *Discretization of the FE model*

Depending on the different age and type of the main parts of the three units, a total of 17 materials (linear elastic and isotropic) are preliminary identified in the baseline model. In order to reduce the number of updating variables, parameters which are likely to be less uncertain and less influential on the global dynamic behavior are excluded from updating. The model is therefore parted in the 6 homogeneous zones represented in Figure 6a. The structural joint between units 1 and 3 is one of them, its nominal value having been manually calibrated to 0.10 GPa in order for the analytical modes' sequence to match the experimental one.

6.2 *Objective function and sensitivity analysis*

The objective (or error) function selected for updating, and therefore used for the sensitivity analysis as well, is defined as (Friswell & Mottershead 1995):

$$\varepsilon(\mathbf{x}) = \sum_{i=1}^{m}\left[\alpha_i\left(\frac{f_{ai}-f_{ei}}{f_{ei}}\right)^2 + \beta\left(\frac{1-\sqrt{MAC_i}}{MAC_i}\right)\right] \quad (1)$$

where $\mathbf{x}$ is the updating parameter vector, f_{ai} and f_{ei} are the analytical and experimental i-th natural frequencies, MAC_i is the Modal Assurance Criterion between the i-th identified mode-shape and the corresponding i-th analytical mode-shape, αi and βi are the weight factors for the frequency and the mode-shape errors, respectively.

The sensitivity analysis is based on the local sensitivity index defined by Saltelli et al. (2000) as:

$$\hat{S}_i = \frac{\ln(\varepsilon)-\ln(\varepsilon_0)}{\ln(x_i)-\ln(x_{i0})} \quad (2)$$

where x_{i0} and $x_i = x_{i0}\cdot(1+d)$ are, respectively, the initial nominal value of the i-th updating parameter and its value incremented of a given percentage δ (here assumed equal to 5%), ε_0 is the error corresponding to the nominal model, and ε is the error corresponding to equaling all parameters to their nominal value while setting the i-th parameter to x_i.

Expressed in terms of percentage values, the relative sensitivity index is reported in Figure 6b. The elastic modulus of the lower stories appears clearly predominant.

Based on the sensitivity analysis, the four most significant parameters have been chosen as the updating parameters. For the city hall of San Romano, these parameters are summarized in Table 4, with their initial nominal values reported in the second column.

In this case, the model-updating procedure has consisted in the numerical minimization of the objective function e in Eq. (1) by means of a genetic algorithm,

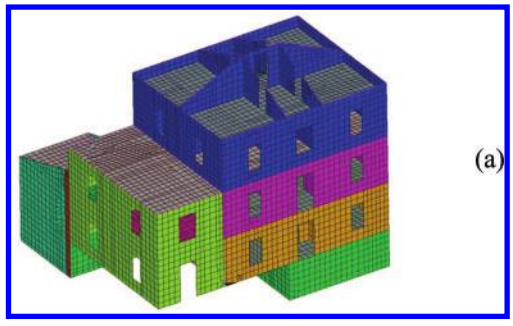


Figure 6a. FE model discretization in 6 homogeneous zones.

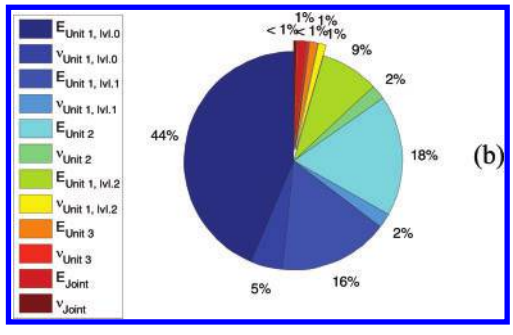


Figure 6b. Sensitivity indexes.

Table 4. Updating elastic moduli of the city hall of San Romano. Second column: nominal values. Third column: updated values

Part	Initial E (GPa)	Updated E (GPa)
1) Masonry of unit 1 – Level 0	1.50	1.84
2) Masonry of unit 1 – Level 1	1.50	1.60
3) Masonry of unit 1 – Level 2	1.50	1.03
4) Masonry of unit 2	1.50	0.78

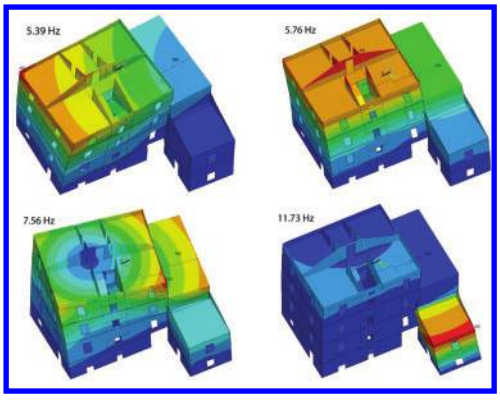


Figure 7. Mode shapes of the updated model of the city hall of San Romano.

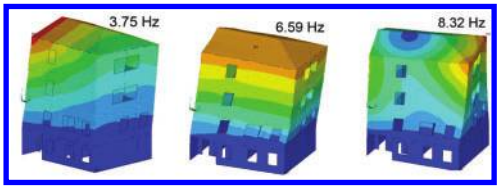


Figure 8. Mode shapes of the updated model of the hospital of Castelnuovo.

Table 5. Updated natural frequencies and frequency errors for the four different buildings.

Mode	Frequency (Hz)	Δf (%)	MAC
CITY HALL OF SAN ROMANO			
1	5.39	1.3%	93%
2	5.76	−5.3%	91%
3	7.56	5.4%	82%
4	11.73	−2.1%	82%
CITY HALL OF CASOLA			
1	5.41	−8.1%	88%
2	5.62	−12.1%	85%
3	8.45	6.5%	91%
HOSPITAL OF CASTELNUOVO DI GARFAGNANA			
1	3.75	0.3%	99%
2	6.39	−3.3%	94%
3	7.74	−1.0%	92%
CHURCH OF S.CATERINA			
1	2.00	1.5%	98%
2	2.49	−5.6%	95%
3	3.61	5.5%	88%

using 15 generations and a population of 300 individuals. Weights α_i and β_i are taken as 0.8 and 0.2, as suggested by Merce et al. (2007). The updated values of the five selected parameters are reported in the third column of Table 4.

The optimal solution is reported in Table 5, which is referred to the four monitored building. A satisfactory agreement between the analytical and the experimental modal models can be appreciated. MAC values between analytical and identified modes, in particular, are always greater than 80%. The first mode-shapes of the updated model are reported in Figure 7 for the building in San Romano. Figure 8 reports the first three vibration modes resulting from the updated model of the hospital monitored in Castelnuovo.

7 CONCLUSIONS

The experimental dynamic identification of four strategic building belonging to the OSS permanent seismic monitoring network is here reported as an example of a larger pilot study including a total of four public buildings monitored during a recent earthquake. The study provides useful indications on how to design monitoring actions and experimentally updated numerical model which can be of help in assessing the current structural seismic safety and in planning future interventions.

ACKNOWLEDGEMENTS

This research has been conducted within the activities of inter-university Italian DPC-ReLUIS 2010-2013 Project – Research line n. 1 “Development of Technologies for Monitoring and Management of the Seismic Risk”.

REFERENCES

Allemang, R.J. 2002. The Modal Assurance Criterion (MAC): twenty years of use and abuse. *Proceeding of 20th International Modal Analysis Conference*. Los Angeles, CA.

Ceravolo, R. and Abbiati, G. 2013. Time Domain Identification of structures: a Comparative Analysis. *ASCE Journal of Engineering Mechanics*.

Friswell, M.I. and Mottershead, J.E. 1995. *Finite Element Model Updating in Structural Dynamics*. Kluwer Academic Publishers.

Larimore, W.E. 1990. Canonical Variate Analysis. *Proceedings of the 29th IEEE Conference on Decision and Control*. Honolulu, Hawaii.

Merce, R.N., Doz, G.N., Vital de Brito, J.L., Macdonald, J.H. and Friswell, M.I. 2007. Finite element model updating of a suspension bridge. *Design and Optimization Symposium*. Florida, USA.

Peeters, B. and DeRoeck, G. 1999. Reference-based stochastic subspace identification for output-only modal analysis. *Mechanical Systems and Signal Processing* 13: 855-878.

Saltelli, A., Chan, K. and Scott, E.M. 2000. *Sensitivity Analysis*. Chirchester (UK): Wiley.

Research and Applications in Structural Engineering, Mechanics and Computation – Zingoni (Ed.)
© 2013 Taylor & Francis Group, London, ISBN 978-1-138-00061-2

A frequency analysis applied to force identification

M. Thiene & U. Galvanetto
Cisas G. Colombo, Università degli studi di Padova, Padova, Italy

M. Ghajari & M.H. Aliabadi
Department of Aeronautics, Imperial College London, South Kensington Campus, London, UK

ABSTRACT: A continuous monitoring of aeronautical structures is essential to guarantee the safety of both airplanes and passengers. Impacts are one of the most important causes of damage in aeronautical structures. The possibility to reconstruct the energy and the forcehistory of an impact on a structure can be a useful technique to determine if possible damage is present. In this paper a frequency domain method is applied to a composite plate in order to reconstruct the force caused by an impact. In the first step the position of the load is considered known its force history is identified.In the second step the impact is applied at hypothetical unknown position and both its location and force history are identified. Analyses considering the influence of noise are also conducted. The influence of energy of the impact, relative location between impact and sensors, and position of sensors is also investigated.

1 INTRODUCTION

Damage detection in aeronautical structures is a key factor for the economy of aeronautical industries as well as for the safety of passengers. The increasing use of composite materials in aircraft applications requires real time monitoring of the performances of critical structural elements. This monitoring cannot be accomplished by standard Non Destructive Techniques (NDTs), which can perform only a local analysis when the airplane is not in flight. Furthermore, NDTs can be long and expensive, while a real time analysis would provide data on the structure as the plane is airborne. This type of analysis is the essential step to go from NDTs to Structural Health Monitoring (SHM). Two main approaches can be used in order to detect the presence of damage in a structure: a passive one, which requires only the acquisition of data, and an active one, which needs also a known external stimulus.

One of the main sources of damage in aeronautical structures is the impact caused by e.g. debris or birds. The reconstruction of the impact energy and location is very important in SHM. It is a passive technique, as the analysis is performed only from data collected by sensors. The main advantage of this approach is that the mathematical background is simple, as a linear relationship can be established between the force applied by the impact and the signal collected by the sensors. The impact force and location can be obtained from sensors' response by applying an inverse transform. The main disadvantage of this approach is that it can be difficult to calculate the exact relationship G between force and signal, especially for complicated structures. Previous papers evaluated this relationship analytically, using a Finite Element Method (FEM) approach or from experiments. They were able to calculate G only for few impact cases. Previous papers (Martin and Doyle 1996) and (Doyle 1997) applied this inverse technique to simple beams and plates, knowing a priori the position of the load. However in real cases the position of the load is unknown so a straight forward method cannot be applied. In (Meo et al. 2005)a method for locating an impact and reconstructing its history based on the estimation of the wave propagation speed was provided; however it is difficult to apply this method to composite panels due to the direction dependence of the wave propagation speed. Other authors(Hu et al. 2007), proposed a method based on a minimization problem to simultaneously reconstruct the force history and find its location. Another research (Park et al. 2009), proposed a technique based on an initial estimation of the impact location, which was then updated with an error minimization method. However the accuracy of the technique was based on the resolution of the grid points used to evaluate the relationship G. Other examples of force reconstruction and calculation of response at different locations can be found in (Wu et al. 1994; Ribeiro et al. 2000; Jacquelin et al. 2003; Liu and Shepard 2006; Chen and Yuan 2010; Law et al. 2011).

In this research a FEM based analysis is conducted in order to calculate G for specific cases. A frequency domain analysis is then performed in order to reconstruct the force. A novel interpolation approach is then applied to extend the validity of the analysis to unknown impact locations. In the first part of the paper

the mathematical background is presented. Then, the numerical model is described. Results of impact simulations and force reconstruction are shown, first for the case in which the position of the impact was known and then for different unknown impact positions. The influence of noise in data on the predictions is investigated in the final part of this paper.

2 METHODOLOGY

The relationship between a dynamic load and the response of the plate at a certain point, assuming that the system is linear time-invariant, is given by a convolution integral:

$$u(t) = \int_0^t g(t-\tau)p(\tau)d\tau \tag{1}$$

In this equation p is the load, u is the response (e.g. displacement, acceleration,…) and g is a transfer function which represents the structure. According to the Convolution theorem, a convolution in the time domain analysis corresponds to a product in the frequency domain analysis. So taking the Fast Fourier Transform (FFT) of the signals leads to:

$$U(f) = G(f)P(f) \tag{2}$$

This is a direct problem; the response is obtained from the force exerted on the structure. However, for SHM application the key point is to reconstruct the force history and possibly its location from the response. This is called an inverse problem. Before continuing with the inverse problem formulation, it is useful to give the definition of Fourier transform. A discrete signal *s(t)* is usually available inside a timewindow$T$. At a fixed time interval ΔT, N samples are obtained. The Discrete Fourier Transform (DFT) provides *S(f)*, a representation of the time domain signal *s(t)* in the frequency domain. The number of frequency components depends both on the number of samples N and time window T, being $T=N\cdot\Delta T$. The frequencies at which frequency components are available are given by the following equation:

$$f_0 = 0, f_1 = \frac{1}{N\cdot\Delta T}, f_2 = \frac{2}{N\cdot\Delta T}, \ldots \\ \ldots, f_{N-1} = \frac{N-1}{N\cdot\Delta T} \tag{3}$$

Each component is given by a summation of the contribution of each sample:

$$S_k = \frac{1}{N}\sum_{n=0}^{N-1} s(n\cdot\Delta T)\cdot e^{-i\frac{2\pi kn}{N}} \tag{4}$$

The frequency representation of a signal is a complex discrete spectrum. Each component refers to a defined frequency, which depends on the window and sampling time. The resolution of the spectrum depends on the window, while the number of components depends on the samples. The FFT is a variation of DFT in which the calculation is done with less time consumption. From equation (4) it is clear that the number of frequency components k can vary, with a maximum value of N. This aspect can be very useful in certain situations when data are corrupted by noise.

A simple inversion of equation (2) is however not always possible, especially when data are obtained experimentally. This is due to the fact that G is a function which can have zeros; in such cases there is no information on the force at certain frequencies. Usually the presence of boundary conditions in the structure amplifies this problem (Martin and Doyle 1996). To overcome this problem, a small amount of random noise can be added to the matrix. Hence, equation (2) is rearranged as:

$$G_k^* \cdot U_k = [G_k^{\,2} + R_k]\cdot P_k \tag{5}$$

Where * indicates the complex conjugate and k indicates the frequency domain component. If two sensors are available, the equation can be written as:

$$P_k = \left[\frac{G_1^* \cdot U_1 + G_2^* \cdot U_2}{G_1^{\,2} + G_2^{\,2} + R}\right]_k \tag{6}$$

The problem consists on finding the correct representation of the function G. This can be evaluated using different techniques such as the impulse response function (IRF) (Jacquelin, Bennani et al. 2003), wavelet deconvolution (Doyle 1997) or frequency response function (FRF) (Martin and Doyle 1996). In this paper the last technique is applied. It is important to underline that the function G depends not only on the mechanical properties of the system or on its boundary conditions, but also on the relative position between the load and the sensor. This is a very important issue because in many real situations it is not possible to know a priori the location of an impact, so the matrix G is not available in that case. In such a situation, it is important to know the matrix at some points in the structure. With this information it can be possible to obtain the required matrix, i.e. the one at the impact location, with an interpolation. Another important issue is then to locate the impactcorrectly.

In this paper the following approach is developed:

1. First a preliminary estimation of the impact position is made using an energy criterion. The inputs to the energy criterion are the sensor signals (out of plane displacements).
2. With this position, G is calculated with a third order interpolation, based on known responses at given locations.
3. Then the force is reconstructed with equation (6).
4. The corresponding displacement is calculated with the direct problem provided by equation (1).

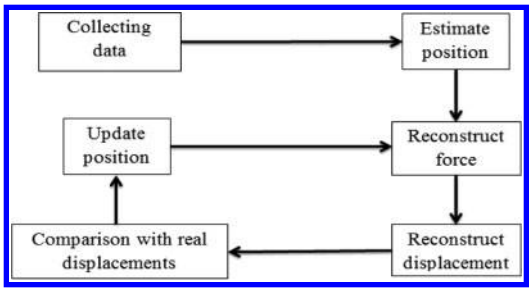


Figure 1. Localization procedure.

5. The calculated displacements are compared to the real ones. If the error is larger than a tolerance,these steps are repeated using new displacements.

The energy criterion is based on the calculation of the integral of the displacements:

$$E_i = \frac{1}{t_f - t_o}\int_{t_0}^{t_f} |u_i(t)|^2\, dt \tag{7}$$

$$\bar{x}_c = \frac{\sum E_i x_i}{\sum E_i} \quad \bar{y}_c = \frac{\sum E_i y_i}{\sum E_i} \tag{8}$$

In the above equations *i=1,2,..., number of sensors*.After each displacement has been reconstructed in step 4, equation (7) is applied and each calculated $E_i$is compared to the real E_i. Based on the maximum difference, the estimated position of the load is updated, defining a Δx or Δy which is added to the previous predicted position in step 1 and the procedure starts again. A schematic representation of this procedure is given in the Figure 1.

3 MODEL OF THE PLATE

The model under investigation is a composite plate, with all the four edges simply supported. All the properties of the plate can be found in table 1. The plate is modeled with 9652 s4r elements provided by Abaqus 6.10. The explicit package was used as the integration method, with duration of *5e-3s* and step of *1e-7s*. This system was selected because an analytical solution, which provides accurate results, is available in literature(Pierson and Vaziri 1996). The finite element solution obtained with the presented model is compared to the analytical one in order to validate the impact model. The Hertzian contact approach is used to model a nonlinear spring, with one end attached to the plate and with the other end attached to a mass of *6.28 kg* with an initial velocity of 1.76 m/s. The value of $k = 0.610^9 \mathrm{N/m}^{0.5}$ used in equation (9) was provided in (Pierson and Vaziri 1996); x is the compression of the spring.

$$F = k \cdot x^{0.5} \tag{9}$$

Table 1. Properties of the system under examination.

System		T800H/3900-2 CFRP plate, simply supported	
Size		$127.0 \times 76.2 \times 4.65\ \mathrm{mm}^3$	
Layup		$[45/90/-45/0]_{3s}$	
Density ρ		$1540\ \mathrm{kg/m}^3$	
E11	129 GPa	G12	3.5 GPa
E22	7.5 GPa	G13	3.5 GPa
V12	0.33	G23	2.6 GPa

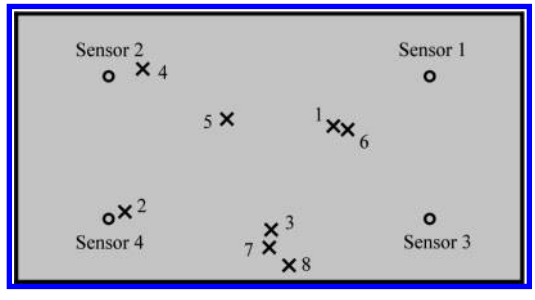


Figure 2. Schematic representation of the plate with sensors (circles) and impact positions (crosses).

Table 2. Positions of impacts and of sensors.

Position	X [m]	Y [m]
1	0,016	0,006
2	−0,036	−0,018
3	0	−0,028
4	−0,0315	0,022
5	−0,0105	0,008
6	0,0195	0,005
7	0,0005	−0,023
8	0,005	−0,033
Sensor1	0.04	0.02
Sensor2	−0.04	0.02
Sensor3	0.04	−0.02
Sensor4	−0.04	0.02

In the first simulation, the position of the impact is known, so the matrix G is available at the correct location. This simulation is useful to derive some important considerations on the capabilities of the method, as well as some limitations. The velocity of the mass was reduced to 1 m/s in the following simulations; the reason will be explained in the results section. In order to obtain the required information to reconstruct the force, the FRF of the system was calculated at four chosen locations, highlighted in Figure 2. These points also represent the output locations at which displacements were obtained during the analysis.

In the second case the position of the load was moved on the plate, but the FRF corresponding to a

load in that position was not calculated. In this case the four points denominated as "sensors" represent both the positions of the output and the position of the load in the FRF calculation. In this way 16 matrices G are available for the analysis: 4 matrices for each load case. This step can be considered a training of the system. This is the first step needed to reconstruct the force applied at an unknown position.

Eight different positions of the impact were chosen, with the same mass and velocity described before. For each impact, the procedure described in the previous section was applied and the force reconstructed. As it is possible to see from Figure 2, these positions lay both inside the rectangle formed by the sensors and outside. This is an important aspect, which will be underlined in the following section.

In order to determine the convergence of the method, as the real force is considered unknown, the convergence is checked on the calculated displacements. They are compared to the real one and, according to the sensors which suffers the greatest error, a Δx or Δy is defined in order to update the position. Their values decrease as the error decreases.

Both for the displacements and for the position of the impact, the error is calculated with equation (10). In the displacement case the *value* is the energy of the displacement, evaluated with equation (7), while in the position case, it is the distance between the point and the center of the plate.

$$error = \left| \frac{value_{calculated} - value_{true}}{value_{true}} \right| \qquad (10)$$

4 RESULTS AND DISCUSSION

4.1 *Known position of the impact*

As described previously the first simulation was done knowing the position of the impact, hence being able to calculate previously the FRF at that location. In this way equation (4), rearranged in order to consider 4 sensors, can be applied straightforward without any interpolation approach. From Figure 3 it is possible to see the analytical, FEM and reconstructed solution for the impact. Comparing the analytical and FEM solutions,it is clear that the FEM model accurately predicts the real impact force.

What is interesting to highlight is the difference between the FEM and reconstructed force. The overall shapes of the loads are very similar but the maximum amplitudes are significantly different. The reason behind this mismatch lies on the large deflection (nonlinear response) of the plate under the impact force. A demonstration of this can be done by running the analysis without considering the nonlinear geometrical effect and then reconstructing the force. The result is given in Figure 4. As it is possible to notice, the two loads considered in this case match completely. The reason behind this different behavior relies on equation (1). As this equation is only applicable to linear

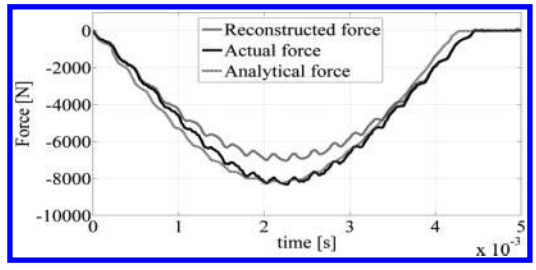


Figure 3. Comparison between analytical, FEM and reconstructed force for an impact at 1.76 m/s.

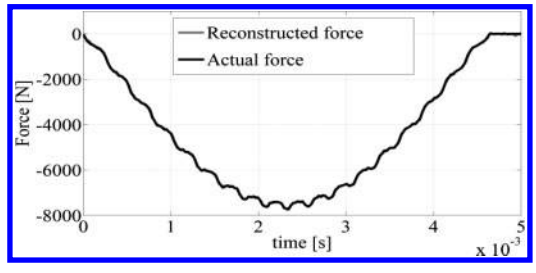


Figure 4. Comparison between FEM and reconstructed force for an impact at 1.76 m/s, linear analysis.

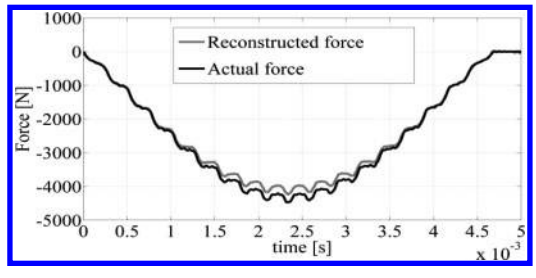


Figure 5. Comparison between FEM and reconstructed force for an impact at 1,m/s.

systems, any large deflection of the plate under a certain force cannot be reconstructed correctly. In order to reduce the amount of nonlinearity in the process, the analysis was conducted with a reduced impact, 1 m/s. The result for this case is given in Figure 5. In this case a small mismatch is still present but the level is much lower than in the previous case. In the following analysis this velocity is considered for the impact.

4.2 *Unknown position of the impact*

This part of the analysis is certainly the most challenging as it represents most of the real cases. The analysis results showed that the presented approach is suitable for the purpose of both localizing and reconstructing the impact under certain circumstances. In particular, it was found that the relative position between the impact and the sensors can influence the final results. In some cases the position of the load was wrongly calculated and so the interpolation of the transfer matrix was incorrect. However, for certain cases, the results

were accurate in terms of both force and displacement reconstruction.

The convergence of the method is very good in the first 100 iterations while a plateau in the error appears after those. This probably means that the parameters used in the position updating procedure are suitable at the beginning of the analysis but they need to be updated when the error is small. In Figure 6,one result is presented. It is clear that the force is reconstructed correctly. The convergence of the reconstructed displacement at one sensor to the real one is also shown in Figure 7.

In Figure 8 one case in which the approach fails to reconstruct the force is presented. When the impact was located outside the rectangle formed by the sensors, the interpolation approach gave incorrect results. This was due to an error in the position calculation, which was much different than the real one. An explanation is given in Figure 9 in which the error in position calculation of all the cases under exam is presented. While for most of the cases this error is low, for three impact cases it is really high. In order to investigate the method also when the load was applied at those positions, the output locations were changed and the area of that rectangle increased. However the results were not satisfactory, probably because of the proximity of the boundary condition which affected the FRF. Analyses on plates with bigger dimensions are under development in order to better understand the effect of relative position of sensors, boundaries and impacts on estimating the impact location.

4.3 *Influence of noise*

One of the greatest difficulties in the application of the inverse problem is that, during experiment, data can be corrupted by noise. If the level of disturbances is too high, the possibility to reconstruct correctly the force history can be greatly affected. In this section the proposed method is applied to one of the cases shown previously, after a certain amount of white noise was added to data with the command *'awgn'* of Matlab. This is also the opportunity to underline an important aspect of this approach. Recalling equation (4), the inverse problem involves calculating the value of the FFT of the force at each frequency component. The number of these components depends on the number of frequency components of the displacements, so on the sampling frequency. However not all of them must be used. In certain cases it can be useful to apply the analysis using only the low frequency content of the data. In this way the values at the highest frequencies, which can often be corrupted by noise, are not taken into account. In the following figures an example of the reconstruction at position 5 is given using all the frequency components and by using only first 20 components. Data were corrupted with a signal to noise ratio (SNR) of 20. The results are compared in Figures 10 and 11. These figures suggest that by using a few frequency components of the response, noise can be filtered and the impact force can be reconstructed accurately.

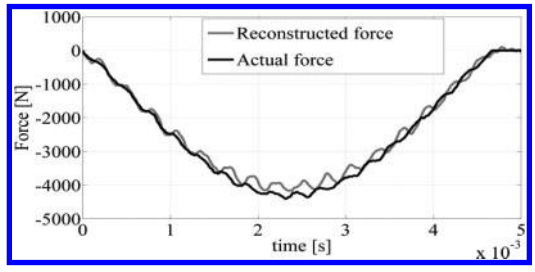


Figure 6. Result obtained for an impact at position 5

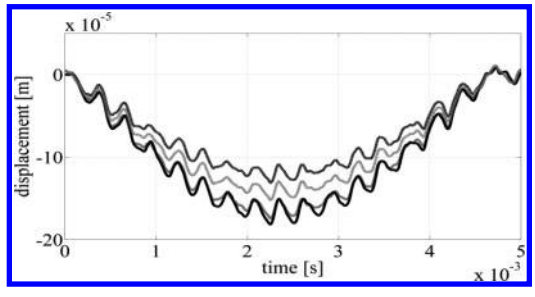


Figure 7. Example of convergence of the reconstructed displacement. Black dash 1st iteration, grey dash 10th iteration, grey solid final iteration, black solid actual displacement.

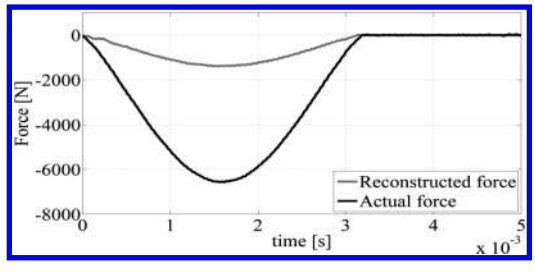


Figure 8. Result obtained for an impact at position 8.

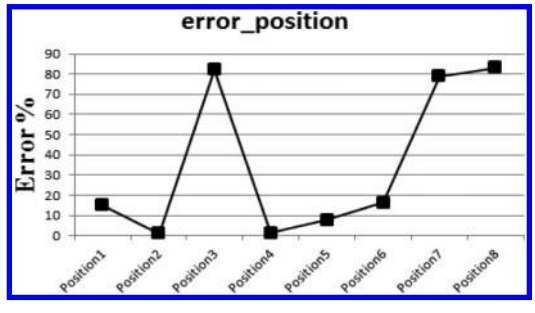


Figure 9. Error in the position calculation.

5 CONCLUSIONS

This paper presents a frequency domain approach to the inverse problem of force reconstruction. The application of the method to a case in which the position of the impact was known indicated that this technique is suitable to reconstruct the impact forcehistory.

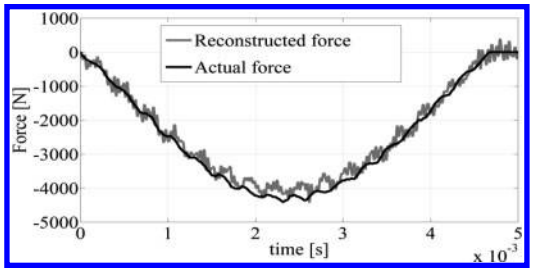


Figure 10. Reconstruction of force after the addition of noise using all frequency components.

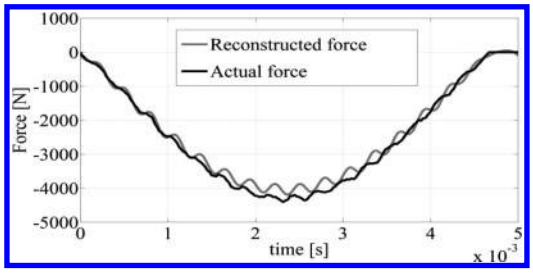


Figure 11. Reconstruction of force after the addition of noise using all frequency components.

However it also revealed that the method fails in reconstructing the correct amplitude of the load when its intensity leads to large deflection of the structure. The application to a case in which the position of the load was unknown provided useful information about the optimal mutual position between sensors and impact. In particular it highlighted how the proposed method fails to reconstruct correctly the force if the load is applied outside the sensors' grid area. However increasing this area did not provide better results, probably because of the proximity of the boundaries of the plate.The influence of noise was also investigated; the use of a few frequency components revealed that this noise can be filtered in order to obtain a better result.Further analyses are being conducted on a plate with wider dimensions in order to perform a deeper analysis on the position of the impact.

REFERENCES

Chen, C. and F. G. Yuan (2010). "Impact source identification in finite isotropic plates using a time-reversal method: theoretical study." *Smart Materials and Structures* 19(10): 105028.

Doyle, J. F. (1997). "A wavelet deconvolution method for impact force identification." *Experimental mechanics* 37(4): 403-408.

Hu, N., S. Matsumoto, et al. (2007). "Identification of impact forces on composite structures using an inverse approach." *Structural Engineering and Mechanics* 27(4): 409–424.

Jacquelin, E., A. Bennani, et al. (2003). "Force reconstruction: analysis and regularization of a deconvolution problem." *Journal of Sound and Vibration* 265(1): 81–107.

Law, S., J. Li, et al. (2011). "Structural response reconstruction with transmissibility concept in frequency domain." *Mechanical Systems and Signal Processing* 25(3): 952–968.

Liu, Y. and W. S. Shepard (2006). "An improved method for the reconstruction of a distributed force acting on a vibrating structure." *Journal of Sound and Vibration* 291(1): 369–387.

Martin, M. and J. Doyle (1996). "Impact force identification from wave propagation responses." *International journal of impact engineering* 18(1): 65–77.

Meo, M., G. Zumpano, et al. (2005). "Impact identification on a sandwich plate from wave propagation responses." *Composite structures* 71(3): 302–306.

Park, J., S. Ha, et al. (2009). "Monitoring impact events using a system-identification method." *AIAA journal* 47(9): 2011–2021.

Pierson, M. O. and R. Vaziri (1996). "Analytical solution for low-velocity impact response of composite plates." *AIAA journal* 34(8): 1633–1640.

Ribeiro, A., J. Silva, et al. (2000). "On the generalisation of the transmissibility concept." *Mechanical Systems and Signal Processing* 14(1): 29–35.

Wu, E., J. C. Yeh, et al. (1994). "Impact on composite laminated plates: an inverse method." *International journal of impact engineering* 15(4): 417–433.

Research and Applications in Structural Engineering, Mechanics and Computation – Zingoni (Ed.)
© 2013 Taylor & Francis Group, London, ISBN 978-1-138-00061-2

Influence of multiple cracks upon the dynamic behavior of beams

Z.I. Praisach & G.R. Gillich
Universitatea "Eftimie Murgu" Resita, Resita, Romania

ABSTRACT: This paper presents the way how multiple damages influence the dynamic behavior of beam-like structures, in terms of natural frequencies, mode shapes and stiffness. The analyzed cases include asymmetric supported beams with rectangular cross-section. The undamaged beams are considered with constant cross-section; damages are in form of open, transversal cracks. The analyses permitted to clearly define the relation between damage depth and location, respective frequency changes. As a significant result, we succeed to find a single mathematical relation describing the frequency changes for all bending vibration modes, involving one term defining damage's location and one defining its depth. While the first term changes for different modes, being defined by the mode shape curvature, the second maintain its value for all modes, being affected just by damage depth. Afterwards, scenarios for multiple cracks were analyzed and compared with the results obtained for these cracks considered one-by-one.

1 INTRODUCTION

Since the early 1980s the subject of damage detection using vibration data has received attention from the engineering and research communities.

In the context of Structural Health Monitoring (SHM) it can distinguish two methods for damage identification: local and global methods. Local methods inspect the structure in a relatively small area by using classical methods of Non-Destructive Testing (NDT), for example the ultrasonic methods, magnetic field methods, radiography, eddy-current methods, thermal field methods. All of these experimental techniques require that the vicinity of the damages known *a priori* and the portion of the structure being inspected is readily accessible (Doebling, et al. 1998). The inspection procedure can be very expensive and time consuming, especially when it involves components at inaccessible locations.

The global model-based damage identification is considered as a special application of system identification methodology. The damage causes characteristic local changes in stiffness, damping and/or mass, and, as a consequence of these changes, shifts of the dynamic characteristics, such as eigenfrequencies, modal damping and mode shapes, occur. The deviations between the actual dynamic properties and the undamaged state it used to detect the damage and diagnose its location and extent (Balageas et al. 2006).

The dynamic behavior of cracked structures has been investigated by many researches. Dimaragonas presented a review on the researches have been done on the issue of vibration of cracked structures until 1996 (Dimaragonas 1996). Doebling et al. provided an overview of methods to detect, locate and characterize damage in the structural and mechanical systems by examining changes in measured vibration responses (Doebling et al. 1998).

There are two approaches in using natural frequencies for damage detection: numerical and analytical. The numerical approaches by using Finite Element Analysis (FEA) is performed on a numerical model with the stiffness of the elements in the model changed systematically until the natural frequencies of the numerical model matches those measured on the real structure. The disadvantage is that an accurate numerical model of the structure is needed, which is not always easy to generate. In the analytical approach, the damage is modeled as a spring when formulating the vibration theory, assuming that it produces a discontinuity in stiffness (Rizos et al. 1990).

This paper presents the way how multiple damages influence the dynamic behavior of beam-like structures, in terms of natural frequencies, mode shapes and stiffness. The method considers a large series of weak-axis bending vibration modes for the damaged and undamaged beam. The natural frequency shifts of these modes for each crack constituting a unique signature (Gillich & Praisach 2012).

2 THE ANALYTICAL APPROACH

The research was conducted to find how the natural frequencies of several weak-axis bending vibration modes changes by occurrence of a crack. In the prior authors researches, it was demonstrated that for any vibration modes there are particular locations in which a damage do not affect the natural frequency of the respective vibration mode. These locations are identical with the inflection points of the mode shape

curvature (Fig. 1b). These locations x are different for the different vibration modes. The locations x, in which no frequency changes due damage occur, are similar for all beams identically supported. At these locations no bending occurs and consequently no strain energy is stored in the beam. There are also locations in which main frequency changes occur (Fig. 1c). These locations are identical with the points of extreme of the mode shape curvatures. These locations, x are also different for the different vibration modes, but similar for a given vibration mode for identically supported beams. The location of these points is dependent of the mode shape and its second derivative and is specific for different boundary conditions (Gillich et al. 2012a).

Comparing the frequency changes for various positions along the beam with the strain energy of slices placed on those locations:

$$dU_i(x) = \frac{1}{2} EI\left(\phi_i''(x)\right)^2 dx \tag{1}$$

where $U_i(x)$ = the strain energy of a slice dx located at distance x from the origin axis (Fig. 1a) for the vibration mode i and $\Phi_i''(x)$ = the mode shape curvature for mode i at that location.

Taking in consideration the above remarks and considering that between frequency changes of a certain vibration mode i and the corresponding mode shape curvature there is a direct relation:

$$f_{i_D}(x,a) = f_{i_U}\left[1-\gamma(0,a)\cdot\left(\overline{\phi}_i''(x)\right)^2\right] \tag{2}$$

where $f_{i_D}(x,a)$ = the frequency of the damaged beam with damage located at distance x and having a = the depth value and f_{i_U} = the frequencies of the undamaged beam for the i-th bending vibration mode. $\gamma(0,a)$ is a term depending on the damage severity and $\Phi_i''(x)$ = the mode shape curvature of the i-th mode. In Equation (2) we used the normalized mode shape curvature. The term $\gamma(0,a)$ = the stiffness loss at the location where the curvature achieves maxima and has the same value for all bending vibration modes for a given beam. It has the expression (Gillich et al. 2012b):

$$\gamma(0,a) = 1-\sqrt{\frac{v_{U\max}}{v_{D\max}}} \tag{3}$$

where v_{Umax} = the maximum deflection of the undamaged beam and v_{Dmax} = the maximum deflection of the damaged beam under own load, the damage being located at the place where the bending moment has the maximum value. Damages are in form of open transversal cracks. It is also possible to use, in stand of Equation (3), one derived from the fracture mechanics theory (i.e. that presented by Ostachowicz & Krawczuk 1991)

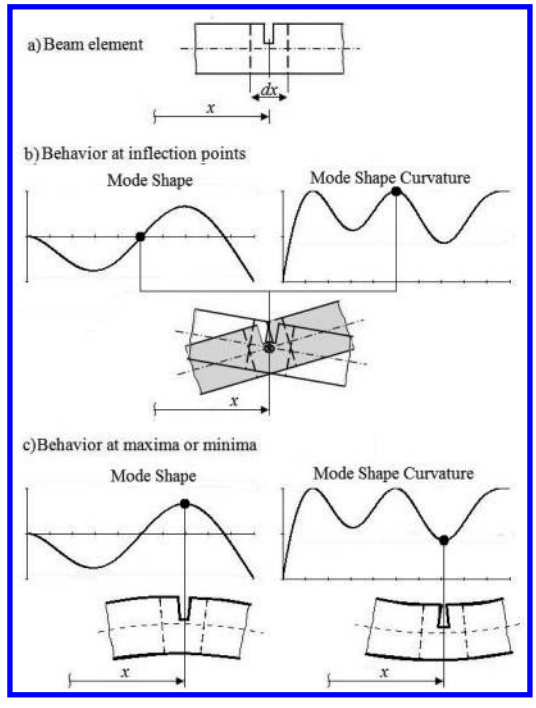


Figure 1. Behavior of the mode shape curvature points at the inflection point (b) and at the maximum or minimum points (c).

The natural frequency shifts for any damage location can be found from the modified form of Equation (2):

$$\Delta f_i(x,a) = f_{i_U} - f_{i_D}(x,a) = f_{i_U}\left[\gamma(0,a)\cdot\left(\overline{\phi}_i''(x)\right)^2\right] \tag{4}$$

or, dividing by f_{i-U} result the *relative frequency shift*, as:

$$\Delta f_i^*(x,a) = \frac{f_{i_U} - f_{i_D}(x,a)}{f_{i_U}} = \gamma(0,a)\cdot\left(\overline{\phi}_i''(x)\right)^2 \tag{5}$$

The relative frequency shift represent a single line matrix with i terms and uniquely characterize a crack in terms of depth a and location x for asymmetric structures.

3 THE NUMERICAL APPROACH

3.1 *Dynamic behavior of beam with one crack*

The chosen type of beam is a steel beam having: mass density $\rho = 7850\,\text{kg/m}^3$; Young's modulus $E = 2.0 \cdot 10^{11}\,\text{N/m}^2$; Poisson's ratio $\nu = 0.3$.

The geometrical characteristics of the beam: wide $b = 0.05$ m; height $h = 0.005$ m and consequently, for the undamaged state the cross-section $A = 250 \cdot 10^{-6}\,\text{m}^2$, moment of inertia $I = 520.833 \cdot 10^{-12}\,\text{m}^4$.

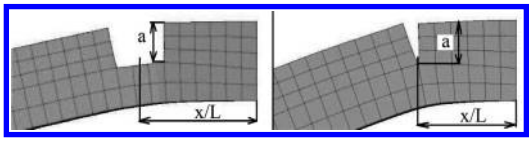


Figure 2. Left side – damage width of 3 mm and right side – damage width of 0 mm.

Were considered two dimensions of beam length 0.6 m, respectively 1 m and four type of supporting ends: clamped – free, clamped – clamped, hinged – sliding and clamped – hinged.

The medium dimension of the mesh element was 1 mm and the first ten natural frequencies of the weak-axis bending modes for the undamaged beams were determined. Afterwards, a series of damages placed separately one after the other on 200 locations along the whole length of the beam were modeled with 9 (nine) levels of depth, reducing the cross-section by: 8%, 17%, 25%, 33%, 42%, 50%, 58%, 67% and 75%, respectively. The first ten natural frequencies of the weak-axis bending modes for each case of the damaged beam were determined. Damages are in form of open transversal cracks with 3 (three) cases: 3 mm damage width, 2 mm damage width and 0 mm (Fig. 2).

The Equation (5) was verified and validated. For the first ten natural frequencies, at each location of the damage and each depth of the damage, are calculated the relative frequency shift and the results are represented in diagrams (Fig. 3). The curves formed by segments unifying this pair of values just indicate the tendency of the shift in frequency and are used to make easier comparison with the shift of natural frequencies obtained by measurements. These diagrams, for each location of damage and each level of depth have a unique signature, or pattern, in the natural frequency shift spectrum for asymmetric supported beams. For symmetric supported beams, due to the effect of symmetry, there are always two location providing one pattern.

Example, a steel cantilever beam with geometrical dimensions 50 × 5 × 600 mm. Analytical results for the first ten natural frequencies for undamaged and damaged beam are presented in Table 1 and the numerical results are presented in Table 2. The damage is located at $x / L = 0.2$ from clamped end with $a = 0.25h$ damage depth and 2mm damage width.

Figure 3 presents the relative frequency shift using the results from Table 1 and Table 2.

Analyzing Figure 3 it can observe a good correlation between analytic approach and numeric approach.

Table 1. Analytical results

Vibration Mode i	Natural frequency f_{i_U} [Hz]	Natural frequency f_{i_D} [Hz]	Relative frequency shift [%]
1	11.325	11.227	0.865
2	70.971	70.965	0.008
3	198.721	198.314	0.205
4	389.413	387.182	0.573
5	643.727	640.350	0.525
6	961.617	960.163	0.151
7	1,343.085	1,342.774	0.023
8	1,788.131	1,780.696	0.416
9	2,296.756	2,278.325	0.802
10	2,868.958	2,850.275	0.651

Table 2. Numerical results

Vibration Mode i	Natural frequency f_{i_U} [Hz]	Natural frequency f_{i_D} [Hz]	Relative frequency shift [%]
1	11.384	11.282	0.895
2	71.308	71.311	−0.003
3	199.655	199.273	0.191
4	391.427	389.037	0.585
5	647.118	643.739	0.522
6	967.033	965.642	0.144
7	1,350.994	1,350.665	0.024
8	1,798.764	1,791.883	0.383
9	2,309.933	2,292.446	0.757
10	2,883.932	2,866.083	0.619

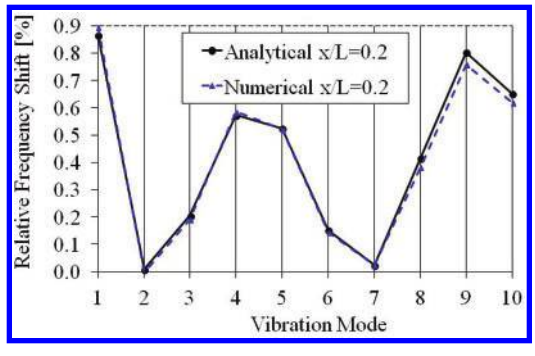


Figure 3. Relative Frequency Shift.

3.2 *Dynamic behavior of beam with multiple cracks*

In physics and systems theory, the superposition principle, also known in the literature as the superposition property, states that, for all linear systems, the net response at a given place and time caused by two or more stimuli is the sum of the responses which would have been caused by each stimulus individually (Valerie Illingworth (ed), 1991). Mathematically, for a linear system F, defined by $F(x) = y$, where x stay for input and y for output or response, the superposition (i.e., sum) of inputs yields a superposition of the respective responses:

$$F(x_1 + x_2 + \cdots) = F(x_1) + F(x_2) + \cdots \tag{6}$$

This principle applies to any linear system, including algebraic equations, linear differential equations, and systems of equations of those forms.

Table 3. Numerical results. Damage location $x_1/\mathrm{L} = 0.077$ and $a_1 = 0.5h$ damage depth

Vibration Mode i	Natural frequency f_{i_U} [Hz]	Natural frequency f_{i_D} [Hz]	Relative frequency shift [%]
1	4.090	3.931	3.875
2	25.627	25.146	1.876
3	71.754	71.216	0.750
4	140.627	140.434	0.138
5	232.520	232.574	−0.023
6	347.452	346.840	0.176
7	485.458	482.439	0.622
8	646.562	639.157	1.145
9	830.783	817.750	1.569
10	1038.109	1019.335	1.809

Table 4. Numerical results. Damage location $x/L = 0.351$ and $a_2 = 0.25h$ damage depth

Vibration Mode i	Natural frequency f_{i_U} [Hz]	Natural frequency f_{i_D} [Hz]	Relative frequency shift [%]
1	4.090	4.079	0.275
2	25.627	25.580	0.183
3	71.754	71.515	0.334
4	140.627	140.629	−0.001
5	232.520	231.748	0.332
6	347.452	346.337	0.321
7	485.458	485.444	0.003
8	646.562	644.093	0.382
9	830.783	828.739	0.246
10	1038.109	1037.831	0.027

By using the Equation (5) of relative frequency shift definition, the superposition principle for a damaged beam with multiple cracks can be applied.

In the first case it is considered a steel cantilever beam with geometrical characteristics 50 × 5 × 1000 mm heaving three open cracks of 2 mm width located from clamped end at $x_1/L = 0.077, x_2/L = 0.351$ and $x_3/L = 0.5$. First and third crack have $a_1 = a_3 = 0.5h$ damage depth, the second crack is of $a_2 = 0.25h$ damage depth.

The natural frequencies for the first ten vibration mode were determined for the undamaged beam and for the damaged beam one by one. In other words, the right terms of Equation (6) will be determined. The results are presented in Table 3 for damage located at $x_1/L = 0.077$ and $a_1 = 0.5h$ damage depth, in Table 4 for damage located at $x_2/L = 0.351$ and $a_1 = 0.25h$ damage depth and in Table 5 for damage located at $x_3/L = 0.5$ and $a_3 = 0.5h$ damage depth.

The relative frequency shift for each location of the damage are presented in Table 3, 4 and 5 and the relative frequency shift tendency is illustrated in Figure 4.

Table 5. Numerical results. Damage location $x_3/L = 0.5$ and $a_3 = 0.5h$ damage depth

Vibration Mode i	Natural frequency f_{i_U} [Hz]	Natural frequency f_{i_D} [Hz]	Relative frequency shift [%]
1	4.090	4.067	0.564
2	25.627	25.017	2.378
3	71.754	71.755	−0.001
4	140.627	137.479	2.239
5	232.520	232.520	0.000
6	347.452	339.973	2.152
7	485.458	485.446	0.002
8	646.562	633.123	2.079
9	830.783	830.730	0.006
10	1038.109	1016.669	2.065

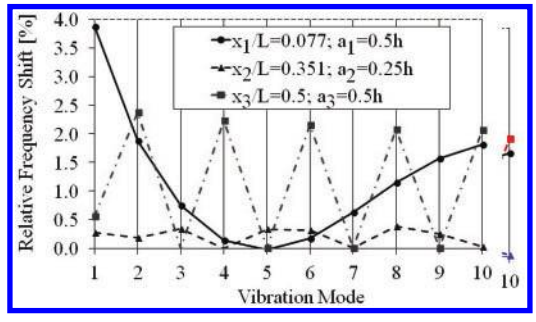


Figure 4. Relative Frequency Shift for three locations of damage.

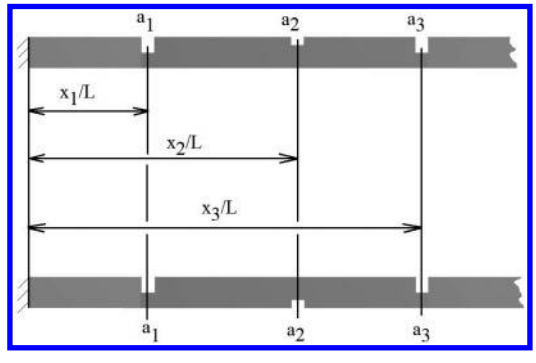


Figure 5. Damaged beam with three open cracks: top – the cracks are located on the upper side of the beam; down – the second crack is located on the lower side of the beam.

Now, we consider the damaged beam with three open cracks located at: $x_1/L = 0.077$ with $a_1 = 0.5h$ damage depth, $x_2/L = 0.351$ with $a_1 = 0.25h$ damage depth and $x_3/\mathrm{L} = 0.5$ with $a_3 = 0.5h$ damage depth.

Are considered two situations: first – all three open cracks are located on the upper side of the beam, second – first and third open cracks located on the upper side of the beam and the second crack is located on the lower side of the beam.

Table 6. Numerical results. Three damages location: $x_1/L = 0.077$ with $a_1 = 0.5h$ damage depth; $x_2/L = 0.351$ with $a_2 = 0.25h$; $x_3/L = 0.5$ with $a_3 = 0.5h$ damage depth, damages located on upper side of the beam

Vibration Mode i	Natural frequency f_{i_U} [Hz]	Natural frequency f_{i_D} [Hz]	Relative frequency shift [%]
1	4.090	3.901	4.619
2	25.627	24.493	4.425
3	71.754	70.969	1.095
4	140.627	137.257	2.396
5	232.520	231.787	0.315
6	347.452	338.252	2.648
7	485.458	482.364	0.637
8	646.562	624.018	3.487
9	830.783	815.786	1.805
10	1038.109	996.885	3.971

Table 7. Numerical results. Three damages location: $x_1/L = 0.077$ with $a_1 = 0.5h$ damage depth; $x_2/L = 0.351$ with $a_2 = 0.25h$; $x_3/L = 0.5$ with $a_3 = 0.5h$ damage depth, second damage located on lower side of the beam

Vibration Mode i	Natural frequency f_{i_U} [Hz]	Natural frequency f_{i_D} [Hz]	Relative frequency shift [%]
1	4.090	3.900	4.647
2	25.627	24.475	4.492
3	71.754	70.968	1.097
4	140.627	137.178	2.453
5	232.520	231.790	0.314
6	347.452	338.059	2.703
7	485.458	482.350	0.640
8	646.562	623.701	3.536
9	830.783	815.901	1.791
10	1038.109	995.865	4.069

The natural frequencies for the first ten vibration mode for the damaged beam with three open cracks located on the upper side of the beam are presented in the Table 6 and natural frequencies for the first ten vibration mode for the damaged beam with three open cracks with second crack located on lower side of the beam are presented in Table 7.

The superposition principle is shown in Figure 7 by using relative frequency shift. The three curves represents: the values of relative frequencies shift presented in Table 6, the values of relative frequencies shift presented in Table 7 and sum of the relative frequencies shift from Tables 3, 4 and 5. It can be observed that the results are very close.

In the second case it is considered a steel cantilever beam with geometrical characteristics 50 × 5 × 600 mm heaving two closed cracks (Fig. 7) located from clamped end at $x_1/L = 0.0055$, $x_2/L = 0.01$ with $a = 0.5h$ damage depth.

The relative frequency shift for: damaged beam with damage located at $x_1/L = 0.0055$ and $a = 0.5h$ damage depth, damaged beam with damage located at $x_2/L = 0.01$ and $a = 0.5h$ damage depth and damaged beam with two damages located at $x_1/L = 0.0055$ and $x_2/L = 0.01$ having $a = 0.5h$ damage depth are presented in Table 8 and the relative frequency shift tendency is illustrated in Figure 8.

Analyzing the Figure 8 it can be observed that for the vibration modes 1 and 2 there is a small deviation between sum of the relative frequency shift and relative frequency shift obtained for damage beam with two closed cracks. Anyhow, the superposition principle can be applied for damaged beams with multiple closed cracks.

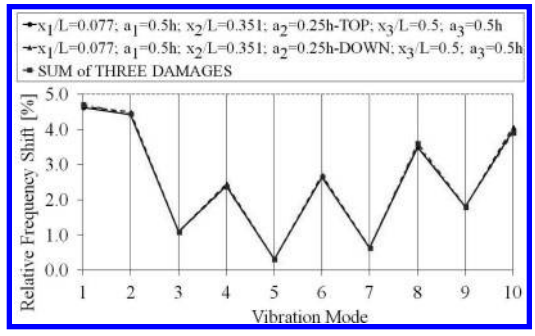


Figure 6. Superposition principle. Beam with three open cracks.

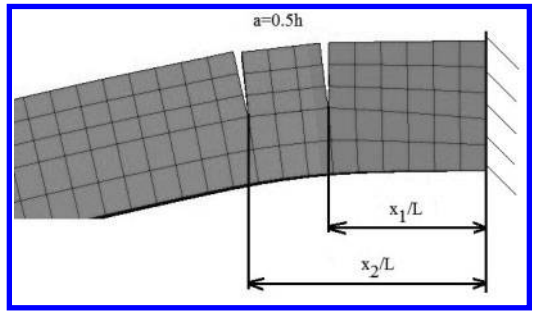


Figure 7. Beam with two closed cracks, first crack located at $x_1/L = 0.0055$ and second crack located at $x_2/L = 0.01$, both having $a = 0.5h$ damage depth.

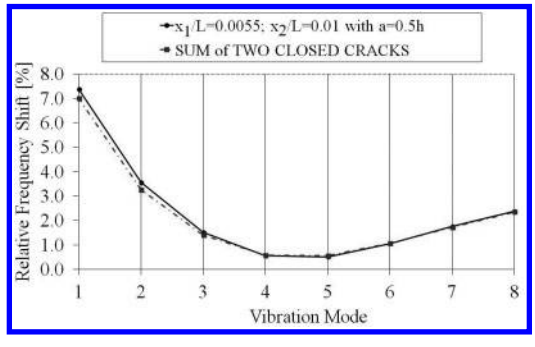


Figure 8. Superposition principle. Beam with two closed cracks.

Table 8. Numerical results. Relative frequency shift: $x_1/L = 0.0055$, $x_2/L = 0.01$ with $a = 0.5h$ damage depth

Vibration Mode i	Natural frequency f_{i_U} [Hz]	Natural frequency f_{i_D} [Hz]	Relative frequency shift [%]
1	3.907	3.473	7.008
2	2.288	1.271	3.263
3	1.259	0.260	1.407
4	0.554	0.010	0.585
5	0.150	0.368	0.568
6	0.006	1.048	1.062
7	0.092	1.664	1.719
8	0.398	1.981	2.350

4 CONCLUSIONS

The superposition principle presented in this paper, applicable to beams with open cracks or closed cracks, is based on certain phenomena characteristic to the dynamic behavior of beams, highlighted as a result of several numerical and experimental studies developed by the authors.

This property can be used to detect and assess damages in beams, even for complex cases.

Researches performed this direction revealed that it is a clear dependency between deflection and frequency changes, what makes deflection an important feature of beam behavior, usable in damage assessment.

To verify the applying the superposition principle were analyzed many locations of the damages on the beam. For open cracks, the small differences between sum of the relative frequencies shift and the values obtained for damaged beams with multiple cracks are insignificant. There are some small deviations for closed cracks, especially for first, second and third vibration modes between sum of relative frequencies shift for each closed crack and relative frequencies shift for damaged beam with multiple closed cracks.

ACKNOWLEDGMENTS

The research was co-funded by the Sectoral Operational Programme Human Resources Development 2007-2013 of the Romanian Ministry of Labour, Family and Social Protection through the Financial Agreement POSDRU/89/1.5/S/62557.

REFERENCES

Balageas, D., Fritzen, C.P. & Güemes, A. 2006. *Structural Health Monitoring*, London ISTE Ltd.

Dimarogonas, A.D. 1996. Vibration of cracked structures-A state of the art review, *Engineering Fracture Mechanics,* Vol. 5, 831-857.

Doebling, S.W., Farrar, C.R. & Prime, M.B. 1998. A summary review of vibration based damage identification methods, *Shock Vibration Digest* 30(2), 91–105.

Rizos, P.F., Aspragathos, N. & Dimarogonas, A.D. 1990. Identification of crack location and magnitude in a cantilever beam from the vibration modes, *Journal of Sound and Vibration,* 138(3), 381–388.

Gillich, G.R. & Praisach, Z.I. 2012. Robust method to identify damages in beams based on frequency shift analysis, *SPIE Conference on Health Monitoring of Structural and Biological Systems,* San Diego CA, Article Number 83481D.

Gillich, G.R., Praisach, Z.I. & Iavornic, C.M. 2012a. Reliable method to detect and assess damages in beams on frequency changes, *Proceedings of the ASME 2012 International Design Engineering Technical Conference & Computers and Information in Engineering Conference,* Chicago IL, Article Number DETC2012-70094.

Gillich, G.R., Minda, P.F., Praisach, Z.I. & Minda, A.A. 2012b. Natural frequencies of damaged beam – a new approach, *Romanian Journal of Acoustic and Vibration*, Vol. IX, issue 2/2012, 101-108.

Ostachowicz, W.M. & Krawczuk, C. 1991. Analysis of the effect of cracks on the natural frequencies of a cantilever beam, *Journal of Sound and Vibration,* 150(2), 191–201.

Valerie Illingworth (ed), 1991.*The Penguin Dictionary of Physics*, London: Penguin Books.

Research and Applications in Structural Engineering, Mechanics and Computation – Zingoni (Ed.)
© 2013 Taylor & Francis Group, London, ISBN 978-1-138-00061-2

Structural health monitoring of continuously welded underground pipelines based on quasi-distributed wireless inclinometers

Suzhen Li, Ming Zhao & Naihui Gao
College of Civil Engineering and the State Key Laboratory of Disaster Research in Civil Engineering, Tongji University, Shanghai, China

ABSTRACT: For the convenience of distribution and construction, most pipelines are buried underground. Besides corrosion, crack and material flaw, failures occurring in buried pipelines are particularly associated to structural damages externally induced by surface loading or permanent ground deformation. In the framework of structural health monitoring (SHM), this paper presents a real-time technique for safety evaluation of continuously welded underground pipelines subjected to external interference by using quasi-distributed wireless inclinometers. Based on the multiple inclination measurements, the location of abnormal surface loading and permanent ground deformation can be identified. Structural deflections are then derived based on the infinite beam model on elastic foundation and cubic spline interpolation for the estimation of pipeline behavior. Numerical simulations are conducted to investigate the effectiveness of the proposed method for detection and localization of external intrusive events as well as the influence of sensor placement and measurement error.

1 INTRODUCTION

With the rapid development of economic and industry, it is of great significance to monitor and maintain the integrity and reliability of the increasingly extensive pipeline network to ensure the smooth transportation of oil, gas and other energy sources over long distances. For the convenience of distribution and construction, most pipelines are buried underground. Besides corrosion, crack and material flaw, failures occurring in buried pipelines are particularly associated to structural damages externally induced by surface loading or permanent ground deformation (PGD), which is sometimes unavoidable in the case of nearby superstructure construction or foundation pit excavation.

A distinct consequence that either surface loading or PGD brings to the pipeline is the supervention of longitudinal bending. The flexural deflection is an important parameter for pipeline health monitoring and safety evaluation. Different from the case of other beam structures like bridges, the measurement and estimation of pipeline flexural deflection faces some specific challenges: (1) LVDT (Linear variable differential transformer) is inconvenient to be installed onto a underground pipeline; (2) The traditional leveling process is high labor cost and low measuring precision; (3) The unexpected external interference makes the load pattern unknown, and so as the deflection pattern. The number and the placement of sensors should be carefully designed.

In the framework of structural health monitoring (SHM), this paper presents a real-time technique for safety evaluation of continuously welded underground pipelines subjected to external interference by using quasi-distributed wireless inclinometers. Based on the multiple inclination measurements, the location of abnormal surface loading and permanent ground deformation can be identified. Structural deflections are then derived based on the infinite beam model on elastic foundation and cubic spline interpolation for the estimation of pipeline behavior. Numerical simulations are conducted to investigate the effectiveness of the proposed method for detection and localization of external intrusive events as well as the influence of sensor placement and measurement error.

2 A PIPELINE SHM SYSTEM USING WIRELESS INCLINOMETERS

2.1 *System architecture*

The overview of an integrated SHM system for underground pipeline using wireless inclinometers is given in Figure 1. To identify the pipeline deflection due to surface loading or construction excavation, dual axis inclinometers are attached onto the top surface of the pipe in series along the longitudinal length. A few sensors consist of a set in charge of a certain area (e.g. Zone-1) and via cables are connected to a local RTU (Remote Terminal Unit). Based on wireless transmission techniques (GPRS, Zigbee or 3G), the on-site data can be sent to the management center for pipeline health monitoring and safety evaluation. This system is expected to work as a subsystem integrating to gas or water SCADA (Supervisory Control and Data Acquisition System).

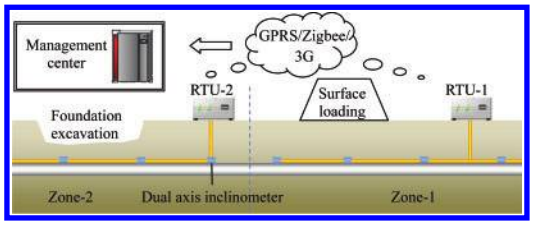


Figure 1. A pipeline SHM system using wireless inclinometers.

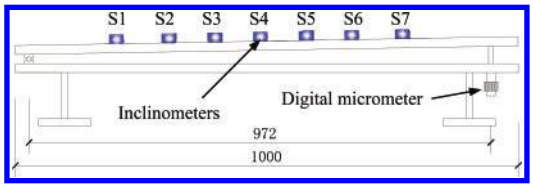


Figure 2. Calibration table for wireless inclinometers.

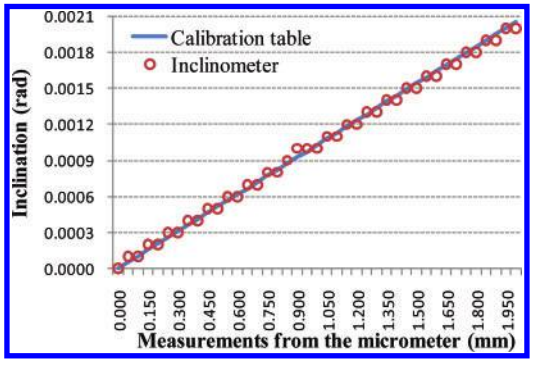


Figure 3. Characterization of the developed inclinometer.

2.2 *Wireless inclinometers*

A wireless inclinometer is recently developed in our laboratory by using MEMS (Micro Electro Mechanical systems) technique. To characterize the performance of the developed sensor, a calibration table is designed as shown in Figure 2. The total length of the table is 1m with a hinge at one hand and a digital micrometer at the other. Since the precision of the micrometer is 0.001 mm, the precision of the table is higher than 0.0001 degree, which is good enough for sensor characterization.

Seven inclinometers are selected as testing samples. The calibration result of a sensor (S3) is illustrated in Figure 3. It can be found the measurements from the developed sensor agree well with the data set by the calibration table.

Taking the set data from calibration as a reference, the errors of the measured inclinations at different measuring range can be calculated. The maximum error in the all testing cases is defined as the precision of the sensor. It can be seen from Table 1 that all the seven sensors achieve a high measuring precision. The largest error is 0.005 degree for S5. Most of the sensors achieve the precision of 0.003 degree. For the following analysis, the measuring precision of the developed inclinometer is conservatively determined as 0.005 degree.

Table 1. Sensor precision (unit: degree)

Sensors	S1	S2	S3	S4	S5	S6	S7
Precision	0.002	0.004	0.002	0.003	0.005	0.003	0.003

3 DEFLECTION ESTIMATION OF A BEAM BASED ON MULTIPLE INCLINATION MEASUREMENTS

3.1 *Basic idea*

Consider a typical gas pipe with abutting ends welding together large quantities of pipe segments. It is reasonable to simplify the pipe as a beam model of homogeneous material and geometric properties. According to mechanics of materials, the deflection (y) and rotation (θ) of a beam over the length (x) have the relation as:

$$y = \int \theta dx + C \tag{1}$$

Here, C is integration constant determined by boundary conditions.

If load pattern and boundary conditions are given in advance, which means the deflection and rotation pattern of the beam model is known as well, the rotation measured at a few locations can determine the deflection distribution. This method is widely used in the case of periodic inspection on simply supported beam bridge. The maximum deflection of the bridge under the concentrated stack loading at the mid-span can be identified by one-point rotation measurement, based on which the structural performance of the bridge can be further evaluated.

The significant difference of pipeline structural health monitoring from the above case lies in the fact that the load pattern is unpredictable and so as the deflection pattern. Numerical interpolation is a good solution to the reconstruction of rotation and deflection distribution using multiple inclination measurements. The number and the placement of sensors should be carefully designed.

3.2 *Deflection estimation method based on cubic spline interpolation*

Since the rotation function in terms of x for a beam under various load patterns is normally cubic or less, it is applicable to use cubic spline interpolation to construct rotational function θ(x).

For a given table

x	x_0	x_1	…	x_n
$S(x)$	θ_0	θ_1	…	θ_n

with $a = x_0 < x_1 < \ldots < x_n = b$, if the function $S(x)$ holds:

(1) $S_i(x)$ for each sub-range $[x_{i-1}, x_i]$ $(i = 1,2,\ldots,n)$ can be written as a cubic polynomial;
(2) $S(x)$,$S\prime(x)$,$S\prime\prime(x)$ are all continuous at $[a, b]$;
(3) $S(x_i) = \theta_i (i = 1, 2, \ldots, n)$, i.e., inclination measurements ; $S(x)$ is the cubic spline interpolation function regarding the knots $x_0, x_1, \ldots, x_n$.

A key issue to determine the polynomial coefficients is the adoption of boundary conditions. Regarding the actual mechanic behavior of a pipeline, the following equations are included in this work:

$$\begin{cases} S'''(x_1 - 0) = S'''(x_1 + 0) \\ S'''(x_{n-1} - 0) = S'''(x_{n-1} + 0) \end{cases} \tag{2}$$

Its physical meaning is that the first two sub-ranges are subjected to the exactly same external load and so as the last two, which is a reasonable assumption for buried pipelines since the external inference is usually localized.

For the efficient numerical computation, a standard procedure is followed. Suppose it holds:

$$S''(x_i) = M_i (i = 0,1,2,\cdots,n) \tag{3}$$

As $S_i(x)$ for the sub-range $[x_{i-1}, x_i]$ is a cubic polynomial, $S\prime_i(x)$ is linear and can be written as:

$$S_i''(x) = M_{i-1}\frac{x_i - x}{h_i} + M_i\frac{x - x_{i-1}}{h_i}, x \in [x_{i-1}, x_i] \tag{4}$$

with

$$h_i = x_i - x_{i-1} \tag{5}$$

The double integrals of Eq.(4) lead to:

$$S_i(x) = M_{i-1}\frac{(x_i - x)^3}{6h_i} + M_i\frac{(x - x_{i-1})^3}{6h_i} + A_i(x - x_{i-1}) + B_i \tag{6}$$

Here, A_i, B_i is the integral constant, which can be determined based on $S(x_{i-1}) = \theta_{i-1}$ and $S(x_i) = \theta_i$ as:

$$\begin{cases} A_i = \dfrac{\theta_i - \theta_{i-1}}{h_i} - \dfrac{1}{6}(M_i - M_{i-1})h_i \\ B_i = \theta_{i-1} - \dfrac{1}{6}M_{i-1}h_i^2 \end{cases} \tag{7}$$

Substitute Eq.(7) to Eq.(6):

$$S_i(x) = M_{i-1}\frac{(x_i - x)^3}{6h_i} + M_i\frac{(x - x_{i-1})^3}{6h_i} + \left(\theta_{i-1} - \frac{1}{6}M_{i-1}h_i^2\right)\frac{x_i - x}{h_i} + \left(\theta_i - \frac{1}{6}M_i h_i^2\right)\frac{x - x_i}{h_i} \tag{8}$$

Regarding $S\prime_i(x_i - 0) = S\prime_{i+1}(x_i + 0)$, it is established

$$\mu_i M_{i-1} + 2M_i + \lambda_i M_{i+1} = g_i \qquad (i = 1,2,\ldots,n-1) \tag{9}$$

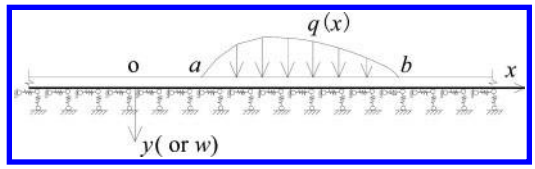


Figure 4. Infinite beam model on elastic foundation

Here,

$$\begin{cases} \mu_i = \dfrac{h_i}{h_i + h_{i+1}} \\ \lambda_i = \dfrac{h_{i+1}}{h_i + h_{i+1}} = 1 - \mu_i \\ g_i = \dfrac{6}{h_i + h_{i+1}}\left(\dfrac{\theta_{i+1} - \theta_i}{h_{i+1}} - \dfrac{\theta_i - \theta_{i-1}}{h_i}\right) \end{cases} \tag{10}$$

Two more equations can be included according to the boundary conditions given in Eq.(2)

$$\begin{cases} \lambda_1 M_0 - M_1 + \mu_1 M_2 = 0 \\ \lambda_{n-1} M_{n-2} - M_{n-1} + \mu_{n-1} M_n = 0 \end{cases} \tag{11}$$

The combination of Eq.(9) and Eq.(11) yields

$$\begin{bmatrix} \lambda_1 & -1 & \mu_1 & & & & \\ \mu_1 & 2 & \lambda_1 & & & & \\ & \ddots & & \ddots & & \ddots & \\ & & & \mu_{n-1} & 2 & \lambda_{n-1} & \\ & & & \lambda_{n-1} & -1 & \mu_{n-1} & \end{bmatrix} \begin{bmatrix} M_0 \\ M_1 \\ \vdots \\ M_{n-1} \\ M_n \end{bmatrix} = \begin{bmatrix} 0 \\ g_1 \\ \vdots \\ g_{n-1} \\ 0 \end{bmatrix} \tag{12}$$

Based on Eq.(12), the solution of $M_0, M_1, M_2, \cdots, M_n$ can be achieved. The rotation function $S(x)$ and the deflection function y(x) can be finally calculated regarding Eq.(8) and Eq.(1).

4 STRUCTURAL HEALTH MONITORING OF BURIED PIPELINE SUBJECTED TO EXTERNAL INTERFERENCE

4.1 *Analytical model for buried pipeline*

The infinite beam model for a continuously welded underground pipeline on elastic foundation can be found in Figure 4. It is simplified as a 2-D problem within the vertical plane. The methodology is exactly same to detect the vertical and lateral interference on the pipeline by using the measurements from dual axis inclinometers. The elastic foundation is considered by applying a series of springs vertically supported to the beam model.

4.2 *Numerical simulations*

Regarding external interference, structural health monitoring of underground pipeline is supposed to

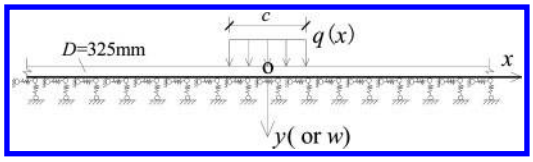


Figure 5. The pipeline model for numerical simulations.

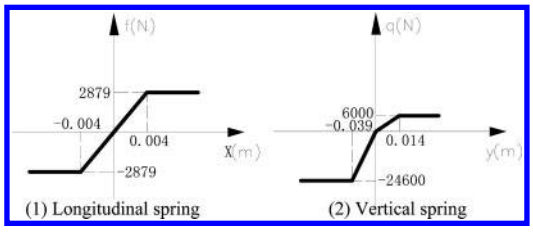


Figure 6. Stiffness of the springs for elastic foundation.

achieve three-level targets: (1) detection of interference; (2) localization of interference; (3) to evaluate the effect on pipelines. In this work, the three targets can be integrated to detect and assess the abnormal deflection. Based on the model for buried pipeline, numerical simulations are conducted to investigate the effectiveness of the proposed method in Section 3.2 for detection and localization of external interference as well as the influence of sensor placement and measurement error.

Consider a buried pipe with the outside diameter of 325 mm and the wall thickness of 10 mm. Since most of the external interferences on the buried pipe act in the form of additional soil pressure, the load can be approximately simplified as the uniformly distributed load (see Figure 5), which has no essential influence on the verification of the effectiveness of the proposed method. As the external interference is usually localized, the vertical displacement of the pipe can be assumed to be zero as long as the distance from the interference is far away enough.

According the guidelines for the seismic design of pipeline system from ASCE, the stiffness of the longitudinal and vertical spring given in Figure 6 is adopted. Suppose the volume weight of the backfill soil is 19 kN/m^3; the internal friction angle is 30deg; the pipe-soil friction coefficient is 0.55; the buried depth is 1.2 m.

Numerical studies are conducted based on the commercial software ANSYS. The pipe is modeled by PIPE16 with the element size of 0.2m. The longitudinal and vertical springs are applied to each node by using the element COMBIN39.

4.3 *Sensor placement*

For the given model in Figure 5, the identified results may be affected by two parameters including the distance (d) of sensors and the distributed length (c) of loads.

Consider the case of $c = 1$ m and the maximum deflection of 20 mm. The deflection and rotation of the pipe structure can be calculated based on the forward analysis using ANSYS. Suppose the sensors are installed on the pipeline at different distances ($d = 1$ m, 2 m, 3 m, 4 m, 5 m). The rotations at the corresponding positions can be then used as the measurements for deflection identification.

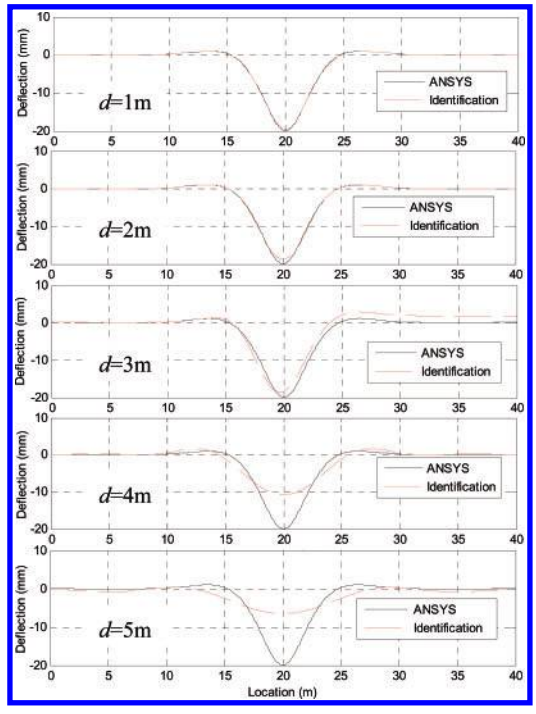


Figure 7. Identified deflections ($c = 1$ m).

According to the method proposed in Section 3.2, the pipeline deflection can be estimated using the multiple inclination measurements. The identified results are illustrated in Figure 7, by comparing with the set deflections based on forward analysis. It can be seen that the deflection is almost exactly recovered when $c = d$=1m. With the increase of the sensor distance, the identification precision is getting worse. It is indicated that the abnormal deflection due to external inference can be detected and located even when the sensor distance is five times the distributed length of loads.

Consider the case of $d = 3$ m and still the maximum deflection of 20 mm. Assuming the distributed length (c) of loads is 1 m, 3 m, 6 m, 9 m respectively, the pipeline deflections are identified and compared with the deflection calculated by ANSYS. As shown in Figure 8, the identified results achieve very good accuracy when $c \geq d$. If the external interference is more localized than sensor distribution, the identified accuracy is degraded but still good enough to locate the abnormal event. It also verifies the effectiveness of the method to identify permanent ground deformation and the potential application in early-warning of nearby foundation pit excavation.

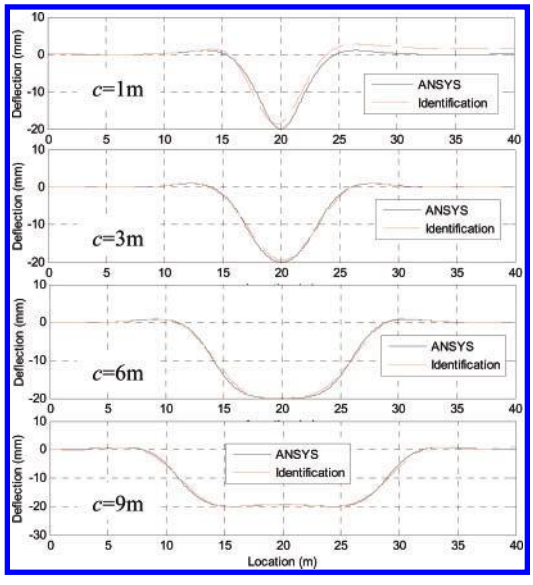


Figure 8. Identified deflections ($d = 3$ m).

4.4 *Measurement error*

In a general way, the measurement error has a significant influence on the inverse analysis for parametric identification. It is always important to investigate the feasibility of the method using the noise contaminated signals.

Suppose $d = 3$ m and $c \geq d$. Totally 200 simulation cases are conducted with the maximum deflection increasing to 20 mm. As characterized in Section 2.2, the precision of the developed inclinometer is 0.005 degree. The measurement error here is simulated as a random number of absolute value less than 0.005, which is artificially introduced to the rotation calculated by ANSYS.

Based on the inclination measurements including random noise, the pipeline deflections are identified for the all 200 cases. The absolute error can be obtained from the difference of the identified deflection and the calculated one. For each case, the largest error is taken and plotted in Figure 9. It is indicated from this statistical chart that the identified accuracy of deflection can get to 1 mm, 0.8 mm, 0.6 mm to ensure a probability of guarantee of not lower than 98%, 95%, 90%. It is a very good precision in comparison with most of current techniques for deflection measurement.

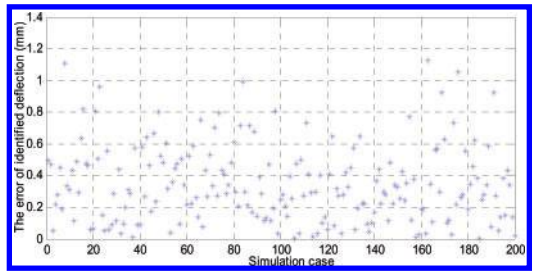


Figure 9. The statistical chart of the absolute errors of identified deflections.

5 CONCLUSIONS

Failures occurring in buried pipelines are particularly associated to structural damages externally induced by surface loading or permanent ground deformation. The flexural deflection is an important parameter for pipeline health monitoring and safety evaluation. This paper presents a safety monitoring technique for continuously welded underground pipelines subjected to external interference by using quasi-distributed wireless inclinometers. Some conclusions are summarized as follows: (1) Based on the infinite beam model on elastic foundation and cubic spline interpolation, pipeline deflection can be determined by multiple inclination measurements regardless of load pattern; (2) The developed wireless inclinometer has been testified and characterized as the measuring precision of 0.005 degree; (3) Numerical studies verify that the identified deflection can achieve very good accuracy if the sensor distribution is more localized than external interference. The identified accuracy of deflection can get to 1mm, 0.8mm, 0.6mm to ensure a probability of guarantee of not lower than 98%,95%,90%.

ACKNOWLEDGEMENTS

The authors are grateful to the Ministry of Science and Technology of China (Project: 2011BAK02B04) and the National Natural Science Foundation of China (Project: 51008236) for the financial support of this research project.

Research and Applications in Structural Engineering, Mechanics and Computation – Zingoni (Ed.)
© 2013 Taylor & Francis Group, London, ISBN 978-1-138-00061-2

Cable break detection in pre-stressed bridges, parking decks and girders

B. Hillemeier
Technische Universität Berlin, Germany

S. Knapp
IFDB, Berlin

ABSTRACT: The Remanent Magnetism Method (RM-method) is a non-destructive method to identify potentially unsafe conditions in pre-tensioned and post-tensioned concrete structures. The RM-method identifiesfractures in single pre-stressing wires, even when they are bundled with intact wires. Fractures produce characteristic magnetic leakage fields, which are measured with Hall-Effect sensors. The magnetic field of the tendons is measured at the concrete surface, once they have been pre-magnetized with an electromagnet.The parameters associated with fractured wires are the intensity of the magnetic poles, the distance between tendon and concrete surface and the crack width.The knowledge of these parameters allows drawing conclusions about the reduction of the cross-sectional area or the number of fractured wires in a tendon.The method has been evaluated by the German Federal Highway Research Institute (BundesanstaltfürStraßenwesen, BASt) and is going to be described in a DGZfP directive (German Association for non-Destructive Testing).The test results are indicated just in time in a gray-scaled magnetic laptop picture.

1 DEVELOPMENT OF BRIDGE EXAMINATION IN GERMANY

88 percent of the about 120.000 bridges in Germany are reinforced or pre-stressed concrete bridges. Probably in all countries as well as in Germany traffic infrastructure is chronically underfunded. 46% of the bridge decks in Germany are only sufficient or worse weighted according to the condition notes of the German Federal Highway Research Institute (BASt). Estimates assume that about 7 billion € are needed for examination and repair within the next ten years (Naumann 2011).

Within the years 2008/2009 the German BASt-Institute has carried out a nationwide evaluation of the stock. The condition data have been evaluated after a list of criteria. For each structure an object-related priority number has been determined. Relevant features are rated using grades between 1 (very good) and 4 (unsatisfactory) for structural stability, traffic safety and durability.

Pre-stressed concrete bridges, built between 1960 and 1985 and bridges with the condition note less than 3.0 have urgently to be examined.

1.1 *Pre-stressed concrete damages*

The reasons for corroded pre-stressing wires very often are poorly injected sheathings, the diffusion of chlorides by deicing salts, or chemical components in former grouting systems promoting corrosion. Pre-stressing wires in Germany were frequently made from tempered steel of strength class St 1420/1570, beeing technically approved until the mid 1960s. Damage analysis showed characteristic features of fracture mechanisms. Steel strengthening methods could lead to residual stresses dependingon an unsuitable hardening process leading to a retarded crack propagation. Other probable causes for defects of pre-stressing steel are hydrogeneembrittlement, untightwaterproofingwithchloride penetration, fatigue and overloading of structures, e.g. bridges.

1.2 *The magnetic detection of fractures in pre-stressing wires*

A magnetized pre-stressing wire is comparable to a bar magnet. At the positions where the magnetization starts and ends intense magnetic end-poles are generated and remanently memorized in the pre-stressed steel. At the location of a fracture, a dipole is formed, a magnetic north pole and south pole are generated (Fig. 1). The stray field of the dipole is measured at the concrete surface. The intensity of the signal is directly proportional to the reduction in cross-section of the pre-stressing strand. The signal level is also influenced by the concrete cover, the arrangement of mild reinforcement or embedded steel fittings (Hillemeier 1993, 1995; Hillemeier & Scheel 1998; Scheel & Hillemeier 1997).

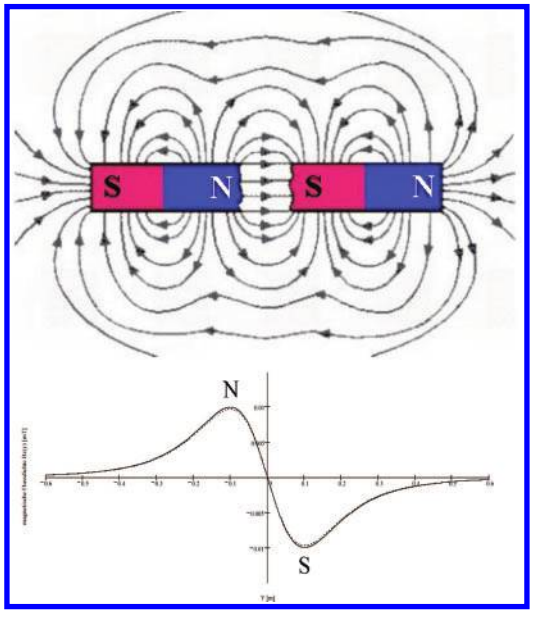


Figure 1. Locating fractures in pre-stressing wires. The curve of the measuring signal shows a characteristic graph. The inflection point of the curve is located exactly between the two magnetic poles (extreme values) and precisely defines the center location of the fracture.

1.3 *The working steps*

The following steps are involved during inspection of pre-stressed concrete components for possible fractures in pre-stressing wires:

- Accessibility to the building
- Locating the pre-stressing wires, e.g. by radar
- Installation of a mechanical guidance system to run the magnet and sensor along the member, Fig. 2
- Magnetization of the pre-stressing wires
- Measuring the magnetic field of the remanently magnetized pre-stressing wires
- Signal processing
- Interpretation of data

1.4 *The magnetization*

The pre-stressing steel should get best possible magnetized up to its magnetic saturation. Prestressing wires could have been exposed to magnetic fields prior to their installation. Such magnetic contaminations are eliminated by full saturation. Full saturation will be accomplished by using a 30 kg electromagnet (Fig. 2) within depths of up to 30 cm concrete cover. In the case of a tendon with a sufficiently large cross-section ($A \geq 50\,\text{mm}^2$) and with distances between the installed mild reinforcement bars which vary not too much, fractures can be detected up to a concrete cover of 30 cm. In the case where a tendon consists of 40 single wires with a small cross-section each (about $20\,\text{mm}^2$) mounted behind a dense mild reinforcement, the detectability of single steel fractures (one fracture



Figure 2. Measurement devices fixed under a girder for inspection. Bridge beams, factories and indoor pools, post-tensioned bridge slabs, pre-stressed parking decks and circumferential tendons of oil tanks have been inspected.

in a cross-section) might be restricted to a concrete cover of 10 cm only. The detectability always depends on the concentration and the local arrangement of the reinforcement. In a seven-wire-strand one fractured wire leads to a cross-section reduction of about 13% which is representing a good distinguishability.

1.5 *The equipment*

The pre-stressing wires are magnetized using specially developed electromagnets which are operated by a power supply unit that runs on continuous and alternating current.

The magnetic flux density is measured using Hall-Effect sensors. This type of sensors shows a fairly high sensitivity and robustness and is easily manageable in the field. The measured magnetic flux signals are stored in a computer in order to get evaluated attentively later. Immediate data evaluation also takes place by visualizing the magnetic pole situation in a gray scaled picture. (Fig. 3).

To guide the equipment precisely along the path of the pre-stressing wire, auxiliary fixtures are available for inspecting the upper, lower, and sideway surfaces of a concrete structure. A standard power supply with conventional connection specifications of 230 Volts and 16 Amps is sufficient.

2 TESTING OF PRE-STRESSED CONCRETE BRIDGE DECKS AND PARKINGSTRUCTURES

Location of pre-stressing steel fractures in bridge decks and parking structures involves the following processes:

– For bridge investigations under traffic, minimum two lanes must be blocked for traffic for each measurement line
– The works on bridges have to be prepared meticulously. Positioning of small magnets supported by conveying are prerequisites for a required exact

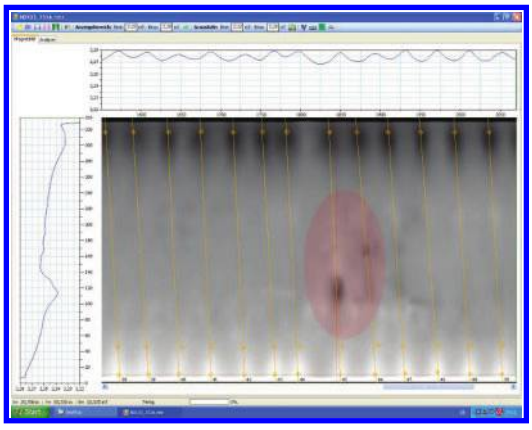


Figure 3. Fast data evaluation during the measurement. The result gets visualized in a gray scaled picture mathematically produced by a computer software. The black poles (north) are connected virtually with the white poles (south). Changing of polarity on an intersection line indicates a fracture, here to be seen inside the pink ellipse.

position indication of fractures within a millimeter range
- It is beneficial to classify the measurement tracks in 50 m to 100 m sections in order ensure data security due to the high amount of data
- Magnetization of the pre-stressing steel and scanning of the magnetic flux density according to the pre-mentioned modifications can increase the measurement speed on bridge decks up to 600 m/h
- Data acquisition and processing
- Data interpretation

The position of the tendon has to be known along the entire magnetized length within a tolerance of about 10 cm. Consequently, it is often necessary to locate the tendons using ground penetration radar before the magnetization may start.

The disadvantage of using small electro-magnets is the time consuming magnetization procedure, because the magnets have to be moved several times along the tendons until a satisfactory magnetization for evaluation is achieved.

2.1 *Single-step-magnetization*

In cases where measurements can be performed from the top surface of the concrete component, the use of larger magnets is feasible.

As a consequence a big electromagnetic unit of 3,50 m length has been developed (Fig. 4). The legs of the electromagnetic yoke have a height of about 1 m and consist of iron cores and coils with an inner diameter of 35 cm. The magnetic yoke with a mass of approximately 3,0 t is operated with a controllable DC power supply with a maximum power output of approximately 16 kW. With this magnet, whose length corresponds to the width of one traffic lane (3,75 m), it is possible to magnetize a 3 m long section of a tendon in one step.



Figure 4. The big line scanner driven by the big magnet on a highway-bridge in Germany.

With this, a fast procedure for locating pre-stressing steel fractures in transverse tendons of bridge decks or tendons in large plane structures, such as parking decks, has become available. The measuring speed has been increased by magnitudes. As a result, structural testing of the pre-stressing steel, required to maintain structural safety, could be performed without severe disruption of traffic.

An array of 335 Hall-effect sensors in a straight line of 3.35 m would be the most obvious solution to this task. Coping with the difficulties for calibration a 3 m long big line scanner has been developed in 2011. 120 Hall-sensors are mounted in six 50 cm long single elements driven extremely near to the testing surface. The robustness of measurement, the resolution of the signal and the speed could be enhanced significantly compared to the previously used rotating system since 2006 (Szielasko et al. 2006). Fig. 4 shows a photograph of the new equipment on a highway-bridge in Germany.

3 MATHEMATICAL EVALUATION OF FRACTURES

Innovations with the MFL-technique can be expected by mathematical simulation of reinforcement arrangements and their magnetic responses. Fractures in a steel bar can be visualized with their specific magnetic flux density. The PhD-thesis of Chol-I Pak delivered advantages in this respect (Pak 2009). The pre-stressing tendon got magnetized up to its magnetic saturation and though to its full remanence. Equivalent magnetic charges are introduced into the reinforcing bar in accordance with Fig. 5.

The magnetic flux density at point P(x,y,z), where e_1, e_2 and S in Fig. 5 meet, can be investigated according to the following formula (1), with B=magnetic field, P=position point P, Q=charge, r=distance of P from charge Q, m_0= 4p x 10^{-7} Tm/A, m = magnetization, A=area, d=diameter of the bar, z=depth of

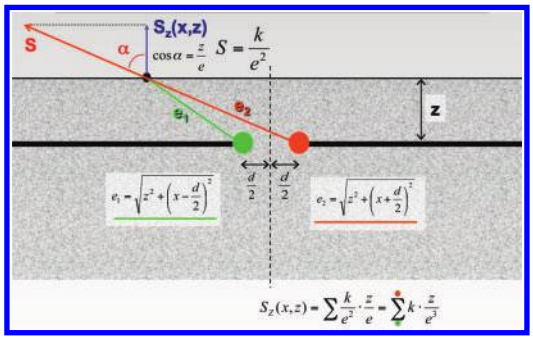


Figure 5. Magnetic charges +Q(green) and –Q(red) are implemented at the positions –d/2and +d/2distance of the fracture of the bar. The bar is oriented along the y-axis, the concrete cover is z.

the bar (vertical distance of measurement), x=position (x=0 over the bar), y=position along the bar.

$$\boldsymbol{B}(\mathrm{P}) = -\frac{\mu_0}{4\pi}\sum_{i=1}^{2}\frac{Q_i}{r_i^2}\cdot\boldsymbol{e}_{r_i}$$

$$Q = \int_A \boldsymbol{m}\,dA = \frac{B_{R,S}}{\mu_0}\cdot\frac{\pi d^2}{4}$$

$$B_z(x,y,z) = -\frac{\mu_0 Q}{4\pi}\left(\frac{z}{\left[x^2+(y-y_1)^2+z^2\right]^{3/2}} + \frac{z}{\left[x^2+(y-y_2)^2+z^2\right]^{3/2}} - \frac{z}{\left[x^2+(y-y_3)^2+z^2\right]^{3/2}} - \frac{z}{\left[x^2+(y-y_4)^2+z^2\right]^{3/2}}\right), \quad (1)$$

Mathematical derivations (Hillemeier & Pak 2012) show that the distance in y-direction between the two extreme values is identical with the depth z(at x = 0) of the bar representing the concrete cover.

$$\frac{\partial \Delta B_{Bruch}}{\partial y} = 0$$

$$-\frac{3B_{R,S}\cdot d^2\cdot z\cdot l_B\cdot(x^2-4y^2+z^2)}{16\left(x^2+y^2+z^2\right)^{7/2}} = 0$$

$$y_{Peak} = \pm\frac{1}{2}\sqrt{x^2+z^2} \quad (2)$$

The distance between the two peaks at x=0 (projection line of the axis of the bar onto the concrete surface) equals z, the concrete cover of the bar. Figure 6 visualizes the fact which is important concerning the evaluation of fractures in reinforcing bars.

4 GIRDER EXAMINATION

The following example shows the investigation of a roof construction of a sports hall in Bavaria, Germany, with a combined measurement unit by magnet and sensors, the so called “small” line-scanner. The roof construction consisted of eight roof girders with the shape of hyperboloid shells (HP-shells). The hall has been built in the years 1970/71 and was prestressed

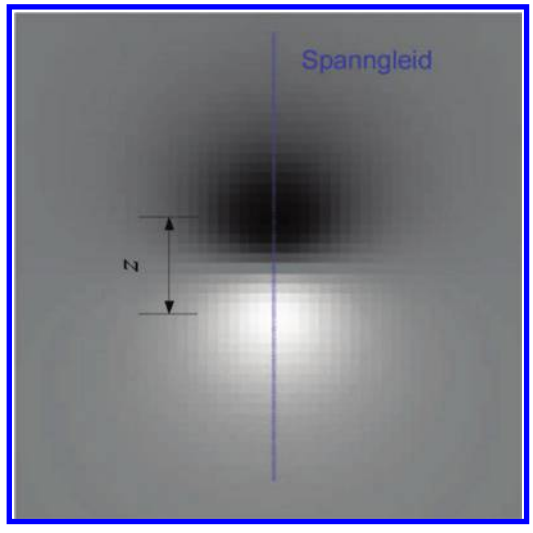


Figure 6. Typical fracture signal measured two-dimensionally. The distance of maxima equals the depth of the bar. See formula (2) with explanations.



Figure 7. Magnet-Sensor-Unit, adapted by a substructure in order to follow along straight lines the curvature of the double curved HP-shells

with prestressing steel St 1500/1700. The span of the girders is 18 m, the width 2.70 m and the thicknesses 10 cm at the ends and 6 cm in the center. Altogether 30 prestressing wires are arranged crosswise in two prestressing ribbons with 15 wires each. The prestressing wires have a diameter of 7.5 mm and a distance to each other of 30 mm.

Worrying deformations of the roof let the assumption arise that these damages resulted of broken prestressing wires. The accessibility to the structure was the most difficult task, to lead the magnet-sensor-unit along the bent ceiling girders. The special construction is shown in Fig. 7 and the pictorial representation of the magnetic stray flux in Fig. 8. The change of the magnetic north pole to the magnetic south pole at a fracture is seen in a sharp black-and-white transition.

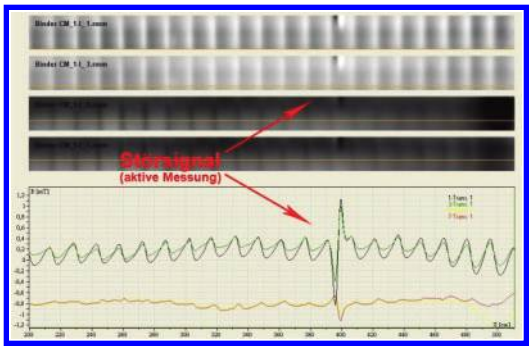


Figure 8. The upper curves are generated by an active field. The lower curves represent the effect of a de- and re-magnetization, suppressing signals from transversal reinforcement. The peak-signal does not show the characteristics of a fracture signal, it represents the signal of a specific steel item.

5 OUTLOOK

The MFL-testing method will show continuous improvement by the development of the magnetization device, the sensor equipment and the mathematical analysis of the complex arrangements of the reinforcement in real structures. Learning by doing is getting a deeper sense also in this challenging field of checking safety and durability of existing pre-stressed structures.

REFERENCES

Naumann, Joachim. 2011. Brückenertüchtigung jetzt – Ein wichtiger Beitrag zur Sicherung der Mobilität auf Bundesfernstraßen. *Heft 22, Deutscher Beton- und Bautechnik-Verein E.V.* Berlin.

Hillemeier, B. 1993. Das Erkennen von Spanndrahtbrüchen an einbetonierten Spannstählen. *Betontag 1993, Deutscher Beton-Verein E.V.* Wiesbaden

Hillemeier, B. 1995. Assessment of Structural Stability of Pre-stressed Concrete by Non-Destructive Detection of Steel Fractures, In G. Schickert & H. Wiggenhauser (eds), *Proceedings Vol. 1 of the International Symposium Non-Destructive Testing in Civil Engineering (NDT-CE)*; *Deutsche Gesellschaft für zerstörungsfreie Prüfung e. V. (1995) 23-29*

Hillemeier, B. & Scheel, H. 1998. Magnetische Ortung von Spanndrahtbrüchen in Spannbeton. *Materials and Corrosion 49, 799-804*

Pak, Chol-I. 2009. Optimierung des Remanenzmagnetismus-Verfahrens zur Stahlbruchortung in Bauwerken – Theoretische Weiterentwicklung. *PhD-thesis, Fachgebiet Baustoffe und Baustoffprüfung, Technische Universität Berlin*

Scheel, H. & Hillemeier B. 1997.Capacity of the remanent magnetism method to detect fractures of steel in tendons embedded in pre-stressed concrete. *NDT&E International, Vol. 30, No. 4; 211-216*, Elsevier Science Ltd.

Szielasko, K. &Kloster, A. &Dobmann, G. &Scheel, H. & Hillemeier, B. 2006.High-Speed, High-Resolution Mag-netic Flux Leakage Inspection of Large Flat Surfaces. *European Conference on Nondestructive Testing 2006*

Taffe, A. & Hillemeier, B. & Walther, A. 2010. Condition Assessment of a 45-year old pre-stressed concrete bridge using NDT and verification of the results.*NDE/NDT forHighways and Bridges: Structural Materials Technology (SMT) 2010, New York, 16-20 August 2010.*

Hillemeier, B. &Pak, Chol-I. 2012. Magnetic localization of fractures of broken wires in pre-stressing cables of bridges and parking decks. *Proceedings of the sixth international conference on bridge maintenance, safety and management, Stresa, Lake Maggiore, Italy, 8-12 July 2012*

Research and Applications in Structural Engineering, Mechanics and Computation – Zingoni (Ed.)
© 2013 Taylor & Francis Group, London, ISBN 978-1-138-00061-2

Detection of damage due to salt crystallization through the Scaling Subtraction Method

P. Antonaci, P.G. Bocca, A.S. Gliozzi & M. Scalerandi
Politecnico di Torino, Turin, Italy

ABSTRACT: A laboratory procedure aimed at generating a progressive deterioration of the interface between brick and mortar layers in controlled experimental conditions was developed at the Non Destructive Testing Laboratory of the Politecnico di Torino. It was carried out to explore the role of salt crystallization due to water infiltration and is intended as a preliminary stage in the design of a pre-qualification procedure to be applied to repair mortars for restoration of historical masonry buildings. The evolutionary phenomenon of mortar de-bonding generated in the lab was analyzed through a non destructive technique denoted as Scaling Subtraction Method (SSM), which is based on the detection and post-processing of the nonlinear response of the system to prescribed ultrasonic excitations. The results obtained are able to describe the experimental evidence correctly, thus allowing to characterize the mechanical behavior of the interface. Further than providing a better understanding of the mechanical degradation process under consideration, they highlight the effectiveness and potentialities of the non destructive technique used and therefore substantiate the use of the SSM to predict de-bonding phenomena also in problems characterized by different boundary conditions or damage mechanisms.

1 INTRODUCTION

Some of the most important problems affecting masonry structures are related to rising damp and to the presence of soluble salts into capillary water (Rirsch & Zhang 2010, Lubelli *et al.* 2004, Fassina *et al.* 2002): due to repeated wet-dry cycles, some salts tend to crystallize in the form of expansive compounds, causing progressive cracking and de-bonding phenomena, especially at the interfaces between different material layers, where such compounds tend to collect. An early diagnosis of the onset of such damage phenomena would make it possible to perform corrective actions promptly, thus optimizing repair costs and structural performances during service life. For this reason, it is crucial to have effective and reliable diagnostic tools, offering high resolution in detection, so as to properly identify early symptoms. A full non-destructive character is additionally required in order to keep the building functionality during inspection and monitoring.

Among these tools, ultrasonic inspection techniques (such as those based on attenuation or pulse velocity measurements) are currently widely used for damage characterization in the Building Engineering field (McCann & Forde 2001, Kim & Kim 2009), because of the close interaction between the ultrasonic wave propagation properties and the material mechanical/elastic properties.

Recent studies have revealed that the elastic excitation of cracks at the micro- or meso-scale can induce the generation of nonlinear terms in the ultrasonic wave propagating through the damaged element (Guyer & Johnson 1999, Guyer *et al*. 1999). Such terms are specifically related to damage, since they cannot be ascribed to heterogeneity or geometrical flaws of the element tested, and for this reason nonlinear ultrasounds can be significantly more sensitive to the degradation of the material mechanical properties than traditional linear ultrasonic techniques, yet in the early stages of damage (Van den Abeele *et al.* 2001, Solodov & Busse 2007, Antonaci *et al.* 2010). Therefore, improving experimental methods to properly excite a structural element and extract the full nonlinear signature in the resulting ultrasonic output signals can lead to more effective diagnostic tools to test its integrity.

Based on the above considerations, the present work aimed to check the effectiveness of a nonlinear ultrasonic technique recently developed by the authors and denoted as Scaling Subtraction Method (SSM) (Scalerandi et al. 2008, Bruno et al. 2009), when applied to the characterization of damage induced by the crystallization of expansive salts in masonry systems.

A damage protocol consisting in performing repeated cycles of imbibition in a salt solution followed by a drying phase was carried out to produce salt crystallization in coupled brick-mortar specimens. SSM measurements were made at the end of each cycle, so as to follow the evolution of damage with progressive crystallization. Mass measurements were also performed in order to produce a control indicator to be used as a reference to evaluate the SSM outcome.

2 MATERIALS AND METHODS

2.1 *Specimens*

Two masonry systems, each one constituted of an assembly of a clay brick with two external layers of restoration mortar, were considered in this study. Their final geometry is reported in fig. 1.

The bricks were selected among those commercially available in order to be representative of most common building products. Similarly, the mortar chosen was a typical example of de-humidifying mortar, as commonly used in restoration works. In particular, it was a cement-free prepacked mortar, with a base of hydrated lime and hydraulic lime, natural fine sand, polyacrylonitrile fibers and additives.

The external layers of repair mortar were not applied in complete adhesion to the brick support, on the contrary they were applied in symmetrical and regular discontinuity, created in the casting phase through the interposition of a thin steel leaf. These discontinuities behave as notches which are able to trigger multiple crack propagations.

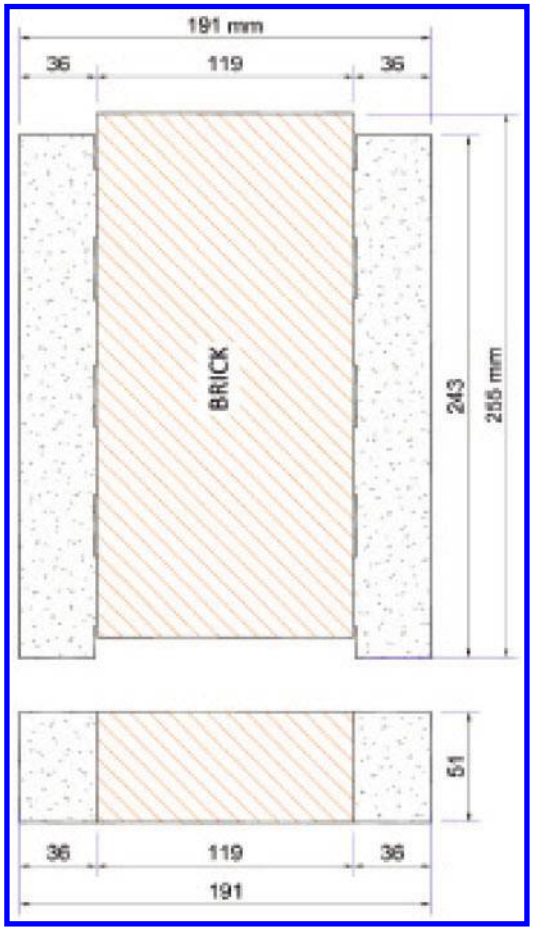


Figure 1. Geometry of specimens.

The samples thus produced were water-cured for 28 days and subsequently air-cured in indoor environment up to the time of testing.

2.2 *Salt crystallization protocol*

In accordance with Standard UNI EN 12370, after verification of mass stability, the specimens were subjected to a damage protocol consisting in immersion in a solution of Sodium Sulfate Decahydrate in deionized water for 2 hours at a temperature of 20°C, subsequent oven-heating at 85°C for approx. 14 hours, further oven-heating at 105°C for additional 4 hours, final cooling down at room temperature for a duration of approx. 2 hours. This process of imbibition followed by a drying phase tends to make the salt crystallize, with consequent alteration of the stress state due to the salt expansive action.

At the end of the cooling phase, the specimens were subjected to mass measurements to assess the amount of salt crystallization, and to SSM measurements, as described in the following. Then the damage protocol was repeated in successive steps, each one always followed by mass measurements and ultrasonic tests, until final rupture occurred due to complete de-bonding of either one or both the external mortar layers.

2.3 *SSM measurements and data processing*

As mentioned before, at the end of each step of the salt crystallization protocol described above, ultrasonic characterization tests were performed. They were carried out with the aid of two identical narrowband piezoelectric transducers with working frequency of 55.5 kHz, placed at the center of two opposite longitudinal faces of the specimen and used one as an emitter and the other as a receiver. An arbitrary waveform generator forced the emitter to vibrate according to a prescribed sine burst law, while a high voltage linear amplifier properly amplified the excitation signals. Finally, a digitizing oscilloscope was used for data visualization and acquisition. The entire setup is schematically shown in fig. 2.



Figure 2. Setup for nonlinear ultrasonic tests.

The linearity of the testing apparatus was preliminarily verified in the proper range of strain amplitudes and frequency using a reference steel sample. Salol was used as a coupling agent.

Ultrasonic measurements were performed injecting sets of sinusoidal bursts with varying amplitudes as input signals, and recording the related response of the system, in terms of received waveforms. Each input burst was composed of 10 sine cycles with the same amplitude and frequency of 55.5 kHz; then the excitation amplitude was progressively increased for successive bursts: for each damage step, 15 input amplitudes (in the range $[1 \div 20]$ V, before amplification) were used to excite the system. A time window of 200 μs was used for the acquisition of the received waveforms, even though, as described below, only first arrivals were considered in the analysis.

For the generic step i, the weight of the sample was monitored before ultrasonic measurements and the mass value was indicated as m^i. Recorded ultrasonic output signals representing the response of the system to the input excitation of amplitude A_k were denoted as $u_k^i(t)$, with i damage step index and k input amplitude index.

A post-processing of the recorded data was required to characterize the progression of damage due to salt crystallization in terms of nonlinearity evolution of the system. To do so, the established Scaling Subtraction Method (SSM) was used (see Bruno 2009 as a reference). Such a method is based on the detection of the loss of proportionality between input and output signals caused by nonlinear elastic effects in the ultrasonic waves propagation. In consolidated granular media, as well as in similar media such as brick, mortar, concrete and most building materials, these nonlinear elastic effects are highly amplified in the presence of cracks at the micro- and meso-scale and consequently tend to become more and more marked with increasing damage. Considering a generic damage step i and an excitation amplitude A_k, if the system was linear the response to that excitation amplitude would be expected to be $u_{ref}^i(t) = A_k/A_1 \cdot u_1^i(t)$, where A_1 is the lowest excitation amplitude and $u_1^i(t)$ is the corresponding response, that can be measured experimentally.

Since nonlinear effects tend to be negligible for low excitation amplitudes, it can be argued that the nonlinear signature contained in the output signal at the amplitude k is entirely expressed through the SSM signal defined as $w_k^i = u_k^i - u_{ref}^i$. Considering a small time window of the recorded signal around the first arrivals ($\Delta t = 60$ μs), the nonlinear effect can be quantified as:

$$\theta_k = \max_{\Delta t} \left| w_k^i \right| \tag{1}$$

Such a nonlinear effect must always be related to the amount of energy used to excite the specimen, which can be expressed as:

$$\eta_k = \max_{\Delta t} \left| u_k^i \right| \tag{2}$$

When plotting the experimental data for varying excitation amplitudes in terms of θ vs. η plots, a power-law dependence of θ on η is observed:

$$\theta = a\eta^b \tag{3}$$

where the parameters a and b can be estimated by best fitting of the experimental data. Finally, a proper nonlinearity indicator can be defined as the value of θ corresponding to a given amount of excitation energy η_0, as obtained from eq. 3. In this analysis, a nonlinearity indicator related to each damage step i was obtained as $\Theta^i = a\eta_0^b$, with $\eta_0 = 2$ V and a and b best fitting parameters.

3 RESULTS

As a first consideration, it is interesting to analyze the mechanism of damage caused by salt crystallization and its evolution with increasing imbibition/drying cycles, as resulting from mass measurements. Considering the percent mass variation with respect to the corresponding initial value for the elements tested (see fig. 3), it can be seen that both specimens underwent final rupture due to complete de-bonding of the external mortar layers when their mass increased by approx. 5%. Actually, in both cases visual inspection revealed that significant decay occurred even before the ultimate rupture, involving prevalently the brick component of the specimens, with surface exfoliation and partial material disintegration. The consequent mass loss related to these phenomena could not be measured during the experiments: this aspect should be taken into account when evaluating the actual mass increase due to salt crystallization, which is expected to be eventually slightly larger than the measured one.

The two specimens differ somehow from each other in terms of mass variation rate with increasing damage steps, especially at the beginning of the damage procedure: they could be ascribed to possible casual

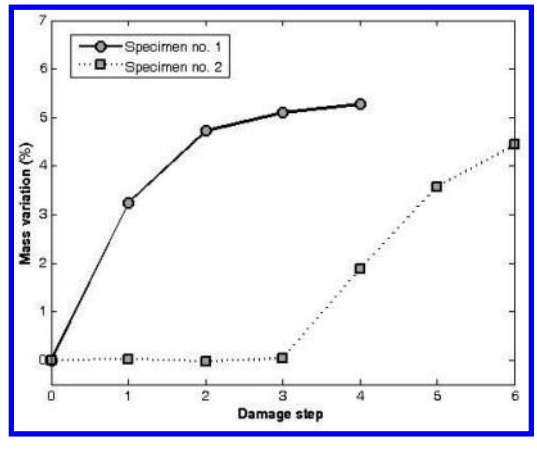


Figure 3. Percent mass variation with increasing damage steps.

discrepancies in manufacturing, resulting in a better brick-mortar adherence for specimen no. 2. This is probably the cause for a delay in the onset of the mass increase due to salt crystallization, which is perfectly reflected by the SSM data analysis, as it will be shown in the following. Nonetheless, as soon as the crystallization process takes place, the mass increase rate is almost the same for both specimens, leading to rupture in about 4 cycles.

It must be noticed that there is no evidence of any precursory trend in the percent mass variation with approaching failure: indeed, the mass increase due to progressive salt crystallization is probably balanced by the mass loss caused by partial material disintegration with increasing damage steps. As a consequence, the mass variation trend globally assumes a quite flat profile, which cannot provide any useful indication about the onset of de-bonding phenomena occurring in the element under investigation.

A clearer view of damage evolution can be obtained considering the results of the ultrasonic tests as a function of increasing salt crystallization. Based on the SSM analysis illustrated in Section 2, the evolution of decay can be described in terms of Θ curves as a function of damage steps, and accordingly in fig. 4 the variation of the Θ indicator with respect to the intact state is reported for both specimens in a logarithmic scale. When considering the behavior of specimen no. 1, it can be noticed that the nonlinear content of the output response increases with increasing damage, in agreement with the mass variation trend.

The same goes for specimen no. 2: here again the nonlinear effects caused by damage accumulation make the Θ curve rise as a function of damage steps, except for steps no. $1 \div 3$, where it tends to be roughly constant. On the other hand, it can be observed that during the same damage steps almost no mass variation occurred, meaning that the brick-mortar adherence for this specimen was strong enough to ensure a very good resistance to damage growth during the initial imbibition-drying cycles. Therefore, the SSM analysis turned out to be reliable in describing the evolution of the system, in agreement with the mass variation measurements.

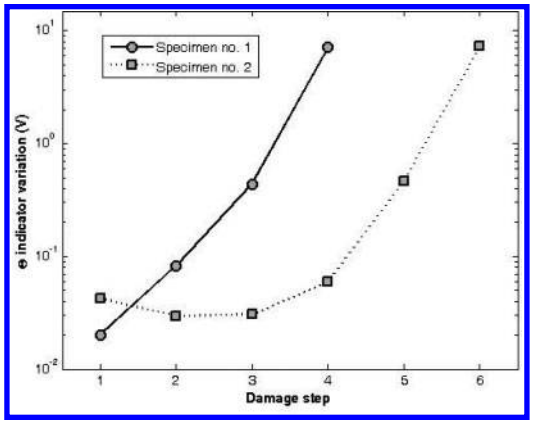


Figure 4. Variation of the nonlinearity indicator Θ as a function of increasing damage steps.

As a whole, the nonlinearity trend is similar for the two elements analyzed, but the most important feature to be observed is that in both cases the Θ variation curves show a faster growth when approaching rupture. This is a very interesting characteristics because, unlike mass variation curves, it potentially allows to make a prediction about the residual lifetime of the bond between the mortar layers and the underlying brick support under the effects of expansive salt crystallization, or at least to provide an early warning in the framework of a monitoring system. This makes nonlinear ultrasonic characterization methods, and particularly the SSM data analysis, very attractive in view of the development of highly efficient monitoring methodologies.

4 CONCLUSIONS

A lab-scale masonry system constituted by a traditional hand-made brick coupled with external layers of dehumidifying mortar was subjected to repeated imbibition-drying cycles inducing progressive crystallization of an expansive salt at the interface between brick and mortar, eventually leading to complete debonding. Such a damage protocol was set up in order to simulate the detrimental effects of rising damp in masonry buildings, in the presence of soluble salts into capillary water.

The evolution of damage was described by means of a mass variation indicator and a nonlinearity indicator experimentally derived from nonlinear ultrasonic tests based on the Scaling Subtraction Method. The experimental evidence revealed that the type of damage here investigated causes an increase in the nonlinear response of the system to an ultrasonic excitation, in a similar way as already attested in the scientific literature for several other forms of degradation. The use of a nonlinearity indicator such as the one here proposed proved to be very useful for the purposes of damage monitoring, since it showed a high sensitivity to the appearance of decay and was able to provide precursory indications with approaching failure.

REFERENCES

Rirsch, E. & Zhang, Z. 2010. Rising damp in masonry walls and the importance of mortar properties. *Constr Build Mat* 24:1815–1820.

Lubelli, B. *et al*. 2004. The role of sea salts in the occurrence of different damage mechanisms and decay patterns on brick masonry. *Constr Build Mat* 18:119–124.

Fassina, V. *et al*. 2002. Evaluation of compatibility and durability of a hydraulic lime-based plaster applied on brick wall masonry of historical buildings affected by rising damp phenomena. *J Cult Her* 3:45–51.

McCann, D.M. & Forde, M.C. 2001. Review of NDT methods in the assessment of concrete and masonry structures. *NDT&E Int* 34:71–84.

Kim, B.C. & Kim, J.Y. 2009. Characterization of ultrasonic properties of concrete. *Mech Res Commun* 36:207–214.

Guyer, R.A. & Johnson, P.A. 1999. Nonlinear mesoscopic elasticity: Evidence for a new class of materials. *Phys Today* 52:30–36.

Guyer, R.A. *et al*. 1999. Hysteresis and the Dynamic Elasticity of Consolidated Granular Materials. *Phys Rev Lett* 82:3280–3283.

Van den Abeele, K. et al. 2001. Micro-damage diagnostics using nonlinear elastic wave spectroscopy (NEWS). *NDT&E Int* 34:239–248.

Solodov, I. & Busse, G. 2009. Nonlinear air-coupled emission: The signature to reveal and image microdamage in solid materials. *Appl Phys Lett* 91:251910.

Antonaci, P. *et al*. 2010. Evolution of damage-induced nonlinearity in proximity of discontinuities in concrete. *Int J Sol Struct* 47.1603–1610.

Scalerandi, M. *et al*. 2008. A scaling method to enhance detection of a nonlinear elastic response. *Appl Phys Lett* 92:101912.

Bruno, C.L.E. *et al*. 2009. Analysis of elastic nonlinearity using the Scaling Subtraction Method. *Phys Rev B* 79:064108.

Research and Applications in Structural Engineering, Mechanics and Computation – Zingoni (Ed.)
© 2013 Taylor & Francis Group, London, ISBN 978-1-138-00061-2

A damage evaluation method for bridge substructures using longitudinal impact dynamic responses

J.W. Zhan, H. Xia & N. Zhang
School of Civil Engineering, Beijing Jiaotong University, Beijing, China

ABSTRACT: A two-stage damage evaluation method for bridge substructures is proposed. The damage indices based on frequency response functions of the longitudinal dynamic responses under impact loads are used to determine whether damage exists in bridge substructures. The damage extents are determined by finite element model updating method with the longitudinal modal parameters as inputs. The damage evaluation criteria for bridge substructures are suggested based on the limit values of damage indices. The proposed damage evaluation method is verified by an engineering case.

1 INTRODUCTION

Substructures are very important members to support the superstructures in bridges. Most researches, however, focused on the damage evaluation of superstructure, but very little attention paid to the substructures. Various damage identification methods have been proposed utilizing either static parameters or dynamic responses. Damage in bridges can result in changes of their mechanical properties such as mass, stiffness, damping and boundary conditions, which can be reflected by changes in their dynamic characteristics. Damage identification based on the dynamic characteristics of structures has become currently an active research topic in civil engineering (Pandey 1991, Salawu 1997, Hassiotis 2000, Palacz 2002, Wang 2001, Ren 2001). Among the vibration properties, the dynamic responses and natural frequencies are the most sensitive indicators of damage and can be used for the condition evaluation of substructures.

In many countries, the vibration amplitudes and the natural frequencies of bridge substructures are restricted to the allowable ranges. If they are beyond the limit values, then the substructures are judged unsafe (China 2004). According to some studies, however, it is not easy to use the measured amplitudes to evaluate the damage because they are related to the type, weight, length and running speed of vehicles. It is often difficult to consider all these factors in processing the measured amplitudes (Nishimura 1992, 2001). Due to the complexity of vehicle excitation, it is also difficult to obtain the natural frequencies of substructures by train-induced dynamic responses.

In this paper, the vibration of the substructure body, bearing stiffness and subsoil stiffness are used as condition parameters. The sensitivities of longitudinal responses under impact forces to damage are analyzed. The frequency response functions (FRF) based damage index signature assurance criterion (SAC) is used to judge whether damage exist and to determine the global damage extent. With the tested longitudinal impact responses and modal parameters as objectives, the bearing parameters, stiffness parameters and the subsoil parameters are obtained by the finite element model updating method. Thus, the working states of the bridge substructures can be evaluated.

2 SUBSTRUCTURE DAMAGE EVALUATION USING DYNAMIC RESPONSES

The damage of bridge substructures includes structural false, bearing deterioration and subsoil degradation, which usually result in the change of lateral or longitudinal dynamic responses. For most highway bridges, the lateral deformation is main shearing. On the other hand, the constraints of superstructure and bearings are very strong due to the integrity of superstructure, so the lateral modal parameters and dynamic responses are not very sensitive to damage. In contrast, the longitudinal stiffness of substructures is small and the vibration in the longitudinal direction is bending, so it is very easy to excite their local vibration by impact forces. Under the strong constraints of the superstructure in the longitudinal direction, the longitudinal responses under impact forces are transient and local, and the substructures can be simplified as cantilever models with subsoil and bearing constraints (see Fig. 1).

Different from the complicated vehicle excitations, the impact forces executed by the weight hammers and the frequency response functions can be measured simultaneously. The impact forces can be applied on the columns or the bent caps in the longitudinal or lateral direction.

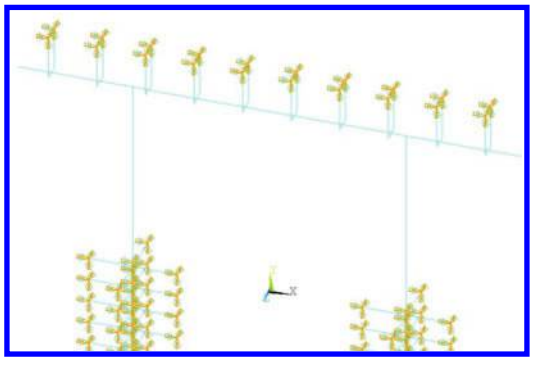


Figure 1. Simplified model in the longitudinal direction.

The soundness index (SI) of the substructure is defined as:

$$\mathrm{SI} = \frac{\text{measured frequencies}}{\text{benchmark values}} \tag{1}$$

In this formula, the benchmark frequency of the tested substructure is computed by the benchmark frequency formula or adopted as its initial test value in the healthy condition. For the symmetrical double-column highway bridge substructures, if the bearings, column body and subsoil are intact, the longitudinal natural frequencies and dynamic responses of the two columns should be the same. When SI is below 0.90, it indicates that damage exists in the structure (Zhan 2005).

Under the impact forces, the motion equation of the substructure can be expressed as:

$$\mathbf{M}\ddot{\mathbf{X}} + \mathbf{C}\dot{\mathbf{X}} + \mathbf{K}\mathbf{X} = \mathbf{P} \tag{2}$$

where: **M**, **K** and **C** are, respectively, the mass, stiffness and damping matrices of the structure; **P** is the impact force vector acted on the substructure.

When the impact force is a unit one, the frequency response function is:

$$H_{pl}(\omega) = \sum_{r=1}^{n} \frac{\phi_{lr}\phi_{pr}}{(\omega_r^2 - \omega^2 + 2j\zeta_r\omega_r\omega)M_r} \tag{3}$$

where: p and l denote the force point and the response point, respectively; M_r is the r-order modal mass.

The signature assurance criterion (SAC) is usually used to describe the similarity of the FRFs of different points:

$$\mathrm{SAC}_{pij} = \frac{(|\{u\}^{\mathrm{T}}\{v\}|)^2}{(\{u\}^{\mathrm{T}}\{u\})(\{v\}^{\mathrm{T}}\{v\})} \tag{4}$$

where: nf is the total number of frequency point; $\{u\}^T = \{H_{pi}(\omega_1), H_{pi}(\omega_2), ..., H_{pi}\omega_{nf})\}$ is the FRF vector of point i; $\{v\}^T = \{H_{pj}(\omega_1), H_{pj}(\omega_2), ..., H_{pj}(\omega_{nf})\}$ is the FRF vector of point j.

If SAC = 1.0, the FRFs of two points are fully linearly related and no structural damage exists, and if SAC = 0.0, the two points are totally unrelated and severe damage emerged in the structure. SAC is not related to the amplitude, but the shape of FRF, so the error induced by the incorrectness of modal shapes can be overcome. Damage Index (DI) based on SAC value is defined as:

$$\mathrm{DI} = 1 - \mathrm{SAC} \tag{5}$$

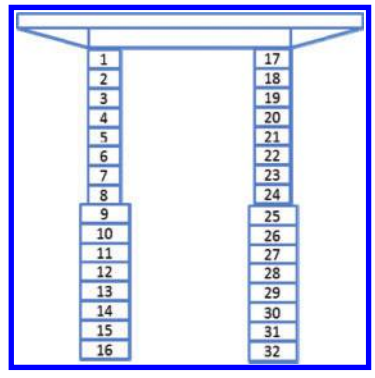


Figure 2. Finite element model of the substructure.

Table 1. DI in different damage scenarios.

Damage element	DI at different damage extents			
	20%	50%	65%	80%
1	0.06	0.25	0.40	0.56
2	0.04	0.14	0.24	0.41
3	0.03	0.07	0.13	0.26
4	0.03	0.05	0.07	0.15
5	0.03	0.05	0.07	0.15
6	0.03	0.06	0.11	0.22
7	0.03	0.09	0.16	0.31
8	0.04	0.11	0.21	0.40
9	0.03	0.08	0.15	0.33
10	0.03	0.08	0.16	0.33

A symmetrical highway bridge substructure shown in Fig. 2 is used to analyze the influence of damage on DI. The subsoil surface is near point 9. The lateral responses of symmetrical points on the two columns, for example 1 and 17, are compared and DI is obtained. Different elements are damaged with different extents in turn. The damage scenarios shown in Table 1 are investigated.

It can be seen that DI of the substructure increases with the damage extents and that the damage near the subsoil has more influence on DI than the others. According to Table 1, the following evaluation criteria for bridge substructures are suggested.

3 QUANTITATIVE DAMAGE EVALUATION OF BRIDGE SUBSTRUCTURES

For bridge management, soundness index SI is an indicator of damage, which can point out the integral damage extents of substructures. However, it is

Table 2. Suggested damage evaluation criteria.

DI range	Measures	Judgment rank
$0 \le DI < 0.05$	sound	1
$0.05 \le DI < 0.10$	damage exists but does not influence the serviceability	2
$0.10 \le DI < 0.20$	condition monitoring should be conducted	3
$0.20 \le DI < 0.40$	reinforcement should be done	4
$0.40 \le DI$	severe damage exist, detailed inspection and reinforcement should be conducted	5

more important to know the location of damage and determine the damage extent.

In recent years, the finite element (FE) model updating technique has become a powerful tool to identify the real parameters of structures and evaluate the damage extents. Many researches have focused on this area (Teughels 2002).

The procedure of updating a finite element model uses measurement data as reference. The estimated natural frequencies and mode shapes are usually considered and the modeling parameters are updated to minimize the differences between experimental and numerically calculated modal parameters. In essence, this is an optimization problem.

The optimization parameters of bridge substructures are chosen as elastic modulus E of substructure body, m value of subsoil and bearing coefficient K. The objective function F comprises two terms, one related to the natural frequencies of global and local modes, and another related to the MAC values of global and local modes:

$$F = \sum_{i=1}^{nmode} w_{fi}\left[\frac{(2\pi f_{ti}^2 - 2\pi f_{ai}^2)}{(2\pi f_{ti}^2)}\right]^2 + \sum_{i=1}^{nmode} w_{\phi i}[1 - \mathrm{MAC}(\phi_{ai}, \phi_{ti})]^2 \quad (6)$$

where: w_{fi} and $w_{\varphi i}$ are, respectively the weighing factors of natural frequencies and mode shapes; f_{ti} and f_{ai} are the i-order experimental and analytical frequencies; ϕ_{ti} and ϕ_{ai} are the vectors containing the experimental and numerical modal information regarding the mode i; $nmode$ is the number of used modes.

The constrained optimization problem can be expressed as:

$$\min : F = F(x) \quad (7)$$

The constrained conditions are:

$$F_k(P) \le \xi \quad \text{and} \quad |F_{k+1} - F_k| / F_k \le \varepsilon \,\&\, k \le N \quad (8)$$

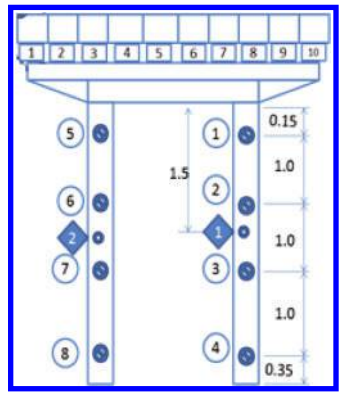


Figure 3. Longitudinal elevation of test substructure.



Figure 4. Measurement and impact point arrangement.

where: ξ is the allowable error of objective function, ε is the convergence coefficient, N is the designated iteration number.

4 ENGINEERING CASE OF SUBSTRUCTURE DAMAGE EVALUATION

4.1 *Sketch of the test bridge*

The bridge shown in Fig. 3 is a substructure of a two-way bridge with 10 spans of simply-supported box-girders. Two impact points are arranged in the middle of the left column and right column, respectively. The sensors on the columns and the impact points are shown in Fig. 4. The columns were impacted in the longitudinal direction.

4.2 *Damage evaluation*

The time-domain dynamic response and frequency spectrum of point ⑤ are shown in Fig. 5. According to the principle of impact vibration test method

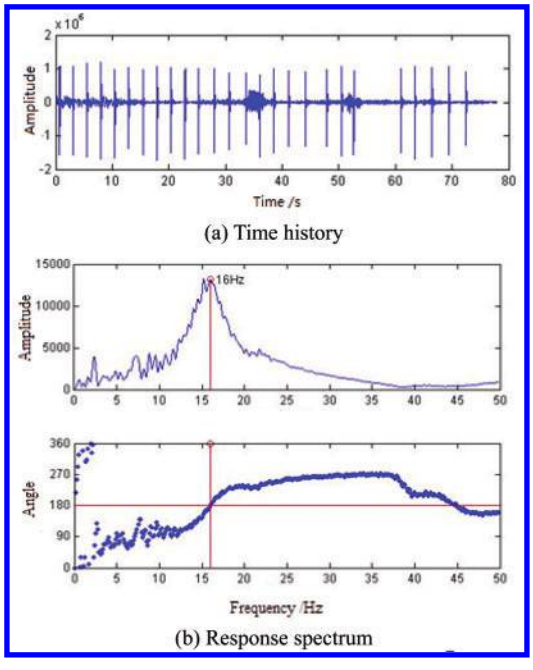


Figure 5. Dynamic response and spectrum of point ⑤.

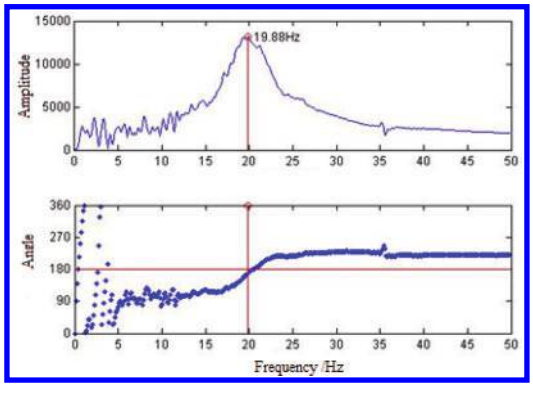


Figure 6. Response spectrum of point ①.

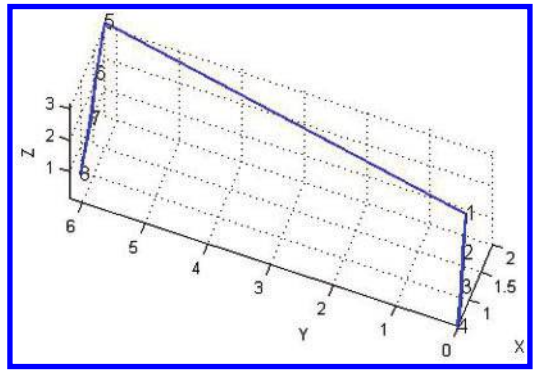


Figure 7. Left column dominating mode (16.0 Hz).

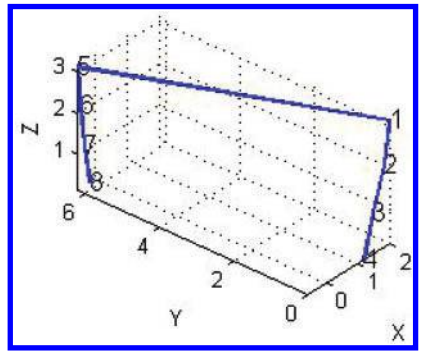


Figure 8. Right column dominating mode (19.88 Hz).

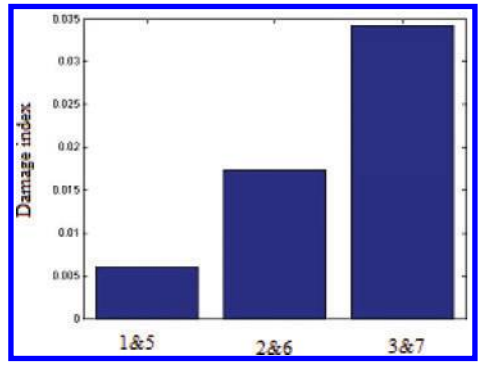


Figure 9. Damage index of the substructure.

(IVTM), the natural frequency of left column is determined as 16.0 Hz (Zhan 2005). Similarly, the natural frequency of right column is 19.88 Hz (Fig. 6). The mode shapes corresponding to the two frequencies are shown in Figs. 7 and 8, respectively.

According to the design, the two columns have the same height, same material and same bearing constraints. Therefore, if the two columns are sound, they should have similar frequency and mode shape, otherwise, damage must exist in the substructure.

If the condition of the right column is assumed good and its natural frequency is used as benchmark value, the soundness index of the left column is SI=16/19.88=0.8. It is blow the safety limit value 0.90, so it can be estimated that the damage happens in the left-column side. To find out the damage type, the bent cap is impacted by a 30 kg hammer in the lateral direction and the damage index DI is analyzed. The DI of three-group points in Fig. 9 is all near zero. According to the evaluation criterion in Table 2, a conclusion is drawn that the substructure belongs to rank 1 and no structural damage in the columns.

Because there is no structural damage in column, possible damage is bearing deterioration or subsoil degradation. The finite element model updating method is used to evaluate the damage. In the analysis, three natural frequencies and mode shapes in the longitudinal direction are used as objective data. The ten bearing of

girders are classified into two groups, i.e. the left five bearing and the right five bearings, whose stiffness are k_1 and k_2, respectively. The m value of the subsoil,k_1,k_2 and the elastic modulus E of the column body are used as variables in the updating analysis.

After the system identification, the true values of the designed variables are obtained and following conclusions can be drawn:

(1) The elastic modulus E of the column body is 3.50×10^4 MPa, which is bigger than the design value of 3.25×10^4 MPa, so the column body is sound.
(2) According to the design and the corresponding code, the m value of the subsoil is 5000 kN/m^4. The identified value is 5921 kN/m^4 The safety coefficient is 1.19 so it can be seen that the subsoil can satisfy the service requirements
(3) The identified horizontal and vertical stiffness for the left 5 bearings are 26989.2 kN/m and 13154736.0 kN/m, which are far smaller than the identification values (60102.0 kN/m and 29294160.0 kN/m) of right 5 bearings. A possible explanation is that different settlements of the two columns cause uneven forces of the bearings. The site investigation proved the substructure inclined to the left side and the left column settles down more than the right one.

5 CONCLUSIONS

In this paper, a damage evaluation method for bridge substructures is proposed. Compared with the lateral responses, longitudinal responses of substructures are easier to measure and sensitive to damage, so the responses and modal parameters in the longitudinal direction are used to evaluate the working state of substructures. The method uses the stiffness of substructure body, the stiffness of bearing and the m value of the subsoil as variables. The signature assurance criterion (SAC) that describes the similarity of FRFs of points is used to quantify the integral damage. The whole identification procedure is divided into two stages: (1) Use the damage indexes based on SAC to determine whether damage exists. (2) Identify the damage extents by finite element model updating method with the longitudinal modal parameters as inputs. A highway bridge substructure engineering case indicates that the proposed damage evaluation method using the longitudinal dynamic responses can effectively judge the damage type and quantify the damage.

ACKNOWLEDGEMENTS

This study is sponsored by the National Natural Science Foundation of China (No. 51208028) and the Fundamental Research Funds for the Central Universities (Grant No. 2012JBM080).

REFERENCES

Pandey, A.K. & Biswas, M. S. 1991. Damage detection from changes in curvature mode shapes. *Sound & Vibration* 145: 321-332.

Salawu, O.S. 1997. Detection of structure damage through changes in frequency: a review. *Engineering Structures* 19: 718-723.

Hassiotis, S. 2000. Identification of damage using natural frequencies and Markov parameters. *Computers & Structures* 74: 365-373.

Palacz, M. & Krawczuk, M. 2002. Vibration parameters for damage detection in structures. *Sound & Vibration* 249(5): 999-1010.

Wang, X. 2001. Structural damage identification using static test data and changes in frequencies. *Engineering Structures23*: 610-621.

Ren, W.X. & De Roeck, G. 2001. Structural damage identification using modal data. I: Simulation Verification. *Structural Engineering* 128(1): 81-95.

Zhan J.W., Xia H. & Yao J.B. 2004. Safety evaluation for foundations of existing railway bridges. *Proc. ISSST'2004*, Shang'hai: 1952-1958.

Zhan J.W., Xia H. & Yao J.B. 2005. An impact vibration test method for measuring natural frequencies of existing piers. *Journal of Beijing Jiaotong University* 29(1): 14-17.

Nishimura A. & Nakano. 1987. Grasping the vibration characteristics of structures by impact vibration test. *Proc. the 19th Japan national conference on soil mechanics and foundation engineering*. Tokyo: 563-569.

Nishimura A. 1992. *Research on The Diagnosis Method of Integrity for Existing Bridge Foundations*. Tokyo: Railway Technical Research Institute.

Nishimura A. 2001. Examination of bridge substructure for integrity. *Proc. TIVC'2001*, Beijing: 131-142

Zhou H.L. 2000. Experimental and finite element analysis of bridge pier with high-rising pile cap under dynamic train loading. *Railway Engineering Society* 3: 36-40.

Chow Y.K. 1987. Three-dimensional analysis of pile groups. *Geotechnology Engineering* 113(6): 637-651

Ministry of Railways P.R. China. 1999. *Code for Design on Subsoil and Foundation of Railway Bridge and Culvert*. Beijing: China Railway Publishing House.

Ministry of Railways P.R. China. 2004. *Code for Rating Existing Railway Bridges*. Beijing: China Railway Publishing House.

Teughels, A., Maeck, J. and De Roeck G2002. Damage assessment by FE model updating using damage functions. Computers and Structures 80:1869-1879

Research and Applications in Structural Engineering, Mechanics and Computation – Zingoni (Ed.)
© 2013 Taylor & Francis Group, London, ISBN 978-1-138-00061-2

Structural damage identification in small scale models of bridge decks

R. Carrazedo & T. M. Juliani
University of São Paulo, São Carlos School of Engineering, São Carlos, Brazil

ABSTRACT: As a nondestructive technique, experimental dynamic analysis offers many advantages on structural integrity evaluation than conventional destructive methods. No damage with the extraction of samples is necessary and the test can be repeated as many times as needed. Natural frequencies and modal shapes are important information on the global response of a structure that can be obtained by experimental dynamic analysis. Once a localized damage affects this global response, its detection is possible. In this paper vibration measurements were carried out on small scale models of a bridge deck to obtain their fundamental dynamic properties. The measurements were carried out through accelerometers placed in strategic positions to obtain the relevant modal data of both slabs and beams of the deck. Unknown excitation forces were applied, simulating operational conditions. Post processing of experimental data was carried out using specialized routines in order to precisely obtain the experimental natural frequencies and mode shapes. On the other hand, theoretical models were developed with the Finite Element Method (FEM) to establish the ideal conditions of the undamaged structure. Comparison between theoretical and experimental models allowed damage identification based on Modal Assurance Criterion (MAC) and Coordinate Modal Assurance Criterion (COMAC).

1 INTRODUCTION

Experimental dynamic analysis has been extensively used as a tool for integrity evaluation of existing structures. For many types of structures the measurements can be implemented with ambient vibrations, simplifying test procedures.

This is the case of bridges, where the traffic induced vibrations can be measured and experimental modal analysis can be performed to identify natural frequencies and mode shapes.

However, many questions regarding measurement procedures, post-processing of the results and comparison to theoretical models are still interesting subjects of research, especially the use of modal data to structural assessment.

In this paper an experimental / numerical dynamic analysis of small scale bridge decks is described as well as the results obtained in structural damage identification through modal data.

A reinforced concrete beam bridge with a central span of 16.8 m and two cantilever spans of 3.7 m was selected for this analysis. Fig. 1 shows the geometry of this bridge, a common structural configuration in Brazilian roads. It is a simple geometry with two longitudinal beams (0.4 m x 1.2 m), five transverse beams (0.2 m x 1.2 m) and a 0.18 m slab.

Instead of dealing with measurements in a real scale bridge subjected to traffic induced vibrations the authors preferred in this initial phase of the research to develop a study with small scale models of the bridge deck under laboratory conditions. With this approach the operations related to the measurements are extremely simplified and the number of situations to be tested can be increased. Every effort was tried to simulate the field conditions in the laboratory with a reasonable agreement.

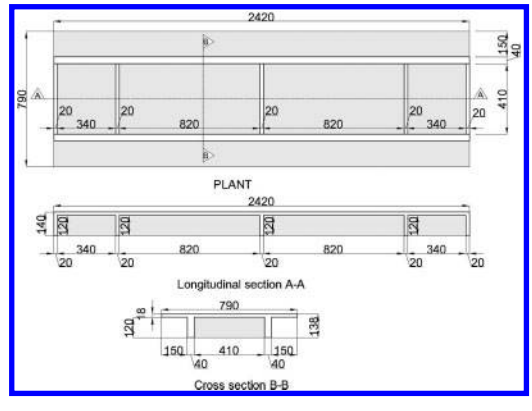


Figure 1. Dimensions of the real scale bridge (in cm).

2 METHODOLOGY

2.1 *Small scale specimens*

A 1/20 scale was selected for the models. With this scale, the models were light enough to allow easy handling (18 kg) and large enough to allow pouring a cement mortar into the forms.

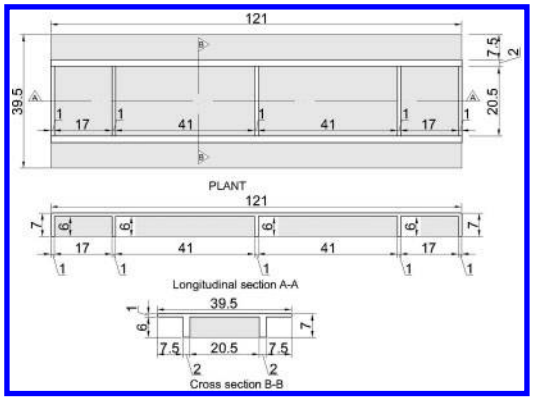


Figure 2. Dimensions of the small scale specimens (in cm).



Figure 3. View of small scale specimens.

Besides this, Harris and Sabnis (1999) mentioned previous studies showing accurate estimates of natural frequencies and mode shapes in 1/3 scale models, although inaccuracies on determination of viscous damping were reported. Successful research works on dynamic behavior of small scale models of bridges (1/30 and 1/33.3 scale) were also described.

Considering these facts and the nature of the present analysis (based only on modal shapes and frequencies) the use of the 1/20 scale was considered an adequate approach. The dimensions of the small scale model are shown in Fig. 2.

The small scale specimens were produced so that model 1 would be an undamaged model and model 2 had structural defects in the form of cracks shown in Fig. 3 (one at the mid section and other near to the corner). These cracks were filled with epoxy resin to simulate a retrofitting process (less than 1 mm of epoxy thickness was used).

A cement mortar with 323 kg/m^3 of Type III - Portland Cement (according to ASTM C150), 1615 kg/m^3 of natural sand and 300 kg/m^3 of water was used. This mortar had a density of 2065 kg/m^3.

The dynamic modulus of elasticity was obtained through resonant acoustic tests with the equipment Sonelastic and in accordance with ASTM C215-08. An impact was applied in one face of the cylinder and

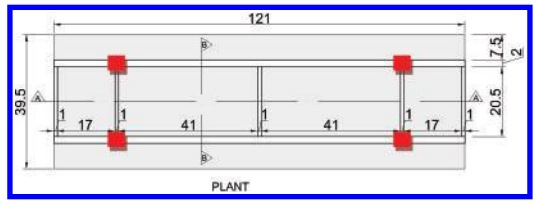


Figure 4. Bottom view of small scale specimens with the polymer pads.

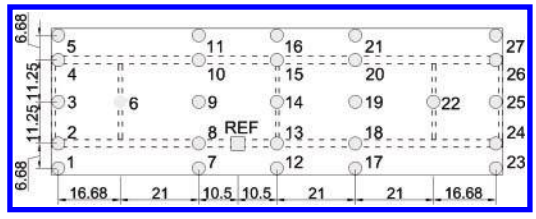


Figure 5. Reference and measuring positions.

the sound was measured by a microphone in the opposite face. Analysis of the sound spectrum allowed clear identification of the frequencies associated to the first longitudinal and first flexional modes of the cylinder. The dynamic elastic modulus was of 23120 MPa, as average of 3 cylinders. Only one batch was used to produce concrete for the two models and control cylinders.

Polymer pads with dimensions of 6 mm x 26 mm and 52 mm were used as supports of the deck in four positions shown in Fig.4. The dynamic stiffness of these pads were also obtained through resonant acoustic tests, based on rigid body motion of a steel disk supported by these pads. The steel disk had 190 mm of diameter and 98 mm of thickness. The total mass of this disk was similar to the bridge model mass. As a consequence the dynamic stiffness of the pads was determined under the same level of stress of the bridge models. The vertical stiffness was of 174571 N/m and the horizontal stiffness was of 300000 N/m.

2.2 *Experimental program*

Bruel Kjaer accelerometers model 8344 were used connected to an acquisition/conditioning system from Vishay Measurements Group – System 6000.

During all tests one accelerometer was fixed at the reference position while the other was positioned at one of the several measurement positions described in Fig. 5

Excitation was applied by impacts of a hammer with a rubber point. The impacts were applied in several locations along the axis where the traffic lanes would be in a real situation. The excitation force was not measured and no exact control of the applied force was possible.

The acceleration x time history was recorded by the acquisition system with a sampling frequency of 2000 Hz. A low pass filter of 800 Hz was applied to reduce noise.

2.3 *Post processing of the measured data*

Post processing of the acquired data was developed with special routines developed with the open source software Scilab.

Power spectral densities were estimated through the pspec function, which is based on the Welch's averaging modified periodogram. A rectangular window with 1000 points of length and 100 points of offset was used. Auto and cross spectra were calculated (PSD and CPSD).

Phase, coherence and transmissibility between the signals in the reference (i) and measurement (j) positions were determined with spectral densities based on the equations of Felber (1993).

The phase angle was calculated as:

$$\theta_{ij} = \arctan\left(\frac{imag(CPSD_{ij})}{real(CPSD_{ij})}\right) \quad (1)$$

while the coherence function was evaluated as:

$$coherence_{ij} = \frac{CPSD_{ij}^2}{PSD_i \cdot PSD_j} \quad (2)$$

and the transmissibility ratio as:

$$TR_{ij} = \frac{real(CPSD_{ij})}{real(PSD_i)} \quad (3)$$

Some of these values were used to check the quality of the acquired data. The phase angle should assume values near to 0^o or 180^o while the coherence should be close to 1 for the natural frequencies. The transmissibility ratio was used to construct the experimental mode shapes.

2.4 *Numerical simulations*

A Finite Element Model (FEM) was created with the software Abaqus version 6.12 to evaluate the properties of an ideal undamaged structure with the properties described in the item 2.1. Solid elements with quadratic interpolation and reduced integration were used (C3D20R). The used mesh is shown in Fig. 6.

A modal analysis was performed identifying all eigenvalues and eigenvectors in the frequency range of interest.

2.5 *Damage identification*

Damage identification was possible through comparison between numerical and experimental frequencies and mode shapes, using MAC (see Allemang and Brown, 1982) and COMAC (see Lieven and Ewins, 1988) coefficients.

The Modal Assurance Criterion (MAC) was used to verify the correspondence between the analytical (i) and experimental (j) mode shapes. The comparison

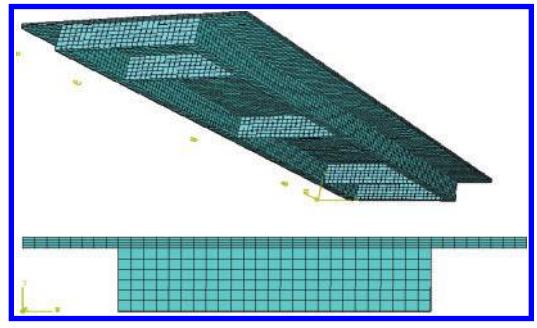


Figure 6. Mesh of the Finite Element Model.

for the same mode should give a MAC close to 1. On the other hand the MAC coefficient between different modes should be close to 0. The MAC coefficients were calculated as:

$$MAC_{ij} = \frac{\left|\{\Phi_i^a\}^T \{\Phi_j^e\}\right|^2}{\left(\{\Phi_i^a\}^T \{\Phi_i^a\}\right)\left(\{\Phi_j^e\}^T \{\Phi_j^e\}\right)} \quad (4)$$

where Φ_i^a is the vector of analytical modal coordinates of mode i and Φ_j^e is the vector of experimental modal coordinates of mode j.

The Coordinate Modal Assurance Criterion (COMAC) was used to identify for each modal coordinate (j) the match between the analytical and experimental data for the n identified modes.

$$COMAC_j = \frac{\left(\sum_{i=1}^{n} \Phi_i^a(j)\Phi_i^e(j)\right)^2}{\left(\sum_{i=1}^{n} \Phi_i^a(j)\Phi_i^a(j)\right)\left(\sum_{i=1}^{n} \Phi_i^e(j)\Phi_i^e(j)\right)} \quad (5)$$

where Φ_i^a and Φ_j^e are the analytical and experimental vectors of modal coordinates of mode i.

3 RESULTS AND DISCUSSION

3.1 *Numerical results – undamaged model*

In Fig. 7 the numerical mode shapes are shown together with the natural frequencies. Rigid body modes were not considered.

Contour plots of the deformed shapes however were more valuable for comparisons of these modes with the experimental counterparts. Some of the contour plots are shown in Fig. 8.

3.2 *Experimental Results*

3.2.1 *Time domain*

Figure 9 shows an acceleration x time curve where the results of several impacts are shown. It is possible to notice a good resolution of the signal compared to the noise floor.

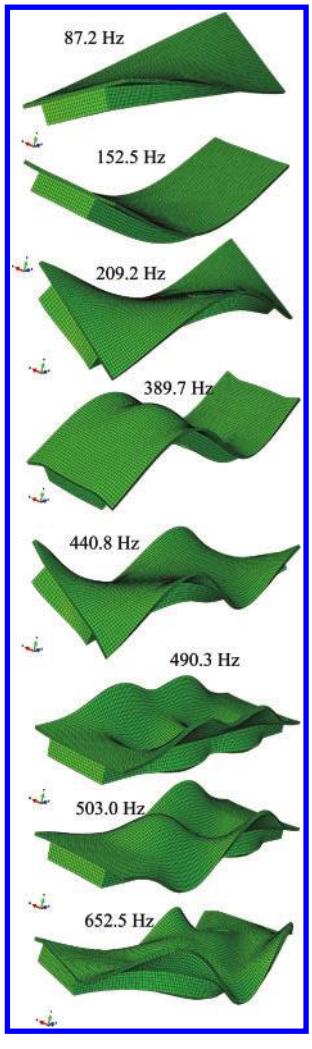


Figure 7. Mode shapes and natural frequencies obtained with the numerical model

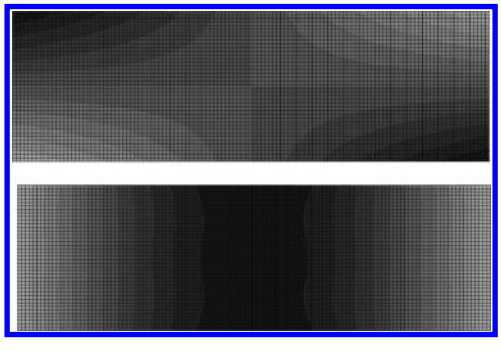


Figure 8. Contour plot of numerical mode shapes – model 2.

3.2.2 *Vibration spectra, phase and coherence*

Typical vibration spectra obtained for the reference position and one measuring position are shown in

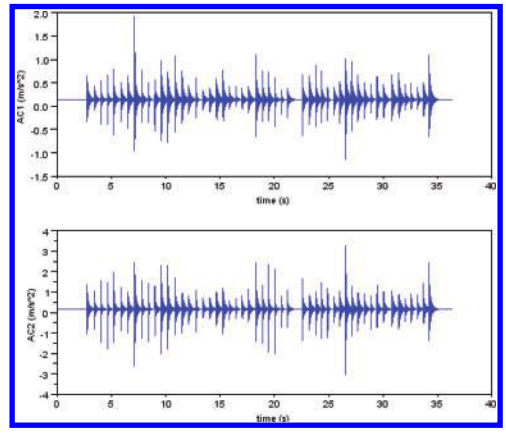


Figure 9. Acceleration × time curves.

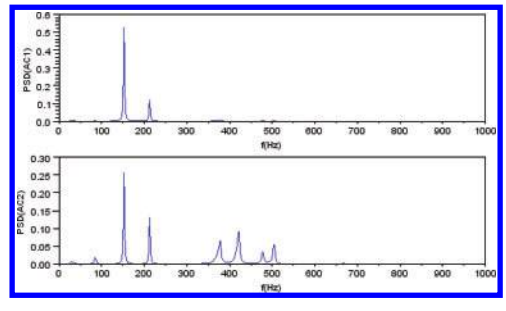


Figure 10. Power Spectral Density (PSD) × frequency curves.

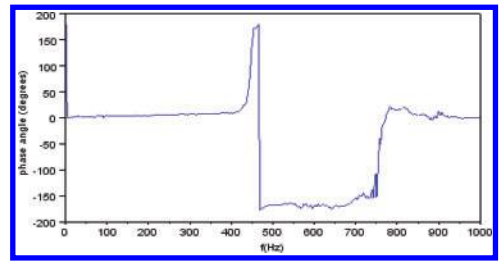


Figure 11. Phase angle × frequency curve.

Fig. 9. As shown several peaks were clearly identified for the measuring positions PSD(AC2). The same peaks were not so clear, but could also be identified in the reference position PSD(AC1).

Plots of phase and coherence functions are also shown in Fig. 10 and 11. The phase angle assumed values close to 0^o or $\pm\ 180^o$, as expected. The coherence was close to unity for most of the frequencies of interest.

3.2.3 *Natural frequencies*

The frequency peaks identified in spectral analysis are shown in Table 1. Only modes with coherence close to unity and experimental modal shapes in reasonable agreement with the numerical ones are shown. It is important to notice that the experimental frequency

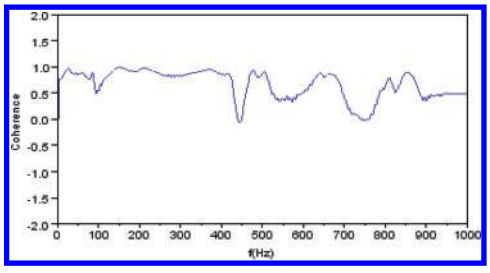


Figure 12. Coherence × frequency curve.

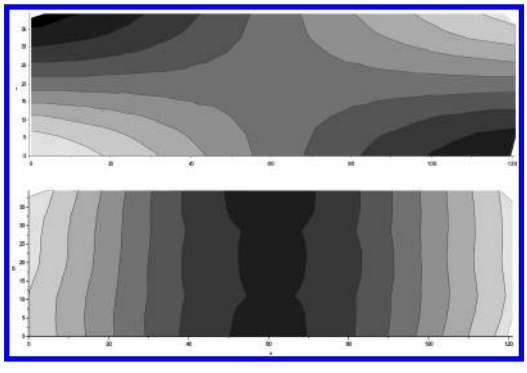


Figure 13. Contour plot of experimental mode shapes – mod. 2.

Table 1. Natural frequencies – numerical x experimental.

		Experimental	
Mode	Numerical	Model 1	Model 2
1	87.2	84	84
2	152.5	136*	150
3	209.2	208	210
4	389.7	-	376
5	440.8	-	426

of the second mode in model 1 (marked with *) was significantly lower than the numerical. This may be caused by structural damage.

3.2.4 *Mode shapes*

Experimental mode shapes were evaluated through contour plots such as the shown in Fig. 12, which were compared to their numerical counterparts such as Fig. 8. In this case a reasonable representation of the theoretical mode shape was observed.

3.2.5 *MAC coeficients*

Tables 1 and 2 show the MAC coefficients calculated for model 1 and 2. It is possible to notice that the first three experimental mode shapes were in good agreement with the numerical ones in both models.

3.2.6 *COMAC coeficients*

The COMAC coefficients were calculated based on the first three modes of both models. A contour plot of

Table 2. MAC coefficients for model 1.

	Experimental frequencies (Hz)		
Num. f(Hz)	84	136	208
87.2	**0.975**	0.026	0.000
152.5	0.000	**0.942**	0.032
209.2	0.007	0.012	**0.940**

Table 3. MAC coefficients for model 2.

	Experimental frequencies (Hz)				
Num. f(Hz)	84	150	210	376	426
87.2	**0.984**	0.002	0.004	0.029	0.032
152.5	0.001	**0.995**	0.003	0.000	0.016
209.2	0.002	0.001	**0.983**	0.005	0.026
389.7	0.000	0.000	0.001	**0.865**	0.030
440.8	0.223	0.001	0.002	0.065	**0.616**

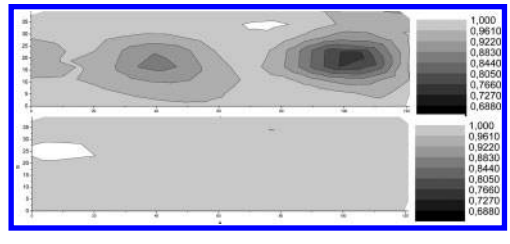


Figure 14. COMAC values calculated for model 1 and 2, respectively.

COMAC values in Fig. 13, showed: possible damaged zones on model 1 (COMAC ranging from 0.688 to 0.999) and almost no damaged zones in model 2 (COMAC ranging from 0.965 to 0.999).

4 CONCLUSIONS

The comparison between experimental and numerical frequencies indicated a possible damage in model 1 (the experimental frequency of mode 2 was significantly lower than the numerical). Besides, the COMAC plot of model 1 showed probable damage zones. As no damage was imposed to model 1 a possible explanation was a significantly higher local water/cement ratio in the slabs due to bleeding. High water content (300 kg/m^3) was used and excessive vibration may have occurred in model 1.

On the other hand, model 2, which initially had cracks, was then retrofitted with epoxy resin and behaved as an undamaged model during the tests. A

close agreement between experimental and numerical frequencies was observed and also for MAC and COMAC coefficients.

The final conclusion was that the dynamic experimental analysis was capable of identifying structural damages in model 1 although these damages were not intentionally imposed to the specimens. At the same time the technique showed that the retrofitting process in model 2 reestablished totally the flexural stiffness of the deck.

5 FUTURE IMPLEMENTATIONS

The results shown here are part of an ongoing research project. Several tests with small scale models will be carried out in a near future simulating different types of structural damages in bridge decks.

Based on these partial results some necessary improvements were identified in the experimental procedures and will be implemented in the remaining tests:

- A more careful control of mortar mix proportions (lower water content), filling and vibration is necessary to avoid bleeding or undesired lack of homogeneity;
- A higher sample frequency and longer acquisition times will be adopted to improve frequency resolution and the accuracy of the results;
- The location of the reference and measuring positions will be further analyzed to improve the number and the quality of experimental mode shapes.

ACKNOWLEDGEMENTS

The authors express their sincere gratitude to FAPESP (São Paulo State Foundation for Research) for the financial support.

REFERENCES

Allemang, R. J., Brown, D. L., "A Correlation Coefficient for Modal Vector Analysis," Proceedings, International Modal Analysis Conference, pp. 110-116, 1982.

AMERICAN SOCIETY FOR TESTING AND MATERIALS, C150/C150M-12: Standard Specification for Portland Cement. Pennsylvania, 2012.

AMERICAN SOCIETY FOR TESTING AND MATERIALS. C215 – 08: Standard Test Method for Fundamental Transverse, Longitudinal, and Torsional Resonant Frequencies of Concrete Specimens. Pennsylvania, 2008.

Felber, A.J. 1993. Development of a hybrid bridge evaluation system. Vancouver, Canada: The University of British Columbia.

Harris, H.G. & Sabnis, G.M. (2.ed.) 1999. *Structural modeling and experimental techniques.* Boca Raton, Florida: CRC Press LLC.

Lieven, N. A. J., Ewins, D. J., "Spatial Correlation of Mode Shapes, The Coordinate Modal Assurance Criterion (COMAC)," Proceedings, International Modal Analysis Conference, pp. 690-695, 1988.

Research and Applications in Structural Engineering, Mechanics and Computation – Zingoni (Ed.)
© 2013 Taylor & Francis Group, London, ISBN 978-1-138-00061-2

An application of the local flexibility method to hyper-static beams using non-local virtual forces

Ting-Yu Hsu
National Center for Research on Earthquake Engineering, Taipei, Taiwan

Shen-Yuan Shiao & Wen-I Liao
National Taipei University of Science and Technology, Taipei, Taiwan

Chin-Hsiung Loh
National Taiwan University, Taipei, Taiwan

ABSTRACT: Vibration-based damage detection methods try to apply structural features extracted from vibration signals to perform damage diagnosis. The local flexibility method (LFM), which can determine local stiffness variations of beam structures using measured modal parameters, is one of the promising approaches. The LFM method is founded on virtual forces that cause nonzero stresses within a local part of the structure. In this study, non-local virtual forces which cause concentrated stresses in a local part and nonzero stresses in the other parts of a structure are employed. The theoretical basis of the proposed pseudo local flexibility method (PLFM) which uses the non-local virtual forces is derived. The effects of the number of modes on damage detection results of three damage scenarios of a numerical hyperstatic beam are studied. The results show that much fewer modes are required for the PLFM to estimate the damage locations and extents with acceptable accuracy. Therefore, the feasibility of the PLFM is higher due to limited number of high quality modes can be identified in real world application, especially for ambient vibration measurement.

1 INTRODUCTION

Many vibration-based structural damage detection techniques which perform damage diagnosis of a structure based on structural dynamic characteristic parameters have been proposed in the last two decades. Toksoy and Aktan (1994) first tried to detect damage locations based on structural flexibility matrices of a beam structure. However, the damage detection algorithms based on flexibility matrices lack a solid theoretical background until the damage location vector method which can locate damage was developed by Bernal (2002). Reynders and De Roeck (2010) further developed the local flexibility method (LFM) with a robust theoretical background to not only detect damage locations but also damage extents.

The LFM utilizes flexibility matrices of a beam structure constructed by lateral displacement mode shapes. Combined with corresponding load configurations which cause stress fields within a local region of the beam structure, the damage extent of the local region can be estimated. The LFM does not require a finite element model of the beam structure. The structural modal parameters identified from the ambient vibration signals both before and after damage are the key information for the LFM. The number of modes necessary for the LFM is usually quite small, especially for a simply supported beam where only the first mode could be sufficient. However, for a hyperstatic beam, the number of modes required for estimation of the damage could be much higher. This makes the feasibility of the LFM much lower because in practice only the first few modes could be identified with high quality using ambient vibration signals. Therefore, in this study, non-local virtual forces which cause concentrated stresses in a local part and nonzero stresses in the other parts of a structure are employed. The theoretical basis of the proposed method which uses non-local virtual forces is derived. The effects of the number of modes on damage detection results of three damage scenarios of a numerical hyperstatic beam are studied. The proposed method is named as the pseudo local flexibility method (PLFM) and is explained and validated in the following sections.

2 PSEUDO LOCAL FLEXIBILITY METHOD

The local flexibility method (Reynders & De Roeck, 2010) considers a structure with volume $\boldsymbol{\Omega}$ and boundary $\boldsymbol{\Gamma}$ which is subjected to the Dirichlet boundary conditions along part of the boundary. A first load system $\boldsymbol{f}^1$ is applied at a limited number of r DOFs where response can be measured. The first load system for the PLFM is chosen such that the induced stress field $\boldsymbol{\sigma}^1$: (1) can be calculated from the loading without knowledge of the structure's stiffness; and (2) consists of

concentrated stresses in a small volume $\boldsymbol{\Omega}_p$ and also stress outside $\boldsymbol{\Omega}_p$. Note that $\boldsymbol{f}^1$ is assumed only causes non-zero stress within $\boldsymbol{\Omega}_p$ for the LFM. Based on the virtual work principle with the body force neglected:

$$\int_{\Gamma} \boldsymbol{t}^T \delta \boldsymbol{x} d\Gamma = \int_{\Omega} \boldsymbol{\sigma}^T \delta \boldsymbol{\varepsilon} d\boldsymbol{\Omega} \tag{1}$$

where $\boldsymbol{t}$ is the vector with applied tractions, $\boldsymbol{\sigma}$ is the corresponding stress vector, $\delta \boldsymbol{x}$ is a virtual displacement field that obeys the Dirichlet boundary conditions and $\boldsymbol{\varepsilon}$ is the corresponding virtual strain vector. If the virtual displacement field is chosen as the one that is induced by the first load system $\boldsymbol{f}^1$ while the forces and the stresses are due to the second load system $\boldsymbol{f}^2$ which obeys the boundary condition of the system, one has that:

$$\sum_{j=1}^{r} f_j^2 x_j^1 = \int_{\Omega_p} (\boldsymbol{\sigma}_p{}^2)^T \boldsymbol{\varepsilon}_p{}^1 d\boldsymbol{\Omega}_p + \int_{\Omega_q} (\boldsymbol{\sigma}_q{}^2)^T \boldsymbol{\varepsilon}_q{}^1 d\boldsymbol{\Omega}_q \tag{2}$$

where x_j^1 is the displacement at DOF j corresponding to the first load system. Assume that the structure is linear elastic and that $\boldsymbol{\sigma}^1$ is proportional to $\boldsymbol{\varepsilon}^1$ with stiffness constant K. If the virtual work is calculated before and after damage has occurred, one has that:

$$\frac{\sum_{j=1}^{r} f_j^2 x_j^1}{\sum_{j=1}^{r} f_j^2 x_{jd}^1} = \frac{\frac{1}{K_p}\int_{\Omega_p} (\boldsymbol{\sigma}_p{}^2)^T \boldsymbol{\sigma}_p{}^1 d\boldsymbol{\Omega}_p + \frac{1}{K_q}\int_{\Omega_q} (\boldsymbol{\sigma}_q{}^2)^T \boldsymbol{\sigma}_q{}^1 d\boldsymbol{\Omega}_q}{\frac{1}{K_p+\Delta K_p}\int_{\Omega_p} (\boldsymbol{\sigma}_p{}^2)^T \boldsymbol{\sigma}_p{}^1 d\boldsymbol{\Omega}_p + \frac{1}{K_q+\Delta K_q}\int_{\Omega_q} (\boldsymbol{\sigma}_q{}^2)^T \boldsymbol{\sigma}_q{}^1 d\boldsymbol{\Omega}_q} \tag{3}$$

If the energy within $\boldsymbol{\Omega}_p$, denoted as $\boldsymbol{E}_p$ or $\boldsymbol{E}_{pd}$, is much smaller than the energy within $\boldsymbol{\Omega}_q$, denoted as $\boldsymbol{E}_q$ or $\boldsymbol{E}_{qd}$, Equation (2) can be derived as:

$$\frac{\sum_{j=1}^{r} f_j^2 x_j^1}{\sum_{j=1}^{r} f_j^2 x_{jd}^1} = \frac{E_p + E_q}{E_{pd} + E_{qd}} \cong \frac{E_p}{E_{pd}} = \frac{K_p + \Delta K_p}{K_p} \tag{4}$$

where $\Delta \boldsymbol{K}_p$ is the change in the stiffness parameter in $\boldsymbol{\sigma}_p$ due to damage. It is assumed that $\boldsymbol{K}_p$ and $\Delta \boldsymbol{K}_p$ are constant within $\boldsymbol{\Omega}_p$, while $\boldsymbol{K}_q$ and $\Delta \boldsymbol{K}_q$ are not necessary to be constant within $\boldsymbol{\Omega}_q$.

For a beam structure, suppose the shear deformation can be neglected, Equation (2) can be modified as:

$$\frac{\sum_{j=1}^{r} f_j^2 x_j^1}{\sum_{j=1}^{r} f_j^2 x_{jd}^1} = \frac{\frac{1}{(EI)_p}\int_0^{\ell_p} M_p^2 d\ell + \frac{1}{(EI)_q}\int_0^{\ell_q} M_q^2 d\ell}{\frac{1}{(EI)_p+(\Delta EI)_p}\int_0^{\ell_p} M_p^2 d\ell + \frac{1}{(EI)_q+(\Delta EI)_q}\int_0^{\ell_q} M_q^2 d\ell} \tag{5}$$

where EI is the bending rigidity, M is the bending moment and l is the length of a beam. Similarly, if the strain energy within $\boldsymbol{\Omega}_q$ is neglected, Equation (4) can be derived as:

$$\frac{\sum_{j=1}^{r} f_j^2 x_j^1}{\sum_{j=1}^{r} f_j^2 x_{jd}^1} \cong \frac{EI_p + \Delta EI_p}{EI_p} \tag{6}$$

The virtual displacement vector $\boldsymbol{x}^1$ under the first load system $\boldsymbol{f}^1$ can be obtained using the following equation:

$$\boldsymbol{x}^1 = \boldsymbol{H}\boldsymbol{f}^1 \tag{7}$$

where $\boldsymbol{H}$ is the flexibility matrix. With the assumption of lumped and approximately equally distributed mass, the flexibility matrix can be estimated using the identified unscaled modal parameters as (Reynders & De Roeck, 2010)

$$\boldsymbol{H} \cong \boldsymbol{H}^n = -\boldsymbol{\Phi}\boldsymbol{\Lambda}_c^{-1}(\boldsymbol{\Lambda}_c{}^H \boldsymbol{\Phi}^H \boldsymbol{\Phi}\boldsymbol{\Lambda}_c + \boldsymbol{\Phi}^H\boldsymbol{\Phi})^{-1}\boldsymbol{\Lambda}_c{}^H\boldsymbol{\Phi}^H \tag{8}$$

where $\boldsymbol{\Phi}$ is the matrix of mode shapes, $\boldsymbol{\Lambda}_c$ is the diagonal matrix of system poles and ^{H} is the Hermitian transpose. If only the first n modes are available, then the flexibility matrix is truncated, denoted as $\boldsymbol{H}^n$. Note that the contribution of the modes in the flexibility matrix is proportional to the inverse of square of the system poles. The influence of the higher modes is much smaller than the one of lower modes. As a result, the number of truncated modes needed to approximate a non-truncated flexibility matrix is much smaller than the ones needed to approximate a non-truncated stiffness matrix. This benefits the practical cases where only limited number of lower modes can be identified with acceptable accuracy, especially using ambient vibration signals.

The calculation of both the LFM and PLFM includes: (1) using the identified modal parameters to construct the truncated flexibility matrix; and then (2) multiply the truncated flexibility matrix and the virtual forces together. The truncated flexibility matrix and the second load system $\boldsymbol{f}^2$ for LFM and PLFM are identical. The only difference of the calculation between LFM and PLFM is the first load system $\boldsymbol{f}^1$.

Based on the theory above, the two main sources of error when estimating rigidity reduction using PLFM are: (1) the truncation error of flexibility matrix due to limited number of modes, denoted as ER_E; and (2) the neglect of virtual strain energy within $\boldsymbol{\Omega}_q$ in Equation (3), denoted as ER_E. Note that for the LFM only exists, while for the PLFM both ER_H and ER_E exist. The key point of the PLFM is that if the non-local first load system $\boldsymbol{f}^1$ can reduce ER_H for a large amount and at the same time induce ER_E which is much smaller than ER_H, the chosen of the non-local first load system should benefit the damage detection results.

3 NUMERICAL STUDIES

We use the same numerical beam model in (Reynder and De Roeck's 2010) to illustrate the feasibility of the proposed PLFM. A hyperstatic IPE100 of 6m length is modeled by 48 beam elements of equal length. It is assumed that only the vertical accelerations at the 25 equidistant points are measured (Figure 1). Totally three damage scenarios are considered. The first two damage scenarios are: (1) a bending rigidity reduction

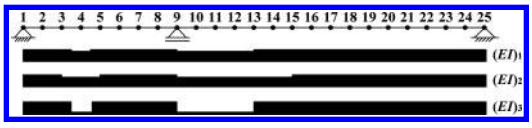


Figure 1. Measurement points and EI distribution of the three damage scenarios of a hyperstatic beam.

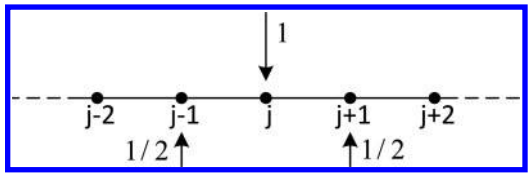


Figure 2. A load configuration of a beam structure that causes concentrated virtual stresses within the region between node j−1 to node j+1.

of 5% at the 2 elements adjacent to measurement point 4 and the elements between points 9 and 13; and (2) a bending rigidity reduction of 10% between elements 3 and 5 and between points 9 and 15. The last damage scenario is the same as the first damage scenario but the stiffness reduction ratio increases to 90%.

At each measurement point, the force configuration in Figure 2 and Figure 3 is applied as $\boldsymbol{f}^1$ for the PLFM and LFM, respectively. The corresponding displacements at the measured DOFs are calculated using the truncated flexibility matrices constructed by different number of modes. For both methods, the force configuration in Figure 2 is applied as $\boldsymbol{f}^2$. Figure 4 shows the estimated relative bending rigidity, denoted as R, estimated with the first 2 unscaled modes using the PLFM and LFM, as well as the reference value which can be calculated using the exact flexibility matrix and the virtual forces. It is evident that the estimated relative bending rigidity using the LFM is quite close to the reference value only at measurement points 6, 7, 9, 11, 13 and between 15 and 23. The estimated relative bending rigidity using the LFM at the other points is far from the reference value. These points are at the measurement points where nonzero stresses exist at both damaged and undamaged locations. On the other hand, the estimated relative bending rigidity using the PLFM is quite close to the reference value at any locations. The relative bending rigidity estimated using the LFM becomes acceptable if the first 12 unscaled modes are used, as shown in Figure 5. Note that the relative bending rigidity estimated using the PLFM is even more accurate than the one estimated using the LFM at most of the points. Similar phenomenon can be observed from the second damage scenario as shown in Figure 6 and 7. In Figure 6, the estimated rigidity reduction ratio using the LFM at point 4, 6, 8, 10, 14 and 16 is far from the reference value. Again, these points are also at the measurement points where nonzero stresses exist at both damage and undamaged locations. The estimated rigidity reduction ratio at point 16 is 4.2, which is outside the limit of the vertical-axis. In the damage scenario 3, the damaged beam becomes more complex

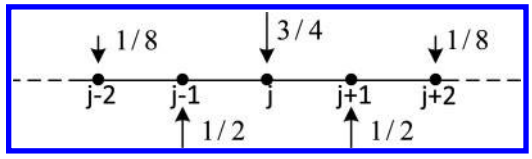


Figure 3. A load configuration of a beam structure that causes non-zero virtual stresses only within the region between node j−2 to node j+2.

because the bending rigidity reduction ratio increases to 90%. As a result, in order to estimate the relative bending rigidity, the required number of modes for the PLFM increases to 9 as shown in Figure 8, while the required number of modes for the LFM increases to 16 as shown in Figure 9.

Obviously, based on the numerical results above, the PLFM can estimate the relative bending rigidity much closer to the reference value if the same number of modes are used. Much fewer modes are required for the PLFM to estimate the rigidity reduction ratios. The merit of PLFM can be explained via the following two reasons.

The first reason is that the error caused by the neglect of strain energy within $\boldsymbol{\Omega}_q$ in Equation (3), i.e. ER_E, is quite small comparing to ER_H. For instance, when the load configuration in Figure 2 is applied at the measurement point 9 of the intact beam as the first load system $\boldsymbol{f}^1$, the strain energy within $\boldsymbol{\Omega}_q$ is 20.6% of the strain energy within $\boldsymbol{\Omega}_p$. When the same load is applied at the same point of the beam with damage scenario 1, the strain energy within $\boldsymbol{\Omega}_q$ becomes 21.2% of the strain energy within $\boldsymbol{\Omega}_p$. The error ER_E caused by neglect of the strain energy within $\boldsymbol{\Omega}_q$ is only 2.8%, which is the largest for damage scenario 1. The smallest ER_E for damage scenario 1 is 0.0% when the load configuration in Figure 2 is applied at the measurement point 2. As long as the ratio between the strain energy within $\boldsymbol{\Omega}_p$ and $\boldsymbol{\Omega}_q$ do not change too much, the error ER_E caused by the neglect of strain energy within $\boldsymbol{\Omega}_q$ in Equation (2) is quite small. It is evident that this ratio could change more if larger rigidity reduction is induced. Taking the damage scenario 3 for example, the maximum ER_E is at point 10 whose error increases to 18.5%. Even though, the rigidity reduction ratio estimated using the PLFM is still much better than the LFM using the same number of modes, as shown in Figure 8.

The second reason is that the accuracy of flexibility matrix required by the first virtual load system $\boldsymbol{f}^1$ for the LFM is much higher than the one for the PLFM. For the PLFM, the first virtual load system $\boldsymbol{f}^1$ is much simpler. As a result, the exact virtual displacement caused by the $\boldsymbol{f}^1$ can be estimated using a truncated flexibility matrix constructed with fewer modes. On the contrary, for the LFM, the first virtual load system $\boldsymbol{f}^1$ is more complex, which causes the exact virtual displacement also more complex. Therefore, the exact virtual displacement could not be estimated with acceptable accuracy using a rough flexibility matrix constructed with fewer modes.

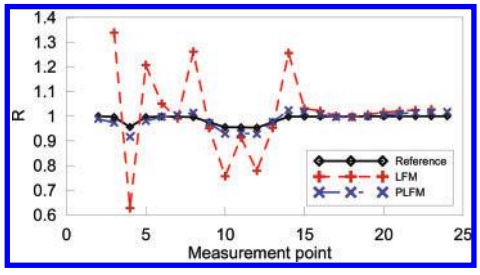


Figure 4. Estimated rigidity reduction ratio for damage scenario 1 using the first 2 unscaled modes.

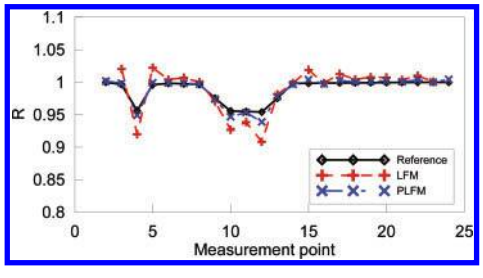


Figure 5. Estimated rigidity reduction ratio for damage scenario 1 using the first 12 unscaled modes.

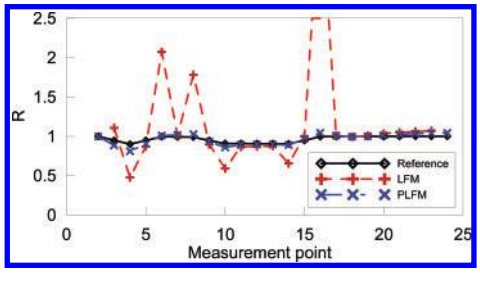


Figure 6. Estimated rigidity reduction ratio for damage scenario 2 using the first 2 unscaled modes.

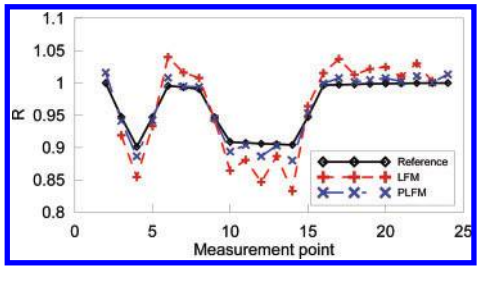


Figure 7. Estimated rigidity reduction ratio for damage scenario 2 using the first 12 unscaled modes.

4 CONCLUSIONS

In this paper, a pseudo local flexibility method (PLFM) to localize and quantify the damage of a hyperstatic beam structure is proposed.The PLFM breaks the constraint of the LFM that only virtual forces which cause

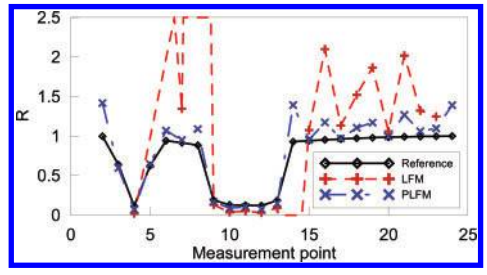


Figure 8. Estimated rigidity reduction ratio for damage scenario 3 using the first 9 unscaled modes.

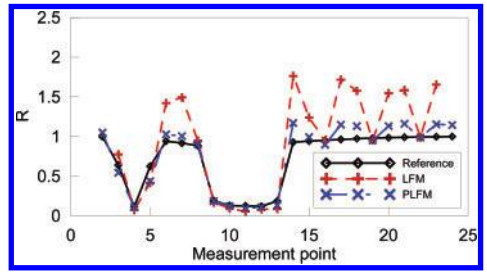


Figure 9. Estimated rigidity reduction ratio for damage scenario 3 using the first 16 unscaled modes.

nonzero local stress within a small part of a structure can be applied. That is, non-local virtual forces which cause a global but concentrated stress filed of a structure is valid for the PLFM. The release of the constraint on the virtual forces makes a simple force configuration possible. The results of numerical studies of a hyperstatic beam show that much fewer modes are required for the PLFM to estimate the damage location and extent with acceptable accuracy. Therefore, the feasibility of the PLFM is higher due to limited number of high quality modes can be identified in real world application, especially for ambient vibration measurement.

ACKNOWLEDGEMENT

We thank E. Reynders & G. De Roeck who provided valuable assistance to our research. This research was supported in part by the National Science Council of the Republic of China under the grant No NSC 101-2625-M-492-007.

REFERENCES

Bernal D. 2002. Load Vectors for Damage Localization. *Journal of Engineering Mechanics* 128(1): 7–14.

Reynders E. & De Roeck G. 2010. A Local Flexibility Method for Vibration-based Damage Localization and Quantification. *Journal of Sound and Vibration*. 329(12): 2367–2383.

Toksoy T. & Aktan A.E. 1994. Bridge-condition assessment by modal flexibility. *Experimental Mechanics*. 34(2): 271–278.

Research and Applications in Structural Engineering, Mechanics and Computation – Zingoni (Ed.)
© 2013 Taylor & Francis Group, London, ISBN 978-1-138-00061-2

Effect of load redistribution of a steel truss bridge due to fracture of a truss member on vibration-based fault detection

C.W. Kim, S. Kitauchi, K. Hashimoto & K. Sugiura
Department of Civil and Earth Resources Engineering, Graduate School of Engineering, Kyoto University, Kyoto, Japan

M. Kawatani
Department of Civil Engineering, Graduate School of Engineering, Kobe University, Kobe, Japan

ABSTRACT: This study is intended to investigate how damage in a steel truss member results in load redistribution and the fault detection from the traffic-induced vibration data of the bridge. A damage experiment is carried out on a real nine-span-continuous steel-truss bridge. Stress redistribution of truss members due to cut in a diagonal member was observed under live load as well as dead load. Frequencies and damping constants led to a low fault-detection performance. Nonetheless there exists a possibility to detect a fault utilizing changes in frequencies and damping constants, of which success substantially varies amongmodes. On the other handan improved performance in fault detection was observed by the damage-sensitive feature derived from linear system parameters of an AR model.

1 INTRODUCTION

The collapse of the I-35W Mississippi River bridge in Minneapolis, Minnesota, USA on August 1, 2007, was an unprecedented shock to the civil engineering community. (National Transportation Safety Board 2008) After the event bridge inspections in Japan also observed damages at members of steel truss bridges. The importance and need for bridge inspection and monitoring has increasingly become more apparent aftermath of these events. Among the inspection and monitoring, bridge owners have been captivated by the vibration-based bridge health monitoring (BHM) since the vibration-based BHM is expected to provide more efficient way of BHM comparing to visual inspections. (*e.g.*Salawu 1997, Doebling et al. 1998)

In the vibration-based BHM of truss bridges, an important point that must be clarified is how the possible load redistribution of the bridge due to damage on a truss member affects the success of fault detection in terms of the vibration-based BHM. How to excite the bridge economically, reliably and rapidly is another technical issue in the vibration-based BHM with short to medium span. For small to medium span bridges moving vehicles on the bridge are dominant external sources for vibrations of the bridges. The bridge vibration induced by moving vehicles is called as traffic-induced vibration of bridges which is a kind of non-stationary vibration. (e.g. Kim & Kawatani 2008, Chang et al. 2013) Despite of the non-stationary property of the traffic-induced vibration, the idea of using the traffic-induced vibration data in the BHM is that parameters identified repeatedly under moving vehicles may provide a pattern and give useful information about fault detection. (Kim et al. 2013)

This study investigates how damage in a steel truss member results in load redistribution, and also to examine how the load redistribution affects fault detection utilizing the traffic-induced vibration data of anine-span continuous steel truss bridge. This study deemsthe Mahalanobis distances (MD) of frequency, damping constant and damage indicator derived from linear system parameters of a time series model as damage-sensitive features. Potential changes in the damage-sensitive features due to damage are emphasized by the Mahalanobis-Taguchi system (MTS) (Taguchi & Jugulum 2000).

2 ON-SITE DAMAGE EXPERIMENT

On-site damage experiments were conducted on a real nine-span-continuous steel-truss bridge shown in Figure 1. The observation span was the sixth span from the A1 abutment. The roadway roughness condition was poor for the bridge has not been maintained for quite a long time. Figure 2 shows the experiment-setup and a diagonal member before and after severing the member. Acceleration responses of the bridge were measured and utilized in fault detection. Strain gages were also deployed to measure stress changes before and after severing the member. Accelerometers

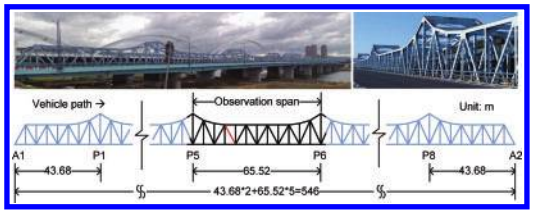


Figure 1. Elevation view of the bridge.

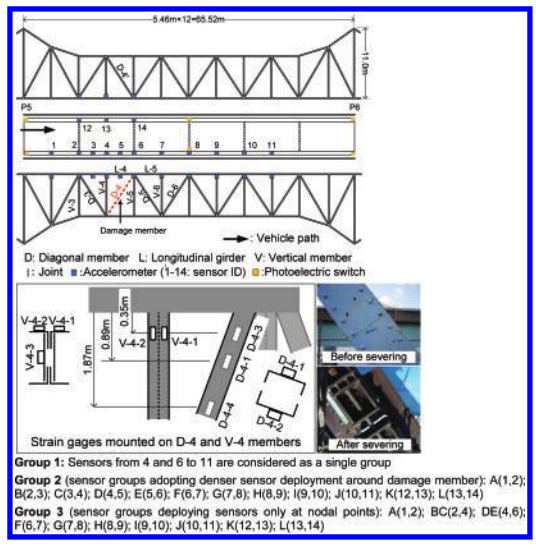


Figure 2. Sensor deploying map.

aremore densely installed around the damage member. It is noteworthy that an excessive displacement of the damage member was controlled by wrapping a safety member around the damage member and installingtension bars in the safety member to prevent abrupt release of tensile force of the damage member and any possible bridge collapse during the damage experiment.

The MTS requires larger number of observations than the number of variables/sensors. However only a limited number of runs were carried out in the field experiment in order to reduce time and cost. Therefore this study utilizes data from sensor groups to reduce the number of sensors which is considered as the number of variables in MTS since reducing the number of variables in MTS results in a similar effect of increasing the number of observations relatively. Three different sensor groups which is also depicted in Figure 2 are considered in fault detection by means of MTS: Group 1 utilizes all the observation data from the 7 observation points, 4 and from 6 to 11, for the damage detection; Group 2 utilizes the data from two adjacent observation points for detecting even the damage location; Group 3 utilizes the observation points except the two observation points, 3 and 5, near the damage member to examine the feasibility of damage-location detection without using data of the sensors which are densely installed near the damage member.

The same vehicle was used in the campaign of experiments in two days, even though vehicle weights were slightly altered from 253 kN to 258 kN. However effects of the small difference of the vehicle's axle load to the bridge response were negligible. Photoelectric switches mounted on the entrance, center and end of the span were used to estimate location and average speed of the passing vehicle. The vehicle-drop test showed that natural frequencies of the vehicle were 3.0 Hz and 3.5 Hz for bounce motions of the front axle and rear axle respectively. Those for hop motions appeared around 12 Hz for the front axle and 14 Hz for the rear axle.

Vehicle-induced vibrations of the bridges before and after severing the member were measured and utilized in fault detection of the bridge.During the experiment, 18 runs were carried out for the intact bridge which comprises 4 runs under vehicle speed of 10 km/h, 7 runs under vehicle speed of 20 km/h and 7 runs under vehicle speed of 40 km/hr. For the damage bridge, 15 runs were carried out for intact bridge which comprises 3 runs under vehicle speed of 10 km/h, 6 runs under vehicle speed of 20 km/h and 6 runs under vehicle speed of 40 km/h.

3 LOAD REDISTRIBUTION

Load redistribution due to severing the diagonal member is examined utilizing the stress redistribution estimated from strain measurements. Table 1 shows change of stresses of observed members due to damage under dead load: tensile stress of the D-4 member was released to 60Mpa in average; on the other hand, the average tensile stress increased to 56Mpa at the V-4 member; for other members such as D-3, D-5, and V-5 increase of compressive stress was observed. An interesting point is that increase of both compressive and tensile stresses were observed at D-4', L-4 and L-5 members as the out-of-plane behavior led to bending moments at the members.

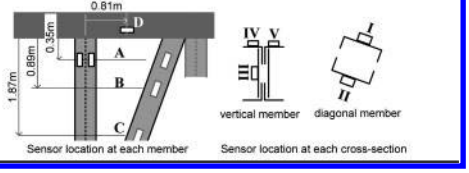
Static and dynamic responses of the truss members, D-4 and V-4, under vehicle load are shown in Figures 3 and 4. Figure 3 shows the static and dynamic strain responses measured at the diagonal member (D-4 in Figure 2) which was cut after the experiment on the healthy bridge. The horizontal axis indicates the position of the front axle of the vehicle from the P5 pier. Applying the damage on the member reduced strains of the member down to half of the strain of the intact member. One reason for strains of the damaged member do not converge to zero after severing the member may be that usually truss members are distorted by out-of-the-plane behavior of the bridge due to damage of the member, but nonetheless the safety member prevents the out-of-the-plane behavior and raises a bending stress in the severed member.

Those strain responses on the vertical member (V-4 in Figure 2) which is adjacent to the damaged

Table 1. Stress change due to damage under dead load.

Sensor ID	Strain change ($\times 10^{-6}$)	Stress change (MPa)	Sensor location	
			Cross section	Member
D-3	-41	-8.2	I	A
D-4-1	-288	-57.6	I	B
D-4-2	-214	-42.8	II	B
D-4-3	-400	-80.0	I	A
D-4-4	-313	-62.6	I	C
D-4'-1	111	22.2	I	B
D-4'-2	-40	-8.0	II	B
D-4'-3	91	18.2	I	A
D-5	-155	-30.9	I	A
V-4-1	222	44.4	III	A
V-4-2	410	82.1	IV	A
V-4-3	223	44.5	V	A
V-5-1	-158	-31.7	III	A
V-5-2	-25	-4.9	IV	A
L-4-1	-32	-6.4	I	D
L-4-2	42	8.3	II	D
L-5-1	3	0.6	I	D
L-5-2	-105	-21.0	II	D

+: Increase of tension, -: Increase of compression, - (for D-4): decrease of tension



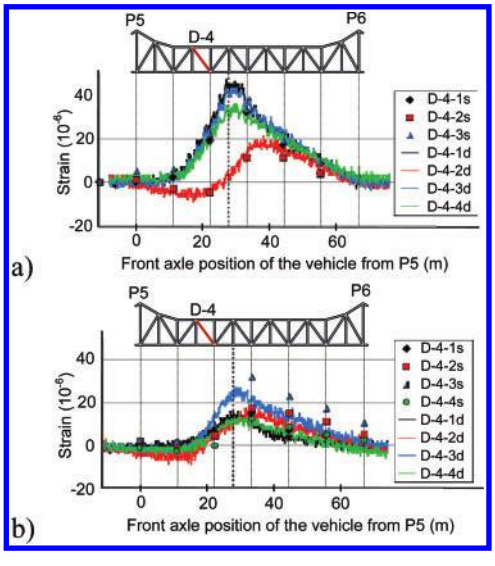


Figure 3. Strain responses of the diagonal member (D-4): a) Intact; and b) Damage. (s: static response; d: dynamic response).

member are shown in Figure 4. Differently from the damaged member no obvious change of peak strains was observed. However, strain responses following the peak response showed larger strains than those strains before applying the damage, which demonstrates stress redistribution under vehicle load. It implies that vehicle-induced vibrations of the bridge hold an indication of some sort of change.

4 CHANGE OF DYNAMIC PARAMETERS

4.1 *Fault detection using MTS*

The MTS is one of the pattern recognition methods, which is used in diagnostic applications to make

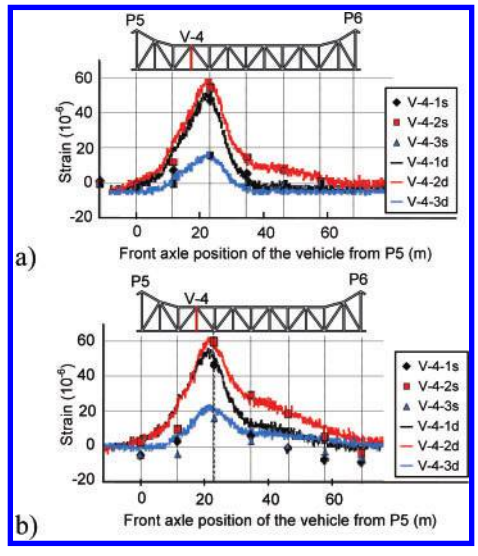


Figure 4. Strain responses of the vertical member (V-4): a) Intact; and b) Damage. (s: static response; d: dynamic response).

quantitative decisions by constructing the multivariate measurement scale MD. (Taguchi & Jugulum 2000) In the MTS, the Mahalanobis space (MS) is obtained using the standardized variables of normal data. The MS can be used to discriminate between normal and abnormal data.

In applying MTS, firstly a measurement scale with MS needs to be constructed as a reference: this is done using the data from a normal group and calculating their MDs, whose value should be close to 1. The standardized normal data are obtained using Equation 1.

$$z_i^p = \frac{x_i^p - \mu_i}{\sigma_i} \tag{1}$$

where z_i^p indicates the standardized p-th tuple of normal data for j-th variable; z_i^p, the p-th tuple of normal data for i-th variable; μ_i, mean value of the i-th variable; and, σ_i, the standard deviation of i-th variable. Those mean and standard deviation values are estimated from Equations 2 and 3 respectively.

$$\mu_i = \frac{1}{n}\sum_{p=1}^{n} x_i^p \tag{2}$$

$$\sigma_i = \frac{1}{n}\sqrt{\sum_{p=1}^{n}\left(x_i^p - \mu_i\right)^2} \tag{3}$$

If $\mathbf{Z} = (z_1^p, z_2^p, \ldots)z_k^p$, and denotes $\mathbf{C} \in \mathbb{R}^{k\times k}$ correlation matrix for k standardized variables, then MD calculated for the p-th tuple of normal data in a sample size n with k variable is given by

$$MD_p = D_p^2 = \frac{1}{k}\mathbf{Z}_p^T\mathbf{C}^{-1}\mathbf{Z}_p \tag{4}$$

Next, the signal space is obtained from abnormal data or newly observed data. Abnormal data are also standardized utilizing mean and standard deviation values of the normal data as

$$y_i^p = \frac{w_i^p - \mu_i}{\sigma_i} \tag{5}$$

The $\overline{MD_p}$ of the normalized abnormal data, $\mathbf{Y}_p = (y_1^p, y_2^p, \ldots, y_k^p)$, in the signal space can be defined by Equation 6 from the normalized abnormal data and $\mathbf{C}$, which is obtained from known data.

$$\overline{MD}_p = \overline{D^2}_p = \frac{1}{k}\mathbf{Y}_p^T \mathbf{C}^{-1}\mathbf{Y}_p \tag{6}$$

If newly monitored data is abnormal $\overline{MD_p}$ should be considerably greater than one.

The required conditions to utilize the MTS are as follows: the number of variables k of normal data is equivalent to that of abnormal data; the number of observation data n is larger than that of variable k; and the standard deviation of normal data σ_i is not zero.

4.2 *Fault detection using dynamic characteristics*

The linear dynamic system can be modeled by the AR model (autoregressive model) (*e.g.* Ljung 1999, Kim et al. 2012) as

$$y(k) + \sum_{i=1}^{p} a_i y(k-i) = e(k) \tag{7}$$

where $y(k)$ denotes the output of the system, a_i is the i-th order AR coefficient and $e(k)$ indicates the error term.

This study also adopts the AR model to model vibrations of the bridge and to identify dynamic characteristics of the bridge. The stabilization diagram combined with the singular value spectrum taken from the frequency domain decomposition (FDD) (Brincker et al. 2000) is also used to choose dynamic parameters to be monitored. The MDs of frequencies and damping constant corresponding to the 1.96Hz and 7.64Hz were considered as damage-sensitivity features. The mode shapes corresponding to the mode near 1.96Hz and 7.64Hz were also considered to detect damage location.

Results of applying the frequency and damping of the Group 1 into the MTS are shown in Figure 5, in which the red horizontal line denotes the threshold. In deciding the threshold, the largest and smallest values of MD taken from the cross-validation were removed, and the trimmed mean value was adopted as the threshold using (n-2) MD distances to reduce the effect of outliers on the MDs.The n-fold cross-validation was also adopted for assessing how the results of a statistic analysis will generalize to an independent data set. (Bishop 2006) Figure 5 demonstrated difficulty of

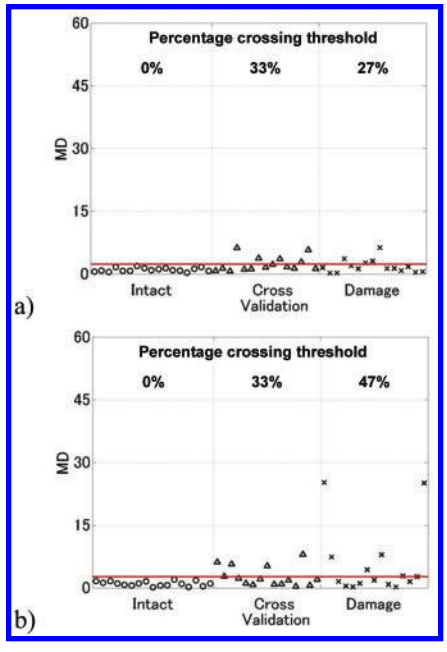


Figure 5. MDs of frequencyof Group1: a) 1.96 Hz; b) 7.64 Hz.

detecting anomalous event from the MDs of 1.96Hz, while MDs of 7.64Hz led to a little higher probability to detect an anomalous event compared to that of 1.96Hz. As shown in Figure 6, for those of damping constants corresponding to 1.96Hz, the MDs led to a higher possibility than those corresponding to of 7.64Hz differently from tendency of the frequency.

The COMAC (Coordinate Modal Assurance Criterion) (Lieven & Ewins1988)value is estimated to identify the damage location. Figure 7 shows the plot of COMAC value at each observation point of the Group 3 and clearly provides the suspected damage location. Two modes associated with 1.96Hz and 7.64Hz were considered.For those COMAC values taken from considering all the 14 observation points (Group 2), no clear difference were observed compared to the result from the 12 observation points shown in Figure 7, and omitted for brevity.

The modal assurance criterion (MAC) values (Ewins 1984)of Group 3 were changed from 0.9913 to 0.9905 for the mode corresponding to 1.96Hz, and from 0.938 to 0.865 for the mode corresponding to 7.64Hz.The MAC values considering all the 14 observation points (Group 2) led to changes from 0.991 to 0.990 for the mode corresponding to 1.96Hz, and from 0.934 to 0.861 for the mode corresponding to 7.64Hz, but no obvious difference with the MAC values from Group 3 was observed.

4.3 *Fault detection using damage indicator*

The coefficient a_p of the AR model shown in Equation 7 is related to the pole of the system since the

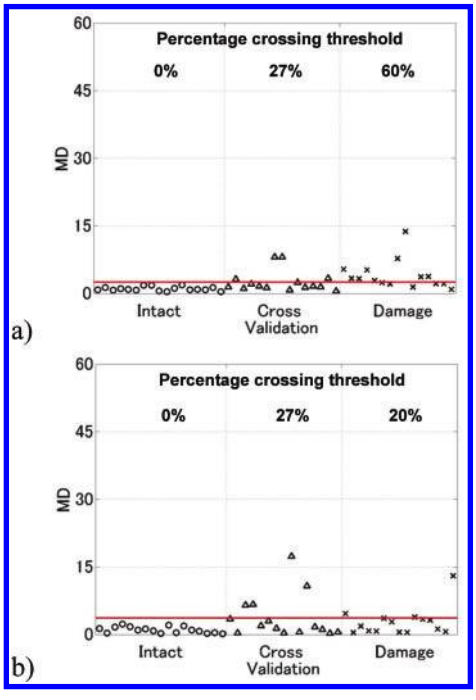


Figure 6. MDs of damping constant of Group1: a) 1.96 Hz; b) 7.64 Hz.

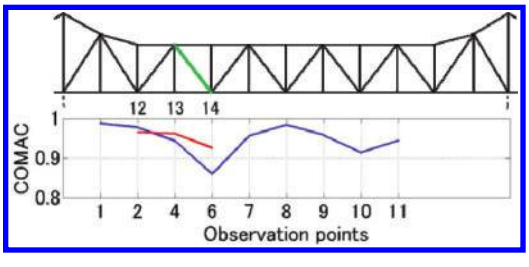


Figure 7. COMAC from modes corresponding to two dominant frequencies 1.96Hz and 7.64Hz.

z-transformation of Equation 7 can be written as (*e.g.* Oppenheim et al. 1996)

$$Y(z) = H(z)E(z) = \frac{1}{1+\sum_{i=1}^{p} a_i z^{-i}} E(z) \quad (8)$$

where $Y(z)$ and $E(z)$ are z-transformations of $y(k)$ and $e(k)$, $H(z)$ is the transfer function of the system in the discrete-time complex domain, and z^{-i} denotes the forward shift operator.

Values of z in which the elements of the transfer function matrix show infinite values are the poles. This means that the denominator of the transfer function is the characteristic equation of the dynamic system, given as

$$z^p + a_1 z^{p-1} + a_2 z^{p-2} + \cdots + a_{p-1} z + a_p = 0 \quad (9)$$

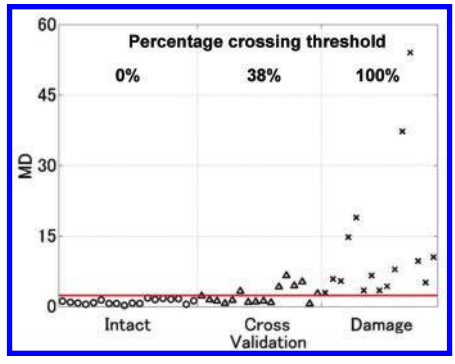


Figure 8. MDs of DI from Group1.

The poles on the complex plane are associated with the frequency and damping constant of the dynamic system of structures. The poles z_k of Equation 9 are obtained by finding the roots of the AR coefficient polynomial in the denominator of $H(z)$. The number of poles in the z -plane equals the AR model order. It should be noted that AR coefficients can be defined by sums and products of its roots z_k according to Vieta's formula. (*e.g.* Bold 1982) In other words, AR coefficients are directly associated with the modal parameters, and AR coefficients are also affected by damage (Kim et al. 2013). Therefore the MD of the parameter which is obtained from AR coefficients as shown in Equation 10 (Nair et al. 2006) is adopted as a damage-sensitive feature.

$$\mathrm{DI} = \frac{|a_1|}{\sqrt{\sum_{i=2}^{3} a_i^2}} \quad (10)$$

where a_i denotes the i-th AR coefficient and DI is the damage indicator that considers up to the third AR coefficient.

The fault detection of the bridge is also carried out by means of the MTS. Figure 8 shows that all of MDs of the DI crossing the threshold, and indicates high possibility of detecting anomalous events of the bridge. It is obvious that the DI acts more sensitively against potential faults compared to the result derived utilizing frequency and damping constants shown in Figures 5 and 6.

Detecting the damage location is carried out using the Group 2, and the results are summarized in Figure 9a). Apparently the probability of crossing the threshold was higher at the sensor group which contains the observation points near the damaged member. The success of detecting the damage location is natural since the stress drastically decreased only at the damaged member as shown in Figures 3 and 4 and two additional sensors installed near the damage member store more information about the damage.

However, it is a rather unrealistic idea to predict the damage suspected member and install sensors around the damage suspected member for monitoring. A remaining question, thus, to be answered would be

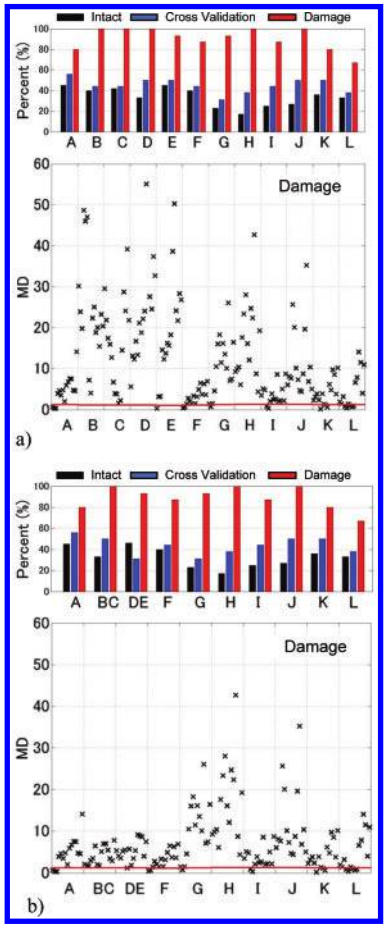


Figure 9. MDs of DI and percentage of MDs crossing the threshold: a) Group 2; and b) Group 3.

the feasibility to detect damage location when sensors are installed at the panel points. Therefore, this study examines the feasibility of detecting damage location utilizing Group 3 in which the two observation points near damage member, points 3 and 5, are not considered. The results are summarized in Figure 9b), and it shows difficulty of detecting the damage location without considering sensors near the damage. However, it is still obvious from the percentage of MDs crossing the threshold that the DI can provide an effective damage-sensitive feature for fault detection.

5 CONCLUDING REMARKS

This study investigates feasibility of a vibration-based bridge health monitoring of a real steel truss bridge utilizing traffic-induced vibrations of the bridge.This study uses the MDs of damage indicator (DI) from linear system parameters of an AR model,frequencies and damping constants as damage-sensitive features. The MTS is applied to emphasize potential change of the damage-sensitive feature due to damage.

Obvious load redistribution was observed even under live load as well as dead load. The most obvious stress change was observed at the damaged member as expected. Load redistribution to other members due to the damage even under live load implies that vehicle-induced vibrations of the bridge have an indication of some sort of change and moreover signals measured at a location away from the damage member also have an indication of change in the bridge.

Frequencies and damping constants led to a low fault-detection performance. Nonetheless there exists a possibility to detect a fault utilizing changes in frequencies and damping constants, of which success substantially varies among modes. On the other handan improved performance in fault detection was observed by DI.

Denser sensor deployment near the damage member led to success of detecting damage location by means of MTS. On the other hand damage location detection was unsuccessful after excluding the sensors near the damage member in the damage detection procedure.

More comprehensive investigations are needed to clarify the reason of failure to detect damage location after removing the sensors near the damage member in consideration.Deciding the optimal number of sensors is another future research. However the proposed fault detection approach is nonetheless applicable to BHM of real truss bridges.

ACKNOWLEDGEMENT

This study is partly sponsored by JSPS, Grant-in-Aid for Scientific Research (B) under project No. 24360178. Such financial aid is gratefully acknowledged.

REFERENCES

Bishop, C M. 2006. *Pattern Recognition and Machine Learning*, Springer.

Bold, B. 1982. *Famous problems of geometry and how to solve them*. New York, Dover.

Brincker, R, Zhang, L and Andersen, P. 2000. Modal identification from ambient responses using frequency domain decomposition.in Proc. *IMAC 18, International Modal Analysis Conference*, San Antonio, USA.

Chang, KC, Kim, CW and Kawatani, M. 2013. Feasibility Investigation for Bridge Damage Identification through Moving Vehicle Laboratory Experiment. *Structures and Infrastructure Engineering*, DOI:10.1080/15732479.2012.754773.

Doebling, SW, Farrar, CR, Prime, MB and Shevitz, DW. 1998, A review of damage identification methods that examine changes in dynamic properties.*Shock and Vibration Digest*, 30(2): 91–105.

Ewins, DJ. 1984. *Modal testing: theory and practice*. Research Studies Press Ltd., Letchworth, Hertfordshire, England.

Kim, CW and Kawatani, M. 2008.Pseudo-static approach for damage identification of bridges based on coupling vibration with a moving vehicle. *Structure and Infrastructure Engineering*, 4(5): 371–379.

Kim, CW, Kawatani, M and Hao, J. 2012. Model parameter identification of short span bridges under a moving vehicle by means of multivariate AR model. *Structure and Infrastructure Engineering*, 8(5): 459–472.

Kim, CW, Isemoto, R, Sugiura, K, Kawatani, M. 2013. Structural fault detection of bridges based on linear system parameter and MTS method.*Journal of JSCE*, JSCE, 1: 32–43.

Lieven, NAJ and Ewins DJ. 1988. Spatial correlation of mode shapes, the Co-ordinate Modal Assurance Criterion (COMAC). Proceedings of the 6th International Modal Analysis Conference, 1: 690–695

Ljung, L. 1999. *System identification-Theory for the user, 2nd Ed.* PTR Prentice Hall, Upper Saddle River, N. J.

Nair, KK, Kiremidjian, AS and Law, KH. 2006. Time series-based damage detection and localization algorithm with application to the ASCE benchmark structure.*J. of Sound and Vibration*, 291(1-2): 349-368.

National Transportation Safety Board. 2008. Collapse of I-35W Highway bridge, Minneapolis, Minnesota, August 1, 2007. Highway Accident Report NTSB/HAR-08/03. Washington, DC.

Oppenheim, AV, Willsky, AS and Nawab, S.H. 1996. *Signlas & Systems, 2nd Ed.* Prentice Hall, Upper Saddle River, N.J.

Salawu, OS. 1997. Detection of structural damage through changes in frequency: A review. *Engineering Structures*, 19:791–808.

Taguchi, G and Jugulum, R. 2000. New trends in multivariate diagnosis.*Indian Journal of Statistics,* 62(B): 233–248.

Research and Applications in Structural Engineering, Mechanics and Computation – Zingoni (Ed.)
© 2013 Taylor & Francis Group, London, ISBN 978-1-138-00061-2

A system model for lifecycle monitoring of bridges

M. Wild & O. Fischer
Chair of Concrete and Masonry Structures, Technische Universität München, Germany

G. Dori & A. Borrmann
Chair of Computational Modeling and Simulation, Technische Universität München, Germany

ABSTRACT: In current bridge maintenance practice, condition grades are assigned to individual bridges, based on regularly performed inspections. The main limitations to this approach are the time-discrete and also subjective nature of grade assignment. To overcome this issue, major bridge authorities are developing new methods for condition assessment, based on collecting and evaluating sensor data in real time. In this research, a system model-based approach has been developed to accurately model the correlations between the deterioration mechanisms and the measurement values indicating the progress of the deterioration. A major challenge in this context is to correctly model the impact of local deterioration on the condition of the bridge as a whole. The actual state propagation mechanism is achieved by means of logical connection elements. The resulting impact tree can be used for propagating the condition assignments from the leaf nodes (the sensors) to the top (the entire bridge).

1 INTRODUCTION

In most industrialized countries, large parts of the infrastructure were erected during the 1960's and 1970's. As a result they are now facing an increasing aging stock of infrastructure buildings. To maintain the infrastructure safe and at the same time to keep the impact on public budget at a tolerable level, an elaborate management scheme for these buildings, including inspections, maintenance and repairs is necessary.

In current bridge maintenance practice, condition grades are assigned to individual bridges, based on regularly performed inspections. Some of the main limitations of this approach are the time-discrete and also subjective nature of grade assignment, resulting in significantly diverging grades for bridges in the same condition. To address this issue, major bridge authorities are developing new methods for condition assessment, based on collecting and evaluating sensor data in real time. In this context it is essential to correctly model the impact of local deterioration on the state of the entire bridge.

In this paper we introduce a system-model based approach which is used to precisely model (1) the correlations between the deterioration mechanisms and the measurement values indicating the progress of the deterioration and (2) the impact of the condition of individual bridge components on the condition of the overall bridge system. The resulting impact tree can be used for simulating deterioration mechanisms as well as for determining the actual condition of bridge, based on sensor measurements. To this end, condition assignments are propagated from the leaf nodes (the sensor measurements) to the top node (the entire bridge). A major function of this propagation mechanism is provided by the logical connection elements which are located between the different layers of the impact tree and model rules for state propagation. These rules can either be based on empirical models or probabilistic or deterministic approaches.

2 COMMON MODELING APPROACHES

Some system modeling methods are already used to describe real bridge structures (Sianipar & Adams 1997, LeBeau & Wadia-Fascetti 2000). These approaches have in common that the investigated bridge is subdivided into single structural components, which are linked by logical conjunctions to obtain the entire bridge system model. The level of detail for a structural component depends on the relevance of the element for the structure. Commonly used modeling approaches in the context of reliability analyses are reliability block diagrams, fault tree analysis and event tree analysis (Klinzmann 2008).

In the abovementioned modeling approaches, structural elements can be set to the states "in service" or "default". This binary description is based on Boolean operators. The relevance of each element depends on the particular problem (stability, durability etc.) and the system structure. The individual elements have to be placed in their position in the system model and linked to each other, according to their task in the real bridge system. Complex systems can be modeled in this way as serial or parallel system or as combination

of the two. The systems structure function can be set up using state variables of individual elements and, based on this function, the failure probability of the system can be evaluated.

The reduction of complex interrelationships to a binary notation leads to a significant limitation in system modeling of bridge structures. It is not possible to capture partially deteriorated or damaged structural elements in this model. In addition, time dependent modeling of damage processes (e.g. corrosion of reinforcement) are not taken into consideration by the abovementioned approaches.

3 IMPACT TREE

3.1 *The system model approach*

The key idea of the new approach is to generate a system model which takes into account dependencies of structural components as well as interactions between damage mechanisms. It is important to avoid "black-box" systems in order to obtain a better understanding of deterioration processes and their interactions (Neumann &Haardt 2012). The developed system model is able to identify causes of damage and to determine the criticality of damage as well as their impact on individual bridge components and on the bridge itself.

The newly introduced impact tree model enables the analysis of condition and damage potential for both single structural components and complete systems. Implemented in software the impact tree can be used for condition assessment of structures in real time. Also it is possible to simulate certain deterioration processes by variation of input parameters to identify critical damage hot-spots at the planning stage of a bridge.

The impact tree is an improvement of the above mentioned fault tree. It uses a new rating system and more flexible connection elements than those used in the binary description of the fault tree (Reay & Andrews 2002).

The impact tree is composed of three hierarchical ordered levels: (1) the structure level, (2) the damage level and (3) the parameter level (Fig. 1).The elements can be grouped to modules to simplify the process of modeling an impact tree. All elements of each level can show their actual condition as output value. So the cause of a condition change of the whole bridge can be determined exactly.

3.2 *Structure level*

The structure level of the new modeling approach comprises all aspects of the bridge regarding the static system, relevant structural components and, at the lowest level, the building materials.

In the course of structure level preparation the bridge is fragmented into functionally smaller and smaller structural elements and ordered into a hierarchical way according to their role in the system of the bridge.These components are named structure elements of the system model. The bridge itself is represented by the top element of the impact tree.

As shown in the example below structure elements of particular interest, e.g. the bridge superstructure can be subdivided in several uniform elements. This will facilitate the allocation of condition changes in significant parts of the system model.

3.3 *Damage level*

The next level, which extends the structure level, is the damage level. Here, possible damage mechanisms which could occur on a structural component are allocated as damage elements to the corresponding (lowest) elements of the structure level. A damage element could be e.g. failure of reinforcement. The connection of a damage element to a structural element defines the exact allocation of the specific damage. This enables a functional system analysis. Using sophisticated building information modeling approaches the connection of damage elements to structure elements could be done by using a 3D model of the structure (Borrmann et al. 2012 & Lukas et al. 2012).

Damage elements which may have more than one cause will be hierarchically divided into sub-elements. As an example corrosion of reinforcement can be subdivided into elements regarding to the cause of corrosion: chloride respectively carbonation inducement. Damage elements are visualized by dash-dotted boxes within the impact tree model.

3.4 *Parameter level*

A further subdivision of the damage elements leads to the finest level of the impact tree: the parameter level. Parameters, which constitute an indication of beginning or further propagation of damage, will be allocated to the corresponding lowest element of the damage level. They can be a precondition or a cause of damage. Also parameters which indicate the propagation of damage are located in the parameter level.For reinforcement corrosion one precondition parameter is humidity. In contrast, the spalling of the concrete surface can already indicate onset or progression of reinforcement corrosion. All these parameters provide input values for the system analysis.

Wherever possible, all necessary parameters should be a part of a suitable monitoring concept that can feed the system model real time data to determine the condition of the bridge. Another approach to fill the system model with input data is to manually define the necessary or missing parameters. Although the parameters within the system model are linked to a damage element and thus bounded to a structure element, there is no need to locate them on the corresponding component of the bridge. For example the settlement of a pier can provide information about the condition of superstructure elements. Therefore, the measuring process actually takes place on the pier,

but the impact is considered at the superstructure element. Parameter elements are depicted as dotted boxes within the impact tree model.

3.5 *Connection elements*

A difficulty in creating an impact tree is the limited number of reliable described damage mechanisms. There are some damage mechanisms and correlations which have been investigated in detail (e.g. Sudret 2008), but the broad scope cannot be described by available realistic models.

For the newly introduced system model, interconnections between elements can be described by freely definable calculation rules. The main difference between the impact tree and the fault tree are these interconnections called logical connection elements (logic). In contrast to connections by Boolean operators of a fault tree,the logic element of the impact tree can describe different relationships between elements in a very flexible manner. These relationships are defined as a combination of equations and rules that describe the propagation of damage from one element to another.

There is the possibility to apply the following models and approaches:

- physicalmodels with deterministic approaches
- chemicalmodels with deterministic approaches
- probabilistic approaches
- empirical approaches
- etc.

As an example for a physical model, the description of fatigue behavior of reinforcing steel by a Wöhler curve can be mentioned. In this case parameter elements contain stress range and number of load cycles. This input values enable us to draw conclusions on the condition of the structure element (reinforcing steel) by the use of the hypothesis of damage accumulation according to (Palmgren 1924 & Miner 1945). The calculation rule is implemented in the connection element.

A probabilistic deterioration model for the description of reinforcement corrosion applied for life cycle management can be seen in (Gehlen 2000).

On basis of empirical values or statistical analysis decision-matrices can be set up without any detailed background knowledge about the damage process itself. In this type of matrix input parameters were correlated to each other in consideration of their consequences on the condition of the connected structure element. The defined relationships determine the output values of the logic elements - the grade of damage of a structure element.

When no calculation models or applicable descriptions of damage propagation are available, logic elements can be defined according to the currently used - inspection based - grade assignment methodology. Thus, a stepwise transition from the current approach to a full reliability based procedure can be realized in practice.

4 CONDITION EVALUATION BY THE IMPACT TREE

4.1 *Evaluation process*

The condition of individual elements can be represented on a rating scale. For example a ten-stage scale or a scale of warning colors similar to traffic lights (green: insignificant, yellow: warning, red: critical) can be implemented to elements of an impact tree. The condition, indicated by the scale, depends on stepwise predefined lower or upper limit values, e.g. maximum chloride content. The classification of the condition on a scale is independent of the calculation rule implemented in the logic element. Thus a consistent format can be used to show the condition of all elements.

The process using an impact tree for condition evaluation goes from bottom to top. The input values of parameter elements are checked and updated constantly during the evaluation. In the connected superordinate logic operation, these values are evaluated by predefined calculation rules. The easiest calculation rule is a comparison to limit values. If the values are below the limit, the rating scale shows an insignificant state (green light). Exceeding predetermined limit values leads to a warning or critical state based on the exaggeration of the limit by measuring values. The damage element will be activated if a signal of the subordinate parametric element shows a warning or critical value. The rating scale of the structure element gives notice of its condition which is calculated by the connected logical element. The condition evaluation process continues in loops until the parameter values change and an uncritical state is reached or until the top element in the structure level (which symbolizes the bridge itself) is reached.

4.2 *Sample application of the impact tree*

Using the example of a single span reinforced concrete bridge the application of the impact tree approach is explained in the following.

4.2.1 *Deterioration mechanisms*

As a representative deterioration mechanism corrosion of longitudinal reinforcement is chosen in this example. In the damage level of the impact tree (Fig. 1) are shown the subelements “chloride induced corrosion” and “carbonation induced corrosion” according to the cause of damage.

In this example an approach by (Novak et al. 2002) was selected to model the deterioration mechanisms. This approach is implemented in the connection elements “logic 6a” and “logic 6b” of the impact tree in form of a decision matrix. The incorporated input values are carbonation, concrete cover and chloride content (Tab. 1 & 2).

4.2.2 *Structure of the impact tree*

The top element of an impact tree is always the structure as a whole – in our example the bridge. In the next division the bridge is subdivided according to its

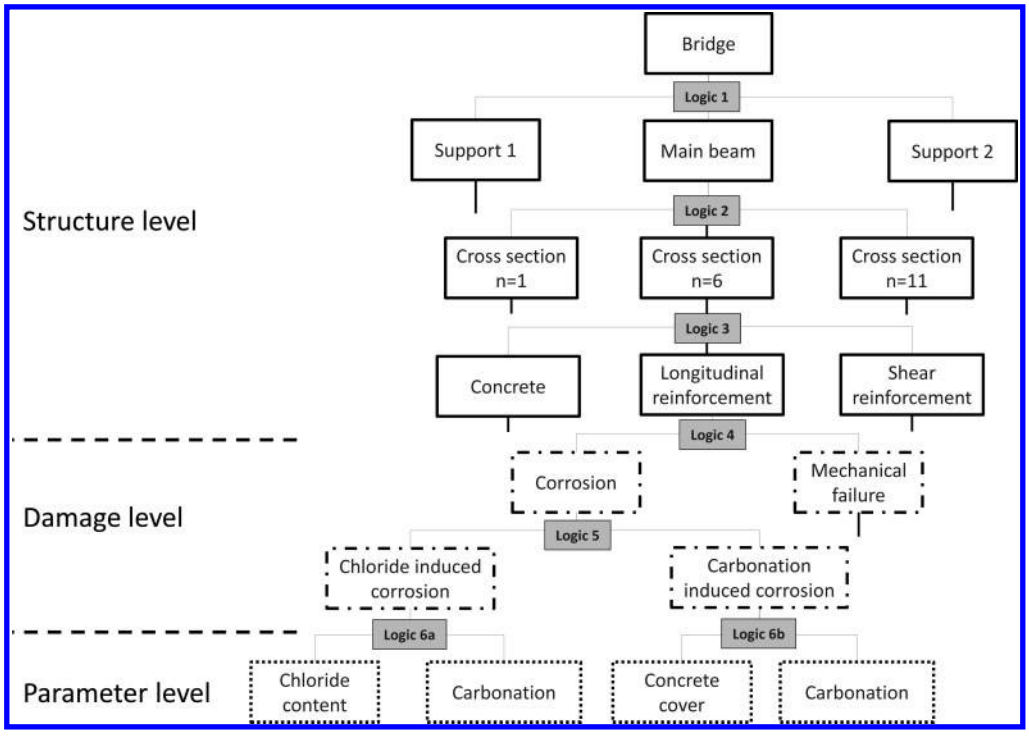


Figure 1. Example: condition evaluation by the impact tree.

Table 1. Corrosion rate due chloride induced corrosion (Novak et al. 2002)

Carbonation	Chloride content M%	Corrosion rate μm/a
yes	0,5	100
	2,0	150
no	0,5	10
	2,0	50

Table 2. Corrosion rate due carbonation induced corrosion (Novak et al. 2002)

Carbonation	Concrete cover d cm	Corrosion rate μm/a
yes	$d \leq 2$	60
	$2 < d \leq 4$	20
	$d > 4$	30
no	-	0

static system in the supports and the main beam. In this example the focus is on the main beam. Hence the beam is modeled as combination of several cross sections. At each of them the lowest partition of structure level is built of the used materials.

By the element "logic 4" structure and damage level are connected. In this case study corrosion processes of longitudinal reinforcement are discussed. The remaining branches of the impact tree are neglected. According to the used approach of the corrosion process, subordinated damage elements with their appropriate parameter elements are modeled.

The elements of the impact tree are linked by connection elements (logic 1-6) as shown in Figure 1. The resulting impact tree can be used for propagating the condition from the parameter level to the top element. In the following the main logical connection elements are specified. The logic elements 6a and 6b have two input parameters each. Based on the decision matrices of Table 1 & 2 the appropriate corrosion rate is defined as output value for further considerations. Also the logic calculates the criticality of the damage element. In the next step, in "logic 5", the interaction of both damage mechanisms is determined. In the current example the processes are assumed as accumulative. The remaining cross section of reinforcement is calculated in "logic 4" in consideration of the determined corrosion rate and a certain time period. In "logic 3" the statically required reinforcement is calculated and compared to the remaining cross section of reinforcement. Depending on this comparison the condition of the structure element (cross section *n*) is shown on the connected rating scale. Due to the fact that the system is statically determined, the condition of the cross section is identical to the condition of the main beam and the entire structure.

4.2.3 *Analysis by the impact tree*

The impact tree system model facilitates the analysis of deterioration processes and causes in the examined structure. There are different aspects on which we will focus further on.The first step of an impact tree analysis in the given example is to determine structural

hot-spots. For this parameter elements are kept constant at a certain default value, while the structural element under investigation (main beam) is subdivided in a certain number of cross sections. To get a continuous significant curve in the result diagram, we introduce a variable longitudinal coordinate x. The corrosion rate is independent of the longitudinal coordinate x, because the input values of all connection elements of parameter and damage level are equal. So the critical cross section depends only on the load applied on the main beam. Assuming a uniformly distributed load, the bending moment in the middle is at its maximum. A comparison of the required to the remaining reinforcement by the implemented calculation rule leads to the result that the middle part of the beam is identified as most critical. This method easily can be transferred to more complex structures.

The prediction of future condition states is another possible application of an impact tree. A precondition is here a time dependent definition of deterioration processes. In the example the corrosion process is time dependent due to the corrosion rate in micrometer per year. The variation of the input parameter time leads as a result to time-condition diagrams of all elements. By means of this result the critical moment of structure elements or the bridge as a whole can be determined.

The influence of different damage mechanisms or some measuring values can also be investigated by the impact tree. For this application parameter elements of interest can be varied. The consequences of parameter variation can be seen on the rating scale of the appropriate element. In the given example variation of chloride content with or without present carbonation is a suitable parameter to determine the influence of measuring values (parameter level) on the deterioration process.

The determination of the actual condition of the structure is one of the most important applications of the impact tree. In combination with an appropriate monitoring system condition assessment can be executed in real time. Measuring devices applied at identified hot-spot areas deliver the input values for the system analysis by the impact tree. But also further locations have to be taken into account by planning a monitoring concept. Due to the fact that each element of the impact tree, whether structure element, damage element or parameter element, is connected to a rating scale which is representing its condition, it is not only possible to determine the condition of the bridge itself; moreover causes of damage (parameter level) and the propagation of damage can be recognized.

5 CONCLUSION

In this paper is introduced a system model based approach for determining the condition of bridges, based on sensor measurements. The impact tree model consists of three different levels (structure level, damage level and parameter level). The modeling approach considers correlations between the deterioration mechanisms and the measurement values indicating the progress of the deterioration and also the impact of the condition of individual bridge components on the condition of the overall bridge system.

There are different possible applications of the impact tree. It can be used to simulate deterioration mechanisms by variation of parameter elements as input values during the planning phase of a bridge to detect critical damage mechanisms or structural components – so called hot-spots. Also it is possible to determine the actual condition of a bridge, based on sensor measurements in real time. On the basis of this information the impact tree model can be used as well to propagate future condition states by varying significant input values. For all applications, condition assignments are propagated from the leaf nodes (the sensor measurements) to the top node (the entire bridge).The most important function in this propagation mechanism is provided by the logical connection elements which are introduced between the different layers of the impact tree and model rules for state propagation. These logic elements are able, in contrast to Boolean interconnections of the fault tree, to describe different and flexible relationships between elements using a combination of equations and rules that describe the propagation of damage from one element to another. Thus, the impact tree can represent the next generation of modeling approaches for bridge maintenance problems.

New investigations of damage mechanisms can be implemented easily in the logic connection elements of an impact tree.Future work will concentrate on developing logical connection elements for a broad range of deterioration mechanisms and different approaches to condition assessment (deterministic/probabilistic).

ACKNOWLEDGEMENTS

This report is based on parts of the research project carried out at the request of the Federal Ministry for Transport, Construction and Town Planning, represented by the Federal Highway Research Institute, under research project No. 15.0538/2011/ARB.The author is solely responsible for the content.

REFERENCES

Borrmann, A., Lukas, K., Zintel, M., Schießl, P. & Kluth, M. 2012. BIM-based life-cycle management for reinforced concrete buildings.*International Journal of 3D Information Modeling 1(1), 1-24.*

Gehlen, C. 2000. Probabilistische Lebensdauerbemessung von Stahlbetonbauwerken. Zuverlässigkeitsbetrachtungen zur wirksamen Vermeidung von Bewehrungskorrosion. *Deutscher Ausschuss für Stahlbeton, Heft 510,* Berlin.

Klinzmann, C. 2008. Methodik zur computergestützten, probabilistischen Bauwerksbewertung unter Einbeziehung von Bauwerksmonitoring. Braunschweig, Germany.

LeBeau, K. H. & Wadia-Fascetti, S. J. 2000. A fault treemodel of bridge deterioration. *Specialty Conference on Probabilistic Mechanics and Structural Reliability.*

Lukas, K. & Borrmann, A. 2012.Integrated Bridge Management from 3D-Model to Network Level.*Proc. of the 6th Int. Conf. on Bridge Maintenance, Safety and Management.* Lake Como, Italy.

Miner, M.-A.1945.Cumulative Damage in Fatigue.*Journal of Applied Mechanics, Jg. 12, S. A159-A164.*

Neumann, T.& Haardt, P. 2012. Intelligent Bridges - Adaptive Systems for Information and Holistic Evaluation in Real Time.Proc. of the 6th European Workshop on Structural Health Monitoring - We.4.C.3 – Dresden, Germany.

Novak, B.,Brosge, S. & Reichert, F. 2002. Weiterentwicklung von Verhaltensmodellen im Rahmen des BMS. *Bundesanstalt für Straßenwesen.*

Palmgren, A. 1924. Die Lebensdauer von Kugellagern. *Zeitschrift des Vereins Deutscher Ingenieure, Jg. 68, S. 339–341.*

Reay, K. A. & Andrews, J. D. 2002.A fault tree analysis strategy using binary decision diagrams. *Reliability Engineering & System Safety, Volume 78, Issue 1, 45-56.*

Sianipar, P. R. M. & Adams, T. M.1997. Fault-Tree Model of Bridge Element Deterioration Due to Interaction.*Journal of Infrastructure Systems, No. 3, ASCE Press, 103-110.*

Sudret, B. 2008. Probabilistic models for the extent of damage in degrading reinforced concrete structures. *Reliability Engineering and System Safety, 93 (3), 410–422.*

Research and Applications in Structural Engineering, Mechanics and Computation – Zingoni (Ed.)
© 2013 Taylor & Francis Group, London, ISBN 978-1-138-00061-2

The opportunities of blind source separation techniques in the automation of modal identification for vibration based SHM

C. Rainieri & G. Fabbrocino
Structural and Geotechnical Dynamics Laboratory StreGa, DiBT Dept., University of Molise, Termoli, Italy

ABSTRACT: Accurate and effective methods for estimation of modal properties of civil structures in operational conditions play a relevant role in a number of applications ranging from validation of numerical models to Structural Health Monitoring (SHM). Several Operational Modal Analysis (OMA) methods are available and several successful applications are reported in the literature. Beside the classical time domain and frequency domain techniques, the use of Blind Source Separation techniques for output-only modal analysis is rapidly spreading. In the present paper their theoretical background is reviewed and attention is focused on the Second Order Blind Identification (SOBI) and the effect of analysis parameters on response time and accuracy of modal identification results. These aspects are of interest in view of the automation of the method and its integration within vibration-based SHM systems. The herein discussed results have suggested criteria for setting of the analysis parameters able to reduce the computational efforts and provide accurate estimates. The latter topic is of interest also when single modal identification tests are carried out. The proposed rule of thumbs has also been validated against some experimental case studies. They are representative of the different levels of complexity usually encountered during real modal tests. Comparisons with modal estimates provided by well-established OMA techniques have confirmed the potentialities of SOBI in this field.

1 INTRODUCTION

Several algorithms for automated identification (Rainieri & Fabbrocino 2010) and tracking (Rainieri et al. 2011) of modal parameters based on Operational Modal Analysis (OMA) methods have been developed in recent years. As a consequence, modal based damage detection techniques (Doebling et al. 1996) are again gaining in popularity, even if they suffer limitations in terms of damage localization and, above all, quantification, as well as drawbacks related to sensitivity to measurement quality and environmental and operational factors. Nevertheless, continuous monitoring of modal parameters has a large potential in performance and health assessment of civil engineering structures (Rainieri et al. 2010). Applications range from prompt detection of damage and degradation phenomena to post-earthquake health assessment and emergency management.

In this framework, the encouraging results obtained from the application of Blind Source Separation (BSS) techniques (Ans et al. 1985), and in particular Second Order Blind Identification (SOBI) (Belouchrani et al. 1997), as innovative tools for OMA has led to an increasing attention on their modal identification performance and on the opportunities of automation provided by these new data processing techniques.

In the present paper, after a review of the basics of BSS and, in particular, SOBI, attention is focused on this last method and on the results of some sensitivity analyses aimed at the assessment of the effect of analysis parameters on computational time and accuracy of modal identification estimates. The results of sensitivity analyses will lead to the formulation of basic guidelines for application of SOBI to output-only modal identification. In particular, a rule of thumbs for the setting of the analysis parameters aimed at an accurate estimation of the modal parameters and a control of the computational efforts is suggested. It allows for an automatic setting of the analysis parameters and, as a consequence, it points the way towards the automation of the modal identification process, for instance in combination with the strategy proposed in Poncelet et al. (2008). On the other hand, the separation of the modal contributions makes the analysis easier and can support the development of hybrid strategies for the automation of OMA (Rainieri & Fabbrocino 2013, Rainieri & Fabbrocino 2011).

The proposed criterion for parameter setting is herein applied to a number of experimental case studies. They are selected in order to provide examples of the different levels of complexity, which can be encountered during real modal tests. The comparison with the modal parameter estimates provided by well-established OMA procedures will lead to the identification of potentialities and limitations of SOBI in the field of dynamic identification on a rational basis.

2 BSS FOR MODAL IDENTIFICATION

BSS techniques allow for the extraction of a set of signals, the sources, from observations of their mixtures (Ans et al. 1985). In the last decade an increasing number of applications to structural dynamics have appeared in the literature. However, their use in this field is still a challenge (Antoni 2005). Nevertheless, different BSS algorithms have shown a potential in the field of output-only modal analysis, and a physical interpretation and prove of their applicability are given in (Kerschen et al. 2007).

In the context of modal identification, BSS techniques can be referred to as time domain methods. Moreover, since no model is fitted to data, they can be classified as non-parametric. The absence of stabilization charts to be interpreted or model parameters to be set makes BSS techniques an interesting alternative to classical time domain modal identification methods, such as Stochastic Subspace Identification (SSI) (Van Overschee & De Moor 1996). Thus, a performance assessment of BSS techniques for OMA of civil structures is of interest. However, some limits in the use of BSS for modal identification can be traced back to the basic assumptions of the different techniques. In fact, they may have different degree of compatibility with the dynamic systems of interest.

BSS techniques can be classified as linear (Belouchrani et al. 1997) or non-linear (Storck & Deco 1997), depending on the type of combination of the sources. Moreover, linear simultaneous (static) mixing (Belouchrani et al. 1997) and convolutive mixing (Thi & Jutten 1995) can be considered. The dynamic response of a system is given by the convolution product of the impulse response function and the external forcing vector but the problem of a convolutive mixture of sources is not completely solved yet. However, the response of a dynamic system can be also interpreted as a static mixture of sources (Kerschen et al. 2007). Assuming linear and static mixtures, the noisy model can be expressed in matrix form (Poncelet et al. 2007):

$$\{x(t)\} = [A]\{s(t)\} + \{\sigma(t)\} \tag{1}$$

where {x(t)} represents the recorded data, {s(t)} are the source signals, {σ(t)} is the noise corrupting the data and [A] is referred to as the mixing matrix. BSS has the goal of recovering the sources {s(t)} from their observed mixtures {x(t)}, based on a poor knowledge of the mixing matrix [A] and general assumptions about the sources. Applicability of BSS to vibration data is demonstrated by the comparison of Eq. (1) with the relation between physical response {x(t)} and modal response {q(t)} via the modal matrix [Φ]:

$$\{x(t)\} = [\Phi]\{q(t)\} \tag{2}$$

Thus, under given assumptions, the modal coordinates may act as virtual sources (Poncelet et al. 2007). No mathematical model is assumed to describe the process that produced the measured data. The mixing model is the only assumption, confirming that BSS techniques can be referred to as non-parametric procedures for modal identification.

In the case of static mixing, two approaches can be identified: the first is based on higher-order statistics, if sources are statistically independent and no more than one source is Gaussian (Comon 1994); the second relies upon second-order statistics, if sources are uncorrelated (Belouchrani et al. 1997). In both cases separation is affected by some indeterminacies related to the order of the sources (any permutation of the sources is also a solution of the blind identification problem) and their amplitude.

The first application of BSS to modal identification (Feeny & Kappagantu 1998) was based on Principal Component Analysis (PCA). However, the required knowledge of the mass matrix limited its applicability (Kerschen et al. 2007). Independent Component Analysis (ICA), instead, seems to be more promising in this field. The main assumptions in ICA are the mutual independence and non-Gaussianity of the sources. Under this assumptions, source separation is obtained by maximizing the non-Gaussianity of the sources through the solution of an optimization problem based on a given cost function. The main drawbacks of ICA are related to the use of high-order statistics, whose computation is computational demanding and difficult in the presence of a scarcity of data, and to some limitations strictly related to modal identification. In fact, ICA works well only in the case of weakly damped systems, characterized by damping ratios lower than 1% (Kerschen et al. 2007). These reasons make ICA unattractive for modal identification purposes.

Methods based on second-order statistics of the observed signals assume that sources are uncorrelated for all delays and have different spectra. Among these, the Algorithm for Multiple Unknown Signal Extraction (AMUSE) (Tong et al. 1991) and SOBI are based on a similar theoretical background. In fact, they exploit the information contained in covariance matrices. However, while SOBI jointly diagonalizes several time-shifted covariance matrices, AMUSE relies upon eigenvalue decomposition of the covariance matrix evaluated at one time lag. Thus, SOBI overcomes the shortcoming of AMUSE related to an eventual inappropriate choice of the time lag. This can result in two similar eigenvalues and makes unfeasible the identification of the sources. It has been shown that SOBI is also much more robust to noise than AMUSE (Zhou & Chelidze 2007). When SOBI is applied to vibration data, the real valued mixing matrix implies real valued mode shape estimates. This can be a drawback of the method in the presence of complex modes. An evolution of SOBI able to deal with complex modes is the Blind Modal Identification (BMID) algorithm (McNeill & Zimmerman 2008).

Taking into account the superior potential of SOBI for dynamic identification with respect to other BSS

techniques (PCA, ICA, AMUSE...) and that civil structures often show real modes, attention is herein focused on SOBI and its performance for output-only modal analysis of civil structures. In the context of output-only modal identification, SOBI can be classified as a non-parametric, low order time domain method. As a consequence, a number of sensors larger than or equal to the number of active modes is required for their identification. This is a common limitation of BSS techniques when applied to OMA. Moreover, unlike other two-step modal identification methods, SOBI provides mode shape estimates at the first step, while natural frequencies and damping ratios are recovered in a second step through post-processing of the obtained sources.

From a practical viewpoint, SOBI is based on a pre-processing step aiming at centering and whitening of data, and on the Joint Approximate Diagonalization (JAD) (Belouchrani et al. 1997, Cardoso & Souloumiac 1996) of a number of time-shifted covariance matrices. Once the measured data are centralized by removal of the mean value, whitening is obtained by the eigenvalue decomposition of the covariance matrix at $\tau = 0$:

$$[R_x(0)] = [E][D][E]^T \tag{3}$$

where [E] is the orthogonal matrix of eigenvectors and [D] is the diagonal matrix of eigenvalues; the whitened data vector is obtained as follows:

$$\{z(t)\} = [D]^{-1/2}[E]^T\{x(t)\} = [W]\{x(t)\} \tag{4}$$

The mixing matrix [A], providing the mode shape estimates for the structure under test (as pointed out by the comparison between Equation 1 and Equation 2), is obtained by JAD of p time-shifted covariance matrices. It looks for a matrix [Ψ] that approximately diagonalizes the time-shifted covariance matrices through the solution of an optimization problem. The matrix [Ψ] is iteratively identified by minimizing the sum of all off-diagonal terms of $[\Psi]^T[R_z(\tau_i)][\Psi]$, i=1,…,p, for the p time-shifted covariance matrices:

$$\min_{[\psi]} \sum_{i=1}^{p} off\left([\psi]^T[R_z(\tau_i)][\psi]\right) \tag{5}$$

A numerical algorithm based on Jacobi rotation technique (Cardoso & Souloumiac 1996) is adopted to this aim. Under the assumption that [Ψ] is orthogonal, the JAD of the p time-shifted covariance matrices allows for the identification of the de-mixing matrix [U] and the mixing matrix [A]:

$$[U] = [\Psi]^T[W] \tag{6}$$

$$[A] = [W]^{-1}[\Psi] \tag{7}$$

The natural frequency and damping ratio of the modes are finally extracted from the resulting sources after demixing. This can be done according to different procedures (single-degree-of-freedom curve fit, spectral analysis, and so on). In this study the natural frequency of the i-th mode is estimated by a linear regression on the zero crossing times of the associated source, while damping ratio is calculated through the logarithmic decrement technique, in agreement with another well-established OMA technique, the Enhanced Frequency Domain Decomposition (EFDD) (Gade et al. 2005).

Table 1. Modal properties of the simulated 6-DOF system.

Mode #	Natural frequency [Hz]	Damping ratio [%]
I	1.509	1.00
II	2.823	0.80
III	3.810	0.81
IV	4.737	0.87
V	5.593	0.95
VI	6.167	1.00

3 JAD PARAMETERS AND MODE ESTIMATES

In this section the results of some sensitivity analyses are summarized. They are aimed at the assessment of the effect of the parameters governing the JAD on response time and accuracy of modal estimates provided by SOBI. A rule of thumbs is proposed for the automation of SOBI when it is applied for OMA and vibration based SHM of civil structures. It is also applied to a number of experimental case studies related to civil structures and characterized by increasing degree of complexity. Comparisons with the modal estimates provided by well-established OMA methods are reported to further validate the rule.

The problem of the definition of mechanisms for noise rejection and, therefore, for the prior identification of the expected number of sources associated to structural modes is out of the scope of the present paper. Here a number of sources equal to the number of measurement channels are extracted, in agreement with similar OMA applications reported in the literature (Poncelet et al. 2007). Noise sources are eliminated in the second step of analysis aimed at the estimation of natural frequencies and damping ratios from the sources. The effect of the parameters governing the JAD (the number p of time-shifted covariance matrices to be jointly diagonalized, and the threshold t used to stop JAD) on accuracy of modal estimates and response time has been quantified by sensitivity analyses. The benchmark is represented by a simulated 6-DOF system (whose modal properties are reported in Table 1) subjected to a Gaussian white noise. Rayleigh damping is adopted.

The response of the system has been simulated at all the six DOFs and it has been sampled at 20 Hz. White noise has also been added to the time series in order to simulate measurement noise. A signal-to-noise ratio of 5 dB has been considered. The adopted

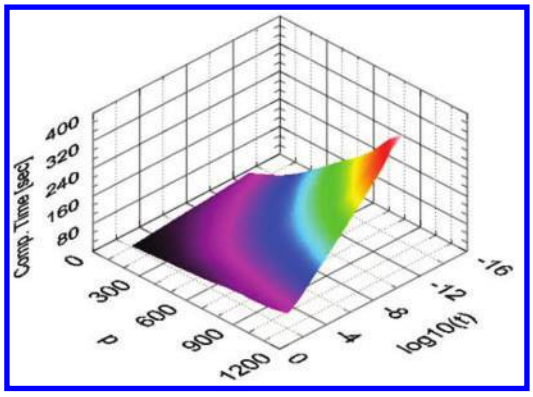


Figure 1. Sensitivity of response time to t and p (sample plot).

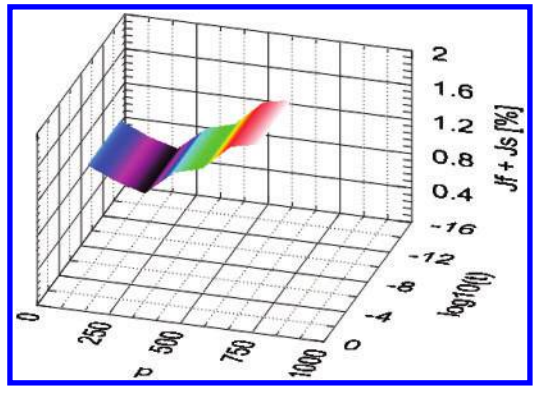


Figure 2. Sensitivity of overall accuracy to t and p.

sampling frequency leads to the extraction of four modal responses and two noise sources.

About parameter settings, a careful literature review has provided a suggested value for t. In particular, Cardoso & Souloumiac (1996) stated that very small values for t have no sense because the diagonality criterion is approximate itself. Thus, it is usually unnecessary to push the accuracy of the rotation matrix to the machine precision, but a value equal to its square root is suggested. However, this value has been determined according to a theoretical framework and not in view of OMA. Even if the response time might not be a problem for single modal identification tests, its control can be of interest for continuous, automated monitoring. The response time can range from fractions of seconds to several minutes or hours depending on the settings of t and p and the number of measurement channels. Figure 1 shows the dependence of the response time from p and t for a real dataset consisting of 12 measurement channels. As expected, it increases when p becomes larger and t decreases. Moreover, the larger the number of measurement channels, the higher the response time. Thus, the assessment of the influence of t and p on the modal parameter estimates can provide effective hints to ensure their accuracy or reduce the response time with little or no accuracy losses. To this aim, the simulated dataset has been processed by SOBI, the four modes in the range 0-10 Hz have been identified and compared with the theoretical values for different settings of t and p. The overall accuracy of the modal identification results in terms of natural frequencies and mode shapes has been quantified by the cumulative frequency scatter J_f and the cumulative discrepancy between corresponding mode shapes J_s:

$$J_f = \sum_{i=1}^{N_m} \left| \frac{f_i^{SOBI} - f_i^{ref}}{f_i^{ref}} \right| \cdot 100 \qquad (8)$$

$$J_s = \sum_{i=1}^{N_m} \left[1 - MAC\left(\{\psi_i^{SOBI}\}, \{\psi_i^{ref}\} \right) \right] \cdot 100 \qquad (9)$$

and their combination. N_m is the number of identified modes, while the MAC (Allemang & Brown 1982) between theoretical and estimated mode shapes is given by:

$$MAC\left(\{\phi_i^{SOBI}\}, \{\phi_i^{ref}\} \right) = \frac{\left| \{\phi_i^{SOBI}\}^T \{\phi_i^{ref}\} \right|^2}{\left(\{\phi_i^{SOBI}\}^T \{\phi_i^{SOBI}\} \right)\left(\{\phi_i^{ref}\}^T \{\phi_i^{ref}\} \right)} \qquad (10)$$

The plot of J_f+J_s vs. p and t for the simulated dataset is shown in Figure 2. It is possible to recognize that accuracy is mainly influenced by p, while a weak variation with t can be observed. Moreover, for t not larger than 1E-8, results do not change anymore. This limit value for t is expected to be data dependent. However, similar sensitivity analyses carried out on real datasets have provided the same results. Even if it is impossible to extrapolate a general rule, the obtained results seem to confirm that this value can be assumed as reference to obtain very stable results. Moreover, the little effect of t on the accuracy of estimates allows to set a threshold larger than 1E-8 in order to reduce the response time. In particular, it can be increased up to 1E-4 with negligible effects on the estimates but relevant reduction of response time, in particular when the number of measurement channels is larger. Above that value the approximations start inducing major effects on the estimates.

About the effect of p on accuracy, the analysis of the individual contributions J_f and J_s has pointed out that the trend in J_f+J_s depends on the trend of J_f vs. p, since J_s monotonically and slowly decreases with increasing values of p (even if for the single mode the 1-MAC vs. p plot can be not monotonic). This is consistent with the higher robustness of SOBI to noise with respect, for instance, to AMUSE, as a consequence of the joint diagonalization of several time-shifted covariance matrices. On the other hand, the trend of J_f can be probably addressed to the larger effect of disturbance beyond a certain decay level. As a final result, an optimal setting for p able to maximize the overall accuracy of modal estimates can be obtained from the minimum of the J_f+J_s function. Repeating the sensitivity analysis

Table 2. Test cases, modal identification results and comparisons.

Case study	Characteristics	Channels	(f_s [H_z], p)	Mode #	f_{SOBI} [H_z]	f_{ref} [H_z]	MAC
6-DOF system	Simulated data	6	(10, 400)	I	1.51	1.51	0.998
				II	2.82	2.82	0.999
				III	3.81	3.81	0.999
				IV	4.73	4.74	0.998
Tower of the Nations (Naples)	Well separated modes	8	(5, 360)	I	1.81	1.81	=1
				II	1.38	1.38	=1
				III	1.66	1.66	=1
Carmine's Bell Tower (Naples)	Close modes, noisy data	12	(5, 300)	I	0.70	0.70	=1
				II	0.76	0.76	=1
School of Engi-neering (Naples)	Close and coupled modes	12	(10, 400)	I	0.92	0.92	=1
				II	0.99	0.99	0.999
				III	1.30	1.30	=1

for different values of the sampling frequency, in order to change the number of modes in the frequency range of interest, the trend of the J_f+J_s function is kept, but the value of p corresponding to its minimum changes, as expected. However, when the sampling frequency changes by a factor of x with respect to that of the original dataset, the optimal setting for p changes by the same factor. Focusing the attention on the fundamental mode, which is obviously present in all the analyses, and on the decay level associated to this value of p, this was found to be the same for different values of the sampling frequency. Thus, the time to observe a certain amplitude decay more than the number of samples plays a major role in determining the accuracy of estimates. This is consistent with the change of the optimal setting of p with the adopted sampling frequency and with the increasing effect of noise when p is set much too large. The analysis of the decay level associated to the optimal setting for p seems to suggest the following rule for its evaluation. Taking into account the results of sensitivity analyses and that all the sources always start from a value of the amplitude equal to 1, the optimal setting of p has been associated to a ratio between the maximum amplitude of the i-th cycle and that of the first cycle (occurring at t>0) in the order of 10% for the fundamental mode (Fig. 3). As a consequence, the optimal value of p can be determined in a couple of iterations starting from a trial value and changing it in a way able to fulfil the suggested rule.

The rule has been validated against four real datasets. Reference modal parameters have been extracted according to well-established techniques, such as FDD (Brincker et al. 2000) and SSI, which provided very consistent estimates in terms of both natural frequencies and mode shapes. Even if SOBI and its variants have already been applied to the modal identification of real civil structures (Hazra 2010), to the best of the authors' knowledge this study represents its first systematic application to modal identification problems typically encountered in civil engineering and characterized by different degree of difficulty. Relevant information and details for each case study are reported in Table 2.

More details can be found elsewhere (Rainieri & Fabbrocino 2010). Taking into account how the value

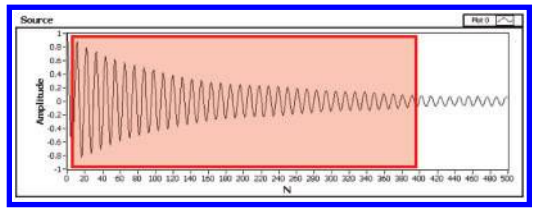


Figure 3. Illustration of the rule of thumbs to set p.

of t influences the accuracy, a value of 1E-8 has been adopted in the analysis of the real measurements. For each dataset, the optimal value of p has been determined according to the above mentioned rule of thumbs. The obtained modal identification results are reported in Table 2 in comparison with reference estimates provided by other, well-established OMA methods. A very good agreement can be observed, confirming that SOBI can be effectively applied for output-only modal identification of civil structures.

In order to validate the proposed rule for the setting of p, the real datasets have been analyzed also for different values of p. The function J_f+J_s vs. p has been evaluated around the estimated optimal value of p and considering as reference values of the natural frequencies and mode shapes those provided by the SSI (however, the same results are obtained considering the modal estimates provided by FDD as references, since they are very consistent with the corresponding estimates by SSI). Its plot (Fig. 4) shows that the proposed rule has been able to properly evaluate the optimal setting of p even in the case of real datasets.

4 CONCLUSIONS

In the present paper OMA by BSS has been reviewed, focusing the attention on SOBI. The moderate complexity and computational demand of the algorithm and the separation of modal contributions make it suitable for automation and integration into SHM systems. In this perspective the influence of JAD parameters on accuracy of modal estimates and response time

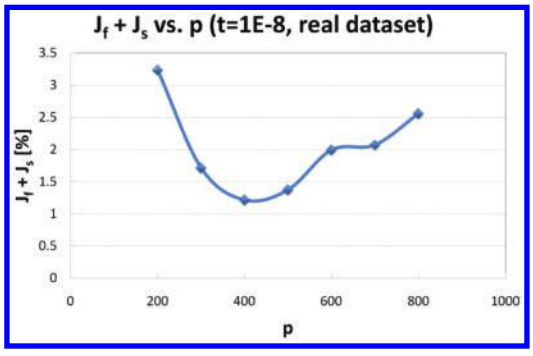


Figure 4. Validation of the proposed rule for setting of p.

has been analyzed. Rules of thumbs for their setting have been identified and validated. The good agreement of SOBI estimates with those of well-established OMA techniques, such as FDD and SSI, confirms the effectiveness of SOBI for OMA of civil structures. However, the typical limit of low order methods in the presence of a reduced number of sensors has to be taken into account.

REFERENCES

Allemang, R.J. & Brown, D.L. 1982. A correlation coefficient for modal vector analysis. In *Proceedings of the 1st SEM International Modal Analysis Conference*, Orlando, FL, USA.

Ans, B., Hérault, J. & Jutten, C. 1985. Adaptive neural architectures: detection of primitives. *COGNITIVA '85*: 593–597.

Antoni, J. 2005. Blind separation of vibration components: principles and demonstration. *Mechanical Systems and Signal Processing* 19: 1166–1180.

Belouchrani, A., Abed-Meraim, K., Cardoso, J.F. & Moulines, E. 1997. A blind source separation technique using second-order statistics. *IEEE Transactions on Signal Processing* 45: 434–444.

Brincker, R., Zhang, L. & Andersen, P. 2000. Modal identification from ambient responses using frequency domain decomposition, In *Proceedings of the 18th SEM International Modal Analysis Conference*, San Antonio, USA.

Cardoso, J.F. & Souloumiac, A. 1996. Jacobi angles for simultaneous diagonalization. *SIAM Journal of Matrix Analysis and Applications* 17:161–164.

Comon, P. 1994. Independent component analysis, a new concept?. *Signal Processing* 36: 287–314.

Doebling, S.W., Farrar, C.R., Prime, M.B. & Shevitz, D.W. 1996. Damage Identification and Health Monitoring of Structural and Mechanical Systems from Changes in their Vibration Characteristics: A Literature Review. *Technical Report LA-13070-MS*, UC-900, Los Alamos National Laboratory, New Mexico 87545, USA.

Feeny, B.F. & Kappagantu, R. 1998. On the physical interpretation of proper orthogonal modes in vibrations, Journal of Sound and Vibration 211: 607–616.

Gade, S., Møller, N.B., Herlufsen, H. & Konstantin-Hansen, H. 2005. Frequency domain techniques for operational modal analysis, In R. Brincker & N. Moller (eds.), *Proceedings of the 1st International Operational Modal Analysis Conference*, Copenhagen, Denmark.

Hazra, B. 2010. *Hybrid Time and Time-Frequency Blind Source Separation Towards Ambient System Identification of Structures*, Ph.D. Thesis, University of Waterloo, Waterloo, Canada.

Kerschen, G., Poncelet, F. & Golinval, J.C. 2007. Physical interpretation of independent component analysis in structural dynamics. *Mechanical Systems and Signal Processing* 21: 1561–1575.

McNeill, S.I. & Zimmerman, D.C. 2008. A framework for blind modal identification using joint approximate diagonalization. *Mechanical Systems and Signal Processing* 22: 1526–1548.

Poncelet, F., Kerschen, G., Golinval, J.C. & Verhelst, D. 2007. Output-only modal analysis using blind source separation techniques. *Mechanical Systems and Signal Processing* 21: 2335–2358.

Poncelet, F., Kerschen, G. & Golinval, J.C. 2008. In-orbit vibration testing of spacecraft structures, In *Proceedings of the International Conference on Noise and Vibration Engineering ISMA 2008*, Leuven, Belgium.

Rainieri, C. & Fabbrocino, G. 2010. Automated output-only dynamic identification of civil engineering structures. *Mechanical Systems and Signal Processing* 24: 678–695.

Rainieri, C., Fabbrocino, G. & Cosenza, E. 2010. Integrated seismic early warning and structural health monitoring of critical civil infrastructures in seismically prone areas. *Structural Health Monitoring – An International Journal* 10: 291–308.

Rainieri, C. & Fabbrocino, G. 2011. Validation of a hybrid automated modal identification algorithm for structural health monitoring applications. In F.K. Chang (ed.) *Structural Health Monitoring 2011: Condition-Based Maintenance and Intelligent Structures; Proceedings of the 8th International Workshop on Structural Health Monitoring*, Stanford, USA.

Rainieri, C., Fabbrocino, G. & Cosenza, E. 2011. Near real-time tracking of dynamic properties for standalone structural health monitoring systems. *Mechanical Systems and Signal Processing* 25: 3010–3026.

Rainieri, C. & Fabbrocino, G. 2013. Accurate damping estimation by automated OMA procedures. In F.N. Catbas, S. Pakzad, V. Racic, A. Pavic & P. Reynolds (Eds.) *Topics in Dynamics of Civil Structures, Volume 4; Proceedings of the 31st IMAC, A Conference on Structural Dynamics,* Garden Grove, USA.

Storck, J. & Deco, G. 1997. Nonlinear independent component analysis and multivariate time series analysis. *Physica, D* 108: 335–349.

Thi, H.L.N. & Jutten, C. 1995. Blind source separation for convolutive mixtures. *Signal Processing* 45: 209–229.

Tong, L., Liu, R.W., Soon, V.C. & Huang, Y.F. 1991. Indeterminacy and identifiability of blind identification. *IEEE Transactions on Circuits and Systems* 38: 499–509.

Van Overschee, P. & De Moor, B. 1996. *Subspace Identification for Linear Systems: Theory – Implementation – Applications*. Kluwer Academic Publishers, Dordrecht, the Netherlands.

Zhou, W. & Chelidze, D. 2007. Blind source separation based vibration mode identification. *Mechanical Systems and Signal Processing* 21: 3072–3087.

Research and Applications in Structural Engineering, Mechanics and Computation – Zingoni (Ed.)
© 2013 Taylor & Francis Group, London, ISBN 978-1-138-00061-2

Transducers frequency influence on ultrasonic velocity measurements in concrete specimens

G. Concu, B. De Nicolo, N. Trulli & M. Valdés
Department of Civil Engineering, Environmental and Architecture, University of Cagliari, Italy

ABSTRACT: Ultrasonic testing is a non invasive surveying technique suggested for concrete quality control. European standards concerning the determination of ultrasonic velocity in concrete take into account measurements stability, repeatability and reproducibility, and address the main factors influencing velocity measurements, but no exhaustive suggestion is given about the frequency characteristics of the transducers to be used in the test. Commercial measurements systems offer several types of transducers with different frequency characteristics, the choice of which is left with the operator, who has to decide without clear standards or guidelines. This work reports the preliminary results of an experimental campaign aimed at establishing the influence of transducers natural frequency on ultrasonic velocity measurements in concrete. Several concrete specimens have been made and tested by using transducers with different natural frequency. The correlation between transducers frequency and ultrasonic velocity has been exploited and discussed, also with relation to curing stage and concrete compressive strength.

1 INTRODUCTION

Non-destructive techniques based on ultrasonic wave propagation are generally used in structural diagnosis and also suggested for concrete quality control. They are applied directly in the field for investigations of a wide range of structures and infrastructures, and in laboratory for materials characterization.

Traditional application of UT is based on measurements of the velocity V of acoustic waves propagating through the material. UT is preferentially carried out applying the Direct Transmission Technique, in which the wave is transmitted by an emitter transducer through the test object and received by a receiver transducer on the opposite side. This allows to measure the time T the wave needs to travel through the object's thickness, from the emitter to the receiver, along a path of length L; the average velocity of the wave is then obtained from the ratio L/T. The wave velocity is directly related to structures elastic parameters, e.g. dynamic modulus of elasticity, Poisson's ratio and density, so that its analysis provides information on physical and mechanical properties of the material, crucial for materials quality control and on site structural performance assessment (Camplani, 2008; Cannas, 2008; Concu, 2006; De Nicolo, 2005).

Standards concerning the determination of ultrasonic velocity in concrete, e.g. European EN 12504-4, take into account the problems of measurements stability, repeatability and reproducibility, and address the main factors influencing velocity measurements. Nevertheless, no exhaustive suggestion is given about the natural frequency of the transducers to be used in the test. The only given information is that transducers natural frequency should normally be within the range 20 kHz to 150 kHz, and that it is preferable to use high frequency transducers (60 kHz to 200 kHz) for short path lengths (down to 50mm) and low frequency transducers (10 kHz to 40 kHz) for long path lengths (up to a maximum of 15m). However, commercial measurements systems often offer several types of transducers with different frequency characteristics, the choice of which is left with the operator, who have to decide without clear standards or guidelines. This paper reports the preliminary results of an experimental campaign aimed at establishing the influence of transducers frequency characteristics on ultrasonic velocity measurements in concrete.

Several concrete cubic specimens have been prepared and tested by using transducers with different natural frequency. Correlations between transducers frequency and ultrasonic velocity have been analyzed also taking into account both curing stage and concrete compressive strength.

2 EXPERIMENTAL CAMPAIGN

The experimental campaign has been carried out on 27 cubic specimens 150mm sized, casted by using a C 40/50 strength class concrete (NTC, 2008).

Ultrasonic measurements have been performed using the ultrasonic test equipment Pundit Lab+, developed by Proceq. This testing equipment includes:

- four pairs of standard transducers with natural frequency respectively of 24 kHz, 54 kHz, 150 kHz and 250 kHz for emitting and receiving signals;

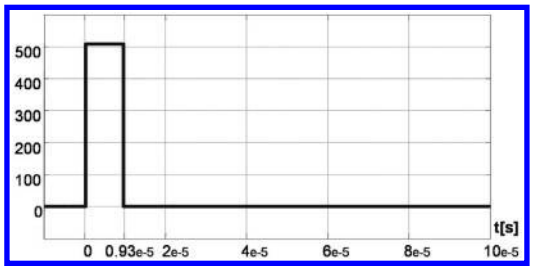


Figure 1. The energizing signal. Amplitude is measured in Volts.

– a unit for signals generation, acquisition and preliminary analysis;
– a PC for data storage and further signal processing;
– a dedicated software Pundit Link which unlocks the full capabilities of the ultrasonic test system.

The energizing signal is a square wave with high input voltage of 500 V (Fig. 1), which allowed signals to be detected even if strongly attenuated.

UT has been carried out on specimens during the curing stage at 7, 14 and 28 days. For each specimen, three measures of velocity have been performed for each couple of opposite sides. The velocity value associate with a specimen is the average of all the value measured on that specimen.

After 28 days of curing compressive tests have been carried out according to UNI EN 12390-3.

3 RESULTS

Table 1 shows a summary of velocity values measured at the selected different curing times by using 24 kHz, 54 kHz, 150 kHz and 250 kHz natural frequency transducers. Figures 2-5 show how ultrasonic velocity varies with curing time and with transducers natural frequency.

From Table 1 and figures 2–5 it can be inferred that ultrasonic velocity increases with curing time independently on the resonant frequency of the applied transducers. The increase is of about 150 m/s after 28 days of curing. Average and standard deviation values are quite similar for the various resonant frequencies.

Table 2 reports specimens compressive strength and density determined at 28 days of curing.

3.1 *Regression analysis*

A regression analysis has been performed in order to evaluate the reliability of ultrasonic velocity measured at 28 days of curing with the different resonant frequency transducers in predicting compressive strength. Figures 6-9 show the correlation between velocity and compressive strength for the different natural frequencies. Table 3 reports regressions parameters.

Table 1. Ultrasonic signal velocity.

Transducer	V*[m/s]	SD*[m/s]	COV* [%]
7 DAYS OF CURING			
24 kHz	4472	26.48	0.59
54 kHz	4499	29.38	0.65
150 kHz	4464	31.38	0.70
250 kHz	4474	35.74	0.80
14 DAYS OF CURING			
24 kHz	4578	73.91	1.61
54 kHz	4546	42.00	0.92
150 kHz	4544	37.59	0.83
250 kHz	4532	36.08	0.80
28 DAYS OF CURING			
24 kHz	4618	29.93	0.65
54 kHz	4638	31.37	0.68
150 kHz	4636	29.42	0.63
250 kHz	4650	28.89	0.62

*V = Average of all samples, SD = Standard deviation, COV = coefficient of variation.

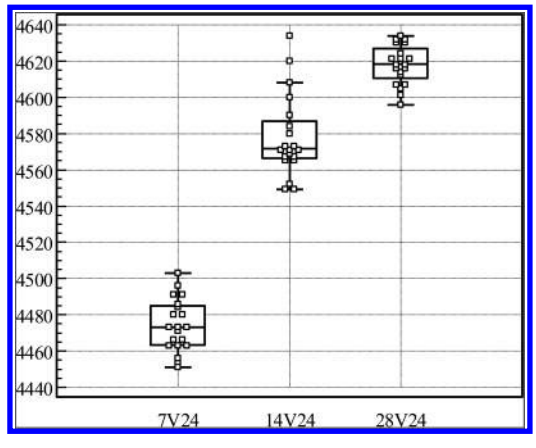


Figure 2. Average velocity V at 7, 14 and 28 days of curing. Measures performed with 24 kHz natural frequency transducers.

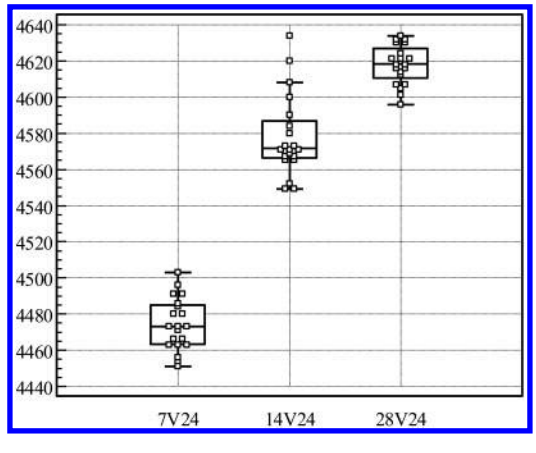


Figure 3. Average velocity V at 7, 14 and 28 days of curing. Measures performed with 54 kHz natural frequency transducers.

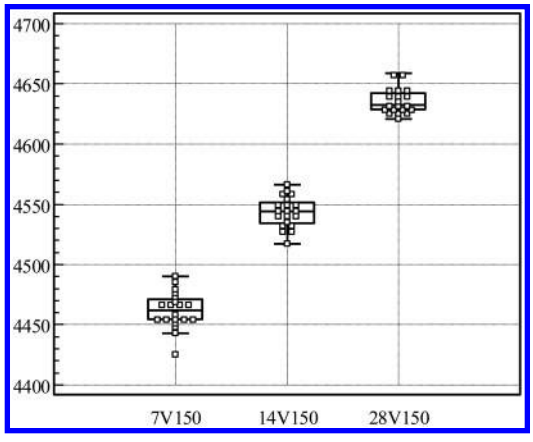


Figure 4. Average velocity V at 7, 14 and 28 days of curing. Measures performed with 150 kHz natural frequency transducers.

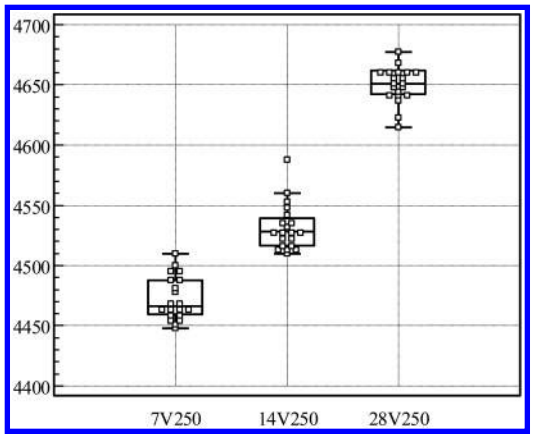


Figure 5. Average velocity V at 7, 14 and 28 days of curing. Measures performed with 250 kHz natural frequency transducers.

Table 2. Specimens compressive strength and density.

28 days of curing	
Compressive Strength	
Average [N/mm^2]	56.23
SD* [N/mm^2]	1.84
COV* [%]	3.27
Density	
Average [kg/mm^3]	2323
SD* [kg/mm^3]	10.89
COV* [%]	0.47

*SD = Standard deviation, COV = Coefficient of variation.

Correlations between average velocity and compressive strength are represented by quadratic polynomial curves with a coefficient of determination R^2 ranging from 0.4453 to 0.9010. The best correlation is provided by ultrasonic tests in which the 250 kHz resonant frequency transducers have been used.

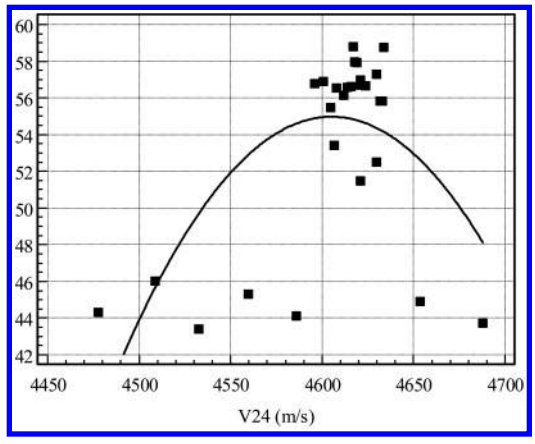


Figure 6. Correlation between 28 days average velocity and compressive strength. Measures performed with 24 kHz natural frequency transducers.

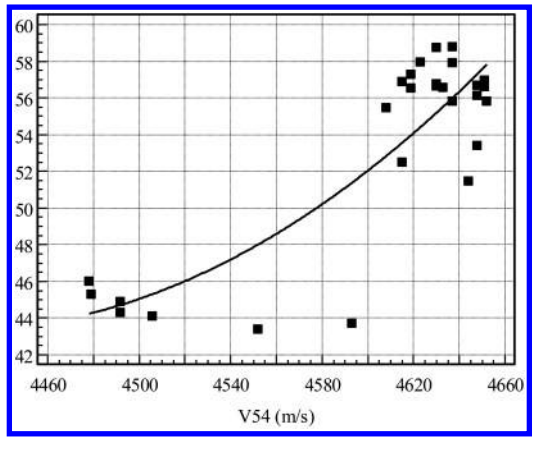


Figure 7. Correlation between 28 days average velocity and compressive strength. Measures performed with 54 kHz natural frequency transducers.

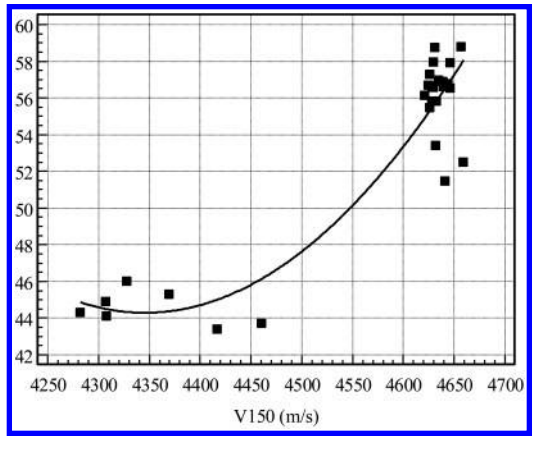


Figure 8. Correlation between 28 days average velocity and compressive strength. Measures performed with 150 kHz natural frequency transducers.

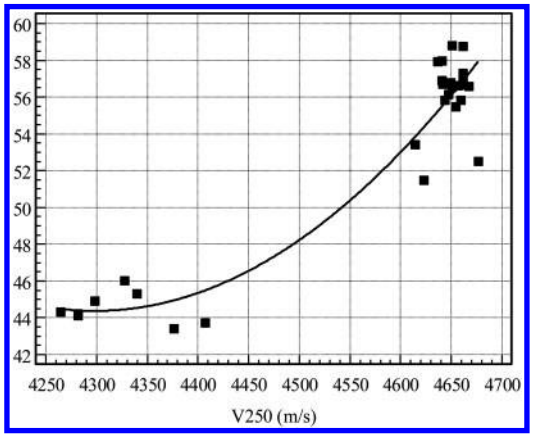


Figure 9. Correlation between 28 days average velocity and compressive strength. Measures performed with 250 kHz natural frequency transducers.

Table 3. Regressions parameters.

Freq.	Equation	R^2
24 kHz	$y = -21192{,}6353 + 9{,}2282x - 0{,}0010 \times^2$	0,4453
54 kHz	$y = 5317{,}6823 - 2{,}3864x + 0{,}0003 \times^2$	0,7237
150 kHz	$y = 2688{,}6725 - 1{,}2171x + 0{,}0001 \times^2$	0,8685
250 kHz	$y = 1800{,}5781 - 0{,}8172x + 0{,}0001 \times^2$	0,9010

4 CONCLUSION

An experimental campaign has been started with the aim of establishing the influence of transducers natural frequency on ultrasonic velocity measurements in concrete.

Several concrete specimens have been prepared and tested by using couple of transducers with resonant frequency of 24 kHz, 54 kHz, 150 kHz and 250 kHz respectively.

The correlation between transducers natural frequency and ultrasonic velocity has been exploited and discussed, also with relation to curing stage and concrete compressive strength.

Results achieved since now highlighted that ultrasonic velocity increases with curing time independently on the resonant frequency of the applied transducers. This increase is of about 150 m/s after 28 days of curing. Average velocity and standard deviation values are quite similar for measurements performed by using the different resonant frequencies.

A simple statistical elaboration of the acquired data pointed out the reliability of ultrasonic velocity measured at 28 days of curing in predicting compressive strength. With the exception of the 24 kHz transducers, in the other cases (54 kHz, 150 kHz and 250 kHz transducers) the coefficient of determination R^2 for the regression equation correlating ultrasonic velocity and compressive strength is significantly high, the best correlation being provided by the 250 kHz resonant frequency transducers. This outcome is not in unison with the European standard UNI EN 12504-4, which states that it is preferable to use high frequency transducers (60 kHz to 200 kHz) for short path lengths (down to 50 mm) because high frequency pulses become attenuated more rapidly than pulses of lower frequency.

REFERENCES

Cannas, B. et al. *Features extraction techniques for sonic and ultrasonic NDT on building materials*. Proc. of 1st International Symposium on Life-Cycle Civil Engineering, Varenna, Lake Como, Italy, June 11–14, 2008.

Camplani, M. et al. 2008. Acoustic NDT on building materials using Features extraction techniques. In ICCSA 2008, Part II. *Springer Lecture Notes in Computer Science* 5073: 582–595.

Concu, G. et al. 2006. *Ultrasonic test methods for assessment of concrete strength during construction*. Proc. of 10th International Conference on Inspection Appraisal Repairs & Maintenance of Structures – Hong Kong, October 24–26, 2006.

De Nicolo, B. et al. 2005. *NDT ultrasonic evaluation of early compressive strength in SCC.* Proc. of 9th International Conference on Inspection Appraisal Repairs & Maintenance of Structures – Fuzhou, China, October 19–21, 2005.

NTC 2008. Italian Standards for Constructions.

UNI EN 12504-4. 2005. Testing concrete. Part 4: Determination of ultrasonic pulse velocity.

UNI EN 12390-3. 2009. Testing hardened concrete. Part 3: Compressive strength of test specimens.

Research and Applications in Structural Engineering, Mechanics and Computation – Zingoni (Ed.)
© 2013 Taylor & Francis Group, London, ISBN 978-1-138-00061-2

Application of SHM system based on modal filtration to the truss structure

K. Mendrok, T. Uhl & W. Maj
AGH University of Science and Technology, Department of Robotics and Mechatronics, Krakow, Poland

ABSTRACT: The paper presents the application of damage detection technique based on modal filtration to the monitoring of the truss structure model. Test object was a scaled down version of typical element of a roof structure. It was mounted in the specially built hydraulic test stand. During the tests the structure was loaded with increasing force until the damage occurred. In the paper the method and developed SHM system are briefly presented together with the results of the tests for civil engineering-like structure.

1 INTRODUCTION

1.1 *Vibration based damage detection*

One of the groups of damage detection algorithms used in nondestructive testing and structural health monitoring is the group of the so-called vibration methods, i.e. methods that use data in the form of accelerations of vibrations in time or frequency domains. They are based on the observation of changes in the system's vibration responses, which result from damage occurrence. The methods' main idea is model-based diagnostics defined in the following way: the model of a particular system in an undamaged state is given, and this model is compared to the model identified from the data measured on the object in the current state. Differences between these two models indicate the object modification (e.g. stiffness or mass decrease), which may be caused by damage. A detailed description of some of the methods mentioned above, together with its verification can be found in Mendrok & Uhl (2004), Doebling et al. (1998) and Carden & Fanning (2004). The most convenient model, which can be applied in the described approach, is a modal model. It is relatively easy to identify and, by means of operational modal analysis, may be identified only from response data; it is, therefore, very useful in diagnostics. Apart from its advantages, application of modal model-based diagnostics within damage detection has several limitations and faults. First of all, there is a serious problem distinguishing between the changes in parameters resulting from damage and those caused by environmental changes e.g. temperature or humidity. That is especially visible in civil engineering structures monitoring. A further limitation of modal model-based diagnostics involves difficulties with the automation of procedures. Despite the current development of autonomous modal analysis procedures in many scientific centers, the total independence of an engineer's interference is still problematic in practice. Additionally, diagnostic symptoms in the form of natural frequencies, modal damping coefficients and modal vectors are estimated periodically, and depend on the subjective assessment of a testing team. Also the computational cost required by the modal parameters estimation algorithms is rather high, and makes problematic its implementation on the embedded diagnostic systems.

There is however a method which uses vibration data as well as a modal model of the object and, in addition, overcomes all mentioned above limitations. This is the advantage of modal filtering applied to the data recorded on the object.

1.2 *Modal filtration*

A modal filter is a tool used to extract the modal coordinates of each individual mode from a system's output (Meirovitch & Baruh 1982, Zhang et al. 1990). It decomposes the system's responses into modal coordinates, and thus, on the output of the filter, the frequency response with only one peak, corresponding to the natural frequency to which the filter was tuned, can be obtained. The modal filter was used for the first time for damage detection and structural health monitoring by Slater & Shelley (1993). Later on also Gawronski & Sawicki (2000) and El-Ouafi Bahlous et al. (2007) applied it in this field. One more way of using modal filtering for structural health monitoring is presented by Deremeker & Preumont (2006) and later by Mendrok & Uhl (2010a). The frequency response function of an object filtered with a modal filter has only one peak corresponding to the natural frequency to which the filter is tuned. When a local change occurs in the object – in stiffness or in mass (this mainly happens when damage in the object arises), the filter stops working and, on the output characteristic, other peaks start to appear, corresponding to other imperfectly filtered natural frequencies. On the other hand, a global change in entire stiffness or mass matrix

(due to changes in ambient temperature or humidity) does not corrupt the filter and the filtered characteristic still has one peak, although it is slightly moved in the frequency domain. Such an approach has also been applied in this paper due to its advantages over the classical modal model based methods: robustness for environmental changes, low computational cost, autonomous operation.

2 SHM SYSTEM BASED ON THE MODAL FILTRATION

2.1 *General assumptions*

The authors decided to implement modal filtration as a practical measuring – diagnostic system. Its main assumption was that it should be completely independent. It means that the user should be able to perform full diagnostic procedure without necessity of usage of any additional measuring device or software. To fulfill above requirement the original 16-teen channel measuring – diagnostic unit was designed and the dedicated modal analysis and modal filtration software was developed. Generally the system composed of both hardware and software is supposed to work in one of the three modes: operation in dynamic signal analyzer mode for the purposes of the modal testing, operation in diagnostic mode (acceleration of vibration measurements, frequency characteristics estimation modal filtration of the characteristics, damage index calculation) operation in monitoring mode (the same activities as in diagnostic mode but performed periodically).

2.2 *Measuring unit and modal analysis software*

In order to develop the SHM system, dedicated measuring device has been designed and built. The device's logic structure contains CPU and FPGA modules connected with each other and with some additional peripheral devices. CPU module is included mainly for control purposes – it implements user interface together with some peripheral devices like keyboard, LCD display and communication units. FPGA module on the other hand, contains all logic modules necessary for implementation of desired method. The device structure contains also 16 A/D converters which moves analog input signal delivered from vibration sensors into digital domain, and two high speed synchronous RAM modules needed for data buffering and data processing needs. FPGA goal is to provide synchronous signal acquisition from all 16 channels and maintain all functionality necessary for measurement process like triggering, configuration, over condition detection and many others. The FPGA also contains data processing module, so it is also responsible for desired algorithm implementation. Thanks to that, CPU task is limited mainly to maintain control and auxiliary functions only. This is very important from power consumption point of view, because CPU device does not need to be fast (and complicated), and therefore it consumes much less power. Of course FPGA device also consumes power, but it's power consumption can be precisely controlled during operation. Thanks to that the whole device can work fully independently in diagnostic mode (without any PC connected to it), and it can be battery powered, which is very important especially in portable applications.

The main goal of the software written for the described SHM system is the estimation of the modal filter coefficients. For this purpose, the application provides the following functionalities:

- Geometrical model definition of the tested object.
- Measurement points definition, namely the assignment of specific points of a geometric model to the sensors placed on an object.
- Execution of measurement and presentation of the results (time histories, PSD, FRF and coherence), and data archiving.
- Execution of modal analysis by:
  - calculation of stabilization diagram,
  - estimation and visualization of mode shapes for selected poles,
  - estimation of modal filter coefficients and visualization of filtration results.

The application was created in the .Net Framework 3.5 environment with use of additional external libraries.

3 PERFORMED TESTS

3.1 *Test stand description*

The measurements could be successfully accomplished thanks to courtesy of interested staff members of the Faculty of Automotive and Construction Machinery Engineering at Warsaw University of Technology. The object of the test was a single truss shown in Figure 1 mounted on a specially built test stand in the laboratories of the Faculty of Automotive and Construction Machinery Engineering at Warsaw University of Technology (Galezia et al. 2012, Szulim et al. 2012). It is a typical element usually found in roof constructions, and it's damage may directly lead to roof crash. During the experiment a force was applied to the truss as shown in the figure.

The main goal of the test was to proof that modal filtration and designed system can be successfully used for damage detection for such objects. The photo of measuring stand is presented below in Figure 2.

A set of sensors was installed on the bottom beam of the truss. A significant advantage of this approach

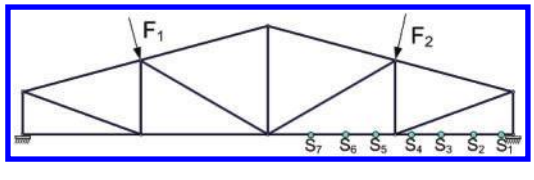


Figure 1. Object of tests.



Figure 2. Photo of the laboratory test stand.

is that it is not necessary to place a large number of sensors on examined object even if it is large. The user can place only a few sensors evenly distributed on the object. The result in damage detection efficiency would be very similar. However a bit of experience is needed from the user to choose a proper area and sensors number. What is more, position of each sensor cannot be changed during measurements, as it would affect damage detection quality (Mendrok & Uhl 2010b). As a matter of fact this method can be successfully used in applications where the measures are performed periodically. In this case sensors doesn't need to be installed permanently, however user have to ensure that every sensor is mounted exactly in the same point of the object as it was during reference measure. This can be achieved by using dedicated spacers (between object and sensors) mounted permanently on tested object.

3.2 *Preliminary tests*

At the very beginning measuring unit was connected to PC (with dedicated analytic software installed) in order to calculate modal filter coefficients for object in reference state. The reference state is defined as a state of object without damage in it's typical working conditions. In this case it was assumed a state of truss mounted on test stand with no force applied to it. The photo of hardware unit connected to the PC with installed software is presented in Figure 3.

To obtain the modal model and from it the modal filter coefficients, the impulse test was performed. The 0.1 kg modal hammer with force sensor was used to excite the structure. The responses were measured in the 7 points shown in Figure 1 by one-axis accelerometers. The following parameters were used



Figure 3. Hardware unit connected to the PC.

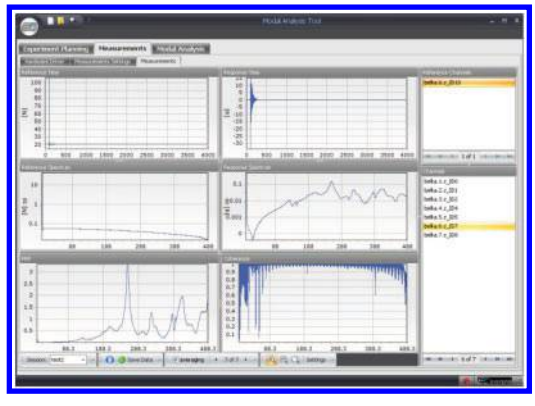


Figure 4. Exemplary results of modal testing.

during the measurements: bandwidth – 500 Hz, spectral resolution – 0.25 Hz. The frequency response functions together with power spectral densities averaged 9 times in frequency domain were recorded. The exemplary view of graphical user interface during measurements is placed in Figure 4. In the last step the results of measurements were verified for their correctness. The ordinary coherence function and repeatability of the driving point frequency response function were the quality criteria.

In the next step the modal parameters were estimated with use of the LSFD algorithm, which is implemented in the software. The results obtained during the identification process are presented in Figure 5.

The last step of the reference data preparation consists in modal filter coefficients estimation. After model extraction user is able to verify quality of designed filter (which is shown below in Figure 6).

As the result, three modal filters had been calculated, each for different natural frequency and corresponding mode shape. Coefficients of these filters were then transferred to MDU, which enabled it to work independently and calculate damage index values for each defined filter.

3.3 *Damage measurements*

During the experiment, load was slowly increased in several steps. The reference measurements were

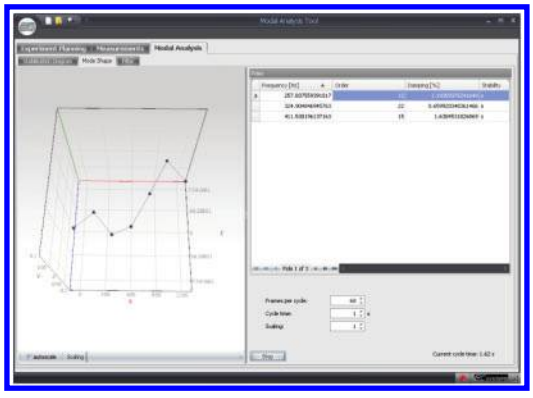


Figure 5. View of the software GUI for the mode shape visualization.

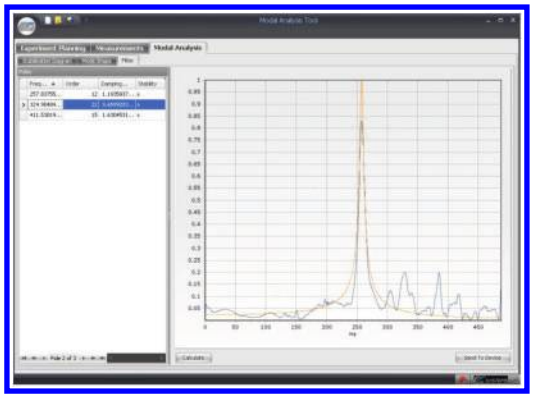


Figure 6. View of the software GUI for the filter quality verification.

performed without load and next load was applied with use of hydraulic drives. The load was increased up to 35 kN. Every 5 kN the diagnostic procedure was launched and damage index was calculated. The 35 kN load caused serious deformation of the tested truss. To see if the deformation is in the elastic range the load was released and increased again. At the level of 35 kN the damage occurred. One of the clamps was broken and that ended the experiment. In Figure 7 deformed frame with 35 kN load in first load cycle is shown. In Figure 8 the broken clamp after second load cycle is presented.

As it was stated above, every 5 kN the damage index values were calculated. They are gathered together in Table 1.

For better visualization of the results are presented as plot in Figure 9.

Both Table 1 and Figure 9 exhibits very clear trend of the damage index value. It grows together with load increase. Especially the modal filter tuned to Mode shape 3 presents linear dependency. It indicates that the method and SHM system based on it can detect not only damage but also the load change. This is very useful information for the roof monitoring system because it can give the information about too big snow layer.

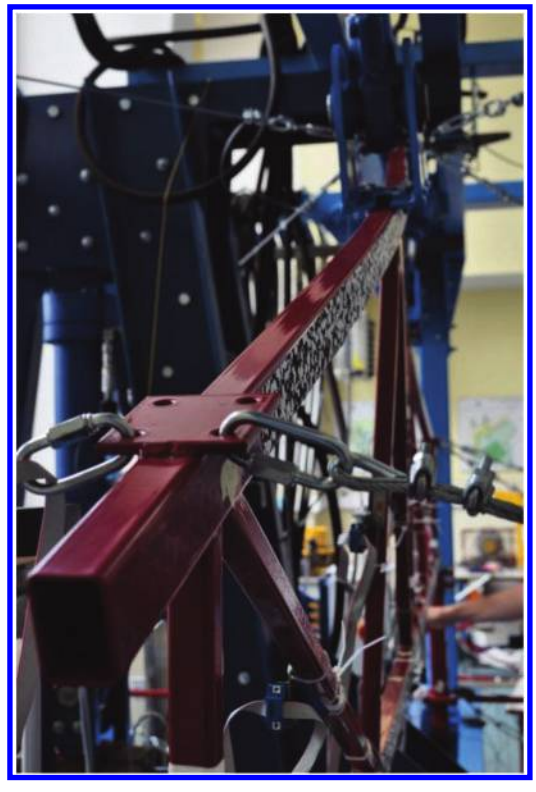


Figure 7. Deformed frame after first load cycle.



Figure 8. The broken clamp after second load cycle.

Another interesting information is that after complete load release the damage index did not returned to the 0 value. It means that the 35 kN load introduced some structural changes to the structure. This results were confirmed by the camera-based measurements of the structure deflection. After the load release the truss did not returned to its original shape.

Table 1. Values of damage index (DI) calculated for modal filter (MF) tuned to consecutive mode shapes

	Measurement Results			
No	DI(MF 1)	DI(MF 1)	DI(MF 1)	Load
1	1.46E−02	4.53E-02	2.82E-02	F = 0 kN
2	8.07E−01	8.17E−01	4.00E−01	F = 5 kN
3	8.83E−01	7.59E−01	4.80E−01	F = 10 kN
4	9.60E−01	9.24E−01	6.98E−01	F = 20 kN
5	1.03E+00	1.11E+00	7.52E−01	F = 25 kN
6	1.11E+00	1.30E+00	8.31E−01	F = 30 kN
7	1.44E+00	1.31E+00	1.34E+00	F = 35 kN
8	8.54E−01	8.71E−01	7.10E−01	F = 15 kN
9	2.07E−01	4.39E−01	3.50E−01	F = 0 kN
10	1.35E+00	1.16E+00	1.13E+00	F = 35 kN

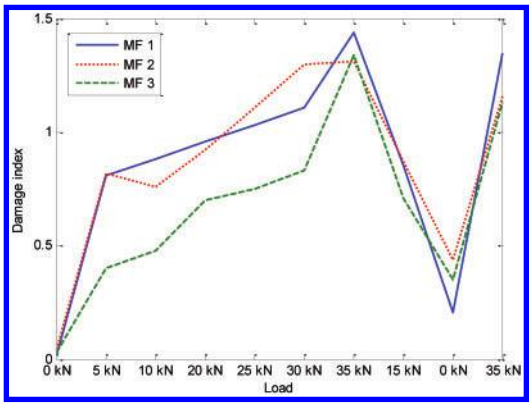


Figure 9. Values of damage index in function of load.

4 CONCLUSIONS

The paper presents the results of laboratory tests for a damage detection procedure and monitoring system based on modal filtration. The object of test was a single truss mounted on specially build laboratory test stand, which imitate real working conditions for this object.

A general conclusion is that the developed SHM system detects damage with good sensitivity and it is suitable for the truss like structures. Apart from detection of damage it also provides information on load changes, which can be very useful in roof structure monitoring. It can detect not only the cracks or other damages but also the excessive load, e.g. due to the snow layer.

In the further development of the SHM system based on modal filtration, authors plan to install it on other type of real structures such as bridge to verify its monitoring ability.

ACKNOWLEDGEMENTS

Research funding from the Polish research project MONIT (No. POIG.01.01.02-00-013/08-00) is acknowledged by the authors

Authors would like to also express their special thanks to Professor Stanislaw Radkowski, dr Jedrzej Maczak and Adam Galezia for the possibility and help in measurements on the stand in Warsaw University of Technology.

REFERENCES

Carden P., Fanning P., (2004), "Vibration Based Condition Monitoring: A Review", Structural Health Monitoring, 3(4), 355–377.

Deraemaeker A., Preumont A. (2006), "Vibration-based Damage Detection Using Large Array Sensors and Spatial Filters," *Mechanical Systems and Signal Processing*, 20 (7), 1615–1630.

Doebling S. W., Farrar C. R., Prime M. B., (1998), "A Summary Review of Vibration-Based Damage Identification Methods", *The Shock and Vibration Digest*, 30 (2), 91–105.

El-Ouafi Bahlous S., Abdelghani M., H. Smaoui, S. El-Borgi (2007), "Modal Filtering and Statistical Approach to Damage Detection and Diagnosis in Structures Using Ambient Vibrations Measurements," *Journal of Vibration and Control*, 13 (3), 281–308.

Gałęzia A., Gontarz S., Jasiński M., Mączak J., Radkowski S., Seńko J., (2012), Distributed system for monitoring the large scale infrastructure structures based on changes analysis of its static and dynamic properties, *Key Engineering Materials*, 518, 106–118.

Gawronski W., Sawicki J. (2000), "Structural Damage Detection Using Modal Norms," *Journal of Sound and Vibration*, 229 (1), 194–198.

Meirovitch L., Baruh H. (1982), "Control of Self-Adjoint Distributed Parameter System," *Journal of Guidance Control and Dynamics*, 8 (6), 60–66.

Mendrok K., Uhl T. (2004), "Overview of Modal Model-based Damage Detection Methods," *Proceedings of 2004 ISMA*, Leuven, Belgium.

Mendrok K., Uhl T. (2010a), "The application of modal filters for damage detection", *Smart Structures and Systems*, 6 (2) 115–133.

Mendrok K., Uhl T., (2010b), "Numerical tests of a damage detection procedure based on modal filtration", In F. Casciati, M. Giordano (eds) *Proceedings of the fifth European workshop Structural Health Monitoring 2010 : June 28–July 4, 2010,* 982–987.

Slater G. L., Shelley S. J., (1993), "Health monitoring of flexible structures using modal filter concepts", *Proceeding of SPIE*, vol. 1917, 997–1008.

Szulim P., Lubikowski K., Mączak J., Rokicki K., (2012) Low-budget magnetic field transducers for construction diagnosis, *Proceedings of the Institute of Vehicles*, 3(89).

Zhang Q., Allemang R.J., Brown D.L. (1990), "Modal Filter: Concept and Applications," *Proceedings of International Modal Analysis Conference*, 487–496.

Research and Applications in Structural Engineering, Mechanics and Computation – Zingoni (Ed.)
© 2013 Taylor & Francis Group, London, ISBN 978-1-138-00061-2

System identification of masonry buildings in Vienna

F. Kopf, D. Schäfer, M. Pietsch & H. Wenzel
VCE – Vienna Consulting Engineers, Vienna, Austria

ABSTRACT: Intensive scientifical works in the field of earthquake research caused the classification of new earthquake zones in wide areas of Europe, also in Austria. The introduction of the compulsory Eurocode 8 changed the estimation of earthquake risk for buildings in Austria's cities significantly. The endangerment by earthquakes for buildings in the Vienna Basin became a deciding factor, not only in planning, but also financially. In order to eliminate this problem for the real estate economy, the research project SEISMID was launched and thanks to financial contribution of the "Technologieagentur der Stadt Wien (ZIT)" it could be finished successfully on 31.12.2010. This project was the first step to compensate the lack of knowledge and experience in this sector in Austria. Historical masonry buildings are very complex structures. Their global dynamic behavior is affected by many components (foundings, walls…), that consist of many sub-components themselves (bricks, joints, etc.). There are many constraints for the dynamic system identification of the micro- and macro-behavior while taking measurements. This article describes the technical aspects of the measurements, which was acquired within SEISMID and could be tested successfully.

1 INTRODUCTION

Proofing the stability of collapse of buildings under seismical loads is mostly performed with numerical methods because of increasing non-linear effects of material response, which also causes nonlinearity regarding the stiffness and damping of structures.

Any attempt to analyze the stability of buildings under conditions similar to real earthquakes would require enormous loading devices and yield undesirable damages of the buildings which then would have to be assessed. For these reasons the dynamical response of buildings is analyzed with numerical models. This is usually possible for modern buildings with a known geometry and controlled material properties. Problems emerge with old masonry buildings which have a great dispersion of material properties, accomplishments, joins etc. In this case it is mostly impossible to make sufficiently accurate assumptions, required for numerical models. For such cases it turned out, that measurements done with small amplitudes in the linear elastic range can be used for the calibration of numerical models. The calibration with this kind of data improves the accuracy of numerical models significantly even in the non- linear-elastic range.

2 MEASUREMENT METHODS

For analyzing the spectrum of single measurement points it would be sufficient to make measurements completely independent from each other. For analyzing the behavior of entire buildings it is not sufficient to focus on single measurement points. The signals have to be observed together, it is necessary to analyze their relation in space and time. For this kind of analysis the signals have to be absolutely synchronized. A possible workaround would be to work with one reference-sensor remaining on one place, whereas the other sensors can be re-positioned. With synchronized measurement devices (Brimos Wireless Recorder) it is possible to use many sensors and recording units on different places; the quality of synchronization is comparable to an assembly made with only one central recording device. The main advantage of the Brimos Wireless Recorder system is its flexibility and the lack of long cables that would be difficult to handle.



Figure 1. Acceleration sensor (left) and geophone (right).

3 SIGNAL COMBINATION IN TIME DOMAIN ANALYSIS IN FREQUENCY DOMAIN

3.1 *Signal combination in time domain*

The used sensors usually take measures in three spatial directions. In this way, the translatory movement of the

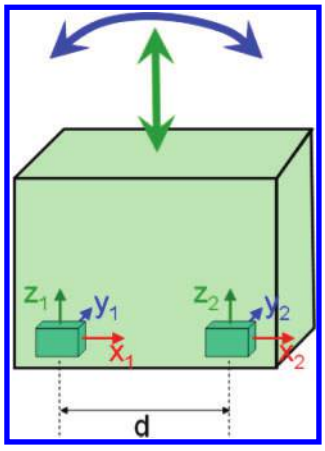


Figure 2. Translatory and rotatory movement of a structure.

measured building point is documented, but in order to find out the composition of the various building movements for each single measurement point it is useful to analyze the relations between discrete sensors synchronized in time.

If we assume a translatory movement, superposed with a rotatory movement around the y-axis, these movements will be recorded by the sensors drafted on figure 2, but they cannot be interpreted immediately. If we are only interested in the vertical movement, then we can calculate the mean value of the vertical signals.

$$z_translation = \frac{z_1 + z_2}{2} \quad (1)$$

The rotatory movement would be equalized, if the center of rotation is exactly between both sensors. In this case, the vertical movement of the structure can be interpreted from the two combined signals. The rotatory oscillation around the y-axis causes diametrically opposed vertical oscillations (z-direction). The linearized angle of rotation (in radiant) can be calculated from the given signal-combination within a defined time interval in the following way:

$$y_rotation = \frac{z_1 - z_2}{d} \quad (2)$$

This formula can be applied to measure rotatory oscillations around any axis that is perpendicular to the plane mounted by the line between the sensors and the vertical z-axis. These combined signals can now be treated as one signal, recorded by an imaginary sensor that would be placed exactly between the sensors and could measure vertical and rotatory movements around the y-axis.

3.2 *Analysis in the frequency domain*

If Fourier Transformation is applied to those previously combined signals, it is possible to determine the frequencies of the vertical and rotatory movements separately. Of course, these frequencies are also visible as peaks in the FFT-diagram of the original sensors, but with signal-combination they can be assigned to the separate oscillation-components. In the following, some useful signal combinations for building-measurements and its applications will be discussed.

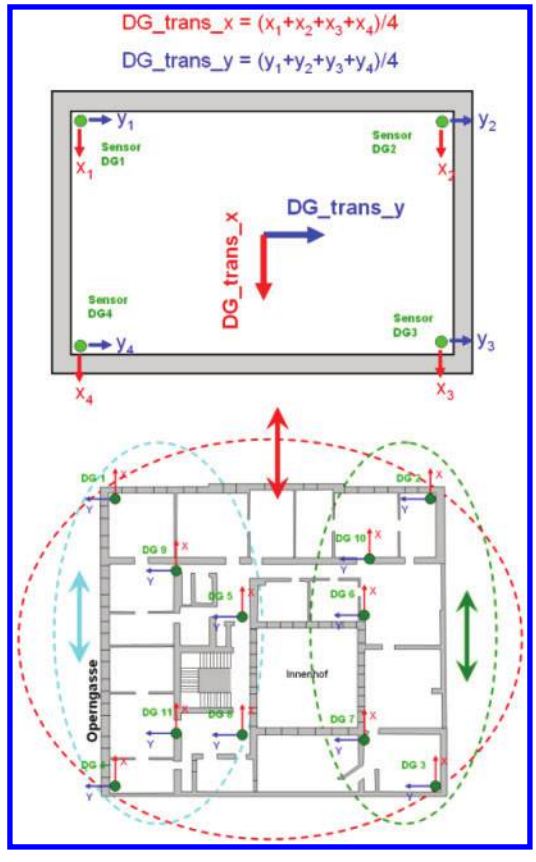


Figure 3. Translatory building movement in plan view.

4 SIGNAL COMBINATIONS

4.1 *Translatory movements*

Normally the roof-layer of wilhelminian style buildings is the place where measurements should be made. If the roof level is in an original state (no additional flats built on top), it is mostly easy to have access. Besides, the displacements caused by oscillations are strongest in the roof level which yields very significant signals.

Figure 3 shows a simplified ground sketch of a roof level. In all four corners of the building a sensor that measures the accelerations in three directions was placed. If a mean value of the signals of these four sensors for all three directions in space is built, then this combined signal equals the translatory movements of the roof level in its center. The combined signals can be seen as a virtual sensor placed exactly between the four

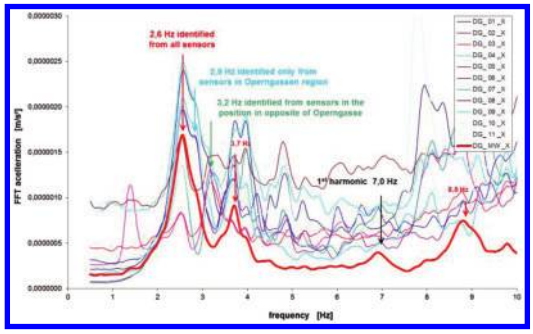


Figure 4. Translatory building movement in x-direction in frequency domain.

real sensors. Thus, this is only the case, if the entire roof level behaves like a rigid structural element. In buildings built during the Wilhelminian era, this will never be the case, thus the mean vertical signals are mostly useless. In horizontal direction, the assessability is dependent on the shear rigidity of the slabs. In many cases, the shear rigidity of the slabs can be assessed by comparing the discrete signals with the mean values. In the following example, a big number of sensors were placed in the roof level of a wilhelminian style building and the mean value in horizontal direction was compared with each single signal (ground sketch is given in figure 3).

Figure 4 shows the analysis of the signals in x-direction of all sensors after FFT-analysis in frequency domain. The mean value of these signals was computed in the time domain and after that FFT – analysis was applied. In figure 4 one can see it in bold. A basic oscillation of 2.6 Hz in x-direction of the building is obvious in the mean value and can also be identified from each single measurement positions. But to assume, that a building from the Wilhelminian era would accomplish a rigid movement is not appropriate. Therefore the shear rigidity of the roof level is too weak. Very often, parts of a building have a „dynamic life of its own". It is recognizable, that the part of the building along the Operngasse is oscillating at about 2.9 Hz, whereas in the part averted from the Operngasse, this 2.9 Hz oscillation is not recorded but one with 3.2 Hz. It is interesting to see that almost every sensor captures a peak at 4.8 Hz, but the mean signal does not. In this part of the building a very significant oscillation around 4.8 Hz was recorded, but the mean value does not show a peak in this frequency range. This indicates, that the oscillation is not translatory, the sensors obviously oscillate in an opposed way and equalize in the mean value. Below we want to introduce these kinds of oscillations.

4.2 *Rotatory movements in rooftop level*

Also for regarding the rotatory movement we have to assume a shear resistant plate in the roof top level. A center of rotation is being assumed (in the case of a rectangular form it's middle point), the connecting lines to the sensor positions are drawn (in a case of a rectangular form the diagonals). Now, the two horizontal components of the sensor's signals are vectorially composed in a way that the direction is perpendicular to the connecting line and clockwise around the center. The components obtained for each sensor are averaged to an "entire rotational signal", which shows the rotatory wave forms around the vertical axis by FFT-analysis. In the case of a rectangular ground form, the position of the center of rotation is easy to find, and the sensors placed in the corners of the building are placed nearly in the same distance from the rotational center. If additional sensors are used and if they have different distances to the assumed center of rotation, the single components of the rotational signal have to be divided by the sensor's distance to the rotational center in order to describe the kinematics in a correct way. But in this case it might be a problem, that the effect of the components of those sensors are overestimated, which are close to the rotational center. In their signals there will be hardly significant components of the rotational oscillation. For this reason it is better to take only components of those sensors into consideration, whose distance to the rotational center is big and more or less equal. Then it's not necessary to regard the distance to the rotational center, because all components get the same weight. Also the dependency of the accurate position of the assumed rotational center is neglectable in this case.

For the building shown in figure 5, two kinds of rotatory movements were investigated. Once, four sensors placed in the corners of the buildings were used (outer corners), another time the corners close to the court in the middle (inner corners). Both rotatory signals were investigated and are shown in bold (figure 6). The frequency domain analysis shows some peaks that do not coincide with peaks of other types of oscillation. The rotation at the outer corners coincides very well with the rotation at the inner corner. This can be seen as an acknowledgement of the method.

4.3 *Deviatory movements in the roof level*

Different from translatory and rotatory wave forms; in case of deviatory movement, rigid movement caused by shear resistance of the slabs, does not have to be assumed. In opposite, in this case dynamic shear movements are made measurable. According to figure 7, those horizontal signal components are determined, that either point to each other or point to opposite directions at the other diagonal line. By combining these components, it is possible to show a waveform that is significant for the dynamic shear movements of the entire roof floor (black dashed line in the sketch). If there is only rigid movement, this waveform must not exist and the deviation signal must theoretically equal zero. The example for this waveform is from a house from the Wilhelminian era, which was first measured in its original state. Afterwards, the shear resistance of the existing wooden slab was improved by assembling a composite slab, that was connected to the outer

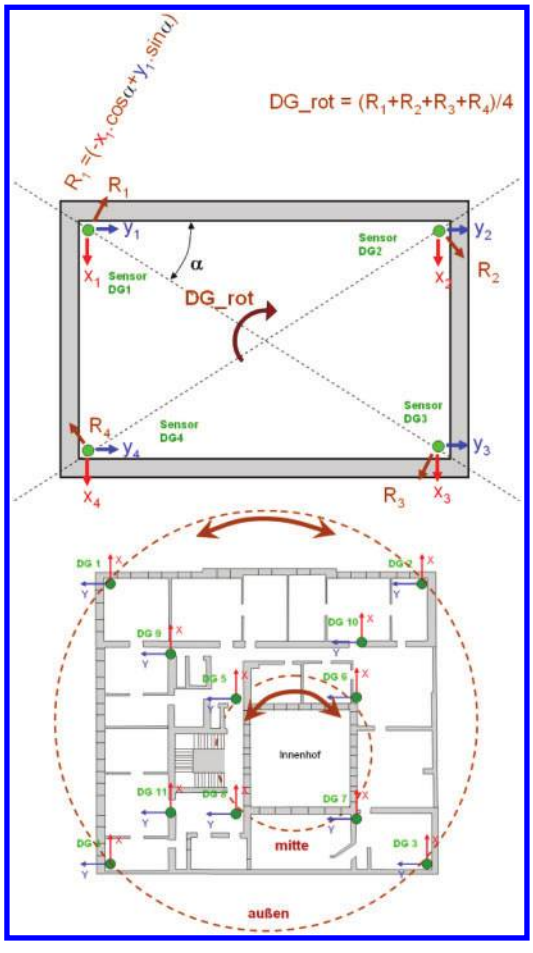


Figure 5. Rotatory building movement in ground view.

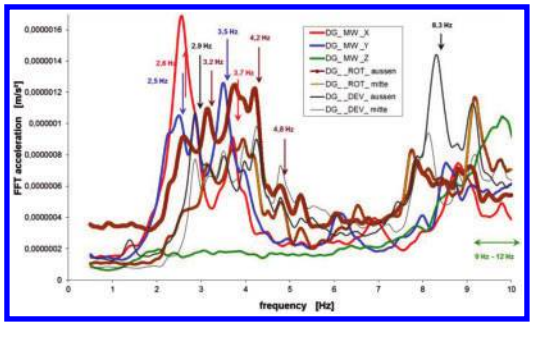


Figure 6. Rotatory building movement around the vertical axis in frequency domain

walls. This didn't change the mass of the structure, but improved the shear resistance. The following figures show the change of the wave forms by assembling a composite slab.

The interpretations of changes caused by the assembly of a shear resistant slab are shown in figure 7. They show the waveform analysis with combined signals in an effective way. If there were used single sensors

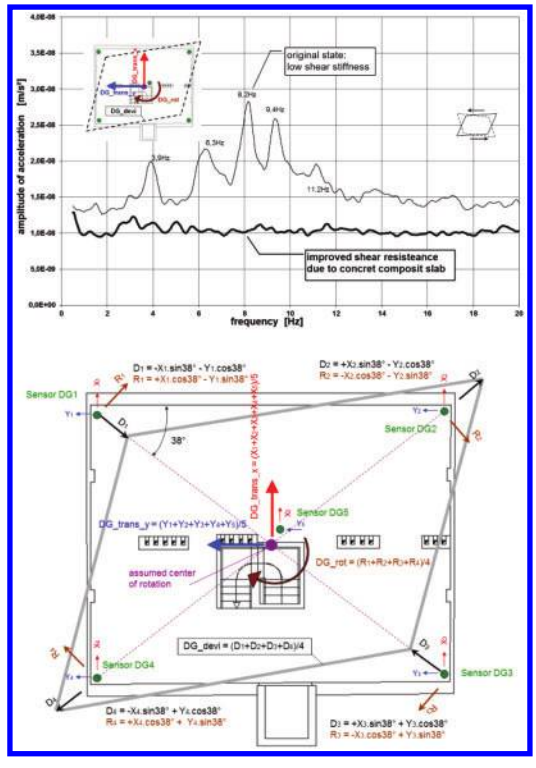


Figure 7. Deviatory building movement.

only, the interpretation would have been much more difficult and far more speculative.

4.4 *Determination of the first harmonic in the building cross section*

If the frequency of the first harmonic can be easily determined by applying a spectral analysis (FFT) from the first obvious peak in the low frequency range, this does not mean, that the following peaks are the following harmonics. The first harmonic in the building's cross section is shown in figure 8 and characterized by the fact that the horizontal oscillation of the 2nd story and the roof level occur in a reverse phase. This "opposite oscillation" of the two stories can be useful for the analysis.

Figure 8 shows the horizontal acceleration of each floor of building in frequency domain. The basic harmonic at 2.6 Hz is easily recognizable. The amplitudes of the upper stories are higher than those of the lower stories. For determination of the first harmonic, we focus on the "opposite oscillation" of the stories OG_02 (blue line) and OG_05 (red line). Instead of comparing the phases via FFT and getting a confusing image, a more stable algorithm was developed. The opposite oscillation is characterized by the difference between the signals (OG_5 - OG_2). This difference has a maximum (thin black line L1 in diagram). If the two stories oscillate in the same phase and have a different amplitude in the basic oscillation, then the FFT

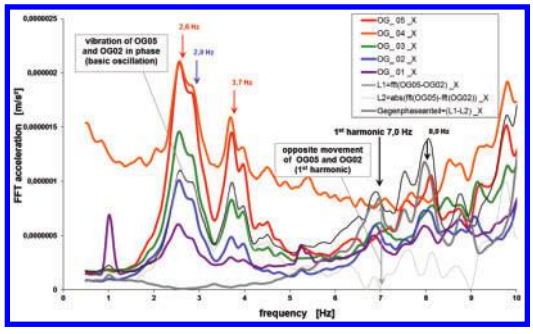


Figure 8. Basic oscillation and first harmonic in a building's cross section.

of the difference-signal shows a peak, that is equal to the difference of the FFT analyses of both signals (L2 = abs(FFT(OG_5) FFT(OG_2)), thin grey line in diagram). The conclusion is, that the difference of those lines (L1-L2) is an appropriate indicator for phase reverse oscillation of both stories. This line is shown in the diagram with a thick grey line. It's first significant maximum is at 7 Hz. This is the frequency of the first harmonic.

5 DYNAMIC MEASUREMENTS FOR THE DETERMINATION OF PROPOERTIES OF WALL STRUCTURES

5.1 *Wave dispersion in elastic media*

In an elastic and isotropic medium, the compression- and shear waves propagate with different but constant velocities that are independent of the frequency of the wave and also from the structure's geometry. They depend only on the material properties. The velocity of compression waves v_p can be determined with the following formula, where E_s is the elastic modulus (with prevented lateral strain) and ρ is the density of the material.

$$v_p = \sqrt{\frac{E_s}{\rho}} \tag{3}$$

The shear wave velocity v_s can be calculated via the modulus of elasticity in shear G and the material density ρ in the following way.

$$v_s = \sqrt{\frac{G}{\rho}} \tag{4}$$

With the following formulas, we can transform the values into such for isotropic linear-elastic material, whereas υ is the radial strain coefficient, E is the Youngs Modulus and G is the modulus of elasticity in shear.

$$E = \frac{(1+\upsilon)(1-2\upsilon)}{1-\upsilon} \cdot E_s = 2(1-\upsilon) \cdot G \tag{5}$$

$$G = \frac{1-2\upsilon}{2(1-\upsilon)} \cdot E_s = \frac{1}{2(1+\upsilon)} \cdot E \tag{6}$$

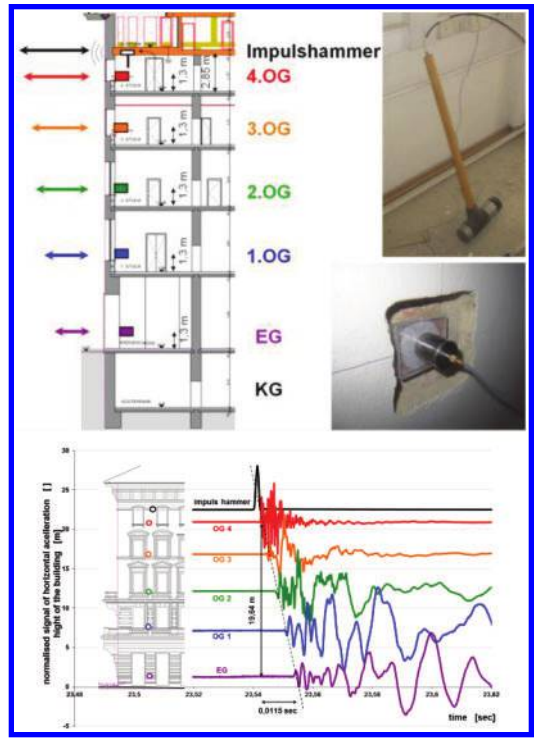


Figure 9. Experiment for wave dispersion in masonry wall.

5.2 *Measurement of wave dispersion in masonry walls*

The idea to measure the wave dispersion in masonry walls was to determine its properties in its undisturbed entity. Laboratory tests with bore cores and samples of mortar and bricks can only selectively assess the different components of masonry walls. Goal of this experiment was to capture the in situ properties of masonry walls in today's conditions after decades of loading. In order to measure the wave dispersion in masonry walls, sensors were placed along a masonry pillar in every story. The dynamic impact was realized in the top story with an impulse hammer. Hoping to be able to differentiate the shear wave from the compression wave, the sensor were placed horizontally, also the dynamic stroke was done in the horizontal direction.

Figure 9 shows the progression of the recorded measurement signals (horizontal acceleration) according to the vertical position of the sensors in the measured masonry pillar. The dispersion velocity can be recognized by the time delay between the sensors.

$$v = \frac{19{,}64\ m}{0{,}0115\ s} = 1708\ m/s \tag{7}$$

Before the arrival of the wave, the signal is completely homogenous and shows no agitation. This means, that the wavefront can be assigned to the compression wave. This compression wave causes also

Table 1. Different wave-velocities because of non-linear and amplitude-dependent material properties.

	Medium impact	Strong impact	Difference
Pillar 1	1363 m/s	1315 m/s	−3,5%
Pillar 2	1546 m/s	1502 m/s	−2,9%
Pillar 3	1650 m/s	1583 m/s	−4,1%
Average	1519 m/s	1466 m/s	−3,5%

vertical oscillations, but obviously the horizontal component is dominant. Therefor it is not possible to recognize the following shear wave. Using formulas for linear elastic, isotropic materials it is possible to estimate the material properties.

$$v_p = \sqrt{\frac{E_s}{\rho}} \tag{8}$$

In dependency of the radial strain coefficient, the other material parameters can be determined. Table 1 shows the result from measurements at different pillars in the same building. Various light strokes and various strong strokes with the impulse hammer were accomplished. The nonlinearity of the material parameters is obvious. The greater the amplitudes, the lower the stiffness of the material, which yields smaller wave velocities.

As we have seen, it is relatively easy to measure the compression wave in a masonry pillar. The shear wave can be slightly recognized in the top story, but it is strongly damped. Because of the anisotropy of the masonry wall it would be good to be able to measure the compression wave going vertically through the pillar, as well as the shear wave, which is propagating with horizontal oscillations through the pillar in vertical direction. In this case it would be possible to determine the relevant parameters directly. No assumption for the radial strain coefficient would have to been taken. A comparison with this dynamic method for determination of material properties with conventional methods has not yet been undertaken.

REFERENCES

G. Achs, “Erdbebengefährdung von Gründerzeithäusern. Beurteilung, Klassifizierung und experimentelle Untersuchungen”. Dissertation. Technische Universität Wien, 2011

H. Waller, R. Schmidt, “Schwingungslehre für Ingenieure”, Mannheim/Wien/Zürich, Wissenschaftsverlag, 1989

Seismid Bericht, “Zustandsbeurteilung Wiener Gründerzeithäuser,” interner Bericht im Projekt SEISMID, www.seismid.com

Seismid Bericht, “Messtechnische Untersuchung Gründerzeithäuser”, interner Bericht im Projekt SEISMID, www.seismid.com

J. Studer, J. Laue, M. Koller, “Bodendynamik”, 3. Auflage, Springer Verlag, 2007

R. Flesch, “Baudynamik”, Band 1, Bauverlag, 1993

G. Achs et al, “Erdbeben im Wiener Becken” 2011

Research and Applications in Structural Engineering, Mechanics and Computation – Zingoni (Ed.)
© 2013 Taylor & Francis Group, London, ISBN 978-1-138-00061-2

Shear wave travel times in multi-story buildings for system identification and damage detection

E. Şafak, E. Çaktı & E. Zengin
Boğaziçi University, Kandilli Observatory and Earthquake Research Institute, Istanbul, Turkey

ABSTRACT: Seismic response of multi-story buildings can be formulated as a one-dimensional wave propagation problem in terms of wave velocities and frictional damping values at each story, and the wave reflection and transmission coefficients at each floor. When compared to commonly used modal analysis and its parameters (i.e., modal frequencies, damping values, and mode shapes), the wave propagation approach provides a better insight into the response and its parameters are more sensitive to damage. A critical parameter of the wave propagation approach is the wave velocities (or, wave travel times) in the building. The commonly used approaches to calculate wave travel times from vibration records have been to use the phase shift of a characteristic peak in the records, or the delay time for the peak of the cross-correlation function of the records. These two approaches do not give accurate wave velocities, because the damping in the building also alters the phase of the records. This paper presents a methodology to calculate the velocity of seismic waves in multi-story buildings more accurately than the current procedures. The methodology involves utilization of the envelopes of the impulse response functions with respect to roof, and can separate the phase shifts due to damping and the wave travel time. As an example, seismic wave velocities in three instrumented multi-story buildings are calculated by using their earthquake records and the methodology presented.

1 INTRODUCTION

Although common approach has been modal analysis, seismic response of multi-story buildings can also be formulated as a one-dimensional wave propagation problem in terms of wave velocities and fricitonal damping values at each story, and the wave reflection and transmission coefficients at floor levels (Safak, 1999). Recorded responses from instrumented buildings clearly show the propagation characteristics of seismic response in buildings.

As an example, Figure 1 shows the recorded E-W accelerations of a 17-story steel frame building in Los Angeles during the M = 4.7 Yorba Linda earthquake of 3 September 2002. The building, known as the Factor Building, is located at the University of California campus in Los Angeles (UCLA), and instrumented with 72 acceleration sensors. With four channels at every floor, the building is one of the most densely instrumented buildings anywhere in the world, providing continuous data at 500 Hz (Kohler et al., 2007). Although the propagation of waves is not clear from the full time histories of the response shown in the figure, it becomes very clear if one takes a closer look to a short time interval. To see the waves, we consider a one-second long segment of the records, as depicted with a pink band in Figure 1, and deconvolve the records with the basement and roof records. The deconvolution gives the impulse-response functions for a basement and roof impulse. The reason for looking at the impulse-response functions is that they are independent of soil-structure interaction effects and provide a much clearer view of the wave propagation (Safak, 1995). Figures 2a and 2b show the impulse-response functions with respect to the basement and the roof in 3D view. Horizontal axes are the time and the floor number, and the vertical axis is the impulse response. The figures clearly show the propagation of waves in the building. It takes about 0.4 second for the waves to reach from the ground to the roof.

It can be shown that the deconvolution by the roof record eliminates the upgoing wave components in the signals, resulting in a simple downgoing wave (Snieder and Safak, 2006; Safak and Cakti, 2009b). In comparison, the signals deconvolved by the foundation-level records include both upgoing and downgoing waves, resulting in more complex impulse-response functions. This is clearly seen in the figures. The roof record is simply twice the upgoing wave at the top story (i.e., the free-surface reflection because of the air above), whereas the records at other floors are a sum of upgoing and downgoing waves (Safak, 1999). Thus, deconvolution by the roof record eliminates all upgoing waves in the signals.

When analysing vibration records from instrumented structures, it has been shown that, for system

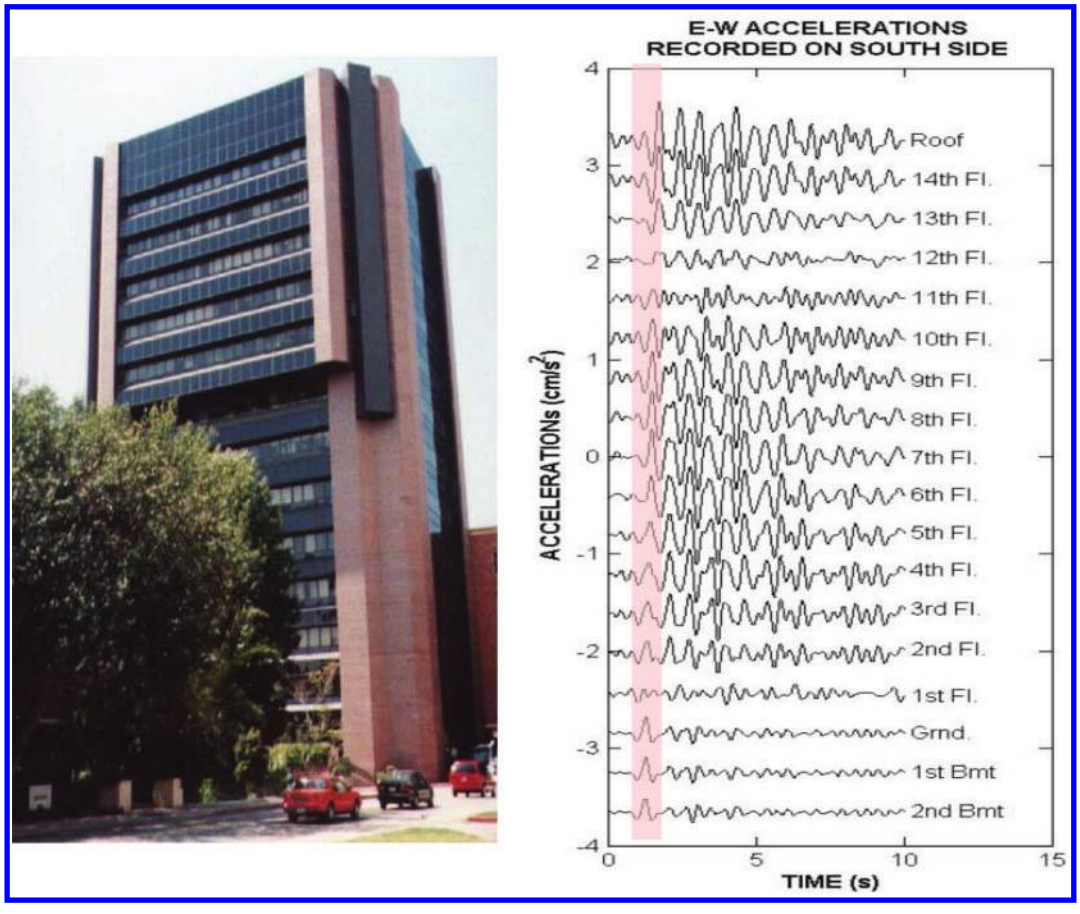


Figure 1. Factor Building and recorded acceleration from the M = 4.7 Yorba Linda earthquake.

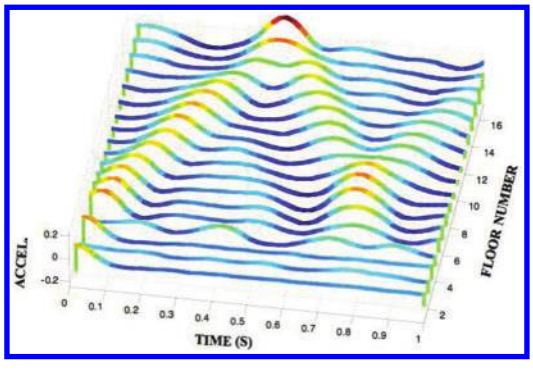


Figure 2a. Propagation of seismic waves, after deconvolution by the basement record, during a one-second interval in Factor Building.

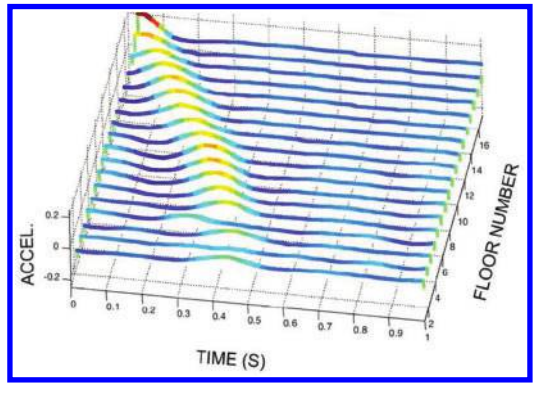


Figure 2b. Propagation of seismic waves, after deconvolution by the roof record, during a one-second interval in Factor Building.

identification and damage detection, the wave propagation parameters are more reliable and robust than modal parameters, and also more sensitive to damage (Safak, 1998). This is particularly true for older, historical structures because these structures do not meet the requirements of the classical modal analysis, such as elasticity, linearity, mass and/or stiffness proportional damping (Safak and Cakti, 2009a).

In this paper, first a new methodology is introduced to calculate the wave velocities in multi-story buildings. The methodology provides a more accurate estimation of wave velocities than the commonly

used other methods, for it eliminates the phase shifts introduced by damping. Next, the velocities of seismic waves in three instrumented multi-story buildings are calculated by using their vibration records during earthquakes.

2 CALCULATION OF WAVE VELOCITIES

A critical step in using wave travel times for identification and damage detection is the accurate calculation of wave travel times. This first requires a high-quality and high-sample-rate recording. For multi-story buildings, the sampling interval in the records should be at least 1/10th of the shortest travel time between any two successive floors. Wave travel times cannot be calculated accurately from the raw data, because the noise in the signals alters the peak amplitudes and phases. The two processing steps that help to increase the accuracy in wave travel time calculations are band-pass filtering and deconvolution. Band-pass filters should be selected such that the filtered signal has a much higher signal-to-noise ratio than the original signal. This is accomplished by selecting the pass-band to keep only the resonant frequencies of the building. The band-pass filters should be either a zero-phase filter, or the filter should be applied twice, first forward and then backward, so that the phase content of the signal is not altered. As discussed above, the deconvolution of the records by the roof record eliminates the upgoing components in the signals, resulting in a simple downgoing wave. This process gives a much cleaner signal for calculating wave velocities.

The standard approach to calculate the wave travel times between two recording points have been either to use the time difference for a characteristic peak in the signal, or to determine the time lag where the cross-correlation of the signals has a maximum. These methods are acceptable for non-dispersive, non-attenuating media, where the waveforms do not change their shape as they travel. In structures, the waves attenuate due to damping. The attenuation changes the shape (i.e., the phase) of the waves. In other words, the phase shifts in two records are caused by the combined effects of wave travel times, plus the phase distortions due to damping (Safak and Cakti, 2009a). A rigorous theoretical analysis of wave dispersion in an attenuating medium can be found in Aki and Richards (1980).

It is possible to eliminate the phase shifts introduced by damping on the calculated wave travel times. This can be accomplished by calculating the time shifts from the envelopes of the signals, rather than the original signals. The envelope functions are determined by taking the Hilbert transforms of the signal, and then calculating the corresponding analytic function. It can be shown that for narrow-band signals that are propagating in a frequency-dispersive medium, the envelope functions are not affected by the dispersive properties of the medium (Safak and Cakti, 2009a).

Table 1. Seismic wave velocities at Factor Building.

Dominant Direction	Frequency (Hz)	Travel time (s) for h = 74.77 m	Velocity (m/s)
East-West	0.40	0.52	145
North-South	0.50	0.42	180
Torsion	1.70	0.23	330

3 EXAMPLES

Using the methodology presented above, seismic wave velocities in three buildings are calculated from their earthquake-induced vibration records. The first building is the UCLA's Factor Building, which is described above. From the inspection of the Fourier amplitude spectra of the EW and NS accelerations, it was concluded that the building has three dominant frequencies, and the corresponding mode shapes are three-directional (i.e., modes include two translations and a rotation. In order to determine the dominant directions of the modes, we band-pass filtered the roof records around the resonant frequencies and plotted the corresponding particle displacements of the roof. Next, we calculated the envelopes of roof impulse-response functions and the wave velocities for each direction. The identified wave velocities are summarized in Table 1 below.

The second building is the 10-story, reinforced-concrete Millikan Library at the Caltech's campus in Pasadena, California, as shown in Figure 3 (Snieder and Safak, 2006; Clinton et al., 2006). The building has three accelerometers at every floor and continuous recording. By using the records from the same Yorba Linda earthquake, the dominant frequencies of the building are identified from the Fourier amplitude spectra of the EW and NS accelerations. The roof particle displacements, calculated by band-pass filtering the records around the resonant frequencies, show that the modes are mainly uni-directional with not much torsional component. Thus, from the envelopes of roof impulse-response functions for each direction, the wave velocities are calculated as shown in Table 2 below.

The third building is the 62-story, reinforced-concrete Sapphire Building in Istanbul (Figure 4). With a height of 261 meters, it is currently the tallest building in the city. The building is being monitored continuously with 30 accelerometers, placed as shown in Figure 4. The wave travel times are calculated by using the data from the M = 6.2, Aegean Sea earthquake of 8 January 2013. The dominant modes of the building are determined from the Fourier amplitude spectra and the corresponding particle displacements of the roof. The particle motions have shown that the building's motions are dominated by torsion. This is probably due to the fact that the building is much wider in the NS direction. For each horizontal direction and rotation, the wave velocities are calculated from the envelopes of roof impulse-response functions. The results are summarized in Table 3 below.

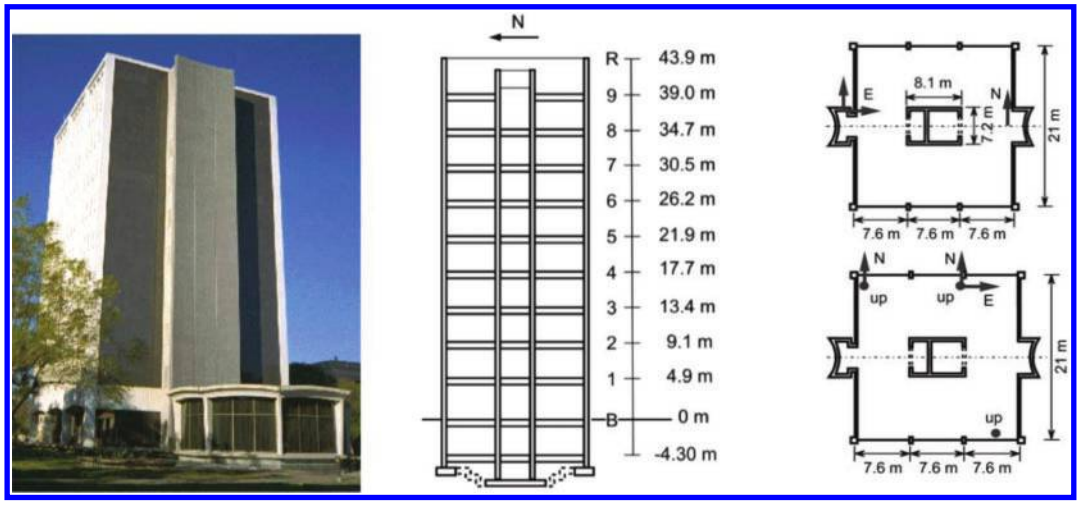


Figure 3. Millikan Library, vertical cross-section, and typical floor and basement sensor locations.

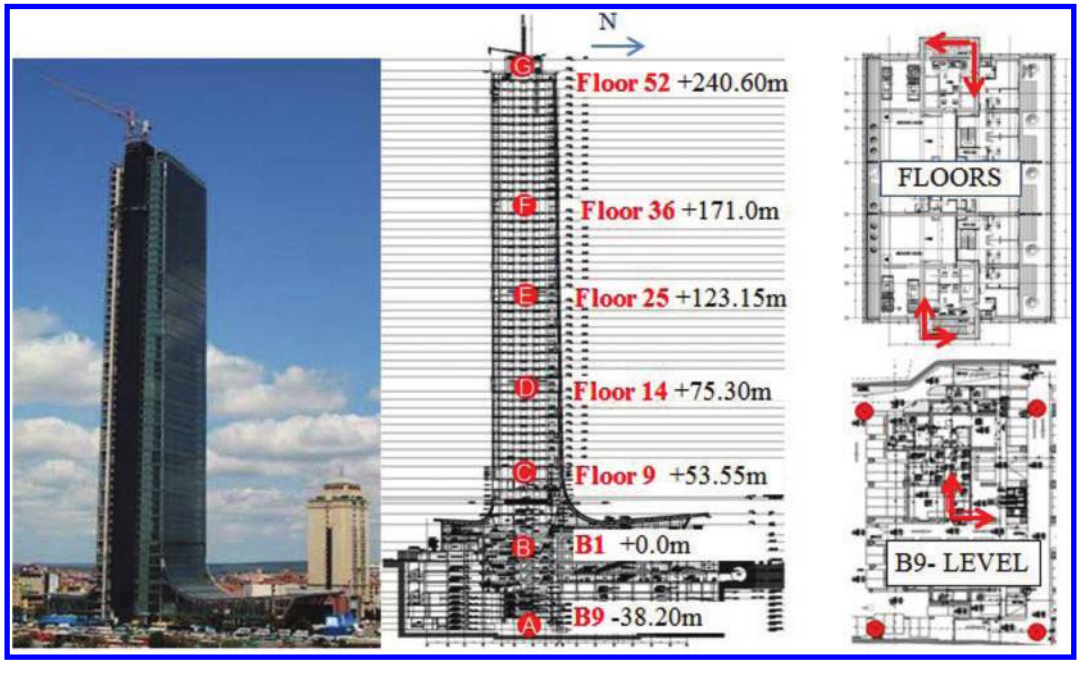


Figure 4. Sapphire Building, vertical cross-section, and typical floor and basement sensor locations.

Table 2. Seismic wave velocities at Millikan Library.

Dominant Direction	Frequency (Hz)	Travel time (s) for h = 39 m	Velocity (m/s)
East-West	1.00	0.25	156
North-South	1.70	0.16	243

Table 3. Seismic wave velocities at Sapphire Bldg.

Dominant Direction	Frequency (Hz)	Travel time (s) for h = 187 m	Velocity (m/s)
East-West	1.90	0.52	145
North-South	0.40	0.42	197
Torsion	0.80	0.23	1247

4 CONCLUSIONS

The wave travel times in multi-story buildings give a critical insight into the behaviour of multi-story buildings, as well as superior tools for system identification and damage detection. Impulse-response functions provide much clearer signals than the original records for the calculation of wave travel times.

The roof impulse-response functions are better than the commonly used foundation impulse-response functions, because the former one leads to a simple downgoing wave in multi-story buildings. The story damping alters the phase characteristics of the waves as they propagate up and down the building. This may create an error in the calculation of wave travel times. To eliminate the phase shifts due to damping, the wave travel times should be calculated from the envelope functions of the impulse response functions.

The calculated wave velocities from the earthquake records of three buildings indicate that the wave velocities are around 150 to 250 m/sec. for translational motions, and higher for torsional motions.

REFERENCES

Aki, K. and Richards, P.G. 1980. *Quantitative Seismology: Theory and Methods, Volume I,* W.H. Freeman and Company, San Francisco.

Clinton, J.F., Bradford, S.C., Heaton, T.H., and Favela, J. 2006. The Observed Wander of the Natural Frequencies in a Structure, *Bulletin of the Seismological Society of America* Vol. 96, pp.237–257.

Kohler, M.D., Davis, P.M. and Safak, E.2005. Earthquake and Ambient Vibration Monitoring of the Steel Frame UCLA Factor Building, *Earthquake Spectra*, Vol. 21, No. 3, August 2005, pp.715–736.

Safak, E. 1995. Detection and identification of soil-structure interaction in buildings from vibration recordings, *Journal of Structural Engineering*, ASCE, Vol.121, No.5, May 1995, pp.899–906

Safak, E. 1998. Detection of seismic damage in multi-story buildings by using wave-propagation analysis, *Proceedings (in CD-ROM) of the Sixth U.S. National Conference on Earthquake Engineering*, Seattle, Washington, May 31-June 4, 1998, Elsevier Science Inc., New York, NY.

Safak, E. 1999. Wave propagation formulation of seismic response of multi-story buildings, *Journal of Structural Engineering*, ASCE, Vol. 125, No. 4, pp.426–437.

Safak, E. and Cakti, E. 2009a. Seismicwave velocities in historical structures: A new parameter for identification and damage detection, *Proceedings of the 3rd International Operational Modal Analysis Conference- IOMAC'09*, 4–6 May, 2009, Ancona, Italy.

Safak, E. and Cakti, E. 2009b. A Simple Approach to Develop Analytical Models For Multi-Story Buildings by Using Earthquake Response Records,*Proceedings of the 3rd International Operational Modal Analysis Conference, IOMAC'09*, 4–6 May, 2009, Ancona, Italy.

Snieder, R and Safak, E.2006. Extracting the building response using interferometric imaging: Theory and application to the Millikan Library in Pasadena, California, *Bulletin of the Seismological Society of America* Vol. 96, pp.586–598.

Research and Applications in Structural Engineering, Mechanics and Computation – Zingoni (Ed.)
© 2013 Taylor & Francis Group, London, ISBN 978-1-138-00061-2

Application and developments of the infrared thermography in the building construction sector

S. Knapp
IFDB – Professor Hillemeier & Knapp GmbH, Berlin, Germany

B. Hillemeier
Technische Universität Berlin, Germany

ABSTRACT: This paper gives an overview of active thermography methods for investigation of building structures. It briefly describes the theory of thermography and discusses the development and optimization of pulse-thermography concerning the detection of reinforcement, voids and inhomogeneities in concrete and brickwork components. The following examples illustrate the development and application of this method.

1 INTRODUCTION

Infrared thermography is an image producing technique that measures the infrared radiation from the surface of a body and associates the distribution of radiation or temperature in a false-color image. Thermography differs in passive and active methods. In passive thermography the temperature differences develop in a natural way, as the temperature distribution by the sun or the cooling process during the night (Hillemeier 2012). To obtain more significant results, temperature differences can also be forced artificially. Thereby unsteady temperature profiles are produced by artificial decrease or supplying heat. This is known as active thermography methods. With the aid of a thermography camera, the normal or generated temperature profile is observed and recorded digitally over a period of time.

Thermography is used primarily in the construction physics sector as a passive process. Snap-shots of outdoor and indoor areas from building elements are produced to illustrate the surface temperature and the surface distribution (Fouad & Richter 2008). These recordings give conclusions on thermotechnical construction defects or irregularities, like thermal bridges, different air flows and moisture contents, which can be evaluated in terms of energysaving thermal insulation and possibly eliminated.

However, thermography can be also used for the localization of inhomogeneities or defects in components. In this case, active thermography techniques are used, in which the surfaces to be examined are heated with an appropriate heat source and the temperature profile and the temperature change is detected with a thermography camera. Depending on the respective heat sources, the following different methods are used (Maierhofer at al. 2002).

At the impulse thermography structural components are irradiated with a heat source and subsequently, the cooling behavior observed on the surface with a thermography camera. In this case the pulse duration of the heat source can vary between seconds to several hours. The thermal conductivity, heat capacity and density of the respective component could be influenced by subsurface inhomogeneities; thus, it could be localized by the temporal behavior of the cooling surface.

At the lock-in-thermography, the surface temperature would be taken after a periodic heating of the structural component with a camera. With the help of periodic temperature signals amplitude and phase images can be calculated. The depth image is independent of the emissivity of the surface and concerning to the frequency of the heating period it is linked with depth information.

A combination of mentioned methods represents the pulse-phase-thermography. The structural component is heated as the pulse-thermography method. Afterwards a Fourier transformation is determined from the time-dependent temperature profile, whereby as in the lock-in-thermography, the amplitudes and phase images can be evaluated. A big advantage of this method is the possibility to obtain the information of temperature from a depth greater than the lock-in-thermography.

The following examples give an insight into different areas of applications of the thermography method, which has become indispensable due to its non-destructive application in the construction sector.

2 DETECTION OF REINFORCEMENT

Another active thermography method is the induction thermography. In contrast to the direct irradiation of the entire concrete surface by use of heat sources, this method only heats in the construction lying reinforcing bars via electromagnetic induction. Even bars with



Figure 1. Performance of the induction thermography.

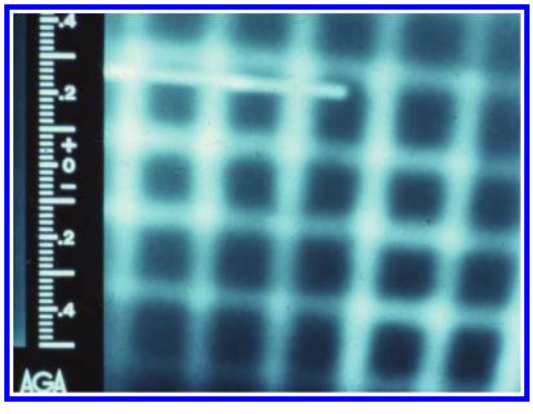


Figure 2. Thermography image of a reinforcement arrangement.

a concrete cover of 10 cm can be heated sufficiently (Hillemeier & Müller-Run 1980).

The heat of the inductively heated rebar spreads in the region of the rods and the heat front migrates to the concrete surface. With a thermography camera that heat propagation is observed on the surface and recorded (Figure 2). The apparent heat lines indicate the position of the individual rods and can be marked directly on the concrete. Through the analysis of temporal change in temperature the respective depths of the reinforcement bars can also be determined.

Further advantages of this method are:

→ the location of the bars can be determined with millimeter accuracy,
→ the thickness of concrete and the degree of reinforcement does not affect the applicability,
→ the necessary heating of the reinforcing rods will not take more than 1 minute depending on power of the induction system,
→ depending on the diameter of the rods up to four layers can be detected.

On the other hand, as a disadvantage, the induction procedure requires huge devices (Figure 1), so it



Figure 3. Measurement setup of the thermography camera and concrete sample with built-in inhomogeneities.

is replaced by the more portable magnetic and radar equipment very quickly.

3 STRUCTURE AND MOISTURE INVESTIGATIONS WITH THE IMPULSTHERMOGRAPHY

Due to the increasing importance of the pulse thermography in the building sector further investigations were performed in the course of a research project of the German Research Foundation (DFG) between the Technical University of Berlin (TUB) and the Federal Institute for Materials Research and Testing (BAM) (BAM & TUB 2005). The intention of this research project was to optimize, develop and apply the pulse-thermography in the field of nondestructive testing in civil engineering. Besides the adaptation of heat sources to different building structures and their materials with different thermal properties, the priority set on the possibility to detect inhomogeneities in concrete and masonry structures (Figure 3). Furthermore, the defects determined from temperature-time curves should be quantitatively assessed by comparisons with numerical simulations and analytical approaches.

For heating the surface of the building component, ideally, a heat source would be necessary to produce a homogeneous temperature field on the radiating surface of the component. Depending on the type of heat transport to the surface, there are three general heating methods: irradiation units, convection units and contact units. As a part of this research project four different heat sources were examined: infrared heater, hot air blower, heat mats and sunlight. An induction heating would have been possible (see above), however, because of the huge equipment this application is not very practical, and therefore the investigation of this heat method was not more pursued.

According to a common comparison the infrared radiator stood out due to the applied power and the uniform temperature distribution as the most suitable option. Starting from the surface, the heat pulse

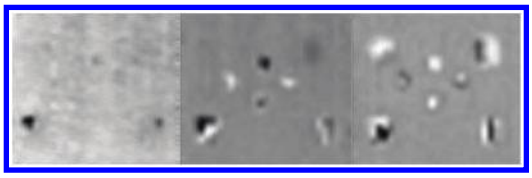


Figure 4. Illustration of the inhomogeneities inside the concrete sample in different depths.

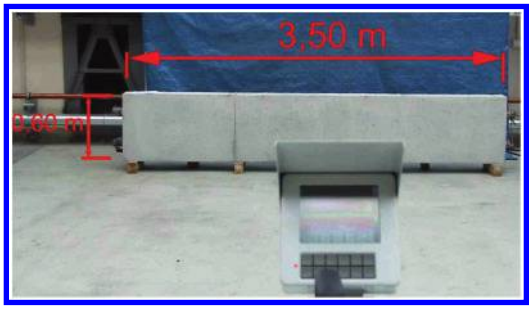


Figure 5. Test samples with incomplete grouted tendons.

of the pulse-thermography causes a transient thermography heat flow into the structural component. Depending on the thermal properties of the component (thermal conductivity λ, specific heat capacity cp, bulk density ρ), the engraved heat is spreading out. If inhomogeneities or defects with different material properties exist within this part, then the heat flow will change accordingly in this area. If voids are producing measurable temperature differences on the surface of the component as a result of the modified heat flow, they can be localized by the time variation of the temperature distribution with a help of an infrared camera. The data were analyzed with thermal images and the cooling curves of the individual data points on the surface were adjusted with different functions. By the application of the pulsephase-thermography a contrast improvement of the graphical illustration of the inhomogeneities has been reached. The determined phase images contain information about the time variation of the heat flow, which, in contrast to pulse-thermography, make deeper structures recognizable and a high-contrast display of the geometry defects is possible.

The results of the performed tests and the numerical calculations and simulations also showed an influence of different material parameters (degree of hydration, porosity, reinforcement density and percentage of steel fibers) to the detection and quantitative assessment of in homogeneities by using pulse-thermography.

Another interesting application in the context of this research project were the studies of the TUB concerning concrete structures with grouted tendons. Here, beam-like samples with tendons and different degrees of reinforcement were provided, whereby the grouting had several voids (Figure 5). On the one hand the test samples were heated by electric heaters; and on the other hand only the tendons were heated directly on

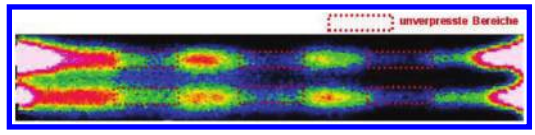


Figure 6. Thermography image of not-grouted areas of the tendons.

the exercise of its electrical resistance. Despite the relatively high concrete cover (5 to 8 cm) and the cladding tube, with both alternatives it was possible to detect the voids very well with the infrared camera. With the direct heating of the tendons, additional statements about the shape and the size of the non-pressed areas could be taken (Figure 6). The influence of the normal reinforcement was negligible in these studies.

The results of the research project have shown that the pulse-thermography is well suited for the detection of inhomogeneities or defects in concrete and masonry components and multilayer systems. However, it should be noted, that the efficiency of this method is limited to the near-surface region (about 10 cm) of the structural component. Measurements of deeper elements would take longer time (up to 1.5 hours).

4 PRACTICAL APPLICATION OF LOCATING VOIDS

As noted in the upper section, the pulsethermography is well suited for locating voids in structures. Partly due to the high cost of equipment (heat sources and infrared camera), however, more practical units of magnetic and radar technology are used. At inspections with an examination area of several thousand square meters, it is worth from an economic perspective to apply a corresponding active thermography method.

Corresponding structures in such a size are industrial floors of warehouses or similar (Walther & Hasenstab 2012). The floors of warehouse and production facilities are subjected to very high loads such as storage and forklift traffic. These heavy-duty floors are often designed as cementitious hardscreed with thicknesses up to 10 mm and can take loads up to 40 N/mm^2 in the respective base course. In general, these ground systems are produced by using of the "wet-on-wet" technique, i.e. that the screed layer is applied to the still fresh concrete base. By inadequate planning, the necessary steps and quality requirements are often not observed for a single-piece composite, which has a negative effect on the compound structure properties of the floor system. Poorly valued shrinkage behavior or incorrectly dimensioned concrete sections can damage the bond between the concrete and screed layer. The consequences are voids in the composite structure and shrinkage cracks.

To save time and cost in investigation of an industrial floor with an area of about 20,000 m^2, the pulsed-thermography was used instead of usual methods. An appropriate heater and an infrared camera were



Figure 7. Measurement of an industrial floor with the pulse-thermography.

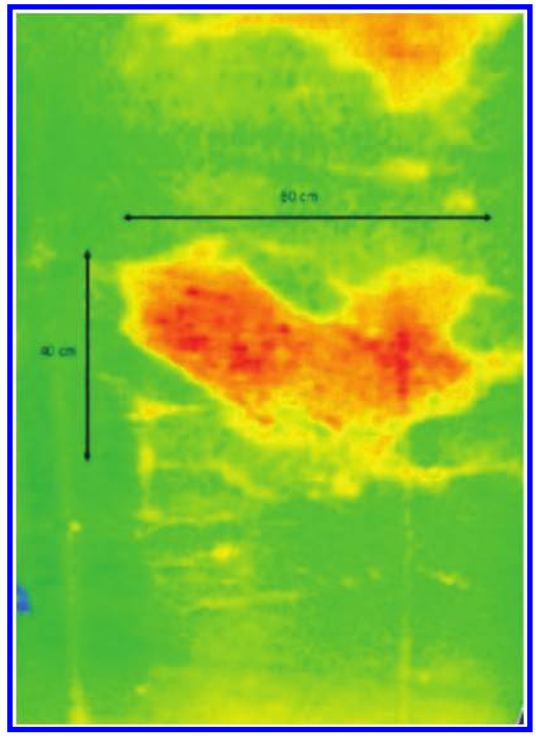


Figure 8. Thermography representation of voids in the floor area of an industrial hall.

installed on a trolley and the entire floor area of the hall has been investigated in a specific grid (Figure 7). The changes of respective coordinates were processed on a computer in conjunction with the associated infrared image, whereby a planar thermography image of the industrial floor was formed.

5 CONCLUSION

Active thermography methods such as the pulsethermography or the induction thermography can be successfully used for non-destructive testing in building structures.

These thermography methods allow among others the location of:

- voids and inhomogeneities in concrete structures up to 10 cm depth,
- delamination of screeds and coatings,
- injection faults in subsequent grouted tendons,
- the arrangement of reinforcement in concrete structures.

These are effective methods which can be used contactless; and also imaging and quantitative analysis of the results in connection with numerical simulations are possible.

REFERENCES

BAM & TUB (Bundesanstalt für Materialforschung und –prüfung & Technische Universität Berlin, Fachgebiet Baustoffe und Baustoffprüfung) 2005. *Struktur- und Feuchteuntersuchungen von Bauteil- und Bauwerksoberflächen mit der Impuls-Thermografie* (Abschlussbericht zum DFGProjekt Impuls-Thermografie. Berlin

Fouad, N.A. & Richter, T. 2008. Infrarot-Thermografie zur Schadensdiagnostik im Bauwesen – Möglichkeiten und Grenzen. *Der Bausachverständige* 2/2008: 10–18

Hillemeier, B. & Müller-Run, U. 1980. Bewehrungssuche mit der Thermografie. *Beton- und Stahlbetonbau* 4/1980: 83–85

Hillemeier, B. 2012. Bauwerkdiagnostik und ihre Bedeutung im Bauwesen. *Bauphysik Kalender - Gebäudediagnostik* 2012:3–19

Maierhofer, C. & Brink, A. & Röllig, M. & Wiggenhauser, H. 2002. *Anwendung der Impuls-Thermografie als quantitatives zerstörungsfreies Prüfverfahren im Bauwesen*. DGZfPJahrestagung

Walther, A. & Hasenstab, A. 2012. Zerstörungsfreie Prüfverfahren zur Bestimmung von Materialparametern im Stahlund Spannbetonbau. *Bauphysik Kalender - Gebäudediagnostik* 2012: 157–202

Research and Applications in Structural Engineering, Mechanics and Computation – Zingoni (Ed.)
© 2013 Taylor & Francis Group, London, ISBN 978-1-138-00061-2

Automated devices for inspection and maintenance

Eric Kuhn
CEO, Alpin Technik und Ingenieurservice GmbH, Leipzig, Germany

Carsten Zimmermann
Division manager, Alpin Technik und Ingenieurservice GmbH, Leipzig, Germany

ABSTRACT: Efficiency, minimum shut-downs, less traffic interruptions and the least amount of required time are key factors in construction and maintenance of small and large projects. Automated systems such as robots for inspection and maintenance of bridge stay cables and tunnels, however, can offer significant potential for efficiency and cost reduction. Use of such automated systems will enhance the operation safety as well as extending the useful life of the structures while the cost is reduced.

1 INSTRUCTIONS

Buildings, particularly infrastructural buildings like cable bridges, often not only combine high technical and design demands but are also particularly sensitive to impairment caused by inspection and maintenance measures due to their function. High direct costs from the actual measure and indirect costs due to impairment, e.g. of traffic, are associated with them. This often leads to the delay or non-performance of urgent inspections and maintenance work, which leads to a repair backlog, a delay and over proportional increase of future cost.

2 PREVIOUS APPROACHES

2.1 *Tasks*

In Germany, buildings like bridges are subject to the strict provisions of DIN 1076 that provide for the manner in and the intervals at which the buildings must be inspected (at least one main inspection every 6 years). In other EU states and elsewhere, building maintenance is provided for according to similar directives. The objective is achieving the originally planned service life of the buildings and to warrant that the building can be operated securely across this period. In particular the cable-stayed bridges used as examples here pose considerable challenges to operators and auditors, since the structural elements are often very difficult to reach, complicated in their forms and impairments of building operation are undesired and subject to high economic damage.

In addition to regular building inspections, regular maintenance and repair work is required for bridge cables and other structural elements to achieve the expected service life of the building and to prevent an accumulation of investments. This work is a particular challenge, since practical services are listed in addition to the already-high access effort already high during inspection due to material transport and removal.

2.2 *Time expenditure effect and consequences*

Traditionally and to this day, comprehensive scaffolding, heavy access lifts and cable lifts, cranes and cherry pickers are installed when working at cable-stayed bridges to take staff and technology to the construction site.

The procedures named often block setup areas during long construction and removal times, lead to considerable traffic impairment and thus to considerable access costs even before the actual work has started. A traffic-relevant consequence of conventional planning and setup of scaffolding can be explained using the example of the renovation measure of the Speyer bridge. A congestion of 17 km has been happening every day for the last year. Due building inspections have often been delayed or cancelled because availability of access technology, such as bridge cable inspection devices was limited and the time for setting up the device with its weight of several tons was up to 2 weeks.

In addition to the time aspects, practical aspects in implementation of the actual task are dealt with as well. The conventional access procedures often considerably limit the ability to work. Cables, for example, can only be inspected very conditionally across their entire circumference and, in particular, documented completely. Access lifts that move right on the cables and often weigh between 500 and 1300 kg may damage any possible coating, impair processing of the cable as such and may cause considerable damage particularly in PE-coated strand bundles at the anchors of the PE-pipes, as well as at the extruded corrosion protection sleeve of the upper strand layer in the PE coating when the radial welding seams are run over.



Figure 1. Traditional access methods for cable maintenance.



Figure 2. Traditional cable car system for cable inspection.erection time up to three weeks.

Cranes and cherry pickers are the most progressive ones among the conventional methods. They require an increasing setup area depending on the necessary height and reach. They lead to impairment of the traffic flow. Their use is limited particularly in bridges with cable fans or cable harps running diagonally from the centre of the bridge to the outside. These systems, as well as the access lifts, cannot or only with difficulty be integrated into processing of a bridge cable (e.g. corrosion protection).

3 AUTOMATED SYSTEMS

3.1 *General Approach*

Considering the complex interrelations between maintenance requirements, operating requirements of the



Figure 3. Heavy cable gantry.

building, costs, time budgets, safety aspects, weather aspects, quality requirements, the question will arise of whether some of these aspects can be positively influenced by the development and use of state-of-the-art machines and technologies.

Generally, “extra tasks”, repeating tasks, safety-critical tasks and tasks with a claim to high, consistent quality are considered in more detail.

The positive potentials of automation of processes are particularly in the above tasks. Another aspect that is of importance in assessment is the examination of technologies. Only the willingness to break open “old and loved” processes and changing them by use of state-of-the-art devices, such as robots, and to change processes, will permit considerable increase of efficiency. An example would be the introduction of digital cameras. Once, lots of time was used to frame slides of just a few images. Now, a lot more time is needed to manage a multiple of images. Instead of saving time and dealing with things that may be more pleasant, the new technology has clearly increased time effort without adjustment of own photographing and archiving conduct. Transferred to the use of automatic systems, this means that their true success will only be possible if adjacent processes are adjusted. This is explained by the example of a visual cable inspection with documentation with an ATIS cable robot by untangling previous processes.

3.2 *Automated Visual Inspections*

Once,an cable inspection was executed in that way that a costly access system was installed (bride cable inspection device, crane, cherry picker) before a cable inspection. Than the inspector had to document and measure the cable manually, assess and categorise the damage, move the access system and often only had the chance of recording the entire cable surface with a mirror. Documentation of the intact surfaces or surfaces almost assessed as damage, was impossible. However, documentation of the intact or borderline surfaces is sensible as well in particular in the light of later assessment of possible damage development. Earlier results

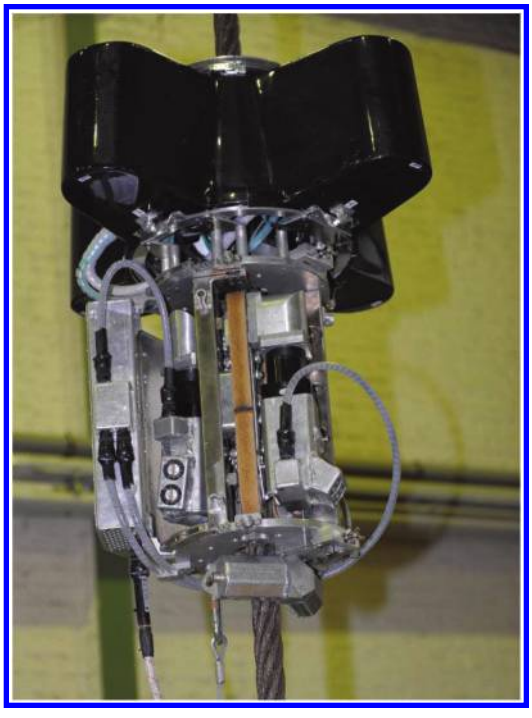


Figure 4. ATIS cable robot with 360° visual inspection module.

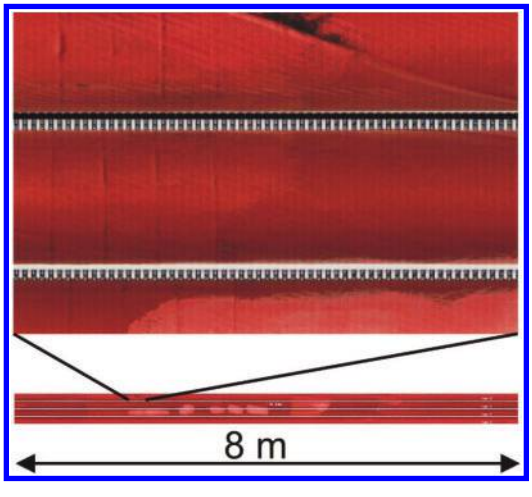


Figure 5. 8 m 360° panorama image and zoomed section.

thus can be compared to current ones and conclusions to damage mechanisms can be drawn. Only the automated visual inspections with robots offer these options. A 360° panorama image of the whole cable surface is usually drawn up to map the original cable length and the complete surface.

This high-resolution figure then can be viewed and assessed in a special viewer and processed into a report.

The panorama images can also be printed on endless paper partially or as a whole.

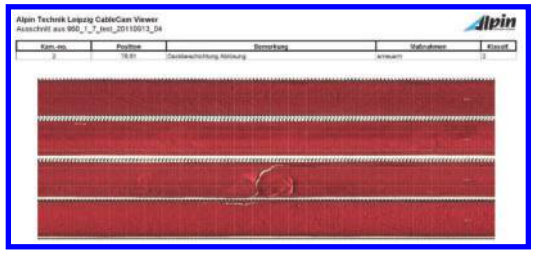


Figure 6. Sheet of a report created with panorama viewer.



Figure 7. A printed section of a cable surface 1:1 scale.

The results of later examinations can be mapped in addition to the results of earlier inspections and permit reliable assessment.

Systems like those described offer the possibility of illustrating other measuring results, such as layer thickness measurement, magnet-inductive results, etc. as well and to thus warrant good assignment to the visual results. Not only cables, but any kind of geometrically equal components, such as tunnels, shafts, facades and pillars, can be inspected and monitored with automated visual inspection methods.

3.3 *Automated Corrosion Protection Methods at Cables*

Automation is available for tasks that require a high degree of repeating, high time-dependence in performance and high secondary costs, such as access costs and high quality claims. These tasks include coating of full locked cables such as bridge cables.

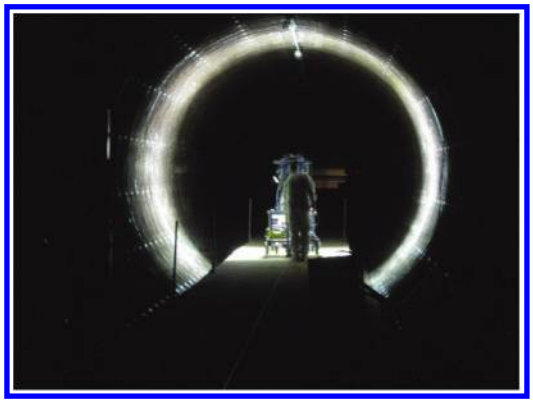


Figure 8. Automated visual inspection of a tunnel with creation of 360° panorama images.



Figure 9. Corrosion protection for cables ATIS Cableskin®, Description

There are diverse reasons for additional coating. In most cases, the causes are in damage to the outer corrosion protection of the cables during construction, the age of present cables and the connected abrasion of the zinc-plating and design reasons. Usually, such cables are protected from outward climatic conditions with multi-layered coating systems after preparation of the substrate by sand blasting and elaborate scaffolding with casings. Application is a synonym for considerable costs, long performance duration, high potential environmental strain and a service life limited to 25 years at most.

Due to these factors, a robot-supported procedure that permits application of butyl rubber-based corrosion protection tapes that have proven their worth for more than 45 years to the cables was introduced in 2008. The tapes optimised for this application form a sleeve virtually impenetrable for water vapour and oxygen with a thickness of approx. 2.6 mm. Their outer, visible layer of UV-stabilised PE can be coloured. Their service life is at least 35 years, with the present experience and independent barrier effect of 4 tape systems, leading to a longer expected service life. Butyl rubber welds into a completely homogeneous sleeve based on interdiffusion once the layers were wrapped with a 50% overlap.

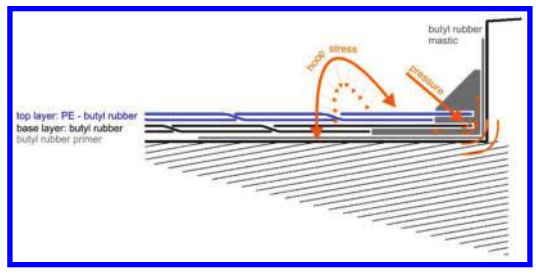


Figure 10. Connection of ATIS Cableskin® with an anchor.



Figure 11. ATIS cable robot with wrapping module for butylrubber tapes on Obere Argen Bridge, Germany.

The system with the brand name ATIS Cableskin® is generally technically approved by construction supervision in Europe as well as in Germany.

Since no requirements are posed to the underground pre-treatment so that sand blasting is not required, drying and airing-off times do not need to be observed, the procedure is perfect for time-critical use. The high plasticity of the butyl rubber provided by the integrated PE films at concurrently high resistance that, e.g., escaping grouting agent and the movement of cables can be easily compensated. The plasticity in particular and the ring tension of the belts that is applied during coiling generate a longitudinal movement conduct of the corrosion protection system that ensures permanent transfers at connection to anchors or interim anchors.

Automation of the process with robots now permit coating work in approx. 10% of the usual time and at approx. 15%–80% of the usual coating costs at clearly increased service life of the system.

Another application area of the butyl rubber based corrosion protection system system is use on PE-coating of parallel wire bundles and parallel strand systems in extend the service life if the plastic is damaged by UV-light.

3.4 *Automated Plastic Welding Methods at Cables*

Not only full locked cables, but also PE-sheathed parallel strands and parallel wire systems require regular maintenance. In particular the outer protective cover



Figure 12. Changing of red color to white due to environmental reasons and composition of PE.



Figure 13. Broken duct after strong vibration.

of these cable systems is subject to diverse strain. This includes UV irradiation, mechanical strain resulting, e.g., from the elongation, creeping for example from the continuous load on the lower sections in systems that move at the top.

Access systems were designed and used until now for running on such cable systems. They have dead weights between 800 kg and 1500 kg. These systems are pulled by steel cable winches, run on rolls and are asymmetrically loaded due to their geometric design. This leads to forces between the system and PE-duct that may cause considerable longitudinal forces.

Another problem is running over radial welding seams that may be present. Usually, the seams have welding beads on the inside of the pipes. The beads push the important corrosion-protecting extrusion of the upper, outer strands when run over and may penetrate this layer. The consequence of this may be the corrosion of the affected strands.

The problems named were, among others, the reason for development of automated methods and robots for the cable test and cable repair in such state-of-the-art cable systems.

3.4.1 *PE-Welding of ducts*

There are diverse reasons for having to weld PE ducts. On the one hand, these may be assembly-technology reasons that require welding hemispheres on present strand bundles longitudinally as well as radially. Furthermore, damages to present cables (UV-resistance



Figure 14. Damage due to impact.



Figure 15. Too short ducts.



Figure 16. Automated longitudinal and radial PE-welding with ATIS cable robot and PE-welding module

not applicable, broken pipes,outer damage or assembly defects) may require performance of sophisticated welding in exposed situations.

Specialists can use robots to implement PE welding in high quality in such situations in state-of-the-art light-weight cableway systems.

Additionally, they can complete repairs in very short times without expensive scaffolding and traffic impairment. A mandatory requirement is highly qualified staff that combines expert knowledge in the areas of cableway construction, plastic welding methods and rope access technology.

3.4.2 *Subsequent Helical Welding*

Rain-wind-induced vibrations of cables are a known but still complex phenomenon. To eliminate this kind of vibration, it is important to right the causes before dealing with the symptoms. An important and particularly effective measure is providing for the assembly of helixes on the cable surface in addition to the structural design of the entire building. Older buildings that



Figure 17. Subsequent welding of helical fillets wit ATIS cable robot and PE-welding module.

did not intend for this measure yet tend to suffer more badly under the harmful vibrations. Therefore, development of a robot that permits subsequent application of a helix like this to the cable surface was important.

This process is fully automatic, so that no person must be in direct proximity of the welding robot. A particular challenge is the underground preparation of the helical seam, since the cables to be processed are often aged and subject to environmental contamination (e.g. diesel adherences). The robots used use, among others, a special procedure that mixes the materials to be welded together and does not cause any significant abrasion of the old material. If such systems are used, this not only avoids traffic impairment but also reduces the direct repair costs and in particular the subsequent maintenance costs.

4 COMPARISON

Renovation of the cables of the Obere Argen Bridge in Germany, for example, would have required blocking of the entire busy motorway A96 more than 40 times. The costs for the scaffolding alone would have corresponded to the final complete cable renovation.

The renovation measure of the cable-stayed bridge in Speyer would have not only led to a clear increase of the coating system's service life with state-of-the-art renovation methods. It would not have taken far more than one year, but only 3 months.

The costs for renovation of the Köhlbrandbrücke cables, including all secondary work and double complete automated cable inspection corresponded to one third of the forecast alternative scaffolding costs.

Without use of robots, the subsequent welding of ca. 35.000 m helixes to the ANZAC bridge in Sydney, Australia would not have been impossible.

5 SUMMARY

Automated machines like robots, in combination with state-of-the-art access systems and expert know-how, offer enormous potentials in maintenance of buildings. According to the current status, significant cost savings concur with a clear quality increase at concurrently low impairment of operations (e.g. traffic) and the shortest duration of execution.

Cable maintenance and other measures at large infrastructure projects do not need to be tantamount with time- and cost-critical activities. The quality of the work to be performed can be much increased as compared to conventional methods.

REFERENCES

– Figures 1, 3-17 *Alpin Technik und Ingenieurservice GmbH*
– Figure 2 *http://www.teupe-hebetechnik.de/core/cms/upload/bilder/referenzen/befahranlage/178_Brueckenseilbesichtigungsgeraet.jpg*

Research and Applications in Structural Engineering, Mechanics and Computation – Zingoni (Ed.)
© 2013 Taylor & Francis Group, London, ISBN 978-1-138-00061-2

Structural health monitoring of the Basilica S. Maria di Collemaggio

V. Gattulli, F. Graziosi, F. Federici, F. Potenza & A. Colarieti
CERFIS, University of L'Aquila, L'Aquila, Italy

M. Lepidi
DICCA, University of Genoa, Genoa, Italy

ABSTRACT: The work deals with the main findings obtained during the development of a permanent structural health monitoring system for a monumental church, the Basilica S. Maria di Collemaggio, strongly damaged by the 2009 L'Aquila earthquake. Ongoing studies on the causes of the partial collapse occurred in the transept area have accompanied the monitoring system design and field testing. Benefits and critical issues related with the use of the wireless sensor networks technology are analyzed in the specific case of monumental buildings monitoring. The specific features of the implemented system, purposely designed to detect low-amplitude earthquake-induced vibrations, are discussed. The information collected during one-year data acquisition is summarized, together with critical observations on the operating system. The modal signature extracted from the acceleration measurements has been compared with finite element models, furnishing valuable results to evaluate the effectiveness of the temporary scaffolding structures. Finally, specific features concerning a secondary wireless network of crack propagation sensors are presented.

1 INTRODUCTION

Structural health monitoring is an emerging tool for reliable structural assessments. Efficient monitoring programs may help in the characterization of the progressive decay of structural performances, both in the short and in long term, providing useful information for optimized maintenance and safety.

Although the importance of monitoring action is widely recognized, the deployment of monitoring systems is still limited by some critical factors: high costs of the measurement equipment, difficulty in installation due to large instruments size and need of a wired communication and power infrastructure.

In recent years, wireless communication, low power computing and sensing technology has paved the way to overcome these problems, with the application of Wireless Sensor Networks technology to face Structural Health Monitoring problems (Federici et al 2012, Liu et al. 2012).

The paper describes the design, deployment and validation of a wireless sensor network for structural monitoring of a monumental structure, the Basilica Santa Maria di Collemaggio at L'Aquila, Italy. The system is specifically designed for seismic and dynamic response analysis based on acceleration, crack opening and wall inclination measurements.

Since 1999 the Structural Engineering Department (DISAT) of the University of L'Aquila pursued a wide campaign of experimental measurement on the building, leading to the formulation and updating of finite element models (Antonacci et al. 2001).

In April 2009 a 6.3 Mw earthquake struck the city of L'Aquila, causing considerable damage to the Basilica. A partial collapse occurred in the transept area, caused the breakdown of the dome, and dramatically altered the whole structural characteristics.

The assessment of the changes occurred in structure's behavior, together with the analysis of the structural modifications coming out from successive consolidation and restoration interventions, required the setup of a permanent monitoring system. Such a monitoring system is part of a wide monitoring program supported by the Italian Civil Protection, and it is one of the first totally based on Wireless Sensor Networks technology (Antonacci et al. 2011).

The system development can be broadly divided into two distinct phases: the design and deployment of an accelerometric monitoring network (essentially designed to capture the global seismic response) and the design and deployment of a second network for wall inclination and crack width local measurement.

The paper is structured as follows: Section 2 briefly summarizes the state-of-the-art of monitoring systems of infrastructure, specifically concerning systems based on wireless sensor networks. Section 3 briefly describes the operational scenario and details the implementation of the monitoring networks. Section 4 illustrates the analysis of the data collected. Concluding remarks are finally pointed out.

2 WIRELESS SENSOR NETWORKS FOR STRUCTURAL HEALTH MONITORING

In recent years, progressive developments in wireless communication, low power computing and sensing technology has led to the application of Wireless Sensor Networks technology to Structural Health Monitoring problems.

A wireless sensor network consists of multiple autonomous sensing devices communicating to each other via a radio connection. New generation sensors (e.g. MEMS technology based accelerometers, fiber optic sensors, piezoelectric sensors) with small size and low power consumption provide greater deployment flexibility.

Wireless technology, however, presents some serious drawbacks: for example, measure synchronization can be extremely more problematic than in the wired case. Moreover, battery-powered nodes heavily relies on duty cycling techniques for energy saving. This aspect is extremely limiting for long term monitoring applications (Park et al. 2005). Several solutions have been presented in literature to address these issues (Paek et al. 2005, Niu et al. 2010, Boyle et al. 2011). Illinois Structural Health Monitoring Project presented a hardware and software wireless sensing platform specifically designed for structural health monitoring applications. The solution (Mechitov et al. 2006) is based on a general purpose wireless communication and computation platform, the Imote2 wireless node manufactured by Memsic. The platform is supplemented by a sensor board (SHM-A) specifically designed for structural monitoring. A custom management software (ISHMP Toolsuite) based on TinyOS operating system allows easy management of sensor data acquisition and communication. The software tool suite integrates a multi-hop routing protocol (AODV) in addition to an original data synchronization protocol, which combines FTSP network synchronization and a specially developed local delay correction algorithm (Rice et al. 2011). ISHMP solution has been successfully employed in Korean Jindo Bridge monitoring project (Nagayama et al. 2011, Cho et al. 2011).

Anyhow, the experimental applications of wireless sensor networks are still limited, with traditional monitoring solution remaining on a dominant position. The Italian Department of Civil Protection maintains and utilizes an extensive accelerometric monitoring network (Spina et al. 2011). The system is often integrated and strengthened by temporary monitoring networks (e.g. after catastrophic events in order to monitor relevant or strategic sites during the post-catastrophe emergency phase), which are managed also by the Department, by local governments or other entities, such as Universities. OSS main monitoring network is an accelerometric monitoring system installed on public buildings, bridges and dams. Each structure is monitored by up to 32 force balance accelerometers wired connected to a central acquisition and transmission unit. Recently, the RAMSES monitoring system, comprising three MEMS accelerometer based sensing wireless unit per building has been introduced. Moreover, a GSM communication based mobile monitoring system (OSM) is frequently used in post-disaster damaged buildings monitoring.

3 STRUCTURAL HEALTH MONITORING OF THE BASILICA DI COLLEMAGGIO

The basilica S. Maria di Collemaggio is the most important church in the city of L'Aquila, Italy. The church has a central nave, which measures 61 m in length and 11.3 m in width and two side aisles measuring 7.8 m and 8.0 m in width respectively. Naves and side aisles are separated by two series of seven columns with a height of 5.3 m and an average central section of about 1 m in diameter. Four external walls, with a masonry thickness varying from 0.95 m to 1.05 m are connected on two sides with the church façade and transept area. Other adjacent structures are partially connected with the Basilica main body: an octagonal tower connected on one side of the façade and another masonry building adjacent for about 40% of the external walls. The church has a wooden roof supported from trusses placed in a cross-sectional direction respect external walls. The dynamic behavior of the Basilica was characterized by means of numerical and experimental studies conducted before the occurrence of the 2009 L'Aquila earthquake. The earthquake caused a partial collapse of the structure in the transept area.

The will to deepen collapse possible causes and to investigate possible modification of structure dynamics response after retrofitting has led to the development and successive deployment of a structural monitoring system along the damaged church. In order to explore possible advantages arising from the use of innovative technologies (e.g. wireless communication and innovative sensing elements), the system has been based on a wireless sensor network. According to the project requirements, the work consists in the implementation of two main system: an accelerometric network for dynamic response measurement and a secondary network for crack width and wall inclination monitoring.

3.1 *Accelerometric Monitoring System*

The first phase of the system deployment has included the design, implementation, installation and test of an accelerometric monitoring network. The main goal was an accurate measurement of the building dynamic response, both to environmental actions and to the low-amplitude seismic events which occasionally continue to interest the site.

Memsic Imote2 wireless communication platform, along with ISHMP derived SHM-A board were chosen as main monitoring platform. Each SHM-A board includes ST microelectronics LIS344ALH MEMS triaxial accelerometer, Sensirion SHT11 temperature

Table 1. LIS344ALH mechanical characteristics.

Feature	Value
Input Range	±2, ±6g
Sensitivity	V_{dd}/5@±2 g V_{dd}/15@±6 g
Bandwidth	1.8 KHz
Noise Density	50 μg/$\sqrt{}$Hz
Non linearità	±0.5 % FS
Cross Axis	± 2 %

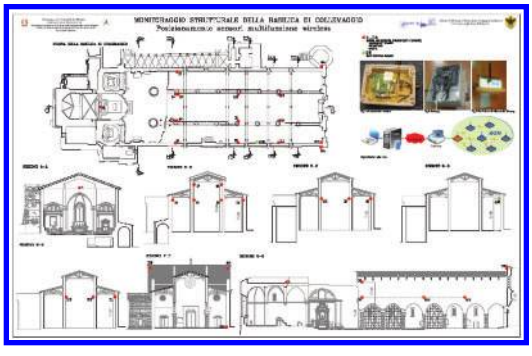


Figure 1. Drawings for the placement of the 16 smart sensors installed at the Basilica di S. Maria di Collemaggio.

and humidity sensor, and TAOS 2561 luminosity sensor. The board features also an advanced 16 bit analog to digital converter, the QF4A512 model by QuikFilter. Performance characteristics of MEMS accelerometer relevant to the present analysis are resumed in Table 1.

Imote2 wireless communication platform includes Marvell Xscale PXA271 processor and Texas Instruments CC2420 2.4 GHz, 802.15.4 compliant radio transceiver. Processor chip features a processor core with a clock frequency of up to 416 MHz, with the possibility of radical downscaling (down to 13 MHz) for low power consumption, SRAM and Flash memory bot for an amount of 32 MB.

The board is actively supported by TinyOS operating system, both in 1.x and 2 versions. ISHMP developed a software tool-suite based on TinyOS 1.x, which address specific problems of Structural Health Monitoring application. Implemented wireless sensor nodes, along with FTSP based synchronization and AODV multi-hop routing from ISHMP tool-suite are the main software components used in the accelerometric monitoring system.

A total of 16 sensor nodes, conveniently installed in custom IP-45 compliant packages, were deployed along the church on June 2011.

The majority of sensor nodes were placed inside the structure, ten along the main nave, one at the base of a column base and one in the transept area. Two sensor nodes were instead placed externally, at the top corners of the church facade (Fig.1).



Figure 2. Installation phases of the monitoring system: a) b) sensor positioning on the central walls of the nave, c) sensor positioning beyond the facade, d) f) sensor views, g) on-site testing, h) sensor positioning at the end of the nave walls.

A single board computer, connected with a network apparatus, acts as monitoring system gateway. The network apparatus guarantees 3G connectivity (for the automatic uploading of the measurement results to a remote server) and Wi-Fi local connectivity (for the direct access to the monitoring system; this feature is useful when performing local tests – as the operator don't needs an internet access to interact with the network – and as a backup redundant system in case of down of the 3G network access).

The gateway is connected to an Imote2 node, which acts as sink for the network: it forwards operating commands from the gateway to the leaf nodes and collects measurements data. Each leaf node communicates with the sink by means of a multi-hop routing protocol, thus allowing to effectively cover the wide area of the church. The central gateway runs a measurement scheduling application, which automatically handles data acquisition on leaf nodes, measured data collection, data compression and load on a remote server machine.

Both the gateway subsystem and leaf nodes are network powered. This choice, apparently counterintuitive, has two main motivations. First, the research for a coverage of the dynamic response as far as possible temporally extended prevents from the use of duty cycling energy savings techniques. Moreover, any maintenance intervention (such as node battery replacement) requires the use of heavy-duty vehicles (trucks and cranes are needed to reach the heights at which sensor nodes are placed), and should then be avoided given the precarious state of the Basilica. An Uninterruptible Power Supply Device guarantees the continuity of monitoring system operability. Reduced possibility of TinyOS 1.x scheduler prevents the sensor nodes from simultaneously acquire data from sensor and transmit data to the sink node. A scheduling algorithm able to alternate two groups of node in the mentioned operation was developed. In such way it is still possible to obtain a continuous coverage of the dynamic response of the building.



Figure 3. Light model (scale 1:3) of modular steel-made 3D frame: (a) basic configuration, (b) sensor-node of wireless network; (c) comparison with sensor of traditional wired network.

3.2 *Crack and wall inclination monitoring system*

Phase two of the monitoring system development involves the deployment of crackmeter and inclinometer sensors in the Basilica. Some of the limitations described in section 3.1 (especially those related to software implementation), along with the end of commercial life cycle of Imote2 platform has led to the development of a novel custom sensing platform. The developed wireless sensing platform is currently at a prototype stage and is going to be installed in the Basilica in the near future. The node is based on Atmel Zigbit 900 module, which features Atmel AT86RF212 868 MHz, 802.15.4 compliant radio transceiver. Software stack won't be based on TinyOS system and will fully implement 802.15.4 protocol stack. Nodes will be battery powered: this choice is appropriate in case of crack width and inclination measurements, as the reduced measurement frequency allows an extensive use of duty cycle power saving techniques. The possibility of implementing energy saving techniques in the case of accelerometric time-extended measures will be also further investigated.

4 DATA COLLECTION AND ANALYSIS

The analysis of the data collected by the monitoring system has been anticipated by a preliminary phase, devoted to compare the performance of each single wireless node with a reference wired sensor in a controlled laboratory environment (Fig.3).

4.1 *Preliminary validation phase*

The validation phase of the monitoring system had two main goals: the characterization of each wireless sensor node performances and the analysis of the structural dynamic response by means of the measured acceleration signals.

Two different types of test have been conducted using a modular structural steel frame to characterize a SHM-WSN in a laboratory environment. In the first series a direct comparison between a single wireless sensor (the above described IMOTE 2 type) and a wired accelerometer (SA107LN-Columbia) has been conducted (Fig. 3). With this configuration the frame responses both to a little impulse in longitudinal direction and under environmental noise have been recorded. Others tests have been made using six wireless sensors, two for each slab, placed at diagonally opposite corners. This particular experimental setup has been used to identify the main modal frequencies, shapes and damping. Again both impulsive and ambient tests have been performed. The results, here not reported for sake of brevity, were largely satisfying to the project purposes.

4.2 *Available on-site pre-earthquake data*

Before the occurring of the 2009 earthquake a numerical and experimental study permitted to characterize the dynamic behavior of the Basilica (Antonacci et al. 2001). The experimental data were firstly used to identify a modal model and then to determine suitable FE models of the church. Preliminary numerical analyses were carried out on the basis of several assumptions regarding: (1) mechanical parameters of masonry, (2) timber trusses of the roof, (3) restraints in walls and columns, (4) links among structural components. Afterwards the Basilica was excited at low vibration levels by an instrumented hammer and a tunable, mono-frequent mechanical exciter (vibrodyne). Several tests have been carried out, with different positions of the instruments and impact locations, in order to excite and to measure as many modes as possible.

The vibrodyne was located on the top of a lateral wall. The frequency responses were directly measured around the first two modes; these are the most important ones that describe the dynamic response of the church. Experimental data were used to identify natural frequencies, modal displacements and damping factors. The first campaign of tests permitted to recognize at least four major resonance peaks in the in the frequency range $0.8 \div 3.0$ *Hz*. The first two peaks were close to the frequency values 1.25 and 1.7 *Hz*. Other peaks were present over 2 *Hz*. Two of them, around 2.5 and 2.7 *Hz*, were well defined in all tests. Secondary peaks, around 2.2, 2.3 and 2.6 *Hz*, were not always visible in all the responses; they indicated highly coupled modes. These peaks, however, were estimated to be less important: numerical analysis indicated that the participating mass of first two modes is at least 85% of total mass in the transverse direction of the church.

After retrofitting, all peaks were shifted to higher frequencies. The first two moved around 1.45 *Hz* and 2.12 *Hz* respectively. Other peaks were clearly visible around 2.6 and 2.95 *Hz*. Secondary peaks, which were not always visible in all the responses, were recognizable even in this case. Higher frequencies were a consequence of the increasing stiffness brought about by retrofitting. Other dynamic testing, performed on the façade, permitted to evidence that out-of-plane

Table 2. Recorded response of Basilica di Collemaggio.

Earthquake	Date	Time (UTC)	Magnitude	Peak Response Acceleration [g]
Main Shock Emilia	May 5th 2012	2:03 AM	5.9	0.0054
Aftershock Emilia	May 5th, 2012	1:18 PM	5.1	0.0018
Shock Ravenna	June 6th, 2012	6:08 AM	4.5	0.0014
L'Aquila	October, 14, 2012	4:32 PM	2.8	0.0072
L'Aquila	October 10, 2012	2:52 AM	3.6	0.0073
L'Aquila	November, 11, 2012	3:37 AM	3.2	0.0082

local modes of this element were in a frequency range higher than the transversal mode of the nave. Recently, the available data from the previous on-site dynamic campaign have been used to develop complete finite element models of the Basilica, able to reproduce the main modal identified characteristics and the collapse scenario (Gattulli et al. 2013). A campaign of numerical simulations has been conducted to evaluate the dynamic response of the Basilica together with the temporary retrofitting under small earthquakes.

4.3 *Experimental on-site post-earthquake data*

During the months following the installation, the monitoring system has been continuously enhanced and brought to complete and automatic management to sense seismic induced vibrations. During this path, test campaigns have been conducted with different induced source of vibrations such as hammer, ambient vibrations and free-vibration tests.

To date, six major events have been detected. Three are associated with the Emilia region and three are local events at L'Aquila. Table 1 shows the maximum accelerations registered during each earthquake. Recorded structural responses show prevailing out-of-plane oscillations of the nave walls.

Low magnitude events furnish a sufficient level of energy to overcome the noise threshold of the monitoring system, allowing acceleration data recording characterized by sufficient vibration signature. Consequently, spectral analysis has been used to extract preliminary information from recorded data clearly evidencing the change in the main natural frequencies with respect the values measured in the pre-earthquake configuration. Table 3 summarizes the main findings emerging from spectral analysis of the recorded data. The main peak frequency of the out-plane acceleration spectra at different sensors located on each macro-element (Fig. 4a) are reported in Table 3, as

Table 3. Main peak frequency of measured acceleration spectra.

Earthquake	Macro-element D (Hz)	Macro-element C (Hz)	Macro-element B (Hz)
20/5/2012 (main)			0.85
20/5/2012 (after)	0.95	0.95	
06/6/2012			1.02
14/10/2012	0.95	0.95	
30/10/2012	1.00	1.00	
16/11/2012			1.00

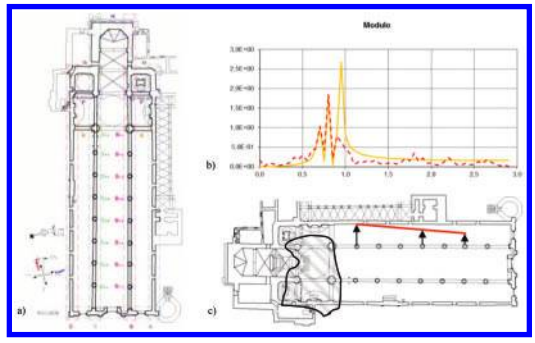


Figure 4. Basilica S. Maria Collemaggio: a) macro-elements definition, b) amplitude of the experimental transfer function c) identified modal shape.

extracted by different occurred earthquakes. Similar frequency values have been obtained for the first mode of the finite element model of Basilica in the post-earthquake configuration, including temporary scaffolding structures.

Fig. 4b compares the amplitude of the experimental transfer function (red dotted) with the transfer function amplitude of a modal model identified through the modal identification results obtained by the Goyder technique.

Additional information is provided by the comparison of pre- and post- earthquake experimental data. A stiffness reduction of the current configuration with respect to the pre-earthquake is evident. The current configuration is more flexible, since the principal mode period moves from 0.69*s* to 0.95*s*, suffering therefore a 37% increase.

4.4 *Numerical models*

Structural analyses have been conducted through a finite element model (Fig.5a,c), allowing the characterization of the seismic adequacy, in the pre-earthquake state (Gattulli et al. 2013) and in the post-earthquake taking into account temporary scaffolding structures (Fig.5b,d). Pre-earthquake linear structural analyses using the design response spectrum provided by the Italian code have evidenced the strong vulnerability of the nave walls, especially the interior ones, with respect to transversal seismic actions,

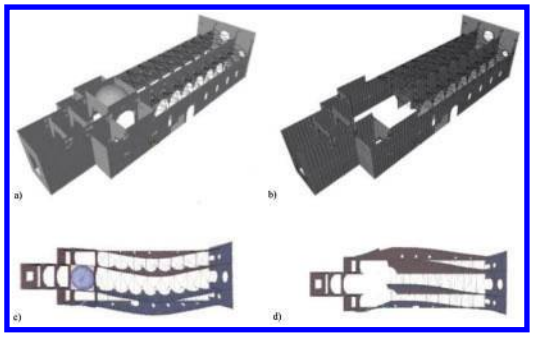


Figure 5. Finite element model and first mode shape: a), c) pre-earthquake, b), d) post-earthquake.

Table 4. Modal period and frequency inferred from Basilica finite elements model, pre and post earthquake comparison.

	Pre-earthquake model		Post-earthquake model	
Mode	Period [s]	Frequency [Hz]	Period [s]	Frequency [Hz]
1	0,6902	1,4490	0,9488	1,0540
2	0,4520	2,2123	0,5161	1,9375
3	0,4048	2,4701	0,4209	2,3758
4	0,3450	2,8986	0,3703	2,7005
5	0,3268	3,0604	0,3365	2,9719

even in the presence of the light steel bracing systems connecting them.

The absence of the transverse main arch due to the collapse of the transept reduces the transversal seismic adequacy.

5 CONCLUSIONS

This paper described the design, deployment and verification of a structural health monitoring system for a monumental building, the Basilica S.Maria di Collemaggio in L'Aquila, Italy. Measured and numerical data have been continuously integrated during one-year activity in order to perform a safety assessment before and after the earthquake, which struck the structure in 2009. It has been possible to analyze various critical issues related to the use of a wireless network of sensors, such as synchronization issues and MEMS sensors noise. Among the main results, monitoring action has allowed to identify reliable finite element model which have permitted the evaluation of the seismic adequacy according to the Italian code.

REFERENCES

Antonacci, E., Beolchini, G. C., Di Fabio, F. & Gattulli, V. 2001. The dynamic behavior of the basilica S. Maria of Collemaggio, *Proc. 2nd Intern. Congr. on Studies in ancient Structures*, Instanbul, Turkey, 2001.

Antonacci, E., Ceci, A., Colarieti, A., Gattulli, V., Graziosi, F., Lepidi, M. & Potenza, F. 2011. Dynamic testing and health monitoring via wireless sensor networks in the post-earthquake assessment of structural condition at L'Aquila. *8th European Conference on Structural Dynamics, Eurodyn11*, Leuven, Belgium, 2011.

Boyle, D., Magno, M., O'Flynn, B., Brunelli, D., Popovici, E. & Benini, L. 2011. Towards persistent structural health monitoring through sustainable wireless sensor networks. *Intelligent Sensors, Sensor Networks and Information Processing (ISSNIP), 2011 Seventh International Conference on,* Pages 323–328, 6-9 Dec. 2011

Cho, S., Park, J., Jo, H., Sim, S. H., Mechitov, K., Jung, H. J., Yun, C. B. & Spencer Jr., B. F. 2011. Structural Health Monitoring of a Cable-stayed Bridge Using Wireless Smart Sensor Network. *Engineering Mechanics Institute Conference (EMI2011)*, Boston, 4–2 June 2011.

Federici, F., Graziosi, F., Faccio, M., Gattulli, V., Lepidi M., & Potenza, F. 2012. An integrated approach to the design of Wireless Sensor Networks for structural health monitoring. *International Journal of Distributed Sensor Networks*, Article ID 594842.

Gattulli, V., Antonacci, E. & Vestroni, F. 2013. Field observations and failure analysis of the basilica S. Maria di Collemaggio after the 2009 L'Aquila earthquake. *Engineering Failure Analysis,* in press 2013.

Liu, W., Fei, X., Tang, T., Wang, P., Luo, H., Deng, B. & Yang, H. 2012. Application specific sensor node architecture optimization. Experiences from field deployments. *Design Automation Conference (ASP-DAC), 2012 17th Asia and South Pacific.*

Mechitov, K., Kim, W. Y., Agha, G. & Nagayama T. 2006. High-Frequency Distributed Sensing for Structure Monitoring. *Trans. of the Society of Instrument and Control Engineers (SICE)*, vol. E-S-1, no. 1.

Nagayama, T., Ushita, M. & Fujino, Y. 2011. Suspension Bridge Vibration Measurement Using Multihop Wireless Sensor Networks. *Procedia Engineering*, Volume 14, Pages 761–768

Niu, J., Deng, Z., Zhou, F., Cao, Z., Liu, Z. & Zhu, F. 2009. A Structural Health Monitoring System Using Wireless Sensor Network. Wireless *Communications, Networking and Mobile Computing, 2009. 5th International Conference on.*

Paek, J., Chintalapudi, K., Govindan, R., Caffrey, J. & Masri, S. 2005. A Wireless Sensor Network for Structural Health Monitoring: Performance and Experience. *Embedded Networked Sensors, 2005. EmNetS-II. The Second IEEE Workshop on.*

Park, C., Xie Q., Chou, P.H. & Shinozuka, M. 2005. , DuraNode: wireless networked sensor for structural health monitoring. *Sensors, 2005 IEEE*, Oct. 30 2005-Nov. 3 2005.

Rice, J. A. & Spencer Jr., B. F. 2008. Structural health monitoring sensor development for the Imote2 platform. *Proc. SPIE Smart Structures/NDE*.

Spina, D., Lamonaca, B. G., Nicoletti, M. & Dolce, M. 2011. Structural monitoring by the Italian Department of Civil Protection and the case of 2009 Abruzzo seismic sequence. *Bulletin of Earthquake Engineering*, Volume 9, Issue 1, pp 325–346

Research and Applications in Structural Engineering, Mechanics and Computation – Zingoni (Ed.)
© 2013 Taylor & Francis Group, London, ISBN 978-1-138-00061-2

Experimental study on bridge damage identification based on wavelet packet energy curvature difference method

Zhu Yu, He Xia & Jiawang Zhan
School of Civil Engineering, Beijing Jiaotong University, Beijing, China

ABSTRACT: Among those damage identification methods, the Wavelet Packet Energy Curvature Difference (WPECD) Method is an effective one. However, most of the existing methods rely on numerical simulation and are unverified via experiment, and very few of them have been applied to practice. In this paper, the validity of WPECD in structural damage identification is verified by a numerical example. A damage simulation experiment is taken on a real replaced girder from a road bridge in Cangzhou, China. Two damage cases are applied and the acceleration responses at the measuring points are obtained, based on which the damages are identified with the WPECD Method and the influence of wavelet function and decomposition level is studied. The results show that the WPECD Method can identify structure damage efficiently and can be put into practice.

Keywords: wavelet packet analysis, WPECD, damage identification, experiment

1 INTRODUCTION

The key components of structures will get accumulative damage and defect along with the service, which will influence structure safety. For this reason, Structural Healthy Monitoring (SHM) becomes quite important to the performance evaluation of engineering structure. Generally speaking, SHM can be divided into Local Detection and Integral Detection. Local Detection obtains the damage information via technologies such as infrared and ultrasonic inspection, while Integral Detection evaluates the damage by the change of structure vibration characteristics. As for most of the traditional damage identification methods which are based on structure vibration, the modal parameters are obtained by means of Fourier Transform. However, Fourier Transform is insufficient in high frequency modal analysis and it will lose the time domain information during the transform. As a result, it is impossible to evaluate the damage characteristic accurately.

The Wavelet Transform (WT) is a signal analysis method which can overcome the shortcoming mentioned above. Wavelet is composed of a cluster of primary functions which can describe the signal local characteristic whatever in time or frequency domain. Due to this reason, wavelet analysis can reflect the damage information hidden in the test data. There are many research results on damage identification based on WT. However, the WT resolution in high-frequency range is at a low level.

In order to overcome this disadvantage, the Wavelet Packet Transform (WPT) is proposed which can provide integral decomposition of different levels. Ding and Li et al. apply Wavelet Packet Energy Spectrum to structure damage alerting. Sun et al. takes the wavelet packet signal energy as the input of neural network to identify structure damage. Han and Ren propose a damage identification index as Energy Gradient based on WPT and verify it by lab experiment.

Among these method based on WPT, most of them are during theoretical research and a few of them are verified under laboratory condition. However, the actual damage is relatively more complex. In this paper, a method based on Wavelet Packet Energy Curvature Difference (WPECD) is proposed. By means of numerical simulation and site test, this method is verified.

2 DAMAGE IDENTIFICATION BASED ON WAVELET PACKET ANALYSIS

2.1 *Introduction to Wavelet Packet Theory*

As for WT with multiresolution, it only decomposes the low-frequency part of the signal, leading the bad resolution in high-frequency signal. Therefore it is not applicable for all kinds of signals. However, WPT decomposes every sub-band into two bands at every level, covering whatever high or low frequency part, shown in Fig. 1

For this reason, WPT can provide a more accurate signal analysis method, which can improve the resolution.

The wavelet packet function can be expressed as $\psi^i_{j,k}$, where i,j,k are modulation, scale and translation parameter respectively.

$$\psi^i_{j,k}(t) = 2^{j/2}\psi^i(2^j t - k) \quad i = 1,2,\ldots\ldots \tag{1}$$

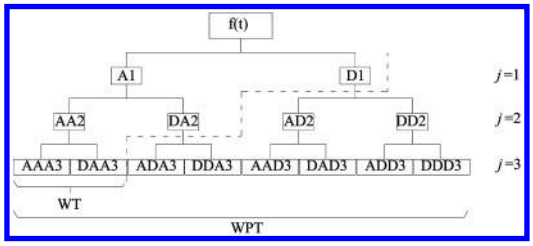


Figure 1. Wavelet Transform and Wavelet Packet Transform.

Here, ψ^i can be obtained by the following recurrence relation.

$$\psi^{2i}(t)=\sqrt{2}\sum_{-\infty}^{+\infty}h(k)\psi^i(2t-k) \tag{2}$$

$$\psi^{2i+1}(t)=\sqrt{2}\sum_{-\infty}^{+\infty}g(k)\psi^i(2t-k) \tag{3}$$

where ψ is the Mother Wavelet, $h(k)$ and $g(k)$ are integral mirror filter coefficients which are correlative to scale function and Mother Wavelet.

The recurrence relations of the jth and $j+1$th wavelet packet decomposition are shown as follows,

$$f_j^i(t)=f_{j+1}^{2i-1}(t)+f_{j+1}^{2i}(t) \tag{4}$$

$$f_{j+1}^{2i-1}(t)=Hf_j^i(t) \tag{5}$$

$$f_{j+1}^{2i}(t)=Gf_j^i(t) \tag{6}$$

where H and G are filter operators corresponding to $h(k)$ and $g(k)$ respectively.

$$H\{\bullet\}=\sum_{k=-\infty}^{\infty}h(k-2t) \tag{7}$$

$$G\{\bullet\}=\sum_{-\infty}^{\infty}g(k-2t) \tag{8}$$

The initial signal $f(t)$ can be expressed as follows via jth wavelet packet decomposition.

$$f(t)=\sum_{i=1}^{2^j}f_j^i(t) \tag{9}$$

The wavelet packet component signal $f_j^i(t)$ can be expressed as the linear combination of wavelet packet function.

$$f_j^i(t)=\sum_{-\infty}^{+\infty}c_{j,k}^i(t)\psi_{j,k}^i(t) \tag{10}$$

The wavelet packet coefficient $c_{j,k}^i$ can be derived as follows,

$$c_{j,k}^i=\int_{-\infty}^{+\infty}f(t)\psi_{j,k}^i(t)dt \tag{11}$$

where these coefficients meet the orthogonality condition.

$$\psi_{j,k}^m(t)\psi_{j,k}^n(t)=0 \quad when \quad m\neq n \tag{12}$$

In practice, wavelet packet decomposition is often applied in the energy monitoring. The energy of wavelet packet signal can be defined as

$$E_f=\int_{-\infty}^{\infty}f^2(t)dt=\sum_{m=1}^{2^j}\sum_{n=1}^{2^j}\int_{-\infty}^{\infty}f_j^m(t)f_j^n(t)dt \tag{13}$$

Substitute Eq. (10) to (13), with the orthogonality condition in Eq. (12), one obtains

$$E_f=\sum_{i=1}^{2^j}E_{f_j^i} \tag{14}$$

where the wavelet packet component energy E_{fj} can be regarded as the energy stored in component signal $f_j^i(t)$.

$$E_{f_j^i}=\int_{-\infty}^{\infty}f_j^i(t)^2dt \tag{15}$$

As for Eq. (14), it can be explained that the total energy of the signal is the sum of wavelet packet component energy corresponding to different frequency bands.

The component energy is very sensitive to the change of signal characteristic, which can reflect the inherent feature of signal. If there is damage in the structure, a certain frequency of response will fluctuate, thus the energies of some signal components will change. Therefore, the change of energy distribution of measured response signal can be used to identify structure damage.

2.2 *Solution of unevenly spaced curvature*

In practice, curvature can be obtained by second order difference of dependent variable, which is the gradient of slope, as shown in Fig. 2.

For unevenly spaced case the curvature can be expressed as

$$K_i=y_i^{''}=\frac{\frac{y_{i+1}-y_i}{h_{i+1}}-\frac{y_i-y_{i-1}}{h_{i-1}}}{\frac{h_{i+1}+h_{i-1}}{2}} \tag{16}$$

where the numerator is the slope difference of the two curves around the node and the denominator is the space of the two curves. If the nodes are evenly spaced, that is $h_{i-1}=h_{i+1}$, then

$$K_i=y_i^{''}=\frac{\frac{y_{i+1}-y_i}{h}-\frac{y_i-y_{i-1}}{h}}{h}=\frac{y_{i+1}-2y_i+y_{i-1}}{h^2} \tag{17}$$

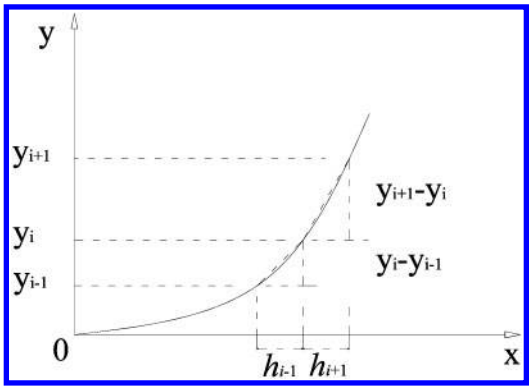


Figure 2. Curvature sketch.

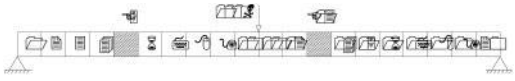


Figure 3. Sketch of the damaged girder.

which is just the formula to solve curvature with Second Order Finite Difference Method.

Substitute wavelet packet energy $E_{f_j^i}$ for y in Eq. (16), one can get the Wavelet Packet Energy Curvature (WPEC). The Wavelet Packet Energy Curvature Difference (WPECD) is the difference of WPEC under undamaged and damaged cases, defined as

$$\Delta K_i = K_i^u - K_i^d \tag{18}$$

where K_i^u and K_i^d are WPEC under undamaged case and damaged case respectively. This index will be applied to structure damage identification.

3 NUMERICAL EXAMPLE

Take a 20 m simply-supported girder for example, as shown in Fig. 3 with $E = 1 \times 10^8$ Pa, $\rho = 2500$ kg/m^3, $A = 1$ m^2, $I = 0.083$ m^4. There are altogether 20 elements with 21 nodes. An exciting force of 100 N is imposed on the middle point of the girder. Then transient analysis is done by ANSYS. Here, damage is simulated as the decrease of stiffness. Assume the stiffness of elements E5 and E13 decreases by 5% and 10%, respectively. Take WPT on responses of all the 21 nodes under the exciting force before and after damage respectively. The Daubechies Wavelet with order $N = 15$ (Db 15) is chosen as the wavelet function and the decomposition level is 7. The WPECDs of the first 8 components are shown in Fig. 4.

It can be observed that the magnitude of the first component energy is much higher than those of others. The sum of these 8 components is calculated, shown in Fig. 5.

It can be seen that there are peaks on the WPECD curves where there are damage. Even the damage is quite slight (E5), the peak is still obvious, which proves

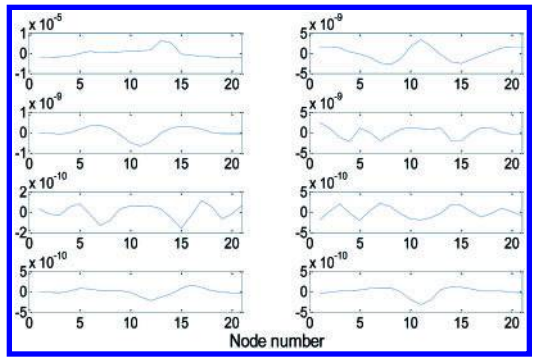


Figure 4. WPECD of damaged girder (First 8 components).

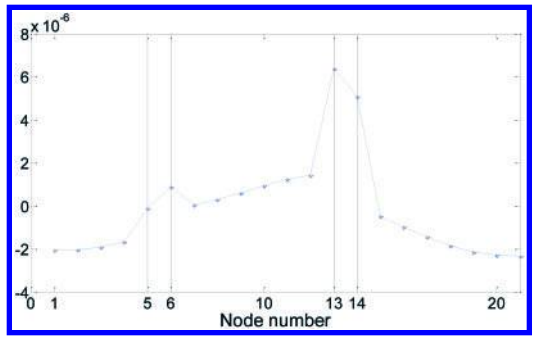


Figure 5. Sum of the first 8 WPECD components.

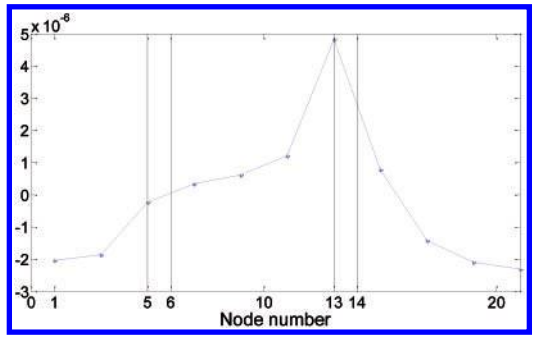


Figure 6. WPECD under sparse measuring points.

that this method is sensitive to damage. Besides, the peak of E13 is higher than that of E5, which indicates the fact that the damage degree in E13 (10%) is higher than E5 (5%).

The influence of sparse measuring points is investigated. Only 11 nodes (1, 3, 5, …, 21) are taken as measuring points and the result is shown in Fig. 6.

It can be seen that the damage of E13 can still be identified. However, the damage information of E5 is not as obvious as before, since the damage degree is too slight. This shows that there is some influence of fewer measuring points on slight damage and in actual test the measuring points should be as intensive as possible where there may be some damage.

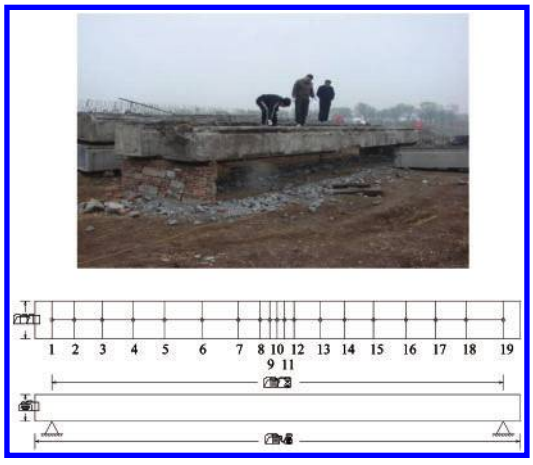


Figure 7. Sketch and measurement arrangement of the girder.



Figure 8. Excitation of hammer.

4 EXPERIMENTAL STUDY

4.1 *Experimental introduction*

The experimental girder is removed from a bridge located on the Ziyaxin River, Cangzhou, China, as shown in Fig. 7.

The length and width of the girder are 12.06 m and 1 m, respectively. There are 19 accelerometers fixed on the middle line of the girder, and those near the midspan (damage location) are relatively intensive. The girder is excited by a hammer between Node 14 and 15. The hammer free falls from the same height every time in order to make sure that the forces are the same in different cases.

4.2 *Damage cases*

There are two steps to simulate the damage.

Case 1: The 10-cm-thick concrete at the bottom of mid-span is removed and 2 steel bars on one side of the midspan bottom are cut. There is no visible crack on the girder. The damage location is corresponding to Node 10 in Fig. 7

Case 2: More steel bars are cut, only two left. A whole-length crack appears with the width 3 mm at the bottom.



Figure 9. Damage case (left: Case 1; right: Case 2).

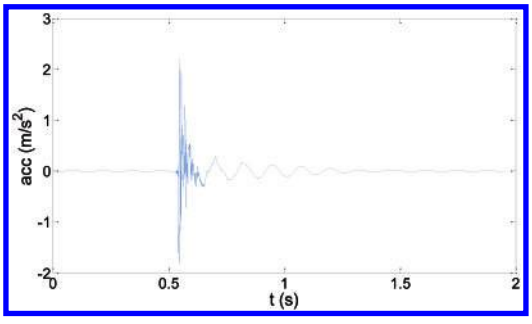


Figure 10. Measured acceleration time-history.

Table 1. The 1st order frequency and variation of the girder.

Case	1st freq. (Hz)	1st freq. variation V^*	Damage location
Undamaged	8.704	—	—
Damage 1	8.192	−5.88%	Node 10
Damage 2	6.144	−29.4%	Node 9, 10

As for damage Case 2, although the steel bars are cut at midspan, the actual crack appears to 25 cm left of the midspan, shown in Fig. 9. Thus the actual damage location should be between Node 9 and 10, and more likely to be in Node 9.

4.3 *Vibration measurement*

The accelerations of the 19 measuring points under undamaged case and the two damaged cases are measured. Take Node 14 as an example, the acceleration time history under Case 1 is shown in Fig. 10. Moreover, the frequencies under the 3 cases are shown in Table 1, in which $V^* = (f_d - f_u)/f_u$, where f_d and f_u are frequencies under undamaged and damaged cases

The reduction of frequency can be used to indicate the appearance of damage. The more the frequency reduces, the more the damage is. However, the damage location should be paid more attention.

4.4 *Damage identification based on WPECD*

Take WPT on all of the node responses under the undamaged case and the two damaged cases with 7 decomposition levels. The wavelet function is Db 15. The WPECDs of the two damage cases are shown in Fig. 11.

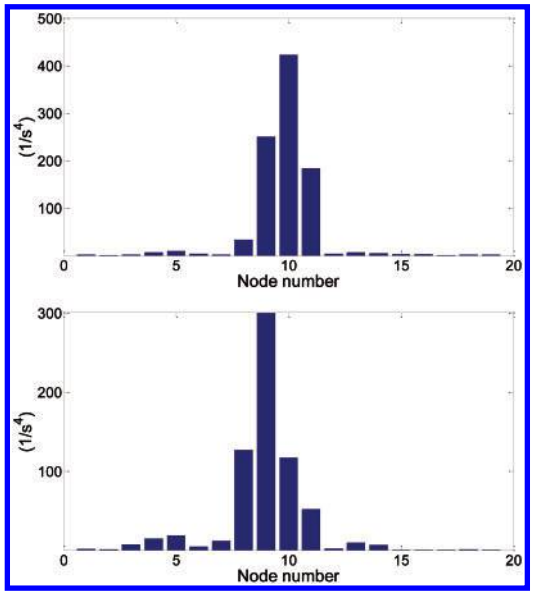


Figure 11. WPECD (upper: Case 1; lower: Case 2; db15).

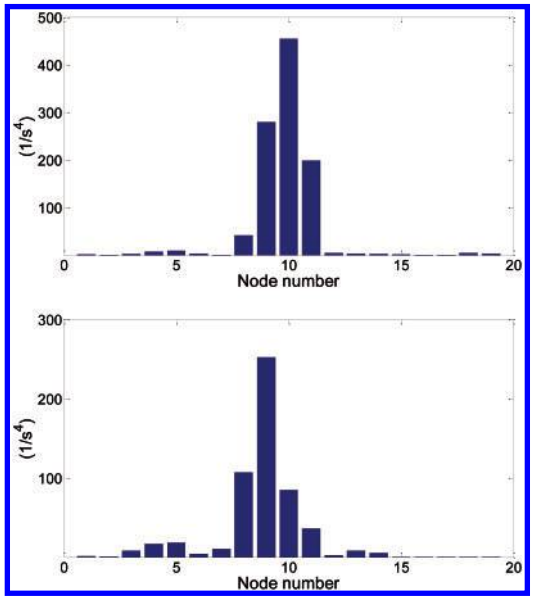


Figure 12. WPECD (upper: Case 1; lower: Case 2; coif5).

It can be noticed that for damage Case 1 there is an obvious peak at Node 10 where the damage appears, while for Case 2 the peak appears at Node 9 where the crack just locates, which suggests WPECD is quite effective in damage localization.

4.4.1 *Influence of wavelet function*

The wavelet function Coif with order $N = 5$ (Coif 5) is chosen and the decomposition level is still 7. The result is shown in Fig. 12.

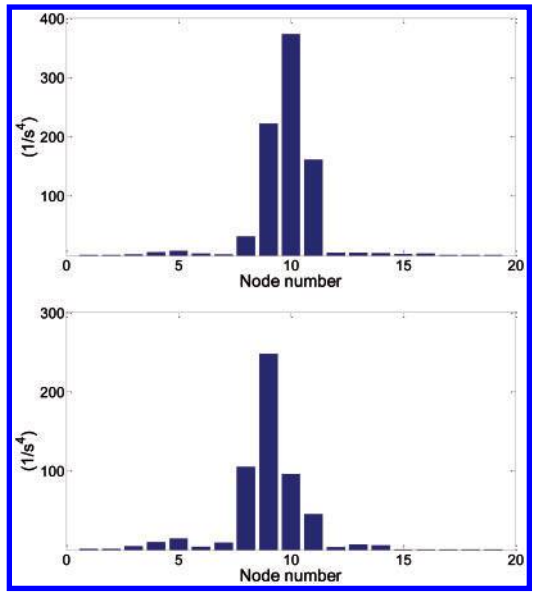


Figure 13. WPECD (upper: Case 1; lower: Case 2; db15).

Compared with Fig. 11, the difference is quite small. Both of the two wavelet-functions can achieve reasonable results. Moreover the calculation time for Db 15 and Coif 5 are also very close, those are 50s and 48s, respectively. Thus these two wavelet functions are both effective and can be verified each other.

4.4.2 *Influence of decomposition level*

Generally speaking, the more the decomposition level, the better the result, but the more the calculation time will be. Still take Db 15 as wavelet function while the decomposition level is 8 and the result is shown in Fig. 13.

Compared with Fig. 11, the peak value is a little smaller but the identification results are the same. As for calculation time, it is 101s, nearly two times of that when decomposition level is 7. That is because when the decomposition level increases, the number of wavelet packet components will double, which will make calculation time increase. For this reason, an appropriate level should be chosen to guarantee the identification quality as well as reduce calculation time as much as possible. In this example, level 7 has already met the requirements.

4.4.3 *Summary of damage identification method based on WPECD*

Based on the analysis above, the procedure of damage identification based on WPECD can be summarized as follows.

(1) Measure the vibration responses of concerned nodes when structure is undamaged.
(2) Monitor the node responses of structure in service.
(3) Chose appropriate wavelet function and decomposition level, take WPT on responses under relevant cases.

(4) Calculate the WPECD of each node. Where there is a peak on the WPECD curve there may be some damage, which should be paid attention.

5 CONCLUSIONS

In this paper, a numerical simulation is taken to indicate the effectiveness of WPECD on damage localization, and an experiment on a real bridge girder is taken to verify this method. The conclusions are as follows.

(1) Numerical calculation shows that WPECD is sensitive to damage and is effective to identify the damage even when the damage is slight (5%). However, if the measuring points are quite sparse, the slight damage information may be hidden.
(2) The WPECD Method is verified by an experiment on a real bridge girder which provides references for structure healthy monitoring.
(3) Different wavelet functions can be chosen for damage identification and verified each other.
(4) Higher decomposition level will cost more calculation time, so an appropriate decomposition level should be chosen to guarantee the identification quality as well as calculation efficiency.

REFERENCES

Doebling S W, Farrar C R, Prime M B. 1998. A summary review of vibration-based damage identification methods. *Shock Vib. Dig*., 30(2):91–105.

Farrar C R, Jauregui D A. 1998. *Comparative study of damage identification algorithms applied to a bridge.I. Experiment*. Smart Mater. Struct. 7:704–719.

Farrar C R, Jauregui D A. 1998. *Comparative study of damage identification algorithms applied to a bridge. II. Numerical study*. Smart Mater. Struct. 7:720–731.

Hou Z, Noori M, et al. 2000. Wavelet-based approach for structural damage detection. *Eng. Mech. Div.*, ASCE, 12(7):677–683.

Kitada Y. 1998. Identification of nonlinear structural dynamics systems using wavelets. *Eng. Mech. Div.*, 124 (10): 1059–1066.

Ding Y L, Li A Q, et al. 2006. Investigation on the structural damage alarming method based on wavelet packet energy spectrum. *Engineering Mechanics*, 23(8):42–48. (in Chinese)

Liu T, Li A Q, et al. 2009. Experimental study on structural damage alarming method based on wavelet packet energy spectrum. *Journal of vibration and shock*, 28(4): 4–8. (in Chinese)

Fan Y F, Hu Z Q, et al. 2008. Study on damage state of ribbed arch bridge using wavelet packet analysis. *Engineering Mechanics*, 25(5):182–188. (in Chinese)

Sun Z, Chang C C. 2002. Structural damage assessment based on wavelet packet transform. *Journal of Structural Engineering*, 128 (10):1354–1361.

Han J G, Ren W X, et al. 2006. Experimental study on structural damage identification based on wavelet packet analysis. *Journal of vibration and shock*, 25(1): 47–50. (in Chinese)

Jiang Z G, Qu W L, et al. 2006. Damage Localization of structures by wavelet packet analysis. *Journal of Wuhan University of Technology*, 28(11):94–97. (in Chinese)

Yuan Y, Zhou A H. 2008. *Theory and Application of Structure Damage Identification*. China Land Press, Beijing. (in Chinese)

Wang Z L, Nie G H. 2008. A method for structure damage defection based on curvature mode and wavelet packet transformation. *Journal of vibration and shock*, 27(1):124–126. (in Chinese)

Research and Applications in Structural Engineering, Mechanics and Computation – Zingoni (Ed.)
© 2013 Taylor & Francis Group, London, ISBN 978-1-138-00061-2

Damage detection on reinforced concrete framed structures using a band-variable filter

F.C. Ponzo, R. Ditommaso, G. Auletta & A. De Muro
School of Engineering, University of Basilicata, Potenza, Italy

ABSTRACT: Structural Health Monitoring (SHM) aims to increase the knowledge about linear and non linear dynamic behaviour of structures in order to develop accurate strategies of analysis for the safety assessment. Particularly, structural monitoring, especially for structures located in seismic prone areas, assumed great importance for the possibility to provide useful information about the state of the health of strategic structures and infrastructures over time and to perform an objective quick estimate of the damage occurred on structures just after a seismic event. It is known that the occurrence of structural damage, for any kind of structure, it is able to changes its dynamic characteristics over time. Generally, the main parameters conditioned by this problem are periods of vibration, equivalent viscous damping factors and mode shapes. Several authors showed that also the variations of the modal curvature are strictly related to the damage occurred on a structure. Moreover, using the mode curvature as a control parameter it is also possible to localize where the damage occurred along the height of the structure. In order to analyze the nonlinear behaviour of a general structure, and localize a possible damage, a band-variable filter based on the Stockwell Transform has been proposed. Basing on the results of nonlinear numerical analyses and shaking table tests on a scaled model, this paper shows some example of application of the proposed methodology to identify and localize damage occurred on framed reinforced concrete structures after an earthquake.

1 INTRODUCTION

Structural Health Monitoring (SHM) aims to increase the knowledge about time-varying bahavoiur of structures, especially after seismic events, in order to develop accurate strategies of analysis for the safety assessment. Especially for structures located in seismic prone areas, SHM assumed great importance, for the possibility to provide useful information about the state of the health of strategic structures and infrastructures over time and to perform an objective quick estimate of the damage occurred on structures just after a seismic event. SHM performed on both weak and strong motion can also facilitates the understanding of structural behaviour during earthquakes and related damage mechanisms. In the last years many researchers worked to set-up new methodologies for Non-destructive Damage Evaluation (NDE) based on the variation of the dynamic behaviour of structures under seismic loads (Dinh *et al*., 2012; Bisht and Singh, 2012, Ponzo *et al*., 2010).

The NDE methods can be classified into four different levels (Stubbs *et al*., 2000) as a function related to the type of information provided by the different approach (Rytter, 1993):

- **First level methods:** only able to evaluate the presence of a possible damage to the structure;
- **Second level methods:** able to assess the presence of any damage on the structure providing also information about the related position;
- **Third level methods:** able to identify any possible damage occurred on the structure by providing information about both location and severity of the damage;
- **Fourth level methods:** able to detect the presence of damage on the structure, estimate severity and position as well as providing information related to the impact that impairment has on the structure.

Each method, according to the level where it takes place, requires information and algorithms characterized by an increasing in complexity when the level increases. Therefore, the development of high level refined methodologies requires, in general, high costs, great computational effort and often needs experts people to understand the complex results. Using a complex approach it can result very difficult to control a relevant number of structures and infrastructures, especially in automatic way. This kind of approach is indicated to perform scientific studies or more in depth control on a limited number of structures. It is, then, clear the importance to set-up fast and simplified methodologies for SHM and NDE. These methodologies must be based exclusively on few sensors installed within the structure and able to capture the main modes

of vibration characteristics. Most of methods proposed in the past were based on the eigenfrequencies variations of the structure, but it is now well know that frequency variation could be related to other factors also, as well as the external temperature variations or the soil-structure interaction (Xia *et al*., 2012).

2 THE STOCKWELL TRANSFORM AND THE NONLINEAR FILTER

This paper discusses the possibility to use a Band-Variable Filter (Ditommaso *et al*., 2012) to point out the evolution of the dynamic characteristics of systems, over the time, by acting simultaneously in both time and frequency domain. The filter was built using the properties of convolution, linearity and invertibility of the S-Transform. As discussed in Ditommaso *et al*. (2012), the proposed band-variable filter can be written as:

$$h_f(t) = \int_{-\infty}^{+\infty} \left(\int_{-\infty}^{+\infty} [S(\tau, f) \cdot G(\tau, f)]\, d\tau \right) \cdot e^{i \cdot 2 \cdot \pi \cdot f \cdot t}\, df \qquad (1)$$

Where $S(\tau,f)$ is the S-Transform of the signal $h(t)$, $G(\tau,f)$ is the filtering matrix and $h_f(t)$ is the filtered signal. A generic k-th column $G(\tau,f)$ identifies a filtering window at a given time step. In order to better clarify the filtering procedure a worked example will be provided in the next section. The definition of the filtering matrix could be a time-demanding process, since each filtering window should be defined over a varying frequency recursively with a fixed time lapse. Moreover, the band-pass portion of the filter must be enlarged or reduced for each time step according to the desired bandwidth and the rectangular shape of the matrix. In order to simplify this process, it is convenient to try to automate it. We propose an implementation that defines the filtering matrix using a graphical user interface (GUI) that visualizes the amplitude spectra of the S-transform of the signal allowing for a point-and-click selection of the desired portion of the time-frequency domain. The routine is designed so that the user can select a few points and the computer performs a cubic spline interpolation. In order to build the filtering matrix we used the *pimf* function of MATLAB©, which is a convenient approximation of a boxcar function. This spline-based curve is so named because of its Π shape. It is possible to obtain more details about this function from www.mathworks.com. The matlab routine of the proposed Band Variable Filter can be downloaded from http://roccoditommaso.xoom.it.

3 MODE SHAPES EVALUATION AND DAMAGE LOCATION

The band-variable filter discussed in the previous section gives the possibility to extract from a non-stationary and/or non-linear signal just the energy content of interest, preserving both amplitude and phase in the region of interest, as discussed by Ditommaso *et al*. (2012). Using this kind of approach and a suitable distribution of sensors along the height of the monitored structure it is possible to extract the time-varying behaviour of each mode of vibration starting from a nonlinear signal recorded on a damaging structure during an earthquake. The proposed procedure has been applied on reinforced concrete framed structure to detect and localize the damage occurred after an earthquake. As mentioned before, the basic idea is to identify, using the band-variable filter (Ditommaso *et al*., 2012), the fundamental mode shape over time and evaluate its changes in temrs of shape and related curvature. It is possible to demonstrate that mode curvature variation is strongly related with the damage occurred on a structure (Pandey *et al*., 1991). To apply the proposed procedure it is necessary to focus the attention on three most important instants for a structure subjected to an earthquake: (A) before the earthquake, (B) the instant of maximum inter-storey drift and (C) after the earthquake. Comparing the mode shapes characteristics evaluated in the instant A, B and C it is possible to unserstand if damage occurred after the earthquake and to localize it on the structure. The instant A is the reference instant and it is necessary to compare the difference in terms of mode curvature between B-A and C-A. In order to better explain the proposed procedure two examples have been considered. The former is related to a nonlinear numerical model of a reinforced concrete framed structure (plant 15 × 12 m), regular in plan and in elevation, with five floors, as shown in Figure 1. The considered structure has been designed following the criteria of the Italian seismic code (NTC2008)

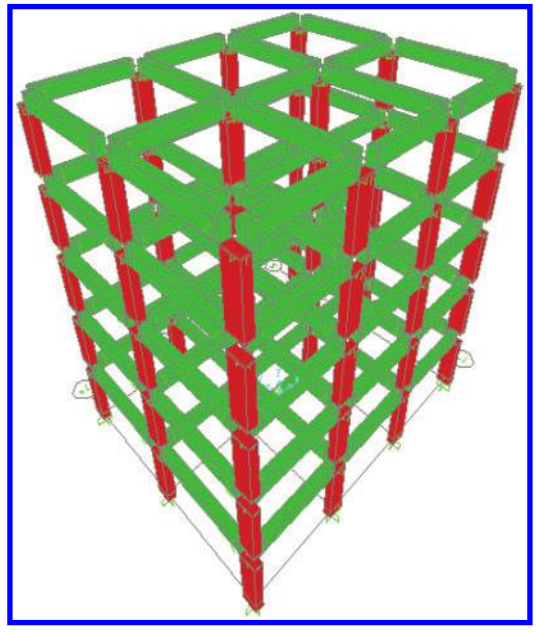


Figure 1. Numerical model.

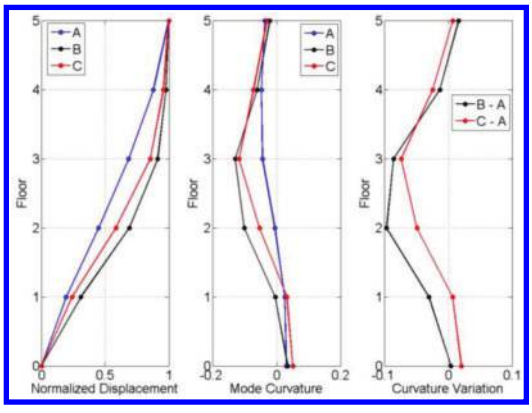


Figure 2. From The Left: Mode Shapes And Curvatures evaluated at time instances A, B and C, And Curvature Variations B-A And C-A.

for high ductility class (CDA), high seismic intensity (PGA 0.35g) and for soft soil type D. The height of each storey is 3m, for a 15m total height of the building. In order to take into account the presence of infill panels within the structural R/C frames and their interaction with the columns, both the masonry strength and stiffness contribution have been considered (Mainstone R.J. 1974) by inserting two equivalent structural elements in the models. Using SAP2000 finite elements program, these elements were modelled by means of multi-linear plastic link, with a Takeda hysteretic behaviour. It is possible to find more details about this numerical model in Ponzo *et al.* (2010). The Figure 2 shows the mode shapes evaluated over time: Mode Shape B has a curvature bigger than Mode Shapes A and C. It is known that mode curvature is strongly linked to the building damage during a seismic event (Pandey *et al*., 1991). Therefore, being able to evaluate the mode curvature during the maximum excursion in nonlinear field and isolating it from superimposed signals, we can achieve a better understanding of the mechanisms of damage as well as a more precise location of the damage on the structure. In this example the maximum curvature variation (B-A) is located at the second floor where the maximum interstory drift occurred. On the contrary, using the curvature variation associated to the mode shapes A and C, related to the stationary behaviour before and after the earthquake, the maximum curvature variation is associated to the third level, but it is in contrast with the maximum measured intersory drift (Figure 2). The latter example is related to a 1:4 reinforced concrete scaled experimental model, designed for vertical loads only and tested at the Structural Laboratory of the University of Basilicata in Potenza, as part of the POP project (Dolce *et al*. 2005), through the mono-axial shaking table test (Figure 3a). The model was tested using two different conditions: fixed base (phase I) and with isolation system (phase II). With regards to the tests in the fixed-base configuration mentioned above, the effective peak acceleration of the table was progressively increased from 0.05 up to 0.35 g, using different

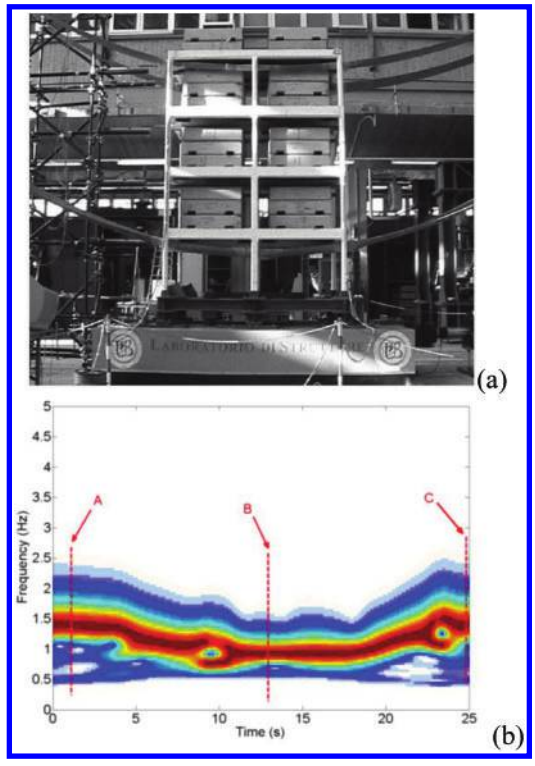


Figure 3. (a) POP model (Ponzo et al. – 2010) (b) Normalized S-Transform and selection of the time instants A, B and C.

spectral shapes. All floor displacements were measured through Temposonic digital transducers, fixed to an external steel reference frame.

The floor accelerations were acquired through a system of horizontal servo accelerometers. Figure 3b shows the S-Transform related to the accelerometric recordings at the last level of the structure.

The starting frequency is 1.4 Hz, the minimum frequency is 0.90 Hz and the final frequency is 1.35 Hz. Figure 3b shows also the time-point from which the mode shapes were evaluated: Mode Shape A, B and C (starting frequency, minimum frequency and final frequency). In order to highlight the frequency evolution of the POP model a normalized S-Transform has been used. Figure 4 shows the mode shapes evaluated over time. In order to compare the performance of the proposed technique the variations of the modal curvature were calculate for both numerical and experimental models and compared with those evaluated using a classical band-pass filter to isolate the dynamic characteristics related to the fundamental mode.

The results obtained using the classical approach are coherent with those related to the time-instants A and C, but are very different from those related to minimum frequency (B) reached during the nonlinear phase of the motion. This kind of result was expected because the classical approach, commonly adopted to analyze the stationary motion of a system, fails when

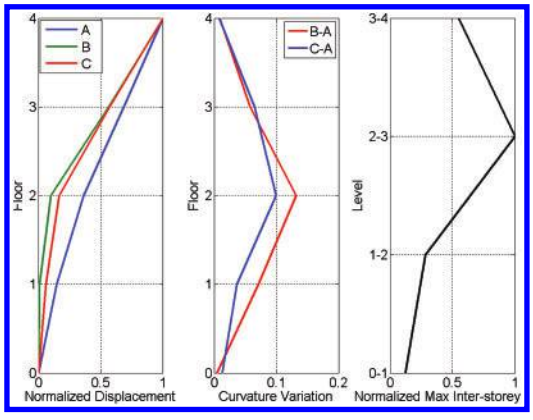


Figure 4. From The Left: Mode Shapes And Curvatures Variations B-A And C-A And Normalized Max Inter-storey.

it is used to analyze the nonstationary behaviour of the same system. The results obtained for both numerical and experimental models highlight the capacity of the proposed approach of evaluating the fundamental mode shapes during the maximum excursion in the plastic field (minimum frequency reached over time). This is a crucial aspect for a correct detection and localization of the damaged occurred on the structure during the strong motion phase. In fact, the results obtained from the experimental model shown that also using the modal curvature variation (C-A) it is possible to localize the damaged floor, but the amplitude of this kind of variation is very different from those obtained using the modal curvature variation evaluated using the approach proposed in this paper (B-A), that better approaches the real variation reached during the nonlinear motion.

How can be seen from Figure 4, the maximum modal curvature variation occurs in correspondence of the same plane in which the maximum inter-storey drift focuses. Using the band-variable filter, taking into account the possibility to evaluate the maximum mode shapes variation over time, further study are necessary to find a relationship to link the damage level with the maximum modal curvature variation reached during the nonlinear motion of the structure forced by a strong earthquake.

4 DISCUSSION AND CONCLUSIONS

Techniques based on Fourier transform provide good results when the response of the system is stationary, but fail when the system exhibits a non-stationary, time-varying behaviour. To hamper classical techniques, it is not necessary that a building reaches damage: even the non-stationarity of the input and the possible interaction with the ground and/or adjacent structures can show the inadequacy of classic techniques (Ditommaso *et al*., 2010). In 1996, Stockwell introduced a new powerful tool for the signals analysis: the S-Transform (Stockwell *et al*., 1996). Compared with the classical techniques for time-frequency analyses, this transformation shows a much better resolution and also offers a range of fundamental properties such as linearity and invertibility (Ditommaso *et al*., 2012). By exploiting these properties, it was possible to develop a filter whose band varies both in time and in frequency domains, being very useful to study the characteristics of non-stationary signals (Ditommaso *et al*., 2012). As discussed in the previous sections, this tool becomes necessary when one wants to isolate the response of individual time-varying modes of vibration of soil and buildings (e.g., when their dynamic characteristics evolve over time as a result of seismic events). The ability to investigate the non-stationary response of structures opens new scenarios, giving the opportunity to explore new possibilities. For example, the ability to isolate individual modes of vibration of a building make possible to explore their variation over time, evaluating the change in mode curvature. It is known that this parameter is strongly linked to the building damage during a seismic event (Pandey *et al*., 1991). Therefore, the possibility of evaluation of the modal curvature during the maximum excursion in nonlinear field and isolating it from superimposed signals, allows for a better understanding of the mechanisms of damage as well as for a more precise location of both structural and non-structural damage.

In this paper the results of the proposed procedure for damage detection and localization have been proposed. The methodologie appears able to localize the damage occurred on a reinforced concrete framed structure after a strong earthquake. Particularly, the methodologie has been tested on both a numerical model and a 1:4 reinforced concrete scaled model damaged using several shaking table tests. It is worth noting that the procedure is completely based only on accelerometric data, then, it is not necessary to integrate the data to evaluate velocities or dislacements. In this way the damage localization is very fast. Using the band-variable filter, taking into account the possibility to evaluate the maximum mode shapes variation over time, further study are necessary to find an empirical relationship to link the damage level with the maximum modal curvature variation reached during the nonlinear motion of the structure forced by a strong earthquake.

ACKNOWLEDGEMENT

This study was partially funded by the Italian Civil Protection Department under the project DPC-RELUIS 2010-2013 (Task 3.1).

REFERENCES

Bisht Saurabh S. and Singh Mahendra P. (2012). Detecting sudden changes in stiffness using high-pass filters. *Struct. Control Health Monit.* **19,** 319–331. DOI: 10.1002/stc.433.

Dinh H. M., Nagayamaz T. and Fujinoy Y. (2012). Structural parameter identification by use of additional known masses and its experimental application. *Struct. Control Health Monit.* **19,** 436–450. DOI: 10.1002/stc.444.

Ditommaso, R., Parolai, S., Mucciarelli, M., Eggert, S., Sobiesiak., M., and J. Zschau (2010). Monitoring the response and the back-radiated energy of a building subjected to ambient vibration and impulsive action: the Falkenhof Tower (Potsdam, Germany). *Bull Earthquake Eng.* **8: 3**, 705–722. DOI: 10.1007/s10518-009-9151-4.

Ditommaso Rocco, Marco Mucciarelli, Felice Carlo Ponzo (2012). Analysis of non-stationary structural systems by using a band-variable filter. *Bulletin of Earthquake Engineering.* DOI: 10.1007/s10518-012-9338-y.

Dolce M, Cardone D, Di Cesare A, Moroni C, Nicoletti M, Ponzo FC, Nigro D (2005). Dynamic tests on a 1:4 scaled R/C existing building: comparison of several isolation systems. *9th Assisi, Kobe*.

Mainstone R.J. (1974). Supplementary note on the stiffness and strength of infilled frames. Current paper CP13/74. Build. Res. Establishment. London.

NTC (2008). Nuove Norme Tecniche per le Costruzioni. DM 14 gennaio 2008, pubblicato sulla Gazzetta Ufficiale n. 29 del 4 febbraio 2008 - Suppl. Ordinario n. 30

Pandey, A. K., M. Biswas, M. M. Samman (1991). Damage detection from changes in curvature mode shapes. *Journal of Sound and Vibration*. **Vol. 145: Issue 2,** pp. 321–332.

Ponzo F. C., Ditommaso R., Auletta G., Mossucca A. (2010). A Fast Method for Structural Health Monitoring of Italian Strategic Reinforced Concrete Buildings. *Bulletin of Earthquake Engineering.* DOI: 10.1007/s10518-010-9194-6.

Rytter A. (1993). Vibrational based inspection of Civil Engineering Structures. Ph.D. Thesis, University of Aalborg, Denmark.

Stockwell, R. G., L. Mansinha, and R. P. Lowe (1996). Localization of the complex spectrum: the S transform. *IEEE Trans. Signal Process.* **Vol. 44,** pp. 998–1001.

Stubbs N., Perk S., Sikorsky C., Choi S. (2000). A global non-distructive damage assesment methodology for civil engi-neering structures. *International Journal of System Science, 2000.*

Xia Yong, Chen Bo, Weng Shun, Ni Yi-Qing, Xu You-Lin (2012). Temperature effect on vibration properties of civil structures: a literature review and case studies. J Civil Struct Health Monit. DOI 10.1007/s13349-011-0015-7.

Research and Applications in Structural Engineering, Mechanics and Computation – Zingoni (Ed.)
© 2013 Taylor & Francis Group, London, ISBN 978-1-138-00061-2

Damage identification in the mistuned bladed system utilizing the outlier analysis

A.U. Rehman & F.H. Shah
Department of Mechanical Engineering, University of Engineering & Technology, Lahore, Pakistan

K. Worden & J.A. Rongong
Dynamics Research Group, Department of Mechanical Engineering, The University of Sheffield, Sheffield, UK

ABSTRACT: Damage detection in the turbomachinery bladed system is of prime concern as a growing fatigue crack that leads to the blade failure threatens the survival of the entire engine. Therefore damage to the blades needs to be detected primarily during its initiation or early propagation stage before the ultimate failure occurs. In addition to that, the presence of mistuning in the constituent bladed sectors complicates the damage detection procedure because of the associated problems of mode localization and peak splitting in the mistuned bladed structures. This study presents an effectual approach for damage detection in the mistuned turbomachinery bladed system utilising statistical approach to the vibration–based damage detection paradigm involving the Outlier analysis. A simplified bladed disc, in the damage and undamaged conditions, is considered in this work for the varying mistuning levels. Possibility of utilising the frequency domain data (in the form of Frequency Response Functions (FRFs)) and the time domain data (in the form of time signals obtained for swept sine excitation) for the damage detection is explored for varying signal-to-noise ratios. The effectiveness of the developed damage detection strategy is also investigated for the blade tip timing data.

1 INTRODUCTION

Timely detection of damage in bladed structures is of significant importance as growing fatigue damage threatens the survival of whole system. Amongst various damage detection procedures developed over the last few decades, statistical approach to damage identification has been given great attention by the researchers. Statistical approaches to vibration-based damage detection are based on the principle that the vibration response measurements contain damage sensitive features which can be utilized for damage identification by quantifying the observed changes in those features. Therefore, this technique can be regarded as a statistical pattern recognition paradigm. Vibration response measurements usually contain inherent uncertainties, therefore statistical analysis procedures are required to detect whether any deviation in the vibration response is from the damage or due to the operational variability or inconsistency in the measurement chain [1].

The problem of damage detection has a hierarchical structure comprising several levels [2]. In order to satisfy the higher levels, complicated information regarding the expected life of a structure (after a detailed prognosis) is required, but at the lowest level, damage detection is only a two class problem – whether the structure is damaged or not? The requirement of robust low-level damage detection is fulfilled by the principle of "Novelty Detection", which tries to identify if a structure has deviated from the normal condition. Outlier analysis is a novelty detection technique and falls into the unsupervised learning category. It involves processing of a large data set of samples representing the undamaged state of the structure. When a new data set is available, it is compared with that of the undamaged state and the occurrence of a significant deviation from the undamaged state leads to a conclusion regarding the presence of damage in the structure. Outlier analysis highlights the potential outlier from a given data set, which might be thought of being produced due to some different mechanism in comparison to the rest of the data. It also compares the status of any data set against a threshold level. This threshold level is obtained by using a Monte Carlo method. If a data set is lying above the threshold level, this indicates a different mechanism being responsible for generating that data set in comparison to the rest of the data [3, 4].

The outlier analysis technique has been successfully applied to variety of engineering problems in the past. The most important development in the utilization of outlier detection as a possible damage indicator evolved in the three phase experimental damage investigation reported in [5-7], as previously this method was largely only applied to synthetic data. The first phase of this investigation dealt with the experimental verification of the novelty detection method

considering a laboratory structure (an aluminum panel stiffened with ribs and stingers). The features used for this analysis were transmissibility FRFs and the damage was induced by making a progressive saw-cut through one of the stringers. The method was successful in identifying all the damaged states for depth of crack exceeding 5mm. The second phase of the experiment proved successful in highlighting local damage on a full-scale structure (a Gnat aircraft wing). Damages of various forms were introduced in different inspection panels and transmissibility measurements (across the panels) were used to detect damage using outlier analysis. In the last phase of this research, the objective was to move from level 1 (detection) to level 2 (location). A network of sensors was used to establish a set of novelty detectors, each sensitive to different sections of the wing. The results confirmed to establish a level 2 damage detection system (detection and location) using outlier analysis. Since this detailed study, outlier analysis has been successfully applied to detect damage in various applications which include: annular components [8], plates [9], and stiffened composite panels [10].

An important aspect of the vibration-based damage detection is its sensitivity to the uncertainties in the measurement chain. Vibration response measurements are always associated with some form of measurement noise or error. The effect of noise on the damage detection is investigated in detail in [11-13]. The presence of noise in a signal complicates the problem of damage detection and can lead to a faulty diagnosis. In order to reduce the probability of a faulty diagnosis, the effect of noise must be taken into consideration [11]. It has been reported in [12] that the influence of input noise (noise added to the input parameters to the system e.g. force, displacement, velocity etc. input) is slightly less significant on damage detectability as compared to the influence of an output noise (noise added to the response of a system). The effect of input noise is lessened by the structure whereas the effect of output noise is independent at each response location and tries to hide the damage to a larger extent.

For damage detection using outlier analysis, increasing noise level results in complicating of the damage detection [14]. A very promising approach to consider uncertainty, in the form of noise, in the FRFs obtained from dynamic testing is explained in [15]. The confidence bounds, in terms of the standard deviation, for the measured FRFs are obtained in terms of the standard coherence function and the number of averages used to compute the FRF.

In this paper, statistical approach to the vibration-based damage detection is considered for a simple, representative bladed structure. Different mistuning levels are considered along with the cracks of varying depths. Both, frequency and time domain data was acquired from the blades and Outlier analysis was utilized to highlight the damage in one of the blades. Effectiveness of the developed methodology is also examined for the operational uncertainties by adding noise to the data.

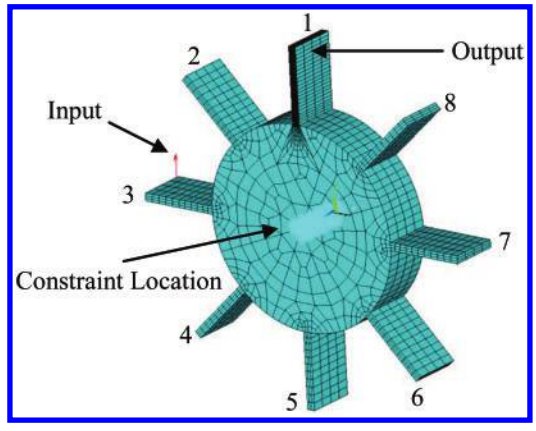


Figure 1. 3D FE model of bladed disc.

2 3D FE MODEL OF BLADED DISC

The 3-D FE model of the bladed disc specimen is shown in Figure 1. It is comprised of eight blades mounted on a thick circular base. The interface between the blade and the circular base was modeled as a rigid single piece to represent the geometry of a blisk. The thickness of each blade was 6 mm; blade length was 60 mm; the inner diameter of the disc was 40 mm and the outer diameter was 160 mm. The bladed disc was meshed using a 3-D 20-node structural solid element with mid-side nodes. The total number of elements along the width of a blade was set to be three for Blades 2-8 and twelve for Blade-1; thirty along the length of the blade and four along the bladed disc thickness. The higher number of elements for Blade-1 was chosen in order to model the cracks of smaller depths precisely without disturbing the mesh density. This resulted in 3356 elements for the whole bladed disc model. The FE model was constrained radially from the centre and the material assigned to it was steel ($E = 200$ GPa, $\upsilon = 0.3$, *density* $= 8000$ Kg/m^3).

The actual blades in a physical bladed disc are always slightly mistuned due to the small differences in the individual blade sectors because of inevitable manufacturing constraints. In order to obtain an equivalent spread of mistuning modes for the numerical bladed disc model, and to simulate the numerical mistuning, different modulus of elasticity (E) ranges were considered. Random E values (equivalent to the number of elements of the blades) were obtained for a given E range and were randomly distributed across all the elements of the blades of the FE model (Figure 2).

3 FREQUENCY DOMAIN DAMAGE DETECTION

3.1 *FRFs of Tuned and Mistuned Bladed Disc*

The FRFs for the varying mistuning levels were obtained by applying a unit force on Blade-3 and the

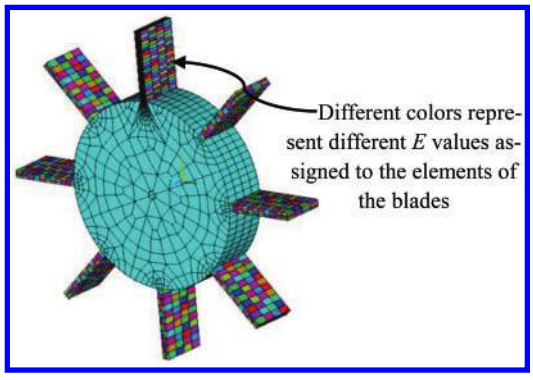


Figure 2. Random distribution of 'E' across the bladed disc.

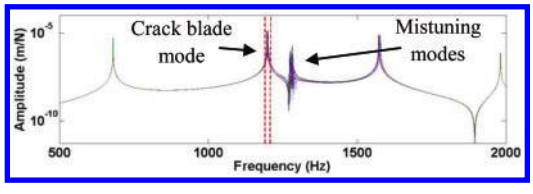


Figure 3. FRF of the bladed disc for a/d = 0.25 crack.

response was taken on Blade-1. The blade numbers and input/response locations are shown in Figure 1. The bladed disc model was considered in the pre-crack condition and also with cracks of varying depths ($a/d = 0.04, 0.08, 0.25, 0.5$), at the first crack location on Blade-1. Crack depth and location parameters were defined in accordance with [16]. The crack was modeled by two separate surfaces resting on each other with no material removal between them. This represented a hair-line crack. The crack depth has minimal effect on the damping levels, which are significantly affected by the increasing excitation levels instead [17]. Therefore, a friction-free contact was considered at the crack interface of the bladed disc. The presence of crack in one of the blades resulted in the occurrence of a crack blade mode peak in the FRF plot. For the larger crack depths ($a/d = 0.25$ and 0.5), the crack blade mode itself can provide useful information about the presence of damage in the structure by just visualizing the FRF plots – for example see Figure 3. But for the smaller crack depths ($a/d = 0.04$ and 0.08) some additional steps are required to highlight the damage in the mistuned environment [18].

3.2 *Outlier Analysis*

For damage detection in the bladed disc model using outlier analysis in the frequency domain, the feature used was the transfer function between Blade-3 (input) and Blade-1 (output). At first, the bladed disc without a crack was considered and 10 FRFs were obtained, each corresponding to a different mistuning level. These FRFs were then sampled at 20 regularly spaced points

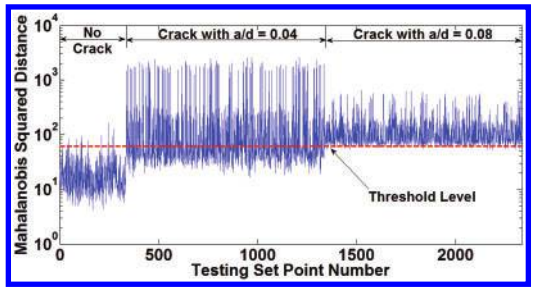


Figure 4. Mahalanobis squared distances for damaged and undamaged cases (Frequency domain).

(a 20 dimensional feature) between the frequency interval of 1270-1290 Hz to provide the pattern to be used as reference/undamaged condition in the analysis. In order to account for the effect of noise in the simulated FRFs, each of the FRFs was corrupted with a noise level corresponding to the coherence estimate, as described in [15]. The coherence level considered was varied from 0.99 to 0.95 within the frequency range of interest (where all the resonance peaks of mistuning modes were lying). The undamaged pattern of each FRF was copied 100 times and each copy was corrupted with a Gaussian noise vector obtained for a given standard deviation corresponding to each mistuned FRF.

The 100 copies for all 10 mistuning levels were concatenated vertically to form a 1000×20 feature matrix for the undamaged bladed disc. Rows of this feature matrix were then randomly rearranged to rectify the block effect of each mistuning level FRFs stacking on the top of each other. Two-thirds of the undamaged data were classified as healthy data and one-third as testing data. These 666 (2/3rd of feature matrix), 20-dimensional observations for the healthy data were used to calculate the mean vector, $\{\bar{x}\}$, and a covariance matrix, [S], for the unfaulted condition. The values for the exclusive MSD measure, D, were then calculated for each row of the testing data. After that, testing data of the undamaged case were subsequently replaced with the feature matrices (each having dimensions of 1000×20) of the damaged cases i.e. the bladed disc specimen with a crack depth ratio of 0.04 and 0.08 and the MSDs were calculated. The results are plotted as shown in Figure 4. To decide about a data set being an inlier or outlier, a threshold value was computed using Monte Carlo simulations. The threshold value for a 1000 observation, 20 dimensional problem was found to be 61.2 after 1000 trails. This process was repeated ten times to obtain an averaged threshold value.

Figure 4 indicates that the undamaged data points are lying below the threshold level and are classified as "inliers", as expected. The bladed disc with a crack having $a/d = 0.04$ was partially detectable as the threshold level was crossing approximately 25% of the MSD values. All the observations corresponding to crack depth ratio 0.08 were diagnosed as "outlier" and are detectable. An interesting point to note is the drop

in the magnitude of MSD for $a/d = 0.08$. This was because of the fact that the frequency range considered for this analysis was 1270-1290 Hz and the FRF peak for the crack having $a/d = 0.08$ was just lying outside this frequency range. When the displaced mode was still within the frequency range there are two sources of discordancy: (a) the mode was not where it should be and (b) the mode was somewhere it shouldn't be. If the mode leaves the frequency range of interest, only the first source of discordancy is present.

4 TIME DOMAIN DAMAGE DETECTION

As the ultimate objective of this paper is to develop a damage detection strategy that utilises blade tip timing data, damage detection in the bladed disc is now addressed considering the time domain data. A discrete convolution integral approach, as described by Equation 1, was utilised to generate the time domain data from the modal properties of the bladed disc, obtained numerically.

$$x(t) = \int_{-\infty}^{\infty} f(t-\tau).h(\tau)\,d\tau \qquad (1)$$

Blade-3 of the bladed disc was subjected to a swept-sine excitation from 1100-1600 Hz for 2 seconds and the response was obtained on Blade-1. One data point per cycle was obtained to represent the tip-timing data obtained from a single sensor attached to the turbomachinery casing. For the two or more sensors, the number of data points per cycles can be increased accordingly.

Once the time domain data was obtained, the outlier analysis was utilised to highlight the crack in the bladed disc. The procedure to obtain the MSD measure, D, was exactly the same as it was in the frequency domain case. The bladed disc without damage was considered first for the 10 mistuning levels. The time domain signal of the bladed disc is shown in the Figure 5. The presence of "beating" phenomenon in the time response of the bladed disc is due to the closely spaced cluster of mistuning modes in the frequency range of 1250 – 1300 Hz. The time interval chosen for the subsequent analysis was from 0.7 – 1 second, which corresponds to the frequency range of the mistuning modes cluster. The time domain signal of the undamaged bladed disc was sampled at 40 regularly spaced points between the selected time interval, resulting in a 40 dimensional feature problem.

Data was then copied 100 times and each copy was corrupted with a Gaussian noise vector having noise-to-signal ratio (NSR) of 0.025%. A 1000×40 dimensional feature matrix was obtained by vertically concatenating the 100 copies of the undamaged time domain data corresponding to 10 mistuning levels. Two-thirds of this feature matrix was designated as healthy data and the rest of the data was classified as testing data. The mean vector, $\{\bar{x}\}$, and a covariance

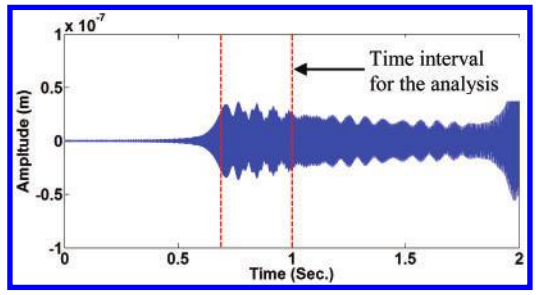


Figure 5. Time domain response of the bladed disc.

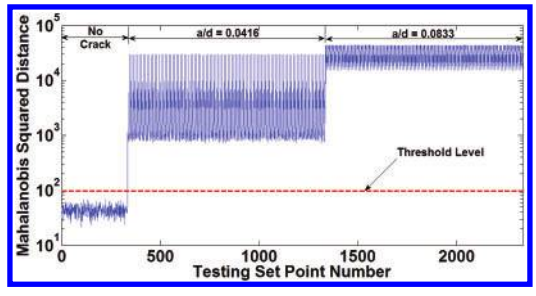


Figure 6. Mahalanobis squared distances for damaged and undamaged cases (Time domain).

matrix, [S], for the unfaulted condition were obtained from the healthy data and the exclusive values of MSDs were calculated. After that, the undamaged testing data were replaced subsequently by the time domain, 1000×40 feature matrix of the damaged bladed disc having cracks of 0.04 and 0.08 depths. The results are plotted in Figure 6.

The threshold level for 1000 observations of a 40 dimensional problem was found to be 96 after 1000 iterations using the same procedure as described earlier. The data points for the unfaulted case occurred below the threshold level. The MSD measures for the bladed disc having $a/d = 0.04$ and 0.08 were lying above the threshold level, indicating that the damage is completely detectable.

The time domain damage detection technique described above worked satisfactorily to highlight the damage in the mistuned environment considering low NSR. In order to investigate the effectiveness of this method when the data is corrupted with the higher levels of noise, two further cases were considered which included: a) NSR – 0.25%, b) NSR – 1.0%. The results for the two noise levels are shown in the Figures 7 (a) and (b) respectively.

Increasing NSR resulted in lower magnitudes of MSDs as the Euclidean distance between the two data sets (faulted and unfaulted) decreases with the increase in noise levels. For NSR – 0.25%, considering $a/d = 0.04$, the threshold level was crossing approximately through 10% of the MSD values. Therefore, the crack having $a/d = 0.04$, was partially detectable. Whereas all the observations for the crack having

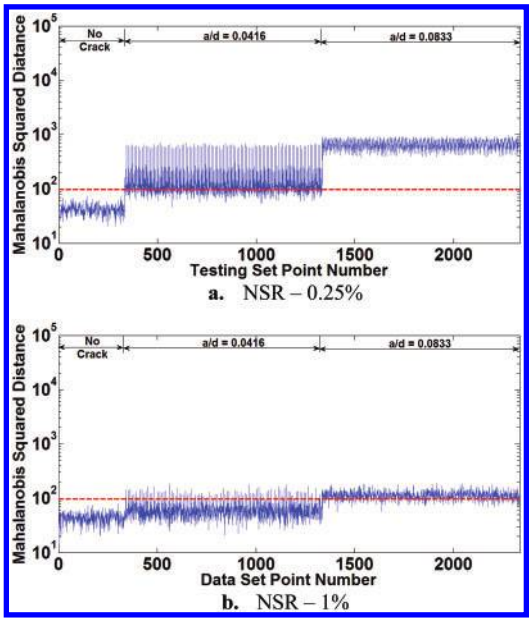


Figure 7. Mahalanobis squared distances for damaged and undamaged cases (Varying noise level).

$a/d = 0.08$ were lying above the threshold level and it was completely detectable. When the noise level was further increased, considering NSR – 1.0%, the majority of the data points for $a/d = 0.04$ were lying below the threshold level and were classified as inliers (not detectable). Whereas, the MSD values obtained for the crack with $a/d = 0.0833$ were lying above the threshold level and the crack was detectable.

5 CONCLUSIONS

The damage detection in the bladed disc was addressed in this paper considering a statistical approach. Outlier analysis was utilized to highlight the damage considering varying mistuning levels present inside the bladed disc. Damage detection was addressed for the frequency domain and for the time domain data (representing the tip timing data). Both the techniques worked satisfactorily in highlighting the damage in the bladed disc. The presence of a varying level of mistuning in the bladed disc resulted in widening the span of mistuning modes. For the frequency domain data, considering larger crack depths, the resonance peaks of the crack blade modes were well separated from the cluster of mistuning modes in the FRF plot and could be easily highlighted. However for smaller cracks, the crack mode merged into the group of mistuning modes and could not be distinguished at all. The outlier analysis successfully detected these smaller crack depths. In addition to that, the frequency domain method also detected the crack whose resonance peak was lying outside the frequency range considered for the analysis. For the time domain data, one data point per cycle was selected to represent the tip timing data from a single sensor. The method also highlighted the cracks in the bladed disc precisely with varying NSRs.

REFERENCES

[1] Fugate ML, Sohn H, Farrar CR. *Vibration-Based Damage Detection Using Statistical Process Control*. Mechanical Systems and Signal Processing, Vol. 15 (4), pp. 707–721, 2001.

[2] Rytter A. *Vibration Based Inspection of Civil Engineering Structures*. PhD Thesis. Aalborg University, Denmark, 1993.

[3] Worden K. *Structural Fault Detection Using a Novelty Measure*. Journal of Sound and Vibration, Vol. 201 (1), pp. 85–101, 1997.

[4] Worden K, Manson G, Fieller NRJ. *Damage Detection Using Outlier Analysis*. Journal of Sound and Vibration, Vol. 229 (3), pp. 647–667, 2000.

[5] Worden K, Manson G, Allman D. *Experimental Validation of a Structural Health Monitoring Methodology: Part I. Novelty Detection on a Laboratory Structure.* Journal of Sound and Vibration, Vol. 259 (2), pp. 323–343, 2003.

[6] Worden K, Manson G, Allman D. *Experimental Validation of a Structural Health Monitoring Methodology: Part II. Novelty Detection on a Gnat Aircraft*. Journal of Sound and Vibration, Vol. 259 (2), pp. 345–363, 2003.

[7] Worden K, Manson G, Allman D. *Experimental Validation of a Structural Health Monitoring Methodology: Part III. Damage Location on an Aircraft Wing*. Journal of Sound and Vibration, Vol. 259 (2), pp. 365–385, 2003.

[8] Mustapha F, Manson G, Pierce SG, Worden K. *Structural Health Monitoring of an Annular Component Using a Statistical Approach*. Strain. Vol. 41, pp. 117–127, 2005.

[9] Chetwynd D, Rongong JA, Pierce SG, Worden K. *Damage Detection in an Aluminium Plate Using Outlier Analysis*. Fatigue and Fracture of Engineering Materials and Structures. Vol. 31, pp. 629–649, 2008.

[10] Chetwynd D, Mustapha F, Worden K, Rongong JA, Pierce SG, Dulieu-Barton JM. *Damage Localisation in a Stiffened Composite Panel*. Strain. Vol. 44, pp. 298–307, 2008.

[11] Cavalini AA, Franco VR, Gonsalez CG, De Melo GP. *Noise Influence on Damage Detection Through Modal State Observers Methodology*, TEMA Tend. Mat. Apl. Comput., Vol. 9 (2), pp. 195–204, 2008.

[12] Overbey LA, Todd MD. *Effects of Noise on Transfer Entropy Estimation for Damage Detection*. Mechanical Systems and Signal Processing. Vol. 23, pp. 2178–2191, 2009.

[13] Escobar J, Rodriguez R, Gomez R. *Effect of Limited Modal and Noise Information on Structural Damage Detection*, 5th WDEAS International Conference on Instrumentation, Measurement, Circuits and Systems, Hangzhou, China, 68–73, 2006.

[14] Worden K, Farrar CR, Manson G, Park G. *The Fundamental Axioms of Structural Health Monitoring.* Proceedings of the Royal Society A, Vol. 463, pp. 1639–1664, 2007.

[15] Worden K. *Confidence Bounds for Frequency Response Functions From Time Series Models.* Mechanical Systems and Signal Processing. Vol. 12 (4), pp. 559–569, 1998.

[16] A. U. Rehman, K. Worden, J. A. Rongong, *Detection of damage in repeating structures*, Proceedings of ASME Turbo-Expo: Power for Land, Sea and Air (GT 2010), Gas Turbine Technical Congress & Exposition, GT 2010-23351,Volume 6: Structures and Dynamics, Parts A and B, pp. 1053–1061, Glasgow, UK.

[17] A. U. Rehman, K. Worden, J. A. Rongong, *Experimental and numerical investigation of damage detection in a mistuned bladed disc*, Structural Health Monitoring, Condition-Based Maintenance and Intelligent Structures, Volume 1, Proceedings of the 8th International Workshop on Structural Health Monitoring, 2011, Stanford, CA, USA.

[18] A. U. Rehman, K. Worden, J. A. Rongong, *Understanding the effects of a breathing crack on the dynamic response of cantilever-type structures for damage detection*, Structural Health Monitoring, Condition-Based Maintenance and Intelligent Structures, Volume 1, Proceedings of the 8th International Workshop on Structural Health Monitoring, 2011, Stanford, CA, USA.

Research and Applications in Structural Engineering, Mechanics and Computation – Zingoni (Ed.)
© 2013 Taylor & Francis Group, London, ISBN 978-1-138-00061-2

Modal characteristics-based damage identification in repeating structures

A.U. Rehman, F.H. Shah & S. Nazar
Department of Mechanical Engineering, University of Engineering & Technology, Lahore, Pakistan

C.E. Lord
Dynamics Research Group, Department of Mechanical Engineering, The University of Sheffield, Sheffield, UK

A. Javed
Department of Physics, The University of Punjab, Lahore, Pakistan

ABSTRACT: Crack initiation and propagation in a bladed system typically alters its overall dynamic response by causing local variation in the stiffness. The presence of a crack in one part of the repeating structure, such as a set of rotor or stator blades, affects the modal characteristics (natural frequencies, mode shapes and modal damping values) of the entire system. Changes in the modal characteristics will differ for each mode as they depend on the size and location of the crack. Thus, there exists an opportunity to utilize modal properties for crack detection. Accordingly, this work includes an investigation of modal characteristics-based damage detection techniques to highlight damage in repeating structures.

Modal Assurance Criterion (MAC) – based damage detection is an effective way to track damage growth in simple repeating structures by comparing the mode shapes of a structure in damaged and undamaged conditions. However, MAC is not a sensitive indicator to identify small damages accurately. To address this issue, further two modal characteristics-based parameters are considered in this work involving the first and second derivatives of the mode shapes – the slope and the curvature. Damage detection sensitivities are then compared for the modal vectors, slope and curvature considering a simple repeating bladed disc structure. Damage is considered in the form of a crack in one blade of the repeating structure which is represented by two crack surfaces resting on each other with no material removal in between. This represents a hair-line crack with no surface breathing or friction as modal analysis ignores any nonlinearity. However, the damage severity is varied by considering different crack depths at varying locations along the length of the blade.

1 INTRODUCTION

Repeating structures, in the form of multiple bladed sectors of a turbomachinery, are widely employed in aerospace, process and power generation industries worldwide [1]. Accurate functioning of any repeating structure depends on the structural integrity of the constituent components, as any damage developed in one part of the repeating structure can destroy the whole system and lead to a catastrophic failure. Therefore, any developing damage in the form of a crack must be timely detected before the ultimate failure occurs [2]. Various damage detection procedures have been developed over the recent decades to address damage detection in turbomachinery bladed system. These procedures involve utilization of various structural health monitoring (SHM) techniques and condition monitoring (CM) methodologies along with non-destructive testing (NDT) routines [3, 4, 5, 6]. Amongst these, modal characteristics of a system have also been given great concentration by the researcher to address damage detection in turbomachinery blades [7].

Modal characteristics of any structure comprise of its natural frequencies, mode shapes and modal damping ratios. These modal properties are highly dependent on the structure's physical and material properties, for example – density, modulus of elasticity, shape and size etc. Any change in these physical and material properties ascertains a corresponding change in the modal characteristics. This statement provides the basis for the modal characteristics – based damage identification in repeating structures [8].

Amongst the modal properties of any physical structure, mode shapes have proved to be a sensitive indicator for damage detection in repeating structures as compared to the shift in natural frequencies due to the presence of damage [turbo-expo paper]. Utilising the natural frequencies of a system for damage detection is reviewed in detail in [10]. The natural frequency is proportional to the square root of stiffness, thus a relatively large stiffness change is required before significant frequency change can be detected. The extent of the drop in the natural frequency depends on the location and position of damage with respect to the

mode shape of a particular mode of vibration [11]. Any damage or crack of a given size would result in a relatively small shift in the natural frequency as compared to the damage or a crack of the same size but located in a region of high stress [12]. This indicates that damage detection using frequency shifts might be unreliable due to the positioning of damage in the structure. Thus, the frequency shifts alone might not provide sufficient information regarding the existence and location of damage in the structure.

Mode shapes are sensitive indicators of the presence of damage in structures. Damage growth tracking can be accomplished by comparing two sets of modes in the experimental and/or numerical domains. The most commonly used method to compare the two sets of mode shapes is the utilization of the Modal Assurance Criterion (MAC). The MAC can take any value between zero and one. If the MAC indicates a value near zero, no correlation exists between two mode shapes. If the MAC indicates a value near one, the two sets of modes are fully consistent [13].

Detection of a structural fault by tracking changes in the mode shapes utilising the MAC was first reported in 1984 [14]. Besides the MAC, different criteria have been used over the years for model correlation. Amongst them, the Coordinate Modal Assurance Criterion (COMAC) attempts to identify the measurement degree of freedom contributing negatively to a low value of MAC. The Inverse Modal Assurance Criterion (IMAC) increases the sensitivity of the MAC to small mode shape changes by taking the inverse of modal coefficients. The Frequency Response Assurance Criterion (FRAC) compares any two frequency response functions having the same input/output relationship. These developments in the MAC have been precisely reviewed in [15]. The model correlation process usually involves a MAC plot, an auto-MAC plot and a natural frequency comparison. These three parameters can be viewed simultaneously using the Frequency-Scaled MAC on (FMAC) [16, 17].

Despite the applicability of the mode shape-based crack detection techniques to a wide range of applications, they still have some drawbacks. Extracted mode shapes are affected by noise issues, inconsistent sensor positions and the choice of the number of chosen sensors and their coordinates. In addition to these, the presence of damage in any structure has a less significant influence on the lower modes that are usually measured from the vibration tests [18], until the damage is severe enough to change the lower modes.

Another technique to detect and locate damage in structures is mode shape curvature and modal strain energy analysis. Mode shape curvature is more sensitive to local reductions in the stiffness due to damage in the structure than the modes shapes themselves. The first derivative of the mode shape is slope while the second derivative is curvature or strain. Both of these quantities suddenly change when damage appears in the structure and are dependent on the size of damage. Investigating any change in these mode shapes derivatives can help detecting and locating the damage inside the structure [19, 20]. The squared ratio of the undamaged structure's modal curvature to the damaged, referred to as the Fault Index (FI), is also found to be a sensitive indicator to the presence of damage but is strongly influenced by the presence of noise in the mode shape measurement [21]. The higher derivatives of the mode shapes are even more sensitive to damage but the experimental variations are amplified in the differentiation process. This problem can be overcome by selecting a mode shape based feature that is sensitive to the fault but insensitive to the noise. The first derivative of the mode shape (slope) has proved to be appropriate to rectify this issue [22]. In the absence of the availability of the undamaged structure's modal data, the possibility of utilising this technique for damage detection is investigated in [23]. Another modal strain energy-based damage detection study is reported in [24] where this method detected and located damage (in the form of a saw-cut crack) with an accuracy of less than 21 mm over a 725 mm stringer. Application of this method to detect damage in repeating structures has not yet been examined and is currently addressed in this paper.

In this paper, modal characteristics–based damage detection is addressed considering a simple repeating structure. Modal vectors, slope and curvature are utilized to compare the effectiveness of the MAC for damage identification. Different mistuning levels and patterns are also considered in addition to the varying crack depth and location along the length of the blade. Damage index, based on tracking the mode shapes, due to increasing damage severity, is correlated to the crack depths and is compared for modal vectors, slope, curvature.

2 FE MODEL OF BLADED DISC

A two dimensional disc type structure was considered as a representative base model for an actual turbomachinery bladed system. It is comprised of eight blades mounted on a thick circular base. The interface between the blade and disc was modeled as a rigid single piece to represent the geometry of a blisk. The geometry of the bladed disc model along with its finite element (FE) model mesh is shown in Figure 1. To keep

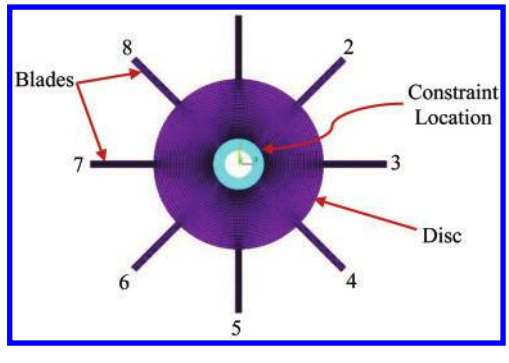


Figure 1. FE model of bladed disc.

the FE model simple, the bladed disc was meshed using 2-D plane stress (eight node quadrilateral) elements with mid-side nodes. The total number of elements in the bladed disc model was 7040. Out-of-plane mode shapes were not considered and the material assigned to this FE model was steel ($E = 200$ GPa, $\upsilon = 0.3$, $density = 8000$ kg/m^3). The model was constrained radially at the centre, indicating a rigid connection between the rotor and the connecting shaft. The blade thickness (d) was 6 mm, blade length (l) was 60 mm, the outer radius of base was 80 mm whereas the inner radius was 20 mm. Crack depth and location parameters were defined according to the guidelines described in [9], considering crack depth ratios (a/d) ranging from 0.01–0.9, at three different locations along the length of the blade ($b/l = 0.14$, 0.5 and 0.8). Cracks were simulated by the material removal crack modeling technique as accomplished in [9].

3 BLADED DISC MISTUNING PATTERN

The presence of mistuning in the bladed disc was simulated by attaching lumped masses to the blade tips. The quantity of these lumped masses and their distribution pattern was varied. It is useful to note here that a 0.1g lumped mass attached to one of the blade tips of the bladed disc results in a frequency drop of approximately 1.23% for the lower modes. In order to investigate the effect of different mistuning patterns in the presence of a crack on the modal characteristics of the whole bladed disc, the following mistuning patterns were considered:

3.1 *No Mistuning Present in the System*

In this scenario, the bladed disc was assumed to be a perfectly tuned system with all the sectors perfectly identical to each other. This case provided a reference for comparing the behaviour of the mistuned system with the tuned one in the presence of a crack in one of the blades of the bladed disc.

3.2 *Arbitrarily Mistuned System (Low Mistuning Level) – Model 1*

In this case, the bladed disc was arbitrarily mistuned by attaching an equal quantity of small lumped masses (0.1g) at the tips of Blades 1, 4 and 6. The purpose was to distinguish between the effects of the alternately mistuned system and tuned system.

3.3 *Arbitrarily Mistuned System (High Mistuning Level) – Model 2*

The bladed disc model was once again arbitrarily mistuned but this time, the level of mistuning was high in comparison to the previous case. Blades 1, 3, 4, 6, 7 and 8 were mistuned by attaching 0.2g, 0.1g, 0.2g, 0.1g, 0.1g and 0.5g respectively.

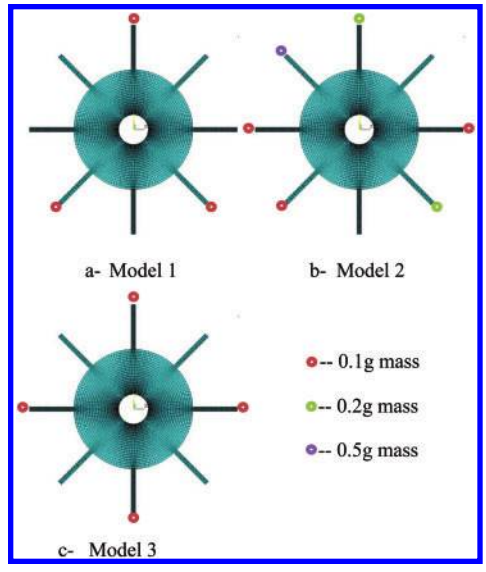


Figure 2. Bladed disc mistuning patterns.

3.4 *Alternately Mistuned System – Model 3*

In the alternately mistuned system, each alternate blade sector was equally mistuned. Blades 1, 3, 5 & 7 were mistuned by attaching 0.1 g of mass.

4 DAMAGE INDEX CURVES

For each of the crack depth ratios ($a/d = 0.01$-0.9) at different crack locations ($b/l = 0.14$, 0.5 and 0.8), displacement vectors were obtained for twenty modes. The MAC matrices were then generated comparing each case with a crack with the reference model (without crack). All mode shape matrices were obtained using data acquired from nodes at the same geometric locations. These MAC matrices were subtracted from the AutoMAC matrix of the reference case. The resulting matrix represents the MAC change and gives a measure of disorder due to the presence of the crack. A single scalar value for this matrix was obtained by calculating its Frobenius norm which therefore provides a measure of the extent of that disorder. The Frobenius norm of a matrix is defined as the square root of the sum of the absolute squares of its elements. Its mathematical definition can be obtained from Equation 1:

$$\|A\|_f = \sqrt{\sum_{i=1}^{m}\sum_{j=1}^{n}|a_{ij}|^2} \quad (1)$$

The Frobenius norm was calculated for each crack depth and location and plotted against crack depth ratios giving three curves, each representing different crack locations. In this way the extent of damage (damage index) due to crack initiation and propagation inside the blade was estimated.

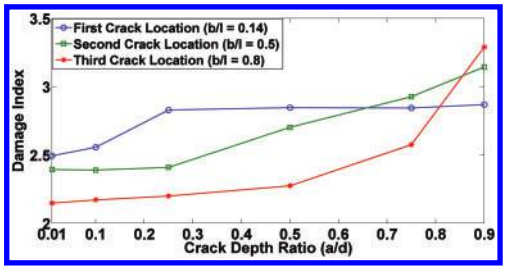


Figure 3. Damage index curves for tuned bladed disc.

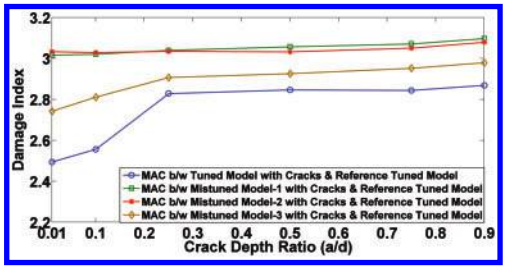


Figure 4. Damage index curves for mistuned bladed disc.

4.1 *Tuned Bladed Disc*

The damage index versus crack depth ratio plot is shown in Figure 3. The magnitude of the damage index for the first crack location represented by $b/l = 0.14$ was higher than for the second ($b/l = 0.5$) and third ($b/l = 0.8$) crack locations. The first crack location, $b/l = 0.14$ gave a steep damage index curve up to a crack depth ratio of 0.25 and then followed a continuous horizontal pattern in the magnitude. For the second crack location near the middle of the blade, $b/l = 0.5$, and third crack location near the blade tip, $b/l = 0.8$, the analysis showed an approximately smooth increase rate in the magnitude of the damage index considering crack initiation and then propagation. It was found that a very minute damage in one of the blades of the bladed disc model resulted in a sudden increase in the magnitude of Frobenius norm and this was indicated by a steep rise in the damage index curve. The extent of this sharp increment is greater for a crack of a certain depth near the blade root as compared to a crack in the middle or tip of the blade.

4.2 *Mistuned Bladed Disc*

In order to investigate the effect of the presence of mistuning on the damage index, the MAC matrix between the perfectly tuned bladed disc without any crack and three mistuned models, having cracks of various depths were computed. That MAC matrix was then subtracted from the AutoMAC of the perfectly tuned bladed disc without a crack. The damage index curves are plotted in Figure 4.

Mistuning causes mode shapes to be highly localized, corresponding primarily to the oscillation of a single blade. Besides this, vibration energy is no longer distributed along all the blades but confined to limited

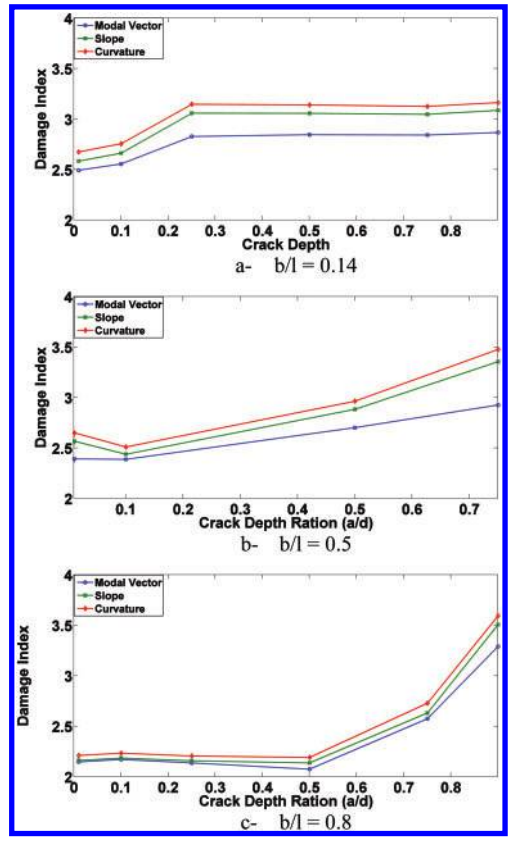


Figure 5. Damage index curves for modal vector, slope and curvature – Tuned bladed disc.

sets of blades. As the damage index plots are strictly dependent on the mode shapes obtained, higher magnitudes of the damage index can be attributed to the presence of localized modes due to mistuning. These localized modes for the tuned system, arbitrarily (low level) mistuned system, arbitrarily (high level) mistuned system and alternately mistuned system are shown in [2, 8].

5 MODAL VECTOR, SLOPE & CURVATURE

In damage index curves for the tuned and mistuned bladed disc, higher magnitudes of damage indices indicates a larger deviation in the modal behaviour of structure having cracks of various depths from the reference model and makes damage detection easier. In order to investigate this, two further parameters were considered to obtain damage index curves for the tuned and mistuned bladed disc. These were slope (first derivative of mode shapes) and curvature (second derivative of mode shapes). Bladed disc models having cracks near the blade root (b/l = 0.14), in the middle of the blade (b/l = 0.5) and near the blade tip (b/l = 0.8) were considered for this study and results for tuned bladed disc are shown in Figure 5a, 5b and

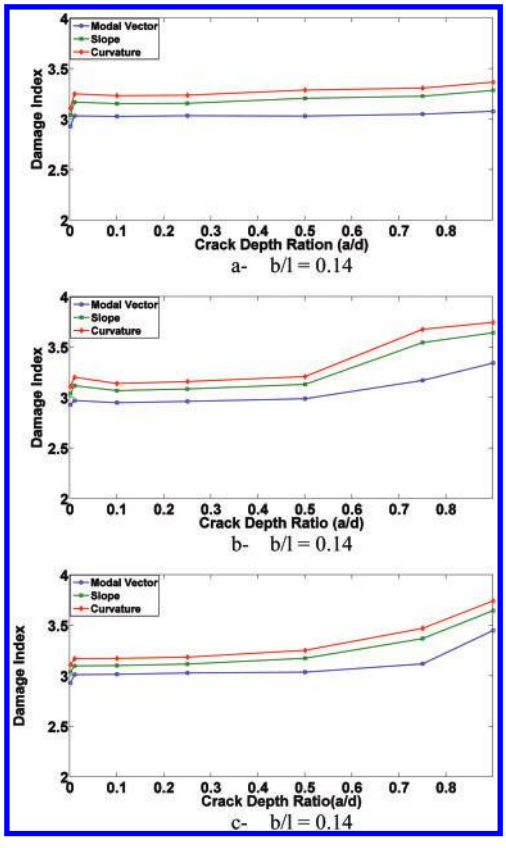


Figure 6. Damage index curves for modal vector, slope and curvature – Mistuned bladed disc.

5c respectively. Second derivative of mode shape, curvature, indicated higher sensitivity to the presence of crack in a blade by resulting in higher magnitudes of damage index as compared to the slope and modal vectors for all the three cases. However, the difference in the trend lines for modal vectors, slope and curvature for b/l = 0.8 is very small as compared to b/l = 0.14 and b/l = 0.5. This indicates that for any crack developed near the blade root or in the middle of blade, modal curvature indicates significantly higher sensitivity towards damage detection. Whereas for a crack near the blade tip, all three parameters indicate almost the same level of sensitivity for damage identification by resulting in similar values for the damage index.

In order to investigate the effect of mistuning on modal vectors, slope and curvature, damage index curves were obtained for a bladed disc having cracks of various depths considering mistuning model 2 (as defined in the previous section). Results are shown in Figure 6. Presence of mistuning resulted in higher magnitudes of damage indices due to mode localization. However, the trend comparison of the modal vector, slope and curvature follows the same pattern as in case of tuned bladed disc. It should also be noted that for the mistuned bladed disc, separation between the damage index curves of the modal vector, slope and

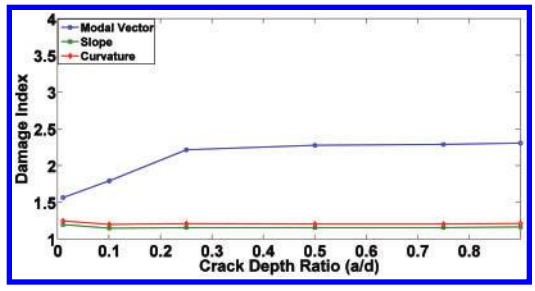


Figure 7. Damage index curves for blade tip data.

curvature is nearly the same for all three crack locations. This indicates that the selection of best suited parameter for damage detection is overwhelmed by the effects of presence of mistuning in the repeating structures. For all the three crack locations, modal curvature may be a better option to estimate crack in mistuned structures.

Applicability of this technique for a reduced data set from the blade tips (representing blade tip data) was also investigated and the results are shown in Figure 7. Slope and curvature indicated less sensitivity towards damage detection considering reduced data set from the blade tips by resulting in smaller damage indices. This is due to the fact that data acquired from the blade tip do not truly represent the actual modal deflection of a blade. Selection of modal vector as a damage detection parameter is a better option in comparison to its counterparts in this case.

6 CONCLUSIONS

A modal characteristics–based damage investigation was carried out in this paper considering a simplified repeating structure in the form of a bladed disc. Three modal parameters (modal vectors, slope and curvature) were considered for this study. It was found that for a tuned system, modal curvature indicated greater sensitivity to the presence of damage if the damage is present in the region between blade root and half way along the length of blade. However, for a crack developed near the blade tip, any of these three parameters can be used for damage estimation. For the mistuned system, the presence of mistuning resulted in similar trends of modal vectors, slope and curvature for any crack location (separation between the damage index curves is similar). For the reduced data set from the blade tips, slope and curvature proved to be insufficient to highlight the damage by resulting in lower damage index magnitudes.

REFERENCES

[1] Soares C. Gas Turbines: *A Handbook of Land, Sea and Air Applications*. Butterworth Heinemann 2007.

[2] A.U. Rehman, K. Worden, J.A. Rongong, *Crack detection in mistuned repeating structures,* ISMA 2010, pp. 1083–1098, Leuven, Belgium.

[3] Worden K, Farrar CR, Manson G, Park G. *The Fundamental Axioms of Structural Health Monitoring.* Proceedings of the Royal Society A, Vol. 463, pp. 1639–1664, 2007.

[4] Doebling SW, Farrar CR, Prime MB. *A Summary Review of Vibration-Based Damage Identification Methods*. The shock and Vibration Digest. Vol. 30, pp. 91–105, 1998.

[5] Auerkari P, Pitkanen J, Pihkakoski M, Muurinen L, Kangas P. *Maintenance of Gas Turbines-Impact and Implications for NDT*. Insight: Non-Destructive Testing and Condition Monitoring, 44(9), pp. 568–571, 2002.

[6] Heo GY. Condition monitoring using empirical models: Technical review and prospects for nuclear application. Nuclear Engineering & Technology, Vol. 4(1), pp. 49–68.

[7] Doebling SW, Farrar CR, Prime MB. *A Summary Review of Vibration-Based Damage Identification Methods*. The shock and Vibration Digest. Vol. 30, pp. 91–105, 1998.

[8] A.U. Rehman, Vibration based condition monitoring of a turbomachinery bladed system. PhD Thesis, University of Sheffield, UK, 2012.

[9] A.U. Rehman, K. Worden, J.A. Rongong, *Detection of damage in repeating structures*, ASME Turbo-Expo 2010, Vol. 6, pp. 1053-1061, Glasgow, UK.

[10] Salawu OS. *Detection of Structural Damage through Changes in Frequency: A Review*. Engineering Structures. Vol. 19, pp. 718–723, 1997.

[11] Moradalizadeh M. *Evaluation of Crack Defects in Frames Structures using Resonant Frequency Techniques*. MPhil Thesis. University of Newcastle Upon Tyne, Newcastle, 1990.

[12] Mirza MS, Ferdjani O, Hadj-Arab A, Joucdar K, Khaled A, Razaqpur AG. *An Experimental Study of Static and Dynamic Responses of Prestressed Concrete Box Girder Bridges*. Canadian Journal of Civil Engineering, Vol. 17(3), 481–493, 1990.

[13] Allamang RJ, Brown DL. *A Correlation Coefficient for Modal Vector Analysis*. International Modal Analysis Conference, pp. 110–116, 1982.

[14] West WM. *Illustration of the Use of Modal Assurance Criterion to Detect Structural Changes in an Orbiter Test Specimen*. Air Force Conference on Aircraft Structural Integrity, pp. 1–6, 1984.

[15] Allemang RJ. *The modal assurance criterion _MAC: Twenty years of use and abuse.* Proc., IMAC-XX: Conf. on Structural Dynamics. Los Angeles, 397–405, 2002.

[16] Fotsch D, Ewins DJ. *Application of Mac in Frequency Domain*, Proceedings of SPIE - The International Society for Optical Engineering 4062, pp. I/-.

[17] Fotsch D, Ewins DJ. *Further applications of the FMAC*. Proceedings of SPIE - The International Society for Optical Engineering. Vol. 4359 (1), pp. 635–639, 2001.

[18] Kim JT, Tyu YS, Cho HM, Stubbs N. *Damage Identification in Beam-Type Structures: Frequency-Based Method vs Mode-Shape-Based Method*. Engineering Structures. Vol. 25, pp. 57–67, 2002.

[19] Chance JC, Tomlinson GR, Worden K. *A Simplified Approach to the Numerical and Experimental Modelling of the Dynamics of a Cracked Beam*. 12th International Modal Analysis Conference, pp 778–785.

[20] Pandey AK, Biswas M, Samman MM. *Damage Detection from Changes in Curvature Mode Shapes*. Journal of Sound and Vibration. Vol. 145 (2), pp. 321–332, 1991.

[21] Ho YK, Ewins DJ. *Numerical Evaluation of the Damage Index*. Structural Health Monitoring, Stanford University, California, USA. pp. 995–1011, 2000.

[22] Ho YK, Ewins DJ. *On the Structural Damage Identification with Mode Shapes.* European COST F3 Conference on System Identification and Structural Health Monitoring, Madrid, Spain, pp. 667–686, 2000.

[23] Stubbs N, Kim JT. *Damage Localization in Structures without Baseline Modal Parameters*. AIAA Journal, Vol. 34 (8), pp. 1644–1649, 1996.

[24] Worden K, Manson G, Wardle R, Staszewski W, Allman D. *Experimental Validation of Two Structural Health Monitoring Methods*. Structural Health Monitoring, Stanford University, California, pp. 784–799, 1999.

Research and Applications in Structural Engineering, Mechanics and Computation – Zingoni (Ed.)
© 2013 Taylor & Francis Group, London, ISBN 978-1-138-00061-2

Research on corrosion monitoring for steel-reinforced concrete structures using fiber optic sensing technique

X.F. Zhao, L. Wang, Q. Liu, S.J. Shan, H. Dong, Y.F. Zhu, Y.H. Jiang & Y. Yu
School of the Civil Engineering, Dalian University of Technology, Dalian, China

ABSTRACT: One novel kind of Brillouin corrosion sensor was proposed and tested in this paper. Distributing strain sensing ability was utilized to monitor the corrosion expansion which is the key reason for concrete corrosion deterioration. Strain sensitivity test was designed to obtain the strain coefficient. And then one kind of Brillouin corrosion sensor packaging structure was designed and developed. The test results show that there is good linear relationship between Brillouin frequency shift and strain, and also corrosion expansion strain can be monitored using corrosion sensor developed precisely.

1 INTRODUCTION

Steel corrosion is the key factor leads to deterioration of steel reinforcement concrete structures and the consequent corrosion of steel will lead to severe damage of structures. The detection and measurement of corrosion are essential for damage evaluation and prevention, and also safety maintenance (Metha 1991, Matta 1992). Lots of research work has been conducted to monitor corrosion. Common corrosion monitoring methods reported are based on electrochemical method, whose durability and stability are the obstacles to long time span corrosion health monitoring. Comparing with traditional corrosion sensing technique, fiber optic sensing technique provides new approach for corrosion monitoring, with its advantages, such as good durability, good stability, electromagnetic interference immunity, high precision, etc (Lee 2003, Gafsi 1999). P. L. Fuhr and D. R. Huston developed the fiber optical chloride detector, whose sensing mechanism relies on spectroscopic analysis of a chemical reaction of chloride and reagents (Fuhr 1996). K. D. Bennett designed a prototype optical fiber sensor for monitoring corrosion on large steel structures and the sensor works by pulling a multimode fiber into a tight bend and securing it with a "corrosion fuse"(Bennett 1995). And Xueming Li proposed a Fiber Optic Corrosion Sensor (FOCS) fabricated by electroplating a Fe-C alloy film onto an optical fiber core within the sensing region (Li 1998). Research works mentioned above need extra packaging structure or sensing materials to transfer corrosion related parameters to fiber optic sensitive parameters detectible, which will affect durability and stability of corrosion sensors, inevitably. Fiber optic Brillouin sensing technique is deployed in this paper to provide one new approach to corrosion monitoring for good durability and stability measurement.

The fiber optic Brillouin sensing technique is based on Brillouin scattering phenomena. Fiber optic is utilized both as sensing element and signal transmission medium. When a short light pulse is launched into and transmitted along the fiber, the frequency of the Brillouin backscattering light can be measured at the same end. The time interval between sending the pulse and backscattering light arriving provides the spatial information, while the frequency of the backscattering light provides information of the temperature or strain distributed along the fiber optic. The backscattered Brillouin frequency is shifted from ... the incident light frequency because of the temperature variation and strain variation along the optic fiber. The Brillouin frequency shift is determined by the following equation (Horiguchi 2002):

$$f_B = 2nv_a / \lambda \tag{1}$$

Where f_B is Brillouin frequency shift, n is refractive index of fiber, v_a is the acoustic wave velocity and λ is wavelength of incident light.

The relationship between the Brillouin frequency shift at a certain location along the fiber and its corresponding temperature and strain change can be described as the following equation:

$$f_B = k_{ft}\Delta T + k_{f\varepsilon}\Delta\varepsilon + C \tag{2}$$

Where ΔT is temperature change, k_{ft} is temperature coefficient, $k_{f\varepsilon}$ is strain coefficient of Brillouin frequency shift, $\Delta\varepsilon$ is strain change and C is a constant.

In the case of pure strain variations, the relation can be simplifies as :

$$f_B = k_{f\varepsilon}\Delta\varepsilon + C_1 \tag{3}$$

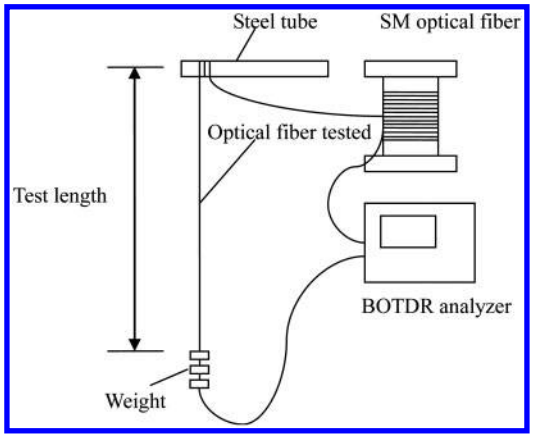


Figure 1. sensitivity test set up.

As a result, by measuring the Brillouin frequency shift we have access to the local temperature and strain conditions along the fiber optic.

When corrosion coursed by Cl- penetration or carbonation happens, there will be one rust accumulation layer on the steel rebar surface with cross section reduction. Generally, rust volume of corrosion is 2–4 times than steel volume lost, which is the reason for corrosion expansion of steel rebar in reinforcement concrete structure. If single mode fiber optic was winded around the steel rebar into coils, the rust expansion will lead to the elongation of fiber optic. According to the sensing principle of Brillouin sensing technique, strain distribution along the fiber optic coils can be detected by Brillouin Optical Time Domain Analysor (BOTDA).

2 STRAIN SENSITIVITY TEST

Single mode fiber optics with sensing lengths of 1 m and 2 m were studied, and strain calibration experiments were designed and conducted to obtain the strain coefficients for monitoring corrosion expansion strain In the experiments, a steel tube with 5 cm of diameter was used to support fiber optics with sensing lengths of 1 m or 2 m, respectively, as Figure 1 shows.

Weight was loaded and unloaded using weights ranging from 0 to 200 g, in increments of 50 g. Two load cycles were conducted for each kind of test length. Spatial resolution of 1 m, and a sampling interval of 0.41 m was used for every experiment. The Brillouin frequency was measured using BOTDA analyzer in every load step.

Diameter of fiber optic is 0.125 mm, and Young's modulus is 0.72×105 N/mm^2. According to elastic theory, there should be uniform strain distribution along the test length of fiber. When the weight of 50 g is loaded at the end of fiber, the strain change along the fiber is 558 $\mu\varepsilon$.

In the fiber optic circuit, only the sensing fiber optic with length of 1 m and 2 m is under extension load.

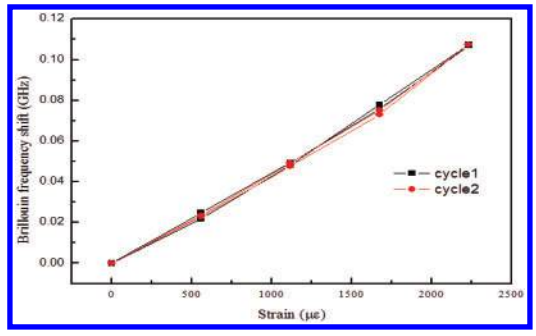


Figure 2. Strain sensitivity result of sensor with length of 1 m.

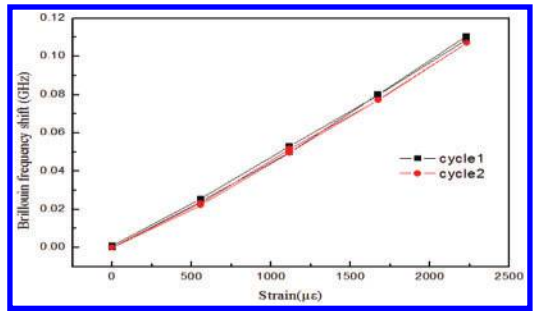


Figure 3. Strain sensitivity result of sensor with length of 2 m.

There is signal change of the Brillouin frequency in the sensing fiber area, and no apparent signal change is found in any other part of fiber optic circuit, as Figure 11 shows. The signal peak grows gradually as loads from 0 g to 200 g were added in increments of 50 g. The maximum value at each signal peak is used to calibrate the strain coefficient.

There were very good linear relationships between load and Brillouin frequency, when test length is 1 m and 2 m, as figure 2 and 3 show Also, good linear relationships between strain loaded and Brillouin frequency are found. Averaging strain coefficient of 0.048 MHz/$\mu\varepsilon$ was obtained.

The strain calibration experimental results show that single mode fiber optics with sensing lengths of 1 m and 2 m can serve as strain sensors. The strain coefficients obtained with the two kinds of length show very good agreement. There is very good linearity of the results with the BOTDA analyzer using the spatial resolution of 1 m and sampling interval of 0.41 m.

3 CORROSION MONITORING TEST

3.1 *Corrosion sensor design*

Design scheme of Brillouin corrosion sensor is illustrated in Figure 4 and sensor packaging method follows the steps as described below: 1) polish the surface of a 50 mm-length part of a steel rebar with diameter of 22 mm(ϕ22), after which the diameter in polishing

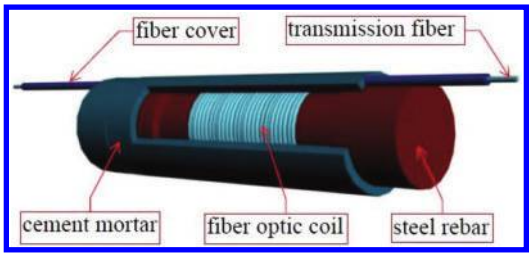


Figure 4. Packaging structure of Brillouin corrosion sensor.

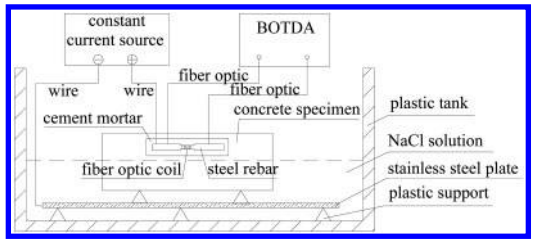


Figure 5. Schematic diagram of the electrochemical corrosion accelerating test system.

area decreased to 18 mm. 2) wind about 50 circles of single mode fiber optic into coils with a little pretension, which will guarantee the close contact of fiber optic and steel rebar surface. The total winding length of the fiber optic is about 3.0 m. 3) fix both ends of the fiber optic on the rebar using epoxy glue, and draw out the fiber optic along the steel rebar. 4) Put one layer of cement mortar with depth of 4 mm outside the fiber optic to prevent damage to fiber optic coil winding. Cement mortar mass mix rate is Cement: Water: Sand = 1:1.15:3.Cement mortar layer can provide better packaging structure with little interference to corrosion interface than other packaging materials, which make the steel rebar inside corrosion sensor have one corrosion development close to real corrosion development. In the sensing structure, fiber optic in coil winding area serves as sensing element, and the other severs as signal wire for light transmission. There are two ends of fiber optic were lead out of the cement mortar layer for connection with BOTDA.

Single mode fiber optic used is Corning G.657.A/B, minimum bending curve radius of the fiber optic is 7.5 mm, which will keep optical loss in a very low level after dozens fiber optic coils were winded.

3.2 *Corrosion test*

In order to study the sensitivity of Brillouin corrosion sensor developed, one electrochemical corrosion accelerating testing system was designed and built to accelerate the steel rebar corrosion process in concrete specimens, as shown in figure 5. In the system, the steel rebar was the a node and the stainless steel plate was the cathode. When electric current was applied, the circuit between the steel rebar and the plate was conducted by Cl^-, which will transport Cl^- ion in the solution to the surface of the rebar continuously. Cl^- is one of the most important factors influencing the corrosion of the steel rebar, and therefore this kind of experiment setup can accelerates the rate of corrosion enormously. During the test, the mass concentration of the solution of NaCl is 5.0%, and the constant current source was applied. The current through the specimen was 0.05A.

Before the test, the corrosion sensor was embedded into concrete specimens by concrete casting. The size of concrete specimen was 100 mm * 100 mm * 300 mm. Ultimate strength of concrete was 30 MPa. The cement using was P.O 32.5, and the concrete mix mass ratio Cement: Water: Sand: Aggregate = 1: 0.4: 1.26: 2.24. One sensor was embedded into concrete specimen, and placed along the axis of the specimen close to upper surface, as shown in figure 5. Half immersing accelerating corrosion method used here can guarantee relatively high corrosion speed and less corrosion rust leakage. The specimen was putted into the steam maintaining room for 10 days, after casting, and kept at room temperature at 22°C for 3 days before it was tested.

BOTDA analyzer used was DiTest STA202-C made by Omnisens Company. It was used to collect monitoring data during the tests, whose sampling interval is 0.41 m, and spatial resolution 1.0 m, and strain resolution is 2 $\mu\varepsilon$. BOTDA analyzer was set up to scan the optical circuit every one hour automatically, during the tests.

3.3 *Result analysis*

Electrochemical corrosion accelerating test was conducted on the specimen continuously until the signal of sensing fiber optic became very week that BOTDA analyzer cannot detect it. The test lasted for 32.5 hours. There is no crack found on surface of specimen after test. Figure 6 shows the relationship between distance and Brillouin frequency at different time sampling point. There is one signal peak of Brillouin frequency shift at the distance 33.78–37.03 m, where is the fiber optic coil of corrosion sensor located in the fiber optic circuit of experiment system. No apparent signal change was detected in other locations of fiber optic. The signal peak grows gradually as the test proceeded. Results reveals that the corrosion sensor can monitor Brillouin frequency variation in fiber optic coil area coursed by the steel rebar corrosion expansion in the specimens.

Frequency value of every sampling point monitored is average Brillouin frequency along area in certain length of fiber optic in backward direction (the length of the area equals to spatial resolution specified).The area is called sampling area of one sampling point. If sampling area is fully located in sensing area, the point is called Valid Monitoring Point (VMP). If only one part of sampling area of one sampling point is located in sensing area, the point is called Invalid Monitoring Point (IMP). The other points are called Transmitting Point (TP). Considering the spatial resolution, sampling interval and length of sensing fiber

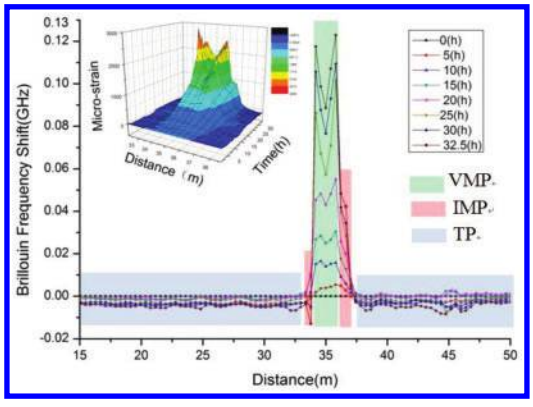


Figure 6. Brillouin frequency result of Brillouin corrosion sensor.

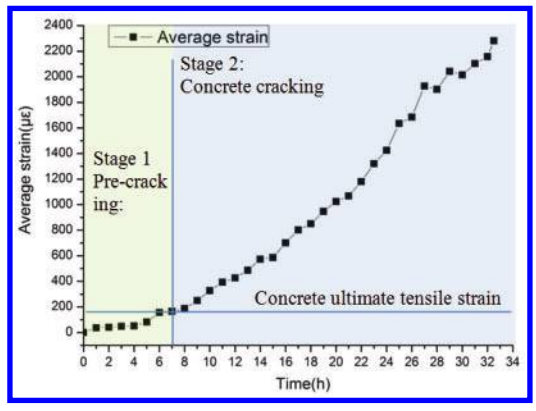


Figure 7. Average strain result of Brillouin corrosion sensor.

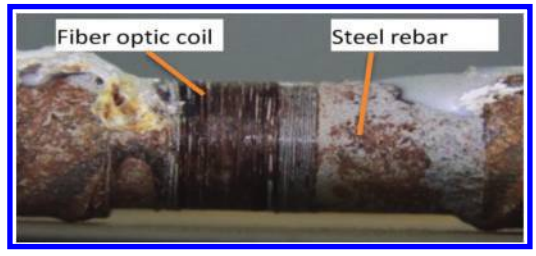


Figure 8. *Corrosion status of steel rebar inside Brillouin corrosion sensor after test.*

optic, five valid monitoring points was selected, as shown in figure 6. Five valid monitoring points were located in 34.18 m, 34.59 m, 35 m, 35.4 m and 35.81 m in fiber optic circuit, respectively. From 3D view of the Brillouin frequency shift monitored, increasing trend of Brillouin frequency can be seen clearly. There are two small peaks in two sides of fiber optic coil area, which means that corrosion expansion monitored is not very evenly distributed along the steel rebar in sensing area. Maximum value of 0.12286 GHz was monitored at sampling point at 35.81. There is little change in transmitting fiber optic area, which is because of that there is little environment temperature change. Because of that there is good linear relationship between Brillouin frequency and strain applied, strain coefficient of 0.048 MHz/$\mu\varepsilon$ obtained from strain calibration test was used here to calculate the expansion strain. Average expansion strain around steel rebar surface was obtained using values from five valid monitoring points, as shown in figure 6. Result show the expansion strain increase gradually as accelerating test proceeded. At very beginning, expansion strain of 37 $\mu\varepsilon$ by corrosion is monitored one hour after test started. And then strain increases gradually. Ultimate tensile strain of concrete is about 160 $\mu\varepsilon$, beyond which expansion crack will occur. Strain monitored at 7th and 8th hour is 156 $\mu\varepsilon$ and 165 $\mu\varepsilon$, respectively. There will be crack occur at this moment, after which bigger expansion strain increasing slope can be observed. Corrosion speed increases as the interface between steel rebar and concrete was damaged by crack development. Then corrosion expansion strain increases with a high speed, until maximum average strain of 2282 $\mu\varepsilon$ is monitored.

Test results show that Brillouin corrosion sensor is very sensitive to corrosion expansion strain, and can detect the strain change at first hour. And also this kind of sensor can capture the corrosion speed different at crack occur moment around concrete ultimate tensile strain value, with which corrosion status can be evaluated to two stages: pre-cracking stage, cracking stage, as shown in figure 7.

After the test, concrete specimen was broken to inspect corrosion status of steel rebar inside. There is one corrosion rust layer on the steel rebar surface, as shown in figure 8; there is no spot corrosion found. The fiber optic coil is not broken, it can be seen that there are rust between fiber optic coil and steel rebar. Reason of the signal detection failure at the end of corrosion accelerating test is the big optical loss by micro bending from corrosion expansion.

4 CONCLUSIONS

One novel kind of cement mortar packaged Brillouin corrosion sensor was proposed in this paper. Single mode fiber optic coil winding with cement mortar protection layer was used to monitor strain change by corrosion expansion of steel rebar. Test results shown that Brillouin corrosion sensor is very sensitive to corrosion expansion strain, can detected the strain change at first hour. And also this kind of sensor can capture the corrosion speed different at crack occur moment around concrete ultimate tensile strain value, with which corrosion status can be evaluated to two stages: pre-cracking stage, cracking stage. And with assumption of even corrosion, diameter of steel rebar can be calculated using average strain monitored. This kind of sensor is featured with low cost, long durability, and expansion strain monitoring ability, which can be used for corrosion monitoring and evaluation of steel reinforcement concrete structures in a long time span.

ACKNOWLEDGMENTS

This research is made possible by the National Natural Science Foundation of China (51278085 and 5092100), Key Projects in the National Science & Technology Pillar Program during the Twelfth Five-Year Plan Period (2011BAK02B02), and the Fundamental Research Funds for the Central Universities.

REFERENCES

Metha, P.K. 1991. Durability of concrete—-fifty years of progress, *Durability of concrete: Second international conference*, Montreal, Canada, 1–32.

Matta, Z. G. 1992. *Chlorides and corrosion in the Arabian gulf environment*, concrete international, 14(5), 47–48.

Lee, B. 2003. *Review of present status of optical fiber sensors*, Optical fiber technology, 9(2), 57–79.

Gafsi, R., Malki, A., Ahdad, F., Lecoy, P., Bures, J. 1997. *Static stress optical-fiber sensor*, Sensors and actuators A: Physical, 62(1), 501–505.

Fuhr, P.L, Huston, D. R. 1996, *Embedded chloride detectors for roadways and bridges*. Proc SPIE, 2719, 229–237.

Bennett, K. D., McLaughlin, L. R. 1995, *Monitoring of corrosion in large steel structures using low cost optical fiber sensors*. Proc SP IE, 2446. 71–82.

Li, X. M. , Chen, W. M. , Huang. Z. Q. et al. 1998. *Fiber optic corrosion sensor fabricated by electrochemical method*. Proc SPIE. 3330–3333.

Horiguchi, T., Shimuzu, K. Kurashima, T. Tateda, M. 1995, Development of a distributed sensing technique using Brillouin scattering, J. Lightwave Technology. 13(5). 12–18

Research and Applications in Structural Engineering, Mechanics and Computation – Zingoni (Ed.)
© 2013 Taylor & Francis Group, London, ISBN 978-1-138-00061-2

Steel reinforced concrete structures dynamic damage monitoring using guided wave testing technique

D.S. Li & J.H. Yuan
School of Civil Engineering, Dalian University of Technology, Dalian, China

W. Yang & W.Y. Zhang
Fujian Academy of Building Research

ABSTRACT: The base theory and principle of ultrasonic guided waves was briefly presented. By using finite element analysis program ANSYS to establish the steel model, and imposed excitation load on the terminal of the steel, to simulate the spread of ultrasonic guided waves and the reflected echo of defects. Through the analysis of the received signal, we could find the position accurately, and systematic analysis of the depth factor and axial length factor. The result of simulation was proved by experiment, The results obtained by numerical simulation agree well with that of experiments previously conducted by former investigators.

1 INTRODUCTION

Steel bars have been widely used in civil engineering, such as anchor bolt in geotechnical engineering, suspender in construction engineering, and steel wire in the cable-stayed bridge. These structures usually play a major bearing role in the project, easily influenced by the external environment, emerging the defects, resulting in huge economic losses and casualties. The detection in the course of using has a very important significance. The most common methods to detect the steel bars corrosion are as follows, drill cores, half-cell measurement, ultrasonic waves and radar [2–3]. But all these methods have their own shortcomings. Drill cores can only get the local information of test point, bringing the damage to the whole structure. Half-cell measurements are easily affected by resistance and pH of concrete. Ultrasonic waves and radar propagate short distance and only sensitive to significant defects. Thus, a more precise and efficient method is urgently needed.

UGW, as a developed tool, have many advantages comparing to traditional detective methods. First, it can propagate a long distance, because of its little attenuation in steel [4]. This characteristic is especially suitable for detection of the long range bridges; Second, high sensitivity is another merit of the method. UGW have many different modes at a single frequency and these modes are sensitive to different defects. Third, UGW have broad coverage. The whole information of the rebar and concrete can be obtained using a pair of transducers. The reason is that the sound field spreads all over the waveguide instead of a single point or surface. Therefore, it is meaningful to investigate the propagation characteristics of UGW.

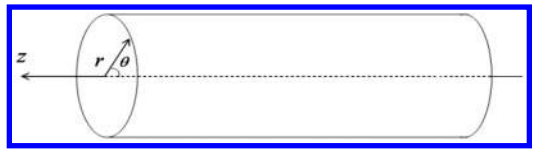


Figure 1. Geometry profile of steel rebar.

2 THE THEORETICAL BASIS

2.1 *Ultrasonic guided waves in rebar*

The propagation of guided waves is in accordance with elastic theory in elastic media, while in non-elastic media, they follow the viscoelastic theory. Pipes, anchor molts, rails and steel rebar are typical waveguides. The geometry profile of rebar is presented in Fig. 1.

There are three different modes propagating in cylindrical waveguide, longitudinal modes L (0, m), torsion modes F (n, m) and flexural modes F (n, m). In this expression, m and n stand for circumferential order and modulus, respectively. The displacement is symmetrical corresponding to $n = 0$, while $n = 1, 2, 3 \ldots$, refer to asymmetrical displacements. Therefore, L (0, m), T (0, m) are symmetrical modes and F (n, m) are asymmetrical modes.

The longitudinal modes that propagate in steel rebar have only two types of displacement, radical displacements and axial displacements. The boundary condition is $u_\theta = 0$, and u_z u_r are independent of θ. Taking into account of the boundary condition $\sigma_{rr} = \sigma_{rz} = 0 (r = a)$, Pochhammer frequency

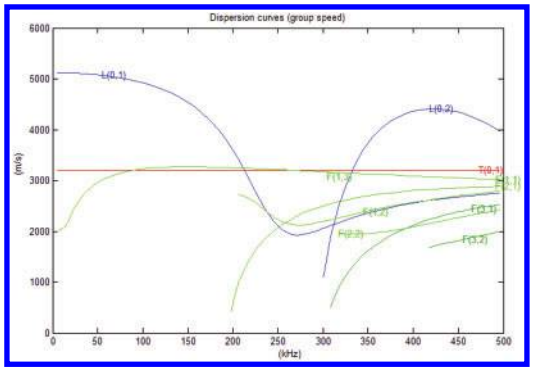


Figure 2. Disperse curve for the 12mm diameter steel.

equation can be achieved by solving the wave equation.

$$\frac{2\alpha}{a}\left(\beta^2+k^2\right)J_1(\alpha a)J1\left(\beta a\right)-\left(\beta^2-k^2\right) J_0(\alpha a)J_1\left(\beta a\right)-4k^2\alpha\beta J_0\left(\beta a\right)=0 \quad (1)$$

where λ is the length of guided waves, ω is angular velocity, k is wave number, J is Bessel function and coefficients $\alpha^2=\omega^2/c_L^2$, $\beta^2=\omega^2/c_T^2-k^2$, c_L is velocity of longitudinal guided waves, c_T is velocity of transverse guided waves , c_P is phase velocity. This is a transcendental equation with independent variables ω and k. Basing on the theory of mathematics, we know there are more than one solution to a single frequency ω. This phenomenon corresponds well with the fact that many modes are existed at a single frequency. This is the multiple modes property of UGW.

2.2 *Dispersion curves*

The curves that depict the relationships between frequency and phase velocity, frequency and group velocity are called dispersion curves. The phase velocity is defined as the speed of the phase of wave propagation in the waveguide while group velocity corresponds to the speed of wave packet propagation. Above definitions are the two fundamental parameters that describe the characteristic of wave propagation. All waveguides, both symmetrical ones and asymmetrical ones, have special dispersion curves.

Take the 18 mm rebar as an example, its area of cross section is 201.1 mm^2, density is $\rho=7858.5$ kg/m^3, and Young's modulus, passion ratio are 206 GPa and 0.28, respectively. We can neglect the influence of ribs when the ratio of diameter to length is less than 0.4. The ratio of diameter to length is 0.025. Thus, we can ignore the effect of steel ribs. Dispersion curves showed in Fig. 2 can be achieved by numerical calculation.

2.3 *Steel rebar corrosion damage detection principle*

When guided wave is propagated in the medium encountering defects, it is occurred reflection, transmission and mode conversion, resulting in the echo which brings the whole structure information. Dealing with the received signal we can determine the location of the defect, Figure 3 for the defect locations principle.

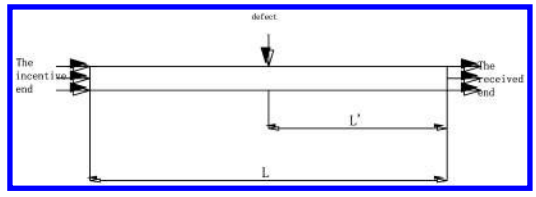


Figure 3. Principle of defect position.

Incentive side and the receive side are both at the end of the rod, the distance between the receiving end of the defects at the distance is L′, time interval between the incentives end and receiving end of the echo signal received is t, time interval between the defect echo and echo is t′, velocity of longitudinal wave is c, using the formula $L=ct'=ct'/2$, we can determine the length of the rod and the location of the defects.

2.4 *Reflection coefficient*

When guided waves speed to the rod-shaped structure defects, it will occur the phenomenon of reflection and transmission .In order to accurately analysis the impact on the detection for of the crack size, define the dimensionless reflection coefficient R.

$$R_c=\frac{V_b}{V_t} \quad (2)$$

Among them, V_b is the peak of the wave packet which defects back, V_t is the peak of the first signal wave packet. The reflection coefficient is a dimensionless parameter, which does not contain the size of the parameters, of the excitation signal, so it can be widely used to characterize the size of the defect echo. The quantitative research of guided-wave defect detection is of great significance.

3 NUMERICAL SIMULATION

3.1 *Steel rebar corrosion damage detection principle*

Numerical Simulation we selected diameter is 12 mm, length 1.2 m, round steel, elastic modulus 210 Gpa, Poisson's ratio is 0.3, the density of 7800 kg, and unit type is solid45 units.

For the transient dynamics analysis type, we select the FULL method, select the superposition of a single audio signal after 5 cycles hanning window regulator, the signal frequency is 100 KHZ, shown in Figure 4. The cell size selection within each wavelength range consists of 10 units to meet the requirements of the calculation accuracy. so we Can calculate the wavelength of $\lambda=4900/100\ 000=0.049$ m $=49$ mm, so choose

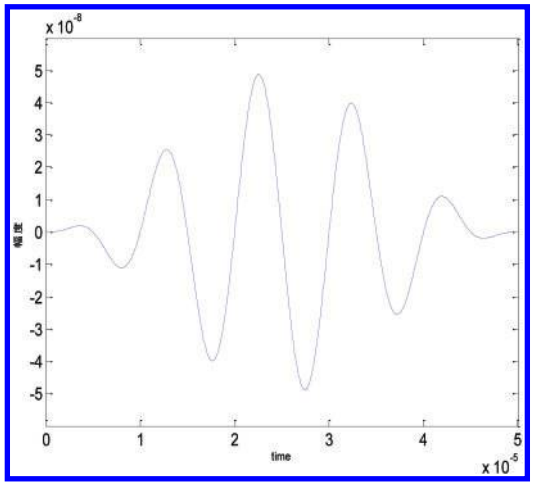


Figure 4. Sketch of exciting signal.

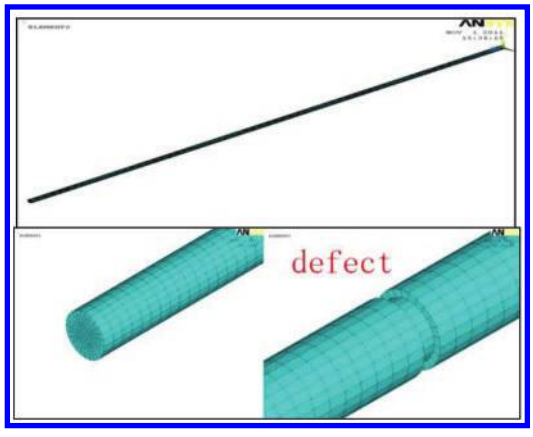


Figure 5. Model and meshing by ANSYS.

the 3mm divided into a unit. The finite element model was shown in Figure 4. The defects are Circumferential defects, and the defect length is divided into an integer multiple of the grid.

4 NUMERICAL SIMULATION

4.1 *Signal processing*

As guided waves is multi-modal, usually includes a variety of modes in its received signal. Simulated depth of 0.6 mm, 1.2 mm and 1.8 mm, the length of 3 mm, 6 mm, 9 mm, 12 mm and 15 mm defects, the results are shown in Figure 6 to Figure 9.

Then simulated two defects, the distance between defect and the receiving end are 600 mm and 300 mm, the length of defect is 3 mm, the depth of the defects were 0.6 mm, 1.2 mm and 1.8 mm. The simulation results are shown in Figure 9.

According to the dispersion curves, around the frequency of 100 kHZ, group velocity is huge difference

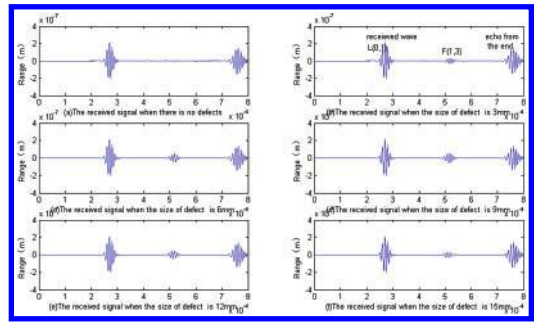


Figure 6. Signal from the terminal, 0.6 mm in defect depth, 3 mm, 6 mm, 9 mm, 15 mm in axial separately.

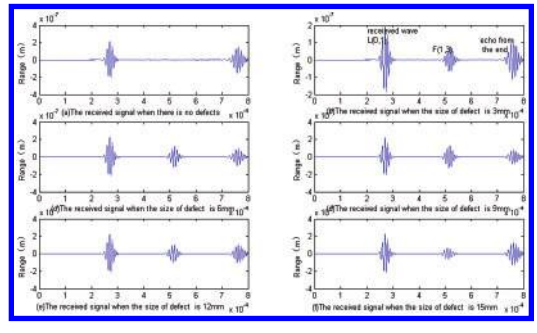


Figure 7. Signal from the terminal, 1.2 mm in defect depth, 3 mm, 6 mm, 9 mm, 15 mm in axial separately.

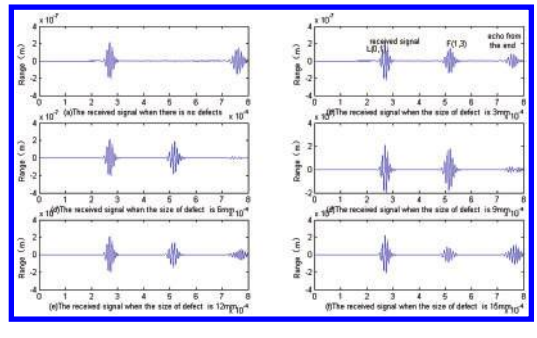


Figure 8. Signal from the terminal 1.8 mm in defect depth 3 mm, 6 mm, 9 mm, 15 mm in axial separately.

between the L (0,1) mode guided wave and F (1,1) mode guided wave difference, so their wave packet will separate ,it is easily indicated, it is easy obtained to identify. In addition, because around 100kHZ group velocity curve is sharper than the other modes, so dispersion phenomena is more serious than the other modes, the length of wave packet is longer for than the other modes wide in the time domain, in Figure 6 to Figure 9, this phenomenon can be found. When the guided wave meet the defects, it will occur modal transformation, and inspire the F (1,3) mode guided wave, at last, it will be received at the receiving end. Figure 6 to Figure 9 also made a corresponding identity. These are consistent with the theoretical analysis of guided wave dispersion.

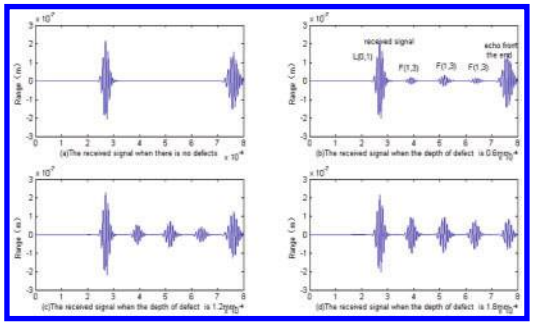


Figure 9. Signal from the terminal, 3 mm in axial, double defects, 0.6 mm, 1.2 mm, 1.8 mm in defect depth.

As for the case of two defects, there will be three defect echoes, because the receipt of the second defect echo, it will continue to reflect, the reflected waves encounter the first defect will occur launch and received, so it will form of the third defect echo. Because it had produced a modal superposition, so it did not get the effect that the margin getting smaller and smaller.

4.2 *Defect detection results and analysis*

In the diameter of 12 mm, length 1200 mm steel rebar, there is a circumferential defect in the distance from the receiving end of 600 mm, Figure 5 to Figure 8 is the echo chart. We can conclude that, guided wave which generated from the incentive side, encountered defects and the transmitted wave reach the receiving end reflect, once again encountered the defect, the defect echo is received by the receiving end. Therefore, the clearer defect echo must be received in the first $L(0,1)$ and the second received L (0,1). when the frequency is100 kHZ , the speed of L (0,1) mode is 4914 m/s, take the defect depth is 0.6 mm, length is 0.3 mm for example, the first wave of the echo signal 0.2444 ms defect echo signal 0.4876 ms calculated, we can see the length of the reinforcement 4 914 * 0.244e-3 = 1.201 m, the location of the defect (0.4828e-3-.2444) * 4914/2 = 05946, the actual length and defect location is 1.2 m and 0.6 m, so the relative error of 0.087% and 0.895% respectively. in the allowable error range. All the calculation results are shown in Table 1.

It should be stated that, the main features of the guided wave technology is the large detection range, long distance detection, for use of defect detection of large-scale structure, the relative error in this article works within the error range. The source of the error is the error of the data read from the time domain graph, and this is the recognition by the human eye. Therefore, the ultrasonic guided wave detection of reinforced length and positioning defect location is feasible.

4.3 *The variation between the reflection coefficient and crack size*

Figure 10 indicate the depth of 0.6 mm, 1.2 mm and 1.8 mm, relationship between axial length of

Table 1. Results of calculation of the reinforcement length and defect location for a single defect.

Items	Calculation the length	Calculation the location of defect	Error for length	Error for defect location
No defects	1.2030	none	0.251%	none
defect length:3 mm depth:0.6 mm	1.2011	0.5951	0.087%	0.813%
defect length:6 mm depth 0.6 mm	1.1971	0.5976	0.240%	0.403%
defect length:6 mm depth: 1.2 mm	1.2030	0.5966	0.251%	0.567%
defect length:6 mm depth: 1.8 mm	1.2050	0.5956	0.415%	0.731%

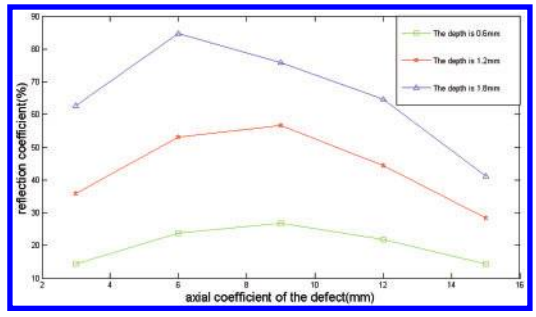


Figure 10. Relationship between the axial length and reflection coefficient.

reinforced the circle distribution defects of and the reflection coefficient.

It can be seen from Figure 10, the reflection coefficient will reach the maximum when the length of defect axial is 6 mm or 9 mm, when the length of defect axial is less than 6 mm or greater than 9 mm, the reflection coefficient reduce. This may be due to the echo in the front section of the defects and in the cross-section of the defects mutual interference. When the distance between back and forth section is even multiple as wavelength of the incentive guided wave, it will occur Mutual enhancement interference, so that the reflection coefficient increases; When the distance between back and forth section is odd multiple as wavelength of the incentive guided wave, it will occur Mutual counteract interference, so that the reflection coefficient is minimum.

Figure 11 shows the axial length of 3 mm, 6 mm, 9 mm, 12 mm and 15 mm, the affection of the defect depth on the reflection coefficient. In figure, the horizontal axis is the ratio between the defect depth and the radius.

It can be seen from Figure 11, the depth coefficient and reflection coefficient are essentially linear

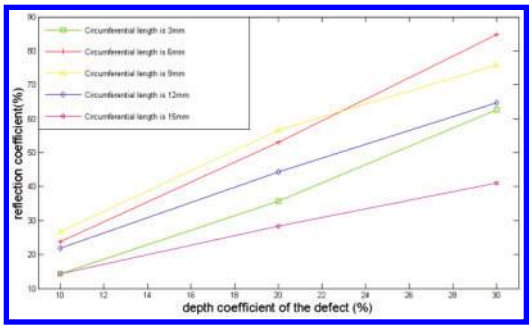


Figure 11. Relationship between the depth and reflection coefficient.

variation. That is, the deeper the defects, the greater the reflection coefficient. This may be due to that along with the defect depth increasing, the guided wave through defects will be reduced, the peak will fall, after echo through the defects, and then return to the receiving end receives, the defects increases, the peak of the defect echo will increase, therefore, the reflection coefficient will increase.

5 CONCLUSIONS

Through theoretical analysis, numerical calculation and experimental research can draw the following conclusions:

(1) The time of cracks reflected wave can accurately determine the crack location. The time of cracks reflected wave has nothing to do with crack size, but with crack position and material parameters.

(2) With the increase of axial length of defects, the emission coefficient changes erratically; when the defect depth changes, the emission coefficient is of linear change. That is, it is not sensitive to the axial width of the axial crack width for the reflection coefficient.

The main error comes from the calculation of material constants (such as wave velocity, density, etc.) different with the experimental material constants and the error of the defect echo time read from the oscilloscope.

REFERENCES

Barros J A O, Fortes A S. 2005. Flexural strengthening of concrete beams with CFRP laminates bonded into slits. *Cement and Concrete Composites*, 27: 471–480

Saud A, Ammar A O, Ashraf B. 2009. Accelerated weathering effects on the mechanical and surface properties of CFRP composites. *Materials and Design*, 30:833–837

Kolesnikov B, Herbeck L, Fink A. 2008. CFRP/titanium hybrid material for improving composite bolted joints. *Composite Structures*, 83: 368–380

Rose, J. L. 2003. Dispersion curves in guided wave testing. Materials Evaluation. 1:20–22

Research and Applications in Structural Engineering, Mechanics and Computation – Zingoni (Ed.)
© 2013 Taylor & Francis Group, London, ISBN 978-1-138-00061-2

Structural condition assessment based on modal flexibility from operational modal analysis and model updating

L.-M. Zhang, T. Wang & X.-K Lin
Dynamic Testing & Analysis Center, Nanjing University of Aeronautics & Astronautics, P.R. China

ABSTRACT: The deflection of a bridge under predetermined loading is widely utilized for bridge condition assessment. A modal flexibility method based on advanced operational modal analysis (OMA) and finite-element model (FEM) updating is proposed. Modal frequencies and mode shapes can be identified directly from OMA based on traffic-induced bridge vibration response measurements. In order to obtain modal masses accurately, a fine FE model of the bridge is built followed by model updating using modal parameters obtained from OMA. Flexibility matrix, and hence deflection shape with known static loading, can then be derived and applied for condition assessment instead of running an expensive and time consuming static testing. Both narrow band and broadband OMA techniques, based on frequency-spatial domain decomposition (FSDD) and polyreference Right Matrix Fraction Polynomial (RMFP) modal identification algorithms, are utilized for OMA. The influence of traffic mass loading and modal truncation to the accuracy of the final deflection results are studied via computational simulation based on updated FE model. Finally, modal flexibility method, which combines OMA and FEM updating, is utilized for structural condition assessment. The method has been successfully applied to a few prestressed concrete box-girder highway bridges. The modal flexibility method is validated via comparison of deflection derived with the ones obtained directly from static reflection testing. Encouraging results are obtained with major deflection errors less than 5%. Issues to be answered and further studied relating to structural condition assessment are summarized in the concluding remarks.

1 INTRODUCTION: STRUCTURAL HEALTH MONOTORING AND CONDITION ASSESSMENT

Structural health monitoring (SHM) has obtained increasingly attention in recent years due to associated potential for significant life-safety and economic benefits (Doebling et al. 1996, Farrar et al. 2001, Sohn et al. 2003). SHM can be referred to a process of implementing damage identification or detection for engineering structures. Damage can, in general term, be defined as changes to the material and/or geometric properties of the structures, including boundary conditions and structural connectivity, which adversely affect the structure's performance. As the damage grows and reaches a point where it affects the system operation and is no longer acceptable to the user. This point is referred to as failure.

Damage can be detected by local non-destructive evaluation (NDE). However, the majority of SHM research conducted over the last three decades has attempted to identify damage in structures on a more global basis. SHM involves the spaced measurements of a structure over time, the extraction of damage-sensitive features, or damage indices, from these measurements and the statistical analysis of these features or condition indices to determine the current state of system health.

On the other hand, visual inspection is typical routine applications for condition assessment of civil engineering structures (CES) for evaluating vulnerability post typhoon and earthquake damage or after accidents.(Catbas et.al. 1998, Akta et al. 2000, Brownjohn 2007) However, the relation between such visible signs of damage and the corresponding "condition" or "reliability" of the structure is often very difficult to establish. Civil engineering community has long been aware of the limitations and shortcomings of the visual inspection with subjective condition assessment. Objective condition assessment for making meaningful management decision and for cost-effective management has drawn great attention in the last 30 years.

One of the most important issues of damage or condition assessment for CES is to device appropriate features or damage indices. The selected feature, or damage index, should be effectively related to structural damage with small dimension and can be analytically predicted from computational model, and derived from field measurement of the structure as well. An array of dynamic features (or damage indices) has been developed for damage detection and condition

assessment. However, quite a few of them, e.g. modal parameters, are insensitive to the damage, and, hence, cannot be effectively applied for the damage detection or condition assessment.

In the bridge engineering static load testing is conducted to measure deflection shape, which is acceptable for condition assessment. However, such static testing has serious drawbacks, such as high cost, time consuming, and blogging normal traffic.

Modal or dynamic flexibility approach is proposed based on operational modal analysis (OMA). Dynamic flexibility, which actually is the frequency response function of the structure, can be synthesized via modal parameters identified via OMA of the structure subjected to, e.g. traffic excitation. Static flexibility, the elements of which is the displacement influence factors of the structure, can easily be obtained as special case of FRF as dynamic flexibility. Deflection shape is then calculated from flexibility matrix multiplying by pre-scribed static loading vector.

2 THEORETICAL BACKGROUND OF STRUCTURAL CONDITION ASSESSMENT BASED ON MODAL FLEXIBILITY

Frequency response function (FRF), or dynamic flexibility, model can be built via identified modal parameters:

$$[H(j\omega)]=\left[\frac{X(j\omega)}{F(j\omega)}\right]=\sum_{r=1}^{n}\frac{\phi_r\phi_r^T}{m_r\left[\left(\omega_r^2-\omega^2\right)+j2\xi_r\omega_r\omega\right]} \quad (1)$$

where flexibility can easily be obtained from dynamic flexibility, i.e. FRF, letting w = 0,

$$\underset{\omega\to 0}{[H(j\omega)]}=[W]=\sum_{r=1}^{n}\frac{\phi_r\phi_r^T}{m_r\omega_r^2} \quad (2)$$

Static deflection shape (d) can then simply be determined from known static load (f) with static flexibility matrix W: $\{d\}=[W]\times\{f\}$. Static flexibility can be determined for modal frequency, mode shape plus modal mass or modal scaling, where $r=1,2\ldots,n$.

Modal parameters can be identified via traditional experimental modal analysis (EMA) or operational modal analysis (OMA). Artificial excitation is required for the EMA, and therefore traffic normally should be blocked, that is unfavorable for the traffic administration. OMA makes use of natural excitation under operational condition. Actually traffic provides appropriate excitation for a bridge, which can be utilized for OMA. A variety of modal identification procedures have been developed for OMA. The 2-stage FD OMA approach would be appropriate for industry application, which estimating power spectrum density (PSD) via digital signal processing of random responses measurements as the first stage, and then conducting modal parameter estimation based on PSD data (Zhang et al. 2005a).

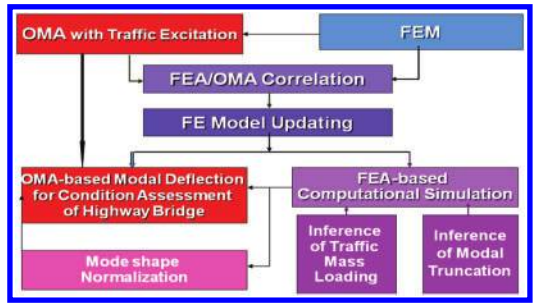


Figure 1. Flow diagram of modal flexibility procedure for bridge condition assessment procedures.

However, due to lack of excitation force measurement, only modal frequencies and unscalled mode shapes can be identified from OMA. In this project, in order to obtain accurate modal scaling factors, a fine finite element model of the structure is built and then updated (calibrated) based on identified modal parameters from OMA. Figure 1 shows flow diagram of the proposed modal flexibility procedure for structural condition assessment.

3 MODAL FLEXIBILITY METHOD APPLIED TO A HIGHWAY BRIDGE

A typical pre-stressed concrete continuous box-girder highway bridge is utilized for flexibility-based structural condition assessment study. The bridge is divided into left and right part, each of which includes a main bridge and two flanking bridges. The main bridge of the right part is composed of three-span pre-stressed concrete continuous box-girder. The total span is 236.33 m (Figure 2).

An operational modal analysis with traffic excitation on the right main bridge was carried out. Force-balanced-type of acceleration sensors were utilized with 32-channel dynamic data acquisition system. The sampling rate is 50 Hz, and all signals were recorded simultaneously with duration of 20 min. Traffic-excided dynamic responses at 30 points with half at left and half at right sides in vertical direction of the bridge were recorder. Fig. 3 gives typical time series recorded and power spectrum density (PSD) estimated via dynamic signal processing based on field measured response data (Zhang et al. 2010).

An advanced modal parameter identification technique, based on Frequency-Spatial Domain Decomposition (FSDD) algorithm (Zhang et al. 2005b), is utilized for modal parameter identification. The modal indication function MIF (Figure 4) of the FSDD shows there are 13 modes were clearly located in the frequency band of 0–25 Hz. The identified modal frequencies, damping ratios and mode shapes are presented in Figure 5.

Since there are no input force measurements in the OMA, only unscaled mode shapes can be obtained. However, flexibility matrix can only be calculated with

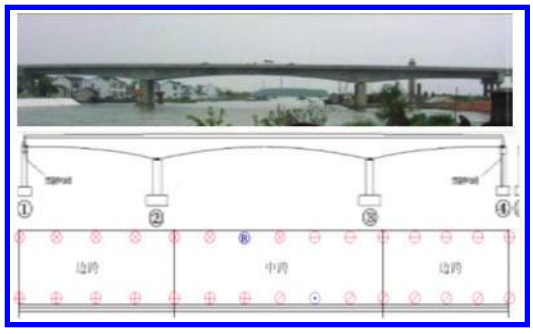


Figure 2. A pre-stressed box-girder bridge and OMA test setups.

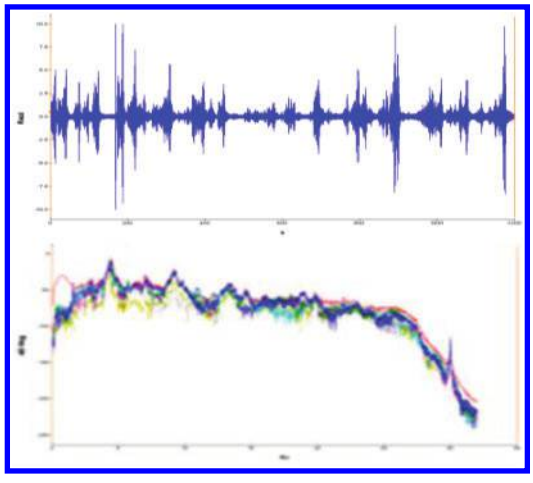


Figure 3. Typical time series and PSDs of the traffic induced dynamic responses of the bridge.

modal frequency and scaled mode shapes. In order to have an accurate modal scaling factor, a fine finite element modeling with model updating (calibration) was conducted based on rather accurately identified modal parameters via OMA.

A full 3-D FEM of the right main bridge is built making use of MSC.Patran, an advanced FEA software widely used in the aerospace and mechanical engineering [10]. The main structure, four piers, lateral guardrails, connections, the layer of bitumen and concrete fiber web, anchor, etc. of the bridge are discretized with different FE types. The main structure of the bridge is modeled by 5149 shell elements with four piers modeled by 288 solid elements and lateral guardrails modeled by 133 beam elements. The connections of the main structure and four piers of the bridge are modeled by 72 MPC (Multiple-point Constraints) elements; the layer of bitumen and concrete fiber web and anchor are merged into the main structure of the bridge. The complete FEM consists of 5,782 nodes and 5,570 elements resulting in 34,692 active degrees of freedom (DOFs) (Lin et al. 2009).

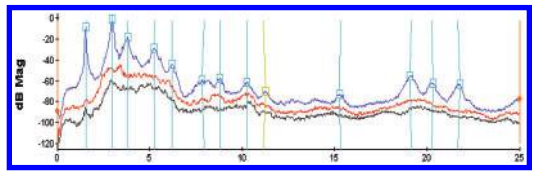


Figure 4. Modal indication functions of FSDD clearly indicate 13 modes in the frequency band of interest.

For the very complicated engineering structure, the maximum difference of modal frequencies computed via FEM to the ones obtained from OMA reaches 30% as shown in Table 1. It evidences the necessity for model updating (calibration). It can also be seen from the Table 1 that modal correlation before and after model updating improved significantly in both modal frequency and mode shape (via MAC values).

There are three key parts for FE model updating. The first key part of FEM updating is appropriate selection of physical parameters to be updated (calibrated) (Zhang 2012). Considering that the shell element is the majority type of elements in FEM, the elastic modulus and equivalent density of pre-stressed concrete and their thickness of geometrical characteristics are highly sensitive to the modal parameters, and they are selected as updated parameters. MPC elements between four piers and main structure are important factors affecting the precision of the FEM and also be selected as updated parameters.

The second key part of model updating is the selection of updating criterion which is closely related to the feature for model updating. Modal frequency and mode shape are classical features for model updating. For this project flexibility of the bridge is applied for structural condition assessment, and therefore, it is also utilized as dynamic feature for model updating. The third key part for model updating is to select an appropriate optimization algorithm to minimize the residue of selected feature/index. A real-coded accelerating genetic algorithm (RAGA) is applied to solve the minimization problem. Table 1 also shows the errors in modal frequencies and mode shapes, represented by MAC after updating. It can be seen, the FEM have been improved significantly after model updating (calibration). Except the 6-th torsional mode, the most modal frequency errors are less than 5%, and MAC values increased to more than 0.9. Figure 6 gives comparisons of the first six modes from OMA and updated FEA.

From updated FEM, modal scaling factor is extracted and modal flexibility is then calculated together with modal frequencies and unscaled mode shapes identified from OMA. Deflection shape under predefined external static loading is finally obtained. To study the impacts of the modal truncation and traffic mass loading to the accuracy of the deflection obtained from modal flexibility, computational simulations are conducted based on updated FEM. It has been shown

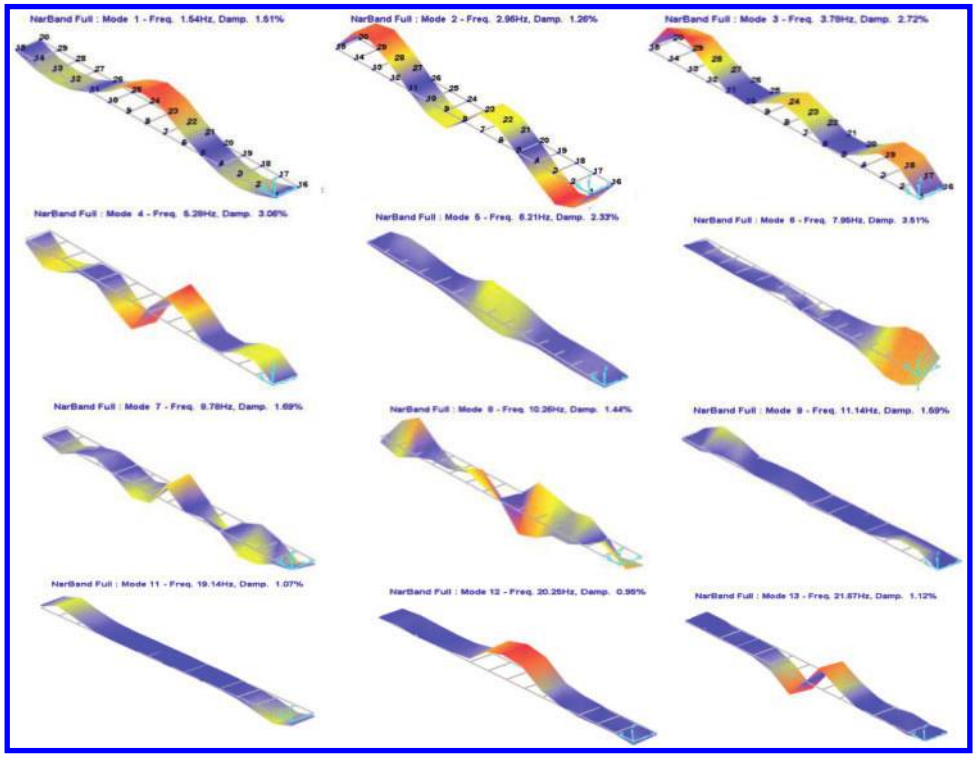


Figure 5. OMA identified 12 modes based on FSDD.

Table 1. Modal frequencies and MAC identified from OMA and predicted by initial and updated FEM.

No.	f_{Exp} Hz	f_A Hz	f_U Hz	ε_{fA} %	ε_{fU} %	$\varepsilon_{\phi A}$	$\varepsilon_{\phi U}$
1	1.54	1.45	1.59	−5.63	2.91	0.994	0.995
2	2.96	2.53	2.81	−14.4	−5.15	0.871	0.88
3	3.79	3.7	4.05	−2.41	6.4	0.965	0.939
4	5.28	5.18	5.59	−1.85	4.53	0.958	0.969
6	7.95	5.53	6.74	−30.4	−15.1	0.583	0.919
7	8.78	8.14	9.09	−7.26	3.41	0.892	0.929
8	10.3	8.41	9.84	−17.9	−4.05	0.828	0.893
10	15.3	13.3	15.2	−13.0	−0.47	0.87	0.87
12	20.3	15.7	18.5	−22.69	−8.7	0.927	0.958
13	21.7	19.2	21.2	−11.51	−2.04	0.977	0.982

that the errors due to modal truncation and traffic mass loading are all within engineering tolerance (Zhang et al. 2010).

To validate the accuracy of the modal flexibility approach, a static truck-loaded testing is conducted and compared with predicted deflection based on modal frequency, mode shape identified from OMA and modal scaling factor calculated from updated FEM. Fig. 7 shows the deflection shapes predicted by the modal flexibility method and 8 deflection points measured in four sections of the bridge by static traffic-loading tests. The errors are mostly within 5% with a largest one near to 10% error, which are within the engineering tolerance.

4 CONCLUDING REMARKS

A modal flexibility method is proposed to obtain deflection shape under pre-described static loading based on operational modal analysis (OMA) and updated finite element model (FEM), and applied to a pre-stressed concrete continuous box-girder highway bridge. Modal frequencies and mode shapes are identified from dynamic response measurements of the bridge subjected to traffic excitation. A fine FEM is built and updated based on modal parameters identified from OMA. Modal scaling factors are calculated from fine updated finite element model. Modal flexibility is then synthesized from modal frequencies and scaled mode shapes. Rather accurate deflection shape under pre-described static loading is then obtained to replace the one normally measured via expansive and time consuming static loading test for bridge condition assessment.

The modal flexibility method based on OMA and FEM updating for structural condition assessment has been validated via comparison of deflection shape obtained from identified modal parameters with mode shape normalization using updated FEM and

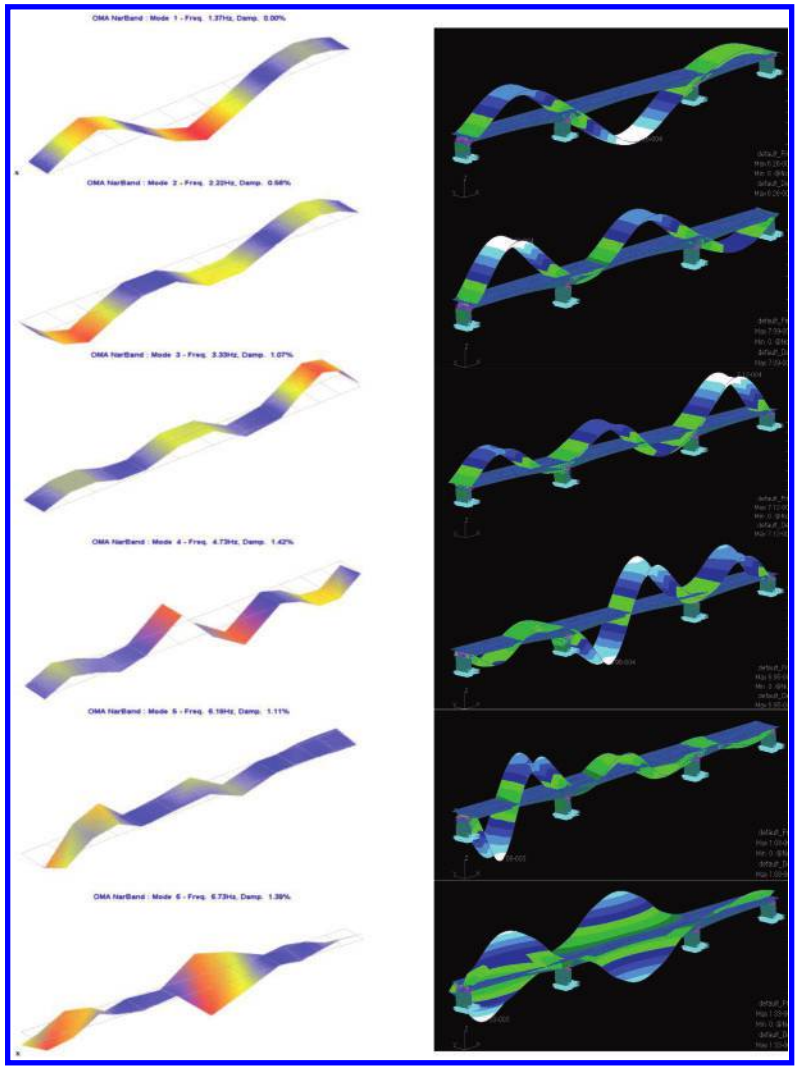


Figure 6. Comparisons of 6 the first 6 modes from OMA and updated FEM.

deflection directly measured from static truck-loading testing. The errors of deflection shape between them are within 5% at the 7 points with largest error at rest one point near 10%, which are within engineering requirement

To study the errors due to modal truncation and traffic mass loading, a series computational simulations based on updated FEM is conducted. It is shown that the approximation introduced by modal truncation and mass loading is within engineering tolerance.

In the bridge engineering, static deflection shape under pre-described loading is widely applied as indices for bridge condition assessment. However, many issues still remain to be solved between the deflection shape and damage, reliability, serviceability and life-cycle safety. Other condition indices should also be studied with following questions to be answered: What are the most suitable condition indices for global health, preferably by correlating to structural reliability for serviceability and safety. How stationary are the directly measurable condition indices? What are their sensitivity thresholds to various type of damage? Is it possible to assess condition and damage without a baseline? How can we optimally integrate various experimental approaches and related technologies such as modal testing, controlled load testing and instrumented monitoring for condition assessment of constructed structures? Besides, better understanding the civil engineering structure, foundation and soil characteristics, the load paths, critical load carrying capacities, and possible failure mechanisms are important for condition assessment of civil engineering structures, such as bridges and buildings.

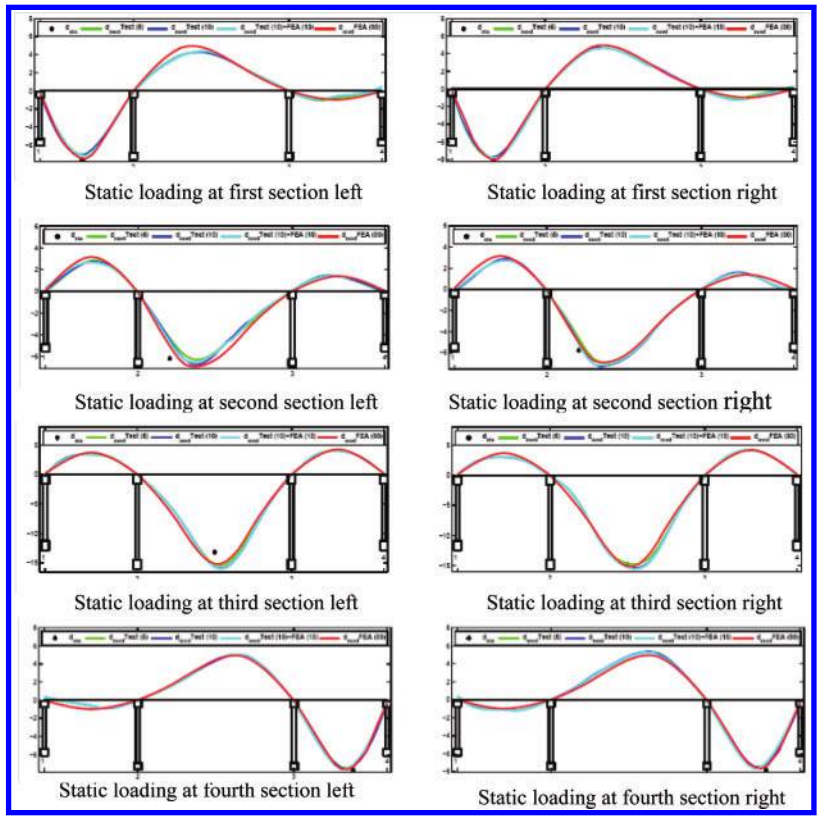


Figure 7. Validation of deflection shape obtained from OMA and updated FEM and static truck-loading tests. Where the results from static tests are denoted with black dots in four sections.

REFERENCES

Aktan, A. E., Catbas, F. N. Grimmelsman, K. A. & Tsikos, C. 2000. Issues in infrastructure health monitoring for management. *J. Eng. Mech.*: 711–724.

Brownjohn, J. M. W. 2007. Structural health monitoring of civil infrastructure. *Phil. Trans. R. Soc. A 365*: 589–622.

Catbas, F. N. et al. 1998. Damage detection and condition assessment of Seymour bridge. *Proc. 16th Int. Modal Analysis Conf.*: 1694–1702, Society of Experimental Mechanics, Bethel, Conn.

Doebling, S. Farrar, C. Prime, M. & Shevitz, D. 1996. Damage identification and health monitoring of structural and mechanical systems from changes in their vibration characteristics: A literature review. *Rep. No. LA-13070-MS, Los Alamos National Laboratories*, Los Alamos, N.M.

Farrar, C. Doebling, S & Nix, D. A. 2001, Vibration-based structural damage identification. Phil. Trans. R. Soc. A 359, 131–149.

Lin, X.Q. Zhang, L.M., Guo, Q.T. & Zhang, Y.F. 2009. Dynamic Finite Element Model Updating of Pre-stressed Concrete Continuous Box-Girder Bridge, *Earthquake Engineering and Engineering Vibration*, 8(3): 399–407.

Sohn, H. Farrar, C. Hemez, F. M. Czarnecki, J. Shunk, D. Stinemates, D. & Nadler B. R. 2003. A Review of Structural Health Monitoring Literature *Los Alamos National Laboratory Report*, LA-13976-MS: 1996–2001.

Zhang, L.M. Brincker, R. & Anderson, P. 2005a. An Overview of Operational Modal Analysis: Major Development and Issues, *The first International Conference on Operational Modal Analysis (IOMAC)*, Copenhagen, Denmark, April, 2005

Zhang, L.M. Wang, T. & Tamura, Y. 2005b. Frequency-spatial Domain Decomposition Technique with Application to Operational Modal Analysis of Civil Engineering Structures, *IOMAC*, Copenhagen, Denmark, April, 2005

Zhang, L.M. et al. 2010a. *Final Technical Report on the Modal Flexibility Method for Highway Bridge Condition Assessment* (In Chinese), Nanjing University of Aeronautics and Astronautics and Jiangsu Highway Transportation Research Institute.

Zhang, L.M. et al. 2010b. An operational modal analysis (OMA) technique for bridge structure condition assessment, *The Third National Conference on Structural Health Monitoring and Condition Assessment of long-span Bridge*, Nanjing, Jiangsu Prov. China, Oct. 2010

Zhang, L.M. 2012. Advances of Structural System Identification and its Potential for Wind Engineering Application, *Lecture notes II, for the 9th Advance School in Wind Engineering, sponsored by the G-COE program*, Tokyo Polytechnic University, Manila, Philippine, August 13–16, 2012.

31. Structural assessment, damage assessment, failure analysis, forensic engineering, disaster management

Research and Applications in Structural Engineering, Mechanics and Computation – Zingoni (Ed.)
© 2013 Taylor & Francis Group, London, ISBN 978-1-138-00061-2

The art of the forensic engineer

Donald Charrett
Chairman, AMOG Consulting

ABSTRACT: The first part of the paper discusses the role of the forensic engineer in investigating and determining the causes of structural failures, and how that role differs from that of the design engineer. The forensic engineer's "deliverables" and "clients" require specialised skills directed to answering and communicating "why" the failure occurred. Recommendations are made for the appropriate engagement of a forensic engineer. The second part of the paper reviews the application of forensic engineering in the public reports of several structural failures. The direct "technical" causes of failure were accompanied by contractual and project execution deficiencies that did not prevent or detect the onset of disaster before it was too late. The "non-technical" lessons learnt include implementing the appropriate contractual mechanisms for managing the project risks, the appropriate engagement of the design and checking engineers, the designer's involvement during the construction, and the ongoing requirement for monitoring and inspection of constructed facilities.

1 THE ROLE AND ENGAGEMENT OF THE FORENSIC ENGINEER

1.1 *Introduction*

One definition of forensic engineering is: the application of the art and science of engineering in the jurisprudence system, requiring the services of appropriately qualified and experienced professional engineers. Forensic engineering may include investigation of the physical causes of accidents and other sources of claims and litigation, preparation of engineering reports, testimony at hearings and trials in administrative or judicial proceedings, and the delivery of advisory opinions to assist the resolution of disputes affecting life or property (Carper 2001).

However, the scope of forensic engineering is broader than in connection with the legal system, as forensic engineers may also be required to provide a report to a client as to the cause and reasonable options for replacement or repair, or desirable procedural changes to avoid future failures.

Forensic engineers are usually, although not exclusively, involved in investigations of "failures", where a failure is an "*unacceptable difference between expected and observed performance"* (Leonards 1982). Perceived "failure" of a structure is thus not confined to a failure to carry the required load, but includes any shortcoming in meeting the client's expectations in respect of time, cost or quality.

1.2 *The forensic engineer's role in legal disputes on structural "failures"*

There are two distinct roles that a forensic engineer may undertake in connection with a (potential) legal dispute – an expert consultant who acts as part of a legal "team", and an independent expert who is not part of the legal team, and gives testimony in a court or arbitration hearing on the basis of his/her independent assessment of the cause of the failure.

It is important that a forensic engineer understands clearly the role that she/he has been engaged for, as it determines how she/he is engaged and instructed, what documents are provided, what investigations should be conducted and what type of report will be required.

1.2.1 *Expert consultant*

An expert consultant acts as a member of a legal "team", and accordingly may be privy to confidential details about the legal "case", including the client case theory and the opinions of other experts acting for the client. Given such close association with the legal preparation of the client's case, it may be difficult for an expert consultant to be seen by a judge or arbitral tribunal to exercise his/her independent judgement, without regard to the exigencies of the case.

An expert consultant (sometimes referred to as a "dirty" expert) can provide forensic engineering advice at all stages of a dispute on a structural failure, including the identification and engagement of suitable independent experts. However, because such an expert consultant may be perceived as "tainted" by the client's case, she/he is usually not the appropriate person to give forensic engineering evidence in court or before an arbitral tribunal.

1.2.2 *"Independent" or "clean" experts*

An independent (or "clean") expert who is not part of the legal team and is not privy to confidential aspects of the client's case will be suitable to provide an expert opinion on forensic engineering issues that will be seen

by a tribunal to be independent. To maintain the independence of such an expert, it will be necessary to ensure that she/he is appropriately briefed, does not have any inappropriate contact with the legal team and is not provided with any documents that could taint his/her independence or ability to express an independent view.

Engagement of an independent expert requires careful documentation by the legal team so that all communications are transparent and the evidentiary material on which the expert opinion is based is clear. Independent experts in some jurisdictions have obligations to formally acknowledge that they have formed an independent opinion, and that they are not acting as an advocate for their client's case.

1.3 *The forensic engineer's skills*

Forensic engineering, in common with every other branch of engineering, involves the application of both science and art.

The fundamental skill needed by a forensic engineer is a deep knowledge of the science of engineering relevant to the issues that need to be investigated. This is gained through training, study and experience. A perceived lack of this relevant expertise by a legal tribunal may disqualify an independent expert from giving expert evidence.

Equally important to the science of engineering is the "art" of how a forensic engineer should apply his/her engineering knowledge to prepare and conduct investigations to determine the facts, apply the relevant engineering principles to effectively determine the cause of failure, and to prepare reports or testimony that are soundly based, relevant, cogent and persuasive.

The art of the forensic engineer who is required to investigate and report on a failure is fundamentally different to the art of the engineer who designs a facility. The fundamental question addressed by the design engineer is "how" to apply the art and science of engineering to synthesise all the required elements into a functional and operating whole to satisfy the client's requirements. By contrast, the fundamental question addressed by the application of the forensic engineer's skills is "why" did the failure occur. The forensic engineer must keep an open mind whilst making observations, collecting evidence and planning and conducting the necessary investigations. She/he may need to carry out complex and sophisticated analyses to determine why the failure occurred. The results of theoretical analyses will need to be reconciled with all the available evidence of the failure.

The forensic engineer needs to have refined observation and recording skills, to take note of and document all possibly relevant features observed at a site inspection of a "failed" structure. It is important that a forensic engineer takes note of all matters that may have an influence on the cause of the "failure", whether or not they appear to be consistent with a particular theory of failure.

The "art" of the forensic engineer importantly includes good written and oral communication skills. The design engineer communicates the design to be constructed by means of drawings and specifications to those in the construction industry who understand the "language". The forensic engineer usually communicates his/her findings to those not knowledgeable in engineering or construction – a Board of Directors, corporate counsel or a judge. The ability to communicate complex engineering concepts in simple understandable terms is an essential aspect of the art of the forensic engineer. Appropriate photographs, models or simplified diagrams or animations are usually more effective in communicating complex technical issues to lay people than a detailed technical description. A brief but comprehensive executive summary at the start of a report is important to convey the fundamental findings to senior people.

A forensic engineer may be engaged to provide an opinion as to whether the original design was prepared on a reasonable basis. In such a case the forensic engineer should have relevant recent design experience and maintain an analytical approach to determining whether the original designer acted reasonably, rather than opining on what the forensic engineer might have done if she/he was the designer.

This emphasises the importance of the forensic engineer maintaining the highest professional and ethical standards. A forensic engineering report may have dire consequences for the professional career of the designer of a failed structure. A further aspect of the forensic engineer's ethics is the obligation to advise the client if she/he does not possess all the skills required for the investigation.

1.4 *Engagement of a forensic engineer*

A forensic engineer is usually engaged by a lawyer acting on behalf of a client with an interest in a structure to be investigated. This is particularly important if legal professional privilege is to be asserted. If it is not known whether or not litigation or arbitration might ensue, it may be appropriate in the first instance to engage an expert consultant who can assist the legal team in whatever manner is appropriate and to the fullest extent possible, recognising that an independent expert may have to be engaged at a later time.

In principle, engagement of a forensic engineer is no different to engaging an engineering consultant for any design or construction task. It is necessary to define the scope of the forensic engineer's work, select a forensic engineer with the appropriate skill and experience to carry out the scope of work, and execute a consulting agreement with appropriate terms and conditions that specify the requirements of time, cost and quality.

Defining scope with precision is fundamental to selecting the most appropriate forensic engineer, because it is the scope that determines the threshold issue of the skills required. Of course, the scope may evolve over time: the engaging lawyer may not understand the full ramifications of the issue at the outset, or

have insufficient knowledge of the technical requirements, or the forensic engineer's investigations may go in a different direction to that initially anticipated.

Part of the scope of the forensic engineer may be to define the full scope of services required, after an initial investigation of the facts and the issues. Nevertheless, the initial scope should be defined by the engaging lawyer as clearly as possible, particularly what are the "deliverables": those outputs of the forensic engineer's intellectual property provided to the client, e.g. a report on the causes of failure, or a presentation to senior management as to the recommended further investigations necessary.

Inevitably there is a trade-off between the conflicting demands of completing the scope to the appropriate quality within the required time frame at an acceptable cost. In selecting the most appropriate forensic engineer, the engaging lawyer will have to make his/her own value judgment on where the appropriate balance lies. In this author's experience, the emphasis should undoubtedly be on the quality of the forensic engineer and his/her support organisation, and not on ad hoc determinations of budget cost or timeframe. Typically, the skills and experience that will be required for a high-level forensic investigation will only be available in very senior individuals with years of experience. Such individuals are usually very busy, and inevitably have a high charge rate, particularly in circumstances where they are required to commit significant periods of time for court appearances.

It is suggested that typically, a forensic engineer should be selected on the basis that she/he can provide the required quality, and the conditions of engagement should be tailored to ensure that the services are delivered within the required time and budget. Detailed suggestions for the engagement of forensic engineers are made by Charrett & Potts (2012).

2 PUBLIC INQUIRIES INTO STRUCTURAL FAILURES

2.1 *Introduction*

Public inquiries into structural failures are important not only for establishing the causes of the failures, but for identifying changes that need to be made to avoid future failures from similar causes. Such public inquiries invariably rely heavily on forensic engineers to assist the investigating tribunal to determine the causes of failure, both technical and non-technical. This paper draws on some reports of public inquiries into high profile structural failures to identify some relevant "non-technical" issues that have invariably accompanied the direct "technical" causes of failure.

Public inquiries have a number of unique features that make them an especially valuable resource for the assessment of structural failures. Although only conducted for a small number of high profile failures, typically involving loss of life, public inquiry reports are of greater significance then their conclusions on the particular failure. In contrast to the judicial inquiry a judge or arbitrator makes in civil litigation to determine legal liability for failure as between the litigants, a public inquiry is an administrative process in which the objective is to determine the cause of the failure and the lessons learned from it, in order to guide actions in the future to avoid a repetition. Typically, the report of a Public inquiry contains detailed technical information on the engineering "state of the art" relevant to the failure.

In the common-law world, public inquiries are conducted along similar lines to adversarial court proceedings. Counsel are appointed to assist the tribunal, and interested parties engage their own counsel to represent their interests in the inquiry. Lay and expert evidence is adduced in a similar way to court proceedings. Forensic engineers may be called as expert witnesses on behalf of the inquiry itself, or a party whose interests may be affected by the outcome of the inquiry.

The details of the failures discussed in this paper, as revealed by the reports of the public inquiries that ensued, highlight many issues relevant to the contracts and the execution of those contracts. In each case the direct "technical" causes of failure were accompanied by contractual and project execution deficiencies that did not prevent or detect the onset of failure before it was too late. No doubt all of the disasters had their genesis in human failings, generally and perhaps invariably in a combination of individual failures. The importance of identifying the "non-technical" issues contributing to failures is in determining what changes to project execution procedures and contractual arrangements are required to prevent a repetition of failures from similar causes.

The failures listed in the following sections all resulted in loss of life, and were followed by public inquiries that determined and documented both the technical and non-technical causes of failure. Following a brief description of each of the failures and its subsequent inquiry, some of the lessons learned from these failures are discussed. The discussion of lessons learned highlights the similar findings on important contractual and procedural issues that have contributed to the different failures. Further details on the public inquiry reports referred to can be found in Charrett (2008), Charrett (2009) and Charrett (2012).

It will be noted that most of these failures occurred a long time ago, and are still remembered by structural engineers today for the technical issues they identified, and the impact they have had on the practice of structural design. However, in this author's view, the contractual and procedural lessons learned appear to be forgotten by subsequent generations. Revisiting these historical reports reinforces the importance of designing and constructing structures within contractual arrangements that encourage and support clear lines of authority and communication, with appropriate allocation of risks and an appropriate balance between the required time, cost and quality for project execution.

2.2 *Québec Bridge, Canada (1907)*

The Québec Bridge over the St Lawrence River is a steel cantilever bridge with a main span of 548 m. It was procured by a company specifically incorporated to finance, build and operate a toll bridge, which called tenders on minimal documentation, including a clearance diagram and specifications. The company's consulting engineer, Theodore Cooper, recommended an increased span and increases in the allowable steel stresses, significantly above those in common use at the time.

The construction contractor, Phoenix, entered into a contract to design and construct the bridge to the satisfaction of Cooper and the company's engineer. Whilst Phoenix was responsible for preparing the design, Cooper approved all of the designs on behalf of the company. However, he was only concerned with the bridge in its final constructed configuration, and had no involvement with the erection engineering, or with any inspections in the shop or in the field, and made no inspections during construction.

During erection of the suspended span the south anchor arm of the bridge collapsed completely, resulting in the death of 74 men. Many of the joints were not fully riveted, and major compression members suffered from increasing lateral deflections, which gave prior warning of substantial structural distress. Unfortunately, the site personnel did not have sufficient experience to recognise the impending danger, and Cooper was only made aware of it too late.

After the collapse, the Government appointed a Royal Commission, comprising two practicing civil engineers, and a professor of engineering. The Commission's report determined the technical causes of the failure, and made a number of observations on the contractual and procedural issues that were relevant. This report was for many years regarded as a classic of its kind, and many of its conclusions are still relevant to the practice of structural engineering today.

The technical reason for the collapse was the failure of the lower chords in the anchor arm near the main pier, due to their defective design. The stresses that caused the failure were not due to abnormal weather conditions or accident, but arose because of the errors in judgment on the part of the designer and Cooper.

The collapse of the bridge is still remembered by engineers because it drew attention to the lack of knowledge on the behaviour under load of built up columns with lattice bracing. It is interesting to note that although considerable theoretical work on the design of large compression members was carried out after the failure of the Québec Bridge, testing of major compression members were still regarded as prudent in structures designed in the 1920s such as the Sydney Harbour Bridge.

2.3 *Westgate Bridge, Melbourne Australia (1970)*

Westgate Bridge comprises a total of 21 concrete spans, with five steel box girder spans over the Yarra River. It was procured under a forerunner of modern Public-Private Partnership. The design of the steel box girder spans was prepared by consulting engineers engaged directly by the Principal, and contractors under the consulting engineer's supervision carried out fabrication and construction.

After the original contractor for fabrication and erection fell seriously behind schedule, the Principal appointed an erection contractor to complete the erection under a "cost plus" labour management contract. The method of erection chosen by the original contractor was unusual, using two half spans jacked into position and joined along the longitudinal centreline. The erection contractor experienced difficulties because of unequal deflections of the half spans, and applied kentledge to correct the difference in camber. The application of this additional weight caused a buckle near a splice at the middle of span 10–11. In an attempt to eliminate this buckle, about 30 bolts were removed. The span collapsed and 35 workers died.

The Government appointed a Royal Commission, comprising a Supreme Court judge, a professor of civil engineering and a distinguished bridge engineer. The Royal Commission sat for 80 days, hearing evidence from 52 witnesses. It was required to enquire into and report on the circumstances surrounding and the cause or causes direct and indirect of the failure of span 10-11, and whether any aspect of the design was inadequate or undesirable.

The Royal Commission found that the immediate cause of the collapse was the removal of the bolts. However it made forthright comments that the design was approached in a "*disorganised and unsystematic manner and without any real guidance being given to the engineers doing the work*" and "*the calculations contain a great many errors of arithmetic and engineering principle*". It found that the primary cause of the collapse was that the consulting engineer "*failed altogether to give a proper and careful regard to the process of structural design*".

2.4 *Milford Haven Bridge, Wales UK (1970)*

Westgate Bridge collapsed shortly after the steel box girder Milford Haven Bridge in Wales (now the Cleddau Bridge) collapsed during construction. The UK Government appointed a technical Committee of Inquiry to investigate the collapse of the Milford Haven and West Gate bridges, their terms of reference being to consider whether it was necessary to reconsider the design and method of erection of box girder bridges about to be erected in the UK, to draw up technical guidelines for bridge engineers, to advise on any special matters affecting contract procedures and to recommend further research and development.

The 5 man Committee was chaired by Dr Merrison, whose name is often associated with the technical recommendations on the design of box girder bridges made by the Committee. It concluded that the collapse of the bridge was caused by the inadequacy of the design of a vertical pier support diaphragm, which failed in compression over the column.

The lessons from Milford Haven primarily concerned the inadequacy of the design methods used for the permanent design and checking the safety during erection. The "Merrison Rules" in the final report, comprehensive design and workmanship rules for the stress analysis and design of steel box girder bridges, are still used today in the design and checking of steel box girder bridges.

In its Final Report, the Committee accepted the Royal Commission's assessment of events which led to the collapse of the Westgate Bridge, and drew considerable support from its recommendations on contractual and procedural aspects: *"While there were also fundamental defects in the erection procedure and permanent design of the West Gate Bridge, we regard the failures of site organisation and of communication between the principal parties – client, engineers and contractors – as of more general significance in this case."*

2.5 *De La Concorde Overpass, Quebec Canada (2006)*

The de la Concorde Overpass was a prestressed concrete bridge, built in the 1970s and designed and constructed generally in accordance with the prevailing standards. In 2006 a span collapsed under light traffic load, killing five people. The Government established a Commission of Inquiry, with an attorney President and two engineer Commissioners.

The Commission conducted its inquiry in accordance with the principles defined by the Canadian Supreme Court, and concluded that, whilst there were a number of defects and shortcomings, both technical and procedural, none of those by itself would have caused the collapse which resulted from a chain of causes.

The reason for the failure of the overpass was a shear failure in a reinforced concrete cantilever slab, the concrete of which had deteriorated over the years. The reinforcement design satisfied the code requirements at the time, but would not do so now, nor would the detailing of the reinforcement be regarded as satisfactory today. The weakness of the detail was due to errors in placement of the reinforcement (a quality-control failure during construction), and low quality concrete that was not suitable to resist freeze-thaw cycles (arising from ambiguity in the specification). There were further contributing causes that the thick slab was not watertight (the specified waterproof membrane had apparently not been installed) either originally or during subsequent refurbishment), and refurbishment work in 1990 caused damage that was not evaluated.

In addition to these technical issues, the Commission identified a number of procedural failures in respect of both design and construction.

2.6 *Procedural and contractual lessons*

The following are some of the contractual and project execution lessons relevant to major engineering projects extracted from the public inquiry reports discussed above.

2.6.1 *Quebec bridge*

- The difficulties and time involved in raising finance for a project should not preclude sufficient time allowance for the preparation of initial studies, the design, tender documentation and the execution of the works.
- Unquestioning reliance on the skill and experience of an individual engineer may be misplaced without adequate peer review.
- A project owner requires adequately qualified and experienced technical staff with the appropriate authority for both the design and erection phases, even if it procures its project via a design and construct contract.
- An independent engineer should review the engineering design of a major project, without reference to the designer's calculations.
- The scope of the engineer's engagement should include responsibility for both design and erection, with compensation commensurate with the proper execution of that scope.
- An owner with limited financial resources may be subject to cost pressures that result in inappropriate engineering decisions.
- The construction contractor needs to have an appropriately qualified and experienced erection engineer on site with an understanding of the design and full authority for the erection.
- Appropriate allowances should be made for the additional risks inherent in unusual structures or structures of a scale not attempted before, and this may require testing of components.

2.6.2 *Westgate bridge and Milford Haven bridge*

- The client must be assured that the engineer will have adequate and appropriate resources.
- A certified independent check should be carried out to confirm that the permanent design is adequate and complies with the relevant technical requirements.
- There should be a clear division of responsibilities between engineer and contractor, and the contracts between the parties in a major project should reflect their practical engineering relationship.
- A certified independent check of the erection method should be performed by an engineer independent of the design engineer, who should be given full details of the erection method and have a right of veto over it.
- The contractor should submit a construction programme to the engineer for its approval.
- The independent checks of the permanent design and of the erection method should be complete when work starts and the erection of the relevant part of the superstructure starts respectively.
- The contractor should be allowed sufficient time to prepare itself for the start of work and the client

and the engineer should be prepared to consider a revision of the programme in the event of slippage.
- The engineer should carefully monitor the progress of construction to ensure compliance with the agreed erection method, and should scrutinise the contractor's site staff and where necessary exercise the powers under the contract.
- The client should satisfy itself as to the adequacy of the engineer's site representatives, and the functions and tasks of the engineer's site representatives should be defined in writing.

Note the close similarity to the issues identified by the Quebec Bridge Royal Commission, 65 years previously.

2.6.3 *De La concorde overpass*

- A transparent process should be used for selecting consulting engineers based on competency and past performance, with cost only considered for those firms meeting the competence criteria.
- A responsible engineer should validate the concept, drawings and calculations of structural designs.
- Contractors should be prequalified on the basis of their ability for the type of structure to be built, with cost only considered for contractors meeting the competence criteria.
- When awarding contracts for consulting engineering or construction, it is important to ensure that the key personnel on which prequalification was based will be available for the duration of the work.
- Subcontracting requirements should be identified in bids, and contractors required to produce a work quality control plan for their own and subcontract work.
- On completion, an engineer should certify that the structure was built in accordance with the drawings and specifications and all the documents associated with the work and structure should be assembled and kept during the entire life of the structure to assist with inspection and maintenance programs.
- Owners of structures need to evaluate the performance of consulting engineering firms and contractors on completion of a project, and keep the evaluations on record.

REFERENCES

Carper, K.L. 2001. Forensic engineering – the perspective from N. America. In Campbell, Peter (ed). *Learning from Construction Failures: Applied Forensic Engineering*: 2. Scotland: Whittles Publishing.

Charrett, D.E. 2008. Contractual lessons from construction failures: part one. *Construction Law International* V3 No 4: 15.

Charrett, D.E. 2009. Contractual lessons from construction failures: part two, *Construction Law International* V4 No 2: 19.

Charrett, D.E. 2012. Construction Failures – Have We Learned the Lessons of History? *Australian Construction Law Newsletter* 143: 40.

Charrett D.E. & Potts A.E. 2012. What corporate counsel need to know about engaging forensic engineers" *International In-house Counsel Journal* V5 No 19: 1.

Leonards, G.A. 1982. Investigation of Structural Failures. *Journal of the Geotechnical Engineering Division (ASCE)* GT2: 108.

Research and Applications in Structural Engineering, Mechanics and Computation – Zingoni (Ed.)
© 2013 Taylor & Francis Group, London, ISBN 978-1-138-00061-2

Lessons for structural engineers: The Hillsborough disaster

R.A. Smith
Department of Mechanical Engineering, Imperial College London, UK

ABSTRACT: Although the Hillsborough disaster occurred more than 20 years ago, new evidence is still being evaluated. In particular, the extensive findings of the Hillsborough Independent Panel have removed blame from the spectators onto deficiencies of the ground, the arrangements on the day, the response of the emergency services after the accident and attempts by the police to smear the spectators involved. However, this short paper concentrates on the generic lessons to be learned for engineers who are concerned with advising about safety at venues where large crowds are expected.

1 INTRODUCTION

1.1 *Personal involvement*

The author was living and working in Sheffield at the time of the Hillsborough Football Stadium disaster in 1989. He was invited to assist inspectors from the Health & Safety Executive, also by coincidence located in Sheffield, in their investigations of technical aspects of the disaster.

His personal view is that the various inquiries that have taken place have underplayed the technical deficiencies of the ground and the arrangements, in their concentration on spectator behavior, police actions and the response of the emergency services. However the most recent inquiry report, of the so-called Hillsborough Independent Panel, has spotlighted some of these concerns, and the purpose of this paper is to draw some conclusions of a general applicability for engineers working and advising on situations which involve crowd management.

1.2 *Background description*

On 15 April 1989, a football match between Liverpool and Nottingham Forest was to be played as the semi-final of the Football Association Challenge Cup competition. By tradition, such games are played on neutral grounds; in this case Hillsborough Stadium, the home of Sheffield Wednesday, was chosen. After only six minutes of play, the game was stopped when it was realised that a major incident was occurring behind one of the goals. Ninety-five people died during the incident, one death occurred four years later, and over 400 people received hospital treatment.

1.3 *The development of the stadium*

Sheffield Wednesday, a club named because it played its early fixtures in mid-week, moved to Hillsborough in 1899. The area was then an out-of-town greenfield site, but the provision of a tram line provided the necessary transport to allow spectators to reach the ground. Over the intervening years, the site has become extremely constrained, see Fig.1, surrounded as it is by roads, a river and houses. The tram line was removed in 1950's, only to be replaced by a modern system in 1995, some six years after the accident of 1989. Parking for cars (now, of course, the dominant mode of transport) is extremely limited and difficult, and for most spectators necessitates a considerable walk after finding a parking space in a back street some distance from the ground.

The Stadium itself has developed over the years. The two tiered South Stand on one side of the ground is the largest of the stands and is of attractive lines. It was originally opened in 1914 and was designed by the famous football ground architect Archibald Leitch. Named after a hill that was the scene of a famous battle in the Second South African Boer War, the Spion Kop is built into a natural hill at the east end of the ground. In 1914 concrete terracing was installed on the bank, which was further extended in 1927. The final expansion of the hill came in 1954.

A new cantilever North Stand was built in 1961; the West Stand was added in 1965, in time for the ground to be a venue for World Cup games, when the competition was hosted (and won!) by England in 1966. The much admired North Stand established the popular view that Hillsborough was one of the leading grounds in the country, "There is not a misplaced line in this remarkable stand. From any angle (it) is quite breathtaking. It is *like an architect's model of the dream* stand of the future, a space age stand." Finally, the West Stand was originally built at the turn of the last century as a covered terrace housing up to 3,000 fans. In the 1920s this was joined by the North West terrace before the Leppings Lane stand was replaced by a 12,000 capacity partially covered terrace. Before the 1966 World Cup the West Stand was demolished again

and replaced by a two-tiered structure with 4,471 seats in the upper tier and retaining a terrace in front of the stand, its condition at the time of the accident.

Referring again to Fig. 1, before 1965 the Leppings Lane end consisted entirely of terracing (i.e. stepped standing space). The new West Stand (i.e. seating accommodation built over the rear of the terrace), truncated the space available and restricted access to a tunnel under the West Stand and passages round both ends of the stand.

During the early 1970s, the problems of hooliganism and pitch invasions made it necessary to prevent access to the playing area and caused perimeter fences to be erected in 1977. In an FA Cup semi-final in 1981, incidents of crushing occurred and the police suggested that the terrace be divided into sections by the erection of radial fences, which were fitted in November 1981. The idea was that these sub-divisions would enable a more even distribution of the crowd to be achieved and would allow the segregation of opposing supporters, if necessary by having an empty 'pen' (as a sort of no-man's land) between them. The consequences for pens 2 and 3, see Fig. 1, should have been obvious. Entry to these pens was via the tunnel under the West Stand. Because of the upward slope of this tunnel, spectators could not judge the condition of crowding in the pens until they had exited the tunnel and arrived on the terrace. Further, and crucially important, pens 2 and 3 now formed closed boxes, since the only access to the larger pens 1 and 4 at either side was by small gates at the back of each pen–gates which were extremely difficult of access for spectators in crowded conditions. In view of the closed-box nature of these pens, and the fact they would be attractive positions for spectators immediately behind the goal, it was imperative that a method should be available for monitoring the numbers entering and cutting off further access when the pens were judged to be full. No such method existed.

2 INQUIRY TIMELINE

In the immediate aftermath of the disaster an inquiry was instigated under Lord Justice Taylor. An preliminary interim report was produced by August 1989 in which the police were criticised for failing to close off the tunnel leading to the pens where supporters had been crushed and for failing to control the build up of fans outside the stadium. In January 1990 the second final part of Lord Taylor's report recommended the removal of terrace fences and the introduction of all-seater stadia in the UK. Subsequent history has shown that these changes were the catalyst for a major revolution in UK football and led to, inter alia, to the establishment of the Premier League. In March 1991 after lengthy inquests into the deaths of the victims of the accident a verdicts of accidental death were recorded and a ruling that they were all dead by 3:15 pm on the day of the tragedy.

In June 1997 following a TV dramatized reconstruction the then Home Secretary Jack Straw ordered evidence to be re-scrutinised. A report by Lord Justice Stuart-Smith failed to uncover any new compelling evidence. However, the following year the Hillsborough family support group brought private manslaughter charges against two police officers who had been in charge on the day of the disaster. In July 2000 following a six week trial a jury found one of the police officers not guilty and failed to reach a verdict on the other but the judge refused permission for a retrial.

In April 2009 the Hillsborough Independent Panel was set up in the wake of the 20th anniversary of the tragedy. This panel reported in September 2012. Its major finding being that the police orchestrated a cover up, falsified documents and blamed innocent supporters. It further found that up to 40 of the fans who died might have been saved if action had been taken sooner and the report cleared supporters of wrongdoing or blame for the disaster. Following this report the Director of Public Prosecutions announced that he was looking at all the new evidence unearthed to see if it could support charges that the authorities chaotic response led to lives being unnecessarily lost.

The report of the Hillsborough Independent Panel was a major publication of nearly 400 pages: it was generated from an archive of an exhaustive mountain of accumulated evidence. It contained dramatic evidence of a police conspiracy to tamper with evidence in order to shift the blame onto Liverpool spectators. It also contained severe criticism of the organization and delivery of emergency services following the disaster it led to the quashing of the original inquest findings and re-opening of new inquests.

Of particular relevance to this paper the Panel's report contained details of the physical shortcomings of the ground itself and of the arrangements for the admission and distribution of spectators within the ground. It noted that in 1981 in a previous FA cup semi-final played at Hillsborough there was severe and serious congestion at the Lepping's Lane turnstiles and crushing on the confined outer concourse there was also a serious crush on the terraces in which many people were injured and fatalities narrowly avoided at that time lateral fences did not divide the terrace into pens and funds were able to move sideways thus escaping the consequences of the crush. Further problems arose at semi finals played at the ground in both 1987 and 88. The serious accusation was made that these experiences had not been used to improve safety matters by the club and their safety engineers.

3 LESSONS TO BE LEARNED

Amongst the lessons to be learnt from the engineering background of the Hillsborough disaster, the following are of importance:

3.1 The dangers of ad hoc and piecemeal developments over a long period of time. Unless rigorous

system wide thinking is employed, the law of an unintentional consequences can kick in. In this case the installation of dividing terraces and a perimeter fence at different times had the effect of confining the spectators without egress routes from the terracing. Furthermore the layout of the crush barriers on the terracing was modified by the installation of the fences and had consequence on reducing the number of spectators that could be comfortably accommodated.

3.2 Although the testing of crush barriers was covered by instructions in the then current edition of the Green Guide for the design of sports grounds, the methods suggested were open to considerable freedom of interpretation and were inadequate. It is not unreasonable to have anticipated that engineers in charge of such testing would be questioning and critical of the then requirements. Even cursory examination of the barriers at Hillsborough led to the discovery of significant areas of rust which in some cases extended right through the steel tubes which comprised the barrier structure. In almost all cases this rust was in the load bearing joints of the barrier structure and arguably should have led to the condemning of the so affected barriers and their replacement by new ones. The heights of the barriers in the ground were extremely variable, ranging from upper chest height to lower groin height for an average build of spectator.

3.3 It was a matter of simple arithmetic to calculate the terms style capacity needed for crowd entry in a reasonable time before the start of the game. The maintenance of the turnstiles left much to be desired and they were unable to operate at their best capacity because of the pressure of the waiting crowd causing the turnstiles to in effect jam it was therefore inevitable that the numbers entering the ground on this occasion would cause huge congestion at the areas immediately before the turnstiles and in fact this was a trigger which caused the police to open large gates usually used for egress in order to relieve crowd outside the ground. That a crush outside the ground in the area immediately in front of the turnstiles was inevitable can be seen at a glance when the converging area between Leppings Lane and the turnstiles is examined on Figure 1. The turnstiles marked A-G are clearly inadequate for the large number of spectators due to enter the standing areas marked 1-4 in front and to the wings of the West Stand.

Furthermore it was also a matter of simple arithmetic to calculate the capacity of the various parts of the ground and the reductions in that capacity caused by the installation of radial fences and the perimeter fence. The fact that there was no formal method of estimating the number of people entering sub division of the ground and closing such sections when they were full is quite in explicable.

3.4 The prior organization of major crowd events for example, like a football match or a pop concert, should lead to a clear understanding of the division of responsibilities of the various parties involved in the case of Hillsborough there was a confusion of responsibility between the club and its stewards and the police. Were the police there to maintain order or to assist in the disposition of the crowd? Did the police have different roles outside the ground or within (where they were guests of the club)?

3.5 Complacency prior to the disaster was an attitude shared by both the club and the police. We have organized and hosted major games before and therefore it is a matter of routine to do the same once again. The lessons of near-misses of previous crowd disasters in 1981, 1987 and 1988 were largely ignored.

3.6 It was the responsibility of the Sheffield City Council to inspect the ground and to issue a safety certificate. There is evidence that this process was inadequate and less than rigorous. Following the disaster, the system has been tightened and augmented by a national system of licensing to enforce the application of uniform standards for the all-seater accommodation of major stadia.

3.7 In general there was a blurring of the recognition of the role of the spectators. On the one hand they were paying guests on whom the club depended: on the other they were potential troublemakers who were to be offered minimal comfort facilities within the ground. It is perhaps one of the few positive legacies of the Hillsborough disaster that grounds have been rebuilt and reorganized and now spectators are offered considerably more comfortable accommodation.

4 BIBLIOGAPHY

The literature produced in the wake of the Hillsborough disaster is enormous and still growing. It includes several books, reports of the various investigations, endless articles from newspapers and magazines and comment on the many types of social media now available.

The best and most convenient single source is the website of the Hillsborough Independent Panel inquiry http://hillsborough.independent.gov.uk/

Here can be found an archive of material disclosed to the enquiry. Complete copies of the original Taylor reports and the collected volume of technical evidence gathered by the Research and Laboratory Services division of the Health and Safety Executive are available. The report of Lord Justice Stuart-Smith on his scrutiny of evidence is also available together with the extremely detailed report of the Hillsborough Independent Panel which was published in September 2012.

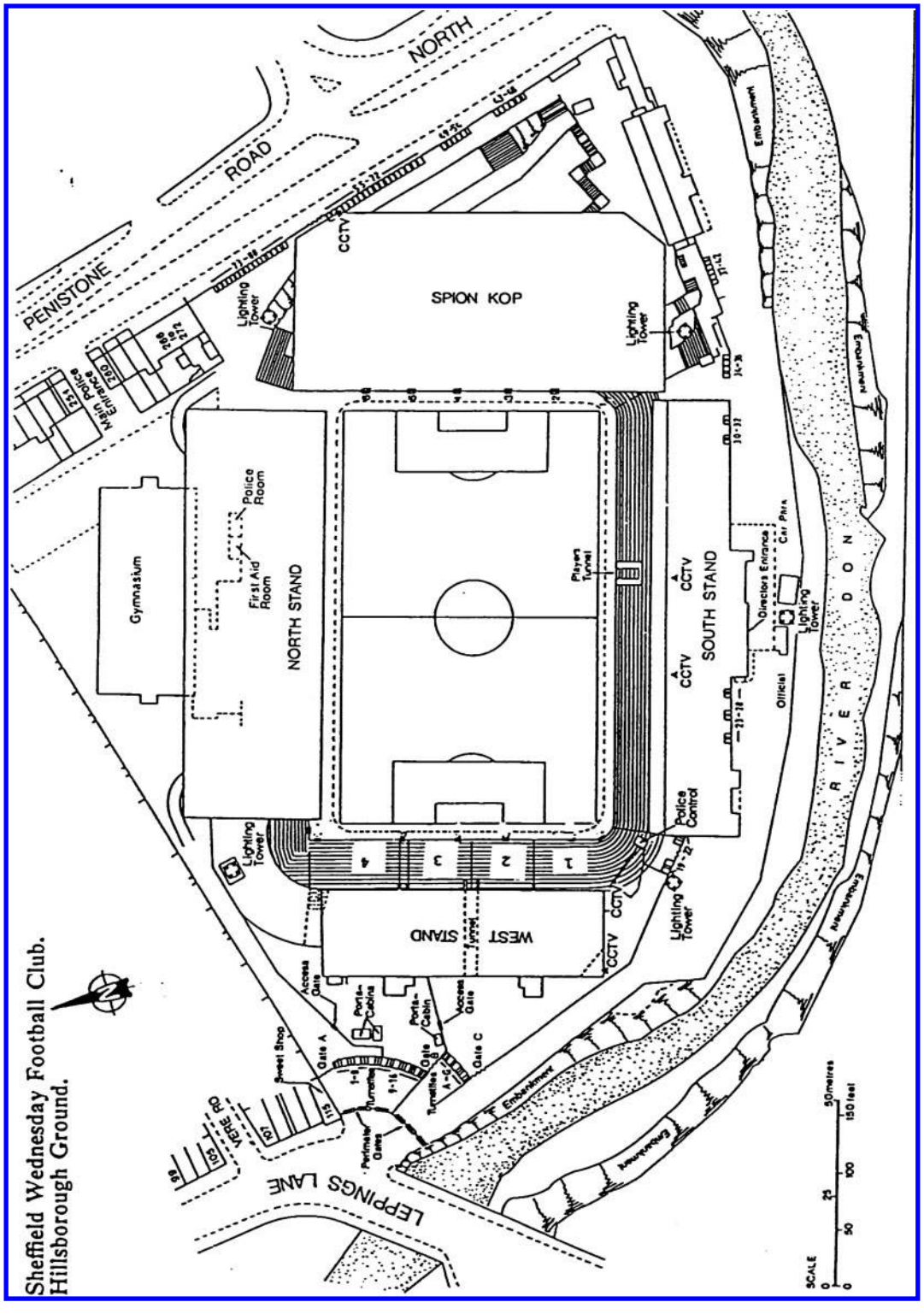


Figure 1. The Hillsborough Ground of Sheffield Wednesday Football Clob.

5 APPENDIX

An eyewitness account was published in The Times on September 15 2012. The author, Adrian Tempany, was on the terraces in Sheffield that day, and this is a shortened account of his experiences. It is reproduced here not for sensationalism, but to be a stark reminder of the responsibilities we have in trying to design a safe environment for people attending large events.

On April 15, 1989, I walked through a set of creaking turnstiles, on to a dilapidated concourse and down a tunnel into Hillsborough. At the end of the tunnel stood a radial fence, and I turned right, into pen three. I took my usual position on a terrace, about halfway up and to the right of the right-hand goalpost. As the sun beat down, a beach ball was launched along the terrace. People stood to read their programmes. FA Cup semi-final day. Where would you rather be, I thought?

But by 2.35 pm, we were fixed in position, and this seemed to be getting tight. People around me began to jockey for space, and by 2.40 pm, sweating and increasingly agitated, men, women and children were using their heads, shoulders or knees to try to move people off them. Someone's breath was blowing hot on my head. Around me, the same cry, "Please, get off me". And the reply, always the same: "Sorry lad, I can't move."

The entire Leppings Lane terrace was designed to hold 10,100 people. Lord Justice Taylor found that if its capacity was exceeded that day it was by no more than 24. However, poor signposting and an absence of police supervision meant that pens three and four — the two behind the goal — were filled with about 3,000 people; Lord Justice Taylor ruled in 1989 that they should have held 1,693.

The crush in pen three began at about 2.35 pm, 25 minutes before the kick-off. It would go on, getting worse, until at least 3.10 pm, when the gates in the perimeter fence were finally unlocked. Many people died, slowly and agonisingly, over the course of nearly 40 minutes. Some died over the course of at least an hour.

The next time you watch a game of football, imagine being crushed for almost the entire first half of that match. How badly? Well, take an old red phone box, strip out the phone and the fittings, and settle yourself in. Now the door opens behind you, and a group of people are shoved in. How many? Talking to fellow survivors, we reached a conservative estimate of seven, at least. So, you are now one of at least eight people in a phone box. The door is closed again. It will not be opened for half an hour.

By 2.50 pm, I was trapped in that box. The paralysis was terrifying; but there was something else. I could feel an energy building up behind me: it would swirl and grind, and as it broke, 50 or 60 of us were picked up, one lump of tangled, compacted limbs, and ground against each other; the crush barriers, the fence. "I got through that," I thought, but I was tiring.

Two minutes later, 2,000 people were invited to enter a large exit gate by the turnstiles, to relieve a crush simultaneously building up outside the stadium. Without anyone to direct them elsewhere, they headed for that tunnel. A bottleneck developed, and because that tunnel had a 1 in 6 downward gradient they were picked up and thrown down it, in a wave of limbs, into the two already overcrowded pens behind the goal.

Arms were now bent at impossible angles. One survivor recalls people being driven off their feet, into the air, and deposited on his head; another how the glass face on his watch popped out. But there was no release for us: the new influx of fans created an even bigger swirl of energy.

We were lifted up again, and like garments in an overfull washing machine, slowly we went, round and round, ground and ground. We couldn't see where this was coming from, or why. I could move my mouth and my eyes, and no more. Occasionally a hand popped up in front of me — mine — and I tried to manoeuvre a shoulder away from my face, to stick my head into a patch of air. But my arm was dragged down again, and I was starting to lose hope.

With my head twisted to the left, I could see through the gap between the North Stand and the huge Spion Kop at the far end, and out to the hills around Sheffield. Cars were pottering along country lanes; people were going to the shops, for a spring drive. I wondered if they were listening to the radio. If they knew we were in trouble, they might call the police.

What exactly were the police doing that day? One of the lines now being trotted out is that Hillsborough couldn't happen today, because communications are so much better than they were in 1989. Certainly, police radios broke down at Hillsborough, and communication was patchy. But surely the police did not need technology to realise that people were dying in front of their eyes in pens three and four. Our fans at the front were crushed into the metal perimeter fence with such impact the fence was bulging towards the pitch. The blue paint on the fence was ground to spots of powder on their cheeks.

Behind them, 10 or 12 feet back, I was one of hundreds of people screaming for my life — for half an hour. In those two pens, people were turning blue, their faces contorted in pain, and confusion. Some were crying. Others had vomit trailing from their chins. There was a smell of excrement and urine, as people's organs began to fail.

I do not want to talk here about what it is like to accept that your life is over. But I had to. I was 19, and it is a long way back from there. Suffice to say that after trying to resist that crush for half an hour, and failing to escape, I gave up. I was exhausted, and I made my peace and said my goodbyes. Only at about 3.10 pm, four minutes after the match was abandoned, was the gate in the perimeter fence finally opened. Drifting in and out of consciousness, I heard a voice in my head, "If you can hang on for another two minutes, you'll live."

I did, to fight for this day.

Research and Applications in Structural Engineering, Mechanics and Computation – Zingoni (Ed.)
© 2013 Taylor & Francis Group, London, ISBN 978-1-138-00061-2

Causal models for the forensic investigation of structural failures

S. Arangio, C. Crosti & F. Bontempi
Sapienza University of Rome, Italy

ABSTRACT: The structural collapses are rare events that are characterized by complex dynamics: the identification of their causes and the explanation of their developments are not straightforward processes and depend on numerous different factors. A fundamental aspect is that, even if sometimes it is possible to identify the trigger that have materially caused the collapse, usually there is a complex background of situations that have made the event possible and that need to be accurately analyzed. The investigation of the interrelated aspects and concurrent causes is a fundamental task to assign conveniently the civil and criminal responsibilities. Starting from these considerations, the aim of this paper is to present some concepts that, in the Authors' opinion, constitute a basis for the framework of the investigation activities. In the first part of the work two concepts are discussed. The first one is the concept of structural complexity, which is an attribute of the civil constructions that are characterized by significant interactions, strong nonlinearities, and large uncertainties. The second concept regards the extension to the Civil Engineering field of a model for the development of failures proposed by Reason (Swiss Cheese Model, 1990). In the second part of the paper some operational approaches are briefly introduced: the breakdown of the problem and the analysis of the timeline; they are essential tools for the assignment of the various responsibility profiles. At the end of the contribution, the concept of structural dependability is recalled as an antidote to avoid failures providing high-quality structural design.

1 INTRODUCTION

The investigation of the causes of a structural failure is a delicate and challenging process that bares the intimate behavior of a structure and points out its relationships with the project environment.

The forensic engineer should be able to identify and explain the causes of the structural failures, intending with "failure" not only the catastrophic collapses that may even result in loss of life, but including all those situations where there is an unacceptable difference between the expected and observed performance.

The solution is found in an iterative way, through the accurate examination of all the available documents, including the declarations of the involved people, and by carrying out the necessary experimental and numerical analyses. On the whole, it is an incremental and nonlinear process that needs precise strategies for its convergence. In fact, even if sometimes it is possible to identify the trigger that has materially caused the collapse, usually there is a complex background of situations that have made the event possible.

A fundamental task of the investigation process is the analysis of the conduct of the various involved parts (designers, managers, contractors, users, etc). Their civil and criminal responsibilities have to be attributed according to the relevance of the consequences of the failure for the Civil Society (Carper, 2002).

The aim of this paper is to present some concepts that, in the Authors' opinion, constitute a basis for the framework of the investigation activities. The first one is the concept of structural complexity while the second one regards a model for the development of failures adapted from the Reason's Swiss Cheese Model (1990).

These two concepts can be profitably applying by making use of some operational tools, which are briefly discussed in the second part of the paper: the breakdown of the problem and the analysis of the timeline; they are essential tools for the convenient assignment of the responsibility profiles.

At the end of the contribution the concept of structural dependability is proposed as an antidote to avoid failures providing an effective approach for a high-quality structural design.

2 COMPLEXITY

2.1 *Definition of complexity*

An interesting definition of complexity (of a system or a problem), that can be easily interpreted in an operational way, comes from the graph in Figure 1 (adapted by Perrow, 1984). The plot shows a three dimensional reference system where the axes indicate:

1. The *nonlinearities* of the system/problem. In the structural field, the nonlinearities affect the behavior at different levels: at a detailed micro-level, for example, they influence the mechanical properties of the materials; their effect depends on the type of materials: it is weak in case of ductile materials

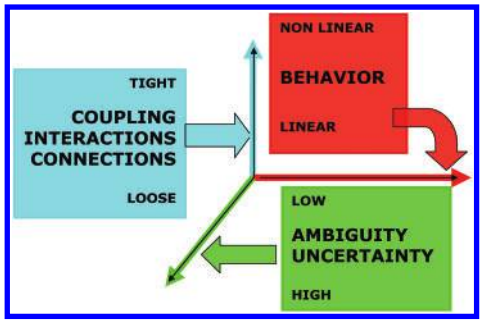


Figure 1. Aspects that increase the complexity of a problem.

while it is significant for example in case of no-tensile materials; at a macro-level the nonlinearities have effects on single elements or even on the entire structure; an example is given by the instability phenomenon that can lead to strong nonlinear behavior.

2. The *interactions* and the *connections* between the various parts: if they are tight, the situations is considered complex while when the connections are slack some tolerance exists.
3. The intrinsic *uncertainties* of the problem/system; they could have both stochastic and epistemic nature.

In this reference system the overall complexity of the problem/system increases as the values in the axes increase, so passing from linear to nonlinear behavior, from loose to tight interactions, from low to high uncertainty.

In the Civil Engineering field, a practical (and also common) case that presents the three components of complexity indicated above, is the intervention on existing adjacent masonry buildings.

According to the Eurocode 8-3, when we are dealing with existing masonry buildings there are some general aspects that should be carefully examined:

- physical condition of masonry elements and presence of any degradation or modification respect to the original situation;
- configuration of the masonry elements and their connections, as well as the continuity of load paths between lateral resisting elements; it is important to keep in mind that the buildings show the level of knowledge at the time of their construction and some defects in the design or in the manufacturing can exist, even if it is not evident at a first sight;
- properties of in-place materials of masonry elements and connections;
- the presence of nonstructural components and the distance between partition walls;
- information on adjacent buildings potentially interacting with the building under consideration.

For the definition of the structural models it should be considered that:

- the geometry, the details and the dead load are assigned but our knowledge depends on the available documents and on the accuracy of the investigations;
- the knowledge on the mechanical properties of the material are related to the accuracy and reliability of the investigation;
- the design approach depends on the completeness and reliability of the gathered information. In order to take into account the uncertainties, the capacity parameters can be modified by using specific confident factors that vary according to the level of knowledge.



Figure 2. Example of an aggregate of buildings and identification of a single structural unity (from Borri and De Maria, 2009).

From these recommendations it is evident that, in case of interventions on existing adjacent buildings, a preventive evaluation of the interactions between the buildings and an accurate and reliable investigation are necessary. Moreover, even if the works will affect only one of the buildings, the entire design process should be carried out considering the effects of the various steps of the work on the adjacent ones.

The Italian Building Code (NTC 2008), that could be considered as a draft of the Italian national annex of the Eurocodes, is even more specific on this topic. Particular attention is devoted to the assessment of the historical heritage and it is introduced the concept of "aggregate of buildings" in order to standardize the procedure for dealing with adjacent buildings.

An "aggregate of buildings" is delimited by an open space and it is composed by various adjacent non-uniform constructions (Figure 2). The constituting buildings have been built in different epochs, with different materials. They had different owners and usually experienced different uses and modifications during time. In the analysis of a single structural unit it is necessary to take into account the possible interactions arising from the structural contiguity with the adjacent buildings. Neglecting these aspects can have significant consequences on the structures even up the occurrence of catastrophic collapses (Figure 3).

Among the possible interactions between adjacent buildings, it should be considered the influence of loads (both vertical and horizontal) transmitted by floors or walls of adjacent units and the actions of arches or vaults that belong to contiguous buildings. The accurate representation of the unit under investigation through plants and sections will allow the evaluation of the stress distribution and the effect of the interactions. In addition to the standard procedure that are carried out for isolated buildings, in case of adjacent buildings it should be evaluated also



Figure 3. An example of an aggregate of building that experience a catastrophic collapse: some interventions on an internal unit were carried out without taking into account the interactions with the adjacent units (Barletta, Italy, 2011).

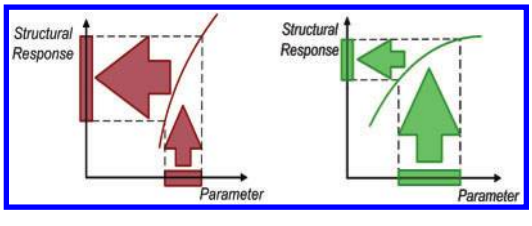


Figure 4. Sensibility of the structural response to the variation of a parameter.

the local effects due to not non-aligned floors or facades, the influence of differences in height or stiffness between adjacent units, the possibility of rotations or translations of the external walls of aggregate.

2.2 *Sensibility and structural robustness*

There are two other aspects that are strictly related to the complexity of a system/problem.

The first one regards the sensibility of a response to a specific parameter: Figure 4 shows the difference in the structural response between a parameter that strongly influences the behavior (on the left) and another one that needs a large variation for changing significantly the results (on the right).

The mechanical interpretation of the concept of sensibility lead to the concept of structural robustness, which is schematically represent in Figure 5. The graph shows the variation of the quality (y-axis) in time (x-axis) of two different structural systems. The first



Figure 5. Variation in time of the performance of a robust system (in blue) and a not robust system (in green).

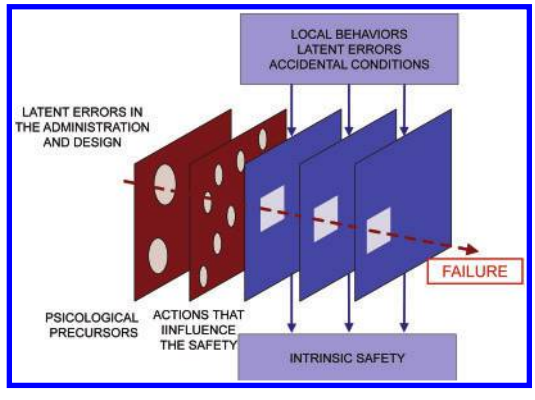


Figure 6. General model for the development of a failure – Swiss Cheese Model (Reason, 1991).

one (green curve) shows a better performance at the beginning respect to the other one (blue curve), however its performance decreases rapidly in time and it crosses the threshold that represents the minimum required performance earlier. On the other hand, the blue one, even if it shows a lower level of performance at the beginning, it is able to maintain it longer and after time it is still above the limit also in presence of some damage. The blue curve is representative of a system with a robust behavior.

Those structural situations that show to be very sensible to some parameters or that are lacking of robustness will exhibit a complex behavior and would need specific investigations (Bontempi et al., 2007).

3 SWISS CHEESE MODEL

It is interesting to observe that, even if the accidental situations have different nature and each one has peculiar characteristics, a general model able to represent in a synthetic way the origin and the development of a failure can be proposed.

According to Reason (1991), it is possible to consider a model of development composed by various steps. They can be conceptual or actual steps and can regard material aspects or human behaviors: each of them can be seen as an ideal layer (Fig. 6).

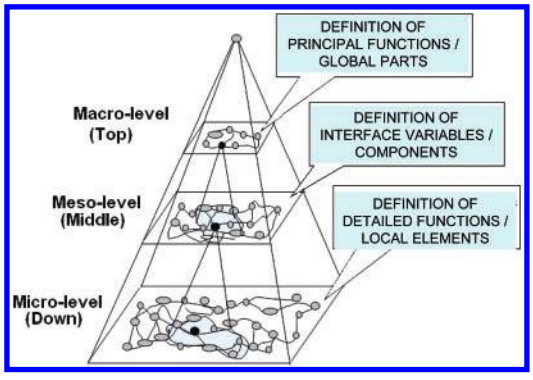


Figure 7. Functional/hierarchical breakdown of a problem/system.

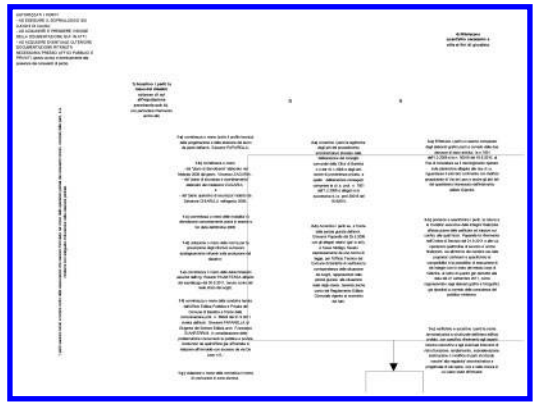


Figure 8. Example of the logical breakdown of the question asked by the magistrate to the expert witness (the details are not visible for privacy issues).

Actually, each layer has imperfections and deficiencies that represent fault and errors for the system (Minato, 2003; Chong & Low, 2006). In Figure 6, these are represented by holes in the layers. The model predicts that, also if a single shortage is not critical, an alignment of these weaknesses (hazards), can lead to a failure. The graphical representation of the model explains its original name: the Swiss Cheese model (Reason, 1991).

4 BREAKDOWN

The previous sections dealt with the concept of complexity and with the extension of a model for representing the development of a structural failure. This framework is still missing the operational point of view; two operational tools that can significantly help in the investigation are the spatial decomposition of the problem (*breakdown*) and the analysis of its temporal evolution (*timeline*).

The hierarchical/functional breakdown of a problem (or a system) can be represented graphically (as shown in Figure 7) by a pyramid, set up with various objects positioned in a hierarchical manner. The peak of the pyramid represents the goal (the whole problem), the lower levels represent a description of fractional objects (the sub-problems in which the problem can be divided), and the base corresponds to basic details. By applying a *top-down* approach, a problem can be decomposed by increasing the level of details one level at a time. On the other hand, in those situations where the details are the starting point, a *bottom-up* approach is used for the integration of low-level objectives into more complex, higher-level objectives. In common practice, however, actual problems are unclear and lack of straightforward solutions. In this case, the strategy becomes a mixed recipe of top-down and bottom-up procedures that may be used alternately with *reverse-engineering* approaches and *back analysis* techniques.

The expert witness applies the breakdown approach to the various phases of the forensic investigation. A first application is the decomposition of the question asked by the magistrate. Usually these questions are complex and need to be accurately analyzed and deconstructed.

An example is shown in Figure 8; for privacy issues the details are not visible, but it is possible to identify clearly three main tasks with 7, 2, and 3 subtasks respectively.

5 TIMELINE

In the previous section a first operation toll has been discussed, the hierarchical breakdown.

Another useful tool for the investigation of an event is the analysis of its timeline.

An example in shown in Figure 9 where it is shown the timeline of an event that started as a demolition and reconstruction of a building but ended with a catastrophic collapse. The chain starts with the conception of the intervention and the relative administrative practices needed to have the feasibility of the work verified by the public administration; then, there is the design phase that lasts up to the realization. For each phase the attention is focused on different aspects and different people are involved:

1) during the administrative practices, the technicians of the public administration should verify the feasibility of the intervention from the point of view of the existing city plan;
2) during the design phase (considering both architectural and structural design) the attention is focused of the conception of the work; the entire project will be analyzed and the respect of the codes will be verified by architects and engineers. In this phase, specific aspects, as for example the influence of adjacent building, should be investigated in detail;
3) during the realization phase, the attention is focused both on the people that materially make the works and on the managers of the site; specific documents and plans need to be drafted (as the safety plan and

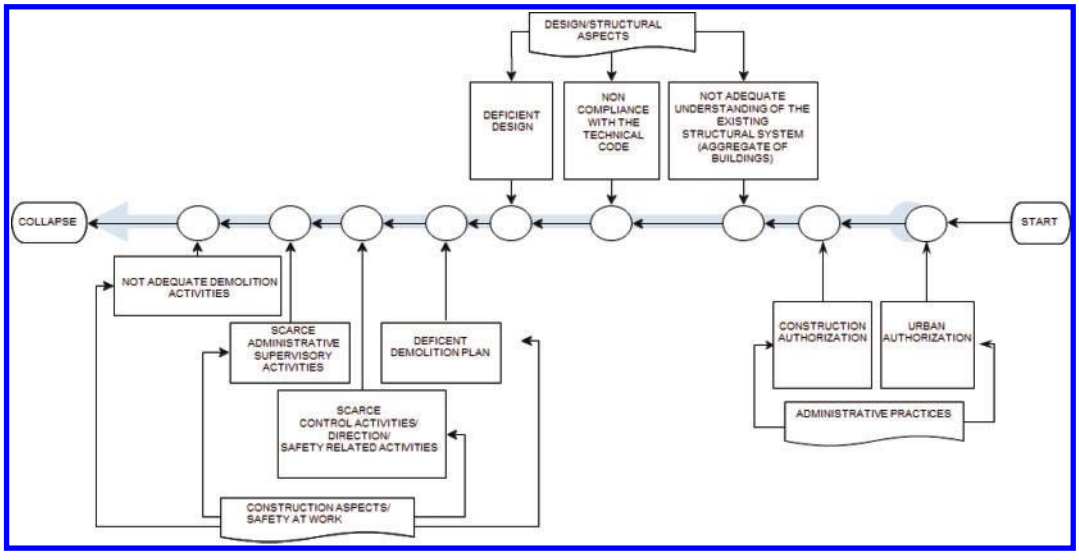


Figure 9. Example of timeline for the analysis of a work of demolition and reconstruction that turned into a collapse.

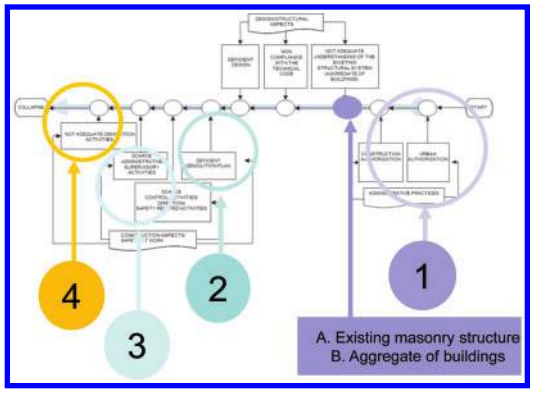


Figure 10. Example of the identification of the causal joint of the timeline in Figure 9 and definition of the various triggers.

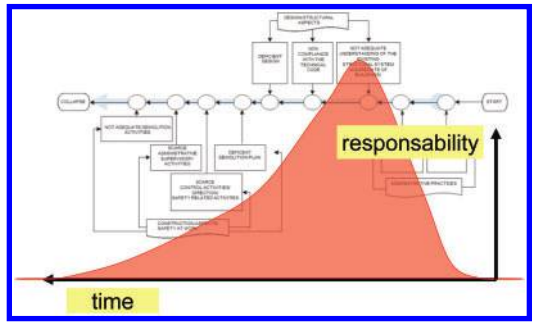


Figure 11. Example of the responsibility profile associated to the timeline of Figure 9.

the demolition plan); all the involved people (contractors, managers, designers, etc) have to carry out activities of control. Also some representatives of the institutions should carry out supervisory activities.

Even if the phases are represented separate and sequential, between them numerous overlapping and mutual influences exist (Suraji et al., 2001).

An accurate analysis of the entire process will show that one of these steps plays a central role: this one can be considered the causal joint of the entire process; all the events that led to the collapse rotate around this point.

Once the causal joint is identified, the other steps, that led to the failure, can be consequently ordered and the entire event is understood (Figure 10).

It is important to point out that, according to Reason's model, even if the collapse has been materially activated by a specific trigger (number 4 in the Figure), it was prepared and made possible by other acts, that sometimes are also distant in time, and that usually cannot be detected by a superficial interpretation of the event (Augenti & Parisi, 2009; Brady, 2012; Love, 2008; Petrosky, 1992).

6 RESPONSABILITY PROFILE

Starting from the timeline in Figure 9 and according with the identified causal joint, it is possible to define a profile that measures the responsibility of the involved people, as schematically shown in Figure 11.

It is possible to note that also this representation is coherent with Reason's model that states that it is not the last actor that necessarily should be considered the most, or even the only, responsible of the disaster, but the whole process should be evaluated.

7 CONCLUSIONS

In this work, some general concepts that, in the Authors' experience, constitute a basis for the framework of the forensic investigation activities have been discussed. It has been shown that it is necessary to start analyzing the peculiar complexities that characterize each problem. In this sense it is often useful to evaluate the sensibility to specific parameters and the existence (or not) of structural robustness. Then, Reason's model for the development of failures has been extended to the case of Civil Engineering structures, showing that a failure is usually caused by multiple concurrent causes. Even if a collapse is materially activated by a specific trigger, its initial causes should look for in other acts, which sometimes are also distant in time. This aspect should be considered also when the various responsibilities are assigned.

Tragic events as the structural collapses make the technicians reflect on the approach that are commonly used for the structural design and facilitate the introduction of new concepts, as that of structural *dependability* that has been recently proposed. It is a global concept that describes the aspects assumed as relevant to describe the quality of a system and their influencing factors (Bentley, 1993). It has been originally developed in the Computer Science field but it can be reinterpreted in the Civil engineering (Arangio et al., 2010). The dependability reflects the user's degree of trust in the system, i.e., the user's confidence that the system will operate as expected and will not 'fail' in normal use: the system shall give the expected performance during the whole lifetime.

The use of this concept would include the structural Performance-Based Design in a holistic framework.

ACKNOWLEDGMENTS

The team www.francobontempi.org from Sapienza University of Rome is gratefully acknowledged. This work was partially supported by StroNGER s.r.l. from the fund "FILAS – POR FESR LAZIO 2007/2013 – Support for the research spin off".

REFERENCES

Arangio S., Bontempi F., Ciampoli M. (2010), *Structural integrity monitoring for dependability*, Structure and Infrastructure Engineering, 7, 75–86, 2011.

Augenti, N. and Parisi, F., Learning from Construction Failures due to the 2009 L'Aquila, Italy, Earthquake. J. *Perform. Constr. Facil.*, 24(6), 536–555, 2010.

Bontempi, F., L. Giuliani, and K. Gkoumas, Handling the exceptions: dependability of systems and structural robustness, *Proc., 3rd International Conference on Structural Engineering, Mechanics and Computation* (SEMC), 2007.

Bentley, J.P. An Introduction to Reliability and Quality Engineering, Longman, Essex, 1993.

Borri A., De Maria A., Eurocode 8 and Italian Code. A comparison about safety levels and classification of interventions on masonry existing buildings, *Eurocode 8 – Perspectives from the Italian Standpoint Workshop*, 2009.

Brady S.P., Role of the Forensic Process in Investigating Structural Failure, *Journal of Performance of constructed facilities*, 26: 2–6, 2012.

Carper K., *Forensic Engineering*, CRC Press, 2002.

Chong W. K., Low S. P., Latent buildings defects: causes and design strategies to prevent them, Journal of Performance of Constructed facilities, 20(3), 213–221, 2006.

HANDLING EXCEPTIONS, Roma 2008 – 2010, http://www.francobontempi.org/handling.php

Love P. E. D., Edwards J., Irani Z., Forensic Project Management: An Exploratory Examination of the Causal Behavior of Design-Induced Rework, *IEEE Transactions on Engineering Management*, 55(2), 234–247, 2008.

Minato T., Representing causal mechanism of defective designs: a system approach considering human errors, *Construction Management and Economics*, 21, 297–305, 2003.

Norme Tecniche delle Costruzioni 2008 (NTC 2008), D.M. 14/01/2008

Perrow C., *Normal Accidents: Living With High Risk Technologies*, University Press, 1984.

Petrosky H., *To engineer is human – The role of failure in successful design*, Vintage Books edition, Random House: New York, 1992.

Reason J., *Human Error*, Cambridge University Press, 1990.

Suraji A., Duff R., Peckitt S., J., Development of causal model of construction accident causation, *J. Constr. Eng. Management*, 127:337–344. 2001.

UNI EN 1998–3:2005, Design of structures for earthquake resistance: assessment and retrofitting.

Research and Applications in Structural Engineering, Mechanics and Computation – Zingoni (Ed.)
© 2013 Taylor & Francis Group, London, ISBN 978-1-138-00061-2

Capacity assessment of damaged school buildings after 2011 Van earthquake

R.A. Oyguc
University of Illinois at Urbana-Champaign, Illinois, USA
Istanbul Technical University, Istanbul, Turkey

ABSTRACT: On October 23, 2011 a devastating earthquake with M_w of 7.2 hit Van province, which is located in the east of Turkey. The epicenter was Tabanlı village which is 30 km far from the city. 16 days afterwards the first earthquake, a second earthquake with M_w 5.6 again hit Van province. This time the epicenter was 18 km far from the city. Due to the large number of unqualified structures, the damage was more than expected. In this study, 3 damaged school buildings which were subjected to Van earthquakes were chosen. To overcome the soil effects, the buildings were chosen in the same era. Although they had the same structural properties, 1 of them were heavily damaged, 2 had minor damages and were in use. After conducting time-history analysis on the 3D models of the selected buildings, the reasons of the damages were discussed according to the assessed capacities.

1 INTRODUCTION

Two earthquakes, on October 23, 2011 (10:41 GMT) and November 9, 2011 (19:23 GMT) hit Van province, which is located in the eastern part of Turkey between Lake Van and the Iranian border. It is 20000 square km in area and has a population of 1million approximately. The peak ground acceleration values of the earthquakes were measured as 178.5 gal in the north-south direction and 102.6 gal in the east-west direction respectively. According to the governmental reports at least 600 people died, and more than 4000 are injured due to the earthquakes. More than 2000 houses are heavily damaged or collapsed. Comprehensive data about the earthquakes can be found in Table 1.

To carryout reconnaissance studies in the region, Government of Van signed a protocol with wide-known universities of Turkey. They want to know which buildings they should demolish and which they should support credits for retrofitting. Figure 1 shows the epicentral distances of the earthquakes.

Table 1. October 23, 2011 and November 9, 2011 Van earthquakes characteristics.

Earthquakes	October 23		November 9	
Source	KOERI	USGS	KOERI	USGS
Latitude (N)	38.757	38.691	38.429	38.42
Longitude (E)	43.360	43.497	43.234	43.22
Depth (km)	5.0	16.0	5.0	5.0
M. Magnitude	7.2	7.1	5.6	5.6

2 SEISMO-TECTONIC CHARACTERISTIC OF THE REGION

It is known by the seismologist that Lake Van is a key factor in the Arabian-Eurasian plate boundary. It lies near the intersection of two transform fault zones and a subduction zone. It is also assumed by NASA that, the southern edge of Lake Van lies along the extension of the right-lateral strike slip North Anatolian fault (Fig. 2). The Dead Sea and East Anatolian fault zones are classified as left-slip faults. Central Turkey is being squeezed west (to the right) by the northward movement of the Arabian Plate. Beyond Lake Van are the folds and thrust faults straddling the boundary between the Arabian Plate from the Eurasian Plate (NASA).

It is also reported that, the region had affected from the historical earthquakes between the periods 1101-1900 B.S. The intensity of them were in the range V-X. It was a known fact that there had been a fault trace

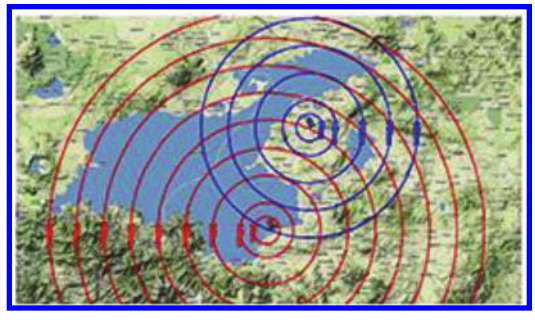


Figure 1. Epicentral distances of Van earthquakes.



Figure 2. NASA picture of Lake Van (NASA).

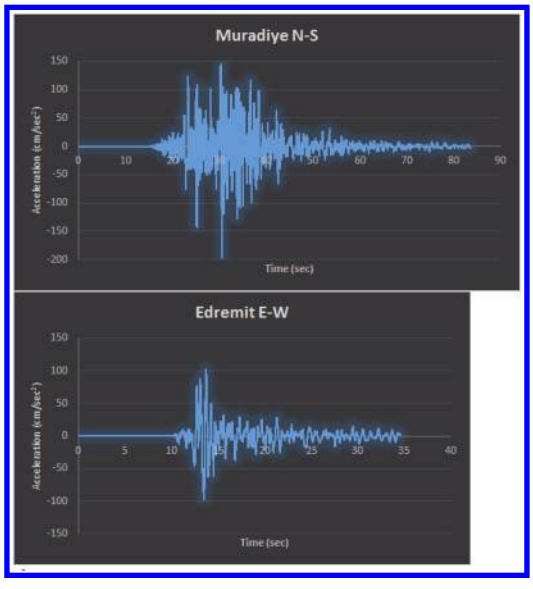


Figure 3. Filtered earthquake records of Muradiye and Edremit.

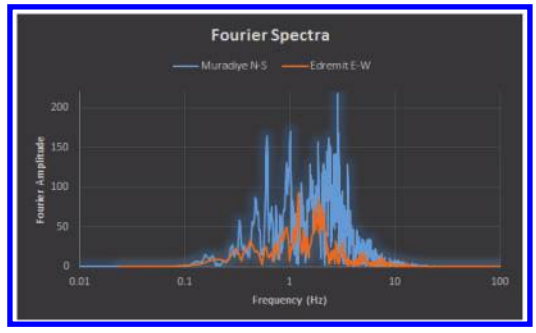


Figure 4. Fourier spectra of Muradiye and Edremit earthquakes.

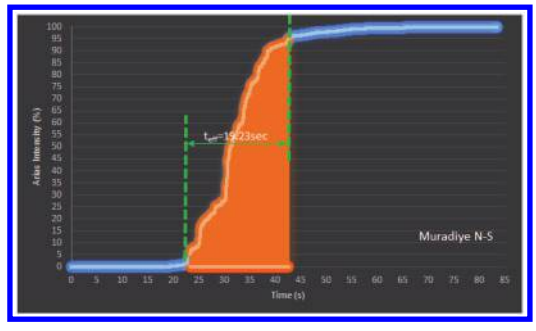


Figure 5. Arias intensity of Muradiye N-S component.

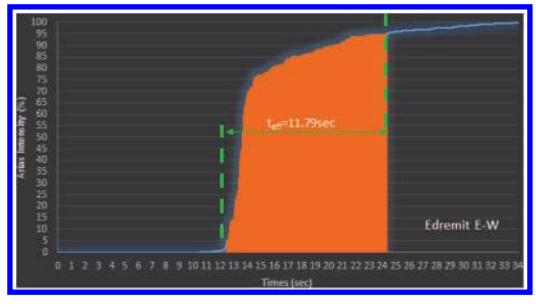


Figure 6. Arias intensity of Edremit E-W component.

in the region, it did not accepted as an active fault in the 1992 dated map of MTA (Mineral Research and Exploration Institute) though.

Regarding this issue, it is later accepted and marked in the seismological maps that there is an active left-lateral strike slip fault line called Van Fault.

The gathered ground motion records from Muradiye and Edremit stations were then filtered using *Seismo-Signal* (Seismosoft) program respectively. It was first performed baseline correction to the records. Later on, in order to bypass the undesirable noise contents in the records, quadratic Butterworth band filter had been applied to the acceleration records. Since N-S components of Muradiye and E-W of Edremit had the peak ground acceleration values, the processed values of those records are given in this paper. Figure 3 shows the acceleration-time graphs of the mentioned earthquakes.

The comparison of Fourier spectrums for both earthquakes are given in Figure 4. The effective durations of the horizontal components are determined assuming that the effective time is the time interval between the 95% and 5% values on the Arias intensity curves. The calculated effective times for Muradiye and Edremit records are shown on Arias Intensity plots on Figure 5 and Figure 6. The effective time for Muradiye N-S and Edremit E-W records are calculated as 19.23sec, 11.79sec respectively.

For the 5% damped acceleration response spectra of the filtered ground motions recorded at Muradiye and Edremit are compared with the design spectrum defined in Turkish Earthquake Resistant Design Code

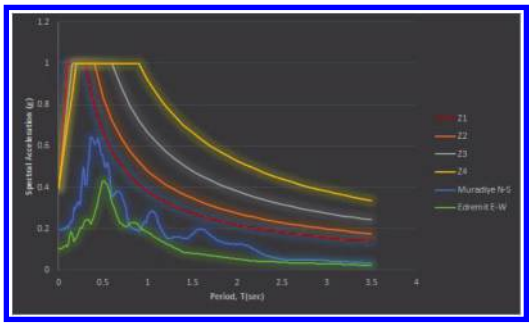


Figure 7. Comparison of acceleration response spectra with the design spectra of TERDC.

(Ministry of Public Works, 2007) for all soil types. Figure 7 shows the comparison plot. Here Z1 represents the most stiff soil and Z4 the softest one.

It can easily be seen from Figure 7 that, the gathered 5% damped elastic response spectrums are all below the design spectrum values defined in TERDC, for all types of soils. Due to this fact, it can be stated that it is in fact not the earthquake that demolished the structures, it was the result of poor designed structures. Not obeying the engineering rules, using out of standard materials were the cause of the damage.

3 DAMAGE ASSESSMENT

3.1 *General characteristics of the building stock*

The building stock of Van can be categorized in to two, the reinforced buildings and the masonry ones. It can be stated that, the scene is not so much different from the other parts of Turkey indeed. Majority of the buildings were lack of engineering care. Most of the citizens of the province build up their own buildings without obeying engineering rules.

After the reconnaissance studies completed in the field, the reasons causing the damage in the reinforced buildings due to the earthquake excitation were resulted as follows;

a) It was just after 1999 Marmara earthquake that ready-mixed concrete started to use in the east of Turkey. The tested core samples of the 6–7 story buildings were astonishing. The strength results of the concrete samples were found to be 3–4 MPa.
b) Poor detailing of reinforcing bars can be stated as the second factor. The stirrups and the loops were not curved due to the regulations. There were also no stirrups in the column-beam connections.
c) Usually ribbed slabs were preferred. To overcome the rigidity deficiency of ribbed slabs, structural wall elements were not implemented in the buildings.
d) In the majority of the high-rise apartments, the entrance floors were used as car galleries or supermarkets. To expand free space in this floors the middle columns were cut off.

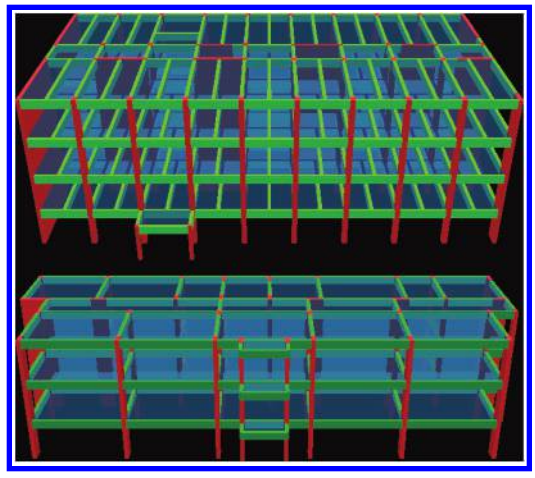


Figure 8. 3-D model of Building of (a) A and B (b) C.

e) Irregularity effects were not taken into account in the design.
f) The non-structural elements, clads, ceramics etc fell with the started excitation and caused injuries.
g) Adjacent buildings. There were no dilation. Due to hammering effect of different story levels, majority of the buildings were destroyed.

When the masonry buildings investigated, the causes of the failures can be stated as;

a) Heavy clay roofs due to protect the residents from bad weather condition caused the most damage in masonry structures.
b) Poor quality of the mud mortar binder.
c) Inadequate corner connections of the walls.
d) Excessive lengths of walls without any lateral support.
e) Majority of the brick masonry structures were unreinforced. They did not have any vertical and horizontal tie beam elements.

After the reconnaissance studies completed, the Government started to demolish the poor qualified structures and maintain the minor damaged ones. The reconnaissance field observations were not limited to residential buildings, as well as the school and governmental buildings. After the studies were completed, the retrofitting stage started in the region.

3.2 *Selected school buildings for assessment*

The selected school buildings were all built as three story, 12-class, and they were constructed in the same region. They all had structural shear-wall elements since they were school buildings. Two of them had been detailed using the same structural project prepared by the Ministry of Education of Turkey. Their design concrete strength was 20 MPa and design steel strength was 420 Mpa. The 3-dimensional ETABS (CSI) models of the selected buildings are given in Figure 8.

Table 2. Material properties of the selected school buildings.

Building name	Concrete strength (MPa)	Steel strength (MPa)
A	8	420
B	14	420
C	12	420

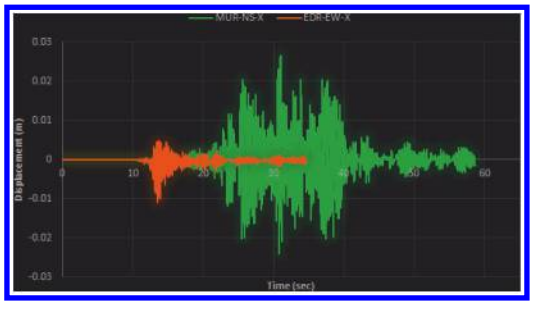


Figure 9. Time history trace of Building A for X-direction.

Concrete core samples were taken from the buildings implementing the stated procedures in TERDC. The test results were found to be different from the design projects. The concrete strength of the buildings which had the structural detailed projects by the Ministry of Education had been found to be 12 MPa and 8 MPa. The other school buildings concrete strength was found as 12 MPa. The experimental results of the concrete and the rebar samples were given in Table 2.

Here in the paper, the building with the lowest strength will be named as "Building-A", the highest one as "Building-B" and the other one as "Building-C".

3.3 *Time-history analysis results*

Time-history analysis were implemented on the selected three school buildings using the filtered ground excitations of Muradiye-NS and Edremit-EW. Following the sequence of the earthquakes, the buildings were first subjected to Muradiye-NS earthquake and then Edremit-EW in both X and Y-directions. Figure 9-11 shows the time-history displacement trace of the buildings. The displacement traces of the building were found to be slightly different in X and Y directions, so that only X-direction had been chosen to plot.

The earthquakes peak ground acceleration values were not big enough to produce large energy. The established displacements were not found to be considerable though.

After completing the time-history analysis, the probability of failure in the structural elements according to the implemented analysis, were matched with the reconnaissance observations in the following section.

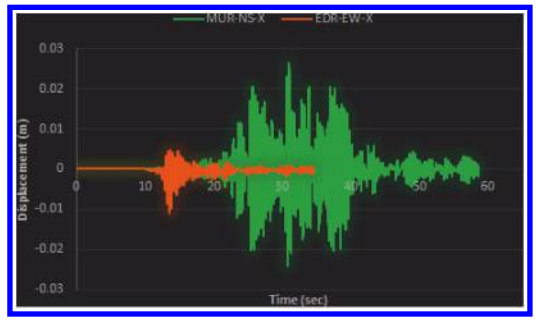


Figure 10. Time history trace of Building B for X-direction.

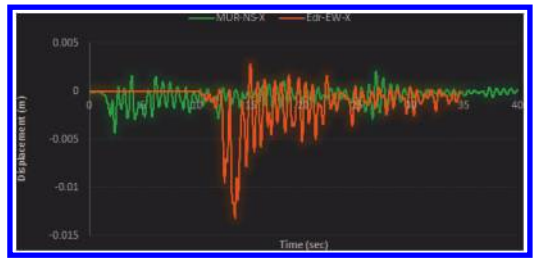


Figure 11. Time history trace of Building C for X-direction.

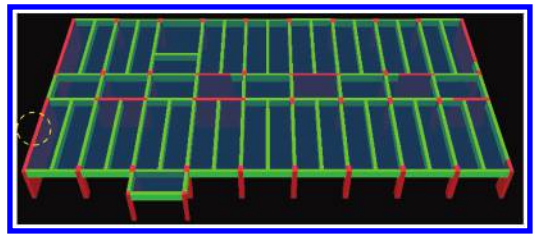


Figure 12. Plan view of Building-A.

3.4 *Matching the results with the field observations*

The results showed that even if the structural system properties were the same, the concrete strength and quality of workmanship directly effects the performance of the buildings. Building-A, with the lowest concrete strength showed the worst performance. Its companion one Building-B had just minor cracks and were in use. Also Building-C was not damaged heavily.

Figure 12 shows the plan view of heavily damaged Building-A. The damage was excessive though to the shear-walls. The interior walls were demolished, and there were diagonal cracks in the shear-walls.

Figure 13 shows the outer view of the school building and the identified damages inside the building. The damaged shear wall were marked in Figure 12.

4 CONCLUSIONS

Three school buildings were selected to be analyzed to betray the behavior of buildings due to Van-Turkey 2011 earthquakes. Three buildings were established in



Figure 13. Outer and inside view of the school building.

the same region. Two of them were built conducting the same static detailed projects prepared by the Ministry of Education of Turkey. All of them were 3-storied and had shear-walls. Their design concrete strength was 20 MPa. The buildings had irregularity in one-direction.

The earthquakes record were filtered and scaled before using them. The unnecessary noisy parts were pulled out. After conducting time-history analysis on the selected buildings, the followings were resulted.

a) The peak ground accelerations of the earthquake records were found to be 178.5 and 102.6 gal. That was below the design limits. In Figure 7 it was shown that the earthquakes acceleration response spectra were below the design spectra of TERDC 2007. The damage caused by the ground motions on the buildings were astonishing though.
b) The majority of the buildings concrete strengths were found to be different and considerable lower than their design strengths. This is believed to be the main reason of the determined damage.
c) In the analyzed 3 school buildings, the building with the lowest concrete strength had the most damage, the interior walls were demolished and the shear-walls had diagonal cracks, the building did not collapse though. The one from the same executed project (A and B) with a higher concrete strength were in good position after the same earthquakes.
d) It can be concluded that, whether if the detailed project is perfectly designed, the application of that project on the field is another concern. Poor quality of the established buildings in the region made the damage excessive.
e) Not using ready-mixed concrete and not properly detailing the reinforced elements may be classified as the most important deficiencies.
f) It is believed that if the analyzed buildings were built-up with higher stories they would collapse, like the others, due to their deficiencies.

In many parts of Turkey and many other countries there are many non-engineered buildings indeed. To betray the future possible damage in this type of buildings, they should be demolished or strengthened before earthquakes demolishes them.

REFERENCES

NASA, www.nasa.gov
MTA, Mineral Research and Exploration Institute
http://kyh.deprem.gov.tr/ftpe.htm
Seismosignal, Seismosoft
Turkish Earthquake Resistant Design Code, Ministry of Public Works and Settlement, Ankara, 2007
ETABS (CSI)

Research and Applications in Structural Engineering, Mechanics and Computation – Zingoni (Ed.)
© 2013 Taylor & Francis Group, London, ISBN 978-1-138-00061-2

Structural failures and monitoring of structural health with use of WiSeNe^{MONIT} system

S. Wierzbicki, M.A. Gizejowski & Z. Stachura
Warsaw University of Technology, Warsaw, Poland

ABSTRACT: Extreme loading events associated with climatic conditions can have a severe impact on building structures leading to local damage that can trigger the instant failure or progressive collapse. Extreme wind action associated with a high wind speed and gust may cause a local damage to façades and roof claddings or even the total destruction of lightweight building load bearing systems. Extreme snowfall, snow-on-ice, rain-on-snow or rainfall ponding actions may lead to catastrophic roof failures. In this paper, the outcome of studies related to forensics of specific climatic-induced failures is summarized. Such events would have in many cases been avoided if certain safety measures were applied. One of the most effective tools of safety assurance is to install an efficient structural health monitoring system that could inform about the actual state of the structure and warn in advance about forthcoming dangerous situations. In case of snowfalls, an early warning sign would initiate an immediate action for the arrangement of snow removal procedure, or in case of a heavy snow storm - a snow removal procedure combined with the building evacuation. In this paper, the WiSeNe^{MONIT} monitoring system is presented together with its pilot installation. The system was customized for the purpose of monitoring of large span steel roof in a hypermarket located on north-east of Poland. The data recorded from sensors distributed over the roof area is evaluated for periods between December 2011 and February 2013, and presented in the paper together with some practical observations.

1 1 INTRODUCTION

Warehouses, factories, exhibition halls and commercial buildings of lightweight bearing systems, especially those of flat large span roofs, are among the most common low-rise buildings affected by failure incidents. Failures were attributed to many factors, mainly arising from unforeseen climatic conditions and errors undetected during design or/and execution processes. Among climatic actions, the excessive wind speed and gust, overloading by snow, rain-on-snow mixes, and rain water ponding are the causes of building damages with reported fatalities and injuries. There is a trend of increasing number of such events said to be associated with accelerating global climate change influencing the patterns of snowfall and rainfall frequency and density.

There have been many research papers dealing with climatic actions and their influence on buildings; Gizejowski et al. (2011), Geis et al. (2012) & Goliger et al. (2013). The latter one deals with wind loading while the former one examines the risk of building failure and damage due to snow loading, characterizing the relative susceptibility of different types of structures as well as the human and economic impacts of these incidents. High profile American building failures due to snow have included the Hartford Arena in Connecticut and the C.W. Post College Theater on Long Island, both taking place in 1978. Reported international failures include the collapse of the Basmanny Marketplace in Russia and the Katowice Exhibition Hall in Poland, both of which occurred in the spring of 2006, killing a total of 131 people.

In the first part of this paper, the issues related to survey of failure causes are reported. In some countries, including Poland, there is an obligation requiring timely inspections of certain large span roof structures by building owners in order to monitor their technical conditions and to eventually react in an early stage. The other failure preventive measure is to install the structural health monitoring system (SHM system). Structural design execution strategies cannot define a priori all the extreme actions the structure may be subjected to during service that may lead to a danger of structural collapse. The only reliable information about the actual performance can be obtained from the SHM system controlling climatic actions and the most important action effects of structural response.

In the second part of this paper, issues related to monitoring systems that can prevent structural failures are addressed. WiSeNe^{MONIT} monitoring system is dealt with in details that allows for controlling vertical deflections of building roof structures due to winter climatic loads, as well as due to temperature of structural elements. Temperature of individual structural elements is interpolated from records obtained in the points of deflection measurements. The laser distance measurement and multi-hop radio data

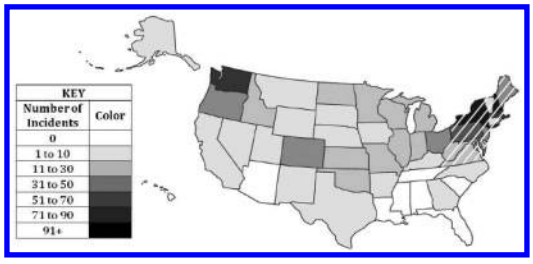


Figure 1. Distribution of the U.S. database failure incidents; Geis et al. (2012).

transmission are utilized for monitoring of deflections. The WiSeNe^{MONIT} system systematically collects, processes and evaluates information about the response of the roof structure, i.e. change of representative deflections due to climatic loads such as snow, ice or rain water, taking into account the effect of temperature on the deflection.

Moreover, the WiSeNe^{MONIT} SHM system supports the maintenance management process by providing users with the warning signals to take preventive actions of snow or rain water removal at the right time, therefore reducing the number of unnecessary operations and avoiding the risk of damages caused during the operational processes.

2 STRUCTURAL FAILURES

2.1 *Survey conducted by Geis et al. (2012)*

Factors such as building location, time of year, and weather patterns affecting a building's susceptibility to extreme snow loads were considered in research. Incidents were reported in all the U.S. states and clustered in northern regions of the country (Fig. 1). The majority of reported incidents (58%) occurred in the Mid-Atlantic and New England states, delineated in Figure 1.

The study has also been conducted to relate semimonthly periods of snowfalls and the number of failure incidents. A positive relationship was observed between snowfalls in a semimonthly period and the number of incidents in a semimonthly period, with increasing snowfalls tending to be associated with a larger number of incidents (Fig. 2). Data points along the vertical axis showing incidents without any record of snowfall may reflect snow build-up on roofs over days or weeks before the incident, or the additional weight from rain and ice in addition to snow, which could not be determined from available weather data. Large snow depths causing no incidents for data points located along the horizontal axis may represent snow falling on unpopulated areas, or less-dense or quickly-melting snow that imparts smaller loads to buildings. Using the available weather data, it was not possible to determine whether or not snow loads exceeded code design loads for any particular incident.

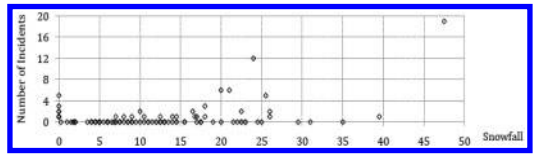


Figure 2. Database failure incidents vs. snowfall depth (in.) for Massachusetts between 1993 and 2009; Geis et al. (2012).

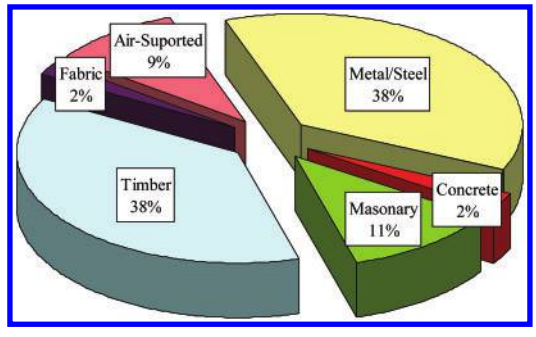


Figure 3. U.S. reported database incidents by construction type.

Other considered features of buildings impacted by failures were structural systems, function and age up to the event occurrence. Of the total number of 1,029 snow-induced building failure incidents in the U.S. between 1989 and 2009, and 91 international incidents between 1979 and 2009, 233 (23%) incidents were identified with information about construction type. Figure 3 represents the classification of the number of database incidents in the U.S. by construction type.

The majority of impacted buildings are reported by Geis et al. (2012) to be metal/steel (38%) and timber (38%) constructions. Steel structures of low-rise buildings consist of various combinations of lightweight cold-formed and hot-rolled steel members for roof systems with different types of walls. As was clearly indicated in Geis et al. (2012), such buildings are subjected to a high live to dead load ratio and are particularly at risk under snow loads. The number of air-supported and fabric structures reported in the database is also notable, although these structures make up a relatively small percentage of the overall considered building stock. They are at risk due to their small dead load, vulnerability to uneven loading, and difficulty associated with clearing snow and ice when overloaded (Geis et al. 2012).

Figure 4 presents the classification of the number of database incidents outside of the U.S. by construction type (Geis et al. 2012).

Although the number of incidents considered in this case are relatively narrow, the same tendency is observed like in case of a broader survey done for the U.S.

2.2 *Survey conducted within the MONIT project*

In the framework of MONIT Project led by the Warsaw University of Technology and carried out by several

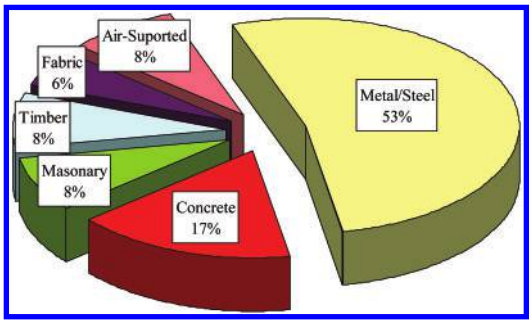


Figure 4. Internationally reported database incidents by construction type.

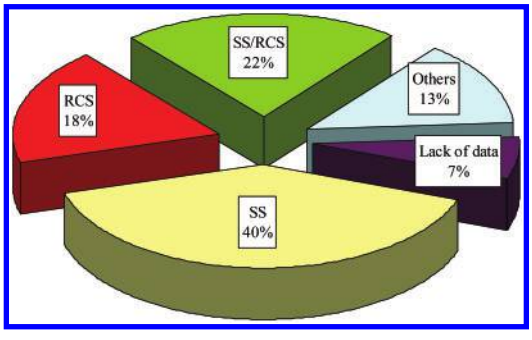


Figure 5. MONIT database incidents by construction type.

partners (see http://www.monit.pw.edu.pl/), a task of collection of building failures and collapse events in Poland in the years 1995-2010 has been completed. From the building surveillance offices, the data of 443 officially submitted cases were reported. Because only 12 of them were concerned with large span roof buildings, independent investigations were undertaken in order to bring this number closer to reality. The additional 48 cases of incidents reported for large span roof buildings were included from other sources, giving the number of 60 in total.

Figure 5 presents the MONIT database incidents by construction type. It is indicative from this survey that failures and collapses of buildings with steel structural load bearing systems (SS) or with mixed reinforced concrete supports and steel roofs structural systems (RCS) have been dominant. Although the incidents reported above were in majority related to climatic actions resulting from snow-ice overloading events, the real causes of failures and collapses would be somewhat different. Figure 6 indicates what are the factors responsible for structural failures and collapses.

The total number of reported cases for which the factors responsible for incidents were given is shared almost equally between all three selected types of reasons, namely design, execution and exploitation.

The most dangerous factors are related to errors inherited in the structure during the phase of execution because they are difficult to detect after the construction has been finished and their existence appears

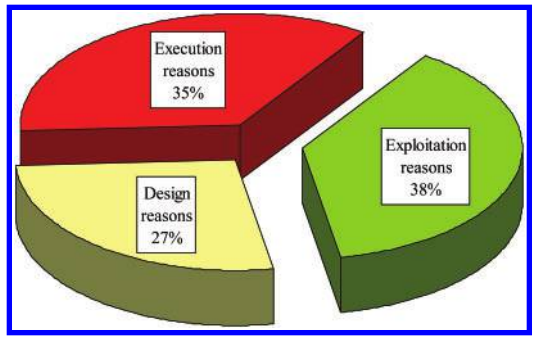


Figure 6. MONIT database factors responsible for building incidents.

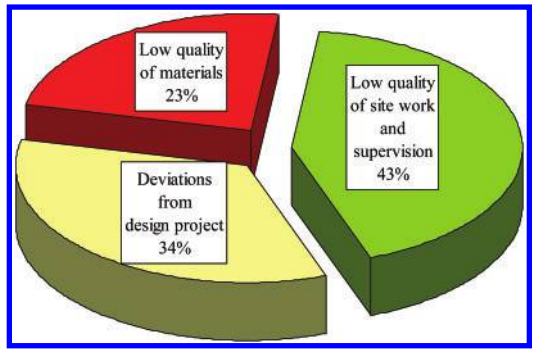


Figure 7. MONIT database factors affecting the execution reasons.

suddenly and frequently under climatic overloading. Figure 7 shows the factors affecting the execution reasons relating incidents of failure or collapse to execution reasons. The low quality of site work and supervision are the dominant factors.

3 MONITORING OF STRUCTURAL HEALTH USING THE SYSTEM DEVELOPED WITHIN THE MONIT PROJECT

3.1 *General*

One of the most efficient means of controlling the amount of snow or rain-water ponding loads on building flat roofs is to monitor the temperature and structural response in terms of deflections and compare them with deflection limits evaluated on the basis of calibrated numerical model of the whole structural system (Gizejowski et al. 2012). This idea has resulted in the development of SHM systems that control online the safety and serviceability criteria, enabling the recalculation of the structural deflection limits in relation to monitored temperature of structural elements. In the last decade, wireless sensing network technologies became superior monitoring solutions because of low installation cost, fast communication time and efficient online assessment capability.



Figure 8. Integrated measuring device mounted on the purlin.

3.2 *WiSeNe*^{MONIT} *structural health monitoring system*

The monitoring system WiSeNe^{MONIT} consists of two main subsystems, namely the on-line subsystem and the off-line subsystem that supports the former one by a numerical module (Gizejowski et al. 2012). The on-line subsystem is responsible entirely for recording, storing and evaluating the structural deflections under climatic actions (snow, ice, rainwater) in representative number of nodal points, and recording the temperature changes in respective structural elements. The off-line subsystem utilizes the temperature data from the on-line subsystem and performs numerical evaluation of action effects, displacements in all the nodes and stress resultants in all the line elements of the monitored structure.

On-line subsystem consists of three types of hardware devices interconnected in a radio multi-hop data transmission network. They are integrated measuring devices, retransmitting devices and central controlling unit (for details refer to Gizejowski et al. 2012).

Figure 8 shows the integrated measuring device installed over the bottom chord of truss purlin being the secondary element of roof structure transferring the load onto the main frameworks. The measurements of displacements are done by the laser's optical device evaluating the distance between the point to which is attached and the stable point that is not subjected to movements, or its movement can be related to the other reference point of known displacements. This device is equipped with a radio transmission capability so that it serves as a node in radio network being able to communicate with other such devices, as well as with retransmitting devices and central controlling unit. The other task of measuring device is to integrate the displacement related measurements with the temperature. The temperature is recorded inside the measuring device and outside it with use of a satellite thermometer (see Fig. 8). Measuring devices are mounted by means of special slings seen in Figure 8 to secondary and primary substructures of building roof or to other reference points in order to avoid obstacles disturbing the laser's optical axis to go through.

Table 1. Reaction levels corresponding to four threshold levels of structure health assessment.

	System state		End user state	
Displacement state*	Reaction type	Sampling frequency	Signal	Activity
$\delta \leq$ L1	Normal	T	None	None
L1 $< \delta \leq$ L2	Raised	T/2	Alert	Observation
L2 $< \delta \leq$ L3	High	T/4	Warning	Inspection
L3 $< \delta \leq$ L4	Higher	T/8	Alarm	Intervention
$\delta >$ L4	Highest	T/8	Closure	Evacuation

* δ – displacement due to climatic actions.

The calculated values of deflection are compared with threshold values to determine the corresponding climatic action level for the roof structure. Based on the results of this evaluation, the subsystem sends an appropriate message of different types, namely the information type, warning type or alarm type. The four threshold levels (levels L1-L4; for details refer to Gizejowski et al. 2012) correspond to five reaction levels that are given in Table 1. It is important to note that the sampling interval time T (see the third column of Table 1) at which all the displacements controlling the actual state of the structure safety are recorded, is not of a constant value but is implemented in the system as a variable value being dependent on the season and upon reaching the threshold values of displacements of representative structure nodes. The base value T is being set in accordance with the consultation with the owner/user of building subjected to monitoring.

3.3 *Pilot installation*

Pilot installation of WiSeNe^{MONIT} system was done for a large span steel roof of hypermarket located in the north-east of Poland, in the region of usually severe snowfalls in wintertime.

The on-line subsystem installed in the considered building consists of 18 measuring devices, 9 retransmitting devices and one controller with ratio module and GSM router. Figure 9 shows the distribution of measuring devices over the roof structural elements. As one can note, measuring devices are distributed over the entire roof structure and installed on both the secondary structural elements (truss purlins) and main structural elements (rafters of rigid frames transferring loads from purlins onto the foundations). Installation was done in December 2011 when there was no snow on roof, and the initial measurement of roof elements deflected profile was evaluated for known permanent loading conditions. On the basis of this initial record, the off-line numerical model of the entire structure (consisting of both secondary and primary elements) was constructed and calibrated to conform with initial measurements. The numerical model was

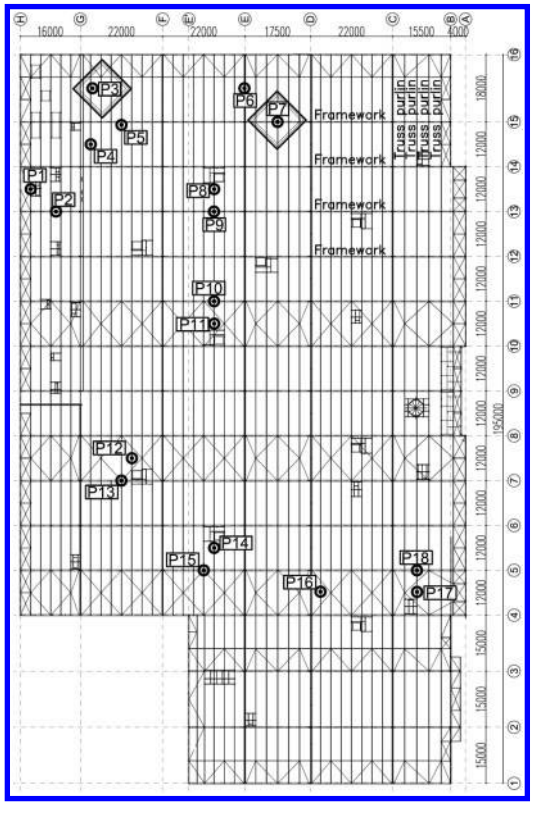


Figure 9. Location scheme of integrated measuring devices.

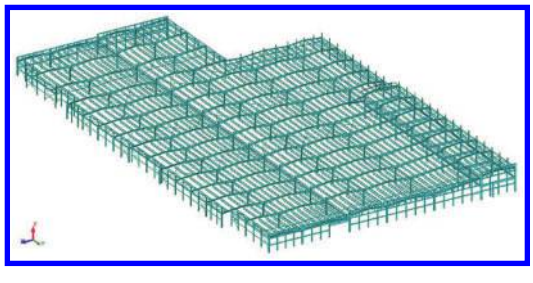


Figure 10. Printout of constructed numerical model from the off-line subsystem of WiSeNe^{MONIT}.

developed with help of Autodesk Robot Structural Analysis Professional software and it is shown in Figure 10.

It consists of 19041 elements and 12783 nodes, and the number of equations needed to be solved is 75600. Because the constructed model consists of cable elements, the nonlinear structural analysis option is applied together with a Newton-Raphson solver.

The calibrated numerical model was used for the evaluation of displacements produced by permanent and climatic load combinations.

Figure 11 shows the displacement coordinates for all the measuring devices corresponding to the uniformly distributed snow load of 0.91 kN/m^2 that corresponds to the displacement of approximately 5 mm

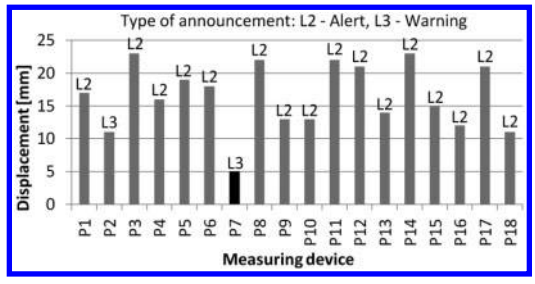


Figure 11. Displacement coordinates for measuring devices corresponding to a chosen value of snow load.

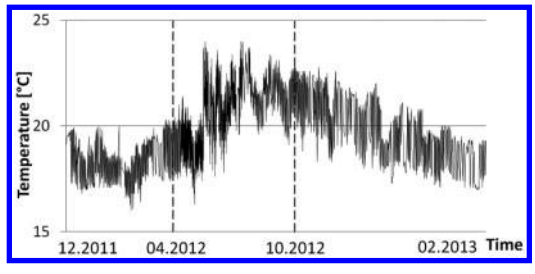


Figure 12. Temperature records from the measuring device P3.

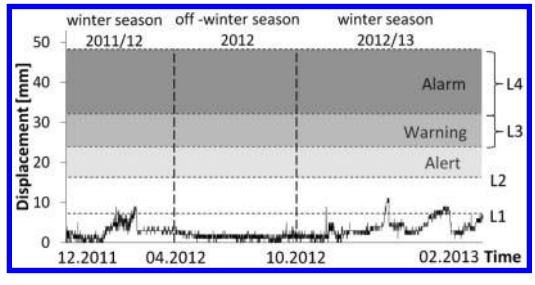


Figure 13. Displacement records from the measuring device P3.

for the measuring device P7. This snow load level is about to activate the warning announcement from two measuring devices while the others are in an alert state.

Since the pilot installation of WiSeNe^{MONIT} monitoring system, the results are constantly recorded and interpreted for the client. Typical records for the winter season 2011–2012, off-winter season 2012 and consecutive winter season 2012–2013 are presented herein. Both winter seasons were not associated with very heavy snowfalls. Figures 12 & 13 show the records of the temperature and displacement from the measuring device P3. The similar illustrations of the records from the measuring device P7 are given in Figures 14 & 15.

The temperature of roof steel structure varies from about 16°C in winter season and rises up to about 24°C in summer. As it has been indicated by the off-line numerical module, this change of temperature results in the displacement change of around plus/minus 1 mm, so that it is in the range of measurement tolerances. The effect of temperature may

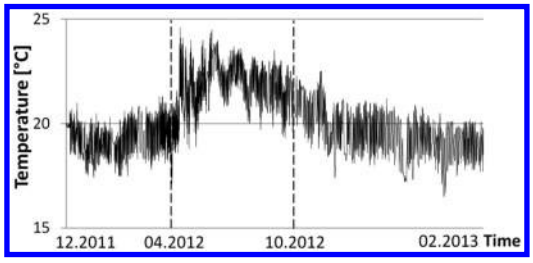


Figure 14. Temperature records from the measuring device P7.

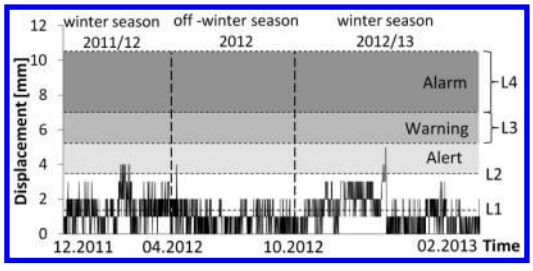


Figure 15. Displacement records from the measuring device P7.

threfore be omitted in monitoring of considered roof structure. It has to be noted that the effect of temperature is generally important in controlling the structural behavior since the residual deflections due to temperature may have a significant influence on the deflection level in statically determinate structures and both on the deflection and stress levels in case of structures with a high degree of structural redundancy.

Because the winter season 2011–2012 was in Poland without substantial snowfalls, the picks of displacements are for this season below those indicative to reaching the bottom line of warning signals. Contrarily, the winter season 2012–2013 resulted once in a more heavy snowfall. The pick of displacement for the measuring device P7 almost reached at this time that corresponding to the bottom line of warning signals. Although it was not yet the situation requiring the inspection, the building owner decided to remove snow from the roof. The fact of snow removal is clearly visible from the records of device P7 because the pick value suddenly drops down to the level oscillating around quasi-permanent load level.

4 CONCLUDING REMARKS

Topics related to structural catastrophic events and monitoring of structural health are dealt with. Independent databases of reported structural incidents indicate that lightweight large span steel roofs, especially those flat and composed of segments placed at different heights, are the most vulnerable systems to failures and collapses.

The monitoring system WiSeNe^{MONIT} is developed for typical single-storey buildings of steel lightweight roof structures. It facilitates the assessment of safety criteria allowing for suitable maintenance procedure to be undertaken during service.

REFERENCES

Geis, J.M., Strobel, K.M. & Liel, A.B. 2012. Snow-Induced Building Failures, *Journal of Performance of Constructed Facilities*, August.

Gizejowski, M.A., Wierzbicki, S., Stachura, Z. 2012. *Structural health monitoring as a tool assisting the structural robustness assessment.* Proc. Twin Inter. Conf. 5th BR12 & 13th RB12, 28–29 July, Wuyishan, China.

Gizejowski, M.A., Wilde, K., Uziak, J., Wierzbicki, S. 2011. On a necessity of monitoring systems for sustainable development of mechanical and civil engineering infrastructure. *Botswana Journal of Technology* 2(10): 9–20.

Goliger, A., Zuranski, J., Gizejowski, M., Gaczek, M., Retief, J., Kruger, A., Dunaiski, P., Fisher, S., Cwik, M. 2013. Wind climates of Poland and South Africa; the related damage and implications of adopting the Eurocode for wind action on buildings. *Archives of Civil Engineering* (in press).

Research and Applications in Structural Engineering, Mechanics and Computation – Zingoni (Ed.)
© 2013 Taylor & Francis Group, London, ISBN 978-1-138-00061-2

Approaches to quantify the safety gain for existing concrete bridges due to surveillance

C. Siegert, L. Eckfeldt & M. Empelmann
Institute for Building Materials, Concrete Construction and Fire Protection (iBMB), Concrete Construction Department, TU Braunschweig, Germany

ABSTRACT: If the recalculation of an existing bridge due to deficient verifications is not successful, in Germany, the recalculation guide for existing road bridges offers the possibility of arranging compensatory measures. The guide differentiates between traffic-oriented compensatory measures and compensatory surveillance. The safety gain due to traffic-oriented compensatory measures is already well quantifiable. However, objective methods to quantify the safety gain due to compensatory surveillance, especially of permanent monitoring, are rare and not very detailed. Therefore, in this paper general approaches based on the probability theory are shown. With the help of these approaches compensatory surveillance can be used by roadway authorities as a sensitive but effective measure in the future.

1 INTRODUCTION

New design standards as well as increasing traffic on German motorways produce high demands in recalculating existing bridge structures. The recalculation of road bridges is regulated in Germany in the recalculation guide (BMVBS 2011). Experience shows that the design checks often show shortfalls of safety. To preserve structural integrity, the guide offers the possibility of arranging compensatory measures. The definition of a compensatory measure is that it ensures the continued use of a structure for a given bearing capacity. Thus, it causes a safety gain. The guide differentiates between traffic-oriented compensatory measures and compensatory surveillance.

Traffic-oriented compensatory measures may include bans on passing, minimum distances, speed and weight limits. Typically, roadway authorities enforce these kinds of compensatory measures. However, if such measures cause difficulties, like an undesired influence on the traffic, or if they compensate the given deficit insufficiently, compensatory surveillance can be another option to maintain an existing bridge without the need of strengthening.

Experience shows that avoiding bridge collapse is closely related to its surveillance. The better and more systematic the surveillance is conducted, the greater is the likelihood that damaged components are identified, assessed and, if necessary, measures are taken before an actual bridge collapse occurs. Thus, surveillance can be used as compensatory measure as well. Currently, various compensatory surveillance measures are undertaken. However, due to the lack of knowledge, decision makers do not base their decision pro or contra compensatory surveillance on a precise assessment of the expected safety gain, but on intuition. Thus, to verify objectively the target failure probability, strategies to quantify the safety gain are of great interest.

2 BASICS OF THE APPROACHES

A reliable quantification of the safety gain due to compensatory surveillance measures can be performed by using the probability theory.

2.1 *Basics of the probabilistic design*

The reliability of a structure can be expressed by the limit state equation:

$$G = R - E \tag{1}$$

where R = resistance and E = effect. Thus, G is the difference between the resistance and the effect.

As the resistance and the effect are generally subjected to scatter, there is always a possibility that for the realizations $r < e$ is true. Thus, the region $G < 0$ describes the failure region (grey area in Fig. 1). The failure probability P_f can therefore be expressed as:

$$P_f = P[G < 0] = P[(R - E) < 0] \tag{2}$$

As the failure probability P_f in construction engineering is generally very small and sensitive to variations of the input parameters, the reliability index β

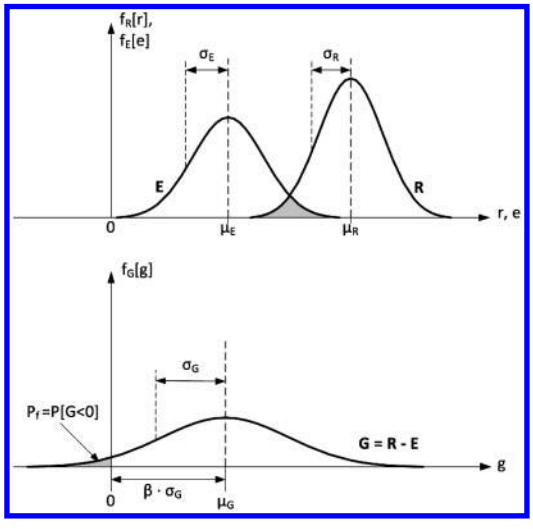


Figure 1. Definition of probability of failure P_f and reliability index β.

is often used for designs. The reliability index β is given by:

$$\beta = \frac{\mu_G}{\sigma_G} \tag{3}$$

where μ_G = mean value of G and σ_G = standard deviation of G (cf. Fig. 1).

The design method directly based on this concept is called the 'full probabilistic concept'. An acceptable reliability of the structure is verified, if the calculated failure probability of the analyzed structure P_f is lower than the target failure probability $P_{f,t}$ (resp. if its reliability index β is higher than the target reliability index β_t):

$$P_f \leq P_{f,t} \quad resp. \quad \beta \geq \beta_t \tag{4}$$

Target reliability indexes β_t are usually defined in standards (i.e. EC 0).

2.2 *Quantification of a safety gain due to compensatory surveillance*

According to the definition of compensatory surveillance, a compensatory surveillance system compensates deficits. That means that the arrangement of a compensatory surveillance system on a bridge in deficit leads to a safety gain for it.

In the full-probabilistic context, the safety gain $\Delta P_{f,s}$ can be expressed as the decrease of the failure probability due to the surveillance measure. Thus, it is obtained by subtracting the failure probability of the structure that takes the surveillance into consideration $P_{f,s}$ from the failure probability of the structure without compensatory surveillance P_f:

$$\Delta P_{f,s} = P_f - P_{f,s} \quad resp. \quad \Delta\beta_s = \beta_s - \beta \tag{5}$$

The compensatory surveillance measure is successful, if the safety gain $\Delta P_{f,s}$ is as high or higher than the investigated deficit ΔP_f:

$$\Delta P_{f,s} \geq \Delta P_f \quad resp. \quad \Delta\beta_s \geq \Delta\beta \tag{6}$$

3 TYPES OF COMPENSATORY SURVEILLANCE

Compensatory surveillance systems can be generally differentiated according to their temporal arrangement into:

- singular compensatory surveillance measures,
- recurring compensatory surveillance measures and
- continuous compensatory surveillance measures.

3.1 *Singular compensatory surveillance measures*

Singular compensatory surveillance measures performed on existing concrete bridges are for example:

a) the determination of the compressive strength of the concrete,
b) the determination of the force of the prestressing steel,
c) the geodetic survey of the geometry,
d) the determination of the actually existing traffic on the bridge and
e) the execution of a load test.

During the design process of a bridge, assumptions have to be made regarding the statistical description of the variables of the limit state equation. Those assumptions are usually based on experience. All of the singular aforementioned compensatory measures have in common that they deliver additional information to the ones based on experience for the statistical description of the input variables.

In detail, the measures a) to d) deliver additional samples to describe the statistical distribution of a specific input variable. With the help of this information, a Bayesian Update can be performed for the investigated variable. The idea of the update is to enhance the original statistical description of the variable due to the new information gained. Usually that leads to a decrease of the standard variation of the variable and thus to lowered failure probability of the structure and to a safety gain, while recalculating the investigated existing structure. For the computation algorithm of a Bayesian Update it is i.e. referred to Faber (2012).

The new information gained by executing a load test, in which the bridge is surcharged until a test target load, which is higher than the calculated maximum, measure e), has to be assessed differently. In this case, the part of the uncertainty of the resistance up to the test target load is eliminated, so that the concerning part of the failure probability disappears and thus the failure probability decreases. For a more detailed description and the probabilistic quantification of the enhanced failure probability and the safety gain it is referred to Spaethe (1994) and Siegert et al. (2012).

3.2 *Recurring compensatory surveillance measures*

Examples of recurring compensatory surveillance measures performed on concrete bridges are:

a) in time intervals recurring inspections (i.e. bridge inspection according to the standard with reduced intervals) and
b) recurring load tests.

Bridges have to be inspected in regular time intervals according to the existing standards. The aim of these inspections is to detect serious damage in time to be able to react before an actual bridge collapse occurs. Both aforementioned recurring compensatory surveillance measures have in common that the probability of detecting serious damage in time is higher than for the regular inspection plan. Structures, for which a recurring compensatory surveillance measure is applied, thus exhibit a lower failure probability.

The Probabilistic Model Code of the JCSS (JCSS 2001) contains the basics of a probabilistic approach for considering the effect of recurring compensatory surveillance while determining the failure probability of a structure. The safety gain due to performing inspections with reduced intervals can then be derived from the comparison of the failure probability of the structure under consideration of performing inspections according to the existing standards and the failure probability of the structure under consideration of performing inspections with reduced intervals. For computational details it is referred to Siegert et al. (2012).

The safety gain due to recurring load tests can be determined analogously.

3.3 *Continuous compensatory surveillance measures*

Continuous compensatory surveillance measures performed on concrete bridges are for example:

a) threshold value monitoring and
b) traffic-weight control.

The idea of a threshold value monitoring is to directly monitor the limit state in deficit and in the case of exceeding a threshold value triggering an alert. An example is the exceedance of a defined crack width which heralds an imminent failure of the monitored bridge.

A threshold value monitoring is the most effective compensatory surveillance measure for an existing bridge as it relates directly to the limit state. Therefore, the uncertainties of both the effect on the bridge and the resistance of the bridge are affected. However, threshold value monitoring is only possible in case of the existence of an adequate monitoring system that announces the failure of the structure in time. Threshold value monitoring for deficits with brittle failure modes is therefore difficult to set up. Another difficulty is the determination of the threshold values for the monitoring system.

Recurring inspections relate directly to the limit state as well. However, in the case of the arrangement of an adequate monitoring-system, the failure probability of the threshold value monitoring is significantly lower than the one of the recurring inspections.

The concept of a traffic-weight control is the determination of potential traffic loads on the investigated bridge (i.e. by a Weigh-in-Motion System) before they actually impact on the bridge. In the case of an exceedance of a threshold weight, the bridge is blocked before the detected vehicle can pass (i.e. with the help of a barrier or a traffic light system).

An extensive literature review with the topic of approaches to quantify the safety gain provided by continuous compensatory surveillance shows that available methods are rare. The only approaches known to the authors are by Allen (1992) and Bergmeister & Santa (2004). Both follow the approach of reducing the target reliability in dependence of the intensity of the surveillance. However, the quantification of the reduction is based on experience and is only available for the categories “no surveillance”, “regular surveillance” and “continuous surveillance”. Thus, a consideration of neither the type of the surveillance (e.g. threshold value monitoring or traffic-weight control) nor the value of its failure probability is possible.

3.4 *System identification*

Both a threshold value monitoring and a load test offer the possibility of gathering more information about the bridge in order to gain an advanced knowledge of it. An improved model can not only be used to recalculate the structure, moreover, the standard deviations of the model uncertainties, which have to be applied in a full-probabilistic analysis, can be reduced as well.

Both the resistance R and the effect E are described using models. Such a model is complete and accurate, if the model returns exactly the experimental results. As most models do not fulfill this demand, usually two multiplicative model uncertainty factors are introduced into the limit state equation (one on the effect and one on the resistance side). Is the model improved by a system identification, the model uncertainties decrease so that the standard deviations of the model uncertainty factors can be reduced. On the effect side, examples for causes of a decrease are a better knowledge of the support conditions and of changing stiffness ratios of the examined concrete bridge. On the resistance side, an example is the time dependent concrete behavior. The decrease of the standard deviations of the model uncertainty factors results in lower variations of the effect and the resistance and thus in a calculative reduction of the failure probability of the bridge.

A study that investigates the safety gain due to a decrease of model uncertainty due to system identification is unknown to the authors.

3.5 *Conclusion*

Several varying compensatory surveillance measures for existing concrete bridges are available. All of them

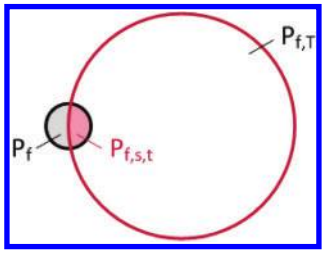


Figure 2. Failure probability under consideration of threshold value monitoring $P_{f,s,t}$.

require different methods to quantify the resulting safety gain. Quantification approaches for singular and recurring compensatory measures exist. However, for the continuous compensatory surveillance measures, which are the most effective compensatory surveillance measures, no sensitive quantification approaches exist. Therefore, in the following section such quantification approaches are developed mathematically. Moreover, the idea of a safety gain due to a decrease of model uncertainty by system identification is analyzed.

4 SAFETY GAIN DUE TO COMPENSATORY SURVEILLANCE

4.1 *Safety gain due to threshold value monitoring*

The safety gain due to threshold value monitoring can be derived analogously to the safety gain due to inspection. However, in a figurative sense only one inspection is performed, but this one continuously.

Based on the law of total probability, the failure probability under consideration of the threshold value monitoring $P_{f,s,t}$ is given by:

$$P_{f,s,t} = P[G < 0 \mid T > 0] \cdot P[T > 0] + P[G < 0 \mid T < 0] \cdot P[T < 0] \tag{7}$$

where T is the result of the threshold value monitoring (negative values represent the detection of damages).

Under the assumption that in the case of surpassing the threshold value the structure is refurbished Equation 7 reduces to:

$$P_{f,s,t} = P[G < 0 \mid T > 0] \cdot P[T > 0] \tag{8}$$

Reformulated, the failure probability under consideration of the threshold value monitoring $P_{f,s,t}$ results from the cut-set of the failure probability of the structure without surveillance P_f and the failure probability of the threshold value monitoring to detect serious damage successfully $P_{f,T}$. This context is illustrated in Figure 2. The corresponding calculation formula is:

$$P_{f,s,t} = P[G < 0 \cap T > 0] = P_f \cap P_{f,T} \tag{9}$$

If both failure probabilities are fully uncorrelated, the total failure probability $P_{f,s,t}$ results from the multiplication of the individual failure probabilities. Therefore, the total failure probability $P_{f,s,t}$ is reduced and a safety gain is created.

$$P_{f,s,t} = P_f \cdot P_{f,T} \tag{10}$$

However, if both failure probabilities are fully correlated, the total failure probability $P_{f,s,t}$ equals the minimum of the individual failure probabilities. A safety gain can only be created if the failure probability of the threshold value monitoring $P_{f,T}$ is very small. This is rather unlikely.

$$P_{f,s,t} = \min[P_f;\ P_{f,T}] \tag{11}$$

In reality, the individual failure probabilities are neither fully uncorrelated nor fully correlated. Therefore, the total failure probability lies between the following bounds:

$$\min[P_f;\ P_{f,t}] \leq P_{f,s,t} \leq P_f \cdot P_{f,T} \tag{12}$$

The safety gain due to threshold value monitoring is given by the comparison of the failure probability of the structure without monitoring P_f and the failure probability under consideration of the threshold value monitoring $P_{f,s,t}$:

$$\Delta P_{f,s,t} = P_f - P_{f,s,t} \quad resp. \quad \Delta\beta = \beta_{s,t} - \beta \tag{13}$$

The required safety gain in order to comply with the given target failure probability $P_{f,t}$ determines the maximum admissible failure probability of the threshold value monitoring max $P_{f,T}$. For the fully uncorrelated case it is:

$$\max P_{f,T} = 1 - \frac{\text{pres}\,\Delta P_f - P_{f,t}}{P_f} = 1 - \frac{\text{req}\,\Delta P_{f,s,t}}{P_f} \tag{14}$$

In Figure 3 the relationship between the present reliability index pres β and the resulting maximum admissible failure probability of the threshold value monitoring max $P_{f,T}$ is illustrated for varying target reliabilities β_t for the fully uncorrelated case. One can see the exponential decrease of max $P_{f,T}$ with decreasing pres β. Thus, for severe deficits a very low failure probability of the threshold value monitoring max $P_{f,T}$ is necessary to compensate for deficits in compliance with standards.

Resuming, for the design of a reasonable threshold value monitoring with the aim of compensating for deficits the knowledge about its reliability is necessary. However, for a given probability of failure of the measure $P_{f,T}$ the effectiveness of it can already be ensured in the planning stage.

4.2 *Safety gain due to traffic-weight control*

In the context of the probability theory the safety gain due to a traffic weight-control resembles the safety

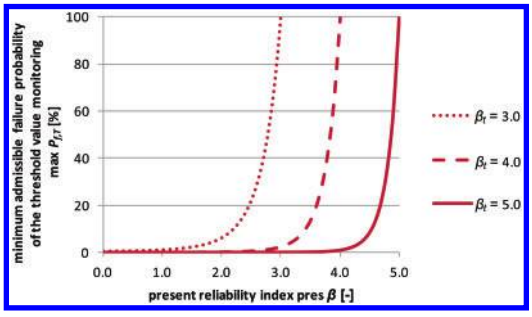


Figure 3. Admissible failure probability of the threshold value monitoring max $P_{f,T}$ versus present reliability index pres β (fully uncorrelated case).

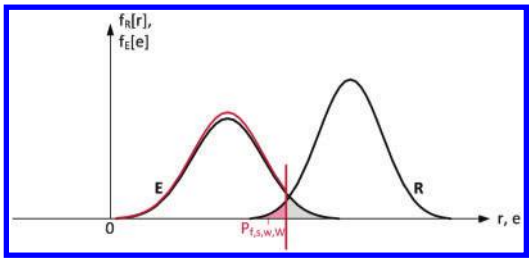


Figure 4. Failure probability under consideration of traffic-weight control $P_{f,s,w}$.

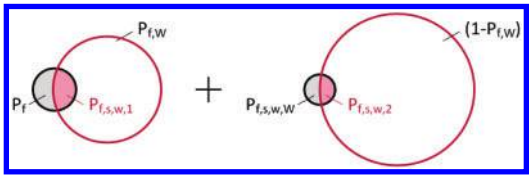


Figure 5. Failure probability under consideration of traffic-weight control $P_{f,s,w}$.

gain due to a load test. In a simplified consideration, the difference is that instead of part of the uncertainty on the resistance side part of the uncertainty on the load side is eliminated. That is the part above the threshold value of the weight-control system. This relationship is illustrated in Figure 4. E represents the acting load and R the load the bridge can bear.

The approach just described is simplified as a traffic-weight-control can fail with a certain failure probability $P_{f,W}$. For example, the Weigh-in-Motion System or the barrier system may be defect. Taking into account this fact, the failure probability under consideration of a traffic-weight control $P_{f,s,w}$ results as well according to the law of total probability. In Figure 5 the context is shown graphically.

Two different cases have to be distinguished: The first case represents the non-serviceability of the traffic-weight control. The corresponding probability is $P_{f,W}$. The second case represents the complementary event, the serviceability of the traffic-weight control. The corresponding probability is (1-$P_{f,W}$).

In case of a default of the traffic-weight control the structure fails with its original failure probability P_f. A partial failure probability of $P_{f,s,w,1}$ results.

In contrary, is the traffic-weight control functioning, the structure fails with a probability of $P_{f,s,w,W}$ (see Fig. 4). The partial failure probability is $P_{f,s,w,2}$.

The total failure probability $P_{f,s,w}$ is then given by the sum of the two partial failure probabilities $P_{f,s,w,1}$ and $P_{f,s,w,2}$. The calculation formula is:

$$P_{f,s,w} = P[G < 0 \mid W > 0] \cdot P[W > 0] + P[G < 0 \mid W < 0] \cdot P[W < 0] \quad (15)$$

where W is the result of the traffic-weight control (negative values represent the serviceability of the control measure). Rephrased it is:

$$P_{f,s,w} = P_f \cap P_{f,W} + P_{f,s,w,W} \cap (1 - P_{f,W}) \quad (16)$$

where:

$$P_{f,s,w,W} = P[G < 0 \mid G_W > 0] \quad (17)$$

$$G_W = R - E_W \quad (18)$$

where E_w is the threshold value of the weight-control-system.

The safety gain due to traffic-weight control is given by the comparison of the failure probability of the structure without traffic-weight control P_f and the failure probability under consideration of a traffic-weight control $P_{f,s,w}$:

$$\Delta P_{f,s,w} = P_f - P_{f,s,w} \quad resp. \quad \Delta\beta = \beta_{s,w} - \beta \quad (19)$$

Resuming, the resulting safety gain can be controlled by both the reliability of the traffic-weight control and its set load limit. For a given reliability of the traffic-weight control the necessary load limit to compensate for the existing deficit can be determined directly. Thus, if the required safety gain can be achieved by the traffic-weight control, it can already be checked in the planning stage.

4.3 *Safety gain due to system identification*

A decrease of the standard deviations of the model uncertainty factors θ_E and θ_R due to system identification results in lower variations of the resistance R and the effect E and thus into a reduction of the failure probability of the structure $P_{f,s,i}$. This context is illustrated in Figure 6.

The failure probability under consideration of a decrease of model uncertainty factors due to system identification $P_{f,s,i}$ is obtained by the following equation:

$$P_{f,s,i} = P[G_i < 0] \quad (20)$$

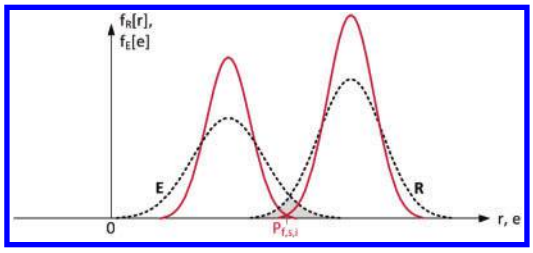


Figure 6. Failure probability under consideration of system identification $P_{f,s,i}$.

where:

$$G_i = R_i - E_i \tag{21}$$

$$R_i = \theta_{R,i} \cdot R \tag{22}$$

$$E_i = \theta_{E,i} \cdot E \tag{23}$$

The safety gain due to system identification thus results from:

$$\Delta P_{f,s,i} = P_f - P_{f,s,i} \quad resp. \quad \Delta\beta = \beta_{s,i} - \beta \tag{24}$$

The difficulty within this approach is that model uncertainty factors can only be described insufficiently in the required degree of detail by the current state of knowledge. For example, a manual calculation with the help of design charts and a FE-calculation should require the use of two different model uncertainties. However, due to lack of experience and only recipient research this is not performed in practice. Appropriate investigations that allow a hedged quantification of reduced model uncertainties exist barely. Further research is needed.

Thus, with the help of system identification basically two different safety gains can be achieved. On the one hand improved models, which describe the behavior of the structure, lead to a safety gain. This benefit cannot be determined in the planning stage, but it is dependent on the results of the surveillance. The second safety gain due to a decrease of the model uncertainty factors could be determined in advance. However, the current state of knowledge does not allow quantification.

5 SUMMARY AND PROSPECTS

Compensatory surveillance is nowadays not used on a precise, objective assessment of the expected safety gain. The reason is the lack of knowledge of detailed quantification methods. This paper shows general approaches to quantify safety gains due to continuous surveillance measures based on the probability theory. The approaches are set up in the full-probabilistic concept and allow the consideration of the type of the surveillance measure and its failure probability. Further research steps are the quantification of the failure probabilities of the surveillance measures and the transformation of the approaches into the semi-probabilistic concept.

With the help of quantifiable compensatory surveillance, roadway authorities have a sensitive but effective measure available to compensate for deficits and therefore to be able to preserve large parts of the aging bridge portfolio in the future.

ACKNOWLEDGEMENT

This report is based on parts of the research project carried out at the request of the Federal Ministry for Transport, Construction and Town Planning, represented by the Federal Highway Research Institute, under research project No. FE 15.0544/2011/LRB. In the first part of the research project the theoretical background of designing compensatory surveillance is developed, in the second part the methods are analyzed on a practical example. The author is solely responsible for the content.

REFERENCES

Allen, D. E. 1992. Canadian highway bridge evaluation: reliability index. *Canadian Journal of Civil Engineering* 19 (6): 987–991.

Bergmeister, K. & Santa, U. (2004): Brückeninspektion und- überwachung. *Betonkalender* 2004: 407–481 Berlin: Ernst & Sohn (in German).

BMVBS, Road Construction Departement 2011. *Richtlinie zur Nachrechnung von Straßenbrücken im Bestand (Nachrechnungsrichtlinie)* (in German).

Faber, M. H. 20012: *Statistics and probability theory – In Pursuit of Engineering Decision Support*. Dordrecht: Springer.

JCSS 2001. *Probabilistic Model Code*.

Siegert, C.; Empelmann, M.; Holst, A.; Budelmann, H. (2012): *Überwachungskonzepte für Bestandsbauwerke aus Beton als Kompensationsmaßnahme zur Sicherstellung von Standsicherheit und Gebrauchstauglichkeit.* 1st interim report to the research project FE 15.0544/2011/LRB funded by the BMVBS (in German).

Spaethe, G. 1994. Die Beeinflussung der Sicherheit eines Tragwerkes durch Probebelastung. *Bauingenieur* 69 (12): 459–467 (in German).

Research and Applications in Structural Engineering, Mechanics and Computation – Zingoni (Ed.)
© 2013 Taylor & Francis Group, London, ISBN 978-1-138-00061-2

An investigation on the collapse sequence of an RC frame during L'Aquila 2009 earthquake

M.G. Mulas, L. Martinelli & F. Perotti
Department of Civil and Environmental Engineering, Politecnico di Milano, Milano, Italy

ABSTRACT: The partial collapse of a seven-story reinforced concrete building designed in 1965 is investigated starting from previous results. The building was hosting a university dorm, named "Casa dello Studente", and suffered the partial collapse of one of its three wings during the April 6, 2009 earthquake of L'Aquila (Italy). Two distinct collapse zones were detected in the collapsed wing: a soft/weak story mechanism at the ground floor, and the failure of three columns along the height. In a previous study, encompassing only linear analyses, the lack of flexural strength of ground story columns was detected as the main cause of the collapse. Here non-linear static analyses of a refined numerical model of the structure, including the reinforcement data, allow for a better insight on the disproportionate effects that the partial soft-story collapse had. The results clarify the role of lack of shear strength of a beam on the collapse of the three columns.

1 INTRODUCTION

On April 6th 2009 at 3.32 am a magnitude Mw 6.3 earthquake struck Central Italy, with devastating effects in the city of L'Aquila and causing the failure of several reinforced concrete (RC) buildings in the urban area. Among them, the "Casa dello Studente" building (CdS, in the following), located at about 6 km from the epicenter, suffered a partial collapse. The death toll was very high, with eight students killed and one suffering serious injury.

The CdS building is a seven-story RC building hosting a University dorm ("Casa dello Studente" means Student House, in Italian). It was designed in 1965, following the Italian Seismic Codes of 1937 and 1962 (RDL 2105, L 1684), for a mixed use (residential/commercial). The plan of the residential part, in the upper four stories, was subdivided in three wings, connected through the stairwell. Ground story and basement were common to all the wings. A second underground level was present below the South wing. In 1979 the building was bought by a University Institution to be used as student house, and in 1982 it became a property of the Abruzzo Region, in force of State and Region Laws. A wide refurbishment intervention, not covering the structural system, was performed during the years 1999–2001.

The partial collapse of the building was limited to the North wing (see Figure 1). Within this wing two distinct collapse zones were detected, from both pictures of the collapsed part and on-site observations: the failure of all the columns at the ground floor, with a soft/weak story mechanism, and that of three columns along the height of the building. A previous study, reported in (Mulas et al. 2012, 2013), performed for legal reasons, showed that neither the poor quality of material properties nor the ground motion at the building site could be considered – from the Italian laws viewpoint – among the causes of the collapse. The most likely collapse sequence was established by crossing the design criteria adopted in 1965, the results of modal analyses of the building in its original configuration and after refurbishment, and all the experimental data coming from the analysis of damage in the part of building that survived the earthquake. The lack of flexural strength of ground story columns was detected as the main mechanical cause of the collapse itself.



Figure 1. Aerial view of the building in the configuration at the date of the 2009 seismic event.

Starting from the previous results, the collapse sequence has been investigated further in this study. The availability of data on the geometry of the reinforcement has allowed the derivation of a complete and refined numerical model. Non linear static analyses are performed to compute the capacity curve of the structure, with the aim to further investigate on the disproportioned effect that arose by the partial soft-story collapse at ground floor. The results obtained help to clarify the role played by the lack of shear strength of a beam at floors 1–4 on the collapse of the three columns along the height of the building.

2 THE BUILDING AND ITS RENOVATION

The CdS building is a 7-story (including two underground floors) RC framed structure (see Mulas et al. 2013) having an irregular T-shaped plan composed by three nearly rectangular "wings" (Figs 1, 2a, b).

The building was designed for a mixed use (residential/commercial) in 1965. The code adopted in the structural design was the Italian Seismic Code of 1937 (RDL 2105), even though newer provisions were enforced by the Seismic Code of 1962 (L. 1684).

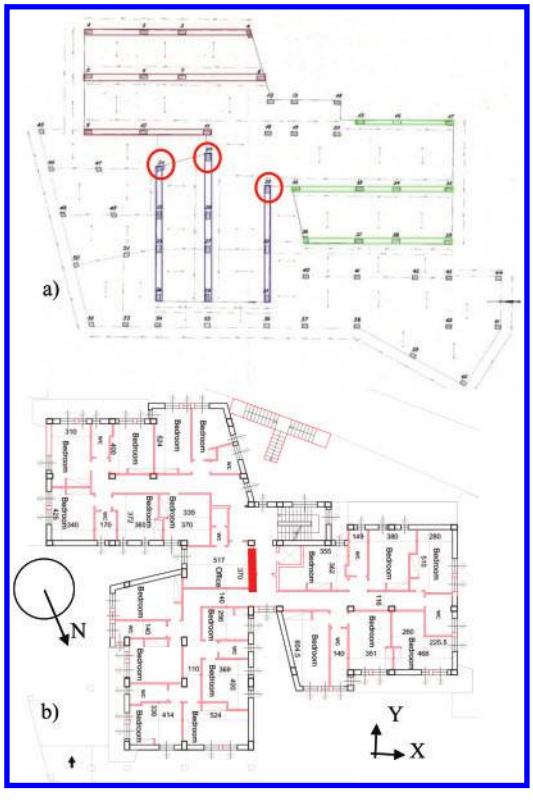


Figure 2. (a) layout of the vertical members. The colored lines highlight the positions of the main frames, circles show the collapsed columns # 21, 25 and 29. (b) typical plan of the building after refurbishment in 2000. The thick line marks the position of a fire resistant wall on Beam 18–29 which triggered the collapse of this beam at several floors.

The design principles of both Codes were based on the application, at the centre of mass of each floor, of a set of equivalent static forces, equal to 7% (as prescribed by the 1962 Code of permanent loads plus 1/3 of variable loads. These forces should have been applied both in transverse and longitudinal directions according to the 1937 Code; in any horizontal direction according to the 1962 Code. Vertical loads had to be computed as the maximum between a) 1.25 times the sum of permanent loads and 1/3 of variable loads, b) the sum of permanent loads and variable loads. These criteria were used for designing the main lateral load resisting system, i.e. the three longitudinal moment-resisting RC frames located in each wing (Figure 2a). However, horizontal loads acting on each frame were apparently derived according to tributary areas Given the building plan configuration, the procedure led to substantial underestimation of seismic forces in the NS direction encompassing only three longitudinal frames.

A wide refurbishment intervention, not covering the structural system, was performed during the years 1999–2002. The layout of the internal partitions was changed to better adapt the building to its use as a university dormitory. To comply with fire safety regulations, a fire resistant wall (denoted, from the French acronym, as "REI wall" in the following) composed of lightweight concrete hollow blocks, 20 cm thick, was placed at floors from the first to the fourth (thick red line in Figure 2b). This wall spans from column 18 on roughly half of the beam 18–29, that in turn is part of the beam that connects columns 18, 29, 30, and the corner column 31 (beam 18-29-30-31).

The role that this non-structural element, inserted in a non-engineered way, had on the collapse will be investigated in the following.

3 EARTHQUAKE GROUND MOTION AT THE BUILDING SITE

The ground motion at the CdS site was estimated according to the procedure described in (Mulas et al. 2013). The elastic response spectra along the principal directions of the CdS building (namely: N23°E and E23°S; directions Y and X, respectively in Fig. 2) are plotted for a 5% damping ratio in Figure 3. The prevailing amplitude of the N23°E component at the

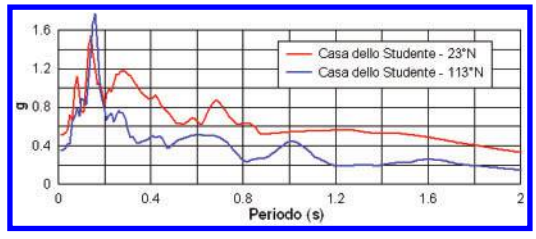


Figure 3. Reconstructed elastic response spectra along the principal directions of the building: 23°N = N23°E, 113°N = E23°S.

longer periods is a consequence of the directionality of earthquake ground motion in L'Aquila records along the fault normal direction, as pointed out by different studies (e.g., Paolucci & Smerzini 2010). The estimated motion has been deemed compatible (Mulas et al. 2013) with the magnitude of the static horizontal forces, equal to 7% of gravity loads, prescribed by the 1962 Code (L. 1684) in a design process based on a working stress approach.

A ratio close to 3 to 1 can be assumed for the spectral ordinates in the likely ranges of period (0.83–1.63 s and 0.81–1.45 s, respectively), estimated in Mulas et al. 2012, 2013 for the first and the second mode. This is confirmed by the ratio of the extreme values of ground acceleration: the acceleration in direction E23°S was 35% of that in direction N23°E. This fact will be accounted for in the direction the capacity curves are computed.

The wide period ranges depend on the boundary conditions assumed for the model, on the amount of reduction of member stiffness and on the presence of the added fire resistant wall. The boundary conditions addressed the action of the basement wall towards XX Settembre street.

4 NUMERICAL MODEL OF THE BUILDING

In previous studies (Mulas et al. 2012, Mulas et al. 2013) a comprehensive model was developed to achieve an accurate representation of the geometry and masses of structural and non-structural elements, and of the stiffness of the structural ones. The geometry of the structural elements (beam, columns and floor slabs) derives from both the results of on site surveys and the blueprints recovered by State and County archives damaged by the April 6th, 2009 earthquake. Blueprints describes both the original design and the renovations of the building.

A modification of this model was derived for the static non-linear analyses, to reduce the number of degrees of freedom. The new model retains the total mass but disregards the balconies (their weight and mass is applied to the perimeter beams). Moreover, the floor system is considered to be sufficiently rigid in its plane to act as a diaphragm. A view of the solid model is depicted in Figure 4. The new model has been validated by comparison with the previous one in terms of modal periods and correlation of the modal shapes. As in the linear models, the REI wall on beam 18–29 is modeled through 2D quadrilateral and triangular plane-stress (membrane) elements.

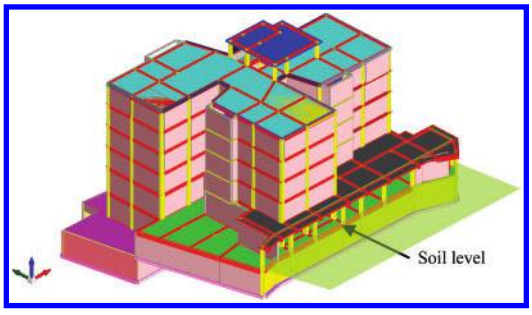


Figure 4. Geometrical model obtained by disregarding the cantilevered balconies.

A static non linear analysis, involving non linear material behavior, requires that beams and columns are properly discretized to avoid strain localization effects. In this work beams and columns were discretized in elements of length 20 cm and 40 cm, near the members ends and elsewhere respectively. The cross-sections were discretized in rectangular sub-domains having the longest side less than 7 cm (see Fig. 5). The computer code (SISMICAD v.12) used in the static non linear analyses assigns 9 Gauss points per sub-domain to follow locally the stress-strain law of the concrete material. A single Gauss point is assumed at the location of a reinforcing bar, as well as perfect bond between concrete and reinforcement. Concrete follows different laws depending on the confinement (confined or unconfined concrete). The elements behave nonlinearly for axial force and in bending only, being elastic in shear.

4.1 *Materials models and values of the mechanical parameters*

Concrete has no strength in tension and follows a parabola-rectangle law in compression up to a strain value ε_{c0}. Compression failure is attained at a strain value ε_{cu}. Unconfined concrete has the design nominal values of strength and strain $f_{ck} = 16$ MPa, $\varepsilon_{c0} = 0.2\%$, $\varepsilon_{cu} = 0.35\%$. Confinement has a small effect, due to the low amount of stirrups in columns and in beams, and to a larger extent to the lack of longitudinal reinforcement along the long sides of the rectangular cross-sections. Confinement effectiveness, estimated on a sample column cross-section, accounts for the following values of strength and deformation: $f_{ck.c} = 1.033\, f_{ck}$, $\varepsilon_{c2,c} = 1.067\varepsilon_{c2}$ and $\varepsilon_{cu2,c} = \varepsilon_{cu2} + 0.13\%$.

Steel reinforcement follows an elastic-plastic law, symmetric in tension and compression, and has nominal strength and Young's modulus values $f_{yk} = 380$ MPa, $E_s = 2.6$ GPa.

Analyses were carried out with both the nominal design values of the mechanical parameters and the average values coming from on-site and laboratory material testing: concrete average compression

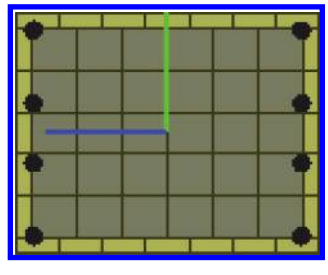


Figure 5. Sample or cross-section discretization for the static non-linear analyses. A lighter color denotes unconfined concrete.

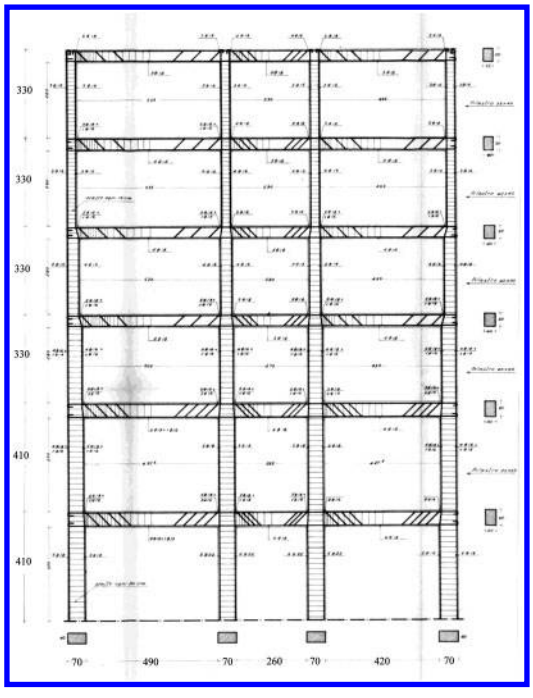


Figure 6. Reinforcement and dimensions of typical main frame.

strength $f_{cm} = 13.3$ MPa, steel average yielding strength $f_{ym} = 388$ MPa. While the yielding strength of the steel reinforcement corresponds to the prescribed value, the one of the concrete is far lower than its prescribed value corresponding to a concrete of class C8/10, instead of C16/20, according to the classification in the Italian code D.M. 14.01.2008 (NTC2008).

4.2 *Details of reinforcement*

Original design drawings (as in Fig. 6), on-site surveys and typical details from manuals of the time allowed to define the reinforcement distributions in the members of the primary frames (colored lines in Fig. 2a). As an example, Figure 7 details the reinforcement considered for the critical beam 18–31 in the span that supports the REI wall. This span failed in shear at the location of the REI wall.

Bending reinforcement at mid-span is $4\phi18$ mm + $1\phi16$ mm in the lower part of the cross-section, $3\phi18 + 1\phi6$ in the upper part. The symbol ϕ denotes the bar diameter in mm. At the supports, bending reinforcement is $6\phi18 + 3\phi16$ in the upper part and $2\phi18$ in the lower part. Shear reinforcement is provided by $\phi6$ stirrups at a variable spacing: 240 mm in the central part of the beam and in between 50–75 mm at the supports.

Table 1 lists the geometry, at ground floor, of the cross-sections of the columns of the North Wing. The reinforcement is located along each short side of the rectangular cross-section of the columns

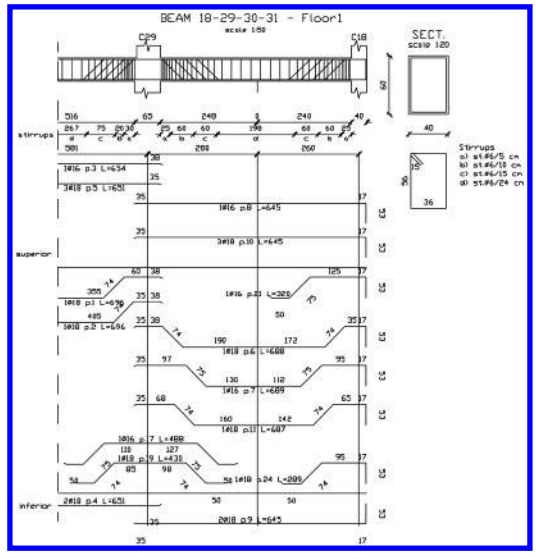


Figure 7. Detail of the reinforcement in beam 18-31 at first floor.

Table 1. North Wing columns reinforcement at ground floor.

Column	Dimensions cm	Reinforcement* N. bars	Diam. mm
21	65 × 40	5	18
22	40 × 65	4	18
23	40 × 65	4	18
24	40 × 65	4	18
25	40 × 65	5	18
26	40 × 65	5	18
27	40 × 65	5	18
28	40 × 65	5	18
29	40 × 65	5	18
30	40 × 65	4	18
31	40 × 65	4	18
1	65 × 40	4	18
9	65 × 40	4	18
17	65 × 40	4	18
39	65 × 40	4	18

*The reinforcement is located along each short side of the rectangular cross-section.

(see Fig. 5). Shear reinforcement for the columns is provided by 6 mm diameter closed stirrups. On average, the stirrups spacing is 200 mm for most of the columns, without provisions for closer spacing at the ends.

5 NON-LINEAR STATIC ANALYSIS OF THE BUILDING

The non linear static analysis procedure in the code NTC2008 has been adopted to compute the capacity curves for the CdS building, to the aim to gain a better

insight on the disproportioned effect that arose by the partial soft-story collapse at ground floor.

The nonlinear static analysis, or pushover analysis, in NTC2008, has to be performed applying to the structure first the gravity loads and then, for the considered direction of the seismic action, a fixed pattern of horizontal forces proportional to the inertia forces and having as resultant (base shear) the force F_b. The horizontal forces, acting at the floors, are increased monotonically up to the condition of local or global collapse. The horizontal displacement d_c of a control point, located at the center of mass of the last level, is monitored and the diagram F_b-d_c is the capacity curve of the structure.

According to NTC2008, this analysis has to be performed with two different distributions of horizontal forces, named primary (Group 1, GR1), and secondary (Group 2, GR2) force distribution The force distributions relate to the largest value of participating mass of the natural modes for a chosen direction of the seismic action.

Whenever the largest participating modal mass is less than 75% of the building mass in the seismic configuration and the period of the first mode is larger than the corner period T_c between the constant–spectral–acceleration and the constant–spectral–pseudo–velocity ranges of the response spectrum, as it is the case here, the GR1 force distribution is derived from the seismic floor shears calculated in a linear dynamic analysis for the chosen direction of the seismic action. Group 2 distribution adopts a uniform distribution of forces, that would correspond to a uniform distribution of accelerations along the height of the building.

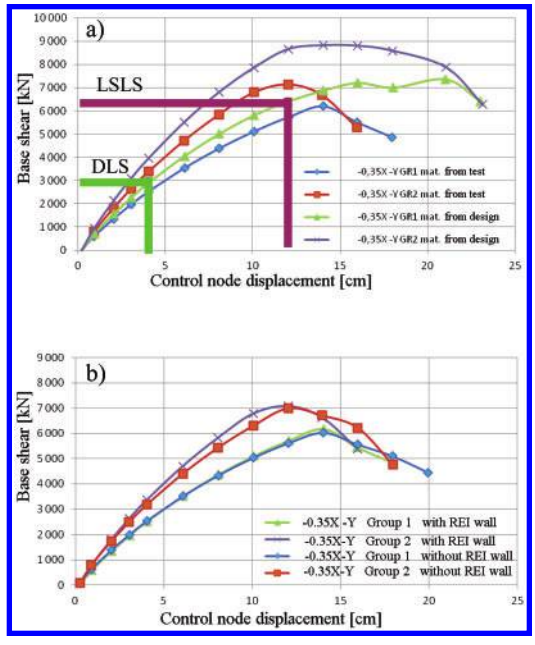


Figure 8. Capacity curves for Group 1 and Group 2 forces distributions: (a) REI wall included, material parameters from design and from tests; (b) with and without the REI wall, material parameters from tests.

5.1 *Analysis details*

The nonlinear static analysis is carried out on a three-dimensional model of the structure, derived from the geometrical model in Figure 4, discretized in elements with distributed inelasticity. Axial force is released at one end for all members having both nodes belonging to the same "rigid floor" to avoid spuriously enhancing the bending strength due to moment-axial force interaction.

Two structural configurations were analyzed, namely: with and without the REI wall on beam 18–29. In addition, two sets of material parameters were considered, derived either from design specifications or from material testing. For each structural configuration and set of material parameters, several pushover analyses were carried out applying the seismic action in different directions. The floor forces were obtained from linear dynamic analyses with the NTC2008 response spectrum, combining the effects of the seismic action in the X and Y direction (see Figure 2b) as it follows ±X, ±Y, ±0.3X, ±0.3Y. The most severe combination turned out to be as −0.30X−Y. This combination is very close to that corresponding to the extreme values of the ground acceleration at the site, characterized by an X-acceleration that is 35% of the Y-acceleration. For this ratio of seismic actions the effects of accidental eccentricities equal to 5% of the floor X and Y dimensions were also introduced.

6 ANALYSES RESULTS

For the sake of brevity, only the results obtained for a direction of the seismic action −0.35X−1.0Y will be presented in the following. Figure 8 depicts the capacity curves of the structure, for GR1 forces distribution, as well as the estimate of the displacement demands at the Damage Limit State (DLS) and the Life Safety Limit State (LSLS). The last one corresponds to the ultimate limit state for seismic loading in EN 1998-1:2005. Figure 9 shows the displaced configurations with and without the REI wall for a displacement of the control node $d_c = 23$ cm.

Absence of the REI wall, however, would probably not have saved the building, as the estimated displacement demands in Figure 8 clearly highlight.

From the analysis of the sequence of local collapses, it can be observed that, when the REI wall is included, the beam 18–29 fails in shear at the first floor for a displacement of the control node $3 \le d_c \le 4$ cm, then at the upper stories for $4 \le d_c \le 6$ cm. The collapse of the North wing columns at ground floor starts at $4 \le d_c \le 6$ cm with failure in shear of column #29. The structural configuration without the REI wall sees the first collapse at a displacement of the control node $6 \le d_c \le 8$ cm, when some of the North wing columns at ground floor fail in shear.

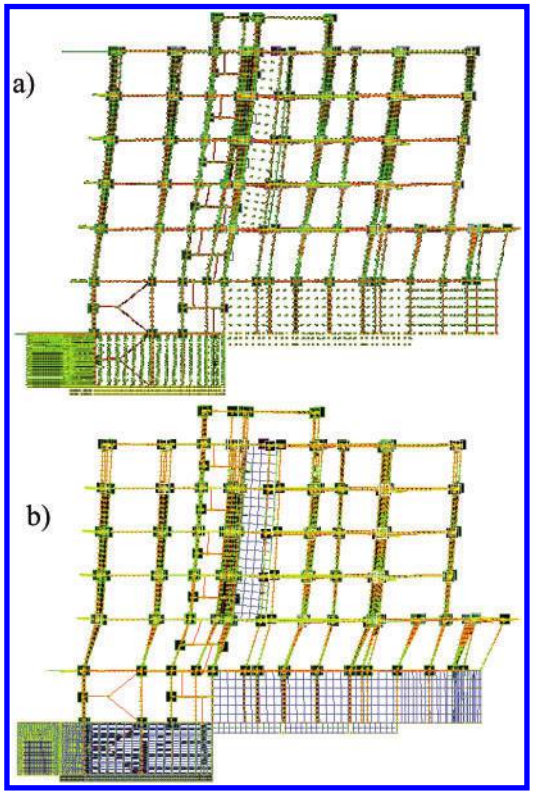


Figure 9. Displaced structure for Group 1 forces distribution and seismic action −0.35X−1.0Y without the REI wall (a). With the REI wall (b). Displacement of control node is in both cases 23 cm.

As Figure 9 also points out, the presence of the REI wall tends to exacerbate formation of a soft story at ground floor and induces early failure in shear of beam 18–29. The failure of this beam accounts for the collapse of portion of the floor system in the zone from the end of the REI wall to column #29. This failure can be clearly detected at several floor in the pictures taken immediately after the seismic event of April 6th, before the remains of the North wing were taken down. The collapse of column #29 can be ascribed to the increased shear force at the beam interface, causing ultimately the collapse of the column joints in shear.

7 CONCLUSIONS

The results of the pushover analyses confirm the activation of a partial collapse mechanism, restricted to the part of the building where it actually took place, as already found from linear analyses and simple hand computation in Mulas et al (2013). From the numerical results here presented the effects that the REI wall, inserted during refurbishment works, had on the structural behavior are well highlighted. The collapse sequence points out that the combined effect of the REI wall and of the lack of shear strength of beam 18–29 is responsible for the collapse of one of the three failed columns, column #29. For the other two, the collapse can be ascribed to the soft/weak story mechanism at the ground floor, in turn triggered by shear failure of the columns. A partial soft story collapse would have taken place also in the original configuration of the building.

The numerical code here adopted detects a shear failure according to the rules of the Italian Code NTC2008, and accounts for a linear behavior in shear even after detecting a failure. Further analyses with a research oriented code are thus needed to better describe the collapse sequence.

DISCLAIMER AND ACKNOWLEDGEMENTS

The content of the paper reflects the Authors opinion and does not intend to anticipate any legal conclusion. Andrea Iadanza e Matteo Rossato performed the numerical analyses as a part of their MS thesis in Civil Engineering under the guidance of the second Author. The educational license of SISMICAD is gratefully acknowledged.

REFERENCES

EN 1998-1:2005. Eurocode 8: design of structures for earthquake resistance – Part 1: general rules, seismic actions and rules for buildings. Bruxelles, Belgium: European Committee for Standardization, 2005.

L 1684. Legge n. 1684, 25 November 1962. Provvedimenti per l'edilizia, con particolari prescrizioni per le zone sismiche (in Italian).

Mulas, M.G. Coronelli, D. Martinelli, L. Paolucci, R. Perotti, F. Pavesi, A. 2012. Analysis of the "Casa dello Studente" collapse during the L'Aquila 6th April 2009 earthquake. In *Proceedings of 15th World Conference on Earthquake Engineering*, *Lisboa, 24–28 September 2012*. Paper #5833.

Mulas MG., Perotti F., Coronelli D., Martinelli L., Paolucci R., 2013. The partial collapse of "Casa dello Studente" during L'Aquila 2009 earthquake. *Engineering Failure Analysis*, http://dx.doi.org/10.1016/j.engfailanal.2013.02.031 (in press)

NTC2008. D.M. 14 January 2008. Nuove norme tecniche per le costruzioni (in Italian).

Paolucci, R. Smerzini, C. 2010. Strong ground motion in the epicentral region of the MW 6.3, Apr 6 2009, L'Aquila earthquake, Italy. In: *Proc. 5th int. conf. on recent advances in geotechnical earthquake engineering and soil dynamics*, *San Diego, CA, May 24–29 2010*, paper EQ4.

RDL 2105. Regio Decreto Legge n. 2105, 22 November 1937. Nuove norme tecniche di edilizia per tutti i comuni del regno e speciali norme tecniche di edilizia asismica per i paesi colpiti da terremoti (in Italian).

SISMICAD v.12, Concrete S.r.L., Padova, Italy.

Research and Applications in Structural Engineering, Mechanics and Computation – Zingoni (Ed.)
© 2013 Taylor & Francis Group, London, ISBN 978-1-138-00061-2

Structural assessment during the demolition of an arch bridge by advanced modal techniques

K. Islami
Department of Civil, Environmental & Architectural Engineering, University of Padua, Padua, Italy

R. Betti
Department of Civil Engineering and Engineering Mechanics, Columbia University, New York City, NY, USA

ABSTRACT: An old arch bridge was subject to demolition due to life-cycle damage and environmental issues, in a central-east region of Italy. During the demolition process, several dynamic tests were executed in order to evaluate the structural behavior before, during and after the demolition. The classical Modal Analysis methods revealed difficulty in determining the modal parameters, so these results were validated with a newly developed technique of modal parameter identification and then verified with sophisticated finite element models. The structure revealed some relatively surprising results in the dynamic characteristics before and after the partial demolition.

1 INTRODUCTION

Many bridges, due to intrinsic weakness, deterioration process and environmental changes, showed inadequate structural performance and necessity to be upgraded to current standards. Structural characterization via dynamic tests is an immediate and cheap technique for bridges in order to understand the structural behavior and damage of the structure. The dynamics of the system are represented by a set of matrices that are not based on physical laws. These kinds of models are derived from realization theory and their only requirement is to relate the input-output data without any consideration of physical parameters, like mass, damping and stiffness. Various methods that perform in frequency domain (Brincker et al., 2001) or in time domain (Peeters and Roeck, 2001) can be used to identify the global modal parameters such as natural frequencies, damping ratios and mode shapes. Most of the modal techniques show great achievement in detecting the amplified modes but are unsuccessful to detect the modes that are not well excited. An overcome to this problem is the realization of stabilization diagrams (Peeters and Ventura, 2003) and clustering analysis, by observing the sensitivity of modal properties of a mode to the change in the model's order and so discrimining structural modes from the noise modes. When considering damaged structures, a modification of the response due to damage is observed. Variations in the behaviour of the system can be associated with the decay of mechanical properties.

In the context of this study, an arch bridge was subject to a demolition process, after the construction of a new steel bridge. During the demolition progression, several dynamic tests were carried out with different kinds of measurement sensors and different configurations. The main aim of the study is to give a dynamic assessment of the structure by evaluating its modal parameters from ambient output-only measurements, observing the effects of the damaging process. Therefore, it is appropriate to evaluate the modal parameters of the bridge, before and after the partial demolition, not only with the classical modal techniques aforementioned but also with a recently developed approach (Hong, 2010), called Enhanced Canonical Correlation Analysis. This technique, together with an advanced cluster analysis developed, will help to get consistent results which will confirm the unexpected behavior of the bridge before and after the partial demolition. All the experimental data are then used to update FE models representing the demolition procedure that will validate what has been captured in the field measurements.

2 DEMOLITION PROCESS

The bridge was composed of 5 spans with an overall length of nearly 80 m and each of 15.5 m. In transverse direction, its width was about 11.0 m and composed of two parallel concrete arches connected together with a reinforced concrete slab. The average thickness of the arch was 0,60 m. The maximum height of the piers was 6.5 m and their section was rectangular with dimensions 2.5×12.50 m (Figure 1). The upper structure was carried by masonry piers and abutments that had a core made of infill material with poor mechanical

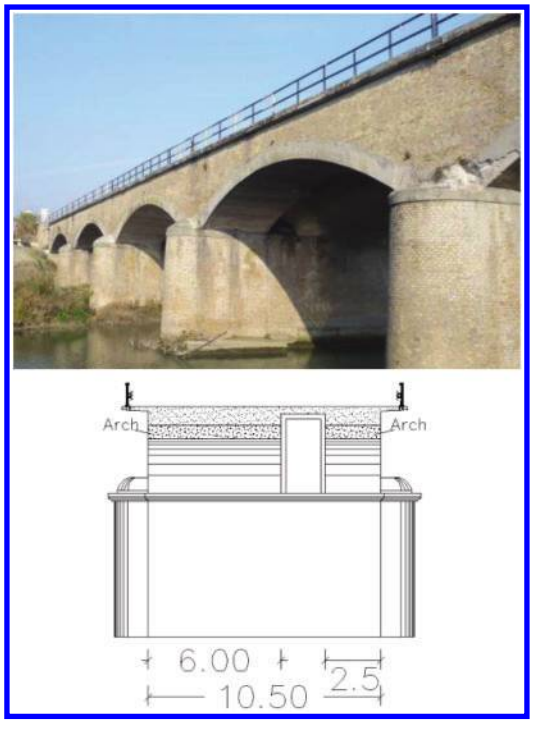


Figure 1. Photo and cross section of the analyzed bridge.

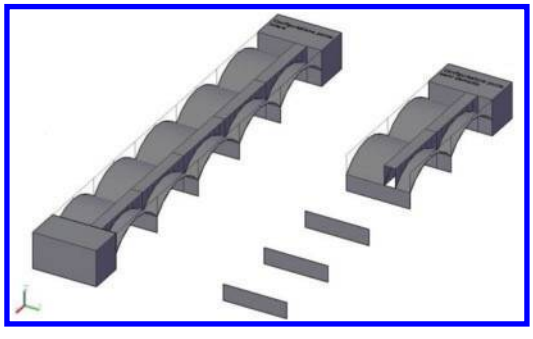


Figure 2. Two principal demolition configurations: a) five spans with some infill material, b) two spans without infill.

characteristics, containing loose material, stones and pebbles.

The demolition process began on the 14th of November 2011 and the first step was to remove the pavement and the roadbed. After a few surveys and core drillings for testing the strength of concrete, the contractor began to empty the infill material present above the arches of the old bridge. The four principal sequences of the demolition process were:

- Removal of the roadbed and emptying of the infill material.
- Demolition of the first three arches (Figure 2).
- Demolition of the first three piers.
- Demolition of the two remained arches and their piers.



Figure 3. Sequential demolition process of the bridge.

3 MEASUREMENT CAMPAIGNS

Dynamic identification allows us to determine modal parameters (natural frequencies, mode shapes, damping ratios) from experimental data. In Operational Modal Analysis the natural excitation (wind or vibrations induced by traffic) is used as an excitation source in order to capture the response of all possible modal contributions. In our case, the natural excitation was represented by traffic on the adjacent new bridge, but also the demolishing machines and excavators near the tested structure. The tests of the entire bridge were performed In November 2011, while the tests on the partly demolished bridge were executed in December 2011. The side on which the tests were performed, is the part which was demolished at the end, in hypotheses to repeat the measures after the demolition of three spans. In this description, configurations will be considered in order to evaluate the differences encountered before and after the demolition of the 3/5ths part of the bridge. In the first case, the measurements were recorded with 16 velocity sensors for nearly 4 minutes with a sampling frequency of 200 Hz.

In the second case, three of the five spans were demolished, and two spans remained. Tests were performed in overlapping, but not simultaneously, with velocity and acceleration sensors (Figure 4).

4 MODAL ANALYSIS BEFORE AND AFTER THE PARTIAL DEMOLITION

As previously mentioned, measurements have been taken before and after the demolition of three spans. In fact, the different results will be presented in this paragraph in terms of analysis conducted before and after the partial demolition. As a first step, the extraction of modal parameters from ambient vibration data was carried out by using standard methods as Frequency Domain Decomposition (FDD) developed by (Brincker et al., 2000), and the data-driven Stochastic Subspace Identification (SSI) technique (Peeters and Ventura, 2003). The analysis included frequencies corresponding to several Eigen-modes, but considering more accurate the first 4 values (Figure 5). From the very beginning it was seen that noisy data were recorded and the structure was not sufficiently excited in order to capture its dynamic characteristics, so it was difficult to get clear results.

The plots in Figure 5 present similar features but more importantly show a shift in the natural frequency

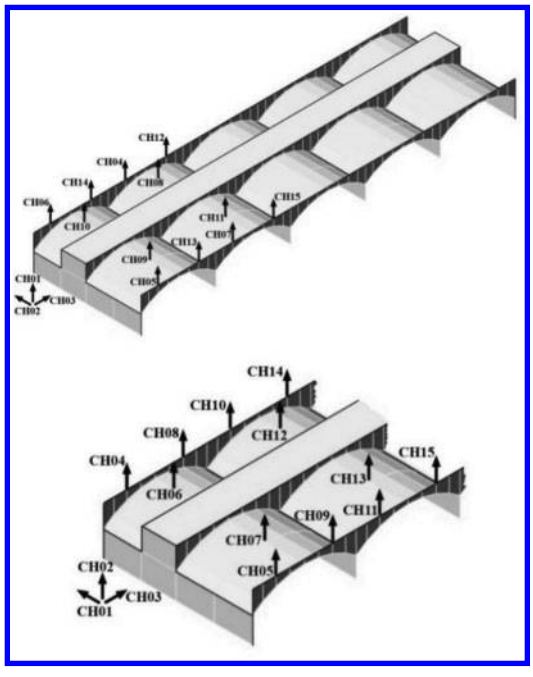


Figure 4. Example of local configurations: before and after the demolition.

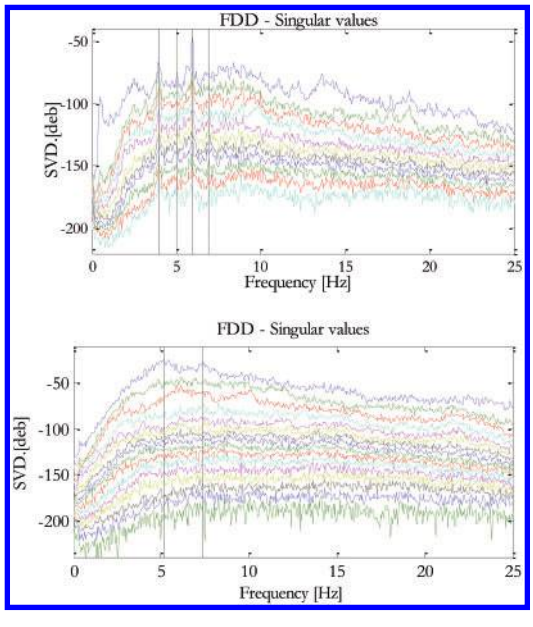


Figure 5. The FDD method with velocity data before and after the partial demolition.

values. In particular the first peak present in the first graph has a shift of nearly 1 Hz in relation to the second graph, resulting in an increase from 3.97 to 5.20 Hz, respectively before and after the partial demolition.

Although, the SSI and FDD methods weren't capable of identifying many natural frequencies (noisy results), they revealed that the structure after the partial demolition seems to be more rigid than the entire structure. These surprising results will be reviewed and exalted in the next paragraphs, but also validated with a theoretical model that represents the demolition process. While already in the first plot of Figure 5 the selection of the modes was not simple, when we consider the second plot, regarding the tests after the demolition, it is impossible to identify more than two modal modes. For this reason, another study and some cluster analyses will be developed to get the best results from this interesting demolition process.

5 MODAL PARAMETER IDENTIFICATION VIA ECCA CLUSTER ANALYSIS

During the previous analysis with the standard modal methods we encountered some difficulties in finding the principal modal parameters of the studied structure. In this paragraph, some of the results obtained from the analysis with the Enhanced Canonical Correlation Analysis (Hong, 2010) method will be shown. In this case, it was possible to identify more dynamic parameters and at the same time confirm the previous results. The stabilization diagram permits to identify the modes whose properties do not change significantly when varying the model order. Modes classified as "stable" are considered as structural modes. However, such modal parameter estimates, particularly the damping ratios, are influenced by the particular selection of the model order, as presented in Figure 6. It can be noticed how the frequency values related to the model order number show a stable trend, especially for the first modes. In the frequency range of 3–30, 11 structural modes were identified with the ECCA (far more than the standard techniques). The results reveal again that every vibrating mode, after the partial demolition, has a shift towards higher values. This might be an unpredicted result that can complicate the demolition processes for this kind of structures.

5.1 *Cluster analysis*

In order to develop this automated technique, the initial ideas have been taken not only from the stabilization diagram of the SSI method, but they are also based on the advanced SSI technique called ECCA. Essentially, the main element, which detects the stable modes, in this case is the damping vs. frequency plot. As will be described in the following paragraphs, the procedure consists in applying the modal analysis for varying parameters, by obtaining a large amount of system identification data. Then, after cleaning the data by specific rules, some cluster analyses are performed to consistently determine the structural modal parameters. Finally, the technique is repeated for each dataset (which is filtered and overlapped) coming from a possible SHM system.

Some of the parameters which can influence the identification results are the number, i, of the block

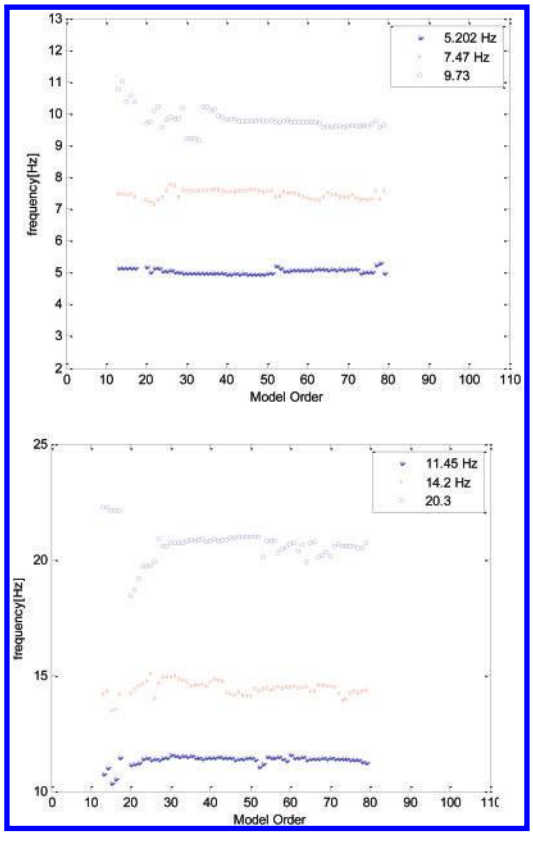


Figure 6. Natural frequencies identified vs. system's model order (after demolition).

rows of the output data matrix and the model's order, n. So, by combining these parameters in infinite ways, we can get different results, but as we know, only the stable modes can be considered as structural modes (Ubertini et al., 2011). The presented approach for automatic estimation of modal parameters is composed by the following steps: (a) run modal analysis with different values, i, and the model's order, n; (b) apply rules in order to clean the noise modes; (c) apply a cluster analysis; (d) plot frequency vs. damping results of stable modes; (d) determine mean values of structural modes and their 95% confidence intervals; (e) loop the cycle for all the recorded data and extract the modal parameters for the entire monitored period.

Modes are identified from each analysis conducted by using a different pair of (i, n). Among the identified poles from all the possible pairs (i, n), modes that can be considered as noise ones are eliminated first, then, the remaining modes are grouped with respect to their frequencies and mode shape vectors. Noise modes can be detected by considering the fact that:

- the estimation of structural modes is not affected by the specific selection of i and n;
- mode shapes corresponding to structural modes are likely to be similar in different analysis;
- and probably large damping values belong to noise frequencies.

A single mode should be identified within a single cluster at least 30 times using different combinations of n and i.

5.1.1 *Cleaning and clustering the identified poles*

In order to lead to a more evident mode selection, before applying the clustering rules, a cleaning procedure has been developed. First of all, after extracting all the poles from all analyses, modes whose damping ratio is negative or larger than 14% are eliminated. In our case, similar noise eliminating rules used in a stabilization diagram are applied; however, these include not only variations of model's order, but also the number of block rows. Considering only modes remaining from the previous step, the identified modes are compared: modes are grouped on the basis of analogous frequency, damping and mode shape values, and after that, modes having frequencies that differ from each other by more than 1% are eliminated. The algorithm distinguishes only stable modes which are stored in a matrix. Among all the poles identified with the previous analyses, only *some* of them are considered to be physical modes and meet frequency, Δf_{lim}, damping ,$\Delta \xi_{lim}$ and Modal Assurance Criterion, MAC_{lim} tolerances. The *n-th* mode is said to be stable when it is similar, in terms of frequency, damping ratio and mode shape to a minimum number of other modes.

To remove further noise modes, at this point, mode shapes, that show irregular behavior in relation to the group, are eliminated by operating with the following cluster analysis containing only those poles that correspond to the same mode. The aim of cluster analysis is to group all modes, cleared from the previous step, into separate sets belonging to the same structural mode. At the end, each cluster will contain only the stable frequency, damping and mode shape of the particular mode. The separation procedure is obtained by the use of a mutual distance between all clusters as follows:

$$d(j,l) = | f_j - f_l | + 1 - MAC(\phi_j, \phi_l)$$

where f_j and f_l are frequencies of modes j and l and $\Phi_j$and Φ_l the corresponding mode shapes.

At this point, two clusters that are close together are collected in a single cluster, and the mutual distance between all clusters is recomputed. As a last step, the average of the elements of all clusters is calculated and the clusters that contain less than the average value are eliminated. Clusters containing a minimum number are selected for the candidate modes, otherwise they are rejected. The merged cluster available can now be described by means of statistical parameters. Each modal parameter is characterized by a mean value (f, ξ), standard deviation σ and its 95% confidence intervals can be calculated.

5.1.2 *Cleaning and clustering the identified poles*

In this study, considering values of the model's order n ranging from 40 to 160 with increments of 5, and by

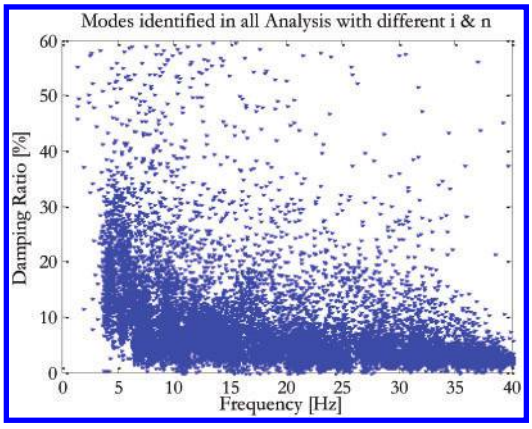


Figure 7. All damping ratios for all the modes identified.

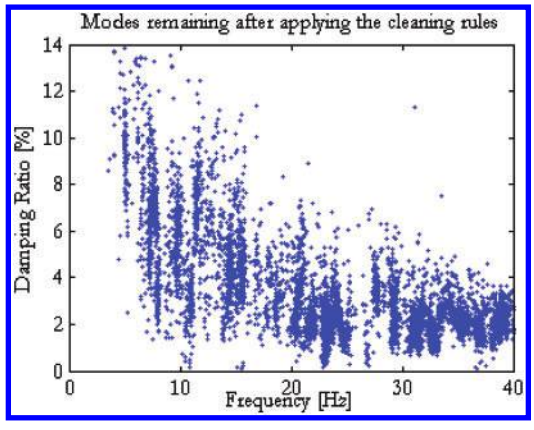


Figure 8. All values of damping ratios for all the modes identified.

considering the value of *i* number of blocks ranging from 40 to 120 with increments of 4, a total of 480 analyses have been conducted (Figure 7). The results of clustering steps are presented in Figure 7 – Figure 9, where modal properties are plotted in terms of frequency and damping ratio. Figure 7 shows all modes that have been identified by the total parametric analysis and Figure 8 shows modes remaining after eliminating modes with damping larger than 14% and after applying the cleaning rules (similar to a stabilization diagram, but with the damping values in the y axis).

Figure 9 is showing the modes identified with the cluster analysis. A total of 20 groups were identified, indicating that a total of 20 structural modes are recognized from the cluster analysis. Mean values and confidence intervals (Table 1) confirm the estimated modal parameters with very small uncertainties. In such analysis, even close modes seem to be well distinguished whereas noise modes are efficiently eliminated. Comparing Figure 7 and Figure 9, most of the noisy modes are eliminated by inspecting the consistency between modes estimated using different pairs of *n* and *i*.

With regard to modal parameters estimation, the natural frequencies and damping ratios can be calculated from the individual groups in relationship to their statistical properties (e.g. mean, standard deviation). Table 1 presents the mean and standard deviation values of 12 natural frequencies identified in this study from the cluster analysis.

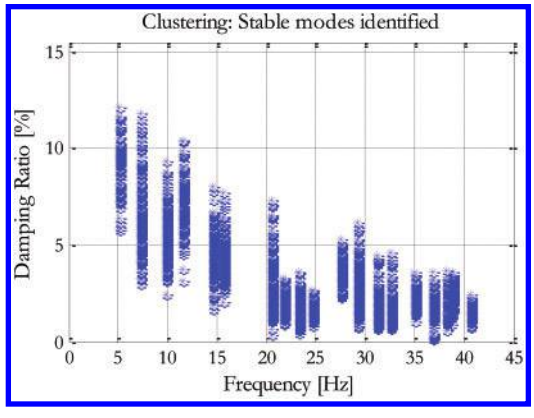


Figure 9. All values of damping ratios for all the modes identified.

Table 1. The identified frequencies [Hz] from the cluster analysis for the experimental problem.

Mode	Freq. mean [Hz]	Freq. Std	Num of times found
1	5.2049	0.0280	98
2	7.4666	0.0441	230
3	9.7291	0.0489	210
4	11.4604	0.0563	155
5	14.2099	0.0887	232
6	15.5820	0.0563	255
7	20.3015	0.0936	205
8	21.5218	0.1206	94
9	23.1927	0.0671	345
10	24.6084	0.0942	452
11	27.6969	0.1311	112
12	29.4251	0.1249	392

6 VALIDATION OF THE DEMOLITION PROCESS WITH FE ANALYSIS

In this case, the FE model was not only updated from the experimental results, but also served as a means of demolition scenario validation. In order to create the same situation existing during the tests, only the standing spandrel walls and part of the infill material were modeled, without the roadbed or slab. After defining the base model and updating it according to the experimental data, a second model group has been generated. This model wants to reproduce what was left in site after the demolition of three spans of the bridge; from the previous model only the first

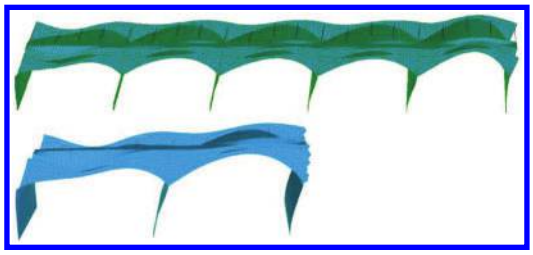


Figure 10. First mode of the entire model and the partly demolished one.

Table 2. Comparison between experimental and theoretical models **before** and **after** the demolition.

	Experimental		MAC	FEM	
Mode	Before	After	Exp.	Before	After
1	3.959	5.204	0.46	3.989	5.226
2	5.949	7.466	0.56	6.011	7.264
3	6.950	9.729	0.60	6.413	8.245
4	10.58	11.460	–	10.02	10.25
5	12.95	14.209	–	12.50	13.42

two spans were present and a small portion of the infill material was extracted. In summary, we have two groups of models representing the bridge before and after the partial demolition, in accordance with the measurement configurations.

Figure 10 and Table 2 show the results of what was carried out from the model updating and demolition scenario. In Figure 10 it can easily be noticed that the first mode shapes and natural frequencies of the entire structure are similar to the results that were captured during the dynamic tests before the demolition of the three spans.

A better view of what happened in both cases of the experimental and analytical model, before and after the demolition, is shown in Table 2, where one can notice that the overall frequency values in both cases have augmented. We can now state that what was observed in the field from the experimental tests is also confirmed by the FE models. This result, at the beginning unexpected, is probably due to the order change of the mode shapes, to the different boundary conditions and small change of material present before and after the demolition.

7 CONCLUSIONS

In this work, detailed analysis of the ambient dynamic response of an existing arch bridge has been carried on, starting from the identification of its modal parameters from field measurement during its demolition process and ending with a calibrated FE model that has been used to reproduce the demolition scenarios. Measurements before and after the demolition of three, out of five, spans were recorded. The principal scope of this study was to understand the dynamic behavior of this kind of structure and to validate the results with a newly developed technique of modal analysis.

The first principal mode shapes were difficult to be identified through the FDD and the SSI methods. It was observed immediately that the structure revealed higher values of natural frequencies after the demolition, which was surprising because the opposite thing was expected. Straightaway, the results aroused some inquiring doubts that needed further study of the event. Modal parameter identification via Enhanced Canonical Correlation Analysis technique and cluster analysis has been implemented in order to better detect what the noisy data contained.

From the analysis with different combinations of the model order and the number of rows of the output block matrices was observed that most noisy modes are eliminated. In the frequency range of 3–30, a total of 20 structural modes have been identified. This cluster analysis and another similar data elaboration established clearly the principal mode shapes involved in the structural change of the bridge before and after the demolition.

Finally the natural frequencies of an updated FE model of the Bridge have been compared with the ones of the field test models in the cases of the entire bridge and also in the case of the partially demolished one. The comparison confirmed once again the initial affirmation that the structure was behaving in a different way: the overall frequency values in both cases of analytical and experimental models have increased.

REFERENCES

Brincker, R., Zhang, L., & Andersen, P. 2001. Modal identification of output-only systems using FDD. *Smart Material and Structures* 10: 441–445.

Hong, A. L. 2010. *Wheiting matrices and model order determination in stochastic system identification for civil infrastructure systems*, Ph.D thesis, Columbia University, New York.

Hong, A. L., Ubertini, F. and Betti, R. 2011. Wind analysis of a suspension bridge: Identification and FE model simulation, *ASCE J. Struct. Eng.*, 137:133–142.

Peeters, B. and De Roeck, G. 1999. Reference-based stochastic subspace identification for output-only modal analysis, *Mechanical Systems and Signal Processing* 13(6): 855–878.

Peeters, B. and Ventura, E. E. 2003. Comparative study on modal analysis techniques for bridge dymanic characteristics, *Mechanical Systems and Signal Processing* 17(5): 965–988.

Strand7, *Structural software HSH s.r.l.*, Padova, Italy.

Ubertini F., Gentile C. and Materazzi A. 2011. "On the automatic identification of modal parameters by subspace methods," in *4th International Conference on Experimental Vibration Analysis of Civil Engineering Structures*, Varenna, Italy.

Research and Applications in Structural Engineering, Mechanics and Computation – Zingoni (Ed.)
© 2013 Taylor & Francis Group, London, ISBN 978-1-138-00061-2

EQvis: A consequence based risk management software tool

D. Schäfer, M. Pietsch & H. Wenzel
VCE – Vienna Consulting Engineers ZT GmbH, Vienna, Austria

ABSTRACT: The possible applications of disaster-management-software are not reduced to theoretical case-studies. Contrariwise, one of the main aims while developing EQvis was to cover also the needs and ease the work of rescue-teams. Severe earthquakes can be accompanied by a partly or total breakdown of communication, failure of road networks, electrical power supply systems, sewerage systems, water supply systems etc. Embedded in the platform are various plug-ins. In general the platform comprises a consequent based risk management tool for seismic events. The field of analyses that can be performed with EQvis is very large, e.g. Hazard Computation, Structural Damages, Functionalities, Repair Cost Estimations, Cost Benefit Analyses, Utility Network Damages, Multi Attribute Utility Analyses, Shelter Needs, Social Vulnerability, Temporary Housing, etc. The modularity of EQvis is the key for such a successful software tool. The earthquake real-time simulations admit the quick generation of an overview with the detail of the estimated damages to structures or buildings, as soon as magnitude data and epicentre coordinates are available. With this data, a simulation can be run and results can be obtained within some minutes. Inspection teams are sent out to the most damaged structures (indicated by EQvis) in order to confirm or controvert the results of the simulation, by reporting their observations. The IRIS-exercise in Hungary has shown how the effectiveness of rescue workers can be improved with the help of an appropriate disaster-simulation-program.

1 INTRODUCTION

Catastrophic events, particularly natural disasters have devastating consequences on society.

The damages occurring in case of an earthquake do not depend exclusively on the earthquake-resistance of buildings and infrastructures. The most severe earthquakes that occurred in the last years show that many victims are caused by secondary impacts. A faster organization of rescue facilities such as availability of medical services, drinking water, allocation of emergency accommodations etc., could have contributed to avoid many victims.

When handling all helping hands, the decisions time has to be minimized. This achievement can be pursued by developing realistic disaster-scenarios within which the efficiency of rescue teams can widely improve. By training in those situations, the rescue teams can develop a better interaction with other subjects involved, with a consequent improvement and optimization of their response in emergency situations. The development of evacuation plans requires emergency managers to understand the potential impacts in terms of location, direct and secondary consequences, the needs of society both short- and long-term, as well as economic ramifications. Analytical impact assessments for natural disasters provide the potential to inform emergency managers and support the development of appropriate and effective response plans for catastrophic events. In the case of analytical earthquake impact assessment, models and data are used to provide estimates of damage to infrastructures and network performance, as well as secondary damage due to cascading effects, social impacts and uncertainty quantifications.

2 DESCRIPTION OF EQVIS MODELLING

EQvis is an advanced seismic loss assessment, and risk management software which stands on the Consequence-based Risk Management (CRM) methodology. CRM provides the philosophical and practical bond between the cause and effect of the disastrous event and mitigation options. EQvis follows the CRM methodology using a visually-based, menu-driven system to generate damage estimates from scientific and engineering principles and data, test multiple mitigation strategies, and support modelling efforts to estimate higher level impacts of earthquake hazards, such as impacts on transportation networks, social, or economic systems. It enables policy-makers and decision-makers to ultimately develop risk reduction strategies and implement mitigation actions. In EQvis, a wide range of user-defined parameters are introduced. The breadth of user-defined parameters enables emergency planners to model a virtually unlimited number of scenarios.

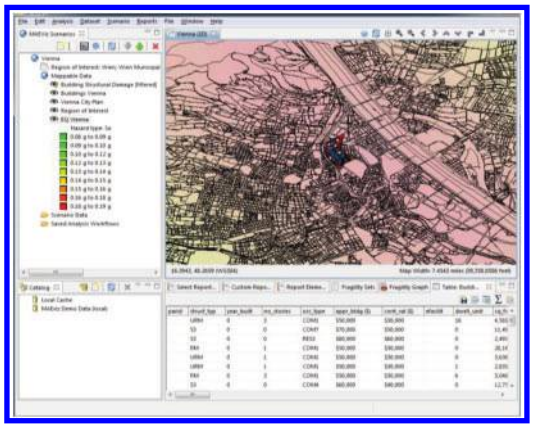


Figure 1. Interactive surface of EQvis: scenario manager, data catalogue, tables, hazard map.

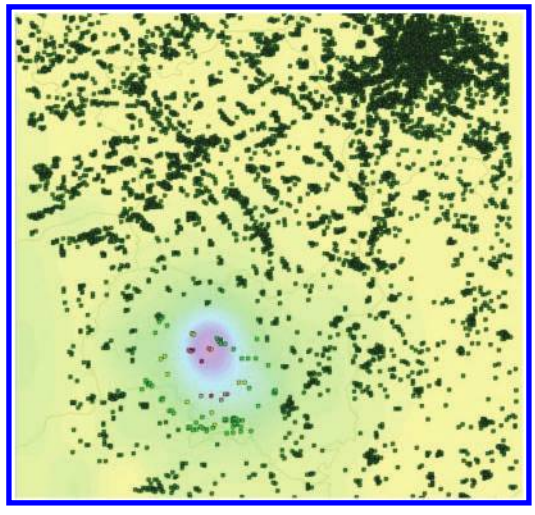


Figure 2. Built areas in Central Hungary represented with building-aggregates; the map also shows the results from an earthquake-simulation in the region of Tolna county.

3 APPLICATION OF EQVIS DURING THE IRIS-EXERCISE 2011 IN TOLNA COUNTY/HUNGARY

The possible applications of disaster-management-software are not reduced to theoretical case-studies. Contrariwise, one of the main aims while developing EQvis was to cover also the needs and ease the work of rescue-teams. Severe earthquakes can be accompanied by a partly or total breakdown of communication, failure of road networks, electrical power supply systems, sewerage systems, water supply systems etc. An additional problem is very often panic among inhabitants.

The earthquake real-time simulations admit the quick generation of an overview with the detail of the estimated damages to structures or buildings, as soon as magnitude data and epicentre coordinates are available. With this data, a simulation can be run and results can be obtained within some minutes. Inspection teams are sent on the most damaged structures (indicated by EQvis) in order to confirm or controvert the results of the simulation, by reporting their observations.

By means of these inputs, the operation controllers can better identify the rescue priorities in order to decide where to send the rescue staff, and if it is necessary to ask for more help. On the other hand, the observation team reports could also be used to refine and calibrate the computer-model. Other simulations could be subsequently run in order to get more accurate results.

On 24th of May 2011, EQvis was tested under realistic conditions in the region of Tolna County/Hungary. Tolna county is situated west of the Danube river, south of Budapest. It covers an area of 3703 km^2 with a population of 238400 inhabitants. It is remarkable, that Hungary's only nuclear power station is situated in Tolna County close to the city of Paks. Its four reactors produce more than 40 % of the electrical power generated in Hungary. All rescue and observation teams, that participated in the exercise on 24th of May 2011 were coordinated from the county's fire brigade headquarter situated in the city of Szekszard (capital of Tolna county).

3.1 *Population density*

It was necessary to gain information about the allocation of the population in a certain area. As a first approach, the public census data can be used. The problem about census data is that the inhabitants are assigned to counties, districts, and communities. Since these administrative units cover also unpopulated areas, this would cause the falsification of the results. Exactly for this reason, the census data were combined with satellite data from satellite-image-recognition. Satellite images of Tolna County were used indeed to distinguish the populated areas, using algorithms developed in-house by VCE. In combination with the available census-data, a more accurate population-density-map has been drawn.

3.2 *Building inventory*

VCE developed a routine to update fragility functions by visual assessment. The aim was to find a routine which enables anybody to perform the assessment, only after a short period of instructions and training. The assessment-routine was developed according to international standards (as FEMA 154 *Rapid Visual Screening of Buildings for Potential Seismic Hazards*) and was applied to 150 selected buildings in the cities of Szekszard, Tamasi and Paks. The aim consists in the application of this visual screening to all of the buildings within the regions with high seismic hazard. In case there is no chance to scan the buildings, an extrapolation of the results can be discussed. Of course, visual assessment cannot replace more detailed investigations as they have to be made for essential



Figure 3. Building assessment: photo, map, assessment-protocol.

structures. The advantage of the visual assessment is that usually it does not take more than 15 minutes per building and it is not necessary to access the building, which would not be possible in many cases.

3.3 *Soilmap*

During a seismic event, the structures react in a variety of ways. Oftentimes substantial differences in damage are discovered in buildings in close vicinity. The reason for such deviations is the variation of the subsoil supporting the structures and various local geological discrepancies. The design codes support a certain classification of subsoil to incorporate differences in seismic loading. The basic classification parameter in the Eurocode is the $V_{S,30.}$ This value represents the average shear wave velocity of the upper 30 metres of the stratum. To accurately determine the value of this variable, a sound estimation of the seismic performance of the designed structure is essential. . The direct measure of the shear wave velocity is invasive and expensive. This is the reason why this research was oriented to assess the local soil conditions in an unintrusive way.

The methodology to reconstruct the soil profile is based on surface testing, mathematical modelling and inverse calculation. The connecting feature between these parts is the dispersion curve.

Generally, the subsoil can be described by a great number of parameters. When dealing with wave propagation only a number of parameters are used. To fully describe the propagation of waves in an elastic medium the compressional wave velocity, shear wave velocity, density and Poisson's ratio are sufficient. Of these the shear wave velocity is the parameter that is most descriptive of possible site related specifics of which amplification is the most notable.

VCE developed and approved a procedure to determine $V_{S,30}$-values using field tests within the SEISMID-project. SEIMSID measurements consist mainly of 3 parts:

- Impact measurements
- Harmonic measurements



Figure 4. Assumed earthquake event in Tolna county used for the IRIS-exercise 2011.

- Ambient measurements

Due to time and in particular space restriction it was possible to perform the impact and the harmonic measurements, which in this case is not a problem.

In the IRIS 2011 Demonstration one task was the ground characterization of the nuclear power plant in Paks. For this reason some measurements have been performed.

3.4 *Sequence of events during the IRIS-exercise in Tolna county/Hungary 2011*

At 7:30 the simulation started with the assumption of an earthquake with epicentre in the Country of Tolna. Data about magnitude, location and depth were transmitted to the fire brigade's headquarter. Additionally to the main earthquake an aftershock was also assumed.

The acquired earthquake-data, including the data of the aftershock, were implemented to simulate the emergency scenario.

After some minutes, the results of the scenario computation were shown on the GIS-map. The computed damage can be shown within the geographic content in EQvis or either be exported as a shapefile and then be used in any GIS-application.

The degree of damage is displayed using different colours. Additionally, a damage-report for every single building or structure can be calculated.

Based on the results of the damage-calculation, two teams were sent out to the most likely damaged objects. Due to full interoperability with other GIS-applications as ArcGIS, the shortest route to all of the highlighted objects was calculated taking into account possible damaged streets. At 9:58 am, after the first instructions, the building inspection team left the headquarters in Szekszard.

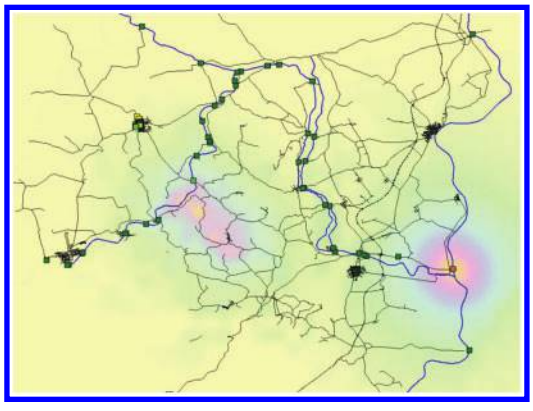


Figure 5. Computed and displayed scenario earthquakes in EQvis.



Figure 6. Building-damage protocol generated by EQvis.

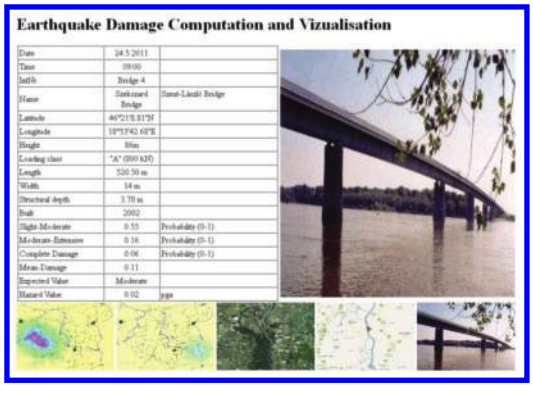


Figure 7. Bridge-damage protocol generated by EQvis.

At 10:32 the headquarters in Szekszard was informed of an accident in the chemical factory of Pincehely. Toxic gas escaped from the factory; because of its diffusion in atmosphere, roads had to be closed within a wide area. The building inspection team was informed immediately and the route was changed.

In the framework of the IRIS Demonstration, one of the biggest task was the simulation of the toxic cloud

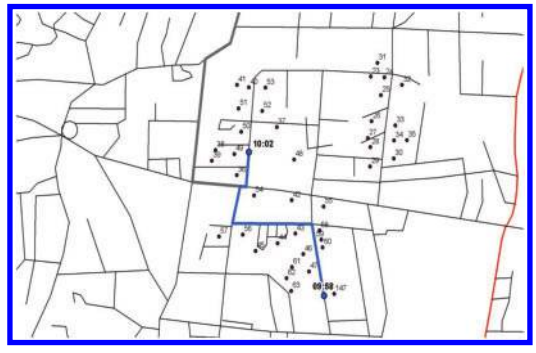


Figure 8. Route of the building inspection team (first minutes).



Figure 9. Route of the building inspection team; the toxic cloud coming from an accident in Pincehely had to be circumvented.

and the consequent management of all the linked difficulties. As the primary attempt was to create smoke and simulate the cloud. Due to uncertain wheather conditions, the creation of a back-up plan was decided.

In detail, the idea was to lay out markers in predefined positions. These markers represent the extension of the simulated cloud. 5 points were identified to mark the extension of the cloud. The identified points were white colored and they had the big size of 30×30 meters, in order to ease their recognition by the RapidEye satelite. Paper stripes where identified as the best technical solution to be used as markers. These stripes were carried to the point in rolls with 30×2 meters and were rolled out in the morning. The paper was fixed with earth material.

The markers worked very well and the points were visible from the airplane as well as from the satellite. The airplane took off in Tolna and was going south to the Szeksard bridge where a car accident was simulated. The next destination was the area around the chemical plant in Pincehely. The aim of the airplane was to first detect and collect information about the smoke cloud. The cloud did not perform as expected and the visibility was very poor, as one can see on the pictures. The plane did a few circles around the area of Pincehely in order to detect the smoke and the marker positions. The marker positions were photographed



Figure 10. Route of the airplane.



Figure 11. Markers simulating a toxic cloud in the area of Pincehely.

and documented. Also a message to the Management Team was sent out via SMS when a marker has been found. The Management Team documented the times and the coordinates and got a good impression how long it took to find all the marker positions. Around the area of Pincehely there have only been 3 Markers. 2 other markers were placed southwest with respect to the chemical plant. The pilot knew the wind direction and tried to find the rest of the markers. After finding all the markers, the plane was flying north again and looked at all the important bridges across the Danube. These bridges match with the bridges where damage calculations were performed in the simulation software. These bridges were also inspected by the Bridge Inspection Team.

This is the final flight route of the airplane. As one can see the important places were the marker positions around the chemical plant in Pincehely, then the

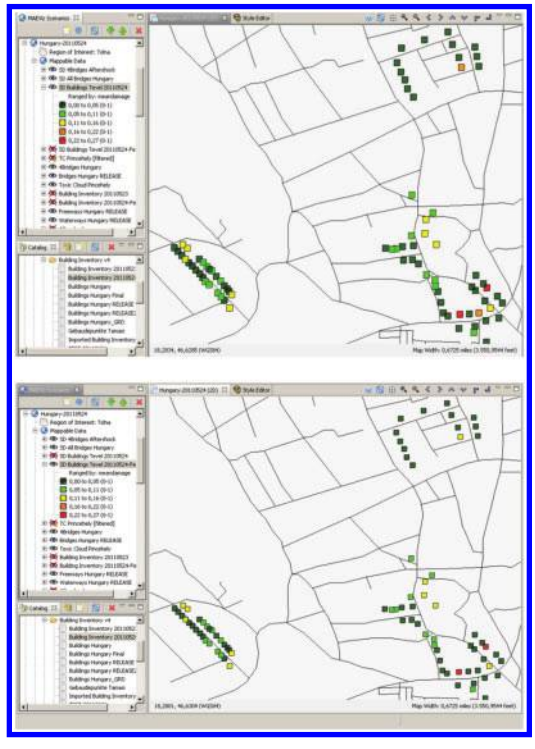


Figure 12. Damaged buildings in Tamasi, Tolna county before (upper image) and after (lower image) model update.

3 marker points southwest of the Picehely area, and the most important Danube bridges.

The inspection of all the probably damaged buildings finished at 11:50. The outcomes of the building inspection team were immediately transmitted to the headquarters in Szekszard and they were used for the model-updating.

4 CONCLUSIONS

EQvis enables to study the earthquake resistance of buildings in an analytical way. The weakest points of the infrastructure can be shown up and in this manner it is helpful for decision makers to make necessary improvements.

Whether modelling disaster consequences or alerting residents to impending disaster-events, GIS-driven maps and applications help emergency personnel to save lives, mitigate property damage, and speed recovery. The key to effective emergency management is situational awareness. EQvis is designed to be used not only by earthquake-engineers, it can also support the work of rescue workers.

The IRIS-exercise in Hungary should show how the effectiveness of rescue workers can be improved with the help of an appropriate disaster-simulation-program. This could be proven in an impressing way, and also many suggestions for further improvements could be formulated.

REFERENCES

Achs, G. et al, 2010, *Erdbeben im Wiener Becken*, Wien, www.seismid.com

DeMeritt, Matthew, 2012, *Sim Disaster - a better approach to disaster consequence management*, ArcUser magazine

Duenas-Osorio, L.A. (2005). *Interdependent Response of Networked Systems to Natural Hazards and Intentional Disruptions*. Ph.D. Dissertation, Georgia Institute of Technology.

Flesch, R., 1993, *Baudynamik Band 1*, Bauverlag

Genctürk, B. (2007*). Improved Fragility Relationships for Populations of Buildings Based on Inelastic Response*. MS Thesis, Department of Civil and Environmental Engineering, University of Illinois at Urbana-Champaign, Urbana, IL.

Genctürk, B., Elnashai, A. S., and Song, J. (2008). *Improved Fragility Relationships for Populations of Buildings Based on Inelastic Response*. The 14th World Conference on Earthquake Engineering. Beijing, China. October 12–17.

Kim, Y.S. (2007). *Seismic Loss Estimation and Mitigation of Critical Urban Infrastructure*. Ph.D. Dissertation, University of Illinois at Urbana-Champaign.

Kim, Y.S., Spencer, B.F., Song, J., Elnashai, A.S., Stokes, T. (2007). *Seismic Performance of Interdependent Lifeline Systems*, Mid-America Earthquake Center, University of Illinois at Urbana-Champaign, CD Release 07-16, September.

Kim, Y., B. F. Spencer, and A.S. Elnashai (2008). *Seismic loss assessment and mitigation for critical urban infrastructure systems* (NSEL-007). Newmark Structural Engineering Lab, Urbana, IL: University of Illinois.

Mid-America Earthquake Center, 2009*, Impact of New Madrid Seismic Zone Earthquakes on the Central USA*, MAE Center Report No. 09-03

Seismid – Bericht 48, 2010 *Boden-Gebäude Interaktion*, 2011, interner Bericht im Projekt Seismid, www.seismid.com

Sheffi, Y. (1985). *Urban transportation networks: Equilibrium analysis with mathematical programming methods*. Englewood Cliffs, NJ: Prentice-Hall.

Studer, J., Laue, M., Koller, 2007, *Bodendynamik*, 3. Auflage, Springer Verlag

Wardrop, J.G. (1952). Some theoretical aspects of road traffic research. Proceedings of Institute of Civil Engineers (part II), v 1, 325–378.

Wen, Y.K, B.E. Ellingwood and J. Bracci (2003). "*Vulnerability Function Derivation for Consequence-Based Engineering.*" Mid-America Earthquake Center Report.

Wen, Y.K. and C.L. Wu (2001). *Uniform Hazard Ground Motions for Mid-America Cities*. Earthquake Spectra. v 17, 359–384.

Youd, T.L. and D.M. Perkins, (1978), *Mapping of Liquefaction Induced Ground Failure Potential.* Journal of the Geotechnical Engineering Division, ASCE. v 104, n 4, 433–446.

Research and Applications in Structural Engineering, Mechanics and Computation – Zingoni (Ed.)
© 2013 Taylor & Francis Group, London, ISBN 978-1-138-00061-2

Measuring degree of interdependencies at the infrastructure level during emergencies

D. Solari & G.P. Cimellaro
Department of Structural, Building and Geotechnical Engineering, (DISEG), Politecnico di Torino, Turin, Italy

A.M. Reinhorn
Department of Civil Structural and Environmental Engineering, University at Buffalo, Buffalo, NY, USA

ABSTRACT: Communities today have a complicated structure, in which various infrastructures overlap and depend on each other. Infrastructures have a certain degree of interdependency at different levels: national, regional, local, etc. This is highlighted when the community is subject to a shock (earthquakes, hurricanes, floods, etc.). Measuring the degree of interdependency is crucial to take appropriate actions on various infrastructures before, during and after the event, in order to minimize the loss of functionality of the various infrastructure networks, thereby reducing severe social and economic losses and optimizing the interventions on the existing infrastructures. In this article we use time series analysis based on cross-correlation functions as a tool for the evaluation of the degree of interdependency at the infrastructure level, on the basis of data provided from the restoration curves of power, natural gas and water supply networks in different regions of Japan after March 11th, 2011 earthquake in Japan.

1 INTRODUCTION

In the last years the scientific community increased the interested in lifelines interdependencies and resilience evaluation (Cimellaro et al., 2010a,b, Cimellaro 2013). In literature there are several papers related to the evaluation of the interdependency index among infrastructures (Arcidiacono et al., 2012). All the articles mainly concentrate on the last decade and they are all using the taxonomy of lifeline interdependencies which is given in the fundamental work by Rinaldi et al. (2001). Paton & Johnston (2006) have given a numerical quantification of the dependencies among different infrastructures, by using an empirical approach in which the degree of dependency among different infrastructures is function of the strength of dependency (high, medium, low dependence). Bigger et al. (2009) have collected different interdependent lifeline information associated with the 2004 hurricane season in Florida. Delamare et al. (2009) have studied the potential effect of interdependencies that may occur between the telecommunication and the electrical network and they have proposed a model that describes the behavior of these interdependent systems. More recently Kakderi et al. (2011) summarizes the available methodologies and models for the vulnerability and risk assessment of systems of systems. They reported illustrations, identification and definitions of the interaction of complex dependencies available in literature. The classification schemes of dependencies are reviewed, and the available methods for the simulation of interdependencies are summarized and classified in five categories. Furthermore, the main characteristics, ad-vantages and limitations of each category of interdependency are also reported. Instead, in the work proposed by Kongar & Rossetto (2012) it is provided a review of the literature using a matrix approach, describing the gaps in knowledge. Based on the review outcomes it conceives a methodological framework for the assessment of infrastructure vulnerability accounting for interdependencies. Kjølle et al. (2012) have used contingency analysis (power flow), reliability analysis of power systems and cascade diagrams for investigating interdependencies, while Poljansek et al. (2012) have studied the seismic vulnerability of the European gas and electricity transmission networks from a topological point of view; network interdependency is evaluated using the strength of coupling of the inter-connections, together with the seismic response. Recently Dueñas-Osorio & Kwasinski (2012) have proposed an approach based on the post-analysis of the restoration curves. The interdependency index between infrastructures is calculated with an empirical equation that depends on the maximum positive value of the cross correlation function (CCF) of the two data series. In this article it is proposed a method to evaluate resilience of a region affected by a disaster considering infrastructure interdependency. The resilience index of every infrastructure in the region is combined with others through weight coefficients, which are calculated starting from a modified version of the interdependence index

proposed in the work of Dueñas-Osorio & Kwasinski (2012) where the cross correlation functions (CCF) are adopted. A new method to evaluate interdependency index is proposed and compared with other methods available in literature. The regional resilience index is evaluated taking in account the weights coefficients which are evaluated for every region and infrastructure considered in the analysis. Finally, a method for the treatment of the restoration curves is proposed where aftershocks are included in the restoration curves. The method is described using the restoration curves (Nojima, 2012) of the physical infrastructures of the twelve regions in Japan which were affected by March 11th 2011 Tohoku Earthquake.

2 RESTORATION CURVES OF PHYSICAL INFRASTRUCTURES AFTER 2011 TOHOKU EARTHQUAKE

The proposed method for the evaluation of the interdependency index and the weights coefficients necessary to evaluate the regional resilience index is based on the evaluation of the CCF among different restoration curves. In this paper, the restoration curves used for the analysis are the time series recorded during March 11th 2011 Tohoku Earthquake (Nojima, 2012), in the twelve Japanese regions which are: Miyagi, Ibaraki, Fukushima, Yamagata, Akita, Ibaraki, Tochigi, Aomori, Chiba, Gunma, Saitama and Kanagawa (listed according to the distance from the epicenter). In particular, are available the restoration curves of three different types of lifelines (Power delivery, Water supply, City Gas delivery) for the regions of Miyagi, Iwate, Fukushima, Ibaraki, Aomori and Saitama. Instead for the region of Yamagata, Akita, Tochigi and Gunma are available only the data of Power delivery and Water supply, whereas for Chiba and Kanagawa prefecture are available only the restoration curves of the Power delivery and City Gas delivery. In this restoration curves it can observe the effects of two main aftershocks, which occurred on April 7th (M=7.2) and on April 11th (M=7.0), on the different infrastructures and regions respectively. The first aftershock reduced the serviceability in the regions located near the epicenter of the main shock and the first aftershock, whereas the second aftershock reduced the serviceability of the lifelines in Fukushima prefecture only. City Gas delivery were not influenced from the two aftershocks in any region.

3 EVALUATION OF INTERDEPENDENCY INDEX

In order to calculate the CCF functions of the different restoration curves, it is necessary that the time series would be at least weakly stationary (Shumway & Stoffer, 2006). To minimize the effects of non-stationary and obtain meaningful statistical analyses, the time series data have been logarithmically transformed and second-differenced (Figure 1a). This transformation stabilizes the variability, and the mean

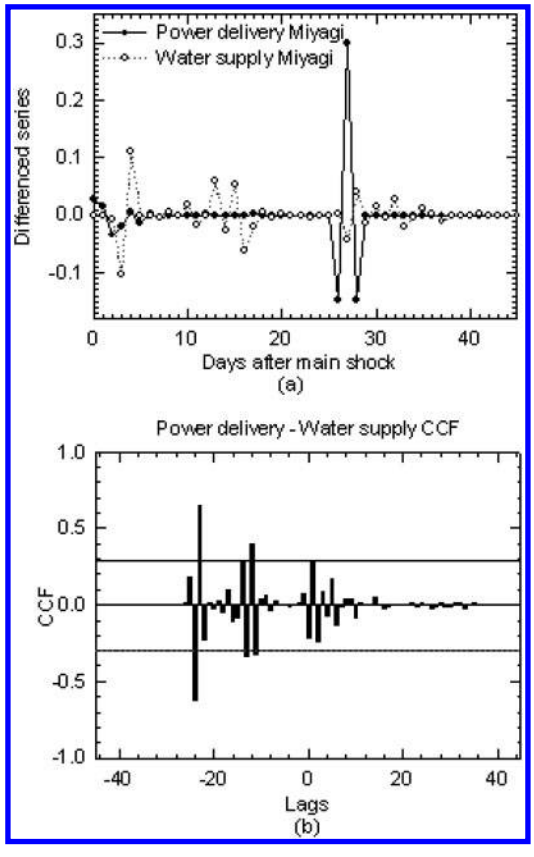


Figure 1. Miyagi power delivery and water supply restoration curves logarithmically transformed and second differenced (a); Cross correlation function of power delivery and water supply in Miyagi region (b).

value which remains constant through the time, while the auto-covariance values decay rapidly and only depends on the time-difference $h = t_1 - t_2$ between the data series, where t_1 and t_2 are arbitrary points in time (Shumway & Stoffer, 2006). An example of the results of the transformation, about Power delivery and water supply for Miyagi region is shown in Figure 1a. After the logarithmical transformation and the second-differenced of the data series, it is possible to evaluate the CCF functions ($\rho_{i,j}(h)$) for different combinations of the restoration curves. In Figure 1b is shown an example of CCF function between Power delivery and water supply for Miyagi region. Four equations for the evaluation of the interdependency index $S_{i,j}$ among different infrastructures are proposed (Eq. (2), (3), (4), (5)), and compared with the results of Equation (1) which has been proposed by Dueñas-Osorio & Kwasinski (2012).

$$S_{i,j} = \begin{cases} \dfrac{\rho^{+}_{i,j}(h)}{1+\sqrt{|h|}} \times \mathrm{sgn}(h) & when \quad h \neq 0 \\ \rho^{+}_{i,j}(h) & when \quad h = 0 \end{cases} \qquad (1)$$

where $\rho^{+}_{i,j}(h)$ corresponds to the maximum positive CCF value, which occurs at the peak lag time value h with absolute value $|h|$, and the sign function (sgn) is used to keep track of the dominant system. The ith system leads [lags] the restoration of the jth system when $S_{i,j}$ is positive [negative] (Dueñas-Osorio & Kwasinski, 2012).

$$S_{i,j} = \begin{cases} \dfrac{\rho^{+}_{i,j}(h)}{h} & when \quad h \neq 0 \\ \rho^{+}_{i,j}(h) & when \quad h = 0 \end{cases} \tag{2}$$

$$S_{i,j} = \frac{1}{N}\sum_{k=1}^{N}\left(\begin{cases} \dfrac{\rho(h_k)}{1+\sqrt{|h_k|}} \times \mathrm{sgn}(h_k), when \quad \rho(h_k) \geq \rho_{tr} \cup h_k \neq 0 \\ \rho(h_k) \qquad\qquad , when \quad \rho(h_k) \geq \rho_{tr} \cup h_k = 0 \end{cases} \right) \tag{3}$$

$$S_{i,j} = \frac{1}{N}\sum_{k=1}^{N}\left(\begin{cases} \dfrac{\rho(h_k)}{h_k} & when \quad \rho(h_k) \geq \rho_{tr} \quad and \quad h_k \neq 0 \\ \rho(h_k) & when \quad \rho(h_k) \geq \rho_{tr} \quad and \quad h_k = 0 \end{cases} \right) \tag{4}$$

$$S_{i,j} = \left|A_{i,j}\right|^{\frac{1}{N}} \cdot \mathrm{sgn}\left(A_{i,j}\right) \tag{5}$$

where

$$A_{i,j} = \frac{1}{N}\sum_{k=1}^{N}\left(\begin{cases} \dfrac{\rho(h_k)}{\sqrt{|h_k|}} \times \mathrm{sgn}(h_k) & when \quad \rho(h_k) \geq \rho_{tr} \quad and \quad h_k \neq 0 \\ \rho(h_k) & when \quad \rho(h_k) \geq \rho_{tr} \quad and \quad h_k = 0 \end{cases} \right) \tag{6}$$

and where $\rho^{+}_{i,j}(h)$ corresponds to the maximum positive CCF value, which occurs at the peak lag time value h, $\rho(h_k)$ corresponds to the CCF values which occur at lag time h_k, ρ_{tr} is the value of the positive threshold of statistical significance (the threshold is shown in Figure 1b with the two horizontal solid lines), N corresponds to the number of CCF values that exceed the upper bound of statistical significance. n-infrastructure restoration curves are analyzed and the results are organized in a matrix of dimension (n × n) in which every element ranges between −1 and 1. Positive values of this index shows that the ith infrastructure (row) leads the restoration process of the jth infrastructure (column), while negative value of the index shows that the ith infrastructure (row) is lags behind the restoration process of the jth infrastructure (column). The magnitude of the dependence is given by the absolute value of the index, which, when it is close to 1 the dependency is high, while when it is close to 0 the dependency is weak (zero value indicates absence of dependency). The results of March 11th 2011 Tohoku Earthquake are shown in Table 1, while in Figure 2 is shown the comparison of the different interdependency indices $S_{i,j}$ evaluated with the different equations for the regions of Miyagi and Iwate respectively. Equation (5) generally gives the highest values of the interdependency index, while the other equations have lower values of $S_{i,j}$. Equations (3) and (4) have the lowest values of the interdependency index, because the $S_{i,j}$ index are evaluated from the average of the values of the CCF function which exceed the positive threshold of statistical significance. From Table 1 it is observed that the interdependency index relative to the Power-delivery evaluated with the different equations using the restoration curves of 47 days, often has negative value, which has no physical meaning. This behavior is well highlighted also in Figure 2 where are reported the interdependency index resulting from all the different equations taken into consideration. All equations used for the evaluation of the $S_{i,j}$ index have a sign agreement, while differences are observed in the absolute values.

Table 1. Comparison of different interdependency indices from different equations (T_{LC}=47 days)

Region		Eq. (1)	Eq. (2)	Eq. (3)	Eq. (4)	Eq. (5)
	P - W	−0.11	−0.10	−0.03	−0.03	−0.35
Miyagi	P - G	−0.15	−0.15	−0.05	−0.05	−0.19
	W - G	0.10	0.03	0.04	0.00	0.31
	P - W	0.33	0.07	0.66	0.21	0.55
Iwate	P - G	−0.10	−0.13	−0.03	−0.08	−0.56
	W - G	−0.10	−0.04	−0.08	−0.03	−0.38
	P - W	0.22	0.04	0.44	0.14	0.47
Fukushima	P - G	−0.11	−0.10	−0.02	−0.03	−0.35
	W - G	−0.15	−0.15	−0.11	−0.11	−0.23
Yamagata	P - W	−0.13	0.02	−0.03	0.16	0.31
Akita	P - W	0.46	0.46	0.93	0.93	0.93
	P - W	0.14	0.14	0.09	0.09	0.20
Ibaraki	P - G	0.19	0.16	0.12	0.12	0.49
	W - G	0.87	0.87	0.87	0.87	0.87
Tochigi	P - W	0.29	0.29	0.26	0.26	0.45
	P - W	−0.13	−0.13	−0.03	−0.03	−0.15
Aomori	P - G	−0.11	−0.11	−0.03	−0.03	−0.13
	W - G	0.72	0.72	0.72	0.72	0.72
Chiba	P - G	0.15	0.15	0.11	0.11	0.23
Gunma	P - W	0.26	0.26	0.23	0.23	0.40
	P - W	0.29	0.29	0.27	0.27	0.46
Saitama	P - G	1.00	1.00	1.00	1.00	1.00
	W - G	−0.29	−0.29	−0.27	−0.27	−0.46
Kanagawa	P - G	0.28	0.28	0.55	0.55	0.55

4 DISCUSSION REGARDING THE PROPOSED EQUATIONS

The following discussion aims to find a mathematical formula that improves Equation (1) proposed by Dueñas-Osorio & Kwasinski (2012) for the calculation of the interdependency index ($S_{i,j}$). Equations (1), (3) and (5) have the denominator term proportional to the square root of |h| that has the effect of amplifying the interdependency index with respect to Equations (2) and (4) that have the denominator term proportional to h (Figure 2). This happens because the equations that have the denominator term proportional to the square root of |h| give more importance to the terms far from lag 0 with respect to the equations that have the

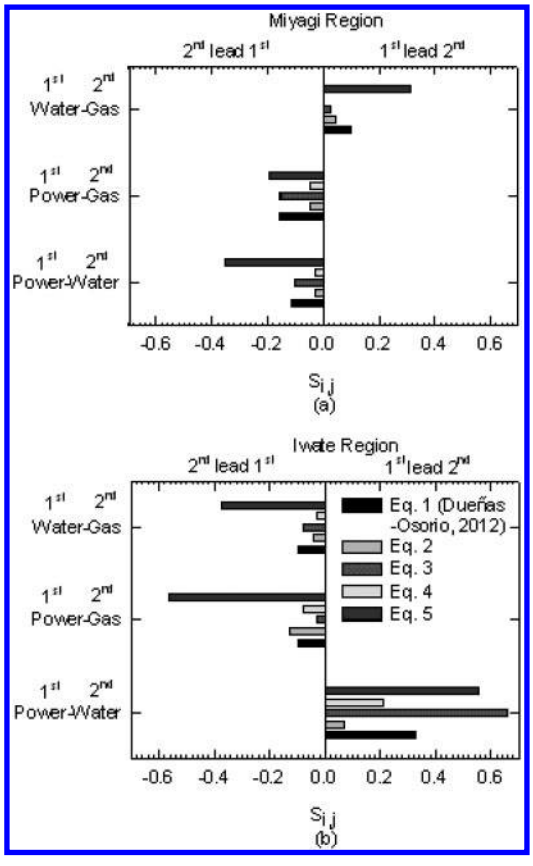


Figure 2. Comparison of different interdependency index proposed for Miyagi (a) and Iwate regions (b).

denominator term proportional to h. If CCF function has only one peak to lag ±1 (most common for CCF function about power delivery), Equations (1) and (3) give a value of $S_{i,j}$ that is a half of that which would be obtained using Equations (2), (4) and (5). Equations (1) and (2) take into consideration only one value (the positive peak) of the CCF function, without taking into account the threshold of statistical significance of the same function CCF, while the Equations (3), (4) and (5) take into account all the positive values of CCF function over the positive threshold, which is a more meaningful approach, because all values below the threshold might not have any statistical significance. This last consideration leads to discard the Equations (1) and (2), and focusing the analysis on the other remaining equations. Equation (3) give a value of $S_{i,j}$ that is half of what would be obtained using equation (4) and (5), if CCF function has only one peak to lag ±1. This behavior (that is due to the mathematical composition of the denominator) leads to low value of $S_{i,j}$ for CCF functions in which for example one infrastructure is power delivery. This happens because, immediately after the main shock, power delivery suffering a rapid drop of the functionality curve that precedes the loss of functionality of the other infrastructures (Nojima, 2012); and it is also the first lifeline that is repaired after a disaster. This behavior is due to the physical nature of electric network and because other lifelines in the community depend on electricity, therefore if it fails they reduce their functionality. These considerations lead to disregard also Equation (3).

The structure of the denominator of Equation (4) makes it less sensitive to the values of CCF far from lag 0, and, in general, gives a low value of interdependency index with respect to the other equations as is it shown in Figure 2. Moreover, if the CCF function has more than one value over the positive threshold (which is often a low value, because it is distant from lag 0), the structure of the formula, which considers the average (1/N) among these values, always provides a low value of interdependency index, in this way, instead of increasing the index of interdependence for those lifelines that have more than one value of the CCF function beyond the positive threshold, it is obtained the opposite effect. These considerations lead to reject Equation (4). Equation (5) is the only one that provides a value of $S_{i,j}$ higher, compared to Equation (1), when there is more than one value of the CCF function over the positive threshold of statistical significance. Furthermore, as shown in Figure 2b, Equation (5) provides the highest $S_{i,j}$ value for power delivery and lowest values (maximum negative values of $S_{i,j}$) for other infrastructures dependent on this. Equation (5) is the only one that provides meaningful results on the basis of the considerations so far shown and it is there-fore adopted for the calculation of the interdependency indices $S_{i,j}$.

In Cimellaro et al. (2013) is shown the behavior of Equation (5) for different hypothetical CCF functions, in order to test its sensitivity with respect to the Equation (1) proposed by Dueñas-Osorio & Kwasinski (2012). Figure 3 shows the value of the behavior threshold, based on the ratio between the CCF value at lag 0 and the CCF value at lag 1; if the value of this ratio is less than the curved line, it follows that Equation (5) gives a lower value with respect to Equation (1). If the value of this ratio is located on the curve, it follows that Equation (5) gives the same result of Equation (1). If the value of this ratio is higher than the curved line, it follows that Equation (5) gives a higher value compared to Equation (1).

Finally, if the first value of the CCF function at lag 0 is comprised between 0 and 0.5, the Equation (5) provides a greater result with respect to Equation (1) for any positive value assumed by the CCF function at lag 1. This theoretical analysis of the response of Equation (5) as a function of the first two values of the CCF function to positive lag has been developed in order to test its confidence limits of the equation in order to highlight some potentialities (such as an increasing of the index of interdependency in case more than one value of the CCF function exceeds the threshold of statistical significance), and some limits (such as the negative effect of the Equation (5) on the index of interdependency when the ratio between the value of the CCF function at lag 1 and the value of the CCF

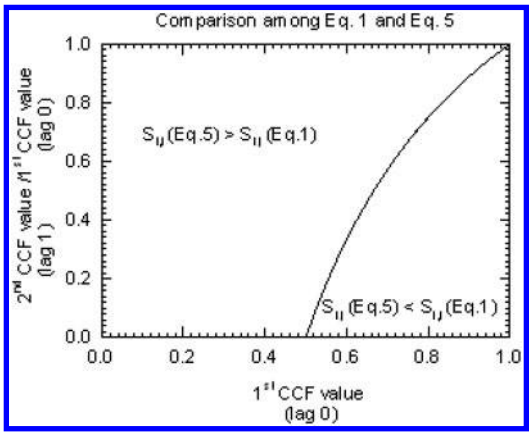


Figure 3. Comparison of CCF values between Equation (1) proposed by Duenas-Osorio & Kwasinski (2012) and Equation(5)

function to lag 0 is situated below the curve shown in Figure 3). Equation (1) does not take into account the information given by the threshold of statistical significance. Equation (5) is more conservative because if no value of the CCF function exceeds the positive threshold, the index of interdependence relative to those two lifelines is equal to zero.

5 DECOMPOSITION OF THE RESTORATION CURVES IN INTERVALS RANGING BE-TWEEN TWO CONSECUTIVE SHOCKS

From the critical analysis of the results shown in Figure 2a an anomalous behavior of the interdependency index in Miyagi region was observed, which gives a negative value for the combinations Power-Water and Power-Gas. This means that Power delivery is controlled by Water supply and Gas delivery. This does not have any physical meaning, because normally electricity leads the other networks (for example electricity is needed for the operation of pumps, valves, etc. which are them-selves essential for the proper functioning aqueducts, gas pipelines, etc.). This behavior of the inter-dependency index appears also in Figure 2b for Iwate region, in which the index of interdependency gives a negative value for the combination Power-Gas. This anomaly affects all equations considered, including the one proposed by Dueñas-Osorio & Kwasinski (2012) and it might be caused by the nature of the restoration curves under consideration. The problem is in the data collected after the main shock in which have occurred two strong after-shocks. These events have affected the functionality of lifelines, perturbing the restoration curves.

The problem can be solved by dividing the data into homogeneous parts of the restoration curves corresponding to the elapsed time between two consecutive strong shocks (Cimellaro & Solari 2013). For each period, the cross-correlation analysis of the restoration curves are performed after the logarithmic transformation and the second differences as described above. In Table 2 are shown the S matrices calculated using Equation (5) for two different time intervals: 47 days and 27 days respectively, which are the maximum duration of the series of recordings and the time interval between the main shock and the first strong aftershock which occurred on April 7th. In the same table, the values of interdependency which pass from negative values to positive values when moving from 47 to 27 days are highlighted in gray, for the row pertaining to the Power delivery. It should be noted that the interdependency index of a given lifeline with respect to itself is 1, therefore all the terms of the diagonal in the matrix in Table 2 are 1. It is observed how the interdependency indices of the row corresponding to the Power delivery have a positive value, if one considers the interval of 27 days to compute it. So the interdependency index has physical meaning when the time interval is shorted to 27 days. The same operation is repeated using Equation (1) proposed by Dueñas-Osorio & Kwasinski (2012). If only the data range between the main shock and the first strong aftershock is considered, the index of interdependence assumes a meaning that is related to the physical nature of the problem, regardless of the type of equation which is used for the calculation of the index $S_{i,j}$.

Table 2. Comparison of interdependency index among different time: in gray are highlighted the values that increase.

Region		Eq.(5) 47 days	Eq.(5) 27 days
	Power - Water	−0.35	**0.00**
Miyagi	Power - Gas	−0.19	**0.20**
	Water - Gas	0.31	0.31
	Power - Water	0.55	0.23
Iwate	Power - Gas	−0.56	**0.13**
	Water - Gas	−0.38	0.51
	Power - Water	0.47	0.00
Fukushima	Power - Gas	−0.35	**0.49**
	Water - Gas	−0.23	−0.27
Yamagata	Power - Water	0.31	0.35
Akita	Power - Water	0.93	0.20
	Power - Water	0.20	0.20
Ibaraki	Power - Gas	0.49	0.27
	Water - Gas	0.87	0.87
Tochigi	Power - Water	0.45	0.45
	Power - Water	−0.15	**0.42**
Aomori	Power - Gas	−0.13	**0.33**
	Water - Gas	0.72	0.80
Chiba	Power - Gas	0.23	0.23
Gunma	Power - Water	0.40	0.40
	Power - Water	0.46	0.46
Saitama	Power - Gas	1.00	1.00
	Water - Gas	−0.46	−0.46
Kanagawa	Power - Gas	0.55	0.54

6 CONCLUSIONS

In this article, a detailed analysis of the interdependency index is performed and a new equation for the

calculation of the interdependency index using CCF function among different restoration curves has been proposed. The proposed equation takes into account the level of statistical significance for each CCF function, considering only the values above it. It is also given more weight not only to the peak value, but to the number of times in which the CCF function exceeds the threshold of statistical significance. The proposed methodology has been developed using the restoration curve data of 2011 Tohoku Earthquake. Numerical results may have been influenced by the reduced number of restoration curves of only three lifelines used in the analysis. Further research may clarify this behavior testing the proposed methodology for the calculation of the regional interdependency index using more than three restoration curves for each region.

REFERENCES

Arcidiacono, V., Cimellaro, G. P., Reinhorn, A. M., and Bruneau, M., 2012. Community Resilience Evaluation including interdependencies. 15th World Conference on Earthquake Engineering (15WCEE), Lisbon, Portugal, September 24–28th, 2012.

Bigger, J. E., Willingham, M. G., Krimgold, F., and Mili, L., 2009. Consequences of critical infrastructure interdependencies: Lessons from the 2004 hurricane season in Florida, *International Journal of Critical Infrastructures* 5(3), 199–219.

Cimellaro, G. P., 2013. Computational framework for Resilience-Based Design (RBD) CH11. U. o. B. C. Seismic risk analysis and management of civil infrastructure systems, ed., Edited by S Tesfamariam, Canada and K Goda, University of Bristol, UK, ed., Woodhead Publishing Limited, 80 High Street, Sawston, Cambridge, CB22 3HJ, UK, 810.

Cimellaro, G. P., Reinhorn, A. M., and Bruneau, M., 2010a. Framework for analytical quantification of disaster resilience, *Engineering Structures* 32(11), 3639–3649.

Cimellaro, G. P., Reinhorn, A. M., and Bruneau, M., 2010b. Seismic resilience of a hospital system, *Structure and Infrastructure Engineering* 6(1-2), 127–144.

Cimellaro, G. P., D. Solari, et al. (2013) Community resilience index integrating network interdependencies. In: *Proceedings of the 2013 Structures Congress (SEI 2013)* ASCE, Pittsburgh, Pennsylvania, May 2–4, 2013.

Cimellaro, G. P., Solari, D., and Bruneau, M. (2013). "Interdependency and regional resilience index after 2011 Tohoku earthquake in Japan." *Earthquake Engineering and Structural Dynamics*, in review.

Cimellaro, G. P., and Solari, D., 2013. Considerations about the optimal period range to evaluate the weight coefficient of coupled resilience index, *Engineering Structures* in review.

Delamare, S., Diallo, A. A., and Chaudet, C., 2009. High-level modelling of critical infrastructures' interdependencies, *International Journal of Critical Infrastructures* 5(1-2), 100–119.

Duenas-Osorio, L., and Kwasinski, A., 2012. Quantification of Lifeline System Interdependencies after the 27 February 2010 M-w 8.8 Offshore Manic, Chile, Earthquake, *Earthquake Spectra* 28, S581–S603.

Kakderi, K., Argyroudis, S., and Pitilakis, K., 2011. *State-of-the-art literature review of methodologies to assess the vulnerability of a "system of systems"*, *D*2.9, Aristotle University of Thessaloniki.

Kjolle, G. H., Utne, I. B., and Gjerde, O., 2012. Risk analysis of critical infrastructures emphasizing electricity supply and interdependencies, *Reliability Engineering & System Safety* 105, 80–89.

Kongar, I., and Rossetto, T., 2012. A framework to assess the impact of seismic shocks on complex urban critical infrastructure networks. 15th World Conference on Earthquake Engineering (15WCEE), Lisbon, Portugal, September 24–28, 2012.

Nojima, N., 2012. Restoration Processes of Utility Lifelines in the Great East Japan Earthquake Disaster, 2011. 15th World Conference on Earthquake Engineering (15WCEE), Lisbon, Portugal, September 24–28, 2012.

Paton, D., and Johnston, D., 2006. *Disaster resilience an integrated approach*, Charles C Thomas publisher LTD, pp.

Poljanšek, K., Bono, F., and Gutiérrez, E., 2012. Seismic risk assessment of interdependent critical infrastructure systems: The case of European gas and electricity networks, *Earth. Eng.& Struct. Dyn.* 41(1), 61–79.

Rinaldi, S. A., Peerenboom, J. P., and Kelly, T. K., 2001. Identifying, understanding, and analyzing critical infrastructure interdependencies, *Ieee Control Systems Magazine* 21(6), 11–25.

Shumway, R. H., and Stoffer, D. S., 2006. *Time Series Analysis and Its Applications*, Springer, New York, pp.

Solari, D., and Cimellaro, G. P. (2013). "A comprehensive methodology for the evaluation of infrastructure interdependencies." 4th International Conference on Computational Methods in Structural Dynamics and Earthquake Engineering (COMPDYN2013), Kos Island Greece, June 12–14th, 2013.

Research and Applications in Structural Engineering, Mechanics and Computation – Zingoni (Ed.)
© 2013 Taylor & Francis Group, London, ISBN 978-1-138-00061-2

Back-analysis of the collapse of a metal truss structure

C. Crosti & F. Bontempi
School of Civil and Industrial Engineering, Department of Structural and Geotechnical Engineering, Sapienza University of Rome, Italy

ABSTRACT: This paper is organized in two parts. The first one describes a case history of few collapses of metal truss structures designed to be used as entertainment structures for which the structural safety gains therefore much more importance due to the people that can be involved in the collapse. In the second part, a specific case of the collapse of an entertainment structure made by aluminum is taken under study. A back analysis of the collapse of this metal truss structure is developed and produces a flowchart that points out the possible causes that led the structure to the collapse. By means of non linear analyses by Finite Element Model (FEM) the failure sequence of this particular structure is shown and forensic investigation concerning the whole phase of the construction phase is performed, starting from the design one, through the assembling and ending with the rigging phase.

1 INTRODUCTION

Particular attention recently has been given to the design and to the construction of entertainment structures due to the recent collapses that have had them as object.

Those kinds of structures are defined as temporary demountable structures and most of the time used as stages for music concerts. The stability of these structures becomes therefore important especially because of the need to assure the safety of people (Andi and Minato 2003).

The preparation of these kinds of structures for an event can be divided into separate phases:

- Management and Administration, where all the agreements necessary for the construction are obtained;
- Design, where it is contemplates the analysis of suspended loads and the design of the supporting structure;
- Build-up, that means the construction of the structures;
- Load in, that includes the rigging and installation of sound, light, and similar equipment (including artist specific stage equipment);
- The event;
- Load out, removal of sound, light, video, etc;
- Break down or deconstruction, dismantling and removal of temporary demountable structures.

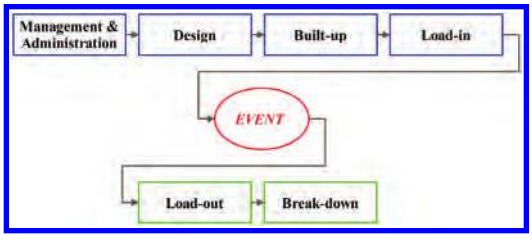


Figure 1. Phases for the construction of an entertainment structure.

Errors that could lead the structure to the collapse can be found in each of the phases above described.

2 CASE HISTORY

Unfortunately, there have been recent collapses of temporary stage structures in the United States and in Europe during entertainment events. These have resulted in fatalities and numerous injuries, below few cases are listed:

- 2007, June 15th, Parco San Giuliano di Venezia, Italy, Heineken Jammin' Festival;
- 2009, July 20th, Marseille, France, Madonna's concert;
- 2009, August 1nd, Camrose North America, Big valley Jamboree;
- 2011, August 14th, Indianapolis, USA, Country music concert;
- 2011, December 12th, Trieste, Italy, Jovanotti's concert;
- 2012, March 5th, Reggio Calabria, Italy, Pausini's concert;
- 2012, June 16th, Toronto, Canada, Radiohead's concert.

Most of these listed collapses define wind as a contributory cause of the collapse. These temporary



Figure 2. Collapses of entertainment structures.

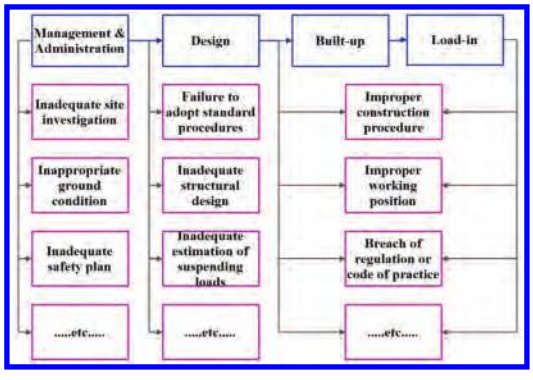


Figure 3. Most frequent errors in the phases before the event.

structures are exposed to vertical imposed loadings from attached lighting and sound equipment and also, when outdoor, to lateral loadings resulting from wind.

The risk is that when the structure is subjected to combined vertical equipment loads, to the horizontal wind loads and to the eccentric vertical loads, the resulting forces can cause catastrophic failures which may result in collapse if the structure is not competently designed, constructed, and managed in use.

Learning from the past it is possible to point out some frequent errors which could lead structures to collapse, (Sebastiani, 2012), (Sgambi, 2012).

Where error is defined as "something that has been done, which was: not intended by the author; not desired by a set of rules or an external observer; or that lead the task or system outside its acceptable limits" (Senders, 1991).

Focusing on the phases previous the event Figure 1 shows some of the most frequent errors that could be seen as principal factors for structural failure. Most of them can be classified as human errors due to the poor knowledge, to the carelessness and negligence (Love, 2008).

Inadequate site investigation, inappropriate ground condition, inadequate structural design, failure to adopt standard procedures or failure in realizing what prescribed in the design and in the regulations, are all factors that can contribute to a catastrophic event, (Suraji, 2001).

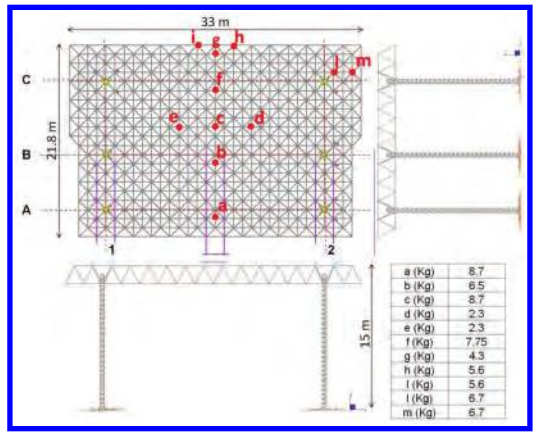


Figure 4. Structure under study.

3 CASE STUDY: NUMERICAL MODELING

The structure under study is an entertainment structure that collapsed skidding on the stage left before the event had started.

The structure was made by precast aluminum elements which composed a space roof, six vertical towers and a small truss necessary for suspending scenographic lighting, speakers and videos, Arangio (2011).

The structure was built with EN AW-6082 T6, with modulus of elasticity (E) equal to 7×10^{10} Pa, density (ρ) of 2700 Kg/m^3, elastic limit for the strength (σ_y) of 2.5×10^8 Pa and ultimate strength (σ_u) of 2.9×10^8 Pa, (Mazzolani, 2012), EN1993 1-1 (2005).

Using Strand7/Straus7, a Finite Element Model is defined as shown in Figure 4, with 2148 nodes and 5275 beams.

In order to take account of the weight of the connection between the elements, made in cast iron, an additional uniform pressure of 115 Pa is considered on the roof. The suspending loads present at the moment of the collapse are applied as shown in Figure 4. In this way, the weight of the whole structure is about 28.5 tons.

4 INVESTIGATION ON TECHINAL CAUSES OF THE COLLAPSE

Three are the main aspects investigated to individuate the cause of the collapse of the structure: failure to adopt standard procedures, inadequate structural design, improper construction procedure, see Figure 2.

4.1 *Failure to adopt standard procedures*

A failure to adopt standard procedures could have been for example to design the structure not including in the global analyses the nonlinearities, in particular the

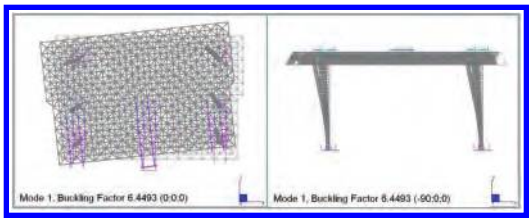


Figure 5. Deformed shape of the first mode of buckling.

geometric ones. The EN 1993-1-1: 2005 at point 5.2.1 says that:

"*The effects of the deformed geometry (second-order effects) should be considered if they increase the action effects significantly or modify significantly the structural behavior*"

This consideration can be neglected only when:

$$\alpha_{cr} = \frac{F_{cr}}{F_{Ed}} \geq 10; \text{for elastic analysis} \quad (1)$$

Where α_{cr} is the factor by which the design loading have to be increased to cause elastic instability in a global model, F_{ED} is the design loading on the structure and F_{cr} is the elastic critical buckling load for global instability mode based on initial elastic stiffnesses.

Running linear buckling analysis on this specific structure, the buckling factor α_{cr} is 6.44, Figure 5. Since it is smaller than 10 the second order effects have to be taken into account in the global analyses. In the next paragraph it will shown how much difference gives to neglect them.

4.2 *Inadequate structural design*

Another important aspect investigated is that the structure is designed to be indoor; therefore the structural elements were designed to carry vertical loads but may not have been designed for lateral loads. That could be an important consideration in the design phase, in fact, following what prescribed in the UNI ENV 1999-1-1:2007, in order to run global analyses, it is necessary to take account of horizontal forces due to the imperfections of the elements composing the structure.

At point C4.1 of the UNI ENV 1999-1-1:2007 it is explained how to take into account of the imperfection in the global analyses. Therefore, rather than applying to each element a lateral imperfection, three horizontal forces, in correspondence of lower elements composing the space roof have been applied to the structure.

4.3 *Improper construction procedure*

The latest consideration will be conducted on the possibility of improper construction procedures.

The attention is focused on the realization of restraints between the paving and the columns in order to assess how and how much an error in defining or in realizing them could compromise the whole structural behavior, (Crosti, 2012).

Table 1. Horizontal forces applied to simulate the imperfections.

ϕ	0.005	
kc	1.225	> 1
n_c	1.000	
ks	1.225	> 1
n_s	1.000	
ϕ_0	0.005	
$N_{dead\ load}$	2.25E+05	N
ϕN	1.13E+03	N

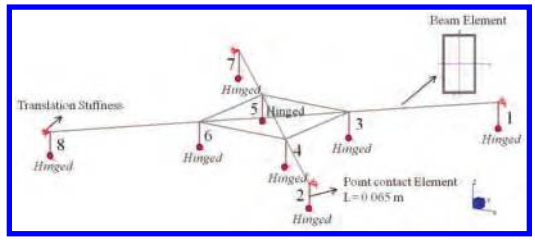


Figure 6. Unilateral restraint on the bottom of each column.

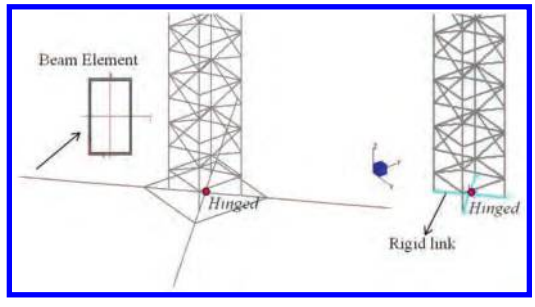


Figure 7. Cases with hinged restraints, on the left with outriggers and on the right with no outriggers.

Three different models are considered in order of taking account of some aspects:

- the possibility that, due to horizontal displacements caused by the structural imperfections, the outriggers could lose the contact with the paving. To simulate this case, eight point-contact elements are set to simulate the contact between those elements and the paving, Figure 6. The point contact element in the Finite Element Code Strand7/Straus7 is used to model a gap between two surfaces or edges, stiffness is provided in compression but zero stiffness is given in tension;
- it could happen that during the phase of the construction for example, what it is designed to be a rigid connection, could be realized for a while as able to rotate. To simulate this aspect hinged restraints are considered on the bottom of each column, Figure 7; and

Table 2. Definition of the studied models.

Model	GNL	MNL	Imperfection	Restraint	Outriggers	ULf
0	X			Fixed	X	6.942
1	X	X		Fixed	X	4.000
2	X	X	X	Fixed	X	3.946
3	X	X	X	Unilateral	X	4.019
4	X	X	X	Hinged	X	1.122
5	X	X	X	Hinged		0.853

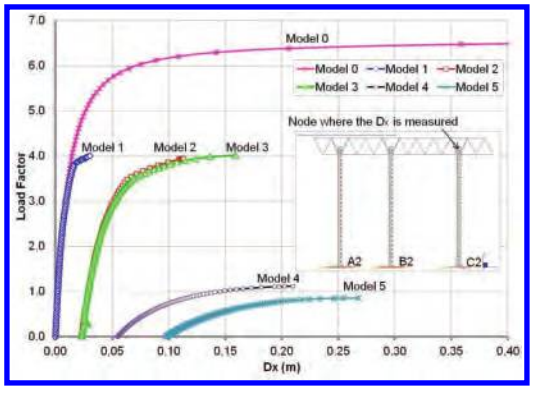


Figure 8. Load Factor-Horizontal Displacement of the node.

– the case where hinged restraints are on the bottom of each column but no outriggers are set, Figure 7.

5 NUMERICAL RESULTS

Five different models were run in order to assess the influence that the above mentioned errors give to the global response of the structure under study.

Table 2 summarizes the different models considered, where MLN means Nonlinear Material, GNL stays for Nonlinear Geometry, Imperfection means that horizontal forces simulating the structural imperfection defined by Eurocodes are applied, Unilateral means that the bottom column is modeled with unilateral restraint, see Figure 6, Hinged considers as restraint the ones in Figure 7 and U.L.F. stays for Ultimate Load Factor.

Looking at Figure 8 it is possible to recognize that Model 1 has the classical bifurcation trend, while Model 2, thanks to the introduced imperfections, shows an asymptotic one. Reaching the peak load at both ends of the columns, the elements are in an intermediate condition, being neither elastic nor having a fully developed plastic hinge mechanism, therefore laborious step-by-step elastic-plastic analyses were necessary to obtain the failure load (ULF) of 3.95.

Moreover, interesting is to point out that there is no difference in terms of Ultimate Load Factor as well as of horizontal displacement trend between Model 2 and Model 3. Modeling the contact between the outriggers and the paving does not seem to be a relevant issue in terms of global response of the structure. In fact,

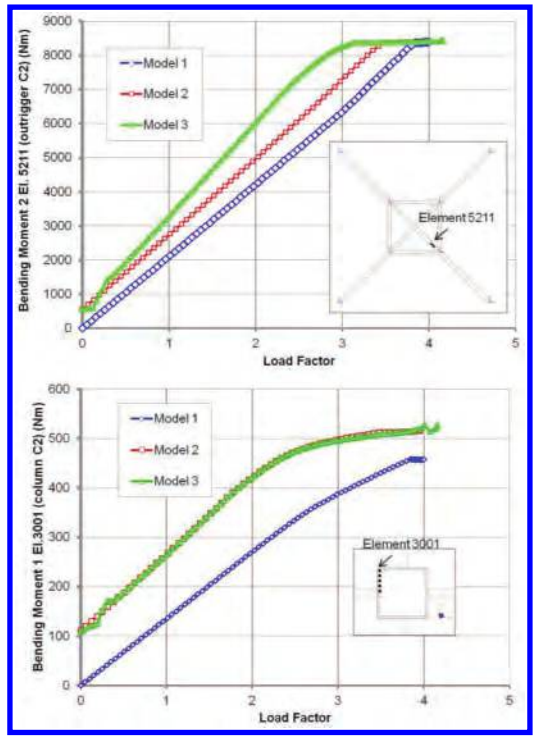


Figure 9. Comparison of the Bending Moment trend for element 5211 of the outrigger and element 3001 of the column.

looking at Figure 10, it is possible to assess that as soon as the horizontal loads are applied to simulate the structural imperfections, the external points of the outriggers lose the contact with the paving not giving any contribution to the stability of the structure.

Model 1, 2 and 3 have more or less the same Ultimate Load Factor at that peak load they reach the same cause of collapse: elastic-plastic failure of the outriggers and of the column elements where the roof is connected, this allows the structure to rotate much more and to buckle.

Figure 9 shows the reaching of the elastic-plastic failure for the two elements mainly stressed with the increasing of the Load Factor.

Figure 10 shows instead a comparison in terms of deformed shape and of maximum vertical displacements reached in the outriggers behind column C2 at the moment of the collapse.

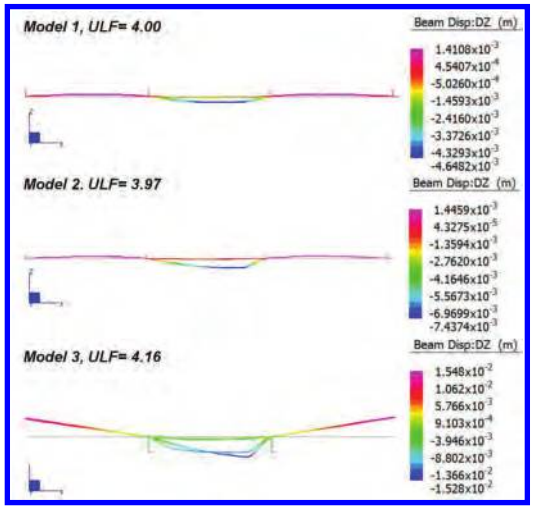


Figure 10. Deformed shape (20%) of the outrigger elements of column C2.

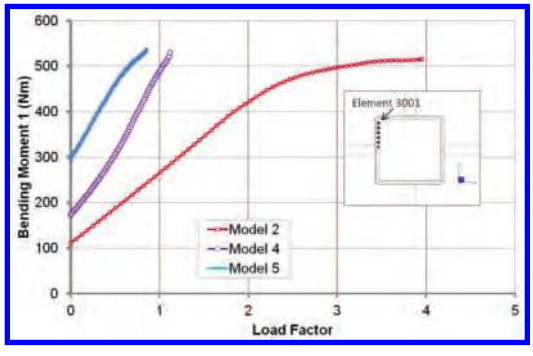


Figure 11. Bending moment 1 trend of element 3001 (column C2).

A different case is the one of Model 4 that, having different restraints on the bottom of the columns, reaches an Ultimate Load Factor of 1.122 which means the structural collapse is due just to the nominal loads applied.

In this particular configuration once the columns reach the yielding stress the structure loses its stability and the analyses cannot find the solution.

The difference shown in Figure 8 between Model 4 and Model 5 is given by the presence of the outriggers. Their presence does not give much contribution in terms of structural stability: in fact the Ultimate Load Factor for Model 5 is 23% smaller than the one of Model 4; however looking at the initial displacement their presence decreases them of about 50%.

From Figure 11 it is possible to evaluate that for Model 4 and 5, due to the different restraints, as soon as the element reaches the yielding load, the analyses stop, while Model 3 shows a better redistribution of the stresses when they reach the failure load.

This large difference in terms of ultimate load shown going from Model 0 to Model 5 shows the

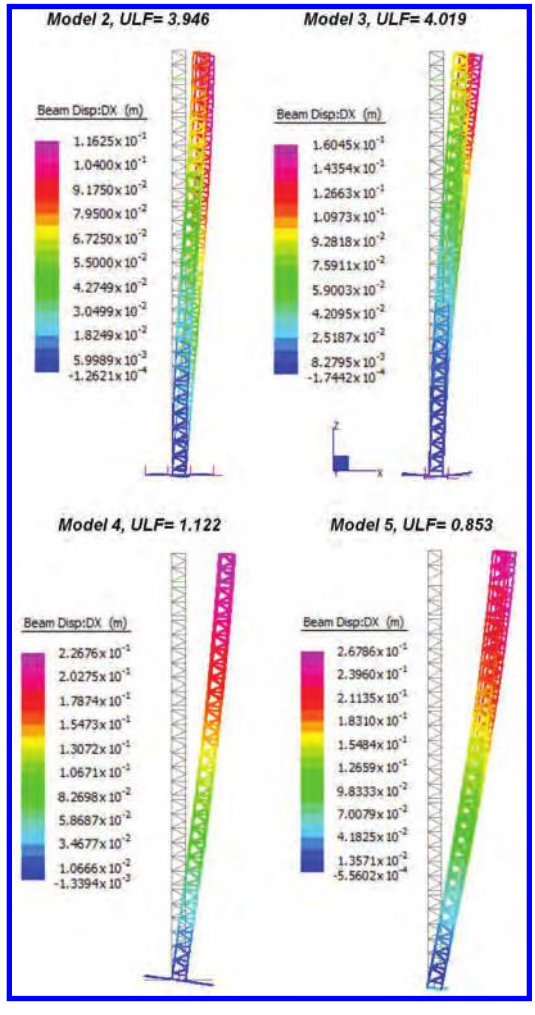


Figure 12. Deformed shape of column C2 at the corresponding Ultimate Load Factor.

sensitivity of the structure to the modeling of the restraints which involve the columns.

6 CONCLUSION

Following the whole construction process of entertainment structures, some of the most frequent errors that can be present in it, have been taken under consideration and applied to a specific metal structure.

By means of Finite Element Analyses it has been possible to point out that:

- Linear analysis can be used just for evaluation of structure critical buckling load, but then, especially for these kinds of structures, proper nonlinear analyses should have been run.
- Not accounting of the initial imperfection, leads the results to be different from the real structural behavior that they have especially when the restraints are subjected to improper construction procedures.

– The importance of taking into account, even in the design phase, of what can happen during the built up phase. Particular importance has to be done to the restraints on the bottom of the columns, which represent the key elements for this structure. During the phase of construction for example, what it is designed to be a rigid connection (Model 1 ad 2), could be realized for a while as able to rotate (Model 4 and 5). That shows the need of considering the design in all the cases which could make a modification in the static scheme of the structure. Introducing bracing member for example, the designers could defend the structure from such possible changes in the structure and avoid failure, (Arangio, 2012). This solution could be especially effective in cases where the structures are not designed for horizontal forces that are the indoor ones.

A further development could be to take into account of the stiffness of the paving which can be an issue that compromises the structural stability.

ACKNOWLEDGEMENTS

The authors would like to acknowledge our research team, www.francobontempi.org, the research spin-off StroNGER S.r.l. for the support and Eng. Piergiorgio Perin for providing the use of the Finite Element Code Strand7/Straus7.

REFERENCES

Andi & Minato, T., (2003). "Representing causal mechanism of defective designs: a system approach considering human errors." Construction Management and Economics, 23, 297–305.

Arangio, S., (2012). "Reliability based approach for structural design and assessment: performance criteria and indicators in current European codes and guidelines." International Journal of Lifecycle Performance Engineering, 1(1), 64–91.

Arangio S., Bontempi F., and Ciampoli M. (2011). "Structural integrity monitoring for dependability." Struct. Infrastruct. E., 7(1), 75–86.

Arangio S., Crosti C., Zampetti M., (2011). "Design of aluminum structures for the entertainment industry and analysis of the behavior in fire conditions." Proc. of the 7th Greek National Conference on Metal Structures, Greece, Volos, September 29–October 1 2011.

Bontempi, F., Arangio, S., Gkoumas, K., (2008). "Systemic approach for the maintenance of complex structural systems." Struct. Infrastruct. E., 4(2), 77–94.

Crosti, C., Duthinh, D. (2012). "Simplified gusset plate model for failure prediction of truss bridges." Proc. of the 6th IABMAS Conf., Italy, Stresa, 8–12 July.

Crosti, C., Duthinh, D., Simiu, E., (2012). "Risk Consistency and Synergy in Multihazard Design." J Struct Eng-ASCE, 137(8), 844–849.

Giuliani, L., (2012). "Structural safety in case of extreme actions." Int. J. Lifecycle Performance Engineering, 1(1), 22–40.

EN1993-1-1 (2005) Design of steel structures – Part 1-1: General rules and rules for buildings. Comité Européen de Normalisation (CEN)

Kim, T., Kim, J., Park, J., (2009). "Investigation of Progressive Collapse-Resisting Capability of Steel Moment Frames Using Push-Down Analysis." J. Perform. Constr. Facil., 23, 327–335.

Horne M.R., Merchant W., "The stability of frames". Pergamon Press. (1965).

Love, P. (2008). "Forensic Project Management: An Exploratory Examination of the Causal Behavior of Design-Induced Rework." IEEE T. Eng. Manage., 55(2), 234–247.

Mazzolani F.M., (2012). "La progettazione strutturale delle leghe in alluminio". Officine grafiche.

Novoselac, S. (2012). "Linear and nonlinear buckling and post buckling analysis of a bar with the influence of imperfections." Technical Gazette, 19(3), 695–701.

Petrini F., Bontempi F. (2011), "Estimation of fatigue life for long span suspension bridge hangers under wind action and train transit." Struct Infrastruct E, 7(7–8), 491–507.

Sebastiani, P.E., Petrini, F., Franchin, P., Bontempi, F., (2012). "Back Analysis for Earthquake Damaged Bridges. Part I: a general procedure" Proc. of the 6th IABMAS Conf., Italy, Stresa, 8–12 July.

Senders, J.W. (1991). "Human Error: Cause, Prediction, and Reduction." Lawrence Erlbaum Associates, Inc., Hillsdale, New Jersey.

Sgambi, L., Gkoumas, K., and Bontempi, F. (2012). "Genetic Algorithms for the Dependability Assurance in the Design of a Long-Span Suspension Bridge". Comput-Aided Civ. Inf., 27(9), 655–675.

Suraji, A. (2001). "Development of causal model of construction accident causation." J.Constr. Eng. Manage, 127, 337–344.

Strand7/Straus7, Sydney, NSW, Australia (2010) http://www.hsh.info/

UNI ENV 1999-1-1:2007. "Eurocode 9: Design of aluminum structures – Part 1-1: General structural rules."

Research and Applications in Structural Engineering, Mechanics and Computation – Zingoni (Ed.)
© 2013 Taylor & Francis Group, London, ISBN 978-1-138-00061-2

FE models for evaluating damages in churches hit by L'Aquila earthquake

G. Brando, E. Criber & G. De Matteis
Department of Engineering and Geology, University "G. d'Annunzio" of Chieti-Pescara, Italy

ABSTRACT: The behavior of churches during an earthquake is very complex, mainly due to the peculiarities of the buildings, which usually were conceived more for pursuing stylistic aims rather than structural goals. On the other hand, churches are often the result of continuous stratifications generated during their life, which led to constructions characterized by heterogeneous parts working with different modalities. As a consequence, the observation of damages produced by earthquakes could represent a rare occasion for improving the knowledge about the structural behavior of these buildings. In this framing, the current paper deals with the interpretation of the vulnerabilities observed, after the 2009 seismic event, on a church belonging to the district of L'Aquila, the St. Gemma Church in Goriano Sicoli. In a first step a careful analysis of the damage revealed after the 2009 earthquake on similar churches belonging to the same regional area is provided. Then, a suitable FEM numerical model, able to reproduce the revealed damages and properly calibrated by means of Ambient Vibration Tests, is set up for the church under consideration, with the aim of providing a sophisticated tool for weighing up the most important phenomena of failures and to provide some information about the most appropriate retrofitting techniques to be adopted.

1 INTRODUCTION

The small town of Goriano Sicoli represents a typical example of historical urban center belonging to L'Aquila district which was severely stricken by the 2009 seismic event. One of the most interesting building in the village is surely the church of St. Gemma, which due to both architectonic and structural features, can be considered as a representative sample of a wide population of churches erected in the same regional area in the last ten centuries. As the last earthquake proved, such churches are very vulnerable and they are characterized by a complex structural response that need to be deeply investigated. In addition, the significant stratifications carried out after the seismic event of the pasts have to be duly accounted for, with the aim of defining specific retrofitting strategies to be implemented for their conservation.

In view of this demand, in the immediate aftermath of the 2009 seismic event, the authors carried out a wide post-earthquake survey (Criber et al., 2011), in order to detect recurrent damages and failures mechanisms. The attention has been focused on the south-east area of the L'Aquila district, also known as the territory of the Sulmona-Valva Diocese, where three nave churches have been investigated by means of kinematic analyses that allowed justifying the main observed damages (Brando et al., 2011). Furthermore, Ambient Vibration Tests have been conducted on two of these churches, i.e. St. Gemma and St. Maria Nova Church, both located in the centre of Goriano Sicoli (Tashkov et al., 2010). Then, on the basis of these tests, a sophisticated FEM model has been defined for the St. Gemma case study (De Matteis et al., 2011).

In this paper, the main outcomes of a response spectrum linear dynamic analysis are presented, with the aim of validating the above modeling process, by a comparison of the model parts subjected to the most severe stress concentrations and the church zones in which damage has been identified.

2 DAMAGE IDENTIFICATION

2.1 *Territorial analysis*

The Sulmona-Valva Diocese is one of the three administrative area of the Roman Curia in the Abruzzi region. It is composed by 49 municipalities, where almost 250 religious buildings are nowadays present. Among these, rural churches, churches belonging to religious institutes (convents) and cathedral churches have been identified. Rural churches are usually composed by one nave only (80% of the investigated cases, see figure 1), whereas the later ones can be classified as "central plan" (2%), "two-", "three-" and "five-"naves churches (3%, 14% and 1% respectively).

With particular regard to the three-naves typology, a set of 20 churches has been considered. These are characterized by almost homogeneous geometric features, as it is shown in figure 2, where both the plant Length/Width (most frequent value equal to almost 2) and Façade Length/Height ratios (most frequent value equal to almost 1.3) are depicted.

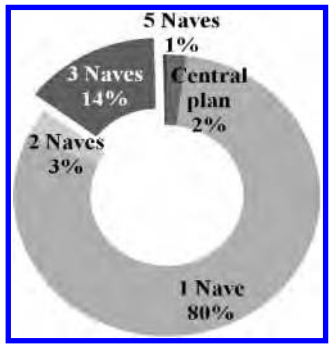


Figure 1. Percentage of structural typologies of churches in Sulmona-Valva Diocese.

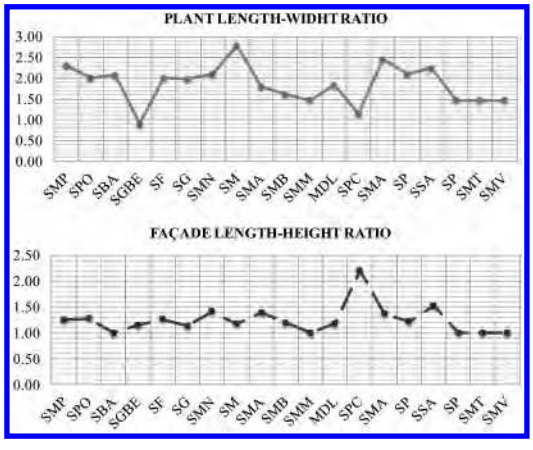


Figure 2. Geometrical ratios characterizing the observed churches: a) plant length/span and b) façade length/height.

The most recurrent damages revealed on the above churches have been therefore observed and classified according to the Guidelines for the Cultural Heritage (Circular n.26, 2010).

2.2 *Revealed damage mechanisms*

In order to identify typical damage mechanisms, macro-elements behaviors have been critically analyzed and compared, this allowing to note that, in most of cases, the churches having the same distance from the earthquake epicenter and characterized by both the same geometrical ratios and architectonic features (type of vaults, pillars cross section shape, etc.), apart from the cases in which different retrofitting techniques have been applied, presented the same damage level. Cross diagonal cracks have been recurrently found on lateral walls, bell towers and domes (fig. 3), owing to the composition of the masonry fabric, which, in the great part of cases, resulted poor and chaotically organized.

As far as the vault systems is concerned, the elliptical vaults resulted to be the most vulnerable. For these elements, fractures along both the diagonal directions and the circular spring-lines have been highlighted

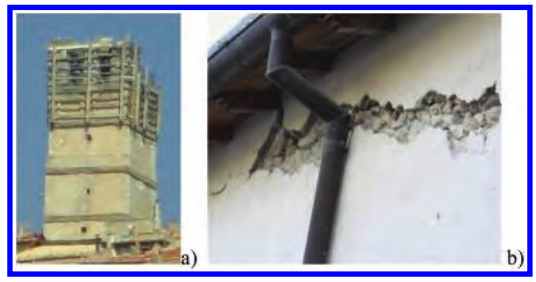


Figure 3. Observed damages on a) bell tower of St. Marco Evangelista in Castel del Monte and b) lateral wall.

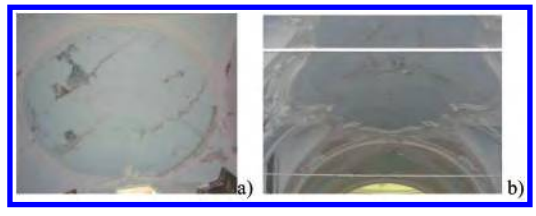


Figure 4. Observed damages on a) elliptical vaults and b) barrel vaults of St. Maria Nova church in Goriano Sicoli.

(Fig. 4a). Different type of damage have been found at the top of the barrel vaults, where longitudinal cracks along the key-vault recurred in a more or less extended way according to the presence of ties in the orthogonal direction (Fig. 4b). Lower damage levels have been detected on the groin vaults, where some fractures developed along the diagonal lines.

With regard to the pillars, vertical cracks due to crushing phenomena have been sometimes surveyed, as in the case of St. Gemma church in Goriano Sicoli. These have been probably induced by the increasing compression stresses, due to the earthquake vertical component, which, even far from the epicentre, resulted significant during the 2009 seismic event. The above failures are particularly evident on those columns built with rubble masonry techniques, where cracks along the mortar, often followed by significant vertical openings on the elements, have been highlighted (Fig. 5a). On the contrary, in the case of monolithic pillars, built with superimposed stones, none damage has been found (Fig. 5b).

Heavy sliding damages have been detected on the churches where reinforced concrete roof or beams have been built in past years (Fig. 6a). This obsolete practice provoked damages on arches (fig. 6b) also, because of the outward thrust of the heavy roof, amplified by the horizontal seismic component. The presence of iron ties certainly constrained this effect; nevertheless, in some cases, punching phenomena of the ties-key (Fig. 6c) or breaking of ties have been detected (fig. 6d).

Out-of-plane mechanisms were very dangerous for the global stability of the buildings, when these resulted not correctly endowed with a proper number of well dimensioned ties. For the churches under investigation, three main out-of-plane phenomena

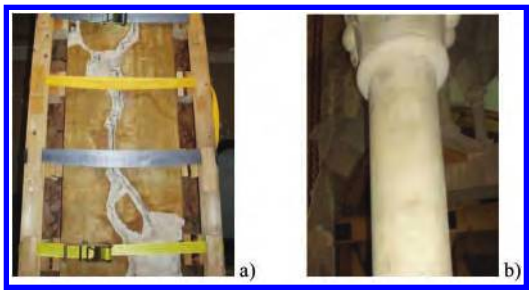


Figure 5. Observed damages on the a) rubble masonry pillars of St. Gemma church in Goriano Sicoli and b) not damaged monolithic columns in St. Pietro ad Oratorium, Capestrano.

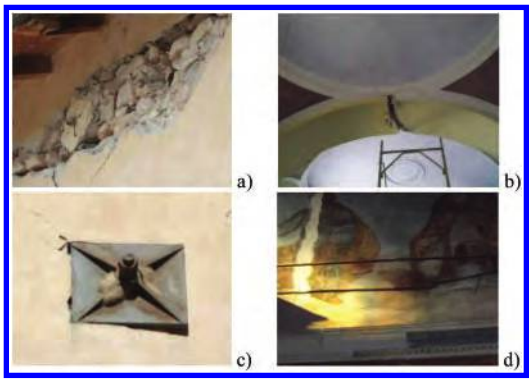


Figure 6. a) Sliding cracks due to the reinforced concrete roof; b) damages on arches, c) punching phenomena and d) tie breacking.

have been recognized: the rigid facade overturning, the facade top-corner overturning and the apse overturning.

For the first type, only one church (St. Gemma church in Goriano Sicoli) showed a mechanism completely developed, where a detachment between the wall and the orthogonal ones of about the thickness of the facade has been revealed (Fig. 7). In other cases the longitudinal ties constrained the rigid overturning, even though the corner connection was clearly inefficient. On the analyzed buildings, in fact, a material discontinuity between the lateral walls and the facade is often recognizable, probably due to the fact that this element was generally built at the end of the church erection process, with different material and different techniques.

Another typical rigid mechanism is the apse overturning, generally due to bad connections or wide openings. For example, in the case of St. Martino church in Gagliano Aterno, both the diagonal crack along the apse and the breaking of one tie demonstrated the activated overturning (Fig. 8a). As far as the façade top corner overturning is of concern, this type of mechanism has been clearly recognized on the majority of the flat facades through diagonal cracks (Fig. 8b), where efficient devices to contain the mechanism usually are not present.



Figure 7. Façade overturning in St. Gemma church.

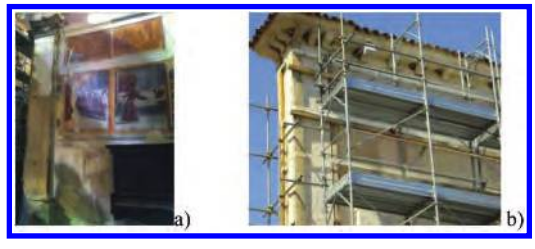


Figure 8. a) Apse overturning on St. Martino church in Gagliano Aterno and b) top-corner overturning on St. Maria della Pace church in Capestrano.

3 THE CASE STUDY OF ST. GEMMA CHURCH IN GORIANO SICOLI

3.1 *General*

Among the observed cases, the St. Gemma church in Goriano Sicoli represents the one with more intense damage. This is due to the many collapse mechanisms developed, probably due to site effects ascribable to the subsoil structure.

Considering that this church is representative also of the others in terms of geometrical features and structural elements type, it has been selected as case study for a deeper comprehension of its behavior, to be pursued by means of a sophisticated FEM numerical model.

3.2 *Architectonic features*

The current building configuration is a clear example of architectonic stratification, often observed in the Abruzzi region for others churches. The global space is a typical Renaissance space, with the intersection between nave and transept (Latin cross).

The church plant is constituted by tree naves, a transept and a dome. The central nave is covered by a barrel vault with lunettes, supported by cross section shaped masonry columns connected by arches. The aisles present characteristic elliptical vaults on arches, constrained by ties. The transept has plane ends and is surmounted by barrel vaults. It crosses the central nave in its central span, which is towered above by a 5.50 m diameter dome. The latter is supported by a circular drum with lateral squinches. On the two sides of the apse, two small compartments covered by pavilion

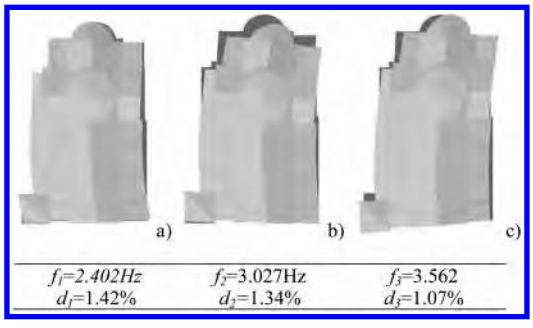


Figure 9. Main mode shapes of the St. Gemma church.

vaults are present. In these, two sacristies are included. The façade has a central part crowned by a tympanum. On the left of the façade a three storey tower bell is present. Behind this, there is a stretched corridor with a reinforced concrete roof supported by reinforced concrete ring beams. The same roof typology has been revealed also on the other lateral aisle.

3.3 *Ambient vibration test*

For the dynamic characterization of the Santa Gemma church, non destructive ambient vibration tests have been conducted. Three seismometers Ranger type were used and the measured signal was amplified by four channel Signal Conditioner. The amplified and filtered signals from the seismometers were then collected by a high-speed data acquisition system which transforms the analogical signals to digital. A special software for on-line data processing has been used to plot the time history and the Fourier amplitude spectra of the response at any measuring point. After recording, the ARTEMIS software was used to define the Spectra density curves and mode shapes of the structures. In Figure 9 the measured first three mode shapes are depicted.

In the same figure, the main natural frequencies f with the associated damping values d are also shown. The first mode ($f_1 = 2.402$ Hz, $d_1 = 1.42\%$) is mainly translational in the transversal direction, the second in the longitudinal one ($f_2 = 3.027$ Hz, $d_2 = 1.34\%$), the third is a torsional mode characterized by a natural frequency of $f_3 = 3.562$ Hz and a modal damping of $d_3 = 1.07\%$ (Tashkov et al. 2010).

3.4 *FEM model set up and analysis results*

The in-situ test outcomes allowed the calibration of a suitable linear FE numerical model, aimed at providing a more refined interpretation of the occurred damages (De Matteis et al. 2011). In a first phase, this has been assembled by referring to the current conditions of the building, namely by reproducing both the geometrical features and the revealed crack patterns of the damaged structure (Fig. 10). The ABAQUS 6.7 software has been used to this purpose. The geometrical model has been suitably meshed by finite tetrahedral solid C3D4 elements of sizes ranging between 0.3m and 0.4m, validated by sensitivity analyses.

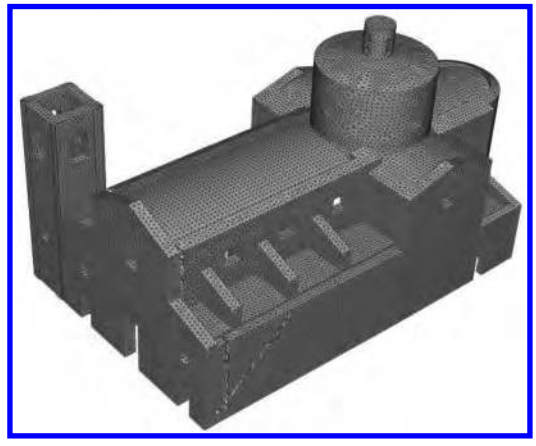


Figure 10. The Fem model of the cracked church.

Table 1. Materials mechanical properties.

Material	E	Id	Ee
Poor mortar Masonry	870 MPa	−40%	522 MPa
Good mortar Masonry	1305 MPa	−30%	914 MPa
Brick Masonry	2400 MPa	−60%	960 MPa
RC beam	20000 Mpa	−0%	20000 MPa

The reinforced concrete roof has been considered as a load weighting the RC beams, whereas its diaphragm action has been simulated by coupling-kinematic constraints. To simulate the iron rod ties, a wire type connector has been defined and a preload force of 50% of its yielding strength has been imposed. The most significant local cracks have been reproduced by deleting the finite elements of the corresponding parts. The material elastic modulus has been selected depending on the quality of the masonry fabric, as listed in Table 1. This values have been taken by the Italian Code "Circolare n.26", on the basis of visual inspections, and modified in a proper way. In detail, they were firstly amplified in order to account for the possible presence of good mortar (increase of 50%, as indicated by the code), and then reduced by a proper "damage reduction factor" I_d in order to account for the diffused cracks revealed during inspections

In order to validate the model, a modal analysis has been run. In Table 2 the data of the first six modes are given, compared with the AVT results. The reliability of the model is proved by the fact that numerical results well fit the experimental ones.

3.5 *Response spectrum linear dynamic analysis*

On the basis of the above model, a response spectrum linear dynamic analysis has been implemented, with the aim of giving a more careful interpretation of the seismic response of the church occurred during the L'Aquila earthquake. To this aim, the continuity of the model, which was broken in some parts during the calibration process, has been re-established. Moreover,

Table 2. Eigenvalue extraction analysis.

Mode	Frequency (AVT)	Frequency (FEM)	Δ%
1	–	2.006 Hz	–
2	–	2.019 Hz	–
3	2.402 Hz	2.391 Hz	−0.45 %
4	3.027 Hz	3.105 Hz	+2.58%
5	3.652 Hz	3.827 Hz	+4.79%
6	–	4.277 Hz	–

Table 3. Materials mechanical properties.

Material	Compression f_{Cmax}	Tension f_{Cmax}
Poor mortar Masonry	0.87 MPa	0.09
Good mortar Masonry	1.30 MPa	0.13
Brick Masonry	2.40 MPa	0.24
RC beam	–	–

the elastic modulus values have been incremented, by setting to 1.0 the above reduction damage reduction factors I_d. On the basis of these values, both the maximum and the minimum stresses of the masonry materials, which will be useful for the interpretation of the analysis results, have been found. In absence of in situ direct tests, the maximum compressive stress has been conventionally assumed equal to f_{Cmax} =E/1000, whereas the maximum stress in tension is given by $f_{Tmax} = f_{Cmax}/10$ = E/10000 (see Table 3).

In a first stage a static analysis under permanent loads only has been carried out, so to establish the state of the church immediately before the main- shock. The revealed tension-compression stress distribution highlighted a satisfying global condition for the structure, with tensile stress always lower than the above limits (figure 11). Then, a response spectrum analysis has been carried out. Due to the absence of time-history registrations of the 2009 earthquake in Goriano Sicoli, both the horizontal and the vertical spectra used for the analysis have been referred to the data retrieved by the closest station (Ortucchio, ORC. Fig. 12). The horizontal spectrum has been therefore scaled to the PGA equal to 0.150 g, which has been previously evaluated by means of attenuation laws.

Moreover, the vertical PGA has been scaled to the value of 0.061g, which has been assessed considering that the crushing of the columns could be provoked only by this level of vertical acceleration.

The seismic input has been applied in the three directions, 100% in X, 30% in Y and 100% in Z. The modal results have been combined by applying the SRSS (Square-Root-of-Sum-of-Squares) summation method. The obtained outcomes have been therefore superimposed to the effects of gravity loads.

In figure 13 some results are described in terms of maximum principal stresses. It is possible to observe that the peak values are concentrated in those zones on which the most important damages have been revealed. For example, with reference to the aisle triumphal

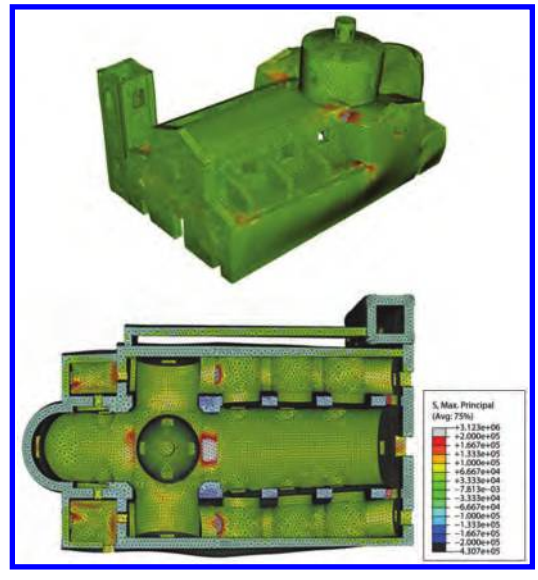


Figure 11. State of the church for gravity loads only.

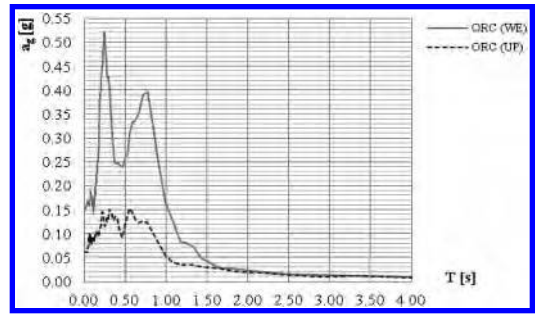


Figure 12. The scaled response spectra of the ORC (Ortucchio) Station used for the analysis.

arcs, maximum tensile stresses of 0.62 MPa have been detected, where deep cracks at the keystone have been surveyed. Also, in the vaults tensile principal stresses equal to five times the limit stress have been revealed, as they appeared the most damaged parts of the church. Finally, the model shows that on both the bell tower and the façade, the maximum tensile stresses evidenced by the numerical model (around 0.33 MPa vs. a limit value of 0.13 MPa) are consistent with the diffused state of crack provoked by the 2009 seismic event.

What has been stated above means that, although both the proposed analysis and modeling process are not able to capture the non linear behavior of the building, they allow to predict where the damages occur, giving important indications to well detect the possible interventions to be applied for retrofitting purposes.

4 CONCLUSIONS

This paper has provided a careful investigation on the damages provoked by the 2009 L'Aquila earthquake



Figure 14. Numerical stresses vs. revealed damages.

on the St. Gemma church in Goriano Sicoli, which has been selected as a representative sample of a wide population of churches belonging to the Sulmona-Valva diocese. After a careful survey conducted at regional level in order to highlight the main vulnerabilities activated during the seismic event on other similar buildings, the main outcomes obtained by Ambient vibration tests on the church under consideration have been described. These has allowed to put in evidence the presence of local modes of single macro-elements, as well as to calibrate a suitable FEM model that, subjected to a response spectrum linear analysis, provided a more careful interpretation of the occurred damages. These have been completely reproduced, as proved by the comparison between the model parts characterized by higher stresses and the cracked church zones. The validation of the proposed model allows to state that it is reliable for carrying out further analyses devoted to the identification of the most appropriate retrofitting techniques.

REFERENCES

Brando, G., Criber, E., De Matteis, G., (2011). "Interpretazione del Danno Indotto dal Terremoto Aquilano: il Caso Studio della Chiesa di Santa Gemma a Goriano Sicoli". Proc. del "Workshop on Design for Rehabilitation of Masonry Structures- Modellazione e progetto di interventi sul costruito in muratura- Wondermasonry 2011". Firenze (Na) 10–11 Novembre.

Criber, E., Brando, G., De Matteis, G. Structural individuation of damages occurred on St. Gemma church in Goriano Sicoli during the 2009 L'Aquila earthquake (2011). Applied Mechanics and Materials, 82, pp. 816–821.

De Matteis, G., Criber, E., Brando, G. Development of a finite element model of a church damaged during the 2009 L'Aquila earthquake (2011) Proceedings of the 13th International Conference on Civil, Structural and Environmental Engineering Computing.

Ministry of Heritage and Cultural Activities, Circular n.26, Italian Code for protection of cultural heritage. Linee Guida per la valutazione e la riduzione del rischio Sismico del patrimonio culturale con riferimento alle norme tecniche per le costruzioni. Prot 10953 of 02/12/2010.

Tashkov, L., Krstevska, L., Naumovski, N., De Matteis, G., Brando, G. Ambient vibration tests on three religious buildings in Goriano Sicoli damaged during the 2009 L'Aquila earthquake (2010) COST ACTION C26: Urban Habitat Constructions under Catastrophic Events - Proceedings of the Final Conference, pp. 433–438.

32. Repair, strengthening, retrofitting, sustainable construction

Research and Applications in Structural Engineering, Mechanics and Computation – Zingoni (Ed.)
© 2013 Taylor & Francis Group, London, ISBN 978-1-138-00061-2

The strengthening and widening of the Okavango River Bridge in Northern Namibia

W. Martin
SMEC South Africa, Consulting Engineers

ABSTRACT: The Okavango River Bridge in northern Namibia near Divundu was originally designed and constructed in the 1970's to carry a 60 tonne army tank on a deck width of 5.5 m. The route across the bridge has become a major access between the harbour at Walvisbay and Zambia. This required the bridge to be widened to two lanes plus sidewalks and strengthened to carry abnormal loads. The prestressed concrete box girder deck was widened by extending the cantilevers along with a deck overlay. The strengthening was done using external prestressing inside the box along with vertical prestressing bars to increase shear capacity.

1 INTRODUCTION

The Okavango River Bridge is located in Northern Namibia at the start of the Caprivi Strip near the village of Divundu. The Okavango River drains southern Angola, passing through Rundu, then turning south at the start of the Caprivi Strip and finally flowing into the Okavango Delta.

The bridge, constructed in the 1970's, was originally designed to carry a 60 tonne army tank on top of the 5.5 m wide deck and to allow army troops to walk through inside the deck. As a result, all structural elements are robust and heavily reinforced.

The bridge was constructed via the Incremental Launching Method (ILM) with only concentric prestressing in the top and bottom slabs. There was no secondary stage draped prestressing after launching. This approach is rare in ILM decks. The long section of the bridge is shown in **Figure 1** while the deck cross-section before widening is shown in **Figure 2**.

After the construction of the Zambezi River Bridge near Katima Mulilo, this road now became a major access for heavy and abnormal vehicles travelling

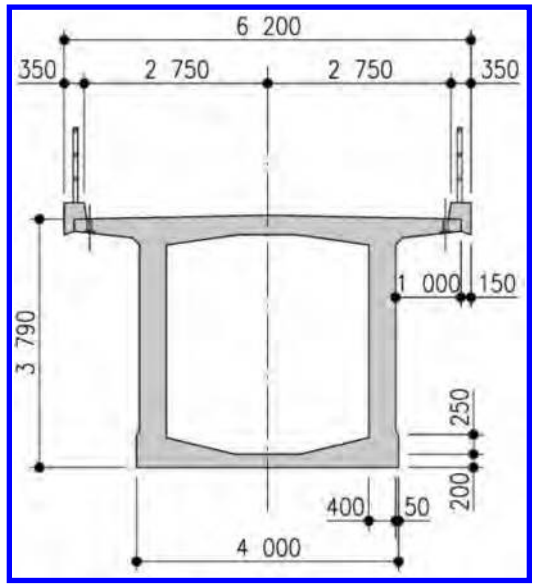


Figure 2. Deck cross-section before widening.

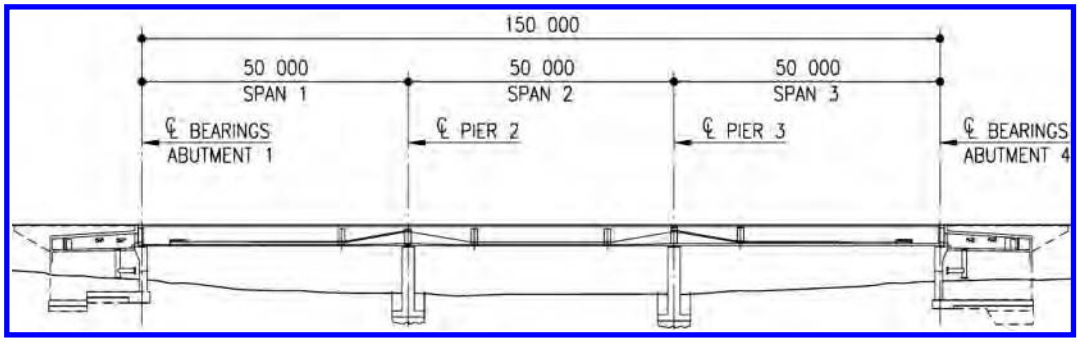


Figure 1. Long section of bridge.

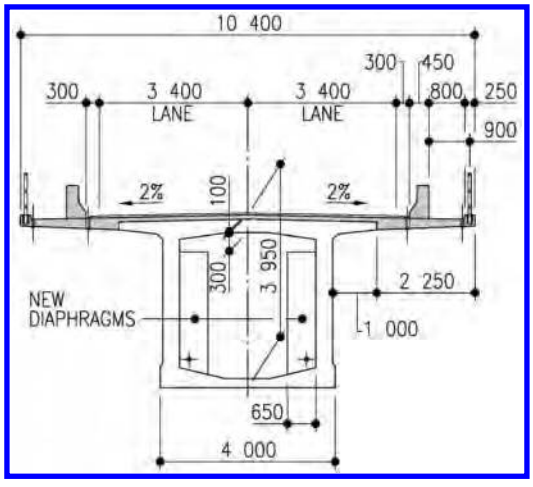


Figure 3. Widened bridge deck.

from the harbour at Walvisbay to Zambia and beyond, especially the Zambian Copper Belt.

The roadway on the existing bridge consisted of two lanes of 2.75 m, giving a total deck width of 5.5 m. This meant that when a heavy vehicle was on the bridge, traffic had to slow right down to allow vehicles to safely pass each other. As pedestrians also used the bridge, the increase in traffic volume made it unsafe for the pedestrians. The bridge therefore had to be widened to carry traffic and pedestrians as well as be strengthened to carry abnormal and heavy loads. Photographs of the bridge before, during and after the construction are given in **Figures 5 to 12**.

2 PRELIMINARY DESIGN

The bridge widening had to accommodate two lanes of traffic plus pedestrian traffic. After examining various standards including the Namibian Roads Agency standards, the Southern African Transport and Communications Commission (SATCC) standards and other southern African standards, the following road widths for the widening was agreed to: 2/3.4 m lanes, 2/0.3 m shoulders and 2/0.9 m sidewalks. To reduce loading on the widened portion, a 700 mm high concrete traffic barrier was placed between the traffic lane and the sidewalk as opposed to the more conventional position of outside the sidewalk. This prevented vehicles from accidently encroaching onto the sidewalk and reduced the design load on the sidewalk from vehicle traffic to pedestrian traffic. The trafficked way would therefore increase from 5.5 m to 7.4 m and pedestrians would be separated from vehicular traffic. The deck cross-section of the widened deck is shown in **Figure 3**.

This layout significantly improved the safety of the new bridge as the original bridge did not have any parapets to retain traffic on the deck, even though the deck was in excess of 10 m above the water level.

With regards increasing the capacity of the bridge, the piers and abutments could carry additional load but the deck could not. Several options were examined for the widening and strengthening. These included:

- Concrete overlay with external prestressing inside the box: Differential shrinkage and the low concrete design strength of 30 MPa made it difficult for this option to work;
- Cutting the concentric prestressing where not required, namely at the top at the mid-spans and at the bottom at the supports: this would reduce the high P/A and increase the capacity to carry additional load;
- Adding piers: This would reduce the forces associated with the live load. Having concentric prestressing would mean that no additional prestressing would be required;
- Shortening the end-spans by extending the abutments: The span configuration of 50-50-50 m is not ideal for carrying live load. As the end spans work the hardest under this configuration, shortening them will increase the capacity of the deck;
- Internal frame inside the box: This would consist of a steel frame over the supports extending to the quarter points of the spans where load would be "picked up" and transferred to the piers via this separate structure;
- Take pedestrians off the bridge by constructing a separate pedestrian bridge;
- Take pedestrians off the top of the deck by suspending a pedestrian walkway under one of the deck cantilevers;
- Take pedestrians off the top of the deck by allowing them to walk through the box, which was the original intention for soldiers crossing the bridge;
- For the widening with a concrete overlay, various options of supporting the widened cantilevers were examined including stiffening with transverse beams under the cantilever, propping off the bottom of the box and thickening the cantilever root to take the additional bending moment.

What was clearly obvious when examining the various options in greater detail was that the original concrete design strength for the deck of 30 MPa was a limiting factor. This low strength severely restricted the allowable bending stress and shear that the bridge could carry. It would also limit the design concepts that could be used for the widening and strengthening. It was therefore important to know what the actual strength of the deck was.

To verify the strength of the existing deck, twelve cores were taken and tested. These gave a mean strength of 55.6 MPa with a standard deviation of 4.6 MPa. This yielded a characteristic strength of 48 MPa. We could now increase the design stresses on the concrete by up to 60% without exceeding capacity. This opened new possibilities for the options for strengthening and widening.

After a comparison of the various options, the chosen option was to widen the deck using a concrete

overlay than extended the cantilevers. To carry the additional load, external prestressing inside the box would be added and the bearings would be replaced as the original bearings could not carry the additional load.

3 STRENGTHENING USING EXTERNAL PRESTRESSING:

In examining the forms of strengthening, both external and internal prestressing options were considered. External prestressing has the advantages of ease of installation, lower weight and replaceability. The advantages of increased durability are less significant in Southern Africa as de-icing salts are not used on our roads. However, external prestressing is infrequently used on Southern Africa with very few contractors and suppliers having experience in this. Internal prestressing is more conventional and more familiar to contractors: For internal prestressing, reinforced concrete beams containing the prestressing ducts can be dowelled into the webs of the deck inside the box. This does increase the weight of the structure. After examining the options, external prestressing was chosen, mainly for the lower increase in dead load.

There are some fundamental differences between external and internal prestressing: Firstly, external prestressing is un-bonded – at serviceability limit state (SLS), the behaviour is quite similar to internal prestressing. However at ultimate limit state (ULS), the stress in the prestressing does not increase as much as internal prestressing and with severe cracking and deformation, the eccentricity at mid-span can actually decrease, depending on the placement of the deviators. Therefore there is generally very little additional bending capacity at ULS. Secondly external prestressing is generally installed between the top and bottom slabs, resulting in it not having the higher eccentricities that internal prestressing would have by extending into the bottom and top slabs. This is not as significant in deep decks but becomes quite significant as the deck depth decreases.

4 DETAILED DESIGN

The design loading for the widened bridge included:

- Dead load (25.5 kN/m^3) and superimposed dead load;
- 100 mm asphalt overlay: This was to allow for future asphalt overlays. The actual surfacing placed on the deck was a 19 mm double seal;
- Full abnormal traffic loading consisting of NA (36 kN/m per lane decreasing with loaded length along with a 144 kN knife-edge load), NB36 (Four axles of 360 kN each) and NC30 (30 kN/m^2 on a loaded area of 5 m by 40 m) loading;
- Earthquake analysis using equivalent load method (3.3 kN/m);
- Temperature range (+/−21°C) and gradient;
- Braking (2.7 kN/m) and accidental skidding (250 kN);
- Wind (1.5 kN/m^2) and flood action (180 kN plus 20 kN/m);

The analysis of the deck incorporated a full beam FEM model including the following phenomena:

- The deck was modelled as a composite section whereby the differential creep and shrinkage between the original deck and the overlay widening was examined at various stages during construction and under traffic;
- External prestressing is un-bonded. Therefore the behaviour at ultimate limit state is non-linear;
- Bearing eccentricities and fixities were accurately modelled using spring elements and rigid connections;
- Moment rounding at supports was taken into account by using a 45 degree spread from the centre of the bearing to the centroid of the section. This reduces the theoretical peak bending moment that occurs directly above a bearing when modelling the deck as elements with no thickness, a weakness when using beam elements;
- NA traffic loading was modelled as a series of line loads and point loads positioned to give the maximum eccentric loading. This causes maximum torsion in the deck and maximum bearing loads.
- Staged construction, creep and shrinkage in the deck were modelled from the construction of the original deck to the construction of the new top slab in stages and on to 100 years design life. The relevant creep and shrinkage factors are applied by the program, dependent on the creep and shrinkage model chosen and time steps between the various stages of construction.

In combining the various permanent actions, traffic loads, supplementary actions and imposed deformations, a matrix of combinations was set up at each end of each element. The six matrix columns consisted of N, Vy, Vz, T, My and Mz, representing the beam end-forces. The twelve rows of the matrix consisted of the maximum and minimum values of each of the above. After doing the combinations, the first row consisted of the maximum N with associated forces, the second row consisted of the minimum N what associated forces and so on to the last line which consisted of minimum Mz with associated forces. This method avoids the conservative approach of combining the maximum of each force, irrespective of whether they can occur concurrently.

The strength of the deck at ultimate limit state was checked using a post-processor written in-house using Pascal. This took the combination matrix from the program and checked the various combinations for combined bending, shear and torsion in a box girder. The program has subsequently been rewritten in Excel using Visual Basic, making it more transparent and easier to verify.

The effect of creep and shrinkage due to the additional external prestressing and the differential creep

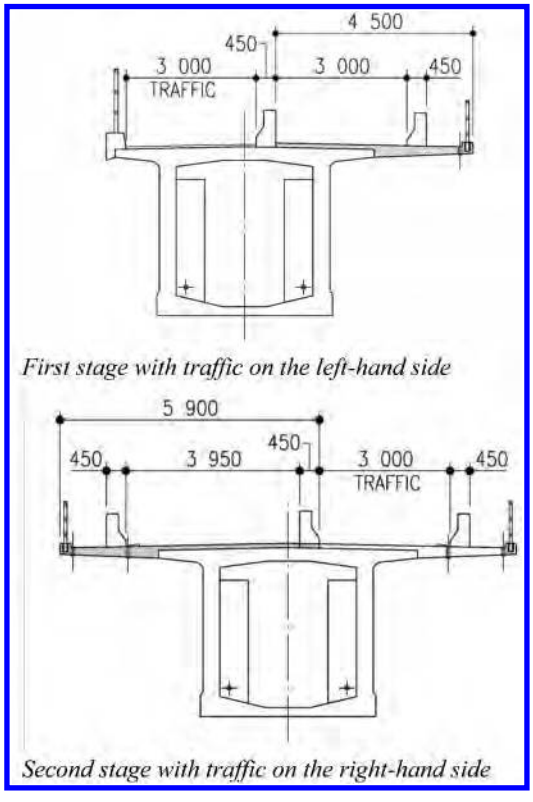


Figure 4. Bridge deck during construction.

and shrinkage due to the concrete deck widening was carefully modelled in the FEM model. As the original deck was in excess of 20 years old, creep and shrinkage effects in it were quite small once the axial shortening due to additional prestressing had taken place. Differential creep and shrinkage was significant due to the age difference between the widening and the original deck. This resulted in the stresses induced by the additional dead load becoming quite small in the widening, especially with time. However, under traffic the section behaves compositely with the additional stress being linear though the full depth of the section.

This also meant that the deck movement due to creep and shrinkage was quite small, resulting in less movement being required in the bearings and expansion joints than was required in the original deck

The longitudinal external prestressing was installed through reinforced concrete deviators above the piers, at the quarter points and at the deck ends as shown in **Figure 1**. The load was transferred from the deviators to the deck via dowels and through shear using Dywidag bars to create the normal reaction. As the concrete surface to the deck was scabbled before casting the deviators, the co-efficient of friction was taken as 1.0. The prestressing strand was cement-grouted in HDPE sheathing which passed though galvanized steel deviator tubes. These had bell-ends to accommodate construction tolerances. The external prestressing can be seen in **Figure 8**.

There was insufficient shear reinforcement in the existing webs close to the piers to carry the additional load. Vertical prestressing bars were installed inside the webs as shown in **Figure 8**. There was sufficient transverse reinforcement in the deck cross-section to carry this additional transverse bending.

On this project, traffic accommodation was a particular challenge. If the bridge were closed to traffic during construction, the detour for traffic from Walvisbay to Zambia would be several hundred kilometres longer and a ferry service would have to be provided for local traffic. The design therefor included the construction of the deck widening in two halves while keeping a 3.0 m lane open to traffic. This is shown in **Figure 4**.

During the construction of the first stage, a solid barrier was placed down the centre of the road to create a 3.0 m traffic lane while protecting the construction staff from traffic. The slab was dowelled into the exiting deck during this stage to ensure stability. The strength of the existing deck, the strength of the bearings and the stability of the whole structure had to be checked during the construction of this stage.

The deck widening was then completed during the second stage.

5 CONSTRUCTION

At the time of the design, funding for construction was limited and it was decided to do the construction in two stages: firstly strengthen the bridge to take abnormal loads, then secondly, when further funds became available, widen the deck. However, to keep overall construction costs down, it was decided to avoid duplication of construction actions in the two contracts as much as possible. The following design decisions were made in order to satisfy these requirements:

- Install all the external prestressing in the first contract.
- Replace the bearings in the first contract with bearings that would be able to carry the increased loads of the widening as well.

Fortunately the client was able to acquire sufficient funds resulting in both contracts going out as one contract.

Late delivery of the final bearings meant that the contractor had to replace the bearings while the top slab was being cast. This increased the load to be jacked and temporarily supported while the existing bearings were removed and replaced. This gave him little room to work in.

The contractor added an additional construction stage to the casting the top slab. The original design had this done in two stages. The contractor did this in three stages, giving him more space to work in. This also allowed more space for pedestrians to use the bridge at the same time as vehicle traffic.

The contractor was able to meet the very high specification for concrete mix design and curing.



Figure 5. Location of the bridge in the sparsely populated Caprivi Strip of northern Namibia.



Figure 6. The bridge before widening. The understrength and narrow deck has to share pedestrian traffic and heavy vehicle traffic.



Figure 7. Inside the box girder before strengthening. The inside was kept clear to allow people to walk through the deck.

This resulted in almost no plastic shrinkage cracks in the deck or subsequent differential shrinkage cracks. The deck surface was sprayed with bitumen before the double-seal surfacing was applied. This further reduced water-loss in the overlay, reducing shrinkage effects.



Figure 8. Inside the box girder after strengthening. Diaphragms, external prestressing and vertical prestressing is visible. Dywidag bars were used in the deviator diaphragms to increase the load transferred by shear.



Figure 9. Widening of the left-hand side under traffic. Panels were cast in lengths of 5 m.



Figure 10. Widening of the right-hand side of the deck under traffic: A cantilever frame was used above the deck to support the widening.

6 CONCLUSION

Widening and strengthening of large bridges do not happen too often so there is not much literature available



Figure 11. Bearing replacement after completion of the deck. Access platforms were used to finish off the cantilever soffits after removal of the formwork. Limited space for bearing replacement presented a challenge on site.



Figure 12. The widened bridge deck can now carry two lanes of vehicle traffic with two 900 mm sidewalks separated with a concrete barrier.

to assist in decision making. Some valuable lessons learnt from this project include:

- Deck width: in choosing the width for widening, the cost, additional load and most important of all, the long-term level of service needs to be considered. It is short-sighted to design for the next 10 years when the remaining design life is in excess of 50 years. At the time of design, the pedestrian traffic was quite low, hence the sidewalks of 900 mm. However, pedestrian traffic has increased significantly and the sidewalks are a little narrow when groups of people are passing each other;
- When adding diaphragms for strengthening, rather make them larger. The additional cost and weight is quite small compared to the increased flexibility and robustness. In attempting to keep the loads down, we made the diaphragms as small as possible. By making them a little larger, we would have made life easier for the contractor; and
- The vertical prestressing bars to carry additional shear did affect the construction programme as the top of the bar had to be anchored in the overlay slab. Access to the bottom anchor also presented a problem and at one stage the bottom anchor interfered with the installation of the replacement bearings. Alternative forms of strengthening such as steel plates or carbon-fibre sheets would have avoided these problems.

By providing an innovative deck overlay and external prestressing, we were able to prolong the life of a bridge without significant disruption to traffic during construction.

Research and Applications in Structural Engineering, Mechanics and Computation – Zingoni (Ed.)
© 2013 Taylor & Francis Group, London, ISBN 978-1-138-00061-2

CFRP strengthening of steel I-beam against local web buckling: A numerical analysis

M.A. Ghareeb
Bemco Steel Industries, Saudi Arabia

M.A. Khedr
Faculty of Engineering, Benha University, Egypt

E.Y. Sayed-Ahmed
The American University in Cairo and Professor (on leave), Ain Shams University, Egypt

ABSTRACT: The use of Carbon Fibre Reinforced Polymers (CFRP) in strengthening of steel structural elements is growing every year. CFRP laminates offer an economic strengthening alternative for steel I-beams. The common method of using CFRP laminates in strengthening steel beams is by bonding the laminates (usually high modules type) to the lower flange of the beam to increase its flexural strength. However, for thin walled "slender" I-section steel beams, the risk of local buckling failure is also a major concern. Recently, it was found that bonding CFRP laminates to steel slender I-section web can enhance the local buckling of the steel section. Here, a numerical investigation is performed to investigate the effect of bonding CFRP laminates to the webs of I-section steel beams on the beam's flexural strength. The main advantage of this technique is delaying the onset of local buck-ling of the beam's web thus allowing the slender I-section to reach its yield flexural capacity. The study reveals that bonding the CFRP laminates to the web of I-sections significantly increases the critical load and may allow the beam to reach its yield capacity.

1 INTRODUCTION

Traditional strengthening techniques of steel beams involve an expensive process of welding/bolting steel plates to the beams' cross section. These plates are heavy, impractical and face many difficulties in site-installation. Fibre Reinforced Polymers (FRP) which are characterized by their high strength to weight ratio may offer an attractive strengthening alternative. FRP laminates/strips are currently adopted as one of the most successful strengthening techniques for different reinforced and prestressed concrete elements. On the other hand, investigations on strengthening steel structures using FRP are still limited, in most cases, to applying the laminates/strips to the tension flange of the beam in order to increase its flexural strength (Miller et al. 2001; Liu et al. 2001; Teng and Podolny 1998; Chajes and Swinehart 2002; Miller 2000; Moy 2001; West 2001; Cadei et al. 2004).

Furthermore, for thin walled I-section beams the risk of buckling failure is also a major concern. Steel I-sections subject to flexure are classified into compact, non-compact and slender sections. Compact sections of can develop the cross-section full plastic moment while non-compact sections are guaranteed only to develop the cross-section yield moment, then the section would fail by local buckling of its component plate elements before reaching the plastic moment. Slender sections suffer local buckling of the component plate elements before reaching the yield moment. FRP laminates may offer a good strengthening technique for slender section by delaying its local buckling and as such, changing the section class.

On another front, steel plate girders are widely used in buildings and bridges. They have good flexure capacity and serviceability performance due their deep webs. Environmental effects and substandard maintenance of plate girders can cause their main strength element to rust. Rehabilitation of such damaged sections could be very tricky. The traditional rehabilitation techniques are based on welding steel plates and stiffeners to the damaged web. However, one of the many disadvantages of this technique is the resulting elevated temperature due to the welding process which may cause more damage to the steel section. So FRP laminates may offer an attractive alternative in such cases.

Failure modes of CFRP strengthened steel I-section beams may take place via steel yielding, flange and/or web local buckling, rupture of the CFRP laminates, and/or de-bonding of CFRP laminates from the section (Buyukozturk et al. 2004). In most cases, an interactive failure mode between more than one of the previously mentioned modes may govern failure of the FRP

strengthened steel I-beam. An experimental investigation conducted by Lam and Clark, 2003 showed that bonding CFRP laminates to the tension flange of a compact I-section is not as effective as it is thought to be: only 9% increment on the strength of the compact section were achieved. The final and sudden failure occurred by shattering of the epoxy layer after the steel had reached its yield strength. The strength of the CFRP laminates was not fully utilized. The investigation also pointed-out that bonding CFRP laminates to the web of non-compact I-section beam increased the ultimate load by about 23% and also improved the buckling behaviour. Similar numerical investigation was conducted by Sayed-Ahmed (2004, 2006) which yielded the same previously mentioned conclusions.

More interestingly, the non-compact sections with web-bonded CFRP laminates in some cases were able to achieve steel yielding followed by formation of plastic hinge, and then the CFRP laminates deboned from the steel sections. It was found that bonding CFRP strips in such configuration may increase the critical load by a ratio ranging between 20% and 60% (Sayed-Ahmed 2004, 2006).

Here, a numerical model is developed based on the finite element technique and solved using a commercially available FE package. The model is used to analyse the effect of bonding Carbon Fibre Reinforced (CFRP) laminates to webs of slender steel I-beams. The numerical analysis is also used to investigate web buckling of these strengthened I-beams. The main objective of this work is to investigate the benefit of using high modules CFRP laminates in strengthening steel I-beams. The study also investigated the effect of increasing the thickness of the adhesive layer on the web stability of the CFRP strengthened I-beams.

2 FINITE ELEMENT MODEL

Steel beam composed of a built-up section (Figure 1) with a total length of 12.0 m is numerically modeled. The beam's web depth is 573 mm with a thickness varying between 2 mm and 12 mm which corresponding to compact, non-compact and slender sections. The two flanges of the beams are composed of 229 mm × 20 mm plates. Sections proprieties for the analyzed beams are listed in Table 1.

The beam is subjected to four points loading with points of applications shown in Figure 1. CFRP laminates are bonded to the beam's web with the configuration shown in Figure 1.

To prevent lateral torsional buckling, the beam is laterally supported every 3.0 m. The beam is simply supported at both ends. It is restrained against rotation around its longitudinal (weak) axis.

As shown in Figures 1 and 2, horizontal CFRP laminates are bonded to the web at mid height (mimicking plate girder's horizontal stiffeners). Other vertical CFRP laminates mimicking plate girder's vertical stiffeners are welded to the web in the configuration shown in Figures 1 and 2. All the CFRP strips are 100 mm wide by 1.4 mm thick. To study the effect of increasing the thickness of the adhesive layer which bonds the laminates to the steel web, two thicknesses are assumed, 1.0 mm and 1.4 mm.

Layered shell element (Figure 3) is adopted for modelling the steel and both the adhesive and the CFRP laminates. The element has 8 nodes with 6 degrees of freedom per node. For the web parts with the bonded CFRP laminates, five layers are used: central steel layer modelling the steel web, two layers modelling the epoxy adhesive and two outer layers modelling the CFRP laminates.

The constitutive model of steel beam follows a bilinear elastic-plastic stress-strain curve which has identical behaviour in tension and compression. The strain hardening modulus was assumed to be 5% of Young's modulus. The assumed initial yield stress of the steel material is 300 MPa and the Young's modulus was taken as 200 GPa. Poisson's ratio of 0.3 was adopted.

Two types of CFRP laminates are modelled: normal modulus laminates (S), and high modulus laminates

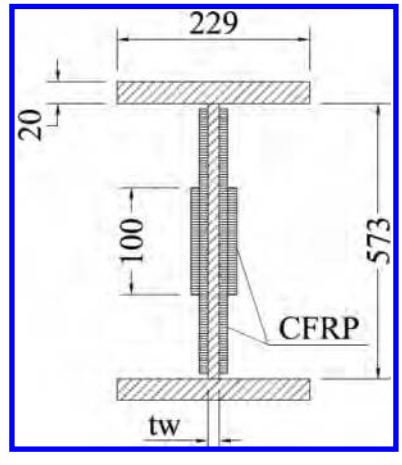


Figure 1. Strengthened steel beam's cross-section.

Table 1. Mechanical properties of the analysed beams.

Beam	t_w (mm)	h_w/t_w	Sec Class	A ($\times 10^3$) mm^2	I_x ($\times 10^6$) mm^4	I_y ($\times 10^6$) mm^4
B1	12	47.75	1	16.04	993.2	40.1
B2	6	95.50	2	12.60	899.0	40.0
B3	4	143.25	3	11.50	567.7	40.0
B4	2	286.50	4	10.30	836.3	40.0

Beam	r_x mm	r_y mm	S_x ($\times 10^3$) mm^3	S_y ($\times 10^3$) mm^3	Z_x ($\times 10^6$) mm^3	Z_y ($\times 10^6$) mm^3
B1	249	50.0	3241	350	3699	545
B2	267	56.4	2934	349	3207	529
B3	275	59.1	2832	349	3043	527
B4	285	62.3	2730	349	2961	526

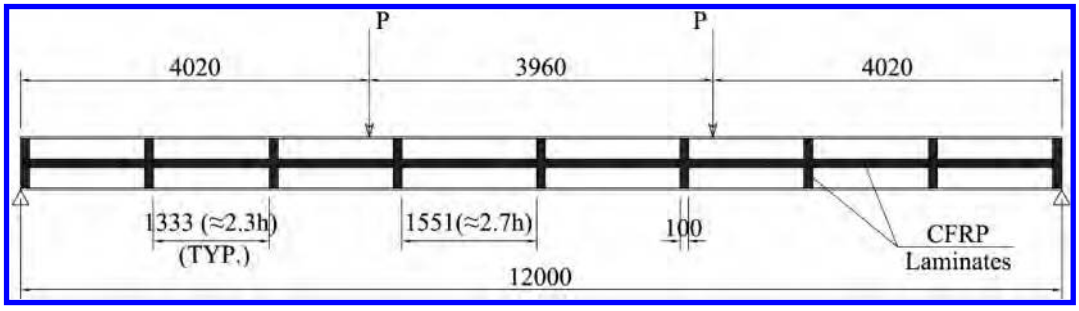


Figure 2. Strengthened steel beam: loading, boundary conditions and CFRP laminates configuration.

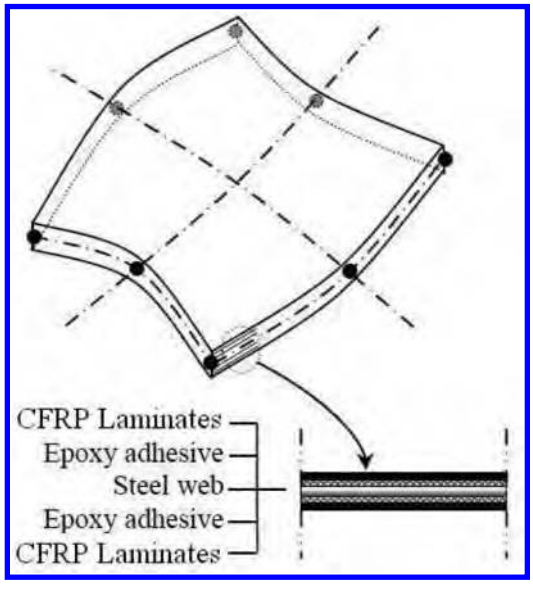


Figure 3. Layered shell element adopted in the analyses.

Table 2. Properties of the CFRP laminates.

Mechanical properties	St. Modulus Laminates (S) MPa	High Modulus Laminates (H) MPa
Tensile Modulus	167,000	300,000
Tensile Strength	2,800	1,500

(H). The mechanical proper-ties of the CFRP laminates and the epoxy are shown in Table 2. Table 3 shows the mechanical properties of the adhesive material.

The layered shell element requires linear isotropic and multi-linear isotropic material properties to properly model the adhesive. The multi-linear isotropic material uses the von-Mises failure criterion (Willam and Warnke 1974). The modulus of elasticity of the adhesive and Poisson's ratio are obtained from the manufacturer's datasheet. Implementation of the material material model requires 9 constants to be defined. Only 4 constants are affecting the behaviour of the adhesive layer: shear transfer coefficients for an open

Table 3. Properties of the epoxy adhesive.

Mechanical properties	Value MPa
Tensile Strength	26
Compressive Strength	85
Shear Strength	18
Bond Strength	21
Tensile Modulus	11,200

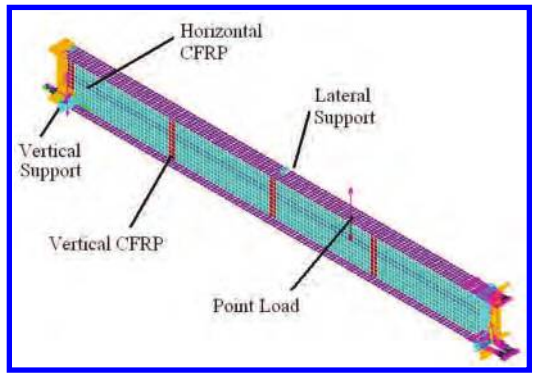


Figure 4. Finite element model (because of symmetry, only half the beam is shown and modelled.

crack, shear transfer coefficients for a closed crack, uni-axial tensile cracking stress, (assumed to be 5.9), and uni-axial crushing stress (assumed to be 1.0). Typical shear transfer coefficients range from 0.0 to 1.0, with 0.0 representing a smooth crack (complete loss of shear transfer) and 1.0 representing a rough crack (no loss of shear transfer). The shear transfer coefficients for open and closed cracks are assumed to be 0.2 and 1.0, respectively. The adopted finite element mesh, boundary conditions and loading are shown in Figure 4.

3 RESULTS AND DISCUSSION

A linear elastic buckling analysis on each steel beam is performed to evaluate the critical loads which initiate web buckling.

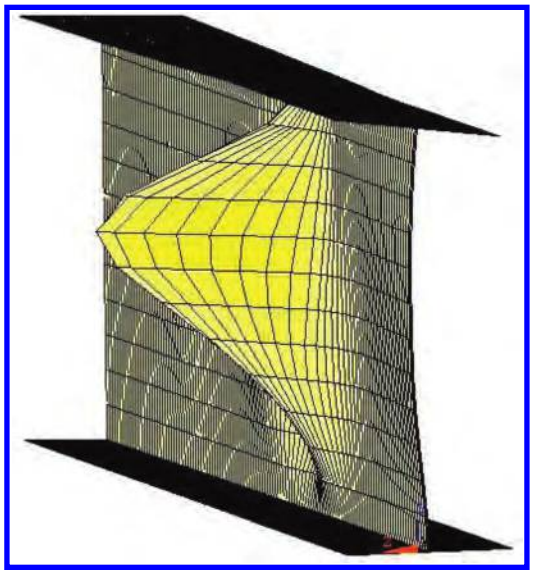


Figure 5. Modelled steel beam deformed shape at web buckling.

For each class of beams, five types of beams are analyzed. The first type (D1) is the control beam with no CFRP laminates bonded to it. The second type (D2-S-1) is strengthened with normal modulus CFRP laminates with the CFRP arrangement shown in Figures 1 and 2: the thickness of the adhesive layer is 1.0 mm. The third type (D2-S-1.4) has the same CFRP laminates arrangements and the same laminates type but the thickness of the adhesive layer is 1.4 mm. The forth type (D2-H-1) has the same CFRP laminates arrangements as the third beam but the type of laminates is high modulus CFRP: the thickness of the adhesive layer is 1.0 mm. The fifth type (D2-H-1.4) has the same CFRP laminates arrangements and the same type of laminates but the thickness of the adhesive layer used is 1.4 mm.

Eigen buck-ling analysis was performed for all the beams: Figure 5 shows the deformed shape of the one of the analyzed beams. The full results of these analyses are shown in Table 4. The Table reveals that bonding the CFRP strips to web of slender sections significantly delayed web buckling and increased the critical load by about 31%. For non-compact section, the enhancement in the critical load is in the order of 16%.

Table 4. Results of Eigen buckling analyses.

			D1	D2-S-1		D2-S-1.4		D2-H-1		D2-H-1.4	
Beam No.	h_w/t_w	Section Classification	P_{cr} kN	P_{cr} kN	% of Incr.	P_{cr} kN	% of Incr.	P_{cr} kN	% of Incr.	P_{cr} kN	% of Incr.
B1	47.75	Compact	1342.0	1380.0	3.0%	1395.0	4.0%	1384.0	3%	1400.0	4.3%
B2	95.50	Compact	292.0	316.0	8.0%	322.0	10.0%	319.0	9%	325.0	11.0%
B3	143.25	Non-compact	102.6	115.0	12.0%	117.1	14.1%	116.9	14%	118.9	15.8%
B4	286.50	Slender	15.2	18.9	24.3%	19.2	26.3%	19.6	29%	19.9	31.0%

Table 5. Failure moment to plastic moment and yield moment.

Beam No.	h_w/t_w	Section Classification	M_y kN·m	M_P kN·m	M_f kN·m	M_f/M_y	M_f/M_p
B1-D1	47.75	Compact	972.3	1109.7	5394.8	5.55	4.86
B1-D2-S1	47.75	Compact	972.3	1109.7	5547.6	5.71	5.00
B1-D2-S14	47.75	Compact	972.3	1109.7	5607.9	5.77	5.05
B1-D2-H1	47.75	Compact	972.3	1109.7	5563.7	5.72	5.01
B1-D2-H14	47.75	Compact	972.3	1109.7	5628.0	5.79	5.07
B2-D1	95.50	Compact	880.2	962.1	1173.8	1.33	1.22
B2-D2-S1	95.50	Compact	880.2	962.1	1270.3	1.44	1.32
B2-D2-S14	95.50	Compact	880.2	962.1	1294.4	1.47	1.35
B2-D2-H1	95.50	Compact	880.2	962.1	1282.4	1.46	1.33
B2-D2-H14	95.50	Compact	880.2	962.1	1306.5	1.48	1.36
B3-D1	143.25	Non-compact	849.6	912.9	412.5	0.49	0.45
B3-D2-S1	143.25	Non-compact	849.6	912.9	462.3	0.54	0.51
B3-D2-S14	143.25	Non-compact	849.6	912.9	470.7	0.55	0.52
B3-D2-H1	143.25	Non-compact	849.6	912.9	469.9	0.55	0.51
B3-D2-H14	143.25	Non-compact	849.6	912.9	478.0	0.56	0.52
B4-D1	286.50	Slender	819.0	888.3	61.1	0.07	0.07
B4-D2-S1	286.50	Slender	819.0	888.3	76.0	0.09	0.09
B4-D2-S14	286.50	Slender	819.0	888.3	77.2	0.09	0.09
B4-D2-H1	286.50	Slender	819.0	888.3	78.8	0.10	0.09
B4-D2-H14	286.50	Slender	819.0	888.3	80.0	0.10	0.09

Using high modules CFRP laminates in the configurations shown in Figures 1 and 2 increased the critical load from 24% to 29% for slender sections. Increasing the adhesive layer thickness from 1.0 mm to 1.4 mm had no significant effect on the critical load: only a 2% strength enhancement is achieved. Table 5 shows a comparison between the calculated yield moment M_y and the calculated plastic moment M_p to the failure moment obtained from the finite element analyses. The results show that for beam no. 3, the use of the suggested strengthening technique increased the ratio of the failure moment to the yield moment from 0.49 to 0.56. For beam no. 4, the ratio is increased from 0.07 to 0.10.

4 CONCLUSIONS

The effect of bonding CFRP strips to the webs of thin-walled I-section steel beams on the beam's flexural strength is numerically investigated. The main advantage of this detail is delaying the local buckling of the beam's web. Nonlinear finite element analyses were performed on steel I-section beams with different web height-to-thickness ratios. The effect of bonding 100 mm × 1.4 mm CFRP strips on the critical load initiating web buckling is evaluated. It is found that bonding CFRP strips in such configuration may increase the critical load by a ratio of 24%. Increasing the tensile modules of CFRP strips will enhance the performance of the configurations by additional 5%. The effect of increasing the adhesive layer thickness is also studied and was found to be negligible.

REFERENCES

Buyukozturk, O. Gunes, O. and Karaca E., 2004. Progress on understanding debonding problems in reinforced concrete and steel members strengthened using FRP composites," Construction and Building Materials, Vol. 18, No. 1, pp. 9–20.

Cadei, J.M.C., Stratford, T.J., Hollaway, L.C. and Duckett W.G., 2004. Strengthening metallic structures using externally-bonded Fibre-Reinforced-Polymers – C595, CIRIA, London, UK.

Chajes, M., and Swinehart, M., 2002. Bridge rehabilitation Using advanced composites: Ashland Bridge SR-82 over Red Clay Creek. Center for Innovative Bridge Engineering, University of Delaware, Newark, Delaware, USA.

Lam, D. and Clark, K.A., 2003. Strengthening of steel sections using carbon fibre reinforced polymers laminates," Proceedings, Advances in Structures: Steel, Concrete, Composite and Aluminum ASSCCA'03, Sydney, Australia, pp. 1369–1374.

Liu, X. Silva, P.F. and Nanni, A., 2001. Rehabilitation of steel bridge members with FRP composite materials. Proc. of the Composite in construction, Porto, Portugal, pp. 613–617

Miller, T. C., 2000. The rehabilitation of steel bridge girders using advanced composite materials." MSc. Thesis. University of Delaware, Newark, Delaware. USA.

Miller, T.C., Chajes, M.J., Mertz, D.R., and Hastings, J., 2001. Strengthening of a steel bridge girder using CFRP plates. Journal of Bridge Engineering, ASCE, Vol. 6, No. 6, pp. 514–522.

Moy, S.S.J. (ed), 2001. FRP composites – Life extension and strengthening of metallic structures – ICE design and practice guide, Thomas Telford, London, UK.

Tang, B. Podolny, W. Jr., 1998. A successful beginning for Fibre Reinforced Polymer (FRP) composite materials in bridge applications. FHWA Proceedings, International Conference on Corrosion and Rehabilitation of Reinforced Concrete Structures, Orlando, FL. USA.

Sayed-Ahmed, E.Y. 2004. Strengthening of Thin-Walled Steel I-Section Beams Using CFRP Strips. Proceedings, 4th International Conference on Advanced Composite Materials in Bridges and Structures (ACMBS IV), Calgary, Alberta, Canada – CD Proceedings.

Sayed-Ahmed, E.Y. 2006. Numerical Investigation into Strengthening Steel I-Section Beams Using CFRP Strips. Proceedings, 2006 Structures Congress, ASCE, St. Louis, USA, 18–20 May 2006.

West, T., 2001. Enhancements to the bond between advanced composite materials and steel for bridge rehabilitation. MSc. Thesis. University of Delaware, Newark, Delaware. USA.

Willam, K.J., and Warnke, E.P., 1974. Constitutive Model for Tri-axial Behaviour of Concrete. Seminar on Concrete Structures Subjected to Tri-axial Stresses, International Association of Bridge and Structural Engineering Conference, Bergamo, Italy, 1974; p. 174.

Research and Applications in Structural Engineering, Mechanics and Computation – Zingoni (Ed.)
© 2013 Taylor & Francis Group, London, ISBN 978-1-138-00061-2

Timber beams with external strengthening based on CFRP and GFRP composites

M. Karmazínová
Brno University of Technology, Brno, Czech Republic

ABSTRACT: The paper is focused on the possibilities of the usage of fibre-reinforced polymers or polymer composites respectively, to strength timber structural members of load-bearing civil engineering structures, in the case of reconstructions, for example. Strengthening timber beams using external reinforcement based on carbon-fibre-reinforced or glass-fibre-reinforced polymer (CFRP or GFRP) composites appears the advanced way. The paper deals with the problems of the application of externally bonded lamellas based on CFRP and GFRP composites for strengthening timber beams to increase their load-carrying capacity and stiffness, in the case of reconstructions of existing building constructions (e.g. historical buildings), for example. During the process of the beam resistance investigation the attention is mainly paid to increasing load-bearing capacity in connection with increasing stiffness of the beams strengthened by lamellas mentioned. In the paper, mainly the information obtained from the experimental research is presented, that means especially outcomes of the experimental verification of the actual behaviour, failure mechanism and load-bearing capacity of the beams strengthened. For this reason, loading tests of two sets of timber beams strengthened by CFRP lamellas have been performed and subsequently test results have been elaborated and statistically evaluated. For the solution of this problem the theoretical analyses using analytical and numerical tools and experimental verification using loading and material tests including advanced methods of the test results evaluation are used. The research has been oriented to several particular problems and in connection with this, to the following arising results: (i) results of the parametric and comparative studies to choose the available beam cross-sections for experimental investigations, (ii) results of the loading and material tests to obtain actual objective resistances and material properties for subsequent numerical analysis, (iii) the efficiency of the application of CFRP and GFRP for strengthening timber beams including their comparison.

1 INTRODUCTION

The strengthening lamellas considered are being developed and produced by the company of PREFA KOMPOZITY, Inc. at Brno city in Czech Republic. The examples of some available products – CFRP reinforcement commercially named PREFACARB, in the forms of lamella and matting, are shown in Fig. 1. These types of the lamellas are usually based on epoxy resin reinforced by carbon fibres.

Usually and recently even on a mass scale, these lamellas are being used for strengthening masonry and concrete load-bearing structures, especially to strength floor structures of existing building constructions. To the contrary, their usage for strengthening timber load-bearing members is not so wide, and for strengthening steel members, CFRP lamellas are used very sporadically only and GFRP lamellas are not used at all. In the case of strengthening steel structural members, the problematic usage is caused by GFRP and CFRP material properties in relation with material properties of steel. Carbon-fibre and also glass-fibre reinforced polymers have a high tensile strength, which is (much) higher than steel tensile strength, but the Young's modulus of elasticity is not so high, especially in the case of GFRP, even much less than steel modulus.

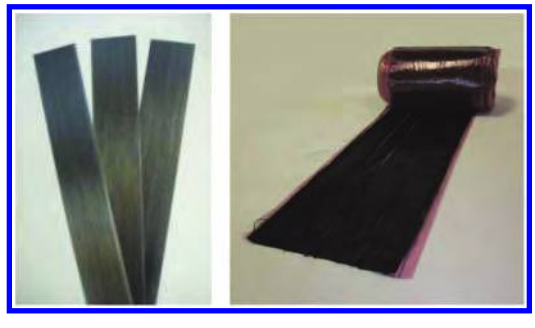


Figure 1. Examples of CFRP reinforcement PREFACARB (see www.prefa-kompozity.cz): a) lamella, b) matting.

For that, CFRP and GFRP usage for steel beams strengthening can give a higher load-bearing capacity, but not adequately high flexural stiffness, which negatively influences the deflections. However for timber beams strengthening, the values of tensile strength and Young's modulus of CFRP and GFRP composites are enough high in relation to the corresponding properties of timber.

2 EXTERNAL NON-METAL REINFORCEMENT BASED ON CFRP AND GFRP COMPOSITES

Non-metal reinforcements based on CFRP or GFRP are applied in the form of lamella externally bonded to the surface of the strengthened structural member.

In standard case, CFRP lamella material contains epoxy resin and high-strength carbon fibre reinforcement. The dimensions of cross-sections of produced lamellas vary in the range from 30×1.0 mm to 50×1.4 mm; the density of this CFRP composite is approximately in the range of 1 600–1 800 kgm^{-3}. The mean value of CFRP tensile strength derived from producer performed material tests is declared as $f_{CFRP} =$ 3 000 MPa, the mean value of Young's modulus of elasticity is given as $E_{CFRP} = 155$ GPa.

The material of GFRP lamella usually consists of polyester or vinyl ester (usually, for difficult long-term applications) resin and glass-fibre reinforcement. Usual produced GFRP lamella cross-sections are in the same range as CFRP lamella dimensions; the density is in the range from about of 2 000 kgm^{-3} (usually) to 3 000 kgm^{-3} (exceptionally). The mean value of GFRP tensile strength is $f_{GFRP} = 1\,000$ MPa, the mean value of Young's modulus of elasticity is $E_{GFRP} = 55$ GPa.

CFRP and GFRP lamella reinforcements mentioned above are used for the additional strengthening of concrete, timber, metal and other load-bearing structural members. The product may be used to increase the load-bearing capacity of existing constructions if the load has been increased, the load-bearing members have been damaged, and the improvement of utility properties or changes of static behaviour are required. The load increasing can be caused, for example, by operational loading effects increasing or heavy equipment adding. The damage of load-bearing structural members can occur as a result of the accidents (vehicle impacts, fire), degradation of building materials, corrosion of steel reinforcement in concrete, initiation and propagation of cracks and others. The improvement of utility properties means, for example, the requirement to decrease the deflections or to increase the ride height. The changes of the static behaviour can be caused by decreasing of the support number or creating new holes in horizontal and vertical structures.

The usage of composite reinforcement is appropriate in the field of the material properties, but also in the field of the realization. CFRP and GFRP composites have a low weight, which allows the simple installation and easy manipulation without supporting during glue hardening and application to vertical walls and to bottom side of floor structures. Due to the small thickness it is possible to cross the lamellas; the maintenance requirements are minimal due to the high resistance to environment influences. The most important advantages of reinforcing element are the high strength and high fire, chemical and corrosion resistance. Polymer composites also have a low temperature conductivity and are electrically non-conductive and electro-magnetic transparent.

3 THEORETICAL ANALYSIS OF LOAD-BEARING CAPACITY FOR "FRP-TIMBER"

For the determination of load-bearing capacity of the beam strengthened by externally bonded CFRP or GFRP lamella the approach similar to steel-concrete composite beams offers to be applied. However, it is necessary to take into account the actual behaviour of the strengthened beam regarding the character of the material of basic cross-section, i.e. timber. Due to the non-plastic character and inability of the full plastic behaviour, no typical plastic zones can occur in timber beams. For that, assumptions of the elastic behaviour have been applied to the determination of the load-bearing capacity of the strengthened beam.

3.1 *Normal stress*

Assuming the rigid shear connection between timber and FRP lamella the relative deformations of timber and FRP reinforcement in the contact are the same, i.e. $\varepsilon_{timber} = \varepsilon_{FRP}$. Then, for the calculation of normal stresses and determination of bending moment capacity, the general concept of composite ideal (substitute) cross-section (Ascione et al. 2007, Cadei et al. 2004, Gilfillan et al. 2003) based on parameter n

$$n = \frac{E_{timber}}{E_{FRP}}, \tag{1}$$

where E_{timber}, E_{FRP} are Young's modulus of elasticity of timber and FRP reinforcement, can be applied.

The assumed normal stress distribution in "FRP-timber" cross-section based on the elastic approach is shown in Fig. 1, where σ_{timber} is timber stress on the tensile edge of the beam and σ_{FRP} is the stress in FRP reinforcement. The values of normal stresses in the cross-section can be generally calculated as:

$$\sigma_{timber} = \frac{M}{I_i} \cdot z_{timber}, \tag{2}$$

$$\sigma_{FRP} = \frac{M}{n \cdot I_i} \cdot z_{FRP}, \tag{3}$$

where M is the bending moment, I_i is the second moment of area of the ideal cross-section, and z_{timber} and z_{FRP} are the corresponding distances from the gravity centre of the substitute cross-section.

Basic characteristics of the ideal cross-section of the composite member that means cross-section area A_i and the second moment of area I_i are generally given as follows:

$$A_i = A_{timber} + \frac{A_{FRP}}{n}, \tag{4}$$

$$I_i = I_{timber,i} + \frac{I_{FRP,i}}{n}, \tag{5}$$

Of course, the formulas for the cross-section characteristics of FRP parts and for normal stresses in

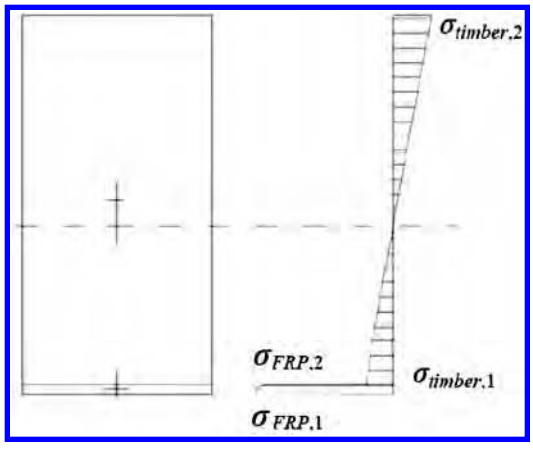


Figure 2. Elastic distribution of normal stress in "FRP-timber" cross-section.

FRP parts include parameter n, which arises from the principle described above and it is also evident from equations (3), (4), (5).

3.2 *Longitudinal shear stress*

Based on the ideal cross-section conception, the longitudinal shear force V_{long} (per unit of the length) at the interface between FRP reinforcement and timber can be calculated as

$$V_{long} = \frac{V \cdot S_i}{I_i} \quad [\mathrm{Nmm^{-1}}], \tag{6}$$

where V is the (transverse) shear force, S_i is the first (static) moment of the cut off part of the area, I_i is the second moment of area. Then, the longitudinal shear stress in the interface between timber and FRP can be given as

$$\tau_{long} = \frac{V \cdot S_i}{b \cdot I_i}, \tag{7}$$

where b is the width in the corresponding place of the cross-section, that means in this case it is the width of the glued area, i.e. the width of FRP lamella, because it is bonded over its all the width.

4 EXPERIMENTAL VERIFICATION OF LOAD-BEARING CAPACITY FOR "CFRP-TIMBER"

4.1 *Loading tests arrangement and realization*

For the experimental verification timber beams with CFRP lamellas have been chosen. The specimens of following geometrical and material parameters have been tested: (i) timber beams of rectangular cross-sections 100 / 220, 100 / 200, 100 / 180, 100 / 160, 100 / 140, 100 / 120 have been used; two spans in dependence of cross-section dimensions have been

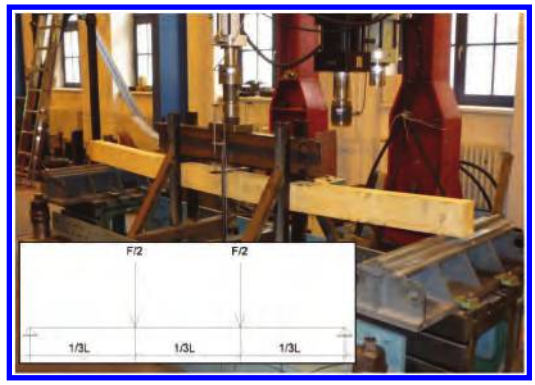


Figure 3. Arrangement and performance of loading tests.



Figure 4. CFRP lamella and strain gauges bonded to bottom (tensile) beam edge.

considered, i.e. $L = 4$ m (cross-sections of 100 / 220, 100 / 200, 100 / 180) and $L = 3$ m (cross-sections of 100 / 160, 100 / 140, 100 / 120); the grade of used timber was declared as the class of C 24 – timber quality of timber has been verified by material tests, that characteristic strength of 24 MPa and Young's modulus of elasticity 10 GPa have been confirmed; (ii) CFRP lamellas of cross-section of 50×1.2 with the tensile strength of 3 000 MPa and Young's modulus of elasticity of 155 GPa have been used.

Totally 18 non-strengthened timber beams (3 test specimens for each cross-section mentioned above) and 18 CFRP-strengthened timber beams (the same cross-sections with 3 specimens in each group) have been tested. The test specimens have been simply supported and loaded by the force F introduced as forces F / 2 to the beam span thirds, that means 4-points bending has been applied (see scheme and illustration in Fig. 3).

Illustration of the arrangement and realization of loading tests is shown in Fig. 3, CFRP lamella and strain gauges bonded to the bottom beam edge are seen in Fig. 4, as well as the examples of typical failure mechanisms, which are shown in Fig. 5.

4.2 *Particular test results*

Actual load-bearing capacities of "CFRP-timber" beams, that means ultimate moments obtained from loading tests, are listed in Table 1, as well as the predicted theoretical load-bearing capacities calculated as elastic bending moments with mean values



Figure 5. Examples of typical failure mechanisms.

Table 1. Load-bearing capacity of "CFRP-timber" beams: theoretical elastic moment capacity $M_{u,th}$ vs. experimental ultimate moments $M_{u,exp}$

Cross section	$M_{u,th}$ kNm	$M_{u,exp}$ kNm		
100 / 220-C	31.35	36.44	33.14	31.54
100 / 200-C	26.09	30.71	26.64	28.73
100 / 180-C	21.30	24.69	17.42	21.37
100 / 160-C	19.56	23.13	19.76	20.13
100 / 140-C	15.60	18.00	16.35	16.37
100 / 120-C	11.32	14.32	9.88	14.02

of measured timber strength and with mean values of Young's modulus of both materials.

In Figs. 6 and 7, the relationships of the deflections to bending moments during loading progress – "M – w" diagrams, are drawn. The theoretical elastic load-bearing capacities are added to these diagrams.

"M – w" diagrams mentioned may be used for the investigation of the rigidity of strengthened beams, to determine the actual flexural stiffness EI and the second moment of area I_i of the ideal cross-section, respectively. Using the actual moment I_i the interaction between CFRP lamella and base timber beam, among others, can be verified. The mutual interaction of both section parts, ensuring sufficient cross-section stiffness, assumes the fully rigid shear connection between both parts and is the necessary condition for the rightness of the elastic calculating approach based on the ideal (substitute) cross-section.

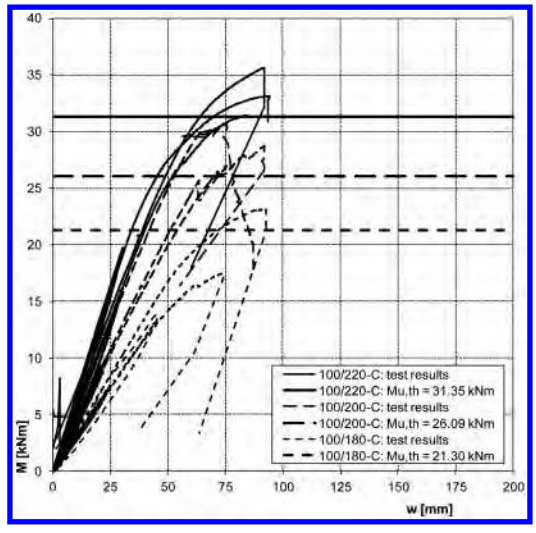


Figure 6. Test results and theoretical elastic capacities $M_{u,th}$: "CFRP-timber" sections 100/220-C, 100/200-C, 100/180-C.

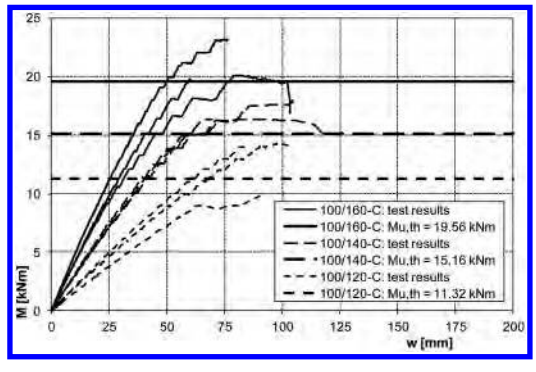


Figure 7. Test results and theoretical elastic capacities $M_{u,th}$: "CFRP-timber" sections 100/160-C, 100/140-C, 100/120-C.

From the deflection of simply supported beam loaded by forces F / 2 in the span thirds (4-points bending – see above), the flexural stiffness is

$$EI_i = \frac{23}{648} \cdot \frac{(F/2) \cdot L^3}{w} = \frac{23}{216} \cdot \frac{M \cdot L^2}{w}. \quad (8)$$

In the format (8), the ratio M / w can be substitute using this dependence taken from the linear part of "M – w" diagrams. Then, considering Young's modulus of timber by the value of 10 GPa (as above), the second moment of area can be expressed from the stiffness EI_i. The actual second moments of area $I_{i,exp}$ calculated according to the formula (8) using test results, in comparison with the theoretical second moments of area $I_{i,th}$, are listed in Table 2.

From Table 2 it is seen, that the actual second moments of area obtained rom the tests using formula (8) are in average by 2.4 % less only, than the theoretical. For comparison, the corresponding values have

Table 2. Second moment of area of "CFRP-timber" beams: theoretical $I_{i,th}$ vs. experimental $I_{i,exp}$

Cross section	$I_{i,th}$ mm^4	$I_{i,exp}$ mm^4	$I_{i,exp}/I_{i,th}$ —
100 / 220-C	$99.65 \cdot 10^6$	$102.22 \cdot 10^6$	1.026
100 / 200-C	$75.66 \cdot 10^6$	$77.44 \cdot 10^6$	1.024
100 / 180-C	$55.86 \cdot 10^6$	$52.15 \cdot 10^6$	0.934
100 / 160-C	$39.84 \cdot 10^6$	$39.12 \cdot 10^6$	0.982
100 / 140-C	$27.21 \cdot 10^6$	$25.90 \cdot 10^6$	0.952
100 / 120-C	$17.57 \cdot 10^6$	$16.52 \cdot 10^6$	0.940
Mean value of $I_{i,exp}/I_{i,th}$			0.976

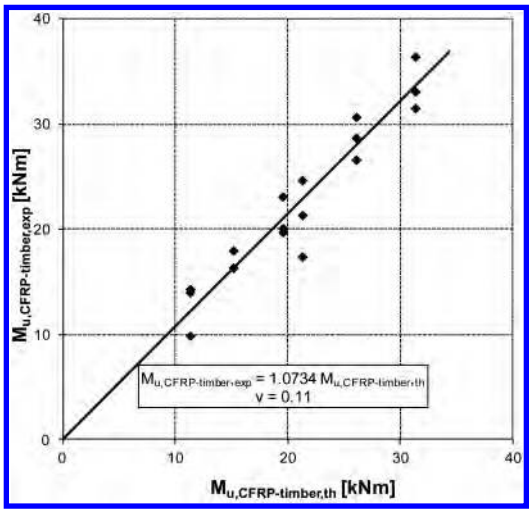


Figure 8. Comparison of experimental and theoretical load-bearing capacities (i.e. elastic moment capacity calculated for actual material properties) of "CFRP-timber" beams.

been also derived from the normal stresses measured on the surface of CFRP and timber on the bottom edge of the beams. The stresses have been obtained from the strains measured by strain gauges. The stress analysis going, among others, to the flexural stiffness, is in detail described in (Karmazínová 2013), for example. Based on that stress analysis, the mean value of the actual second moment of area derived from the tests was by 2.2 % more than the theoretically calculated value. The insignificant difference is probably caused by the errors of measuring instruments, which usually vary in the range of about from 2 % to 3 % and fully covers the differences. Thus, these two methods how to determine actual stiffness and the interaction of both cross-section parts give the same results and may be considered as essentially equivalent. In addition, using both procedures the results of one of them can be verified by the second one.

According to the experimental results described above, it may be assumed, that the concept of the capacity calculation arising from the elastic approach based on the ideal cross-section is applicable and appropriate. It can also be proved by Fig. 8 (see also test

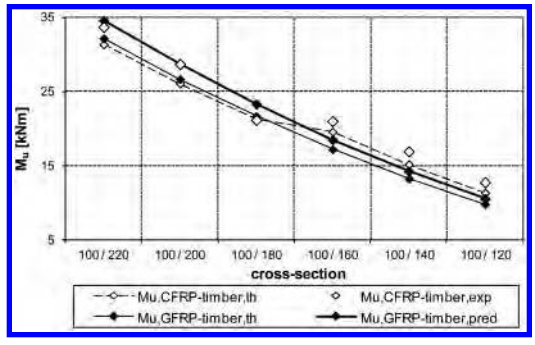


Figure 9. Comparison of load-bearing capacities: theoretical and experimental capacity of "CFRP-timber" beams; theoretical and predicted capacity of "GFRP-timber" beams.

evaluation in Karmazínová 2012a), where the comparison of test results with elastic calculation is seen and relationship and variation coefficient also show the suitability of elastic approach.

The effect of CFRP strengthening to the timber beams resistance increasing is significant related to the elastic behaviour only, if the lamellas of given geometrical and material parameters used; then, the usage of GFRP lamellas could be probably more effective because of more appropriate material properties, and thus because of more efficient utilization.

5 THEORETICAL PREDICTION OF LOAD-BEARING CAPACITY FOR "GFRP-TIMBER"

Because the configuration and technology of timber structural members strengthened by GFRP lamellas, here "GFRP-timber" beams, are practically identical with "CFRP-timber" beams, it may be expected, that the behaviour is very similar. So that, it is assumed, that the load-bearing capacity of both types of FRP-strengthened timber beams may be calculated according to the same approaches and principles.

Therefore, the theoretical prediction of expected load-bearing capacity of "GFRP-timber" beams is also based on the elastic concept using ideal (substitute) cross-section. The load-bearing capacities of "GFRP-timber" beams have been determined for the same timber and GFRP lamella cross-sections and the same timber properties as for "CFRP-timber" beams, and for the following material parameters of GFRP lamella: tensile strength of 1 000 MPa and Young's modulus of elasticity of 55 GPa.

To predict the expected load-bearing capacities of "GFRP-timber" beams, it is possible to arise from experimentally verified results of "CFRP-timber" beams, which confirm, that the actual bending moment capacity is about by 7.5 % higher (see Fig. 8) in comparison with theoretically calculated capacity. Because the cross-section configuration of "GFRP-timber" beams is analogical and the technology is the same as in the case of "CFRP-timber" beams, it may be concluded, that increasing in load-bearing capacity also

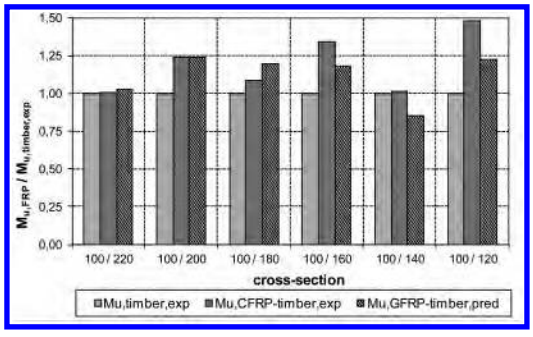


Figure 10. Relative comparison of load-bearing capacities: experimental capacities of "CFRP-timber" beams and predicted capacities of "GFRP-timber" beams in relation to experimental capacities of timber (only) beams.

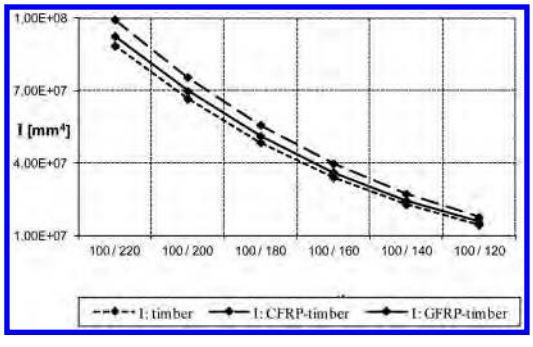


Figure 11. Comparison of second moments of area: "CFRP-timber", "GFRP-timber", timber only.

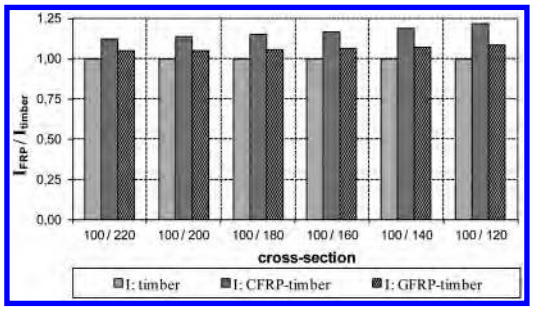


Figure 12. Relative comparison of second moments of area: "CFRP-timber" and "GFRP-timber" in relation to timber only.

can be in the range from about 7 % up to 10 % maximally, related to the theoretical elastic calculation, as shown in Figs. 9 and 10.

The same principle can be also used for the prediction of the second moment of area. In the text above it is seen, the actual second moment of area of "CFRP-timber" section is practically the same as the theoretical value based on the ideal cross-section principle. Then, the second moment of area of "GFRP-timber" section can be also calculated using the elastic approach based on ideal cross-section concept. The comparison of the second moments of area is depicted in Figs. 11 and 12.

6 CONCLUSIONS

From particular results verified experimentally, for "GFRP-timber" or "CFRP-timber" beams following partial conclusions may be deducted: (i) actual load-bearing capacity can be derived using the elastic calculation and increased about by 7 to 10 %; (ii) actual flexural stiffness can be determined as the stiffness of the ideal cross-section, practically exactly.

ACKNOWLEDGEMENT

The paper has been elaborated within the solution and financial support of the research projects of the Czech Ministry of Education, Youth and Sports: CZ.1.05/2.1.00/03.0097 (Centre of "AdMaS") and FAST S-11-32/1252 (university specific research).

REFERENCES

Ascione, L., Barbieri, A., Benedetti A. et al. 2007. *Guidelines for the Design and Construction of Externally Bonded FRP Systems for Strengthening Existing Structures*. National Research Council: Rome.

Cadei, J.M.C., Stratford, T.J., Hollaway, L.C. & Duckett, W.G. 2004. *Strengthening Metallic Structures Using Externally-Bonded Fibre-Reinforced-Polymers*, CIRIA: London.

Gilfillan, J.R., Gilbert, S.R. & Patrick, G.R.H. 2003. The use of FRP composites in enhancing the structural behaviour of timber beams. *Journal of reinforced plastics and composites*, Sage publications, Vol. 22, Issue 15, pp. 1373–1388.

Karmazínová, M. 2012a. Theoretical analysis and experimental verification of moment resistance of steel and timber beams strengthened by external CFRP composites. *Intl. Journal of Mechanics*, Vol. 6, Issue 3, pp. 168–178. ISSN 1998-4448.

Karmazínová, M. 2012b. Analysis of the actual behaviour, stress and moment capacity of composite beams composed of steel and glass-fibre-concrete, *International Journal of Mechanics*, Vol. 6, Issue 2, pp. 158–167. ISSN 1998-4448.

Karmazínová, M. 2013. Actual behaviour of composite externally CFRP-reinforced timber beams – stress analysis. *Intl. Jl. of Mechanics*, Vol. 7, Issue 1, pp. 1–9. ISSN 1998-4448.

Melcher, J., Karmazínová, M. & Pozdíšek, J. 2009. Experimental verification of behaviour of composite steel and glass-fibre-concrete beam. In *Proceedings of the 9th Intl. Conf. on Steel-Concrete Composite and Hybrid Structures ASCCS 2009* held in Leeds, Singapore: Research Publishing Services, 2009, pp. 390-395. ISBN 978-981-08-3068-7.

Research and Applications in Structural Engineering, Mechanics and Computation – Zingoni (Ed.)
© 2013 Taylor & Francis Group, London, ISBN 978-1-138-00061-2

Bond characterization between historical concrete substrate and SRG/SRP strengthening systems

E. Stievanin, F. da Porto, M. Panizza, E. Garbin & C. Modena
Department of Civil, Environmental, Architectural Engineering, University of Padova, Italy

ABSTRACT: Strengthening of existing reinforced concrete structures by using composite materials has been growing in popularity, since they are characterized by high strength-to-weight ratios and good versatility. Recently, beside common Fibre-Reinforced Polymers (FRP) that consist in various types of fibres (e.g. carbon, glass, aramid, basalt, etc.) embedded in a plastic matrix, mostly epoxy, new composites have been introduced; they are characterized by the use of small high-strength twisted steel wires as resisting elements, combined either with cementitious grouts (SRG) or epoxy (SRP) as matrix. Epoxy resins are widespread as composites matrix and adhesive, however they require special attentions like fireproof and UV protections; moreover, their substantial impermeability might cause compatibility problems, especially in the case of historical RC structures. Based on these observations, SRG have been developed to combine traditional materials, i.e. cementitious mortars and steel, in order to reach structural performances comparable to FRP materials, and meet additional requirements such as a lower cost, a simpler application and an improved compatibility with the original substrates. However, the structural performance of such strengthening systems strongly relies on the bond between reinforcement and substrate. The present work deals with the bonding performance of both SRP and SRG composites applied to a historical concrete substrate, investigated through pull-off and tangential shear tests. The influence of steel fibres and matrix (organic or inorganic) has been studied by combining two types of steel wires with either epoxy or cementitious mortar. Concrete samples were removed from the decommissioned St. Francesco bridge in Veneto (Italy), built in the Fifties: this allows testing the reinforcement bond performances on an historical concrete characterized by a mix design completely different from current ones. Pull-off and shear tests were carried out after a preliminary phase of material characterization, aimed at identifying materials mechanical properties, namely substrate, cementitious mortar and steel fibres.

1 INTRODUCTION

Repair of existing structures is often coupled with interventions needed to increase their load bearing capacity or their resistance against seismic actions.

The use of FRP (Fibre Reinforced Polymers) has become widespread during last decades (Meier 1995, Valluzzi 2008) for the strengthening of concrete and masonry structures. They are characterized by high strength, also in fatigue (Kim et al. 2008), and stiffness, low density, and versatility of application (da Porto et al. 2012). They exhibit excellent properties against corrosion and wear, combined with a low impact due to their good structural performances, related to very high strength-to-weight and elastic modulus-to-weight ratio.

FRP consist of fibres (mostly carbon and glass, but also aramid, basalt, and others) coupled to organic matrices (mostly epoxy) that bind fibres together and transfer stresses between fibres and substrate. On the other hand, these materials present some shortcomings to be accounted for, like an overall linear elastic behaviour until failure, a low shear resistance (perpendicularly to the fibres), a certain vulnerability to high temperatures, beside the absence of vapour permeability and relatively high costs.

Moreover, epoxy resins require certain additional precautions during their application. Catalysis reactions of the epoxy resin are strongly influenced by temperature: above 25–30°C, they considerably accelerate, while below 5°C the hardening hardly triggers. The presence of moisture can worsen the normal catalysis reaction as well, therefore substrates should be dry and possibly protected from rain. Skilled manpower and protective equipment are required, as epoxy resins have a certain toxicity.

Furthermore, in case of fire, high temperatures change epoxy properties and may compromise the effectiveness of the strengthening, therefore fireproof systems and protective coatings are required.

To overcome some of the limitations related to FRP, the use of steel fibres as resisting element, or composite materials with inorganic matrices, has been promoted in recent years (Huang et al. 2004). These systems are generally obtained coupling thin high-strength steel wires with either epoxy (SRP) or cementitious grouts (SRG), or adopting meshed fibres element suitable to be impregnated with mortars

Table 1. Cementitious mortars compared to epoxy resins as matrices for composite materials

	matrix type	
behaviour to high temp.	cementitious as the substrate	epoxy resin loss of consistence above 80°C
substrate moisture	helps adhesion	must be absent
workability	good	quick curing; temp. dependent
vapour permeability	yes	no
viscosity	high (tricky impregnation)	rather low
toxicity	rather low	protective equipment required

(TRM). A comparison of the main features / differences between cementitious and epoxy matrices is depicted in Table 1 (Stievanin 2012).

2 SCOPE

This paper presents and analyses the preliminary results of an experimental investigation about the effects of matrix type and steel fibres type on the bonding performance between historical concrete substrates and steel-based composite materials. Two commercially available thin steel wires (labelled as *fid* and *db*) were used as resisting element, while a cementitious mortar and a bi-component epoxy resin were adopted as matrix, thus obtaining four matrix/fibres combinations. Concrete samples used as substrate were extracted from the deck of St. Francesco bridge, a decommissioned structure located in Veneto (Italy) and built in the Fifties, therefore having mix design and mechanical properties rather different from modern concrete elements.

The experimental program was carried out in two phases. In the first one, pull-off tests were carried out on two strips of composite materials made by the cementitious mortar coupled with the two types of steel wires; epoxy was not tested since its behaviour is supposed to be known and, therefore, not relevant in this case. In the second phase, eight tangential bond tests (shear tests) were performed using four combinations of matrices (organic and inorganic) and steel fibres.

3 MATERIALS

3.1 *Concrete substrate*

In order to test concrete mechanical properties, nine cores were cut from a piece of slab obtained during the demolition of the bridge: six of them tested in compression (according to UNI EN 12390-3: 2003), the other three used to measure the elastic modulus (according to UNI 6556: 1976).

Table 2. Mechanical properties of concrete substrate and cementitious mortar (matrix).

ID	f_c [N/mm^2]	f_f [N/mm^2]	E_c [N/mm^2]
concrete	52.5	4.46*	33500
mortar	26.7	5.43	17800

* estimated according to Italian Building Code

Values of compressive strength (f_c), flexural strength (f_t) and elastic modulus (E_c) are shown in Table 2.

3.2 *Mortar matrix*

The cementitious mortar used as matrix is characterized by a fine particle size (less than 0.8 mm) to allow an easier and more effective impregnation of the steel fibres.

Compressive strength, flexural strength and elastic modulus were obtained by testing prismatic specimens ($40\times40\times160$ mm^3), according to UNI EN 1015-11: 2007 and UNI EN 13412: 2007, respectively.

Average values ?are listed in Table 2.

3.3 *Steel fibres*

The tested strengthening systems were made using two different steel reinforcements, characterized by similar mechanical properties, but different density and strand geometry.

The first one, Fidsteel 3X2-B 4-12-500 (herein labelled *fid*) is produced by Hardwire LLC. It is made of unidirectional twisted wires of Ultra High Tensile Strength Steel (UHTSS), about 6 mm spaced (1.57 strands/cm). Each steel strand is made by 5 wires: 3 straight filaments wrapped together by other 2 having a high curvature radius.

The second steel reinforcement (labelled *db*) was provided by Dalla Betta Group. It is composed by brass-coated unidirectional steel cords, about 3 mm spaced (3.15 strands/cm). Each strand is made by 19 wires twisted together.

For each reinforcement type, characterization tests were performed on both single wires and strands, according to ISO 6892-1.

Results are summarized in Table 3.

4 PULL-OFF TESTS

4.1 *Specimens preparation*

A concrete slab 16 cm thick, extracted from the deck of St. Francesco bridge, was used as substrate for the application of two SRG systems made coupling *fid* and *db* steel reinforcements to the inorganic matrix. Concrete surface was mechanically roughened to facilitate the adhesion of the composite materials. Dust was

Table 3. Mechanical properties of steel fibres

	fid 1 strand = 5 wires	*db* 1 strand = 19 wires
wire		
maximum load	320 N*	105 N*
tensile strength	2939 N/mm^2	3220 N/mm^2
elastic modulus	206 000 N/mm^2	-
wire area	0.1076 mm^2	0.0326 mm^2
strand		
strand area	0.538 mm^2	0.620 mm^2
n° strand/cm	1.57 strands/cm	3.15 strands/ cm
specific mass	670 g/m^2	750 g/m^2
equivalent thickness	0.084 mm	0.152 mm
failure load	1630 N*	2086 N
tensile strength	3033 N/mm^2	2766 N/mm^2
elastic modulus	190 000 N/mm^2	162 000 N/mm^2
strain at failure	1.50%	1.78%

* value from experimental tests

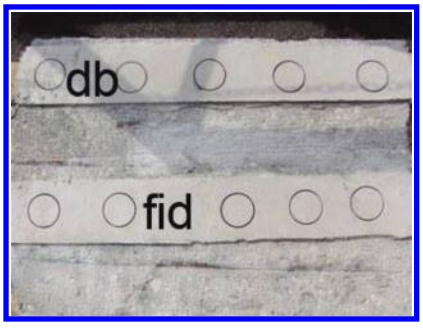


Figure 1. SRG strips applied to the concrete slab, after the cuts.

accurately removed using compressed air, and the surface was properly wet to avoid an excessive absorption of the matrix mixing water.

Two strips of SRG, 60 mm wide, were applied to the concrete substrate. After a curing period of 28 days, 5 circular cuts (50 mm of diameter) were made on the surface of each SRG system (Figure 1), several millimetres deep into the substrate, according to EN 1542 (2000).

4.2 *Pull-off test method*

Compared to other tests, the pull-off test is a simple and popular way to basically evaluate adhesion properties of layered materials (such as plasters or composites), in terms of failure modes and tensile strength (Bonaldo et al. 2005).

This test consists in applying a force, normal to materials' plane, to a metallic plate glued to the external surface of an area isolated by a cut that goes through materials' layers into the substrate.

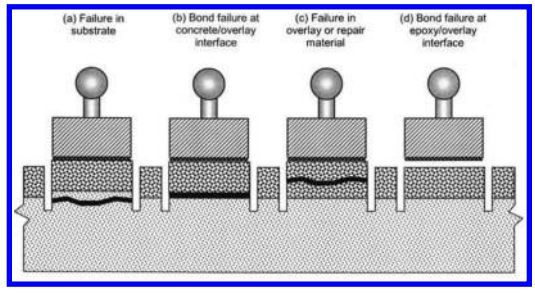


Figure 2. Pull-off failure modes (ASTM C 1583-04: 2004).

In this work, a core diameter of 48 mm, cut approximately 15 mm deep into the substrate, was adopted.

The pull-off strength f_h is defined as the maximum tensile force F_h divided by the area of the cut (Eq. 1, where D = cut diameter).

$$f_h = \frac{4F_h}{\pi D^2} \quad (1)$$

Possible types of failure, according to the American standard ASTM C 1583-04 (2004), are shown in Figure 2.

4.3 *Results*

Pull-off tests showed mainly failure type "b", that is bond failure at concrete/overlay interface (Figure 2). This failure indicates that there are no weaker elements in the strengthening system, being the matrix able to bind the steel strands together.

Photos in Table 4 show that traces of mortar and concrete coexist on both the failure surfaces.

The strengthening system with fibres type *fid* reached a slightly higher average tensile strength, 1.25 N/mm^2, compared to fibres type *db* (1.11 N/mm^2). Actually, being the failure located at the mortar-to-concrete surface, density and strand geometry of steel fibres should not affect the measured pull-off strength, therefore this difference could be imputed to factors like local superficial differences, preparations, etc.

Pull-off strengths and related photos of failure modes are reported in Table 4.

5 SHEAR TESTS

5.1 *Specimens preparation*

Eight concrete prisms 145 mm wide, 280 mm long and 110 mm thick, taken from St. Francesco bridge deck, were used as concrete substrate for tangential bond tests (shear tests).

Four strengthening systems were tested, made coupling each steel reinforcement (the same used for pull-off tests) either to the cementitious mortar or to an epoxy resin. Composite strips were 60 mm wide, hence, according to the different reinforcement density, 10 strands of *fid* fibres and 19 strands of *db*

Table 4. Summary of failure modes

ID *fid*	Pull-off strength (N/mm^2)	Photo	Failure type
FID1	0.57		B
FID2	1.32		B
FID3	1.20		B/C
FID4	1.36		B
FID5	1.81		B
Average:	1.25		

ID *db*	Pull-off strength (N/mm^2)	Photo	Failure type
DB1	1.08		B
DB 2	1.21		B
DB 3	1.00		B
DB 4	1.08		B
DB 5	1.18		B
Average:	1.11		

fibres were applied. Specimens details are reported in Table 5.

The surface of concrete prisms was mechanically roughened before bonding SRP and SRG strips, then dust and any trace of dirt was accurately removed before the application of composites (the surface was properly wet in the case of inorganic matrix). A reinforcement strip was applied on each prism, bonded for 250 mm along the main axis. About 200 mm of steel, protruding out above the prism edge, were used to clamp the reinforcement to the universal machine used for tests.

Table 5. Shear test matrix

ID	Steel fibres	Matrix
TCA_FID_01	*fid* (Fidsteel)	cem. mortar
TCA_FID_02		
EPO_FID_01		epoxy resin
EPO_FID_02		
TCA_DB_01		cem. mortar
TCA_DB_02	*db* (Dalla Betta)	
EPO_DB_01		epoxy resin
EPO_DB_02		

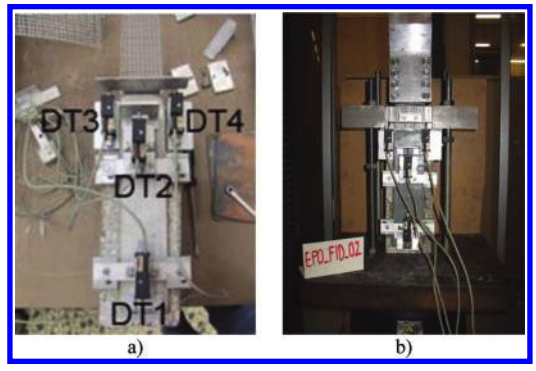


Figure 3. An instrumented specimen (a) and a sample ready to be tested (b).

5.2 *Shear test method*

Shear tests consist in reproducing the typical load condition of composite materials (reinforcement in tension) in order to produce tangential stresses at the composite-to-concrete interface and therefore test their bonding behaviour.

Force was recorded by a load cell, while four displacement transducers (Fig. 3a) were adopted to measure the mutual slip between substrate and reinforcement.

Specimens (Fig. 3b) were blocked into a universal machine by means of two stiff steel plates, and the protruding reinforcement was clamped to the moving beam in order to apply the axial load.

5.3 *Results*

The predominant failure mode was the debonding at the interface between concrete substrate and strengthening system. This happened for all samples, except *db* fibres coupled to mortar matrix, which showed a relevant slippage of strands into the matrix, without failing at the composite-to-concrete interface. The debonding mechanism was rather brittle, but reached higher load values.

Diagrams of axial force (P) vs. total displacement (δ) are given in Figure 4, while maximum loads and

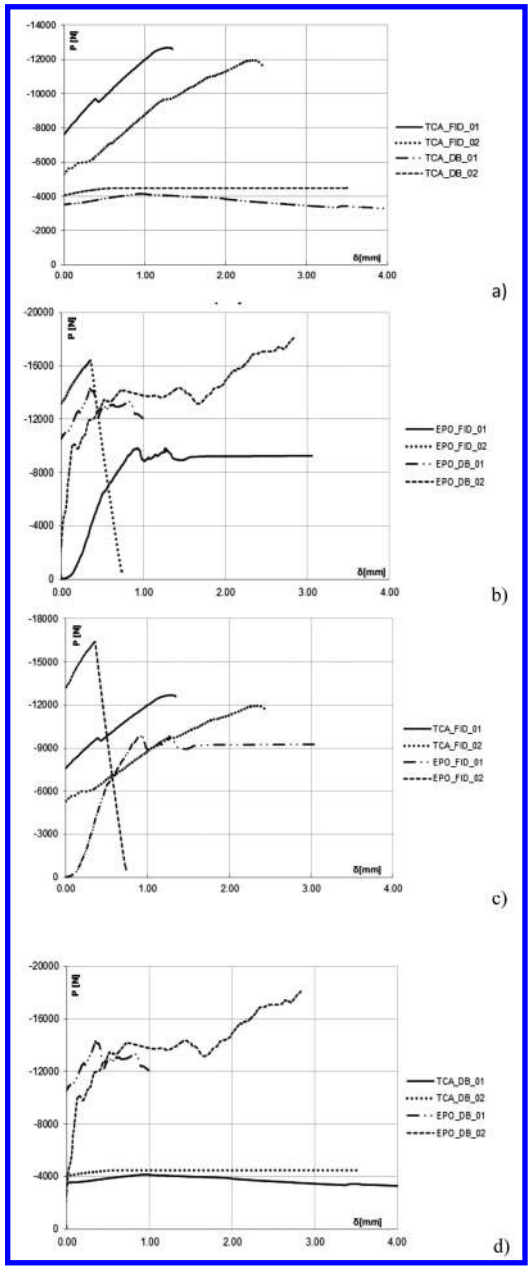


Figure 4. Load –displ. plots for: cementitious matrices (a); epoxy matrices (b); *fid* steel fibres (c) and *db* steel fibres (d).

related displacements are listed in Table 6. Charts in Figg.4-5 were obtained from data recorded by transducers DT3 and DT4 (Fig. 3). DT1, placed at the bottom, did not record displacement of composite material until failure, whereas DT2, located at the top of the strip, showed that the SRG/SRP slip became relevant only close to maximum load values, as shown in Figure 5.

All *fid* fibres showed a brittle failure (debonding failure or steel rupture), and allowed reaching load

Table 6. Shear tests: result summary

ID	P_{max} (kN)	δ_{max} (mm)	failure mode
TCA_FID_01	12.70	1.30	
TCA_FID_02	11.96	2.35	interface failure
average	12.33	1.83	
EPO_FID_01	9.48	0.85	fiber failure
EPO_FID_02	16.42	0.36	interface failure
average	12.95	0.61	
TCA_DB_01	4.16	0.97	
TCA_DB_02	4.48	0.70	fiber slip
average	4.32	0.84	
EPO_DB_01	14.31	0.35	
EPO_DB_02	18.16	2.84	interface failure
average	16.24	1.60	

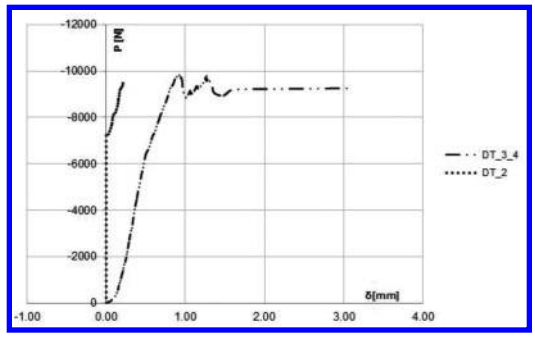


Figure 5. Example of displacements measured by DT3-4 compared to DT2.

values higher than in case of *db* fibres. Moreover, maximum loads were similar for mortar and epoxy matrix, 12.33 kN and 12.95 kN respectively. Reinforcement made of *db* fibres and mortar achieved lower values of maximum load (4.32 kN) and after the peak load *db* fibres slipped into the mortar matrix without reaching the bonding failure. On the other hand, steel type *db* coupled with epoxy reached an average maximum load of 16.23 kN, even higher than *fid* fibres, showing a brittle debonding failure at the composite-to-concrete interface.

6 CONCLUSIONS

This paper presents the preliminary results of an experimental activity aimed at investigating the bond between steel-based composite materials and historical concrete substrates, taking into account the effects of matrix (organic/inorganic) and type of steel fibres. The experimental program included the investigation of bond along normal (pull-off test) and tangential (shear tests) direction. The historical concrete substrate was extracted from the deck of a decommissioned bridge built in the Fifties.

About pull-off tests, specimens with *fid* steel fiber exhibited average pull-off strength of 1.25 N/mm^2, whereas average pull-off strength of SRG with *db*

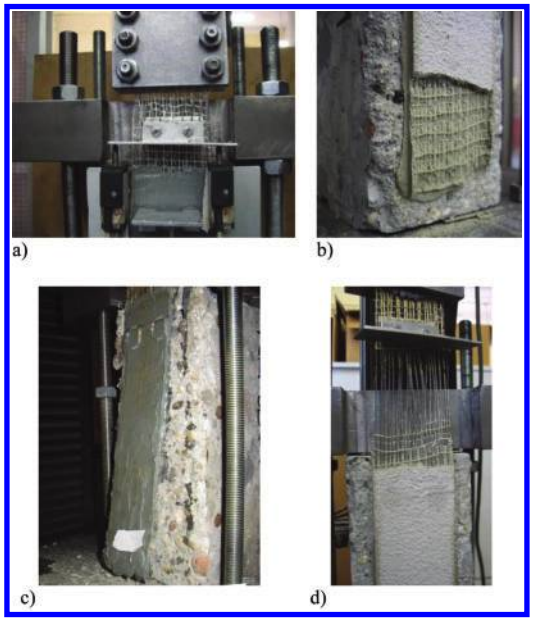


Figure 6. Fibres tensile failure (a); fibres slip into the mortar matrix (b, d); interface debonding (c).

fiber was slightly lower (1.11 N/mm^2). In general, failure occurred at the mortar-to-concrete interface, highlighting a rather good adhesion of the composite materials to substrate.

In the case of shear tests, *fid* fibres revealed a good adhesion with the matrix which caused debonding failure at the concrete interface. On the other hand, *db* fibres, although no particular problem was shown by pull-off tests, exhibited a loss of adhesion when impregnated with mortar which produced high slippage values, at rather low loads. This was probably due to a less effective strands arrangement and probably too low strands spacing that may worsen the impregnation with mortar.

REFERENCES

ASTM 2004. ASTM C 1583-04 – *Standard Test Method for Tensile Strength of Concrete Surfaces and the Bond Strength of Concrete Repair and Overlay materials by Direct Tension (Pull-off Method)*, American Society for Testing and Materials, 2004, West Conshohocken, Pa

Bonaldo, E., Barros, J.A.O., Lourenço, P.B. 2005. Bond characterization between concrete substrate and repairing SFRC using pull-off testing, *International Journal of Adhesion & Adhesives* 25: 463–474.

da Porto, F., Stievanin, E., Garbin, E., Valluzzi, MR. 2012. SRG application for structural strengthening of RC beams. In ACI (eds), *A fracture approach for FRP-concrete structures*; *ACI Special Publication 286, 1 May 2012*: 1–14.

Huang, X., Birman, V., Nanni, A. 2005. Properties and potential for application of steel reinforced polymer and steel reinforced grout composites, *Composites: Part B, Elsevier, 36* (2005) pp. 73–82.

ISO 2009. ISO 6892-1 – *Metallic materials – Tensile testing – Part 1: Method of test at room temperature*, International Organization for Standardization, Geneva, Switzerland

Kim, Y.J. and Heffernan, J. 2008. Fatigue behaviour of externally strengthened concrete beams with fiber-reinforced polymers: state of the art, *Journal of composites for construction, ASCE, May/June 2008*, pp. 246–256.

Meier, U. 1995. Strengthening of structures using carbon fibre/epoxy composites, *Construction and building materials, V.9, No.6, 1995,* pp. 341–351.

Stievanin, E. 2012. *PhD thesis – Retrofitting of Reinforced Concrete Moment Resisting Frames*. Dept. of Civil, Environmental, Architectural Eng., Univ.of Padova, Italy

UNI 1976. UNI 6556 – *Tests of concretes. Determination of static modulus of elasticity in compression*, Ente Italiano di Unificazione, March 1976, Milan.

UNI 2000. UNI EN 1542 – *Products and systems for the protection and repair of concrete structures. Measurement of bond strength by pull-off*, Ente Italiano di Unificazione, December 2000, Milan.

UNI 2003. UNI EN 12390-3 – *Testing hardened concrete. Compressive strength of test specimens*, Ente Italiano di Unificazione, August 2003, Milan.

UNI 2007. UNI EN 13412 – *Products and systems for the protection and repair of concrete structures. Determination of modulus of elasticity in compression*, Ente Italiano di Unificazione, January 2007, Milan.

UNI 2007. UNI EN 1015 – *Methods of test for mortar for masonry. Part 11: Determination of flexural and compressive strength of hardened mortar*, Ente Italiano di Unificazione, March 2007, Milan.

Valluzzi, M.R. 2008. Strengthening of masonry structures with Fibre Reinforced Plastics: from modern conception to historical building preservation", keynote lecture, *Proc. of VI Int. Conf. on Structural Analysis of Historic Constructions – SAHC08, Bath (UK)*, pp. 33–45.

Research and Applications in Structural Engineering, Mechanics and Computation – Zingoni (Ed.)
© 2013 Taylor & Francis Group, London, ISBN 978-1-138-00061-2

Methods of silo strengthening walls in practice.

M. Kaminski & M. Maj
Institute of Building Engineering Technical University of Wroclaw, Poland

ABSTRACT: Same methods of strengthening of concrete reinforced silo walls are presented in this article. Some methods of repairing silo are used in the same type of silo construction: external pressurising by using type "x" of connecting tendons, application of a discharge device reducing pressure of material, gunite with additional reinforced steel bars, using pressurised methods by external steel hooping. Additional the reliability of this strengthened silo were computed for rape silo with 19 diameter and about 30 m of height which were erected in '70 last century. The durability of strengthened silo walls were discussed. The article present discussion of increasing safety of silo construction by European Standards.

1 INTRODUCTION

After many years of exploitation some silos constriction need to be reconstructed, strengthened or changed in their static solution. It caused by such parameter as degradation of property of existing construction materials, increase standards alive loads as pressure, temperature, patching loads, decreasing value of parameters of construction designing materials, changing functions of silo etc. It is almost certain than each silo built more than twenty years ago must be strengthened. Strengthening of silo construction (silo walls, bottom, foundations or overlap) can be carried out generally in two ways, according to formula (Kaminski & M. Maj, M 2000):

$$A_c <= R_e \quad (1)$$

where A_c = effect of designed acting loads against silo construction (ex. tension), R_e = designed effect of resistant of silo contraction (ex. strength).

Decreasing of value of left side of this equation and increasing value of right side of this equation separately or simultaneously makes silo construction more safety.

Decreasing value of A_c can be achieved by decreasing mean value of loads or decreasing the value of coefficient of variation of loads separately or simultaneously. It follows from formula of design loads, which are function of mean value of load and coefficient of variation of loads and loads coefficient. The first simplest solution used for silo is reducing the level of filling of the silo of material stored in silo. The second solution is using perfect control of kinematic of discharging material. This allows to predict characteristic value of pressure and using appropriate load factors.

Perfect control of parameters of stores material as bulk density, moisture, internal temperature etc. reduce the value of coefficients of variation. Changing the flow material to chimney flow during discharging, what is possible for the discharging device, decrease value of material pressure. The same applies to reduce the flow velocity of the material.

The value of right side of discussed equation can be higher by such solutions as increasing the size of the silo wall, using materials of higher strength or strengthening of silo construction (adding new elements to the structure). The value of right side of equation (smaller or larger) is connected with static scheme used by designer and with designer's engineering experience, of course.

All these presented above methods were used by Authors to strengthen silo wall in their engineering and scientific practise.

2 CONCRETE RAPE SILO

There are 4 rape companies in Poland where are built the same rape batteries, i. E. in Bodaczów, Brzeg, Kruszwica and Pyrzyce. Concrete battery of 18 freestanding rape silos was built in '60 last century (Figure 1, 2) . Silo diameter is 19 m, high of silo is about 30 m, silo thickness is 0,25 m (Figure 1). Authors of this paper were involved in research of loads of pressure of rape against silo wall. They investigated the basic parameters of wall strength either. Pressure was investigated by sensors inserted into stored material. The sensor is presented on Figure 3.

Measured pressure was compared with the pressure calculated according to silos codes. Comparison of this values of pressure are shown on Figure 4. where; z = distance from the top surface of the filling, D = diameter of silo, α = no dimension coefficient from the formula for pressure $p_h = \alpha\gamma_s D$: where γ_s = specific weight of stored material, 1 = pressure according to the guidelines of the 60s last century, 2 = pressure adopted in the design of the silo in the 70 s of last century, 3 = experimental pressure by (Borcz &

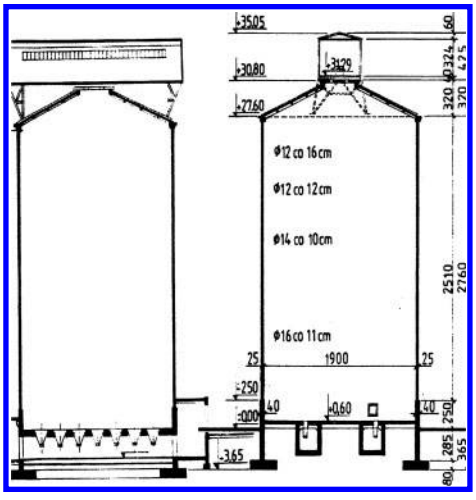


Figure 1. Cross section of reinforced concrete rape silo.



Figure 2. View of silo battery.



Figure 3. Sensor for measuring pressure into material.

Maj &Trochanowski 1991), 4 = pressure calculated for discharge device according to (Eurocode 1), 5 = calculated by polish code (PN-89/B-03262), 6 = pressure calculated according to (Eurocode 1).

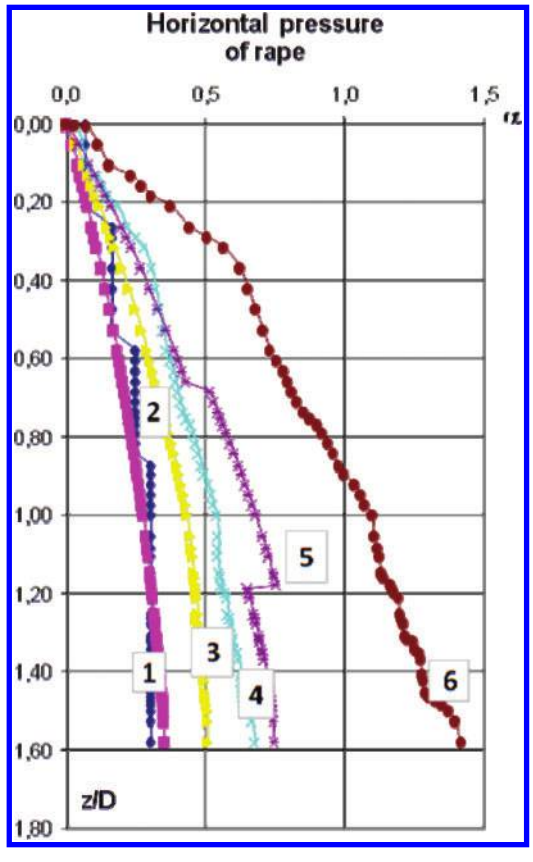


Figure 4. Pressure Comparison by different sources.

3 METHODS OF SILO STRENGTHENING WALLS IN PRACTICE OF 4 SILO BATTERIES

These batteries in each of the said four places were taken into account by experts and engineers from the beginning, when it was built for the period between 1995 to 2012. After first few years of exploitations their decided to strengthen silo walls. It was caused by changing standards requirements for the material pressure. Additional quality of silo wall was poor: many defects, imperfection, deficiencies in the number of horizontal reinforcement steel bars, low strength concrete. During the test of strength parameters of the silo walls it was found that values of coefficients of variation of parameters as steel bar diameter, distance between bars, concrete cover, concrete strength are rather high. They achieve value 0,4 and more. That means that significantly is reduced the value of strength of silo walls. Silo walls were strengthened using different technique. sby additional prestressed steel rings. After next 10 years of exploration appeared cracks on silo wall. In this time was developed the first polish silo code in 1984. From this time during next 30 years silo codes modified three times. In accordance with the requirements of the new standards increased value of silo pressure, loads caused by temperature etc. There were changed requirements for construction

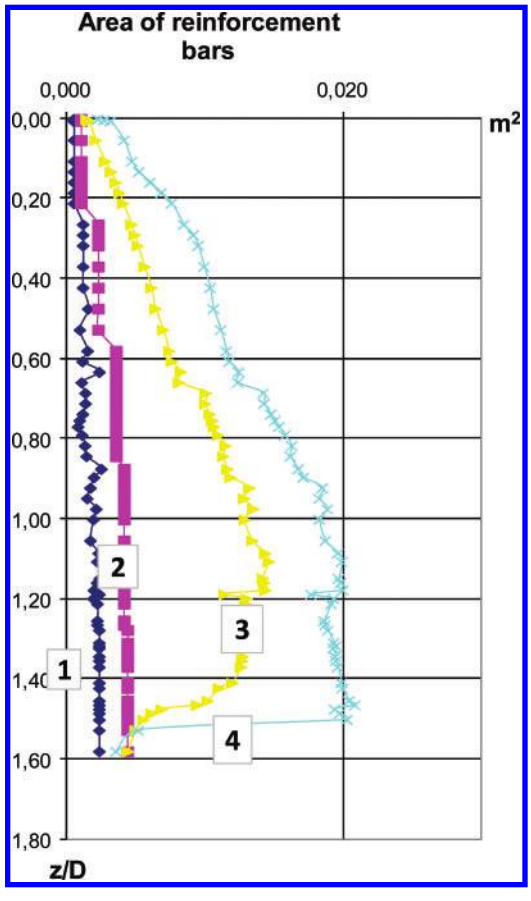


Figure 5. Comparison of reinforcement steel bars in rape silo.



Figure 6. Rape silos strengthened by steel hops.



Figure 7. Corrosion of steel hoops after more than 40 years of exploitation.

i.e for reinforcing bar diameters, laps, concrete cover, minimal concrete class for silo wall etc. Authors of this paper took part in strengthening these batteries in this period time. Depend on financial condition, depending on the strength of the walls of the silo, various methods have been used in strenghtening silos. The following methods of strengthening the silos:

1 shotcrete with additional reinforcement
2 prestresing tendons combined with the strengthening of concrete
3 reprofiling walls and cleaning reinforcement steel bars and supplemnt missing bars
4 using steel hoops instead of prestresing tendons
5 using low-height discharge device. It allow for decreasing pressure of flowing material about 20% – 30%.
6 reprofiling and reduce the level of filling a silo.

In this way in Bodaczów was used method of shotcrete and partially prestresing tendomns. In Kruszwica were used reprofilation and installation of low-height discharge device. In Brzeg three solutions were used prestresing tendons, steel hoops and low-height discharge device. On silos non repaired was used limited filling of silo to a designated height of the silo. In Pyrzyce reprofiling and low-height discharge device and limited filling of silo to a designated height of the silo.

On Figure 5 is shown amount of reinforcement steel bars existing and expected according to calculation, where 1 = area of existing reinforcement bars in silo wall before renovation, 2 = area of design reinforcement bars more than 40 years ago, 3 – area of reinforcement bars calculated according to polish code (PN-89/B-03262), 4 – area of reinforcement bars calculated according to (Eurocode 1).

In the silo battery repaired in Brzeg used all ways of reparation except the shotcrete. On Figure 6 it is shown silos strengthened by steel hops

After many years steel hoops and joins rings have corrosion, which is shown on Figure 7.

During renovation corroded parts were listed. Steel used before many years had a large relaxation and during renovation was changed to steel stronger. Some of

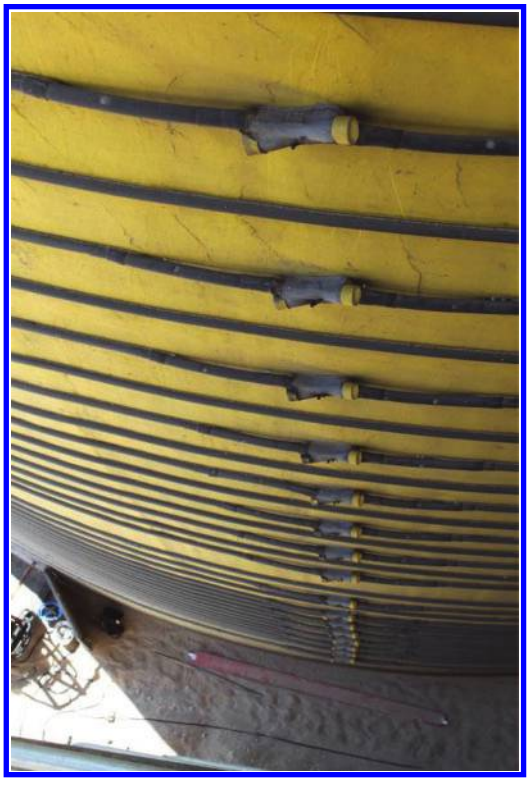


Figure 8. Silo wall strengthened by prestresing tendons.



Figure 9. Framework placed on the whole silo wall.

silos renovated in “90 last century were strengthened by prestresing tendons, which is shown on Figure 2, 8.

Figure 4 shows value if pressure of material against rape silo wall for different codes. Based on Authors investigation.

In the case of prestressing tendons concrete wall must be carefully prepared. Weak concrete must be replaced with a stronger. Reinforcement bars have again reinforced by welding and and re-connected with the concrete. This reparation presents Figure 9.



Figure 10. Framework placed on the whole silo wall.

Repair works are very complex and costly. Repair shall be subject to all of the silo wall. It shown on Figure 10.

4 CONCLUSIONS

Almost each silo after twenty years of service is suitable for repair Silo repair techniques depend on the changing standards first at all. The choice of the optimal service consists of a number of factors, including economic. In Poland, enjoying great success method mixed, including strengthening by tendons, using discharging devices, reduce the amount of filling materials stored etc.

In the decision of choice of strengthening methods are very useful own measurements of pressure and resistance parameters. The authors of this paper who are members of the research team in the Institute of Building Engineering of the Technical University of Wroclaw, for more than 40 years have been carrying out researches on silos for bulk materials. They had big influence on preparing polish silo codes . These investigations were carried out on silo batteries, free-standing silos and silo models. The researches include the evaluation of value of pressure and temperature field on the silo wall as well as temperature gradient, registration of simultaneity of these loads The researches include either the evaluation of influences of the wall stiffness and wall inclination on pressure changes, parameters connected with silo strength and geometry etc. (Kaminski, M. Maj, M 2006).

REFERENCES

Kaminski, M. Maj, M 2000 Reliability analysis of the global safety index design for conrete silo., The 3d Israeli Conference for Conveying and Handling of Particulate Solids, Dead Sea, Israel,

Borcz, A Maj, M. Trochanowski, A 1995, Guiding principles of silo designing, construction and operating, Prace Naukowe Instytutu Budownictwa Politechniki Wroclawskiej, Wroclaw 1991,

PN-89/B-03262, "Silosy zelbetowe na materialy sypkie. Obliczenia statyczne i projektowanie"

Eurocode 1 — Actions on structures — Part 4: Silos and tanks

Kaminski,M. Maj,M 2006 .Experimental and design loads of pressure of bulk materials against silo wall, Bulk Europe 2,Spain, Barcelona

Research and Applications in Structural Engineering, Mechanics and Computation – Zingoni (Ed.)
© 2013 Taylor & Francis Group, London, ISBN 978-1-138-00061-2

Study on mechanical behavior of circular concrete columns confined by HFRP under axial compressive load

Li-Juan Li, Shun-De Xu, Lan Zeng & Yong-Chang Guo
School of Civil and Transportation Engineering, Guangdong University of Technology, Guangzhou, Guangdong, China

ABSTRACT: The mechanical property of CFRP, BFRP, GFRP and their hybrid FRP were analyzed. The elastic module and compressive strength of CFRP, BFRP, GFRP and their hybrid FRP were tested. The experiment results show that the elastic module of hybrid FRP agree well with theoretical mixing rule while the tensile strength does not. The bearing capacity, peak strain, stress-strain relation of circular concrete columns confined by CFRP, BFRP, GFRP and hybrid FRP were analyzed under axial compressive load. The confining effectiveness of hybrid FRP on concrete columns was analyzed. Testing results show that the bearing capacity and ductility of concrete columns can be efficiently improved through hybrid FRP confining. A strength simulation model and a stress-strain whole process simulation model of hybrid FRP confined concrete columns were presented. The new stress-strain model has good simulation accuracy and does not need piecewise fitting compared with other hybrid FRP model. The new stress-strain simulation model is also suitable for single FRP confinement cases and is simple for use in design of structures.

1 INTRODUCTION

The superior mechanical properties of the fiber reinforced polymer (FRP) composite material, such as light weight, high strength, nice corrosion resistance, and its applicability to broad range of structural members, such as beams, columns, slabs, masonry and walls, led to the fast development of research of FRP materials (Teng et al. 2002, Saadatmanesh and Ehsani 1991, Sundarraja and Prabhu 2012). The advantages and disadvantages of using one kind of FRP materials, such as carbon fiber reinforced polymer (CFRP) glass fiber reinforced polymer (GFRP), or basaltic fiber reinforced polymer (BFRP) to strengthen concrete columns are obvious (Meier et al. 1993, Guo et al. 2009). Recently, research work about FRP strengthening method is focused on hybrid strengthening program, in which different FRP materials are used to achieve expected strengthening results (Chen et al. 2008, Li et al. 2009, Mosallam et al. 2012, Vanaja and Rao 2002), and obtain FRP confined new members (Guo et al. 2009).

The study on hybrid fiber reinforced polymer (HFRP) to confine concrete members had been mainly focused on HFRP reinforced concrete beams and columns (Li et al. 2009, Chen et al. 2012, Guo et al. 2012, Teng et al. 2012, Lau and Pam 2010, Rousakis and Karabinis 2012). To study the behavior of HFRP reinforced concrete structures, the fundamental step is to understand the basic mechanical behavior of the constitutive materials, reinforced concrete and FRP, separately. The nonlinear behavior of reinforced concrete such as concrete cracking, tension stiffening, shear retention, concrete plasticity and yielding of reinforcing fiber have been extensively studied by many researchers and numerous proper constitutive laws have been proposed (Chen 1982, Meyer and Okamura 1985, Hu and Schnobrich 1989, 1990). However, the studied on mechanics of HFRP confined concrete structures especially columns is limited. While, the stress-strain relation of HFRP confined concrete columns is necessary in design of structures especially for aseismic design of structures. Different stress-strain models of FRP confined concrete materials were presented by Farids and Khalili (1982), Miyauchi et al. (1999) and Samaan et al. (1998), however the most common one is the model presented by Teng et al. (2002), which had been accepted by most of the researches so far, but the model is still too completed to be used to engineering design easily. Therefore, appropriate modeling of the nonlinear behavior of HFRP confined concrete is still crucial.

2 TEST ON HFRP CONFINED CONCRETE COLUMNS

2.1 *Design of specimens*

In this paper, 30 cylinder specimens with diameter of 150 mm and height of 300 mm were cast for test, which is shown in Figure 1. The cubic compressive strength of concrete measured was 38.73 MPa. The frames of

Table 1. Mechanical properties of fibers Setting

Type of FRP	Tensile strength (MPa)	Elastic modulus (GPa)	Elongation (%)	Thickness (mm)
CFRP	4833	254.16	1.71	0.167
BFRP	1575	83.98	2	0.153
GFRP	1079	69.45	2.23	0.111



Figure 1. Specimen columns. (a) Specimen un-wrapped (b) Specimen wrapped.

specimens were removed in 24 hours after pouring, and the specimens were maintained in standard curing room for 28 days to attach HFRP, including CFRP, BFRP and GFRP. The related mechanical properties of the three fibers were measured in the test and are shown in Table 1.

2.2 *Wrapping and loading approach*

By using the method of wet sticking paste, HFRP was pasted on the surface of columns with resin completely infiltrated. The confining HFRP has a width of 300 mm. There is no lapping joint for HFRP in height of columns. The lapping joint length was set 150 mm in circumferential direction and joints were deliberately offset. Two layers of CFRP with 50 mm width were pasted on ends of FRP sheets in order to prevent the pre-fracture of top of columns. Specimen number and the types of FRP are shown in Table 2.

3 TEST RESULTS AND ANALYSIS

3.1 *Compressive strength and deformation*

The bearing capacity, circumferential and longitudinal strains of concrete columns were measured from the test and are shown in Table 3.

Compared with specimen P0 without FRP confinement, the compressive strength of specimen C1G1, C1B1and B1G1 with two layers of fibers is increased by 134%, 136% and 67% respectively. The compressive strength of C1G1 and C1B1 are nearly the same,

Table 2. Types of FRP confining

Specimen	Fiber wrapping approach	Numbers of specimen	Types of FRP
P0*	None	3	—
C2	Two layers of CFRP	3	1
B2	Two layers of BFRP	3	1
G2	Two layers of GFRP	3	1
C1B1**	One layer of CFRP/ one layer of BFRP	3	2
C1B2	One layer of CFRP/ two layers of BFRP	3	2
C1G1	One layer of CFRP/ one layer of GFRP	3	2
C1G2	One layer of CFRP/ two layers of GFRP	3	2
B1G1	One layer of BFRP/ one layer of GFRP	3	2
C1B1G1	One layer of CFRP/ one layer of BFRP/ one layer of GFRP	3	3

* P0 refers to the normal concrete specimen, while B, G, C refers to BFRP, GFRP and CFRP respectively.
** C1B1 means that the specimen is wrapped by one layer of CFRP and one layer of BFRP from inner to outside, and the others are the same.

but the circumferential strain of fiber in C1G1 is obviously better than that in C1B1, which suggests that if the fiber elongations are appropriate, C1G1 can take the advantage of the fiber with high elongation and delay the FRP damaging more effectively, which makes full use of the ductility of fibers and increases the strength of specimens.

The strength of concrete columns confined by three layers of FRP is higher than that by two layers. Moreover, the compressive strength of C1G2 and C1B2 is higher than that of C1B1G1 which is higher than that of C1B1 only by 1.57 MPa. It is suggested that the ways of bonding and connection have effect on specimens, but the confining effectiveness will not increase with the increase of fiber types. It is suggested that three kinds of fibers are not suitable to be used together in practice.

The circumferential strains of C2, G2 and B2 are 1.11%, 1.23% and 1.22% respectively when broken, while the circumferential strains of C1G1 and C1B1 are 1.39% and 1.26%, which is obviously higher than that of single type fiber, such as C2, G2 and B2, the reason is that hybrid fibers can make full use of the property of high elongation to enhance the ductility of specimens. However, the circumferential strain of B1G1 is lower than that of B2 and G2. The reason why the hybrid effect of B1G1 is not so well may result from the different material characteristics of BFRP and GFRP, such as GFRP is rather smooth on surface while BFRP is relatively rough. The mechanical properties of specimens are affected by the different properties of fiber surface along with the bonding and connection between fibers. The circumferential strains of the concrete columns confined by three layers of

Table 3. Experimental results

Specimen	Bearing Capacity	Relative value (MPa)	Longitudinal strain	Relative value (10^{-6})	Circumferential strain	Relative value (10^{-6})
P0	31.72	1.00	3017	1.00	2118	1.00
C2	92.87	2.93	27937	9.26	11173	3.70
G2	47.63	1.50	10805	3.58	12252	4.06
B2	57.29	1.81	13403	4.44	12254	4.06
C1G1	74.19	2.34	20277	6.72	13870	4.60
C1G2	83.81	2.64	21569	7.15	14088	4.67
C1B1	74.73	2.36	20597	6.83	12551	4.16
C1B2	87.77	2.77	24000	7.95	13106	4.34
B1G1	53.12	1.67	12153	4.03	11990	3.97
C1B1G1	75.56	2.38	20153	6.68	12869	4.27

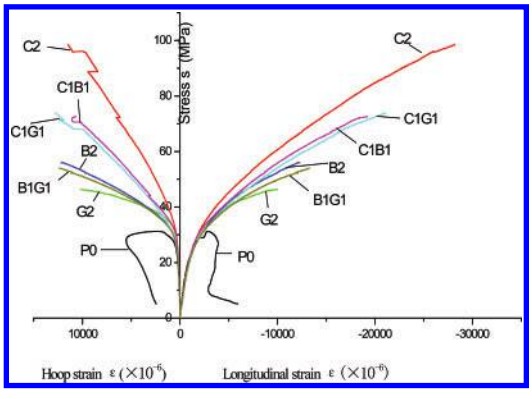


Figure 2. Stress-strain whole process curves of specimens with 2 layers of FRP.

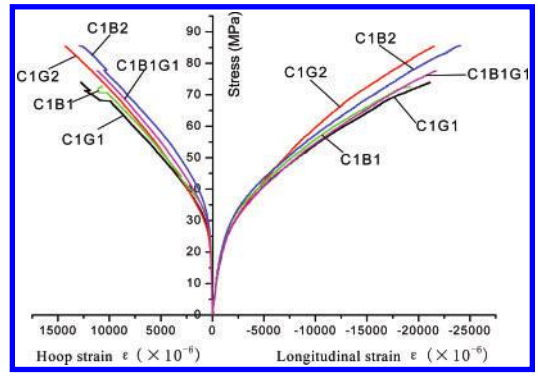


Figure 3. Stress-strain whole process curves of specimens with 3 layers of FRP.

HFRP, such as C1G2 and C1B2 are higher than that by two layers, such as C1G1 and C1B1 when broken, which indicates that with the increase of layers of FRP, the hybrid effect can be fully developed and the ductility of concrete columns confined by HFRP can be improved.

3.2 *Effects of fiber layers on stress-strain relations*

Stress-strain whole process curves of specimens are shown in Figure 2 and Figure 3. The longitudinal strain is calculated by the average value of LVDT, while the circumferential strain is calculated by the average value of circumferential strains.

It can be seen from Figure 2, that compared with columns without FRP, the stress-strain curves of circular concrete columns confined by FRP are nearly the same when the circumferential strains is smaller than peak strain of P0. The circumferential strain of concrete is small before reached peak strength and will increase greatly after peak point. At the period before peak point, the circumferential expansion of concrete was not big enough, and the confining effect of FRP could not be acted. When the strength reached pick strength of P0, the compressive strength of concrete columns rises considerably, but the slopes of stress-longitudinal strain curves dropped sharply, and are far more below than that of the first segment. The slopes of the curves in the second segment are related with the stiffness of HFRP, it seems a linear relationship basically. The intersection point of the extension line in the second segment of curve's with the stress axis is close to the peak strength of P0.

For the concrete columns confined by 2 layers of FRP, the slopes of longitudinal strain are nearly the same. That is to say, the trends of longitudinal strain are similar, but the slopes of circumferential strain are significantly different, whose trends are affected by types of hybrid fibers. The stiffness of the circumferential strain in the reinforced segment can be divided into four groups as (1) C2, (2) C1B1 and C1G1, (3) B2 and B1G1, (4) G2. The stiffness of specimen in hardening section has a little difference, and decrease from the first group to the fourth group. As to the stress-circumferential strain relation curves of columns confined by HFRP, the stiffness in the hardening segment is determined mainly by the fiber of low elongation, and affected by fiber of the high elongation. Circular concrete columns can take the advantage of inhibiting fiber cracks from extending of high elongation fiber, which helps the redistribution of internal stress in HFRP, decreases the development of circumferential strain and delays the fracture of structures.

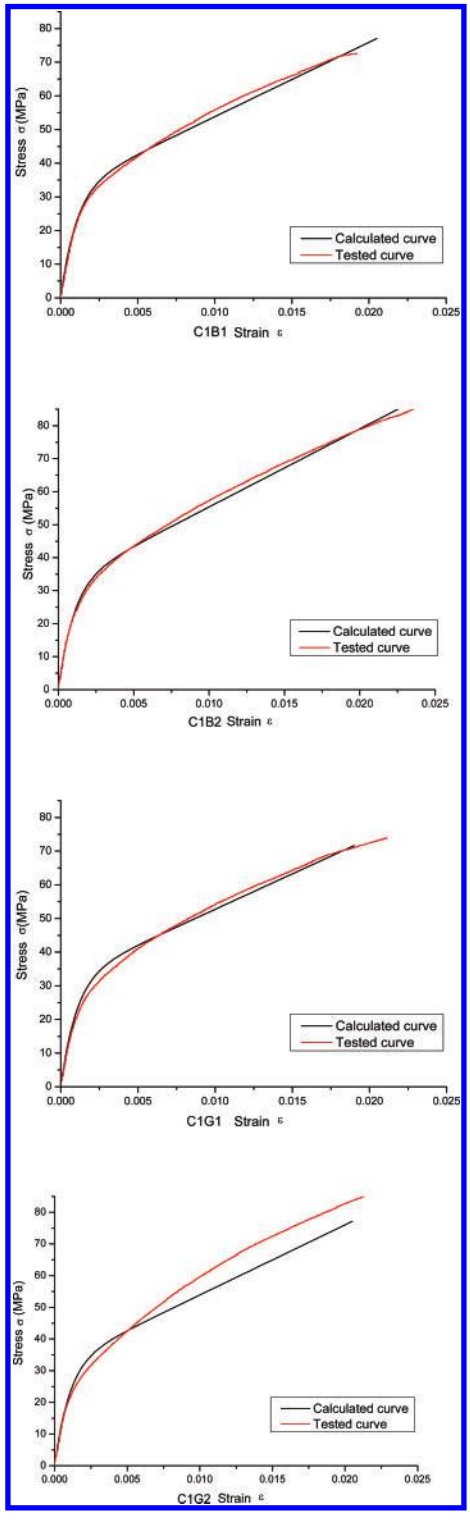


Figure 4. Stress-strain curves of HFRP confined concrete columns obtained in this paper.

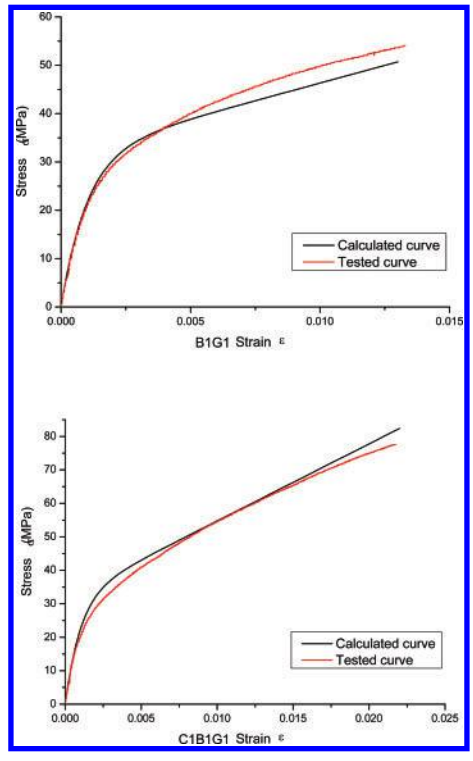


Figure 4. (*Continued*)

It can be seen from Figure 3, the stiffness of C1G2 and C1B2 in the hardening segment increases compared with that of C1B1and C1G1 when columns are confined by 3 layers of FRP. The increase of stiffness of specimen in the hardening segment can be achieved by increase of fiber layers and thus the effect of confinement can be improved. However, compared with that of C1B1, the slope in the hardened segment of C1B1G1 is not increased, which indicates that too many types of fibers may have a negative influence on confinement effect because of too many different fiber bonding and connections.

As for stress-circumferential strain relation curves of columns confined by HFRP, the stiffness in the hardening segment is various. It can be seen from Fig. 2 that the circumferential stiffness can be sorted as C1B2 > C1B1G1 > C1G2 > C1B1 > C1G1 when confinement increased from 2 layers to 3 layers, which matched the confining stiffness of FRP well. That is to say, the hybrid approach of fibers has great effects on the development of the hardening stiffness in circumferential direction. The bearing capacity of circular concrete columns confined by HFRP is controlled by the fibers of low elongation, while the fibers with high elongation helps to enhance the ductility of columns mainly, thus reduces the speed of development of the circumferential strain in hardening segment and postpones the fracture.

4 STRESS-STRAIN RELATION MODEL

According to the test results, a simple and accurate index model of stress-strain relation for concrete confined by HFRP is presented in this paper. The model is given as follows:

$$\sigma_c = f_{co}^{'}(1 - e^{-1000\varepsilon}) + E_2\varepsilon, when 0 \le \varepsilon \le \varepsilon_{cc} \quad (1)$$

$$E_2 = \frac{f_{cc}^{'} - f_{co}^{'}}{\varepsilon_{cc}} \quad (2)$$

where, E_2 is the slope of the second segment.

The stress-strain relations obtained from simulation model and test are presented in Figure 4. It can be seen from Figure 4 that the theoretical model presented in this paper agree well with experimental results of stress-strain relationship of concrete confined by HFRP.

5 CONCLUSION

The high elongation property of glass fiber can be fully used to prevent cracks from stretching if it is used by HFRP reinforcement to confine concrete columns. The fracture strain of hybrid FRP confined concrete columns can be obviously improved than that of single fiber confined columns. The fracture of columns can be delayed by reducing the speed of the development of circumferential strain. On the other hand, the stiffness of circular concrete columns confined by HFRP can be improved by taking the advantage of the low elongation of carbon fibers.

The confinement effectiveness is influenced by the bonding and connections of fibers, but does not increase with the increase of types of fibers. It seems using three or more kinds of hybrid fibers to confine concrete components cannot get better results. the confinement effectiveness of C1G2 is the best within the test extents of three-layer fibers.

6 ACKNOWLEDGMENTS

This research was funded by the National Natural Science Foundation of China (Project No. 51278129) and the Foundation of Guangdong Provincial Transportation Department (Project No. 2012-04-013).

REFERENCES

Chen, G.M., Chen, J.F. & Teng, J.G. (2012). Behaviour of FRP-to-concrete interfaces between two adjacent cracks: A numerical investigation on the effect of bondline damage, *Const. Build. Mater.* 28: 584–591.

Chen, W.F. (1982). *Plasticity in reinforced concrete.* McGraw-Hill.

Chen, Z.F., Wan. L.L. & Lee. S. (2008). Evaluation of CFRP, GFRP and BFRP material systems for the strengthening of RC slabs. *J. Reinfo. Plas. Compos.* 27(12): 1233–1243.

Farids, M.N. & Khalili, H. (1982). FRP-Encased concrete as a structural material, *Magaz. of Concr. Rese.* 34(121): 191–202.

Guo, Y.C., Huang, P.Y., Yang, Y. & Li, L.J. (2009). Experimental studies on axially loaded concrete columns confined by different materials, *Key Eng. Mater.*: 400–402, 513–518.

Guo, Y.C., Li, L.J., Chen, G.M. & Huang, P.Y. (2012). Influence of hollow imperfections in adhesive on the interfacial bond behaviors of FRP-plated RC beams, *Const. Build. Mater.* 30: 597–606.

Hu, H.T. & Schnobrich, W.C. (1989). Constitutive modelling of concrete by using nonassociated plasticity, *J. Mater. Civil. Eng. (ASCE)* 1(4):199–216.

Hu, H.T. & Schnobrich, W.C. (1990). Nonlinear analysis of cracked reinforced concrete, *ACI Struct. J.* 87(2): 199–207.

Li, L.J., Guo, Y.C., Huang, P.Y., Liu, F., Deng. J. & Zhu, J. (2009). Interfacial stress analysis of RC beams strengthened with hybrid CFS and GFS, *Const. Build. Mater.* 23(6): 2394–2401.

Meier, U., Deuring, M., Meier, H. & Schwegler, G (1993). *Strengthening of structures with advanced composites. Alternative materials for reinforcement and prestressing of concrete*. Glasgow, Scotland: J.L. Clarke/Chapman & Hall.

Meyer, C. & Okamura, H. (1985). Finite element analysis of reinforced concrete structures, *ASCE*.

Miyauchi, K., Inoue, S., Kuroda, T. & Kobayashi, A. (1999). Strengthening effects of concrete columns with carbon fiber sheet,*Transa. Japan Concr. Insti.* 21: 143∼150.

Mosallam, A., Taha, M.M.R., Kim, J.J. & Nasr, A. (2012). Strength and ductility of RC slabs strengthened with hybrid high-performance composite retrofit system, *Eeg. Struct.* 36: 70–80.

Rousakis, T.C. & Karabinis, A.I. (2012). Adequately FRP confined reinforced concrete columns under axial compressive monotonic or cyclic loading, *Mater. Struct.* 45(7): 957–975.

Saadatmanesh H. & Ehsani M.R. (1991). RC beams strengthened with FRP plates II: analysis and parametric study, *J. Struct. Eng. (ASCE)* 117(11): 3434–55.

Samaan, M., Mirmira, A. & Shahawy, M. (1998). Model of concrete confined by fiber cComposites, *J. Struct. Eng. (ASCE)* 126(9): 1025–1031.

Sundarraja, M,C. & Prabhu, G.G. (2012). Experimental study on CFST (concrete filled steel tubular) members strengthened by CFRP composites under compression, *J. Constr. Steel Res.* 72: 75–83.

Teng, J.G., Chen, .J.F., Smith, S.T. & Lam, L. (2002). *FRP-Strengthened RC Structures.* John Wiley & Sons, Ltd.

Teng, J.G., Zhao, J.L., Yu, T., Li, L.J. & Guo, Y.C. (2012). Recycling of coarsely-crushed concrete for use in FRP tubular columns, *The First International Conference on Performance-based and Life-cycle Structural Engineering,* December, HongKong.

Vanaja & Rao, RMVGK. (2002). Fibre fraction effects on thermal degradation behaviour of GFRP, CFRP and hybrid composites, *J. Reinf. Plasti. Compos.* 21(15): 1389–1398.

Research and Applications in Structural Engineering, Mechanics and Computation – Zingoni (Ed.)
© 2013 Taylor & Francis Group, London, ISBN 978-1-138-00061-2

Research on concrete repair materials

G. Lagoda
Warsaw University of Technology, Warsaw, Poland

T. Gajda
Road and Bridge Research Institute, Warsaw, Poland

ABSTRACT: The methodology and the repair materials essential research activity, which could ensure reliability of bridge structures, should be the choice base and the realization of investigations, which was simulated of material behaviour in time. The test to hasten age of the concrete repair materials, which estimates the durable adhesiveness executed layers to the concrete base and the mechanical properties change is investigated in freeze resistant test performed in the climate chamber. The freeze resistance test methods (cyclic freezing and thawing) may be different, as exemplified by tests repair mortars in accordance to the EN 1504-3 and tests commonly used in the Polish market according to the Polish Guidelines. The paper presents the most important issues concerning repair materials test methods used in Poland, which simulate their behavior during the cyclic freezing and thawing.

1 INTRODUCTION

The concrete bridge structures repair work durability is the main issue from the user point of view, when assessing the effectiveness of repair materials. As the durability one should understand the repaired structure ability to ensure the performance, not worse than before the repair, and to guarantee reliability in the assumed service life with the minimum maintenance costs. The greatest impact on the repair durability, with the use of repair materials, in Polish conditions has the resistance to the cyclic freezing and thawing. This is directly connected with the location of Poland in the transitional climate, which is something between temperate oceanic climate in the west and the moderate continental climate in the east of the country. The consequence of this location is a big difference in temperatures between winter and summer - summer temperature reaches above 30°C, and in winter often fall below −20°C. Additionally there are frequent passages through the freezing/thawing temperature 0°C. There are about 100 such passages through the temperature 0°C yearly in Polish climate. The use of concrete repair material characterized by the lack of resistance to cyclic freezing and thawing is often the main cause of repair failure. The structures damage repair caused by cyclic freezing and thawing are long-lasting and expensive. This is in particular important in case of bridge structures, which are most exposed to the temperature and weather conditions changes. It is therefore very important task to select the appropriate repair materials, which are characterised by high resistance to cyclic freezing and thawing for restoring the concrete structures.

Usually, the repair assessment, carried out on the basis of the immediate investigation, is based on the two elements. The one judges whether the repairing material adhesives to the repaired component and the other whether the fixing material has the required mechanical properties. The problem, however, is that no one is interested in the immediate adhesion which is the adhesion determined straight forward after the application, neither the immediate strength, determined usually after 28 days of hardening. Finding this values is not a problem at all, usually. The problem is that the durable adhesion has to be assessed, which is the repairing material adhesion presented after several or several tens of years. Moreover the material change strength properties in that time has to be predicted as well. Therefore, the implemented methodology and the repair materials essential research activity, which could ensure reliability of bridge structures should be focused on defining and implementation of ageing tests, which simulate the material behavior over the time in the best way. Further in this article there will be the methodology and the repair materials ageing tests types used in Poland presented.

2 CLASSIFICATION OF MATERIALS FOR REPAIRS

Repair materials for concrete bridge structures are used for example:

– to fill the losses in load-bearing elements, which have arisen as a result of mechanical damage and caused by the corrosion;

– to lay the levelling layer on bridge deck, in particularly loaded with pedestrian or vehicle traffic;
– to retrofit and level (smooth) carrying elements concrete surface;
– to replace damage elements.

The materials for concrete bridge structures repair can be divided into three groups, depending on type of used binders:

– CC (Cement Concrete) type hydraulic mortar and concrete – mortars and concretes based on hydraulic binder, which is blended together with graded aggregates and may include admixtures and additions and which, when mixed with water, set by a hydration reaction;
– PCC (Polymer Concrete Cement) type polymer hydraulic cement mortars or concretes - hydraulic mortars or concretes modified by the addition of polymer additives, which are added in sufficient quantity to give specific properties. The most commonly used polymers are:
  – acrylic, methacrylate or modified acrylic resins as water-soluble powders or aqueous dispersions,
  – vinyl mono-polymers, co-polymers and ter-polymers as water-soluble powders or aqueous dispersions;
  – styrene butadiene rubber as aqueous dispersions
  – natural rubber lattices;
  – epoxies;
– PC (Polymer Concrete) type polymer mortar and concrete – blended mixtures of polymer binder and graded aggregates which are set up by polymerisation reaction.

Due to the application objectives one can specify the following concrete bridge structures repair materials (mortar):

– smoothing mortars – mortars intended for laying the coatings to a thickness of 5 mm;
– repair mortars – mortars intended for laying the coatings to a thickness of 40 mm;
– fast acting mortars – mortars characterized by a very rapid increase in strength, such as the mortar used for tunnels leaks impound, manhole covers deposition;
– special mortars – mortars with unusual properties for special applications, e.g. to perform bearings grout, self-compacting.

According to the standard EN 1504-3, depending on user requirements, repair materials are divided into two groups:

– for non-structural repair, in which one can distinguish R1 and R2 class materials;
– for structural repair, in which one can distinguish R3 and R4 class materials.

The compressive strength is the main criterion for classifying repair material class according to the EN 1504-3 standard. According to this criterion, the compressive strength of repair materials for the relevant class should be at least:

- – 10 MPa in case of the class R1,
- – 15 MPa in case of the class R2,
- – 25 MPa in case of the class R3,
- – 45 MPa in case of the class R4.

In Poland, the concrete bridge structures are usually made of concrete from C25/30 to C50/60 class according to the PN-EN 206-1. Therefore, the repairs are performed with the use of repair materials class R3 or R4.

3 AGING TESTS OF REPAIR MATERIALS

The freeze resistance test in climate chamber is widely used for decades concrete repair materials ageing investigation in Poland. On the basis of that test the repairing layers and the base material durable adhesion and their strength properties changes are assessed.

The test is completed on the basis of the Road and Bridge Research Institute test procedures developed on the basis of the freeze resistance investigation according to the Polish standard PN-88/B-06250 *Concrete*.

The test is performed under the following conditions:

– temperature changes from $-18°C \pm 2°$ C to $18°C \pm 2°C$;
– the specimens thawing completed in the water;
– freezing specimens are soaked with the water, with the water pumped out form the chamber;
– there are 200 number of freezing and thawing cycles.
– freezing and storage in water cycle takes 4 h, while the defrosting one between 2 h and 4 h

There are following values identified on the basis of the above test:

– peel strength with the use of the pull-off method, after 200 cycles of freezing and thawing in water at the temperature of $-18 \pm 2°C / +18 \pm 2°C$;
– freeze resistance after 200 cycles of freezing and thawing in water, at the temperature $-18 \pm 2°C / +18 \pm 2°C$ (weight loss, flexural strength decrease and compressive strength decrease).

In case of repair mortars peel strength determination, in other words their adhesion, after freeze resistance testing, the mortar are laid on the frost-resistant C25/30 class concrete slabs. The minimum concrete slabs dimensions are 300 × 300 × 5 mm. There should be at least two slabs, which are covered with the repair material or repair complete system. After seasoning, one slab is tested for freeze resistance and the other one is kept in the laboratory. After finishing the required number of freezing and thawing cycles, which are usually 200 cycles, on both slabs 50 mm diameter discs are glued to perform adhesion test of the layer laid. The "pull-off" method is employed



Figure 1. The specimen after test “pull-off”.



Figure 2. The specimen after 200 freezing and thawing cycles – visible cracks grid.



Figure 3. The specimens that pass 200 freezing and thawing cycles.



Figure 4. The specimens that were damaged during 200 freezing and thawing cycles.

The basic criteria for assessing the repair mortar adhesion test are as follows:

– average adhesion repair mortar to the substrate after 28 days of hardening, which is the value of adhesion of the material not exposed to freezing and thawing cycles should be not less than 2.0 MPa (in case of smoothing mortar $\geq$ 1.5 MPa);
– average adhesion of the material exposed to the freezing and thawing cycles should be not less than 1.5 MPa (in case of smoothing mortar $\geq$ 1.2 MPa).

The figure 1 shows the repair mortar specimen after test "pull-off", and the figure 2 after 200 freezing and thawing cycles - visible cracks grid.

The freeze resistance determination is the test, which allows to assess the strength properties change in time, including drop in bending and compressive strengths as well as weight loss of the repair and re-profile concrete material.

The tested repair materials specimens are formed as 4 × 4 × 16 cm beams. There are 12 specimens in one test. After the stabilizing, all specimens are soaked in water to a solid mass, and then six specimens are stored in a climate chamber, and six other specimens are stored in water in the container. After completing the required number of freezing and thawing cycles, which is usually after 200 cycles, all specimens are weighed and tested for bending and compressive strength according to the PN-EN 1015-11/A1:2007. The mortar freeze resistance assessing criterions are:

– decrease of compressive strength should not exceed 20%;
– decrease of bending strength should not exceed 20%;
– weight loss should not exceed 5%.

The figure 3. shows specimens made of repair mortar, which passed 200 freezing and thawing cycles and the figure 4. – damage specimens while freeze durability tested the climate chamber after 200 freezing and thawing cycles.

Both ageing tests described above are contained in the Recommendations of the Road and Bridge Research Institute and fulfilling its requirements is the main decision criteria on issuing the Technical Approval.

The set of Standards EN 1504 *Products and systems for the protection and repair of concrete structures*,

together with the sheet EN 1504-3 *Part 3: Structural and non-structural repair* introduction to use, was to arrange and adapt to the current state of knowledge the repair materials test and requirements choice.

The durable repair material layer adhesion to the base material might be assessed on the basis of performing below listed tests, which concern thermal compatibility tests (after the EN 1504-3) according to the EN 1504-3:

– determination of resistance to freeze-thaw cycling with de-icing salt immersion according to the EN 13687-1;
– determination of resistance to thunder-shower cycling (thermal shock) according to the EN 13687-2;
– determination of resistance to dry thermal cycles according to the EN 13687-4;

However if the material meets the requirements concerning the freezing and thawing in saturated NaCl solution, according to the EN 13687-1, it should be deemed to satisfy the requirements of the other two tests.

Therefore, the test examination: resistance to thunder-shower cycling according to the EN 13687-2 and resistance to dry thermal cycles in accordance with the EN 13687-4 can be omitted if one receives a positive test result in freeze resistance according to EN 13687-1. In that case both mentioned test are treated as supplementary, performed exceptionally.

In case of resistance to freeze-thaw series according to the EN 13687-1 determination the repair material is applied on the concrete sample, prepared in accordance with the EN 1766. After seasoning, the specimen is exposed to cyclic temperature rapid changes between $+21 \pm 2°C$ and $-15 \pm 2°C$, together with the immersion in the de-icing salts saturated solution, the special set of test chambers (Figure 5-6).

If the temperature change cycles are finished, the noticeable spoils are recorded and the material or system repair to concrete basis adhesion is determined, with the use the of the "pull-off" method. Each test requires three samples, of which one is left as the reference specimen. When the specimens are ready, two of them should be immersed in the water and kept there for 24 h. After that period the proper test begins and lasts for 4 hours and includes following stages:

– immersion in the tank containing saturated sodium chloride solution at the temperature $-15 \pm 2°C$ for 2 h;
– storage in the water tank at the temperature $+21 \pm 2°C$ for 2 h.

When the test (50 cycles) is finished the repair layer adhesion is investigated. The repair materials adhesion should reach at least:

– 1.5 MPa for mortar for compressive strength $\geq$ 25 MPa (R3 class mortar according to the EN 1504-2);
– 2.0 MPa for mortar for compressive strength $\geq$ 45 MPa (R4c lass mortar according to the EN 1504-2).

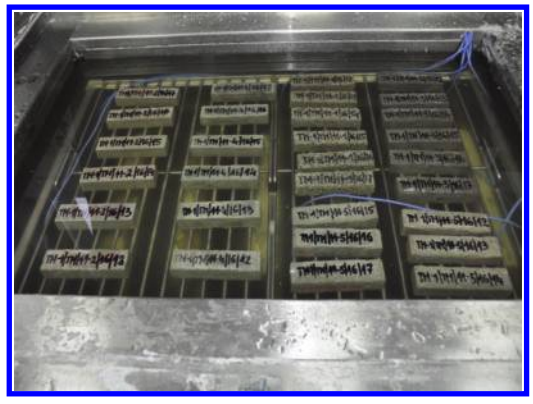


Figure 5. A set of special chambers for test according to the EN 13687-1.



Figure 6. The specimens during freezing in a saturated salt solution.

The PN-EN 1504-3 standard ignores mortar mechanical properties (compressive strength and bending strength) determination, once the freeze resistance in a saturated solution of NaCl is tested or the other two ageing test are performed. It must be stressed either that the flexural strength test was omitted in the PN-EN 1504-3 standard, though as an immediate test.

4 CONCLUSION

A new approach in accordance with the EN 1504-3 for ageing tests was to a new standard in the repair materials testing. According to the EN 1504-3 in the concrete repair materials testing and assessment the permanent repairing layers adhesion one may assess after the ageing test concerning the thermal compatibility execution. The basic thermal compatibility test is a new test method –cyclic freeze-thaw in NaCl saturated solution durability determination, which has not been known to the most repair materials manufacturers. Ageing tests listed in the PN-EN 1504-3 are focused primarily on repair materials used in general civil engineering, where one is dealing with the structure, usually heated on one side, and exposed

to climatic factors on the other. In bridge engineering, the entire structure is exposed to the climate factors.

Due to the EN 1504-3 new approach to the repair materials ageing test, a very important issue was to compare the two types of ageing investigation. Road and Bridge Research Institute has begun laboratory activity to assess the effectiveness (validity) of the two freeze resistance test methods. The comparison related to both values: bond strength of mortar, as well as determination the strength properties of mortar after 200 cycles of freezing and thawing in water, and after 50 cycles of freezing in a saturated de-icing salt solution and defrosting in water.

The hitherto obtained results confirm indirectly described in the literature dependence of de-icing salts concentration and its influence on the concrete damage. In case of de-icing salts (NaCl or $CaCl_2$) activity, the biggest frost damage occur when the concrete is exposed to relatively low concentrations of salts (solution of 2 to 4%). However, the higher is the salt concentration, then its influence is smaller. The highest compliance results trends were obtained in case of mortar adhesion test after 200 cycles of freezing and thawing in water, and after 50 cycles of freezing in a saturated de-icing salt solution and defrosting in water. The smallest trend compliance recorded in case of the bending and compressive strength test results, after 50 cycles of freezing in a saturated de-icing salt solution and defrosting in water, where the often significant increase of flexural strength was recorded, with the decrease in compressive strength.

Currently in Poland, the basic ageing research on the basis of frost resistance investigation, which should be performed for any repair material are:

- peel strength determination with the use of the pull-off method, after 200 freezing and thawing cycles in the water at the temperature of $-18 \pm 2°C$ / $+18 \pm 2°C$;
- freeze resistance determination after 200 freezing and thawing cycles in the water, at the temperature $-18 \pm 2°C$ / $+18 \pm 2°C$ (weight loss, flexural strength decrease and compressive strength decrease).

Performing these tests allow to assess materials for repairing concrete, regarding permanent adhesion of layers made of them to the base and their strength properties change in time, which in fact allows to assess the durability and effectiveness of repair made with the use of them.

REFERENCES

PN-88/B-06250:1988 Concrete

Neville, A.M. 2000. Properties of Concrete, Polski Cement, Kra-ków

EN 12190:2000 Products and systems for the protection and re-pair of concrete structures – Test methods – Determination of compressive strength of repair mortar.

EN 13687-1:2002 Products and systems for the protection and repair of concrete structures – Test methods – Determination of thermal compatibility – Part 1. Freeze-thaw cycling with de-icing salt immersion

EN 13687-1:2002 Products and systems for the protection and repair of concrete structures – Test methods – Determination of thermal compatibility – Part 1. Freeze-thaw cycling with de-icing salt immersion

EN 1504-1:2005 Products and systems for the protection and re-pair of concrete structures - Definitions, requirements, quality control and evaluation of conformity

EN 1504-3:2005 Products and systems for the protection and re-pair of concrete structures - Definitions, requirements, quality control and evaluation of conformity – Part 3: Structural and non-structural repair

Germaniuk, K. & Gajda, T. & Królikowska, A. 2010. Recommendations IBDiM Technical Approval No. Z/2009-03-019 Products and systems for the repair of concrete structures, Is-sue II, IBDiM, Warszawa, 2010

Germaniuk K.: 2009 Comments the bridge engineer for the PN-EN 1504. Article discussion, Materialy budowlane Nr 2/2009, 5-7

Germaniuk, K.: 2009. Experience in the use of materials for repair and re-profiling of concrete bridges and protection of method of hydrophobization in Poland. International Conference, Modern corrosion protection systems for bridges, Kielce 2009, 15–30.

Lagoda, G. & Gajda, T. 2011. Test of repair materials of bridge construction, Autostrady 10/2011, 56–59

Lagoda, G. & Gajda, T. 2011. Research materials for repair of bridges, International Conference, Structural Failures, Miedzyzdroje 2011, Volume I, 1127–1135

Research and Applications in Structural Engineering, Mechanics and Computation – Zingoni (Ed.)
© 2013 Taylor & Francis Group, London, ISBN 978-1-138-00061-2

Energy harvesting for the sustainability of structures and infrastructures

K. Gkoumas, F. Petrini, S. Arangio & C. Crosti
Sapienza University of Rome, Rome, Italy

ABSTRACT: In an energy sustainability context, and in the upward trend of renewable energy growth, several proposals have been made concerning energy harvesting in civil engineering structures and infrastructures. After a literature review on the topic, in the first part of this research, focus is given to the definition of an energy harvesting taxonomy in the civil engineering field and to the classification of energy extraction schemes. After that, this study focuses on the energy sustainability of complex structural systems. Within this topic, the possibility of using the air flow as an energy resource is explored.

1 INTRODUCTION

It is a common understanding that the society requires enhanced structures and infrastructures for the people's needs. Besides safety and functional requirements collectively defined in the so-called Performance-based Design (PEBBUH, 2005), today the attention focuses on the sustainability in the broader and profound sense of the word (Ehrenfeld, 2008). In this sense, the modern construction embraces the concept of smart structural systems that behave optimally with respect to the human needs, being at the same time coherently collocated in the environment (Srinivasan & McFarland, 2001) and inserted in a context of resilient cities.

Energy Harvesting (EH), i.e. the process of extracting energy from the environment or from a surrounding system and converting it to useable electrical energy, is a prominent research topic, with many promising applications nowadays in structural and infrastructural systems. Its areas of application are currently focused – though not limited – to powering small autonomous wireless sensors (thus eliminating the need for wires), while more recently proposals have been made concerning higher power EH devices, in the upward trend of renewable energy growth. In the latter case, the main objective is to supply power to auxiliary systems (e.g. road lights or information panels, in the case of transportation infrastructures), thus satisfying the requirement for sustainable structures and infrastructures.

EH is part of a global clean energy trend that encompasses other aspects, and focuses on the use of renewable energy sources. Advantages from the reduction of fossil fuel usage can be obtained at various levels, starting from a more sustainable (in terms of environmental sustainability) development (Adams, 2006), something that leads to CO_2 and greenhouse gas emissions reduction.

The idea of harvesting freely available energy is not new, and dates back to the windmills and watermills, in use since the ancient times. These have found their contemporary counterparts respectively in the form of wind turbines – solely in Europe, by the year 2020, wind energy is expected to account for most part of the 20% target share of renewable sources set by the European Community (EU, 2010) – and wave farms or underwater energy systems, currently at a proposal phase. Similarly, there great interest in wind power in the U.S., with wind power capacity representing more than 20% of the world's installed wind power (AWEA, 2012).

In what said above, the main objective is to produce a great amount of energy in order to supply the electrical grid. On the other hand, EH as intended nowadays, focuses in providing energy for powering sensors or other small electronic devices that require small amounts of energy, with the main purpose the elimination of traditional wire connections (e.g. in the case of sensors), while recently, the possibility to extract higher amounts of energy is possible, also with piezoelectric materials.

This study focuses on recent developments that highlight the possibility to extract energy in structures using the wind flow something that could specifically contribute to the energy sustainability of high-rise buildings. Before that, some aspects of energy sustainability of complex structural systems are inquired together with a literature review in the civil engineering field.

2 SUSTAINABILITY OF STRUCTURES

Sustainability in the urban and built environment is a key issue for the wellbeing of people and society. Sustainable development, defined as the "development that meets the needs of the present without

compromising the ability of future generations to meet their own needs" (UN, 1987) is nowadays a first concern for public authorities and the private sector, and is shaped by incentives and sanctions. Although sustainability goals are not uniquely identified, a total plan for sustainability requires, in a cost efficiency balance (ISE, 1999):

- Reduction of emission of greenhouse gases;
- More efficient use (and reuse) of resources;
- Minimization and constructive reuse of waste;
- Reduction of harmful effects from construction activities and building occupation.

The design, construction and operation of "green" buildings is nowadays regulated by international guidelines, codes and standards (see for example the green building evaluation and certification system USGBC, 2009). What emerges is a variety of widely acknowledged and recognizable standards, especially for what regards ranking and certification systems (Nguyen and Altan, 2011). In fact the whole concepts of "sustainable development" and "sustainable building" are cumbersomely defined, with different and sometimes contrasting definitions. Berardi (2013) deeply discusses several aspects of sustainable development (namely its time dependency, its multi-space and multi-scale levels, its multiple dimensions and its social dependencies) and arrives at a definition of what is a sustainable building by means of a number of principles.

It is important to add that even though sustainability has mostly a social character, benefits of sustainable design are not only to the general public but also for the building stakeholders, including owners, who benefit from the increased value of the property.

Sustainable design leads to innovation since it demands inventive solutions, and eventually is supported by a cultural shift, evident from national level reviews and surveys (Robin and Poon, 2009; Tae and Shin, 2009). Sustainability issues are wide-ranging, in the building industry but the main focus is the reduction of energy consumption in construction and use. Although the trend is to arrive to a so-called Net Zero Energy Buildings, for which a balance between energy flow and renewable supply options is established, the path to this goal is still very long (Srinivasan et al. 2011).

Ramesh et al. (2010) provide a breakdown of energy use in the various phases of building lifecycle (manufacture, use and demolition), and highlight the higher contribution of the operating phase, and the variability of the results for different climates, different building uses etc.

This is especially important for structural parts and systems, where recycling, reusing and material minimization can be important aspects (Vezzoli and Manzini, 2008). In the tall building design of diagrid and braced tube structures for example, stiffness provision is an important aspect of the design, and a material saving design methodology can be based on this aspect (Moon, 2010). In fact the diagrid structural scheme (with a perimeter structural configurations characterized by a narrow grid of diagonal members involved both in gravity and in lateral load resistance) has emerged as a new design trend recently for tall-shaped complex structures due to aesthetics and structural performance (Moon, 2011; Mele et al. 2012).

A second issue is the energy sustainability of structures and infrastructures, in terms of auto efficiency. For one thing it is possible to intervene on the energy balance of the structure using passive insulation systems. Alternatively, renewable energy sources could be implemented that contribute to the energy balance of the structure through "on-site" energy generation.

Several proposals and applications can be found in literature and practice, mostly using solar and wind energy. The latter is of particular interest for high-rise buildings, due to the superior characteristics of the wind field. The trend nowadays it to have a fully integration of aesthetically appealing wind turbines to the building, in harmony with its architectonic form.

Proposals are in the form of vertical wind turbines (Müller et al. 2009; Balduzzi et al. 2012a; Chong et al. 2013), innovative design and architectural integration (Sharpe and Proven, 2010), integration of wind turbine/solar generators (Chong et al. 2012). There are still some problems to overcome. The energy potential in urban environments is not fully assessed, and actually several researches focus on this issue. Walker (2011) provides a commented review of urban wind speed estimations, theoretical power curves and power production estimations for building mounted wind turbines. Balduzzi et al. (2012b) investigate by means of CFD the energy potential of rooftop wind turbines, focusing on the influence to the flow velocity of different geometric characteristics of the urban settlement (building height, distance between buildings etc.).

From what said above, the following principal sustainability measures can be identified for buildings.

- Passive systems. Focus is primarily on the use of more energy efficient materials and on the optimized design of structural and non-structural elements. The first mostly for the thermal isolation, the second for the minimization of the quantity of materials. Recently, innovative thermal isolation methods have been proposed (in the form of e.g. green roofs).
- Active systems. Focus is on the "on-site" energy production, something that leads to a lower energy need from the grid. Most applications so-far are in the form of wind turbines and photovoltaics. These applications can be considered as a part of a broader EH agenda.

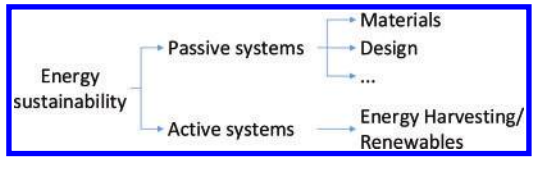


Figure 1. Sustainability measures.

Since EH is a rather innovative concept with many potential applications, it is useful to provide a taxonomy, based on the desired outcomes and the future potential.

3 ENERGY HARVESTING TAXONOMY

EH applications in structures and infrastructures can be divided in three groups:

- EH on a macro-scale
- EH on a meso-scale
- EH on a micro-scale

The proposed classification helps setting the framework for possible future applications, the assessment of their efficiency and their prospects.

Focusing on meso-scale EH applications, and in order to evaluate the energy production efficiency of the system, as a first step it is important to define the energy extraction patterns. In this sense, Section 4 focuses on energy production schemes (the reader is referred to Gkoumas et al. 2012 for additional details). Section 5 focuses on a meso-scale application that could use piezoelectric devices for harvesting the wind flow.

3.1 *Energy harvesting on a macro-scale*

Generally with macro-scale EH is in-tended the energy production for supplying the electrical grid. The produced energy is commonly known as renewable energy (the current exploitation of the energy sources does not affect their availability in the future). Geothermal, hydroelectric, solar thermal, geothermal, marine and wind energy are examples of renewable types of energy. Currently the produced energy is in the range of MWs.

3.2 *Energy harvesting on a meso-scale*

It is possible to define as H on a me-so-scale all those applications that have as an objective the supply of power to systems otherwise powered by the electrical grid. The energy produced in excess could supply the electrical grid. The energy sustainability of houses, structures and infrastructures provide an example of meso-scale EH implementation. Currently the produced energy is in the range of W/kWs.

Examples of meso-scale EH include piezoelectric roads and railways (see for example Innowattech, 2011) in which the movement of vehicles induces a strain to piezoelectric materials underneath the pavement or the railway track, thus producing energy. The East Japan Railway Company (JR East) is carrying out tests on piezoelectric floors in the Tokyo subway station, and the produced energy could be used to run the automatic ticket gates and electronic display systems (Techon, 2008). The duality is evident with the common practice of regenerative brake energy recovery in trains and cars (Robertson & Markham, 2007) or the energy that could be harvested inside a moving vehicle (e.g. a train) from vibrations (Romani et al. 2010). Numerous other applications are found in specialized journals, mostly in the form of conceptual design. Some worth mentioning are based on special wind turbines that can harvest wind-induced energy from passing vehicles in freeways. These are placed either over the road track (horizontal axis turbines – Ecofriend, 2011) or on the side (vertical axis turbines – Energy Harvesting Journal, 2010).

3.3 *Energy harvesting on a micro-scale*

Micro-scale EH aims to the powering of sensors or other small electronic devices, including those based on MEMS (Micro Electro Mechanical Systems) that require small amounts of energy. The objective is the elimination of traditional wire connections (in the case of sensors) and to provide an alternative to traditional limited energy sources (e.g. batteries). Currently the produced energy is in the range of μW/mWs.

Even though a great progress took place in the last decade, there are still issues to be solved and margins for improvement in the efficiency of micro-scale EH. Some of the key issues (power storage efficiency, communication standards, integration of devices, cost of ownership) are discussed in Kompis & Aliwell (2008). The same authors provide an overview of international centers of expertise in this field.

Applications in the last decade in the civil engineering field focus on the Structural Health Monitoring (SHM) of long span bridges and skyscrapers.

4 CLASSIFICATION OF THE ENERGY PRODUCTION SCHEME

This Section focuses primarily on the energy production schemes, typically for meso-scale EH applications, adapting findings from Gkoumas et al. (2012).

In order to evaluate the energy production of the system, as a first step it is important to define the energy extraction patterns. Consequently, the energy efficiency can be assessed.

4.1 *Definition phase of the scheme*

The energy production scheme can be classified following the scheme proposed in Table 1, based on the energy resource and the extraction system.

The first classification regards the resource type, in terms of the maximum extractable energy (E_H) and the energy cost of the structural system (E_C^{SS}). If the resource is natural (renewable resources such as wind and sun), E_H is infinite (since it is assumed that resources in nature are infinite) and E_C^{SS} is zero (since the sole purpose of the structure is the energy extraction). If the resource is artificial (e.g. bridge joints with piezoelectric devices), E_H is finite, since artificial resources are not infinite (e.g. in the case of energy extraction from a structural motion, since the latter

Table 1. Classification of the energy production schemes (adapted from Gkoumas et al. 2012).

RESOURCE Defined in terms of E_H, E_C^{SS} +		From natural resources $E_H = \infty; E_C^{SS} = 0$	From artificial resources $E_H < \infty; E_C^{SS} > 0$	From natural resources, modified by artificial systems $E_H = ?; {}^{*}E_C^{SS} > 0$ * Greater than if a system of extraction was implemented
EXTRACTION SYSTEM Defined in terms of E_C^{ES} =		Magnetic induction converter; Thermal energy converter; Electrostatic converter; Photovoltaic converter; RF converter; Piezoelectric converter; Radian energy converter; …		
COUPLED SYSTEM Defined in terms of E_C, $\hat{E}_H$, ΔE		Example: wind turbines for a wind farm.	Example: piezoelectric converters placed on deformable joints of a flexible structure.	Example: wind turbine on a skyscraper (the source is natural but it is placed in high attitude due to the skyscraper).
ΔE	ACTIVE (ΔE>0)	SUCCESSFUL[1]	SUCCESSFUL[3]	SUCCESSFUL[3]
	PASSIVE (ΔE<0)	UNSUCCESSFUL	SUCCESSFUL[1] UNSUCCESSFUL $\hat{E}_H - E_C^{ES} > 0$ $\hat{E}_H - E_C^{ES} < 0$	SUCCESSFUL[1] UNSUCCESSFUL $\hat{E}_H - E_C^{ES} > 0$ $\hat{E}_H - E_C^{ES} < 0$
	BALANCED (ΔE=0)	UNSUCCESSFUL	SUCCESSFUL[2]	SUCCESSFUL[2]

SUCCESSFUL[1]: Production of energy; SUCCESSFUL[2]: Production of an amount of energy equal to the one consumed;
SUCCESSFUL[3]: Production of an amount of energy higher than the one consumed
Definitions: E_H ~ Maximum extractable energy; E_C^{SS} ~ Energy cost of the structural system;
E_C^{ES} ~ energy cost of the extraction system; E_C ~ Total energy cost of the coupled system; $\hat{E}_H$ ~ Effective extracted energy of the coupled system; ΔE ~ Energy balance of the coupled system; ΔE' ~ Energy balance of the extraction system

is finite, accordingly it will be the extracted energy). E_C^{SS} is higher than zero since it is identified with the energy spent for construction and maintenance (illumination, etc.). A third case consists in natural resources modified by artificial systems. In this case E_H is indefinable since the resource is infinite but extractable only partially (this is the case, for example, of a wind turbine placed on a skyscraper, where only the part of wind flowing in the turbine location contributes to the produced energy). E_C^{SS} is higher than zero, and higher with respect to the same structure without an energy extraction system (additional cost is due to structural adjustment for the energy extraction).

The second classification regards the extraction system, defined in terms of the energy cost of the extraction system (E_C^{ES}). The extraction system of choice is specific to the resource type and consists in different parts, with the principal being the converter (e.g. piezoelectric, photovoltaic etc.).

The combination of the first two classification schemes leads to the definition of the coupled system. Therefore, the coupled system is essentially defined in terms of:

- the total energy cost of the coupled system (EC), which is the sum of ECSS and ECES;
- of the effective extracted energy of the coupled system ($\hat{E}H$); and,
- of the energy balance of the coupled system (ΔE).

The last one is defined as the balance between $\hat{E}_H$ and E_C.

4.2 *Evaluation of the system efficiency*

Based on the definitions given in paragraph 3.1, and with reference to Table1, the evaluation of the system efficiency is performed in terms of the energy balance of the coupled system ($\Delta E = \hat{E}_H - E_C$) and the energy balance of the extraction system ($\Delta E' = \hat{E}_H - E_C^{ES}$).

Regarding the first, if $\Delta E > 0$, the energy cost is lower than the produced energy, and the energy balance is active. If $\Delta E < 0$, the energy cost is higher than the produced energy and the energy balance is passive. Finally, if $\Delta E = 0$, the energy cost is equal to the produced energy and the energy of the coupled system is balanced.

Regarding the second, if $\Delta E' > 0$, the energy cost of the extraction system is lower than the produced energy. If $\Delta E' < 0$, the energy cost of the extraction system is higher than the produced energy.

Consequently, it is possible to define different "success levels", in order to obtain a qualitative view of the system efficiency.

For natural systems:

- If $\Delta E > 0$: Energy production
- If $\Delta E \leq 0$: Unsuccessful coupling

For artificial systems:

- If $\Delta E > 0$: Energy production
- If $\Delta E \leq 0$: Unsuccessful coupling

For natural resources modified by artificial systems:

- If $\Delta E > 0$: Energy production higher than the consumed energy
- If $\Delta E < 0$ and $\Delta E' > 0$: Energy production
- If $\Delta E < 0$ and $\Delta E' < 0$: Unsuccessful coupling
- If $\Delta E = 0$: Energy production equal to the consumed energy

Some limitations to this scheme are worth noting. The first one is that the energy balance refers to the system in operation and not for the entire lifecycle. The second and most important is that it doesn't take into account non-monetary aspects. Therefore, the decision to invest on a coupled system is often based on questions that are either non-monetary or driven by specific social or other interests.

The following section focuses on a meso-scale application, at the conception phase, that could use piezoelectric devices that harvest the wind flow.

5 EH AND SUSTAINABILITY USING PIEZOELECTRIC DEVICES

A very up to date research issue for Civil Engineering Structures is the sustainability of tall buildings, for example skyscrapers with 60-80 floors or more.

The main idea is to extract energy from the air flows in several parts of this complex system. Ventilation is an important part of the design of a high-rise building, and it is usually controlled by HVAC (heating, ventilation and air-conditioning) systems. Alternatively, natural ventilation is used, either in the form of the stack effect or using the wind. Regarding wind-driven ventilation, Khan et al. 2008 provides an overview of methods and applications, while Saadatian et al. (2012) review windcatcher technologies.

The implementation of EH from the air flow considers the allocation of a series of fins composed of piezoelectric materials ideally optimized in form and specifically characterized by special aerodynamics appendices consisting in small flexible elements. These modules immersed in the airflow channels, will lead to the extraction of energy, being able to develop all the necessary nonlinear and resonant behavior. An adaptive control strategy could be implemented to optimize in real time the flexible elements.

Such kind of application is not entirely new. Weinstein et al. (2012) investigate the possibility to extract energy by means of piezoelectric materials from the air flow in HVAC. In their study they focus on flow speeds of 2.5 and 5.0 m/s, and on using the vortex shedding effect from a bluff body placed in the air flow ahead of piezoelectric fins. Hobs and Hu (2012) propose piezoelectric cylinders placed in air flows of 1.8-4.3 m/s, where the ones upstream function as bluff bodies for those downstream so that they generate a Kármán vortex street. Energy-harvesting based on vibration induced by Kármán vortex street has been proposed recently also by Wang et al. (2012) at a smaller scale.

6 CONCLUSIONS AND DISCUSSIONS

Since this study focuses on an overview of sustainability issues and EH opportunities, no conclusions are provided in this stage. However, there are many other aspects that need to be inquired: the optimum (and cost effective) use of piezoelectric materials, the energy storage options, etc. However, the opportunity of using piezoelectric materials for EH is interesting, also for producing energy at remote locations. This has obvious advantages for powering micro-electronic devices, but the soundness for meso-scale applications needs to be tested.

ACKNOWLEDGEMENTS

The team www.francobontempi.org from Sapienza University of Rome is gratefully acknowledged. This work was partially supported by StroNGER s.r.l. from the fund "FILAS – POR FESR LAZIO 2007/2013 – Support for the research spin-off". Fruitful discussions with Prof. Alessandro De Stefano of Politecnico di Torino are also acknowledged.

REFERENCES

Adams, W.M. 2006. The Future of Sustainability: Re-thinking Environment and Development in the Twenty-first Century. *Report of the IUCN Renowned Thinkers Meeting*, 29–31 January 2006.

AWEA. 2012. U.S. Wind Industry Annual Market Report Year Ending 2011.

Balduzzi, F., Bianchini, A., Carnevale, E.A., Ferrari, L. & Magnani, S. 2012. Feasibility analysis of a Darrieus vertical-axis wind turbine installation in the rooftop of a building. *Applied Energy* 97: 921–929.

Balduzzi, F., Bianchini, A. & Ferrari, L. 2012. Microeolic turbines in the built environment: Influence of the installation site on the potential energy yield. *Renewable Energy* 45: 163–174.

Berardi, U. 2013. Clarifying the new interpretations of the concept of sustainable building. *Sustainable Cities and Society*. http://dx.doi.org/10.1016/j.scs.2013.01.008

Chong, W.T., Fazlizan, A., Poh, S.C., Pan, K.C., Hewb, W.P. & Hsiao, F.B. 2013. The design, simulation and testing of an urban vertical axis wind turbine with the omni-direction-guide-vane. *Applied Energy*, in press. http://dx.doi.org/10.1016/j.apenergy.2012.12.064

Chong, W.T., Fazlizan, A., Poh, S.C., Pan, K.C. & Ping, H.W. 2012. Early development of an innovative building integrated wind, solar and rain water harvester for urban high rise application. *Energy and Buildings* 47: 201–207.

Ecofriend. 2011. What's next in wind energy harvesting systems?. Accessed online on 12.2012, http://www.ecofriend.com/entry/whats-next-in-wind-energy-harvesting-systems

Energy Harvesting Journal. 2010. Air movement on highways to produce energy. Accessed online on 12.2012,

http://www.energyharvestingjournal.com/articles/air-movement-on-highways-to-produce-energy-00002706.asp
Ehrenfeld, J.R. 2008. *Sustainability by Design: A Subversive Strategy for Transforming Our Consumer Culture*. Yale University Press.
EU. 2010. *Energy 2020: A strategy for competitive, sustainable and secure energy*. COM 639 final.
Environmental Leader. 2010. London's Strata Tower Integrates 3 Wind Turbines into Façade. Accessed online on 03.2013, http://www.environmentalleader.com/2010/03/17/londons-strata-tower-integrates-3-wind-turbines-into-facade
Gkoumas, K., Petrini, F. & Bontempi, F.. Energy harvesting for the life-cycle of structures and infrastructures. *Life-Cycle and Sustainability of Civil Infrastructure Systems*. Oct 2012, 2102–2109.
Hobbs, W.B. & Hu, D.L. 2012. Tree-inspired piezoelectric energy harvesting. *Journal of Fluids and Structures* 28: 103–114.
Innowattech. 2011. The Innowattech Piezo Electric Generator (IPEG™). Accessed online on 12. 2012, http://www.innowattech.co.il/techInfo.aspx
ISE – Institution of Structural Engineers November 1999. Building for a sustainable future: Construction without depletion 96 pages, ISBN 1-87466-50-6, 30.
Khan, N., Su, Y. & Riffat, S.B. 2008. A review on wind driven ventilation techniques. *Energy and Buildings* 40(8): 1586–1604.
Kompis, C. & Aliwell, S. (eds.). 2008. Energy Harvesting Technologies to enable remote and wireless Sensing. *Sensors and Instrumentation KTN Report*.
Mele, E., Toreno, M., Brandonisio, G. & Del Luca, A. 2012. Diagrid structures for tall buildings: case studies and design considerations. The Structural Design of Tall and Special Buildings. *Wiley Online Library*, DOI: 10.1002/tal.1029
Moon, K.S. 2010. Stiffness-based design methodology for steel braced tube structures: A sustainable approach. *Engineering Structures* 32: 3163–3170.
Moon, K.S. 2011. Diagrid Structures for Complex-Shaped Tall Buildings. *Procedia Engineering* 14: 1343–1350.
Müller, G., Jentsch, M.F. & Stoddart, E. 2009. Vertical axis resistance type wind turbines for use in buildings. *Renewable Energy* 34(5): 1407–1412.
Nguyen, B.K. & Altan, H. 2011. Comparative review of five sustainable rating systems. *Procedia Engineering* 21: 376–386.
PEBBUH. 2005. *Performance Based Building Thematic Network*. Funded by EU 5th Framework Research Programme Managed by CIB.
Ramesha, T., Prakasha,R. & Shuklab, K.K. 2010. Life cycle energy analysis of buildings: An overview. *Energy and Buildings* 42:1592–1600.
Robertson, S.J.T. & Markham, J. 2007. *The regenerative braking story*. Venture Publications Ltd, United Kingdom.
Robin, C.P.Y. & Poon, C.S. 2009. Cultural shift towards sustainability in the construction industry of Hong Kong. *Journal of Environmental Management* 90: 3616–3628.
Romani, A., Paganelli, R.P. & Tartagni, M. 2010. A scalable micro-power converter for multi-source piezoelectric energy harvesting applications. *Procedia Engineering*, 5: 782–785.
Saadatian, O., Haw, L.C., Sopian, K. & Sulaiman, M.Y. 2012. Review of windcatcher technologies. *Renewable and Sustainable Energy Reviews* 16(3): 1477–1495.
Sharpe, T. & Proven, G. 2010. Crossflex: Concept and early development of a true building integrated wind turbine. *Energy and Buildings* 42: 2365–2375.
Srinivasan, R.S., Brahamb, W.W., Campbell, D.E. & Curcija, C.D. 2011. Re(De)fining Net Zero Energy: Renewable Emergy Balance in environmental building design. *Building and Environment* 47:300–315
Srinivasan, A.V. & McFarland. D.M. 2001. *Smart Structures*, Cambridge University Press.
Tae, S. & Shin, S. 2009. Current work and future trends for sustainable buildings in South Korea. *Renewable and Sustainable Energy Reviews* 13: 1910–1921.
Techon. 2008. Revamped 'Power Generating Floor' to Be Tested at Tokyo Station. Accessed online on 12. 2011, http://techon.nikkeibp.co.jp/english/NEWS_EN/20081204/162357
UN – United Nations. 1987. Report of the World Commission on Environment and Development. General Assembly Resolution 42/187, 11 December 1987. Retrieved: 2013-02-04.
USGBC – United States Green Building Council. 2009. *LEED for New Construction and Major Renovations*, version 3.0. Green Building Council, Washington, D.C
Vezzoli, C. & Manzini, E. 2008. Design for Environmental Sustainability. Springer-Verlag London.
Walker, S.L. 2011. Building mounted wind turbines and their suitability for the urban scale – A review of methods of estimating urban wind resource. *Energy and Buildings* 43:1852–1862.
Wang, D-A., Chiu, C-Y. & Pham, H-T. 2012. Electromagnetic energy harvesting from vibrations induced by Kármán vortex street. *Mechatronics* 22(6): 746–756.
Weinstein, L.A., Cacan, M.R., So P.M. & Wright P.K. 2012. Vortex shedding induced energy harvesting from piezoelectric materials in heating, ventilation and air conditioning flows. *Smart Materials and Structures* 21(4): 10p.

Research and Applications in Structural Engineering, Mechanics and Computation – Zingoni (Ed.)
© 2013 Taylor & Francis Group, London, ISBN 978-1-138-00061-2

Sustainability considerations for tunnel projects

J. Sauer & O. Fischer
Chair of Concrete and Masonry Structures, Technische Universität München, Munich, Germany

ABSTRACT: Sustainability and the associated environmental protection is one main issue in present time. The question of sustainability is also interesting in civil engineering. So far the most research projects focused on sustainability of building structures. However infrastructure projects, especially tunnel construction, are not considered. Many public databases are available to get ecological parameters like CO_2E-emissions for construction materials and processes. Concrete is one of the most important materials for tunnel construction. The CO_2E-emissions of concrete are just given for a few different concrete strength classes in the considered databases GEMIS and Ökobau.dat. Exemplary mix designs are made for different concrete and cement strength classes to calculate the CO_2E-emissions and to evaluate the influence for the overall CO_2E-emissions of tunnel construction. The CO_2E-emissions will be evaluated monetarily to compare them with production costs and therewith life cycle costs. Indirect effects resulting from traffic situations and related indirect costs have to be taken into account.

1 INTRODUCTION

Sustainability and the associated environmental protection is one main issue in present time. The question of sustainability is also interesting in civil engineering. Most structures are made of concrete and therefore cement. During production process of 1000 kg cement nearly 1000 kg CO_2 will be released (Ulm 2012). For this reason the cement industry has a big influence on the releasing of CO_2-emissions worldwide (about 5%). The aim is to reduce the global warming potential (GWP) which is described by the CO_2-equivalent (CO_2E).

So far the most research projects focused on sustainability of building structures. However infrastructure projects, especially tunnel construction, are not considered. Concrete is one of the most important materials for tunnel construction. The relevance of different concrete and cement strength classes on the overall CO_2E-emissions will be analyzed for one exemplary tunnel project in this paper. The emissions will be evaluated monetarily to show the influences on the overall life cycle costs of tunnel projects. Additionally construction and maintenance works may have an impact on the traffic leading to an increase of 'indirect' emissions, so called indirect effects. These effects have to be taken into account.

2 DATABASES

Many databases are available to get ecological parameters like CO_2E-emissions for construction materials and processes like GEMIS (= Global Emissions Model for integrated Systems) (IINAS 2013) and Ökobau.dat (BMVBS 2013). Both are freely accessible programs but with one main difference: with GEMIS it is possible to model new materials and processes from the first step to the last which are not included in the given database. For example the mining of minerals is the first step in the process chain for the production of concrete. The product concrete is the last step. Many sub steps can be modeled with different input e.g. electricity. It is also possible to add transport routes of admixtures. In the end the CO_2E-emissions are calculated over the whole process chain. With Ökobau.dat it is not possible to model new materials. Fixed materials are included and their characteristics cannot be changed.

The CO_2E-emissions of concrete are just given for a few different concrete strength classes in both databases. As it is not possible to model new materials with Ökobau.dat the CO_2E-emissions for different concrete strength classes will be modeled and calculated with GEMIS in this paper.

3 CO_2E-EMISSIONS OF CONCRETE

To model different concrete strength classes with GEMIS it is necessary to have information about the mixture of each concrete strength class. For this reason exemplary mix designs for concrete strength classes C12/15 to C50/60 are made, which are not directly derived from current projects.

For the mixture portland cement (CEM I) is used. Three types of cement strength classes are available: 32.5 N/mm^2, 42.5 N/mm^2 and 52.5 N/mm^2. Mix designs with these three cement strength classes are made for every concrete strength class. For the

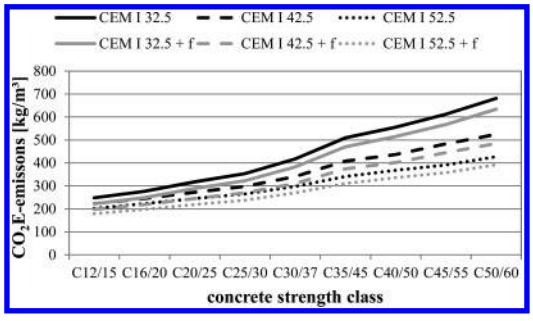


Figure 1. CO_2E-emissions for different concrete strength classes with different cement strength classes with and without fly ash (f).

aggregate a grain size distribution with maximum grain size Ø 16 is used. This grain size distribution often is used at our laboratory at Technische Universität München. The CO_2E-emissions are calculated for each concrete strength class with different cement strength classes. Additionally mix designs with fly ash are made for each concrete and cement strength class (Fig. 1).

With increasing concrete strength classes the CO_2E-emissions increase. Depending on the cement strength class the CO_2E-emissions of concrete C50/60 are 2–3 times bigger than for C12/15. The reason for this is the increasing cement content for higher concrete strength classes within one cement strength class. With increasing cement strength classes the CO_2E-emissions decrease in a certain concrete strength class due to the reduction of required cement content. However from Figure 1 it can be seen that the CO_2E-value for C30/37 with 32.5 N/mm^2 cement strength is in the range as for C45/55 with 52.5 N/mm^2 cement strength. This aspect is going to be discussed in the following sections.

The CO_2E-value of concrete is mainly influenced by the cement content of concrete. From our results it can be stated that a concrete mixture with e.g. 200 kg cement produces CO_2E-emissions in a range of 200 kg/m^3. Further process steps like mining of minerals have a very small influence and they could be neglected for a simple assessment of the greenhouse effect for concrete. Admixtures like fly ash reduce the cement value and with it the CO_2E-emissions for concrete (Fig. 1).

4 EFFECTS FOR TUNNEL PROJECTS

4.1 *Example project*

For the relevance of CO_2E-emissions for different concrete strength classes and their influence on the overall CO_2E-emissions for tunnel projects one example project is used.

The example project is a highway section in a region with varying topography closed to the Alps. In a study of alternatives six different options of alignment

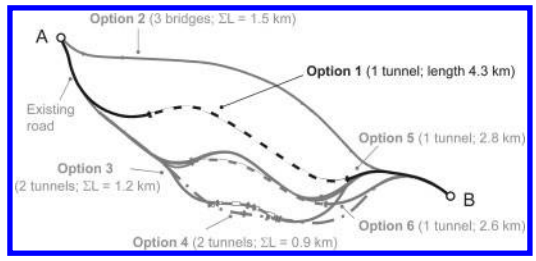


Figure 2. Scheme of options (TUM 2012).

were designed according to the German guideline "Richtlinie für die Anlage von Autobahnen" (RAA) (FGSV 2008): Five options have road and tunnel sections; option 2 has only road and bridge sections. Figure 2 shows a scheme of these in an abstract ground view.

The tunnel section of option 1 will be considered for the evaluation of CO_2E-emissions. The tunnel length is 4.3 km each for north and south tube. The standard cross section of the tunnel is defined as RQ 36t according to RAA. This cross section has three lanes of 3.50 m width per direction and no emergency lane which leads to other traffic safety measures. The tunnel has to be equipped according to the German guideline "Richtlinie für die Ausstattung und den Betrieb von Straßentunneln" (RABT) (FGSV 2006). According to the tunnel length the RABT determines the emergency equipment (number of breakdown bays, emergency call stations and cross passages). The tunnel is built with shotcrete method (NATM).

4.2 *Results*

For the relevance of CO_2E-emissions for different concrete and cement strength classes we will first consider the inner concrete lining of our example project. Resulting from chapter 3 we know that the CO_2E-value for C30/37 with 32.5 N/mm^2 cement strength is in the range as for C45/55 with 52.5 N/mm^2 cement strength. With a higher concrete strength it will be possible to reduce the depth of the inner concrete lining. A thinner inner lining reduces the structural bending stiffness. Accordingly the bending moments will be reduced leading to an increase of deformations and additional lateral subsoil bedding reactions. The influence on the normal forces is insignificant.

Based on the values from Table 1 the CO_2E-emissions are calculated for the reinforced inner concrete lining. The depth of the inner lining is varied from 0.50 m to 0.35 m (hereby also the required amount of reinforcement is considered depending on the depth). For the depth of 0.50 m lower concrete strength classes of C25/30 and C30/37 are used. For C30/37 also the cement strength class is varied from 32.5 to 42.5 N/mm^2. For the thinner inner lining of 0.35 m a higher concrete strength class of C50/60 with cement strength of 52.5 N/mm^2 is used.

Corresponding to the results of chapter 3 (Fig. 1) higher emissions for C30/37 with cement strength of

Table 1. Values of inner concrete lining for calculation of CO_2E-emissions.

	Cement strength	Depth of inner lining
	N/mm²	m
C25/30	32.5	0.50
C30/37	32.5	0.50
C30/37	42.5	0.50
C50/60	52.5	0.35

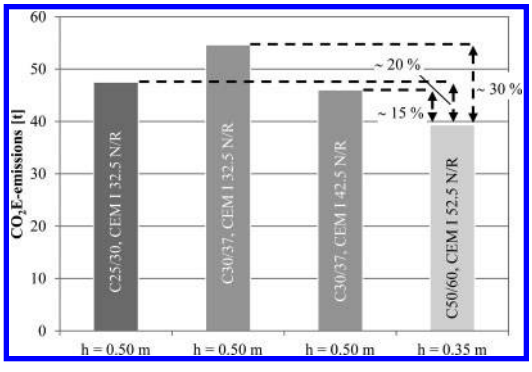


Figure 3. CO_2E-emissions for different concrete and cement strength classes with respect to the depth of the inner concrete lining including reinforcement for our example.

32.5 N/mm² are resulting than for C25/30 (Fig. 3, two columns on the left side). As the volume of concrete is not changing because of the same depth of the inner lining (0.5 m), the reason is still the higher cement content for C30/37 with 32.5 N/mm² cement strength. Lower CO_2E-emissions are resulting for C30/37 if we change the cement strength to 42.5 N/mm² (Fig. 3, third column from left) because of lower cement content for higher cement strength. The lowest CO_2E-emissions are resulting for C50/60 with 52.5 N/mm² cement strength and depth of the inner lining of 0.35 m for our example. The reason is the reduced volume of concrete by using nearly the same CO_2E-value as for C30/37 with 32.5 N/mm² cement strength.

With respect to the depth of the inner lining, the concrete and cement strength it is possible to save CO_2E-emissions of about 15–30% resulting from concrete for our example. The amount of saving is not a fixed value because it is depending on the cross section of the tunnel. It is reasonable to analyze the influence of using a thinner inner lining with a higher concrete strength class for tunnel projects to reduce the CO_2E-emissions. A higher concrete strength class is not necessarily related to higher CO_2E-emissions resulting from the production process of the structure. The same conclusion is drawn by Ulm (2012) for structures in general.

In order to illustrate the relevance of CO_2E-emissions we have evaluated them monetarily. Thus we can compare them with production costs and

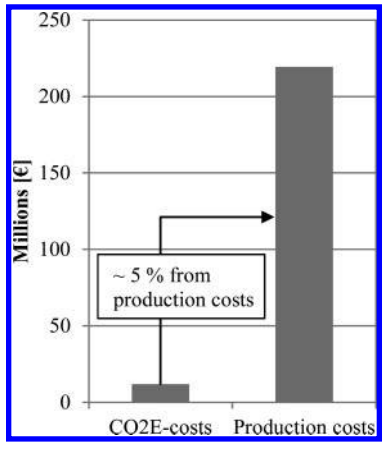


Figure 4. Comparison of CO_2E-costs and production costs.

therewith life cycle costs. To convert CO_2E-emissions into costs, a value of 70 €/t-CO_2E is used, which is a value from a report "Ökonomische Bewertung von Umweltschäden: Methodenkonvention zur Schätzung externer Umweltkosten" published by the Federal Environment Agency (UBA 2007). For the comparison with production costs the CO_2E-emissions for the whole production process of the tunnel (including emergency equipment e.g. cross passages and construction phases e.g. blasting) are calculated. From Figure 4 it can be seen that the CO_2E-costs are just in a range of some 5% in relation to the production costs.

The tunnel in our example is built with shotcrete method. Calculations from another project have shown that it is possible to save more CO_2E-costs by using the TBM-tunneling method utilizing precast segments, only, than the shotcrete method (TUM 2012). Main reason is the overall reduced volume of concrete of the segmental lining.

The production costs do not include costs occurring from maintenance work. Adding these costs on top of the production costs, the influence of CO_2E-costs from production process is getting more and more negligibly small although there are additional CO_2E-costs induced by maintenance works. Extending our point of view from the tunnel section to the whole route additional effects have to be taken into account. These effects are so called indirect effects resulting from the traffic situation. Emissions from only a free traffic flow exceed the CO_2E-emissions from production process in short time. Considering traffic jam situations leads to higher CO_2E-emissions and they are more significant. Influencing parameters on indirect effects are technical quality of construction and process quality which enable traffic flow or in contrast cause traffic interferences (Fig. 5).

5 CONCLUSION

In this paper we have analyzed the influence of different concrete and cement strength classes for

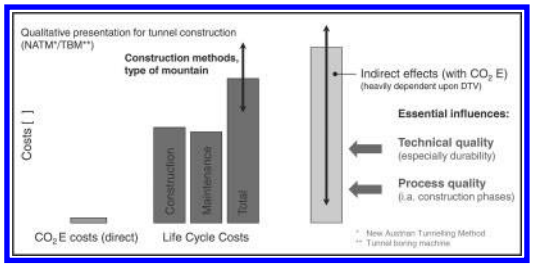


Figure 5. CO_2E-emission costs compared to life cycle costs and indirect effects (TUM 2012).

CO_2E-emissions of tunnel projects. We have calculated the CO_2E-emissions for concrete strength classes C12/15 to C50/60 with cement strength of 32.5 N/mm^2, 42.5 N/mm^2 and 52.5 N/mm^2. For a simple assessment of the greenhouse effect it can be said that a concrete mixture with e.g. 200 kg cement produces CO_2E-emissions in a range of 200 kg/m^3.

We have applied the results on an exemplary tunnel project. The depth of the inner concrete lining of the example project was varied and the CO_2E-emissions were calculated and analyzed for different concrete and cement strength classes. In order to illustrate the relevance of CO_2E-emissions we have evaluated them monetarily. Applying this parameter allowed us to compare the CO_2E-emission costs with production costs and therewith life cycle costs.

The results have shown that it is reasonable to analyze the influence of different concrete and cement strength classes for CO_2E-emissions of tunnel projects. A higher concrete strength class is not necessarily related to higher CO_2E-emissions. For a higher concrete strength class higher cement strength is used and with this the cement content of concrete is reduced. By using higher concrete strength it is possible to reduce structural dimensions leading to decreased concrete quantities and furthermore to a reduced volume of cement. The cement industry represents a large share on releasing CO_2E-emissions worldwide and these emissions could be reduced. Additionally with a thinner inner lining the excavated cross-section will be reduced. This leads also to reduced CO_2E-emissions and higher environmental protection.

In general it can be said that it is useful to reduce CO_2E-emissions during construction phase but it is more useful to optimize the life cycle of infrastructure projects during planning process. The CO_2E-emissions are mainly related to indirect effects resulting from traffic situations. These effects have to be reduced which is possible with an optimized life cycle of infrastructure projects. It is important to use sustainable materials but it is even more important to build more robust and durable structures with less maintenance work which enable traffic flow and cause traffic interferences. Direct production costs and also indirect costs resulting from maintenance and refurbishment can be saved. During planning process it is necessary to choose an optimum alignment with small longitudinal gradients or shorter routes to reduce emissions resulting from traffic situations and the use of fuel.

REFERENCES

BMVBS – Bundesministerium für Verkehr, Bau und Stadtentwicklung 2011. *Ökobau.dat*. http://www.nachhaltiges bauen.de/baustoff-und-gebaeudedaten/oekobaudat.html.

FGSV – Forschungsgesellschaft für Straßen- und Verkehrswesen 2006. *Richtlinie für die Ausstattung und den Betrieb von Straßentunneln – RABT*. Köln: FGSV-Verlag.

FGSV – Forschungsgesellschaft für Straßen- und Verkehrswesen 2008. *Richtlinie für die Anlage von Autobahnen – RAA*. Köln: FGSV-Verlag.

IINAS – International Institute for Sustainability Analysis and Strategy 2013. *GEMIS – Global Emissions Model for integrated Systems*. http://www.iinas.org/gemis-de.html.

TUM – Technische Universität München, Lehrstuhl für Massivbau und Lehrstuhl für Verkehrswegebau in Zusammenarbeit mit der Ingenieurekammer-Bau 2012. *Ganzheitliche Beurteilung der Nachhaltigkeit und Energieeffizienz bei der Planung und dem Bau von Infrastrukturprojekten*. Munich: Bayerisches Staatsministerium für Umwelt und Gesundheit, Report – unpublished.

UBA – Umweltbundesamt 2007. *Ökonomische Bewertung von Umweltschäden: Methodenkonvention zur Schätzung externer Umweltkosten*. Dessau, 2007.

Ulm, F.-J. 2012. Innovationspotential Beton: Von Atomen zur Grünen Infrastruktur. *Beton- und Stahlbetonbau 107*, Volume 8: 504–509.

Research and Applications in Structural Engineering, Mechanics and Computation – Zingoni (Ed.)
© 2013 Taylor & Francis Group, London, ISBN 978-1-138-00061-2

Challenges in rehabilitation techniques in strengthening cracked concrete beams

M. Keshava Murthy
UVCE, Bangalore University, Bangalore, India

N. Munirudrappa
Dayananda Sagar College of Engineering, Bangalore, India

Showkath Ali Khan Zai, J. Guruswamy & S. Krishnan
UVCE, Bangalore University, Bangalore, India

ABSTRACT: The feasibility of Epoxy to repair of cracks such as Flexural cracks and Shear cracks of various widths in the concrete were examined. The main focus of research investigation is in the areas of the concrete Repair and Rehabilitation which have been formulated by injection of Epoxy Resin under high pressure for their behaviour. The bonding characteristics of rehabilitated beams were suitably analyzed for their behaviour. The first stage of experimental programme involves studying the static behaviour of flexural member under two point static loading to obtain the load deflection behaviour having sectional dimensions 150 × 230 mm with an effective span of 2000 mm. Three test beam specimens were tested at 100%, 70% and 40% of the ultimate loads respectively to create flexural and shear cracks. Energy absorption capacity, toughness index and ductility index were evaluated. The second stage of experimental investigation involves flexural test of rehabilitated failed test specimen after epoxy resin injection. It is experimentally evident that the rehabilitated beams behaved much better with respect to the first crack load, energy absorption capacity, toughness index and ductility index as compared to the beam before rehabilitation. The proposed technique is simple and economical to execute and has resulted in an adhesively bonded joints without any additional effort such as jacketing or shear connectors.

Keywords: Epoxy resin injection, rehabilitated, flexural cracks, toughness index, ductility index.

1 INTRODUCTION

The present investigation deals with the studies on repair and rehabilitation of flexural member using synthetic resins such as epoxy. The relevant literature review available in this area has been critically studied and discussed on the use of polymers (Epoxy) for Repairs and Rehabilitation of RCC Structures. Most widely used polymers for the application in cementations repair work are urethane, modified acrylics, poly vinyl acetates, styrene butadiene rubber (SBR), chloroprene rubber (CR) poly acrylic ester (PAE), poly ethylene vinyl acetate

(EVA or VAE), poly styrene acrylic ester (SAE), in cementations mixture improves a host of properties (El-Hawary 2000, M. Haider 2007). Amongst the Epoxy resins (R. D. Maksimov1995) when cured with different hardeners offer a wide range of application to bond plastic concrete to hardened concrete, bond rigid materials to each other, enhanced resistance to crack propagation, increased tensile, flexural and bond strength resistance etc. Injection material epoxy resin (Paolo Gazzarrini1998) is traditionally used for filling cracks in concrete structures. The function of the injected material is mainly two fold - fill the crack to prevent water ingress and act as a structural filler to transfer loads across the crack were exploited for innovative repairs at a high security establishment. For repairing of concrete slabs (Alexander 2000, C. Li 2004) deteriorated due to the remarkable increase of traffic roads, the reinforcement of those defective slabs by bonding steel from underside using epoxy resins are recently becoming popular. Polymer being the costliest input in any repair and rehabilitation job, the selection of an appropriate brand assumes importance. Due to the rapid deterioration of concrete structures, more and more repair and rehabilitation works are being taken up. The majority of structures surveyed have been repaired, using a variety of technologies with varying degrees of success. Repaired materials included conventional concrete, fiber reinforced concrete, polymer concrete. In many instances, materials have been prototype repairs with limited or no laboratory evaluation of their effectiveness in the particular application. In practice a flexural member is usually subjected to combined flexure and shear and very rarely is under the action of pure shear since the performance of reinforced concrete member can be judged from the load

deformation characteristics of a member the same will be studied to understand the behaviour of the test beam specimen. Hence an attempt has been made in the present work to evaluate a detailed study on Flexural cracks and shear cracks which were experimentally created on the test beam specimen and rehabilitating the same using epoxy injection innovative technique.

2 MATERIALS

In the present work Special Grade Portland cement (53-S) conforming to IRS/T-40-1985, crushed granite angular aggregate of size 20 mm passing, conforming to IS 383 having specific gravity 2.67, natural river sand confirming to IS 383, Zone II, having specific gravity 2.63, water confirming to IS 456:2000 and Mix Design proportions 1:1.59:3.22 with w/c ratio 0.5 having target strength of 29.6 N/mm^2 for M20 grade of design were used. Fe 415 bars of 12,10,8 mm diameter as reinforcement for main, hangar bars and stirrups respectively. Synthetic Epoxy Resin a solventless crack injection material composed of suitable viscous liquid epoxy resin & amine hardener system were used to seal the cracks and bring the structure to stronger state. Epoxy resin adhesive for the pressure injection of cracks consists of

i. Component "A" shall be a modified epoxy resin of the epichlorohydrin biphenol A type containing suitable viscosity control agents.
ii. Component "B" shall be primarily a reaction product of a selected amine blend with an epoxy resin of the epichlorohydrin bisphenol A type containing suitable viscosity control agents and accelerators.
iii. The Component "A" and Component "B" shall be taken by 2:1 ratio by volume. Capping were carried out using Universal mortar which consists of modified cement mortar with Polypropylene fibre.

3 TEST PROGRAM

A series of three test beam specimen of size 150×230×2200 mm with effective span of 2000 mm were tested as shown in figure 1 under two point load condition in the loading frame of capacity 300 kN. The load increment was applied with a 200 kN capacity jack. The test beam specimens are loaded up to 100%,70%, 40% of ultimate load and then the failed test beam specimen is rehabilitated by using epoxy resin injection technique under high pressure to enhance the load carrying capacity of the test beam specimen as similar to the virgin beams.

4 METHOLODY ADOPTED FOR REPAIR WORK IN THE PRESENT INVESTIGATION

The repair work is focused on applying epoxy resin injection technique to the major diagonal cracks and



Figure 1. Test Setup.



Figure 2. Rehabilitated Beam with capping.

other cracks formed along the beam after the test specimen is subjected to loads, while hairline cracks are ignored because of their insignificant effect and the practical difficulty in treating them. The procedure for application of Epoxy resin injection involves the following steps.

1. Surface Preparation: Cleaning of the cracks that have been contaminated with oil, grease, dirt, or fine particles of concrete which prevents epoxy penetration and bonding.
2. Fixing of nozzles: The method entails drilling a hole into the crack into which a fitting such as a pipe nipple or tire valve stem is bonded. The surface of the cracks in between the nipples should be sealed with concrete repair mortars of 30-40 mm wide & 2-3 mm thick band.
3. Mixing the epoxy: This is done either by batch or continuous method. In batch mixing the adhesive components A and B are premixed usually with the use of a mechanical stirrer.
4. Inject the epoxy: Epoxy resin Injection grout should be used with standard injection equipment. As shown in figure 3. The injection pressure should be at least 0.2 N/mm^2 otherwise the use of excessive pressure may propagate the existing cracks, causing additional damage. After completion of the injection work, the injection system shall be allowed for 24 hours curing and shall be left undisturbed.
5. Capping: After the injected epoxy has cured the surface seal should be capped as shown in figure 2 for nozzles depending upon methodology adopted.



Figure 3. Epoxy Injection to damaged beams.

Table 1. Mechanical Properties of concrete.

Properties		M20 Grade concrete
Compressive strength (N/mm^2)	3 days	15.83
	7 days	22.55
	28 days	29.66
Split tensile strength (N/mm^2)	3 days	0.93
	7 days	1.43
	28 days	2.07
Flexural strength (N/mm^2)	3 days	1.42
	7 days	2.35
	28 days	2.85

5 TEST RESULTS

The test results obtained for Ductility index, energy absorption capacity, toughness index were evaluated from load deflection curve for the test beam specimen B1, B2, B3 and the rehabilitated beams specimen B1R, B2R (Beam B2, B2R are discussed) and the table 1. shows the properties of concrete matrix used.

5.1 *Load-Deflection Behaviour*

Typical load-deflection curves for test beam specimen beams, B1, B2, B3 and retrofitted beams B1R,B2R beams are shown in figure 4. The major stages are observed on load deflection curves as first cracking load, Yield point load and ultimate load respectively.

5.2 *Ductility Index* (μ_d)

The term ductility is defined as the ability of the material or member to sustain deformation beyond the elastic limit, while maintaining a reasonable load-carrying capacity before total collapse. Generally is defined in the case of member subjected to flexure as Ultimate Deformation to deformation at first yield. The Values of ductility are given in table 2.

5.3 *Energy Absorption Capacity*

The values of energy absorption capacity were computed from the area of load deflection curve for beam B2 are given in table 3. It is seen that the rehabilitated beam B2R has increased the energy absorption capacity as compared to the test beam specimen B2.

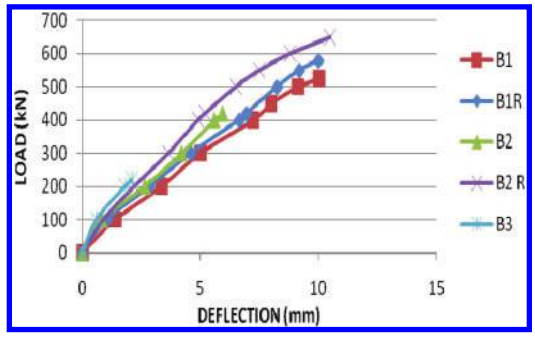


Figure 4. Load-Deflection Behaviour.

Table 2. Ductility Index.

Beam	P_U(KN)	Δ_U(mm)	P_y(KN)	Δ_y(mm)	μ_d
B2	420	5.95	315	3.89	1.21
B1-R	580	10.00	400	8.25	1.24
B2-R	600	10.50	420	7.90	1.40

Table 3. Energy absorption capacity.

Beam	Energy absorption capacity (KN-mm)
Test Beam specimen-B2	2.961
Rehabilitated beam-B2R	3.318

Table 4. Toughness Index.

Type of beam	Toughness Index
Test Beam specimen-B2	1.80
Rehabilitated beam-B2R	2.62

5.4 *Toughness Index*

It is defined as the ratio of area under the curve up to ultimate load to area under the curve up to first crack load. The value of Toughness index for different concrete mix under investigation and are given in table 4.

6 CONCLUSIONS

- The beam retrofitted with epoxy resin injection shows more deflection in B2R compared to B2. The cracking load and ultimate load carrying capacity increases significantly.
- As per the results tabulated in the table 2, it indicates that the ductility index increases by 14%, toughness



Figure 5. Details of Epoxy Resin Injection Treatment.

index increases by 25% energy absorption capacity increases by 10.75%. The enhancement in the strength level is observed in B2R among other retrofitted beams.

- In general all the retrofitted beams exhibits much load carrying capacity and the structural integrity due to epoxy injection.
- In the retrofitted beam no reopening of cracks were observed even at 70% of the ultimate load due to stiffness compared to before retrofitting.

REFERENCES

Abdel-Fattah, H., and El-Hawary, M. M., 1999,"Flexural Behavior of Polymer Concrete," Construction and Building Materials, Vol. 13, No. 5,pp. 253–262.

Alexander M. Vaysburd and peter H. Emmons 2000, "Effect of Elevated Temperature on the Residual Fracture Toughness of Epoxy Modified Concrete," *Kuwait Journal of Science and Engineering*, Vol. 27, No. 1, pp. 29–40.

C. Li, K. Potter, M. R.Wisnom, and G. Stringer, , 2004 "In-situ measurement of chemical shrinkage of MY750 epoxy resin by a novel gravimetric method", Compos. Sci. Technol. 64(1),pp. 55.

Causes, evaluation, and repair of cracks.1984, ACI Committee 224. *ACI*, Vol. 81, No. 3, American Concrete Institute, Detroit, MI,. ACI224.lR-84.

El-Hawary, M. M., Al-Khaiat, H., and Fereig, S.,2000, "Performance of Epoxy- Repaired Concrete in Marine Environment," Cement and Concrete Research, Vol. 30, No. 2, pp. 41–42.

Hand book on repair and rehabilitation of RCC buildings, 2002, CPWD, New Delhi, pp. Vo1-49.

M. Haider, P. Hubert, and L. Lessard, 2007, Cure shrinkage characterization and modeling of a polyester resin containing low profile additives, Compos. A: Appl. Sci. Manufact. 38 (3), pp. 994–1009.

Maintenance and repair of concrete and concrete structures US Army Corps of Engineers, Washington, DC, 1979 Engineer Manual 1110-2-2002.

Paolo Gazzarrini, 1998, "Effect of Temperature on the Mechanical Behavior of Resin Concrete," *Proceedings of the Arab Conference on Repair and Rehabilitation of Structures,* Cairo, Egypt, pp. 397–410.

R. D. Maksimov, L. Jirgens,J. Jansons, and E. Plume S. V. Muzumdar, and L. J. Lee, 1995, "Analysis of volumetric changes of unsaturated polyester resins during curing", Polymer Engg., Science 35(10), pg. 852.

Selvaraj, R. Vedalakshmi, R. And S. Srinivasan, October 2002, "Critical test methods for evaluating structural repair materials", *The Indian Concrete Journal,* Vol. 76, No. 10, pp. 653–659.

Terro, M. J., and El-Hawary, M. M., 1998, "Mechanical Behavior of Reinforced Concrete at Elevated Temperature," *Proceedings of the International Conference on Civil Engineering*, Helwan University, Cairo, Egypt, pp. 115–131.

John Trout, Nov. 2005 "Tips for Epoxy Resin Injection" *Concrete International*, Vol. 27, No. 11, pp. 44–48

33. Soil-structure interaction, foundations, geotechnical engineering

Research and Applications in Structural Engineering, Mechanics and Computation – Zingoni (Ed.)
© 2013 Taylor & Francis Group, London, ISBN 978-1-138-00061-2

The second order solution of Boussinesq's problem

E. Ferretti
DICAM, School of Engineering and Architecture – University of Bologna, Bologna, Italy

ABSTRACT: In this document, we have proposed a second order solution to Boussinesq's problem (Boussinesq 1885), which allows us to account for the new experimental evidence (Ferretti & Bignozzi 2012, Ferretti 2012b) on the stress field induced by aircraft traffic in concrete pavements. In particular, the second order solution is able to describe the tensile state of stress acquired in the proximity of the contact area and not accounted for in the classical solution of Boussinesq's problem for a homogeneous linear-elastic and isotropic half-space. The second order solution also allows us to evaluate the effect of the elastic constants on the stress field, improving the solution of Boussinesq in this second case also.

1 THE FIRST ORDER ELASTIC SOLUTION

1.1 *First integral of the equilibrium problem*

The first solution of Boussinesq is based on the similarity between the equilibrium equations in terms of displacements, with the body forces per unit volume, f_x, f_y and f_z, set equal to zero:

$$\begin{cases} (\lambda+\mu)\dfrac{\partial I_{1\varepsilon}}{\partial x}+\mu\nabla^2 u=0 \\ (\lambda+\mu)\dfrac{\partial I_{1\varepsilon}}{\partial y}+\mu\nabla^2 v=0 \\ (\lambda+\mu)\dfrac{\partial I_{1\varepsilon}}{\partial z}+\mu\nabla^2 w=0 \end{cases} \tag{1}$$

where $I_{1\varepsilon}$ is the bulk strain, and the three equations:

$$\begin{cases} \dfrac{\partial}{\partial x}\left(2\dfrac{\partial P}{\partial z}\right)-\nabla^2\dfrac{\partial(zP)}{\partial x}=0 \\ \dfrac{\partial}{\partial y}\left(2\dfrac{\partial P}{\partial z}\right)-\nabla^2\dfrac{\partial(zP)}{\partial y}=0 \\ \dfrac{\partial}{\partial z}\left(2\dfrac{\partial P}{\partial z}\right)-\nabla^2\dfrac{\partial(zP)}{\partial z}=0 \end{cases} \tag{2}$$

that are satisfied by any potential function P for which the Laplacian is equal to zero:

$$\nabla^2 P=\frac{\partial^2 P}{\partial x^2}+\frac{\partial^2 P}{\partial y^2}+\frac{\partial^2 P}{\partial z^2}=0\,. \tag{3}$$

The use of the equilibrium equations with the body forces set equal to zero for studying the stress field induced in the soil by a point-load is allowed by the superposition principle: assuming a linear-elastic behavior for the soil, we can separately analyze and superpose the stress field induced in the soil by the point-load and the stress field induced in the soil by the weight of the soil itself.

The similarity between the two systems of Equations 1 and 2 is established in the assumptions:

$$u=-\frac{\partial}{\partial x}(zP),\quad v=-\frac{\partial}{\partial y}(zP),\quad w=-\frac{\partial}{\partial z}(zP)+KP, \tag{4}$$

$$\frac{\lambda+\mu}{\mu}I_{1\varepsilon}=2\frac{\partial P}{\partial z}\,. \tag{5}$$

The function P chosen by Boussinesq is the logarithmic potential Ψ for the prefixed point (x, y, z) of the semi-space under the surface, at the distance r from the point $Q \equiv (x_1, y_1, 0)$ of the load surface:

$$r=\sqrt{(x-x_1)^2+(y-y_1)^2+z^2}\,, \tag{6}$$

$$P=\Psi=\int\log(z+r)\,dm\,, \tag{7}$$

where dm is given by $\rho(x_1, y_1)$, the mass density for unit surface at the point Q:

$$\int dm=\int\rho(x_1,y_1)\,dx_1dy_1\,. \tag{8}$$

The solution of the equilibrium problem in terms of potentials is:

$$(u,v)=-\frac{\partial}{\partial(x,y)}(z\Psi),\quad w=-\frac{\partial}{\partial z}(z\Psi)+K\Psi\,. \tag{9}$$

Since Equations 9 satisfy the conditions of equilibrium but do not provide the right displacement field for

$z \to \infty$ (Boussinesq 1885), Boussinesq used the first derivative $\partial\Psi/\partial z$ instead of the logarithmic potential Ψ for the potential P in Equations 2, which is allowable since $\partial\Psi/\partial z$ still gives a Laplacian equal to zero:

$$P = \frac{\partial \Psi}{\partial z} = \int \frac{dm}{r}, \tag{10}$$

$$(u,v) = -z\frac{\partial}{\partial(x,y)}\frac{\partial \Psi}{\partial z},\ w = -z\frac{\partial^2 \Psi}{\partial z^2} + \frac{\lambda+3\mu}{\lambda+\mu}\frac{\partial \Psi}{\partial z} \tag{11}$$

$$\begin{cases} \tau_{xz} = -2\mu\dfrac{\partial}{\partial x}\left(\dfrac{\mu}{\lambda+\mu}\displaystyle\int\frac{dm}{r} + z\int\frac{z dm}{r^3}\right) \\ \tau_{yz} = -2\mu\dfrac{\partial}{\partial y}\left(\dfrac{\mu}{\lambda+\mu}\displaystyle\int\frac{dm}{r} + z\int\frac{z dm}{r^3}\right) \\ \sigma_z = -2\mu\displaystyle\int\left(\frac{\mu}{\lambda+\mu}\frac{z}{r^3} + 3\frac{z^3}{r^5}\right)dm \end{cases} \tag{12}$$

For the points of the surface, Boussinesq provides the results:

$$u = 0,\ \ v = 0,\ \ w = \frac{\lambda+3\mu}{\lambda+\mu}\int\frac{dm}{r}, \tag{13}$$

$$I_{1\varepsilon} = -4\pi\frac{\mu}{\lambda+\mu}\rho(x,y), \tag{14}$$

$$\begin{cases} (p_x, p_y) = \lim\limits_{z\to 0} -2\dfrac{\mu^2}{\lambda+\mu}\dfrac{\partial}{\partial(x,y)}\displaystyle\int\frac{dm}{r} \\ p_z = 4\pi\mu\dfrac{\lambda+2\mu}{\lambda+\mu}\rho(x,y) \end{cases} \tag{15}$$

The third of Equations 15 and the first two of Equations 13 tell us that this is the case in which the boundary conditions consist in giving the normal component of the load and assuming the horizontal displacements on the surface to be equal to zero.

A discussion of the original treatment of Boussinesq (Boussinesq 1885) can be found in Ferretti (2012a), where it is pointed out how it seems unnecessary to perform integrals on the whole load surface – as Boussinesq does – since the aim of the treatment is to find the solution for a single point-load, and not for a distributed load. In effect, after obtaining the general solution, Boussinesq gives the point-load solution by substituting the integrals with their integrands, that is, by causing the dimensions of the load surface to vanish. It therefore seems possible, besides being simpler, to build the point-load solution directly, by defining the potentials for the infinitesimal superficial neighborhood of the point:

$$\psi = \log(z+r)\,dm, \tag{16}$$

$$P = \frac{\partial \psi}{\partial z} = \frac{1}{r}dm. \tag{17}$$

The solution following by the position in Equation 17 is:

$$\begin{cases} u = \dfrac{z(x-x_1)}{r^3}dm,\ \ v = \dfrac{z(y-y_1)}{r^3}dm \\ w = \dfrac{r^2(\lambda+3\mu)+z^2(\lambda+\mu)}{r^3(\lambda+\mu)}dm \end{cases} \tag{18}$$

$$I_{1\varepsilon} = -\frac{2\mu}{\lambda+\mu}\frac{z}{r^3}dm, \tag{19}$$

$$\begin{cases} \tau_{xz} = 2\mu(x-x_1)\dfrac{\mu r^2 + 3(\lambda+\mu)z^2}{(\lambda+\mu)r^5}dm \\ \tau_{yz} = 2\mu(y-y_1)\dfrac{\mu r^2 + 3(\lambda+\mu)z^2}{(\lambda+\mu)r^5}dm \\ \sigma_z = -2\mu z\dfrac{\mu r^2 + 3(\lambda+\mu)z^2}{(\lambda+\mu)r^5}dm \end{cases} \tag{20}$$

For $z \to 0$ (points of the surface), we find:

$$u = 0,\ \ v = 0,\ \ w = \frac{\lambda+3\mu}{r(\lambda+\mu)}dm \tag{21}$$

$$I_{1\varepsilon} = \begin{cases} 0 & \text{for } r > 0 \\ -\dfrac{2\mu}{\lambda+\mu}\rho(x_1,y_1) & \text{for } r \to 0 \end{cases}, \tag{22}$$

$$\begin{cases} p_x = \dfrac{2\mu^2}{\lambda+\mu}\dfrac{x-x_1}{r^3}dm,\ \ p_y = \dfrac{2\mu^2}{\lambda+\mu}\dfrac{y-y_1}{r^3}dm \\ p_z = \begin{cases} 0 & \text{for } r > 0 \\ 2\mu\dfrac{\lambda+2\mu}{\lambda+\mu}\rho(x_1,y_1) & \text{for } r \to 0 \end{cases} \end{cases} \tag{23}$$

1.2 *Second integral of the equilibrium problem*

The second solution follows from the position:

$$u = \frac{\partial P}{\partial x},\ \ v = \frac{\partial P}{\partial y},\ \ w = \frac{\partial P}{\partial z}. \tag{24}$$

Due to Equation 3, in this second case the bulk strain is equal to zero:

$$I_{1\varepsilon} = \frac{\partial u}{\partial x} + \frac{\partial v}{\partial y} + \frac{\partial w}{\partial z} = \nabla^2 P = 0, \tag{25}$$

and the equilibrium equations expressed by Equations 1 are identically satisfied.

By using the logarithmic potential given in Equation 16 instead of Ψ, the second solution of Boussinesq is substituted by the following (Ferretti 2012a):

$$\begin{cases} u = \dfrac{\partial \psi}{\partial x} = \dfrac{x - x_1}{r(z+r)} dm \\ v = \dfrac{\partial \psi}{\partial y} = \dfrac{y - y_1}{r(z+r)} dm \\ w = \dfrac{\partial \psi}{\partial z} = \dfrac{1}{r} dm \end{cases} \tag{26}$$

$$\begin{cases} (\tau_{xz}, \tau_{yz}) = -2\mu \dfrac{\partial}{\partial (x,y)} \left(\dfrac{1}{r} \right) dm \\ \sigma_z = 2\mu \dfrac{\partial}{\partial z} \left(\dfrac{1}{r} \right) dm = -2\mu \dfrac{z}{r^3} dm \end{cases} \tag{27}$$

and, for the points of the surface:

$$\begin{cases} u = \dfrac{\partial \psi}{\partial x} = \dfrac{x - x_1}{r^2} dm \\ v = \dfrac{\partial \psi}{\partial y} = \dfrac{y - y_1}{r^2} dm \\ w = \dfrac{\partial \psi}{\partial z} = \dfrac{1}{r} dm \end{cases} \tag{28}$$

$$\begin{cases} p_x = 2\mu \dfrac{x - x_1}{r^3} dm, \quad p_y = 2\mu \dfrac{y - y_1}{r^3} dm \\ p_z = \begin{cases} 0 & \text{for } r > 0 \\ 2\mu\rho(x_1, y_1) & \text{for } r \to 0 \end{cases} \end{cases} \tag{29}$$

1.3 *Third integral of the equilibrium problem*

For the third solution, Boussinesq assumes:

$$u = -\frac{\partial P}{\partial y}, \quad v = \frac{\partial P}{\partial x}, \quad w = 0 \tag{30}$$

which are the plane strain conditions.

As for the second solution, in this case also, the bulk strain is equal to zero and the equilibrium equations are identically satisfied, due to Equation 3

Since the bulk strain is equal to zero, the condition of plane strain implies plane stress in each point of the body. The stress field is given by:

$$\tau_{xz} = \mu \frac{\partial^2 P}{\partial y \partial z}, \quad \tau_{yz} = -\mu \frac{\partial^2 P}{\partial x \partial z}, \quad \sigma_z = 0, \tag{31}$$

where:

$$\frac{\partial \tau_{xz}}{\partial x} + \frac{\partial \tau_{yz}}{\partial y} = 0. \tag{32}$$

This is the solution for the case in which the normal component of the external load is set equal to zero and the two shear components stand in the relationship represented by Equation 32. The displacements take place horizontally.

1.4 *Elastic solution for a point-load perpendicular to the surface*

Due to the superposition principle, it is always possible to find further solutions to the equilibrium problem by combining the former three solutions with each other. Along these lines, Boussinesq formed two linear combinations of Equations 11 and 24. The linear combination giving the solution of the point-load perpendicular to the surface is obtained by multiplying Equations 11 by the inverse of $-4\pi\mu$ and Equations 24 by the inverse of $-4\pi(\lambda + \mu)$. The multiplying factors of the linear combination have been chosen specifically to equal p_z and $\rho(x, y)$:

$$p_z = \lim_{z \to 0} -\frac{1}{2\pi} \frac{\partial^2 \Psi}{\partial z^2} = \rho(x, y). \tag{33}$$

and, consequently, also the external load dF and dm:

$$dF = p_z dx_1 dy_1 = \rho(x_1, y_1) dx_1 dy_1 = dm. \tag{34}$$

Due to the superposition principle, the same multiplying factors can be taken to build a second linear combination, providing the solution in terms of stresses. In the case of infinitesimal load surface, the well-known solutions of Boussinesq for a point-load perpendicular to the surface is:

$$\begin{cases} \tau_{xz} = \dfrac{3}{2\pi} \dfrac{z^2}{r^5} (x - x_1) dF \\ \tau_{yz} = \dfrac{3}{2\pi} \dfrac{z^2}{r^5} (y - y_1) dF \\ \sigma_z = -\dfrac{3}{2\pi} \dfrac{z^3}{r^5} dF \end{cases} \tag{35}$$

where the stresses are independent of the elastic coefficients of the medium.

In Ferretti (2012a), the elastic solution for a point-load perpendicular to the surface has been derived as linear combination of Equations 18 and 26, for displacements, and of Equations 20 and 27, for stresses, providing:

$$\begin{cases} u = \dfrac{x - x_1}{2\mu} \left[\dfrac{z}{r^3} - \dfrac{\mu}{\lambda + \mu} \dfrac{1}{r(z+r)} \right] dF \\ v = \dfrac{y - y_1}{2\mu} \left[\dfrac{z}{r^3} - \dfrac{\mu}{\lambda + \mu} \dfrac{1}{r(z+r)} \right] dF \\ w = \dfrac{1}{2\mu r} \left[\dfrac{\lambda + 2\mu}{\lambda + \mu} + \dfrac{z^2}{r^2} \right] dF \end{cases} \tag{36}$$

$$I_{1\varepsilon}=\frac{1}{\lambda+\mu}\frac{d}{dz}\left(\frac{1}{r}\right)dm=-\frac{1}{\lambda+\mu}\frac{z}{r^3}dF\,, \tag{37}$$

$$\begin{cases}\tau_{xz}=3\dfrac{z^2}{r^5}(x-x_1)\,dF\\ \tau_{yz}=3\dfrac{z^2}{r^5}(y-y_1)\,dF\\ \sigma_z=-3\dfrac{z^3}{r^5}dF\end{cases} \tag{38}$$

for a point inside the soil, and

$$\begin{cases}u=-\dfrac{1}{2(\lambda+\mu)}\dfrac{x-x_1}{r^2}dP\\ v=-\dfrac{1}{2(\lambda+\mu)}\dfrac{y-y_1}{r^2}dP\\ w=\dfrac{\lambda+2\mu}{2\mu(\lambda+\mu)}\dfrac{1}{r}dP\end{cases} \tag{39}$$

$$I_{1\varepsilon}=\begin{cases}0 & \text{for } r>0\\ -\dfrac{1}{\lambda+\mu}\rho(x_1,y_1) & \text{for } r\to 0\end{cases} \tag{40}$$

$$\begin{cases}p_x=0,\;\; p_y=0\\ p_z=\begin{cases}0 & \text{for } r>0\\ \lim\limits_{z\to 0}-\dfrac{\partial^2\psi}{\partial z^2}=\rho(x_1,y_1) & \text{for } r\to 0\end{cases}\end{cases} \tag{41}$$

for the points of the surface.

2 THE SECOND ORDER ELASTIC SOLUTION

2.1 *A second order solution of the first integral*

Following the spirit of the superposition principle and noting that the partial derivatives of any arbitrary order of the function ψ, defined in Equation 16, have a zero Laplacian (i.e. they satisfy the condition $\nabla^2=0$), it is possible to refine the elastic solution of Boussinesq by adding to it a further solution of Equations 2, obtained by substituting ψ with one of its derivatives of second order. This observation will be used here in order to find a further form of the first integral, which, combined to the former form and the second integral, could provide a stress solution to the vertical point-load problem that also depends on the elastic constants of the soil.

Assuming:

$$P=\frac{\partial^2\psi}{\partial z^2}=-\frac{z}{r^3}dm\,, \tag{42}$$

we find:

$$\begin{cases}u=-3\dfrac{z^2(x-x_1)}{r^5}dm\\ v=-3\dfrac{z^2(y-y_1)}{r^5}dm\\ w=-\dfrac{z}{r^3}\left(3\dfrac{z^2}{r^2}+\dfrac{2\mu}{\lambda+\mu}\right)dm\end{cases} \tag{43}$$

$$I_{1\varepsilon}=\frac{2\mu}{\lambda+\mu}\left(3\frac{z^2}{r^5}-\frac{1}{r^3}\right)dm\,, \tag{44}$$

$$\begin{cases}\tau_{xz}=\dfrac{6\mu}{\lambda+\mu}\dfrac{(x-x_1)z}{r^5}\left[\lambda-5(\lambda+\mu)\dfrac{z^2}{r^2}\right]dm\\ \tau_{yz}=\dfrac{6\mu}{\lambda+\mu}\dfrac{(y-y_1)z}{r^5}\left[\lambda-5(\lambda+\mu)\dfrac{z^2}{r^2}\right]dm\\ \sigma_z=-2\mu\left(\dfrac{\lambda+2\mu}{\lambda+\mu}\dfrac{1}{r^3}+\dfrac{6\lambda+3\mu}{\lambda+\mu}\dfrac{z^2}{r^5}-15\dfrac{z^4}{r^7}\right)dm\end{cases} \tag{45}$$

inside the soil, and:

$$u=0,\;\; v=0,\;\; w=0, \tag{46}$$

$$I_{1\varepsilon}=\begin{cases}-\dfrac{2\mu}{\lambda+\mu}\dfrac{1}{r^3}dm & \text{for } r>0\\ -\infty & \text{for } r\to 0\end{cases} \tag{47}$$

$$\begin{cases}p_x=0,\;\; p_y=0\\ p_z=\begin{cases}2\mu\dfrac{\lambda+2\mu}{\lambda+\mu}\dfrac{1}{r^3}dm & \text{for } r>0\\ \infty & \text{for } r\to 0\end{cases}\end{cases} \tag{48}$$

for $z\to 0$.

Since p_x and p_y are equal to zero, Equations 45 may be added to the combined solution of first order without changing the nature of the solved problem, which still is a vertical point-load problem. Moreover, due to the infinite value achieved by p_z for $z, r\to 0$, the second form of the first integral seems to be useful for building the combined solution in all the points of the soil apart from the one of load application.

2.2 *Combined solution*

The combined solution of second order is built by multiplying Equations 45 for $-C$ and adding the result to Equations 38. The resulting stress field (for $r\neq 0$) is

now in relationship with the elastic constants of the soil:

$$\begin{cases} \tau_{xz} = 3\dfrac{(x-x_1)z}{r^5}\left[z + 2C\mu\left(5\dfrac{z^2}{r^2} - \dfrac{\lambda}{\lambda+\mu}\right)\right]dm \\ \tau_{yz} = 3\dfrac{(y-y_1)z}{r^5}\left[z + 2C\mu\left(5\dfrac{z^2}{r^2} - \dfrac{\lambda}{\lambda+\mu}\right)\right]dm \\ \sigma_z = -\dfrac{1}{r^3}\left[3\dfrac{z^3}{r^2} + 2C\mu\left(15\dfrac{z^4}{r^4} - 3\dfrac{2\lambda+\mu}{\lambda+\mu}\dfrac{z^2}{r^2} - \right.\right. \\ \left.\left. - \dfrac{\lambda+2\mu}{\lambda+\mu}\right)\right]dm \end{cases} \tag{49}$$

As far as the third of Equations 49 is concerned, we may easily verify that the new terms (the ones which are multiplied for C) significantly modify the normal stress when approaching the surface, while they are negligible at great depths. Indeed, for $z \to 0$:

$$-p_z = \lim_{z\to 0}\sigma_z = 2C\mu\frac{\lambda+2\mu}{\lambda+\mu}\frac{1}{r^3}dm, \tag{50}$$

while, for $z \to \infty$, the third of Equations 49 gives the combined solution of Section 1.4.

$$\lim_{z\to\infty}\sigma_z = -3\frac{z^3}{r^5}dm. \tag{51}$$

From the comparison between Equations 50 and 51, it is clear that, for $C > 0$, the normal stress for $z \to 0$ is opposite in sign to the normal stress for $z \to \infty$:

$$\operatorname{sign}\left(\lim_{z\to 0}\sigma_z\right) = -\operatorname{sign}\left(\lim_{z\to\infty}\sigma_z\right). \tag{52}$$

Therefore, near to the surface, the compressed soil is subjected to a normal stress of traction. This is a result not accounted for in the solution of Boussinesq and, together with the dependence of σ_z on the elastic constants, represents the most important novelty of the combined solution of second order.

From Equation 52 we can also argue that, as σ_z is a continuous function, there exists a finite value of depth for which the normal stress is equal to zero. Setting $z_0 = z_0(r, C, \lambda, \mu)$, the function giving the depth for which $\sigma_z = 0$, from Equations 49 we find the relationship:

$$z_0^2\left(10C\mu\frac{z_0^2}{r^4} + \frac{z_0}{r^2} - 2C\mu\frac{2\lambda+\mu}{\lambda+\mu}\frac{1}{r^2}\right) = \frac{2}{3}C\mu\frac{\lambda+2\mu}{\lambda+\mu} \tag{53}$$

in which the banal solution:

$$\sigma_z = 0 \quad \text{for } r \to \infty, \tag{54}$$

has been eliminated.

As can be easily verified, for $z \to \infty$ the combined solution of second order is equal to the solution of Boussinesq even for the displacement field.

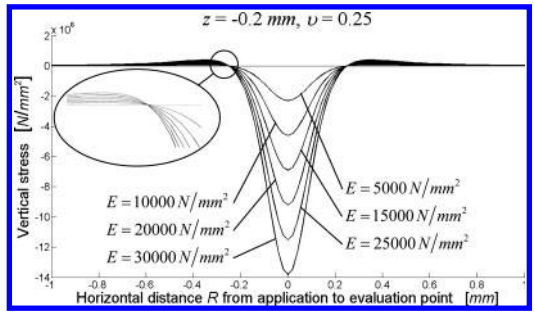


Figure 1. Parametric analysis on the Young modulus, E.

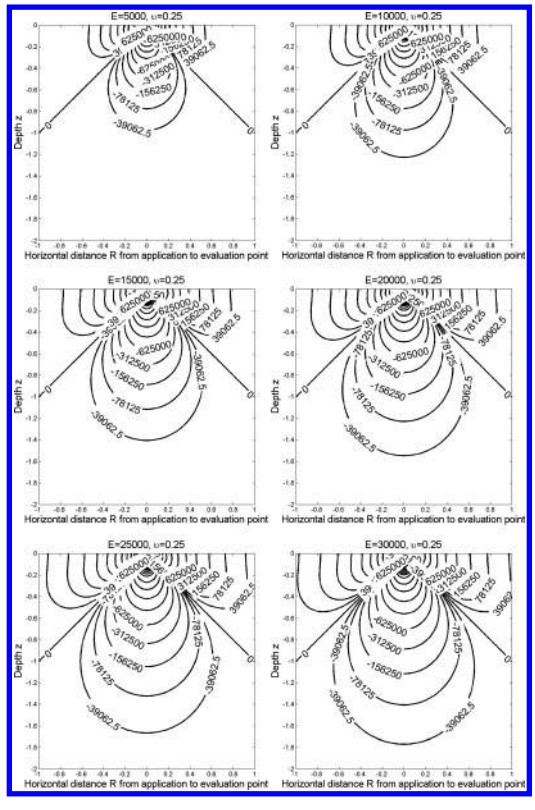


Figure 2. Parametric analysis on the Young modulus, for the vertical stress contours on the vertical cross-section (all distances are in *mm*).

3 NUMERICAL RESULTS

3.1 *Point-load perpendicular to the surface*

The plots of the vertical stress and the vertical stress contours of second order for a prefixed Poisson's ratio, υ, and variable values of Young's modulus, E, are given in Figure 1 for a plane near to the surface and in Figure 2 for a vertical cross-section passing through the point load, respectively. The parametric analysis on the Poisson's ratio for a prefixed E is shown in Ferretti (2012a).

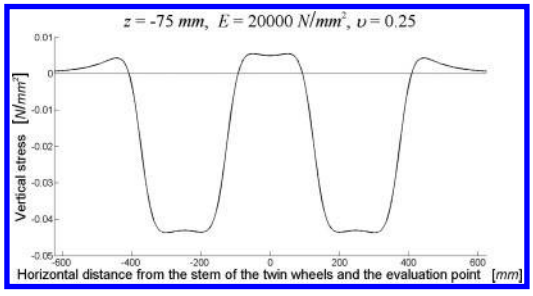


Figure 3. Vertical stress under the twin wheels of an aircraft for rectangular contact areas and uniform load.

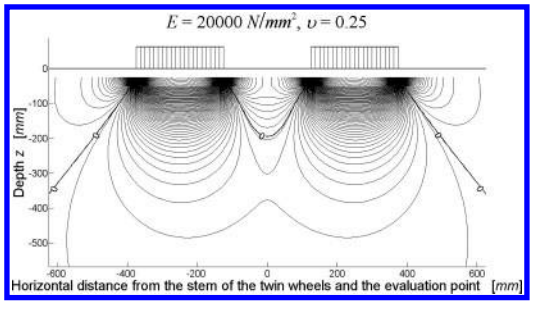


Figure 4. Vertical stress contours on the vertical cross-section for rectangular contact areas and uniform load (twin wheels).

The numerical solution of second order shows two positive peaks of vertical stress in the proximity of the application point of compression load (Fig. 1), in total agreement with the experimental data for vehicular loading shown in Ferretti & Bignozzi (2012) and Ferretti (2012b). This result gives a numerical proof that a tensile state of stress arises on the surface of soils and pavements when subjected to compression loads, with the point in which the vertical stress change in sign that is also a point in which the vertical stress does not depend upon the value of E (Fig. 1). Since both soil and concrete are assumed as not being resistant to traction – to be on the safe side – the tensile state of stress must be considered with particular attention in these materials.

Due to the tensile state of stress, there exist two families of stress contours (Fig. 2): one family for the tensioned soil and one family for the compressed soil, with the two families separated by straight lines. Moreover, the parametric analysis on the vertical cross-section shows that greater values of E increase the vertical stresses at each depth without modifying the shape of the iso-lines of stress, which change in size homothetically (Fig. 2).

3.2 *Distributed load perpendicular to the surface*

In order to evaluate which the interaction effect is of two adjacent loaded areas, the vertical stress and the vertical stress contours of second order for a vertical load that is uniformly distributed over two contact areas of rectangular shape have been plotted in Figures 3, 4, respectively. All the dimensions in Figures 3, 4 are those typical of two twin wheels in an aircraft. The existence of a tensile state of stress near the wheels is well evident even in this last case. Moreover, the interaction effect make particularly severe the positive stresses between the wheels.

Further results for contact areas of circular, rectangular and elliptic shape together with uniform and parabolic laws of external pressure distribution may be found in Ferretti (in prep.).

4 CONCLUSIONS

In this paper, we have discussed Boussinesq's solution in the light of new experimental findings on the stress distribution in a half-space subjected to point-loads. The original work of Boussinesq has been extended to provide a second order solution.

The second order solution has shown that a compression load always generates positive stresses at the surface, in the proximity of the load. The existence of a tensile state of stress, not accounted for in Boussinesq's solution, could explain the several observed mechanisms of premature damage that affect concrete pavements subjected to vehicular loading, particularly when twin wheels are involved.

The second order solution also allows us to evaluate the effect of the elastic constants on the stress field, which, in this second case also, is an improvement to Boussinesq's solution.

REFERENCES

Boussinesq, M.J. 1885. *Application des potentiels a l'étude de l'équilibre et du mouvement des solides élastiques, avec des notes étendues sur divers points de physique mathématique et d'analyse*. Paris: Gauthier-Villard imprimeur libraire.

Ferretti, E. 2012a. A Higher Order Solution of the Elastic Problem for a Homogeneous, Linear-Elastic and Isotropic Half-Space Subjected to a Point-Load Perpendicular to the Surface. *CMES: Computer Modeling in Engineering & Sciences* 86(5): 435–468.

Ferretti, E. 2012b. Waste Tire Rubberized Concrete Plates for Airport Pavements: Stress and Strain Profiles in Time and Space Domains.*CMC: Computers, Materials, & Continua* 31(2): 87–111.

Ferretti, E., in prep. A Higher Order Solution of the Elastic Problem for a Homogeneous, Linear-Elastic and Isotropic Half-Space Subjected to a Distributed Load Perpendicular to the Surface.*CMES: Computer Modeling in Engineering & Sciences.*

Ferretti, E. & Bignozzi, M.C. 2012. Stress and Strain Profile along the Cross-Section of Waste Tire Rubberized Concrete Plates for Airport Pavements.*CMC: Computers, Materials, & Continua* 27(3): 231–274.

Research and Applications in Structural Engineering, Mechanics and Computation – Zingoni (Ed.)
© 2013 Taylor & Francis Group, London, ISBN 978-1-138-00061-2

Upper and lower bound calculations of the bearing capacity of strip footings near slopes in cohesionless soil

Sven Krabbenhoft & Lars Damkilde
Department of Civil Engineering, Aalborg University, Esbjerg, Denmark

Kristian Krabbenhoft
Department of Civil, Surveying and Environmental Engineering, University of Newcastle, Australia

ABSTRACT: The calculation of the bearing capacity of a strip foundation located on the edge of or near a slope is commonly based on the well known bearing capacity equation applying so called slope factors, and expressions for these factors have been proposed by amongst others Brinch Hansen and Vesic. These factors only take into account the inclination of the slope, whereas other parameters, which may play a role, such as the distance from the footing to the slope, the width of the footing and the strength of the soil are ignored. The present work comprises finite element based upper- and lower-bound calculations, using the software OptumGEO, considering the influence of these factors for vertical loads, and also the effect of a possible surcharge is investigated. The results are given as design charts and tables suitable for practical design.

1 INTRODUCTION

The bearing capacity of a vertically and centrally loaded strip foundation located at the crest of a slope in cohesionless soil can be found from the bearing capacity equation proposed by Hansen (1970) and Vesic (1975) :

$$q_{ult} = 0.5\gamma B N_\gamma d_\gamma g_\gamma + q_s N_q d_q g_q \qquad (1)$$

where q_{ult} is the bearing capacity per unit area of the foundation, γ is the effective soil unit weight, B is the width of the foundation, N_γ and N_q are bearing capacity factors, d_γ and d_q are depth factors, which are always greater than unity and very often they are assumed equal to unity, as will be done in this study, q_s is the vertical effective stress at the foundation base level and g_γ and g_q are slope factors which are functions of the inclination of the slope. For the slope factors the following empirical expressions have been proposed by Hansen (1970):

$$g_\gamma = g_q = (1 - 0.5\tan\beta)^5 \qquad (2)$$

and by Vesic (1975) :

$$g_\gamma = g_q = (1 - \tan\beta)^2 \qquad (3)$$

where in both equations β is the inclination of the slope to the horizontal. The slope factors are independent of the magnitude of the friction angle of the soil and for a footing located a distance away from the crest of the slope neither Hansen nor Vesic gives any guidelines.

Gemberline (1988) carried out a large number of centrifuge tests on model footings located both at various distances from the crest of the slope and at various distances from the top of the slope and on that basis he proposed the following equation for the bearing capacity:

$$q_{ult} = 0.5\gamma B N_{\gamma q} \qquad (4)$$

where the factor $N_{\gamma q}$ depends on the friction angle of the soil, the distance of the foundation from the crest of the slope and the distance from the top of the slope to the level of the foundation base.

The bearing capacity of foundations near slopes has also been investigated by Saran et al (1989), Sarma and Chen (1996) and Castelli and Motta (2010) who all used the limit equilibrium method.

The results of the above authors for a surface foundation located at the crest of a slope are given in Figure 1 for a slope inclination 1:3 ($\beta = 18.44°$).

From Figure 1 it can be seen, that according to Hansen, Vesic and Gemberline the slope factor g_γ is independent of the friction angle of the soil, whereas the other authors all find some dependence of the friction angle on the slope factor. Sarma and Chen and Saran et al. have found decreasing values of the slope factor for increasing values of the friction angle and the opposite is the case with the findings of Castelli and Motta and roughly there is a discrepency up to about 100% between the smallest and the largest values.

The aim of the present study is – within an accuracy acceptable for practical design – to find the bearing capacity of a strip footing located near a slope, and also it is of interest to investigate, whether the

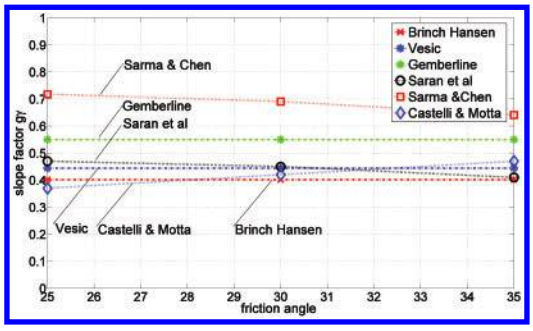


Figure 1. Slope factors g_γ for slope inclination 1:3

traditional bearing capacity equation (1) is providing results, that are reasonably accurate. For that purpose a series of numerical upper- and lower-bound limit analyses using the software package OptumGEO (2012) of the bearing capacity of a strip footing located near a slope in cohesionless soil with varying surcharges have been performed. The analyses are carried out for friction angles 30, 35 and 40° and slope inclinations of 1:2 ($\beta = 26.57°$), 1:3 ($\beta = 18.44°$) and 1:4 ($\beta = 14.04°$). The bearing capacity equation assumes, that the total bearing capacity can be found as the sum of the contributions from the selfweight of the soil and the surcharge and therefore also separate analysis have been done, making it possible to determine both g_γ and g_q and thus the dependency of the friction angle ϕ on the slope factors. The results are reported as tables and graphs suitable for practical design.

2 LIMIT ANALYSIS

2.1 *OptumGEO*

OptumGEO is a finite element program dedicated to geotechnical applications. A key feature of the program is that it allows for the calculation of rigorous upper and lower bound solutions to plasticity problems. The gap between the calculated upper- and lower-bound solutions can be reduced by using the automatic adaptive remeshing procedure available in OptumGEO. For typical problems, the gap between the upper- and lower-bound values of a specific problem can thus be reduced to a few percent or less.

2.2 *Soil characteristics and geometry*

All the simulations were performed for friction angles $\varphi = 30, 35$ and 40° and the unit weight γ of the soil was taken equal to 20 kN/m^3.

The geometry of the slope and the footing is shown in Figure 2. The total area of the domain was chosen large enough to avoid any effects from the boundaries. Likewise the height of the slope was chosen large enough in order for the bottom of the slope not to have any influence on the results.

The width B of the strip foundation was taken equal to 1.00 metre and the calculations were carried out for values of the distance a from the crest of the slope to

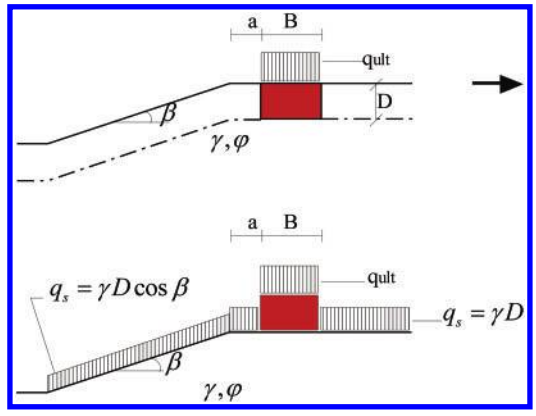


Figure 2. Geometry of slope and nomenclature

the edge of the footing in the interval 0-15 metres. The base of the footing was considered perfectly rough and for cases where the base of the footing is below ground level, the effect of the soil above the base is considered equivalent to a vertical uniform surcharge at base level as shown in Figure 2.

The surcharge is expressed by the surcharge ratio λ defined by:

$$\lambda = \frac{q_s}{\gamma B} \tag{5}$$

where $q_s$is the surcharge; i.e. the weight of the soil from the base of the footing to ground level, γ is the soil unit weight and B is the width of the foundation. For footings having the same value of the surcharge ratio λ and the same value of the relative distance a/B the bearing capacity can be normalized with respect to the quantities B and γ as shown by Krabbenhoft et al (2012).

3 RESULTS FROM THE ANALYSIS

The analyses yielded both upper- (UB) and lower-bound (LB) values of the bearing capacity of a strip foundation and these are given in Table 1, 2, 3 and 4 where the values in Table 4 are for weightless soil and a surcharge equal to unity. The values are given as functions of the relative distance a/B, the surcharge ratio λ and the friction angle φ and as can be seen from the tables the bearing capacity increases with an increase in any of these three parameters. Shadings of the values of the bearing capacities indicate, that for this particular combination of a/B, λ and φ there is no further increase in the bearing capacity even for an increase of the relative distance a/B. From the tables it can be seen, that the greater the friction angle the greater the discrepancy (also percentage-wise) between the upper- and lower-bound values. The relative discrepancy is taken as the difference between the upper bound values and the mean values divided by the mean value. For all slope inclinations the largest discrepancies occur in the case of no surcharge (5.4% for $\varphi = 40°$) and the smallest for a surcharge ratio

Table 1. Bearing capacities [kPa] for slope inclination 1:2

a/B	λ	$\varphi = 30°$		$\varphi = 35°$		$\varphi = 40°$	
		LB	UB	LB	UB	LB	UB
	0	34.8	35.5	82.0	84.0	186.0	191.5
0	0.2	61.3	61.9	132.6	134.3	280.7	309.4
	0.5	94.4	95.2	195.2	197.4	398.5	436.0
	1.0	146.6	147.7	293.2	296.2	580.7	632.9
	0	72.5	74.0	154.6	158.4	325.8	336.6
0.5	0.2	96.8	97.6	198.8	202.0	404.2	410.6
	0.5	136.8	138.0	269.8	273.5	530.9	541.5
	1.0	198.5	199.8	382.1	386.5	738.1	747.4
	0	102.0	103.9	202.1	214.3	429.9	444.4
1.0	0.2	132.1	133.4	259.9	263.0	512.8	521.9
	0.5	176.0	177.2	333.1	342.3	655.1	664.5
	1.0	245.4	247.0	463.8	467.7	878.3	889.0
	0	133.0	138.8	270.9	280.2	550.8	573.1
2.0	0.2	196.0	198.3	372.0	377.3	717.1	731.7
	0.5	253.3	255.4	471.6	476.6	889.8	902.5
	1.0	338.9	341.3	621.9	627.3	1151.2	1166.3
	0	146.5	149.9	334.8	345.1	694.0	720.4
3.0	0.2	250.4	253.9	471.5	480.9	906.2	926.5
	0.5	326.8	330.0	597.3	604.8	1114.4	1134.0
	1.0	430.9	434.3	776.0	783.6	1418.3	1439.1
	0	146.5	149.9	334.8	345.1	800.1	842.6
4.0	0.2	263.0	270.1	539.0	560.1	1068.8	1102.1
	0.5	388.7	394.3	710.3	720.5	1324.7	1352.2
	1.0	518.1	523.0	923.2	933.7	1678.3	1704.0
	0	146.5	149.9	334.8	345.1	817.3	907.8
5.0	0.2	263.0	270.1	539.0	560.1	1182.9	1248.9
	0.5	393.9	405.3	793.2	815.4	1515.4	1552.8
	1.0	592.4	601.2	1058.0	1071.9	1925.0	1960.0
	0	146.5	149.9	334.8	345.1	817.3	907.8
10.0	0.2	263.0	270.1	539.0	560.1	1237.9	1318.6
	0.5	393.9	405.3	793.2	815.4	1712.6	1815.6
	1.0	598.2	610.9	1153.5	1203.5	2470.2	2565.4

Table 2. Bearing capacities [kPa] for slope inclination 1:3

a/B	λ	$\varphi = 30°$		$\varphi = 35°$		$\varphi = 40°$	
		LB	UB	LB	UB	LB	UB
	0	66.2	68.5	140.1	144.0	317.6	329.0
0	0.2	119.7	121.2	229.3	232.9	483.8	494.1
	0.5	182.7	184.5	335.8	340.0	681.5	693.6
	1.0	280.1	282.7	500.2	506.0	985.8	1001.4
	0	97.8	100.2	204.6	210.3	439.4	455.2
0.5	0.2	154.8	156.5	302.7	305.1	613.6	626.4
	0.5	220.1	221.9	417.5	419.5	822.4	836.6
	1.0	322.2	324.5	596.2	598.3	1145.9	1163.4
	0	120.9	123.6	248.7	256.0	529.5	552.3
1.0	0.2	189.3	191.5	362.1	368.2	729.1	745.7
	0.5	260.7	264.4	485.7	493.0	952.5	970.8
	1.0	373.8	376.3	678.9	685.7	1299.8	1319.7
	0	143.8	149.7	305.8	327.1	669.8	700.8
2.0	0.2	238.1	246.0	451.8	473.7	874.9	949.1
	0.5	331.7	335.1	609.5	617.8	1180.1	1203.4
	1.0	463.4	467.2	830.2	838.7	1567.9	1592.6
	0	143.8	149.7	325.5	351.8	748.1	813.3
3.0	0.2	262.7	270.2	526.9	540.1	1071.2	1099.6
	0.5	383.9	388.6	709.8	721.2	1373.3	1400.9
	1.0	540.3	545.3	964.3	976.1	1806.7	1836.7
	0	143.8	149.7	325.5	351.8	826.7	875.9
4.0	0.2	262.7	270.2	546.9	573.4	1171.6	1228.8
	0.5	395.0	405.4	769.7	799.6	1532.1	1578.0
	1.0	595.8	605.7	1078.4	1093.3	2033.4	2073.1
	0	143.8	149.7	325.5	351.8	826.7	875.9
5.0	0.2	262.7	270.2	546.9	573.4	1235.7	1310.0
	0.5	395.0	405.4	796.3	824.6	1635.8	1717.7
	1.0	601.4	610.5	1155.3	1185.0	2214.6	2267.5
	0	143.8	149.7	325.5	351.8	826.7	875.9
10.0	0.2	262.7	270.2	546.9	573.4	1235.7	1310.0
	0.5	395.0	405.4	796.3	824.6	1743.9	1818.5
	1.0	601.4	610.5	1155.3	1185.0	2456.7	2564.6

Table 3. Bearing capacities [kPa] for slope inclination 1:4

a/B	λ	$\varphi = 30°$ LB	$\varphi = 30°$ UB	$\varphi = 35°$ LB	$\varphi = 35°$ UB	$\varphi = 40°$ LB	$\varphi = 40°$ UB
	0	85.3	86.1	179.1	183.3	409.5	425.3
0	0.2	151.2	152.5	291.3	296.3	618.8	637.4
	0.5	229.1	231.0	423.2	429.3	870.2	886.8
	1.0	349.2	351.3	626.1	633.9	1249.4	1271.5
	0	112.2	114.4	237.1	244.0	523.9	546.5
0.5	0.2	182.4	184.7	355.4	364.5	745.3	765.0
	0.5	261.8	264.2	497.2	503.7	1003.5	1022.3
	1.0	384.4	387.6	711.8	719.7	1393.8	1424.0
	0	130.3	132.9	274.5	283.5	565.4	601.0
1.0	0.2	212.0	214.3	411.1	419.1	848.3	869.7
	0.5	298.2	301.2	560.8	568.6	1120.1	1142.1
	1.0	429.4	432.8	787.5	796.5	1533.3	1560.6
	0	145.2	150.0	322.2	334.5	708.3	744.8
2.0	0.2	246.9	257.4	485.3	507.9	987.2	1047.8
	0.5	355.9	359.9	666.0	676.7	1322.3	1351.1
	1.0	506.7	511.5	920.5	932.5	1777.6	1810.1
	0	145.2	150.0	336.7	351.7	795.4	841.1
3.0	0.2	261.0	270.1	539.6	556.1	1129.3	1171.1
	0.5	392.7	399.5	738.1	759.1	1486.7	1522.2
	1.0	552.7	574.3	1031.8	1047.3	1991.6	2029.6
	0	145.2	150.0	336.7	351.7	799.5	879.6
4.0	0.2	261.0	270.1	552.2	573.6	1205.7	1266.9
	0.5	394.3	405.6	791.7	814.9	1602.2	1661.1
	1.0	596.1	610.5	1116.8	1140.3	2121.7	2220.9
	0	145.2	150.0	336.7	351.7	820.4	880.6
5.0	0.2	261.0	270.1	552.2	573.6	1220.2	1316.1
	0.5	394.3	405.6	791.7	814.9	1684.2	1763.7
	1.0	596.1	610.5	1165.2	1202.4	2303.3	2371.4
	0	145.2	150.0	336.7	351.7	820.4	880.6
10.0	0.2	261.0	270.1	552.2	573.6	1231.7	1319.9
	0.5	394.3	405.6	791.7	814.9	1736.6	1819.5
	1.0	596.1	610.5	1165.2	1202.4	2456.1	2566.5

Table 4. Bearing capacities [kPa] weightless soil, $q_s = 1$ kPa

a/B	λ	$\varphi = 30°$ LB	$\varphi = 30°$ UB	$\varphi = 35°$ LB	$\varphi = 35°$ UB	$\varphi = 40°$ LB	$\varphi = 40°$ UB
	1:2	5.0	5.0	9.5	9.5	17.3	18.2
0	1:3	9.1	9.1	15.2	15.3	27.6	27.9
	1:4	11.0	11.1	18.5	18.7	33.9	34.3
	1:2	6.0	6.1	10.7	10.9	19.2	19.4
0.5	1:3	9.5	9.6	16.5	16.5	29.5	29.8
	1:4	11.3	11.4	19.6	19.8	35.6	36.0
	1:2	6.8	6.8	11.9	12.0	21.0	21.2
	1:3	10.4	10.4	17.6	17.8	31.4	31.8
1.0	1:4	12.0	12.1	20.6	20.8	37.2	37.6
	1:2	8.1	8.2	14.0	14.1	24.3	24.6
2.0	1:3	11.7	11.8	19.7	19.9	34.6	35.0
	1:4	13.3	13.4	22.5	22.7	40.0	40.6
	1:2	9.3	9.4	16.0	16.1	27.3	27.6
3.0	1:3	13.0	13.1	21.6	21.8	37.3	37.9
	1:4	14.4	14.5	24.2	24.5	42.7	43.3
	1:2	10.4	10.4	17.7	17.8	30.0	30.4
4.0	1:3	14.0	14.1	23.2	23.5	40.1	40.6
	1:4	15.5	15.6	25.8	26.1	45.2	45.9
	1:2	11.4	11.5	19.4	19.4	32.6	33.0
5.0	1:3	15.1	15.2	24.9	25.1	42.6	43.4
	1:4	16.5	16.6	27.3	27.6	47.6	48.4
	1:2	16.0	16.1	26.5	26.7	43.9	44.7
10.0	1:3	18.2	18.5	31.9	32.3	54.0	54.9
	1:4	18.3	18.5	32.9	33.6	58.1	59.2

λ equal to 1.0 (0.30% for $\varphi = 30°$). This tendency for the relative discrepancy to decrease with increasing surcharge can be explained by the fact, that the determination of the bearing capacity factor N_γ associated with the selfweight of the soil poses a much harder challenge, than do the bearing capacity factor N_q and consequently the greater the contribution from the surcharge to the total capacity the more exact the result.

The bearing capacity equation (1) assumes, that the total bearing capacity can be found as the sum of the two contributions due to the selfweight of the soil and

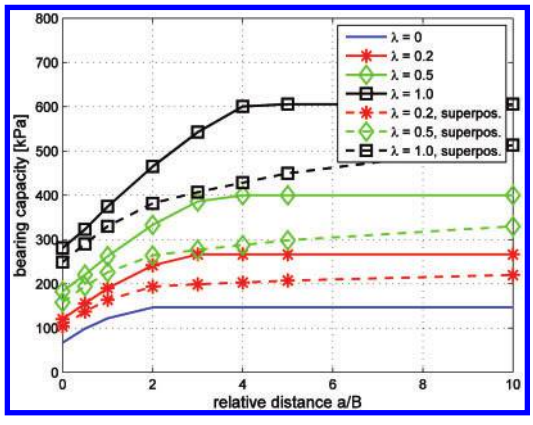


Figure 3. Bearing capacity, slope inclination 1:3, $\varphi = 30°$.

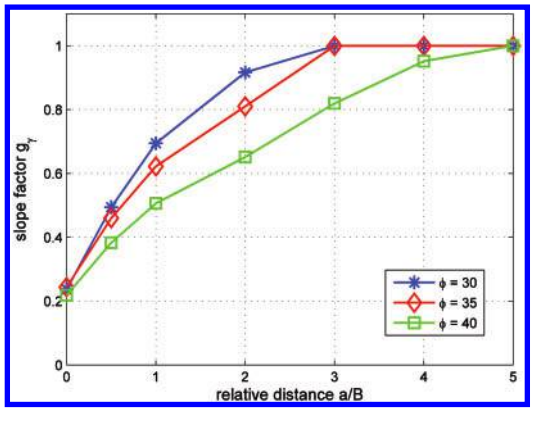


Figure 4. Slope factor g_γ for slope inclination 1:2

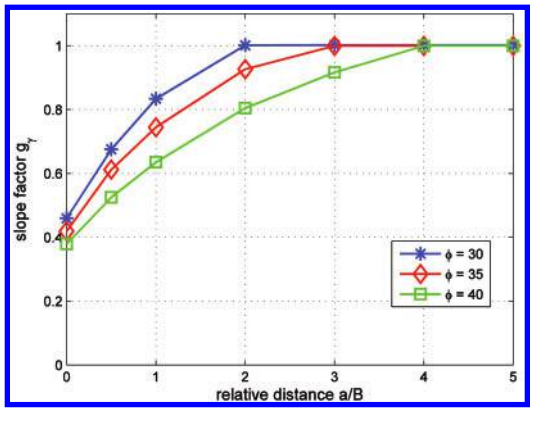


Figure 5. Slope factor g_γ for slope inclination 1:3

the surcharge, and as reported by amongst others Zhu et al. (2003) this assumption yields results that are conservative. The results from the present analyses confirm this fact and as a typical example the results for a slope inclination 1:3 and a friction angle equal to 30° are graphed in Figure 3. It can be seen that superposition gives results which are always the lesser

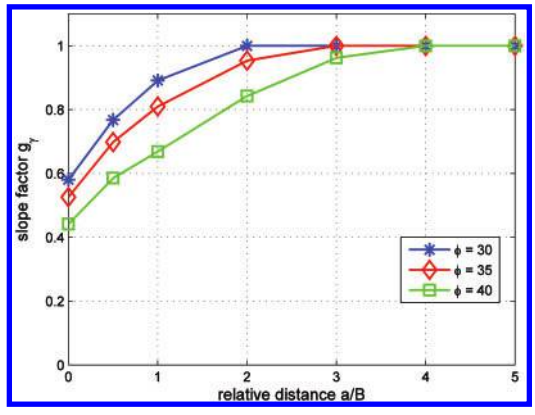


Figure 6. Slope factor g_γ for slope inclination 1:4

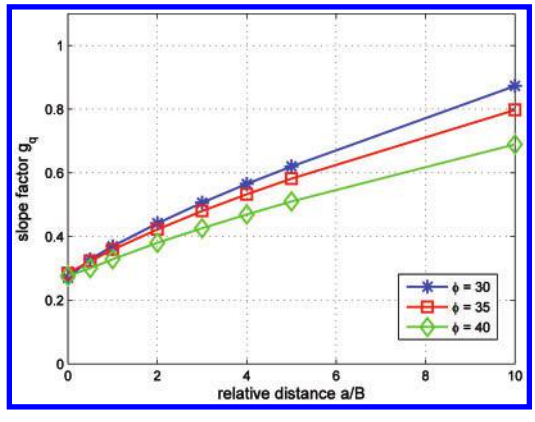


Figure 7. Slope factor g_q for slope inclination 1:2

but for smaller values (0–1) of the relative distance a/B, the discrepancy, being of the order of 10–20%, is acceptable for practical design.

As to the effect of the presence of the slope on the bearing capacity it can be seen from Table 1, 2 and 3, that the smaller the values of the surcharge ratio λ, the friction angle ϕ and the slope inclination angle β the smaller the value of the relative distance a/B where the slope has an importance and for a/B values greater than 5 the effect is ignorable in any case.

On the basis of the values in Table 1,2,3 and 4 diagrams showing the slope factors as functions of the slope inclination, friction angle and the relative distance have been prepared, and these are shown in Figure 4 through 9. It can be seen, that there is some dependency of the friction angle on the slope factors and that the greater the friction angle, the stronger the relative effect of the slope on the bearing capacity.

4 EXAMPLE

A strip foundation, B = 2.50 m is located at a distance a = 1.50 m from the crest of a slope. The inclination of the slope is 1:3 ($\beta = 18.44°$) and the foundation level is 1.00 m below ground level. The angle of friction is

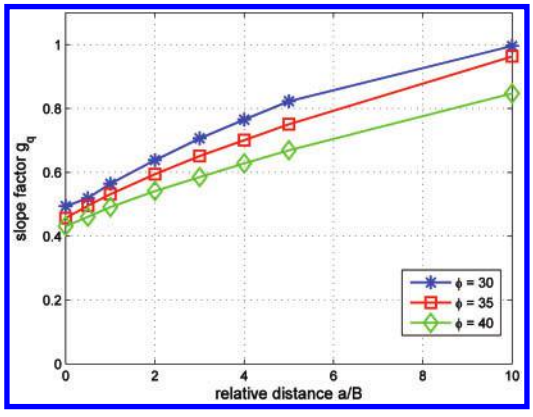


Figure 8. Slope factor g_q for slope inclination 1:3

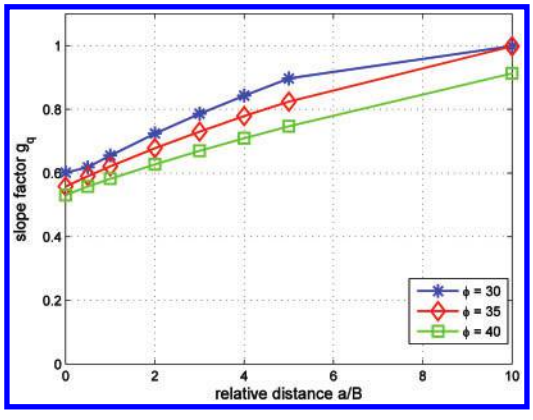


Figure 9. Slope factor g_q for slope inclination 1:4

33° and the soil unit weight is 18 kN/m^3. Determine the vertical bearing capacity.

This can be found by using the bearing capacity equation where the slope factors are found from Figure 5 and 8 or by using the values in Table 2. Only the first method is demonstrated.

From Figure 5 and 8 for a/B= 0.60 is read : $g_\gamma = 0.68$, $g_q = 0.53$.

$$N_q = \frac{1+\sin\varphi}{1-\sin\varphi} e^{\pi\tan\varphi} = 26.09 \quad \text{(Reissner 1924)}$$

$$N_\gamma = 1.5(Nq-1)\tan\varphi = 24.44 \quad \text{(Hansen 1970)}$$

$$q_{ult} = \frac{1}{2} 18kN/m^3 \cdot 2.50m \cdot 24.44 \cdot 0.68 + 18kN/m^3 \cdot 1m \cdot 26.09 \cdot 0.53 = 632.8kPa$$

This result has been verified by OptumGEO, which gives a bearing capacity of 749.0 kPa and the failure mechanism is shown in Figure 10.

When the tables are used to find the bearing capacity interpolation becomes necessary and it has been verified by the authors that linear interpolation can be used for a/B, λ and the slope inclination angle β whereas

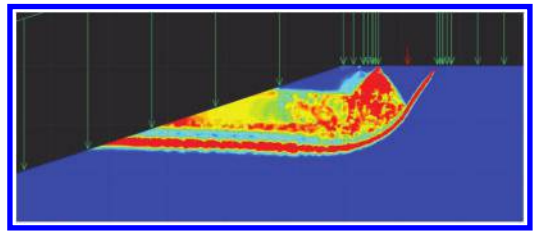


Figure 10. Failure mechanism, OptumGEO.

for the friction angle an interpolation function of the form $y = a \cdot e^{b \cdot x}$ is recommended.

5 CONCLUSIONS

Lower- and upper-bound, finite element based calculations of a vertically, centrally loaded strip foundation in cohesionless soil with friction angles 30, 35, 40° have been carried out for slope inclinations 1:2, 1:3 and 1:4 and these calculations have resulted in tables and graphs suitable for practical design. It has been shown, that the conventional slope factors depend on the friction angle of the soil, and that the greater the friction angle the greater the effect of the slope. A sample example shows, that the bearing capacity equation, i.e. using superposition, may produce a bearing capacity that is approximately 20% lower than found by limit analysis without using superposition.

REFERENCES

Castelli, F. & Motta, E. 2010. Bearing capacity of strip footings near slopes. *Geotech Geol Eng, 28, 187–198.*

Gemberline, M. C. 1988. Centrifuge modeling of shallow foundations. *Proc., 11th Int. Conf. on Soil Mech. and foundation Engrg., Balkema, Rotterdam, the Netherlands,* 2, 33–36.

Hansen, J. B. 1970. A revised and extended formula for bearing capacity. *The Danish Geotechnical Institute, Bulletin no. 28.*

Krabbenhoft, S., Damkilde, L. and Krabbenhoft, K. 2012. Lower-bound calculations of the bearing capacity of eccentrically loaded footings in cohesionless soil, *Canadian Geotechnical Journal,* 49, 298–310.

OptumGEO. 2012. Optum Computational Engineering. Theory, Version 1.0.

Reissner, H. 1924. Zum erddruckproblem. In *Proceedings first international congress of applied mechanics,* delft, The Netherlands, pp. 295–311.

Saran, S., Sud, V. K. and Handa, S. C. 1989. Bearing capacity Of footings adjacent to slopes. *Journal of Geotechnical Engineering,* Vol. 115, No. 4, April, 1989.

Sarma, S. K. & Chen, Y. C. 1995. Seismic bearing capacity of shallow strip footings near sloping ground. *European seismic design practice, Elnashai (ed.)* 1995 Balkema, Rotterdam. ISBN 9054105887.

Vesic, A. S. 1975. Bearing capacity of shallow foundations. In H. F. Winterkorn & H.-Y. Fang (eds.) *Foundation engineering handbook.* Van Nostrand Reinhold, chap. 3.

Zhu, D.Y., Lee, C. F., and Law, K.T. 2003. Determination of bearing capacity of shallow foundations without using superposition approximation. *Canadian Geotechnical Journal*, 40, 450–459.

Research and Applications in Structural Engineering, Mechanics and Computation – Zingoni (Ed.)
© 2013 Taylor & Francis Group, London, ISBN 978-1-138-00061-2

Stress state of massive foundation slabs – Measurements and simulation

K. Stopp
Department of Civil Engineering, University of Wuppertal, Germany

ABSTRACT: Foundation slabs are generally calculated by using the plate theory. In the industrial sector some slabs are constructed with plate thicknesses of more than 2 meters. By taking their building area into account the criteria of a thin structure is fulfilled otherwise a massive cross-section exists. Against this background and under consideration of the soil-structure-interaction the use of the plate theory needs to be questioned. The paper will present measuring results and verifying simulations for a foundation slab of the main buildings of a power plant unit. It will discuss the considerable influences of seasonal temperature variations on the structural response of the slab during a construction period of 3 years where the stress state is much more caused by seasonal temperature than by loading during construction and extension of the boiler house.

1 1 INTRODUCTION

Plate structures are normally calculated providing the Kirchhoff-Love theory, straight lines normal to the mid-surface remain normal and straight during the deformation, which means that the strains are linear across the thickness. For bigger plate thicknesses this assumption is not valid anymore. Furthermore, the mechanical model assumptions of the plate theory provide that there exist no stresses perpendicular to the surface. For big slab thicknesses with a massive cross section on the one hand and related large slab dimensions on the other hand, it is not known for sure, how the load transfer from the column through the foundation slab occurs. Depending on the soil stiffness compression arches or compression struts may result. Because of simplifying assumptions – especially for the subsoil – numerical studies carry the risk of representing the reality insufficiently. They can be used as a supportive instrument but they have to be verified by respective measurements.

Experimental studies on the long-time behavior of shallow foundations in the serviceability state hardly exist. Conducted experiments had their focus on the punching behavior. On subsoil only single foundations were analyzed, but their behavior differs significantly from foundation slabs. Here only a small part of the soil pressure appears within the supporting area, whereas a huge part of the shear forces derive from the span area. Small-scale experiments of extensive foundation slabs in the laboratory are over-simplistic and do not accurately reflect the interaction of subsoil and extensive structure; therefore in-situ measurements are necessary, which were previously non-existent.

A research and development project, financed by the power company Vattenfall Europe Generation AG, has been initiated to monitor and analyze the load bearing and deformation behavior of a massive foundation slab, which has a thickness of 3.80 m, for carrying the main buildings of a new power plant unit in Boxberg/Germany. The aim is to verify existing soil-structure-interaction models and to get an idea about the settlement behavior and its influence on the total structure. As part of this project a monitoring concept for measuring the strains and temperatures inside the foundation slab and the stresses at intersection between boiler column and slab has been developed by the University of Wuppertal.

The analysis and evaluation of the measured values showed a highly unexpected impact of seasonal temperature variations on the stress state of the foundation slab during construction and extension. At this time heat of hydration no longer exists.

2 MEASURING PROGRAM

2.1 *Concept*

The research team consists of Bergische Universität Wuppertal, Erdbaulaboratorium Essen ELE and Gesellschaft für Montan- und Bautechnik GMB. An impression about the dimensions of the mainly investigated slab (140 m long, 80 – 100 m wide and 3.80 m thick) is given in Figures 1-2.

Geotechnical measurements with soil pressure pads, extensometers and inclinometers (Fig. 3) are conducted to examine the deep and broad effect of the foundation and the stress distribution in the foundation plane. With the example of the boiler column load scientific knowledge about the load transfer of big single loads through massive foundation slabs in the ground shall be made. Furthermore the activation of the stress in the slab shall be examined by

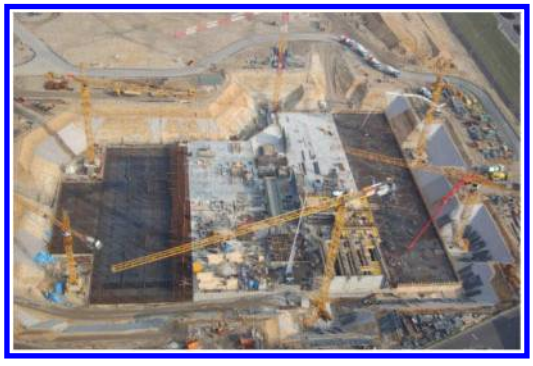


Figure 1. General view of the foundation slab under construction.



Figure 2. Reinforcement cage of the foundation slab.

measuring the strain distribution of the cross section in decisive places. In a measuring point additionally stress measurements are taken for comparison reasons. Furthermore the actual boiler column load will be validated by stress measurements with pressure pads in the base of the column. In order to derive a more general valid and accepted geotechnical model, additional measurements are taken at a medium and small sized foundation slab on site. All measurements should enable a formulation which is independent of scaling factors. For a detailed description of the whole measuring program and for a theoretical background of the modeling of the soil-structure-interaction as well see (Harte & Stopp 2008, Stopp 2010).

This paper will present selected measurement results only for the strains in the foundation slab. Figure 4 shows the principle arrangement of the built-in sensors in an idealized cross-section of the slab in the vicinity of the boiler column. At each measuring point the concrete strains are measured at the upper face and in the center of the slab in three directions perpendicular to each other, the steel strains at the horizontal reinforcement layers for plate bending in two directions and at the vertical bars for the punching proof in one direction.

The measuring points are arranged in three axes rotated by 45°. At one of the measuring points there

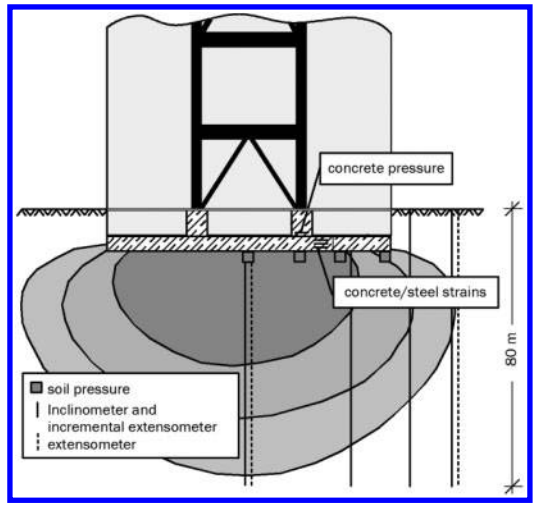


Figure 3. Cross section of the boiler house with built-in sensors.

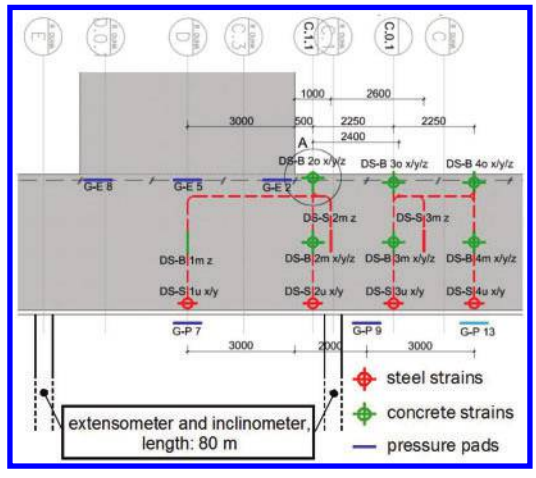


Figure 4. Measuring points in the vicinity of the boiler column.

are 8 strain and temperature sensors in plate thickness direction instead of only 3.

2.2 *Strain gauges*

The strains will be measured in the concrete and at the horizontal reinforcement layers for plate bending and at the vertical bars for the punching proof as well. The measuring devices are based on the principle of vibrating wire, which has proved long-term stability and robustness. All strain gauges have a measurement length of 250 mm and are equipped with a thermal element. The ends of the steel transducers are welded to the bars whereas the concrete transducers have been installed movable within the fresh concrete by hanging them at the reinforcement mesh (Fig. 5).

Strain gauges based on the principle of vibrating wire directly measure stress-generating strains. For



Figure 5. Built-in strain gauge.

non-constrained deformable structures under thermal effects no strains are monitored, if strain gauge and respective material have equal thermal coefficients and thus they will deform simultaneously. To receive real, existing strains ε_{real} the measured strains ε_{meas} need to be completed by the thermal strains of the strain gauge wire according to Equation 1.

$$\varepsilon_{real} = \varepsilon_{meas} + \alpha_{T_{wire}} \cdot \Delta(T_0) \tag{1}$$

In fully constrained structures a strain gauge will indicate thermal strains. They represent the stress-generating strains due to thermal changes, under the presumption that strain gauges and respective material are characterized by the same thermal coefficient. Otherwise the measured strains have to be corrected according to Equation 2.

$$\varepsilon_{stress} = \varepsilon_{meas} + (\alpha_{T_{wire}} - \alpha_{T_{object}}) \cdot \Delta(T_0) \tag{2}$$

3 TEMPERATURE MEASUREMENTS

3.1 *Temperature profile*

The temperature characteristics of all sensors vary with the season. The strength of the variation at the local measuring point $\Delta(T_0)$ is decisively dependent on the depth position of the sensor in the slab. Due to the heat input in summer and the cooling down in winter respectively there are more significant variations at the upper face of the slab. In Figure 6 the seasonal differences for all 8 sensors of a cross-section in the year 2008 are shown. At this time, the hydration of concrete and the corresponding heat evaluation have already vanished, characterized by comparable temperatures at the beginning and at the end of the year. During the year, the temperature distribution turns over twice. Due to the non-stationary heat transfer in the slab the full turn-over of the thermal gradient will appear in spring and autumn. As maximal temperature changes have occurred: $\Delta(T_0) \approx +18,5-1,0 = 17,5\,\mathrm{K}$ at the slab's upper face, $\Delta(T_0) \approx +17,0-4,0 = 13,0$ K at



Figure 6. Temperature profile across the slab thickness.

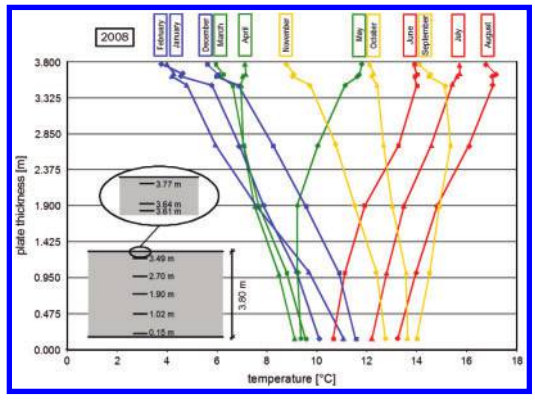


Figure 7. Seasonal development of the temperature gradient.

the height of the upper reinforcement layer and at the slab's lower face only $\Delta(T_0) \approx +14,0-9,0 = 5,0\,\mathrm{K}$. Visible are the almost identical changes in temperature in the first 20 cm from the upper face of the slab whereas compensation only starts in a depth of 30 cm from the upper face downwards to the lower face.

3.2 *Temperature gradient*

Figure 7 shows the seasonal pattern of the temperature gradient across the thickness of the slab as it appears after the cooling down of the slab arising from heat of hydration during the construction period. In winter there are the lowest temperatures at the upper face, whereas the lower face has not already cooled down yet. While the temperatures rise at the upper face during spring they still drop at the lower face. The same effect occurs in summer and autumn, but with a sign being reversed. The resulting gradient is all the time more or less linear across the slab thickness with exception of May and September. At this time there are the zero crossings of the gradient which means that the sign changes. The seasonal temperature difference $\Delta(\Delta T) = T_o - T_u$ between slab upper and lower face varies from about $-7,5$°C in January 2008 to $+4,5$°C in August 2008. The differences in January are comparable to the ones one month after the concreting of the slab in April 2007.

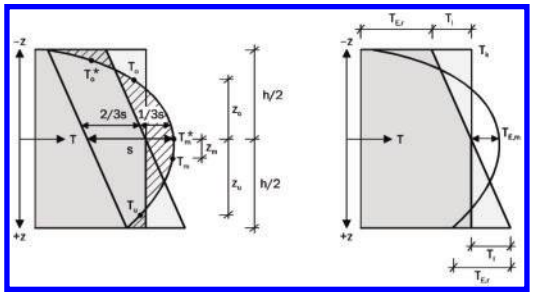


Figure 8. Separation of the temperature profile.

3.3 *Temperature parts*

For the interpretation of the resulting stress state of the slab due to the temperature its temperature profile was separated into a constant, linear and non-linear part. By means of the measured values it could be proven, that a parabolic separation is sufficient for this one dimensional temperature profile. Nevertheless a consideration of the exact location of each measured value is essential (Fig. 8). For massive structures with slab thicknesses of 3–4 m the determination of the temperature constraint of the curvature can be done by neglecting the non-linear parts in the upper 20–30 cm of the slab.

4 STRAIN MEASUREMENTS

4.1 *Temperature induced stress state*

In Figure 9 the real strains and in Figure 10 the stress-generating strains are shown during year 2008 (measuring point 2 in section C1.1 according Fig. 4). Both are given at the slab's upper and lower face and refer to the start of mounting of the boiler house. They are compared with the separation of their strain profile into constant, linear and non-linear parts. The thermal profile has been separated as well and the resulting thermal strains have been calculated. The clear correlation between the constant part of the real strains and the calculated constant thermal strains as well as the stress-generating strains and the calculated linear thermal strains are obvious. That means that the longitudinal extension of the slab is unconstrained whereas its curvature is constrained. In Figure 10 the calculated linear constraint strain part is bigger than the measured value because the linear temperature part refers to the upper face of the slab whereas the sensor is located 15 cm inside of the slab. The exact evaluation of the constraint degree of the linear part is complex, as the stress-generating strains due to temperature are superposed both by strains due to loading and by constraints due to soil friction at the slab-soil-interface. It is further difficult to identify the dependence on the respective thermal strain profile because of the continuously changing load situation due to the site activities. Additionally the degree of the constraint of the curvature is dependent on stiffness ratio of subsoil

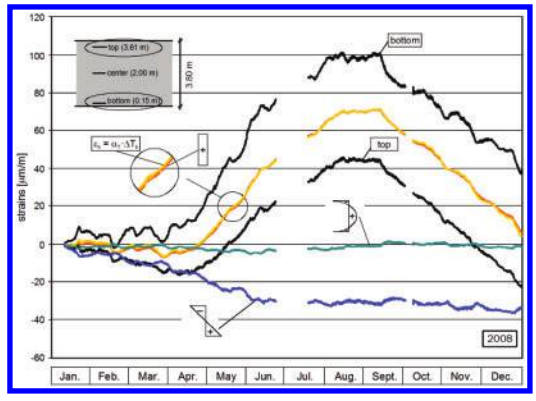


Figure 9. Real strains in axis C.1.1.

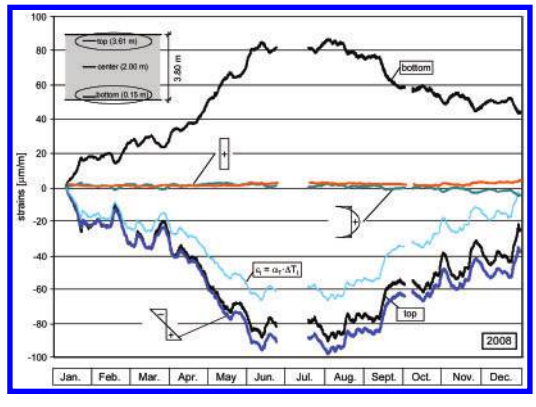


Figure 10. Stress-generating strains in axis C.1.1.

and structure. But nevertheless it is obvious, how significant the seasonal temperature changes affect the stress state in the foundation slab – much more than the load during construction of the boiler house. The residual stresses can be neglected.

The determination of the influence of the temperature for each of the local measuring points is not possible because of the superposition of the different impacts. In consideration of the before mentioned dependencies and the fact that there are almost no periods without construction activity to determine the degree of constraint, the following procedure has proven to be appropriate. For each measuring point both temperature and strain profiles are separated into their constant, linear and non-linear part. Calculating the regression line for each part, the related constant can be obtained and it is possible to derive the temperature caused strains for each local measuring point. This procedure was executed for both stress-generating and real strains. From a comparison of constant temperature and strain part (index k), linear temperature and strain part (index l) and non-linear temperature and strain part (index E) the dependencies and therefore the corresponding degree of constraint can be determined. Hence the resulting strain curve due to loading can be calculated for each local measuring point according

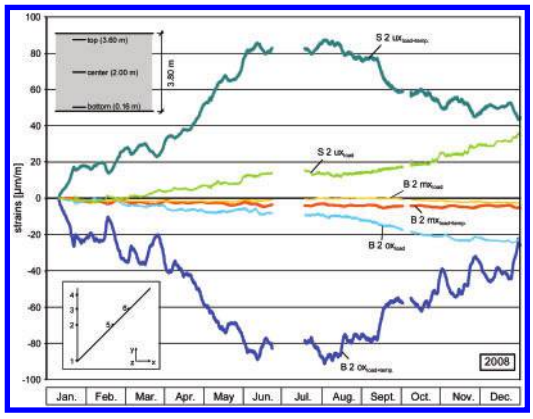


Figure 11. Influence of temperature gradient on the stress state.

to Equation 3 – presented as an example for the local measuring point 2 ox.

$$\varepsilon_{load}^{2ox} = \varepsilon_{\sigma}^{2ox} - C_k^{*2x}\Delta T_k^{MP2} - C_l^{*2x}\Delta T_l^{MP2}k_l^{ox} - C_E^{*2x}\Delta T_E^{MP2}k_E^{ox} \qquad (3)$$

The temperature constants correspond to the upper face of the slab (T_l) and to the center of the slab (T_E). The factors k_l and k_E consider the differing positions of the strain gauges. With the aid of simple geometric relations the location of each gauge can be considered through a percentage of the total value.

As a result of this procedure, Figure 11 shows the strains exclusively resulting from load. In addition, the actual stress-generating strains due to load and temperature are still given. To the end of the year, when the temperature conditions are equivalent to the reference value in January, both curves show comparable values as expected.

In summer the strain gauges at this local measuring point detect stress-generating strains resulting from temperature which are four times bigger than those resulting from loads. This result is rather caused by the small strains due to load than caused by big strains due to temperature. But it shows clearly the importance of the identification of the temperature strains to determine the size and nature of the stress state of the foundation slab.

The true scale of the restraint stresses, and therefore the scale of relaxation, is only identifiable in combination with stress measurements in concrete at the same measuring point. Figure 12 shows a comparison of directly measured stresses and stresses derived from measured strains at the upper face of the slab at measuring point 7 for the year 2008. The difference between the measured stresses σ_{meas} and the calculated stressesdue to the stress-generating strains $\sigma_{meas}^{*} = E \cdot \varepsilon_{meas}$ is obvious (elasticity modulus: 28,300 MN/m^2). Only about 50 % of the constraint stresses remain in the cross-section. By comparing the measured stresses with the ones calculated with the identified load strains $\sigma_{load}^{*} = E \cdot \varepsilon_{load}$, the total

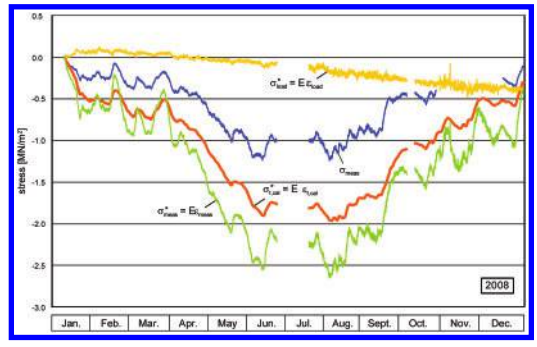


Figure 12. Comparison of derived and measured stresses.

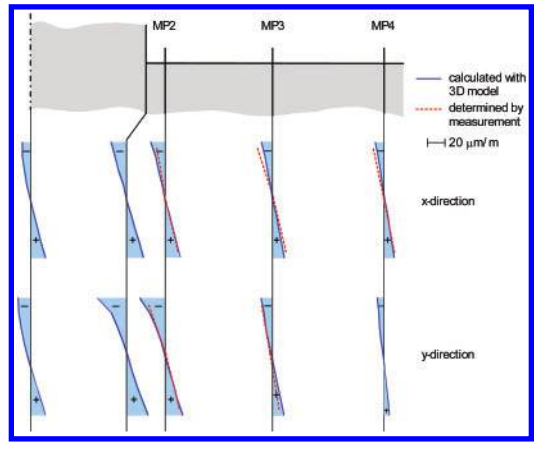


Figure 13. Comparison auf measured and calculated strains.

stress of load and temperature is still much bigger than the part of the stress resulting from load. Additionally the curve of the constrained temperature stresses $\sigma_{t,cal}^{*} = E \cdot \varepsilon_{t,cal}$, calculated by using the identified constraint temperature strains of the linear and non-linear part, is added.

5 COMPARATIVE SPATIAL ANALYSES

In comparative spatial analyses the qualitative stress distribution caused by the boiler column load and the seasonal temperature effects could be demonstrated and the quantitative load strains for discrete time steps could be determined in agreement with the measured values. The cross-section remains plane. Only in the area of the load transmission there are slight local variations, but those can be modeled via a volume model. For the design of the foundation slab the simplifying assumption of a plate is valid.

Figure 13 shows the comparison of measured and calculated strains for the 14th of June 2008. At this time the measured boiler column load was P = 10,000 kN. For the determination of the boiler column load temperature effects had to be considered as well. The separation of the temperature induced stresses at the base of the column is not as simple as the separation of the

temperature induced strains in the slab. The reason for this is a superposition of several non-linear influences. By means of a pragmatic approach the constrained stresses can be eliminated and the load can be continuously derived by integration (Stopp 2010). This load is taken for the numerical 3D analysis. The calculated strains in the area of the boiler column are compared to the strains due to load determined by the measurement with the explained procedure in Section 4. The determination of the load strains was only possible for measuring points with 3 local measuring points across the thickness. That is why the comparison is not made for all points. In addition, the calculated distributions are given for the face and the centre of the column.

6 CONCLUDING REMARKS

Knowledge about the load transfer behavior of massive foundation slabs is an important part for the understanding of the soil-structure-interaction of large-scale founded structures. While evaluating and interpreting the measured strain values it turned out, that the influence of the seasonal stresses due to temperature are much more significant than expected. During the construction period not only heat of hydration has to be considered but also seasonal temperature changes. After going into operation these changes will be minimized as the outside air will no longer have direct access to the foundation slab and the basement will be heated. Because of the successful separation and identification of the stress parts due to load and due to temperature, the investigation of the spatial load transfer was possible. Hereby scientific knowledge about the dependency of the structural behavior on soil stiffness, construction stage and redistribution effects could be achieved.

ACKNOWLEDGEMENT

The financial support of Vattenfall Europe Generation in Cottbus/Germany for installing the measuring devices and for evaluating the measuring results is gratefully acknowledged.

REFERENCES

Harte, R. & Stopp, K. 2008. Monitoring of Power Plant Foundations for Analysing the Soil-Structure-Interaction, In Jirova, J. (ed.), *New trends in Experimental Methods together with advanced numerical modelling. Proc. XIth Bilateral Czech/German Symposium, Liblice, Czech Republic, 28–30 May 2008*: 75–78.

Stopp, K. 2010. *Structural and deformation behavior of large-scale founded RC structures under consideration of the soil-structure-interaction* (in German). Ph.D.-thesis, Bergische Universität Wuppertal, IKIB 16, ISBN 978-3-940795-15-1.

Research and Applications in Structural Engineering, Mechanics and Computation – Zingoni (Ed.)
© 2013 Taylor & Francis Group, London, ISBN 978-1-138-00061-2

Soil-structure-interaction: Analysis through measurements

F. Kopf
FCP– Fritsch, Chiari & Partner, Vienna, Austria

D. Schäfer
VCE – Vienna Consulting Engineers ZT GmbH, Vienna, Austria

J. Pistrol
TU – University of Technology, Vienna, Austria

ABSTRACT: In common buildings the Soil-Structure-Interaction (SSI) is governed by the elastic behavior of the building. The best conditions to see the soil effect predominate would be a dynamic rigid body movement of a massive building. For this reason measurements were carried out on an old anti-aircraft tower from World War II on typical Viennese soil conditions. The dynamic properties of the soil could be determined in two different ways. The first one is the common way using the dispersion of the Rayleigh waves on the soil surface and the back calculation to shear wave profiles. The second approach is the back calculation of the soil stiffness based on the soil-structure-interaction.

With the simultaneous measurement of the dynamic movement of the building the kinematic behavior of the SSI could be determined. The tilting oscillations of the tower in both directions with different frequencies transmitted to the soil could be measured in the surroundings. The decay of these vibrations and their influence on the H/V-method results was studied.

The results of the dynamic measurements were compared with different methods of numerical simulation. The benefits and the disadvantages of the methods can be compared. The calculation values of the numerical models could be calibrated with the real dynamic properties of the measured SSI-system.

1 INTRODUCTION

The Leitturm in Augarten (Vienna) was part of an anti-aircraft defense system in World War II. It has not been used since those times. For the rigidity of the structure and its tall shape it is considered to be an ideal test object. Since there is a quiet park surrounding this building it was the ideal test field to carry out the measurements.

Measurements for the soil structure interaction were carried out separately on the soil surface for assessment of soil parameters and on the tower structure to record the building movements. The next step was to measure the influence of the tower oscillation on the soil and the decay of this influence with distance.

Numerical simulations were carried out based on different methods. The calibration of these methods with the measured conditions led to scientific findings and the opportunity to evaluate the different methods.



Figure 1. The Leitturm in Augarten, Vienna, built during World War II (left) and aperture in the 2.5 m concrete wall of the tower seen from inside (right).

2 MEASUREMENTS ON THE SOIL SURFACE

The vibrations of the soil surface were measured for the documentation of the surface wave propagation. The phase velocity of Rayleigh waves on the surface is not constant but it depends on the frequency of the wave. Usually the Rayleigh waves with low frequencies are faster than those with higher frequencies. This results in the fact that a vibration signal containing a wide frequency spectrum changes shape with the propagation. This phenomenon is called the dispersion of the wave because low frequency waves will reach

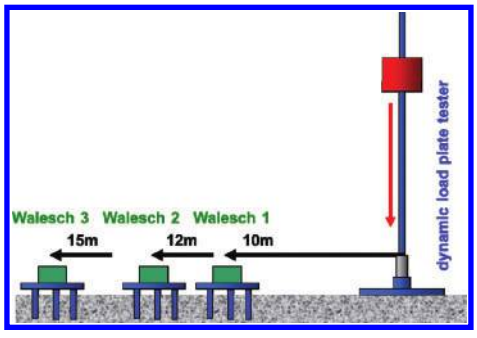


Figure 2. Surface-wave dispersion test setup with artificial impulse excitation using a light falling weight device.

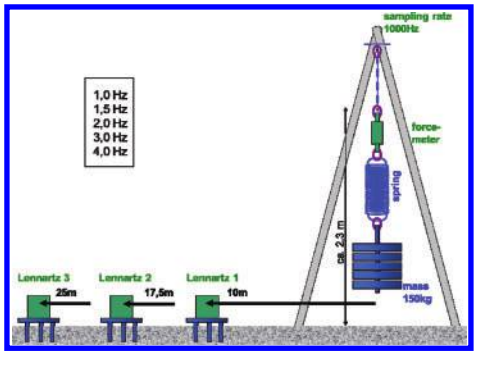


Figure 3. Surface-wave dispersion test setup with artificial harmonic excitation using a "shaker" as a mass-spring-system.

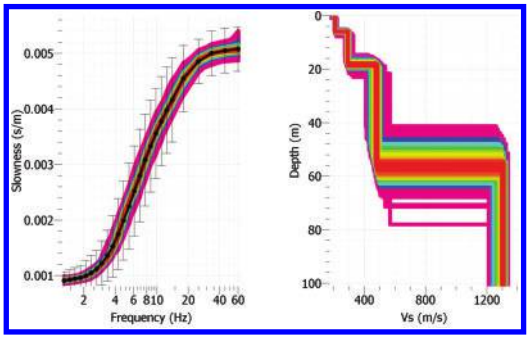


Figure 4. Triangle setup: dispersion of best fitting profiles (left) and shear wave velocities of best fitting profiles (right).

a measurement point distanced from the impact first and the high frequencies will follow later. To measure this effect, two artificial excitation types: an impulse (for the high frequencies) and a harmonic excitation of the soil (for the low frequencies) were applied. The ambient vibrations were recorded in several triangular setups with different dimensions.

By analyzing the measured vibrations the dispersion curve could be evaluated.

Since the natural soil is no homogeneous infinite half-space but consists of different layers of soil types

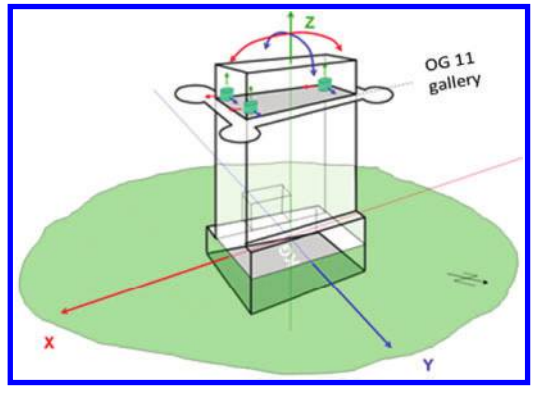


Figure 5. Sensor setup for the measurement on the gallery level inside the tower.

with diverse soil properties, the dispersion curve of the surface waves is influenced by this.

By means of numerical simulations of different layered soil profiles the corresponding dispersion curves can be evaluated. The artificial dispersion curve best fitting to the measured one can be found by a special optimization algorithm. This inverse analysis method does not give a unique result but a most likely soil profile can be found.

The results of these tests are the shear wave velocity profiles of the soil. The shear wave velocity is the leading parameter for assessment of the dynamic soil properties. The shear wave velocity is a real material parameter and it is constant for all frequencies (shear waves do not disperse).

3 MEASUREMENTS ON THE TOWER

The ambient vibrations of the Leitturm-structure were measured with three very sensitive geophones (Lennartz LE-3D-5s) on different levels. The Fast Fourier Transformation (FFT) analysis of the measured data of vibrations on the 11th floor shows the eigenfrequency of 1.6 Hz for the tilting motion in the "weak", y-direction (blue) and 2.0 Hz in the "stiffer", x-direction (red). The peak of the vertical oscillation is not as significant but can be found at 3.9 Hz. Because of the tower's rigid structure the soil-structure interaction behavior is governed by the mass of the tower and the stiffness of the soil.

By use of the Random Decrement Technique (RDT), the damping ratio of the vibrations can be detected for each frequency separately. The algorithm analyses ambient vibrations and looks for "events" in the signal. Averaging all detected events lead to an artificial event, where the decay of vibration can be evaluated and the damping ratio of the relating vibration mode can be determined.

The artificial excitation with impulses of a medicine ball (5 kg) on the gallery of the Leitturm (mass about 40.000.000 kg) could be detected inside the tower with its 2.5 m thick walls and a ceiling with more than 3.5 m

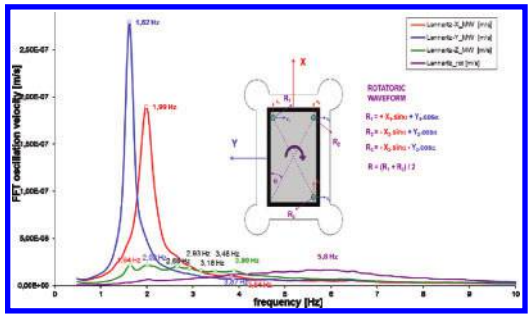


Figure 6. FFT-analysis of combined values from measure-ments in the corner of the gallery.

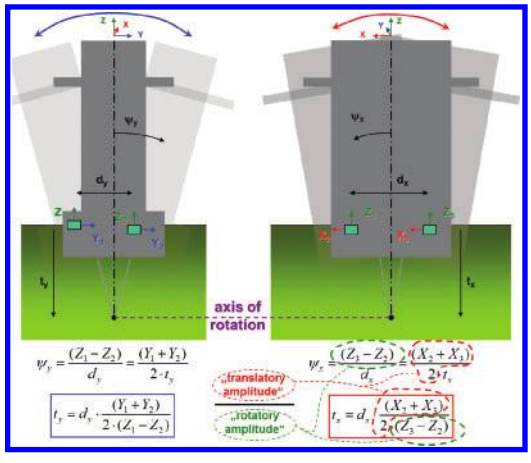


Figure 7. Determining the rotatory center of the rigid body by analyzing signals from two sensors on one level.

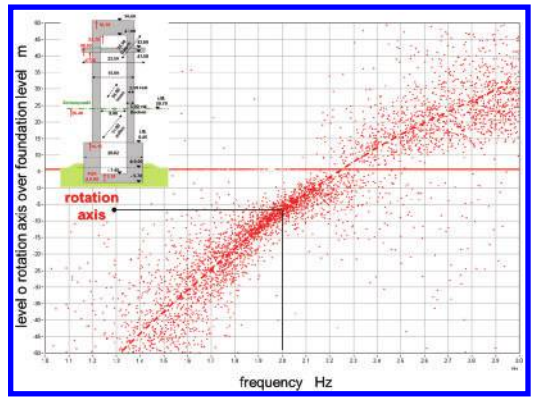


Figure 8. Level of the rotatory center for tilting oscillations in x-direction depending on the frequency. Only the oscillations in phase or out of phase are considered.

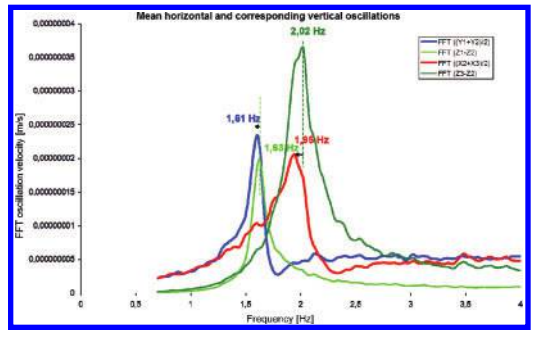


Figure 9. Translational and rotatory oscillation components of tilting oscillation whose maxima have different positions.

concrete slab. Each individual impact could be clearly detected. The analysis gives the natural frequencies caused by the soil-structure interaction in the low frequency domain, and after a gap without any significant peaks, the internal vibrations of the building in the high frequency domain.

It is the metrological evidence for the separation of internal vibration of the building from the global movements caused by the soil-structure interaction in this special Leitturm case. At usual buildings both effects are overlapping which leads to mixed effects in the measurement signals and difficulties for the interpretation.

In a first approximation the soil structure interaction of the Leitturm can be understood as a rigid body motion of a concrete block socketing in an elastic half space of soil. To answer the question if a center of rotation exists for both tilting modes and to find its position, vibration measurements in the cellar of the Leitturm were analyzed by the following procedure. Combining the signals of two sensors the tower movement can be divided in a translational and a rotatory component. The relationship of these components will lead to the position of the center of rotation in relation to the measurement level. A fixed rotation center exists only if both, the translational and the rotatory oscillation components are oscillating either exactly in phase or exactly out of phase.

The evaluation of the level of the center of rotation for the tilting movement of the Leitturm for each sample or the FFT analysis with correct phasing is shown in the Figure 8 as a cloud of red dots. The position of the rotation center at the eigenfrequency of the tower (2.0 Hz) is found. It is the highest density within the red dotted cloud in this domain.

It can be seen that a fixed center of rotation does exist but the position depends on the frequency. This moving center is the reason, why the frequency at the maximum of the translational component (red, blue) is lower than the related rotatory components (green) in Figure 9. That is not trivial because both of the peaks indicate the frequency of the same oscillation mode and should be exactly the same. But since there are also frequencies besides the eigenfrequency and the translational component is also influenced by the distance to the rotation center, the peak of this component is shifted according to the sketch.

3.1 *Measurements of soil structure interaction*

According to the soil-structure interaction mechanism the soil stiffness influences the movements of the

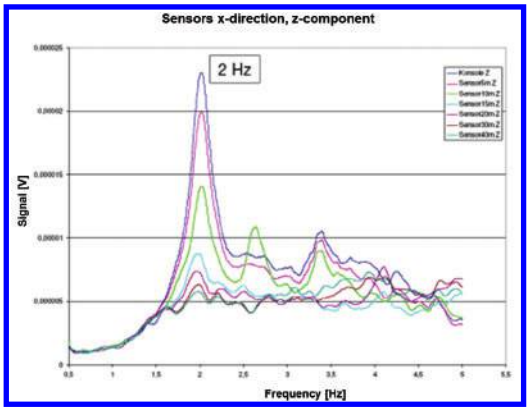


Figure 10. Acceleration measurements for the x-direction array: z-component of the sensors.

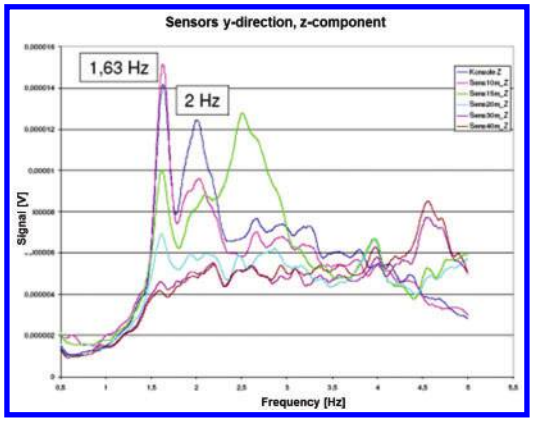


Figure 11. Acceleration measurements for the y-direction array: z-component of the sensors.

building just as well the building affects the soil. To measure the effect of movement in the interaction, the tower oscillation and the vibration on the soil surface was measured simultaneously. One sensor was fixed on the tower and the others placed in a line on the soil in both axis direction.

In the FFT-analysis of these measurements the influence of the tower with its significant eigenfrequencies of 1.6 Hz and 2.0 Hz can be detected. This influence (velocity V) decreases with the distance r to the tower. According to the influence depth of the different modes there is more damping in the propagation function in the y-direction. The deeper the influence, the less is the decay, which can be seen in the value of the damping exponent in this function.

Due to the eccentricity of the sensor setup in y-direction the peak of the x-direction (2.0 Hz) movement can be also detected in Figure 11. Due to the different damping exponents in the formula of propagation the effect of y-movement becomes dominant with increasing distance to the tower.

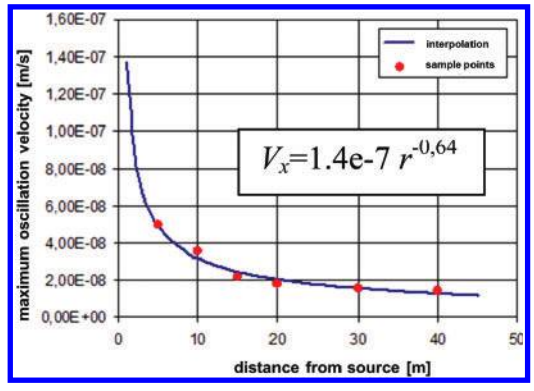


Figure 12. Damping function in x-direction of the tower.

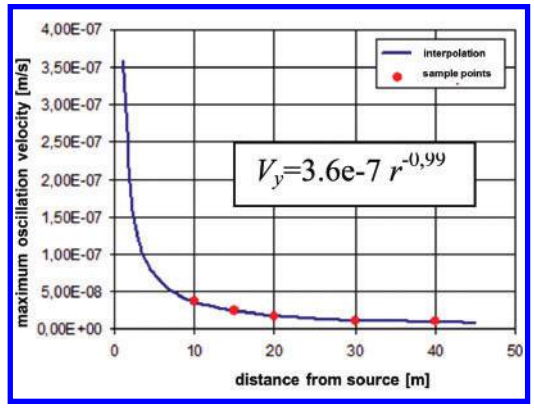


Figure 13. Damping function in y-direction of the tower.

4 NUMERICAL SIMULATION

4.1 *Method of modulus of subgrade reaction*

The method of modulus of subgrade reaction is the most common method. The effect of the soil is simulated by linear elastic springs distributed on the horizontal projection. The modulus of subgrade reaction k_s is this spring stiffness per square meter and it is not a real soil parameter because the geometry, shape, scale of the building and influence depth for layered soil profiles has to be taken into account.

The problem of the method of modulus of subgrade reaction is evident in Figure 15. There is no value for the modulus of subgrade reaction to fulfill all the oscillation mode frequencies measured in the field on the same soil conditions. This effect can be explained by showing the different soil loading and influence depth of the modes. The method is theoretically and practically not able to describe the real physical situation. It can only be used for simple estimations within the frame of existing experiences.

4.2 *Stiffness method*

The deformation of a single point in the area of contact between soil and tower depends on the loading of

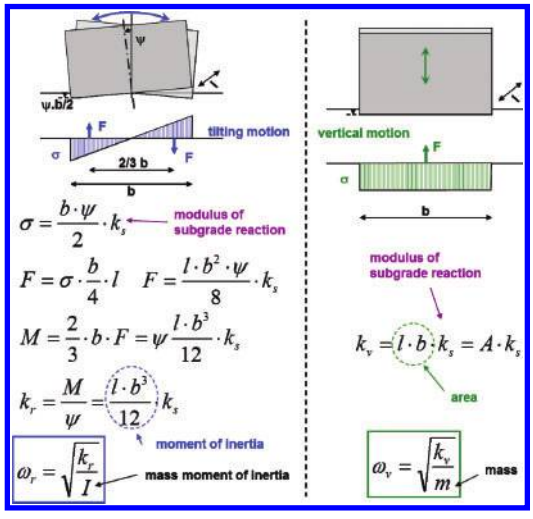


Figure 14. Eigenfrequencies with dynamical modulus of subgrade reaction method: tilting motion and vertical motion.

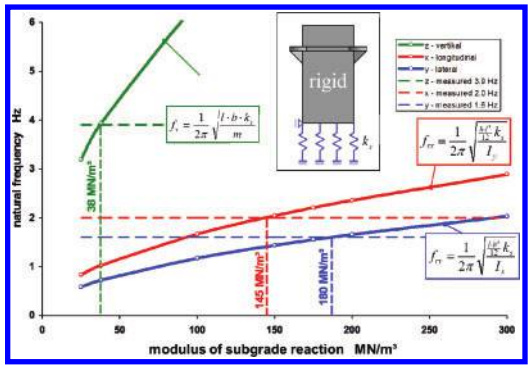


Figure 15. Coherence between modulus of subgrade reaction and eigenfrequency for different oscillation modes, comparison with measured values.

the point itself as well as the loading of the surrounding area. Moreover it is possible to take the flexibility of the tower structure into consideration. The method is based on the oedometric modulus, a real physical soil parameter. The oedometric modulus is assumed to be constant for the whole soil domain influenced by the foundation. A stress-dependency of the oedometric modulus and a layered soil structure were not taken into account. For the stiffness method the geometry of the tower is segmented into n single, finite elements. To determine the deformation characteristics of the interacting soil - tower system, a single element i is loaded with the single load $p = 1$, which causes a settlement trough with its maximum c_0 under the loaded element i. The settlement under the adjacent elements $(i-1)$ and $(i+1)$ is c_1 et cetera.

The settlement c_0 is evaluated for the characteristic point. The actual settlements can be calculated with these lines of influence and the real loads for each element. For the natural frequency of the vertical motion

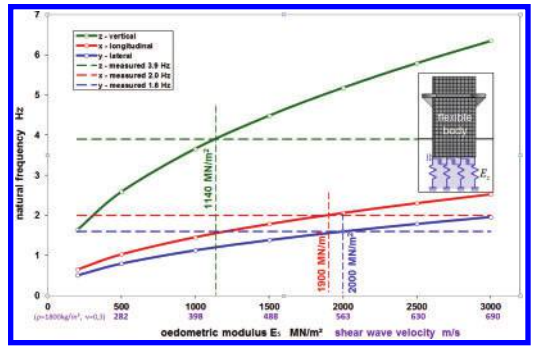


Figure 16. Results of back-calculation of eigenfrequencies with the stiffness method.

the settlements under the dead load of the tower are calculated. An equivalent stiffness per square meter k_s can be derived from the mean settlement w_m. The total equivalent stiffness can be written as

$$k_v = k_s \cdot A$$

where A is the ground area of the building. With the buildings mass m, the natural frequency of the vertical motion is d*efined as*

$$\omega_v = \sqrt{\frac{k_v}{m}} \quad .$$

The angle ψ of rotation is calculated for a tilting moment of $M = 1$ to evaluate the natural frequency for the tilting motions, which can be written as

$$\omega_r = \sqrt{\frac{k_r}{I}} \quad .$$

with $k_r = M/\psi$ and the mass moment of inertia I of the building.

4.3 *Analytic formulas for circular rigid body on linear elastic half-space*

Using analytic formulas for circular rigid bodies on linear elastic half-space provides reliable results if the foundation of the building is rigid and can be described with a corresponding circular shape. The method is based on real physical soil parameters (shear modulus). The results are corresponding very well with the measured tilting modes from the field test. The relationship between the damping ratios fits with the test results, but not the absolute values, because of the small amplitudes.

4.4 *Finite Element Method (FEM)*

The Finite Element Method (FEM) was used for two separate analyses. First, the method of modulus of subgrade reaction was carried out with FEM to take into consideration the flexibility of the tower structure. The problem of this method still exists. A modulus which

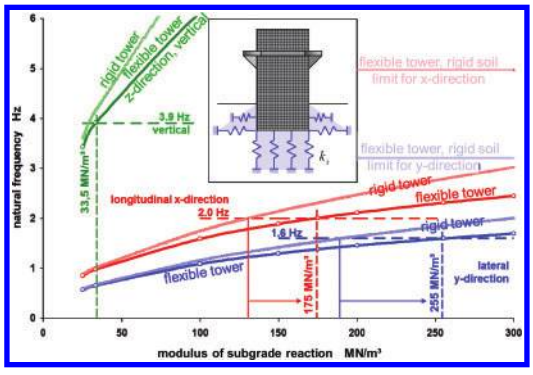


Figure 17. Coherency between modulus of subgrade reaction and eigenfrequency for different modes of vibration for rigid body movement and elastic building characteristic; comparison of FE-computations with measured results.

could fulfill the real dynamic soil conditions for all modes at the same time cannot be found.

In the second analysis with FEM the soil was modeled by linear elastic elements. Especially for the small amplitudes of the ambient measurements this is feasible. With updating the model according to the measured dynamic soil profile and by changing soil stiffness, it was possible to find a solution fulfilling the tilting mode frequencies, the position of the rotation center and the damping exponent for vibration decay with distance. The soil properties of the updated model are stiffer leading to higher shear wave velocities than the measurements in the field but with a fitting relationship between the layers.

5 CONCLUSION

The target of the research work was to find a method to determine dynamic soil parameters using dynamic surface measurements, to find calculation parameters for different numeric simulations and to check the results with dynamic measurements of soil-structure interaction on a simple test object. There are two main reasons for the demonstrated differences between the measured soil properties in the adjacent domain and the stiffer soil behavior from the back calculation: The water content of the soil has no relevant effect to the shear wave velocity (just the mass difference) but it is important for the dynamic compression stiffness of the soil because of the pore water pressure. The considered modes are dominated by the compression stiffness of the soil. The second reason for the stiffer soil properties beneath the Leitturm building is the soil consolidation. The average soil pressure of 610 kN/m^2 of the foundation slab of 31 m times 21 m has been loading the soil for the last 66 years. The measurements for the shear wave profiles were carried out on unaffected soil conditions in the adjacent park. Summarizing the experiments in and around the Leitturm in Augarten in Vienna led to two different metrological approaches for determination of the dynamic soil properties connected with numerical inverse analysis. The power and the disadvantages of several numerical methods which are used in engineering practice could be pointed out. There is a difference between the dynamic soil structure interaction for the usual load cases (live loads, ambient excitation) and for the extraordinary conditions of earthquake; the shear wave velocity profile and the H/V-method are developed for these conditions.

REFERENCES

Seismid Bericht, “Boden-Gebäude Interaktion”, interner Bericht im Projekt SEISMID, www.seismid.com

J. Studer, J. Laue, M. Koller, “Bodendynamik”, 3. Auflage, Springer Verlag, 2007

R.Flesch, “Baudynamik”, Band 1, Bauverlag, 1993

G. Achs et al, “Erdbeben im Wiener Becken” 2011

Research and Applications in Structural Engineering, Mechanics and Computation – Zingoni (Ed.)
© 2013 Taylor & Francis Group, London, ISBN 978-1-138-00061-2

Numerical calculation of damping for monopile foundations under cyclic load during steady-state vibration

M. Bayat, L.V. Andersen, S.M. Andersen & L.B. Ibsen
Department of Civil Engineering, Aalborg University, Aalborg, Denmark

ABSTRACT: Dynamic loading and fatigue has significant effects on offshore wind turbine foundations. To obtain a proper design of a turbine and its foundation it is therefore important to understand how the structure and soil interact regarding damping. Especially, this paper demonstrates the damping and stiffness of the saturated soil within the seabed due to pore water flow generated by the cyclic motion of a monopile. The concept of a Kelvin-Voigt model is employed and combined with a Finite Element Method (FEM) model of the pile. The two-dimensional analysis of each individual soil layer is performed in ABAQUS by coding input files, utilizing Python and MATLAB. A parametric study is performed to illustrate the effects of model size, soil properties such as permeability, void ratio, Young's modulus, bulk modulus, and load parameters such as amplitude and frequency. It is found that by increasing the bulk modulus, the damping and stiffness in the soil increase; however, the increase is small. Further, it is observed that Young's modulus has a significant effect on the dynamic response of the soil. Finally, the permeability of the seabed has a strong influence on the damping of wind-turbine-tower vibrations.

1 INTRODUCTION

The recent developments of offshore industries such as offshore wind turbine foundations and also structures for oil and gas extraction lead to a growing demand for realistic predictions of the behavior of offshore structures. As the use of offshore foundations increases, new methodologies need to be developed to characterize and analyze offshore structural components due to dynamic loads.

Dynamic behavior of offshore structures is one of the most important parts in the design of such structures. The dynamic response varies significantly in time and is affected by inertial, damping and kinematic effects as well as the stiffness of the structure and the underlying soil. Large shear strains (greater than 10^{-4}%), pile–soil interaction, dynamic load rates and nonlinear material behavior lead to nonlinearity in the dynamic response (Ahangar et al. 2011). Dynamic analysis is carried out theoretically by numerical methods, analytical or semi-analytical methods.

In the case of analytical methods, Nogami & Konagai (1987) implemented nonlinear conditions in the time domain for dynamic response of pile foundations subjected to harmonic and transient load. Kazama & Nogami (1991) described the dynamic behavior of saturated two-phase layered media. They found that the permeability and loading rate (loading frequency) are critical factors to control the dynamic behavior of saturated soil. Bea (1992) described the effects of cyclic loadings on the axial capacity of piles driven in cohesive soils and supporting offshore platforms. An advanced analytical procedure was developed to estimate pile penetration and to evaluate the pile performance when a platform is subjected to intense cyclic loading. Bea (1992) found that loading rates, the ratio of steady to cyclic load amplitudes, the sequencing and numbers of cycles of loading, and the relative pile–soil stiffness are all important parameters that determine the pile performance. Chang et al. (2000) analyzed the time-dependent damping model by employing integration technique, an alternative time-dependent damping model was proposed by Chang & Yeh (1999) in modeling the pile response from direct wave equation analyses. Lanzo et al. (2003) presented frequency and time domain analyses by using computer codes PROSHAKE, DESRAMOD and QUAD4M. They have considered viscous damping which is generally assumed to be of the Rayleigh type, i.e. stiffness- and mass proportional, or in a simplified form, only stiffness-proportional. They have shown the dependency of damping from frequency. On the other hand, the numerical methods can be useful and implement easily.

Rajashree & Sitharam (2001) applied a FEM in order to present the nonlinear soil behavior by a hyperbolic relation for static load conditions and a modified hyperbolic relation which includes both degradation and gap for cyclic loads. They used an incremental-iterative procedure where the pile was idealized as beam elements and the soil as elastoplastic spring elements. Klar and Frydman (2002) presented 3-D models and Winkler models based on the commercial 2-D finite difference code FLAC under static, seismic,

and lateral dynamic loading. Karim et al. (2002) analyzed a saturated porous elastic soil layer under cyclic loading by using a 2-D mesh free Galerkin method by having periodic conditions. Liang et al. (2007) applied a 3-D FEM and presented the parametric study of laterally loaded drilled shafts in clay. A hyperbolic p-y criterion was developed for cohesive intermediate geometrical. Harada et al. (2008) employed a multi-Winkler model based on soil traction for nonlinear soil–foundation interaction during cyclic loading. The integration of the traction over the foundation area was efficiently treated numerically by employing the fiber element method. Al-Wakel et al. (2011) implemented a model of frequency-dependent damping by using 3-D FEM while a rectangular footing on saturated soil was subjected to cyclic and harmonic force. The coupled dynamic equations with an u-p formulation based on the dynamic consolidation theory were used to simulate the soil skeleton. The Beam on Nonlinear Winkler Foundation can be modeled in ABAQUS while the interaction nonlinearity can be accounted for. Trochanis (1991) presented the response of laterally loaded piles by using ABAQUS and compared the results with 3-D FEM. Boulanger et al (1999) employed ABAQUS to present the dynamic results of piles and validated the results with centrifuge experimental tests. Commercial software such as ABAQUS can be versatile, economical and friendly user software for various complicated conditions in a simple manner.

It may be noted that the existing literature on offshore monopile foundations as cited above presents experimental and theoretical solutions based on numerical or analytical approaches. To the best of our knowledge, no work has been reported till date that presents a comprehensive parametric study of offshore foundations by using FEM with presence of the pore pressure that is developed due to dynamic load. The influence of different parameters such as pore pressure, load amplitudes and frequencies, the bulk modulus of the grains, the permeability of the seabed and void ratio of the seabed, and Young's modulus of the matrix material are investigated. The FEM and a Kelvin-Voigt model are employed for analysis of a 2-D saturated soil model.

2 MODEL DESCRIPTION

Consider an axisymmetric solid circular cylinder with radius R, as shown in Figure 1. The arc-boundary which represents the common border between the solid cylinder and the saturated soil is subject to harmonically varying forced displacement with the cyclic frequency ω and applied in the horizontal (x) direction. The two-dimensional analysis of each individual soil layer is performed.

2.1 *Soil modeling*

The soil is considered as an isotropic and elastic material. For saturated soil, the permeability, specific weight and void ratio, porous bulk moduli (which encompass the bulk modulus of grains and the bulk modulus of fluid) are defined. The mesh consists of 4-noded quadrilateral elements with linear interpolation of the displacement and pore pressure (CPE4P).

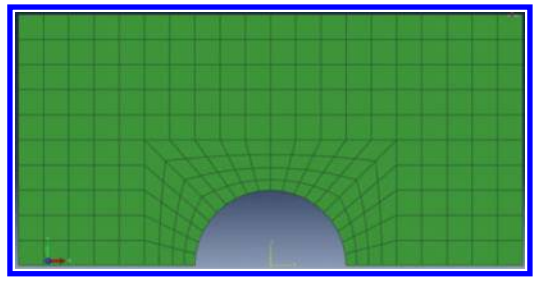


Figure 1. Two-dimensional finite-element model of an offshore wind turbine foundation and the surrounding soil.

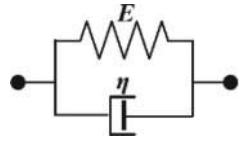


Figure 2. Kelvin-Voigt model.

2.2 *Theoretical approach*

The numerical calculation for dynamic analysis of offshore monopile foundations based on a one dimensional Kelvin-Voigt model by using FEM is presented. The dynamic analysis has been implemented within the framework of ABAQUS. Different model size for symmetry pile are applied. A numerical solution for the reaction force on the pile is given.

In the Kelvin-Voigt model as shown in Figure 2, the equation of motion can be written as:

$$C\dot{x} + Kx = F. \tag{1}$$

Here C, K and F are the damping, stiffness and reaction force, respectively, while x and $\dot{x}$ are the displacement and the velocity. By applying sinusoidal force-displacement, the reaction force F could be in sinusoidal form with phase angle respect to applied displacement, however the amplitude of force and applied displacement are different. By calculating the phase angle from numerical results in ABAQUS (Dassault Systèmes Simulia Corp. 2012) and using the flowchart as shown in Figure 3, the damping and stiffness can be calculated.

2.3 *Boundary conditions*

The pore pressure and displacement at the exterior boundary should be zero. Symmetry of the solution should apply across the center line of the model, while for the semi-circle carve, the sinusoidal periodic displacement in horizontal direction is applied as shown in Figure 4.

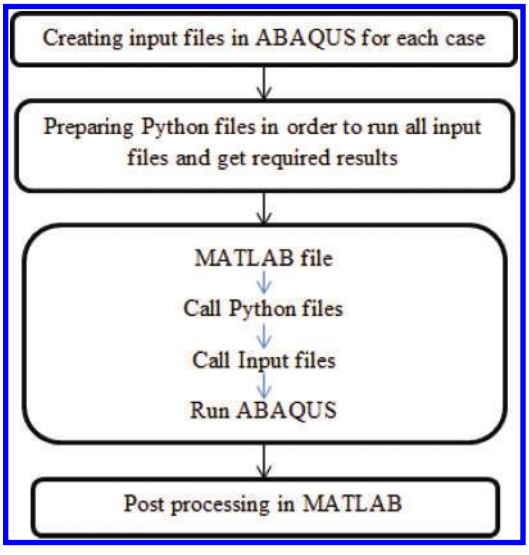


Figure 3. Flowchart of computer program.

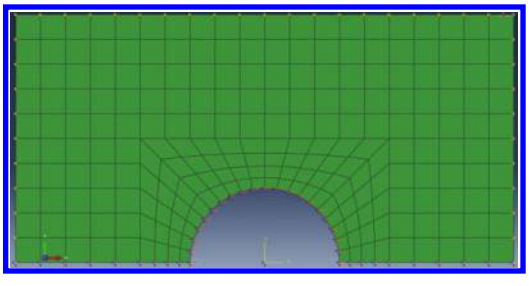


Figure 4. Boundary conditions for the soil block.

Table 1. Material properties of soil.

Young's modulus (N/m^2)	1×10^8
Poisson's ratio	0.25
Void ratio	0.50
Bulk modulus of grain (N/m^2)	3.6×10^{10}
Bulk modulus of fluid (N/m^2)	2×10^9

3 NUMERICAL RESULTS

For numerical illustration of the elastic solutions of this study, a solid cylinder with radius $R = 3.0$ m is considered. The material properties listed in Table 1 are considered. A soil block with a circular cavity subjected to sinusoidal periodic displacement is analyzed, using different geometry and soil properties in order to illustrate the effects of changes.

3.1 *Results for different geometries*

Figure 5 (top and middle) illustrates the damping and stiffness due to sinusoidal periodic load for different geometry of the soil block around the pile. It can be seen from Figure 5 that for each dimension of the

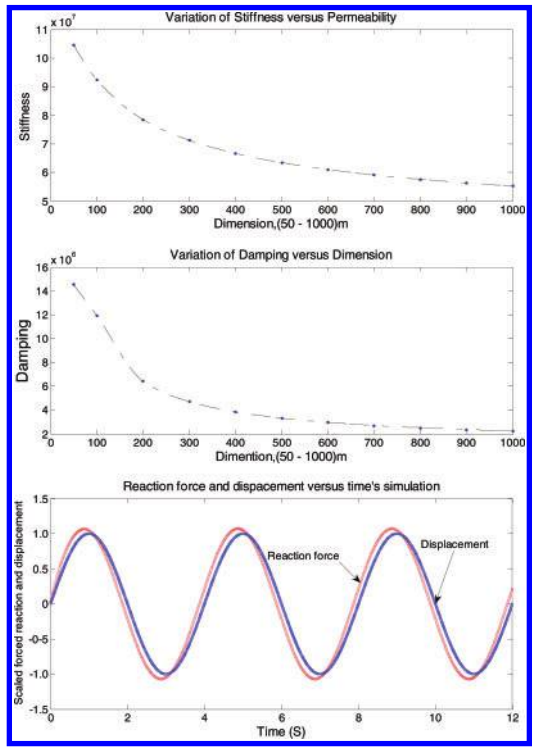


Figure 5. Variation of stiffness and damping versus model dimensions, and variation of scaled reaction force and displacement versus time.

model, the stiffness and damping have their maximum value for the smaller size of the model. It is seen that for large sizes of the model, the variations of the mentioned properties become small. As expected, the effect of the exterior boundary condition for large sizes of the model became smaller than those for a small model.

The graphs in Figure 5 (top and middle) are calculated based on reaching steady state conditions. The simulation is carried for 12 s as shown in Figure 5 (bottom) and then by calculating the phase angle between two graphs the damping is determined. It is worth to mention that the stiffness and damping are calculated after two periods in order to have the steady state results. It can be concluded that a bigger model can make better results by avoiding the effect of outer boundary conditions. Thus, in the rest of the analyses the larger model of this study is considered.

3.2 *Results for different void ratio*

Figure 6 illustrates the variation of stiffness and damping due to periodic loading for different values of the void ratio. It is seen that the values of stiffness and damping decrease by increasing the void ratio. It is noted that the variation of damping versus void ratio is greater than the variation of the stiffness.

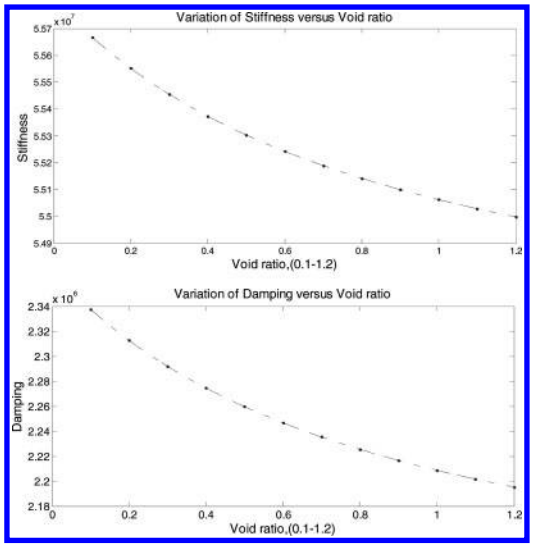


Figure 6. Variation of stiffness and damping versus variation of the void ratio.

3.3 *Results for different permeability*

The variation of stiffness and damping due to periodic load for saturated soil for different values of permeability are presented in Figure 7 (top and middle). As it can be seen the by increasing the permeability the damping increases, and for specific values of the permeability the maximum damping occurs, whereas for further increasing permeability the damping decreases. The stiffness decreases with increasing the permeability. A decrease of almost 30% can be identified. The following values of the permeability have initially been examined in the study: 0.5, 0.4, 0.2, 0.1, 0.07, 0.05, 0.03, 0.01, 0.005, 0.001, 0.0005, 0.0001, 0.00005, and 0.00001 (m/s). The behavior of damping makes awareness to investigate the variation of damping using smaller increments in the permeability. The following values have been applied in Figure 7 (bottom): 0.01, 0.02, 0.03, …, 0.27, 0.028, 0.29, 0.30 (m/s). The graph suggests that the maximum damping for the soil material properties and pile geometry occurs for a permeability of 0.15.

3.4 *Results for different load frequencies*

Figure 8 shows the variation of stiffness and damping in the soil due to harmonic forced displacement with different values of the excitation frequency. It is evident that the dynamic soil stiffness increases with increasing load frequency in the entire range of frequencies, the damping decreases with an increase of the excitation frequency. It can be noted that the relative variation of the damping in the considered frequency range is more than four times bigger than the relative variation of the stiffness, which means that the damping is much more sensitive to a variation of the load frequency than the stiffness.

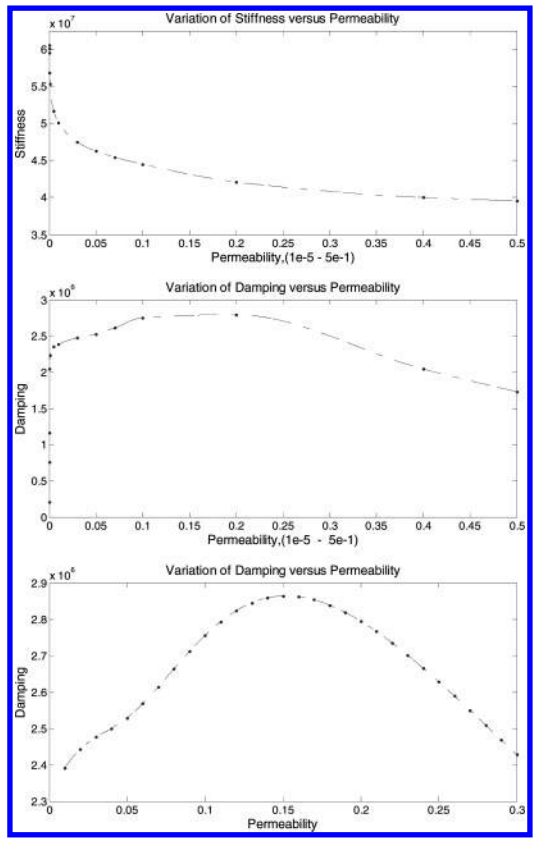


Figure 7. Variation of stiffness and damping versus variation of the permeability.

3.5 *Results for different load amplitudes*

Figure 9 illustrates the variation of stiffness and damping due to time-harmonic excitation with different values of load amplitudes. As it can be seen, the behavior of stiffness and damping are similar: by increasing load amplitudes, the stiffness and damping related to the soil increase up to the specific value of amplitude = 0.6 m. Hereafter they are going to decrease. It can be mentioned that the variations of the stiffness are very small, whilst the variations of damping are slightly greater with respect to the load amplitude variation.

3.6 *Results for different grain bulk moduli*

The variation of stiffness and damping due to harmonic loading for soil with different grain bulk moduli are presented in Figure 10. As expected the values of stiffness and damping increase with an increase of the grain bulk modulus. The relative variations of stiffness and damping are almost the same, and only small variations are observed.

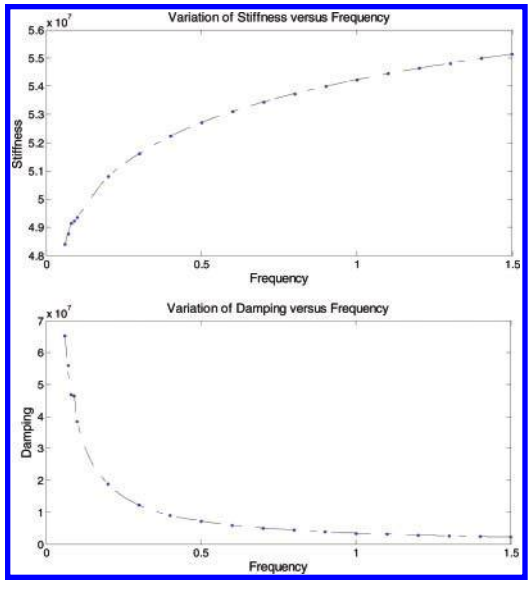


Figure 8. Variation of stiffness and damping versus variation of the load frequency.

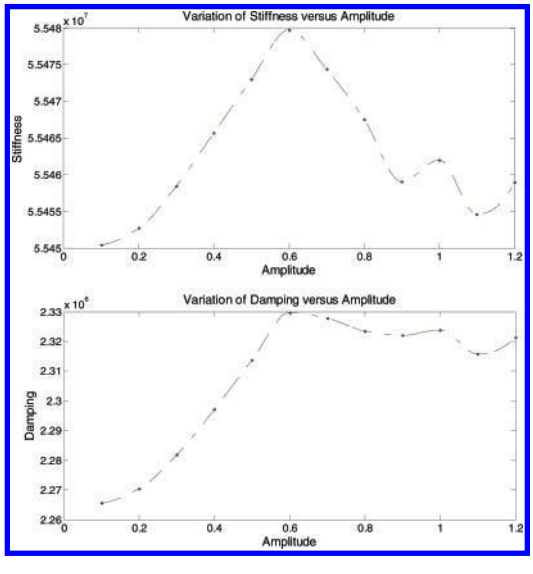


Figure 9. Variation of stiffness and damping versus variation of the load amplitude.

3.7 *Results for different Young's moduli*

It is evident from Figures 11(a) and 11(b) that the variation of stiffness and damping is almost linear versus the variation of Young's modulus.

As expected, by increasing the Young's modulus the stiffness and damping in soil increase. It is worth to mention that the variation of stiffness is higher than the variation of damping versus the variation of Young's modulus. For the mentioned model, the relative variation of the stiffness is about 1.5 times higher than

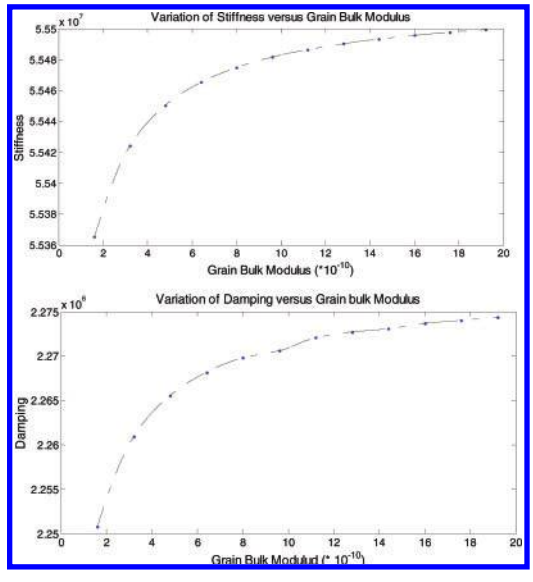


Figure 10. Variation of stiffness and damping versus different grain bulk modulus.

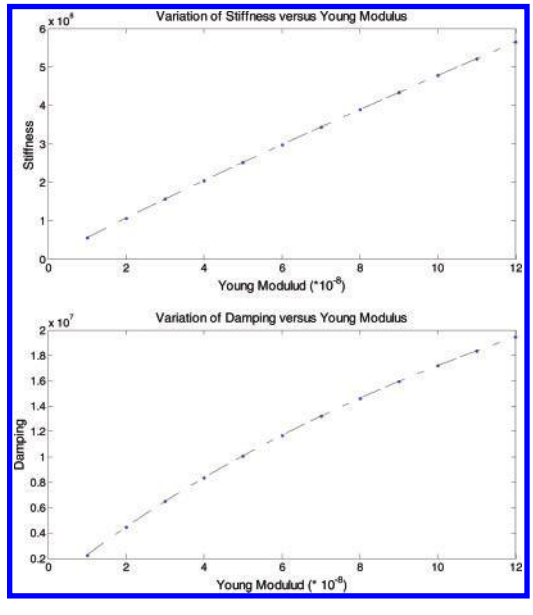


Figure 11. Variation of stiffness and damping versus different Young's moduli.

the relative variation of the damping. This implies that the stiffness is more sensitive than the damping with respect to variations of Young's modulus.

4 CONCLUSIONS

The dynamic response of isotropic elastic saturated soil is presented by using a finite-element model. The effects of model size, soil properties (such as Young's

modulus, bulk modulus of grain, void ratio, and permeability), load frequency and amplitude on the dynamic stiffness and soil damping are investigated.

Numerical results are presented by using the finite-element method by coding the input file and using Python scripting in ABAQUS and MATLAB. A sinusoidal forced displacement is applied and the simulation is carried out within 12 second.

Some general observations of this study can be summarized as follows:

- Dynamic stiffness and damping decrease with increase of void ratio and the variation of damping versus void ratio is greater than variation of stiffness versus void ratio.
- Damping increases to certain value for specific value of permeability and then decreases by increasing the permeability, whilst stiffness decreases by increasing permeability.
- Dynamic stiffness increases with increasing load frequency, whilst the damping decreases with the increase of load frequency.
- Dynamic stiffness is more sensitive than damping with respect to variation of Young's modulus.

Results of the frequency-dependent damping and dynamic stiffness are similar and in the same line to the results reported in Chang et al. (2000) and Kazama & Nogami (1991), respectively.

5 ACKNOWLEDGEMENT

The authors highly appreciate the financial support provided by Danish Energy Development and Demonstration Programme via the project "Monopile cost reduction and demonstration by joint applied research".

REFERENCES

Ahangar, M. & Bargi, K. & Sharifian, H. & Safarnezhad, M. 2011. Dynamic nonlinear behavior of fixed offshore jacket piles. *International journal of civil and structural engineering* 2(1): 260–269.

Al-Wakel, S.A.F. & Fattah, M.Y. & Karim, H.H. 2011. Dynamic Analysis of Foundations on Saturated Clay Using an Energy Absorbing Layer. *Eng. & Tech. Journal*, 29 (11): 2189–2201.

Bea, R.G. 1992. Pile capacity for axial cyclic loading. *Journal of Geotechnical Engineering, ASCE*, 118(1): 34–50.

Boulanger, R.W. & Curras, C.J. & Kutter, B.L. & Wilson, D.W. & Abghari, A. 1999. Seismic Soil-Pile-Structure Interaction Experiments and Analyses. *Journal of Geotechnical and Geoenvironmental Engineering, ASCE*, 125(9): 750–759.

Chang, D.W. & Roesset, J.M. & Wen, C.H. 2000. A time-domain viscous damping model based on frequency-dependent damping ratios. *Soil Dynamics and Earthquake Engineering* 19: 551–558.

Chang, D.W. & Yeh, S. H. 1999. Time-domain wave equation analysis of single piles utilizing transformed radiation damping. *Soils and Foundations, JGS* 39(2): 31–44.

Dassault Systèmes Simulia Corp. (2012). *Abaqus 6.12 Analysis User's Manual*. Providence, RI, USA: Dassault Systèmes Simulia Corp.

Harada, T. & Nonaka, T. & Wang, H. & Magoshi, K. & Iwamura, M. 2008. A nonlinear dynamic soil foundation interaction model using fiber element method and its application to nonlinear earthquake response analysis of cable stayed bridge. *The 14th World Conference on Earthquake Engineering October 12–17 Beijing China.*

Karim, M.R. & Nogami, T. & Wang, J.G. 2002. Analysis of transient response of saturated porous elastic soil under cyclic loading using element-free Galerkin method. *Int. J. of Solids and Struct* 39: 6011–6033.

Kazama, M. & Nogami, t. 1991. Effects of permeability and loading rate on dynamic stiffness of saturated soil, *GEO-Cost* 91. 3–6 *Sep.:459–462.*

Klar, A. & Frydman, S. 2002. Three-Dimensional Analysis of Lateral Pile Response using Two-Dimensional Explicit Numerical Scheme. *Journal of Geotechnical and Geoenvironmental Engineering,ASCE*, 28(9): 775–784.

Lanzo, G. & Pagliaroli, A. & D'Elia, B. 2003. Numerical study on the frequency-dependent viscous damping in dynamic response analyses of ground. *Transactions on the Built Environment* 72, *WIT Press, www.witpress.com, ISSN* 1743–3509.

Liang, R. Y. &Shatnaw, E.S. & Nusaira, J. 2007. Hyperbolic P-Y Criterion for Cohesive Soils. *Jordan Journal of Civil Engineering* 1(1): 38–58.

Nogami, T. & Konagai, K. 1987. Dynamic response of vertically loaded nonlinear pile foundations, *Journal of Geotechnical and Geoenvironmental Engineering, ASCE*, 113(2): 147–160.

Rajashree, S.S. & Sitharam T.G. 2001. Nonlinear finite element modeling of batter piles under lateral load. *Journal of Geotechnical and Geoenvironmental Engineering, ASCE*, 127(7): 604–612.

Trochanis, A.M. & Bielak, J. & Christiano, P. 1991. Three-dimensional Nonlinear Study of Piles. *ASCE Journal of* Geotechnical Engineering 117(3): 429–447.

Research and Applications in Structural Engineering, Mechanics and Computation – Zingoni (Ed.)
© 2013 Taylor & Francis Group, London, ISBN 978-1-138-00061-2

Improved subgrade reaction model in designing embedded piles exposed to static lateral head loads

Matthias Pulsfort & Tim Welskopf
Bergische Universitaet Wuppertal, Germany

ABSTRACT: Based upon the results of recent model tests with vertical piles exposed to lateral head loads, some new findings upon soil-pile head interaction are reported here. The bearing behavior of piles carrying off lateral loads at the pile head towards the surrounding soil is determined by the development of horizontal reaction stresses, as in prototype scale for instance at bridge abutments, in offshore piling (cyclic loading with low frequency due to wave excitation) or cantilevers of noise load reduction walls as to highspeed railway tracks (dynamic loading due to higher frequencies of wind shock waves). In daily design practice the pile-soil-interaction is commonly disregarded or represented in extremely simplified forms, like linear subgrade reaction models with stepwise control of the equilibrium between reaction stresses and passive earth pressure to be mobilized. This usually leads to an uneconomic - but safe sided - design, because a strong restraining effect at the toe of the pile is disregarded.

The main focus in this contribution is a simple approach to assess the development and redistribution of reaction stresses along the pile-axis due to the imposed head displacement of the pile in static monotonic loading.

1 INTRODUCTION

1.1 *Regarded Problem*

The bearing behavior of vertical piles exposed to lateral head loads can be physically studied in prototype scale with very expensive large scale measurements or in small scaled model tests, while taking into account the effect of the installation method - by means of driving or boring technique. The real excitations are for instance in offshore piling (in form of a cyclic loading with low frequency due to wave excitation) or cantilevers of noise load reduction walls as to high-speed railway tracks (dynamic loading due to higher frequencies of wind shock waves). But also static loading can be dominant for instance in foundations of bridge abutments (FLEMING et.al. 2009).

To study the latter, single floating piles were regarded in small-scaled physical simulation tests in a sand box with dry sand of different initial densities; the model piles were exposed to static lateral head loads by means of constant deformation velocity, leading to results like static load-displacement-curves of the pile top and the distribution of the bending moments, which were counted back from strain measurements at certain points along the pile shaft. The observed distribution of bedding stresses along the pile shaft could be recalculated from these measured strain values by means of inverse methods like IFEM.

1.2 *Physical Modeling*

The geometrical scale in the physical model was chosen to 1:12, representing in prototype scale a driven cylindrical pile made from reinforced concrete of 30 cm in diameter and 5 m in embedded length.

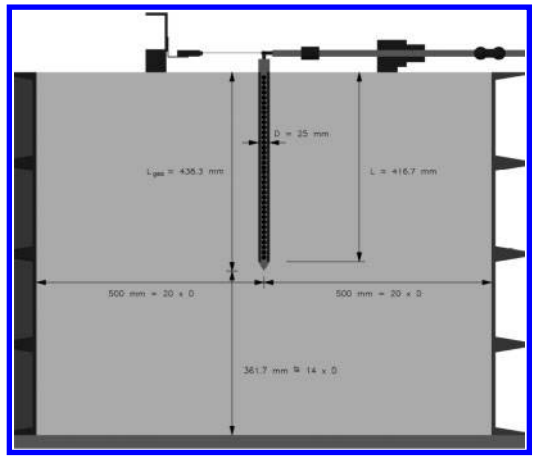


Figure 1. Cross section through sand box with model test loading equipment.

The model piles (diameter D=25 mm) were constructed from brass tubes surrounded with epoxy resin to assure a correctly scaled bending stiffness as well as the scaled geometric width of the pile according to the modeling theory. The concerning bending stiffness of the model piles has been measured to EI=486,69 kNcm^2.

The brass pile shafts were equipped with triple sets of strain gauges in 3 different depths. The model soil was dry medium coarse grained quartz sand, which



Figure 2. Physical model testing equipment.

was installed in layers by means of curtain raining method to achieve different initial densities between loose and very dense. The model piles were driven by means of a guided pushing process into the soil mass. Due to this, the effect of the installation process is taken into account. In this procedure, already a certain clamping effect could be observed.

1.3 *Theoretical approach*

Based upon the observations and results of these test series as well as numerical investigations by means of the Finite Element Analysis under three-dimensional conditions (using a hypoplastic material law for the surrounding soil) in this presentation an improved non-linear subgrade reaction model is proposed, taking into account the observed strong restraining effect at the piles toe. This calculation proposal is compared with the so called p- y- method, which is often used in the design of offshore piles, and it can be shown, that both methods lead to similar design results.

2 RESULTS OF MODEL TESTS

2.1 *Sand Installation*

The dry sand could be installed with 4 different methods of sand placement – varying in the effective falling height – leading to 4 different initial densities between very dense state ($I_d \geq 0{,}81$, method 1), dense (method 2, $I_d = 0,60 - 0,70$), medium dense (method 3, $I_d = 0,27 - 0,35$) and loose state ($I_d = 0,09 - 0,18$, method 4). Fig. 3 shows a satisfying reproducibility of these initial states.

2.2 *Pile Installation*

The model piles were installed vertically by means of a threaded control bar in a guiding frame, pushing the pile 43,83 cm deep into the soil. The development of the mobilized axial pile resistance with installation depth is shown in Fig. 4 for the different initial densities (in detail see WELSKOPF 2013).

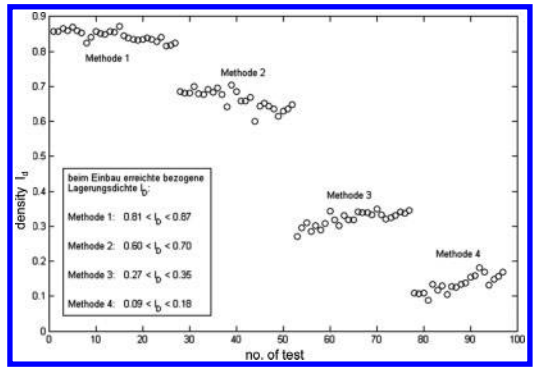


Figure 3. Initial density I_d of the sand due to 4 different methods of sand raining (1= loose to 4 = very dense) for all model tests (static, cyclic and dynamic loading).

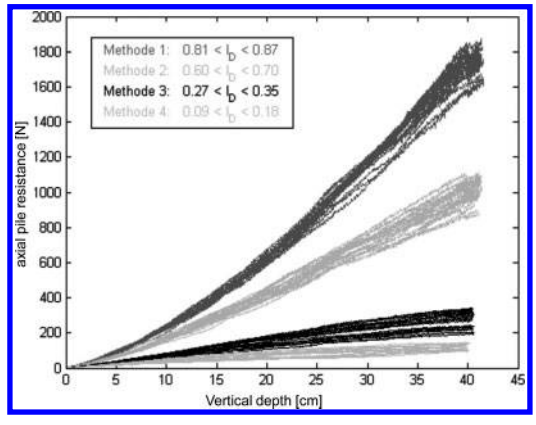


Figure 4. Mobilized axial pile resistance due to installation depth for 4 different methods of sand raining resp. initial densities.

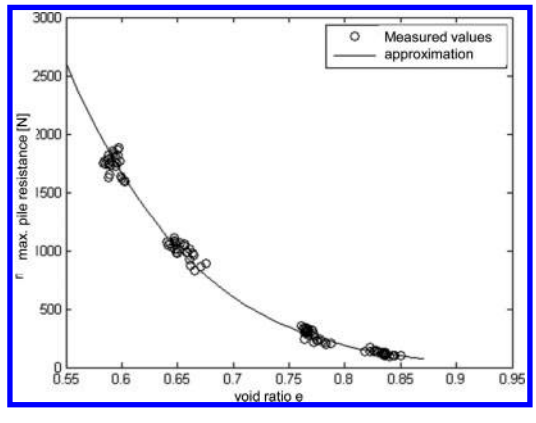


Figure 5. Max. axial pile resistance due to the different initial densities.

The maximum axial pile resistance at the final installation depth in each and any of the in total 100 model tests (Fig. 5) can be very well fitted by an exponential approximation curve as given in eq. (1):

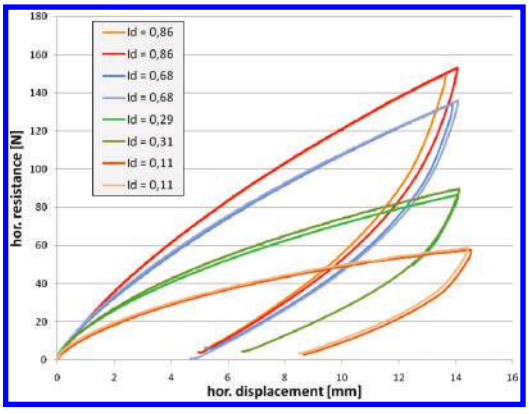


Figure 6. Displacement – load curves.

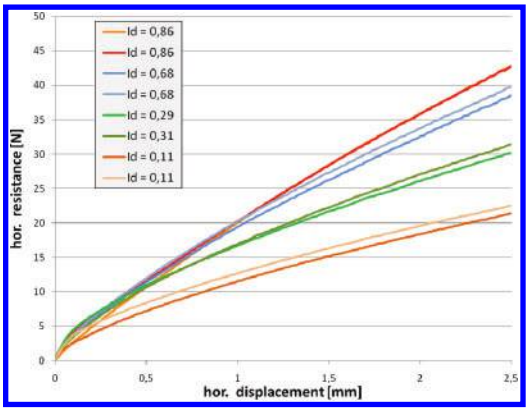


Figure 7. Zoomed displacement-load curves below u/D=0,10.

$$R_p = \alpha * \exp(\beta * e^2) \quad (1)$$

with e= initial void ratio and α, β as parameters to be determined statistically by means of correlation to α =27564 N and β =7,797.

2.3 *Displacement-load curves*

The excitation by the horizontal head load was realized by means of a connection rod (see Fig. 1) to a horizontal pneumatic pulser cylinder, where the reaction load of the pile due to the imposed deformation rate can be measured according to the imposed head movement. The tests were performed with constant horizontal displacement rate, whereas the horizontal head load at the pile top was measured as effect of the "horizontal pile resistance". Typical results for the different initial densities I_d are given in Fig. 6, showing, that the tests have been conducted up to very large dimensionless deformation values of u/D > 0,50, which means in practice an approach to the ultimate limit state (ULS).

Suitable serviceability states in practice will be limited to dimensionless values of u/D< 0,10, so in detail, the lower parts of these curves are zoomed in Fig. 7 up

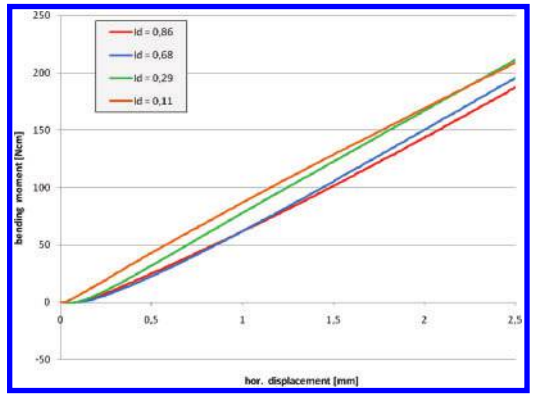


Figure 8. Development of the bending moment in the central point of the initial pile embedding length.

to a horizontal displacement u= 2,5 mm, meaning a dimensionless value u/D=0,10. Even though a strong effect of the initial density of the soil can be observed.

2.4 *Development of bending moments*

The development of the bending moment has been measured at the upper quarter point, middle point and lower quarter point of the pile length, leading to moment-displacement-curves as given in Fig. 8 for the middle point of the pile length. Depending on the initial density, a change in the freeboard value at the pile top could be observed, heaving like a soil wave for initially dense soil, but settlements for initially loose to medium dense soil. This results in a certain change of the effective cantilever length above the actual soil surface.

As can be seen in Fig. 8, the bending moment for the stiffer kinds of soil are beginning with a development of small negative values, whereas the bending moment for the looser soils are only increasing from zero. This is a clear sign for a certain clamping effect due to the installation process, because especially the piles in the stiff soils show a softening effect in the first deformation increments, obviously due to a loosening of the inherent stress condition due to the installation restraint (see Fig. 9).

3 NUMERICAL EVALUATION

3.1 *Method*

The following trial functions have been considered to implement an approximation of the measured values using the theory of beam bending, to be accommodated to the boundary conditions as measured in the 3 points and as given at the top and the toe of the pile.

$$f_1(\xi) = p_0 + p_1 \cdot \xi + p_2 \cdot \xi^2 + p_3 \cdot \xi^3 + p_4 \cdot \xi^4 + p_5 \cdot \xi^5 + p_6 \cdot \xi^6 \quad (2)$$

$$f_2(\xi) = p_0 + p_1 \cdot \xi + p_2 \cdot \xi^2 + p_3 \cdot \xi^3 + p_4 \cdot \xi^4 + p_5 \cdot \xi^5 + p_6 \cdot \xi^6 + p_7 \cdot \xi^7 \quad (3)$$

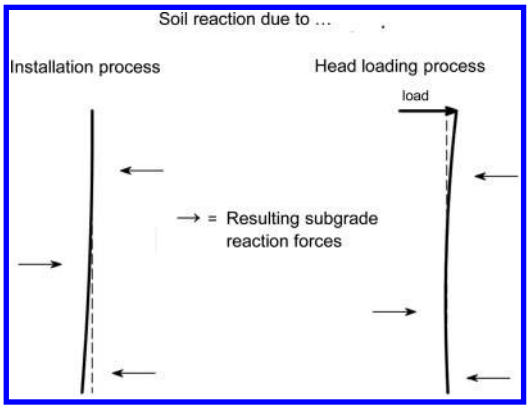


Figure 9. Interpretation of clamping effect due to the installation process.

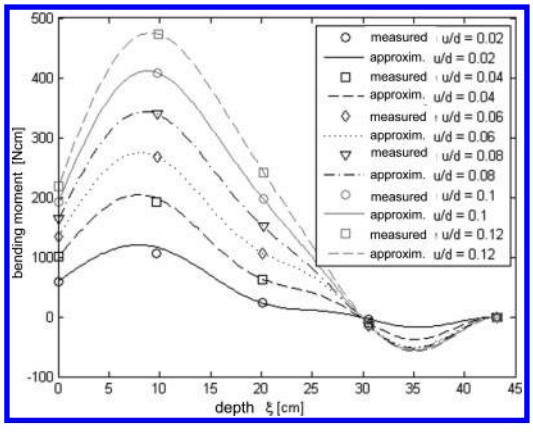


Figure 10. Distribution of bending moments in dense soil (I_d = 0,68) for different displacement stages up to u/D = 0,12.

$$f_3(\xi) = a_0 + b_0 \cdot \xi + a_1 \cdot \cos\left(\frac{2 \cdot \pi}{c_0} \cdot \xi\right) + b_1 \cdot \sin\left(\frac{2 \cdot \pi}{c_0} \cdot \xi\right) + a_2 \cdot \cos\left(\frac{4 \cdot \pi}{c_0} \cdot \xi\right) + b_2 \cdot \sin\left(\frac{4 \cdot \pi}{c_0} \cdot \xi\right) + a_3 \cdot \cos\left(\frac{6 \cdot \pi}{c_0} \cdot \xi\right) \quad (4)$$

$$f_4(\xi) = a_0 + b_0 \cdot \xi + a_1 \cdot \sin\left(\frac{2 \cdot \pi}{c_0} \cdot \xi\right) + b_1 \cdot \cos\left(\frac{2 \cdot \pi}{c_0} \cdot \xi\right) + a_2 \cdot \exp\left(-\left(\frac{\xi - c_1}{c_2}\right)^2\right) \quad (5)$$

with ξ = depth coordinate. By means of differentiation of these functions, the boundary conditions concerning bending moment, shear forces and deformations can be taken into account. This best fit analysis has been executed by a suited MATLAB-routine for all 4 trial functions and showed, that equation (5) leads to the highest degree of clamped support at the toe, at least for initially dense soil. An example of this evaluation is given in Fig. 10.

The distribution of bending moments shows a considerable increase of the negative clamping moment at the pile's toe with increasing deformation.

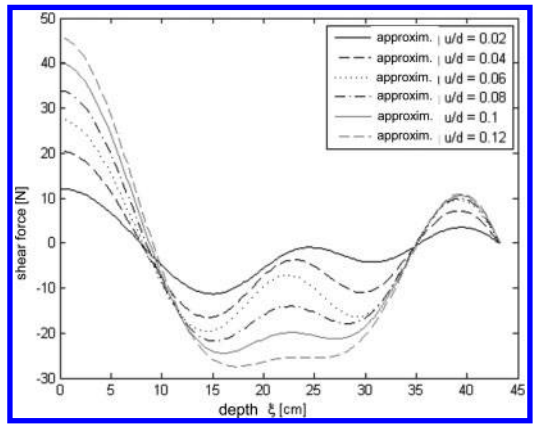


Figure 11. Distribution of shear forces in dense soil (I_d = 0,68) for different displacement stages up to u/D=0,12.

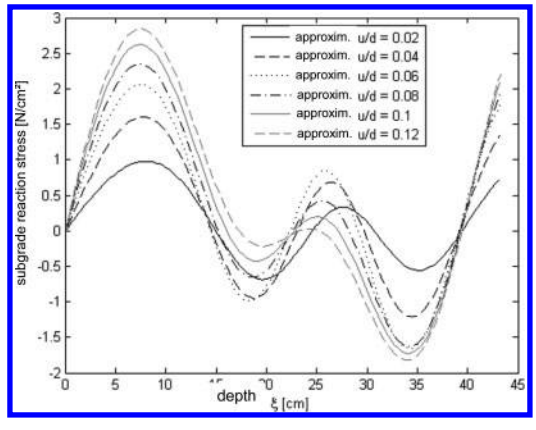


Figure 12. Distribution of subgrade reaction stresses in dense soil (I_d = 0,68) for different displacement stages up to u/D=0,12.

3.2 *Evaluation of subgrade reaction stresses*

Using eq. (5) one can achieve the distribution of shear forces and subgrade reaction stresses by means of multiple differentiation as shown in Fig. 11 and Fig. 12.

In Fig. 12 there can be seen 4 different areas of subgrade reaction stresses, combined with 4 zero points, whereas the classical suggestion allows only one. This apparent contradiction confirms the observation, that a strong clamping effect due to the installation is present in the model tests in dense or very dense sand.

4 CONCLUSION FOR PRACTICAL PURPOSE

The results of the model tests can be compared with a classical (see POULOS 1973), but nonlinear subgrade reaction calculation, performed in the model scale as well (for instance see Fig. 13), but combined with a substantial step increase in stiffness in the lower third

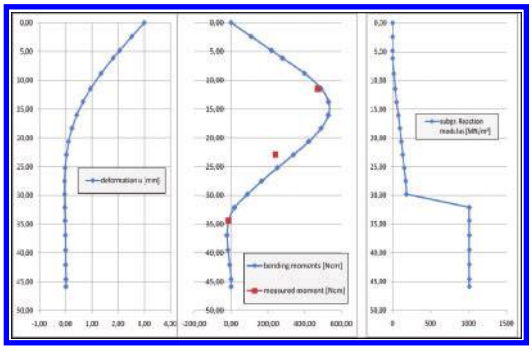


Figure 13. Results of classical subgrade reaction calculation with adopted distribution of subgrade reaction modulus for dense soil (I_d =0,68) and displacement stage u/D= 0,10.

of the pile. In this calculation, the passive earth pressure stress in relation to the depth has been used as plastic yield criteria, leading to a stepwise reduced subgrade reaction modulus at the top quarter of the pile length. The comparison between the calculated bending moment and the measured values at the three quarter points is rather satisfying.

In conclusion, a practical design calculation of a pile under statical and monotonous head loads can be performed with an adopted subgrade reaction modulus, concentrating a very high stiffness in the lower third of the pile.

The behavior of piles due to cyclic or really dynamic head loads, has been regarded e.g. in ABDEL-RAHMAN/ACHMUS (2005) and PULSFORT/ WELSKOPF (2010). In this cases, a subgrade reaction model is not sufficient due to loading/unloading effects, so a 3D-FEM analysis is necessary, using the hypoplastic material law for the soil behavior as published by NIEMUNIS/Herle (1997).

REFERENCES

Abdel-Rahman & K., Achmus, M. 2005: Finite Element Modelling of Horizontally Loaded Monopile Foundations for Offshore Wind Energy Converters in Germany. *International Symposium on Frontiers in Offshore Geotechnics*, Perth.

Cox, W.R., Reese, L.C. & Grubbs, B.R. 1974: Field Testing of Laterally Loaded Piles in Sand. *Offshore Technology Conference*, 459–472. R.

Cudmani, R.O. 2001: Statische, alternierende und dynamische Penetration in nichtbindigen Böden. *Publications of the Inst. for Soil Mech. and Rock Mech., Universität Fridericiana* in Karlsruhe/Germany, Vol. 152.

De Beer, E. 1977: Piles Subjected to Static Lateral Loads. State of the Art Report, Vol. 10, *Rijksinstituut voor Grondmechanika*, Gent/Belgium.

Fleming, W.G.K., Weltman, A.J., Randolph M.F. & Elson, W.K. 2009: *Piling Engineering*. Surrey University Press, London.

Meier, T. 2009: Application of Hypoplastic and Viscohypoplastic Constitutive Models for Geotechnical Problems. *Publications of Inst. for Soil Mechanics and Rock Mech., Universität Fridericiana* in Karlsruhe/Germany, Vol. 171.

Niemunis, A., Herle, I. 1997: Hypoplastic model for cohesionless soils with elastic strain range. *Mechanics of Cohesive- Frictional Materials*, Vol. 2, 279.

Poulos, H.G. 1973: Load-Deflection Prediction for Laterally Loaded Piles. *Australian Geomechanics Journal*, 1–8.

Pulsfort, M., Welskopf, T. 2010: Bearing behavior of embedded piles due to caclic and dynamic lateral head loads. *AProceedings of the 4. SEMC, Cape Town,* p. 345 ff. Ed. A. Zingoni. Taylor and Francis Group, London.

Welskopf, T. 2013: Untersuchungen zum Tragverhalten von Pfählen unter aktiver Horizotnalbelastung (in German, meaning consideration of bearing behavior of piles due to active head loads). Dissertation. *Report No. 33, issued by the Geotechnical Inst. at Bergische Universität Wuppertal/Germany.*

Research and Applications in Structural Engineering, Mechanics and Computation – Zingoni (Ed.)
© 2013 Taylor & Francis Group, London, ISBN 978-1-138-00061-2

Field test of soil-steel arch with ribs and calculation of internal forces on the basis of measured strains

B. Kunecki & L. Korusiewicz
Wrocław University of Technology, Wrocław, Poland

ABSTRACT: Flexible corrugated steel culverts have been used in engineering for many years. This paper describes full-scale field tests and internal forces analysis of one of two identical large-span flexible structures built on the A4 motorway in Poland. The structures serve as a wildlife crossing. The tested 75 m long culvert is a low-profile steel arch with a span of 19.5 m and a rise of 6 m. The experimental results were used to verify the response computed using software called "Tunel2" based on the finite difference method. The basic input data include the material and geometrical characteristics of the tested culvert and the circumferential stresses calculated on the basis of the measured strains. The main procedures used in the software are described. The results of computations performed by the software for an experimental case are presented. The research project was sponsored by the European Community under Marie Curie European Reintegration Grants.

1 INTRODUCTION

Flexible metal culverts have been gaining in popularity in recent years. In Europe they have been used for over 40 years. Examples of such structures can be found in Janusz & Madaj (2007) and Machelski (2008).

As a result of the increased demand for culverts with large spans, varying barrel shapes and backfill depths, the suitability of the existing semi-empirical procedures for analysing the stress, strain and deflection characteristics of soil-conduit systems subject to both static (soil weight) and live vehicular loads has been questioned. Therefore, several full-scale tests have been carried out in the field to validate the long-term performance and great load bearing capacity of these structures (Vaslestad 1994, Flener & Karoumi 2009, Yeau et al. 2009, Korusiewicz & Kunecki 2012). The experimental results give an insight into the actual behaviour of such structures under service conditions and form the basis for creating and verifying computational models. The progress in finite element methods has contributed to the implementation of a new generation of soil-shell structures with spans of over 20 m.

2 TESTED STRUCTURE

In 2008 twin flexible large-span structures were built on the A-4 motorway in Poland (Figure 1). The structures are low-profile metal arches with a span of 19.5 m and a rise of 6.0 m. Each of the two structures, serving as wildlife crossings over the motorway, is about 75 m long.

An additional spiral type metal pipe was installed between the two main arches. The relief steel pipe with a diameter of 2.40 m was closed at its ends and covered with soil and a top layer of humus to a height of 2.60 m above the crown. The main structures were similarly backfilled with soil and humus to a height of 2.25 m above the crown. The twin metal arches were erected on three reinforced concrete footings. The steel material conformed to European Standard PN-EN 10025-2:2007, having the minimum yield stress of 315 MPa. The dimensions of a single corrugation were 381×140 mm and the steel was 7.0 mm thick. The steel plates were joined with 20 mm diameter bolts of grade 8.8. Over the crown and the haunch region the arches were intermittently reinforced with additional 5.5 mm thick corrugated plates, as shown in Figure 2. A detailed description of the tested culvert can be found in Kunecki & Korusiewicz (2010).



Figure 1. View of complete structures.

3 MEASUREMENTS

The behaviour of one of the arches during backfilling was to be closely monitored. This was done by taking measurements after each backfill layer was placed on both sides of the arches.

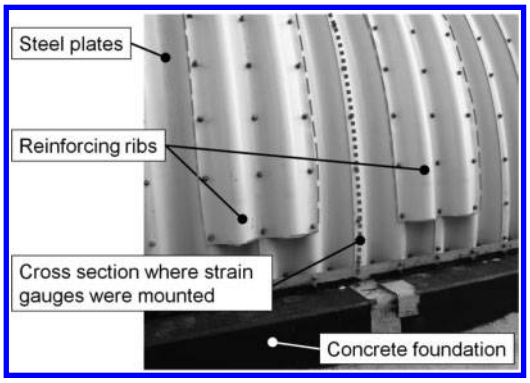


Figure 2. Reinforcing ribs on arch exterior.

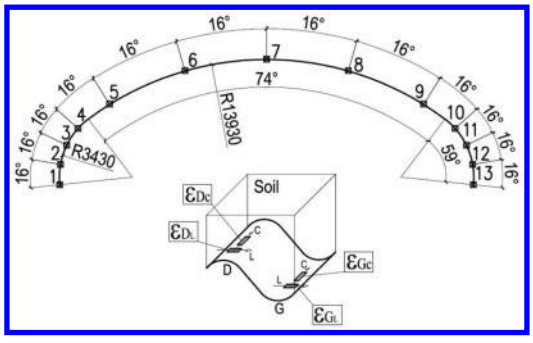


Figure 3. Location of strain gauges on inner side of structure.

Strain gauges were placed in 13 locations inside the west arch in the middle of the structure. Four gauges were fitted in each location: two at the crest of the corrugation and two in its valley (in total 52 strain gauges). Thanks to this configuration strains could be measured in longitudinal and latitudinal directions. Location of strain gauges is shown in Figure 3. The strains in each measuring point were used to calculate the axial and bending stresses from the equations derived by Korusiewicz and Kunecki (2011).

An example of the stress points distribution for the crown and final backfill level is shown in Figure 4. The axial and bending stresses of the tested steel arch for the crown and final backfill level are shown in Table 1 and 2, respectively. The experimental results are comprehensively presented elsewhere (Kunecki & Korusiewicz, in press).

4 DESCRIPTION OF SOFTWARE

The software, under the working name of "Tunel2", computes load intensities on the surface and generalized cross-sectional forces in the lining of a tunnel (culvert) on the basis of the circumferential stresses measured in two layers of the tunnel lining. Data from measuring points (in cross sections) uniformly distributed on the lining's average contour are input into the software. The software comprises two subprograms called: "Tunel2-D" and "Tunel2-O".

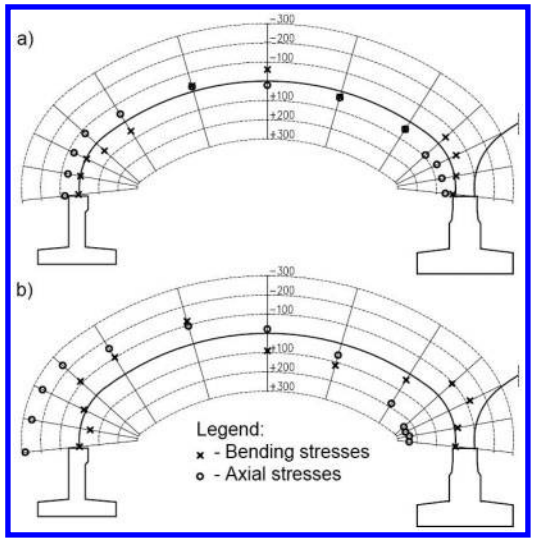


Figure 4. Stress distribution for (a) crown backfill level and (b) final backfill level.

Table 1. The axial and bending stresses of the tested steel arch for the crown backfill level.

Point	s_i	Stresses	
		Axial stresses	Bending stresses
	m	MPa	MPa
1	0,000	−76,85	−5.65
2	0,958	−64,45	0,25
3	1,916	−69,95	2,75
4	2,874	−77,90	55,90
5	4,747	−47,25	56,25
6	8,637	−25,95	−30,05
7	12,527	21,15	−60,95
8	16,417	33,20	28,10
9	20,307	45,35	44,75
10	22,180	90.00	−49,30
11	23,138	69,20	−41,60
12	24,096	66,75	−8,65
13	25,054	52,15	13,75

4.1 *Subprogram "Tunel2-D"*

This program is used to create a data file for program "Tunel2-O". The input data are:

- the task identifier,
- the number of strain gauge pairs (the number of measuring points) –*lpt*,
- the Young modulus of the culvert material – E,
- the lining membrane stiffness in the circumferential direction – D_φ,
- the lining flexural rigidity in the circumferential direction – K_φ,

Table 2. The axial and bending stresses of the tested steel arch for the final backfill level.

Point	s_i	Stresses	
		Axial stresses	Bending stresses
	m	MPa	MPa
1	0,000	−295,13	−1,15
2	0,958	−254,95	51,35
3	1,916	−250,95	−13,35
4	2,874	−234,40	−111,90
5	4,747	−155,25	−101,85
6	8,637	−95,00	−121,40
7	12,527	−22,35	90,95
8	16,417	62,25	116,95
9	20,307	180,30	36,50
10	22,180	241,90	−93,90
11	23,138	249,90	−121,30
12	24,096	237,40	−15,10
13	25,054	186,95	3,05

– the distance of measuring points D_i from the middle layer (the distance is positive for points D_i within the average contour of the lining) – g_{Di},
– the distance of measuring points G_i from the middle layer (the distance is negative for points G_i outside the average contour of the lining) – g_{Gi} ($g_{Di} = g_D =$ const and $g_{Gi} = g_G =$ const are assumed in the program),
– the length of the average lining contour – *SKOT* (the average lining contour should be understood as the arc of a curve, being the geometric locus of the centres of gravity of the considered tunnel lining segment cross sections).

For the next control (measuring) cross sections bearing numbers $i = 1, 2,\ldots, lpt$ and ordered according to increasing length s_i the following quantities are entered:

– the distance of a given measuring point from the adopted starting point, measured along the average lining contour – s_i,
– the radius of curvature of the average lining contour – ri,
– the circumferential stress in points D_i and G_i –σ_{Di} and σ_{Gi}.

Moreover, the program requires that it be specified whether the average lining contour is an open or closed curve and whether the radius of curvature along the whole length of the average contour is intervalwise constant. If so, the number of intervals in which the radius of curvature is constant needs to be input.

Into the program, data can be entered in the interactive mode and saved to a file with a name given by the user or read in from a file indicated by the user.

The terms used in program "Tunel2-D" are explained in Figure 5.

Circumferential stresses σ_{Di} and σ_{Gi} are calculated on the basis of the strains measured in the measuring points. If bidirectional strain rosettes are used,

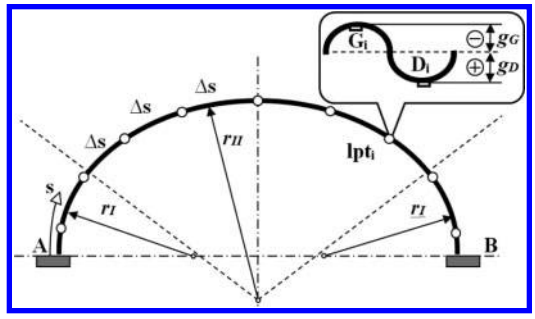


Figure 5. Diagram of terms used in program.

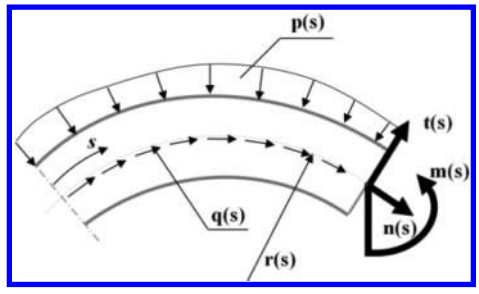


Figure 6. Internal and external forces acting on culvert structure.

the circumferential stresses are calculated from the following relation:

$$\sigma_D = \frac{E}{1-\nu^2}\left(\varepsilon_{D_C} + \nu\varepsilon_{D_L}\right), \tag{1}$$

$$\sigma_G = \frac{E}{1-\nu^2}\left(\varepsilon_{G_C} + \nu\varepsilon_{G_L}\right) \tag{2}$$

Membrane stiffness D_φ and flexural rigidity K_φ for corrugated culverts are expressed by the equations:

$$K_\varphi = E\,I_f, \tag{3}$$

$$D_\varphi = E\,A_f \tag{4}$$

where A_f and I_f stand for respectively the area and moment of inertia of the cross section (fold) per width unit.

4.2 *Subprogram "Tunel2-O"*

This computational program uses the data saved in program "Tunel2-D". The internal forces in the culvert shell and the external forces acting on the culvert shell from the surrounding ground are computed. The results of the computations are displayed in the form of tables and diagrams on the computer screen.

The symbols in Figure 6 stand for: $p(s)$ – the normal stress per middle lining layer unit area; $q(s)$ – the static load per middle lining layer unit area; $m(s)$, $n(s)$ and

$t(s)$ – the bending moment, the normal force and the shearing force in the cross section of the lining per cross sectional unit width.

First the program calculates bending moments m_i and normal forces n_i ($i = 1, 2, \ldots, lpt$) in the control (measuring) cross sections from the formulas:

$$m_i = \frac{K_\varphi}{E\left(g_{Di} - g_{Gi}\right)}\left(\sigma_{D_i} - \sigma_{Gi}\right)$$
$$n_i = \frac{D_\varphi}{E\left(g_{Di} - g_{Gi}\right)}\left(g_D\,\sigma_{Gi} - g_G\,\sigma_{Di}\right) \tag{5}$$

Then the coefficients of the Fourier-Bessel series of functions $m(s)$ and $n(s)$ are calculated and taking into account the statics conditions:

$$t = -\frac{\mathrm{d}m}{\mathrm{d}s} \tag{6}$$

$$p = \frac{\mathrm{d}^2 m}{\mathrm{d}s^2} + \frac{n}{r} \tag{7}$$

$$q = -\frac{\mathrm{d}n}{\mathrm{d}s} - \frac{t}{r} \tag{8}$$

the coefficients of the Fourier-Bessel series of functions $t(s)$, $p(s)$ and $q(s)$ are calculated. The user can choose the trigonometric interpolation method or the trigonometric approximation method. The program correctly solves the interpolation problem only when the distances between the control cross sections are constant $\Delta s = \text{const}$.

Two approximation selection methods: a standard method and a statistical method are available in the program. In both cases, the so-called approximation defect is calculated for successive tentative values of the number of harmonic components (LSH) in expansions $m(s)$ and $n(s)$ into Fourier-Bessel series. As the proper LSH value the user should select the value above which the approximation defects no longer significantly decrease. In the standard method one uses an approximation defect defined as the ratio of the sum square of the measured ordinate deviations from the calculated ordinates in the control cross sections to the sum square of the ordinates measured in the control cross sections. In the statistical method the approximation defect is an approximation error variance defined in the monograph by A. Ralston (1971).

The user can select from three methods of calculating the derivatives of functions in the nodes, mainly the method of Fourier series differentiation, the finite difference method with the five-point scheme and the finite difference method with the three-point scheme.

The calculation results can be saved to a file with a name given by the user as "Results table I" in which values m_i and n_i calculated from formulas (5) are stored and as "Results table II" which for j uniformly distributed cross sections (j – a number selected by the user, lower than 362) stores values $m(s)$ and $n(s)$ determined by the trigonometric interpolation method together with values $m(s)$, $n(s)$ and $t(s)$ determined (depending on the user's needs) by the trigonometric approximation or interpolation method and values $p(s)$ and $q(s)$ determined by the trigonometric approximation method or the trigonometric interpolation method.

A detailed description of the programs can be found in Korusiewicz (2012).

4.3 *Numerical calculation.*

The following case was used to calculation. For the structure shown in Figure 3 the following parameters values were adopted:

- area of the cross section A_f = 8,867 mm^2/mm per width unit,
- moment of inertia of the cross section I_f =21897, 45 mm^4/mm per width unit,
- length of arc AB = 25054 mm,
- number of strain gauge pairs lpt = 13,
- Young modulus E =205000 N/mm^2,
- membrane stiffness D_φ =1817735 N/mm,
- flexural rigidity K_φ = 4488977250 Nmm^2/mm,
- distance g_D =73,5 mm,
- distance g_G = −66,5 mm,
- radius r$_I$ = 3430 mm,
- radius r$_{II}$ = 13930 mm.

The results of the computations performed by program "Tunel2" (the interpolation method, the derivatives calculated by the finite difference method with the five-point scheme) are shown in Figure 7 and 8. Interpolation method was used to compute the quantities.

5 SUMMARY

The main goal of this paper was to present the results of field measurements of a super-span low-profile metal arch culvert in a twin-arch configuration and to describe the software based on the finite difference method. The tested culvert is one of the largest in Europe.

Strains (stresses) in 13 points on the steel plates were measured in the course of backfilling. The measured strain implied the maximum absolute axial stress of 295 MPa for the final backfill level on the side of the arch. The maximum absolute bending stress for the final backfill level amounted to 121 MPa. The distributions of bending and axial stress at this stage were asymmetrical.

The computer software for calculating the internal bending moments and normal and shearing forces in corrugated culverts was presented. The basic input data include the material and geometrical characteristics of the tested culvert and the circumferential stresses calculated on the basis of the measured strains. The results of computations performed by the software for a theoretical case are presented in Korusiewicz

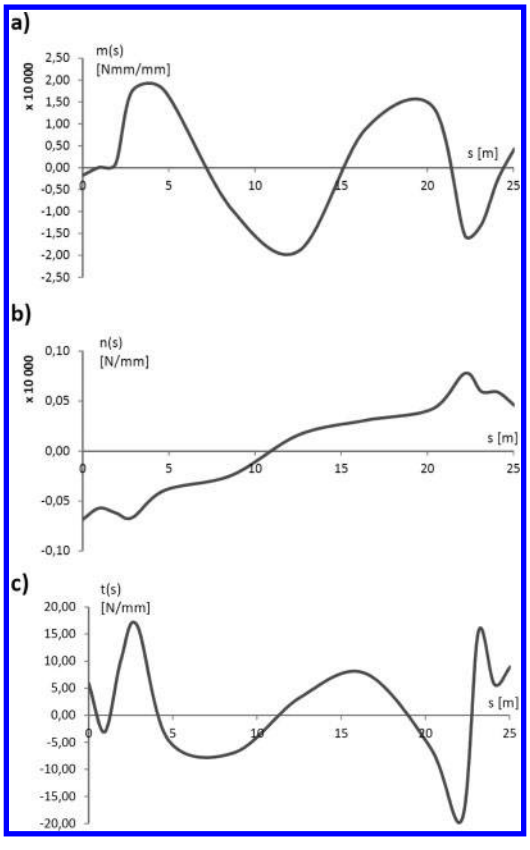


Figure 7. Internal forces distribution for crown backfill level (6.27 m): (a) the bending moment, (b) the normal force and (c) the shearing force in the cross section of the lining per cross sectional unit width.

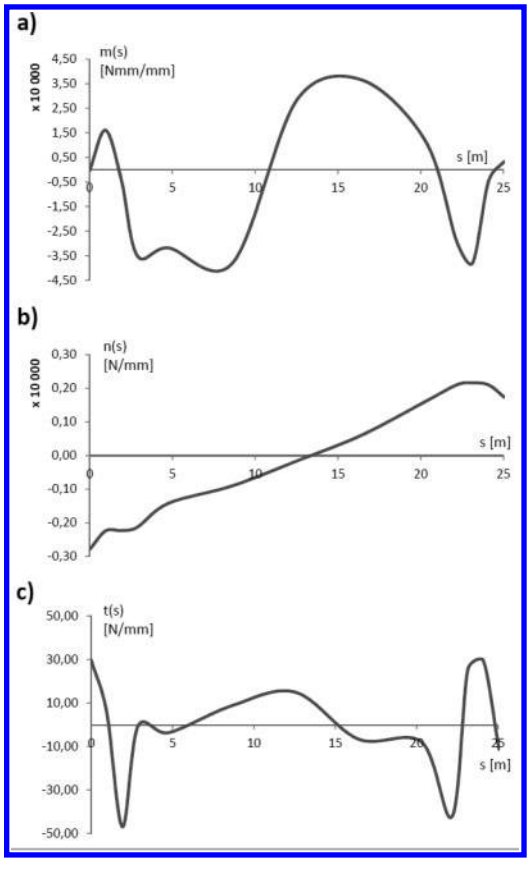


Figure 8. Internal forces distribution for final backfill level (8.31 m): (a) the bending moment, (b) the normal force and (c) the shearing force in the cross section of the lining per cross sectional unit width.

(2012) and a comparison of results shows that the theoretical and the ones computed are in very good agreement. Present paper shows the results of computations performed by the software for an experimental case.

According to the graph (Figure 7a and 8a) bending moments are changing in the range of −19100 to 17600 Nmm/mm for crown backfill level and from −38000 to 36600 Nmm/mm for final backfill level. The distributions of bending moments at both stages were asymmetrical and fluctuated.

The distributions of axial forces (Figure 7b and 8b) are changing in the range of −690 to 780 N/mm for crown backfill level and from −2800 to 2160 N/mm for final backfill level. Reasonably uniform axial forces change is observed.

Distribution of shear forces (Figure 7c) at the crown backfill level is asymmetric and it changes in the range of −19 to 17 N/mm, in contrast to final backfill level, where the distribution is more symmetrical and changed in the range of −47 to 30 N/mm (Figure 8c). The shear forces are not significant in comparison to other internal forces.

6 ACKNOWLEDGEMENT

The tests reported in this paper were supported by funding from The European Community under a Marie Curie European Reintegration Grants: Super-span soil-steel bridge (animal crossing) – backfill and long-term monitoring (EC Contract no: PERG03-GA-2008-230913).

REFERENCES

Flener, E.B. & Karoumi, R. 2009. Dynamic testing of a soil-steel composite railway bridge. *Engineering Structures* 31(12): 2803–2811.

Janusz, L. & Madaj, A. 2007. *Civil engineering structures made from corrugated plates*. Warsaw: WKL (in Polish).

Korusiewicz, L. 2012. Computer software for calculating internal and external forces in corrugated culverts on the basis of measured strains. *Archives of Institute of Civil Engineering* 12: 109–116.

Korusiewicz, L. & Kunecki, B. 2011. Behaviour of the steel box-type culvert during backfilling. *Archives of Civil and Mechanical Engineering*, XI (3): 637–650.

Korusiewicz, L. & Kunecki, B. 2012. Field test of a large-span soil-steel arch without stiffeners during backfilling operations. *Archives of Institute of Civil Engineering* 12: 133–139.

Kunecki, B. & Korusiewicz, L. 2007 Laboratory test of a full-scale soil-steel box-type culvert under road loads. *New horizons and better practices, Long Beach, California, Proceedings of the ASCE Structures Congress, 16–19 May 2007*.

Kunecki, B. & Korusiewicz, L. 2010. Field test of super-span metal twin arches during backfilling. *TRB 89th Annual Meeting, Washington D.C., 10–14 January 2010*, Paper No. 10-1467.

Kunecki, B. & Korusiewicz, L. 2013. Fidel tests of large-span metal arch culvert during backfilling. *Roads and Bridges* (in press).

Machelski, Cz. 2008. *Modelling of soil-shell bridge structures*. Wroclaw: DWE (in Polish).

Ralston A. 1971. *An introduction to numerical analysis*. Warsaw: PWN (in Polish).

Vaslestad, J. 1994. Long-term behaviour of flexible large-span culverts. *Publication No.74*: 38–56. Oslo: Norwegian Public Roads Administration.

Yeau, K.Y., Sezen, H., Fox, P.J. 2009. Load performance of in situ corrugated steel highway culverts. *Journal of Performance of Constructed Facilities* 23(1): 32–39.

Research and Applications in Structural Engineering, Mechanics and Computation – Zingoni (Ed.)
© 2013 Taylor & Francis Group, London, ISBN 978-1-138-00061-2

Alternative shape of suction caisson to reduce risk of buckling under high pressure

S. Madsen, L.V. Andersen & L.B. Ibsen
Department of Civil Engineering, Aalborg University, Denmark

ABSTRACT: Using large suction caissons for offshore wind turbines is an upcoming technology also referred to as bucket foundations. During operation the bucket foundation is loaded by a large overturning moment from the wind turbine and the wave loads. However, during installation the bucket is loaded by uniform external pressure and vertical forces. The bucket foundation does not require heavy installation equipment, but since it is constructed as a thin steel shell structure, instability, in the form of buckling, becomes a crucial issue during installation. Typically, the bucket foundation is a large cylindrical monopod foundation made of steel. In this paper, an alternative design/shape of the suction caisson, having a smaller risk of buckling under high pressure is presented. The risk of structural buckling is addressed using numerical methods to determine the buckling pressures of the re-designed bucket foundation during installation. Further, the effect of the lateral restraint offered by the surrounding soil on the buckling pressures is analysed. It is found that the new design enables a significantly larger buckling load compared to the traditional design.

1 INTRODUCTION

The expenses related to the foundations of an offshore wind farm constitute about one third of the total cost. For wind turbines located on deeper waters, the cost of the foundations might be even higher. Thus, a new technology is needed to reduce the total cost of offshore wind turbines. This technology could be the bucket foundation. The first part of the seabed penetration is caused by self-weight. Secondly, suction is applied inside the bucket chamber. The suction creates a differential pressure across the bucket lid as shown in Figure 1, effectively increasing the downward force on the bucket while the water flow reduces the skirt tip resistance. As a result, this foundation does not require heavy installation equipment.

In deeper waters, the diameter of the bucket must be increased in order to accommodate the larger forces on the foundation. This leads to a larger aspect ratio between the skirt diameter and the wall thickness. Thus, instability in the form of buckling becomes a vital issue during installation.

A crucial buckling incident occurred in Wilhelmshaven, Germany, in 2005 (Bakmar 2009). To support a large offshore wind turbine, a bucket foundation was to be installed by both suction and skirt tip injection. The bucket had a skirt length of 15 m and a diameter of 16 m. However, as the skirt had penetrated 6.8 m into the soil, the bucket foundation buckled. Consequently, the installation failed completely.

By use of the commercial finite element package ABAQUS (Dassault Systèmes Simulia Corp. 2011), the authors have introduced a three-dimensional, nonlinear, finite element analysis including the "real" structure of the bucket lid. The soil is considered linear elastic. Previous work by the authors has shown that introducing an imperfect geometry based on the first linear buckling mode shape can increase the nonlinear buckling load significantly, if a sufficiently large scaling of the mode shape is introduced (Madsen, Andersen, & Ibsen 2011).

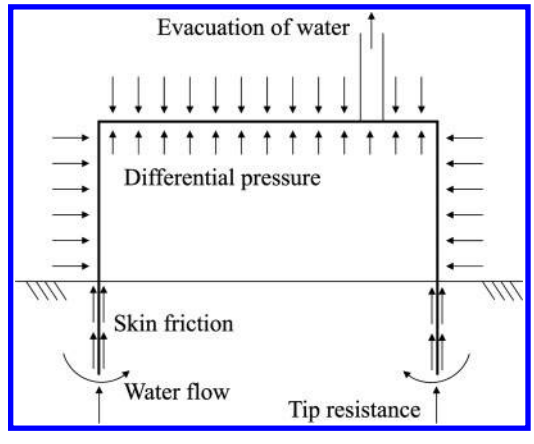


Figure 1. Principle sketch of the downward pressure on lid and skirt due to suction.

Instead of increasing the wall thickness to decrease the risk of buckling, an alternative cross section is presented in Figure 2. The cross section is denoted "multi-shell", since it is constructed of several shell panels with a radius smaller than the overall radius. The shell panels are joint together at the flanges of HEM profiles.

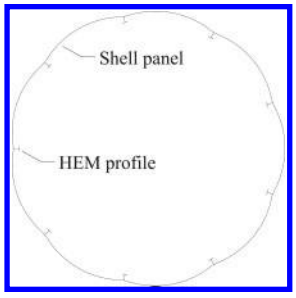


Figure 2. Cross section of the multishell.

During installation, the bucket skirt becomes partly embedded, and the degree of skirt fixation increases due to the lateral restraint offered by the surrounding soil. The lateral restraints provided by the soil to the embedded skirt may increase the buckling loads significantly. In the initial installation phase, the free height of the skirt above the seabed is large and a low suction pressure is needed. For subsequent installation phases, a larger pressure is required. Thus, a critical embedded depth, leading to the minimum difference between the required suction and the buckling load, can be identified.

2 METHODS OF ANALYSIS

Two kinds of boundary conditions are considered. In Section 3, the "classical" boundary condition S3 is used. The end displacements are axially free but circumferentially restrained in-plane (zero tangential deflection). This makes the ends free to warp. In Section 4, the surrounding soil and the "real" structure of the bucket lid is included.

2.1 *Geometry*

The multi-shell considered in this paper has 9 shells of radius 5 m joint together in HEM 300 profiles. The reference diameter is 15 m leading to a maximum diameter of 15.4 m. A cross section of the multi-shell is shown in Figure 4.

The bucket lid is made of a 50 mm steel plate and 9 stiffening ribs with flanges, as shown in Figure 4.

2.2 *Matrial Properties*

The bucket foundation consists of steel with a Young's modulus of $E = 210$ GPa, a Poisson's ratio of $\nu = 0.3$, and an initial yield stress of $\sigma_{y0} = 355$ MPa. The elastic properties of the surrounding soil are defined by Young's modulus $E = 25 \cdot 10^6$ Pa and Poisson's ratio $\nu = 0.25$.

2.3 *Numerical buckling analysis*

The steel is modelled as a linear elastic-perfect plastic material with yielding defined by the von Mises yield criterion. For S3 boundary conditions, the multi-shell

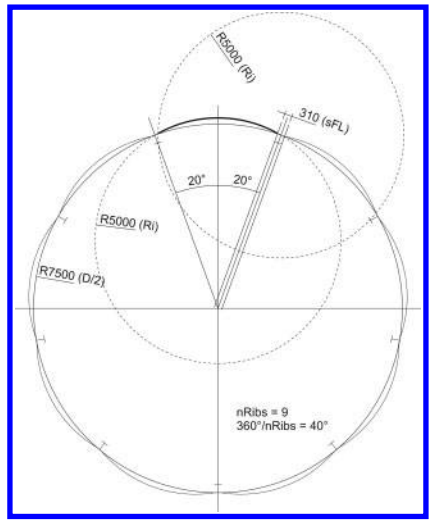


Figure 3. Cross section of the multishell.

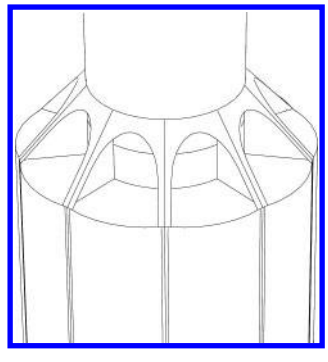


Figure 4. Geometry of the multi-shell bucket lid structure.

is modelled using 8-noded quadrilateral shell elements with quadratic interpolation and reduced integration (S8R).

When the surrounding soil is included the multi-shell bucket foundation is modelled using 4-noded quadrilateral shell elements with linear interpolation and reduced integration (S4R). The surrounding soil is modelled using 8-noded solid elements with linear spatial interpolation and reduced integration . The shell elements of the bucket are coupled to the solid elements of the soil by tie constraints which fuse together the surfaces of two regions even though they have dissimilar meshes and different degrees of freedom.

The numerical buckling analysis is made in two steps. Step one is a linear eigenvalue buckling analysis used to find an estimate of the initial imperfect geometry based on buckling mode shapes (eigenvectors). Also found in step one is a linear prediction of the buckling load (eigenvalue). Step two is a nonlinear analysis where an imperfection in the geometry is introduced by adding the buckling mode shapes determined in step one to the "perfect" geometry.

The linear eigenvalue problem solved is given by

$$\left(K_0^{NM} + \lambda_i K_\Delta^{NM}\right) v_i^M = 0, \tag{1}$$

where K_0^{NM} is the stiffness matrix to the base state including the effects of the preloads P^N, K_Δ^{NM} is the differential initial stress and load stiffness matrix due to the incremental loading pattern Q^N, λ_i are the eigenvalues, v_i^M are the buckling mode shapes, M and N are the degrees of freedom for the whole model. The Lanczos Eigensolver is used to extract the eigenvalues in this analysis.

Since the multi-shell is not a convex structure, as is the case for a circular cylinder, negative eigenvalues can emerge indicating internal pressure. Since external pressure is of interest, only positive eigenvalues are considered. Thus, in this paper, mode 1 refers to the first mode with a positive eigenvalue.

The buckling mode shape from the eigenvalue buckling analysis is introduced as an imperfect geometry. The imperfection has the form

$$\Delta x_i = \sum_{i=1}^{M} w_i \psi_i, \tag{2}$$

where ψ_i is the i^{th} mode shape (nodal displacements normalised to 1) and w_i is the imperfection scale factor, given by

$$w_i = \frac{u_{imp,i}}{U_{max,i}} = \alpha, \tag{3}$$

where $u_{imp,i}$ is the magnitude of the imperfection, and $U_{max,i}$ is the maximum deflection of the i^{th} linear buckling mode. Note that $U_{max,i} \geq 1$ since the nodal displacements of the mode shape are normalised to 1.

When the surrounding soil is included, the buckling mode shape corresponding to a certain penetration depth is introduced as an imperfection for each penetration depth. So, the imperfect geometry is different for each penetration depth.

A uniformly distributed pressure is applied incrementally, and the buckling load is determined as the load level where no further strain energy can be accumulated. Yielding is allowed.

Both the *Static, General* method, which uses the *Newton Rapson* solver, and the *Static, Riks* method, which uses an *arc-length* solver, are tested for comparison. The solutions from both solvers are found to be convergent. The *Static, General* method is used to find the nonlinear buckling load since this method enables automation of the numerical simulations more easily.

2.4 *Analytical solution to the buckling load of a circular cylinder*

The von Mises equation for the critical elastic pressure for a cylindrical shell subjected to uniform external lateral pressure (Windenburg & Trilling 1934, Eq. 2

$$p_c = 2E\frac{t}{D}\left(\frac{(t/D)^2}{3(1-\nu^2)}\left[n^2 - 1 + \frac{\lambda^2(2n^2-1-\nu)}{n^2+\lambda^2}\right] + \frac{\lambda^4}{(n^2-1)(n^2+\lambda^2)^2}\right) \tag{4}$$

where n is the number of circumferential lobes formed at collapse, and $\lambda = (\pi D)/(2L)$.

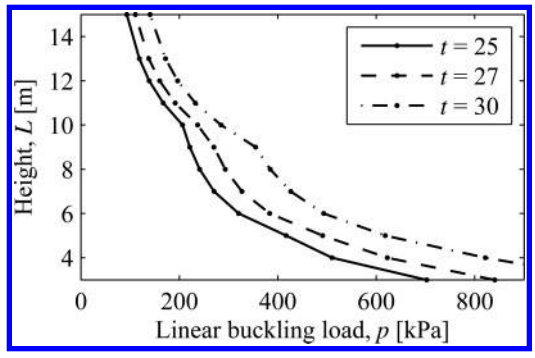


Figure 5. Buckling load versus skirt height at three different skirt thicknesses.

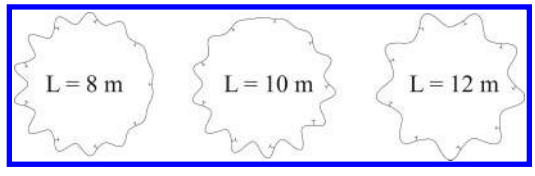


Figure 6. Cross section of buckling mode shape 1 for three different skirt he

ights. Wall thickness $t = 25$ mm.

3 LATERALLY LOADED MULTI-SHELL WITH S3 BOUNDARY CONDITIONS

In this section, the "classical" boundary condition S3 is used, and the shell is loaded by uniformly distributed lateral pressure.

3.1 *Linear bifurcation analysis*

In this section, the results of the linear bifurcation analysis are presented. In Figure 5, the linear buckling pressure is shown as function of the skirt height for three different skirt thicknesses.

From Figure 5 it seems that the linear buckling load follows one expression for skirt lengths lower than 10 m (9 m for $t = 30$ mm) and another expression for skirt lengths longer than 10 m (9 m for $t = 30$ mm). In Figure 6 the first buckling mode shape is shown for $L = 8$ m, $L = 10$ m and $L = 12$ m.

Apparently the circumferential lobes of the first mode shape for skirt lengths longer than 10 m are

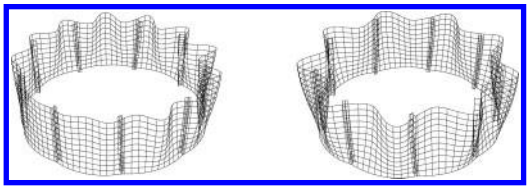


Figure 7. Buckling mode shape 1. Only half the model is shown. Left: $L = 10$ m. Right: $L = 11$ m. Wall thickness $t = 25$ mm.

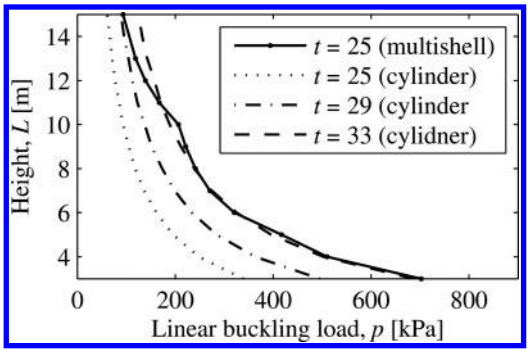


Figure 8. Buckling load as a function of the skirt length for both multi-shell and circular cylinder.

periodic, indicating overall global buckling. On the contrary, the opposite is the case for skirt lengths shorter than 10 m where mode one indicates a more localized failure mode.

In Figure 7 an isometric view of the first buckling mode shape is shown for $L = 10$ m and $L = 11$ m. From both Figures 6 and 7 it is clear that the HEM profiles warp.

3.2 *Equivalent circular cylinder*

A multi-shell cross section with 9 shells, HEM 300 columns, and of dimensions $D = 15$ m, $Ri = 5$ m, $t = 25$ mm has a cross-sectional area of 1.40 m^2 and a surface length of 107.1 m. The maximum diameter is 15.4 m. A circular cylinder of diameter 15.4 m and wall thickness of 29 mm also has a cross-sectional area of 1.40 m^2. In Figure 8 the buckling load is shown as a function of the skirt length for a multi-shell with a wall thickness of 25 mm and for cylinders of various wall thicknesses. The buckling loads for the cylindrical cross section are calculated using Eq. (4).

From Figure 8 it appears that the buckling load of a multi-shell of thickness $t = 25$ mm is equivalent to the buckling load of a circular cylinder of thickness $t = 33$ mm as long as the length is shorter than 10 m. For shells longer than 10 m, it seems that the buckling load for the multi-shell goes asymptotically towards that of a circular cylinder of thickness $t = 29$ mm.

3.3 *Nonlinear analysis with imperfect geometry*

In Figure 9 the nonlinear buckling load is plotted as a function of the imperfection amplitude for a

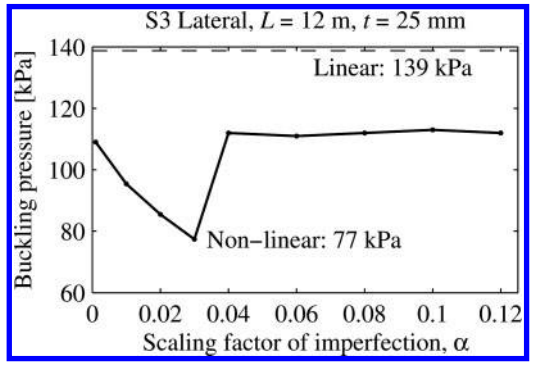


Figure 9. Nonlinear buckling load as a function of imperfection size. Skirt height $L = 12$ m.

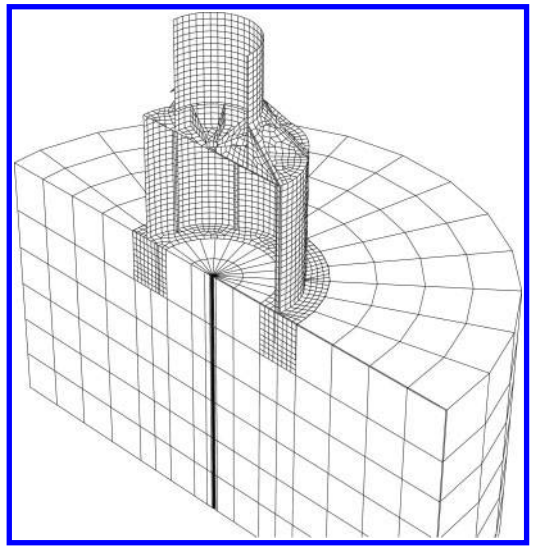


Figure 10. Mesh of multi-shell bucket and surrounding soil. Only half the model is shown.

skirt length of 12 m. Even for very small imperfection amplitudes, the nonlinear buckling load is significantly lower than the linear bifurcation load.

For $L = 12$ the nonlinear buckling load for an imperfection amplitude of 0.001 is 78.5% lower than the linear bifurcation load.

4 SOIL AND LID STRUCTURE BOUNDARY CONDITION

In this section, the "real" structure of the bucket lid is included. Also considered is the surrounding soil. For the soil, "interface elements" are added. The interface elements have similar element size as the bucket skirt. The interface soil elements are extended 2 m below the skirt tip. The mesh of the multi-shell bucket and the surrounding soil is shown in Figure 10.

A bucket with skirt height $L = 15$ m is considered. Penetration depths of $h = 3, 6, 9$ and 12 m are analysed.

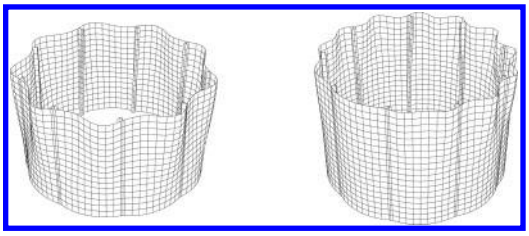


Figure 11. Linear bifurcation mode shape 1. $L = 15$, Soil stiffness is 25 MPa. Soil is omitted and the cylinder is cut at half the free height. Left: $h = 6$ m. Right: $h = 3$ m.

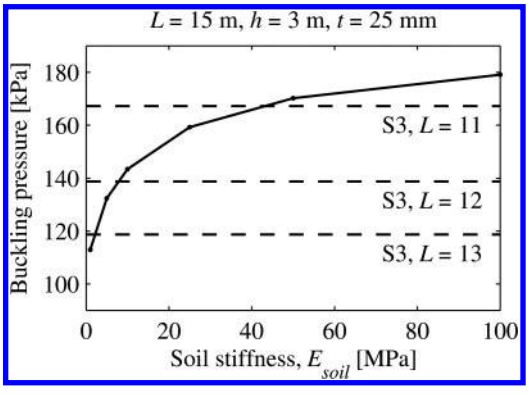


Figure 12. Linear bifurcation load as function of soil stiffness. Skirt height is 15 m and penetration depth is 3 m, i.e. the free height is 12 m.

4.1 *Linear bifurcation analysis*

From Figure 11 it is evident that the penetrated part of the HEM profiles is prevented from warping. Further, in Figure 11 it can be observed that the first buckling mode shape is periodic and symmetric for $h = 3$ m by contrast to the first buckling mode shape for $h = 6$ which is asymmetric. Buckling mode shapes for $h = 9$ and 12 are not shown here, but the first mode shape for $h = 9$ is asymmetric by contrast to the first mode shape for $h = 12$ which is symmetric.

In Figures 12 and 13, the linear bifurcation load is shown as a function of the soil stiffness for penetration depths of 3 and 6 m.

From Figure 12 it can be observed that the multi-shell surrounded by a soil with stiffness as low as 8 MPa corresponds to a pinned-pinned (S3) multi-shell of length equal to the free heigth (12 m).

From Figure 13 it seems that the multi-shell surrounded by soil with a stiffness as low as 5 MPa corresponds to a pinned-pinned (S3) multi-shell of length equal to the free heigth (9 m).

4.2 *Nonlinear analysis with geometric imperfections*

In Figures 14–17 the nonlinear buckling load is shown as a function of the imperfection amplitude.

From Figures 14–17 it is seen that the critical imperfection amplitude varies with the penetration depth. Also, there is a similar tendency of the imperfection

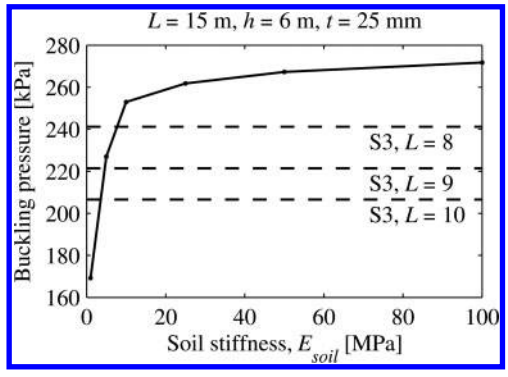


Figure 13. Linear bifurcation load as function of soil stiffness. Skirt height is 15 m and penetration depth is 6 m, i.e. the free height is 9 m.

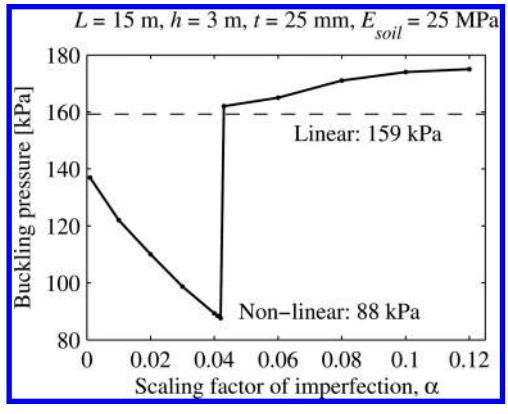


Figure 14. Critical buckling load as a function of imperfection size. Skirt height is 15 m and penetration depth is 3 m, i.e. the free height is 12 m.

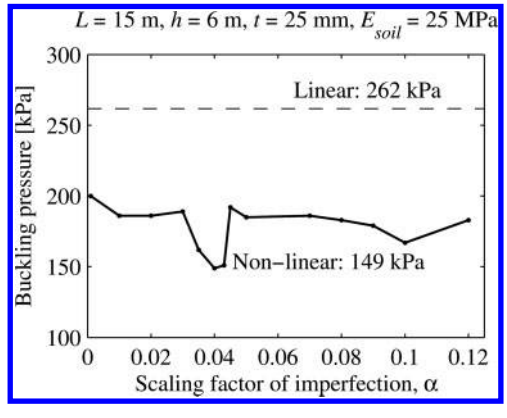


Figure 15. Critical buckling load as a function of imperfection size. Skirt height is 15 m and penetration depth is 6 m, i.e. the free height is 9 m.

sensitivity for the symmetric buckling mode shapes ($h = 3$ and $h = 12$). That is, for "small" imperfection amplitudes the buckling load is reduced significantly and a critical imperfection amplitude gives the lowest

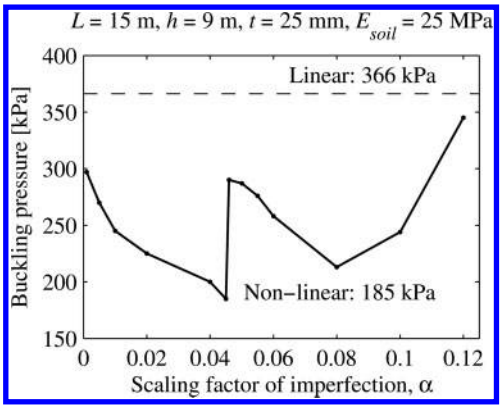


Figure 16. Critical buckling load as a function of imperfection size. Skirt height is 15 m and penetration depth is 9 m, i.e. the free height is 6 m.

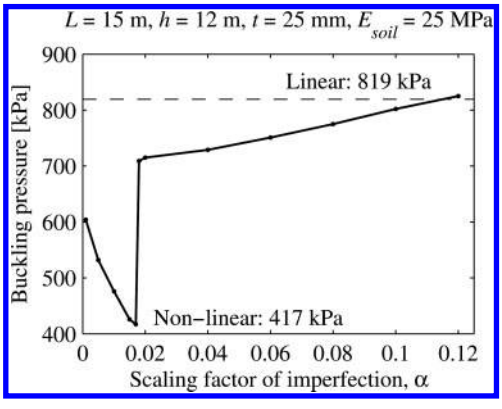


Figure 17. Critical buckling load as a function of imperfection size. Skirt height is 15 m and penetration depth is 12 m, i.e. the free height is 3 m.

buckling load. But, as the size of imperfections is increased above this critical value, the introduced imperfections act as stiffeners raising the nonlinear buckling load even beyond the linear bifurcation load.

In Figure 18 the linear bifurcation load as well as the nonlinear buckling load are shown as function of the penetration depth. These curves are to be compared with the suction required to penetrate the bucket. The penetration resistance of the bucket is the sum of the skin resistance and end resistance as shown in Figure 1.

5 CONCLUSIONS

This paper has introduced an alternative cross section to the bucket foundation called "multi-shell". The linear bifurcation load as well as the nonlinear buckling pressure has been found for both S3 boundary conditions and more realistic boundary conditions, taking into account the bucket lid and the lateral restraint from the surrounding soil. The buckling load of the multi-shell has been found to be significantly larger than

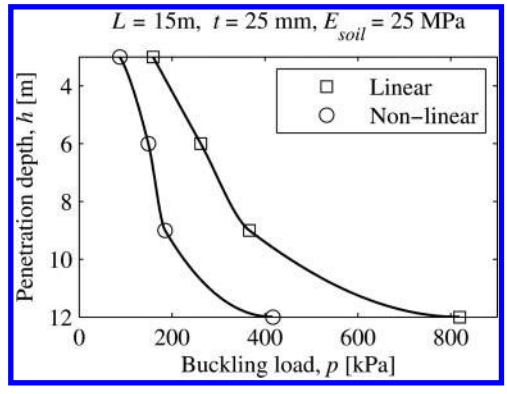


Figure 18. Buckling load as a function of penetration depth. Skirt height is 15 m. Both linear bifurcation load and nonlinear buckling load is shown.

that of a traditional circular cylindrical cross section with similar cross-sectional area. In terms of material consumption, it therefore provides a cost-effective alternative to a circular bucket foundation.

5.1 *Future research*

Instead of introducing the lowest linear buckling mode shape as the initial geometric imperfection for the nonlinear buckling analysis, several imperfect geometries could be considered to reveal the most critical mode shape if not the first. Also, an initial imperfect geometry obtained by combining two or more buckling modes could be considered if a single mode shape does not provide the worst case.

ACKNOWLEDGEMENTS

The work presented is funded by the Danish Advanced Technology Foundation project "Cost-effective deep water foundations for large offshore wind turbines".

REFERENCES

Bakmar, C. L. (2009). *Design of Offshore Wind Turbine Support Structures: Selected topics in the field of geotechnical engineering.* DCE Thesis. Aalborg University. Department of Civil Engineering.

Dassault Systèmes Simulia Corp. (2011). *Abaqus 6.11 Analysis User's Manual.* Providence, RI, USA: Dassault Systèemes Simulia Corp.

Galambos, T. V. (1998). *Guide to Stability Design Criteria for Metal Structures 5th ed.* New York: Wiley.

Madsen, S., L. Andersen, & L. B. Ibsen (2011). Buckling analysis of bucket foundations for wind turbines in deep water. In B. Topping and Y. Tsompanakis (Eds.), *Proceedings of the Thirteenth International Conference on Civil, Structural and Environmental Engineering Computating*, Civil-Comp Proceedings. Civil-Comp Press.

Windenburg, D. F. & C. Trilling (1934). Collapse by instability of thin cylindrical shells under external pressure. *Trans. ASME* 56, 819.

Research and Applications in Structural Engineering, Mechanics and Computation – Zingoni (Ed.)
© 2013 Taylor & Francis Group, London, ISBN 978-1-138-00061-2

Qualitative and quantitative assessment of liquefaction in a saturated road embankment

A. Borowiec
Cracow University of Technology, Cracow, Poland

K. Maciejewski
Kielce University of Technology, Kielce, Poland

ABSTRACT: The paper deals with the liquefaction susceptibility of a saturated cohesionless soil subjected to dynamic loading. The analyzed soil structure is a road embankment built across a shallow water reservoir. Two cases of dynamic loading are examined: cyclic point loading (induced by a vibratory roller working on the top of the embankment) and an earthquake. In order to asses the liquefaction phenomenon, a Factor of Safety is introduced as a ratio of yield shear strength and shear stress in the soil.

1 INTRODUCTION

Liquefaction is a phenomenon most frequently observed in medium and fine grained saturated cohesionless soils subjected to dynamic loading. Due to rapid cyclic straining, the free drainage can not occur and the gravity loadings are transferred from the soil skeleton to the pore water. As a result, an increase of pore pressure is observed along with the reduction of shear strength and the capacity of the soil to sustain loading.

Liquefaction may lead to uneven and significant settlements of buildings, failures of soil structures such as road embankments and dams, landslides and other hazardous phenomena. In that context, there is still a lack of its quick and simple assessment in geotechnical practice.

2 CASE STUDY

The literature mentions a case of a failure of an road embankment across the Ackerman Lake induced by six Vibroseis vehicles conducting a geophysical survey (Jeffries). A Vibroseis is used to excite the ground via a vibrating metal plate moved by an eccentric weight. As the trucks were spread out over 74 m along embankment, they were set to operate in phase for 8 seconds. The excitation frequency changed linearly from 8 to 58 Hz to give a sum of 264 cycles. Soon after the equipment was activated the saturated soil liquefied sinking five trucks. The failure was rapid enough to cause 4.5 m wave on the waters of Ackerman Lake.

In the paper a similar case is examined. A road embankment built across a shallow water reservoir is analyzed in terms of susceptibility to liquefaction.

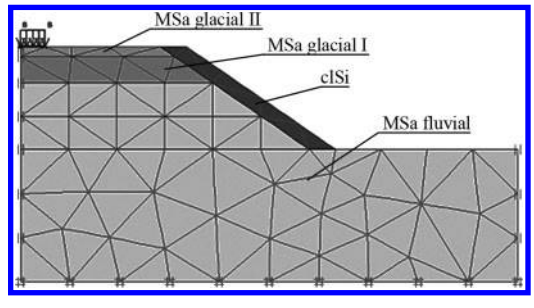


Figure 1. Model geometry and finite element mesh.

Two types of dynamic loadings are considered: first corresponding to an operation of a vibratory roller and second to an earthquake.

2.1 *Geometry*

The embankment is three meter high above the reservoirs bed with a ten meter wide crest. The structure has a slope of 1.5H : 1V with a approx. 0.8 m facing of clayey soil. The embankments core is mainly made of fluvial medium density, medium - grained sands topped by two layers of glacial dense sands (see Figure 1). The surface of water is set to 1 m and 2 m above the reservoir bottom giving the Water Table Level (WTL) at 5 m and 6 m respectively.

2.2 *FEM model in Plaxis 2D*

The 15-node Finite Elements are used to generate the mesh. Average element size less then 1.0 m is sufficient for this dynamic problem. To prevent the reflection and refraction of propagating waves, viscous boundary is introduced.

Table 1. Soil properties.

Soil	MSa fluvial	MSa glacial I	MSa glacial II	clSi	Units
Soil model	HS	HS	HS	M-C	-
D_r	0.6	0.7	0.8	-	-
γ	16	17	18	16	kN/m^3
γ'	18	19.5	20	20	kN/m^3
c	0.1	0.1	0.1	5	kPa
φ	35°	37°	40°	24°	-
ψ	5°	7°	10°	-	-
ν	0.2	0.2	0.2	0.35	-
m	0.5	0.5	0.5	-	-
E	-	-	-	2000	kPa
E_{50}^{ref}	35,000	40,000	45,000	-	kPa
E_{oed}^{ref}	35,000	40,000	45,000	-	kPa
E_{ur}^{ref}	10,500	12,000	13,500	-	kPa

The full geometry is used for modeling soil behavior during earthquake while for cyclic point load only a half of the embankment is considered. Thus both Plane Strain and Axisymmetry are employ.

2.3 *Materials*

The plastic behavior of the cohesionless soils is modeled by means of Hardening Soil constitutive relationship, implemented in Plaxis software. Soil parameters are accordingly modified but based on those found in the literatures (Tiznado). Material properties along with the model parameters, for each layer are specified in the Table 1.

2.4 *Types of loading*

In the first case a cyclic load simulating an operation of vibratory roller is introduced. The load positioned at the center of the embankments crest interacts with the soil through a stiff plate element 1.5 m wide. The loading itself has two components: static with a magnitude of 119 kN/m and harmonic with an amplitude of 350 kN/m and frequency of 55 Hz.

The second case of load is an earthquake excitation of magnitude 5.4 on the Open-Ended Richter Scale. Epicentral distance is 5.0 km and peak acceleration 240 cm/s^2. In Plaxis 2D, like in most FEM programs, earthquake is modeled by imposing prescribed displacements at the bottom boundary, here calculated from accelerogram.

3 FACTOR OF SAFETY CALCULATION

Simple and practical approach is to define a factor of safety against triggering of liquefaction as:

$$FS_{Triggering} = \frac{s_u(yield)}{\tau_{driving} + \tau_{dynamic} + \tau_{other}} \quad (1)$$

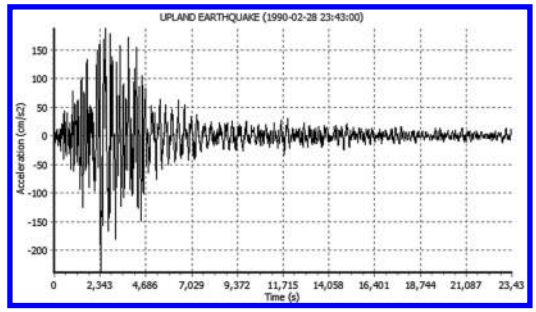


Figure 2. Earthquake accelerogram.

where $s_u(yield)$ = undrained yield shear strength; $\tau_{driving}$ = static shear stress; $\tau_{dynamic}$ = shear stresses caused by dynamic loading; τ_{other} = other shear stresses.

The undrained yield shear strength can be derived from the yield strength ratio expressed as:

$$\frac{s_u(yield)}{\sigma'_{v0}} = \tan\phi_y \quad (2)$$

where σ'_{v0} = vertical or normal effective stress; φ_y = mobilized yield friction angle.

Based on the field test regarding relationship between SPT blowcounts and CPT tip resistance and the yield strength ratio, the mobilized yield friction angle of the analyzed soils (MSa fluvial) can be of $\varphi_y = 13°$ (Olson).It can also be determine with *phi-c* reduction procedure during numerical analysis.

Having normal effective stresses and rewriting Equation 2 it is possible to compute the yield shear strength:

$$s_u(yield) = \tan\phi_y \sigma'_{v0} \quad (3)$$

The $FS_{Triggering}$ is therefore dependent only on two unknown variables: shear stress and vertical effective stress. For the considered structure they are calculated using finite element method program, here Plaxis 2D.

Eventually the factor of safety against triggering liquefaction at point $P_{x,y}$ can be written as:

$$FS_{Triggering}(P_{x,y}) = \frac{\tan\phi_y \sigma'_{v0}(P_{x,y})}{\tau_{dynamic}(P_{x,y})} \quad (4)$$

where $\sigma'_{v0}(P_{x,y})$ = vertical effective stress at point $P_{x,y}$; $\tau_{dynamic}(P_{x,y})$ = sum of dynamic and static shear stresses at point $P_{x,y}$.

4 CRITICAL TIME DETERMINATION

As the stress tensor varies in time during dynamic excitation, the $FS_{Triggering}$ has to be calculate for some particular moment of time when liquefaction is most likely to occur. For the purposes of this paper it is

named a critical time and established for reference point in which the pore pressures where traced in time. The reference point is located in the one-third of the embankment height, close to its core. The critical time takes place when pore pressure reaches its peak value. In case of cyclic point load (vibratory roller) the critical time is established as 0.08 second.

Finding critical time for earthquake excitation is much more demanding, though. It is well known that liquefaction can occur not only during the earthquake but also after it finishes. In the modeled embankment pore pressure is building up at the beginning and reaches its peak value, for the first time in the 9th second of excitation. Then, after showing some drop, it grows again. In order to select proper critical time, factor of safety distribution was generated – in the way described in the following paragraph – for the 9th and the 24th second of excitation, i.e. when the first peak occurs and after the earthquake is finished.

5 RESULTS FOR CYCLIC LOAD

Factor of safety distribution inside embankment is generated on the base of vertical effective stress and sum of dynamic and static shear stresses. Both stresses are taken from cross sections put up along the embankment in 1.0 m spacing, at the critical time.

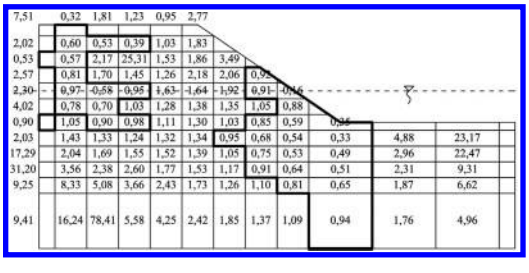


Figure 3. Factor of safety distribution inside embankment for cyclic load (WTL at 5 m).

The allocation of $FS_{Triggering}$ for cyclic load depending on water table is shown at Figure 3 and Figure 4. The liquefaction occurs when $FS_{Triggering}$ is lower than 1.0 and the areas susceptible to it are bold outlined.

In case of cyclic point loading regardless the water table level two regions of the embankment are especially exposed to liquefaction. As long as these two regions are separated the overall stability should be kept. Although very low values of $FS_{Triggering}$, at the foot of the slope indicate to the local stability loss which also can lead to total failure of the structure. Embankment sections lying straight below the dynamic loading are the second exposed to the risk of liquefying. Area prone to liquefaction observed on Figure 3 spreads above the free water surface due to suction in these glacial Medium Sands.

Map of those areas (created from slices of 1.0 m width around cross sections mentioned) with calculated $FS_{Triggering}$, gives qualitative and quantitative assessment of liquefaction in a saturated road embankment.

6 RESULTS FOR EARTHQUAKE EXCITATION

Analogical procedure is apply to asses liquefaction susceptibility of road embankment under earthquake excitation. Only the higher water table is considered as it is the most unfavorable.

Factors of Safety at 9th second do not indicate any possible liquefaction in any area so its distribution is not included in this paper. Figure 5 illustrates map of $FS_{Triggering}$ inside the structure at 24th second of earthquake excitation thus practically after it has finished. Despite short epicentral distance liquefaction do not penetrate into embankment core, influencing only the soil on the base of both slopes along with isolated local areas on the slope edges.

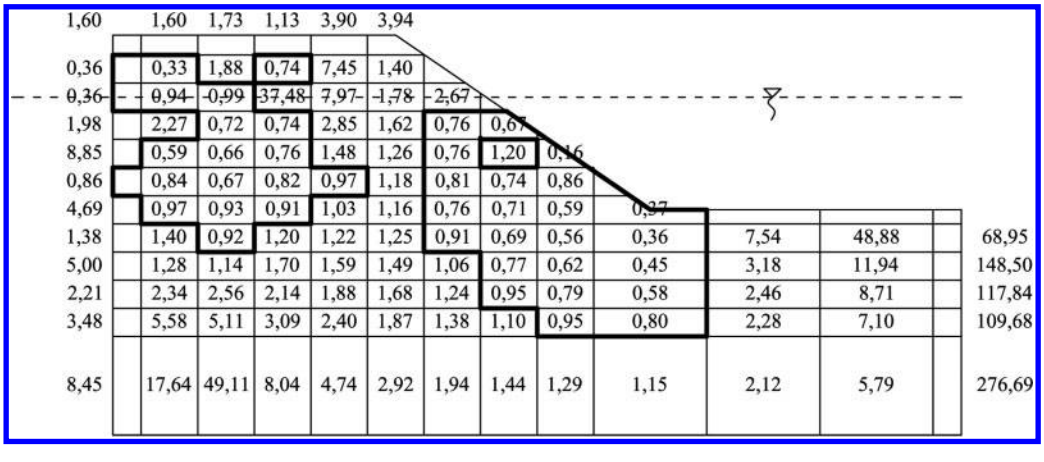


Figure 4. Factor of safety distribution inside embankment for cyclic load (WTL at 6 m).

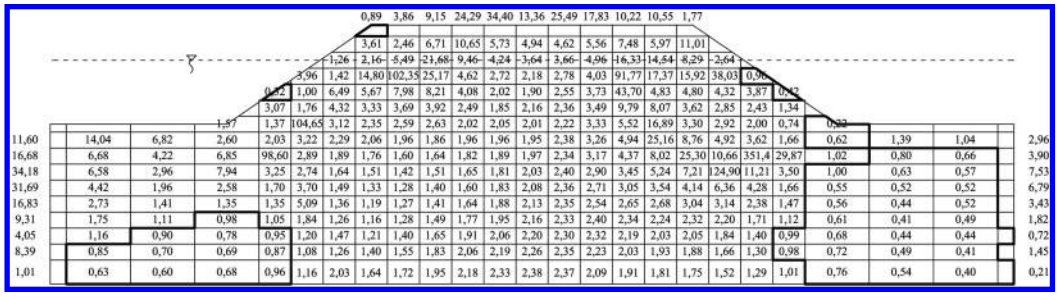


Figure 5. Factor of safety distribution inside embankment for earthquake excitation (WTL at 6 m).

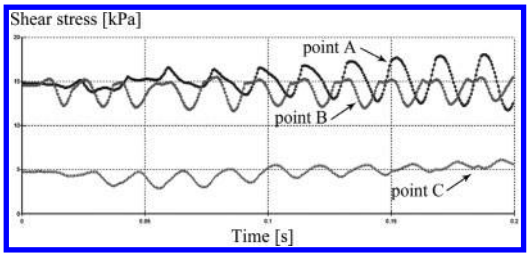


Figure 6. Shear stresses for cyclic loading in Plane Strain.

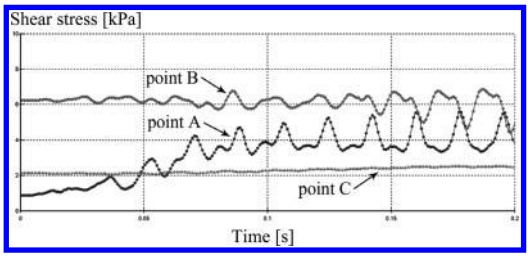


Figure 7. Shear stresses for cyclic loading in Axisymmetry.

7 PLANE STRAIN VERSUS AXISYMMETRY

In order to model properly wave propagation, as it is mentioned in the second paragraph, plane strain as well as axisymmetry is used.

Waves reflection and refraction is best illustrated by shear stress changes in time for points A, B and C. Those points are located at the bottom part of embankment in such way that propagating wave should reach them one by one starting from point A. But as it can be observed on Figure 6, representing Plane Strain, the negative phase displacement takes place.

Besides only in the Axisymmetry (see Figure 7) absorption is clearly visible and correctly modeled.

8 CONCLUSIONS

For the modeled structure, earthquake excitation appears not to be as dangerous as cyclic point load.

Method introduced in the paper presents an clear and easy way to locate and estimate liquefaction susceptibility of soil (not only in the road embankment). In that content it could be very helpful in geotechnical practice, as long as the stresses are obtained from program based on Biot's theory of dynamic consolidation.

REFERENCES

Borowiec, A. (2010) Numerical Analysis of Wave Propagation in Two-Phase Soil Medium. *Soil Dynamics and Earthquake Engineering. GeoShanghai International Conference 2010 Proceedings*: 252–262. ASCE

Das, B. M. 1993. *Principles of Soil Dynamics*. Pacific Grove: Brooks/Cole.

Jeffries, M. & Been, K. 2006. *Soil Liquefaction. A critical state approach*. Taylor & Francis.

Olson, S. M. & Stark, T. D. 2003. Yield Strength Ratio and Liquefaction Analysis of Slopes and Embankments. *Journal of Geotechnical and Geoenvironmental Engineering,* 129(8): 727–737. ASCE

Tiznado, J.C. & Rodriguez-Roa, F. 2011. Seismic lateral movement prediction for gravity retaining walls on granular soils. *Soil Dynamics and Earthquake Engineering*, 31: 391–400. Oxford: Elsevier.

Research and Applications in Structural Engineering, Mechanics and Computation – Zingoni (Ed.)
© 2013 Taylor & Francis Group, London, ISBN 978-1-138-00061-2

A study of frictional interface properties between typical South African sands and construction materials

Z. Bhengu, D. Kalumba & F.C. Chebet
Department of Civil Engineering, University of Cape Town, Cape Town, Western Cape, South Africa

ABSTRACT: Numerous approximations are used to determine the footing material-soil interface friction angle for the design of foundations. The approximations are generalised and very often result in inaccurate estimations for respective soil/foundation materials interactions. This study investigated the interface properties of two common South African sandy soils and three different foundational construction materials with a view of obtaining more representative values so as to provide a possible guide to the local industry. A direct shear apparatus was used to conduct the interface tests to obtain the angle of interface friction between the soils and the foundation materials. As expected, it was found that the type and the degree of roughness of a foundation material greatly influenced the interface frictional resistance, and so did the soil's particle size and grading. It was also found that the typical interfacefriction values used in design are conservative estimations of the actual values for respective sands.

1 INTRODUCTION

The interfacial interaction between construction materials and soil is fundamental for the stability of structural foundation systems. Determination of soil-foundation material interface properties is therefor eessential to ensure the reliability of structural foundations dependent on the frictional resistance of the construction material relative to the soil material. Soil in contact with a dissimilar solid material exerts frictional resistance known as the interface friction which changes with each foundation material type. The values of frictional resistance which consists of the angle of friction and the interface friction are used directly in equations relating to foundations and retaining structures. The angle of friction, φ, also referred to as inter particle friction, is the main source of a soil's strength providing soil with the ability to resist failure to due shear (Powrie, 2004). Celik *et al.* (2011) maintain that in order to make a good estimation of the axial capacity of a pile foundation, the angle of interface friction, δ, must be established. This angle can be determined by conducting experiments in a controlled laboratory environment, from field observations, or from the pile driving resistance (Ampera & Aydogmus, 2005).

In engineering design, the angle of interface friction has been approximated as a function of the angle of internal friction for different foundation materials (Meidema, 2012). It is often estimatedto be $2/3\varphi$ as applied in the Coulomb theory of lateral earth pressures. This study was therefore undertaken to determine the critical relationship between the angle of internal friction and the interface friction in order to validate and facilitate improvement of current estimations particularly with regard to typical South African sands, Klipheuwel and Cape Flats sand relative to selected foundation construction materials.

2 LITERATURE REVIEW

2.1 *Interface friction*

The magnitude of frictional resistance changes with the degree of roughness of the surface with which the soil is in contact; the value of friction for smoother surfaces being lower than for rougher surfaces. However, the angle of interface friction between various materials will vary depending on the soil's characteristics. It is common practice to express the angle of interface friction (δ) in terms of the angle of internal friction (φ). Some researchers express it as a ratio while others deduce empirical formulae with various additional parameters. Subba Rao *et al.*(1988) proposed a correlation between the ratio of the peak interface friction angle, the peak angle of internal friction of sand and the relative roughness shown in Equation 1 below:

$$\delta/\varphi = 1.0 - 0.8\exp(-1.5R^{0.54}) \quad (1)$$

Where R is the relative roughness defined by the ratio of the average roughness, Ra, to the weighted average particle size of the soil.

According to Al-Mhaidib (2006), the preceding equation yielded values close to the average values obtained from laboratory tests conducted hence proving it a reliable method to deduce the angle of interface friction.

Table 1. Table 1. Interface Friction Angles (Meidema, 2012)

Interface friction angle	Material	Source
$0.67\varphi - 0.83\varphi$	Piles	USACE
20°	Steel piles	NAVFAC*
		B. B. Broms
$3\varphi/4$	Concrete piles	B. B. Broms
$2\varphi/3$	Timber piles	B. B. Broms
$2\varphi/3$	Piles	M. R. Lindeburg
$2\varphi/3$	Concrete walls	Coulomb Theory

*Naval Facilities Engineering Command.

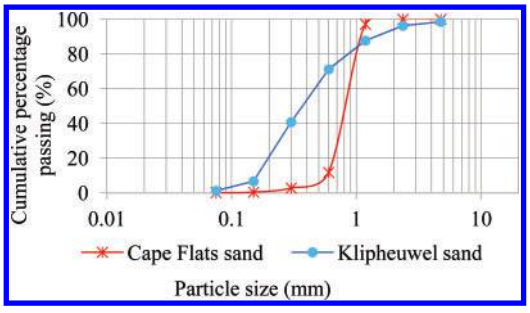


Figure 1. Particle distribution chart.

Table 1 provides a summary of the ratios of interface friction angle in terms of the internal friction angle, as determined by the respective researchers and engineering institutions. For some ratios, the soil types are not specified, thus disregarding the effect of particle size and grading. These ratios may not be accurate since it has been established that the angle of interface friction is a function of the particle size and distribution of a soil(Ampera and Aydogmus, 2005). The angle of interface friction is largely influenced by the relative roughness of the construction material which is also not specified.

3 RESEARCH MATERIALS AND METHOD

3.1 *Soil material*

Two soils were used in this research: Klipheuwel and Cape Flats sands. The Soils were cleaned and oven dried before the testing process commenced. The mechanical properties of each were determined using classification methods prescribed in the British Standards 1377:1990. The grading curves obtained from particle size distribution analysis of the soils is shown in Figure 1.

Cape flats sand is light grey quartz, uniformly graded coarse grained sand. The soil particles are predominantly of one particle size and therefore the sample is classified as poorly graded sand with little fines (SP). Klipheuwel sand is reddish brown quartz sand. It is poorly graded coarse grained soil. It is made up of a wider range of particle sizes with relatively more fines than Cape Flats sand. A summary of the soil mechanical properties are listed in Table 2.

Table 2. Soil mechanical properties of sands.

Properties	Cape Flats	Klipeuwel
Specific gravity	2.76	2.72
Optimum moisture content (%)	15.0	6.7
Maximum dry density (kg/m^3)	1710	1985
Particle size range (mm)	0.075–2.36	0.075–4.75
Mean grain size D_{50}	0.80	0.36
Coefficient of uniformity C_u	1.534	2.647
Coefficient of curvature C_c	0.977	0.753
Angle of friction	37°	40°

3.2 *Construction materials*

Common local construction materials such as South African pine timber, bright mild steel and concrete were selected for the tests conducted.

The concrete mixture was prepared to a ratio of1 kg 52.5 PPC cement, 1.5 kg Klipheuwel sand and 1.5 kg9.5mm stone aggregate. A water-cement ratio of 0.58 was used to obtain a compressive strength of at least 30 MPa at 28 days.

The concrete samples covered three ranges of surface roughness (i.e. smooth, medium-rough and rough). Specific techniques were employed to produce each of the desired three surface finishes. The smooth concrete surface was produced by finishing the wet concrete surface with a smooth metal plate. The medium-rough concrete surface was obtained by imprinting the wet concrete sample surfaces with a P40 sandpaper. This sandpaper has an average particle diameter of 0.425 mm (ISO 6344-2:1998). Cape Flats sand of particle size 0.600 mm–2.36 mm was used to imprint the finish of the rough surface.

3.3 *Methodology*

Direct shear interface tests were conducted to determine the shear deformation characteristics of the different soils at the interface of the different construction materials. The procedures according to the British Soil Classification System were used to conduct all laboratory experiments: BS 1377:1990 *Part 7: Shear Strength Test (Total Stress)*. The Wykeham Farrance SB1 constant strain rate direct shear apparatus was used, with a 100 mm × 100 mm shear box. An electric motor speed of 1.32 mm/min was used.

A total of 36 direct shear tests were conducted; 6control tests (internal friction tests) and 30 interface friction tests. The soils were prepared at optimum moisture content to achieve maximum dry densities for the samples tested. . Three normal stresses 25, 50 and 100 kPa were used in the testing schedule to obtain the Mohr-Coulomb failure envelope for analysis of the results.

The interface friction direct shear tests were conducted by placing the construction material at the bottom half of the shear box and the soil placed in the tophalf of the shear box. For timber, the blocks were placed in the shear box such that the direction of the grade of the timber was perpendicular to the shearing movement to which it was subjected. The other construction materials were uniform and had no lines of gradation.

3.4 *Data capturing and processing*

The readings were taken from the dial gauge of the direct shear apparatus in 10 seconds intervals, and entered into spreadsheets which were used to Compute the shear strength corresponding to the respective horizontal displacement. The relationship between the shear strength and the horizontal displacement of the specimen was determined from the results and the shear strength parameters obtained using the Mohr-Coulomb failure envelope (Equation 2 and 3).

$$\sigma = \tau \tan \varphi + c \quad (2)$$

$$\sigma = \tau \tan \delta + c_a \quad (3)$$

where σ: normal stress, τ: shear strength
φ : internal friction angle, c: cohesion
δ : interface friction angle, c_a: adhesion

4 RESULTS AND ANALYSIS

4.1 *Cape Flats sand: Shear strength and horizontal displacement*

The shear stress of the Cape Flats sand reached peak shear strength (τ_p) for all the normal stresses and gradually decreased as the shear displacement increased eventually reaching residual shear strength (τ_r).

The shear strength resulting from the interaction between Cape Flats sand and timber showed a similar pattern to that of the sand only control test, in which the shear stress increased rapidly to peak shear stress and then decreasing to a constant value. The residual shear strength was reached at a lower horizontal displacement of 2.0–2.4 mm, whereas in the control test the residual shear strength was reached at 5 mm horizontal displacement. Both the peak shear strength and residual shear strength for timber and Cape Flats sand test were found to be lower than that of the control test. The interface shear strength results are shown in Figure 2 below.

The Cape Flats sand and steel shear strength did not peak. The residual shear strength was lower than that of the control test, with an average drop of 4.63 kPa for normal stresses 25 kPa and 50 kPa, and a drop of 11.94 kPa for normal stress 100 kPa. There was interface peak shear stress exhibited. (Figure 3).

The smooth surface concrete responded in a similar manner as the Cape Flats sand-steel results with no peak shear strength. However, the shear strength

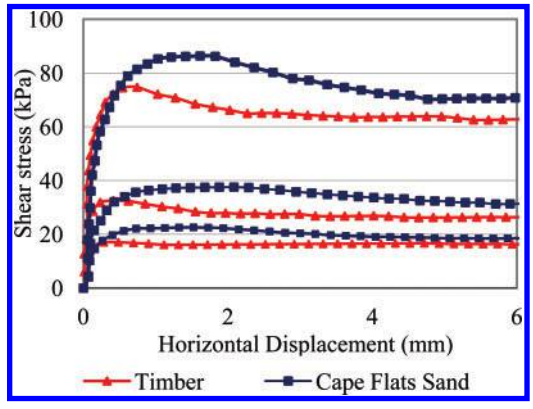


Figure 2. Cape Flats sand and timber shear stress and horizontal displacement relationship.

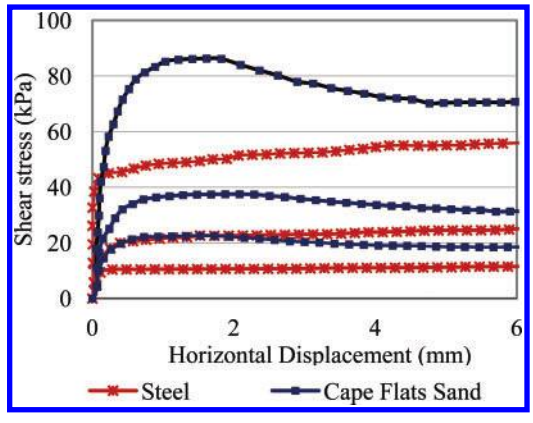


Figure 3. Cape Flats sand and steel shear stress and horizontal displacement relationship.

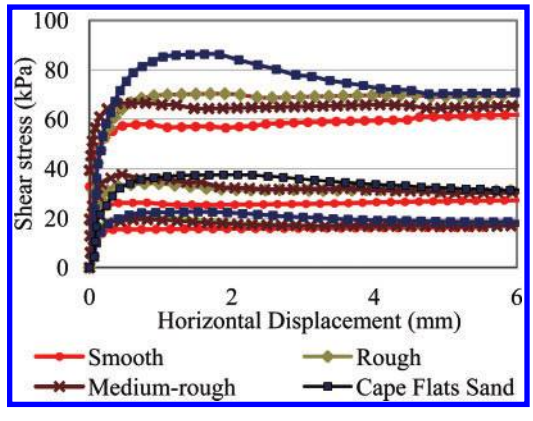


Figure 4. Cape Flats sand and concrete (smooth, medium-rough and rough) shear stress and horizontal displacement relationship.

results for the medium-rough and the rough concrete surfaces exhibited peak shear strength before gradually reaching residual shear strength. The difference between the peak and residual shear strengths were marginal as shown in Figure 4 below.

Table 3. Cape Flats sand interface peak shear strength.

Normal stress (kPa)	Shear strength (kPa)					
	Sand	Timber	Steel	CS*	CM *	CR*
25	22.6	17.1	13.5	16.3	19.5	20.3
50	37.5	32.6	27.1	27.6	37.7	34.0
100	86.3	74.6	62.0	62.0	66.6	71.3

*Where CS = Smooth concrete, CM = Medium-rough concrete, CR = Rough concrete, Sand = Cape Flats sand.

Table 4. Cape Flats sand interface residual shear strength.

Normal stress (kPa)	Shear strength (kPa)					
	Sand	Timber	Steel	CS*	CM *	CR*
25	18.4	15.0	13.5	16.3	16.7	17.2
50	31.5	27.6	27.1	27.6	30.8	31.7
100	73.9	60.8	62.0	62.0	65.6	71.1

*Where CS = Smooth concrete, CM = Medium-rough concrete, CR = Rough concrete, Sand = Cape Flats sand.

Overall, the peak shear strength of Cape Flats sand-concrete was lower than that of the control test. At normal stresses 25 kPa and 50 kPa, the residual shear strength was close to the value of the sand only test; however at 100 kPa there was a noticeable decrease in shear strength compared to the control test. The rough surface finish remained very close to the control test values with a drop of only 2.8kPa. The results of peak and residual shear strengths with the corresponding normal stresses are listed in Table 3 and 4.

4.2 *Klipheuwel sand: Shear strength and horizontal displacement*

For Klipheuwel sand, the shear strength rapidly increased however it did not reach a peak. As the shear displacement increased the shear stress eventually reached residual shear strength (τ_r). At a normal stress of 25 kPa, the shear strength resulting from the composition of timber and Klipheuwel sand was larger than the internal shear strength of the soil. However, as the normal stress increased the shear strength between the two materials became lower than the soil shear strength (Figure 5).

The shear resistance between Klipheuwel sand and steel was lower than that exhibited by timber and sand. The shear stress between the two materials did not at tain a peak value for all normal stresses. Contrary to the control test results, the interface tests for smooth and rough concrete yielded results in which the shear strengths reached a peak and then gradually decreased up to the residual shear strength(Figure 6).

The peak shear strength from the interface tests was generally larger than that of the sand. However, the residual shear strength of the materials in contact with Klipheuwel sand was lower than the value for sand

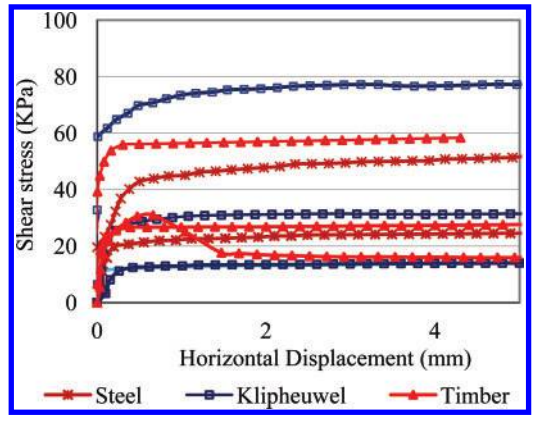


Figure 5. Klipheuwel sand, steel and timber shear stress and horizontal displacement relationship.

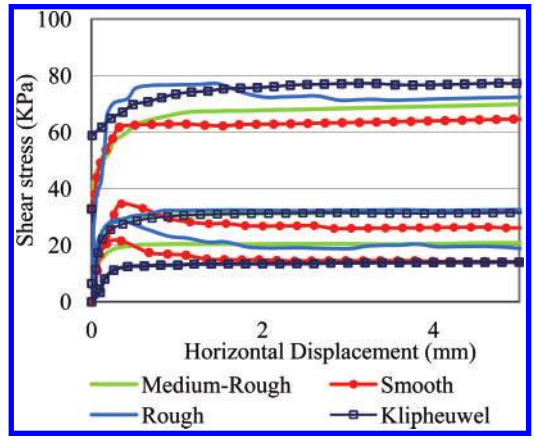


Figure 6. Klipheuwel sand and concrete (smooth, medium-rough and rough) shear stress and horizontal displacement relationship.

Table 5. Klipheuwel sand interface residual shear strength.

Normal stress (kPa)	Shear strength (kPa)					
	Sand	Timber	Steel	CS*	CM *	CR*
25	14.0	15.4	14.7	13.9	20.0	18.9
50	31.9	27.8	25.5	26.1	32.5	33.2
100	76.7	58.2	53.8	64.6	69.6	74.1

*Where CS = Smooth concrete, CM = Medium-rough concrete, CR = Rough concrete, Sand = Klipheuwel sand.

alone. The residual shear strengths results are as listed in Table 5.

4.3 *Angle of interface friction*

Klipheuwel sand yielded the higher angle of internal friction of 40.2° : It was better graded than the Cape Flat sand with more particles of varying sizes which interlock resulting in a greater resistance against sliding. Cape Flats sand had a peak angle of internal

Table 6. Interface friction angles.

	Sand	Timber	Steel	CS*	CM*	CR*
Cape Flats sand						
Peak	41.0°	37.9°	33.2°	31.1°	31.9°	34.6°
Residual	37.1°	31.7°	33.2°	31.1°	33.4°	36.1°
Klipheuwel sand						
Peak/Residual	40.2°	29.9°	28.8°	34.6°	33.9°	36.8°

*Where CS = Smooth concrete, CM = Medium-rough concrete, CR = Rough concrete, Sand = Klipheuwel sand.

friction of 41.0° , and a residual angle of internal friction of 37.1° . The interface friction resulting from the interaction between Cape Flats sand and the construction materials generally yielded lower values than that of the internal friction of sand only. Timber tests yielded the greatest value of interface friction while the smooth concrete had the lowest value which, however increased as the surface finish became rougher. The angle of interface friction at peak and at residual shear strength did not differ considerably; generally this angle was greater at residual strength than at peak shear strength, with the exception of timber where the angle was 37.9° at peak and 31.7° at the residual strength. The friction parameters are presented in Table 6. The interface shear strengths for all the construction materials and Klipheuwel sand were lower than the internal shear strength of the sand. It was observed that the angle of interface friction increased as the surface became rougher. Steel yielded the lowest interface friction with an angle of 28.8°, followed by timber at 29.9° .

4.4 *Relationship between the angle of internal and interface friction*

The relationship between interface friction and internal friction is commonly quantified using the ratio: δ/φ. Strength the ratios δ_r/φ_r and δ_p/φ_p were used to determine the relationship for the residual and peak shear parameters respectively. For Cape Flats sand, the lowest interface friction ratio was obtained from tests involving smooth concrete. At peak shear strength, the timber interface yielded the highest ratio, however at residual shear strength rough concrete yielded the highest with the ratio tending towards the internal angle of friction as the foundation material became rougher. The ratios foreach material are presented in Figure 7 and 8.

The highest strength ratio was achieved for tests ona rough concrete surface with Klipheuwel sand while the steel material yielded the lowest ratio(Figure 9). From the results, it can be deduced that the angle of interface friction tends towards the angle of internal friction with increasing surface roughness.

4.5 *Angle of interface friction ratios*

The interface friction ratios commonly used in design were compared with the ratios obtained from this

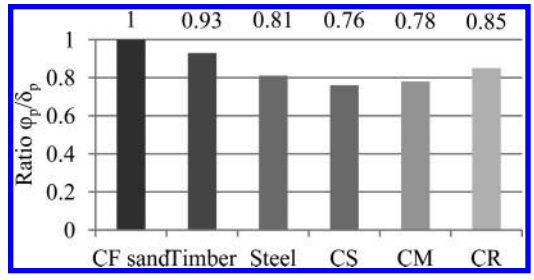


Figure 7. Bar chart of interface friction angle ratios for Cape Flats sand at peak shear strength.

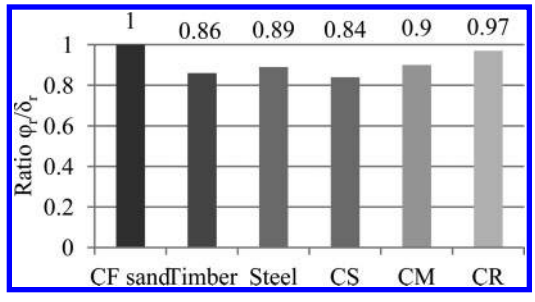


Figure 8. Bar chart of interface friction angle ratios for Cape Flats sand at residual shear strength.

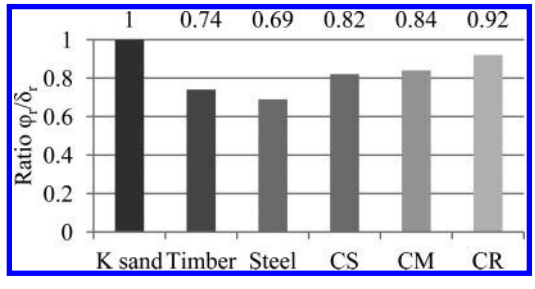


Figure 9. Bar chart of interface friction angle ratios for Klipheuwel sand.

study (Table 7). The values from the study were all found to be greater than the typical interface friction angles used in design (i.e. $2/3\varphi$), which are relatively more conservative estimations of the actual interface friction. The interface friction angles obtained from Klipheuwel sand tests were generally greater than $3/4\varphi$, and greater than $4/5\varphi$ for Cape Flats sand tests.

Overall, from the results obtained in the study, the internal friction angle of Klipheuwel sand was found to be 40° and the interface friction angles ranged between 29°–37° for the construction materials tested and while for Cape Flats sand the value of the internal friction angle was determined as 37° and the interface friction values were between 31°–36° . The various concrete finishes exhibited increasing angles of interface friction as the contact surface with the soils became rougher. A coarser texture achieved a larger shear resistance than a smooth surface due to the increased contact and interlocking of particles. The

Table 7. Comparison of angle interface friction ratios at shear strength.

Material	Cape FlatsSand		Klipheuwelsand	Typical
	Peak	Residual	Peak/Residual	value*
Timber	0.92ϕ	0.85ϕ	0.74 ϕ	0.67 ϕ
Steel	0.81 (41°)	0.89 (33°)	0.69 (29°)	20°
Smooth concrete	0.76ϕ	0.84 ϕ	0.82 ϕ	0.67–0.75 ϕ
Medium-rough concrete	0.78ϕ	0.90 ϕ	0.81 ϕ	0.67–0.75 ϕ
Rough concrete	0.85ϕ	0.97 ϕ	0.92 ϕ	0.67–0.75 ϕ

*see Table 1 for references.

rough concrete surface had the highest shear strength, and therefore the highest angle of interface friction for both sands.

5 CONCLUSION

A series of direct shear interface tests were undertaken on two locally sourced sands (Klipheuwel and Cape Flats sand) and three typical foundation materials (timber, steel and concrete)in order to examine and review the soil-construction material interfacial frictional properties. The values of interface friction determined from the study were found to be greater than the ratios currently used in practice which are conservative estimates possibly with an inherent factor of safety. The angle of interface friction obtained for Cape Flats sand and the construction materials ranged from 0.76φ–0.97φ and for Klipheuwel sand, from 0.69φ–0.92φ. The results of this study suggest that the design values of interface friction in common use approximated between0.67φ–0.75φ are not an accurate representation of the actual angle of friction at a soil-foundation interface. It is essential to establish the true values of interfacial interaction between the soils and the structures in order to avoid instances of over design based on ultra conservative estimates.

REFERENCES

Al-Mhaidib, A. I., 2006. Influence of shearing rate on interfacial friction between sand and steel. *Engineering Journal of the University of Qatar,* Volume 19.

Ampera, B. & Aydogmus, T., 2005. *Skin Friction between Peat and Silt Soils with Construction Materials,* s.l.: EJGE.

Celik, F., Canakci, H., Yavuz, H. E. & Gullu, H., 2011. *Interface between organic soil and construction materials,* Turkey

Craig, R. F., 2004. Chapter 4: Shear Strength. In: *Craig's soil mechanics.* 7th ed. New York: Spon Press.

Das, B. M., 2010. Chapter 12: Shear Strength of Soil. In: *Principles of Geotechnical Engineering.* 7th ed. Stamford: Cenage Learning, pp. 365-423.

Meidema, A. S., 2012. *Dredging Processes: The Cutting of Sand, Clay & Rock – Soil Mechanics,* Netherland

Powrie, W., 2004. Chapter 2: Soil Strength. In: *Soil Mechanics: Concepts & Applications.* 2nd ed. New York: Spon Press.

Sobhee, L., 2010. *Soil Reinforcement using perforated plastic (polyethylene) waste,* Department of Civil Engineering, University of Cape Town, Cape Town

Subba, Rao, K.S., Allam, M.M. and Robinson, R.G, 1988. *Interfacial Friction between Sand and SolidSurfaces. Proceedings of the Institution of Civil Engineers, Geotechnical Engineering*, Vol. 131, pp. 75–82.

Tan, W. H., Lee, C. Y. & Sivadass, T., 2008. Behaviour of Clay-Steel Interfaces. *International conference on construction and building technology,* Volume 2, pp. 11–20

Research and Applications in Structural Engineering, Mechanics and Computation – Zingoni (Ed.)
© 2013 Taylor & Francis Group, London, ISBN 978-1-138-00061-2

Dynamic soil structure interaction behaviour of building frames with raft foundation

G. Narayana
Department of Civil Engineering, S.J.C. Institute of Technology, VTU, Chickaballapur, Karnataka, India

H. Sharada Bai
Department of Civil Engineering, U V C E, Bangalore University, Bangalore

M.P. Jyothi
Anagha Engineering Consultant, Design Engineer, Bangalroe, Karnataka, India

ABSTRACT: The soil flexibility effect is generally ignored in seismic design of building frames and the design is carried out based on results of dynamic analysis considering fixed base condition. Flexibility of soil causes lengthening of lateral natural period due to overall decrease in lateral stiffness of the structure. Such lengthening of lateral natural period(T) may considerably alter the seismic response of the building frames resting on Raft foundation. Hence it is necessary to incorporate the flexibility of soil on which the foundation rests during analysis, such study being termed as Soil Structure Interaction.

The present paper deals with dynamic behaviour of building frames asymmetric in plan with Raft footings under seismic forces incorporating soil-structure interaction. The analysis is carried out using FEM software SAP 2000*V14. The structure is idealized as 3D space frame where in beam and column are modeled as 2 noded line elements with six degrees of freedom at each node and slabs are modeled as thin shell with four noded plate elements having six degrees of freedom at each node. The soil is modeled as equivalent springs with single(Winkler) and six degrees of freedom(Modified winkler) the stiffness of which varies with type of soil based on the properties, viz., dynamic shear modulus and poissons ratio of soil.The raft foundation for winkler and Modified Winkler are modeled as thin shells with four noded plate elements having 6 degrees of freedom at each node and is discritised, such that the aspect ratio of the elements are equal to one.

The response in terms of fundamental Natural Period, Seismic Base Shear and Max. Lateral Displacement, for a variety of building frames with and without consideration of soil flexibility is compared to evaluate the contribution of soil structure interaction on building frames. Influence of of parameters such as different soil types(i.e, Soft, Medium and Stiff), different span lengths, number of bays and number of stories are considered in the parametric study for Zone V.

It is found that the effect of soil flexibility on building frames appreciably alters the fundamental lateral natural period and seismic base shear of the system. Due to the effect of soil flexibility, the lateral natural period and seismic base shear increase with the decreasing stiffness of soil. It is also observed that the lateral period and base shear of the building increases with increase in number of bays. The Maximum lateral displacement increases with increase in number bays and stories.

Keywords: Soil structure interaction, Natural period, Base shear, Max. Lateral displacement, Raft footing.

1 INTRODUCTION

When any structure is subjected to seismic force during an earthquake, the waves that reach produce motions in the structure itself. These motions depend on the structure's vibrational characteristics and the building or structural layout. For the structure to react to the motion, it needs to overcome its own inertia, which results in an interaction between the structure and the soil. Such an interdependent behaviour between soil and structure regulating the overall response is referred as Interaction behaviour in the present context.

It has been a common practice to consider the analysis of structure and foundation separately. Typical load distributions within the building frames are calculated based on the assumption that the base of structure is fixed i.e., assumption made that the base of the foundations transfer the load by direct bearing on solid rocky stratum.There is no doubt that, this assumption is generally applicable if the superstructure is much



Figure 1.

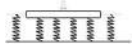


Figure 2.

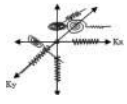


Figure 3.

more flexible/compliant than the underlying soil stratum upon which the foundations rest. However, when the reverse is true i.e., assuming that the structure is much stiffer than the soil medium, then the response of structure can be significantly influenced by the flexibility of soil.

Analyzing the structure with fixed base condition proves to be lower estimation of certain response quantities as highlighted in few earlier researches (Sekhar Chandra Dutta,et.al, Chandrashekar et.al). Soil flexibility may decrease the overall stiffness of the structural systems and hence may increase in natural period of system. So such increase in lateral natural period may considerably alters the response of building frames under the seismic forces. Hence present study has been carried out for dynamic response of building frames resting over Raft foundation incorporating soil flexibility (equivalent springs) with that of a fixed base under the influence of various parameters.

2 MODELING AND ANALYSIS METHOD

For the interaction analysis, the superstructure(3D frame), Raft foundation and soil are considered as single interactive unit and is modeled using SAP2000 V14 FEM structural analysis software package.

Superstructure of building frame is idealized as 3 dimensional space frame consisting of columns in each storey and beams and slabs at each floor level (fig. 1). Two noded line elements with six degrees of freedom at each node represent beams and columns in each storey. Flexible floor diaphragm for slab at each floor level is discretized and is modeled as thin shells with four noded plate elements having six degrees-of-freedom at each node(three translations and three rotations in their respective coordinate directions).

Raft foundation is discretized and modeled as thin shells with four noded plate elements having six degrees-of-freedom at each node.

The soil considered is sandy clay and is idealized using two types of soil models, namely, Winkler Model(WM) as per which one translational spring at each node of foundation along vertical(Z) direction is considered to simulate the effect of soil flexibility (fig.2) and Modified Winkler Model(MWM) as per which three translational and three rotational springs about three mutually perpendicular directions are considered to simulate the effect of soil flexibility (fig.3).

Any torsional effects are automatically considered in the model. The ground motions can be applied in 1, 2 or 3 directions individually or simultaneously. In the present study earthquake load is applied individually along horizontal X and Y directions.

Dynamic analyses (Response Spectrum Method) is carried out as per IS 1893-2002 (part 1) for structure modeled with fixed base(Non Interaction Analysis) and flexible base (Interaction Analysis)using SAP2000 V14.

3 SCOPE OF THE PRESENT STUDY

3.1 *Description of Building Model with Raft Foundation*

For the present study, Two bay Two bay – one, two and four storied reinforced concrete moment resisting frame buildings are chosen (without considering stiffness of infill). The storey height of base story is 4.5m (termed Ratio of Base storey to higher stories Hr=1.5 henceforth) and is kept at 3m for all the other stories in the model. In order to introduce certain amount of unsymmetry in the structures considered, the independent spans of the 2bay 2 bay structure is taken as 6m and 3m (henceforth referred as Ratio of higher to lower span Sr=2). No parapets on the roof storey but all-round brick infill masonry wall (230 mm thick) in the intermediate stories, is considered in the structure. The building is modeled as bare frame; however masses of the walls are included. To study the effect of soil flexibility, lumped mass spring model is used. The stiffness of the springs is used to represent soil flexibility.

3.2 *Input design data for building models with raft foundations*

The material properties considered are: Young's modulus of M25 concrete, E= 25×10^6 kN/m2,Density of Reinforced Concrete = 25 kN/m^3, Density of brick masonry = 20 kN/m^3, Dead load intensities like Floor finishes = 1.0 kN/m^2, Roof finishes = 2.0 kN/m^2, Live load intensities on Roof = 1.5 kN/m^2 and on Floor = 3.0 kN/m^2,Member properties taken are: Thickness of Slab=150 mm,Column size =350 mm × 500 mm, Beam size=250 mm × 600 mm, Thickness of wall=230 mm, Earthquake live load on slab as per clause 7.3.1 and 7.3.2 of IS: 1893-2002 (Part 1) is calculated as: Roof= 0.25 × 1.5 =0.375 KN/m^2,Floor=0.25 × 3.0 = 0.75 KN/m^2.

Seismic data: Seismic Zone V, Response spectra = As per 1893(part 1)2002, Importance factor =1, Response reduction factor = 5.

The foundation dimensions were designed for gravity load and all its load combinations, using STAAD ETC software package, The raft with plan dimensions 11 m × 11 m is adopted for all building models with the thickness of raft being 300 mm,400 mm and 500 mm for Single storey,two storey and four storey building frames respectively.

3.3 *Soil Parameters Considered*

The type of soil considered is sandy clay **(Bowles, 1996)** classified as soft, medium and stiff soil based on Dynamic shear modulus(G). Properties of soil types considered in this study are Stiff(Type-I with μ =0.2 and G=30000 KN/m^2); Medium(Type-II with μ =0.25 and G=20000 KN/m^2)and Soft (Type-IIIwith - μ =0.3 and G=10000 KN/m^2).

4 CALCULATION OF STIFFNESS OF ELASTIC SPRINGS FOR RAFT FOUNDATION-SOIL MODELS

The Raft foundation is discretized such that the aspect ratio of each element is equal to 1.0 and the soil system is idealized by one translational spring at each node for Winkler Model and six springs at each node(three translations and three rotations)for Modified Winkler Model. The area of element of footing influencing each node is considered for calculating stiffness of the spring at that node.

4.1 *Winkler Model*

The stiffness of the spring represented by subgrade modulus of soil (*ks′*)is calculated using Vesic's equation (1961a, 1961b), adopted from Bowles (1996).

$$ks^{I} = 0.65 * \sqrt[12]{\frac{E_s B^4}{E_f I_f}} * \frac{E_s}{1-\mu^2}, \quad kN/m^2$$

$$ks = \frac{ks^{I}}{B}, \quad kN/m^3$$

Where, ks = modulus of Unit subgrade modulus reaction, kN/m^3;E_s,E_f =Elastic Modulus of soil and footing, respect tively, kN/m^2; B=Width of each dicretized element of the Footing, (m); I_f =moment of inertia (m^4) based on cross section (not in Plan); μ = Poisson's ratio and

$$E_s = \frac{2G}{(1+\mu)}$$

Fig.4 shows the global axes direction considered in SAP2000V14.

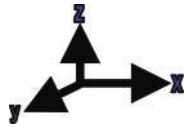


Figure 4. Global axes direction considered in SAP

Table 1. Stiffness of equivalent soil springs along various degrees of freedom (ATC40, adopted from George Gazetas, 1991)

Degrees of freedom	Stiffness of equivalent soil springs
Vertical (Kz) in kN/m	$\frac{GL}{1-\mu}\left[0.73+1.54\left(\frac{B}{L}\right)^{0.75}\right]$
Horizontal (Ky) (Lateral direction) in kN/m	$\frac{GL}{2-\mu}\left[2+2.5\left(B/L\right)^{0.85}\right]$
Horizontal (Kx) (Longitudinal direction) in kN/m	$\frac{GL}{2-\mu}\left[2+2.5\left(B/L\right)^{0.85}\right]-\frac{GL}{0.75-\mu}\left[0.1\left(1-\frac{B}{L}\right)\right]$
Rocking(Krx) (About the longitudinal,x-axis) in kN-m	$\frac{G}{1-\mu}I_x^{0.75}\left(L/B\right)^{0.25}\left[2.4+0.5\left(B/L\right)\right]$
Rocking(Kry) (About the lateral,y- axis) in kN-m	$\frac{G}{1-\mu}I_y^{0.75}\left[3\left(L/B\right)^{0.15}\right]$
Torsion (Krz) in kN-m	$3.5GI_{bz}^{0.75}\left(B/L\right)^{0.4}\left(I_{bz}/B^4\right)^{0.2}$

μ - Poisson's ratio
B, L – width and length of a rectangular foundation respectively, in m.
I_x, I_y, and I_{bz}, Moment of inertia, in m^4 of the foundation area with respect to longitudinal, lateral and vertical axes respectively.
G = Dynamic shear modulus in kN/m^2 , which depends on type of soil.

4.2 *Modified Winkler Model.*

The stiffness of springs in each translational and rotational directions are calculated as suggested by Gazetas(1991) and recommended by ATC-40 and tabulated in Table 1.

Fig. 5 and Fig. 6 show the finite element idealization of the building frame - raft foundation -soil interactive system for WM and MWM respectively.

5 RESULTS AND DISCUSSION

Here, only Fundamental natural period, Base shear and Maximum lateral displacements obtained from

Interaction Analysis(IA) are compared with Non Interaction Analysis (NIA).

5.1 *Lateral Natural Period*

Variation of Fundamental natural period, Tn with shear modulus of three types of soil for Zone V are plotted for the two types of soil models and frame type of 2bay 2bay 1storey,2 storey and 4 storeies with Sr=2 and Hr=1.5 in Figure 7 and shown in Table 1.

For any frame type and soil model considered, there is similar variation in Tn with shear modulus of soil, i.e. it slightly decreases with increase in shear modulus.

In comparison to NIA, Tn substantially increases in the interaction analysis as the structure foundation soil system is rendered flexible. The degree of variation depends on type of soil model and soil type.

Story- wise variation of natural period is as shown in Table 1, and Fig. 10. It is evident that the natural period is relatively higher as number of stories is increased. Tn of all the models are greater than the values of NIA in all types of soils. Between the soil models, WM is observed to predict maximum variation with respect to NIA.

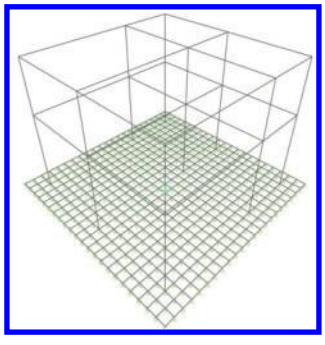


Figure 5. Finite Element idealizations of the building foundation soil interactive system for Winkler model.

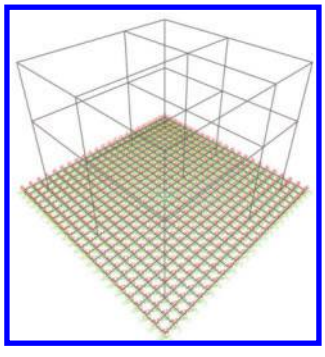


Figure 6. Finite Element idealizations of the building foundation soil interactive system for Modified Winkler Model.

5.2 *Change in Base Shear*

Table 2, Fig.8 and Fig.11 show the resulting base shear(V_B) for different number of stories of the frame and types of soil. It is seen that increase in number of stories increases the base shear. Also observed is the decrease in base shear values from soil type soft to stiff which is more effective for 4 storey than one and two storied structures.

Comparing V_B values of both soil models and also NIA, MWM shows higher values of V_B followed by WM upto 2 storey, where as for 4 storey frame NIA shows higher values of V_B followed by MWM and WM.

5.3 *Maximum Lateral Displacement*

The lateral displacement(Δ) values in the table 3 are those which are obtained as maximum values out of different modes of deformation. As Moment of Inertia along X-direction is high, displacements along Y-direction are relatively higher.

In comparison to Non interaction analysis Fig.9 and Fig.12, Δ substantially increases in the interaction

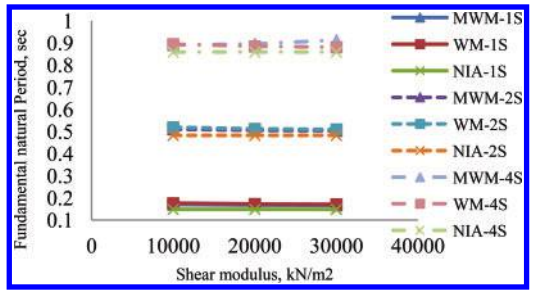


Figure 7. Variation of Fundamental Natural Period with Shear Modulus of Soil

Table 2. Fundamental Natural Period, Sec

Type of Frame	Model Type	Fixed	Spring		
			Stiff	Medium	Soft
2bayx2bay-1Storey: Sr=2	MWM	0.148169	0.16638	0.1675	0.16993
	WM		0.17106	0.1724	0.17572
2bayx2bay-2Storey: Sr=2,Hr=1.5	MWM	0.482751	0.5037	0.5056	0.51003
	WM		0.50946	0.5122	0.51935
2bayx2bay-4Storey: Sr=2,Hr=1.5	MWM	0.85926	0.88123	0.885	0.89515
	WM		0.89014	0.8962	0.91328

Table 3. Base Shear, kN.

Type of Frame	Model Type	Fixed	Spring		
			Stiff	Medium	Soft
2bayx2bay-1Storey: Sr=2	MWM	100.99	103.94	104.8	107.45
	WM		100.99	103.64	103.4
2bayx2bay-2Sroey: Sr=2,Hr=1.5	MWM	315.2	316.86	317.15	317.9
	WM		315.41	315.8	314.66
2bayx2bay-4Storey: Sr=2,Hr=1.5	MWM	702.09	409.23	559.1	654.21
	WM		400.96	543.2	627.95

Table 4. Maximum Lateral Displacement, mm

Type of Frame	Model Type	Fixed	Spring		
			Stiff	Spring Medium	Soft
2bayx2bay-1Storey: Sr=2	MWM	0.7956	1.0188	1.033	1.0692
	WM		1.0692	1.087	1.1232
2bayx2bay-2Storey: Sr=2,Hr=1.5	MWM	9.4536	8.5104	10.38	10.588
	WM		8.5932	10.63	10.966
2bayx2bay-4Storey: Sr=2,Hr=1.5	MWM	24.962	15.415	21.08	26.302
	WM		15.592	21.39	26.932

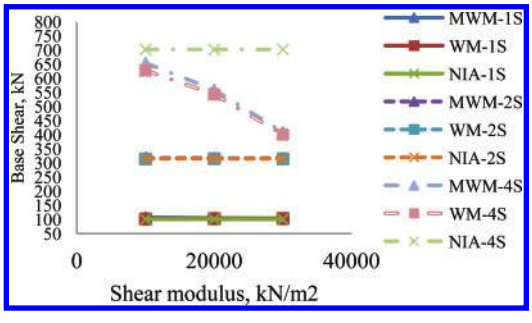


Figure 8. Variation of Base shear with Shear Modulus of Soil

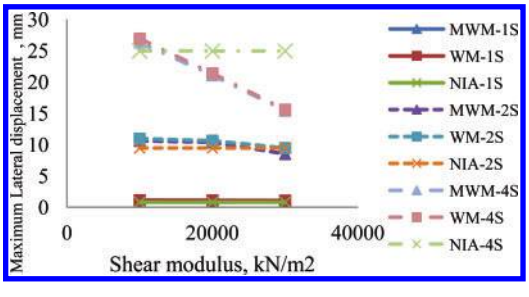


Figure 9. Variation of Max.Lateral Displacement with Shear Modulus of Soil

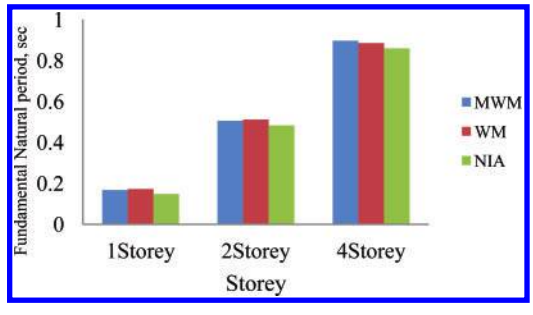


Figure 10. Variation of Fundamental Natural Period with Storey variation for Medium soil(Type II Soil)

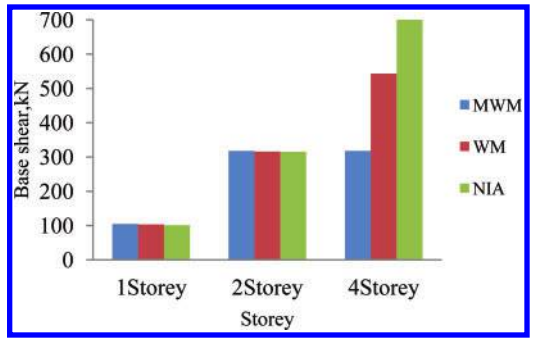


Figure 11. Variation of Base Shear with Storey variation for Medium soil (Type II Soil)

analysis as the structure foundation-soil-system is more flexible than that with fixed ends.

Trend of variation of Maximum lateral displacement with type of soil is almost same for all soil models i.e. it decreases with increase in stiffness of soil. Δ values for NIA are relatively higher than other two models followed by WM and MWM for 2 and 4storey frames where as WM shows higher values in 1 storey frames followed by WM and MWM.

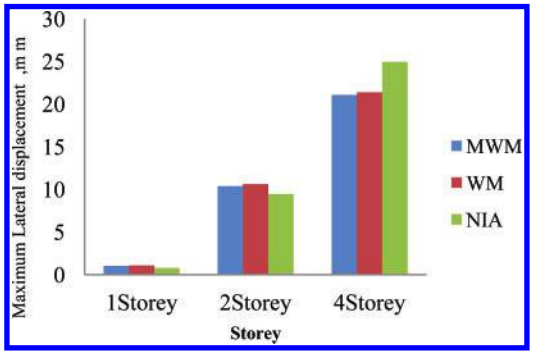


Figure 12. Variation of Max. Lateral Displacement with Storey variation for Medium soil (Type II Soil)

6 CONCLUSIONS

The present study makes an effort to evaluate the effect of soil flexibility on dynamic characteristics of building frames resting on Raft foundation, namely the Lateral natural period , Seismic base shear and Maximum lateral displacement.The study leads to the following conclusions.

The behavior of the structure is rendered flexible due to IA , as a result of which substantial increase in Tn and Δ and moderate increase in V_B, occur. For the sandy clay soil considered, the fundamental natural period of 3D-frames is maximum for type III(soft soil) and decreases as the shear modulus of soil increases. Effect of increase in number of storeys from 1 to 2 and 2 to 4 results in substantial increase in Tn in both IA and NIA.

Base shear values due to Interaction analysis are found to be higher than that of Non-Interaction analysis which is more predominant in longitudinal direction of the 3D frame. As number of storeys increases from 1 to 2 and 2 to 4 base shear increases.

The top storey sway(Δ) values along any of the horizontal directions decreases as the shear modulus of soil increases. For the frame 2bayx2bay-4 storey, as soil changes from soft to hard Δ reduces by 70.62%(MWM) and 72.73%(WM). As number of storeys increases from 1 to 2 and 2 to 4, Δ increases by about 10 & 2.03 times in MWM, 9.78&2.012 times in WM and 11.88 & 2.64 times in NIA.

REFERENCES

Agarwal. P. and Shrikhande. M., 2006. "Earth quake resistant Design of Structures" Prentice-Hall of India Private Limited, New Delhi, India

Allam, M.M., Subbarao, K.S., Subramanya, 1991. "frame soil interaction and Winkler model, journal of institution of civil engineers, part 2, 477–494.

Annigeri.S. A, Hegde Purnchandra S, S. S. Dyavanal, 2007. "performance based seismic evaluation of multistoreyed buildings considering the effect of SSI" Proceedings of International Conference on Recent Developments in Structural Engineering (RDSE-2007), 1361–1368.

ATC-40 (Applied technology council) "Seismic evaluation and retrofit of concrete buildings" Volume 1.

Bowles J.E, 1996. "Foundation Analysis and Design", 5th Edition, *McGraw-Hill International Editions*, Civil Engineering Series, New York,.

Chandrashekar. A, Jayalakshmi B.R, Katta Venkatarama Na, 2005. "Dynamic soil-structure interaction effects on multi storied RCC frames" *Proceedings of International Conference on Advance to structural dynamics and its application* 7-9 December, ICASDA, 454–467.

D. Daniel Thangaraj, K. Illamparuthi, 2010. "Parametric Study on the Performance of Raft Foundation with Interaction of Frame" EDJE, Vol. 15, Bund.H

Edward L Wilson, 2004. "Static & Dynamic analysis of structures",4th edition, *Computers & Structures Inc.,*

Gazetas. G, 1991 "Formula and Charts for impedance of surface and embedded foundations" *Journal of Geotechnical Engineering*, American Society of Civil Engineers 117(9) 1363–1381.

IS:1893 (part 1), 2002."Criteria for Earthquake Resistant Design of Structures" Part 1-General provisions and buildings, fifth revision, Bureau of Indian Standards, New Delhi, India.

Koushik Bhattacharya, Sekhar Chandra Dutta,2004 . "Assessing lateral period of building frames incorporating soil flexibility" *Journal of sound and vibrations* 269795-821.

Sekhar Chandra Dutta, Koushik Bhattacharya, Rana Roy, 2004. "Response of low-rise buildings under seismic ground excitation incorporating soil-structure interaction" *Journal of soil dynamics and earthquake engineering* 24893–914.

Research and Applications in Structural Engineering, Mechanics and Computation – Zingoni (Ed.)
© 2013 Taylor & Francis Group, London, ISBN 978-1-138-00061-2

Using the shear strength reduction method to assess the stability of retaining structures adjacent to excavations for the University of Cape Town's New Engineering Building

C.J. Warren-Codrington & D. Kalumba
University of Cape Town, Cape Town, South Africa

ABSTRACT: The construction of the New Engineering Building (NEB) on the University of Cape Town's (UCT) Upper Campus raised concerns about the stability of the adjacent Ring Road. This busy internal road ran along the western boundary of the site, and was supported by a tapered retaining wall which was 6.3 m at its highest point. Hence, a slope stability analysis was conducted on the critical section of the wall using conventional limit equilibrium (LE) techniques as well as the shear strength reduction (SSR) finite element (FE) method. The results of these analyses were compared and deemed the retaining wall to be safe against a global failure. The benefit of combining the LE and SSR FE methods was highlighted by the correlation between the LE failure surfaces and the development of shear strain behind the wall. Furthermore, the SSR FE analysis yielded a distinct band of shear strain behind the wall which further exemplified the usefulness of the SSR FE technique in modelling the deformation behaviour of the system.

1 INTRODUCTION

1.1 *Background*

Geotechnical engineers are often faced with the problem of assessing the stability of structures adjacent to open excavations. The Finite Element Method, since its first application to geotechnical engineering in 1966, has become very popular in assisting in this regard (Hammah *et al.*, 2005). This is based on the method's ability to predict stresses and deformations, which fall outside of the capabilities of conventional limit equilibrium (LE) techniques.

The University of Cape Town (UCT) in 2010 was faced with the problem of evaluating the response of structures to basement excavations for the New Engineering Building (NEB). The NEB formed part of UCTs three year capital expenditure programme, and required the multi-staged demolition of the former structure in conjunction with the initiation of the construction.

It was established that the proposed basement excavations may undermine the structural integrity of a retaining wall that extended along the western boundary of the site and supported Ring Road – an internal road which serviced vital amenities of UCT. The retaining wall supported 6.3 m of backfill at its highest point. A failure of this system would have had detrimental consequences for Ring Road and possibly the Chemical Engineering Building, which joined the existing wall at its highest point.

Hence, an additional lateral support system was designed and constructed by Esorfranki prior to excavations taking place. This was to provide the required stability to the slope once excavations commenced as well as transfer column loads of the NEB to underlying strata.

These slope stability concerns led to an independent investigation, undertaken by the University of Cape Town's Geotechnical Research Group and centred on good excavation practice, to assess the performance of the Ring Road lateral support system in stabilising the western boundary. This was carried out in light of extensive research into excavation failures, especially by Sowers & Sowers (2004), Chen, Hiew, & Sofianaa, (2000) and Gue & Tan, (2002), which found that inadequacy in design was the main contributing factor to many excavation failures around the world.

1.2 *Aims and objectives*

This study aimed to assess the stability of the western boundary of the NEB site by performing a slope stability analysis. This was done by employing (1) conventional limit equilibrium (LE) techniques, and (2) the Shear Strength Reduction Method (SSRM). In doing so, the study aimed to explore the advantages of combining LE techniques and the SSRM for future slope stability and support structure analyses.

1.3 *Modelling methodology*

Once the site was characterised a cross-section through the site at the highest point of the respective retaining wall was formed. This formed the basis upon which the following modelling was carried out.

The LE techniques adopted included the Fellenius Simplified, Bishop Simplified, Janbu Corrected, Janbu

and Spencer methods. A wide array of LE methods was selected to account for the respective errors accompanying each method as a result of the respective assumptions required to perform each LE analysis. A full description of these methods can be found in texts such as (Gedeon 2003). The LE slope stability analysis was carried out in *Slide*. *Slide* was a comprehensive slope stability package, capable of FE groundwater seepage modelling, rapid drawdown, sensitivity and probabilistic analyses and support design. The average of the results of the LE analysis was calculated and then compared to the output of the SSRM investigation, which was done using *Phase*^{2}. *Phase*^{2} is a powerful two dimensional elasto-plastic FE stress analysis program for underground or surface excavations in rock or soil. Both software packages were developed by *Rocscience*.

The SSRM analysis involved the systematic use of the Finite Element method (FEM) to determine a Shear Strength Reduction Factor (SSRF), or factor of safety which brings the slope to the verge of failure (Hammah *et al.*, 2005). This was done by reducing the strength of respective materials of the slope by the SSRF until the FE analysis did not converge. For a Mohr Coulomb failure criterion, the SSR factor, SSRF, was used as follows to give the reduced material strength parameters, c'^* and φ'^*:

$$\frac{\tau}{SSRF} = \frac{c'}{SSRF} + \frac{\sigma_n tan\phi'}{SSRF} \quad (1)$$

where,

$$\frac{\tau}{SSRF} = c'^* + \sigma_n \tan(\phi'^*) \quad (2)$$

and,

$$c'^* = \frac{c'}{SSRF};\ \phi'^* = \arctan\left(\frac{tan\phi'}{SSRF}\right) \quad (3)$$

2 SITE CHARACTERISATION

2.1 *Material parameters*

The geotechnical report, compiled by Kantey & Templer Consulting Engineers, found the site to be underlain by three distinct material profiles: (1) transported material, (2) reworked residual Malmesbury Group material and (3) intact residual Malmesbury Group material. The bulk unit weights (γ) of the respective materials were determined by a set of laboratory results and are given in table 1, along with the soil strength and stiffness parameters.

This confirmed published geological data that depicted the area to consist of varying thicknesses of transported material emanating from the slope to the west, followed by residual Malmsbury Group shales of the Tygerburg Formation (Brink 1985).

For the colluvial material The Mohr-Coulomb shear strength parameters, cohesion (c′) and internal angle of friction (φ'), were approximated from a back analysis conducted on an exposed cutting on the site. The Mohr

Table 1. Material parameters.

Parameter	Soil Layer (1)	(2)	(3)
γ (kN/m^3)	18	18	18.5
φ' (°)	36	28	28
c′ (kPa)	2	15	25
E (kPa)	25000	20000	20000
υ	0.35	0.3	0.3

Coulomb shear strength parameters for the reworked and intact weathered Malmesbury Group material were determined from relevant literature and case studies, with considerable reference to Brink, (1985) and (Du Plessis and Parrock 2010). The elastic material parameters, Young's Modulus (E) and Poisson's Ratio (υ) were derived from relevant literature, with special reference to Sabatini *et al.*, (2002). The grwound water table profile was determined from a series of boreholes drilled on the site perimeter during the geotechnical investigation. These results were linearly extrapolated across the site.

2.2 *Lateral support*

An anchored soldier pile wall was deemed the most appropriate retaining system for the NEB site, by the design consultants, the construction of which was to last 3 months and began in June 2011. This tied back pile wall included the following components: (1) 750 mm diameter, 17.0–20.0 m long cased auger piles; (2) 300 mm diameter, 7.75 m rotary percussion piles; (3) 1 m wide, 1.2 m deep capping beam; (4) 16.5 m Titan 52/26 permanent ground anchors; (5) steel mesh and gunite arch system.

The piles were arranged with sets of three 300 mm diameter piles in between pairs of 750 mm diameter piles. The 750 mm diameter piles were used to support 5 MN column working loads. The 750 mm diameter piles provided considerable stiffness to the lateral support system.

Once the installation of the piles was complete the capping beam was constructed to provide extra rigidity to the soldier pile wall, and it provided a base upon which ground anchors could be stressed (Figure 1). The primary purpose of the ground anchors was to minimise the deflections of the pile wall and hence to minimise the development of eccentric loads forming at the interface between the capping beam and the columns. The ground anchors also served to reduce the bending stresses in in the soldier piles. Steel mesh gunite arches were adopted to retain the soil between the piles. Wick drains were installed behind these arches to carry seepage to a drain at the basement floor slab level. The arrangement of the support system is illustrated by figure 1 and an overview of the site with the completed bulk excavations and additional lateral support system installed is given by figure 2. Critically, the placement of a crane behind the lateral support structure can be viewed in figure 2. The

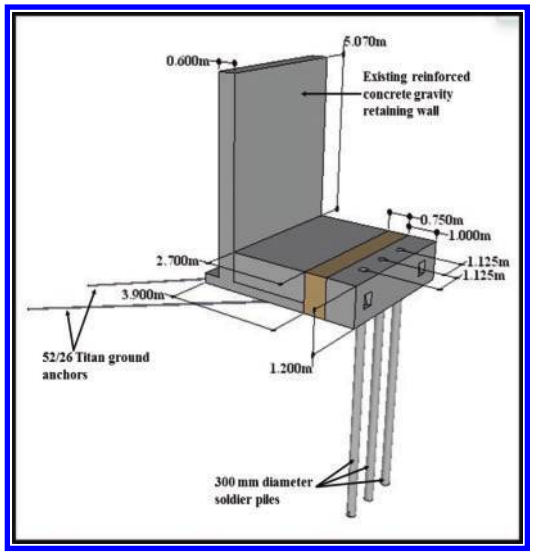


Figure 1. View of the Anchored Soldier Pile Wall.



Figure 2. Completed bulk excavations with pile wall and crane loading visible.

additional loads emanating from this temporary structure were modelled to determine the respective effects on the lateral support.

3 RESULTS

Table 2 gives the slope stability results from the different methods of analysis conducted on the Ring

Table 2. Slope Stability Results.

Analysis	Before Excavation		After Excavation	
	CSF‡	NCSF†	CSF	NCSF
Fellenius	1.799	1.326	1.937	1.322
Simplified Bishop	2.235	1.786	2.319	1.851
Simplified Janbu	1.815	1.663	1.695	1.794
Corrected Janbu	1.976	1.811	2.137	1.941
Spencer	2.237	2.197	2.354	2.316
Average	2.012	1.757	2.142	1.845
SSRF●	2.39		2.28	

‡ Circular Shear Failure Analysis
† Non-circular Shear Failure Analysis

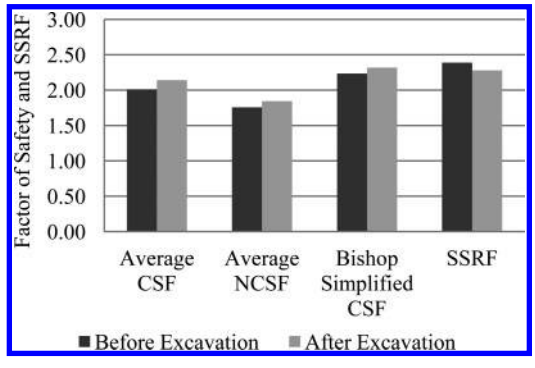


Figure 3. Slope stability analysis results.

Road lateral support. These results are summarised and shown graphically in Figure 3. It is evident from these results that the system was adequately safe both before and after excavation. This conclusion is based on factor of safety and SSRF values greater than 1.50. Furthermore, as anticipated, the stability of the system generally improved with the construction of the anchored pile wall. The SSRF was the only stability proxy to decrease after the excavation process.

On a qualitative level, the importance of the pile wall was illustrated by this analysis. The circular shear failure results (Figure 4) indicate that an overall failure of the system was the most critical mode, whereas, the analyses conducted using non-circular shear surfaces show that the most likely mode of failure was by failure of the ground anchors (Figure 5). An important observation of this was the shear surfaces extending below the pile wall despite breaching the ground anchor. This emphasised the importance of the pile wall in maintaining the stability of the slope.

The FEM SSRM results were compared to the LE analysis by superimposing the circular and non-circular failure surfaces yielded by the LE analysis onto the FEM SSRM results, illustrated by figures 6 and 7. A red and orange dashed line represented the circular and non-circular slip surfaces, respectively.

Figure 7 shows the development of two distinct zones of shear strain behind the tied back wall following excavations. The most prominent shear strain

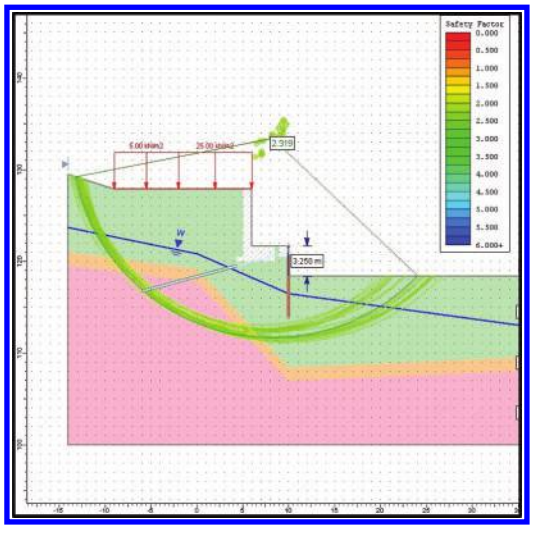


Figure 4. CSFS Slope Stability Results.

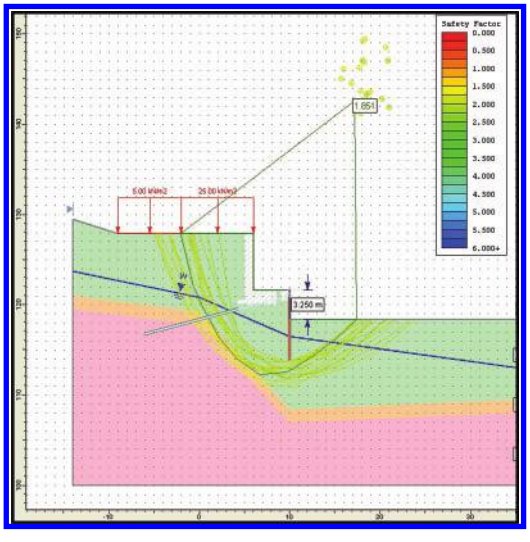


Figure 5. NCSFS Slope stability results.

zone correlated closely to the non-circular slip surface yielded by the LE analysis. The circular shear surface also followed a band of shear strain recognised by the FEM SSRM analysis, but this was less noticeable. Furthermore, Figure 6 depicts the effect of the pile with significant shear strain in front of the pile wall, but a reduced area of shear strain behind the toe of the wall. This demonstrates the mobilisation of the shear stress by the pile wall and how this stress is transferred to the soil in front of the wall.

Superimposing the LE analysis result onto the FE SSR results illustrated the effectiveness of the FE SSRM. Not only does the FE SSRM allow an assessment of the stresses and deformations of the lateral support system, but in doing so provides insight into the material behaviour under different loading

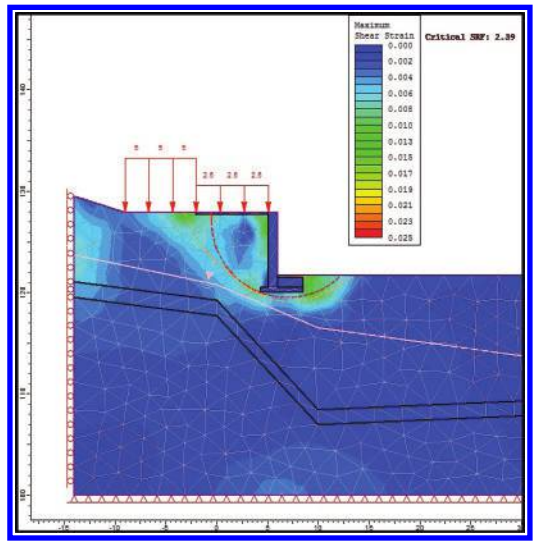


Figure 6. FEM SSR Slope Stability Results – After Demolition, but Before Excavation.

conditions and geometry. With reference to Figure 2, the LE result showed an improved factor of safety with the construction of the pile wall, but the FEM SSR results did not. The difference between the two cases is likely to be due to the increased surcharge loading behind the wall as a result of a construction crane. This was important as it illustrated the system's stability as a function of its geometry, strength parameters and loading, in terms of the material's response to stress. The FEM SSR technique essentially modelled the progressive response of the lateral support to the excavation and modified loading. This is opposed the the LE techniques assessing the likelihood of the entire system failing. In doing so, the FE SSRM highlighted key weaknesses in the material which arose from the system's geometry and loading. Such an analysis is not possible to model using LE techniques, as inter-particle material interactions are not assessed (Hammah *et al.* 2005). Furthermore, LE methods are unable to model the interaction between structural elements, such as the anchored soldier pile wall and the supported soil. FEM techniques, such as the SSRM are capable of doing this, and are able to accurately predict the soil-structure-interaction between the retained material and anchor forces, deformation, shear, sbending and axial stresses.

4 CONCLUSION

The analyses conduced on the western boundary of the NEB bulk excavations found the Ring Road lateral support system to be stable. This conclusion was derived from slope stability analyses, using numerical methods, conducted on the Ring Road lateral support system. The Ring Road lateral support system formed the western boundary to the NEB site.

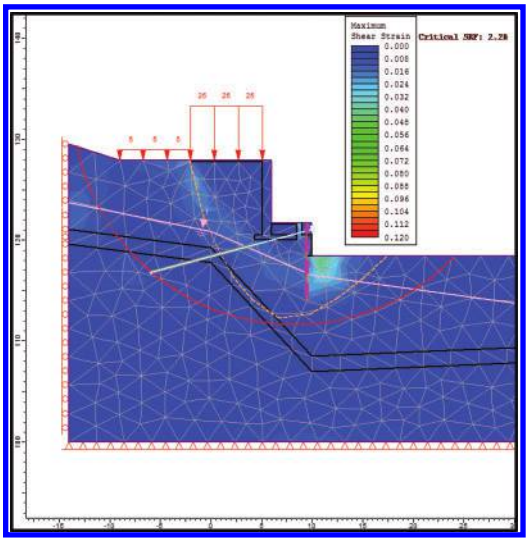


Figure 7. FEM SSR Slope Stability Results – After Excavation.

The slope stability analysis conducted on the Ring Road lateral support system showed that the system was stable based on the factor of safety and SSRF values produced from the LE and FEM SSR analyses, respectively. The section of the Ring Road lateral support that was modelled yielded factor of safety and SSRF values greater than 1.50. Although the SSRF values were found to be adequately high to assure the safety of the system, the development of a zone of increased shear strain was found in the FEM SSR analyses conducted on the Ring Road lateral support system. It is likely that this shear zone was influenced by the surcharge loading behind the wall.

This highlighted the usefulness of combining LE methods with the FEM SSR method in assessing slope stability. Furthermore, this investigation emphasized the effectiveness of using FE methods in the design of lateral support systems. This was based on FE methods being able to model the response of the materials to stress as well as the interaction between the retained soil and the support system.

REFERENCES

Brink, A. B. A. 1985. *Engineering Geology of South Africa*. 1st ed. Pretoria: Building Publications, Pretoria.

Chen, C. S., L. C. Hiew, and B. T. Sofianaa. 2000. "Failures Due to Excavation in Soft Clay." In *Seminar on Failures to Geotechnical Works*, 1–7. Kuala Lumpur: Institute of Engineers, Malaysia.

Gedeon, G. 2003. *Slope Stability*. New York.

Gue, S. S., and Y. C. Tan. 2002. "Prevention of Failures Related to Geotechnical Works on Soft Ground." In *Malaysian Geotechnical Conference*. Kuala Lumpur.

Hammah, R. E., T. E. Yacoub, B. C. Corkum, and J. Curran. 2005. *A Comparison of Finite Element Slope Stability Analysis with Conventional Limit-equilibrium Investigation*. Toronto.

Du Plessis, L., and A. Parrock. 2010. *Lateral Support for Great Westerford Extensions*. Pretoria.

Sabatini, P. J., R. C. Bachus, P. W. Mayne, J. A. Schneider, and T. E. Zettler. 2002. *Evaluation of Soil and Rock Properties*. Vol. 7. Atlanta.

Sowers, G. B., and G. F. Sowers. 1967. "Failures of Bulkhead and Excavation Bracing." *Civil Engineering* 37 (1): 72–77.

34. Structural engineering education

Research and Applications in Structural Engineering, Mechanics and Computation – Zingoni (Ed.)
© 2013 Taylor & Francis Group, London, ISBN 978-1-138-00061-2

Efforts to reduce the drop-out rate in civil and structural engineering programs

U. Quapp & K. Holschemacher
Faculty of Civil Engineering and Architecture, Leipzig University of Applied Sciences, Germany

ABSTRACT: Usually, drop-out rates in engineering courses of studies are higher than in other programs. There are various reasons for this. Because of the already existing lack of well educated civil and structural engineers worldwide, universities and industry are interested in finding out the reasons and developing ideas to reduce the civil and structural engineering students' drop-out. And also a lot of money is at stake. Each student not completing the program costs the taxpayers a lot of money without providing any benefit to society in future. This paper investigates reasons for the high drop-out rate in civil and structural engineering study courses and offers solutions for the problem.

1 INTRODUCTION

Usually, drop-out rates in civil and structural engineering courses of studies are higher than in other programs (Heublein *et al.* 2010). At German universities normally about 50 percent of students withdraw from their civil and structural engineering degree courses (Heublein *et al.* 2010). Currently, there already exists a lack of well educated civil engineers worldwide. In Germany alone, the engineers' unemployment rate is now around 2.4 percent, which means nearly full employment (The Association of German Engineers 2011). Additionally, in the next years more civil and structural engineers will retire than universities are able to graduate. Therefore, universities and industry are interested in finding out the reasons and developing ideas to reduce the civil and structural engineering students' drop-out (The Association of German Engineers 2011).

And also a lot of money is at stake. In Germany, higher education financing is mainly matter of the state. In some Federal States of Germany, the *Länder*, studying to the first cycle degree is for free. In other Federal States students have to pay only up to 1.000 Euros (1.300 US-Dollars) per year. But, every year of civil or structural engineering studying cost the German taxpayer approximately 8.000 Euros (11.000 US-Dollars) per each student (German Federal Statistical Office 2012). Of course, there is an interest that students do not leave the universities without a degree. Further, because of the existing lack of engineers, the ensued financial damage for German economy is around 3 billion Euros (4 billion US-Dollars) which will increase with extension of the lack (The Association of German Engineers 2011).

Not every student leaving university without a degree is unsuitable to become a civil or structural engineer. For some students the conditions are not ideal to complete their studies. That's why universities must work out the reasons for drop-out and try to optimize the study conditions to reduce the number of students not graduating in civil and structural engineering programs without losing education quality.

2 CURRENT STUDY SITUATION IN GERMANY

2.1 *Bologna Process*

As a consequence of the Bologna Process bachelor and master programs were implemented all over Europe during the last years. In Germany the former first cycle degrees leading to the degree *Diplom-Ingenieur* with duration of 4 or 5 years had to be replaced by bachelor programs with duration of 3 or 4 years and master programs of 1 or 2 years (Standing Conference of the Ministers of Education and Cultural Affairs of the *Länder* in the Federal Republic of Germany 2010). Most of the German universities decided for 3 years' bachelor with 2 years' master programs or 3.5 years' bachelor with 1.5 years' master programs. It is worth pointing out that the bachelor degree is the first cycle degree what means that the degree has to qualify the graduates to work professionally. That's why many universities tried to bring all comprehensive contents from the former national programs in the curricula of the new bachelor courses of studies to allow the students to work professionally after graduating (Quapp & Holschemacher 2010).

2.2 *University Admission Law*

German educational policy regarding schools and universities is matter of the German Federal States, the *Länder*. The disadvantage of a federal system is the difference between educational requirements and

school curricula of the various Federal States. Additionally, one out of every seven first year students is a non-national who acquired his or her higher education entrance qualification outside Germany (Federal Ministry of Education and Research Germany 2012). These differences in educational background result in various pupils' knowledge and skills after earning a higher education entrance qualification.

German University Admission Law can be recognized as difficult. Especially for admission to universities of applied sciences, which are higher education institutions with the same rights and tasks just like regular universities, there are several entrance qualifications. These regulations result in a high heterogeneity of first year students regarding knowledge and skills as well.

Currently, by change in the German University Law, additionally to candidates with school diploma corresponding to university entrance level, people without any higher education entrance qualification can be enrolled in study courses under special conditions. These candidates must hold a master craftsman's certificate and must apply for a field of study which relates to his or her profession. Reason for this change in university admission regulations is the worry about the looming shortage of engineers. In consequence, by reducing the admission requirements, it is intended to motivate more people to study engineering sciences to counter the lack of engineers in the long-term and to promote the idea of lifelong learning. In 2012, 12.000 students without higher education entrance qualification were enrolled in study courses at universities and universities of applied sciences in Germany (German Centre for Higher Education 2012).

Some of the students beginning a civil engineering course of studies completed a professional training in the building industry additionally to the higher education entrance qualification. At Faculty of Civil Engineering and Architecture at Leipzig University of Applied Sciences around 20 percent of students with these qualifications are enrolled in the first year. These students combine the knowledge in sciences and technology with experiences from the construction site. For this reason they have fewer problems in the civil engineering bachelor program than students without experience in the building industry.

2.3 *Finance of studies*

Furthermore, a students' survey by the German Federal Ministry of Education shows that 75 percent of the German students must work beside their studies (German Federal Ministry of Education 2010). German engineering students work by an average of 13 hours per week, students of economics or social sciences even more (German Federal Ministry of Education 2010). Students from financially disadvantaged families or which are in need of social support can apply for student loans granted under Germany's Federal Education Assistance Act (Germany's Federal Education Assistance Act – BaföG 2010). Depending from the financial situation of the student he or she have the possibility to receive between 400 and 600 Euros (530 to 800 US-Dollars) monthly. But students associations always complain that this amount of money is not enough for the costs of living. That's why many students are obliged to work while studying.

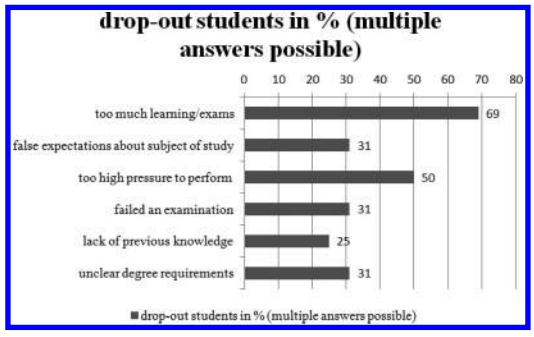


Figure 1. Reasons for drop-out at Faculty of Civil Engineering and Architecture (survey at Leipzig University of Applied Sciences 2010).

3 REASONS FOR DROP-OUT

3.1 *High workload*

One of the reasons for the large number of students not finishing their civil and structural engineering studies in Germany may be the high workload which is often higher than in other programs (Fig. 1). An explanation for the high workload can be the changes caused by the Bologna Process. So many universities overburden programs to optimize the graduates' opportunities for getting a good and well paid job. Anyway, the drop-out rates in the new bachelor programs in civil and structural engineering are higher than in former first cycle degree programs (Heublein *et al.* 2010).

Another difficulty is that at many German universities basic first year classes such as engineering mathematics, physics and chemistry are given by non-engineering lecturers. That is a problem for students because the lecturers' interests and requirements often do not meet the demands of a civil engineering education. So, students complain about theoretical course contents without any practical relevance in civil and structural engineering and high requirements, which are the same for students in sciences and engineering programs.

3.2 *New university admission regulations*

In Germany, there is a high heterogeneity among first year students. The fact that candidates without school diploma corresponding to university entrance level can be enrolled in study courses under special conditions does not make the universities' first year situation easier. This development leads to problems in the study entrance phase because of freshmen's heterogeneity regarding prior knowledge and skills, especially on the field of science and technology. The study programs in civil and structural engineering

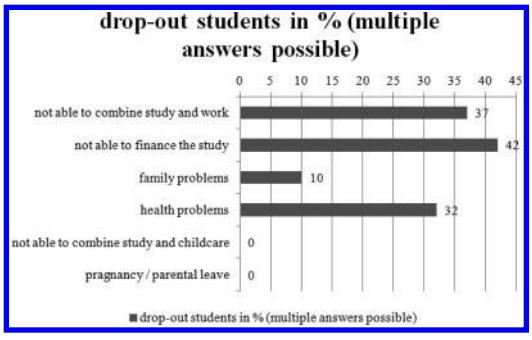


Figure 2. Reasons for drop-out at Faculty of Civil Engineering and Architecture (survey at Leipzig University of Applied Sciences 2010).

fields often require detailed knowledge in mathematics, physics and chemistry which the first year students without school diploma corresponding to university entrance level often do not possess. This causes a feeling of being overburdened among these students and results in a high drop-out rate.

It is understandable that civil and structural engineering fields of study seem very difficult and demanding to many students, containing courses like mathematics, physics, statics and technical mechanics. So, students argue, earning a university degree in social sciences and humanities would be more comfortable and easy than working so hard in engineering programs. Some students begin a civil or structural engineering study without any information about the course contents. While studying, they are surprised about the percentage of science in curriculum. Some students have no interest in science and technology and choose the civil or structural engineering field of study for some other reasons. But it is nearly impossible to complete the difficult and demanding studies if there is no passion for the science and technology which brings the students through some hard times in students' life.

3.3 *Working beside studying*

As mentioned before many students work while studying. One of the reasons why some students must leave university without a degree is that they are not able to combine study and work. Some Students give up their courses voluntarily, for others the lack of time for preparing test and examinations lead to failing definitively and getting expelled by the university administration. Determined through a detailed questionnaire, 37 percent of students leaving Leipzig University of Applied Sciences without a degree gave as the reason not to be able to combine study and work. Over 40 percent could not finance their study (Fig. 2).

4 SOLUTIONS

4.1 *StudiFIT program*

Since 2011 Leipzig University of Applied Sciences offers a program to the first year students specially developed to reduce their orientation problems in the first weeks at university. Another aim of the program is the more successful management of freshmen's heterogeneity regarding prior knowledge and skills, especially on the field of science and technology.

The Program is financed by the German Federal Government until 2016 with more than 3.7 million Euros (4.8 million US-Dollars). With the money coming from the program 12 new jobs are financed. So, 1 Program Leader, 3 Assistants, 1 e-learning consultant and 6 department consultants are responsible for the success of the program. In the first year of the program the StudiFIT team evaluated the reasons for drop-out in the first weeks of the study time. On the basis of the results a package of measures has been developed which contains e.g. extra coaching in courses like mathematics, physics and chemistry given by master students or young civil or structural engineers. Additionally, the program tries to improve the social cohesion between the students by organizing excursions, challenges and parties. The first week at university the freshmen spent together with presentations, parties, challenges and little tests in sciences. The aim is to stimulate the social responsibility under students and to create an atmosphere in which students help each other and look at each other to motivate fellow students not to give up in the early phase of study.

Furthermore the e-learning offers will be improved by the program. Learning management systems can be a valuable support for students who can't attend the classes for various reasons such like illness, work and so on. Online consultation offers, communication platforms or online access to teaching materials may help to manage students' life and reduce the drop-out rate.

A prolongation of the program after 2016 is possible if the efforts had a measurable success.

4.2 *Information*

Detailed information about contents of lessons in civil and structural engineering before starting a study in this field is extremely important in order to avoid surprises in the first year of study. Also information about help and support in sciences and basic subjects can positively influence the decision about starting a civil or structural engineering study and reduce the drop-out rate. Also comprehensive information about the different branches of work, work tasks and the daily routine of a civil or structural engineer may be helpful to introduce the applicants to the civil and structural engineering programs.

4.3 *Entrance examination*

Additionally to the StudiFIT program the selection of candidates suited for a civil or structural engineering program should be improved. Not every person with a good higher education entrance qualification will become a good civil or structural engineering student. Comparable with artistic entrance exams in

architecture there could be an entrance test for civil or structural engineering candidates. Of course, if selecting the candidates the number of freshmen will not be as high as without an entrance test. But it is much wiser to enroll fewer, but good students and reduce the drop-out rate by that measure.

4.4 *Pre-study internship*

As explained before, students with experience in building industry know what they have to expect from a civil or structural engineering program. That's why the Leipzig University of Applied Sciences requires from every undergraduate civil engineering student to prove an 8 weeks pre-study internship before enrollment.

4.5 *Competence center for engineering mathematics, physics and chemistry*

The students' problems with first year courses such as engineering mathematics, physics and chemistry are one more reason for high drop-out rates. Classes given by non-engineering lecturers have been identified as not ideal for students' understanding of the subjects. So, Leipzig University of Applied Sciences decided to establish a competence center for engineering mathematics, physics and chemistry. Lecturers which are engineers themselves should teach subject-related knowledge in sciences to enable students to apply this knowledge in solving subject-specific problems. If the center will be successful to reduce the drop-out rates we will see in the next years.

4.6 *Increase student loans*

As students' associations always complain student loans should be increased. So, students from financially disadvantaged families or who are in need of social support can concentrate on studying and are not or only some hours obliged to work while studying.

5 CONCLUSION

Not everyone who is starting in civil or structural engineering program is good enough to graduate as a civil or structural engineer. Some of them only realize this fact while studying. This means that drop-out can't be eliminated totally. But, in the interests of students who are able to finish their civil or structural engineering studies, it can be reduced.

To reduce the drop-out rate different potential solutions can be found. One of them is the improvement of the students' introductory phase (first year of study) and the offer of natural science classes given by civil and structural engineers. Also the increase of student loans would be helpful to provide students more time for learning and support them to finish their studies.

Of course, it is extremely important to guarantee the quality of the engineering graduates leaving higher education institutions by sorting out these students who are not talented enough to become a civil or structural engineer. For the future and good reputation of Germany as a country of engineering sciences, a few good engineers are better than a lot of bad ones. But regarding the already existing lack of civil and structural engineers, universities should do their best to bring every hard working and talented students to a degree.

The future will show if the efforts and the money invested in the future of the civil and structural engineering education will quickly bear fruit.

REFERENCES

Federal Ministry of Education and Research Germany 2010. *Studiensituation und studentische Orientierung – 11. Studierendensurvey an Universitäten und Fachhochschulen*: 27-29. Bonn, Berlin: W. Bertelsmann Verlag.

Federal Ministry of Education and Research Germany 2012. *Bildung in Deutschland 2012*: 126. Bonn, Berlin: W. Bertelsmann Verlag.

German Centre for Higher Education 2012. http://www.che.de/cms/?getObject=5&getLang=de. Available on website on 21 January 2013.

German Federal Education Assistance Act (Bundesgesetz über die individuelle Förderung in der Ausbildung – BAföG) 2010, BGBL. I p. 1952; 2011 I p. 2592.

German Federal Statistical Office 2012. *Bildungsfinanzbericht 2012*: 57–58. Wiesbaden: German Federal Statistical Office.

Heublein, U.; Richter, J.; Schmelzer, R.; Sommer, D. 2010. *Die Entwicklung der Schwund- und Studienabbruchquoten an den deutschen Hochschulen*: 16–22. Hannover: HIS.

Quapp, U. & Holschemacher, K. 2010. Bologna Process – Friend or Foe – Experience between Change and Tradition. In Zingoni, A. (ed.), *Advances and Trends in Structural Engineering, Mechanics and Computation; SEMC 2010 – The Fourth International Conference on Structural Engineering, Mechanics and Computation*, *Cape Town 6–8 September 2010*. Rotterdam: Balkema.

Standing Conference of the Ministers of Education and Cultural Affairs of the Länder in the Federal Republic of Germany 2010. *Common structural guidelines of the Länder for the accreditation of Bachelor's and Master's study courses*: 2–3. http://www.kmk.org/dokumentation/veroeffentlichungen-beschluesse/wissenschaft-hochschule.html.

The Association of German Engineers 2011. *Positionspapier – Fachkräftemangel und – sicherung*: 5–6. Düsseldorf: VDI.

Research and Applications in Structural Engineering, Mechanics and Computation – Zingoni (Ed.)
© 2013 Taylor & Francis Group, London, ISBN 978-1-138-00061-2

Teaching and learning of fundamentals of structural engineering in undergraduate level

M.R. Karim
Faculty of Engineering and Information Technology, University of Technology, Sydney

ABSTRACT: This paper describes some common problems that students face in grasping the concepts in fundamental engineering subjects such as Engineering Mechanics (Statics and Dynamics), Mechanics of Solids and Structural Analysis. These subjects are taught in the initial years of a student's life. New students might be able to receive information about fundamental principles and concepts, but if they are not exposed to real-world situations it can be hard for them to see their relevance. Thus these subjects can be dry and boring to students or they can be interesting and enjoyable to learn, depending on the teaching methods and strategies used by the lecturer. The author describes in this paper some simple methods and strategies that he has adopted which increase student understanding greatly, thus making learning more effective and enjoyable.

1 INTRODUCTION

In all branches of engineering, there are core subjects, which focus on fundamental principles, concepts and ideas. These are taught in the initial years of students' academic life. Conceptual and practical understanding of each topic in the subjects such as Engineering Mechanics, Mechanics of Solids and Structural Analysis are of utmost importance to almost all engineering disciplines (civil, mechanical, aeronautical, marine, mining engineering and etc.). Application subjects such as Structural Design and Structural Construction require a sound knowledge and skill of a student in the fundamentals of structural engineering. It can thus rightly be said that these fundamental subjects are the building blocks of structural engineering knowledge. A student with poor foundations in these subjects will not only face appreciable difficulty in the subsequent years of his/her studies, but also later in his/her professional life. As such the standard of assessment in these subjects should be high and the academics, who are in-charge of teaching these subjects ought not to contemplate lowering the standard.

The failure rates in Engineering Mechanics, Mechanics of Solids and Structural Analysis in all faculties in Australia and overseas is considerably high. In some faculties failure rates were found to be as high as 35%. Considerable research has been done on why failure rate is so high and how to improve learning in these subjects and many papers were published and presented in engineering education conferences. Goldfinch, Carew and & McCarthy (2008) and Dwight & Carew (2006) did extensive research and presented a very informative table where they summarized the causes of failures and the degree of success of various strategies and methods adopted by many academicians. They could not conclude with any concrete measure how to deal with the problems of students' poor performance in these subjects.

2 PROBLEMS IN LEARNING FUNDAMENTAL PRINCIPLE AND CONCEPTS

In the author's experience, a student has real problems in understanding some fundamental concepts and principles which are abstract in nature. These problems arise from the way in which information is commonly presented in lectures and engineering textbooks. The author describes a few causes that generally create barrier to learning and the measures that he took to improve students' understanding and learning.

2.1 *The Idealized Diagrams*

Subjects like Engineering Mechanics, Mechanics of Solids and Structural Analysis contain numerous abstract concepts, principles and ideas which students need to use to solve problems related to real-world structures. The theory for the subjects can be found in a large number of text books, but it is difficult for students who are generally beginners in gathering knowledge in engineering to connect the idealized diagrams and examples given in the text books to more complex situations found in real-world. To an experienced lecturer and to an experienced professional engineer connecting the real-world structure or structural member with its idealized model may appear very simple. But it can be a barrier to learning to an inexperienced student. If during a lecture a student cannot make the connection, he/she may see little relevance in the model and may lose the motivation to learn deeply and rote learning does occur.

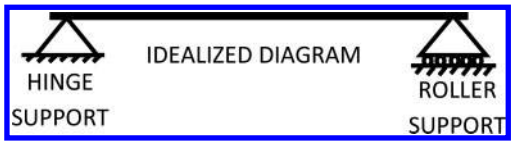


Figure 1. Simply supported beam.

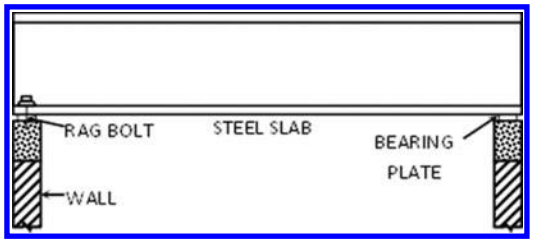


Figure 2. Structural steel beam.

Let us take an example of an idealized diagram of a simply supported beam (Figure 1). Support A is a hinge, support B is a roller. An inquisitive mind of a student would ask where in practice am I going to see such a peculiar supports (a triangle with hatched line, a triangle with circles with hatched line). If the student is not shown the steps before actually arriving at this line with peculiar triangles at the ends, he/she may have difficulty in connecting the idealized models with the real structural member (Figure 2). Such a student may simply rote learn the model, without real understanding. Making the steps explicit is very often ignored by lecturers, because it is not done in conventional engineering mechanics books.

2.2 *The use of assumptions*

Many engineering problems are solved using assumptions which are valid within certain limits. In author's experience he noticed that almost all students had difficulty in understanding what these assumptions mean. They appear to have misconceptions that they can make any assumption rather than use assumptions within defined limits. Let us take a case of one of the valid assumptions that we make in determining the bending stresses in a beam: A plane section remains plane before and after bending. No matter how much the lecturer may talk about this, students find it difficult to grasp this phenomenon. This is a relatively easy concept to demonstrate using three dimensional model beam made of sponge with vertical and horizontal lines drawn on it (Figure 3). Lecturer can explain by showing this to students and students can see that vertical lines remain straight and they do not warp which proves that the assumption is valid.

2.3 *Various names and nomenclatures used in the subjects*

In structural engineering we use many technical names and terms and many students find it difficult to visualise what exactly the members look like. As for example a beam has many names such as girder, joist, rafter, purlin and so on. The non-English speaking students face serious problem to connect the name of the structural members with the concept and principle of the topic. The author prepared a list of such commonly used names of the structural parts with sketches and hand these on to the students. Students are encouraged to buy a dictionary of engineering terms.

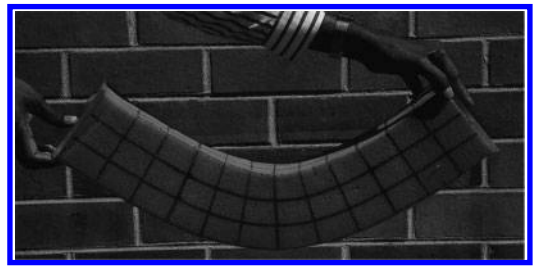


Figure 3. A plane section remains plane before and after bending.

2.4 *Clear understanding of units and to connect with real world situation*

The SI units are scientifically correct but it is difficult to visualize the effect in the context of real structure. As for example, what mental picture a student would form if we tell a student that the crushing strength of engineering brick and concrete is 20 MPa (N/mm^2) and 50 MPa (N/mm^2) respectively. The student would think that the particular concrete block is two and half times stronger than the brick. But question is how strong the brick is. The author poses a question to students to calculate: if the density of bricks is 20 kN/m^3 and if the crushing strength is 20 N/mm^2, how high you can make a brick wall neglecting wind load.

They determine the height to be 1000 m that is 1 km. The students then can comprehend that 20 MPa is a very high stress.

It is quite difficult to comprehend the weight such as N, kN and GN. It was easy with Imperial Units such as pound (lb) and Metric Units such as kg. But in SI units it may be difficult to visualize. The author advises the students that 1 N is approximately weight of an average apple and thus 1 kN is equal to weight of 1000 apple. He also advises students that 1 N/mm^2 is like holding an apple on a tooth-pick of cross sectional area of 1 mm^2 and it is exactly equal to carrying 1 million apple on a surface area of 1 m × 1 m (1 MN/m^2). Figure 4 illustrates this clearly.

2.5 *Responsibility on the part of the faculty*

Engineering Mechanics, Mechanics of Solids and Structural Analysis are the building blocks of engineering knowledge and it is taught in the early years (first year and second year) of any undergraduate degree. Its importance makes it critical that Faculty/Schools are careful in dealing with all aspects of managing these subjects. Very often newly appointed academic staff with no or very little practical knowledge in structural

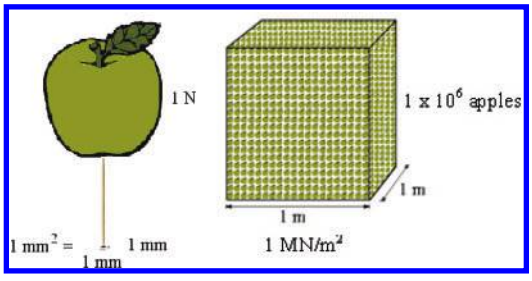


Figure 4. 1 N/mm^2 (1 MN/m^2).

design are assigned to teach these subjects and often it is found that he/she is not an effective teacher for students' learning. To become an effective teacher in these subjects one has to have knowledge and skill in design and construction of structures. These subjects should be taught and managed by senior academician who has practical experience in design and construction of structures.

In many Faculties in Australia lecture classes are very big and typically they are three hours in duration. This long duration, even with break, is not conducive to learning due to the fact that students' concentration decreases with time. Recently (Autumn 2010) in the Faculty of Engineering of UTS Engineering Mechanics (Statics), lecture duration time has been amended from one three hours class to two-two hours classes each week. There has been a marked improvement in students' learning and their performance. Number of failure has been reduced markedly from average 35% per semester previously to 21% in Autumn 2010 when the amendment has been introduced.

2.6 *Effective teaching of fundamental principles*

Lecturers teaching fundamental principles need to consider their goals very carefully in relation to student learning. A lecturer in these fundamental subjects should take into consideration of the fact that the concepts, principles and laws were developed over many centuries by scientists and engineers like Galileo, Verignon, Euler, Columbs, Newton and *et al* and it is hard for a student to grasp all those theories within one semester. Author sees his role:

- To be aware of and help students to overcome the common barriers to learning in fundamental subjects, such as engineering mechanics, mechanics of materials and structural analysis
- To motivate the students to learn the subject and to create enthusiasm and curiosity by bringing examples from real-world structures and structural members;
- To facilitate students' learning by adopting improved methods of teaching and learning: inventing, creating and devising teaching resource materials which illustrate and reinforce concepts;
- To foster students' critical thinking regarding engineering problems by providing choices based on critical assessment of alternatives;
- To create an environment in the tutorial class which is conducive to learning where students are encouraged to participate actively in the class.
- To urge students to form a positive attitude to their studies and future profession and make aware of their social responsibility in designing a structure.

2.7 *Transparencies and use of doc-camera*

The author has experience in teaching fundamental subjects with the help of chalk/markers and black/white board. It has been a successful approach for small classes for many years but it has got limitations for a large class. He has found that teaching with transparencies with the help of two over-head projectors (OHP) or using one OHP and one doc-camera is very effective. In the fundamental subjects there are many machine parts and structural elements which need to be drawn and it is time consuming to draw on the board. The structural elements and machine parts can be drawn beforehand and in the class it is placed on one OHP. The solution of the problem can be done step by step and with ease on another OHP/doc-camera. When compared to Power Point presentation, drawing and solving of problems related to parts of structure and machine on transparencies are more effective for students' learning. Thus using Power Point for these subjects should be discouraged.

2.8 *Handouts*

For conceptually difficult topics in these subjects, handouts which illustrate underlying principles with diagrams and graphics greatly enhance the learning ability of students. Handouts should not be long winded and writing should not be descriptive. In fact it is more effective if you use as little writing as possible and make sure that the topic is not fully discussed in the handout. Handouts should have blank spaces where student can write on the diagrams, sketches and photographs during the lecture.

2.9 *Models*

The usefulness of small physical models in explaining the conceptually difficult principles in Engineering Mechanics, Mechanic of Solids and Structural Analysis cannot be under estimated (Karim 1993). The author believes that these are probably the most effective teaching aids one can use to explain abstract concepts, principles and ideas. A lecturer can easily design, devise and fabricate physical models such as truss models with balsa wood and drinking straw; models of beams made of sponge; plastic rod to explain buckling of columns. A few diagrams of such models are given below (Figure 5, 6, 7 & 8).

2.10 *Practice problems*

To link the foundational learning in the classroom with the application in the real world the Author developed a number of problems (questions) which are directly related to practical engineering problems. A UNESCO



Figure 5. Eccentrically loaded member.



Figure 6. Shear in steel bolt and timber.

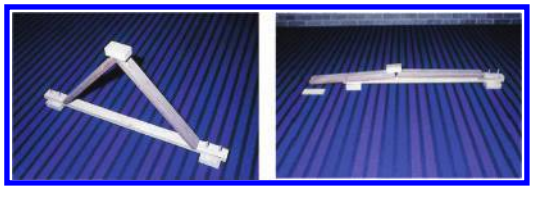


Figure 7. Horizontal and vertical shear in timber.

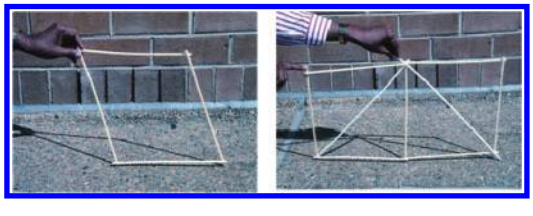


Figure 8. Construction of trusses with straw.

study (Grayson 1977) on the design of curricula has this to say:

" ..One series of studies conducted at the college level reported that 50 percent of the material known when a student finished a certain college course is forgotten within one year, and 80 percent is forgotten in two years. These students also have suggested certain conditions which can greatly reduce the amount that is forgotten. One such condition is the opportunity to use the new knowledge in daily life. This suggests that objectives concentrating on specific knowledge are more attainable, and the results are more permanent, when there are opportunities for the students to use this knowledge in their daily activities"



Figure 9. Vertical Cantilever.



Figure 10. Tension Structures (Outside class room).



Figure 11. Pedestrian Bridge: Member in tension and bending.

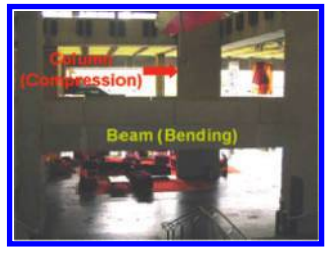


Figure 12. Frame structure (Outside class room).

The author developed some practice problems from structures in and around students' immediate environment (in and around UTS City campus). Some of these structures and structural members from the surrounding environment are given below (Figures 9, 10, 11 & 12)

3 CONCLUSION

It is important that Faculty/School of Engineering does recognize that these subjects like Engineering Mechanics, Mechanics of Solids and Structural Analysis are great important to one to become good professional engineers and senior experienced academicians should teach these subjects. Lecturers who are in charge of these fundamental subjects are to accept the fact that students experience problems in learning these subjects. Once this is recognized, the lecturer can adopt a variety of teaching strategies which make these subjects interesting and comprehensible so that learning can be effective and enjoyable. Experience has shown use of the methods and strategies described in this paper have proved successful in creating interest and enthusiasm, and the author has received consistently positive feedback from students.

REFERENCES

Goldfinch, T., Carew, A.L. & McCarthy, T.J. 2008. *Improving Learning in Engineering Mechanics: The Significance of Understanding*; Proceeding of AaeE Conference. Yeppoon.

Goldfinch, T., Carew, A.L., Gardner, A., Henderson, A., McCarthy, T.J. & Thomas, G. 2008. *Cross-institutional comparison of mechanics examinational: A Guide for the Curious*; Proceeding of AaeE Conference. Yeppoon.

Dwight, R., & Carew, A. 2006. *Investigating the causes of poor student performance in basic mechanics*. Australian Association of Engineering Education 17th Annual Conference. Auckland, New Zealand.

Grayson, P.L. 1977. *The Design of Engineering Curricula*. UNESCO, Paris.

Karim, M.R. 2002. *Teaching fundamentals of engineering, 6th Baltic Region Seminar on Engineering Education & 2nd German Seminar on Engineering Education*. Wismar/Warnmunde, Germany.

Karim, M.R. 1993. *Use of Simple Physical Models to Facilitate Students' Learning, Proc. conf. on Aiming for Quality in Engineering Education.* AAEE, Auckland, New Zealand.

Rezaul K. 1993. *Interesting, Effective and Enjoyable Approaches to Teaching Fundamentals of Engineering. Teaching Quality and Quality of Learning in Professional Courses* (pp. 147–153). Australasian Government Publishing Service, Canberra.

Research and Applications in Structural Engineering, Mechanics and Computation – Zingoni (Ed.)
© 2013 Taylor & Francis Group, London, ISBN 978-1-138-00061-2

Structural stability, and the complement to the differential equation

R.D. Ziemian
Bucknell University, Lewisburg, PA, USA

ABSTRACT: A fundamental understanding of structural stability is a requirement for engineers who design metal structures. Given that sophisticated computer analysis software tools are only now becoming more readily available, the teaching and learning of structural stability has been and continues to be heavily rooted in the development and solution of the related differential equations. For many structural engineering students, who may not be well versed or interested in this level of math, basic structural stability concepts are not being learned because of their perception that an understanding of structural stability requires the ability to be proficient in solving differential equations. To compensate for this and given that in-class physical laboratory testing is often impractical, faculty often resort to descriptions of experimental tests and the results obtained. Although this is a significant step in the right direction, this passive learning approach is not ideal. With this in mind, the author has developed a series of nine stability learning modules that employ readily available and relatively easy to use nonlinear analysis software. Although no statistical data has been gathered, this "virtual" laboratory experience has been in use for the past year at many universities in the U.S. and the results are very encouraging. This paper will provide an overview of these modules, including their consistent format, dissemination, and related instructional YouTube videos. A detailed description of one of the modules, including the simple finite element model employed, is also provided.

1 INTRODUCTION

With high strength-to-weight and stiffness-to-weight ratios, structural metals such as steel and aluminum continue to provide architects with unique opportunities to design elegant systems that are often distinguished by their slender form. This slenderness, however, comes with the need for designers to learn and understand essential topics in structural stability. Unfortunately, many engineering students and practitioners have linked a comprehension of stability concepts to their abilities to solve the differential equations that are often used to describe the related behavior. In cases for which a student's interest in such mathematics is not prominent, important concepts of structural stability are often deemed too difficult to learn and an inherent weakness develops in their abilities and confidence to design metal structures. In response to this, and with the overarching goal of providing students and engineers the opportunity to *see the forest for the trees* when it comes to this topic, the author has developed a series of nine learning modules in which nonlinear computational analysis is used as a virtual laboratory for learning many of the important concepts related to designing for stability. This paper will present an overview of these modules, which include topics such as elastic and inelastic flexural and lateral-torsional buckling, inelastic force redistribution, local buckling, bracing, and second-order effects. The modules have been prepared in a generic form so that many nonlinear analysis software packages could be employed. For those without access to such software or who are unsure as to whether or not their software will suffice, the author has made a nonlinear analysis program available at no cost. This software MASTAN2 (2012) is described below. Having employed these learning modules in undergraduate steel design courses, the author is convinced that the use of a virtual laboratory can significantly compliment current methods for teaching and learning important structural stability concepts.

2 BACKGROUND

The stability learning modules are intended for use in undergraduate and/or graduate level steel design, aluminum design, and/or structural stability courses. Of course, practicing engineers are also encouraged to continue their education by completing these exercises. The modules are independent of one another, and hence, faculty may employ any number of the modules depending on the objectives of their courses.

Although all of the modules can be completed with the nonlinear analysis software MASTAN2, they have been prepared in generic form so that alternative nonlinear analysis software could be employed. Each module is provided as PDF and Microsoft Word files along with accompanying Microsoft Excel spreadsheets. In addition to instructions, questions, and suggestions for further study, these files include links to YouTube videos that demonstrate the use of MASTAN2.

2.1 *Nonlinear analysis software requirements*

Understandably, the key component in this virtual laboratory approach is the structural analysis software. The analytical requirements for modeling structural stability topics may be defined in the following four general categories, with each including specific attributes.

1. Stiffness contributions:
   axial, flexural, and shear deformations
   torsion, including St. Venant and warping resistances
   connection restraint
2. Destabilizing effects:
   second-order effects, including system P-Δ and member P-δ contributions
   imperfections, including frame out-of-plumbness and member out-of-straightness
   partial yielding accentuated by the presence of residual stresses
   plastic hinges based on axial force and major- and minor-axis bending contributions
3. Solution procedures:
   two- and three-dimensional incremental and/or iterative schemes
   critical load (eigenvalue) analysis
4. Stability limit states:
   in/elastic flexural buckling
   in/elastic lateral torsional buckling
   combined in/elastic flexural and lateral torsional buckling
   in/elastic frame buckling
   plastic mechanism(s)

Several software packages are currently available that can handle most, if not all, of the above requirements. Examples of commercial programs available in the U.S. include ABAQUS, ADINA, ANSYS, PERFORM3D, LARSA4D, and SAP2000. There are also several educational programs that meet most of the above criteria, including, OpenSees, FE++2012, GTSABRE, BASP, Arcade, Dr. Frame, GBTUL, and MASTAN2. The author is confident that similar programs have been developed in other parts of the world, including Europe, Asia, and Australia. Factors to consider in deciding which software to employ include, price and availability to students, ease of use and steepness of original learning curve, experiences from other courses that may also make use of analysis software, and which of the stability learning modules are to be accomplished.

2.2 *MASTAN2*

To assure that the stability learning modules can be completed with a minimum amount of overhead to the faculty member and his/her students, the author has made the nonlinear analysis software MASTAN2 available via a web download at no cost. This software is PC and Mac compatible and does not require any third-party software; although it can also be executed on any computing platform in which MATLAB (2013) is available.

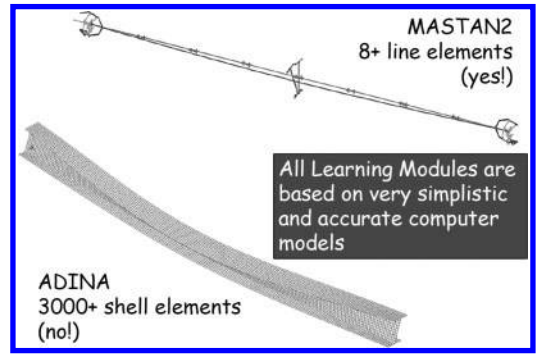


Figure 1. Example of a MASTAN2 model used to learn about in/elastic lateral torsional buckling.

The MASTAN2 software provides an easy to use graphical user interface and all of the analysis capabilities defined in the previous section. To do so, the program employs 14 d.o.f. line elements that include axial, bending, shear, and torsion (both St. Venant and warping) resistances. Second-order effects are modeled through the use of element geometric stiffness matrices and an incremental/iterative solution scheme based on an updated Lagrangian formulation (McGuire *et al.* 2000). A concentrated plasticity model, with a yield criterion that is a function of axial force and major- and minor-axis bending, is used to model material nonlinearity. An additional analysis parameter may be set to invoke a modified tangent modulus approach (Ziemian & McGuire 2004) that will closely approximate partial yielding accentuated by the presence of residual stresses.

To the best of the author's knowledge, all of the universities currently assigning the stability learning modules employ MASTAN2, although its use is not a requirement. It is important to note that very simple finite element models are needed when using MASTAN2 to complete the learning modules (Figure 1).

2.3 *Format of modules*

All of the learning modules are presented in a consistent format. An overview of each module is first provided followed by the learning objectives. The general method for which the objectives will be attained is presented followed by details specific to the use of MASTAN2. A series of questions is then provided to guide the students in thinking critically about what should have been observed in the analytical study. All modules conclude with a section titled *More Fun with Computational Analysis!*. This component provides the student direction for additional studies that can be used for more breadth and/or in-depth understanding of the concepts being learned. All modules also include references to instructional YouTube videos, related literature, and prepared Microsoft Excel spreadsheets to assist with data recording.

All of the modules reference the American Institute of Steel Construction's (AISC) *Specification for Structural Steel Buildings* (2010). Original Microsoft Word and Excel documents are provided for all learning modules thereby allowing them to be easily modified for other non-U.S. steel building codes.

3 OVERVIEW OF LEARNING MODULES

The following nine modules are currently available at the MASTAN2 website or through the American Institute of Steel Construction's Partners in Education website (www.aisc.org). Faculty members may obtain solutions to the learning modules by contacting the author.

3.1 *LM1: Elastic column buckling and the effect of end restraint*

Using critical load (eigenvalue) analyses, the elastic flexural buckling strength of a system of parallel columns with various degrees of end restraint is investigated. By creating an analysis model of six parallel columns that only differ in end restraint (Figure 2), students experience first-hand the changes in column capacities and respective buckling modes that result from varying the support conditions. Students confirm the theoretical effective length K-factors that are given in the literature, including Table C-A-7.1 of the Commentary on the AISC *Specification for Structural Steel Buildings* (2010).

3.2 *LM 2: Factors influencing the flexural buckling strength of compression members*

Using computational analysis as a virtual laboratory, the main factors that impact the in/elastic flexural buckling strength of steel wide-flange sections with nonslender elements are investigated. These factors include member slenderness, material nonlinearity, initial imperfections in geometry (out-of-straightness), and partial yielding accentuated by the presence of residual stresses. Computed strengths are presented in the form of column curves (Figure 3), which are further compared with the corresponding nominal strength curve defined in Chapter E of the AISC *Specification for Structural Steel Buildings* (2010). In completing this study, students further recognize the limitations of the theoretical Euler buckling solution and gain an appreciation of the impact that initial imperfections and partial yielding/residual stresses have separately and collectively on the flexural buckling strength of a column.

3.3 *LM3: Effective length K-factors for frame members*

By preparing and investigating a computational model of a one-story, one-bay planar frame, effective length K-factors for compression members in structural systems are investigated. In addition to studying cases of sidesway inhibited and not inhibited, elastic and inelastic buckling is explored. The computational results are compared with alignment chart methods, thereby allowing the student to assess the applicability of the assumptions made in developing the alignment charts.

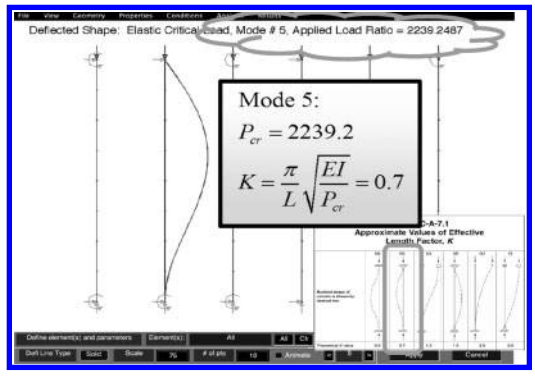


Figure 2. Example results from LM1.

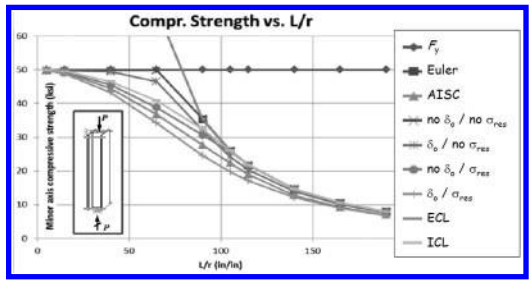


Figure 3. Column capacity curves obtained as part of LM2.

3.4 *LM4: Factors influencing the strength of flexural members*

Using an approach very similar to LM2 and the computational model shown in the upper right portion of Figure 1, the main factors that impact the major-axis flexural strength of an unbraced steel wide-flange section with compact elements are investigated. These factors include unbraced length, partial yielding accentuated by the presence of residual stresses, and initial imperfections in geometry (out-of-plane out-of-straightness). Strength limit states defined by full yielding of the cross-section (plastic hinge) and in/elastic lateral torsional buckling are studied. Computed strengths are presented in the form of beam strength curves (Figure 4), which are further compared with the corresponding nominal strength curve defined in Chapter F of the AISC *Specification for Structural Steel Buildings* (2010).

3.5 *LM5: Lateral-torsional buckling of beams with moment gradient*

The influence of a non-uniform moment distribution on the lateral-torsional buckling capacity of compact wide-flange beams is studied. Equivalent uniform

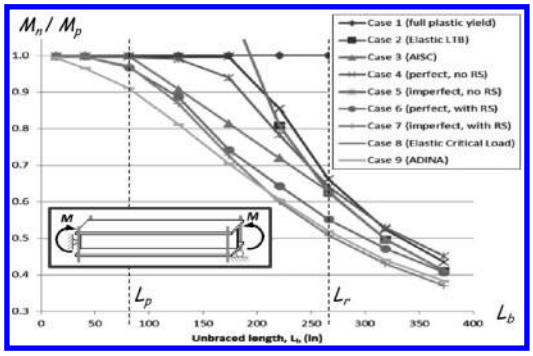


Figure 4. Beam capacity curves obtained as part of LM4.

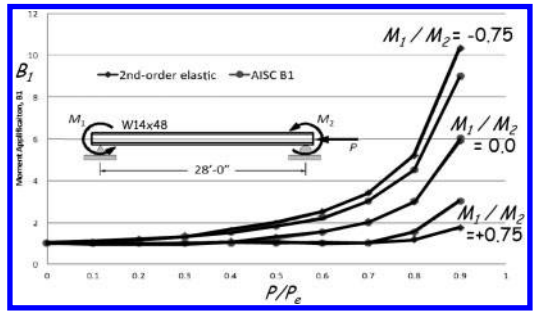


Figure 5. Moment amplification curves obtained in LM7.

moment C_b factors back-calculated from computational analyses are compared with values computed using two longstanding equations, one appearing in Chapter F of the AISC *Specification for Structural Steel Buildings* (2010) and the other in the commentary to the Specification. In addition to investigating several different possibilities of moment gradient, including linear, bi-linear, and parabolic, the impact of providing an interior brace point is also studied.

3.6 *LM6: Continuous beam design by elastic and inelastic analyses*

The design of a three-span laterally braced beam of compact section is investigated using elastic and inelastic analyses. In addition to observing differences in load carrying capacity and efficiency, force and moment redistribution as a result of member yielding is explored. In this learning module, students "compete" against one another in two categories to see who can provide the least weight design for a given load condition. The categories are (1) same section size for all three spans of the continuous beam, and (2) different section sizes may be used in each of the three spans.

3.7 *LM7: Second-order (P-Δ and P-δ) effects*

In this learning module, second-order effects in members subject to the combined effect of compression and flexure (beam-columns) are investigated. Results obtained using rigorous second-order elastic analyses are compared with approximate moment amplification factors given in Appendix 8 of the AISC *Specification for Structural Steel Buildings* (2010) and recommended in the literature. Both frame sway P-Δ and member deforming P-*δ* effects are studied.

Emphasis is placed on the relationship between the amount of moment amplification B_1 in a member and the ratio of axial force resisted to elastic critical load, P/P_e. Students also investigate the impact that single or double (reverse) curvature bending has on the degree of moment amplification (Figure 5).

3.8 *LM8: Strength of Beam-Columns*

Students employ second-order inelastic analyses to study the capacity of beam-columns subject to various

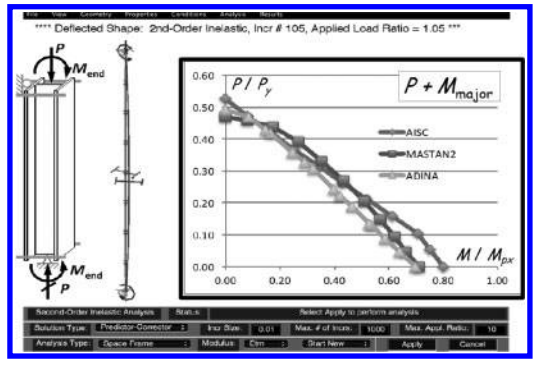


Figure 6. Beam-column capacity curves obtained in LM8.

combinations of axial force and bending moment. Both major- and minor-axis flexure of steel wide-flange sections with compact elements are investigated. Nominal strength interaction curves per the requirements of Chapter H of the AISC *Specification for Structural Steel Buildings* (2010) are compared with equivalent curves based on finite element analysis results (Figure 6). Strength limit states defined by in/elastic flexural and lateral torsional buckling as well as full yielding of the cross-section (plastic hinge) are observed. In all cases, computational analyses account for partial yielding (accentuated by the presence of residual stresses) and initial imperfections in geometry. LM8 is the logical extension of LM2, which studies the strength of compression members, and LM4, which explores the strength of flexural members.

3.9 *LM9: Design by the direct analysis method*

This learning module guides the student through the design of a simple portal frame using a relatively new approach termed the Direct Analysis Method, which is defined in Chapter C of the AISC *Specification for Structural Steel Buildings* (2010). Rigorous second-order analyses are employed to check the adequacy of compact doubly symmetric members subject to axial force and flexure.

The module includes two methods for accounting for initial frame sway imperfections and stiffness reduction due to partial yielding. These methods

include explicit modeling and the use of equivalent notional loads. Students gain competency in using code-based interaction equations to check the adequacy of beam-column members. The use of second-order to first-order drift ratios is also assessed as an indicator of a system's sensitivity to second-order effects.

4 EXAMPLE

The specific details for Learning Module 7 – *Second-order (P-Δ and P-δ) Effects* are provided below. Due to space limitations, the tables and figures are not included herein. Similar details are provided for all of the stability learning modules described above.

4.1 *Overview*

The design of a laterally braced beam of compact section is investigated using elastic and inelastic analyses. In addition to observing differences in load carrying capacity and efficiency, force and moment redistribution as a result of member yielding is explored.

4.2 *Learning Objectives*

- Employ rigorous second-order elastic analysis to determine required strengths in beam-columns.
- Observe the relationship between the amount of moment amplification in a member and its ratio of axial force to elastic critical load.
- Investigate the impact single or double (reverse) curvature bending has on the degree of moment amplification.
- Compute and assess the moment amplification factor B_1 defined in Appendix 8 of the AISC *Specification for Structural Steel Buildings* (2010).

4.3 *Method*

Part 1: Prepare a computational model of the beam-column, assuming the member is a W14x48 (A992) oriented for major-axis bending and fully braced out-of-plane. Varying the amount of axial force P, employ rigorous second-order elastic analysis to complete the provided tables for the three M_1/M_2 ratios given in the header of each table. In addition to computing the amount of amplification observed $|M_{max}|_{span}/|M_{max}|_{end}$, calculate the corresponding moment amplification factor B_1 defined in Appendix 8 of the AISC *Specification for Structural Steel Buildings* (2010).

Part 2: Prepare computational models of a second set of beam-columns, assuming once again that the members are W14x48 (A992) oriented for major-axis bending and fully braced out-of-plane. Perform the rigorous second-order elastic analyses required to complete the tables provided at the end of the module.

Hints:

- Suggested units are kips, inches, and ksi.
- Do not include initial imperfections such as member-of-straightness.
- Do not include the self-weight of the member.

4.4 *MASTAN2 details*

Per a figure provided in the module, the following suggestions are for those employing MASTAN2 to complete the above studies:

- In several cases, the maximum moment may occur at any point along the member span. Thus, it would be ideal to have an element end (node) at every location. Given that this is impossible, subdividing the member into 10 elements should provide adequate sampling points.
- By leaving $A_{yy} = \text{inf}$ and $A_{zz} = \text{inf}$ when defining the section properties, shear deformations are neglected.
- For the second-order elastic analyses, use the following options:
  - Planar frame analysis type
  - Solution type: Predictor-Corrector for $P/P_e < 0.6$ and Work-Control for $P/P_e > 0.6$
  - Load increment size of 0.1
  - Maximum number of increments set to 100
  - Maximum applied load ratio set to 1.0

4.5 *Questions*

Samples of the seven questions provided in Learning Module 7 are provided below.

1. Prepare a single plot that illustrates the relationship between P/P_e (abscissa) and the amount of moment amplification (ordinate) recorded in the data tables. For each of the three moment gradient M_1/M_2 cases, provide two curves; one for the computational ratio $|M_{max}|_{span}/|M_{max}|_{end}$ and the other based on the B_1 factor. *Note to reader – the solution is provided previously in Figure 5*. Comment on the accuracy of the approximate moment amplification B_1 factor. For which moment gradient M_1/M_2 case does the approximate B_1 factor provide the most accurate results? With this in mind, which term in the B_1 equation is most likely the greatest source of error?
2. To confirm the accuracy of the analysis software you employed, please compare the data recorded in the tables with those presented in Figs. C-C2.2 and C-C2.3 of the Commentary to the AISC *Specification for Structural Steel Buildings* (2010). Did your analyses include or neglect shear deformations? Why does AISC provide two sets of results (including and excluding shear deformations)? With this in mind, does the analysis software you employed provide an adequate degree of accuracy to meet the requirements defined by the benchmark problems and solutions given in the AISC Commentary?

4.6 *Additional resources*

This section contains electronic links to (1) a Microsoft Excel spreadsheet to assist with data recording; (2) a

six-minute YouTube video demonstrating the module; (3) the AISC *Specification for Structural Steel Buildings and Commentary* (2010); and (4) the MASTAN2 website.

5 FUTURE DIRECTIONS

There are currently three additional stability learning modules under development. Two of these will be based on frame analysis software such as MASTAN2 and will include investigations of leaning columns and exercises for understanding column and beam bracing. The third module will investigate the stability of cross sections with slender elements (flanges and webs) and will be based on CUFSM, which is computational software based on the finite strip method (Schafer & Ádány 2006) and is also available for download at no cost.

6 SUMMARY

Over the past twenty-five years, the author has learned, both first hand and from many other steel design educators worldwide, that students are not learning (and in some cases not being taught) basic structural stability concepts because of what is perceived as a dual requirement of being proficient in formulating and solving differential equations. In response to this misconception, this paper presents an overview of a series of nine learning modules on structural stability that are based on readily available and easy to use nonlinear finite element analysis software. An additional focus of the modules is to provide a "virtual" laboratory in addition to or as an alternative to more costly (both financially and setup time) physical experiments. The modules have been in use for the past year in undergraduate and graduate school course at many universities in North and South America. Although no statistical data has been formally gathered, the general response to the use of these "hands-on, learn by doing" modules has been very positive in regard to comprehension and retention of fundamental structural stability concepts. In all regards, the author encourages the reader to contact him with comments or to make suggestions for other stability related modules.

REFERENCES

ADINA® (Release 8.9) [Software]. (2013). Available from http://www.adina.com/

AISC 2010. *Specification for structural steel buildings*. Chicago.

CUFSM® (Release 4.05) [Software]. (2012). Available from http://www.ce.jhu.edu/bschafer/cufsm/

MASTAN2® (Release 3.1) [Software]. (2012). Available from http://www.mastan2.com/

Matlab® (Release R2013a) [Software]. (2013). Available from http://www.mathworks.com/

McGuire, W., Gallagher, R.H., & Ziemian, R.D. 2000. *Matrix structural analysis*. 2nd ed. Hoboken: John Wiley & Sons.

Schafer, B.W. & Ádány, S. 2006. Buckling analysis of cold-formed steel members using CUFSM: conventional and constrained finite strip methods. 18th International Specialty Conference on Cold-Formed Steel Structures, Orlando, FL.

Ziemian, R.D. & McGuire, W. (2002). The modified tangent modulus approach, a contribution to plastic hinge analysis. *Journal of Structural Engineering*. 128–10: 1301–1307.

Research and Applications in Structural Engineering, Mechanics and Computation – Zingoni (Ed.)
© 2013 Taylor & Francis Group, London, ISBN 978-1-138-00061-2

International master program in structural engineering at Leipzig University of Applied Sciences (HTWK Leipzig)

K. Holschemacher & U. Quapp
Faculty of Civil Engineering and Architecture, Leipzig University of Applied Sciences, Germany

ABSTRACT: Internationalization has become an increasingly important topic in higher education systems. However, academic globalization can only be achieved by offering courses of studies in English language. The Faculty of Civil Engineering and Architecture at Leipzig University of Applied Sciences took the initiative and created an International Master Program in Structural Engineering. Intention was to generate a course of studies which brings students together from all over the world to study structural engineering in English language. This paper provides information about the International Master Program in Structural Engineering at Leipzig University of Applied Sciences. It informs about development, structure, curriculum and partners.

1 INTRODUCTION

Academic Globalization in Europe has been under way since the Declaration of Bologna in 1999 whose objectives were permeability, higher transparency and acceptance of university degrees across Europe (German Rectors' Conference 2004). But also students from outside of Europe are of interest for German universities. This has been driven by the desire to get a larger share of the academic cake which the major receiving countries of academic mobility, namely the USA and Great Britain, divide up among themselves (Michel-Quapp & Holschemacher 2009).

The most important reason for many students using the chance of academic mobility is to improve their language skills, mostly English language skill. Therefore, a university which is not offering programs in English language is less attractive for foreign students. This was the motivation for the Faculty of Civil Engineering and Architecture at Leipzig University of Applied Sciences to offer an International Master Program in Structural Engineering to students from all over the world.

2 INTERNATIONALIZATION AT GERMAN UNIVERSITIES

One important measure in universities' internationalization strategies is to increase the percentage of foreign students. In the last years, the number of foreign students at Faculty of Civil Engineering and Architecture continuously increased. Now, the Faculty has more than 20 percent foreign students. The main reason for this is a part-time study course in civil engineering which is running in the neighbored country Austria. Its advantage is a high number of foreign but German speaking students. Students from other foreign countries are rather rare. This is caused by universities' high language requirements and the bad students' German language skill. Fewer and fewer students are speaking German language as the first foreign language. Even in countries in which traditionally German language was taught in school such as Eastern Europe or Vietnam, the importance of the German language is decreasing.

Regarding the degree structure, Germany is well prepared for students from all over the world. As a consequence of the Bologna Process, comparable degrees like bachelor and master were implemented during the last years. In Germany, the former first cycle degrees leading to the degree *Diplom-Ingenieur* with duration of four or five years was replaced by bachelor programs with duration of three or four years and master programs of one or two years (Standing Conference of the Ministers of Education and Cultural Affairs of the Länder in the Federal Republic of Germany 2010). Most of the German universities decided for three years' bachelor and two years' master programs or 3.5 years' bachelor and 1.5 years' master programs.

One of the problems German universities have regarding internationalization is the lack of English-speaking lecturers. So, it was not a matter of course that language skills played a role in appointment procedures for professorships or lectureships in the last years. Although universities now pay more attention on language skills of applicants there is still a high number of lecturers who are not able to give courses in English language. This fact leads to difficulties for

a higher education institution to develop a course offer for English-speaking foreign students.

3 PROGRAM INFORMATION

3.1 *Development*

The intention of the Faculty of Civil Engineering and Architecture of Leipzig University of Applied Sciences was to create a program which is not too specialized to be attractive to plenty of students worldwide. Thus, a master in structural engineering seemed to be the right decision. Beside the long faculty's tradition in structural engineering, one of the reasons for creating a master in the field of structural engineering was the great similarity of structural engineering standards used all over the world. Thus, students will be able to apply their new acquired knowledge in all fields of building industry worldwide.

One difficulty in creating an English-speaking structural engineering master program was the small number of structural engineering professors with sufficient English language skills to give courses with. Finally, five professors and the same number of scientific staff members have been willing to engage in this course of studies.

As mentioned before, in Germany a master program lasts from one to two years. In each academic year, students must have the possibility to award 60 credit points according to the European Credit Transfer and Accumulation System (ECTS), while credit points will be awarded for each successful completed course. 60 credit points correspond to 1800 students' working hours (Standing Conference of the Ministers of Education and Cultural Affairs of the Länder in the Federal Republic of Germany 2010). This is plenty of work for the faculty as well as for the students.

The program started in 2010 in cooperation with the first partner which was a partner university in China. In October 2012, the HTWK Leipzig welcomed already students from two nationalities in Leipzig. The study course is supported by an institute for international higher education cooperation that takes care of all organizational issues.

3.2 *General information*

The master course in structural engineering is a two-year's master program offered to students pursuing a specialization in structural engineering. In close cooperation with partner universities the academic education is organized in a 1 year plus 1 year model. The first year must be completed at the home university of the students in accordance with the curriculum of the program. After passing all courses of the first year, students spend the second year at Faculty of Civil Engineering and Architecture at Leipzig University of Applied Sciences. There, all remaining courses must be finished and the master thesis must be elaborated. After successful completion of all courses, the academic degree Master of Science "M.Sc." of Leipzig University of Applied Sciences is granted.

The program is offered only in cooperation with partner universities. These universities teach all first year courses in accordance with the curriculum developed by Leipzig University of Applied Sciences. This is necessary because the second year courses base on the knowledge students gained in the first year at home.

3.3 *Curriculum*

The course content of International Master Program in Structural Engineering covers advanced topics of civil engineering with the focus on structural engineering. It consists of two different kinds of courses, compulsory and elective courses. Both were executed as lectures, tutorials, seminars or practical trainings including computer work and accompanied by individual studies, tutorial tasks and course works. The program contents base on regular civil or structural bachelor programs, for this reason only few scientific basics such as mathematics, material sciences and building physics are taught. Teaching materials will be of course offered in English language.

While the first year, students follow the courses at their home university. There, subjects like numerical methods, Finite Element method and surface structures I, prestressed concrete construction, spread foundation, bridge design, composite structures and structural dynamics are taught. Within this year, students must select five elective courses from the elective subject pool including modern and historical building materials, construction materials and environment, energy efficient and environmentally compatible building, glass and plastic materials for structural engineering, selected topics in steel structures, selected topics in reinforced concrete, three dimensional concrete structures and precast concrete structures.

The second year students spend at Faculty of Civil Engineering and Architecture at Leipzig University of Applied Sciences. Students have to attend courses in Finite Element method and surface structures II, selected topics of structural mechanics, experimental mechanics, reinforced concrete structures and fire protection in structural engineering. Courses completed at the home universities and marks of the first year are recognized at Leipzig University of Applied Sciences.

The improvement of the students' English language proficiencies is one of the aims of the program. That's why students must attend English lessons for the first 1.5 years. While the English courses the focus is on academic English, with the intention to train students in various subject-specific terms in the field of civil and structural engineering as well as in academic writing in the foreign language.

The study program will be completed by passing the final examination, which means a master thesis and a colloquium. For preparing the master thesis 675 students' working hours are necessary, for preparing the colloquium 225 hours. That's why in the fourth

semester no other courses are offered. The intention is that students focus on their master thesis. While preparing the master thesis, students are part of a professor's research team with the possibility to do experiments by their own, to produce specimens made of concrete and so on. In this way students gain research experience and work scientifically as well as practically.

Small groups, currently 15 students, allow the lecturers to work individually with the students. Problems of understanding can be solved quickly and directly. So, students have more benefit from the classes.

Between the arrival in Leipzig and the start of the lessons, a free two-week's German language and regional cultural studies course is offered to the students by the Leipzig University of Applied Sciences. Most of the students are enthusiastic about the German language and continue their German language training at their own expense.

3.4 *Admission regulations*

The program is offered only in cooperation with partner universities. That's why only students from partner universities can apply for the program.

To study the program, applicants must hold a bachelor degree or higher in civil or structural engineering after studying at least three years on university level (Leipzig University of Applied Sciences 2011). For students from various countries like China there is a requirement for a bachelor degree with at least four years study time. This requirement results from the specialty of Chinese Curricula to include interdisciplinary courses such as politics, sports etc. with the consequence of less time for subject-specific courses.

If foreign partner universities award a degree higher than a bachelor degree, some courses can be recognized on the master curriculum. If all courses of the first master's year will be offered in this degree higher than a bachelor degree, students can get recognized the completed courses. The advantage for students is the possibility to be enrolled directly to the second master's year in Leipzig without spending the first master's year at the home university. In this case the recognition of courses is concluded in a written equivalency agreement between the foreign partner university and the Leipzig University of Applied Sciences. For this reason, the program manager of Faculty of Civil Engineering of Leipzig University of Applied Sciences compares the program contents and decides about courses to recognize.

Additionally to the subject-specific qualification, students must prove sufficient English language skills. Non-native English speakers have to verify the level of their language proficiency by TOEFL Test (Test of English as a Foreign Language) or by an equivalent recognized English language test. These language requirements are necessary to guarantee ideal conditions for a successful completion of the degree. Without sufficient language proficiency students can't follow the lectures and are not able to deliver their best performance in examinations.

3.5 *Organizational information*

The program is offered in cooperation with a university institute for international education cooperation. The institute provides support for universities interested in offering international courses of studies.

Important in an international program is, aside from the academic service, also a comprehensive service in all administrative and organizational issues for the international students.

The international students studying in this program often haven't got any or very limited German language proficiency. Therefore, they need support in all organizational things like visa application, insurances, accommodation, transport from the airport and bureaucratic procedures. The institute cares about all students' matters not connected with academic issues. Its stuff accompanies them to the doctor, to the foreigner's registration office, to the bank and so on.

3.6 *Fees*

The academic as well as the full students' service provided by Leipzig University of Applied Sciences and the University Institute for International Education Cooperation is subjected to charges. Currently, the service fee is about 13.200 Euros (18.000 US-Dollars). Included in this fee are all courses and examinations, experiments, the master thesis, the colloquium etc. Furthermore, organizational support such like transport from airport to the dormitory and first equipment package containing food and beverages and so on in the rooms of the dormitory are covered. Additionally, all foreign students must prove to the foreigner's registration office that they can cover living costs of one year. This will be done by a bank deposit. From the bank deposit the rent for the dormitory rooms, the rent deposit, health and liability insurance, fees for residence permit and membership fees for student organization will be paid. From the remaining amount of money on the bank account the student can withdraw money for covering all other personal living costs. After leaving Germany, students will get back the rent deposit.

3.7 *First experience*

In the year 2010, the first group of this program started at the first partner university in China. One year later, these 15 students were welcomed at Faculty of Civil Engineering and Architecture in Leipzig to their program's second year.

Very quickly the first group became familiar with the German life and the procedures at the university. The entire program's staff was surprised about the high activity and independence of the international students. In their free time they traveled around Germany and Europe, continued learning the German language at their own expense and came in contact with other students.

The marks of the examinations after one term were better than expected. Only two students had to repeat an examination. From the first group of 15 students 6 students graduated in 2012. The other students decided to take more time to prepare the master thesis. They will graduate some weeks later.

Also, some leisure time activities were offered to the International students. One of the highlights was a table tennis championship with students, lecturers and academic staff.

In 2012, a Syrian university joined the program and sent some students for the second group. The relationship between Chinese students and Syrian students is friendly and relaxed.

Currently, the faculty is in negotiation with some more interested universities of cooperating in this program.

4 CONCLUSION

Internationalization can work, even if universities do not have a plenty of human or financial resources. Necessary are good concepts, experienced partners and much enthusiasm. The majority of universities already discovered the potential of and the need for internationalization in a globalized academic world.

The future lies in international programs in English language. There is no better and easier way to bring foreign students to universities than International programs. The organizational and academic efforts-benefits-ratio is much higher in the International course of studies than for each individual foreign student coming e.g. with Erasmus program.

With English speaking staff, motivated lectures and intercultural openness everybody, students as well as university staff, will benefit from such a program.

REFERENCES

German Rectors' Conference (ed.) 2004, *Bologna Reader – Bologna Declaration:* 277, Bonn: HRK Service-Stelle Bologna.

Leipzig University of Applied Sciences, Study Regulations for the Structural Engineering International Master's Degree Program 2011. http://structuralengineering.de.

Michel-Quapp, U. & Holschemacher, K. 2009. What contribution does quality assurance make to academic globalization in engineering. *In Proceedings Volume I of the 13th World Multi-Conference on Systemics, Cybernetics and Informatics; The Second International Symposium on Academic Globalization*, *Orlando 10–13 July 2009*. Winter Garden Florida.

Standing Conference of the Ministers of Education and Cultural Affairs of the Länder in the Federal Republic of Germany 2010. *Common structural guidelines of the Länder for the accreditation of Bachelor's and Master's study courses*: 2–3, annex p. 2, http://www.kmk.org/dokumentation/veroeffentlichungen-beschluesse/wissenschaft-hochschule. html.

Research and Applications in Structural Engineering, Mechanics and Computation – Zingoni (Ed.)
© 2013 Taylor & Francis Group, London, ISBN 978-1-138-00061-2

Author index

Abambres, M. 1157
Abdel-Mooty, M.A.N. 1877
Adams, J.M. 835
Adetunji, A.R. 2143
Adewoye, O.O. 2143
Afshan, S. 1471
Aguilar-Ramos, G. 357
Akinluwade, K.J. 2143
Akinyele, J.O. 1599
Ala, M.R.A. 363
Albertyn, H.L. 1261
Albrektsson, J. 1965
Aliabadi, M.H. 2193
Almeida, S.J.C. 1959
Álvarez, J.A. 405
Ambrósio, J. 157
Andersen, L.V. 131, 2497, 2515
Andersen, S.M. 2497
Anderson, J.R.B. 747
Andrade, A. 1059
Andreassen, M.J. 1003
Andres, M. 229
Antonaci, P. 2217
Antretter, T. 505
Arangio, S. 2353, 2457
Arboleda, D. 1567
Ariyanayagam, A. 1993
Arrayago, I. 1435
Arroyo, B. 405
Ashraf, M. 301, 2027
Ashrafi, S.A. 687
Assas, M.M. 1555
Astaneh-Asl, A. 211
Ataei, A. 499
Ataoglu, S. 387
Audebert, M. 2021
Auletta, G. 2303
Azhari, M. 429

Babafemi, A.J. 1593
Baddoo, N.R. 1471
Badet, R.X. 1279, 1285
Bahr, M. 519
Bai, L. 1249
Baier, B. 829
Bakhti, F. 1341
Baldassino, N. 669, 1023
Balzani, D. 411
Banthia, N. 1561
Barandun, A. 1865
Barcewicz, W. 1323
Barnardo-Viljoen, C. 651, 1531, 2065
Barrera, O. 399
Barszcz, A.M. 1183
Basaglia, C. 1029, 1083, 1249
Bathe, K.J. 3
Bayat, M. 2497
Bayat, M.R. 675
Becker, T.H. 591, 609
Becque, J. 933, 1101
Bednář, J. 1943
Bedynek, A. 1189
Beg, D. 1317
Behnam, B. 2027
Belardinelli, P. 469
Bembridge, N. 2137
Benčat, J. 111
Benfratello, S. 241
Berger, A. 149
Berhe, A.T. 1715
Betti, R. 2383
Bhengu, Z. 2525
Bisby, L.A. 1947
Blaise, N. 663
Blondeau-Patissier, R. 1981
Bocca, P.G. 2217
Bogdan, T. 341
Boissonnade, N. 1195, 1201, 1303
Bongiovanni, G. 81
Bontempi, F. 2353, 2401
Boone, S. 2151
Booth, E.D. 235
Borekci, M. 319
Borkowski, G. 741
Borowiec, A. 2521
Borri, A. 1859
Borri, C. 947, 983
Borrmann, A. 2247
Boshoff, W.P. 1593, 1679, 1729, 1895
Bouchaïr, A. 1225, 1359, 1827, 2021
Bradford, M.A. 499, 1373
Braham, C. 295, 341
Brando, G. 511, 2407
Brandrud Næss, O.E. 2053
Brands, D. 411
Brownjohn, J.M.W. 119, 2163
Brüls, O. 149
Buffarini, G. 81
Bukasa, G.M. 1137
Bukashkina, O.S. 853
Bulut, O. 387
Buru, M. 1385, 1409
Busse, D. 1497

Čáchová, M. 1745
Caddemi, S. 565
Caglayan, P.O. 353
Çaktı, E. 2275
Caliò, I. 565
Calzada, J.A. 183
Camotim, D. 17, 1029, 1059, 1071, 1083, 1095, 1119, 1157, 1231, 1249, 1303
Campeanu, B.M. 1937
Candela, M. 1859
Cannizzaro, F. 565
Canor, T. 189, 663
Cao, M.M. 799
Cao, Q. 163
Carino, C. 265
Carli, F. 265
Carlisle, M. 87
Carrascal, I. 573
Carrazedo, R. 2229
Carvalho, E.C. 175
Casafont, M. 1347
Caspeele, R. 705
Casucci, D. 229
Čejka, T. 1503
Čekon, A.M. 1813
Ceravolo, R. 69, 2187
Chan, T.M. 253
Charrett, D. 2341
Chatzi, E.N. 61
Chebet, F.C. 2525
Chen, S. 541
Chen, Y. 1421, 1477
Cheung, M.M.S. 271
Chiaia, B. 585
Chiorean, C.G. 1385, 1409
Chira, A. 1385, 1409
Chira, N. 313, 347, 1219
Chock, G. 247
Chudoba, R. 823
Cicero, S. 573
Cimellaro, G.P. 323, 2395
Clausen, J. 375
Clemente, P. 81, 201
Cocks, A.C.F. 399

Coda, H.B. 1029
Coetzee, G. 1895
Colarieti, A. 2291
Combrinck, R. 1729
Concu, G. 2259
Correa, F.N. 169
Cottam, P. 959
Criber, E. 2407
Cristutiu, I.M. 1255, 1267
Croisier, J.-L. 149
Crosti, C. 2353, 2401, 2457
Cucu, H.L. 1219
Cui, Y. 307
Cundall, P.A. 603
Cwik, M. 645, 657

D'Angelo, L. 757
da Gama, F.O.M. 1213
da Porto, F. 2433
Dagwa, I. 2137
Dall'Asta, A. 341
Damjanac, B. 603
Damkilde, L. 375, 2479
Darby, A.P. 625, 813
Darwich, H. 911
De Backer, H. 579
de Boer, A. 475
de Borst, R. 29
de Freitas, A.M.S. 829
De la Serna-Hernandez, F. 357
De Matteis, G. 511, 2407
De Muro, A. 2303
De Nicolo, B. 2259
De Roeck, G. 43, 125, 1513
De Sortis, A. 81
de Sousa Jr, J.B.M. 829
De Stefano, A. 69, 2187
de Villiers, W. 1779
De Wilder, K. 1513
Debruyne, D. 1513
Degée, H. 295, 341
Del Prado, Z.J.G.N. 175
Denoël, V. 149, 189, 663, 865
Detournay, C. 603
Detournay, E. 597, 865
Dezi, L. 1403
Dhima, D. 1827, 1981, 2021
Di Cesare, A. 1833, 1851
Dickerson, M. 847
Dinis, P.B. 17, 1071, 1095, 1119
Diógenes, H.J.F. 1427
Ditommaso, R. 2303
Dogariu, A.I. 1207
Domaneschi, M. 335
Dong, H. 2321
Dong, W. 1489
Doran, B. 1889
Dori, G. 2247
Dorka, U.E. 2081
Dubina, D. 1015, 1065, 1089, 1207
Dubois, F. 1839
Duffour, P. 959, 2105, 2117
Dulinska, J.M. 289
Dumont, A.-G. 757
Dunaiski, P.E. 1261
Dundu, M. 1107, 1137, 1273, 1415, 2123
Durif, S. 1225

Ecker, W. 505
Eckfeldt, L. 1497, 2371
Egner, H. 547
Egner, W. 547
Ekinci, E.C. 319
El Debs, A.L.H.C. 1427
El Debs, M.K. 1427
Elgohary, H.A. 1555
Empelmann, M. 1497, 2371
Erdogmus, E. 1883, 1907
Eriksen, M.B. 49
Erkmen, R.E. 481
Escobar-Sanchez, J.A. 357
Essack, M. 435
Evbuomwan, N.F.O. 1603, 1611
Evernden, M. 625, 813

Fabbrocino, G. 2253
Fabijanska-Kopacz, M. 289
Faller, G. 1845
Fantilli, A.P. 585
Federici, F. 2291
Fehling, E. 1619, 1673, 1697
Fenart, M.A. 757
Feng, Y.T. 537
Ferreira, P.S. 751, 775
Ferretti, E. 2473
Ferreño, D. 405
Fileccia Scimemi, G. 553
Fischer, G. 631
Fischer, O. 1649, 2247, 2463
Fontana, M. 1915, 1931
Fonti, R. 1859
Forthomme, B. 149
Foster, S.J. 1637
Fournely, E. 1839
Frangi, A. 1915
Franssen, J.M. 1465
Freitas, M.S.R. 1149
Frigo, B. 585
Fromme, P. 959
Fu, F. 717
Fujino, Y. 9, 223, 283

Gajda, T. 2451
Galloway, A. 613
Galvanetto, U. 2193
Gao, N. 2205
Garbin, E. 2433
García, T. 573
Gardner, L. 253, 1035, 1113, 1453, 1471
Gargab, L.O. 259
Gates, P.T. 625
Gattulli, V. 2291
Gentili, F. 1987
Georgakis, C.T. 49, 631
Ghajari, M. 2193
Ghareeb, M.A. 2421
Ghasemi, H. 2157
Gherlone, M. 911
Ghorbanpoor, A. 2151
Giambanco, G. 553
Giancaspro, J. 1567
Gilbert, B.P. 1279, 1285
Gîlia, L. 1089
Gillich, G.R. 2181, 2199
Giovine, T. 323
Giraudo, M. 1937
Giuliani, L. 1937
Gizejowski, M.A. 645, 657, 1183, 1323, 2365
Gkoumas, K. 2457
Glaubitt, A. 1661
Gliozzi, A.S. 2217
Goel, S.C. 675
Goliger, A.M. 645, 657
Gomez-Martinez, R. 357
Gonçalves, P.B. 175
Goqo, S.P. 609
Gordon, R. 2143
Gouverneur, D. 705
Gowda, K.N.N. 1703
Graziosi, F. 2291
Graça, A. 105
Gresnigt, A.M. 1317
Groenwold, A.A. 2095, 2111
Gucunski, N. 2157
Guerreiro, L. 105
Gunalan, S. 2009
Guo, W. 75
Guo, X.K. 2047
Guo, Y.-C. 2445
Guruswamy, J. 2467
Gutiérrez-Solana, F. 405

Haas, T.N. 769, 1261
Hafner, S. 1047
Halabieh, B. 917
Han, L.H. 1483
Han, N. 163
Han, Y. 1755
Hanna, S. 2105, 2117
Harte, R. 953, 1925
Hartmann, D. 989
Hasani, N. 363
Hashimoto, K. 2239
Hassanein, M.F. 1177, 1447
Heath, A.C. 1901
Hegger, J. 823, 1507, 1543
Heidarpour, A. 429, 487, 1353, 2033
Helmus, M. 971, 1807

Hendriks, M.A.N. 1871
Hertz, K.D. 1937
Hidallana-Gamage, H.D. 525
Hillemeier, B. 2211, 2281
Hisdal, J.M. 1573
Hjaji, M.A. 1125, 1131
Hodicky, K. 1655, 1685
Holčapek, O. 1745, 1775
Höffer, R. 965, 989
Holicky, M. 651
Holický, M. 2041, 2065
Hollmann, C. 1721
Holschemacher, K. 2545, 2561
Horová, K. 1999
Hossain, M.R. 301
Hosser, D. 493, 1971
Hou, J.L. 2169
Hradil, P. 1459
Hraška, B.J. 1813
Hsu, T.Y. 2235
Huang, Y. 1441
Hubert, W. 639
Hudson, M.J. 137
Hühne, C. 891, 2089
Hui, C. 1035
Hulin, T. 1655, 1685
Hummam, G. 1397
Huynen, A. 865
Hyzl, P. 1785, 1789

Ibell, T.J. 625, 813
Ibrahim, F.S. 2157
Ibsen, L.B. 2497, 2515
Immelman, D.W. 1779
Islami, K. 2383
Ismail, M. 1673

Jacob, B.P. 169
Jahanshahi, M. 443
Jaini, Z.M. 537
Jankowski, Ł. 2169
Jankowski, M. 531
Javed, A. 2315
Jeffers, A.E. 451
Jeffrey, M.R. 195
Jensen, T.M. 1519
Jiang, Y.H. 2321
Joh, C. 1631
Jönsson, J. 1003
Jowsey, A. 1977
Juliani, T.M. 2229
Juozapaitis, A. 1165
Just, A. 1691
Jyothi, M.P. 2531

Kadioglu, N. 387
Kalender-Wevers, C. 965
Kalousek, M. 1813
Kalu, P.N. 2137, 2143
Kalumba, D. 2525, 2537
Kalyoncuoglu, A. 319, 1889
Kaminski, M. 1739, 2059, 2439
Kanstad, T. 1573
Kapelko, A. 1667
Kapelko, M. 1667
Kapelko, R. 1667
Karaki, G. 2101
Karim, M.R. 2549
Karmazínová, M. 1391, 2427
Kathage, K. 807
Kawatani, M. 2239
Keerthan, P. 1041, 1077, 1993
Keip, M.-A. 393
Kelm, A. 1807
Keppert, M. 1745
Khan, F.A. 1703
Khedr, M.A. 2421
Kilber, S.J. 1243
Kim, B.S. 1631
Kim, C.W. 2239
Kim, G.-D. 897
Kim, S.W. 1631
Kim, Y.J. 1631
Kirkegaard, P.H. 131
Kishiki, S. 307
Kitauchi, S. 2239
Knapp, S. 2211, 2281
Knaust, C. 2003
Knobloch, M. 1915, 1931
Koçak, A. 319, 1889
Koh, K.T. 1631
Kohoutková, A. 1943
Kolář, K. 1745
Köke, H. 891, 2089
Kollegger, J. 1379
Koltsakis, E. 1453
Konvalinka, P. 1745, 1775
Kopf, F. 2269, 2491
Korusiewicz, L. 2509
Kotełko, M. 531
Kousgaard, A. 1883
Krabbenhoft, K. 2479
Krabbenhoft, S. 2479
Krätzig, W.B. 23
Krausche, T. 819
Krause, U. 2003
Krishnan, S. 2467
Kueres, D. 1543
Kuhn, E. 2285
Kunecki, B. 2509
Kuo, H.-C. 681
Kuo, V. 1801
Kwasniewski, L. 859

Labusch, M. 393
Lacalle, R. 405
Lachmann, S. 989
Ladar, I. 313, 347
Ladkany, S.G. 1715
Lagoda, G. 2451
Łagoda, M. 787
Lam, D. 699
Landesmann, A. 1083
Langbecker, T. 2071
Lange, D. 1965
Lange, J. 901, 1311, 1329
Lantsoght, E.O.L. 475
Laußat, L. 971, 1807
Lava, P. 1513
Lechner, T. 1649
Lee, S.-Y. 897
Lee, S.S.M. 1373
Lei, J.Q. 793
Leimbach, K.R. 989
Leira, B.J. 2053
Lenci, S. 469
Leoni, G. 341, 1403
Lepidi, M. 2291
Leutbecher, T. 1673
Li, D.S. 2327
Li, G.Q. 541, 2047
Li, K. 87
Li, L.J. 2445
Li, M. 1489
Li, S. 2205
Li, Y. 1291
Li, Y.Y. 799
Liao, W.-C. 675
Liao, W.I. 2235
Lim, J. 1107
Lim, J.B.P. 2123
Lim, J.H. 2123
Lima, L.R.O. 1213
Lin, X.-K. 2333
Liou, G.S. 681
Liu, D. 1311
Liu, H. 939
Liu, Q. 2321
Liu, S. 1755
Liu, X. 989
Liu, Y.S. 2047
Loganathan, S. 2071
Loh, C.H. 2235
Löhnert, A. 2003
Lombaert, G. 43, 125
Long, E. 217
Lopez-Batiz, O. 357
Lopez-García, D. 323
Lord, C.E. 2315
Lorenz, P. 1697
Lourens, E. 43
Lu, Y. 541, 2175
Lugni, C. 983
Luongo, A. 1009
Lupascu, D.C. 393
Lupi, F. 947

Maciejewski, K. 2521
Madrazo, V. 573
Madsen, S. 2515
Maes, K. 43
Magnucka-Blandzi, E. 879
Magnucki, K. 879

Mahendran, M. 1041, 1077, 1993, 2009
Maher, A. 2157
Maj, M. 1739, 2059, 2439
Maj, W. 2263
Mania, R.J. 531
Manzini, G. 1023
Mao, L. 2175
Marchis, I. 1409
Mariani, V. 1871
Marinkovic, D. 457
Marino, E. 983
Maroney, B. 277
Martin, W. 2415
Martinelli, L. 335, 2377
Martins, A.D. 1095
Masarira, A. 2077
Maślak, M. 2015
Mathias, N. 217
Matta, E. 69, 2187
Mattiello, E. 49
Mbangagoye, B. 1839
Mboya, H.A. 1769
McLeod, C.H. 1549
Mehidi, N. 1359
Mehrabani, R.V. 1537
Meins-Becker, A. 1807
Melcher, J.J. 1391
Mendrok, K. 2263
Mensah, K.K. 1531, 2065
Mi, F. 417
Miah, M.S. 61
Middendorf, B. 1661, 1691
Mikl, M.J. 505
Miláčková, K. 1763, 1795
Mimoune, F.Z. 1359
Mimoune, M. 1359
Mirambell, E. 1189, 1435
Mirzaei, A. 463
Misiunaite, I. 1165
Mmusi, M. 2077
Modena, C. 2433
Mohamed, M.A. 1335
Mohareb, M. 1125, 1131
Mojsilović, N. 1865
Mondschein, P. 1763
Monreal, N. 2003
Monti, A. 1987
Moutou Pitti, R. 1839
Mrema, A.L. 1769
Mühlhausen, A. 2081
Mulas, M.G. 2377
Munirudrappa, N. 1709, 2467
Munro, D.P. 2095
Murthy, M.K. 2467
Muscolino, G. 55
Muthumani, K. 1709

Nader, M. 277
Naess, A. 2053
Nagaraja, P.S. 1703
Nagy, W. 579
Naji, K.K. 93
Nanni, A. 1567
Napier, J.A.L. 597
Narayana, G. 2531
Nasly, M.A. 537
Natário, P. 1231
Naveen, R. 1709
Nazar, S. 2315
Nedelcu, M. 1219
Needleman, A. 29
Nelke, H. 901
Nethercot, D.A. 1035
Neto, J.M. 1959
Neto, M.A. 157
Nicoletti, M. 81
Nielsen, J.H. 1685
Niemann, H.-J. 639, 947
Nigro, D. 1833
Nishikawa, H. 329
Novotny, M. 1735
Nowak, K. 1819
Nowak-Dzieszko, K. 1819
Nseir, J. 1195, 1201, 1303
Nunes, D.L. 1255, 1267
Nunes, E.F. 829
Nunziante, L. 369
Nussbaumer, A. 757
Nyawako, D.S. 137

Obaya, R. 183
Obiała, R. 1953
Obón Santacana, F. 2081
Obręb̨ski, J.B. 841, 871
Ohtsuka, T. 1931
Olawuyi, B.J. 1679
Oliveira Pedro, J.J. 729
Orr, J.J. 813
Ou, J.P. 2169
Øverli, J.A. 1519
Oyguc, R.A. 2359

Páez Chávez, J. 181, 207
Palizzolo, L. 241
Pampanin, S. 1833, 1851
Pan, B. 939
Pan, Y. 271
Panizza, M. 2433
Papán, D. 111
Pariciani, T. 1987
Park, S.Y. 1631
Pasternak, H. 819
Pastor, M.M. 1347
Pau, A. 67
Paul, S.C. 619
Pavic, A. 119, 143, 2163
Pavlovskaia, E.E. 207
Pazoki, M. 429
Pereira, E.B.R. 735
Perera, N.J. 525
Perneş, P. 1065
Perotti, F. 2377
Petrini, F. 1987, 2457
Phan, T.D. 2123
Piccardo, G. 1009
Pietsch, M. 2269, 2389
Pirringer, S. 1379
Pistrol, J. 2491
Pittino, G. 505
Ponzo, F.C. 1833, 1851, 2303
Popa, A.G. 1219
Portilla, J. 405
Potenza, F. 2291
Praisach, Z.I. 2181, 2199
Prodan, O. 313, 347
Providência, P. 1059
Pulsfort, M. 2503

Quapp, U. 2545, 2561
Quattrone, A. 69, 2187

Raabe, D. 411
Racher, P. 1827
Racic, V. 119, 143
Rainieri, C. 2253
Ran, J.H. 799
Ranzi, G. 1009, 1403
Rao, M.N. 885, 907
Rasmussen, K.J.R. 997, 1101, 1279, 1285, 1297
Real, E. 1189, 1435
Rega, G. 175
Rehman, A.U. 2309, 2315
Reichel, M. 1625
Reinhorn, A.M. 2395
Reis, A.J. 729
Reissen, K. 1507, 1543
Reiterman, P. 1745, 1775
Remmers, J.J.C. 29
Renner, A. 1329
Retief, J.V. 651, 1531, 1549, 2065
Reynolds, P. 137
Rinaldis, D. 81, 201
Robertson, I.N. 247
Rodrigues, J.P.C. 1959
Rogers, C.A. 463, 1341
Rojewska-Warchał, M. 1819
Ronagh, H. 2027
Rongong, J.A. 2309
Roos, P. 741
Rossi, B. 1291, 1465
Rossi, G. 81
Rots, J.G. 1871
Roure, F. 1347
Rozvany, G.I.N. 35
Rücker, W. 977
Ruiz, E. 405
Ruta, G. 67
Ryś, M. 547

Sack, K. 423
Şafak, E. 2275
Said, S. 977
Saitta, F. 81, 201
Saleh, A.A.K. 1323
Saloumi, E. 1195, 1201
Sancak, E. 387
Sanchayan, S. 1637
Sansour, C. 423
Santoro, R. 55
Sarkisian, M. 217
Sarmanho Freitas, A.M. 1149
Sarmiento, E.V. 1573
Sarracco, G. 511
Sauer, J. 2463
Sayed-Ahmed, E.Y. 93, 1335, 2421
Scalerandi, M. 2217
Scavazza, F. 1023
Schäfer, D. 2269, 2389, 2491
Scheunemann, L. 411
Schmauder, S. 381
Schmid, W. 977
Schmidt, J.W. 1655, 1685
Schmidt, M. 1643
Schmidt, R. 885, 907
Schnier, G. 613
Schröder, J. 393, 411
Schwartz, C. 149
Schwer, A. 1907
Scott, P. 1977
Šedina, J. 1795
Seema 669
Seidl, G. 1649
Selamet, S. 711
Seman, M.A. 537
Sena Cardoso, F. 1297
Senatore, G. 2105, 2117
Serpilli, M. 929
Sha, W. 2123
Shaat, A.A. 1335, 1365
Shah, F.H. 2309, 2315
Shahabpoor, E. 143
Shan, S.J. 2321
Sharada Bai, H. 2531
Sheehan, T. 253
Shi, C.X. 335
Shiao, S.Y. 2235
Shokouhi, S.K.S. 363
Siburg, C. 1543
Siegert, C. 2371
Siemon, M. 493
Sigrist, V. 519, 1537
Silva, J.G.S. 1213
Silvestre, N. 17, 1157, 1177, 1231, 1447
Simonetti, M. 1833, 1851
Sinaie, S. 2033
Siringoringo, D.M. 9, 223, 283
Sitek, M.A. 657
Sivakumaran, K.S. 917, 1053
Skatulla, S. 423, 435, 609
Skramlik, J. 1735
Slobbe, A.T. 1871
Smith, D. 769
Smith, R.A. 2347
Smith, T. 1833, 1851
Smolka, A. 2081
Sofi, A. 55
Solari, D. 2395
Somalo, M.R. 1347
Song, J. 721
Song, Q.Y. 1353
Song, T.Y. 1483
Sørensen, E.S. 375
Sossou, G. 1749
Souza, F.T. 1149
Spada, A. 553
Srinivas, H.R. 1703, 1709
Stabile, G. 983
Stachura, Z. 2365
Stang, H. 1655, 1685
Staniek, R. 2129, 2133
Stehlik, D. 1785, 1789
Stephen, O.D. 699
Stievanin, E. 2433
Stojadinović, B. 1865
Stopp, K. 2485
Stroetmann, R. 1171
Stull, C.J. 847
Stupazzini, M. 2081
Su, M. 1113
Suda, J. 1795
Sugiura, K. 2239
Suhajda, K. 1735
Surace, C. 911
Surovek, A.E. 1243
Sykora, M. 2065
Szostak, M. 2129, 2133

Tabbuso, P. 241
Taerwe, L. 705
Taig, G. 1009
Takatani, T. 329
Talja, A. 1459
Tan, E.L. 1397
Tanyimboh, T.T. 2123
Tao, Z. 1483
Taras, A. 1047
Tarleton, E. 399
Teh, L.H. 693, 1279, 1285
Thambiratnam, D.P. 525
Thanga, T. 917
Theofanous, M. 1453
Thiene, M. 2193
Thoma, K. 741
Thöns, S. 977
Tichy, R. 505
Tikhonov, V.S. 853
Todd, M.D. 847
Toledo Filho, R.D. 1895
Tomás, J. 1303
Tondini, N. 1465
Torero, J.L. 1919
Toropov, V.V. 699
Torresani, G. 1023
Tremblay, R. 463, 1341
Trulli, N. 2259
Tse, K.T. 721
Tu, Z.G. 2175
Tue, N.V. 1625
Tumkou, J. 1273
Turner, D.Z. 559, 591

Ubaid, U. 137
Ubysz, A. 1739
Uhl, T. 2263
Ungureanu, V. 1065, 1089
Unterweger, H. 1047
Uy, B. 1397
Uziak, J. 1323

Valdés, M. 2259
Valentin, J. 1763, 1795
Van Bogaert, Ph. 579, 763, 781
Van den Broeck, P. 125
van der Veen, C. 475
van der Woerd, J.D. 823
van Huyssteen, S.S. 2111
Van Nimmen, K. 125
van Zijl, G.P.A.G. 619, 1587
Vandewalle, L. 1513
Varaus, M. 1785, 1789
Vaziri Hamaneh, S.V. 181
Vejmelková, E. 1745, 1775
Vellasco, M.M.B.R. 1213
Vellasco, P.C.G.S. 1213
Verhoosel, C.V. 29
Vestroni, F. 67
Vieira, R.F. 735
Virtuoso, F. 105, 751, 775
Virtuoso, F.B. 735
Vodička, J. 1943
Vogel, F. 1745, 1775
Vögeli, C. 1865
Vosoughifar, H.R. 363
Vu, T.D. 885, 907

Wachtling, J. 1971
Wadee, M.A. 1249
Wagner, B. 1907
Walachowski, M. 879
Wald, F. 1943, 1999
Walker, P.J. 1901
Walraven, J.C. 475
Wang, B.M. 1755
Wang, K. 75
Wang, L. 2321
Wang, T. 2333
Wang, X.Q. 1483
Wang, Y. 1513
Wang, Y.L. 799
Warkus, N. 971

Warren-Codrington, C.J. 2537
Weber, F. 61
Weber, U. 381
Weiß, L. 891, 2089
Welskopf, T. 2503
Wenzel, H. 2269, 2389
Wiercigroch, M. 163, 181, 207
Wierzbicki, S. 2365
Wierzbicki, T. 787
Wild, M. 2247
Wille, K. 1721
Winkelmann, U. 965
Winkler, J. 631
Winslow, P. 2105, 2117
Wise, C. 2105, 2117
Witzany, J. 1503
Wium, J. 1801
Wium, J.A. 1549
Woermann, R. 229
Wood, J. 613
Worden, K. 2309
Woźniak, G. 1953
Wu, L. 1525
Wu, S.Y. 1421

Xia, H. 75, 2223, 2297
Xing, J.H. 253
Xiong, F. 271
Xu, M.J. 99
Xu, S.D. 2445

Yadwad, S. 693
Yamada, S. 307
Yan, N.N. 1421
Yan, S. 1143
Yang, C.-Y. 271
Yang, W. 2327
Yao, Z. 997
Ye, D. 417
Yin, X. 417
You, Z. 923
Young, B. 17, 1071, 1113, 1143, 1441, 1477
Yu, Y. 2321
Yu, Z. 2297
Yuan, H. 1525
Yuan, J.H. 2327
Yuan, S. 1567
Yuksek, M. 387

Zai, S.A.K. 1703, 1709, 2467
Žák, J. 1795
Zandonini, R. 669, 1023, 1403
Zanotti Fragonara, L. 69, 2187
Zehfuß, J. 493, 1971
Zehn, M.W. 457
Zeng, L. 2445
Zengin, B. 1889
Zengin, E. 2275
Zeranka, S. 1587
Zhan, J. 2297
Zhan, J.W. 2223
Zhang, B. 923
Zhang, K. 793
Zhang, L.-M. 2333
Zhang, N. 2223
Zhang, R. 259
Zhang, W.Y. 2327
Zhao, M. 2205
Zhao, X.F. 2321
Zhao, X.L. 1353, 2033
Zhao, X.Z. 1421
Zhong, Y. 99
Zhou, F. 1477
Zhu, C.G. 541
Zhu, Y.F. 2321
Ziemian, R.D. 1237, 2555
Zigler, R. 1503
Zimmermann, C. 2285
Zingoni, A. 835
Zirgulis, G. 1573
Zona, A. 341
Zych, T. 1579